EURODYN 2020

XI International Conference on Structural Dynamics

PROCEEDINGS

Volume II

M. Papadrakakis, M. Fragiadakis, C. Papadimitriou (Eds.)

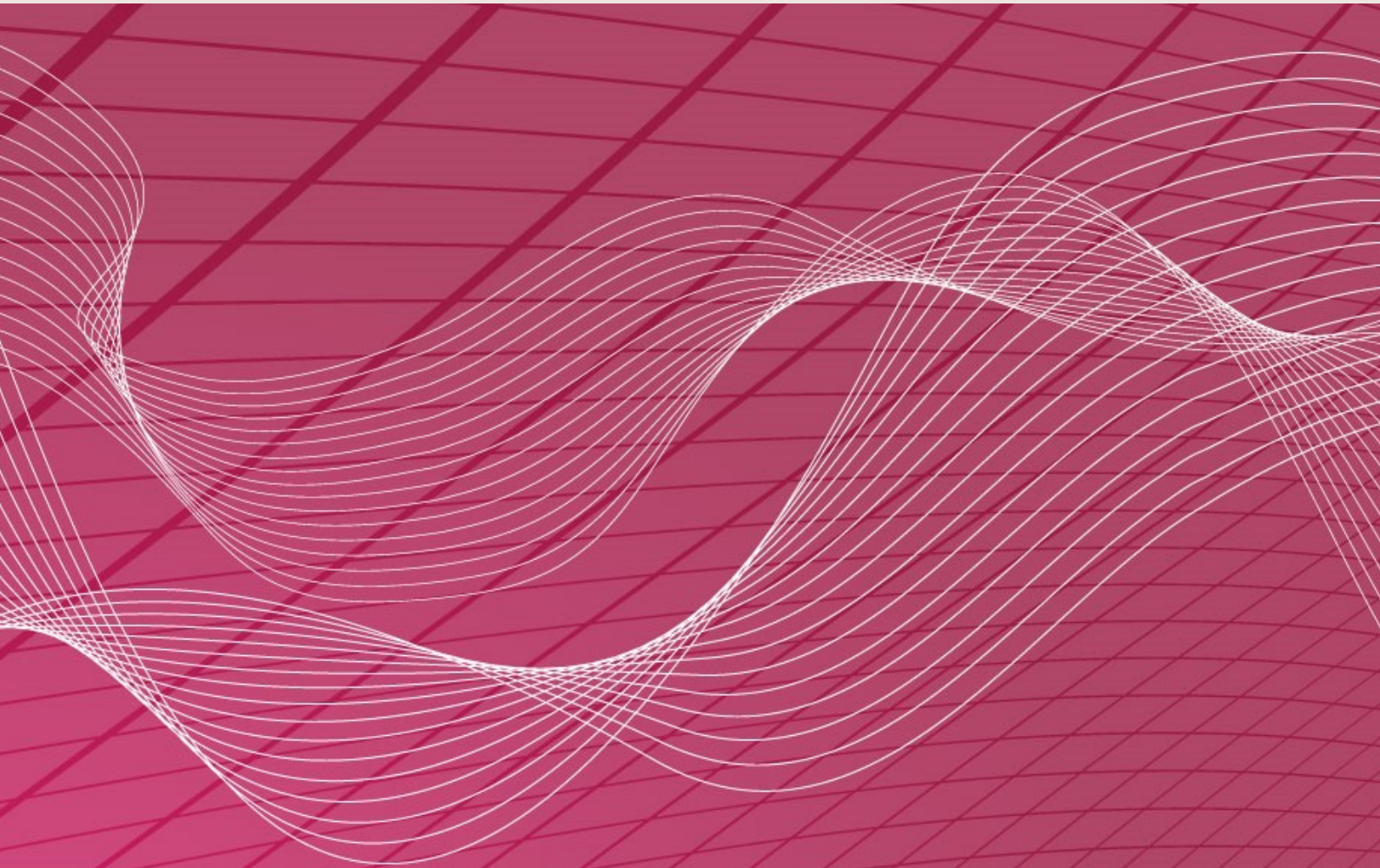

EASD
European Association
for Structural Dynamics

EURODYN 2020

Proceedings of the XI International Conference on Structural Dynamics

Streamed from Athens, Greece

23-26 November 2020

Edited by:

M. Papadrakakis

National Technical University of Athens, Greece

M. Fragiadakis

National Technical University of Athens, Greece

C. Papadimitriou

University of Thessaly, Greece

A publication of:

Institute of Structural Analysis and Antiseismic Research

School of Civil Engineering

National Technical University of Athens (NTUA)

Greece

EURODYN 2020

XI International Conference on Structural Dynamics

M. Papadrakakis, M. Fragiadakis, C. Papadimitriou (Eds.)

First Edition, September 2020

ISBN (set): **978-618-85072-2-7**

ISBN (vol II): **978-618-85072-1-0**

PREFACE

This volume contains the full-length papers accepted for presentation at the XI International Conference on Structural Dynamics EURODYN 2020, streamed online from Athens, Greece on November 23-26, 2020.

EURODYN Conference Series is organized under the auspices of the European Association of Structural Dynamics (EASD). EASD was founded in 1990 as a joint European initiative of experts in Structural Dynamics, with the purpose of sponsoring and overseeing the organization of the EURODYN conferences, scheduled to take place with a three-year interval. The first EURODYN Conference was held in Bochum in 1990, organized by the founding president of EASD Prof. Wilfried Krätzig. Following Bochum, the conferences were held in Trondheim (1993), Florence (1996), Prague (1999), Munich (2002), Paris, (2005), Southampton (2008), Leuven (2011), Porto (2014), Rome in 2017 and this year in Athens, the city where the EURODYN 2020 conference would have taken place in June 2020.

In view of the first signs of the COVID-19 pandemic at the beginning of this year, we were forced to postpone the conference dates at the end of November 2020. This was expected to give the opportunity to the participants to attend the conference either physically or remotely. Unfortunately, and contrary to what we had all anticipated, the COVID-19 was still around at the end of June 2020, and hence we were left with no other choice but to abandon the idea of a physical conference and organize a fully online event. This transition was very painful and created many administration complications. Nevertheless, EASD and the organizing committee have seen this sanitary crisis as an opportunity to organize a different type of event and to propose a new approach for scientific collaboration and communication that respects both the legacy of the conference series and the health of the members of the European Community of Structural Dynamics.

EURODYN conferences have been established as the top scientific events in the area of theoretical, numerical and experimental Structural Dynamics worldwide and are highly-anticipated every three years by the international community of Structural Dynamics. For the 2020 edition of EURODYN series, more than 1000 abstracts were submitted, of which 830 were selected for presentation and among them 400 full-length papers were accepted for publication in the EASD Open Access Procedia, indexed by Scopus Database.

The editors of this volume would like to thank all authors for their contributions. Special thanks go to the 88 colleagues who were involved in the organization of 38 Minisymposia and to the reviewers who contributed to the scientific quality of this e-book with their work.

We would particularly like to thank the Members of the EASD Executive Board, and especially Álvaro Cunha, the President of EASD, Guido De Roeck, the Honorary Chairman of EURODYN 2020 and Fabrizio Vestroni the Chair of the EURODYN 2017, for their valuable advice, suggestions and interest, during the three-year preparation period of EURODYN 2020. Their contributions were significant to the successful outcome of this undertaking.

Manolis Papadrakakis
National Technical University of Athens, Greece

Michalis Fragiadakis
National Technical University of Athens, Greece

Costas Papadimitriou
University of Thessaly, Greece

ACKNOWLEDGEMENTS

The conference organizers acknowledge the support towards the organization of the "XI International Conference on Structural Dynamics", to the following organizations: European Association for Structural Dynamics (EASD), Greek Association for Computational Mechanics (GRACM), Hellenic Society for Earthquake Engineering (HSEE), School of Civil Engineering, National University of Athens (NTUA).

Plenary, Semi-Plenary Speakers and Minisymposia Organizers

We would also like to thank the Plenary and Semi-Plenary Speakers and the Minisymposia Organizers for their help in the setting up of a high standard Scientific Programme.

Plenary Speakers: Geert Degrande, Tracy Kijewski-Correa, Yi Qing Ni

Semi-Plenary Speakers: Eleni Chatzi, Joel P. Conte, Geert Lombaert, Andrei Metrikine, Sotirios Natsiavas, Filippo Ubertini

MS Organizers: I. Antoniadis, M. Arnst, K. Bakalis, B. Balachandran, C.C. Baniotopoulos, M. Barbato, J. Beck, M. Beer, G. Bonnet, C. Borri, C. Boutin, L. Bruno, E. Caetano, F. Casciati, C.A. Castiglioni, E. Chatzi, A. Cicirello, F. Clementi, D. Clouteau, J. Conte, M. Corradi, A. Cunha, G. De Roeck, G. Degrande, V. Denoël, D. Duhamel, J. Edelmann, D. Forcellini, A. Formisano, F. Foti, M. Fragiadakis, V. C. Fragkoulis, V. Fragkoulis, C. Gentile, R. Ghanem, D. Giagopoulos, A. Giaralis, P.B. Gonçalves, R. Höffer, A. Kanyilmaz, I. A. Kougioumtzoglou, S. Lenci, G. Lombaert, F. Magalhães, C. Maniatakis, E. Marino, T. Mazilu, C. E. N. Mazzilli, V. Melissianos, A. Metrikine, A.V. Metrikine, G. Milani, I.P. Mitseas, B. Moaveni, C. Moutinho, H. Mouzakis, H. P. Mouzakis, G. Müller, J. Naprstek, S. Natsiavas, P. Omenzetter, C. Papadimitriou, M. Papadrakakis, I. Papaioannou, A. Pavic, F. Pellicano, F. Perotti, M. Ploechl, I. Psycharis, G. Rega, J. Rodellar, E. Sapountzakis, J-F. Semblat, V. Sepe, C. Soize, S. Sorokin, C. Spyrakos, A. Taflanidis, F. Tubino, D. Vamvatsikos, K.N. van Dalen, P. Van den Broeck, K. Van Nimmen, M. Vasta, P-M. Vasta, I. Vayas, D. Wagg, K. Worden, W.M. Zhai

SUMMARY

Preface..... iii

Acknowledgements..... iv

Contents..... viii

VOLUME I

Minisymposia

MS 1: ADVANCES IN COMPUTATIONAL STRUCTURAL DYNAMICS 1
Organized by B. Balachandran, D. Duhamel, D. Giagopoulos, S. Natsiavas

MS 2: NON-LINEAR DYNAMICS 180
Organized by J. Naprstek, G. Rega

MS 3: DYNAMIC BUCKLING 468
Organized by P.B. Gonçalves, F. Pellicano, C. E. N. Mazzilli

MS 4: DYNAMICS OF COMPOSITE MATERIALS 482
Organized by G. Bonnet, C. Boutin, S. Lenci

MS 5: DYNAMIC FLUID-STRUCTURE INTERACTION 621

MS 6: VEHICLE DYNAMICS 669
Organized by M. Ploechl, J. Edelmann

MS 7: SYSTEM IDENTIFICATION AND DAMAGE DETECTION 785
Organized by E. Chatzi, G. De Roeck

MS 8: STRUCTURAL HEALTH MONITORING 1053
Organized by J. Conte, A. Cunha, G. Lombaert, B. Moaveni, P. Omenzetter, C. Papadimitriou

MS 9: STRUCTURAL CONTROL 1408
Organized by F. Casciati, J. Rodellar

MS 10: ADVANCES ON INERTER-BASED STRUCTURAL VIBRATION CONTROL 1501
Organized by A. Giaralis, A. Taflanidis

MS 11: BRIDGE DYNAMICS 1586

MS 12: FOOTBRIDGE VIBRATIONS 1731
Organized by E. Caetano, F. Tubino, P. Van den Broeck, K. Van Nimmen

MS 13: HUMAN INDUCED VIBRATIONS IN FLOORS, STAIRCASES AND STADIA 1896
Organized by L. Bruno, A. Pavic

MS 14: WIND INDUCED VIBRATIONS OF SLENDER STRUCTURES AND FATIGUE 1944
Organized by V. Denoël, F. Foti, F. Perotti

MS 15: DYNAMICS OF ON- AND OFF-SHORE WIND ENERGY STRUCTURES (WES) 2113
Organized by C. Borri, E. Marino, C.C. Baniotopoulos, R. Höffer, F. Magalhães

MS 16: VIBRATION-BASED ASSESSMENT AND SHM OF CULTURAL HERITAGE STRUCTURES 2244
Organized by C. Gentile

MS 17: VIBRATIONS DUE TO CONSTRUCTION AND INDUSTRIAL ACTIVITIES 2407
Organized by C. Moutinho

VOLUME II

Minisymposia

MS 18: VIBRO-ACOUSTICS 2427
Organized by S. Sorokin

MS 19: BLAST AND IMPACT LOADS 2521

MS 20: MOVING LOADS 2585
Organized by T. Mazilu, A.V. Metrikine, K.N. van Dalen, W.M. Zhai

MS 21: TRAFFIC INDUCED VIBRATIONS 2680
Organized by G. Degrande, G. Lombaert, G. Müller

MS 22: DYNAMIC SOIL-STRUCTURE INTERACTION AND WAVE PROPAGATION 2782
Organized by D. Clouteau, A. Metrikine, G. Müller, J-F. Semblat

MS 23: ASSESSMENT OF INDUSTRIAL STRUCTURES AND INFRASTRUCTURE UNDER NATURAL HAZARDS 3043
Organized by K. Bakalis, V. Melissianos, D. Vamvatsikos

MS 24: SEISMIC PROTECTION OF STEEL STRUCTURES BY MEANS OF DISSIPATIVE SYSTEMS AND COMPONENTS 3079
Organized by C.A. Castiglioni, A. Kanyilmaz, I. Psycharis, H. P. Mouzakis, I. Vayas

MS 25: EXPERIMENTAL EARTHQUAKE ENGINEERING 3174
Organized by M. Fragiadakis, H. Mouzakis

MS 26: UQ AND PROBABILISTIC LEARNING IN COMPUTATIONAL DYNAMICS 3403
Organized by M. Arnst, R. Ghanem, C. Soize

MS 27: STOCHASTIC DYNAMICS AND RELIABILITY ANALYSIS OF STRUCTURAL AND MECHANICAL SYSTEMS UNDER ENVIRONMENTAL EXCITATION 3438
Organized by M. Barbato, M. Vasta

MS 28: UNCERTAINTIES ON MATERIALS AND ENVIRONMENTAL LOADS 3519
Organized by M. Barbato, V. Sepe, P-M. Vasta

MS 29: BAYESIAN UPDATING, FILTERING AND INVERSION FOR DYNAMIC SYSTEMS 3558
Organized by J. Beck, A. Taflanidis, I. Papaioannou

MS 30: RECENT ADVANCES IN PERFORMANCE-BASED ENGINEERING AND DESIGN OF STRUCTURES AND CIVIL INFRASTRUCTURE SYSTEMS SUBJECTED TO SINGLE OR MULTIPLE HAZARDS 3607
Organized by M. Barbato, J. Conte

MS 31: EUROPEAN ETN "DYNAMIC VIRTUALISATION: MODELLING PERFORMANCE OF ENGINEERING STRUCTURES" (DYVIRT) 3803
Organized by M. Beer, V. Fragkoulis, D. Wagg, K. Worden

MS 32: COMPUTATIONAL METHODS FOR STOCHASTIC DYNAMICS 3921
Organized by M. Beer, V. C. Fragkoulis, I. A. Kougioumtzoglou, I.P. Mitseas

MS 33: NUMERICAL SIMULATIONS FOR EARTHQUAKE-RESILIENT SYSTEMS 3939
Organized by D. Forcellini

MS 34: VIBRATION ABSORPTION 4069
Organized by I. Antoniadis, E. Sapountzakis

MS 35: NEW TRENDS IN THE COMPUTATIONAL AND EXPERIMENTAL STRUCTURAL DYNAMICS FOR THE PRESERVATION OF HISTORICAL MASONRY STRUCTURES IN SEISMIC AREAS 4200
Organized by F. Clementi, A. Formisano, G. Milani

MS 36: DAMPING MODELLING AND EXPERIMENTS 4349
Organized by A. Cicirello

MS 37: CONSERVATION, RETROFIT AND STRENGTHENING OF EXISTING STRUCTURES: INNOVATIONS IN APPLIED METHODS AND MATERIALS 4358
Organized by M. Corradi, C. Maniatakis, C. Spyrakos

MS 38: GENERAL SESSION ON STRUCTURAL DYNAMICS, STABILITY AND VIBRATIONS 4418
Organized by G. De Roeck, M. Fragiadakis, C. Papadimitriou, M. Papadrakakis

CONTENTS

VOLUME I

Minisymposia

MS 1: ADVANCES IN COMPUTATIONAL STRUCTURAL DYNAMICS

A MODE MATCHING TECHNIQUE FOR THE SEISMIC RESPONSE OF LIQUID STORAGE TANKS INCLUDING SOIL-STRUCTURE INTERACTION 1
Apostolos Tsouvalas, Timo Molenkamp, Khairina Canny, David Kroon, Marco Versluis, Yaxi Peng, Andrei Metrikine

APPLICATION OF THE WAVE FINITE ELEMENT METHOD TO MULTI-SPAN BRIDGES 15
Gabriele Paratore, Tien Hoang, Gilles Foret, Maria Pina Limongelli, Denis Duhame

A VARIATIONAL APPROACH TO ASYNCHRONOUS TIME-INTEGRATION OF STRUCTURAL DYNAMICS PROBLEMS IN THE CONTEXT OF FETI AND SPURIOUS OSCILLATIONS ON THE INTERFACES 26
Andreas Seibold, Daniel Rixen

DEVELOPMENT AND VALIDATION OF A MULTIBODY DYNAMICS MODEL FOR THE ASSESSMENT OF THE SEISMIC RETROFIT POTENTIAL OF BRIDGE EXPANSION JOINTS 44
Michael Tahedl, Andreas Taras, Fredrik Borchsenius, Daniel Rill

AN DELAYED FREQUENCY PRECONDITIONER APPROACH FOR SPEEDING-UP FREQUENCY RESPONSE COMPUTATION OF STRUCTURAL COMPONENTS 56
Guilherme Jenovencio, Arul Sivasankar, Zeeshan Saeed, Daniel Rixen

NONLINEAR FORCE LAW SELECTION AND PARAMETER UPDATE FOR A CANTILEVER BEAM WITH PERIODICALLY REPEATED IMPACTS 68
Alexandros Arailopoulos, Dimitrios Giagopoulos

SIMULATION-LEAN TRAINING-SETS FOR HYPER-REDUCTION OF PARAMETRIC GEOMETRIC NON-LINEAR STRUCTURES 80
Christian H. Meyer, Daniel J. Rixen

REGULARIZATION METHOD TO INCLUDE MATERIAL SOFTENING IN FIBER BEAM-COLUMN ELEMENTS FOR SEISMIC PERFORMANCE ASSESSMENT OF STEEL FRAMES 93
Sebastián Pozo, Bryam Astudillo, Esteban Samaniego, Francisco Flores

EFFICIENCY OF 1D CNNS IN FINITE ELEMENT MODEL PARAMETER ESTIMATION USING SYNTHETIC DYNAMIC RESPONSES 108
Mohammad Almutairi, Onur Avci, Nikolaos Nikitas

INFLUENCE OF SLENDERNESS RATIO IN THE MODAL ANALYSIS BY ANALYTICAL FORMULATION 121
Jonas Falcão, Rodolfo Carvalho, Renan Ribeiro, Ledymar Moreno, José De Brito

ON SPACE-TIME FORMULATIONS IN STRUCTURAL MECHANICS USING THE PROPER GENERALIZED DECOMPOSITION 136
Franz Bamer, Nima Shirafkan, Abdelbacet Oueslati, Marcus Stoffel, Géry De Saxcé, Bernd Markert

ISOGEOMETRIC COLLOCATION METHODS FOR THE DYNAMICS OF THREE-DIMENSIONAL GEOMETRICALLY EXACT BEAMS 154
Enzo Marino, Josef Kiendl, Laura De Lorenzis

ANALYTICAL-NUMERICAL MODELING OF FLEXIBLE PYLONS FOR STRUCTURAL HEALTH MONITORING 168
George D. Manolis, Georgios Dadoulis, Stylianos Pardalopoulos, Kosmas Dragos

MS 2: NON-LINEAR DYNAMICS

NONLINEAR DYNAMICS OF A NEGATIVE STIFFNESS OSCILLATOR: EXPERIMENTAL IDENTIFICATION AND MODEL UPDATING 180
Dario Anastasio, Alessandro Fasana, Luigi Garibaldi, Stefano Marchesiello

GEOMETRICALLY NONLINEAR FORCED VIBRATIONS OF MULTIPLE-STEPPED EULER-BERNOULLI BEAMS 193
Issam El Hantati, Ahmed Adri, Hatim Fakhreddine, Said Rifai, Rhali Benamar

NONSMOOTH MODAL ANALYSIS WITH BOUNDARY ELEMENT METHOD 205
Tianzheng Lu, Mathias Legrand

SUBSONIC STALL FLUTTER ANALYSIS IN 2D BLADE CASCADE USING HYBRID BOUNDARY ELEMENT METHOD 213
Chandra Shekhar Prasad, Ludek Pesek

GEOMETRICALLY NON-LINEAR FREE AND FORCED VIBRATION OF C-F-C-F RECTANGULAR PLATE AT LARGE TRANSVERSE AMPLITUDES 225
Abdelfattah Majid, El Mehdi Abdeddine, Khalid Zarbane, Zitouni Beidouri

NONLINEAR LONGITUDINAL FREE VIBRATION OF UNIFORM RODS AND RODS WITH SECTIONS VARYING EXPONENTIALLY 239
EL Mehdi Abdeddine, Abdelfattah Majid, Zitouni Beidouri, Khalid Zarbane

DYNAMIC RESPONSE OF TWO INTERACTING EXTENSIBLE BARS IN FRICTIONAL CONTACT 252
Timo Molenkamp, Athanasios Tsetas, Apostolos Tsouvalas, Andrei Metrikine

NUMERICAL STUDY OF DYNAMIC PROPERTIES OF A SELECTED MATERIAL LAYER OF BULLETPROOF SHIELDS 265
Miroslaw Bocian, Krzysztof Jamroziak, Maciej Kulisiewicz, Joanna Pach, Dariusz Pyka

MEASUREMENTS OF NONLINEAR VIBRATIONS OF A BEAM SUBJECTED TO TWO BROADBAND CORRELATED RANDOM EXCITATIONS 273
Sébastien Talik, Maxence Claeys, Jean-Pierre Lambelin, Jean-Jacques Sinou

VIBRATION POWER FLOW TRANSMISSION BETWEEN NONLINEARLY COUPLED OSCILLATORS WITH DUAL FORCE EXCITATIONS 283
Baiyang Shi, Chendi Zhu, Jian Yang

STOCHASTIC DYNAMICAL RESPONSE OF A NON-SMOOTH DYNAMICAL SYSTEM UNDER FILTERED WHITE NOISE 290
Saeed Gheisari Hasnijeh, Arvid Naess

A NEW TIME INTEGRATION SCHEME IN MULTIBODY DYNAMICS INVOLVING FRICTIONAL IMPACT BASED ON A RETURN MAP TO NON-FLAT CONFIGURATION MANIFOLDS 303
Elias Paraskevopoulos, Panagiotis Passas, Sotirios Natsiavas

COMPUTING BACKBONE CURVES FOR NONLINEAR OSCILLATORS WITH HIGHER ORDER POLYNOMIAL STIFFNESS TERMS 318
Ayman Nasir, Neil Sims, David Wagg

TOWARD A SYSTEMATIC CONSTRUCTION OF THE BASIS FOR NONLINEAR GEOMETRIC REDUCED ORDER MODELS 335
X.Q. Wang, Marc Mignolet

NONLINEAR VIBRATIONS OF AN ELASTIC PLATE ON A VISCOELASTIC FOUNDATION MODELLED BY THE FRACTIONAL DERIVATIVE STANDARD LINEAR SOLID MODEL 355
Marina V. Shitikova, Anastasiya I. Krusser

NONLINEAR HARDENING BEHAVIOR OF A HELMHOLTZ RESONATOR 369
Emmanuel Gourdon, Alireza Ture Savadkoohi, Claude-Henri Lamarque

EMPIRICAL EXPRESSION PREDICTING SEISMIC DISPLACEMENT OF SANDY SLOPES IN GREECE IN TERMS OF SOIL PROFILE TYPE USING NON-LINEAR DYNAMIC STICK-SLIP ANALYSIS 382
Loukas C. Katsenis, Constantine A. Stamatopoulos, Vassilis P. Panoskaltsis

SUPPRESSION OF CLASSICAL FLUTTER OSCILLATIONS IN BLADED WHEEL USING INNER DAMPING EFFECT 401
Ludek Pesek, Pavel Snabl, Ch. S. Prasad

THE THEORY OF BODY COLLISIONS IN ROLLING THROUGH GEOMETRY, KINEMATICS AND DYNAMICS OF BILLIARDS 412
Katica Hedrih

THE EFFECT OF BUILDING'S RESPONSE ON THE FRAGILITY OF FREESTANDING SYMMETRIC OR ASYMMETRIC CONTENTS 451
Spyridon Diamantopoulos, Michalis Fragiadakis

MS 3: DYNAMIC BUCKLING

PARAMETRIC INSTABILITY OF PULTRUDED FIBER-REINFORCED POLYMER COLUMNS UNDER AXIAL HARMONIC FORCING 468
Julio C. Coaquira, Daniel C.T. Cardoso, Paulo B. Gonçalves, Diego Orlando

EFFECTS OF INITIAL GEOMETRICAL IMPERFECTIONS ON DYNAMIC STABILITY OF CIRCULAR CYLINDRICAL PANELS 476
Frederico Silva, Wanclaine Vaz, Paulo Gonçalves

MS 4: DYNAMICS OF COMPOSITE MATERIALS

ON THE WAVE DYNAMICS OF MICROSCALE BISTABLE TENSEGRITY STRUCTURES 482
Andrea Micheletti, Zacharias Vangelatos, Narinder Singh, Costas P Grigoropoulos, Fernando Fraternali

PIECEWISE CONSTRUCTION OF WAVE DISPERSION CURVES IN ELASTIC PERIODIC NETWORKS BY ASYMPTOTIC MULTI-SCALE APPROACH 489
Antoine Rallu, Claude Boutin, Stéphane Hans

DEVELOPMENT OF FREQUENCY CURVES FOR CROSS-LAMINATED TIMBER (CLT) FLOORS USING DYNAMIC STIFFNESS METHOD 502
Miroslav Marjanović, Verica Jugović, Marija Nefovska-Danilović

ANALYTICAL SOLUTIONS FOR THE FLEXURAL NATURAL VIBRATION OF THE COMPOSITE GIRDERS WITH CORRUGATED STEEL WEBS 510
Yunsheng Li, Chaoxing Liu, Qingnian Dai, Yanling Zhang

METAMATERIALS WITH FIBERS OF ELLIPTIC CROSS-SECTION 520
Guy Bonnet, Vincent Monchiet

A TWO MODE NON-UNIFORM APPROXIMATION FOR AN ELASTIC ASYMMETRIC SANDWICH 528
Mohammed Alkinidri, Julius Kaplunov, Ludmila Prikazchikova

MODELING OF CFRP STRUCTURES USING MODEL UPDATING TECHNIQUES AND EXPERIMENTAL MEASUREMENTS 536
Ilias Zacharakis, Dimitrios Giagopoulos, Ioannis Zyganitidis, Alexandros Arailopoulos, Olga Markogiannaki

VIBRATION ANALYSIS OF LAMINATED COMPOSITE CYLINDRICAL SHELLS WITH VARIOUS FIBRE ORIENTATIONS ... 551
Chendi Zhu, Baiyang Shi, Chen Zhou, Jian Yang

ACOUSTIC WAVES IN HOMOGENIZED FLUID-SATURATED DEFORMING PERIODIC SCAFFOLDS UNDER PERMANENT FLOW 562
Eduard Rohan, Robert Cimrman, Salah Naili

A NEW ANALYTICAL METHOD FOR FREE VIBRATION ANALYSIS OF SANDWICH BEAMS 578
Lhoucine Boutahar, Zakaria Ibnorachid, Khalid El Bikri

HOMOGENIZED MODEL OF UNCONVENTIONAL DYNAMIC BEHAVIOUR OF PERIODIC PLATES AND EXPERIMENTAL COMPARISONS 589
Pascal Fossat, Claude Boutin, Mohamed Ichchou

A DISCRETE-TO-CONTINUUM APPROACH TO FREQUENCY BANGAPS IN 1D BIATOMIC METAMATERIALS 604
L. Placidi, A. Amendola, M. Miniaci, F. Fraternali

INDUCING DISPERSION CURVES WITH NEGATIVE GROUP VELOCITY IN INERTIALLY AMPLIFIED PHONONIC CRYSTALS THROUGH THE APPLICATION OF AN EXTERNAL STATE OF PRESTRESS 612
M. Miniaci, M. Mazzotti, A. Amendola, F. Fraternali

MS 5: DYNAMIC FLUID-STRUCTURE INTERACTION

SUSCEPTIBILITY OF U-PROFILES WITH DIFFERENT GEOMETRY AND POROSITY TO GALLOPING 621
Stanislav Hračov, Michael Macháček

THE EFFECT OF FOLDING WINGTIPS ON THE FLIGHT DYNAMICS OF AN AIRCRAFT WITH ELASTIC WING 631
Davide Balatti, Hamed Haddad Khodaparast, Michael Friswell, Marinos Manolesos, Mohammadreza Amoozgar
NONLINEAR STRUCTURAL BEHAVIOUR OF AN ARCH DAM UNDER STATIC AND DYNAMIC LOADS 640
Carla Ferreira, Helena Barros

A NEW OPEN SOURCE SOLVER FOR MODELLING FLUID-STRUCTURE INTERACTION: CASE STUDY OF A POINT-ABSORBER WAVE ENERGY CONVERTER WITH POWER TAKE-OFF UNIT 657
Bonaventura Tagliafierro, Rosario Montuori, Ioannis Vayas, Pablo Ropero, Alejandro Crespo, Jose Domınguez, Corrado Altomare, Giacomo Viccione, Moncho Gomez Gesteira

MS 6: VEHICLE DYNAMICS

SPEED DISTRIBUTION ON ROAD TEST SECTIONS FOR THE NEED OF PROFILE GROUND TESTING OF SPECIAL WHEELED VEHICLES 669
Mariusz Kosobudzki

TMEASY 6.0—A HANDLING TIRE MODEL THAT INCORPORATES THE FIRST TWO BELT EIGENMODES 676
Georg Rill

OPTIMIZATION OF NONLINEAR QUARTER CAR SUSPENSION-DRIVER SEAT MODEL USING GA BASED PID CONTROLLER 690
Omar El-Mezayen, Mustafa Qasem, Hesham Ibrahim, Nora Merabet, Zakaria.Elnaggar

ENHANCING ROAD – VEHICLE BEHAVIOR BY IMPLEMENTING ACTIVE - CONTROLLED DRIVER SEAT COMBINED WITH SEMI-ACTIVE GROUND HOOK SUSPENSION SYSTEM 705
Mohamed Ezzat, Hesham Ibrahim, Zakaria Elnaggar, Nora Merabet, Mohamed Salama

AUTO-SAPIENS, AN EXPERIMENTAL AUTONOMOUS DRIVING SYSTEM 718
Maicol Laurenza, Gianluca Pepe, Antonio Carcaterra

IDENTIFICATION OF NONLINEAR ROAD-VEHICLE DYNAMIC BEHAVIOR USING AUTOREGRESSIVE TECHNIQUE ….734
Mohab Anwar, Mostafa Tamer, Mohamed Tawfik, Hesham Ibrahim

EFFICIENT METHODS TO ASSESS LINEAR AND NON-LINEAR AUTOMOTIVE PLATOON CONTROL STABILITY AND PERFORMANCE …… 748
Christian Kalteis, Sebastian Thormann, Alexander Schirrer, Stefan Jakubek

ANALYSIS OF AUTOMOBILE BRAKE CREEP GROAN VIBRATIONS: TEST RIG EXPERIMENTS IN COMPARISON TO FINITE ELEMENT SIMULATIONS …… 758
Manuel Pürscher, Severin Huemer-Kals, Peter Fischer

MS 7: SYSTEM IDENTIFICATION AND DAMAGE DETECTION

VIBRATIONS FOR ESTIMATING BOLTED JOINT INTEGRITY (VEBJI) PROJECT: CHALLENGES AND RESULTS …… 785
Dmitri Tcherniak, Jon Juel Thomsen, Marie Brøns

NONPARAMETRIC NONLINEAR RESTORING FORCE AND EXCITATION IDENTIFICATION WITH LEGENDRE POLYNOMIAL AND DATA FUSION …… 799
Bin Xu, Ye Zhao, Baichuan Deng

REDUCTION OF QUANTIZATION AND CLIPPING ERRORS USING BAYESIAN VIRTUAL SENSORS …… 808
Jyrki Kullaa

VIBRATION-BASED DAMAGE LOCALIZATION WITH DENSITY RATIO ESTIMATION METHOD …… 823
Yulong Zhang, John Macdonald, Paul Harper, Song Liu

PARAMETRIC SPECTRAL ESTIMATION AND DYNAMICS IDENTIFICATION FOR TRAVELING SURFACE VEHICLES ….833
Ilias A. Iliopoulos, Spilios D. Fassois, John S. Sakellariou

SYSTEM IDENTIFICATION AND DAMAGE DETECTION FRAMEWORK USING SIMULATING EXPERIMENTS AND MACHINE LEARNING TECHNIQUES ……..848
Panagiotis Seventekidis, Dimitrios Giagopoulos, Alexandros Arailopoulos, Olga Markogiannaki

AN IN-SITU EXPERIMENTAL SETUP FOR DAMAGE LOCALIZATION AND MECHANICAL PARAMETER ESTIMATION …… 857
Max Vollmering, Ivan Dolbonosov, Armin Lenzen

SUB-WAVELENGTH DAMAGE DETECTABILITY ASSESSMENT IN PERIODIC ASSEMBLIES USING A BLOCH MODELLING FRAMEWORK …… 870
Christophe Droz, Regis Boukadia, Elke Deckers, Wim Desmet

IDENTIFICATION OF DAMAGE TO A TWO-STORY HISTORIC MASONRY BUILDING IN NEPAL DUE TO THE 2015 GORKHA EARTHQUAKE USING NATURAL FREQUENCIES AND MODE SHAPES …… 878
Aiko Furukawa, Junji Kiyono, K. Toki

DEMINING WAR SCENARIOS: A PROJECT BASED ON NEW TECHNOLOGIES 889
Federica Mezzani, Gianluca Pepe, Nicola Roveri, Antonio Carcaterra, Stefano Solferini

LIE SYMMETRIES, OBSERVABILITY AND MODEL TRANSFORMATION OF NONLINEAR SYSTEMS WITH UNKNOWN INPUTS 901
Xiaodong Shi, Manolis Chatzis

VIBRATION TESTING BASED ON EVOLUTIONARY OPTIMIZATION TO IDENTIFY STRUCTURAL FAILURES AND DAMAGE IN GLULAM COMPONENTS 912
Juan Peña-Lasso, Rebeca Sanchez-Ruiz, Alvaro Gaute, Ignacio Lombillo, Ramon Sancibrian, Oscar Ramon Ramos

A METHODOLOGY ON INTERPRETABLE NOVELTY DETECTION 922
Artur Movsessian, David Garcia Cava, Dmitri Tcherniak, R. Janeliukstis

INVESTIGATION ON DAMAGE SENSITIVE FEATURES FOR OPTIMAL SENSOR NETWORKS BASED ON REAL-SCALE RECORDINGS 936
Said Quqa, Michelangelo Malatesta, Panagiotis Martakis, Artur Movsessian

EXPERIMENTAL ASSESSMENT OF VIBRATION-BASED METHODS FOR DAMAGE LOCALIZATION 948
Michal Venglár, Pier Francesco Giordano, Maria Pina Limongelli, Milan Sokol

ON THE PROBLEM OF ON–BOARD VIBRATION–BASED FAULT DETECTION IN RAILWAY SUSPENSIONS UNDER VARYING OPERATING CONDITIONS: A FEASIBILITY STUDY 960
Georgios Vlachospyros, Nikolaos Kaliorakis, Ilias A. Iliopoulos, Spilios D. Fassois, John S. Sakellariou, Alexandros Deloukas, George Leoutsakos, Ilias Chronopoulos, Christos Mamaloukakis

SYSTEM IDENTIFICATION OF CODE CONFORMING LOW-RISE RC BUILDING IN LALITPUR, NEPAL 972
Rajan Dhakal, Rajesh Rupakhety, Dipendra Gautam, Said Elias Rahimi

A DISPERSION-BASED METHODOLOGY FOR THE IN SITU ASSESSMENT OF BENDING STIFFNESS IN BRIDGE CABLES 981
João Rodrigues, Elsa Caetano, João Santos

A PSEUDO-INVERSE APPROACH TO THE PHYSICAL MODEL ESTIMATION PROBLEM. CAPACITIES AND LIMITATIONS 989
Alvaro Magdaleno, Jose M. Soria, Antolin Lorenzana

MODAL IDENTIFICATION OF STRUCTURES DURING STATIC LOAD TESTING: INTERACTION EFFECTS 1002
Antolin Lorenzana, Alvaro Magdaleno, Tomislav Jarak, Roberto Martinez, Antonio Balmori, Luis-Alfonso Basterra, Lara del Val, Juan J. Villacorta, Alberto Izquierdo

AN INTEGRATED VIBRATION-IMAGE PROCEDURE FOR DAMAGE IDENTIFICATION IN STEEL TRUSSES 1011
Marianna Crognale, Vincenzo Gattulli, Salvador Ivorra, Francesco Potenza

MAXIMUM LIKELIHOOD ESTIMATION OF DAMPING IN THE FREQUENCY DOMAIN DECOMPOSITION METHOD 1027
Javier Cara

A NUMERICAL INVESTIGATION OF NEW ALGORITHMS FOR THE DRIVE-BY METHOD IN RAILWAY BRIDGE MONITORING 1033
Lorenzo Bernardini, Marco Carnevale, Claudio Somaschini, K. Matsuoka, Andrea Collina

DAMAGE FEATURE RECOGNITION BASED ON LAMB WAVES DETECTION 1044
Xiaohui Wang, Jinhui Liang, Bin Zhang, Yeping Xiong, Jun Gao

MS 8: STRUCTURAL HEALTH MONITORING

DAMAGE ANALYSIS OF STEEL-CONCRETE COMPOSITE BEAMS UNDER STATIC LOADS 1053
Faraz Sadeghi, Xinqun Zhu, Jianchun Li

SEISMIC STRUCTURAL HEALTH MONITORING FOR REDUCING LIFE CYCLE COST OF ROAD BRIDGES 1063
Michela Torti, Ilaria Venanzi, Filippo Ubertini

ENGINEERED MODEL FOR THE NUMERICAL INVESTIGATION INTO VIBRATION CHARACTERISTICS OF A NOVEL BRIDGE BEARING UNDER FREE-FREE AND FIXED BOUNDARY CONDITION 1075
Pasakorn Sengsri, Charalampos Baniotopoulos, Sakdirat Kaewunruen

VIBRATION–BASED ROBUST DAMAGE DETECTION UNDER ASSEMBLY–INDUCED UNCERTAINTY: THE OUTPUT–ONLY CASE 1084
Andreas Mastakouris, Georgia Andriosopoulou, Kyriakos Vamvoudakis-Stefanou, Spilios Fassois

AUTOMATED OPERATIONAL MODAL ANALYSIS OF A STEEL ARCH BRIDGE FROM DYNAMIC SUB-MICROSTRAIN FIBER BRAGG GRATING DATA 1096
Dimitrios Anastasopoulos, Guido De Roeck, Edwin P.B. Reynders

AN ITERATIVE MULTILEVEL UPDATING SCHEME FOR VIBRATION-BASED DAMAGE ASSESSMENT OF A PRESTRESSED CONCRETE GIRDER BRIDGE 1109
Leqia He, Edwin Reynders, Changgen Deng, Giuseppe C. Marano, Bruno Briseghella, Guido DeRoeck

AN LTE-M OPENTHREAD MESH NETWORK FOR DISTRIBUTED REAL-TIME STRUCTURAL HEALTH MONITORING OF CRITICAL INFRASTRUCTURE IN CANADA 1123
Jason Thornton, Georgios Balomenos

DRIVE-BY RESONANT BRIDGE DETECTION METHOD USING TWO TRACK IRREGULARITIES MEASURED ON THE FIRST AND LAST VEHICLES OF A TRAIN 1138
Kodai Matsuoka, Hirofumi Tanaka, Kyohei Kawasaki, Kazuhiro Kajihara

CHARACTERIZATION OF VIBRATIONS MEASURED IN THE GRONINGEN BUILDING MONITORING NETWORK 1147
Chris Geurts, Okke Bronkhorst, Davide Moretti, Jitse Pruiksma, Ron Snijders

MONITORING FATIGUE DAMAGE ACCUMULATION OF WIND TURBINE TOWERS USING LIMITED NUMBER OF OUTPUT-ONLY VIBRATION MEASUREMENTS 1178
Victor Flores Terrazas, Omid Sedehi, Lambros S. Katafygiotis, Costas Papadimitriou

DYNAMIC CHARACTERISTICS OF A SIX-STOREY STEEL BUILDING EXAMINED FROM STRONG MOTION AND AMBIENT VIBRATION DATA 1189
Toshihide Kashima, Hiroto Nakagawa

REDUCTION OF TEMPERATURE EFFECTS FOR BRIDGE HEALTH MONITORING 1195
Viet Ha Nguyen, Tanja Kebig, Jean-Claude Golinval, Stefan Maas

DISCUSSIONS ON ILL-POSED PROBLEM IN DRIVE-BY PAVEMENT ROUGHNESS IDENTIFICATION 1205
Soichiro Hasegawa, Chul-Woo Kim, K. C. Chang, Naoya Toshi

DAMAGED DETECTION OF A BELL TOWER THROUGH OMA 1221
Simone Castelli, Andrea Belleri, Alessandra Marini, Babak Moaveni

TOWARDS STRUCTURAL HEALTH MONITORING BASED RISK BASED INSPECTION PLANNING FOR OFFSHORE WIND TURBINE SUPPORT STRUCTURES 1230
Simon Tewolde, Ruediger Höffer, Inka Mueller

INVESTIGATION OF EFFICIENT MODAL IDENTIFICATION OF BRIDGES USING BAYESIAN INFERENCE 1242
Yoshinao Goi, Chul-Woo Kim

VIBRATION-BASED STRUCTURAL HEALTH MONITORING OF A REINFORCED CONCRETE BEAM SUBJECT TO VARYING AMBIENT TEMPERATURES USING BAYESIAN METHODS 1254
Patrick Simon, Ronald Schneider, E. Viefhues, S. Said, Ralf Herrmann, Matthias Baeßler

MONITORING MONOPILE PENETRATION THROUGH MAGNETIC STRAY FIELD MEASUREMENTS 1272
Peter Meijers, Apostolos Tsouvalas, Andrei Metrikine

MITIGATION OF ENVIRONMENTAL VARIABILITIES IN DAMAGE DETECTION: A COMPARATIVE STUDY OF TWO SEMI-SUPERVISED APPROACHES 1281
Artur Movsessian, Bilal Ali Qadri, Dmitri Tcherniak, David Garcia Cava, Martin Dalgaard Ulriksen

IMPLEMENTING A STRUCTURAL HEALTH MONITORING SYSTEM USING DIGITAL MODELS OF THE BAM LARGE DROP TEST FACILITY IN HORSTWALDE 1293
Ralf Herrmann, Falk Hille, S. Said, Jens Sterthaus, Karsten Müller, Thomas Quercetti, Frank Wille, J.-A. Paffenholz, Matthias Baeßler

APPLICATION OF A CLASSIFICATION ALGORITHM TO THE EARLY-STAGE DAMAGE DETECTION OF A MASONRY ARCH 1305
Alberto Barontini, Maria Giovanna Masciotta, Paulo Amado Mendes, Luís Ramos, Paulo Lourenço

VIBRATION-BASED DAMAGE DETECTION APPLIED TO A CONCRETE ARCH-DAM 1315
Sérgio Pereira, Filipe Magalhães, Álvaro Cunha, Jorge Gomes, José Lemos

A FULLY AUTOMATED OMA PROCEDURE WITH ADAPTIVE TRACKING OF LONG-TERM MONITORING DATA: AN APPLICATION TO MASONRY TOWERS 1325
Giacomo Zini, Michele Betti, Gianni Bartoli

VIBRATION-BASED ANOMALY DETECTION USING SPARSE AUTO-ENCODER AND CONTROL CHARTS 1335
Rafaelle Finotti, Carmelo Gentile, Flávio Barbosa, Alexandre Cury

DESIGN OF A MONITORING SYSTEM FOR A LONG-SPAN SUSPENSION BRIDGE: OPTIMAL SENSOR PLACEMENT ……..1348
Øyvind Wiig Petersen, Ole Øiseth, Gunnstein Thomas Frøseth

COMPARISON OF ALTERNATIVE DYNAMIC VIBRATION MITIGATION APPROACHES FOR WIND TURBINE TOWERS …….. 1358
Konstantinos A. Kapasakalis, Pyros-Orfeas N. Bollano, Evangelos J. Sapountzakis, Ioannis A. Antoniadis

AN INTEGRATED MONITORING STRATEGY FOR CURRENT CONDITION ASSESSMENT OF HISTORIC BRIDGES …. 1373
Gabriele Ravizza, Rosalba Ferrari, Egidio Rizzi, Vasillis Dertimanis, Eleni Chatzi

APPLICATION OF WAVELET SYNCHRO-SQUEEZED TRANSFORM (WSST) METHOD TO RAILWAY BRIDGE HEALTH MONITORING …… 1388
Neda Mostafa, Richard Loendersloot, Dario Di Maio, Tiedo Tinga

DETECTION OF CLAMPING FORCE LOSS IN BOLTED JOINTS OF RAIL SUPPORTS IN CONSIDERATION OF CHANGING AMBIENT TEMPERATURE …… 1397
Anna-Lena Dreisbach, Volkan Yokaribas, Gerhard Dietrich, Daniel Sahm, Daniel Pak, Claus-Peter Fritzen

MS 9: STRUCTURAL CONTROL

NUMERICAL PERFORMANCE EVALUATION OF A BI-DIRECTIONAL ROLLER SEISMIC ISOLATION BEARINGS …..… 1408
Ricardo González, Nelson Ortiz-Cano, Andrés Nieto-Leal, Carlos Gaviria-Mendoza

CONTROL LAW AND ACTUATOR CAPACITY EFFECT ON THE DYNAMIC PERFORMANCE OF A HYBRID MASS DAMPER; THE CASE OF ROTTWEIL TOWER …… 1422
Lefteris Koutsoloukas, Nikolaos Nikitas, Petros Aristidou, Christian Meinhardt

DOUBLE TUNED MASS DAMPER INERTER FOR SEISMIC RESPONSE REDUCTION OF STRUCTURES …… 1433
Mahdi Abdeddaim, Salah Djerouni, Abdelhafid Ounis, Nassim Djedoui

OPTIMAL FEEDBACK CONTROL LAW FOR VISCOELASTIC MATERIALS WITH MEMORY EFFECTS …… 1445
Gianluca Pepe, Elena Paifelman, Antonio Carcaterra

OPTIMAL DAMPER DISTRIBUTIONS IN SHEAR FRAMES CONSIDERING SOIL CONDITIONS …… 1459
Ersin Aydin, Baki Ozturk, Osman Sivrikaya

A LOCAL ACTIVE NOISE CONTROL SYSTEM BASED ON A NONLINEAR SENSING TECHNIQUE FOR YACHT APPLICATIONS …… 1475
Dimitrios Mylonas, Alberto Erspamer, Andreas Paradisiois, Christos Yiakopoulos, Ioannis Antoniadis

TUNING STRATEGIES AND PLACEMENTS FOR DISTRIBUTED MULTIPLE TUNED MASS DAMPERS FOR WIND-INDUCED VIBRATION CONTROL IN HIGH-RISE BUILDINGS …… 1491
Ahmed Abed, Oum El Khaiat Moustachi

MS 10: ADVANCES ON INERTER-BASED STRUCTURAL VIBRATION CONTROL

OPTIMUM DESIGN OF A TUNED-INERTER-HYSTERETIC-DAMPER (TIHD) FOR BUILDING STRUCTURES SUBJECT TO EARTHQUAKE BASE EXCITATIONS 1501
Predaricka Deastra, David Wagg, Neil Sims

RESPONSE CONTROL OF BUILDINGS USING TMDI UNDER WIND AND EARTHQUAKES 1510
Said Elias, Rajesh Rupakhety, Simon Olafsson

SUPPRESSION OF VIBRATION TRANSMISSION BETWEEN OSCILLATORS COUPLED WITH AN INERTER-BASED JOINT 1521
Zhuang Dong, Jian Yang, Han Meng, Dimitrios Chronopoulos

SEISMIC PROTECTION OF MULTI-STOREY ROCKING STRUCTURES WITH INERTERS 1529
Rodrigo Thiers-Moggia, Christian Málaga-Chuquitaype

THE EFFECTS OF PARASITIC MASS ON THE PERFORMANCE OF INERTER-BASED DYNAMIC VIBRATION ABSORBERS 1545
Hakan Dogan, Neil Sims, David Wagg

VIBRATION CONTROL OF STEEL LIQUID STORAGE TANKS EQUIPPED WITH INERTER-BASED ISOLATION SYSTEMS 1556
Daniele Zahedin Labaf, Maurizio De Angelis, Daniele Pietrosanti

INERTER-BASED VIBRATION ABSORBERS FOR ROTATING WIND TURBINE BLADES 1568
Zili Zhang

MOTION CONTROL PERFORMANCE OF TUNED MASS DAMPER INERTER (TMDI) IN CONTINUOUS WHITE-NOISE EXCITED CANTILEVERED BEAMS WITH VARIOUS SHAPES 1576
Zixiao Wang, Agathoklis Giaralis

MS 11: BRIDGE DYNAMICS

EXPERIMENTAL STUDY OF RAILWAY BRIDGES OF SEVERAL STRUCTURAL TYPOLOGIES 1586
Pedro Galvín, Emma Moliner, Antonio Romero, María Dolores Martínez-Rodrigo

DYNAMIC RESPONSE OF CORRUGATED STEEL CULVERTS FOR RAILWAY LINES 1613
Andreas Andersson, Raid Karoumi

DYNAMIC SOIL-STRUCTURE INTERACTION IN RESONANT RAILWAY BRIDGES WITH INTEGRAL ABUTMENTS 1625
Abbas Zangeneh, Andreas Andersson, Costin Pacoste, Raid Karoumi

A NEW APPROACH TO MODELLING ROCKING MOTION OF POST-TENSIONED SEGMENTAL COLUMNS 1634
Ehsan Ahmadi, Mohammad Kashani

STOCHASTIC DYNAMIC ANALYSIS OF HIGH-SPEED MAGLEV GUIDEWAY COUPLED SYSTEM CONSIDERING VEHICLE PARAMETER 1642
Peng Zhang, Zhi-wu Yu, Jian- feng Mao

RAIL-BRIDGE INTERACTION EFFECTS IN SINGLE-TRACK MULTI-SPAN BRIDGES. EXPERIMENTAL RESULTS VERSUS NUMERICAL PREDICTIONS UNDER OPERATING CONDITIONS 1652
María D. Martínez-Rodrigo, Pedro Galvín, Emmanuela Moliner, Antonio Romero

VERTICAL COUPLING EFFECT OF THE BALLASTED TRACK ON THE DYNAMIC BEHAVIOR OF MULTITRACK RAILWAY BRIDGES COMPOSED BY ADJACENT DECKS 1666
Emmanuela Moliner, Antonio Romero, J.C. Sanchez-Quesada, María Dolores Martínez-Rodrigo, Pedro Galvín

DISPLACEMENT BASED ANALYSIS AND DESIGN OF ROCKING BRIDGES 1680
Michalis F. Vassiliou, Natalia Reggiani Manzo

SEISMIC PERFORMANCE OF BRIDGES ISOLATED WITH DCFP DEVICES 1704
Paolo Castaldo, Guglielmo Amendola, Diego Gino, Elena Miceli

MEASUREMENTS OF AMBIENT VIBRATIONS FOR A CABLE-STAYED BRIDGE INCLUDING THE SOIL-FOUNDATION SYSTEM 1722
Vanni Nicoletti, Davide Arezzo, Sandro Carbonari, Francesca Dezi, Fabrizio Gara

MS 12: FOOTBRIDGE VIBRATIONS

PERFORMANCE OF INERTIAL MASS CONTROLLERS FOR ULTRA-LIGHT FOOTBRIDGES: A CASE STUDY 1731
Carlos M. C. Renedo, Iván M. Díaz, Justin M. Russel, Stana Živanović

INTERVAL SERVICEABILITY ASSESSMENT OF FOOTBRIDGES 1747
Roberta Santoro, Alba Sofi, Federica Tubino

CLOSED—FORM SOLUTION OF THE RESPONSE OF SINGLE PEDESTRIAN INDUCED LOAD FOR CLAMPED—CLAMPED BRIDGES 1756
Daniel Colmenares, Andreas Andersson, Raid Karoumi

NUMERICAL VALIDATION OF THE GENERALISED EQUIVALENT SPECTRAL MODEL THROUGH CROWD DYNAMICS SIMULATIONS 1769
Fiammetta Venuti, Federica Tubino

VALIDATION OF A NOVEL VIRTUAL REALITY PLATFORM FOR INVESTIGATING PEDESTRIAN-PEDESTRIAN INTERACTION IN THE CONTEXT OF STRUCTURAL VIBRATION SERVICE ABILITY 1777
Artur Adam Soczawa-Stronczyk, Mateusz Bocian

MEASURING THE DYNAMIC RESPONSE OF A LIVELY FOOTBRIDGE TO AMBIENT AND WALKING EXCITATION 1791
Alfredo Cigada, Carmelo Gentile, Giulia Lastrico, Maria Gabriella Mulas

DYNAMIC PROPERTIES OF TWO PEDESTRIAN WOODEN BRIDGES INCLUDING SEASONAL EFFECTS 1805
John Hallak Neilson, Aida Ibisevic, Hasanhüseyin Ugur, Jean-Marc Battini, Roberto Crocetti, Costin Pacoste, Maria D. Martinez-Rodrigo

EVALUATION OF HUMAN INDUCED VIBRATIONS IN KJÆRRA BRIDGE 1814
Thomas Tenev, Ole Andre Kristiansen, Emrah Erduran

PERFORMANCE OF BIODYNAMIC MODELS TO REPRESENT THE ACTION OF A PEDESTRIAN IN THE VERTICAL DIRECTION 1824
Rafaela Silva, Roberto Pimentel, Aleksandar Pavic

PEDESTRIAN LATERAL FOOT PLACEMENT AND LATERAL DYNAMIC INSTABILITY OF BRIDGES 1835
Mateusz Bocian, Jeremy Burn, John Macdonald

MOTION-BASED DESIGN OF ACTIVE TUNED MASS DAMPERS TO CONTROL PEDESTRIAN-INDUCED VIBRATIONS IN FOOTBRIDGES UNDER UNCERTAINTY CONDITIONS 1844
Javier Fernando Jiménez-Alonso, Jose Manuel Soria, Carlos Martín de la Concha Renedo, Francisco Guillen González

CONTACT FORCE RECONSTRUCTION ON VIBRATING SURFACES 1854
Jeroen Van Hauwermeiren, Katrien Van Nimmen, B. Vanwanseele, Peter Van den Broeck

AN OPEN ACCESS BENCHMARK DATASET ON PEDESTRIAN-INDUCED VIBRATIONS COLLECTED ON THE EEKLO FOOTBRIDGE 1866
Peter Van den Broeck, Jeroen Van Hauwermeiren, Katrien Van Nimmen

IDENTIFICATION OF HUMAN-STRUCTURE INTERACTION BASED ON FULL-SCALE OBSERVATIONS 1874
Katrien Van Nimmen, Jeroen Van Hauwermeiren, Peter Van den Broeck

A NOVEL METHOD FOR INDIRECT MEASUREMENT OF GROUND REACTION FORCES ON VIBRATING STRUCTURES 1883
Andrei Firus, Roman Kemmler, Hagen Berthold, Steven Lorenzen, Jens Schneider

MS 13: HUMAN INDUCED VIBRATIONS IN FLOORS, STAIRCASES AND STADIA

SIMPLIFIED COMPUTATION OF TIMBER FLOOR VIBRATIONS LEVEL DUE TO HUMAN ACTIVITIES 1896
Thomas Catterou, Jean-Baptiste Castaing, Patrice Garcia

SYSTEM IDENTIFICATION OF HUMAN LEG SPRING STIFFNESS DURING RHYTHMIC JUMPING ON A PERCEPTIBLY MOVING SURFACE 1913
Rory White, Nicholas Alexander, John Macdonald

ENVIRONMENTAL IMPACT OF STRUCTURAL MODIFICATIONS IN OFFICE FLOORS TO SATISFY VIBRATION SERVICEABILITY 1924
Márcio S. Gonçalves, Aleksandar Pavic

ANALYSIS THE LATERAL VIBRATION SERVICEABILITY OF TEMPORARY GRANDSTAND AND HUMAN COMFORT BASED ON EXPERIMENT 1932
Suhui Yu, Jian Yuan, Wei Wang, Chengqiang Gao, Weili Wang, Cong Liu

MS 14: WIND INDUCED VIBRATIONS OF SLENDER STRUCTURES AND FATIGUE

LARGE-SCALE AEROELASTIC TESTING TO INVESTIGATE THE RESILIENCY OF TRANSMISSION INFRASTRUCTURE TO HURRICANE STORMS 1944
Ziad Azzi, Amal Elawady, Arindam Chowdhury

A STUDY ON THE EVALUATION OF WIND INDUCED VIBRATION IN LONG-SPAN SUSPENSION BRIDGES WITH ARTIFICIAL NEURAL NETWORKS 1958
Dario Fernandez, Aksel Fenerci, Ole Øiseth

AUTHORIAL METHOD OF EVALUATING VIBRATIONAL COMFORT OF OCCUPANTS OF HIGH-RISE BUILDINGS BASED ON AEROELASTIC MODEL TESTS 1968
Aleksander Pistol, Łukasz Flaga, Piotr Krajewski, Andrzej Flaga

WIND TUNNEL TESTS ON MOTION-INDUCED VORTEX VIBRATION 1988
Kazutoshi Matsuda, Kusuo Kato, Nade Cao

DYNAMIC STUDY OF PORT CRANES SUBJECTED TO STOCHASTIC WIND ACTIONS 2001
Luigi Solazzi

ON THE VALIDATION AND USE OF A SIMPLIFIED MODEL OF AEOLIAN VIBRATION OF OVERHEAD LINES FOR PARAMETRIC STUDIES 2011
Emmanuel Cieren, John Redford, Maxime Guéguin, Olivier Allix, Christine Yang, Fikri Hafid, Jean-Michel Ghidaglia

FATIGUE LIFE ESTIMATION CONSIDERING THE QUASI-PERIODIC CROSS-WIND RESPONSE OF SLENDER STRUCTURES IN THE LOCK-IN RANGE 2022
Francesca Lupi, Ruediger Höffer, Hans-Jürgen Niemann

MODELING THE INTERACTION OF GALLOPING AND VORTEX INDUCED VIBRATION FOR STEEL-CONCRETE COMPOSITE BRIDGES IN LAUNCHING PHASE 2040
Cong Chen, Niccolo Wieczorek, Julian Unglaub, Klaus Thiele

WIND TUNNEL VIV TESTING OF HELICAL STRAND CABLE MODELS 2054
Arsenii Trush, Stanislav Pospíšil, Hrvoje Kozmar

NUMERICAL AND EXPERIMENTAL STUDY OF A SLENDER CATENARY BRIDGE WITH A NOVEL TENSIONING SYSTEM 2063
Gergely Szabó, Gábor Hochrein

PREDICTION OF THE WIND-INDUCED FATIGUE OF SLENDER STRUCTURES 2077
Michela Damele, Maria Pia Repetto

A STOCHASTIC AND CONTINUOUS MODEL OF AEOLIAN VIBRATIONS OF CONDUCTORS EQUIPPED WITH STOCKBRIDGE DAMPERS 2088
Francesco Foti, Vincent Denoël, Luca Martinelli, Federico Perotti

ENHANCED SERVICE ABILITY PERFORMANCE IN WIND-EXCITED TALL BUILDINGS EQUIPPED WITH OPTIMAL TUNED MASS DAMPER INERTER VIA TOP-STOREY SOFTENING 2103
Zixiao Wang, Agathoklis Giaralis

MS 15: DYNAMICS OF ON- AND OFF-SHORE WIND ENERGY STRUCTURES (WES)

DYNAMICS OF TENSEGRITY SOLAR FAÇADES OPERATING AS MECHANICAL ENERGY HARVESTERS 2113
Raffaele Miranda, Enrico Babilio, Narinder Singh, Diana P. Villamil, Filipe Santos, Fernando Fraternali

TALL OFFSHORE STEEL WIND TURBINE TOWERS UNDER WIND CURRENT AND WAVE LOADING: AN EXPERIMENTAL AND NUMERICAL STUDY 2123
Yu Hu, Jian Yang, Charalampos Baniotopoulos, Xinger Wang, Xiaowei Deng

SPATIAL DISTRIBUTED CHARACTERISTICS OF DYNAMIC RESPONSE OF JACKET SUPPORTED OFFSHORE WIND TURBINES SUBJECTED TO HURRICANE INDUCED ENVIRONMENTAL LOADS 2134
Bowen Jiang, Qingshan Yang, Guoqing Huang, Min Liu

SURROGATE MODEL FORMULATION FOR STOCHASTIC FLUTTER ANALYSIS OF WIND TURBINE BLADES UNDER UNCERTAIN AERODYNAMICS LOADS 2151
Luca Caracoglia

A SYSTEMATIC INVESTIGATION OF COMMON GRADIENT BASED MODEL UPDATING APPROACHES APPLIED TO HIGH-FIDELITY TEST-DATA OF A WIND TURBINE ROTOR BLADE 2159
Johannes Knebusch, Janto Gundlach, Yves Govers

PLATFORM OPTIMIZATION OF LARGE FLOATING OFFSHORE WIND ENERGY STRUCTURES 2175
Giulio Ferri, Enzo Marino, Claudio Borri

DYNAMIC FIELD DATA FROM OFFSHORE MONOPILE WIND TURBINES – ASSESSMENT OF NATURAL FREQUENCIES AND DAMPING 2181
Karin Norén-Cosgriff, Amir M. Kaynia

MONITORING OF OFFSHORE WIND TURBINES UNDER WAVE AND WIND LOADING DURING INSTALLATION 2189
Aljoscha Sander, Christian Meinhardt, Klaus-Dieter Thoben

EXPERIMENTAL EVALUATION OF BENDING MOMENTS AT THE TOWER OF AN ONSHORE WIND TURBINE 2206
João Pacheco, Francisco Pimenta, Álvaro Cunha, Filipe Magalhães

WIND TURBINE ROTOR BLADE VIBRATION – APPLICATION OF TWO ALTERNATIVE MODAL DECOMPOSITION PROCEDURES ……2219
Evgueni Stanoev

MS 16: VIBRATION-BASED ASSESSMENT AND SHM OF CULTURAL HERITAGE STRUCTURES

STATISTICAL PROCESS CONTROL PROCEDURES FOR ONLINE DAMAGE DETECTION OF A MONUMENTAL MASONRY PALACE: THE CONSOLI PALACE IN GUBBIO, ITALY …… 2244
Enrique García Macías, Filippo Ubertini

EFFECT OF NOISE IN THE TIME-FREQUENCY ESTIMATE OF THE PERIDYNAMIC BOND ELASTIC CONSTANT PARAMETER …… 2260
Gaetano Miraglia, Rosario Ceravolo, G. Coletta

DYNAMIC MODELLING OF TRAM-INDUCED VIBRATION ON THE TEMPLE OF MINERVA MEDICA IN ROME …… 2266
Fernando Saitta, Sara Forliti, Alessandro Colucci, Angelo Tatì, Ivan Roselli

ENHANCED CONTINUOUS DYNAMIC MONITORING OF A COMPLEX MONUMENTAL PALACE THROUGH A LARGER SENSOR NETWORK …… 2275
Alban Kita, Ilaria Venanzi, Nicola Cavalagli, Enrique Garcia-Macias, Filippo Ubertini

FE MODEL UPDATING OF MASONRY TOWERS: MODELING AND NUMERICAL ISSUES …… 2285
Riccardo Mario Azzara, Maria Girardi, Cristina Padovani, Daniele Pellegrini, Leonardo Robol

INFLUENCE OF IMPORTANT STRUCTURAL STRENGTHENING ON THE DYNAMIC PROPERTIES OF A MASONRY ARCH BRIDGE …… 2299
Chiara Pepi, Nicola Cavalagli, Massimiliano Gioffrè, Vittorio Gusella

A MULTIDISCIPLINARY APPROACH INTEGRATING GEOMATICS, DYNAMIC FIELD TESTING AND FINITE ELEMENT MODELING TO EVALUATE THE CONSERVATION STATE OF THE GUIMARÃES CASTLE'S TOWER KEEP …… 2310
Luis Javier Sánchez-Aparicio, Maria Giovanna Masciotta, Daniele Pellegrini, Borja Conde, Maria Girardi, Cristina Padovani, Luis Ramos, Belén Riveiro

ENVIRONMENTAL EFFECTS ON THE DYNAMIC CHARACTERISTICS OF A HISTORIC CATHEDRAL …… 2323
Carmelo Gentile, Antonello Ruccolo

A DAMAGE LOCALISATION PROCEDURE FOR MASONRY TOWERS BASED ON FREQUENCY DATA …… 2338
Paolo Borlenghi, Carmelo Gentile, Antonella Saisi

MODAL PARAMETERS IDENTIFICATION ON ENVIRONMENTAL TESTS OF ANCIENT BELL TOWERS AND VALIDATION OF THEIR NUMERICAL MODELS …… 2355
Francesco Clementi, Gianluca Standoli, Ersilia Giordano, Angela Ferrante, Stefano Lenci

MEASUREMENTS OF THE COLOSSEUM RESPONSE TO ENVIRONMENTAL ACTIONS …… 2367
Fabrizio Vestroni, Adriano De Sortis, Annamaria Pau

ASSESSMENT OF THE TRM REINFORCEMENT OF WINDOWED MASONRY WALLS THROUGH OMA IDENTIFICATION 2377
Salvador Ivorra, Domenico Camassa, David Bru, Ignacio Gisbert, Anna Castellano, Aguinaldo Fraddosio, Mario Daniele Piccioni

MODAL IDENTIFICATION OF THE SAN FRANCESCO CHURCH IN PISA, ITALY 2386
Emanuele Lorenzo, F. Canessa, Giuseppe Chellini, Anna De Falco, Carlo Resta, E. Savelli, Giacomo Sevieri

DYNAMIC ANALYSIS OF THE INTERACTION BETWEEN BELLS AND MASONRY STRUCTURES 2400
David Bru, Salvador Ivorra, Michele Betti, Gianni Bartoli, F. Javier, Baeza F. Borja Varona

MS 17: VIBRATIONS DUE TO CONSTRUCTION AND INDUSTRIAL ACTIVITIES

REDUCING IMPACT OF VIBRATIONS FROM COMPACTION ON SLOPE STABILITY 2407
Jörgen Johansson, Joonsang Park, Christian Madshus, Carl Wersäll

VOLUME II

Minisymposia

MS 18: VIBRO-ACOUSTICS

A COUPLED MODELLING APPROACH FOR THE FAST COMPUTATION OF UNDERWATER NOISE RADIATION FROM OFFSHORE PILE DRIVING 2427
Yaxi Peng, Apostolos Tsouvalas, Andrei Metrikine

WAVE-RESOLVING AIRCRAFT FUSELAGE MODEL FOR CABIN NOISE PREDICTIONS UNDER DISTRIBUTED FLUID LOADINGS 2437
Christopher Blech, Sabine C. Langer

NUMERICAL EVALUATION OF THE SOUND TRANSMISSION OF A STRUCTURAL SYSTEM WITH ATTACHED NOISE CONTROL TREATMENTS USING STATISTICAL ENERGY ANALYSIS 2446
Thaynan Oliveira

BAND STRUCTURE OF ELASTIC BODIES WITH PERIODIC NONLOCALITIES 2457
A. S. Rezaei, S. V. Sorokin, F. Mezzani, A. Carcaterra

GLOBAL LONG WAVE APPROXIMATIONS FOR ELASTIC WAVE GUIDES 2464
Kirill Cherednichenko, Julius Kaplunov, Danila Prikazchikov, Leyla Sultanova

A NOVEL VIEW ON THE COMPOSITION OF ENERGY FLOW IN MULTI-MODAL WAVEGUIDES 2475
Lasse S. Ledet, Sergey V. Sorokin

ACOUSTIC BLACK HOLE PROFILE OPTIMIZATION 2482
Horia Cornean, Sergey Sorokin, Benjamin Støttrup

NOISE REDUCTION USING THE CONCEPT OF ACOUSTIC BLACK HOLES DESIGNED BASED ON MODAL ANALYSIS 2489
Bjørnar Saurdal, Daniel Villadsen, Sergey Sorokin, Lasse Ledet

OPTIMIZATION OF PERFORMANCE OF WAVEGUIDES USING THE WAVE FINITE ELEMENT METHOD 2497
Peter Broberg, Mikkel Steffensen, Sergey Sorokin, Lasse Ledet

FAST FREQUENCY SWEEPS FOR UNBOUNDED MEDIA: AN EFFICIENT PERFECTLY MATCHED LAYER FINITE ELEMENT FORMULATION 2508
Romain Rumpler, Antoine Vermeil de Conchard, Huina Mao

MS 19: BLAST AND IMPACT LOADS

IMPACT DAMAGE CHARACTERIZATION AT RC PLATES WITH PLANAR TOMOGRAPHY AND FEM 2521
Deborah Nerger, Robabeh Moosavi, Franz Bracklow, Marcus Hering, Tino Kühn, Manfred Curbach, Falk Hille, Andreas Rogge

MODEL REDUCTION FOR STRUCTURES SUBJECTED TO BLAST LOADING BY USE OF DYNAMIC SUBSTRUCTURING 2544
Linus Andersson, Peter Persson, Kent Persson

2DOF BLAST ANALYSIS OF BUILDINGS 2565
Sander Meijers, Peter Flink, Harm Kraaijenbrink, Meindert Wiersma

PROTECTION OF MASONRY STRUCTURES AGAINST EXPLOSIONS APPLYING LAYERS OF TEXTILE REINFORCED MORTAR 2573
Leonidas Alexandros Kouris, Georgios Valsamos, Savvas Triantafyllou, Vasileios Karlos, Daniel A. Pohoryles, Dionysios A. Bournas, Martin Larcher, Folco Casadei

MS 20: MOVING LOADS

SIMPLIFIED DYNAMIC RESPONSE ANALYSIS OF A RAILWAY BRIDGE CONSIDERING SOIL-STRUCTURE INTERACTION 2585
Christoph Adam, Benjamin Hirzinger

DYNAMIC AMPLIFICATION FACTORS FOR ULTRA-HIGH-SPEED HYPERLOOP TRAINS: VERTICAL AND LATERAL VIBRATIONS 2594
Ehsan Ahmadi, Mohammad Kashani, Nicholas Alexander

MOVING LOAD ON AN ELASTIC HALF-SPACE COATED WITH A THIN VERTICALLY INHOMOGENEOUS LAYER 2601
Saad Althobaiti, Vladimir Bratov, Ali Mubaraki, Danila Prikazchikov

VERIFICATION OF THE VALIDITY OF THE IMPACT FACTOR USED IN THE DESIGN OF PC SLEEPERS 2612
Shintaro Minoura, Tsutomu Watanabe, Kodai Matsuoka, Kenji Narita

DYNAMIC RESPONSE OF SINGLE AND MULTI-SPAN BEAMS UNDER A MOVING LOAD USING DYNAMIC STIFFNESS FORMULATIONS AND GALERKIN'S METHOD 2621
Baran Bozyigit, Sinan Acikgoz, Yusuf Yesilce

THE IN-PLANE STEADY-STATE RESPONSE OF A RING IN RELATIVE MOTION TO A CONSTANT LOAD 2631
Tao Lu, Apostolos Tsouvalas, Andrei Metrikine

TRAIN-WEIGHT-IN-MOTION IDENTIFICATION MEASURING TIME-HISTORIES OF RAIL STRAINS 2638
Annamaria Pau, Fabrizio Vestroni

DYNAMIC EFFECT OF TRAINS WITH ARTICULATED COACHES AND JACOBS BOGIES WITH INTEGER WHEELBASE RATIOS 2646
Pedro Museros, Andreas Andersson, Raid Karoumi

ANALYSIS OF VIBRATIONS INDUCED BY PROXIMATE MASSES TRAVERSING A BEAM SUPPORTED BY A FINITE DEPTH FOUNDATION WITH PARTIAL SHEAR RESISTANCE 2658
Zuzana Dimitrovová

THEORETICAL ASSESSMENT OF VERTICAL INTERACTION BETWEEN A WHEELSET AND TRACK: INFLUENCE OF THE TRACK DAMPING MODEL 2667
T. Mazilu, M.A. Gheți

MS 21: TRAFFIC INDUCED VIBRATIONS

REDUCING VIBRATIONAL IMPACT LATERAL OF A RAILWAY TRACK ON AN URBAN DEVELOPMENT PROJECT 2680
Felix Mertens, Thomas Jaquet

IMPROVED FLOATING SLAB TRACK PERFORMANCE BY ON TOP INSTALLED TUNED MASS DAMPER 2688
Thomas Jaquet, Wang Bo

A MIXED-FRAME-OF-REFERENCE MODEL FOR RAILWAY INDUCED SOIL-STRUCTURE VIBRATION INTERACTION 2700
Paulius Bucinskas, Evangelos Ntotsios, David Thompson, Lars Andersen

THE USE OF MULTIPLE MODELS TO ANALYSE RAILWAY TRACK GROUND DYNAMICS 2718
Panudech Chumyen, David Connolly, Kaitai Dong, Pedro Costa, Paulo Soares, Peter Woodward

OURS - INTRODUCING THE DUTCH FORMAL MODEL FOR RAILWAY VIBRATION 2729
Arnold Koopman

SUBSOIL MODELLING FOR RAILWAY INDUCED VIBRATIONS 2740
Bruno Zuada Coelho, Sven Lentzen, Maarten Pronk, Dirk de Lange, Eleni Smyrniou, Marc Hijma

NUMERICAL ASSESSMENT OF THE INFLUENCE OF BALLAST HETEROGENEITIES ON THE DYNAMIC BEHAVIOR OF RAILWAY TRACKS 2763
Hadrien Pinault, Etienne Balmes, Elodie Arlaud, Régis Cottereau

MITIGATION OF VIBRATION INDUCED BY RAILWAY TRAFFIC USING GRANULAR BARRIERS 2775
Patryk Dec, Régis Cottereau, Baldrik Faure

MS 22: DYNAMIC SOIL-STRUCTURE INTERACTION AND WAVE PROPAGATION

SCATTERING OF ELASTIC WAVES BY TRANSVERSELY ISOTROPIC SPHERE 2782
Ata Jafarzadeh, Peter D. Folkow, Anders Boström

A 2.5D FEM-BEM-MFS METHODOLOGY FOR SOIL-STRUCTURE INTERACTION PROBLEMS IN LAYERED HALF-SPACES 2798
Hassan Liravi, Robert Arcos, Dhananjay Ghangale, Jordi Romeu

A NEW SEMI-ANALYTICAL APPROACH FOR DYNAMIC PILE-SOIL INTERACTION PROBLEM 2807
Kenny Conto, Robert Arcos, Cecília Parente, Pedro Alves Costa, Jordi Romeu

STRUCTURE-SOIL-STRUCTURE INTERACTION ANALYSIS FOR REINFORCED CONCRETE FRAMED STRUCTURES 2817
Reine Fares, Maria Paola Santisi d'Avila, Anne Deschamps, Evelyne Foerster

COUPLED ITM-FEM APPROACH FOR THE ASSESSMENT OF THE MITIGATION EFFICIENCY OF FINITE AND INFINITE OPEN TRENCHES AND SOFT FILLED BARRIERS 2827
Julian Freisinger, Gerhard Müller

SOIL-STRUCTURE INTERACTION OF AN END-BEARING PILE FOUNDATION: DESIGN OF AN EXPERIMENTAL CASE STUDY 2846
Freddie Theland, Jean-Marc Battini, Costin Pacoste, Geert Lombaert, Stijn François, Peter Blom, Fanny Deckner

VIBRATIONS OF RECTANGULAR FLEXIBLE FOUNDATION ON HALFSPACE 2857
Marko Radišić, Mira Petronijević, Gerhard Müller

THE EFFECTS OF MODEL ASSUMPTIONS ON THE DYNAMIC IMPEDANCE FUNCTIONS OF A SHALLOW FOUNDATION 2868
Johan Lind Östlund, Andreas Andersson, Mahir Ülker-Kaustell, Jean-Marc Battini

ANALYSIS OF SEISMIC METASURFACES USING SPECIALISED ASYMPTOTIC MODELS FOR RAYLEIGH WAVES 2882
Peter Wootton, Julius Kaplunov, Danila Prikazchikov

INCREMENTAL DYNAMIC ANALYSES OF BRIDGE PYLONS WITH CONSIDERATION OF THE EFFECT OF SURFACE WAVES 2893
Charisis Chatzigogos, Kristel Meza Fajardo

TRANSIENT ANALYSIS IN HALF-SPACE COMBINING IGA AND THE PERFECTLY MATCHED LAYER METHOD 2909
Arturo Méndez Salas, Margarita Chasapi, Sven Klinkel

NUMERICAL WAVENUMBER INTEGRATION FOR 2.5D WAVE EQUATION SOLUTION 2919
Joonsang Park, Karin Norén-Cosgriff, Amir M. Kaynia

USE OF THE DOMAIN REDUCTION METHOD TO SIMULATE THE SEISMIC RESPONSE OF AN EXISTING STRUCTURE PROTECTED BY RESONATING UNIT CELL METAMATERIALS 2926
Constantinos Kanellopoulos, Boris Jeremić, Ioannis Anastasopoulos, Božidar Stojadinović

THE EFFECT OF SOIL LIQUEFACTION ON THE SEISMIC PERFORMANCE OF A TYPICAL PORT QUAY WALL 2939
Stella Karafagka, Stavroula Fotopoulou, Anna Karatzetzou, Georgia Kroupi, Kyriazis Pitilakis

A 2.5 DIMENSIONAL INDIRECT TREFFTZ METHOD TO MODEL LINEAR ELASTIC SOILS 2955
Hannes Englert, Fei Qu, Gerhard Müller

MITIGATION OF GROUND VIBRATION FROM PILE DRIVING BY CIRCULAR ARRAYS OF RIGID BLOCKS PLACED ON THE GROUND SURFACE 2966
Lars Vabbersgaard Andersen, Peter Persson, Andrew T. Peplow

TIME DOMAIN BEM-FEM COUPLING FOR SEISMIC SOIL-STRUCTURE INTERACTION ANALYSES CONCEIVED FOR AN ANSYS-MATLAB WORKFLOW 2985
Francesca Taddei, Bettina Chocholaty, Gerhard Müller

EXPERIMENTAL IDENTIFICATION OF THE DYNAMIC BEHAVIOUR OF PILE-SOIL SYSTEM INSTALLED BY MEANS OF THREE DIFFERENT PILE-DRIVING TECHNIQUES 3005
Athanasios Tsetas, Sergio S. Gomez, Apostolos Tsouvalas, Kees van Beek, Faraz S. Tehrani, Evangelos Kementzetzidis, Federico Pisano, Ahmed Elkadi, Maxim Segeren, Timo Molenkamp, Andrei V. Metrikine

DEVELOPMENT OF A METAMATERIAL PERIODIC FOUNDATION FOR SEISMIC PROTECTION 3016
Ahmad Saoud, Ahmad Omar, Diogo Queiros-Conde

GENERATION OF ARTIFICIAL ACCELEROGRAMS CONSISTENT WITH EARTHQUAKE-INDUCED GROUND MOTIONS 3027
Federica Genovese, Giuseppe Muscolino, Giovanni Biondi, Ernesto Cascone

MS 23: ASSESSMENT OF INDUSTRIAL STRUCTURES AND INFRASTRUCTURE UNDER NATURAL HAZARDS

FULL SCALE DYNAMIC TESTING OF WALL PANEL CONNECTIONS FOR PRECAST INDUSTRIAL BUILDINGS 3043
Ilaria Venanzi, Laura Ierimonti, Filippo Ubertini, Annibale Luigi Materazzi, Leonardo Casali, Giuseppe Paci

GROUND MOTION MODEL FOR SEISMIC VULNERABILITY ASSESSMENT OF PROTOTYPE INDUSTRIAL PLANTS 3053
Chiara Nardin, Rocco Di Filippo, Roberto Endrizzi, Igor Lanese, Fabrizio Paolacci, Oreste Salvatore Bursi

SIMPLIFIED ESTIMATION OF DESIGN FAULT DISPLACEMENT FOR BURIED PIPELINES AT FAULT CROSSING 3067
Vasileios Melissianos, Dimitrios Vamvatsikos

MS 24: SEISMIC PROTECTION OF STEEL STRUCTURES BY MEANS OF DISSIPATIVE SYSTEMS AND COMPONENTS

INNOVATIVE DISSIPATIVE DEVICES WITH TENSEGRITY ARCHITECTURE AND SUPER ELASTIC BEHAVIOUR FOR THE SEISMIC PROTECTION OF STRUCTURES 3079
Narinder Singh, Ada Amendola, Filipe Amarante Dos Santos, Gianmario Benzoni, Fernando Fraternali

EARTHQUAKE EFFECTS ON LOW PROFILE CONTAINER CRANE WITH SEISMIC ISOLATION DEVICE 3086
Luigi Solazzi

STEEL TRUSS BRIDGE WITH BUCKLING RESTRAINED DAMPER UNDER SEISMIC LOADING 3097
Purevdorj Sosorburam, Eiki Yamaguchi

MONOTONIC AND CYCLIC BEHAVIOUR OF THE BEAM-TOCOLUMN JOINTS OF THE “FUTURE” MOCKUP 3107
Roberto Tartaglia, Mario D'Aniello, Raffaele Landolfo

DAMAGE-AVOIDANCE STEEL ROCKING FRAMES WITH BUCKLING-ENABLED COMPOSITE BRACING 3117
Leena Tahir Kibriya, Christian Málaga-Chuquitaype, Mohammad Mehdi Kashani

OPTIMIZATION OF DISSIPATIVE REPLACEABLE LINK FRAMES BY ELASTIC HIGH STRENGTH STEEL COUPLING BEAMS 3127
Marius Pinkawa, Cristian Vulcu, Benno Hoffmeister, Markus Feldmann

USE OF HIGH-STRENGTH STEEL FOR MULTI-CRITERIA OPTIMIZATION OF DISSIPATIVE DEVICES 3144
Silvia Caprili, Ivan Panzera, Walter Salvatore

ENHANCED STRUCTURAL RESILIENCE THROUGH THE USE OF "LEAF-SPRING" COLUMNS AND REPLACEABLE DISSIPATIVE COMPONENTS 3154
Cristian Vulcu, Marius Pinkawa, Aurel Stratan, Benno Hoffmeister

MS 25: EXPERIMENTAL EARTHQUAKE ENGINEERING

EXPERIMENTAL INVESTIGATION OF THE INFLUENCE OF TENSILE STRAIN ON THE CRACKING OF R/C VERTICAL STRUCTURAL ELEMENTS 3174
Theodoros A. Chrysanidis, Vassilis P. Panoskaltsis

EVALUATION OF CRACKING BEHAVIOR OF R/C VERTICAL COMPONENTS REINFORCED WITH VARYING LONGITUDINAL REINFORCEMENT RATIOS 3186
Theodoros A. Chrysanidis, Vassilis P. Panoskaltsis

GRAPHENE-RUBBER LAYERED COMPOSITES FOR SEISMIC ISOLATION 3198
Maria Rosaria Marsico, Julián Mauricio Londoño Monsalve

CYCLIC PERFORMANCE OF WIND TURBINE TOWER WITH CONCRETE FILLED DOUBLE SKIN STEEL TUBES SECTION UNDER TORSION..... 3204
Yu-HangWang, Shu-Qi Wang, Guo-Bing Lu, Ji-Ke Tan

THE ST. SILVESTRO BELFRY IN L'AQUILA: FROM THE REHABILITATION WORKS TO THE ACTUAL PERFORMANCE IN TERMS OF DYNAMIC PROPERTIES AND FRAGILITY FUNCTIONS ESTIMATION 3218
Ilaria Capanna, Riccardo Cirella, Angelo Aloisio, Rocco Alaggio, Franco Di Fabio, Massimo Fragiacomo

OUT-OF-PLANE SHAKING TABLE TESTS ON DUTCH BUILDING PRODUCTS 3228
Alexander Johannes Bronkhorst, C.P.W. Geurts

AN EXPERIMENTAL STUDY ON THE RELATIONSHIP BETWEEN EARTHQUAKE DAMAGE AND THE NATURAL FREQUENCY OF WOODEN HOUSE 3245
Kazuhiro Hayashi, Ariyoshi Yamada, Yoshiyuki Komiya

PERFORMANCE OF A LINEAR SOLUTION FOR APPROXIMATING NONLINEAR RESPONSE OF REINFORCED CONCRETE STRUCTURES SUBJECTED TO EARTHQUAKE SHAKING 3251
Kevin Kariuki, Tarjei Heen, Lars Halvor Kaasa, Amir Massoud Kaynia

BEHAVIOUR OF REINFORCED CONCRETE STRANDS DURING TENSION TEST INSPECTED WITH DIC 3261
Haukur Eiriksson, Bjarni Bessason

REVIEW OF SITE EFFECT MODELING METHODS CONSIDERING EXPERIMENTAL GEOPHYSICAL DATA 3274
Rita Abou-Jaoude, Nisrine Makhoul, Jean-Alain Fleurisson, Alexandrine Gesret

HYBRID COLLAPSE TEST OF STEEL COLUMNS WITH NONLINEAR FRAME SUBSTRUCTURING AND FORCE REDISTRIBUTION 3291
Konstantinos Skalomenos, Masahiro Kurata, Yoshiki Ikeda

FRF-BASED MODAL TESTING OF HORIZONTALLY SWAYING STRUCTURES USING OCXO SYNCHRONISED WIRELESS ACCELERAMETERS FOR SIMULTANEOUS FORCE AND VIBRATION RESPONSE MEASUREMENTS 3301
Wai Kei Ao, Aleksandar Pavic

TESTING OF ADDITIVELY MANUFACTURED SMALL SCALE RC SPECIMENS FOR STATISTICAL VALIDATION OF STRUCTURAL MODELS IN EARTHQUAKE ENGINEERING 3313
Lorenzo Del Giudice, Rafal Wrobel, Christian Leinenbach, Michalis F. Vassiliou

MEASUREMENT OF SOIL STRAINS UNDER EARTHQUAKE LOADING 3324
Xiaoyu Guan, Gopal Madabhushi, Mark Talesnick

STRUCTURAL PROPERTIES OF UNREINFORCED MASONRY WALLS CONSIDERING CONSTRUCTION QUALITIES 3334
Dong-Hyeon Shin, Hyung-Joon Kim

DIRECT OBSERVATION OF BOND FAILURE OF FATIGUE PULLOUT TEST WITH LIQUID WATER BY USING DIC 3343
Ahmed Okeil, Koji Matsumoto, Kohei Nagai

SHAKE TABLE TEST FOR SEISMIC PERFORMANCE EVALUATION ACCORDING TO ANCHORING INTERVAL OF SUPPORT ELEMENTS PANEL SYSTEM 3355
Jaehan Park, Haeyong Park, Sanghoon Oh

SHAKING TABLE TEST FOR EVALUATION OF SEISMIC PERFORMANCE ACCORDING TO EDGE CLEARANCE OF GLAZING CURTAIN WALL SYSTEM 3367
Jung Woo Yang, Hae Yong Park, Sang Hoon Oh

EXPERIMENTAL SEISMIC ASSESSMENT AND PROTECTION OF MUSEUM ARTEFACTS 3381
M. Fragiadakis, L. DiSarno, A. Saetta, M. G. Castellano, I. Rocca, S. Diamantopoulos, V. Crozet, I. Politopoulos, T. Chaudat, S. Vasic, I.E. Bal, E. Smyrou, I. Psycharis, T.C. Hutchinson, L. Berto

A MACHINE LEARNING APPROACH TO NONLINEAR RESPONSE ANALYSIS OF STRUCTURES 3397
Panagiotis Georgakis, Manolis Georgioudakis, Michalis Fragiadakis

MS 26: UQ AND PROBABILISTIC LEARNING IN COMPUTATIONAL DYNAMICS

IDENTIFICATION OF A STOCHASTIC PROCESS MODELING THE STIFFNESS OF THE VOCAL FOLDS FOR A VOICE PRODUCTION MODEL REPRESENTED BY A NEURAL NETWORK 3403
Edson Cataldo, Christian Soize, R.L. Silva, João Marcos Silva

AIRSHIP GUST RESPONSE PROBABILISTIC MODEL CONSTRUCTION 3413
Fabrice Poirion, Guy Mortchelewicz

STATE-OF-THE-ART REVIEW OF MACHINE LEARNING APPLICATIONS TO GEOTECHNICAL EARTHQUAKE ENGINEERING PROBLEMS 3424
Zeinep Achmet, Luigi Di Sarno

MS 27: STOCHASTIC DYNAMICS AND RELIABILITY ANALYSIS OF STRUCTURAL AND MECHANICAL SYSTEMS UNDER ENVIRONMENTAL EXCITATION

RELIABILITY ASSESSMENT OF THE DYNAMIC BEHAVIOR OF HIGH-SPEED RAILWAY BRIDGES USING FIRST ORDER RELIABILITY METHOD 3438
Reza Allahvirdizadeh, Andreas Andersson, Raid Karoumi

RESPONSE OF ELASTIC SHOCK OSCILLATORS AND ELASTOPLASTIC OSCILLATORS, WHITELY EXCITED, FROM ENERGY BALANCE AND STOCHASTIC ANALYSES 3451
Laurent Borsoi, Philippe Piteau

EFFICIENT ESTIMATION OF THE SKEWNESS OF THE RESPONSE OF A WAVE-EXCITED OSCILLATOR 3467
Margaux Geuzaine, Vincent Denoël

EXTREME DYNAMIC RESPONSE OF EXTENDED BRIDGE STRUCTURES SUBJECTED TO INHOMOGENEOUS ENVIRONMENTAL LOADING 3481
Bernt Leira, Jian Dai

UNCERTAINTY ABOUT ENVIRONMENTAL VIBRATION TESTS: A CASE STUDY 3496
Alice Di Primio, Noemi Fiorini, Daniele Spina, Claudio Valente, Marcello Vasta

RESPONSE OF NONLINEAR SECONDARY OSCILLATORS IN CASCADE TO RANDOM EXCITATION 3507
Stavros Kasinos, Eleni Chatzi, Christian Málaga-Chuquitaype

MS 28: UNCERTAINTIES ON MATERIALS AND ENVIRONMENTAL LOADS

EFFECTS OF MECHANICAL UNCERTAINTIES ON DYNAMIC PROPERTIES OF CROSS-LAMINATED TIMBER FLOORS 3519
Marija Milojević, Marija Nefovska-Danilović, Stana Živanović, Miroslav Marjanović

MODEL UNCERTAINTIES IN NLFEAS OF RC SYSTEMS UNDER CYCLIC LOADS 3527
Paolo Castaldo, Diego Gino, Guglielmo Amendola, Elena Miceli

UNCERTAINTIES IN WIND-INDUCED LOADS ON HYPERBOLIC PARABOLOID ROOFS: WIND-TUNNEL TESTS AND ANALYTICAL MODELS 3548
Fabio Rizzo, Vincenzo Sepe

MS 29: BAYESIAN UPDATING, FILTERING AND INVERSION FOR DYNAMIC SYSTEMS

BAYESIAN MODEL UPDATING FOR EXISTING SEISMIC-ISOLATED BRIDGES USING OBSERVED ACCELERATION RESPONSE DATA 3558
Masaru Kitahara, Matteo Broggi, Michael Beer

NONLINEAR SYSTEM IDENTIFICATION OF CORRODED REINFORCED CONCRETE STRUCTURES BASED ON SEISMIC RESPONSE DATA 3567
Shaghayegh Abtahi, Zhenning Liu, Yong Li

DAMAGE DETECTION OF JOINING TECHNOLOGIES FOR PRINTED CONTROLLER BOARDS IN AUTOMOBILES 3581
Moritz Hülsebrock, Maximilian Herrnberger, Heiko Atzrodt, Roland Lichtinger

REAL-TIME BAYESIAN PARAMETER, STATE AND INPUT ESTIMATION USING OUTPUT-ONLY VIBRATION MEASUREMENTS 3590
Daniz Teymouri, Omid Sedehi, Lambros S. Katafygiotis, Costas Papadimitriou

HIERARCHICAL BAYESIAN UNCERTAINTY QUANTIFICATION OF DYNAMICAL MODELS UTILIZING MODAL STATISTICAL INFORMATION 3599
Omid Sedehi, Costas Papadimitriou, Lambros Katafygiotis

MS 30: RECENT ADVANCES IN PERFORMANCE-BASED ENGINEERING AND DESIGN OF STRUCTURES AND CIVIL INFRASTRUCTURE SYSTEMS SUBJECTED TO SINGLE OR MULTIPLE HAZARDS

RISK-TARGETED MAPS FOR ALICANTE PROVINCE (SPAIN) 3607
Alireza Kharazian, Sergio Molina, Juan Jose Galiana-Merino, Noelia Agea-Medina

EFFECT OF MODELLING ASSUMPTIONS ON THE SEISMIC PERFORMANCE ASSESSMENT OF THIN REINFORCED CONCRETE WALL BUILDINGS 3618
Orlando Arroyo, Dirsa Feliciano, Julián Carrillo, José Colombo

SENSITIVITY OF SPECIAL STEEL MOMENT FRAMES TO THE INFLUENCE OF COLUMN-BASE HYSTERETIC BEHAVIOR INCLUDING GRAVITY FRAMING SYSTEM 3629
Pablo Torres-Rodas, Francisco Flores, Bryam Astudillo, Sebastian Pozo

A MULTI-OBJECTIVE OPTIMAL PARAMETER DESIGN PROCEDURE FOR SLIDE BRIDGE BEARINGS UNDER SEISMIC EXCITATION BASED ON A DETERMINISTIC-STOCHASTIC MODELING APPROACH 3643
Xinhao He, Akira Igarashi

PARAMETRIC ANALYSIS AND COMPARISON OF MODELS USED IN THE ANALYSIS OF STEEL STRUCTURES 3655
Bryam Astudillo, Sebastian Pozo, Francisco Flores

DYNAMIC RESPONSE OF EXISTING STEEL FRAMES WITH MASONRY INFILLS UNDER MULTIPLE EARTHQUAKES 3671
Luigi Di Sarno, Jing-Ren Wu, Fernando Gutiérrez-Urzúa, Fabio Freddi, Mario D'Aniello, Ob-Sung Kwon, Stathis Bousias, Matjai Dol§ek

SEISMIC RESILIENCE ASSESSMENT FOR THE G7 HIGHWAY BRIDGE IN GREECE 3686
Akrivi Chatzidaki, Konstantinos Bakalis, Dimitrios Vamvatsikos

LIMITATIONS OF EUROCODE 8 DUAL DUCTILITY CLASS APPROACH IN SEISMIC DESIGN OF RC HIGH-RISE BUILDINGS 3697
Jelena Pejovic, Nina Serdar, Radenko Pejovic

SEISMIC PERFORMANCE AND RESILIENCE QUANTIFICATION OF A ROCKING BRIDGE FRAME 3709
Anastasios Giouvanidis, You Dong

MODIFIED INTENSITY MEASURES TO IMPROVE ACCURACY IN FRAGILITY ANALYSIS 3724
Matteo Ciano, Massimiliano Gioffrè, Klaus Thiele, Mircea Grigoriu

OPTIMAL VISCOUS DAMPER PLACEMENT TO PREVENT POUNDING OF ADJACENT BUILDINGS 3735
Huseyin Cetin, Baki Ozturk, Ersin Aydin

SEISMIC RELIABILITY-BASED DESIGN OF STRUCTURES EQUIPPED WITH DFPS 3744
Paolo Castaldo, Gaetano Alfano

GLOBAL AND LOCAL PERFORMANCE LEVELS ON THE PROBABILISTIC EVALUATION OF THE STRUCTURAL POUNDING EFFECT BETWEEN ADJACENT RC STRUCTURES 3762
Maria Flegga, Maria Favvata

FRAGILITY CURVES FOR RC FRAMED BUILDINGS SUBJECTED TO EARTHQUAKE-INDUCED LANDSLIDE: COMPARISON BETWEEN 2D AND 3D STRUCTURAL MODELS 3780
Giacomo Miluccio, Fulvio Parisi, Edoardo Cosenza

IMPACT OF CUMULATIVE DAMAGE ON FRAGILITY OF RC FRAMED BUILDINGS SUBJECTED TO EARTHQUAKE-INDUCED LANDSLIDES 3788
Giacomo Miluccio, Fulvio Parisi, Edoardo Cosenza

MS 31: EUROPEAN ETN "DYNAMIC VIRTUALISATION: MODELLING PERFORMANCE OF ENGINEERING STRUCTURES" (DYVIRT)

PARAMETER INVESTIGATION OF RELAXED UNCERTAIN POWER SPECTRA FOR STOCHASTIC DYNAMIC SYSTEMS 3803
Marco Behrendt, Marius Bittner, Liam Comerford, Matteo Broggi, Michael Beer

AN APPLICATION OF GENERATIVE ADVERSARIAL NETWORKS IN STRUCTURAL HEALTH MONITORING 3816
George Tsialiamanis, Eleni Chatzi, N. Dervilis, David Wagg, Keith Worden

A NEAT APPROACH TO STRUCTURAL HEALTH MONITORING 3832
George Tsialiamanis, David Wagg, N. Dervilis, Keith Worden

A PROBABILISTIC APPROACH TOWARDS UNCERTAINTY QUANTIFICATION IN JOINED STRUCTURES 3846
Atmaram Muraleedharan, Robert Barthorpe, Keith Worden

ON THE USE OF NONLINEAR NORMAL MODES FOR NONLINEAR REDUCED ORDER MODELING 3865
Thomas Simpson, Nikolaos Dervilis, Eleni Chatzi

KALMAN-BASED COUPLED RESPONSE-INPUT ESTIMATION DURING ENVIRONMENTAL TESTS ON THE BOX ASSEMBLY WITH REMOVABLE COMPONENT STRUCTURE 3878
Silvia Vettori, Emilio Di Lorenzo, Bart Peeters, Eleni Chatzi

COMPUTATIONALLY EFFICIENT HIERARCHICAL BAYESIAN MODELING FRAMEWORK FOR LEARNING EMBEDDED MODEL UNCERTAINTIES 3886
Xinyu Jia, Omid Sedehi, Costas Papadimitriou, Lambros S. Katafygiotis

ON THE IMPLEMENTATION OF ADAPTIVE INVERSE CONTROL TO VIRTUAL TRANSFER SYSTEMS 3894
Thomas Simpson, Vasilis Dertimanis, Eleni Chatzi

ROBUST BAYESIAN OPTIMAL SENSOR PLACEMENT FOR MODEL PARAMETER ESTIMATION AND RESPONSE PREDICTIONS 3904
Tulay Ercan, Petros Koumoutsakos, Costas Papadimitriou

UNCERTAINTY QUANTIFICATION FRAMEWORK FOR STRUCTURAL MODEL OF WIND TURBINE BLADES 3911
Paulo Gonzaga, Keith Worden, Nikolaos Dervillis, Nevena Stevanovic, Lars Oliver Bernhammer, Henrik Stensgaard Toft

MS 32: COMPUTATIONAL METHODS FOR STOCHASTIC DYNAMICS

SENSITIVITY ANALYSIS OF SAFETY PERFORMANCE OF THE BURIED PIPELINES UNDER SURCHARGE 3921
Zhiqiang Wang, Zhenyu Lei

INCREMENTS AND DIFFERENTIALS IN THE STOCHASTIC ANALYSIS OF FRACTIONAL DIFFERENTIAL EQUATIONS 3931
Mario Di Paola, Antonina Pirrotta

MS 33: NUMERICAL SIMULATIONS FOR EARTHQUAKE-RESILIENT SYSTEMS

A DEVELOPED ANALYTICAL NON-LINEAR MODEL OF ELASTOMERIC BEARINGS VERIFIED WITH NUMERICAL FINDINGS 3939
Konstantinos N. Kalfas, Davide Forcellini

EXPERIMENTAL, THEORETICAL, AND NUMERICAL SIMULATION APPROACHES TO ASSESS THE COMPRESSIVE BEHAVIOR OF ELASTOMERIC BEARINGS 3949
Manuel Guzmán Sánchez, Davide Forcellini, Ricardo Moreno Sánchez, Diego Giraldo-Vásquez

THE ROLE OF NON-LINEARITY IN THE SEISMIC ASSESSMENT OF A BASE ISOLATED BENCHMARK BUILDING WITH SOIL STRUCTURE INTERACTION EFFECTS 3959
Andrea Canini

SENSITIVITY OF DEFORMATION DEMANDS IN BUILDINGS TO MODELING ASSUMPTIONS IN NONLINEAR SEISMIC ANALYSIS 3981
Jørgen Rosmo Roven, Emrah Erduran, Amir M. Kaynia

EFFECT OF THE JOINT STRENGTH ON THE PERFORMANCE OF ORDINARY MOMENT-RESISTING FRAMES UNDER A PROGRESSIVE COLLAPSE SITUATION 3995
Mohammad Ali Mahdavipour, Dmitry Vysochinskiy

NUMERICAL SIMULATIONS OF UNBURIED HP/HT SUBSEA PIPELINES SUBJECTED TO SEISMIC SCENARIOS 4007
Daniele Mina, Davide Forcellini, Hassan Karampour

GRAVITY SYSTEM ENERGY DISSIPATION CONTRIBUTION IN SEISMIC PERFORMANCE OF SPECIAL STEEL MOMENT FRAMES 4023
Francisco Flores, Sebastian Pozo, Bryam Astudillo, Jose Vazquez

SIMULATING THE CYCLIC BEHAVIOUR OF A SINGLE-BAY WIDE-FLANGED STEEL BRACED FRAME 4039
Madhar Haddad, Nigel Shrive

NUMERICAL SIMULATIONS OF ELASTOMERIC BEARINGS BRACED WITH STEEL CABLES UNDER CYCLIC DISPLACEMENT 4049
Hossain Talebi, Mohammad Reza Adibramezani, Nooshin Ghorbani Amirabad

CYCLIC BEHAVIOUR AND FRACTURE OF A SINGLE-BAY WIDE-FLANGED STEEL BRACED FRAME 4059
Madhar Haddad, Nigel Shrive

MS 34: VIBRATION ABSORPTION

EFFECT OF DIFFERENT CONFIGURATIONS OF THE GEOFOAM FILLED BARRIER IN VIBRATION SCATTERING AND ITS OPTIMIZATION BY GENETIC ALGORITHM 4069
Mehran Naghizadehrokni, Martin Ziegler

EXPERIMENTAL INVESTIGATION OF 2D RAINBOW PHONONIC CRYSTALS FOR BROADBAND VIBRATION ATTENUATION 4085
Han Meng, Dimitrios Chronopoulos, Nick Bailey, Zhuang Dong, Jian Yang

ACOUSTIC PERFORMANCE EVALUATION OF A PANEL UTILIZING NEGATIVE STIFFNESS MOUNTING FOR LOW FREQUENCY NOISE CONTROL 4093
Andreas Paradeisiotis, Moris Kalderon, Ioannis Antoniadis, Lina Fouriki

A MACHINE MOUNT BASED ON THE KDAMPER FOR VIBRATION ABSORPTION AT LOW FREQUENCIES 4111
Andreas Paradeisiotis, Konstantinos Tsioumanis, Ioannis Antoniadis, Kalliopi Fouriki

DESIGN OF A BROADBAND ELASTIC METAMATERIAL VIA TOPOLOGICALLY OPTIMIZED INERTIAL AMPLIFICATION MECHANISMS 4125
Osman Yuksel, Cetin Yilmaz

VIBRATION ABSORPTION PERFORMANCE OF METAMATERIAL LATTICES CONSISTING OF IMPACT DAMPERS 4139
Kyriakos Chondrogiannis, Vasilis Dertimanis, Sami Masri, Eleni Chatzi

SEISMIC RESPONSE OF STRUCTURE EQUIPPED WITH A NON-INVASIVE EXTERNAL VISCOUS DAMPING SYSTEM 4150
Antonio Sabino, Antonio Mannella

ADVANCED NEGATIVE STIFFNESS VIBRATION ABSORBERS COUPLED WITH SOIL-STRUCTURE INTERACTION FOR SEISMIC PROTECTION OF BUILDINGS 4160
Konstantinos Kapasakalis, Antonios Alvertos, Antonios Mantakas, Ioannis Antoniadis, Evangelos Sapountzakis

OPTIMAL DESIGN OF ADVANCED NEGATIVE STIFFNESS ABSORBERS 4177
Konstantinos A. Kapasakalis, Ioannis A. Antoniadis, Evangelos J. Sapountzakis

DYNAMIC ANALYSIS OF AN ACTIVE ISOLATION MOUNT USING FEEDFORWARD AND FEEDBACK CONTROL SCHEMES 4189
Grigorios Chatziathanasiou, Nikolaos Chrysochoidis, Dimitris Saravanos

MS 35: NEW TRENDS IN THE COMPUTATIONAL AND EXPERIMENTAL STRUCTURAL DYNAMICS FOR THE PRESERVATION OF HISTORICAL MASONRY STRUCTURES IN SEISMIC AREAS

AN INNOVATIVE VOXEL-BASED APPROACH FOR THE OUT-OF-PLANE HOMOGENIZED LIMIT ANALYSIS OF NON-PERIODIC MULTI-LEAF MASONRY WALLS 4200
Gabriele Milani, Simone Tiberti

EXPERIMENTAL AND NUMERICAL STUDY OF HISTORIC MASONRY WITH BED JOINT REINFORCED REPOINTING 4212
Anastasios Drougkas, Lucia Licciardello, Jan G. Rots, Rita Esposito

SEISMIC VULNERABILITY EVALUATION OF LONGHU PAGODA, SICHUAN, PRC 4226
Peixuan Wang, Jacopo Scacco, Gabriele Milani, Shengcai Li

ADAPTIVE LIMIT ANALYSIS OF HISTORICAL MASONRY STRUCTURES MODELED AS NURBS SOLIDS 4243
Nicola Grillanda, Andrea Chiozzi, Gabriele Milani, Antonio Tralli

AN AUTOMATIC AND FAST PROCEDURE FOR THE NUMERICAL ANALYSIS OF CURVED MASONRY STRUCTURES 4255
Jacopo Scacco, Gabriele Milani, Paulo Lourenço

THE MODELLING OF MULTIPLE LEAF MASONRY WALLS OF THE ARQUATA DEL TRONTO FORTRESS AS A NON-SMOOTH DYNAMICAL SYSTEM 4262
Angela Ferrante, Ersilia Giordano, Francesco Clementi, Vasilis Sarhosis, Gabriele Milani, Stefano Lenci

DAMAGE ASSESSMENT OF CHURCHES IN THE CITY OF CAMERINO AFTER THE 2016 CENTRAL ITALY SEISMIC SEQUENCE 4272
Ersilia Giordano, Angela Ferrante, Francesco Clementi, Stefano Lenci

AUTOMATIC ASSESSMENT OF PARTIAL FAILURE MECHANISMS IN RETROFITTED HISTORICAL MASONRY AGGREGATES THROUGH ADAPTIVE NURBS LIMIT ANALYSIS 4282
Nicola Grillanda, Marco Valente, Gabriele Milani

MITIGATION OF AMPLIFIED RESPONSE OF RESTRAINED ROCKING WALLS THROUGH HORIZONTAL DAMPERS 4292
Fabio Solarino, Linda Giresini, Daniel V. Oliveira

THE SPECTRAL ACCELERATION IN THE SEISMIC VULNERABILITY ASSESSMENT OF A HISTORIC MASONRY BUILDING. A COMPARISON BY USING SEVERAL APPROACHES ON A CASE STUDY 4304
Renato Sante Olivito, Saverio Porzio, Carmelo Scuro

FRAGILITY ASSESSMENT OF UNREINFORCED MASONRY WALLS UNDERGOING EARTHQUAKE-INDUCED LOCAL FAILURE MECHANISMS 4311
Marco Nale, Andrea Chiozzi, Riccardo Lamborghini, Fabio Minghini, Marco Rigolin, Antonio Tralli

SEISMIC VULNERABILITY COMPARATIVE ASSESSMENT OF SOME SAMPLES OF CHURCHES AFFECTED BY LAST ITALIAN EARTHQUAKES 4318
Generoso Vaiano, Michele D'Amato, Antonio Formisano

A MULTIDISCIPLINARY APPROACH FOR THE ASSESSMENT OF THE DYNAMIC AND SEISMIC BEHAVIOUR OF ARCHAEOLOGICAL STRUCTURES IN HIERAPOILIS OF PHRIGYA, TURKEY 4340
F. Lorenzoni, M. Salvalaggio, M.R. Valluzzi, J. Boaga, R. Deiana

MS 36: DAMPING MODELLING AND EXPERIMENTS

VALIDATION OF A STRUCTURAL MODEL OF A LARGE TIMBER TRUSS WITH SLOTTED-IN STEEL PLATES AND DOWELS 4349
Pierre Landel, Andreas Linderholt

MS 37: CONSERVATION, RETROFIT AND STRENGTHENING OF EXISTING STRUCTURES: INNOVATIONS IN APPLIED METHODS AND MATERIALS

SHEAR STRENGTHENING OF MASONRY PANELS USING A GFRP-REINFORCED MORTAR COATING 4358
G. Castori, E. Speranzini, M. Corradi, S. Agnetti, G. Bisciotti

EFFECTS OF IMPULSIVE ACTIONS DUE TO SEISMIC JERK AND LOCAL FAILURES IN MASONRY STRUCTURES 4373
Massimo Mariani, Francesco Pugi

MS 38: GENERAL SESSION ON STRUCTURAL DYNAMICS, STABILITY AND VIBRATIONS

ANALYSIS OF RC CONTAINMENTS OF NUCLEAR PLANTS UNDER AEROPLANE IMPACT LOADS 4418
Mohamed Ihab S. Elmasry, Nabil H. Alashkar, Mostafa M. Hassan

DESIGN AND ANALYSIS OF AN X-STRUCTURED VIBRATION ISOLATION MOUNT (X-MOUNT) WITH WIDER QUASI-ZEROSTIFFNESS RANG 4434
Jing Bian, Xingjian Jing

CALCULATION DISPERSIONS AND ERRORS OF SHIP HULL AND SUPERSTRUCTURE VIBRATIONS 4441
Lech Murawski, Do Van Doan

EVALUATION OF A PUSHOVER PROCEDURE FOR ASYMMETRIC R/C BUILDINGS WITH VARIOUS TORSIONAL PROPERTIES 4451
Grigorios Manoukas, Asimina Athanatopoulou

OPTIMUM STRUCTURAL DESIGN OF A CUBESAT SUBJECTED TO LAUNCHER MECHANICAL ENVIRONMENT 4467
Adham Adel, Amir Tawfik, Eslam Saleh, Hesham Ibrahim

WIND EFFECTS ON LOW-RISE BUILDINGS WITH NEIGHBOURING STRUCTURE AS OBSTACLES 4481
Josue U. Rodriguez-Alcantara, Adrian Pozos-Estrada, Roberto Gomez-Martinez

FLEXURAL PERFORMANCE OF DOUBLE HOOKED END STEEL FIBRE REINFORCED CONCRETE BEAMS UNDER CYCLIC LOADING 4492
Demewoz Menna, Aikaterini Genikomsou, Mark Green

DISCUSSION ON THE CAPACITY DESIGN OF COLUMNS IN LOW-RISE BARE AND INFILLED RC MOMENT FRAMES 4500
Alexios Papasotiriou, Asimina Athanatopoulou

ELASTIC AXIS OF BUILDINGS UNDER EARTHQUAKE EXCITATION 4512
Vasiliki Terzi, Asimina Athanatopoulou

EVALUATION OF VIBRATION CHARACTERISTICS OF RC AND PPC BEAM MEMBERS UNDER CYCLIC TRAIN LOADING 4529
Munemasa Tokunaga

EXPERIMENTAL STUDY ON THE FRACTURE BEHAVIOR OF AN RC PILE GROUP FOUNDATION USING A CENTRIFUGE MODEL 4536
Yuichi Miyachi, Kazuhiro Hayashi, Shuhei Takahashi, Taiki Saito

SSI EFFECTS ON R/C ONE-STOREY BUILDINGS UNDER SEISMIC LOADINGS 4545
Paraskevi K. Askouni, Dimitris L. Karabalis, Dimitri E. Beskos

THE RESPONSE OF DIFFERENT BUILDINGS TO FREE-FIELD EXCITATION – A STUDY USING DETAILED FINITE ELEMENT MODELS …… 4560
Lutz Auersch, Susanne Ziemens

INVESTIGATION OF AN ACTIVELY CONTROLLED ROBOT ARM FOR VIBRATION SUPPRESSION IN MILLING ……..4577
Muhammet Ozsoy, Neil D. Sims, Erdem Ozturk

AN EVALUATION OF THE CURRENT APPROACHES AND RECOMMENDATIONS FOR MORE RATIONAL APPROACHES FOR ASSESSING THE SEISMIC TORSIONAL STABILITY OF BUILDINGS …… 4590
Bryam Astudillo, Francisco Flores, Sebastian Pozo, Finley Charney

VIBRATION CONTROL BY STRUCTURAL COUPLING IN ADJACENT STRUCTURES USING STOCHASTIC ANALYSIS ….4601
Augusto Pippi, José Luis de Brito, Suzana Avila, Graciela Doz

STUDY OF A HYBRID INVERTED PENDULUM TUNED MASS DAMPER BEHAVIOR USING A PID CONTROLLER ……. 4615
Jonas Pereira Falcão, Ledymar Foncault Moreno, José Luis Vital de Brito, Marcus Vinicius Girão de Morais, Suzana Moreira Avila

A COMPARISON OF GAIN DESIGN CRITERIA FOR CLOSED-LOOP MODEL UPDATING …… 4630
Lars Lynge Hansen, Thomas Akselsen, Ünal Korkmaz, Martin Dalgaard Ulriksen

ADEQUACY OF ACCIDENTAL ECCENTRICITY IN ACCOUNTING FOR THE EFFECTS OF THE TORSIONAL COMPONENT OF EARTHQUAKES ON THE SEISMIC DAMAGE …… 4639
Konstantinos Morfidis, Konstantinos Kostinakis, Nikolaos Pneymatikos

SUB-STRUCTURING APPROACH OF THE PREDICTION OF BUILDING VIBRATIONS INDUCED BY RAILWAY TRAFFIC …….. 4651
Chao He, Shunhua Zhou, Peijun Guo, Honggui Di

A TUNED MASS DAMPER INERTER CONTROL DEVICE FOR BASE ISOLATED STRUCTURES …… 4663
Salah Djerouni, Mouncef Eddine Charrouf, Abdelhafid Ounis, Mahdi Abdeddaim, Nassim Djedoui

FUNDAMENTAL PERIOD RELATIONSHIP OF RC-BUILDINGS IN ALICANTE PROVINCE (SPAIN). A FIRST STEP TO SOIL-STRUCTURE RESONANCE MAPS …… 4678
Noelia Agea-Medina, Alireza Kharazian, Sergio Molina, Juan José Galiana-Merino, Juan Luís Soler-Llorens

MEASURING THE DYNAMIC DISPLACEMENTS OF BRIDGES USING GEOPHONE DATA: APPLICATION AND VALIDATION ON A LIVELY FOOTBRIDGE …….. 4687
Paolo Borlenghi, George Piniotis, Harris Perakis, Vassilis Gikas, Carmelo Gentile

SEISMIC RESPONSE OF ADJACENT BUILDING STRUCTURE CONNECTED WITH SUPERELASTIC DAMPER: COMPARISON WITH YIELD DAMPER …… 4696
Sourav Gur, Pranay Singh, Koushik Roy

SURFACE WAVE PROPAGATION FROM DROP-PROJECTILE TESTS: PHYSICAL AND NUMERICAL MODELLING …… 4710
Vipul Kumar, S.P.G Madabhushi

GAP MONITORING IN REFURBISHMENT TASKS IN A FERRONICKEL FURNACE AT CERRO MATOSO SA 4722
Diego Alexander Tibaduiza, Jersson León, Luis Bonilla, Bernardo Rueda, Oscar Zurita, Juan Carlos Forero, Jaime Vitola, Dario Segura, Edwin Forero, Maribel Anaya

ON THE ESTIMATION OF VON MISES EQUIVALENT STRESS IN RANDOM VIBRATION ANALYSIS 4730
Federico Perotti, Francesco Foti, Luca Martinelli

INTERRELATION BETWEEN NEW HILBERT-HUANG TRANSFORM-BASED SEISMIC INTENSITY PARAMETERS AND STRUCTURAL DAMAGE 4739
Magdalini Tyrtaiou, Anaxagoras Elenas

TYPHOON FRAGILITY ANALYSIS AND CLIMATE CHANGE IMPACT ASSESSMENT OF FILIPINO CULTURAL HERITAGE ASSET ROOFS 4763
Giacomo Sevieri, Carmine Galasso

MODAL PROPERTIES OF A FLOOR WITH SINGLE-LEAF PLYWOOD ON TIMBER JOISTS: EXPERIMENTAL AND NUMERICAL MODELLING 4777
Lars Vabbersgaard Andersen, Nina Jørgensen, Gitte Skovlund Iversen, Jannick Balleby Hansen

COMPARATIVE EVALUATION OF THE METHODS PROPOSED BY THE GREEK CODE FOR STRUCTURAL INTERVATION (KAN.EPE.) FOR THE ESTIMATION OF CURVATURE DUCTILITY 4799
Konstantinos Morfidis, Christos Karakostas, Sotiria Stefanidou

SEISMIC PERFORMANCE OF EXISTING BUILDINGS CONCRETE SHEAR WALL 4816
Sk Amjad Hossain, Ashutosh Bagchi

EFFECTS OF ALTERNATING AXIAL FORCES ON THE RECYCLING RESPONSE OF REINFORCED CONCRETE FRAMES STRENGTHENED BY TENSION-TIES 4826
Angelos Liolios, George Hatzigeorgiou, Panagiotis Panetsos, Dimitrios Konstantinidis

CORRECTION OF LASER DOPPLER VIBROMETER MEASUREMENTS AFFECTED BY SENSOR HEAD VIBRATION USING TIME DOMAIN TECHNIQUES 4842
Abdel Darwish, Ben Halkon, Sebastian Oberst, Robert Fitch, Steve Rothberg

THE DISSIPATIVE CHARACTERISTICS OF OBLATE PARTICLES IN GRANULAR DAMPERS 4851
Furkan Terzioglu, Jem A. Rongong, Charles E. Lord

PREDICTION OF BEAM DYNAMICS IN CABLE-BEAM SYSTEMS THROUGH EXPERIMENTAL-NUMERICAL DECOUPLING 4867
Mohammad Hadi Jalali, Geoff Rideout

CONTRIBUTION OF SEISMIC NOISE RECORDINGS TO THE NON-STRUCTURAL VULNERABILITY ASSESSMENT 4878
Konstantinos G. Megalooikonomou

STRUCTURAL HEALTH MONITORING OF A PASSIVE VIBRATION CONTROLLED STRUCTURE 4887
Tsutomu Ochiai, Tetsushi Inubushi, He Ma, Manuel Navarro, Takahisa Enomoto

DYNAMIC RESPONSE OF TALL TIMBER BUILDINGS UNDER SERVICE LOAD – THE DYNATTB RESEARCH PROGRAM …. 4900
Rune Abrahamsen, Magne A Bjertnæs, Jacques Bouillot, Bostjan Brank, Lionel Cabaton, Roberto Crocetti, Olivier Flamand, Fabien Garains, Igor Gavric, Olivier Germain, Ludwig Hahusseau, Stephane Hameury, Marie Johansson, Thomas Johansson, Wai Kei Ao, Blaž Kurent, Pierre Landel, Andreas Linderholt, Kjell Malo, Manuel Manthey, Petter Nåvik, Alex Pavic, Fernando Perez, Anders Rönnquist, Haris Stamatopoulos, Iztok Sustersic, Salue Tulebekova

SEISMIC RISK ASSESSMENT OF A MEDIEVAL TOWER: THE CASE STUDY OF CRACO …… 4911
Michela Lerna, Maria F. Sabbà, Mariella Diaferio, Leonarda Carnimeo, Salvador Ivorra, Dora Foti

DYNAMIC ANALYSIS OF A POMPEIAN DOMUS …… 4922
Michela Monaco, Antonino Iannuzzo, A.Tafuro, Antonio Gesualdo

SHEAR PLASTIC DYNAMIC BEHAVIOUR OF WIND TURBINE TOWERS …… 4930
Antonio Gesualdo, Francesco Penta, Antonino Iannuzzo, Michela Monaco

ON THE AXIAL FORCE IDENTIFICATION IN EULER-BERNOULLI BEAMS WITH UNKNOWN BOUNDARY CONDITIONS …… 4944
Margaux Geuzaine, Francesco Foti, Vincent Denoël

SEISMIC VULNERABILITY ASSESSMENT OF A ROMANIAN HISTORICAL BUILDING UNDER NEAR-FIELD EARTHQUAKE …… 4957
Nicola Chieffo, Antonio Formisano, Marius Mosoarca, Paulo B. Lourenço

VIBRATION MONITORING OF CONSTRUCTION WORK AND INDUSTRIAL ACTIVITIES USING NEW SOLUTIONS OF INSTRUMENTATION …… 4972
Carlos Moutinho, Alvaro Cunha

EURODYN 2020
XI International Conference on Structural Dynamics
M. Papadrakakis, M. Fragiadakis, C. Papadimitriou (eds.)
Athens, Greece, 23–26 November 2020

A COUPLED MODELLING APPROACH FOR THE FAST COMPUTATION OF UNDERWATER NOISE RADIATION FROM OFFSHORE PILE DRIVING

Yaxi Peng[1], **Apostolos Tsouvalas**[1], **Andrei V. Metrikine**[1]

[1]Delft University of Technology
Faculty of Civil Engineering and Geosciences
Stevinweg 1, 2628CN Delft, The Netherlands
e-mail: {y.peng, a.tsouvalas, a.metrikine}@tudelft.nl

Keywords: underwater noise, offshore pile driving, vibro-acoustics, noise propagation, offshore wind.

Abstract. *This paper presents a computationally efficient modelling approach for the prediction of underwater noise radiation from offshore pile driving. A near-source module is adopted to capture the interaction between the pile, fluid and soil, which is based on a previously developed semi-analytical vibro-acoustic model. This module primarily aims at modelling the sound generation and propagation in the vicinity of the monopile. The Green's tensor for an axisymmetric ring source in a horizontally stratified acousto-elastic half-space emitting both compressional and shear waves is derived using the normal modes and branch line integrations. The boundary integral equations are then formulated based on the reciprocity theorem, which forms the mathematical basis of the far-from-source module for the propagation of the wave field at large radial distances. The complete noise prediction model comprises the two modules, which are coupled through the boundary integral formulation with the input obtained from the near-source module. Model predictions are benchmarked against measurement data from an offshore installation campaign.*

1 INTRODUCTION

The anthropogenic noise generated during the installation of the foundation piles for offshore wind farms has raised serious concern over environmental issues. The underwater noise pollution can endanger the lives of marine mammals and fishes [1]. Under the strict environmental regulations imposed by the government in many countries, the offshore industry strives to keep the noise levels to within acceptable limits. To assess the noise levels to be expected and control the hydro-sound emission, underwater noise predictions are required prior to the offshore installation of piles in most projects.

Over the last decades, modeling of the underwater noise generated by offshore pile driving has been studied extensively. Reinhall and Dahl [2] firstly proposed a coupled Finite Element (FE) and Parabolic Equation (PE) model for the prediction of underwater noise for offshore pile driving. The former method (FE) aims at generating the noise in the vicinity of the pile, while the latter one (PE) focus on the long-range propagation of the sound field. The coupling is achieved via a vertical array of phased point sources from FE results. Lippert and Estorff [3] presented a coupled FE and wavenumber integration model and investigated the influence of uncertainties in the sediment parameters through Monte-Carlo simulations. A theoretical benchmark case was then examined by various models discussed in [4]. Similar to [2], a two-step approach is adopted in most available models mentioned in [4, 3, 5] with a FE model to capture the vibration of the pile and a sound propagation model to propagate the field at larger distances (from the pile).

A semi-analytical approach for the prediction of underwater noise from pile driving was developed by Tsouvalas and Metrikine [6] based on a mode-matching technique. In contrast to most of the aforementioned models, this model additionally captured the characteristics of more complex seabed conditions with the soil being described as a three-dimensional elastic continuum. This allows one to examine the influence of the seabed properties on the noise generation and transmission.

In this paper, the authors present a coupled modelling approach for the noise prediction by impact piling with the focus being placed on a computationally efficient approach for the propagation of the sound field at large distances. The method extends the earlier works [7] by a far-range propagation module. The complete model comprises two modules: i) a near-source module aiming at the accurate description of the pile-water-soil interaction together with the sound generation and propagation in the pile vicinity [6], and ii) a far-from-source module aiming at the propagation of the wavefield at larger distances. The input to the far-from-source module is provided by the near-source module through the boundary integral formulation.

Section 2 introduces the mathematical statement of the problem together with the solution technique. In section 3, an experimental benchmark case is presented and measurement results are compared to model predictions. Finally, section 4 gives an overview of the main conclusions of the paper.

2 THEORY

The complete vibro-acoustic model for noise prediction in impact piling is shown in Fig.1. The pile is modelled as linear elastic thin shell occuping the domain $0 \leq z \leq L$. A vertical force $F(t)$ is applied at the top side of the pile. The ocean environment is modelled as an acousto-elastic layered waveguide. The fluid is modelled as a three-dimensional inviscid compressible medium with a compressional wave speed c_f and a density ρ_f occupying the domain $z_0 \leq z \leq z_1$ and $r \geq R$. The soil is described as a three-dimensional horizontally stratified elastic

continuum. Each soil layer is characterised by its density ρ_j, the compressional and shear wave speeds $c_{p,j}$ and $c_{s,j}$, and the compressional and shear damping coefficients $\alpha_{p,j}$ and $\alpha_{s,j}$, respectively. In the near-source module, the soil occupies the domain $z \geq z_1$ and is terminated at a large depth $z = H$ with a rigid boundary which has been shown not to affect the pile vibrations and noise generation in the vicinity of the pile [6]. In the far-from-source module, the soil extends to infinity in the vertical direction to accurately capture the energy loss mechanisms at larger distances from the pile.

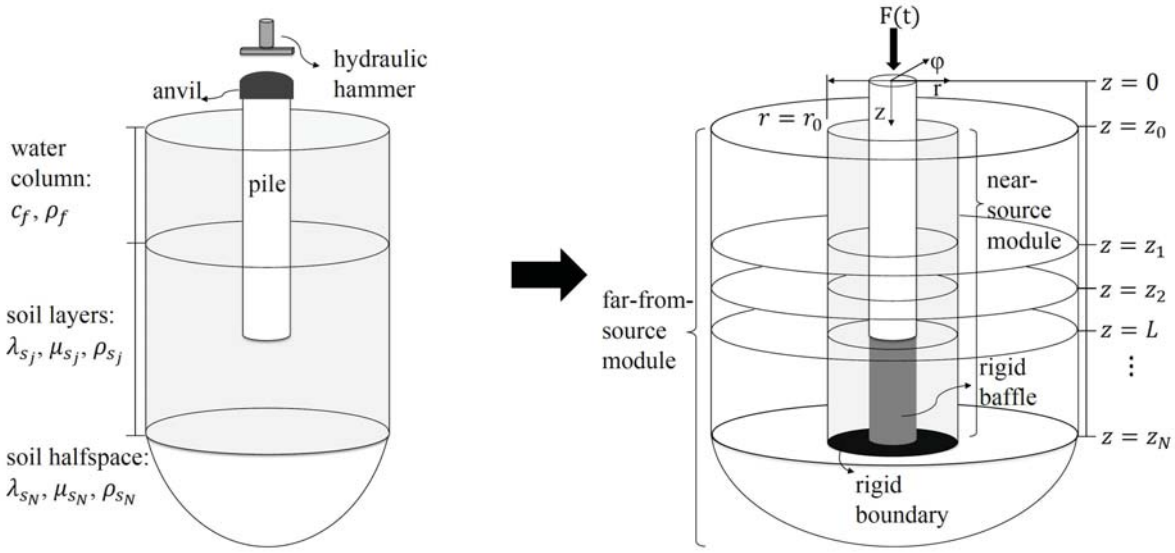

Figure 1: Geometry of the complete system (left) and the coupled modelling approach (right).

2.1 Governing equations

The equations of motion of the pile-soil-water system read [7]:

$$\mathbf{L}\,\mathbf{u}_p + \mathbf{I}_m\,\ddot{\mathbf{u}}_p = -\left[H(z-z_0) - H(z-L)\right]\,\mathbf{t}_s + \mathbf{f} \tag{1}$$

$$G_j\,\nabla^2\mathbf{u}_s^j + (\lambda_j + G_j)\,\nabla\nabla\cdot\mathbf{u}_s^j - \rho_j\ddot{\mathbf{u}}_s^j = \mathbf{0} \tag{2}$$

$$\nabla^2\phi_f(r,z,t) - \frac{1}{c_f^2}\ddot{\phi}_f(r,z,t) = 0 \tag{3}$$

In the equations above, $\mathbf{u}_p = [u_{p,z}(z,t)\ u_{p,r}(z,t)]^{\mathrm{T}}$ is the displacement vector of the mid-surface of the shell, $\mathbf{u}_s^j(r,z,t) = \left[u_{s,z}^j(r,z,t)\ u_{s,r}^j(r,z,t)\right]^{\mathrm{T}}$ is the displacement vector of each solid layer and $\phi_f(r,z,t)$ is a velocity potential introduced for the description of the fluid. The operators $\mathbf{L}$ and $\mathbf{I}_m$ are the stiffness and modified inertia matrices, respectively [6]. The vector $\mathbf{t}_s$ represents the boundary stress vector that takes into account the reaction of the soil and fluid surrounding the shell at $z_0 < z < L$. Naturally, in the domain $z_0 < z < z_1$ this reflects only the normal pressure exerted by the fluid normal to the surface whereas for $z > z_1$ both shear and normal stresses are present. The functions $H(z - z_i)$ are the Heaviside step functions which are used here to account for the fact that the soil and the fluid are in contact with a segment

of the shell in correspondence with Fig.1. The vector $\mathbf{f} = [f_{rz}(z,t)\ f_{rr}(z,t)]^{\mathrm{T}}$ represents the externally applied force on the surface of the shell.

A set of boundary conditions and interface conditions are formulated as follows for $r \geq R$:

$$p_f(r, z_0, t) = 0 \tag{4}$$

$$\sigma^1_{s,zz}(r, z_1, t) + p_f(r, z_1, t) = 0,\ \sigma^1_{s,zr}(r, z_1, t) = 0,\ u^1_{s,z}(r, z_1, t) - v_{f,z}(r, z_1, t) = 0 \tag{5}$$

$$\sigma^{j+1}_{s,zi}(r, z_j, t) - \sigma^{j}_{s,zi}(r, z_j, t) = 0,\ u^{j+1}_{s,i}(r, z_j, t) - u^{j}_{s,i}(r, z_j, t) = 0\,,\ 2 \leq j \leq N-1,\ i = z, r \tag{6}$$

$$u^N_{s,r}(r, z_N, t) = u^N_{s,z}(r, z_N, t) = 0 \tag{7}$$

where $p_f(r, z, t)$ indicates the pressure in the fluid, $\sigma^j_{s,zi}(r, z, t)$ represents the stresses in the soil at the corresponent layer j. In addition to Eqs. (4–7), the radiation condition needs to be satisfied at $r \to \infty$. In the far-from-source module, the boundary conditions at $z = z_N$ are substituted by the radiation condition at $z \to \infty$, which indicates that the bottom soil is modelled as elastic half-space.

2.2 Solution to the coupled problem

The complete solution to the coupled vibroacoustic problem consists of two modules: (i) the near-source module aiming at the noise generation and propagation in the vicinity of the pile; and (ii) the far-from source module aiming at propagating the field at larger distances from the pile.

2.2.1 Near-source module

The near-source module is based on a three-dimensional vibroacoustic model developed by Tsouvalas and Metrikine [6]. The module captures the characteristic of dynamic interactions between the pile and the surrounding media. A modal decomposition is applied both for the shell structure and the acousto-elastic waveguide as:

$$\begin{aligned}
\tilde{u}_{p,k}(z, \omega) &= \sum_{m=1}^{\infty} A_m\, U_{km}(z)\,, \\
\tilde{\phi}_f(r, z, \omega) &= \sum_{p=1}^{\infty} C_p\, H_0^{(2)}(k_p r)\, \tilde{\phi}_{f,p}(z)\,, \\
\tilde{\phi}_s(r, z, \omega) &= \sum_{p=1}^{\infty} C_p\, H_0^{(2)}(k_p r)\, \tilde{\phi}_{s,p}(z)\,, \\
\tilde{\psi}_s(r, z, \omega) &= \sum_{p=1}^{\infty} C_p\, H_1^{(2)}(k_p r)\, \tilde{\psi}_{s,p}(z)\,,
\end{aligned} \tag{8}$$

in which the subscripts p, f, s indicate the pile structure, fluid and soil, respectively, k refers to the displacement components r and z, the index $m = 1, 2, ..., \infty$ represents the mode number.

$H_n^{(2)}$ denotes the n^{th}-order Hankel function of the second kind which ensures that the radiation condition at $r \to \infty$ is satisfied at all times. The expressions for the displacement and the pressure/stress fields can be obtained through Helmholtz decomposition by substituting the potential functions. The coefficients C_p with $p = 1, 2, ..., \infty$ are the unknown modal amplitudes. The coefficients A_m are the modal amplitudes to be determined by solving the coupled problem. The terms k_p denote the horizontal wavenumber obtained by the formulation of the eigenvalue problem of the acousto-elastic region [8]. A system of infinite algebraic equations to the unknown coefficients C_p can be obtained [7]:

$$\sum_{q=1}^{\infty} C_q \left(L_{qp} + k_q \, H_1^{(2)}(k_q R) \, \Gamma_q \, \delta_{qp} - \sum_{m=1}^{\infty} \frac{R_{mq} \, Q_{mp}}{I_m} \right) = \sum_{m=1}^{\infty} \frac{F_m \, Q_{mp}}{I_m} \tag{9}$$

The coefficients of the shell structure are given by:

$$A_m = \frac{F_m + \sum_{p=1}^{\infty} C_p \, R_{mp}}{I_m} \tag{10}$$

The terms L_{qp}, Γ_q, Q_{mp}, R_{mp} and I_m are computed given the expressions in [6], which are omitted here for brevity. The eigenproblem of the shell and the surrounding acousto-elastic medium can be solved independently, which provide flexibilities in examining various configurations of the system.

2.2.2 Far-from-source module

To propagate the axisymmetric disturbances radiated from the pile into the surrounding medium, Green's tensors for a ring source emitting both compressional and shear waves are first derived. Assuming that a ring source is positioned at $\boldsymbol{r}_0 = (r_0, z_0)$, the wave equation in the Fourier-Hankel domain reads [9]:

$$\left[\frac{d^2}{dz^2} + k_{z,\xi}^2 \right] \hat{\Phi}_{\Xi,\xi}^{g}(k_r, z; r_0, z_0, \omega) = \frac{J_0(k_r \, r_0)}{2\pi} \, \delta(z - z_0) S_{\beta}^{\xi}(\omega) \tag{11}$$

in which ξ indicates the type of the sources considered; "f" being a fluid source, "p" a compressional source, and "s" being a shear source. The subscript Ξ represents the position of the receiver in the layered medium. $S_{\beta}^{\xi}(\omega)$ represents the source strength, which will be determined based on a unit impulse in β direction at source point $\boldsymbol{r}_0$ as discussed in section 2.2.3.

The solutions to Eq.(11) for the displacement potentials $\hat{\Phi}_{\Xi,\xi}^{g} = [\hat{\phi}_{f,\xi}^{g}, \hat{\phi}_{s,\xi}^{g}, \hat{\psi}_{s,\xi}^{g}]$ in the wavenumber domain are first derived for an acousto-elastic layered half-space. Applying the inverse Hankel transform yields:

$$\tilde{\Phi}_{\Xi,\xi}^{g}(\boldsymbol{r}; \boldsymbol{r}_0, \omega) = -\frac{1}{2} \int_{-\infty}^{+\infty} (S_{\beta}^{\xi}(\omega) \frac{e^{-\mathrm{i}k_{z,\xi}|z-z_0|}}{4\pi \mathrm{i} k_{(}z,\xi)} + A_{\xi}^{1} e^{\mathrm{i}k_{z,\xi}z} + A_{\xi}^{2} e^{-\mathrm{i}k_{z,\xi}z}) J_0(k_r \, r_0) H_0^{(2)}(k_r \, r) k_r dk_r \tag{12}$$

For $z \geq z_N$, $A_{\xi}^{1} = 0$ to ensure that the downward propagating waves *leave* the soil half-space without reflection. Upon substitution of the Eq.(12) into Eqs.(4–6), it becomes clear that the kernels in the integral representations need to be satisfied. This yields a linear algebraic system of equations with unknowns A_{ξ}^{1} and A_{ξ}^{2}. Once the amplitude coefficients are solved for every

k_r, the Green's tensor for any configuration of compressional or shear source potentials can be obtained.

To evaluate the wavenumber integral given by Eq.(12), the complex contour integration technique is applied. The solution can be expressed as a summation of a finite number of (normal) modes supplemented by Ewing-Jardetsky-Press (EJP) branch line integrations. The final expression of the Green's tensor in modal summation for the acousto-elastic domain considered here reads:

$$\begin{aligned}\tilde{\Phi}^{g}_{\Xi,\xi}(r,z;r_0,z_0;\omega) &= -\pi i \sum_{m=1}^{M}\left[\frac{\hat{\Phi}^{g,num}_{\Xi,\xi}(k_r,z;r_0,z_0)}{f'(k_r)} J_0(k_r\, r_0) H_0^{(2)}(k_r r) k_r\right]^{(m)} \\ &+ \frac{1}{2}\int_{\alpha+\beta} \hat{\Phi}^{g}_{\Xi,\xi}(k_r,z;r_0,z_0) J_0(k_r\, r_0) H_0^{(2)}(k_r r) k_r dk_r\end{aligned} \tag{13}$$

in which $\hat{\Phi}^{g,num}_{\Xi,\xi} = [\hat{\phi}^{g,num}_{f,\xi}, \hat{\phi}^{g,num}_{s_j,\xi}, \hat{\psi}^{g,num}_{s_j,\xi}]$ denotes the numerator of the solutions of the potential functions in Hankel domain. The characteristic equation $f(k_r)$, being the determinant of the coefficient matrix, is used to determine the horizontal wavenumbers $k_r^{(m)}$.

2.2.3 Direct boundary element integral

The direct boundary element method (BEM) is adopted in this model to couple the near-source and far-from-source modules. The solution of the wavefield in both acoustic and elastodynamic field employs Somigliana's identity in elastodynamics and Green's third identity in potential theory [9-11]. The boundary data is specified from the near-source module on a cylindrical surface at $r = r_0$ from the pile, i.e. section 2.2.1, are used as input to the far-from-source module via the BEM.

The fundamental solutions of Green's displacement tensors $\widetilde{U}^{\Xi\xi}_{\alpha\beta}(\boldsymbol{r},\boldsymbol{r}_0,\omega)$ are derived from the potential functions [12] given the receiver point at $\boldsymbol{r} = (r,z)$ (in medium Ξ) in α-direction due to a unit impulse at source $\boldsymbol{r}_0 = (r_0,z_0)$ (in medium ξ) in β-direction:

$$\begin{aligned}\widetilde{U}^{s\xi}_{\alpha\beta}(\boldsymbol{r},\boldsymbol{r}_0,\omega) &= \nabla\tilde{\phi}^{g}_{s_j,\xi}(\boldsymbol{r},\boldsymbol{r}_0,\omega) + \nabla\times W, \quad W = -\frac{\partial\psi^{g}_{s_j,\xi}(\boldsymbol{r},\boldsymbol{r}_0,\omega)}{\partial r} \\ \widetilde{U}^{f\xi}_{\alpha\beta}(\boldsymbol{r},\boldsymbol{r}_0,\omega) &= \nabla\tilde{\phi}^{g}_{f,\xi}(\boldsymbol{r},\boldsymbol{r}_0,\omega)\end{aligned} \tag{14}$$

For the elastic domain, the Green's stress tensors $\widetilde{T}^{\Xi\xi}_{\alpha\beta}(\boldsymbol{r},\boldsymbol{r}_0,\omega)$ related to $\widetilde{U}^{\Xi\xi}_{\alpha\beta}(\boldsymbol{r},\boldsymbol{r}_0,\omega)$ can be obtained through substitution of Eq. (14) into the constitutive equations [12]. The fundamental solution pair $\{\widetilde{U}_{\alpha\beta},\widetilde{T}_{\alpha\beta}\}$ can be obtained once the unknown source strengths $S^{\xi}_{\beta}(\omega)$ are determined. By employing the Green's displacement tensors in Eq.(14), the traction vector can be expressed through stress tensor as,

$$\tilde{\tau}_i = \tilde{\sigma}_{ij} n_j \tag{15}$$

where $\tilde{\tau}_i$ is the traction vector in i direction, n_j is the unit normal vector at the boundary. The condition of a unit impulsive load can be applied in the β-direction at the source $\boldsymbol{r} = \boldsymbol{r}_0$ by setting, :

$$\begin{bmatrix}\tilde{\tau}_\beta \\ \tilde{\tau}_\alpha\end{bmatrix} = \begin{bmatrix}\delta(\boldsymbol{r}-\boldsymbol{r}_0) \\ 0\end{bmatrix} \tag{16}$$

The solution of Eq.(16) yields the coefficients $S^{p}_{\beta}(\omega)$ and $S^{s}_{\beta}(\omega)$.

For the acoustic domain, the conventional boundary integral representation is the Helmholtz integral in terms of pressure or displacement potential. By taking the directional derivative of the displacement potential as stated in Eq.(14), the boundary integral formulation for the displacement can be obtained directly by setting $S^f(\omega) = 1$, which is analogous to the integral formulation in the soil.

By utilizing Betti's reciprocal theorem in elastodynamics [10] and Green's theorem for acoustic problem [11], the complete solution for the acousto-elastic domain reads:

$$\begin{aligned}\tilde{u}_\alpha^\Xi(\boldsymbol{r}) = &\sum_{\beta=r,z}\int_{S^s}\left(\widetilde{U}_{\alpha\beta}^{\Xi s}(\boldsymbol{r},\boldsymbol{r}_0,\omega)\cdot\tilde{t}_\beta^{\boldsymbol{n}}(\boldsymbol{r}_0,\omega) - \widetilde{T}_{\alpha\beta}^{\boldsymbol{n},\Xi s}(\boldsymbol{r},\boldsymbol{r}_0,\omega)\cdot\tilde{u}_\beta(\boldsymbol{r}_0,\omega)\right)dS_0^s(\boldsymbol{r}_0)\\ &+\int_{S^f}\left(\widetilde{U}_{\alpha r}^{\Xi f}(\boldsymbol{r},\boldsymbol{r}_0,\omega)\cdot\tilde{p}(\boldsymbol{r}_0,\omega) - \widetilde{T}_{\alpha r}^{\boldsymbol{n},\Xi f}(\boldsymbol{r},\boldsymbol{r}_0,\omega)\cdot\tilde{u}_r(\boldsymbol{r}_0,\omega)\right)dS_0^f(\boldsymbol{r}_0),\quad \boldsymbol{r}\in V\end{aligned} \tag{17}$$

where $\boldsymbol{n}$ is the outward normal to the cylindrical boundary. The superscripts of the Green's tensors, "f" and "s" indicate fluid and soil domains, respectively.

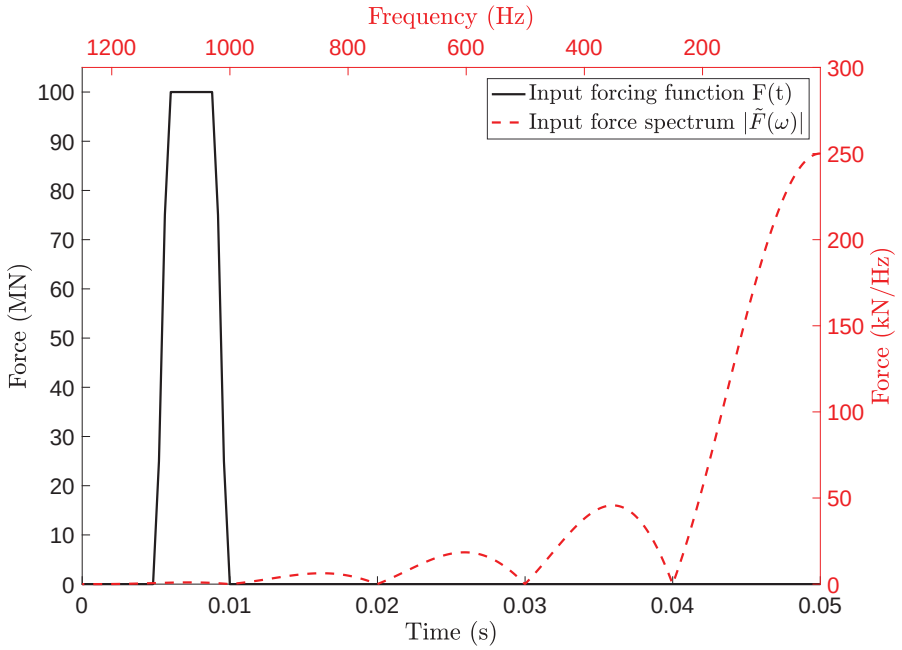

Figure 2: Input forcing function.

3 VALIDATION CASE STUDY

In order to validate the model, a benchmark case is considered with the measurement data recorded at offshore wind farm BARD Offshore 1 [5]. The material properties and the geometry of the model are given in Table 3 [5]. The seabed in the model consists of a thin marine sediment layer overlaying a stiffer soil half-space. The actual penetration depth of the pile was around 20 m. The pile was driven by a hydraulic hammer. The time signature of the applied force is the one shown in Fig.2, which generates approximately 1370 KJ blow energy into the system. The frequency spectrum is also given in Fig.2.

The peak pressure level (L_{peak}) and the sound exposure level (SEL) of receiver points at radial distances up to 1500m are shown in Fig.3. As can be seen, the difference between the

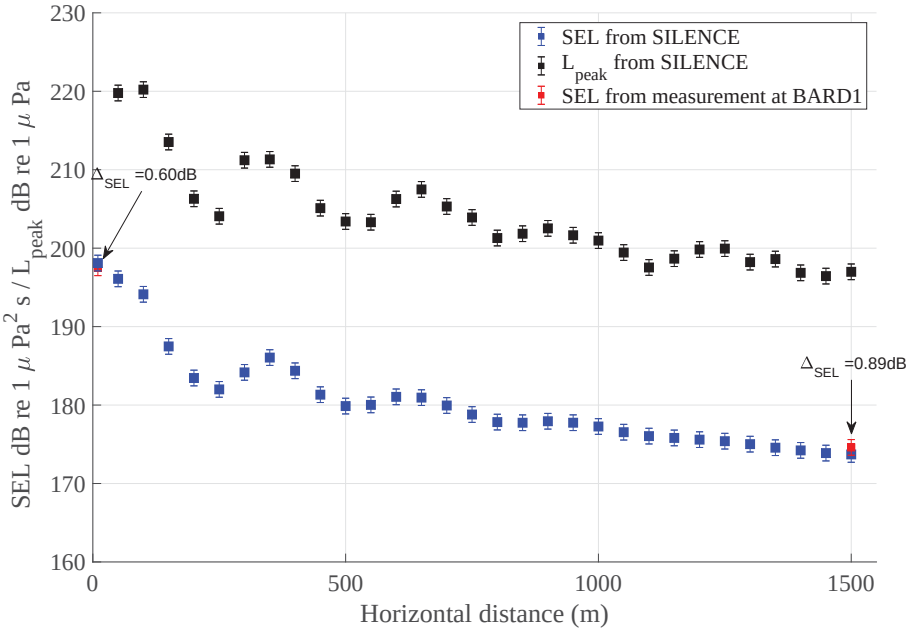

Figure 3: Comparison of SEL and L_{peak} at several radial distances from the pile and 2 m above the seabed.

Parameter	Pile	Parameter	Fluid	Upper soil	Bottom sediment
Length[m]	85	Depth [m]	40	2	48
Density [kg/m^3]	7850	ρ[kg/m^3]	1000	1888	1908
Outer diameter [m]	3.35	c_L [m/s]	1500	1705	1725
Wall thickness [mm]	70	c_T [m/s]	-	186	370
Final penetration depth [m]	20	α_p $[dB/\lambda]$	-	0.91	0.88
Maximum Blow Energy [kJ]	1370	α_s $[dB/\lambda]$	-	1.86	2.77

Table 1: Basic input parameters for the simulations.

predicted SEL and the measured values are 0.60 dB and 0.89 dB at 10m and 1500m radial distances from the pile respectively. The SEL indicates the averaged amount of energy radiated into the surrounding media and L_{peak} evaluates the impulsiveness of the pressure waves from the pile. The results verify the validity of the developed model, which can provide predictions that lies within the accuracy of the measurement equipment ($\pm$ 1 or 2 dB).

Figure 4 shows the pressure levels (dB re $1\mu Pa^2$/Hz) in 1/3-octave bands at various radial distances from the pile. Assuming that the energy in all the defined bandwidths (one-third octave) results from an effective source, the bandwidth energies add directly to give the total energy in one frequency band. The derivation of the sound pressure level in the unit of dB re 1 $\mu Pa^2 s^{-1}$ reads:

$$\mathrm{SPL}_{1/3-octave} = 10\log_{10}\sum_{i=m}^{n}\left(\frac{|\tilde{p}_i(\omega)|^2}{p_0^2}\right) \tag{18}$$

As can be seen in Fig.4, the spectrum shows that most of the energy is distributed at low frequencies, which is consistent with the 1/3-octave band spectrum obtained by measurement data and numerical results from FE-PE model in [5].

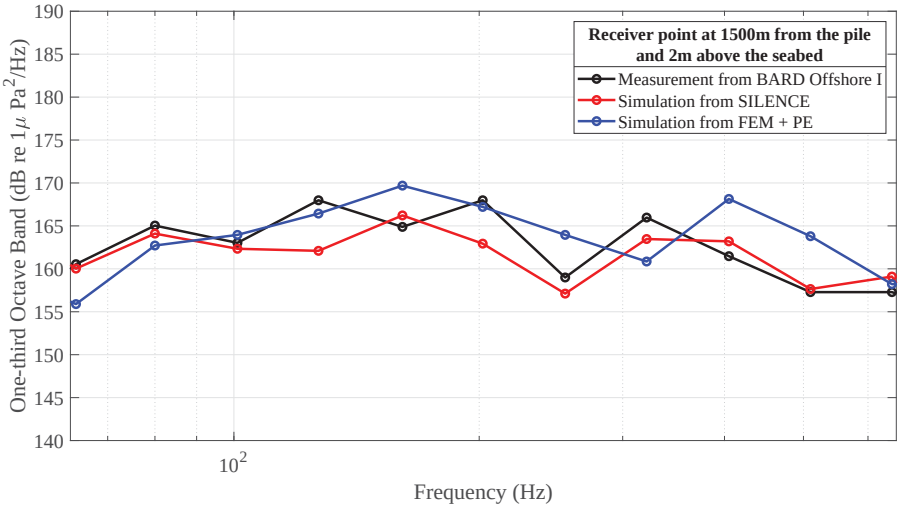

Figure 4: One-third octave band spectrum for a point positioned 2m above the seabed in the fluid and at r = 1500m from the pile.

4 CONCLUSIONS

The paper presents a computationally efficient coupled approach for noise predictions by offshore pile driving. The mathematical background of the generation and propagation of the sound field is given and the adopted method of solution is described. The direct boundary integral equation (BIE) formulation is adopted to propagate the radiated wave field from the near-source module to larger distances. A numerical analysis of a benchmark case is conducted, which verifies the validity of the model for the prediction of underwater noise from offshore pile driving. In the future, model predictions will be benchmarked against both numerical model predictions and available data from other measurement campaigns published in the scientific literature.

5 ACKNOWLEDGEMENTS

The authors gratefully acknowledge the China Scholarship Council (CSC) for financing this research project on the development of a generic underwater noise prediction model for offshore activities.

REFERENCES

[1] H. Bailey, B. Senior, D. Simmons, J. Rusin, G. Picken, and P. M. Thompson, Assessing underwater noise levels during pile-driving at an offshore windfarm and its potential effects on marine mammals, *Marine Pollution Bulletin*, 2010.

[2] P. G. Reinhall and P. H. Dahl, Underwater Mach wave radiation from impact pile driving: Theory and observation, *The Journal of the Acoustical Society of America*, vol. 130, pp. 1209–1216, sep 2011.

[3] T. Lippert and O. von Estorff, The significance of parameter uncertainties for the prediction of offshore pile driving noise, *The Journal of the Acoustical Society of America*, vol. 136, no. 5, pp. 2463–71, 2014.

[4] S. Lippert, M. Nijhof, T. Lippert, D. Wilkes, A. Gavrilov, K. Heitmann, M. Ruhnau, O. von Estorff, A. Schafke, I. Schafer, J. Ehrlich, A. MacGillivray, J. Park, W. Seong, M. A. Ainslie, C. de Jong, M. Wood, L. Wang, and P. Theobald, COMPILE—A Generic Benchmark Case for Predictions of Marine Pile-Driving Noise, *IEEE Journal of Oceanic Engineering*, vol. 41, pp. 1061–1071, 2016

[5] M. B. Fricke and R. Rolfes, Towards a complete physically based forecast model for underwater noise related to impact pile driving, *The Journal of the Acoustical Society of America*, 2015.

[6] A. Tsouvalas and A. V. Metrikine, A three-dimensional vibroacoustic model for the prediction of underwater noise from offshore pile driving, *Journal of Sound and Vibration*, vol. 333, no. 8, pp. 2283–2311, 2014.

[7] A. Tsouvalas and A. Metrikine, Structure-Borne Wave Radiation by Impact and Vibratory Piling in Offshore Installations: From Sound Prediction to Auditory Damage, *Journal of Marine Science and Engineering*, vol. 4, p. 44, 2016.

[8] A. Tsouvalas, K. N. van Dalen, and A. V. Metrikine, The significance of the evanescent spectrum in structure-waveguide interaction problems, *The Journal of the Acoustical Society of America*, 2015.

[9] A. A. Bakr, *Axisymmetric Potential Problems*, pp. 6–38. Berlin, Heidelberg: Springer Berlin Heidelberg, 1986.

[10] D. E. Beskos, Boundary element methods in dynamic analysis, *Applied Mechanics Reviews*, vol. 40, no. 1, pp. 1–23, 1987.

[11] F. Jensen, W. Kuperman, M. Porter, and H. Schmidt, *Computational Ocean Acoustics*, Springer New York, 2011.

[12] J. D. Achenbach, *Wave propagation in elastic solids*. North-Holland series in applied mathematics and mechanics, v. 16, Amsterdam New York: North-Holland Pub. Co.; American Elsevier Pub. Co., 1973.

EURODYN 2020
XI International Conference on Structural Dynamics
M. Papadrakakis, M. Fragiadakis, C. Papadimitriou (eds.)
Athens, Greece, 23–26 November 2020

WAVE-RESOLVING AIRCRAFT FUSELAGE MODEL FOR CABIN NOISE PREDICTIONS UNDER DISTRIBUTED FLUID LOADINGS

Christopher Blech and Sabine C. Langer

TU Braunschweig
Institute for Acoustics
Langer Kamp 19
c.blech@tu-braunschweig.de

Keywords: cabin noise, aircraft, modelling, finite element method, seat, acoustic impedance

Abstract. *For the development of future passenger aircraft comprising novel technologies and designs, a reduction of cabin noise is one major aim. An analysis of the aircraft cabin sound pressure levels can be achieved by mechanical models. In opposite to energy-based methods, wave-resolving models allow a detailed investigation of distributed fluid loadings and the wave propagation within the fuselage. A turbulent boundary layer loading on the outer skin of the aircraft is investigated exemplary. As the loading bring along a specific footprint on the aircraft skin and the model resolves the bending waves, the load input can be applied directly. Besides the outer skin, the aircraft fuselage model considers the stiffeners, the insulation, the inner cabin lining and the cabin fluid of the entire cabin. Each part is validated separately and included in the aircraft fuselage model. The structural and fluid domains are fully coupled and discretised with finite elements using 2D shells and 3D continua resulting in millions of degrees of freedom. The simulation shall not model a specific aircraft, but rather demonstrate on the example of a generic research aircraft the crucial modelling and solving aspects of typical aircraft parts. Within this contribution, a section of the fuselage is presented having a specific focus on the cabin fluid modelling. The damping characteristics of the seats are considered by impedance boundary conditions within the 3D fluid domain and compared to a homogenising approach using a frequency-dependent damping loss factor. The necessary input parameters are measured in a reverberation chamber having available an aircraft seat bench. The numerical comparison of the modelling approaches in the fuselage model shows that local differences can be expected but in general the SPL is decreasing similarly with increasing frequency.*

1 INTRODUCTION

Facing an increasing demand for mobility, the number of flights is expected to raise significantly in future. Many passengers are exposed to cabin noise during flights. Under high noise levels, health and comfort issues may occur. A simulation of cabin sound pressure levels in early design stages can help to avoid a high exposure by integrating sound reduction measures if necessary.

Based on preliminary aircraft design data as provided in the Collaborative Research Center 880 [1], a wave-resolving fuselage model can be derived. The modelling of structure-borne sound waves in the primary and secondary structure and the fluid waves in the insulation and the cabin itself allows a detailed analysis of the sound transfer paths. As waves in all domains are considered, sound reduction measures like, e.g., acoustic black holes and their placement can be studied directly without any assumptions on their efficiency. Discretising and solving the model delivers the sound pressure level (SPL) distribution in the cabin under certain loads. Fluid loads like jet noise or the turbulent boundary layer (TBL) bring along a characteristic footprint on the outer skin. Only a correct consideration of phase differences and amplitudes of such loads ensure a precise prediction of cabin noise. Especially for novel aircraft concepts, resulting sound sources are not known and may be assessable through complex simulations. In [2], e.g., the cabin noise due to jet noise is investigated for a comparison of an UHBR engine with a conventional engine. The model is extended by a TBL load in [3] suggesting that this load might be one of the dominating loads in aircraft with UHBR engines.

However, appropriate modelling assumptions for all fuselage parts are required in order to receive reasonable responses in the cabin. The cabin fluid itself including seats and passengers is expected to play a major role in the entire model. Hence, a comparison of models of different complexity is aimed for in this contribution. Simple approaches considering a homogenised cabin fluid offer a simple and fast modelling procedure. A detailed consideration of seats is more complex but may offer crucial quality differences in the model. A boundary element solution of an aircraft passenger cabin is applied in [4] to the cabin fluid of an aircraft segment. The numerical model is compared to experiments – differences are mainly attributed to the neglected influence of the surrounding structure. In the model applied here, all surrounding structures are considered. Qualitatively, in [4], the numerical sound pressure distribution near the seats matched experimental results under a consideration of impedance boundary conditions for the seat surfaces. Hence, this shall be the local approach applied here within the fuselage model described in the next section.

2 FUSELAGE MODEL

The preliminary design data by the design tool PrADO [1, 5] within the CRC 880 provides a dimensioning of the entire primary structure of a virtual research aircraft for 100 passengers. For the purpose of cabin noise simulations, these information on materials, thickness distribution and cross-sections are automatically transferred into a finite element shell model of the outer skin, the stiffeners and the floor section. In Fig. 1, the FE model of the fuselage is shown. Basically, the model underlies the assumptions of linearity and symmetry. For simplicity, a small model with three seat-rows is applied in this study. Curved sandwich plates fixed to the stiffeners are considered as typical inner sidewall and ceiling panels with a constant thickness of 0.01 m. An aramid honeycomb core is homogenised to a 3D continuum meshed by 27-node quadratic hexahedrons while a glass-fibre-reinforced plastic layer is modelled at each side by shell elements perfectly fixed to the honeycomb core.

The double wall gap between outer skin and inner cabin linings is filled by glass wool. The fibres material is considered as homogenised 3D equivalent fluid volume meshed by hexahedrons as well. The passenger cabin itself is basically filled by air with typical density, temperature and humidity values of the cabin air in cruise. Different modelling approaches for the cabin fluid volume including damping, reflection and refraction of the aircraft seats shall be in focus of this contribution. As visible in Fig. 1, seat domains are already separated in groups in order to apply different modelling approaches keeping the finite element mesh unchanged.

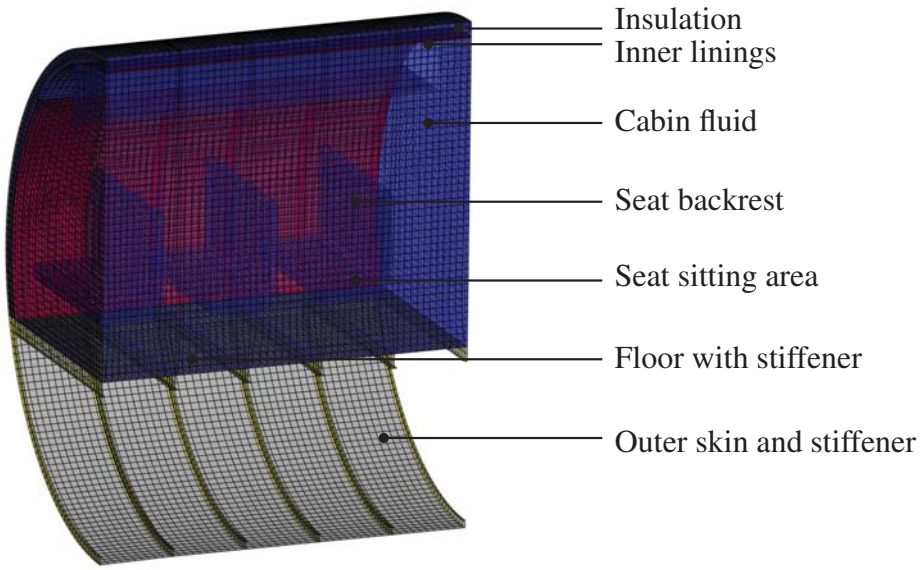

Figure 1: Meshed fuselage section model including structural and fluid domains; Symmetry boundary conditions are applied.

Fluid and structural domains are strongly coupled resulting in a total computational cost of $7.3\,\mathrm{min}$ per frequency step[1]. As exemplary load for a comparison of the cabin models, an artificially generated TBL load is considered as described in detail in [3].

3 MODELLING ASPECTS IN THE PASSENGER CABIN

In previous studies of the aircraft model from Sec. 2 which can be found in [2, 6, 3], a homogeneous constantly damped Helmholtz fluid domain is considered according to Eq. 1. A constant complex speed of sound $\underline{c}$ is applied for the entire fluid in order to consider the damping properties of seats and passengers. $\underline{p}$ is the sound pressure, ω is the angular frequency and $\mathbf{x}$ is the location in the aircraft cabin.

$$\nabla^2 \underline{p}(\mathbf{x},\omega) + \frac{\omega^2}{\underline{c}^2}\underline{p}(\mathbf{x},\omega) = 0 \tag{1}$$

$\underline{c}$ is calculated according to Eq. (2) by use of the fluid loss factor η_f and the imaginary unit i [7].

$$\underline{c}^2 = c^2\,(1 + i\eta_f) \tag{2}$$

[1]Using the direct MUMPS solver and the institute's in-house code elPaSo at 20 cores on the phoenix cluster of TU Braunschweig

In order to assess the consideration of $\underline{c} = const$, the model complexity is increased in this contribution. As the surrounding structures of the cabin (sidewall panels, floor) are considered with material damping properties in the model, the seats and the passengers are mainly expected to influence the cabin fluid domain. For the purpose of experimental studies on the damping characteristics of seats, three aircraft seats are available which are shown in Fig. 2 (a). As sketched in Fig. 2 (b), each seat is transformed to simplified cornered domains and considered as separate block in the FE model. Two approaches are investigated: A frequency-dependent loss factor and an introduction of surface impedances for the seat rows.

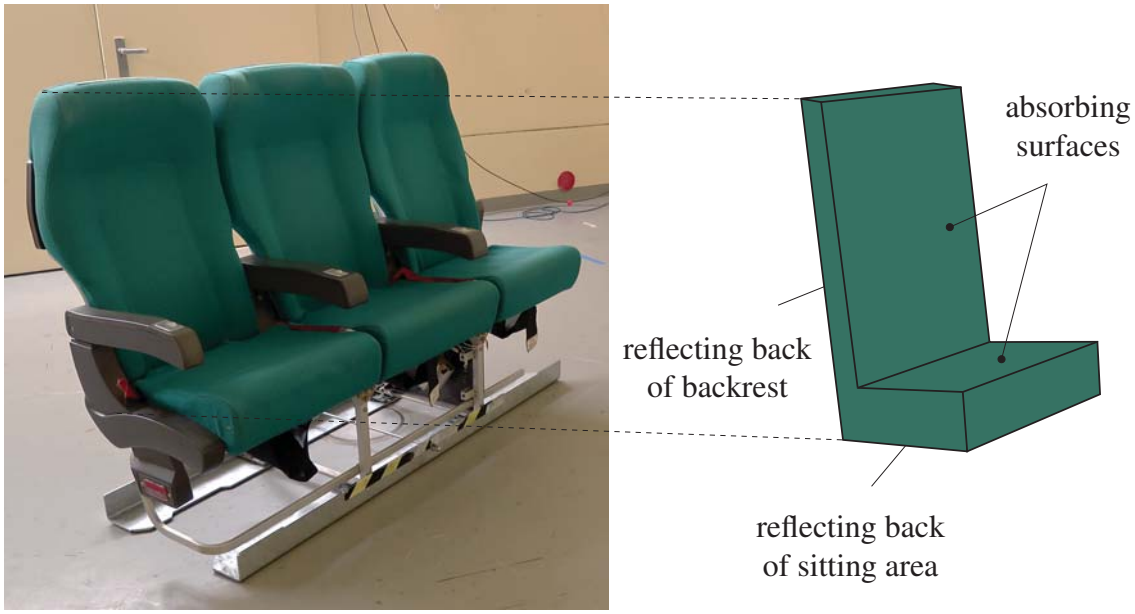

Figure 2: (a) Aircraft seats in reverberation chamber and (b) sketch of simplified seat assembly.

A first extension of the previous model is a consideration of a **frequency-dependent loss factor** $\eta_f(f)$ leading to a frequency-dependent speed of sound $\underline{c}(f)$ (Eq. (2)). The frequency-dependent parameter is yielded by measurements. The reverberation time $T_r(f)$ is measured in a reverberation chamber resulting in the equivalent absorption area $A_t(f)$ according to DIN ISO 354 [8] for the three seats shown in Fig. 2. The equivalent absorption area of three seats is linearly scaled to 100 seats which neglects any influences between seat rows. The effect of passengers has been studied as well, but the change of $A_t(f)$ is not significant. For the equivalent absorption area with 100 seats $A_{t,100}(f)$, the reverberation time $T_{r,\mathrm{cabin}}$ is calculated according to Eq. 3 [8] inserting the properties of the passenger cabin.

$$T_{r,\mathrm{cabin}}(f) = \frac{55.3 V_{\mathrm{cabin}}}{\left(A_{t,100}(f) + 4 V_c m_{\mathrm{cabin}}(f)\right) c} \tag{3}$$

$V_{\mathrm{cabin}} = 118\,\mathrm{m}^2$ is the fluid volume in the cabin and $m_{\mathrm{cabin}}(f)$ is the air absorption coefficient. Finally, $\eta_{\mathrm{cabin}}(f)$ is related to $T_{r,\mathrm{cabin}}(f)$ as given in Eq. (4) [9] with frequency f.

$$\eta_{\text{cabin}}(f) = \frac{2.2}{f T_{r,\text{cabin}}(f)} \tag{4}$$

In Fig. 3, the resulting loss factor is shown. In the low frequency range ($< 250\,\text{Hz}$), a homogenised loss factor of $3\,\%$ can be expected by the seat cushions. With increasing frequency, the loss factor decreases to $1\,\%$ damping at $1000\,\text{Hz}$. As most passenger cabins are similarly designed, a transferability of these results is expected to a certain extent.

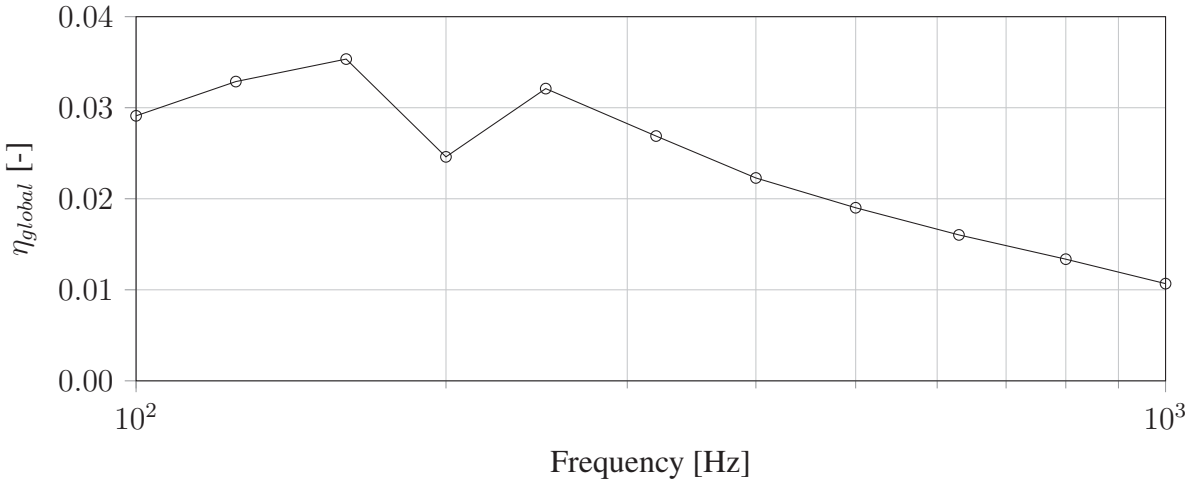

Figure 3: Homogenised loss factor in the cabin with volume $V_c = 118\,\text{m}^2$ for 100 passengers based on measurement of the reverberation time of three seats.

The second approach is similar to the above described approach by [4] – an acoustic **surface impedance** $\underline{Z}_a$ according to Eq. 5 [10] is placed in the fluid domain for the seat's backrest and the sitting area. The seat positions are given by the preliminary design data.

$$\underline{Z}_a(f) = \frac{\underline{p}(f)}{\underline{v}_n(f)} \tag{5}$$

The impedances are experimentally determined in the reverberation chamber as well. By placing an intensity probe near the surface, $\underline{p}$ and $\underline{v}$ are calculated on the basis of the two pressure signals and the cross-correlation of these. This way, the impedances of the surfaces (backrest and sitting area) are approximately given. The results for the $\underline{Z}_a$ are depicted in Fig. 4. In the low frequency range ($< 250\,\text{Hz}$), the values show high variations which is consistent with findings in [11]. In these frequency ranges, rather a smoother curve is expected which can be shown by comparing with porous material models or impedance tube measurements. With increasing frequency, the real part of the impedance converges to the impedance of air (blue curve) which is physically reasonable as the absorption performance of the seat cushion is expected to increase with reduced wave lengths.

As shown in Fig. 5 (b), the meshed cabin fluid volume assigned to the seat row is substituted by the surface impedance. This means, the finite elements in these regions are removed introducing a reflecting surface at the back of each seat cushion besides the impedance at the front of each seat cushion (backrest and sitting area). For the homogenised approach (Fig. 5 (a)), the mesh is the same including the filled gap. Here, no reflecting boundaries are introduced.

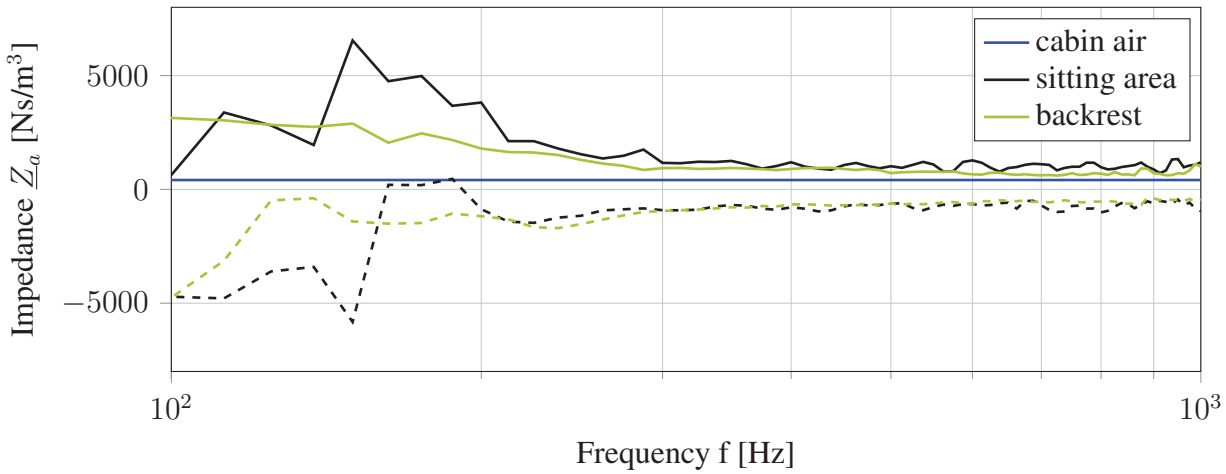

Figure 4: Acoustic impedances measured near the seat surfaces; The dotted lines are the imaginary parts.

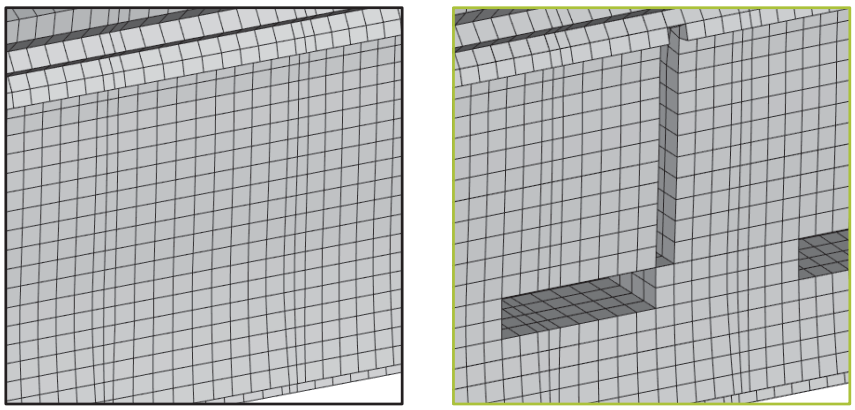

Figure 5: (a) Continuous mesh for homogenised approach; (b) Removed elements in seat region.

By removing the elements in the cabin fluid domain for the seat model, the computational costs are reduced by 17 % in comparison to the homogenised approach. Of course, the modelling effort is higher as the seat volumes must be considered in the model. In the vicinity of the sidewall panels, the meshing procedure is slightly more complex.

4 RESULTS

In Fig. 6, the SPL is plotted for the two described modelling approaches. The position corresponds to the seat in the central row near the sidewall panel. The height is chosen in accordance with a typical passenger ear height. Basically, the two SPL curves are similarly decreasing over frequency and show comparable basic sound levels. The overall damping characteristics seem similar as the dynamics of both curves is comparable as well. For a fast comparison of aircraft configurations (e.g. in third octave bands), the global loss factor may be appropriate in order to save modelling effort and avoid further mistakes during the introduction of impedances and reflecting boundaries. Furthermore, the impedance approach brings along several assumptions

like one impedance value at normal sound incidence which requires a more critical interpretation of results.

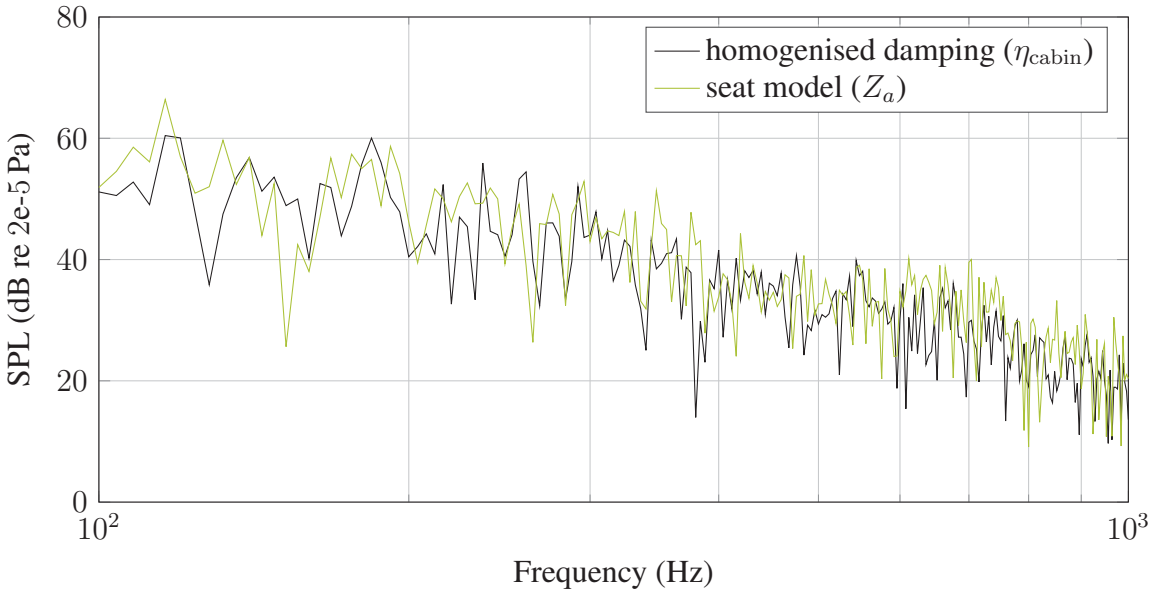

Figure 6: Sound pressure level at central seat position near the sidewall panel under TBL load with two different modelling approaches for the cabin.

Having a closer look, some resonances occur in both approaches (e.g. around 300 Hz and 530 Hz) but in most frequency regions there are local differences up to 10 dB and slightly more resonances in the response of the seat modelling approach. In the case of the local seat model, standing waves between seat rows and acoustic effects near seats can occur besides global resonances of the entire cabin fluid. In Fig. 7, pressure distributions in a cabin slice are shown for several frequencies. For the global pressure distribution at 168 Hz, for instance, only a slight distortion of the global shape is observed. For shapes in longitudinal direction as, e.g. seen at 184 Hz, the backrests of the seats seem to have a major influence. Furthermore, as it can be observed at 232 Hz, local effects (here below the seat sitting area) occur.

Concluding the results, detailed seat models seem necessary for applications or analyses which require a knowledge of local effects. For a rough and global comparison of the sound pressure levels, a global loss factor is appropriate. For active sound reduction measures, like noise cancelling in aircraft cabins, these local information are crucial and a seat model must be considered. Also, for a detailed investigations of tonal components like propeller noise, a seat model should be preferred in order to cover local effects at specific frequencies which might interfere with the tonal noise transferred into the cabin.

5 CONCLUSION

In this contribution, the SPL in an aircraft cabin is simulated using a finite element model of a typical fuselage section under an artificially generated TBL load. A comparison of two different modelling approaches is conducted – a homogenised damping loss factor for the entire cabin fluid is compared to a local modelling of seats introducing local impedances for the seat cushions. Both input parameters are frequency-dependent and received by measurements of a real seat bench. The resulting SPL at one passenger ear delivers comparable results regarding

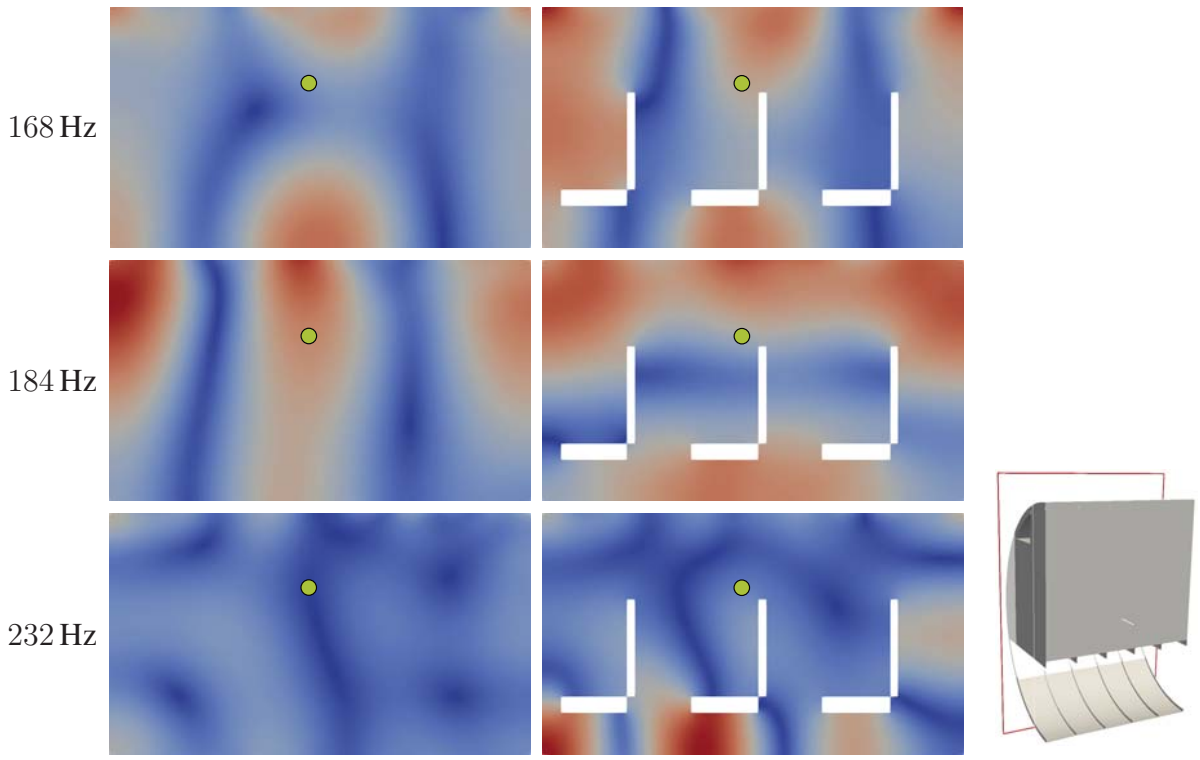

Figure 7: Qualitative pressure distribution in slices of the passenger cabin fluid; Each row refers to one example frequency with identical contour map ranges per row; The evaluation position for Fig. 6 is indicated by the green dots.

basic sound levels and damping performances over frequency. A detailed comparison of the pressure distribution in the cabin shows local effects at and between seat rows which lead to differences up to 10 dB in the model response.

For studies in future, a consideration of few tria elements in the volume mesh and non-coincident meshes in general may reduce the modelling effort. In addition, a consideration of porous material domains for the seat cushions might be a third approach. Furthermore, an experimental setup without surrounding aircraft parts seems reasonable in order to validate the local approach using impedances and reflecting backs of the seats. Finally, a more precise measurement of the seat impedances, especially for lower frequencies, is aimed for in future.

6 ACKNOWLEDGEMENT

The authors would like to thank the Collaborative Research Center 880 (Sonderforschungsbereich 880) of the German Research Foundation (Deutsche Forschungsgemeinschaft) and its graduate research program Graduate College for the financial support.

Special thanks go to the German Aerospace Center (DLR) Braunschweig for providing the aircraft seats and to the Physikalisch-Technische Bundesanstalt (PTB) Braunschweig for conducting measurements in their reverberation chamber.

REFERENCES

[1] C. Werner-Westphal, W. Heinze, P. Horst: Multidisciplinary integrated preliminary design applied to unconventional aircraft configurations. Journal of aircraft 45.2:581-590, 2008.

[2] C. Blech, C.K. Appel, R. Ewert, J.W. Delfs, S.C. Langer: Numerical prediction of passenger cabin noise due to jet noise by an ultra–high-bypass ratio engine. Journal of Sound and Vibration 464: 114960, 2020.

[3] C. Blech, C.K. Appel, R. Ewert, J.W. Delfs, S.C. Langer: Wave-resolving Numerical Prediction of Passenger Cabin Noise Under Realistic Loading, In: Radespiel, R., Semaan, R.: *Fundamentals of High Lift for Future Civil Aircraft: Papers Contributed to the Final Symposium of the Collaborative Research Center 880*, December 17-18, Braunschweig, Germany 2019, Springer (2020)

[4] V. Mallardo, M.H. Aliabadi, A. Brancati, V. Marant: An accelerated BEM for simulation of noise control in the aircraft cabin, Aerospace Science and Technology, 23(1), 418-428, 2012.

[5] Blinstrub, J., Bertsch, L., Heinze, W.: CRC 880 Vehicle Concepts and Comparative Noise Assessment, In: Radespiel, R., Semaan, R.: Fundamentals of High Lift for Future Civil Aircraft: Papers Contributed to the Final Symposium of the Collaborative Research Center 880, December 17-18, Braunschweig, Germany 2019, Springer (2020)

[6] S.C. Langer, C. Blech: Cabin noise prediction using wave-resolving aircraft models, PAMM 19.1:e201900388, 2019.

[7] N. Atalla, F. Sgard: Finite element and boundary methods in structural acoustics and vibration. CRC Press, 2015.

[8] DIN EN ISO 354: Akustik–Messung der Schallabsorption in Hallräumen (ISO 354: 2003). Deutsche Fassung EN ISO 354, 2003.

[9] A.C. Nilsson, B. Liu: Vibro-Acoustics, Volume I, Springer, 2016.

[10] M. Kaltenbacher: Numerical simulation of mechatronic sensors and actuators. Vol. 3. Berlin: Springer, 2015.

[11] E. Brandão, L. Arcanjo and S. Paul: A review of the in situ impedance and sound absorption measurement techniques. Acta Acustica united with Acustica 101.3: 443-463, 2015.

EURODYN 2020
XI International Conference on Structural Dynamics
M. Papadrakakis, M. Fragiadakis, C. Papadimitriou (eds.)
Athens, Greece, 23–26 November 2020

NUMERICAL EVALUATION OF THE SOUND TRANSMISSION OF A STRUCTURAL SYSTEM WITH ATTACHED NOISE CONTROL TREATMENTS USING STATISTICAL ENERGY ANALYSIS

Thaynan A. Oliveira[1]

[1]Univ. Lille, ULR 7512 - Unité de Mécanique de Lille - Joseph Boussinesq (UML)
F-59000 Lille, France
e-mail: {talvesoliv}@univ-lille.fr

Keywords: Vibroacoustics, Noise Control, Statistical Energy Analysis, Numerical Modeling.

Abstract. *Acoustical and structural systems are often found in engineering, whose importance of dynamic responses to random excitation is extended to high frequencies. On vibroacoustics, the prediction of the sound transmission loss and damping of a structural element in full spectral range is important for design purposes in many areas, like the automotive and aerospace industry. In the context of noise control, Statistical Energy Analysis (SEA) coupled with the Transfer Matrix Method (TMM) is widely used in high-frequency modeling of multilayered systems. Two mechanisms are involved in the application of a noise control treatment: the sound insertion loss (IL) and the damping loss factors of the equivalent systems. The first one is related to the transmission loss (TL) of the layers and, conceptually, is defined as the ratio between the acoustic TL of an treated panel over the TL of the panel without the attached treatment. The second one is related to the dissipative part that imposes acoustic or structural damping to the medium in contact with the treatment surfaces. This work presents a theoretical review involving the SEA approach coupled with the TMM for modeling the Sound Transmission Loss of treated subsystems. Additionally, implementing strategies are presented for considering this kind of wave approach in a SEA model. The results obtained from the SEA-Toolbox, a new open-source code developed in this project, are compared with experimental data.*

1 INTRODUCTION

Acoustical and structural systems are often found in engineering, whose importance of dynamic responses to random excitation is extended to high frequencies. Examples of such situations include:

- The structural response of an aerospace payload in flight;
- The vibration result of a structure under diffuse field conditions;
- The calculation of sound pressure into a car;
- The dynamical analysis of an aircraft structure (fuselage) due to jet noise and other dynamical sources;
- The sound transmission between partitions in a building;
- The knowledge of marine structures excited by intense vibration.

Statistical Energy Analysis (SEA) can be used for modeling a given system as an interaction of modes associated with isolated parts of the system (subsystems), considering each mode group as a single-degree-of-freedom oscillator described by the average energy response. The responses are obtained from the analysis of the energy distribution through the system, excited by a power source. This technique is based on the power balance equations for each mode group [1].

Some hypotheses are assumed in the determination of a model in SEA. The most important is that the vibration energy varies from one subsystem to another with a rate proportional to the difference between the modal energy and the proportionally dissipated energy within each subsystem. Another important hypothesis assumes weak coupling between subsystems. The weak coupling condition is valid if the internal dissipation of the subsystem is more important than the coupling path in the total loss of energy. It makes the ratio between the coupling factors and the internal dissipation factors considerably less than 1. Thus, the energy flow between the subsystems may be based on the difference between the energies of the decoupled subsystems [2, 3]. Additionally, it is important to ensure that the input powers are uncorrelated, and they can be simply summed. It guarantees the linearity of the equations that govern the SEA problem.

This paper concerns on the presentation and validation of the SEA Toolbox, an open source code that has been developed in the present project. In this version, the main connection types are implemented between beams, plates and acoustic subsystems. From the coupling between SEA and the Transfer Matrix Method (TMM) [4, 5], it is also possible to model plates and cavities with attached noise control treatments. An overview concerning the implementation of the method is presented and the Transmission Loss of treated subsystems obtained from the in-house code is compared with experimental data collected from the bibliography [6].

2 FUNDAMENTALS

In SEA the system is divided into physical elements in which the vibroacoustic characteristics, such as damping, excitation and coupling properties, can be considered similar. Subsystems directly excited by external sources will transmit a portion of energy to the others by means of coupling characteristics. The main mechanism in SEA is based on the relationship between power inputs and outputs from each subsystem. Figure 1 shows a simple problem of sound transmission loss in the SEA point of view.

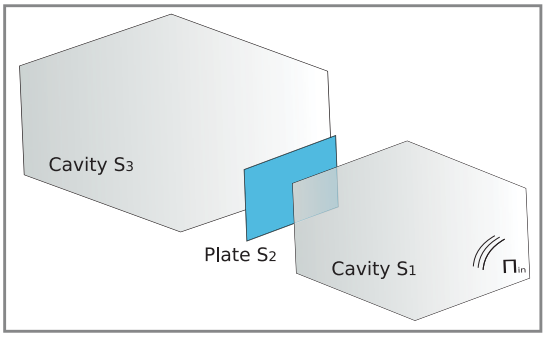

Figure 1: Example of a sound transmission loss problem.

Figure 1 shows the coupling of 3 SEA subsystems. However, it is common to have more robust models with a high number of elements. Considering a subsystem i coupled to a number of n subsystems, the power flow is [1, 2]

$$\Pi_i^{in} = \Pi_i^{\text{absorbed}} + \sum_{j \neq i}^{n} \Pi_{i;j}^{\text{transmited}} \ . \tag{1}$$

Equation (1) shows that there are a dissipated portion of the input power into a subsystem (controlled by the dissipation loss factor) and a transmitted portion of this power, controlled by the coupling loss factors. The transmitted powers by the coupling between subsystems will depend on the radiation characteristics and differences between the environments.

Considering a 3-subsystems problem, where the subsystem 1 is excited by an input power, as shown in Figure 1, the power flow can be illustrated by Figure 2.

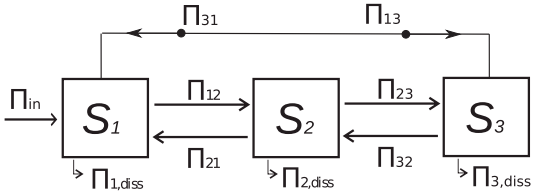

Figure 2: SEA flow for the cavity-plate-cavity problem.

It is possible to obtain the equations of the power flow illustrated in Figure 2, for each subsystem, as

$$\begin{aligned}
&\text{Subsystem 1:} && \Pi_{in} + \Pi_{21,trans} + \Pi_{31,trans} = \Pi_{1,diss} + \Pi_{12,trans} + \Pi_{13,trans} \\
&\text{Subsystem 2:} && \Pi_{12,trans} + \Pi_{13,trans} = \Pi_{2,diss} + \Pi_{21,trans} + \Pi_{31,trans} \\
&\text{Subsystem 3:} && \Pi_{23,trans} + \Pi_{13,trans} = \Pi_{3,diss} + \Pi_{31,trans} + \Pi_{32,trans} \ .
\end{aligned} \tag{2}$$

The power Π is related to the energy from

$$\Pi_i = \omega \eta_i E_i \ , \tag{3}$$

where ω is the angular frequency, η is the loss factor and E is the energy of a subsystem. Then, the dissipated power and the transmitted power will be given by

$$\Pi_{i,diss} = \omega \eta_{i,diss} E_i \qquad [i = 1, 2, 3] \ ; \tag{4}$$

$$\Pi_{ij,trans} = \omega \eta_{ij} E_i \qquad [i \neq j]. \tag{5}$$

being η_{ij} the coupling factor between the subsystems i and j.

Substituting Equation (4) and (5) into (2), the following linear system is obtained

$$\omega \begin{bmatrix} \eta_{1,diss} + \eta_{12} + \eta_{13} & -\eta_{12} & -\eta_{13} \\ -\eta_{21} & \eta_{2,diss} + \eta_{21} + \eta_{23} & -\eta_{23} \\ -\eta_{31} & -\eta_{32} & \eta_{3,diss} + \eta_{31} + \eta_{32} \end{bmatrix} \begin{Bmatrix} E_1 \\ E_2 \\ E_3 \end{Bmatrix} = \begin{Bmatrix} \Pi_{in} \\ 0 \\ 0 \end{Bmatrix} . \tag{6}$$

It can be observed that the SEA method is based on the resolution of linear systems for calculating the energy for each subsystem. The determination of damping variables for more complex systems is based on theoretical models or from direct experimental data. However, if the modal density of the subsystems involved in the problem are known, the coupling loss factor in one direction is required, and the following consistency ratio is valid to complement the damping matrix

$$n_i \eta_{ij} = n_j \eta_{ji} \ , \tag{7}$$

where n_i e n_j are the modal densities of the subsystems i and j, respectively. Theoretical models for the modal densities of flat plates and rectangular cavities can be found in [1, 3].

For the problem illustrated in Figure 1, the mean square value of the pressure inside the cavities $p_i^2 = E_i \rho_i c_i^2 / V_i$ can be recovered from the solution, with ρ_i being the fluid density, c_i the sound velocity and V_i the volume of the cavity $i = 1, 3$. The transmission loss of the partition can be calculated as [7]

$$TL = 10 \log_{10} \left(\frac{p_1^2}{p_3^2} \right) + 10 \log_{10} \left(\frac{S}{A_{eq}} \right) \ , \tag{8}$$

where $A_{eq} = 4 \omega V_3 \eta_{3,diss} / c_3$ is the equivalent absorption area of the reception cavity and S is the area of the panel.

2.1 The cavity-plate-cavity connection

The coupling between the three subsystems showed in Figure 1 is controled by diferent propagation paths. The most important ones are controled by the resonant and non-resonant sound transmission. The first one is affected by the radiation capacity of the structural system and is important in frequencies above the coincidence spectral region of the plate. On the other hand, the non-resonant path is controled by the mass of the structure and it is important for global responses below the coincidence frequency [8]. The radiation loss factor that models the connection between plate s and cavity a is given by

$$\eta_{sa} = \eta_{rad} = \frac{\rho_a c_a S_s}{\omega M_s} \sigma_{rad} \, , \tag{9}$$

with ρ_a being the fluid density, c_a the fluid sound velocity, S_s the area of the partition, M_s the structural mass and σ_{rad} the radiation efficiency of the structural system that can be recovered in theoretical models as that one proposed by Leppington [9]. The non-ressonant loss factor that models the coupling between two cavities i and j is

$$\eta_{ij} = \eta_{mass} = \frac{c_i A_i \tau_m}{4\,\omega\, V_i} \ , \tag{10}$$

where A is the total surface area, V is the volume of the cavity and τ_m is the mass controled transmission coefficient of the system. In this work, the field incidence transmission coefficient presented in [8] was used.

2.2 Noise control treatments modeling using transfer matrices

Multilayer panels are often used in the context of noise control. The mechanisms involved in the application of a noise control treatment (NCT) on a face of a structural system are: the sound insertion loss (IL) that can change the acoustic radiation and the mass law transmission of the structure, the sound absorption seen by the acoustic medium in contact with the surface of the treatment and the added structural damping. The methodology of the Transfer Matrix Method (TMM) [4] is based on the theory of plane wave propagation in a given layer. The material of each layer is assumed homogeneous, transversely isotropic and the surface of the treatment is considered infinite in this formulation. Figure 3 shows an incident plane acoustic wave upon a media with thickness h, at an incident angle θ.

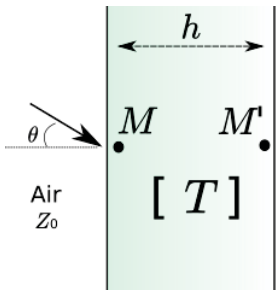

Figure 3: Ilustration of an infinite extent layer on the Tranfer Matrix Method.

The sound propagation inside the layer is represented by a transfer matrix T such that

$$V(M) = [T]V(M') \ , \tag{11}$$

where V is a vector containig the response for each degree of freedom of the media at the points M and M' set close to the foward and the backward of the layer [4]. The matrix T depends on the physical propierties as well as the thickness of the medium. If considering the layer illustrated in Figure 3 as an equivalent fluid, the vector $V = \{p, v\}^{\mathrm{T}}$ is composed by the pressure and the particle velocity. The transfer matrix T^f, in this case, is given by

$$[T^f] = \begin{bmatrix} \cos(k_x h) & \mathrm{j}\,\frac{\omega\rho_0}{k_x}\sin(k_x h) \\ \mathrm{j}\,\frac{k_x}{\omega\rho_0}\sin(k_x h) & \cos(k_x h) \end{bmatrix} \ , \tag{12}$$

where $k_x = \sqrt{k_c^2 - k_0^2 \sin^2(\theta)}$ is the longitudinal component of the wavenumber into the layer, k_c being the propagating wavenumber of the material, k_0 and ρ_0 the wavenumber and density

of the air. The continuity between adjacent layers is applied and a global transfer matrix $[T_g]$ is constructed according to the references [4] and [5]. The acoustic properties depend on the surface impedance computed from the ratio between pressure and velocity $p(M)/v(M)$, obtained from the solution of a linear system $V = [T_g]^{-1}\{F\}$.

2.2.1 Insertion Loss (IL) from the TMM

The Insertion Loss is defined as the ratio between the acoustic TL of a panel with the attached treatment over the TL of the unteated panel. This parameter can be calculated from the TMM simulation if considering a semi-infinite fluid as the boundary condition. The insertion coefficient IC will be given by

$$IC(\omega) = \frac{\int_0^{\theta_f} |T_{NCT}(\omega,\theta)|^2 \sin(\theta)\cos(\theta)\mathrm{d}\theta}{\int_0^{\theta_f} |T_{bare}(\omega,\theta)|^2 \sin(\theta)\cos(\theta)\mathrm{d}\theta} \ , \tag{13}$$

where θ_f is the final incidence angle, T_{NCT} and T_{bare} are the transmission coefficients of the treated and untreated infinite extent systems, respectively. In order to solve this problem, the bare panel is considered as the first solid layer in the TMM simulation. The insertion loss $IL(\omega) = -10\log_{10}(IC(\omega))$ is recovered from the insertion coefficient. Finally, the insertion loss from TMM is applied as a scaling factor to the radiation and the mass law coupling loss factors in the SEA problem [5], then

$$\eta_{rad} = \eta_{rad}\, IC(\omega) = \eta_{rad}(10^{-IL(\omega)/10}) \ ; \tag{14}$$

$$\eta_{mass} = \eta_{mass}\, IC(\omega) = \eta_{mass}(10^{-IL(\omega)/10}) \ . \tag{15}$$

With *SEA-Toolbox*, it is possible to model equivalent fluids, solids and poroelastic materials, over the incidence range from 0 to $\pi/2$.

3 METHODOLOGY

The present study consists of testing the functionality of Statistical Energy Analysis coupled with the Transfer Matrix Method for Transmission Loss problems. The SEA simulation of two acoustic cavities with a multilayered partition was done and the obtained results were compared with experimental data extracted from reference [6]. The experimental study was developed at the Laboratory of Vibration and Acoustics of the Federal University of Santa Catarina - Brazil and folowed the guidelines of the ISO 10140-2 standard [7]. Kulakauskas [6] presented a numerical and experimental evaluation of the sound transmission loss for single and double-wall setups using different porous samples.

In this work, the single and double-wall setups were reproduced in the new open-source code (*SEA-Toolbox*) using two different porous samples, considering the SEA implicit approach. It means that the multi-layer structures were represented by applying the obtained Insertion Loss from the TMM analysis to the SEA coupling factors (see Equations 9 and 10), as illustrated in Figure 4.

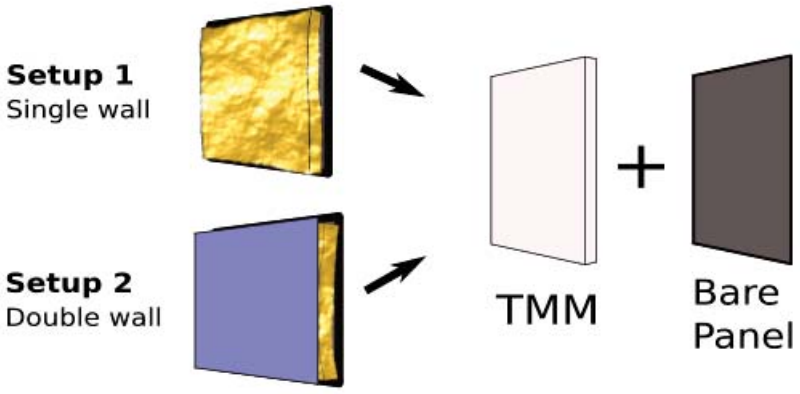

Figure 4: Ilustration of the simulated systems.

Based on the experimental procedure, the porous samples were modeled as simply supported limp fibers. The Johnson-Champoux-Allard model [10, 11] was used for the characterization of the fluid part in addition to the equivalent density calculated from the simplification of the Biot's Theory for low-stiffness framed materials [4]. This approach avoids artificial clamping between the plate and the porous material, but in case of using the full Biot's Theory (poroelastic material), an air gap should be applied between the structure and the foam to simulate the cited mounting condition. The properties for the solid structures and fibers considered in this work are presented in Table 3.

Table 1: Material properties of the setups considered in this work.

	Solid		**Porous**	
	Plate 1	**Plate 2**	**Material A**	**Material B**
Thickness h [mm]	1.0	0.5	50	58
Young's Modulus E [Pa]	71E9		-	-
Poisson's ratio ν [-]	0.33		-	-
Density ρ [kg/m^3]	2700		27	9.6
Flow Resistivity σ [kN/m^4]	-		5	38.72
Porosity ϕ [-]	-		0.89	0.92
Tortuosity α_∞ [-]	-		1.37	1.06
Viscous charac. length Δ [μm]	-		213	37
Thermal charac. length Δ' [μm]	-		288	148

As already mentioned, the SEA simulation consists of 3 subsystems illustrated by Figure 1. The emission (S1) and reception (S3) cavities have a volume of 147.54 m^3 and 199.0 m^3, based on the dimensions of the experimental reverberant chambers [6]. The total surface area A_1 and perimeter P_1 of the cavity S1 are 190 m^2 and 70.44 respectively. For the cavity S3, these geometrical dimensions are $A_3 = 210$ m^2 and $P_3 = 72.0$ m. The total surface area of the bare panel is $S_2 = 1.0$ m^2. An acoustic power source of 1 Watt was applied in the S_1 subsystem. The total mean absorption of the non-treated surfaces of the cavities was considered 1%, as well as the dissipation loss factor of the solid plate.

A propagation way that can be important in experimental procedures is the leakage due to the mounting conditions. According to Beranek [8], this phenomena causes a reduction in the

Insertion Loss that can be simply modeled as

$$\Delta IL_L = IL_s - IL_L \approx 10\log_{10}(1 + \beta\, 10^{TL_s/10}) \tag{16}$$

where IL_s and IL_L are the insertion losses of the sealed and leaky systems, TL_s the transmission loss of the system and β is the leak ratio factor. Experimentally, the influence of this phenomena becomes more important in high frequencies [6]. In this paper, the application of the model presented in Equation 16 was evaluated in the Transmission Loss of the double wall systems, considering $\beta = S_{leak}/S_{plate} = 2.0\,\mathrm{E} - 6$. The determination of S_{leak} was done by adjusting experimental data. The analyses are presented in Section 4.

4 RESULTS

The results were obtained in one third-octave band, from 250 Hz to 8000 Hz. Although the damping of the subsystems in contact with the surfaces of the NCT can be changed when applying the noise control treatment, these parameters are not important for this work. Since the treated acoustic surface is too small if compared to the total surface area of the reception cavity, the mean absorption of the subsystem 3 would not be significantly altered in this scenario. On the other hand, the loss factor of the structural system can be important for the sound transmission on frequencies above the critical frequency ($\approx$ 12 kHz) for this panel. Therefore, the Insertion Loss (IL) of the treatment is the only parameter that contributes significantly to the numerical transmission loss of the complete system. Figure 5 shows the infinite size insertion loss for the single and double-wall setups, considering the Material A and Material B, obtained from the Transfer Matrix Method.

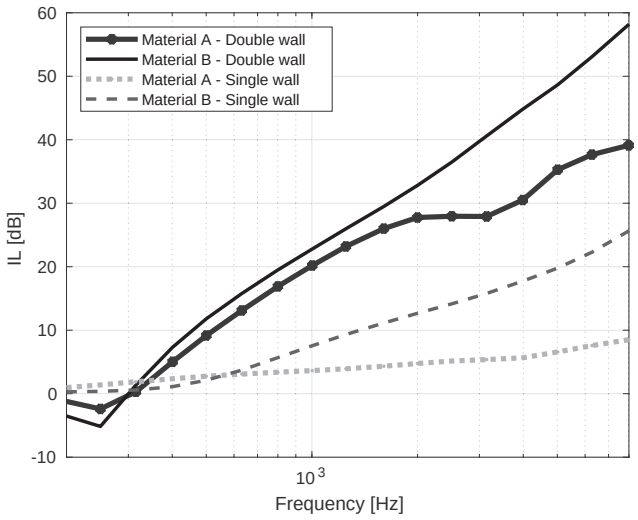

Figure 5: Insertion Loss obtained from the TMM for the studied systems.

It can be noticed in Figure 5 that the formulation of transfer matrices is capable of capturing the poor performance of the double-wall configuration in frequencies below the resonance of the spring-mass system ($f \approx 300$ Hz), represented by a negative value of the IL. The results also show the importance of the flow resistivity parameter for improving the Insertion Loss of the system, which is expected since this parameter controls the barrier capacity of the porous material. The Insertion Loss was applied to the coupling factors, as presented in Equations 10

and 9. The Transmission Loss results calculated for the single-wall configurations (plate + porous) are presented in Figure 6.

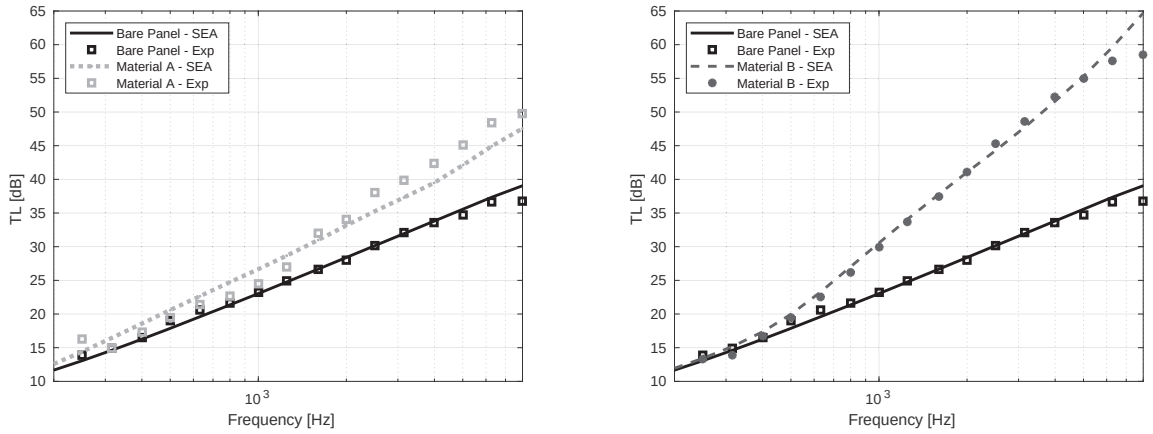

(a) Material A (b) Material B

Figure 6: Sound Transmission Loss obtained for the single-wall configurations.

Figure 6 shows good agreement between numerical and experimental data for the considered single-wall systems, which indicates the efficiency of the presented modeling approach for flat structures. It can be noticed in the obtained result for Material B the drop of TL in high frequency that probably occurs due to the leakage of the sound wave in the experimental condition. This characteristic is more evident in Figure 7, that brings the collected Transmission Loss for the double-wall setups (plate - porous - plate) with and without the leakage correction applied to the numerical data.

Figure 7 shows that the greater the complexity of the multilayers, the more difficult it becomes to obtain a perfectly sealed condition from an experimental point of view. It can be seen in Figures 7 (a) and 7 (c) that the experimental TL of the different systems converges in high frequencies even though it does not occur when the same samples were used in the single-panel setups. It suggests greater importance of leaks in the double wall configurations. Although adjusting the parameter β imposes uncertainties, Figures 7 (b) and 7 (d) shows that the use of a model for considering this propagation path is necessary when the presence of leaks becomes evident in the experimental results. Nevertheless, the method of SEA/TMM can be a useful tool when due care is taken.

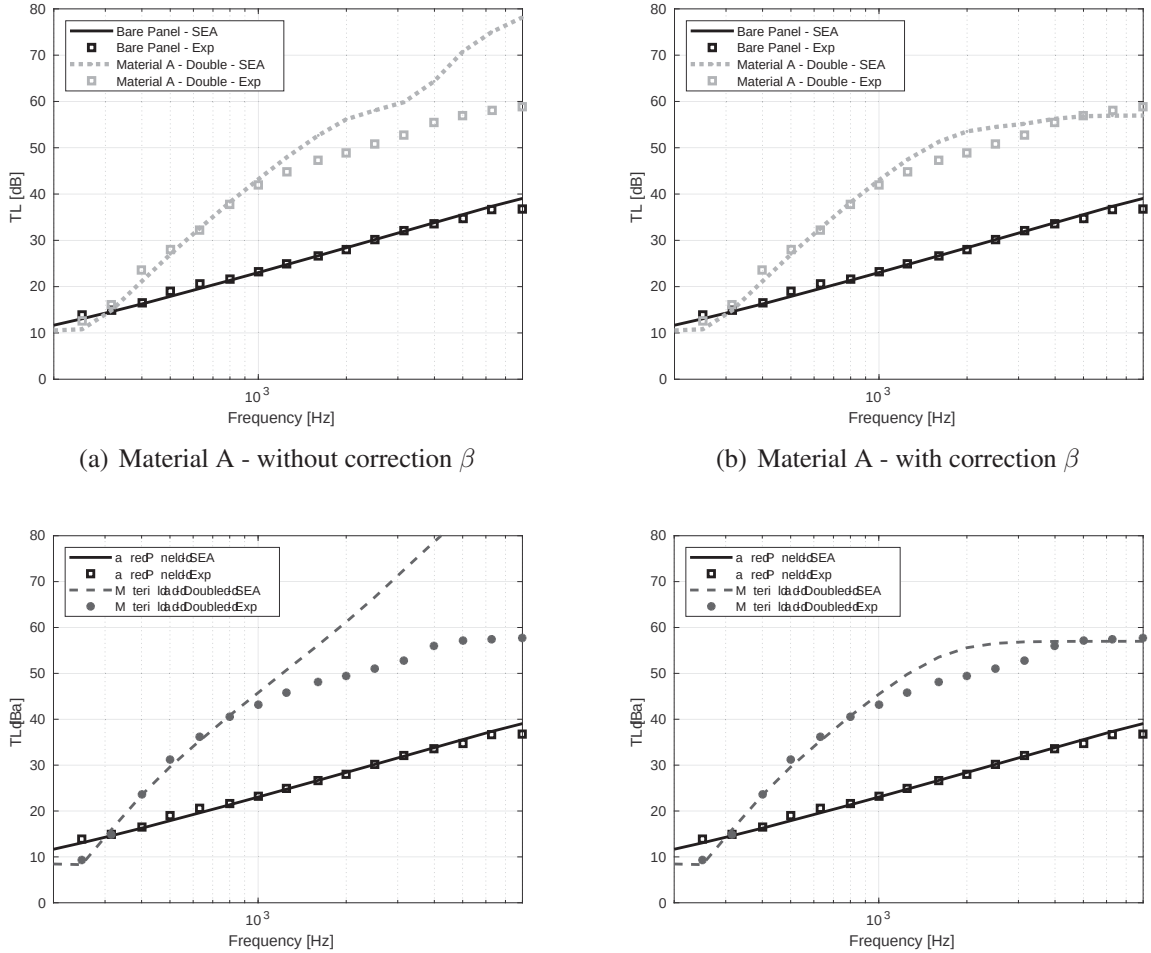

(a) Material A - without correction β

(b) Material A - with correction β

(c) Material B - without correction β

(d) Material B - with correction β

Figure 7: Sound Transmission Loss obtained for the double-wall setups.

5 CONCLUSIONS

This paper presented an overview of the transmission loss characterization of multilayered structures using Statistical Energy Analysis and the Transfer Matrix Method. The Insertion Loss of the treated systems was calculated by using the TMM and applied to the coupling loss factors of the SEA matrix. Additionally, a model for leaks was presented and applied to the TL results for simulating experimental conditions of a double-wall system composed by plate-porous-plate. The results obtained from the $SEA - Toolbox$, an open-source code developed in the present project, demonstrated good agreement with experimental data.

6 ACKNOWLEDGMENTS

The author gratefully acknowledges Professor Mhamed Souli for all the support. Many thanks is also given to Lucas Lobato for important suggestions.

REFERENCES

[1] R. H. Lyon, R. G. DeJong, and M. Heckl, "Theory and application of statistical energy analysis," 1995.

[2] F. J. Fahy, "Statistical energy analysis: a critical overview," *Philosophical Transactions of the Royal Society of London. Series A: Physical and Engineering Sciences*, vol. 346, no. 1681, pp. 431–447, 1994.

[3] K. D. Langhe, *High frequency vibrations: contributions to expiremental and computational sea parameter identification techniques*. PhD thesis, Katholieke Universiteit Leuven, 1996.

[4] J. Allard and N. Atalla, *Propagation of sound in porous media: modelling sound absorbing materials*. United Kingdon: John Wiley & Sons, 2 ed., 2009.

[5] N. Atalla, "Structural and acoustic noise control material modeling," in *Engineering vibroacoustic analysis: methods and applications* (S. A. Hambric, S. H. Sung, and D. J. Nefske, eds.), pp. 230–265, United Kingdom: John Wiley & Sons, 2017.

[6] F. L. V. Q. Kulakauskas, *Avalição do Uso de Materiais Porosos na Perda de Transmissão de Painéis Duplos*. PhD thesis, Universidade Federal de Santa Catarina, 2016.

[7] ISO:10140-2, "Laboratory measurement of sound insulation of building elements: *Measurement of air-borne sound insulation*. International Standard Organization," 2010.

[8] L. L. Beranek and I. L. Ver, *Noise and vibration control engineering: principles and applications*. Cambridge, USA: John Wiley & Sons, Inc., 814 p., 1992.

[9] F. G. Leppington, E. G. Broadbent, and K. Heron, "The acoustic radiation efficiency of rectangular panels," *Proceedings of the Royal Society of London. A. Mathematical and Physical Sciences*, vol. 382, no. 1783, pp. 245–271, 1982.

[10] D. L. Johnson, J. Koplik, and R. Dashen, "Theory of dynamic permeability and tortuosity in fluid-saturated porous media," *Journal of fluid mechanics*, vol. 176, pp. 379–402, 1987.

[11] J.-F. Allard and Y. Champoux, "New empirical equations for sound propagation in rigid frame fibrous materials," *The Journal of the Acoustical Society of America*, vol. 91, no. 6, pp. 3346–3353, 1992.

EURODYN 2020
XI International Conference on Structural Dynamics
M. Papadrakakis, M. Fragiadakis, C. Papadimitriou (eds.)
Athens, Greece, 23–26 November 2020

BAND STRUCTURE OF ELASTIC BODIES WITH PERIODIC NONLOCALITIES

A. S. Rezaei[1], **S. V. Sorokin**[2], **F. Mezzani**[1], **and A. Carcaterra**[1]
[1] *Department of Mechanical and Aerospace Engineering, Sapienza University of Rome*
Via Eudossiana 18, 00184 Rome, Italy
e-mail: {amirsajjad.rezaei, federica.mezzani, antonio.carcaterra}@uniroma1.it

[2] *Department of Mechanical and Manufacturing Engineering, Aalborg University*
Fibigerstrade 16, 9220, Aalborg, Denmark
e-mail: svs@mp.aau.dk

Keywords: Long-range interactions, Periodic nonlocality, Wave propagation, Metamaterials, Floquet theorem.

Abstract. *Investigating the status of travelling waves in systems integrated with periodic means of distant communication, and the possibility of obstructing the energy flow carried via coupled modes, are of interest. The governing system of linear differential equations with periodic coefficients gives the possibility to adopt Floquet theorem, as a powerful framework, to identify the location of stop band frequencies. The generation of gaps in the band structure of the system owing to the newly launched periodic long-range channels is shown. The likelihood of pulling the first stopband to lower frequency bands as a major demand, is examined by raising some assumptions.*

1 INTRODUCTION

The analysis of waves travelling in periodic arrays has grabbed the attention of many researchers over the past few decades, and direct application in electromagnetism and acoustics have been the keynote to most of the investigations. The existence of bandgaps in the band structure of the mechanical systems, within which the transmission of energy is prohibited, is significantly important due to the problems frequently faced in real-life, such as discomforting noise in cars and noise-related health concerns.

In principle, the repetition of subunits with a certain pattern gives birth to some gaps in the band structure of the system [1]. The characteristics of the stopbands, including the width and the location, are totally dependent upon the type of subunits. Several studies concerning the analysis of the vibro-acoustic behaviors of structures composed of periodic attachments, have been conducted [2-4]. Recently, the acoustic metamaterials, typically made of thin-walled segments integrated with simple mechanical subunits such as spring and dampers, have been in the center of attention. A sizable number of studies [5, 6] are devoted to fully describe the features of the foregoing periodic configurations including the effect of resonator type and its placement on the band structure of the array. Although subunits mostly act locally, cases might be imagined in which the distant action between two or several points forms the force exerted by the element. To clarify the effect of nonlocalities on the status of travelling, a handful of investigations have been carried out [7-9]. For instance, in Ref. [9] the arising propagation regimes in a newly proposed waveguide in which distant particles may communicate remotely, is investigated, as the emergence of hypersonic group velocity under certain circumstances.

Although nonlocalities can adopt any topology, one may assume them to be distributed periodically. The recently developed mechanisms are, indeed, new paths for energy transmission through the system. The combination of nonlocality and periodicity might be a fruitful design which guarantees the born of gaps in the band structure of the system as well as other potential phenomena. To put it differently, the coincidence of periodicity and long-range interactions could deliver peculiar behaviors under particular conditions. The potential latent qualities offer the opportunity to tackle problems encountered in the vibro-acoustic field including achieving the ultra-low-frequency bandgaps, which is a hugely demanding task among the academics.

The inclusion of the periodic nonlocalities within the domain of a conventional system, alters the dynamics of the structure, and thereby a strong modification in the behavior of waves travelling through the domain. Using Floquet theorem, a structured investigation of the dependence of the system's response upon the intensity of the long-range effects is presented.

2 THEORY AND FORMULATION

This work investigates the dynamics of a periodic structure, as in Figure 1, composed of an infinite axisymmetric cylindrical shell. Besides, spring-like links let distant points interacting with each other. The inclusion of the periodically allocated axial connections generates new dynamic effects in the dynamic performance. The global dynamic response, by the displacements $\bar{u}(x,t)$ and $\bar{w}(x,t)$ along the axis and along the transverse direction, respectively, is associated by the following coupled differential equations:

$$\begin{aligned} \frac{Eh}{1-\nu^2}\left(\frac{d^2\bar{u}}{dx^2}+\frac{\nu}{R}\frac{d\bar{w}}{dx}\right) &= \rho\frac{d^2\bar{u}}{dt^2} \\ \frac{Eh}{1-\nu^2}\left(\frac{h^2}{12}\frac{d^4\bar{w}}{dx^4}+\frac{\bar{w}}{R^2}+\frac{\nu}{R}\frac{d\bar{u}}{dx}\right) &= \rho\frac{d^2\bar{w}}{dt^2} \end{aligned} \tag{1}$$

with $\rho, E, R, h,$ and ν being the mass density, Young's modulus, radius, thickness and Poisson's ratio, respectively. The nondimensional forms become:

$$\begin{aligned} \frac{d^2u}{dX^2} + \Omega^2 u - \nu \frac{dw}{dX} = 0 \\ \nu \frac{du}{dX} + w + \frac{h^2}{12R^2}\frac{d^4w}{dX^4} - \Omega^2 w = 0 \end{aligned} \tag{2}$$

$X = x/R$ denoting the nondimensional axial coordinate, $u = \bar{u}/R$ and $w = \bar{w}/R$ the nondimensional axial and bending displacements, are introduced. $\Omega = \sqrt{(1-\nu^2)\rho R^2 \omega^2/E}$ is the nondimensional frequency. In the correspondent structure, the energy is carried out via coupled modes due to the coupling between the axial and bending terms in the equations of motion. This may be perceived by inspecting Eq. (2) where both u and w are present in both equations indicating the link between the extensional and flexural modes.

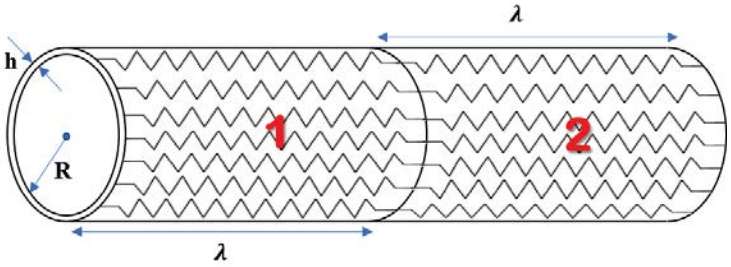

Figure 1: A periodicity cell of a cylindrical shell with periodic nonlocalities

Using modal coefficients τ_i, the general solution for the system of equations (2) is:

$$\begin{aligned} w = \sum_{i=1}^{6} \bar{w}_i \, e^{jk_i x} \\ u = \sum_{i=1}^{6} \tau_i \, \bar{w}_i \, e^{jk_i x} \end{aligned} \tag{3}$$

k_i $(i = 1, 2, \dots, 6)$ are the roots of the dispersion relation for a homogenous and isotropic axisymmetric cylindrical shell. Given the above expressions for the displacements u and w, 24 equations, in total, are necessary to fully characterize the kinematics of both segments. However, only twelve of them are self-sufficient and the rest are indeed connected to the independent ones by the modal coefficients. The modal coefficients are:

$$\tau_i = \frac{j\nu k_i}{k_i^2 - \Omega^2} = j\frac{1 + \frac{h^2 k_i^4}{12R^2} - \Omega^2}{\nu k_i} \tag{4}$$

where j is the imaginary unit. Considering a unit cell of the system, which contains two equivalent shell segments coupled with periodic nonlocalities of stiffness k, the interface conditions between the neighboring segments 1 and 2, in the nondimensional form, are:

$$\begin{aligned} w_1\big]_{X=\lambda} &= w_2\big]_{X=\lambda} \\ \left.\frac{dw_1}{dX}\right|_{X=\lambda} &= \left.\frac{dw_2}{dX}\right|_{X=\lambda} \\ \left.\frac{d^2w_1}{dX^2}\right|_{X=\lambda} &= \left.\frac{d^2w_2}{dX^2}\right|_{X=\lambda} \\ \left.\frac{d^3w_1}{dX^3}\right|_{X=\lambda} &= \left.\frac{d^3w_2}{dX^3}\right|_{X=\lambda} \\ u_1\big]_{X=\lambda} &= u_2\big]_{X=\lambda} \end{aligned} \tag{5}$$

$$\left.\frac{du_1}{dX}\right|_{X=\lambda} + \nu w_1\big]_{X=\lambda} = \left.\frac{du_2}{dX}\right|_{X=\lambda} + \nu w_2\big]_{X=\lambda} + \hat{k}\left[u_1\big]_{X=\lambda} + u_2\big]_{X=\lambda} - \left(u_1\big]_{X=0} + u_2\big]_{X=(1+\gamma)\lambda}\right)\right]$$

where $\hat{k} = kR(1-\nu^2)/E$ denotes the nondimensional spring stiffness. $\lambda = l_1/R$ and $\gamma = l_2/l_1$ are nondimensional length parameters. The above conditions are referring to the continuity of axial and bending displacements, the slopes dw/dX, the flexural moments d^2w/dX^2 and bending forces d^3w/dX^3 at the interface. Besides, the condition regarding the continuity of the axial force, is modified by an additional term $\hat{k}[u_1]_{X=\lambda} + u_2]_{X=\lambda} - \left(u_1]_{X=0} + u_2]_{X=(1+\gamma)\lambda}\right)]$, which brings into the system the effects induced by nonlocalities. To proceed with the analysis, six more equation are required, which are obtained by considering the Floquet periodicity conditions, as:

$$\begin{aligned} w_1]_{X=\lambda/2} &= \Gamma\, w_2]_{X=(1+\gamma/2)\lambda} \\ \left.\frac{dw_1}{dX}\right|_{X=\lambda/2} &= \Gamma \left.\frac{dw_2}{dX}\right|_{X=(1+\gamma/2)\lambda} \\ \left.\frac{d^2w_1}{dX^2}\right|_{X=\lambda/2} &= \Gamma \left.\frac{d^2w_2}{dX^2}\right|_{X=(1+\gamma/2)\lambda} \\ \left.\frac{d^3w_1}{dX^3}\right|_{X=\lambda/2} &= \Gamma \left.\frac{d^3w_2}{dX^3}\right|_{X=(1+\gamma/2)\lambda} \\ u_1]_{X=\lambda/2} &= \Gamma\, u_2]_{X=(1+\gamma/2)\lambda} \\ \left.\frac{du_1}{dx}\right|_{X=\lambda/2} + \nu w_1]_{X=\lambda/2} &= \Gamma\left(\left.\frac{du_2}{dx}\right|_{X=(1+\gamma/2)\lambda} + \nu w_2]_{X=(1+\gamma/2)\lambda}\right) \end{aligned} \tag{6}$$

Here Γ is a standard parameter describing the phase shift in a periodic array [10]. The relations in (6) compare the state vector of neighboring segments. It is apparent how the state vector gets modified from one cell to the next by the parameter Γ. Considering $\Gamma = e^{jK_B}$ with K_B being the Bloch parameter, two possibility for its value may be imagined: real-valued K_B, hence $|\Gamma| = 1$, suggests the propagation is allowed in the structure, complex valued K_B, inducing $|\Gamma| \neq 1$, disclosed the impossibility to project the state vector of one segment on the neighboring, implying the existence of stopband frequencies. Note that, once Γ is defined, its value is constant for any selected periodicity cell. A sixth-order transcendent equation associated with the described system is of the form:

$$\Gamma^6 + A_1\left(\Omega,\hat{k}\right)\Gamma^5 + A_2\left(\Omega,\hat{k}\right)\Gamma^4 + A_3\left(\Omega,\hat{k}\right)\Gamma^3 + A_4\left(\Omega,\hat{k}\right)\Gamma^2 + A_5\left(\Omega,\hat{k}\right)\Gamma + 1 = 0 \tag{7}$$

The above polynomial is the nontrivial solution of a system of equations obtained from the combination of Eqs. (5) and Eqs. (6). Eq. (7) proclaims the existence of three pair of roots possibly determining the energy transmission across the domain. Note that, the coefficients in the preceding equation may not be explicitly extracted and values of Γ are individually calculated for a given frequency Ω.

3 RESULTS AND DISCUSSION

This section is devoted to investigating the band structure of an unbounded axisymmetric cylindrical shell in the presence of periodic nonlocalities governed by the nondimensional stiffness $\hat{k}$. The analysis of the trend of Γ with respect to the nondimensional frequency Ω unveils the existence of several bandgaps induced by the introduction of periodic nonlocalities, occurring whenever $|\Gamma| \neq 1$, spread along the entire frequency domain. Since the bandgaps usually get smaller, the higher the frequency, only the first two bandgaps are here illustrated in Figures (2a) and (2b). In fact, energy transmission is not permitted about $\Omega = 0.96$ (see Figure (2a)) and $\Omega = 1.23$ (see Figure (2b)), where $|\Gamma|$ may adopt any value but unity. Evidently, the first gap is significantly broader with respect to the second one of the widths 0.006.

The figure implicitly points to the fact that the long-range interactions are conveniently beneficial for blocking the energy paths no matter it is being carried by extensional or bending modes.

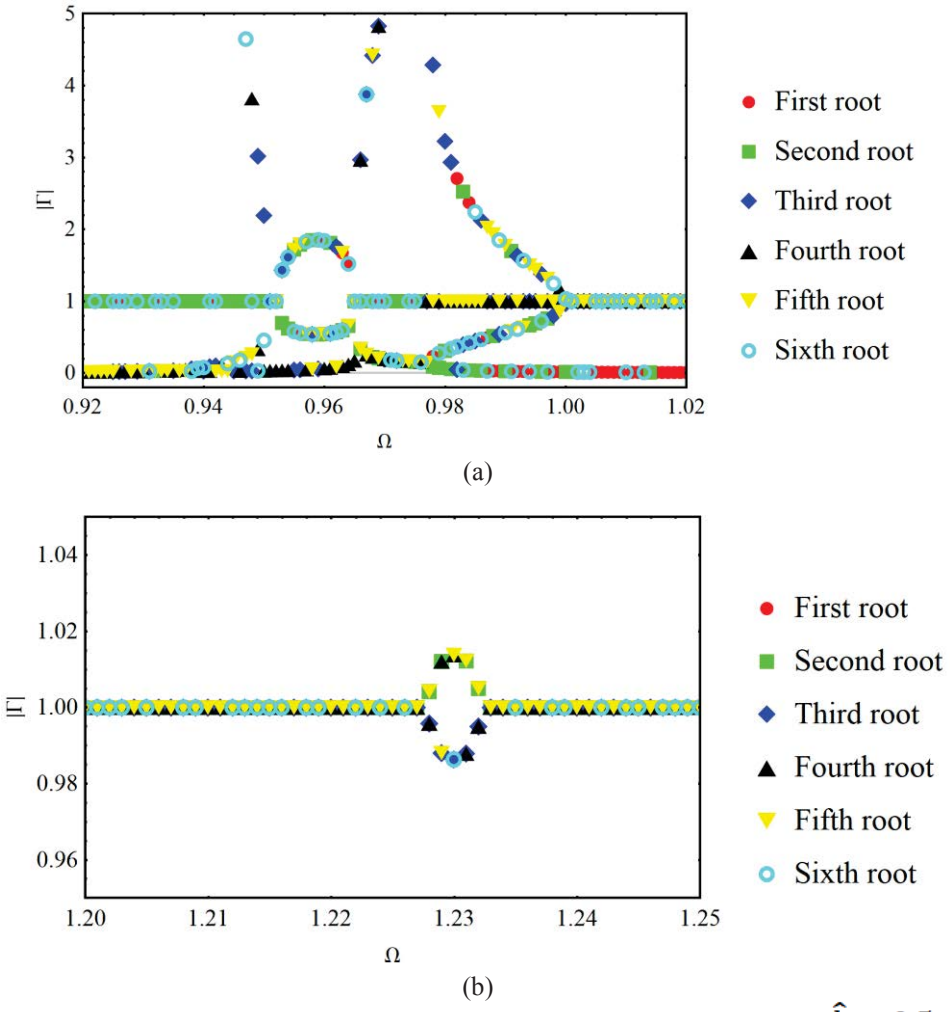

Figure 2: Band structure of an axisymmetric cylindrical shell with periodic nonlocalities ($\hat{k} = 0.5,\ \eta = 0.02$) a) First gap b) Second gap

According to Eq. (2), the response of the system is dependent upon the thickness-radius ratio η=h/R; therefore, the effect of this parameter may sensibly influence the location and the width of the gaps dramatically. Considering other parameters to be fixed as ν=0.3, γ=1, λ=1 and k̂=0.5, for four different value of η, the location of the stopbands is given in Table 1.

η	First gap	Second gap
0.005	$0.94895 < \Omega < 0.95495$	$0.96295 < \Omega < 0.96895$
0.01	$0.94895 < \Omega < 0.95795$	$0.98695 < \Omega < 0.98995$
0.015	$0.94995 < \Omega < 0.96195$	$1.12195 < \Omega < 1.12595$
0.02	$0.95195 < \Omega < 0.96495$	$1.22695 < \Omega < 1.23295$

Table 1: The low-frequency bandgaps in an axisymmetric cylindrical shell with periodic nonlocalities

To extract what is brought in the table, a narrow band $\Omega < 1.5$ is taken into account. Although the change in η roughly influences the width of the gaps, for the case of first stopband, a quite wider gap is met as this ratio increases. In fact, the left border of both gaps is pulled towards higher frequencies as the thickness-length ratio rises. Obviously, the origin of

these gaps may be simply explained by the decoupling of the flexural and longitudinal modes, which are integrated because of the Poisson's ratio and the further discussion is held for the future works.

The frequency dependence of $|\Gamma|$ is demonstrated in Figure 3, for two values of the non-dimensional stiffness, namely $\hat{k} = 0.2$ shown in black and $\hat{k} = 0.5$ in red. Two distinct patterns are observed: those points which resemble non-flat curves are originated from the real roots of Eq. (7), and the roots constructing the flat lines i.e. $|\Gamma| = 1$, are referring to pass band frequencies. Based on the figure, the right border of the stopband, the frequency at which the stop band vanishes, moves towards higher frequencies for higher values of $\hat{K}$. The emerging frequency (seed of the stopband) picks a slightly higher value with respect to the frequency associated with the system having less stiff external links. Given the circumstances, a wider gap is attained.

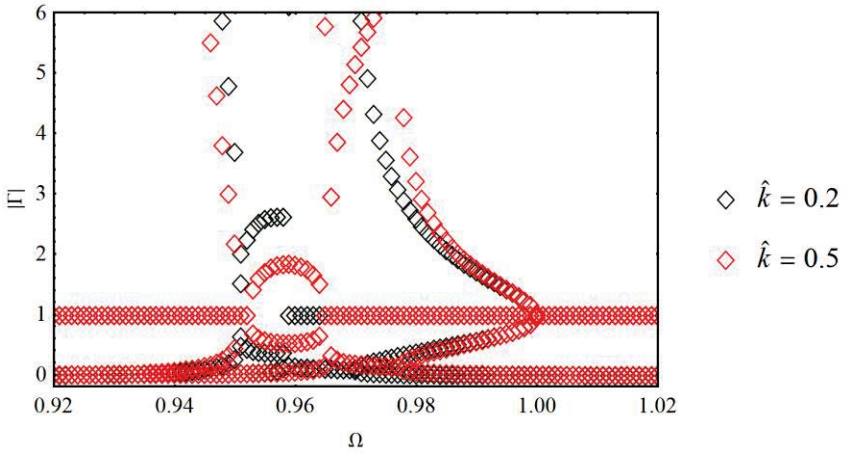

Figure 3: Band structure of an axisymmetric cylindrical shell with periodic nonlocalities for two different values of nondimensional stiffness $\hat{k}$

4 CONCLUSION

To identify the band structure of a hollow axisymmetric cylindrical shell with periodic long-range links embedded, Floquet analysis is carried out. The structure is composed of equivalent shell segments and equivalent axial links, which connect the interface of one pair of segments to the next. To simplify the analysis, the axial links are assumed to be simple extensional springs by which the interaction of distant points is made possible. The results suggest the generation of bandgaps in the band structure of the system and the occurrence of this phenomena may be attributed to the newly introduced periodic external links. Parametric studies show that the major gap (first one) becomes wider as stronger external connections are implemented. Moreover, the presented mathematical formulation shows the possibility of attenuating the flexural and extensional energy owing to solely axial nonlocalities.

REFERENCES

[1] M. S. Kushwaha, P. Halevi, G. Martínez, L. Dobrzynski, and B. Djafari-Rouhani, Theory of Acoustic Band Structure of Periodic Elastic Composites, *Physical Review B* 49, 2313, 1994.

[2] D. J. Mead, Wave Propagation in Continuous Periodic Structures. Research Contributions from Southampton 1964–1995, *Journal of Sound and Vibration* 190, 495–524, 1996.

[3] J. S. Jensen, Phononic Band Gaps and Vibrations in One- and Two-dimensional Mass-spring Structures, *Journal of Sound and Vibration* 266, 1053–1078, 2003.

[4] S. V. Sorokin, O. A. Ershova, Plane Wave Propagation and Frequency Band Gaps in Periodic Plates and Cylindrical Shells with and without Heavy Fluid Loading, *Journal of Sound and Vibration* 278, 501–526, 2004.

[5] H. Sun, X. Du, P.F. Pai, Theory of Metamaterial Beams for Broadband Vibration Absorption, *Journal of Intelligent Material Systems and Structures* 21, 1085-1101, 2010.

[6] R. Zhu, X.N. Liu, G.K. Hu, C.T. Sun, G.L. Huang, A Chiral Elastic Metamaterial Beam for Broadband Vibration Suppression, *Journal of Sound and Vibration* 333, 2759-2773, 2014.

[7] M. Zingales, Wave Propagation in 1D Elastic Solids in Presence of Long-range Central Interactions, *Journal of Sound and Vibration* 330, 3973-3989, 2011.

[8] V.E. Tarasov, Lattice with Long-range Interaction of Power-law Type for Fractional Non-local Elasticity, *International Journal of Solids and Structures* 51, 2900-2907, 2014.

[9] A. Carcaterra, F. Coppo, F. Mezzani, S. Pensalfini, Long-range Retarded Elastic Metamaterials: Wave-Stopping, Negative, and Hypersonic or Superluminal Group Velocity, *Physical Review Applied* 11, 014041, 2019.

[10] C. Kittel, Introduction to solid state physics, *Wiley*, New York, 1996.

EURODYN 2020
XI International Conference on Structural Dynamics
M. Papadrakakis, M. Fragiadakis, C. Papadimitriou (eds.)
Athens, Greece, 23–26 November 2020

GLOBAL LONG WAVE APPROXIMATIONS FOR ELASTIC WAVE GUIDES

Kirill Cherednichenko[1], Julius Kaplunov[2, 3], Danila Prikazchikov[2,3], and Leyla Sultanova[4]

[1] University of Bath
Bath, BA2 7AY, UK
e-mail: k.cherednichenko@bath.ac.uk

[2] Keele University
Keele, Staffordshire, ST5 5BG, UK
e-mail: j.kaplunov@keele.ac.uk, d.prikazchikov@keele.ac.uk

[3] Institute for Problems in Mechanical Engineering, RAS
St. Petersburg, 199178, Russia

[4] WMG, University of Warwick
Coventry, CV4 7AL, UK
e-mail: leyla.sultanova@warwick.ac.uk

Keywords: Long wave, high frequency, uniformly asymptotic, thin layer.

Abstract. *It is well known that the long-wave approximations for thin elastic structures can be separated into local low-frequency and high-frequency ones. The former are given by more conventional plate and shell theories justified near zero frequency, whereas the latter correspond to 2D equations valid over the vicinities of thickness resonances. In this contribution, we develop a more general long-wave procedure for a broad band surface loading resulting in 2D equations involving transcendental expressions of the spectral frequency parameter. These equations are reduced to the aforementioned local approximations in the vicinities of zero and thickness resonance frequencies. As an example, SH waves in a layer loaded along its faces are considered. Comparison with the exact solution of the problem is presented. Similar global approximations could also be constructed for periodic media, due to the analogy for asymptotic schemes for thin and periodic structures.*

1 INTRODUCTION

Dynamic asymptotic theories for thin elastic structures have been investigated in great detail, see e.g. books [6, 15], and references therein. The most focus traditionally has been on low-frequency dynamics corresponding to both classical and refined models, e.g. see [5, 11]. High-frequency long wave approximations got less attention. Nevertheless, the initial efforts in this area [1, 3] later on have found various implementations for fluid-loaded, pre-stressed, layered and curved structures, as well as for thin coating and interfacial layers modelled by imposing Dirichlet, Neumann and mixed boundary conditions along the faces, e.g. see [7, 8, 12, 13, 14, 17, 18, 19, 20].

At the same time, all the mentioned low- and high-frequency long-wave approximations are local ones in a sense, that their range of validity is restricted to the vicinities of zero and thickness resonance frequencies, respectively. Although their interaction was analysed for initial value problems for thin plates [10, 16], a non-local long-wave model covering a broad frequency range has not been developed yet. The previous consideration in [2] studying forced vibrations under arbitrary high-frequency loading did not take into account the peculiarities of near-cut-off behaviour and consequently has not resulted in a lower dimensional partial differential equations of motion.

Below we attempt to derive a non-local long-wave approximation oriented to a broad band surface loading for the simplest setup of anti-plane problem in elasticity for a thin layer with clamped lower face and a prescribed time-harmonic shear force on the upper face. The normalised vibration frequency is assumed to be of order unity meaning that the focus is not on the vicinity of a single chosen thickness resonance frequency as it has been usually done, but on a family of thickness resonances; it is obvious that the clamped lower face does not support low-frequency vibrations. Straightforward asymptotic scheme leads to a 1D differential equation in which the spectral parameter is transcendentally dependent on the vibration frequency, in contrast to all the above mentioned previous considerations on the subject. Various limits of the derived approximations are tackled, including its near- and outside cut-off behaviours. Comparisons with the exact solution and the known approximate results are presented.

2 STATEMENT OF THE PROBLEM

Consider an anti-plane problem of elasticity for a thin isotropic layer, such that the displacements $u_1 = u_3 = 0$ and $u_2 = u_2(x_1, x_3, t)$, see Fig. 1. The governing equations of motion and constitutive relations are given by

$$\sigma_{12,1} + \sigma_{23,3} = \rho u_{2,tt}, \qquad \sigma_{12} = \mu u_{2,1}, \qquad \sigma_{23} = \mu u_{2,3}, \tag{1}$$

where comma denotes differentiation with respect to appropriate spatial or time variable, and ρ and μ are volume mass density and the shear modulus, respectively.

Boundary conditions are taken in the form

$$\begin{aligned} &\sigma_{23} = P, \qquad x_3 = -h, \\ &u_2 = 0, \qquad x_3 = 0. \end{aligned} \tag{2}$$

The exact solution may be easily written for the case of harmonic loading, as well as the associated dispersion relation, see Appendix for more detail.

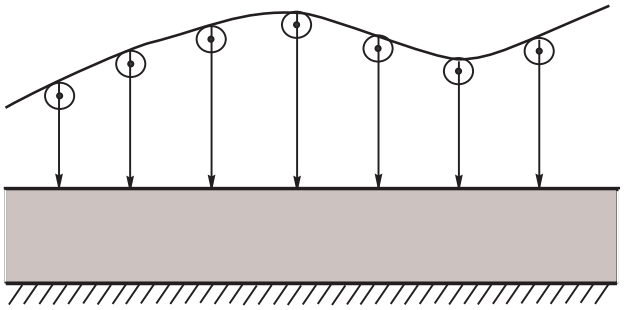

Figure 1: Statement of the problem.

3 ASYMPTOTIC ANALYSIS

The focus is on the long-wave regime, i.e. it is assumed that the thickness of the layer h is small compared to the typical wavelength l, therefore, a small parameter ε is

$$\varepsilon = \frac{h}{l} \ll 1. \tag{3}$$

Then, following the conventional asymptotic integration procedure, the dimensionless variables and parameters are introduced

$$\xi_1 = \frac{x_1}{l}, \qquad \xi_3 = \frac{x_3}{h}, \qquad K = kh, \qquad \Omega = \frac{\omega h}{c_2}, \tag{4}$$

along with the scaling

$$u_2 = hu_2^*, \qquad \sigma_{12} = \varepsilon\mu\sigma_{12}^*, \qquad \sigma_{23} = \mu\sigma_{23}^*, \qquad P = \mu p^*, \qquad \Omega \sim 1, \tag{5}$$

where the quantities with asterisks are assumed to be of the same asymptotic order.

Note that in what follows the time-harmonic motion is assumed, with the factor $e^{-i\omega t}$ omitted for brevity. Using (5), the governing equations (1) are rewritten as

$$\varepsilon^2\sigma_{12,1}^* + \sigma_{23,3}^* + \Omega^2 u_2^* = 0, \qquad \sigma_{12}^* = u_{2,1}^*, \qquad \sigma_{23}^* = u_{2,3}^*, \tag{6}$$

together with boundary conditions (2) represented as

$$\begin{aligned} &\sigma_{23}^* = p^*, \qquad \xi_3 = -1, \\ &u_2^* = 0, \qquad \xi_3 = 0. \end{aligned} \tag{7}$$

We proceed with expanding the scaled displacement and stress components as asymptotic series

$$\begin{pmatrix} u_2^* \\ \sigma_{12}^* \\ \sigma_{23}^* \end{pmatrix} = \begin{pmatrix} u_2^{(0)} \\ \sigma_{12}^{(0)} \\ \sigma_{23}^{(0)} \end{pmatrix} + \varepsilon^2 \begin{pmatrix} u_2^{(1)} \\ \sigma_{12}^{(1)} \\ \sigma_{23}^{(1)} \end{pmatrix} + ... \tag{8}$$

Therefore, at leading order we have

$$\sigma_{23,3}^{(0)} + \Omega^2 u_2^{(0)} = 0, \qquad \sigma_{12}^{(0)} = u_{2,1}^{(0)}, \qquad \sigma_{23}^{(0)} = u_{2,3}^{(0)}, \tag{9}$$

which leads to

$$u_{2,33}^{(0)} + \Omega^2 u_2^{(0)} = 0 \tag{10}$$

subject to the leading order boundary condition

$$u_2^{(0)} = 0, \qquad \xi_3 = 0. \tag{11}$$

Taking into account boundary condition (11) the solution of (10) is given by

$$u_2^{(0)} = C_1(\xi_1)\, \sin(\Omega\xi_3), \tag{12}$$

hence,

$$\sigma_{12}^{(0)} = \frac{dC_1}{d\xi_1} \sin(\Omega\xi_3), \qquad \sigma_{23}^{(0)} = C_1 \Omega \cos(\Omega\xi_3). \tag{13}$$

As may be seen from (12), the corresponding leading order dispersion relation has a term of $\cos\Omega$ degenerating at the cut-off frequencies, see (22) below, hence, consideration of the next order corrector is required.

At next order we have

$$\sigma_{12,1}^{(0)} + \sigma_{23,3}^{(1)} + \Omega^2 u_2^{(1)} = 0, \qquad \sigma_{12}^{(1)} = u_{2,1}^{(1)}, \qquad \sigma_{23}^{(1)} = u_{2,3}^{(1)}. \tag{14}$$

Therefore, from (14) and taking into account $(13)_1$, we obtain

$$u_{2,33}^{(1)} + \Omega^2 u_2^{(1)} = -\frac{d^2 C_1}{d\xi_1^2} \sin(\Omega\xi_3), \tag{15}$$

from which, in view of the boundary condition at $\xi_3 = 0$,

$$u_2^{(1)} = C_3(\xi_1)\, \sin(\Omega\xi_3) + \frac{\xi_3}{2\Omega} \frac{d^2 C_1}{d\xi_1^2} \cos(\Omega\xi_3). \tag{16}$$

Thus, the two-term expansions for the displacement u_2^* and stress σ_{23}^* follow from (8), (12) and (16) as

$$u_2^* = A(\xi_1) \sin(\Omega\xi_3) + \varepsilon^2 \left(\frac{\xi_3}{2\Omega} \frac{d^2 A}{d\xi_1^2} \cos(\Omega\xi_3) \right) + O(\varepsilon^4), \tag{17}$$

and

$$\sigma_{23}^{*} = A(\xi_1)\Omega\cos(\Omega\xi_3) + \varepsilon^2\left(\frac{1}{2\Omega}\frac{d^2A}{d\xi_1^2}\left[\cos(\Omega\xi_3) - \xi_3\Omega\sin(\Omega\xi_3)\right]\right) + O(\varepsilon^4), \quad (18)$$

where $A(\xi_1) = C_1(\xi_1) + \varepsilon^2 C_3(\xi_1)$.
Then, from boundary condition $(2)_1$ the relation between the load and displacement is

$$p^{*} = A\Omega\cos(\Omega) + \frac{\varepsilon^2}{2\Omega}\frac{d^2A}{d\xi_1^2}\left(\cos(\Omega) - \Omega\sin(\Omega)\right) + O(\varepsilon^4). \quad (19)$$

This may be rewritten in dimensional form as

$$h^2\frac{d^2A}{dx_1^2} + f(\Omega)A = g(\Omega)\,\frac{P}{\mu}\,, \quad (20)$$

where

$$f(\Omega) = \frac{2\Omega^2}{1 - \Omega\tan\Omega}, \qquad g(\Omega) = \frac{f(\Omega)}{\Omega}. \quad (21)$$

Thus, the derived approximation is in a sense global over the long-wave region, complementing the previous local long-wave high-frequency theories applicable in the vicinity of a single chosen cut-off frequency [6], however at a cost of a more sophisticated dependence on the spectral parameter $f(\Omega)$.

4 DISCUSSION

Let us compare the obtained approximate results with the exact solution displayed in the Appendix. Let us first examine the dispersion relations. The exact form of the dispersion relation becomes from (A.6) as

$$K^2 = \Omega^2 - \Omega_n^2, \quad (22)$$

which gives the cut-offs at $K = 0$ as $\Omega = \Omega_n$ or $\cos\Omega = 0$.

On setting $A = Ue^{ikx_1} = Ue^{iK\varepsilon^{-1}\xi_1}$ and $P = 0$ in (19), we have

$$K^2 = f(\Omega), \quad (23)$$

with $f(\Omega)$ defined in (21).

Note that (23) naturally gives the same cut-off frequencies as (22), associated with discontinuities of $\tan\Omega$. Indeed, since $\tan\Omega \sim (\Omega_n - \Omega)^{-1}$ in the near cut-off vicinity $\Omega^2 - \Omega_n^2 \ll 1$, the leading order term in the series of (23) around the cut-offs coincides with (22), i.e.

$$\frac{2\Omega^2}{1 - \Omega\tan\Omega} \sim \frac{(\Omega + \Omega_n)\Omega}{1 - \Omega_n(\Omega_n - \Omega)^{-1}} \sim \Omega^2 - \Omega_n^2. \quad (24)$$

At the same time, the form of (23) suggests the approximation will blow up in the vicinity of the roots of the transcendental equation $\tan\Omega = \Omega^{-1}$, which moves the wave number K outside of the long-wave range of validity $(K \ll 1)$. A confirmation of the above may be readily observed from the following illustration, see Fig. 2.

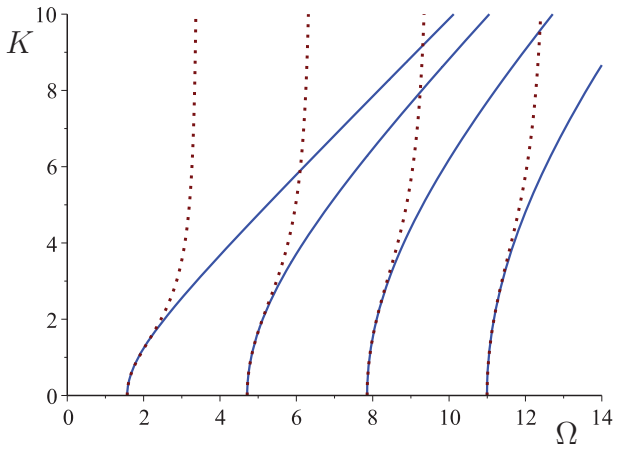

Figure 2: Dispersion curves: comparison of the exact solution (22) (blue solid curves) and approximation (23) (dotted lines).

The first four harmonics of the exact dispersion relation (22) depicted in Fig. 2 by blue solid lines, are compared with their approximation provided by formula (23) shown by dotted lines. On the contrary to known "local" polynomial approximations valid within the vicinity of a given cut-off frequency, see e.g. [6], the approximation derived in the present contribution, involving trigonometric functions of frequency, are "non-local", thus providing approximation in a broad range of frequencies.

Let us now compare the solutions of the forced problem. On setting $A = Ue^{ikx_1}$ and making use of (4) and (5), the exact and approximate displacements follow from (A.3) and (19) as

$$u_2^{ex} = \frac{P_0 h}{\mu} \frac{1}{\sqrt{\Omega^2 - K^2}\cos\sqrt{\Omega^2 - K^2}} \sin\left(\sqrt{\Omega^2 - K^2}\xi_3\right), \tag{25}$$

and

$$u_2^{as} = \frac{P_0 h}{\mu} \frac{1}{\Omega\cos\Omega - \dfrac{K^2}{2\Omega}(\cos\Omega - \Omega\sin\Omega)} \sin\left(\Omega\xi_3\right), \tag{26}$$

respectively, with the factor $e^{i(kx_1-\omega t)}$ omitted for brevity. It is clear that as $K \to 0$, the argument of sine function in (25) coincides with that of (26). Moreover, straightforward Taylor expansion of $\sqrt{\Omega^2 - K^2}\cos\sqrt{\Omega^2 - K^2}$ in (25) around $K = 0$ gives the

appropriate denominator in (26). Moreover, outside the vicinity of cut-offs a simpler approximation is possible as

$$u_2^{as} = \frac{P_0 h}{\mu} \frac{1}{\Omega \cos \Omega} \sin\left(\Omega \xi_3\right), \tag{27}$$

whereas in the vicinity of the cut-offs $|\Omega - \Omega_n| \ll \varepsilon$ we have (similar to [6])

$$u_2^{as} = \frac{P_0 h}{\mu} \frac{2(-1)^{n+1}}{K^2 - (\Omega^2 - \Omega_n^2)} \sin\left(\Omega \xi_3\right). \tag{28}$$

The comparison of the exact solution (25) with the approximations (26), (27) and (28) are presented in the following Figs. 3 and 4.

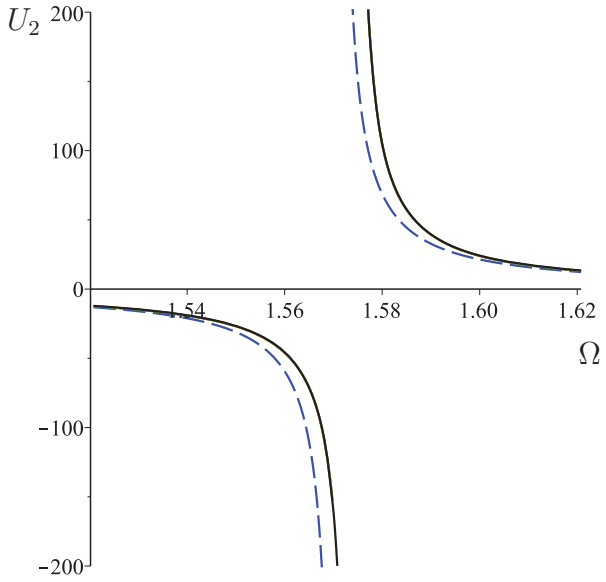

Figure 3: Comparison of the exact solution (25) and its approximations (27), (26) and (28) in the vicinity of the first cut-off frequency.

Fig. 3 demonstrates the variation of the scaled displacement on the upper surface

$$U_2 = \frac{\mu}{P_0 h} u_2\big|_{x_3=-h} \tag{29}$$

on the frequency in the vicinity of the first thickness resonant frequency $\Omega_1 = \pi/2$. The calculations are performed for $K = 0.1$. It may be clearly observed that the elementary leading order approximation (27) shown by dashed line is not capturing the true resonance, confirming its validity outside the cut-off vicinity. At the same time, the approximation (26), and its simplified version aimed at the vicinity of the cut-off frequency

(28), are virtually indistinguishable from the exact solution (25) in the above-mentioned vicinity. Indeed, the three solid lines merge together.

An even more pronounced behaviour may be seen in the following Fig. 4, showing variation of the scaled displacement U_2 on the wave number in case of the exact solution (25) and approximations (27), (26) and (28). The calculations are performed for the frequency value close to the first thckness resonant frequency, i.e. $\Omega - \Omega_1 = 0.1$. As before, the approximations (26) and (28) are extremely close to the exact solution (25), all shown by solid lines, but virtually indistinguishable. At the same time, the rough approximation (27) depicted by dashed line obviously cannot take into account the resonant nature in K, since it is independent of the wave number. This confirms the importance of the differential terms in (20), following from the asymptotic analysis for correctors.

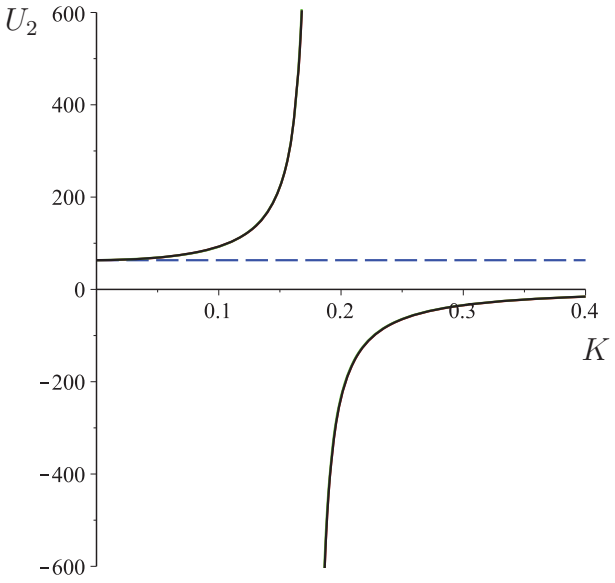

Figure 4: Comparison of the dependence of the exact solution (25) and its approximations (27), (26) and (28) on the wave number.

5 CONCLUSION

The derived long-wave equation (20) with a transcendental dependence of the spectral parameter is valid over a broad frequency band. This equation was implemented to analyse free and forced vibrations. As expected, it involves both the local high-frequency approximations valid near the thickness resonances (28), as well as a simple approximation (27) of the forced amplitude outside the latter. Comparison with the exact solution demonstrates that the obtained equation is robust over the whole long-wave range failing at short-wave domain which is generally not typical for surface loading

of thin structures. The developed methodology has a potential to be extended to more general setups, including plane and 3D problems with boundary conditions along the faces, supporting not only considered long-wave high-frequency vibrations, but also low-frequency ones. Finally, we note that a hierarchy of h-dependent effective hyperbolic problems with sharp-norm estimates for the difference between the appropriate solutions could be obtained using the mathematically rigorous approach in [4].

ACKNOWLEDGEMENT

J. Kaplunov and D. Prikazchikov acknowledge support by the Russian Science Foundation, Grant No. 20-11-20133.

REVIEW

Peer review under the responsibility of the Scientific committee of EURODYN 2020.

REFERENCES

[1] J.D. Achenbach. An asymptotic method to analyze the vibrations of an elastic layer. Journal of Applied Mechanics, 36(1), 65–72, 1969.

[2] L. Aghalovyan. Asymptotic theory of anisotropic plates and shells. World Scientific, Singapore, 2015.

[3] V.L. Berdichevskii. High-frequency long-wave plate vibrations. Doklady Akademii Nauk SSSR 236(6), 1319–1322, 1977.

[4] K. Cherednichenko, I. Velčić. Sharp operator-norm asymptotics for thin elastic plates with rapidly oscillating periodic properties, 29 pp., *arXiv: 1802.02639*

[5] A.L. Goldenveizer, J.D. Kaplunov, E.V. Nolde. On Timoshenko-Reissner type theories of plates and shells. International Journal of Solids and Structures, 30(5), 675–694, 1993.

[6] J.D. Kaplunov, L.Yu. Kossovich, E.V. Nolde. Dynamics of thin walled elastic bodies. San-Diego: Academic Press, 1998.

[7] J.D. Kaplunov, D.G. Markushevich. Plane vibrations and radiation of an elastic layer lying on a liquid half-space. Wave Motion, 17(3), 199–211, 1993.

[8] J.D. Kaplunov, E.V. Nolde. Long-wave vibrations of a nearly incompressible isotropic plate with fixed faces. The Quarterly Journal of Mechanics and Applied Mathematics, 55(3), 345–356, 2002.

[9] J.D. Kaplunov, E.V. Nolde, G.A. Rogerson. An asymptotically consistent model for long-wave high-frequency motion in a pre-stressed elastic plate. Mathematics and Mechanics of Solids, 7(6), 581–606, 2002.

[10] J. Kaplunov, E. Nolde, G.A. Rogerson. An asymptotic analysis of initial-value problems for thin elastic plates. Proceedings of the Royal Society A: Mathematical, Physical and Engineering Sciences, 462(2073), 2541–2561, 2006.

[11] J.D. Kaplunov, E.V. Nolde, B.F. Shorr. A perturbation approach for evaluating natural frequencies of moderately thick elliptic plates. Journal of Sound and Vibration, 281, 905–919, 2005.

[12] J. Kaplunov , D.A. Prikazchikov, L.A. Prikazchikova. Dispersion of elastic waves in a strongly inhomogeneous three-layered plate. International Journal of Solids and Structures, 113, 169–179, 2017.

[13] M.I. Lashhab, G.A. Rogerson, L.A. Prikazchikova. Small amplitude waves in a pre-stressed compressible elastic layer with one fixed and one free face. Zeitschrift für angewandte Mathematik und Physik, 66(5), 2741–2757, 2015.

[14] K.C. Le High frequency vibrations and wave propagation in elastic shells: variational-asymptotic approach. International Journal of Solids and Structures, 34(30), 3923–3939, 1997.

[15] K.C. Le. Vibrations of shells and rods. Springer Science & Business Media. 2012.

[16] E. Nolde. Qualitative analysis of initial-value problems for a thin elastic strip. IMA Journal of Applied Mathematics, 72(3), 348–375, 2007.

[17] E.V. Nolde, G.A. Rogerson. Long wave asymptotic integration of the governing equations for a pre-stressed incompressible elastic layer with fixed faces. Wave Motion, 36(3), 287–304, 2002.

[18] A.V. Pichugin, G.A. Rogerson, G. A. A two-dimensional model for extensional motion of a pre-stressed incompressible elastic layer near cut-off frequencies. IMA Journal of Applied Mathematics, 66(4), 357–385, 2001.

[19] G.A. Rogerson, K.J. Sandiford, L.A. Prikazchikova. Abnormal long wave dispersion phenomena in a slightly compressible elastic plate with non-classical boundary conditions. International Journal of Non-Linear Mechanics, 42(2), 298–309, 2007.

[20] M.Y. Ryazantseva. High-frequency vibrations of symmetrical sandwich plates. Mechanics of Solids, 24(5), 175–181, 1989.

APPENDIX. EXACT SOLUTION FOR TIME-HARMONIC LOADING

Equations (1) imply a conventional wave equation for the non-zero displacement

$$u_{2,11} + u_{2,33} = \frac{1}{c_2^2}\, u_{2,tt}, \tag{A.1}$$

where $c_2 = \sqrt{\mu/\rho}$ is the shear wave speed. We focus on the time-harmonic load of the form and the corresponding anzats for the solutions

$$P = P_0 e^{i(kx_1 - \omega t)}, \qquad u_2 = U f(kx_3) e^{i(kx_1 - \omega t)}, \tag{A.2}$$

where k and ω stand for the wave number and frequency. On substituting (A.2) into (A.1) and satisfying the conditions (2), we obtain

$$u_2 = \frac{P_0}{\mu k \alpha \cos(k\alpha h)}\, \sin(k\alpha x_3)\, e^{i(kx_1 - \omega t)}, \tag{A.3}$$

where

$$\alpha = \sqrt{\frac{\omega^2}{k^2 c_2^2} - 1}. \tag{A.4}$$

The corresponding dispersion relation maybe trivially derived from the solvability of the homogeneous boundary value problem $(P = 0)$, taking the form

$$k\alpha \cos(k\alpha h) = 0, \tag{A.5}$$

implying non-trivial eigensolution for the displacement u_2 for

$$k\alpha h = \Omega_n = \frac{(2n-1)\pi}{2}, \quad n \in \mathbf{N}. \tag{A.6}$$

EURODYN 2020
XI International Conference on Structural Dynamics
M. Papadrakakis, M. Fragiadakis, C. Papadimitriou (eds.)
Athens, Greece, 23–26 November 2020

A NOVEL VIEW ON THE COMPOSITION OF ENERGY FLOW IN MULTI-MODAL WAVEGUIDES

Lasse S. Ledet[1] **and Sergey V. Sorokin**[2]

[1]Grundfos A/S
Poul Due Jensens Vej 7, 8850 Bjerringbro, Denmark
e-mail: lledet@grundfos.com

[2] Department of Materials & Production, Aalborg University
Fibigerstraede 16, 9220 Aalborg East, Denmark
e-mail: svs@mp.aau.dk

Keywords: Energy Flow, Essential state variables, Forces & displacements

Abstract. *In waveguide theory calculating the energy flowing through the guide is often of prime interest and especially within elastodynamics the energy partition between the different transmission paths such as axial, torsion, shear etc. is also of interest. In this paper, we show that the definition of state variables is not unique which make conclusions on energy partition between the various transmission paths somewhat ambiguous. On the other hand, we show that for the various definitions of state variables they all have in common what we denote essential state variables which is the part of the states variables that is responsible for the transmission of energy. The essential variables, therefore, correspond to what can be interpreted as the unique, or essential, part of any definition of the state variables. To illustrate this we use an infinite elastic plate strip simply supported at the edges as an example.*

1 INTRODUCTION

Calculating and interpreting the energy flow in a waveguide provides valuable insight into the behaviour of a waveguide and, at times, reveal interesting phenomena such as tunnelling effects, dominant transmission paths and near field re-distribution of energy between components of the waveguide e.g. between fluid and structure. This topic of energy and transmission path analysis within waveguide theory has become more or less a standard subject. However, there are equally interesting phenomena hidden in the total energy flow that are yet unresolved. For instance, in [1] it was shown how waves in orthotropic shells emit more energy in one direction than the other. Even for symmetric waveguides, where the energy is split into equal shares, there are still open questions such as which sub-components of the force and displacement fields are responsible for energy transmission through the waveguide. A deeper understanding of these issues is the subject of this paper.

For the waveguide governed by a self-adjoint operator, it is not surprising that the total energy flow varies much with frequency, however, it is not so obvious that only specific, or essential, terms of the forces and displacements contribute to the energy flow. Effectively, this negates the need for all remaining, or non-essential, terms and quite surprisingly also negates the effect of Poisson's ratio. This makes calculation of the total energy flow for all such waveguides indisputably simple.

While it is known from [2] that non-essential terms of forces and displacements all contribute to the energy flowing through individual transmission paths, the total energy flowing through the waveguide is completely independent of these, [3]. Showing this constitutes one of the main objectives of this paper. Furthermore, the non-essential terms of the forces are sensitive to the method of derivation, or rather the definition of the state variables. It makes the definition of transmission paths and the energy partition in them somewhat ambiguous. Fortunately, each definition contains the essential part which alone is responsible for the energy flow while the non-essential part can be attributed to the ambiguity. This novel view on the composition of energy flow constitutes the essence of the paper. To clarify this novel view, wave propagation in an infinite straight plate strip is considered.

The paper is structured as follows: In Sec. 2 the governing equations and definition of energy flow for the elastic plate strip are presented. In Sec. 3 two definitions of forces are shown for the example and in Sec. 4 the derivation of the essential state variables from the two definitions is shown. This section we also discuss a generalisation of the formulation of the total energy flow. Finally, Sec. 5 summarizes the results reported in the paper.

2 ENERGY FLOW IN WAVEGUIDES

In classical textbooks wave propagation in elastic solids, dispersion of waves and the energy flow through such waveguides are usually the main scope of the analysis. Moreover, we usually prefer to split the energy flow into its physical constituents (transmission paths) in terms of pairs of state variables e.g. we look at the energy propagating in shear, torsion etc. Thus, we define our state variables as the kinematic states (displacement and rotation) and the associated states of forces/moments, which essentially make up the total energy flow in a waveguide. However, as we shall see shortly the definition of these state variables is non-unique and therefore, particularly in the near-field, the energy distribution will depend on the choice of definition.

To illustrate this we use the infinite simply supported plate strip as an example i.e. we impose boundary conditions $w(x, y, t) = M_y(x, y, t) = 0$, at $y = 0$ and $y = L$. The Equation of Motion

(EoM) within the standard Kirchhoff plate theory is given as

$$D\nabla^4 w(x,y,t) + \rho h \frac{\partial^2}{\partial t^2} w(x,y,t) = q(x,y,t) \tag{1}$$

where $D = \dfrac{Eh^3}{12(1-\nu^2)}$, ρ is density, h the plate thickness, E Young's modulus, ν Poisson's ratio, $w(x,y,t)$ the transverse displacement of the plate strip and $q(x,y,t)$ a distributed driving force.

The solution to this problem is standard and hence all details are omitted. The displacement field is given as

$$w(x,y,t) = W \sin\left(\frac{m\pi}{L} y\right) \exp(kx - i\omega t) \tag{2}$$

where $m \in \mathbb{N}$ is the integer order of the wavenumber in coordinate y, k is the wavenumber in the propagation direction x, ω is the angular frequency, W the amplitude, L the width of the strip and $i = \sqrt{-1}$ the complex operator. (x,y,t) will be omitted in what follows.

Substituting this ansatz into the Equation of Motion with $q = 0$ gives the dispersion equation

$$D\left(k^4 - 2\frac{m^2\pi^2}{L^2}k^2 + \frac{m^4\pi^4}{L^4} - \frac{\rho h}{D}\omega^2\right) = 0 \tag{3}$$

from which we can find the wavenumbers as

$$k_1 = -\sqrt{\left(\frac{m\pi}{L}\right)^2 + \sqrt{\frac{\rho h \omega^2}{D}}} \qquad k_2 = \sqrt{\left(\frac{m\pi}{L}\right)^2 - \sqrt{\frac{\rho h \omega^2}{D}}} \tag{4}$$

where k_1 are evanescent waves and k_2 propagating waves if $\left(\frac{m\pi}{L}\right)^2 < \sqrt{\frac{\rho h\omega^2}{D}}$. Note that since the waveguide is symmetric we consider the right-going waves.

The solution to the inhomogeneous problem with $q \neq 0$ can be obtained straightforwardly, see e.g. [4]. From the inhomogeneous solution we can then easily deduce the state variables (generalised moment, shear force, rotation and displacement) and formulate components of the total energy flow propagating via the different transmission paths, [5].

Following [5] the time-averaged energy flow is defined as in Eq. (5).

$$N = -\frac{1}{2}\mathrm{Re}\left[\int_\Gamma \mathbf{Q} \cdot \left(\frac{\partial}{\partial t}\mathbf{U}\right)^* \mathrm{d}\Gamma\right] \tag{5}$$

where $\mathbf{Q}$ and $\mathbf{U}$ are the state variables on vector form, $\cdot$ the scalar product, Re is the real part, * the complex conjugated and Γ the cross-section of the waveguide.

For the plate strip with $\exp(-i\omega t)$ the formula expands to

$$N(x) = -\frac{\omega h}{2}\mathrm{Im}\left[\int_0^L Q w^* + M\gamma^* \mathrm{d}y\right] \tag{6}$$

where $\gamma = \frac{\partial}{\partial x} w$.

3 AMBIGUITIES IN STATE VARIABLES OF WAVEGUIDES

As already mentioned the definition of state variables in e.g. dynamics of thin plates and shells, is not unique and depends on the applied derivation methodology. Obviously, it does not alter the results in terms of total energy flow but does, however, alter the near-field energy distribution in the individual transmission paths and therefore slightly distorts conclusions of the near-field energy partition. Let us consider the different formulations of state variables for a plate strip.

State variables from infinitesimal volume equilibrium Probably, the most common way of deriving the state variables is to consider an infinitesimal element subjected to stresses and strains and require equilibrium thereof. Doing so, we arrive at the EoM from Eq. (1) and the state variables (relevant for the energy flow in the propagation direction x) given as in Eq. (7), [6].

$$\begin{aligned} \gamma_x &= \frac{\partial w}{\partial x} & \gamma_y &= \frac{\partial w}{\partial y} & M_{xy} &= -D(1-\nu)\frac{\partial^2 w}{\partial x \partial y} \\ M_x &= -D\left(\frac{\partial^2 w}{\partial x^2} + \nu \frac{\partial^2 w}{\partial y^2}\right) & Q_x &= -D\left(\frac{\partial^3 w}{\partial x^3} + \frac{\partial^3 w}{\partial y^2 \partial x}\right) \end{aligned} \tag{7}$$

Except for a few changes in sign convention we arrive at the same result coming from the variational principle, [6].

State variables from Equation of Motion On the other hand, we may also derive the state variables directly from the EoM. To do this we consider the homogeneous EoM in Eq. (1) formulated for $w^{(j)}$ and multiply it by the solution $w^{(n)}$. Then, through *'by parts integration'* following [6], we arrive at

$$\gamma = \frac{\partial w}{\partial x} \qquad M = D\left(\frac{\partial^2 w}{\partial x^2} + \frac{\partial^2 w}{\partial y^2}\right) \qquad Q = D\left(\frac{\partial^3 w}{\partial x^3} + \frac{\partial^3 w}{\partial x \partial y^2}\right) \tag{8}$$

Even from this derivation, we would see that there are several ambiguities in the definition of state variables as they can be derived differently depending on the sequence of *'by-parts integration'*.

The first and, likely, most notable difference between the two formulations of the state variables is the lack of M_{xy} and Poisson's ratio in Eq. (8). Thus, it is indeed far from obvious that no matter which pairs of state variables are substituted into Eq. (5) the total energy flow remains the same. However, the reason why these state variables can be so different and yet still satisfy the same equations was pointed out in [3]. It is because they all have essential state variables in common, while all non-essential terms cancel completely in the reciprocity relation.

4 ESSENTIAL STATE VARIABLES

The essential state variables are not always easily derived and to accomplish this task the reciprocity relation should be used. So before deriving the essential state variables we need to derive the relation between total energy flow and reciprocity since the purpose is to show that the essential state variables constitute the energy-carrying terms.

The reciprocity relation is essentially a product of the state variables from one solution, (n), of the EoM with the state variables from another solution, (j). The inhomogeneous reciprocity

relation associated with the state variables from Eq. (8) is thereby given as

$$\int_\Gamma \left[Q^{(n)}w^{(j)} - Q^{(j)}w^{(n)} + M^{(j)}\gamma^{(n)} - M^{(n)}\gamma^{(j)}\right] \mathrm{d}\Gamma = \int_V qw^{(n)}\mathrm{d}V \tag{9}$$

Although, we proceed with Γ in the following it does in this case reduce to $\int_\Gamma [\quad] \mathrm{d}\Gamma = \int_0^L [\quad]_{x=a}^{x=b} h\mathrm{d}y$.

Then following [5] or [3] we multiply by $-i\omega$, consider only the real parts, take the time average and after some straightforward algebra we arrive at

$$-\frac{\omega}{2}\mathrm{Im}\int_\Gamma \left[Q^{(n)}w^{(j)^*} - Q^{(j)}w^{(n)^*} + M^{(j)}\gamma^{(n)^*} - M^{(n)}\gamma^{(j)^*}\right] \mathrm{d}\Gamma = -\frac{\omega}{2}\mathrm{Im}\left[\int_V qw^{(n)^*}\mathrm{d}V\right] \tag{10}$$

where we immediately notice that the right-hand-side equals the total injected energy, [5], and therefore the left-hand-side must equal the total energy flow through the waveguide and is therefore equivalent to Eq. (5).

Moreover, it was shown in [3] that if n and j are single modes the reciprocity relation in Eq. (9) obeys bi-orthogonality and the left-hand-side is therefore non-zero only when $n = -j$ (where $-j$ means the opposite going wave of j i.e. $k^{-j} = -k^j$). For the inhomogeneous case where each solution, (n) and (j), is an eigenfunction expansion, bi-orthogonality of Eq. (9) converts the reciprocity relation to a quantity for which superposition applies (cross-terms cancel) and thereby proving that the total energy flow in Eq. (10) is a linear quantity. Then, the energy flow in multi-modal waveguides may be calculated straightforwardly as

$$N = -\frac{1}{2}\mathrm{Re}\left[\sum_{n\in\mathbb{N}}\int_\Gamma \mathbf{Q}^{(n)} \cdot \left(\frac{\partial}{\partial t}\mathbf{U}^{(n)}\right)^* \mathrm{d}\Gamma\right] \tag{11}$$

i.e. all cross-products of the state variables' expansions cancel completely. Here (n) counts only propagating waves. See details in [3].

Besides, it was also shown in [3] that Eq. (9) has both spatially invariant real and imaginary parts. It is essential for deriving the modal amplitudes related to the inhomogeneous problem. This immediately leads to a generalised expression for energy flow, while the conventional definition from [5] – Eq. (5), retains only a spatially invariant real part. For details see [3].

4.1 Reciprocity – State variables from equilibrium

As it has already been shown that the reciprocity relation is closely related to the total energy flow we may continue and manipulate the reciprocity relation to simplify the energy expression. Thus, let us consider instead the homogeneous reciprocity relation for the state variables from the equilibrium derivation in Eq. (7). In this case reciprocity is formulated as in Eq. (12), see [6], and for simplicity we consider n and j to be single modes.

$$\int_\Gamma \left[-M_x^{(n)}\gamma_x^{(j)} + M_x^{(j)}\gamma_x^{(n)} - M_{xy}^{(n)}\gamma_y^{(j)} + M_{xy}^{(j)}\gamma_y^{(n)} + Q_x^{(n)}w^{(j)} - Q_x^{(j)}w^{(n)}\right] \mathrm{d}\Gamma = 0 \tag{12}$$

Then, by substituting the state variables into the reciprocity relation using the notation: $\frac{\partial^3 w^{(n)}}{\partial x^3} \equiv w_{xxx}^{(n)}$ and omitting D we get

$$\begin{aligned}\int_\Gamma \big[\left(w_{xx}^{(n)} + \nu w_{yy}^{(n)}\right) w_x^{(j)} - \left(w_{xx}^{(j)} + \nu w_{yy}^{(j)}\right) w_x^{(n)} + (1-\nu)w_{xy}^{(n)}w_y^{(j)} - (1-\nu)w_{xy}^{(j)}w_y^{(n)} \\ - \left(w_{xxx}^{(n)} + w_{xyy}^{(n)}\right) w^{(j)} + \left(w_{xxx}^{(j)} + w_{xyy}^{(j)}\right) w^{(n)}\big] \mathrm{d}\Gamma \quad = 0\end{aligned} \tag{13}$$

and further, substituting the solution from Eq. (2) into the latter we get

$$\int_\Gamma \Big[k^{2(n)}k^{(j)} - k^{2(j)}k^{(n)} - k^{3(n)} + k^{3(j)} + \frac{m^2\pi^2}{L^2}\left[-\nu k^{(j)} + \nu k^{(n)} + (1-\nu)k^{(n)} - (1-\nu)k^{(j)} + k^{(n)} - k^{(j)}\right]\Big] \mathrm{d}\Gamma = 0 \tag{14}$$

from which we see that the bracket must satisfy the equation (for $n \neq -j$, [3]) and we get

$$k^{2(n)}k^{(j)} - k^{2(j)}k^{(n)} - k^{3(n)} + k^{3(j)} + 2\frac{m^2\pi^2}{L^2}\left[k^{(n)} - k^{(j)}\right] = 0 \tag{15}$$

By keeping track of the origin of each cancelled and remaining term we may deduce the essential state variables which are identical to those derived from the EoM in Eq. (8) – For example we see that the first term $k^{2(n)}k^{(j)}$ from Eq. (15) arises from $w_{xx}^{(n)}w_x^{(j)}$ in the first term in Eq. (13) which in turn belongs to $M_x^{(n)}$ and $\gamma_x^{(j)}$, respectively. The second term comes from $M_x^{(j)}$ and $\gamma_x^{(n)}$ and so on. The terms in the last bracket of Eq. (15), however, come from $M_{xy}^{(n)}\gamma_y^{(j)}$.

Then, by comparing the different state variables from, respectively, Eq. (7) and (8) it becomes obvious that it is only the product of the essential part of the forces with the essential part of the kinematic variables that are responsible for the propagation of energy and thus Poisson's ratio is seen to not affect the total energy flow. We may also note that cancellation of the non-essential parts are obvious only in the reciprocity relation while in the conventional definition of total energy flow from Eq. (6) the cancellation is indeed not obvious and here rely, somewhat, on cancellation of numerical values.

Plate in polar coordinates Another interesting example in terms of ambiguous definitions of state variables is a plate in polar coordinates with direction of propagation in r. In this example, the state variables derived from equilibrium and the variational principle are not identical as in the case of the strip. Furthermore, although the EoM is the same for the plate and the plate strip the essential state variables are different as the last terms in Eq. (15) with the factor $2\frac{m^2\pi^2}{L^2}$ in front vanishes for the plate.

4.2 From reciprocity relation to dispersion equation

Besides a close relationship between the total energy flow and the reciprocity relation, there is also a close relation between reciprocity and the dispersion relation from Eq. (3). To show this we take the reduced reciprocity relation from Eq. (15) and multiply by $(k^n + k^j)$ to get

$$k^{4(j)} - k^{4(n)} - 2\frac{m^2\pi^2}{L^2}\left(k^{2(j)} - k^{2(n)}\right) = 0 \tag{16}$$

which in comparison with the dispersion equation is seen to correspond exactly to the dispersion equation formulated for k^n subtracted the dispersion equation for k^j. In other words, we can express the reduced reciprocity relation, which is associated with the total energy flow, directly from the dispersion equation by taking the difference of two different solutions (n and j), divide by $(k^n + k^j)$ and integrate over the contour (cross-section), Γ. Thus, we can deduce, directly from the EoM, the essential state variables.

5 CONCLUSIONS

In this paper, we have shown that there exist several definitions of state variables depending on which methodology is used to derive the governing equations. These definitions slightly distort the view on energy partition between transmission paths. It is shown explicitly here that each of these definitions consist of what we denote a non-essential and an essential part where the non-essential part can be attributed to the various definitions (the ambiguity) while the essential part alone is responsible for the energy transfer through the waveguide. This novel view on the energy flow in waveguides using essential state variables suggests that the energy partition between the transmission paths might be better defined using the essential variables as they are consistent (unique) throughout the various definitions. Finally, the essential state variables also make up the energy balance in Eq. (10) which can be interpreted as a generalised formulation of the energy flow defined in [5] as it has both spatial and temporal invariant real and imaginary parts.

REFERENCES

[1] S. V. Sorokin, E. Manconi, L. S. Ledet & R. Garziera, Wave propagation in helically orthotropic elastic cylindrical shells and lattices, *International Journal of Solids and Structures*, **170**, 11-21, 2019.

[2] Y. Bobrovnitskii, Letters to the editor on the energy flow in evanescent waves, *Journal of Sound and Vibration*, **152**, 175-176, 1992.

[3] L. S. Ledet & S. V. Sorokin, (Bi)-Orthogonality Relation for Eigenfunctions of Self-Adjoint Operators, *Philosophical Transactions. Series A, Mathematical, Physical, and Engineering Sciences*, **377**(2156), 2019.

[4] B. Karp, Generation of symmetric Lamb waves by non-uniform excitations, *Journal of Sound and Vibration*, **312**, 195-209, 2008.

[5] L. Cremer, M. Heckl & B. A. T. Petersson, Structure-Borne Sound, *Springer*, ISBN: 3-540-22696-6, 2005.

[6] C. L. Dym & I. H. Shames, Solid Mechanics – A variational approach, *Springer*, ISBN: 978-1-4614-6035-0, 2013.

EURODYN 2020
XI International Conference on Structural Dynamics
M. Papadrakakis, M. Fragiadakis, C. Papadimitriou (eds.)
Athens, Greece, 23–26 November 2020

ACOUSTIC BLACK HOLE PROFILE OPTIMIZATION

Horia D. Cornean[1], **Sergey Sorokin**[2], **and Benjamin Støttrup**[1]

[1]Department of Mathematical Sciences
Aalborg University
e-mail: {cornean,benjamin}@math.aau.dk

[2] Department of Materials and Production
Aalborg University
e-mail: svs@mp.aau.dk

Keywords: Acoustic Black Holes, Optimization, Calculus of Variations

Abstract. *The effectiveness of a one-dimensional acoustic black hole has often been characterized by its reflection coefficient R and its so-called normalized wave number variation, both of which depend on the height profile of the beam. The underlying assumptions of existence of acoustic black holes require the normalized wave number variation to be small. In this work, we consider an acoustic black hole with fixed parameters of geometry (i.e. length, maximal and minimal height) and pose the variational problem of finding a height profile which minimizes R under the additional constraint of keeping L^{2n} norm of the normalized wave number variation small, since for large n this norm approximates a point-wise estimate. Using the method of Lagrange multipliers, we solve this variational problem and prove that the optimal profile is one of three different types. These profile types can be seen as direct generalizations of the well-researched profile $h(x) = \epsilon x^2$. In the limiting case $n \to \infty$, we obtain closed form expressions for the optimal profiles as well as the corresponding reflection coefficient and the normalized wave number variation. Furthermore, we compare numerically the performance of the optimal profiles and profiles previously considered in the literature. In this comparison, we demonstrate that for comparable reflection coefficients the normalized wave number variation of the optimal profile is far superior to the other profiles.*

1 INTRODUCTION

In [10] M. Mironov showed that if the height of a plate goes sufficiently smoothly to 0 at the edge then bending waves does not reflect from this edge. In particular, Mironov considered a height profile near the edge of the plate given by $h(x) = \epsilon x^m$, for $m \geq 2$ and ϵ small. In reality an edge truncation is always present and in [10] Mironov also demonstrated how a truncation of the edge (see Figure 1) can lead to increased reflection. To combat this problem many different approached have been considered [1, 3, 6–8] and numerous experiments and practical applications have been proposed [3–5, 9, 12].

In this paper we consider the optimal choice of height profile h for acoustic black holes with fixed parameters of geometry. In particular, we will formulate a variational problem for the optimality of a profile and solve this using the method of Lagrange multipliers. In the literature different choices of profiles have been considered. These profiles include $h(x) = \epsilon x^m$ [3,6–8,10,12], $h(x) = \epsilon \sin^m(x)$ [8], and $h(x) = \epsilon x^m + h_0$ [1,11]. Especially noteworthy for our purpose is [11] in which multi-objective optimization algorithm was employed to numerically find an optimal profile of the form $h(x) = \epsilon x^m + h_0$ for an acoustic black hole. Note that our approach to finding optimal profiles is purely analytical and as opposed to [11] we do not restrict our attention to one particular type of profile.

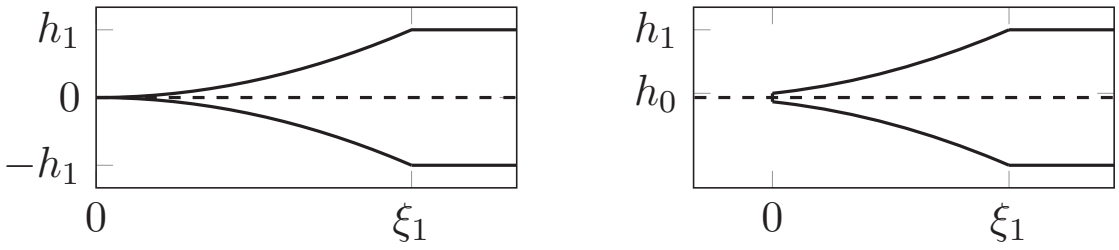

Figure 1: Non-truncated profile (left) and truncated profile (right).

2 SETTING AND PROBLEM STATEMENT

We consider an Euler-Bernoulli beam with *local* wave number given by the equation

$$(k(x))^4 = \frac{12\rho\omega^2}{Eh^2} = \frac{12\omega^2}{c^2h^2(x)}, \tag{1}$$

where $c = (E/\rho)^{1/2}$ is the speed of dilatation wave velocity in beams [7, 8]. We assume a time dependence $e^{-i\Omega t}$ and take energy dissipation into consideration, i.e. $E = E_0(1 - i\eta)$ for some $\eta > 0$. The reflection coefficient of an acoustic black hole, situated between x_0 and x_1 is defined as

$$R = \exp\Big(-2 \int_{x_0}^{x_1} \mathrm{Im}(k(x))\, \mathrm{d}x \Big), \tag{2}$$

under the assumption that the following geometrical acoustics validity condition is satisfied

$$\left| \frac{1}{k^2} \frac{\mathrm{d}k}{\mathrm{d}x} \right| \ll 1, \tag{3}$$

see e.g. [1, 7, 8, 10]. The left hand side of (3) is often referred to as the normalized wavenumber variation (NWV) [1]. The condition (3) has been suggested to be satisfied when the NWV is less that 0.3 [2].

For the rest of this paper we consider dimensionless variables and denote dimensional variables with a tilde. We want to construct an acoustic black hole in the interval $[0, \xi_1]$. We construct a symmetric acoustic black hole (cf. Figure 1) and hence we denote half the maximal (minimal) height by h_1 (h_0). We assume that $h_1 = 1$ and $h_0 \in (0, 1)$, see Figure 1. Additionally, $h(\xi)$ denotes the half beam height at ξ and Ω denotes the dimensionless frequency.

The equivalent problem in dimensional variables is to consider an interval $[\tilde{x}_0, \tilde{x}_1]$ and a function $\tilde{h}$ such that $\tilde{h}(\tilde{x}_0) = \tilde{h}_0$, $\tilde{h}(\tilde{x}_1) = \tilde{h}_1$, and $\tilde{h}(\tilde{x})$ is the half height of the beam at $\tilde{x} \in [\tilde{x}_0, \tilde{x}_1]$. Transformation to non-dimensional variables is done by the formulas

$$h(\xi) = \frac{\tilde{h}(\tilde{x}_0 + \xi\tilde{h}_1)}{h_1}, \quad k(\xi) = \tilde{k}(\tilde{x}_0 + \xi\tilde{h}_1)\tilde{h}_1, \quad h_0 = \frac{\tilde{h}_0}{\tilde{h}_1}, \quad \xi_1 = \frac{\tilde{x}_1 - \tilde{x}_0}{\tilde{h}_1}, \quad \Omega = \frac{\tilde{\omega}\tilde{h}_1}{\tilde{c}},$$

where $\tilde{\omega}$ is the dimensional angular frequency and $\tilde{c}$ it the dimensional longitudinal wave velocity and $\tilde{k}$ is the dimensional local wave number.

Our aim is to find a profile h which minimizes R in (2) while (3) hold. However, for simplicity we will approximate the pointwise bound in (3) with a bound of the L^{2n} norm of the NWV for large n. By noting that R is minimized by maximizing the integral on the right hand side of (2) and using a first order approximation to the non-dimensional form of k in (1) we arrive at the following isoperimetric variational problem: *Given $\eta, \Omega_0 > 0$ find, for every $n \in \mathbb{N}$, a curve h_n which maximizes the functional*

$$h \mapsto \int_0^{\xi_1} \frac{12^{1/4}\Omega_0^{1/2}}{\sqrt{2}h^{1/2}(\xi)} \frac{\eta}{4} \, \mathrm{d}\xi \tag{4}$$

subject to the boundary conditions

$$h_n(0) = h_0, \quad \text{and} \quad h_n(\xi_1) = 1, \tag{5}$$

and the additional constraint that

$$\int_0^{\xi_1} \Big(\frac{\sqrt{2}}{2 \cdot 12^{1/4}\Omega_0^{1/2}} \frac{h_n'(\xi)}{h_n^{1/2}(\xi)} \Big)^{2n} \, \mathrm{d}\xi = L \tag{6}$$

for some $L \ll 1$.

We refer to Ω_0 as the design frequency.

3 RESULTS

By using the method of Lagrange multipliers together with a convenient scaling and the notation $\delta = (-\lambda)^{-1/(2n)}$ we find that a solution to our isoperimetric problem must maximize

$$h \mapsto \int_0^{\xi_1} b\frac{1}{h^{1/2}(\xi)} - \frac{(h'(\xi))^{2n}}{h^n(\xi)} \, \mathrm{d}\xi, \tag{7}$$

where $b = (2\delta)^{2n} 12^{(2n+1)/4} \Omega_0^{n+1/2} \frac{\eta}{8}$. Hence any solution must satisfy the Euler-Lagrange equation

$$h'(\xi) = (2n-1)^{-1/(2n)} (a h^n(\xi) - b h^{n-1/2}(\xi))^{1/(2n)}, \quad \xi \in (0, \xi_1), \tag{8}$$

where a is some constant which must be determined so that the boundary conditions (5) holds. Note that by considering a sequence of oscillating functions with increasing frequency it follows that (7) does not have a minimizer.

3.1 The case $b = 0$

The case $b = 0$ is uninteresting from a practical perspective since it corresponds to minimizing the NWV without any regards for the reflection coefficient. Nevertheless it turns out to be interesting when considering the literature on acoustic black holes. When $b = 0$ the function

$$h(\xi) = \left(\left(1 - \sqrt{h_0}\right)\frac{\xi}{\xi_1} + \sqrt{h_0}\right)^2 \tag{9}$$

is the unique solution to (8) satisfying (5) for all $n \in \mathbb{N}$. This is a generalization of the profile $h(x) = \epsilon x^2$ (which has been used extensively in the literature, see e.g. [1, 4, 7, 8, 10, 11]). Indeed when converting this profile to non-dimensional variables it solves (9) if and only if $\tilde{h}_0\tilde{x}_1^2 = \tilde{h}_1\tilde{x}_0^2$.

3.2 The case $b > 0$

When $b > 0$ solving (8) leads to two possibilities. Specifically, for every $n \in \mathbb{N}$ there exists a number b_n such that:

1. If $b \leq b_n$ there exists a unique $a \geq bh_0^{-1/2}$ such that (8) has a unique $C^\infty([0, \xi_1], [h_0, 1])$ solution satisfying (5).

2. If $b > b_n$ there exists a unique $\xi(b) \in [0, \xi_1]$ and a function $h_b \in C^\infty([\xi(b), \xi_1], [h_0, 1])$ satisfying (8) with the boundary conditions $h_b(\xi(b)) = h_0$ and $h_b(\xi_1) = 1$ such that

$$h(\xi) = \begin{cases} h_0, & \text{if } 0 \leq \xi \leq \xi(b), \\ h_b(\xi), & \text{if } \xi(b) < \xi \leq \xi_1 \end{cases}$$

   is a $C^1([0, \xi_1], [h_0, 1])$ and piecewise $C^\infty([0, \xi_1], [h_0, 1])$ solution to (8).

Note that in both cases the solution must be found numerically as no closed form expression exist. Therefore it is unclear how to choose the parameters δ and n in practical applications.

The parameter n should be large to ensure that the left hand side of (6) approximates a point-wise estimate. By taking n to infinity we obtain the following: If $\Omega_\infty = \left(\frac{1-\sqrt{h_0}}{12^{1/4}\delta\xi_1}\right)^2$, then:

(a) If $\Omega_0 < \Omega_\infty$ then no optimal profile exists.

(b) If $\Omega_0 \geq \Omega_\infty$ then the optimal profile is given by

$$h(\xi) = \begin{cases} h_0, & \text{if } 0 \leq \xi \leq \xi_\infty, \\ \left(12^{1/4}\delta\Omega_0^{1/2}(\xi - \xi_1) + 1\right)^2, & \text{if } \xi_\infty < \xi \leq \xi_1 \end{cases} \tag{10}$$

   where $\xi_\infty = \xi_1 - \frac{1-\sqrt{h_0}}{12^{1/4}\delta\Omega_0^{1/2}}$.

Note that h is a continuous function with a discontinuity in the first derivative at ξ_∞. Furthermore, the simple expression for h makes it possible to determine both R and the NWV explicitly. The NWV for the optimal profile in (10) is given by

$$\left|\frac{1}{k^2}\frac{\mathrm{d}k}{\mathrm{d}\xi}\right| = \begin{cases} 0, & \text{if } 0 \leq \xi \leq \xi_\infty, \\ \sqrt{2}\delta\left(\frac{\Omega_0}{\Omega}\right)^{1/2}, & \text{if } \xi_\infty < \xi \leq \xi_1, \end{cases} \tag{11}$$

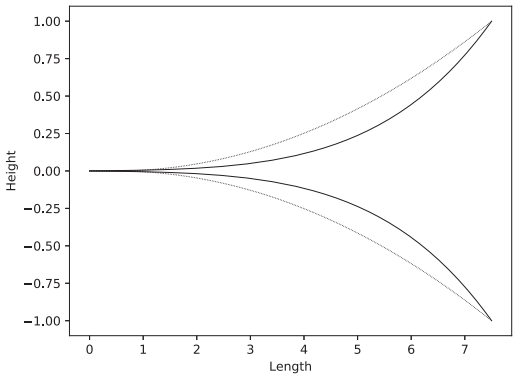

(a) The classical (solid) and optimal (dotted) profile of Section 4.

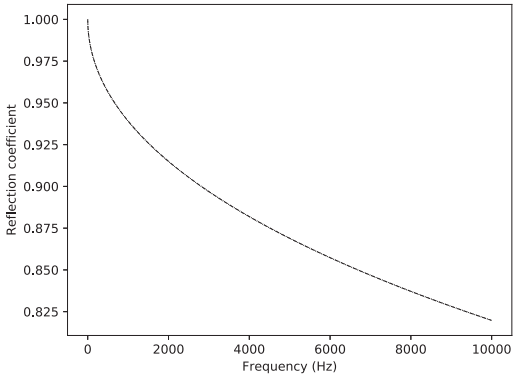

(b) Reflection coefficients for the profiles in Figure 2a. The same line specefications as in Figure 2a have been used.

Figure 2: Classical and optimal profile and their corresponding reflection coefficients.

and the reflection coefficient for the profile in (10) is

$$R = \exp\Big[\frac{\eta\Omega^{1/2}}{2\sqrt{2}}\Big(\frac{\ln h_0}{2\delta\Omega_0^{1/2}} - \frac{12^{1/4}\xi_\infty}{h_0^{1/2}}\Big)\Big]. \tag{12}$$

One strength of the optimal profile in (10) is that its NWV becomes a piecewise constant function of ξ. Hence to make the NWV small it suffices to consider sufficiently large Ω. For example, it is clear that if $\delta = \sqrt{2}/5$ then we have NWV< 0.4 when $\Omega > \Omega_0$. This is not the case for e.g. profiles of the form $h(x) = \epsilon x^m$ with $m > 2$ cf. Section 4.

4 NUMERICAL EXPERIMENTS

In [1] it was demonstrated that increasing m for profiles like $\tilde{h}(\tilde{x}) = \epsilon\tilde{x}^m$ decreases the reflection coefficient but increases the NWV. In this section we demonstrate numerically the difference between an acoustic black hole with profile $\tilde{h}(\tilde{x}) = \epsilon\tilde{x}^m$ for $m = 5$ and the profile in (10). We consider the following dimensional parameters: $\tilde{x}_0 = 5$cm, $\tilde{x}_1 = 20$cm, $\tilde{h}_0 = 0.00195$ cm, $\tilde{h}_1 = 2$cm, $\tilde{c} = 3000$m/s. Furthermore, we assume that the loss factor is $\eta = 0.01$ and let $\delta = \frac{\sqrt{2}}{5}$. We then find Ω_0 such that the optimal profile given by (10) has reflection coefficient similar to that of the non-optimal profile (see Figure 2b). The difference in the shape of the profile (see Figure 2a) leads to the vastly different NWV for the two profiles (see Figure 3). Note that the NWV of the "classical" profile is larger than 0.3 somewhere in the acoustic black hole at most of frequencies considered.

5 CONCLUSIONS

In the present paper the choice of optimal height profile for a one-dimensional acoustic black hole with fixed parameters of geometry has been considered. By regarding the reflection coefficient R as a functional defined on the possible height profiles we have posed the variational problem of minimizing R subject to the constraint that the L^{2n} norm of the NWV equals some small constant. By solving this problem we obtain, that the optimal profile can be of three types: a quadratic polynomial, a smooth function (which has to be determined numerically), or a C^1 function which is comprised of a constant part equal to the minimal height and a smooth part. In the limiting case $n \to \infty$, there is essentially one solution: a continuous piecewise smooth

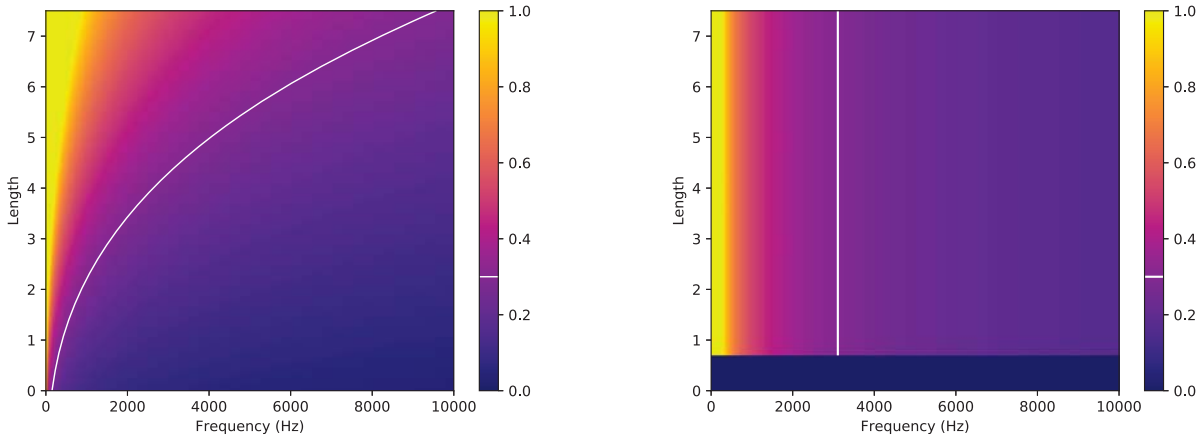

(a) NWV for the classical profile in Figure 2a.

(b) NWV for the optimal profile in Figure 2a.

Figure 3: NWV for the profiles of Figure 2a.

function comprised of a constant part equal to the minimal height and a quadratic part. In fact, we obtain simple expressions for both the quadratic part and the length of the constant part. We have shown that this can be seen as a generalization of the well-known profile $h(x) = \epsilon x^2$. We have numerically compared this optimal profile in the limiting case to a profile of the form $h(x) = \epsilon x^m$ for $m > 2$. This shows that at similar reflection coefficients the NWV differs vastly. For the optimal profile the NWV becomes small for large frequencies but for the other profile NWV is large for most of the frequencies considered.

REFERENCES

[1] P. A. Feurtado, S. C. Conlon, and F. Semperlotti. A normalized wave number variation parameter for acoustic black hole design. *The Journal of Acoustical Society of America*, 136(2):149–152, 2014.

[2] Philip A. Feurtado and Stephen C. Conlon. Investigation of boundary-taper reflection for acoustic black hole design. *J. Noise Cont. Eng.*, 63(5):460–466, 2015.

[3] Vasil B. Georgiev, Jacques Cuenca, Miguel A. Moleron Bermudez, François Gautier, and Laurent Simon. Recent progress in vibration reduction using Acoustic Black Hole effect. In Société Française d'Acoustique SFA, editor, *10ème Congrès Français d'Acoustique*, pages –, Lyon, France, April 2010.

[4] V.B. Georgiev, J. Cuenca, F. Gautier, L. Simon, and V.V. Krylov. Damping of structural vibrations in beams and elliptical plates using the acoustic black hole effect. *Journal of Sound and Vibration*, 330(11):2497 – 2508, 2011.

[5] V. Kralovic and Victor V. Krylov. Some new methods of damping impact-induced vibrations in badminton racquets. In *Proceedings of the Institute of Acoustics, 30 (2)*, pages 155 – 162, 2008.

[6] Victor Krylov. Laminated plates of variable thickness as effective absorbers for flexural vibrations. In *Proc. 17th Int. Congress on Acoustics*, volume 1, pages 270–271, 09 2001.

[7] Victor Krylov. New type of vibration dampers utilising the effect of acoustic 'black holes'. *Acta Acustica united with Acustica*, 90:830–837, 08 2004.

[8] V.V. Krylov and F.J.B.S. Tilman. Acoustic black holes for flexural waves as effective vibration dampers. *Journal of Sound and Vibration*, 274(3):605 – 619, 2004.

[9] V.V. Krylov and R.E.T.B. Winward. Experimental investigation of the acoustic black hole effect for flexural waves in tapered plates. *Journal of Sound and Vibration*, 300(1):43 – 49, 2007.

[10] M. Mironov. Propagation of a flexural wave in a plate whose thickness decreases smoothly to zero in a finite interval. *Sov. Phys. Acoust.*, 34:318–319, 1988.

[11] Micah R. Shepherd, Philip A. Feurtado, and Stephen C. Conlon. Multi-objective optimization of acoustic black hole vibration absorbers. *The Journal of the Acoustical Society of America*, 140(3):EL227–EL230, 2016.

[12] Liuxian Zhao, Stephen C. Conlon, and Fabio Semperlotti. Broadband energy harvesting using acoustic black hole structural tailoring. *Smart Materials and Structures*, 23(6):065021, may 2014.

EURODYN 2020
XI International Conference on Structural Dynamics
M. Papadrakakis, M. Fragiadakis, C. Papadimitriou (eds.)
Athens, Greece, 23–26 November 2020

NOISE REDUCTION USING THE CONCEPT OF ACOUSTIC BLACK HOLES DESIGNED BASED ON MODAL ANALYSIS

Bjørnar Saurdal[1], Daniel Villadsen[1], Sergey V. Sorokin[1], Lasse S. Ledet[2]

[1]Department of Materials & Production, Aalborg University
Fibigerstraede 16, 9220 Aalborg East, Denmark
e-mail: {bsaurd18, dvilla15}@student.aau.dk, svs@mp.aau.dk

[2] Grundfos A/S
Poul Due Jensens Vej 7, 8850 Bjerringbro, Denmark
e-mail: lledet@grundfos.com

Keywords: Noise, Vibrations, Eigenmodes, Acoustic Black Holes, Modal Analysis.

Abstract. *The classical theory of acoustic black holes (ABHs) is quite complex with its application being limited to simple plates and beams. The aim of this paper is to promote ABHs for the community of engineers well familiar with finite element analysis (FEA). Firstly, a validation of FEA as a tool to analyze and design ABHs is done by conventional FE studies replicating experiments, which have already been conducted. Then the concept of modal analysis-based design of ABH is proposed and verified by means of harmonic analysis (both using standard ANSYS software). As the damping layer is an essential part of any real fabricated products utilizing the ABH effect, the influence of its size and thickness are studied by the means of FEM and compared to what has been found in earlier experiments.*

1 INTRODUCTION

ABHs are power-law wedges used to achieve efficient damping of waves. The power-law wedges are described by $h(x) = \varepsilon x^m$, where ε is the wedge parameter and m is the power-law exponent, $m \geq 2$. Under such circumstances, the wave speed gradually decreases and the wave stops in the limit of $h \to 0$ where the height is zero, see Fig. 1, and hence, is not reflected but trapped. However, real fabricated wedges have truncations and it has been shown that the introduction of such truncations only reduce the reflection coefficient to about 50-70%, [1], making them practically useless as ABH dampers. It has been shown, on the other hand, that placing a damping layer in the ABH at the tip of the wedge can reduce the reflection coefficient to only 1-3%, meaning that almost all of the wave energy is absorbed by the damping layer, [1].

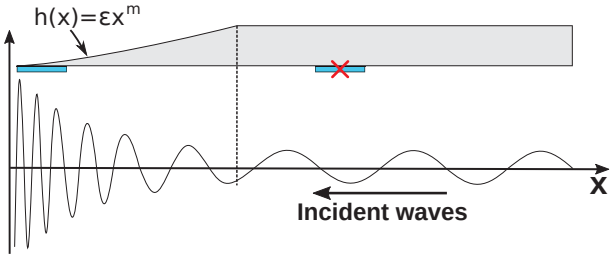

Figure 1: Illustration of the wave as it approaches the tip of the wedge.

The idea of the ABH is illustrated in Fig. 1 i.e. when a wave travelling through the plate reaches the ABHs the wave speed gradually slows down due to the gradual decrease in height, which causes the wavelength to decrease and the amplitude to increase. Thus, by placing a damping layer at the tip where the wavelength is short and the response is high, an efficient damping of the wave energy can be achieved. If, on the other hand, the damping layer is placed outside the ABH, where the wavelength is long and the energy is less concentrated, the damping layer has little to no effect. Thus, as the ABHs rely on sufficiently small wavelengths in the damping layer zone, ABHs are indeed mostly effective at higher frequencies, as also confirmed in literature, [2]. Likewise, it has been shown in [3] that damping layers do not need to cover the entire ABH area but covering just a small area may in fact be more efficient, see e.g. Fig. 6. It was also shown that at higher frequencies a larger damping area was required to retain the strong effect of the ABH which may be somewhat counter intuitive.

In this paper, we begin with simulations conducted using a commercial FEA program on cases, which have already been investigated experimentally by others. This is done to investigate the capability of the FEA program to simulate the ABH effect. Next, we implement ABHs in a physical product in FEA, and interestingly, it is found that design of ABHs can be done using modal analysis alone. The performance of the ABHs can, to some degree, be predicted from the eigenmodes as the damping effect proves to be strongly related to localization of the eigenmodes. This also explains why ABHs are more effective at higher frequencies. Therefore, ABHs of arbitrary shapes have also been tested as they do not need to be circular.

2 ACOUSTIC BLACK HOLES USING FINITE ELEMENT ANALYSIS

ABH theory is typically associated with infinite structures and incident waves while FEA is concerned with finite structures and therefore standing waves. Likewise the experimental work on ABH done in [2] was also based on finite structures with no attempt to make anechoic terminations and thus the effects observed here should be reproducible using e.g. FEA. Thus, to verify the ability of the commercial FE program ANSYS to capture the effect of a plate with ABHs, harmonic analysis has been conducted on cases from [4, 5], which involves both 1D and 2D examples. In [5], several configurations of plates with 2D ABHs are presented, but for brevity, only one of them is presented here. The cases presented here are seen in Fig. 2.

2.1 FEA setup

Meshing has been done following the guidelines from *ANSYS* and the damping layer has density of 1160 $\frac{kg}{m^3}$, stiffness equal to 0.1 of the plate material, [2], Poisson's ratio of 0.48, thickness of 0.2 mm, and a loss factor of 0.4 according to [2, 4, 6]. For the 1D example in Fig. 2, a unit force was applied transversely on the rear edge, while the transverse surface velocity response was measured on a line on top of the uniform section of the plate. Similarly for the 2D case, transverse loading and response measurements were done on two opposite edges of the plate.

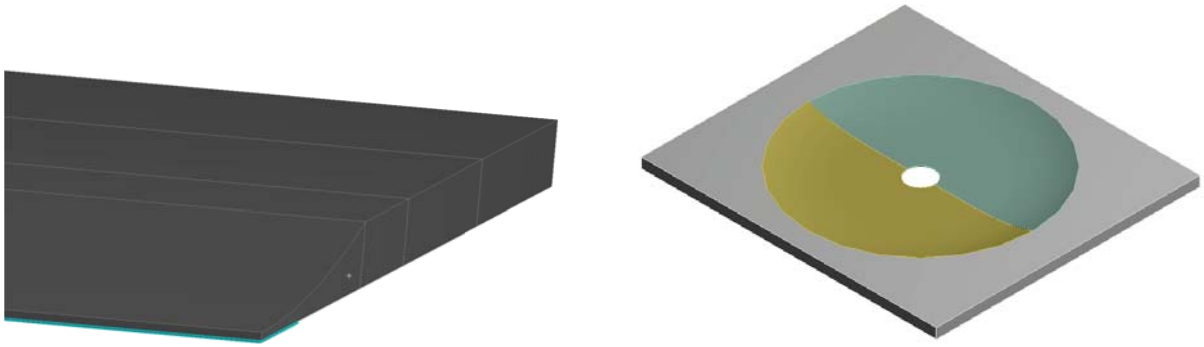

(a) (b)

Figure 2: a) 1D ABH at the end of a plate. b) 2D ABH on a plate. Both in free conditions.

2.2 Harmonic analysis of acoustic black holes

The results from the replicated experiments on plates with 1D and 2D ABHs are plotted in Fig. 3.

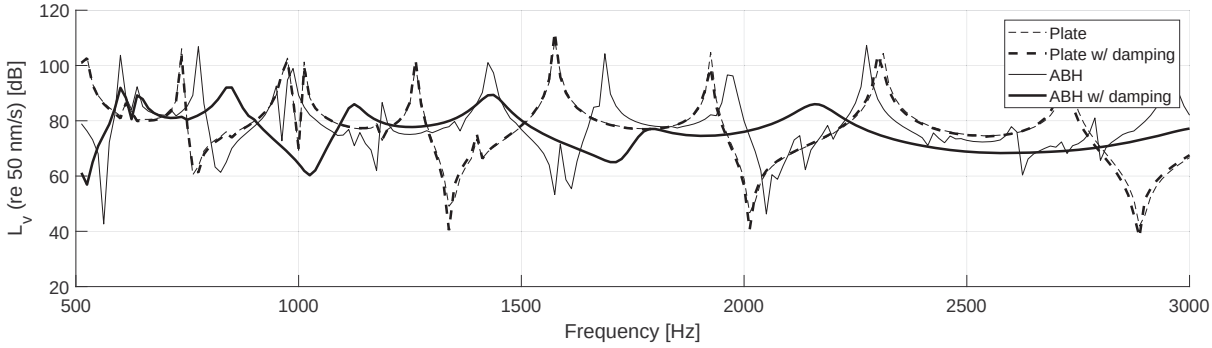

(a)

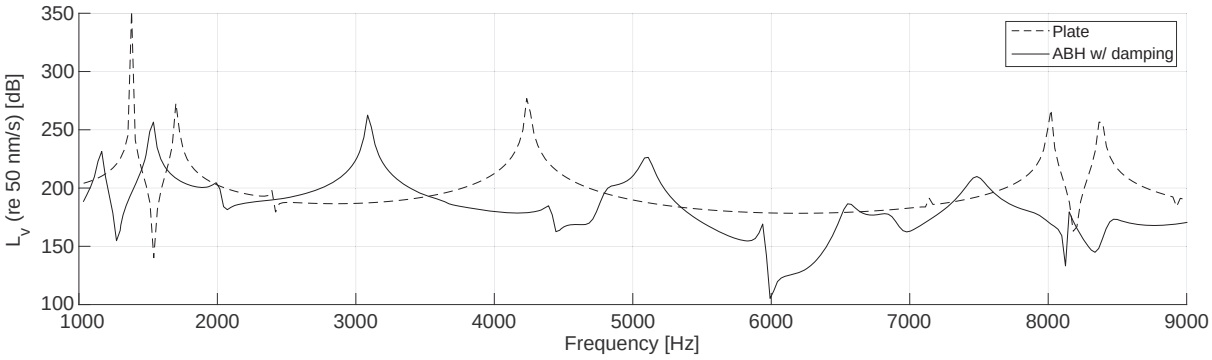

(b)

Figure 3: a) Results from analysis of 1D ABH. b) Results from analysis of 2D ABH. Velocities in dB following ISO 1683, [7].

As can be seen in Fig. 3a, the unmodified plate with a damping layer has almost no effect on the response as mentioned in Sec. 1, while the introduction of ABHs without damping just shifts the eigenfrequencies, but does not significantly damp the response as the reflection coefficient remains within 50-70%, according to Sec. 1. The combination of an ABH with a damping layer, however, damps the response significantly and damping is seen to increase with increasing frequency as also discussed in Sec. 1. This is also observed for the 2D example in Fig. 3b.

In conclusion, we see similar tends of the ABH as those observed in experiments and the ABH theory in Sec. 1 when using standard harmonic analysis. Furthermore, in both graphs, we see that the dB-response is reduced significantly: for the 1D case in Fig. 3a about 20 dB and for the 2D case close to 100 dB.

2.3 Modal analysis of acoustic black holes

From the analyses done in Sec. 2, it has been found that the observed phenomena of the 1D and 2D ABHs, can actually be very well explained through simple modal analyses. In Fig. 4, we see selected eigenmodes from the modal analysis and immediately note that in terms of eigenmodes, the ABHs simply cause the eigenmodes at higher frequencies to localize in the center of the hole. This readily explains why ABHs work only at sufficiently high frequencies but also why adding a damping layer significantly improves the performance. Thus, localizing 'all' higher order modes in one location obviously makes damping by a small damping layer in the ABH very efficient for broad band excitation, in accordance with Sec. 1. Further, we see

that the lower order modes remain global and are thus less affected by the ABH. However, the wave speed still decreases in the ABH and some energy can be damped even at lower frequency as we shall see in Sec. 3.

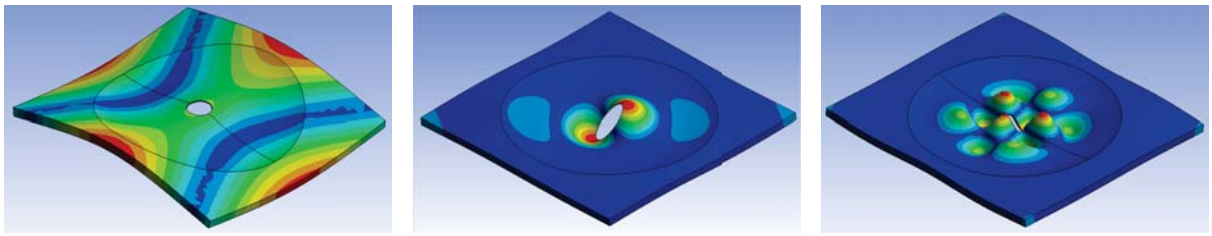

(a) (b) (c)

Figure 4: a) Global eigenmode at 770 Hz. b) Localized eigenmode at 2790 Hz. c) Localized eigenmode at 8165 Hz.

Furthermore, comparing Fig. 4b and 4c we can readily explain the counter intuitive phenomenon that for higher frequencies the localized eigenmodes become spatially less compact and thus require a larger damping layer, as also observed in experiments see e.g. Sec. 1.

Indeed, choosing the right damping layer thickness and size is not trivial. From Fig. 5a, we see that a low coverage can be desirable for these low frequencies, although the peak at 300 Hz is slightly higher for lower coverage. Considering 5b, it is seen that a thicker damping layer lowers the ERPL response, as expected. Therefore, it is believed that a thick and low coverage damping layer would be the optimal design.

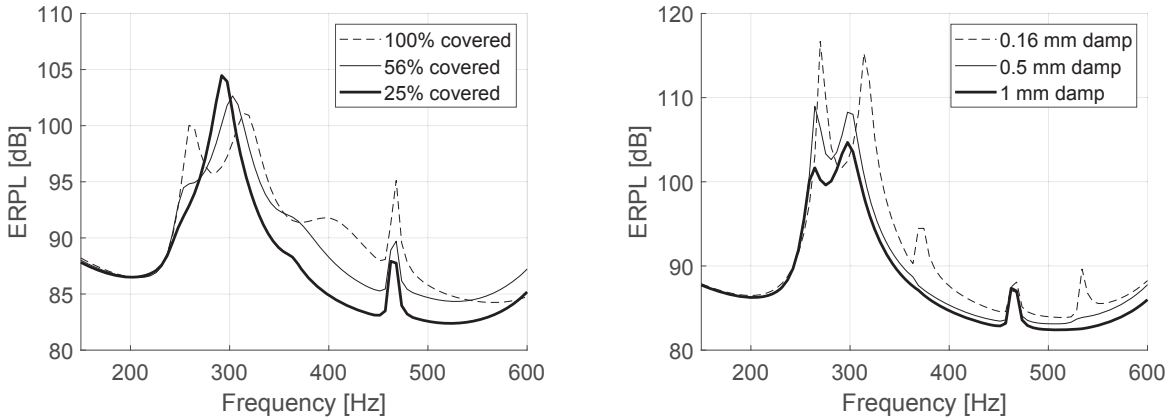

(a) (b)

Figure 5: a) Comparison of damping layer coverage of the ABH. Layer thickness 1 mm. b) Comparison of damping layer thickness. Coverage of ABH: 25%. ERPL (Equivalent Radiated Power Level) is used. Test case: Circular ABH from Fig. 4.

In conclusion, ABHs cause the eigenmodes to localize, thereby producing a large response in a small area, which can then be damped efficiently using only a small patch of damping layer. Thus, for a desired frequency range, the ABH can be designed based on a simple modal analysis and moreover the size of the damping layer be determined by matching the size of the spatially largest mode shape in the spectrum, which will typically be the last mode in the desired range.

At lower frequencies, however, the ABH have only little effect, but as this is usually interesting from a industrial viewpoint this will be the main interest in the following section.

3 ACOUSTIC BLACK HOLES OF ARBITRARY SHAPES

As we have shown in the previous section, the ABH can be evaluated and designed directly from modal analysis, we no longer confine ourselves to think of ABH as wedges or circular holes, nor are we strictly confined to power-laws (though they may likely be the most efficient ones) as long as we ensure localization of the eigenmodes. Therefore, we consider instead arbitrarily shaped ABHs (with power-laws) and study how they perform compared to the regular circular ABHs.

In this paper, two ABHs of 'arbitrary' shape have been considered. The first one is an elliptically shaped ABH, as a simple idea to reduce the size of the ABH without compromising the effect of the ABH, see Fig. 6a. This shape could also be tailored to match specific eigenmodes or shapes of an industrial product. The other type is an acoustic black 'moat', where a power-law profile is swept along a path to create a type of insulator, tailored to a specific lower order eigenmode. The purpose is to prevent waves generated at the source point B, from reaching the receiver point A, see Fig. 6b.

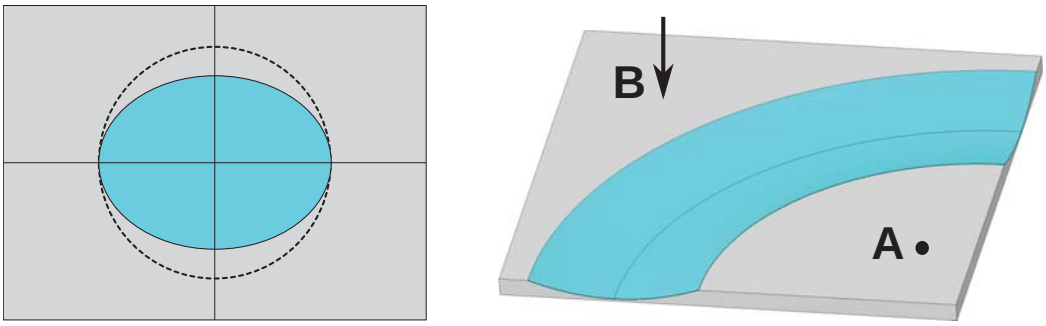

(a) (b)

Figure 6: Conceptual illustrations of arbitrary ABH. a) Elliptical ABH. b) Acoustic black 'moat' with a receiver (A) and source point (B).

To compare the performance of the arbitrarily shaped ABHs, a traditional circular one is used as benchmark. This ABH corresponds to the dotted circle in Fig. 6. For consistency, all ABHs are 100% covered with a 1 mm damping layer. Additionally, these ABHs have been implemented in a physical product and analyzed using the FEA approach elaborated in Sec. 2. The circular, elliptical and moat ABH cover, respectively 56%, 48% and 34% of the total surface area of the product. Further, the material properties have been changed to those of the physical product, which compared to steel, is much more compliant. Furthermore, the frequency range of interest is 150-600 Hz, which is indeed in the low frequency range even for this compliant material.

In Fig. 7, we see that all three cases reduce the ERPL by about 20 dB, even in this lower frequency range. Further, we note, interestingly enough, that the moat performs surprisingly well given a coverage of only 34% compared to the benchmark, which covers 56%. The elliptical ABH (with 48% coverage) also outperforms the circular one. This may be explained by the location and dimensions of the ellipsoid, which has been designed to match a specific mode shape.

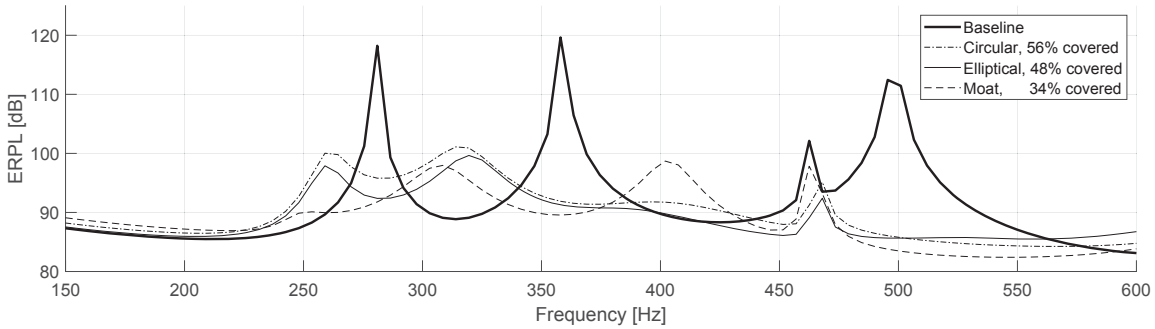

Figure 7: Comparison of ERPL, for the baseline design, a circular ABH, an elliptical ABH, and the acoustic black 'moat'.

Upon closer inspection of the eigenmodes of the moat, it can be seen from Fig. 8 that it does in fact act as an eigenmode-insulator, where the energy is sufficiently damped in the moat before it 'reaches' and excites the mode. The reason for this is explained by the decrease in wave speed, elaborated in Sec. 1. In conclusion, we have shown that we can, even at lower frequencies, benefit from the ABH concept even without having strict localization of the modes, simply by tailoring the ABH shapes to match the modes we are trying to damp, or 'protect', from the source. Thus, we have shown that we can benefit greatly from arbitrarily shaped ABHs designed based on modal analysis.

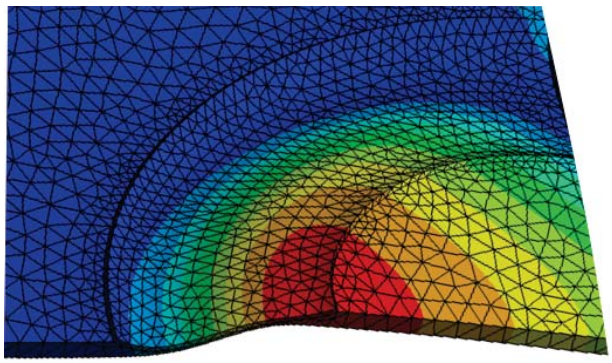

Figure 8: Lower order eigenmode for the acoustic black moat.

4 CONCLUSION

In this paper, we demonstrate that design of acoustic black holes can be done through standard finite element modal analysis of a structure with ABH through the eigenmodes. Further, the phenomena found in experiments conducted by various authors, may conveniently be explained by localization of eigenmodes. If the eigenmodes are not localized, the size of the ABH generally needs to be increased. Respectively, we have shown that the damping layer only needs to cover the area, where the given eigenmodes are localized, as a larger damping layer will have only an insignificant effect. Since localization of eigenmodes has been shown to be the key for designing efficient ABHs, it has been proposed that the shape of the ABHs does not need to be circular, which certainly allows for more freedom in design. This has also led to think of ABHs as moats, e.g. 'insulators' to protect a 'receiver' from a 'source'. This significantly widens the possibilities of using ABHs in industrial applications.

REFERENCES

[1] V.V. Krylov, Acoustic Black Holes: Recent Developments in the Theory and Application, *IEEE Transactions on Ultrasonics, ferroelectrics, and frequency control*, **61(8)** 2014.

[2] V.V. Krylov, R.E.T.B. Winward, Experimental investigation of the acoustic black hole effect for flexural waves in tapered plates, *Journal of Sound and Vibration*, **300(1-2)**, 43–49 2007.

[3] Philip A. Feurtado and Stephen C. Conlon, An Experimental Investigation of Acoustic Black Hole Dynamics at Low, Mid, and High Frequencies, *Journal of Vibration and Acoustics*, **138(6)**, 2016.

[4] V.V. Krylov, F.J.B.S. Tilman, Acoustic 'black holes' for flexural waves as effective vibration dampers, *Journal of Sound and Vibration*, **274(3-5)**, 605–619, 2004.

[5] E.P. Bowyer, D.J. O'Boy, V.V. Krylov, F.Gautier, Experimental investigation of damping flexural vibrations in plates containing tapered indentations of power-law profile, *Applied Acoustics*, **74(4)**, 553—560, 2013.

[6] V. Denis, F. Gautier, A. Pelat, J. Poittevin, Measurement and modelling of the reflection coefficient of an Acoustic Black Hole termination, *Journal of Sound and Vibration*, **349**, 67–79, 2015.

[7] International Organization for Standardization, Preferred Reference Values for Acoustical and Vibratory Levels (ISO Standard No. 1683:2015, 2015).

EURODYN 2020
XI International Conference on Structural Dynamics
M. Papadrakakis, M. Fragiadakis, C. Papadimitriou (eds.)
Athens, Greece, 23–26 November 2020

OPTIMIZATION OF PERFORMANCE OF WAVEGUIDES USING THE WAVE FINITE ELEMENT METHOD

Peter H. Broberg[1], Mikkel T. Steffensen[1], Sergey V. Sorokin[1], and Lasse S. Ledet[2]

[1] Department of Materials & Production, Aalborg University
Fibigerstraede 16, 9220 Aalborg East, Denmark
e-mail: {pbrobe15, msteff15}@student.aau.dk, svs@mp.aau.dk

[2] Grundfos A/S
Poul Due Jensens Vej 7, 8850 Bjerringbro, Denmark
e-mail: lledet@grundfos.com

Keywords: Periodic structures, Stop bands, Optimization, Wave propagation, WFEM.

Abstract. *A classical problem in the design of periodic waveguides is to get stop bands at desired frequencies. In this paper, the problem is addressed by use of optimization within the Wave Finite Element Method (WFEM). Typically, today optimization for stop bands is done using stochastic optimization due to the 'semi-discrete' behavior of the objective function. This method, in-line with previous work, is used as benchmark. This is compared to another method which handles the 'semi-discrete' behavior by a simple manipulation of the objective function into being continuous. This is a novel method that allows for fully gradient based optimization to be used. By comparing the continuous objective function with the benchmark method, it is found, that the continuous objective function outperforms the benchmark, in terms of computational speed and robustness.*

1 INTRODUCTION

This paper is concerned with the general case of wave propagation in waveguides with complex geometry, where analytical solutions might not be available. To accommodate this, we use the wave finite element method (WFEM) which is a well-established numerical method for solving wave propagation problems of complex waveguides, and is described in numerous references, [1–4]. In WFEM a finite waveguide is modelled as being infinite through periodicity by use of continuity and periodicity conditions. Analysis of periodic structures is concerned with Bloch's parameter, K_B, which is a complex number, describing the phase change (Re$\{K_B\}$) and attenuation (Im$\{K_B\}$) of a wave over a unit cell. A description of analysis of periodic structures can be found in classical text such as [5]. To obtain wavenumbers in WFEM, Bloch's parameter is divided with the length of the unit cell. In this paper, however, only Bloch's parameter is of interest. Description of the WFEM is out of scope for this paper, but is described in detail in e.g. [2].

Periodic waveguides have the ability of attenuating waves at certain frequencies, following the phase-closure principle, [6]. This is also known as stop bands. For the industrial partner, Grundfos A/S, the main issue, that can be alleviated by stop bands, is the propagation of waves from pumps into a system, causing noise or damage. It is thus relevant to investigate how stop bands in periodic structures can be moved to or created at desired frequencies. By employing optimization on a parametric model of a waveguide, it is possible to tailor the performance of a waveguide to include stop bands at desired frequencies. In literature, this has been done by use of a stochastic optimization scheme and subsequent gradient based optimization on an analytical model of a waveguide in [7], by use of a pure stochastic optimization on a WFEM model in [8] and a genetic algorithm on an analytical model of a composite in [9]. Common for all papers is that they use zero order optimization algorithms. One of the main pit falls of zero order algorithms is increased computational time for problems involving many design variables. The scope of this paper is to present a novel method for optimization in WFEM using fully gradient based optimization.

The paper is structured as follows; In Sec. 2, optimization of the waveguides is described. This includes a benchmark method based on previous work from literature and a novel method. In Sec. 3, the optimization is carried out on two different examples. Finally, Sec. 4 will contain a discussion on the advantages of using the new method instead of the benchmark method.

2 OPTIMIZATION ON A WFE MODEL

In the optimization it is desired to maximize the attenuation of waves at desired frequencies, hereinafter denoted target frequencies, by including stop bands in a frequency range, corresponding to e.g. the operating frequency range of a pump.

From the WFE program a $2m \times n$ array, $\mathbf{K_B}$, is obtained. This array contains Bloch's parameter for n target frequencies and m different types of waves. To maximize the attenuation at all target frequencies with respect to all wavemodes of interest, corresponds to maximizing the absolute value of the imaginary part of $\mathbf{K_B}$. Mathematically this can be expressed as,

$$\min_{\mathbf{x}} \quad f(\mathbf{x}) = \max[-|\text{Im}\{\mathbf{K_B}\}|] \tag{1}$$

In Eq. (1), $\mathbf{x}$ is the vector of design variables that is put into the WFE model. The problem with the formulation of the objective function from Eq. (1), is that it has a 'semi-discrete' behavior, meaning that gradient information is only available at some points in the frequency spectra, see Fig. 1, where e.g. no gradient information is available at 0-1 kHz and 2-4 kHz. To overcome

this problem literature, [7–9], suggests that a stochastic algorithm must be applied before a gradient based optimization can be carried out. The issue with this method is that the stochastic algorithm is computationally heavy, when there is a large number of design variables, and needs several reruns to ensure robustness.

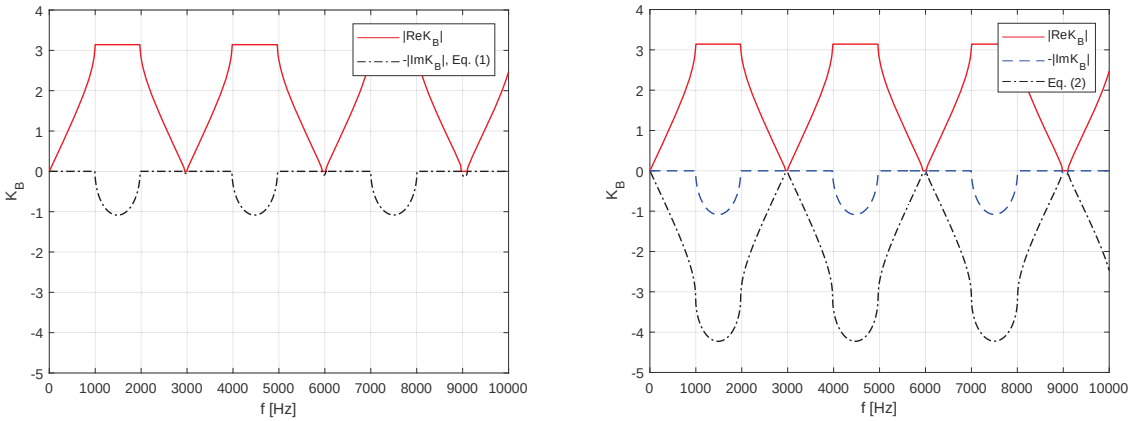

Figure 1: Illustration of the 'semi-discrete' behavior corresponding to Eq. (1) (left) and a function, which is C^1 continuous at almost all frequencies corresponding to Eq. (2) (right). The dispersion diagram is obtained for a two volume functionally graded material model, see Sec. 3, with only propagating longitudinal waves considered.

These issues can be overcome, by a simple manipulation of the objective function as proposed here. This method contains a formulation which is the summation of the real and imaginary part of the complex Bloch parameter. The real and imaginary part of the Bloch parameter is alternating C^1 continuous, and summation of them will yield an expression continuous almost everywhere, see Fig. 1. The continuous problem may thus be formulated as,

$$\min_{\mathbf{x}} \quad f(\mathbf{x}) = \max[-w_1|\mathrm{Im}\{\mathbf{K_B}\}| - w_2|\mathrm{Re}\{\mathbf{K_B}\}|] \tag{2}$$

where w_1 and w_2 are weights for the imaginary and real part, respectively.

Through the rest of this paper, optimization on the objective function in Eq. (1) will be denoted formulation 1, while optimization on the objective function in Eq. (2) will be denoted formulation 2 and will be benchmarked against formulation 1. The controlled random search (CRS) algorithm, [10], is used as the stochastic optimization scheme, in-line with [7], and the sequential quadratic programming algorithm (SQP), [11], instead of the method of moving asymptotes (MMA), for the gradient based optimization. The sensitivities are calculated numerically by use of forward difference approximation. Further, when optimizing with respect to a target frequency range, the frequency range is discretized into a sufficient number of discrete frequencies. To overcome the inherent problem of non-differentiability in the min-max problem of minimizing Eq. (1) and Eq. (2), bound formulation is used, when multiple target frequencies ($n > 1$) and wavemodes ($m > 1$) are considered, [12].

3 EXAMPLES

To compare formulation 2 with the benchmark formulation, two different 1-dimensional examples are considered. The first example is optimization of a waveguide, that consists of elements with fixed geometry and discretely functionally graded material properties. The second example is optimization of a waveguide, consisting of a bi-material composite with fixed

material properties and variable geometry. For both examples optimization is targeted for respectively maximum attenuation at a single target frequency, maximum attenuation at a target frequency range and maximum attenuation at multiple target frequencies. The focus of the optimization is on longitudinal propagating waves. Optimization using formulation 1 is carried out four times to ensure robustness, as the algorithm is stochastic, [7]. Only the solution with the highest attenuation level is presented in the following. For formulation 2, the optimization is made with different weighings. Not all solutions are presented.

3.1 Functionally graded material

In this example, optimization is carried out on a model consisting of n volumes of size 1m×1m×1m, see Fig. 2. Each volume has constant material properties given by the relation,

$$\begin{aligned} E_i &= E_A + x_i(E_S - E_A), \quad i = 1, 2, .., n \\ \rho_i &= \rho_A + x_i(\rho_S - \rho_A), \quad i = 1, 2, .., n \end{aligned} \tag{3}$$

where E_A and ρ_A are the material properties for aluminum, and E_S and ρ_S the material properties for steel, see Tab. 1. x_i are the design variables and have upper and lower bound, $0 \leq x_i \leq 1$. This means that there is an abrupt change in material properties at the volume

Material	Young's modulus E	Poisson's ratio ν	Density ρ
Aluminum	69 GPa	0.30	2700 kg/m^3
Steel	210 GPa	0.30	7800 kg/m^3

Table 1: Material properties used for the functionally graded materials.

boundaries which is needed for the travelling waves to be reflected and stop bands to be created. An industrial application for this example could be an element consisting of sintered metals with changing porosities which would result in this form of functionally graded materials.

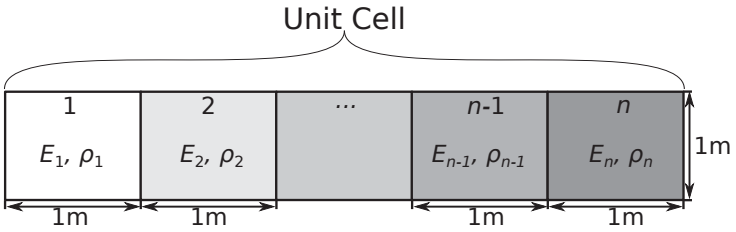

Figure 2: Illustration of the model consisting of n volumes of functionally graded material. Each volume has the dimensions 1m×1m×1m.

For a two volume model, it is the stiffness ratio between the two volumes that determines the stop bands. The stop bands evolve from the critical frequencies or 'seeds' of stop bands, which is described in [13]. The critical frequencies are dependent on the parameter $\tau = \frac{c_1 L_2}{c_2 L1}$, where c_i and L_i is the speed of sound and length of each volume. As the length of each element is fixed and the speed of sound remains constant, it is not possible to change the critical frequencies, see Fig. 1. Optimization is therefore carried out on a model consisting of 8 volumes, as this increases the mobility of the critical frequencies and thus stop bands.

The optimization is carried out for several target frequencies, see Tab. 2, and the starting guess for formulation 2 is a homogeneous material distribution, i.e. $x_i = 0.50$. The optimization for a desired stop band at frequency 2150 Hz, shows that formulation 1 finds a minimum with an

Formulation	x_{min}	f_{min}	Attenuation	Time [s]	nFunEval	w_1	w_2
		Target frequency: 2150 Hz					
1	[0.01, 0.01, 0.92, 0.92, 0.01, 0.01, 0.89, 0.92]	-0.23	0.23	5176	1804	-	-
2	[0.92, 0.01, 0.92, 0.92, 0.01, 0.92, 0.92, 0.01]	-0.15	0.15	1308	389	100	1
		Target frequencies: 275-400 Hz					
1	No solution found	-	-	-	-	-	-
2	[0.00, 1.00, 0.00, 0.90, 0.70, 1.00, 0.00, 0.00]	-1.12E+03	0.13	627	151	1	10
		Target frequencies: 500 Hz, 1000 Hz, 1500 Hz, 2000 Hz, 2500 Hz					
1	No solution found	-	-	-	-	-	-
2	[0.92, 0.01, 0.92, 0.01, 0.92, 0.92, 0.92, 0.24]	-5.02	0.00	533	160	100	1

Table 2: Results for optimization of the eight elements model for various target frequencies. Attenuation describes the lowest attenuation of target frequencies.

attenuation level just above formulation 2, but takes approximately 4 times as long. The result from the optimization, for a stop band in the frequency range 275-400 Hz for formulation 2, are shown in Fig. 3. From the table, it is seen that formulation 1 fails at finding a minimum, while formulation 2 finds a minimum. This is because there is a low number of possible solutions that produce a stop band at this frequency range, which makes the probability for the CRS algorithm to 'guess' a solution lower. In Tab. 2 the results are shown for a desired stop band at

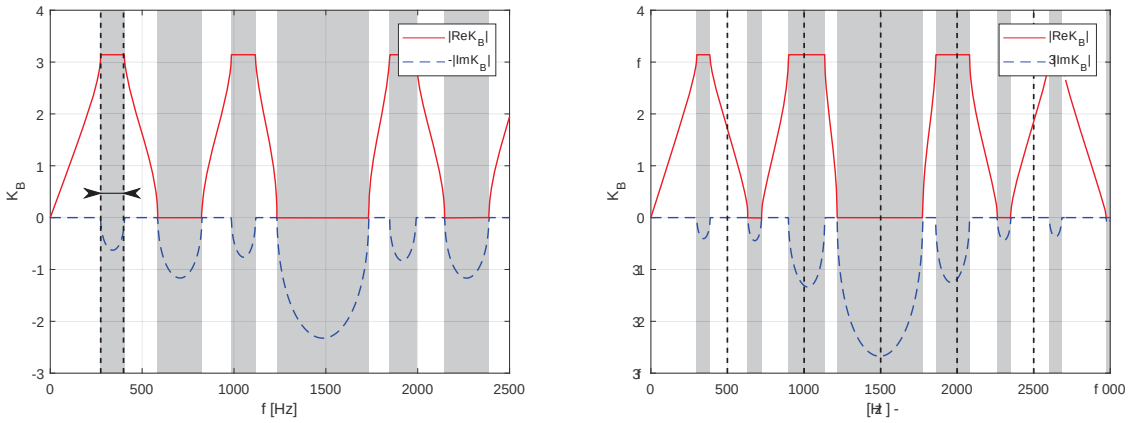

Figure 3: Results with a target frequency range of 275-400 Hz (left) using formulation 2. Results for target frequencies 500, 1000, 1500, 2000 and 2500 Hz using formulation 2 (right). Gray areas indicate stop bands.

500, 1000, 1500, 2000 and 2500 Hz, which corresponds to a fundamental frequency of 500 Hz and its first four harmonics. Formulation 1 fails to find a solution, while formulation 2 finds a solution where some of the target frequencies are, however, not placed in a stop band, see Fig. 3. This result highlights an important property of formulation 2; that it is capable of finding a solution where only some target frequencies are in stop bands, because it might be impossible to place all target frequencies in stop bands for the given mobility. Formulation 2, thus, gives a 'compromise' solution, while formulation 1 gives an 'all or nothing' solution. This implies that formulation 2 is more robust, as it always finds a solution.

3.2 Bi-material composite

This example consists of optimization of a composite consisting of two different materials. The model used is sketched in Fig. 4. The model consists of n layers of repeating fiber and

matrix material, with the material properties listed in Tab. 3. The length of the model is $L = 1$ m and the cross sectional area is $A = 1\text{m}\times 1\text{m}$. The design variables used in this case are the length of the material layers, x_i, where $i = 1, 2, .., n$, while the total length of the layers are constrained by,

$$\sum_{i}^{n} x_i = 1 \tag{4}$$

This means that only $n - 1$ design variables are independent. The lower bound for the design variables are $x_i \geq 0.01$. The starting guess for formulation 2 is in all cases an evenly distributed thickness of all layers, i.e. $x_i = 1/n$. This example is tested for a two and six layer model. The dispersion diagram for the starting guess for these models, are shown in Fig. 5. As the starting guess in both cases are evenly distributed layer thicknesses, one could expect the dispersion diagrams to be identical. However, this is not the case, as seen in Fig. 5, due to the constraint on the length of the model.

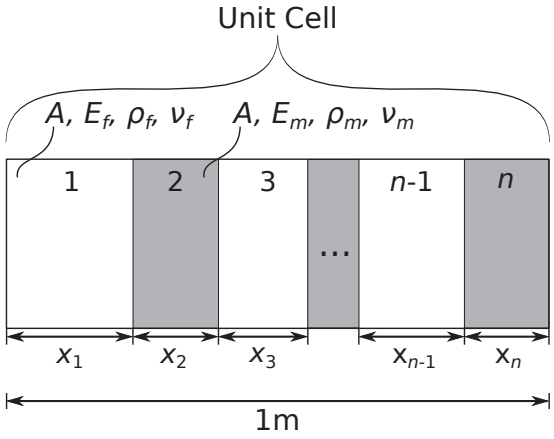

Figure 4: Illustration of the bi-material composite consisting of n repeating layers (left). The length of the composite must sum to 1 m and the cross sectional area is 1 m^2.

Material	Young's modulus E	Poisson's ratio ν	Density ρ
Fiber	72.35 [GPa]	0.22	2500 [kg/m^3]
Matrix	4.09 [GPa]	0.38	1272 [kg/m^3]

Table 3: Material properties used for the composite.

For the two layer model ($n = 2$), the optimization is carried out for a single target frequency at 5000 Hz with different weightings, and a target frequency range at 4000-6000 Hz. The results are listed in Tab. 4. For a target frequency at 5000 Hz the resulting dispersion diagrams for both formulations are shown in Fig. 6. As is observed from the results, the desired frequency is placed in a stop band by use of both formulations. Formulation 2 is as high as 5.2 times faster than formulation 1 depending on the chosen weighing. It is seen that the weight w_1 can be increased to decrease the computational time, but at some values of w_1, local minima may be found, as is the case for $w_1 = 10$ in Tab. 4. Fortunately, the speed is increased when $w_1/w_2 \to \infty$ in which case formulation 2 approaches formulation 1, which is indeed the main objective of the optimization, i.e. to maximize attenuation. Formulation 1 finds a minimum with a slightly higher attenuation and broader stop band than formulation 2. However, the solution

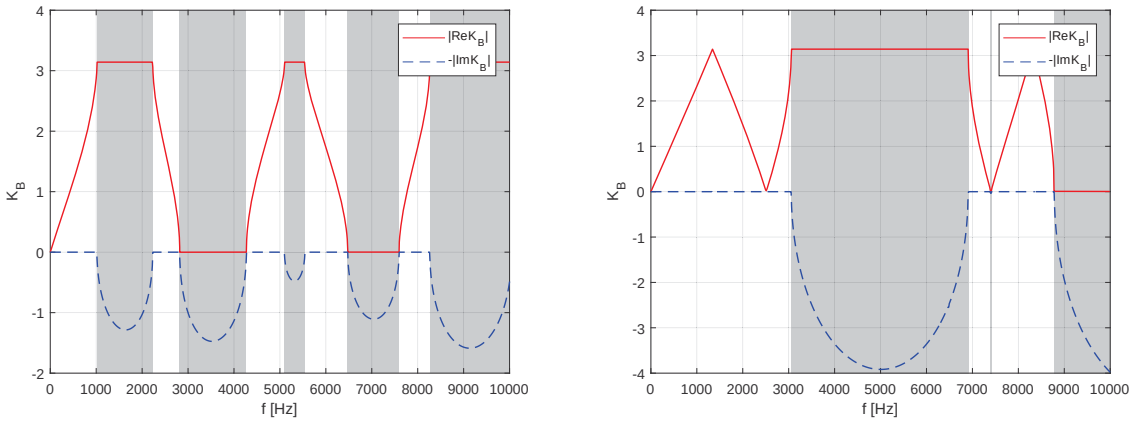

Figure 5: Dispersion diagram for the starting guess (equal volume fiber and matrix) for the two layer model (left) and for the six layer model (right). Gray areas indicate stop bands.

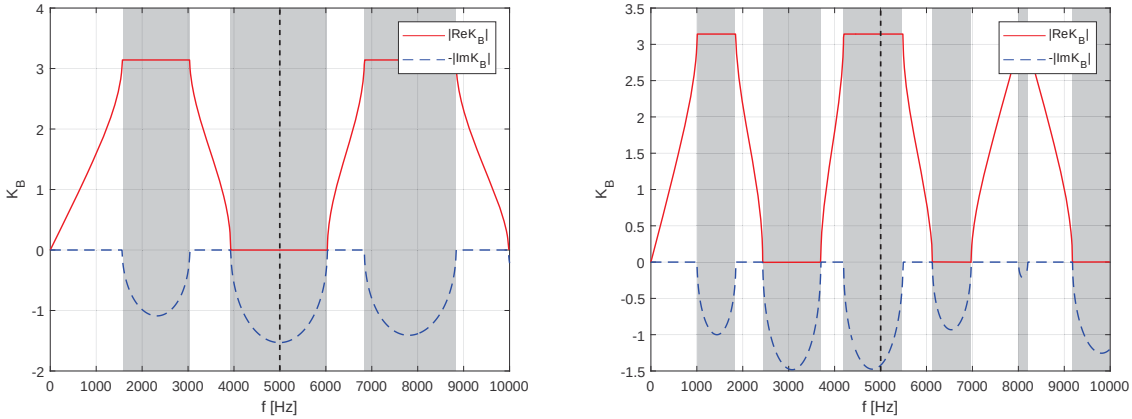

Figure 6: Results with a target frequency at 5000 Hz. (left) shows the dispersion diagram for results obtained using formulation 1 and (right) the results for formulation 2 with weights $w_1 = 100,\ w_2 = 1$. Gray areas indicate stop bands.

Formulation	x_{min}	f_{min}	Attenuation	Time [s]	nFunEval	w_1	w_2
Target frequency: 5000 Hz							
1	0.89	-1.53	1.53	659	222	-	-
2	0.38	-2.29	1.43	396	126	1	1
2	0.12	-0.89	0.97	217	71	10	1
2	0.37	-1.44	1.42	126	41	100	1
Target frequencies: 4000-6000 Hz							
1	0.89	-0.39	0.39	915	276	-	-
2	0.86	-0.24	0.00	218	74	1	1

Table 4: Results for optimization of the two layer composite for various target frequencies. Attenuation describes the lowest attenuation of target frequencies.

found for formulation 2 is closer to the starting guess, see Tab. 4, and thus tries to widen the nearest stop band instead of shifting. This means that formulation 2 finds a minimum, with less change of the original structure, discussed further in Sec. 4. The results for the optimization for a desired stop band at the frequency range 4000-6000 Hz is shown in Fig. 7. Formulation

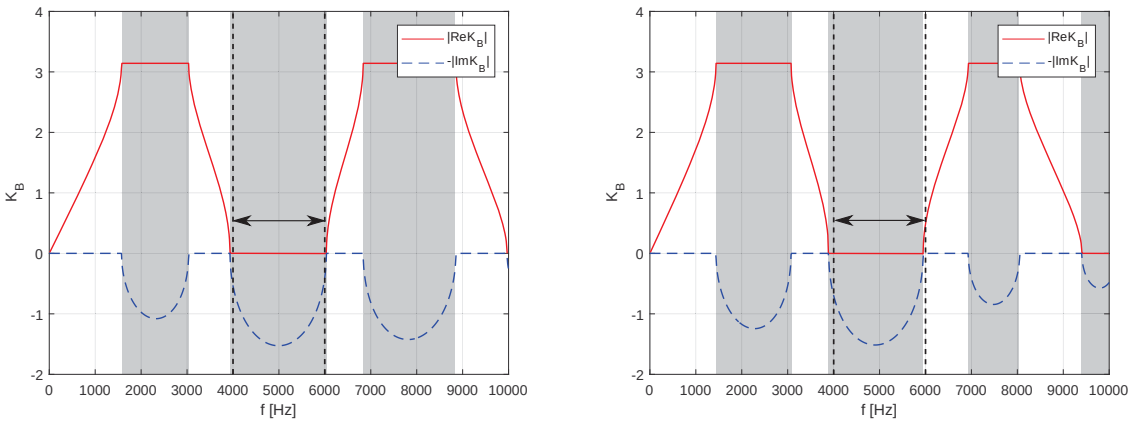

Figure 7: Resulting dispersion diagram for optimizing the two-layer composite for a desired stop band at 4000-6000 Hz, using formulation 1 (left) and formulation 2 (right). The arrow indicates the placement of the desired stop band and the gray areas indicate stop bands.

1 finds the same minimum for a single frequency at 5000 Hz and a frequency range at 4000-6000 Hz. The minimum found by formulation 2 is approximately the same as the one found by formulation 1, but it is slightly offset from the target frequency range, see Fig. 7. This could be fixed by proper weighting. From the results it is observed that by optimizing with respect to a frequency range, formulation 2 is capable of shifting stop band and finding the same minimum as for formulation 1. Formulation 2 thus outperforms formulation 1, in the sense, that it can find the same minimum as formulation 1 but at a much lower computational cost. Furthermore, it shows that formulation 2 is more versatile than formulation 1, because it is able to find different solutions to a single target frequency and a target frequency range.

The next optimization case is for a six layer model. The optimization is carried out for a single target frequency at 2000 Hz and multiple target frequencies with harmonics hereof, i.e. 2000 Hz, 4000 Hz, 6000 Hz, 8000 Hz and 10000 Hz. The results are listed in Tab. 5. The results for a single target frequency at 2000 Hz are shown in Fig. 8. Approximately the same

Formulation	x_{min}	f_{min}	Attenuation	Time [s]	nFunEval	w_1	w_2
Target frequency: 2000 Hz							
1	[0.01, 0.25, 0.01, 0.01, 0.67]	-1.50	1.50	2078	619	-	-
2	[0.01, 0.12, 0.01, 0.01, 0.68]	-1.49	1.47	598	209	100	1
Target frequencies: 2000 Hz, 4000 Hz, 6000 Hz, 8000 Hz and 10000 Hz							
1	[0.27, 0.04, 0.08, 0.22, 0.38]	-6.70	0.89	3566	1007	-	-
2	[0.66, 0.08, 0.01, 0.01, 0.06]	-1.17	0.97	734	240	20	1

Table 5: Results for optimization of the six layer composite for various target frequencies. Attenuation describes the lowest attenuation of target frequencies.

minimum is found for both formulations. Interestingly, it is observed that x_2 in formulation 1

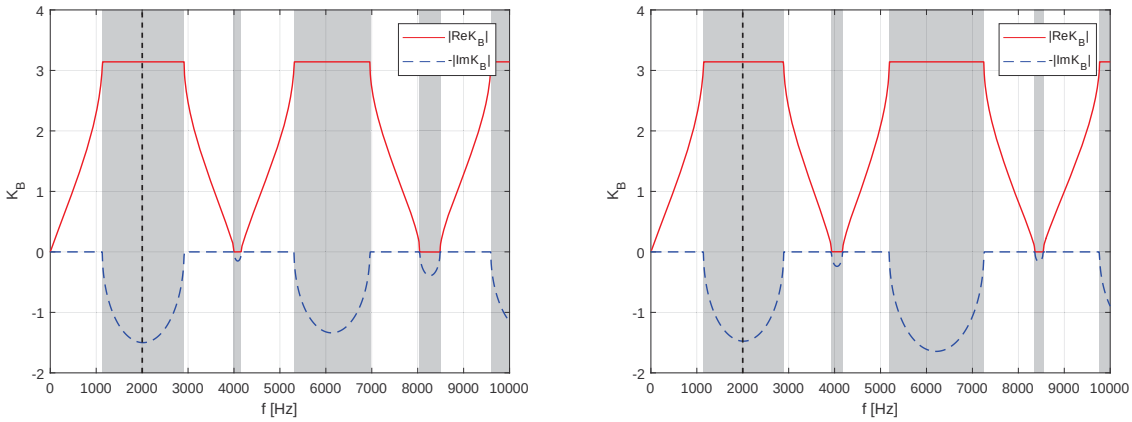

Figure 8: Resulting dispersion diagram for the six layer composite after optimizing for a stop band at 2000 Hz using formulation 1 (left) and formulation 2 (right). Gray areas indicate stop bands.

is approximately twice as large as in formulation 2. This implies, that x_2 in this case is actually irrelevant for the generation of the stop band at 2000 Hz, and hence we see that there exists several almost 'identical' solutions as mentioned in Sec. 3.1. The computational time is still higher for formulation 1, but it is observed that going from 1 to 5 design variables, the computational time for formulation 2 have increased by approximately a factor 5, while it is approximately only a factor 3 for formulation 1. The reason is that there are several solutions that makes a stop band at 2000 Hz. The probability of the CRS algorithm to find a minimum, therefore, significantly increases. For a stop band at target frequencies 2000 Hz, 4000 Hz, 6000 Hz, 8000 Hz and 10000 Hz, the results are shown in Fig. 9. As observed, both formulations finds a minimum that places all the desired frequencies in a stop band. Because less solutions exists for stop bands at these frequencies, the solution time for formulation 1 is much higher than for formulation 2, and in two of the four reruns formulation 1 failed to find a solution. Thus, to retain robustness, the stochastic optimization scheme must have more mobility, i.e. a high number of solutions. Furthermore, formulation 2 finds a minimum with a slightly higher attenuation. This again indicates, that for optimization problems with only few solutions, formulation 2 is indeed superior both on speed and robustness.

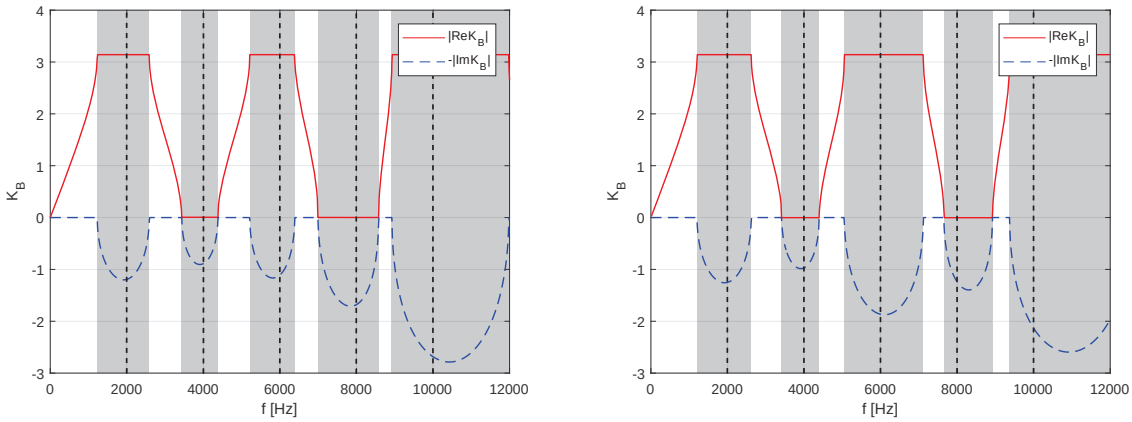

Figure 9: Resulting dispersion diagram for the six layer composite after optimizing for a stop band at 2000 Hz, 4000 Hz, 6000 Hz, 8000 Hz and 10000 Hz using formulation 1 (left) and formulation 2 (right). Gray areas indicate stop bands

4 DISCUSSION

Formulation 1 has the advantage, that if it finds a minimum, all desired frequencies will always be in a stop band. This is due to the stopping criteria for the CRS algorithm, ensuring that all found starting guesses are in a minimum, [7; 10]. The drawback of this, however, is that, if there is only a few number of solutions to the problem, the computational time of the CRS algorithm will increase. Another drawback is that the optimization has to be carried out several times to ensure the robustness of the algorithm, which is increasing the computational time even more. For optimization problems involving a lot of design variables, formulation 1 would thus be most impractical.

The advantages of formulation 2 is that it is much faster than formulation 1. In the examples studied, formulation 2 uses as low as $1/5$ of the time of formulation 1. If analytical expressions can be found for the design sensitivity analysis, this can be reduced even further. Another advantage of formulation 2 is that it gives a compromise if a solution, which has stop bands at all target frequencies, does not exist. This can be improved even further by introducing different weights on the target frequencies, such that the formulation will find the best compromise solution. According to the authors wishes, formulation 2 is thus more robust than formulation 1. The drawback of formulation 2 is, that specific weights are needed for different cases, which increases the computational time as multiple reruns are needed. As multiple reruns also are needed for formulation 1, to ensure the robustness, formulation 2 still outperforms formulation 1 in terms of computational time. One major difference between formulation 1 and 2 is that formulation 2 typically finds the closest local minimum, while formulation 1, due to the CRS algorithm, tends to find a 'more global' minimum with larger attenuation. This, however, can result in large changes in the waveguide optimized compared to the starting guess. In the case of waveguides of the industrial partner, a global minimum is not be desired, as long as there are no constraints on static performance. The reason is, that a global minimum often results in large ratios of stiffness between two elements, which will compromise the structural integrity. If constraints on static performance are added to the optimization problem, a global minimum is desired. However, when introducing constraints on static performance, another analysis is needed for each iteration, which would increase the computational time significantly. As no constraints are introduced in this paper, a minimum that ensures stop bands at the target frequencies with minimal change to the starting guess is desired. This means, that the solutions obtained by formulation 2 are likely better in a structural sense, as changes to the original structure are smaller. The work presented in this paper is work in progress and further improvements to formulation 2 are currently being investigated.

5 CONCLUSION

This paper is concerned with periodic waveguides modelled by the WFEM and two different methods for optimization of the waveguide is tested. One is a conventional benchmark which has a 'semi-discrete' behavior, causing lack of gradient information, and is optimized by a zero-order algorithm (CRS) and subsequent gradient based optimization, in-line with earlier work done by other authors. The other is a novel method which uses manipulation of the objective function such that it becomes continuous with gradient information available. Both methods has been tested on two 1-dimensional examples; one with the design variables associated with material properties in a functionally graded material, and one with the design variables associated with length of layers in a bi-material composite. From the results it was found that the new method solves the problem much faster and is indeed more robust than the benchmark method.

References

[1] D. Duhamel, B.R. Mace, M.J. Brennan, Finite element analysis of the vibrations of waveguides and periodic structures, *Journal of Sound and Vibration*, **294**, 205–220, 2006.

[2] B.R. Mace, D. Duhamel, M.J. Brennan, L. Hinke, Finite element prediction of wave motion in structural waveguides, *Journal of the Acoustical Society of America*, **117**, 2835—2843, 2005.

[3] Alf Søe-Knudsen, Sergey Sorokin, On accuracy of the wave finite element predictions of wavenumbers and power flow: A benchmark problem, *Journal of Sound and Vibration*, **330**, 2694–2700, 2011.

[4] Elisabetta Manconi, Brian R. Mace, Wave characterization of cylindrical and curved panels using a finite element method, *Journal of the Acoustical Society of America*, **125**, 154—163, 2009.

[5] Léon Brillouin, Wave Propagation in Periodic Structures, *Electric Filters and Crystal Lattices*, ISBN: 0486600343, 1946.

[6] D. J. Mead, Waves and Modes in Finite Beams: Application of the Phase-Closure Principle, *Journal of Sound and Vibration*, **171**, 695–702, 1994.

[7] Alf Søe-Knudsen, Design of stop-band filter by use of curved pipe segments and shape optimization, *Structural and Multidisciplinary Optimization*, **44**, 863–874, 2011.

[8] Elisabetta Manconi, Sergey Sorokin, Rinaldo Garziera, Alf Søe-Knudsen, Wave Motion and Stop-Bands in Pipes with Helical Characteristics Using Wave Finite Element Analysis, *Journal of Applied and Computational Mechanics*, **4**, 420–428, 2018.

[9] M.I. Hussein, K. Hamza, G.M. Hulbert, R.A. Scott, K. Saitou, Multiobjective evolutionary optimization of periodic layered materials for desired wave dispersion characteristics, *Structural and Multidisciplinary Optimization*, **31**, 60—75, 2006.

[10] W. L. Price, Global Optimization by Controlled Random Search, *Journal of Optimization Theory and Applications*, **40**, 333–348, 1983.

[11] Jorge Nocedal, Stephen J. Wright, Numerical Optimization, *Second Edition*, ISBN: 9780387303031, 1999.

[12] N. Olhoff, Multicriterion structural optimization via bound formulation and mathematical programming, *Structural Optimization*, **1**, 11–17, 1989.

[13] R.B. Nielsen, S.V. Sorokin, Periodicity effects of axial waves in elastic compound rods, *Journal of Sound and Vibration*, **353**, 135–149, 2015.

EURODYN 2020
XI International Conference on Structural Dynamics
M. Papadrakakis, M. Fragiadakis, C. Papadimitriou (eds.)
Athens, Greece, 23–26 November 2020

FAST FREQUENCY SWEEPS FOR UNBOUNDED MEDIA: AN EFFICIENT PERFECTLY MATCHED LAYER FINITE ELEMENT FORMULATION

Romain Rumpler[1], **Antoine Vermeil de Conchard**[2], **and Huina Mao**[1]

[1]KTH Royal Institute of Technology
The Centre for ECO[2] Vehicle Design
Department of Engineering Mechanics
SE-100 44 Stockholm, Sweden
e-mail: {rumpler,huina}@kth.se

[2] École Centrale de Nantes, Université de Nantes
Department of Mechanics, Materials and Civil Engineering
e-mail: avdc@kth.se

Keywords: Perfectly Matched Layer, Finite Element Method, Exterior Acoustics, Fast Frequency Sweeps, Unbounded Domains

Abstract. *Effective treatment of unbounded domains using artificial truncating boundaries are essential in numerical simulation including unbounded media, such as in the scope of exterior acoustics, sound transmission calculations, ... Among these, Perfectly Matched Layers (PML) have proved to be particularly efficient and flexible, as well as relatively easy to implement using the Finite Element Method (FEM). However, an efficient handling of frequency sweeps is not trivial with such absorbing layers since the formulation inherently contains coupled space- and frequency-dependent terms. Using the FEM, this may imply generating system matrices at each step of the frequency sweep. In this contribution, an approximation is presented in order to allow for efficient frequency sweeps, for instance using Padé-based methods as extensively used by the authors in previous contributions. The performance and robustness of the proposed approximation is presented on an acoustic cases. A generic, robust way to truncate the acoustic domain efficiently is also proposed, tested on a range of test cases and for different frequency regions. It is shown that the approximation, based on a sub-interval approximation of a tuning parameter in the frequency range of interest, provides consistently very good results, close to the costly, original formulations. An a priori estimate of a robust choice for this tuning parameter is also introduced, together with a set of empirical recommendations associated with mesh size, domain size and truncation.*

1 INTRODUCTION

Modelling and simulation of propagating waves in an unbounded domain are necessary in a wide range of disciplines such as acoustics, electromagnetism, solid and fluid mechanics, quantum mechanics, as well as study of earthquakes, water waves propagation, soil-structure or water-structure interaction, *etc.* In a computational environment, such as the Finite Element Method (FEM), the associated models imply a truncation of the unbounded domain with the treatment of artificial boundaries in order to avoid spurious reflections of the outgoing waves within the studied domain. Both for time- and frequency-domain analyses, the accuracy of these non-reflecting conditions under various problem configurations is fundamental. For time-harmonic problems [1], these conditions may be referred to in different ways in the literature, but can generally be classified into three broad families: Absorbing Boundary Conditions (ABCs) [2–7], Infinite elements [8–10], or Absorbing layers such as the Perfectly Matched Layer (PML) [11].

Over the past few decades, several improvements have been brought to these techniques. However, due mostly to complementary strengths and weaknesses, at times problem- and physics-dependent, none of these families has been established as the default option in order to model unbounded media, when considering a range of criteria such as accuracy, computational cost, robustness, and ease of implementation.

Appreciated for their flexibility (suited for a wide range of problems, e.g. including corners or low-incidence outgoing waves, generally less case-dependent performance, and well-suited for standard finite-element implementation [12–14]), PMLs are in focus in the present contribution. Their performance is however largely dependent on their thickness and on the choice of the decay parameter. The latter, due to its dependence on the mesh, on the size of the layer and on its position, may not always be tuned optimally. In short, PMLs require to define and discretize an additional domain whose size and mesh naturally strongly impact the performance and accuracy [15].

In view of the study of propagation of acoustic waves from structures into unbounded acoustic domains, frequency sweeps are an essential part of computational acoustics. However, neither ABCs nor PMLs are naturally adapted to such frequency sweep calculations via the FEM due to their coupled dependence on space and frequency. This dependence requires an update of the assembled system matrices at each frequency step, which has to be performed in a non-trivial way in order to avoid the high computational cost associated with re-assembling these matrices at each step. Furthermore, this coupled dependence on space and frequency makes these formulations difficult to be introduced in the scope of fast frequency sweep techniques, such as the Padé-approximant-based methods widely used by the authors in previous contributions [16,17]. The present contribution details an approximation which allows a frequency-independent generation of the system matrices, but also enables the straightforward use of Padé-based fast frequency sweep techniques for exterior acoustic calculations using the FEM.

First, a selection of PML formulations is presented in view of highlighting the chosen candidate for robust and efficient frequency sweeps, to be combined with Padé-based fast frequency sweep techniques. Then, a simple approximation is introduced, by imposing a piece-wise constant frequency approximation allowing for band-wise frequency-independent system matrices. The impact of this approximation and the choices of band-wide constant frequency parameters is subsequently evaluated on a 2D exterior acoustic case for various frequency ranges. Finally, a tuning procedure of this approximation frequency is proposed.

2 Cartesian Perfectly Matched Layer formulation

In order to take advantage of the geometric versatility of Perfectly Matched Layers as a non-reflecting boundary treatment, several formulations, using a range of different coordinates systems, have been proposed for unbounded wave propagation problems. From the original contribution by Berenger, for the Maxwell system in rectilinear coordinates [11], numerous formulations are available in the literature in order to respond to a range of more specific cases. The approach has been adapted for several types of physical problems, including acoustics [14, 18, 19], among others. The present contribution focuses on an approximation of the unbounded PML formulation initially proposed by Bermúdez $et\ al.$, in [14], for 2D Cartesian problems, enabling its use for fast frequency sweep techniques [20, 21]. In this sense, it relates to the contribution by Lenzi *et. al.* [22], however aiming at an arguably simpler implementation. In order to assess the accuracy of the approximation proposed, it is initially tested against the original, non-approximated, Cartesian coordinate formulation on the same application as presented in [14]. Adapting the approximation to a curvilinear coordinates formulation, though not the focus of this paper, is a natural extension of the present contribution. The problem formulation and its associated approximation are summarized in this section, after the formulation in [14].

2.1 Cartesian formulation

A general problem description is provided in order to introduce the 3D Cartesian formulation of the PML. As presented in Figure 1, the problem consists of a truncated infinite domain Ω_{T}, such that

$$\Omega_{\mathrm{T}} = \left\{(x, y, z) \in \mathbb{R}^3 : |x| \leq L_{\mathrm{T}x}, |y| \leq L_{\mathrm{T}y}, |z| \leq L_{\mathrm{T}z}\right\}.$$

This truncated domain contains an inner acoustic fluid domain Ω_{F} such that

$$\Omega_{\mathrm{F}} = \left\{(x, y, z) \in \mathbb{R}^3 : |x| \leq L_{\mathrm{F}x}, |y| \leq L_{\mathrm{F}y}, |z| \leq L_{\mathrm{F}z}\right\},$$

surrounded by a PML layer Ω_{A} such that $\Omega_{\mathrm{A}} = \Omega_{\mathrm{T}} \setminus \Omega_{\mathrm{F}}$. The interface between the acoustic domain Ω_{F} and the PML layer Ω_{A} is referred to as Γ_{I}, and the outer boundary of the truncated infinite domain as Γ_{D}. An acoustic velocity source is introduced within the acoustic domain, defined by its velocity amplitude g along the normal $\mathbf{n}_{\mathrm{S}}$ to the boundary Γ_{S}.

Following the formulation presented by Bermúdez $et\ al.$ in [14] for a 2D case, the amplitudes of the acoustic pressure fluctuations in the acoustic domain Ω_{F}, denoted p_{F}, and in the PML

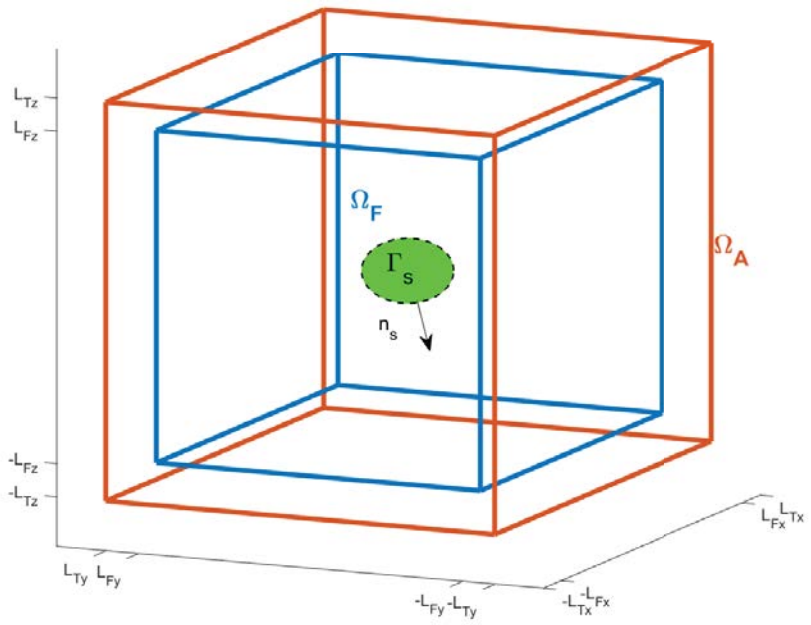

Figure 1: Cartesian PML on 3D scattering problem.

layer Ω_{A}, denoted p_{A}, are solution of the following set of equations:

$$\begin{cases} \Delta p_{\mathrm{F}} + k^2 p_{\mathrm{F}} = 0 \text{ in } \Omega_{\mathrm{F}} \\ \dfrac{\partial p_{\mathrm{F}}}{\partial \mathbf{n}_{\mathrm{S}}} = g \text{ on } \Gamma_{\mathrm{S}} \\ \dfrac{1}{S_x}\dfrac{\partial}{\partial x}\left(\dfrac{1}{S_x}\dfrac{\partial p_{\mathrm{A}}}{\partial x}\right) + \dfrac{1}{S_y}\dfrac{\partial}{\partial y}\left(\dfrac{1}{S_y}\dfrac{\partial p_{\mathrm{A}}}{\partial y}\right) + \dfrac{1}{S_z}\dfrac{\partial}{\partial z}\left(\dfrac{1}{S_z}\dfrac{\partial p_{\mathrm{A}}}{\partial z}\right) + k^2 p_{\mathrm{A}} = 0 \text{ in } \Omega_{\mathrm{A}} \\ p_{\mathrm{F}} = p_{\mathrm{A}} \text{ on } \Gamma_{\mathrm{I}} \\ \dfrac{\partial p_{\mathrm{F}}}{\partial x} + \dfrac{\partial p_{\mathrm{F}}}{\partial y} + \dfrac{\partial p_{\mathrm{F}}}{\partial z} = \dfrac{1}{S_x}\dfrac{\partial p_{\mathrm{A}}}{\partial x} + \dfrac{1}{S_y}\dfrac{\partial p_{\mathrm{A}}}{\partial y} + \dfrac{1}{S_z}\dfrac{\partial p_{\mathrm{A}}}{\partial z} \text{ on } \Gamma_{\mathrm{I}} \\ \dfrac{\partial p_{\mathrm{A}}}{\partial \mathbf{n}_j} = 0 \text{ on } \Gamma_{\mathrm{D}},\ j \in \{x, y, z\} \end{cases} \tag{1}$$

where S_x, S_y, and S_z are decay functions defined in Eqs (3)-(5), and the $\mathbf{n}_j$ are associated with the outer normal unit vectors to the boundary surfaces. For the sake of clarity, the operator $\dfrac{\partial \cdot}{\partial \square}$ is denoted $\partial_{\square} \cdot$ in the following.

Standard arguments in the finite element framework lead to the following discrete problem,

after the weak statement from the strong form of the problem in Eq. (1),

$$\int_{\Omega_\mathrm{T}} \frac{S_y S_z}{S_x} \partial_x p^h \, \partial_x u^h \, x \, y \, z + \int_{\Omega_\mathrm{T}} \frac{S_x S_z}{S_y} \partial_y p^h \, \partial_y u^h \, x \, y \, z + \int_{\Omega_\mathrm{T}} \frac{S_x S_y}{S_z} \partial_z p^h \, \partial_z u^h \, x \, y \, z - \int_{\Omega_\mathrm{T}} S_x S_y S_z k^2 p^h u^h \, x \, y \, z = \int_{\Gamma_\mathrm{S}} g u^h \, \mathrm{S} \tag{2}$$

for all functions u^h, continuous and piecewise linear in Ω_T. The decay functions may be expressed as

$$S_x(x) = \begin{cases} 1, & |x| < L_{\mathrm{F}x} \\ 1 + \dfrac{\sigma}{ik}\gamma(x), & L_{\mathrm{F}x} \leq |x| < L_{\mathrm{T}x} \end{cases} \tag{3}$$

$$S_y(y) = \begin{cases} 1, & |y| < L_{\mathrm{F}y} \\ 1 + \dfrac{\sigma}{ik}\gamma(y), & L_{\mathrm{F}y} \leq |y| < L_{\mathrm{T}y} \end{cases} \tag{4}$$

$$S_z(z) = \begin{cases} 1, & |z| < L_{\mathrm{F}z} \\ 1 + \dfrac{\sigma}{ik}\gamma(z), & L_{\mathrm{F}z} \leq |z| < L_{\mathrm{T}z} \end{cases} \tag{5}$$

where $L_{\mathrm{F}x}$, $L_{\mathrm{F}y}$, $L_{\mathrm{F}z}$ correspond to coordinates referring to inner boundaries of the PML layer and $L_{\mathrm{T}x}$, $L_{\mathrm{T}y}$, $L_{\mathrm{T}z}$ to outer boundaries (see Fig. 1). σ is a decay parameter and $\gamma(x)$, $\gamma(y)$ and $\gamma(z)$ are functions of the space variables, driving the shape of the decay functions. They may take several forms (e.g. constant, linear, quadratic, rational), see *e.g.* [14,23]. In the preliminary implementations leading to this contribution, three common forms have been investigated and are further commented upon in the following. Given a coordinate u associated with one of the axes of the Cartesian coordinate system considered here, *i.e.* $u \in \{x, y, z\}$, these selected functions, for the three chosen PML formulations, may be expressed as

$$\mathsf{PML}_1 : \gamma(u) = \left(\frac{u - L_{\mathrm{F}u}}{L_{\mathrm{T}u} - L_{\mathrm{F}u}} \right), \tag{6}$$

$$\mathsf{PML}_2 : \gamma(u) = \left(\frac{u - L_{\mathrm{F}u}}{L_{\mathrm{T}u} - L_{\mathrm{F}u}} \right)^2, \tag{7}$$

$$\mathsf{PML}_\infty : \gamma(u) = \left(\frac{1}{L_{\mathrm{T}u} - u} \right). \tag{8}$$

Beyond the choice of γ function for the PML formulation, the tuning of the σ parameter is yet another critical aspect to consider, in particular for the PML_1 and PML_2 formulations. For the unbounded formulation PML_∞, Bermúdez *et al.* proposed in [14] a value of the decay parameter, such that $\sigma = 1$, making it a robust, parameter-free formulation. Furthermore, it was shown that this formulation is better suited to absorb outgoing waves on a scattering problem than those associated with the linear and quadratic cases, PML_1 and PML_2 respectively, even when optimal values of σ are available analytically for these cases. Similar conclusions were drawn by Rabinovich *et al.*, in [23], given constant, linear and quadratic decay functions on a very different set of test cases.

Given the ease of tuning for the σ parameter and the robustness of the unbounded formulation in a wide range of cases, this PML_∞ formulation is primarily investigated in the present contribution.

After discretization, the weak form of Eq. (2) leads to a Finite Element (FE) system of the form

$$[\mathbf{K} - k^2\mathbf{M}]\mathbf{p} = \mathbf{f}, \tag{9}$$

where $\mathbf{f}$, the right-hand side (RHS) vector, includes the source terms imposed as Neumann boundary conditions on Γ_S. $\mathbf{K}$ and $\mathbf{M}$ are, following a Galerkin approach, formed by the contributions from elementary matrices $\mathbf{K}^e$ and $\mathbf{M}^e$, respectively, given by

$$\begin{aligned}\mathbf{K}^\text{e}_{ij} = &\int_{\Omega_e} \frac{S_y S_z}{S_x} \partial_x N_i^T \, \partial_x N_j \, \Omega + \int_{\Omega_e} \frac{S_x S_z}{S_y} \partial_y N_i^T \, \partial_y N_j \, \Omega \\ &+ \int_{\Omega_e} \frac{S_x S_y}{S_z} \partial_z N_i^T \, \partial_z N_j \, \Omega,\end{aligned} \tag{10a}$$

$$\mathbf{M}^\text{e}_{ij} = \int_{\Omega_e} (S_y S_z S_x) N_i \, N_j \, \Omega, \tag{10b}$$

$$\mathbf{f}^\text{e}_j = \int_{\Gamma_\text{S}} g N_j \, \text{S}, \tag{10c}$$

where the N_i correspond to the nodal finite element basis of an isoparametric FE formulation and Ω_e to the associated elementary domains.

Obviously, the rational forms involved in the elementary integration associated with the elementary matrices $\mathbf{K}^e$, in Eq. (10a), combining the 3D Cartesian expressions of the decay functions given in Eq. (3)-(5), imply non-separated space-frequency expressions. It implies, in turn, frequency-dependent elementary matrices, critically impacting the efficiency of typical frequency sweeps for acoustic applications. The following section therefore introduces considerations in order to perform frequency-independent integrations of the elementary matrices, leading to formulations suited for the use of fast frequency sweep techniques for exterior acoustics, as previously discussed by the authors [24, 25].

2.2 Approximation for efficient frequency sweep

In order to separate the frequency and space variables, in view of the elementary integrations to be performed in Eq. (10a), several approximations may be sought in the form, for instance, of polynomial expansions with respect to the frequency. The simplest form consists in choosing a constant value such that $f = f^*$, in the terms $\dfrac{1}{S_u}$, $u \in \{x, y, z\}$.

In the Perfectly Matched Layer domain Ω_A, this leads to approximated expressions such that

$$\frac{1}{S_u} \sim \frac{1}{1 + \frac{\sigma}{ik^*}\gamma(u)}, \qquad u = x, y, z, \tag{11}$$

where k^* corresponds to a constant value of the wave number, typically chosen within the range of interest. This may imply piece-wise approximations for a given broad frequency range of interest, which, as further detailed in the result Section 3, may match the need to adapt the FE mesh for frequency sub-intervals in view of the trade-off between accuracy and efficiency.

A number of options have been tested in order to evaluate the potential of such an approximation, i.e. setting $f = f^*$ constant only for some of the S_u terms, since only the denominator

terms in (10a) are critical in order to be able to perform frequency-independent integrations within each element. The simplest, and potentially most severe approximation to be tested, corresponds to setting such constant wavenumbers in all the S_u terms involved in the weak form of the problem, both in Eq. (10a) and Eq. (10b). Interestingly, having provided a satisfying degree of accuracy, and often better accuracy than the other combinations tested, this simple approximation, practical from an implementation point of view, is the focus of the analyses conducted in the following sections.

3 RESULTS AND DISCUSSION

3.1 Definition of the numerical test case

In order to have a reference solution which may be compared to results of the literature, the different formulations are tested on a bi-dimensional test case proposed by Bermúdez $et\ al.$ in [14]. As may be seen in Figure 2, this case corresponds to a scattering problem where the center of the domain is limited by a circle of unitary radius with a totally reflecting boundary. The solution of this problem, with a point source located at (x_0, y_0), is given by

$$p(x,y) = \frac{i}{4}\mathcal{H}_0^{(1)}\left(k\sqrt{(x-x_0)^2+(y-y_0)^2}\right), \tag{12}$$

where $\mathcal{H}_0^{(1)}$ is the Hankel function of the first kind, of order 0.

Note that in Figure 2, the notations used in the original contribution, a and b, correspond to $L_{\mathrm{F}x}$ and $L_{\mathrm{F}y}$ defined in Section 2.1, respectively, and a^* and b^*, to $L_{\mathrm{T}x}$ and $L_{\mathrm{T}y}$, respectively. N stands for the mesh refinement, in Figure 2, where $N = 2$ corresponds to 2 rectangular elements in the thickness of the layer.

Figure 3 introduces the solution of the real pressure field of this scattering problem for two frequencies chosen arbitrarily: $f = 20$ Hz and $f = 1$ kHz.

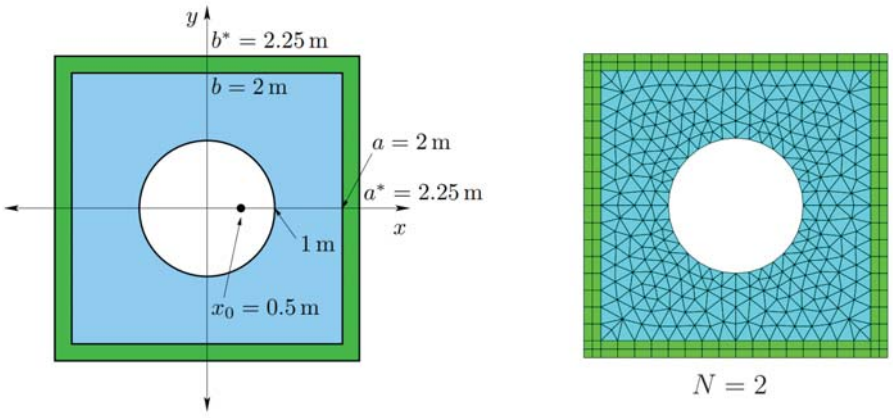

Figure 2: Bermúdez $et\ al.$ Scattering Problem [14].

3.2 Illustration of the approximation

The behaviour of the PML approximation proposed here, with respect to the choice of k^*, is tested on the Bermúdez $et.\ al.$ test case. For this purpose, the pointwise L^2-error with respect to the analytical solution of Eq. (12) is used. For each choice of $f^* = \frac{c_0 k^*}{2\pi}$ in the frequency range of interest, the mean of these L^2-errors over the whole frequency range is calculated.

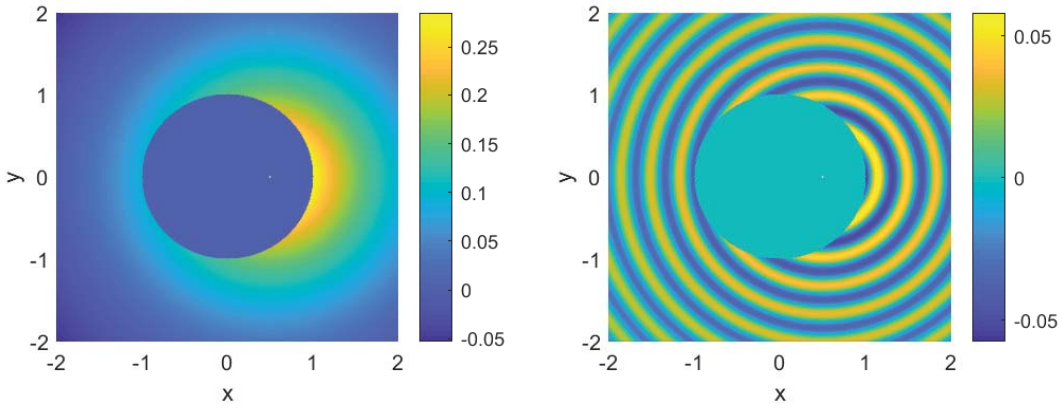

(a) $f = 20$ Hz (b) $f = 1$ kHz

Figure 3: Acoustic pressure field (real part) for the Bermúdez *et al.* scattering problem.

In this way, scanning all frequencies in the range of interest for each chosen value of f^*, an error estimate assessing the quality of the choice is obtained. The outcome of this procedure is presented in Figure 4a in the frequency range $[50 - 400]$ Hz.

In this case the optimal frequency minimizing the error indicator is found to be of $f^* = 130$ Hz. Figure 4b shows the frequency sweep obtained for this choice of $f^* = 130$ Hz, together with the results obtained with the non-approximated PML formulation. Note that the solutions are obviously the same for the value $f = f^*$. In this case, the value of this parameter has a

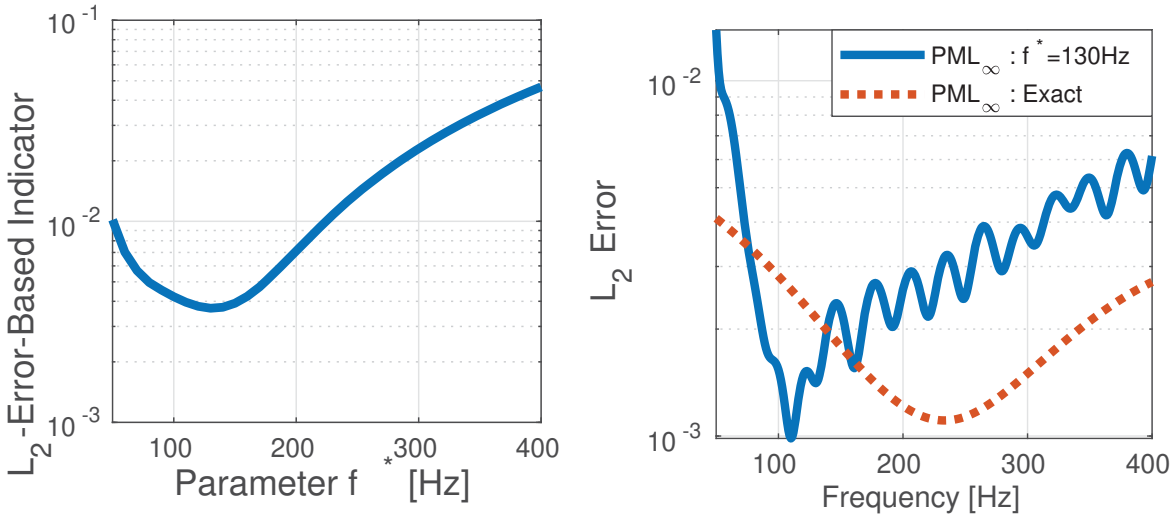

(a) (b)

Figure 4: Impact of the tuning of f^* on the accuracy of the PML approximation: (a) Error with respect to f^*; (b) Comparison with the original PML formulation.

significant impact on the accuracy of the approximation, which leads to the question of choosing an optimal value for a problem without a known analytical solution, a point considered in the following Section.

3.3 A priori indicators for f^*

In the process of attempting to locate, at least qualitatively, the optimal range for f^*, it seems sensible to consider the impact of the f^*-approximation on the decay functions in Eqs. (3)-(5). One suggestion to do so, is to connect f^* to the frequencies which allow to minimize the error between the approximate functions $1/S^*$ or S^*, and the exact ones $1/S$ or S, respectively. This assumption emerges from the fact that, in Eq. (2), the functions $1/S$ are impacting the integrations leading to the PML terms in the $\mathbf{K}$ system matrix, while the functions S are impacting the integrations leading both to PML terms in the $\mathbf{K}$ and the $\mathbf{M}$ system matrices. These reference approximation frequencies may be introduced as

$$f_{\mathrm{S}}^* = \quad argmin_f \left(||S_x - S_x^*||_{L_2} \right), \tag{13}$$

$$f_{1/S}^* = \quad argmin_f \left(\tfrac{1}{S_x} - \tfrac{1}{S_x^*}_{L_2} \right). \tag{14}$$

Provided a systematic and reliable truncation of the PML layers, as proposed and further detailed in Ref. [25], the use of the above a priori approximation indicators is evaluated for different frequency ranges on the selected test cases.

3.4 Approximation of the Bermúdez $et.\ al.$ test case

In order to evaluate the accuracy of the approximation and the impact of the choice of f^*, a number of calculations are performed, for different frequency ranges, and for varying values of f^*. Figure 5 shows the results of these calculations. The calculations are performed in the range $[20, 1000]$ Hz in order to limit the computational burden, given that several sweeps are to be calculated. The size of the domain, the thickness of the layer and the mesh size are defined according to the lowest and the highest frequencies of the range considered, as further detailed in Ref. [25]. In order to limit the computational burden, as realistically done for larger applications, the calculations in the full frequency range of interest are divided into sub-intervals such that the ratio between the upper and lower frequencies remains reasonably small. Three frequency intervals are therefore considered in this range, taking for bounds of these intervals the approximate rule $f_{\mathrm{max}} \leq 10 \cdot f_{\mathrm{min}}$. Note that although two intervals only are necessary in this case, the following intervals are chosen in order to test several configurations for the choice of f^*: $[20, 100]$ Hz, $[50, 400]$ Hz and $[100, 1000]$ Hz.

The Figures 5a, 5c, and 5e plot a measure of the error with respect to the choice of f^*. The same error measure as in Fig. 4a is used here. The impact of the approximation may thus be evaluated for different frequency ranges. The vertical lines correspond to the estimates calculated as detailed in Eqs. (13) and (14). These plots highlight that for most cases or frequency ranges, there may be an optimal value for f^* in order to minimize the approximation error. In connection with this, the *a priori* indicators detailed in Eqs. (13) and (14) seem to provide a fair estimate for a sensible choice of such approximation frequency. In particular, in this case, the estimate according to Eq. (13) clearly provides a higher weight to the low frequencies, as more severely exhibited by the optimal values for this case. It is not surprising that this estimate doesn't necessarily provide the optimal value for f^*, since minimizing the error between the approximate and the exact functions in Eqs. (13) and (14), does not imply optimizing the absorption performance of the PML. Another observation from these plots is that the narrower the frequency range (in term of ratio f_{max}/f_{min}), the less important the impact of the value of f^* on the results. A trivial approach to the problem would therefore be to chose narrower intervals with optimal mesh sizes, and to choose an approximation frequency close to a quarter or third of the frequency span.

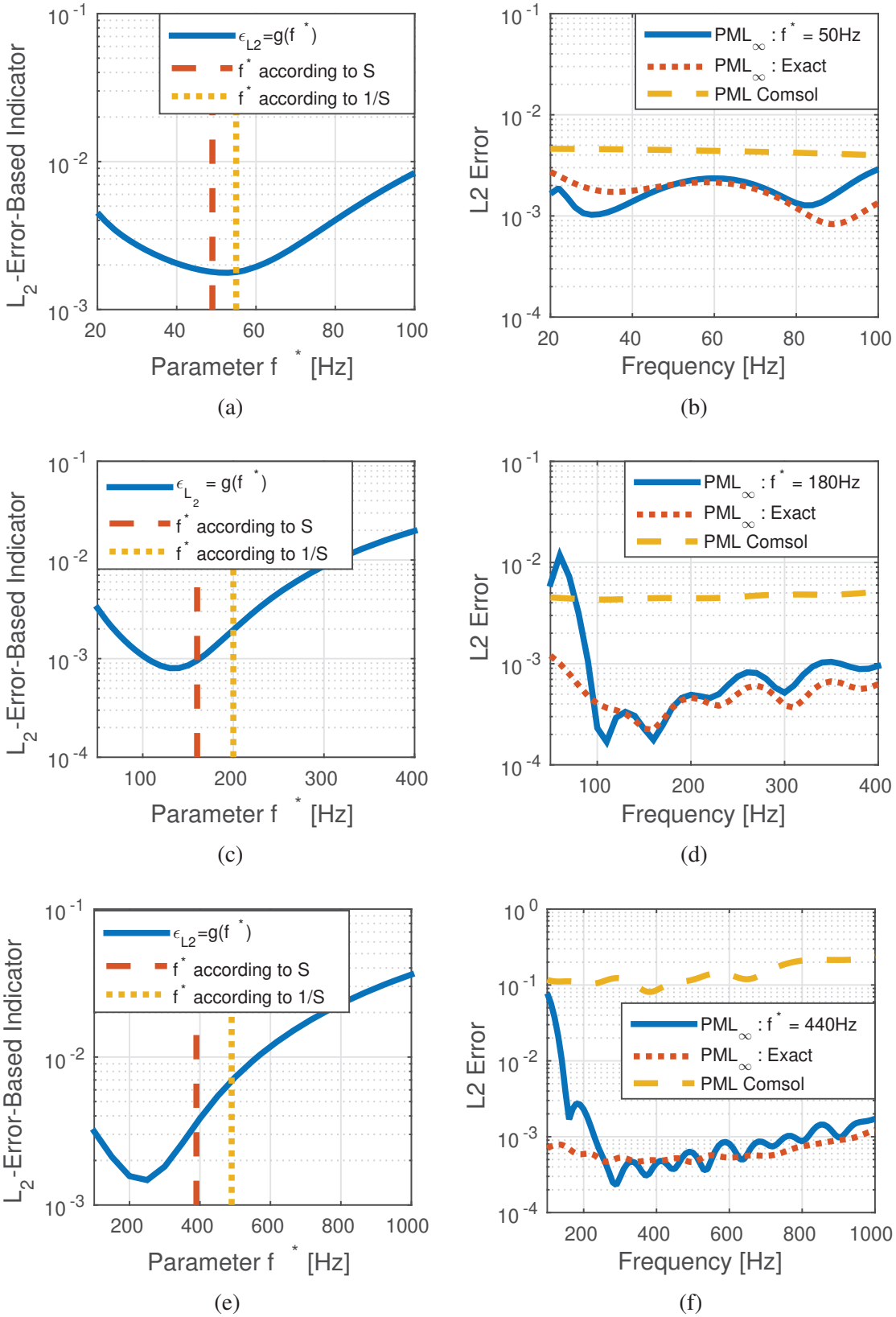

Figure 5: **Bermúdez *et. al.* test case**: Impact of the choice of f^* for different frequency ranges (left), and comparison of the error with the f^*-approximation, the original PML, and the COMSOL implementation (right).

The Figures 5b, 5d, and 5f plot the comparison between the error from the frequency sweep performed without the approximation (*i.e.* updating the assembly of the system matrix $\mathbf{K}$ in Eq. (9)), and the frequency sweep with the approximation where f^* is set as the arithmetic average of the indicators in Eqs. (13) and (14). For the sake of comparison with a commercial implementation, a reference calculation using COMSOL and its implementation of a rational PML formulation [26], with the same discretization and geometry, is also added for this test case. First, although the *a priori* estimate of a suitable value for f^* does not provide the optimal choice, the accuracy of the approximation is overall quite good. It is also noteworthy that the truncation approach detailed in Ref. [25] seems quite robust for all frequency ranges, since the error is kept low for all three plots. Finally, the approximated solution using the approach proposed in this contribution provides, overall, a better accuracy than the reference COMSOL implementation, for this specific case and problem definition (mesh, domain truncations, ...). Despite the value for f^* not being optimal, thus implying in this case a sharp increase of the error in the low-frequency end of the intervals, the maximum error observed for the approximated formulation remains in the range of the lowest error for the reference calculation. These observations may of course be case-dependent, and one may argue that the reference calculation may have the potential to be improved by tweaking the set of parameters available for that specific PML formulation. The objective is however here to estimate the robustness of the proposed approximation with as little prior knowledge about the problem of interest as possible, hence avoiding any specific tuning as available in COMSOL.

4 CONCLUSIONS

In this paper, a simple yet robust approximation of the unbounded PML formulation introduced by Bermúdez *et. al.* [14] is introduced in order to allow for the possibility of computationally efficient and accurate frequency sweeps. The proposed approximation provides results close to the original formulation while enabling for the FE system matrices to be generated once only during the initial assembly step. It is however shown that a tuning of the f^* approximation frequency is necessary for each frequency sub-interval of interest.

An *a priori* estimate of a robust choice for the value of this parameter is therefore proposed. It relies on a cost-effective minimization of the difference between the approximate and exact PML functions. It is shown that the resulting choice provides sensible approximations for the test case considered.

ACKNOWLEDGEMENTS

The first author gratefully acknowledges the financial support provided by the Swedish Research Council (VR Grant 2015-04925) and the Centre for ECO2 Vehicle Design (Sweden's Innovation Agency VINNOVA, Grant Number 2016-05195).

REFERENCES

[1] I. Harari, A survey of finite element methods for time-harmonic acoustics, Computer methods in applied mechanics and engineering 195 (13-16) (2006) 1594–1607.

[2] A. Bayliss, E. Turkel, Radiation boundary conditions for wave-like equations, Communications on Pure and Applied Mathematics 33 (6) (1980) 707–725.

[3] A. Bayliss, M. Gunzburger, E. Turkel, Boundary conditions for the numerical solution of elliptic equations in exterior regions, SIAM Journal on Applied Mathematics 42 (2) (1982) 430–451.

[4] X. Antoine, H. Barucq, A. Bendali, Bayliss–turkel-like radiation conditions on surfaces of arbitrary shape, Journal of Mathematical Analysis and Applications 229 (1) (1999) 184 – 211.

[5] L. L. Thompson, A review of finite-element methods for time-harmonic acoustics, The Journal of the Acoustical Society of America 119 (3) (2006) 1315–1330.

[6] B. Engquist, A. Majda, Radiation boundary conditions for acoustic and elastic wave calculations, Communications on pure and applied mathematics 32 (3) (1979) 313–357.

[7] D. Givoli, High-order local non-reflecting boundary conditions: a review, Wave motion 39 (4) (2004) 319–326.

[8] P. Bettess, Infinite elements, International Journal for numerical methods in engineering 11 (1) (1977) 53–64.

[9] D. S. Burnett, A three-dimensional acoustic infinite element based on a prolate spheroidal multipole expansion, The Journal of the Acoustical Society of America 96 (5) (1994) 2798–2816.

[10] R. Astley, Infinite elements for wave problems: a review of current formulations and an assessment of accuracy, International Journal for Numerical Methods in Engineering 49 (7) (2000) 951–976.

[11] J.-P. Berenger, A perfectly matched layer for the absorption of electromagnetic waves, Journal of Computational Physics 114 (2) (1994) 185 – 200.

[12] E. Turkel, A. Yefet, Absorbing pml boundary layers for wave-like equations, Applied Numerical Mathematics 27 (4) (1998) 533–557.

[13] I. Harari, M. Slavutin, E. Turkel, Analytical and numerical studies of a finite element pml for the helmholtz equation, Journal of Computational Acoustics 8 (01) (2000) 121–137.

[14] A. Bermúdez, L. Hervella-Nieto, A. Prieto, R. Rodrı, et al., An optimal perfectly matched layer with unbounded absorbing function for time-harmonic acoustic scattering problems, Journal of Computational Physics 223 (2) (2007) 469–488.

[15] F. Collino, P. B. Monk, Optimizing the perfectly matched layer, Computer methods in applied mechanics and engineering 164 (1-2) (1998) 157–171.

[16] R. Rumpler, P. Göransson, H. Rice, An adaptive strategy for the bivariate solution of finite element problems using multivariate nested padé approximants, International Journal for Numerical Methods in Engineering 100 (9) (2014) 689–710.

[17] R. Rumpler, Padé approximants and the modal connection: Towards increased robustness for fast parametric sweeps, International Journal for Numerical Methods in Engineering 113 (1) (2018) 65–81.

[18] A. Bermúdez, L. Hervella-Nieto, A. Prieto, R. Rodríguez, An exact bounded pml for the helmholtz equation, Comptes Rendus Mathematique 339 (11) (2004) 803 – 808.

[19] A. Bermúdez, L. Hervella-Nieto, A. Prieto, R. Rodríguez, Perfectly matched layers for time-harmonic second order elliptic problems, Archives of Computational Methods in Engineering 17 (1) (2010) 77–107.

[20] G. A. Baker, P. Graves-Morris, S. S. Baker, Padé approximants, Vol. 59, Cambridge University Press, 1996.

[21] R. Rumpler, P. Göransson, J.-F. Deü, A finite element approach combining a reduced-order system, padé approximants, and an adaptive frequency windowing for fast multi-frequency solution of poro-acoustic problems, International Journal for Numerical Methods in Engineering 97 (10) (2014) 759–784.

[22] M. S. Lenzi, S. Lefteriu, H. Beriot, W. Desmet, A fast frequency sweep approach using padé approximations for solving helmholtz finite element models, Journal of Sound and Vibration 332 (8) (2013) 1897–1917.

[23] D. Rabinovich, D. Givoli, E. Bécache, Comparison of high-order absorbing boundary conditions and perfectly matched layers in the frequency domain, International Journal for Numerical Methods in Biomedical Engineering 26 (10) (2010) 1351–1369.

[24] H. Rice, R. Rumpler, P. Göransson, A development on fast frequency sweep methods for acoustic radiation problems, in: ISMA 2016, 19-21 September, Leuven, Belgium, ISMA, 2016.

[25] A. V. de Conchard, H. Mao, R. Rumpler, A perfectly matched layer formulation adapted for fast frequency sweeps of exterior acoustics finite element models, Journal of Computational Physics 398 (2019) 108878.

[26] COMSOL, COMSOL Multiphysics Reference Manual, version 5.3, 1998–2017.
URL `www.comsol.com`

EURODYN 2020
XI International Conference on Structural Dynamics
M. Papadrakakis, M. Fragiadakis, C. Papadimitriou (eds.)
Athens, Greece, 23–26 November 2020

IMPACT DAMAGE CHARACTERIZATION AT RC PLATES WITH PLANAR TOMOGRAPHY AND FEM

Deborah Nerger[1], Robabeh Moosavi[1], Franz Bracklow[2], Marcus Hering[2], Tino Kühn[2], Manfred Curbach[2], Falk Hille[1] and Andreas Rogge[1]

[1]Federal Institute for Materials Research and Testing (BAM)
Unter den Eichen 87, D-12205 Berlin
e-mail: {deborah.nerger, robabeh.moosavi, falk.hille, andreas.rogge}@bam.de

[2] Institute of Concrete Structures
Technische Universität Dresden, D-01062 Dresden
e-mail: {franz.bracklow, marcus.hering, tino.kuehn, manfred.curbach}@tu-dresden.de

Keywords: post-impact evaluation, damage characterization, planar tomography, reinforced concrete structure, Drucker-Prager, Ansys Autodyn

Abstract. *Prediction of dynamic effects of reinforced concrete structures under impact loading is a technical challenge. This is a consequence of the great variability of the physical properties resulting from the wide adaptability of reinforced concrete and a consequence of the wide range of impact loading. Experiments and numerical investigations are normally used on a small scale to address the problem. In this paper, impact tests on reinforced concrete plates with the lateral dimensions of 1.5 m x 1.5 m and a thickness of 30 cm are presented. In bending reinforcement, besides the velocity two properties are varied, the diameter and the spatial distribution of the rebars. Experiments are performed at the Otto-Mohr-Laboratory of the Institute of Concrete Structures of the Technische Universität Dresden. Due to the accelerated fall of the impactor the velocity ranges between 20 and 70 m/s. In addition to the measured quantities such as bearing forces, accelerations are also measured at 4 different positions on and under the plate, as well as the deflection at several positions. The measured data are used for the analysis of the damage form and the numerical examinations with the program Ansys Autodyn and the material model after Drucker-Prager. Numerical investigations support the tests, with detailed analysis of individual effects. These numerical computations and the planar tomographic investigations were carried out at BAM in Berlin. With the help of planar tomographic evaluation, the damaged structure is made visible and compared with the numerical results. Influences of the bending reinforcement are explained on the basis of damage evaluation in the local area and on selected measured values. In addition to the test evaluation, the tomographic and numerical methods are presented.*

1 INTRODUCTION

Reinforced concrete (RC) is used as a construction material in a wide range of applications in the building industry. This great variability of applications is reflected in the range of physical properties. Due to the variability of the physical properties it is still an engineering challenge to meet all necessary requirements for predicting dynamic effects in structural reinforced concrete members under impact loading. The damage behaviour of RC structures depends on various parameters and cannot be predicted exactly. There are several empirical formulas that give a prognosis for the penetration depth and the minimum thickness of the concrete layer to avoid perforation [1, 2]. Some formulae are anchored in codes of practice and can be used for initial analyses and verification [3]. However, often the real structural behavior is only approximated.

In addition to the analytical approaches, experiments are performed. These are often carried out in a small scale. For example, in [4] RC columns are investigated under hypervelocity impact (500–1700 m/s). In [5] - [9] investigations on impact damage on plates due to small projectiles and cylinders at high velocity (70–500 m/s) are presented. Large-scale tests were carried out with different boundary conditions (target size and shape, impactor velocity and shape) for example at Sandia Laboratories [10, 11], at the VTT (summarized among others in [12]) or [13].

Numerical investigations are performed to investigate parameter studies or to study structures that cannot be investigated destructively. Furthermore, it is possible to implement experiments that are otherwise not or very difficult to realize. Examples can be found at [14] - [18].

Not only the load and its temporal course are relevant for the test evaluation, as described e.g. by [19] and [20]. Also the local damages are interesting. Furthermore, there are many factors that influence the post-impact behaviour, such as the bond properties between concrete and steel. This leads to different damage characteristics due to the impact [2].

Most studies are focussing on investigations of detailed damage analysis after an impact is in the speed range above 100 m/s.

This paper presents some results of a study on damage of plates impacted by moderate impactor velocities. The impact damage was caused by an accelerated fall of the impactor on reinforced concrete plates (1.5 m x 1.5 m). The test setup should be comparable to a part of the scenario of an impact of an aircraft engine. The physical properties of the plates (concrete strength, plate thickness, degree of reinforcement) and the impact properties (energy, weight, speed) were varied.

To identify and characterize the internal crack structures of the RC plates, the innovative planar tomographic method was applied on a unique tomography laboratory test stand. Possible damages, such as cracks, scabbing and spalling, are made visible during the tomographic reconstruction. Numerical simulations are used to identify the physical effects.

2 EXPERIMENTAL INVESTIGATIONS

The experiments were carried out at the Otto-Mohr-Laboratory of the Institute of Concrete Structures of the Technische Universität Dresden. The drop tower facility, which was available for this purpose, was built in a former project part and can be used in two different configurations. In the freefall mode, the impactor moves due to a sledge-rail construction. Through gravity and in dependence of the height of fall, the energy and velocity of the impactor can be controlled. In contrast to this, the impactor in the ballistic configuration is accelerated by air pressure and a guided impact of the plate is realized with a pipe (Figure 1) [21]. At first, the influence of external (impact energy, impactor size) and internal parameters (plate geom-

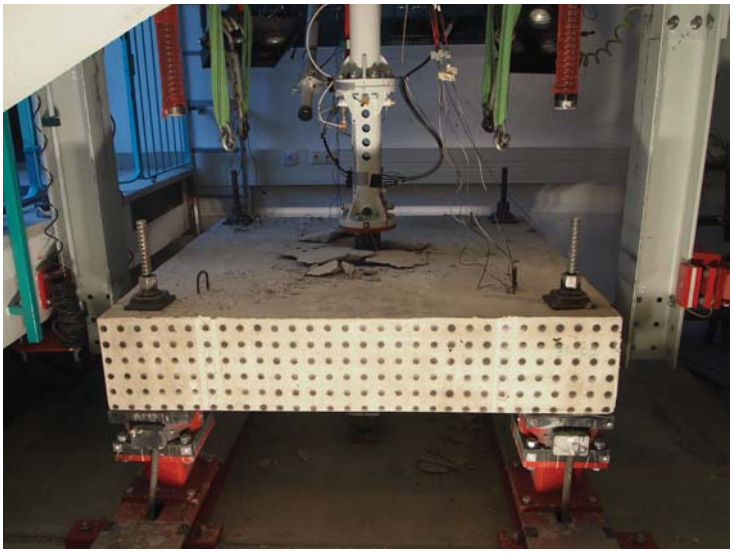

Figure 1: Experimental setup of an accelerated impact test

etry, concrete quality, reinforcement parameters) was investigated in free-fall tests and a first damage analysis was carried out [22, 19, 23]. Currently, a comprehensive investigation of the internal parameters takes place with accelerated experiments. Four test series are planned for this purpose (Figure 2). First of all, experiments with different plate thicknesses were carried

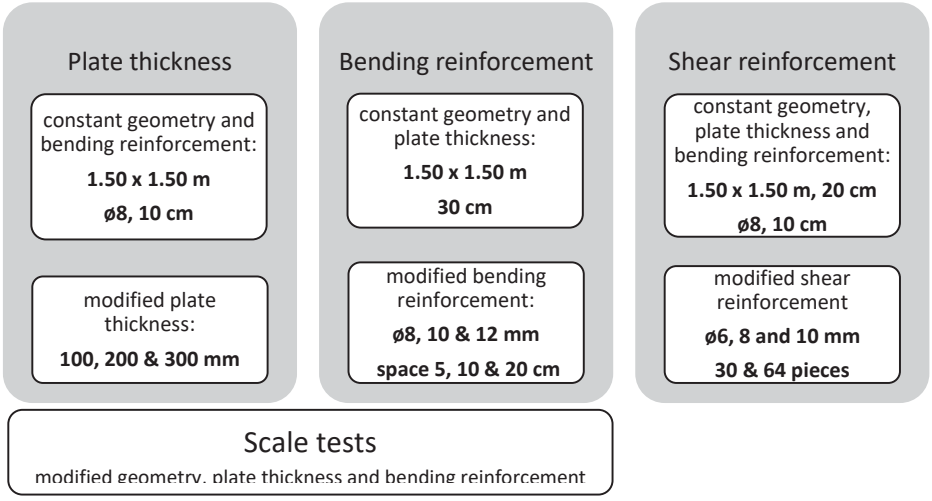

Figure 2: Planned test series

out. Therefore 15 plates with a geometry of 1.50 m x 1.50 m and a thickness of 10, 20 and 30 cm were tested with different velocities. All test specimens were made of concrete C35/45 and reinforcement ø8 with a spacing of 10 cm. These tests are the foundation for further investigations [24].

In the context of a further series of tests, the influence of bending reinforcement variations was investigated. Next to the the diameter, also the influence of the space between the reinforcementbars was examinated. In total, 32 plates with a geometry of 1.50 m x 1.50 m and a thickness of 30 cm were made. With a previous plate series include the reinforcement combinations therefore configurations of ø8 with a spacing of 5 and 20 cm as well as ø10 and ø12

with a spacing of 5, 10 and 20 cm. Four plates per configuration were loaded by impactors with different velocities and compared with the 30 cm thick samples (ø8–10 cm) from the plate thickness variation test series. In total, nine different bending reinforcement configurations could be realized.

Table 1 shows for each specimen (series & number) the respective reinforcement parameters (steel diameter d_r and spatial distribution of the rebars a_r). V_{imp} represents the velocity of the impactor measured in the experiments and I_{imp} the impulse resulting from multiplication of the velocity with the impactor mass.

series	d_r/a_r [mm]/[cm]	v_{imp} [m/s]	I_{imp} [N/s]	series	d_r/a_r [mm]/[cm]	v_{imp} [m/s]	I_{imp} [N/s]	series	d_r/a_r [mm]/[cm]	v_{imp} [m/s]	I_{imp} [N/s]
S31P01	8/5	54.02	1169.98	S31P05	10/5	54.29	1175.83	S32P01	12/5	54.17	1173.31
S31P02	8/5	73.50	1592.01	S31P06	10/5	74.07	1604.44	S32P02	12/5	61.14	1324.34
S31P03	8/5	67.98	1472.45	S31P07	10/5	61.79	1338.34	S32P03	12/5	67.44	1460.66
S31P04	8/5	61.64	1335.08	S31P08	10/5	68.53	1484.36	S32P04	12/5	71.97	1558.86
S29P04	8/10	54.95	1190.28	S32P05	10/10	52.52	1137.64	S33P05	12/10	53.30	1154.39
S29P05	8/10	68.97	1493.79	S32P06	10/10	61.54	1332.92	S33P06	12/10	61.64	1335.09
S29P06	8/10	62.04	1343.80	S32P07	10/10	67.20	1455.49	S33P07	12/10	73.43	1590.52
S30P01	8/10	74.73	1618.64	S32P08	10/10	73.64	1595.12	S33P08	12/10	67.02	1451.64
S33P01	8/20	52.81	1143.96	S34P01	10/20	53.90	1167.49	S34P05	12/20	54.02	1169.98
S33P02	8/20	61.34	1328.62	S34P02	10/20	61.69	1336.17	S34P06	12/20	61.64	1335.09
S33P03	8/20	73.08	1582.85	S34P03	10/20	68.22	1477.70	S34P07	12/20	68.04	1473.73
S33P04	8/20	67.56	1463.25	S34P04	10/20	73.22	1585.90	S34P08	12/20	74.07	1604.44

Table 1: Test properties of all plates of the reinforcement variation, sorted by the diameter (d_r) of the reinforcement bars and its spatial distribution (a_r)

For all experiments, a 38 cm long steel impactor with a mass of 21.66 kg was used. For the impactor tip, a flat shape was chosen. In addition to the support forces and displacements, especially accelerations on the top on rear side of the plates were also measured (Figure 4). To evaluate the plate's damage, the weight of the test specimen was determined before and after the test and the masses of the fragments on the top (spalling) and under the plate (scabbing) were measured (Figure 3). After the experiments, the specimens were cut in the middle and the punching cones were investigated in the cross section. A computer tomographic examination was also carried out (see section 3).

(a) (b)

Figure 3: (a) Spalling damage on the top and (b) scabbing damage on the bottom side of the plate

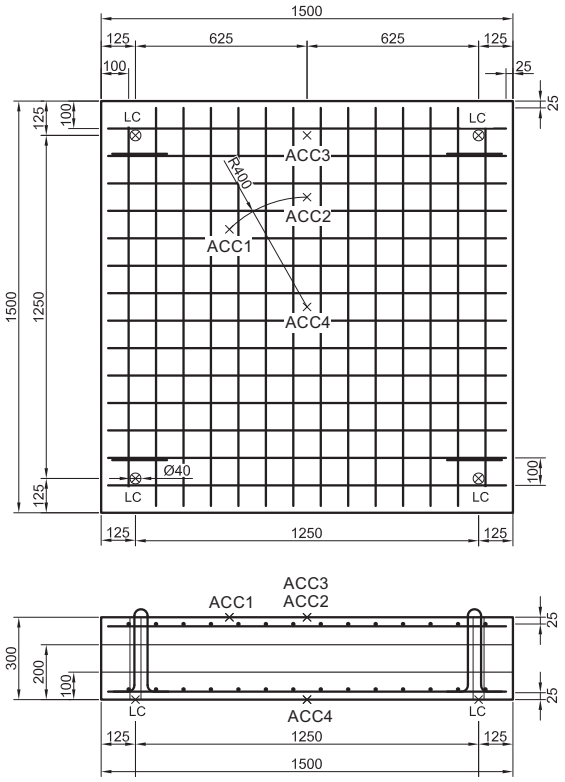

Figure 4: Plan of measuring points of the accelerating data ACC and the load cells LC

3 PLANAR TOMOGRAPHY AND CRACK DETECTION

Planar tomography measurements were performed in the High Energy X-ray Laboratory (HEXY Laboratory) at the Federal Institute for Materials Research and Testing in Berlin (BAM). The manipulator can be controlled by 13 axes, 9 linear and 4 rotational axes, which ensures a different movement of X-ray source, object and detector for 3-dimensional investigations (CT and laminography) (Figure 5). The dimensions of the object can be up to 4 m in length, 1.5 m in height and 2 t in weight. A betatron, an electron accelerator, with an acceleration voltage of 7.5 MV is used. With this energy it is possible to radiate through concrete with a thickness of 0.3 m. The image data was recorded with a high-resolution matrix detector (DDA: Digital Detector Array) from PerkinElmer (XRD1620).

Due to the large dimensions of the concrete plates, the scanning method had to be adapted. With the new method a total of 4392 projections with 2048 x 2048 pixels each can be scanned. The total recording time for half a plate is 17 hours. The volume data of the investigated object are reconstructed using a fast shift-average algorithm [25]. The resulting three-dimensional volume is composed of voxels (a 3D equivalent of a pixel) with a side length of 0.5 mm in lateral direction and 1.5 mm in depth direction of the plate. This resolution allows the visualization of cracks with a minimum width of 0.5 mm.

The methodology of crack detection and segmentation is further explained in [26]. Data in STL format are generated from the segmented cracks in order to compare them with the exported data from the numerical simulations. STL data are a standard format for STereoLithography and contains all necessary geometric information. Figure 6 shows the visualization of the crack structure projected onto a layer of the tomographic data.

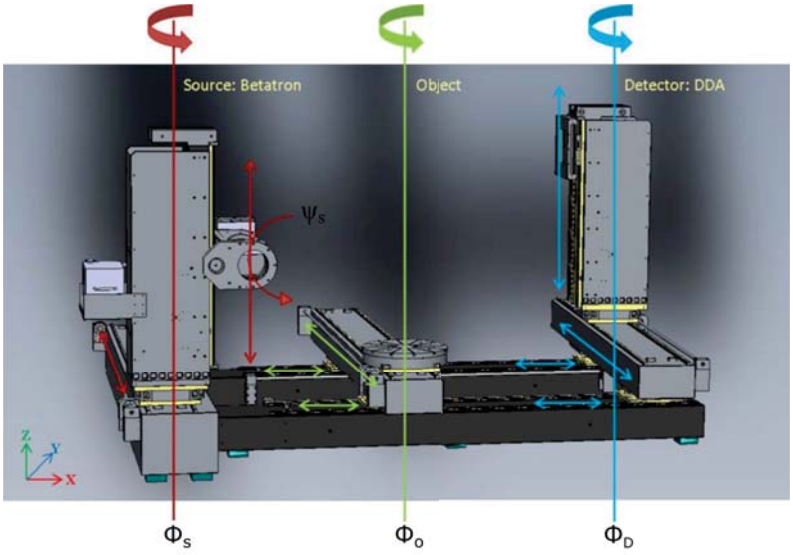

Figure 5: Schematic structure of the HEXY lab with its source, object, detector and its rotational axes [26]

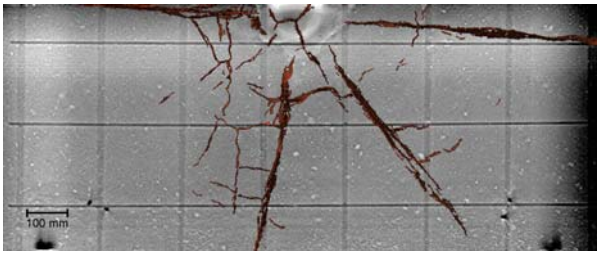

Figure 6: Visualization of the crack map (orange colored) projected on a layer of the tomographic data (gray colored)

4 NUMERICAL SIMULATION

For a numerical analysis the real system is simplified and transferred into a simulation model. The continuous body is reduced to small finite elements. Depending on the selection of the element type the nodes are generated. At each individual node the momentum balance equation is solved in the form of the weak differential equation of second order (Equation 1).

$$\mathbf{M}\ddot{u}(t) + \mathbf{C}\dot{u}(t) + \mathbf{K}u(t) = \mathbf{P}(t) \tag{1}$$

In Equation 1, $\mathbf{M}$ is the mass matrix, $\mathbf{C}$ is the damping matrix and $\mathbf{K}$ is the stiffness matrix of the system. $\mathbf{P}$ describes the externally acting time-variable forces. $u(t)$ describes the deformation which is also dependent on time.

In the explicit solution approach, the current status (time step n) of the deformation, acceleration and stress at each node of the system is determined first. From this, the deformations and velocities of the next time step (n+1) will be derivate. After calculating the internal forces and stresses of the time step (n+1) using the velocity, the external forces will be determined. Accelerations will be get from th forces and are the initial values for the next time step (n+2). This cycle is iteratively be going through until the last time step of the numerical simulation [27].

The impact test is modeled as a full model (Figure 7) with the program Ansys Autodyn. The bearings, the impactor and the plate are described with solids, whereas the rebars are modeled

with line elements. Automatic meshing takes place with a specified element edge length. Hexahedron were primarily used for the solids and beams for the line elements. The given edge length for the bearings is 20 mm and for the other components 10 mm. Thus, the system has 750,000–790,000 nodes and 730,000–810,000 elements when meshed.

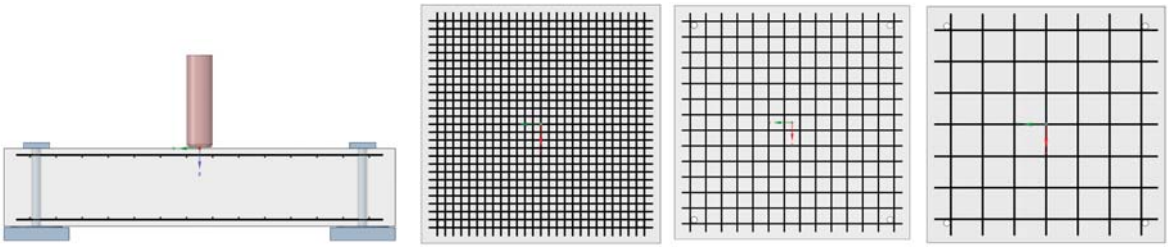

(a) (b) (c) (d)

Figure 7: Side view of the model with the bearings, the plate, the impactor and the reinforcement (a), top view of the plate with the spatial distribution of the reinforcement bars: 5 cm (b), 10 cm (c) and 20 cm (d)

The impactor velocity was determined in the test from the measured data and was initially applied to the modeled impactor. The surfaces of the bearings are assumed to be fixed. Another fixed contact (contact = bonding) is defined between the plate and the four bearings. The impactor hits the center of the plate, whereby the contact is assumed to be frictionless. Previous comparative computations with the friction coefficient of 0.8 determined from the tests showed no relevant difference in the simulation. A reason is presumably the short contact time between impactor and plate. The rebars are modeled into the plate in a smeared pattern and the contact behaviour is defined as 'body interaction, type = reinforcement'. According to this formulation, the reinforcement bars are modeled as line bodies which are tied to each element they intersect.

An elastic material model was used for the structural steel components, since no significant damage to the components was detected during the tests. Concrete is described with the nonlinear material model 'Beton NL'. This model is freely available in the Ansys material library and is based on the strength description according to Drucker-Prager (DP).

The description of the failure surfaces according to Drucker-Prager is an extension of the description according to von Mises and is similar to that of Mohr-Coulomb under certain conditions, [28, 29, 30].

The failure criterion (Equation 2)

$$f(I_1, J_2) = \alpha I_1 + \sqrt{J_2} - k = 0 \tag{2}$$

mit

$$p = -\frac{1}{3} I_1 \tag{3}$$

$$\sigma_{eff} = \sqrt{3 J_2} \tag{4}$$

$$k = f(\varepsilon_{ij}^p) \tag{5}$$

$$d\varepsilon_{ij}^p = d\lambda \frac{\partial g}{\partial \sigma_{ij}} \overset{\text{assoz.}}{=} d\lambda \frac{\partial f}{\partial \sigma_{ij}} \tag{6}$$

is described with the first invariant of the volumetric stress tensor I_1, the second invariant of the deviational stress tensor J_2, the hardening rule k and a material parameter α for the compaction

path. p describes the pressure. σ_{eff} represents the effective or von Mises equivalent stress. ε^p describes the plastic strains in the object. Equation 6 is called flow rule. The derivative of a plastic potential $g(\sigma_{ij})$ multiplied by a proportionality factor $d\lambda$ represents the rule for the kinematic description of inelastic deformation, which is associative according to Drucker and Prager.

For the description of the piecewise linear yield surface of concrete under compression, the points P_i (pressure p / yield stress Y) in the meridian plane can be determined from measurements and comparisons with triaxial tests, see Figure 8. In [30], the appendix is a very extensive summary of about 13 international studies of triaxial tests with variing concrete strength which helps to identify the yield surface of concrete. Further material parameters for the model de-

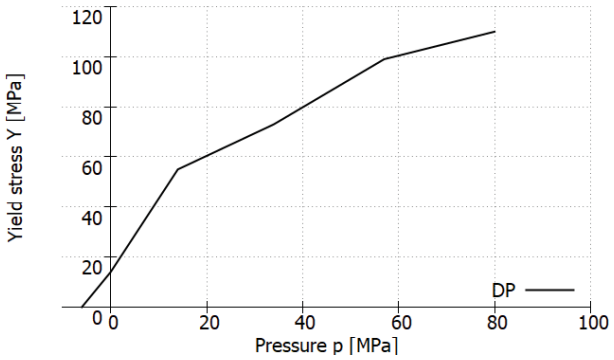

Figure 8: Failure surface after DP as a projection in a meridian plane based on the used test material

scription are shown in table 2. The material parameters for the tested plates are specified in a range. They refer to two different test sets: the plate thickness variation [24] and the bending reinforcement variation described in section 2. These data were used to calibrate the model. Only the tensile strength was adjusted so that the value is outside the range of the test data.

Properties	FEM	Test
Density	2250 $\mathrm{kg/m^3}$	2204–2279 $\mathrm{kg/m^3}$
Young's modulus	32200 MPa	27300–35700 MPa
Poisson's ratio	0.2	0.2
Maximum tensile pressure	6 MPa	2.82–4.58 MPa
Fracture energy Gf	100 $\mathrm{J/m^2}$	

Table 2: Material parameters of the numerical model and the range of the tested data of about 9 series (plate thickness variation [24] and reinforcement variation. The properties are named as in the Ansys program.

Figure 9 shows the process of numerical evaluation of the damage based on the damage structure. The computations were carried out without element erosion (Figure 9a). Using the parameter 'user defined result: damageall', the damage is displayed smeared. The result is shown per element as probability based on the user defined material failure (Figure 9b). For further comparison, elements with a value exceeding 0.93 are isolated and extracted (Figure 9c). This corresponds to a damage probability of 93%. In the SpaceClaim module of Ansys, the data set (STL format) is manually cleaned, replacing failed elements and re-meshing the surface (Figure 9d).

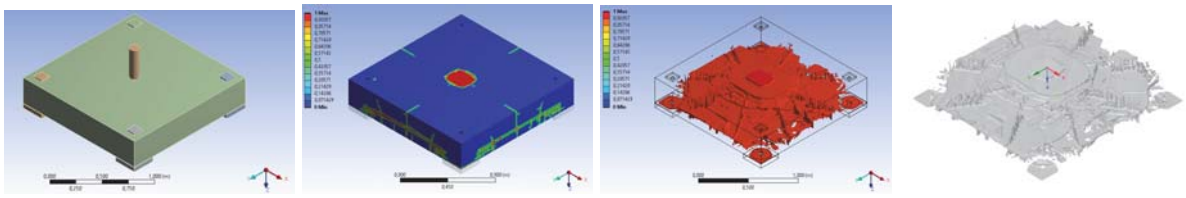

(a) (b) (c) (d)

Figure 9: Visualization of the damage evaluation; (a) geometry of the model, (b) damage pattern based on the material failure, (c) extracted damaged elements (d) cleaned and remeshed damage map

5 EVALUATION

In the following, damages in selected form (penetration depth, total degree of damage, quantity of cracks and impact area) with different emphasis (d_r = const. and a_r = const.) are to be examined on the tested plates. Furthermore, crack structures are evaluated based on tomographic data and comparisons with the numerical results. The bearing forces, the acceleration and the deformation data of the tests are compared with those of the numerical simulations using a plate series.

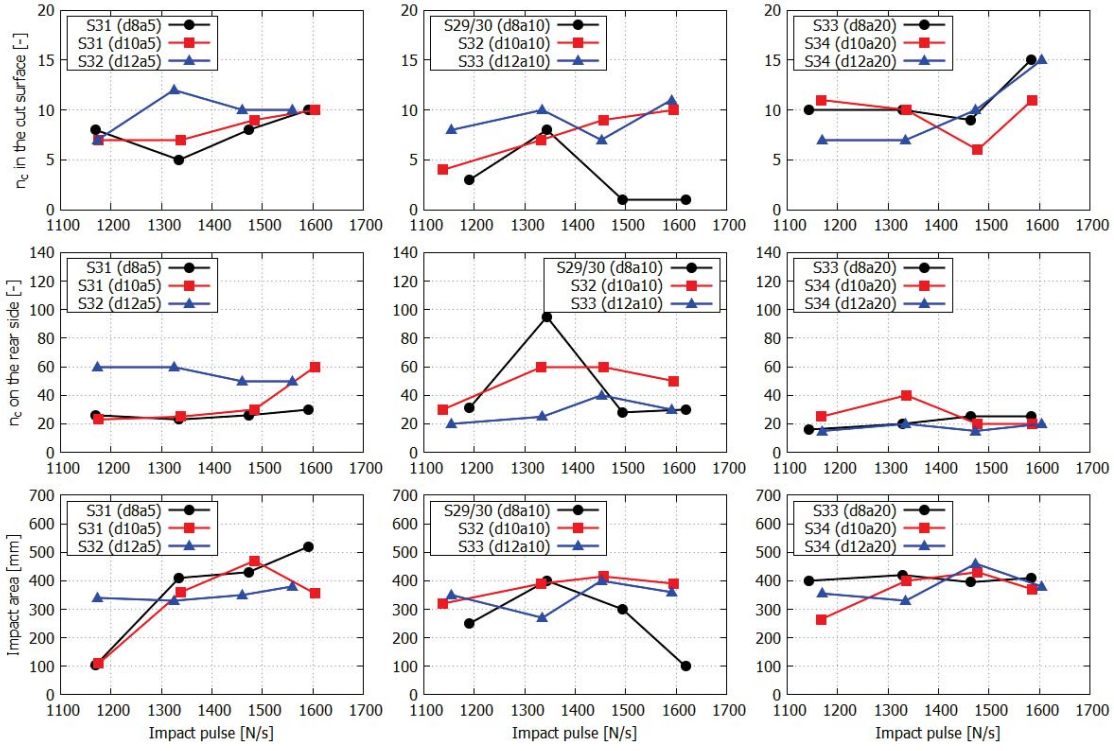

Figure 10: Visualization of the number of cracks (n_c) in the middle cut surface of the plate (top row), number of cracks on the half rear side (middle row) and the diameter of the damaged area of the front side of the plate (bottom row) in series with constant spatial distribution and varying rebar diameter

In Figures 10 and 11, the upper row shows the number of cracks (n_c) in the cut surface and

the middle row shows the cracks on the half rear side, both w.r.t. the impact pulse. In the bottom row, the diameter of the damaged area on the top side of the plate w.r.t. the impact pulse is presented. Cracks are counted as those that can be detected without using tools. This corresponds in some cases to a crack width of 0.1 mm. Every single crack was counted, which results in a large number for some plates.

The impactor mass was identical for all tests of series S29 to S34, see section 2. Therefore, for visualization it makes no difference whether the results are displayed w.r.t. the impact pulse or the impact velocity. For better comparison with other tests the impact pulse was used here.

Three series are compared in each presentation. These differed in the reinforcement's diameter (d = 8/10/12 mm) or it's spatial distribution (a = 5/10/20 cm). Despite of the parameters of the different series, the color representation is identical. The series with the smallest size of the varying parameter is colored black and circles are used for value marking. The series with the middle parameter is colored red and marked with squares, and the series with the highest parameter is colored blue and marked with a triangle.

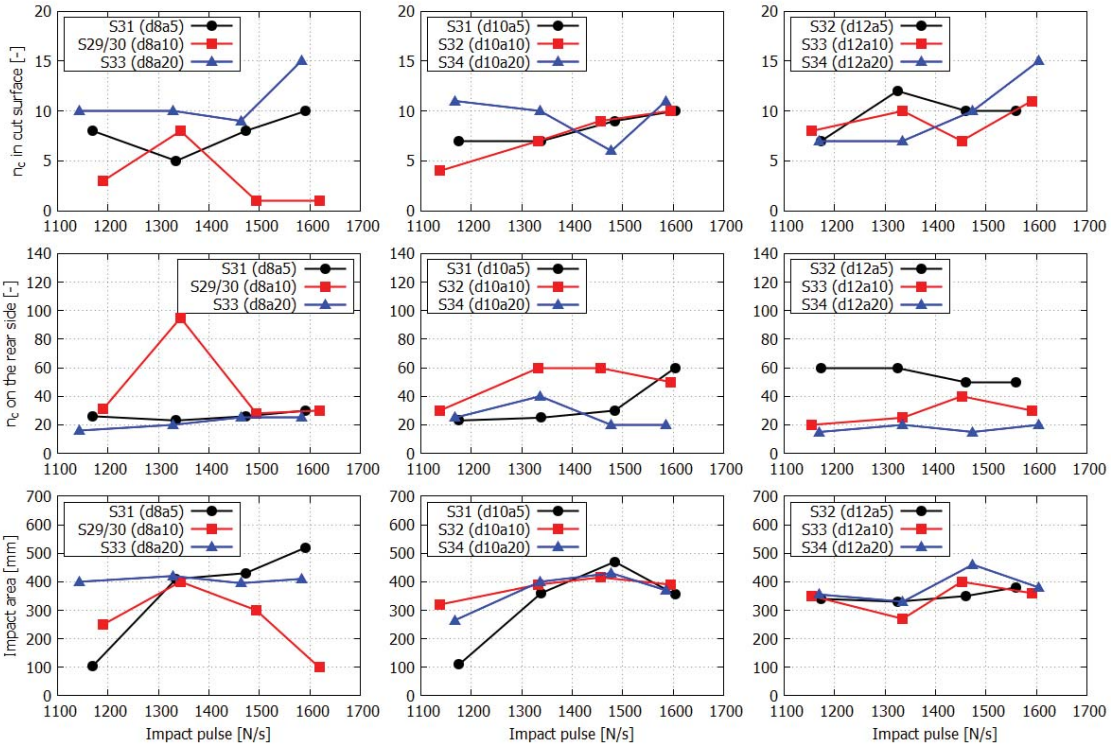

Figure 11: Visualization of the number of cracks in the middle cut surface of the plate (top row), number of cracks on the half rear side (middle row) and the diameter of the damaged area of the front side of the plate (bottom row) in series with varying spatial distribution and constant rebar diameter

In Figure 10, the series are sorted by the spatial distribution of the rebars. In each column, the spatial distribution remains constant and the diameter of the bars varies. In Figure 11, the comparison is the other way round. In the columns, the diameters of the bars remain constant and the spatial distribution varies. The aim is to obtain an overall comparison of the crack damage and to identify potential correlations.

For all combinations, the number of detected cracks is approximately in the same range and, with a few exceptions, increases with rising impact velocity. The number of cracks in the cut surface (upper row in each case) is currently not related to the number of cracks varying with the diameter or the distance between the bars. A similar conclusion can be drawn about the number of cracks on the half underside of the damaged plate.

In the following passages, the individual diagrams are explained in more detail.

At a constant distance of 5 cm, the 'curve' with the bar diameter of 12 mm behaves differently than expected (Figure 10, left diagram). In the comparison above, the plates with medium impact pulse show more cracks than the other plates. In the middle diagram, the whole series (S32 with d = 12 mm and a = 5 cm) shows more cracks. In the lower diagram, the diameter of the damaged surface on the upper side is plotted. In this series the plate with the lowest impact pulse has a much larger damaged area than the other series. With increasing velocity of the impactor, however, this changes slightly. In the three diagrams, the other two series (S31 with d = 8 mm and S31 with d=10 mm) are close together. A possible connection between impact area and number of cracks on the rear side cannot be recognized. At higher velocities the plates of the series S31 display a larger damaged area than that of S32. However, the number of cracks does not increase as expected.

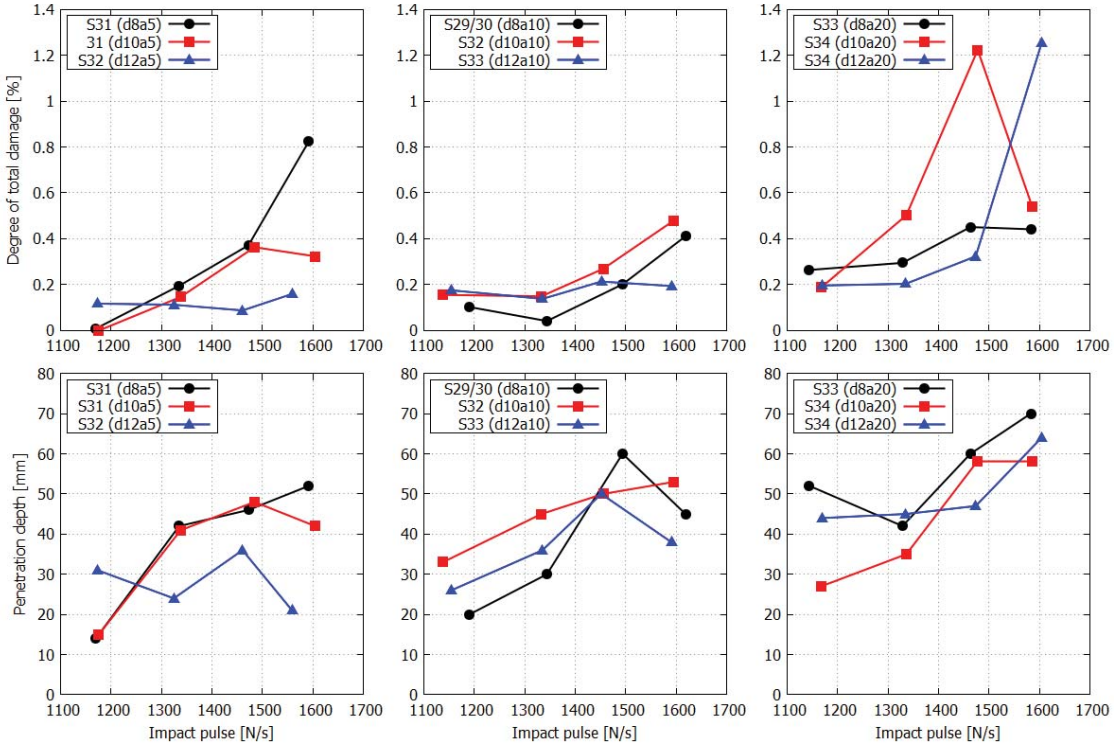

Figure 12: Degree of damage and penetration depth in the series with constant spatial distribution and varying rebar diameter

When comparing the series with constant rebar distance of 10 cm, the series S32 with d = 10 mm and S33 with d = 12 mm are relatively close to each other and show similar behaviour with increasing impact pulse. The series 29/30 with a bar diameter of 8 mm is the exception. A plate of this series with an impact pulse of about 1350 N/s is more damaged by cracks than the other plates of this series. The other three plates of this series are of about the same amount. A further remarkable difference to the two series S32 and S33 is the impact area.

With increasing velocity, the area is significantly smaller than the other plates of the series under the same experimental conditions. In the right column of Figure 10, all results of the plates are close together.

When comparing the series with constant diameter (see Figure 11) of 8 mm, the results of the individual plates differ from each other. When comparing the series with constant diameter of 10 mm and 12 mm, most results are again relatively close. Even if the individual results are not similar in every diagram, the behavior of the individual curves is relatively similar.

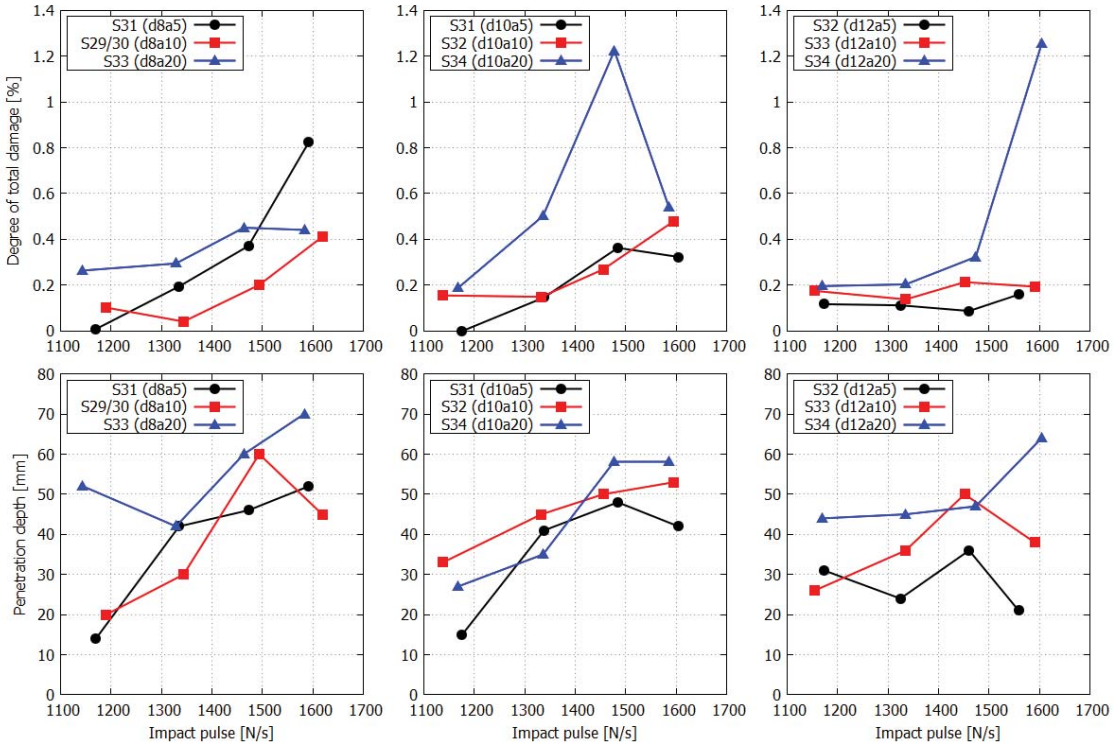

Figure 13: Degree of damage and penetration depth in the series with varying spatial distribution and constant rebar diameter

In the Figures 12 and 13, the total damage and penetration depth is given by the impact pulse. The total damage in this illustration is the ratio of the damaged material to the total volume of the plate and is calculated based on the weight loss. Analogous to the comparisons of the number of cracks, the exceptions to the results in individual series can be observed here.

The results of the series with constant distance a = 5 cm with respect to the impact area can be seen in the total damage and in slight variance in the values of the penetration depth, see Figure 12. When comparing the series with a spatial distribution of 10 cm, the results of the individual series are similar to each other, except for series 29/30 (d = 8 mm and a = 10 cm). The differences in the results of the series with 20 cm bar spacing were greater than expected after considering the previous results. With relatively minor crack damage and small impact area, the results of penetration depth and material loss show a high degree of damage.

Comparing the series with constant diameter (Figure 13), again the two series (S32 with d = 12 mm and a = 5 cm, and S29/30 with d = 8 mm and a = 10 cm) are an exception in the analysis of the results. The results of the series S31 and S33 with a constant diameter of d = 8 mm show expected results for the total damage and the penetration depth. In the S29/30 series, the impact area decreases with higher impact pulses, but the total damage increases.

When evaluating the results with constant diameter of d = 10 cm, the results of the series S31 with a = 5 cm and S32 with a = 10 cm can be explained. The results of series S34 with a = 20 cm cannot be concluded from the previous results. Similarly, this applies to the series with a bar diameter of 12 mm. Here it concerns the series S32 with a = 5 cm and S34 with a = 20 cm.

All the comparisons described here concerning damage (Figures 10 to 13) are based on a relatively small amount of tests. In total, 36 plates were examined. With the varying parameters of impact velocity, rebar diameter and their spatial distribution, one plate per constellation was tested. The individual damage characteristics examined will probably not show a large scattering width per parameter constellation, but it is exactly this scattering width and the reproducibility of damage caused by an impact that is not known.

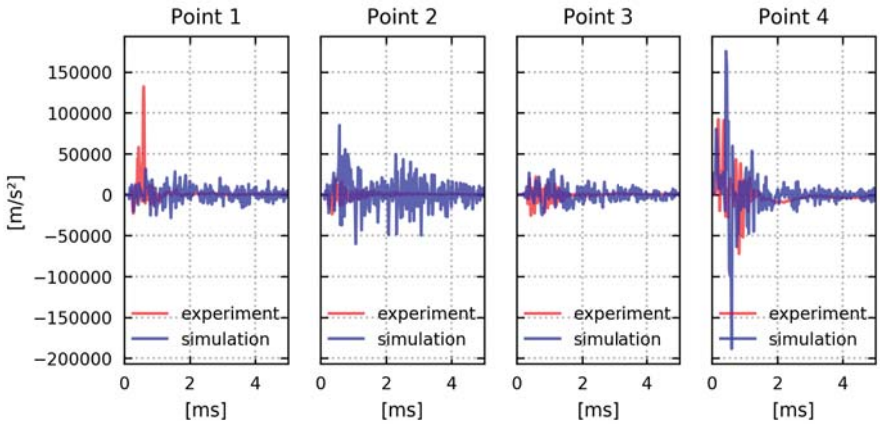

Figure 14: Visualization of the acceleration data in $[\mathrm{m/s^2}]$ comparing the test data with the numerical results of the plate S31P01 for the first 5 milliseconds at 4 measuring positions

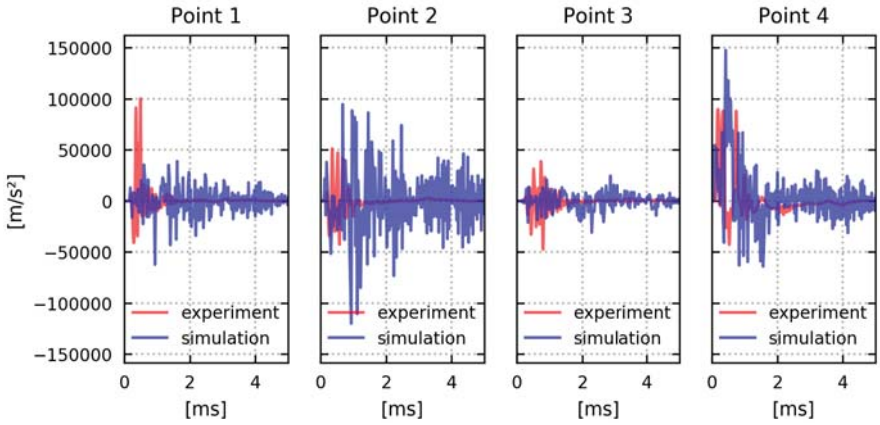

Figure 15: Visualization of the acceleration data in $[\mathrm{m/s^2}]$ comparing the test data with the numerical results of the plate S31P02 for the first 5 milliseconds at 4 measuring positions

The acceleration data were recorded at four positions on the plate, with three sensors mounted on the front and one sensor on the back (Figure 4). The measured data contain a time intervall of 2s. In the diagrams of Figure 14 bis 17, the measured values from the tests are only plotted for the first 5 milliseconds per plate compared to the numerical results based on the used time intervall of the numerical computations. Point 1 corresponds to measuring point ACC1, Point

2 correnspondsto ACC2 and so on. From the acceleration curve w.r.t. the time in every measuring position at every plate, it can be seen that the plate is damped faster than the numerical simulation. Further comparison have to be carried out with all measured data of all plates.

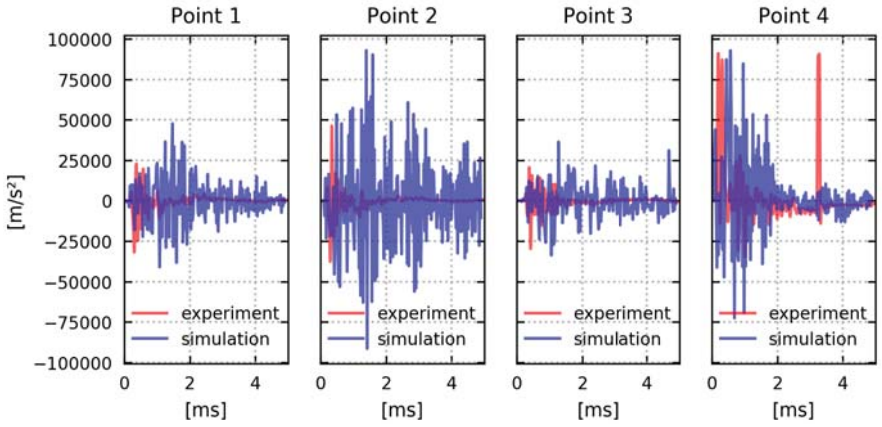

Figure 16: Visualization of the acceleration data in $[\mathrm{m/s^2}]$ comparing the test data with the numerical results of the plate S31P03 for the first 5 milliseconds at 4 measuring positions

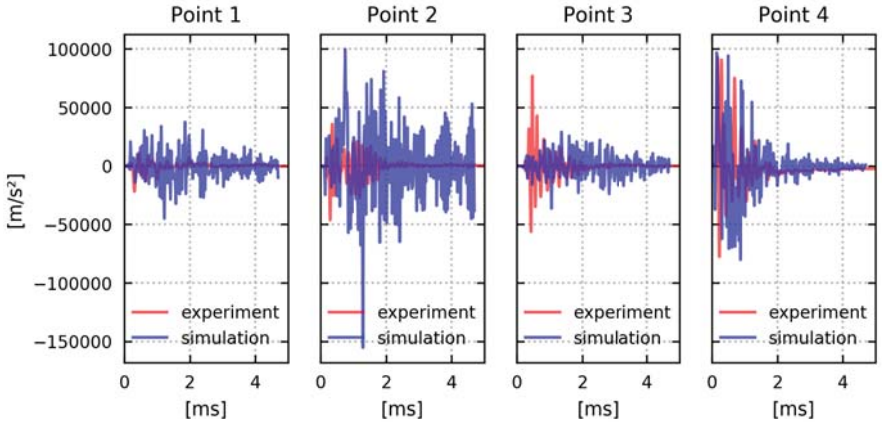

Figure 17: Visualization of the acceleration data in $[\mathrm{m/s^2}]$ comparing the test data with the numerical results of the plate S31P04 for the first 5 milliseconds at 4 measuring positions

In Figure 18, the maximum bearing force measured on the load cells in the tests with the results of the FEM is compared. Analogous to the previous comparisons, the results here are shown with constant bar diameter (left column) or constant spatial distribution (right column) w.r.t. the impact pulse. As in the previous figures, the colouring is black with circles as the second parameter increases, then red with squares and blue with triangles as marking of the measured data. The results from the numerical computations are colored the same. The measured values are marked with crosses for better differentiation.

The maximum forces in the bearings are mostly of the same order of magnitude. In the numerical results, the variance between the individual plates is much smaller than in the tested plates. Further investigations will follow, in which the relationship between the damage and the bearing reaction will also be investigated over time.

Figure 19 displays a selection of the analyzed tomographic results. Not all 36 plates of the reinforcement variation were examined. Here, 4 plates of the series 29/30 with a diameter of

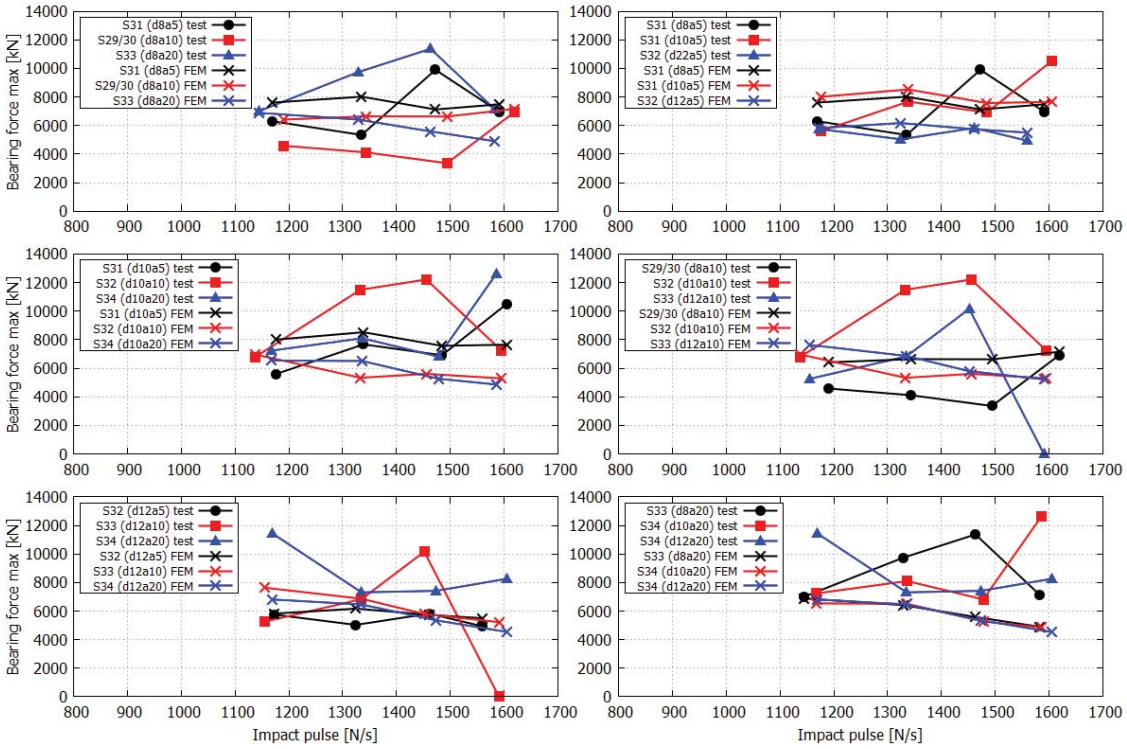

Figure 18: Visualization of the maximum bearing forces on the load cells comparing the test data with the numerical results

8 mm and a spatial distribution of 10 cm are compared to a plate of the series S31 (d = 8 mm and a = 5 cm) and two plates of the series S33 (d = 8 mm and a = 20 cm). In Figure 20, three plates with a spatial distribution of 20 cm and varying bar diameter are compared.

The crack maps (orange-red colored) were generated and in this case mapped to a layer of the radiated plate (gray colored). On some plates, the reinforcement bars are clearly visible (black colored). Only half plates are shown. The upper edge of each plate image corresponds to the middle cut edge of the entire plate. Due to the resolution, hairline cracks and cracks running diagonally into the material are not completely detected.

In table 3, the calculated damage degrees are shown. For a better allocation, the table lists the designation (series and plate), the rebar diameter (d_r), the spatial distribution of the rebars (a_r) and the impact pulse (I_{imp}). The total damage (dod total) is calculated from the material loss normalized to the mass of the total plate. The crack damage is calculated analogously from the crack volume normalized to the total volume. The identified crack volume from the tomographic data is calculated similar to the FEM damage maps. Both degrees of damage are evaluated separately and are based on different forms of damage (spalling and scabbing for one and crack volume for the other). In further steps, the crack maps are compared with the numerically computed damage maps in order to be able to configure the numerical parameters better for the future, also with regard to the damage. In this paper this takes place on the photos of the damaged plates, as shown in the Figures 21 to 23.

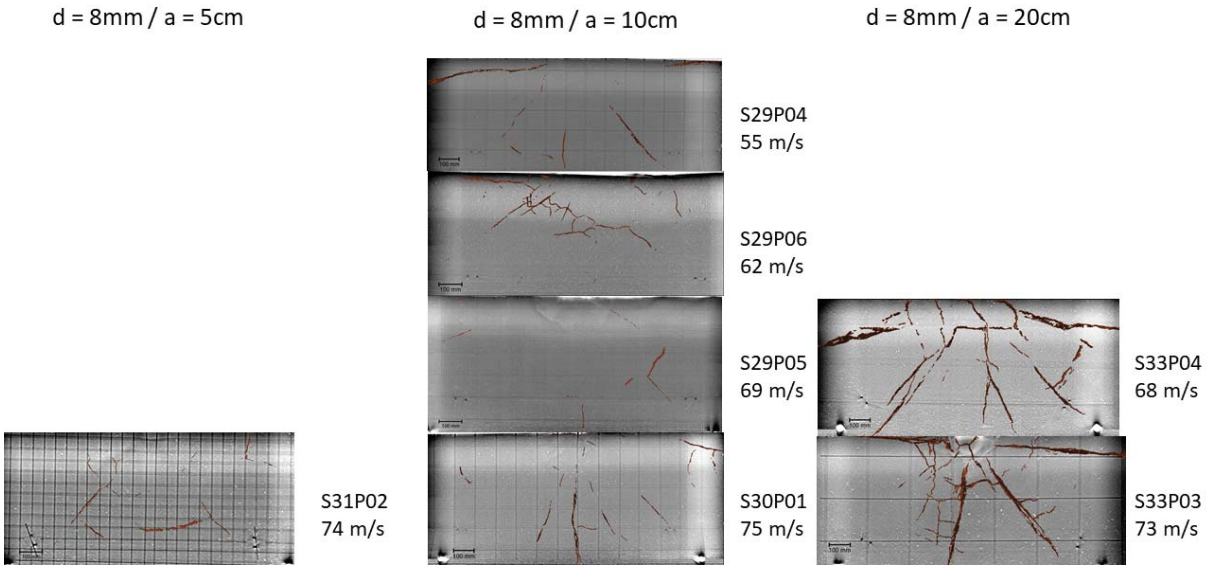

Figure 19: Visualization of the crack maps of the plates with a constant rebar diameter of 8 mm

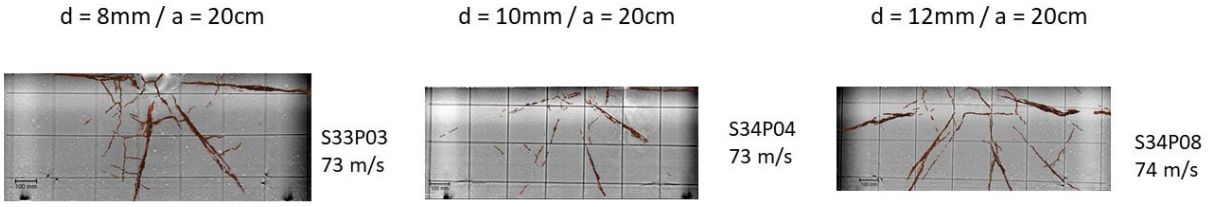

Figure 20: Visualization of the crack maps of the plates with a constant spatial distribution of 20 cm

designation	d_r [mm]	a_r [cm]	I_{imp} [N/s]	dod total [%]	dod crack [%]
S31P02	8	5	1592.01	0.824	0.0070
S29P04	8	10	1190.28	0.103	0.0130
S29P06	8	10	1343.80	0.041	0.0133
S29P05	8	10	1493.79	0.201	0.0007
S30P01	8	10	1618.64	0.411	0.0135
S33P04	8	20	1463.25	0.451	0.1044
S33P03	8	20	1582.85	0.441	0.1145
S34P04	10	20	1585.90	0.539	0.0442
S34P08	12	20	1604.44	1.452	0.0993

Table 3: Summary of the degree of crack damage (dod crack) and total damage (dod total) combined with the test parameters, like rebar diameter (d_r), the spatial distribution (a_r) and the impact pulse (I_{imp})

In the Figures 21 to 23, the results of the numerical simulations are compared to the crack patterns of the plates. On the left side, there is the middle cut surface, and on the right side, there is the half rear side of the plate, where the lower edge of the figure corresponds to the cut edge. The 4 plates of each series are shown sorted from top to bottom according to the impact velocity.

The cracks in the photos are highlighted in black and the spalling and scabbing in red. On

the photos, the individual cracks, the punching cone and the size of the impact area can be seen. The damage patterns of the FEM illustrate the probable damage due to the impactor. A blue coloring corresponds to a probability of 0%. The color gradient goes from blue to green to yellow to red. A red coloring corresponds to a probability of 100% damage of the element. The comparison of the representations (photo and FEM) indicates the difficulty of simulating crack structures if the damage level changes rapidly.

The material model was calibrated on previous plate experiments [21, 22, 19, 24]. The previous plates were not varied in the reinforcement parameters. The diameter remained constant 8 mm and the spatial distribution was 10 cm. For this reason, the correlation between the numerical data of the present plates and the experimental data in this series is better than for the others. Further refinements in the material model and in the contact modeling regarding the influence of the reinforcement will follow.

For a global evaluation of the damage, the external damage and the internal crack structures are of interest. In most cases, the cracks on the rear side of the plate between the numerical investigation and the damaged plate are identical. Difficulties occur in the case of spalling, since they do not appear in the numerical damage analysis. Due to the way the bearing is modeled, the damage to the bearing locations in the numerical model is unusually large.

The conformity of the cracks in the cut surface is less than that of the rear side of the plate. The impact velocities using in the tests are selected in such a way that, if possible, no bending failure and no perforation occurs. The damage area with cracks along the reinforcement and a punching cone due to the high compression force are in the focus. These patterns can be seen on the photos and in the numerical simulation. When comparing the photos with the numerical plots, not all computations show a match of the crack path. In contrast to the tests, the numerical results are reproducible and the models show no imperfections within the material.

In summary, the agreement is better for the plates with a distance of 10 cm than with a smaller or larger distance. The sensitivity of numerical modeling in this context is different from that of the experiments. In the experiments, there is still a lack of studies on the reproducibility of damage in order to be able to define a scattering width.

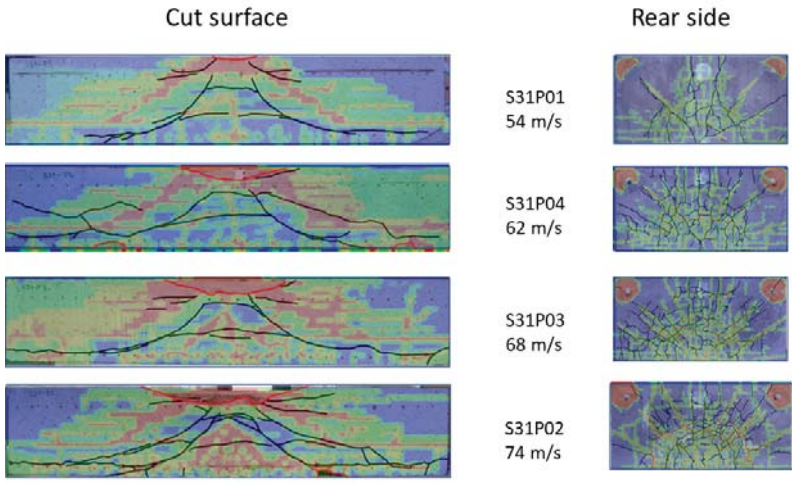

(a) Diameter of 8 mm and spacing of 5 cm

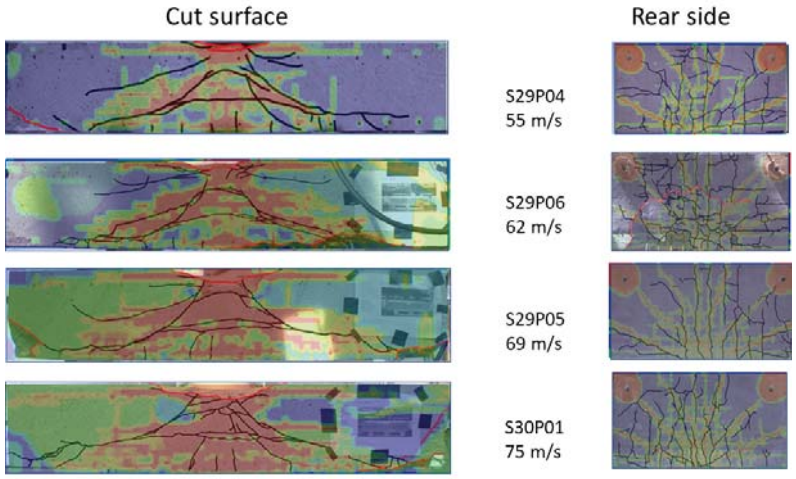

(b) Diameter of 8 mm and spacing of 10 cm

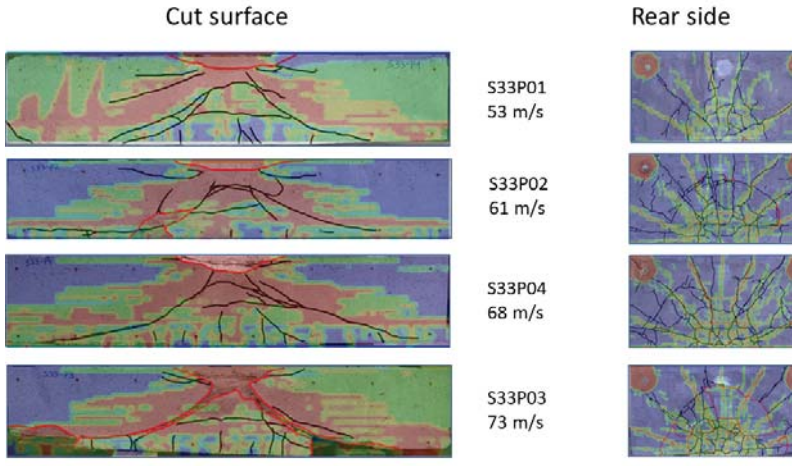

(c) Diameter of 8 mm and spacing of 20 cm

Figure 21: Comparison of the damage maps of the FEM (color map from blue to yellow to red, means from 0% to 100% damage) with the photos of the plates of the series with a constant diameter of 8 mm, left: middle cut surface, right: half rear side, the plates are sorted with raising velocity

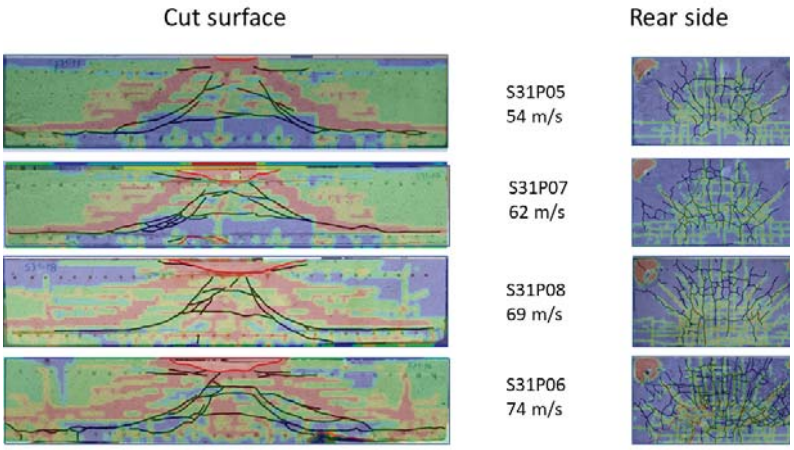

(a) Diameter of 10 mm and spacing of 5 cm

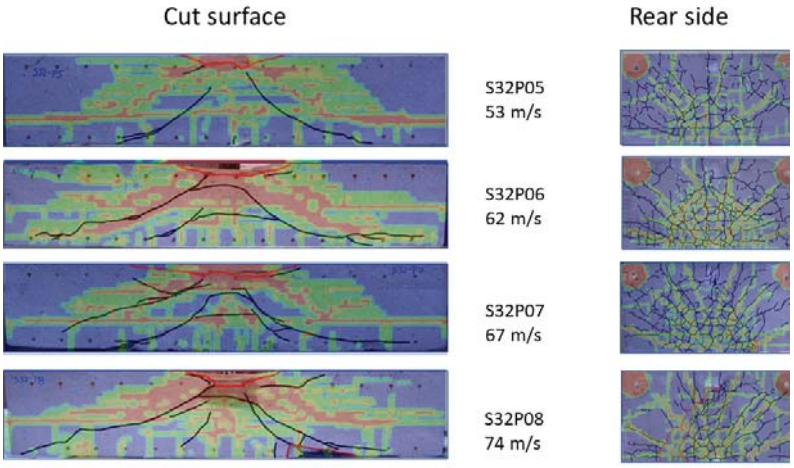

(b) Diameter of 10 mm and spacing of 10 cm

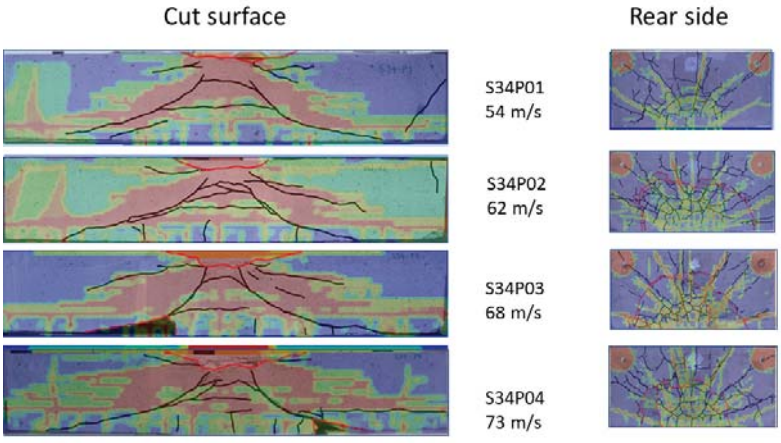

(c) Diameter of 10 mm and spacing of 20 cm

Figure 22: Comparison of the damage map of the FEM (color map from blue to yellow to red, means from 0% to 100% damage) with the photos of the plate of the series with a constant diameter of 10 mm, left: middle cut surface, right: half rear side, the plates are sorted with raising velocity

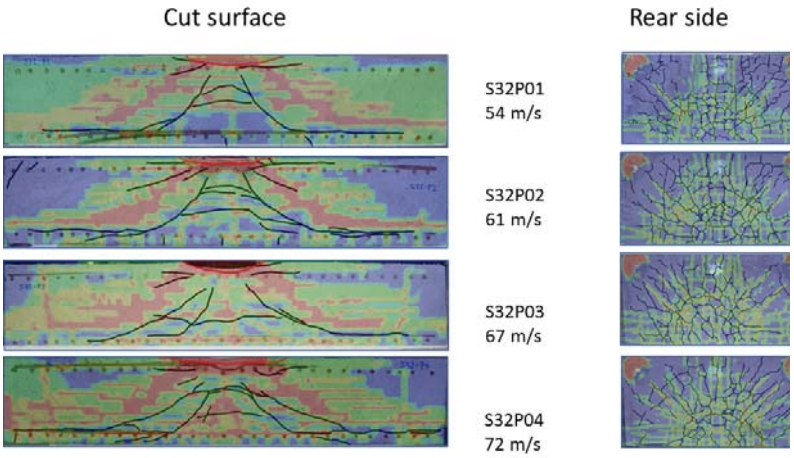

(a) Diameter of 12 mm and spacing of 5 cm

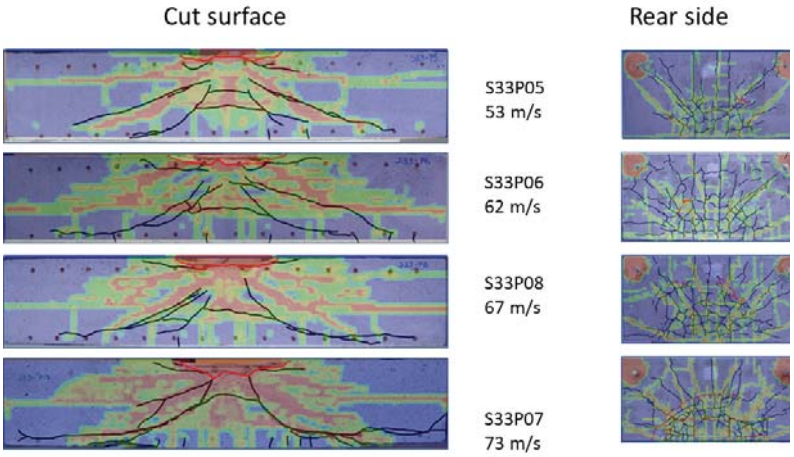

(b) Diameter of 12 mm and spacing of 10 cm

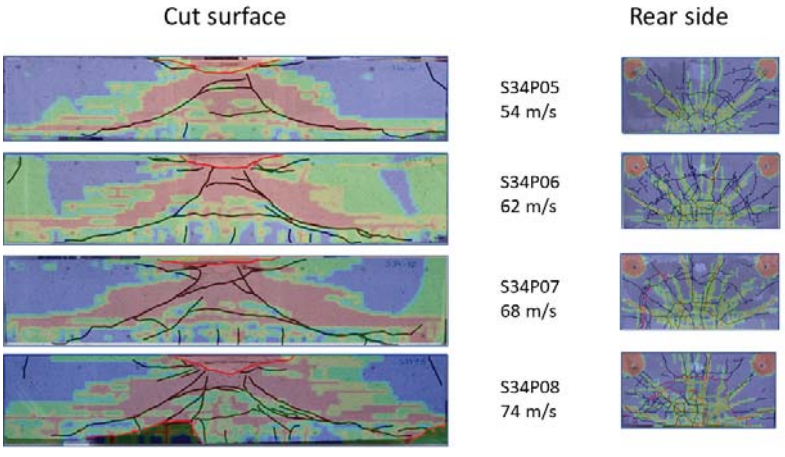

(c) Diameter of 12 mm and spacing of 20 cm

Figure 23: Comparison of the damage map of the FEM (color map from blue to yellow to red, means from 0% to 100% damage) with the photos of the plate of the series with a constant diameter of 12 mm, left: middle cut surface, right: half rear side, the plates are sorted with raising velocity

6 CONCLUSION

- With this variation of the reinforcement parameters, a large number of effects of local damage due to an impact was shown. In all series of reinforcement variation, the increase of damage with the impact velocity is clearly visible. Correlations between individual measured values and the structural behavior of the components were described.

- Further effects that concern the individual damage characteristics must be investigated more intensively. For example: What is the relationship between crack structure, impact area and reinforcement parameters? What about the reproducibility of damage? How large is the scatter range of the damage characteristics?

- The wide range of experiments and the detailed documentation is advantageous for further numerical investigations.

- It was shown that, the evaluation with the help of the combination of methods (direct analysis, tomography and FEM) can illustrate and explain many effects. The results of the combination of the evaluation methods tomography and numerics were presented using crack maps. In both methods, the structures were analyzed with the focus on damage. The damaged structure was identified and extracted. In further investigations the combinability of the tomographic data with the numerical results will be evaluated.

7 ACKNOWLEDGMENT

We thank the technical staff, especially Marcel Grunwald, for his support in the HEXY Lab. This work was funded by the German Federal Ministry of Economic Affairs and Energy under grant number 1501542 on the basis of a decision by the German Bundestag.

REFERENCES

[1] X. W. Chen, X. L. Li, F. L. Huang, H. J. Wu, Y. Z. Chen, Normal perforation of reinforced concrete target by rigid projectile, *International Journal for Impact Engineering*, **35**, 1119–1129, 2008.

[2] Q. M. Li, S. R. Reid, H. M. Wen, A. R. Telford, Local impact effects of hard missiles on concrete targets, *International Journal of Impact Engineering*, **32**, 224–284, 2005.

[3] U.S. Department of Energy, DOE Standard: Accident Analysis for Aircraft Crash into Hazardous Facilities, **DOE-STD-3014-96**, 2006.

[4] T. Atou, Y. Sano, M. Katayama, S. Hayashi, Damage Evaluation of Reinforced Concrete Columns by Hypervelocity Impact, *Procedia Engineering*, **58**, 348–354, 2013.

[5] M. Beppu, K. Miwa, M. Itoh, M. Katayama, T. Ohno, Damage evaluation of concrete plates by high-velocity impact, *International Journal of Impact Engineering*, **35**, 1419–1426, 2008.

[6] P. M. Booker, J. D. Cargile, B. L. Kistler, V. La Saponara, Investigation on the response of segmented concrete targets to projectile impacts, *International Journal of Impact Engineering*, **36**, 926–939, 2009.

[7] A. Lastunen, I. Hakola, E. Järvinen, K. Calonius, J. Hyvärinen, Impact Test Facility, *International Conference Structural Mechanics in Reactor Technology SMIRT19*, **J08/2**, 2007.

[8] M. Sadiq, Z. Xiu Yun, P. Rong, Simulation analysis of impact tests of steel plate reinforced concrete and reinforced concrete slabs against aircraft impact and its validation with experimental results, *Nuclear Engineering and Design*, **273**, 653–667, 2014.

[9] T. Zhang, H. Wu, T. Huang, J.H. Sheng, Q. Fang, F.J. Zhang, Penetration depth of RC panels subjected to the impact of aircraft engine missiles, *Nucl. Eng. Des. 335*, 44–53, 2018.

[10] Sandia National Laboratories SNL, Containment Integrity at Sandia National Laboratories, An Overview, *Sandia National Laboratories*, NUREG/CR-6906, SAND2006-2274P, 2006.

[11] T. Sugano, H. Tsubota, Y. Kasai, N. Koshika, H. Ohnuma, W.A. von Riesemann, D.C. Bickel, M.B. Parks, Local damage to reinforced concrete structures caused by impact of aircraft engine missiles, Part 1. Test program, method and results, *Nucl. Eng. Des.*, **140**, 387–405, 1993.

[12] N. Orbovic, F. Tarallo, J. Rambach, G. Sagals, A. Blahoianu, IRIS2012 OECD/NEA/CSNI benchmark: Numerical simulations of structural impact, *Nuclear Engineering and Design*, **295**, 700–715, 2015.

[13] Z. Duan, L. Zhang, L. Wen, C. Guo, Z. Bai, Z. Ou, F. Huang, Experimental research on impact loading characteristics by full-scale airplane impacting on concrete target, *Nucl. Eng. Des.*, **328**, 292–300, 2018.

[14] J. Leppänen, Concrete subjected to projectile and fragment impacts: Modelling of crack softening and strain rate dependency in tension, *International Journal of Impact Engineering*, **32**, 1828–1841, 2006.

[15] M. Abdel-Kader, Numerical predictions of the behaviour of plain concrete targets subjected to impact, *International journal of protective structures*, **9/3**, 313–346, 2018.

[16] N. Gebbeken, M. Hübner, M. Larcher, G. Michaloudis, A. Pietzsch, Beton und Stahlbetonkonstruktionen unter Explosion und Impakt, *Beton- und Stahlbetonbau*, **108/8**, 515–527, 2013.

[17] T. Duc-Kien, K. Seung-Eock, Numerical simulation of pre-stressed concrete slab subjected to moderate velocity impact loading, *Engineering Failure Analysis*, **79**, 820–835, 2017.

[18] O. Martin, V. Centro, T. Schwoertzig, Finite element analysis on the VTT–IRSN flexural failure test, *Nucl. Eng. Des.*, **252**, 88–95, 2012.

[19] F. Hille, A. Rogge, G. Nery, B. Redmer, Bauteilverhalten unter stoßartiger Beanspruchung durch aufprallende Behälter (Flugzeugtanks): Phase 1B: Quantifizierung der Schädigung des Betongefüges, *Project report BAM*, Berlin, Germany, **GRS1501477**, 2017.

[20] G. Nery, F. Hille, A. Rogge, Post-impact assessment of reinforced concrete plate load capacity, *Proceedings of the International Concrete Sustainability Conference 2016*, 1–9, 2016.

[21] M. Just, M. Curbach, T. Kühn, M. Hering, Bauteilverhalten unter stoßartiger Beanspruchung durch aufprallende Behälter (Flugzeugtanks): Phase 1A: Maßstabseffekte bei stoßartiger Beanspruchung, *Project report TU Dresden*, Dresden, Germany, **GRS1501438**, 2016.

[22] M. Hering, T. Kühn, M. Curbach, Bauteilverhalten unter stoßartiger Beanspruchung durch aufprallende Behälter (Flugzeugtanks): Phase 1B: Quantifizierung der Schädigung des Betongefüges, *Project report TU Dresden*, **GRS1501479**, 2017.

[23] T. Kühn, M. Curbach, Behavior of RC-slabs under impact-loading, *EPJ Web of Conferences*, **94**, 1–6, 2015.

[24] M. Hering, F. Bracklow, T. Kühn, M. Curbach, Impact experiments with reinforced concrete plates of different thicknesses, *Structural Concrete*, 1464–1477, 2019.

[25] A. Deresch, K. U. Thiessenhusen, U. Ewert, C. Bellon, Fast shift-average reconstruction for coplanar translational laminography, *DGZfP-Jahrestagung*, 2014.

[26] R. Moosavi, M. Grunwald, B. Redmer, Crack detection in reinforced concrete, *NDT and E International*, **106**, 2020.

[27] ANSYS INC., ANSYS Explicit Dynamics Analysis Guide, **18.2**, 2017.

[28] A. Haufe, Dreidimensionale Simulation bewehrter Flächentragwerke aus Beton mit der Plastizitätstheorie (Diss.), *Universität Stuttgart - Fakultät Bauingenieur- und Vermessungswesen*, 2001.

[29] W. Riedel, Beton unter dynamischen Lasten, Meso- und makromechanische Modelle und ihre Parameter (Diss.), *Universität der Bundeswehr München*, 2000.

[30] A. Rogge, Materialverhalten von Beton unter mehrachsiger Beanspruchung (Diss.), *Technische Universität München*, 2002.

EURODYN 2020
XI International Conference on Structural Dynamics
M. Papadrakakis, M. Fragiadakis, C. Papadimitriou (eds.)
Athens, Greece, 23–26 November 2020

MODEL REDUCTION FOR STRUCTURES SUBJECTED TO BLAST LOADING BY USE OF DYNAMIC SUBSTRUCTURING

Linus Andersson, Peter Persson, Kent Persson

Department of Construction Sciences, Lund University
P.O. Box 118, SE-221 00 Lund, Sweden
e-mail: {linus.andersson, peter.persson, kent.persson}@construction.lth.se

Keywords: Dynamic substructuring, Blast loading, Direct time-integration, Beam frame structure

Abstract. *In the present study, strategies are developed to enable time-efficient models for structures subjected to blast loading, appropriate for use in a structural design process. Dynamic substructuring is employed to obtain reduced models with localized nonlinearities, such as predefined plastic hinges in a beam–column structure. The parts of the substructures that remains linear elastic are modeled by Ritz-vectors whereas parts with a nonlinear response are retained as physical degrees-of-freedom. Furthermore, a time-stepping method is presented that is shown to be suitable for reduced models including local and predefined rigid–plastic behavior. The proposed methodology is applied and demonstrated in a numerical example of a concrete frame structure. Both the well-established Craig-Bampton method and reduction bases enriched by so-called correction modes are evaluated. For the load case studied, it is shown that the standard Craig-Bampton technique is suitable for reducing the substructures. Furthermore, it is shown that only a few Ritz-vectors are needed to sufficiently describe the deformation of the structure. However, additional modes are needed to ensure an accurate representation of the interface forces between the substructures.*

1 INTRODUCTION

Simplified models, such as equivalent single-degree-of-freedom (SDOF) systems, are often used for design of concrete members subjected to blast loading, an approach proposed already in the mid-1960s [1]. When this simplified approach is used for studying individual structural members, the supporting global structure is often considered as rigid and thus represented by prescribed displacement boundary conditions in the local response analyses. Hence, if a global response analysis is required it is in general performed in a subsequent stage, where the reaction forces computed in the local analyses are applied on the global structure. Such a procedure can be suitable if the stiffness and/or mass of the global structure are relatively large. However, in cases where the structural member is stiff and heavy, or even integrated as a part of the global lateral load-bearing structure, it can be necessary to employ a model of the coupled system. Furthermore, it can be necessary to include higher order modes to accurately capture the force transmitted between individual members and the global structure, in particular if the structure is subjected to a pulse with short duration and large peak pressure, as e.g. discussed in [2].

The dynamic response of a structure can e.g. be computed by use of a nonlinear finite element (FE) model, including the members subjected to external loading and the supporting global structure. However, the design of concrete structures subjected to blast loading is often an iterative process, where the cross-section dimensions and the amount and arrangement of bending reinforcement affect the dynamic response. Therefore, simplified and computationally efficient models are key in the conceptual design phase.

In the present study, strategies are developed to enable time-efficient models for structures subjected to blast loading, appropriate for use in a structural design process. More specifically, reduced models with localized nonlinearities, such as predefined plastic hinges in a beam–column structure, are obtained by use of dynamic substructuring (DS) (for an overview of DS techniques see e.g. [3,4]). Hence, parts that remains linear elastic are reduced and modeled by Ritz-vectors whereas the degrees-of-freedom (DOFs) included in parts with a nonlinear response are retained as physical DOFs. Furthermore, a time-stepping scheme is presented that is shown to be suitable for reduced models including local and predefined rigid–plastic behavior, such as frame structures with plastic hinges.

2 SIMPLIFIED MODELING OF CONCRETE STRUCTURES SUBJECTED TO BLAST LOADING

As for dynamic loading in general, the design of concrete structures subjected to blast loading can be challenging due to that the response is affected by the structure's mass, stiffness and strength. Hence, a modification of the dimensions, the amount and/or arrangement of reinforcement must, in general, be verified by an updated dynamic response analyses. Furthermore, a nonlinear response analysis is often required. The kinetic energy induced by the external pressure is converted into elastic and plastic strain energy, and if the plastic dissipation is omitted in the analysis the response can be inaccurate, e.g. resulting in a very conservative design. Therefore, simplified nonlinear SDOF models are often employed to evaluate the response of individual structural members.

In addition to the design of individual members, the global structure must be designed to resist progressive collapse and to ensure lateral stability. If a nonlinear response analysis is required for studying the global response, it is in general not straight-forward to construct a simplified model. Hence, a more refined nonlinear FE model of the whole structure can be necessary.

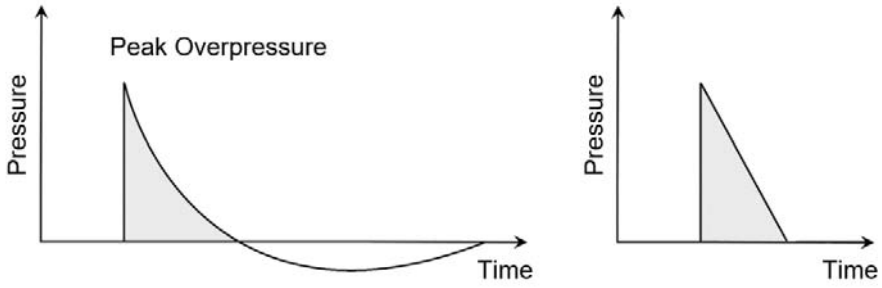

Figure 1: Typical (left) and idealized (right) blast pressure–time history.

2.1 Impulse pressure due to unconfined explosion

An unconfined explosion located on the ground surface results in a ground reflected shock wave that moves radially away from the center of the explosion [5]. If the explosion center is reasonable far from a structure, the pressure acting on the structure can be approximated by a uniform pressure. Upon impact, the initial wave is reinforced and reflected. The reflected impulse pressure acting on the structure is characterized by a very short duration and large peak pressure. For design purposes, the reflected impulse can, in general, be replaced by an equivalent triangular pulse, as shown in Figure 1. The actual duration is then replaced by a fictitious duration, computed from the peak reflected pressure and the reflected impulse.

2.2 Reduced models for design of concrete members

To ensure an adequate design of concrete members, such as beams and plates, subjected to blast loading, both the local response and the semi-global response (i.e. the global response of an individual member) must be considered. Hence, concrete members must be designed to resist local failure modes, such as punching shear failure, scabbing, spalling and penetration. Further, the shear force capacity and rotation capacity must be sufficiently large. Thus, it is crucial to ensure sufficient ductility and to avoid brittle failure modes.

A common procedure when evaluating the semi-global response of beams and plates is to set up an equivalent elasto-plastic SDOF system, where the yield force is derived from the ultimate moment capacity [1]. In fact, the yield force corresponds to the ultimate load, which implies that the maximum shear force in the dynamic response analysis is equal to the shear force given by a static yield line analysis. As e.g. shown in [2], the shear force computed using this simplified approach might be underestimated due to the neglection of higher order modes. Nonetheless, the approach can be reasonably accurate and in accordance with several design codes, such as UFC [5].

Using a simplified equivalent SDOF system implies that the position of the yield lines and/or plastic hinges can by assumed in accordance with a static yield line analysis, where the spatial load distribution correspond to the spatial distribution of the impulse pressure. This assumption is also the basis in the modeling strategies developed in Sections 3 and 4. However, it should be noted that this approach is primarily intended to be used in a conceptual design phase, i.e. a full nonlinear analysis can be necessary to verify the final design.

3 DYNAMIC SUBSTRUCTURING OF STRUCTURES WITH PLASTIC HINGES

By use of dynamic substructuring (DS) the aim is to efficiently compute the dynamic response of a structure by subdivision of the structure into substructures. Solving several substructures can be computationally less expensive than solving one large system. Moreover, DS can be employed to reduce systems with localized nonlinearities, such as predefined plastic

hinges in a beam–column structure. The parts of the structure that remains linear elastic is then reduced and modeled by Ritz-vectors whereas the DOFs included in parts with a nonlinear response are retained as physical DOFs.

In most DS techniques reduction is performed on the substructure level. Hence, the substructure displacements $\mathbf{u}^{(s)}$ are represented by a reduced set of coordinates $\mathbf{q}^{(s)}$, given by

$$\mathbf{u}^{(s)} = \mathbf{T}\mathbf{q}^{(s)} \tag{1}$$

where superscript *s* is the substructure label and $\mathbf{T}$ is a $n^{(s)} \times m^{(s)}$ transformation matrix, whose columns are Ritz-vectors, or so-called component modes. Depending on the DS technique, the reduced vector $\mathbf{q}^{(s)}$ can include physical master (or boundary) DOFs and/or generalized coordinates. Typically, $m^{(s)} << n^{(s)}$.

A FE formulation of a substructure leads to a linear equation of motion of the following form:

$$\mathbf{M}^{(s)}\ddot{\mathbf{u}}^{(s)} + \mathbf{C}^{(s)}\dot{\mathbf{u}}^{(s)} + \mathbf{K}^{(s)}\mathbf{u}^{(s)} = \mathbf{p}^{(s)} \tag{2}$$

where $\mathbf{p}^{(s)}$ is a $n^{(s)} \times 1$ substructure load vector and $\mathbf{M}^{(s)}$, $\mathbf{C}^{(s)}$ and $\mathbf{K}^{(s)}$ are the $n^{(s)} \times n^{(s)}$ substructure mass, damping and stiffness matrices, respectively. By inserting Equation (1) in (2) and pre-multiplying with $\mathbf{T}^{\mathrm{T}}$ the reduced subsystem is given by:

$$\widetilde{\mathbf{M}}^{(s)}\ddot{\mathbf{q}}^{(s)} + \widetilde{\mathbf{C}}^{(s)}\dot{\mathbf{q}}^{(s)} + \widetilde{\mathbf{K}}^{(s)}\mathbf{q}^{(s)} = \tilde{\mathbf{p}}^{(s)} \tag{3}$$

where

$$\widetilde{\mathbf{M}}^{(s)} = \mathbf{T}^{\mathrm{T}}\mathbf{M}^{(s)}\mathbf{T}, \qquad \widetilde{\mathbf{C}}^{(s)} = \mathbf{T}^{\mathrm{T}}\mathbf{C}^{(s)}\mathbf{T}, \qquad \widetilde{\mathbf{K}}^{(s)} = \mathbf{T}^{\mathrm{T}}\mathbf{K}^{(s)}\mathbf{T}, \qquad \tilde{\mathbf{p}}^{(s)} = \mathbf{T}^{\mathrm{T}}\mathbf{p}^{(s)} \tag{4}$$

The size of the reduced system matrices $\widetilde{\mathbf{M}}^{(s)}$, $\widetilde{\mathbf{C}}^{(s)}$ and $\widetilde{\mathbf{K}}^{(s)}$ is thus $m^{(s)} \times m^{(s)}$ and the reduced load vector $\tilde{\mathbf{p}}^{(s)}$ is $m^{(s)} \times 1$ (to simplify the notation the superscript *s* will be left out until Section 3.3, on substructure coupling procedures). The substructures are then reassembled to form a reduced model of the full coupled system, why DS is sometimes referred to as Component Mode Synthesis (CMS).

Arguably the most straight-forward methods within DS are the so-called condensation methods, where only physical master DOFs are included in $\mathbf{q}$. The most common condensation method is Guyan reduction, also referred to as static condensation due to that inertia effects are ignored [6]. The Guyan transformation matrix is given by

$$\begin{bmatrix}\mathbf{u}_i \\ \mathbf{u}_b\end{bmatrix} = \begin{bmatrix}-\mathbf{K}_{ii}^{-1}\mathbf{K}_{ib} \\ \mathbf{I}_{bb}\end{bmatrix}\mathbf{u}_b = \begin{bmatrix}\boldsymbol{\Psi}_{ib} \\ \mathbf{I}_{bb}\end{bmatrix}\mathbf{u}_b = \mathbf{T}_{\mathrm{G}}\mathbf{q} \tag{5}$$

where the subscripts *i* and *b* denotes the *interior* and interface *boundary* DOFs, $\mathbf{T}_{\mathrm{G}}$ is the Guyan transformation matrix and $\mathbf{q}$ contains the physical boundary DOFs. The columns of the transformation matrix are the so-called constraint modes, obtained by prescribing a unit displacement for a boundary DOF, while the interior DOFs are force-free and the other boundary DOFs are held fixed. Using this approach, "exact" results are achieved for static loading. However, due to neglected inertia effects the accuracy can be expected to decrease with an increasing forcing frequency.

Using a similar procedure but replacing the stiffness matrix with the dynamic stiffness matrix, exact result can instead be achieved for a certain forcing frequency, often referred to as dynamic reduction. There are also other more sophisticated condensation methods, such as Improved Reduction System (IRS) and System Equivalent Reduction Expansion Process (SEREP),

where the number of exact resonances is less or equal to the number of boundary DOFs [7]. However, using condensation methods, it is not possible to both obtain a reduced model that is "statically complete" (i.e. a basis for all possible deformations that result from loading at the substructure boundary nodes) and at the same time keeping exact resonances. To achieve this, a CMS approach is required that uses generalized coordinates representing the amplitudes of additional Ritz-vectors.

Several CMS techniques have been developed since the 1960s, which can be divided into *fixed-interface* and *free-interface* methods. The most popular approach, a fixed-interface method, is CMS by Craig-Bampton (C-B), developed in the late 1960s [8]. The C-B method combines fixed-interface normal modes with so-called constraint modes, see further Section 3.1. Free-interface methods, using so-called free-interface component modes, were developed by MacNeal, Rubin and Craig and Chang in the 1970s [9,10,11]. In addition, another free-interface method, the dual Craig-Bampton method, was proposed in the early 2000s which, in contrast to the other free-interface methods, preserves the sparsity of the system matrices [12].

Reducing a structure with plastic hinges, it is important to employ a DS technique where the physical boundary DOFs, namely the rotational DOFs at the plastic hinges, are retained. Therefore, the CMS method proposed by Craig and Chang is excluded due to an assembling procedure that removes the physical boundary DOFs. The dual C-B method is an interesting approach since the interface forces are kept as DOFs in the assembled system. However, this method produces negative eigenvalues which make a stable time integration impossible [13] (an approach to overcome this issue is e.g. proposed in [13], unfortunately this approach includes removing all physical DOFs).

Apart from retaining the physical boundary DOFs at the plastic hinges, the plastic deformations of the assembled system must be resolved. Hence, the reduced subsystems should be "statically complete" and rigid body modes of the subsystems should be included in the reduction basis. Using the C-B method, the rigid body modes are not explicitly included in the reduction basis. However, the rigid body modes are spanned by the constraint modes. In fact, the set of constraint modes is a basis for all possible deformations that result from loading at the substructure boundary nodes [14]. In addition to the C-B method, the free-interface methods by MacNeal and Rubin retains the physical boundary DOFs in the assembled system and explicitly includes the rigid body modes in the reduction basis.

In summary, either the fixed-interface C-B method or the free-interface methods by MacNeal and Rubin are judged to be the most suitable methods for reducing a beam–column structure including predefined plastic joints. A free-interface approach can be expected to be more accurate upon yielding, i.e. when the joint stiffness is zero, whereas a fixed-interface approach can be expected to be more accurate when the joints are fixed, i.e. when yielding does not occur. Based on this observation it is assumed that the classic C-B approach, which preserves the sparsity of the system matrices, is the preferred choice.

3.1 Craig-Bampton method

The Craig-Bampton method combines the retained physical DOFs with generalized coordinates corresponding to the amplitudes of so-called fixed-interface normal modes. Neglecting damping the partitioned mass and stiffness matrices can be written as:

$$\begin{bmatrix} \mathbf{M}_{ii} & \mathbf{M}_{ib} \\ \mathbf{M}_{bi} & \mathbf{M}_{bb} \end{bmatrix} \begin{bmatrix} \ddot{\mathbf{u}}_i \\ \ddot{\mathbf{u}}_b \end{bmatrix} + \begin{bmatrix} \mathbf{K}_{ii} & \mathbf{K}_{ib} \\ \mathbf{K}_{bi} & \mathbf{K}_{bb} \end{bmatrix} \begin{bmatrix} \mathbf{u}_i \\ \mathbf{u}_b \end{bmatrix} = \begin{bmatrix} \mathbf{p}_i \\ \mathbf{p}_b \end{bmatrix} \tag{6}$$

By setting the boundary displacements to zero in Equation (6), the fixed-interface normal modes are obtained by the generalized eigenvalue problem:

$$\left(\mathbf{K}_{ii} - \omega_j^2 \mathbf{M}_{ii}\right)\left\{\boldsymbol{\phi}_i\right\}_j = 0 \tag{7}$$

where $\mathbf{K}_{ii}$ and $\mathbf{M}_{ii}$ are the interior stiffness and mass matrices. The eigenvectors are normalized so that $\boldsymbol{\Phi}_{ii}{}^{\mathrm{T}}\mathbf{M}_{ii}\boldsymbol{\Phi}_{ii} = \mathbf{I}_{ii}$, where $\boldsymbol{\Phi}_{ii}$ is the complete set of fixed-interface normal modes. The physical coordinates can then be represented as:

$$\begin{bmatrix}\mathbf{u}_i \\ \mathbf{u}_b\end{bmatrix} = \begin{bmatrix}\boldsymbol{\Phi}_{ik} & \boldsymbol{\Psi}_{ib} \\ \mathbf{0}_{bk} & \mathbf{I}_{bb}\end{bmatrix}\begin{bmatrix}\mathbf{q}_k \\ \mathbf{u}_b\end{bmatrix} = \mathbf{T}_{\text{C-B}}\mathbf{q} \tag{8}$$

where the subscript k denotes the kept fixed-interface normal modes, $\mathbf{T}_{\text{C-B}}$ is the Craig-Bampton transformation matrix, $\mathbf{q}_k$ is the generalized coordinates and $[\boldsymbol{\Psi}_{ib} \quad \mathbf{I}_{bb}]^{\mathrm{T}}$ is the constraint mode matrix, equivalent to the Guyan reduction basis. Hence, the Craig-Bampton method can be interpreted as an extension of the Guyan reduction where the neglected inertia terms are compensated by including a set of fixed-interface normal modes.

3.2 Craig-Bampton with Modal Truncation Augmentation

The fixed-interface normal modes included in the C-B reduction basis can be augmented by so-called high order static correction modes, which can be interpreted as a form of generalization of the Guyan static modes. The C-B method with so-called Modal Truncation Augmentation (MTA) is presented in [15].

If the internal forces are zero, the top row of Equation (6) can be rewritten as:

$$\mathbf{M}_{ii}\ddot{\mathbf{u}}_i + \mathbf{K}_{ii}\mathbf{u}_i = -\mathbf{M}_{ib}\ddot{\mathbf{u}}_b - \mathbf{K}_{ib}\mathbf{u}_b \tag{9}$$

Hence, the substructure can be considered excited by imposed displacements on its boundary. Further, the internal displacements can be approximated as

$$\mathbf{u}_i = \mathbf{u}_{i,\text{stat}} + \mathbf{y} \tag{10}$$

where $\mathbf{u}_{i,\text{stat}} = -\mathbf{K}_{ii}{}^{-1}\mathbf{K}_{ib}\mathbf{u}_b$ is the quasi-static solution modified by the second term $\mathbf{y}$ to obtain the dynamic response, i.e. similarly to the well-established mode acceleration method, e.g. described in [16]. By inserting Equation (10) into Equation (9) the dynamic response of the relative solution is given by

$$\mathbf{M}_{ii}\ddot{\mathbf{y}} + \mathbf{K}_{ii}\mathbf{y} = -\mathbf{M}_{ii}\ddot{\mathbf{u}}_{i,\text{stat}} - \mathbf{M}_{ib}\ddot{\mathbf{u}}_b = \mathbf{Y}\ddot{\mathbf{u}}_b \tag{11}$$

where $\mathbf{Y} = \mathbf{M}_{ii}\mathbf{K}_{ii}{}^{-1}\mathbf{K}_{ib} - \mathbf{M}_{ib}$, which can be interpreted as inertia forces associated to static modes [15]. This procedure can be continued by replacing $\mathbf{y}$ with a quasi-static solution and a dynamic correction. Hence, a recursive procedure is obtained, indicating that the dynamic response can be approximated as

$$\mathbf{u}_i \approx -\mathbf{K}_{ii}{}^{-1}\mathbf{K}_{ib}\mathbf{u}_b + \sum_{j=1}^{n}\left(-\mathbf{K}_{ii}{}^{-1}\mathbf{M}_{ii}\right)^{j-1}\mathbf{K}_{ii}{}^{-1}\mathbf{Y}\frac{\mathrm{d}^{2j}\mathbf{u}_b}{\mathrm{d}t^{2j}} \tag{12}$$

where n is the number of static corrections.

According to Equation (12) a dynamic response analysis is not included in the approximation. However, if a dynamic analysis including k eigenmodes has been performed, part of the corrections is already considered. The expression for the higher order corrections can then be rewritten as:

$$\mathbf{u}_{i,cor.j} \approx \left(\mathbf{K}_{ii}^{-1} - \sum_{r=1}^{k} \frac{\boldsymbol{\phi}_r \boldsymbol{\phi}_r^{\mathrm{T}}}{\omega_r^2} \right) \left(-\mathbf{M}_{ii} \mathbf{K}_{ii}^{-1} \right)^{j-1} \mathbf{Y} \frac{\mathrm{d}^{2j} \mathbf{u}_b}{\mathrm{d}t^{2j}} \tag{13}$$

where we use that the inverse of the stiffness matrix can be expressed as

$$\mathbf{K}_{ii}^{-1} = \sum_{r=1}^{N} \frac{\boldsymbol{\phi}_r \boldsymbol{\phi}_r^{\mathrm{T}}}{\omega_r^2} = \sum_{r=1}^{k} \frac{\boldsymbol{\phi}_r \boldsymbol{\phi}_r^{\mathrm{T}}}{\omega_r^2} + \sum_{r=k+1}^{N} \frac{\boldsymbol{\phi}_r \boldsymbol{\phi}_r^{\mathrm{T}}}{\omega_r^2} \tag{14}$$

where N is the total number of eigenmodes, and $\boldsymbol{\phi}_r$ and ω_r is the eigenmode and eigenfrequency for mode r. Hence, the space already spanned by the fixed-interface normal modes is removed from the corrections. The total response is then given by

$$\mathbf{u}_i \approx \sum_{r=1}^{k} \boldsymbol{\phi}_r q_r + \sum_{j=0}^{n} \mathbf{u}_{i,cor.j} \tag{15}$$

where $\mathbf{u}_{i,cor.0} = -\mathbf{K}_{ii}^{-1} \mathbf{K}_{ib} \mathbf{u}_b$. Furthermore, the amplitudes $\frac{\mathrm{d}^{2j} \mathbf{u}_b}{\mathrm{d}t^{2j}}$ can be treated as separate DOFs, i.e. instead of high order corrections the modal basis is augmented by high order correction *modes*, also referred to as force-dependent Ritz-vectors or Krylov vectors. Hence, the j-th order correction modes is given by:

$$\mathbf{x}_{i,cor.j} = \left(\mathbf{K}_{ii}^{-1} - \sum_{r=1}^{k} \frac{\boldsymbol{\phi}_r \boldsymbol{\phi}_r^{\mathrm{T}}}{\omega_r^2} \right) \left(\mathbf{M}_{ii} \mathbf{K}_{ii}^{-1} \right)^{j-1} \mathbf{Y} \tag{16}$$

Note that the number of vectors generated in each iteration equals the number of boundary DOFs, why the subspace spanned by the generated vectors is sometimes referred to as a block-Krylov subspace [14]. The static correction modes are both mass- and stiffness-orthogonal to the fixed-interface normal modes. However, they are not mutually orthogonal. This can e.g. be achieved by solving a small eigenvalue problem:

$$(\mathbf{X}_{cor}^{\mathrm{T}} \mathbf{K} \mathbf{X}_{cor}) \mathbf{Z} = (\mathbf{X}_{cor}^{\mathrm{T}} \mathbf{M} \mathbf{X}_{cor}) \mathbf{Z} \boldsymbol{\Lambda} \tag{17}$$

where $\mathbf{X}_{\mathrm{cor}}$ is the correction mode matrix. The eigenvectors are normalized so that $\mathbf{Z}^{\mathrm{T}} \left(\mathbf{X}_{\mathrm{cor}}^{\mathrm{T}} \mathbf{M} \mathbf{X}_{\mathrm{cor}} \right) \mathbf{Z} = \mathbf{I}$ and the orthonormal basis of the correction vectors is then given by $\tilde{\mathbf{X}}_{\mathrm{cor}} = \mathbf{X}_{\mathrm{cor}} \mathbf{Z}$. The relation between the substructure physical DOFs and the reduced coordinate is then given by

$$\begin{bmatrix} \mathbf{u}_i \\ \mathbf{u}_b \end{bmatrix} = \begin{bmatrix} \boldsymbol{\Phi}_{ik} & \tilde{\mathbf{X}}_{cor} & \boldsymbol{\Psi}_{ib} \\ \mathbf{0}_{bk} & \mathbf{0}_{bn} & \mathbf{I}_{bb} \end{bmatrix} \begin{bmatrix} \mathbf{q}_k \\ \mathbf{q}_n \\ \mathbf{u}_b \end{bmatrix} = \mathbf{T}_{\mathrm{C\text{-}B,cor}} \mathbf{q} \tag{18}$$

where $\mathbf{q}_n$ is the amplitudes of the correction modes and $\mathbf{T}_{\mathrm{C\text{-}B,cor}}$ is the C-B transformation matrix augmented by correction modes.

Using the above procedure, correction modes are generated based on interface excitation. Using a similar procedure, the correction modes, or so-called force dependent Ritz-vectors, can also be generated based on external loads applied to the substructure interior DOFs.

3.3 Substructure coupling procedures

Since the physical boundary DOFs are preserved in the C-B reduction process the assembly method is straight-forward, hence each substructure can be treated as a super-element. However, the substructures can either be assembled by eliminating one set of interface DOFs, a so-called *primal* assembled system, or so that all interface DOFs are preserved, a so-called *dual* assembled system.

The block diagonal system matrices for a structure consisting of N_s substructures are given by

$$\mathbf{M} = \text{diag}(\mathbf{M}^{(s)}), \qquad \mathbf{C} = \text{diag}(\mathbf{C}^{(s)}), \qquad \mathbf{K} = \text{diag}(\mathbf{K}^{(s)}) \tag{19}$$

where **M**, **C** and **K** have size $n \times n$ and the superscript s is the substructure label. The equation of motion can then be written as

$$\mathbf{M}\ddot{\mathbf{u}} + \mathbf{C}\dot{\mathbf{u}} + \mathbf{K}\mathbf{u} = \mathbf{p} \tag{20}$$

where **u** is the $n \times 1$ global displacement vector, including all DOFs at the interfaces between substructures. Assuming compatible meshes, constraints enforced between substructures for individual DOF pairs, e.g. $u_i^{(s_1)} = u_j^{(s_2)}$, can be written in matrix form:

$$\mathbf{B}\mathbf{u} = \mathbf{0} \tag{21}$$

where the constraint matrix **B** is a signed Boolean matrix with size $m \times n$, where m is the number of constraints and n is the total number of DOFs.

As e.g. shown in [3], a primal assembly can be enforced by using the so-called Boolean localization matrix **L**, found by computing the null-space for **B**, i.e.

$$\mathbf{L} = \text{Null}(\mathbf{B}) \tag{22}$$

The relation between the global displacement vector and a displacement vector with a unique set of interface DOFs, $\mathbf{u}_P$, is then given by

$$\mathbf{u} = \mathbf{L}\,\mathbf{u}_P \tag{23}$$

By inserting Equation (23) in Equation (20) and pre-multiplying with $\mathbf{L}^T$ the equation of motion for the primal assembled system is given by

$$\mathbf{M}_P\ddot{\mathbf{u}}_P + \mathbf{C}_P\dot{\mathbf{u}}_P + \mathbf{K}_P\mathbf{u}_P = \mathbf{p}_P \tag{24}$$

where

$$\mathbf{M}_P = \mathbf{L}^T\mathbf{M}\mathbf{L}, \qquad \mathbf{C}_P = \mathbf{L}^T\mathbf{C}\mathbf{L}, \qquad \mathbf{K}_P = \mathbf{L}^T\mathbf{K}\mathbf{L}, \qquad \mathbf{p}_P(t) = \mathbf{L}^T\mathbf{p} \tag{25}$$

The number of DOFs in the primal assembled system is thus $n_P = n - m$ and, accordingly, the size of $\mathbf{M}_P$, $\mathbf{C}_P$, $\mathbf{K}_P$ is $[n_P \times n_P]$ and $\mathbf{p}_P$ is $[n_P \times 1]$.

Instead of eliminating one set of DOFs, a dual assembled system can be achieved by enforcing the interface constraints using Lagrange multipliers $\boldsymbol{\lambda}$. The system of equations can then be written as

$$\begin{bmatrix} \mathbf{M} & \mathbf{0} \\ \mathbf{0} & \mathbf{0} \end{bmatrix} \begin{bmatrix} \ddot{\mathbf{u}} \\ \boldsymbol{\lambda} \end{bmatrix} + \begin{bmatrix} \mathbf{C} & \mathbf{0} \\ \mathbf{0} & \mathbf{0} \end{bmatrix} \begin{bmatrix} \dot{\mathbf{u}} \\ \boldsymbol{\lambda} \end{bmatrix} + \begin{bmatrix} \mathbf{K} & \mathbf{B}^T \\ \mathbf{B} & \mathbf{0} \end{bmatrix} \begin{bmatrix} \mathbf{u} \\ \boldsymbol{\lambda} \end{bmatrix} = \begin{bmatrix} \mathbf{p} \\ \mathbf{0} \end{bmatrix} \tag{26}$$

thus, preserving all interface DOFs [17]. Note that $\boldsymbol{\lambda}$ can be interpreted as an interface force vector, i.e. the forces required to enforce equal displacements for interface DOF pairs.

A dual assembled system can also be enforced using the penalty method, e.g. expressed as

$$\mathbf{M}\ddot{\mathbf{u}} + \mathbf{C}\dot{\mathbf{u}} + (\mathbf{K} + \alpha \mathbf{B}^T\mathbf{B})\mathbf{u} = \mathbf{p} \tag{27}$$

where α is the penalty stiffness, chosen sufficiently large so that $\mathbf{Bu} \approx \mathbf{0}$ [17]. Note that this approach corresponds to adding stiff springs between the constrained DOFs.

The preferred assembly method, or constraint enforcement method, depend on several factors such as the analysis type, the output data of interested, etc.

4 TIME-STEPPING METHOD FOR STRUCTURES WITH RIGID–PERFECTLY PLASTIC JOINTS

Simplified models are often used for design of concrete structures where linear elastic beam elements are combined with predefined discrete plastic hinges, approximated as rigid–perfectly plastic. To enforce a rigid–perfectly plastic coupling between two DOFs, namely the rotational DOFs at the plastic hinges, one alternative is to utilize the penalty method, i.e. by introducing a stiff elastic–perfectly plastic rotational spring. However, one obvious problem when using the penalty method is to choose a suitable penalty stiffness—if it is too low, the results will be inaccurate and if it is too large, the system equations will be ill-conditioned with respect to inversion. Furthermore, the highest eigenfrequency of the system can be expected to increase significantly, which can result in a very small critical time increment size in conditionally stable time integration schemes.

Another alternative is to set up a dual assembled system according to Equation (26) and setting a maximum value, corresponding to the plastic moment, for the Lagrange multipliers. The Lagrange multipliers will then be either known, i.e. treated as external forces equal to the plastic moments, or unknown. However, ensuring stability for a system including Lagrange multipliers, for so-called Differential-Algebraic Equations (DAEs), is often found to be problematic in direct time integration of dual assembled systems. For example, a standard Newmark time integration scheme, assuming constant average accelerations, is in this case unconditionally unstable. However, methods to ensure stability exist, see e.g. [18]. Nonetheless the available time integration schemes are somewhat limited.

Instead of using a pure dual or primal formulation, a methodology is proposed where the system is reassembled when yielding of the rigid–perfectly plastic hinges starts or stops. Such a procedure implies that the nonlinear analysis is performed as a series of linear analyses. Hence, the plastic hinges are either modeled as fixed by eliminating one of the rotational DOFs or as external moments applied on both rotational DOFs at the plastic hinges. This approach can be expected to be particularly suitable for systems consisting of reduced substructures, with a limited number of plastic hinges. The critical time increment is then related to the highest eigenfrequency of the assembled substructures, which in turn have already been reduced by a modal truncation on the substructure level, removing the high frequency content. Furthermore, high frequency noise induced by penalty elements is avoided.

4.1 Time-stepping algorithm

Starting with the system in Equation (20), a $m \times n$ signed Boolean matrix $\mathbf{B}$ can be constructed to define all the interface couplings between the substructures. The couplings can either be fixed constraints or rigid–perfectly plastic couplings. The matrix is then partitioned as:

$$\mathbf{B} = \begin{bmatrix} \mathbf{B}_r \\ \mathbf{B}_c \\ \mathbf{B}_y \end{bmatrix} \tag{28}$$

where $\mathbf{B}_r$ defines m_r constraints (or boundary conditions) that are not limited by a yield force, e.g. the translational DOFs at a plastic hinge, $\mathbf{B}_c$ defines the m_c rigid–plastic couplings not yielding and $\mathbf{B}_y$ defines the m_y rigid–plastic couplings currently yielding. Hence, the Boolean matrices $\mathbf{B}_c$ and $\mathbf{B}_y$ must be updated in a time-stepping scheme. The constraints defined by $\mathbf{B}_r$ are enforced using a primal formulation before the time-stepping is initialized, hence by eliminating m_r interface DOFs. The equation of motion for the assembled system can then be written as

$$\widehat{\mathbf{M}}\ddot{\mathbf{u}}_r + \widehat{\mathbf{C}}\dot{\mathbf{u}}_r + \widehat{\mathbf{K}}\mathbf{u}_r = \hat{\mathbf{p}} \tag{29}$$

where

$$\widehat{\mathbf{M}} = \mathbf{L}_r^{\mathrm{T}}\mathbf{M}\mathbf{L}_r, \qquad \widehat{\mathbf{C}} = \mathbf{L}_r^{\mathrm{T}}\mathbf{C}\mathbf{L}_r, \qquad \widehat{\mathbf{K}} = \mathbf{L}_r^{\mathrm{T}}\mathbf{K}\mathbf{L}_r, \qquad \hat{\mathbf{p}} = \mathbf{L}_r^{\mathrm{T}}\mathbf{p} \tag{30}$$

and where the Boolean localization matrix $\mathbf{L}_r = \mathrm{Null}(\mathbf{B}_r)$. To simplify the implementation the eliminated DOFs are then removed from the matrices $\mathbf{B}_c$ and $\mathbf{B}_y$, i.e. by removing the corresponding m_r columns containing zeros. The size of the updated matrices $\widehat{\mathbf{B}}_c$ and $\widehat{\mathbf{B}}_y$ is then $m_c \times (n - m_r)$ and $m_y \times (n - m_r)$, respectively. At the initial stage, the couplings defined by $\widehat{\mathbf{B}}_c$ is enforced in the same manner by computing $\mathbf{L}_c = \mathrm{Null}(\widehat{\mathbf{B}}_c)$. At each time increment $t^{(i)}$, the interface forces $\boldsymbol{\lambda}^{(i)}$ is computed from the expression

$$\widehat{\mathbf{B}}_c^{\mathrm{T}}\boldsymbol{\lambda}^{(i)} = \hat{\mathbf{p}}^{(i)} - \widehat{\mathbf{M}}\mathbf{L}_c\ddot{\mathbf{u}}_c{}^{(i)} - \widehat{\mathbf{C}}\mathbf{L}_c\dot{\mathbf{u}}_c{}^{(i)} - \widehat{\mathbf{K}}\mathbf{L}_c\mathbf{u}_c{}^{(i)} \tag{31}$$

where the relation $\mathbf{u}_r = \mathbf{L}_c\mathbf{u}_c$ has been applied. If the interface force for a coupling is larger than the specified yield force, the Boolean matrices $\widehat{\mathbf{B}}_c$ and $\widehat{\mathbf{B}}_y$ are updated, i.e. the row in $\widehat{\mathbf{B}}_c$ defining the coupling is moved to $\widehat{\mathbf{B}}_y$. Thereafter, the system is reassembled by computing the localization matrix $\mathbf{L}_c = \mathrm{Null}(\widehat{\mathbf{B}}_c)$ and applying it to Equation (29). The couplings currently yielding are then considered by adding the yield forces as external loads, hence

$$\mathbf{L}_c^{\mathrm{T}}\widehat{\mathbf{M}}\mathbf{L}_c\ddot{\mathbf{u}}_c{}^{(i)} + \mathbf{L}_c^{\mathrm{T}}\widehat{\mathbf{C}}\mathbf{L}_c\dot{\mathbf{u}}_c{}^{(i)} + \mathbf{L}_c^{\mathrm{T}}\widehat{\mathbf{K}}\mathbf{L}_c\mathbf{u}_c{}^{(i)} = \mathbf{L}_c^{\mathrm{T}}\left(\hat{\mathbf{p}}^{(i)} - \widehat{\mathbf{B}}_y^{\mathrm{T}}\mathbf{f}_y\right) \tag{32}$$

where $\mathbf{f}_y$ is a $m_y \times 1$ vector containing the specified yield forces. Unloading of the m_y couplings currently yielding is detected by checking the relative velocity sign, i.e. if

$$\mathrm{sign}\left(\left\{\widehat{\mathbf{B}}_y\dot{\mathbf{u}}_r{}^{(i)}\right\}_j\right) \neq \mathrm{sign}\left(\left\{\widehat{\mathbf{B}}_y\dot{\mathbf{u}}_r{}^{(i+1)}\right\}_j\right) \tag{33}$$

where subscript j denotes an element of the column vector $\widehat{\mathbf{B}}_y\dot{\mathbf{u}}_r$. If unloading occurs, the system is updated by moving rows from $\widehat{\mathbf{B}}_y$ to $\widehat{\mathbf{B}}_c$, computing the localization matrix $\mathbf{L}_c = \mathrm{Null}(\widehat{\mathbf{B}}_c)$ and applying it to Equation (29).

The time integration between the system updates can be performed in a standard manner by the Newmark-β method, as e.g. described in [19]. However, for a nonlinear system including both elastic and plastic deformations it is convenient to use incremental quantities,

$$\Delta\mathbf{u}^{(i)} = \mathbf{u}^{(i+1)} - \mathbf{u}^{(i)}, \quad \Delta\mathbf{u}^{(i)} = \mathbf{u}^{(i+1)} - \mathbf{u}^{(i)}, \quad \Delta\ddot{\mathbf{u}}^{(i)} = \ddot{\mathbf{u}}^{(i+1)} - \ddot{\mathbf{u}}^{(i)}, \quad \Delta\mathbf{p}^{(i)} = \mathbf{p}^{(i+1)} - \mathbf{p}^{(i)} \tag{34}$$

In fact, the time-stepping algorithm is constructed so that the computed incremental displacements are always transformed and appended to $\mathbf{u}_r$, thus

$$\mathbf{u}_r{}^{(i+1)} = \mathbf{u}_r{}^{(i)} + \mathbf{L}_c \Delta\mathbf{u}_c{}^{(i)} \tag{35}$$

Consequently, the displacement vector need not to be transformed at the system updates. Merging DOF pairs in couplings where yielding is stopped would certainly be an ambiguous operation, since the displacement in each DOF in general will differ.

Upon yielding, the system is updated so that couplings where yielding is initiated are released. The interpretation of this update is straight-forward since the initial state of the physical quantities (i.e. displacements, velocities, accelerations) in the new configuration is well defined by the previous state. If yielding is stopped, rigid couplings are enforced by eliminating one set of interface DOFs. The velocities for the constrained DOFs are by definition equal when unloading is detected and it is thus straight-forward to eliminate one set of DOFs. The initial acceleration in the updated system is computed as

$$\ddot{\mathbf{u}}_c{}^{(i)} = \left(\mathbf{L}_c^{\mathrm{T}}\widehat{\mathbf{M}}\mathbf{L}_c\right)^{-1}\mathbf{L}_c^{\mathrm{T}}\left(\hat{\mathbf{p}}^{(i)} - \widehat{\mathbf{B}}_y^{\mathrm{T}}\mathbf{f}_y - \widehat{\mathbf{C}}\dot{\mathbf{u}}_r{}^{(i)} - \widehat{\mathbf{K}}\mathbf{u}_r{}^{(i)}\right) \tag{36}$$

Note that the time increment between system updates, $\Delta t^{(i)} = t^{(i)} - t^{(i-1)}$, is zero. Hence, the velocities and deformations are equal in increment i and $i - 1$. However, the accelerations are changed at the system updates in accordance with Equation (36). Even though an instantaneous change of the accelerations might seem unreasonable, this is a consequence of the unphysical assumption of a perfectly rigid connection, which however can be a very useful approximation; in particular when modeling plastic hinges in beam–column structures. Furthermore, it should be noted that both the strain and kinetic energy is preserved.

4.2 Remarks on performance and accuracy

In contrast to a conventional implicit direct time integration, the proposed time-stepping scheme, as presented above, is a non-iterative procedure. However, in general an adjustment of the last increment size before a system update is needed to ensure that the system is updated just before yielding start or stop. This adjustment can be set up in an iterative fashion.

If the system consists of reduced substructures the critical time increment, in a conditionally stable time integration scheme, can be expected to be reasonably large since the high frequency content has been removed in the reduction process on the substructure level. The time increment size prescribed in the analysis is then instead governed by the precision of the requested time-histories. Consequently, the Newmark parameters can be optimized to increase the analysis accuracy (or performance) rather than to ensure stability. For example, setting the parameters to $\beta = 1/12$ and $\gamma = 1/2$ ensures forth-order accuracy and $\beta = 0$ and $\gamma = 1/2$ enables the explicit central difference scheme [19]. Furthermore, if the system at hand is relatively small and if the number of system updates can be assumed rather limited, the critical time increment can be updated based on an eigenvalue analysis of the updated system. However, an alternative is to prescribe a conservative time increment and thereby skip this check.

5 NUMERICAL EXAMPLE: CONCRETE FRAME SUBJECTED TO BLAST LOADING

A concrete frame structure subjected to blast loading is studied to demonstrate the discussed substructuring and time-stepping method. The dynamic response is computed using a simplified two-dimensional model, suitable in a conceptual design phase. Various strategies to reduce the model by use of DS are investigated, both in terms of accuracy and computationally efficiency (i.e. number of DOFs). Focus is primarily on evaluating DS techniques applied to the lateral load-bearing structure that is not subjected to external loading, i.e. the supporting structure consisting of the horizontal beam and the right column, as shown in Figure 2a. The dynamic response is computed using the time-stepping scheme proposed in Section 4. Furthermore, the highest eigenfrequency, which is related to the critical increment size in conditionally stable time-integration schemes, is evaluated for the reduced models.

The concrete frame is subjected to a uniformly distributed reflected impulse pressure of 1500 Pa·s, as shown in Figure 2a. The pulse is approximated by an equivalent triangular pulse with a fictitious duration of 10 ms and a peak reflected pressure of 300 kPa at $t = 0$ s. The length of the frame members is 3 m and the cross-section width and height, for the columns as well as the horizontal beam, are 1000 mm and 200 mm, respectively. Young's modulus for concrete is set to 32 GPa and the density for reinforced concrete is set to 2500 kg/m^3. The ultimate moment capacity for the columns and the horizontal beam is set to 60 kNm.

5.1 Frame structure model reduced by dynamic substructuring

The frame structure is analyzed with a two-dimensional beam model. The positions of possible plastic hinges are predefined and approximated as five discrete rigid–perfectly plastic joints, as shown in Figure 2b. Yielding of the frame corners are approximated by one distinct plastic hinge, i.e. Joints 3 and 4, respectively. However, it should be noted that a more accurate approximation can be achieved by modeling the corners as separate substructures. Moreover, several effects are neglected in the analysis, e.g. catenary effects, reduced stiffness due to concrete cracking etc. Nevertheless, the model is suitable for studying different DS techniques and to evaluate the efficiency of the proposed time-stepping method.

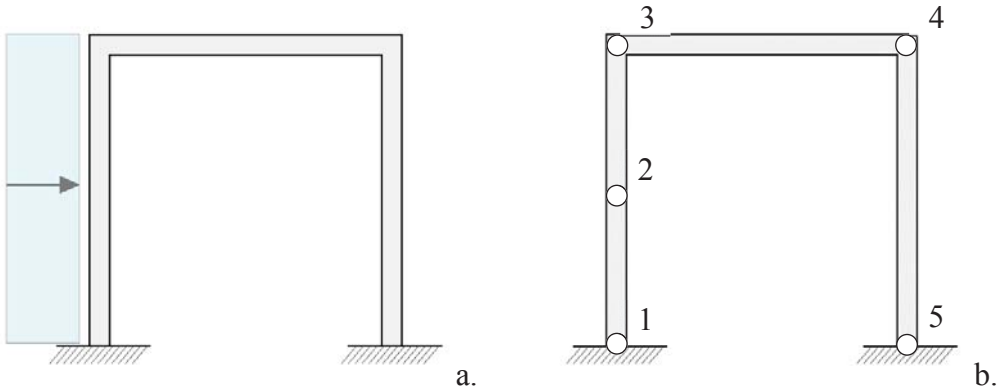

Figure 2: Concrete frame structure subjected to blast loading (a) and locations and labeling of plastic hinges (b).

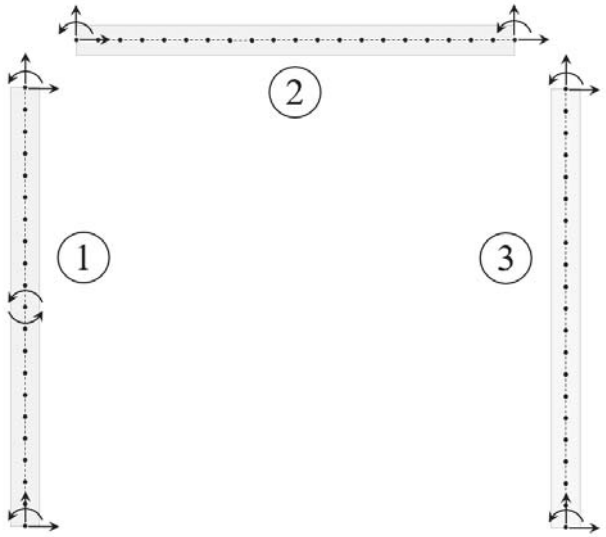

Figure 3: Boundary DOFs and numbering of substructures.

The structure is divided into three substructures, as shown in Figure 3. Each substructure is modeled by 20 Euler–Bernoulli two-node beam elements. Six interface DOFs are retained for Substructures 2 and 3, namely the translational and rotational DOFs at the beam ends. By selecting these boundary DOFs, the fixed-interface normal modes will be the exact mode-shapes of a fixed–fixed beam. Further, eight boundary DOFs are retained for Substructure 1, namely the translational and rotational DOFs at the top and bottom and the rotational DOFs at the joint positioned at midspan. By selecting these boundary DOFs the fixed-interface normal modes will include the exact symmetric modes for a fixed–fixed beam, whereas the antisymmetric modes will be affected by the constrained rotational DOFs at midspan. The fixed-interface normal modes and the constraint modes included in the reduction basis for Substructure 1 is shown in Figures 4 and 5. Note that the antisymmetric modes for a fixed–fixed beam are not excited by a uniformly distributed load. However, since Substructure 1 is not fully supported at the top, some antisymmetric normal modes (modes 2, 5 and 8) are included in the reduction basis.

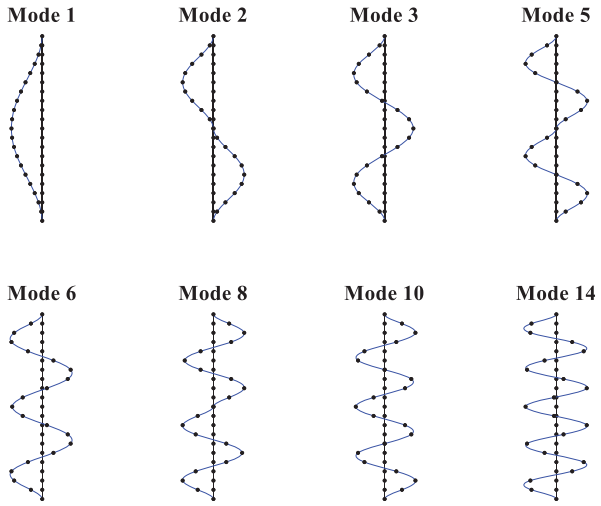

Figure 4: Substructure 1 – fixed-interface normal modes.

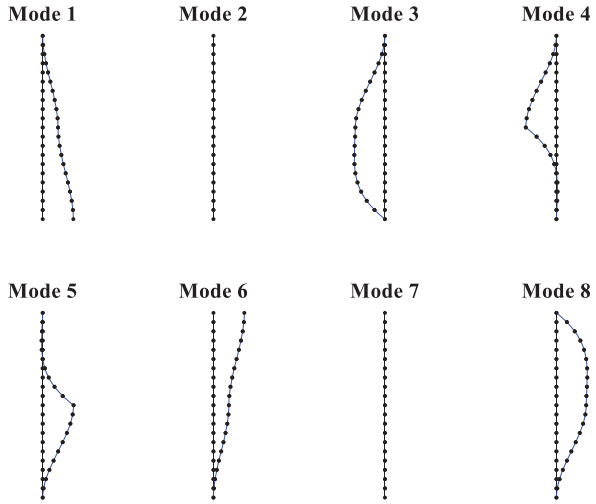

Figure 5: Substructure 1 – constraint modes.

During a dynamic response analysis, the predefined plastic hinges can be either fixed or free, i.e. non-yielding or yielding. A total of five predefined plastic hinges are included in the model, which implies that a response analysis can include up to ten different system configurations. However, to get a rough estimate of the reduced model accuracy two configurations are evaluated—where all joints are either fixed or free, respectively.

The eigenfrequencies for the assembled reduced systems are evaluated by computing the so-called normalized relative frequency difference (NRFD), given by $\text{NRFD} = \left| f_i^{red} - f_i^{full} \right| / f_i^{full}$, that relate the eigenfrequencies of the reduced system to those of the full system. As previously described, the reduction basis for Substructure 1 includes the fixed-interface normal modes and constraint modes shown in Figures 4 and 5, respectively. Five different reduction bases for Substructures 2 and 3 are evaluated. Using a standard C-B approach, reduction is performed including two or four fixed-interface normal modes. Furthermore, reduction bases including two or four correction modes, as described in Section 3.2, are evaluated. The correction modes are generated based on the constraint modes associated to the rotational boundary DOFs at the beam ends. Hence, two modes are generated by computing a set of first-order correction modes and two additional modes are generated by computing a set of second-order correction modes. In addition, the accuracy of a reduction basis including both four fixed-interface normal modes and two first-order correction modes is evaluated. The analyzed models are summarized in Table 1.

Model name	Normal modes	Correction modes[1]	No of DOFs[2]
Mode 1-2	1, 2	-	19
Cor. 1st	-	2 × 1st	19
Mode 1-4	1, 2, 3, 4	-	23
Cor. 1st, 2nd	-	2 × 1st + 2 × 2nd	23
Mode 1-4, Cor.1st	1, 2, 3, 4	2 × 1st	27
Full model	-	-	177

[1] Correction modes associated to rotational boundary DOFs.
[2] Total number of DOFs for model with fixed joints.

Table 1: Normal modes and correction modes for Substructures 2 and 3.

The computed NRFD values are shown in Figures 6 and 7. As shown in the figures, at least, the first seven free and fixed global modes, respectively, are well-described by all the evaluated reduced models; measured as NRFD < 1 %. However, to increase the precision for higher order modes, the constraint modes in Substructures 2 and 3 need to be complemented by at least four modes. However, increasing the number of fixed-interface normal modes and/or correction modes in the reduction basis result in additional generalized DOFs in the reduced system, hence, increasing the computational cost. Moreover, the accuracy when using correction modes and normal modes are comparably, as long as the same number of modes are included in the reduction basis.

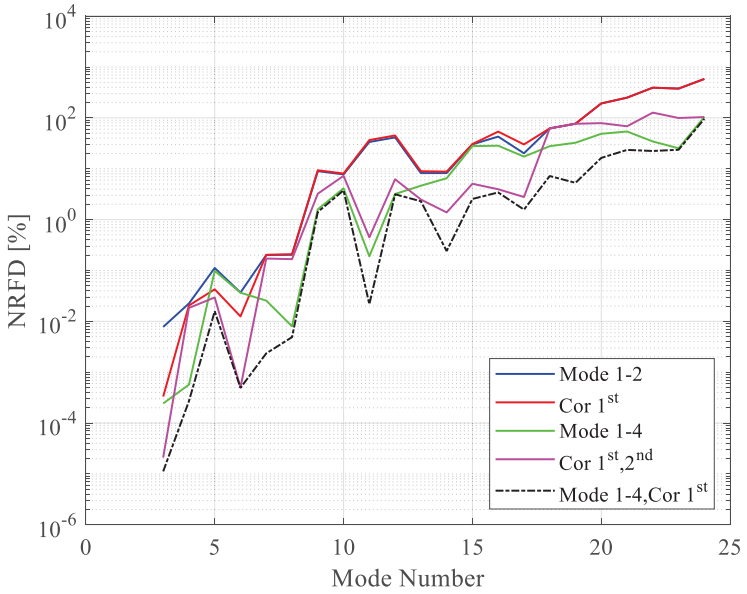

Figure 6: NRFD values for systems with unconstrained rotations at joints.

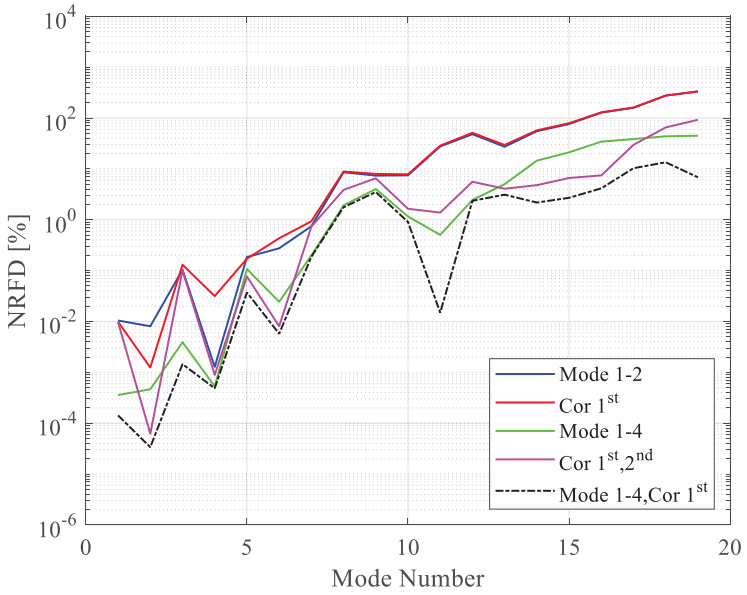

Figure 7: NRFD values for systems with constrained rotations at joints.

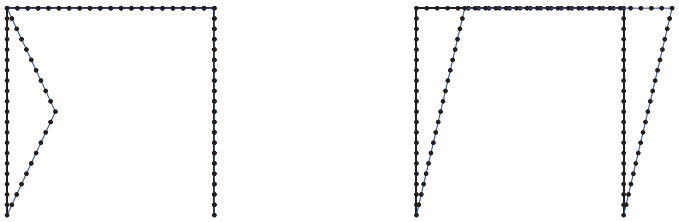

Figure 8: Failure modes spanned by rigid body modes.

Note that the NRFD value is not computed for the first two eigenmodes for the systems with free rotations at the joints. This is due to that the first two modes are rigid body modes with zero frequency. By properly scaling of the rigid body modes, the failure modes, shown in Figure 8, are obtained.

5.2 Dynamic response analysis and results

The dynamic response is computed for the reduced system where the reduction basis for Substructures 2 and 3 includes four normal modes and two first order correction modes. Again, the reduction basis for Substructure 1 includes the normal modes and constraint modes shown in Figures 4 and 5, respectively. The reduced model has a total of 27 DOFs in the initial stage, i.e. when the plastic hinges are fixed, whereas the full model has a total of 177 DOFs. The response is computed using the time-stepping scheme presented in Section 4. Direct time-integration is performed using the Newmark method, with parameters $\beta = 1/12$ and $\gamma = 1/2$ that result in a conditionally stable integration scheme with forth order accuracy [19]. The critical time increment is computed as $dt_{crit} = 2.45/\omega_{max}$. The analysis is performed with a time increment $dt = dt_{crit}/10$ and the analysis time is set to 150 ms.

Snapshots of the deformed shape during the first 50 ms is shown in Figure 9. As shown in the figure, the response of the left column during the first, approximately, 10 ms is similar to that of a fully supported fixed–fixed column due to the inertia of the supporting horizontal beam.

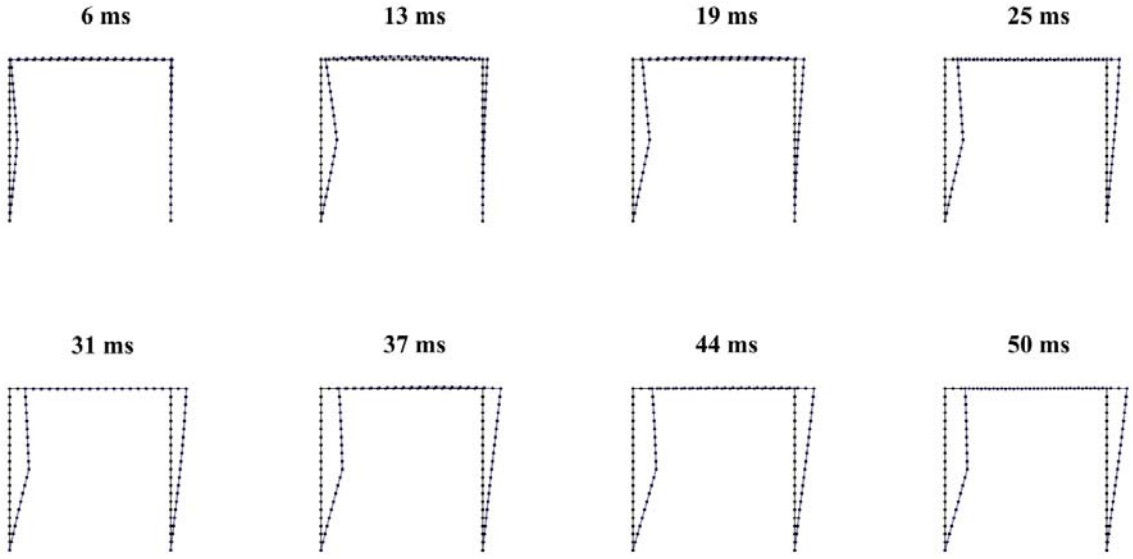

Figure 9: Snapshots of the deformed shape during the first 50 ms. The deformation is scaled by a factor of 15.

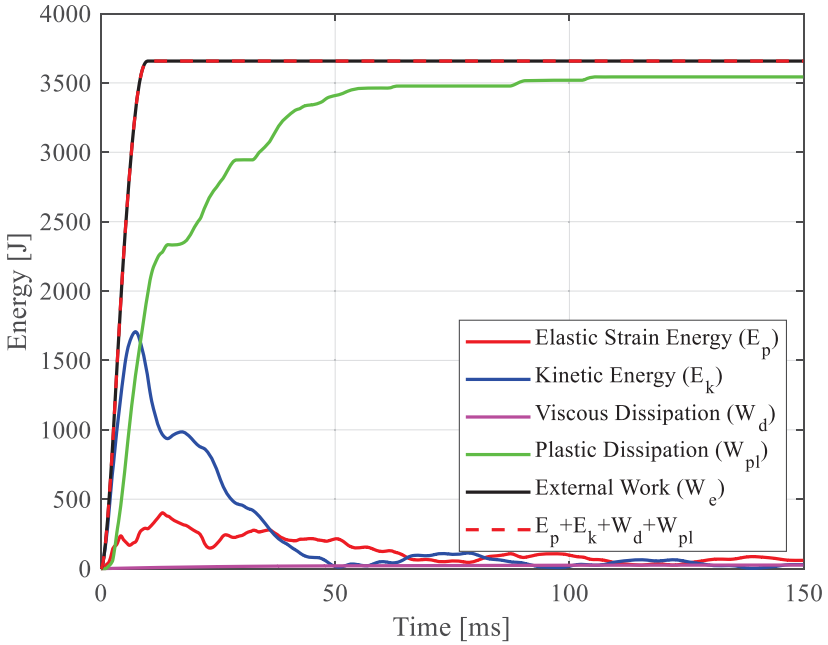

Figure 10: Elastic strain and kinetic energy, plastic and viscous dissipation and external work for the reduced system.

As shown in Figure 10, the energy induced by the external impulse pressure is mainly dissipated by plastic deformations, i.e. by rotation of the predefined plastic hinges. A low Rayleigh beta damping is included in the analysis by setting $\mathbf{C} = 10^{-5} \cdot \mathbf{K}$. As shown in the figure, the viscous dissipation is almost zero.

The relative rotation of the plastic hinges is shown in Figure 11. As shown, most of the plastic dissipation is due to plastic rotation in Joints 1 and 2. The rotation computed with the full model is shown in light gray color. As shown in the figure, the response is almost identical to that of the reduced model. Note that the relative rotation of the plastic hinges is an important parameter in a design calculation, which should not exceed the rotation capacity of the cross-section.

The horizontal displacement at Joints 2 and 4 is shown in Figure 12. The displacement is very close to the displacement computed with the full model. The fundamental eigenfrequency for the non-yielding frame structure is 11.7 Hz, corresponding to a period of 1/11.7 = 85 ms. Clearly, the displacement after approximately 50 ms can essentially be described by the fundamental mode and a plastic displacement.

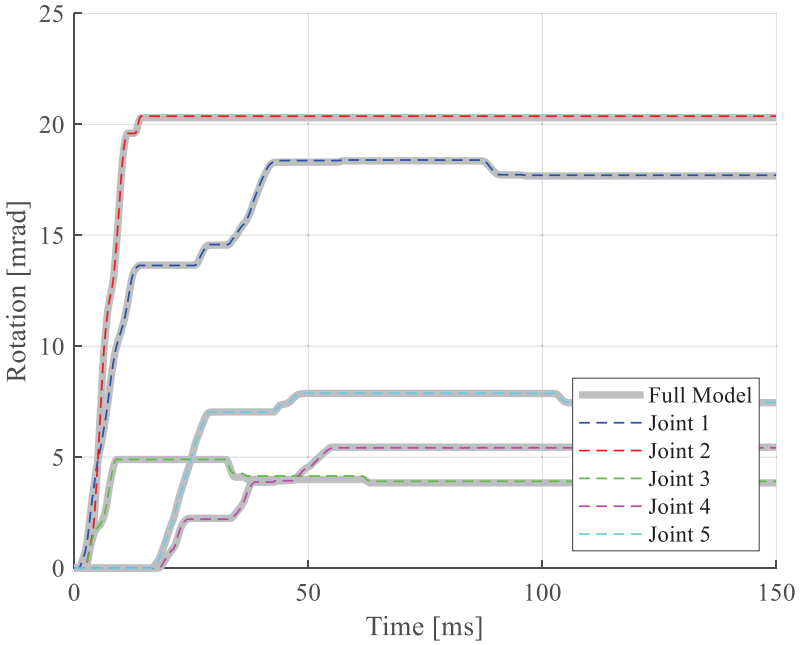

Figure 11: Relative rotations at Joints 1–5, positioned according to Figure 2b.

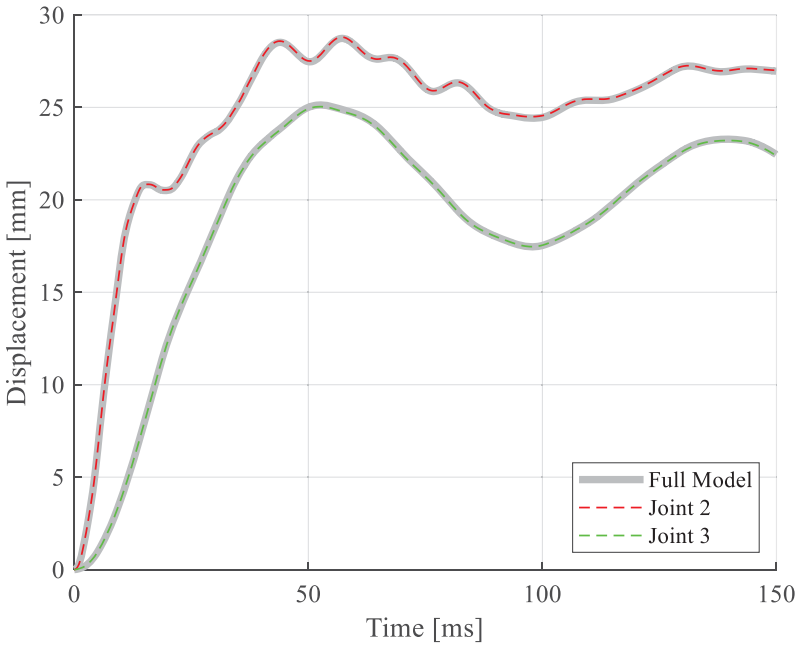

Figure 12: Horizontal displacements at Joints 2 and 3, positioned according to Figure 2b.

If a suitable reduction basis is applied to Substructure 1, to properly describe the application of the external pressure, the global displacements can be well-described by only including two fixed-interface normal modes (or correction modes) for Substructures 2 and 3, as indicated by Figures 11 and 12. However, a more refined reduction basis is needed to properly describe the reaction and interface forces between the substructures. The influence of the reduction basis on the horizontal interface force in Joint 4 is shown in Figure 13. As shown, the constraint modes need to be complemented by at least four modes to obtain a reasonable accurate response. The

accuracy for the models reduced by using fixed-interface normal modes and correction modes, respectively, are comparable. Hence, the correction modes are then the preferred choice since the generation of these modes are less computationally expensive (in this simple example, however, the computational cost of generating either normal modes or corrections modes is negligible).

The critical time increment in a conditionally stable direct time integration method is inversely proportional to the highest eigenfrequency. Consequently, a reduction of a system that removes the high frequency content can result in a more computationally efficient analysis. To get an estimation of how much the eigenfrequency is affected by the reduction bases studied herein, the highest eigenfrequency is computed for the initial state of the reduced systems, i.e. when all joints are fixed.

The highest eigenfrequency of the reduced models including two and four fixed-interface normal modes in the reduction bases for Substructure 2 and 3 is 4.2 kHz and 4.3 kHz, respectively. The highest eigenfrequency when using two and four correction modes is 4.2 kHz and 4.4 kHz, i.e. almost equal to the eigenfrequencies obtained when using normal modes. However, the highest eigenfrequency in the reduced models is in this case most likely governed by Substructure 1, reduced by a more refined reduction basis.

For the reduced model including four fixed-interface normal modes and two first-order correction modes the highest eigenfrequency is 4.7 kHz. In comparison, the highest eigenfrequency of the full model is 74.5 kHz, i.e. a factor of 74.5/4.7 ≈ 16. Furthermore, the highest eigenfrequency for a reduced system where the rigid–perfectly plastic joints are modeled using penalty elements, with a stiffness 10 times the mean stiffness of the corresponding entries in the unreduced stiffness matrix, is 64.4 kHz. Hence, for the model studied herein, the number of time increments can be decreased by a factor 64.4/4.7 ≈ 14 by avoiding penalty elements.

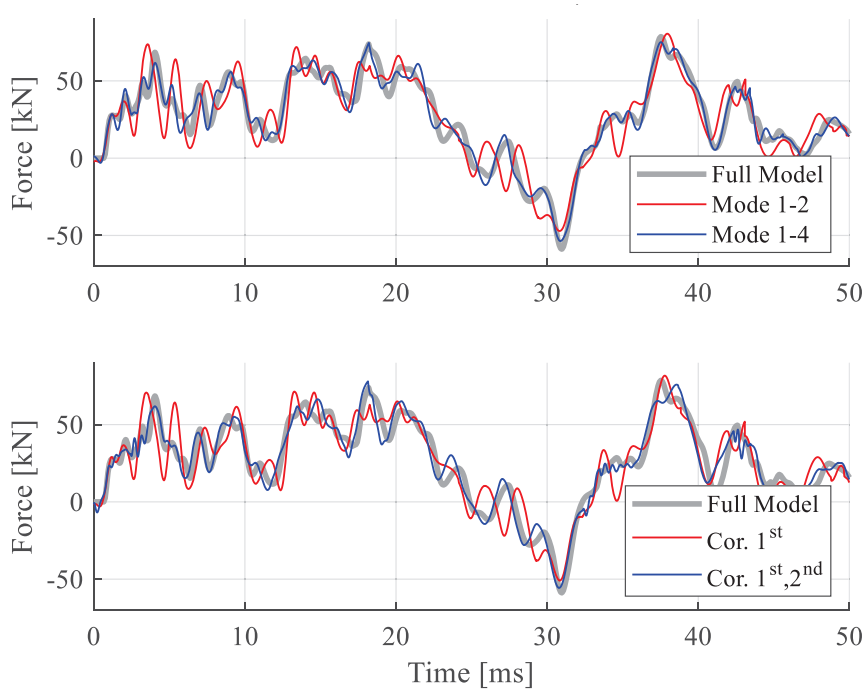

Figure 13: Horizontal interface force at Joint 4.

6 CONCLUSIONS

In the study, strategies are developed to enable time-efficient models for concrete frame structures subjected to blast loading, appropriate for use in a structural design process. Dynamic substructuring is employed to obtain reduced models with localized nonlinearities, such as predefined plastic hinges in a beam–column structure. The parts of the substructures that remains linear elastic are modeled by Ritz-vectors whereas parts with a nonlinear response are retained as physical degrees-of-freedom. Furthermore, a time-stepping scheme is presented that is shown to be suitable for reduced models including local and predefined rigid-plastic behavior.

The proposed methodology is applied and demonstrated in a numerical example of a concrete frame structure. The standard Craig-Bampton method that uses fixed-interface normal modes and constraint modes is evaluated. Furthermore, reduction bases augmented by so-called correction modes are investigated. Various reduction bases are evaluated for the substructures included in the supporting structure, i.e. the substructures that are not subjected to external loading. Two correction modes or two standard fixed-interface normal modes are sufficient to describe the displacement and relative rotations at the plastic hinges. However, to obtain an acceptable accuracy of the interface forces between the substructures, at least four correction modes or four standard fixed-interface modes are needed. For the studied load case, the accuracy when using correction modes and fixed-interface normal modes are comparable.

Moreover, the highest eigenfrequency for the reduced systems, which is related to the critical increment size in conditionally stable direct time integration methods, is evaluated. It is shown that a reduction of the studied model by use of dynamic substructuring can increase the critical time increment by a factor of approximately 16. Furthermore, it is shown that by enforcing a rigid–plastic behavior using the proposed time-stepping scheme, the critical increment size can increase by a factor of approximately 14 compared to a modeling approach where the rigid–plastic behavior is enforced using penalty elements.

The present methodology can be extended further to, for example, consider large deformations and failure, e.g. by considering the rotation capacity of the cross-sections. Furthermore, the methods can be applied and evaluated for larger and more complex structures, e.g. three-dimensional beam–column structures. Also, a more refined modeling approach for frame corners can be investigated, where the corner itself is treated as a separate substructure.

REFERENCES

[1] J.M. Biggs, *Introduction to Structural Dynamics*. McGraw-Hill, New York, 1964.

[2] L. Andersson, P. Persson, P. Austrell, K. Persson, Reduced order modeling for the dynamic analysis of structures with nonlinear interfaces. *Proceedings of the 7th ECCOMAS Thematic Conference on Computational Methods in Structural Dynamics and Earthquake Engineering (COMPDYN 2019)*, Crete, Greece, 24–26 June, 2019.

[3] D. de Klerk, D.J. Rixen, S.N. Voormeeren, General Framework for Dynamic Substructuring: History, Review, and Classification of Techniques, *AIAA Journal*, **46 (5)**, 1169–1181, 2008.

[4] O. Flodén, K. Persson, G. Sandberg, Reduction methods for the dynamic analysis of substructure models of lightweight building structures, *Computers and Structures*, **138**, 49–61, 2014.

[5] Unified Facilities Criteria (UFC), *Structures to Resist the Effects of Accidental Explosions*, U. S. Army Corps of Engineers, Naval Facilities Engineering Command, Air Force Civil Engineer Support Agency, UFC 3-340-02, December 5 2008.

[6] R.J. Guyan, Reduction of Stiffness and Mass Matrices, *AIAA Journal*, **3 (2)**, 380, 1965.

[7] J. O'Callahan, P. Avitabile, R. Riemer, System Equivalent Reduction Expansion Process (SEREP), *Proceedings of the 7th International Modal Analysis Conference*, Las Vegas, Nevada, 1989.

[8] R.R. Craig, M.C.C. Bampton, Coupling of Substructures for Dynamic Analysis, *AIAA Journal*, **6 (7)**, 1313–1319, 1968.

[9] R.H. MacNeal, A Hybrid Method of Component Mode Synthesis, *Computers and Structures*, **1 (4)**, 581–601, 1971.

[10] S. Rubin, Improved Component-Mode Representation for Structural Dynamic Analysis, *AIAA Journal*, **13 (8)**, 995–1006, 1975.

[11] R.R. Craig, C.J. Chang, On the Use of Attachment Modes in Substructure Coupling for Dynamic Analysis. *Proceedings of the 18th Structures, Structural Dynamics and Material Conference*, San Diego, CA, 1977.

[12] D.J. Rixen, A dual Craig–Bampton method for dynamic substructuring, *Journal of Computational and Applied Mathematics*, **168(1–2)**, 383–391, 2004.

[13] F.M. Gruber, M. Gille, D.J. Rixen, Time integration of dual Craig-Bampton reduced systems. *Proceedings of the 6th ECCOMAS Thematic Conference on Computational Methods in Structural Dynamics and Earthquake Engineering (COMPDYN 2017)*, Rhodes Island, Greece, 15–17 June, 2017.

[14] R. Craig, A. Hale, Block-Krylov Component Synthesis Method for Structural Model Reduction. *Journal of Guidance, Control and dynamics, American Institute of Aeronautics and Astronautics*, **11(6)**, 562–570, 1988.

[15] D.J. Rixen, High Order Static Correction Modes for Component Mode Synthesis. *Proceedings of the fifth World Congress on Computational Mechanics*, Vienna, Austria, 7–12 July, 2002.

[16] R.R. Jr. Craig, A.J. Kurdila, *Fundamentals of Structural Dynamics, 2nd Edition*, John Wiley & Sons, New Jersey, 2006.

[17] K. J. Bathe, *Finite element procedures*. Prentice-Hall, 1996.

[18] C. Farhat, L. Crivelli, M. Géradin, Implicit time integration of a class of constrained hybrid formulations—Part I: Spectral stability theory, *Computer Methods in Applied Mechanics and Engineering*, **125 (1–4)**, 71–107, 1995.

[19] M. Geradin, D.J. Rixen, *Mechanical Vibrations: Theory and Applications to Structural Dynamics, Third Edition*. Wiley, New York, 2014.

EURODYN 2020
XI International Conference on Structural Dynamics
M. Papadrakakis, M. Fragiadakis, C. Papadimitriou (eds.)
Athens, Greece, 23–26 November 2020

2DOF BLAST ANALYSIS OF BUILDINGS

Sander J.H. Meijers[1], Peter J. Flink[2], Harm G. Kraaijenbrink[2] and Meindert Wiersma[2]

[1] Royal HaskoningDHV
P.O. Box 8520, 3009 AM Rotterdam, The Netherlands
e-mail: sander.meijers@rhdhv.com

[2] Royal HaskoningDHV
P.O. Box 8520, 3009 AM Rotterdam, The Netherlands
peter.flink@rhdhv.com, harm.kraaijenbrink@rhdhv.com, meindert.wiersma@rhdhv.com

Keywords: Blast, 2DOF, SDOF, Lumped

Abstract. *Blast loading on buildings may originate from various sources and may be redefined during the lifetime of a building. The blast response of buildings is roughly governed by the response of the façade and the main load bearing structure. While a full FEM analysis in the time domain can provide reliable and accurate results for the building response in detail, a quick assessment based on lumped masses is preferred in many cases in practice, either related to early design stages, decision making or to validation of sophisticated models. In such classical single or multi degree-of-freedom approaches the façade and main load bearing structure can be clearly distinguished. In practice both components are usually dealt with individually, conveniently ignoring the effect of the response of the former on the blast load on the latter component. Early graphical tools for the incorporation of non-linear effects have been widely used. Here the results of time-domain analyses of an elasto-plastic 2-degree-of-freedom system in terms of ductility demand are shown and compared to those of corresponding single-degree-of-freedom systems. Explicit results for the interaction of façade members and main load bearing members are obtained and shown for various configurations. It is concluded that representation of structural systems by individual single-degree-of-freedom systems in blast analysis is generally conservative for façade members, but can be unconservative for the main load bearing structure. In practical cases this underestimation is not likely to exceed 10%.*

1 INTRODUCTION

While nowadays non-linear finite element (FEM) analysis can be used to accurately evaluate the impact of blast loading on buildings, still simple analysis of individual structural members represented as single-degree-of-freedom (SDOF) systems is common in engineering practice. Such simple analysis is useful in early design stages and in the validation phase of the more complex calculations. Graphs for the evaluation of ductility demand of non-linear SDOF systems were already presented by Biggs [1] in 1964. However, the assessment of individual members without consideration of their dynamic interaction with other members or the main load bearing structure may entail significant errors. A logical step to assess these errors is to expand the SDOF lumped approach to a non-linear 2-degree-of-freedom (2DOF) system, see Figure 1, bridging the gap between simple SDOF and sophisticated FEM analysis. The first degree-of-freedom (DOF) represents the member that is struck by the blast first, while the second DOF represents its supporting structure.

The blast response of a non-linear 2DOF system is determined by five independent variables, as opposed to two independent variables in a non-linear SDOF system. Furthermore, a 2DOF system is essentially not different from multiple degree-of-freedom systems, i.e. FEM models, while the latter are more difficult to interpret. 2DOF Systems can be easily recognised in buildings, e.g. façade and main load bearing structure or glass panels and supporting mullions. Therefore, the 2DOF system is eligible for assessing the accuracy of SDOF approaches. This will be elaborated in the next sections with focus on ductility demand.

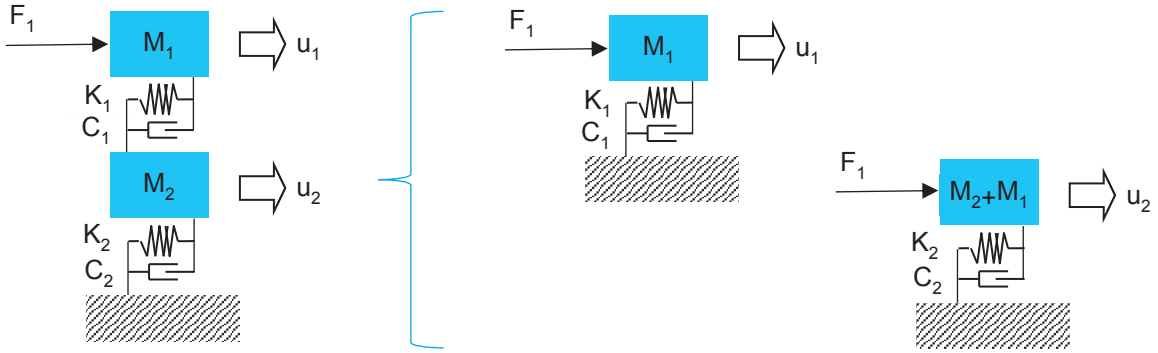

Figure 1: A 2-degree-of-freedom system (left) and its decomposition into two individual single degree-of-freedom systems (right).

2 2DOF SYSTEM FOR BLAST ANALYSIS

The dynamic response of a 2DOF system, as depicted in Figure 1, to a shock wave [1, 2] is governed by:

$$\begin{bmatrix} M_1 & 0 \\ 0 & M_2 \end{bmatrix} \begin{Bmatrix} \ddot{u}_1 \\ \ddot{u}_2 \end{Bmatrix} + \begin{bmatrix} C_1 & -C_1 \\ -C_1 & C_1 + C_2 \end{bmatrix} \begin{Bmatrix} \dot{u}_1 \\ \dot{u}_2 \end{Bmatrix} + \begin{bmatrix} K_1 & -K_1 \\ -K_1 & K_1 + K_2 \end{bmatrix} \begin{Bmatrix} u_1 \\ u_2 \end{Bmatrix} = \begin{Bmatrix} F_1 f_1 \\ 0 \end{Bmatrix} \quad (1)$$

with mass, damping and stiffness coefficients denoted by M_i, C_i and K_i respectively, where i is the related DOF. In order to assess the amount of interaction between the two DOFs that would be overlooked in case of SDOF modelling, a dynamic force is applied only to DOF 1 of the 2DOF system. For blasts this is often simplified as a triangular force-time diagram. The initial (maximum) external force is denoted by F_1 and the function defining its linear decay over duration t_d is denoted by f_1. The last equation is set up for absolute displacements u_i. It is convenient to write the dynamic response in terms of relative displacements w_i:

$$\begin{bmatrix} M_1 & M_1 \\ 0 & M_2 \end{bmatrix} \begin{Bmatrix} \ddot{w}_1 \\ \ddot{w}_2 \end{Bmatrix} + \begin{bmatrix} C_1 & 0 \\ -C_1 & C_2 \end{bmatrix} \begin{Bmatrix} \dot{w}_1 \\ \dot{w}_2 \end{Bmatrix} + \begin{bmatrix} K_1 & 0 \\ -K_1 & K_2 \end{bmatrix} \begin{Bmatrix} w_1 \\ w_2 \end{Bmatrix} = \begin{Bmatrix} F_1 f_1 \\ 0 \end{Bmatrix} \tag{2}$$

where $w_1 = u_1 - u_2$ and $w_2 = u_2$. Symmetry of the matrices can be restored by adding the first row to the second, which yields:

$$\begin{bmatrix} M_1 & M_1 \\ M_1 & M_2 + M_1 \end{bmatrix} \begin{Bmatrix} \ddot{w}_1 \\ \ddot{w}_2 \end{Bmatrix} + \begin{bmatrix} C_1 & 0 \\ 0 & C_2 \end{bmatrix} \begin{Bmatrix} \dot{w}_1 \\ \dot{w}_2 \end{Bmatrix} + \begin{bmatrix} K_1 & 0 \\ 0 & K_2 \end{bmatrix} \begin{Bmatrix} w_1 \\ w_2 \end{Bmatrix} = \begin{Bmatrix} F_1 f_1 \\ F_1 f_1 \end{Bmatrix} \tag{3}$$

Next, the following non-dimensional variables for time t and displacements w_i are introduced, similar to Biggs [1]:

$$\begin{aligned} \tau &= \frac{t}{T_1} \\ \mu_i &= \frac{w_i}{w_{i,el}} \end{aligned} \tag{4}$$

where μ_i is in fact the ductility demand, $w_{i,el}$ the elastic limit displacement and T_1 is the natural period of the upper SDOF subsystem (refer to Figure 1). If damping is neglected, it can then be derived that:

$$\begin{bmatrix} \frac{1}{4\pi^2} & \frac{1}{4\pi^2} \\ \frac{a}{4\pi^2} & \frac{a(b+1)}{4b\pi^2} \end{bmatrix} \begin{Bmatrix} \ddot{\mu}_1 \\ \ddot{\mu}_2 \end{Bmatrix} + \begin{bmatrix} 1 & 0 \\ 0 & 1 \end{bmatrix} \begin{Bmatrix} \mu_1 \\ \mu_2 \end{Bmatrix} = \begin{Bmatrix} \frac{F_1}{R_1} g_1 \\ \frac{F_1}{R_2} g_1 \end{Bmatrix} \tag{5}$$

where the stiffness and mass ratios have been introduced as:

$$\begin{aligned} a &= \frac{K_1}{K_2} \\ b &= \frac{M_1}{M_2} \end{aligned} \tag{6}$$

and plastic resistances as:

$$R_i = K_i w_{i,el} \tag{7}$$

Function $f_1(t)$ has transformed into $g_1(\tau)$ and still describes the linear decay of the shock load. The choice of T_1 for the normalisation of time could also have been T_2, which would lead to a similar result. So, it follows from equation 5 that the blast response of a 2DOF system to a shock wave is completely described by five independent non-dimensional variables: τ, F_1/R_1, F_1/R_2, a and b. Consequently, the maximum response depends on t_d/T_1, F_1/R_1, F_1/R_2, a and b. The last three are additional to the ones already defined by Biggs [1].

The response of the 2DOF system is analysed and subsequently the responses of two individual SDOF systems as shown in Figure 1. These SDOF systems are a decomposition of the 2DOF system and represent practical modelling approaches to the primary (DOF 1) and secondary (DOF 2) load resisting structure. Their natural frequencies are related as follows:

$$\begin{aligned} {f_{2DOF}}^2 &= \tfrac{1}{2} {f_1}^2 \frac{b}{a} \left(\frac{a(b+1)}{b} + 1 \pm \sqrt{\left(\frac{a(b-1)}{b} + 1 \right)^2 + 4\frac{a^2}{b}} \right) \\ {f_2}^2 &= {f_1}^2 \frac{b}{a(b+1)} \end{aligned} \tag{8}$$

and the two mode shapes of the 2DOF system can be written as:

$$\left\{ \begin{matrix} 1 \\ 1 - \frac{1}{2}\frac{b}{a} \left(\frac{a(b+1)}{b} + 1 \pm \sqrt{\left(\frac{a(b-1)}{b} + 1 \right)^2 + 4\frac{a^2}{b}} \right) \end{matrix} \right\} \tag{9}$$

The analysis results of these 2DOF and SDOF systems are presented in the next section.

3 DUCTILITY DEMAND IN 2DOF VERSUS SDOF SYSTEMS

The ductility demand as calculated for SDOF systems which are members of a larger structure, is expected to be different from the one calculated using a sophisticated FEM model with many DOFs. This higher complexity is represented here by a 2DOF system and the ductility demand for each of the two DOFs is compared between the 2DOF system and the SDOF system. This is shown here by means of contour plots of the maximum ductility ratio μ_i, i.e. ductility demand, resulting from 2DOF analysis divided by the maximum ductility ratio resulting from SDOF analysis, see Figure 2 to Figure 5. This means that a value smaller than unity in the contour plots indicates conservative design in case of an SDOF approach, and a value greater than unity indicates unconservative design in case of an SDOF approach. The contour plots are a function of t_d/T_1 and a for constant F_1/R_1, F_1/R_2 and b. If necessary, ratio t_d/T_1 can be readily converted to ratio t_d/T_2 based on equation 8:

$$\frac{t_d}{T_1} = \frac{t_d}{T_2}\sqrt{\frac{a(b+1)}{b}} \tag{10}$$

Since in reality always some damping is present, a small amount of damping, i.e. 2% of critical, has been specified in the calculations for practical purposes. The corresponding damping matrix has not been set up based on modal damping, but rather as a non-proportional damping matrix (refer to equation 1) where the damping coefficients are 2% of the critical damping coefficients of the individual SDOF systems.

Furthermore, economical blast design usually corresponds to resistance F_1/R_1 ratios greater than unity and in practice also the stiffness ratio a is usually greater than unity. In case of vehicle bombs [3] the duration of the blast is mostly shorter than the natural period of the glazing [4], so that the ratio t_d/T_1 is smaller than unity. Depending on the level of aggregation in the 2DOF representation, the mass ratio b may be smaller than unity (e.g. façade and building core) or approximately unity (e.g. glass panels and mullions). Therefore, contour plots are presented here for the constants as listed in Table 1 only, but many more have been generated and interpreted for F_1/R_1 and F_1/R_2 in the range (0.7,…,1.4) and b in the range (0.1,…,10).

Case	Resistance ratio F_1/R_1	Resistance ratio F_1/R_2	Mass ratio b
1	1.4	1.0	0.1
2	1.4	1.0	1.0
3	1.4	1.4	0.1
4	1.4	1.4	1.0

Table 1: Considered cases for evaluation of the ductility demand in a 2DOF system compared to individual SDOF systems.

The numerical solutions have been obtained by a Newmark time stepping scheme with parameters $\beta = 0.25$ and $\gamma = 0.5$, providing unconditional numerical stability. Time steps were constant per analysis and set to the smaller of 1/10th of the lower natural period and 1/50th of the blast duration. The number of time steps per analysis was set to fully cover the blast duration or the upper natural period, whichever was greater. The elasto-plastic response was dealt with by Newton-Raphson iterations with a tolerance of 10^{-4} within each time step.

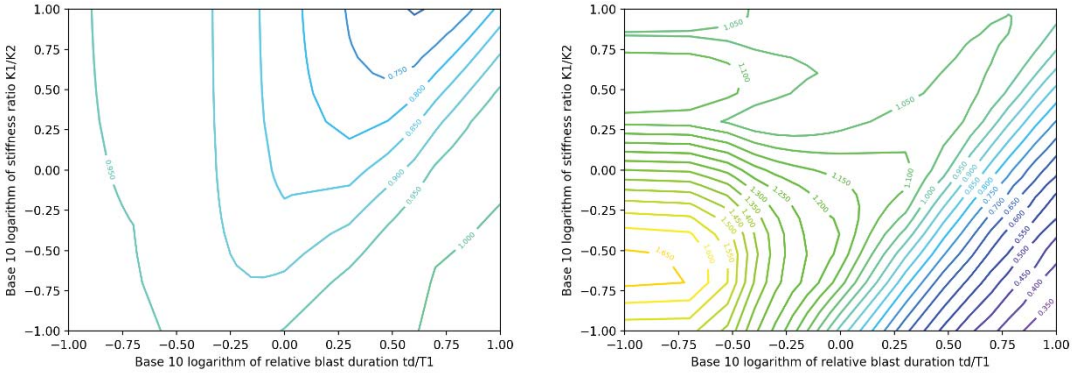

Figure 2: Ductility demand resulting from 2DOF analysis divided by ductility demand resulting from SDOF analysis at DOF 1 (left) and DOF 2 (right) for case 1 (F_1/R_1 = 1.4, F_1/R_2 = 1.0, b = 0.1).

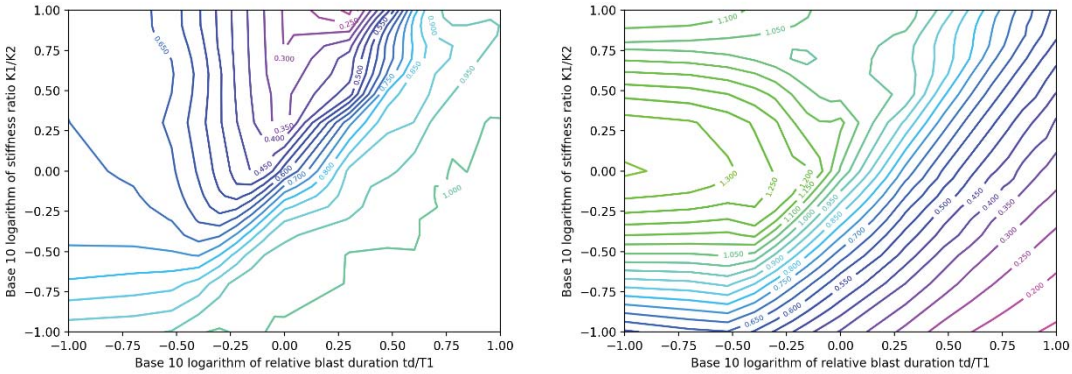

Figure 3: Ductility demand resulting from 2DOF analysis divided by ductility demand resulting from SDOF analysis at DOF 1 (left) and DOF 2 (right) for case 2 (F_1/R_1 = 1.4, F_1/R_2 = 1.0, b = 1.0).

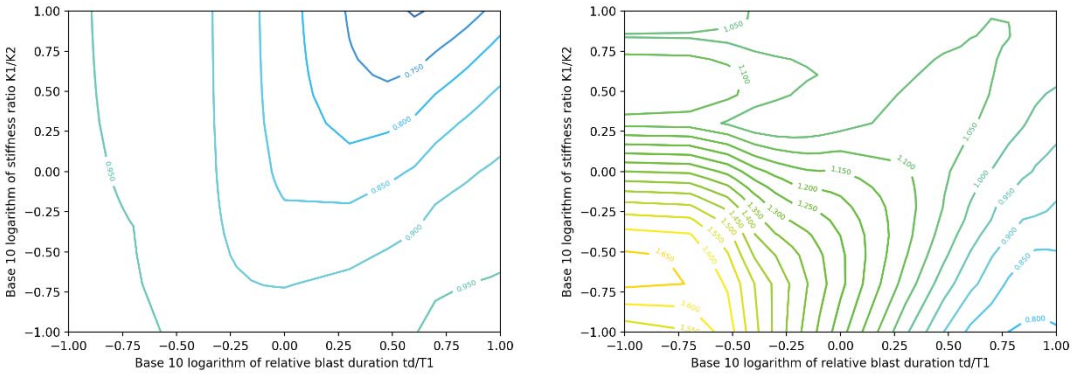

Figure 4: Ductility demand resulting from 2DOF analysis divided by ductility demand resulting from SDOF analysis at DOF 1 (left) and DOF 2 (right) for case 3 (F_1/R_1 = 1.4, F_1/R_2 = 1.4, b = 0.1).

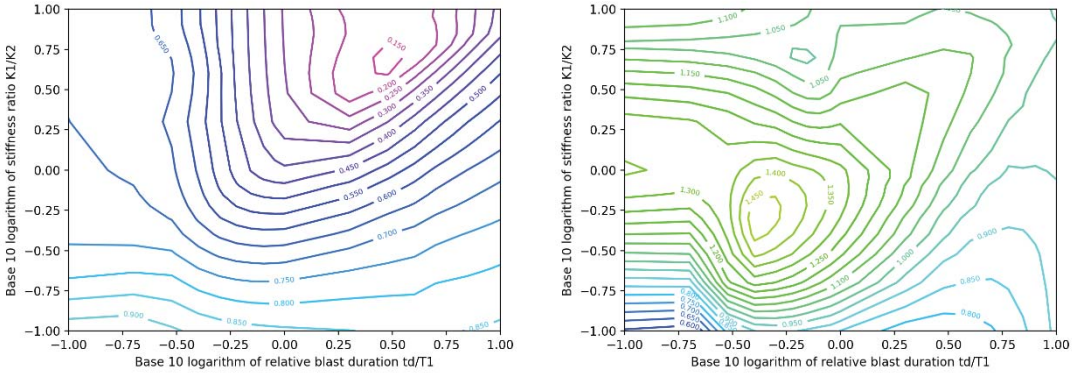

Figure 5: Ductility demand resulting from 2DOF analysis divided by ductility demand resulting from SDOF analysis at DOF 1 (left) and DOF 2 (right) for case 4 (F_1/R_1 = 1.4, F_1/R_2 = 1.4, b = 1.0).

Figure 2 to Figure 5 show that the ductility demand of DOF 1 is always conservatively estimated by an SDOF approach, however this is not a general rule (after inspection of other plots not presented here). Apparently, 2DOF analysis may return only 15% of the ductility demand calculated by SDOF analysis of DOF 1 in some cases. On the other hand, SDOF analysis of DOF 2 roughly tends to produce unconservative results for stiffness ratios a of 1.0 and less and t_d/T_1 ratios smaller than 1.0. It appears that SDOF analysis of DOF 2 may underestimate the ductility demand by 66% in some cases, e.g. for stiffness ratio a = 0.2 and relative blast duration t_d/T_1 = 0.1 in Figure 2 and Figure 4. It should be noted that structures with stiffness ratio a of 1.0 or less are rare cases in practice.

Underestimating the DOF 2 response might not frequently occur in building design. Considering the practical case of glass façades [4] with relative resistances F_1/R_1 = 1.4 and F_1/R_2 = 1.4, mass ratio b = 1.0 (Figure 5), stiffness ratio a = 7.0 and relative blast duration t_d/T_1 = 0.1, this underestimation of DOF 2 is reduced to 8% and the ductility demand of DOF 1 in 2DOF analysis is 69% compared to the one in SDOF analysis. This is shown in the time domain in Figure 6 and Figure 7. Such deviations can be considered fair in early design stages or FEM model validation stages. Note that, obviously, 2DOF analysis and SDOF analysis of DOF 2 (as defined in Figure 1) produce the same results if the stiffness ratio $a \gg 1.0$.

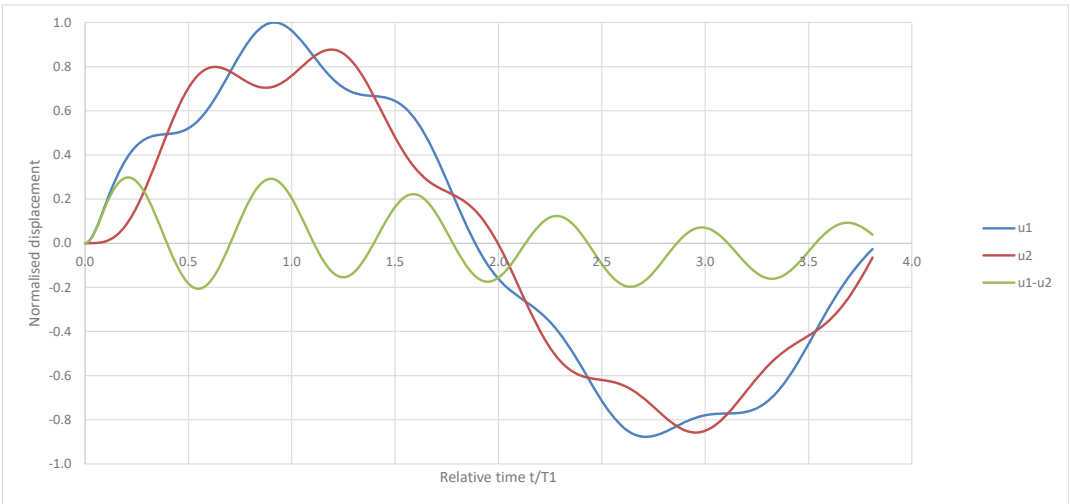

Figure 6: Normalised displacements of the 2DOF system showing the interaction of DOFs for the practical case of F_1/R_1 = 1.4, F_1/R_2 = 1.4, b = 1.0, stiffness ratio a = 7.0 and relative blast duration t_d/T_1 = 0.1.

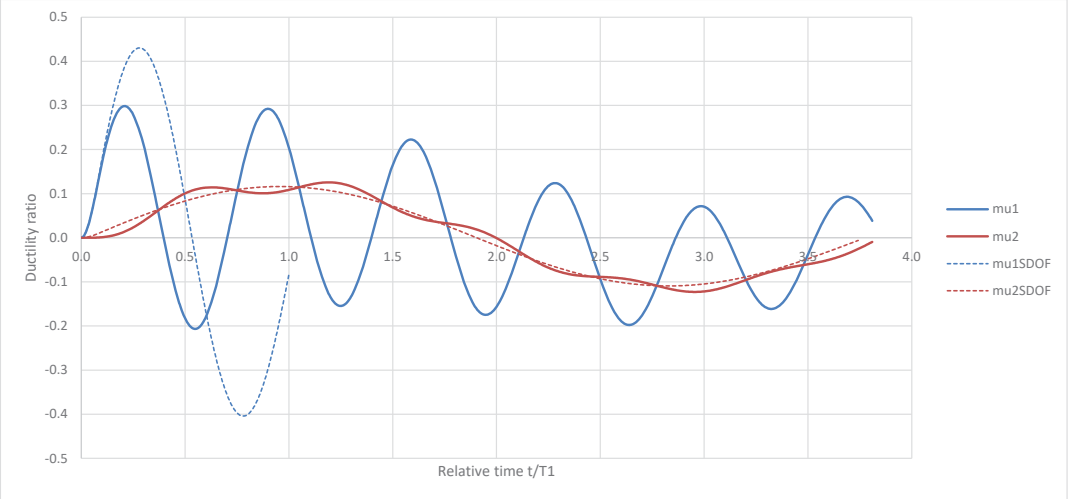

Figure 7: Ductility ratios according to 2DOF (solid lines) and SDOF analysis (dashed lines) for the practical case of $F_1/R_1 = 1.4$, $F_1/R_2 = 1.4$, $b = 1.0$, stiffness ratio $a = 7.0$ and relative blast duration $t_d/T_1 = 0.1$.

Ductility ratios greater than unity (plasticity) and more discrepancy at DOF 2 between 2DOF and SDOF approaches are observed e.g. in the rare case of stiffness ratio $a = 0.2$ combined with relative resistances $F_1/R_1 = 1.4$ and $F_1/R_2 = 1.4$, mass ratio $b = 0.1$ (Figure 4) and relative blast duration $t_d/T_1 = 0.4$. This is further shown in Figure 8 and Figure 9, where it can be seen that the ductility ratio at DOF 2 is actually 150% of the value calculated with an SDOF approach.

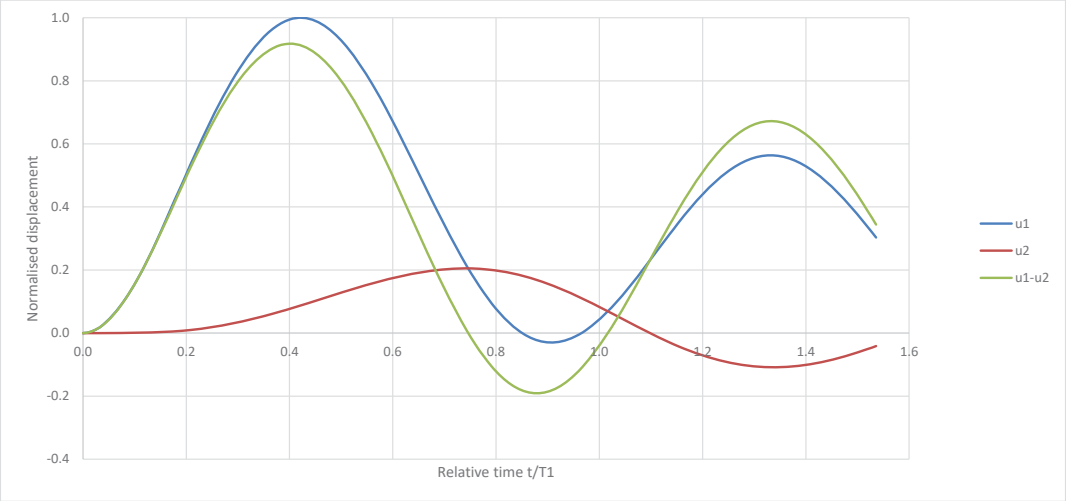

Figure 8: Normalised displacements of the 2DOF system showing the interaction of DOFs for the rare case of stiffness ratio $a = 0.2$ combined with $F_1/R_1 = 1.4$, $F_1/R_2 = 1.4$, $b = 0.1$ and relative blast duration $t_d/T_1 = 0.4$.

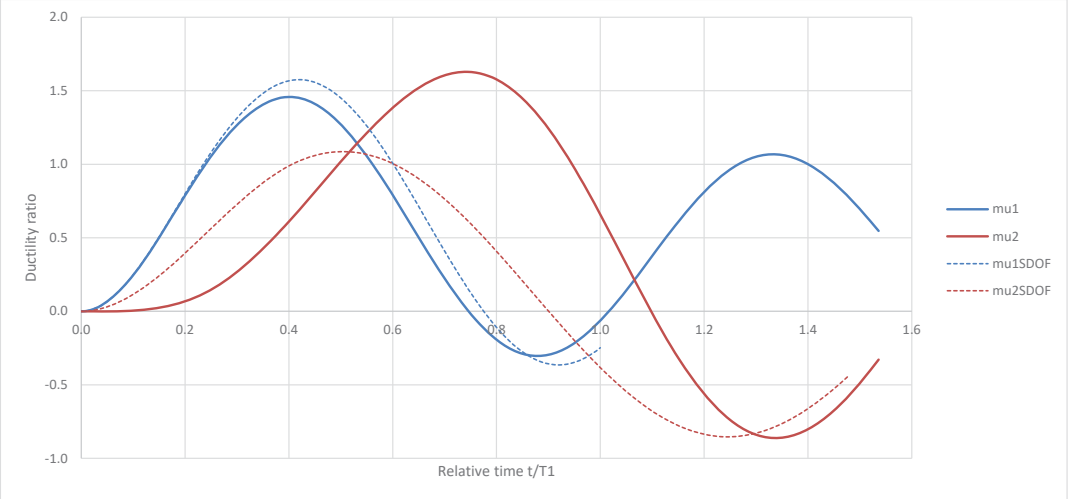

Figure 9: Ductility ratios according to 2DOF (solid lines) and SDOF analysis (dashed lines) for the rare case of stiffness ratio $a = 0.2$ combined with $F_1/R_1 = 1.4$, $F_1/R_2 = 1.4$, $b = 0.1$ and relative blast duration $t_d/T_1 = 0.4$.

4 CONCLUSION

In engineering practice frequent use is made of single-degree-of-freedom (SDOF) approaches to blast-resistant design and evaluation of buildings, either in concept design or in validation of sophisticated finite-element models. While this approach is simple and fast, the omission of the dynamic interaction with other structural members obviously entails some inaccuracy. This inaccuracy has been assessed here by means of a 2-degree-of-freedom (2DOF) system. It appeared that if the member that is struck by the blast first is analysed as an SDOF system, its calculated response in terms of ductility demand will be conservative in most cases. However, the response of the member or structural system that supports this primary system, if calculated using an SDOF approach, may be significantly underestimated in theory. In practical cases some underestimation of its structural response may occur, although this is not likely to exceed 10%.

REFERENCES

[1] J.M. Biggs, Introduction to structural dynamics, *McGraw-Hill*, ISBN: 07-005255-7, 1964

[2] American Society of Civil Engineers, Design of blast-resistant buildings in petrochemical facilities, 2nd ed., *ASCE*, 2010

[3] Glass in building – Explosion-resistant security glazing – Test and classification for arena air-blast loading, *ISO 16933*, 1st ed., 2007

[4] S.F. de Haan, Blast response of glass façades, Retrofit for blast-effect mitigation in the event of a terrorist bombing attack, MSc Thesis, *Delft University of Technology*, The Netherlands, 2017

EURODYN 2020
XI International Conference on Structural Dynamics
M. Papadrakakis, M. Fragiadakis, C. Papadimitriou (eds.)
Athens, Greece, 23–26 November 2020

PROTECTION OF MASONRY STRUCTURES AGAINST EXPLOSIONS APPLYING LAYERS OF TEXTILE REINFORCED MORTAR

Leonidas A. Kouris[1], Georgios Valsamos[1], Savvas Triantafyllou[2], Vasileios Karlos[1], Daniel A. Pohoryles[1], Dionysios A. Bournas[1], Martin Larcher[1] and Folco Casadei[1]

[1] European Commission, Joint Research Centre (JRC)
Via E. Fermi, 2749, I-21027 Ispra (VA), Italy
e-mail: {Leonidas.KOURIS,Georgios.VALSAMOS,Vasileios.KARLOS, Daniel.POHORYLES Dionysios.BOURNAS,Martin.LARCHER, Folco.CASADEI}@ec.europa.eu

[2] National University of Athens
Institute for Structural Analysis and Aseismic Research, School of Civil Engineering, National Technical University of Athens, GR-15780, Greece
e-mail: savtri@mail.ntua.gr

Keywords: Textile reinforced mortar, Blast loads, Explicit model, Experimental calibration

Abstract. *The protection of masonry walls against blast-induced loads by using textile-reinforced mortar (TRM) is investigated herein. Typically the consequences to a structure from explosions (either intentional or accidental) may range from total or partial building collapse due to the direct release of energy to injuries and fatalities due to the created debris. Masonry elements are of stiff and brittle nature and demonstrate considerable resistance in medium-sized compressive loads but degrade dramatically for stronger loads and impacts under tensile stresses. TRM constitutes a novel composite, using open-mesh textiles made from fibre rovings, which has been proven effective as strengthening material to carry the tensile stresses of out-of-plane inertial loading, while satisfying the necessary compatibility, reversibility and durability requirements for masonry buildings. Retrofitting of existing structures with the use of TRM can substantially increase their strength and deformation capacity, providing a sufficient protection to the occupants from blast loads. It should be noted that improving the deformation capacity of masonry can increase the gravitational load bearing capacity of the structure and minimise second order phenomena during a blast event. In this work, we propose a numerical method to accurately predict the various structural effects of explosions on masonry. The focus is to evaluate the developed damage due to impulsive loads and investigate the enhancement of the global dynamic response of a masonry wall before and after retrofitting. Masonry consists of brick units surrounded by mortar joints. The brittle behaviour of this two-phase material is modelled in the EUROPLEXUS explicit finite element code for fast transient phenomena, in complex three-dimensional fluid-structure systems. The performance of masonry is described using plasticity laws for the constituent elements and damage for softening. Geometric non-linearity effects accounting for large displacements and large rotations are also considered. The numerical response is validated using out-of-plane experiments of masonry walletes.*

1 INTRODUCTION

Strong blasts and impact loads on structures result in cracking, fracture, diffusion of debris and may lead to their total or partial collapse. The main cause of injuries and fatalities after the impact of a blast wave on a structure is mainly attributed to the impact of the resulting structural fragments and debris on the occupants [1]. While structural integrity cannot be entirely ensured, damage control can be achieved by applying strengthening techniques. A description of the applied loads on structures due to external explosions is available in [2]. However, in the case of large and complex structures, where shadowing and channeling phenomena take place, advanced numerical modelling techniques are required [1,3] to accurately estimate the effect of strengthening on the dynamic response of the structure.

Masonry walls are amongst the most common building components; they can be distinguished in load bearing and non-load bearing elements as in the case of infill walls in reinforced concrete frame buildings. Masonry walls demonstrate a stiff and brittle nature and, even when designed as non-structural elements, they influence to a great extent the structure's response to external or internal explosions. Few studies are available in the literature for simulating textile reinforced mortar (TRM) strengthened masonry structures under seismic loads, and very limited information exists on the modelling of masonry subjected to blast loads and the simulation of the strengthening. The reason of scarce numerical models of TRM strengthened masonry is the presence of four different materials (brick units, mortar, textile, matrix) and their complicated interactions that give rise to numerous and complex damage modes. These necessitate fine resolutions that render numerical simulation a computationally intensive procedure. Therefore, several simplifications need to be performed in order to strike the right balance between the amount of numerical analysis and exhaustive material characterisation tests.

Focusing only on the TRM external layer, the influence of the imperfections of the in-plane position of the textile, i.e., a curved layer of the textile inside the matrix, on its tensile behaviour was studied in [4] using two-dimensional finite element (FE) models. In this, the mortar was simulated using plane stress elements whereas truss elements were used for the textile. As expected, the higher the imperfect and non-straight placement of the textile in the matrix the higher the change of the stiffness of the TRM. To reduce computational costs, reduced order macro-modelling approaches for TRM strengthened masonry walls were presented based on 2D planar models including either a homogenised non-linear (NL) material calibrated to experimental responses [5,6] or different materials for bricks and mortar [7]. The plane elements can overlap and a perfect bond between the masonry, the inorganic basis and, the textile was assumed [8]. In [9], the authors used fully bonded shell elements for the bricks and the mortar and linear elements arranged in a grid for the TRM; the NL material laws were calibrated using experimental data.

Kyriakides et al. [10] performed an experimental campaign and a corresponding numerical investigation studying the out-of-plane and retrofitting of masonry with an external coat made of steel fibres sprayed in a cementitious mortar, the so-called engineered cementitious composite (ECC), with or without a two-dimensional steel textile [11]. The modelling considers brick units and mortar joints separately simulated, whereas a second more simplified approach merges the two materials while maintaining the interfaces between the homogenised elements to simulate the interaction. A perfect bond between the reinforcement and the inorganic matrix is assumed in both models. Moreover, elastoplastic elements are introduced to simulate the interaction between the coat and the masonry.

Unreinforced masonry walls subjected to blast loads have been investigated both experimentally and numerically. A study investigating masonry materials under high strain rate conditions and their influence on the structural behaviour under blast shows that the strain rate effect has

a substantial impact [12]. Large unreinforced masonry walls 2m × 2m fixed at their base have undergone blast loads up to collapse and the resulting reflected peak pressures have been determined in [13]. A homogenisation model with strain rate effect has been developed for impact loads on unreinforced masonry walls in [14]. A study concerning masonry loaded by near filed detonations investigated the question of fragmentation of masonry [15]. A review of the available numerical models for masonry structures experiencing blast loads can be found in [16].

In [17–19], the effect of impact loads on masonry stack specimens strengthened with composites has been investigated both experimentally and numerically. The finite element simulation was performed on the basis of an implicit dynamic analysis procedure considering material failure via a smeared cracking model and loss of cohesion at the interfaces. The efficiency of elastomeric materials for strengthening masonry walls against blast loads has been investigated in [20]. The masonry specimens are ¼ scaled and made of concrete blocks while the strengthening process involved spraying with a polyurea liner. Single degree of freedom (SDOF) models have been used to simulate masonry performance and estimate their damage producing P-I curves [21].

This study develops a nonlinear FE model in EUROPLEXUS [22], an explicit code, to investigate the strengthening of masonry structural elements using TRM against blast loads.

2 EXPERIMENTAL CAMPAIGN

2.1 Test design and set-up

The test campaign conducted in [23], studying the out-of-plane response of masonry piers strengthened with external layers of TRM in the tension side was simulated in the present study. Kariou et al. 2018 [23] tested a series of eighteen specimens in three-point bending as presented in Figure 1, including two control specimens (unstrengthened). The load is increasing monotonically at the mid-span of the masonry piers which have 18 courses of bricks units in a stretcher bond (Figure 1).

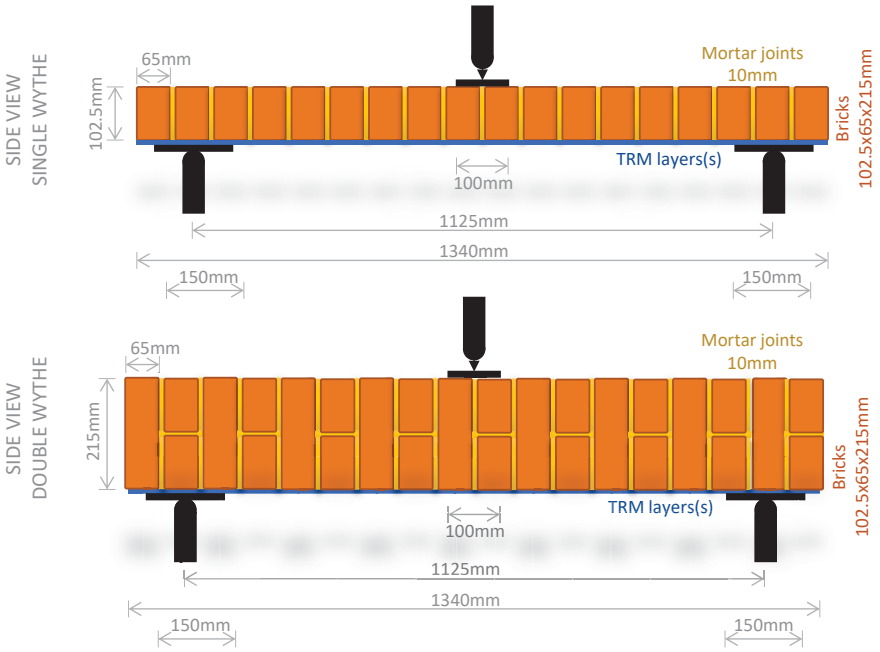

Figure 1. Test set-up and dimensions.

Mortar joints were approximately 10 mm thick, and the specimens' dimensions were 1.34 m long × 0.44 m wide. Wall thickness was a parameter under investigation and therefore, the eight single wythe piers (S) were 0.1025 m thick, while the eight double wythe piers (D) were 0.215 m thick as they include one head mortar joint. Three different fibres were used: (i) carbon (C), (ii) glass (G) and (iii) basalt (B). In this study, only the carbon textile is investigated. Details about the epoxy resin and the impregnation process can be found in [23]. The thickness of the coat is 3 mm for the one-layer carbon textile.

2.2 Material properties

The masonry walls were built using solid clay bricks 65 mm high and with bed face dimensions 215 × 102.5 mm and a mortar with a mix ratio of 1:4 (cement: sand) by volume. The mortar used for the matrix of TRM is made of cement mixed with polymers at a ratio 8:1 while the water to material weight ratio was kept at 0.23.

Material	Strength [MPa]	Elastic modulus [GPa]	Thickness [mm]
Masonry	9.7	2.5	102.5/215
Reinforcing mortar (matrix)	6.0	0.8	3.0
Carbon (C)	3800	225	0.097

Table 1. Material properties: elastic modulus (GPa), strength (MPa) and thickness (mm).

The masonry's vertical Elastic modulus and nominal strength are equal to 2.5 GPa and 9.7 MPa, respectively, estimated from the mean of three compression tests of masonry wallettes [24]. The matrix mortar compressive strength was found 6.0 MPa. Three different composite textiles have been used: (i) carbon with a nominal thickness 0.097 mm, glass with a nominal thickness 0.044 mm and basalt (coated textile) with a nominal thickness 0.037 mm. Measured material properties for all materials are provided in Table 1.

2.3 Test results

Masonry walls usually experience two predominant failure modes or a combination of the two: (i) textile failure (TX), or (ii) masonry failure (MR). The textile failure can occur either as fibre breakage (FB), or textile debonding (DB) and slippage (SL). Masonry failure can be either flexural with vertical cracks (FL), shear with diagonal cracks (SD) or shear sliding of the bricks on the mortar joints (SV) due to loss of bonding. In both cases (i.e. fibres and masonry) a combination of the failure modes is possible. The specimens retrofitted with carbon TRM failed in textile slippage (single wythe specimen) and textile rupture (double wythe specimen).

3 NUMERICAL MODELLING FOR BLAST LOADING

Finite element analysis has been performed to verify the quasi-static experimental results and then obtain a qualitative assessment of the performance of the specimen under blast loading. The simulations herein are carried out using the explicit finite element solver EUROPLEXUS [22] jointly developed by the French Commissariat à l'Energie Atomique et aux Energies Alternatives (CEA Saclay) and the European Commission's Joint Research Centre (JRC Ispra). The main application domain of the software is numerical simulation of fast transient phenomena including non-linear effects, such as explosions and impacts in complex three-dimensional fluid structure systems and therefore, suits perfectly for the masonry blast analysis applied here.

3.1 Numerical setup

The numerical model of the masonry wall was discretized by 8-node linear brick elements with reduced integration to avoid locking phenomena. A uniform element size of 1cm was opted for to also resolve the mortar joints, see Figure 2. The TRM layer has been modelled with 4-node shell elements with 6 DOFs per node, 4 integration points in the plane and 5 integration points through the thickness. A similar element size of 1cm has been employed for the TRM layer which is sharing common nodes with the masonry wall in order to take into account the bonding between the two different components. The specimen was constrained along the vertical direction (parallel to the load) at the support locations. For the quasi-static tests the load has been implemented somewhat faster (constant velocity of 0.05m/s), using time scaling which implies that the simulation run during a shorter time interval than the duration of the physical process of the test. Time scaling increases the strain rates in the structure, therefore rate-sensitivity has been deactivated from the constitutive model.

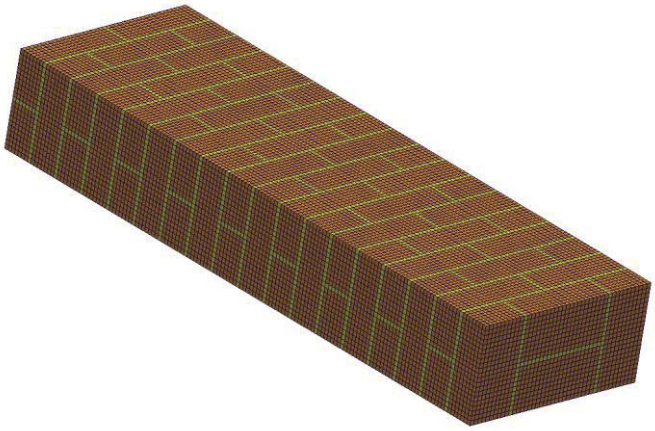

Figure 2. Numerical model of the masonry wall.

3.2 Blast load

An idealized form of a blast pressure-time curve at a certain distance from the detonation point and without intermediate obstacles is presented in Figure 3. The shock wave first reaches the point under consideration at the arrival time t_a (which includes the time of the detonation itself). The pressure reaches its maximum value p_{max} (peak-overpressure) almost instantly and starts decaying until it reaches the ambient pressure p_0 (in most cases the atmospheric pressure) within time t_d, called the positive phase duration. The pressure continues to drop below the ambient pressure reaching its minimum value p_{min}, and then starts to rise again reaching the ambient pressure within time t_n, known as the negative phase duration. The exponential decay of the pressure-time history is represented through the modified Friedlander equation [25], that describes the rate of decrease of the blast pressure values. Depending on the distance of the obstacle from the detonation point and the mass of the explosive charge, the desired parameters (time of arrival, pressure magnitudes, duration and impulses) can be defined using the graphs included in [26].

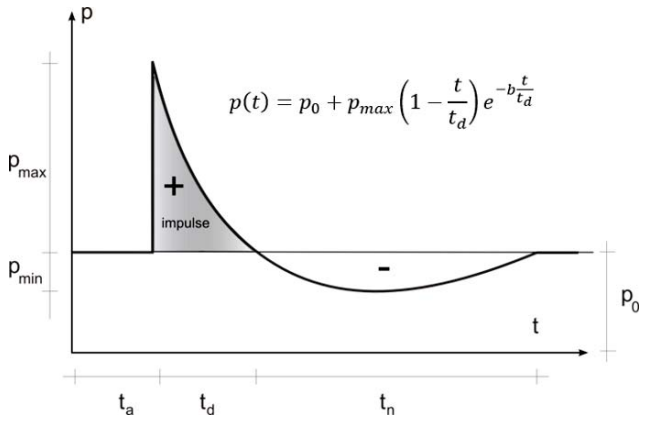

Figure 3. Idealized form of pressure-time history due to explosion (Friedlander equation [25]).

3.3 Material properties and modelling considerations

The response of a perfectly bonded TRM strengthened masonry is generally assumed to be trilinear [27] as shown in Figure 4, where the three subsequent phases I, II_a and II_b are characterised by the moduli E_1, E_2 (=0) and E_3, which can be further simplified to a linear one neglecting the first two phases. However, a complex interaction process between filaments, yarns, the matrix, and the masonry takes place which results in a macroscopic debonding and an uneven stress distribution of the fibres microscopically. To this end an estimation of an 'effective' elastic modulus is opted for in this study, calibrated from the experimental results. The definition of the effective strain is as follows:

$$\varepsilon_{eff} = \varepsilon + \varepsilon_{bond} \tag{1}$$

where ε_{bond} is the macroscopic 'strain' defined as the ratio of the slip to the length of the roving. The TRM coat is modelled assuming only the textile; to this end, the effect of the matrix is introduced as an initial increased stiffness applying the rule of mixtures to reflect its 'presence' prior to cracking and loss of tensile capacity.

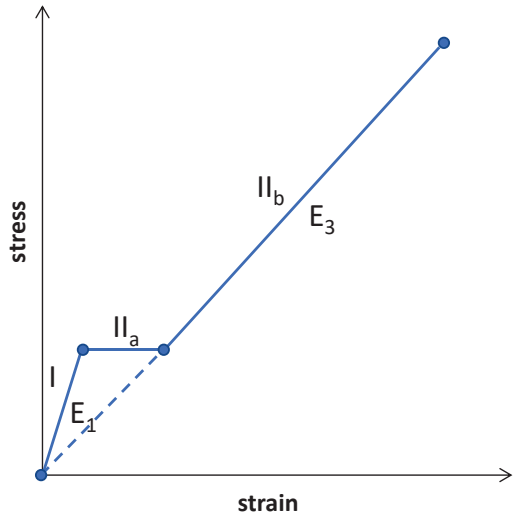

Figure 4. Typical trilinear stress-strain curve of TRM and a simplified linear one [28].

The mortar and the bricks exhibit a brittle behaviour, therefore a three-invariant cap model with mixed hardening has been used [29]. It includes strain rate sensitivity and isotropic damage,

and has been successfully employed in previous studies representing concrete structures [30]. For the TRM layer a Von Mises material law has been used, where elasto-plasticity with isotropic hardening is implemented via a radial return algorithm.

Failure was modelled using element erosion (element excluded from the calculation for the remaining period) that is triggered when all the integration points in the respective element reach a critical value related with the constitutive law. For the brittle material law, the volumetric plastic strain has been used as a failure criterion, while the threshold has been defined after appropriate parametric studies. For the TRM, a criterion based upon the principal strains has been engaged. The criterion is active when the hydrostatic stress is positive (traction), while when the hydrostatic stress is negative (compression) failure is inactive.

4 MODEL CALIBRATION AND BLAST ANALYSES

4.1 Calibration of the proposed model

The numerical model and the assumptions described in Section 3 are applied to the masonry single and double wythe specimens of the experimental campaign presented in Section 2 to calibrate the effective material properties. The calibrated material properties for both specimens retrofitted with a carbon TRM layer are presented in Table 2 and Table 3. It is noted that a uniform weight is applied to all materials as the analysis is explicit. Masonry and mortar joints are modelled using a concrete NL material law applying a Drucker-Prager strain threshold [22].

Material	Density [kg/m³]	Young modulus [GPa]	Poison ratio	Compressive strength [MPA]	Tensile strength [MPa]	Volumetric strain threshold
Brick	2000	6	0.3	15	1.5	0.2
Mortar	1800	0.4	0.2	5	0.5	0.1

Table 2. Material parameters for brittle constitutive law.

Density [kg/m³]	Young modulus [GPa]	Poison ratio [-]	Elastic limit [MPA]	Ultimate stress [MPa]	Ultimate strain [%]
3650	225	0.2	250	1600	1.5

Table 3. Effective material parameters for the carbon TRM layer.

The calibration of the effective material parameters for the carbon textile is shown in Table 3 and the comparison between analytical and experimental results are presented in Figure 5 where an excellent matching is observed. Failure is calibrated with high accuracy in both cases as well as the initial stiffness. A reasonably small variation of the stiffness is observed for the double wythe masonry specimen which can be attributed to local aleatory bonding imperfections.

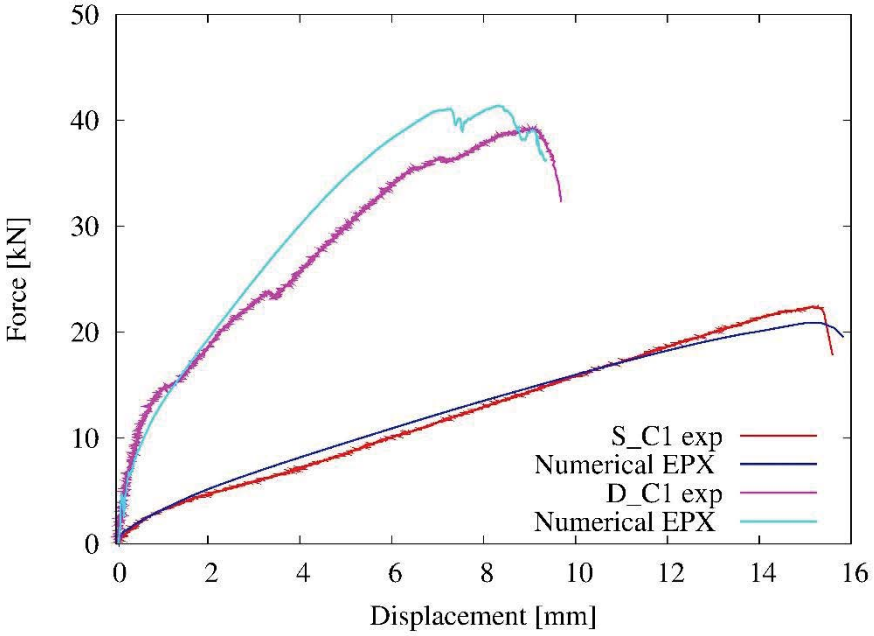

Figure 5. Comparison between experimental results of single (S_C1) and double wythe (D_C1) masonry and numerical model (EPX).

Moreover, comparing the failure mode and the crack propagation among the experimental specimens and the numerical models show a reasonably accurate coincidence as depicted in Figure 6.

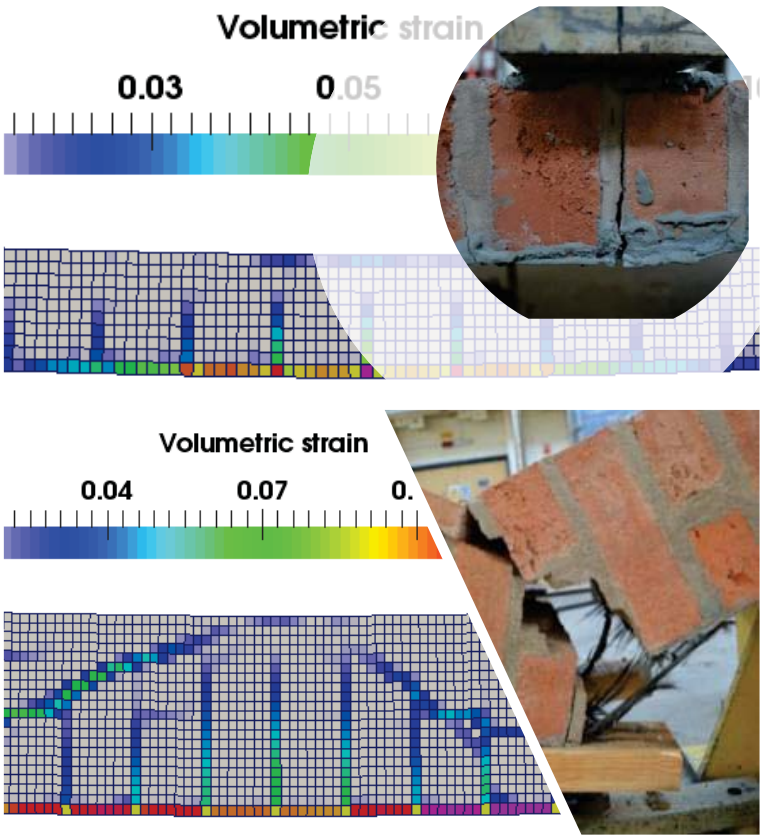

Figure 6. Failure mode of experimental specimens and analytical representation.

4.2 Application of blast loading

A hemispherical blast wave produced from a 80 kg TNT charge at a standoff distance of 5m has been considered to impinge the upper surface of the wall. This scenario implies a Hopkinson-Cranz scaled distance of 1.16 $m/kg^{1/3}$ according to the following Equation:

$$Z = {}^{R}/_{\sqrt[3]{W}} \tag{2}$$

where R is the standoff distance and W is the charge mass.

The materials comprising the masonry wall behave differently under impulsive loading when compared to static or quasi-static loading, due to the effect of the increased strain-rates. Figure 7 presents the comparison of the masonry wall response under blast loading with and without TRM enhancement. The magenta coloured zones indicate the eroded elements after reaching their maximum limit. More accurate representation of the crack propagation needs finer discretisation, but the current one is sufficient to extract qualitative conclusions.

The additional TRM layer appears to prevent the extensive cracking of the mortar. In fact, the opening of the mortar bed joints in the middle zone due to tensile failure is prevented allowing for an additional masonry arch mechanism to develop which, however, is still far from high plastic strains. This additional arch mechanism appears with a moderate diagonal cracking and a compression zone in the middle mortar head joints. Moreover, this mechanism relieves part of the stress and strain tension at the supports.

Monitoring of the number of the failed elements for each case, reveals that the TRM enhanced wall has 20% less eroded elements that is a clear indication of damage reduction. The TRM is not exfoliated, keeping together the individual components of the wall, a characteristic that can contribute towards the reduction of the potential flying debris and their lethal consequences, and thus, increase substantially the safety of the structure.

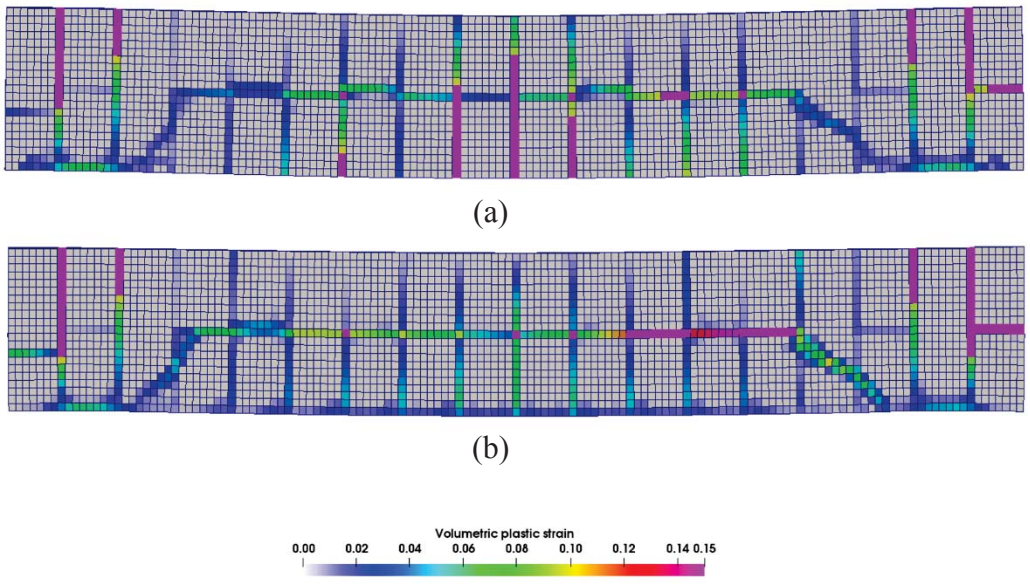

Figure 7. Damage states for: (a) unreinforced masonry, and (b) retrofitted masonry with TRM.

5 CONCLUSIONS

- A model for unreinforced masonry and masonry strengthened with TRM has been developed in an explicit FE code.

- The material models of the simulation have been calibrated using static out-of-plane experiments.
- The materials strain rate effect due to the impulsive loading has been estimated from the literature.
- Unreinforced and retrofitted masonry piers using one layer of carbon textile in inorganic cement-based matrix (TRM) have been exposed to blast loads.
- Application of one layer of TRM (using carbon textile in inorganic matrix) can substantially increase the capacity against impact and blast loads.
- Flying debris is expected to be substantially reduced and thus, increase the occupant safety.

ACKNOWLEDGEMENTS

L. Kouris and D. Bournas gratefully acknowledge the Marie Skłodowska-Curie 'SPEctRUM' project for carrying out this research (Programme/Call: H2020-MSCA-IF-2017; Proposal No: 799593 Individual Fellowship).

REFERENCES

[1] Giannopoulos G, Larcher M, Casadei F, Solomos G. Risk assessment of the fatality due to explosion in land mass transport infrastructure by fast transient dynamic analysis. J Hazard Mater 2010;173:401–8. doi:10.1016/j.jhazmat.2009.08.096.

[2] Karlos V, Solomos G, Larcher M. Analysis of the blast wave decay coefficient using the Kingery–Bulmash data. Int J Prot Struct 2016;7:409–29. doi:10.1177/2041419616659572.

[3] Valsamos G, Casadei F, Solomos G, Larcher M. Risk assessment of blast events in a transport infrastructure by fluid-structure interaction analysis. Saf Sci 2019;118:887–97. doi:10.1016/j.ssci.2019.06.014.

[4] Bertolesi E, Carozzi FG, Milani G, Poggi C. Numerical modeling of Fabric Reinforce Cementitious Matrix composites (FRCM) in tension. Constr Build Mater 2014;70:531–48. doi:10.1016/j.conbuildmat.2014.08.006.

[5] Basili M, Marcari G, Vestroni F. Nonlinear analysis of masonry panels strengthened with textile reinforced mortar. Eng Struct 2016;113:245–58. doi:10.1016/j.engstruct.2015.12.021.

[6] Wang X, Ghiassi B, Oliveira D V., Lam CC. Modelling the nonlinear behaviour of masonry walls strengthened with textile reinforced mortars. Eng Struct 2017;134:11–24. doi:10.1016/j.engstruct.2016.12.029.

[7] Lignola GP, Prota A, Manfredi G. Nonlinear Analyses of Tuff Masonry Walls Strengthened with Cementitious Matrix-Grid Composites. J Compos Constr 2009;13:243–51. doi:10.1061/(ASCE)CC.1943-5614.0000007.

[8] Basili M, Vestroni F, Marcari G. Brick masonry panels strengthened with textile reinforced mortar: experimentation and numerical analysis. Constr Build Mater 2019;227. doi:10.1016/j.conbuildmat.2019.117061.

[9] Parisi F, Lignola GP, Augenti N, Prota A, Manfredi G. Nonlinear Behavior of a Masonry Subassemblage Before and After Strengthening with Inorganic Matrix-Grid Composites. J Compos Constr 2011;15:821–32. doi:10.1061/(ASCE)CC.1943-5614.0000203.

[10] Kyriakides MAA, Hendriks MANAN, Billington SLL. Simulation of unreinforced masonry beams retrofitted with engineered cementitious composites in flexure. J Mater Civ Eng 2012;24:506–15. doi:10.1061/(ASCE)MT.1943-5533.0000412.

[11] Kyriakides MA, Billington SL. Behavior of unreinforced masonry prisms and beams retrofitted with engineered cementitious composites. Mater Struct Constr 2014;47. doi:10.1617/s11527-013-0138-x.

[12] Larcher M, Peroni M, Solomos G, Gebbeken N, Bieber P, Wandelt J, et al. Dynamic Increase Factor of Masonry Materials: Experimental Investigations. ISIEMS, Int. Symp. Interact. Munitions with Struct., Potsdam; Germany: 2013, p. 10.

[13] Ahmad S, Elahi A, Pervaiz H, Rahman AGA, Barbhuiya S. Experimental study of masonry wall exposed to blast loading. Mater Constr 2014;64:e007. doi:10.3989/mc.2014.01513.

[14] Hao H. Numerical modelling of masonry wall response to blast loads. Aust J Struct Eng 2009;10:37–52. doi:10.1080/13287982.2009.11465031.

[15] Dörr A, Gebbeken N, Larcher M, Steyerer M, Haberacker C. The effect of near-field explosions on masonry. 15th Int. Symp. Interact. Eff. munitions Struct., Potsdam, Germany: 2013.

[16] Badshah E, Naseer A, Ashraf M, Shah F, Akhtar K, Bhatti AQ. Review of Blast Loading Models, Masonry Response, and Mitigation 2017. doi:10.1155/2017/6708341.

[17] Pourfalah S, Cotsovos DM, Suryanto B. Modelling the out-of-plane behaviour of masonry walls retrofitted with engineered cementitious composites. Comput Struct 2018;201:58–79. doi:10.1016/j.compstruc.2018.02.004.

[18] Pourfalah S, Cotsovos DM. Enhancing the out-of-plane behaviour of unreinforced masonry walls under impact loading through the use of partially bonded layers of engineered cementitious composite. Int J Prot Struct 2020;11:209–34. doi:10.1177/2041419619866457.

[19] Pourfalah S, Cotsovos DM, Suryanto B, Moatamedi M. Out-of-plane behaviour of masonry specimens strengthened with ECC under impact loading. Eng Struct 2018;173:1002–18. doi:10.1016/j.engstruct.2018.06.078.

[20] Johnson C, Slawson T, Cummins T, Davis J. Concrete masonry unit walls retrofitted with elastomeric systems for blast loads. 2004.

[21] Mayrhofer C. Reinforced masonry walls under blast loading. Int. J. Mech. Sci., vol. 44, Pergamon; 2002, p. 1067–80. doi:10.1016/S0020-7403(02)00014-0.

[22] EUROPLEXUS. Commissariat à l'Energie Atomique & European Commission - JRC. User Manual, 2019:1507. http://www-epx.cea.fr/.

[23] Kariou FA, Triantafyllou SP, Bournas DA, Koutas LN. Out-of-plane response of masonry walls strengthened using textile-mortar system. Constr Build Mater 2018;165:769–81. doi:10.1016/j.conbuildmat.2018.01.026.

[24] EN 1052-1. Methods of test for masonry - Part 1: Determination of compressive strength. Eur Comm Stand 1999.

[25] Baker WE (Wilfred E. Explosion hazards and evaluation. Elsevier Scientific Pub. Co; 1983.

[26] Kingery CN, Bulmash G. Air blast parameters from TNT spherical air burst and hemispherical surface burst. US Army Ballistic Research Laboratory technical report ARBRL-TR 02555. Maryland: Defence Technology Information Center, Ballistic Research Laboratory, Aberdeen Proving Ground; 1984.

[27] Kouris LAS, Triantafillou TC. Design Methods for Strengthening Masonry Buildings Using Textile-Reinforced Mortar. J Compos Constr 2019;23. doi:10.1061/(ASCE)CC.1943-5614.0000906.

[28] Kouris LAS, Triantafillou TC. State-of-the-art on strengthening of masonry structures with textile reinforced mortar (TRM). Constr Build Mater 2018. doi:10.1016/j.conbuildmat.2018.08.039.

[29] Kristoffersen M, Hauge KO, Valsamos G, Børvik T. Blast loading of concrete pipes using spherical centrically placed C-4 charges. EPJ Web Conf 2018;183. doi:10.1051/epjconf/201818301057.

[30] Guilbaud D. Damage plastic model for concrete failure under impulsive loadings XIII International Conference on Computational Plasticity. Fundamentals and Applications. In: Oñate E, Owen DRJ, Peric D, Chiumenti M, editors. XIII Int. Conf. Comput. Plast. Fundam. Appl. COMPLAS XIII , Barcelona, Spain : 2015, p. 1031–1042.

EURODYN 2020
XI International Conference on Structural Dynamics
M. Papadrakakis, M. Fragiadakis, C. Papadimitriou (eds.)
Athens, Greece, 23–26 November 2020

SIMPLIFIED DYNAMIC RESPONSE ANALYSIS OF A RAILWAY BRIDGE CONSIDERING SOIL-STRUCTURE INTERACTION

Christoph Adam[1] **and Benjamin Hirzinger**[1]

[1]University of Innsbruck, Unit of Applied Mechanics
Technikerstr. 13, 6020 Innsbruck, Austria
e-mail: {christoph.adam,benjamin.hirzinger}@uibk.ac.at

Keywords: Bridge dynamics, Maximum bridge acceleration, Soil-structure interaction, Approach and departure phase.

Abstract. *Based on a simple mechanical model, the dynamic response of a railway bridge crossed by a high-speed train is analyzed. The bridge structure is represented by an Euler-Bernoulli beam resting at both ends on spring-damper elements, which model the viscoelastic flexibility of the soil below the bridge foundations. The train is simplified by its axle loads, which cross the beam at constant speed. The influence of the train on the structure during the approach phase and after departure is considered. In an application example the effect of the train speed, the subsoil conditions and the type of train on the peak acceleration of a ballasted bridge is studied.*

1 INTRODUCTION

The bridge structures along high-speed rail lines can be excited to resonance at critical speeds of the crossing train. Resonance leads to considerable acceleration responses of the bridge deck, which has a negative effect on the stability of the ballast bed and the track quality [1]. As a result, the intervals for track maintenance and track servicing must be reduced in order to maintain ongoing operation at the intended operating speed. Consequently, Eurocode 1 [2] specifies limit values for the maximum bridge acceleration, which is for ballasted bridges 3.5 m/s^2 and for non-ballasted bridges 5.0 m/s^2. Such resonance phenomena should be already identified at the planning stage. Therefore, a sufficiently accurate computational prediction of the dynamic bridge response is of great importance in this phase.

The analysis of the structural response is generally based on a mechanical model. For the problem soil-bridge-train interaction, various modeling strategies with varying degrees of detail can be found in the literature [3]. In the more complex models, the bridge structure is converted into a three-dimensional finite element model and the train is represented as a multi-body system [4]. In simple cases, the structure is represented as a beam, which is dynamically loaded by the static axle loads of the passing train [5]. The majority of studies neglect the flexibility of the soil under the bridge bearings and only very few studies (e.g. [6, 7]) deal with the effect of soil-structure interaction on the dynamic bridge response. The soil can be represented simplified by discrete spring-damper elements [8] below the supports.

In this contribution a simple model recently proposed by the authors [9] is used to efficiently predict the dynamic response of a bridge exposed to high-speed trains. The structure is modeled as an *Euler-Bernoulli* beam, whose viscoelastic supported bearings capture the behavior of the soil below the foundations. As a novelty, the approach presented in [9, 10] is used to take into account the effect of the train on the response of the structure while approaching and leaving the bridge. The train is represented in simplified form by the static axle loads moving at the speed of the train. The response of the non-classically damped beam is found by complex modal analysis. For an example problem the influence of the soil-structure interaction on the dynamic response of the bridge structure is studied.

2 MODELING STRATEGY

2.1 Bridge structure, foundation and subsoil

A slender single-span bridge with a constant cross-section over its span L is considered. The bridge structure can be sufficiently accurately represented as an *Euler-Bernoulli* beam with bending stiffness EI and mass per unit length ρA. The lumped masses m located at both beam ends represent the mass of the bridge foundations and the mass of the soil above the foundations. The half-space below the vertically excited rigid foundations is simplified by means of spring-damper elements [11], which are located under the bridge bearings in the model, see Figure 1. Assuming that the half-space is homogeneous, the spring stiffness k and the viscous damping parameter c of these elements are estimated in the present study on the basis of the *Wolf* cone model [12],

$$k = \frac{\rho_b c_w^2 A_0}{z_0} \,, \quad c = \rho_b c_w A_0 \tag{1}$$

where

$$z_0 = \frac{\pi}{4} (1 - \nu) \left(\frac{c_w}{c_s} \right)^2 \tag{2}$$

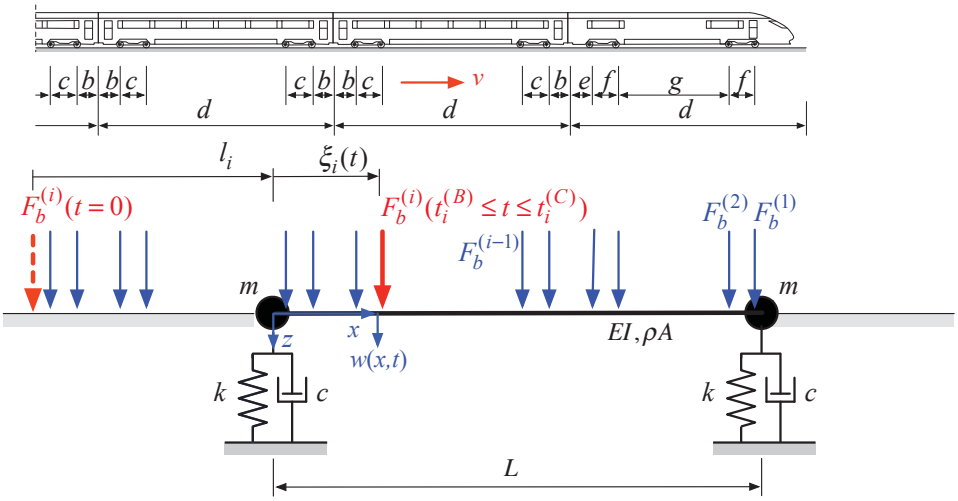

Figure 1: Idealization of the train as a sequence of moving static axle forces and bridge model; from [9].

ρ_b is the density of the soil, A_0 the contact area of the foundation, and $c_s = \sqrt{G/\rho_b}$ the shear velocity with G denoting the shear modulus. For soils with a *Poisson*'s ratio $\nu \le 1/3$, c_w corresponds to the compression velocity,

$$c_w = \sqrt{\frac{E_s}{\rho_b}} \quad , \quad \nu \le 1/3 \tag{3}$$

with the constrained modulus E_s, which is related to the shear modulus G through $E_s = 2G(1-\nu)/(1-2\nu)$.

The time history t of the vertical displacement $w(x,t)$ of the *Euler-Bernoulli* beam at position x satisfies the following partial differential equation [13],

$$\rho A \ddot{w}(x,t) + EI w_{,xxxx}(x,t) = p(x,t) \tag{4}$$

The corresponding boundary conditions of the present beam problem read as [10, 13],

$$\begin{aligned} m\ddot{w}(0,t) + kw(0,t) + c\dot{w}(0,t) + EIw_{,xxx}(0,t) = 0 \ , \ w_{,xx}(0,t) = 0 \\ m\ddot{w}(L,t) + kw(L,t) + c\dot{w}(L,t) - EIw_{,xxx}(L,t) = 0 \ , \ w_{,xx}(L,t) = 0 \end{aligned} \tag{5}$$

The load function $p(x,t)$ in the equation of motion Eq. (4) accounts for the effect of the moving train. It is composed of three portions [9],

$$p(x,t) = p_b(x,t) + p_0(x,t) + p_L(x,t) \tag{6}$$

where $p_b(x,t)$ captures train load when moving on the bridge, $p_0(x,t)$ represents the effect of the train in the approach phase, and $p_L(x,t)$ in the departure phase when the train has already left the bridge. In contrast to a vertically immovable bridge (i.e. on rigid ground), the two contributions $p_0(x,t)$ and $p_L(x,t)$ must be taken into account for this flexibly supported bridge, as described below.

2.2 Train model

2.2.1 Train on the bridge

Since the rail vehicles are generally low tuned, according to Eurocode [2] for the estimation of the dynamic bridge response a train with N_w wheel sets may be described by its N_w static

axle loads $F_b^{(i)}$, $i = 1, ..., N_w$ moving at the train speed v, as shown in Figure 1. If the speed v is constant, the load function $p_b(x,t)$ on the bridge can be expressed as follows [3],

$$p_b(x,t) = \sum_{i=1}^{N_w} F_b^{(i)} \delta(x - \xi_i)[H(t - t_i^{(B)}) - H(t - t_i^{(C)})] \tag{7}$$

The *Dirac* delta function $\delta(x - \xi_i)$ represents the i-th axle load $F_b^{(i)}$ at $\xi_i = vt - l_i$, with l_i denoting the initial position of the force at time $t = 0$ (cf. Figure 1). The *Heaviside* functions H describe the arrival of this force on the bridge at time $t_i^{(B)} = l_i/v$ or its departure at time $t_i^{(C)} = (l_i + L)/v$.

2.2.2 Approach and departure phase of the train

In the common models of viscoelastically supported beam bridges, the beam is suddenly loaded when the i-th axle load of the train is applied. Since the deflection of the beam is still zero when the load arrives at the bridge, an inertial force is suddenly generated which counteracts this axle load. However, the acceleration jump in the model associated with this inertial force has no physical background, but is only caused by the insufficient model, which ignores the approach and departure phase of the train. An appropriate model must consider the lowering of the bridge foundation caused by the deformation of the ground and track when the train approaches the bridge. The acceleration jump is then avoided in the analysis.

The model proposed recently by the authors [9] assumes that at time $t_i^{(A)} = (l_i - L_0)/v$ at the distance L_0 from the left support the i-th static axle load $F_b^{(i)}$ of the train induces the single force $P_0^{(i)}(t)$ at this support. $P_0^{(i)}(t)$ increases linearly with time $t - t_i^{(A)}$ from zero. At time $t_i^{(B)} = l_i/v$ the axle load $F_b^{(i)}$ reaches this support, where $P_0^{(i)}(t_i^{(B)}) = F_b^{(i)}$. This model is based on the assumption that the axle load $F_b^{(i)}$ in the approach phase crosses a rigid massless beam of length L_0, which is simply supported on the left and elastically supported on the right by the soil spring of stiffness k, as shown in Figure 2(a). The force $P_0^{(i)}$ thus represents the quasi-static reaction force of this beam at the flexible support due to the load $F_b^{(i)}$ moving at constant speed. The effect of the N_w axle loads on the left support can be combined to form the total force $P_0(t)$ as [9],

$$p_0(x,t) \equiv P_0(t) = \delta(x) \sum_{i=1}^{N_w} F_b^{(i)} \left(1 + \frac{vt - l_i}{L_0}\right) \left[H(t - t_i^{(A)}) - H(t - t_i^{(B)})\right] \tag{8}$$

The *Dirac* delta function $\delta(x)$ indicates the position of $P_0(t)$ at $x = 0$, i.e. at the left bridge bearing. The ith axis load $F_b^{(i)}$ is activated at the time $t_i^{(A)}$ by the *Heaviside* function $H(t - t_i^{(A)})$, and is deactivated at the time $t_i^{(B)}$ by the *Heaviside* function $H(t - t_i^{(B)})$ when entering the left bridge bearing.

If at time $t_i^{(C)} = (l_i + L)/v$ the axle load $F_b^{(i)}$ leaves the bridge, the force $P_L^{(i)}(t_i^{(C)}) = F_b^{(i)}$ is applied to the right support, which then decreases linearly with increasing distance of $F_b^{(i)}$ until it is zero at time $t_i^{(D)} = (l_i + L + L_L)/v$. L_L represents the influence length behind the bridge. Mathematically, the total force $P_L(t)$ at the right bridge bearing is expressed as [9],

$$p_L(x,t) \equiv P_L(t) = \delta(x - L) \sum_{i=1}^{N_w} F_b^{(i)} \left(1 - \frac{vt - l_i - L}{L_L}\right) \left[H(t - t_i^{(C)}) - H(t - t_i^{(D)})\right] \tag{9}$$

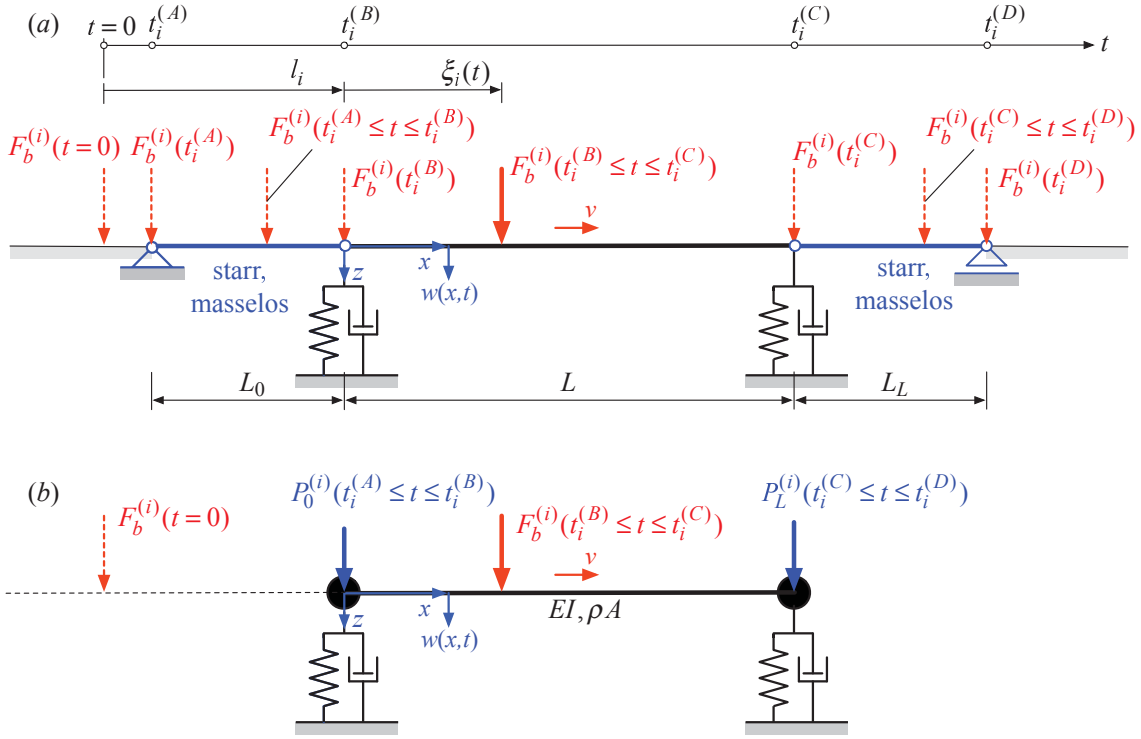

Figure 2: (a) Basic idea of considering the approach and the departure phase of the train, visualized for the ith axle load, whose position is shown at different time instants. (b) Implementation of the approach and departure condition on the viscoelastic supported beam model; modified from [9].

Figure 2(b) illustrates the load on the beam induced by the i-th moving axle load $F_b^{(i)}$. In the approach phase in the period $t_i^{(A)} \leq t \leq t_i^{(B)}$ the force $P_0^{(i)}$ is applied to the left support, in the period $t_i^{(B)} \leq t \leq t_i^{(C)}$ the force $F_b^{(i)}$ crosses the bridge and in the departure phase $P_L^{(i)}$ is applied to the right support.

3 ANALYSIS OF THE STRUCTURAL RESPONSE

The *Euler-Bernoulli* beam described by the equation of motion Eq. (4) is non-classically damped due to the non-classical boundary conditions Eq. (5). Therefore only a complex modal analysis leads to the decoupling of the modal equations. For the complex analysis the equation of motion is transferred to the state space. For details it is referred to [9, 10].

4 APPLICATION

4.1 Bridge and soil parameters

A single-span ballasted steel railway bridge with a span of $L = 21$ m is considered, see also [9]. The corresponding beam model has a bending stiffness of $EI = 2.6 \cdot 10^{10}$ Nm^2 and a mass per unit length of $\rho A = 7083$ kg/m. The modal damping coefficients $\widetilde{\zeta}_r = 0.5\%$, $r = 1, 2, \ldots$ of the vertically immovable steel structure (i.e. the base is rigid) are assumed to be equal to 0.5% according to Eurocode 1 [2]. In contrast, in the viscoelastically supported bridge models the modal damping coefficients for the steel structure are only half of the value proposed in Eurocode 1 [2], i.e. $\widetilde{\zeta}_r = 0.25\%$, because the effect of radiation damping is captured by the viscous dampers.

Five homogeneous soils of different stiffness are considered, whose soil parameters (con-

strained modulus E_s, *Poisson*'s ratio ν, mass density ρ) are summarized in Table 1 [9, 10]. Soil 1 with the lowest stiffness corresponds to a medium stiff soil and soil 5 to a stiff soil (rock). Since the required contact area A_0 of the foundations depends on the soil stiffness (i.e. the stiffer the soil the smaller the required area), the product of the base area of the foundation A_0 and the root of the constrained modulus of the soil E_s is kept constant when determining k and c, i.e. $A_0\sqrt{E_s} = 2.289 \cdot 10^4$ $\sqrt{\text{N}}$m. The foundations are assumed to have the same mass for all soils considered, i.e. $m = 1.5 \cdot 10^5$ kg.

	E_s [MN/m^2]	ν [-]	ρ [kg/m^3]	k [N/m]	c [kg/s]
1	200	0,30	2263	5,895·10^8	1,089·10^6
2	250	0,28	2300	7,662·10^8	1,098·10^6
3	300	0,26	2333	9,495·10^8	1,106·10^6
4	400	0,25	2367	1,284·10^9	1,114·10^6
5	500	0,25	2400	1,605·10^9	1,121·10^6

Table 1: Soil parameters and corresponding parameters of the spring-damper elements [9]

4.2 Maximum dynamic bridge response

In the following, the maximum dynamic response of the bridge subjected to the Austrian high-speed train Railjet and the Intercity-Express train ICE 3, respectively, is studied. The Railjet train with the maximum speed of $v_{max} = 280$ km/h consists of two powercars and twice six wagons with a total length of $L_{train} = 205.4$ m and 56 axles. The considered ICE 3 train is composed of two units (i.e. 16 cars) with a total length of $L_{train} = 400$ m and has 64 axles. The maximum speed of the ICE 3 train is 330 km/h. The amplitude and distances of the axle loads for the Railjet train can be found in [14] and for the ICE 3 train in [15].

As already described in the introduction, in general the maximum acceleration of the bridge deck is decisive for the assessment of the reliability of the bridge structure exposed to high-speed trains. Therefore, in a series of analyses, the acceleration response of the beam model under the effect of the axle loads of the considered trains is computed, increasing in each analysis the speed v stepwise by $\Delta v = 0.1$ m/s. The response is approximated by seven modes. Additionally, the deflection w_r of the beam model is also determined, which is the vertical displacement $w(x,t)$ minus the rigid body displacement due to the lowering of the supports,

$$w_r(x,t) = w(x,t) - \frac{(w(0,t) + w(L,t))}{2} \tag{10}$$

A previous convergence study [9] has shown that the influence length before and after the bridge of $L_0 = L_L = 20$ m is sufficient. Plotting the maximum bridge acceleration a and the maximum deflection w_{rel}, respectively, observed in the period $T = (l_1 + L_{train} + L_0 + L + L_L)/v$,

$$\begin{aligned} a(v) &= \max\{|\ddot{w}(x,t,v)| : 0 \le x \le L, 0 \le t \le T\} \\ w_{rel}(v) &= \max\{|w_r(x,t,v)| : 0 \le x \le L, 0 \le t \le T\} \end{aligned} \tag{11}$$

against the train speed v, yields the response spectra of the bridge structure induced by the Railjet train (Figure 3) and the ICE 3 train (Figure 4), respectively. In the Figures 3 and 4 the maximum accelerations are shown on the left and the maximum deflections on the right. The maximum spectral values occur at the critical speeds $v_l^{(r)}$ (also referred to as resonance speeds), which

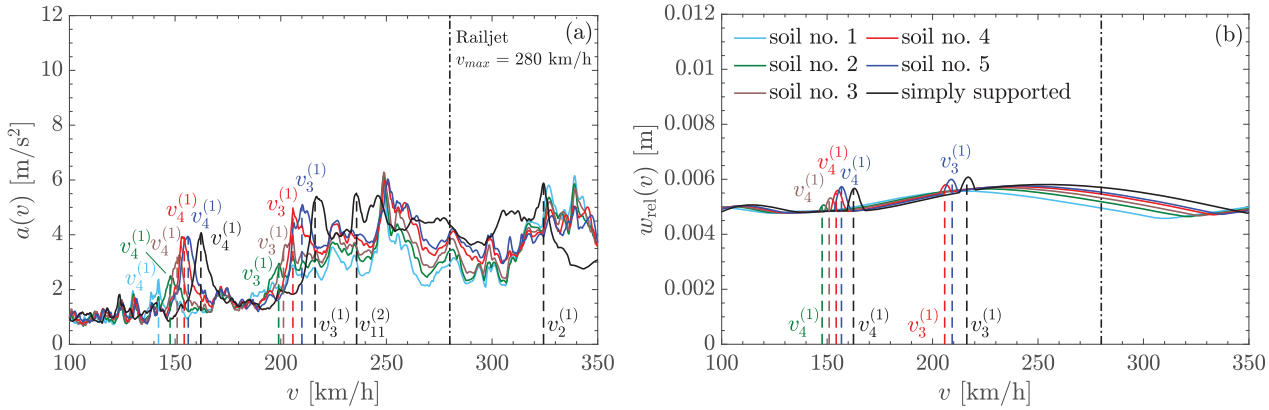

Figure 3: (a) Maximum acceleration and (b) maximum deflection of the bridge with respect to the speed of the Railjet train for different subsoil conditions.

are defined as [3] $v_l^{(r)} = df_r/j,\ j = 1, 2, 3, ...$ These resonance phenomena are a consequence of the excitation of the structural modes by the moving axle loads with constant distance d. f_r denotes the r-th natural frequency of the bridge and j is an integer variable. The distance d, which corresponds to the car length, is 26.5 m for the Railjet train and 24.78 m for the ICE 3 train.

As can be seen from Figure 3, the first two main resonance speeds $v_4^{(1)}$ and $v_3^{(1)}$ of the Railjet train in the ranges between 150 to 160 km/h and 200 to 230 km/h are a consequence of the excitation of the fundamental mode. The decrease of the soil stiffness is accompanied by a reduction in the fundamental frequency and consequently in the corresponding critical speeds. Thus, for the simply supported beam (rigid soil) the critical speed $v_4^{(1)}$ is 162.4 km/h, but for the structure on medium stiff soil 1 only $v_4^{(1)} = 142.2$ km/h. In the first case the maximum acceleration is $a(v_4^{(1)}) = 4.08$ m/s^2, in the latter case only $a(v_4^{(1)}) = 2.37$ m/s^2.

According to Figure 3(a), for the simply supported beam on rigid soil as well as for the structure on soils 4 and 5 at critical speeds $v_4^{(1)}$ and $v_3^{(1)}$ the acceleration threshold for ballasted bridges according to the Eurocode 1 [2] of 3.5 m/s^2 is exceeded. This is due to the low first mode damping for this combination of structure and soil properties. From this figure two main effects of the soil-structure interaction can already be seen. The critical speeds become smaller with lower soil stiffness, but at the same time the corresponding maximum accelerations are reduced because the overall damping increases. In contrast to the acceleration spectra, which show numerous local peaks, a minor amplification of the maximum deflection is only observed at the previously mentioned resonance speeds, as shown in Figure 3(b). However, these amplifications are not critical.

As the spectra of Figure 4(a) shows, the ICE 3 train induces resonance accelerations for all subsoil conditions that are a multiple of the acceleration threshold of 3.5 m/s^2. The critical speeds of the ICE 3 train, at which this limit acceleration is exceeded, start at about 220 km/h. These critical speeds excite the first and second mode ($v_2^{(1)}$, $v_{10}^{(2)}$, $v_{11}^{(2)}$) of the simply supported structure (on rigid soil), and the first and fourth mode ($v_2^{(1)}$, $v_{10}^{(4)}$) of the beam on flexible subsoil, as can be seen from Figure 4(a). As observed, the rigidly supported bridge model exceeds for the first time the limit acceleration of 3.5 m/s^2 at the speed $v_{11}^{(2)} = 220$ km/h, which is at a lower speed than with the models with flexible soil. The largest maximum acceleration of 9.6 m/s^2 occurs at $v_2^{(1)}$ of the model with soil 5, because the damping of the first mode is smaller with this model than with the simply supported beam. The deflection, on the other hand, is significantly

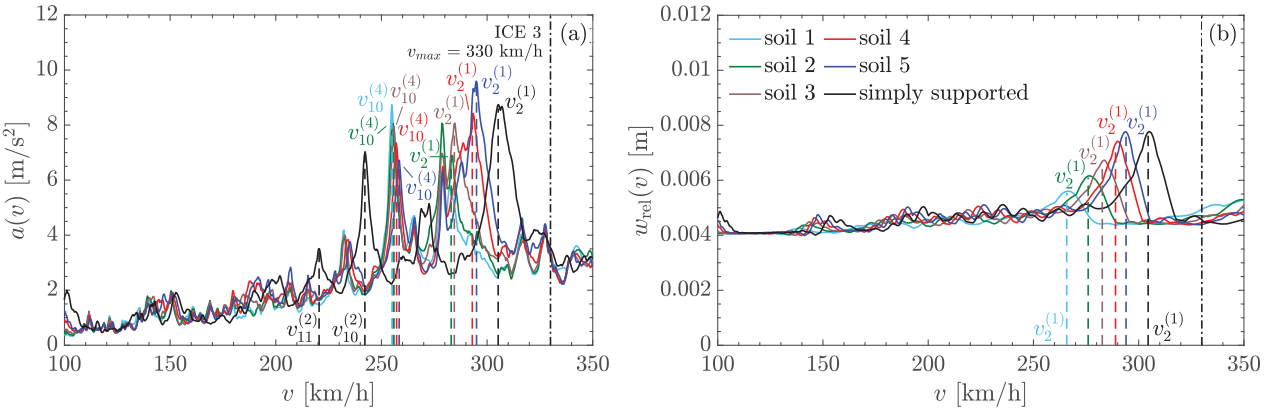

Figure 4: (a) Maximum acceleration and (b) maximum deflection of the bridge with respect to the speed of the ICE 3 train for different subsoil conditions.

increased by the ICE 3 train only at the critical speed $v_2^{(1)}$, see Figure 4(b).

5 CONCLUSIONS

The results of this study on the soil-bridge-train system are based on a simplified model in which the structure is represented as a beam, the subsoil as spring-damper elements below the bearings, and the train as moving axle loads. A corresponding consideration of the approach phase and the departure phase of the train is decisive for physically meaningful outcomes of this model.

This study shows the influence of soil-structure interaction on the numerically predicted acceleration response of a bridge structure exposed to a high-speed train. In general, the maximum accelerations become smaller due to the radiation damping of the ground. In many cases the resonance speeds are also reduced as the fundamental frequency of the bridge decreases due to the decreasing overall stiffness. As in the case of the considered bridge crossed by the ICE 3 train, additional resonance peaks can occur when taking into account the soil-structure interaction, since additional modes emerge in the interacting system due to the flexibility of the soil.

6 ACKNOWLEDGEMENT

The research of B. Hirzinger was partly supported by the Tyrolean Science Fund (project no DB-NR: 302222).

REFERENCES

[1] H. Xia, N. Zhang, W.W. Guo, Analysis of resonance mechanism and conditions of train-bridge system, *Journal of Sound and Vibration*, **297**, 810–822, 2006.

[2] Eurocode 1., EN 1991-2, Eurocode 1: Actions on Structures, 2003.

[3] Y.B. Yang, J.D. Yau, Y.S. Wu, *Vehicle-Bridge Interaction Dynamics*, World Scientific Publishing Company Incorporated, 2004.

[4] P. Salcher, C. Adam, Modeling of dynamic train-bridge interaction in high-speed railways, *Acta Mechanica*, **226**, 2473–2495, 2015.

[5] L. Fryba, *Vibration of Solids and Structures Under Moving Loads* (3. ed.), Thomas Telford, 1999.

[6] A. Romero, M. Solís, J. Domínguez, P. Galvín, Soil-structure interaction in resonant railway bridges. *Soil Dynamics and Earthquake Engineering*, **47**, 108–116, 2013.

[7] A.M. Gharad, R.S. Sonparote, Study of direct finite element method of analysing soil-structure interaction in a simply supported railway bridge subjected to resonance. *Iranian Journal of Science and Technology, Transactions of Civil Engineering*, **43**, 273–286, 2019.

[8] C. Svedholm, A. Zangeneh, C. Pacoste, S. François, R. Karoumi, Vibration of damped uniform beams with general end conditions under moving loads, *Engineering Structures*, **126**, 40–52, 2016.

[9] C. Adam, B. Hirzinger, Ein Modell mit Boden-Bauwerk-Interaktion zur dynamischen Berechnung von Eisenbahnbrücken (in German) [A model with soil-structure interaction for the dynamic analysis of railway bridges], *Bauingenieur*, 2020.

[10] B. Hirzinger, C. Adam, P. Salcher, Dynamic response of a non-classically damped beam with general boundary conditions subjected to a moving mass-spring-damper system, under review.

[11] J.A. Studer, J. Laue, M.G. Koller, *Bodendynamik* (3. ed.) (in German) [Soil Dynamics], Springer, 2004.

[12] J.P. Wolf, A.J. Deeks, *Foundation Vibration Analysis: A Strength-of-Materials Approach*, Elsevier, 2004.

[13] R.W. Clough, J. Penzien, *Dynamics of Structures* (2. ed.), McGraw-Hill, 1993.

[14] P. Salcher, *Reliability assessment of railway bridges designed for high-speed traffic: Modeling strategies and stochastic simulation*, Dissertation, University of Innsbruck, 2015.

[15] Peterson, C., Werkle, H. *Dynamik der Baukonstruktionen* (2. ed.) (in German) [Dynamics of Civil Structures], Springer Vieweg, 2017.

EURODYN 2020
XI International Conference on Structural Dynamics
M. Papadrakakis, M. Fragiadakis, C. Papadimitriou (eds.)
Athens, Greece, 23–26 November 2020

DYNAMIC AMPLIFICATION FACTORS FOR ULTRA-HIGH-SPEED HYPERLOOP TRAINS: VERTICAL AND LATERAL VIBRATIONS

Ehsan Ahmadi[1], Mohammad M. Kashani[2] and Nicholas A. Alexander[3]

[1] Postdoctoral Research Associate
University of Southampton, United Kingdom
e-mail: e.ahmadi@soton.ac.uk

[2] Associate Professor
University of Southampton, United Kingdom
mehdi.kashani@soton.ac.uk

[3] Associate Professor
University of Bristol, United Kingdom
nick.alexander@bristol.ac.uk

Keywords: Hyperloops, Ultra-high-speed trains, Dynamic amplification factors, Vertical and lateral vibration

Abstract. *The ultra-high-speed (UHS) Hyperloop is the next-generation mode of passenger/freight transportation, and is composed of a tube or a system of tubes through which a pod travels free of friction. The entire system must be supported by piers (multi-span viaducts), where the tubes act as the bridge deck. The UHS moving Hyperloops can exert large dynamic effects to the supporting pier-deck system both vertically and laterally. Particularly, asymmetric Hyperloop loading can generate significant lateral vibrations. Therefore, for safe design of a bridge pier-deck system for UHS trains, it is of great importance to explore dynamic interaction of bridge deck and piers under UHS moving Hyperloops. Hence, this paper analytically summarizes the dynamic amplification factors of the Hyperloop-deck-pier system for vertical and lateral vibrations. It was found that the UHS Hyperloop trains result in higher dynamic effects compared to the high-speed trains.*

1 INTRODUCTION

The Hyperloops suggested initially by Tesla, and later by TransPod, are ultra-high speed (UHS) trains that move and transport passengers at (UHSs) [1]. As shown in Figure 1, the train travels inside a vacuum tube (continuous beams) free of air resistance and friction. In addition, this UHS idea uses magnetic levitation and linear accelerators to push the train forward. The suggested operating speed of these trains are around 970 km/h, with a maximum

speed of 1200 km/h. This compares with mean operating speed of 270km/h for high-speed (HS) trains.

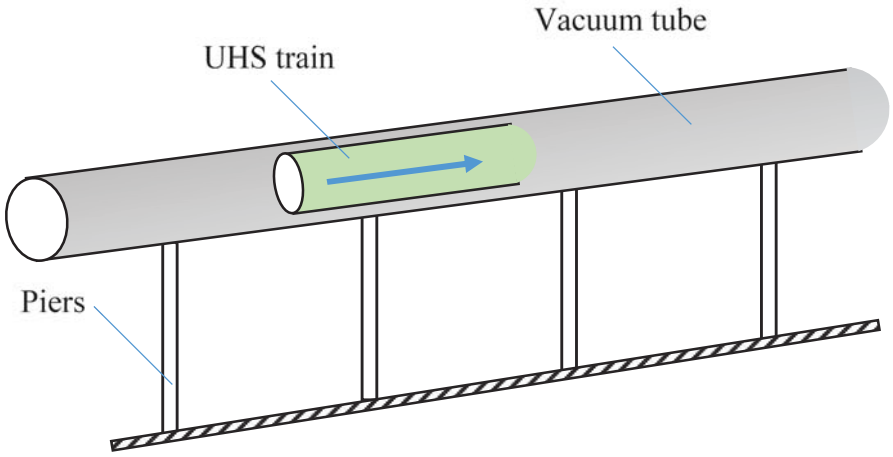

Figure 1: Preliminary concept of Hyperloop trains.

The present UK network rail guideline for design and assessment of bridge structures [2] does not take into account dynamic effects of moving loads for train speeds less than 160 km/h or vertical dynamic amplification factor (DAF) of 1. Nonlinear analysis of existing UK railway bridges also recommends that dynamic effects of train loading are very pronounced for train speeds over 160 km/h [3, 4]. Eurocode EN 1991-2 [5] recommends similar vertical DAFs for train speeds below 200 km/h. However, for train speeds higher 200 km/h, Eurocode EN 1991-2 [5] suggests further advanced dynamic analysis to determine vertical DAFs.

Analytical approaches for moving load problems are very appropriate for parametric analyses. However, it should be noted that all moving force problems cannot be analytically described and more rigorous numerical approaches are necessary to calculate dynamic effects of moving loads [6]. Dynamic effects of moving loads can be substantial particularly for HS trains. Thus, DAFs are defined as dynamic-to-quasi static peak deflection due to the dynamics of moving loads. A solid literature review on DAFs of road bridges for vertical motion can be found in [7]. Currently, there is lack of sufficient knowledge on the UHS Hyperloop trains, and hence, no design recommendations exist to design bridges and accommodate the next-generation UHS transport system. Therefore, this study summarizes DAFs of Hyperloop train-bridge-pier systems for vertical and lateral vibrations already published in [8, 9].

2 ANALYTICAL MODELLING

In this section, the equations of motion of a train composed of a set of moving masses traveling at any speed across a continuous beam of any span length with any number of spans is analytically studied. Consider a set of moving masses traveling at some group velocity V across a continuous beam of n spans of length L as illustrated in the Figure 2. The beam has a uniform mass per unit length m and flexural rigidity EI_b. In addition, for lateral vibration, lateral flexural rigidity of each column (bridge pier) of height h is EI_c. Small deflection theory and linear elastic analysis are used to formulate the lateral motion of the deck. Torsional and vertical oscillations are also ignored in this analysis.

To derive governing equations of vertical and lateral motions of the bridge deck, the Lagrangian formulation is used. The kinetic energy of the system is composed of kinetic energy of the beams and of the moving trainset, and the potential energy of the system includes the internal flexural strain energy of the beam and the external work done by the gravitational load of the train for vertical vibration. However, for lateral vibration due to vertical moving

load eccentricity, the flexural energy of the laterally deformed cantilever piers is also added to the potential energy. Then, the minimization of action principle is employed to derive equations of vertical and lateral motion separately:

$$\left(M_{ij}^{b,v}+M_{ij}^{t,v}\right)\ddot{Z}_i+C_{ij}^{v}\dot{Z}_i+K_{ij}^{v}Z_i=F_j^{t,v} \tag{1}$$

$$\left(M_{ij}^{b,l}+M_{ij}^{t,l}\right)\ddot{Y}_i+C_{ij}^{l}\ddot{Y}_i+\left(K_{ij}^{b,l}+\eta K_{ij}^{c}\right)Y_i=F_j^{t,l} \tag{2}$$

Equations (1) and (2) are respectively for vertical and lateral vibrations; *M, C* and *K* are mass, damping and stiffness matrices respectively; superscripts *b*, *t*, *v*, and *l* stand for beam, train, vertical and lateral; η is the pier-to-deck stiffness ratio; *Z* and *Y* are non-dimensional vertical and lateral deflections:

$$Z=gz/\omega_{1v}^2;\qquad Y=gy/\omega_{1l}^2 \tag{3}$$

where ω_{1v} and ω_{1l} are the first natural frequencies of the unloaded bridge respectively for vertical and lateral motions. For more information on the parameters and assumptions taken, you can see [8, 9].

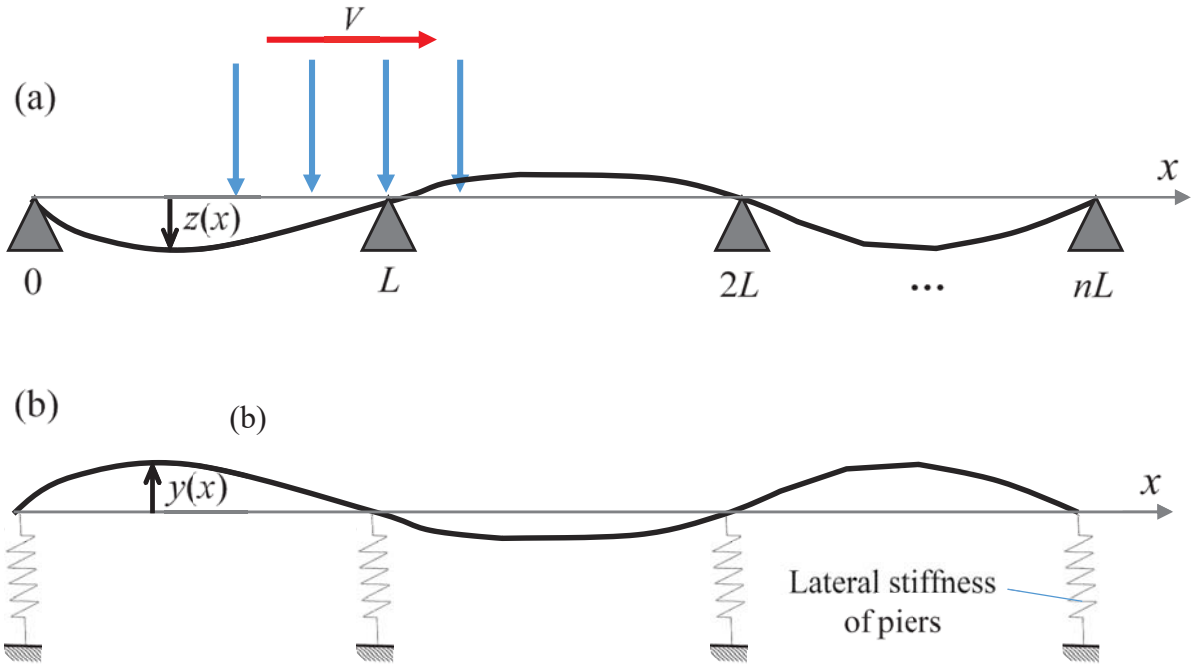

Figure 2: A train set of moving point masses traveling across an *n* span continuous beam: (a) vertical vibration, and (b) lateral vibration.

3 DYNAMIC AMPLIFICATION FACTORS

To study the effects of moving train on vertical and lateral motions of the pier-deck system, dynamic amplification factor (DAF), η, is determined and compared for a wide range of key parameters, $\eta = y_d^{max}/y_s^{max}$ where y_d^{max} and y_s^{max} are dynamic and quasi-static vertical/lateral deflections. The key parameters of the bridge deck-pier systems are: (1) vertical/lateral non-dimensional speed, $\Omega = \pi V/\omega_1 L$, (2) number of spans of length *L*, *n* (3) single train-to-single span bridge mass ratio, α, and (5) the spacing ratio between moving loads to span length, *s*.

Figure 3 shows the effects of single span to multi-span beams on dynamic amplification factors for both vertical and lateral motions. Vertical and lateral DAFs are plotted versus non-dimensional speed for single-span to 5-span beams. This figure is for case of single moving

mass on a continuous beam. The results show a clear maximum which increases for higher number of spans for vertical vibration. For lateral vibration, the increase in the peak is far less than the vertical motion. The increase in the peak is because of the train loading being in contact with the beam for more cycles of loading. The, the higher the number of span is, the more dominant the resonant response is. The peak speed limits for HS trains and Hyperloop trains form regions for lateral vibration as the natural frequency of the unload bridge changes for different number of spans for the lateral motion. It is desirable that the current maximum speed for HS trains is below this resonance.

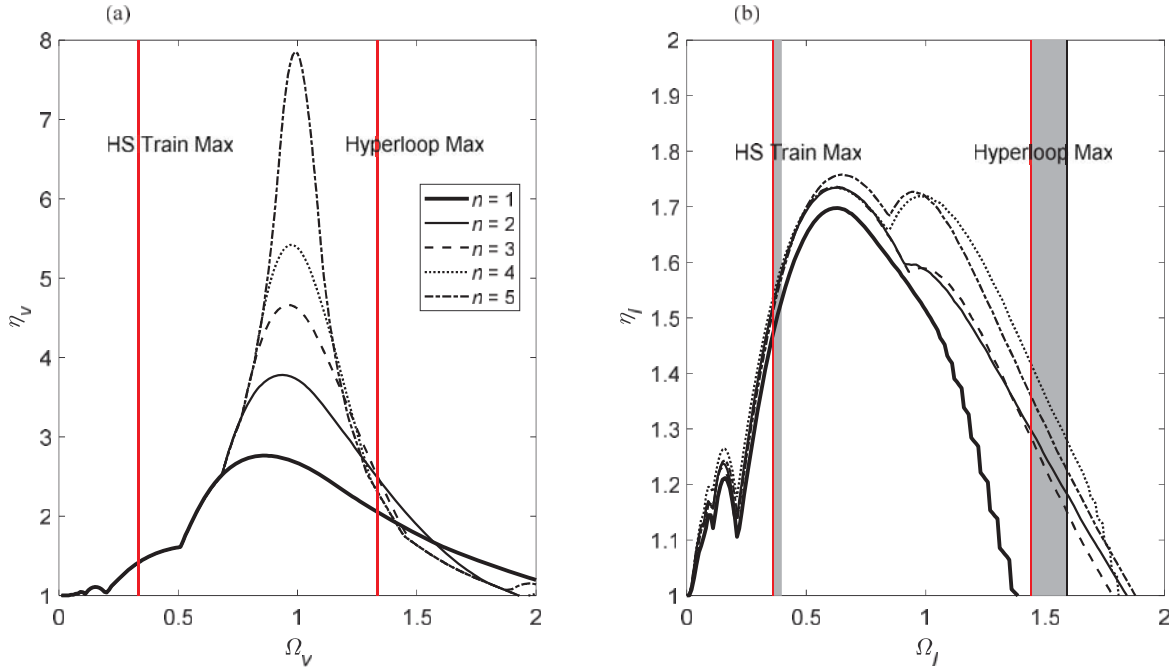

Figure 3: Dynamic amplification factors for single mass crossing multi-span continuous beam: (a) vertical vibration, and (b) lateral vibration.

Figure 4 illustrates vertical and lateral DAFs of a beam with different train-to-bridge mass ratios, α. Different train-to-bridge mass ratios show difference between a moving force (very small mass ratio, $\alpha = 0.01$) and a moving mass (larger mass ratios, $\alpha = 0.1$, 0.5, and 1.0). The maximum speed limits for HS trains and Hyperloop trains are constant for both lateral and vertical motions as the natural frequency of the unload bridge remains unchanged for different mass ratios. At $\alpha = 0.01$, there is a very small difference between moving force and moving mass problems, and for higher mass ratios, this difference becomes far more significant. It is worth noting that as the mass ratio increases, the lateral DAF does so. Moreover, the maximum vertical and lateral DAFs shift toward lower non-dimensional speed with the increase of mass ratio. Comparison of the vertical DAF range with those pf lateral motion shows that DAFs of vertical vibration are much larger than those from lateral vibration. This was expected as the magnitude of bridge lateral vibration due to the train loading eccentricity is much smaller than the vertical vibration of the bridge. Figure 5 illustrates vertical and lateral DAFs versus non-dimensional speed and spacing for a train of 9 equidistance masses. In the case where s is zero, a single moving mass travels the bridge while for $s = 0.25$, the mass of each moving load is divided by 9. The maximum vertical and lateral DAFs are roughly similar to a single moving mass case ($s = 0$). Further, the speed at which the maximum vertical and lateral DAFs occur depends on the spacing ratio. As spacing ratio increases, the maximum lateral DAF moves towards higher non-dimensional speeds for both vertical and lateral

vibrations. For normal HS trains, this is very desirable as it pushes the resonance further away from their operating speed limit. However, for Hyperloop trains, it is adverse as this effect pushes the resonance close to their operating speed limit.

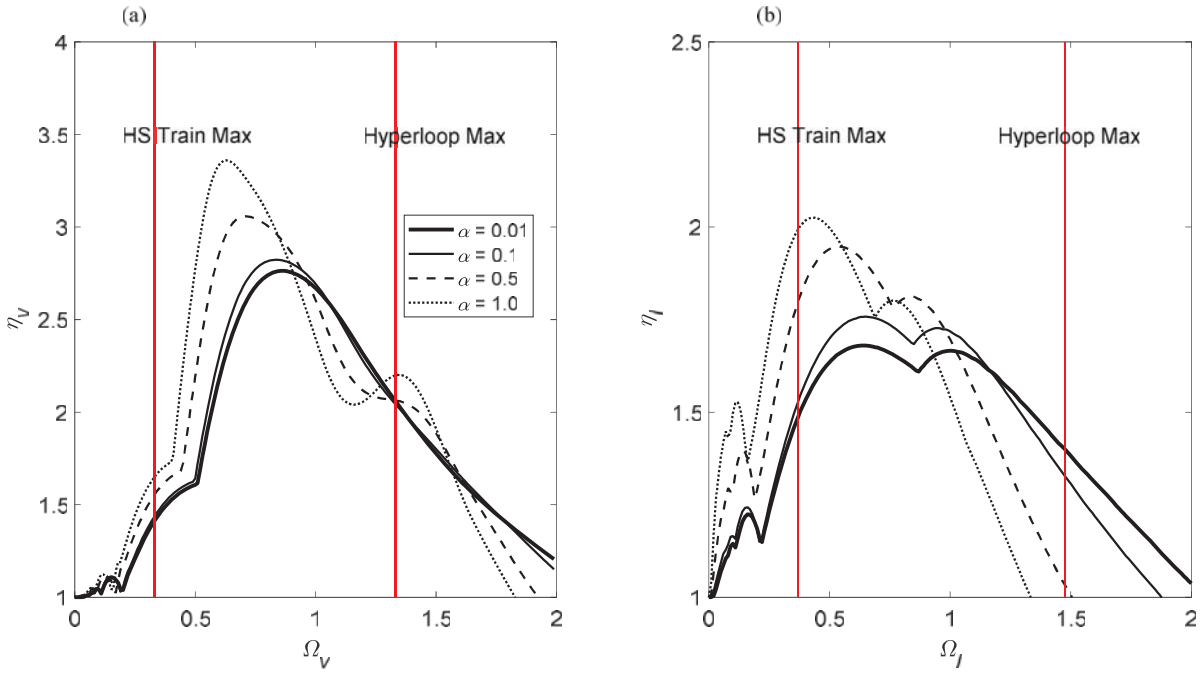

Figure 4: Dynamic amplification factors for different mass ratios, α: (a) vertical vibration, and (b) lateral vibration.

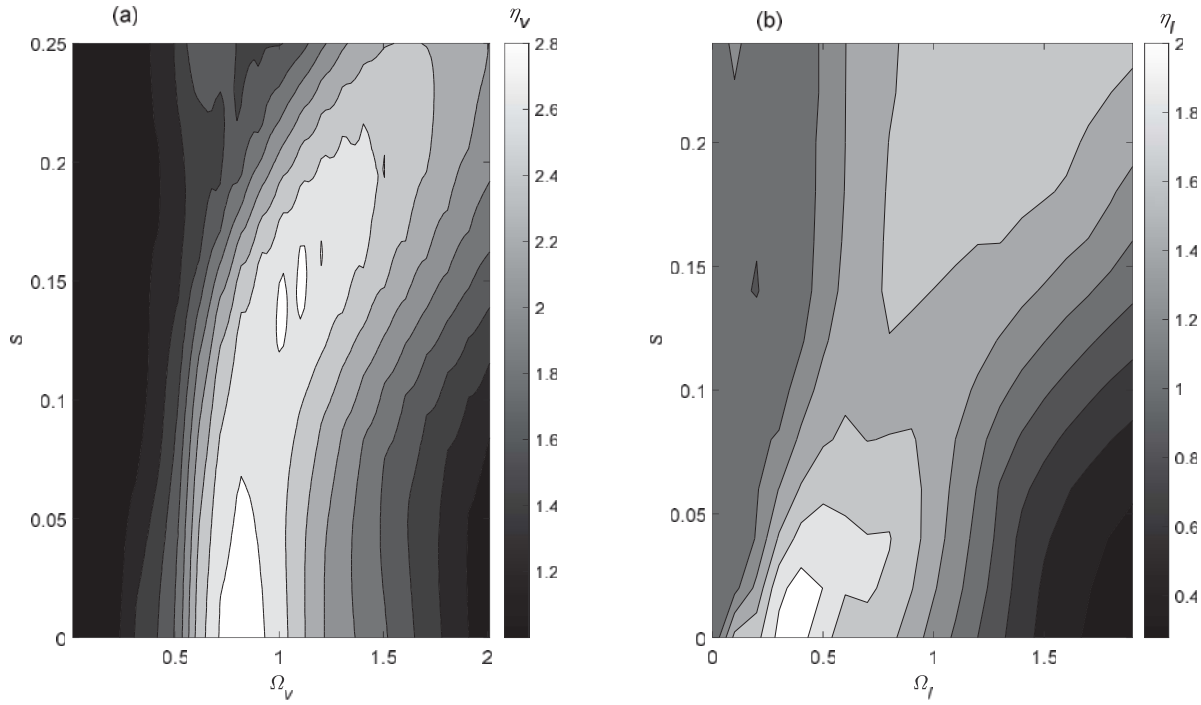

Figure 5: Dynamic amplification factors for different loading spacing values, s: (a) vertical vibration, and (b) lateral vibration.

From Figures 3 and 4, it is easy to understand that the DAFs at the operating speed limit can be used to design the structural system. This is correct for the HS train as the maximum DAF occurs for its maximum operating speed. However, for the Hyperloop train, the max DAF occurs below its max operating speed and all DAFs up to its maximum operating speed have to be taken into account. This is because there are bound to be accelerations, decelerations, emergencies and faulty trains and the designed structural system must be able to safely support all those speeds up to its maximum operating one.

4 CONCLUSIONS

This study addresses and summarizes the Dynamic amplification factors of Hyperloop trains for both vertical and lateral vibrations. It was found that the vertical and lateral DAFs of the system are highly dependent on the train speed, number of spans, train-to-bridge mass ratio, and train loading spacing. The DAFs of the lateral vibration are much smaller than the vertical vibration. Therefore, this work highlights the significance of vertical and lateral vibrations of the Hyperloop train-bridge-pier systems which needs be considered in future design guidelines. Given the significantly large dynamic amplification factors of the vertical vibration, it is necessary to highly stiffen the bridge spans and incorporate large damping in the form of viscous and tuned mass dampers.

5 ACKNOWLEDGEMENT

The first author acknowledges the support received by the UK Engineering and Physical Sciences Research Council (EPSRC) for a Prosperous Nation [grant number EP/R039178/1]: SPINE: Resilience-Based Design of Biologically Inspired Columns for Next-Generation Accelerated Bridge Construction].

REFERENCES

[1] R. Janzen, TransPod Ultra-High-Speed Tube Transportation: Dynamics of Vehicles and Infrastructure, *Procedia Engineering*, 8–17, 2017.

[2] Anon, *Network Rail*, NR/GN/CIV/025 Issue 3, Guidance note – the structural assessment of underbridges, 2006.

[3] G. Parke, N. Hewson, *ICE manual of bridge engineering*, 2nd edition Thomas Telford publishing, 2008.

[4] L. Canning, MM. Kashani, Assessment of U-type wrought iron railway bridges, *Proceedings of the ICE - Engineering History and Heritage*, 169, 2, 2016.

[5] Anon, British Standard, EN 1991-2: Eurocode 1: Actions on structures in: Part 2: Traffic loads on bridges, *European Committee for Standardization*, 2003.

[6] M. Olsson, On the fundamental moving load problem, *Journal of Sound and Vibration*, 145, 299–307, 1991.

[7] P. Paultre, O. Chaallal, J. Proulx, Bridge dynamics and dynamic amplification factors — a review of analytical and experimental findings, *Canadian Journal of Civil Engineering*, 19, 2, 260–278, 1992.

[8] NA Alexander, MM. Kashani, Exploring Bridge Dynamics for Ultra-high-speed, Hyperloop Trains, *Structures*, 14, 69–74, 2018.

[9] E. Ahmadi, MM. Kashani, NA. Alexander, Lateral dynamic bridge deck-pier interaction for ultra-high-speed Hyperloop train loading, Journal of Bridge Engineering-Institution of Civil Engineers (ICE), E-ISSN 1751-7664, 2019.

EURODYN 2020
XI International Conference on Structural Dynamics
M. Papadrakakis, M. Fragiadakis, C. Papadimitriou (eds.)
Athens, Greece, 23–26 November 2020

MOVING LOAD ON AN ELASTIC HALF-SPACE COATED WITH A THIN VERTICALLY INHOMOGENEOUS LAYER

Saad Althobaiti[1], Vladimir Bratov[2], Ali Mubaraki[1,3], and Danila Prikazchikov[3]

[1] Taif University
Saudi Arabia, Taif, Taif University, 21944
e-mail: salthobaiti@tu.edu.sa

[2] Saint-Petersburg State University
Russia, Saint-Petersburg, Universitetsky Pr., 28, 198504
e-mail: vladimir.bratov@gmail.com

[3] Keele University
Keele, Staffordshire, ST5 5BG, UK
e-mail: a.m.a.mubaraki@keele.ac.uk, d.prikazchikov@keele.ac.uk

Keywords: Moving load, asymptotic model, Rayleigh wave, inhomogeneous, thin coating.

Abstract. *The study is focussed on the near-critical regimes of the moving load on a coated elastic half-space. The material properties of the coating are assumed to be depending on the vertical coordinate. The analysis relies on the hyperbolic-elliptic formulation for the Rayleigh wave induced by prescribed surface loading, containing an elliptic equation for the elastic potential governing its decay over the interior, and a singularly perturbed wave equation on the interface between the layer and the substrate. This scalar formulation allows significant simplifications, including in particular, classification of the near-resonant regimes. The method of fictitious absorption is then used in order to incorporate the effect of poles, associated with the radiation of energy from the moving source. Finally, numerical illustrations of results for several types of vertical inhomogeneity are presented.*

1 INTRODUCTION

Moving load problems on elastic structures have been studied for around a century now, see e.g. [12], [25] and possess important industrial applications, in particular, in high-speed train operation [4]. Solution for steady-state regime of a moving load on an elastic half-space has been first presented in [6], see also [14]. Moving load on a coated half-space has been seemingly first considered by [2]. More realistic modelling motivates development of studies oriented to dynamics of multi-layered and vertically inhomogeneous half-space, see e.g. [15] and [22].

At the same time, sophisticated structure of the exact solution stimulates development of effective approximations. In view of the well-known fact of the Rayleigh wave speed being the critical speed of the moving load, the near-resonant formulation for surface wave field, allowing explicit solutions seems a prospective approach. The current work is based on the long-wave asymptotic formulation presented in [7], which has been applied to problems on a moving load for elastic half-space [17, 10, 8, 26], see also [18] for a more systematic exposition of the methodology of hyperbolic-elliptic models for surface waves. Recent advances of the approach include in particular extensions incorporating the effects of anisotropy [13] and pre-stress [21], composite models for elastic layers [9], as well as development of seismic meta-surfaces [29] and the second-order refined model [30].

The described asymptotic model [18] is focused on the contribution of the Rayleigh wave to the overall dynamic response. It is derived as a slow-time near-resonant perturbation of the self-similar solution by [5] and hence allows reduction of the vector problem of elasticity to a scalar problem for the Laplace equation in respect of the longitudinal elastic potential, with the boundary condition on the surface presented in the form of the forced wave equation. In case of the coated half-space the presence of the layer is reflected by the appropriate pseudo-differential operator, thus, the boundary condition describing the near-surface dynamics is a singularly perturbed wave equation, see e.g. [7].

The focus of the current contribution is on the near-resonant steady-state regimes of a moving line load on a half-space coated by a vertically inhomogeneous thin coating. The corresponding extension of the hyperbolic-elliptic model has been recently suggested in [24]. The study of a singularly perturbed hyperbolic equation at the interface allows classification of the regimes of the moving load, pointing out typical behaviours depending on the speed of the load and the combinations of material parameters.

The paper is organized as follows. The problem is formulated in Section 2. The analytic treatment of the pseudo-differential equation on the interface between the layer and the substrate and classification of regimes of the moving load is carried out in Section 3. Finally, numerical illustrations of the results are presented in Section 4.

2 FORMULATION OF THE PROBLEM

Consider a linearly isotropic, elastic half-space over the domain $-\infty < x_1, x_2 < \infty$ and $x_3 \geq 0$, coated by a thin layer of thickness h described by $-\infty < x_1, x_2 < \infty$ and $-h \leq x_3 \leq 0$, see Fig. 1.

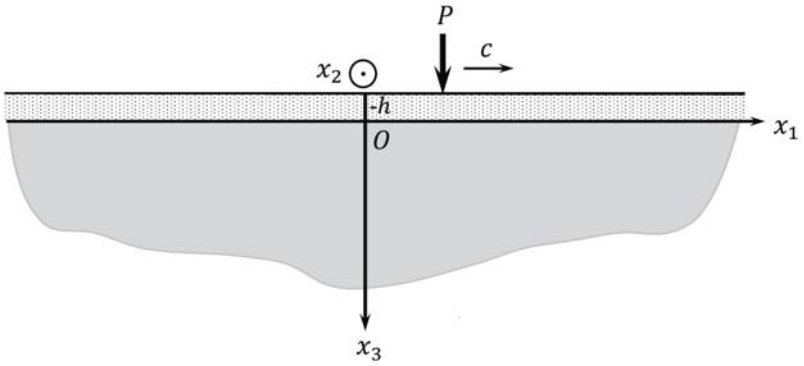

Figure 1: Moving load on a coated elastic half-space.

The properties of the coating are assumed to be dependent on the transverse variable x_3, so that

$$\lambda_c = \lambda(x_3), \quad \mu_c = \mu(x_3), \quad \rho_c = \rho(x_3) \tag{1}$$

denote the Lamé elastic parameters and volume mass density, respectively. The substrate is assumed homogeneous, with the associated material parameters given by λ_s, μ_s and ρ_s. The governing equations of motion and the constitutive relations of linear isotropic elasticity are conventionally written as

$$\sigma^q_{ij,j} = \rho_q u^q_{i,tt}, \qquad \sigma^q_{ij} = \lambda_q u^q_{k,k} + \mu_q \left(u^q_{i,j} + u^q_{j,i}\right), \tag{2}$$

where σ^q_{ij} and u^q_i $(i,j = 1,2,3)$ are the Cauchy stress and displacement components of the coating and substrate $(q = c, s)$, comma indicates differentiation with respect to appropriate spatial or time variable, and the Einstein summation convention is adopted. Here we restrict the consideration to plane-strain formulation, for which $u^q_2 = 0$ and the components $u^q_1 = u^q_1(x_1, x_3, t)$ and $u^q_3 = u^q_3(x_1, x_3, t)$ are independent of x_2.

The loading on the surface of the coating is prescribed in the form of a line vertical force P, moving at a constant speed c, hence the boundary conditions are written as

$$\sigma^c_{31} = 0, \qquad \sigma^c_{33} = P_0\, \delta\left(x_1 - ct\right), \qquad \text{at} \quad x_3 = -h, \tag{3}$$

see Fig.1. Perfect bonding on the interface is assumed, giving $(m = 1, 3)$

$$u^s_m = u^c_m, \qquad \sigma^s_{3m} = \sigma^c_{3m}, \qquad \text{at} \quad x_3 = 0. \tag{4}$$

Below, the long-wave assumption is adopted, i.e.

$$\epsilon = \frac{h}{L} \ll 1, \tag{5}$$

where L is the typical wave length.

We consider the steady-state problems focusing on the near-resonant regimes, when the speed of the moving load is close to that of the resonant Rayleigh wave c_R in the substrate, namely

$$\left| \frac{c}{c_R} - 1 \right| \ll 1. \tag{6}$$

Then, the contribution of the Rayleigh wave to the overall dynamic response is dominant compared to that of body waves, hence, the hyperbolic-elliptic model for the Rayleigh wave is applicable.

The corresponding asymptotic formulation for a vertically inhomogeneous coated half-space has been recently proposed in [24], extending the previous results in [7]. Within this framework, efficient boundary conditions are derived by means of the asymptotic integration technique, see e.g. [11] and [19], then serving as a starting point for slow-time perturbation procedure.

For the current problem, the proposed model for surface wave contains an elliptic equation for the interior $x_3 > 0$

$$\frac{\partial^2 \phi}{\partial x_3^2} + \alpha_R^2 \frac{\partial^2 \phi}{\partial x_1^2} = 0, \tag{7}$$

where ϕ is the longitudinal Lamé elastic potential in the substrate and

$$\alpha_R = \sqrt{1 - \frac{\rho_s c_R^2}{\lambda_s + 2\mu_s}}. \tag{8}$$

The boundary condition at $x_3 = 0$ is given by a singularly perturbed 1D hyperbolic equation

$$\frac{\partial^2 \phi}{\partial x_1^2} - \frac{1}{c_R^2} \frac{\partial^2 \phi}{\partial t^2} - bh \sqrt{-\frac{\partial^2}{\partial x_1^2}} \left(\frac{\partial^2 \phi}{\partial x_1^2} \right) = -\frac{1 + \beta_R^2}{2\mu B} P_0 \, \delta(x_1 - ct), \tag{9}$$

where

$$B = \frac{\alpha_R}{\beta_R} \left(1 - \beta_R^2\right) + \frac{\beta_R}{\alpha_R} \left(1 - \alpha_R^2\right) - 1 + \beta_R^4, \qquad \beta_R = \sqrt{1 - \frac{\rho_s c_R^2}{\mu_s}}, \tag{10}$$

and the constant b is given by

$$b = \frac{(1 - \beta_R^2)}{2\,\mu\,B} \left[\tilde{\rho}\, c_R^2 \, (\alpha_R + \beta_R) - \beta_R \, \tilde{\gamma} \right], \tag{11}$$

with the integral quantities accounting for vertical inhomogeneity

$$\tilde{\gamma} = \frac{4}{h} \int_{-h}^{0} \frac{\mu_c \left(\lambda_c + \mu_c\right)}{\lambda_c + 2\mu_c} \, dx_3, \qquad \text{and} \qquad \tilde{\rho} = \frac{1}{h} \int_{-h}^{0} \rho_c \, dx_3. \tag{12}$$

It is worth noting that the pseudo-differential operator $\sqrt{-\frac{\partial^2}{\partial x_1^2}}$ is an essential feature of the problem, associated with the dispersion of waves within the coating layer. Moreover, the sign of the coefficient b is associated with the sign of the group velocity in the long-wave limit, see [28] for more detail.

Once the longitudinal potential ϕ is determined from the scalar formulation (7), (9), the transverse potential ψ may be found as its harmonic conjugate, see e.g. [18], originating from [5]

$$\psi\left(x_1, \beta_R x_3, t\right) = \frac{2\alpha_R}{1+\beta_R^2} \, \phi^*\left(x_1, \beta_R x_3, t\right), \tag{13}$$

where the asterisk denotes the Hilbert transform.

Now, the boundary value problem (7), (9) may be rewritten in the moving coordinate system $(\xi, x_3) = (x_1 - ct, x_3)$, hence the steady-state limit is governed by

$$\frac{\partial^2 \phi}{\partial x_3^2} + \alpha_R^2 \frac{\partial^2 \phi}{\partial \xi^2} = 0, \tag{14}$$

subject to

$$\eta \frac{\partial^2 \phi}{\partial \xi^2} - b\, h \sqrt{-\frac{\partial^2}{\partial \xi^2}} \left(\frac{\partial^2 \phi}{\partial \xi^2}\right) = -\frac{1+\beta_R^2}{2\mu B} \, P_0 \, \delta(\xi) \qquad \text{at} \qquad x_3 = 0, \tag{15}$$

where

$$\eta = 1 - \frac{c^2}{c_R^2}.$$

3 ANALYSIS ON THE INTERFACE

Let us concentrate on the analysis of equation (15) on the interface $x_3 = 0$. Note that on setting $h = 0$ the problem formulation (14), (15) will reduce to that for an uncoated elastic half-space which is the leading order Taylor expansion of the exact solution [6], for more details see [18].

Another observation which immediately follows from (15) is the presence of two small parameters, a geometric one, associated with the long-wave approximation, as well as η corresponding to the near-resonant vicinity.

Now, let us introduce the dimensionless coordinate $\zeta = \left|\frac{\eta}{b}\right| \frac{\xi}{h}$ along with a scaled quantity

$$\chi = -\frac{2\mu\, B\, b\, h}{(1+\beta_R^2)\, P_0} \frac{\partial^2 \phi}{\partial \xi^2}. \tag{16}$$

Then, the equation (15) takes the form

$$\text{sgn}\,(b\,\eta)\ \chi - \sqrt{-\frac{\partial^2}{\partial \zeta^2}}\,(\chi) = \delta(\zeta), \tag{17}$$

The solution of the latter can be obtained by using the Fourier integral transform

$$\chi = \frac{1}{2\pi} \int\limits_{-\infty}^{\infty} \frac{e^{i\omega\zeta}\, d\omega}{\text{sgn}\,(b\,\eta) - |\omega|}. \tag{18}$$

From (18) it may be observed that the analysis splits in two sub-cases, depending on the value of $\text{sgn}\,(b\,\eta)$.

3.1 SUB-CASE 1: NO POLES ON THE REAL AXE

Consider first the situation $b\eta < 0$, in which

$$\chi = \frac{1}{2\pi} \int_{-\infty}^{\infty} \frac{e^{i\omega\zeta}\, d\omega}{-1 - |\omega|} = \mathcal{F}\,(|\zeta|)\,, \tag{19}$$

where

$$\mathcal{F}\,(x) = \frac{1}{\pi}\,[\text{si}(x)\sin x + \text{Ci}(x)\cos x]\,, \tag{20}$$

with si and Ci denoting the sine and cosine integral functions, respectively, i.e.

$$\text{si}(x) = -\int\limits_{x}^{\infty} \frac{\sin t}{t}\, dt, \qquad \text{Ci}(x) = -\int\limits_{x}^{\infty} \frac{\cos t}{t}\, dt,$$

see e.g. [1]. Note that this case occurs either in the the sub-Rayleigh regime $(c < c_R)$ with local minimum of the phase velocity at the Rayleigh wave speed $(b < 0)$, or in the super-critical regime $(c > c_R)$ combined with local maximum of the phase velocity $(b > 0)$, for more detail see [7].

3.2 SUB-CASE 2: POLES ON THE REAL AXE

The second sub-case $b\eta > 0$ of poles on the real axis of the integral (18) may be treated using the limiting absorption principle, see e.g. [27, 16].

In case of the sub-critical regime $(c < c_R)$, when $(b > 0)$, formula (18) yields

$$\chi = \frac{1}{2\pi} \int_{-\infty}^{\infty} \frac{e^{i\omega\zeta}\, d\omega}{1 - |\omega|} = -2\, H\,(-\zeta) \sin\zeta + \mathcal{F}\,(|\zeta|)\,, \tag{21}$$

whereas in the case of the super-Rayleigh regime $(c > c_R)$ the solution becomes

$$\chi = 2\, H\,(\zeta) \sin\zeta + \mathcal{F}\,(|\zeta|)\,, \tag{22}$$

with $\mathcal{F}$ defined in (20) and $H(\zeta)$ denoting the Heaviside function.

4 NUMERICAL RESULTS

In this section, the illustrations of the obtained results are presented. We consider the dependence of the Young's modulus E_c of the coating layer on the vertical coordinate x_3 of exponential form, see e. g. [22]

$$E(x_3) = E_c\, e^{\beta\, x_3}, \;\; \beta = \frac{1}{h} \ln\!\left(\frac{E_s}{E_c}\right), \tag{23}$$

providing a smooth variation from the value E_c on the surface of the coating to the Young's modulus E_s of the homogeneous substrate. In the computations below we also take $h = 1$ and assume constant mass densities $\rho_c = \rho_s = 1$, and Poisson's ratios $\nu_c = \nu_s = 0.25$, with the sub-Rayleigh and super-Rayleigh regimes computed for $c = 0.9\, c_R$, and $c = 1.1\, c_R$, respectively.

Consider first the case of a relatively hard coating layer, when $E_c/E_s = 10$. The associated graphs in Fig. 2 show the dependence of the quantity χ on the scaled moving coordinate ζ. In this case, the constant b may be computed using (11), resulting in $b \approx -1.32$. In Fig. 2(a) the super-Rayleigh regime is depicted $(\eta > 0)$, corresponding to the case of no poles in (18), whereas Fig. 2(b) illustrates the sub-Rayleigh regime $(\eta < 0)$, clearly showing the effect of poles in (18) for positive ζ, i.e. radiation of energy in front of the moving source.

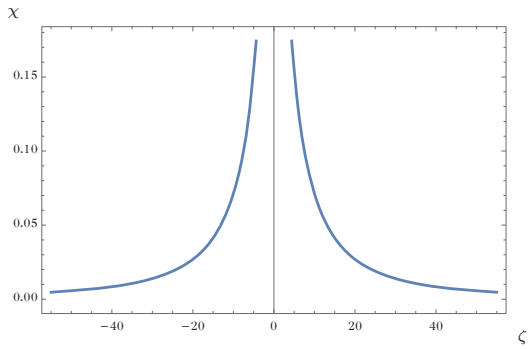

(a) $\eta > 0$.

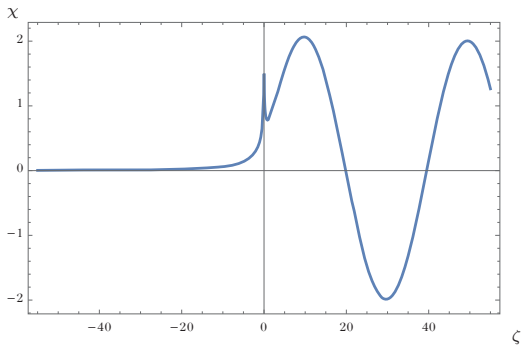

(b) $\eta < 0$.

Figure 2: Dependence of the quantity χ on the moving coordinate ζ for the case of softening within the layer $(E_c/E_s = 10)$.

The following Figs. 3 (a) and (b) illustrate another typical scenario, when the coating layer is relatively soft compared to the substrate and stiffens gradually with depth, when $E_c/E_s = 0.1$. The calculation of the constant b according to (11) gives $b \approx 0.276$. The plots in Fig. 3(a) and 3(b) show the variation of the quantity χ on the moving coordinate ζ. Now, the energy radiation behind the moving load is observed in the super-Rayleigh regime in Fig. 3 (a).

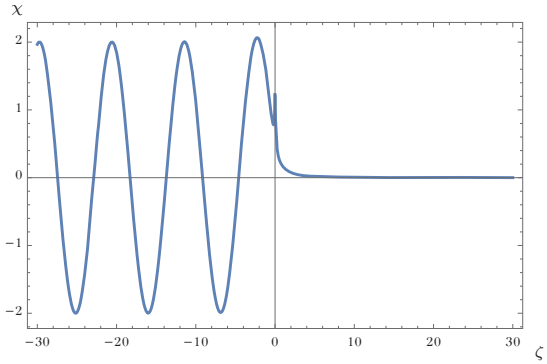

(a) $\eta > 0$.

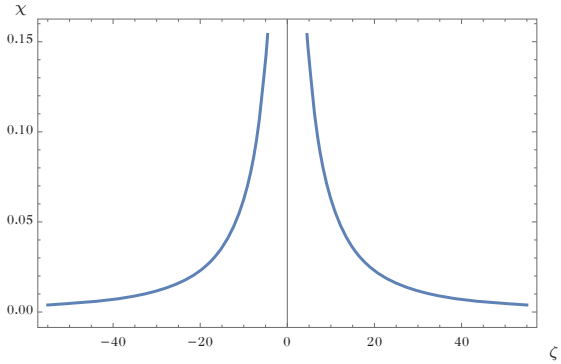

(b) $\eta < 0$.

Figure 3: Dependence of the quantity χ on the moving coordinate ζ for the case of hardening within the layer $(E_c/E_s = 0.1)$.

5 CONCLUSIONS

The steady-state problem for a moving line load on a half-space coated by a thin vertically inhomogeneous layer has been analysed. The hyperbolic-elliptic formulation for the Rayleigh wave field allowed an explicit solution, as well as a clear classification of the regimes.

Further possible developments include addressing transient problems [17], generalizations to coatings with more sophisticated mechanical properties, taking into account

the effects of viscosity, curvature, long-wave high-frequency waves [20], as well as a more general treatment of a vertically inhomogeneous half-space, see e.g. [3]. We also mention potential applications for seismic metabarriers [23]

ACKNOWLEDGEMENT

This work has been supported by the Russian Science Foundation under grant Nr. 20-49-08002.

REFERENCES

[1] M. Abramowitz, I. A. Stegun. Handbook of mathematical functions. New York, NY: Dover, 1982.

[2] J. D. Achenbach, S. P. Keshava, G. Herrmann. Moving load on a plate resting on an elastic half space. Journal of Applied Mechanics, 34, 910–914, 1967.

[3] I. Argatov, I., A. Iantchenko. Rayleigh surface waves in functionally graded materials – long-wave limit. Quarterly Journal of Mechanics and Applied Mathematics 72(2) 197–211 (2019).

[4] Y. Cao, H. Xia, Z. Li. A semi-analytical/FEM model for predicting ground vibrations induced by high-speed train through continuous girder bridge. Journal of Mechanical Science and Technology, 26(8), 2485–2496, 2012.

[5] P. Chadwick. Surface and interfacial waves of arbitrary form in isotropic elastic media. Journal of Elasticity, 6, 73–80, 1976.

[6] J. Cole, J. Huth. Stresses produced in a half plane by moving loads. Journal of Applied Mechanics, 25, 433–436, 1958.

[7] H.-H. Dai, J. Kaplunov, D. A. Prikazchikov. A long wave asymptotic model for surface wave in a coated elastic half-space.Proceedings of the Royal Society A: Mathematical, Physical and Engineering Sciences 466, 3097–3116, 2010.

[8] N. Ege, B. Erbaş. Response of a 3D elastic half-space to a distributed moving load. Hacettepe Journal of Mathematics and Statistics, 46(5), 817–828, 2017.

[9] B. Erbaş, J., Kaplunov, E., Nolde, M. Palsü. Composite wave models for elastic plates. Proceedings of the Royal Society A: Mathematical, Physical and Engineering Sciences, 474(2214), 20180103, 2018.

[10] B. Erbaş, J. Kaplunov, D. A. Prikazchikov, O. Şahin. The near-resonant regimes of a moving load in a three-dimensional problem for a coated elastic half-space. Mathematics and Mechanics of Solids, 22(1), 89-100, 2017.

[11] B. Erbaş, B., E. Yusufoglu, J. Kaplunov. A plane contact problem for an elastic orthotropic strip. Journal of Engineering Mathematics, 70(4), 399–409, 2011.

[12] L. Fryba. Vibration of solids and structures under moving loads. London: Thomas Telford, 1999.

[13] Y. Fu, J. Kaplunov, D. A. Prikazchikov. Reduced model for the surface dynamics of a generally anisotropic elastic half-space. Proceedings of the Royal Society A: Mathematical, Physical and Engineering Sciences, 476(2234), 20190590, 2020.

[14] H. G. Georgiadis, J. R. Barber. Steady-state transonic motion of a line load over an elastic half-space. The corrected Cole/Huth solution. ASME Transactions Series E Journal of Applied Mechanics, 60, 772–774, 1993.

[15] E. V. Glushkov, N. V. Glushkova, S. I. Fomenko, C. Zhang. Surface waves in materials with functionally gradient coatings. Acoustical Physics, 58(3), 339–353, 2012.

[16] V. V. Kalinchuk, T. I. Belyankova. Dynamics of the surface of inhomogeneous media. Moscow: Fizmatlit, 2009.

[17] J. Kaplunov, E. Nolde, D. A. Prikazchikov. A revisit to the moving load problem using an asymptotic model for the Rayleigh wave. Wave Motion, 47, 440–451, 2010.

[18] J. Kaplunov, D. A. Prikazchikov. Asymptotic theory for Rayleigh and Rayleigh-type waves. Advances in Applied Mechanics, 50, 1–106, 2017.

[19] J. Kaplunov, D. A. Prikazchikov, L. Sultanova. Justification and refinement of Winkler–Fuss hypothesis. Zeitschrift für Angewandte Mathematik und Physik, 69(3), 80, 2018.

[20] J. Kaplunov, D. A. Prikazchikov, L. Sultanova. Rayleigh-type waves on a coated elastic half-space with a clamped surface. Philosophical Transactions of the Royal Society A, 377(2156), 20190111, 2019.

[21] L. A. Khajiyeva, D. A. Prikazchikov, L. A. Prikazchikova. Hyperbolic-elliptic model for surface wave in a pre-stressed incompressible elastic half-space. Mechanics Research Communications, 92, 49–53, 2018

[22] R. Kulchytsky-Zhyhailo, A. S. Bajkowski. Three-dimensional analytical elasticity solution for loaded functionally graded coated half-space. Mechanics Research Communications, 65, 43–50, 2015.

[23] S. V. Kuznetsov. Seismic waves and seismic barriers. Acoustical Physics, 57(3), 420–426, 2011.

[24] A. Mubaraki, D. Prikazchikov. Explicit model for surface waves on an elastic half-Space coated by a thin vertically inhomogeneous layer. Proceedings of the 9th International Conference Dynamical Systems-Theory and Applications DSTA, 2019.

[25] G. B. Muravskii. Mechanics of non-homogeneous and anisotropic foundations. Springer, Berlin, Heidelberg, 2012.

[26] O. Şahin. Analysis of the Rayleigh wave field due to a tangential load applied on the surface of a coated elastic half-space. Communications Faculty of Sciences University of Ankara Series A1 Mathematics and Statistics, 69(1), 158–171, 2020.

[27] J. R. Schulenberger, C. H. Wilcox. The limiting absorption principle and spectral theory for steady-state wave propagation in inhomogeneous anisotropic media. Archive for Rational Mechanics and Analysis, 41, 46–65, 1971.

[28] A. L. Shuvalov, A. G. Every. On the long-wave onset of dispersion of the surface-wave velocity in coated solids. Wave Motion, 45, 857–863, 2008.

[29] P. T. Wootton, J. Kaplunov, D. J. Colquitt. An asymptotic hyperbolic–elliptic model for flexural-seismic metasurfaces. Proceedings of the Royal Society A: Mathematical, Physical and Engineering Sciences, 475(2227), 20190079, 2019.

[30] P. T. Wootton, J. Kaplunov, D. A. Prikazchikov. A second-order asymptotic model for Rayleigh waves on a linearly elastic half-plane. IMA Journal of Applied Mathematics, 85, 113–131, 2020.

EURODYN 2020
XI International Conference on Structural Dynamics
M. Papadrakakis, M. Fragiadakis, C. Papadimitriou (eds.)
Athens, Greece, 23–26 November 2020

VERIFICATION OF THE VALIDITY OF THE IMPACT FACTOR USED IN THE DESIGN OF PC SLEEPERS

Shintaro Minoura[1], **Tsutomu Watanabe**[1], **Kodai Matsuoka**[2], **and Kenji Narita**[2]

[1] Track Dynamics Laboratory, Railway Dynamics Division, Railway Technical Research Institute
2-8-38 Hikari-cho, Kokubunji-shi, Tokyo, Japan
e-mail:{minoura.shintaro.51, watanabe.tsutomu.30}@rtri.or.jp

[2] Structural Dynamics Laboratory, Railway Dynamics Division, Railway Technical Research Institute
2-8-38 Hikari-cho, Kokubunji-shi, Tokyo, Japan
e-mail:{matsuoka.kodai.13, narita.kenji.97}@rtri.or.jp

Keywords: PC sleeper, Impact load, On-site measurement, Wheel load, Railway track

Abstract. *The purpose of this study is to identify the actual load environment of train loads acting on PC sleepers in order to perform effective maintenance and optimize design of PC sleepers. In Japan, the design load for PC sleepers is calculated by multiplying the static wheel load by impact factor, which is a factor for considering the impact load (generally 2.0) and this value has been conventionally used since the beginning of the use of PC sleepers in Japan. However, considering the improvement of current track and vehicle maintenance technology, it is considered that wheel flats and track irregularities that cause impact loads have been reduced. Therefore, it is necessary to identify the impact factor based on the field tests. In this study, the wheel load was measured in the long rail section of the conventional line, and the actual condition of the impact factor was investigated. As a result, the current impact factor 2.0 is in a safer side to freight trains. Furthermore, for commuter trains, we confirmed that the impact factor for the static design wheel load in Japan (generally 80kN) can be lower than the current value.*

1 INTRODUCTION

PC sleepers are an essential component that contributes to the safety, stability and high-speed transportation of modern railways. PC sleeper is a component made of prestressed concrete which is laid under the rails of railway track. Its main role is to keep the distance between the two rails constant and to properly distribute the load of the passing train transmitted through the rails to the gravel called ballast. In addition to PC sleepers, there are wooden sleepers and iron sleepers. PC sleepers have advantages such as mass production and high durability.

Figure 1 shows an example of a PC sleeper laid on a railway track in Japan. Although there are differences in the distance between rails (track gauge) and the size of PC sleepers, the structure of railway track is generally the same throughout the world. Mass introduction of PC sleepers in Japan began around the 1960s and the cumulative number the cumulative number of installations has exceeded 39.5 million only for Japanese National Railways (JNR) and JR companies which took over most of the assets of the JNR after privatization. The life expectancy of PC sleepers is usually 50 years. However, in recent years, PC sleepers which exceeded this life expectancy have also increased and studies for appropriate maintenance and replacement guidelines have been promoted [1][2].

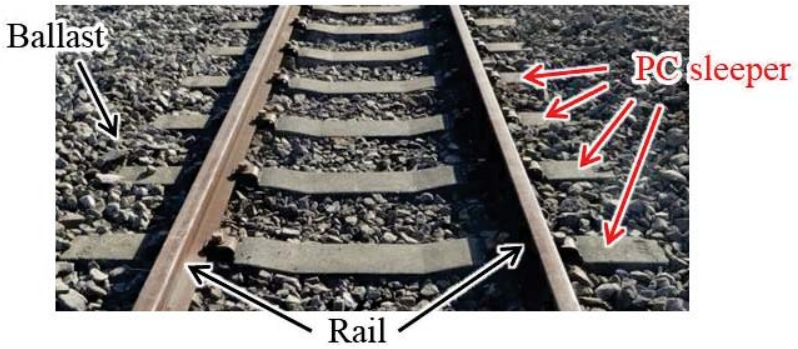

Figure 1: Example of a PC sleeper laid on a railway track

Figure 2 shows the method of design of PC sleepers in Japan. The PC sleeper is designed so that the PC sleeper does not crack under a predetermined design load. In Japan, the design load for PC sleepers is calculated by multiplying the train load transmitted via wheels (static wheel load) by impact factor, which is a factor for considering the impact load (generally 2.0) [3]. However, this value has been conventionally used since the beginning of the use of PC sleepers in Japan. The impact load is generated by unevenness of the wheel (wheel flat) and irregularities [4]. Since the track and vehicle maintenance technology advance in recent years, it seems that wheel flats and track irregularities causing impact loads have been reduced compared to the past time. Therefore, the value of this impact factor may not be in accordance with the actual situation. In order to evaluate the remaining life and to make an optimal design of track members such as PC sleepers, it is required to properly understand the load condition.

In this study, the wheel load was measured in the long rail section of the conventional line, and the actual condition of the impact factor was investigated.

Design load = static wheel load × impact factor (2.0) × dispersion dactor (0.5)

Figure 2: Method of design of PC sleepers in Japan

2 ON-SITE MEASUREMENT

2.1 Target site and PC sleeper

Figure 3 shows the track conditions of measurement site and Figure 4 shows the type 3 PC sleeper which is installed the site. The measurement site is a straight continuous welded rail section. The rail used in the site is a "60kg N-rail", which is specified in Japan industrial standards (JIS). The target PC sleeper is a "Type 3 PC sleeper" specified in JIS. This type of PC sleeper is for a straight section and a curved section with a radius of 800m or more, and is one of the most popular PC sleepers Japan. The No. 3 PC sleeper is designed under the condition of a design wheel load of 160kN with the impact factor of 2.0. The default interval of PC sleepers in the target section is 41 sleepers per 25m, but the each interval between sleepers varies by several tens of mm.

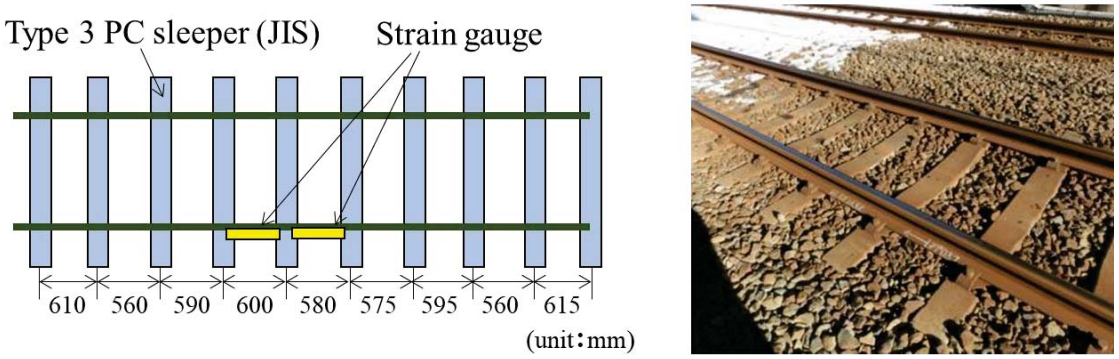

Figure 3: conditions of measurement site

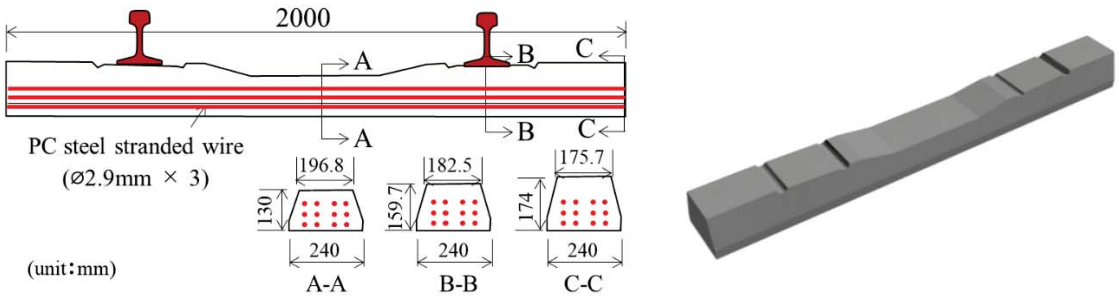

Figure 4: Type 3 PC sleeper

2.2 Measurement method

Figure 5 shows the method of measuring wheel load. In this measurement, a strain gauge for measuring the wheel load was attached to the side surface of the rail. The wheel load was measured by converting the measured strain. A piezoelectric accelerometer was installed on a PC sleeper about 30m away from the measurement point in the direction of train arrival, and used it as a trigger to start measurement. The strain gauge was connected to the National Instruments modules and stored in a PC via a LAN cable. The sampling rate was 10kHz. The recording program was constructed by LabVIEW. In this measurement, wheel load of both commuter trains and freight trains were measured. The measurement period is 50 days in total, and the number of measurement cases is 6042 for commuter trains and 2107 for freight trains.

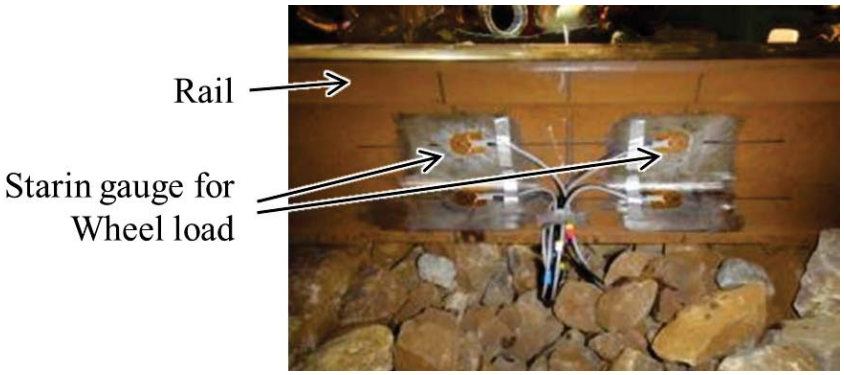

Figure 5: Sensor for measuring wheel load

3 MEASUREMENT RESULTS

Figure 6 shows the time-series data of the measured wheel load, and Figure 7-9 shows the wheel load of commuter train for each time. The data in Figure 9 is obtained by averaging wheel load for every 30 minutes. The average wheel load is 51.9kN for commuter trains and 87.2kN for freight trains, and the maximum wheel load is 105.9kN for commuter trains and 154.0kN for freight trains. The wheel load of commuter trains on weekdays tends to increase at commuter hours, from around 7:00 to 8:00 and from 18:00 to 20:00. On holidays, wheel load of commuter trains tends to increase around 16:30. According to Figure 9, the wheel load at around 18:00, which is the maximum on weekdays, was 1.15 times larger the wheel load at around 14:00 on weekdays, the wheel load at around 16:30, which is the maximum on holydays, was 1.13 times larger than that at 14:00.

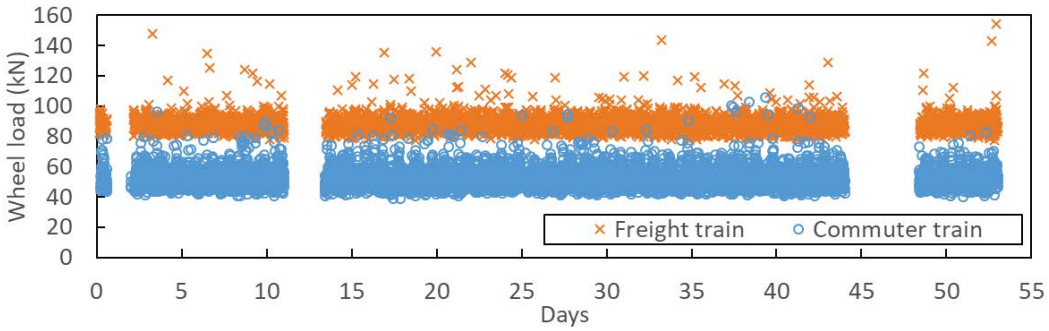

Figure 6: Time-series data of the measured wheel load

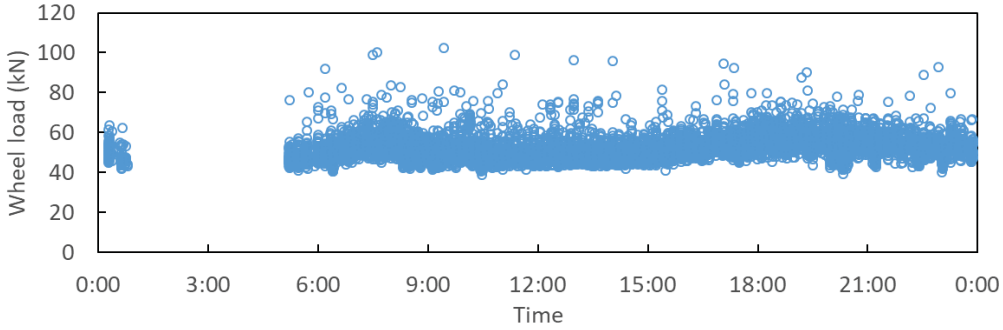

Figure 7: Wheel load for each time (Weekdays)

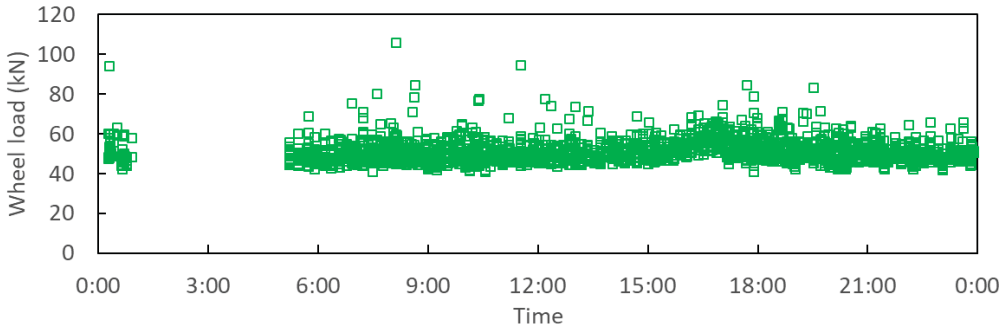

Figure 8: Wheel load for each time (Holydays)

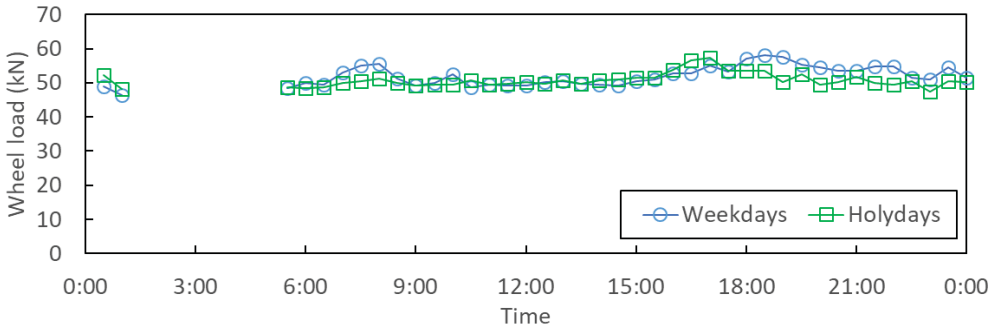

Figure 9: Wheel load for each time (averaging wheel load for every 30 minutes)

Figure 10 shows the minimum, average, and maximum values of wheel load measured by each trains in order to evaluate the variation of the wheel load in the same train. The minimum and average values of the wheel load of each train is similar value, but the maximum wheel load varies widely. From this, there is a possibility that a significant wheel load is caused by a wheel flat generated on a specific train.

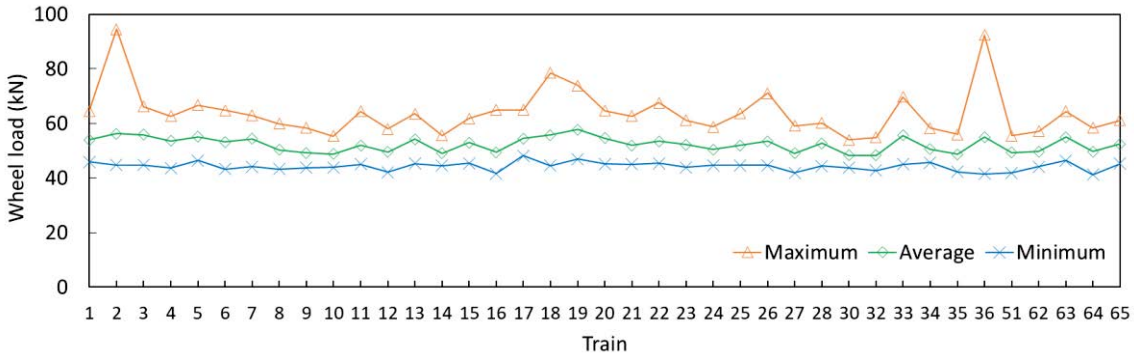

Figure 10: Wheel load measured by each trains

Figure 11-12 shows the probability distribution of wheel loads for commuter and freight trains. The same graph also shows a probability density function following a log-normal distribution. From this graph, the measured wheel load generally followed a log-normal distribution. The mode of wheel load for commuter trains was 48-49kN, and the mode of wheel load for freight trains was 88-89kN.

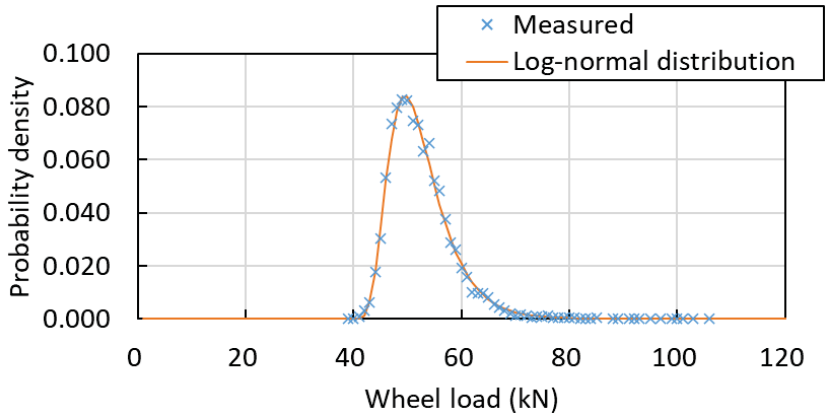

Figure 11: Probability distribution of wheel loads for commuter train

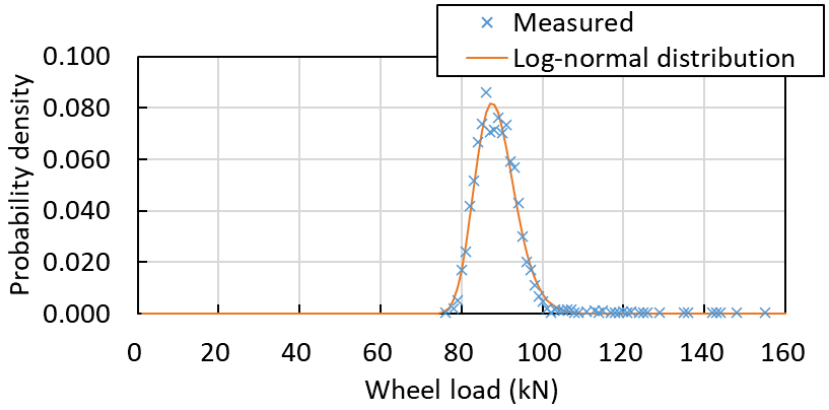

Figure 12: Probability distribution of wheel loads for freight train

Figure 13-16 shows the excess probabilities of measured wheel load and impact factor. The excess probability obtained from the probability density function following a lognormal distribution was also shown in the figure. From figure 13 and figure 14, it is confirmed that

wheel load of commuter train measured in the field test exceeding 90kN are approximately 0.1% or less, which is significantly smaller than the design wheel load considering the impact load (160kN). Similarly, when converted wheel load to an impact factor for a static wheel load of 80kN, impact factor which exceeds 1.2 are 0.1% or less. The main reason for this is the weight of the vehicle of a recent commuter train is lighter than the designed wheel load. For freight trains, percentage of wheel load which exceeds 140kN is less than 0.1%, and also impact factor which exceeds 1.8 is less than 0.1%, which is close to the value used in the design (2.0). In addition, the excess probability distribution of commuter trains roughly matches the excess probability by the log-normal distribution. On the other hand, for freight trains, the log-normal distribution underestimated the excess probabilities especially in the region where the wheel load was more than 110kN. This means that commuting trains run only the same type of train and the variation of train speed passing the site is relatively small. Whereas, for of freight trains, there are many types of locomotives and freight wagons, and the variation in passing speed is larger than the commuter train.

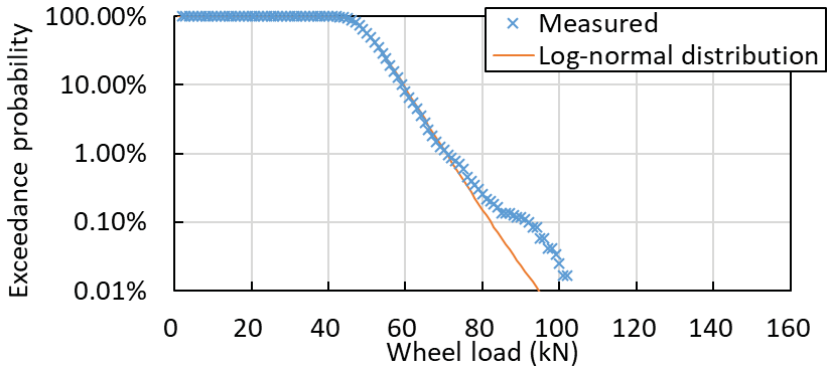

Figure 13: Excess probabilities of measured wheel load for commuter train

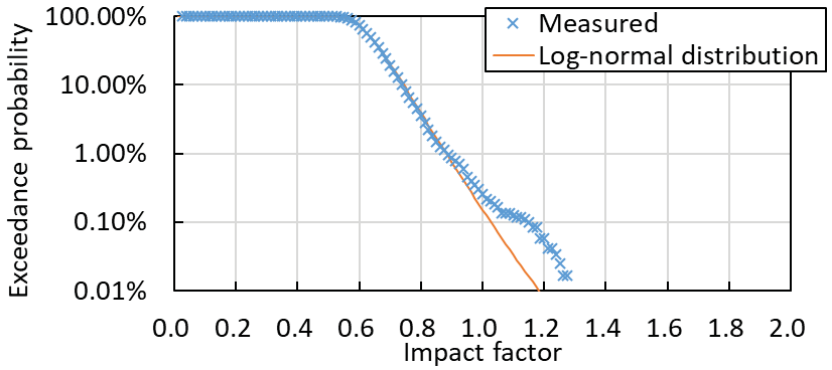

Figure 14: Excess probabilities of measured impact factor for commuter train

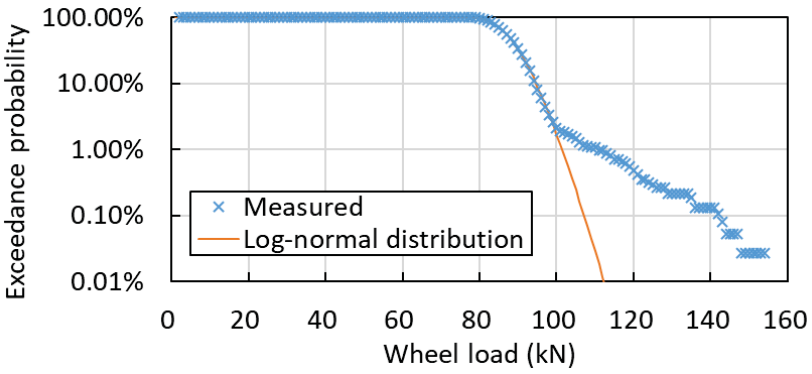

Figure 15: Excess probabilities of measured wheel load for freight train

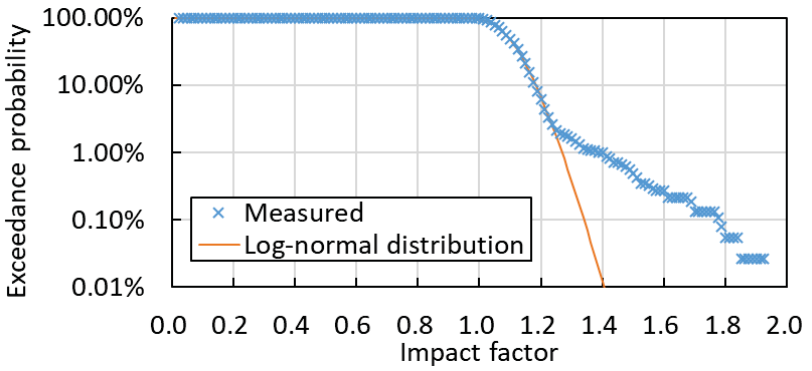

Figure 16: Excess probabilities of measured impact factor for freight train

4 CONCLUSION

The purpose of this study is to identify the actual load environment of train loads acting on PC sleepers in order to perform effective maintenance and optimize design of PC sleepers. In the study, the wheel load was measured in the continuous welded rail section of the conventional line, and the actual condition of the impact factor was investigated. The conclusions obtained are as follows.

- The maximum wheel load measured in the study is 105.9kN for commuter trains and 154.0kN for freight trains.
- On weekdays, the average wheel load during commuting hours was 1.18 times higher than the wheel load measured during the daytime.
- The impact factor of 2.0, which has been used in the design of the PC sleeper, is generally appropriate for freight trains. However, for commuter trains, the design wheel load was large compared to the measured wheel load.
- For commuter trains, the probability of occurrence of the wheel load considering the impact load could be roughly estimated by log-normal distribution. Based on this, it can be used for future design and prediction of fatigue life.

REFERENCES

[1] H. Wakui, H. Okuda, A study on limit state design method for prestressed concrete sleepers, *Concrete library of JSCE*, No. 33, 1–25, June, 1999.

[2] S. Minoura, T. Watanabe, K. Matsuoka, H. Yamane, Study on impact load response of the pc sleeper for rail joint using three-dimensional numerical analysis model, Proceedings of the 6th ECCOMAS thematic conference on computational methods in structural dynamics and earthquake engineering (COMPDYN 2017), 3748-3755, January, 2017

[3] T. Watanabe, K. Goto, K. Matsuoka, S. Minoura, Validation of a dynamic wheel load factor and the influence of various track irregularities on the dynamic response of prestressed concrete sleepers, Proceedings of the Institution of Mechanical Engineers, Part F: Journal of Rail and Rapid Transit, 1-10, December, 2019

[4] T. Watanabe, K. Matsuoka, S. Minoura, Numerical analysis for the dynamic response characteristics of the prestressed concrete sleeper, Proceedings of VII European Congress on Computational Methods in Applied Sciences and Engineering, June, 2016

EURODYN 2020
XI International Conference on Structural Dynamics
M. Papadrakakis, M. Fragiadakis, C. Papadimitriou (eds.)
Athens, Greece, 23–26 November 2020

DYNAMIC RESPONSE OF SINGLE AND MULTI-SPAN BEAMS UNDER A MOVING LOAD USING DYNAMIC STIFFNESS FORMULATIONS AND GALERKIN'S METHOD

Baran Bozyigit[1,2], Sinan Acikgoz[2], and Yusuf Yesilce[1]

[1] Department of Civil Engineering, Dokuz Eylul University, Izmir, Turkey
{baran.bozyigit,yusuf.yesilce}@deu.edu.tr

[2] Department of Engineering Science, University of Oxford, Oxford, United Kingdom
{baran.bozyigit,sinan.acikgoz}@eng.ox.ac.uk

Keywords: Dynamic stiffness method, Bernoulli-Euler beam, Free vibration, Moving load, Multi-span beam

Abstract. *This paper is concerned with the dynamic response analysis of single and multi-span beams under moving point loads. The Dynamic Stiffness Method (DSM) is used to calculate the mode frequencies and shapes of single, two and four-span Bernoulli-Euler beams. The exact mode shapes obtained from dynamic stiffness formulations are used to derive generalized mass, stiffness and force terms for normal modes using Galerkin's method. This enables efficient and accurate calculation of the time-history response of the investigated structures. This is demonstrated by comparing the results from this study with advanced finite element simulations of the same problem from the literature. The results validate the accuracy of this approach and demonstrate how this technique can be used to model dynamic amplification of bridges under the influence of moving loads.*

1 INTRODUCTION

The dynamic response of structures assembled from beam elements under moving loads is commonly encountered in bridge engineering applications. Fryba's textbook [1] summarises the pioneering work carried out on the dynamic behaviour of beams under moving loads. This includes analytical and computational work carried out on the response of solitary beams with different moving loads (e.g. point loads and sprung masses) and boundary conditions (simple or fixed supports), as well as work on more complex beam assemblies (e.g. frame structures and curved beams). For complex structures assembled from multiple beams, the free vibration characteristics of the system play an important role in reliable prediction of time-history response. Therefore, it is important to perform free vibration analysis of beam assembly systems accurately and use these to predict the dynamic response.

There has been significant research activity in the last few decades on simulating the response of beam assemblies to moving loads. For instance, Henchi et al. [2] applied the DSM to free vibration and time-history analyses of multi-span Bernoulli-Euler beams under moving load by using a fast Fourier transform (FFT) approach. Ichikawa et al. [3] combined direct integration method and analytical solutions to obtain the dynamic response of multi-span Bernoulli-Euler beams under a moving mass. Mahmoud [4] investigated the effects of cracks on the dynamic response of simply supported Bernoulli-Euler beams subjected to a concentrated moving load. Uzzal et al. [5] obtained the dynamic response of an infinite Bernoulli-Euler beam resting on a Pasternak foundation under the influence of a moving load. Mazilu [6] investigated the dynamics of infinite beams on bilinear viscoelastic foundation under constant and harmonic moving loads by using Bernoulli-Euler beam theory (BET). Beskou and Muho [7] investigated the dynamic response of a simply supported Bernoulli-Euler beam resting on a Winkler foundation considering a moving load on its surface with variable speed. Yang and Wang [8] performed time-history and stability analysis of an inclined beam subjected to a moving vertical concentrated load by using BET. Dynamic behaviour of various types of Timoshenko beams under moving loads and different boundary conditions were also investigated [9-12]. Kim and Lee [13] applied modified spectral element method (SEM) to the time-history analysis of single and multi-span Timoshenko beams and the results were presented in comparison with finite element method (FEM) results.

In this study, a simple approach is used to predict the dynamic response of multi-span beams under moving loads. In particular, continuous parameter models and DSM are used to identify mode frequencies and shapes of assembled structures. These exact mode shapes are then used to derive the dynamic time history response of the structure under the influence of moving loads using Galerkin's method. The use of theoretically exact mode frequencies and shapes for complex assemblies allow capturing the dynamic response efficiently and accurately. To demonstrate this, free vibration analyses of single, two and four-span Bernoulli-Euler beams are performed. First five natural frequencies and mode shapes are presented for all models. Then, time-history responses under a load moving with a constant speed are calculated for the single and two-span beams. Additionally, for the four-span beam model, an accelerating concentrated load is considered. The natural frequencies and time-history responses are compared to published studies from the scientific literature for validation purposes. The conclusion section summarizes the findings and provides a brief discussion on extending these models to simulate dynamic amplification in bridges.

2 FREE VIBRATION RESPONSE

The single, two and four span Bernoulli-Euler beams presented in Figure 1 are considered in this study. In Figure 1a, x describes the local beam coordinate, $S(t)$ is current position of the

load, *P* is a concentrated load, *v* is the velocity of this load, *t* is time and *a* is the constant acceleration of the load. For this preliminary study, the following assumptions are made: i) The behaviour of beams is linear elastic, ii) the material of beams is isotropic, iii) damping is neglected, and iv) axial deformations of the beam are not considered.

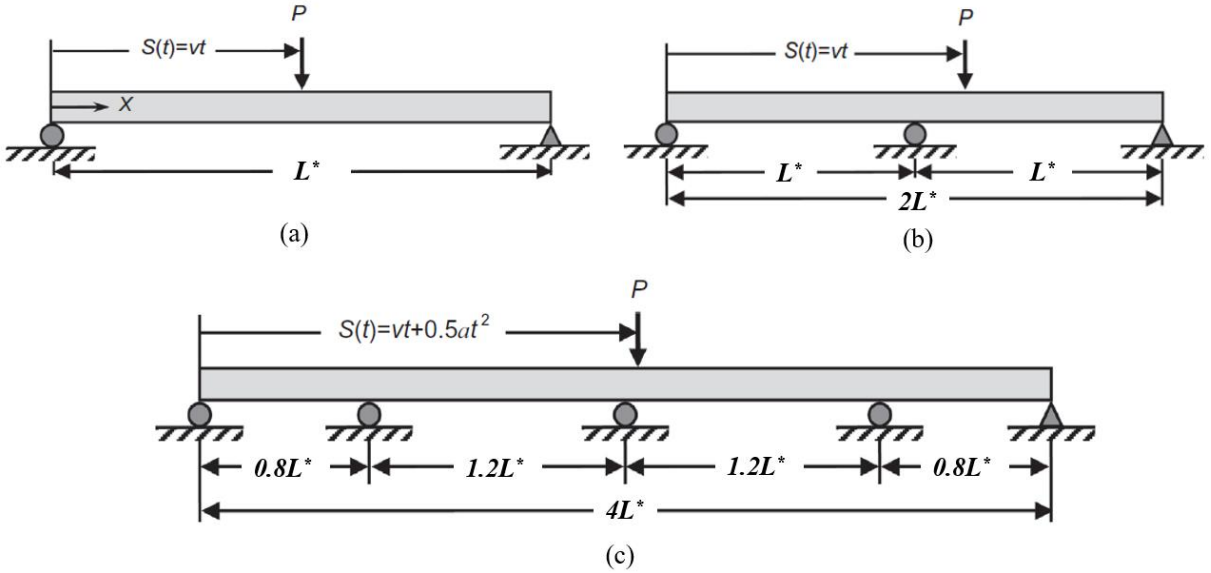

Figure 1: (a) Single-span Bernoulli-Euler beam under moving load (b) Two-span Bernoulli-Euler beam under moving load (c) Four-span Bernoulli beam under accelerating load [13]

The governing equation of motion of a single Bernoulli-Euler beam in free vibration can be written as [14]:

$$EI\frac{\partial^4 y(x,t)}{\partial x^4}+\bar{m}\frac{\partial^2 y(x,t)}{\partial t^2}=0 \tag{1}$$

where *y(x,t)* is transverse displacement function of the beam, $\bar{m}$ is mass per unit length, *E* is modulus of elasticity, *I* relevant area moment of inertia. If the bending motion of the beam is harmonic, Eq.(2) is obtained by applying the separation of variables method:

$$\frac{d^4 y(x)}{dx^4}-\frac{\bar{m}\omega^2}{EI}y(x)=0 \tag{2}$$

where ω is natural circular frequency.

It is assumed that the solution to Eq.(2) is of the form:

$$y(x)=\{C\}e^{isx} \tag{3}$$

where $\{C\}$ is a vector of integration constants, *s* represents the characteristic roots of equation and *i* is the imaginary number.

Substituting Eq.(3) into Eq.(2) leads to the following solutions for the transverse displacement and cross-section rotation functions in Eqs.(4) and Eq. (5), respectively:

$$y(x)=(C_1e^{is_1x}+C_2e^{is_2x}+C_3e^{is_3x}+C_4e^{is_4x}) \tag{4}$$

$$\theta(x)=(is_1C_1e^{is_1x}+is_2C_2e^{is_2x}+is_3C_3e^{is_3x}+is_4C_4e^{is_4x}) \tag{5}$$

where C_1, C_2, C_3 and C_4 are integration constants.

Bending moment function *M(x)* and shear force function *T(x)* can then be defined as follows:

$$M(x) = (EIs_1^2 C_1 e^{is_1 x} + EIs_2^2 C_2 e^{is_2 x} + EIs_3^2 C_3 e^{is_3 x} + EIs_4^2 C_4 e^{is_4 x}) \tag{6}$$

$$T(x) = (EIis_1^3 C_1 e^{is_1 x} + EIis_2^3 C_2 e^{is_2 x} + EIis_3^3 C_3 e^{is_3 x} + EIis_4^3 C_4 e^{is_4 x}) \tag{7}$$

In order to determine the eigenmodes of the assembled beam structure, its dynamic stiffness matrix needs to be assembled. To do this, the dynamic stiffness matrix of a single span element first needs to defined. This is achieved by the following procedure described below [15]:

i) a closed form solution for the free vibration problem is obtained, using Eqs. (2) – (3);

ii) the nodal degrees of freedom and forces are determined in terms of the natural vibration frequencies and boundary conditions;

iii) a frequency dependent dynamic stiffness matrix of the element is formulated by relating generalized nodal forces to generalized nodal displacements.

Following this procedure, the nodal degrees of freedom of the element and the arbitrary integration constants can be written in matrix form follows:

$$\delta = \begin{bmatrix} y_0 & \theta_0 & y_L & \theta_L \end{bmatrix}^T \tag{8}$$

$$\{C\} = \begin{bmatrix} C_1 & C_2 & C_3 & C_4 \end{bmatrix}^T \tag{9}$$

where $y_0 = y(x=0), \theta_0 = \theta(x=0), y_L = y(x=L), \theta_L = \theta(x=L)$. Here, L represents the length of a Bernoulli-Euler beam element. The nodal force vector (F) is given in Eq.(10) as:

$$F = \begin{bmatrix} T_0 & M_0 & T_L & M_L \end{bmatrix}^T \tag{10}$$

The sign convention utilised for the displacements and forces is shown in Fig. 2.

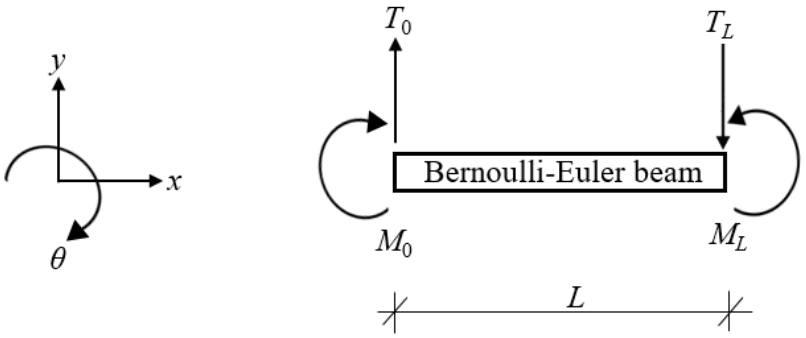

Figure 2: Positive sign convention for displacements and forces for a Bernoulli-Euler beam

The relations of $\delta = \Delta C$ and $F = \kappa C$ are obtained by using Eqs.(8-10) where Δ and κ represent coefficient matrices. Using these, the dynamic stiffness matrix of the single-span beam model is constructed by establishing a relationship between δ and F as follows:

$$F = \kappa(\Delta)^{-1}\delta \tag{11}$$

$$K^* = \kappa(\Delta)^{-1} \tag{12}$$

where K^* represents the dynamic stiffness matrix of the single-span Bernoulli-Euler beam.

The global dynamic stiffness matrix of the two-span and four-span beam models are obtained by assembling dynamic stiffness matrices from each element using standard assembly procedures:

$$\begin{Bmatrix} F_1 \\ F_2 \\ F_3 \\ . \\ . \\ . \\ F_j \end{Bmatrix}_{j\times 1} = \left[DSM_{glob} \right]_{j\times j} \begin{Bmatrix} \delta_1 \\ \delta_2 \\ \delta_3 \\ . \\ . \\ . \\ \delta_j \end{Bmatrix}_{j\times 1} \tag{13}$$

where j equals to the number of nodes multiplied by 2. Correspondingly, F_i and δ_i are the jth nodal force and degree of freedom of the system, respectively, and DSM_{glob} represents global dynamic stiffness matrix of the whole vibrating system. The DSM_{glob} is reduced to $DSM_{glob,red}$ matrix by removing rows and columns of inactive degrees of freedom according to displacement constraints arising from the boundary conditions.

The natural frequencies of the assembled structure are obtained by equating the determinant of the global dynamic stiffness matrix $DSM_{glob,red}$ to zero. A standard root finding algorithm (based on an iterative bisection approach) is used for obtaining the natural frequencies. This allows the calculation of the mode shape of each element of the structure for a given natural frequency. These are then normalized in a consistent manner, considering compatibility between nodal displacements and rotations to obtain the mode shape of the whole structure.

3 MOVING LOAD RESPONSE

The differential equation of a single Bernoulli-Euler beam element subjected to a moving concentrated load can be written as [4]:

$$EI\frac{\partial^4 y(x,t)}{\partial x^4} + \bar{m}\frac{\partial^2 y(x,t)}{\partial t^2} = P\delta^D\left(x - S(t)\right) \tag{14}$$

where δ^D is the Dirac delta function. Galerkin's method can be used to minimize the error in satisfying Eq.(14) with the following expansion for $y(x,t)$ [16]:

$$y(x,t) = \sum_{n=1}^{\infty} y_n(x) q_n(t) \tag{15}$$

where n is mode number, $y_n(x)$ and $q_n(t)$ are a chosen set of functions which approximate the eigenmodes and generalized displacements of the system, respectively. These need to satisfy boundary conditions of the model. When the chosen eigenmode functions are exact and orthogonal, Galerkin's method yields exact results. In this paper, the exact mode shape $y_n(x)$ of the whole structure is obtained from continuous parameter models using DSM, following the procedures discussed in the previous section.

Substituting Eq.(15) into (14) and assuming normal modes, Eq.(16) is obtained.

$$\bar{m}^* \ddot{q}_n(t) + k^* q_n(t) = Q(t) \tag{16}$$

In Eq.(16), $\bar{m}^*$ is generalized mass, k^* is generalized stiffness and $Q(t)$ is generalized force which are defined as follows [4]:

$$\bar{m}^* = \int_0^L y_n(x)^2 dx;$$

$$k^* = \int_0^L EI\left(\frac{d^2 y_n(x)}{dx^2}\right)^2 dx; \tag{17}$$

$$Q(t) = \int_0^L P\delta^D\left(x - S(t)\right) y_n(x) dx = P y_n\left(S(t)\right)$$

By using Eqs.(16) and (17), the dynamic response of the single-span beam can be obtained in terms of the generalized displacements for each vibration mode. Then, by using Eq. (15), the displacements at any desired location on the beam can be determined. For the two and four span beams, Eq.(17) is used to calculate generalized mass, stiffness and force values for each span separately. Then, these values are summed to obtain the total generalized mass, stiffness and force terms.

4 NUMERICAL CASE STUDY

To illustrate the numerical modelling procedure, the response of simple beam assemblies from the scientific literature will be discussed in this section. The following material and geometric properties are considered for each span of the model [13]: $L^* = 4$ m, width × height of the cross-section: 0.06 m × 0.02 m, unit weight of the beam: 7850 kg/m^3, $E = 2\times10^8$ kN/m^2.

In the free vibration analysis part of numerical case study, the first five natural frequencies and mode shapes are obtained by using DSM. Table 1 compares the first five natural frequencies of single, two and four-span beam models determined in this study to detailed finite element simulations conducted in an earlier study [13]. A very good agreement is observed where the maximum relative error between the results is less than 1%. It should be noted that the results from [13] are based on Timoshenko beam theory. However, as the cross-section of the beam is thin, the effects of rotational inertia and shear deformations are negligible. The accompanying mode shapes for single, two and four-span beam models are presented in Figure 3(a)-(c).

Model	Method	1st mode	2nd mode	3rd mode	4th mode	5th mode
Single-span beam	DSM	17.8047	71.2787	160.2420	284.8747	445.1167
	[13]	17.9755	71.8935	161.7267	287.4325	448.9480
	Error (%)	0.95	0.86	0.92	0.89	0.85
Two-span beam	DSM	17.8047	27.8143	71.2187	90.1361	160.2420
	[13]	17.9755	28.0796	71.8935	90.9805	161.7267
	Error (%)	0.95	0.94	0.94	0.93	0.92
Four-span beam	DSM	15.0807	21.5993	34.6706	36.9614	57.7196
	[13]	15.2254	21.8059	35.0013	37.3130	58.2663
	Error (%)	0.95	0.95	0.94	0.94	0.94

Table 1: First five natural frequencies (rad/sec) and relative errors for single-span, two-span and four-span beam model

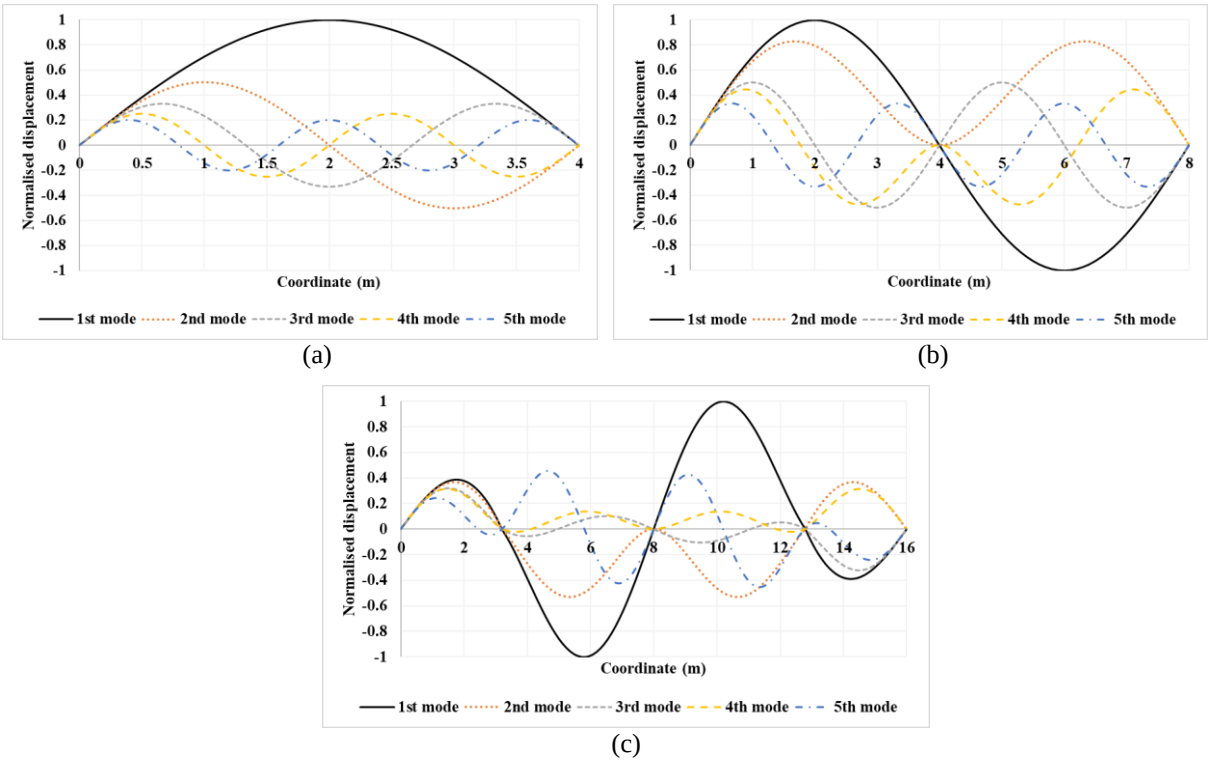

Figure 3: First five mode shapes of (a) Single-span Bernoulli-Euler beam model (b) Two-span Bernoulli-Euler beam model (c) Four-span Bernoulli beam model

After obtaining exact mode shapes, the dynamic response of the beam models can be calculated by using Eqs.(16)-(17). In this study, Eq.(16) is solved numerically using the ode45 function in Matlab, which is based on an explicit Runge-Kutta formulation [17]. The time-history responses of single and two-span Bernoulli-Euler beams under loads moving at constant velocity are presented in Figures 4 and 5. Both figures show the displacement at the middle of the first span. For the single span in Figure 4, accurate results could be achieved by considering only a single vibration mode. In contrast, for the two-span beam in Figure 5, the first two modes need to be considered to achieve good agreement with the published results.

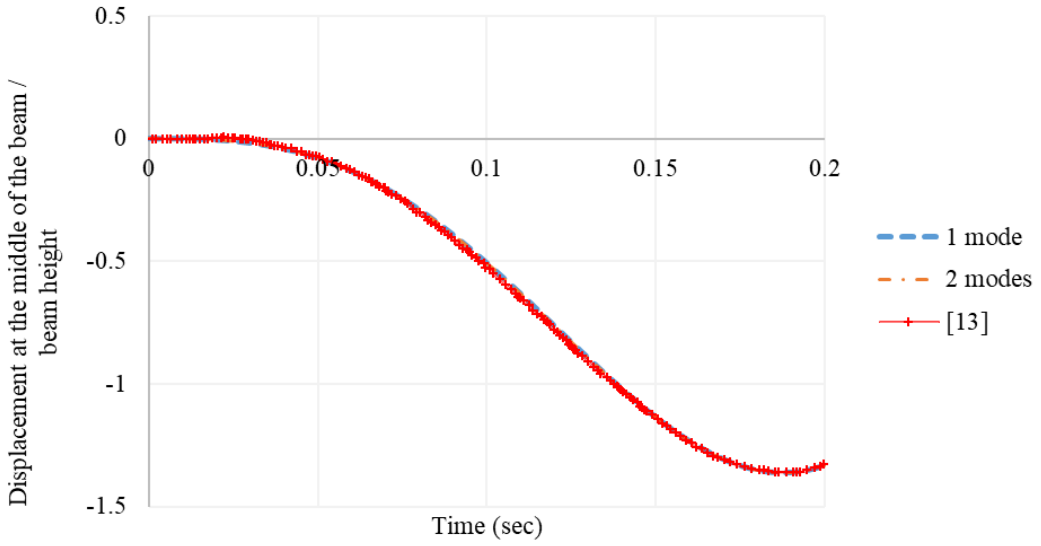

Figure 4: Time-history response of single-span beam model taking v = 20 m/s, P = 100 N

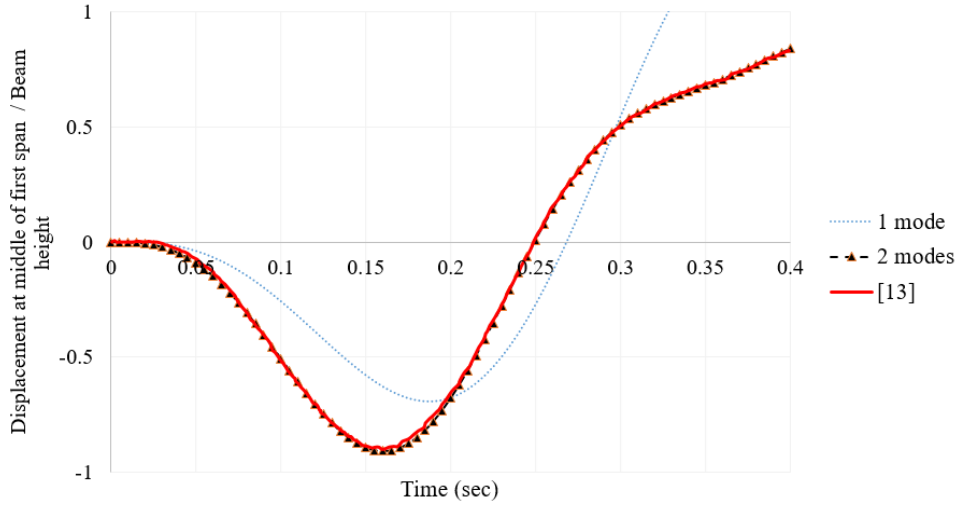

Figure 5: Time-history response of two-span beam model taking v = 20 m/s, P = 100 N

The proposed approach can also be used to calculate the dynamic response of beams under accelerating concentrated loads. Figure 6 shows the displacement time history at the middle of the second span of the four-span beam for an accelerating load. In this case, at least the first four modes need to be taken into account to capture the dynamic time history response of the multi-span beam structure accurately.

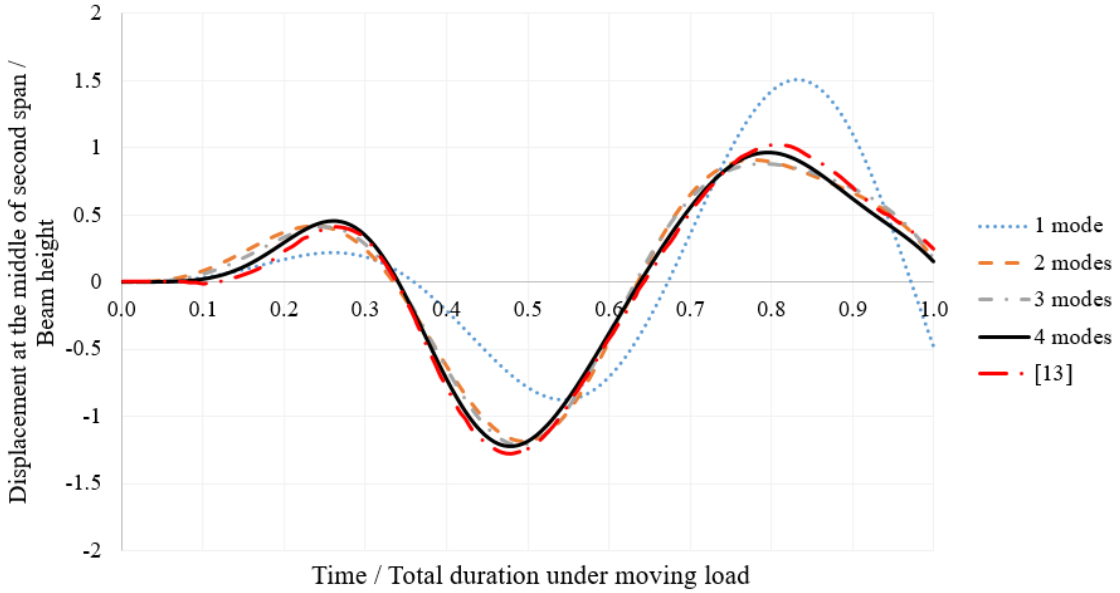

Figure 6: Time-history response of four-span beam model taking v = 20 m/s, a = 10 m/s^2 and P = 100 N

5 CONCLUSIONS

- In this paper, the dynamic stiffness approach, which is based on theoretically exact mode shapes, is combined with Galerkin's method for time-history response analysis of Bernoulli-Euler beams under moving loads. This enables the study of complex beam assemblies under the influence of moving loads in a computationally efficient manner.
- To demonstrate the numerical method, single, two and four-span beam models were considered for free vibration and dynamic response analysis under a concentrated moving load. Moving loads with constant velocity or constant acceleration have been considered.

- The estimation of natural frequencies and mode shapes from the DSM method demonstrate excellent agreement with detailed finite element simulations from the published literature.
- The time-history responses under the influence of moving load also demonstrate excellent agreement. The results show that increasing span number increases the number of modes that should be taken into account to achieve sufficient accuracy.
- The proposed approach is rigorous but simple. It can be easily extended to account for more advanced beam models (considering shear deformability) and geometries (e.g. arch frames) to investigate dynamic amplification in bridges under the influence of moving loads. This requires conducting a DSM analysis and using the identified mode shapes to calculate generalized mass, stiffness and force values to simulate the time history response of the structure.

ACKNOWLEDGEMENT

The authors would like to acknowledge the support of the Scientific and Technological Research Council of Turkey (TUBITAK) 2214-A International Doctoral Research Fellowship Programme.

REFERENCES

[1] L. Fryba, Vibration of solids and structures under moving loads, Thomas Telford, London, 1999.

[2] K. Henchi, M. Fafard, G. Dhatt, M. Talbot, Dynamic behaviour of multi-span beams under moving loads, *Journal of Sound and Vibration* 199(1), 33-50, 1997.

[3] M. Ichikawa, Y. Miyakawa, A. Matsuda, Vibration analysis of the continous beam subjected to a moving mass, *Journal of Sound and Vibration* 230(3), 493-506, 2000.

[4] MA. Mahmoud, Effect of cracks on the dynamic response of a simple beam subject to a moving load, *Proceedings of the Institution of Mechanical Engineers, Part F: Journal of Rail and Rapid Transit* 215(3), 207-215, 2001

[5] RUA. Uzzal, RB. Bhat, W. Ahmed, Dynamic response of a beam subjected to moving load and moving mass supported by Pasternak foundation, *Shock and Vibration* 19, 205-220, 2012.

[6] T. Mazilu, The dynamics of an infinite uniform Euler-Bernoulli beam on bilinear viscoelastic foundation under moving loads, *Procedia Engineering* 199, 2561-2566, 2017.

[7] ND. Beskou, EV. Muho, Dynamic response of a finite beam resting on a Winkler foundation to a load moving on its surface with variable speed, *Soil Dynamics and Earthquake Engineering* 109, 222-226, 2018.

[8] D. Yang, CM. Wang, Dynamic response and stability of an inclined Euler beam under a moving vertical concentrated load, Engineering Structures 186, 243-254, 2019.

[9] RT. Wang, Vibration of multi-span Timoshenko beams to a moving force, *Journal of Sound and Vibration* 207(5), 731-742, 1997.

[10] MH. Kargarnovin, D. Younesian, Dynamics of Timoshenko beams on Pasternak foundation under moving load, *Mechanics Research Communications* 31, 713-723, 2004.

[11] C. Yunmin, W. Changjing, Steady-state response of a Timoshenko beam on an elastic half-space under a moving load, *Acta Mechanica Solida Sinica* 19(1), 26-39, 2006.

[12] J.Jiang, W. Chen, Y. Pao, Reverberation-ray analysis of a continous Timoshenko beams subjected to moving loads, *Journal of Vibration and Control* 18(6), 774-784, 2011.

[13] T.Kim, U.Lee, Dynamic analysis of a multi-span beam subjected to a moving force using the frequency domain spectral element method, *Computers and Structures* 192, 181-195, 2017.

[14] M.Paz, YH. Kim, Structural Dynamics, *Theory and Computation*, ISBN: 978-3-319-94742-6, 2019.

[15] B.Bozyigit, Y.Yesilce, MA. Wahab, Single variable shear deformation theory for free vibration and harmonic response of frames on flexible foundation, *Engineering Structures* 208, 110268, 1-14.

[16] H.Ding, L.Chen, S.Yang, Convergence of Galerkin truncation for dynamic response of finite beams on nonlinear foundations under a moving load, *Journal of Sound and Vibration* 331(10), 2426-2442, 2012.

[17] MatlabR2019b, MathWorks Inc., USA, 2019.

EURODYN 2020
XI International Conference on Structural Dynamics
M. Papadrakakis, M. Fragiadakis, C. Papadimitriou (eds.)
Athens, Greece, 23–26 November 2020

THE IN-PLANE STEADY-STATE RESPONSE OF A RING IN RELATIVE MOTION TO A CONSTANT LOAD

Tao Lu[1], **Apostolos Tsouvalas**[1], **and Andrei V. Metrikine**[1]

[1]Faculty of Civil Engineering and Geosciences, Delft University of Technology
Stevinweg 1, 2628 CN Delft, the Netherlands
e-mail: {T.Lu-2,A.Tsouvalas,A.Metrikine}@tudelft.nl

Keywords: Rotating ring, Moving load, High-order model, Steady-state response, Resonance.

Abstract. *Ring-like structures are very commonly used in civil, mechanical and aerospace engineering. Typical examples of such structures are components in turbomachinery, compliant gears, conventional pneumatic tires and more recent non-pneumatic tires, to name a few. In this paper, a ring on elastic foundation is considered. The foundation, modelled as distributed springs, connects the inner surface of the ring to an immovable axis. Focus is placed on the in-plane response of the ring subjected to in-plane load only. A high-order ring model, which accounts for the through-thickness variations of displacements is adopted for the study. Two loading situations of a ring structure are of interest in practice: (i) a stationary ring subjected to a circumferentially moving constant load; and (ii) a rotating ring under a stationary constant load. For the first situation, it is well-known that resonances occur when the rotational speeds of the load satisfy certain conditions. In a series of recent investigations, such resonance speeds have been predicted for a rotating ring subjected to a stationary load. In this paper the case of the rotating ring under a stationary constant load and that of a stationary ring subjected to a moving load are compared in terms of their resonance speeds, as well as the steady-state responses for various parameters. It is found that these two cases are distinguishable even for system parameters which result at similar critical speeds.*

1 INTRODUCTION

The in-plane vibration of rings is a classical problem in solid mechanics due to the broad applications of ring-like structures in practice. It is usually the case that the ring and the load acting on it are in relative motion. Two particular situations, namely a stationary ring subjected to a circumferentially moving load (hereafter it is termed as moving load case) and a rotating ring under a stationary load (hefeafter it is termed as rotating ring case) are commonly encountered in engineering. Despite the absence of consensus on the existence of resonances of a rotating ring subjected to a stationary load with constant magnitude [1, 2], a seemingly conclusive result has been obtained in [3] according to which resonance can occur in rotating rings. Modes which are stationary as observed in a space-fixed reference system, are excited by the load [4] when a ring rotates at high speeds, resulting in a steady-state response which is time-invariant to a space-fixed observer. The experimental evidence of such a response is the occurrence of the so-called "standing waves" in rolling tires [5]. Similar wave phenomena have been reported in soft calenders of paper machines [6]. On the contrary, there is no doubt in the literature that resonances of a stationary ring subjected to a circumferentially moving constant load occur when the rotational speeds of the load equal to one of the natural frequencies divided by the corresponding mode number. Investigations of the steady-state responses in such a case can be found in [6, 7].

To what extent the moving load case and the rotating ring situation can be treated as equal is of interest and some deliberations on the topic can be found in the literature. It is concluded in [6] that the effect of rotation is negligible and the rotating ring under stationary load and stationary ring under moving load can be treated as equal. In this work, the steady-state deflection patterns of the ring when the speed of the relative motion is lower and higher than the minimum resonance speed are investigated for both moving load and rotating ring cases. The high-order model adopted from [3] is employed to simulate the in-plane response of rings on elastic foundation in relative motion with a load. The primary aim is to critically study the earlier suggested equivalence between the two cases. The responses of the two cases are compared in terms of their resonance speeds, as well as the steady-state responses for various parameters. It is shown that these two cases need to be distinguished especially when the foundation stiffness is relatively large.

2 HIGH-ORDER RING MODEL

A ring on elastic foundation subjected to a point load is shown in Fig. 1. The ring and the load are in relative motion with Ω_r being the rotating speed of the ring and Ω_p the velocity of the load. The inner surface of the ring is connected to an immovable axis by distributed radial springs k_r and circumferential springs k_c. The in-plane radial and circumferential displacements of the ring are designated by $w(z,\theta,t)$ and $u(z,\theta,t)$. A space-fixed coordinate system (r,θ) is adopted to describe the motions of the ring. It is assumed that the mean radius of the ring is R. An auxiliary coordinate z is introduced as $z = r - R$. The material properties of the ring are: the density ρ, Young's modulus E, shear modulus G, Poisson's ratio ν, Lamé constants λ and μ. The dissipation in the ring material is considered by replacing E by $E^* = E(1 + \zeta \mathrm{d}/\mathrm{d}t)$ in which ζ is a loss factor of the material. In addition, A is the cross-sectional area, I is the cross-sectional moment of inertia, b is the width of the ring. A constant point load $P(t) = P_0$ is applied on the outer surface of the ring.

The high-order model of the ring developed in [3] is employed. Plane strain configuration is assumed for the model. The external load is incorporated in the governing equations by the

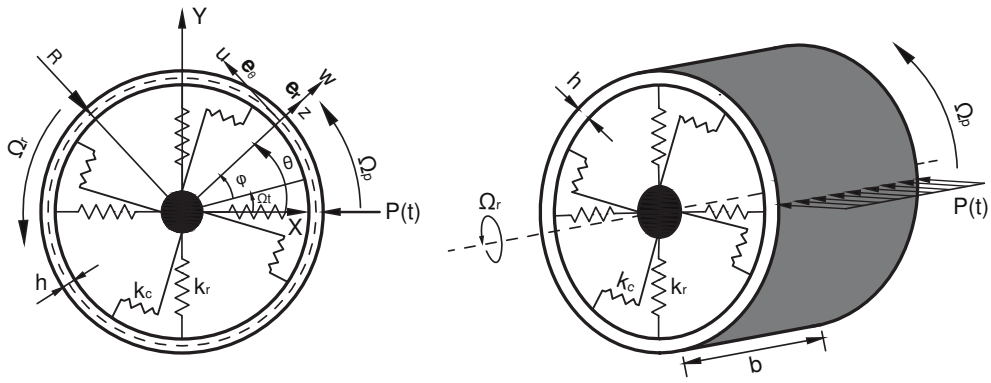

Figure 1: An elastic ring on elastic foundation in relative motion with a point (line) load. Ω_r and Ω_p are the rotational speeds of the ring and the load, respectively: left figure for front view; right figure for side view.

Hamilton's principle. One is referred to [8] for details of the derivation procedure. According to [3], the displacement fields are expressed as polynomial functions of the ring thickness z:

$$w(z,\theta,t) = \sum_{l=0}^{l=N_1} w_l(\theta,t)\, z^l,\; u(z,\theta,t) = \sum_{q=0}^{q=N_2} u_q(\theta,t)\, z^q \tag{1}$$

in which l, q are integers and $l \geq 0$, $q \geq 0$. N_1 and N_2 are the orders of the polynomials of the displacement fields. Assuming a radial point load of constant amplitude is applied on the outer surface of a rotating ring, the equations of motion that govern the small vibrations of the ring around the static equilibrium in the radial direction are:

$$\begin{aligned} &\int_{\frac{-h}{2}}^{\frac{h}{2}} (\mathrm{I}_1^{\mathrm{lin}}\, z^l)\, \mathrm{d}z + \rho \int_{\frac{-h}{2}}^{\frac{h}{2}} \left(r(\dot{v}_1 + \Omega_r\, v_1' - \Omega_r\, v_2) z^l\right) \mathrm{d}z + \left(f_1^{\mathrm{lin}} - f_2^{\mathrm{lin}}(-1)^l\right) \left(\frac{h}{2}\right)^l \\ &= -\left(\frac{h}{2}\right)^l P(t)\delta(\theta) = -\left(\frac{h}{2}\right)^l P_0\, \delta(\theta), \quad (l = 0,1,2,3...N_1). \end{aligned} \tag{2}$$

The dimension of P_0 is N.m^{-1} and δ is the Dirac delta function.

The linearised equations of motion of a rotating ring in the circumferential direction are:

$$\begin{aligned} &\int_{\frac{-h}{2}}^{\frac{h}{2}} (\mathrm{I}_2^{\mathrm{lin}}\, z^q)\, \mathrm{d}z + \rho \int_{\frac{-h}{2}}^{\frac{h}{2}} \left(r(\dot{v}_2 + \Omega_r\, v_2' + \Omega_r\, v_1) z^q\right) \mathrm{d}z + \left(f_3^{\mathrm{lin}} - f_4^{\mathrm{lin}}(-1)^q\right) \left(\frac{h}{2}\right)^q = 0, \\ &(q = 0,1,2,3...N_2). \end{aligned} \tag{3}$$

The details of the governing equations including the expressions for $\mathrm{I}_1^{\mathrm{lin}}$, $\mathrm{I}_2^{\mathrm{lin}}$, $f_1^{\mathrm{lin}} - f_4^{\mathrm{lin}}$ and the velocities v_1 and v_2 of a differential element of the ring in radial and circumferential directions in the left-hand side of Eqs. (2-3) can be found in [8]. For the case of a stationary ring subjected to a circumferentially moving load of constant amplitude, the governing equations can be obtained by setting Ω_r and the static equilibrium to zero on the left side of Eqs. (2-3) and altering $P_0\, \delta(\theta)$ to $P_0\, \delta(\theta - \Omega_p t)$ on the right-hand side of Eq. (2).

The following dimensionless parameters are introduced [3]:

$$k = \sqrt{I/A},\; \bar{k} = k/R,\; \bar{\gamma} = n\,\bar{k},\; \bar{\omega} = \omega\, k/c_0,\; \bar{v}_{(r,p)} = R\,\Omega_{(r,p)}/c_0,\; \bar{k}_{(r,c)} = k_{(r,c)}k^2/(Eh), \tag{4}$$

where $c_0 = \sqrt{E/\rho}$ is the speed of the longitudinal wave in the rod, $I = bh^3/12$ is the cross section area moment of inertia and $\bar{k}$ is the non-dimensional radius of gyration. $\bar{\theta} = \theta/\bar{k}$ and $\tau = c_0 t/k$ are the dimensionless angle and temporal variables, respectively. $\bar{P} = P_0\,\bar{k}/(Eh)$ is the dimensionless load amplitude.

3 MOVING LOAD VERSUS ROTATING RING

The load speeds causing resonance of a stationary ring subjected to a constant point load moving circumferentially are well known [7], namely $\Omega_p = \omega_n/n$ in which n is the circumferential mode number and ω_n is the nth natural frequency of the ring. The minimum resonance speed (the critical speed) is the lowest value of ω_n/n. Resonance speeds of a rotating ring subjected to a stationary constant load satisfy the condition $\bar{\omega}_n = 0$ in which $\bar{\omega}_n$ is the natural frequency calculated in a space-fixed reference system [3]. By substituting $\bar{\omega}_n = 0$ into the frequency equation [3], one can solve for resonance speeds for each circumferential wavenumber.

Theoretically, resonances of the moving load case always exist. However, in practice the load speed can not always reach the resonance speeds, especially for stiff rings since their resonance speeds are high. On the contrary, resonance occurs only for certain parameters of a rotating ring subjected to a stationary load of constant magnitude. Specifically, resonances of a rotating ring may only occur for relatively soft rings. For example; for a ring made of steel, resonance speeds do not exist for the rotating ring case whereas resonance speeds of such a ring for the moving load case do exist but are extremely large. One needs to bear in mind that if a ring is stiff, the responses of the ring for the rotating ring and moving load cases are similar. The reason is that in the operational speed range, the translational rigid-body like motion governs the response in both cases. Thus, only soft rings are considered in this section because resonance speeds exist for such rings for both moving load and rotating ring cases.

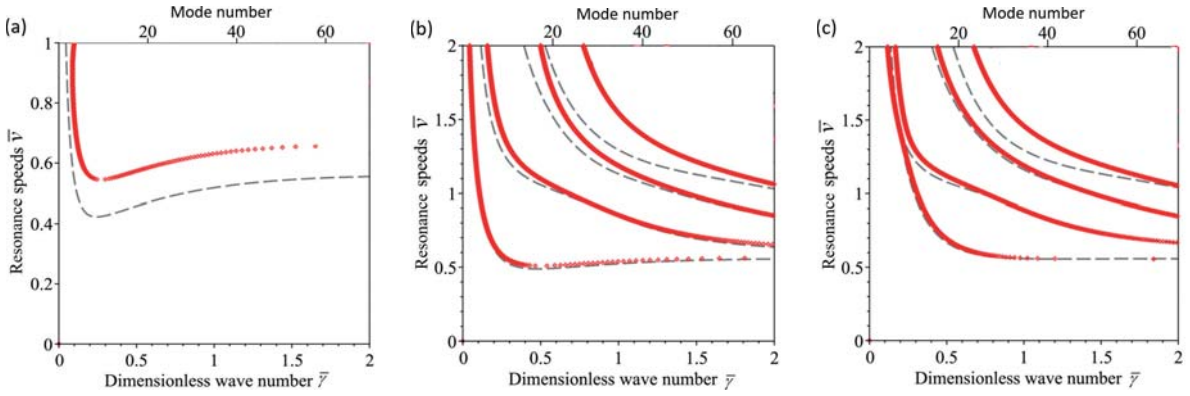

Figure 2: Comparison of resonance speeds, $h/R = 0.1, \bar{k}_c = 0.1$ using the high-order model with increasing stiffness of radial springs. Grey dashed line for moving load case; Red dotted lines for rotating ring case: (a) $\bar{k}_r = 0.001$; (b) $\bar{k}_r = 0.01$; (c) $\bar{k}_r = 0.1$.

3.1 Comparison of resonance speeds between both cases for relatively soft rings

Fig. 2 shows the comparisons of resonance speeds, as functions of the mode number, between moving load and rotating ring case with different values of the foundation stiffness. Since high-order theory is used, there are several curves representing higher order motions of the ring. In the figure, the lower abscissa in each plot is the dimensionless wavenumber, whereas the upper abscissa is the corresponding discrete circumferential mode number n. All the chosen

parameters represent relatively stiff foundation (soft ring) configuration since only in this case resonance speeds of rotating rings exist.

In Fig. 2 the upper limit of the plots is set at $\bar{v} = 1$ and therefore only the lowest branch of resonance speeds is shown. The reason is that at higher speeds, the predictions of other branches are not accurate since the rotation-induced hoop tension is approaching unrealistically high value. Generally, rotation stiffens the ring, therefore, the resonance speeds of rotating rings are larger than those in the moving load case as shown in Fig. 2(a). With increasing $\bar{k}_r$, the resonance speeds for the two lower branches of both cases become close as shown in Figs. 2(b)(c). For the two higher branches of resonance speeds, the differences are still large. The minimum resonance speed in Fig. 2 is a critical speed at which a wave-like steady-state deformation pattern is initiated. For the parameters shown in Figs. 2(b)(c), the critical speed converges to the Rayleigh wave speed with increasing wavenumber and a Rayleigh wave resonance is expected when a stationary constant load is applied [6].

3.2 Steady-state response for soft rings on stiff elastic foundation

The steady-state responses of a ring in relative motion to a constant point load is investigated in this section for a soft ring. The parameters are chosen the same as in Fig. 2(b). For this set of parameters, resonance speeds in the two cases are close, especially for the lower order motion. The dynamic responses are derived using the so-called "method of the images" described in [7, 8].

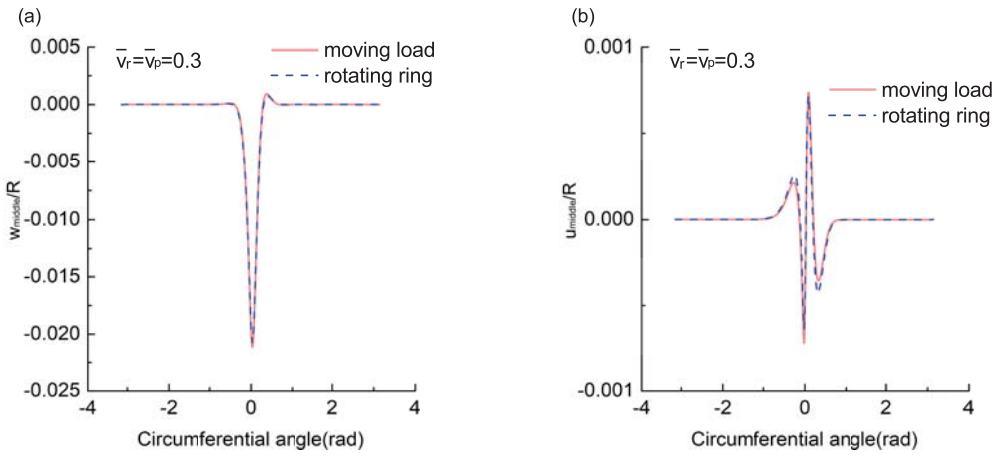

Figure 3: Displacements at the middle surface of the ring for $\bar{v}_r = \bar{v}_p = 0.3$, $\bar{k}_r = 0.01$, $\bar{k}_c = 0.1$, $\zeta = 0.002$, $\bar{P} = 0.002$: (a) Normalised radial displacement; (b) Normalised circumferential displacement.

As shown in Fig. 2(b), the minimum resonance speed in both cases is the same, namely $\bar{v}_{cr} \approx 0.5$. Therefore, two velocities of the relative motion are chosen: $\bar{v}_r = \bar{v}_p = 0.3$ as a sub-critical speed and $\bar{v}_r = \bar{v}_p = 0.7$ as a super-critical one. Fig. 3 shows the displacements (normalized with respect to the ring radius at the middle surface) at the middle surface of the ring for the two cases. It can be seen that the responses are very close. In this case, the stiffening effect due to rotation for the rotating ring case is not obvious. When the speeds increase, for the rotating ring case, the static expansion due to rotation becomes large, resulting in high hoop tension. This tension stiffens the ring, especially it suppresses the radial displacement of the rotating ring comparing to the moving load case as shown in Fig. 4(a) for the super-critical case $\bar{v}_r = \bar{v}_p = 0.7$. However, the stiffening effect is not obvious on the circumferential displacement

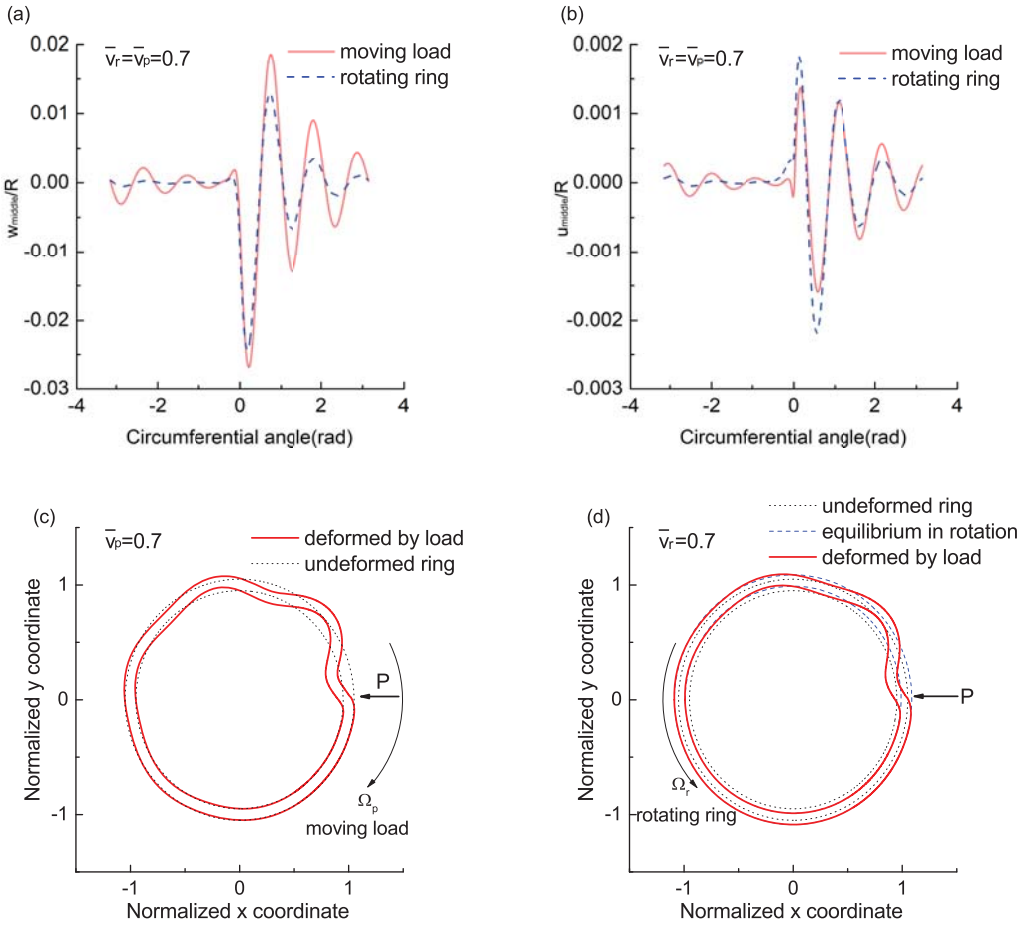

Figure 4: Displacements at the middle surface of the ring for $\bar{v}_r = \bar{v}_p = 0.7$, $\bar{k}_r = 0.01$, $\bar{k}_c = 0.1$, $\zeta = 0.002$, $\bar{P} = 0.002$: (a) Normalized radial displacement; (b) Normalized circumferential displacement; (c) Ring deformation, moving load; (d) Ring deformation, rotating ring. The ring deformations are scaled by 5.

(Fig. 4(b)). In Figs. 4(c)(d), the ring deformations in both cases are illustrated. Besides the different patterns, the rotating ring shows static radial expansion caused by rotation. In addition, the effect of damping is more pronounced in the rotating ring case as the displacements decay fast along the circumference away from the loading point.

3.3 Maximum deflection of the ring versus velocity

The maximum displacement at the middle surface ($D_{\max}$ is defined as $\max\{\sqrt{{w_0}^2+{u_0}^2}\}$ in which w_0 and u_0 are the radial and circumferential displacements at the middle surface, respectively) for a ring with the same parameters as used in section 3.2 is shown in Fig. 5(a). For the chosen parameters, the resonance speeds of both cases are quite similar as shown in Fig. 2(b). However, the responses are different under the same load as shown in Fig. 5(a), especially when the relative speeds between the load and the ring exceed the minimum resonance speed. For rotating ring case, the rotation of the ring stiffens the ring, resulting in smaller responses. In Figs. 5(b) and (c), the maximum middle surface displacements in the radial and circumferential directions are demonstrated, respectively. It can be seen that the responses are mainly governed by the radial motion. To conclude, for the moving load and rotating ring cases which have similar resonance speeds, their responses are in large disagreement at higher speeds of the

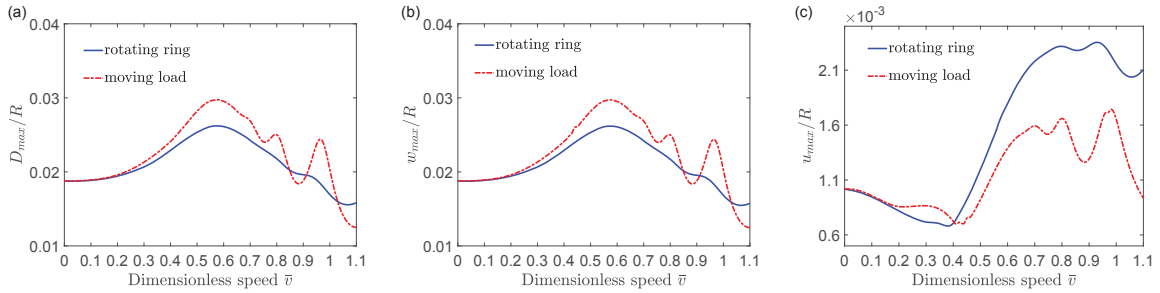

Figure 5: Comparison of maximum deflection at the middle surface versus velocity, $\bar{k}_r = 0.01$, $\bar{k}_c = 0.1$: (a) $D_{\max}$; (b) maximum radial displacement; (c) maximum circumferential displacement.

relative motion between the load and the ring.

4 CONCLUSIONS

The equivalence of the rotating ring under a stationary constant load case and a stationary subjected to a moving constant load case are discussed by comparing their resonance speeds, as well as the steady-state responses. It is found that these two cases need to be distinguished even for system parameters which result in similar critical speeds. The moving load on stationary ring and the rotating ring under stationary load cases can only be considered equivalent when the relative speeds between the ring and the load are low or the responses are mainly governed by the $n = 1$ mode. First, if resonance speeds exist, these can be very different in the two cases under consideration, which will result in different dynamic responses. Second, even for system parameters which result in similar critical speeds, the responses under the same load can be different due to the rotation effects.

References

[1] S. Huang, W. Soedel, Effects of Coriolis acceleration on the free and forced in-plane vibrations of rotating rings on elastic foundation, Journal of Sound and Vibration 115 (2) (1987) 253–274.

[2] J. Lin, W. Soedel, On the critical speeds of rotating thick or thin rings, Mechanics of Structures and Machines 16 (4) (1988) 439–483.

[3] T. Lu, A. Tsouvalas, A. V. Metrikine, A high-order model for in-plane vibrations of rotating rings on elastic foundation, Journal of Sound and Vibration 455 (2019) 118–135.

[4] W. Soedel, Vibrations of Shells and Plates, CRC Press, 2004.

[5] A. Chatterjee, J. P. Cusumano, J. D. Zolock, On contact-induced standing waves in rotating tires: experiment and theory, Journal of Sound and Vibration 227 (5) (1999) 1049–1081.

[6] A. Karttunen, Resonance phenomena of polymer-covered cylinders under rolling contact, Ph.D. thesis, Aalto University (2015).

[7] A. Metrikine, M. Tochilin, Steady-state vibrations of an elastic ring under a moving load, Journal of Sound and Vibration 232 (3) (2000) 511–524.

[8] T. Lu, A. Tsouvalas, A. Metrikine, The steady-state response of a rotating ring subjected to a stationary load, International Journal of Solids and Structures 202 (2020) 319–337.

EURODYN 2020
XI International Conference on Structural Dynamics
M. Papadrakakis, M. Fragiadakis, C. Papadimitriou (eds.)
Athens, Greece, 23–26 November 2020

TRAIN-WEIGHT-IN-MOTION IDENTIFICATION MEASURING TIME-HISTORIES OF RAIL STRAINS

Annamaria Pau[1], **Fabrizio Vestroni**[2]

[1]Department of Structural and Geotechnical Engineering,
Sapienza University of Rome
via Gramsci 53, 00197 Roma, Italy
e-mail: annamaria.pau@uniroma1.it

[2]Department of Structural and Geotechnical Engineering,
Sapienza University of Rome
via Eudossiana 18, 00184 Roma, Italy
e-mail: vestroni@uniroma1.it

Keywords: load identification, rail monitoring, rail strains.

Abstract. *This paper deals with the identification of the weight of a train in motion, based on the measurement of the time-history of the response in terms of strains at the foot of the rail. The direct problem is initially addressed: the response of a rail modelled as a one-dimensional Euler-Bernoulli beam with constant properties, resting on a linear elastic foundation with viscous damping and subjected to a Dirac delta load travelling at constant speed is considered. For the model described, a closed-form expression of the solution can be obtained, which permits to investigate the sensitivity of the response to the main mechanical parameters. Analytical strains are compared to their experimental counterpart, showing their practical ability to describe the real phenomenon. As a second step, the inverse problem consisting in the identification of the loads for a given time-history of measured strains is addressed. The solution of the inverse problem is set up as a minimization problem whose objective function is based on the difference between experimental and model time-histories of strains. This inverse problem is nonlinear, and its solution can be pursued by the Newton method, which requires recursive application of a linearized expression for the evaluation of the optimal parameters. The Bayesian formulation enables to investigate identifiability of parameters and minimum number of measurements, and leads to conclude that the identification process must begin with an improving of the interpretative model. This model updating can be achieved by evaluating the model parameters, using the time-history of a train whose weight is known. After that, the actual identification of the loads can be performed. The procedure proposed is applied to experimental strains recorded at the foot of a rail on a stretch of line run by a locomotor moving at a low constant speed. The identified loads were in good agreement with the expected value, with errors smaller than 4%.*

1 INTRODUCTION

Increased standards of safety in railway transport require awareness of the loads actually travelling on railway lines, in particular when freight trains running. This enables to timely schedule maintenance and monitor rail wear, as well as to check unbalanced loads which can affect vehicle safety, and requires the development of methods for the identification of travelling loads. This paper deals with the identification of the weight of a train in motion, based on the measurement of the time-history of the response in terms of strains at the foot of the rail.

To solve this inverse problem, it is first useful to address the direct problem. Here, the rail is modelled as a one-dimensional Euler-Bernoulli beam with constant geometrical and mechanical properties, resting on a linear elastic foundation with viscous damping and subjected to a Dirac delta load travelling at constant speed. The same model was used in the past to describe the response of rocket test tracks [1] and train tracks [2]. This model has proved its ability to describe the real experimental response and, since it enables obtaining a closed-form solution, it is used here as a reference model, enabling to investigate the response sentitivity to the main mechanical parameters. More complex models involving 2D descriptions of the elastic foundation were also proposed [3], but they seem not suitable for this inverse problem.

On accepting the simplified modelling of the travelling load as a Dirac delta, its identification involves the evaluation of its amplitude only. We approach this inverse problem using an estimator which minimizes the difference between the experimental response and the response provided by the described mechanical model of the rail. An overview of the different approaches presented in the literature for the solution of load identification problems can be found in the work by Ouyang [4]. Among these, it is worth citing the approach proposed by Trujillo and Busby [5], based on dynamic programming, not only the forcing term which provides the best match is sought, but also that which has a certain degree of smoothness according to Tikhonov's regularization. An application of dynamic programming to train load identification is presented by Zhu et al. [7]. Among other possible approaches, Ronasi et al. [6] calculate the minimum of an objective function measuring the distance between experimental and analytical data. In the framework of an algebraic solution, Meli and Pugi [8] made hypotheses to simplify the load time-histories and adopted a multibody model for the railway vehicle. We develop here a load identification procedure within the framework of a Bayesian approach, also addressing problems of optimal choice of parameters and measurements [9, 10, 11]. Based on the results obtained from the investigation of the Fisher matrix, we were able to conclude that the load identification problem can be better formulated in two steps. The first step consists in a model updating performed on the grounds of the knowledge of the response to a known load. The second step is the actual load identification.

Experimental tests were used for validation: they consist of field measurements of the rail strain time-histories due to the transit of a two-axis locomotor at low speed.

2 DIRECT PROBLEM

The rail is represented as a plane beam with constant geometrical and mechanical properties resting on a linearly elastic foundation with viscous damping, and subjected to a Dirac delta load of amplitude P moving at constant speed v. On setting E the Young's modulus of the cross section, I its moment of inertia, the solution to this problem in terms of transverse displacement w as a function of time t and space z can be written in closed form:

$$w(z,t) = \begin{cases} \frac{P}{EI}\left(\frac{e^{(z-vt)k_3}}{(k_3-k_4)(k_3-k_1)(k_3-k_2)} + \frac{e^{(z-vt)k_2}}{(k_2-k_4)(k_2-k_1)(k_2-k_3)}\right) & z \leq 0 \\ -\frac{P}{EI}\left(\frac{e^{(z-vt)k_4}}{(k_4-k_3)(k_4-k_2)(k_4-k_1)} + \frac{e^{(z-vt)k_1}}{(k_1-k_3)(k_1-k_2)(k_4-k_1)}\right) & z > 0. \end{cases} \quad (1)$$

where k_1, k_2, k_3 and k_4 are wavenumbers. The time-history of the response at $z = 0$ for $P = 1$ N resulting from Equation (1) is represented in terms of curvatures $\chi(z,t) = \partial^2 w/\partial z^2$ in Figure 1, for different speeds and damping. Curvature is the observed quantity, since in the experimental tests we will measure the strain at the foot of the rail, which is tied to the curvature by the linear relation $\epsilon = h_G \chi$, valid under the hypothesis of small displacements, with h_G distance between the center of mass of the cross-section and the foot of the rail. Figure 1a shows that, for speeds of 28 km/h, approximately corresponding to 0.1 of the critical speed v_{cr}, the dependence of the maximum amplitude on damping is very limited. The critical speed $v_{cr} = (4kEI/(\rho A)^2)^{1/4}$, with k stiffness of the soil, ρ mass density, and A area of the cross-section, is the lowest speed at which a free wave can propagate in the rail [1]. When the speed increases, the response is no longer symmetric, and the maximum amplitude more and more depends on the train speed (Figure 1b). When the speed equals the critical velocity, a resonance occurs: the maximum response increases and strongly depends on damping (Figure 1c).

Figure 2a shows the analytical time-history of the strains due to a series of ten Dirac loads with P=78400 N, which is approximately the load insisting on one wheel of an unalden ETR324, obtained using Equation 1 for a travelling speed of 28 km/h. Figure 2 b reports, for comparison, the experimental time-history of an ETR324, travelling at around 30 km/h. The pattern of the time-history obtained from the model satisfactorily agrees with the time-history observed experimentally.

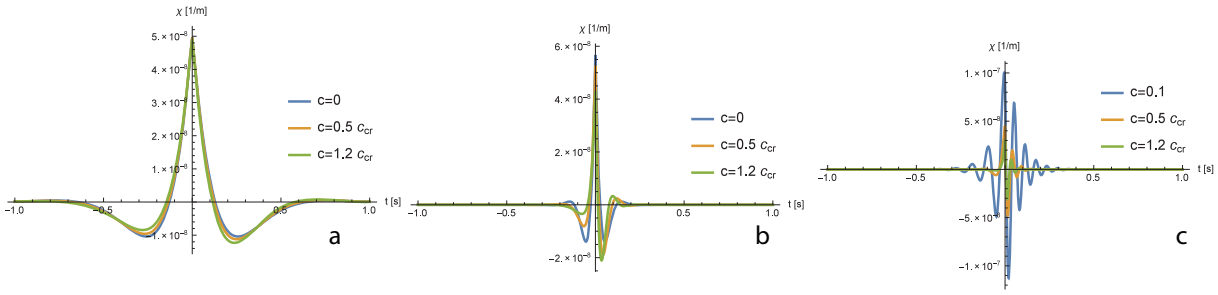

Figure 1: Time-histories of curvatures for different values of damping and speed: 28 km/h=$0.1v_{cr}$ (a), 140 km/h=$0.5v_{cr}$ (b), 280 km/h=v_{cr} (c). $c_{cr} = 2(k\rho A)^{1/2}$

3 INVERSE PROBLEM

The goal of the solution of the inverse problem consists in the identification of the amplitude of the Dirac deltas representing train loads. It must be considered that the model contains several parameters, whose values may be more or less uncertain, and that have an influence on the result of the load identification. Some parameters are mechanical and geometrical characteristics of the model, that is ρA, EI, k, c, while others concern the load: P and v. We will be dealing with recordings made at low speed, therefore we will assume $c = 0$, and, also, that v is known, since it is easily measurable. The vector of unknown parameters will be $\mathbf{x} = \{\rho A, EI, k, P\}^T$.

Let us call $\boldsymbol{\epsilon}(\mathbf{x})$ the vector of observed quantities as a function of the vector of parameters $\mathbf{x}$, and $\mathbf{z}$ the vector of corresponding measured quantities, that is, the time-discretized experimental

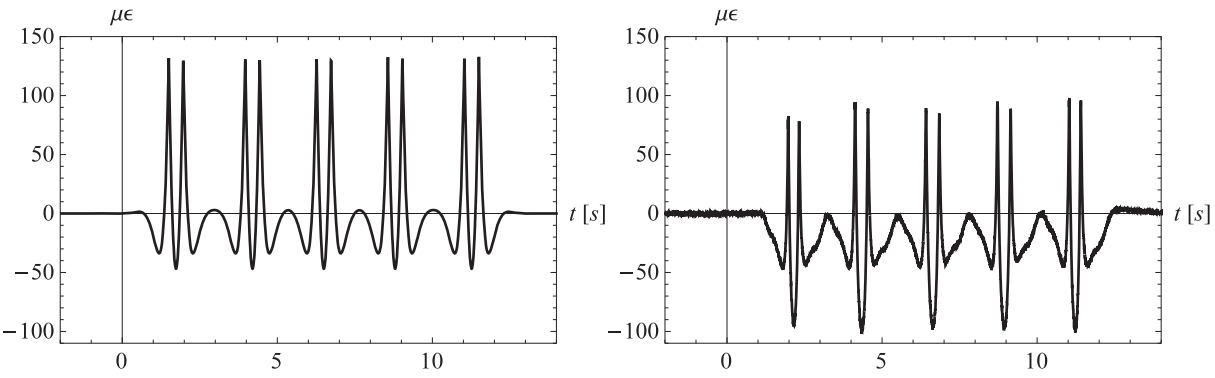

a) b)

Figure 2: Analytical (a) and experimental (b) microstrain time-histories of an ETR324.

response at a given location. The vector of observed quantities is an m-element vector $\boldsymbol{\epsilon}(\mathbf{x}) = \{\epsilon_1(\mathbf{x}), ...\epsilon_m(\mathbf{x})\}$, whose i-th element represents the strain at a given abscissa and at the i-th time instant.

Within a Bayesian approach, parameters are random variables, and measured quantities satisfy the relationship

$$\mathbf{z} = \boldsymbol{\epsilon}(\mathbf{x}) + \mathbf{n} \tag{2}$$

where $\mathbf{n}$ is a vector of stochastic noise, independent of $\mathbf{x}$. Assuming a multivariate normal distrubution for $\mathbf{x}$ and $\mathbf{n}$, and being $\mathbf{S_x}$ and $\mathbf{S_n}$ the covariance matrices of the initial estimate of the parameters and of the noise, respectively, the maximum of the probability $p(\mathbf{x}|\mathbf{z})$ is attained for the optimal $\hat{\mathbf{x}}$ of $\mathbf{x}$ which minimizes the objective function:

$$l(\mathbf{x}) = \frac{1}{2}[\mathbf{z} - \boldsymbol{\epsilon}(\mathbf{x})]^T \mathbf{S_n}^{-1}[\mathbf{z} - \boldsymbol{\epsilon}(\mathbf{x})] + \frac{1}{2}(\mathbf{x} - \mathbf{x}_0)^T \mathbf{S_x}^{-1}(\mathbf{x} - \mathbf{x}_0). \tag{3}$$

Assuming that the initial estimate $\mathbf{x}_0$ is not too far from $\hat{\mathbf{x}}$, a linearization of the relationship between observed quantities and parameters provides a recursive formula whose iterative application enables to reach the minimum of the objective function:

$$\hat{\mathbf{x}} = \mathbf{x}_0 + (\mathbf{H}^T \mathbf{S_n}^{-1} \mathbf{H} + \mathbf{S_x}^{-1})^{-1} \mathbf{H}^T \mathbf{S_n}^{-1} (\mathbf{z} - \boldsymbol{\epsilon}(\mathbf{x}_0)), \tag{4}$$

where $\mathbf{H}$ is the sensitivity matrix whose components are $H_{ij} = \partial \epsilon_i / \partial x_j$, and $\mathbf{S} = (\mathbf{H}^T \mathbf{S_n}^{-1} \mathbf{H} + \mathbf{S_x}^{-1})^{-1}$ is the a posteriori covariance matrix. Within this linearized framewok, the Hessian matrix associated to $l(\mathbf{x})$ is $\mathbf{H}_e = \mathbf{H}^T \mathbf{S_n}^{-1} \mathbf{H} + \mathbf{S_x}^{-1}$, whose first term is the Fisher or information matrix $\mathbf{A} = \mathbf{H}^T \mathbf{S_n}^{-1} \mathbf{H}$.

Figure 3a reports the time-history of the change of the curvature for a 10% variation of each of the three model parameters EI, ρA and k. These time-histories are, in practice, the columns of the sensitivity matrix each multiplied by the variation of the related parameter, and divided by h_G. Figure 3a shows that the parameters which play the most important role are EI and k, while ρA has a scarce influence. Identifiability is the actual possibility to determine a single set of optimal parameters $\hat{\mathbf{x}}$ such that the objective function is at a minimum. Some information about it is provided by $\mathbf{H}$, whose rank indicates the maximum number of identifiable parameters: in

our case, the rank of $\mathbf{H}$ is 3, independently of the number of time samples, which are as many as the rows of the sensitivity matrix.

More precise information on the choice of parameters and measurements is provided by the Fisher matrix, which must be invertible for the solution (4) to be calculated. The list of its eigenvalues can put the parameters, or more often, their linear combination, in order of importance. This is displayed by the shape of the eigenvectors, which enables to point out possible coupling between parameters. Observing the eigenvectors of the Fisher matrix, which are reported in Figure 3b, it can finally be concluded that the parameters EI and k are coupled, while ρA is an independent parameter with scarce influence on the response, in fact, it is associated with the smallest eigenvalue and the related eigenvector has only the first component different from zero. In such situation, it seems to be appropriate to obtain the solution of the inverse problem in two steps: first the optimal parameters EI and k are sought using the response to a known load, then the updated model is used to determine the amplitude P, the real unknown of the problem.

The Fisher matrix also provides information on the choice of measurements by means of its Fisher inflow, which is the value of the terms on the principal diagonal as a function of the number of measurements. In fact, on assuming that $\mathbf{S_n}$ is a diagonal matrix, that is the noise is uncorrelated, the terms on the principal diagonal can be written as: $A_{ii} = \sum_k (\sigma_k^4)^{-1} (\partial \epsilon_k / \partial x_i)^2$. Since the summation occurs over the time instants, in the limit of the time instant between two samples tending to zero, it is obtained $A_{ij} = (1/T) \int_0^T (\sigma^4)^{-1} (\partial \epsilon / \partial x_i)^2 dt$, where T is the duration of the phenomenon. The terms on the principal diagonal of the Fisher matrix provide then an approximation of this integral, and tend to stabilize when the sampling frequency is sufficient, indicating that further samples do not provide further information. This is shown in Figure 4 a and b, where also the trace of $\mathbf{A}$ is reported, showing that a number of 40 measurements will provide a stable estimate of the covariance matrix, for our purposes, with a variation smaller than 5% for an increase of the number of measurements.

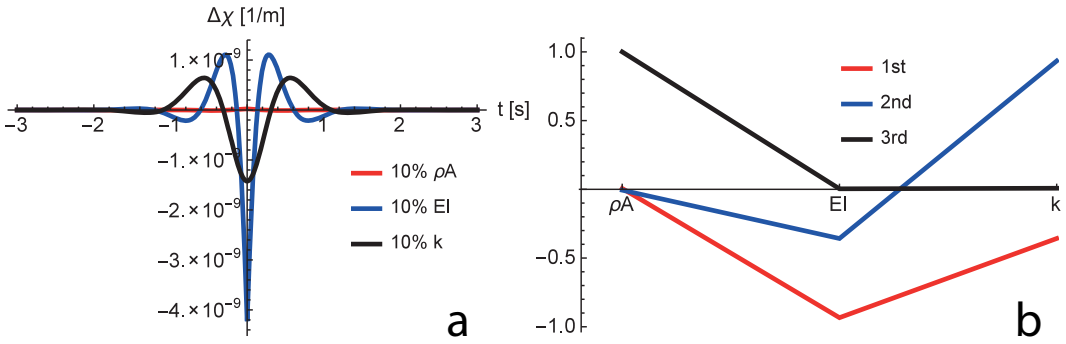

Figure 3: Time-histories of the change of curvature for a 10% variation of mechanical parameters (a) and eigenvalues of the Fisher matrix (b).

As proposed, we proceed to the identification of EI and k using 40 samples of a pseudo-experimental time-history generated by a known load. In the absence of noise and starting from initial parameters with a 30% error, we obtain convergence to the exact values within five iterative applications of Equation 4, according to the Newton method. The objective function is smooth and has a unique minimum, as it is shown in Figure 5. Using the identified parameters, if we proceed to the identification of the load, we obtain the exact value with a single application of Equation (4), in fact, since the dependence of the response on P is linear, Equation (4)

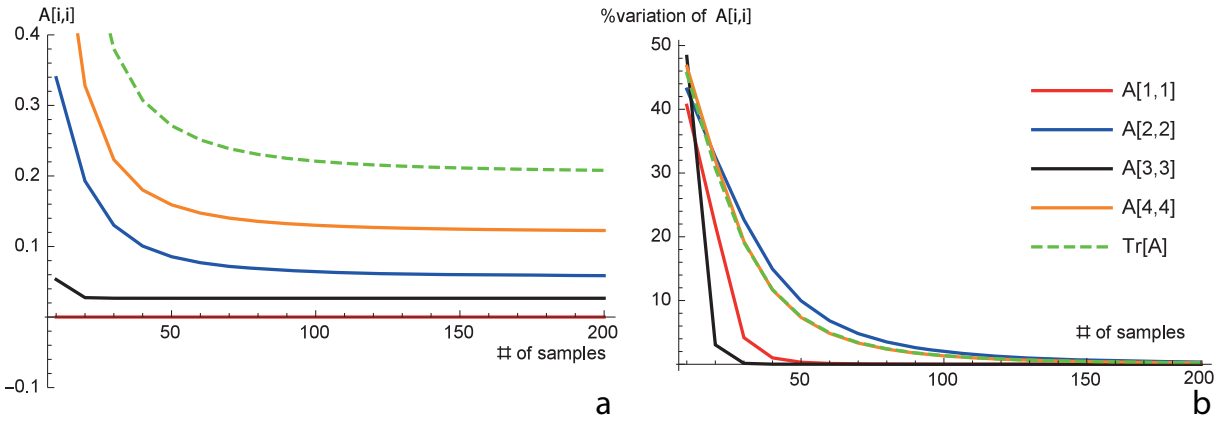

Figure 4: Fisher inflow and trace of the Fisher matrix (a), and % variation of their values (b) as a function of the number of samples.

does not constitute an approximation when the unknown parameter is P. It is instead an exact relationship, which does not requires iterations.

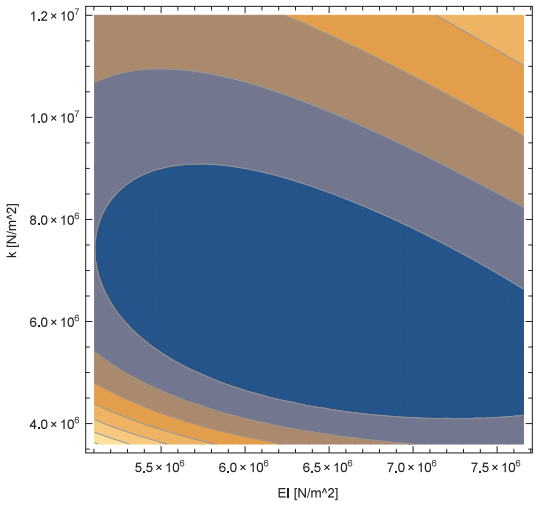

Figure 5: Contourplot of the objective function for pseudo-experimental data in the absence of error.

4 EXPERIMENTAL RESULTS

The procedure proposed is applied to experimental strains recorded at the foot of a rail on a stretch of line run by a locomotor moving at low constant speed. The weight of the locomotor is known and equal to 154.22 kN, so that two time-histories are firstly used to identify the soil stiffness. The resulting objective function is reported in Figure 6a, showing a distinct minimum. Then, a total of 10 locomotor transits with different constant speeds in the range 5-25 km/h were investigated. The updated model was used to identify the loads considered, at this stage, as unknowns, and the resulting identified values are reported in Table 1. These loads are in good agreement with the expected ones, with a mean error of 3.82%. The dispersion of errors, varying from -10.3 to 3.6%, can be ascribed to the simple interpretative model and to the the fact that experimental measurements were performed on one rail only, disregarding possible unbalance of the load. Figure 6b shows the comparison between the experimental time-histories of strains and those obtained from the updated model and the identified loads.

transit	1	2	3	4	5
weight	154.68	144.29	138.28	155.35	154.44
error [%]	0.3	-6.4	-10.3	0.7	0.14
transit	6	7	8	9	10
weight	155.46	144.63	157.71	142.73	159.73
error [%]	0.8	-6.2	2.3	-7.5	3.6

Table 1: Identified weights [kN] in the different transits and related error.

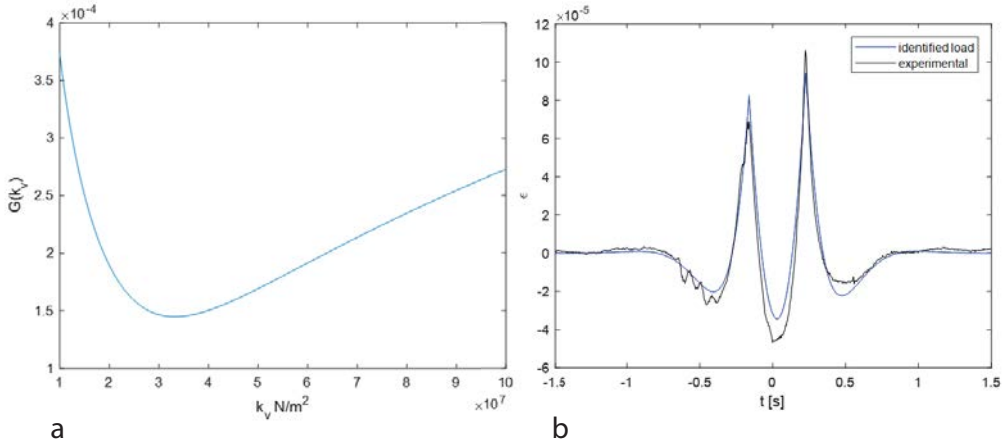

Figure 6: Objective function (a) and comparison between experimental and numerical time-histories of strains (b).

5 CONCLUSIONS

- We applied an approach for the identification of travelling loads of freight trains based on the minimization of the difference between the experimental time-history of strains at the base of the rail and their analytical counterpart. The model describing the response is a one-dimensional Euler-Bernoulli beam resting on a linearly elastic soil. The load is modelled as a Dirac delta load travelling at constant speed, whose amplitude is unknown and is the final goal of the identification procedure.

- As a result of a sensitivity analysis, among the model parameters, the soil and the beam stiffness resulted to be the most relevant, while damping was proved to be not significant for an appropriate description of the response in range of speeds away from the critical value. The procedure of identification is then performed in two steps, first updating the model using the response to a known load, then identifying the intensity of travelling loads.

- Experimental field tests were performed, in which the strains at the foot of the rail due to the transit of a locomotor at low speed were recorded. Making reference to the known loads, the model was updated by identifying the optimal value of the soil stiffness and, afterwards, used as interpretative model to identify the weight of the locomotor, now assumed as unknown. The loads were then identified with satisfactory accuracy, with a mean error smaller than 4%.

6 ACKNOWLEDGEMENTS

The authors would like to thank the company Ace System for collaboration in performing the experimental tests. This work was partially funded by PRIN 2015.

REFERENCES

[1] J.T. Kenney, Steady-state vibration of beam on elastic foundation for moving load, *Journal of Applied Mechanics*, **76**, 359-364, 1954.

[2] X. Lei, Analytic method for dynamic analysis of the track structure, *High Speed Railway Track Dynamics*, 37- 56, Springer, 2017.

[3] M. Shamalta, A.V. Metrikhine, Analytical study of the dynamic response of an embedded railway track to a moving load, *Archive of Applied Mechanics*, **73**, 131-146, 2003.

[4] H. Ouyang, Moving-load dynamic problems: A tutorial (with a brief overview), *Mechanical Systems and Signal Processing*, **25**, 20392060, 2011.

[5] D.M. Trujillo, H.R. Busby, *Practical Inverse Analysis in Engineering*, CRC press, 1997.

[6] H. Ronasi, H. Johansson, F. Larsson, A numerical framework for load identification and regularization with application to rolling disc problem, *Computers & Structures*, **89**, 38-47, 2010.

[7] T. Zhu, S. Xiao, G. Yang, M. Wang *Estimation of wheel/wail contact forces based on an inverse technique, 13th International Conference on Fracture*, Beijing, China, 2013.

[8] E. Meli, L. Pugi, Preliminary development, simulation and validation of a weigh in motion system for railway vehicles, *Meccanica*, **48**, 25412565, 2014.

[9] H.W. Sorenson, *Parameter Estimation: Principles and Problems*, Marcel Dekker inc., New York, 1980.

[10] D. Capecchi, F. Vestroni, Identification of finite element models in structural dynamics, *Engineering Structures*, **15**, 21-30, 1993.

[11] A. Pau, F. Vestroni, E. Duca, M. Platini, *Identification of freight train loads using time-histories of rail strains, 12th World Congress on Railway Research*, Tokyo, Japan, 2019.

EURODYN 2020
XI International Conference on Structural Dynamics
M. Papadrakakis, M. Fragiadakis, C. Papadimitriou (eds.)
Athens, Greece, 23–26 November 2020

DYNAMIC EFFECT OF TRAINS WITH ARTICULATED COACHES AND JACOBS BOGIES WITH INTEGER WHEELBASE RATIOS

Pedro Museros[1], Andreas Andersson[2], and Raid Karoumi[2]

[1]Universitat Politècnica de València
Camino de Vera s/n, 46022 València, Spain
e-mail: pmuseros@mes.upv.es

[2] Royal Institute of Technology
Brinellvägen 23, SE-100 44 Stockholm
e-mail: adde@kth.se; raidk@kth.se

Keywords: Railway bridge, high-speed train, bogie wheelbase, train spectrum.

Abstract. *This paper deals with the dynamic response of railway bridges traversed by articulated trains, specifically the interaction effect between the coach length D and bogie distance d_{BA}. Current design code EN 1991-2 stipulate that the ratio D/d_{BA} should not be close to an integer value, but no further guidance is given. By using train signatures and a so-called bogie factor, the combined effect is illustrated in a non-dimensional domain. The results are also presented by realistic examples which show that integer ratios of D/d_{BA} are not necessarily worse than non-integer ratios. This is further confirmed by a parametric study of simply supported beams and ranges of train parameters according to EN 1991-2 Annex E.*

1 INTRODUCTION

Excessive vibrations may occur in railway bridges if the load frequency coincides with the natural frequency of the bridge. In the design of railway bridges, especially on high-speed lines, the dynamic response is analysed using a set of universal trains, named as HSLM in EN 1991-2 [1]. These train load models were developed within ERRI D214.2/RP6 [2] and should also cover ranges for different real trains, as defined in EN 1991-2 Annex E. Excessive vibrations are likely to occur at resonance, where the load frequency depends on the axle spacings or any of its integer multiples.

This paper focus specifically on the articulated train (AT) with *jacobs bogies*, where the coach length D and bogie distance d_{BA} are the main parameters. In EN 1991-2 Annex E it is stipulated that D/d_{BA} should not be close to an integer value. No further guidance is given on how close to an integer value such ratio is allowed, or how to assess its effect. The main aim of this study is therefore to explore the interaction effect between D and d_{BA} in terms of the resulting dynamic response. This is done by a parametric study of simply supported bridges and a non-dimensional approach based on train signatures and a so-called bogie factor, further explained in this paper.

2 MOTIVATION OF THE RESEARCH

A typical example is presented first, in order to motivate the reasons for this investigation. Let a theoretical simply supported (S-S) railway bridge have first natural frequency $n_0 = 7.0\,\mathrm{Hz}$, which is a usual value for spans between some 12.5 and $30\,\mathrm{m}$. Consider also an AT (see Figure 1) with characteristic distances $D = 18\,\mathrm{m}$ (carriage length) and $d_{BA} = b = 3\,\mathrm{m}$ (bogie wheelbase) travelling over the bridge. For the moment, the presence of the power cars (1) in Figure 1 is ignored, and it is admitted that all passenger coaches of type (2) and (3) have the same distances D and b. These hypotheses allow one to focus on the possible resonant coupling caused by integer values of the D/b ratio.

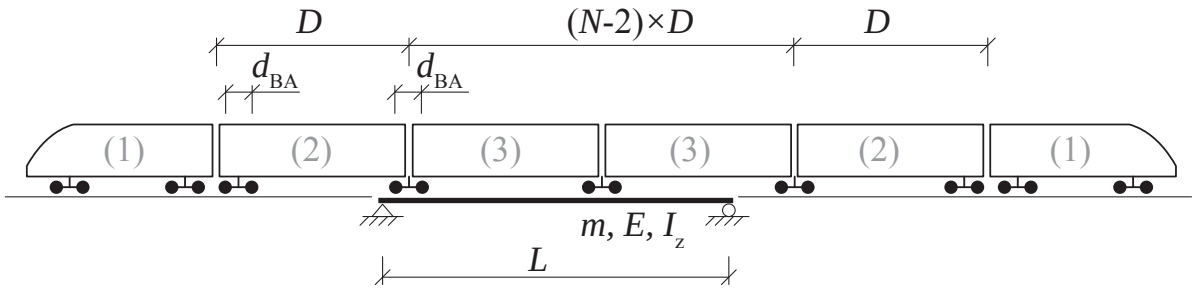

Figure 1: Articulated train passing over a S-S bridge.

Any mode of vibration of the bridge that is excited by the passing train will remain in *free vibration* once the train has left the bridge. The passage of each axle load generates such kind of free vibrations, that will accumulate with the free vibrations generated by the subsequent passing loads, in a way that may lead to (i) resonance in the case of in-phase addition, (ii) cancellation if the addition is in counter-phase, or (iii) addition to some intermediate degree in the rest of cases. If damping were absent, which is only possible from a theoretical point of view, resonance and cancellation phenomena would be ideally perfect for axle loads of equal

intensity adding in-phase or counter-phase, respectively. All these aspects were dealt with in depth in previous research works [3].

The relevance of an eventual integer value of D/b is apparent: in a two-axle bogie, if the vibrations of the second axle add in phase with those of the first axle, this means that the time interval b/V, where V is the speed of the train, is an integer multiple of the period T of the vibration mode of interest. For the fundamental mode, this entails

$$b/V = n/n_0 \qquad n = 1, 2, 3, \ldots \tag{1}$$

In equation (1) $n = 1$ is referred to as the *first bogie resonance*, while for $n = 2, 3, \ldots$ one speaks of *second resonance*, *third resonance*, etc. With the values presented above, one gets

$$V_{n=1} = \frac{b\, n_0}{1} = \frac{3 \cdot 7}{1} = 21\,\mathrm{m/s} = 75.6\,\mathrm{km/h} \tag{2}$$

It is apparent that for speeds equal to integer fractions of $75.6\,\mathrm{km/h}$, one will get the second, third, etc. resonances of the bogie. Because of damping, the amplitude of the resulting vibration from each of them will decrease as n increases. Moreover, speeds around $75.6\,\mathrm{km/h}$ are nowadays considered low speeds, and particular bridge vibration problems are not expected in regular operation of railway vehicles at such speeds.

In the sample case presented here, when the first resonance of the bogie takes place, then also a *sixth* resonance of the carriage takes place, because, in a way analogous to equation (2), one has, for characteristic distance $D = 18\,\mathrm{m}$:

$$V_{n=6} = \frac{D\, n_0}{6} = \frac{(6 \cdot 3) \cdot 7}{6} = 21\,\mathrm{m/s} = 75.6\,\mathrm{km/h} \tag{3}$$

Of course, if damping were high enough, such *sixth sub-harmonic* of the carriage resonance would have little effect, but it should also be born in mind that damping can be higher or lower depending on the bridge type and condition.

For free vibrations to accumulate, cancellation of the vibration mode (for each axle) must not take place [4], [3]. Therefore, the nondimensional speed K must be different from $1/(2i+1)$ if the bridge is S-S, of span equal to L. Integer i is referred to as the *order of the cancellation of the influence line*, since it yields the order of the corresponding zeros of the free vibration amplitude response (see figure 2 in reference [3]). Consequently, the condition to be verified to avoid cancellation is as follows:

$$K = \frac{V}{2n_0 L} \neq \frac{1}{2i+1} \quad i = 1, 2, \ldots \tag{4}$$

With the reference data employed above, cancellation would happen at $75.6\,\mathrm{km/h}$ for the spans listed in Table 1. So, one can select a span equal to $L = 15\,\mathrm{m}$ and be sure that is neatly far from cancellation, and indeed very close to a point of maximum free vibration. In such case, the addition of successive axle loads will lead to a *maximum resonance* phenomenon (see section 4 in reference [3]).

Figure 2 shows the response of the above described bridge under the circulation of a series of $2k = 20$ loads, arranged in $k = 10$ equidistant bogies with two loads $P = 170\,\mathrm{kN}$ in each bogie. The linear mass of the bridge is set to $m = 12\,\mathrm{t/m}$, which is a realistic value for a concrete, single-track, beam bridge of $15\,\mathrm{m}$ span, and damping ratio is $\zeta = 1.0\%$. Damping

i	1	2	3	4	5	6	7
$L(\mathrm{m})$	4.5	7.5	10.5	13.5	16.5	19.5	22.5

Table 1: Span lengths for i-th cancellation of the 1^{st} mode at $75.6\,\mathrm{km/h}$ in a S-S bridge with $n_0 = 7.0\,\mathrm{Hz}$.

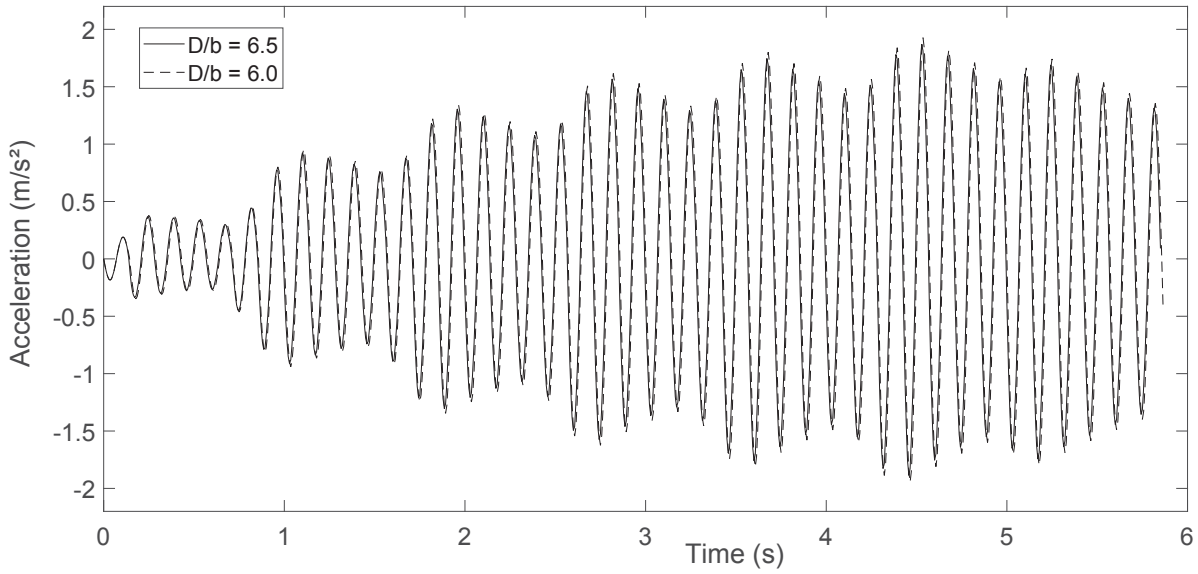

Figure 2: Time-history response of a S-S bridge under a sequence of 10 equidistant, two-axle bogies with $D = 18\,\mathrm{m}$, and $P = 170\,\mathrm{kN}$. $L = 15\,\mathrm{m}$, $n_0 = 7.0\,\mathrm{Hz}$, $m = 12\,\mathrm{t/m}$, $\zeta = 1.0\%$. $b = 3\,\mathrm{m}$ for the dashed line; $b = 2.769\,\mathrm{m}$ for the solid line.

should probably be somewhat higher for a bridge of such span, but the vibration effects will be better illustrated with the selected value.

Figure 2 shows a response that is clearly resonant, with six cycles between maximum peaks as expected from equation (3). Two time series are displayed: the dashed line corresponds to a slightly higher response, obtained with $b = 3\,\mathrm{m}$, so that $D/b = 6.0$; conversely, the solid line has been obtained with $b = 2.769\,\mathrm{m}$, which leads to $D/b = 6.5$. It should be noticed that in the latter case, the $D/b = 6.5$ ratio is *as far as possible* from being integer, but still the observed resonant response is almost identical in both cases. So the following question arises: From the point of view of bridge vibrations, is it reasonable to consider that ATs where $D/b = D/d_{BA}$ is close to integer are more critical than others? This question is dealt with in greater detail in the following sections.

3 NONDIMENSIONAL APPROACH BASED ON TRAIN SIGNATURE AND BOGIE FACTOR

3.1 Signature of a set of equidistant loads

Based on superposition of effects in linear regime, in reference [2] the following approach was presented for the computation of the acceleration level in a S-S bridge due to the passage of a train:

$$a_{max} = \Gamma_{max}(mL, \zeta, K) \cdot G(F_i, d_i, \lambda, \zeta) \tag{5}$$

where the term $G(F_i, d_i, \lambda, \zeta)$ is the *signature* or *train spectrum* for a series of loads F_i with spacing d_i measured from the first load ($d_1 = 0$). The wavelength $\lambda = VT$, where T is the period of the vibration mode, and $\Gamma_{max}(mL, \zeta, K)$ is the influence line for the fundamental mode of a S-S bridge. Because the influence line will vary between different types of structures, it is convenient to keep it as a separate factor, as in equation (5). In so doing, one can concentrate in the values of the signature; those values depend only on damping and the train type for each wavelength. Plots as a function of wavelength will then provide a quick view of the phenomena involved.

In reference [5], a new expression of the signature is presented for a group of k equidistant, unit loads:

$$\begin{aligned} G_E(k, \Lambda, \zeta) &= k \qquad \text{if } \zeta = 0 \text{ and } \Lambda = 1, 1/2, 1/3, ...\text{(resonance)} \\ G_E(k, \Lambda, \zeta) &= \sqrt{\frac{\sigma^{2(1-k)} f_k(\sigma, \Lambda)}{f_1(\sigma, \Lambda)}} \qquad \text{otherwise.} \end{aligned} \tag{6}$$

where

$$\begin{aligned} f_k(\sigma, \Lambda) &= (1 + \sigma^{2k} - 2\sigma^k \cos(2k\pi/\Lambda)) \\ \sigma &= e^{\zeta 2\pi/\Lambda} \geq 1 \\ \Lambda &= \lambda/D = VT/D \end{aligned}$$

and $f_1 = f_k(k = 1)$. Such expression can be computed very efficiently because it neither involves summations of out-of-phase loads, nor it involves taking the maximum among *subtrains* as prescribed in [2]. Conversely, it has the disadvantage that the power cars are not taken into account. The nondimensional wavelength Λ represents the fraction of D travelled in one period of the free vibration.

In order to get the complete signature for a series of carriages supported on bogies as it is usual in an AT, one has to multiply the signature given in equation (6) by the *bogie factor* or bogie spectrum. This factor is also introduced as a function of a nondimensional wavelength in reference [5], as explained next.

3.2 Bogie factor

The bogie factor is a multiplying function that can vary in the interval $[0, 2]$, and provides an exact, equivalent amplitude of the effect of two consecutive loads separated by distance $b = d_{BA}$. The equivalence is established in terms of the addition of the free vibrations created by each of the two loads, when they pass over a flexible structure at speed V:

$$\begin{aligned} f_B(\mu, \zeta) &= \sqrt{1 + e^{-\zeta 4\pi/\mu} + 2e^{-\zeta 2\pi/\mu} \cos(2\pi/\mu)} \\ \mu &= \lambda/b = VT/b \end{aligned} \tag{7}$$

In the same way that $\Lambda = 1/n_D = 1, 1/2, 1/3, ..$ implies resonance or sub-resonance or order n_D associated to distance D (carriage resonance), $\mu = 1/n_b = 1, 1/2, 1/3, ..$ implies resonance or sub-resonance of order n_b associated to distance b (bogie resonance). Also, when $\mu = 2, 2/3, 2/5, ..$ bogie cancellation occurs. Conversely, above $\mu = 2.0$, $f_B \to 2.0$ monotonically, in a way similar to the signature in equation (6), which tends to kF when $\Lambda \to \infty$ (F is the value of the constant axle loads different from unity).

In case of bogie resonance, integer ratios $D/b = l$ would lead to

$$\Lambda = \frac{VT}{D} = \frac{VT}{b} \cdot \frac{b}{D} = \frac{1}{n_b} \cdot \frac{1}{l} = \frac{1}{n_D} \tag{8}$$

As it is apparent, $n_D = n_b \times l$ is integer and (higher order) resonance of the carriage would also be induced. For this reason, the D/b integer ratios may initially be considered more aggressive, as explained in previous section.

3.3 Combined effect of signature and bogie factor

The signature or spectrum of a set of k two-axle bogies of constant loads F can be obtained exactly by multiplication of F times equations (6) and (7). Such signature will represent the vibration coupling of a series of carriages of an AT, where the power cars are neglected and all carriages are assumed to have constant length D. Therefore, the main coupling phenomenon between D and b can be analysed at once.

The signature can be suitably plot as a function of Λ and μ. In such approach it is convenient to realise that any constant ratio $\eta = D/b$, will lead to a inclined line in the $[\Lambda, \mu]$ plane, since

$$\mu = \frac{VT}{b} = \frac{VT}{D} \cdot \frac{D}{b} = \Lambda \cdot \eta \tag{9}$$

Therefore, in log-log axis the lines corresponding to constant η ratios will appear as inclined parallel lines, as shown in Figure 3. The upper limits in Figure 3 are set by considering that $n_0 = 7.0\,\mathrm{Hz}$, $V_{\text{max}} = 350\,\mathrm{km/h}$, $D_{\text{min}} = 18\,\mathrm{m}$ and $b_{\text{min}} = 2.5\,\mathrm{m}$, which are all usual values for high-speed articulated trains. Damping has been neglected, which leads to maximum values of the spectrum equal to 20, since the number of unit loads in the trainset is $2k = 20$.

In Figure 3 the three inclined lines correspond to $\eta = D/b$ equal to $5.5, 6.0$ and 6.5. It is seen that the critical point (where $\Lambda = 1/6$ and $\mu = 1$) reaches a maximum amplitude of 20 for $D/b = 6.0$, but the amplitudes for $D/b = 5.5$ and $D/b = 6.5$ are very similar. This is the theoretical explanation to the very small difference in the amplitude of vibrations levels displayed in Figure 2.

The peak response in Figure 2 can be also analysed for a wider range of speeds, as it is shown in Figure 4, where sub-resonances of the carriage are visible for $n_D = 2$ at $226.8\,\mathrm{km/h}$ to $n_D = 8$ at $56.7\,\mathrm{km/h}$, except for $n_D = 3$ that cancels exactly (indeed it cancels *twice*: $i = 2$ in equation 4, and also $\mu = 2$).

All predictions from Figure 3 are confirmed in Figure 4. The highest peak for the sixth sub-resonance corresponds to $D/b = 6$, while the other two curves give very similar response in this case, even if they are as far as possible from being integer. Besides, the peaks for the eighth, seventh and second sub-resonances are higher for $D/b = 6.5$, while the peaks for the fourth and third sub-resonances are higher for $D/b = 5.5$.

The conclusions of the studies presented in this section are generalised next for a wide ensemble of S-S bridges and articulated trains that cover the vast majority of cases of interest.

4 PARAMETRIC STUDIES

4.1 Hypotheses and methods

In order to confirm that integer values of D/b are not necessarily more aggressive than non-integers as regards the coupling of carriage-induced and bogie-induced vibrations, a comprehensive parametric study has been carried out with the following characteristics.

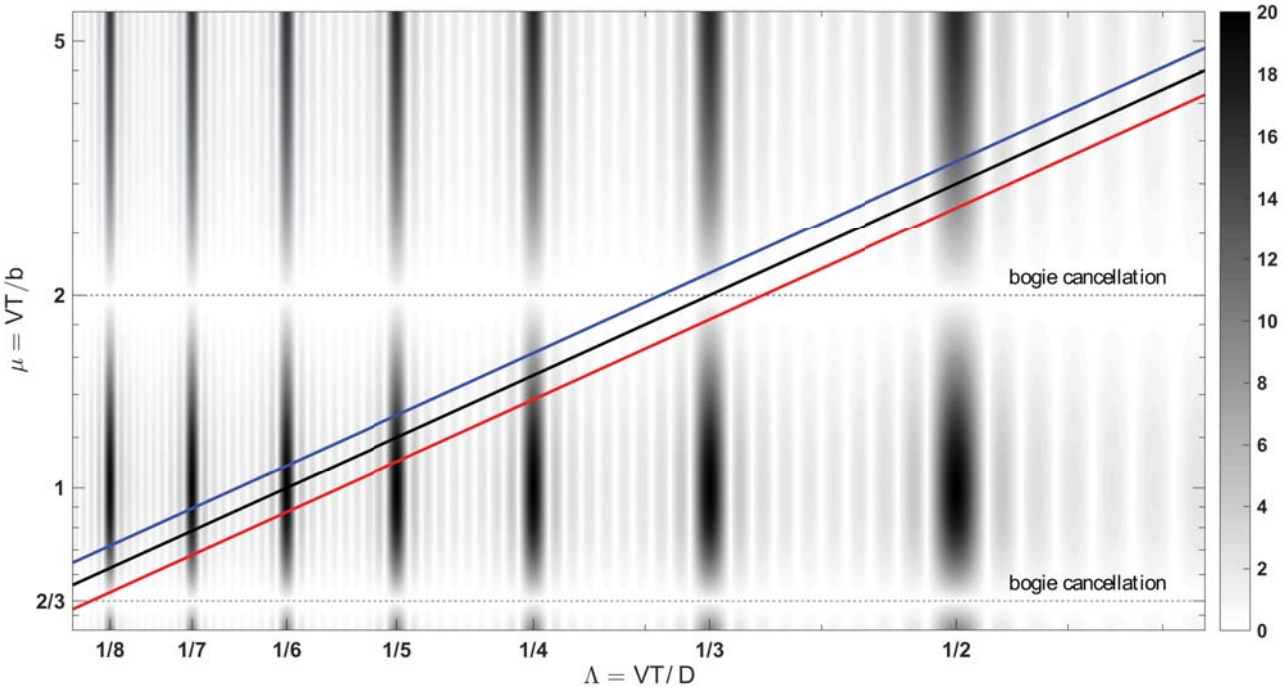

Figure 3: Signature of a sequence of $k = 10$ equidistant, two-axle bogies of unit loads (log-log axis). Red, black and blue lines correspond to $\eta = D/b$ equal to 5.5, 6.0 and 6.5, respectively.

Prestressed bridges of S-S type on rigid supports are analysed under sequences of $(10-1) = 9$ carriages supported on equidistant bogies. Therefore, $k = 10$ as in Figure 4 and each train has 20 constant, concentrated loads travelling at a constant speed V.

According to Table 2, the carriage length D is varied in a discrete manner from $18\,\mathrm{m}$ to $27\,\mathrm{m}$ in steps of $0.5\,\mathrm{m}$, in line with the limits in Annex E from EN1991-2 [1]. Providing that the bogie wheelbase b is limited to the interval $[2.5\,\mathrm{m}, 3.5\,\mathrm{m}]$ as stated also in Annex E from [1], the number of combinations of D and b that can produce integer ratios is limited to 51 different cases. Such cases are shown in Table 2, particularly in the two columns headed by symbol b; the integer $D/b = l$ value for each case is also shown in the corresponding row.

Also in Table 2, 51×2 bogie wheelbases are gathered where D/b is as far as possible from being integer. For instance, in the first row of the table, $D/b = l = 6$ for $D = 18\,\mathrm{m}$ corresponds to $b = 3\,\mathrm{m}$, while $b^- = 3.273\,\mathrm{m}$ corresponds to a smaller ratio $D/b = 6 - 0.5 = 5.5$. Analogously, $b^+ = 2.769\,\mathrm{m}$ corresponds to a larger ratio $D/b = 6 + 0.5 = 6.5$.

It can be seen in Table 2 that some of the values of b^- and b^+ lie outside the interval $[2.5\,\mathrm{m}, 3.5\,\mathrm{m}]$, but such interval is never exceeded by more than $9\,\%$, so the values in the table can be deemed acceptable for the purpose of this study.

Spans from $L = 5\,\mathrm{m}$ and $L = 30\,\mathrm{m}$ have been analysed under the action of such 51×3 trains, and the response under the trains with integer D/b values (column b) has been compared with the one due to the trains with non-integer D/b values (columns b^- and b^+). Damping values for the prestressed bridges have been selected according to [1]. Clearly, the possible carriage-bogie resonant coupling situation would take place for $n_D = n_b \times l$, as explained from equation (8) in section 3.2. In such case, the *resonance order for the carriage* (*length*) is a multiple of the *resonance order for the bogie* (*wheelbase*).

If the speeds involved were to be close to $200\,\mathrm{km/h}$ or higher, which is the usual range

$D/b = l$	D	b	b^-	b^+	$D/b = l$	D	b	b^-	b^+
6	18	3.000	3.273	2.769	7	23	3.286	3.538	3.067
7	18	2.571	2.769	2.400	8	23	2.875	3.067	2.706
–	–	–	–	–	9	23	2.556	2.706	2.421
6	18.5	3.083	3.364	2.846	7	23.5	3.357	3.615	3.133
7	18.5	2.643	2.846	2.467	8	23.5	2.938	3.133	2.765
–	–	–	–	–	9	23.5	2.611	2.765	2.474
6	19	3.167	3.455	2.923	7	24	3.429	3.692	3.200
7	19	2.714	2.923	2.533	8	24	3.000	3.200	2.824
–	–	–	–	–	9	24	2.667	2.824	2.526
6	19.5	3.250	3.545	3.000	7	24.5	3.500	3.769	3.267
7	19.5	2.786	3.000	2.600	8	24.5	3.063	3.267	2.882
–	–	–	–	–	9	24.5	2.722	2.882	2.579
6	20	3.333	3.636	3.077	8	25	3.125	3.333	2.941
7	20	2.857	3.077	2.667	9	25	2.778	2.941	2.632
8	20	2.500	2.667	2.353	10	25	2.500	2.632	2.381
6	20.5	3.417	3.727	3.154	8	25.5	3.188	3.400	3.000
7	20.5	2.929	3.154	2.733	9	25.5	2.833	3.000	2.684
8	20.5	2.563	2.733	2.412	10	25.5	2.550	2.684	2.429
6	21	3.500	3.818	3.231	8	26	3.250	3.467	3.059
7	21	3.000	3.231	2.800	9	26	2.889	3.059	2.737
8	21	2.625	2.800	2.471	10	26	2.600	2.737	2.476
7	21.5	3.071	3.308	2.867	8	26.5	3.313	3.533	3.118
8	21.5	2.688	2.867	2.529	9	26.5	2.944	3.118	2.789
–	–	–	–	–	10	26.5	2.650	2.789	2.524
7	22	3.143	3.385	2.933	8	27	3.375	3.600	3.176
8	22	2.750	2.933	2.588	9	27	3.000	3.176	2.842
–	–	–	–	–	10	27	2.700	2.842	2.571
7	22.5	3.214	3.462	3.000	–	–	–	–	–
8	22.5	2.813	3.000	2.647	–	–	–	–	–
9	22.5	2.500	2.647	2.368	–	–	–	–	–

Table 2: Definition of 51×3 ATs for the parametric study.

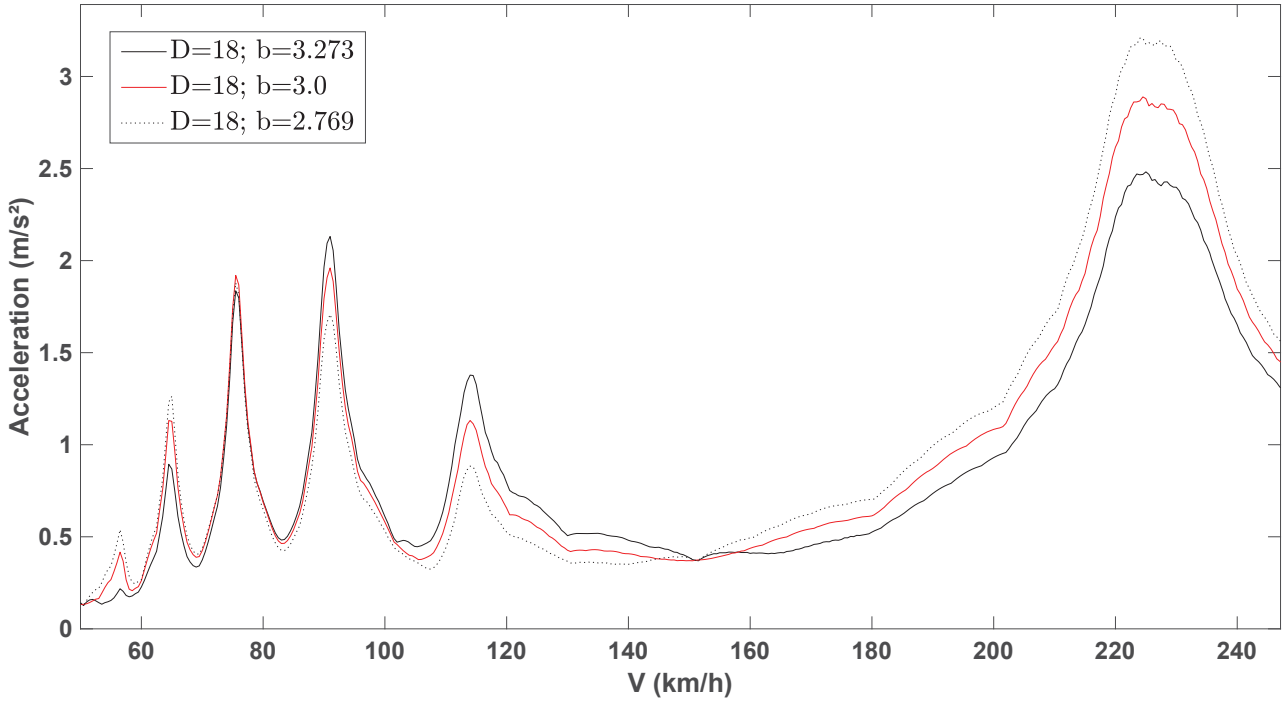

Figure 4: Acceleration envelope for a sequence of $k = 10$ equidistant, two-axle bogies of $F = 170\,\mathrm{kN}$. Values of b corresponding to $\eta = D/b$ equal to $5.5, 6.0$ and 6.5.

for dynamic analysis, $n_b \geq 2$ would correspond to very stiff elements and/or higher modes of frequencies above some $30\,\mathrm{Hz}$, for $b \in [2.5\,\mathrm{m}, 3.5\,\mathrm{m}]$. Moreover, $n_b \geq 3$ would correspond to frequencies above $45\,\mathrm{Hz}$, approximately. These are not the cases of main interest for the present study, which is focussed in the behaviour of principal structural elements. With such perspective, and given that for speeds lower than $200\,\mathrm{km/h}$ vibrations have traditionally not been considered a key concern in railway bridges [6], such cases will be left out of this study; accordingly, the resonance order of the bogie will be limited to $n_b = 1$. However, a closer nondimensional analysis such as the one presented in Figure 3 reveals that the conclusions for $n_b = 1$ and $n_b = 2$ are very similar.

Because resonance is a consequence of the addition of free vibrations, for a relevant resonant peak to occur the speeds of the trains must be carefully chosen in order to avoid cancellations of the influence line, as prescribed by equation 4. Therefore, the values of nondimensional speed $K = \hat{K}_i$ selected for the analysis can be taken as the average ones for every two consecutive cancellations, *i.e.*:

$$\hat{K}_i = \frac{V}{2n_0 L} = 0.5\left(\frac{1}{2i+1} + \frac{1}{2i+3}\right) \quad i = 1, 2, \ldots \tag{10}$$

Equation (10) yields nearly maximum free vibrations for each speed range between cancellations. In addition to those values $\hat{K}_i$, also one extra point has been selected above the first cancellation, named as $\hat{K}_1^m = 0.386$ in reference [3]. Only the fundamental mode of vibration has been considered, since the addition of free vibrations for every mode obeys the same physical rules that the addition for the fundamental mode. As for the integration of the equations of motion, Duhamel's integral has been used throughout.

From previous considerations, it is clear that each train with a $D/b = l$ integer ratio will

present maximum response when $n_D = n_b \times l = 1 \times D/b$. Consequently, the sub-resonances for $\Lambda = 1/n_D = b/D$ from Table 2 are the ones to be analysed. This objective has been accomplished by selecting 41 different, equally spaced speed values between $\Lambda = 1/(n_D + 0.5)$ and $\Lambda = 1/(n_D - 0.5)$, which captures the resonant peak with the required precision.

The frequency of the bridges has been taken from the lower bound of the frequency band in section 6.4.4 from [1]. This only entails that the nominal speed depends linearly on such frequency for the analyses, but it does not affects the spans involved.

The spans are selected to avoid resonance, by using the values $\hat{K}_i$ obtained previously. Because sub-harmonic n_D is the mid-point of the speed range for each analysis, then $V_{target} = n_0\, D/n_D$ is such mid-point. Given the definition of K, it is straightforward to obtain the associated span for each possible $\hat{K}_i$, which should lie within the range $L \in [5\,\mathrm{m}, 30\,\mathrm{m}]$, or is otherwise discarded. This procedure follows the concept of the maximum resonance described in section 4 of reference [3]:

$$L = \frac{D}{2\,\hat{K}_i\, n_D} \tag{11}$$

A total of 442 spans can be derived from the procedure explained above, which cover in a nearly continuous fashion the full range $L \in [5\,\mathrm{m}, 30\,\mathrm{m}]$, with very few minor exceptions that stem from the discretisation procedure adopted in the different ranges of parameters.

4.2 Results and discussion

Figures 5 and 6 summarise some of the main results of the parametric study. In each figure, the horizontal axes are merely counters of the number of different speeds (41) and number of different spans (442). The vertical axis shows the normalised maximum acceleration for every speed, obtained from time-histories of accelerations similar to the one in Figure 2.

The normalisation procedure is as follows. First, the analyses for wheelbase b corresponding to $D/b = l$ integer ratios are run and, for each span L_k, the maximum resonance acceleration is computed ($a^b_{max}(L_k)$, where $k = 1, 2, \ldots 442$). Then, the response envelope for span L_k is divided by $a^b_{max}(L_k)$ and represented in Figure 5; therefore, the maximum value of all curves for every span in Figure 5 is equal to unity. Since the response values at minimum and maximum speeds display variations among different spans that render the plot too jagged, the spans have been rearranged with a view to give an appearance as smooth as possible.

Second, the analyses for wheelbase b^- corresponding to $D/b = l - 1/2$ non-integer ratios are run and, for each span L_k, the maximum resonance acceleration is normalised against the value $a^b_{max}(L_k)$ previously computed. In such way, the maxima of the curves for every span in Figure 6 are not equal to unity, but only slightly smaller. This phenomenon was previously demonstrated to happen for a particular case in Figure 4 (sixth sub-resonance).

From Figures 5 and 6 the comparison of maximum response values for each span has been carried out. In so doing, the conclusion is that the largest observed difference is $4.2\,\%$, which is caused by the difference between b and b^-. A similar comparison has also been carried out among the results corresponding to b and b^+, which produces a largest difference of $3.2\,\%$.

In conclusion, the parametric study conducted here shows that the peak response of sequences of equidistant bogies where D is a multiple of b is not significantly larger than for sequences of bogies where the ratio D/b is as far as possible from being integer, when the first resonance case of the bogie n_b is considered.

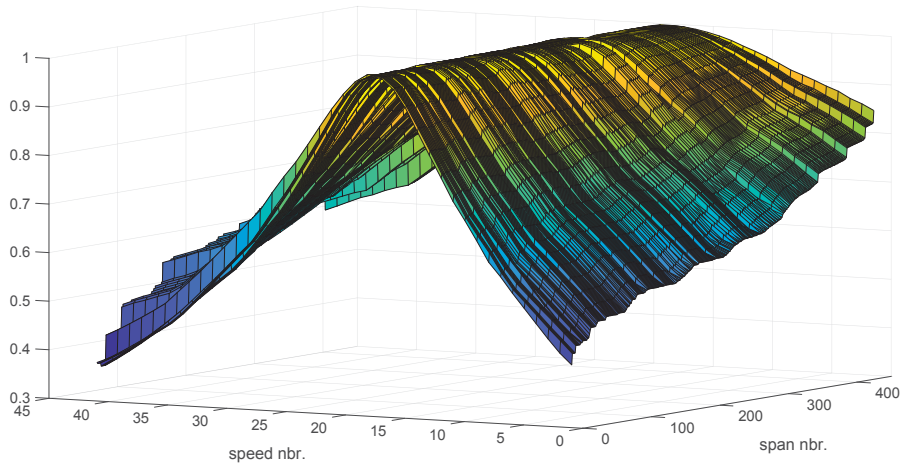

Figure 5: Envelope of maximum normalised accelerations for wheelbase b, corresponding to $D/b = l$ integer ratios.

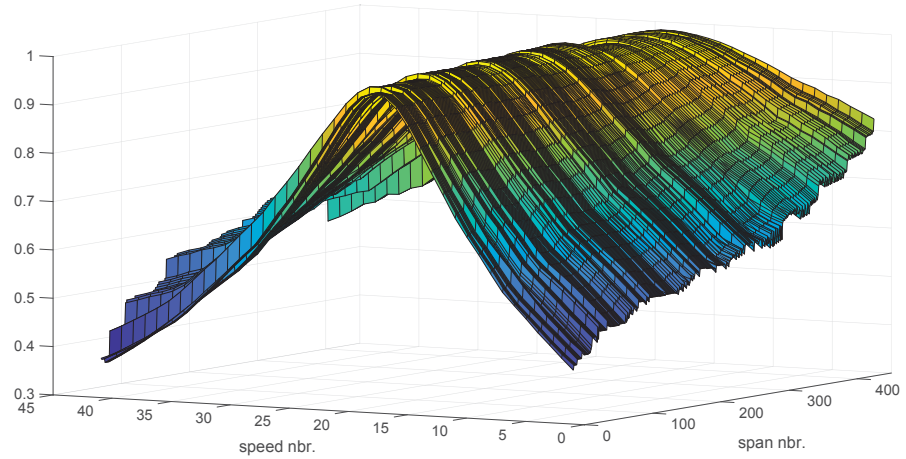

Figure 6: Envelope of maximum normalised accelerations for wheelbase b^-, corresponding to $D/b = l - 1/2$ non-integer ratios.

5 CONCLUSIONS

The coupled resonance effect of sequences of equidistant *Jacobs bogies* has been analysed in this article. The following conclusions can be drawn from the analyses carried out in this research work:

- The addition of the free vibrations created by series of $2k$ constant loads arranged in two-axle bogies that travel through a flexible structure can be carried out in an exact manner, by means of the multiplication of the signature (or spectrum) of a series of k equidistant loads times the signature of the bogie (*bogie factor*). Closed-form expressions for such signatures are summarised in this paper, and were either introduced or discussed in previous works [5].

- The multiplication of the signature of a series of k equidistant loads times the bogie factor yields the signature of an *articulated train* (power cars are neglected). Such signature can be represented in two-dimensional contour plots as a function of normalised wavelengths.

- The two-dimensional signature of the articulated train shows that the response of a train where the ratio between carriage length D and bogie wheelbase b is an integer value l is critical for sub-resonance order $1/l$, in case of first resonance of the bogie wheelbase.

- Both from a theoretical perspective as well as from a comprehensive parametric study, it has been shown that actual articulated trains (as described in Annex E from EN 1991-2) are not significantly more critical when D/b takes integer values than if such ratio is non-integer. This situation has been examined thoroughly for the first resonance of the bogie wheelbase.

- A closer analysis to the two-dimensional signature of the articulated train demonstrates that the preceding conclusions are also valid for the second resonance of the bogie wheelbase, which takes place at half the speed of the first one.

6 ACKNOWLEDGEMENTS

This research was partially developed during a stay performed by Pedro Museros at the *KTH Royal Institute of Technology*, within the Division of Structural Engineering and Bridges (Stockholm, Sweden). The financial support of the *Generalitat Valenciana*, through the program BEST2019 for research stays (*Subvenciones para estancias de personal investigador doctor en centros de investigación radicados fuera de la Comunitat Valenciana*), as well as the permission obtained from the *Universitat Politècnica de València* to carry out such stay, are gratefully acknowledged.

REFERENCES

[1] European Committee for Standardisation (CEN). *EN1991-2. Eurocode 1: Actions on structures. Part 2: General Actions – Traffic Loads on Bridges.* September 2003.

[2] European Rail Research Institute (D-214 Committee, ERRI D-214), *Rail bridges for speeds $>$ 200 km/h. Calculations for bridges with simply supported beams during the passage of a train (RP6)*, Technical Report, 1999.

[3] P. Museros, E. Moliner, L. Martínez-Rodrigo, Free vibrations of simply-supported beam bridges under moving loads: Maximum resonance, cancellation and resonant vertical acceleration, *Journal of Sound and Vibration*, **332**, 326–346, 2013.

[4] P. Museros, E. Moliner, Comments on Vibration of simply supported beams under a single moving load: A detailed study of cancellation phenomenon by C.P. Sudheesh Kumar, C. Sujatha, K. Shankar [Int.J.Mech.Sci.99(2015) 4047,doi:10.1016/j.ijmecsci.2015.05.001], *International Journal of Mechanical Sciences*, **128-129**, 709–713, 2017.

[5] P. Museros, A. Andersson, V. Martí, R. Karoumi, Dynamic behaviour of bridges under critical articulated trains: Signature and bogie factor applied to the review of some regulations included in EN 1991-2, *Journal of Rail and Rapit Transit*, (submitted for publication), 2020.

[6] European Rail Research Institute (D-214 Committee, ERRI D-214), *Rail bridges for speeds $>$ 200 km/h. Final report (RP9)*, Technical Report, 1999.

EURODYN 2020
XI International Conference on Structural Dynamics
M. Papadrakakis, M. Fragiadakis, C. Papadimitriou (eds.)
Athens, Greece, 23–26 November 2020

ANALYSIS OF VIBRATIONS INDUCED BY PROXIMATE MASSES TRAVERSING A BEAM SUPPORTED BY A FINITE DEPTH FOUNDATION WITH PARTIAL SHEAR RESISTANCE

Zuzana Dimitrovová[1,2]

[1] Department of Civil Engineering, NOVA School of Science and Technology, NOVA University of Lisbon
2829-516 Caparica, Portugal
e-mail: zdim@fct.unl.pt

[2] IDMEC, Instituto Superior Técnico, University of Lisbon, Lisbon, Portugal
1049-001 Lisbon, Portugal

Keywords: Moving masses, foundation with partial shear resistance, unsteady solution, semi-analytical methods, dynamic amplification due to proximity

Abstract. *In this paper, analysis of vibrations induced by proximate moving masses traversing a beam supported by a finite-depth foundation with partial shear resistance is presented. This model is simple enough to be handled by semi-analytical approaches and has a counterpart in modal expansion, which is suitable for finite beams [1]. The model can acceptably approximate vibrations recorded experimentally as shown in [2] and provides results sufficiently close to the ones obtained on more sophisticated models [3].*

The semi-analytical analysis is based on developments related to massless foundation presented in [4-7]. The method is extended, and additional aspect of dynamic amplification due to the proximity of moving masses are included. Final solution is presented in convenient form where most terms are analytical, and thus can be easily evaluated. This form also clearly identifies each part contribution. Main part of the solution is harmonic, composed from steady and unsteady parts of the solution. The unsteady part needs identification of induced frequencies. These frequencies are also important indicators of the onset of instability of the moving masses. Generally insignificant transient part of the solution has to be obtained numerically.

The possibility of analysing same situation on finite beams is very important for results validation. In addition, because it is easy to determine vibration modes for beams with abrupt change in foundation stiffness, this additional feature can also be analysed.

The main new contribution of this paper is detailed analysis of dynamic amplification effects due to masses proximity and conclusion that, as far as the instability is concerned, its onset is not influenced by increasing number of masses.

1 INTRODUCTION

In recent years, due to increased computational power, there is a tendency to overlook analytical and semi-analytical solutions, despite their inherent and undoubtable advantages. Nevertheless, at the same time, this computational facility also amplified possibility of symbolic and high-precision calculation with adaptable number of digits precision. This way, after numerical identification of exact values of some key parameters, final results can be presented as closed-form formulas, evaluable in places of interest without the full-time history, and without the necessity of testing discretization parameters ensuring the results convergence.

The aim of this contribution is to fill the gap in available semi-analytical solutions related to wave propagation induced by moving loads, with practical applications of high-speed rails. Many works over the years were directed to moving force problems with a beam as a guiding structure, placed on simplified foundation models. However, when there is no inertia in the moving system, then there is a lack of dynamic interaction and important issues like instability of the moving object are completely hidden. Either inertia is considered in the supporting structure or not, in case of longitudinally homogeneous structure the solution related to moving force with constant velocity rapidly achieves its steady-state form. In case of linearity, superposition is possible.

When inertia is added to the moving object, the problem becomes inherently non-linear and therefore the question of proximate moving objects is relevant and important from a practical point of view. There are several published works on similar subjects, but the question of proximity is rarely considered.

In [7], some preliminary results related to the effect of proximity of two moving masses travelling over an infinite beam supported by a two-parameter visco-elastic foundation are presented. It was concluded that is it possible to define two limiting distances between the masses, identifying an interval for which full solution is strictly necessary. For higher distances, i.e. when masses are sufficiently apart, the error introduced by results superposition is negligible; while when masses are very close to each other, it would be better to replace the two masses by one single doubled mass. It was also concluded that these limiting distances can be determined from analysis of induced frequencies and the corresponding amplitudes. In addition, it was shown that the instability region is not affected in an undamped case and the onset of instability occurs exactly at the critical velocity, as for one moving mass.

In [2] it was proven that the classical critical velocity related to moving force on an infinite beam is not realistic. It was also shown that quite satisfactory foundation model can be obtained by considering finite depth foundation with partial shear resistance. Then the critical velocity is determined as a function of the mass ratio defined as square root of the ratio of the beam mass over the dynamically activated foundation mass. Such simplified model gives quite a good approximation of the full more sophisticated models as shown in [3].

It is therefore interesting to see how the preliminary conclusions from [7] will be affected by more realistic foundation model. In Section 2 the model under consideration is described. Some indications about the way how the semi-analytical solution is obtained are given in Section 3. Numerical results are presented in Section 4 and the paper is concluded in Section 5.

2 MODEL SPECIFICATIONS

In this paper it is assumed that a homogeneous beam is placed either on massless two-parameter visco-elastic foundation or on a foundation with finite depth and partial shear resistance under plan strain condition. The beam is subjected to two moving masses, acted on by constant force with harmonic component each. Both masses are moving at a constant velocity and the contact between the beam and each mass is rigid. The influence of the distance

between these masses is subject of analysis. The model is depicted in Figure 1. Part a) is showing the massless foundation and part b) the foundation with finite depth.

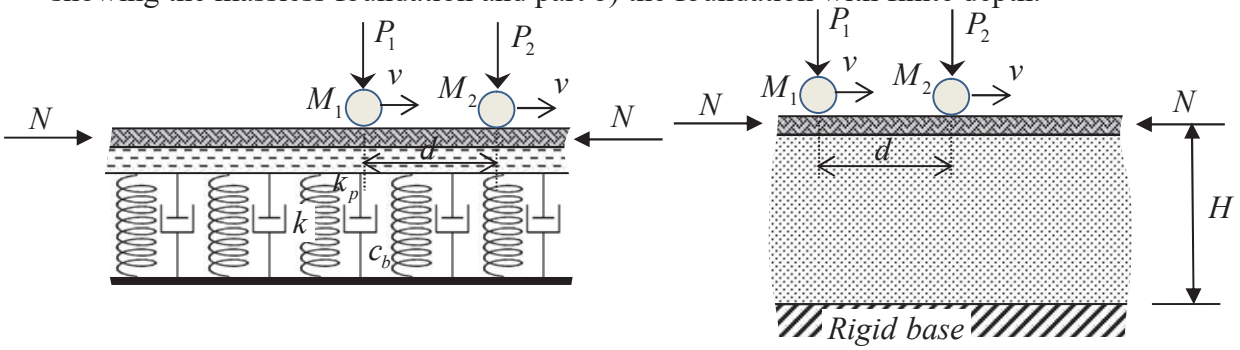

Figure 1: The model under consideration with supporting medium as: a) massless two parameter visco-elastic foundation; b) finite-depth foundation with partial shear resistance under plane strain condition.

It is further assumed that at zero time the beam is at rest and all deflections are measured from static position of the involved parts, excluding from further analysis beam and foundation weight. As the problem has applications in railways, the moving force acting on the point mass may not be coincident with the mass weight. The beam will be treated according to the Euler-Bernoulli theory. Foundation model, as described in [1-3], corresponds to a foundation strip of a finite width b and a finite depth H under plane strain condition and with neglected horizontal displacements, however, the shear resistance is included in its simplified form by the part of the shear stress coming from vertical displacements. This means that in finite element models, the foundation can be modelled by plane strain continuum without horizontal displacements.

3 GOVERNING EQUATIONS AND THE SOLUTION METHOD

The solution method follows the previous publications by this author. The governing equation for determination of the beam deflection field $w(x,t)$ reads:

$$EIw_{,xxxx}(x,t)+Nw_{,xx}(x,t)+mw_{,tt}(x,t)+c_b w_{,t}(x,t)+p(x,t)=F(x,t) \tag{1}$$

where EI, m, and N stand for the bending stiffness and mass per unit length of the beam, and a normal force acting on the beam normal axis. c_b is the coefficient of viscous damping, $p(x,t)$ is the foundation pressure and $F(x,t)$ is the loading term. x is spatial coordinate and t is the time. Derivatives are designated by the respective variable in subscript position, preceded by a comma. The foundation pressure in case of two parameter foundation is given by

$$p(x,t)=kw(x,t)-k_p w_{,xx}(x,t) \tag{2}$$

where k and k_p are Winkler's and Pasternak's moduli of the foundation. In case of foundation of finite depth, dynamic equilibrium in the vertical direction of the foundation has to be solved to determine the foundation pressure. In such a case

$$(\lambda+2\mu)u_{z,zz}(x,z,t)+\mu u_{z,xx}(x,z,t)=\rho u_{z,tt}(x,z,t) \tag{3}$$

where $u_z(x,z,t)$ is the vertical displacement field in the foundation and z is the vertical downward oriented spatial coordinate. Further:

$$\lambda=\lambda_0(1+c_f\bullet_{,t}),\ \mu=\mu_0(1+c_f\bullet_{,t}) \tag{4}$$

where c_f is the coefficient of viscous damping of the foundation and λ_0, μ_0 are basic values of Lame's constants. After determination of the displacement field, using also the boundary condition that states zero displacement at the bottom of the foundation depth and the interface condition establishing that the beam deflection is equal to the soil deflection on the top, foundation pressure is calculated from basic equation of elasticity.

The loading term is in both cases reads:

$$\begin{aligned} F(x,t) &= \left(P_{1c} + P_{1a}\sin\left(\omega_{f1}t + \varphi_{f1}\right) - M_1 w_{01,tt}(t)\right)\delta(x - x_1) \\ &+ \left(P_{2c} + P_{2a}\sin\left(\omega_{f2}t + \varphi_{f2}\right) - M_2 w_{02,tt}(t)\right)\delta(x - x_2) \end{aligned} \tag{5}$$

where, according to Figure 1, M_1 and M_2 are the rear and front mases, respectively, and

$$P_1 = P_{1c} + P_{1a}\sin\left(\omega_{f1}t + \varphi_{f1}\right),\ P_2 = P_{2c} + P_{2a}\sin\left(\omega_{f2}t + \varphi_{f2}\right) \tag{6}$$

P_{1c}, P_{2c} designate the constant forces; P_{1a}, P_{2a} are the amplitudes of the harmonic components, ω_{f1}, ω_{f2} are forced frequencies and φ_{f1}, φ_{f2} are phases of the harmonic terms. δ is the Dirac delta function, marking location of the load at positions x_1 and x_2. As rigid contact is assumed, then

$$w_{01}(t) = w(x_1,t) = w(vt,t),\ w_{02}(t) = w(x_2,t) = w(d + vt,t) \tag{7}$$

For proper problem statement, initial conditions must also be stated. It is assumed for the beam that

$$w(x,t)\big|_{t=0} = 0,\ w_{,t}(x,t)\big|_{t=0} = 0 \quad \forall x \tag{8}$$

and also, for the foundation that at zero time there are no initial displacements or velocities in the full domain. Boundary conditions are defined as

$$w(x,t) = 0,\ w_{,x}(x,t) \quad \forall t, x \to \pm\infty \tag{9}$$

It will be important to validate the final solution with solution on finite beams. In such a case, the boundary conditions must be altered. The advantage of the foundation model with finite depth specified above is that it can be conveniently represented on finite beams by separation in vibration modes, as shown in [1]. This is particularly advantageous, because in moving inertial object problems, where the supporting structure is composed of a beam on a foundation, there is an intimate connection between finite and infinite beams. Therefore, results obtained on finite beams are very good approximation of the infinite scenario, as already demonstrated in [4-7]. For finite beams it is necessary to start actuation of the load further from the initial support, to eliminate its influence. This also means that the most convenient supports can be used. These are undoubtably simple supports due to analytical version of the vibration modes described by numerically stable sine function without involvement of hyperbolic ones. Then the boundary conditions are

$$w(x,t)\big|_{x=0} = 0,\ w_{,xx}(x,t)\big|_{x=0} = 0,\ w(x,t)\big|_{x=L} = 0,\ w_{,xx}(x,t)\big|_{x=L} = 0 \quad \forall t \tag{10}$$

where L is the beam length.

Basic steps to be followed to obtain for solution on finite beams are presented in [1, 7]. In [7] construction of time dependent matrices is given. In [1] is it explained and proven how to determine vibration modes and how to define the orthogonality condition for the case of foundation with finite depth. The loading term is the same as for the massless foundation.

Disadvantage of the solution on finite beams is that quite a high number of modes must be used for good approximation of the results, which is particularly aggravated in the case of finite-depth foundation. Due to the moving inertial terms, equations in modal space are coupled, which makes the numerical solution of the modal coordinate computationally demanding. Nevertheless, it is possible to reorganize the terms in governing time-dependent matrices in a way that the computational effort is significantly reduced. The advantage of solution on finite beams is that it inherently includes all parts of the solution from the very beginning, therefore vibration patterns are not reduced directly to the steady-state solution as would result from the double Fourier transform. This way it forms convenient form for validation of infinite beams, where vibration patterns are considered also from the very start.

Solution on finite beams is conveniently rescaled to dimensionless parameters, which have same base for both types of foundations due to the possibility of introduction of an equivalent Winkler constant for the finite-depth foundation

$$k=\frac{\left(\lambda_0+2\mu_0\right)b}{H},\ \chi=\sqrt[4]{\frac{k}{4EI}},\ w_{st}=\frac{P\chi}{2k},\ v_{cr}=\sqrt[4]{\frac{4kEI}{m^2}}=\frac{1}{\chi}\sqrt{\frac{k}{m}} \tag{11}$$

Further in Eq. (11): χ is the inverse of the characteristic length, w_{st} is the maximum static displacement exhibited by the beam under constant still force P when the beam is supported by Winkler foundation characterized by modulus k. v_{cr} is the critical velocity related to the same case, but with the force moving by constant velocity. These values can be used to define dimensionless velocity α, time τ, spatial coordinate ξ and displacement, respectively

$$\alpha=\frac{v}{v_{cr}},\ \tau=\chi v_{cr}t=t\sqrt{\frac{k}{m}},\ \xi=\chi x,\ \widehat{w}=\frac{w}{w_{st}} \tag{12}$$

It is useful to remark that α=1 does not necessarily mean critical velocity of the problem, because even for massless foundation, the true critical velocity of the problem depends on the effect of the normal force and Pasternak's modulus, and in the case of foundation with finite depth, the critical velocity depends also on the mass ratio R

$$R=\sqrt{\frac{\rho bH}{m}} \tag{13}$$

where ρ is the soil density.

Basic steps for solution on infinite beams follow [1,4-6]. It is convenient to introduce the moving coordinate, and then in Eq. (12), instead of fixed coordinate x, r=x-vt is used. Final solution is presented as a sum of the steady-state solution, the unsteady harmonic solution and the transient vibration. As in previous works, the transient part can be mostly disregarded and affects the solution in initial times to force the full solution to match the initial conditions.

Main equation that determines the induced frequencies necessary for the unsteady part is

$$\left(\pi-2\eta_{M_1}q^2K\left(0,q\right)\right)\left(\pi-2\eta_{M_2}q^2K\left(0,q\right)\right)-4\eta_{M_1}\eta_{M_2}q^4K\left(\widehat{d},q\right)K\left(-\widehat{d},q\right)=0 \tag{14}$$

where q is the unknown complex induced frequency and $\widehat{d}=d\chi$ is the dimensionless distance between the masses. Further in Eq. (14):

$$K\left(\xi,q\right)=\int_{-\infty}^{\infty}\frac{\mathrm{e}^{\mathrm{i}\xi p}\mathrm{d}p}{D\left(p,q\right)},\ \eta_{M_1}=\frac{M_1\chi}{m},\ \eta_{M_2}=\frac{M_2\chi}{m} \tag{15}$$

Polynomial expression from Eq. (15) is given by

$$D(p,q) = p^4 - 4p^2\left(\eta_N - \eta_S + \alpha^2\right) - 4q^2 + 8\alpha pq + 8\mathrm{i}\,\eta_b\left(q - \alpha p\right) + 4 \tag{16}$$

for massless foundation. For foundation with finite depth the formulation is the same, only the effect of Pasternak modulus is removed, and the last number 4 is replaced by

$$4\eta_d \bar{C}_f / \tan\left(\bar{C}_f / \eta_d\right) \tag{17}$$

Formulations for other parameters can be consulted in previous author's works.

4 EXAMPLES

In this section, vibrations induced by two masses of equal value acted on by constant forces of equal value and without harmonic component are analysed. At first, a case with massless foundation is shown. As an example, the case with input data given in [4], where it is designated as Case 1, is used. In Figure 2 deflections of the contact point are plotted with respect to the dimensionless time. It is assumed that the masses are distanced by $\widehat{d} = 2\chi$.

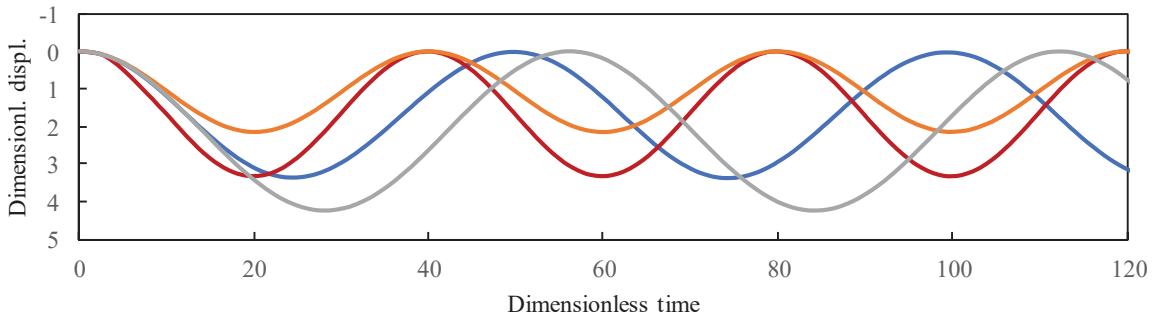

Figure 2: Deflections of the contact point of the rear mass with respect to dimensionless time for massless foundation (orange: one moving mass, grey: solution for doubled force and mass, red: approximate solution obtained by superposition, blue: correct solution).

The results in Figure 2 clearly show that, in case of proximate masses, superposition cannot be used. It is seen that the red line, which corresponds to the results superposition, is quite deviated from the blue one. Moreover, it exhibits the same frequency as one single mass. Full solution represented by the blue line is getting closer to the grey one obtained for the doubled mass and force with decreasing distance between the masses. It is important to remark that for the sake of comparison same static displacement as of one single force is used to scale the grey line results, because it was also used for the other results.

Next case is related to foundation with finite depth, mass ratio R=2 is selected. Results presented were obtained on finite beams. For the sake of simplicity, the number of foundation modes was reduced to one. For the correct solution more modes should be used, nevertheless, the general tendencies are the same. At first, foundation with no shear resistance is examined. This means that the foundation acts as a set of closely located columns with no mutual interaction. This is similar to Winkler's foundation, but here, mass inertia of the foundation is activated in the vertical direction. In Figures 3-5 deflection of the contact point is plotted for both masses, orange curve is for the front mass and the blue one for the rear mass. Effect of distance between mases is analyzed. In the first case, shown in Figure 3, the distance is very low. Both deflections are very similar and with almost steady amplitude. In Figure 4, deflections look like there were out of phase and thus the amplitude is also almost steady. Nevertheless, when the distance between the masses is between these two values, like in Figure 5, it is

seen that the dynamic interaction is affecting the amplitudes; firstly the rear mass is dominant, then the front mass is dominant and then they switch their roles again. Such dynamic interaction is very strong and can be deduced from the values of the induced frequencies.

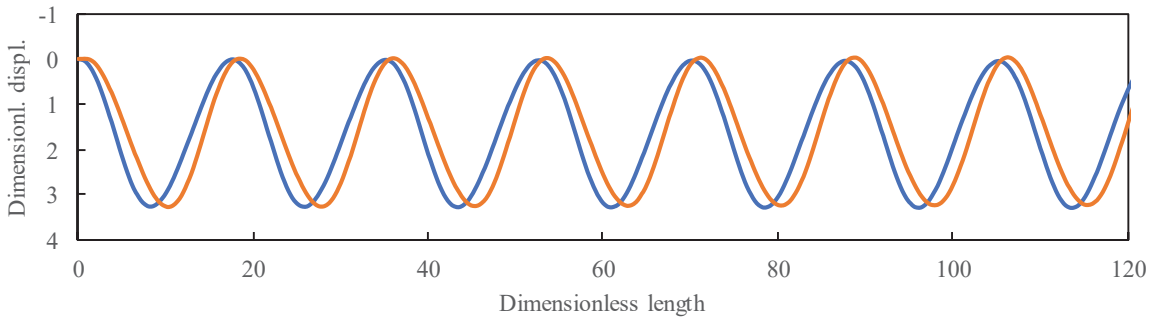

Figure 3: Deflections of the contact points of two masses distanced by $\hat{d} = 2\chi$ with respect to the dimensionless length (orange: front mass, blue: rear mass).

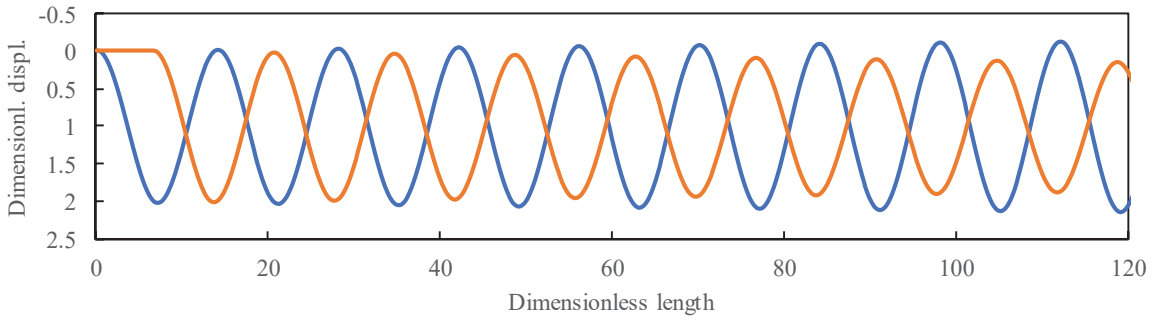

Figure 4: Deflections of the contact points of two masses distanced by $\hat{d} = 15\chi$ with respect to the dimensionless length (orange: front mass, blue: rear mass).

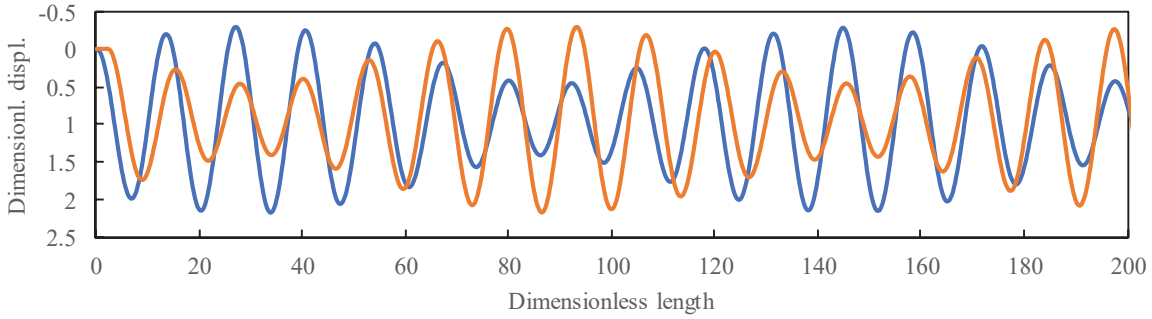

Figure 5: Deflections of the contact points of two masses distanced by $\hat{d} = 5\chi$ with respect to the dimensionless length (orange: front mass, blue: rear mass).

Finally, the influence of the shear resistance of the foundation on the dynamic interaction described above is analyzed. By increasing the shear resistance, it is seen that the dynamic interaction is reduced and the effect on the amplitudes is not so pronounced. This is shown in Figure 5 where three cases are plotted at the same time. They are for ϑ_s=0; 0.2 and 0.4, where

ϑ_s is defined as the ratio of the velocity of propagation of the shear waves in the foundation over the critical velocity. The larger ϑ_s the more moderate influence on the amplitudes.

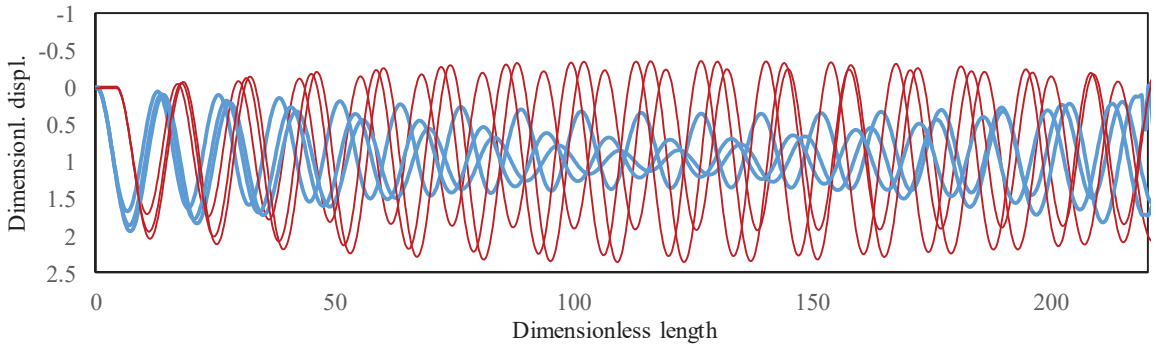

Figure 6: Deflections of the contact points of two masses distanced by $\widehat{d} = 10\chi$ with respect to the dimensionless length (red: front mass, blue: rear mass); different cases are for $\vartheta_s = 0; 0.2; 0.4$.

Together with the analysis of induced frequencies, the onset on instability and its relation the critical velocity was examined. As expected, the instability can take place only in the subcritical range, nevertheless, the critical velocity must be considered in the form as proven in [1-3].

5 CONCLUSIONS

In this paper it is shown how proximity of moving masses affects the beam deflection shape and what differences can be observed in vibration patterns when solution on massless two-parameter visco-elastic foundation and the one on finite-depth foundation with partial shear resistance are compared. Besides the confirmation of strong non-linearity of the problem itself which is demonstrated by impossibility of results superposition of proximate masses, it is shown that in the case of foundation with finite depth, additional frequency is controlling the vibration amplitudes. This effect can be reduced by increasing the shear resistance of the foundation.

Quite obvious conclusion was confirmed, namely, when masses are sufficiently apart, the results superposition is generally acceptable, but when masses are very close, it would be better to replace them by one load with doubled mass and force. The correct solution involving directly both masses is necessary only when masses are at an intermediate distance. In addition, it was shown that the instability region is not affected and in an undamped case, the onset of instability occurs exactly at the critical velocity, as for one moving mass.

The paper demonstrates that by using semi-analytical solutions, several analyses on the quality of the vibrations induced by the moving loads can be performed quickly and accurately without testing numerical convergence of discretized models. This way, it is possible to obtain straightforwardly accurate results in dimensionless forms, and thus encompassing in few graphs results related to all possible parameter combinations.

6 ACKNOWLEDGEMENTS

This work was supported by FCT, through IDMEC, under LAETA, project UIDB/50022/2020.

REFERENCES

[1] Z. Dimitrovová, "Semi-analytical approaches to vibrations induced by moving loads with the focus on the critical velocity and instability of the moving system", pp. 97-152, in Ground Vibration from High Speed Railways, V.V. Krylov (Ed), ICE Publishing, Thomas Telford Ltd. ISBN: 9780727763792.

[2] Z. Dimitrovová, "Critical velocity of a uniformly moving load on a beam supported by a finite depth foundation", Journal of Sound and Vibration (JSV), 366, pp. 325–342, 2016.

[3] Z. Dimitrovová, "Analysis of the critical velocity of a load moving on a beam supported by a finite depth foundation", International Journal of Solids and Structures (IJSS), 122–123, pp. 128-147, 2017.

[4] Z. Dimitrovová, "New semi-analytical solution for a uniformly moving mass on a beam on a two-parameter visco-elastic foundation", International Journal of Mechanical Sciences (IJMS), 127, pp. 142–162, 2017.

[5] Z. Dimitrovová, "Semi-analytical solution for a problem of a uniformly moving oscillator on an infinite beam on a two-parameter visco-elastic foundation", Journal of Sound and Vibration (JSV), 438, pp. 257-290, 2019.

[6] Z. Dimitrovová, "Complete semi-analytical solution for a uniformly moving mass on a beam on a two-parameter visco-elastic foundation with non-homogeneous initial conditions", International Journal of Mechanical Sciences (IJMS), 144, pp. 283-311, 2018.

[7] Z. Dimitrovová, "Semi-analytical approaches to vibrations induced by moving loads", in *Proceedings of the 14th International Conference on Vibration Engineering and Technology of Machinery* (VETOMAC XIV), MATEC Web of Conferences **211**, 11005, 2018 (eds. Maia, N. and Dimitrovová, Z.)

EURODYN 2020
XI International Conference on Structural Dynamics
M. Papadrakakis, M. Fragiadakis, C. Papadimitriou (eds.)
Athens, Greece, 23–26 November 2020

THEORETICAL ASSESSMENT OF VERTICAL INTERACTION BETWEEN A WHEELSET AND TRACK: INFLUENCE OF THE TRACK DAMPING MODEL

T. Mazilu[1], **M. A. Gheți**[2]

[1] University Politehnica of Bucharest, Romania,
Splaiul Independenţei no. 313, 6th District, Bucharest, Romania
e-mail: traian.mazilu@upb.ro

[2] University Politehnica of Bucharest, Romania
Splaiul Independenţei no. 313, 6th District, Bucharest, Romania
marius_alin.gheti@upb.ro

Keywords: wheelset, track, hysteretic model, viscous model, receptance, contact force

Abstract. *The paper presents a comparative analysis of the wheelset/track vertical interaction considering two track damping models, the hysteretic model and viscous model, respectively. To this end, a simple track model consisting in two independent infinite Euler-Bernoulli beams, each of them resting on a foundation with two elastic layers and an inserted inertial layer is used. The wheelset model has asymmetrical structure such as a driving wheelset. The axle is modelled using a free-free Euler-Bernoulli beam, and the wheels and driven wheel are considered rigid bodies. Regarding the parameters of the track model, given the values of the elastic foundation with hysteretic damping, the values of the parameters for the viscous damping model are calculated by applying the least square method in terms of rail receptance at acting point. The stiffnesses and damping constants of the viscous damping model minimize the sum of squared residuals, where the residual is the difference between the receptance modulus of the hysteretic model, and the receptance modulus of the viscous model at a certain angular frequency. Receptance modulus calculated with the viscous damping model matches the receptance derived from the hysteretic model excepting a limited frequency range around the antiresonance frequency of the rail. For simplicity, wheelset/track interaction is modelled applying the moving irregularity model. Interaction between wheelset and track is analyzed based on the numerical results. It is shown that the contact force predicted with the viscous damping model elastic overestimates the results delivered by the hysteretic damping model around the bounce-roll natural frequencies of the wheelset/track system. On the other hand, the results produced by the two models are in satisfactory agreement at lower and higher frequency.*

1 INTRODUCTION

The study of the wheel-rail interaction based on theoretical models is important in order to find solutions to many practical problems such as: rolling noise, rail corrugation and wheel out-of-roundness, ballast settlement etc.

Two kind of track models are used in numerical simulations depending on the track structure and frequency range: infinite beam on continuous elastic foundation [1] and infinite beam on discrete foundation, respectively [2]. In this context, the damping model of the track plays a role, since it has a strong impact on the magnitude of the wheel/rail contact force. From this perspective, the hysteretic and viscous damping models are the most common used due to their simplicity for the rail pad and ballast [3, 4].

Viscous damping model is a linear one and can be applied in both frequency and time-domain. However, the accuracy of the numerical simulations is affected by the fact that the dynamic stiffness increases with the frequency. Hysteretic damping model provides a better agreement with the test results – the dynamic stiffness doesn't depend on frequency, but it can be applied in the frequency-domain only [5]; it doesn't satisfy the causality requirement [6].

Despite the shortcomings mentioned above, the two damping models will still be used in the wheel/rail problem and the question is what kind of results we should expect when using one or the other. To answer this question, a theoretical investigation regarding the influence of the track damping model - hysteretic versus viscous - upon the magnitude of the interaction between a wheelset and track in the presence of the irregularities of the rolling surfaces is presented in this paper.

For simplicity, simple models for track and wheelset have been adopted: two infinite continuous beams on independent elastic foundation for track model and free-free beam with attached rigid bodies for wheelset model.

Values of the parameters of the viscous damping model are derived from those of the hysteretic damping model parameters applying the least square method regarding the difference between the rail receptance modulus at acting point calculated with the hysteretic damping model and the rail receptance modulus at acting point derived from the viscous damping model.

To evaluate the magnitude of the wheelset/tract interaction, the power spectral density (PSD) of the irregularities of the rolling surfaces are calculated starting from rail roughness limit spectrum [7].

Finally, the wheelset/track interaction is analyzed in terms of the PSD of the wheel/rail contact forces and wheel/rail displacements.

2 WHEELSET/TRACK MODEL

Fig. 1 shows the model of the interaction between a wheelset and track when the rolling surfaces exhibit small irregularities - roughness.

The wheelset is considered as an asymmetrical structure, corresponding to a driving wheelset, and consisting of two wheels and a driven gear rigidly fixed on the axle. The axle is modelled using a uniform free-free Euler-Bernoulli beam of $2l$ length, EI_a bending stiffness, where E is Young's modulus and I_a is the moment of inertia of the cross-section, and of m_a is the mass per length unit. The wheels and driven gear are considered rigid bodies of M_w mass and J_w mass moment of inertia for wheels, and M_g mass and J_g mass moment of inertia for the driven gear. Distance between wheels is $2e$ and the distance between a wheel and the corresponding axle end is a. The drive gear is located at the distance b from the left end of the axle.

Equation of motion for the driving wheelset is

$$EI_a \frac{\partial^4 w_a(y_a,t)}{\partial y_a^4} + M_w \left[\frac{\partial^2 w_a(a,t)}{\partial t^2} \delta(y_a - a) + \frac{\partial^2 w_a(l-a,t)}{\partial t^2} \delta(y_a - l + a) \right] -$$
$$J_w \left[\frac{\partial^3 w_a(a,t)}{\partial y_a \partial t^2} \delta'(y_a - a) + \frac{\partial^3 w_a(l-a,t)}{\partial y_a \partial t^2} \delta'(y_a - l + a) \right] + \quad (1)$$
$$M_g \frac{\partial^2 w_a(b,t)}{\partial t^2} \delta(y_a - b) - J_g \frac{\partial^3 w_a(b,t)}{\partial x \partial t^2} \delta'(y_a - b) +$$
$$m_a \frac{\partial^2 w_a(y_a,t)}{\partial t^2} = -Q_1(t)\delta(y_a - a) - Q_2(t)\delta(y_a - l + a),$$

where $w_{ao}(y_a, t)$ is the axle displacement in the cross section at the distance y_a from the left end of the axle at the t time moment and $Q_{1,2}(t)$ are the dynamic components of the wheel/rail contact.

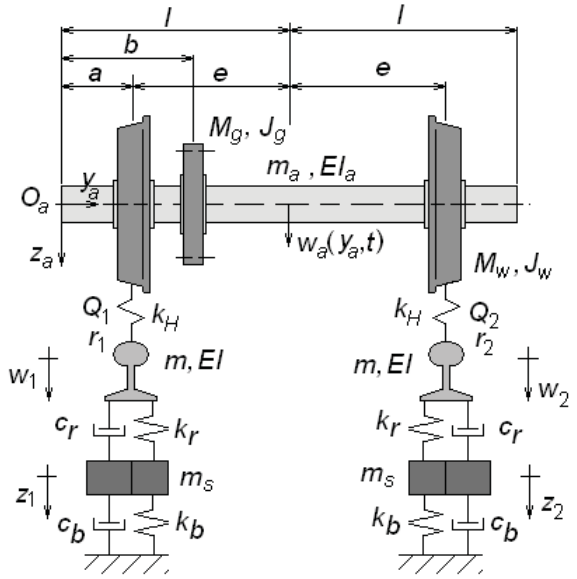

Fig. 1. Wheelset/track model.

Using the modal analysis method, the axle deflection becomes

$$w_a(y_a,t) = w_{ao}(t) + (y_a - l/2)\theta_{ao}(t) + \sum_{n=1}^{\infty} Y_n(y_a) T_n(t) \quad (2)$$

where $w_{ao}(t)$ and $\theta_{ao}(t)$ represent the axle motions as rigid body, and $T_n(t)$ and $Y_n(y_a)$ are the time coordinate and the eigenfunction of the n^{th} elastic vibration mode.

In the following, the axle motion is described by the rigid vibration modes and the first two elastic vibration modes. In this context, Eq. (1) transforms into the below matrix equation

$$\mathbf{M}\ddot{\mathbf{q}} + \mathbf{K}\mathbf{q} = \mathbf{Q}, \quad (3)$$

where $\mathbf{q} = [w_{ao}\ \theta_{ao}\ T_1\ T_2]^T$ is the column vector of the modal coordinates, **M** and **K** are the inertia and stiffness 4×4 matrix and **Q** is the column vector of the four modal forces.

When the steady-state harmonic behaviour is considered (frequency-domain), Eq. (3) becomes

$$\left(-\omega^2\mathbf{M}+\mathbf{K}\right)\bar{\mathbf{q}}=\bar{\mathbf{Q}}\,, \tag{4}$$

where $\bar{\mathbf{q}}=\left[\,\bar{w}_{ao}\quad \bar{\theta}_{ao}\quad \bar{T}_1\quad \bar{T}_2\,\right]^T$ is the column vector of the complex amplitude of the modal coordinates and $\bar{\mathbf{Q}}$ is the column vector of the complex amplitudes of the modal forces.

Solving Eq. (4), the complex amplitudes of the axle displacements at the two wheels may be calculate

$$\bar{w}_{a1,2}=\bar{w}_{ao}\mp e\bar{\theta}_{ao}+\sum_{n=1}^{2}Y_n(y_{an})\bar{T}_n \tag{5}$$

where $y_{a1,2}=l\mp e$.

After some calculations, it holds

$$\begin{aligned}\bar{w}_{a1}&=-\left(\bar{\alpha}_{11}\bar{Q}_1+\bar{\alpha}_{12}\bar{Q}_2\right)\\ \bar{w}_{a2}&=-\left(\bar{\alpha}_{21}\bar{Q}_1+\bar{\alpha}_{22}\bar{Q}_2\right),\end{aligned} \tag{6}$$

where $\bar{\alpha}_{ij}$ with i,j = 1,2 is the axle receptance corresponding to the i wheel due to the unit harmonic force acting at the j wheel, and $\bar{Q}_{1,2}$ is the complex amplitude of the wheel/rail harmonic force.

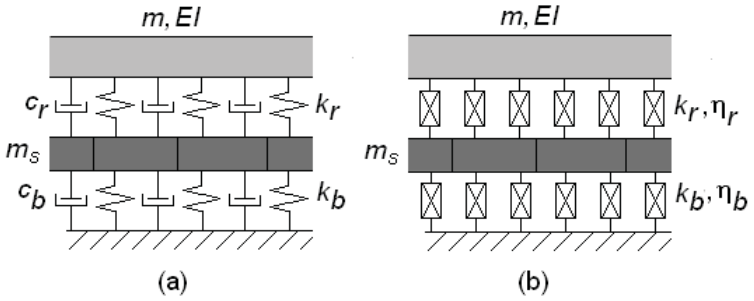

Fig. 2. Track model: (a) viscous damping; (b) hysteretic damping.

Ignoring the weak coupling between the two rails dynamics via sleepers, and the effect of the equidistant supports represented by sleepers, the track model is reduced to two identic infinite Euler-Bernoulli beams, each of them supporting on continuous foundation including two elastic layers and an intermediate inertial layer. The beams model the rails, and the continuous foundation introduces the elasticity of the rail pads and the ballast and the inertia of the sleepers. Such track model can be applied up to 6-700 Hz [7].

Regarding the damping of the track model, two kind of models are taken into consideration, viscous damping model and hysteretic damping model (fig. 2).

Parameters for the track model are the bending stiffness of the rail EI, where E is Young's modulus and I is the moment of inertia of the rail cross-section, the rail mass per unit length m, the railpad stiffness and damping constant per unit length k_r and c_r, the sleeper mass per unit length m_s, the ballast stiffness and damping constant per unit length k_b and c_b; the stiffnesses and damping constants correspond to the visco-elastic model for the foundation.

The track model with viscous damping can be applied in both time and frequency-domain and the equations of motion are given below.

Equations of motion for the time-domain:

$$\begin{aligned} &EI\frac{\partial^4 w_{1,2}(x,t)}{\partial x^4}+m\frac{\partial^2 w_{1,2}(x,t)}{\partial t^2}+c_r\left(\frac{\partial w_{1,2}(x,t)}{\partial t}-\frac{\partial z_{1,2}(x,t)}{\partial t}\right)+\\ &+k_r\left[w_{1,2}(x,t)-z_{1,2}(x,t)\right]=Q_{1,2}(t)\delta(x)\\ &m_s\frac{\partial^2 z_{1,2}(x,t)}{\partial t^2}+c_r\left(\frac{\partial z_{1,2}(x,t)}{\partial t}-\frac{\partial w_{1,2}(x,t)}{\partial t}\right)+c_b\frac{\partial z_{1,2}(x,t)}{\partial t}+\\ &+k_r\left[z_{1,2}(x,t)-w_{1,2}(x,t)\right]+k_b z_{1,2}=0. \end{aligned} \tag{7}$$

where $w_i(x,t)$ is the i rail displacement and $z_i(x,t)$ is the i sleeper displacement.

Equations of motion in the frequency-domain

$$\begin{aligned} &EI\frac{\mathrm{d}^4\overline{w}_{1,2}}{\mathrm{d}x^4}+\left(-\omega^2 m+k_r+i\omega c_r\right)\overline{w}_{1,2}-\left(k_r+i\omega c_r\right)\overline{z}_{1,2}=\overline{Q}_{1,2}\delta(x)\\ &\left[-\omega^2 m_s+k_r+k_b+i\omega\left(c_r+c_b\right)\right]\overline{z}_{1,2}-\left(k_r+i\omega c_r\right)\overline{w}_{1,2}=0. \end{aligned} \tag{8}$$

where the notations with bar are complex amplitudes, and $i^2=-1$.

When the hysteretic damping model is considered, the parameters for the two elastic layers are: k_r and k_b – the stiffness for the rail pad and ballast, η_r – the loss factor of the rail pad and η_b – the loss factor for the ballast.

Equations of motion of the track model with hysteretic damping can be written in the frequency-domain only

$$\begin{aligned} &EI\frac{\mathrm{d}^4\overline{w}_{1,2}}{\mathrm{d}x^4}+\left[-\omega^2 m+k_r\left(1+i\eta_r\right)\right]\overline{w}_{1,2}-k_r\left(1+i\eta_r\right)\overline{z}_{1,2}=\overline{Q}_{1,2}\delta(x)\\ &\left[-\omega^2 m_s+k_r\left(1+i\eta_r\right)+k_b\left(1+i\eta_b\right)\right]\overline{z}_{1,2}-k_r\left(1+i\eta_r\right)\overline{w}_{1,2}=0. \end{aligned} \tag{9}$$

The rails displacements at the acting points (x=0) are

$$\overline{w}_{1,2}=\overline{\alpha}_r\overline{Q}_{1,2}, \tag{10}$$

where $\overline{\alpha}_r$ is the rail receptance calculated for the section of the unit harmonic force.

Wheel/rail contact forces can be calculated applying linearized Hertz's contact theory

$$Q_{1,2}=k_H\left(w_{a1,2}-w_{1,2}-r_{1,2}\right), \tag{11}$$

or, for the frequency-domain,

$$\overline{Q}_{1,2}=k_H\left(\overline{w}_{a1,2}-\overline{w}_{1,2}-\overline{r}_{1,2}\right), \tag{12}$$

where $r_{1,2}$ are the rolling surfaces irregularities and k_H stands for the Hertzian contact stiffness.

Inserting Eqs. (6) and (10) in Eq. (8), it holds

$$\begin{aligned} &\left(\overline{\alpha}_{11}+\overline{\alpha}_r+\overline{\alpha}_H\right)\overline{Q}_1+\overline{\alpha}_{12}\overline{Q}_2=-\overline{r}_1\\ &\overline{\alpha}_{21}\overline{Q}_1+\left(\overline{\alpha}_{22}+\overline{\alpha}_r+\overline{\alpha}_H\right)\overline{Q}_2=-\overline{r}_2, \end{aligned} \tag{13}$$

where $\bar{\alpha}_H = 1/k_H$ is the receptance of the wheel/rail contact.

Problem solution is as follows:

- contact forces

$$\bar{Q}_1 = \frac{-\bar{r}_1(\bar{\alpha}_{22}+\bar{\alpha}_r+\bar{\alpha}_H)+\bar{\alpha}_{12}\bar{r}_2}{(\bar{\alpha}_{11}+\bar{\alpha}_r+\bar{\alpha}_H)(\bar{\alpha}_{22}+\bar{\alpha}_r+\bar{\alpha}_H)-\bar{\alpha}_{12}\bar{\alpha}_{21}}$$
$$\bar{Q}_2 = \frac{-\bar{r}_2(\bar{\alpha}_{11}+\bar{\alpha}_r+\bar{\alpha}_H)+\bar{\alpha}_{21}\bar{r}_1}{(\bar{\alpha}_{11}+\bar{\alpha}_r+\bar{\alpha}_H)(\bar{\alpha}_{22}+\bar{\alpha}_r+\bar{\alpha}_H)-\bar{\alpha}_{12}\bar{\alpha}_{21}} \quad (14)$$

- wheelset displacement at wheels level

$$\bar{w}_{a1} = \frac{\left[\bar{\alpha}_{11}(\bar{\alpha}_{22}+\bar{\alpha}_r+\bar{\alpha}_H)-\bar{\alpha}_{12}\bar{\alpha}_{21}\right]\bar{r}_1+\bar{\alpha}_{12}(\bar{\alpha}_r+\bar{\alpha}_H)\bar{r}_2}{(\bar{\alpha}_{11}+\bar{\alpha}_r+\bar{\alpha}_H)(\bar{\alpha}_{22}+\bar{\alpha}_r+\bar{\alpha}_H)-\bar{\alpha}_{12}\bar{\alpha}_{21}}$$
$$\bar{w}_{a2} = \frac{\left[\bar{\alpha}_{22}(\bar{\alpha}_{11}+\bar{\alpha}_r+\bar{\alpha}_H)-\bar{\alpha}_{12}\bar{\alpha}_{21}\right]\bar{r}_2+\bar{\alpha}_{21}(\bar{\alpha}_r+\bar{\alpha}_H)\bar{r}_1}{(\bar{\alpha}_{11}+\bar{\alpha}_r+\bar{\alpha}_H)(\bar{\alpha}_{22}+\bar{\alpha}_r+\bar{\alpha}_H)-\bar{\alpha}_{12}\bar{\alpha}_{21}} \quad (15)$$

- rails displacement at acting points

$$\bar{w}_1 = \bar{\alpha}_r \frac{-\bar{r}_1(\bar{\alpha}_{22}+\bar{\alpha}_r+\bar{\alpha}_H)+\bar{\alpha}_{12}\bar{r}_2}{(\bar{\alpha}_{11}+\bar{\alpha}_r+\bar{\alpha}_H)(\bar{\alpha}_{22}+\bar{\alpha}_r+\bar{\alpha}_H)-\bar{\alpha}_{12}\bar{\alpha}_{21}}$$
$$\bar{w}_2 = \bar{\alpha}_r \frac{-\bar{r}_2(\bar{\alpha}_{11}+\bar{\alpha}_r+\bar{\alpha}_H)+\bar{\alpha}_{21}\bar{r}_1}{(\bar{\alpha}_{11}+\bar{\alpha}_r+\bar{\alpha}_H)(\bar{\alpha}_{22}+\bar{\alpha}_r+\bar{\alpha}_H)-\bar{\alpha}_{12}\bar{\alpha}_{21}}. \quad (16)$$

In the following section, the same roughness is considered on the two wheel/rail pairs.

3 NUMERICAL APPLICATION

In this section, the parameters corresponding to the wheelset of the electric 060 EA locomotive in service on CFR (Romanian Railway) are considered. The values of these parameters are as follows: m_a= 244,4 kg/m, E = 210 GPa, I_a = 7.7136□10-5 m^4, 2l = 2.11 m, a = 0,305 m, b = 0.52 m, e = 0.75 m, M_w = 500 kg, J_w = 48.8 kgm^2, M_g = 550 kg (including the part of the gear housing resting on the axle), J_g = 17.7 kgm^2.

To point out the impact of the track damping model upon the assessment of the wheelset/track interaction, the hysteretic damping model is considered as reference and two kind of rail pad are considered: stiff rail pad with the stiffness of 350 MN/m and soft rail pad with the stiffness of 60 MN/m (both per half sleeper). Loss factor of the rail pad is η_r = 0.25. The other parameters of the track model are: rail mass per length unit of 60 kg/m, the inertia moment of the rail cross-section of 3.055□10^{-5} m^4, half sleeper mass of 132 kg, ballast stiffness corresponding to a half sleeper 50 MN/m, ballast loss factor of 1.00 and the sleeper bay of 0.55 m. Values per length unit for the rail pad and ballast stiffness are obtained by dividing the stiffness per half sleeper to the sleeper bay. Similar, the sleeper mass per length unit is calculated. The wheel/rail contact stiffness is k_H = 1.5 GN/m.

Figure 3 shows the receptance of the wheelset calculated at the two wheels when the harmonic unit force acts on left/right wheel. The receptance at the left wheel ($\bar{\alpha}_{11}$) is lower than the right wheel receptance ($\bar{\alpha}_{22}$) due to the inertial influence of the driven gear and housing gear which are mounted next to the left wheel. The natural frequencies of the wheelset bending modes taken into consideration in the model are at 86.5 and 187.3 Hz. The

left wheel receptance has antiresonance frequencies at 83.8 and 186.8 Hz, and the right wheel receptance, at 84.8 and 181.3 Hz. The cross-receptance of the wheelset ($\bar{\alpha}_{12} = \bar{\alpha}_{21}$) reflects the coupling between the vibration modes of the wheelset.

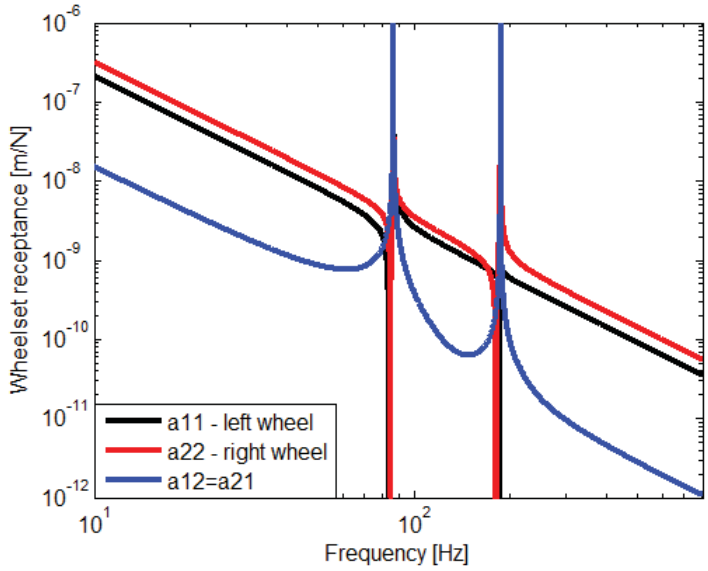

Fig. 3. Receptance of the wheelset calculated at each wheel.

The values of the parameters for the viscous damping model are calculated by applying the least square method in terms of rail receptance at acting point. The stiffnesses and constants damping of the viscous damping model minimize the sum of squared residuals, where the residual is the difference between the receptance modulus of the hysteretic model, and the receptance modulus of the viscous model at a certain angular frequency,

$$S(k_{rv}, c_{rv}, k_{bv}, c_{bv}) = \sum_{\omega_{min} \le \omega_i \le \omega_{max}} \left(\left|\bar{\alpha}_{rh}(\omega_i)\right| - \left|\bar{\alpha}_{rv}(\omega_i)\right| \right)^2 , \tag{17}$$

where the index *h* or *v* denotes the hysteretic damping model or the viscous damping model, and ω_{min} and ω_{max} are the limits of the angular frequency range.

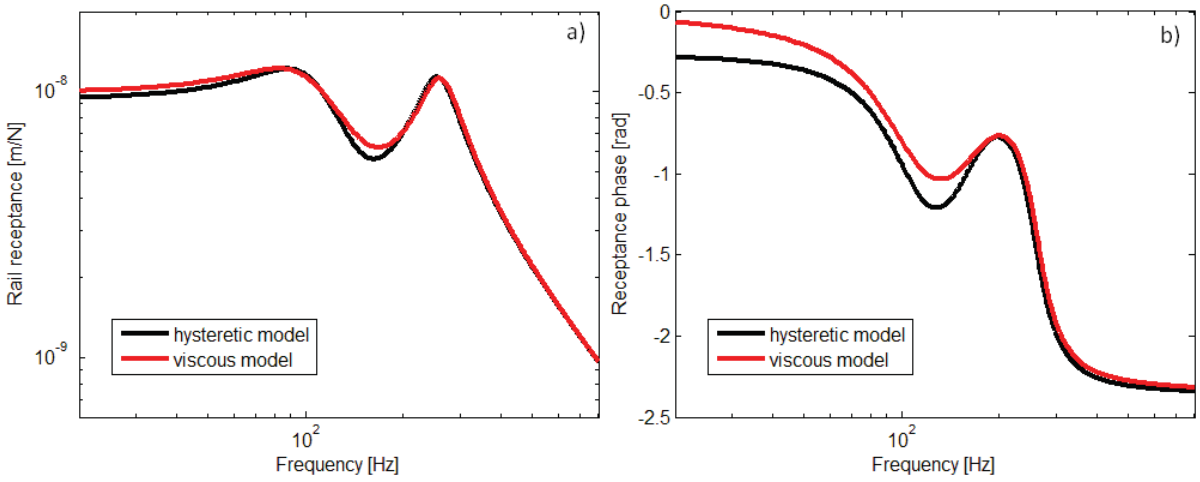

Fig. 4. Rail receptance for soft rail pad: a) receptance modulus; b) receptance phase.

Optimal parameters values can be found by setting the gradient to zero or by mapping the S function using the numerical calculation. Applying former approach, the results are displayed in Figs 4 and 5 for soft and stiff rail pad.

In Fig. 4, the optimal parameters values per half sleeper for the viscous model are: k_{rv} = 70.33 MN/m, c_{rv} = 7.596 kNs/m or ζ_r = 0,0788, k_{bv} = 68.77 MN/m, c_{bv} = 82.15 kNs/m or ζ_b = 0.4327, where the damping ratio for rail pad, ζ_r, and for the ballast, ζ_b, are defined as

$$\zeta_r = \frac{c_{rv}}{2\sqrt{k_{rv}m}}, \qquad \zeta_b = \frac{c_{bv}}{2\sqrt{k_{bv}m_s}}.$$

The rail receptance exhibits two peaks corresponding to the natural frequencies of the track, one at 86.2 Hz, and the other one at 244.7 Hz, and a deep at 145.9 Hz – the anti-resonant frequency due to the dynamic absorber effect produced by sleeper. The results derived from the viscous damping model well matches the results from hysteretic damping model, excepting the range around the anti-resonant frequency, where the maximum error can reach about 10 %.

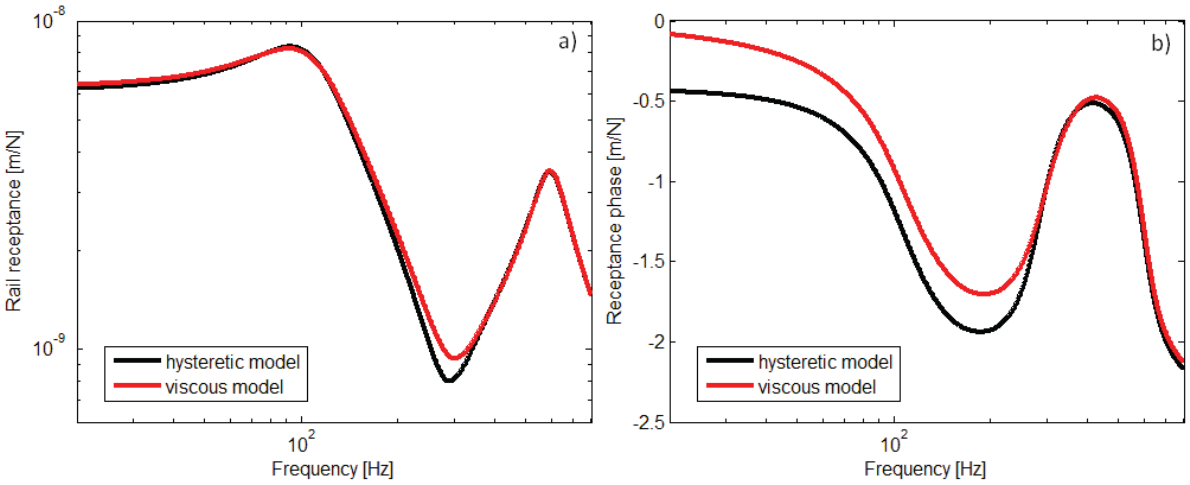

Fig. 5. Rail receptance for stiff rail pad: a) receptance modulus; b) receptance phase.

In the stiff rail pad case, the optimal parameters values per half sleeper for the viscous model are: k_{bv} = 374.28 MN/m, c_{rv} = 20.415 kNs/m or ζ_r = 0,0788, k_{bv} = 76.500 MN/m and c_{bv} = 76.500 kNs/m or ζ_b = 0.4327. Track natural frequencies take the frequency of 87.6 Hz and 581.7 Hz, respectively. The anti-resonant frequency is 278.1 Hz. The viscous damping model ensures results very close to those of the hysteretic damping model, especially around the natural frequencies of the track and at higher frequencies. However, there is a narrow frequency interval around the anti-resonance frequency where the errors are bigger. Receptance phase from the viscous damping model shows significant difference at lower frequencies in relation to that obtained from the hysteretic damping model.

The roughness of the rolling surfaces can be represented as the power spectral density function depending on the wave number. Starting from the rail roughness limit spectrum (fig. 6), power spectral density function can be derived considering the fourth-power dependence like in ref. [9] and adding a linear term in numerator

$$S(\Omega) = \frac{A + B\Omega}{\Omega^n}, \; \Omega_{j-1} < \Omega < \Omega_j, \tag{18}$$

where Ω is the wave number, A [rad^{n-1}/m^{n-3}] and B [rad^{n-2}/m^{n-4}] – constants, Ω_{j-1} and Ω_j are the limit frequencies delimiting a 1/3 octave interval and n is an exponent ($n = 4$).

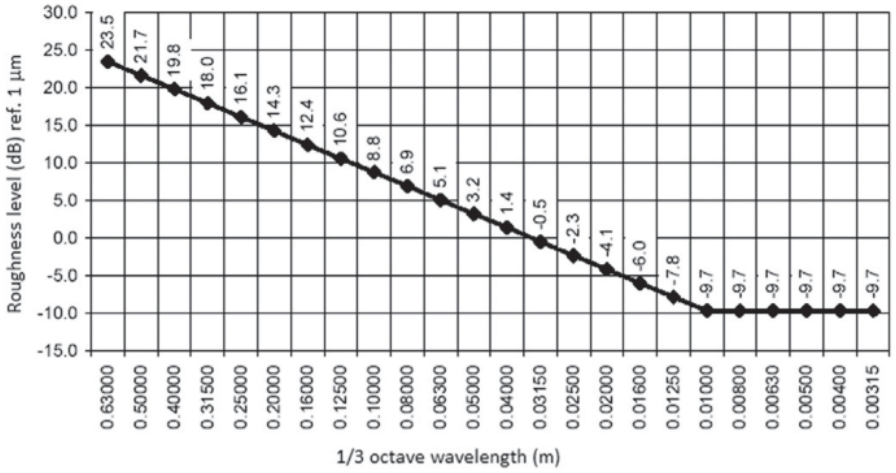

Fig. 6. Roughness limit spectrum [8].

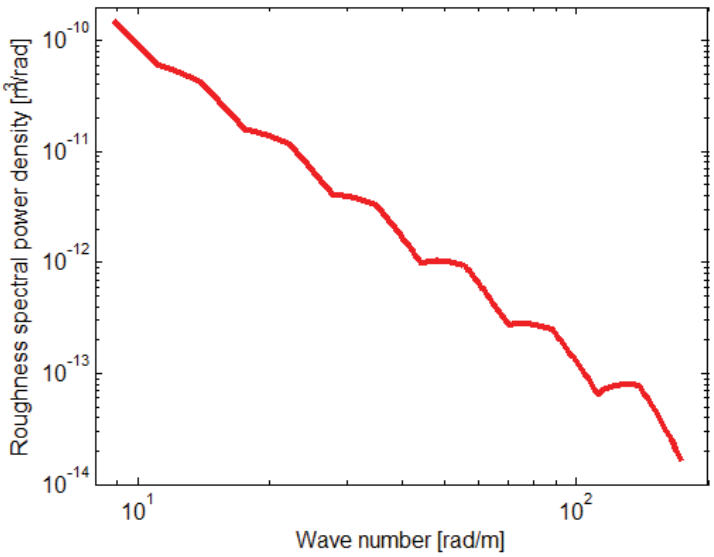

Fig. 7. Spectral density spectrum of the roughness.

Fig. 7 shows the power spectral density of the roughness of the rolling surfaces derived from the limit spectrum of the roughness, which has been extended from the wavelength of 0.63 m to the wavelength of 2 m in order to cover the lower frequencies.

When the wheelset travels along the track with the speed V, the power spectral density of the rolling surfaces roughness becomes ω dependent function, where $\omega = V\Omega$ is the angular frequency,

$$G(\omega) = \frac{S(\omega / V)}{V} = \frac{A + B\omega / V}{V(\omega / V)^n}. \tag{19}$$

The wheel/rail displacement power spectral density (PSD) can be calculated applying the following equation

$$G_{w_{a1,a2},w_{1,2}}(\omega)=\left|\bar{H}_{w_{a1,a2},w_{1,2}}(\omega)\right|^2 G(\omega)\,, \tag{20}$$

where $\bar{H}_{w_{a1,a2},w_{1,2}}(\omega)$ is the frequency response function of the wheel/rail displacement.

Similar, PSD of the contact force can be obtained

$$G_{Q_{1,2}}(\omega)=\left|\bar{H}_{Q_{1,2}}(\omega)\right|^2 G(\omega)\,, \tag{21}$$

where $\bar{H}_{Q_{1,2}}(\omega)$ is the frequency response function of the wheel/rail contact force.

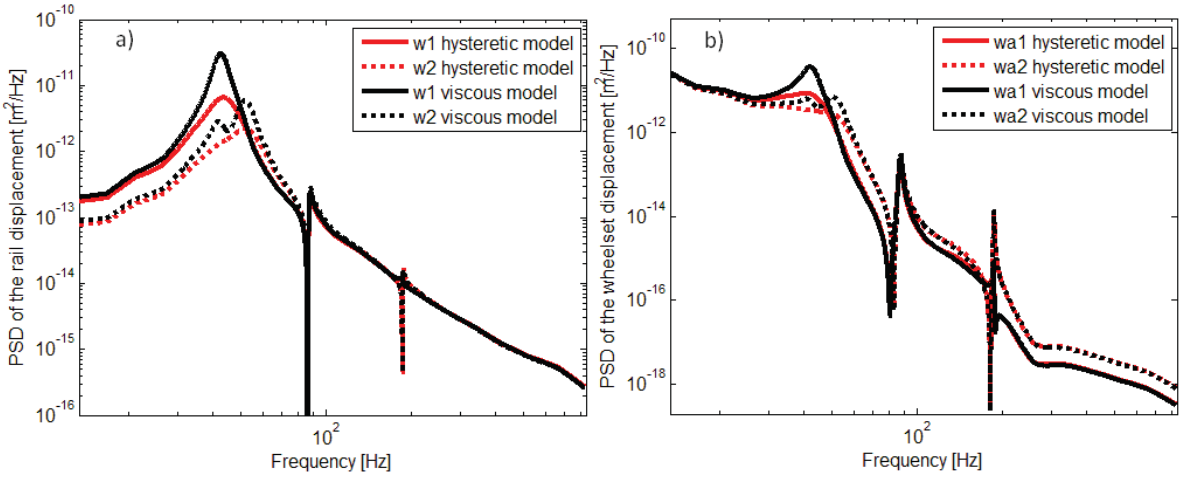

Fig. 8. PSD of the wheel/rail displacement at 30 m/s– soft rail pad.

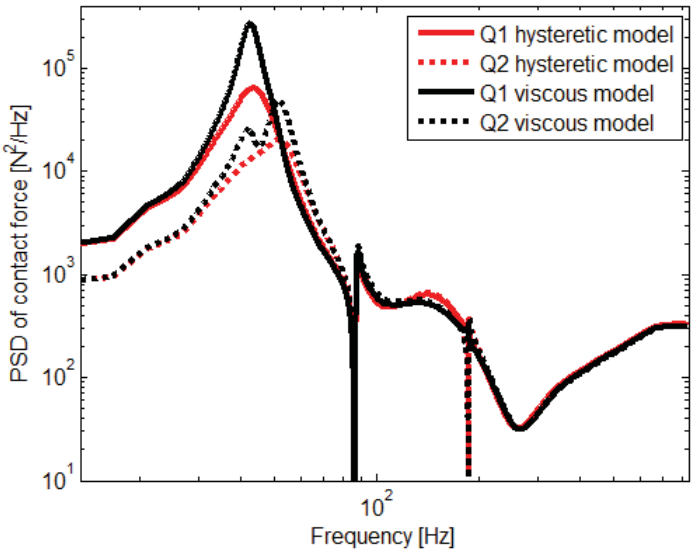

Fig. 9. PSD of the wheel/rail contact force at 30 m/s– soft rail pad.

Figs 8 and 9 shows the PSD of the wheel/rail displacements and contact force for both track damping models considering that the wheelset is moving along a track with soft rail pad at 30 m/s. Wheelset/track dynamics exhibits two resonance frequencies in the interval of 35-50 Hz (depending on the damping model) due to the bounce and roll motions of the wheelset on the track. However, instead of two peaks corresponding to the two resonance frequencies,

the PSD calculated with the hysteretic damping model shows one peak for the left wheel (at lower frequency) and other one for the right wheel (at higher frequency) due to the damping. When the viscous damping model is used, the left wheel has one peak, and the right wheel shows two peaks. It can be observed that the left side of the wheelset/track system vibrates more intense at low frequency due to the higher inertia. In general, the results obtained with the two damping models are close, but a significant difference can be identified in the range of resonance frequencies due to wheelset bounce-roll on the track.

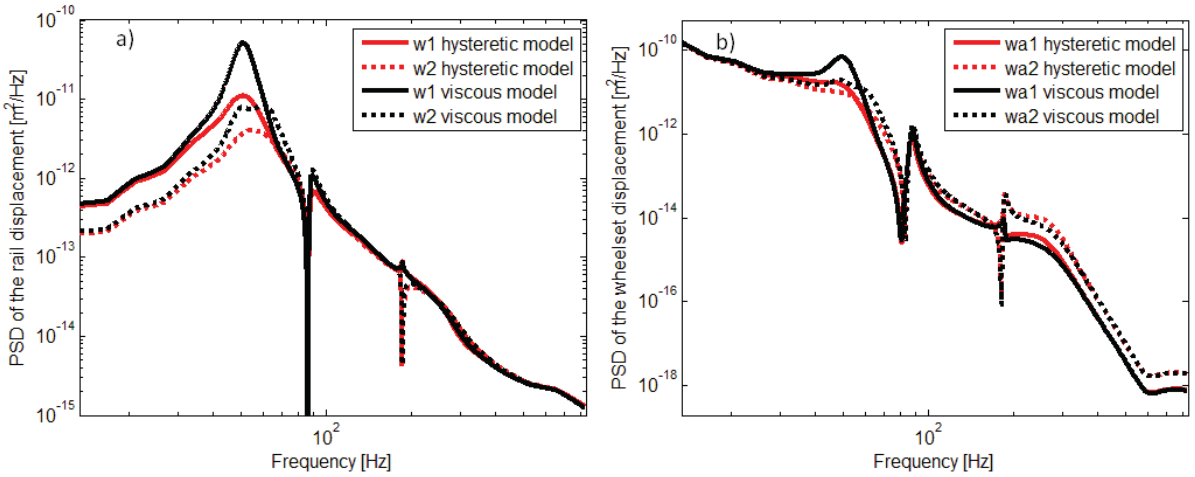

Fig. 10. PSD of the wheel/rail displacement at 30 m/s– stiff rail pad.

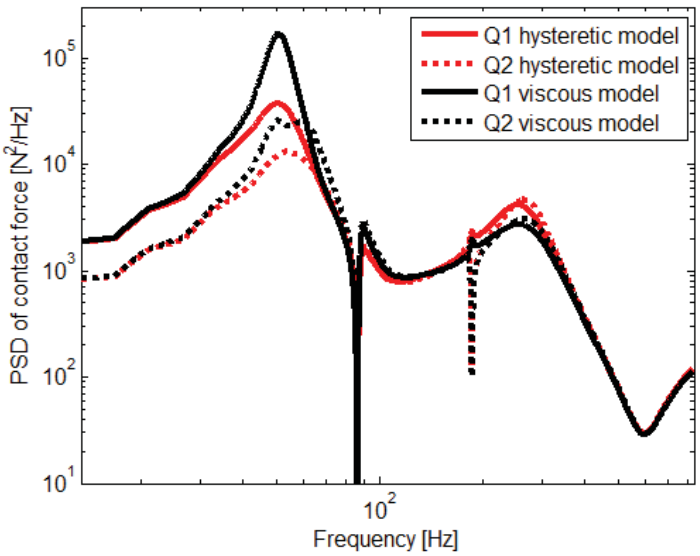

Fig. 11. PSD of the wheel/rail contact force at 30 m/s– stiff rail pad.

Similar comments can be drawn from the Figs 10 and 11 which show the results for the case of the track with stiff rail pad.

4 CONCLUSIONS

Theoretical investigation of the interaction between a wheelset and track is interesting from many practical reasons.

From the track modelling perspective, the most used damping models are the hysteretic and viscous models.

It was shown that the values of the parameters of the track model with viscous damping can be determined applying the least squares method to obtain the best approximation of the rail receptance given by the track model with hysteretic damping.

The results regarding the wheelset/track interaction in the presence of rolling surface irregularities calculated with the track model with viscous damping approximate well the results provided by the track model with hysteretic damping especially at lower and higher frequencies than the resonant frequencies due to the bounce-roll motion of the wheelset on track.

However, the viscous damping model overestimates the magnitude of the rail/wheel interaction in relation to the results obtained with the help of the hysteretic damping model in the range of resonant frequencies due to the bounce-roll motion of the wheelset on the track.

ACKNOWLEDGMENTS

The paper is financed by the Polytechnic University of Bucharest, through the project "Engineer in Europe" in online system, registered at MEC under no. 457/GP/06.08.2020, by using the fund for financing special situations that cannot be integrated in the form of financing higher education state institutions.

REFERENCES

[1] Z. Dimitrovová, New semi-analytical solution for a uniformly moving mass on a beam on a two-parameter visco-elastic foundation, *International Journal of Mechanical Sciences* 127, 142-162, 2017.

[2] S. Zhanga, G. Chenga, X. Sheng, D. J. Thompson, Dynamic wheel-rail interaction at high speed based on time-domain moving Green's functions, *Journal of Sound and Vibration* 488, 115632, 2020.

[3] T. X. Wu, D. J. Thompson, A double Timoshenko beam model for vertical vibration analysis of railway track at high frequencies, *Journal of Sound and Vibration* 224, 329-348, 1999.

[4] B. E. Croft, C. J. C. Jones, D. J. Thompson, Modelling the effect of rail dampers on wheel–rail interaction forces and rail roughness growth rates, *Journal of Sound and Vibration* 323, 17-32, 2009.

[5] N. Maia, Reflections on the hysteretic damping model, *Shock and Vibration* 16, 529–542, 2009.

[6] S. N. Crandall, The Hysteretic Damping Model in Vibration Theory, Proceedings of the Institution of Mechanical Engineers, Part C: Journal of Mechanical Engineering Science 205, 23-28, 1991.

[7] S. L. Grassie, R. W. Gregory, D. Harrison, K. I. Johnson, The dynamic response of railway track to high frequency vertical excitation, Journal Mechanical Engineering Science 24, 77-90, 1982.

[8] EN ISO 3381:2011, Railway applications – Acoustics – Measurement of Noise Inside Railbound Vehicles.

[9] E. K. Bender, P. J. Remington, The influence of rails on train noise, *Journal of Sound and Vibration* 46, 321-334, 1974.

EURODYN 2020
XI International Conference on Structural Dynamics
M. Papadrakakis, M. Fragiadakis, C. Papadimitriou (eds.)
Athens, Greece, 23–26 November 2020

REDUCING VIBRATIONAL IMPACT LATERAL OF A RAILWAY TRACK ON AN URBAN DEVELOPMENT PROJECT

Felix Mertens[1] **and Thomas Jaquet**[2]

[1] Affiliation of Felix Mertens
Peutz Consult GmbH, Borussiastraße 112, 44149 Dortmund
e-mail: fm@peutz.de

[2] Affiliation of Thomas Jaquet
Merensiepen 24 b, 58453 Witten
e-mail: Thomas.jaquet1@web.de

Keywords: Structural Dynamics, Traffic-induced Vibrations, Ground Vibrations

Abstract. *Perceptible vibration effects in adjacent buildings due to passing trains on a near-by track are usually expected in distances lower than one-hundred meters. Railway vibrations in distances of more than two-hundred meters are generally not considered to be a relevant emission source which could affect the living conditions in planned buildings of urban development projects.*

This paper focuses on a real-estate project in a German city to develop a new residential district with an almost identical structural design. Surprisingly, after completion of the first buildings in distances even further away than two-hundred meters to the next railway track, residents on higher floors complained about shaking ceiling lamps and substantially shocks in their apartments.

As a first approach, long-term monitoring revealed building vibrations with higher vibration velocity peaks, which can also be categorized perceptible for humans. The vibrational source could be identified quickly by frequently passing freight trains on the faraway track. A further aspect of the monitored data showed that the discomforting situation was caused by horizontal building movements in a low-frequency domain, especially on higher floors. To solve this vibrational problem, the dynamic behavior of the already constructed buildings, as well as the characteristic of the wave-propagation on the terrain, were measured.

Freight train induced horizontal vibrations correspond to the horizontal eigenmodes of the constructed buildings and amplifies the vibration level within the structure significant. In the early stage of the project, optimization of the construction has been required to detune the dynamic properties of planned buildings from the train vibrations. The paper represents the vibrational situation described above, the detailed numerical studies to find the critical points of the building design as well as the optimization process of the building structure.

Furthermore, this example should also give a short guideline on how the unintended effect of an increased vibrational impact lateral of a railway track can be avoided in future urban development projects.

1 INTRODUCTION

Perceptible vibration effects in adjacent buildings due to passing trains on a nearby track are usually expected in distances lower than one hundred meters. Railway vibrations in distances of more than two hundred meters are generally not considered to be a relevant emission source which could affect the living conditions in planned buildings of urban development projects.

This paper focuses on a real-estate project in a German city to develop a new residential district with almost identical building design. Surprisingly, after the construction of the first buildings in distances of more than two hundred meters to the next railway track, residents on higher floors complained about shaking ceiling lamps and substantially shocks in their apartments.

Studies and detailed investigations were launched to improve the vibrational situation for further planned buildings and give a short guideline of how the unintended effect of an increased vibrational impact can be reduced for future urban development projects.

2 URBAN DEVELOPMENT PROJECT

The project area is subdivided into several sections and located on sandy soil in a larger distance from the next railway line (see Figure. 1). The building design mainly consists of multistory buildings with five to six floors. The construction process started on the opposite side of the track and evolved spatially towards the track over several years.

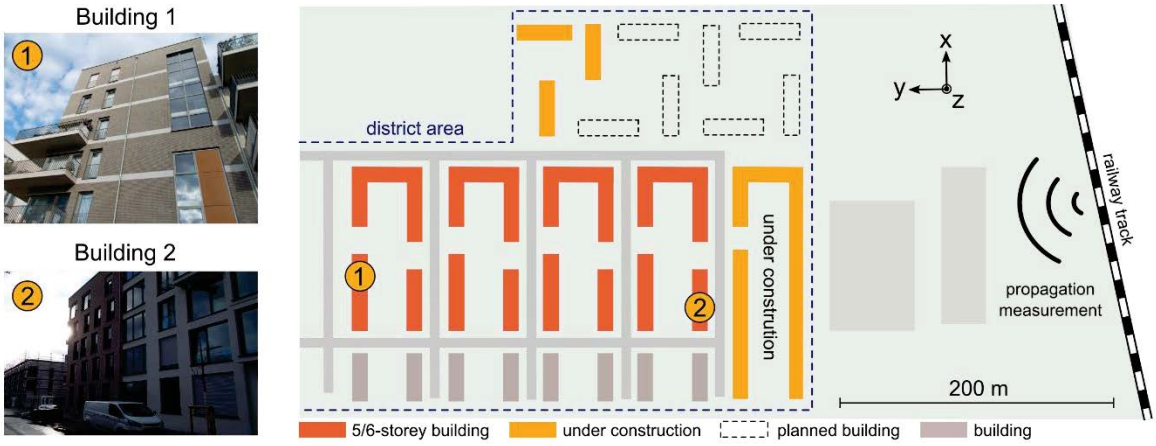

Figure 1: Building design and layout of the district area. The distance between the railway track and district area accounts for more than 200 meters.

A potential impact due to traffic vibrations on planed buildings is usually estimated in a preliminary stage of an urban development project. In the case of floor vibrations and secondary airborne sound, the attenuation of shock waves over distances of one hundred meters is commonly sufficient to avoid disruptive vibrations inside of living spaces.

However, residents on the upper floor in *Building 2* in even more than two hundred meters to the next railway track complain about perceptible shocks in their apartments especially during the night times.

3 VIBRATION MONITORING

Long-Term monitoring in *Building 2* revealed higher vibration velocity peaks which can also be categorized as perceptible (see Figure. 2). The vibrational source could be quickly identified by frequently passing freight trains on the faraway track.

A further aspect of the monitored data revealed that the discomforting situation is caused by horizontal building movements in a low-frequency range at around 4 Hz, especially on higher floors. Floor vibrations in vertical direction were not monitored during the corresponding events.

A more detailed monitoring-study in the apartments revealed up to 60 passing freight-trains in the night and 100 during the daytime. The relevant frequency-weighted velocity values for night and day do not exceed the requirements of the underlying vibrational standards [1].

However, more detailed investigations of the vibrational phenomena were launched to improve the living situation for future residents on higher floors of further planned buildings in the district area.

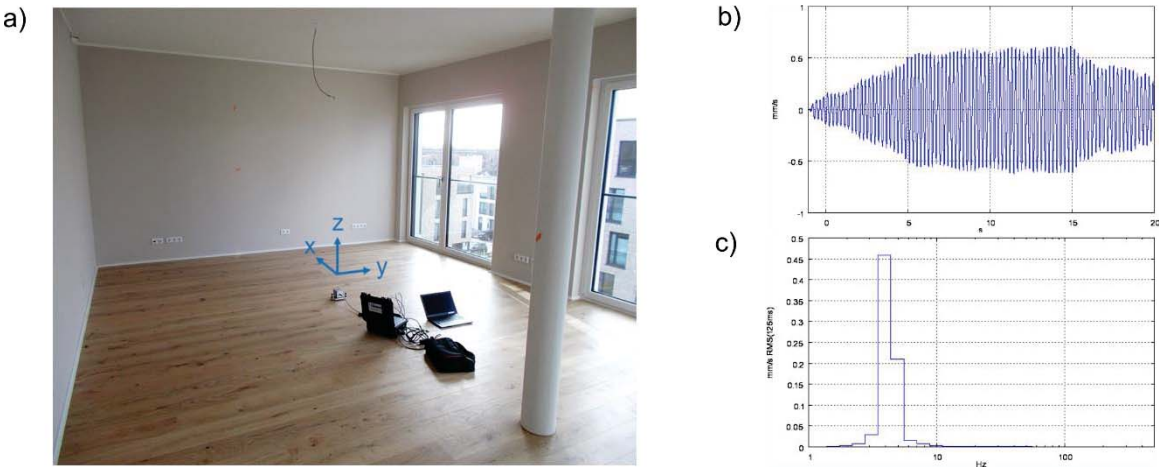

Figure 2: a) Vibration monitoring in an upper floor apartment of Building 2. b) - c) Monitored data in the time and frequency domain reveal horizontal building oscillations in the y-direction with vibration velocities of v_{max} = 0,63 mm/s and v_{rms} = 0,46 mm/s at 4 Hz.

4 FREIGTH TRAIN VIBRATIONS AND WAVE PROPAGATION

Ground vibrations of freight trains in the immediate range of the railway track and the wave-propagation on the terrain were measured. The averaged vibration spectra of freight trains are depicted in Figure 3 as 1/3 octave band values.

A combination of the driven train velocity, the weight and bogie spacing of freight-wagons as well as irregularities of the track superstructure lead to shock wave vibrations in a low-frequency regime laterally to the track. Additionally, sandy soils represent an ideal propagation medium for Rayleigh waves having longer wavelengths within a range of 20 to 40 meters.

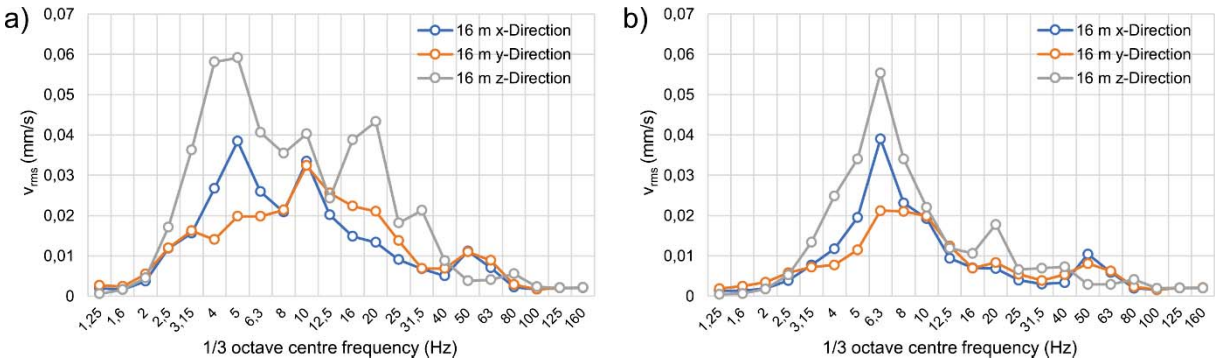

Figure 3: a) – b) Ground vibrations (averaged 1/3 octave values) of freight trains on track 1 (left) and track 2 (right) in the immediate range (16 m) of the railway track.

The reduction exponents of wave propagation on the terrain are depicted in Figure 4. For the purpose of interpretation, these exponents are summarized into three categories. The frequency domains relate to vibrational effects of building dynamics, floor vibrations and secondary airborne sound

On the basis of this rough interpolation, it is evident that the district area is exposed by low-frequency Rayleigh waves. Vibration components in the horizontal and vertical direction are present below the ground level [2]. Instead, higher frequency ranges reveal larger attenuations and corresponding vibrational effects in distant apartments are not estimated.

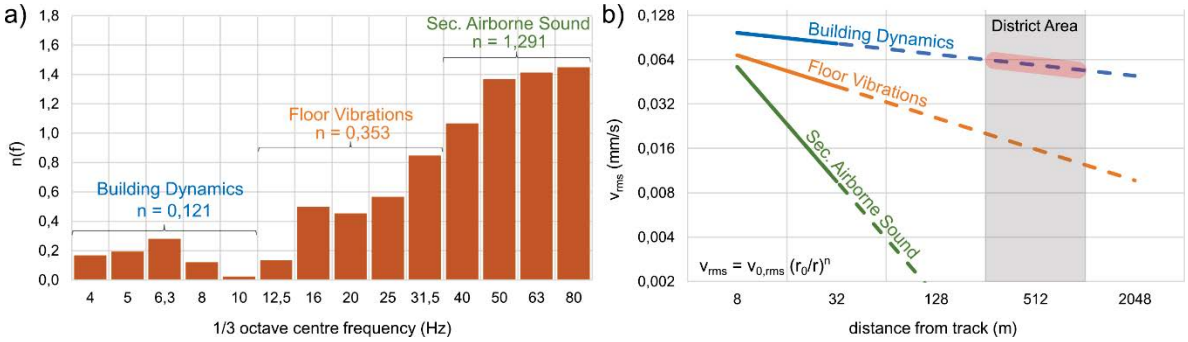

Figure 4: a) Reduction exponents n(f) for the wave propagation in sandy soil. b) Rough interpolation of the vibrational impact on the district area regarding building dynamics (red), vertical floor vibrations and secondary airborne sound.

5 DYNAMIC RESPONSE OF THE BUILDING STRUCTURE

In the next step, the dynamic response of the building structure on the horizontal wave excitation is examined. Vibration sensors were placed on various floors from the basement to the top level. The principal setup and basic concept for detection and interpretation of horizontal oscillations are described in Figure 5. Two different buildings were selected for closer examination (see Figure 1).

Building 1 is subdivided into six floors above the basement. The exterior wall construction consists entirely of reinforced concrete and a wall thickness of 0.2 meters. *Building 2* has one floor less and the exterior wall is executed in the masonry of calcareous sandstone.

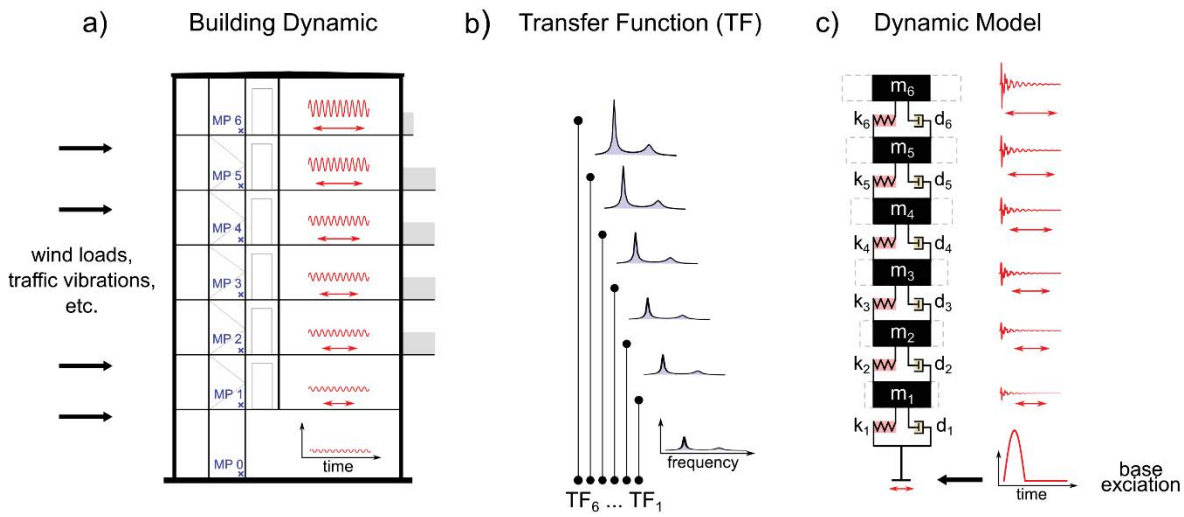

Figure 5: a) – b) Principal set up to detect horizontal transfer functions TFi which represents the dynamic response of the building structure on external excitations. c) A simple dynamic model to emulate the dynamic behavior of bearing structures.

The transfer functions TF_i from the basement to of each floor are plotted in Figure 6 a) and b). In addition, Figure 6 c) shows the transfer behavior derived from the dynamic model. The parameters for stiffness *k* and mass *m* of the coupled system have been tuned to reach an eigenfrequency of around 4 Hz. A numerical method was used to calculate the temporal development of the system [3].

The magnification factors for lateral vibrations of the building structures are depicted in Figure 7. In addition, the model-like behavior for different attenuation ratios ξ of around 1,3%, 2,5% and 5% of the mass oscillations are plotted.

In contrast to the dynamic response of *Building 1* in Figure 7 a), the model-like behavior does not fit well with the transfer magnification of *Building 2* in Figure 7 c). *Building 1* exhibits a better-natured transfer behavior due to its constructive design. Structural damping in between 2,5% and 5% match with the expected attenuation for structures of reinforced concrete [4]. Larger amplification within the structure of *Building 2* in y-direction leads to rocking movements and a higher vibration level on the upper floors.

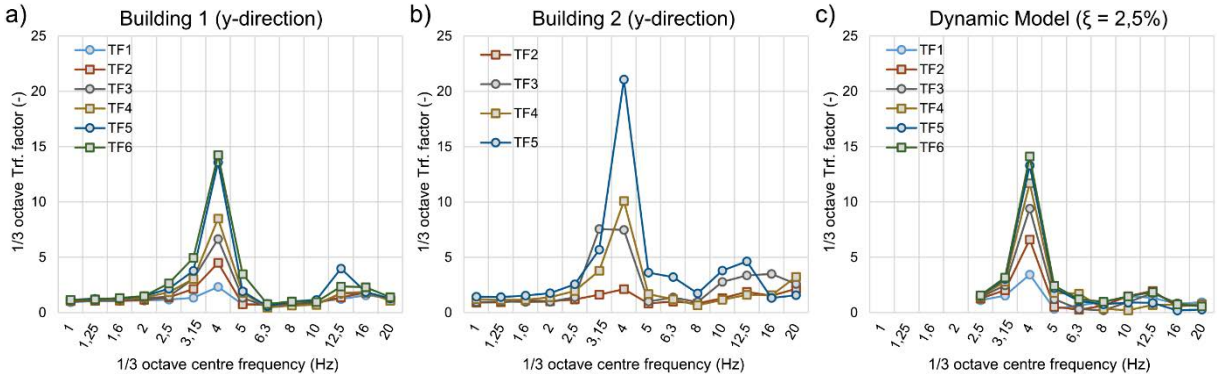

Figure 6: a) – b) Transfer functions TF_i of Building 1 and Building 2 in y-direction. c) Numerical results of the dynamic model with an attenuation ratio of about 2,5% for mass oscillations m_i. (model parameter: $m_i = 1$ to, $k_i = 1100$ kN/m, $d_i = 21.75$ kNs/m).

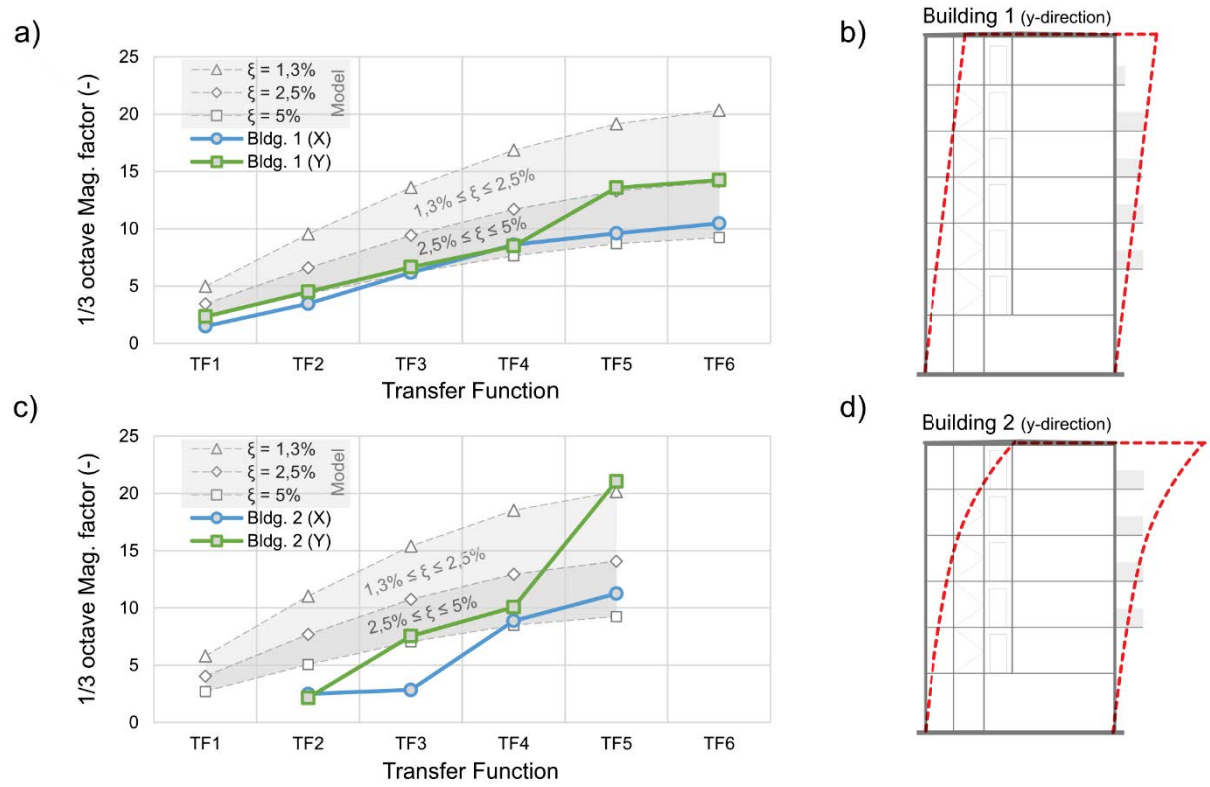

Figure 7: a), c) 1/3 octave magnification factors of Building 1 and Building 2. Besides, numerically gained results from the dynamic model and for different attenuation ratios are depicted. b), d) represent the horizontal deflection of the building schematically.

In summary, disruptive vibrations on upper floors in *Building 2* are caused by an interaction between freight-train vibrations at the track, wave propagation in sandy soils as well as the horizontal oscillation amplification within the building structure which is partially made of calcareous sandstone. A stiffer design should increase structural stability and lead to a model-like response.

On the basis of this knowledge gained, a more detailed FEM study was targeted to improve the dynamic performance of the structural design and to find an optimized constructive design for the district area the dynamic performance of the structural design and to find an optimized constructive design for the district area.

6 OPTIMIZED BUILDING DESIGN

Future area development involves the construction of further multi-story buildings. Fundamental measures to improve the vibrational situation for the whole area could be implemented at the railway track as well as on the propagation path between track and buildings.

An upgrade of the train track and strengthening of the railway superstructure could reduce vibrations at the track. A subterraneous curtain on the path works as a propagation barrier, but these options appeared to be unrealistic due to long approval processes, technical reasons, and economic inefficiency.

Modal analysis in the low-frequency range in Figure 8 reveals basic movement patterns of the building structure in a horizontal direction. The eigenfrequency of Rocking modes matches the experimental results and corresponding resonance magnifications should be minimized.

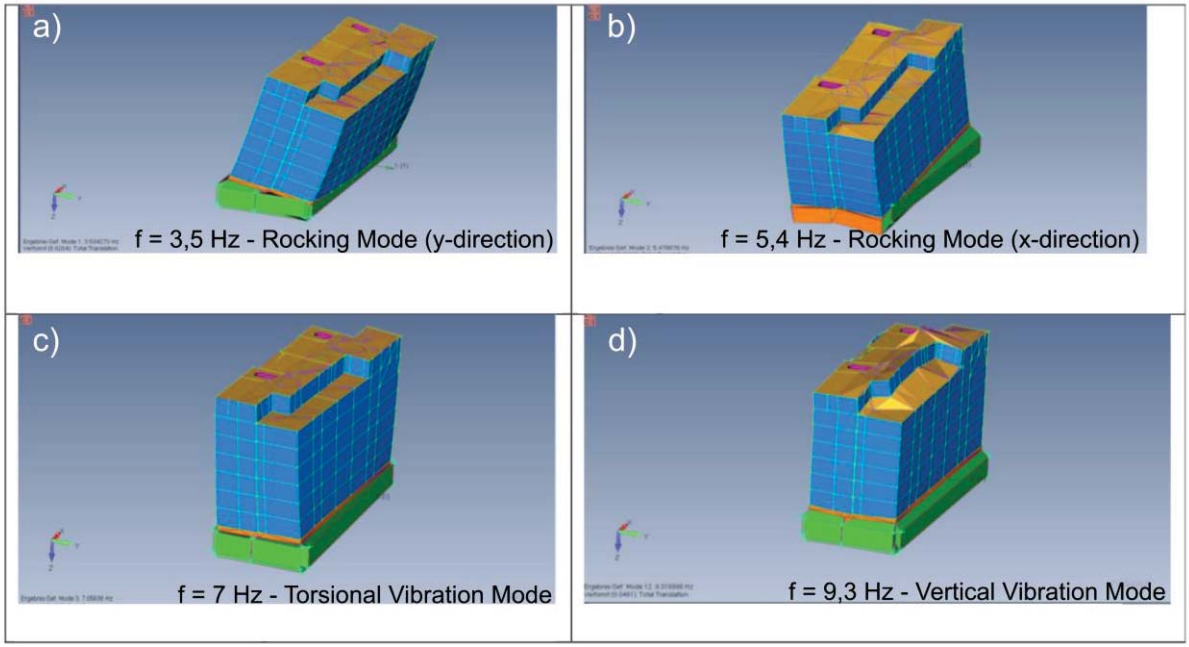

Figure 8: Modal analysis of the building structure having regard to the sandy foundation. a) - b) Rocking modes match with the experimental results and cause horizontal movement patterns. c) – d) In addition, torsion and vertical modes are present in the low-frequency range.

A detailed FEM study instead was launched which is based upon the prior approach. The structural building design and foundation soil were modeled in FEM and a detailed analysis of the building dynamics depending on its parameter was conducted.

Figure 9 depicts the transfer behavior of a construction made of calcareous sandstone (blue). Besides a shift towards higher eigenfrequencies, a stiffer wall construction of a thickness of 0.2 meters (red) made of reinforced concrete leads to a transfer reduction of 33%. These numerical gained results match the experimental results in Figure 7. Furthermore, an increased exterior wall thickness of 0.3 (yellow) meter only reduces the amplification by 40%.

As a result, a stiffer wall construction of thickness 0.2 meter represents a cost-effective solution to reach a reduced vibration level within planned apartments on higher floors.

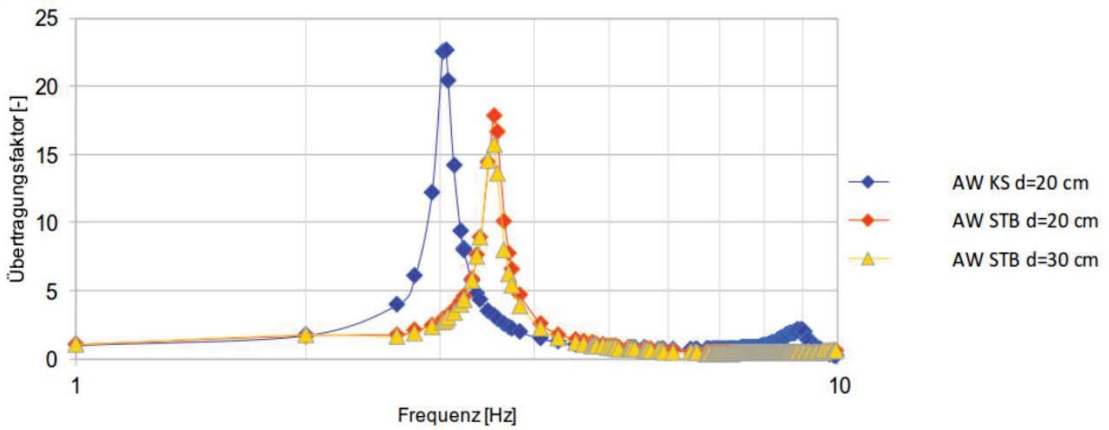

Figure 9: Transfer functions for three different constructive building designs derived from FEM. The transfer behavior for an exterior wall made of calcareous sandstone (blue), reinforced concrete wall of thickness 0.2 meters (red) and 0.3 meters (yellow).

7 SUMMARY

Shock-waves from the faraway railway track lead to horizontal oscillations of the building structure. Buildings are exposed by low-frequency Rayleigh waves which match with the Rocking modes of the constructional design. The design leads to higher amplification of the vibration level within the structure.

The dynamic response of two different constructional designs exhibits that the structural stability of the exterior wall construction is decisive for the amount of amplification within the structure. The optimized structure was determined within a FEM model. A reinforced concrete wall can reach a cost-effective reduction of the vibration level in contrast to a masonry construction of calcareous sandstone.

In general, this case-study indicates, that the constructional design of planned buildings should be investigated more precisely if dynamical risk factors like soft ground, higher building constructions, and a low-frequency shock-wave exposition lateral of a railway track occur.

REFERENCES

[1] DIN 4150-2:1999-06, Vibration in Buildings – Part 2: Effects on persons in buildings, *Beuth*, 1999.

[2] German Geotechnical Society, Empfehlungen des Arbeitskreis Baugrunddynamik, *Ernst & Sohn*, ISBN: 978-3-433-03198-8, 2018.

[3] F. Mertens, T. Göddenhenrich, A. Schirmeisen., Resonant cantilever response of static-to-sliding transitions in dynamic friction force microscopy, *Applied Physics Letters* 104, 113105, 2014

[4] C. Petersen, H. Werkle, Dynamik der Baukonstruktionen, *Springer Vieweg*, ISBN: 978-3-8348-2109-6, 2017

EURODYN 2020
XI International Conference on Structural Dynamics
M. Papadrakakis, M. Fragiadakis, C. Papadimitriou (eds.)
Athens, Greece, 23–26 November 2020

IMPROVED FLOATING SLAB TRACK PERFORMANCE BY ON TOP INSTALLED TUNED MASS DAMPER

Thomas Jaquet, Wang Bo,

Zhejiang Tiantie Industry Co., Ltd
No. 928, Renmin East Road, Tiantai, Zhejiang, China
email: Thomas.jaquet@tiantie.cn

Zhejiang Tiantie Industry Co., Ltd
No. 928, Renmin East Road, Tiantai, Zhejiang, China
email: wangb@tiantie.cn

Keywords: Floating Slab Track, Tuned Mass Damper, Viscous Damper, Insertion Gain

Abstract.
Floating Slab Track (FST) are proven to provide the best mitigation for railway vibration. The inertia of the floating slab balances the excitation of the train pass. Floating Slab on discrete bearing usually provides a system frequency lower than 10 Hz. Although the system frequency is low, FST shows at higher modes, especially in the typical ground-borne noise frequency band of about 63 Hz smaller performances as normally expected. Higher modes of the slab itself amplify train vibration because these modes will not be damped adequately by the support bearings or springs. The solution is an on these specific disturbing frequencies tuned TMD mounted on top of the slab, which balances this problem expertly. The case study at the Metro line 4 shows the application of this combined mitigation measure.

1 INTRODUCTION

In China, the metro network has been rapidly expanded over the past 15 years. A wide variety of noise and vibration measures were also applied in order to protect nearby residential houses. In particular, mass-spring-systems (MSS) were completed in many urban areas in China. An MSS supported by steel springs is a standard mitigation measure in China now. In some areas of the line, however, these systems did not show the isolation effect in practice that could theoretically be expected. This may be due to mistakes during the design phase or construction phase.

2 VIBRATION ATTENUATION BY FLOATING SLAB TRACK

There is no doubt that the best performances in terms of vibration attenuation can be achieved by floating slab track systems if they are well designed by experienced engineers. These mass-spring-systems (MSS) consist of floating slabs with the rails mounted on top. The slabs

are usually constructed of reinforced concrete. Together with the dead load of rails, sleepers and fastenings (and the ballast, if any), they form dynamically active masses that are isolated from the sub-structure by elastic mounts which may be of rubber, elastomeric material or steel. The performance of an MSS depends on a number of factors. Besides the vertical tuning frequency, the bending natural frequencies of the slabs are of significant importance. In addition, the system damping, as well as the stiffness of the sub-structure, has a clear influence. Finally, the success of an MSS can also depend on the dynamics of the tunnel itself. In certain cases there is little advantage to be obtained by using a medium-frequency (say above 15 Hz) floating-slab track construction in railway tunnels. Since the tuning frequency depends on the static spring deflection, it is obvious that the spring stiffness is the most important issue. Fig. 2 shows the transmissibility factor VF over the tuning factor η. The tuning factor is defined as the ratio of the excitation frequency f divided by the natural frequency f_0. It clearly shows that the attenuation of vibration transmission takes place only if the factor is beyond the value of $\sqrt{2}$. There is no reduction of dynamic forces possible when the natural frequency (= tuning frequency) of an MSS is close to or above the relevant excitation frequencies. For an undamped single degree of freedom system (SDOF), the dynamical amplification V being the ratio between dynamic and static force equals:

$$V = \sqrt{\frac{1 + 4D^2\eta^2}{(1-\eta^2)^2 + 4D^2\eta^2}}$$

With
η = f/fo
D = Damping

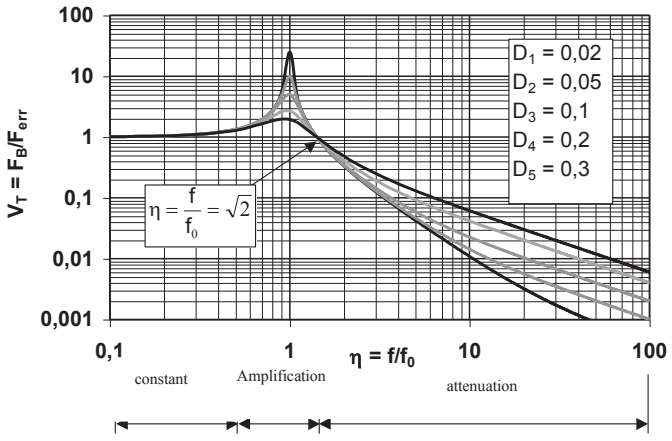

Figure 1: transmissibility curve depending on the damping

Typical vibration frequencies induced by trains are found in a range of 10 - 80 Hz. The frequency spectra usually reveal a concentration of higher peaks in the 60 Hz area, e.g. due to wheel-rail interaction. However, quite often there are high vibration levels between 10 and 30 Hz as well.

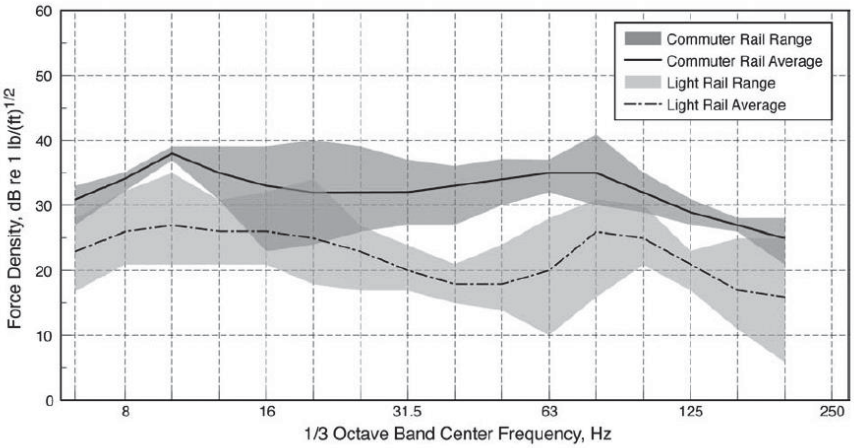

Figure 2: Force density levels for Commuter Train and LRT

In the case of a standard track bed, these frequencies might cause severe vibration problems in nearby buildings showing resonance frequencies just in that range.

A' low-tuned ' mass-spring-system on steel springs can be relied on to provide a tuning frequencies 4 to 10 Hz. Since the tuning frequency of a floating slab track is so important, it has to be explained how it is defined. As a first approach, the extension of the slab can be neglected and all spring stiffnesses of a direction can be united as one common spring. This results in a single-mass-system with 6 degrees of freedom. With respect to the direction of the dominant train excitations, the vertical translation natural frequency is the most relevant one, here referred to as the 'tuning frequency'. A linear spring elasticity provided, the tuning frequency f0 of the non-damped system can easily be calculated by the following simplified equation:

$$f_0 = \frac{5}{\sqrt{\delta_{[cm]}}}(Hz) \qquad \text{with} \quad \delta = \frac{F}{k_z}$$

Although the actual correlations are much more complex, the tuning frequency can be used to evaluate the efficiency of a floating trackbed system at a first view.
Sometimes the non-suspended part of the rolling stock is added to the mass leading to a lower tuning frequency. This part is usually chosen as 10% to 15% of the axle loads contributing to the sprung system.
A more realistic result is achievable by modeling the slab according to the Finite- Element-Method (FEM). In this case, the flexural modes of the slab are taken into consideration. This is of special importance when the 1.-order bending natural frequency of a slab is in the same range as the tuning frequency resulting in coupled modes. The tuning frequency will be shifted, and a diminished tuning factor might result in a reduction of the isolation efficiency of the system.

Vertical Loading	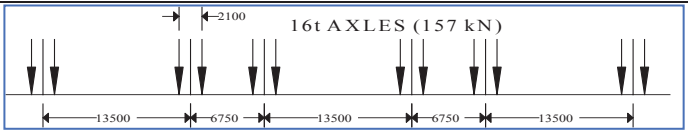
Dynamic Factor	Phi = 1.3 (multiplying the static load and considering the dynamic of a rolling stock)

Horizontal Loading	Curve	$P_H = P \cdot \frac{v^2 \cdot f}{127 \cdot r}$
	Nosing	30 - 100 kN
	Braking	25% of vertical loading

Table 1: Usual train loading for the FST design

3 DESCRIPTION OF THE METRO LINE

The metro line 4 in a Chinese city with a total length of about 42 km was inaugurated in 2017. This line goes from North to South and connects residential areas downtown. The line is constructed as a bored tunnel with a China typical inner diameter of 5.4 m. The tunnel depth is in the range of -20 m (T/R). The subsoil condition is mostly soft clay. Due to the close vicinity between Metro line and dwelling areas and also the very soft soil condition the need for mitigation measures can be normally expected. At the residential area, the predicted vibration level was 72 dB > 62 dB (accepted value for residential buildings).

Figure 3: *Alignment of Metro Line 4 and affected residential buildings*

区域 Applicable Zone	昼间 Daytime	夜间 Nigthtime
特殊住宅区 Special Residential Area	65	62
居住、文教区 Residential &Cultural&Education Area	65	62
居住、商业混合区，商业中心区 Mixed Zone&Bussiness Center District	70	67
工业集中区 Industrial Concentration District	75	72
交通干线道路两侧 Both Sides of Traffic Trunk Road	75	72

Table 2: Accepted limits according to JGJ/T170-2009, Aw= 65 dB (aref=1e-6 m/s)

Due to the predicted vibration level, an FST on steel spring with a system frequency of f=10 Hz was required. Spring supported Floating Slab Tracks are the common mitigation measure in China to attenuate Noise & Vibration from Metro lines.

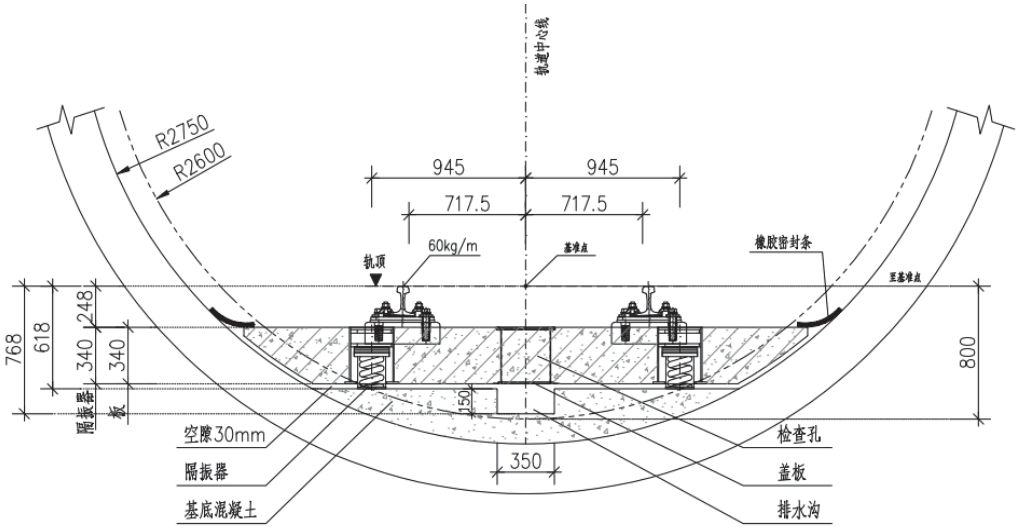

Figure 4: Cross Section of the installed Floating Slab Track

Although an FST on springs was installed the residentials complain about noticeable rumbling noise during the train pass-by. A comprehensive measurement campaign was carried out to identify the reason for the rumbling noise. The measured spectrum at the tunnel wall and within the residential building clearly shows a main peak in the spectra at the 63 Hz 1/3 octave band. The installed FST on springs was not able to mitigate significantly the vibration from the wheel/rail interaction.

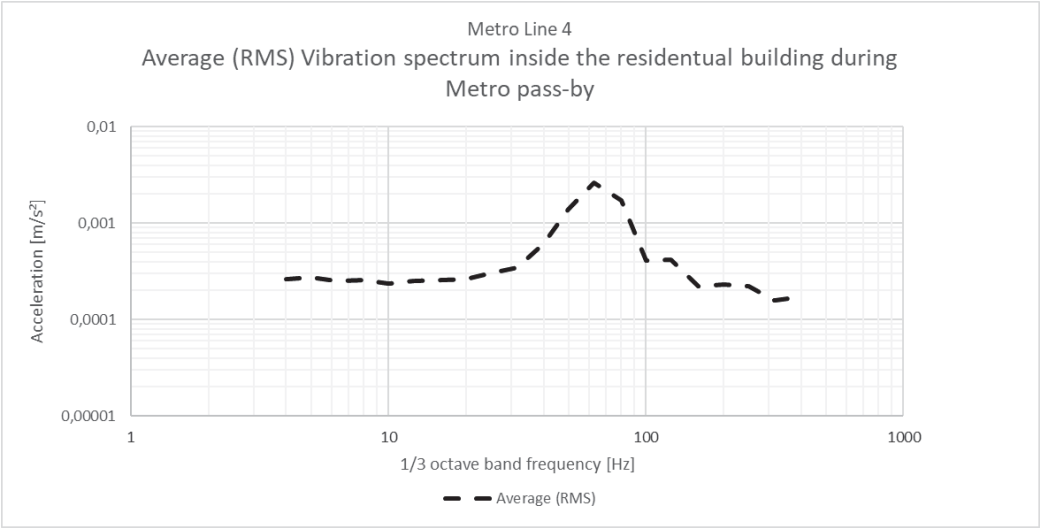

Figure 5: Vibration spectrum inside the affected building on the second floor

Measurements at the tunnel wall confirmed the results of the buildings. Due to the rail wheel interaction, a major peak at 63 Hz on the slab and at the tunnel wall is visible.

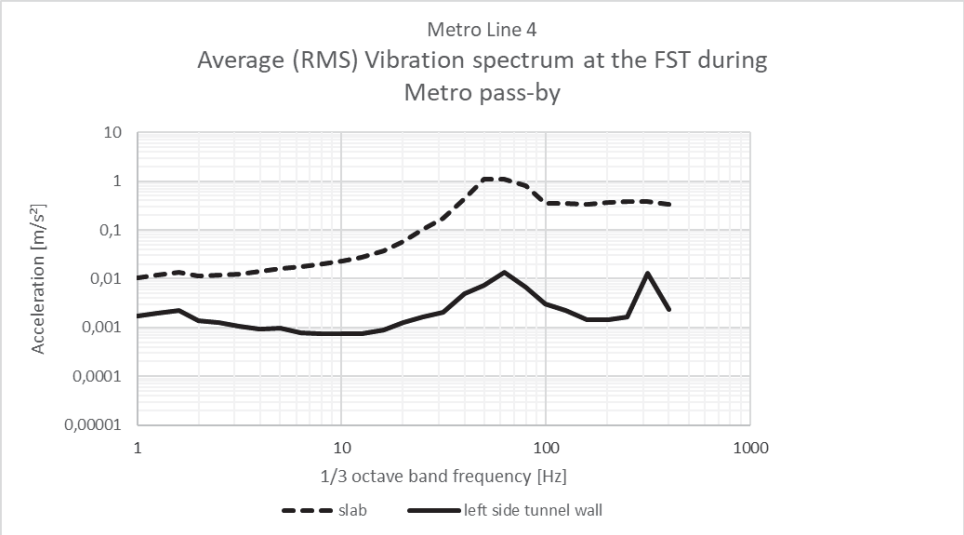

Figure 6: Measured vibration at the tunnel

4 POTENTIAL MITIGATION MEASURES

4.1 Damping of the FST

In order to mitigate the vibration level at 63 Hz, several options were investigated. Damping is an essential factor for all mitigation systems. At railways systems, the standard mitigation materials provide hysteretic and viscous dampers.
The introduction of more viscous damping into the spring cans would increase the damping but would also result in a higher system frequency due to the stiffening effect of the viscous liquid. Real viscous dampers provide only at low frequencies < 10 Hz enough damping, therefore higher structural modes usually are not damped by viscous dampers.

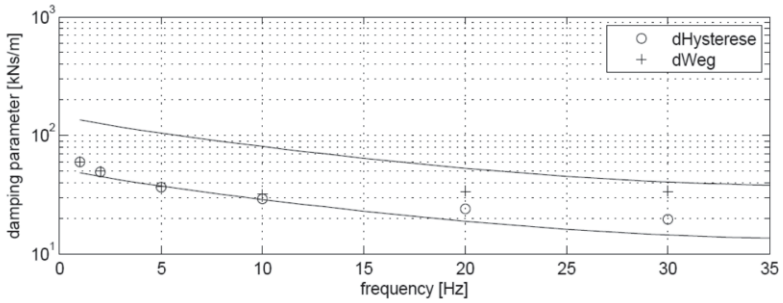

Figure 7: Typical damping behavior of a viscous damper (real measurement)

A theoretical analysis of the expected vibration level at the tunnel wall for an FST with ideal viscous damping and the consideration of the real damping can be seen in figure 8.

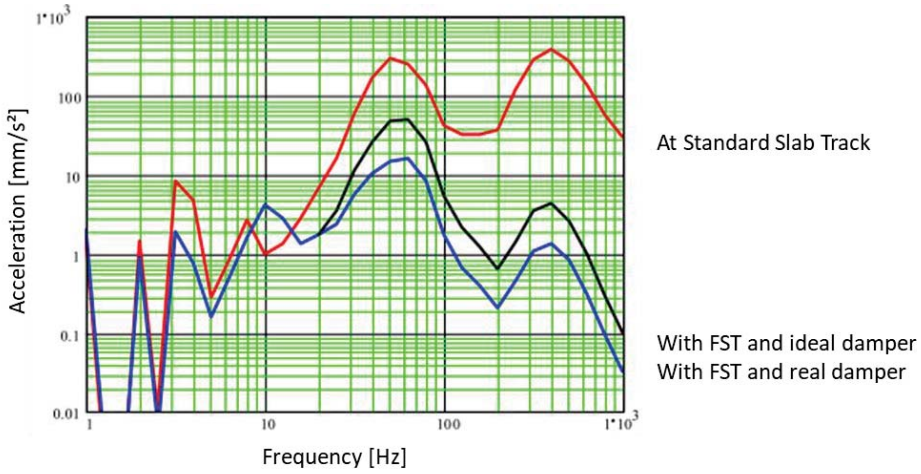

Figure 8: Calculated vibration level at the tunnel wall depending on the applied damping model

4.2 Lower FST system frequency

A lower support frequency can increase the mitigation effect. FST on springs allows due to the permanent access from above to change the springs easily. Softer ones can replace the current springs. Due to the given dimensions, spring stiffness can be varied in the range of +- 20%, which means approx. 10% lower system frequency. It has to be checked whether softer springs would also in compliance with the permissible deflection of the FST (e.g. effect on rail stress) and the static design pf the slab itself (e.g. installed reinforcement).

4.3 Application of a Tuned Mass Damper

A standard method of introducing damping or balancing forces is the application of so-called Tuned Mass Damper (TMD). Excitation forces are compensated by mass forces so that parts of the structure (main construction) remain almost at rest in a certain frequency range. In vibration damping, an additional oscillator consisting of mass and stiffness (undamped absorber) or of mass, stiffness, and damping (damped absorber) is attached to the main structure to be calmed.

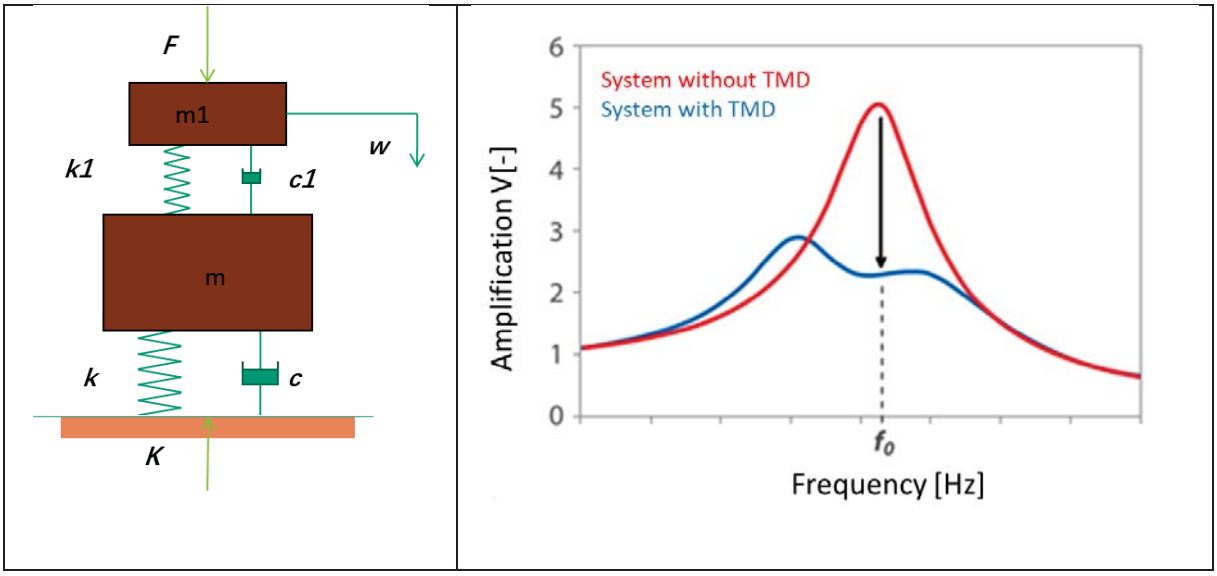

Figure 9: Structure with a Tuned Mass Damper

The undamped absorber is usually used for stationary harmonic oscillation problems, where the absorber natural frequency T is tuned to the excitation frequency. Theoretically, the vibration amplitudes of the main system can be reduced to zero if no damping is present.

For stationary broadband excitation, which is essential in the range of a natural system frequency, the use of an optimally damped absorber is useful. The natural frequency and the damping ratio D_{opt} of the optimally damped absorber can be designed according to [Petersen] with the mass ratio as follows

According to Den Hartog

$$\mu = \frac{m_T}{m}$$

$$\omega_T = \sqrt{k_T/m_T}$$

$$\omega_{T,opt} = \omega \sqrt{\frac{1}{1+\mu}}$$

$$D_{opt} = \sqrt{\frac{3\mu}{8(1+\mu)^3}}$$

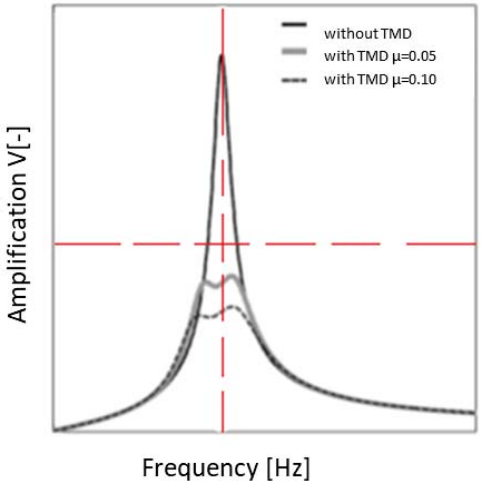

Figure 10: Effect of the TMD mass on the primary system

The above figure shows the effect of an optimally damped absorber with different mass ratios. In order to achieve enough vibration reduction, mass ratios of 0.05 to 0.15 are recommended. The analysis of a 63 Hz TMD leads to the following results:

- The insertion gain can be improved at 63 Hz (from 10 Hz to 65 Hz) with the disadvantage of lower mitigation between 70 and 100 Hz.
- A reduction of -6 dB can be achieved in the 63 Hz 1/3 octave band
- A weakly damped TMD has a stronger narrowband effect.
- The double-weight absorber performs twice as strong and more broadband.
- Minimum damping of 15% is recommended to ensure reliable TMD amplitudes and transmitted forces

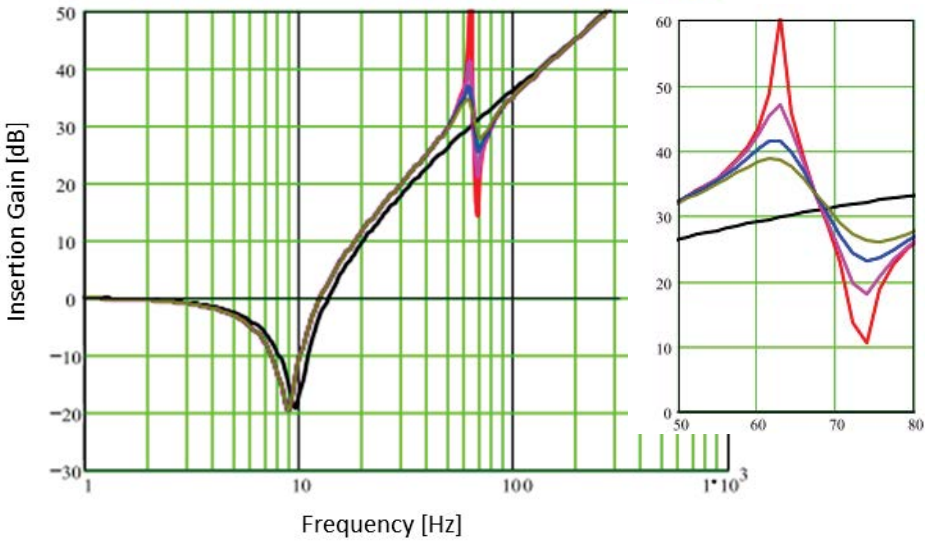

Figure 11: Calculated Insertion Gain for an FST/TMD combination

5 PREFERRED SOLUTION (COMBINED FST / TMD APPLICATION)

Due to the advantages of the TMD compared to the other options, it was decided to continue with the design of the TMD. The following requirements have to be considered to ensure the absolutely safe operation of the track line.

- A low profile of the TMD, it must be designed in between the rails
- No coverage of drainage checking holes
- No obstruction of rescue vehicles

These requirements result in a compact TMD design. The TMD consist mainly of steel plates supported by rubber strips. The system frequency can be adjusted by the specific bedding modulus of the strips and the related strip size. Metal brackets prevent the steel plates from lifting off. A total of 100 m per direction was equipped with these TMD.

Host frequencies	10 Hz (vertical FST system frequency) / 63 Hz (rail / wheel interaction)
Total length of equipped FST per direction	100 m
Number of TMD	88
Installation time per TMD	2 h
TMD Mass	970 kg
Mass ratio	0,15
1. TMD frequency (Theory, Measured)	8.74 Hz / 12.5 Hz
1. TMD Damping (Optimum/ Measured)	18.9 % / 15%
2. TMD frequency (Theory, Measured)	48 Hz / 50 Hz

Table 3 Overview of the design parameter

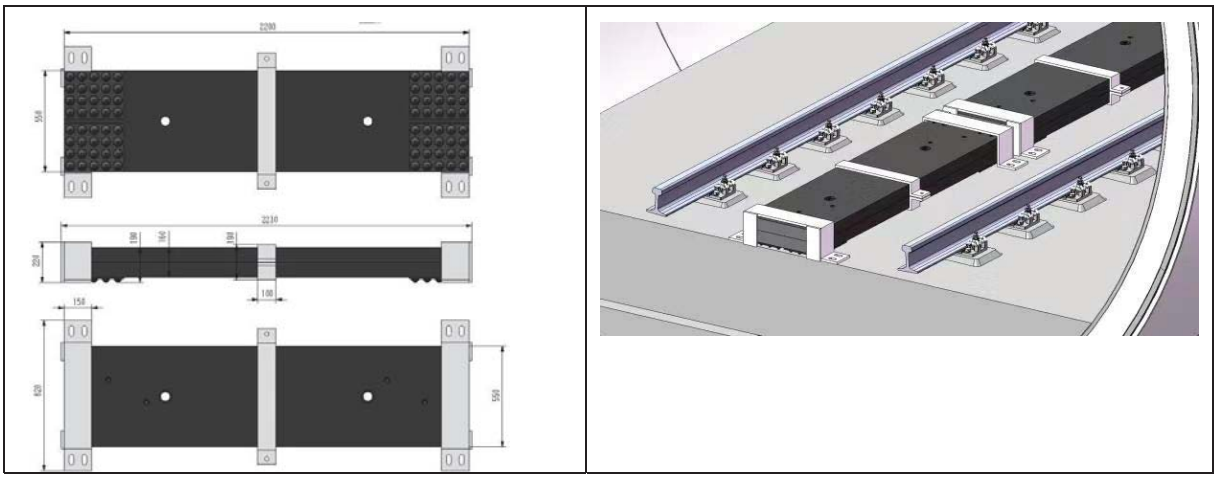

Figure 12: Design of TMD on top of the floating slab track

Figure 13: Installed TMD on the FST

6 ON-SITE RESULTS

Vibration measurements have been performed to check the performance of the installed TMD. In particular, the vibration level at the rail, on the slab, at the TMD, and at the tunnel wall was measured before and after the installation of the TMD. Simultaneously also measurement in residential buildings nearby has been carried out. It was figured out that the effect of the TMD on the tunnel wall vibration shows only low mitigation but measurements within the building show the expected reduction. The TMD itself shows peaks at its eigenmodes which reveals the operation of the TMD itself during train pass-by.

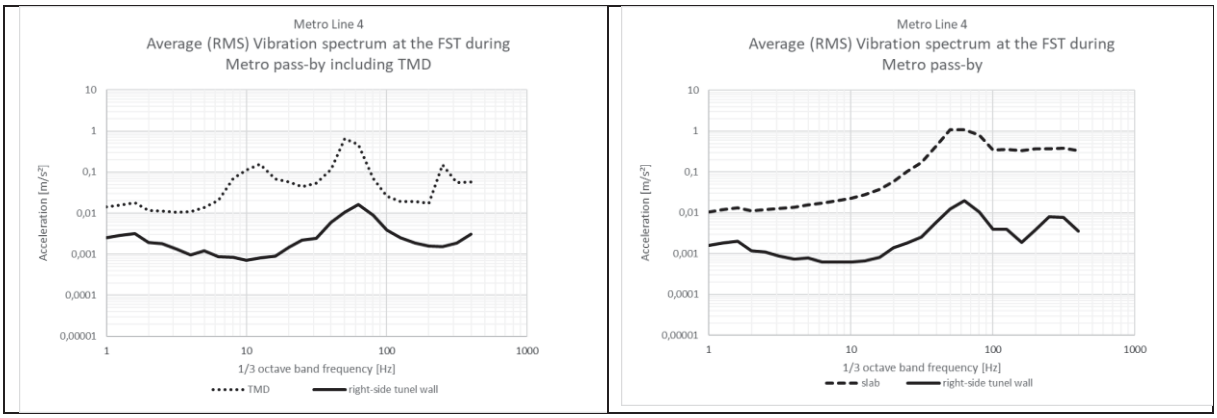

Figure 14: Vibration Level at the tunnel site with and without TMD

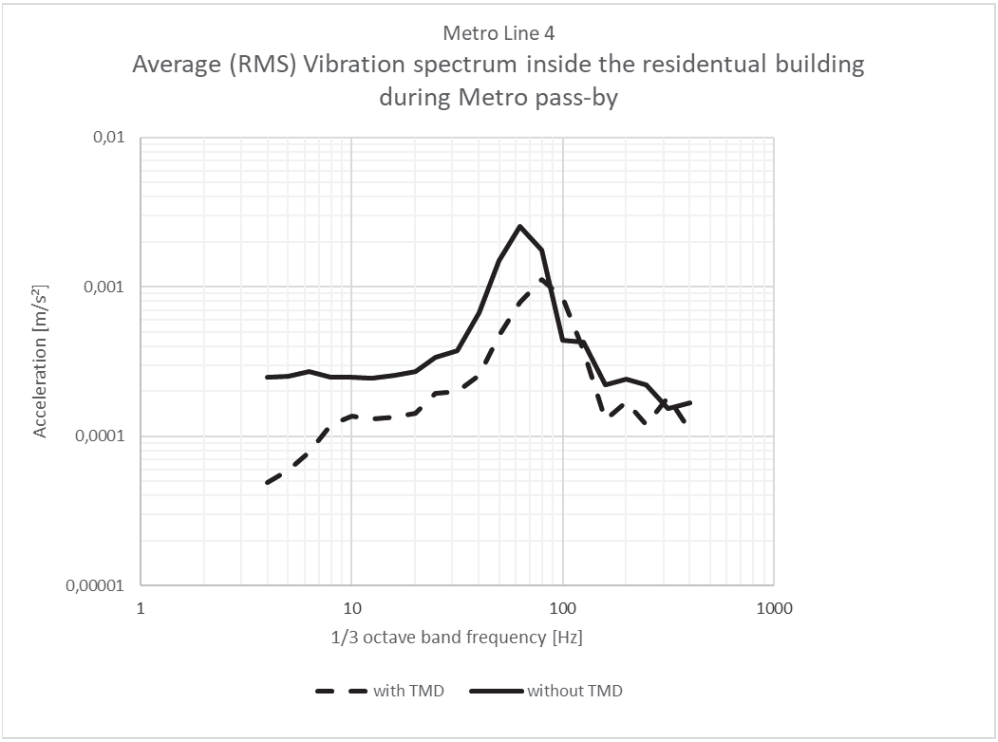

Figure 15: Measured vibration level inside the building with and without TMD

A noticeable reduction mainly at the 63 Hz (1/3 octave band frequency) was measured and confirmed the balancing effect of the TMD on the vibration level. The mitigation effect is even a little bit higher and might result due to the additional inertia of the TMD mounted on the FST.

7 CONCLUSION

Floating Slab Track (FST) are proven to provide the best mitigation for railway vibration. The inertia of the floating slab balances the excitation of the train pass. Floating Slab on discrete

bearing usually provides a system frequency lower than 10 Hz. Although the system frequency is low, FST shows at higher modes, especially in the typical ground-borne noise frequency band of about 63 Hz smaller performances as normally expected. A TMD mounted on top of the slab and tuned on these specific disturbing frequencies can balances this problem expertly. The Case Study at the Metro Line 4 in a Chinese city shows clear vibration mitigation in nearby residential housings due to the installed TMD over 100 m track length.

- The theoretical analysis shows a reduction of – 6dB at the 63 Hz 1/3 octave band. On-site measurements show in the nearby residential housel a slightly higher mitigation effect compared to the theory. The reason might be due to a higher inertia effect of the TMD.
- The design has to consider the requirement/clearance of the track
- Minimum damping of 15% is recommended to ensure reliable TMD amplitudes and transmitted forces
- A TMD mass ratio of 15% is recommended

REFERENCES

[1] Transit Noise and Vibration Impact Assessment Manual, SEPTEMBER 2018

[2] GB/T 50452-2008 Technical specification for protection of historic buildings against man-made vibration, China

[3] Petersen, Schwingungsdämpfer im Ingenieurbau, *ISBN 3-00-008059-7, digitalisierte Neuauflage Oktober 2010*

EURODYN 2020
XI International Conference on Structural Dynamics
M. Papadrakakis, M. Fragiadakis, C. Papadimitriou (eds.)
Athens, Greece, 23–26 November 2020

A MIXED-FRAME-OF-REFERENCE MODEL FOR RAILWAY INDUCED SOIL-STRUCTURE VIBRATION INTERACTION

Paulius Bucinskas[1], Evangelos Ntotsios[2], David J. Thompson[2] and Lars V. Andersen[1]

[1] Department of Engineering
Aarhus University
Denmark
(pb, lva)@eng.au.dk

[2] Institute of Sound and Vibration Research
University of Southampton
United Kingdom
e.ntotsios@soton.ac.uk, djt@isvr.soton.ac.uk

Keywords: Soil-structure interaction, train induced vibration, mixed frame of reference

Abstract. *When modelling the railway induced vibration in a building, three main aspects of the problem have to be considered: the vibration generation at the moving vehicle-track interaction points, the vibration propagation in the underlying infinite soil, and the vibration reception inside the building. This study proposes a computational modelling approach for predicting the full vibration propagation path from the train vehicles up to the building structure. The method includes a moving train model that is directly coupled to a stationary building structure, with interaction between them through the underlying soil using a single step solution procedure. A semi-analytical model is utilized to model the soil to which rigid objects and structures modelled by finite elements (FE) are coupled. The system is excited by a multi-body vehicle model passing over an irregular track. The proposed modelling approach uses the frequency-domain solution with some parts, such as the railway track, formulated in the moving frame of reference (FOR) and other parts, such as building structures, formulated in a fixed FOR. The coupling terms between the two FORs are found by utilizing an analytical formulation of receptance between the two FORs. It is shown that due to the coupling between the fixed and moving FORs, the previously uncoupled discrete frequencies become coupled through the other FOR as a result of the Doppler effect and wave scattering. Two solution procedures of the full system are proposed: partial coupling, where some secondary effects from reflected waves propagating through soil are disregarded, and full coupling, where the vehicle, track, soil and structure are modelled as a fully coupled system. Both proposed solution procedures offer a single-step approach for solving the whole system in the frequency-spatial domain. The application of the model is demonstrated and validated in two example cases: one analyzing a simple building structure near a railway track, using the partial coupling solution procedure, and another analyzing the behaviour of a vehicle model passing over a rigid block embedded inside the soil, using the full coupling solution procedure.*

1 INTRODUCTION

One of the important environmental impacts of existing and future railway lines occurs due to the ground-borne vibration induced by the trains. When a train runs on the track, its wheels induce vibration in the track structure. This vibration then propagates through the ground into nearby buildings where it is perceived either directly, due to motion of floors and walls, or indirectly as re-radiated noise. This causes disturbance to occupants, potential loss of building functionality (e.g. interference with sensitive equipment), loss of real estate value and, in worst case, leading to structural damage.

The impact of railway-induced vibrations has been investigated since the beginning of the previous century and much work has been done to understand and simulate the dynamic interactions between the train, track, tunnel (for underground railways) and ground resulting in models which can predict ground-borne vibration around the railway system. The exact propagation mechanism of environmental vibration is an extremely complex phenomenon, and thus proper evaluation of its effects is difficult. Several different numerical models have been developed for predicting vibration from surface and underground railways in the last few decades. They are mainly based on numerical or semi-analytical methods. Each approach has its own merits. Semi-analytical models are simpler, requiring less input parameters, but they are not able to represent the full details of a given situation. Conversely, numerical models can represent more detailed geometry but require a larger number of input parameters and greater computational effort. The results are then specific to this particular situation and cannot be generalized easily. There are also important limitations in the use of either type of model, due to the modelling simplifications and parameter uncertainty. A comprehensive overview of the state of the art on railway-induced ground vibration models and the underlying excitation mechanisms can be found in [1].

When modelling the environmental vibration in a building induced by railway traffic, three main parts of the problem need to be considered: the vehicle-track system which is the vibration source, the underlying soil through which the vibration propagates, and the building structure which is the vibration receiver. Ideally, all the parts would be combined into a single model, including all coupling terms. However, due to complex analytical formulation needed and the limitations of computational models, this is rarely performed. Most often, parts of the model are coupled together; for example, a coupled vehicle-track-soil model is calculated, and the obtained results propagate to the building structure [2 - 9]. This way, the secondary coupling terms are excluded from the system, such as the effect of the building structure to the response of the track and the vehicle. This is acceptable, as these coupling terms do not influence the system significantly [10]. For example, Fiala et al. [2] used a two-step approach to obtain the response of a building structure by splitting the problem into a vehicle-track-soil source model and a structure-soil receiver model. With a similar approach, François et al. [3] studied road-traffic-induced vibration. The work also proposed a methodology to exclude the soil-structure interaction problem for cases of soft structures resting on stiff soils. A so-called sub-modelling technique was proposed by Hussein et al. [6], where the response of the soil surface from a tunnel structure was modelled using the 'pipe-in-pipe' model [11] to find the response of a 2D frame. An almost identical system assembly method was also used by Lopes et al. [5]; however, the soil surface response from a tunnel structure was modelled using a 2.5D FEM-PML (perfectly matched layers) model and a 3D building structure was analyzed. In [9], Kuo et al. use a similar numerical approach and the model developed in [10] to investigate the effect of dynamic soil characteristics, surface foundation type, and building geometry on the building's response to railway induced vibrations and compare with the FRA empirical adjustment factors [12].

The aim of this work is to model the full vibration propagation path from the vehicle up to the building structure. The proposed method includes a moving vehicle model that is directly coupled to a stationary building structure, with interaction between them through the infinite underlying soil, without needing a multiple step solution. At the same time, the method offers a relatively quick and flexible solution procedure. A fully 3D system is modelled, with structures modelled using FE, allowing a wide variety of configurations. To limit the computational times needed, the semi-analytical soil formulation is utilized, with a surface railway track, using the model originally proposed by Sheng et al. in [13, 14] and later extended in [15]. A multi-body vehicle model passing over an irregular track excites the system. The work introduces an approach of solving the coupled vehicle-track-soil-building system using a single step solution procedure. Two system assembly and solution methods are presented: *partial coupling* and *full coupling*. With the *partial coupling* procedure disregarding some effects caused by the reflected waves for a more computationally efficient solution, and the *full coupling* procedure including all the coupling terms. Additionally, the methodology for modelling rigid objects and FE structures interacting with the soil is described with its implementation into the proposed solution approaches. To show the capabilities of the proposed modelling approach two example cases are analyzed: (i) for a simple building structure near a railway track, using the partial coupling solution procedure, and (ii) the behaviour of a vehicle model passing over a rigid block embedded inside the soil, using the full coupling solution procedure.

2 SEMI-ANALYTICAL SOIL MODEL

A semi-analytical soil model is used in the present work. The model utilizes a well-known approach based on an analytical solution to the Green's function in the frequency-wavenumber domain. For the linear hysteric half-space $z \leq 0$, the displacement field in time–space domain can be obtained using a convolution integral:

$$u_i(x,y,z,t) = \int_{-\infty}^{t}\int_{-\infty}^{0}\int_{-\infty}^{\infty}\int_{-\infty}^{\infty} g_{ij}(x-x',y-y',z,z',t-t')\, p_j(x',y',z',t')\, \mathrm{d}x'\, \mathrm{d}y'\, \mathrm{d}z'\, \mathrm{d}t' \quad (1)$$

where the Green's function g_{ij} relates the displacement component u_i at the point (x, y, z) and time t to the loads p_j applied in direction j at all positions and times up to and including the time t. The soil is assumed invariant and infinite in both horizontal directions, while the material properties vary over depth due to stratification.

The Green's function is challenging to find analytically in time-space domain for a layered half-space. Thus, a triple Fourier transformation can be performed, transforming the two horizontal coordinates into the wavenumbers k_x andk_y, and time into the circular frequency ω. By introducing a discretization into a number of depths z_n, $n = 1,2,3,\ldots,N_z$, Eq. (1) simplifies into

$$\bar{U}_i(k_x,k_y,z,\omega) = \sum_{n=1}^{N_z} \bar{G}_{ij}(k_x,k_y,z,z_n,\omega)\, \bar{P}_{n,j}(k_x,k_y,\omega) \quad (2)$$

where $\bar{U}$ and $\bar{G}_{ij}$are components of the displacement vector and the Green's function tensor, respectively, in the frequency-wavenumber domain. After the discretization over depth, $\bar{P}_{n,j}$ signifies the traction applied on a horizontal interface placed at the depth z_n. In the following, upper case symbols indicate Fourier transforms with respect to time, whereas overbar indicates Fourier transforms with respect to the horizontal spatial coordinates.

There are two major approaches used to assemble multiple soil layers and express analytically the Green's functions $\bar{G}_{ij}$ appearing in Eq. (2): the flexibility approach and the stiffness

approach. The flexibility approach is based on the original work proposed by Thomson [16] and Haskell [17]. The stiffness approach was introduced by Kausel and Roësset [18] and extends the original transfer matrix, as derived in [16, 17] by reordering it into a stiffness expression equivalent to those used in the FEM, assuming that the interface between two layers is interpreted as a connecting node. Multiple layers can be assembled by overlapping the stiffness matrices at the connecting interfaces.

In this work, both methods have been utilized: the flexibility approach with numerical stabilization for the fixed FOR soil model and the stiffness approach for the moving FOR model. The reason that the flexibility approach is used for the fixed FOR and the soil-structure interaction is because it enables the application of structure-to-soil interaction forces without increasing the size of the involved matrices (that is always six by six) for foundations that are embedded in the ground (i.e. piled foundations). For the moving FOR problem, only the Green's functions for a surface load (i.e. the track) are needed and thus the stiffness approach is used which is free of numerical instabilities at higher frequencies, that are more prominent due to the moving of the load. Any instabilities occurring in the flexibility approach are dealt using stabilization techniques that are based on the orthonormalization method [19] and by splitting very thick layers (if any) into multiple smaller layers with the same material properties.

After the displacements in the frequency-wavenumber domain are obtained, a double inverse Fourier transformation is performed into frequency-space domain

$$U_{\mathrm{f}\,i}(x_{\mathrm{f}}, y, z, \omega_{\mathrm{f}}) = \frac{1}{4\pi^2}\int_{-\infty}^{\infty}\int_{-\infty}^{\infty}\overline{U}_i(k_x, k_y, z, \omega_{\mathrm{f}})\,\mathrm{e}^{\mathrm{i}(k_x x_{\mathrm{f}} + k_y y)}\,\mathrm{d}k_x\,\mathrm{d}k_y. \tag{3}$$

This equation is used when both the load and the response in a fixed FOR is considered. The load is applied at a circular frequency ω_{f} and coordinate x_{f}, with subscript 'f' indicating a fixed FOR. Here, the inverse Fourier transformation can be carried out in semi-discrete form by adopting polar coordinates, since the integration with respect to the azimuthal angle can be done in closed form, leading to Bessel functions in the components of the Green's function.

When the whole system is considered in a moving FOR, the Green's function and, at the same time, the response in the frequency-wavenumber domain lose the polar symmetry around the origin of the wavenumber domain, compared to a purely fixed FOR. Hence, a fully discrete inverse Fourier transformation from wavenumber domain into spatial domain is necessary. Assuming that a load is moving in the positive x-direction, the frequency used to compute the Green's function becomes wavenumber dependent. In that case, the inverse double Fourier transformation into frequency–space domain is defined as

$$U_{\mathrm{m}\,i}(x_{\mathrm{m}}, y, z, \omega_{\mathrm{m}}) = \frac{1}{4\pi^2}\int_{-\infty}^{\infty}\int_{-\infty}^{\infty}\overline{U}_i\big(k_x, k_y, z, \omega_{\mathrm{m}} - k_x v\big)\mathrm{e}^{\mathrm{i}(k_x x_{\mathrm{m}} + k_y y)}\,\mathrm{d}k_x\,\mathrm{d}k_y \tag{4}$$

where v is the velocity at which the moving FOR travels through the fixed FOR. Subscript 'm' indicates values in the moving FOR.

Since the methodology presented in this work uses both moving and fixed FOR, a mixed FOR is used, where the displacement response observed in a fixed FOR from a load applied at a stationary point in the moving FOR and vice versa are needed in order to obtain the coupling terms between the two FORs.

Following a similar analysis with [13], the displacements $U_{\mathrm{f}\,i}$ at x_{f} for fixed FOR from a harmonic moving load of circular frequency ω_{m} can be expressed as

$$U_{\mathrm{f}\,i}(x_{\mathrm{f}}, y, z, \omega_{\mathrm{m}}, \omega_{\mathrm{f}}) = \frac{1}{v}\mathrm{e}^{\mathrm{i}\beta x_{\mathrm{f}}}\frac{1}{2\pi}\int_{-\infty}^{\infty}U_i\big(\beta, k_y, z, \omega_{\mathrm{m}} - \beta v\big)\mathrm{e}^{\mathrm{i}k_y y}\mathrm{d}k_y\,,\ \ \beta = \frac{\omega_{\mathrm{m}} - \omega_{\mathrm{f}}}{v} \tag{5}$$

where ω_f is the receiving frequency at the fixed FOR.

Alternatively, using an equivalent analysis for a stationary harmonic load of circular frequency ω_m received in a moving FOR at $x_\mathrm{m} = x_\mathrm{f} - vt$ the displacements $U_{\mathrm{m}\,i}$ can be expressed as:

$$U_{\mathrm{m}\,i}(x_\mathrm{m}, y, z, \omega_\mathrm{f}, \omega_\mathrm{m}) = \frac{1}{v}\mathrm{e}^{\mathrm{i}\beta x_\mathrm{m}}\frac{1}{2\pi}\int_{-\infty}^{\infty} U_i(\beta, k_y, z, \omega_\mathrm{f})\mathrm{e}^{\mathrm{i}k_y y}\mathrm{d}k_y\,, \qquad \beta = \frac{\omega_\mathrm{m} - \omega_\mathrm{f}}{v}. \quad (6)$$

Comparing Eqs. (5) and (6) it is evident that the expressions are equivalent. That is, the displacements originating from a moving source and observed in a fixed FOR are equivalent to the displacements caused by a stationary source and observed in a moving frame:

$$U_{\mathrm{m}\,i}(x_\mathrm{m}, y, z, \omega_\mathrm{f}, \omega_\mathrm{m}) = U_{\mathrm{f}\,i}(x_\mathrm{f}, y, z, \omega_\mathrm{m}, \omega_\mathrm{f}) \quad (7)$$

given that the horizontal coordinates x_m and x_f have the same numerical value. In practice, this means that only Eq. (5) or Eq. (6) needs to be evaluated. Then the integral part of the equation is reused for the other FOR combination, with changed *x*-coordinate.

3 STRUCTURES INTERACTING WITH SOIL IN A SINGLE FRAME OF REFERENCE

To couple the semi-analytical soil model to a FE model of one or more structures, a dynamic stiffness matrix of the soil is established. Firstly, the desired geometry of the soil-structure interface is discretized into a number of 'soil–structure interaction' (SSI) nodes. The response is requested at a range of 'observation' nodes. The dynamic stiffness matrix is established using the SSI nodes, which is then coupled to structures and used to obtain the system displacements.

To establish the dynamic stiffness matrix of the soil, a global flexibility matrix relating all the degrees of freedom is needed. For a three-dimensional case, each SSI node has three degrees of freedom. Therefore, the receptance matrix $\mathbf{R}_{\mathrm{ss}}(\omega)$, also called the flexibility matrix, is a square matrix with three times more rows and columns than the number of nodes in the system. To create the receptance matrix, a unit harmonic load $\bar{P}_{0,s_j}$ is applied to a single degree of freedom, s_j, and the resulting displacements are observed at all SSI degrees of freedom, including the loaded one. The procedure is repeated for every degree of freedom in the system. This way, the receptance relating all degrees of freedom to the loaded degree of freedom is established. The receptance between degrees of freedom $s_i$and s_j is found as

$$R_{s_i,s_j}(\omega) = \int_{-\infty}^{\infty}\int_{-\infty}^{\infty} \bar{G}_{d_i d_j}(k_x, k_y, z_{n_i}, z_{n_j}, \omega)\,\hat{\bar{P}}_{n_j,s_j}(k_x, k_y, \omega)\,\mathrm{e}^{\mathrm{i}\left(k_x(x_{n_i}-x_{n_j})+k_y(y_{n_i}-y_{n_j})\right)}\,\mathrm{d}k_x\,\mathrm{d}k \quad (8)$$

where $\hat{\bar{P}}_{n_j,s_j}(k_x, k_y, \omega)$ is the double spatial Fourier transform of a distributed harmonic load $\hat{P}_{n_j,s_j}(x, y, \omega)$ of unit magnitude acting within the frequency domain at the depth z_{n_j} in degree of freedom s_j. The same procedure can be performed in both fixed and moving FORs. The obtained results are placed in a single column of the receptance matrix and the process is repeated for every degree of freedom. Assuming there is a total of S SSI degrees of freedom in the system, the assembled receptance matrix becomes:

$$\mathbf{R}_{\mathrm{ss}}(\omega) = \begin{bmatrix} R_{s_1,s_1}(\omega) & R_{s_1,s_2}(\omega) & \cdots & R_{s_1,s_S}(\omega) \\ R_{s_2,s_1}(\omega) & R_{s_2,s_2}(\omega) & \cdots & R_{s_2,s_S}(\omega) \\ \vdots & \vdots & \ddots & \vdots \\ R_{s_S,s_1}(\omega) & R_{s_S,s_2}(\omega) & \cdots & R_{s_S,s_S}(\omega) \end{bmatrix}. \quad (9)$$

The receptance matrix can be established for the moving and fixed FORs. However, only in the fixed FOR, the matrix is symmetric, assuming that the applied load $\hat{P}_{n_j,s_j}(x,y,\omega)$ is the same for all degrees of freedom. If no external structures are connected to the semi-analytical soil model, it is possible to apply the loads and obtain the system displacements $\mathbf{U}_\mathrm{s}$ directly as

$$\mathbf{U}_\mathrm{s}(\omega) = \mathbf{R}_\mathrm{ss}(\omega)\,\mathbf{P}_\mathrm{s}(\omega) \tag{10}$$

where $\mathbf{P}_\mathrm{s}$ is the vector of load magnitudes. It is implied here that the load acting in degree of freedom s_j has a spatial distribution defined by $\hat{P}_{n_j,s_j}$ and a magnitude defined by element j of $\mathbf{P}_\mathrm{s}$.

3.1 FE models interacting with the soil

To couple the soil model with an FE model of one or more structures, the dynamic stiffness matrix of the soil $\mathbf{K}_\mathrm{ss}(\omega)$ is needed. It can be obtained by inverting the receptance matrix. Including the dynamic stiffness matrix $\mathbf{K}_\mathrm{FE}$ of the FE model the dynamic stiffness in the single frame of reference (SFOR) can be assembled as:

$$\mathbf{K}_\mathrm{SFOR}(\omega) = \begin{bmatrix} \mathbf{K}_\mathrm{ss}(\omega) + \mathbf{K}_\mathrm{FE}^\mathrm{ss}(\omega) & \mathbf{K}_\mathrm{FE}^\mathrm{sn}(\omega) \\ \mathbf{K}_\mathrm{FE}^\mathrm{ns}(\omega) & \mathbf{K}_\mathrm{FE}^\mathrm{nn}(\omega) \end{bmatrix} \tag{11}$$

where superscript ‘s’ denotes the degrees of freedom through which the FE model interacts with the soil, while superscript ‘n’ denotes the degrees of freedom that are internal to the FE model. Combinations of superscripts ‘sn’ and ‘ns’ denote the coupling terms. Due to symmetry of the FE system matrices, $\mathbf{K}_\mathrm{FE}^\mathrm{ns}(\omega) = [\mathbf{K}_\mathrm{FE}^\mathrm{sn}(\omega)]^\mathrm{T}$. In addition, the matrix $\mathbf{K}_\mathrm{FE}^\mathrm{sn}(\omega)$ is usually sparsely populated.

The displacements of the system can then be obtained by solving the system of equations:

$$\mathbf{K}_\mathrm{SFOR}(\omega)\,\mathbf{U}_\mathrm{SFOR}(\omega) = \mathbf{P}_\mathrm{SFOR}(\omega). \tag{12}$$

To obtain the displacements of the observation degrees of freedom, a flexibility matrix relating the SSI and observation degrees of freedom is needed. Assuming that the numbering of observation degrees of freedom is stored in a set $o = \{o_1, o_2, \ldots, o_O\}$ with the number of degrees of freedom being O, the flexibility matrix will have O rows and S columns. The flexibility matrix for observation degrees of freedom is assembled as:

$$\mathbf{R}_\mathrm{os}(\omega) = \begin{bmatrix} R_{o_1,s_1}(\omega) & R_{o_1,s_2}(\omega) & \cdots & R_{o_1,s_S}(\omega) \\ R_{o_2,s_1}(\omega) & R_{o_2,s_2}(\omega) & \cdots & R_{o_2,s_S}(\omega) \\ \vdots & \vdots & \ddots & \vdots \\ R_{o_O,s_1}(\omega) & R_{o_O,s_2}(\omega) & \cdots & R_{o_O,s_S}(\omega) \end{bmatrix}. \tag{13}$$

To find the displacements of the observation nodes, the observation flexibility matrix $\mathbf{R}_\mathrm{os}$ is multiplied by the soil displacements at the SSI degrees of freedom $\mathbf{U}_\mathrm{s}$, which are extracted from the whole system displacement vector $\mathbf{U}_\mathrm{SFOR}$:

$$\mathbf{U}_\mathrm{o}(\omega) = \mathbf{R}_\mathrm{os}(\omega)\,[\mathbf{R}_\mathrm{ss}(\omega)]^{-1}\,\mathbf{U}_\mathrm{s}(\omega) = \mathbf{R}_\mathrm{os}(\omega)\,\mathbf{K}_\mathrm{ss}(\omega)\,\mathbf{U}_\mathrm{s}(\omega). \tag{14}$$

3.2 Rigid structures interacting with the soil

The semi-analytical soil model allows also modelling of completely rigid objects interacting with the soil. This is useful when modelling structures that are much stiffer than the surrounding material, for example building foundations. To create a three-dimensional rigid object, the object shape is discretized into a number of SSI nodes. The global flexibility matrix is created in

the same way as in the previous subsection and inverted to obtain the dynamic stiffness matrix. However, condensation of the stiffness matrix must be performed in order to reduce the system such that the response can be determined in terms of the rigid body modes rather than the original degrees of freedom of the SSI nodes. This is achieved by assuming that SSI nodes belonging to the same rigid object are fixed relatively to each other and move together with the degrees of freedom of a reference master node that defines the motion of the rigid object. In principle, the master node can be placed at any position. However, it is most conveniently placed in the point at which coupling to an FE model should be done. That is, for example, in the centre of the topside of a footing. In the most common three-dimensional case, separate SSI nodes have three degrees of freedom each, i.e. three lateral displacements, while each rigid object has six degrees of freedom: three for lateral displacements and three additional rotational degrees of freedom of the reference node. For a single rigid object composed of a number of SSI nodes, the transformation matrix $\mathbf{T}_{0,i}$ is created. Multiple rigid objects can also be a part of the same system. The global transformation matrix for a system with N rigid objects can be assembled as:

$$\mathbf{T}_\mathrm{s} = \begin{bmatrix} \mathbf{T}_{0,1} & \mathbf{0} & \cdots & \mathbf{0} \\ \mathbf{0} & \mathbf{T}_{0,2} & \cdots & \mathbf{0} \\ \vdots & \vdots & \ddots & \vdots \\ \mathbf{0} & \mathbf{0} & \cdots & \mathbf{T}_{0,N} \end{bmatrix}. \tag{15}$$

The system can also contain non-associated ‘free’ SSI nodes, which are not part of any rigid object. In that case, the local transformation matrix for such nodes will be the identity matrix with the same number of rows and columns as the number of degrees of freedom associated with the free node.

To obtain the condensed stiffness matrix of the soil, , the dynamic stiffness matrix of the soil $\mathbf{K}_{\mathrm{ss}}(\omega)$ is modified:

$$\mathbf{K}_\mathrm{s}(\omega) = [\mathbf{T}_\mathrm{s}]^\mathrm{T}\, \mathbf{K}_{\mathrm{ss}}(\omega)\, \mathbf{T}_\mathrm{s}. \tag{16}$$

The matrix can then be coupled to FE structures in the same way as described previously. Due to condensation of some SSI nodes, Eq. (14) is also modified by introducing the transformation matrix

$$\mathbf{U}_\mathrm{o}(\omega) = \mathbf{R}_{\mathrm{os}}(\omega)[\mathbf{R}_{\mathrm{ss}}(\omega)]^{-1}\, \mathbf{T}_\mathrm{s}\, \mathbf{U}_\mathrm{s}(\omega) = \mathbf{R}_{\mathrm{os}}(\omega)\mathbf{K}_{\mathrm{ss}}(\omega)\mathbf{T}_\mathrm{s}\, \mathbf{U}_\mathrm{s}(\omega). \tag{17}$$

3.3 Vehicle, railway track and wheel-rail interaction

The system is excited by one or more vehicles travelling across a railway track. The vehicles can be modelled using various multibody systems, with varying complexity, depending in the application case. Vehicles are only modelled in two dimensions and only the vertical wheel-rail interaction forces are considered. The dynamic stiffness matrix of the vehicle $\mathbf{K}_{\mathrm{vv},i}(\omega_\mathrm{m})$ is created in a moving FOR by combining the vehicle stiffness, damping and mass matrices. If multiple vehicles are needed, it is assumed that there is no direct interaction between vehicles and the dynamic stiffness matrix becomes:

$$\mathbf{K}_\mathrm{v}(\omega_\mathrm{m}) = \begin{bmatrix} \mathbf{K}_{\mathrm{vv},1}(\omega_\mathrm{m}) & \mathbf{0} & \cdots & \mathbf{0} \\ \mathbf{0} & \mathbf{K}_{\mathrm{vv},2}(\omega_\mathrm{m}) & \cdots & \mathbf{0} \\ \vdots & \vdots & \ddots & \vdots \\ \mathbf{0} & \mathbf{0} & \cdots & \mathbf{K}_{\mathrm{vv},I}(\omega_\mathrm{m}) \end{bmatrix}. \tag{18}$$

Here it is assumed that there is a total number I of vehicles in the system. Further, there is no coupling between separate vehicles through the vehicle stiffness matrix, i.e. each car of a train acts like a separate vehicle.

A layered track structure containing the rails, rail-pads, sleepers and ballast is used. It is coupled to the underlying soil in the frequency-wavenumber domain as described in [15]. By using the stiffness matrix for the rails $\mathbf{K}_\mathrm{r}(\omega_\mathrm{m})$ and the diagonal stiffness matrix $\mathbf{K}_\mathrm{H}$ for the wheel-rail contact interaction the coupled vehicle–track system response from a unit amplitude unevenness is given as:

$$\begin{bmatrix} \mathbf{K}_\mathrm{v}^{\mathrm{uu}}(\omega_\mathrm{m}) & \mathbf{K}_\mathrm{v}^{\mathrm{uw}}(\omega_\mathrm{m}) & \mathbf{0} \\ \mathbf{K}_\mathrm{v}^{\mathrm{wu}}(\omega_\mathrm{m}) & \mathbf{K}_\mathrm{v}^{\mathrm{ww}}(\omega_\mathrm{m}) + \mathbf{K}_\mathrm{H} & -\mathbf{K}_\mathrm{H} \\ \mathbf{0} & -\mathbf{K}_\mathrm{H} & \mathbf{K}_\mathrm{r}(\omega_\mathrm{m}) + \mathbf{K}_\mathrm{H} \end{bmatrix} \begin{Bmatrix} \mathbf{U}_\mathrm{v}^{\mathrm{u}}(\omega_\mathrm{m}) \\ \mathbf{U}_\mathrm{v}^{\mathrm{w}}(\omega_\mathrm{m}) \\ \mathbf{U}_\mathrm{r}(\omega_\mathrm{m}) \end{Bmatrix} = \begin{Bmatrix} \mathbf{0} \\ K_\mathrm{H}\,\mathbf{d}(\omega_\mathrm{m}) \\ -K_\mathrm{H}\,\mathbf{d}(\omega_\mathrm{m}) \end{Bmatrix} \tag{19}$$

where $\mathbf{d}(\omega_\mathrm{m}) = \exp\left(\frac{\omega_\mathrm{m}}{v}\,\mathbf{x}_\mathrm{w}\right)$ is the vector containing the unit unevenness for all wheel positions $\mathbf{x}_\mathrm{w}$ in the moving FOR. In Eq. (19), the vehicle degrees of freedom are split into two parts: those relating to the wheels, denoted with the superscript ‘w’, and those that are not coupled to the track, denoted with superscript ‘u’. It is assumed that each vehicle wheel has the same linearized Hertzian spring stiffness K_H when calculating the acting forces. Solving Eq. (19) for the unknown displacement vector $\mathbf{U}$ produces the system behaviour. Note that in this case, the effects of external structures coupled to the railway track through the soil are not accounted for.

The stiffness matrix for the rails in Eq. (19) can be found by inverting the flexibility matrix $\mathbf{R}_\mathrm{rr}(\omega_\mathrm{m})$ relating the rail displacements between all vehicle wheel sets positions is constructed. This is achieved in a similar manner as described in the previous section, assuming a single degree of freedom of a rail in a moving FOR for every wheel. The matrix is later used to establish the stiffness matrix of a coupled-domain stiffness matrix.

4 ASSEMBLY AND SOLUTION OF GLOBAL SYSTEM

Parts of the model described in the previous sections are combined into a single global system. The resulting system combines parts formulated in a moving FOR, such as the vehicle and the track, and parts formulated in the fixed FOR, such as the structures interacting with the soil. To couple the two FORs together, the relation described in Section 2 is used. For this purpose, the receptance matrix $\widetilde{\mathbf{R}}_\mathrm{sr}$, providing the interaction between the degrees of freedom of the rails and the degrees of freedom of the soil, is established. The matrix $\widetilde{\mathbf{R}}_\mathrm{sr}$ couples the moving and fixed FORs, and it is therefore dependent on two frequencies: ω_m and ω_f. The tilde indicates that the quantity is defined in the mixed FOR.

4.1 Partly coupled global system

The flexibility matrix, assembled in the fixed FOR and connecting all the degrees of freedom interacting with the soil, is added to the system. Using the created matrices, the full flexibility matrix for the so-called ‘global’ (indicated by subscript ‘g’) system can be constructed

$$\widetilde{\mathbf{R}}_\mathrm{g}(\omega_\mathrm{m}, \omega_\mathrm{f}) = \begin{bmatrix} \mathbf{R}_\mathrm{rr}(\omega_\mathrm{m}) & \widetilde{\mathbf{R}}_\mathrm{rs}(\omega_\mathrm{f}, \omega_\mathrm{m}) \\ \widetilde{\mathbf{R}}_\mathrm{sr}(\omega_\mathrm{m}, \omega_\mathrm{f}) & \mathbf{R}_\mathrm{ss}(\omega_\mathrm{f}) \end{bmatrix}. \tag{20}$$

If no rigid bodies are present in the soil model, the global flexibility matrix may be inverted to obtain the stiffness matrix of the global system $\widetilde{\mathbf{K}}_\mathrm{g}(\omega_\mathrm{m}, \omega_\mathrm{f})$. When the system contains rigid objects, which are formulated as described in Section 3.2, the global stiffness matrix can be constructed using the global transformation matrix

$$\mathbf{T}_{\mathrm{g}} = \begin{bmatrix} \mathbf{I} & \mathbf{0} \\ \mathbf{0} & \mathbf{T}_{\mathrm{s}} \end{bmatrix} \tag{21}$$

where $\mathbf{I}$ is the identity matrix with dimensions equal to the number of rail degrees of freedom. It is assumed that there are no rigid bodies modelled in the moving FOR. In theory, it is possible to model rigid bodies in both the moving and the fixed FORs, given that the reference nodes for these bodies are not shared between the two FORs.

After the stiffness matrix of the system has been obtained, the vehicle and the FE structures can be also added to the global system. The governing equation for partial coupling in the mixed FOR becomes:

$$\widetilde{\mathbf{K}}(\omega_{\mathrm{m}}, \omega_{\mathrm{f}})\widetilde{\mathbf{U}}(\omega_{\mathrm{m}}, \omega_{\mathrm{f}}) = \widetilde{\mathbf{F}}(\omega_{\mathrm{m}}, \omega_{\mathrm{f}}) \tag{22}$$

where

$$\widetilde{\mathbf{K}}(\omega_{\mathrm{m}}, \omega_{\mathrm{f}}) = \begin{bmatrix} \mathbf{K}_{\mathrm{v}}^{\mathrm{uu}}(\omega_{\mathrm{m}}) & \mathbf{K}_{\mathrm{v}}^{\mathrm{uw}}(\omega_{\mathrm{m}}) & \mathbf{0} & \mathbf{0} & \mathbf{0} \\ \mathbf{K}_{\mathrm{v}}^{\mathrm{wu}}(\omega_{\mathrm{m}}) & \mathbf{K}_{\mathrm{v}}^{\mathrm{ww}}(\omega_{\mathrm{m}}) + \mathbf{K}_{\mathrm{H}} & -\mathbf{K}_{\mathrm{H}} & \mathbf{0} & \mathbf{0} \\ \mathbf{0} & -\mathbf{K}_{\mathrm{H}} & \widetilde{\mathbf{K}}_{\mathrm{g}}^{\mathrm{rr}}(\omega_{\mathrm{m}}, \omega_{\mathrm{f}}) + \mathbf{K}_{\mathrm{H}} & \widetilde{\mathbf{K}}_{\mathrm{g}}^{\mathrm{rs}}(\omega_{\mathrm{f}}, \omega_{\mathrm{m}}) & \mathbf{0} \\ \mathbf{0} & \mathbf{0} & \widetilde{\mathbf{K}}_{\mathrm{g}}^{\mathrm{sr}}(\omega_{\mathrm{m}}, \omega_{\mathrm{f}}) & \widetilde{\mathbf{K}}_{\mathrm{g}}^{\mathrm{ss}}(\omega_{\mathrm{m}}, \omega_{\mathrm{f}}) + \widetilde{\mathbf{K}}_{\mathrm{FE}}^{\mathrm{ss}}(\omega_{\mathrm{f}}) & \mathbf{K}_{\mathrm{FE}}^{\mathrm{sn}}(\omega_{\mathrm{f}}) \\ \mathbf{0} & \mathbf{0} & \mathbf{0} & \mathbf{K}_{\mathrm{FE}}^{\mathrm{ns}}(\omega_{\mathrm{f}}) & \mathbf{K}_{\mathrm{FE}}^{\mathrm{nn}}(\omega_{\mathrm{f}}) \end{bmatrix} \tag{23}$$

and

$$\widetilde{\mathbf{U}}(\omega_{\mathrm{m}}, \omega_{\mathrm{f}}) = \begin{Bmatrix} \widetilde{\mathbf{U}}_{\mathrm{v}}^{\mathrm{u}}(\omega_{\mathrm{m}}, \omega_{\mathrm{f}}) \\ \widetilde{\mathbf{U}}_{\mathrm{v}}^{\mathrm{w}}(\omega_{\mathrm{m}}, \omega_{\mathrm{f}}) \\ \widetilde{\mathbf{U}}_{\mathrm{g}}^{\mathrm{r}}(\omega_{\mathrm{m}}, \omega_{\mathrm{f}}) \\ \widetilde{\mathbf{U}}_{\mathrm{g}}^{\mathrm{s}}(\omega_{\mathrm{m}}, \omega_{\mathrm{f}}) \\ \widetilde{\mathbf{U}}_{\mathrm{FE}}^{\mathrm{n}}(\omega_{\mathrm{m}}, \omega_{\mathrm{f}}) \end{Bmatrix}, \qquad \widetilde{\mathbf{F}}(\omega_{\mathrm{m}}, \omega_{\mathrm{f}}) = \begin{Bmatrix} \mathbf{0} \\ K_{\mathrm{H}}\mathbf{d}(\omega_{\mathrm{m}}) \\ -K_{\mathrm{H}}\mathbf{d}(\omega_{\mathrm{m}}) \\ \mathbf{0} \\ \mathbf{0} \end{Bmatrix}. \tag{24}$$

The superscripts relate to the degrees of freedom of: ‘w’-wheels, ‘r’-rails, ‘s’-soil in the fixed FOR, ‘n’-parts of FE structures not coupled to the soil and ‘u’-vehicles uncoupled from the track (e.g. the vehicle body). Vectors $\widetilde{\mathbf{U}}_{\mathrm{v}}$, $\widetilde{\mathbf{U}}_{\mathrm{g}}$ and $\widetilde{\mathbf{U}}_{\mathrm{FE}}$ store the displacements for the vehicle, global railway track–soil system and the FE structure, respectively.

After the system has been solved, the displacement for the observation degrees of freedom in the fixed FOR can be obtained. When the displacements for both the global and the observation degrees of freedom have been obtained, the effects from J_{m} discrete excitation frequencies ω_{m} can be added together to obtain the total response in the fixed FOR:

$$\mathbf{U}_{\mathrm{FE}}(\omega_{\mathrm{f}}) = \frac{1}{2\pi}\sum_{j=1}^{J_{\mathrm{m}}} \widetilde{\mathbf{U}}_{\mathrm{FE}}\left(\omega_{\mathrm{m},j}, \omega_{\mathrm{f}}\right) D(k_{\mathrm{m},j})\, \Delta k_{\mathrm{m}} \tag{25}$$

where $D(k_{\mathrm{m},j})$ is the rail unevenness obtained from a power spectral density (PSD) according to the wavenumber $k_{\mathrm{m},j}$, and Δk_{m} is the wavenumber step size.

The time-domain response for the degrees of freedom associated with the fixed FOR can be obtained by performing an inverse discrete Fourier transformation of the displacements $\mathbf{U}_{\mathrm{FE}}(\omega_{\mathrm{s}})$:

$$\mathbf{u}_{\mathrm{FE}}(t) = \frac{1}{2\pi}\sum_{j=1}^{J_{\mathrm{f}}} \mathbf{U}_{\mathrm{FE}}\left(\omega_{\mathrm{f},j}\right)\mathrm{e}^{\mathrm{i}\,\omega_{\mathrm{f},j}\,t}\,\Delta\omega_{\mathrm{f}} \tag{26}$$

where J_{f} is the number of discrete frequencies in the fixed FOR. Note that J_{f} and J_{m} need not be equal. However, the step sizes $\Delta\omega_{\mathrm{f}}$ and Δk_{m} must be small enough, and the number of frequencies J_{f} and J_{m} large enough, to ensure proper discretization of peaks in the loads and resonances

of the system while, at the same time, avoiding violation of the periodicity inherent in the frequency-domain solution.

4.2 Fully coupled global system

Using the matrices already created for the previously described solution procedure, it is also possible to assemble a fully coupled global system. Such a system will account for the frequency spreading of the reflected waves due to the Doppler effect and might be useful for certain cases where the full coupling between the vehicle (the source) and the structures (the receivers) cannot be discarded. In such a system, the previously uncoupled frequencies in a single FOR are now coupled through the other FOR and the matrix $\mathbf{K}_{\mathrm{g}}$ will be fully populated. The system can be solved by applying loads in either FOR or both FORs at the same time. However, the computation of the fully coupled system is an extremely computationally demanding process, which involves double inversion of very large matrices. Thus, it should only be used when the secondary coupling effects are an important factor.

5 VALIDATION AND APPLICATIONS

The methodology described in this paper is validated by comparisons with other state-of-the-art computational approaches. By considering a system with no structures or rigid objects interacting with the soil, the described system assembly and solution procedures provide identical results to the approach provided by Sheng et al. in [13, 14]. This is expected, as the proposed method here utilizes the same vehicle-track-soil interaction model, and, with no other structures interacting with the soil, the coupling terms cancel out. Modelling of rigid objects interacting with the soil was validated by comparison with BE and FEM-PML models. It was determined that the semi-analytical model provides a very good match, especially with the FEM-PML model, where even the secondary coupling terms show very good agreement. To demonstrate the capabilities of the proposed fully-coupled modelling approach, an example case was set up where the modelled structure is close to the railway track.

5.1 Coupling between moving and fixed frames of reference

In order to validate the coupling terms between the two FORs and especially the symmetry between when a load is applied in the moving FOR and the displacements observed in a fixed FOR and vice versa, two test cases were set up. The proposed mixed-FOR model was simplified by removing the railway track, the vehicle and the FE/rigid structures interacting with the soil. This way, the effects of a single load with a single excitation frequency acting directly on the soil surface can be observed. The ground was modelled as a homogenous elastic half-space of dense sandy-type soil, with 250 MPa Young's modulus, 0.25 Poisson's ratio, 2000 kg/m^3 mass density and 0.05 loss factor. A stationary point in the fixed FOR was placed 3 m from the line along which the load was moving.

A moving vertical load with constant speed v and frequency f_{m} was modelled. The vertical displacements were observed within a fixed FOR for a range of frequencies f_{f}. The system was modelled using the simplified mixed-FOR model. For the analysed case, only the coupling terms between the moving and the fixed FORs, as described in Section 2, have an effect for the obtained results. For comparison, a full model was established, modelled only in the moving FOR, using the semi-analytical approach.

Using the created model, the displacement field of the soil surface in the moving FOR and within the time domain was obtained for a single excitation frequency. Then, a time signal for displacements of an observation point moving through the displacement field with speed $-v$ was found, considering that for every time step the position of the observation point changed.

Fourier transforming the obtained time signal into frequencies f_s, the displacement spectra for a stationary observation point was obtained. Two combinations of speed and frequency in the moving FOR were investigated: Case 1 with $v = 20$ m/s and $f_m = 20$ Hz, and Case 2 with $v = 40$ m/s and $f_m = 10$ Hz. The comparison of both approaches are shown in Figure 1 where it can be seen that the two approaches agree, confirming the analytical derivation presented in Section 2.

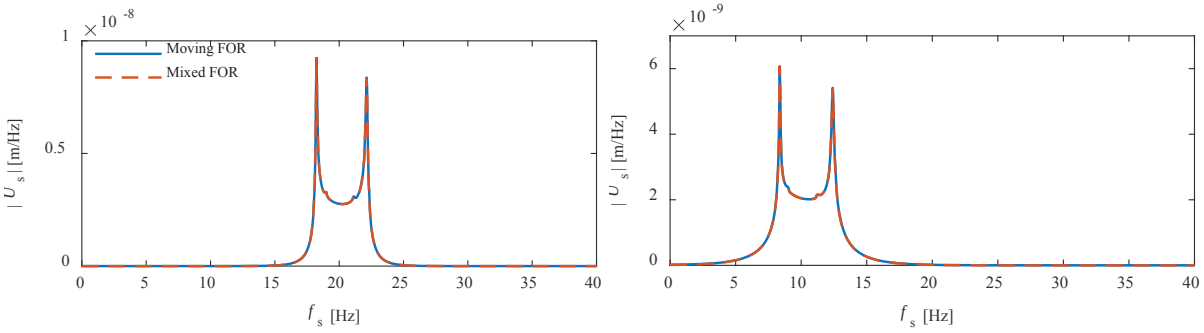

(a) (b)

Figure 1: Displacements in a fixed FOR from a unit load applied in a moving FOR: (a) $v = 20$ m/s and $f_m = 20$ Hz; (b) $v = 40$ m/s and $f_m = 10$ Hz.

A similar validation example was created to analyse the coupling between a load in a fixed FOR and the resulting displacements in a moving FOR. Here, the mixed FOR model was compared to a full solution formulated only in a fixed FOR. In the same way as for the previous validation case, using the full model, the displacement field of the soil surface was found in time domain. Then the vertical displacements for a moving observation point were obtained by changing the position of the point for every time step. Fourier transforming the time-domain response for frequencies f_m, the displacement spectra for a moving observation point were obtained. Two combinations of speed and stationary frequency were again investigated: Case 1 with $v = 20$ m/s and $f_s = 20$ Hz; Case 2 with $v = 40$ m/s and $f_s = 10$ Hz. Results of both approaches are given in Figure 2. Once again, the results agree well, this time confirming the derivation given in Section 2.

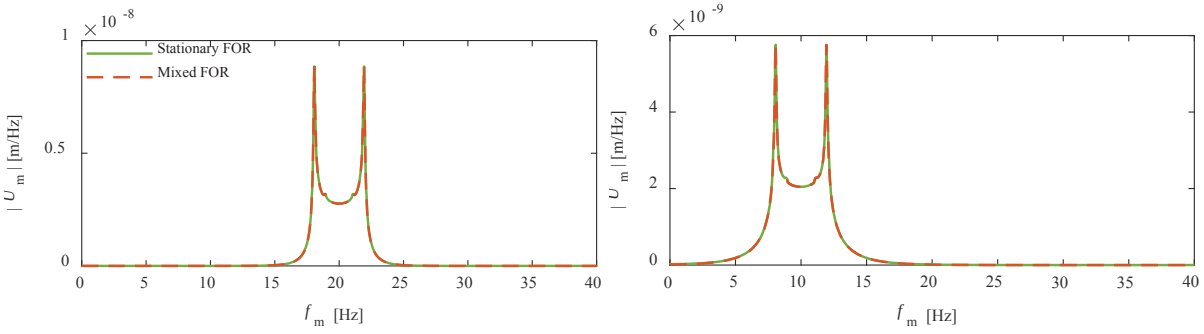

(a) (b)

Figure 2: Displacements in a moving FOR from a unit load applied in a fixed FOR.: (a) $v = 20$ m/s and $f_s = 20$ Hz; (b) $v = 40$ m/s and $f_s = 10$ Hz.

Comparing the two validation examples, it is evident that the response spreads out through the observer frequencies due to the Doppler effect, independently of which FOR the load was

applied in. The range of affected frequencies dependent on the speed of the moving FOR. However, a load applied in the fixed FOR produces two symmetric peaks around the excitation frequency, when observed in a moving FOR, while a load applied in a moving FOR produces two peaks in the fixed FOR. Further, comparing the results of Case 1 for both cases, it can be observed that the result in Figure 4 at $f_s = 20$ Hz and the result in Figure 5 at $f_m = 20$ Hz show exactly the same response. This confirms the symmetry between the two FORs implied by Eq. (7). The same result is obtained by comparing the responses of Case 2 for both cases.

5.2 Validation of the modelling approach

To validate the modelling approach presented in this paper, it was compared to a sub-modelling technique, as described in [6]. A similar modelling approach was also used in [5]. In both cases the sub-modelling approach was used to model an underground railway tunnel with a vehicle travelling through it, in turn exciting a building structure above the soil. However, the solution procedure can also be applied to surface railways and the system analysed in this work. The method uses the free-field displacements of the soil caused by a passing vehicle, which are later modified by introducing the building structure. Ensuring equilibrium and compatibility between the degrees of freedom connecting the building and the soil, a solution for the building displacements can be found.

Comparing the methodology proposed in this work with the sub-modelling technique, it becomes evident that the basic parts used for both solution procedures are identical. For example, the free-field displacements from a moving load used in the two-step approach are identical to the flexibility matrix used here. However, the assembly and solution of the full system is somewhat different, with the proposed methodology allowing a wider range of applications, such as modelling rigid inclusions or allowing a two-way coupling between the two FORs. Further, the sub-modelling technique, as applied in this work, is a two-step solution approach, as the wheel-rail interaction forces are obtained in the moving FOR before being used to obtain the displacements in the fixed FOR.

As, both approaches use the same basic parts, it is relatively easy to compare them. For comparison, a building structure, with six columns supporting two floors was used. The building is facing the railway track with its narrow side, which is 8 m wide, and the building is supported by two columns at either side. The length of the building is 10 m in the direction orthogonal to the track. In addition to the four columns placed at the corners, a column is placed in the middle of each of the longer sides. Each storey is 4 m high. The whole building structure is constructed from concreate with a Young's modulus of 30 GPa, a Poisson's ratio of 0.15, a mass density of 2400 kg/m3, and loss factor of 0.03. The columns have square cross-sections, with one side equal to 0.3 m, while the floors are 0.25 m thick slabs. Since the sub-modelling technique cannot directly model rigid objects, a flexible slab footing lies underneath the whole building with the same thickness as the building floors. 3D beam elements were used to model the columns, using Euler-Bernoulli beam theory to account for bending. The floors and the foundation slab of the building were modelled using Mindlin-Reissner shell elements, accounting for bending as well as shear. All FE parts of the model were discretized with mesh size of 0.5 m, resulting in 4841 degrees of freedom in the system.

The soil is modelled as a half-space of sand, with the same properties as in Section 5.1. Both systems were excited by a single passing vehicle, travelling at 40 m/s, exposed to a unit rail unevenness, with a 4 m wavelength corresponding to an excitation frequency of 10 Hz. For analysis, only a single excitation frequency is used, as the effects from multiple excitations

frequencies are just added together due to the principal of superposition. Thus, a single excitation frequency is enough to evaluate how well both models perform. The test case is illustrated in Figure 3.

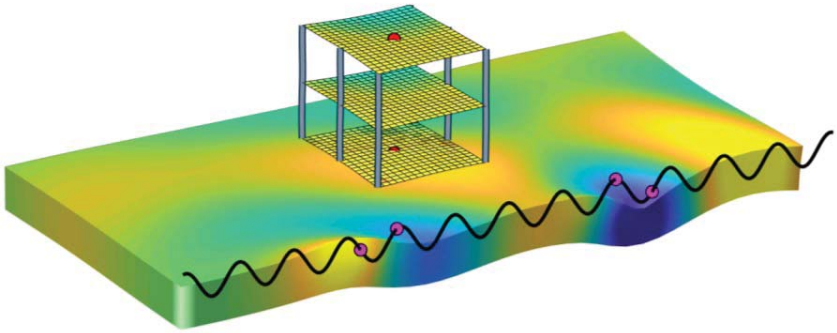

Figure 3: Investigated case for validating the modelling approach. The vehicle is travelling from left to right, with magenta nodes indicating the wheel positions. The red nodes indicate the observation points, while the shades of colour indicate the vertical displacements (bright yellow is up, dark blue is down). Track unevenness is not scaled.

Figure 4 shows the displacements of the building structure obtained at the centre of the ground floor and the second floor where both approaches provide almost identical results, showing that the proposed method is performing well. At the same time, almost identical results indicate that the back-coupling of the building structure to the railway track is insignificant. Thus, for at least for the considered case, there is no significant difference whether on or the other approach is considered.

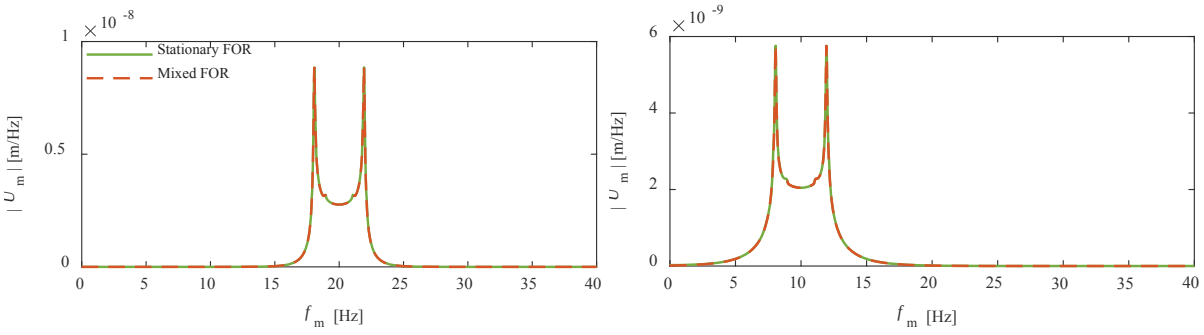

(a) (b)

Figure 4: Displacements in a moving FOR from a unit load applied in a fixed FOR.: (a) $v = 20$ m/s and $f_s = 20$ Hz; (b) $v = 40$ m/s and $f_s = 10$ Hz.

5.3 Fully coupled system

A fully-coupled system solution approach might be necessary in cases where the modelled structures are close to the railway track, introducing a significant change of dynamic stiffness along the track. In that case, the re-scattered waves can have an effect on the vehicle behaviour and the obtained wheel-rail interaction forces. Problems where these effects are important could include modelling of tunnels underneath buildings, railway stations and various structures nearby the tracks. Several such cases have been investigated by Coulier et al. [20], finding that while the axial loads are not effected significantly, the vibration insertion gain for source–receiver transmission can be affected up to 10 dB, when using a fully coupled solution procedure.

Another set of problems could include the sudden change of stiffness underneath the track, e.g. when a concreate passage is constructed underneath the railway track.

To examine such a case, a test case was set up modelling a single vehicle traveling across a railway track, as shown in Figure 5. The speed of the vehicle was 40 m/s. The vehicle and the track properties are given in Tables 1 and 2. The soil was modelled as a 5 m layer of soft clay sitting over a stiffer half-space of sand. The clay had a Young's modulus of 80 MPa, a Poisson's ratio of 0.48, a mass density of 2100 kg/m3, and a loss factor of 0.05. The underlying sand had the same properties as in Section 5. Underneath the track, at a depth of 1 m, a rigid block was embedded within the soil. The block was centred at the position, where the travelling vehicle centre line was located at time 0. The block was modelled as a 2D plate, placed in the horizontal plane with one side equal to 2 m. It was discretized into 36 discretization nodes, with three degrees of freedom per node. The system was excited by the deadweight of the vehicle only applied at $f_{\mathrm{m}} = 0$ Hz, with no excitation from the rail unevenness. The system was assessed by the fully-coupled modelling approach. As only the quasi-static effects of the vehicle were modelled, the considered frequency ranges are reduced. The one-sided frequency range of the moving FOR was 0-30 Hz, and the one-sided frequency range of the fixed FOR is 0-25 Hz. In the computation, negative as well as positive frequencies were considered for either FOR, and each range was split into 200 discrete frequencies.

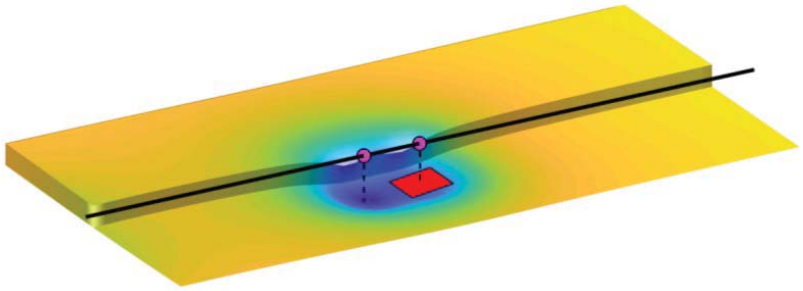

Figure 5: Vehicle passing over a buried rigid block, at an instance where the leading wheel of the vehicle is directly above the centre of the rigid block. The vehicle is travelling at 40 m/s from left to right. The black line indicates the vehicle traverse line, with the magenta nodes indicating the positions of the vehicle wheel sets. Only the two wheel sets of the front bogie are shown.

Rail mass per unit length	60.0 kg/m
Rail bending stiffness	$6.4 \cdot 10^6$ N/m^2
Rail loss factor	0.01
Railpad stiffness	$5.0 \cdot 10^8$ N/m
Railpad loss factor	0.1
Sleeper spacing	1 m
Sleeper mass per unit length	542.0 kg/m
Ballast vertical stiffness	$4.64 \cdot 10^9$ N/m^2
Ballast mass per unit length	1740 kg/m
Ballast loss factor	0.04
Track width	3.2 m

Table 1: Railway track properties.

Figure 6 shows the velocities obtained for the vehicle in the moving FOR as well as the rigid block in the fixed FOR. It can be observed that the vehicle passing over a rigid block introduces a significant excitation into the system, with the rigid block as well as the vehicle reacting to the passage. In this system, the observed excitation of the vehicle is purely due to the weak

coupling effects that are disregarded in the two-step procedure. The waves generated by the passing vehicle are scattered by the rigid block in the fixed FOR and in turn excite a range of frequencies in the moving FOR. These effects would not be accounted for when the weak coupling between the vehicle and structures is not modelled.

Mass of car body	40000 kg
Mass of bogie	5000 kg
Mass of wheel set	1800 kg
Car body pitch moment of inertia	$2.0 \cdot 10^6$ kg·m^2
Bogie pitch moment of inertia	6000 kg·m^2
Primary suspension stiffness	$2.4 \cdot 10^6$ N/m
Secondary suspension stiffness	$6.0 \cdot 10^5$ N/m
Primary suspension damping	$30 \cdot 10^3$ N·s/m
Secondary suspension damping	$20 \cdot 10^3$ N·s/m
Distance between bogies' centers	19.0 m
Distance between bogie's wheels sets	2.7 m
Herztian constant	$5.14 \cdot 10^{-8}$

Table 2: Vehicle properties.

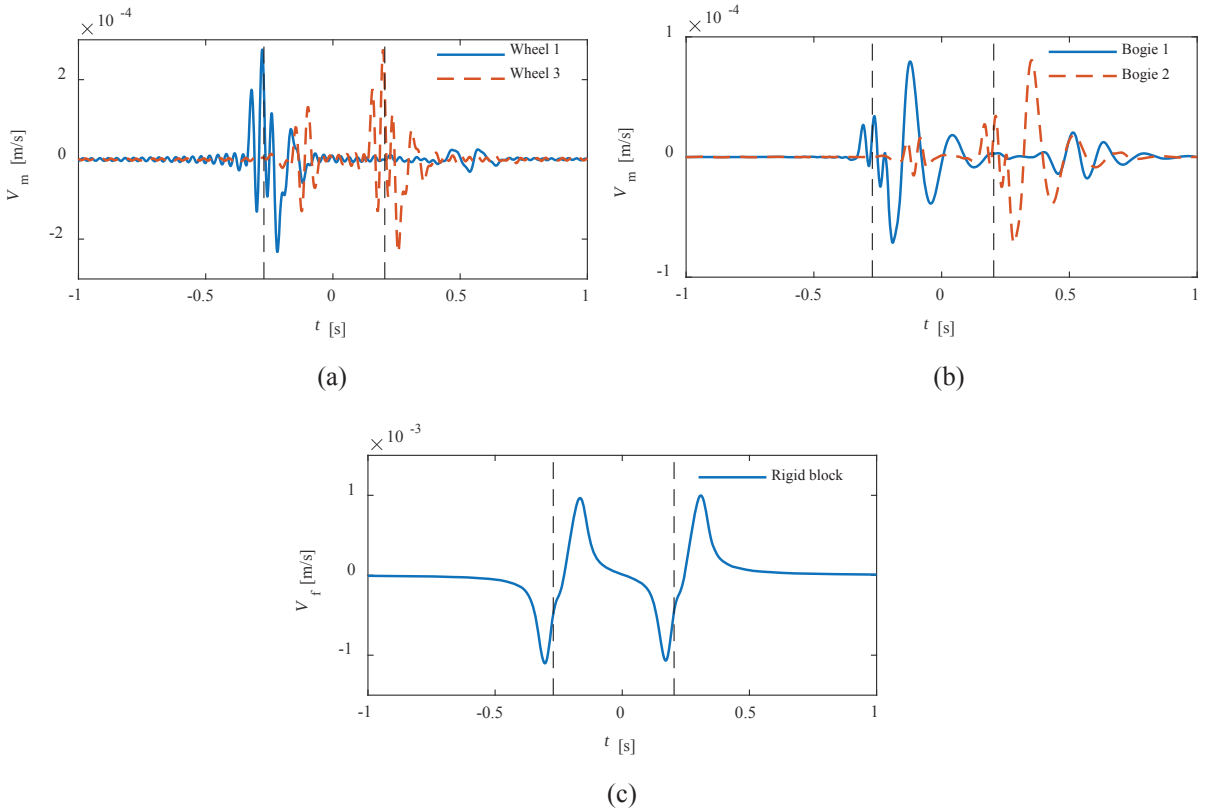

Figure 6: Vertical velocities for parts of the vehicle (in moving FOR) and the rigid block underneath the track (in fixed FOR). The vertical dashed black lines indicate time instance when the first and third vehicle wheels are directly above the centre of the rigid block. The response is shown for: (a) the first and the third vehicle wheels; (b) both vehicle bogies; (c) rigid block underneath the track.

From the wheel velocities shown in Figure 6(a), it can be seen that both leading wheels of separate bogies produce very similar results. However, the excitation due to the first wheel passage over the rigid block generates a wave that excites the third vehicle wheel, even before

it reaches the rigid block. A similar effect is also observed after the third wheel passes over the rigid block, where the generated wave travels forward and excites the first vehicle wheel. A very similar behaviour is also observed on the bogies. When comparing these secondary excitations, it can be seen that the reaction of the third wheel due to the first wheel passage is higher than the excitation of the first wheel due to third wheel passage. This is due to the Doppler effect of the wave travelling through the rail, as the third wheel is travelling towards the wave propagating form the first wheel, while the wave generated by the third wheel must 'catch up' to the first wheel. From the rigid block displacements, it can be observed that the largest velocities are reached just before the leading wheel of a bogie reaches the centre of block. Interestingly, to obtain the same displacements of the rigid block, a fully-coupled system solution approach is unnecessary, as the partly coupled solution provides results that are almost identical. For the analysed case, it can beconcluded that the fully coupled solution approach is only necessary if the vehicle behaviour is of interest, for example for assessment of driver and passenger comfort, or if the track and wheel wear is to be assessed.

6 CONCLUSIONS

- The paper introduced a new modelling approach for the estimation of environmental vibration resulting from railway traffic. A model of a coupled vehicle-track-soil-building system was introduced with two approaches proposed for assembly and solution of the whole system: the partly-coupled approach and the fully-coupled approach. Both solution approaches use a single step procedure with one approach considering a fully-coupled system, while the other approach discards some secondary coupling effects for a more computationally efficient solution procedure.
- A semi-analytical model was utilized to model the soil to which rigid objects and structures modelled by the FE were coupled. The proposed modelling approach uses the frequency-domain solution with some parts, such as the railway track, formulated in the moving FOR and other parts, such as building structures, formulated in a fixed FOR. The coupling terms between the two FORs are found by utilizing an analytical formulation of receptance between the two FORs. It has been established that due to the coupling between the fixed and moving FORs, the previously uncoupled discrete frequencies become coupled through the other FOR as a result of the Doppler effect and wave scattering. Thus, additional consideration is needed when modelling such systems.
- The proposed methodology is a robust approach that does not suffer from numerical instabilities, due to the usage of frequency domain solutions. A wide range of cases can be assessed, including the modelling of rigid objects in or on the ground and flexible structures modelled by the FEM, interacting with the soil. Using the proposed partly-coupled solution approach, the computations can be easily parallelized, thus providing a relatively fast and efficient computational method. Further, the suggested fully-coupled solution procedure is useful in cases where the weak coupling between the vehicle and structures cannot be discarded.
- The analytically derived coupling terms between the two FORs were validated by comparing with models formulated in a single FOR. Further, the partly coupled solution procedure of the full system was compared to a solution procedure in which the weak coupling is completely discarded. The two solution procedures have been found to provide almost identical results, validating the proposed partly coupled solution procedure while, at the same time, indicating insignificant back-coupling in the considered case.

- To demonstrate the capabilities of the numerical model and the potential of the fully-coupled solution procedure, the response of a vehicle passing over a buried rigid block was investigated. It was been found that the fully coupled solution procedure can predict the weak coupling effects between the vehicle and the structure, producing a vehicle response distributed through frequencies, when the load is applied only at a single frequency. Thus, in the present example, the modes of the vehicle were excited parametrically by the waves scattered from the rigid inclusion as a result of the passing deadweight of the vehicle.

REFERENCES

[1] D.J. Thompson, G. Kouroussis, E. Ntotsios, Modelling, simulation and evaluation of ground vibration caused by rail vehicles, *Vehicle System Dynamics* 57, 69-110, 2019.

[2] P. Fiala, G. Degrande, F. Augusztinovicz, Numerical modelling of ground-borne noise and vibration in buildings due to surface rail traffic, *Journal of Sound and Vibration*, 301, 718-738, 2007.

[3] S. François, L. Pyl, H.R. Masoumi, G. Degrande, The influence of dynamic soil-structure interaction on traffic induced vibrations in buildings, *Soil Dynamics and Earthquake Engineering* 27, 655-674, 2007.

[4] G. Kouroussis, L. Van Parys, C. Conti, O. Verlinden, Prediction of ground vibrations induced by urban railway traffic: an analysis of the coupling assumptions between vehicle, track, soil, and buildings, *International Journal of Acoustics and Vibration* 163, 163-172, 2013.

[5] P. Lopes, P.A. Costa, M. Ferraz, R. Calçada, A.S. Cardoso, Numerical modeling of vibrations induced by railway traffic in tunnels: From the source to the nearby buildings, *Soil Dynamics and Earthquake Engineering* 61-62, 269-285, 2014.

[6] M.F.M. Hussein, H. Hunt, K. Kuo, P.A. Costa, J. Barbosa, The use of sub-modelling technique to calculate vibration in buildings from underground railways, *Proceedings of the Institution of Mechanical Engineers, Part F: Journal of Rail and Rapid Transit*, 229, 303-314, 2015.

[7] D. López-Mendoza, A. Romero, D.P. Connolly, P. Galvín, Scoping assessment of building vibration induced by railway traffic, *Soil Dynamics and Earthquake Engineering*, 93, 147-161, 2017.

[8] D.P. Connolly, P. Galvín, B. Olivier, A. Romero, G. Kouroussis, A 2.5D time-frequency domain model for railway induced soil-building vibration due to railway defects, *Soil Dynamics and Earthquake Engineering*, 120, 332-344, 2019.

[9] K.A. Kuo, M. Papadopoulos, G. Lombaert, G. Degrande, The coupling loss of a building subject to railway induced vibrations: Numerical modelling and experimental measurements, *Journal of Sound and Vibration*, 442, 459-481, 2019.

[10] P. Coulier, G. Lombaert, G. Degrande, The influence of source-receiver interaction on the numerical prediction of railway induced vibrations, *Journal of Sound and Vibration*, 333(12), 2520-2538, 2014

[11] M.F.M. Hussein, H.E.M. Hunt, A numerical model for calculating vibration from a railway tunnel embedded in a full-space, *Journal of Sound and Vibration*, 305, 401-431, 2007.

[12] C. Hanson, D. Towers, L. Meister, Transit Noise and Vibration Impact Assessment, Report FTA-VA-90-1003-06, U.S. Department of Transportation, Federal Transit Administration, Office of Planning and Environment, 2006.

[13] X. Sheng, C.J.C. Jones, M. Petyt, Ground vibration generated by a load moving along a railway track, *Journal of Sound and Vibration*, 228, 129-156, 1999.

[14] X. Sheng, C.J.C. Jones, D.J. Thompson, A theoretical model for ground vibration from trains generated by vertical track irregularities, *Journal of Sound and Vibration*, 272, 937-965, 2004.

[15] E. Ntotsios, D.J. Thompson, M.F.M. Hussein, The effect of track load correlation on ground-borne vibration from railways, *Journal of Sound and Vibration*, 402, 142-163, 2017.

[16] W.T. Thomson, Transmission of elastic waves through a stratified solid medium, *Journal of Applied Physics*, 21, 89-93, 1950.

[17] N.A. Haskell, The dispersion of surface waves on multilayered media, *Bulletin of the Seismological Society of America*, 43, 17-43, 1953.

[18] E. Kausel, J.M. Roësset, Stiffness matrices for layered soils, *Bulletin of the Seismological Society of America*, 71, 1743–1761, 1981.

[19] R. Wang, A simple orthonormalization method for stable and efficient computation of Green's functions, *Bulletin of the Seismological Society of America*, 89, 733-741, 1999.

[20] P. Coulier, G. Lombaert, G. Degrande, The influence of source–receiver interaction on the numerical prediction of railway induced vibrations, *Journal of Sound and Vibration*, 333, 2520–2538, 2014.

EURODYN 2020
XI International Conference on Structural Dynamics
M. Papadrakakis, M. Fragiadakis, C. Papadimitriou (eds.)
Athens, Greece, 23–26 November 2020

THE USE OF MULTIPLE MODELS TO ANALYSE RAILWAY TRACK GROUND DYNAMICS

P. Chumyen[1], D.P. Connolly[1], K. Dong[2], P.A. Costa[3], P.J. Soares[3] and P.K. Woodward[1]

[1] Institute for High-Speed Rail and System Integration
School of Civil Engineering, University of Leeds, UK
{ml16p3c, D.connolly, P.K.Woodward}@leeds.ac.uk

[2] Institute for Infrastructure and Environment
Heriot Watt University, UK
kd11@hw.ac.uk

[3] Faculty of Engineering
University of Porto, Portugal
{pacosta,psoares}@fe.up.pt

Keywords: High-speed railway, Track-ground dynamics behaviour, Analytical modelling, Numerical Modelling, Critical Velocity

Abstract. *With the increases in train speed in recent decades, it is important to define the track-ground critical velocity to prevent high track dynamic amplification. This is affected by wave propagation in the soil layers and track supporting the moving load. Therefore, this paper investigates the important variables that influence the critical velocity and dynamic amplification based on three case studies of track-ground dynamic problems, which are: the presence of low stiffness soil layer, track shakedown and soil improvement. Three modelling strategies (analytical, hybrid analytical-numerical and 2.5D numerical) are used to analyse the different track-soil problems. The findings provide a better understanding of critical velocity and dynamic amplification. These are useful when considering a new track-ground design or improving the existing railway lines.*

1 INTRODUCTION

In recent decades, global railway transportations put a great effort into providing the service with higher train capacity and faster journey time; thus, the increase of operational train speed is required. This can bring the problems to engineering practice when the increased train speed approaches to the critical velocity of the track-ground system. By definition, the critical velocity is the minimum threshold speed of the moving and non-oscillating load that wave commences propagation within the supporting track-ground ([1], [2], [3],[4], [5]).

At critical velocity, high levels of dynamic track-ground amplification occur and lead to the accelerated track degradation, including the elevated ground-borne vibration in the free-field ([6], [7]). These phenomena are undesirable on the railway line because they directly concern the safety risk and require the various expensive and advanced solutions to remediate [8]. To prevent such negative impacts, it is essential to define the influential variables related to track-ground dynamics issues, in particular, critical velocity and dynamic amplification. This is because the behaviour and response of track-ground dynamics can become more significant when experiencing high-speed moving load [9].

Existing railway standards for high-speed track attempt to consider the track behaviour and using a basic function of static response and speed to calculate dynamic response [10]. However, this concept is insufficient to achieve an accurate assessment of the complexity of wave propagation within track and soil because of the variety of track types and ground conditions.

Several models have been developed and proposed in the literature, aimed to investigate the dynamic track behaviour due to the moving load. Basically, [11] used analytical methods to model the problem by considering the moving load over an elastodynamic medium. With this approach, the dispersion characteristics of track and ground can be analysed, and the critical velocity can also be derived from the dispersion curves ([12],[13]). Better than the pure analytical simulation, the problem has been modelled semi-analytically ([14],[15]) where the analytical methods are applied for only track structure whereas the 3D soil is simulated using the Green's functions in terms of wavenumber-frequency domain [16]. These simulations are useful to achieve a better understanding of the relationship between moving speed and dynamic displacement amplification while the computation requirements are relatively low. However, when the track structures are more complex, they are still unable to overcome those limitations and complexities.

Alternatively, the 2.5D model has been developed which assumed the track as an invariant structure in the direction of train passage. With this simulation, the number of degrees of freedom are reduced by discretising the track into 2D slices and then capture the response in 3D using a transform ([6],[17],[18], [19],[20]). This is beneficial because it is capable of analysing a relatively complex track and soil conditions, with much lower run times compared to 3D model [21]. For the non-repetitive geometry (for example, transition zones or singular defects), 3D modelling has become an attractive alternative, presenting with a series of brick elements for individual track-ground components. Thus, ensuring the more accurate results in stress and strain field ([22], [23],[24],[25]).

In this paper, the effect of track-soil problems (a presence of low-stiffness soil layer, track shakedown and soil improvement) on dynamic track-soil behaviour, particularly, dynamic amplification and critical velocity will be investigated and analysed. Due to the complexity of such problems, track and soil geometry can be considered repetitive. Therefore, an analytical, semi-analytical and 2.5D numerical model are sufficient to perform the analysis above. The remaining sections of this paper are arranged in order as follow. In section 2, three modelling approaches are described. The modelling analysis of three track-soil problems will be presented in section 3.

2 MODELLING STRATEGIES

In this paper, three different approaches have been developed individually to analyse each problem. The detail of each modelling strategy is described as follows.

Strategy 1 (Analytical): As outlined in [13], analytical expressions are used to compute the dispersion relationship between track and ground. Once the dispersion curves have been plotted, the critical velocity can be identified. For example, the track and soil dispersion curve in terms of wavenumber and phase velocity, as shown in Figure 1, derived from the concrete slab track model with two-layered soil support. Both sub-figures point out that the critical velocity occurs at the intersection point between track and soil dispersion line. For phase velocity, it is straightforward to read to critical velocity, whereas the calculation is required for wavenumber representation, using the frequency divided by wavenumber.

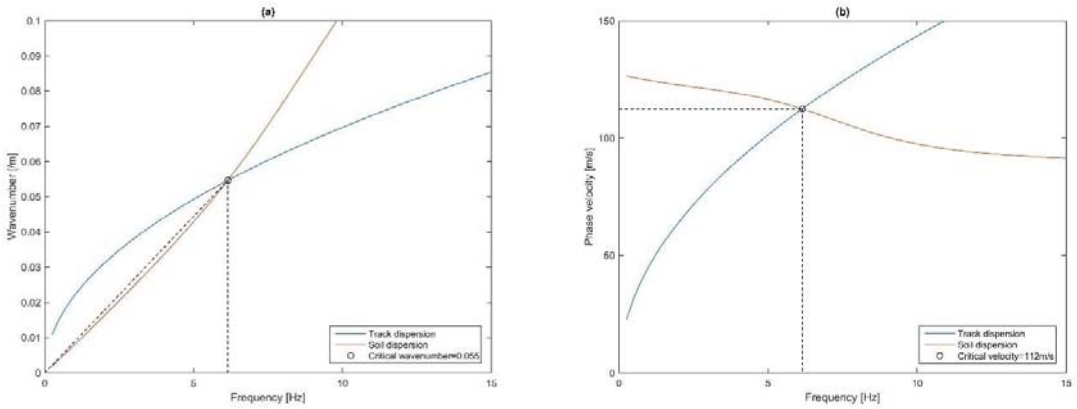

Figure 1: Dispersion relation (a) Wavenumber (b) Phase Velocity

Strategy 2 (Semi-analytical): The track and soil are modelled separately using different methods. An analytical approach is applied to model the track while the ground is modelled using the thin-layer element method (TLM). The thin-layer element and Green's function of soil are used to compute the equivalent soil stiffness in the wavenumber-frequency domain, and such stiffness is then used within a track model to compute the coupled track-ground response, as shown in Figure 2 [26].

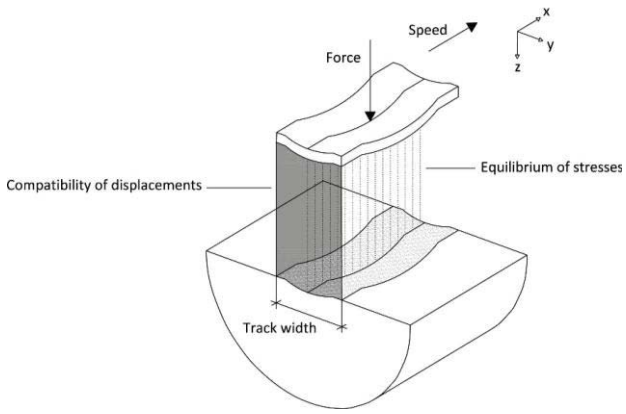

Figure 2: Track-ground interface of a semi-analytical model

Strategy 3 (2.5D numerical): The 2D geometry of track and soil structure are defined using eight-node quadratic finite elements and solving in the frequency domain Absorbing bounda-

ries are created to alleviate the reflection at boundaries, as presented in Figure 3, and the transform is then used to capture the 3D response ([18],[27]).

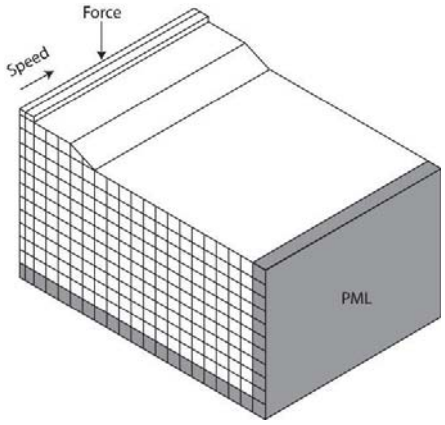

Figure 3: Simplified model of 2.5D modelling method

3 MODELLING ANALYSIS

3.1 Modelling parameters

To generate less complicated models and simulations, only slab track is used throughout this paper, with the properties as shown in Table 1. For the soil properties, Young's modulus is varied in each section depending upon the purpose of informing discussion, and the Poisson's ratio and density are constant at 0.35 and 2000 kg/m3 respectively. Regarding the analysis layout, the soil problem with low stiffness magnitude are presented first, followed by the track shakedown, and remediation solutions for soil are given in the last section.

Component	Properties	Value
Rail	Bending stiffness (Nm^2)	$1.29x10^7$
	Mass (kg/m)	120
Railpad	Stiffness (N/m)	$5x10^8$
	Damping (Ns/m)	$2.5x10^5$
Slab	Height of slab (m)	0.35
	Young's modulus (MPa)	30,000
	Half-track width (m)	1.25
	Density (kg/m^3)	2500

Table 1: Track material properties

3.2 Low stiffness soil layers

In general, the stiffness of soil stratum increases with depth because of the historical earth pressure. An example of dispersion curves for the typical soil layers, which the upper layer contains low stiffness soil (30, 75 and 100 MPa) overlying high stiffness soil (150 MPa) are illustrated in Figure 4(a). It is seen that the soil phase velocity is relatively low when the small magnitude of soil stiffness occurs. In contrast, with the natural processes [28] or localised soil improvement [26], the low-stiffness layers can arise below the top surface zones, possibly causing an increase in soil phase velocity. To illustrate the effect of this scenario on track and

earthwork design, the example of an upper layered soil with 100 MPA stiffness and 6m depth overlying an infinite thickness of soil layer with 50 MPA stiffness is generated. The result of the relationship between train speed and maximum rail displacement is shown in Figure 4(b). It is seen that two peaks occur at similar speeds to the shear wave velocities of two different soil layers. The first peak can be defined as critical velocity which the elastodynamic wave energy commences propagating in low-stiffness layers and the train moving speed is located at the second peak with the highest dynamic amplification. Apart from the theoretical impact, it also affects the engineering practice because the expensive and advanced solutions are required for soil improvement.

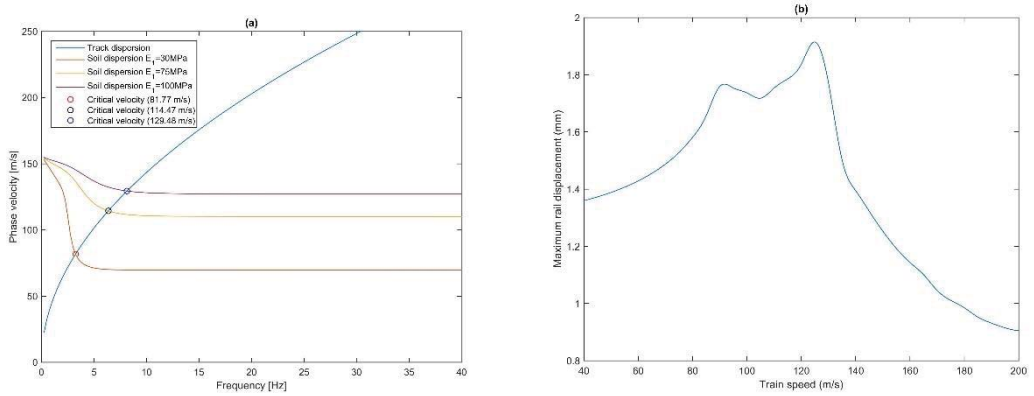

Figure 4 : A presence of low stiffness soil layer: (a) dispersion curves when low-stiffness overlying high-stiffness, (b) Maximum rail displacement curve when low-stiffness underlying high-stiffness

3.3 Track shakedown

With the repeated passages of moving train, track deformations can be both elastic and plastic. Its response can be classified into three main stages: elastic, elastic shakedown, cyclic plasticity and ratcheting depending on moving train loading as presented in Figure 5 ([29],[30],[31]).

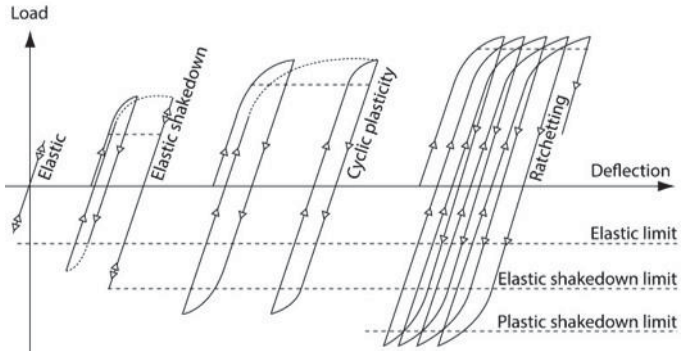

Figure 5: Elastic- Perfectly Plastic behaviour during cyclic loading

For the early stage of elastic, this happens when the train loading is low and does not exceed the elastic yield limit. The permanent track settlement does not appear because the track behaviour is fully elastic with no accumulated strain.

The more adverse stage is elastic shakedown. When train loading is high and exceeds the elastic yield limit for initial train passages, the track will settle with the short period and then return to elastic. The additional train passages at the same loading have no significant impact

on the permanent settlement unless the train loading increase. The reason is that the total stress field (resulting from the combination between the accumulated remaining stress during the initial load cycles, incremental stress from train loading and at-rest stress field) does not affect the yield limit.

The last stage is cyclic plasticity and ratcheting, which is the most critical scenario because the permanent strains occur during each train passage due to the very high train loading exceeding the elastic limit. Such strains, then, induce the instability of track permanent deformation, leading to the increased permanent settlement and ultimate failure.

Regarding the stage of track deformations above, it points out that the elastic shakedown stage plays an important role in track failure because the failure will occur when train loading equal or exceed the elastic shakedown limit. The influential factor for defining this limit are the material properties of track & subgrade, loading aspects (for example, speed and geometry) and level of track dynamic during train passages. To investigate the relationship between the elastic shakedown limit and train speed, an example of the homogenous ground with Young's modulus of 71 MPA and varying friction angle, ϕ = 20˚-35 ˚ are created [32]. The results are plotted, as presented in Figure 6. It is seen that the elastic shakedown limit tends to decrease when the train speed increase for all varying friction angles and the minimum value of shakedown limit can be found at critical speed of 116 m/s. Therefore, the track failure can occur at equal to higher than this speed. However, the analysis above is based on a single moving load, and if considering full train geometries, the shakedown limit will likely be reduced.

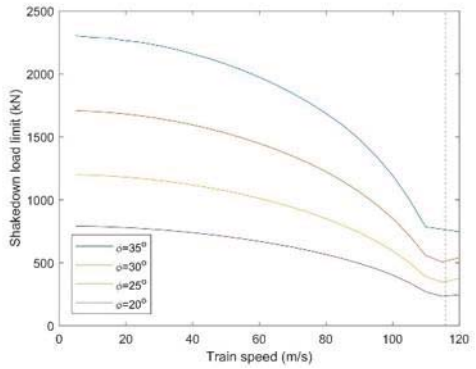

Figure 6: The relationship between train speed and elastic shakedown limit

3.4 Soil improvement

As mentioned in section 3.2, sandwiched low stiffness layers can cause the multiple dynamic amplification factor (DAF) peak generation and significant stiffness contrast. This is challenging to find out the reasonable solutions that can increase the soil stiffness while the cost is needed to be optimised. Therefore, in this section, two main solutions will be considered and discussed.

- Soil replacement

  This is the fundamental practice to improve the soil stiffness by replacing the existing softer soil with the stiffer soil throughout the localised layer. The challenging tasks are to determine the optimisation between the magnitude of stiffness improvement and replacement depth, with respect to construction cost.

  To illustrate this, the example of an original homogenous half-space soil with the stiffness of 45 MPa is created. Then, the soil is locally stiffened by varying five discrete depths (1 to 5 m) and three stiffer magnitudes (100, 200 and 300 MPa). After

simulating the model, the results of all variation cases are plotted, as shown in Figure 7. It is seen that the improvement depth and stiffness magnitude have a non-linear relationship with track deflection. When considering the improvement depth of 1 m, only 300 MPa of stiffness results in lower rail displacement compared with the benchmark case with no improvement (see the dashed line in Figure 7). The reasons are that the train speed is higher than the critical velocity of the original soil, including the increased stiffness shifts the DAF peak closer to train speed [26].

Apart from at 1 m depth above, it is seen that the lower deflections occur when the stiffness magnitude increase. Interestingly, the complex relationships between improvement depth and magnitude stiffness are found at a different level of deflections. For example, 1 m of 300 MPa improvement presents a similar displacement as 2m of 100 MPa, as well as 2 m of 300 MPa and 5 m of 100 MPa. Therefore, to maximise performance and minimise cost, different combinations of both variables are essential to be considered.

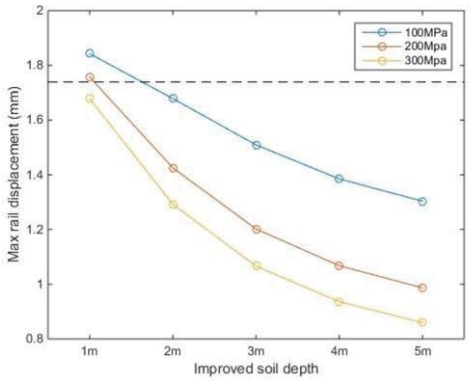

Figure 7: Soil replacement optimisation considering improvement depth and stiffness magnitude

- Discrete soil stiffening

In contrast with soil replacement, soil can be stiffened discretely by either placing stone columns or performing jet grouting. To investigate the performance of both methods, two-layered soil models are created with the thickness of 4 m and 102 MPa of stiffness for the upper layer while the infinite depth of lower layer is modelled with 468 MPa. Then, nine stone columns with diameter of 0.8 m and a stiffness of 160 MPa were placed at the top layers with 1.6 m of spacing while the jet grouting was performed at five locations at 3.48 m of spacing in top layer with 0.7 m of diameter and stiffness of 1 GPa for another model as shown in Figure 8.

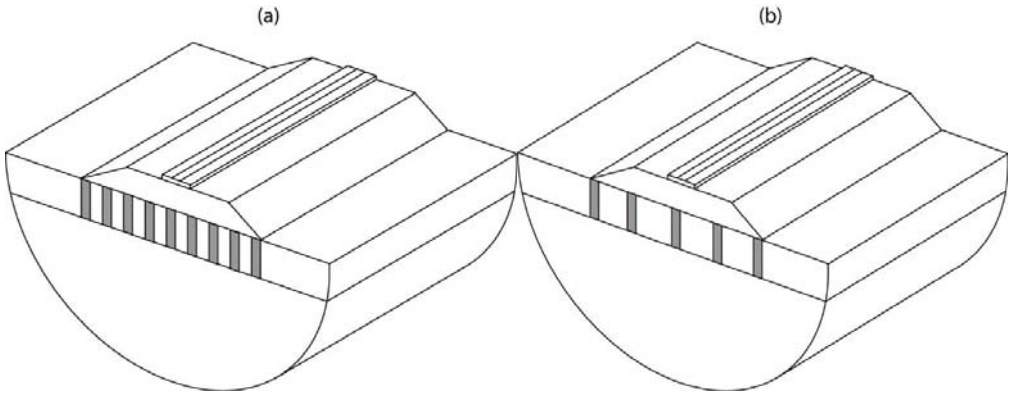

Figure 8 : Discrete soil stiffening model (a) stone column, (b) jet grouting

The results of dynamic amplification for both methods, including the non-improvement case (considered as benchmark case) are plotted, as shown in Figure 9. Such curves from two methods have been normalised as regard to the static displacement of the benchmark. When considering dynamic amplification aspect, using stone column and jet grouting provides a benefit of 12% and 39% respectively compared to the benchmark. Besides, both methods also offer an advantage on critical velocity, 7% when using stone column and 22% for jet grouting. However, these benefit can be affected if the quantity, dimension and stiffness of stone column and jet grouting are changed. Therefore, these three variables above are required to consider when optimising cost and performance of these two methods.

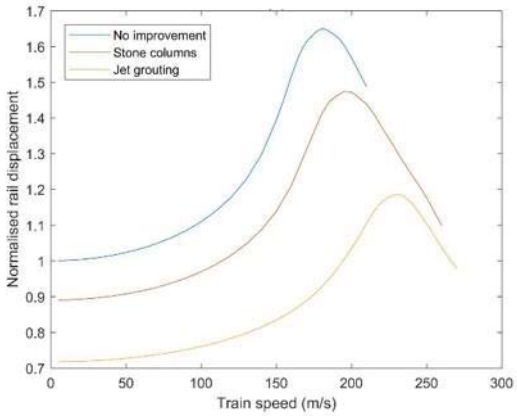

Figure 9: Normalised rail displacement curve when using a stone column and jet grouting

4 CONCLUSION

This paper aims to analyse the dynamic behaviour due to various track and soil problems which involve low-stiffness soil layers, track shakedown and soil improvement. Three types of modelling strategies which consist of analytical, semi-analytical and 2.5D numerical model are developed individually to simulate an example for each problem.

The analysis shows that the presence of sandwiched low stiffness layers can result in a higher level of complexity of soil wave dispersion, with respect to critical velocity. For track shakedown issue, it is found that the elastic shakedown limit is considered as an important factor for the likelihood of track failure due to train loading. Besides, the shakedown limit is highly sensitive when train speed increase. Soil improvement is also examined with two remediation solutions which are soil replacement and discrete soil stiffening. For soil replace-

ment, an improvement depth and stiffness magnitude of replacing soil are essential variables for optimisation of the cost and performance. The relationship between these two variables and track deflection are both non-linear. Lastly, the stone column and jet grouting are considered as discrete soil stiffening method. Two solutions can increase the critical velocity and reduce the dynamic amplification, while jet grouting has a more significant impact on such parameters compared to the stone column.

REFERENCES

[1] R. F. Woldringh and B. M. New, "Embankment design for high speed trains on soft soils," *Proceeding 12th Eur. Conf. Soil Mech. Geotech. Eng.*, pp. 1703–1712, 1999.

[2] D. P. Connolly, P. A. Costa, G. Kouroussis, P. Galvin, P. K. Woodward, and O. Laghrouche, "Large scale international testing of railway ground vibrations across Europe," *Soil Dyn. Earthq. Eng.*, vol. 71, pp. 1–12, 2015.

[3] P. Wang, K. Wei, L. Wang, and J. Xiao, "Experimental study of the frequency-domain characteristics of ground vibrations caused by a high-speed train running on non-ballasted track," *Proc. Inst. Mech. Eng. Part F J. Rail Rapid Transit*, vol. 230, pp. 1131–1144, 2015.

[4] D. P. Connolly, G. Kouroussis, P. K. Woodward, P. A. Costa, O. Verlinden, and M. C. Forde, "Field testing and analysis of high speed rail vibrations," *Soil Dyn. Earthq. Eng.*, vol. 67, pp. 102–118, 2014.

[5] V. Krylov, A. Dawson, M. Heelis, and A. Collop, "Rail movement and ground waves caused by high- speed trains approaching track-soil critical velocities," *Proc.Inst.Mech.Eng.Part F J. Rail Rapid Transit*, vol. 214, pp. 107–116, 2000.

[6] P. Galvín, D. L. Mendoza, D. P. Connolly, G. Degrande, G. Lombaert, and A. Romero, "Scoping assessment of free- field vibrations due to railway traffic," *Soil Dyn. Earthq. Eng.*, vol. 114, pp. 598–614, 2018.

[7] G. Kouroussis, K. E. Vogiatzis, and D. P. Connolly, "Assessment of railway ground vibration in urban area using in-situ transfer mobilities and simulated vehicle-track interaction in-situ transfer mobilities and simulated vehicle-track interaction," *Int. J. Rail Transp.*, vol. 6, pp. 113–130, 2018.

[8] G. Holm, B. Andreasson, P. Bengtsson, A. Bodare, and H. Erikkson, "Mitigation of Track and Ground Vibrations by High Speed Trains at Ledsgard,Sweden," *Rep. 10*, 2002.

[9] D. P. Connolly and P. A. Costa, "Geodynamics of very high speed transport systems," *Soil Dyn. Earthq. Eng.*, vol. 130, 2020.

[10] B. J. Van Dyk, J. R. Edwards, M. S. Dersch, C. J. R. Jr, and C. P. L. Barkan, "Evaluation of dynamic and impact wheel load factors and their application in design processes," *Proc. Inst. Mech. Eng. Part F J. Rail Rapid Transit*, vol. 231, pp. 33–43, 2017.

[11] H. Lamb, "On the propagation of tremors over the surface of an elastic solid," *Philos. Trans. R. Soc. London. Ser.A, Contain. Pap. a Math. or Phys. Character*, vol. 203, pp. 1–42, 1904.

[12] P. A. Costa, A. Colaço, R. Calçada, and A. S. Cardoso, "Critical speed of railway tracks . Detailed and simplified approaches," *Transp. Geotech.*, vol. 2, pp. 30–46, 2015.

[13] S. B. Mezher, D. P. Connolly, P. K. Woodward, O. Laghrouche, J. Pombo, and P. A. Costa, "Railway critical velocity – Analytical prediction and analysis," *Transp. Geotech.*, vol. 6, pp. 84–96, 2016.

[14] F. Barros and J. E. Luco, "Stresses and displacement in a layered half-space for a moving line load," *Appl.Math.Comput.*, vol. 67, pp. 103–134, 1995.

[15] X. Sheng, C. J. C. Jones, and D. J. Thompson, "A comparison of a theoretical model for quasi-statically and dynamically induced environmental vibration from trains with measurements," *Sound Vib.*, vol. 267, pp. 621–635, 2003.

[16] G. Lombaert, G. Degrande, J. Kogut, and S. Francois, "The experimental validation of a numerical model for the prediction of railway induced vibrations," *Sound Vib.*, vol. 297, pp. 512–535, 2006.

[17] H. H. Hung, G. H. Chen, and Y. B. Yang, "Effect of railway roughness on soil vibrations due to moving trains by 2.5D finite / infinite element approach," *Eng. Struct.*, vol. 57, pp. 254–266, 2013.

[18] P. A. Costa, R. Calcada, A. S. Cardoso, and A. Bodare, "Influence of soil non-linearity on the dynamic response of high-speed railway tracks," *Soil Dyn. Earthq. Eng.*, vol. 30, pp. 221–235, 2010.

[19] J. Barbosa, J. Park, and E. Kausel, "Perfectly matched layers in the thin layer method," *Comput. Methods Appl. Mech. Eng.*, vol. 217–220, pp. 262–274, 2012.

[20] D. P. Connolly, P. Galvín, B. Olivier, A. Romero, and G. Kouroussis, "A 2.5D time-frequency domain model for railway induced soil-building vibration due to railway defects," *Soil Dyn. Earthq. Eng.*, vol. 120, pp. 332–344, 2019.

[21] K. Dong, D. P. Connolly, O. Laghrouche, P. K. Woodward, and P. A. Costa, "Non-linear soil behaviour on high speed rail lines," *Comput. Geotech.*, vol. 112, pp. 302–318, 2019.

[22] E. Arlaud, S. C. D'Aguiar, and E. Balmes, "Receptance of railway tracks at low frequency : Numerical and experimental approaches," *Transp. Geotech.*, vol. 9, pp. 1–16, 2016.

[23] H. Chebli, R. Othman, D. Clouteau, M. Arnst, and G. Degrande, "3D periodic BE – FE model for various transportation structures interacting with soil," *Comput. Geotech.*, vol. 35, pp. 22–32, 2008.

[24] D. P. Connolly, A. Giannopoulos, W. Fan, P. K. Woodward, and M. C. Forde, "Optimising low acoustic impedance back-fill material wave barrier dimensions to shield structures from ground borne high speed rail vibrations," *Constr. Build. Mater.*, vol. 44, pp. 557–564, 2013.

[25] D. P. Connolly, A. Giannopoulos, and M. C. Forde, "Numerical modelling of ground borne vibrations from high speed rail lines on embankments," *Soil Dyn. Earthq. Eng.*, vol. 46, 2013.

[26] K. Dong, D. P. Connolly, O. Laghrouche, P. K. Woodward, and P. A. Costa, "The stiffening of soft soils on railway lines," *Transp. Geotech.*, vol. 17, pp. 178–191, 2018.

[27] A. Colaço, P. A. Costa, and D. P. Connolly, "The influence of train properties on railway ground vibrations," *Struct. Infrastruct. Eng.*, vol. 12, pp. 517–534, 2016.

[28] C. Madshus and A. M. Kaynia, “High-Speed railway lines on Soft Ground: Dynamic Behaviour at critical train speed,” *Sound Vib.*, vol. 231, pp. 689–701, 2000.

[29] I. F. Collins and M. Boulbibane, “Geomechanical Analysis of Unbound Pavements Based on Shakedown Theory,” *J. Geothech. Geoenvironmental Eng.*, vol. 126, pp. 50–59, 2000.

[30] M. Boulbibane, I. F. Collins, D. Weichert, and L. Raad, “Shakedown analysis of anisotropic asphalt concrete pavements with clay subgrade,” *Can.Geotech. J.*, vol. 37, pp. 882–889, 2000.

[31] S. F. Brown, H. S. Yu, S. Juspi, and J. Wang, “Validation experiments for lower-bound shakedown theory applied to layered pavement systems,” *Geotechnique*, vol. 62, pp. 923–932, 2012.

[32] P. A. Costa, P. Lopes, and A. S. Cardoso, “Soil shakedown analysis of slab railway tracks : Numerical approach and parametric study,” *Transp. Geotech.*, vol. 16, pp. 85–96, 2018.

EURODYN 2020
XI International Conference on Structural Dynamics
M. Papadrakakis, M. Fragiadakis, C. Papadimitriou (eds.)
Athens, Greece, 23–26 November 2020

OURS – INTRODUCING THE DUTCH FORMAL MODEL FOR RAILWAY VIBRATION

Arnold Koopman

Level Acoustics & Vibration
De Rondom 10, Eindhoven, The Netherlands
e-mail: arnold@levelav.nl

Keywords: Railway, Vibration, Modeling, Emission, Measurement

Abstract. *Assessment of environmental vibration of railway lines can take many forms, often depending on the skills and tools of whoever carries it out. In order to protect stakeholders from this arbitrariness and to reduce assessment costs, the Dutch government has commissioned the design and implementation of a screening model for railway vibration. After a study on the state-of-the-art of different methods a methodology has been chosen. This has been carried out and the model is now taken into service.*

In our state of the art study we found that the best approach is to combine a database of vibration forces of different train types for different soil conditions with a numerical model of the soil and an analytical model of the building. This is also given by the type of data that is usually available in environmental impact studies. Key parts are the existence of an extensive soil database in the Netherlands as well as a 6-monthly update of the track geometry. An important issue we addressed was controlling train-track-soil interaction in such a hybrid model given the soft soils that are typical for the Netherlands. We also gave a thorough treatment of all the variations and uncertainties.

What is achieved now is a model where users input general information like geometry of the track and the types, speeds and number of trains into the model. The model itself collects detailed information from various databases, builds an FEM model and runs its calculations resulting in expected exposure values and their bandwidth. Validation will show to what extend this model can be used.

This paper focusses on the schematization of the problem and the measurement of vibration forces.

1 INTRODUCTION

Current procedure in The Netherlands for environmental vibration impact studies of railway projects is the common three step approach: 1. scoping (setting a distance contour around the project and finding relevant buildings); 2. screening (identifying possible exceedance of criteria); 3. detailed predictions (targeting identified locations). As the third step can be quite costly, a good screening procedure is very important. As most projects involve existing lines (to be upgraded), measurements as a central part of the screening is a possibility and in fact the main method right now. Any model to replace that should at least deliver the same quality, in terms of the avoidance of false positives (wrongly identifying buildings) and false negatives (missing the right buildings). It implies that the model should be especially at his best around the criteria levels and that the model should provide information about its reliability, for users to make it possible to choose the level of certainty that suits their purpose. Another important requirement is that it does not need more input than is available in a screening phase. A nice to have for a screening model is that it is also of use for detailed predictions, for instance by allowing parts of the screening model to be replaced by alternative modelling. That way a detailed study can focus on a part without the burden of building a complete alternative model.

A state of the art study [1] learned that such a model, applicable to typical Dutch soils (ranging from very soft to sandy), is not readily available nor can be easily derived from existing similar models. For instance: an existing Dutch commercial screening model[1], completely based on empirical data, lacks information about its reliability. The Swiss model VIBRA-2 is not applicable to soft soils. Current procedures involving the combination of a train-track-soil model, a ground-propagation model and a building response model require too much details.

The models that are available, according to the state of the art study, fall into three categories:

1. Empirical models. They often offer solutions for the complete problem: source, soil propagation, building response. However they lack known reliability and cannot be transposed from their empirical base to other soils, trains, etc.
2. Detailed models. They offer only solutions for parts of the problem: either the source, or a part of the propagation. Their use requires input that is often not available during screening.
3. Machine learning models. As with empirical models loads of measurement data are statistically treated but instead of deriving closed expressions or look-up tables, networks (neural nets, random forests, etc.) are trained on it. They require a quantity and quality of empirical data that is not yet available in The Netherlands.

It has become clear that any new screening model would involve a combination of models. Empirical models suit the level of detail during screening, detailed models make it possible to transpose the empirical models, statistics is needed to learn about the resulting reliability.

2 SCHEMATIZATION OF *OURS*

OURS[2] is built up like noise models used for environmental assessment:

- The source part is empirical
- The propagation part is detailed

[1] VibraDyna, Movares

[2] OURS is an acronym, *Ontwikkeling Uniform Rekenmodel Spoortrillingen*, which is Dutch for "development of a uniform calculation model for railway vibration"

- The building response is empirical/detailed

Different from noise models is that the propagating medium, the soil, influences both the source and the building response. The detailed soil module therefore also feeds into the source module and the building module.

Similar to noise models, each part of problem is described in the frequency domain. Modules generate octave band spectra with mid frequencies 2, 4, 8, 16, 32 and 63 Hz. The main metrics that the model needs to produce are of a peak nature: Vmax and Vtop. They are the maximum over a week of the maximum of each pass-by. The model works with an average over a week of the root-mean-square of each pass-by. This supports the use of spectral analysis. The peak metrics are derived afterwards based on statistical assumptions about the distribution of the vibration amplitude during a pass-by and the distribution of peak levels among pass-bys.. That procedure is already in use for common railway vibration measurements in the Netherlands [2].

2.1 Source

The kinetic energy of the forward moving train is the actual source of environmental vibration. Irregularities, like track unevenness, track stiffness variation, discontinuities, wheel out of roundness, etc. transform part of this energy into propagating waves. Quasi static excitation caused by the moving axle load only lead to propagating waves above a certain critical speed but also generate a near field below that speed which for soft soils can be considerable. The mechanics of the train, the track and local soil influence how much power is injected into the ground and at which frequencies. OURS does not model all that in detail. Instead, the combined source mechanisms are modelled as one “equivalent” point force on the track, equivalent in the sense that it generates the same vibration levels at a given distance, of 25 meter, from the track. The assumption is that the source power is proportional to the square of the excitation force of the train-track system on the soil.

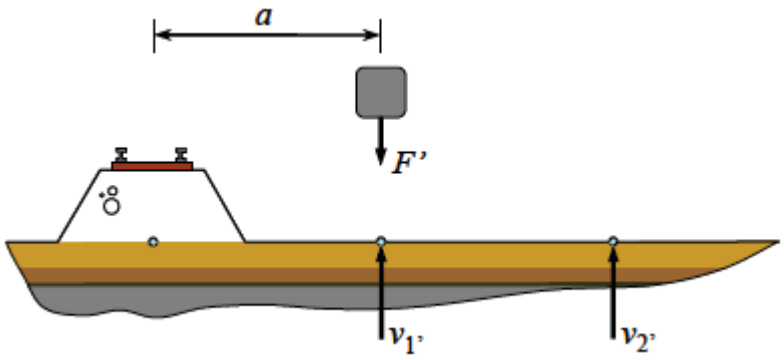

Figure 1: Measurement procedure for use of the equivalent force characterization of a railway track. Using a drop weight the transfer mobility from point 1 to point 2 is measured. Assuming translational symmetry of the ground and regarding the embankment as part of the source, that transfer mobility is taken to be valid also for the train-track system towards point 1.

The distance of the evaluation point (distance *a* in Figure 1) is determined from a sensitivity study performed by Hoving [3]. In that study, a physically complete, though simplified numerical model of the train-track-soil system is set up to determine the minimal distance *a* where the transfer mobility from track to point 1 is not influenced by the train and the track. That distance can be considered the border between source and propagation path and the evaluation point for an equivalent force method.

A drop weight generating a force F on point 1, 25 meter from the track, leads to a velocity response v of point 2 at a distance of 25 meter from point 1. The ratio is the transfer mobility over 25 meter, denoted by Y_{25}:

$$Y_{25} = \frac{v_2}{F_1} \tag{1}$$

Assuming translation invariation, Yo also describes the transfer mobility from a point directly under the embankment to point 1. Measuring the velocity at point 1 during a train passby, a force can be calculated that is characterizes the active train-track-system as a source equivalent to a drop weight:

$$F_{eq} = \frac{v_1}{Y_{25}} \tag{2}$$

The force levels are determined from in situ measurements. How this is done precisely is described in chapter 3. It leads to a database of force spectra for a range of train types, with different speeds, on certain measurement locations. This database constitutes the main part of the source module of OURS. However, this is not enough for describing the source.

Equivalent forces are characteristic for the measurement circumstances under which they are determined: of course train speed and track conditions, but also soil conditions. An algorithm is needed to transpose the measurement data to different conditions. For train speed, that can be a simple case of interpolation between measurement data, given that sufficient speed variation is available in the database. For track conditions, the force can be scaled, given that condition measurements from monitoring trains are available. However, for the embankment as well as for soft soils there is a problem that cannot be solved as easily.

When the receiving system, especially the soil, is relatively soft, the assumption that the source power is proportional to the excitation forces breaks down. The relative mobilities of source system and receiving system influence the actual power injection. This interaction has to be taken into account. In structural acoustics, this is done by introducing a coupling function that is dependent on de mobilities of the subsystems. For railways lines this is difficult: the two dimensional interface between the subsystems complicate the coupling function and complicate the measurement of the needed mobilities.

For OURS, a more simple approach is chosen to take the influence of the soil on vibration generation into account. For each type of train, the equivalent force is determined on two very different soils: a very stiff one and a very soft one. The soil mobility of each of those two locations, already needed to determine forces from measured velocities, become part of the source description. For any location where a prediction is needed, the equivalent fore is determined by interpolation between the two measurement sites based on the mobility of the prediction site. The latter mobility is determined by the same module that calculates the ground propagation.

The interpolation parameter that weights the relative contribution of the soft soil measurements and the stiff soil measurements is determined as follows:

$$s_i = \frac{-\lg(\hat{Y}^{\square}_{25,i}\hat{Z}^{\square}_{25,i,\downarrow})}{\lg(\hat{Z}^{\square}_{25,i,\uparrow}/\hat{Z}^{\square}_{25,i,\downarrow})} \tag{3}$$

In this formula, Z with an arrow up is the transfer impedance (reciprocal of the transfer mobility) of the stiff soil and Z with the arrow down likewise for the soft soil, i is the index for fre-

quency bands, Y_{25} is the calculated transfer mobility of the soil. Given that soil mobilities can differ by an order of magnitude or more, a logarithmic scaling is chosen.

For a certain situation to be evaluated, the equivalent force of a train can thus be calculated from the measured equivalent forces at two sites:

$$F_{eq} = s_i \cdot F_{z,i,\uparrow} \left(\frac{v}{v_{\uparrow}}\right)^{n_{\uparrow}} + (1 - s_i) \cdot F_{z,i,\downarrow} \left(\frac{v}{v_{\downarrow}}\right)^{n_{\downarrow}} \quad (4)$$

In this formula, V stands for the train speed. The exponent n for the influence of the train speed on the equivalent force is also determined at the two measurement sites, each with their own appropriate reference speed (being the median speed at that location).

2.2 Ground propagation

A rather unique opportunity for soil characterization, needed for any propagation model, is the availability in The Netherlands of an extensive and continuously growing database of cone penetration tests (CPT's). For about 80% of the railway system, at least one CPT is available within 600 meter distance. This trove of input data makes it feasible to employ a detailed numerical model. Chosen is to start with implementing a 2D axial symmetric finite element method. Possibly this will be accompanied in the future by a full 3D FEM implementation, for instance for assessing tracks not on grade, mitigation measures, etc.

After drawing from the CPT database, a 2D FEM is built, meshed and solved in the frequency domain. This automated process is implemented into OURS and does not require any commercial FEM code.

The ground module generates transfer functions, for use of calculating the decay over distance as well as point mobilities. These point mobilities are used for taking soil-structure interaction into account, for the source as well as for the building. For the source, the calculated mobility amplitude is used to interpolate between the measured ground mobilities in the source database (see paragraph 2.1). For the building, the calculated complex mobility is combined with a calculated complex building mobility to determine a coupling function (see paragraph 2.3). Also, at the position of the building, the speed of the incoming waves, of whatever nature, is determined for use of the building response.

Choosing a 2D solution over 3D has the benefit of fast calculation but has the drawback that the actual 3D geometrical decay is not represented fully in the 2D solution. This is remedied by imposing the missing extra dimension afterwards.

Choosing to describe the soil with a 2D model in the frequency domain has the drawback that the moving load effect cannot be represented correctly. The near field decay related to the pass-by of an axle cannot be determined from a transfer function. This can be helped by treating the moving load effect completely separately in the time domain, adding axle loads to the source database and using the FEM representation for static deflection tests. This is not implemented in OURS yet.

The ground module is described in more detail in another paper of this Proceedings.

2.3 Building response

The assessment of environmental vibration mainly involves annoyance. To a lesser degree, for railway vibration, structural damage is also an aspect to be accounted for. According to the Dutch regulation [4] in use for annoyance, vibration possibly leading to annoyance is evaluated at the floors of buildings. Vibration possibly leading to structural damage is evaluated at the foundation of the building, according to a generally excepted guideline [5]. In ei-

ther case, a building response model is needed and should take account of soil – structure interaction. To calculate vibration levels on floors, the dynamics of the building structure as well as those of the floors need to be described.

The building response module of OURS is an analytical model in the frequency domain. It takes in information about the nature of the structure and the floors as well as the point mobility and the wave speed in the ground as a function of frequency. From that input, it calculates transfer functions from a green field soil to the foundation and to the floors.

A more detailed description is outside the scope of this paper.

3 MEASUREMENT METHOD FOR SOURCE DESCRIPTION

3.1 General

In OURS, a train type is described by at least two locations, each delivering an equivalent force and the mobility of the soil on which this force is measured. Force and mobility are octave spectra. The mobility is a transfer mobility over 25 meter, determined from a drop weight test. The force is the root-mean-square (rms) of the ground velocity during pass-by, on 25 meter distance from the track, divided by the mobility.

To reduce the influence of varying soil conditions at the measurement location as much as possible, the following precautions are made:

- locations on one side of a track are used with an area of about 200 meter by 200 meter that only contain grass land, without ditches or elevations
- 9 vibration measurements points are used, each at least 2D, preferably 3D. The horizontal of a 2D sensor is oriented towards the source (track or drop weight), a horizontal of the 3D sensor is oriented towards the track.
- for placing the measurement equipment, first the top layer, often about 25 cm, is removed

The drop weight test is performed at each of the 9 measurement points, not only to then later average mobilities, but also to identify possible deviated local soil conditions, to be taken into account during post processing.

To reduce the influence of variation between trains of the same type, at least 50 pass-by's are required, which are averages later. In practice, the measurements continue for at least 2 weeks.

To determine train type and track number a webcam is used and software is trained on the resulting images. To determine train speed a speed radar is installed.

3.2 Measurement procedure

At each measurement location, after careful selection of such a location, the following procedure is followed.

1. A mesh of 3x3 of 50 by 50 meter is set out on 25 meter from the nearest rail of a railway track. See Figure 2.
2. At the 9 mesh points vibration equipment is installed. After removal of the top layer, first a sufficiently stiff plate (first mode>160 Hz, size 30 cm x 30 cm) is positioned and on top of that the sensor is placed. The hole is covered to avoid sensor excitation by rainfall.
3. Webcam and speed radar are installed close to the track and set to run and save continuously.
4. The area is closed down: no cattle or farming or humans allowed.

5. Triggered by a pass-by, full time signals of all 9 points are collected and saved with a pretrigger and posttrigger of 2 seconds.
6. After at least two weeks of measurements, at the last two days a drop weight of at least 300 kg is brought and used to perform the mobility measurements. The drop weight is equipped with an accelerometer to determine the excitation force. The weight is dropped on a plate of about 1 m^2, near each of the 9 measurement points. At least 6 drops at each point: 3 at maximum impulse and 3 at 30% of maximum impulse. Each time the full time signals of all measurement points are collected. In addition to the 9 fixed vibration sensors, there are 4 1D vibration sensors that accompany the drop weight and are positioned around it.
   At least 8 seconds of signal, including a pretrigger of 1 second, is recorded.

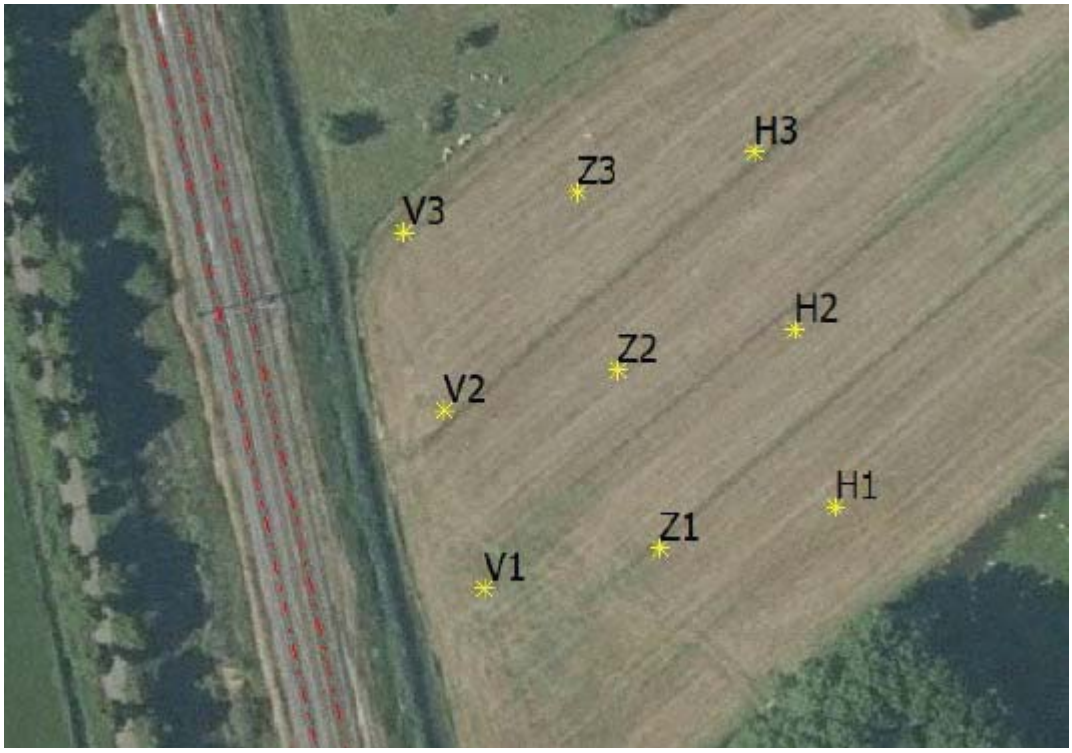

Figure 2: Measurement grid, next to the track. The lines V, Z and H are on a distance of resp. 25, 50 and 75 meter from the nearest rail

The equipment needs to fulfill the next requirements:

- Vibration measurement equipment must fulfill the requirements according to the Dutch guideline SBR B [6] (a.o.: measurement range of 1 to 80 Hz, with a resolution of 0.01 mm/s). The four extra sensors placed around the drop weight need to have a resolution of 0.001 mm/s.
- For the pass-by measurements, the sample frequency is at least 500 Hz. Synchronization between the sensors of 1 second is sufficient.
- For the drop weight measurements, the sample frequency is at least 1000 Hz and all sensors need to be in sync.
- The drop weight should be able to generate a maximum impulse of at least 1000 Ns.

3.3 Post process procedure

First the drop weight tests are processed.

- For each drop, the time signals of the four “traveling” sensors are averaged to one signal.
- For each drop weight test location, the transfer function estimate from the accelerometer on the drop weight to each of the measurement channels is determined. Preferably the estimate is based on a pwelch procedure.
- If in the field accelerometers instead of velocity sensors are used, the transfer functions are divided by the angular frequency.
- The transfer functions are divided by the mass of the drop weight, resulting in a mobility.
- The transfer functions are spectrally averaged to octave band spectra.
- Along with the transfer function estimate, the coherence is determined. The coherence can turn out to be insufficient for large parts of the spectrum, for instance because the drop weight bounces too much or local deformation of the soil underneath the drop weight plate occurs. In that case, instead of determining transfer function estimates, each measurement channel is filtered to octave bands and spectra are generated bases on the root-mean-square of the full signal. The mobilities are derived from the ratio of the spectra, after corrected for drop weight mass. If in the field accelerometers are used, the time signals are first integrated.
- For each test location, the point mobilities (derived from the 4 traveling sensors) is compared to the mobility derived from the vertical direction of the field sensor at that location to investigate the validity of the field sensor. In case of a considerable deviating spectrum, that sensor is removed from all measurements, including the pass-by’s.
- The 9 point mobilities are also compared mutually to find outliers to be removed from all measurements.
- From the remaining mobilities, all the 25-m “neighbor” mobilities for the vertical direction are selected. The inverse is taken to yield the impedance. These impedances are averaged, thus resulting in what is called, in OURS, Zo. Multiplication of Zo with a velocity measurement on a 25 meter distance gives an equivalent force.
- From the neighbor mobilities the horizontal in the direction of the drop weight is divided by its vertical. These are averaged, resulting in what is called, in OURS, Yratio. That parameter is used to derive a vertical force to horizontal velocity mobility from Zo.

Then the pass-by’s are processed.

- The time signals are put through an octave filter bank.
- The signals, including the original unfiltered one, are further treated according to SBR B: the frequency weighting related to human perception is applied in the time domain, the signal is convoluted with an exponential filter with a decay time of 1/8 second, resulting in a DC signal.
- For each channel from the unfiltered but SBR-B treated signal the moment that the maximum (called “Veff,max” by SBR-B) occurs is determined. For that moment and 5 seconds (±2.5 seconds) around it, the root mean square of the octave filtered and SBR-B treated time traces is determined. This results in what is called, in OURS, a Vrms,5s per octave band per measurement point per vibration direction per pass-by.
- The decay over distance, from 25 to 50 and 75 meters from the track, for the vertical and the horizontal vibration directions, is determined by curve fitting an exponential decay on each pass-by and average the results.

- The Vrms,5s spectra are multiplied with correction spectrum that accounts for the amount that the local track geometry deviates from the Dutch mean as determined by the most recent visit from a track monitoring train.
- Using the distance decay, the Vrms,5s on 50 and 75 meter are translated to a prospected spectrum at 25 meter. For multiple tracks, pass-by's on the tracks further from the field are translated to the first track, using that same distance decay relation.
- Each Vrms,5s is multiplied with Zo to yield an equivalent force spectrum.
- Per type of train, all force spectra of that type are collected to fit the exponential of the relationship between train velocity and equivalent force. This exponential becomes part of the source database.
- After applying train speed correction, for each type of train all equivalent force spectra are averaged, yielding Feq, which becomes part of the source database.

4 MEASUREMENT RESULTS

In 2018, specialists from the company Cauberg-Huygen have carried out source measurements at 3 locations in the Netherlands: Best, Schalkwijk and Nijkerk. Best and Nijkerk are chosen for their stiff soil (sandy), Schalkwijk for its very soft soil (clay).

From this experience, some lessons are learned. One involves the drop weight. Applying an elastic layer under a drop weight is an often used method to skew the excitation spectrum. Varying that layer makes it possible to "scan" a considerable frequency range. Eventually it turned out, for this procedure, that just using one very stiff rubber (of unknown Youngs's modulus though) is sufficient.

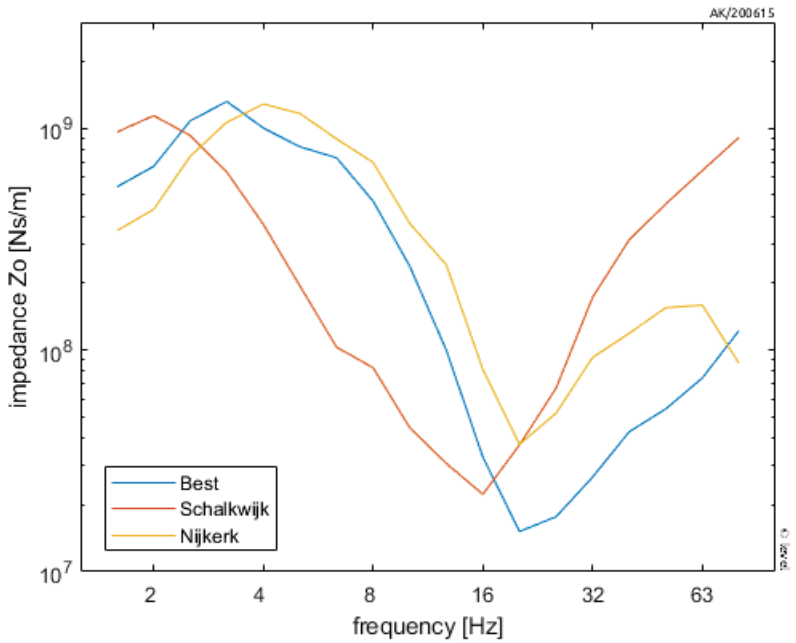

Figure 3: Impedance over 25 meter Zo, as determined by drop weight tests on three different locations in The Netherlands. The variation coefficient in each band is about 30%.

Some results are presented in figures 3, 4 and 5. First the measured impedances are shown. For the purpose of investigation, the impedances are evaluated for third octaves instead of octave. Around 8 Hz, an important frequency for railway vibration on soft soils, the difference between the stiff soils and the soft soil is an order of magnitude. Around 63 Hz, the soft soil has a much higher impedance over 25 meter.

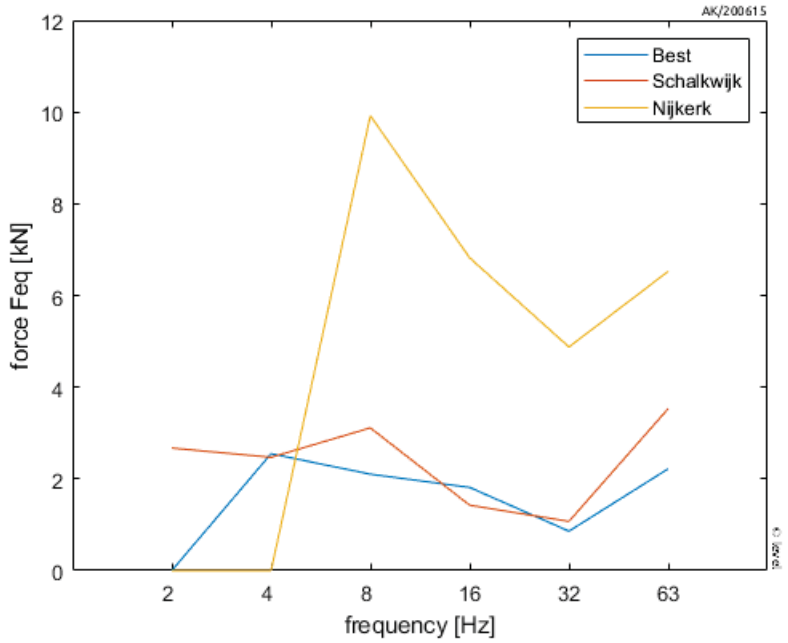

Figure 4: Equivalent force of a VIRM passenger train at 135 km/hr as determined on three different locations. The variation coefficient in each band is about 30%.

The equivalent force for a very common and very significant train type, the double deck passenger train VIRM, is shown in 4, for each of the three locations. It illustrates the influence of the soil on the equivalent force. Remarkable is that for the main part of the frequency range, not the one soft location but one of the two stiff locations stands out: Nijkerk. From a stiffer soil higher forces are expected so the current assumption is that it is actually the other stiff location, Best, that is deviating from expectations. Either way, these results are not fully explained yet and are still under investigation.

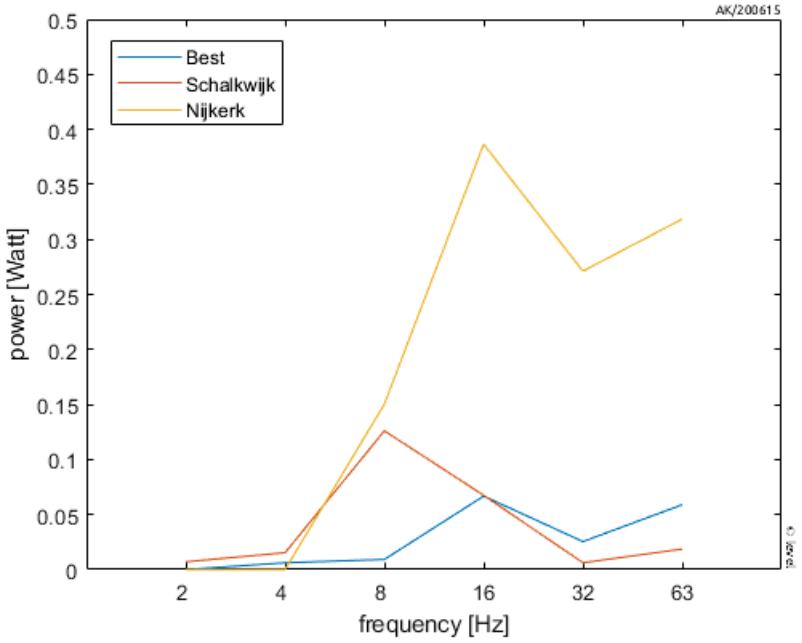

Figure 5: Power, injected into propagating waves, by VIRM passenger trains with a speed of 135 km/hr, on three different locations. The variation coefficient in each band is about 50%.

Finally, the power injected into propagating waves is determined from the equivalent force and resulting response at 25 meters from the track. It illustrates the influence of the soil on injected power and therefor the need to incorporate the soil influence into a source characterization. Again, Nijkerk stands out. This can partially be explained by the high forces that are generated there. Schalkwijk shows why 8 Hz is such an important frequency for soft soils: most of the power is in that octave band. It can be explained by the relatively low soil impedance there which leads to a stronger coupling with the train-track system.

5 CONCLUSIONS

This paper describes the physical schematization that OURS uses to describe the generation and propagation of railway vibration. An important aspect is the influence of the stiffness of the soil on the vibration generation. This led to a measurement procedure that is described in this paper. That procedure has been carried out at three locations, to fill the source database of OURS.

The measurement results show that the injected power indeed depends on the soil conditions and that the equivalent force as a descriptor of a source is only valid under similar soil impedances.

Two similarly stiff locations generate different injected and different equivalent forces though. This is not understood yet.

The full implementation of OURS, the installer as well as all the code, which is released under an open source license, can be found on Github [7].

6 ACKNOWLEDGEMENTS

This work is commissioned by the Dutch Ministry of Infrastructure and Watermanagement to the National Institute for Public Health and the Environment (RIVM) and carried out in a consortium of RIVM, Deltares, DGMR, Cauberg-Huygen, Movares and Level Acoustics & Vibration.

REFERENCES

[1] D. de Gruijter et al., Een uniform rekenmodel voor spoortrillingen 2016, *RIVM briefrapport 2016-0209*, 2016

[2] A. Koopman, C. Ostendorf, Meetmethode Vmax,Bts, *Level Acoustics & Vibration memo LA.131001a.M04*, 2018

[3] J.S. Hoving, A.V. Metrikine, Evaluation of the Effect of Embankment on the Transfer Functions of Soil Vibrations, *Delft University of Technology Technical Report*, 2008

[4] Beleidsregel trillinghinder spoor, *Staatscourant 2014, nr 821*

[5] SBR trillingsrichtlijn A : schade aan bouwwerken : 2017, Stichting Bouwresearch guideline

[6] SBR trillingsrichtlijn B : hinder voor personen in gebouwen : 2002, Stichting Bouwresearch guideline

[7] https://github.com/rivm-syso/OURS

EURODYN 2020
XI International Conference on Structural Dynamics
M. Papadrakakis, M. Fragiadakis, C. Papadimitriou (eds.)
Athens, Greece, 23–26 November 2020

SUBSOIL MODELLING FOR RAILWAY INDUCED VIBRATIONS

B. Zuada Coelho[1], S. Lentzen[2], M. Pronk[1], D. de Lange[1], E. Smyrniou[1], and M. Hijma[1]

[1]Deltares
Boussinesqweg 1, 2629HV Delft
e-mail: {bruno.zuadacoelho, maarten.pronk, dirk.delange, eleni.smyrniou, marc.hijma}@deltares.nl

[2] Level.Tools
De Rondom 10, 5612AP Eindhoven
e-mail: sven@leveltools.nl

Keywords: Soil, Wave Propagation, Finite Elements, Vibrations.

Abstract. *Nuisance due to railway induced vibrations has been receiving increased attention in the Netherlands, as a recent study has found that a significant part of the population living in the vicinity of railway tracks in the Netherlands, experiences excessive vibrations levels. As a result, the Dutch government has commissioned the design and implementation of a screening model for the estimation of railway induced vibrations at a network level. Within this screening model, attention has been paid to the characterisation of the subsoil. This paper focuses on the methodology developed to perform a semi-stochastic subsoil characterisation, based on publicly available datasets for the Netherlands. The method uses a countrywide cone penetration test database and the Dutch geomorphological map to define, at a specific location, a set of possible subsoil schematisations, their likelihood of occurrence, and the corresponding subsoil parameters. The effect of soil variability on the vibration levels is assessed by computing the transfer function at different distances from the source. The transfer functions are computed with a newly developed finite element model kernel. The kernel is optimised to specifically compute layered half-spaces. The results show that the subsoil schematisation plays a significant role on the vibration level, which shows that it is paramount to perform a correct characterisation of the subsoil when trying to estimate induced vibration.*

1 INTRODUCTION

Railway induced vibrations are found to cause public nuisance to inhabitants living on the vicinity of railway tracks. In the Netherlands it is estimated that 20% of the inhabitants living within 300m of a railway track experience severe nuisance due to railway induced vibrations [27].

In order to better characterise the environmental levels of exposure to railway induced vibrations the Dutch government has commissioned a screening model. In 2016 the desire for a robust calculation model was expressed by the minister of the Ministry of Infrastructure and the Environment (currently the Ministry of Infrastructure and Water Management). In response the Dutch National Institute for Public Health and the Environment (RIVM) started a project to answer the following questions:

1. What is the quality of available calculation methods?
2. Can the available methods be improved?
3. What calculation model could best be developed that is suited for railway induced vibrations in the Netherlands?

In an inventory on the state-of-the-art of railway induced vibration models [8], 17 calculation models were considered (10 foreign and 7 domestic). The main conclusion of this study was that none of these models were directly suited to be used in the Netherlands, but a combination of methods could be applied to create a calculation method that fits the requirements for accuracy and reproducibility.

The lead to the development of a new screening model : OURS (a detailed description of the model can be found in [13]). At the heart of the OURS model lies the soil independent source characterisation as developed in [26]. This enables the generation of a database with source parameters that only depend of parameters such as train speed, weight and wagon types. Once a database is filled, then the source terms are convoluted with the transfer admittance through the soil and the vibration levels can be predicted at the foundation of the buildings.

One of the major components of admittance modelling corresponds to the subsoil modelling. Even in countries with abundant information about the subsurface, such as the Netherlands, the data density is in most cases not high enough for reliable deterministic subsoil schematisations. The challenge is to produce a reliable subsoil schematisation and parametrisation, with the available information.

The development of OURS screening model had the following requirements:

- The method needs to be applicable in the entire county;
- The method needs to provide unique response (independent of the user);
- The method needs to provide, for a specific location, subsoil layering and subsoil parameters (Young modulus, soil density, Poisson ratio and damping ratio).

During the past years, a methodology has been developed for flood defences [10] that uses subsurface build up scenarios to characterise the subsurface for a certain assessment. This approach combines data from e.g. boreholes, cone penetration test (CPTs) and geological maps with expert knowledge about the natural pattern in the build-up of the subsurface. The result

is a stochastic subsoil schematisation that, at a certain location, provides the possible subsoil schematisations and its likelihood of occurrence.

Although this methodology has successfully been adopted in flood defences, it cannot be translated into the current project, as it requires expert knowledge in order to derive the subsoil schematisations. The proposed methodology for OURS uses the concepts defined in the flood defences methodology, such as the concept of subsoil scenario [10], but the derivation of the subsoil scenarios is purely based on public datasets.

The second major component of the development of the admittance modelling consists of the creation of a finite element analysis (FEA) kernel. The admittance can be modelled using several methodologies. One of the fastest options is to deploy a semi-analytical description of a layered halfspace. However, the flexibility of such a model is very low. It can only be used in very homogeneously distributed layers. A slightly slower, and a more flexible option are Boundary Element models (BEM). This is a fully numerical method in which only the enclosing surfaces of the layers are discretized. When introducing many thin layers or irregularities, the BEM methods becomes slower. The most flexible and unfortunately slowest option corresponds to Finite Element Method (FEM). In FEM the complete soil domain under consideration has to be discretised. This generally leads to a large number of unknowns to be solved. However, the system of equations to be solved is sparse (in contrary to BEM) and when deploying an explicit scheme to solve the differential equations, only a diagonal matrix has to be inverted.

The major advantage of using FEM is its flexibility. Although it is not foreseen within the scope of this project, it should be easy to improve the method to also model e.g. countermeasures to prevent nuisance. Only FEM is able to easily model these geometric constructs.

This paper the methodology for subsoil modelling and admittance computation in OURS and it is organised as follows: section 2 describes the principles of subsoil modelling, section 3 presents the development of the FEM kernel for the analysis, and section 4 illustrates the application of the methodology in a case study.

2 SUBSOIL MODELLING

2.1 Public datasets for subsoil modelling

The model for the subsoil schematisation and parametrisation developed for OURS has been developed with the following public datasets:

- The Netherlands Hydrological Instrument (NHI);
- Geomorphological map;
- Cone Penetration Test (CPT).

The following sections show the description of these different datasets, and its interpretation (when applicable).

2.1.1 NHI dataset

In the Netherlands the NHI [3] provides the targeted water level for the entire country. This information is used to compute the phreatic level depth, z', and therefore estimate the vertical effective stresses, σ'_{v0}, which are of importance to perform the subsoil schematisation and parametrisation (see Section 2.2.2).

Figure 1 illustrates the targeted water level for the Netherlands. This value is displayed in NAP level (Normaal Amsterdams Peil), which corresponds to the reference surface for vertical positions for the Netherlands. From the Figure 2 it follows that the east and southeast part of the Netherlands have a higher target water level than the western part. This is related to the higher elevation of this region.

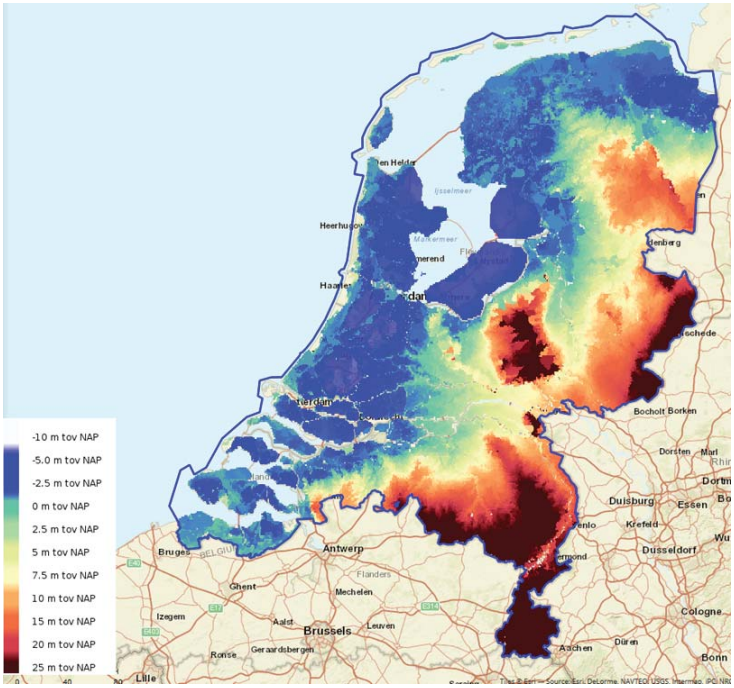

Figure 1: Yearly targeted ground water level for the Netherlands [3].

2.1.2 Geomorphological map

In the Netherlands the geomorphological map has been developed by the Wageningen Environmental Research (Alterra). This map is freely available through PDOK [21]. The geomorphological map provides a detailed overview of the altimetry, origins and formations of the Dutch subsoil (e.g. moraines, river valleys; old river beds), as well as abnormal geological depositions and elevation details. Moreover, the geomorphological map provides information about active geomorphological processes, such as dune formation due to aeolian transport and sedimentation and erosion along rivers and tidal processes.

Figure 2 illustrates the geomorphological map of the Netherlands. Each colour corresponds to an independent geomorphological entity. These geomorphological entities can be interpreted as geological formations that have a similar build-up process. From the figure it follows that the eastern part of the Netherlands has more complex morphology than the western part. Areas as Flevoland have little variability, as they are the result of land reclamation activities.

2.1.3 CPT tests

The CPTs tests are generally the main information used to perform the subsoil schematisation and parametrisation in geotechnical engineering, therefore have been adopted as the main dataset for the development of the subsoil modelling in OURS.

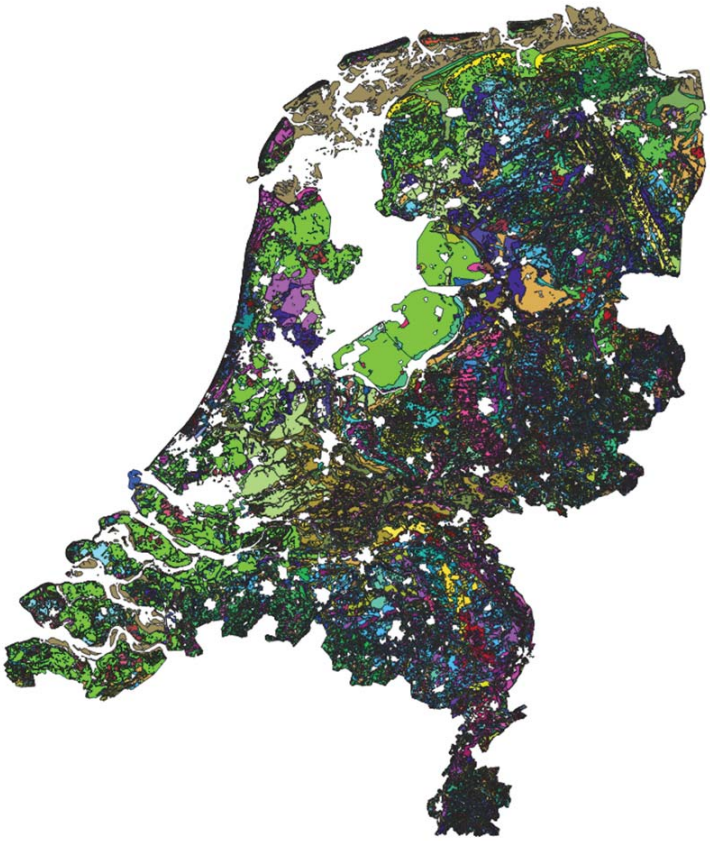

Figure 2: Geomorphological map of the Netherlands [21].

In the Netherlands a public database containing CPTs is freely available (BRO: Basisregistratie Ondergrond [2]), and it is maintained by the Dutch government. This database is being continuously updated with new CPT data, as in the Netherlands it is compulsory to add the CPTs tests into the BRO database for projects funded by the public works.

Figure 3 shows the CPT dataset available in the BRO (February 2020), alongside with the Dutch railway network. In total there are 97732 CPTs tests. It follows that the Randstad has a higher density of CPT tests than the rest of the Netherlands. Nevertheless, the amount of CPT tests will increase with time, as more data will become available in the BRO, which will lead to an overall increase in the density of CPT tests across the country.

2.2 CPT interpretation

2.2.1 CPT: subsoil layering definition

The CPT tests were used to perform the subsoil layering definition. This layering was performed in accordance to the methodology presented in Robertson and Cabal [23]. This is the most established classification system for soils found in literature. This methodology for the calculation is described in Procedure 1.

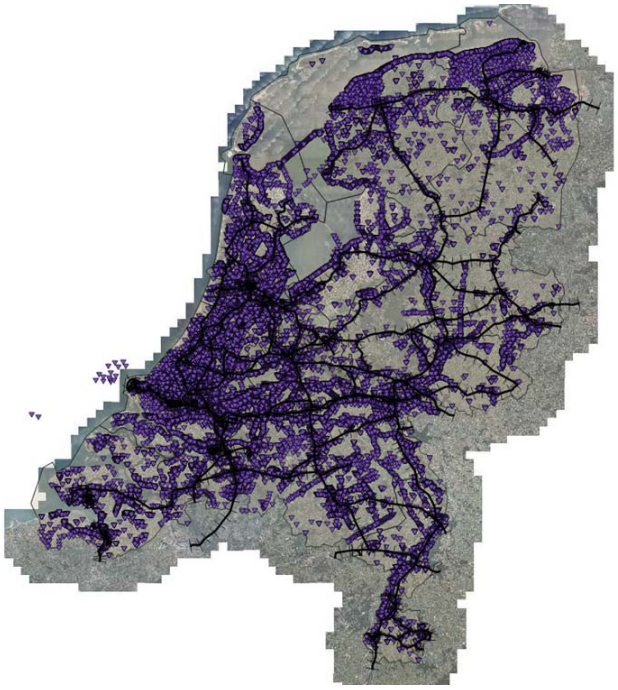

Figure 3: Overview of the CPT distribution in the Netherlands [2]. ▼ represents a CPT and $\neq$ the Dutch railway network.

Procedure 1

1. Read CPT file from BRO
2. Read phreatic level from NHI
3. Compute soil volumetric weight (see Section 2.2.2)
4. Compute total and effective stresses
5. Compute lithology according to [23]

2.2.2 CPT: subsoil parametrisation

For the analysis of wave propagation problems, not only the subsoil layering is of importance, but also the geomechanical parameters associated with each layer. In the model of OURS the wave propagation analysis is done by means of FEA, which has the following geomechanical parameters as input: soil density, ρ; Poisson ratio, ν; small strain shear modulus, G_0; and damping ratio, D_r. Table 1 provides the overview of the correlations used to estimate the geomechanical parameters. Further information about the choice of the correlations, and parameters can be found in [22].

Different correlations exist to establish the relation between CPT data and soil volumetric weight, γ. In OURS the correlation proposed by Lengkeek *et al.* [15] was adopted. This consists of a specific correlation developed for the Netherlands, based on the interpretation of 300 CPT tests, that accounts for the very soft and highly organic soils, typical of the region.

Very little literature is available on the correlation between CPT testing and Poisson ratio. However, this parameter does not vary greatly [14]. From the literature [7, 24, 11, 16] it follows

Property	Correlation	Note
volumetric weight γ	$\gamma = \gamma_{ref} - \beta \cdot \frac{\log\left(\frac{q_{t,ref}}{q_t}\right)}{\log\left(\frac{R_{f,ref}}{R_f}\right)}$	from [15]
soil density ρ	$\rho = \frac{\gamma}{g}$	-
Poisson ratio ν	0.495	clay / loam undrained behaviour
	0.25	silty / sandy clay
	0.3	silty sand
	0.3	sand
	0.375	dense sand
shear wave velocity v_s	$v_s = \sqrt{10^{0.55 \cdot IC + 1.68} \cdot \left(\frac{q_t - \sigma_{v0}}{Pa}\right)}$	from [23]
small strain shear modulus G_0	$G_0 = \rho / v_s^2$	-
damping ratio D_r	$D_r = 2.512 \cdot \left(\frac{\sigma'_{v0}}{Pa}\right)^{-0.2889}$	peat [30]
	$D_r = 0.8005 + 0.0129 \cdot I_p \cdot OCR^{-0.1069} \cdot \left(\frac{\sigma'_{v0}}{Pa}\right)^{-0.2889} \cdot (1 + 0.2919 \ln f)$	clay [6]
	$D_r = 0.55 \cdot C_u^{0.1} \cdot D_{50}^{-0.1069} \cdot \left(\frac{\sigma'_{v0}}{Pa}\right)^{-0.05}$	sand [18]

Table 1: Overview of the correlations for CPT interpretation.

that several authors provide a range of admissible values for the Poisson ratio in the different types of soils.

The value of the shear modulus G depends on the level of shear strain experienced by the soil. For problems involving wave propagation through the subsoil it is generally assumed that the material behaves in elastic regime and that the strain levels are very small. The shear deformations are the result of particle distortion rather than sliding and rolling between particles. Such deformation is almost linearly elastic. This behaviour can be quite accurately simulated by means of the small strain shear modulus, G_0, which is the shear modulus that is mobilised at very small strains [9]. Most of the correlations between CPT and small strain shear modulus are performed through the shear wave velocity, v_s. In OURS the adopted correlation for the shear wave velocity is one proposed by Robertson and Cabal [23], as it is a very well established correlation, and has the advantage of being an universal correlation for all the different soils types.

The value of the damping ratio, D_r, similarly to the shear modulus, is related to the shear strain level. However, while the shear modulus decreases with the increase of the shear strain, the damping ratio increases with the increase of the shear strain. This is related to the dissipation of energy due to hysteretic damping [20]. The damping ratio is estimated for very small shear strains, the reasoning being the same as presented before for the shear modulus. The correlation used to compute the damping depends on the type of soil material.

2.3 Scenario schematisation

2.3.1 Methodology for subsoil scenario schematisation

The methodology devised for the subsoil schematisation was based on the methodology that has been developed for flood defences in the Netherlands [10].

For flood defences, the subsoil is schematised by dividing the subsurface into build-up scenarios that characterise the subsurface for a certain assessment (e.g. macrostabilily, piping). This approach combines data from e.g. boreholes, CPTs and geological maps with expert knowledge about the natural pattern in the build-up of the subsurface. This is relevant, because it important the order of deposition of the sediments (e.g. sediments deposited in a dynamic river-mouth area or at the bottom of the sea). The environment in which the sediments were deposited gives information about what build-up to expect, how much variability is possible, over what distances relevant changes in build-ups can occur and what are the expected geotechnical properties.

One of the requirements for the development of OURS is that the methodology is independent of expert knowledge, so that at any given location the results are always the same, independently from the user.

In order to achieve this, the methodology proposed in [10] for flood defences has been modified. The concept of subsoil scenarios with a defined probability of occurrence remains, however the methodology for its derivation has been modified.

The subsoil scenarios have been computed by combining the information of the geomorphological map with the CPT tests. At the analysis location (x,y) all the CPT tests are gathered for all the geomorphological entities that are in the vicinity of the analysis location (600 m). Each geomorphological entity is a different subsoil scenario (with a probability of occurrence), and the soil properties for the scenario are derived from all the CPT tests that are contained in the geomorphological entity.

In order to keep the FEA computations into a reasonable computational time the scenarios were schematised with a minimum layer thickness of 0.5 m. This means, that layers that are thinner than 0.5 m are merged together. This method is further elaborated in Procedure 2.

Procedure 2

1. Define circle with a radius of 600 m, with centre at the railway analysis location
2. Intercept circle with geomorphological map
3. Identify all the geomorphological entities contained in the interception
4. Read and process all CPTs within each geomorphological entity
5. Read and process remaining CPTs contained in the circle that are not part of any geomorphological entity
6. Schematise in scenarios
   (a) Each geomorphological entity is considered one scenario
   (b) If there is a region in the circle without a geomorphological entity, this region is also considered a scenario
   (c) The probability of occurrence of each scenario is the ratio between the area of the geomorphological entity within the circle and the area of the 600 m radius circle
7. Perform interpolation at the house analysis location. The interpolation is performed to determine the geomechanical properties of each scenario at the analysis point. The interpolation is performed by means of the inverse distance method

Figure 4 shows this procedure in a schematic example. In this example three scenarios: exist Scenario 1, that corresponds to Geomorphological #1 (containing CPT1, CPT2 and CPT3), Scenario 2, that corresponds to Geomorphological #2 (containing CPT6 and CPT7) and Scenario 3 with corresponds to the remaining part of the circle without a geomorphological entity (containing CPT 4 and CPT5).

The geomechanical properties of each scenario will be calculated by interpolating the CPTs contained within each scenario at the calculation point.

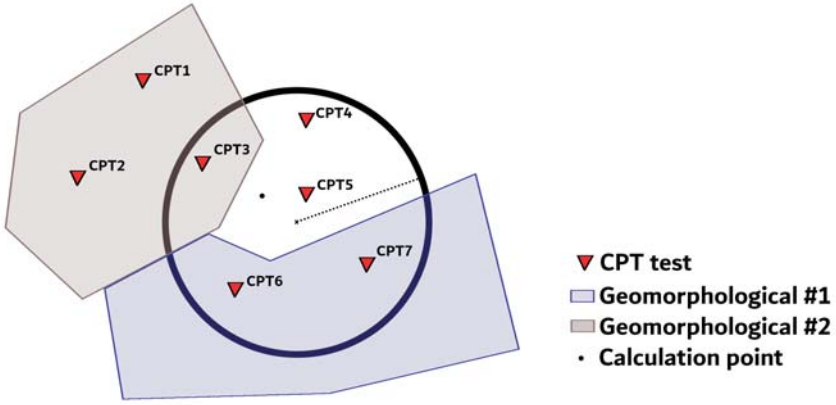

Figure 4: Example of the subsoil scenario schematisation.

The variability in the subsoil parameterisation has been done following the methodology first proposed by Vanmarcke [28], and further developed for the specifics of the Dutch situation by Calle [4].

The methodology is derived from a time series analysis, in which a time varying signal is assumed as one realisation from a stationary stochastic function. Signal characteristics, such as scale of fluctuation and irregularities, are determined by means of the autocorrelation function.

The method is based on the assumption that that at each location (x,y) along the line infrastructure (e.g. dike, road, railway) the spatial variability along the horizontal directions can be described as the random fluctuation, in relation to the average value along the vertical direction. In other words, the average value is random at each location in the (x,y) plane and it is assumed as a stochastic function with average value and standard deviation. These average and standard deviation are called regional parameters, and correspond to the representative values for the soil layer within the area of interest (local fluctuations within a layer, z direction, are averaged out). On the model schematisation of OURS the material parameterisation corresponds to the regional parameters.

3 FINITE ELEMENT ANALYSIS

There is a multitude of options to determine the admittance spectra of a layered half space. The fastest option consists of analytical models. However, analytical models are not flexible enough to eventually simulate mitigation techniques to reduce the vibration levels. On the other end of the spectrum the numerical methods (especially FEM), offer a slow but very flexible alternative.

The modelling of mitigation techniques does not lie within the scope of this project. However, in order to account for the future developments of the model, it is chosen to implement a FEM methodology to determine the admittances.

Within the scope of this project it is sufficient to implement an axisymmetric FEM procedure. Axisymmetric FEM models are impractical when modelling mitigation techniques (which are generally not axisymmetrically oriented around the source of vibrations. However, axisymmetric FEM models do require a similar infrastructure as 3D FEM models do, and thus it can easily be upgraded to a 3D environment.

Further constraints are imposed to the choice of the transmission model by the geometrical dimensions and the maximum frequencies in which the admittances are determined. The admittances are to be determined within a maximum range of 150m to 200m with soils characterised to a depth of 50m. The maximum required frequency is set at 80Hz to 100Hz. These numbers determine whether the system matrices of the FEM model can be assembled and kept in RAM, or be only directly translated into force vectors each time step in an explicit procedure. With these dimensions the system matrices of the axisymmetric models can easily be determined once and stored in RAM. This is determinative for the implemented solving procedures.

When eventually switching to 3D FEM models, the solving procedures need to be adapted. In this light an explicit procedure and an optimal assemblage procedure are developed which can be used when implementing 3D models.

3.1 Finite Element formulation

Several Finite Elements have been implemented in the code. There is naturally an axisymmetric element to determine the stiffness, mass and damping of the soil. There are also elements that determine the stiffness and the damping and the so-called infinite boundaries. For efficiency

reasons the equations have been incorporated analytically on finite element level. This is made possible by assuming that all elements constitute a rectangular geometry. The numerical equations are first fully written out and after summarising all terms, the number of floating point operations are reduced. The resulting analytical equations are rather lengthy and they are therefore not presented in this paper. The resulting number of floating point operations per element are roughly equal to the implementation of the axisymmetric iso-P elements in commercially available explicit software packages. The present element is based on incompatible modes which offers the advantage of a locking free behaviour. The aforementioned iso-P elements suffer greatly from locking (i.e., added parasitic non-physical stiffness caused by improper interpolation of the displacement strains) and this is generally alleviated by reducing the order of numerical integration. The downside of low-order numerical integration is the exhibition of so-called zero energy or hourglass modes. These modes, which consume no energy hence the name, add a zig-zag form of displacements to the solution and are generally battled by adding a numerical damping to the solution procedure.
By analytically incorporating the incompatible mode or Enhanced Assumed Strain element [25], the need of adding artificial damping can be circumvented without consuming additional CPU time.

3.1.1 Axisymmetric stiffness matrix

The strain and stress component vectors of an axisymmetric elements are defined in Voigt notation as

$$\boldsymbol{\varepsilon} = \begin{Bmatrix} \varepsilon_{rr} \\ \varepsilon_{zz} \\ \varepsilon_{\varphi\varphi} \\ 2\varepsilon_{rz} \end{Bmatrix}, \quad \boldsymbol{\sigma} = \begin{Bmatrix} \sigma_{rr} \\ \sigma_{zz} \\ \sigma_{\varphi\varphi} \\ \sigma_{rz} \end{Bmatrix}, \tag{1}$$

where φ denotes the hoop direction.
The strain and stress vector are coupled by the constitutive equations. In this case the linear elastic-isotropic Hooke's law is chosen

$$\boldsymbol{\sigma} = \frac{E}{(1+\nu)(1-2\nu)} \begin{bmatrix} 1-\nu & \nu & \nu & 0 \\ \nu & 1-\nu & \nu & 0 \\ \nu & \nu & 1-\nu & 0 \\ 0 & 0 & 0 & \frac{1-2\nu}{2} \end{bmatrix} \boldsymbol{\varepsilon} = \boldsymbol{D}\boldsymbol{\varepsilon}, \tag{2}$$

where E is the Young's modulus, and ν is the Poisson ratio.
The strain components are kinematically linked to the displacements as

$$\varepsilon_{rr} = \frac{\partial u_r}{\partial r},\ \varepsilon_{rr} = \frac{\partial u_r}{\partial r},\ \varepsilon_{rr} = \frac{\partial u_r}{\partial r}, \text{and } \varepsilon_{rr} = \frac{\partial u_r}{\partial r}. \tag{3}$$

The displacements $\boldsymbol{u}(\xi,\, \eta)$ within the element are interpolated with bilinear interpolation shape functions $H_I(\xi,\, \eta)$

$$\boldsymbol{u}(\xi,\, \eta) = \begin{Bmatrix} u_r(\xi,\, \eta) \\ u_z(\xi,\, \eta) \end{Bmatrix} = \sum_{I=1}^{4} H_I(\xi,\, \eta)\, \boldsymbol{u}_I, \tag{4}$$

where the index I denotes the node number of the element and

$$H_I(\xi,\, \eta) = \frac{1}{4}(1+\xi_I\xi)(1+\eta_I\eta). \tag{5}$$

In order to alleviate the locking effect, the strain components are enhanced with so-called incompatible modes [25] as

$$\boldsymbol{\varepsilon}\left(\xi,\,\eta\right)=\boldsymbol{B}\left(\xi,\,\eta\right)\boldsymbol{u}_I+\boldsymbol{M}\boldsymbol{\alpha}, \tag{6}$$

where $\boldsymbol{B}$ is the so-called strain-displacement matrix resulting from the above kinematic expressions. The enhanced strain components are determined as $\boldsymbol{M}\boldsymbol{\alpha}$, where

$$\boldsymbol{M}=\begin{bmatrix} \xi-\bar{\xi} & 0 & 0 & 0 & 0 \\ 0 & \eta-\bar{\eta} & 0 & 0 & 0 \\ 0 & 0 & \xi-\bar{\xi} & \eta-\bar{\eta} & 0 \\ 0 & 0 & 0 & 0 & \xi\eta\dfrac{J\left(\xi,\,\eta\right)}{r\left(\xi,\,\eta\right)}J\left(0\right) \end{bmatrix} \tag{7}$$

The element averaged coordinates are denoted with a bar $\left(\bar{\xi},\,\bar{\eta}\right)$, and J is the determinant of the Jacobian matrix

$$\boldsymbol{J}=\begin{bmatrix} \dfrac{\partial r}{\partial\xi} & \dfrac{\partial z}{\partial\xi} \\ \dfrac{\partial r}{\partial\eta} & \dfrac{\partial z}{\partial\eta} \end{bmatrix} \tag{8}$$

THe additional enhanced strain components should not generate additional internal work. Therefore

$$\int_V\boldsymbol{\sigma}^T\boldsymbol{M}\boldsymbol{\alpha}\,dV=0 \tag{9}$$

It can be shown that the above interpolation matrix $\boldsymbol{M}$ fulfils this constraint.
The internal virtual work δW^i can be expressed in terms of the stiffness matrix $\boldsymbol{K}^\alpha$ as

$$\delta W^i=\int_V\delta\boldsymbol{\sigma}\cdot\boldsymbol{\varepsilon}\,dV=\delta\begin{Bmatrix}\boldsymbol{u}\\ \boldsymbol{\alpha}\end{Bmatrix}^T\begin{bmatrix}\boldsymbol{K}^e & \boldsymbol{L}^T\\ \boldsymbol{L} & \boldsymbol{Q}\end{bmatrix}\begin{Bmatrix}\boldsymbol{u}\\ \boldsymbol{\alpha}\end{Bmatrix}=\delta\boldsymbol{q}^T\boldsymbol{K}^\alpha\boldsymbol{q} \tag{10}$$

where

$$\boldsymbol{K}^e=\int_V\boldsymbol{B}^T\boldsymbol{D}\boldsymbol{B}\,dV,\;\boldsymbol{L}=\int_V\boldsymbol{M}^T\boldsymbol{D}\boldsymbol{B}\,dV,\;\boldsymbol{Q}=\int_V\boldsymbol{M}^T\boldsymbol{M}\boldsymbol{B}\,dV \tag{11}$$

The coefficient vector $\boldsymbol{\alpha}$ is constant within one finite element and discontinuous across the element border. Therefore these degrees of freedom can be statically condensated on element level, and the element stiffness matrix $\boldsymbol{K}$ becomes

$$\boldsymbol{K}=\boldsymbol{K}^e-\boldsymbol{L}^T\boldsymbol{Q}^{-1}\boldsymbol{L} \tag{12}$$

Due to the static condensation the above type of EAS finite elements (Enhanced Assumed Strain) is numerically very expensive in the assembling process. The advantage of these elements is that they lack any kind of locking. The cheapest of avoiding locking is by introducing mixed integration schemes, such as SRI (Selective Reduced Integration), which dictates that the shear terms in the internal virtual work are integrated with a reduced Gauss quadrature scheme. One of the disadvantages is that the finite element suffers from hourglassing caused by the incapability of capturing the strain energy in these so-called hourglassing deformation modes of the element. In the present code the EAS formulation does not produce unacceptably large CPU times, because:

- The matrices are only assembled once, and

- The assemblage is optimised by constructing $\boldsymbol{K}$ with an analytical expression
- This is possible, since all finite elements are rectangularly shaped
- The finite elements in one column of one layer are described by the same stiffness matrix

3.1.2 Axisymmetric mass matrix

The construction of the mass matrix $\boldsymbol{M}$ is more straightforward than the construction of the stiffness matrix. The mass matrix should represent the kinetic virtual work δW^k as

$$\delta W^k = \int_V \rho \delta \boldsymbol{u} \cdot \ddot{\boldsymbol{u}} \, dV = \delta \boldsymbol{u}^T \boldsymbol{M} \ddot{\boldsymbol{u}} \tag{13}$$

With the interpolation function of Eq. 5 the construction of the mass matrix $\boldsymbol{M}$ is fully defined. Usually a full integration scheme iwth four integration points n at ξ_n, $\eta_n = \pm\sqrt{1/3}$ is deployed. However, when the integration points are located at the nodal positions ξ_n, $\eta_n = \pm 1$ then a diagonalized or lumped mass matrix is generated. This matrix could alternatively be constructed by summing all columns j in each row i of the original (or consistent) mass matrix and by replacing the respective diagonal component with the result

$$M_{lumped,ij} = \delta_{ij} \sum_{j=1}^{all} M_{consistent,ij} \tag{14}$$

The application of the lumped mass matrix in a explicit central difference method leads to a very efficient implementation.

3.1.3 Axisymmetric damping matrix

In dynamic analysis of FEM models, the treatment of damping has to be considered carefully. The standard case of viscous damping (i.e., velocity proportional damping) leads to frequency dependent behaviour. A common methodology is to apply Rayleigh damping, by constructing the damping matrix $\boldsymbol{C}$ from a mass proportional part and a stiffness proportional part

$$\boldsymbol{C} = \alpha \boldsymbol{M} + \beta \boldsymbol{K} \tag{15}$$

The resulting damping ratio ζ then becomes

$$\zeta = \frac{\alpha}{2\omega} + \frac{\beta\omega}{2} \tag{16}$$

which is dependent on the circular frequency ω. Alternatively, the Caughey damping could be deployed as viscous damping model [1]. However, this leads to a fully occupied damping matrix (a lot of RAM is needed), and it requires the determination of all eigenmodes (a lot of CPU time is needed at assemblage).
As the input data of the soil properties assumes frequency independent damping, hysteretic damping seems to be the appropriate choice here. Hysteretic damping is described by assuming a complex Young's modulus leading to a certain amount of phase difference between the displacements and the resulting elastic reaction forces

$$E^{tot} = E\,(1 + i\eta) \tag{17}$$

For relatively small amount of damping (up to 15 % damping ratio) the hysteretic damping η is related to the viscous damping ratio ζ as

$$\eta = 2\zeta \tag{18}$$

to simulate a comparable amount of energy loss per cycle. The hysteretic damping matrix $\boldsymbol{C}_{hyst}$ can now easily be constructed as

$$\boldsymbol{C}_{hyst} = \eta \boldsymbol{K} \tag{19}$$

In the frequency domain analysis, modelling hysteric damping is straightforward. In the time domain analysis special attention has to be given to describing the complex part of the reaction forces. The hysteretic damping force $\boldsymbol{F}^d$ is computed as

$$\boldsymbol{F}^d = i\boldsymbol{C}_{hyst}\boldsymbol{u} \tag{20}$$

The hysteretic damping matrix is thus multiplied with a vector $i\boldsymbol{u}$ which is in phase with the velocity vector (i.e., in the same multi-dimensional direction), but which has the same length as the displacement vector. Therefore the hysteretic damping forces can be obtained as [19]

$$\boldsymbol{F}^d = \boldsymbol{C}_{hyst}\frac{\|\boldsymbol{u}\|}{\|\dot{\boldsymbol{u}}\|}\dot{\boldsymbol{u}} \tag{21}$$

3.1.4 Infinity boundary elements

In order to simulate infinite boundaries are characterised by the fact that elastic waves (primary and secondary) move from the interior to the exterior only. This can be simulated by absorbing the incoming wave energy. For the primary waves this is best approximated by imposing a normal stress σ as [17]

$$\sigma = \rho\, V_P \dot{u}_n \tag{22}$$

and for the secondary waves this is best approximated by imposing a shear stress τ as

$$\tau = \rho\, V_S \dot{u}_t \tag{23}$$

Here V_P and V_S are the wave velocities of the primary and the secondary waves [5]

$$V_P = \sqrt{\frac{E\,(1-\nu)}{(1+\nu)\,(1-2\nu)\,\rho}},\; V_S = \sqrt{\frac{E}{2\,(1+\nu)\,\rho}} \tag{24}$$

and $\dot{u}_n$ and $\dot{u}_t$ are the velocity components normal and tangential to the infinite boundary, respectively. The damping force $\boldsymbol{F}^c$ is expressed in terms of an infinite damping matrix $\boldsymbol{C}^\infty$ as

$$\boldsymbol{F}^c = \boldsymbol{C}_n^\infty \dot{\boldsymbol{u}}_n + \boldsymbol{C}_t^\infty \dot{\boldsymbol{u}}_t = \boldsymbol{C}^\infty \dot{\boldsymbol{u}} \tag{25}$$

where the force vector is constructed as the surface integral of the stresses and therefore

$$\boldsymbol{C}_n^\infty = \int_A^\infty \rho\, V_P\, dA,\; \boldsymbol{C}_t^\infty = \int_A^\infty \rho\, V_S\, dA \tag{26}$$

The integrals are numerically evaluated by Gauss integration over two integration points. The final result is expressed and implemented as an analytical/parametric equation.
The disadvantage of solely applying dashpots at the infinity boundaries, is that the model can

potentially become statically underdetermined. Therefore it is suggested that an additional stiffness needs to be introduced at these boundaries. It is found that the following additional stresses have minimal contribution to wave reflection [12]

$$\sigma = \frac{\rho V_P^2}{2R} u_n, \ \tau = \frac{\rho V_S^2}{2R} u_r \tag{27}$$

where R denotes the distance to the source of excitation. The elastic force $\boldsymbol{F}^k$ is expressed in terms of an infinite stiffness matrix $\boldsymbol{K}^\infty$ as

$$\boldsymbol{F}^k = \boldsymbol{K}_n^\infty \boldsymbol{u}_n + \boldsymbol{K}_t^\infty \boldsymbol{u}_t = \boldsymbol{K}^\infty \boldsymbol{u} \tag{28}$$

where the force is constructed as the surface integral of the stresses and therefore

$$\boldsymbol{K}_n^\infty = \int_A^\infty \frac{\rho V_P^2}{2R} \, dA, \ \boldsymbol{K}_t^\infty = \int_A^\infty \frac{\rho V_S^2}{2R} \, dA \tag{29}$$

3.2 Solving the system of equations

The equation to be solved reads

$$\boldsymbol{M}\ddot{\boldsymbol{u}}\left(t\right) + \boldsymbol{C}^\infty \dot{\boldsymbol{u}}\left(t\right) + \left[\boldsymbol{K} + \boldsymbol{K}^\infty + i\boldsymbol{C}_{hyst}\right] \boldsymbol{u}\left(t\right) = \boldsymbol{F}^{ext}\left(t\right) \tag{30}$$

where $\boldsymbol{F}^{ext}\left(t\right)$ denotes the time dependent externally applied force vector. This equation is solved either in the frequency domain as a harmonic response analysis, or in explicitly in the time domain by the central difference method.
At the basis of the harmonic response analysis lies the decomposition of the linear response into multiple and independent exp-functions of circular frequency ω

$$\boldsymbol{u}\left(\omega\right) = \hat{\boldsymbol{u}} \exp i\omega t, \ \boldsymbol{F}^{ext}\left(\omega\right) = \hat{F}\hat{\boldsymbol{F}} \exp i\omega t \tag{31}$$

where $\hat{\boldsymbol{u}}$ is the vector of amplitudes, $\bar{\boldsymbol{F}}$ is the normalised excitation vector, $\hat{F}$ is the force amplitude and i is the complex unit. With this decomposition the equation to be solved becomes

$$\left[-\omega^2 \boldsymbol{M} + i\omega \boldsymbol{D}^\infty + \boldsymbol{K} + \boldsymbol{K}^\infty + i\boldsymbol{C}^\infty\right] \hat{\boldsymbol{u}} = \hat{F}\bar{\boldsymbol{F}} \tag{32}$$

Introducing the system matrix $\boldsymbol{A}$ representing the bracket terms on the left-hand side, it follows

$$\frac{\hat{\boldsymbol{u}}\left(\omega\right)}{\hat{F}\left(\omega\right)} = \boldsymbol{A}^{-1}\bar{\boldsymbol{F}} \tag{33}$$

The code is developed in Python and the Pardiso solver is used to solve the equation directly. The Python interface to Pardiso (i.e., pyPardiso) only support real matrices and therefore the solution vector $\hat{\boldsymbol{u}}$, the complex system matrix $\boldsymbol{A}$ and the external force vector are extended as

$$\hat{\boldsymbol{u}}^* = \begin{Bmatrix} \hat{\boldsymbol{u}}_{real} \\ \hat{\boldsymbol{u}}_{imag} \end{Bmatrix}, \ \boldsymbol{A}^* = \begin{bmatrix} \boldsymbol{A}_{real} & -\boldsymbol{A}_{imag} \\ \boldsymbol{A}_{imag} & \boldsymbol{A}_{real} \end{bmatrix}, \ \bar{\boldsymbol{F}}^* = \begin{Bmatrix} \bar{\boldsymbol{F}}_{real} \\ \bar{\boldsymbol{F}}_{imag} \end{Bmatrix} \tag{34}$$

Solving the system of equations explicitly with the central differences method is based on the Taylor series approximation of the first and the second derivative

$$\dot{\boldsymbol{u}}^{n+\frac{1}{2}} = \frac{\partial \boldsymbol{u}^{n+\frac{1}{2}}}{\partial t} = \frac{\boldsymbol{u}^{n+1} - \boldsymbol{u}^n}{\Delta t}, \ \ddot{\boldsymbol{u}}^n = \frac{\partial^2 \boldsymbol{u}^n}{\partial t^2} = \frac{\boldsymbol{u}^{n+1} - 2\boldsymbol{u}^n + \boldsymbol{u}^{n-1}}{\Delta t^2} \tag{35}$$

where n is an index to a position in time, and Δt is the time increment with which the differential equation of motion is integrated through time.
With the aforementioned approximation of the hysteretic damping, the system of equations to be solved becomes

$$\ddot{\boldsymbol{u}}^n = \boldsymbol{M}^{-1}\left(\boldsymbol{F}^{ext,n} - \left(\boldsymbol{K} + \boldsymbol{K}^{\infty}\right)\boldsymbol{u}^n - \boldsymbol{C}_{hyst}\frac{\|\boldsymbol{u}\|}{\|\dot{\boldsymbol{u}}\|}\dot{\boldsymbol{u}}^{n-\frac{1}{2}} - \boldsymbol{C}^{\infty}\dot{\boldsymbol{u}}^{n-\frac{1}{2}}\right) \tag{36}$$

In linear systems the central difference scheme becomes unconditionally stable when

$$\Delta t \leq \frac{2}{\omega_{n,max}} \tag{37}$$

where $\omega_{n,max}$ denotes the maximum undamped eigenfrequency of the system. However, due to the approximation of the hysteretic damping, this conditions has proven not to be strict enough. In general the above maximum time increment has to be reduced by a factor of 0.6.

3.3 Verification

One of the undertaken verification cases consists of the calculation of the compliance of a rigid disk with a radius of 1 m on a 20 m thick homogeneous layer of soil with non-reflecting boundary conditions at $r \to \infty$, see Figure 5.

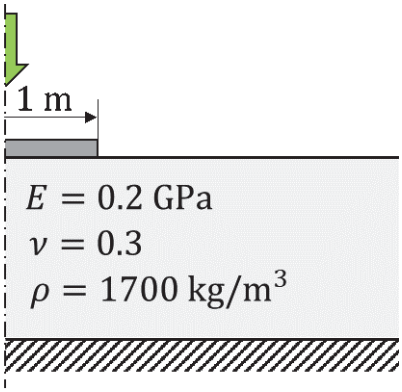

Figure 5: Illustration of the verification case

The soil is excited dynamically by applying a vertical force on the circular rigid disk. A damping of 5 % is assumed and the maximum frequency is set to 100 Hz. The infinitely stiff disk is modelled by coupling the underlying soil nodes in vertical direction to one degree of freedom.
The compliance experienced by the disk is computed with both the central difference method as well as the harmonic response analysis. The results are compared with those obtained by the semi-analytical Wolf model [29]. It is shown (see Figure 6) that the harmonic response analysis agrees well with the results obtained with the Wolf model. In amplitude the central difference method agrees well with the Wolf model. The agreement is less when comparing the phase. It should be noted though that only the amplitude results are relevant for the calculations of the train induced vibrations.

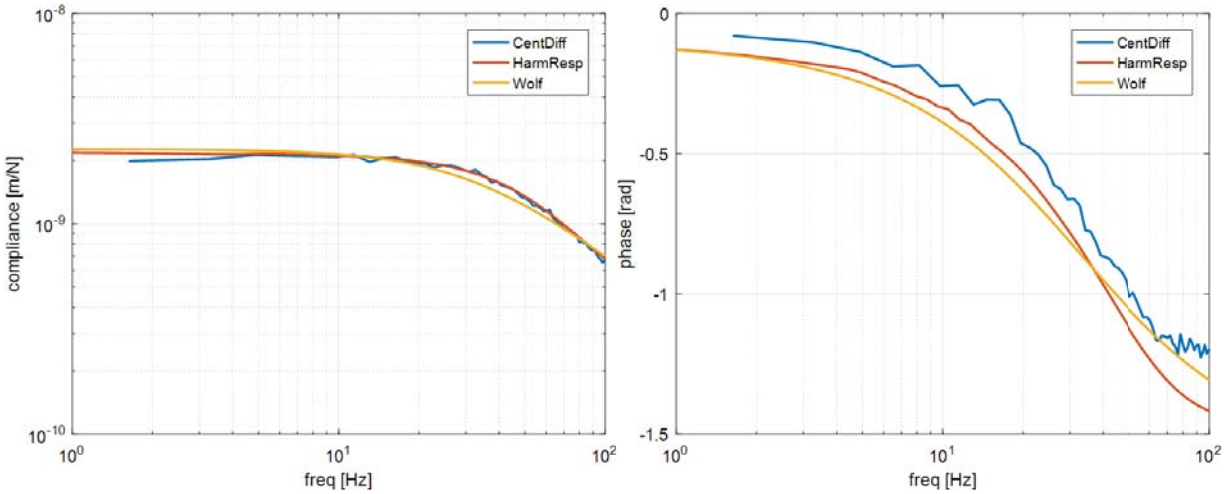

Figure 6: Results of the verification case

4 CASE STUDY

In order to illustrate the proposed methodology for subsoil modelling and FEA admittance calculation, the model developed for OURS has been applied to two locations in the Netherlands: Delft and Tilburg.

Figure 7 shows the subsoil scenario schematisation for the two locations. It follows that the subsoil schematisation in Delft exhibits more variable than the subsoil schematisation in Tilburg. Although for both locations 4 scenarios exist, the variability in the build-up layer formation is bigger in Delft. For Tilburg the subsoil consists of two soil types, sand and sand mixtures, while in Delft it consists of at least six different soil types, ranging from sand to clay layers.

The location in Tilburg is dominated by two scenarios (scenario 3 and 4) that together form 96 % probability of occurrence. The location in Delft is dominated by three scenarios (scenarios 2, 3 and 4 form 99 % probability of occurrence).

The subsoil parametrisation is illustrated in Figure 8 for both locations. Although all geomechanical parameters have a mean and standard deviation, the figure only shows the mean value, for the sake of readability. Similarly to the layering schematisation, the location in Delft exhibits more variation in the geomechanical parameters than the location in Tilburg.

Figure 10 shows the vertical and radial admittance results for both locations at three different distances from the source: 10, 50 and 100m. The results for all the different scenarios are represented as well as the results for the weighted mean admittance. As it would be expected, the admittance is found to reduce with the distance from the source.

The results are also different for the two locations. For Delft it is found that the admittance is constant for the point located at 10m from the source, but for the points further away from the source (50 and 100m) the admittance exhibits a linear reduction with the frequency, i.e. the admittance attenuates linearly with the frequency. This behaviour is less visible in Tilburg. This is related with the presence of soft soil layers in Delft, that cause an higher attenuation of the high frequencies.

Figure 10 shows the mean vertical and radial admittance obtained for the two location. It is clear that the admittance attenuates with the distance, in the entire frequency range.

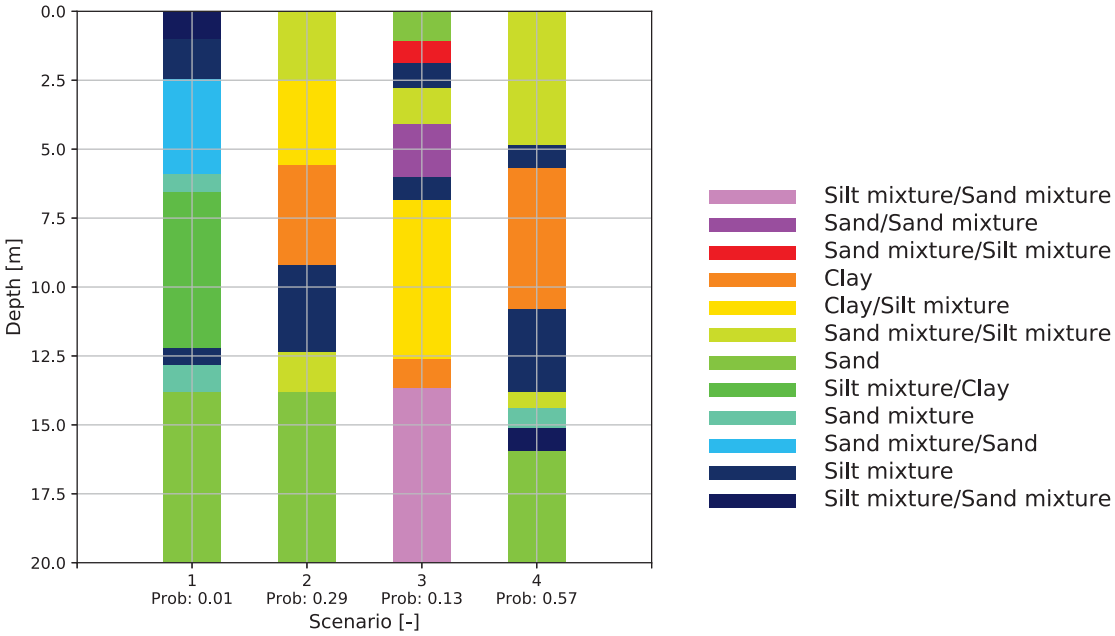

(a)

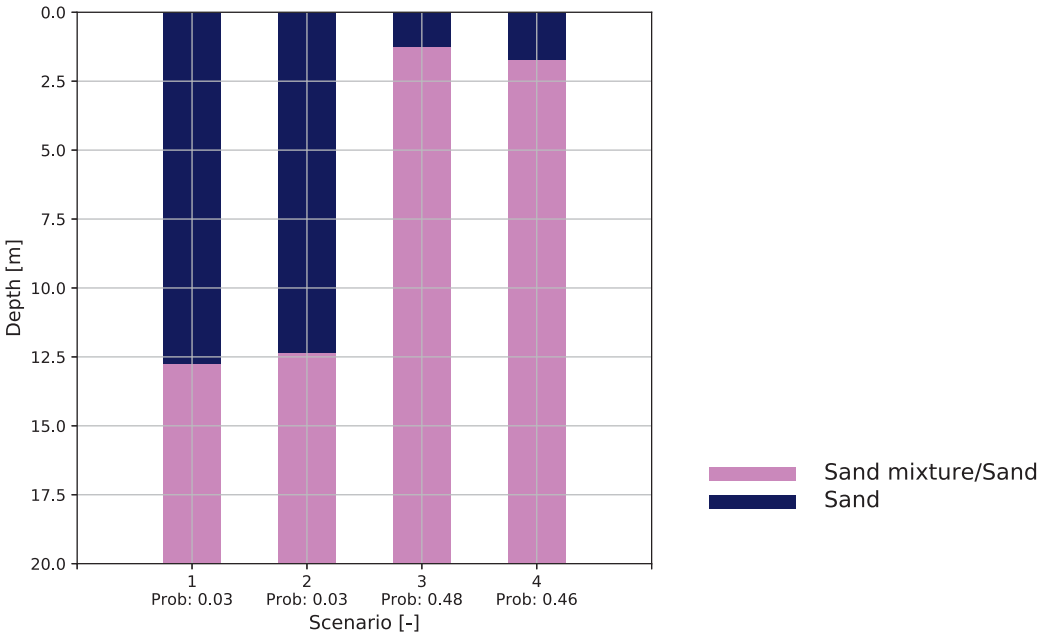

(b)

Figure 7: Subsoil schematisation from OURS: (a) location Delft, (b) location Tilburg.

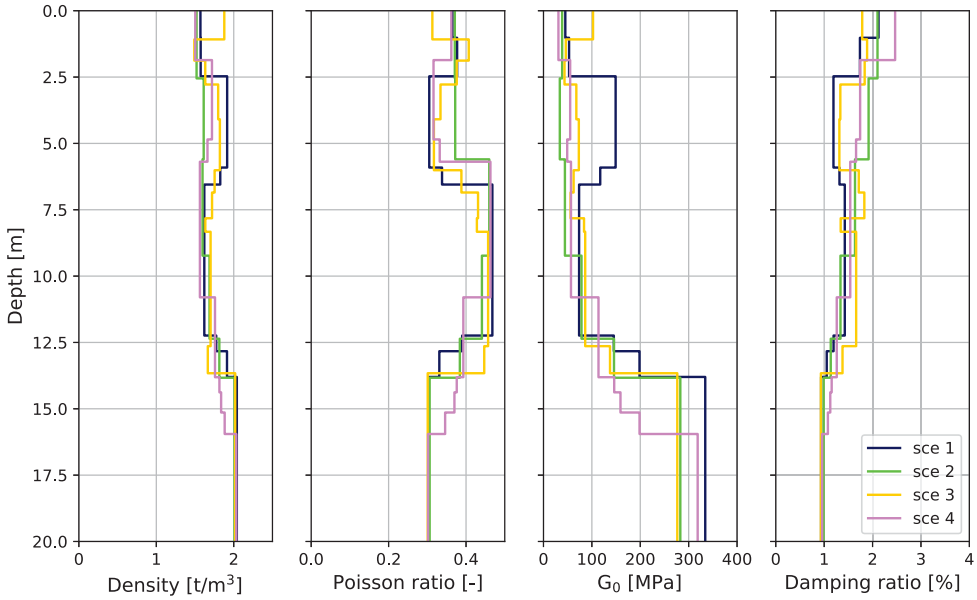

(a)

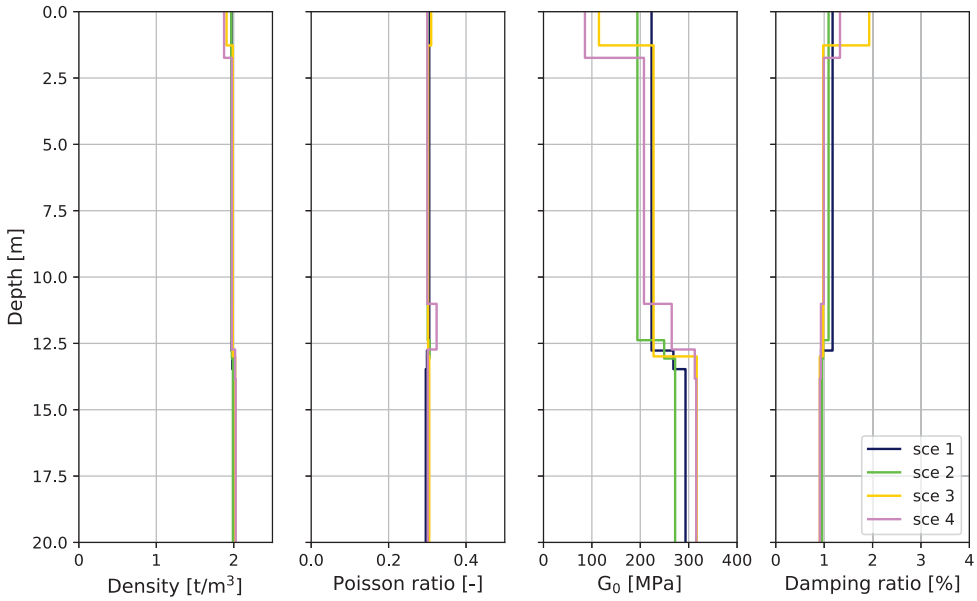

(b)

Figure 8: Subsoil geomechanical parameters (mean values): (a) location Delft, (b) location Tilburg.

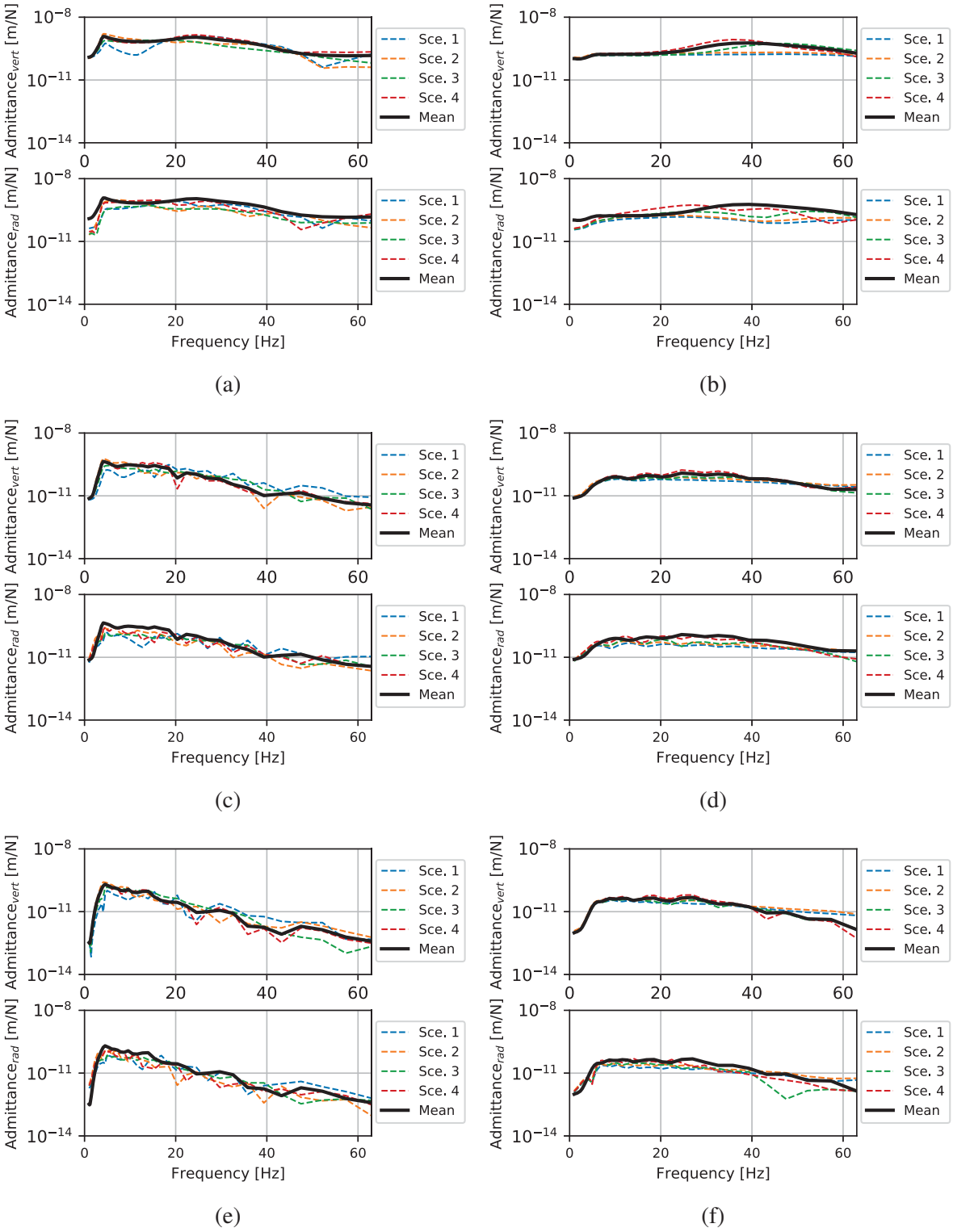

Figure 9: Vertical and radial admittance for points located at 10m (a, b), 50m (c, d) and 100m (e, f) from the source. Figures (a, c, e) are at location Delft and figures (b, d, f) are at location Tilburg.

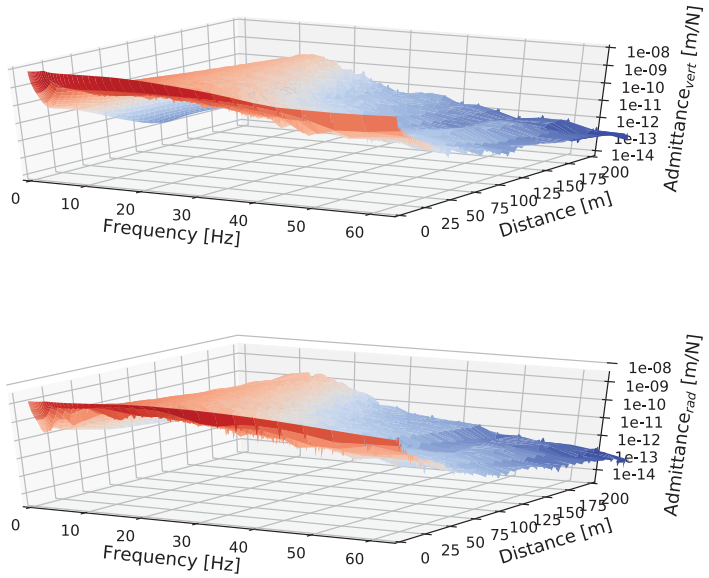

(a)

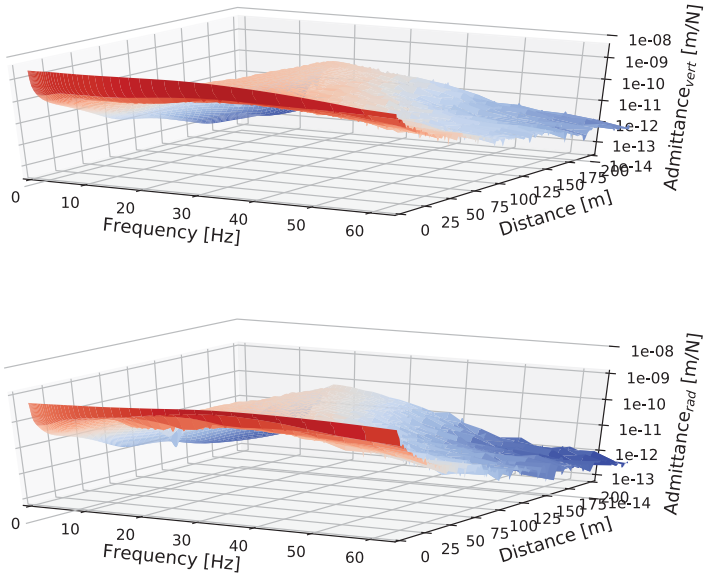

(b)

Figure 10: Vertical and radial admittance: (a) location Delft, and (b) location Tilburg.

5 CONCLUSIONS

This paper presented the methodology developed in OURS to model the subsoil and compute the admittance, between source and receiver.

The subsoil modelling is done by combining public datasets to provide a semi-stochastic subsoil schematisation and parametrisation. The admittance is computed by means of a FEA kernel that has been develop to optimise calculation speed.

The application of the methodology of OURS has been illustrated in two locations (Delft and Tilburg).

6 REFERENCES

References

[1] K. Bathe. *Finite Element Procedures*. Prentice Hall, 2nd edition, 2006.

[2] BRO. Basisregistratie Ondergrond, 2020.

[3] BRO. Nederlands Hydrologisch Instrumentarium, 2020.

[4] E. Calle. Prostab, een computer programma voor probabilistische analyse van stabiliteit van taluds. Technical Report CO 266484-32., GeoDelft, 1990.

[5] L. Cremer, M. Heckl, and B. A. Petersson. *Structure-Borne Sound*. Springer-Verlag, 3rd edition, 2005.

[6] M. Darendeli. *Development of a new family of normalized modulus reduction and material damping curves*. PhD thesis, University of Texas, 2001.

[7] V. Davidovici. *Gènie parasismique*. Ècole Nationale des Ponts et Chaussées, 1985.

[8] D. de Gruijter, A. Koopman, E. Verheijen, S. Lentzen, H. Boshuizen, and J. Bolte. Een uniform rekenmodel voor spoortrillingen 2016. Technical Report 2016-0209, RIVM, 2016.

[9] G. Gazetas. *Foundation Vibrations*. Springer, 1991.

[10] P. Hijma, R. van der Meij, and K. Lam. Grasping the heterogeneity of the subsurface: Using buildup scenarios for assessing flood risk. In *Geotechnical Safety and Risk V*, pages 924–929. IOS Press, 2015.

[11] M. Karray and G. Lefebvre. Significance and evaluation of poisson's ratio in rayleigh wave testing. *Canadian Geotechnical Journal*, 45(5):624–635, 2008.

[12] L. Kellezi. Local transmitting boundaries for transient elastic analysis. *Soil Dyn. and Earthquake Eng.*, 19:533–547, 2000.

[13] A. Koopman. OURS – introducing the Dutch formal model for railway vibration. In *EuroDyn 2020. XI International Conference on Structural Dynamics*, 2020.

[14] F. Kulhawy and P. Mayne. Manual on estimating soil properties for foundation design. Technical report, Cornell University, 1990.

[15] A. Lengkeek, J. d. Greef, and S. Joosten. Cpt based unit weight estimation extended to soft organic soils and peat. In *Cone Penetration Testing (CPT'18)*, pages 389–394. CRC Press, 2018.

[16] P. Lubking. *Grondgedrag: feiten, normen en waarden met betrekking tot grond in de praktijk van de geotechniek*. StudioWAT, 2004.

[17] J. Lysmer and R. L. Kuhlemeyer. Finite dynamic model for infinite media. *J. Eng. Mech. Division*, 95:859–878, 1969.

[18] F. Menq. *Dynamic properties of sandy and gravelly soils*. PhD thesis, University of Texas, 2003.

[19] G. B. Muravskii. On frequency independent damping. *J. Sound and Vib.*, 274:653–668, 2004.

[20] D. Okur and A. Ansal. Stiffness degradation of natural fine grained soils during cyclic loading. *Soil Dynamics and Earthquake Engineering*, 27(9):843 – 854, 2007.

[21] PDOK. Publieke Dienstverlening Op de Kaart, 2020.

[22] RIVM. Single calculation model for railway vibrations. detailed description. Technical report, RIVM, 2020.

[23] P. Robertson and K. Cabal. *Guide to cone penetration testing*. Gregg Drilling & Testing, Inc., 6th edition, 2015.

[24] H. Sharma, M. Dukes, and D. Olsen. Field measurements of dynamic moduli and poisson's ratios of refuse and underlying soils at a landfill site. In *Geotechnics of Waste Fills—Theory and Practice*, pages 57–70. ASTM International, 1990.

[25] J. C. Simo and M. S. Rifai. A class of mixed assumed strain methods and the method of incompatible modes. *Int. J. Num. Meth. Eng.*, 29:1595–1638, 1990.

[26] R. Steenbergen, S. Lentzen, and A. Koopman. Betrouwbare trillingsmaatregel: Standaard rekenmethode voor trillingen (SMR-T), referentieafstand en variatiestudie. Technical Report TNO-034-DTM-2009-03700, TNO, 2009.

[27] I. van Kamp, E. van Kempen, H. van Wijnen, E. Verheijen, T. Istamto, O. Breugelmans, E. Dirven, and A. Koopman. Wonen langs het spoor : Gezondheidseffecten van trillingen door treinen. Technical Report 2014-0096, RIVM, 2014.

[28] R. Vanmarcke. Reliability of earth slopes. *Journal of the Geotechnical Engineering Division*, 103(11):1247–1265, 1977.

[29] J. P. Wolf and A. J. Deeks. *Foundation Vibration Analysis: A Strength-of-Materials Approach*. Elsevier, 1st edition, 2004.

[30] C. Zwanenburg, M. Konstadinou, P. Meijers, M. Goudarzy, D. König, R. Dyvik, B. Carlton, J. van Elk, D. Doornhof, and M. Korff. Assessment of the dynamic properties of holocene peat. *Journal of Geotechnical and Geoenvironmental Engineering*, Accepted for publication, 2020.

EURODYN 2020
XI International Conference on Structural Dynamics
M. Papadrakakis, M. Fragiadakis, C. Papadimitriou (eds.)
Athens, Greece, 23–26 November 2020

NUMERICAL ASSESSMENT OF THE INFLUENCE OF BALLAST HETEROGENEITIES ON THE DYNAMIC BEHAVIOR OF RAILWAY TRACKS

Hadrien Pinault[1,2], Etienne Balmes[2,3], Elodie Arlaud[1] and Régis Cottereau[4]

[1] SNCF Réseau, Direction Générale Industrielle et Ingénierie
6 avenue François Mitterrand, 93574 La Plaine St Denis Cedex, France
e-mail: {hadrien.pinault, elodie.arlaud}@reseau.sncf.fr

[2] Laboratoire PIMM, Arts et Métiers, CNRS, CNAM, HESAM
151 boulevard de l'Hôpital, 75013 Paris, France
e-mail: {hadrien.pinault, etienne.balmes}@ensam.eu

[3] SDTools
44 rue Vergniaud, 75013 Paris, France
e-mail: balmes@sdtools.com

[4] Aix-Marseille Univ, CNRS, Centrale Marseille, LMA UMR 7031
4 impasse Nikola Tesla, CS 40006, 13453 Marseille Cedex 13, France
e-mail: cottereau@lma.cnrs-mrs.fr

Keywords: Ballasted track, Heterogeneous medium, Periodic structures, Model reduction.

Abstract. *In most numerical models of railway tracks, the ballast (i.e. the granular layer in which the sleepers lie) is modeled by a homogeneous medium. This assumption allows an easier implementation within a Finite Element (FE) code, yet may not be justified. In fact, considering the results of in-situ measurements, the global response of the track varies significantly before and after ballast tamping, even at low frequencies (< 100 Hz). After having analyzed these experiments, this paper proposes to include in a track model a heterogeneous medium for the ballast, fully compatible with the FE framework. Samples of random fields (previously fitted to Discrete Elements simulations) are taken for the mechanical properties of the ballast layer. Because the heterogeneous properties require a refined mesh, a model reduction strategy is then proposed to ensure a reasonable computation cost: a learning procedure to construct a reduced basis from several heterogeneous samples. Finally, time-based computations on the track model are performed. It is shown that the heterogeneity does not significantly alter the global response of the track below 30 Hz, yet generates local modifications which are relevant to characterize for the track settlement analysis.*

1 INTRODUCTION

The majority of railway tracks are nowadays ballasted, i.e. covered by a layer of a granular material (typically 0.3 m thick) composed of coarse crushed stone of calibrated size [1]. The main roles of the ballast layer are to transfer the dynamic load caused by the train to the soil and provide elasticity and vibration damping, while facilitating maintenance and water draining. Like other granular materials, ballast mechanical behaviour is not fully understood yet and subject of much research [2–4].

Characterizing the dynamic behavior of the ballast is an industrial issue for the conception and the maintenance of railway tracks. The experimental approaches are mainly a triaxial test on a ballast sample [5] or a full-scale model in laboratory [6, 7]. However, these experiments have a limited range of study due to the boundary conditions of the model and are costly to set up. Thus, numerical studies of railway ballast are also frequent. An extensive approach consists in modeling every ballast grain and the interactions between them (contact, friction, impact...). This method is known as Discrete Element Method (DEM), and is mainly implemented in NSCD (Non-Smooth Contact Dynamics) codes [8–10] or in Molecular Dynamics [11]. However, this granular approach requires huge computational power (a week per computation for [8]), is limited to low frequencies (< 40 Hz) and to a small sample of ballast, and is not easily coupled with soil Finite Element (FE) models.

When a larger scale study is required and lower computational cost desired, continuous models of the railway track are prefered. The ballast layer is then considered as a homogeneous medium, and FE approches are considered [12–19]. These models are coupled with soil behaviour or even train dynamics. To reduce the computational cost, model reduction strategies are accessible, with a periodicity assumption along the track axis [12, 18, 19]. The ballast layer mechanical behavior is often considered linear elastic, yet a non-linear approach is used by Alves Costa et al. [15].

The objective of this paper is to determine the frequency range of influence of the heterogeneity of the ballast layer, neglected without proof in classical FE approaches. A heterogeneous track model has been developed by Abreu Corrêa and al. [20]. The idea of this model consists in mapping the ballast mechanical properties from a sample of 3D random fields. The result is a deterministic model where the mechanical properties at each integration point are different. In [20], the resolution is made by Spectral Element Method (SEM), which is well-suited for large-scale problems especially in seismic wave prediction [21]. The model has been compared successfully to an equivalent DEM model solved by NSCD. However, this approach has not been yet extensively studied in a full-scale track model, which is one purpose of this paper. Another issue of [20] is the high computational cost required.

The first section of this paper will motivate the study of heterogeneous ballast by presenting experimental results. The global responses of the track after ballast tamping, with and without dynamic stabilization, are compared. In a second section, the model from [20] is adapted to a piecewise periodic reduced FEM model, first developped by Arlaud et al. [18]. The influence of the heterogeneity can thus be studied with a much smaller computation cost. In a third part, hammer impact and pass-by of vehicles are simulated for the heterogeneous track model and compared to a homogeneous one.

2 OBSERVATION OF THE EFFECT OF BALLAST HETEROGENEITY

According to standard maintenance operations on French ballasted tracks, the ballast layer is mechanically packed under sleepers by a tamping machine and then stabilized by a dynamic stabilizer. To assess the efficiency of these operations, a track survey was carried out in Évres, Grand Est region, France, on the East-European High Speed Line (EE-HSL) linking Paris and Strasbourg. Two areas distant of 50m were surveyed before and after tamping. Only the second zone was stabilized.

A vertical accelerometer is placed at the end of a bi-block sleeper (blue dot on figure 1) and the rail is excited by an instrumented hammer (red star). The hammer and the accelerometer are synchronized, and the measurements are sampled at a sampling frequency of 16 kHz.

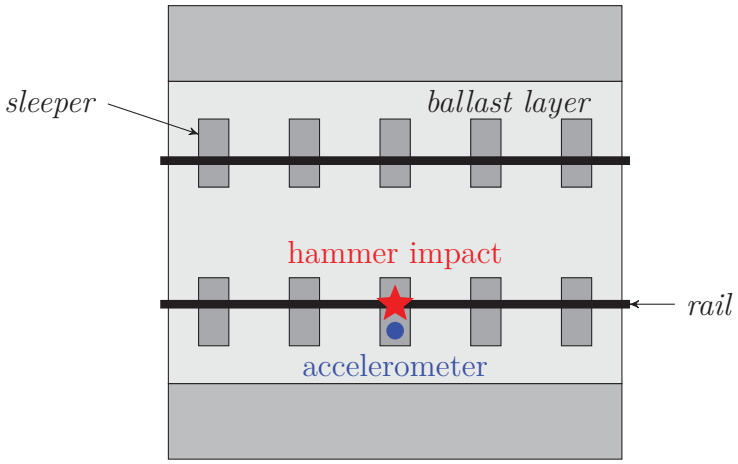

Figure 1: Scheme of the receptance test on a high-speed line.

20 hammer strokes were recorded and the *receptance* is post-processed, i.e. the transfer between the vertical displacement of the sensors $u_z(t)$ and the force exerted by the hammer $f(t)$:

$$R(\omega) = \frac{U_z(\omega)}{F(\omega)} \ . \tag{1}$$

The main interest of this survey is that all frequencies are excited at a similar level by the hammer. The 20 tests are highly repeatable, thus the mean value of these tests will be considered. The coherence between the signals of the sensor and the hammer was above 90% only above 20 Hz. As the focus of this study is only medium frequencies, the results are shown in figure 6 between 20 and 200 Hz.

Before ballast tamping (dotted line in figure 6), the receptances of the two zones have a similar shape with a very broad peak and a identically decreasing phase until 80 Hz, but a very different magnitude (around 60 %), even if the zones are as close as 50m. After ballast tamping, the magnitudes have similar levels, increased 5 times compared to magnitude before tamping. However, without dynamic stabilization (plain blue curve in figure 6), an additional peak appears at 80 Hz. These experiments show that the the ballast layer settlement can then have a high impact on the magnitude level.

These observations are a clear motivation to study the impact of the ballast heterogeneity (mean stiffness and variability), within a numerical model.

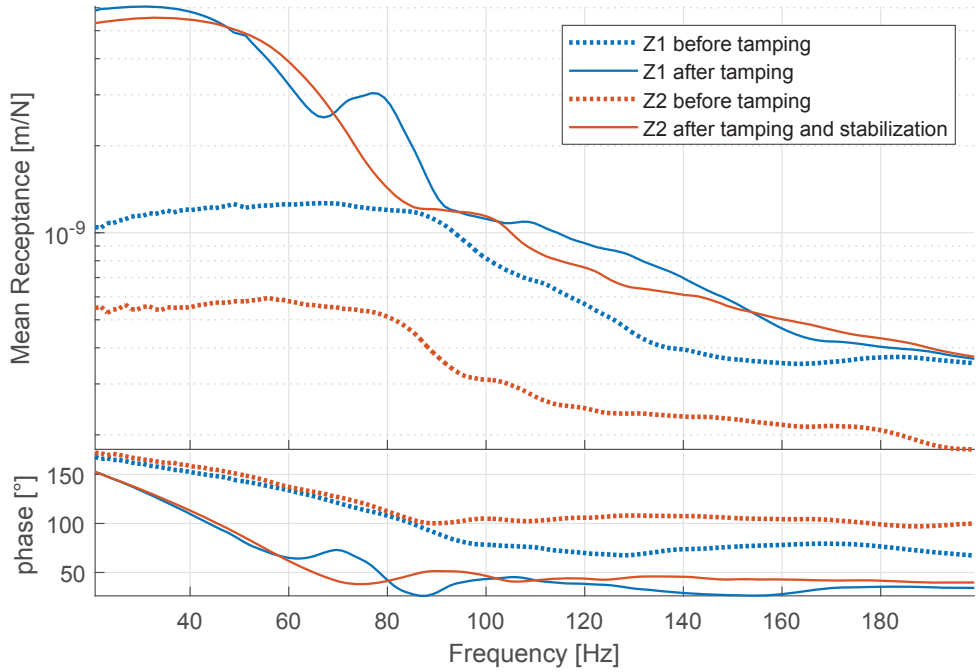

Figure 2: Receptance of the track on two zones (Z1 in blue and Z2 in orange) before (dotted lines) and after ballast tamping (plain lines). On Z1, only ballast tamping is done, on Z2, ballast tamping and dynamic stabilization.

3 REDUCED TRACK MODEL WITH HETEROGENEOUS BALLAST

3.1 Meshing of the slice model

A geometrically periodic track model is considered, adapted from [18]. A reference cell Ω_0 of width $x_0 = 60$ cm, the distance between two sleepers as shown on figure 3, is meshed with hexahedral quadratic elements. The mesh size is defined to ensure 6 nodes per wavelength for the shortest shear wave propagating in the track.

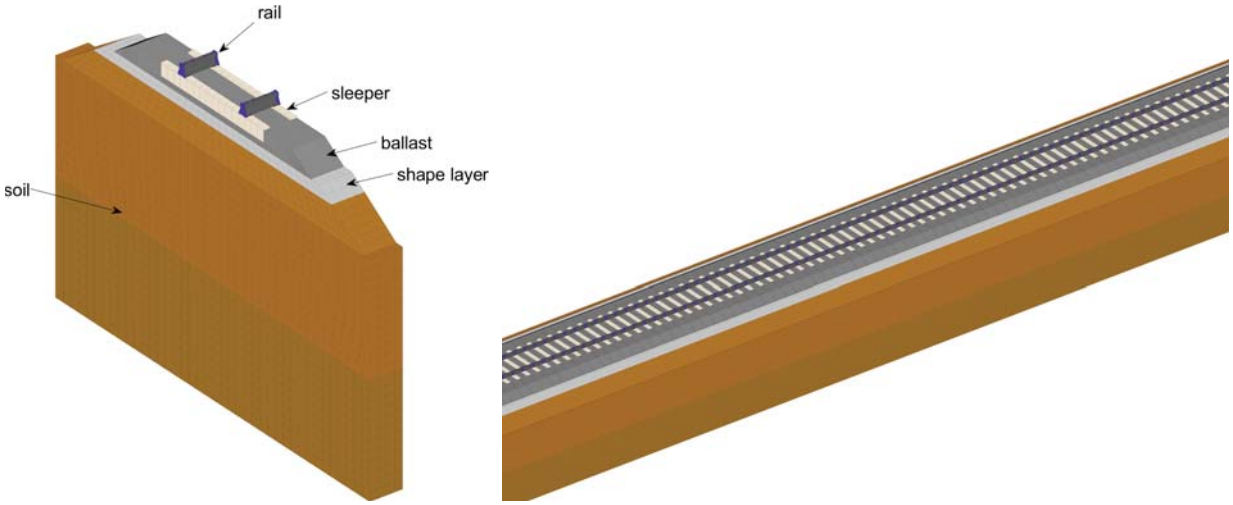

(a) Reference cell. (b) Closeup to periodic track structure.

Figure 3: 3D view of the periodic track model.

To build a heterogeneous model for the ballast layer, the following procedure is used

1. 3D periodic random fields are generated for the density ρ, the bulk modulus $K = \frac{E}{3(1-2\nu)}$ and shear modulus $G = \frac{E}{2(1+\nu)}$ (where E and ν are respectively the Young modulus and Poisson ratio). The choice of these mechanical parameters ensures real-valued shear and pressure wave velocities. These fields are not correlated, and follow a log-normal distribution, ensuring positive values, with parameters taken from table 1. They are efficiently generated with a spectral method proposed by Shinozuka and Deodatis [22]. For example, the density random field $\rho[x]$ is calculated from

$$\rho[x] = \mathbb{E}_\rho(x) + 2\sum_{n=1}^{N_{\text{rand}}} \zeta_n \sqrt{\mathbb{S}_\rho(n\Delta k)\Delta k}\cos(n\Delta k x + \varphi_n), \tag{2}$$

where $\mathbb{E}_\rho$ and $\mathbb{S}_\rho$ are the expectation and autocorrelation of ρ, ζ_n standard normal fields, φ_n uniform fields on $[-\pi\ \pi]$ and Δk the step in wavenumber. The correlation model for each field between the 3 directions of space is chosen gaussian, only determined by a correlation length λ_{corr}, equal to 7 cm. These values are taken from [20], and were identified to a DEM simulation.

Property	**Mean value**	**Standard deviation**
Bulk modulus K	139 MPa	417 MPa
Shear modulus G	104 MPa	312 MPa
Density ρ	1700 kg/m^3	5100 kg/m^3

Table 1: Properties of the heterogeneous beam.

2. Samples of these random fields are generated. A 3D view of a sample of the density field in a block of size $0.25\times0.25\times0.6$ cm^3 is presented in figure 4. The isosurfaces are represented for 80% and 99% of the maximal density. This representation highlights harder points (in red) included in a softer medium (transparent). The periodicity of the field ensures the continuity of the mechanical properties by taking only $\Delta k = \frac{2\pi}{x_0}$ in equation (2).

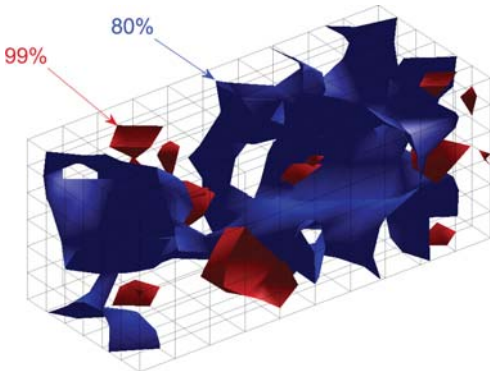

Figure 4: Sample of 3D random field for density. Isosurfaces for 80% and 99% of maximal density are plotted respectively in blue and red.

3. The values of the sample generated in a block bigger than the ballast layer are interpolated linearly at the integration points of the mesh. In order to keep a good representativeness, the mesh in the ballast layer is refined down to $\frac{\lambda_{\text{corr}}}{3}$. This refined

mesh is connected with the coarser mesh with Multiple Point Constraint (MPC): the refined surface of the ballast is forced to have the displacement of the surface below.

The pad between the sleeper and the rail is 9 mm thick, and has a dynamic stiffness of 180 kN/mm. As a volumic element, it is modeled with an anistropic behavior, with an equivalent stiffness 100 times higher in the vertical direction and a damping ratio of 20%.

Finally, every other part of the track model has linear elastic behavior shown in table 2. For the reduction phase, an hysteretic damping model is used by taking a complex modulus $E^* = E\,(1 + i\eta)$. For time simulations, an equivalent viscous model is built. The natural soil has been chosen with an artificially low density to avoid unwanted soil modes. A clear perspective is to include PML elements to model properly the radiation of waves in the soil.

Part	E [MPa]	ν [-]	G [MPa]	ρ [kg/m^3]	η [%]
Under ballast layer	360	0.35	133	1700	7
Shape layer	544	0.35	201	2000	1
Embankment	1290	0.3	496	1990	1
Natural soil	67	0.3	26	1.8	10
Sleeper	$3 \cdot 10^4$	0.25	$1.2 \cdot 10^4$	2400	0
Rail	$2.1 \cdot 10^5$	0.285	$8.2 \cdot 10^4$	7800	0

Table 2: Properties of the homogeneous track components (in order: Young modulus, Poisson ratio, shear modulus, density, damping ratio).

3.2 Building of reduced heterogeneous slice models

The implementation and validation of the reduced methodology used in this paper is fully detailed in [23]. A summary is presented here for reference.

At the end of the meshing phase, the matrix problem in the reference cell Ω can be expressed after assembly as

$$\left(-\omega^2\,[M] + [K]\right)\{q(\omega)\} = [b]\,\{f(\omega)\}\ , \tag{3}$$

where $[M]$ is the mass matrix, $[K]$ the stiffness matrix (taken with complex values $E(1+i\eta)$ to include damping behavior), $\{q\}$ the displacement at the Degrees of Freedom (DOF), and $[b]\,\{f\}$ the external forces applied to the track (contact force of train wheels for example).

When expressing the problem in the wavenumber domain at a fixed wavenumber $\kappa_0 = \frac{x_0}{\lambda_0}$ (where λ_0 is the wavelength), the periodicity condition between Ω_0 and its adjacent cell can be expressed as

$$[c(\kappa_0)] \begin{Bmatrix} \mathrm{Re}\left(Q(\kappa_0,\omega)\right) \\ \mathrm{Im}\left(Q(\kappa_0,\omega)\right) \end{Bmatrix} = \{0\}\ , \tag{4}$$

where matrix $[c]$ is independent of frequency. Then the constrained problem can be written as

$$[T_c]^T \begin{bmatrix} Z & 0 \\ 0 & Z \end{bmatrix} [T_c] \begin{Bmatrix} \mathrm{Re}\left(Q_c\right) \\ \mathrm{Im}\left(Q_c\right) \end{Bmatrix} = [T_c]^T \begin{bmatrix} b & 0 \\ 0 & b \end{bmatrix} \begin{Bmatrix} \mathrm{Re}\left(F\right) \\ \mathrm{Im}\left(F\right) \end{Bmatrix}\ , \tag{5}$$

where $[T_c]$ is a basis of the kernel of $[c]$, and $\{Q_c\}$ the reduced coordinated such as $\{Q\} = [T_c]\{Q_c\}$. The equation (5) can be solved by a classical modal approximation [24], after having computed the modes $\left(\{\phi_j(\kappa_0)\}, \omega_j(\kappa_0)\right)_j$ of the structure Ω_0 for each κ_0.

The key proposition of the reduction procedure is to compute the modes only for few κ ($\kappa = \frac{1}{2}, \frac{1}{5}$ and $\frac{1}{50}$ cell^{-1} in this paper), considering that the modes vary slightly as a function of κ. The main contributing modes for these 3 values of κ are selected with a Singular Value Decomposition (SVD) procedure. Adding the static contribution, and after some manipulations to ensure the periodicity of the selected modes, the reduced basis for the slice (noted $[T]$) is constructed. As examples, two chosen modes are presented in figure 5: a global bending mode (a) for $\kappa = \frac{1}{50}$ cell^{-1} and $f = 17.8$ Hz, and a local ballast shoulder mode (b) for $\kappa = \frac{1}{2}$ cell^{-1} and $f = 168.3$ Hz. The name '*local*' denotes that only a small portion of the track is moving.

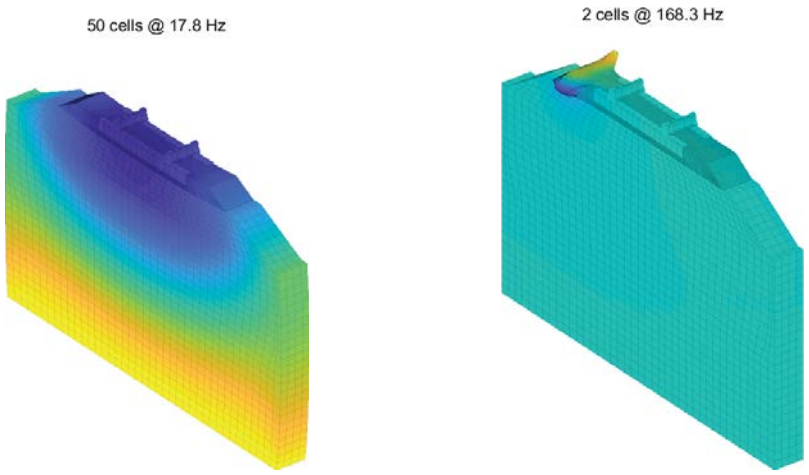

(a) Global track bending mode. (b) Local ballast shoulder mode.

Figure 5: Examples of slice modes selected during the learning phase. Blue corresponds to minimal value of vertical displacement, yellow to the maximal value.

This procedure is performed for three different samples of the ballast layer and the final reduced basis is the result of the SVD for all samples. Then, problem (5) can be expressed and solved in reduced coordinates (208 DOF per slice) instead of physical coordinates (464,919 DOF), thus reducing the computational cost by a factor of more than 2000.

3.3 Assembly of the track from slice models

At this step, heterogeneous slice models have been constructed. However, if one of this slice model is repeated to assemble the track model, the track will remain periodic, which is not the case in reality, with a full random ballast layer.

To avoid this issue, the second key proposition is to consider for each repetition of the slice mesh a random combination of the heterogeneous models. First, reduced matrices $[M_a]$ and $[K_a]$ are assembled by selecting only elements that have homogeneous properties (i.e. the whole track except the ballast layer). These matrices are independent of the heterogeneous sample. Similarly, reduced matrices $[M_{b,j}]$ and $[K_{b,j}]$ are assembled from elements with heterogeneous properties, for each sample j. To obtain the reduced matrices

$[M_n]$ and $[K_n]$ of the n-th slice of the track model, a random combination of coefficient $\left(\alpha_j^n\right)_j$ such as $\sum_j \alpha_j^n = 1$ is sampled with a uniform law on [0 1]

$$[M_n] = [M_a] + \sum_j \alpha_j^n \, [M_{b,j}] \ , \qquad [K_n] = [K_a] + \sum_j \alpha_j^n \, [K_{b,j}] \ . \tag{6}$$

With this procedure, each slice of the assembled track model is different, though taken from the same reduced basis. The numerical gain is even more dramatic between a full 3D track model of 100 slices (more than 40 millions of DOF), and the reduced model (12,880 DOF), i.e. a reduction of a factor more than 3000.

Moreover, to avoid reflection of waves at the end of the track model, the 3 first and 3 last slices are modified to include a damping gradient. If α is the desired damping (here $\alpha = 0.1$), the real-valued part of the stiffness matrix $[K_j]$ of the j-th slice of the 3 edge slices is substituted by the damping matrix $\mathrm{i}\omega\frac{j\alpha}{3}\,[K_j]$ ($j = 3$ corresponding to the first or last slice of the track). The mass matrix $[M_j]$ is untouched.

4 NUMERICAL SIMULATION RESULTS

4.1 Simulation of hammer impact on a track

The first study case is a simulation of the impact experiment presented in section 2. A track of 60 m (i.e. 100 slices) is modeled with the procedure described in section 3. Following the setup in figure 1, an impact is applied on the exterior rail in the middle of the model (i.e. 30 m from the edges or in the 50th slice) and the displacement is measured on the sleeper. The impact is modeled by a Ricker impulse of time 10 ms, with a weight of 10 kg. The temporal integration is done by a Newmark implicit scheme with a time step of $\delta t = 1$ ms and a simulation time of $t_f = 0.8$ s. The receptance (defined in equation (1)) is computed and shown in figure 6. The heterogeneous track model is compared for reference to a homogeneous model, constructed from the same mesh and reduction procedure with the mean values for ballast properties (see figure 1).

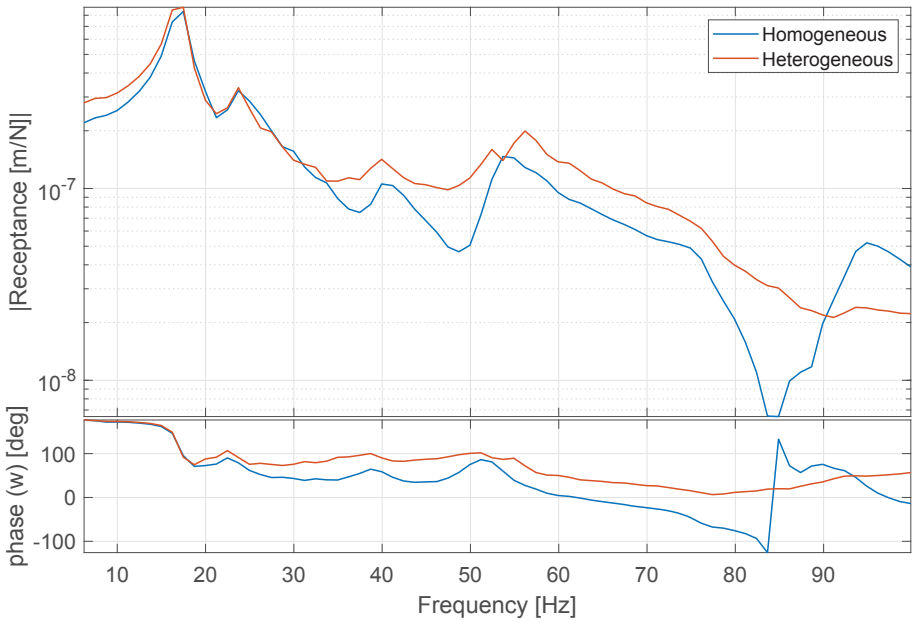

Figure 6: Computed receptance of the track for a heterogeneous model (plain orange curve), and for a homogeneous model (dotted blue curve).

It can be seen that the receptance is very similar at low frequencies (until 25 Hz), especially the phase. The static level (around 0 Hz) is increased by 30%, i.e. 30% softer, which can be explained by a local difference in properties of the ballast layer under the considered sleeper of the heterogeneous model. At higher frequencies (> 25 Hz), the difference is more noticeable. In particular, the peak at 55 Hz is split into two for the heterogeneous model, and the anti-resonance at 83 Hz is shifted to higher frequencies.

This first simulation shows that the difference generated by the heterogeneity of the ballast layer can be non-negligible for higher frequencies than 30 Hz. An immediate continuation of this work is to analyze the discrepancies between impacts at different position in the same track model, and between several track models constructed from different random samples.

4.2 Simulation of bogie pass-by

Another simulation of interest for railway engineering is the pass-by of a vehicle on the track. As a first approach, the pass-by of a single bogie is considered. The bogie is modeled by a assembly of Standard Linear Solid (SLS) models (composed of two springs $K_1 = K_2 = 1.226 \cdot 10^6$ N/m and a damper $C_1 = 10^3$ Ns/m) and beams (represented in blue in figure 7) which have the properties of steel (as the rail in table 2). The masses for the wheels are $M_{\text{wheel}} = 595.5$ kg, for the axles $M_{\text{axle}} = 1024$ kg, and for the bogie $M_{\text{bogie}} = 6780$ kg. These values are representative of a French high speed train. The contact on the rail between the vehicle model and the track model is performed with a functional gap force representation.

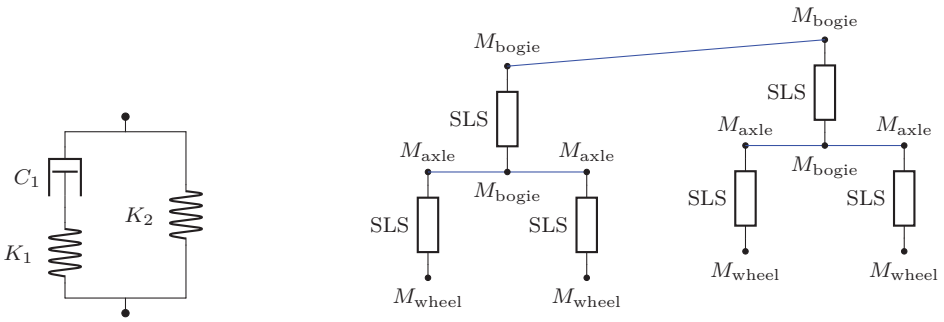

(a) SLS (Standard linear solid model). (b) Scheme of the bogie model (beams in blue).

Figure 7: Scheme of the vehicle used in the simulation.

In the simulation (at a time step of $\delta t = 0.1$ ms), the bogie passes by at $v_0 = 80$ km/h on a 60 m track (i.e. 100 slices) with heterogeneous ballast. The displacement of the 5 middle sleepers (48th to 52th slices) is measured and plotted in figure 8 for the heterogeneous and homogeneous track. The 5 curves are superimposed to show dispersion, with a rescaled time axis $\left\{t_j^*\right\} = \{t\} + \frac{jx_0}{v_0}$.

The displacement for the heterogeneous model is lower than for the homogeneous model, and the spread is bit wider. This means that this zone of the heterogeneous ballast is globally stiffer than the homogeneous properties. This seems to be contradictory to the result for the impact simulation (see figure 6), where it is softer. However, the excitation is very different between both simulations: for the impact, all frequencies are equivalently excited on a small portion of ballast below the concerned sleeper, and

for the bogie pass-by, the excitation is dominated by low frequencies and a larger portion of ballast (around 5 sleepers) are excited. It is possible that the mean stiffness of the ballast layer excited by the impact is lower than the mean properties, but the mean stiffness of the ballast layer excited by the bogie pass-by is higher. This is a first effect of heterogeneity, which would not be represented by a fully homogeneous track model.

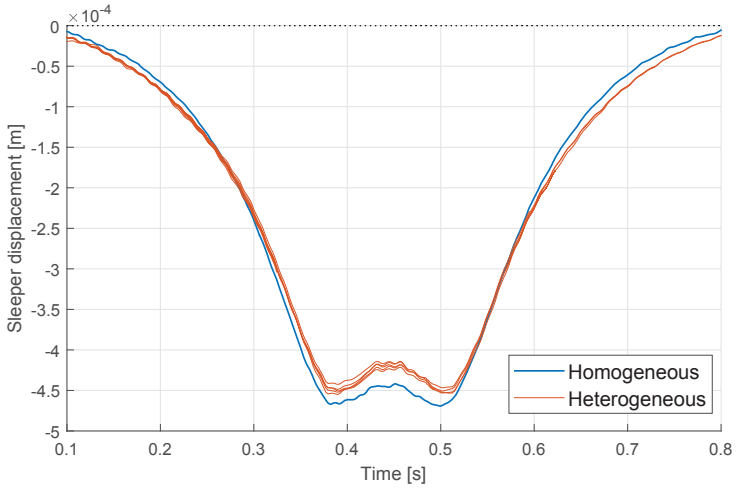

Figure 8: Displacement on 5 consecutive sleepers for a homogeneous (in blue) and heterogeneous track model (in orange), with a rescaled time axis.

The second noticeable effect is the dispersion of the displacement at a pass-by. For the homogeneous model (blue curve in figure 8), the displacement curves on 5 consecutive sleepers are near identical (0.17% of standard deviation from the mean value). This observation validates that the bogie simulation is at an established regime. For the heterogeneous model (orange curve), the displacement curves have a 16 times higher dispersion (2.8%), which is visible by the spread of the curves at the minimum values. This second effect is explained by the local discrepancies of ballast properties, and is also not captured by a homogeneous track model.

5 CONCLUSION

In this paper, the construction of a heterogeneous track model has been presented. The ballast layer is modeled by a heterogeneous, continuous medium whose mechanical properties are taken randomly. A reduced basis for the slice models is constructed from modes computed at few wavenumbers. The slices are then combined randomly to obtain a track model where the ballast layer has lost periodicity. Two type of simulations have been introduced: a hammer impact which excites the track at all frequencies and thus gives an estimation of the critical frequencies, and a vehicle pass-by which is the design case for railway engineering. These first simulations highlight the dispersion added by the heterogeneity, which cannot be obtained from a homogeneous model.

A first clear perspective is to better characterize this dispersion by considering several randomly generated tracks, simulating impacts at different positions along the track, and passages at different speeds. A second development is to add absorbing boundaries (PML) to the soil edges to take into account the radiation in our model. In particular, the remaining effect of heterogeneity while taking into account the radiative behavior of the soil should be checked.

REFERENCES

[1] V. Profillidis, Railway Management and Engineering, 3rd Edition, routledge Edition, 2006.

[2] K. Iwashita, M. Oda, Mechanics of Granular Materials: An Introduction, Taylor & Francis, 1999.

[3] N. Ouhbi, C. Voivret, G. Perrin, J.-N. Roux, Railway Ballast: Grain Shape Characterization to Study its Influence on the Mechanical Behaviour, Advances in Transportation Geotechnics 143 (2016) 1120–1127.

[4] H. Laubie, F. Radjai, R. Pellenq, F.-J. Ulm, Stress Transmission and Failure in Disordered Porous Media, Physical Review Letters 119 (7) (2017) 075501.

[5] A. Suiker, E. Selig, R. Frenkel, Static and Cyclic Triaxial Testing of Ballast and Subballast, Journal of Geotechnical and Geoenvironmental Engineering 131 (6).

[6] S. Kaewunruen, A. Remennikov, Experimental simulation of the railway ballast by resilient materials and its verification by modal testing, Experimental Techniques 32 (2008) 29–35.

[7] P. Anbazhagan, S. Lijun, I. Buddhima, R. Cholachat, Model track studies on fouled ballast using ground penetrating radar and multichannel analysis of surface wave, Journal of Applied Geophysics 74 (4) (2011) 175 – 184.

[8] G. Saussine, C. Cholet, P. E. Gautier, F. Dubois, C. Bohatier, J. J. Moreau, Modelling ballast behaviour under dynamic loading. Part 1: a 2D polygonal discrete element method approach, Computer Methods in Applied Mechanics and Engineering 195.

[9] H. Huang, E. Tutumluer, Discrete element modeling for fouled railroad ballast, Construction and Building Materials 25 (2011) 3306–3312.

[10] E. Azéma, R. Radjai, R. Peyroux, F. Dubois, G. Saussine, Vibrational dynamics of confined granular materials, Physical Review E 74 (2006) 031302.

[11] M. Allen, D. Tildesley, Computer Simulation of Liquids: Second Edition, OUP Oxford, 2017.

[12] H. Chebli, D. Clouteau, L. Schmitt, Dynamic response of high-speed ballasted railway tracks: 3D periodic model and in situ measurements, Soil Dynamics and Earthquake Engineering 28 (2) (2008) 118–131.

[13] S. Gupta, G. Degrande, G. Lombaert, Experimental validation of a numerical model for subway induced vibrations, Journal of sound and vibration 321 (2009) 786–812.

[14] S. François, M. Schevenels, P. Galvín, G. Lombaert, G. Degrande, A 2.5D coupled FE–BE methodology for the dynamic interaction between longitudinally invariant structures and a layered halfspace, Computer Methods in Applied Mechanics and Engineering 199 (23–24) (2010) 1536 – 1548.

[15] P. Alves Costa, R. Calçada, A. S. Cardoso, A. Bodare, Influence of soil non-linearity on the dynamic response of high-speed railway tracks, Soil Dynamics and Earthquake Engineering 30 (2010) 221–235.

[16] P. Alves Costa, R. Calçada, A. S. Cardoso, Track–ground vibrations induced by railway traffic: In-situ measurements and validation of a 2.5D FEM-BEM model, Soil Dynamics and Earthquake Engineering 32 (1) (2012) 111 – 128.

[17] D. P. Connolly, G. Kouroussis, O. Laghrouche, C. L. Ho, M. C. Forde, Benchmarking railway vibrations - Track, vehicle, ground and building effects, Construction and Building Materials.

[18] E. Arlaud, S. Costa D'Aguiar, E. Balmes, Receptance of railway tracks at low frequency: Numerical and experimental approaches, Transportation Geotechnics 9 (2016) 1–16.

[19] M. Germonpré, G. Degrande, G. Lombaert, A track model for the prediction of ground-borne vibrations due to parametric excitation, Procedia Engineering 199 (2017) 2663–2668.

[20] L. de Abreu Corrêa, J. C. Quezada, R. Cottereau, S. Costa d'Aguiar, C. Voivret, Randomly-fluctuating heterogeneous continuum model of a granular medium, Submitted for publication in Computational Mechanics.

[21] D. Komatitsch, J. Tromp, Introduction to the spectral element method for three-dimensional seismic wave propagation, Geophysical Journal International 139 (3) (1999) 806.

[22] M. Shinozuka, G. Deodatis, Simulation of Multi-Dimensional Gaussian Stochastic Fields by Spectral Representation, Applied Mechanics Reviews 49 (1) (1996) 29–53.

[23] H. Pinault, E. Arlaud, E. Balmes, A general superelement generation strategy for piecewise periodic media, Journal of Sound and Vibration 469 (2020) 115–133.

[24] C. Harris, Shock and Vibration Handbook, MacGraw-Hill Pub. Co., New York, N.Y., 1988.

EURODYN 2020
XI International Conference on Structural Dynamics
M. Papadrakakis, M. Fragiadakis, C. Papadimitriou (eds.)
Athens, Greece, 23–26 November 2020

MITIGATION OF VIBRATION INDUCED BY RAILWAY TRAFFIC USING BARRIERS

Patryk Dec[1,2], Régis Cottereau[1], and Baldrik Faure[2]

[1]Aix-Marseille Univ, CNRS, LMA, UMR7031, Centrale Marseille
4 impasse Nikola Tesla, 13013 Marseille, France
e-mail: {dec,cottereau}@lma.cnrs-mrs.fr

[2] SNCF, Innovation and Research Department,
1/3 avenue François Mitterrand, 93212 La Plaine Saint Denis, France
e-mail: baldrik.faure@sncf.fr

Keywords: Railway induced vibrations, Wave propagation, Wave barrier, Spectral Element Method

Abstract. *This paper presents the experimental and numerical evaluation of the barrier's efficiency to mitigate vibration induced by railway traffic. A full-scale in situ experimental setup in France for trains passages on a commercial track is presented. The performance to mitigate vibration of both open and in-filled trench with different materials for different size of trenches is investigated. A numerical model is also introduced in order to understand the phenomena involved and to enable improvements to the design of the barriers to be proposed. A moving load representing a train pass-by is considered. Under the assumptions of linearity and periodicity the response induced by a train pass-by can be reconstructed from the response of a single bogie on a single sleeper.*

1 INTRODUCTION

Railway traffic induces vibrations that can be detrimental to industrial activities and cause annoyance to people in the neighboring buildings. One method to mitigate these waves is to use open trenches or soil barriers (filled trenches). Main conclusions of previous studies about trenches and fill materials of different types highlight that open trenches isolate better than barriers [4] and that trench depth is the main controlling parameter of efficiency [2]. However, the depth of open trenches is limited by stability : rainwater filling, risk of collapse. The use of filling materials improves the stability of the barrier but reduces it efficiency. A main parameter of the efficiency of the barrier is the impedance ratio between soil and the barrier. In this paper, we will study different filling materials and different configurations of the barrier.

First, the experimental campaign that is being set up in France to study the efficiency of the barriers for different parameters of the barriers is presented. Then, a numerical model will be used to understand the details of the experiments and to enable improvements to the design of the barriers to be proposed.

2 EXPERIMENTAL SETUP

With the increase in rail traffic the problems related to noise and vibrations have started to be largely studied. Within the framework of the European research and development project RIVAS, SNCF has carried out a measurement compaign to assess the influence of solutions to reduce vibrations generated by rail traffic. Another experimental campaign is being set up to characterize the efficiency of a barrier on the transmission path to mitigate railway waves. The frequencies of interest are in the range of 10-250 Hz. The test site selected to test the barrier is the same that has been used for RIVAS project. It is located in Florange, France. The track is used for commercial purposes and trains running on this track are TER (Regional Express Trains) and Intercity trains. About ten trains run on this track every day.

2.1 Description of the measurements

Before any works are carried out, a characterization of track and soil is required. The tested site has been already partially characterized during experiments realized for the RIVAS project. As the roughness is the source of vibrations induced at the wheel/rail contact, measurements of rail roughness were realized. Accelerometers were installed on the track and in the soil at 8 m, 16 m and 32 m from the track as presented Fig. 1. Using hammer impacts on the rail and receivers in the soil measurements of track receptances and track/soil transfer functions were realized. The soil/soil transfert functions are estimated from excitations from hammer strikes on an aluminum plate. Others experiments such as for instance the MASW (Multiple Analysis of Surface Waves) to deduce shear wave velocity variations in the soil are carried out to determine soil's properties.

Two areas are defined: a reference section and a test section in which barriers is dug. Measurements are performed for three configurations: before any works, for open trenches and for trenches filled with a different materials. The repeatability of the measurements are verified by comparison of acquisitions results for the same type of trains. Barriers are 20 m long. The first one will be 5 m deep and 3 m wide and the second one 3 m deep and 5 m wide. About fifty acquisitions in each configuration are performed.

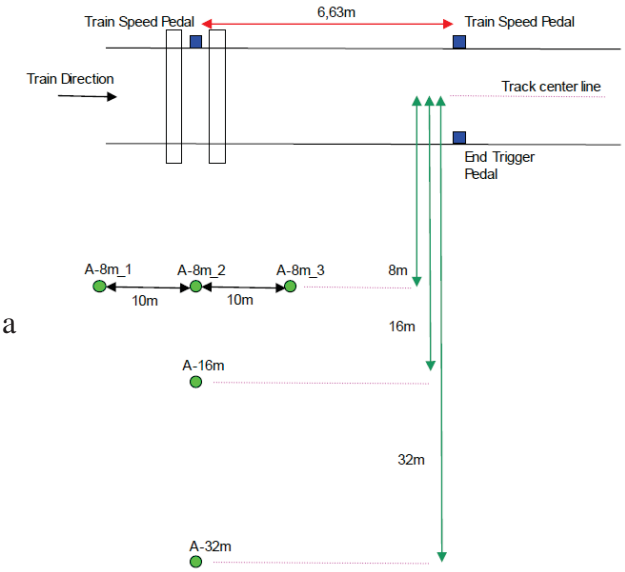

a

Figure 1: Position of receivers in the soil

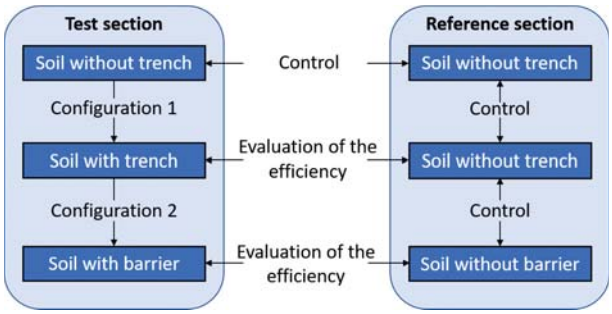

Figure 2: Principle of the test section

2.2 Usefulness of measurements

Before any works are carried out, acquisitions in both areas are compared in order to verify that the responses of the soil for a passing train are similar. The influence of the trench and the barrier on the vibration field is evaluated using the insertion losses defined by :

$$IL(\mathbf{x},\omega) = 20\log_{10}\left|\frac{\hat{a}_Z^{ref}(\mathbf{x},\omega)}{\hat{a}_Z^{Trench}(\mathbf{x},\omega)}\right| \tag{1}$$

where $\hat{a}_Z^{ref}(\mathbf{x},\omega)$ is the vertical acceleration at the reference section and $\hat{a}_Z^{Trench}(\mathbf{x},\omega)$ is the vertical acceleration at the test section. The test section has two functions : to be a reference in the estimation of barrier efficiency and to ensure that the zone was not affected by works in the test section (Fig. 2).

These experiments allow to compare the efficiency of an open trench with these of a barrier, but also to the influence of parameters such as depth, width of the trench and the filling material.

3 WAVE PROPAGATION PROBLEM IN THE PRESENCE OF A BARRIER FOR A MOVING LOAD

In this section, a numerical model is used to understand the phenomena observed during the experiments and propose improvements to the design of the barrier. First, the numerical model is introduced. Then, the modeling of the source is presented. A moving load representing a train pass-by is considered. We show that the response induced by a passing train can be reconstructed from the response of a single bogie on a single sleeper under the assumptions of linearity and periodicity (sleepers spaced regularly). Signals corresponding to a dynamic loading can be easily introduced. Simulations are realized in the time domain.

3.1 Description of the model

Wave propagation problems are solved using the SEM software developed in partnership by CentraleSupelec, Institut de Physique du Globe de Paris and the Commissariat à l'Énergie

Atomique et aux énergies alternatives. SEM is a 3D solver based on the spectral element method (Komatitsch et al. [5] or Cohen [1]). The spectral element method is Finite Element Method (FEM) that uses Lagrange polynomials of high order. The nodes of the Lagrange polynomials are those of the Gauss-Lobatto-Legendre (GLL) quadrature.

A simple model of the track has been considered in this study. Indeed, only the soil, the ballast layer and the sleepers are taken into account (see Fig. 3). In this part, all materials are

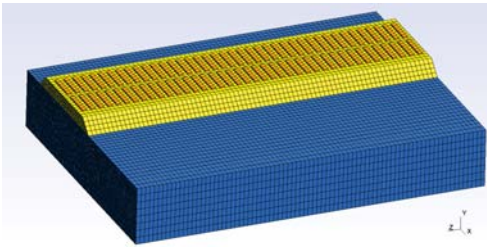

Figure 3: 3D model of the track

assumed to be isotropic linear elastic and follow the Hooke's law. The sleepers are regularly spaced every 0.6 m.

An explicit time scheme is used to solve the problem of wave propagation, the time step Δt is calculated in SEM from the courant number $C < 1$ by :

$$\Delta t = C \frac{\min \Delta x_{nodes}}{c_{p,max}} \tag{2}$$

where $\min \Delta x_{nodes}$ is the minimum distance between two nodes and $c_{p,max}$ is the maximum velocity of materials considered in the model. Then, the time step will be very small for a small mesh or too high velocities.

3.2 Response to a train pass-by obtained from the response of a single bogie

The train is modeled as a set of 13 bogies with different weights. Vibrations produced by a train pass-by can be separated into a quasi-static and dynamic excitation. The quasi-static excitation is related to the static components of the moving axles loads whereas the dynamic excitation is related to the wheel/rail interaction. For a train passing at a speed lower than the wave speed in the soil, vibrations induced by the dynamic excitation are higher than those induce by the quasi-static excitation [8]. For barriers close to the track, the vibration produced by a quasi-static load must be taken into account. The moving axle load can be decomposed in the time domain into a static component and a dynamic component [7].

Under the assumptions of linearity and periodicity, the acceleration at a point $\mathbf{x}$ due to a quasi-static load of a passing train is equal to the sum of accelerations produced by the pass-by of each bogie. It is given by:

$$a_{\text{Train}}(\mathbf{x}, t) = \sum_{k=0}^{12} a_{Bk}(\mathbf{x}, t) = \sum_{k=0}^{12} \alpha_k a_B(\mathbf{x}, t + \tau_k) \tag{3}$$

where a_{Bk} is the acceleration produced by the bogie B_k, τ_k the time delay of the k-th passing bogie with respect to the first one, α_k is the ratio of the weight of bogie k with respect to bogie

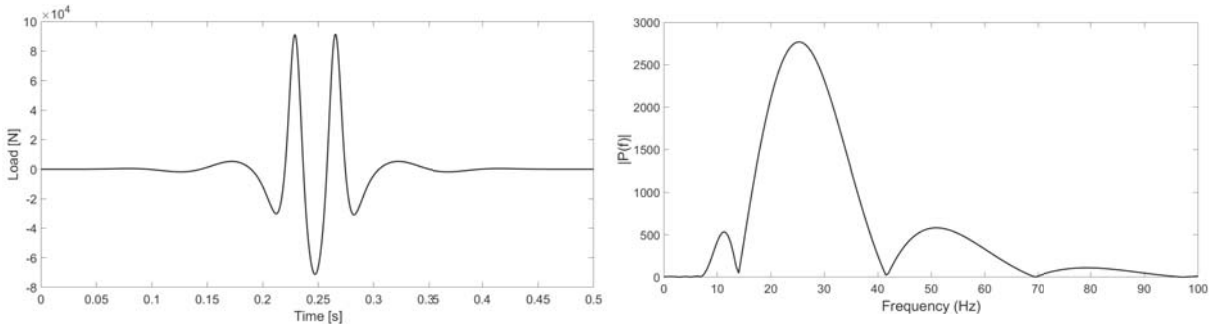

Figure 4: (Left) Loading time function on a single sleeper (Right) Fourier Transform of the loading.

0, $\alpha_0 = 1$, and $a_B = a_{B0}$. The spectrum of a train pass-by is thus given by :

$$\hat{a}_{\text{Train}}(\mathbf{x}, \omega) = \sum_{k=0}^{12} \hat{a}_{Bk}(\mathbf{x}, \omega) = \hat{a}_B(\mathbf{x}, \omega) \sum_{k=0}^{12} \alpha_k \exp(i\omega\tau_k) \tag{4}$$

where $\hat{a}_B$ is the spectrum of the first bogie. The spectrum due to a quasi-satic excitation for a full train can then be analytically calculated from the spectrum of a single passing bogie.

The input force representing the quasi-static load of a bogie is determined using the approach of Hoang et al. [3]. The rail is modeled as an Euler-Bernoulli beam, supported by a periodic elastic support modeling the rail pads on the sleepers. The total force applied on the beam can be expressed as a function of the moving load and reaction forces of sleepers (Fig. 4). By performing a double Fourier transform in time and space of the vertical displacement u_z, given by a dynamic equation, an analytical expression of the 2D-Fourier transform is obtained. The estimation of the dynamic excitation for an axle due to track unevenness characterized by its power spectral density is presented in [7]. The contribution of the dynamic excitation has not been taken into account yet.

For a point force of constant amplitude moving at constant sub-Rayleigh speed along an ideally flat surface of an elastic half-space there are only quasi-static localized displacements moving along with the force that are generated and no elastic waves [6]. However Rayleigh waves are generated if the railway is supported by sleepers. The Fig. 5 presents displacement induced in the soil by a bogie pass-by on 100 sleepers. Three waves can be identified: a

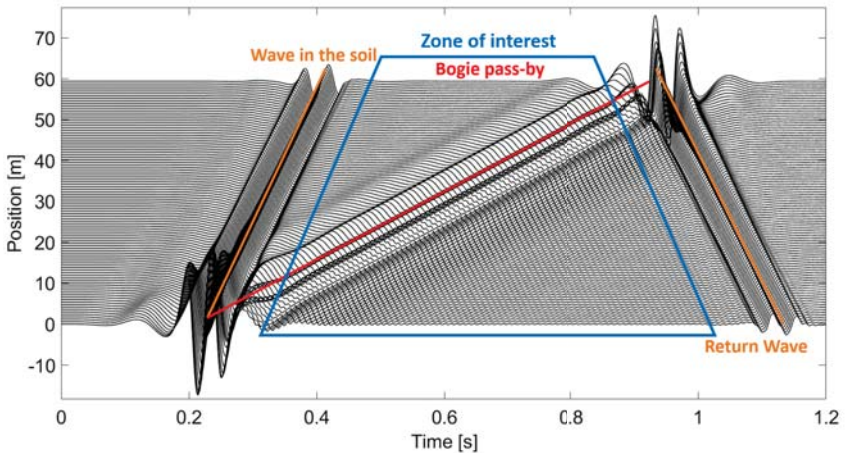

Figure 5: Displacement in the soil obtained for a simulation with 100 sleepers.

wave propagating in the soil at the Rayleigh waves velocity, a wave corresponding to the bogie

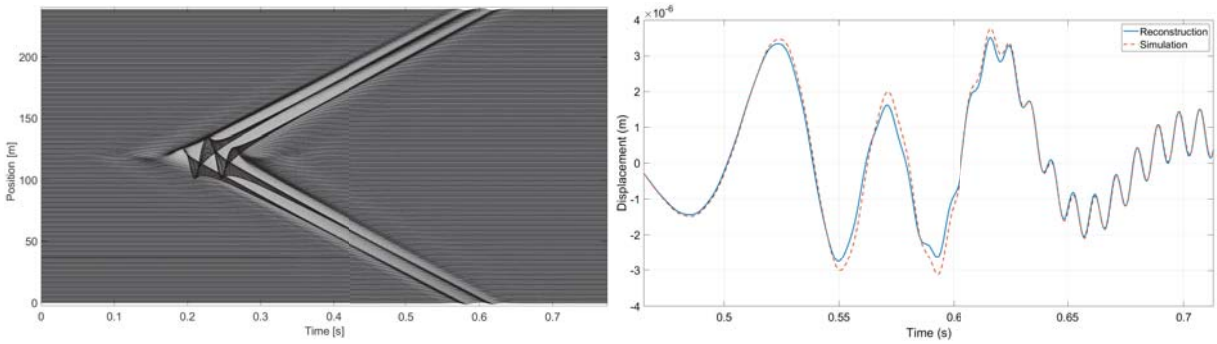

Figure 6: (Left) Displacements (magnified by 5e5) in the soil for a bogie loading on a single sleeper (Right) Reconstructed and simulated displacements in the soil for a bogie pass-by through the simulated domain.

pass-by and a return wave in the soil. The wave in the soil and the return wave appear in the simulations because of the limited size of the track. The loading is applied from the first to the last sleeper and there is no time history of the loading neither before nor after the simulated time. Then, the load on the first bogie generates one wave in the soil and another one which corresponds to the bogie pass-by. The signal of interest is obtained after the removal of these two waves. Oscillations can be seen after the bogie pass-by. They correspond to interference between the displacement induced by a load on one sleeper and displacements induced by loads on the following sleepers. So since there is no loading history above the simulated domain the wave in the soil induced by a load on the last sleeper doesn't interfere with any other wave and a return wave appears in our simulation.

The acceleration at point x for a moving bogie at speed v can be reconstructed from the acceleration measured in sensors distributed along the track with the same periodicity d that sleeper and excited by a non-moving loading applied on only one sleeper using formula :

$$a_B(x,t) = \sum_{k\in\mathbb{Z}} a_0\left(x - kd, t - k\frac{d}{v}\right) \tag{5}$$

where $a_0(x,t)$ is the acceleration at point x at time t produced by a loading at point x_0 at instant t_0. In order to be able to carry out this reconstruction it is necessary to simulate a bogie loading on one single sleeper for a great number of sleepers. The simulation is realized for 40 sleepers. Assuming that wave form are conserved and that the only difference between measurements is in their amplitudes, results are extrapolated beyond the simulated domain. The Fig. 6 (Left) represents the displacement in the soil for a bogie loading on a single sleeper. The reconstructed displacements for a moving bogie along the track are presented in the Fig. 6 (Right). The reconstructed displacements (bleu line) are in good agreement with displacements obtained from the simulation (orange dashed line) of a bogie pass-by.

4 CONCLUSION

A planned experience that aims to evaluate the efficiency of a barrier on the transmitted waves induced by a railway traffic was presented. Different sizes of trenches and materials will be tested. Concerning numerical simulations, they will be used to understand the phenomena that occur on the experiments. The use of a single bogie loading on only one sleeper allowed to reduce the numerical costs. The response of the passing bogie and the spectrum of the train pass-by can then be reconstructed from the simulation results of only a standing bogie in one sleeper.

REFERENCES

[1] G. Cohen. *Higher-Order Numerical Methods for Transient Wave Equations*. Scientific Computation. Springer Berlin Heidelberg, 2013.

[2] D Connolly, A Giannopoulos, W Fan, PK Woodward, and MC Forde. Optimising low acoustic impedance back-fill material wave barrier dimensions to shield structures from ground borne high speed rail vibrations. *Construction and Building Materials*, 44:557–564, 2013.

[3] T. Hoang, D. Duhamel, G. Foret, H.P. Yin, P. Joyez, and R. Caby. Calculation of force distribution for a periodically supported beam subjected to moving loads. *Journal of Sound and Vibration*, 388:327–338, 2017.

[4] HH Hung, YB Yang, and DW Chang. Wave barriers for reduction of train-induced vibrations in soils. *Journal of Geotechnical and Geoenvironmental Engineering*, 130(12):1283–1291, 2004.

[5] D. Komatitsch and J. Tromp. Introduction to the spectral element method for three-dimensional seismic wave propagation. *Geophysical Journal International*, 139(3):806, 1999.

[6] Victor Krylov. Stochastically rough surfaces as seismic barriers against railway-induced ground vibrations. In *Ground Vibrations from High-Speed Railways: Prediction and mitigation*, pages 337–358. ICE Publishing, 2019.

[7] G. Lombaert and G. Degrande. Ground-borne vibration due to static and dynamic axle loads of InterCity and high-speed trains. *Journal of sound and vibration*, 319:1036–1066, 2009.

[8] X Sheng, CJC Jones, and DJ Thompson. A comparison of a theoretical model for quasi-statically and dynamically induced environmental vibration from trains with measurements. *Journal of Sound and Vibration*, 267(3):621–635, 2003.

EURODYN 2020
XI International Conference on Structural Dynamics
M. Papadrakakis, M. Fragiadakis, C. Papadimitriou (eds.)
Athens, Greece, 23–26 November 2020

SCATTERING OF ELASTIC SH WAVES BY TRANSVERSELY ISOTROPIC SPHERE

Ata Jafarzadeh[1], **Peter D. Folkow**[1], **and Anders Boström**[1]

[1]Chalmers University of Technology, Department of Mechanics and Maritime Sciences, Horsalsvagen 7, SE-412 96 Gothenburg, Sweden
e-mail: {jata, peter.folkow, anders.bostrom}@chalmers.se

Keywords: Scattering, Transversely isotropic, Sphere, SH waves, $\mathbf{T}$ matrix.

Abstract. *The scattering by a transversely isotropic sphere in a three-dimensional, homogeneous, isotropic and infinite elastic medium is considered. The problem is a scalar one and is phrased as a scattering problem for an incident SH elastic waves propagating in the direction parallel to the axis of material symmetry. The elastodynamic equations inside the sphere are transformed to spherical coordinates and the displacement field is expanded in associated Legendre functions in the polar coordinate and powers in the radial coordinate. This leads to recursion relations for the expansion coefficients inside the sphere. Using the boundary conditions on the surface of the sphere results in a system of equations for all the expansion coefficients for the fields outside and inside the sphere. As a result, the transition ($\mathbf{T}$) matrix elements are calculated and given explicitly for low frequencies.*

1 INTRODUCTION

Scattering of a wave by a single obstacle has been of much interest in physics and mathematics. This includes the study of scattering for acoustic waves, electromagnetic waves, and elastic waves, where the latter are of interest in this article. There is a wide body of literature on elastodynamic wave scattering in isotropic media. In the treatise on theoretical physics, Morse and Feshbach include several aspects of continuum mechanics and elastic wave propagation [1]. A comprehensive overview of scattering of acoustic, electromagnetic and elastic waves is presented in a unified way by de Hoop [2] and Varadan et al. [3]. However, there exist many natural and synthetic materials, which are not isotropic. This may be fibers in a composite, the grains in a metal, or, on a larger scale, natural soils and rocks or an anisotropic formation in the ground. If the materials are anisotropic the classical series expansion methods for circles and spheres are not applicable any longer and the problem becomes more complicated.

The study of waves in unbounded or semi bounded anisotropic media has mostly been treated in Cartesian and cylindrical coordinates. It is then straightforward to investigate the propagation of waves in layered media. For bounded anisotropic media, where the present focus lies, not so much has been done by analytical methods. However, spherically and cylindrically anisotropic obstacles have been considered by some authors [4–8]. For the case when the obstacle is anisotropic in Cartesian coordinates most interest seems to arise for electromagnetic problems, not mechanical ones. Thus, Wu and Ren [9] investigate the scattering by an anisotropic circle in an isotropic medium using cylindrical wave functions in anisotropic electromagnetic media. Similar wave functions have been used to treat the scattering by a sphere, and to derive the null field approach ($\mathbf{T}$ matrix method) [10–12]. The basic idea in the derivation of these wave functions is a plane wave expansion that is transformed into polar or spherical coordinates, which leads to quite complicated expressions involving integrals that have to be computed numerically. It seems that the method has not been used for mechanical scattering problems. Zharnikov and Syresin [13] develop a very different approach which leads to a Riccati equation for the impedance operator, and they determine the modes in an anisotropic elastic waveguide. Recently, investigations have been performed for scattering of elastic waves by anisotropic obstacles in the 2D case for an orthotropic circle for incident SH waves [14] and P-SV waves [15], using the same type of method as in the present article.

In this paper the scattering problem is considered for a single transversely isotropic spherical obstacle contained in a three-dimensional, homogeneous, isotropic and infinite elastic medium. This is a problem that finds applications in particle composites and in grain scattering in metals (see Boström and Rudá [16]). This canonical problem is here investigated in the simplest case with an incident plane SH wave propagating in the z direction which is scattered by a transversely isotropic sphere with the axis of material symmetry perpendicular to the xy plane (see Figure 1). Therefore, the problem becomes rotationally symmetric and the displacement and stress fields are independent of the azimuthal angle φ. Based on the polarization of the incident wave the problem reduces to a scalar one, relating only to motion in the azimuthal φ direction. The first step is to state the elastodynamic equations in spherical coordinates which leads to expressions containing trigonometric functions in the polar θ coordinate. Expanding the displacement field in associated Legendre functions in θ leads to coupled ordinary differential equations which can be solved by a power series expansion in the radial r coordinate. An expansion in the spherical vector wave functions outside the sphere is employed and using the boundary conditions on the surface of the sphere results in a system of equations for all the expansion coefficients of the fields outside and inside the sphere. The method is in particular well

suited for low frequencies and in this case it is possible to give the elements of the transition matrix in simple analytical form. Some numerical examples are given showing the scattered wave in the far field.

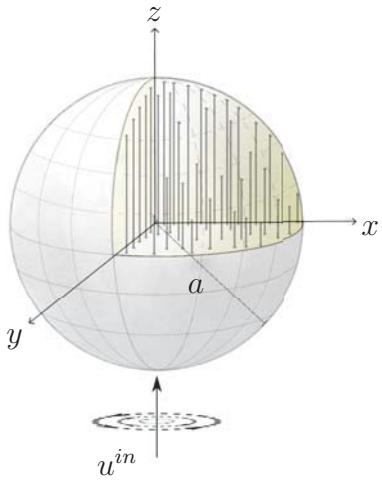

Figure 1: Transversely isotropic sphere with radius a, and incident torsional wave.

2 STATEMENT OF PROBLEM

Consider an anisotropic sphere with radius a surrounded by a homogeneous isotropic elastic infinite medium with density ρ and Lamé parameters λ and μ. Due to the geometry of the problem, it is convenient to use spherical coordinates (r, θ, φ). Considering a time harmonic situation and suppressing the time factor $e^{-i\omega t}$, it is convenient to introduce the spherical vector wave functions of the surrounding medium [3]

$$\boldsymbol{\psi}^0_{1\sigma ml}(r,\theta,\varphi) = \frac{1}{\sqrt{l(l+1)}}\nabla\times\left(\boldsymbol{r}j_l(k_sr)Y_{\sigma ml}(\theta,\varphi)\right) = j_l(k_sr)\boldsymbol{A}_{1\sigma ml}(\theta,\varphi), \tag{1}$$

$$\begin{aligned}\boldsymbol{\psi}^0_{2\sigma ml}(r,\theta,\varphi) &= \frac{1}{\sqrt{l(l+1)}}\nabla\times\nabla\times\left(\boldsymbol{r}j_l(k_sr)Y_{\sigma ml}(\theta,\varphi)\right)\\ &= \left(j_l'(k_sr)+\frac{j_l(k_sr)}{k_sr}\right)\boldsymbol{A}_{2\sigma ml}(\theta,\varphi)+\sqrt{l(l+1)}\frac{j_l(k_sr)}{k_sr}\boldsymbol{A}_{3\sigma ml}(\theta,\varphi),\end{aligned} \tag{2}$$

$$\begin{aligned}\boldsymbol{\psi}^0_{3\sigma ml}(r,\theta,\varphi) &= \left(\frac{k_p}{k_s}\right)^{3/2}\frac{1}{k_p}\nabla\left(j_l(k_pr)Y_{\sigma ml}(\theta,\varphi)\right)\\ &= \left(\frac{k_p}{k_s}\right)^{3/2}\left((j_l'(k_pr)\boldsymbol{A}_{3\sigma ml}(\theta,\varphi)+\sqrt{l(l+1)}\frac{j_l(k_pr)}{k_pr}\boldsymbol{A}_{2\sigma ml}(\theta,\varphi)\right).\end{aligned} \tag{3}$$

Here the first index 1, 2 and 3 on the wave functions indicates SH, SV and P waves, respectively. The spherical harmonics $Y_{\sigma ml}(\theta,\varphi)$ are defined as

$$Y_{\sigma ml}(\theta,\varphi) = \sqrt{\frac{\epsilon_m(2l+1)(l-m)!}{4\pi(l+m)!}}P_l^m(\cos\theta)\left\{\begin{array}{c}\cos m\varphi\\ \sin m\varphi\end{array}\right\}, \tag{4}$$

where $P_l^m(\cos\theta)$ is an associated Legendre function of order $m = 0, 1, 2, ..$ and degree $l = m$, $m+1, m+2, ...$, which has the following definition in terms of the Legendre polynomial

$$P_l^m(x) = (-1)^m(1-x^2)^{\frac{1}{2}m}\frac{d^m P_l(x)}{dx^m}. \tag{5}$$

In eq. (4), $\sigma = e$ for the upper row which is even with respect to φ or $\sigma = o$ for the lower row which is odd with respect to φ. ϵ_m is the Neumann factor, $\epsilon_0 = 1$ and $\epsilon_m = 2$ for $m = 1, 2, 3, ...$ The upper index 0 on the wave functions denotes that they are regular containing spherical Bessel functions j_l, while outgoing waves containing spherical Hankel functions of the first kind $h_l^{(1)}$ are denoted by an upper index $+$. The longitudinal and transverse wave numbers are $k_p = \omega\sqrt{\rho/(\lambda+2\mu)}$ and $k_s = \omega\sqrt{\rho/\mu}$, respectively. Finally, the vector spherical harmonics $\boldsymbol{A}_{\tau\sigma ml}(\theta,\varphi)$, $\tau = 1, 2$ and 3, form a vector basis system for vector-valued functions on the unit sphere which are mutually orthonormal and are defined as

$$\begin{aligned}
\boldsymbol{A}_{1\sigma ml}(\theta,\varphi) &= \frac{1}{\sqrt{l(l+1)}}\nabla\times(\boldsymbol{r}Y_{\sigma ml}(\theta,\varphi)) \\
&= \frac{1}{\sqrt{l(l+1)}}\left(\boldsymbol{e}_\theta\frac{1}{\sin\theta}\frac{\partial}{\partial\varphi}Y_{\sigma ml}(\theta,\varphi) - \boldsymbol{e}_\varphi\frac{\partial}{\partial\theta}Y_{\sigma ml}(\theta,\varphi)\right), \\
\boldsymbol{A}_{2\sigma ml}(\theta,\varphi) &= \frac{1}{\sqrt{l(l+1)}}r\nabla Y_{\sigma ml}(\theta,\varphi) \\
&= \frac{1}{\sqrt{l(l+1)}}\left(\boldsymbol{e}_\theta\frac{\partial}{\partial\theta}Y_{\sigma ml}(\theta,\varphi) + \boldsymbol{e}_\varphi\frac{1}{\sin\theta}\frac{\partial}{\partial\varphi}Y_{\sigma ml}(\theta,\varphi)\right), \\
\boldsymbol{A}_{3\sigma ml}(\theta,\varphi) &= \boldsymbol{e}_r Y_{\sigma ml}(\theta,\varphi).
\end{aligned} \tag{6}$$

Usually it is necessary to have the traction vector on a surface for applying boundary conditions. The traction vector $\boldsymbol{t}^{(r)}$ on the spherical surface $r = a$ with normal $\boldsymbol{e_r}$ is needed to solve the scattering problem, and can be derived directly from the displacement field $\boldsymbol{u}$ by

$$\boldsymbol{t}^{(r)} = \boldsymbol{e}_r\lambda\nabla\cdot\boldsymbol{u} + \mu\left(2\frac{\partial\boldsymbol{u}}{\partial r} + \boldsymbol{e}_r\times(\nabla\times\boldsymbol{u})\right), \tag{7}$$

The first vector wave function (SH waves) and its traction only depend on the first vector spherical harmonic while the second and third wave functions (P-SV waves) only depend on the second and third vector spherical harmonics. Therefore, the scattering problem can be solved for SH waves and P-SV waves separately.

The scattering problem for an incoming wave scattered by the sphere is determined by the constitutive and governing equations inside the sphere (as described later) and the boundary conditions on the sphere, which here are taken as continuity of displacement and traction. Solving the problem, the scattering by the sphere can be represented by the transition ($\mathbf{T}$) matrix which gives the relation between the expansion coefficients of the scattered waves and incoming waves. The incoming and scattered waves can be expanded in the vector wave functions

$$\boldsymbol{u}^{in}(\boldsymbol{r}) = \sum_{\tau\sigma ml} b_{\tau\sigma ml}\boldsymbol{\psi}^0_{\tau\sigma ml}(\boldsymbol{r}), \tag{8}$$

$$\boldsymbol{u}^{sc}(\boldsymbol{r}) = \sum_{\tau\sigma ml} g_{\tau\sigma ml}\boldsymbol{\psi}^+_{\tau\sigma ml}(\boldsymbol{r}), \tag{9}$$

where the expansion coefficients of the incoming wave $b_{\tau\sigma ml}$ can be regarded as known and the expansion coefficients of the scattered wave $g_{\tau\sigma ml}$ are to be determined. The $\mathbf{T}$ matrix is defined as the linear relation between $b_{\tau\sigma ml}$ and $g_{\tau\sigma ml}$

$$g_{\tau\sigma ml} = \sum_{\tau'\sigma'm'l'} T_{\tau\sigma ml,\tau'\sigma'm'l'} b_{\tau'\sigma'm'l'}. \tag{10}$$

Inside the sphere the material is assumed to be transversely isotropic with density ρ_1, such that the axis of anisotropy is perpendicular to the xy plane. Therefore, the constitutive equations in Cartesian coordinates are

$$\begin{Bmatrix} \sigma_{xx} \\ \sigma_{yy} \\ \sigma_{zz} \\ \sigma_{yz} \\ \sigma_{zx} \\ \sigma_{xy} \end{Bmatrix} = \begin{bmatrix} C_{11} & C_{12} & C_{13} & 0 & 0 & 0 \\ C_{12} & C_{11} & C_{13} & 0 & 0 & 0 \\ C_{13} & C_{13} & C_{33} & 0 & 0 & 0 \\ 0 & 0 & 0 & 2C_{44} & 0 & 0 \\ 0 & 0 & 0 & 0 & 2C_{44} & 0 \\ 0 & 0 & 0 & 0 & 0 & C_{11}-C_{12} \end{bmatrix} \begin{Bmatrix} \epsilon_{xx} \\ \epsilon_{yy} \\ \epsilon_{zz} \\ \epsilon_{yz} \\ \epsilon_{zx} \\ \epsilon_{xy} \end{Bmatrix}. \tag{11}$$

The equations of motion in spherical coordinates inside the sphere are

$$\frac{\partial\sigma_{rr}}{\partial r} + \frac{1}{r}\frac{\partial\sigma_{r\theta}}{\partial\theta} + \frac{1}{r\sin\theta}\frac{\partial\sigma_{\varphi r}}{\partial\varphi} + \frac{1}{r}\left(2\sigma_{rr} - \sigma_{\theta\theta} - \sigma_{\varphi r} + \cot\theta\sigma_{r\theta}\right) = -\rho\omega^2 u_r, \tag{12}$$

$$\frac{\partial\sigma_{r\theta}}{\partial r} + \frac{1}{r}\frac{\partial\sigma_{\theta\theta}}{\partial\theta} + \frac{1}{r\sin\theta}\frac{\partial\sigma_{\theta\varphi}}{\partial\varphi} + \frac{1}{r}\left(\cot\theta\left(\sigma_{\theta\theta} - \sigma_{\varphi\varphi}\right) + 3\sigma_{r\theta}\right) = -\rho\omega^2 u_\theta, \tag{13}$$

$$\frac{\partial\sigma_{\varphi r}}{\partial r} + \frac{1}{r}\frac{\partial\sigma_{\theta\varphi}}{\partial\theta} + \frac{1}{r\sin\theta}\frac{\partial\sigma_{\varphi\varphi}}{\partial\varphi} + \frac{1}{r}\left(3\sigma_{\varphi r} + 2\cot\theta\sigma_{\theta\varphi}\right) = -\rho\omega^2 u_\varphi, \tag{14}$$

where the strains ϵ_{ij} in spherical coordinates are

$$\begin{aligned} \epsilon_{rr} &= \frac{\partial u_r}{\partial r}, \quad \epsilon_{\varphi\varphi} = \frac{1}{r\sin\theta}\frac{\partial u_\varphi}{\partial\varphi} + \frac{\cot\theta}{r}u_\theta + \frac{u_r}{r}, \\ \epsilon_{\theta\theta} &= \frac{1}{r}\frac{\partial u_\theta}{\partial\theta} + \frac{u_r}{r}, \quad \epsilon_{\theta\varphi} = \frac{1}{2r}\left(\frac{\partial u_\varphi}{\partial\theta} - \cot\theta u_\varphi + \frac{1}{\sin\theta}\frac{\partial u_\theta}{\partial\varphi}\right), \\ \epsilon_{\varphi r} &= \frac{1}{2}\left(\frac{1}{r\sin\theta}\frac{\partial u_r}{\partial\varphi} + \frac{\partial u_\varphi}{\partial r} - \frac{u_\varphi}{r}\right), \quad \epsilon_{r\theta} = \frac{1}{2}\left(\frac{\partial u_\theta}{\partial r} - \frac{u_\theta}{r} + \frac{1}{r}\frac{\partial u_r}{\partial\theta}\right). \end{aligned} \tag{15}$$

By using the transformation of the stresses and strains between Cartesian and spherical coordinates the stress-strain relations in spherical coordinates become

$$\begin{aligned} \sigma_{rr} = &\left(\alpha_1 + 2\alpha_2\right)\epsilon_{rr} + \alpha_1\epsilon_{\theta\theta} + \left(\alpha_1 - \beta_2 + \beta_3\right)\epsilon_{\varphi\varphi} - 2\beta_1\left(\epsilon_{rr}\cos 2\theta - \epsilon_{r\theta}\sin 2\theta\right) \\ &- \beta_3\left(\epsilon_{\varphi\varphi}\cos 2\theta\right) + \beta_2\left(\left(\epsilon_{rr} - \epsilon_{\theta\theta}\right)\cos 4\theta - 2\epsilon_{r\theta}\sin 4\theta\right), \end{aligned} \tag{16}$$

$$\begin{aligned} \sigma_{\theta\theta} = &\left(\alpha_1 + 2\alpha_2\right)\epsilon_{\theta\theta} + \alpha_1\epsilon_{rr} + \left(\alpha_1 - \beta_2 + \beta_3\right)\epsilon_{\varphi\varphi} + 2\beta_1\left(\epsilon_{\theta\theta}\cos 2\theta + \epsilon_{r\theta}\sin 2\theta\right) \\ &+ \beta_3\left(\epsilon_{\varphi\varphi}\cos 2\theta\right) + \beta_2\left(\left(\epsilon_{\theta\theta} - \epsilon_{rr}\right)\cos 4\theta + 2\epsilon_{r\theta}\sin 4\theta\right), \end{aligned} \tag{17}$$

$$\begin{aligned}\sigma_{\varphi\varphi} = &(\alpha_1 + 2\alpha_2 + 2\beta_1 + \beta_2)\,\epsilon_{\varphi\varphi} + (\alpha_1 - \beta_2 + \beta_3)\,(\epsilon_{\theta\theta} + \epsilon_{rr}) \\ &+ \beta_3\,((\epsilon_{\theta\theta} - \epsilon_{rr})\cos 2\theta + 2\epsilon_{r\theta}\sin 2\theta)\,,\end{aligned} \tag{18}$$

$$\sigma_{\theta\varphi} = \alpha_3\epsilon_{\theta\varphi} + \beta_4\,(\epsilon_{\theta\varphi}\cos 2\theta + \epsilon_{\varphi r}, \sin 2\theta)\,, \tag{19}$$

$$\sigma_{\varphi r} = \alpha_3\epsilon_{\varphi r} - \beta_4\,(\epsilon_{\varphi r}\cos 2\theta - \epsilon_{\theta\varphi}\sin 2\theta)\,, \tag{20}$$

$$\begin{aligned}\sigma_{r\theta} =&2\alpha_2\epsilon_{r\theta} + \beta_1\,((\epsilon_{\theta\theta} + \epsilon_{rr})\sin 2\theta) + \beta_3\,(\epsilon_{\varphi\varphi}\sin 2\theta) \\ &+ \beta_2\,((\epsilon_{\theta\theta} - \epsilon_{rr})\sin 4\theta - 2\epsilon_{r\theta}\cos 4\theta)\,,\end{aligned} \tag{21}$$

where

$$\begin{aligned}&\alpha_1 = \frac{1}{8}(C_{11} + 6C_{13} + C_{33} - 4C_{44}), \quad \alpha_2 = \frac{1}{8}(C_{11} - 2C_{13} + C_{33} + 4C_{44}), \\ &\beta_1 = \frac{1}{4}(C_{11} - C_{33}), \quad \beta_2 = \frac{1}{8}(C_{11} - 2C_{13} + C_{33} - 4C_{44}), \quad \beta_3 = \frac{1}{2}(C_{12} - C_{13}), \\ &\alpha_3 = \frac{1}{2}(C_{11} - C_{12} + 2C_{44}), \quad \beta_4 = \frac{1}{2}(C_{11} - C_{12} - 2C_{44}).\end{aligned} \tag{22}$$

Here, $\alpha_1, \alpha_2, \beta_1, \beta_2$ and β_3 are five linearly independent coefficients that are sufficient to describe the transversely isotropic medium. However, for simplicity, two more coefficients α_3 and β_4 are defined for the case of incident SH waves. They can easily be written in terms of the other coefficients

$$\alpha_3 = 2\alpha_2 + \beta_1 - \beta_3, \qquad \beta_4 = 2\beta_2 + \beta_1 - \beta_3. \tag{23}$$

In the isotropic limit $\beta_i = 0, i = 1, 2, 3, 4$, $\alpha_1 = \lambda_1$ and $\alpha_3 = 2\alpha_2 = 2\mu_1$, with μ_1 and λ_1 being the Lamé parameters of the sphere, and eqs. (16) to (21) reduce to the isotropic case.

3 SCATTERING OF INCIDENT TORSIONAL WAVES

The simplest form of the defined scattering problem occurs for a plane SH wave (or torsional wave) propagating parallel to axis of material symmetry in the z direction. Due to the uncoupling of the SH waves, the displacement field outside the sphere can be written in terms of the first spherical vector wave function (eq. (1)). Such a rotationally symmetric incident wave together with the symmetrical geometry of the media simplify the problem to an axisymmetric situation. Consequently, the displacement and stress fields are φ independent and the vector wave function only consists of $m = 0$ terms (which only have an even part $\sigma = e$). For such an incident plane wave the displacement field outside the sphere, which can be divided into incident and scattered waves, only consists of displacement in the azimuthal direction and is from eqs. (8) and (9)

$$u_\varphi^{in}(r,\theta) = \sum_{l=1}^{\infty} b_{1l}\boldsymbol{\psi}_{1e0l}^0(r,\theta)\cdot\boldsymbol{e}_\varphi = \sum_{l=1}^{\infty} b_{1l}w_l j_l(k_s r)P_l^1(\cos\theta), \tag{24}$$

$$u_{\varphi}^{sc}(r,\theta)=\sum_{l=1}^{\infty}g_{1l}\boldsymbol{\psi}_{1e0l}^{+}(r,\theta)\cdot\boldsymbol{e}_{\varphi}=\sum_{l=1}^{\infty}g_{1l}w_{l}h_{l}^{(1)}(k_{s}r)P_{l}^{1}(\cos\theta), \tag{25}$$

where $w_l=\sqrt{(2l+1)/(4\pi l(l+1))}$.

The radial traction outside the sphere is equal to zero for the r and θ directions and it only has a φ component which is derived from eq. (7) for the incident and scattered waves

$$\begin{aligned}\sigma_{\varphi r}^{in}&=\sum_{l=1}^{\infty}b_{1l}\mu r w_{l}\frac{d}{dr}\left(\frac{j_{l}(k_{s}r)}{r}\right)P_{l}^{1}(\cos\theta),\\ \sigma_{\varphi r}^{sc}&=\sum_{l=1}^{\infty}g_{1l}\mu r w_{l}\frac{d}{dr}\left(\frac{h_{l}^{(1)}(k_{s}r)}{r}\right)P_{l}^{1}(\cos\theta).\end{aligned} \tag{26}$$

In order to find the linear relation between g_{1l} and b_{1l}, the continuity conditions on the surface of the sphere must be applied, and eqs. (12) to (14) must be satisfied inside the sphere. Since there is only traction and displacement components in the φ direction and they are φ independent as well, substituting eqs. (19) and (20) into eq. (14) and using the strain relation in spherical coordinates (eq. (15)) lead to the following partial differential equation to be satisfied inside the sphere

$$\begin{aligned}&\frac{\partial^{2}u_{\varphi}}{\partial r^{2}}+\frac{2}{r}\frac{\partial u_{\varphi}}{\partial r}+\frac{1}{r^{2}}\nabla_{p1}^{2}u_{\varphi}+\beta\cos 2\theta\left[-\frac{\partial^{2}u_{\varphi}}{\partial r^{2}}+\frac{2}{r^{2}}u_{\varphi}+\frac{1}{r^{2}}\nabla_{p1}^{2}u_{\varphi}\right]\\&\quad+\beta\sin 2\theta\left[\cot\theta\left(\frac{1}{r}\frac{\partial u_{\varphi}}{\partial r}-\frac{2}{r^{2}}u_{\varphi}\right)+\frac{\partial}{\partial\theta}\left(\frac{2}{r}\frac{\partial u_{\varphi}}{\partial r}-\frac{1}{r^{2}}u_{\varphi}\right)\right]+k^{2}u_{\varphi}=0,\end{aligned} \tag{27}$$

where $\beta=\beta_4/\alpha_3$ is a measure of the degree of anisotropy, with $\beta=0$ in the isotropic case, $k=\omega\sqrt{2\rho_1/\alpha_3}$ is the wave number in the anisotropic sphere determined with the mean stiffness of the sphere $\alpha_3/2$, and

$$\nabla_{pm}^{2}=\frac{\partial^{2}}{\partial\theta^{2}}+\cot\theta\frac{\partial}{\partial\theta}-\frac{m^{2}}{\sin^{2}\theta}. \tag{28}$$

The differential equation for the Legendre functions of order m can be written in terms of this operator

$$\nabla_{pm}^{2}P_{l}^{m}(\cos\theta)+l(l+1)P_{l}^{m}(\cos\theta)=0. \tag{29}$$

Due to the appearance of ∇_{p1}^2, it is useful to expand the displacement field inside the sphere in terms of the associated Legendre functions of order 1

$$u_{\varphi}(r,\theta)=\sum_{l=1}^{\infty}f_{l}(r)P_{l}^{1}(\cos\theta). \tag{30}$$

Substituting eq. (30) into eq. (27) and using multiple angel formulae for trigonometric functions and the differential equation for the associated Legendre function of order 1 (eq. (29)) lead

to the following relation

$$\sum_{l=1}^{\infty}\Bigg[P_l^1(\cos\theta)\left[(1+\beta)f_l''(r)+\frac{2}{r}f_l'(r)-\left(l(l+1)+\beta\left(2-l(l+1)\right)\right)\frac{1}{r^2}f_l(r)\right]$$
$$+P_l^1(\cos\theta)\cos^2\theta\left[2\beta\left(-f_l''(r)+\frac{1}{r}f_l'(r)-l(l+1)\frac{1}{r^2}f_l(r)\right)\right] \tag{31}$$
$$+\frac{dP_l^1(\cos\theta)}{d\cos\theta}\sin^2\theta\cos\theta\left[2\beta\left(-\frac{2}{r}f_l'(r)+\frac{1}{r^2}f_l(r)\right)\right]+k^2f_l(r)P_l^1(\cos\theta)\Bigg]=0,$$

where a prime denotes differentiation with respect to r. Equation (31) contains terms including multiplication of the associated Legendre functions and trigonometric functions. However, it is convenient to write them in terms of orthogonal functions. For this purpose, the following recursion relations can be used

$$\begin{aligned}(l-m+1)P_{l+1}^m(x)&=(2l+1)xP_l^m(x)-(l+m)P_{l-1}^m(x),\\(-1)^m(1-x^2)\frac{dP_l^m(x)}{dx}&=lxP_l^m(x)-(l+m)P_{l-1}^m(x).\end{aligned} \tag{32}$$

It can be concluded that

$$\begin{aligned}\cos^2\theta P_l^1(\cos\theta)&=c_{1l}P_l^1(\cos\theta)+c_{2l}P_{l+2}^1(\cos\theta)+c_{3l}P_{l-2}^1(\cos\theta),\\\frac{dP_l^1(\cos\theta)}{d\cos\theta}\sin^2\theta\cos\theta&=s_{1l}P_l^1(\cos\theta)+s_{2l}P_{l+2}^1(\cos\theta)+s_{3l}P_{l-2}^1(\cos\theta),\end{aligned} \tag{33}$$

where

$$\begin{aligned}c_{3l}&=\frac{l(l+1)}{(2l+1)(2l-1)},\qquad c_{2l}=\frac{l(l+1)}{(2l+1)(2l+3)},\qquad c_{1l}=\frac{l-1}{l}c_{3l}+\frac{l+2}{l+1}c_{2l},\\s_{3l}&=(l+1)c_{3l},\qquad s_{2l}=-lc_{2l},\qquad s_{1l}=\frac{l-1}{l}s_{3l}+\frac{l+2}{l+1}s_{2l}.\end{aligned} \tag{34}$$

Consequently eq. (31) turns into

$$\sum_{l=1}^{\infty}\left[P_l^1(\cos\theta)R_{1,l}(r)+P_{l+2}^1(\cos\theta)R_{2,l}(r)+P_{l-2}^1(\cos\theta)R_{3,l}(r)\right]=0, \tag{35}$$

which is an expansion only in terms of the associated Legendre functions. It is noted that there is coupling between different degrees of the associated Legendre functions. Here

$$\begin{aligned}R_{1,l}(r)&=(1+\beta-2\beta c_{1l})f_l''(r)+2(1+\beta c_{1l}-2\beta s_{1l})\frac{1}{r}f_l'(r),\\&\quad+\left(r^2k^2-l(l+1)-\beta\big(2-l(l+1)\big)-2\beta c_{1l}l(l+1)+2\beta s_{1l}\right)\frac{1}{r^2}f_l(r),\\R_{2,l}(r)&=-2\beta c_{2l}f_l''(r)+2\beta(c_{2l}-2s_{2l})\frac{1}{r}f_l'(r)+2\beta\big(-l(l+1)c_{2l}+s_{2l}\big)\frac{1}{r^2}f_l(r),\\R_{3,l}(r)&=-2\beta c_{3l}f_l''(r)+2\beta(c_{3l}-2s_{3l})\frac{1}{r}f_l'(r)+2\beta\big(-l(l+1)c_{3l}+s_{3l}\big)\frac{1}{r^2}f_l(r).\end{aligned} \tag{36}$$

Using the orthogonality of the Legendre functions, the following relation must be satisfied inside the sphere for all values of $l=1,2,3,...$ with the condition $f_0(r)=f_{-1}(r)=0$,

$$R_{1,l}(r)+R_{2,l-2}(r)+R_{3,l+2}(r)=0. \tag{37}$$

This is a system of coupled ordinary differential equations for the functions $f_l(r)$. To solve this system of equations, $f_l(r)$ are expanded in power series in r. In order to achieve a solution that is analytical at the origin, the functions $f_l(r)$ must behave as r^l when r approaches the origin and must also contain only even or odd powers of r. Thus, the following series expansion can be made

$$f_l(r) = \sum_{j=l,l+2,\ldots} q_{j,l} r^j. \tag{38}$$

Inserting eq. (38) into eq. (37), results in

$$\sum_{j=l,l+2,\ldots} \left[\left(q_{j,l} M_{1j,l} + q_{j,l+2} M_{2j,l} + q_{j,l-2} M_{3j,l} + q_{j+2,l} k^2 \right) r^{j-2} \right] = 0, \tag{39}$$

where

$$\begin{aligned} M_{1j,l} =& \frac{(j + j^2 - l(1+l))\,(-3 + 4l + 4l^2 + 3\beta)}{-3 + 4l + 4l^2}, \\ M_{2j,l} =& -\frac{2\,(6 + 5l + l^2)\,(3 + j^2 + 4l + l^2 + 2j(2+l))\;\beta}{(3+2l)(5+2l)}, \\ M_{3j,l} =& -\frac{2\,(j^2 - 2j(-1+l) + (-2+l)l)\,(2 - 3l + l^2)\,\beta}{3 - 8l + 4l^2}. \end{aligned} \tag{40}$$

Finally, the linear independence of the powers of r leads to the following equation for all $l = 1, 2, ..,$ and $j = l, l+2, ..,$ with the condition $q_{j,l} = 0$ for all $j > l$

$$q_{j,l} M_{1j,l} + q_{j,l+2} M_{2j,l} + q_{j,l-2} M_{3j,l} + q_{j+2,l} k^2 = 0. \tag{41}$$

This system of equations can be used to determine all $q_{j,l}$ for $j = l+2, l+4, ..$ in terms of $q_{l,l}$. Thus the solution inside the sphere is complete and only contains the unknown coefficients $q_{l,l}$.

Furthermore, for solving the scattering problem, the continuity conditions at the boundary of the sphere must be considered. Substituting the expanded displacement field into the constitutive relation (eq. (20)), the following stress inside the sphere is evaluated

$$\begin{aligned} \frac{2}{\alpha_3}\sigma_{\varphi r} = \sum_{l=1}^{\infty} & (1+\beta)\left(f_l'(r) - \frac{f_l(r)}{r} \right) P_l^1(\cos\theta) - 2\beta\cos^2\theta P_l^1(\cos\theta) f_l'(r) \\ & - 2\beta \frac{dP_l^1(\cos\theta)}{d\cos\theta} \sin^2\theta \cos\theta \left(\frac{f_l(r)}{r} \right), \end{aligned} \tag{42}$$

which again contains terms including multiplication of trigonometric and Legendre functions. However, in order to apply the continuity condition it is convenient to derive the stress inside the sphere in terms of the associated Legendre functions of order 1, the same as the one outside the sphere. Therefore using the same recursion relations as eq. (33) the stress inside the sphere can be rewritten

$$\begin{aligned} \frac{2}{\alpha_3}\sigma_{\varphi r} = \sum_{l=1}^{\infty} & \left[(1+\beta)\left(f_l'(r) - \frac{f_l(r)}{r} \right) - 2\beta\left(c_{1l} f_l'(r) + s_{1l} \frac{f_l(r)}{r} \right) \right] P_l^1(\cos\theta) \\ & + \left[-2\beta\left(c_{3l} f_l' + s_{3l} \frac{f_l(r)}{r} \right) \right] P_{l-2}^1(\cos\theta) \\ & + \left[-2\beta\left(c_{2l} f_l'(r) + s_{2l} \frac{f_l(r)}{r} \right) \right] P_{l+2}^1(\cos\theta). \end{aligned} \tag{43}$$

Considering the expansion of $f(r)$ in terms of powers as in eq. (38), the stress becomes

$$\frac{2}{\alpha_3}\sigma_{\varphi r} = \sum_{l=1}^{\infty} \sum_{j=l,l+2,\ldots} \Big[q_{j,l} N_{1j,l} + q_{j,l+2} N_{2j,l} + q_{j,l-2} N_{3j,l} \Big] r^{j-1} P_l^1(\cos\theta), \tag{44}$$

where

$$\begin{aligned} N_{1j,l} &= \frac{3 + 9\beta - 2l(2+3\beta) - 2l^2(2+3\beta) + j\left(-3 + 4l + 4l^2 + 3\beta\right)}{-3 + 4l + 4l^2}, \\ N_{2j,l} &= -\frac{2(3 + j + l)\left(6 + 5l + l^2\right)\ \beta}{(3+2l)(5+2l)}, \\ N_{3j,l} &= -\frac{2(2 + j - l)\left(2 - 3l + l^2\right)\beta}{3 - 8l + 4l^2}. \end{aligned} \tag{45}$$

Due to the orthogonality of the associated Legendre functions, the boundary condition for the displacement on the surface of the sphere $r = a$ for $l = 1, 2, ...$, gives from eqs. (24), (25), (30) and (38)

$$\sum_{j=l,l+2,\ldots} q_{j,l} a^j = b_{1l} w_l j_l(k_s a) + g_{1l} w_l h_l^{(1)}(k_s a). \tag{46}$$

The stress boundary condition likewise gives from eqs. (26) and (44)

$$\begin{aligned} \sum_{j=l,l+2,\ldots} \Big[q_{j,l} N_{1j,l} + q_{j,l+2} N_{2j,l} + q_{j,l-2} N_{3j,l} \Big] a^{j-1} =& \gamma r b_{1l} w_l \frac{d}{dr}\left(\frac{j_l(k_s r)}{r}\right)\Big|_{r=a} \\ &+ \gamma r g_{1l} w_l \frac{d}{dr}\left(\frac{h_l^{(1)}(k_s r)}{r}\right)\Big|_{r=a}, \end{aligned} \tag{47}$$

where $\gamma = 2\mu/\alpha_3$ is the ratio of the stiffness outside the sphere and the mean stiffness inside the sphere. These equations together with eq. (41) are sufficient to find all the unknowns g_{1l} and $q_{j,l}$ expressed in terms of the incident wave coefficients b_{1l}. Therefore, the solution outside the sphere in the isotropic medium can be derived using eqs. (24) and (25)

$$u_\varphi(r,\theta) = \sum_{l=1}^{\infty} \Big(b_{1l} j_l(k_s r) + g_{1l} h_l^{(1)}(k_s r) \Big) w_l P_l^1(\cos\theta). \tag{48}$$

Here the coefficients g_{1l} of the scattered field are to be determined by using the derived system of equations, where the expansion coefficients of the incoming field are known. For incident plane SH wave, the b_{1l} are

$$b_{1l} = i^l \sqrt{2\pi(2l+1)}. \tag{49}$$

4 THE RAYLEIGH LIMIT

A scattering problem can be simplified by considering extreme values of the geometrical or physical parameters that enter the scattering process. For instance, when the size of the sphere is much smaller than the wavelength of the incident wave, or in other words, when the sphere disturbs only a small fraction of the full incident plane wave, only lower degrees of the scattered wave are significant. This is known as low-frequency scattering, also known as the Rayleigh

limit. For such a problem, the interior displacement field can be expanded to a specific (low) order j_{max} and the regularity condition requires that $l_{max} \leq j_{max}$. Here, $j_{max} = l_{max} = 4$ is considered. The problem can be decoupled into $l = 1, 3$ and $l = 2, 4$. For the $l = 1, 3$ part the following equations are derived from the continuity conditions given in eqs. (46) and (47)

$$q_{1,1}a + q_{3,1}a^3 = b_{11}w_1 j_1(k_s a) + g_{11}w_1 h_1^{(1)}(k_s a), \tag{50}$$

$$q_{3,3}a^3 = b_{13}w_3 j_3(k_s a) + g_{13}w_3 h_3^{(1)}(k_s a), \tag{51}$$

$$\begin{aligned}\frac{2}{5}(5+3\beta)q_{3,1}a^2 - \frac{24}{5}\beta q_{3,3}a^2 =& b_{11}\gamma a w_1 \frac{d}{dr}\left(\frac{j_1(k_s r)}{r}\right)\Big|_{r=a} \\ &+ g_{11}\gamma a w_1 \frac{d}{dr}\left(\frac{h_1^{(1)}(k_s r)}{r}\right)\Big|_{r=a},\end{aligned} \tag{52}$$

$$\begin{aligned}-\frac{8}{15}\beta q_{3,1}a^2 + (2 - \frac{6}{5}\beta)q_{3,3}a^2 =& b_{13}\gamma a w_1 \frac{d}{dr}\left(\frac{j_3(k_s r)}{r}\right)\Big|_{r=a} \\ &+ g_{13}\gamma a w_3 \frac{d}{dr}\left(\frac{h_3^{(1)}(k_s r)}{r}\right)\Big|_{r=a},\end{aligned} \tag{53}$$

which contains the five unknowns $g_{11}, g_{13}, q_{1,1}, q_{3,1}$ and $q_{3,3}$. The additional equation needed comes from eq. (41) which is zero identically for $l = 1, j = 1$ and $l = 3, j = 3$, and is as follows for $l = 1, j = 3$

$$k^2 q_{1,1} + 2(5+3\beta)\beta q_{3,1} - 24\beta q_{3,3} = 0. \tag{54}$$

For solving the system of equations, it is convenient to use the series expansion of the spherical Bessel and Hankel functions, where at low frequencies two terms at most are sufficient. Solving the system of equations the $\mathbf{T}$ matrix is derived based on eq. (10) for elements relating to SH waves ($\tau = 1$) and for $m = 0, \sigma = e$ and different values of l. These matrix elements are simply denoted $T_{ll'}$ and has the following value for T_{11}

$$T_{11} = -\frac{ik_s^3 a^5(-k^2 + \gamma k_s^2)}{45\gamma} = -\frac{ik_s^5 a^5}{45}(1 - \frac{\rho_1}{\rho}). \tag{55}$$

As $l = 1$ corresponds to a rigid body rotation at low frequencies, this element only depends on the density of the sphere, not on the stiffness properties of the sphere. Consequently, this element is identical to the one for an isotropic sphere with the same density.

The $l = 2, 4$ part gives

$$q_{2,2}a^2 + q_{4,2}a^4 = b_{12}w_2 j_2(k_s a) + g_{12}w_2 h_2^{(1)}(k_s a), \tag{56}$$

$$q_{4,4}a^4 = b_{14}w_4 j_4(k_s a) + g_{14}w_4 h_4^{(1)}(k_s a), \tag{57}$$

$$(1-\beta)q_{2,2}a-\frac{1}{7}(-21+5\beta)q_{4,2}a^3-\frac{40}{7}\beta q_{4,4}a^3 = b_{12}\gamma a w_2\frac{d}{dr}\left(\frac{j_2(k_sr)}{r}\right)\Bigg|_{r=a} + g_{12}\gamma a w_2\frac{d}{dr}\left(\frac{h_2^{(1)}(k_sr)}{r}\right)\Bigg|_{r=a}, \tag{58}$$

$$-\frac{24}{35}\beta q_{4,2}a^3+(3-\frac{9}{7}\beta)q_{4,4}a^3 = b_{14}\gamma a w_4\frac{d}{dr}\left(\frac{j_4(k_sr)}{r}\right)\Bigg|_{r=a} + g_{14}\gamma a w_4\frac{d}{dr}\left(\frac{h_4^{(1)}(k_sr)}{r}\right)\Bigg|_{r=a}, \tag{59}$$

which contains five unknowns $g_{12}, g_{14}, q_{2,2}, q_{4,2}$ and $q_{4,4}$. The additional equation from eq. (41) for $l=2, j=4$ is

$$k^2q_{2,2}+2(7+\beta)\beta q_{4,2}-40\beta q_{4,4}=0. \tag{60}$$

The result of solving the system of equations for the first $\mathbf{T}$ matrix element T_{22} (using the asymptotic form of the spherical Bessel and Hankel functions) is

$$T_{22}=-\frac{ik_s^5a^5(\beta+\gamma-1)}{45(\beta-4\gamma-1)}. \tag{61}$$

In the isotropic limit $\beta=0$ and $\gamma=\mu/\mu_1$, this is in agreement with the corresponding isotropic $\mathbf{T}$ matrix element.

To determine other elements of the $\mathbf{T}$ matrix $T_{ll'}$, it is necessary to truncate the expansion of the displacement field inside the sphere at l_{max} in which $l_{max}>l+2$ and $l_{max}>l'+2$, since there is coupling between the $l, l-2$ and $l+2$ degrees of the associated Legendre functions inside the sphere. For instance to evaluate T_{13}, T_{31} and T_{33}, $l_{max}\geq 5$ must be considered. Expanding the displacement field inside the sphere to $j_{max}=l_{max}=5$, the following result for the $\mathbf{T}$ matrix elements is obtained

$$\begin{aligned}
T_{11} =& -\frac{ik_s^5a^5}{45}(1-\frac{\rho_1}{\rho}) \\
&+\frac{ik_s^3a^7}{23625}\left(125k_s^4-\frac{175k^2k_s^2}{\gamma}+\frac{k^4\left(-70\beta^2+87\beta\gamma+5(7+3\gamma)(2+5\gamma)\right)}{\gamma^2L_1}\right), \\
T_{13} =& T_{31}=\frac{i4\sqrt{2}k^2k_s^5a^7}{1125\sqrt{7}}\frac{\beta}{L_1}, \quad T_{33}=-\frac{i2k_s^7a^7}{7875}\frac{5\left(-1+\beta^2\right)+(5+3\beta)\gamma}{L_1}, \\
T_{22} =& -\frac{ik_s^5a^5(\beta+\gamma-1)}{45L_2}+\frac{ik_s^5a^7}{189}\frac{3k^2\gamma+k_s^2\left(\beta^2-5\gamma^2-\beta(2+\gamma)+\gamma+1\right)}{L_2^2},
\end{aligned} \tag{62}$$

where

$$L_1=2\left(-1+\beta^2\right)-(5+3\beta)\gamma, \qquad L_2=\beta-4\gamma-1, \tag{63}$$

This is all $\mathbf{T}$ matrix elements that are of order $(k_sa)^5$ and $(k_sa)^7$, higher order elements are all smaller, going at least as $(k_sa)^9$.

5 Numerical Results

The numerical implementation is straightforward, the only parameter to check is the truncation j_{max} and l_{max}. The validity of the computations can be checked in three ways. The first is to look at the special case of isotropy and this is exactly fulfilled as the method reduces to the standard separation-of-variables solution for this case. The other two is to check the T matrix for symmetry and "hermicity" [17], which are both only valid for lossless media, i.e. real stiffnesses. Symmetry is due to reciprocity and is exactly fulfilled in the Rayleigh limit and more or less exactly fulfilled numerically. "Hermicity" is due to energy conservation and this gives the following relation for the T matrix (in matrix notation)

$$T^{\dagger}T = -\mathrm{Re}T \tag{64}$$

where the dagger denotes the Hermitian conjugate (taking both the transpose and the complex conjugate). This is a very good nonlinear check (but of course it is only necessary, not sufficient). This check is not possible to apply in the Rayleigh limit as the leading order terms are all imaginary and the leading order real terms are much smaller and are thus not calculated. For higher frequencies it is possible to perform this check numerically and this has been done with a very satisfactory result. For $k_s a = 5$, for instance, this relation is satisfied to 4 digits when the truncation $j_{max} = 20, l_{max} = 10$ is used and to 7 digits for $j_{max} = 24, l_{max} = 12$.

One physical quantity that is often calculated is the far field amplitude which is defined according to

$$u^{sc} = F(\theta)\frac{e^{ik_s r}}{k_s r}, \tag{65}$$

where the asymptotic behaviour of the spherical Hankel function for the scattered field is used and the far field amplitude is

$$F(\theta) = \sum_{l=1} i^{l+1} g_{1l} w_l P_l^1(\cos\theta). \tag{66}$$

For numerical illustration, the absolute value of the far field amplitude for cases with the material of the sphere denser and stiffer than the surrounding is calculated. Therefore, $\rho_1/\rho = 2$ and $\gamma = 0.2$ is assigned for all cases. The degree of anisotropy is given by the parameter $\zeta = (C11 - C12)/(2C44)$, which is the quotient between the two shear stiffnesses inside the sphere. The frequency is specified by the parameter $k_s a$. The computations are performed both numerically and in the Rayleigh limit to order $(k_s a)^5$ and $(k_s a)^7$.

First the validity of the Rayleigh limit is examined for an anisotropic sphere with stiffness quotient $\zeta = 0.2$. Figure 2 shows the normalized far field amplitude of the sphere in the $\theta = 3\pi/4$ direction as a function of frequency. As the T matrix goes as $(k_s a)^5$ for low frequencies the normalization is $F(3\pi/4)/(k_s a)^5$. The Rayleigh limit with only $(k_s a)^5$ is shown dashed and with including $(k_s a)^7$ is shown dash-dotted, and the numerical result with $j_{max} = 24, l_{max} = 12$ is shown dotted. These are also compared with the far field amplitude of the isotropic sphere when $\zeta = 1$ (full-drawn). A good agreement between the Rayleigh limit and the numerical result is observed for low frequencies (approximately $k_s a < 0.3$ by considering $(k_s a)^5$ terms and $k_s a < 0.8$ by including $(k_s a)^7$ terms). Also, the effect of anisotropy is considerable even for low frequencies.

To illustrate the effect of anisotropy, Figure 3 shows a polar plot (for $0 \leq \theta \leq \pi$) of the absolute value of the far field amplitude of the anisotropic sphere for $k_s a = 2$ and different

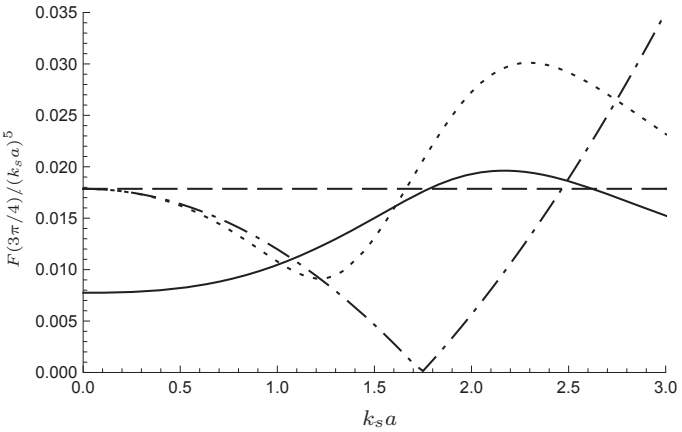

Figure 2: The normalized far field amplitude as a function of frequency $k_s a$ in the $\theta = 3\pi/4$ direction for the density ratio $\rho_1/\rho = 2$ and stiffness ratio $\gamma = 0.2$. Curves are given for a transversely isotropic sphere with stiffness quotient $\zeta = 0.2$, both with numerical computations (dotted) and in the Rayleigh limit (two curves, one with only $(k_s a)^5$ terms (dashed) and one with including also $(k_s a)^7$ terms (dash-dotted)). Also the result for an isotropic sphere ($\zeta = 1$, full-drawn) is included.

values of the stiffness quotient: $\zeta = 10$ (full-drawn), 2 (dashed), 0.5 (dotted), 0.1 (dash-dotted). This is also compared with the isotropic case (i.e. $\zeta = 1$) on the left side of the figure. Figure 4 illustrates the same situation for the higher frequency $k_s a = 5$, which shows somewhat stronger effects due to the anisotropy.

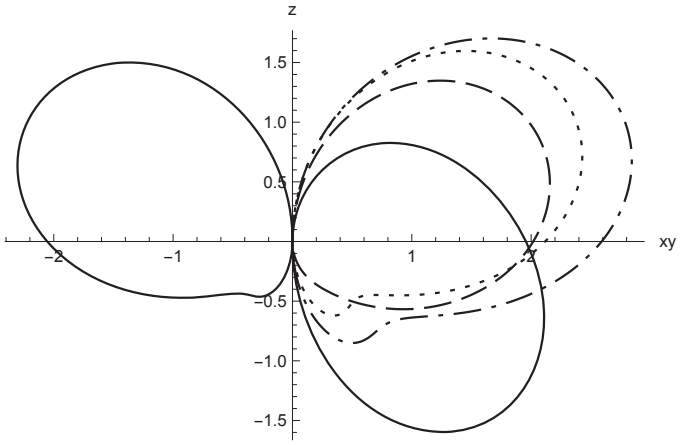

Figure 3: The far field amplitude for the frequency $k_s a = 2$, density ratio $\rho_1/\rho = 2$ and stiffness ratio $\gamma = 0.2$ for the isotropic sphere ($\zeta = 1$) on the left side and transversely isotropic sphere with stiffness quotient $\zeta = 10$ (full-drawn), 2 (dashed), 0.5 (dotted), 0.1 (dash–dotted), on the right side.

6 CONCLUSIONS

The scattering problem for a transversely isotropic sphere inside an isotropic medium for an incident SH wave in the z direction is considered. Transformation of the constitutive equations from Cartesian to spherical coordinates results in complicated expressions for the equations of motion and stresses inside the sphere. Expanding the displacement field in associated Legendre functions of order 1 in θ and power series expansions in r, leads to recursion relations for the expansion coefficients that couple different polar degrees (in contrast to an isotropic sphere where there is no such coupling). Applying the boundary conditions on the sphere the $\mathbf{T}$ matrix elements can be obtained. Explicit expressions are obtained for the $\mathbf{T}$ matrix elements for low

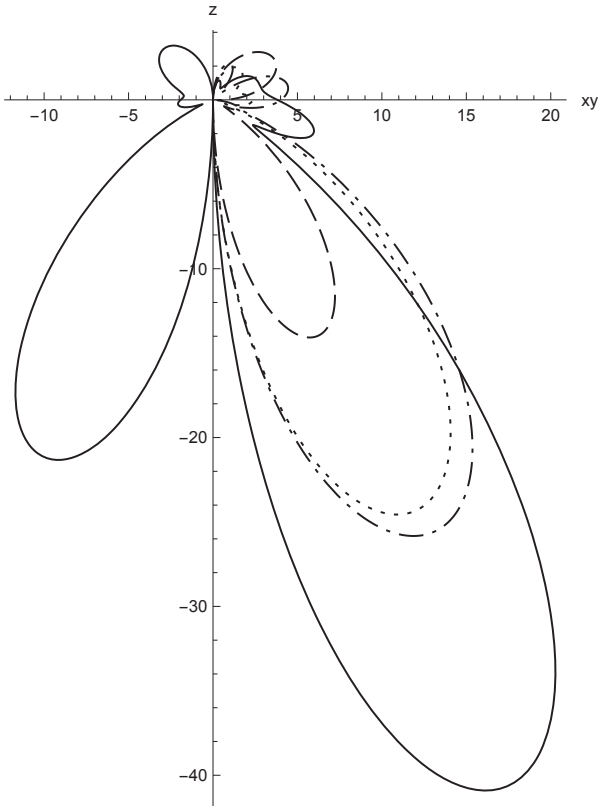

Figure 4: The far field amplitude for the frequency $k_s a = 5$, density ratio $\rho_1/\rho = 2$ and stiffness ratio $\gamma = 0.2$ for the isotropic sphere ($\zeta = 1$) on the left side and transversely isotropic sphere with stiffness quotient $\zeta = 10$ (full-drawn), 2 (dashed), 0.5 (dotted), 0.1 (dash–dotted), on the right side.

frequencies.

The present calculations for the SH waves in low frequencies are of limited interest as these $\mathbf{T}$ matrix elements are not of leading order (the P-SV waves are expected to behave as $(ka)^3$ as they do in the isotropic case). However, the present article also includes the necessary expressions for the stresses expressed in spherical coordinates for the general case. The present approach is applicable to this general case as well and such work is in progress.

The calculated $\mathbf{T}$ matrix elements can be used for various purposes. One important application is in the estimation of damping and phase velocities in polycrystalline materials, typically metals. The grains in such materials are far from spherical, but at low frequencies (when the grains are much smaller than the wavelength) the grain shape is not very important as the scattering is mainly a volume effect. For damping calculations in 2D this approach has been shown to give excellent agreement with FEM computations (Boström and Rudá [16]).

REFERENCES

[1] PM Morse and H Feshbach. *Methods of Theoretical Physics*. McGrow-Hill, New York, 1953.

[2] AT de Hoop. *Handbook of radiation and scattering of waves: acoustic waves in fluids, elastic waves in solids, electromagnetic waves.* Academic Press, San Diego, 1995.

[3] VV Varadan, A Lakhtakia, and VK Varadan. *Field representations and introduction to scattering*. North-Holland, Amsterdam, 1991.

[4] PA Martin and JR Berger. Waves in wood: free vibrations of a wooden pole. *Journal of the Mechanics and Physics of Solids*, 49:1155–1178, 2001.

[5] SM Hasheminejad and M Maleki. Acoustic resonance scattering from a submerged anisotropic sphere. *Acoustical Physics*, 54:168–179, 2008.

[6] AN Norris and AL Shuvalov. Elastodynamics of radially inhomogeneous spherically anisotropic elastic materials in the Stroh formalism. *Proceedings of the Royal Society A: Mathematical, Physical and Engineering Sciences*, 468:467–484, 2012.

[7] MD Guild, A Alù, and MR Haberman. Cloaking of an acoustic sensor using scattering cancellation. *Applied Physics Letters*, 105:023510, 2014.

[8] MY Chung. Stress amplification/shielding phenomena of spherically anisotropic and radially inhomogeneous linear elastic hollow spheres. *The Quarterly Journal of Mechanics and Applied Mathematics*, 72:535–544, 2019.

[9] XB Wu and W Ren. Wave-function solution of plane-wave scattering by an anisotropic circular cylinder. *Microwave and Optical Technology Letters*, 8:39–42, 1995.

[10] C Wan and H Li. Analytical method and semianalytical method for analysis of scattering by anisotropic sphere: A review. *International Journal of Antennas and Propagation*, 2012:782320, 2012.

[11] A Doicu. Null-field method to electromagnetic scattering from uniaxial anisotropic particles. *Optics communications*, 218:11–17, 2003.

[12] JJ Wang, YP Han, L Han, and ZW Cui. Electromagnetic scattering from gyroelectric anisotropic particle by the T-matrix method. *Journal of Quantitative Spectroscopy and Radiative Transfer*, 135:20–29, 2014.

[13] TV Zharnikov and DE Syresin. Formulation of the Riccati equation for the impedance operator in cylindrical coordinates for inhomogeneous anisotropic waveguides with the example of rectilinear anisotropy. *Wave Motion*, 52:1–14, 2015.

[14] A Boström. Scattering by an anisotropic circle. *Wave Motion*, 57:239–244, 2015.

[15] A Boström. Scattering of in-plane elastic waves by an anisotropic circle. *The Quarterly Journal of Mechanics and Applied Mathematics*, 71:139–155, 2018.

[16] A Boström and A Ruda. Ultrasonic attenuation in polycrystalline materials in 2D. *Journal of Nondestructive Evaluation*, 38:47, 2019.

[17] PC Waterman. Matrix theory of elastic wave scattering. *The Journal of the Acoustical Society of America*, 60:567–580, 1976.

EURODYN 2020
XI International Conference on Structural Dynamics
M. Papadrakakis, M. Fragiadakis, C. Papadimitriou (eds.)
Athens, Greece, 23–26 November 2020

A 2.5D FEM-BEM-MFS METHODOLOGY FOR SOIL-STRUCTURE INTERACTION PROBLEMS IN LAYERED HALF-SPACES

Hassan Liravi[1], Robert Arcos[1,2], Dhananjay Ghangale[1], and Jordi Romeu[1]

[1]Acoustical and Mechanical Engineering Laboratory (LEAM), Universitat Politècnica de Catalunya (UPC).
c/ Colom, 11, 08222 Terrassa (Barcelona), Spain.
e-mail: {hassan.liravi,dhananjay.ghangale,jordi.romeu}@upc.edu

[2] Serra Húnter Fellow, Universitat Politècnica de Catalunya (UPC).
c/ Colom, 11, 08222 Terrassa (Barcelona), Spain.
e-mail: robert.arcos@upc.edu

Keywords: Method of fundamental solutions, elastodynamics, soil-structure interaction, railway tunnels, layered half-space.

Abstract. *In this paper, a new prediction methodology to deal with longitudinally invariant soil-structure interaction problems in elastodynamics is presented. The method uses the finite-element method to model the structure, the boundary-element method to model the local soil surrounding the structure and the method of fundamental solutions to model the wave propagation through the soil. All those methods are formulated in the two-and-a-half-dimensional domain. The methodology is firstly verified in the framework of a homogeneous half-space system by comparing the results of the current method with those computed by the semi-analytical solution of this problem. Secondly, the methodology is verified against a two-and-a-half-dimensional finite element-boundary element approach, for two calculation examples: a tunnel embedded in a homogeneous half-space and a tunnel embedded in a layered half-space. This comparison also shows that this novel methodology reduces the computational costs of such simulations without compromising the accuracy of the results. The increase on the computational efficiency is due to the use of the method of fundamental solutions to account for the wave propagation in the medium, and it is even higher when the number of evaluations points increases.*

1 INTRODUCTION

In the framework of soil-structure interaction problems, some structures can be considered as longitudinally invariant systems that can be assessed by two-and-half-dimensional approaches. Structures like at-grade railway tracks [4], tunnels [1], roads [2] or bridges [3] are some examples of soil-structure problems where the structure can be modelled as longitudinally invariant system. A review of the literature indicates that there are several works that contributed to the study of this kind of soil-structure interaction problems. Among them, coupled 2.5D finite element-boundary element methodology (2.5D FEM-BEM) is a well-known numerical approach for the assessment of the soil-structure interaction problems. François et al. [2] presented a 2.5D FEM-BEM model in frequency domain. They proposed this method to study the wave propagation in soil induced by railway or road traffic using this method. Galvín et al. [4] used the same method to analyse two different applications: a ballasted track over a layered half-space and a tunnel embedded in a layered half-space. Lopes et al. [5] proposed an alternative method where a 2.5D FEM with 2.5D perfect matched layers (PML) is used to assess the ground-borne vibration response of a building. Later, the re-radiated noise inside the building was investigated using a 2.5D MFS in acoustics weakly coupled with the building vibration field obtained with the method presented in [5] [6]. More recently, Ghangale and his colleagues [7] presented a method for the prediction of the energy flow radiated by underground railway infrastructures based on a 2.5D FEM-BEM method to model the tunnel and the locally surrounding ground and on the semi-analytical solutions of a cylindrical cavity to model the wave propagation on the soil.

The MFS is a collocation method which approximates the solution within an elastic medium employing a combination of fundamental solutions of the medium governing equations. It is specially interesting for dealing with wave propagation problems in unbounded or partially unbounded domains. Its application is based on a distribution of collocation points, which evaluates the boundary conditions at discrete positions, and on a distribution of source points (or virtual forces, in elastodynamic problems), which are obtained by complying the boundary conditions at the collocation points. The collocation points are located on the boundary and the source points outside the domain. Godinho et al. [11] presented two-dimensional FEM-MFS modelling approach for these types of problems. An extension of this to longitudinally invariant systems was presented by Amado-Mendes and his colleagues [1], where a methodology that models the structure using 2.5D FEM and the surrounding soil with 2.5D MFS is proposed. For many years, it has been a concern of the researchers to find the optimal distance between collocation and source points, particularly in complicated shapes. An incorrect selection of this distance may lead to large errors of the numerical method [9]. Besides, it should be noted that the amount of source points affects the numerical convergence and stability of the results [10].

In this study, a 2.5D FEM-BEM-MFS method in frequency domain is presented. The 2.5D FEM-BEM is used to obtain the displacement field on the boundary and the 2.5D MFS is used as a post-processing tool to obtain the displacement and traction fields on the soil from the displacement field on the soil-structure interaction boundary. The main novelty of the current method is, thus, the way MFS is applied, which leads to two global benefits. On the one hand, the application of this methodology results to an increase of the computational efficiency of the method respect to traditional 2.5D FEM-BEM approaches and this is mostly significant when many evaluator points are to be analysed. On the other hand, a significant difference between the work of Amado-Mendes et al. [1] and the current method is related about how the dynamic stiffness matrix of the soil at the soil-structure interaction boundary is obtained.

2 Description of the methodology

In this study, the calculations are performed in two general steps. Firstly, the displacements on the boundary are computed through a 2.5D FEM-BEM method. In this 2.5D FEM-BEM approach, the FEM is used to model the structure and the BEM is used to model the locally surrounding soil. The formulation of the 2.5D FEM-BEM used here is based on [2]. The response of the soil-structure system can be calculated by

$$\left[\mathbf{K}_0 - \mathbf{i}k_x\mathbf{K}_1 + {k_x}^2\mathbf{K}_2 + \bar{\mathbf{K}}_s - \omega^2\mathbf{M}\right]\bar{\boldsymbol{U}} = \bar{\boldsymbol{F}}, \tag{1}$$

where $\mathbf{K}_0$, $\mathbf{K}_1$, $\mathbf{K}_2$ and $\mathbf{M}$ are the stiffness and mass matrices related to the 2.5D FEM domain, $\bar{\mathbf{K}}_s$ is the dynamic stiffness matrix of the soil obtained by 2.5D BEM model, k_x is the longitudinal wavenumber and ω is the angular frequency. Moreover, $\bar{\boldsymbol{U}}$ and $\bar{\boldsymbol{F}}$ are the vectors of displacements and applied external forces along the mesh of the structure, respectively. Thus, the displacements $\bar{\boldsymbol{U}}_{\boldsymbol{b}}$ on the boundary can be extracted from $\bar{\boldsymbol{U}}$.

Secondly, the displacement and traction fields in the soil are calculated using a 2.5D MFS for elastodynamics. For this aim, the displacements on the boundary ($\bar{\boldsymbol{U}}_{\boldsymbol{b}}$) are considered as the boundary conditions of the MFS. Then, the virtual source strengths can be computed as

$$\bar{\boldsymbol{S}}_v = \bar{\mathbf{H}}_{cs}^{-1}\bar{\boldsymbol{U}}_c, \tag{2}$$

where $\bar{\boldsymbol{S}}_v$ is the vector of virtual source strengths, $\bar{\mathbf{H}}_{cs}$ represents the matrix of displacement Green's functions on the collocation points due to the virtual sources and $\bar{\boldsymbol{U}}_c$ represents the displacements at the collocation points. If the collocation points are considered to be directly the nodes of boundary mesh, $\bar{\boldsymbol{U}}_c = \bar{\boldsymbol{U}}_b$. If the configuration is different, the displacement in the collocation points $\bar{\boldsymbol{U}}_c$ should be obtained by interpolation along the boundary from $\bar{\boldsymbol{U}}_b$. In this study, the Green's function are computed by the ElastoDynamics Toolbox for MATLAB [8]. Given the source strengths, the displacement and traction fields can be calculated as

$$\bar{\boldsymbol{U}}_f = \bar{\mathbf{H}}_{fs}\bar{\boldsymbol{S}}_v, \quad \bar{\boldsymbol{T}}_f = \bar{\mathbf{H}}_{fs}^{\tau}\bar{\boldsymbol{S}}_v, \tag{3}$$

where $\bar{\mathbf{H}}_{fs}$ and $\bar{\mathbf{H}}_{fs}^{\tau}$ represent the source-evaluators Green's functions for displacements and tractions, respectively, and $\bar{\boldsymbol{U}}_f$ and $\bar{\boldsymbol{T}}_f$ stand for the displacement and traction of the evaluation points, inside the domain.

In order to improve the computational efficiency of the method, a mapping technique is used. In this technique, the Green's displacement and Green's traction fields are calculated for the unique values of the sources depth and relative distances of the source-receiver points. Then, these Green's functions are mapped into the original configuration of sources and evaluation points by performing the required coordinate rotations [7].

3 Verification of the method for a homogeneous half-space problem

The proposed method is firstly verified for a solid cylinder with a radius of 3 m embedded in a homogeneous half-space, a system illustrated in Fig. 1. In order to compare with the semi-analytical solutions of a homogeneous half-space for verification purposes, the solid cylinder is assumed to be defined by the exact same mechanical parameters than the soil. The mechanical parameters of the soil are defined in Table 1. The vertical displacements obtained with the new

method are plotted against the results obtained by the semi-analytical solution of the problem and by the 2.5D FEM-BEM approach for a wavenumber of 0.1 rad/m. Results of this verification are shown in terms of displacement Green's functions in the wavenumber-frequency domain, presented in dB based on reference of 10^{-12} m/(N/m).

Type	E [MPa]	ρ [kg/m^3]	ν	Damping
Cylinder	108	1800	$1/3$	0.05
Soil	108	1800	$1/3$	0.05

Table 1: Mechanical parameters of the solid cylinder and the soil.

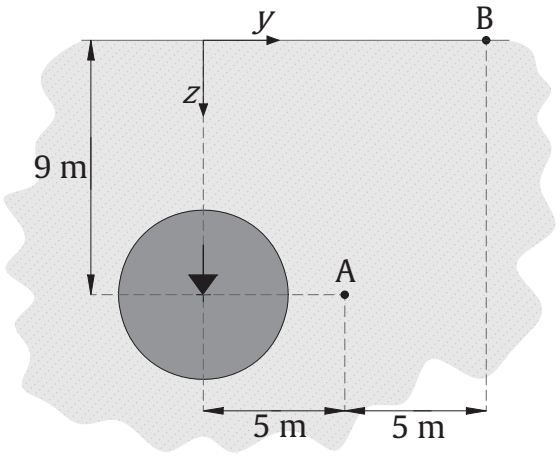

Figure 1: Geometry of the system studied, based on a solid cylinder in a homogeneous half-space. A and B represent the field points on the soil where the results will be obtained. The input vertical force applied at the center of the cylinder is represented by a big arrow.

According to the results presented in Fig. 2, very good agreement of the results is observed between the three methods compared. The results of the current method and those obtained by 2.5D FEM-BEM method are almost exactly matched. However, a slight difference can be observed between the results of the proposed method and semi-analytical solution, particularly at frequencies higher than 60 Hz, due to the mesh size.

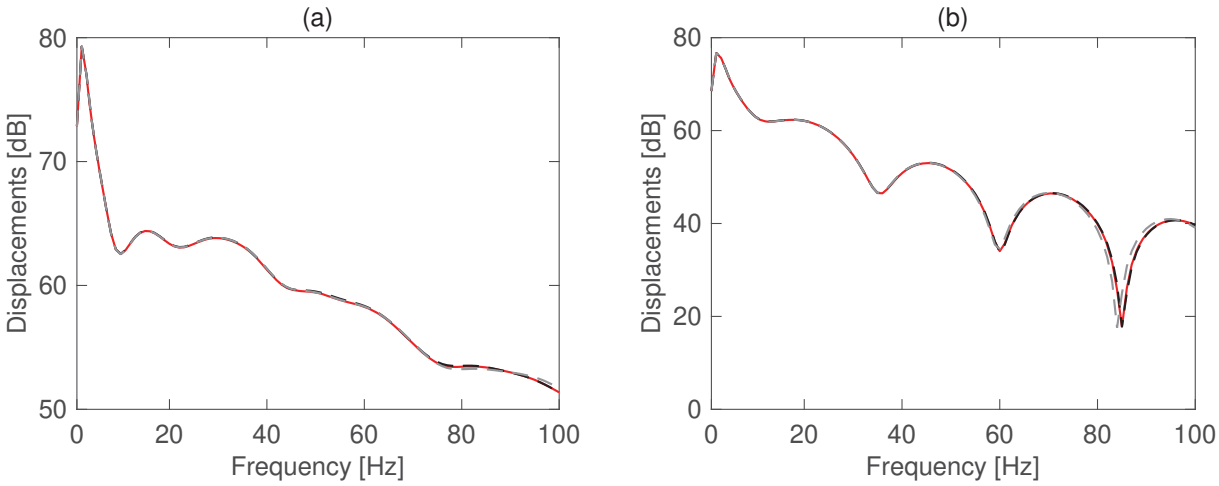

Figure 2: Vertical displacement Green's functions at evaluation points A (a) and B (b). Methods: 2.5D FEM-BEM (solid red line), 2.5D FEM-BEM-MFS (dashed black line) and semi-analytical solution (dashed gray line).

4 Verification of the method for the case of a tunnel embedded in a half-space

In this section, the methodology is verified against a 2.5D FEM-BEM approach, for two calculation examples: a tunnel embedded in a homogeneous half-space and a tunnel embedded in a layered half-space. In these examples, the comparison is done in terms of the displacement Green's function due to a vertical force applied in the bottom of the tunnel and for the wavenumber of 0.1 rad/m. The mechanical parameters of the soil and tunnel are presented in Table 2 and Table 3 for the homogeneous and layered half-space cases, respectively. In the example of a tunnel embedded in a layered half-space, the soil is divided into three layers.

Type	E [MPa]	ρ [kg/m^3]	ν	Damping
Tunnel	31000	2500	0.2	0.001
Medium	108	1800	$1/3$	0.05

Table 2: Mechanical parameters of the tunnel and the soil for the homogeneous half-space case.

Type	E [MPa]	ρ [kg/m^3]	ν	Thickness [m]	Damping
Tunnel	31000	2500	0.2	–	0.001
Soil layer 1	50	1900	0.3	4	0.05
Soil layer 2	180	1980	0.3	9	0.05
Soil layer 3	400	2050	0.3	∞	0.05

Table 3: Mechanical parameters of the tunnel and the soil for the layered half-space case.

4.1 A tunnel embedded in a homogeneous half-space

The application of the methodology for a tunnel embedded in a homogeneous half-space is studied. As shown in Fig. 3, a tunnel embedded in a homogeneous half-space at a depth of 9 m

from the ground surface is assumed. The external radius and the lining thickness of the tunnel are 3 m and 0.3 m, respectively. A single vertical point load is considered to be acting on the bottom surface of the tunnel. Two evaluation points, one on the near field (A), one in the far field (B) are assumed in the soil. The vertical displacements obtained by the proposed methodology are compared with those obtained by the 2.5D FEM-BEM approach. This comparison is shown in Fig. 4, where the left graph represents the vertical displacements in the point A and right figure denotes the vertical displacements at point B.

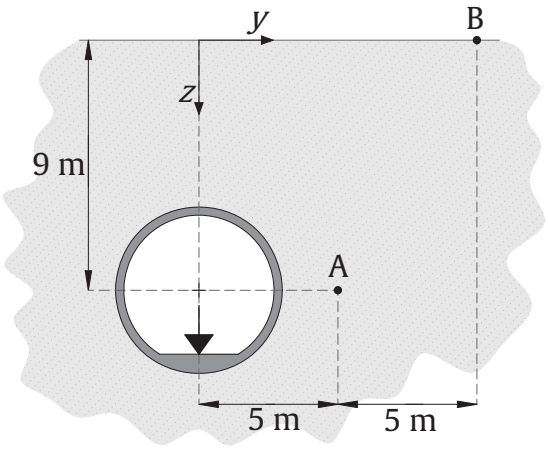

Figure 3: Geometry of the second system studied, based on a tunnel embedded in a homogeneous half-space. A and B represent the field points on the soil where the results will be obtained. The input vertical force is represented by a big arrow.

As presented in Fig. 4, the vertical displacements obtained by the 2.5D FEM-BEM-MFS are in a very good agreement with respect to those obtained with the 2.5D FEM-BEM approach.

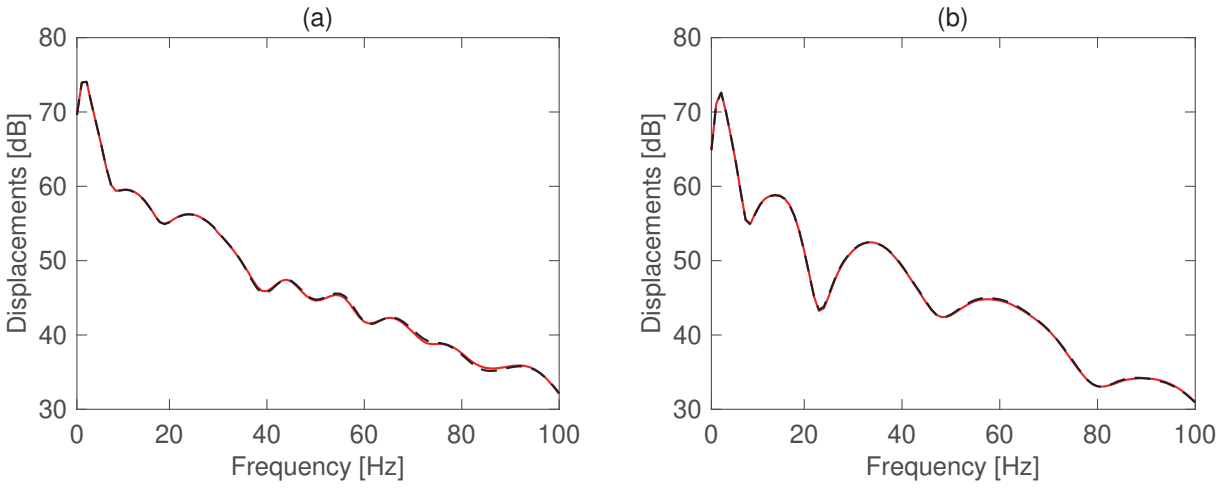

Figure 4: Vertical displacement Green's functions for the system in Fig. 3. Methods: 2.5D FEM-BEM (solid red line) and 2.5D FEM-BEM-MFS (dashed black line).

4.2 A tunnel embedded in a layered half-space

In order to investigate the performance of the method for a tunnel embedded in a layered half-space, another example is presented in this section. As can be observed in Fig. 5, a tunnel structure is located in the second layer and two field points are assumed in the soil (A and B). The geometry of the tunnel is the same as previous example.

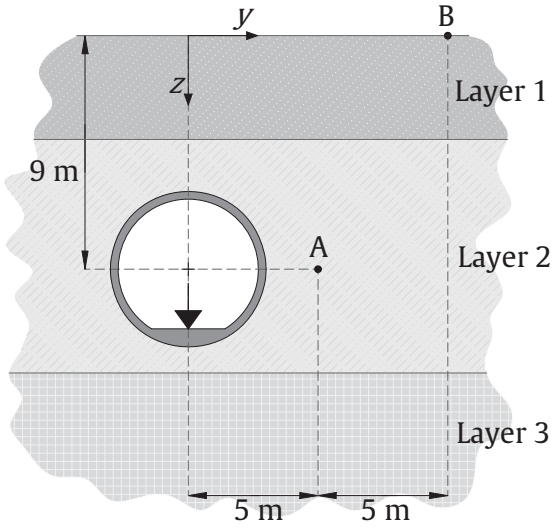

Figure 5: Geometry of the third system studied, based on a tunnel embedded in a layered half-space. A and B represent the field points on the soil where the results will be obtained. The input vertical force is represented by a big arrow.

The results confirms that the proposed methodology can be used for the case of layered half-space. Based on Fig. 6, the results of the current methodology are again consistent with the results of the 2.5D FEM-BEM approach. However, a slight difference can be observed at frequencies higher than 60 Hz for the point A.

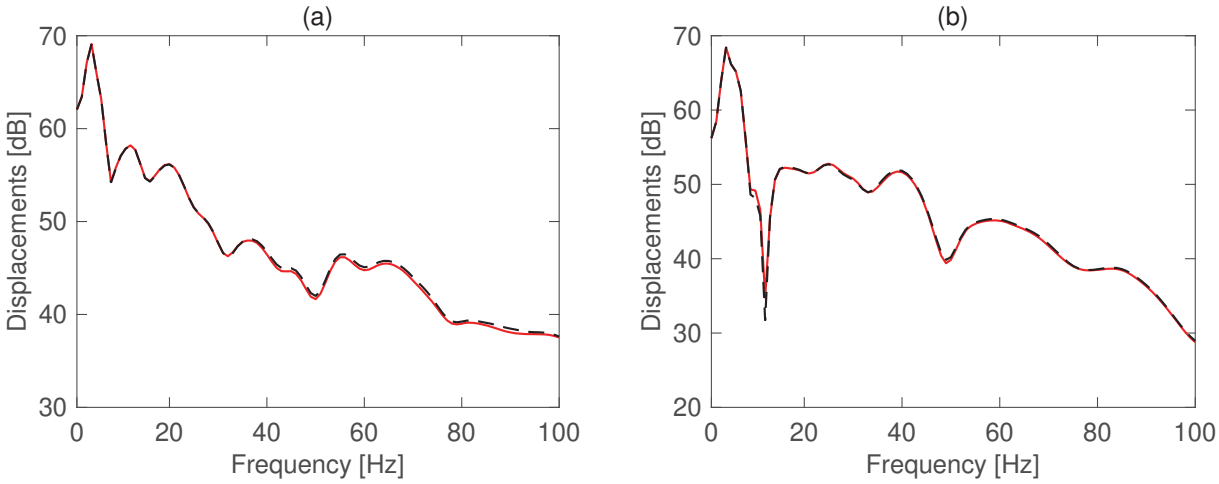

Figure 6: Vertical displacement Green's functions for the system in Fig. 5 at evaluation points A (a) and B (b). Methods: 2.5D FEM-BEM (solid red line) and 2.5D FEM-BEM-MFS (dashed black line).

5 CONCLUSIONS

In this study, a methodology is presented to deal with longitudinally invariant soil-structure interaction problems in elastodynamics. The methodology is firstly verified for the case of a solid cylinder embedded in a homogeneous half-space, having the structure and the soil the same mechanical parameters. Then, the performance of the model is investigated by presenting two calculation examples; a tunnel embedded in a homogeneous half-space and a tunnel embedded in a layered half-space. The results obtained for the three cases studied confirm that the accuracy of the new 2.5D FEM-BEM-MFS method is in agreement with those obtained by 2.5D FEM-BEM, especially in the far field results. Furthermore, the inclusion of the MFS as a post-processing tool has found to be very simple to be implemented. However, it is also found, as was expected, that the accuracy of the 2.5D FEM-BEM-MFS strongly depends on the accuracy of the boundary conditions obtained by 2.5D FEM-BEM method. Moreover, the displacement and traction Green's functions in the field points can be obtained in x, y and z directions. However, in this paper, only the vertical displacements are presented.

The accuracy of the results can be improved considerably by controlling the robustness of the method. To do so, a check point can be assumed in the domain and the distance between virtual sources and collocation points can be optimised by minimising the relative error between the current method and 2.5D FEM-BEM approach at this control point.

REFERENCES

[1] Amado-Mendes, P., Alves Costa, P., Godinho, L. M. C., Lopes, P., 2.5D MFS-FEM model for the prediction of vibrations due to underground railway traffic, *Engineering Structures*, **104**, 141–154, 2015.

[2] François, S., Schevenels, M., Galvín, P., Lombaert, G., Degrande, G., A 2.5D coupled FE–BE methodology for the dynamic interaction between longitudinally invariant structures and a layered halfspace, *Computer Methods in Applied Mechanics and Engineering*, **199**(23–24), 1536-1548, 2010.

[3] Tongaonkar, N. P., Jangid, R. S., Seismic response of isolated bridges with soil-structure interaction, *Soil Dynamics and Earthquake Engineering*, **23**(4), 287–302, 2003.

[4] Galvín, P., François, S., Schevenels, M., Bongini, E., Degrande, G., Lombaert, G., A 2.5D coupled FE-BE model for the prediction of railway induced vibrations, *Soil Dynamics and Earthquake Engineering*, **30**(12), 1500–1512, 2010.

[5] Lopes, P., Alves Costa, P., Ferraz M, Calçada, R. Cardoso, A. Silva., Numerical modeling of vibrations induced by railway traffic in tunnels: From the source to the nearby buildings, *Soil Dynamics and Earthquake Engineering* **61–62**, 269–285, 2014.

[6] Colaço, A., Alves Costa, P., Amado-Mendes, P., Godinho, L., Calçada, R., Mitigation of vibrations and re-radiated noise in buildings generated by railway traffic: A parametric study, *Procedia Engineering*, **199**, 2627–2632, 2017.

[7] Ghangale, D., Arcos, R., Clot, A., Cayero, J., Romeu, J., A methodology based on 2.5D FEM-BEM for the evaluation of the vibration energy flow radiated by underground railway infrastructures. *Tunnelling and Underground Space Technology*, 2020.

[8] Schevenels, M., François, S., Degrande, G., EDT: An ElastoDynamics Toolbox for MATLAB, *Computers and Geosciences*, **35**(8), 1752–1754, 2009.

[9] Alves, C. J. S., On the choice of source points in the method of fundamental solutions, *Engineering Analysis with Boundary Elements*, **33**(12), 1348–1361, 2009.

[10] Sun, Y., Marin, L., An invariant method of fundamental solutions for two-dimensional isotropic linear elasticity, *International Journal of Solids and Structures*, **117**, 191–207, 2017.

[11] Godinho, L., Amado-Mendes, P., Pereira, A., Soares, D., A coupled MFS-FEM model for 2-D dynamic soil-structure interaction in the frequency domain, *Computers and Structures*, **129**, 74–85, 2013.

EURODYN 2020
XI International Conference on Structural Dynamics
M. Papadrakakis, M. Fragiadakis, C. Papadimitriou (eds.)
Athens, Greece, 23–26 November 2020

A NEW SEMI-ANALYTICAL APPROACH FOR DYNAMIC PILE-SOIL INTERACTION PROBLEM

Kenny F. Conto[1], Robert Arcos[2], Cecília Parente[3], Pedro Alves Costa[4] and Jordi Romeu[1]

[1]Acoustical and Mechanical Engineering Laboratory (LEAM), Universitat Politècnica de Catalunya (UPC)
Carrer Colom, 11, 08222 Terrassa (Barcelona), Spain
e-mail: kenny.fernando.conto,jordi.romeu.upc@upc.edu

[2]Serra Húnter Fellow, Acoustical and Mechanical Engineering Laboratory (LEAM), Universitat Politècnica de Catalunya (UPC)
Carrer Colom, 11, 08222 Terrassa (Barcelona), Spain
e-mail: robert.arcos@upc.edu

[3]Mota-Engil Engenharia e Construção, S.A.
Rua do Rego Lameiro, 38, 4300-454 Porto, Portugal
e-mail: cparente@fe.up.pt

[4]CONSTRUCT, Faculty of Engineering (FEUP), University of Porto
Rua Dr. Roberto Frias, s/n 4200-465 Porto, Portugal
e-mail: pacosta@fe.up.pt

Keywords: Dynamic pile-soil interaction, Pile foundations, substructuring method.

Abstract. *This paper proposes a new semi-analytical approach for the computation of the dynamic response of a pile embedded in a half-space when it is subjected to a vertical harmonic load applied at the pile head or to loading from an incident wave field. The proposed approach considers the soil as an elastic half-space medium. In order to capture all essential dynamic behaviour of the pile-soil interaction avoiding large computational efforts, the system is modelled using the substructuring method in which the displacements and forces in a set of uniformly distributed points along the pile shaft are compatibilized with another set of coupling points in the soil also uniformly distributed along the virtual interaction area between the pile and the soil. The paper aims to study the accuracy and computational efficiency of this approach in comparison with two other methodologies: a numerical approach based on axisymmetric finite elements and perfect-matched layers, and against the approximate analytical approach based on linear elasticity developed by Novak. These comparisons reveal that the dynamic response for driving-point, far-field or incident wave-field problems can be predicted with acceptable accuracy and computational efficiency when the number of interaction points in the system increases.*

1 INTRODUCTION

Ground-borne vibration is an important cause of annoyance to nearby buildings inhabitants, malfunction on precision devices in surrounding facilities or even structural damage. These negative effects occurs when the ground-borne vibration incident wave-field excites the building structure through its foundations, being piled foundations one of the most common types. There are different models used to study the dynamic response of a single pile embedded in a half-space, which can be classified into three broad groups [6]. First group is based on the dynamic Winkler foundation approach, attributed as earliest building foundations dynamic models. In that method, the soil medium is modelled by infinitesimally, thin, independent, horizontal layers, meaning that waves can be only propagated in horizontal direction. This approach is adopted in the Novak's benchmark research [10], where the dynamic response of single piles is found throughout an Euler-Bernoulli beam and axial rod models of the pile for the lateral and vertical responses, respectively, which include the soil reaction directly in their differential equations of motion. The second type of methods are based on modelling the soil as an elastic medium. They are proposed to account for wave propagation in the soil in all directions. A relevant model of this method was presented by Kaynia and Kausel [3], where a general formulation for the prediction of the dynamic response of single piles and pile groups embedded in a layered half-space is presented. In this method the soil is also modelled as an elastic half-space while the piles are modelled as Euler-Bernoulli beams and axial rods. Furthermore, forces and displacements of each substructure (soil and pile) are compatibilised in a set of coupling points in order to compute the response of the system. These coupling points are defined when the whole traction acting on the virtual soil-pile interface is segmented along the pile shaft. Where, each segment is identified by a node and placed in its center. Therefore, each node represents either the load acting on the lateral surface of the pile (called barrel load distribution), or the load which is related to the pile-tip surface (called disk load distribution). Recently, the PiP model developed by Forrest [2] was adapted by Kuo et al. [7, 8] in order to create a three-dimensional single-pile dynamic model, which is formulated in the wavenumber domain and uses mirror-image sources to simulate a half-space and the finite length of the piles. Ntotsios et al. [11] developed two methods for the dynamic response of piled foundations where the approach for the coupling technique is similar to the one proposed by Kaynia in [3]. Euler beam and axial rod formulations are again used to model the pile. The dynamic compatibility between the pile and the soil is performed by distributing the displacements and forces in discrete points along the pile shaft over an annulus on the soil, with mean radius equal to the pile radius and a thickness of one-tenth of that, except for the pile-tip, where the distribution is done over a circular disk with the same radius than the pile. On their first method, the response of the soil is computed using the thin layer method (TLM), while in the second approach, the boundary element method (BEM) is used to model the soil medium with the pile cavity. Finally, numerical approaches are also an interesting modelling option for piled foundations. With the finite element method (FEM) [5, 4], the non-linear behaviour of the soil and its interaction with the pile can be introduced. However, the computation of FEM models requires large computational efforts, mostly when high frequency analysis is performed. Furthermore, the FEM applied to wave propagation problems in the soil requires the implementation of energy-absorbing boundaries to simulate an unbounded medium [1]. The BEM is another alternative to be used for this type of problems in order to model the soil, where the use of energy-absorbing boundaries is not required.

In some piled foundation problems where only the pile-driving response is required, the Winkler foundation approach could be enough to compute the dynamic response. When the soil

response is required or when the coupled response between piles is desired to be computed, the low accuracy of this method for these problems releases the numerical approach as the most suitable method to compute the dynamic response without decreasing accuracy. However, the usage of these methods is usually complex and they inherently have high computational requirements. For these reasons, the aim of this paper is presenting a new semi-analytical approach for the computation of the dynamic response of a single pile embedded in a half-space when it is subjected to a vertical harmonic load applied at the pile head or to the action of an incident wave-field. The benefits are its computational efficiency keeping high accuracy levels and the simplicity of its implementation in a computer algorithm, becoming a suitable tool for design use by practising engineers.

2 SINGLE PILE-SOIL MODEL

The current section starts describing the assumptions adopted in the present work. Then, the resulting formulation of the pile-soil model presented here is described. This pile-soil model is mainly constructed using dynamic substructuring techniques. Thus, the dynamic behaviour of each substructure (the pile and the soil) is analysed separately to be later assembled using a coupling procedure. The assumptions followed here are:

- The pile is assumed to be perfectly elastic and it is modelled as a structural column member for the axial response. Lateral motion is not considered in the present work.
- The soil is considered to be a perfectly elastic homogeneous half-space.
- The non-linear effects associated to the soil-pile contact interaction, high strain levels or liquefaction of the soil are neglected.
- The coupling of sub-systems is performed in the basis of equilibrium of forces and compatibility of displacement conditions.

Fig. 1 illustrates the system of a single piled foundation embedded in a homogeneous half-space, which is the problem considered in this study. The system is subjected to a external time-harmonic vertical point load applied either at the pile head or on the soil. In the framework

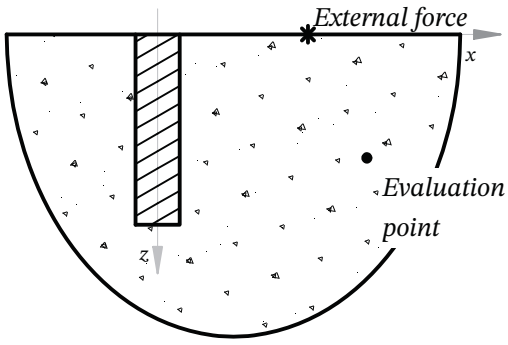

Figure 1: Single pile model.

of dynamic substructuring, the coupling between the pile and the soil is proposed to be done in a set of uniformly distributed coupling points. To do so, the soil-pile interaction traction,

distributed along the the soil-pile interface, is divided into $N+1$ segments (see Fig. 2a) and each of these segments is identified by its corresponding node, placed at the centre of each segment, at the pile shaft. First N nodes are related to the segments of traction acting on the lateral soil-pile surface (barrel loads, see Fig. 2b) while the segment associated to the node $N+1$ refers to the traction acting on the pile-tip (disk load, see Fig. 2c). Therefore, soil-pile interaction will be performed at those points, called coupling points, in where the force equilibrium and compatibility of displacement conditions are complied. The resulting compatibility equations are:

$$\mathbf{P}_p^c + \mathbf{P}_s^c = 0, \tag{1a}$$

$$\mathbf{U}_p^c = \mathbf{U}_s^c. \tag{1b}$$

where

$$\mathbf{P}_p^c = \begin{bmatrix} P_p^{c_1} & P_p^{c_2} & \dots & P_p^{c_{N+1}} \end{bmatrix}^{\mathrm{T}}, \tag{2a}$$

$$\mathbf{P}_s^c = \begin{bmatrix} P_s^{c_1} & P_s^{c_2} & \dots & P_s^{c_{N+1}} \end{bmatrix}^{\mathrm{T}}, \tag{2b}$$

$$\mathbf{U}_p^c = \begin{bmatrix} U_p^{c_1} & U_p^{c_2} & \dots & U_p^{c_{N+1}} \end{bmatrix}^{\mathrm{T}}, \tag{2c}$$

$$\mathbf{U}_s^c = \begin{bmatrix} U_s^{c_1} & U_s^{c_2} & \dots & U_s^{c_{N+1}} \end{bmatrix}^{\mathrm{T}}. \tag{2d}$$

The subscripts described in equations of the current section are referred to the corresponding substructure of the system (s, soil or p, pile). Coupling points, evaluation point or external force are referred by the superscripts c, e and f, respectively. Thus, in Eq. (1), $\mathbf{P}_p^c$ and $\mathbf{P}_s^c$ represent the vectors of vertical interaction forces acting on the pile and the soil, respectively (Eq. (2a),(2b)), while, $\mathbf{U}_p^c$ and $\mathbf{U}_s^c$ are referred to the vector of vertical displacements at the coupling points of the pile and soil, respectively (Eq. (2c),(2d)).

2.1 Response due to an external force applied in the pile head

Based on the dynamic system presented in the previous section, the displacements at the coupling points when the system is excited by an external vertical force applied in the pile head can be written as

$$\mathbf{U}_p^c = \mathbf{H}_p^{cf} F_p + \mathbf{H}_p^c \mathbf{P}_p^c, \tag{3a}$$

$$\mathbf{U}_s^c = \mathbf{H}_s^c \mathbf{P}_s^c, \tag{3b}$$

where the $\mathbf{H}_p^c$ and $\mathbf{H}_s^c$ represents the receptance matrices of the pile and the soil, respectively, at the coupling points, having a dimension of $(N+1) \times (N+1)$. The vector $\mathbf{H}_p^{cf}$ represent the receptance of the coupling points due to the external force F_p, which is applied at the pile head. Thus, the interaction forces at the coupling points in the pile can be obtained combining Eq. (3) with Eq. (1), that is

$$\mathbf{P}_p^c = -(\mathbf{H}_p^c + \mathbf{H}_s^c)^{-1} \mathbf{H}_p^{cf} F_p. \tag{4}$$

Finally, if the dynamic response of the system is required at the pile head, its driving-point response U_p is expressed by Eq. (5a), while if the evaluation points is placed on the soil, then its responses U_s is defined by Eq. (5b).

$$U_p = \mathbf{H}_p^{ec} \mathbf{P}_p^c + H_p^{ef} F_p, \tag{5a}$$

$$U_s = -\mathbf{H}_s^{ec} \mathbf{P}_p^c, \tag{5b}$$

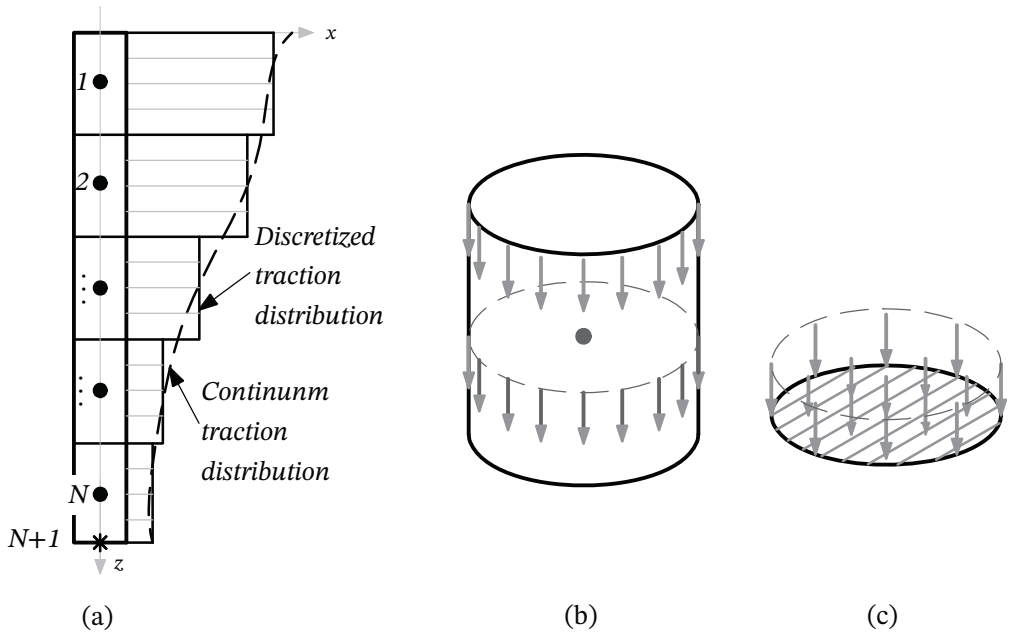

Figure 2: Discretisation of the pile-soil interaction traction (a), where segment from 1 to N represent to barrel type loads (black dots representing the coupling points) while the last segment $N+1$ depicts the disk type load (coupling point represented by star dot). Continuum barrel traction for the firsts N segments (b). Continuum disk traction for the last segment $N+1$ (c).

where $\mathbf{H}_p^{ec}$ and $\mathbf{H}_s^{ec}$ refers to the vector of receptances relating the response in the evaluation point, placed at the pile head or at the soil, respectively, due to the interaction forces $\mathbf{P}_p^c$, while the H_p^{ef} is the receptance of the evaluation point due to the external force F_p applied in the pile.

2.2 Response due to an external force applied in the soil

In the previous section, the system was subjected to an external force placed at the pile head. In the current section, the response of the pile to an incident wave-field due to an external vertical point load in the soil is formulated. In this case, the displacements in the coupling points in the point of view of the pile and the soil are

$$\mathbf{U}_p^c = \mathbf{H}_p^c \mathbf{P}_p^c, \tag{6a}$$

$$\mathbf{U}_s^c = \mathbf{H}_s^{cf} F_s + \mathbf{H}_s^c \mathbf{P}_s^c, \tag{6b}$$

respectively, being F_s the force applied on the soil and $\mathbf{H}_s^{cf}$ the receptance matrix that relates the displacement at the coupling points with the applied external force. Therefore, the corresponding interaction forces of the system are equal to:

$$\mathbf{P}_p^c = (\mathbf{H}_p^c + \mathbf{H}_s^c)^{-1} \mathbf{H}_s^{cf} F_s. \tag{7}$$

Thus, the dynamic response of the pile at the pile head U_p under an incident wave-field produced by F_s is given by:

$$U_p = \mathbf{H}_p^{ec} \mathbf{P}_p^c. \tag{8}$$

2.3 Soil receptance matrices

In order to compute the soil receptance matrices appearing in the previous sections, the soil-pile interaction traction in the point of view of the soil is discretised in a set of N_s uniformly

distributed points placed along the virtual pile perimeter for each pile segment, as shown in Fig. 3. This can be seen as a discretised form of the method proposed by Kaynia and Kausel [3]. The corresponding receptance matrix associated to all these points $\mathbf{H}_{sg}^{c}$ of $M \times M$ dimensions,

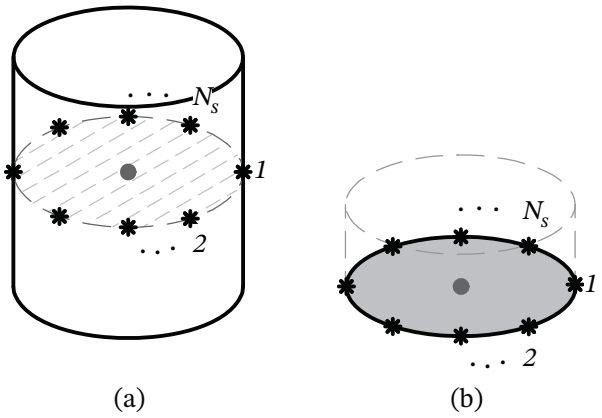

Figure 3: Traction segment discretised into N_s points for a: a) barrel type traction element. b) disk type traction element.

being $M = (N+1)N_s$, can be condensed into $\mathbf{H}_{s}^{c}$ by the expression:

$$\mathbf{H}_{s}^{c} = \mathbf{W}_d \mathbf{H}_{sg}^{c} \mathbf{W}_f \tag{9}$$

where $\mathbf{W}_d$ is the matrix which condense all N_s displacement values of each segment into a corresponding equivalent displacement. The matrix $\mathbf{W}_f$ applies the same concept for the case of the interaction forces. In both cases, this research is developed assuming a uniform distribution. Similarly, when an external force is applied in the soil, this procedure can be extended to compute the soil receptance matrix $\mathbf{H}_{s}^{cf}$. Finally, The Green's functions of the soil required to construct $\mathbf{H}_{sg}^{c}$ and the remaining soil receptances are computed using the ElastoDynamics Toolbox for MATLAB [12], which uses the direct stiffness matrix method to deal with wave propagation problems in horizontally layered media.

2.4 Pile receptance matrices

The receptance matrices related to the pile can be found assuming that the pile can be modelled as a simple rod structural member. Thus, the differential equation for the axial vibration of the pile in the time domain is described as

$$m_p \frac{\partial^2 u_z}{\partial t^2} - E_p A_p \frac{\partial^2 u_z}{\partial z^2} = 0. \tag{10}$$

In Eq. (10), the mass per unit of length is defined by m_p, while A_p and E_p are the cross-section area and the elastic modulus of the pile, respectively. Therefore, if an external force F_z is applied at the pile in some position z_1 of its shaft, the solution of Eq. (10) in the frequency domain for free-free rod is given by

$$\frac{U_z(z)}{F_z} = -\frac{\cos(\alpha z)[\cos(\alpha z_1) + \sin(\alpha z_1)\tan(\alpha L)]}{E_p A_p \alpha \tan(\alpha L)} \qquad 0 \quad \leq z \leq z_1, \tag{11a}$$

$$\frac{U_z(z)}{F_z} = -\frac{\cos(\alpha z_1)\cos(\alpha z)}{E_p A_p \alpha \tan(\alpha L)} - \frac{\cos(\alpha z_1)\sin(\alpha z)}{E_p A_p \alpha} \qquad z_1 \leq z \leq L, , \tag{11b}$$

$$\alpha = \frac{m_p \omega^2}{A_p E_p}, \tag{12}$$

in where L is the total length of the pile and ω is the circular frequency in which the dynamic analysis is performed.

3 COMPARISON OF THE MODEL

In this section, the accuracy of the new semi-analytical approach is analysed in order to demonstrate its applicability in different pile problems. The methods presented for the comparison are the new semi-analytical approach, the extended Novak approach [10] proposed by Kuo [7, 8] and an axisymmetric FEM-based approach with perfect matched layers (aFEM-PML). The aFEM-PML is based on an axissymmetric version of the method presented by [9] considering eight-noded square elements of 25 cm of side. In the extended Novak approach, the approximate far-field response using the Novak approach is obtained by the assumption that only cylindrical SV-waves can spread from the pile through the soil and just in radial direction [7, 8]. The parameters used to compute the results are as following: the pile has a length of $L = 20$ m and radius $r_p = 0.354$ m and it is made of concrete with density $\rho_p = 2800$ kg/m^3, Young's modulus $E_p = 40$ GPa, Poisson's ratio $\nu_p = 0.3$ and hysteretic damping ratio $\beta = 0.01$; while the soil is modelled as a homogeneous half-space elastic medium with density $\rho_s = 2250$ kg/m^3, shear modulus $G_s = 90$ MPa, Poisson's ratio $\nu_s = 0.4$ and hysteretic damping ratios for S- and P-waves equals to $D_s = 0.03$, $D_p = 0.03$, respectively. Furthermore, the range of frequency considered to perform the comparison is from 1 Hz to 80 Hz.

Plots in Fig. 4 show the driving-point response of the pile head. These responses are computed using different values of N and N_s and the results are compared with the outcomes from the Novak method. In this figure, a poor agreement in the response is observed when the pile has $N = 5$ coupling points, as shown in Fig. 4a, where the difference between the two methods rise until 11 dB over the frequency range of 80 Hz. Likewise, if the the number of coupling points is increased to $N = 10$ or $N = 15$ (see Fig. 4b and Fig. 4c) the response of the system presents a good agreement respect to results obtained by the Novak method (less of 2dB of variation) furthermore, the response computed by the current approach shows a smooth curve for the whole range of frequency. Finally, high accuracy is achieved (0.6 dB of variation) when the new semi-analytical method is applied with $N = 25$ coupling points, see Fig. 4d. This can be also seen in Fig. 5a, where the results obtained with the aFEM-PML method are also added in the comparison.

In Fig. 5, the new method is compared with the Novak and the aFEM-PML methods in terms of the response at the soil due to the action of a vertical harmonic force at the pile head. The response in the soil has been computed at the ground surface and at distances of 5 m, 10 m and 20 m from the pile shaft. For this comparison, the new method is applied assuming $N = 25$ and $N_s = 4$. It is observed that the Novak method shows large discrepancies with respect to the aFEM-PML model, mostly at large distances from the pile. That is due to the assumption adopted by Novak in his model and the consequent inaccuracy of the wave-spreading equations [7] in where the wave propagation in the soil due to the axial pile action is assumed to be based only on SV-waves. By other hand, the new semi-analytical model shows less than 2 dB, 1.5 dB and 1 dB of variations in comparison with the aFEM-PML method when the evaluation point and the pile shaft are at a distance of 5 m, 10 m, and 20 m, respectively. This shows that the agreement in the results for axial vibrations is good in the whole frequency range of interest.

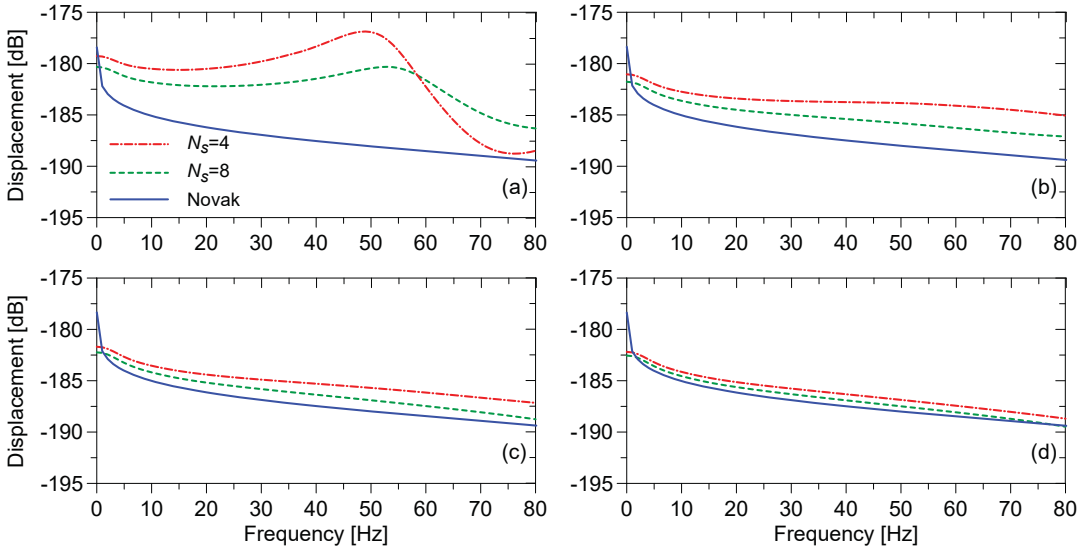

Figure 4: Driving-point response in dB (with a reference of 1 m/N). Cases: $N = 5$ (a), $N = 10$ (b), $N = 15$ (c) and $N = 25$ (d) coupling points.

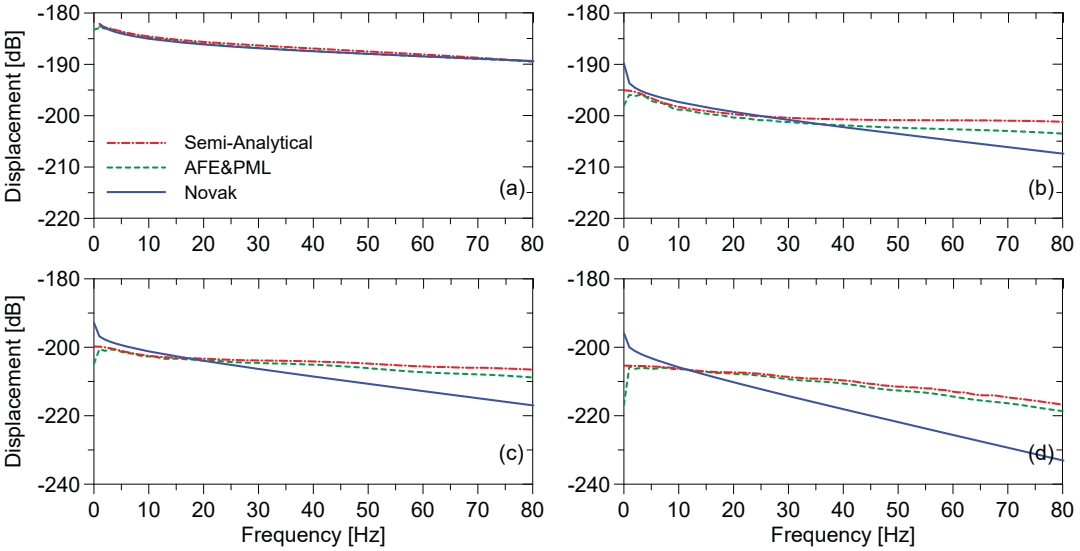

Figure 5: Displacement response in dB (with a reference of 1 m/N) due to an external force applied at the pile head considering with $N = 25$ and $N_s = 4$ for the semi-analytical approach. Cases: Driving-point response (a); response at 5 m (b); response at 10 m (c); and response at 20 m (d).

4 CONCLUSIONS

In this paper, a new semi-analytical modelling approach for the dynamic response of a single pile embedded in a half-space is presented. This new semi-analytical model captures the driving-point response of the pile reasonably well, with some differences at high frequencies (less than 1.5 dB) when the results obtained are compared against the Novak's method [10]. That agreement is obtained when the number of coupling points is equal to 25 and when the number of points used to discretise the traction distribution of each segment is eight. If the number of coupling points is less than 25, the differences in the dynamic response are high for the whole range of frequency.

When the response of the soil due to a force in the pile is required, the results obtained with the new approach present a good agreement in comparison with the aFEM-PML model. The aFEM-PML is an accurate numerical model that requires considerable computational costs, while the new approach is able to reach similar levels of accuracy using quite less resources and time, due to its semi-analytical nature. Novak method, in contrast, is showing a poor agreement with respect to the aFEM-PML method, an expected result due to simplifications on soil modelling inherent to the Novak's method. It can be concluded, then, that the new proposed semi-analytical method can provide accurate results on the soil response, being this feature of the method a significant benefit with respect to Novak's method.

ACKNOWLEDGEMENTS

This research has been carried out with the financial support of three research projects:

- Project VIBWAY: Fast computational tool for railway-induced vibrations and re-radiated noise assessment, with reference RTI2018-096819-B-I00, supported by the Ministerio de Ciencia e Innovación, Retos de Investigación 2018.

- Project NVTRail: Noise and Vibrations induced by railway traffic in tunnels: an integrated approach, funded by FEDER funds through COMPETE2020 (Programa Operacional Competitividade e Internacionalizacão (POCI)) and by national funds (PIDDAC) through FCT/MCTES, with grant reference POCI-01-0145-FEDER-029577.

- Project POCI-01-0145-FEDER-029634 funded by FEDER funds through COMPETE2020 Programa Operacional Competitividade e Internacionalizao (POCI) and by national funds (PIDDAC) through FCT/MCTES.

- The author would like to thank PRONABEC (`www.pronabec.gob.pe`) for the financial support given through the scholarship: "Beca Presidente de la Repblica"

REFERENCES

[1] A. J. Deeks and M. F. Randolph. Axisymmetric time-domain transmittings boundaries. *Journal of Engineering Mechanics*, 120(1):25–42, 1994.

[2] J. A. Forrest and H. E. M. Hunt. A three-dimensional tunnel model for calculation of train-induced ground vibration. *Journal of Sound and Vibration*, 294(4-5):678–705, jul 2006.

[3] A. M. Kaynia and E. Kausel. Dynamics of piles and pile groups in layered soil media. *Soil Dynamics and Earthquake Engineering*, 10(8):386–401, 1991.

[4] R. Kuhlemeyer. Static and dynamic laterally loaded floating piles. *Journal of the Geotechnical Engineering Division, Proceedings of the American Society of Civil Engineers*, 105(GT2):289–304, 1979.

[5] R. Kuhlemeyer. Vertical vibration of piles. *Journal of the Geotechnical Engineering Division, Proceedings of the American Society of Civil Engineers*, 105(GT2):273–287, 1979.

[6] K. Kuo and H. Hunt. Dynamic models of piled foundations. *Applied Mechanics Reviews*, 65(May 2013):9, 2013.

[7] K. A. Kuo. *Vibration from underground railways: considering piled foundations and twin tunnels*. PhD thesis, University of Cambridge, 2010.

[8] K. A. Kuo and H. E. M. Hunt. An efficient model for the dynamic behaviour of a single pile in viscoelastic soil. *Journal of Sound and Vibration*, 332(10):2549–2561, may 2013.

[9] P. Lopes, P. A. Costa, M. Ferraz, R. Calçada, and A. S. Cardoso. Numerical modeling of vibrations induced by railway traffic in tunnels: From the source to the nearby buildings. *Soil Dynamics and Earthquake Engineering*, 61-62:269–285, jun 2014.

[10] M. Novak. Dynamic stiffness and damping of piles. *Canadian Geotechnical Journal*, 11(4):574–598, 1974.

[11] E. Ntotsios, W. I. Hamad, D. J. Thompson, M. F. M. Hussein, H. E. M. Hunt, and J. P. Talbot. Predictions of the dynamic response of piled foundations in a multi-layered half-space due to inertial and railway induced loadings. In *5th ECCOMAS Thematic Conference on Computational Methods in Structural Dynamics and Earthquake Engineering*, 2015.

[12] M. Schevenels, S. François, and G. Degrande. EDT: An ElastoDynamics Toolbox for MATLAB. *Computers and Geosciences*, 35(8):1752–1754, 2009.

EURODYN 2020
XI International Conference on Structural Dynamics
M. Papadrakakis, M. Fragiadakis, C. Papadimitriou (eds.)
Athens, Greece, 23–26 November 2020

STRUCTURE-SOIL-STRUCTURE INTERACTION ANALYSIS FOR REINFORCED CONCRETE FRAMED STRUCTURES

Reine Fares[1*], Maria Paola Santisi d'Avila[2], Anne Deschamps[3] , Evelyne Foerster[1]

[1] DES-SEMT, CEA, Université Paris-Saclay
F-91191, Gif-sur-Yvette, France
{reine.fares, evelyne.foerster}@cea.fr

[2] Université Cote d'Azur, Polytech'Lab, UPR 7498
06410 Biot, France
msantisi@unice.fr

[3] Université Côte d'Azur, CNRS, IRD, OCA
06560 Valbonne, France
anne.deschamps@univ-cotedazur.fr

Keywords: Structure-soil-structure interaction, seismic wave propagation, 3D finite element model.

Abstract. *The seismic response of buildings is generally obtained by modeling structures as isolated from surroundings. However, the structural vibration contributes through the soil to the excitation of adjacent structures and vise-versa. In this research, the structure-soil-structure interaction (SSSI) is studied questioning the influence of an adjacent construction, whose interference passes through the soil. Beneficial and detrimental cases are distinguished.*

The one-directional three-component wave propagation in a T-shaped soil profile (1DT-3C) is adopted as modeling technique to explore the effects of coupling seismic site effects, due to the local soil stratigraphy, with the SSSI, taking into account the foundation deformability and rocking. A three-dimensional model of each structure is adopted to estimate the seismic response taking into account the different mode shapes. This approach allows an easy analysis of SSSI to inspire the design of seismic risk mitigation tools and urban organization.

The seismic response of a reinforced concrete framed structure is numerically simulated by accounting for the effect of an adjacent structure in the linear elastic regime, in both cases of seismic loading exciting the target structure or the adjacent structure. The target to adjacent structure fundamental frequency ratio, is adopted as a key parameter influencing the SSSI phenomenon. In some cases, the effect of the adjacent structure resonance is more detrimental to the target structure than its own resonance as a single building. In other cases, a beneficial effect is obtained by the presence of the adjacent structure. The obtained results can be extended to understand the effect of an adjacent vibration control device.

1 INTRODUCTION

Nowadays, constructions tend to be built more closely to save space especially in big cities, although building codes still consider purely isolated structures in the design phase.

Structure-soil-structure interaction (SSSI) investigations to understand the effect of a nearby building have been undertaken by Luco and Contesse [1] using a two-dimensional analytical model. The effects of an existing second structure are more important for the case of a stiffer structure located close to a more deformable one. In particular, in case of resonance of the stiffer structure, its seismic base motion is significantly different from the one obtained when ignoring the 2nd nearby more deformable structure.

Warburton et al. [2] have found, through an analytical study, that the unexcited mass affects only slightly the response of the excited mass. On the other hand, the unexcited mass is largely influenced by the excited mass even for significant inter-distance. When the adjacent mass has no more influence (increasing inter-distance), the soil-structure interaction (SSI) increases with decreasing soil frequency.

A parametric numerical analysis undertaken by Aldaikh et al. [3], for three adjacent oscillators coupled through the soil, showed that there are detrimental and beneficial configurations of dynamic characteristics of buildings adjacent to the building under consideration. The authors considered that a central building is much more influenced by two adjacent buildings than when there is only one adjacent building. Regardless of the earthquake event features, the interaction generally amplifies the seismic energy seen by a building with two adjacent taller buildings. On the other hand, the effect of two adjacent slightly lower buildings was beneficial in their study.

Mizuno [4] has experimentally observed the SSSI with the consequent variation and possible increase of the structural response caused by the radiation waves from a nearby structure. Moreover, the excitation of a nearby structure induces energy dissipation. Under ambient vibration, the response of the building having low fundamental mode becomes larger than that of a single building, while the response of the building having high natural modes has an opposite trend.

Trombetta et al. [5] investigate the SSSI by centrifuge tests. During strong shaking, SSSI is found to be less significant; this could be due to a combination of superstructure yielding and saturation of footing forces. Consequently, from a design perspective, the results suggest that SSSI effects should be considered for low-to-moderate levels of earthquake shaking.

Nateghi and Rezaei-Tabrizi [6] use a two-dimensional FE model to study the nonlinear dynamic response of two adjacent tall framed buildings. When the soil and structure fundamental modes are close, the interaction between adjacent structures increase the nonlinear response, so it cannot be neglected.

According to Vicencio and Alexander [7], SSSI effects increase when considering loose soil and closely spaced buildings. The most adverse effects on building displacement occur when there is a big difference of height between the adjacent buildings. Moreover, soil nonlinearity can modify SSSI effects in adverse or beneficial way, so it should be accounted for. The nonlinear SSSI response acceleration is amplified for the case of a lower building flanked by a taller one; a beneficial effect can occur for the taller building but this reduction is not assured for the entire range of aspect ratios.

Exploiting SSSI, a device called vibration barrier (ViBa) behaving as an oscillator is proposed by Cacciola et al. [8]. The ViBa is able to reduce the seismic energy on its neighborhood structures and their seismic response. Tombari et al. [9] shows a reduced structural seismic response using a ViBa buried in the soil.

In this research, a parametric analysis is carried out to investigate the interference of an adjacent structure (AS) in the seismic response of a target structure (TS). The modeling technique proposed by Fares et al. [10] is adopted, consisting of a one-directional three-component seismic wave propagation in a T-shaped soil domain (1DT-3C).

2 1DT-3C WAVE PROPAGATION MODEL FOR SSSI

The soil basin is assumed as horizontally layered and infinitely extended. Shear and pressure waves propagate vertically from the top of the underlying elastic bedrock to the soil surface. The one-directional propagation of a three-component seismic wave in a T-shaped soil domain, assembled to one or more 3D building, is modeled in a finite element (FE) scheme, as proposed by Fares et al. [10]. A fully 3D soil domain is modeled until a fixed depth h, where SSI is not negligible. A one-dimensional model is then used for deeper layers, until the underlying elastic bedrock, represented by dashpots.

The soil domain area A is selected as the smallest for which the peak of the building base to bedrock transfer function corresponds to the soil column fundamental frequency in the free-field case (Santisi d'Avila and Lopez-Caballero [11]). Depth h is defined by a preliminary analysis defining the variation in stresses and strains in the soil due to SSI, compared with the free-field case (Fares et al. [10]). A constraint equation is assigned to condense out the degrees of freedom at the base of the 3D soil domain to those at the top of the unit area soil column. No strain variation is considered in the horizontal directions and, for this reason, a periodic lateral boundary condition is imposed at the lateral boundary surfaces.

The 3D frame structure is modeled using Timoshenko beam elements. The building shallow foundation is rigidly connected to the soil, node-by-node. The rotational degrees of freedom of nodes at the base of building columns are blocked. The damping due to structural and non-structural elements is taken into account by the damping submatrix related to the building that is assumed as mass and stiffness proportional, according to Rayleigh approach [12].

The discrete dynamic equilibrium equation is solved directly for the assembly of soil-foundations-structures (Figure 1). The dynamic process is solved step-by-step by the implicit Hilber-Hughes-Taylor algorithm [13]. Numerical damping is provided by the α-method using the parameters $\alpha = -0.1$, $\beta = 0.25(1-\alpha)^2 = 0.3025$ and $\gamma = 0.5 - \alpha = 0.6$ that guarantee an unconditionally numerical stability. The time step is automatically selected in the range between 10^{-4} s and the time step used for the input signal sampling. More details about the model are given by Fares et al. [10].

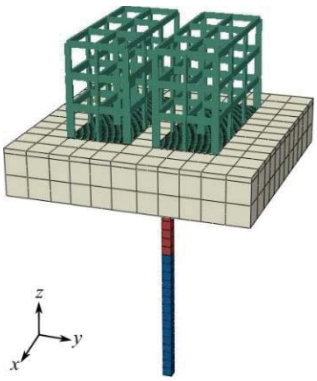

Figure 1: 1DT-3C model for structure-soil-structure interaction analysis.

3 INPUT DATA

A parametric analysis is carried out to study the influence of an AS on the dynamic response of a TS for various target to adjacent structure frequency ratio f_{TS}/f_{AS}, in linear elastic regime.

3.1 Soil profiles

Two soil profiles are used for the analysis, whose stratigraphy and mechanical parameters are given in Table 1. The profile shear velocity v_s is selected to obtain ground types C and D according to the Eurocode 8 classification [14]. The density ρ and the compressional wave velocity v_p are calculated according the relationships proposed by Boore [15]. Soil properties are assumed constant in each soil layer.

A squared soil area $A = 25\ \text{m} \times 25\ \text{m}$ is selected. A 3D soil domain is modeled until a depth $h = 5\ m$, that corresponds to the interface between the first and second soil layer, and a 1D model is used in deeper soil layers.

		Profile C $v_{s30} = 225\ \text{m/s}$, $f_s = 2.0\ \text{Hz}$			**Profile D** $v_{s30} = 173\ \text{m/s}$, $f_s = 1.5\ \text{Hz}$		
Depth	**Thickness**	**ρ**	**v_s**	**v_p**	**ρ**	**v_s**	**v_p**
m	m	kg/m^3	m/s	m/s	kg/m^3	m/s	m/s
5	5	1930	180	1293	1930	160	1256
15	10	1930	210	1347	1930	170	1275
30	15	1930	250	1417	1930	180	1293
>30		2100	1000	2449	2100	1000	2449

Table 1: Stratigraphy and mechanical properties of the analyzed soil profiles.

3.2 Reinforced concrete framed buildings

Five 3D framed structures are modeled. The number of stories is determined in order to obtain various building fundamental frequencies (Table 2). The floor area is defined arbitrarily because it has a negligible influence on the building fundamental frequency.

The column orientation and the floor plan dimensions are indicated in Figure 2. The structural elements size is given in Table 3. The load (sum of dead and live ones) is $700\ \text{kg/m}^2$. It is distributed on beams in x-direction, according to their influence area, as mass per unit length. The inter-story height is 3.2 m. All the analyzed buildings have a translational motion as first mode shape, in y-direction.

Building	**Floors**	**Floor plan**	**Frequency** Hz
1	3	b	4.6
2	3	a	3.8
3	5	b	2.6
4	5	a	2.2
5	7	a	1.5

Table 2: Fundamental frequency of fixed-based framed structures, corresponding to a translational mode shape in y-direction.

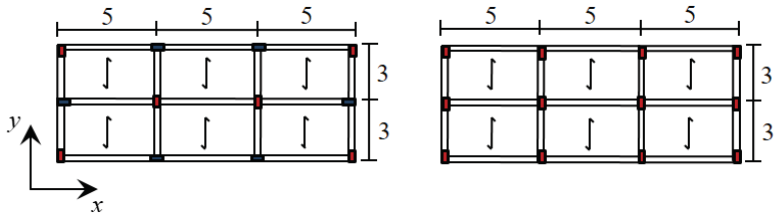

Figure 2: Floor plans of the analyzed buildings in the cases of same (a) and different (b) inertia to horizontal motion in the two orthogonal directions x and y. The buildings have the same floor dimensions but different column orientation.

	Buildings 1-2		Buildings 3-4		Building 5	
Floor	**Beam**	**Column**	**Beam**	**Column**	**Beam**	**Column**
	cm	cm	cm	cm	cm	cm
1	30×80	30×70	30×70	30×80	30×80	30×70
2	30×70	30×70	30×70	30×70	30×70	30×70
3	30×60	30×60	30×60	30×60	30×60	30×60
4			30×60	30×60	30×60	30×60
5			30×60	30×60	30×60	30×60
6					30×60	30×60
7					30×60	30×60

Table 3: Dimensions of rectangular cross-section beams for the analyzed buildings.

The concrete mechanical properties considered are the elastic compression modulus $E_c = 31220\ \mathrm{N/mm^2}$ and the Poisson ratio $\nu_c = 0.2$. For reinforced concrete (RC) beam elements, it is assumed a shear correction factor $\chi = 0.857$, a density $\rho = 2500\ \mathrm{kg/m^3}$ and a damping ratio $\zeta = 5\%$. The foundation, embedded in the soil, is a RC slab which is 16 m long, 7 m wide and 0.5 m deep.

Each of the five framed buildings in Table 2 are assembled with the two T-shaped soil profiles described in Table 1. Moreover, 25 models are obtained, for each soil profile, where each building (Table 2) is close to a similar building and to the others. The distance between the shallow foundations in y-direction (Figure 1) is assumed to be equal to 0.1 m. The SSSI analysis is compared to the single building case (SSI). The models produced when assuming as TS, the building with fundamental frequency $f_{TS} = 1.5$ Hz, are shown in Figure 3.

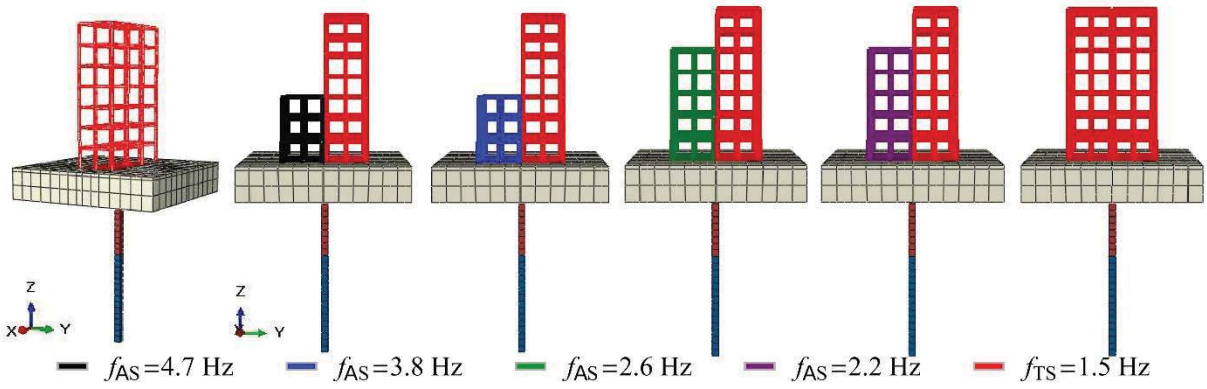

Figure 3 Soil-building systems for SSSI analysis, compared with SSI analysis (left). This figure represents the case where the target structure has fundamental frequency $f_{TS} = 1.5$ Hz.

3.3 Synthetic narrow-band seismic loading

The seismic loading is applied at the soil-bedrock interface in terms of viscous force, proportional to the motion velocity. In this research, a synthetic wavelet is used as input motion for the SSSI analysis, whose predominant frequency corresponds to the building fundamental mode.

The incident motion at the soil-bedrock interface is expressed in terms of velocity [16] as:

$$v_0(t) = v_{0\max}/2\left[1+\cos\left(2\pi f_q/n\,(t-t_0)\right)\right]\cos(2\pi f_q(t-t_0)) \qquad (1)$$

The motion duration is $2t_0$, where $t_0 = n/(2f_q)$ is the time of peak envelope, the predominant frequency is f_q and $n = 5$ is the number of cycles. The incident motion amplitude $v_{0\max}$ corresponds to a peak acceleration $a_{0\max} = 0.1\ \mathrm{m/s^2}$. The loading is applied in the y-direction (Figure 1).

4 SSSI ANALYSIS

In a first part of this parametric analysis, the seismic response of a TS is investigated in the case where the seismic loading excites its fundamental frequency f_{TS}. This means that the synthetic signal has predominant frequency $f_q = f_{TS}$. The ratio between the peak accelerations for SSSI and SSI analyses (a_{SSSI}/a_{SSI}), obtained at the top of the TS, with respect to the TS to AS fundamental frequency ratio f_{TS}/f_{AS}, is shown in Figure 4 for the two selected soil profiles.

At the resonance ($f_q = f_{TS}$), the response for a stiffer TS is not affected by the presence of the AS: it is similar to the single building case. On the contrary, when the AS is stiffer, the TS response is reduced by 30%, compared with the single building case.

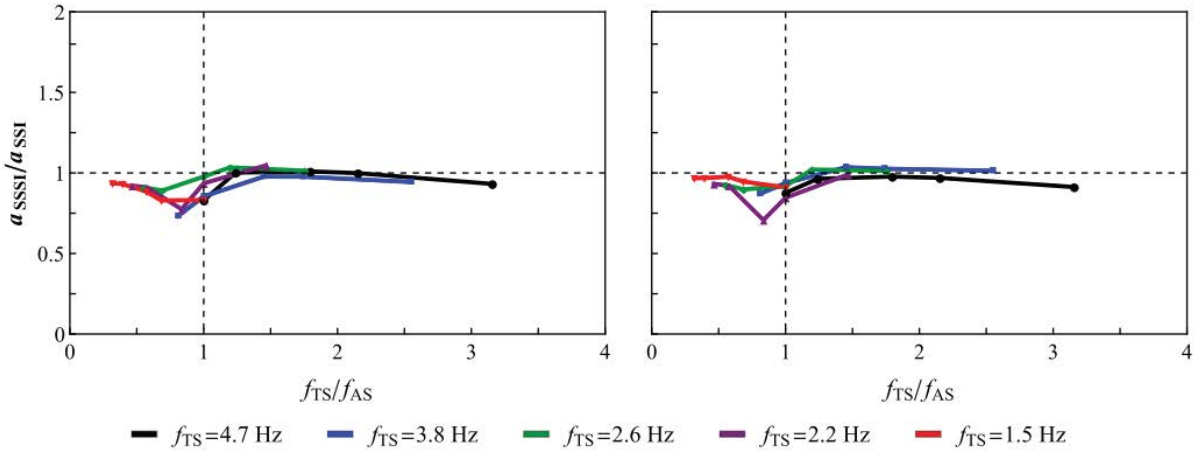

Figure 4: Ratio between the peak acceleration at the top of the target structure (TS) in a SSSI analysis and that in a SSI analysis (single excited building) versus the target to adjacent structure fundamental frequency ratio f_{TS}/f_{AS}, at the resonance of the TS ($f_q = f_{TS}$): soil profile having natural frequency $f_s = 1.5$ Hz (left) and $f_s = 2$ Hz (right).

In a second part of this analysis, the seismic response of a TS is investigated in the case where the seismic loading excites the fundamental frequency f_{AS} of the AS. This means that the synthetic signal has predominant frequency $f_q = f_{AS}$. Figure 5 presents the ratio between the SSSI and SSI peak accelerations (a_{SSSI}/a_{SSI}), obtained at the top of the TS, with respect to the TS to AS fundamental frequency ratio f_{TS}/f_{AS}, for the two selected soil profiles.

At the resonance of the AS ($f_q = f_{AS}$), when the TS is stiffer, its response is increased up to 50% due to the presence of an AS, compared to the single building case. In this situation, the

TS, as a single building, is also loaded by an input signal exciting the fundamental frequency f_{AS} of the AS. On the contrary, when the AS is stiffer, the TS response is reduced by 25%, compared with the single building case.

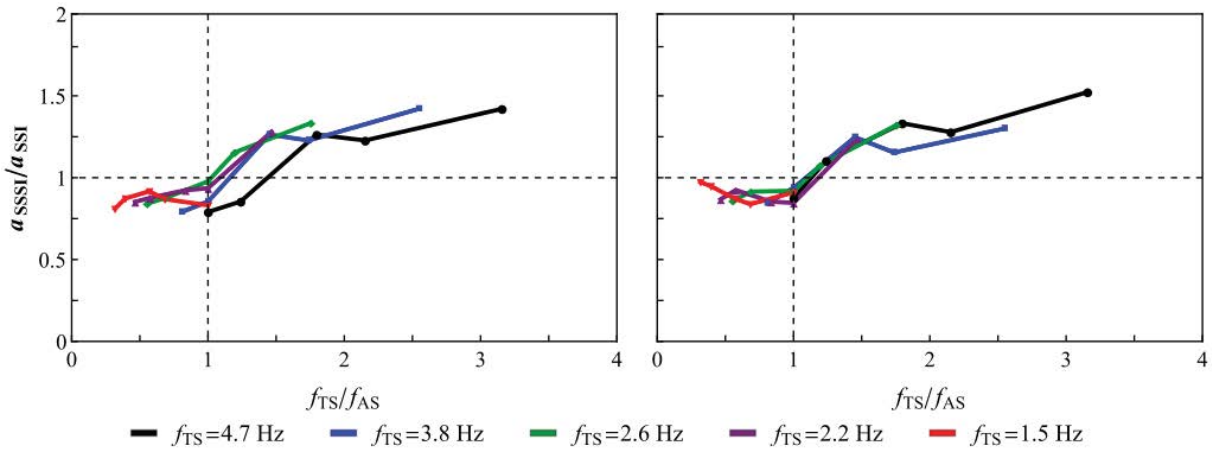

Figure 5: Ratio between the peak accelerations at the top of the target structure (TS) for SSSI (with adjacent strure AS) and SSI (single excited building) analyses when the AS is excited at its resonant mode ($f_q = f_{AS}$), vs. the TS to AS fundamental frequency ratio f_{TS}/f_{AS}, considering two soil profiles with different natural frequencies (left: $f_s = 1.5$ Hz; right: $f_s = 2$ Hz).

The TS response for SSSI analysis is then compared in both cases of TS and AS resonance (Figure 6). The TS response is higher at its resonance than at the resonance of the AS, except in the case of stiffer TS having fundamental frequency close to that of the AS. The TS response at its resonance is lower than at the resonance of the AS, for target to adjacent frequency ratio f_{TS}/f_{AS} in the range $[1 - 1.5]$.

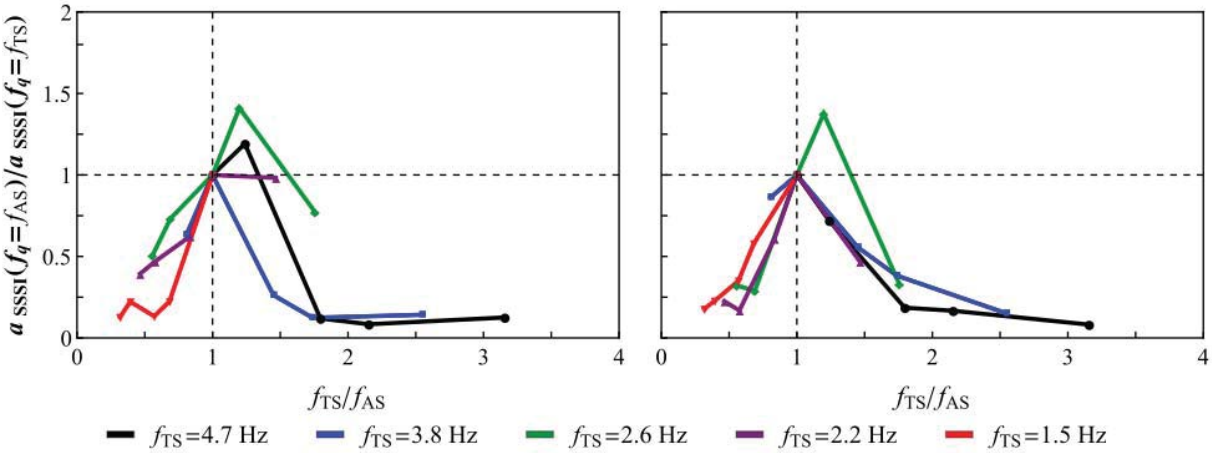

Figure 6: Ratios between the peak accelerations at the top of the TS for SSSI and SSI analyses when the AS is excited at its resonant mode, vs. the TS to AS fundamental frequency ratio f_{TS}/f_{AS}, considering two soil profiles with different natural frequencies (left: $f_s = 1.5$ Hz; right: $f_s = 2$ Hz).

The TS seismic response is compared for both cases: at its resonant mode ($f_q = f_{TS}$) as a single building and at the AS resonant mode ($f_q = f_{AS}$). In the first case (TS as a single building at resonance), TS response is generally higher than in the latter case except when the TS is stiffer with fundamental mode close to the AS one (Figure 7). However, the TS response for

the second case (resonance of an AS) is higher for TS to AS frequency ratio f_{TS}/f_{AS} in the range $[1-1.5]$.

These results are useful to identify the range of fundamental modes which a vibration reduction device should have to produce to obtain a beneficial effect in the vicinity of a TS.

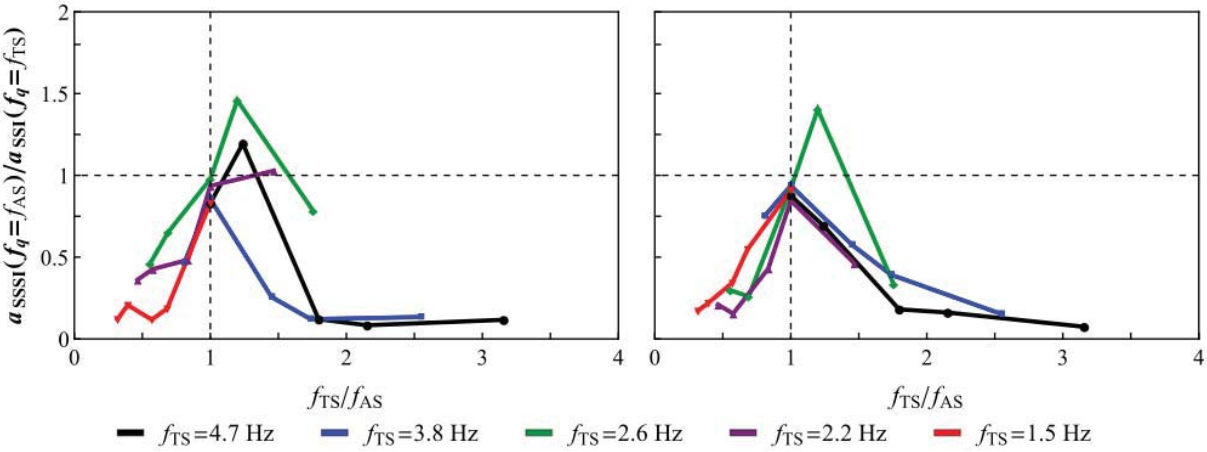

Figure 7: Ratio between the peak accelerations at the top of the TS for a SSSI analysis when the AS is excited and for a SSI analysis (single excited TS building), vs. to the TS to AS fundamental frequency ratio f_{TS}/f_{AS}, considering two soil profiles with different natural frequencies (left: $f_s = 1.5$ Hz; right: $f_s = 2$ Hz).

5 CONCLUSIONS

A parametric study has been carried out to investigate the effect of an adjacent structure (AS) on the seismic response of a target structure (TS). The seismic response is analyzed in the case of a single TS and in the presence of a nearby one.

The 1DT-3C wave propagation approach allows simulating the response of soil and structures to a three-component seismic motion, in a finite element scheme, accounting for foundation deformability, rocking effect, soil-structure interaction and interaction between close structures. Two reinforced framed structures having shallow foundation are assembled with a T-shaped soil domain.

In a structure-soil-structure interaction (SSSI) analysis, each building is modeled as close to a similar building and to others having various height and fundamental frequency. A similar trend is obtained for the seismic response of all the analyzed structures.

In this research, the focus is put on the TS top response. The variation of the peak acceleration versus the TS to AS fundamental frequency ratio is investigated, for SSSI and SSI analyses.

When the TS is stiffer, at its resonant mode, the response is not modified by the presence of the AS: it is similar to the single building case. On the contrary, at the AS resonant mode, the TS response is amplified due to the presence of an AS, compared to the single building case.

When the AS is stiffer, the TS response is reduced compared to the single building case in both cases of resonance (for TS and AS).

When comparing the TS response in both cases (TS or AS resonance), the acceleration at the top of the TS structure is higher for the TS resonance case when it is modeled as single building, except when considering a stiffer TS with fundamental mode close to the AS one. In this case of stiffer TS having fundamental frequency close to that of the AS, the highest response of the TS is obtained when it is modeled nearby the AS structure, at the resonance of the AS structure.

The proposed approach for SSSI analysis can be used to identify the range of fundamental modes which a vibration reduction device should have to produce to obtain a beneficial effect in the vicinity of a TS.

6 ACKNOWLEDGMENTS

This research was performed using HPC resources from GENCI-[CINES] (Grant 2019-[A0070410071]).

REFERENCES

[1] J. E. Luco et L. Contesse, Dynamic structure-soil-structure interaction, *Volume 63: Bulletin of the Seismological Society of America*, 4, 1289-1303, 1973.

[2] G. B. Warburton, J. D. Richardson, et J. J. Webster, Harmonic Response of Masses on an Elastic Half Space, *Volume 1: J. Eng. Ind*, 1, 193-200, 1972.

[3] H. Aldaikh, N. A. Alexander, E. Ibraim, et O. Oddbjornsson, Two dimensional numerical and experimental models for the study of structure–soil–structure interaction involving three buildings, *Volume 150: Computers & Structures*, 79-91, 2015.

[4] H. Mizuno, Effects of structure–soil–structure interaction during various excitations, *Volume 5: Proceedings of the 7th World Conference on Earthquake Engineering*, 149-156, 1980.

[5] N. W. Trombetta, H. Benjamin Mason, T. C. Hutchinson, J. D. Zupan, J. D. Bray, et B. L. Kutter, Nonlinear soil–foundation–structure and structure–soil–structure interaction: engineering demands, *Volume 141: Journal of Structural Engineering*, 7, 04014177, 2014.

[6] F. Nateghi‐A et A. Rezaei‐Tabrizi, Nonlinear dynamic response of tall buildings considering structure–soil–structure effects, *Volume 22: The Structural Design of Tall and Special Buildings*, 14, 1075-1082, 2013.

[7] F. Vicencio et N. A. Alexander, Dynamic interaction between adjacent buildings through nonlinear soil during earthquakes, *Volume 108: Soil Dynamics and Earthquake Engineering*, 130-141, 2018.

[8] P. Cacciola, M. G. Espinosa, et A. Tombari, Vibration control of piled-structures through structure-soil-structure-interaction, *Volume 77: Soil Dynamics and Earthquake Engineering*, 47-57, 2015.

[9] A. Tombari, M. G. Espinosa, N. A. Alexander, et P. Cacciola, Vibration control of a cluster of buildings through the Vibrating Barrier, *Volume 101: Mechanical Systems and Signal Processing*, 219-236, 2018.

[10] R. Fares, M. P. Santisi d'Avila, et A. Deschamps, Soil-structure interaction analysis using a 1DT-3C wave propagation model, *Volume 120: Soil Dynamics and Earthquake Engineering*, 200-213, 2019.

[11] M. P. Santisi d'Avila et F. Lopez-Caballero, Analysis of nonlinear soil-structure interaction effects: 3D frame structure and 1-Directional propagation of a 3-Component seismic wave, *Volume 207: Computers & Structures*, 83-94, 2018.

[12] A. K. Chopra, Dynamics of structures: Theory and applications, 2001.

[13] T. J. R. Hughes, The finite element method - linear static and dynamic finite element analysis, *Prentice Hall Englewood Cliff*, 490–567, 1987.

[14] CEN, EN 1998-5: Eurocode 8: Design of structures for earthquake resistance - Part 5: Foundations, retaining structures and geotechnical aspects, 2003.

[15] D. M. Boore, Notes on relating density to velocity for use in site amplification calculations. http://www.daveboore.com/daves_notes.html, 2015.

[16] G. P. Mavroeidis et A. S. Papageorgiou, Near-source strong ground motion: characteristics and design issues, *Volume 21: Proceedings of The 17th US National Conference on Earthquake Engineering*, 25,2002.

EURODYN 2020
XI International Conference on Structural Dynamics
M. Papadrakakis, M. Fragiadakis, C. Papadimitriou (eds.)
Athens, Greece, 23–26 November 2020

COUPLED ITM-FEM APPROACH FOR THE ASSESSMENT OF THE MITIGATION EFFICIENCY OF FINITE AND INFINITE OPEN TRENCHES AND INFILLED BARRIERS

Julian Freisinger[1], **Gerhard Müller**[1]

[1] Chair of Structural Mechanics, Technical University of Munich
Arcisstr. 21, 80333 Munich, Germany
e-mail: julian.freisinger@tum.de, gerhard.mueller@tum.de

Keywords: Soil Dynamics, Soil-Structure-Interaction(SSI), Integral Transform Method, Finite Element Method, Wavenumber-Frequency Domain, Vibration Mitigation

Abstract. *In order to determine the wave propagation in unbounded media considering the interaction of structures with the soil and thus also their influence on the resulting wave field, an appropriate model is necessary. A efficient approach to account for the infinite extension of the soil by the analytical solutions of the Integral Transform Method (ITM) and for the irregular geometries of the structures by the Finite Element Method (FEM) is presented. The coupled ITM-FEM approach is applied for the assessment of the mitigation efficiency of infinite open or infilled trenches using a computationally profitable 2.5D approach. For spatially limited trenches a complete three dimensional model is used. Amplitude reduction factor and insertion loss are calculated for different combinations of soil and barrier material. The accuracy of the method is shown by comparison to analytical solutions and literature results.*

1 INTRODUCTION

In the modern urban environment, vibrations are caused by a variety of sources such as rail and road traffic, industrial- or construction machinery. These vibrations are transmitted into the soil causing disturbances in adjacent structures and annoyance of nearby residents. In order to attenuate the disrupting effects, mitigation measures can be installed at the source or the receiving structure. However, as a big part of the vibratory energy is transported by Rayleigh waves propagating in an area close to the ground surface, introducing suitable wave barriers in the transmission path leads to an appropriate reduction in the amplitude of the elastic waves on the side of the barrier averted from the source. Usually both, open and soft or stiff infilled trenches act as vibration isolating screens by reflecting and diffracting the incident waves.
A comprehensive amount of studies on the mitigation efficiency of open and infilled trenches can be found in literature. First field tests on the screening effect of rectangular open and bentonite filled trenches were conducted by Dolling [1]. Further measurements were performed by Woods [2], who clearly distinguished between active isolation, installing the open trench in the near field very close to the source, and passive isolation placing the trench in the far field, where the Rayleigh wave dominates the wave field. Numerical studies investigating the amplitude reduction of Rayleigh waves by open or concrete filled trenches using the Finite Element Method (FEM) in the frequency domain were presented by Segol et al. [3] and Haupt [4]. Later, the Boundary Element Method (BEM) was employed by Emad and Manolis [5] as well as Beskos et al. [6], Dasgupta et al. [7], Leung et al. [8], who used it to investigate the efficiency of open and infilled trenches due to harmonic sources. Ahmad and Al-Hussaini [9] performed an extensive parametric study on the effects of the dimensions and the filling material of trenches and barriers situated in a homogeneous as well as a layered soil. To be able to include more complex barrier and source compositions, still satisfying the radiation condition for infinite media, different FEM-BEM formulations were developed and used to predict the reduction of ground vibrations by wave barriers due to moving loads [10, 11, 12]. Mitigation measures aiming on the reduction of railway induced vibrations can be assumed to be longitudinally invariant. Coulier et al. [13] and François et al. [14] used a coupled 2.5D FEM-BEM approached based on [15] to investigate the effect of soft and stiff wave barriers, open trenches and subgrade stiffening next to the track.
In this paper an efficient domain decomposition method to model the three dimensional Soil-Structure-Interaction (SSI) is presented using a coupled Integral Transform Method (ITM) - Finite Element Method approach. The infinite soil is described by the analytical solutions of the ITM avoiding any non-physical reflections at artificial boundaries, whereas the FEM is used to model structures of more complex geometry and material distribution. Fully or partially embedded cylindrical or spherical cavities can be modeled, thus enabling the coupling of finite or longitudinally invariant structures within a matching FEM subsystem.
The outline of the paper is as follows. In section 2 firstly the fundamental solutions are introduced and superposed in order to obtain the stiffness matrix of the ITM subsystems in the respective reference system. Subsequently the dynamic stiffness of the FEM subsystems is presented, followed by the coupling of the substructures. A validation of the proposed method is shown in section 3 by comparison with the analytical solution of the homogeneous halfspace. In section 4, a 2.5D ITM-FEM approach is used to model infinite open trenches and infilled barriers. First, the results for a concrete filled trench and subgrade stiffening next to the track are checked against literature results. Second a comparison of the mitigation efficiency of very

soft or stiff barriers and an open trench is presented. Furthermore a 3D ITM-FEM model is used to investigate the screening efficiency of a spatially limited open trench for different load positions and frequencies. Finally the results for the length invariant open trench are directly opposed to those for the finite open trench.

2 ITM-FEM FORMULATION FOR ELASTODYNAMICS

2.1 Fundamental solutions

The dynamic behavior of an linear elastic, homogeneous and isotropic continuum can be described by the Lamé differential equation, which consists of three coupled partial differential equations

$$\mu u^i|^j_j + (\lambda + \mu)\, u^j|^i_j - \rho \ddot{u}^i = 0 \tag{1}$$

with the displacement field u^i, the Lamé constants μ and λ and the density ρ. Using a Helmholtz decomposition $u^i = \Phi|^i + \Psi_l|_k\, \varepsilon^{ikl}$ and thereby expressing the displacement field by the sum of the gradient of a scalar field Φ and the rotation of a vector field $\mathbf{\Psi}$, the system of equations turns into three decoupled wave equations in dependency of the wave velocities of the compressional c_p and the shear wave c_s (setting $\Psi_z = 0$ cp. [16]).

$$\Phi|^j_j - \frac{1}{c_p^2}\ddot{\Phi} = 0 \qquad\qquad \Psi_i|^j_j - \frac{1}{c_s^2}\ddot{\Psi} = 0 \tag{2}$$

The fundamental solutions for the systems halfspace, fullspace with cylindrical cavity and fullspace with spherical cavity are derived from (2) transforming the equations into the appropriate basis and then applying the respective local and non-local boundary conditions.

The system halfspace is solved in Cartesian coordinates (x, y, z) by using a threefold Fourier transform into the wavenumber-frequency domain (k_x, k_y, z, ω). Thus the coupled partial differential equations can be transformed into three decoupled ordinary differential equations that can be solved analytically with an exponential approach [17]:

$$\hat{\Phi} \;= A_1\, e^{\lambda_1 z} + A_2\, e^{-\lambda_1 z} \tag{3}$$

$$\hat{\Psi}_\alpha = B_{\alpha 1}\, e^{\lambda_2 z} + B_{\alpha 2}\, e^{-\lambda_2 z} \tag{4}$$

with $\alpha = x, y$, $\lambda_1 = \sqrt{{k_x}^2 + {k_y}^2 - k_p^2}$, $\lambda_2 = \sqrt{{k_x}^2 + {k_y}^2 - k_s^2}$ and $k_p = \frac{\omega}{c_p}$, $k_s = \frac{\omega}{c_s}$.

The system fullspace with cylindrical cavity is solved in cylindrical coordinates (x, r, φ) under application of a Fourier transform with respect to $x \circ\!\!-\!\!\bullet\, k_x$ and $t \circ\!\!-\!\!\bullet\, \omega$ as well as performing a Fourier Series expansion along the circumferential direction $\varphi \to n$. Furthermore the vector field $\mathbf{\Psi} = \Psi \mathbf{g}^1 + \chi|^j \varepsilon_{ij1} \mathbf{g}^i$ is expressed by two independent scalar fields. The respective system of equations is solved with Hankel functions of first and second kind [18]:

$$\hat{\Phi}\,(k_x, r, n, \omega) = C_{1n}\, H_n^{(1)}\,(k_1 r) + C_{4n}\, H_n^{(2)}\,(k_1 r) \tag{5}$$

$$\hat{\psi}\,(k_x, r, n, \omega) = C_{2n}\, H_n^{(1)}\,(k_2 r) + C_{5n}\, H_n^{(2)}\,(k_2 r) \tag{6}$$

$$\hat{\chi}\,(k_x, r, n, \omega) = C_{3n}\, H_n^{(1)}\,(k_2 r) + C_{6n}\, H_n^{(2)}\,(k_2 r) \tag{7}$$

with ${k_1}^2 = {k_p}^2 - {k_x}^2$ respectively ${k_2}^2 = {k_s}^2 - {k_x}^2$.

The system fullspace with spherical cavity is solved in spherical coordinates (r, φ, ϑ). All quantities on the spherical boundary are transformed into series of spherical harmonics $(\varphi, \vartheta \to$

$m, l)$ and a Fourier transform into the frequency domain is carried out. Thus the wave equations are solved in the (r, m, l, ω) domain by spherical Hankel functions of first and second kind [19]:

$$\hat{\Phi}\left(r, m, l, \omega\right) = C_{1lm}\; h_m^{(1)}\left(|k_p| r\right) + C_{4lm}\; h_m^{(2)}\left(|k_p| r\right) \tag{8}$$

$$\hat{\psi}\left(r, m, l, \omega\right) = C_{2lm}\; h_m^{(1)}\left(|k_s| r\right) + C_{5lm}\; h_m^{(2)}\left(|k_s| r\right) \tag{9}$$

$$\hat{\chi}\left(r, m, l, \omega\right) = C_{3lm}\; h_m^{(1)}\left(|k_s| r\right) + C_{6lm}\; h_m^{(2)}\left(|k_s| r\right) \tag{10}$$

For all three systems local stress boundary conditions are applied respectively on the halfspace surface Λ, the cylindrical cavity surface Γ_c or the spherical cavity surface Γ_s. Additionally employing the Sommerfeld radiation condition [20] the vector of unknown coefficients $\mathbf{C}_i$ can be determined for each system separately and the stresses and displacements due to unit load states at the surfaces can be calculated by $\hat{\boldsymbol{\sigma}}_i = \hat{\mathbf{K}}_i \mathbf{C}_i$ and $\hat{\mathbf{u}}_i = \hat{\mathbf{H}}_i \mathbf{C}_i$, where $i = hs, c, s$ stands for the different fundamental systems and $\hat{\mathbf{K}}_i$, $\hat{\mathbf{H}}_i$ are the matrices including the fundamental solutions, kinematic and material relations linking the unknowns with the stresses and the displacements. A detailed derivation of the solutions of the fundamental systems as well as the matrices for the calculation of the $\hat{\boldsymbol{\sigma}}_i$ and $\hat{\mathbf{u}}_i$ can be found in [21, 22] and [23].

2.2 Superposition of fundamental systems

The superposition of two of the fundamental systems each is now used to satisfy the boundary conditions of the complete system at both surfaces. Therefore the halfspace is superposed with the fullspace with cylindrical cavity resulting in a halfspace with cylindrical cavity. Furthermore the halfspace is superposed with the fullspace with spherical cavity to obtain the system of a halfspace with spherical cavity. For this reason fictitious surfaces $\delta\Lambda$ resp. $\delta\Gamma_j$ (with $j = c, s$ for the cylinder resp. the sphere) are introduced into the fundamental systems allowing a superposition at the common surfaces as depicted in Figure 1. Thus, loading the halfspace with unit stress states $\hat{\boldsymbol{\sigma}}_\Lambda$ at Λ for each wavenumber combination (k_x, k_y), the stresses $\hat{\boldsymbol{\sigma}}_{\delta\Gamma_j}^{(\Lambda)}$ at the fictitious surface $\delta\Gamma_j$ can be determined. The other way round, the stresses $\hat{\boldsymbol{\sigma}}_{\delta\Lambda}^{(\Gamma_j)}$ at $\delta\Lambda$ due to unit stress states $\hat{\boldsymbol{\sigma}}_{\Gamma_j}$ at Γ_j for each of the respective series members (n resp. m, l) can be calculated. The sum of the stresses at Λ and Γ_j has then to be equal to the external loads $\hat{\boldsymbol{p}}_\Lambda$ and $\hat{\boldsymbol{p}}_{\Gamma_j}$ acting on the complete system. Thus the scaling factors $\mathbf{C_{ITM}}$ for the unit stresses and the

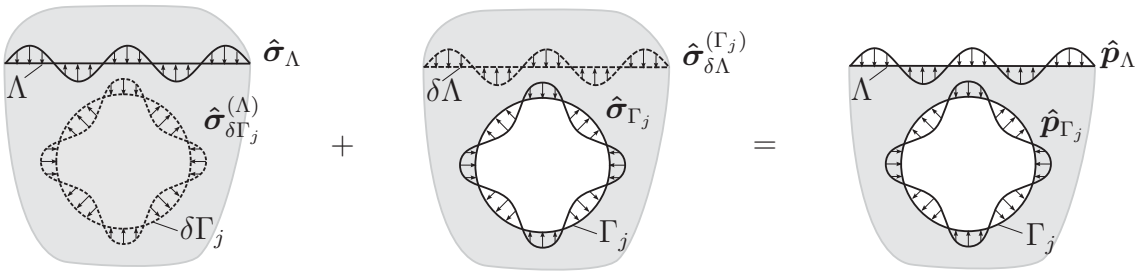

Figure 1: Fictitious surfaces and stresses at the surfaces due to unit stress states.

stresses at the fictitious boundaries, gathered in $\hat{\mathbf{S}}_{\mathbf{ITM}}$, can be determined in dependency of the total external load $\hat{\mathbf{P}}_{\mathbf{ITM}}$ on Λ and Γ_j as:

$$\mathbf{C_{ITM}} = \hat{\mathbf{S}}_{\mathbf{ITM}}^{-1} \hat{\mathbf{P}}_{\mathbf{ITM}} \tag{11}$$

Subsequently, also the resulting displacements $\hat{\mathbf{u}}_{\mathbf{ITM}}$ at Λ and Γ_j can be calculated from the displacements due the unit stresses, gathered in $\hat{\mathbf{V}}_{\mathbf{ITM}}$, scaled with the amplitudes $\mathbf{C}_{\mathbf{ITM}}$:

$$\hat{\mathbf{u}}_{\mathbf{ITM}} = \hat{\mathbf{V}}_{\mathbf{ITM}}\, \mathbf{C}_{\mathbf{ITM}} \tag{12}$$

Combining equations (11) and (12) the stiffness matrix $\hat{\mathbf{K}}_{\mathbf{ITM}} = \hat{\mathbf{S}}_{\mathbf{ITM}} \hat{\mathbf{V}}_{\mathbf{ITM}}^{-1}$ of the ITM subsystem for a halfspace with cylindrical or spherical cavity is obtained giving a direct relation between the displacements and the external loads:

$$\underbrace{\begin{bmatrix} \hat{\mathbf{K}}_{\mathbf{\Lambda\Lambda}_{\mathbf{ITM}}} & \hat{\mathbf{K}}_{\mathbf{\Lambda\Gamma}_{\mathbf{j\,ITM}}} \\ \hat{\mathbf{K}}_{\mathbf{\Gamma}_{\mathbf{j}}\mathbf{\Lambda}_{\mathbf{ITM}}} & \hat{\mathbf{K}}_{\mathbf{\Gamma}_{\mathbf{j}}\mathbf{\Gamma}_{\mathbf{j\,ITM}}} \end{bmatrix}}_{\hat{\mathbf{K}}_{\mathbf{ITM}}} \underbrace{\begin{pmatrix} \hat{\mathbf{u}}_{\mathbf{\Lambda}_{\mathbf{ITM}}} \\ \hat{\mathbf{u}}_{\mathbf{\Gamma}_{\mathbf{j\,ITM}}} \end{pmatrix}}_{\hat{\mathbf{u}}_{\mathbf{ITM}}} = \underbrace{\begin{pmatrix} \hat{\mathbf{P}}_{\mathbf{\Lambda}_{\mathbf{ITM}}} \\ \hat{\mathbf{P}}_{\mathbf{\Gamma}_{\mathbf{j\,ITM}}} \end{pmatrix}}_{\hat{\mathbf{P}}_{\mathbf{ITM}}} \tag{13}$$

The systems halfspace with cylindrical or spherical indentation can be derived analogously by shifting the cavity to the halfspace surface. Further details can be found in [24].

2.3 Finite Element Implementation

The FEM structures that shall be coupled to the previously introduced ITM subsystems need to match with the shape of the respective cavity surface Γ_j. Therefore the dynamic stiffness matrix of a FEM mesh with a cylindrical and a spherical outer boundary have to be computed. Applying the 2.5D approach, the stiffness of the halfspace with cylindrical cavity was calculated in the (k_x, ω) domain. This allows to represent the 3D response on a two dimensional mesh. Thus quadrilateral finite elements with linear shape functions are used to discretize the cross section of the FEM substructure. However, the FEM formulation has to be adopted to the wavenumber frequency domain as presented in [18]. To enable a direct stiffness coupling with the ITM later on, the nodes need to be equally distributed along the cylindrical boundary.
For the spherical FEM structure usual three dimensional, eight node solid elements can be used and the dynamic stiffness matrix is computed in Cartesian coordinates and in the frequency domain as well (x, y, z, ω). The FEM nodes on the spherical boundary must be situated on the intersections of latitudes and longitudes to be able to transform the FEM stiffness matrix into the basis of the ITM subsystem for the coupling. Thereby the z-coordinates of the latitudes are chosen as the Gauß points along the diameter and the longitudes are equally distributed along the circumference [22].

$$\begin{bmatrix} \bar{\mathbf{K}}_{\mathbf{\Gamma}_{\mathbf{j}}\mathbf{\Gamma}_{\mathbf{j_{FE}}}} & \bar{\mathbf{K}}_{\mathbf{\Gamma}_{\mathbf{j}}\mathbf{\Omega}_{\mathbf{FE}}} \\ \bar{\mathbf{K}}_{\mathbf{\Omega\Gamma}_{\mathbf{j_{FE}}}} & \bar{\mathbf{K}}_{\mathbf{\Omega\Omega}_{\mathbf{FE}}} \end{bmatrix} \begin{pmatrix} \bar{\mathbf{u}}_{\mathbf{\Gamma}_{\mathbf{j\,FE}}} \\ \bar{\mathbf{u}}_{\mathbf{\Omega}_{\mathbf{FE}}} \end{pmatrix} = \begin{pmatrix} \bar{\mathbf{P}}_{\mathbf{\Gamma}_{\mathbf{j\,FE}}} \\ \bar{\mathbf{P}}_{\mathbf{\Omega}_{\mathbf{FE}}} \end{pmatrix} \tag{14}$$

2.4 Coupling of Substructures

The coupling of the ITM and the FEM substructure is carried out at the cylindrical respectively the spherical boundary of the substructures. On the coupling surface the continuity of displacements as well as the equilibrium of forces are used as transition conditions. As reference system for both cases the basis of the ITM subsystem is chosen. Therefore the dynamic stiffness matrix of the cylindrical FEM subsystem on Γ_c needs to be transformed into the (k_x, r, n, ω) domain by applying a twofold Fourier transform as well as a Fourier series expansion along the circumference. The spherical FEM structure is transformed into the (r, m, l, ω) domain by transforming the dynamic stiffness on Γ_s into spherical coordinates, conducting a Fourier transform into the frequency domain and developing it into series of spherical harmonics. The FEM

formulation inside the structure Ω is kept in the (x, y, z, ω) domain.

$$\begin{bmatrix} \hat{\mathbf{K}}_{\mathbf{\Lambda\Lambda_{ITM}}} & \hat{\mathbf{K}}_{\mathbf{\Lambda\Gamma_{j_{ITM}}}} & 0 \\ \hat{\mathbf{K}}_{\mathbf{\Gamma_s\Lambda_{ITM}}} & \hat{\mathbf{K}}_{\mathbf{\Gamma_j\Gamma_{j_{ITM}}}} + \hat{\mathbf{K}}_{\mathbf{\Gamma_j\Gamma_{j_{FE}}}} & \bar{\mathbf{K}}_{\mathbf{\Gamma_j\Omega_{FE}}} \\ 0 & \hat{\mathbf{K}}_{\mathbf{\Omega\Gamma_{j_{FE}}}} & \bar{\mathbf{K}}_{\mathbf{\Omega\Omega_{FE}}} \end{bmatrix} \begin{pmatrix} \hat{\mathbf{u}}_{\mathbf{\Lambda_{ITM}}} \\ \hat{\mathbf{u}}_{\mathbf{\Gamma_j}} \\ \bar{\mathbf{u}}_{\mathbf{\Omega_{FE}}} \end{pmatrix} = \begin{pmatrix} \hat{\mathbf{P}}_{\mathbf{\Lambda_{ITM}}} \\ \hat{\mathbf{P}}_{\mathbf{\Gamma_j}} \\ \bar{\mathbf{P}}_{\mathbf{\Omega_{FE}}} \end{pmatrix} \tag{15}$$

3 VALIDATION

The systems halfspace with partly embedded cylindrical or spherical cavity are verified in this section by a comparison with the analytical solution of a homogeneous halfspace. Therefore in the coupled ITM-FEM system the cavity is homogeneously filled with finite elements. Same material parameters are chosen for the FEM substructure and the surrounding soil modeled by the ITM. The system is excited by a vertical harmonic load with $f = 12$ Hz at the halfspace surface $\hat{\mathbf{P}}_{\mathbf{\Lambda}}$ with block size 2x2 m and amplitude $P_0 = 1 \frac{\mathrm{N}}{\mathrm{m}^2}$ at $y_{\mathrm{load}} = -10$ m outside of the FEM inclusion with radius $R = 4$ m. (Figure 2). The soil material parameters are chosen as Soil A given in Table 2.

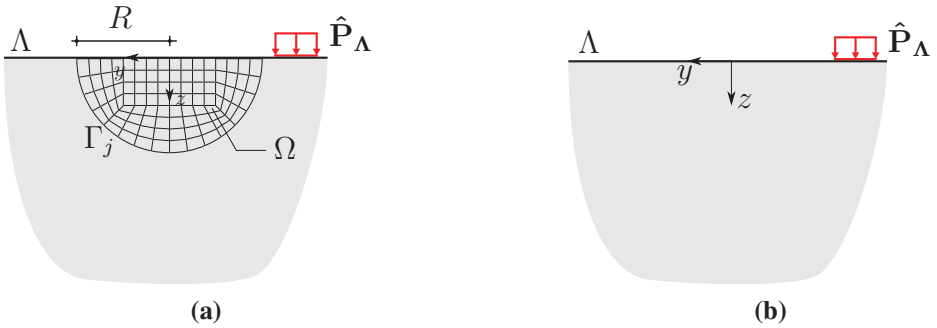

Figure 2: Setup for comparison of coupled ITM-FEM system (a) with analytical solution for homogeneous halfspace (b).

The results for the absolute value of the vertical displacement on the halfspace surface are presented normalized with the load resultant in Figure 3. A very good agreement of the coupled ITM-FEM approach with the benchmark solution can be stated for both, the 2.5D and the 3D model.

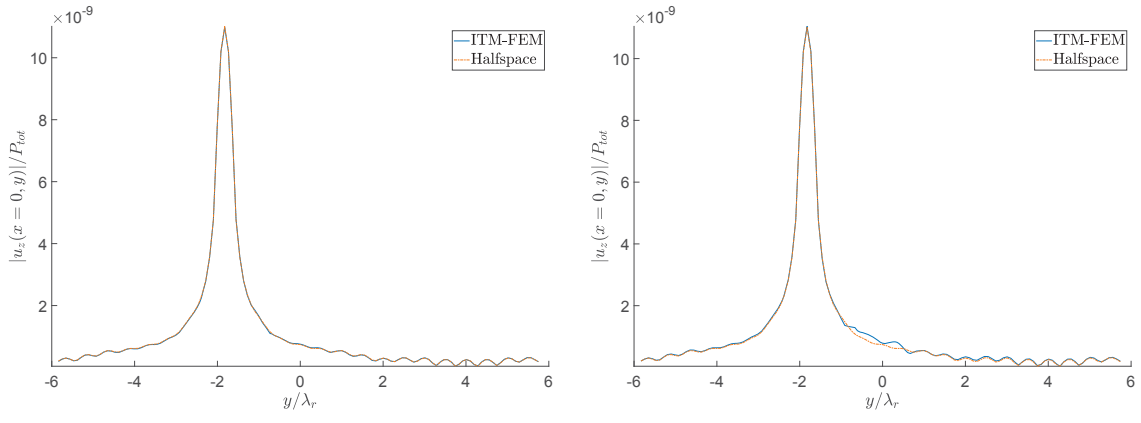

Figure 3: Comparison of $|u_z(x = 0, y, z = 0, \omega)|$ between analytical solution for homogeneous halfspace and (a) halfspace with cylindrical FEM inclusion (2.5D), (b) halfspace with spherical FEM inclusion (3D).

4 NUMERICAL RESULTS

4.1 Infinite open trenches and infilled barriers (2.5D)

In this section numerical results for length invariant open trenches and infilled barriers are presented applying the proposed 2.5D ITM-FEM approach for a halfspace with cylindrically shaped FE substructure. Firstly the results gained with the proposed methodology for a concrete filled trench are compared with those available in published literature. Second the effect of subgrade stiffening as wave impeding barrier is shown followed by a comparison of the mitigation efficiency and the mechanism of action of open trenches and soft or stiff barriers.

Concrete filled trench

In this example the Rayleigh wave diffraction by a rectangular trench, infilled with concrete, in the transmission path, as depicted in Figure 4a, is investigated with the ITM-FEM approach. The results are compared with those obtained by Haupt [4] with the FEM, and Beskos et al. [6] with a constant element based BEM implementation. As the literature results were calculated for a 2D case, the ITM-FEM solution was also done only for wavenumber $k_x = 0$, which means constant conditions in longitudinal direction x. A vertical harmonic load with amplitude $P_0 = 1\ \frac{\mathrm{N}}{\mathrm{m}^2}$ and a width of $b_{\mathrm{y,load}} = 2\ \mathrm{m}$ is applied at a distance of $y_{\mathrm{load}} = -16\,\mathrm{m}$ from the trench with a frequency of $f = 30\ \mathrm{Hz}$ resulting in a Rayleigh wavelength of $\lambda_r = 3.18\ \mathrm{m}$. The width and depth of the barrier were chosen to $w_{\mathrm{tr}} = 1.25$ m and $d_{\mathrm{tr}} = 3.25$ m, prescribed by the FE discretization. Therefore the normalized dimensions result to $W_{\mathrm{tr}} = 0.39$, $D_{\mathrm{tr}} = 1.02$ and $L_{\mathrm{load}} = 5.03$, which almost coincide with the dimensions used in [4, 6]. The further discretization and geometry parameters are given in Table 1 as well as the material parameters of the soil (Soil B) and the concrete filling (Infill A) in Table 2.

	$N_x = N_y$	$B_x = B_y$	N_φ	R	$d_x = d_y = d_{x,\mathrm{FE}}$	$d_{y,\mathrm{FE}}$
Concrete filled trench	2^9	128	128	8	0.25	0.125
Subgrade stiffening	2^9	128	96	8	0.25	0.333
Comp. soft-stiff-open	2^8	64	192	8	0.25	0.166

Table 1: Discretization and geometry parameter for coupled ITM-FEM approach.

	$E\ \left[\frac{\mathrm{N}}{\mathrm{m}^2}\right]$	$\nu\ [-]$	$\rho\ \left[\frac{\mathrm{kg}}{\mathrm{m}^3}\right]$	$\zeta\ [-]$	$c_p\ \left[\frac{\mathrm{m}}{\mathrm{s}}\right]$	$c_s\ \left[\frac{\mathrm{m}}{\mathrm{s}}\right]$	$c_r\ \left[\frac{\mathrm{m}}{\mathrm{s}}\right]$
Soil A	$26.00 \cdot 10^6$	0.30	2000	0.05	132.5	70.8	65.7
Soil B	$46.12 \cdot 10^6$	0.25	1720	0.03	179.5	103.6	95.3
Soil C	$21.60 \cdot 10^7$	0.33	2000	0.05	400.5	201.7	188.0
Infill A	$15.81 \cdot 10^8$	0.25	2356	0.05	914.6	528.1	485.8
Infill B	$15.12 \cdot 10^8$	0.248	2000	0.025	950.7	550.3	506.1
Infill C	$30.00 \cdot 10^9$	0.2	2600	0.01	3580.5	2192.6	1998.9
Infill D	$25.00 \cdot 10^4$	0.4	700	0.05	27.6	11.3	10.6

Table 2: Material parameters of different soils and infill materials

In Figure 4b the amplitude reduction factor A_r for the absolute value of the vertical displacement $|u_z(x = 0, y, z = 0, \omega)|$ at the halfspace surface is shown at $x = 0$ over the dimensionless distance y/λ_r. A_r is defined as the amplitude in presence of the trench $|u_{z,\mathrm{tr}}|$ divided by the amplitude in absence of the trench $|u_{z,\mathrm{ref}}|$. Thus values of A_r smaller than one mean a reduction of the vibration amplitudes of $(1.0 - A_r) \cdot 100$ percent. Significant amplifications are observed

in front of the trench caused by the constructive or destructive interference of the incident and reflected Rayleigh waves due to their phase difference [9], which is indicated by the peak distances being very close to $\lambda_r/2$. On the load remote site, a substantial amplitude reduction due to the concrete barrier of $50-70\%$ is achieved. A very good agreement between the literature results and the ITM-FEM approach can be stated.

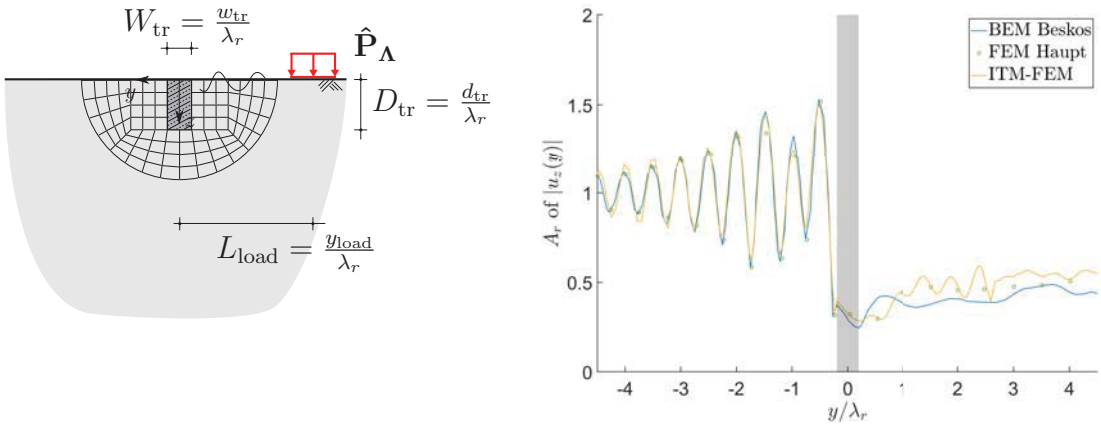

(a) **(b)**

Figure 4: (a) ITM-FEM model for concrete filled trench in transmission path. (b) Comparison of ITM-FEM results for amplitude reduction factor A_r of the vertical displacement $|u_z|$ with BEM solution of Beskos et al. [6] and FEM solution of Haupt [4].

Subgrade stiffening as wave impeding barrier

In this section the 2.5D ITM-FEM approach is used to investigate the efficiency of subgrade stiffening as mitigation measure in the transmission path. The setup depicted in Figure 5a is adopted from Coulier et al. [13], who used a 2.5D FEM-BEM methodology to analyze subgrade stiffening next to the track for the mitigation of railway induced vibrations. A block of stiffened soil (Infill B) with a width and depth of $w_{\mathrm{tr}} = d_{\mathrm{tr}} = 2$ m located within a homogeneous halfspace (Soil C) is investigated. The discretization parameters are given in Table 1. The material parameters for the surrounding and the stiffened soil, leading to the same wave velocities as in [13], are presented in Table 2. A quadratic, harmonic block load with $P_0 = 1\ \frac{\mathrm{N}}{\mathrm{m}^2}$ and a width of $b_{\mathrm{x,load}} = b_{\mathrm{y,load}} = 1$ m is applied at a distance of $y_{\mathrm{load}} = -6$ m from the barrier. The absolute value of vertical displacements and the insertion loss $\bar{\mathrm{IL}}_z$ over the total surface were evaluated for the reference case $|u_{\mathrm{z,ref}}|$ without subgrade stiffening and the situation in presence of the stiffened block $|u_{\mathrm{z,tr}}|$. Therefore positive values of the insertion loss

$$\bar{\mathrm{IL}}_z(x, y, z = 0, \omega) = 20 \log_{10} \frac{|u_{\mathrm{z,ref}}|}{|u_{\mathrm{z,tr}}|}\ [\mathrm{dB}] \tag{16}$$

indicate a reduction compared to the reference case without mitigation measure.

Coulier et al. [13] showed by an investigation of the insertion loss in the wavenumber-frequency domain, that the block of stiffened soil can act as a wave impeding barrier. Considering the stiffened block as infinitely long Timoschenko beam, it was demonstrated that the wave impeding effect depends strongly on the relation of the projection of the Rayleigh wave length in the soil in longitudinal direction λ_x and the free bending wave length in the beam λ_b. The transmission of plane waves in the soil with $\lambda_x < \lambda_b$ is impeded, as the response of the

beam is then dominated by its bending stiffness and the amplitude decreases proportionally to k_y^{-4} for a given frequency.

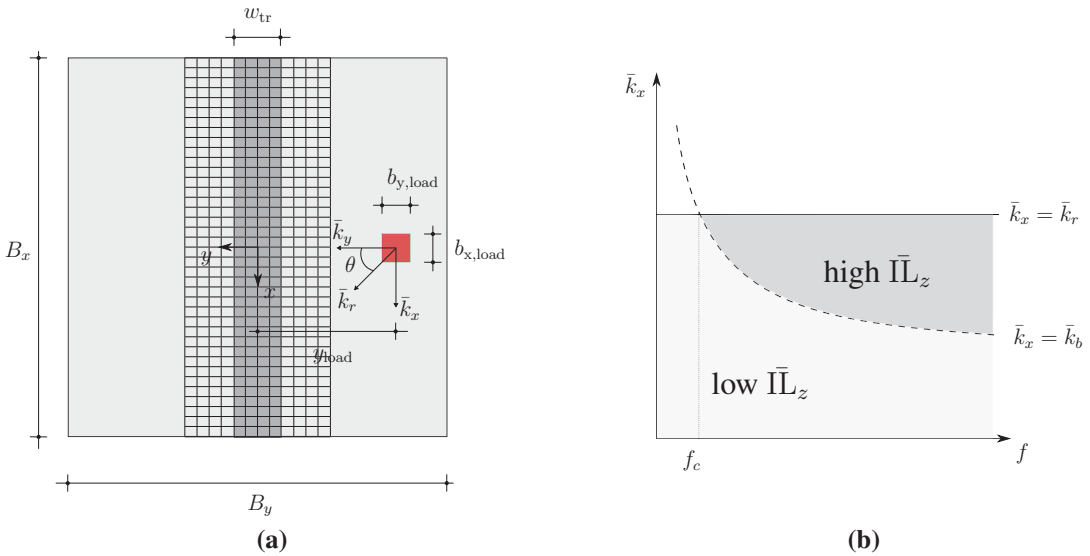

Figure 5: (a) Topview of setup for comparison of coupled ITM-FEM system with 2.5D FEM-BEM model of Coulier et al. [13]. (b) Schematic sketch of the dispersion curves of the free bending wave in a Timoschenko beam and the Rayleigh wave in a homogeneous halfspace.

Figure 5b shows a schematic sketch of the insertion loss $\bar{\mathrm{IL}}_z(\bar{k}_x, y, z = 0, \omega)$ over the dimensionless wavenumber $\bar{k}_x = k_x c_s/\omega$ and the frequency f as presented in [13]. A high insertion loss is obtained for wavenumbers $\bar{k}_x$ smaller than the dimensionless Rayleigh wavenumber $\bar{k}_x = \bar{k}_r = c_s/c_r$ and bigger than the free bending wavenumber $\bar{k}_b$. The contribution of wavenumbers $\bar{k}_x > \bar{k}_r$ to the total response and especially the response in lateral direction is quite limited. This is due to the fact, that the value of the transfer function of a homogeneous halfspace in the wavenumber frequency domain for wavenumbers $k_x^2 + k_y^2 > k_r^2$ is quickly decreasing with increasing wavenumbers and thus, as the propagation direction in the $x-y$ plane is given by $\theta = \tan^{-1}(\bar{k}_x/\bar{k}_y)$, for $\bar{k}_x > \bar{k}_r$ the waves traveling in y-direction have only comparatively small amplitudes. The propagation direction of the Rayleigh wave, which makes up the largest part of the overall response results as $\theta_r = \sin^{-1}(\bar{k}_x/\bar{k}_r)$. For wavenumbers $\bar{k}_x < \bar{k}_b$ follows $\lambda_x > \lambda_r$ and thus the Rayleigh wave is able to propagate through the stiffened block with low transmission loss, whereas for $\bar{k}_x > \bar{k}_b$ the waves are impeded by the barrier because λ_x gets smaller than λ_b. Therefore a critical frequency f_c, when the mitigation measure becomes effective, can be determined by the intersection of the Rayleigh wave and the free bending wave dispersion curves [13]:

$$f_c = \frac{c_r^2}{2\pi}\sqrt{\frac{\rho A}{EI}}\sqrt{\frac{E\mu\kappa}{(E-\rho c_r^2)(\mu\kappa-\rho c_r^2)}} \tag{17}$$

where E is the Young's modulus, μ the shear modulus, ρ the density, A the cross sectional area and I the moment of inertia of the beam. κ is the shear coefficient and can be set to $\kappa = 5/6$ for rectangular cross sections. c_r is the Rayleigh wave velocity in the soil. This critical frequency strongly depends on the stiffness contrast between the soil and the block of stiffened soil. Thus subgrade stiffening is more effective in soft soils. For the given material parameters the critical frequency results to $f_c = 12.37$ Hz.

The propagation direction of the Rayleigh waves is given by θ_r. Beyond a critical angle of $\theta_c = \sin^{-1}(\bar{k}_b/\bar{k}_r)$ and assuming $\omega > \omega_c$, the wavenumbers $\bar{k}_x$ are bigger than $\bar{k}_b$ and thus $\lambda_x < \lambda_b$ holds. Therefore the impinging plane waves with $\theta > \theta_c$ are impeded by the barrier. The critical angle in dependency of the frequency is given by [13] as:

$$\theta_c(f) = \arcsin\left(c_r \sqrt{\rho \left(E + \mu\kappa \pm \sqrt{(E-\mu\kappa)^2 + \frac{4E(\mu\kappa)^2 A}{\rho I(\omega/2\pi)^2}} \right) (2E\mu\kappa)^{-1}} \right) \tag{18}$$

Figure 6a and 6c show the real part of the vertical displacement $u_z(x, y, z = 0, \omega)$ due to a harmonic load with $f = 5$ Hz $< f_c$ for the reference case and the case when subgrade stiffening was applied. The Rayleigh wave length λ_r is much larger than the depth of the barrier and thus a significant part of the Rayleigh wave is able to pass beneath it. For all waves impinging at the stiffened block, $\bar{k}_x > \bar{k}_b$ holds and therefore they are not impeded. The wave field in both cases is very similar and the corresponding insertion loss $\bar{\mathrm{IL}}_z$ in Figure 6e is almost zero over the whole surface. The real part of the vertical displacements for a excitation frequency of $f = 30$ Hz $> f_c$ is shown in Figure 6b and 6d. In the reference case cylindrical wave fronts are observed, whereas, if subgrade stiffening is applied, the wave field is not cylindrical anymore due to the interaction of the barrier and the soil. All waves hitting the barrier at an angle greater than the critical angle θ_c are impeded, leading to a significant reduction of vibrations in the areas with $\theta > \theta_c$. Hence, large values of the insertion loss, partly exceeding $10\,\mathrm{dB}$, are observed there. The critical angle, which results to $\theta_c = 43.26°$ at $f = 30$ Hz, is sketched in Figure 6f.
However, below the critical angle the amplitude reduction is rather small due to the relatively shallow barrier (only $0.32\,\lambda_r$ at $f = 30$ Hz) and the not so pronounced stiffness contrast between the barrier and the soil. Although lines of increased $\bar{\mathrm{IL}}_z$ can be observed in this area due to the partial destructive interference caused by the phase shift of the waves passing below the barrier and the waves transmitted through the barrier with much higher wave velocity, which appears mainly for thick barriers of lower depth [25]. For larger depth of the barrier and an increased stiffness contrast also for angles $\theta < \theta_c$ a significant reduction can be achieved, as more reflections occur at the left face of the barrier and less vibrations are transmitted. Furthermore a smaller part of the Rayleigh wave passes below the barrier. On account of this in the following section the mitigation efficiency for an open trench, a soft and a stiff barrier are compared, assuming adequate dimensions and a sufficient stiffness contrast.

Stiff and soft barriers vs. open trench

The vibration screening efficiency of open trenches massively depends on the trench depth. A satisfactory screening efficiency of $A_r < 0.25$ can be achieved for depths d_{tr} greater than about $1.2\lambda_r$ of the soil [2]. Due to stability reasons the construction of ideal open trenches with vertical sides is limited to shallow depths. For this reason, trenches are often filled with soft material that must be able to withstand the horizontal soil stresses while still providing adequate insulation [26]. Open trenches achieve their vibration reduction effect by the reflection of the incident Rayleigh waves. As no energy can be transferred across the open trench the vibration reduction usually is higher than for infilled trenches, where a part of the wave energy is transmitted through the barrier. If a very soft infill material is used the behavior of the filled trench resembles that of open trench [27], which also yields for the mitigation efficiency.
However, the physical mechanism, which is responsible for the vibration reduction changes, when it comes to stiff barriers. Additionally to the reflected and transmitted Rayleigh waves,

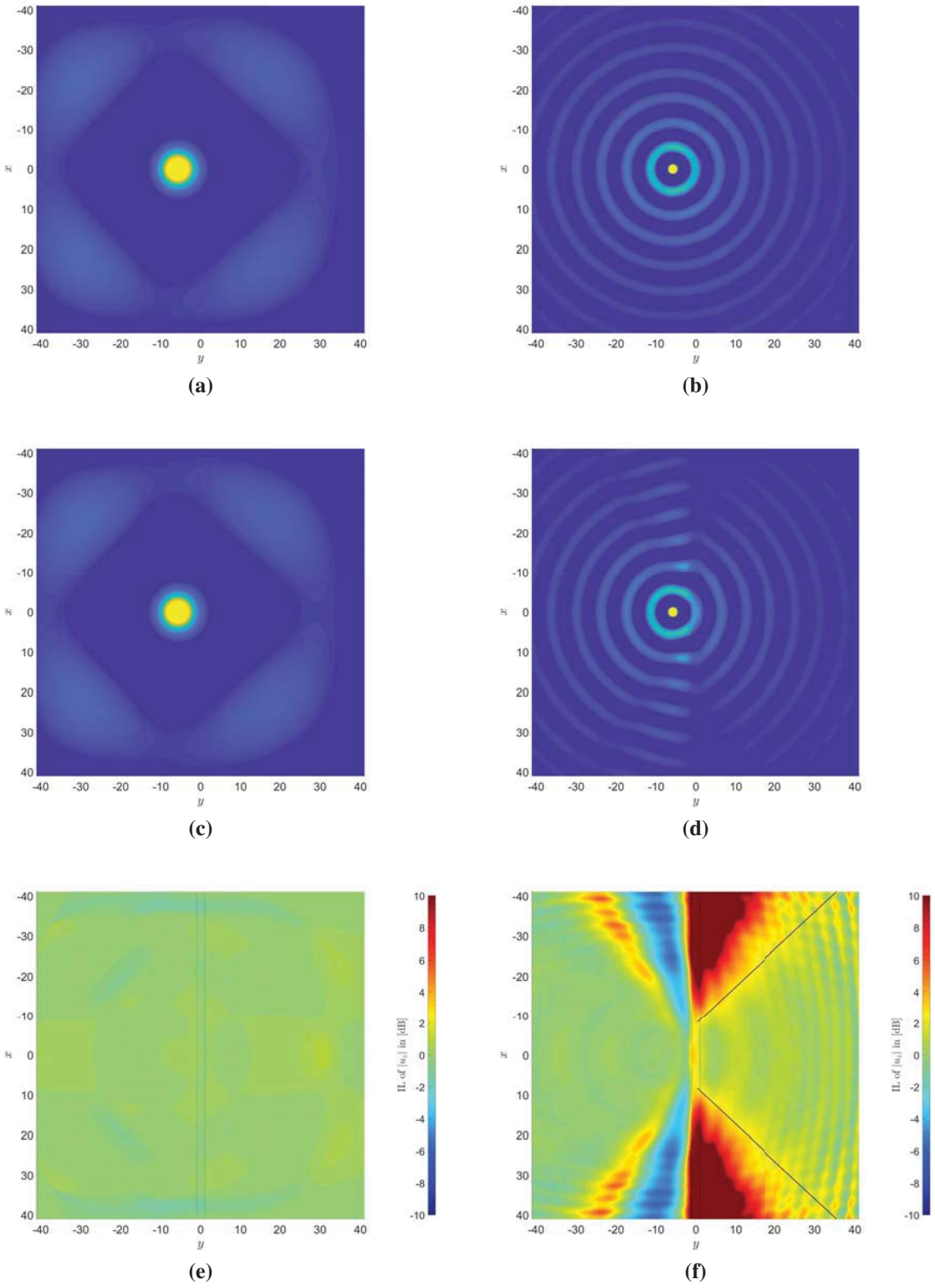

Figure 6: Real part of the vertical displacement $u_z(x, y, z = 0, \omega)$ due to harmonic excitation with block load at $y = -6$ m in the reference case (a,b) and in the case with subgrade stiffening (c,d) as well as the corresponding insertion loss $\bar{\mathrm{IL}}_z$ (e,f). Left column for $f_c > f = 5$ Hz and right column for $f_c < f = 30$ Hz.

the presence of the barrier gives rise to body (P- and S-) waves, that are also reflected and transmitted [9]. Furthermore body waves radiating downward the barrier occur, acting like a new wave source at the lower end of the stiff barrier, emitting body waves into the interior of the halfspace [25]. This transformation of Rayleigh waves into body waves is called mode conversion. The screening effect of a stiff barrier with adequate depth therefore is partly based on the reflection of the Rayleigh waves and partly on its transmission into the interior of the halfspace. For fixed dimensions, the decisive parameter for the vibration mitigation efficiency of a stiff barrier is the stiffness difference between soil and infilled trench rather than the impedance [13]. The material damping of the infill material has no significant effect on the on the screening performance [28]. Therefore, very stiff barriers in relatively soft soils have a mitigation efficiency close to that obtained by an open trench [14].

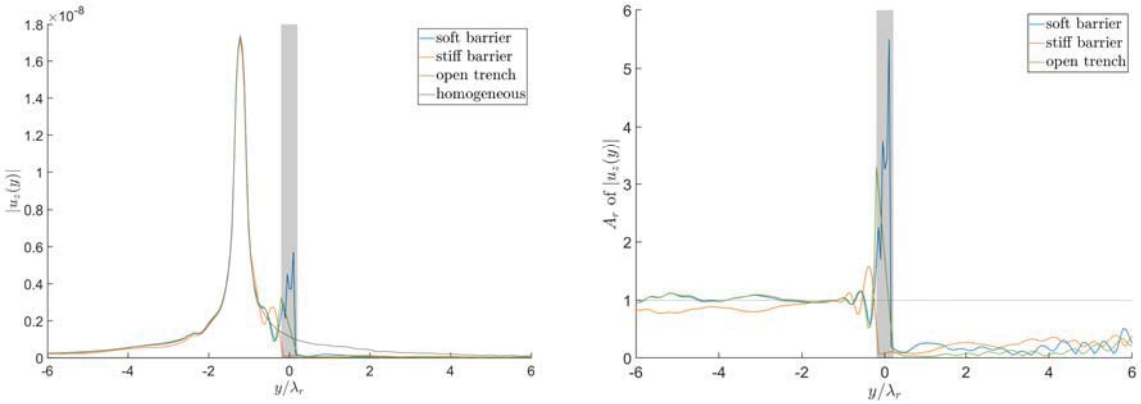

(a) **(b)**

Figure 7: (a) Absolute value of vertical displacement $|u_z(x = 0, y, z = 0, \omega)|$ due to harmonic excitation with $f = 20$ Hz by a 1x1 m block load at $y_{\text{load}} = -4$ m for soft barrier, stiff barrier, open trench, homogeneous halfspace and (b) the corresponding amplitude reduction factor A_r. The gray bar indicates the area enclosed by the open trench resp. the barrier.

Figure 7a shows the vertical displacement $|u_z(x = 0, y, z = 0, \omega)|$ for an extremely stiff (Infill C) and a very soft (Infill D) barrier as well as an open trench and the reference case of a homogeneous halfspace (Soil A). The material properties of the barriers and the soil are given in Table 2, the used discretization in Table 1. Again a 1x1 m block load with $P_0 = 1\ \frac{\text{N}}{\text{m}^2}$ located at $y_{\text{load}} = -4$ was chosen. For the excitation frequency of 20 Hz, λ_r results to 3.3 m and therefore the normalized dimensions of the trench respectively the barrier account for $D_{\text{tr}} = 1.2$ and $W_{\text{tr}} = 0.4$. The soft barrier and the open trench show large displacement amplitudes at the load sided edge, whereas in case of the stiff barrier the deformation is almost zero. This also reflects in the amplitude reduction factor depicted in Figure 7b, exhibiting $A_r \gg 1$ for the open trench and the soft barrier and a very small A_r for the stiff barrier. Behind the trench a significant reduction of vibrations is observed for all three cases, albeit the open trench performs best over the largest part of the considered range.
This tendency is also visible in Figures 8(a,c,e), where the amplitude reduction factor A_r over the surface with dimensions normalized by λ_r is depicted. In the graphs, the area occupied by the barrier is marked by the white lines. The open trench shows the greatest reduction effect over the entire area on the load averted side. Nearly the same pattern of A_r develops on the load facing side for the open trench and the soft filled barrier, which can be explained by the similar physical mechanism for the vibration screening, relying almost solely on the reflection of the impinging Rayleigh waves.

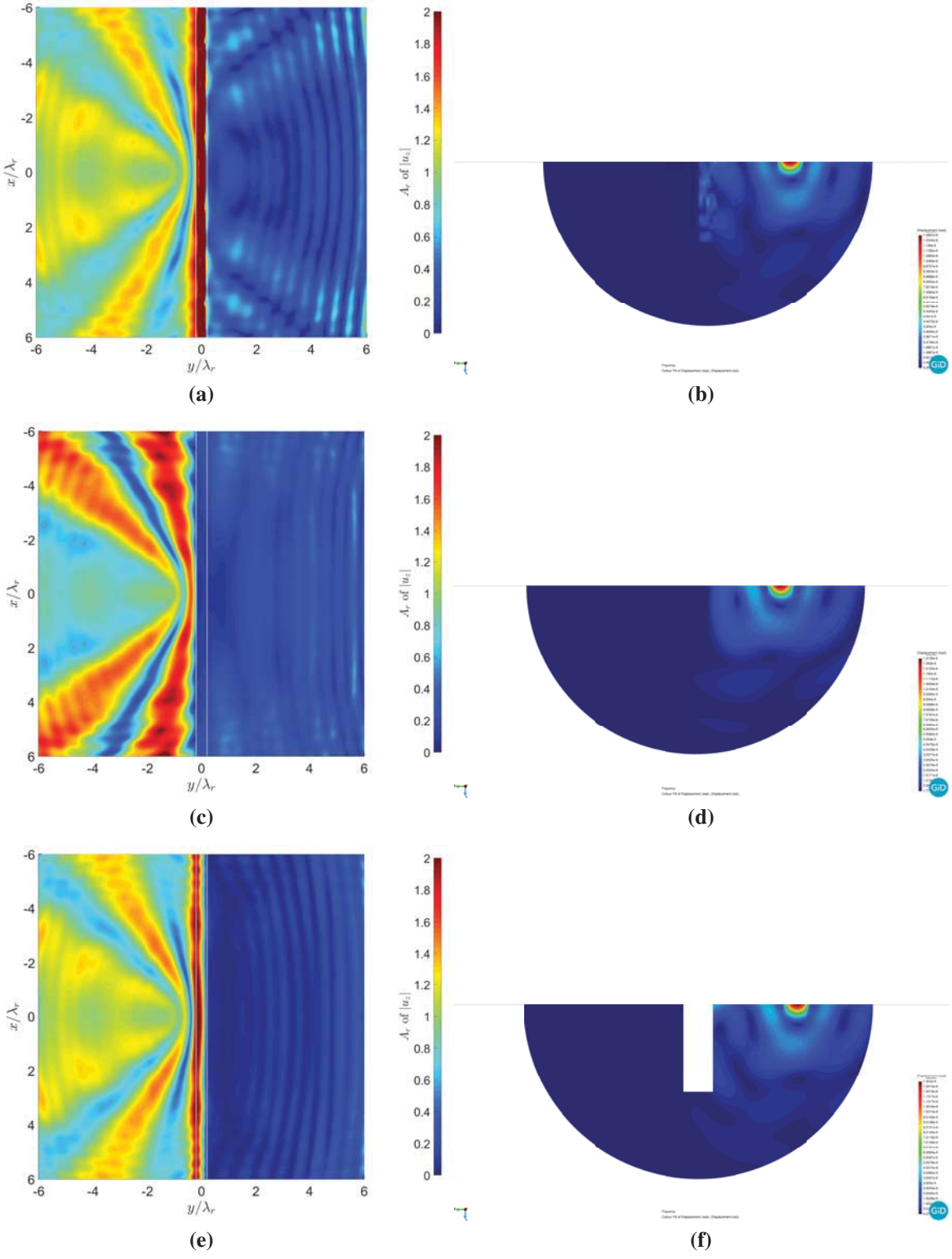

Figure 8: Left column: Amplitude reduction factor A_r, right column: Resultant of displacements $\mathbf{u}(x, y, z, \omega) = \sqrt{u_x^2 + u_y^2 + u_z^2}$ for (a,b) soft barrier, (c,d) stiff barrier and (e,f) open trench.

However, in case of the stiff barrier, due to the very different ratio of wave velocities in the soil and the barrier compared to the soft infill material as well as larger amount of mode conversion, a very different interference pattern of the reflected waves occurs before the bar-

rier. Moreover, in Figures 8(b,d,f) the pseudo resultant of the displacements $\mathbf{u}(x, y, z, \omega) = \sqrt{u_x^2 + u_y^2 + u_z^2}$ within the FEM substructure is illustrated for all three cases in a section at $x = 0$. In the considered frequency range the wave lengths in the soil are considerably larger than the barrier width and thus impose their displacements to the barrier quasi statically [14]. It is clearly visible that with the soft filling material, large deformations occur at the edge and within the barrier, similar to the limit case of the reflection of the incident waves at the free end, as for an open trench. In contrast the stiff barrier shows no deformation at all and therefore almost acts as fixed boundary [11].

4.2 Finite open trench (3D)

Unlike the previously presented 2.5D approach, dealing with infinitely long mitigation measures in longitudinal direction, the 3D approach allows the investigation of spatially limited open trenches or barriers, closer to practical applications. For the length invariant structures the energy transmission is restricted over the whole length, whereas in case of finite vibration shielding measures much more complex wave interference phenomena occur, as additionally to the lower trench end diffraction effects arise also at side edges [7]. Thus, regions with reduced or increased vibration amplitudes on the ground surface can clearly be observed as depicted in Figures 10c and 10d.

For the investigation of the finite open trench, the three dimensional ITM-FEM approach is applied, whereby the open trench is modeled within the half spherically shaped FEM substructure as displayed in Figure 9. A radius of $R = 6$ m was chosen for the sphere and a open trench with $d_{\mathrm{tr}} = 3.8$ m, $w_{\mathrm{tr}} = 1.2$ m and $l_{\mathrm{tr}} = 4.8$ m included. A total region of $B_x = B_y = 64$ m was investigated using $N_x = N_y = 2^7$ Fourier series members on the halfspace surface as well as $N_l = 40$ longitudes and $N_m = 20$ latitudes for the discretization of the sphere, leading to a finite element size of $d_{x,\mathrm{FE}} = d_{y,\mathrm{FE}} = 0.6$ m along the surface. The Material properties of Soil A, given in Table 2, were used for the calculations. In the FEM subsystem solid elements

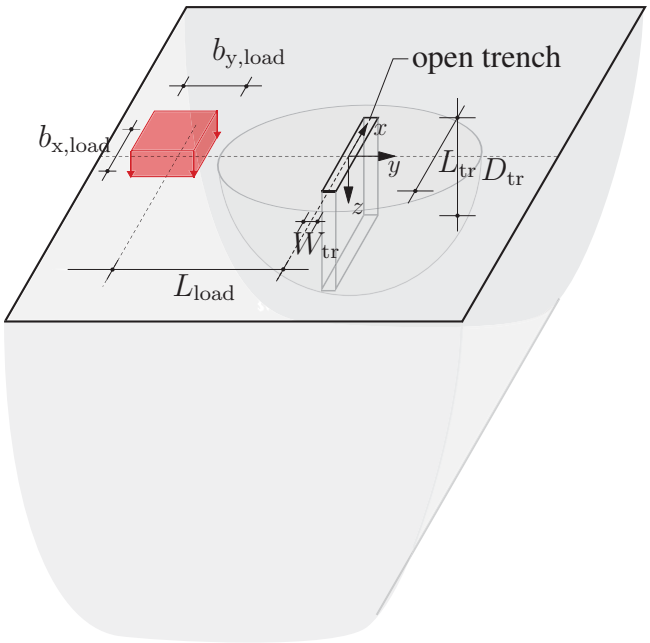

Figure 9: Sketch of the three-dimensional ITM-FEM system for the vibration isolation by an finite open trench.

with linear shape functions were used, which, in general, are not as accurate as higher order elements, if it comes to stress concentrations or detailed results for the displacement amplitude in the near field around the load are of interest. However, for the assessment of the vibration mitigation efficiency, the response behind the trench is more important than the deformation of the trench itself or the stress concentrations around it [7]. Therefore satisfactory precision is reached for the investigated problem, using the ITM-FEM approach.
In the following sections the influence of the trench length and depth as well as the distance of the load from the trench is investigated and finally compared to results obtained for the infinite trench.

Variation of the excitation frequency

Figure 10a shows the absolute value of the vertical displacements at $x = 0$ over the y due to a harmonic $1.2\,\mathrm{x}\,1.2$ m block load located at $y_{\mathrm{load}} = -3$ m with excitation frequencies of 12 Hz and 22 Hz. The corresponding amplitude reduction factor A_r is depicted in Figure 10b. As the frequency changes, also the Rayleigh wavelength and therefore the relative dimensions of the open trench vary. At $f = 12$ Hz, λ_r results in 5.5 m and thus $D_{\mathrm{tr}} = 0.69$, $W_{\mathrm{tr}} = 0.22$ and $L_{\mathrm{tr}} = 0.87$, whereas for $f = 22$ Hz the Rayleigh wave length is $\lambda_r = 2.9$ m and thereby $D_{\mathrm{tr}} = 1.31$, $W_{\mathrm{tr}} = 0.41$ and $L_{\mathrm{tr}} = 1.65$. The amplitude reduction for 12 Hz, depicted in Figure 10e, is rather limited as a significant part of energy passes below the open trench. With increasing frequency the penetration depth of the Rayleigh wave reduces and therefore the mitigation efficiency rises, as can be seen in Figure 10f showing A_r for an excitation frequency of 22 Hz. Amplifications of the displacement amplitudes can be observed in front of the trench and at the sides as well as a reduction behind the trench. For small ratios $l_{\mathrm{tr}}/\lambda_r$ amplifications occur also directly behind the open trench, a phenomenon which was also observed by Woods [2] experimentally. Due to the small trench length, especially for lower frequencies, the waves travel around the trench thereby causing this amplifications, as can clearly be seen in Figure 10c. With increasing dimensionless length and depth the mitigation efficiency rises and thus the shadow zone enlarges and gets more defined.

Variation of load position

Dolling [1] showed that above a certain trench length the shielding effect no longer changes significantly and concluded that an radiation angle of $45° - 56°$ leads to an effective vibration reduction. Also Woods [2] found that larger trenches are required at greater distance from the source to achieve a certain amplitude reduction. Therefore in this section the variation of the load position with a fixed open trench length, depth and width is investigated as depicted in Figure 11a. This leads to a variation of the radiation angle

$$\alpha = \tan^{-1}\left(\frac{L_{\mathrm{tr}}/2}{L_{\mathrm{load}} - W_{\mathrm{tr}}/2}\right) \tag{19}$$

of the waves on the open trench of $45°$ for $y_{\mathrm{load}} = -3$ to $10°$ for $y_{\mathrm{load}} = -14$ and therefore a different shielding zone and mitigation efficiency. Figure 11b shows the amplitude reduction factor $A_r(x = 0, y, z = 0, \omega)$ for load positions $y_{\mathrm{load}} = -3,\ -8,\ -14$ due to an excitation with $f = 22$ Hz. With increasing y_{load} the amplitude reduction at some distance behind the trench decreases substantially, which fits well to Woods's [2] statement, that the screening efficiency is larger, if the trench is positioned close to the source.

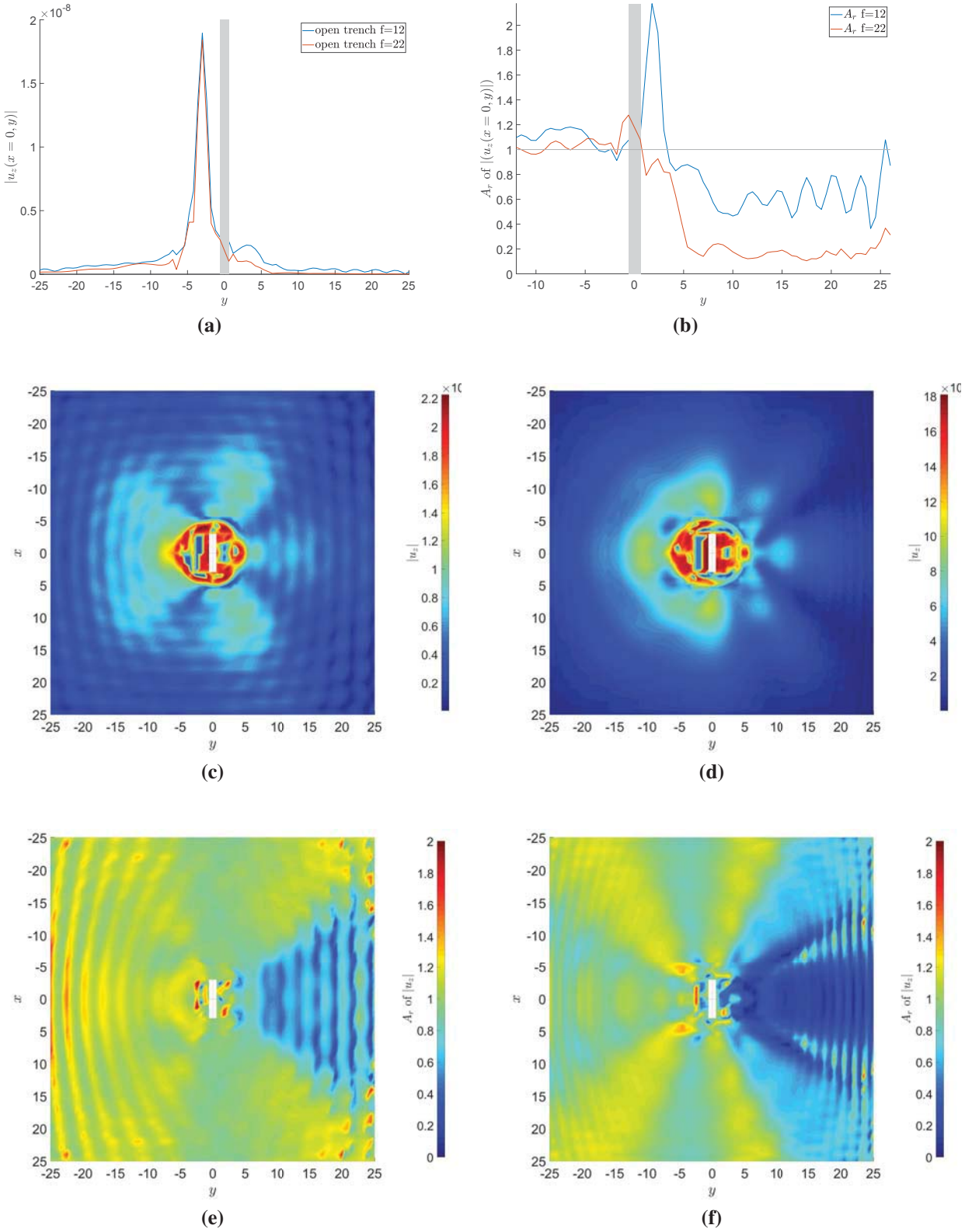

Figure 10: (a) Absolute value $|u_z(x = 0, y, z = 0, \omega)|$ and (b) corresponding A_r. (c,e) Real part of the vertical displacement $u_z(x, y, z = 0, \omega)$ and A_r of $|u_z(x, y, z = 0, \omega)|$ for $f = 12$ Hz and (d,f) for $f = 22$ Hz.

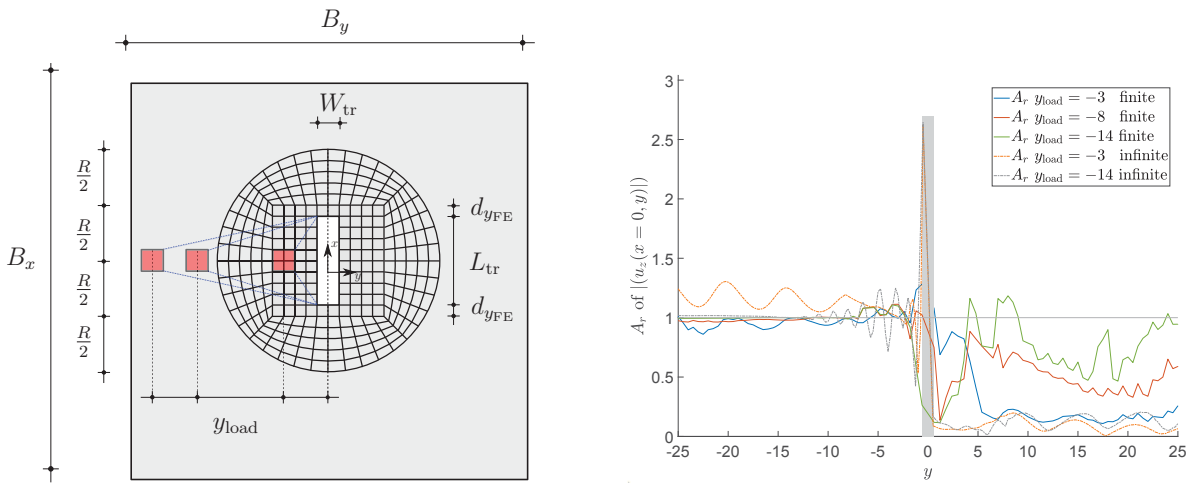

Figure 11: (a) Setup for variation of load position and radiation angle (blue lines). (b) Amplitude reduction factor A_r of $|u_z(x = 0, y, z = 0, \omega)|$ for different load positions y_{load} for the finite and the infinite open trench.

This is further confirmed, when the amplitude reduction factors for different load positions considering the infinitely long trench is opposed to the ones obtained for the finite open trench as depicted also in Figure 11b as well. The variation of A_r due to different load positions is very small for the length invariant open trench because the radiation angle is not relevant in this case, as there is no possibility for the waves to travel around open trench. A more exposed peak in front of the trench can be observed in the 2.5D case because a bigger part of the incoming waves is reflected leading to a lower A_r over the whole length behind the trench.

5 CONCLUSIONS

In this paper a coupled Integral Transform Method - Finite Element Method approach for the Soil Structure Interaction of length invariant (2.5D) and finite (3D) structures has been presented. Therefore fundamental solutions of the Lamé differential equation were superposed in order to gain the systems halfspace with partially or fully embedded cylindrical or spherical cavity. At the cavity boundaries a FEM substructure is coupled to the ITM using a direct stiffness coupling by enforcing the continuity of displacements and the equilibrium of forces. The proposed methodology was validated by comparison with the analytical solution of a homogeneous halfspace for the 2.5D and the 3D approach.
Within the FEM region, structures with more complex geometry and material distribution can be modeled. This was used to investigate the vibration reduction efficiency of longitudinally infinite open trenches and barriers with soft or stiff infill material. The normalized depth of the barrier and the stiffness contrast between infill material and soil are found to be the most important parameters for the performance of the screening measure. More shallow barriers with less pronounced stiffness contrast, as in case of subgrade stiffening, act as wave impeding barrier up from a critical frequency and provide a significant insertion loss within an area delimited by a critical angle. For deeper stiff or soft filled barriers with distinct stiffness contrast the performance is similar to an open trench.
In case of spatially limited open trenches also the dimensionless length plays an important role. As diffraction occurs at the sides of the trench additionally to the bottom, more complex wave interference patterns occur. The radiation angle and therefore the distance of the source from the trench has fundamental impact on the mitigation efficiency, which is not the case for length invariant trenches.

REFERENCES

[1] H.-J. Dolling, Die Abschirmung von Erschütterungen durch Bodenschlitze, Disseration, TU Berlin, Berlin, 1969.

[2] R. D. Woods, Screening of surface waves in soils, Soil mechanics and foundations division (1968) 951–980.

[3] G. Segol, J. F. Abel, P. C. Y. Lee, Amplitude reduction of surface waves by trenches, Journal of the Engineering Mechanics Division 104 (1978) 621–641.

[4] W. A. Haupt, Surface-waves in non-homogeneous halfspace, Proc. Dyn. Meth. in Soil and Rock Mech. (1978) 335–367.

[5] K. Emad, G. D. Manolis, Shallow trenches and propagation of surface waves, Journal of Engineering Mechanics 111 (1985) 279–282.

[6] D. E. Beskos, B. Dasgupta, I. G. Vardoulakis, Vibration isolation using open or filled trenches, Computational Mechanics (1986) 43–63.

[7] B. Dasgupta, D. E. Beskos, I. G. Vardoulakis, Vibration isolation using open or filled trenches part 2: 3-d homogeneous soil, Computational Mechanics 6 (1990) 129–142.

[8] K. L. Leung, D. E. Beskos, I. G. Vardoulakis, Vibration isolation using open or filled trenches, Computational Mechanics 7 (1990) 137–148.

[9] S. Ahmad, T. M. Al-Hussaini, Simplified design for vibration screening by open and in–filled trenches, Journal of Geotechnical Engineering 117 (1991) 67–88.

[10] G. Pflanz, K. Hashimoto, N. Chouw, Reduction of structural vibrations induced by a moving load, Journal of Applied Mechanics 5 (2002) 555–563.

[11] L. Andersen, S. Nielsen, Reduction of ground vibration by means of barriers or soil improvement along a railway track, Soil Dynamics and Earthquake Engineering 25 (2005) 701–716.

[12] M. Adam, O. von Estorff, Reduction of train-induced building vibrations by using open and filled trenches, Computers & Structures 83 (2005) 11–24.

[13] P. Coulier, S. François, G. Degrande, G. Lombaert, Subgrade stiffening next to the track as a wave impeding barrier for railway induced vibrations, Soil Dynamics and Earthquake Engineering 48 (2013) 119–131.

[14] S. François, M. Schevenels, B. Thyssen, J. Borgions, G. Degrande, Design and efficiency of a composite vibration isolating screen in soil, Soil Dynamics and Earthquake Engineering 39 (2012) 113–127.

[15] S. François, M. Schevenels, P. Galvín, G. Lombaert, G. Degrande, A 2.5d coupled fe–be methodology for the dynamic interaction between longitudinally invariant structures and a layered halfspace, Computer Methods in Applied Mechanics and Engineering 199 (2010) 1536–1548.

[16] C. F. Long, On the completeness of the lamè potentials, Acta Mechanica 3 (1967) 371–375.

[17] G. Müller, Ein Verfahren zur Erfassung der Fundament-Boden Wechselwirkung unter Einwirkung periodischer Lasten, Dissertation, Technische Universität München, München, 1989.

[18] M. Hackenberg, M. Dengler, G. Müller, Implementation of the finite element method in the fourier-transformed domain and coupling with analytical solutions, in: Cunha A., Caetano E., Ribeiro P., Müller G (Ed.), Eurodyn.

[19] A. C. Eringen, E. S. Suhubi, Elstodynamics, Vol. II.(Linear Theory), Academic Press: New York, 1975.

[20] A. Sommerfeld, Partial differential equations in physics, volume 1 of */Pure and applied mathematics*, Acad. Pr, New York, 1964.

[21] G. Frühe, Überlagerung von Grundlösungen in der Elastodynamik zur Behandlung der dynamischen Tunnel-Boden-Bauwerk-Interaktion, Dissertation, Technische Universität München, München, 2010.

[22] M. Hackenberg, A Coupled Integral Transform Method - Finite Element Method Approach to Model the Soil-Structure-Interaction, Dissertation, Technische Universität München, München, 2016.

[23] J. Freisinger, M. Hackenberg, G. Müller, A coupled integral transform method - finite element method approach to model the soil structure interaction of finite (3d) and length invariant (2.5d) systems, Journal of Sound and Vibration 482 (2020) 115443.

[24] J. Freisinger, G. Müller, Modellierung eines halbraums mit sphärischem oder zylinderförmigem hohlraum für dreidimensionale boden-bauwerk-interaktion, Forschung im Ingenieurwesen 83 (2019) 31–42.

[25] W. A. Haupt, Wave propagation in the ground and isolation measures, International Conferences on Recent Advances in Geotechnical Earthquake Engineering and Soil Dynamics (1995).

[26] D. J. Thompson, J. Jiang, M. Toward, M. Hussein, E. Ntotsios, A. Dijckmans, P. Coulier, G. Lombaert, G. Degrande, Reducing railway-induced ground-borne vibration by using open trenches and soft-filled barriers, Soil Dynamics and Earthquake Engineering 88 (2016) 45–59.

[27] P. Coulier, A. Dijckmans, S. François, G. Degrande, G. Lombaert, A spatial windowing technique to account for finite dimensions in 2.5d dynamic soil–structure interaction problems, Soil Dynamics and Earthquake Engineering 59 (2014) 51–67.

[28] T. Bose, D. Choudhury, J. Sprengel, M. Ziegler, Efficiency of open and infill trenches in mitigating ground-borne vibrations, Journal of Geotechnical and Geoenvironmental Engineering 144 (2018) 04018048.

EURODYN 2020
XI International Conference on Structural Dynamics
M. Papadrakakis, M. Fragiadakis, C. Papadimitriou (eds.)
Athens, Greece, 23–26 November 2020

SOIL-STRUCTURE INTERACTION OF AN END-BEARING PILE FOUNDATION: DESIGN OF AN EXPERIMENTAL CASE STUDY

Freddie Theland[1], Jean-Marc Battini[1], Costin Pacoste[1], Geert Lombaert[2], Stijn François[2], Peter Blom[3], and Fanny Deckner[4]

[1]KTH Royal Institute of Technology
Brinellvägen 23, 100 44 Stockholm, Sweden
e-mail: {freddie.theland, jean-marc.battini, costin.pacoste}@byv.kth.se

[2]KU Leuven
Kasteelpark Arenberg 40, 3001 Leuven, Belgium
e-mail: {geert.lombaert, stijn.francois}@kuleuven.be

[3]ACAD-International AB
Sveavägen 151, 113 46 Stockholm, Sweden
e-mail: peter.blom@acad.se

[4]Geomind KB
Hesselmans Torg 5, 131 54 Nacka, Sweden
e-mail: fanny.deckner@geomind.se

Keywords: End-bearing piles, Pile group, Dynamic soil-structure interaction, Ground vibrations.

Abstract. *The construction of apartment and office buildings close to road or rail traffic is becoming more frequent in urban areas. These sites are however prone to issues of disturbing vibrations in nearby buildings induced by traffic. In Sweden, designing building foundations with pre-fabricated end-bearing concrete piles is often a necessary and economical measure when soil conditions are poor. Although pile groups have been studied extensively in the context of seismic analysis, there are limited experimental results on the response of end-bearing pile groups due to ground vibration evoked by sources acting on the soil's surface. This paper presents the design of an experimental case study of an end-bearing pile group, aimed at validating models for predicting vibration levels in piled buildings. The test site is presented with results from geotechnical and geophysical site investigations. The experimental setup is outlined, describing measurements taken at each stage of construction of the pile group. Results from numerical simulations demonstrate a different behaviour of the pile group in comparison to an equally large surface foundation.*

1 INTRODUCTION

The densification of the urban environment drives the desire to build on previously unused land close to railway lines or heavily trafficked major roads. When utilizing land close to traffic lines for apartment or office buildings, the risk for comfort disturbing vibrations induced by traffic becomes imminent. Therefore, assessment of expected vibration levels should be carried out prior to construction. In the Stockholm area, and in many other regions in Sweden, the railway network is partially constructed in areas with relatively shallow glacial clay deposits overlaying a high quality bedrock. On such sites, end-bearing pre-fabricated concrete piles are commonly used when constructing building foundations. Soil-structure interaction of different types of pile foundations has been extensively analysed in the literature through numerous numerical models and experiments. However, the vast majority of experimental studies available in the literature have mainly been focused on the local behaviour of floating piles and pile groups. There is limited experimental data presented in the literature on the response of end-bearing pile groups, and especially considering the response due to distant sources acting on the ground surface. Moreover, most studies consider only the narrow frequency range of interest in earthquake engineering, and there are few studies covering the full frequency range 1–80 Hz, relevant for the analysis of traffic induced vibrations [5].

This paper presents the design of an experimental case study with the purpose of validating prediction models for the transmission of vibrations through soil to end-bearing pile foundations. The experiment concerns the dynamic response of a 2×2 pile group with pre-fabricated end-bearing concrete piles subjected to controlled dynamic excitation in the frequency range 1–80 Hz. The experiment is performed in phases of staged construction at a site with a minimum of outside disturbance, allowing to isolate the influence of the addition of the foundation to the site. To determine the ability of numerical models to capture the influence of the embedment in the soil on the bending behaviour of the piles, and thereby the kinematic interaction, measurements are performed at various depths along the center lines of the piles. The objective of the paper is to document and motivate the design of the proposed experiment. The site is presented in section 2 with the identified soil properties obtained from site investigations. Section 3 describes the measurement setup, the geometry of the test foundation and the data to be acquired. Section 4 presents numerical predictions of the expected response of the pile foundation. Finally, section 5 concludes the paper.

2 MEASUREMENT SITE

2.1 Location

The measurement site is located in Brottby, about 40 km north of Stockholm, Sweden, at a remote field that has not been cultivated for more than five years. There is a small private road adjacent to the site and a single inhabited house close by. Thereby, the experimental environment is considered to have a high degree of control while maintaining realistic field conditions. An overview of the site is presented in fig. 1.

2.2 Stratification

An extensive geotechnical site characterization has been performed at the site, consisting of weight probing, bedrock probing, cone peneration tests (CPT) and laboratory testing of undisturbed soil samples. The soil profile at the site consists of a top 1 m thick layer of stiff dry-crust clay, a 3.5 m body of soft clay and 2 m layer of moraine on top of a stiff bedrock. A summary

Figure 1: Overview of the experimental site in Brottby outside of Stockholm.

of the clay profile properties obtained from laboratory measurements of the clay is presented in table 1 and the interpreted soil profile is presented in fig. 2, where the points and depths of investigation are indicated.

Depth	Density	Water content	PI	τ_{cu}	OCR	K_0
[m]	[kg/m^3]	[%]	[%]	[kPa]	[-]	[-]
1	1880	31.8	-	54.4	5*	-
2	1570	78.2	34	19.6	2.6	0.86
3	1720	53.6	29	19.2	1.9	0.74
4	1780	47.2	24	23.1	1.9	0.66

* Estimated from CPT correlations.

Table 1: Clay soil properties obtained from laboratory measurements.

2.3 Dynamic soil properties

The small strain dynamic properties that characterise the mechanical behaviour of the soil are the soil density ρ, P- and S-wave velocities C_{p} and C_{s} and the corresponding damping ratios β_{p} and β_{s}. The soil density of the clay is obtained directly from the laboratory measurements, while the underlying moraine and bedrock densities are assumed using typical values used in geotechnical design. The P- and S-wave velocities of the soil are estimated from in-situ and laboratory testing. Material damping ratios are assumed equal for P- and S-waves and are estimated from the geophyscial tests. The oedometer and triaxial aparatuses used in the laboratory testing were additionally equipped with bender elements (BE), allowing to determine S-wave velocities of undisturbed soil samples reloaded to their in-situ stress states. The material samples were taken at point 13 in fig. 2, where the pile group is constructed. In addition to the laboratory measurements, in-situ testing has been performed by means of two seismic cone penetration tests (SCPT) carried out at points 13 and 8 in fig. 2, a seismic refraction test and spectral analysis of surface waves (SASW) based on the vertical acceleration responses of the soil along a line between points 9 and 12 in fig. 2. The seismic refraction test yields estimates of P-wave velocities while the SCPT and SASW tests yield S-wave velocities. However, P-wave velocities

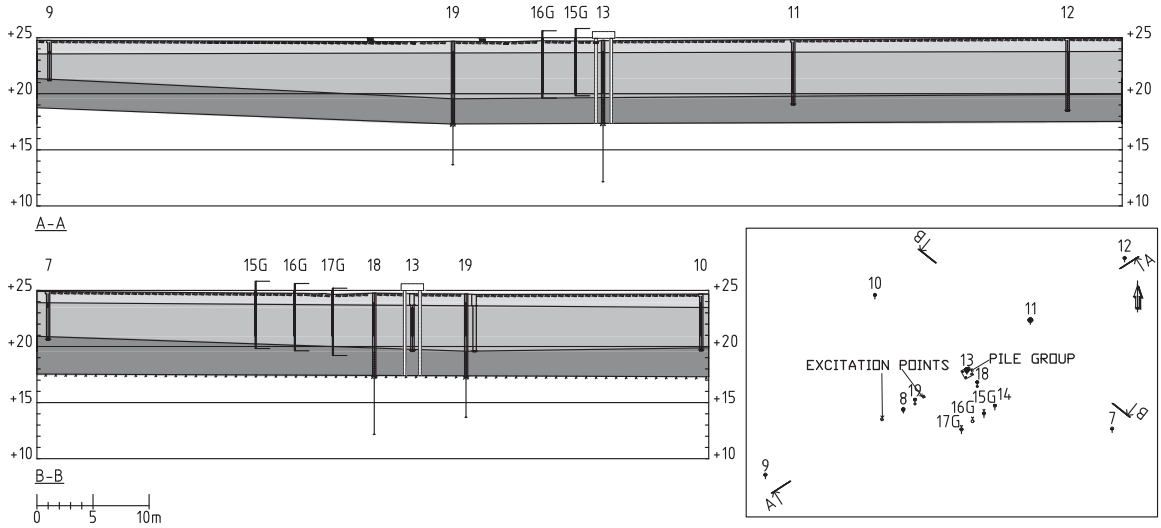

Figure 2: Geotechnical investigation points (numbered) in topview (down-right corner) and sections with shading indicating the interpreted stratification at the site with moraine (bottom), clay (mid-layer) and dry-crust and topsoil (top-layer). The position of the pile group and excitation points on the soil surface are indicated in relation to the investigation points.

are assumed uniform below 1 m depth, due to the full saturation of the clay. A summary of the estimated small-strain dynamic properties of the profile based on the aforementioned tests is presented in table 2.

Depth	Layer thickness	ρ	C_p	C_s	β_p	β_s
[m]	[m]	[kg/m^3]	[m/s]	[m/s]	[-]	[-]
0.66	0.66	1880	129	66	0.05	0.05
1.08	0.42	1880	420	139	0.02	0.02
1.73	0.65	1720	1450	103	0.02	0.02
4.23	2.5	1780	1450	84	0.02	0.02
6.23	2	2300	1450	600	0.02	0.02
∞	∞	2700	3500	2500	0.02	0.02

Table 2: Estimated dynamic soil properties at the test site in Brottby.

3 EXPERIMENTAL SETUP

The investigation concerns a 2×2 pile group constructed of prefabricated concrete piles with a square 235×235 mm cross section, illustrated in fig. 3. The pile cap is cast so that it is slightly elevated from the ground. Thereby, only the piles are in contact with the soil. The four plies are driven to bedrock at a depth of approximately 6.5 m and are separated by a distance of 1365 mm. To enable measurements to be performed at depth, a $\varnothing 76$ mm plastic pipe is cast along the center line of each pile. To replicate the case of vibrations induced by nearby sources at the surface, two positions on the surface with a distance 10 and 20 m to the front of the pile cap are considered. At each position, a concrete foundation of dimension 0.5×0.5×0.2 m is cast

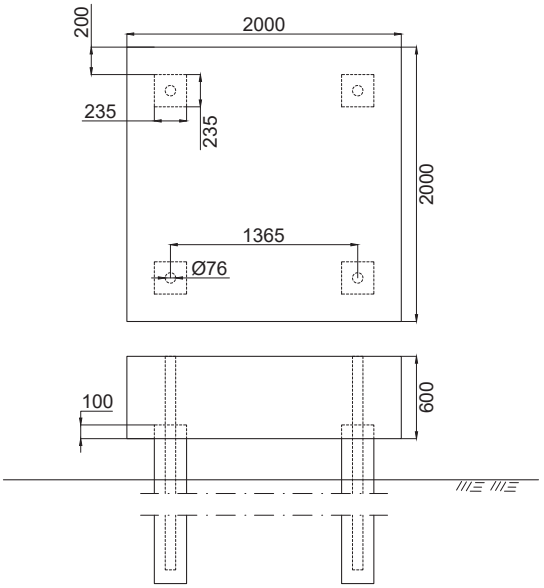

Figure 3: Dimensions in millimetres of the case-study pile foundation.

in place to allow for dynamic excitation (see fig. 5b). Accelerometers are mounted at the soil's surface in the vertical direction and in the horizontal direction, aligned with the propagation path between the excitation points and the construction site. Additional sensors are placed symmetrically at a distance 20 m perpendicularly from the line between the excitation points, to serve as reference points to control for temporal variations in between measurements. Figure 4 presents an illustration of the setup.

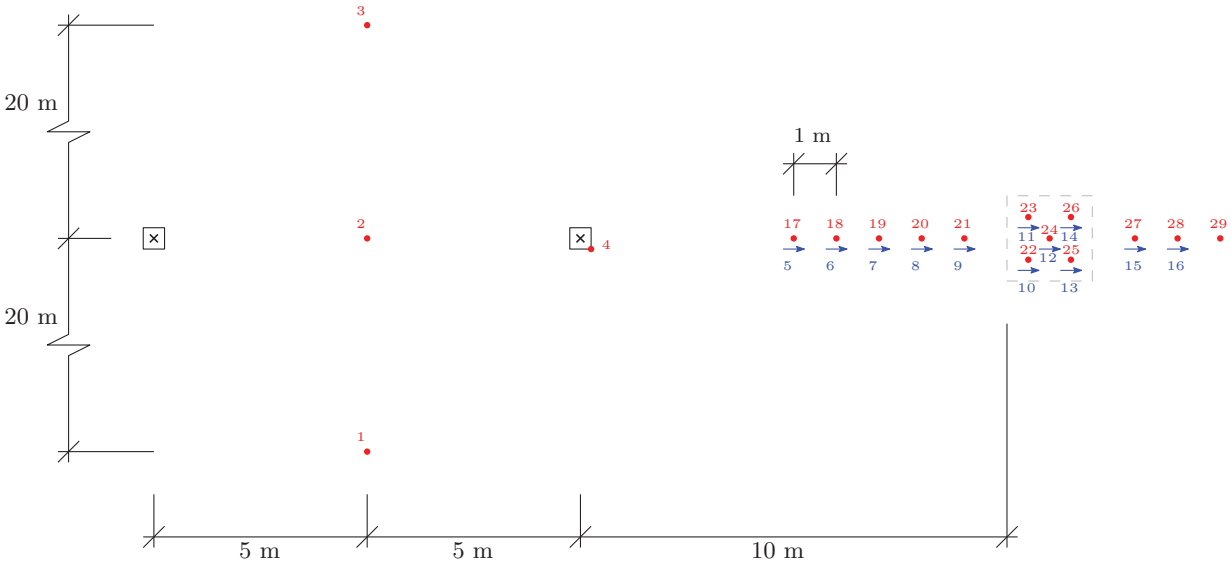

Figure 4: Measurement setup in Brottby. Excitation positions are indicated by an $\times$, vertical measurement channels by a dot and horizontal channels by an arrow.

To reduce the uncertainty regarding the stiffness of the piles, an experimental modal analysis test has been carried out in the factory after the casting of the piles, suspending one of the piles in flexible springs to simulate free-free boundary conditions. In order to identify the material

properties of the reinforced concrete beam, the experimentally obtained natural frequencies and bending modes are matched with an analytical model of the free-free beam. The model updating yield an equivalent modulus of elasticity $E_{\mathrm{p}} = 39$ GPa with a Poisson's ratio $\nu_{\mathrm{p}} = 0.2$ and density $\rho_{\mathrm{p}} = 2400$ kg/m^3 for the concrete piles.

3.1 Dynamic measurements

The dynamic force is applied to the soil by means of a Wölfel BD.5 inertial shaker. The inertial shaker supplies a constant amplitude force over a frequency range 0.5–200 Hz with harmonic or band-limited noise excitation. Thereby, possible non-linearities can be investigated for the frequency band of interest by varying the excitation amplitude. The shaker is firmly mounted on the cast in place concrete foundations by means of threaded fittings. Additionally, an impact sledgehammer Dytran 5803 series is used for impact testing whenever mounting the shaker in place is infeasible, e.g. when determining pile impedances. The responses on the soil's surface are measured by 20 PCD 393A03 and 9 PCB 393B31 accelerometers, with sensitivities 1 and 10 V/g, respectively. The more sensitive sensors are used for the most distant vertical measurements. The accelerometers are mounted on aluminium pickets with a curciform section of dimensions $40 \times 40 \times 300$ mm and are shown mounted in the soil in fig. 5c. The soil-picket-sensor dynamic system is verified experimentally to have a natural frequency well above the frequency band of interest (1-80 Hz) when mounted at site, according to the recommendations given by Degrande et al. [2] and Hunaidi and Rainer [4]. After installation of the sensor pickets in the ground, they are left in place to ensure that the position and mounting is the same in between measurement sessions. Responses in the piles at depth are measured with sensors attached to a pneumatic device, equipment originally designed for seismic exploration in boreholes (see e.g. [8]). The cavity along the centreline of the piles makes it possible to mount the sensors at arbitrary depth, allowing to determine the frequency response at any number of measurement points along the piles with a limited amount of sensors.

(a) (b) (c)

Figure 5: Dynamic measurement equipment: (a) Wölfel BD.5 inertial shaker, (b) Dytran 5803 series impact sledge hammer and (c) PCB 393A03 accelerometers mounted on aluminium pickets.

3.2 Measurements at different phases of construction

For the purpose of response prediction, it is desirable to relate the foundation response to the free-field response measured at the surface prior to installation of the foundation. As the dynamic behaviour of the system is modified at each phase of construction, the influence of the piles and the interaction through the union of the pile tops in the pile cap are tracked by performing response measurements at three different stages of construction (with reference to fig. 6):

1. At the soil surface prior to construction due to distant excitation (P_1) from L =10 and 20 m.
2. On the pile tops and in the surrounding soil due to excitation of the piles in three directions (P_2) as well as excitation vertically (P_1) from the two distances $L = 10$ and 20 m.
3. On the pile cap and in the surrounding soil due to excitation of the pile group in three directions (P_2) as well as distant vertical excitation (P_1) for $L = 10$ and 20 m.

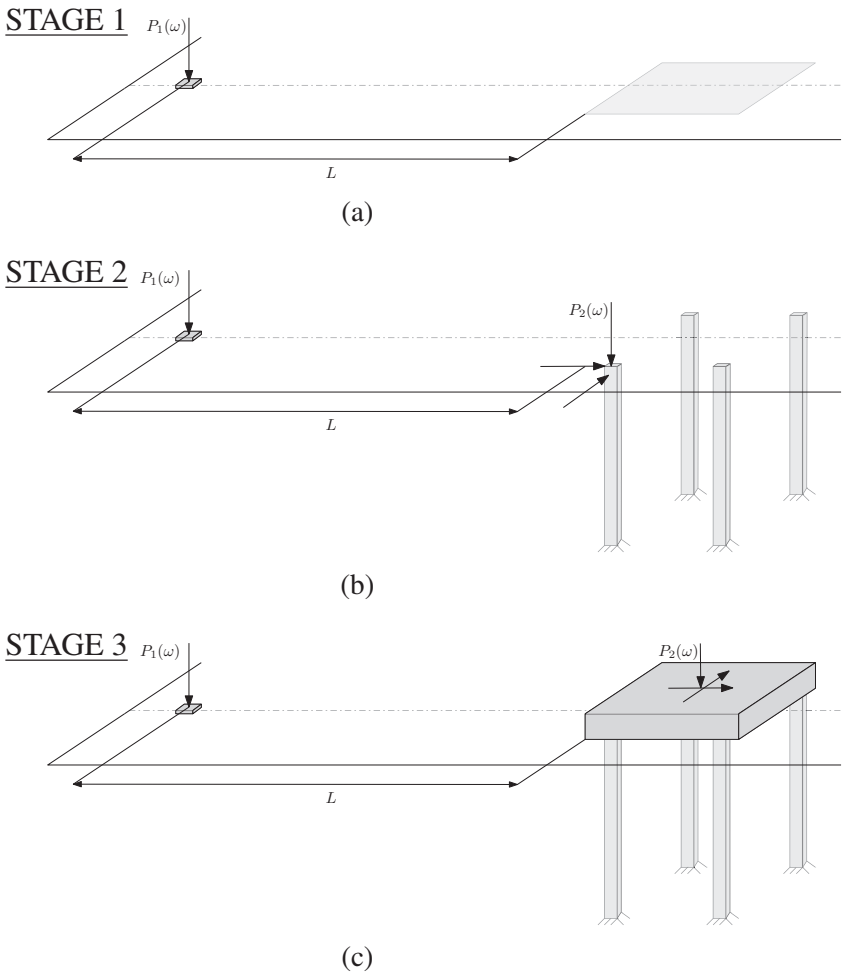

Figure 6: Illustration of the measurements during the different construction stages (a) in the free field, (b) where only piles are installed and (c) where the full pile group is constructed.

Measuring at the different phases of construction of the foundation allows to extract the responses and impedances of the individual piles and the impedance of the pile group when joined

through the cap. This way, data is collected at each step in the construction process whenever additional complexity is added to the system. Thereby, model validation can be performed at each stage of construction. Furthermore, prediction methods using the information acquired in the first or second construction stage to make predictions of the joined pile group's behaviour can be analysed and evaluated. Such methods can be purely empirical models or hybrid models that merge experimental data and numerical predictions, e.g. the strategy followed by François et al. [3] using the method of joining subsystems [6], where hybrid predictions are made based on experimentally obtained pile top impedances and pile top responses due to distant excitation, in combination with a numerical model of the structure joining the pile tops.

4 NUMERICAL PREDICTIONS

To assess the experimental setup, preliminary numerical simulations are performed using a numerical model of the site and the pile group. A comparison is made to the case where instead of a pile foundation, a surface foundation of the same size as the pile cap is considered. Additionally, the corresponding response at the free ground surface at the position of the foundation is considered as a reference to both cases, highlighting the differences of the responses of the two foundation types in relation to the measured velocity at the free surface.

4.1 Numerical model

Simulations are conducted based on the assumption of small strains, so that the soil can be considered linear elastic. A finite element model is constructed to simulate the response of the pile group due to dynamic excitation using the software `Comsol Multiphysics`. The model is composed of solid elements to model both the pile group and the soil. The pile group material properties are set to the experimentally identified ones presented in section 3. The soil layer material properties are defined in accordance with table 2, except for the bedrock which is replaced by a fixed boundary condition. As the problem is symmetric along the path between the source and the receiver, a symmetry condition is applied. The radiation condition is fulfilled by using Perfectly Matched Layers (PML), applied in a zone closest to the boundary in fig. 7, attenuating any outgoing waves before hitting the fixed outer boundary of the model. The PML stretch functions are defined in accordance with the ones proposed by Basu and Chopra [1] and have been verified to efficiently absorb outgoing waves when compared to Green's functions of the profile, corresponding to the exact solutions of a point load, computed with the Direct stiffness method using the Matlab toolbox EDT [7].

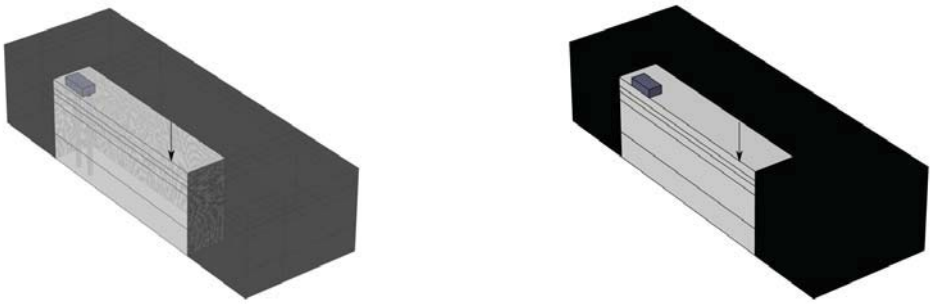

(a) (b)

Figure 7: Geometry of single symmetric finite element model of the (a) pile foundation and (b) surface foundation. The arrow indicates the position and direction of the applied load at the offset 10 m and the outer black partitions of the model correspond to the zone of Perfectly Matched Layers (PML).

4.2 Simulation results

The vertical and horizontal responses of the pile- and surface foundation due to a vertical point load applied at the soil surface at a 10 m distance are compared to the responses at the free surface corresponding to the mid-point of the foundations. Figure 8 compares the velocity responses of the reference points for all three cases. The surface foundation amplifies both the vertical and horizontal responses in the lower frequency range, while acting as a filter at higher frequencies where the dimensions of the foundation are comparable to the wavelengths of the surface waves.

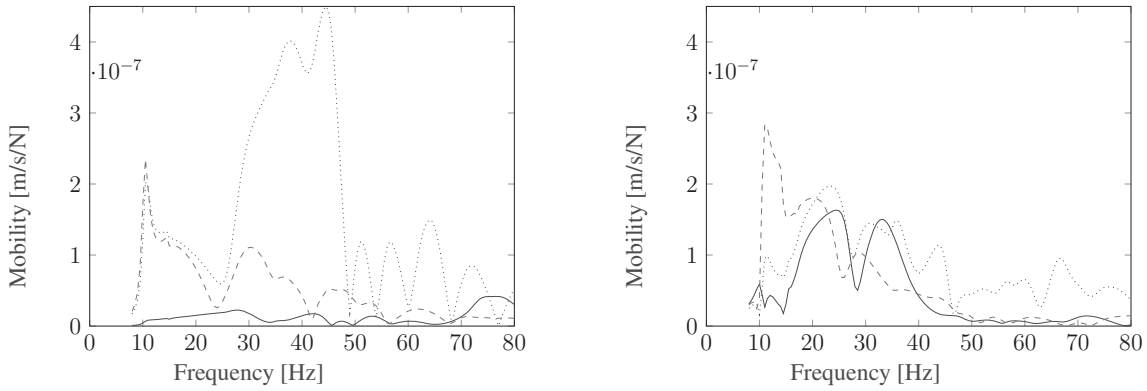

(a) (b)

Figure 8: Velocity response at a 10 m distance from the source at the free surface (dotted line), mid-point surface foundation (dashed line) and mid-point pile cap (solid line) in the (a) vertical direction and (b) horizontal direction.

The pile group, on the other hand, presents a different behaviour, where the vertical response in the lower frequency range is suppressed, while a higher response is found in the frequency range 70–80 Hz, compared to the surface foundation. The horizontal motion of the pile group shows a similar response as the free surface in the frequency range 10–40 Hz. The horizontal

motion of the surface foundation shows a similar trend as the vertical motion, where an amplification of the response is found for lower frequencies while higher frequencies are attenuated.

5 CONCLUSION

Traffic induced vibrations are becoming a concern when constructing apartment or office buildings in the vicinity of major roads or railway lines. When building on sites with poor soil conditions, pre-fabricated concrete piles are an economical choice for constructing the foundation. Although many different modelling approaches exist for making predictions of the response of piled foundations, there is a lack of experimental evidence of the ability to predict the response of end-bearing piles when subjected to distant excitation on the soil's surface.

The design of an experimental campaign investigating the dynamic response of a pile group due to small strain incident loading is presented. The aim of the experiment is to validate models used for the prediction of traffic induced vibrations in buildings. The experiment is conducted at a remote site in the vicinity of Stockholm, where no outside disturbance or construction activity is present. The site's soil profile consists of a shallow layer of soft clay on top of a bottom layer of moraine resting on a high quality bedrock. Multiple geophyscial tests are performed, yielding dynamic soil parameters used as input for model predictions. At this site, a 2×2 concrete pile group is constructed using conventional pre-fabricated concrete piles, joined by a $2 \times 2 \times 0.6$ m concrete pile cap.

Controlled dynamic excitation is applied at the construction site from distances of 10 and 20 m at different stages of construction. Measurements are taken at the undisturbed soil surface before construction, after the piles are driven and finally when the pile tops are joined in the pile cap. Responses are measured along the propagation path in the soil, along the center line of the embedded piles and on top of the pile cap. Numerical simulations of the experimental setup show a different behaviour of the pile group compared to a surface foundation of the same dimensions, demonstrating that the foundation type has a large influence on the transmission of vibrations for the proposed setup.

6 ACKNOWLEDGEMENTS

This work is supported by the Development Fund of the Swedish Construction Industry, SBUF. The funding for experiments and site investigations is received from Vinnova, the Richertska foundation and Trafikverket. The financial support is gratefully acknowledged. The authors would like to thank the Swedish Geotechnical Institute (SGI) for assisting with the laboratory analysis of the soil samples.

REFERENCES

[1] U. Basu and A. K. Chopra. Perfectly matched layers for time-harmonic elastodynamics of unbounded domains: theory and finite-element implementation. *Computer Methods in Applied Mechanics and Engineering*, 192(11):1337 – 1375, 2003. ISSN 0045-7825. doi: https://doi.org/10.1016/S0045-7825(02)00642-4.

[2] G. Degrande, P. Van den Broeck, and D. Clouteau. A critical appraisal of in situ vibration measurements. In *3rd European conference in Structural Dynamics*, pages 1107–1116, Florence, 2014. Balkema. ISBN 9054108134.

[3] S. François, M. Schevenels, G. Lombaert, and G. Degrande. Numerical modeling and in situ vibration measurements during the design and construction of low vibration floors at

the Corelab 1B research facility. *Proceedings of ISMA 2014 - International Conference on Noise and Vibration Engineering and USD 2014 - International Conference on Uncertainty in Structural Dynamics*, pages 935–950, 2014.

[4] O. Hunaidi and J. H. Rainer. Evaluation of measurement limits of transducer mountings in the ground. *Canadian Acoustics*, 18:15–27, 01 1990.

[5] K. Kuo and H. Hunt. Dynamic models of piled foundations. *Applied Mechanics Reviews*, 65:031003, 05 2013.

[6] P. Ropars. *Modélisation des vibrations d'origine ferroviaire transmises aux bâtiments par le sol*. PhD thesis, Universit Paris-Est, 2011.

[7] M. Schevenels, S. François, and G. Degrande. Edt: An elastodynamics toolbox for matlab. *Computers & Geosciences*, 35(8):1752 – 1754, 2009. ISSN 0098-3004. doi: https://doi.org/10.1016/j.cageo.2008.10.012.

[8] F. Thomas, J. von Ketelhodt, and Z. Lin. S-wave borehole tomography - a tool for geotechnical site characterization. In *7th International Conference on Environment and Engineering Geophysics and Summit Forum of Chinese Academy of Engineering on Engineering Science and Technology*, 2016/06. ISBN 978-94-6252-192-6.

EURODYN 2020
XI International Conference on Structural Dynamics
M. Papadrakakis, M. Fragiadakis, C. Papadimitriou (eds.)
Athens, Greece, 23–26 November 2020

VIBRATIONS OF RECTANGULAR FLEXIBLE FOUNDATION ON HALFSPACE

Marko Radišić[1], Mira Petronijević[1], and Gerhard Müller[2]

[1]University of Belgrade
Bulevar kralja Aleksandra 73, 11000 Belgrade, Serbia
e-mail: {mradisic,pmira}@grf.bg.ac.rs

[2] Technical University of Munich
Arcisstr. 21, 80333 Munich, Germany
e-mail: gerhard.mueller@tum.de

Keywords: Integral Transform Method, Dynamic Stiffness Method, Fourier Transforms, Modal Superposition Method, Substructure Method

Abstract. *A semi-analytical method deals with vertical vibrations of a massive, flexible rectangular foundation smoothly jointed to an elastic, homogeneous halfspace is presented. The method is based on the solution in frequency domain that represents a combination of the Integral Transform Method (ITM) used for the soil and the Dynamic Stiffness Method (DSM) used for the foundation. The coupling of the foundation and the soil is established using the modal superposition technique. The influence of the foundation mass and the foundation stiffness on the response of the system is analyzed. The accuracy of the results obtained by using the proposed technique is also discussed.*

1 INTRODUCTION

The dynamic response of rigid foundations on the elastic halfspace has been investigated extensively since the beginning of the last century [1]. The assumption that the foundation is rigid simplifies the solution. However, it is not applicable in the general case, since foundations exhibit flexural behavior. The response of the flexible foundation-soil system is affected by many factors, such as the foundation-soil stiffness ratio, the load distribution, the foundation mass, etc. The studies of the dynamic response of flexible foundations are mostly performed using a combined finite element method and Green's function [2, 3, 4, 5, 6, 7]. This is a computationally demanding approach, especially in the high frequency range. A more efficient technique is the one based on modal analysis that uses free vibration mode shapes of a plate and the modal stiffness matrix of the soil. This technique is used by Chen and Hou [8] to solve the problem of vibrations of circular flexible foundation. It requires the usage of the Bessel functions and the closed form stiffness matrices for wave propagation problems in layered media.

In this paper the solution for vertical vibrations of rectangular flexible foundations smoothly jointed to an halfspace is obtained. The Integral Transform Method (ITM) [9, 10], used to compute impedance functions of the soil, is combined with the Direct Stiffness Method (DSM) [11, 12], used to calculate the dynamic stiffness of the foundation plate, to obtain the response of flexible surface foundation in the frequency domain.

The ITM is based on solving Lamé's differential equations of motion, decoupling them using the Helmholtz decomposition and transforming them from partial to ordinary differential equations by a threefold Fourier Transform. The ordinary differential equations are solved in the transformed wavenumber-frequency domain by taking into account the boundary conditions of the system. The solution is transferred in the original space-time domain by using threefold inverse Fourier Transform.

The DSM is based on the exact solution of the governing differential equations of motion in the space-frequency domain. Consequently, the dynamic stiffness matrix of the element is frequency dependent. It can be developed explicitly for one-dimensional beam elements and Levy-type plates. In the case of plates with arbitrary boundary conditions, the plate displacements are presented in infinite series form, and the boundary problem is solved using the Projection method [15].

The soil-foundation interaction problem (FSI) is solved using the substructure approach and the modal superposition technique [8, 13, 14].

The proposed method is used to analyze the influence of the foundation mass and the foundation stiffness on the response of the system. Both perfectly flexible massive foundation and massive rigid foundation are analyzed. The obtained results are compared with the results from the literature.

2 FORMULATION OF THE PROBLEM

The formulation is derived by observing a steady state vertical vibrations of a rectangular flexible foundation on the surface ($z = 0$) of an elastic, homogeneous and isotropic half-space, Figure 1. It is assumed that the foundation behaves as a Kirchhoff plate and that the contact between the foundation and the soil is smooth. The foundation-soil system represents the assemblage of two substructures, namely the soil and the foundation. The solution is obtained using the substructure approach, i.e. each medium is considered separately and finally combined taken into account the equilibrium and compatibility conditions at the contact surface. In order to reduce the numerical effort the modal superposition is introduced. The displacement

field of the foundation is represented by a set of modal coordinates corresponding to free vibration mode shapes of a rectangular plate, while the influence of the soil reaction forces on the foundation is considered by introducing modal soil impedance functions. The response of the system is obtained in the frequency domain, (x, y, ω). Regarding the steady state analysis, the ω variable is omitted in the notation of the functions.

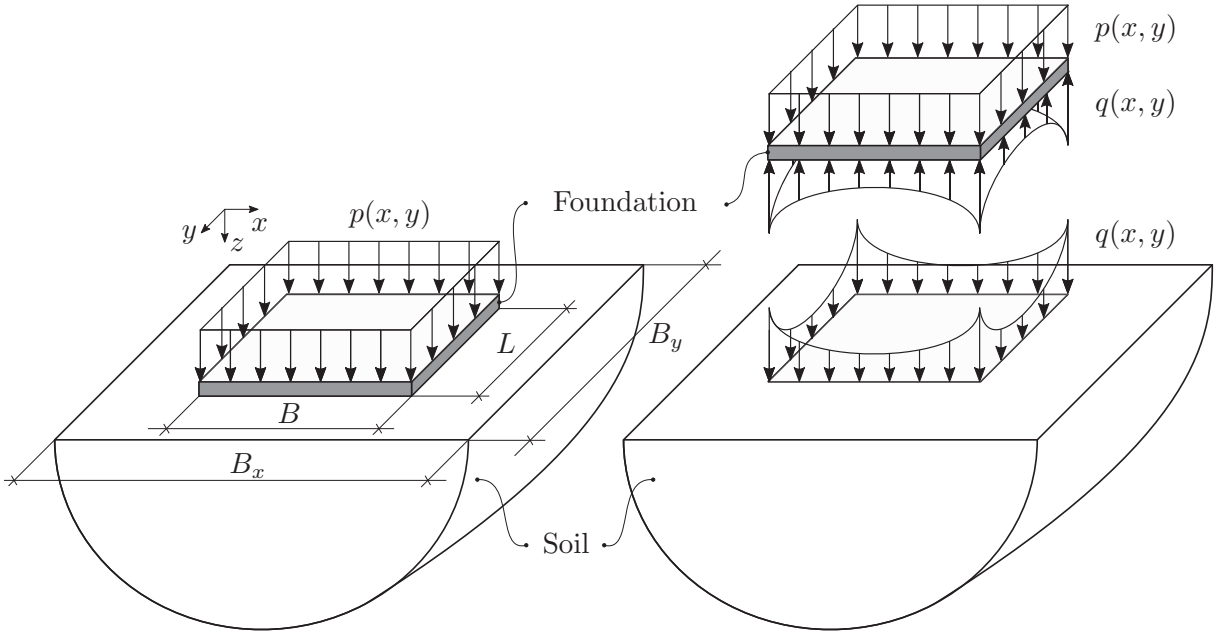

Figure 1: Disposition of the problem.

The differential equation of the problem in (x, y, ω) domain is given by

$$D\left(\frac{\partial^4 w(x,y)}{\partial x^4} + 2\frac{\partial^4 w(x,y)}{\partial x^2 \partial y^2} + \frac{\partial^4 w(x,y)}{\partial y^4}\right) - \rho h \omega^2 w(x,y) = p(x,y) - q(x,y) \tag{1}$$

where ω is the excitation frequency, D denotes the bending stiffness of the plate, $w(x, y)$ is the displacement field, ρ is the material density and h is the thickness of the plate. The bending stiffness of the Kirchhoff plate is defined as

$$D = \frac{Eh^3}{12(1-\nu^2)} \tag{2}$$

where E is Young's modulus, ν is Poisson's coefficient of the foundation. The functions $w(x, y)$, $p(x, y)$ and $q(x, y)$ are the transverse deflection of the foundation, the vertical load and the soil reaction, respectively. They can be expanded in a series of free vibration modes as follows:

$$w(x,y) = \sum_{n=0}^{N} Y_n \phi_n(x,y) \tag{3}$$

$$p(x,y) = \sum_{n=0}^{N} P_n \phi_n(x,y) \tag{4}$$

$$q(x,y) = \sum_{n=0}^{N} Q_n \phi_n(x,y) \tag{5}$$

where ϕ_n represents the orthonormalized mode shape of the foundation for the n^{th} mode and Y_n , P_n and Q_n are modal coefficients:

$$Y_n = \int_{x=0}^{B} \int_{y=0}^{L} w(x,y)\phi_n(x,y)dxdy \tag{6}$$

$$P_n = \int_{x=0}^{B} \int_{y=0}^{L} p(x,y)\phi_n(x,y)dxdy \tag{7}$$

$$Q_n = \int_{x=0}^{B} \int_{y=0}^{L} q(x,y)\phi_n(x,y)dxdy \tag{8}$$

The mode shapes of the foundation are obtained for the case of free vibrations of the completely free plate, solving the eigenvalue problem by using the DSM [11]. The general solution of the problem is of the form

$$\phi_n(x,y) = e^{k_{xn}x}e^{k_{yn}y} \tag{9}$$

where k_{xn} and k_{yn} are wavenumbers in x and y direction, such that

$$k_{xn}^2 + k_{yn}^2 = \pm\omega_n\sqrt{\frac{\rho h}{D}} \tag{10}$$

and ω_n is the n^{th} natural frequency of the plate. The problem is solved by introducing an infinite series of base solution in the (k_x^2, k_y^2) plane [15]. Figure 2 shows the first eight mode shapes of a Kirchhoff plate. The first mode is a translational mode. Substituting equations (6) and (9) into

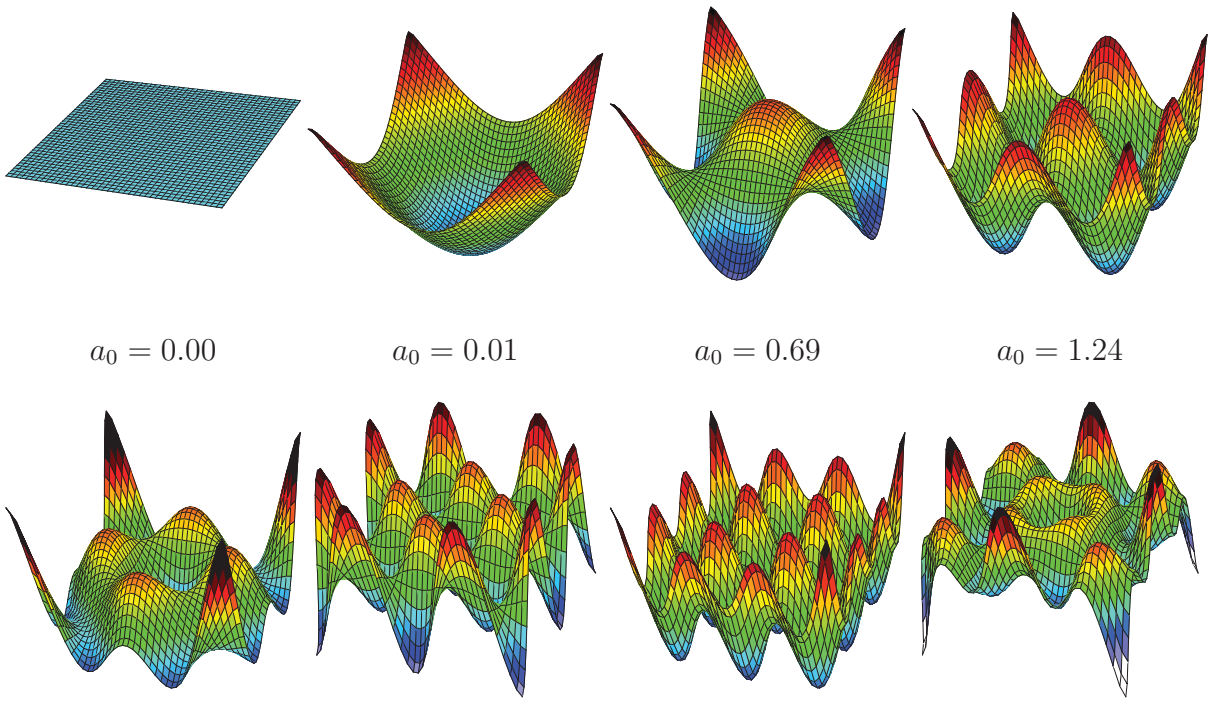

$a_0 = 0.00$ $a_0 = 0.01$ $a_0 = 0.69$ $a_0 = 1.24$

$a_0 = 1.75$ $a_0 = 2.96$ $a_0 = 3.05$ $a_0 = 3.54$

Figure 2: Free vibrations mode shapes of a rectangular foundation.

equation (1) gives

$$\sum_{n=0}^{N}\left(D(k_{xn}^4+2k_{xn}^2k_{yn}^2+k_{yn}^4)-\rho h\omega^2\right)\phi_n(x,y)Y_n=\sum_{n=0}^{N}\phi_n(x,y)P_n-\sum_{n=0}^{N}\phi_n(x,y)Q_n \quad (11)$$

Since the mode shapes ϕ_n are orthonormal, for a uniform mass distribution, equation (11) can be decoupled into N equations by multiplying with the mode shape ϕ_n and integrating over the area of the foundation. That gives the system of N equations, written in matrix form:

$$\left[D\left[\mathbf{k^4}\right]-\rho h\omega^2[\mathbf{I}]\right]\{\mathbf{Y}\}=\{\mathbf{P}\}-\{\mathbf{Q}\} \quad (12)$$

where $\{\mathbf{Y}\}$, $\{\mathbf{P}\}$ and $\{\mathbf{Q}\}$ are coefficient vectors of the modal displacement, the load and the soil reaction, respectively, $[\mathbf{I}]$ is the identity matrix and $[\mathbf{k^4}]$ is the pure bending wavemode wavenumber matrix of the plate

$$\left[\mathbf{k^4}\right]=\begin{bmatrix}0 & 0 & \cdots & 0\\ 0 & \rho h\omega_1^2 & & \vdots\\ \vdots & & \ddots & 0\\ 0 & \cdots & 0 & \rho h\omega_N^2\end{bmatrix} \quad (13)$$

where $\omega_1,\ldots,\omega_N$ are natural frequencies of the plate, obtained using the DSM [11].

Relation between displacements and soil reaction coefficient vectors can be defined as follows

$$[\mathbf{K_s}]\{\mathbf{Y}\}=\{\mathbf{Q}\} \quad (14)$$

where $[\mathbf{K_s}]$ is the modal impedance matrix of the soil, obtained using ITM [16]. Substituting (14) into (12) the equation of motion becomes

$$\left[D\left[\mathbf{k^4}\right]-\rho h\omega^2\left[\mathbf{I}\right]+\left[\mathbf{K_S}\right]\right]\{\mathbf{Y}\}=\{\mathbf{P}\} \quad (15)$$

Once the modal impedance matrix of the soil is formed, the displacement coefficient vector Y is obtained by solving the system of equations (14) and finally the displacement field $w(x,y)$ is obtained by using equation (3). To obtain the displacement field spectrum, the procedure should be repeated for every frequency ω in a desired frequency range. A computer program based on this formulation is developed in MATLAB [17]. In order to achieve numerical stability of the ITM, it is necessary to introduce a small damping into the system. This is accomplished by using a complex moduli

$$E^*=E(1+2i\xi) \quad (16)$$

$$G_s^*=G_s(1+2i\xi) \quad (17)$$

where G_s is soil medium shear modulus, i is imaginary unit and $\xi=1\%$ is the damping ratio.

3 NUMERICAL RESULTS

In order to investigate the influence of the mass and stiffness of the foundation on the response of the system it is good to rewrite equation (15) as

$$\left[\left[\mathbf{K_p}\right]+\left[\mathbf{K_m}\right]+\left[\mathbf{K_s}\right]\right]\{\mathbf{Y}\} \;=\; \{\mathbf{P}\} \quad (18)$$

$$(19)$$

where

$$[\mathbf{K_p}] = D\left[\mathbf{k^4}\right] \tag{20}$$

$$[\mathbf{K_m}] = -\rho h\omega^2\,[\mathbf{I}] \tag{21}$$

Two extreme cases are analyzed: a rigid foundation and a perfectly flexible foundation. The obtained results are presented in terms of main system parameters: the dimensionless stiffness ratio K, the dimensionless mass ratio M, the dimensionless frequency a_0 and the dimensionless response parameter - the displacement $\overline{\Delta}$ [7]

$$K = \frac{Eh^3(1-\nu_s)}{12(1-\nu^2)G_s(B/2)^3} \tag{22}$$

$$M = \frac{h\rho}{(B/2)\rho_s} \tag{23}$$

$$a_0 = \frac{\omega(B/2)}{c_s} \tag{24}$$

$$\bar{\Delta} = \Delta\frac{G_s(B/2)}{(1-\nu_s)\sum F_{ext}} \tag{25}$$

where ω is the excitation frequency, foundation parameters are: modulus E, Poisson's ratio ν, density ρ, thickness h, width B and soil medium parameters are: shear modulus G_s, shear wave velocity c_s, Poisson's ratio $\nu_s$and density ρ_s. A set of steady state analyses is performed, for $a_0 \in [0.1, 6]$ with an increment of 0.05.

In the case of rigid foundation ($K \geq 3.3$) the displacement field is uniform and spatially independent. The stiffness $[\mathbf{K_p}]$ vanishes since $[\mathbf{k^4}] = 0$. The usage of only the first, translational mode shape participates in the solution, $n = 0$. The system of equations (27) is reduced to a single equation:

$$(K_{s0} + K_{m0})Y_0 = P_0 \tag{26}$$

After obtaining Y_0 from equation (26) the response of the system is calculated as

$$\Delta = Y_0\phi_0 \tag{27}$$

The response of rigid foundation is analyzed for $M = 0$ and $M = 1$. The results are presented in Figures 3 and 4 in terms of absolute values of dynamic stiffness and dynamic flexibility of the system, respectively. Figure 3 shows the absolute values of the components of dynamic stiffness matrix: K_{m0}, K_{s0} and $K_{m0} + K_{s0}$. It is shown that the mass of the foundation decreases the stiffness of the system for $a_0 < 3$ and increases the stiffness of the system for $a_0 > 3$. Figure 4 shows the absolute values of vertical displacement $\overline{\Delta}$ of massive foundation $M = 1$ and the foundation without the mass $M = 0$. The vertical displacement of massive foundation is higher than the vertical displacement of massless foundation for $a_0 < 3$, while for $a_0 > 3$ is the opposite.

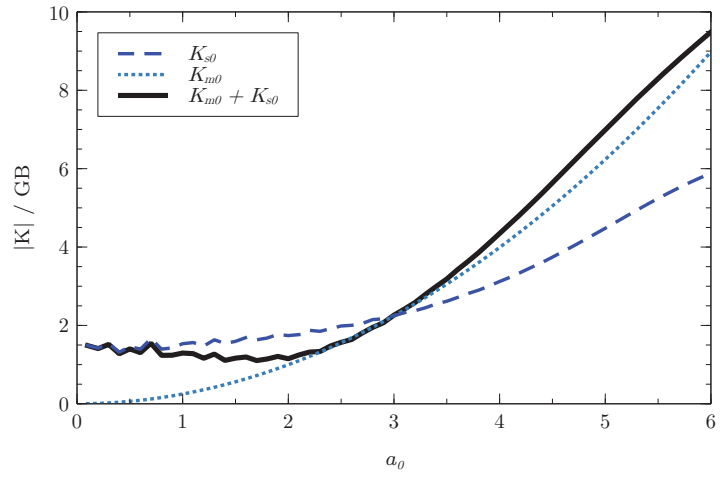

Figure 3: The influence of foundation mass on dynamic stiffness $[\mathbf{K}]$ of rigid foundation.

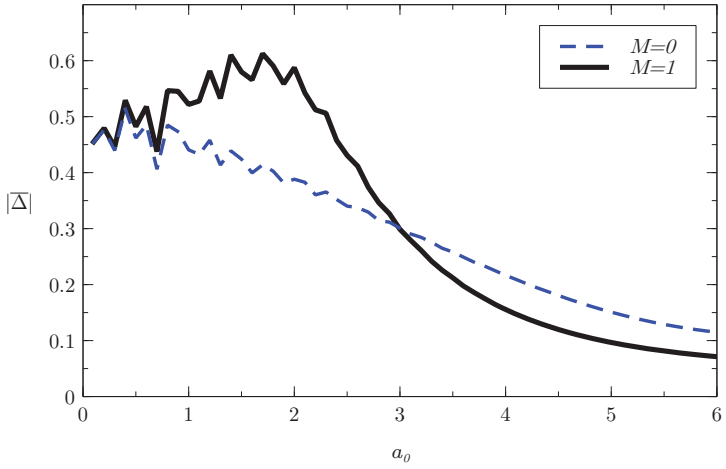

Figure 4: The influence of foundation mass on dynamic flexibility $\overline{\Delta}$ of rigid foundation.

In the second case a perfectly flexible massive foundation is analyzed, $K = 0$, $M = 1$. The influence of the number of mode shapes n on the response of the system is analyzed and compared with the results from the literature [7]. The first eight mode shapes, Figure 2, are taken into account. Absolute values of vertical displacement of the center of the foundation are shown in Figure 5. It is obvious that as the number of mode shapes increases the results converge. Six natural frequencies of the system are distinguished by using eight free vibration mode shapes of the plate, $n = 8$. The corresponding natural mode shapes of the system are shown in Figure 6. There is no resemblance between the natural mode shapes of the flexible foundation, 6, and the natural mode shapes of the flexible plate, 2.

The third and fourth natural frequency, $a_0 = 3.75$ and $a_0 = 4.15$, does not occur in the literature [7]. In the comparison with the rigid massive foundation, Figure 4, the flexible foundation performs similar within the frequency range $0 \leq a_0 \leq 2.5$. However, for $a_0 > 2.5$, the absolute displacement of the flexible foundation does not decrease with the frequency as in the case of rigid foundation.

The deviation of the results obtained using the proposed method is visible in figures 3, 4 and

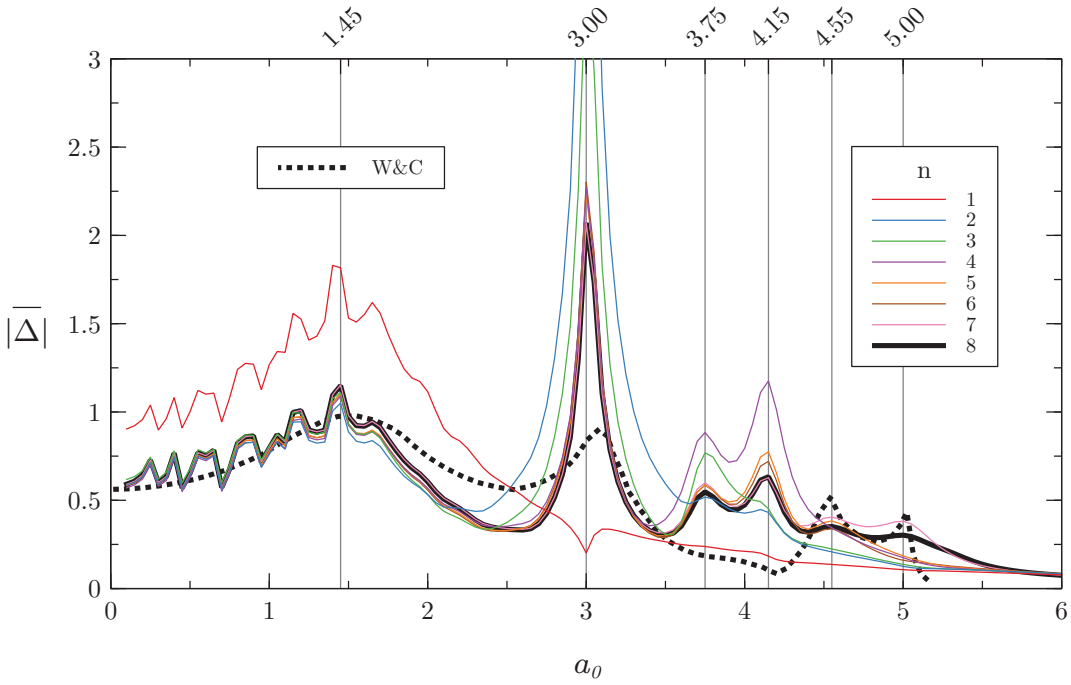

Figure 5: The influence of the number of mode shapes on the response of the system involving the flexible foundation, $K = 0$, $M = 1$, plotted against the results from the literature [7].

5 for $a_0 \in [0, 1.5]$. For small damping ratios, especially in the low frequency range, it is hard to avoid the aliasing effect of Fourier Transforms without a significant computational effort. The solution could be the application of the method of residue [18, 19] but this is still to be investigated.

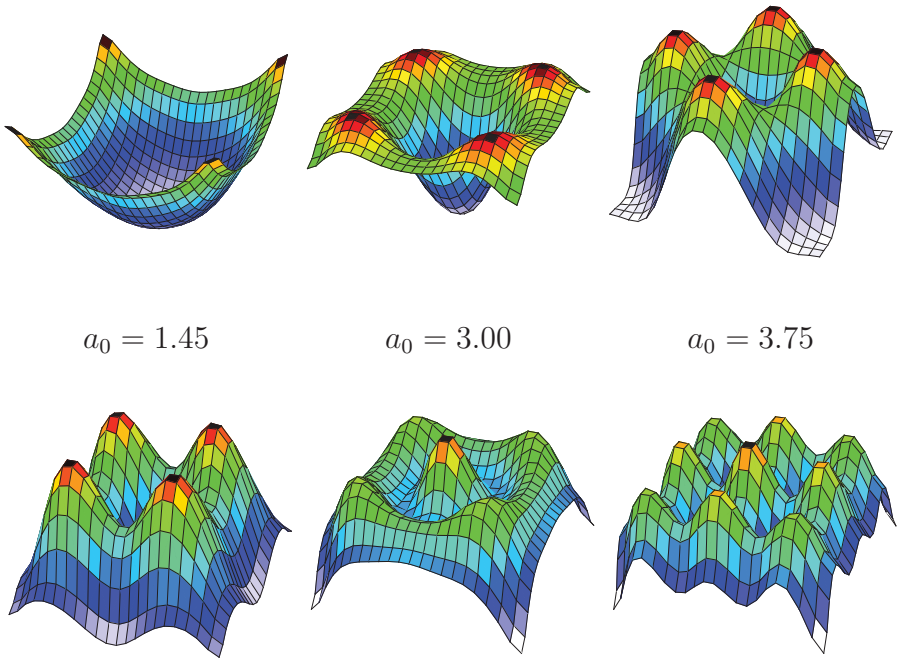

$a_0 = 1.45$ $a_0 = 3.00$ $a_0 = 3.75$

$a_0 = 4.15$ $a_0 = 4.55$ $a_0 = 5.00$

Figure 6: Displacement shapes of the flexible foundation at characteristic peaks, $K = 0$, $M = 1$.

4 CONCLUSIONS

This paper presents a semi-analytical method for solving the problems of massive flexible rectangular foundations resting on the surface of the soil. It is a hybrid method based on coupling Dynamic stiffness method (DSM) and Integral transform method (ITM) using substructuring approach and modal superposition technique. Both DSM and ITM are based on the analytical solution of governing equations of motion in space-frequency or wavenumber-frequency domain. The presented study shows the differences between the analysis of a massive rigid and flexible foundation. In the case of rigid foundation, the influence of the mass could be added to the system separately, while in the case of flexible foundation, the analysis must be carried out simultaneously. The response of a perfectly flexible massive foundation is analyzed. Regarding the nature of the presented method, the number of mode shapes used for the calculation is important for the convergence of the results. The results of the analysis are compared with the results from the literature. More natural frequencies are discovered in the spectrum of vertical displacements of the foundation central point using the proposed method. The deviation of the results obtained using the ITM-DSM is visible in the low frequency range, $a_0 < 2.5$. The solution to this problem is discussed, and it is to be investigated.

5 ACKNOWLEDGMENTS

This research is carried out within the Project TR36046 supported by the Ministry of Science and Technology, Republic of Serbia.

REFERENCES

[1] G. Gazetas, "Analysis of machine foundation vibrations: State of the art," *Soil Dynamics and Earthquake Engineering*, vol. 2, no. 1, pp. 2–42, 1983.

[2] M. Iguchi, J. E. Luco, and O. N. An, "Dynamic response of flexible rectangular foundations on an elastic half-space," *Earthquake Engineering and Structural Dynamics*, vol. 9, no. 3, pp. 239–249, 1981.

[3] M. Iguchi and J. E. Luco, "Vibration of Flexible Plate on Viscoelastic Medium," *Journal of the Engineering Mechanics Division*, vol. 108, no. 6, pp. 1103–1120, 1982.

[4] F. T. Kokkinos and C. C. Spyrakos, "Dynamic Analysis of Flexible Strip-Foundations in the Frequency Domain," *Computers & Structures*, vol. 39, no. 5, pp. 473–482, 1991.

[5] M. Mohammadi and D. L. Karabalis, "3-D soil-structure interaction analysis by BEM: Comparison studies and computational aspects," *Soil Dynamics and Earthquake Engineering*, vol. 9, no. 2, pp. 96–108, 1990.

[6] C. Spyrakos and D. Beskos, "Dynamic response of flexible strip-foundations by boundary and finite elements," *Soil Dynamics and Earthquake Engineering*, vol. 5, pp. 84–96, Apr. 1986.

[7] W. L. Whittaker and P. Christiano, "Dynamic Response of Plate on Elastic Half-Space," *Journal of the Engineering Mechanics Division*, vol. 108, no. 1, pp. 133–154, 1982.

[8] S. S. Chen and J. G. Hou, "Modal analysis of circular flexible foundations under vertical vibration," *Soil Dynamics and Earthquake Engineering*, vol. 29, no. 5, pp. 898–908, 2009.

[9] M. Hackenberg, *A Coupled Integral Transform Method - Finite Element Method Approach to Model the Soil-Structure-Interaction*. PhD Thesis, Technischen Universität München, Munich, Germany, 2016.

[10] J. Rastandi, *Modelization of Dynamic Soil-Structure Interaction Using Integral Transform-Finite Element Coupling*. PhD thesis, Technical University Munich, Munich, 2003.

[11] M. Nefovska-Danilović, *Dynamic Analysis of Soil-Structure System Using Spectral Element Method*. PhD Thesis, University of Belgrade, Belgrade, Serbia, 2012.

[12] M. Nefovska-Danilovic and M. Petronijevic, "In-plane free vibration and response analysis of isotropic rectangular plates using the dynamic stiffness method," *Computers & Structures*, vol. 152, pp. 82–95, May 2015.

[13] S.-S. Chen and J.-G. Hou, "Response of circular flexible foundations subjected to horizontal and rocking motions," *Soil Dynamics and Earthquake Engineering*, vol. 69, pp. 182–195, Feb. 2015.

[14] M. A. Oien, "Steady Motion of a Rigid Strip Bonded to an Elastic Half Space," *Journal of Applied Mechanics*, vol. 38, pp. 328–334, June 1971.

[15] P. H. Kulla, "High precision finite elements," *Finite Elements in Analysis and Design*, vol. 26, pp. 97–114, June 1997.

[16] M. Radišić, *ITM-Based Dynamic Analysis of Foundations Resting on a Layered Halfspace*. PhD Thesis, University of Belgrade, Belgrade, Serbia, 2018. UDC: 624.04:624.151(043.3).

[17] MathWorks, "MATLAB 2013a." MathWorks Inc. The Language of Technical Computing, 2013.

[18] M. Eskandari-Ghadi, "A Complete Solution of the Wave Equations for Transversely Isotropic Media," *Journal of Elasticity*, vol. 81, pp. 1–19, Oct. 2005.

[19] Rahimian Mohammad, Eskandari-Ghadi Morteza, Pak Ronald Y., and Khojasteh Ali, "Elastodynamic Potential Method for Transversely Isotropic Solid," *Journal of Engineering Mechanics*, vol. 133, pp. 1134–1145, Oct. 2007.

EURODYN 2020
XI International Conference on Structural Dynamics
M. Papadrakakis, M. Fragiadakis, C. Papadimitriou (eds.)
Athens, Greece, 23–26 November 2020

THE EFFECTS OF MODEL ASSUMPTIONS ON THE DYNAMIC IMPEDANCE FUNCTIONS OF A SHALLOW FOUNDATION

Johan Lind Östlund[1,2], Andreas Andersson[1,3], Mahir Ülker-Kaustell[1,2], and Jean-Marc Battini[1]

[1]Division of Structural Engineering and Bridges, KTH Royal Institute of Technology
Stockholm, Sweden
e-mail: joost@kth.se, {andreas.andersson, mahir.ulker, jean-marc.battini}@byv.kth.se

[2]Tyréns AB
Stockholm, Sweden

[3]Swedish Transport Administration
Solna, Sweden

Keywords: Dynamic impedance functions, Permanent load, Dynamic soil–structure interaction, Soil dynamics.

Abstract. *The effects of model assumptions on the dynamic impedance functions of shallow foundations are investigated using finite elements. The shallow foundations are considered massless and rigid and are positioned in strata of frictional soil on top of bedrock. Two studies are established. The first investigates the combined effects of model assumptions including the variation of modulus with depth, the embedment of the foundation, and permanent load acting on the foundation. The second study is a parametric analysis investigating the effects of permanent load considering strata with varying soil modulus coefficients and with varying soil depths. Functions describing the small-strain modulus and the modulus reduction of frictional soil are used in an iterative process to update the spatial modulus distribution of the soil due to the permanent load. The results show that model assumptions can have a large effect on the impedance functions. The static stiffness coefficients vary substantially, in some instances by more than 100 %. The impedance functions, normalized with the static stiffness coefficients, match each other well in the frequency range below the fundamental frequency. However, in the frequency range above the fundamental frequency, the normalized impedance functions differ substantially from each other. Further, the results show that the effect of the permanent load is largest in the case of shallow and stiff soil strata, both regarding normalized impedance functions as well as the static stiffness coefficient, which was increased up to 67 %. The variation in fundamental frequency is however small.*

1 INTRODUCTION

In the design of high-speed railway bridges, a dynamic assessment is required. The boundary conditions of these bridges are in many design situations modeled with fixed supports. However, the flexibility of the supports, due to the dynamic soil–structure interaction (SSI), may significantly change the dynamic properties of the bridges. One method of considering the SSI is by decoupling the models and calculating impedance functions. Instead of computing the complete soil–foundation–structure system, the model is decoupled and impedance functions are calculated from the soil–foundation subpart before being applied to the structure. This sub-structuring of the system enables faster calculations, especially at train loading analysis, as compared to the calculation of the complete system.

The impedance function is commonly expressed in complex numbers:

$$Z(\omega) = k_d(\omega) + i\omega c_d(\omega) \tag{1}$$

where k_d is the dynamic stiffness coefficient, c_d is the dashpot coefficient, ω is the cyclic frequency of excitation, and $i = \sqrt{-1}$.

Impedance functions have been published in many journal papers and are compiled in handbooks to give structural engineers simple tools to take SSI into account in design (see e.g. [1] or [2]). Although the studies given in the literature fully explore the effects of one or two of the specific features in each paper, when it comes to combinations of features that are not given in the literature, it may be difficult for the engineer to find the relevant model assumptions to use in a specific project and what consequences to expect. To fill that gap, this paper investigates the effects of the embedment of the foundation, the variation of the modulus with the depth, and the depth of the stratum on bedrock in different combinations. Further, the effects of applying a permanent load to the soil–foundation system and updating the spatial distribution of the modulus before performing linear dynamic analyzes are introduced.

The purpose of this paper is to show the effects of model assumptions on the dynamic impedance functions of shallow foundations. The article aims at filling the gap in the literature by investigating the combined effects of model assumptions from a practical point of view. Two main objectives of the study are defined. The first was to study the implications of model assumptions, including the embedment of the foundation, the variation of the modulus with the depth, and the permanent load. Impedance functions calculated from the models with varying levels of idealization are compared in the paper. The second objective was to quantify the influence of permanent load in relation to the soil modulus coefficient and stratum depth. A parametric study was performed for this purpose. To fulfill the objectives, numerical models using finite elements (FE) were created. The shallow foundation was assumed to be rigid and massless and was given a fixed geometry. The soil strata consisted of frictional soil supported by bedrock. Whereas the permanent load of the structure was included in the soil–foundation FE model in order to consider its effect on soil properties, the mass of the structure was not. This mass will be taken into account when the impedance functions are attached to the structure. The spatial variation of the modulus of elasticity caused by the permanent load was updated for each element, considering functions for the low-strain modulus and modulus reduction. Linear dynamic analyses were then performed on the updated models, and the impedance functions were calculated. The dynamic loading was assumed to affect the soil within the linear elastic range, and the impedance functions are valid in the serviceability limit state.

The soil and foundation parameters were chosen in the context of high-speed railway (HSR) bridges and Swedish soil conditions. Swedish geology is dominated by glacial soil masses

on top of high-quality bedrock [3]. At many locations, lodgment moraine overlays bedrock, possibly covered by clay or silt layers. For shallow strata consisting of frictional soil, shallow foundations may be suitable for HSR bridges. Such soil deposits are limited in depth, and the maximum depth considered in this study was assumed to be 8 m. The embedment depth of a foundation is typically determined by the frost-free depth, which in Sweden is considered at 1.1-2.5 m.

2 SOIL PROPERTIES

2.1 Small-strain shear modulus

The small-strain shear modulus of soil has been studied empirically by several authors for soil types ranging from cohesive to frictional, and many suggestions for formulas have been proposed [4–6]. Seed and Idriss [7] suggested a simplified formula for the small-strain shear modulus of frictional soil:

$$G_0 = K_0(\sigma')^d \tag{2}$$

where K_0 is the soil modulus coefficient, d is the stress exponent, and σ' is the mean effective stress. K_0 and d are soil type-specific constants. The Swedish design recommendations [8] have adopted this formula and adjusted it for Swedish conditions. In the recommendations, K_0 ranges from 15,000 to 30,000 where the first value corresponds to sand and the latter to crushed fill material. Furthermore, $d = 1/2$, and the stress is inserted in kPa.

The mean effective stress σ' can be subdivided into two additive parts. For frictional soil, the stress in the undisturbed in situ soil is commonly estimated by the confined effective stress based on the coefficient of lateral earth pressure [9]:

$$\sigma'_0 = \sigma'_v \frac{1+2k}{3} \tag{3a}$$

where this approximate relationship can be used:

$$k = 1 - \sin(\phi') \tag{3b}$$

Here, σ'_v is the effective vertical stress, k is the coefficient of lateral earth pressure, and ϕ' is the drained friction angle. Assuming no groundwater, the effective vertical stress σ'_v can be calculated with $\rho g z$ where ρ is the density, g is the gravity constant, and z is the depth from the soil surface. External load adds to σ' by the mean effective stress

$$\sigma'_{\mathrm{m}} = \frac{\sigma'_x + \sigma'_y + \sigma'_z}{3} \tag{4}$$

where σ'_x, σ'_y, and σ'_z are the effective normal stresses. Finally, the resulting stress becomes

$$\sigma' = \sigma'_0 + \sigma'_{\mathrm{m}} \tag{5}$$

2.2 Normalized modulus reduction

The reduction of modulus and increase of material damping ratio due to loading have been evaluated empirically in numerous studies for soil gradations ranging from cohesive to frictional soils [10–12]. In recent decades, researchers have aimed at collecting data from empirical studies and describing nonlinear relationships using statistical tools. In [13], a statistical analysis of empirical data from resonant column tests was conducted. This produced a set of 18 dimensionless parameters describing the normalized modulus reduction curves and material damping ratio

curves. The 18 parameters can be chosen to get either mean values or variances of the curves, and their values are dependent on the soil type. The normalized modulus reduction curve is calculated with

$$\frac{G}{G_0} = \frac{1}{1 + \left(\frac{\gamma}{\gamma_\mathrm{r}}\right)^a} \tag{6}$$

where γ is the current shear strain, γ_r is the reference shear strain, and a is the curvature coefficient. The formulas for γ_r and a are found in [13] and require, in addition to the 18 dimensionless parameters, the plasticity index, over-consolidation ratio, and stress in the soil. Only soils with gradations ranging from clay to sand were included. However, the difference in normalized modulus reduction curves between different gradations of frictional soils is relatively small [12, 14]. A comparison between the mean normalized modulus reduction curve of gravelly soils by Rollins et al. [12] and the corresponding curve for sand in [13] shows good agreement.

The shear strain can be calculated from the effective octahedral shear strain [15],

$$\gamma = \frac{\alpha}{3}\sqrt{(\varepsilon_x - \varepsilon_y)^2 + (\varepsilon_x - \varepsilon_z)^2 + (\varepsilon_y - \varepsilon_z)^2 + 6(\gamma_{xy}^2 + \gamma_{xz}^2 + \gamma_{yz}^2)} \tag{7}$$

where ε_i and γ_{ij} are components of the strain vector and $\alpha = 0.65$. This shear strain measure has been used in previous studies [16, 17].

3 NUMERICAL STUDIES

A fixed geometry of the foundation was used in all numerical simulations, and an overview of the FE model including the dimensions of the foundation is presented in Figure 1. The foundation was regarded as massless and rigid. The dimensions of the foundation are as follows: $L = 9.4$ m, $B = 3.3$ m, the thickness of the slab is 1.0 m, the length of the support wall is 7.0 m, and the thickness of the support wall is 0.9 m. H_1 is the soil depth underneath the bottom of the foundation, H_2 is the embedment depth and R is the radius of the FE model. The FE model is further described in section 4.1.

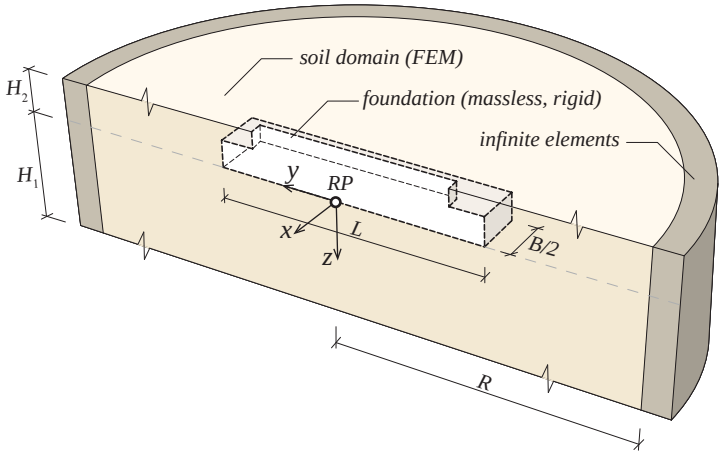

Figure 1: A cross-section of the finite element model.

The material properties of the soil were chosen from typical values of frictional lodgment moraine [18] and were assumed constant in all calculations. The following material properties were chosen for all cases: material damping ratio $\xi = 2.0$ %; density $\rho = 2000$ kg/m^3; Poisson's

ratio $\nu = 0.25$; friction angle $\phi' = 45$ deg; stress exponent $d = 1/2$, and gravity constant $g = 9.81$ m/s^2.

The permanent load was applied as a force P. In order to relate the load to the size of the foundation, the load is presented as a pressure q obtained from dividing the force P with the foundation's bottom surface area. The following values were taken: $q = (0, 220, 500)$ kPa. According to the Swedish design requirements, the upper limit on the pressure of shallow foundations on top of lodgment moraine on bedrock is 600 kPa [19].

The modulus at the surface of the stratum goes toward zero due to Eq. 2. This can cause poor conditioning of the elements because elements with high modulus are next to elements of low modulus, which can be particularly sensitive in the calculation of impedance functions from surface foundations. To avoid this, a lower limit for the modulus corresponding to the value at a depth of 0.2 m was chosen.

3.1 Model assumptions study

The effects of the model assumptions on the impedance functions were studied by investigating four cases as shown in Figure 2. It was decided that the fundamental frequency of all cases should be the same. This choice was made based on the fact that the behavior of the soil–foundation system is essentially different at frequencies below compared to above the fundamental frequency of the soil stratum, and fixing it was considered to be the best way to compare the models. In order to get the fundamental frequency of the homogeneous stratum to match the fundamental frequency of the stratum with a modulus varying with depth, the modulus value of the homogeneous soil stratum can be obtained by calculating an equivalent depth z_{eq} [20, 21]. z_{eq} determines the depth at which the equivalent modulus value G_{eq} of the modulus varying with the depth $G(K_0, \sigma'_0)$ is taken from. G_{eq} is then applied to the homogeneous stratum and the equivalent wave speed v_{eq} gives the fundamental period $T = 4H/v_{\text{eq}}$, where H is the total stratum depth. In this work, since $d = 1/2$ in Eq. 2, the equivalent depth was calculated to $z_{\text{eq}} = 0.64H$.

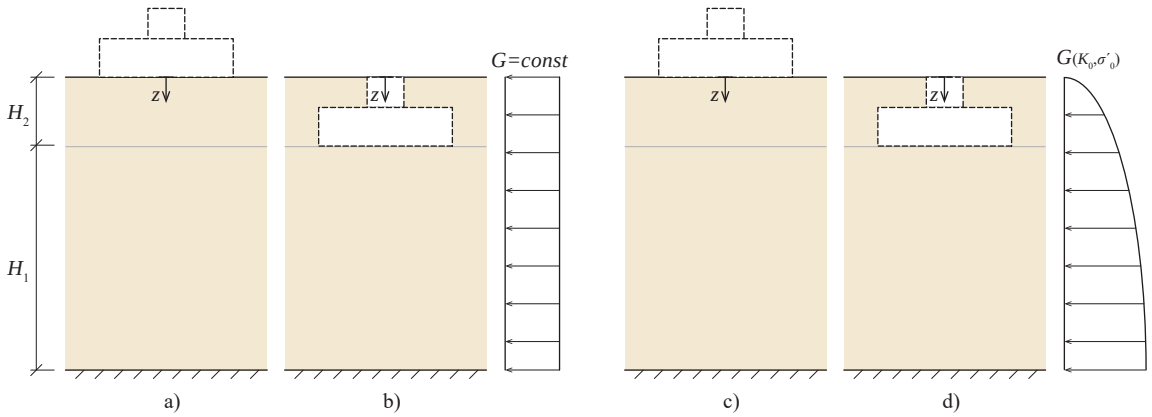

Figure 2: Cases considered in the model assumptions study.

The model assumption cases had the following properties:

- Case (a): A surface foundation on a stratum of homogeneous soil. No permanent load.
- Case (b): An embedded foundation in a stratum of homogeneous soil. No permanent load.

- Case (c): A surface foundation on a stratum with modulus varying with the depth. Includes permanent load P.
- Case (d): An embedded foundation in a stratum with modulus varying with the depth. Includes permanent load P.

The following parameters were chosen for all the models: $H_1 = 8$ m and $K_0 = 30{,}000$, corresponding to a deep soil stratum consisting of stiff lodgment moraine. The embedment depth was fixed at $H_2 = 1.6$ m. The modulus of Case (a) and Case (b) was calculated to G_{eq} = 240 MPa.

3.2 Parametric study

The effect of the permanent load was studied for the strata with varying depth H_1 and soil modulus coefficient K_0 in the parametric study. All the models had the configurations of Case (d) in Figure 2. Eighteen combinations were analyzed based on the following parameters: $q =$ (0, 220, 500) kPa, $H_1 =$ (2, 4, 8) m, and $K_0 =$ (15,000, 30,000). The embedment depth was fixed at $H_2 = 1.6$ m.

4 NUMERICAL MODEL

4.1 FE model

The numerical model of the soil–foundation system was created in the commercial FE software Abaqus [22], and an overview of the FE model is presented in Figure 1. The soil domain was created as a disk with a thickness equal to the stratum depth, and the bedrock was made infinitely stiff by constraining the bottom surface of the disk against translations. A void within the soil domain was created with the geometry of the embedded foundation. Then, rigid connections were applied to the surfaces of the soil facing the void linking them to a reference point (RP) positioned at the midpoint on the bottom surface. In the case of a surface foundation, no void was created and the single surface at the interface between soil and foundation was rigidly connected to the RP. Loading was applied and output was taken at the RP. The damping of the soil was applied as rate-independent structural damping which is incorporated in the complex modulus as $\boldsymbol{K}^* = \boldsymbol{K}(1 + i2\xi)$, where $\boldsymbol{K}$ is the stiffness matrix.

Quadratic tetrahedral solid elements were used. The mesh size at the center of the soil domain at the foundation was 0.25 m. From the center, the mesh size was gradually enlarged along the radius toward the boundary of the model. The radius of the model was R = 200 m. At the boundary, the mesh size was 20 m. Due to the gradual enlargement of the elements, the computational time was reduced without causing spurious waves that can occur due to large size differences between elements. Infinite elements [23] were attached to the outer surface boundary of the model domain.

4.2 Calculation procedure

The updating of the G-modulus in each of the elements due to permanent load and the calculation of impedance functions were performed as follows:

1. Initially, the unloaded modulus was assigned: Calculate σ_0' (Eq. 3) and G_0 (Eq. 2). In this state, $G/G_0 = 1$ (Eq. 6), and the shear modulus is $G = G_0$.
2. Apply permanent load P to the RP in Figure 1 and run a static analysis.

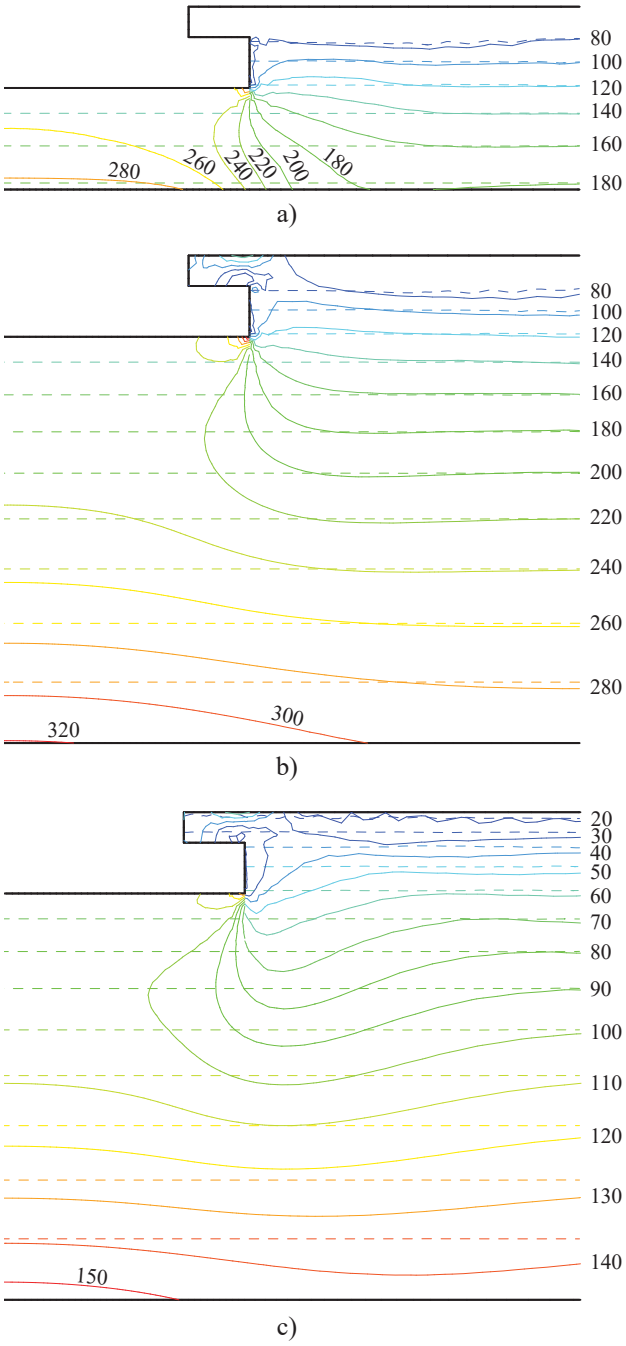

Figure 3: Updating of the shear modulus distribution due to permanent load. Values given in MPa. a) $H_1 = 2$ m, $K_0 = 30{,}000$, b) $H_1 = 8$ m, $K_0 = 30{,}000$ and c) $H_1 = 8$ m, $K_0 = 15{,}000$. Dashed lines: Unloaded soil. Solid lines: Updated soil.

3. Successively calculate: σ_0' (Eq. 3), σ_m' (Eq. 4), σ' (Eq. 5), G_0 (Eq. 2), γ (Eq. 7), and G (Eq. 6).

4. Repeat steps 2 and 3 until convergence of the distribution of shear modulus G is reached.

5. Calculate impedance functions.

Direct steady-state calculations were performed in order to obtain the impedance functions.

Harmonic unit loads were individually applied at the RP displayed in Figure 1 to each of the six degrees of freedom in a given frequency range. The compliance functions U were obtained from the model. The impedance functions were then calculated by the inverse of the compliance functions $Z = U^{-1}$. Only the values of the diagonal of the impedance function matrix were analyzed.

The converged distributions of the shear modulus for three of the models are shown in Figure 3, and the cuts are taken along the y–z plane. The models were configured as in Section 3.2 with $q = 220$ kPa. An increase of the permanent load results in two opposite effects on the modulus: an increase of G_0 due to the increase of σ' and a reduction by G/G_0 due to the increase of γ. In the volume between the foundation and the bedrock, the permanent load caused an increase in the modulus. The influence is large for shallow stratum depths. Just outside of this volume, the modulus can be either reduced or increased from permanent load depending on the stress–shear strain interaction.

5 RESULTS

The real part of the impedance function is denoted with $\mathrm{Re}(Z_j)$, whereas the imaginary part is denoted with $\mathrm{Im}(Z_j)$. The degrees of freedom are indicated by the subscript j and the coordinate axes are defined in Figure 1. The compliance functions, $|U_j|$, are denoted in the same way as the impedance functions and are given as absolute values. All functions are presented with the dimensionless frequency $a_0 = \omega w/v_{s,\mathrm{eq}}$ where $w = B/2$ and $v_{s,\mathrm{eq}} = \sqrt{G_{\mathrm{eq}}/\rho}$ is the equivalent shear wave velocity of the strata (without the influence of the permanent load). Impedance functions are normalized with the static stiffness coefficients $k_{j,\mathrm{stat}}$, and the compliance functions are normalized by the static displacements $u_{j,\mathrm{stat}}$.

5.1 Model assumptions study

The normalized impedance functions from the model assumptions study are presented in Figure 4 including the x and z degrees of freedom. The corresponding static stiffness coefficients are given in Figure 5. The following observations are made:

- The static stiffness coefficients range from 3 to 9 GN/m depending on the model case. The embedment of the foundation increases the static stiffness coefficient as compared to the static stiffness coefficient of the corresponding surface foundation, as shown by comparing Case (a) to Case (b), and Case (c) to Case (d). This is explained by the reduced distance to the bedrock. Strata with a modulus varying with the depth have lower static stiffness coefficients than strata with homogeneous modulus. This is evident when comparing Case (a) to Case (c) and Case (b) to Case (d). With increasing permanent load, the values of the static stiffness coefficients in Cases (c) and (d) are increased but they do not exceed the static stiffness coefficients of the homogeneous cases of (a) and (b).

- In the pre-resonance state, i.e. before wave propagations are initiated, the impedance functions are proportional to the static properties of the soil–foundation system. The normalized impedance functions can be described by a single degree of freedom system. The real part of this system is $(k_{j,\mathrm{stat}} - \omega^2 m_{j,\mathrm{stat}})/k_{z,\mathrm{stat}}$, where $m_{j,\mathrm{stat}}$ is the mass of the system, and the imaginary part is constant and is equal to $i2\xi$. The normalized impedance functions are thus very similar in the pre-resonance frequency range, however, they differ substantially at higher frequencies. In the post-resonant frequency range, the impedance is highly influenced by wave propagations and the single degree of freedom system can

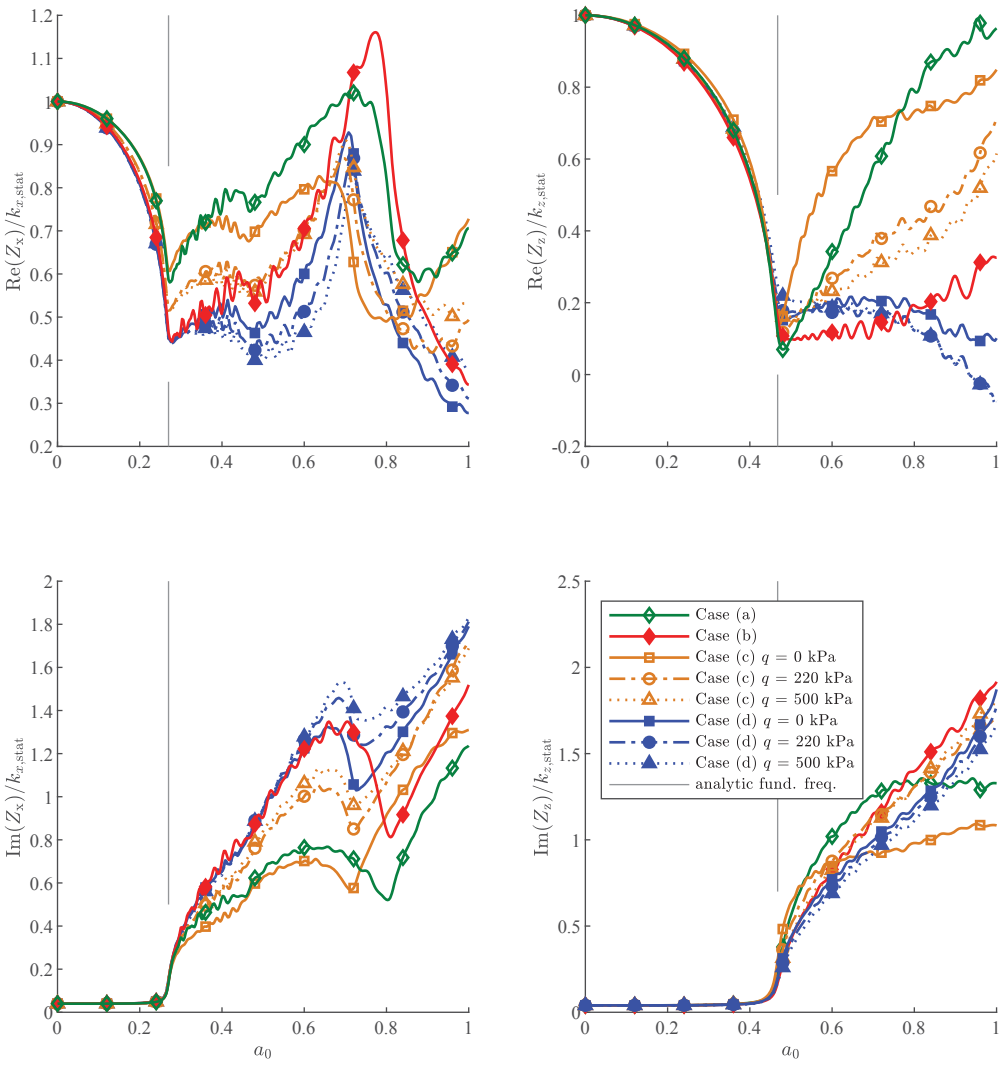

Figure 4: Normalized impedance functions from the model assumptions study.

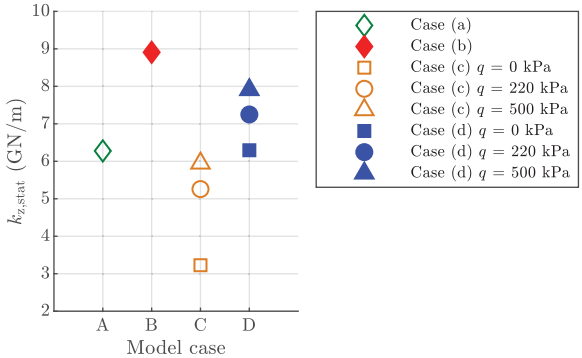

Figure 5: Static stiffness coefficients of the four model cases.

no longer describe the impedance functions. The imaginary part is increased significantly due to the radiation damping, and the differences in impedance between the cases are large.

- All cases had the same fundamental frequency which was also the same as the analytical fundamental frequency of the soil strata [20]. The fluctuations in impedance that can be observed for all cases at $a_0 \approx 0.7$ in the x-direction are due to the second mode of vibration of the soil, which for a homogeneous stratum has the natural frequency of three times the fundamental frequency according to $T_n = (4H/v)/(2n-1)$ were v is the wave speed and n is the mode number. The natural frequencies of the second mode for the strata with modulus varying with the depth are somewhat lower than the natural frequencies of the strata with homogeneous soil. The fundamental frequencies of the strata are not changed by the local influence that the permanent loads have on the soil moduli.

- For surface foundations on top of strata with modulus varying with the depth, as in Case (c), very low static stiffness coefficients are obtained with $q = 0$. This shows the consequences of omitting permanent load in combination with a very low modulus at the surface of the model. Adding the permanent load to Case (c) increases the static stiffness coefficient considerably. This effect is also shown for the normalized impedance functions, where an increase of the permanent load leads to a decrease of the real part of the impedance and an increase of the imaginary part.

5.2 Parametric study

Normalized impedance functions in the z-direction are presented in Figure 6. The static stiffness coefficients of each case, normalized with the static stiffness coefficients with q = 0 kPa, are given in Figure 7. The static stiffness coefficients with q = 0 kPa are given in Table 1 as a reference. Normalized compliance functions are presented in Figure 8. The following observations are made:

- For most cases, the static stiffness coefficient increases with the permanent load, in particular for shallow strata with a high soil modulus coefficient, see Figure 7. This can be explained by the high pressure and the small shear strain that mainly increase the modulus, see Figure 3 (a)–(b). The maximum increase of the static stiffness coefficient is 67 %. In the case of the deep strata with a low soil modulus coefficient ($H_1 = 8$ m and $K_0 =$ 15,000), the static stiffness coefficient decreases with an increased permanent load. The reduction is small (4 %) and is likely due to the high shear strains beside and under the foundation, which reduces the modulus (see Figure 3 (c)).

- In the pre-resonance frequency range, the system acts as a single degree of freedom system, as described in section 5.1. The real part of the normalized impedance can however be significantly influenced by the permanent load in this range, especially for shallower strata. This is clearly visible in Figure 6 in the case of H_1 =2 m where $(k_{j,\mathrm{stat}} - \omega^2 m_{j,\mathrm{stat}})/k_{z,\mathrm{stat}}$ is less steep for increasing permanent load, which is explained by a larger $k_{z,\mathrm{stat}}$ in relation to $m_{z,\mathrm{stat}}$. In the case of the deep soil, the effect of the permanent load on the pre-resonance impedance is low.

- In the frequency range above the fundamental frequency, the effect of the permanent load can lead to both an increase and a decrease of the normalized impedance at different

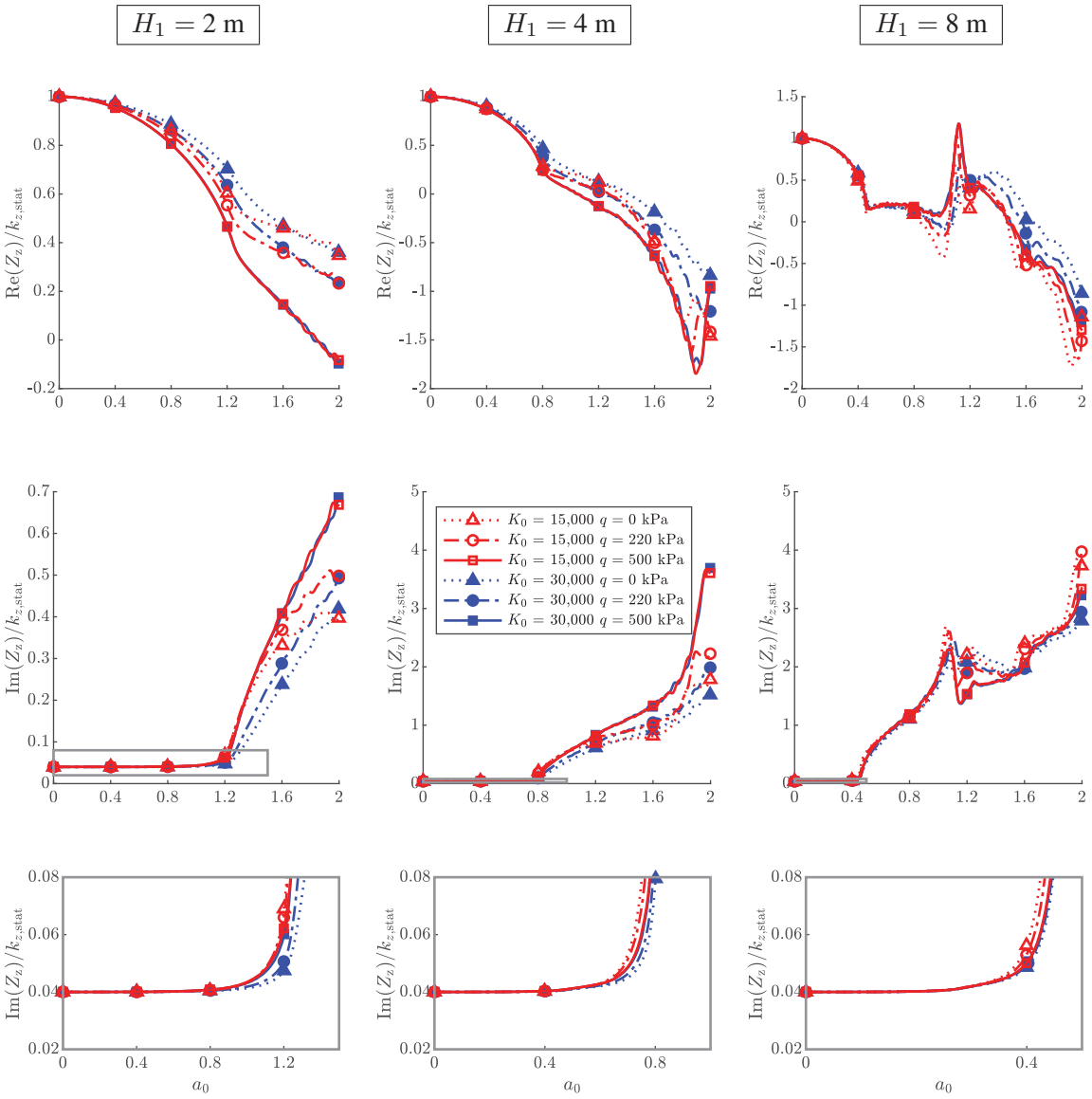

Figure 6: Normalized impedance functions and the effects of the permanent load.

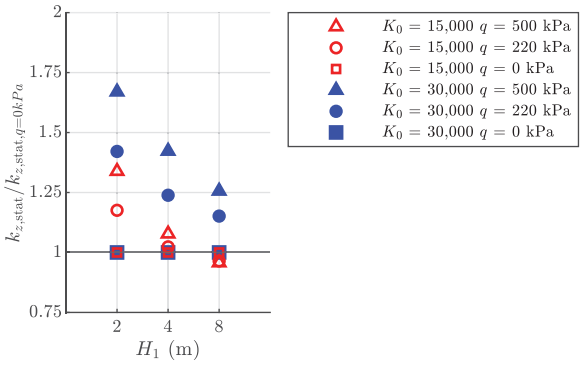

Figure 7: Static stiffness coefficients normalized with $k_{z,\mathrm{stat},q=0kPa}$.

Table 1: Static stiffness coefficients $k_{z,\mathrm{stat},q=0kPa}$ (GN/m).

K_0	H_1 (m)		
	2	4	8
15,000	5.7	4.0	3.1
30,000	11.4	7.9	6.3

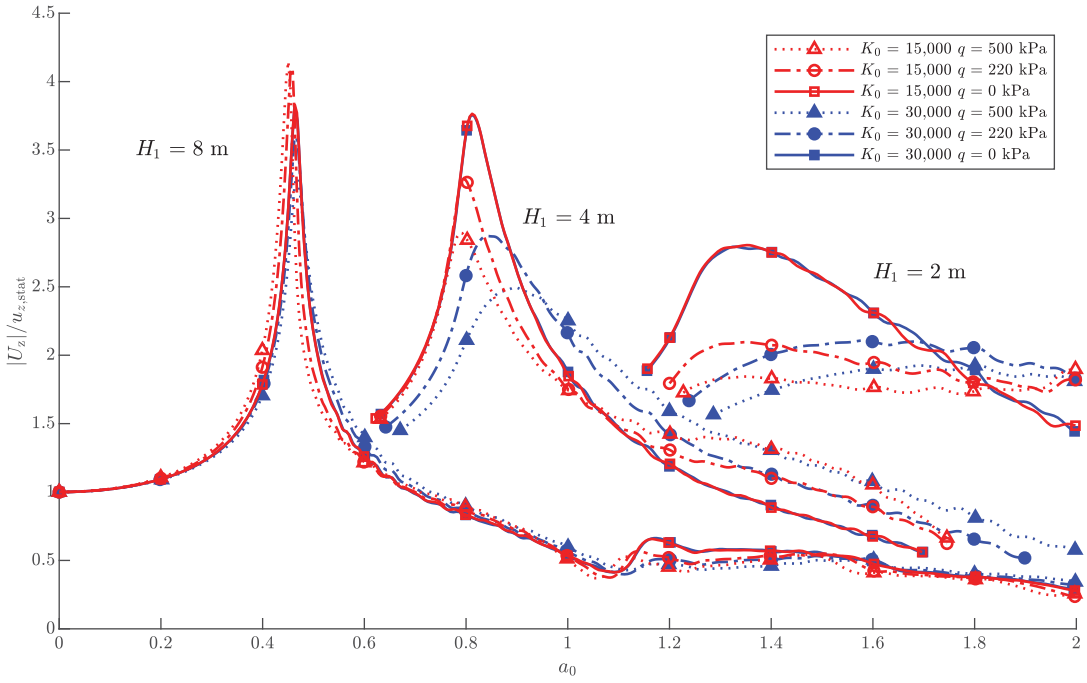

Figure 8: Normalized compliance functions from the parametric study.

frequency ranges. In the case of the shallower strata however, the real part of the normalized impedance is generally increased from the additional permanent load, whereas the imaginary part is decreased. Whereas the effect of the permanent load on the static stiffness coefficients can be quite large, the effect on the normalized impedance functions is relatively small, especially for the deeper strata and at lower frequencies.

- The effect of the permanent load on the fundamental frequency is small, see Fig 8. In the case of $K_0 = 15{,}000$, the fundamental frequency decreases with an increasing permanent load, whereas it increases in the case of $K_0 = 30{,}000$. The effect is smaller for deeper soil strata and increases with shallower depths. However, the variations of the fundamental frequency due to the permanent load are small when compared to the ones that are due to the stratum depth and the soil modulus coefficient.

- In most cases, the resonances of the normalized compliance functions decrease with an increasing permanent load, see Figure 8. The decrease is larger in the cases with stiffer and deeper soils. The resonance peaks for these cases are less distinct, whereas the resonance peaks become pointier for deeper and softer soils. The largest reduction of the normalized resonance peak is however observed in the case of the intermediate depth of $H_1 = 4$ m with a stiff soil $K_0 = 30{,}000$ and is 34 %. In the case of the soft and deep soil stratum ($H_1 = 8$ m with $K_0 = 15{,}000$), a small increase of the normalized resonance (8 %) due to the permanent load is observed.

6 CONCLUSIONS

The conclusions from the presented studies are summarized in the following main points:

1. The model assumptions can have a great influence on the impedance functions. The con-

sidered combinations of model assumptions produced normalized impedance functions that are similar in the frequency range below the fundamental frequency. However, in the frequency range above the fundamental frequency, the normalized impedance functions are very different. Further, the static stiffness coefficients of the models differ with more than 100 %.

2. The parametric study showed that the permanent load has a significant influence on the normalized impedance functions, especially in the cases of shallow soil strata with high soil modulus coefficients. In most of the cases, an increase of the permanent load leads to an increase of the static stiffness coefficient (with up to 67 %). However, in the case of the deep and soft soil, it leads to a small decrease of 4 %. The normalized impedance functions are in some cases relatively uniform, especially for the deeper strata.

3. The permanent load has a small effect on the fundamental frequency of the soil–foundation system.

ACKNOWLEDGEMENT

This work was supported financially by the Swedish Transport Administration and the KTH Railway Group.

REFERENCES

[1] G. Gazetas, Formulas and charts for impedances of surface and embedded foundations, *Journal of Geotechnical Engineering*, **117(9)**, 1363–1381, 1991.

[2] J.-G. Sieffert, F. Cevaer, *Handbook of impedance functions*, Presses Acadeémiques, 1992.

[3] Geological survey of Sweden (SGU), Geology of sweden, Available from: https://www.sgu.se/en/geology-of-sweden/, February 2020.

[4] B. Hardin, V. Drnevich, Shear modulus and damping in soils: Design equations and curves, *Journal of the Soil Mechanics and Foundations Division*, **98(7)**, 667–692, 1972.

[5] Prange, B., Resonant column testing of railroad ballast, Technical report, Institute of Soil and Rock Mechanics, University of Karlsruhe, 1981.

[6] Y. Higuchi, Y. Umehara, H. Ohneda, Evaluation of soil properties of the sand deposits under deep sea bed, *Proceedings of the 36th annual convention of the Japanese Society for Civil Engineering*, **3**, 50–51, 1981.

[7] H. B. Seed, I. Idriss, Soil moduli and damping factors for dynamic response analyses (report no. eerc-70/10), Technical report, University of California, 1970.

[8] Swedish Transport Administraion, Trafikverkets tekniska råd för geokonstruktioner-tr geo 13 (swedish), 2016.

[9] J. Jaky, The coefficient of earth pressure at rest, *Journal of the Society of Hungarian Architects and Engineers*, **7**, 355–358, 1944.

[10] R. Dobry, M. Vucetic, Dynamic properties and seismic response of soft clay deposits, *Proceedings: International Symposium on Geotechnical Engineering of Soft Soils*, **2**, 52–57, 1987.

[11] I. Ishibashi, X. Zhang, Unified dynamic shear moduli and damping ratios of sand and clay, *Soil and Foundations*, **33(1)**, 182–191, 1993.

[12] K. M. Rollins, M. D. Evans, N. B. Diehl, W. D. D. III, Shear modulus and damping relationships for gravels, *Journal of Geotechnical and Geoenvironmental Engineering*, **124(5)**, 396–405, 1998.

[13] M. B. Darendeli, *Development of a New Family of Normalized Modulus Reduction and Material Damping Curves*, Dissertation, University of Texas, 2001.

[14] H. B. Seed, R. T. Wong, I. Idriss, K. Tokimatsu, Moduli and damping factors for dynamic analyses of cohesionless soils, *Journal of Geotechnical Engineering*, **112**, 1016–1032, 1986.

[15] J. Lysmer, T. Udaka, C. F. Tsai, H. B. Seed, Flush - a computer program for approximate 3-d analysis of soil–structure interaction problems (report no. pb–259332), Technical report, University of California, 1975.

[16] A. M. Halabian, M. H. El Naggar, Effect of non-linear soil–structure interaction on seismic response of tall slender structures, *Soil Dynamics and Earthquake Engineering*, **22**, 639–58, 2002.

[17] P. A. Costa, R. Calçada, A. S. Cardoso, A. Bodare, Influence of soil non-linearity on the dynamic response of high-speed railway tracks, *Soil Dynamics and Earthquake Engineering*, **30**, 221–235, 2010.

[18] R. Larsson, Information 1 jords egenskaper (swedish), Technical report, SGI - Swedish Geotechnical Institute, 2008.

[19] Swedish Transport Administraion, Trafikverkets tekniska krav för geokonstruktioner-tk geo 13 (swedish), 2014.

[20] G. Gazetas, Vibrational characteristic of soil deposits with variable wave velocity, *International Journal for Numerical and Analytical Methods in Geomechanics*, **6**, 1–20, 1982.

[21] R. Dobry, I. Oweis, A. Urzua, Simplified procedures for estimating the fundamental period of a soil profile, *Bulletin of the Seismological Society of America*, **66(4)**, 1293–1321, 1976.

[22] Dassault Systèmes, *ABAQUS/Standard: user's manual*, Providence, RI, USA., 2017 edition, 2016.

[23] J. Lysmer, R. L. Kuhlemeyer, Finite dynamic model for infinite media, *Journal of the Engineering Mechanics Division*, pages 859–877, 1969.

EURODYN 2020
XI International Conference on Structural Dynamics
M. Papadrakakis, M. Fragiadakis, C. Papadimitriou (eds.)
Athens, Greece, 23–26 November 2020

ANALYSIS OF SEISMIC METASURFACES USING SPECIALISED ASYMPTOTIC MODELS FOR RAYLEIGH WAVES.

Peter T. Wootton[1], **Julius Kaplunov**[2,3] **and Danila Prikazchikov**[2,3]

[1] University of Glasgow
Glasgow, G12 8QQ, UK
e-mail: peter.wootton@glasgow.ac.uk

[2] Keele University
Keele, Staffordshire, ST5 5BG, UK
e-mail: j.kaplunov@keele.ac.uk, d.prikazchikov@keele.ac.uk

[3] Institute for Problems in Mechanical Engineering, RAS
St. Petersburg, 199178, Russia

Keywords: Rayleigh wave, seismic, meta-surface, flexural.

Abstract. *Previous work has considered the effect that an array of periodic flexural resonators formed from Euler-Bernoulli beams attached to the surface of a linear elastic half-space has on Rayleigh wave propagation, using a specialised leading order asymptotic model for the Rayleigh-like wave motion induced by applied surface stresses. In this work we consider the same beam-like flexural resonators but instead apply a recently developed second order model as a correction to the leading order model. The higher order model is shown to be straightforward to apply and obtains an explicit dispersion relation, albeit one that is significantly less concise than obtained from the leading order model. This explicit dispersion relation is shown to give a significant improvement over the leading order model for cases with either a vertical or horizontal stress only, but not when a mixed stress is applied. As in previous work, special attention is devoted to the effect of various junction conditions between the half-space and resonators.*

1 INTRODUCTION

Recently, there have been several analytical [3, 6], numerical [5, 14], and experimental [2] studies on the use of sub-wavelength resonators for the control of surface waves on elastic substrates. Notable features of such resonant arrays include filtering, focusing, rainbow trapping, and mode-conversion of surface waves to bulk waves [4]. Numerical approaches are computationally intensive and require extensive GPU computing facilities [5], while complete analytical studies present their own significant challenges [6].

Unlike bulk waves, these surface waves do not have an explicit wave equation; they are instead 'hidden' through the equations of linear elasticity. This makes both finding the exact solution or undertaking numerical analysis for a system dominated by surface waves difficult. A leading order asymptotic model has been developed for the Rayleigh-type waves produced by forcing along the surface of a linearly elastic half space, relying on a slow-time perturbation procedure applied to the eigensolution expressed in terms of a single plane harmonic function, see [1, 12]. Within the described asymptotic formulation, the propagation of the Rayleigh wave along the surface is described by a hyperbolic equation, whereas the decay over the interior is governed by an elliptic equation for one of the elastic potentials. A systematic exposition of the asymptotic models for the Rayleigh and Rayleigh-type wave may be found in [11].

This model has been applied to multiple problems including moving loads [10, 8], surface arrays of rod-like resonators [7]. In each, the asymptotic model has produced a simple but remarkably accurate approximation of the exact solution. The formulation has also been recently extended to anisotropic media [13, 9].

While the asimptotic model for the Rayleigh wave has proven to give close representations of the exact solution in many cases, as the problems become more involved the deviation between the exact solution and result from the leading order model will increase. Previous consideration of a system of a surface array of beam-like resonators has shown notable deviations when there are stresses both parallel and perpendicular to the surface [15]. As such it is necessary to investigate this system further, making use of a newly developed higher order model [16].

2 PROBLEM STATEMENT

First we make use of the same system of flexural resonators introduced previously [15]. Shown in Figure 1, this consists of a periodic array of vertically arranged Euler-Bernoulli beams of length L and spacing l attached to the surface of a linearly elastic half-space.

Classically, these Euler-Bernoulli beams have governing equation

$$B_b I_b \frac{\partial^4 u_b}{\partial z^4} + M_b \frac{\partial^2 u_b}{\partial t^2} = 0, \tag{1}$$

where u_b is perpendicular displacement, B_b and M_b are the bending stiffness and mass

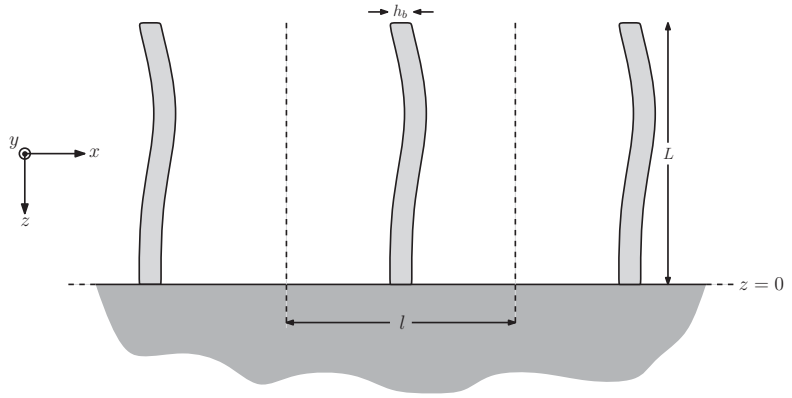

Figure 1: An array of beam-like resonators of length L and diameter h_b periodically attached with spacing l to the surface of a semi-infinite linearly elastic half space.

per unit length of the resonators respectively, and

$$I_b = \frac{\pi h_b^4}{64}, \quad B_b = \frac{E_b}{1-\nu^2} \tag{2}$$

where h_b is the diameter of a beam E_b and ν are the Young modulus and Poisson ratio respectively. This gives the dispersion relation as,

$$K = \left(\frac{64 M_R}{B_b \pi h_b^4}\right)^{\frac{1}{4}} \sqrt{\omega}. \tag{3}$$

In order to investigate the effect on the half-space, these resonators have boundary conditions for displacement, bending angle, bending moment and horizontal force respectively at $z = 0$,

$$u_b = u_1, \qquad \frac{\partial u_b}{\partial z} = \frac{\partial u_3}{\partial x} \qquad \frac{\partial \sigma_{33}}{\partial x} = -B_b \frac{\partial^2 u_b}{\partial z^2}, \qquad H = I_b B_b \frac{\partial^3 u_b}{\partial z^3}, \tag{4}$$

where the half-space displacement is $\mathbf{u} = (u_1, u_2, u_3)$, $\boldsymbol{\sigma}$ is the usual stress tensor and H is the out-of-plane force in the x-direction.

Since the width of each beam is much less than the separation length l we can assume to a good approximation that the stress from the beams will be distributed evenly.

2.1 ASYMPTOTIC MODEL

Suppose that waves are near the classical Rayleigh wave speed. Then a small parameter is defined by the difference between the wave speed c and the classical Rayleigh speed c_R, such that $|c - c_R| \ll 1$. For the sake of simplicity, below we focus on the plane-strain case. Then, at leading order, the elastic bulk has governing equations,

$$\frac{\partial^2 \phi}{\partial z^2} + \alpha_R^2 \frac{\partial^2 \phi}{\partial x^2} = 0, \qquad \frac{\partial^2 \psi}{\partial z^2} + \beta_R^2 \frac{\partial^2 \psi}{\partial x^2} = 0. \tag{5}$$

where ϕ and ϕ are longitudinal and shear displacement potentials respectively and,

$$\alpha(c) = \sqrt{1 - \frac{c^2}{c_1^2}}, \qquad \beta(c) = \sqrt{1 - \frac{c^2}{c_2^2}} \tag{6}$$

with $\alpha_R = \alpha(c_R)$, $\beta_R = \beta(c_R)$ and c_1, c_2 being the bulk longitudinal and shear wave speeds respectively.

Depending on whether the half-space is subject to a normal or tangential stress, we obtain different boundary conditions. In the case of a tangential stress at $z = 0$, $\sigma_{33} = 0$ and

$$\Box\psi = -\frac{1 + \beta_R^2}{2\mu B}\sigma_{31}, \tag{7}$$

while for a normal stress at $z = 0$, $\sigma_{31} = 0$ and

$$\Box\phi = \frac{1 + \beta_R^2}{2\mu B}\sigma_{33}, \tag{8}$$

where $\Box$ is the D'Alambertian operator

$$\Box = \frac{\partial^2}{\partial x^2} - \frac{1}{c_R^2}\frac{\partial^2}{\partial t^2},$$

and B is a material constant arising from the perturbation scheme, given by

$$B = \frac{\beta_R}{\alpha_R}(1 - \alpha_R^2) + \frac{\alpha_R}{\beta_R}(1 - \beta_R^2) - (1 - \beta_R^4). \tag{9}$$

Following the same approach as for the leading order model we obtain new second order boundary conditions. In the case of a normal stress, at $z = 0$,

$$\Box\phi_{,11} = \frac{1 + \beta_R^2}{2\mu B}\,\Box_1\sigma_{33} \tag{10}$$

and similarly for a tangential stress,

$$\Box\psi_{,11} = -\frac{1 + \beta_R^2}{2\mu B}\,\Box_1\sigma_{31}. \tag{11}$$

where the operator $\Box_1$ is defined as

$$\Box_1 = \frac{\partial^2}{\partial x^2} + A_R\Box$$

and the constant A_R is given by,

$$A_R = \frac{1 - \beta_R^2}{1 + \beta_R^2} + \frac{1}{4B}\left(2(1 - \beta_R^2)^2 + \frac{(\alpha_R^2 - \beta_R^2)^2}{\alpha_R^3\beta_R^3}\right). \tag{12}$$

3 NORMAL OR TANGENTIAL STRESS

Similar to the previous approach, we consider three distinct sets of junction conditions. The first two of these arrays, with simply supported and beam on a rail junction conditions, produce only a tangential and normal stress respectively.

3.1 SIMPLY SUPPORTED BEAMS

Begin the treatment of this array with simply supported beams. Then choose the junction conditions for simply supported connections to be,

$$u_b = u_1, \qquad -B_b \frac{\partial^2 u_1}{\partial z^2} = 0, \qquad H = I_b B_b \frac{\partial^3 u_b}{\partial z^3}, \tag{13}$$

which gives the horizontal stress on the half-space as as,

$$\sigma_{31} \approx \frac{H}{l^2} = B_b \frac{\pi h_b^4}{64 l^2} K^3 u_H \frac{\cos(KL)\cosh(KL) - 1}{\cosh(KL)\sin(KL) - \cos(KL)\sinh(KL)}, \tag{14}$$

Then introduce a scaled stress $\hat{H}$,

$$\frac{H}{l^2} = K^3 \hat{H} u_H = -k K^3 \hat{H} \beta_R \frac{1 - \beta_R^2}{1 + \beta_R^2} \psi, \tag{15}$$

where the full unimodal dispersion relation is

$$\begin{aligned} \left((\lambda + 2\mu)k^2\alpha^2 - \lambda k^2\right) \left(-\mu k^2 \left(1 + \beta^2\right) - k K^3 \hat{H} \beta\right) \\ = \left(2\,\mu k^2 \alpha + k K^3 \hat{H}\right) \left(-2\mu k^2 \beta\right). \end{aligned} \tag{16}$$

and the asymptotic dispersion relation is given by,

$$k^2 + k K^3 \hat{H}\ \beta_R \frac{1 - \beta_R^2}{2\mu B}\ - \frac{\omega^2}{c_R^2} = 0. \tag{17}$$

Following the same approach but for the higher order model yields,

$$k^3 + k^2 K^3 (A_R + 1) \hat{H}\ \beta_R \frac{1 - \beta_R^2}{2\mu B}\ - k \frac{\omega^2}{c_R^2} + K^3 A_R \hat{H}\ \beta_R \frac{1 - \beta_R^2}{2\mu B} \frac{\omega^2}{c_R^2} = 0. \tag{18}$$

The comparison of these dispersion relations is given in Figure 2. This plot shows a uniform improvement on the accuracy of the asymptotic model, becoming near indistinguishable to the full unimodal solution for lower frequencies. However, this improved accuracy comes at the cost of increased complexity in the dispersion relation; while the quadratic dispersion relation is less accurate, it yields a straightforward closed form solution. Although the new cubic dispersion relation still produces a closed form solution, it is more difficult to intuitively interpret.

3.2 BEAMS ON RAILS

Next take the junction conditions for connections of a beam moving freely on a rail

$$\frac{\partial u_b}{\partial z} = \frac{\partial u_3}{\partial x}, \qquad \frac{\partial \sigma_{zz}}{\partial x} = -B_b \frac{\partial^2 u_1}{\partial z^2}, \qquad I_b B_b \frac{\partial^3 u_\eta}{\partial \zeta^3} = 0, \tag{19}$$

so the vertical stress is given by,

$$\sigma_{33} \approx \frac{V}{l^2} = i\frac{K}{k}\frac{\pi h_b^2}{4l^2} B_b \, u_{V,x} \frac{1 - \cos(KL)\cosh(KL)}{\cosh(KL)\sin(KL) + \cos(KL)\sinh(KL)} \tag{20}$$

Introduce a scaled stress $\hat{V}$ defined by

$$\frac{V(x,y,t)}{l^2} = i\frac{K}{k}\hat{V} u_{V,x} = -iKk\hat{V}\frac{1-\beta_R^2}{2}\psi, \tag{21}$$

leading to the full unimodal dispersion relation,

$$\mu k^2 \left(1+\beta^2\right)\left(\lambda k^2 - (\lambda+2\mu)k^2\alpha^2 + kK\hat{V}\alpha\right) = 2\mu k^2 \alpha \left(-2\mu k^2 \beta + kK\hat{V}\right) \tag{22}$$

and the approximate dispersion relation,

$$k^2 - k\,\frac{\alpha_R}{\mu B} K\hat{V}\frac{1-\beta_R^2}{2} - \frac{\omega^2}{c_R^2} = 0. \tag{23}$$

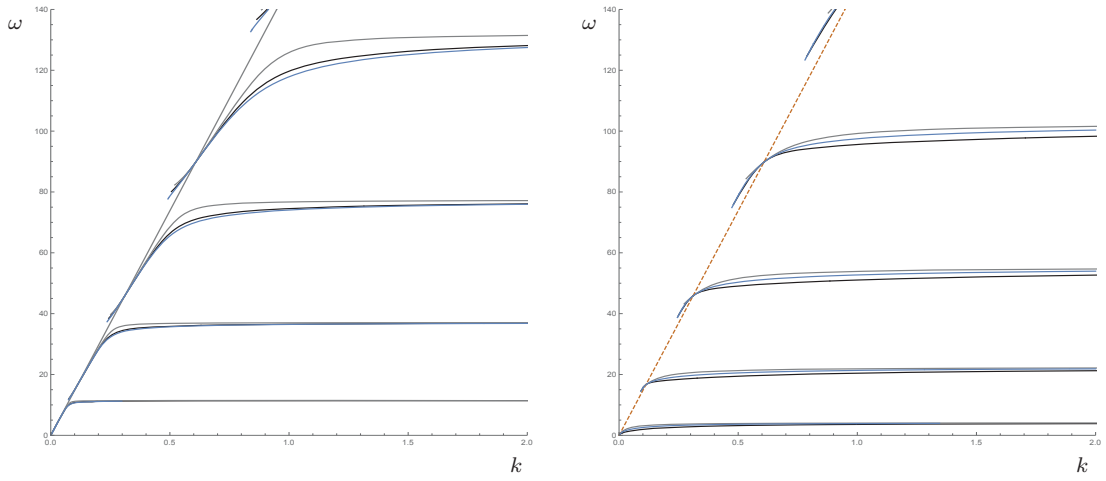

Figure 2: Dispersion curves (frequency ω vs. wavenumber k) for surface waves on the half-space coated with simply supported beam like resonators (left) and beam-like resonators on a rail (right). Solid blue lines show the full unimodal solution, solid black lines the higher-order asymptotic solution and solid gray lines the leading order asymptotic solution.

For the higher order model, using the same approach as before, we obtain the dispersion relation,

$$k^3 - k^2 \frac{\alpha_R}{\mu B} K(A_R + 1)\hat{V}\frac{1-\beta_R^2}{2} - k\frac{\omega^2}{c_R^2} - \frac{\alpha_R}{\mu B} K A_R \hat{V}\frac{1-\beta_R^2}{2} = 0. \tag{24}$$

The comparison of these dispersion relations is again given in Figure 2. Unlike the simply supported array, this plot does not show a uniform improvement for the full range of frequencies. It does, however, show greatly improved accuracy in the immediate vicinity of the Rayleigh line, in particular being much more accurate at predicting the locations of the band gaps. This is also again a cubic dispersion relation, with added complexity over the lower order model.

4 MIXED NORMAL AND TANGENTIAL STRESS

Finally we consider the case where all relevant quantities between the resonators and half plane are conserved. Matching all junction conditions (4) gives the multi-stress condition,

$$\begin{aligned} \sigma_{31} \approx \frac{H}{l^2} &= \frac{\pi h_b^4}{64 l^2} B_b K^2 (\xi u_{V,x} + K\eta u_H), \\ \sigma_{33} \approx \frac{V}{l^2} &= i\frac{\pi h_b^2}{4 l^2} B_b \frac{K}{k} (\zeta u_{V,x} + K\xi u_H), \end{aligned} \tag{25}$$

where,

$$\xi = \frac{\sin(KL)\sinh(KL)}{\cos(KL)\cosh(KL)+1}, \tag{26}$$

$$\eta = \frac{\cosh(KL)\sin(KL) + \cos(KL)\sinh(KL)}{\cos(KL)\cosh(KL)+1}, \tag{27}$$

$$\zeta = \frac{\cosh(KL)\sin(KL) - \cos(KL)\sinh(KL)}{\cos(KL)\cosh(KL)+1}. \tag{28}$$

This gives the full unimodal solution as

$$\begin{aligned} &\left(\mu k^2\left(1+\beta^2\right) + \frac{\pi h_b^4}{64 l^2} B_b k\left(K^3\beta\eta - K^2 k\xi\right)\right) \\ &\qquad = \left((\lambda+2\mu)k^2\alpha^2 - \lambda k^2 + \frac{\pi h_b^2}{4 l^2} B_b\left(K^2\xi - Kk\alpha\zeta\right)\right) \end{aligned} \tag{29}$$

However the existing asymptotic model is not formulated to account for both a normal and tangential stress. Naively combining the previous leading order asymptotic models yields the multi-stress model,

$$\Box\psi = -\frac{1+\beta_R^2}{2\mu B}\sigma_{31} - i\frac{\alpha_R}{\mu B}\sigma_{33}. \tag{30}$$

However, this new model inherits the assumption that at coincidence with the Rayleigh line the stresses tend to zero. This does not take into account for cross interaction between stress terms. Hence to find the predicted inaccuracy with the model at $c = c_R$ first assume that the stresses have the decomposition

$$\sigma_{31} = H_\phi \phi + H_\psi \psi, \qquad \sigma_{33} = V_\phi \phi + V_\psi \psi. \tag{31}$$

so that substitution into the classical Rayleigh denominator gives,

$$\begin{aligned} &-(1+\beta^2)^2 - 4\alpha\beta \\ &\quad = i\frac{2\beta}{\mu k^2} H_\phi + \frac{1+\beta^2}{\mu k^2} H_\psi - \frac{1+\beta^2}{\mu k^2} V_\phi + i\frac{2\alpha}{\mu k^2} V_\psi + \frac{H_\phi V_\psi - V_\phi H_\psi}{\mu^2 k^4} \end{aligned} \tag{32}$$

from which a leading order expansion about the Rayleigh line yields,

$$\left(k^2 - \frac{\omega^2}{c_R^2}\right)\psi = \frac{1+\beta_R^2}{2\mu B}\sigma_{31} + i\frac{\alpha_R}{\mu B}\sigma_{33} - \frac{V_\phi H_\psi - H_\phi V_\psi}{2\mu^2 B k^2}\psi. \tag{33}$$

and so at leading order we predict an inaccuracy of the order of $V_\phi H_\psi - H_\phi V_\psi$. Therefore when the two applied stresses are similar this will tend to zero, but will give a significant deviation when the stresses are more distinct.

The use of this new model gives the leading order asymptotic dispersion relation as,

$$\begin{aligned} 0 = {} & k^2\left(1 + \frac{1+\beta_R^2}{2\mu B l^2}\frac{\pi h_b^4}{64} B_b K^2 \frac{1-\beta_R^2}{2}\,\xi\right) \\ & - k\left(\frac{\alpha_R}{\mu B l^2}\frac{\pi h_b^2}{4} B_b K \frac{1-\beta_R^2}{2}\,\zeta - \frac{1+\beta_R^2}{2\mu B l^2}\frac{\pi h_b^4}{64} B_b K^3 \beta_R \frac{1-\beta_R^2}{1+\beta_R^2}\,\eta\right) \\ & - \left(\frac{\omega^2}{c_R^2} + \frac{\alpha_R}{\mu B l^2}\frac{\pi h_b^2}{4} B_b K^2 \beta_R \frac{1-\beta_R^2}{1+\beta_R^2}\,\xi\right). \end{aligned} \tag{34}$$

We can combine the higher order model in a similar way to produce a multi-stress model,

$$\Box\psi_{,11} = \Box_1\left(-\frac{1+\beta_R^2}{2\mu B}\,\sigma_{31} - i\frac{\alpha_R}{\mu B}\,\sigma_{33}\right), \tag{35}$$

which on substitution of the stresses yields the higher order dispersion relation,

$$
\begin{aligned}
0 = {} & k^4 \left(1 + (A_R+1)\frac{1+\beta_R^2}{2\mu B l^2}\frac{\pi h_b^4}{64} B_b K^2 \frac{1-\beta_R^2}{2}\,\xi\right) \\
& - k^3 (A_R+1)\left(\frac{\alpha_R}{\mu B l^2}\frac{\pi h_b^2}{4} B_b K \frac{1-\beta_R^2}{2}\,\zeta - \frac{1-\beta_R^2}{2\mu B l^2}\frac{\pi h_b^4}{64} B_b K^3 \beta_R \eta\right) \\
& - k^2 \left(\frac{\omega^2}{c_R^2} + (A_R+1)\frac{\alpha_R}{\mu B l^2}\frac{\pi h_b^2}{4} B_b K^2 \beta_R \frac{1-\beta_R^2}{1+\beta_R^2}\,\xi\right) \\
& + k^2 A_R \left(\frac{1+\beta_R^2}{2\mu B l^2}\frac{\pi h_b^4}{64} B_b K^2 \frac{1-\beta_R^2}{2}\,\xi\right)\frac{\omega^2}{c_R^2} \\
& - k A_R \left(\frac{\alpha_R}{\mu B l^2}\frac{\pi h_b^2}{4} B_b K \frac{1-\beta_R^2}{2}\,\zeta - \frac{1-\beta_R^2}{2\mu B l^2}\frac{\pi h_b^4}{64} B_b K^3 \beta_R \eta\right)\frac{\omega^2}{c_R^2} \\
& - A_R \left(\frac{\alpha_R}{\mu B l^2}\frac{\pi h_b^2}{4} B_b K^2 \beta_R \frac{1-\beta_R^2}{1+\beta_R^2}\,\xi\right)\frac{\omega^2}{c_R^2}.
\end{aligned}
\tag{36}
$$

This dispersion relation is shown with the leading order and full unimodal solutions in Figure 3. While the higher order model is a significant improvement over the leading order model, particularly for lower frequencies, both models show the same divergence from the unimodal solution at the Rayleigh line. While this inaccuracy can be calculated, this would significantly reduce the simplicity of the model.

Furthermore, this higher order dispersion relation is significantly more complicated than the leading order relation. While the quartic dispersion relation can still have a closed form solution, it will be significantly less concise or simple to interpret.

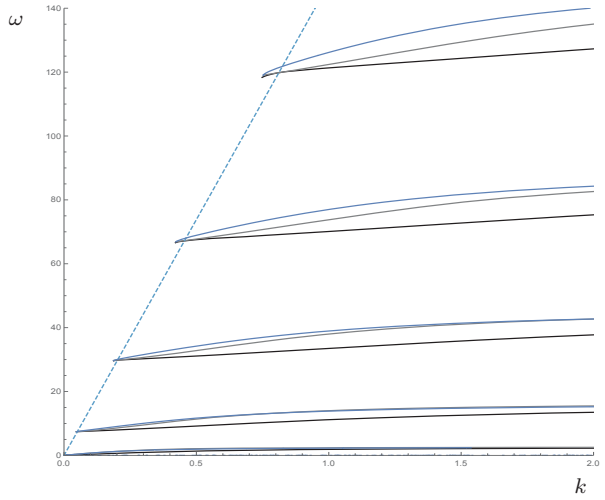

Figure 3: Dispersion curves (frequency ω vs. wavenumber k) for surface waves on the half-space coated with fully matched beam-like resonators. Solid blue lines show the full unimodal solution, solid black lines the higher-order asymptotic solution and solid gray lines the leading order asymptotic solution.

5 CONCLUSION

The refined model for Rayleigh waves has been successfully applied to the array of beam-like resonators for a range of junction conditions. While this showed a general improvement in accuracy compared to the leading order model, it also made the solutions obtained more complicated. This is particularly notable for the fully matched model where the increase in accuracy was only shown away from the Rayleigh line, where there is a fixed deviation from the unimodal solution. This deviation is fundamentally related to the formulation of the model and forms of the stresses so cannot be reduced by taking higher order models.

Overall, the results show the scope of the use of the higher order model. Accurate, closed form solutions in terms of scalar variables can be obtained for a significantly reduced amount of computing power. However, as the complexity of these systems increases, it may not be possible to produce closed form solutions.

ACKNOWLEDGEMENT

J. Kaplunov and D. Prikazchikov acknowledge support by the Russian Science Foundation, Grant No. 20-11-20133.

REVIEW

Peer review under the responsibility of the Scientific committee of EURODYN 2020.

REFERENCES

[1] P. Chadwick. Surface and interfacial waves of arbitrary form in isotropic elastic media. *Journal of Elasticity*, 6(1):73–80, 1976.

[2] A. Colombi, V. Ageeva, R. J. Smith, A. Clare, R. Patel, M. Clark, D. Colquitt, P. Roux, S. Guenneau, and R. V. Craster. Enhanced sensing and conversion of ultrasonic Rayleigh waves by elastic metasurfaces. *Scientific Reports*, 7:6750, 2017.

[3] A. Colombi, D. Colquitt, P. Roux, S. Guenneau, and R. V. Craster. A seismic metamaterial: The resonant metawedge. *Scientific Reports*, 6:27717, 2016.

[4] A. Colombi, R. V. Craster, D. Colquitt, Y. Achaoui, S. Guenneau, P. Roux, and M. Rupin. Elastic wave control beyond band-gaps: shaping the flow of waves in plates and half-spaces with subwavelength resonant rods. *Frontiers in Mechanical Engineering*, 3:10, 2017.

[5] A. Colombi, P. Roux, S. Guenneau, P. Gueguen, and R. V. Craster. Forests as a natural seismic metamaterial: Rayleigh wave bandgaps induced by local resonances. *Scientific Reports*, 6:19238, 2016.

[6] D. Colquitt, A. Colombi, R. Craster, P. Roux, and S. Guenneau. Seismic metasurfaces: Sub-wavelength resonators and Rayleigh wave interaction. *Journal of the Mechanics and Physics of Solids*, 99:379–393, 2017.

[7] N. Ege, B. Erbaş, J. Kaplunov, and P. Wootton. Approximate analysis of surface wave-structure interaction. *Journal of Mechanics of Materials and Structures*, 13(3):297–309, 2018.

[8] B. Erbaş, J. Kaplunov, D. Prikazchikov, and O. Şahin. The near-resonant regimes of a moving load in a three-dimensional problem for a coated elastic half-space. *Mathematics and Mechanics of Solids*, 22(1):89–100, 2017.

[9] Y. Fu, J. Kaplunov, and D. Prikazchikov. Reduced model for the surface dynamics of a generally anisotropic elastic half-space. *Proceedings of the Royal Society A: Mathematical, Physical and Engineering Sciences*, 476(2234):20190590, 2020.

[10] J. Kaplunov, E. Nolde, and D. Prikazchikov. A revisit to the moving load problem using an asymptotic model for the Rayleigh wave. *Wave Motion*, 47(7):440–451, 2010.

[11] J. Kaplunov and D. Prikazchikov. Asymptotic theory for Rayleigh and Rayleigh-type waves. *Advances in Applied Mechanics*, 50:1–106, 2017.

[12] A. Kiselev and D. Parker. Omni-directional Rayleigh, Stoneley and Schölte waves with general time dependence. *Proceedings of the Royal Society A: Mathematical, Physical and Engineering Sciences*, 466(2120):2241–2258, 2010.

[13] A. Nobili and D. A. Prikazchikov. Explicit formulation for the Rayleigh wave field induced by surface stresses in an orthorhombic half-plane. *European Journal of Mechanics-A/Solids*, 70:86–94, 2018.

[14] A. Palermo, S. Krödel, A. Marzani, and C. Daraio. Engineered metabarrier as shield from seismic surface waves. *Scientific Reports*, 6:39356, 2016.

[15] P. Wootton, J. Kaplunov, and D. Colquitt. An asymptotic hyperbolic-elliptic model for flexural-seismic metasurfaces. *Proceedings of the Royal Society A: Mathematical, Physical and Engineering Sciences*, 475(2227), 2019.

[16] P. Wootton, J. Kaplunov, and D. Prikazchikov. A second order asymptotic model for Rayleigh waves on a linearly elastic half plane. *IMA Journal of Applied Mathematics*, doi:10.1093/imamat/hxz037, 2020.

EURODYN 2020
XI International Conference on Structural Dynamics
M. Papadrakakis, M. Fragiadakis, C. Papadimitriou (eds.)
Athens, Greece, 23–26 November 2020

INCREMENTAL DYNAMIC ANALYSES OF BRIDGE PYLONS WITH CONSIDERATION OF THE EFFECT OF SURFACE WAVES

Charisis T. Chatzigogos[1] **and Kristel C. Meza Fajardo**[2]

[1] Géodynamique & Structure
Montrouge, France
e-mail: charisis.chatzigogos@geodynamique.com

[2] Bureau de Recherches Géologiques et Mineurs
Orléans, France
k.mezafajardo@brgm.fr

Keywords: bridge pylon design, surface waves, nonlinear soil-structure interaction, surrogate models, incremental dynamic analyses

Abstract. *The impact of surface waves on long-period structures remains among the less well understood aspects in the earthquake-resistant design of civil structures. Surface waves are typically characterized by rich low-frequency content and long durations and accordingly they can be particularly damaging for long-period structures, such as high-rise buildings, bridge pylons, liquid storage tanks, telecommunication masts etc. It is understood that an insufficient seismic design may be obtained for this class of structures if the effect of surface waves is not taken into account in the definition of earthquake loading. The present paper proposes a concise surrogate mechanical model for the study of the seismic nonlinear response of bridge pylons with and without the consideration of the effect of surface waves on dynamic response. The model is fully parametrizable based on a reduced number of dimensionless parameters that allow generating a large set of different structural and foundation configurations. The model couples a multi-fiber beam model for the bridge pylon with a nonlinear macroelement for the pylon foundation, accounting for sliding, uplifting and partial or full loss of bearing capacity in the foundation soil. This coupled pylon-foundation model is subjected to three cases of record sets for performing Incremental Dynamic Analyses (IDA), in which the records may preserve or not the surface wave components in the horizontal and rotational degrees-of-freedom of the incident motion. The IDA methodology is exploited for presenting in a synthetic manner the overall dynamic response for two characteristic bridge pylon designs and for highlighting the situations in which the non-consideration of surface waves may indeed lead to an insufficient design.*

1 INTRODUCTION

A common assumption in normative seismic studies of civil structures is to establish ground motions (to be used as incident excitations at the foundation level) via 1D site response analyses, in which the vertical propagation of shear waves is studied along an idealized soil column (1D model). Despite its efficiency, this approach wipes out the effects of real 3D topography of the subsoil and, in particular, the eventual presence of surface waves (Rayleigh waves / Love waves). Surface waves are typically generated in geological settings such as sedimentary basins and are characterized by rich low-frequency content and long durations. For example, presence of Rayleigh waves in the incident motion will lead to an increase in horizontal spectral accelerations (translational component) in the low-frequency range and also will generate a rotational component that cannot be obtained via 1D site response analyses.

Notwithstanding the ubiquitous principle, already anticipated by Biot [1] in the 1930's (*cf*. Trifunac [2]) that under favorable conditions (long waves), rotational seismic motions are small and can be neglected, several recent strong earthquakes (*e.g*. Chi-Chi 1999, Chuetsu 2004, El Mayor 2010, Tohoku 2011) have revealed significant rotational motions related to the passage of surface waves. These motions can be detrimental for long-period structures such as high-rise buildings, bridge pylons and liquid storage tanks, to name the most important ones.

Available studies for assessing the impact of surface waves on long-period structures are rather scarce. In two recent papers [3], [4], Meza & Papageorgiou have studied the effect of surface waves on the response of tall buildings and have shown that Rayleigh waves can increase the damage levels in such structures because of period elongation due to nonlinear response, extended shaking duration and risk of resonance. Concerning the effect of surface waves on bridge pylons, Chatzigogos *et al*. [5] have recently proposed a simplified surrogate model with consideration of nonlinear response in the pylon and/or in the foundation. The model is used for studying different soil-pylon configurations and for quantifying the increase in seismic demand (with respect to several performance criteria) due to the consideration of surface waves.

The present paper aims to extend the initial results obtained by Chatzigogos *et al*. [5] by probing -in a more systematic way- the impact of surface waves on nonlinear response of selected soil-pylon configurations via the technique of Incremental Dynamic Analysis (IDA) [6]. IDA is by now a well-established method for gaining insight into nonlinear seismic response for increasing levels of shaking. The studied bridge pylons are subjected to various records of increasing intensity and this allows plotting Damage Measures (DM) of interest as functions of appropriately selected seismic Intensity Measures (IM). The analyses are performed with and without consideration of the surface wave component of the considered records and this allows quantifying the additional distress provoked by the incidence of surface waves.

2 SURROGATE MODEL FOR BRIDGE PYLONS

2.1 General principles

In the following, we concentrate on the study of bridge pylons as shown on Figure 1. The surrogate model proposed by Chatzigogos *et al*. [5] will be used hereafter for studying the response of two characteristic pylon configurations with the IDA methodology. The model is intended for studying the transverse dynamic response of single-branch pylons (piers) and it is formulated in 2D kinematics. The pier supports at its top a part of the bridge deck and the deck-pier connection is concretized via a local spring-dashpot element. The pier foundation is a shallow footing resting at the ground surface (the footing embedment is neglected). Basic features of the surrogate model are the following:

- *Consideration of full nonlinear pier response in bending*. This is achieved by discretizing the pier into 2-noded multi-fiber beam elements. The cross-section of the pier is equally discretized into a number of fibers that are assigned an appropriate 1D nonlinear law. For the application presented hereafter, the nonlinear model for the fibers will be a simple elastoplastic law, with initial elastic stiffness E_p, yield stress f_y and post-elastic stiffness $E'_p = \alpha_k E_p$ (α_k: proportionality constant). In terms of global behavior, parameters E_p and f_y give rise to yield bending moment $M_{p,y}$ and yield curvature κ_y of the pier section.
- *Nonlinear response at the foundation level*. This is achieved via a dedicated nonlinear foundation macroelement following Chatzigogos *et al*. [7]. This model is briefly presented in §2.3.
- *Translational and rotational seismic excitation*. The excitation is introduced as imposed displacement to a control point at the base of the model. Following [5], three scenarios will be studied hereafter: a) only horizontal excitation without surface wave effect, b) only horizontal excitation, enriched with surface wave effect and c) horizontal and rotational excitations with full consideration of surface wave effects. For simplicity, vertical component of seismic motion is neglected in the presented analyses.
- *Solution in time domain.* The resulting dynamic equilibrium equation is integrated in time domain using an unconditionally stable Newmark scheme under the assumption of small displacements. Calculations are run in the open-source FEM platform Code_ASTER [8].

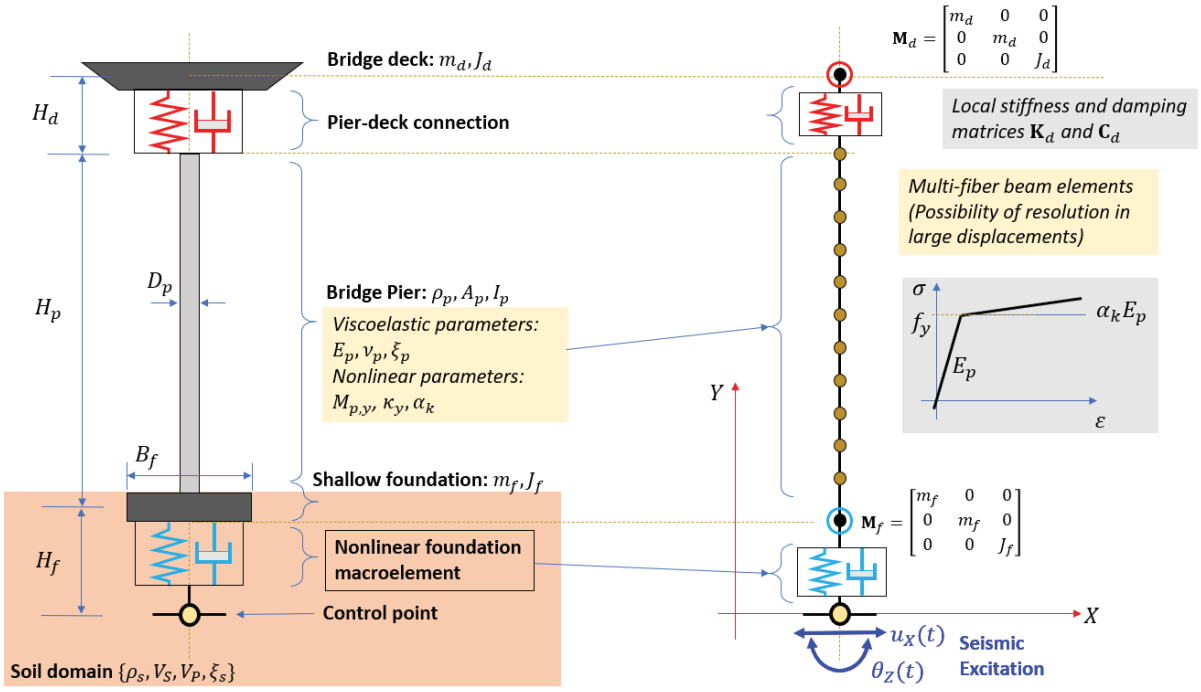

Figure 1: Surrogate model for studying the effects of surface waves on bridge pylons.

2.2 Geometric and mechanical characterization

The proposed surrogate model is intended for efficiently generating a large number of different pylon-foundation configurations, in the search for those cases that are particularly vulnerable in the incidence of surface waves. Each instance of the surrogate model can accordingly be obtained via a set of geometric and mechanical parameters that are organized into vector **a** that groups a limited number of dimensional parameters and into vector **b** that groups all other governing quantities that are either dimensionless or expressed as normalized parameters. In

the definition of governing model parameters, we use subscripts p, d, f and s to designate respectively the pier, the deck, the foundation and the soil. Normalized parameters are designated with a tilde (~).

The vector of dimensional parameters reads:

$$\mathbf{a}^{\mathrm{T}} = \{H_p, m_p, A_p, E_p, T_p, M_{p,y}, W_{\mathrm{tot}}\} \tag{1}$$

with the following definitions:

- H_p : height of bridge pier
- m_p : mass of bridge pier
- A_p: cross-sectional area of pier (considered uniform in the entire height)
- E_p : Young's modulus of bridge pier (initial elastic stiffness)
- T_p : fundamental period of vibration of the pier considering fixed-base conditions
- $M_{p,y}$: yield bending moment of pier section
- $W_{\mathrm{tot}} = g(m_p + m_d + m_f)$: total weight of the structure

The definition of the surrogate model is completed by 17 additional parameters that are either dimensionless or are normalized and are grouped in vector **b**, which reads:

$$\mathbf{b}^{\mathrm{T}} = \{\widetilde{H}_d, \widetilde{D}_p, \widetilde{H}_f, \tilde{B}_f, \widetilde{m}_d, \widetilde{m}_f, \tilde{J}_d, \tilde{J}_f, \xi_p, \xi_s, \nu_p, \nu_s, \tilde{\rho}_s, \tilde{V}_S, \widetilde{N}_{f,\max}, \tilde{V}_{f,\max}, \widetilde{M}_{f,\max}\} \tag{2}$$

with the following definitions:

- $\widetilde{H}_d = H_d/H_p$: normalized height of the bridge deck (form pier top to the center of gravity of bridge deck, *cf*. Figure 1)
- $\widetilde{D}_p = D_p/H_p$: normalized bridge pier diameter (or equivalent diameter for non-circular pier sections)
- $\widetilde{H}_f = H_f/H_p$: normalized foundation height (from pier base to the center of gravity of bridge footing)
- $\tilde{B}_f = B_f/H_p$: normalized characteristic footing dimension
- $\widetilde{m}_d = m_d/m_p$: normalized mass of bridge deck supported by the pier
- $\widetilde{m}_f = m_f/m_p$: normalized mass of bridge foundation
- $\tilde{J}_d = J_d/m_p H_p^2$: normalized rotational inertia of bridge deck
- $\tilde{J}_f = J_f/m_p H_p^2$: normalized rotational inertia of foundation
- ξ_p : critical damping ratio for the bridge pier (in the linear viscoelastic range)
- ξ_s : critical material damping ratio in the soil (in the linear viscoelastic range)
- ν_p : Poisson's ratio for the bridge pier
- ν_s : Poisson's ratio in the soil
- $\tilde{\rho}_s = \rho_s/(\frac{m_p}{A_p H_p})$: normalized soil mass density
- $\tilde{V}_S = V_S/(\frac{H_p}{T_p})$: normalized shear wave velocity (rigidity contrast between soil and structure)
- $\widetilde{N}_{f,\max} = N_{f,\max}/W_{\mathrm{tot}}$: maximum centered force supported by the foundation
- $\tilde{V}_{f,\max} = V_{f,\max}/W_{\mathrm{tot}}$: maximum horizontal force supported by the foundation
- $\widetilde{M}_{f,\max} = M_{f,\max}/M_{p,y}$: maximum overturning moment supported by the foundation

The above definitions for the pylon foundation imply that it is possible to determine dynamic impedance terms (computed at the fundamental SSI frequency of the pylon) assuming equivalent foundation dimension B_f and the homogenized linear viscoelastic soil domain with parameters $\{\rho_s, \nu_s, V_S, \xi_s\}$. For a surface footing (anticipating negligible off-diagonal impedance terms) and 2D kinematics, three stiffness terms $\{K_{NN}, K_{VV}, K_{MM}\}$ and the corresponding damping terms $\{C_{NN}, C_{VV}, C_{MM}\}$ are obtained.

2.3 Nonlinear foundation macroelement

An important feature of the proposed model is the use of a dedicated macroelement for description of nonlinear response at foundation level. The implemented foundation macroelement follows the formulation proposed by Chatzigogos *et al*. [7]. The foundation macroelement is an advanced link element that is placed at the base of the model and aims at reproducing nonlinear foundation response under earthquake action. The macroelement provides a phenomenological constitutive law for relating the increment of foundation displacements $\dot{\mathbf{u}}_f$ to the corresponding increment of work-conjugate force parameters $\dot{\mathbf{Q}}$. For obtaining the macroelement constitutive law, total displacement increment is decomposed into the linear elastic counterpart $\dot{\mathbf{u}}_{\text{lin}}$ that is computed from impedance terms, and counterparts for three independent nonlinear mechanisms: sliding ($\dot{\mathbf{u}}_{\text{sl}}$), foundation uplifting ($\dot{\mathbf{u}}_{\text{up}}$) and soil plasticity ($\dot{\mathbf{u}}_{\text{sp}}$). Total displacement increment $\dot{\mathbf{u}}_f$ thus reads:

$$\dot{\mathbf{u}}_f = \dot{\mathbf{u}}_{\text{lin}} + \dot{\mathbf{u}}_{\text{up}} + \dot{\mathbf{u}}_{\text{sl}} + \dot{\mathbf{u}}_{\text{sp}} \tag{3}$$

Each nonlinear mechanism is described independently by an appropriate model. In particular, sliding mechanism is described by the standard Coulomb friction criterion with a non-associative flow rule. Soil plasticity is described by a bounding surface hypoplastic formulation [10] that can easily be adapted to soil behavior (cohesive, frictional or combination of the two). Finally, uplift mechanism is described by a phenomenological nonlinear elastic model that respects the perfect reversibility of this mechanism and depends solely on foundation geometry. Coupling between nonlinear mechanisms is achieved by solving simultaneously the nonlinear equations of each mechanism (with only minor adjustments in the formulation of each mechanism) for the same force increment. A detailed presentation of the foundation macroelement model implemented in this study is provided in references [5] and [7].

3 STUDIED CONFIGURATIONS

The analyses presented hereafter are performed for two pylon configurations corresponding to two types of seismic design philosophy for the foundation. The first configuration corresponds to what would be a conventional design, in which the foundation is designed with an over-strength (in terms of overturning moment) with respect to the bending moment capacity at the pylon base. Such a design implies that damage will be concentrated at the base of the bridge pylon, while the foundation should exhibit a quasi-linear response.

In the second configuration, the foundation dimension is reduced, inviting for development of nonlinear response at the foundation level (via activation of sliding, uplifting and soil plasticity mechanisms). Such an "inversion" in conventional capacity-design of interacting foundation-superstructure systems has been proposed by many researchers (*e.g.* [12]) as a viable means of seismic protection of structures with an affordable scheme for foundation design. The price to pay is the irreversible foundation response and the pronounced displacements at the top of the pylon (due to uplifting and high foundation rotations) that must be shown to remain in acceptable limits.

Table 1 presents the geometric and mechanical parameters that define the two studied configurations. Given that the pier height is $H_p = 30$m, the configurations are designated "P30-Large" or simply P30L and "P30-Small" or simply P30S.

P30L exhibits a foundation with characteristic dimension $B_f = 11.0$m. For P30S, $B_f = 7.0$m. Table 1 provides the dimensional (vector **a**) and dimensionless parameters (vector **b**) defining the studied configurations. For convenience, Table 1 also provides the dimensional parameters corresponding to vector **b**.

PHYSICAL QUANTITY		SYMBOL	UNIT	P30 (LARGE)	P30 (SMALL)
Dimensional	Column height	H_p	[m]	30.0	30.0
	Total mass of the pier	m_p	[kt]	0.530	0.530
	Pier cross-sectional area	A_p	[m²]	7.1	7.1
	Young modulus of pier	E_p	[MPa]	30000	30000
	Fundamental period (fixed-base conditions)	T_p	[sec]	2.036	2.036
	Yield moment of pier section	$M_{p,y}$	[MNm]	43.0	43.0
	Total weight of bridge pier	W_{tot}	[MN]	22.91	19.38
Dimensionless / Normalized	Pier-deck connection height (normalized)	$\tilde{H}_d$	[-]	0.0	0.0
	Pier section diameter (normalized)	$\tilde{D}_p$	[-]	0.1000	0.1000
	Foundation height (normalized)	$\tilde{H}_f$	[-]	0.0667	0.0667
	Foundation characteristic dimension (normalized)	$\tilde{B}_f$	[-]	0.3667	0.2333
	Mass of the deck (normalized)	$\tilde{m}_d$	[-]	2.2642	2.2642
	Mass of the foundation (normalized)	$\tilde{m}_f$	[-]	1.1415	0.4623
	Moment of inertia of the deck (normalized)	$\tilde{J}_d$	[-]	0.0491	0.0491
	Moment of inertia of the foundation (normalized)	$\tilde{J}_f$	[-]	4.334E-04	1.730E-04
	Basic damping ratio of pier	ξ_p	[%]	5.0	5.0
	Basic damping ratio of soil	ξ_s	[%]	5.0	5.0
	Poisson's ratio of pier	ν_p	[-]	0.2	0.2
	Soil Poisson's ratio	ν_s	[-]	0.3	0.3
	Soil mass density (normalized)	$\tilde{\rho}_s$	[kt/m³]	0.643	0.643
	Soil shear wave velocity (effective) (normalized)	$\tilde{V}_S$	[m/s]	17.29	17.29
	Maximum centered vertical force at the foundation (normalized)	$\tilde{N}_{f,\max}$	[MN]	4.84	2.35
	Maximum horizontal force at the foundation (normalized)	$\tilde{V}_{f,\max}$	[MN]	0.79	0.38
	Maximum overturning moment at the foundation (normalized)	$\tilde{M}_{f,\max}$	[MN]	3.11	0.80

Dimensional			
SYMBOL	UNIT	P30 (LARGE)	P30 (SMALL)
H_d	[m]	0.0	0.0
D_p	[m]	3.0	3.0
H_f	[m]	2.0	2.0
B_f	[m]	11.0	7.0
m_d	[kt]	1.2	1.2
m_f	[kt]	0.6	0.2
J_d	[ktm²]	23.4	23.4
J_f	[ktm²]	0.207	0.083
ξ_p	[%]	5.0	5.0
ξ_s	[%]	5.0	5.0
ν_p	[-]	0.2	0.2
ν_s	[-]	0.3	0.3
ρ_s	[kt/m³]	0.0016	0.0016
V_S	[m/s]	254.8	254.8
$N_{f,\max}$	[MN]	110.81	45.5
$V_{f,\max}$	[MN]	18.15	7.4
$M_{f,\max}$	[MNm]	133.77	34.5

Table 1: Geometric and mechanical parameters of studied bridge pier configurations.

Quantity	Symbol	Unit	P30 (LARGE)	P30 (SMALL)
Yield curvature of pier section	$\kappa_{p,y}$	[1/m]	0.00036	0.00036
Equivalent yield stress of pier fibers	f_y	[MPa]	16.22	16.22
Hardening parameter for pier fibers	α_k	[MPa]	0.001	0.001
Fundamental period of system with SSI	T_{SSI}	[sec]	2.167	2.506
Soil Young's modulus (effective)	E_s	[MPa]	270.00	270.00
Soil shear modulus (effective)	G_s	[MPa]	103.85	103.85
Soil P-wave velocity (effective)	V_P	[m/s]	476.60	476.60
Lysmer's analog velocity	V_{La}	[m/s]	393.88	393.88
Soil layer depth	d_s	[m]	25.00	25.00
Soil cohesion	c_u	[MPa]	0.150	0.15

(a)

PARAMETER DESCRIPTION	SYMBOL	UNIT	P30 (LARGE)	P30 (SMALL)
Footing dimension	B_f	[m]	11.00	7.00
Maximum centered vertical force	$N_{f,\max}$	[MN]	110.81	45.52
Maximum horizontal force	$V_{f,\max}$	[MN]	18.15	7.35
Maximum overturning moment	$M_{f,\max}$	[MNm]	133.77	34.47
Bounding surface parameter ψ	ψ	[-]	0.16	0.16
Bounding surface parameter ξ	χ	[-]	0.11	0.11
Footing elastic rigidity (vertical direction)	K_{NN}	[MN/m]	4247.64	2577.32
Footing elastic rigidity (horizontal direction)	K_{VV}	[MN/m]	3688.98	2193.60
Footing elastic rigidity (rotational direction)	K_{MM}	[MNm]	92178.41	23443.05
Footing dashpot coefficient (vertical direction)	A_{NN}	[MNs/m]	76.26	30.88
Footing dashpot coefficient (horizontal direction)	A_{VV}	[MNs/m]	5.43	2.20
Footing dashpot coefficient (rotation)	A_{MM}	[MNms]	0.00	0.00
Plastic parameter for virgin loading	h_o/K_{NN}	[-]	4.00	4.00
Plastic parameter for reloading	p	[-]	0.50	0.50
Non-associative parameter	p_g	[-]	5.00	5.00
Uplift initiation parameter (strip footing geometry)	α	[-]	4.00	4.00
Uplift parameter	γ	[-]	1.00	1.00
Uplift parameter	δ	[-]	1.00	1.00
Uplift parameter	ε	[-]	0.20	0.20
Uplift - plasticity coupling parameter	ζ	[-]	1.50	1.50

(b)

Table 2: Additional geometric and mechanical parameters of studied bridge pier configurations.

It is interesting to note that the maximum foundation overturning moment is $M_{f,\max} = 133.7$MNm for P30L and only $M_{f,\max} = 34.5$MNm for P30S. Yield bending moment of the pier section is $M_{p,y} = 43.0$MNm for both configurations.

Tables 2(a) and 2(b) provide some additional parameters characterizing the two configurations. In particular, Table 2(b) provides the parameters for the definition of foundation macro-element, following [5] and [7].

4 RECORD SET FOR INCREMENTAL DYNAMIC ANALYSES

The implementation of IDA requires the definition of a concise set of seismic records that correspond to a prescribed earthquake scenario (defined, for example, by the couple {Magnitude, distance} and given geotechnical conditions). The number of records in this set must be large enough to cover uncertainties related to the obtention of a representative acceleration time history in terms of spectral accelerations, strong phase duration, characteristic intensity measures *etc*. In standard IDA applications (*cf*. [6]), calculations are performed for a set comprising at least 30 records. Once such a record set has been defined, uniform scaling is applied to all records to achieve a preselected range of values for one or more characteristic intensity measures. In most cases, scaling is performed with respect to PGA, but other intensity measures can be used, as for example, Arias intensity, CAV *etc*.

Notwithstanding the necessity of a dense record set compatible with a specific earthquake scenario, the following IDA implementations will be performed for a record set comprising 12 signals that have been obtained from different recent earthquakes exhibiting variable characteristics. This record set comes from the studies of Meza & Papageorgiou [3], [4] and, in the present context, offers the advantage that for the selected records, it has been possible to extract the surface wave components in the definition of the translational and rotational ground motions. Consequently, for the two degrees-of-freedom of interest for the presented analyses, three separate signals are provided:

a) total motion q_{tot}, which corresponds to what has been recorded *in situ*
b) extracted motion q_{SW}, which corresponds to the contribution of surface waves in the recorded motion
c) body wave motion q_{BW}, which is the motion exempt of the effect of surface waves ($q_{\mathrm{BW}} = q_{\mathrm{tot}} - q_{\mathrm{SW}}$); it is thus understood that q_{BW} comprises exclusively the effect of body waves

In the above definitions, we use q to designate generically either horizontal translation u or rotation θ about a horizontal axis (rocking). The signals are provided in terms of displacements; velocities and accelerations are obtained by differentiation. The method for extracting the surface wave component of the recorded signals has been exhaustively presented in [13] and [14].

Table 3 presents main properties and intensity measures of the selected records. For each record, we provide the seismic event of origin and some basic features (year, location, magnitude, depth), the time step dt used for definition of the provided signal and corresponding Nyquist frequency f_{N}. Then, for each of the two retained degrees-of-freedom (translation / rotation), Table 3 provides characteristic intensity measures for total motion q_{tot}, extracted motion q_{SW} and body wave motion q_{BW}, with $q \equiv u$ for horizontal translation and $q \equiv \theta$ for the rocking. The provided intensity measures are: a) maximum acceleration, b) maximum velocity, c) maximum displacement, d) Arias Intensity I_A, e) Cumulative Absolute Velocity CAV and f) effective duration t_f. Definition of I_A, CAV and t_f for rotational motions is extrapolated from corresponding definitions for translations.

The presented IDA analyses are performed for five PGA levels defined with reference to motions u_{BW} : The considered intensity levels are: {0.1g, 0.2g, 0.3g, 0.4g, 0.5g}. All other

motions are scaled accordingly so that the above PGA levels are assured for motion u_{BW}. Basic scaling factor as reported in Table 3, is the coefficient that multiplies the initial signal so that PGA of motion u_{BW} becomes equal to 0.1g.

	N/N	[-]	1	2	3	4	5	6	7	8	9	10	11	12
Record	Earthquake	[-]	Niigata-ken Chuetsu	Niigata-ken Chuetsu	Niigata-ken Chuetsu	Niigata-ken Chuetsu	El Mayor-Cucapah	El Mayor-Cucapah	Chi-Chi aftershock 1803	Chi-Chi aftershock 1803	Chi-Chi aftershock 1803	Chi-Chi aftershock 1803	Tohoku	Tohoku
Record	Year	[-]	2004	2004	2004	2004	2010	2010	1999	1999	1999	1999	2011	2011
Record	Magnitude	M	6.8	6.8	6.8	6.8	7.2	7.2	6.2	6.2	6.2	6.2	9.0	9.0
Record	Depth	[km]	300	300	300	300	206.7	206.7	60	60	60	60	29	29
Record	Record Name	[-]	CHB026	CHB013	SIT011	TKY015	GVDA10	GVDA00	TCU140	TCU145	TCU118	TCU112	TKY020	TKY018
Record	Time Step	[dt]	6.5096E-02	6.5096E-02	6.6879E-02	6.6879E-02	5.0397E-02	5.0397E-02	3.5073E-02	3.5073E-02	3.1398E-02	3.1398E-02	4.0002E-02	4.0002E-02
Record	Nyquist frequency	[Hz]	7.68	7.68	7.48	7.48	9.92	9.92	14.26	14.26	15.92	15.92	12.50	12.50
BASIC SCALING FACTOR			16.68	13.45	3.90	6.76	9.13	6.40	3.18	2.79	2.78	3.95	0.93	0.70
u_{tot} Total Translation	Maximum Acceleration	[m/s2]	0.0600	0.0743	0.2566	0.1477	0.1789	0.1732	0.3624	0.3970	0.4547	0.3559	1.1494	1.7348
u_{tot} Total Translation	Maximum Velocity	[m/s]	0.0131	0.0136	0.0320	0.0279	0.0349	0.0326	0.1630	0.1419	0.1470	0.1169	0.2516	0.3572
u_{tot} Total Translation	Maximum Displacement	[m]	0.0123	0.0103	0.0199	0.0227	0.0570	0.0410	0.1322	0.1203	0.1030	0.0891	0.1004	0.1032
u_{tot} Total Translation	Arias Intensity	[m/s]	0.0022	0.0019	0.0175	0.0134	0.0094	0.0103	0.1097	0.0853	0.0912	0.0613	0.9748	2.0134
u_{tot} Total Translation	CAV	[m/s]	1.556	0.830	2.686	3.170	1.717	1.666	6.349	5.438	4.631	3.630	23.282	32.197
u_{tot} Total Translation	Effective Duration	[s]	243.3	87.9	70.2	157.7	46.0	40.8	58.3	62.0	47.8	43.3	103.3	95.4
u_{SW} Extracted Translation	Maximum Acceleration	[m/s2]	0.0153	0.0103	0.0442	0.0415	0.1691	0.0665	0.1486	0.2079	0.1655	0.1691	0.5674	0.7527
u_{SW} Extracted Translation	Maximum Velocity	[m/s]	0.0110	0.0065	0.0200	0.0249	0.0321	0.0323	0.1140	0.0811	0.1101	0.0800	0.0688	0.1299
u_{SW} Extracted Translation	Maximum Displacement	[m]	0.0100	0.0056	0.0133	0.0228	0.0457	0.0405	0.0883	0.0656	0.0843	0.0694	0.0356	0.0466
u_{SW} Extracted Translation	Arias Intensity	[m/s]	0.0002	0.0001	0.0010	0.0012	0.0040	0.0021	0.0297	0.0193	0.0196	0.0185	0.1325	0.4033
u_{SW} Extracted Translation	CAV	[m/s]	0.204	0.106	0.376	0.454	0.681	0.623	2.947	2.386	1.952	1.951	8.614	13.342
u_{SW} Extracted Translation	Effective Duration	[s]	34.6	17.1	25.8	24.2	17.6	29.4	49.8	53.5	30.9	37.1	128.7	92.3
u_{BW} Translation (without SW)	Maximum Acceleration	[m/s2]	0.0599	0.0743	0.2565	0.1479	0.1096	0.1562	0.3144	0.3587	0.3591	0.2530	1.0730	1.4249
u_{BW} Translation (without SW)	Maximum Velocity	[m/s]	0.0108	0.0104	0.0315	0.0242	0.0130	0.0127	0.0973	0.0801	0.1076	0.0746	0.2335	0.2860
u_{BW} Translation (without SW)	Maximum Displacement	[m]	0.0102	0.0087	0.0151	0.0154	0.0232	0.0068	0.0768	0.0738	0.0734	0.0582	0.0980	0.0960
u_{BW} Translation (without SW)	Arias Intensity	[m/s]	0.0019	0.0018	0.0157	0.0118	0.0045	0.0068	0.0614	0.0505	0.0574	0.0290	0.6896	1.2349
u_{BW} Translation (without SW)	CAV	[m/s]	1.424	0.778	2.509	2.976	1.360	1.361	4.729	4.062	3.620	2.431	19.011	25.262
u_{BW} Translation (without SW)	Effective Duration	[s]	261.9	81.1	76.0	170.5	78.4	51.6	61.9	64.5	49.4	50.2	96.9	95.1
θ_{tot} Total Rotation	Maximum Acceleration	[rad/s2]	1.759E-04	1.097E-04	2.478E-04	4.567E-04	3.023E-04	2.523E-04	1.019E-03	5.487E-04	9.246E-04	4.760E-04	2.507E-03	7.042E-03
θ_{tot} Total Rotation	Maximum Velocity	[rad/s]	1.322E-05	7.946E-06	1.538E-05	2.587E-05	1.867E-05	2.105E-05	4.359E-05	4.758E-05	7.110E-05	4.613E-05	1.195E-04	2.460E-04
θ_{tot} Total Rotation	Maximum Rotation	[rad]	1.013E-05	5.214E-06	3.312E-06	5.409E-06	9.823E-06	1.047E-05	3.174E-05	3.038E-05	2.195E-05	1.680E-05	2.227E-05	2.584E-05
θ_{tot} Total Rotation	Arias Intensity	[rad/s]	6.216E-09	5.207E-09	1.927E-08	4.276E-08	1.373E-08	2.055E-08	1.368E-07	1.007E-07	1.854E-07	9.337E-08	2.323E-06	1.562E-05
θ_{tot} Total Rotation	CAV	[rad/s]	1.784E-03	1.214E-03	2.314E-03	3.253E-03	1.814E-03	2.096E-03	5.471E-03	4.719E-03	5.284E-03	3.638E-03	3.097E-02	7.194E-02
θ_{tot} Total Rotation	Effective Duration	[s]	100.0	77.8	40.1	22.9	29.8	31.2	48.5	81.6	28.7	19.7	56.9	44.8
θ_{SW} Extracted Rotation	Maximum Acceleration	[rad/s2]	1.504E-05	7.080E-06	5.310E-06	6.875E-06	6.595E-06	6.693E-06	8.414E-05	1.587E-04	8.952E-05	8.698E-05	8.859E-05	9.218E-05
θ_{SW} Extracted Rotation	Maximum Velocity	[rad/s]	1.172E-05	5.822E-06	4.043E-06	5.762E-06	7.905E-06	8.148E-06	3.401E-05	3.001E-05	2.434E-05	2.491E-05	3.982E-05	3.399E-05
θ_{SW} Extracted Rotation	Maximum Rotation	[rad]	9.942E-06	4.927E-06	3.141E-06	4.752E-06	9.815E-06	1.031E-05	2.677E-05	2.289E-05	1.336E-05	1.470E-05	1.896E-05	1.574E-05
θ_{SW} Extracted Rotation	Arias Intensity	[rad/s]	1.845E-10	3.993E-11	2.542E-11	3.825E-11	3.598E-11	3.739E-11	4.853E-09	6.305E-09	3.508E-09	2.807E-09	1.543E-08	1.448E-08
θ_{SW} Extracted Rotation	CAV	[rad/s]	2.203E-04	8.719E-05	7.867E-05	8.834E-05	8.262E-05	8.377E-05	1.250E-03	1.318E-03	8.142E-04	7.555E-04	3.736E-03	3.387E-03
θ_{SW} Extracted Rotation	Effective Duration	[s]	23.0	15.2	21.5	17.0	14.3	14.1	57.6	137.5	30.9	37.2	189.1	160.1
θ_{BW} Rotation (without SW)	Maximum Acceleration	[rad/s2]	1.758E-04	1.096E-04	2.475E-04	4.566E-04	3.010E-04	2.513E-04	1.028E-03	5.241E-04	8.587E-04	4.920E-04	2.512E-03	7.055E-03
θ_{BW} Rotation (without SW)	Maximum Velocity	[rad/s]	8.059E-06	8.092E-06	1.533E-05	2.587E-05	1.834E-05	2.149E-05	4.466E-05	4.607E-05	6.670E-05	4.836E-05	1.092E-04	2.422E-04
θ_{BW} Rotation (without SW)	Maximum Rotation	[rad]	1.831E-06	1.331E-06	3.040E-06	3.085E-06	1.957E-06	2.405E-06	1.968E-05	1.859E-05	1.259E-05	8.066E-06	1.818E-05	1.973E-05
θ_{BW} Rotation (without SW)	Arias Intensity	[rad/s]	6.023E-09	5.163E-09	1.925E-08	4.271E-08	1.369E-08	2.051E-08	1.289E-07	9.291E-08	1.787E-07	8.948E-08	2.306E-06	1.560E-05
θ_{BW} Rotation (without SW)	CAV	[rad/s]	1.688E-03	1.170E-03	2.303E-03	3.239E-03	1.805E-03	2.091E-03	5.089E-03	4.180E-03	5.141E-03	3.415E-03	2.968E-02	7.128E-02
θ_{BW} Rotation (without SW)	Effective Duration	[s]	67.0	67.6	40.0	22.7	29.7	31.1	36.6	77.7	28.8	18.0	54.7	44.7

Table 3: Record set for IDA: Intensity measures for translational and rotational components

Some additional comments deserve to be noted for the selected records:

- Motion u_{BW} is used as reference motion for scaling: this is the motion that would be felt by the structure if no effect of surface waves were to be considered for the translational component and if rocking (θ_{BW}) were to be neglected following Biot's principle. Incidence of surface waves will modify the horizontal motion from u_{BW} to u_{tot} ; moreover, it will induce the amplified rotational motion θ_{tot} (with respect to θ_{BW})
- The effective durations, especially for motion u_{tot}, are particularly large, with values that may exceed 4min at least for one record (CHB026: $t_f = 243$s). This is because emphasis is to be given in the surface wave component, which is characterized by low frequencies (below 1Hz) that tend to increase duration if several cycles are contained in the signal

- Accordingly, time step dt used for the definition of signals is rather large (ranging between 40msec and 70msec, with corresponding Nyquist frequencies f_N ranging between 7.5Hz and 16Hz). This implies that high-frequency content is poorly described in the signals but this is a deliberate choice for reducing the number of time steps and, accordingly, computational cost
- Total rotations θ_{tot} in the selected signals are rather limited and this is line with Biot's principle, which postulates quasi-negligible rocking motions. For example, record CHB026 presents $\max\{\theta_{tot}\} \approx$ 1e^{-05}rad, which after scaling for the highest intensity level ($\max\{\ddot{u}_{BW}\}$ = 0.5g) yields: $\max\{\theta_{tot}\} = 5\times16.68\times$1e^{-05}rad = 0.8mrad. This value corresponds to an imposed drift at the base of the pylon of only 0.8‰.

Figure 2 presents the response spectra of the 12 signals for motions u_{BW}, u_{tot} and θ_{tot} after scaling of u_{BW} to 0.1g. Characteristic frequencies of u_{BW} motions are contained between 0.5Hz and 4Hz. For u_{tot}, this interval increases from 0.2Hz to 4Hz with higher spectral accelerations, especially for the first characteristic peak of the spectrum. Characteristic frequencies for total rotations are between 2Hz and 8Hz. Finally, it is interesting to note that, although all u_{BW} motions are scaled at 0.1g, PGA values for u_{tot} may range from 0.1g to 0.15g, the difference highlighting the increase in PGA due to the surface wave component.

It is recalled that IDA analyses are performed for three hierarchical motion scenarios:

- Scenario 1: Only horizontal translation u_{BW} is applied at the pylon base
- Scenario 2: Only horizontal translation u_{tot} is applied at the pylon base - scenario 2 adds the translation surface wave effect with respect to scenario 1
- Scenario 3: Horizontal translation u_{tot} and rotation θ_{tot} are applied at the base - scenario 3 adds the total rotational effect with respect to scenario 2

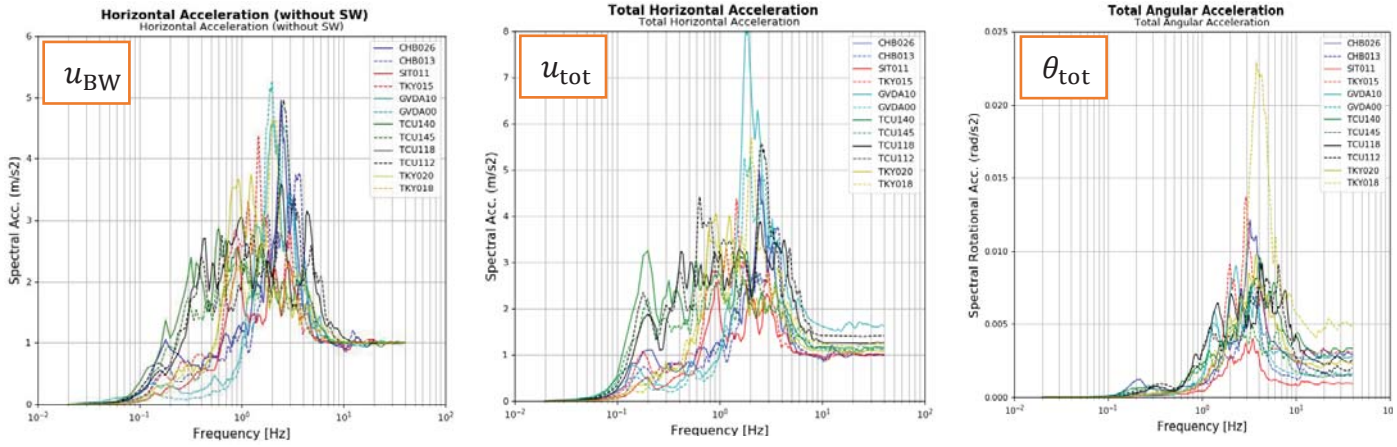

(a) (b) (c)

Figure 2: Record set for IDA: (a) Response spectra of horizontal translations without SW (motion u_{BW}) scaled at 1m/s², (b) Response spectra of total horizontal translations (motion u_{tot}), (c) Response spectra of total rotations (motion θ_{tot})

5 IMPLEMENTATION AND RESULTS

5.1 Organization of computations and results

The computations required for IDA analyses are performed with open-source FEM platform Code_ASTER [8]. The total number of performed analyses is N = 2 pylon configurations × 3 excitation scenarios × 12 records × 5 intensity measures = 360 nonlinear analyses. The calculations are performed in time domain under the assumption of small displacements.

IDA analyses give rise to so-called IDA curves, which present the evolution of a given damage measure (DM) or performance criterion as function of a preselected intensity measure. Following [5], seven damage measures (DM) are used for producing IDA curves and probing the performance of bridge pylon in nonlinear range. The selected DMs are (acronyms are provided in parentheses):

1. Maximum total drift of the deck (MTD) that is obtained from the sum of three components: horizontal displacement of the foundation, foundation rotation and structural drift due to pier deformation
2. Maximum structural drift of the deck (MSD); this is the component of deck displacement which is due exclusively to pier deformation
3. Residual total drift of the deck (RTD); this is deck displacement obtained at the end of excitation. Assuming that pylon vibration has been completed at the end of nonlinear analysis, RTD corresponds to the irreversible components due to sliding and permanent rotation at the foundation and also due to permanent structural drift of the pier
4. Residual structural drift of the deck (RSD), which can be high if the pier response is strongly nonlinear
5. Maximum ductility demand (DD) obtained at the base of the pylon, defined as:

$$\mathrm{DD} = \max\left\{1;\ \frac{\kappa(t)}{\kappa_y}\right\} \tag{4}$$

   where $\kappa(t)$ the developed curvature at the pylon base and κ_y the yield curvature, corresponding to the first exceedance of yield stress in the outer fiber of pier section. If DD = 1, the response is elastic
6. Maximum moment (MM) developed at the base of the pier
7. Accumulated foundation settlement (FS) at the end of loading. Pronounced FS is an indicator of a bearing failure at the foundation, eventually combined with significant permanent rotation

The provided Damage Measures characterize the global behavior and allow identifying significant nonlinear response at the pier or at the foundation. Global parameters are MTD and RTD. Parameters pertaining to the superstructure are MSD, RSD, DD and MM. Finally, FS is an indicator of damage level at the foundation. In what regards the definition of intensity measures, we provide the IDA curve set pertaining to the basic IM used for scaling, which is PGA of motion u_{BW}.

5.2 IDA curves for global DMs

Figures 3 and 4 present the obtained IDA curves for the two global DMs, namely maximum total drift (MTD) and residual total drift (RTD) of bridge deck. For presentation of IDA curves, the same figure setup is always adopted. Each presented figure contains two plots: in the left side, results for P30S (small foundation) are plotted, in the right side for P30L (large foundation). IDA curves are plotted in space {DM, IM}, where horizontal axis corresponds to the studied DM and vertical axis to the selected IM, which is PGA of u_{BW} varying from 0.1g to 0.5g. Each plot contains the following data:

- The raw data from transient analyses corresponding to 3 scenarios, 5 intensity levels and 12 records. These data are plotted as grey circles; each plot contains 180 data points;
- For each excitation scenario, a statistical treatment allows plotting the median value together with 16% and 84% percentiles of studied DM as function of increasing IM. Median values are presented with continuous lines, percentiles are presented with dotted lines. Each excitation scenario is represented by a specific color. Scenario 1 (excitation with u_{BW}) is represented in blue; scenario 2 (excitation with u_{tot}) is represented in green;

scenario 3 (excitation with u_{tot} and θ_{tot}) is represented in red. In the following we may refer to scenario 1 as SC1 (respectively for 2 and 3). SC2-3 will indicate scenarios 2 and 3 together.

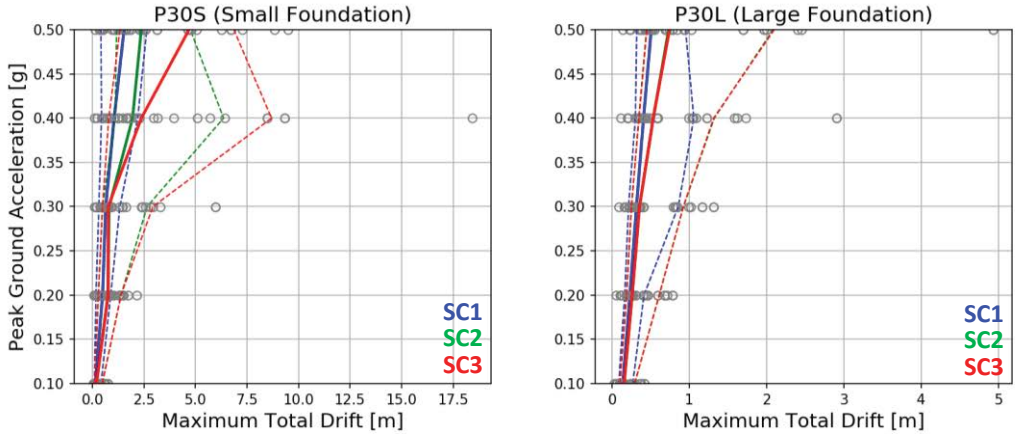

Figure 3: IDA curve for global parameter MTD (Maximum total drift)

IDA curves for global parameter MTD, as presented on Figure 3, indicate a sharp contrast in response for the two studied configurations. For P30S, maximal MTD can be as high as 17.5m for the most critical data point. Despite the fact that this is an isolated value, it certainly indicates development of a bearing failure mechanism at foundation level, accompanied by pronounced rotations. For P30L, maximal MTD is 5m and this is due to nonlinear pier response in bending. For P30S, median curves are all increasing with increasing IM and it is interesting to note that up to 0.30g, there is little difference between SC1 and SC2-3. Beyond 0.3g however, the difference between the three scenarios is more pronounced and one can notice an initial increase from SC1 to SC2, then an additional distress when passing to SC3. This indicates that both the total rotational component and the translational component of surface waves can have an impact on the response for very strong events, in case of yielding foundation systems. On the contrary, in P30L, median curves show a slight increase in MTD when passing from SC1 to SC2, but no additional distress when passing to SC3. Actually, SC3 curves are strictly superimposed to SC2 curves, implying that the consideration of θ_{tot} has no impact on the final result even for very high intensities. Finally, the extent of percentile curves is an indicator of variability in response. In P30S, SC2-3 present clearly larger variabilities than SC1 and this is due to highly nonlinear foundation response. For P30L, there is still a difference in variability between SC1 and SC2-3, but it is less pronounced.

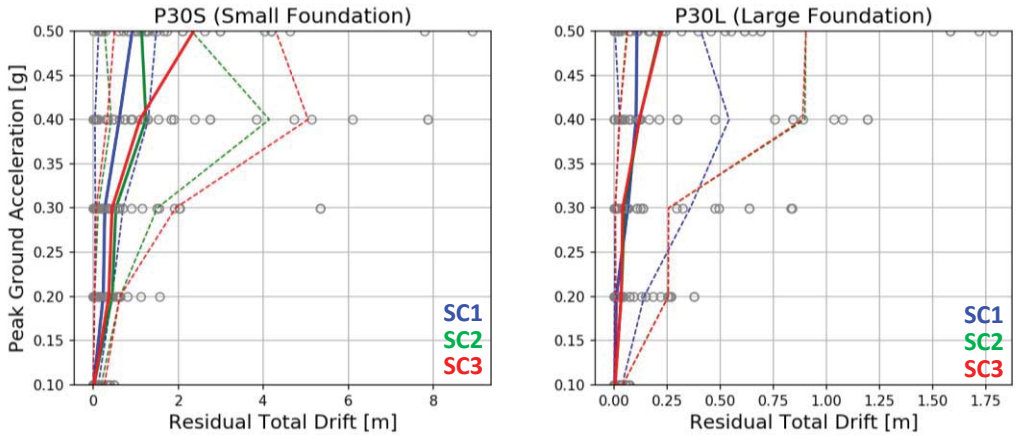

Figure 4: IDA curve for global parameter RTD (Residual total drift)

Figure 4 presents the obtained IDA curves for residual total drift (RTD). Again, the performance of P30S is much more critical than for P30L. The maximal obtained RTD value for P30S can be as high as 8m or more for a very strong earthquake and obviously this corresponds to a failure at foundation level that leads to non-tolerable residual displacements at bridge deck. In terms of mean values, it is interesting to note that SC1 leads to RTDs that increase slightly with intensity and remain less than 1m even at 0.50g. When the effect of surface waves is considered (SC2-3), RTD may be increased by factor 2 or more with respect to SC1. Rocking component (SC3) can lead to even higher RTD values for very strong events.

RTD evolution for P30L seems to remain independent of considered scenario for intensities up to 0.40g. It is needed to reach 0.50g to see a difference between SC1 and SC2-3. As for MTD, SC2-3 are strictly superimposed (both median and percentile curves are almost identical).

5.3 IDA curves for structural DMs

Figures 5 to 8 present IDA curves for four DMs pertaining to the response of the pier, namely maximum structural drift (MSD), residual structural drift (RSD), ductility demand at pylon base (DD) and maximum developed bending moment at the base (MM). All four DMs are clear indicators of the "isolation effect" offered by the reduced foundation design in P30S as compared to P30L.

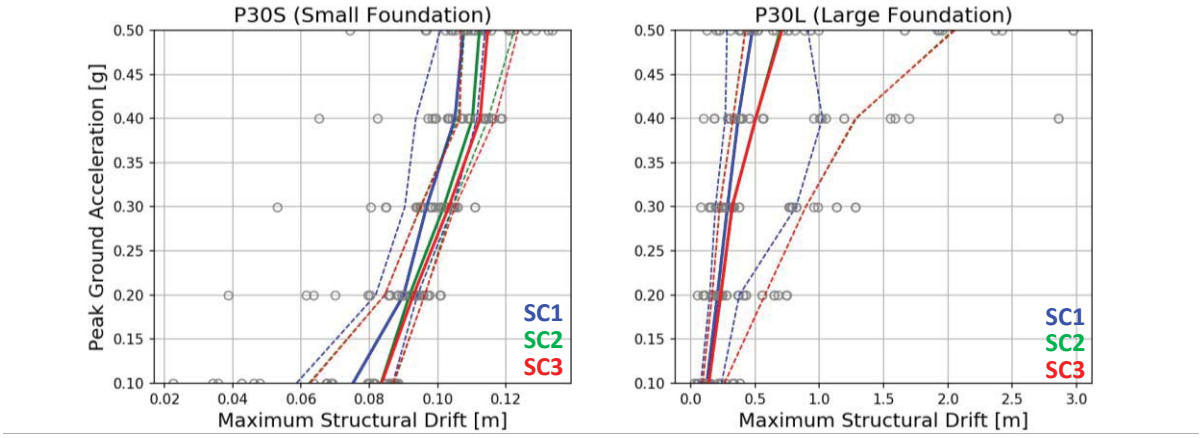

Figure 5: IDA curve for structural parameter MSD (Maximum Structural Drift)

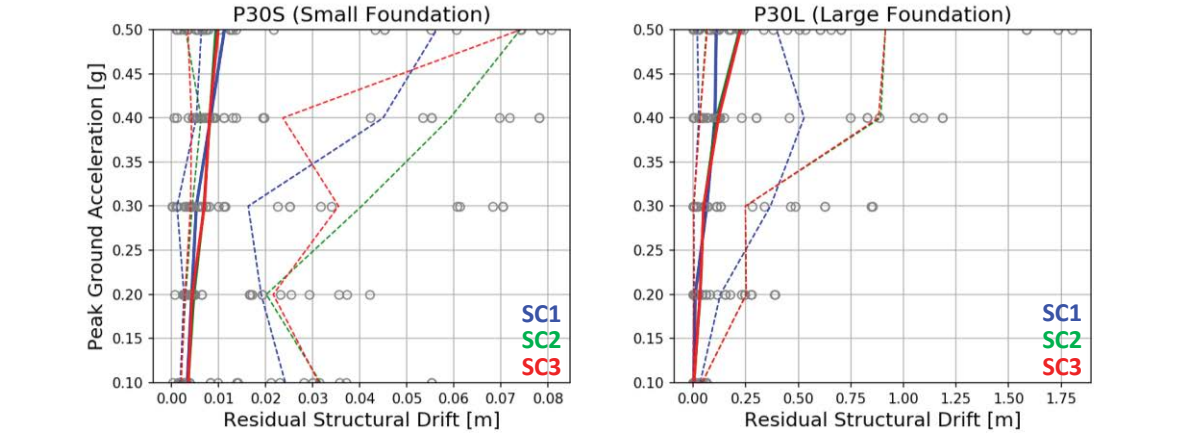

Figure 6: IDA curve for structural parameter RSD (Residual Structural Drift)

More specifically, Figure 5 presents IDA curves for maximum structural drift (MSD). For P30S, MSD values are limited, not exceeding 15cm for the most severe case in the data set. On

the contrary, MSD values for P30L can be as high as 3m (isolated data point). In terms of influence of surface waves, MSD increases slightly from SC1 to SC2 and then to SC3 for P30S for all intensities beyond 0.2g. In the case of P30L, SC2-3 are strictly superimposed (both median and percentile curves). The passage from SC1 to SC2 leads to an increase in distress, which is amplified as intensity increases.

Figure 6 presents IDA curves for residual structural drift (RSD). It is recalled that residual values are the ones obtained at the end of transient analysis and it is supposed that pylon vibration has been completed. For P30S, median RSD values on Figure 6 are less than 1cm and present significant variability: these values are actually "spurious" and originate from the fact that pylon vibration has not been perfectly dissipated by the final time step in transient analyses; if the analyses were to be continued further, RSD curves for P30S would be excepted to fall identically to zero. Results for P30L are almost identical to the results for RTD presented on Figure 4. This implies that RTD in case of P30L is only obtained from the structural component while the foundation contribution is negligible (as expected, since the foundation response is quasi-linear).

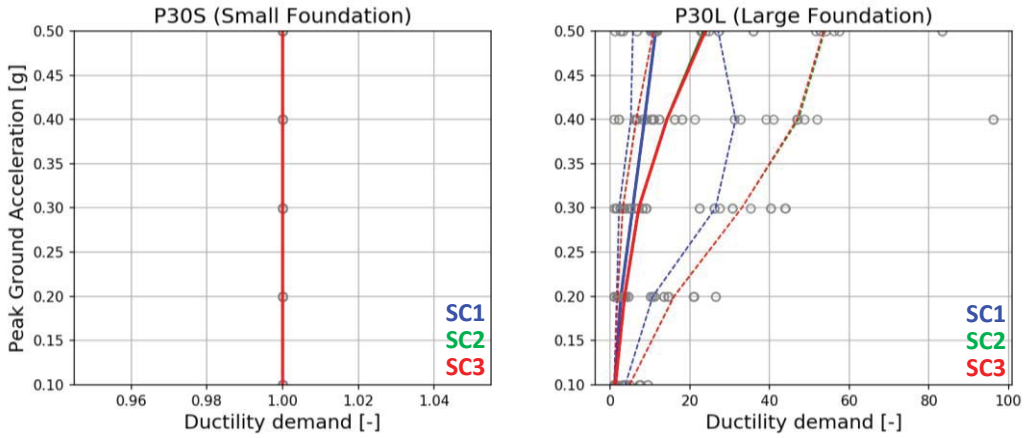

Figure 7: IDA curve for structural parameter DD (Ductility Demand at pier base)

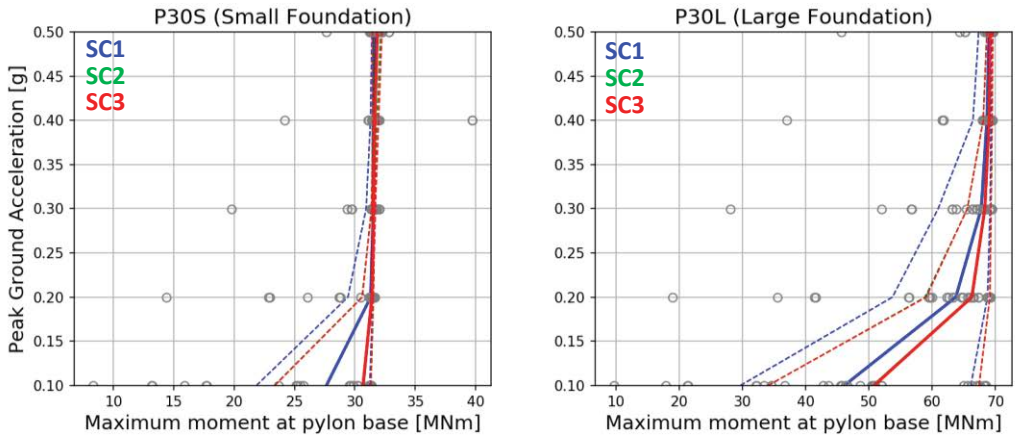

Figure 8: IDA curve for structural parameter MM (Maximum bending moment at pier base)

Figure 7 presents IDA curves for ductility demand (DD) at the pylon base. The result for P30S is very clear: all DDs are strictly equal to 1, which means that the pylon response remains elastic for all intensity levels. This a clear manifestation of the "capacity-design" approach, which guides all damage to a structural element (here, the foundation) and thus protects another structural element (here, the pier). In case of P30L, "capacity-design" is inversed. Consequently,

median DD curves at the pylon base are quickly raising with intensity level and may reach the value 10 for SC1 at 0.5g. The effect of surface waves increases even further median DD values, exceeding the value 20 at 0.5g. As in the previous cases for P30L, SC2-3 are superimposed: the effect of surface waves comes from the translational component. The rotational component induces no further distress on the system.

Figure 8 presents the obtained IDA curves for maximum bending moment developed at the pylon base (MM). An interesting feature of these curves is that, contrary to the previously examined DMs, here the variability is larger for smaller intensities. As IM is increased, IDA curves (both median and percentiles) tend asymptotically to a characteristic value. For P30S, this value is 34.5MNm (*cf*. Table 2b) and corresponds to the foundation overturning moment capacity. For P30L, this value is almost 70MNm and corresponds to the bending moment capacity of the pier. Recall, that for P30L, the overturning capacity at the foundation is 133.7 MNm (*cf*. Table 2b).

5.4 IDA curve for DMs pertaining to foundation response

As a final result, Figure 9 presents IDA curves for foundation settlement (FS), which is a performance indicator of foundation response. As expected, response for P30L is very favorable, with median settlements not exceeding 2cm for the strongest intensity level. The effect of surface waves is almost negligible and median curves for SC1 and SC2-3 are almost superimposed. On the contrary, the performance for P30S is -as expected- much more severe. Median settlements for SC1 are 0.25m at 0.5g but exhibit very high variability. Corresponding 84% percentile value is at least 4 times larger (>1.0m). The effect of surface waves almost doubles median FS for high intensities and one can observe a slight additional distress in passing from SC2 to SC3.

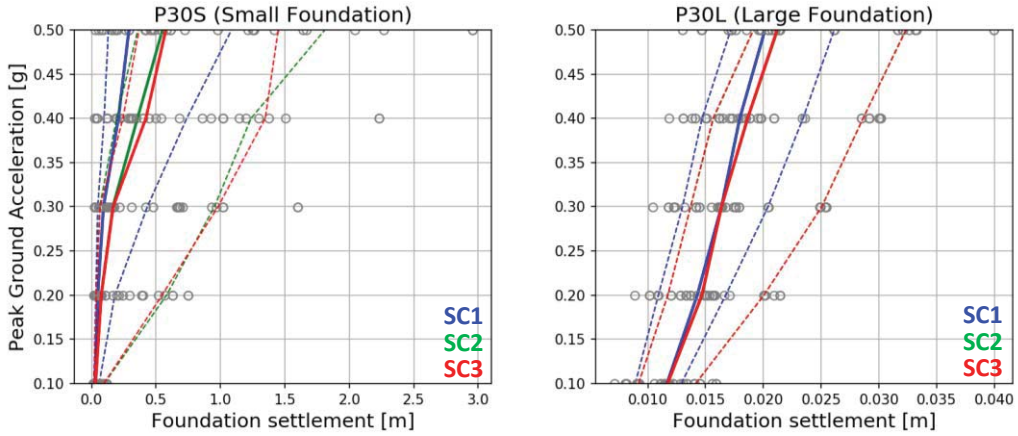

Figure 9: IDA curve for foundation parameter FS (accumulated Foundation Settlement)

6 CONCLUSIONS AND PERSPECTIVES

The present work has focused on the assessment of detrimental effects that surface waves may induce on bridge pylons. Two pylon configurations were studied, with emphasis on two variants for foundation design: a) conventional design, in which the foundation exhibits overstrength with respect to bridge pylon base section, b) inversed capacity-design, in which foundation dimension is reduced so as to concentrate nonlinear response at the foundation and thus protect the superstructure. The pylons have been studied via the IDA technique using a set of twelve records, in which it has been possible to isolate the effect of surface waves for horizontal translation and rocking. Basic conclusions of the study are the following:

- The detrimental effect of surface waves is mainly due to the horizontal motion component, at least for the record set used in this study. Even so, the effect of surface waves may lead to a significant increase in demand for both studied configurations. For the pylon with yielding superstructure, ductility demands at the pylon base section may be doubled due to surface waves. For the pylon with yielding foundation, foundation settlements may equally be doubled because of surface waves
- Detrimental effects of surface waves become more severe as seismic intensities increase. For seismic levels up to 0.20g, the response seems to be slightly altered by the incidence of surface waves
- An observable effect of the rocking motions has only been obtained for very high intensities and only for the configuration with yielding foundation. In the case of yielding superstructure, rocking motions have induced no further damage with respect to horizontal translations
- Bridge pylons designed with yielding foundations remain an interesting option for seismic design as a means for avoiding excessive damage in the superstructure. However, these systems seem to be more vulnerable to the effect of surface waves than conventional systems.

The presented results constitute the preliminary step for a detailed assessment of the effect of surface waves on bridge pylons within the framework or French research project ANR MODULATE. Prospective research works can focus on the following topics:

- A parametric investigation of a large number of pylon configurations (exploiting the proposed surrogate) model and confrontation with real cases
- Further IDA analyses and construction of fragility curves for record sets enriched with new records. As a matter of fact, one of the main objectives of the research project is to generate such records, both from post-processing of natural recordings and by large-scale numerical computations in realistic and canonical subsoil topographies. A further understanding is required as to the influence of rocking motions and as to how large rocking motions (induced by surface waves) can be. IDA analyses can further be investigated as to the selection of most relevant damage and intensity measures for the studied problem
- Last but not least, the studies can be extended to analyses for large displacements, which is a more rigorous hypothesis for systems near instability, foundation failure or extensive structural damage. Another possible extension is towards more realistic modeling of mechanical behavior in the concrete pier. Some selected pylon configurations can become the object of detailed 3D analyses.

7 ACKNOWLEDGEMENTS

This research work has received funding from the French National Research Project ANR MODULATE (2018 - 2022). More details and updates on ANR MODULATE can be accessed through the project website: https://modulate.brgm.fr.

REFERENCES

[1] Biot MA (1933): Theory of elastic systems vibrating under transient impulse with an application to earthquake-proof buildings. Proc Natl Acad Sci 1933; 19(2); 262-268

[2] Trifunac MD (2009): The role of strong motion rotations in the response of structures near earthquake faults. Soil Dynamics and Earthquake Engineering, 29 (2009); 382-393

[3] Meza Fajardo KC, Papageorgiou AS (2018): Response of tall buildings to base rocking induced by Rayleigh waves. Earthquake Engineering & Structural Dynamics, 2018; 47:1755-1773, https://doi.org/10.1002/eqe.3040.

[4] Meza Fajardo KC, Papageorgiou AS (2019): Ductility demands of tall buildings subjected to base rocking induced by Rayleigh waves. Earthquake Engineering & Structural Dynamics, 2019; 1-21, https://doi.org/10.1002/eqe.3179.

[5] Chatzigogos CT, Meza Fajardo KC, Papageorgiou AS (2020): Nonlinear response of bridge pylons to surface wave passage. Proceedings of 17WCEE, Sendai, Japan, September 13-18, 2020

[6] Vamvatsikos D, Cornell CA (2002): Incremental Dynamic analysis. Earthquake Engineering and Structural Dynamics, 31:491-514

[7] Chatzigogos CT, Figini R, Pecker A, Salençon J (2011): A macroelement formulation for shallow foundations on cohesive and frictional soil. International Journal for Numerical and Analytical Methods in Geomechanics, 2011; 35: 902-931

[8] Code_ASTER - Analyse des Structures et Thermo-Mécanique pour des Etudes et des Recherches (https://www.code-aster.org)

[9] Gazetas G (1991): Foundation vibrations. In Foundation Engineering Handbook, Chapter 15, Fang HY(ed.), Van Nostrand Reinhold, NY.

[10] Dafalias YF, Hermann LR (1982): Bounding surface formulation of soil plasticity. In Soil Mechanics - transient and cyclic loading, Pande GN, Zienkiewicz PC (eds.), Wiley, pp. 173-218.

[11] Chatzigogos CT, Pecker A (2009): Project DARE - Soil-Foundation-Structure systems beyond conventional seismic failure thresholds, GDS Internal report 32-09_N1A.

[12] Anastasopoulos I, Gazetas G, Loli M, Apostolou M, Gerolymos N (2010): Soil failure can be used for seismic protections of structures. Bulletin of Earthquake Engineering, 8:309-326

[13] Meza Fajardo KC, Papageorgiou AS (2016): Estimation of rocking and torsion associated with surface waves extracted from recorded motions. Soil Dynamics and Earthquake Engineering, 2016; 80:225-240

[14] Meza Fajardo KC, Papageorgiou AS, Semblat JF (2015): Identification and extraction of surface waves from three‐component seismograms based on the normalized inner product. Bulletin of Seismological of America 2015; 105(1):210-229

EURODYN 2020
XI International Conference on Structural Dynamics
M. Papadrakakis, M. Fragiadakis, C. Papadimitriou (eds.)
Athens, Greece, 23–26 November 2020

TRANSIENT ANALYSIS IN HALF-SPACE COMBINING IGA AND THE PERFECTLY MATCHED LAYER METHOD

Arturo Méndez Salas[1], **Margarita Chasapi**[1], **and Sven Klinkel**[1]

[1]Chair of Structural Analysis and Dynamics, RWTH Aachen University
Mies-van-der-Rohe-Str.1, 52074 Aachen, Germany
e-mail: {mendez.salas,chasapi,klinkel}@lbb.rwth-aachen.de

Keywords: numerical methods, isogeometric analysis, dynamic analysis, finite element method, B-Splines, perfectly matched layer, elastic wave.

Abstract. *This contribution is concerned with a numerical approach to represent the elastic half-space subjected to dynamic forces. The proposed numerical solution is achieved by combining the advantages of the isogeometric analysis concept and the absorbing boundary technique, Perfectly Matched Layer (PML). Due to the nature of the half-space modeling, the attenuation or propagation of the wave motion to infinity as well as an optimal representation of the dynamic response of the media must be validated. Both conditions are needed to obtain acceptable results for dynamic analysis. In this contribution, the PML in combination with the B-Splines is adopted. On one hand, B-Splines is capable of describing more precisely the geometry, dynamic effects and the unknown field of the problem. On the other hand, the spurious reflections are avoided employing the PML method. This is defined using an artificial layer surrounding the computational domain. Using these two formulations, a better representation of the half-space domain can be achieved with less computational effort and higher accuracy. In order to evaluate the performance of this approach, a numerical example is presented for the 2D case considering a homogeneous linear elastic domain. The equation of motion is solved using the displacement-based formulation and approximated by an implicit time integration method. The variation of spatial and temporal refinement of the selected domain, the order of interpolation functions and geometrical properties of the absorbing layer are the considered aspects to investigate the performance of this approach. The results are also compared with the standard FEM.*

1 INTRODUCTION

The success for the representation of unbounded domains in transient analysis relies mainly in two aspects: the validation of the energy propagation and a well-representation of the wave. Depending on the considered problem, solution approaches are commonly based on numerical, analytical or semi-analytical methods.

In numerical methodologies, the most common practice to fulfill the first condition is imposing artificial conditions in order to imitate the behaviour of the far field. Among the most common techniques are those where mechanical methods based on spring and dash-pot models or sufficiently extended domains are used. There are others where preferably absorbing boundary conditions are imposed.

The Perfectly Matched Layer (PML) belongs to the last category. The particularity of PML is that the waves are attenuated inside of an artificial medium without generating any reflection during the transition at incidence plane, see Fig.1. This approach was introduced by Beregner in studies of the electromagnetic field to solve Maxwell's Equations [1].Afterwards this was extended for the modelling of other unbounded media, such as media in elastodynamics [2] [3]. This method has evolved considerably resulting in complex formulations where the equations to be solved include convolutional terms. Those formulations are efficient but certainly costly.

On the other side, not only the energy dissipation must be guaranteed but also the best way to depict the geometry problem and dynamic effects. The Finite Element Analysis is famous for its high potential to model complex media. However, a fine discretization is commonly needed to achieve the desired approximation of the solution. This fact is a major concern generally in time-domain analysis. Therefore, here, the isogeometric analysis is employed not only because of its easy way to catch the geometry but also because it avoids spurious results in dynamics analysis. For example, *optical branches* occurring in standard FEM for high order interpolation functions are eliminated using the IGA approach. The use of IGA has great advantages since the high order basis functions used in numerical analysis demonstrate superior approximation behaviour. That is basically because it possesses higher continuity in comparison with the standard FEA [4] [5]. The basis functions or B-Splines are used not only to depict the geometric but also to approximate the unknown field of the problem to be treated.

In this contribution, the Perfectly Matched Layer Method in combination with the isogemetric analysis (IGA-PML), is used primarily as twofold for unbounded media modelling. Firstly, the use of PML eliminates the influence of reflected wave coming back to the domain of interest. Secondly, isogeometric analysis is used to achieve a better representation of the wave propagating through the media and to capture PML effects all over the computational domain.

2 ISOGEOMETRIC ANALYSIS

The isogeometric analysis concept is an analysis procedure supported by a representation using CAD [4]. The basic idea is to define as good as possible a geometry model to be used in a direct way into an analysis model. The most common computational geometry technologies used for that purposes are the Non-Uniform Rational B-Splines (NURBS), however there are others approaches which can be employed instead. NURBS functions are a strong engineering design tool due to their capability to represent almost directly curved shapes. Other advantages for using NURBS as basis functions are their flexibility to reach a better refinement by knot insertion procedure, their C^{p-1} continuity for p-th order NURBS, and a higher continuity along the described geometry. This avoids some shortcomings in dynamic analysis due to the fact that no abrupt changes occur in the approximated geometry.

The parameter space using NURBS is determined by using patches instead of elements; therefore, the mapping itself is global to the whole patch. Regularly, the domain contained in each patch is homogeneous and uniform. For heterogeneous media additional patches can be added.

The NURBS basis funtions, based on B-Splines, are defined using the Cox-de Boor Recursion formula. For more details see [4], [5]. In case that $p = 1$, the B-Splines functions are the same like those used for standard piece-wise linear element functions. For higher order basis functions no similar equivalence is shown. Those functions are piece-wise non-negative through the domain. Another relevant aspect, and among the most important features of these functions, is the $p - 1$ continuous derivatives across the element boundary for each p^{th} order function.

In this contribution, a single patch is used to depict the geometry of the half-space containing the absorbing boundary layer. Then, the approximation of the geometry and the unknown filed are continuous along the domain of interest and the perfectly matched layer.

3 PERFECTLY MATCHED LAYER FORMULATION

The perfectly matched layer is an artificial absorbing boundary method, see Fig. 1. It is based on creating a layer surrounding the domain of interest where outgoing waves from the source are exponentially attenuated. This effect is achieved using *analytic continuation* to map the equation of motion into a complex plane [6]. This modification is accomplished by changing the coordinate system of the problem. Hence, spurious reflections are avoided at the interface between the layer and the domain with an additionally imposed attenuation along this layer. This PML approach is achieved in terms of a *complex coordinate stretching* but it is in fact mathematically equivalent to the original *split-field* and *perfectly matched anisotropic absorbers* approaches [7].

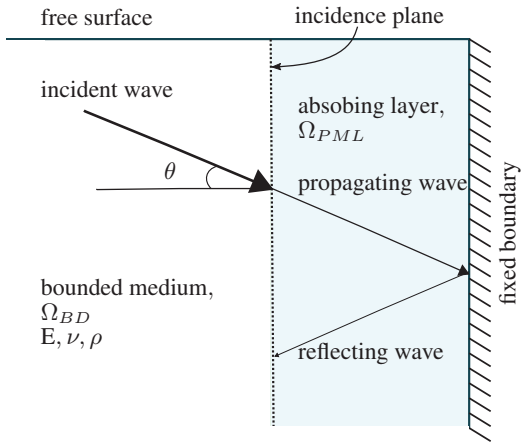

Figure 1: Scheme of perfectly matched layer method. θ denotes incidence angle of the wave.

Here, the complex coordinate stretching approach is adopted for a two dimensional case under plane strain motion. For more detailed information see e.g. [1],[2],[3],[8],[9].

PML equations are naturally developed in the frequency domain. For an elastic medium undergoing time-harmonic motion whose displacements of the form, $\mathbf{u}(\mathbf{x}, t) = \bar{\mathbf{u}}(\mathbf{x})\exp(i\omega t)$

the governing equations, without material damping and body forces, are

$$\begin{aligned} \text{div}\bar{\boldsymbol{\sigma}} &= \omega^2 \rho \bar{\mathbf{u}} \\ \bar{\boldsymbol{\sigma}} &= \mathbb{C}\bar{\boldsymbol{\varepsilon}} \\ \bar{\boldsymbol{\varepsilon}} &= \tfrac{1}{2}\left\{\text{grad}(\bar{\mathbf{u}}) + \text{grad}(\bar{\mathbf{u}})^T\right\}, \end{aligned} \tag{1}$$

where, $\bar{\boldsymbol{\sigma}}$ is the stress tensor, ρ material density, $\bar{\boldsymbol{\varepsilon}}$ contains the strains, $\mathbb{C}$ is the elasticity matrix, and ω is the angular frequency. These quantities are mapped into an orthogonal real coordinate system. The Eq.1 accepts body-wave solutions of the form,

$$\bar{\mathbf{u}}(\mathbf{x}) = \mathbf{q} e^{-ik_r \cdot \mathbf{x} \cdot \mathbf{p}}, \tag{2}$$

where, $\bar{\mathbf{u}}$ are the displacements at position vector $\mathbf{x}$, k_r is the wavenumber, $k_r = \omega / c_r$, with, c_r wave velocity for r-wave type: $r \in \{p, s\}$ for P and S-waves, respectively. $\mathbf{p}$ is unit vector for the propagation direction and $\mathbf{q} = \pm\mathbf{p}$ is the particle motion, see [2].

The wave described by Eq. 2 will travel without any variation or attenuation in an unbounded medium. With the intention of avoiding that effect, an additional attenuation is imposed to the wave response.

3.1 Complex stretch coordinate system

In order to impose the desired attenuation for outgoing waves, the wave equation solution is modified using a transformation into a complex coordinate system. This means that the dependent variable $\mathbf{x}$ is defined with a real and an imaginary part. A simple representation of this conversion is given as,

$$\lambda(\mathbf{x}) = \tilde{\mathbf{x}} = a(\mathbf{x}) - ib(\mathbf{x}). \tag{3}$$

If Eq.3 is used into Eq.2, replacing $\mathbf{x}$, the wave solution in Eq. 2 is transformed as,

$$\bar{\mathbf{u}}(\tilde{\mathbf{x}}) = \mathbf{q} e^{-ik_r \cdot \tilde{\mathbf{x}} \cdot \mathbf{p}} = \mathbf{q} e^{-ik_r \cdot (a(\mathbf{x}) - ib(\mathbf{x})) \cdot \mathbf{p}} = \mathbf{q} e^{-k_r b(\mathbf{x}) \cdot \mathbf{p}} e^{-ik_r a(\mathbf{x}) \cdot \mathbf{p}}. \tag{4}$$

The function $b(\mathbf{x})$ in Eq. 4 imposes an additional attenuation in the wave solution if it is bigger than zero but exponential amplification if it is smaller than zero [6]. In this paper, a and b functions are defined as $a(x_i) = 1 + f(x_i)/b_0 k_i$, and $b(x_i) = f_i(x_i)/b_0 k_i$, where $i \in \{1, 2\}$ defines the direction in which the wave is attenuated. The term b_0 is the characteristic length of the problem. The function $f_i(x_i)$ is called *attenuation function*. These functions impose the rate of attenuation at the position x_i. Evanescent and propagating waves are attenuated by $a(x_i)$ and $b(x_i)$, respectively. The Eq. 3 is considered for the determination of,

$$\tilde{x_i} = \int_0^{x_i} \lambda(\xi) \mathrm{d}\Omega_\xi, \tag{5}$$

where λ is the complex value coordinate stretching function. This relation implies the following mathematical change,

$$\frac{\partial \tilde{x_i}}{\partial x_i} = \lambda(x_i) \rightarrow \frac{\partial}{\partial \tilde{x_i}} = \frac{1}{\lambda(x_i)} \frac{\partial}{\partial x_i}. \tag{6}$$

Finally, the transformation of the coordinate system is done by applying Eq.6 into Eq. 1 for all $\partial / \partial x_i$. It results in,

$$\begin{aligned} \text{div}(\bar{\boldsymbol{\sigma}}\tilde{\boldsymbol{\Lambda}}) &= \omega^2 \rho \lambda_1(x_1) \lambda_2(x_2) \bar{\mathbf{u}} \\ \bar{\boldsymbol{\sigma}} &= \mathbb{C}\bar{\boldsymbol{\varepsilon}} \\ \bar{\boldsymbol{\varepsilon}} &= \tfrac{1}{2}\left\{\text{grad}(\bar{\mathbf{u}})\boldsymbol{\Lambda} + \boldsymbol{\Lambda}^T \text{grad}(\bar{\mathbf{u}})^T\right\} \end{aligned} \tag{7}$$

The terms $\tilde{\mathbf{\Lambda}}$ and $\mathbf{\Lambda}$ are called *stretch tensors* defined as,

$$\tilde{\mathbf{\Lambda}} = \begin{bmatrix} \lambda_2(x_2) & 0 \\ 0 & \lambda_1(x_1) \end{bmatrix}, \; \mathbf{\Lambda} = \begin{bmatrix} 1/\lambda_1(x_1) & 0 \\ 0 & 1/\lambda_2(x_2) \end{bmatrix} \tag{8}$$

The subindex 1 and 2 in Eq. 7 and 8 denotes the direction of attenuation, and

$$\bar{\boldsymbol{\sigma}} = \begin{bmatrix} \sigma_{11} \\ \sigma_{22} \\ \sigma_{12} \end{bmatrix}, \; \bar{\boldsymbol{\varepsilon}} = \begin{bmatrix} \varepsilon_{11} \\ \varepsilon_{22} \\ 2\varepsilon_{12} \end{bmatrix} \tag{9}$$

The system of equations in 7 is formulated with respect to a rotated orthogonal system with basis $\mathbf{e}'_i$. Afterwards, these functions are mapped to the orthogonal basis system $\mathbf{e}_i$ using the rotated matrix $\mathbf{Q}$ whose components are $Q_{ij} = \mathbf{e}_i \cdot \mathbf{e}'_j$.

The time domain equations are obtained through the inverse Fourier transform of Eq. 7 after the change of basis. The resulting equations are,

$$\begin{gathered} \operatorname{div}\left(\boldsymbol{\sigma}\tilde{\mathbf{F}}^e + \mathbf{\Sigma}\tilde{\mathbf{F}}^p\right) = \rho f_m \ddot{\mathbf{u}} + \frac{c_r \rho}{b_0} f_c \dot{\mathbf{u}} + \frac{\mu}{b_0^2} f_k \mathbf{u} \\ \boldsymbol{\sigma} = \mathbb{C}\boldsymbol{\varepsilon} \\ \left(\mathbf{F^e}\right)^T \dot{\boldsymbol{\varepsilon}} \mathbf{F^e} + \left(\mathbf{F^p}\right)^T \boldsymbol{\varepsilon} \mathbf{F^e} + \left(\mathbf{F^e}\right)^T \boldsymbol{\varepsilon} \mathbf{F^p} + \left(\mathbf{F^p}\right)^T \mathbf{E} \mathbf{F^p} = \\ \frac{1}{2}\left\{ \left(\mathbf{F^e}\right)^T \left(\operatorname{grad} \dot{\mathbf{u}}\right) + \left(\operatorname{grad} \dot{\mathbf{u}}\right)^T \mathbf{F^e} \right\} + \frac{1}{2}\left\{ \left(\mathbf{F^p}\right)^T \left(\operatorname{grad} \mathbf{u}\right) + \left(\operatorname{grad} \mathbf{u}\right)^T \mathbf{F^p} \right\} \end{gathered} \tag{10}$$

The terms $\mathbf{F}^n$ and $\tilde{\mathbf{F}}^n$, assuming $n \in \{e, p\}$, contain the components of the stretching tensors for e, evanescent and p, propagating wave, see [3]. μ is the shear modulus, $\mathbf{E}$ and $\mathbf{\Sigma}$ are the integration of stresses and strains over the time, respectively. $\dot{\boldsymbol{\varepsilon}}$, $\dot{\mathbf{u}}$ and $\ddot{\mathbf{u}}$ is the derivative of strains, displacements and velocities with respect to time, respectively. The constants, f_m, f_c and f_k are,

$$\begin{aligned} f_m &= \left[1 + f_1^e(x'_1)\right]\left[1 + f_2^e(x'_2)\right], \\ f_c &= f_1^p(x'_1)\left[1 + f_2^e(x'_2)\right] + \left[1 + f_1^e(x'_1)\right] f_2^p(x'_2), \\ f_k &= f_1^p(x'_1) f_2^p(x'_2), \end{aligned} \tag{11}$$

where the quantities with prime denote the direction of attenuation in the orthogonal system with basis $\mathbf{e}'_i$.

4 NUMERICAL APPROXIMATION WITH B-SPLINES

The above mentioned equations are approximated in space and time by employing IGA and the Newmark's Method.

The weak form of the equations in 10 is obtained using an arbitrary test function, $\mathbf{v}$ and integrating the system throughout the computational domain Ω. The geometry and all unknown fields are approximated using NURBS basis functions such as,

$$\mathbf{u}^h(\xi, \eta) = \bar{\mathbf{N}}\mathbf{u}, \quad \mathbf{x}^h(\xi, \eta) = \bar{\mathbf{N}}\mathbf{x} \tag{12}$$

where, $\bar{\mathbf{N}} = \mathbf{N}(\xi)\,\mathbf{M}(\eta)$, with $\mathbf{N}$ and $\mathbf{M}$ containing the B-Splines basis functions for parametric directions, ξ and η, respectively. The superscript h indicates the approximated term.

The approximation in time is carried out with the Newmark's method. It is important to mention, that due to the nature of new quantities generated by the complex coordinate stretching, which associate the attenuation functions, the equation to be solved must be linearised at the time step t_{i+1}. Therefore, the Newton-Raphson method is employed to solve the system at each time step, Δt, confer e.g. [3]. Due to the use of Newmark's method, the system is solved through increments using an effective stiffness and forces. In piece-wise element representation, the effective stiffness matrix is,

$$\tilde{\mathbf{k}}^e_{i+1} = (\mathbf{k}^e + \bar{\mathbf{k}}^e) + \frac{\gamma}{\beta\Delta t}(\mathbf{c}^e + \bar{\mathbf{c}}^e) + \frac{1}{\beta\Delta t^2} \tag{13}$$

and effective vector of forces,

$$\tilde{\mathbf{p}}^e_{i+1} = \mathbf{m}^e\dot{\mathbf{u}}_{i+1} + \mathbf{c}^e\dot{\mathbf{u}}_{i+1} + \mathbf{k}^e\mathbf{u}_{i+1} + \mathbf{p}^e_{i+1} \tag{14}$$

where,

$$\begin{gathered}\mathbf{m}^e = \int_{\Omega^e} \rho f_m \bar{\mathbf{N}}\bar{\mathbf{N}}\mathrm{d}\Omega^e, \quad \mathbf{c}^e = \int_{\Omega^e} \frac{c_s\rho}{b_0} f_c \bar{\mathbf{N}}\bar{\mathbf{N}}\mathrm{d}\Omega^e, \quad \mathbf{k}^e = \int_{\Omega^e} \frac{\mu}{b_0^2} f_k \bar{\mathbf{N}}\bar{\mathbf{N}}\mathrm{d}\Omega^e \\ \bar{\mathbf{c}}^e = \int_{\Omega^e} \tilde{\mathbf{B}}\mathbb{C}\mathbf{B}^\epsilon \mathrm{d}\Omega^e, \qquad \bar{\mathbf{k}} = \int_{\Omega^e} \tilde{\mathbf{B}}\mathbb{C}\mathbf{B}^\rho \mathrm{d}\Omega^e\end{gathered} \tag{15}$$

The operators, $\mathbf{B}^\epsilon, \mathbf{B}^\rho$, and $\tilde{\mathbf{B}} = \mathbf{B}^e + \Delta t\mathbf{B}^p$, contain the derivatives of the basis functions modified by the components of the attenuation tensors, see [3]. The terms β and γ are constants of the Newmark's method. The element internal forces, $\tilde{\mathbf{p}}^e_{i+1}$ are expressed by,

$$\tilde{\mathbf{p}}^e_{i+1} = \int_{\Omega^e} \tilde{\mathbf{B}}^T \cdot \hat{\boldsymbol{\sigma}}_{i+1}\mathrm{d}\Omega^e + \int_{\Omega^e} \tilde{\mathbf{B}}^{p^T} \cdot \hat{\boldsymbol{\Sigma}}_{i+1}\mathrm{d}\Omega^e \tag{16}$$

with,

$$\begin{gathered}\hat{\boldsymbol{\Sigma}}_{i+1} = \hat{\boldsymbol{\Sigma}}_i + \Delta t\hat{\boldsymbol{\sigma}}_{i+1}, \\ \hat{\boldsymbol{\sigma}}_{t+1} = \mathbb{C}\hat{\boldsymbol{\varepsilon}}^h_{t+1}, \\ \hat{\boldsymbol{\varepsilon}}^h_{i+1} = \tfrac{1}{\Delta t}\left[\mathbf{B}^\epsilon\dot{\boldsymbol{u}}_i + \mathbf{B}^\rho\mathbf{u}_{i+1} + \tfrac{1}{\Delta t}\hat{\mathbf{F}}^\epsilon\hat{\boldsymbol{\varepsilon}}_i - \hat{\mathbf{F}}^\rho\hat{\mathbf{E}}_i\right]\end{gathered} \tag{17}$$

Being unique for each PML-element, the terms $\hat{\mathbf{F}}^\epsilon$ and $\hat{\mathbf{F}}^\rho$ contain only the components of the attenuation functions for evanescent and propagating waves, respectively.

The computational domain and the PML layer are defined in the same patch using B-Splines basis functions. Due to the influence of control points over each element for higher order, the standard PML technique is modified since the attenuation property can be activated directly before of the delimited physical border between the adjacent computational medium and absorbing layer. Let us set this assumption using Fig. 2. The right element is in charge to represent the absorbing layer, and the left two elements the bounded domain. Then, for linear order, the influence of absorbing property of the wave starts immediately at the boundary between the bounded and PML domain. This fact can change when higher order basis functions are employed, where the participation of attenuation functions also influences the control points belonging to the PML-Element allocated just before of the delimited boundary. This aspect is discussed further in the numerical application.

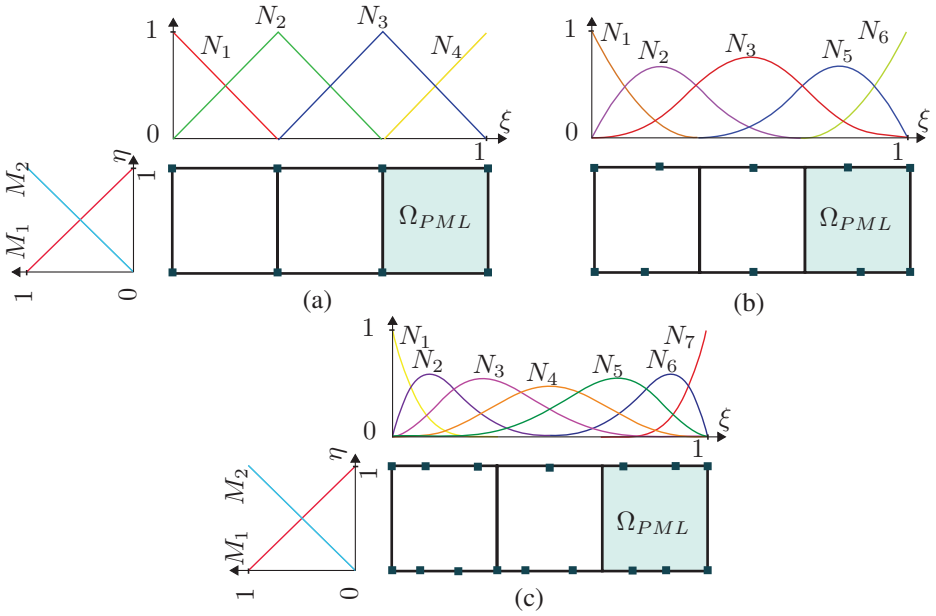

Figure 2: IGA-PML. Influence of basis functions in ξ parametric direction beyond the absorbing layer for order; (a) q =1 , (b) q =2, and (c) q =4. N_i and M_j are the basis functions along ξ- and η-parametric direction, respectively. Subscripts $i, j \in 1, 2, ..., N_{cp}$, where N_{cp} is the number of basis functions. Square dots are the control points.

5 NUMERICAL EXAMPLES

A 2D case for a band geometry is presented, see Fig 3. This is subjected at its left side to a sinusoidal time-dependent displacement, $u(t) = 0.01\sin(16\pi t)$ [m] for $t \in [0, 0.25]$ [s] and $u(t) = 0$ [m] for $t \in (0.25, 1.00]$ [s]. Its right side is fixed. The medium possesses a Young's moduls, $E = 10$ [kPa], density, $\rho = 10$ [kg/m^3] and Poisson's ratio, $\nu = 0$ [-]. No material damping is considered. The approximation of the geometry is based on the standard displacement based formulation using linear elements as reference solution. The density mesh in horizontal direction is quantified based on the wavelength, λ_ω, as, $\Delta x = \lambda_\omega/9$, see [10]. Δy=2 [m] since the wave only travels along x-direction. For this example, the incidence angle of propagating wave, θ is zero. The used time step is Δt =0.001 [s].

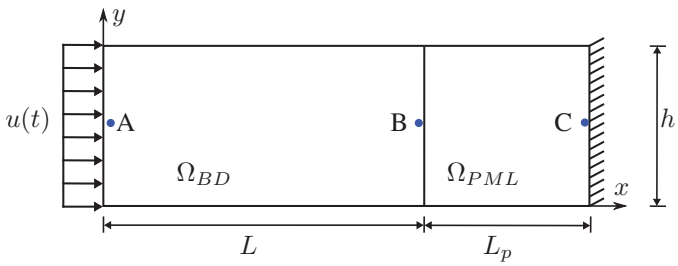

Figure 3: Band geometry. L=10 [m], and Lp=h=5 [m]. Ω_{BD} and Ω_{PML} are the bounded and PML layer domain, respectively. A, B and C are reference points.

The mesh density used in *IGA-PML* is the same as in the reference solution, FEM with Lagrange Interpolation Functions, but not the basis functions. The order of B-Splines basis functions, p and q, is the same in both parametric directions for *IGA-PML*, with $p = q$ =1, 2 and 4. As reference solution, the standard approximation used for the PML is also considered. The results are presented in Fig.4, 5 and 6, for the horizontal displacements of the system at

point A, B and C, see Fig. 3.

The displacements at point A, are shown in Fig.4. These are quite similar for all cases at $t < 0.6$[s]. By using the standard FEM, the system continues oscillating since no attenuating or absorbing boundary is used. In order to prevent this issue, the domain is usually extended.

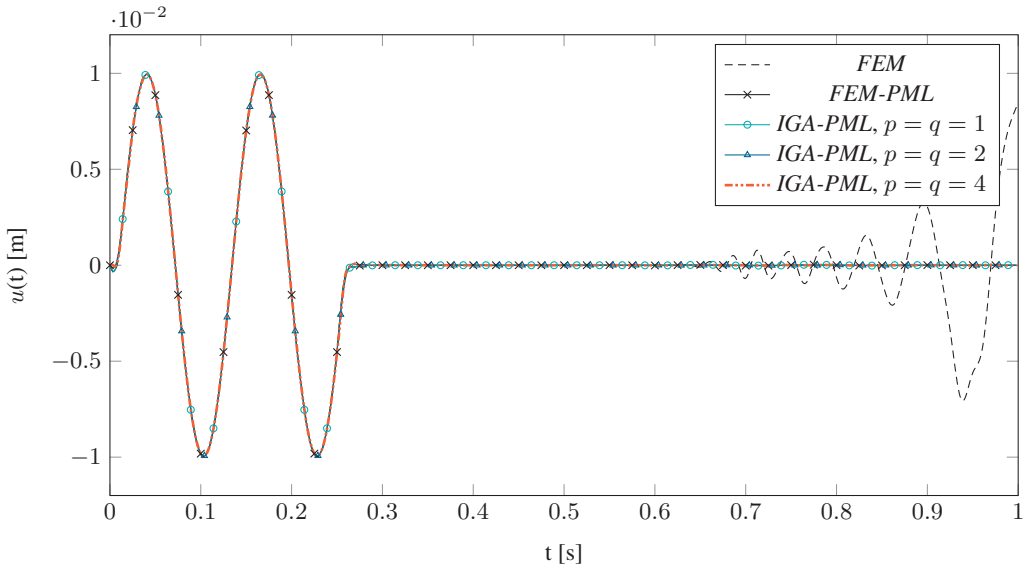

Figure 4: Horizontal displacement of system at point A (0.3 , 2.5) [m]

At the point B the wave amplitude is slightly attenuated in these cases where the PML method is used. However, this small difference could be neglected since all displacements are artificial beyond this point. Furthermore, this effect could be removed using a smaller integration step.

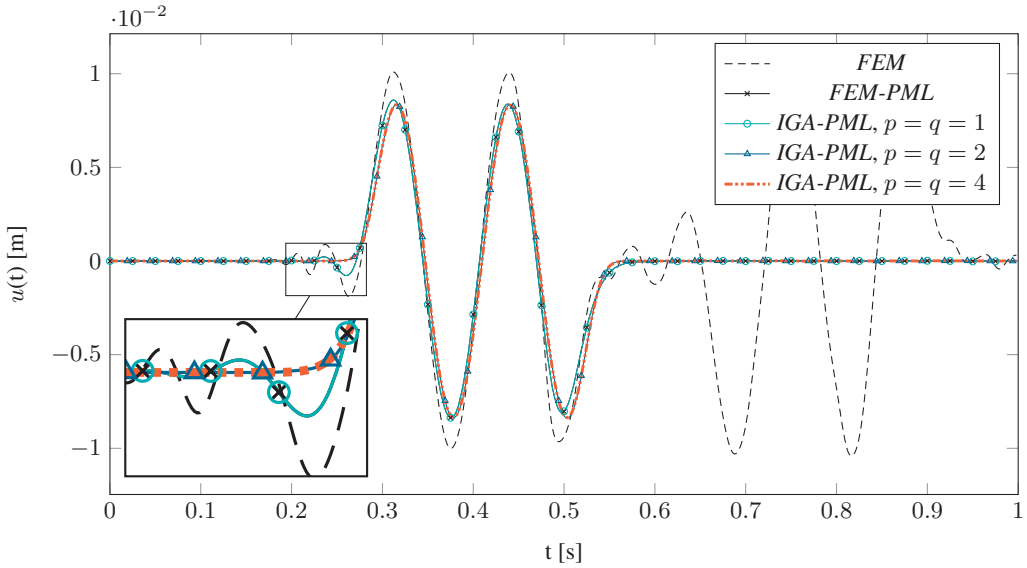

Figure 5: Horizontal displacement of system at point B (9.9 , 2.5) [m]

Another aspect to analyse in Fig.5 is the description of the wave. For the linear FEM, *FEM-PML*, and *IGA-PML*, it is noticed that the transition of the wave between 0.18 and 0.28 [s] has some small oscillations. These spurious effects are absent when higher order B-Splines basis

functions are used. This numerical error is commonly avoided when the mesh refinement is increased keeping a small time step calculation.

In Fig.6 the displacements, corresponding to point C, are plotted for *IGA-PML* of order $p = q =$1, 2 and 4. Even when these displacements are small in the range of $1.5\text{x}10^{-5}$ and $0.2\text{x}10^{-5}$ [m], there are still some differences when the order is increased. Presumably, this fact is due to the high-continuity presented in the basis functions.

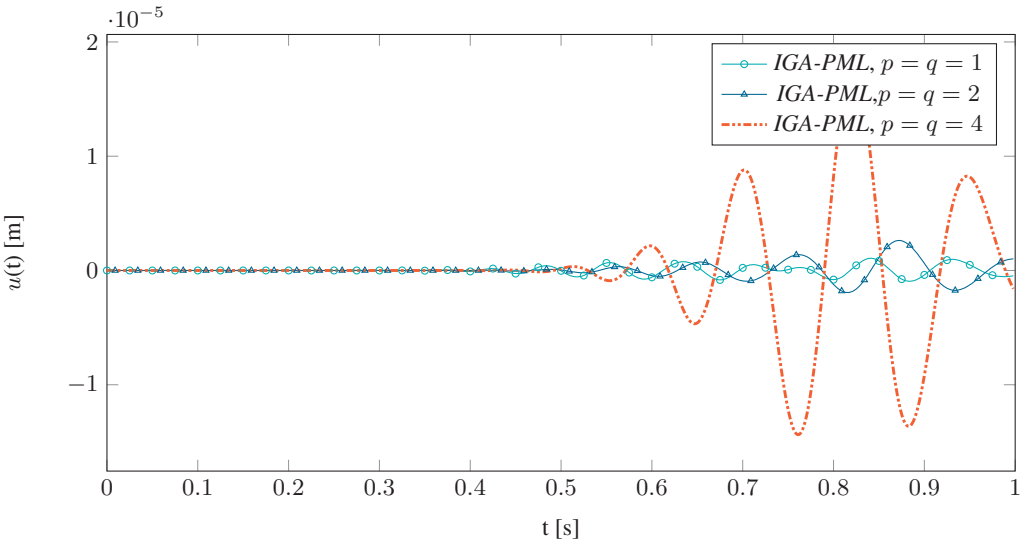

Figure 6: Horizontal displacement of system at point C (14.7 , 2.5) [m]

Additionally, the displacements using *IGA-PML* at different instants of the time calculation are plotted in Fig. 7. These figures correspond to the case with interpolation function of order, $p = q =$2. It is noticed that the displacements at the end of the calculation, Fig.7.d, are in general zero, but small displacements are presented. However, these could be neglected in comparison with the initial imposed displacement amplitude, see Fig. 4.

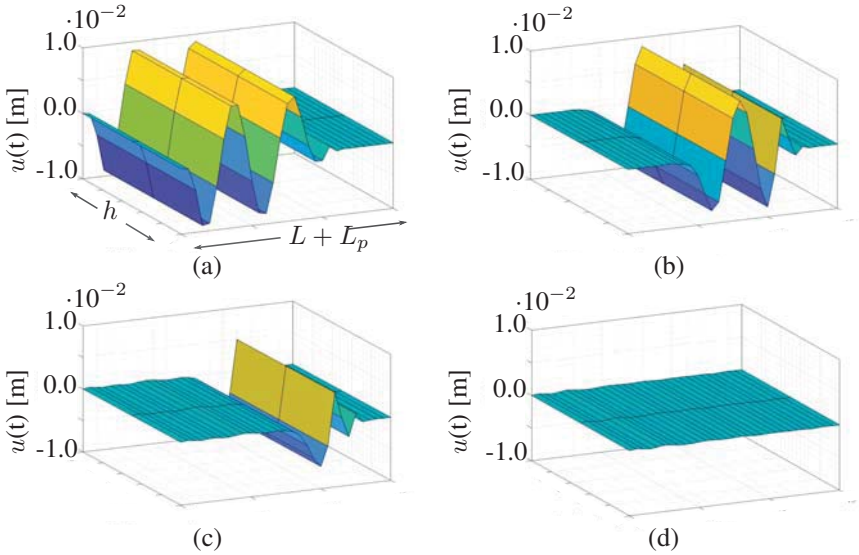

Figure 7: Displacement of horizontal degrees of freedom at: (a) $t = 0.25$, (b) $t = 0.38$, (c) $t = 0.50$, and (d) $t = 1.00$ [s]

6 CONCLUSIONS

- Combination of PML using high order basis functions based on IGA is carried out for two dimensional cases for elastic, homogeneous unbounded domains.
- The attenuation effects of the absorbing layer are slightly imposed just before the incidence border if mesh is considerably fine. However, an absorbing influence beyond the PML border can be expected when a coarse mesh is used. This assumption can be considered for further studies.
- The effects of the basis functions are tested near the fixed boundary where it is observed that, even when the displacements are minimal, the attenuation rate increases with higher order B-Splines basis functions, Fig.4.
- Due to discretization in time, the solution depends strongly on time step. The smaller this interval is, the better the wave approximation is for both FEM and IGA-PML.

REFERENCES

[1] J.P. Berenger, A perfectly matched layer for the absorption of electromagnetic waves, *Journal of Computational Physics*, **114(2)**, 185-200, 1994.

[2] U. Basu, A.K. Chopra, Perfectly matched layers for time-harmonic elastodynamics of unbounded domains: theory and finite-element implementation, *Computer Methods in Applied Mechanics and Engineering*, **192(11-12)**, 1337-1375, 2003.

[3] U. Basu, A.K. Chopra, Perfectly matched layers for transient elastodynamics of unbounded domains, *International Journal for Numerical Methods in Engineering*, **59(8)**, 1039-1074, 2004.

[4] J. A. Cottrell, T. J. Hughes, Y. Bazilevs, Isogeometric analysis: toward integration of CAD and FEA. *John Wiley and Sons*, 2009.

[5] L. Piegl, W. Tiller, The NURBS book, *Springer Science and Business Media*, 2012.

[6] G. Bunting, A. Prakash, T. Walsh, C. Dohrmann, Parallel ellipsoidal perfectly matched layers for acoustic Helmholtz problems on exterior domains, *Journal of Theoretical and Computational Acoustics*, **26(02)**, 2018.

[7] L. Knockaert, D. De Zutter, On the stretching of Maxwell's equations in general orthogonal coordinate systems and the perfectly matched layer, *Microwave and Optical Technology Letters*, **24(1)**, 31-34, 2000.

[8] S.G. Johnson, Notes on perfectly matched layers (PMLs), *Lecture notes, Massachusetts Institute of Technology, Massachusetts*, **29**, 2008.

[9] W.C. Chew, W.H. Weedon, A 3D perfectly matched medium from modified Maxwell's equations with stretched coordinates, *Microwave and Optical Technology Letters*, **7(13)**, 599-604, 1994.

[10] L. Kellezi, Local transmitting boundaries for transient elastic analysis, *Mechanical Systems and Signal Processing*, **28(7)**, 533-547, 2000.

EURODYN 2020
XI International Conference on Structural Dynamics
M. Papadrakakis, M. Fragiadakis, C. Papadimitriou (eds.)
Athens, Greece, 23–26 November 2020

NUMERICAL WAVENUMBER INTEGRATION FOR 2.5D WAVE EQUATION SOLUTION

J. Park[1], K. Norén-Cosgriff[1], and A.M. Kaynia[1]

[1] Norwegian Geotechnical Institute
Sognsvien 72, Oslo, 0855, Norway
e-mails: joonsang.park@ngi.no; karin.noren-cosgriff@ngi.no; amir.m.kaynia@ngi.no

Keywords: Wavenumber integration, 2.5D FE, Time-harmonic wave equation

Abstract. *In this study, we propose and implement a convergence scheme for the numerical wavenumber integration in the context of 2.5D FE solution and validate it through a numerical example. In brief, the scheme is to estimate the convergence based on the relative difference between two interpolations for a given set of wavenumbers, which is done iteratively by refining the wavenumber sampling until the relative difference becomes no greater than a specified value. We evaluate the performance and convergence of the numerical integration scheme by comparing the results of the responses of a tunnel in a layered ground due to a concentrated harmonic load using both a full 3D model and a 2.5D model, including computational time aspect. Finally, we consider applying the same scheme to other relevant numerical integrations.*

1 INTRODUCTION

Most problems in structural and soil dynamics are defined in 3D space. However, in a mathematical framework quite a few among those problems can be simplified in such a way that the geometry and material properties (i.e. density, stiffness, damping, etc.) of the media of interest are invariant along a particular axis. It is then possible to solve some of these 3D problems via the so-called 2.5D numerical approach (e.g. Galvin et al., 2010). For instance, wave propagation due to moving load along a tunnel structure built in layered soil media is a good example where the given geometry and material properties are often assumed constant along the track direction (Say y-axis), while they vary along the other two directions (x and z). Thanks to the y-direction invariance of both geometry and property, all the differentiations with respect to the y coordinate in the 3D wave equation can be replaced by the y-direction wavenumber (k_y) without any loss of accuracy in describing the features in the 3D problems. Then, as in discrete methods such as finite element (FE) method, the solution can be obtained by a spatial discretization only along the x- and z-axes, effectively reducing the number of degrees of freedom (DOF) to solve. On the other hand, this formulation requires that the resulting 2D FE equation be solved for many wavenumbers k_y in the FE context. This can be time-consuming but is still much less demanding than a full 3D FE analysis, provided that one employs a procedure that ensures efficient convergence of the associated wavenumber integration. Therefore, it is important to optimize the sampling and number of k_y's to solve so that one can calculate accurate and converged results, while the computational time is reasonable. Particularly for calculation of high frequency (~100Hz) dynamic response at far offset along the y-axis, the 2.5D FE solution indeed becomes essential in comparison to a full 3D FE solution due to the computational memory requirement.

In this study, we implement a convergence scheme for the numerical wavenumber integration in the context of 2.5D FE solution and validate it through a numerical example. In brief, the scheme is to estimate the convergence based on the relative difference between two interpolations (e.g. linear and spline) for a given set of wavenumbers, which is done iteratively by refining the wavenumber sampling until the relative difference becomes no greater than a specified value (e.g. 0.01). We discuss the performance and convergence of the numerical integration scheme by considering various aspects. At the end, we also discuss to apply the same scheme to other relevant numerical integrations e.g. wavenumber integration for the fully analytical solution.

All the FE calculations in the current study are performed by means of the commercial software *COMSOL Multiphysics*™. The relevant 2.5D wave equation is implemented and solved in the module of *2D Coefficient Form PDE*. In order to avoid artificial reflection from the computational domain boundary, a perfectly matched layer technique (Park and Kaynia, 2017) is deployed in the current study.

2 PROPOSED WAVENUMBER INTEGRATION METHOD

The numerical wavenumber integration is a common and necessary step in calculation of the analytical-solution for elastic wave propagation in layered media (e.g. Apsel and Luco, 1983; Park and Kaynia, 2018) to obtain dynamic response in the spatial domain from the wavenumber domain. There are two associated challenges: 1) handling of the pole singularities in the kernels of wavenumber integration; and 2) controlling of the convergence of numerical integration. The former challenge, which is the most critical in the analytical solution, is due to the extremely large and singular value of kernels at the propagation poles. A similar procedure for numerical wavenumber integration is required in the 2.5D FE solution. However, the challenge is related mainly to the convergence control, because the pole singularity doesn't exist or is not so strong

in the 2.5D FE solution. In the following, we discuss these features through an example of wave response in a homogeneous half-space.

Figure 1 compares two kernels calculated via a fully analytical solution (red thin solid line) by Park and Kaynia (2018) and the corresponding 2.5D FE solution (blue thick solid line). Both of the kernels are for the same homogeneous half-space subjected to a harmonic vertical load with frequency 100 Hz applied at the surface. The kernels are calculated exactly at the loading point. It is clearly shown in Figure 1 that the kernel of the 2.5D FE solution looks rather moderate without any strong singularity near the Rayleigh pole (black thin dashed vertical line). On the other hand, that of the analytical solution shows a strong and sharp singularity near the Rayleigh pole, subsequently requiring very-densely-sampled wavenumbers to calculate accurately. It is shown that the challenge in relation to the pole singularity is less significant (or almost negligible) in the 2.5D FE solution than the analytical solution. Therefore, it is expected that interpolation of the kernels of the 2.5D FE solution is feasible, even near the poles, which in turn can save significantly the computation effort in the 2.5D FE solution. Yet, we still need to make sure the convergence of the wavenumber integration by optimizing the sampling and number of wavenumbers to include into the 2.5D FE calculation.

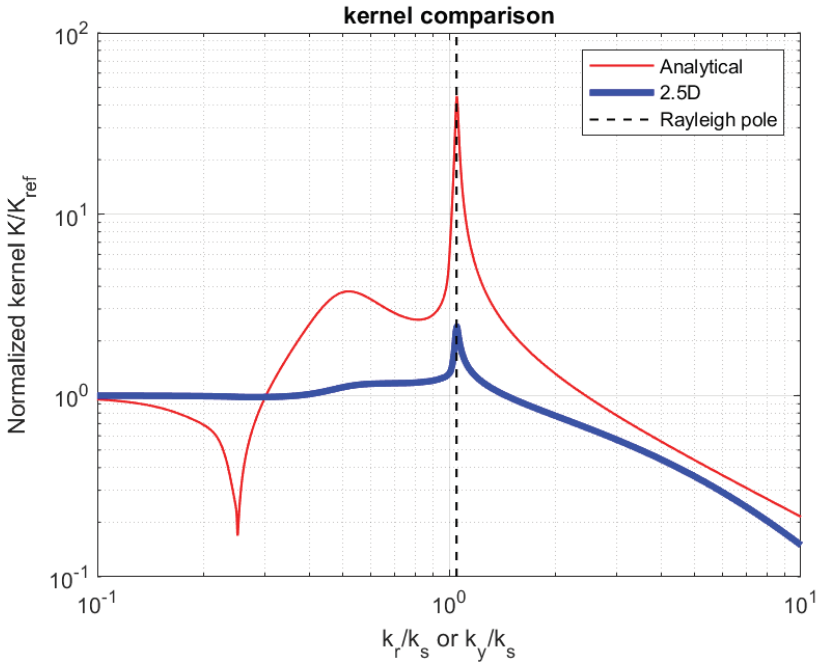

Figure 1. Comparison of two kernels calculated by means of analytical and 2.5D solutions, normalized with respect to the reference kernel calculated at the zero wavenumber. Note that the *x*-axis is the normalized wavenumber with respect to the shear wavenumber k_s; and k_r and k_y are the radial- and y-direction wavenumbers, respectively, used in the analytical and 2.5D FE solutions.

Based on the observations made through the example in Figure 1, we propose a convergence controlling scheme. The scheme a simple approach, consisting of the following steps:

1. Initialize a wavenumber sampling of k=[0:Δk:k_{max}]. Here, k_{max} should be so large that the kernels at k_{max} is small enough. Note that as shown in Figure 1, the kernels decay quickly for k>$k_{Rayleigh}$. In addition, Δk could be large enough such that the total number of k's is no so high e.g. < 10. Alternatively, the sampling can be done logarithmically, while using the same k_{max}.
2. Calculate the kernels for the given wavenumber sampling k by 2.5D FE solution procedure.

3. Interpolate the kernels by means of two different interpolations (e.g. linear and spline).
4. Estimate the relative differences between the interpolated values of the two different interpolation methods at the middle points of individual wavenumber sampling intervals.
5. Collect the middle-point wavenumbers (say $k_{>0.01}$) where the relative differences are greater than a specified criterion (e.g. 0.01).
6. Re-calculate the true kernels for those collected middle-point wavenumbers $k_{>0.01}$ by 2.5D FE solution procedure.
7. Repeat Steps 3-6 by updating k with accumulatively adding $k_{>0.01}$, until $k_{>0.01}$ does not exist.

Once Step 7 above is completed, we perform an inverse Fourier transform from k_y-domain to y-domain in order to calculate the final wave response in the spatial domain. We have found through numerical experiments that the number of wavenumbers after Step 7 is around a few 100's. If, on the other hand, we in a brute force manner use an equally-spaced wavenumber sampling for k=[0,k_{max}], the total number of wavenumbers could be in the order of $>10^4$.

3 NUMERICAL EXAMPLES

We validate the wavenumber integration scheme proposed in the study by solving a simple example of a tunnel embedded in a two-layered soil medium. Figure 2(a) shows the full 3D model described with 2 symmetric planes used at x=0m and y=0m. The tunnel is located in the upper soil layer of 16m thickness, and the tunnel bottom is close to the lower bedrock layer of infinite thickness. The thickness of the tunnel wall varies between 0.6m to 1.0m along the perimeter, shown in Figure 2. The harmonic excitation load of 100 Hz is applied in the middle of the tunnel base and in the vertical direction, red arrow in Figure 2(b). The material properties and geometry in the example problem is shown in Table 1. In addition, Figure 2(b) shows four lines highlighted in blue, where we extract the displacement results and compare with a full 3D FE simulation. Figure 3(a) and (b) show the FE meshes used in calculation, respectively, for the 2.5D and 3D analyses. The numbers of DOFs used in each model are around 43×10^3 and 1250×10^3, respectively.

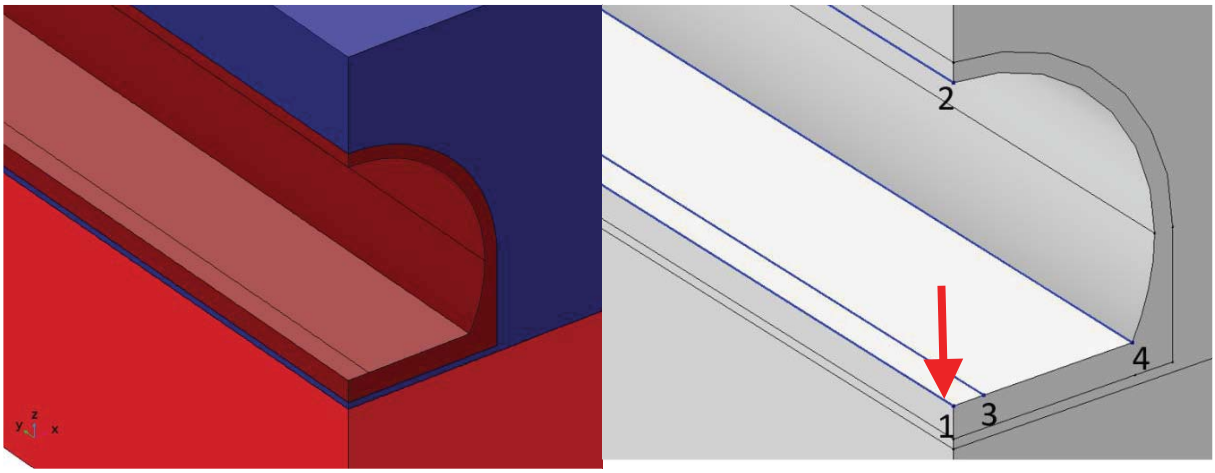

(a) (b)

Figure 2. (a) Example problem of a tunnel imbedded into two-layered soil medium (modelled with two symmetric planes at x=0m and y=0m); (b) 4 lines (blue) on the tunnel surface where responses are calculated and compared. Red arrow shows where the vertical point load of 100Hz is applied on Line 1.

Material	Density [kg/m^3]	Shear/Compression velocity [m/s]	Thickness [m]
Upper layer	1500	500/2000	16
Lower layer	3000	2000/4000	inf
Concrete tunnel	2300	2128/3475	0.6 (bottom: 1.0)

Table 1. Material properties and geometry in the example problem in analysis. A uniform viscous damping of 1% is applied to all the materials.

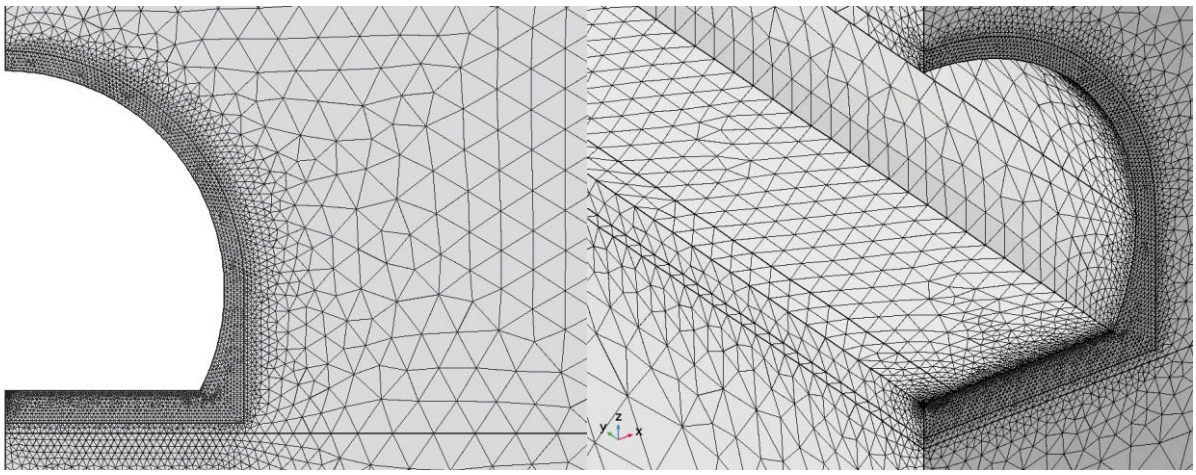

(a) (b)

Figure 3. FE meshes used: (a) for 2.5D simulation; (b) for 3D simulation

Figure 4 compares the two results of the 2.5D and 3D FE simulations, calculated along the 4 lines highlighted with blue lines in Figure 2(b). The solid and dashed lines are, respectively, for the 2.5D and 3D FE solutions, and the blue and red colors denote, respectively, the real and imaginary parts of the time-harmonic response. It is clearly shown that the agreement between the 2.5D and 3D FE simulations is perfect for Line 1, 3 and 4. Namely, the solid and dashed lines are exactly on the top of each other. The agreement for Line 2 (line along the tunnel crown) is also very good but not as much as the other lines, which is believed to have to do with the wavenumber sampling near the Rayleigh (or generally, wave propagation) pole(s). The improvement on this issue is under investigation.

It is mentioned earlier that k_{max} should be so large that the kernels at k_{max} is small enough, making sure that the numerical integration is converged. Furthermore, we have also found out that k_{max} depends on the relative position of (or distance between) load and receiver points. Figure 5 shows the normalized kernels for the four response lines in Figure 2(b) whose distances to the vertical load are different. Line 1 has zero distance to the load point, and Lines 3, 4 and 2 have 1m, 6m and ca 11m distance, respectively. It is easily noticed in Figure 5 that the decaying rate of the kernels is proportional to the distance between the load and response points. Therefore, we may conclude that the longer the distance is, the smaller k_{max} is needed.

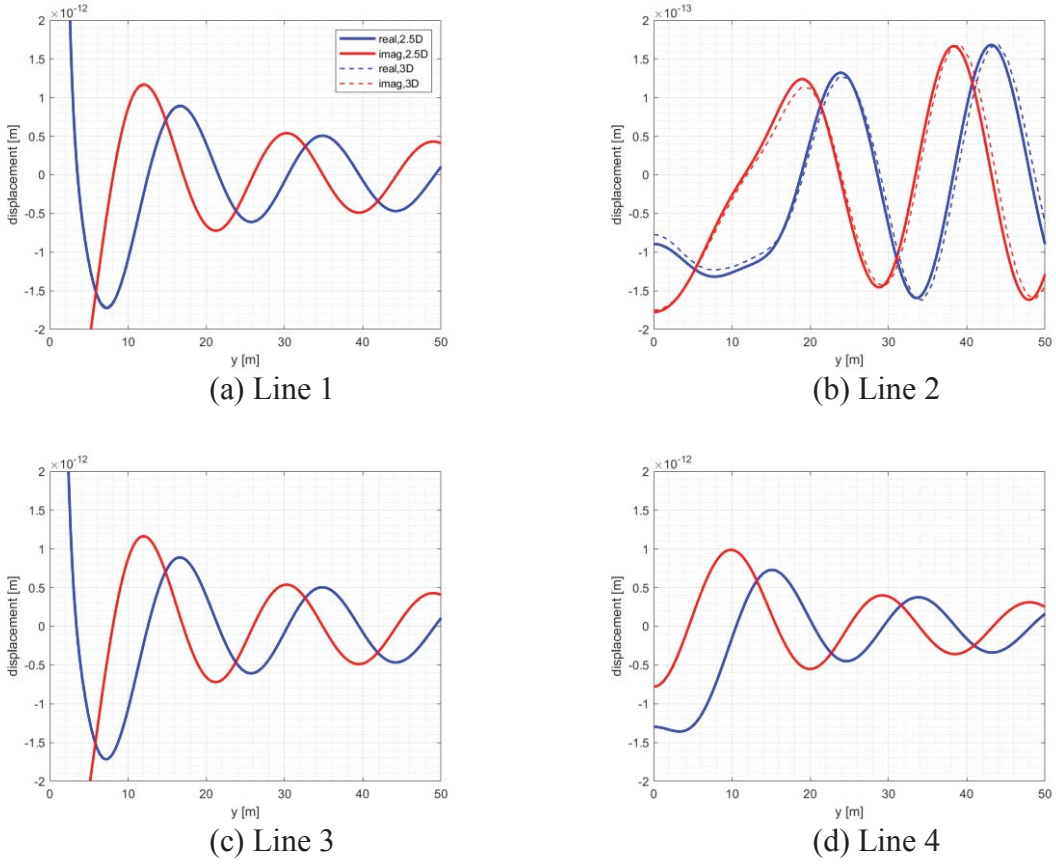

Figure 4. Comparison of 2.5D (solid lines) and 3D (dashed lines) simulation results in displacement along 4 lines on the tunnel surfaces (defined in Figure 2). Note that the Y-axis scale of Plot (b) is 10 time smaller than that of the other three plots.

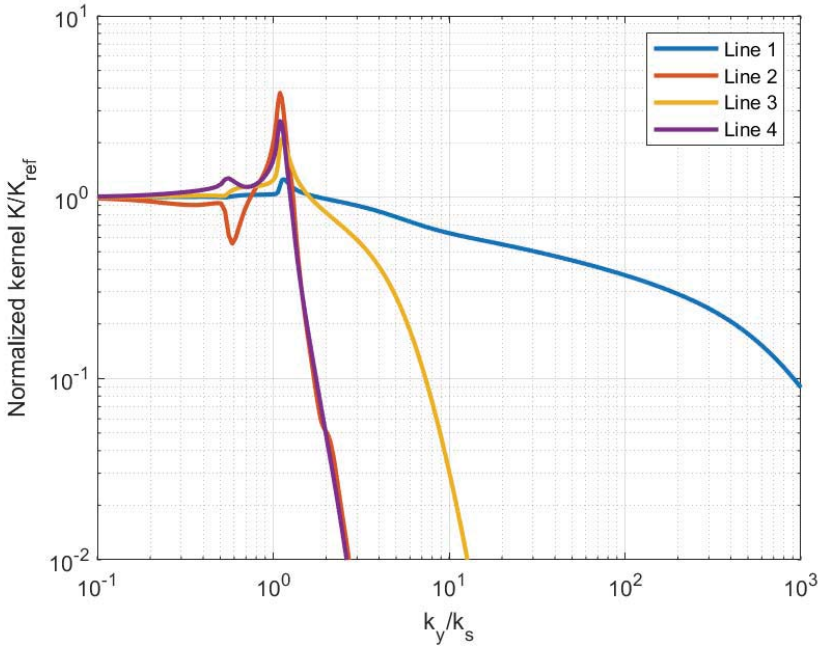

Figure 5. Comparison of kernels calculated for the four lines on the tunnel surfaces (defined in Figure 2). Note that the kernels are normalized with respect to the reference kernel calculated at the zero wavenumber. In addition, the *x*-axis is the normalized wavenumber with respect to the shear wavenumber k_s of concrete (~0.295).

4 CONCLUSIONS

In this study, we propose a simple scheme with which we can efficiently integrate the wavenumber integration in the context of 2.5D FE solution for a full 3D wave equation. The scheme consists of 7 steps and controls iteratively the convergence of the integration. The satisfactory performance of the proposed integration scheme is demonstrated by comparing the results of the responses of a tunnel in a layered ground due to a concentrated harmonic load using both a full 3D model and a 2.5D model. In addition to comparison of the displacements, information about computational time is provide. One of the key parameters in the proposed scheme is the maximum wavenumber to be used in the analysis (k_{max}). Analyses indicate that the longer the distance between load and response points, the smaller k_{max} is required.

Herein, we have applied successfully the proposed integration technique to the 2.5D FE wave equation. Nevertheless, it is worthwhile to mention that the same technique can also be applied to any numerical integration e.g. numerical wavenumber integration for the fully analytical solution by Park and Kaynia (2018), replacing a brute force integration with equally-spaced wavenumbers and saving computation time by >10 times. A related study is in progress.

5 ACKNOWLEDGEMENT

The study is financed by the Research Council of Norway (RCN) through NGI's Basis Grant No. 20190251.

REFERENCES

[1] R.J. Apsel and J.E. Luco, On the Green's functions for a layered half-space. Part II, Bulletin of the Seismological Society of America, 73(4), 931-961, August 1983.

[2] P. Galvín, S. François, M. Schevenels, E. Bongini, G. Degrande, G. Lombaert, A 2.5D coupled FE-BE model for the prediction of railway induced vibrations, Soil Dynamics and Earthquake Engineering, 30, 1500-1512, 2010.

[3] J. Park and A.M. Kaynia, FE simulation of steady state wave motion in solids combined with a PML approach, X International Conference on Structural Dynamics, EURODYN 2017, Procedia Engineering, 199, 1556-1561, 2017.

[4] J. Park and A.M. Kaynia, Stiffness matrices for fluid and anisotropic soil layers with applications in soil dynamics, Soil Dynamics and Earthquake Engineering, 115, 169-182, 2018.

EURODYN 2020
XI International Conference on Structural Dynamics
M. Papadrakakis, M. Fragiadakis, C. Papadimitriou (eds.)
Athens, Greece, 23–26 November 2020

USE OF THE DOMAIN REDUCTION METHOD TO SIMULATE THE SEISMIC RESPONSE OF AN EXISTING STRUCTURE PROTECTED BY RESONATING UNIT CELL METAMATERIALS

Constantinos Kanellopoulos[1], Boris Jeremić[2], Ioannis Anastasopoulos[3] and Božidar Stojadinović[1]

[1] ETH Zurich
Stefano-Franscini-Platz 5, 8093 Zurich, Switzerland
e-mail: {kanellopoulos, stojadinovic}@ibk.baug.ethz.ch

[2] University of California, Davis
One Shields Avenue, Davis, CA 95616
e-mail: jeremic@ucdavis.edu

[3] ETH Zurich
Stefano-Franscini-Platz 5, 8093 Zurich, Switzerland
e-mail: ixa@igt.baug.ethz.ch

Keywords: Domain Reduction Method; Seismic Metamaterials; Resonating Unit Cells; Dynamic Soil-Structure Interaction

Abstract. *Metamaterials have been successfully used during the past decade in the field of electromagnetism to control the propagation of electromagnetic waves. Interesting and possibly practically useful phenomena, such as negative refraction and generation of frequency bandgaps, may be induced in metamaterials. Recently, remarkable attempts have been made to bring this concept to the civil engineering scale in order to control the incoming seismic waves, mitigate their effects on structures and enhance seismic resilience of communities. A study on the potential of installing multiple resonating unit cells around an existing structure to improve its seismic performance is presented in this paper. Taking advantage of the 180^o phase difference that occurs right after the resonance of the unit cell masses, bandgaps can be generated at frequencies of interest for earthquake engineering applications. The Domain Reduction Method (DRM) is employed to realistically model the wave field (vertically propagating shear waves in this case). The model is verified and key features of DRM important for modeling the seismic response of metamaterials are exemplified.*

1 INTRODUCTION

Use of metamaterials to control the propagation of electromagnetic waves was initially proposed by Pendry et al. [1]. Since then, many researchers applied this concept in different science and engineering fields, where the wavelengths are orders of magnitude larger, as in the case of mechanical waves in solids. In particular, earthquake engineers have considered locally resonant metamaterials or resonating unit cells or resonators (multiple unit cells with a vibrating mass inside each one of them), embedded into the soil as the means to guide the incoming seismic waves in certain frequency ranges (i.e., wave lengths) away from the structure to be protected. Most of these studies ([2], [3], [4], [5]) have shown, either numerically or experimentally, that this is feasible for the case of surface waves. Such waves couple with the resonators and are transmitted downwards before reaching the structure.

However, as shown by Zaccherini et al. [6], in case of more realistic inhomogeneous soil layers with depth-increasing stiffness, the initially downward-transmitted waves will eventually bend upwards and travel back towards the ground surface. This implies that the successfully diverted surface waves (aiming to protect one structure) may cause additional damage to neighboring structures. Such unintended "transfer" of seismic risk needs to be thoroughly addressed if seismic metamaterials are to find their way into civil engineering practice.

Most importantly, only a few studies ([7], [8]) have dealt with the other critical seismic wave component: the body shear waves. In contrast to surface waves, body waves propagate almost vertically through the soil, inciting the structure from below. A debate on which waves (surface or body) are more destructive is still ongoing in the earthquake engineering community. However, with a realistic model of the seismic wave field generated by the rupturing seismic fault, the relative importance of the different types of seismic waves can be assessed based on the basis of sound seismic risk analysis principles.

This study employs the Domain Reduction Method (DRM) ([9], [10]) that realistically models both body and surface waves. The DRM is a Finite Element (FE) analysis method that aims at reducing a large computational domain that includes the entire problem (including the seismic fault, the bedrock, the soil, and the structure), to a much smaller computational domain that only includes local soil and structure, using appropriate boundary and initial conditions, and interface layers [11]. The energy generated by oscillations of the structure is radiated back into the domain and dissipated using so-called damping elements at the DRM model boundary. DRM enables accurate modelling of all 6 components of seismic waves.

The paper focuses on a 2D (plane strain) domain, vertically propagating horizontal shear waves, and a structure represented by an elastic single degree of freedom (SDOF) system responding to horizontal base excitation, and metamaterial resonators similar with those ones proposed by Colombi et al. [7]. The aim is to showcase the effectiveness of the DRM in modelling soil–structure–metamaterial seismic response. Emphasis is placed on the importance of model verification and validation, and the illustration of some of the most powerful and useful features of the DRM, as implemented in the Real-ESSI Simulator [12].

2 FINITE ELEMENT MODEL

The in-plane linear elastic FE modelling is conducted using the Real-ESSI Simulator [12], in which the DRM is already incorporated and can be easily applied. The FE model is illustrated in **Fig. 1**, where the DRM elements are highlighted with orange color. The FE model is part of a one-to-two orders of magnitude larger domain that includes the rock and the remaining soil through which the seismic waves propagate. The seismic motions are inserted into the FE model by applying "effective" forces on the DRM elements. To calculate these effective forces, one needs to calculate the displacement and acceleration time histories for each node of the DRM

elements using the free-field response of the larger domain and the known mass and elastic stiffness matrices of the FE model. This can be done either analytically ([13], [14]) or numerically, using one of the available commercial packages to calculate free-field response. This complex process is automated in Real-ESSI, obliviating the need to manually calculate the effective forces on DRM elements. In this way, the only necessary input is the acceleration and displacement time histories of the seismic motion.

A second important part of the FE model are the damping elements (shown with dark-grey color in **Fig. 1**), which surround the DRM elements (orange). Note the different damping ratio values assigned to the damper element zones on the sides and under the soil domain. The purpose of the damping elements is to damp out any waves generated by oscillations of the structure by artificially applying high values of Rayleigh viscous damping on such inciting waves. In the absence of a structure (free-field), the damping elements remain inactive, as there are no radiated waves entering their domain.

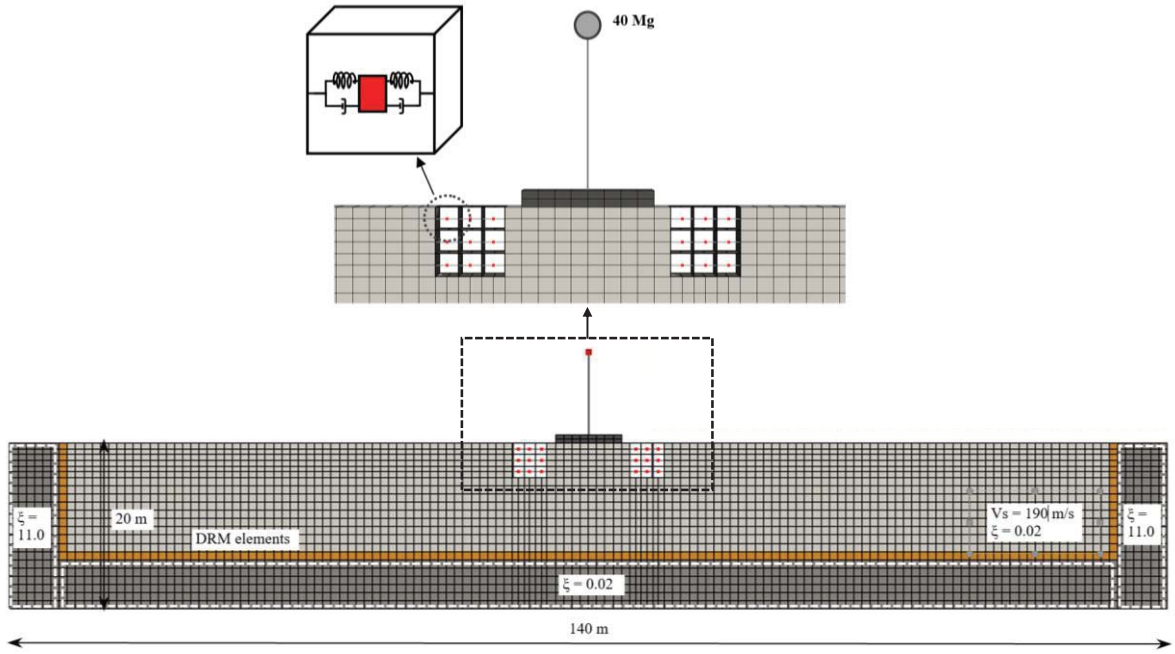

Fig. 1. Geometry of the FE model including the resonating unit cells and the structure.

2.1 Soil, structure, and metamaterial properties

A uniform and relatively soft soil layer of 20 m depth is considered, with V_s = 190 m/s (shear wave velocity), ν = 0.3 (Poisson's ratio), ρ = 1.6 Mg/m^3 (mass density), resting on rigid bedrock; the resulting horizontal natural period is 0.42 s. The soil is modelled using 8-node elastic solid brick elements (2D modelling with 3D elements, i.e. a 3D slice), sufficiently discretized to properly capture wave field response (at least 10-elements per wavelength [15], [16]). Since rigid bedrock is assumed at 20 m depth, the radiated waves from the structure and the resonators should not be damped out by the damping elements at the bottom of the model. In this particular case, radiated waves propagating to the bottom boundary of the FE model should get fully reflected back towards the ground surface, and continue propagating (downwards and upwards), until they gradually dissipate or get artificially damped out by the lateral damping elements (this is why ξ = 0.02 damping ratio is used for the damping elements in the horizontal zone under the soil, same as for the soil above, as shown in **Fig. 1**).

At this point, it should be noted that this is not how damping elements are supposed to be used. According to the DRM, damping elements should be used to damp out internally

generated and radiated waves, not allowing them to go back into the main domain. A deeper FE model would be required for this purpose, also including the rock layer above the DRM elements, so that any radiated waves would be naturally reflected at the soil–rock interface.

An idealized SDOF system is used to represent an existing shear building, lying on a rigid surface foundation of 8 m width, which is modelled with 8-node elastic brick elements. The SDOF system of 10 m height is modelled with elastic beam elements, assumed to be massless, and a 40 Mg lumped mass on top. The stiffness of the beam is defined, so that the resulting natural period of the SDOF system is 0.45 s. A Rayleigh viscous damping of 5% was assumed.

The resonating unit cells are placed at the sides of the structure, embedded into the soil. Each unit cell (18 in total), is a hollow reinforced concrete (RC) box, containing a mass element (at the centre), connected to the sides of the box through two pairs of springs and dashpots, as shown in **Fig.1**. The RC box is modelled with elastic shell elements of h = 0.2 m thickness, Young's modulus E = 25 GPa, v = 0.2, and ρ = 2.5 Mg/m^3, while a Kelvin-Voigt truss element is used to model each pair of springs and dashpots. The spring stiffness and the mass are determined so that the natural vibration period of each unit cell is 0.5 s – just above the 0.45 s period of the SDOF system (the reason of this selection will be explained in Section 2). Hence, assuming a mass of 2.5 Mg for each unit cell, the spring stiffness should be 197.4 kN/m. As discussed later on, the increase of the mass of the resonating unit cells leads to increase of their efficiency. Finally, a damping ratio of 6% is assumed for the unit cells.

Concerning the boundary conditions of the FE model, all degrees of freedom of the outer (lateral and bottom) boundaries of the damping elements are fixed. In addition, since a one-component ground motion excitation is employed (i.e., vertically propagating horizontal shear waves), the soil element nodes are allowed to move only horizontally. The same applies to the lumped mass at the top of the SDOF system and the vibrating masses inside the unit cells (i.e., no rotations or vertical motions are allowed). Finally, the foundation-soil and resonators-soil interfaces are modelled using full contact bonded elements.

2.2 Input motion

As shown in **Fig. 2**, the desired base excitation of the SDOF system is a Ricker pulse of 0.42 s period and 0.1 g peak amplitude. The input motion, applied on the DRM elements, is calculated to create such a wave field that will result in the targeted motion at the ground surface. Generation of the free-field wave field (by first performing deconvolution of the Ricker pulse down to the bedrock) to create the "effective" forces for the DRM elements is done automatically in Real-ESSI, using the analytical solutions described in [13] and [14].

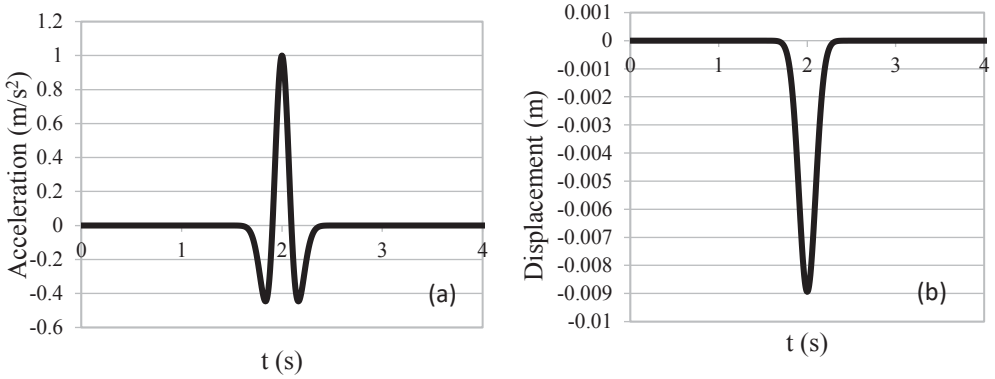

Fig. 2. Ricker pulse (0.42 s, 1 m/s^2): (a) horizontal acceleration; and (b) horizontal displacement time histories.

2.3 Verification of the FE model

2.3.1 Free-field response

The free-field model of **Fig. 3** is developed and used to verify that the excitation at the ground surface is, indeed, the targeted Ricker pulse of **Fig. 2**. The developed free-field model is exactly the same as before, but the SDOF structure and the resonating cells are removed. **Figure 4a** depicts the deformed FE mesh with superimposed horizontal displacement contours for $t = 2$ s. At this specific instant, the model surface attains the maximum negative displacement amplitude (-0.0089 m), as it should. Exactly the same deformed FE mesh is shown in **Fig. 4b**, but with exaggerated horizontal displacement scaling, to verify that the soil layer deforms in its first vibration mode shape, as it should, since the dominant period of the Ricker pulse (0.42 s) coincides with the natural period of the soil column (0.42 s).

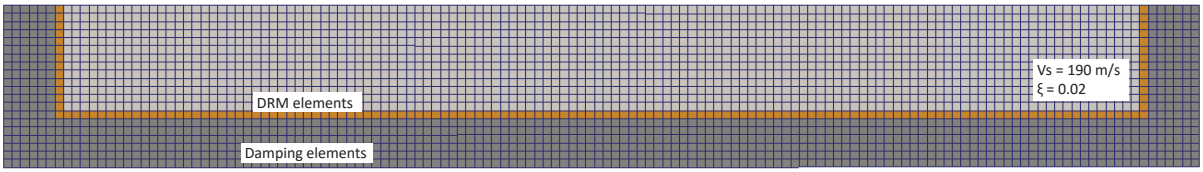

Fig. 3. FE model developed to verify the free-field response.

The effect of numerical damping is examined in more detail looking at the ground surface acceleration time histories (**Fig. 5**). Numerical damping can be tuned using the parameter γ of the Newmark integration method [17]. At this point, it should be noted that numerical damping has nothing to do with the physical damping mechanisms. Such *algorithmic* damping was introduced by Newmark [17] in order to damp out the non-realistic high frequencies stemming from model discretization. Such numerical damping should be employed cautiously, as its improper use could also damp out the real response of the model.

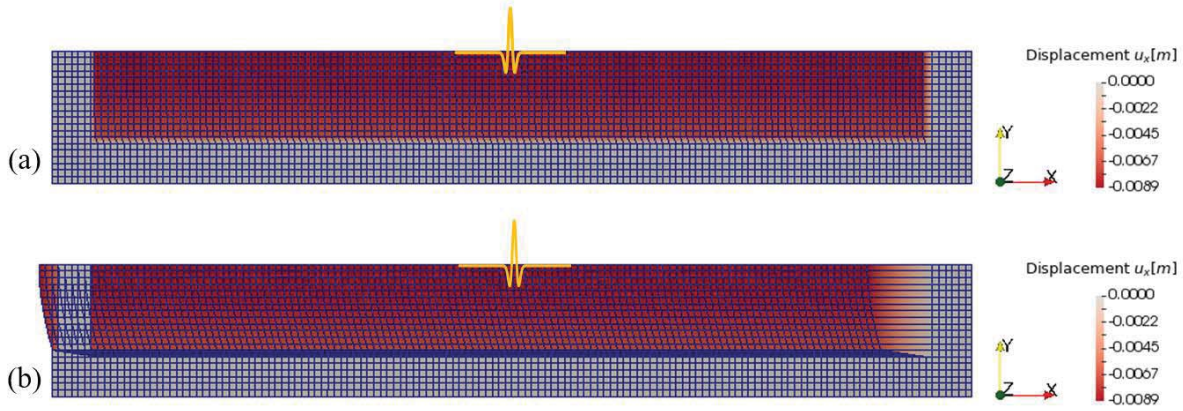

Fig. 4. Free field analysis – deformed FE mesh with superimposed horizontal displacement contours for $t = 2$ s: (a) consistent scaling; (b) exaggerated horizontal displacements.

As shown in **Fig. 5a**, in the absence of numerical damping ($\gamma = 0.5$), the targeted Ricker wavelet is "contaminated" by spurious oscillations after the main pulse. These oscillations vanish with a slight increase of numerical damping ($\gamma = 0.6$), while the main pulse remains unaffected (**Fig. 5b**). Further increase to $\gamma = 1.0$ leads to improper reproduction of the main pulse and to spurious oscillations (**Fig. 5c**). It is therefore essential to conduct a short sensitivity analysis at the beginning of a DRM study, to fine tune the necessary numerical damping. A

similar sensitivity analysis is conducted for the complete model (including the SDOF structure and the resonators), concluding that no numerical damping is necessary (i.e., $\gamma = 0.5$).

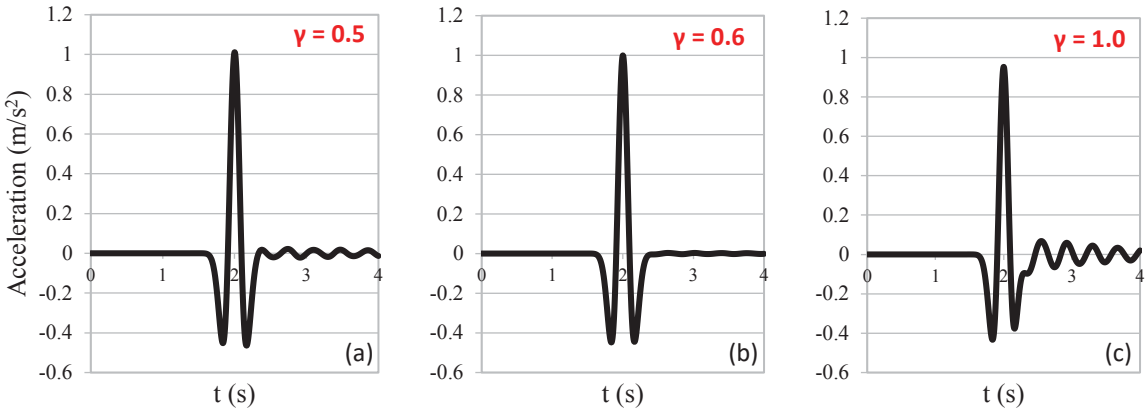

Fig. 5. Time histories of horizontal accelerations at the ground surface for three different values of numerical damping: (a) $\gamma = 0.5$ (no numerical damping); (b) $\gamma = 0.6$; and (c) $\gamma = 1.0$

2.3.2 Damping of the DRM elements

As previously discussed, since the damping elements at the bottom of the FE model are not active, waves radiated from the structure can propagate downwards and upwards, being reflected at the bottom boundary (bedrock) and at the ground surface, respectively. The same Rayleigh viscous damping ($\xi = 0.02$) is used for the soil and the damping elements under the DRM elements, while a higher ξ is employed for the lateral damping elements (**Fig. 1**).

A short sensitivity study is conducted to better understand the importance of damping elements. For this purpose, the Rayleigh viscous damping of all damping elements (including those under the DRM elements) is progressively increased until the response of the SDOF structure (in terms of horizontal accelerations at the mass) is not affected any more (**Fig. 6**). Such convergence is observed for $\xi = 9$ (900%), as the response remains unaffected with further increase of damping to $\xi = 11$ (1100%). This implies that, with $\xi = 9$, all radiated waves from the SDOF structure and the unit cell resonators are fully absorbed by the damping elements.

Figure 7 compares the response for $\xi = 11$ applied to all damping elements, to the case where the same high value of ξ is applied only to the lateral damping elements. The acceleration time histories at the top of the SDOF structure are shown in **Fig. 7a**. Except from the non-negligible difference between the two cases, it can also be observed that that the structural response becomes more intense when the radiated waves are fully absorbed, which is not intuitive. As discussed later on, this is attributed to the response of the resonating unit cells. The vibrating masses inside the unit cells are moving out-of-phase with respect to the SDOF structure. As a result, the radiated waves from the resonators, propagate downwards to bedrock, being reflected back towards the ground surface. And since they are out-of-phase, this leads to a decrease of the acceleration of the SDOF structure. This is why the accelerations of the SDOF structure increase when the radiated waves are damped out.

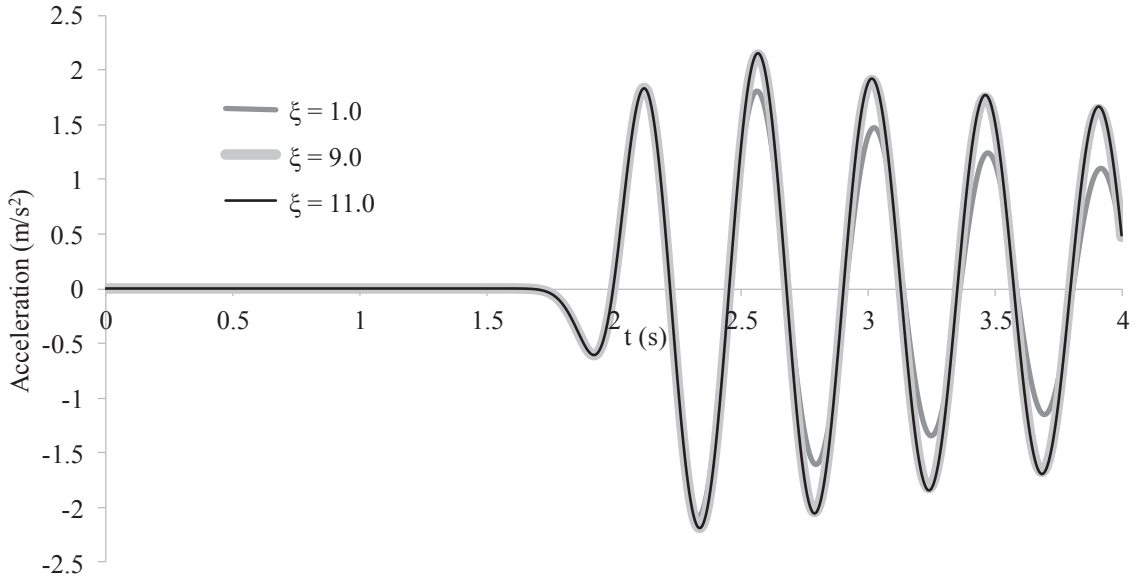

Fig. 6. Time histories of horizontal acceleration at the top of the SDOF structure for three different values of damping ratio (ξ = 1, 9, and 11) of the damping elements in the FE model.

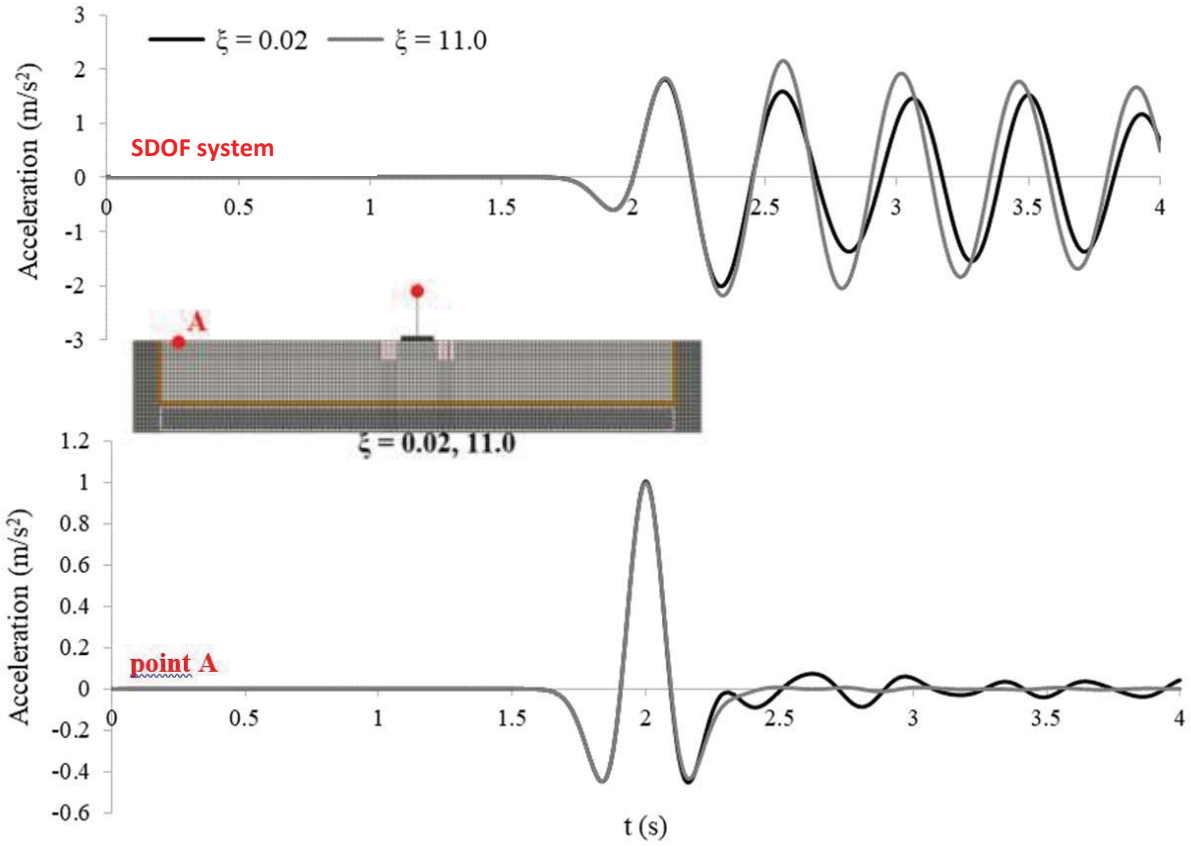

Fig. 7. Time histories of horizontal acceleration: (a) at the top of the SDOF structure; and (b) at the ground surface (point A). For the lateral damping elements, $\xi = 11$ (i.e., laterally propagating waves are fully absorbed); for the damping elements under the DRM elements (inside the white box of the embedded figure), $\xi = 11$ is compared to $\xi = 0.02$ (i.e., practically no damping).

Figure 7b offers a comparison of free-field ground surface accelerations (at Point A, away from the structure). When ξ = 11 for all damping elements, the response at point A is the targeted Ricker pulse (free-field response). However, when only the lateral damping elements are "active", the radiated, from the structure and the resonators, waves are not damped, leading to the development of spurious oscillations after the main pulse. These waves will eventually be damped out when they reach the lateral damping elements. Ideally, those waves should have been able to continue propagating sideways, as shown in **Fig. 8**. The latter plots the FE model strain energy density for four different snapshots, showing the waves, generated by the vibration of the SDOF structure and the resonators, travelling laterally.

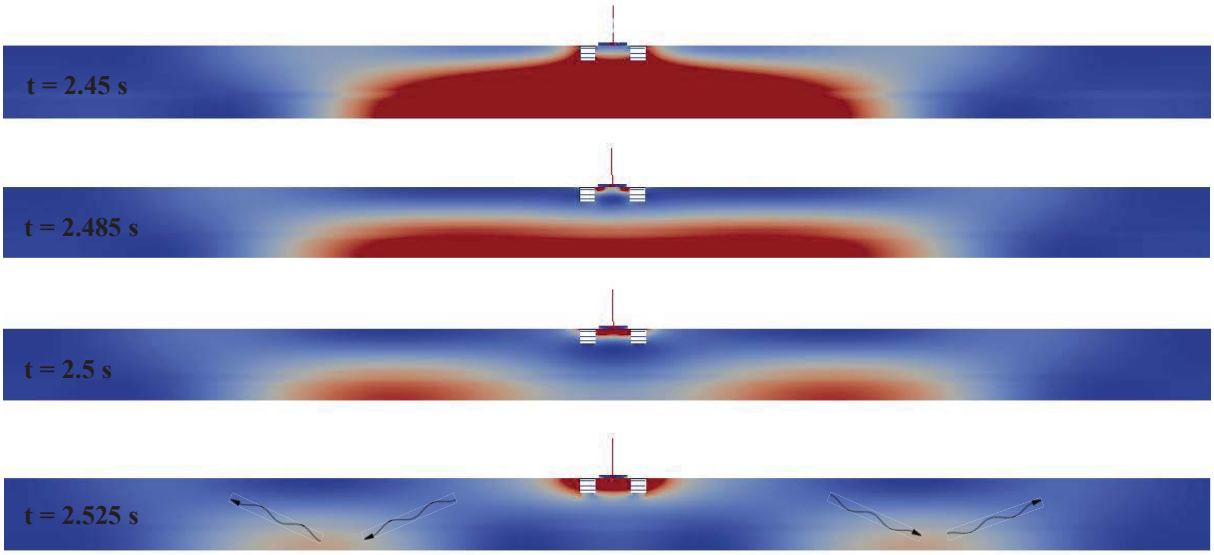

Fig. 8. Snapshots (t = 2.45, 2.485, 2.5 and 2.525 s) of strain energy density contours, showing the lateral propagation of waves radiated from the SDOF structure.

2.3.3 Lateral boundaries of the FE model

An additional sensitivity analysis is conducted to explore the effect of the FE model length. The length is gradually increased until the response of the SDOF structure is not affected any more. As shown in **Fig. 9**, this is achieved when the FE model length becomes equal to 780 m, as further increase to 880 m does not seem to cause any changes in response. This leads to an extremely large FE model, which may be computationally affordable in 2D, but not in 3D. However, faster wave attenuation in 3D along with additional damping due to material nonlinearities [18] may allow significant reduction of the required length.

3 RESULTS

Before presenting some of the key results, it is important to explain a simple property of resonating unit cells that leads to decreased accelerations in the surrounding soil and, consequently, to a reduction of the seismic response of the structure. When a SDOF system resonates under harmonic base excitation, it moves with a 90^o phase difference with respect to the excitation displacement signal. If the harmonic excitation frequency is slightly changed, the displacement phase difference will rapidly drop to 0^o or jump to 180^o, provided that the viscous damping ratio of the SDOF system is relatively low. In the FE model studied herein, the resonating unit cells have a slightly smaller resonant frequency (2Hz = 1/0.5s) than the SDOF structure (2.22 Hz = 1/0.45 s); the Ricker excitation is slightly larger (2.38Hz = 1/0.42 s). Thus, the resonant unit cell masses and the soil will move out-of-phase (with 180^o phase difference).

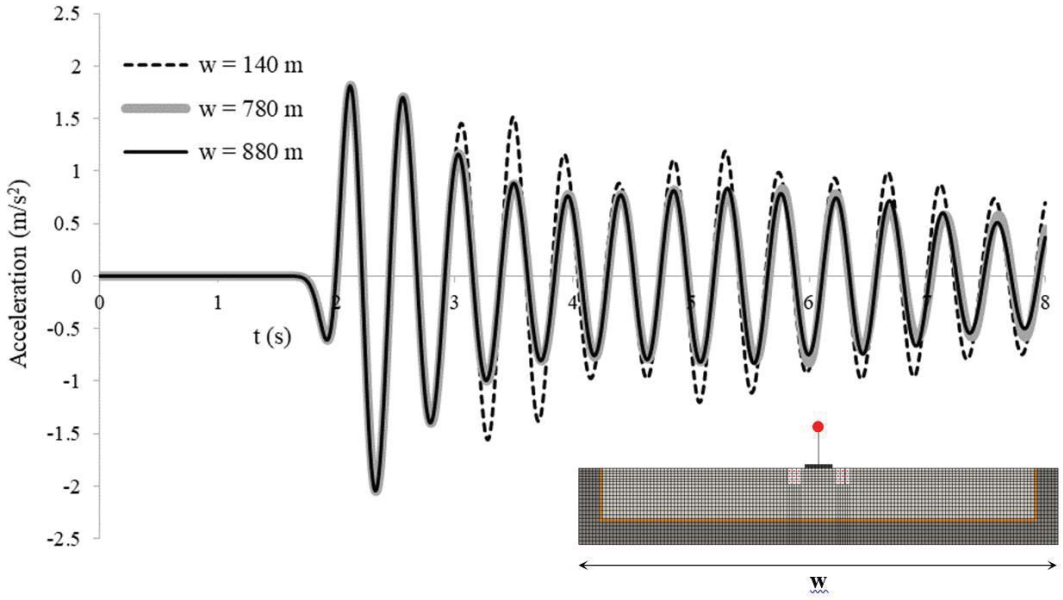

Fig. 9. Horizontal accelerations at the top of the SDOF structure for three different FE model lengths.

Such opposing motion will reduce the accelerations at the ground surface, leading to the desired reduction of the response of the SDOF structure. Out-of-phase resonator systems are more effective for continuous multi-cycle excitations, such as harmonics. The Ricker pulse was deliberately chosen (because of its similarity to the main pulse of recorded ground motions) to examine the efficiency of unit cell resonators for such short pulse signals.

Figure 10 compares the response of the SDOF structure, in terms of acceleration, with and without unit cell resonators. Two cases are examined with respect to the vibrating mass inside the unit cells: 2.5 Mg and 5 Mg. The corresponding stiffness of the unit cell springs is appropriately adjusted, so that their natural period remains 0.5 s. The peak response of the SDOF structure is barely affected by the unit cell resonators. A decrease in response can be observed only after the third cycle, revealing that the effectiveness of resonating unit cells increases with the number of excitation cycles.

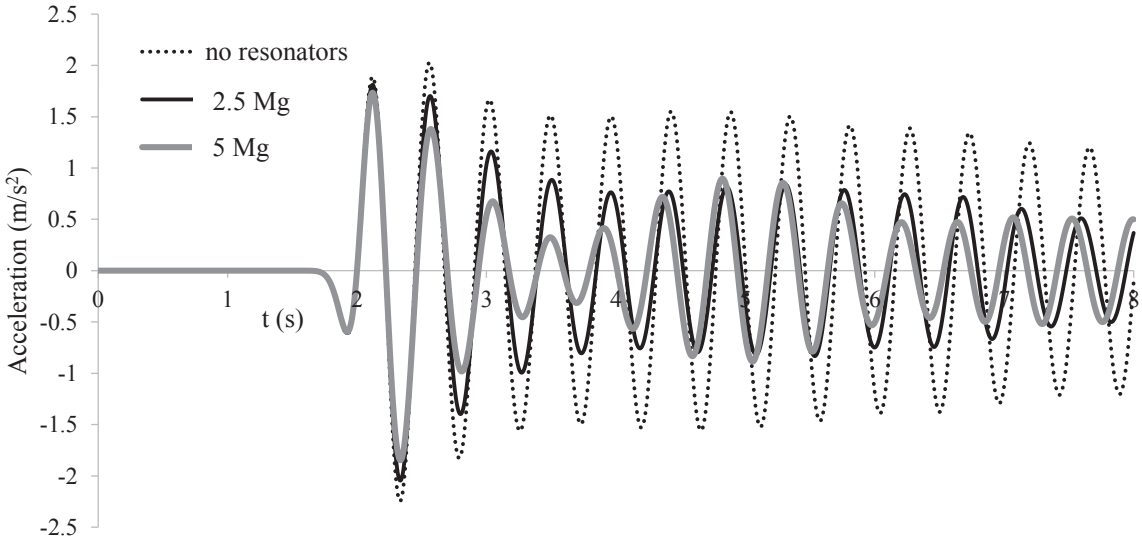

Fig. 10. Horizontal accelerations at the top of the SDOF structure with and without resonators. The vibrating mass in each unit cell is varied from to 2.5 Mg to 5.0 Mg.

Figure 11 compares the acceleration at the top of the SDOF structure to that of the unit cell vibrating mass (2.5 Mg). Right after the end of the transient part (Ricker pulse), both the building and the resonators experience free vibration. Since the mass of the SDOF structure (40 Mg) is approximately equal to the total mass of the resonators (18 x 2.5 Mg = 45 Mg), the inertia forces of the two system components (SDOF structure and resonators) will be proportional to their accelerations. The acceleration of the SDOF structure gradually decreases, reaching a minimum at t = 4 s, when the resonators are moving exactly out of phase. For t > 5 s, the acceleration of the resonators is significantly reduced due to their internal viscous damping (ξ = 0.06). After this point, the free-vibrating SDOF structure becomes the excitation source for the resonators, which are henceforth excited at the natural vibration period of the SDOF structure (0.45 s). And since their natural vibration period of 0.5 s is a bit longer, their masses are, again, going to move out of phase with the SDOF structure. In this way, the resonators continue playing a protective role, reducing the response of the SDOF structure.

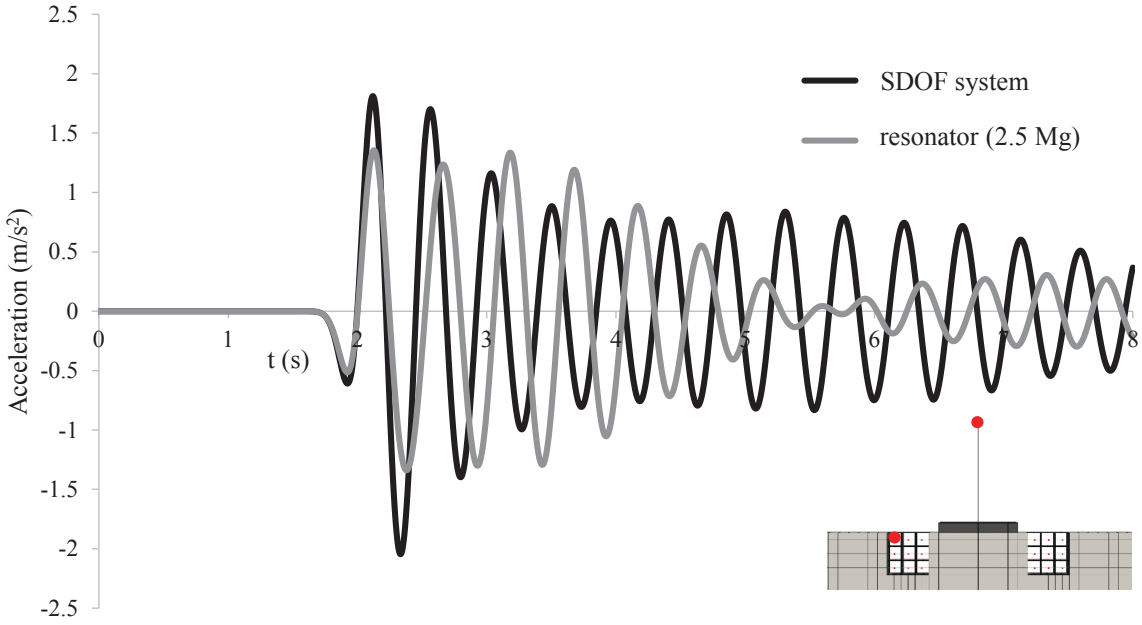

Fig. 11. Horizontal accelerations at the top of the SDOF system, compared to the mass of the top left resonator.

Figure 12 compares the horizontal displacement contours with and without resonators (of 2.5 Mg unit cell mass) for a snapshot at t = 3 s, when the systems are subjected to free vibration (same displacement scale factor). In the absence of resonators (**Fig. 12a**), the displacements are visibly larger compared to the case with 2.5 Mg resonators (**Fig. 12b**), both for the soil and the SDOF structure. Observe also that the unit cell masses are moving in the opposite direction to that of the SDOF structure, which explains their protective function.

4 CONCLUSIONS

The paper has presented a preliminary study on the potential of installing multiple resonating unit cells around an existing structure to improve its seismic performance. The following key conclusions are summarized as follows:

- The Domain Reduction Method (DRM) was used within the Real-ESSI Simulator to realistically model both body and surface waves in FE models, and investigate soil-structure-metamaterial interaction. Some of its powerful features, such as the possibility to damp out waves radiating from the vibrating structures, were demonstrated.

- The importance of conducting short sensitivity analyses to determine the parameters of the FE model was stressed. In this study, the sensitivity of the FE model to numerical damping and the length of the FE model were studied in detail. It was shown that (for this particular case) the lateral boundaries of the FE model should be placed at a considerable distance from the structure in order not to affect its response. It was also shown that adding numerical damping in the analysis to mitigate the spurious high-frequency response due to model discretization might also damp out real frequency components of response.
- The resonating unit cell metamaterials were effective in reducing the free-vibration response of an existing structure for the specific case analysed. It was shown that such metamaterials are effective thanks to the out-of-phase vibration of the unit cell masses with respect to the soil and the structure. This is achieved by tuning the resonator unit cell vibration periods to be slightly longer than the fundamental natural vibration period of the protected structure. Their effectiveness increases with increasing unit cell mass, provided they remain properly tuned.

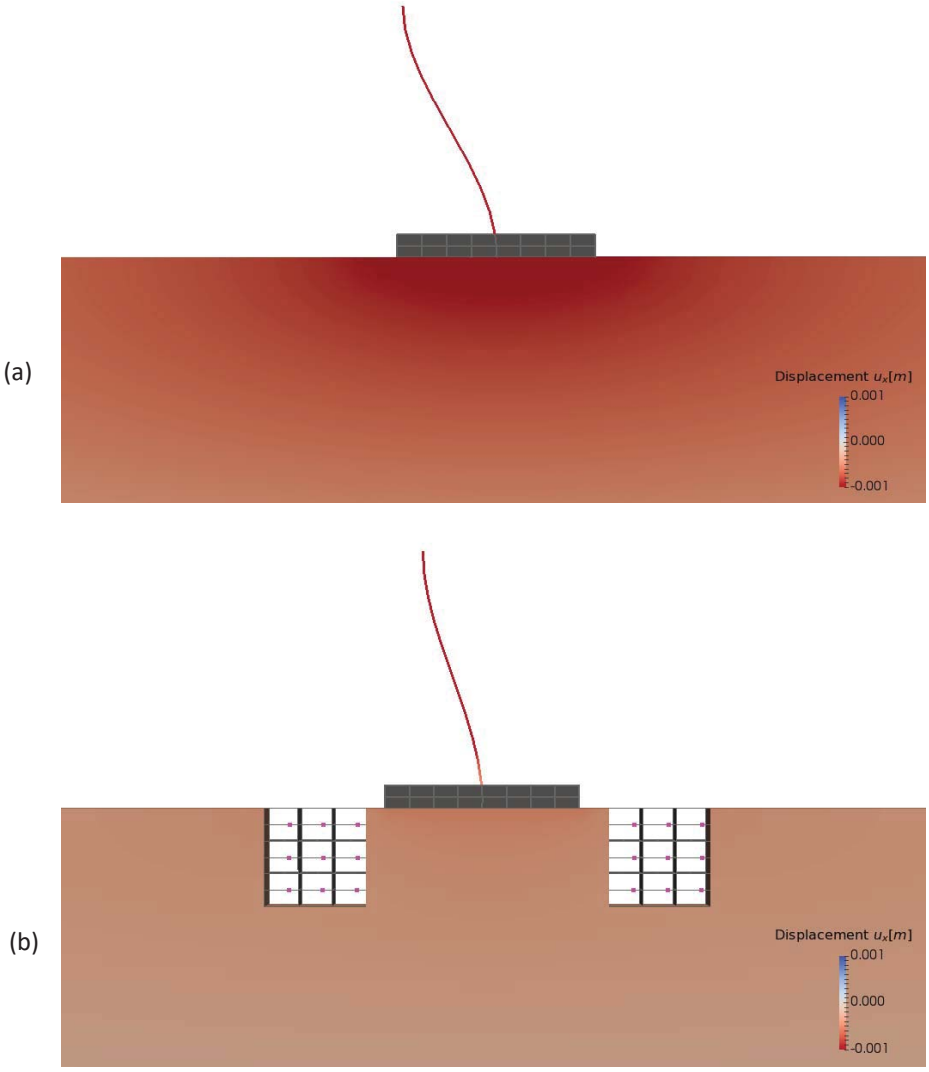

Fig. 12. Horizontal displacement contours: (a) no resonators; compared to (b) resonating unit cells (2.5 Mg).

Acknowledgements

This work lies within the "INSPIRE" EU program. This project has received funding from the European Union's Horizon 2020 research and innovation program under grant agreement No 813424.

REFERENCES

[1] J. B. Pendry, D. Schurig and D.R. Smith. Controlling electromagnetic fields. Science **312**, 1780–1782, 2006.

[2] A. Palermo, S. Krödel, A. Marzani and C. Daraio. Engineered metabarrier as shield from seismic surface waves. Scientific Reports 6, 1–10, https://doi.org/10.1038/srep39356, 2016.

[3] A. Palermo, S. Krödel, K. H. Matlack, R. Zaccherini, V. K. Dertimanis, E. N. Chatzi, A. Marzani, and C. Daraio. Hybridization of guided surface acoustic modes in unconsolidated granular media by a resonant metasurface. Phys. Rev. Appl. **9**, 054026, 2018.

[4] A. Palermo, M. Vitali and A. Marzani. Metabarriers with multi-mass locally resonating units for broad band Rayleigh waves attenuation. Soil Dyn Earthq Eng 113:265, 2018.

[5] S. Krödel, N. Thomé and C. Daraio. Wide band-gap seismic metastructures. Extreme Mech Lett **4**(September):111–117, 2015.

[6] R. Zaccherini, A. Colombi , A. Palermo , V. K. Dertimanis , A. Marzani , H. R. Thomsen , B. Stojadinovic and E. N. Chatzi. Locally resonant metasurfaces for shear waves in granular media. Phys. Rev. Appl. **13**, 034055, 2020.

[7] A. Colombi, R. Zaccherini and A. Palermo. Mitigation of seismic waves: metabarriers and metafoundations bench tested. arXiv:1908.02056 [physics.geo-ph]

[8] P. Cacciola and A. Tombari. Vibrating barrier : a novel device for the passive control of structures under ground motion Subject Areas: Proc. R. Soc. A Math. Phys. Eng. Sci. **471**, 2015.

[9] J. Bielak, K. Loukakis, Y. Hisada and C. Yoshimura. Domain reduction method for three-dimensional earthquake modelling in localized regions. part I: Theory. Bulletin of the Seismological Society of America, **93**(2):817-824, 2003a.

[10] C. Yoshimura, J. Bielak and Y. Hisada. Domain reduction method for three-dimensional earthquake modelling in localized regions. part II: Verification and examples. Bulletin of the Seismological Society of America, **93**(2):825-840, 2003a.

[11] Jeremic et al. Nonlinear Finite Elements: Modelling and Simulation of Earthquakes, Soils, Structures and their Interaction. UCD and LBNL, CA, USA, (1989-2020) ISBN: 978-0-692-19875-9.

[12] Real-ESSI Simulator release version is Global Release, 20.01, Jan2020, http://real-essi.us/

[13] W. T. Thomson. Transmission of elastic waves through a stratified solid medium. J. Appl. Phys., **21**, 89-93, 1950.

[14] N. A. Haskell. The dispersion of surface waves on multilayered media. *Bulletin of the seismological Society of America*, **43**(1):17–34, 1953.

[15] J.-F. Semblat and A. Pecker. *Waves and Vibrations in Soils: Earthquakes, Traffic, Shocks, Construction works*. IUSS Press, first edition, 2009.

[16] K. Watanabe, F. Pisanò and Boris Jeremić. A numerical investigation on discretization effects on seismic wave propagation analyses. *Engineering with Computers*, **33**(3):519–545, Jul 2017.

[17] N. M. Newmark. A method of computation for structural dynamics. ASCE Journal of the Engineering Mechanics Division, **85**, 67-94, July 1959.

[18] K. Kanellopoulos and G. Gazetas. Vertical static and dynamic pile-to-pile interaction in non-linear soil. Géotechnique, **70**, No. 5, 432-447, https://doi.org/10.1680/jgeot.18.P.303, 2020

EURODYN 2020
XI International Conference on Structural Dynamics
M. Papadrakakis, M. Fragiadakis, C. Papadimitriou (eds.)
Athens, Greece, 23–26 November 2020

THE EFFECT OF SOIL LIQUEFACTION ON THE SEISMIC RESPONSE OF A TYPICAL QUAY WALL

Stella V. Karafagka[1], Stavroula D. Fotopoulou[1], Anna C. Karatzetzou[1], Georgia E. Kroupi[1], and Kyriazis D. Pitilakis[1]

[1] Aristotle University of Thessaloniki
e-mail: stellak@civil.auth.gr

Keywords: Liquefaction, Seismic performance, Port quay wall, Effective stress analysis, Numerical modelling, OpenSees

Abstract. *Quay walls are one of the key elements of the port facilities. Experience obtained from past strong seismic events has demonstrated the increased seismic vulnerability of port facilities due to ground shaking as well as the important economic and societal losses (e.g. the 1995 Kobe earthquake. The most significant source of earthquake-induced damage to port facilities is the increase of induced earth pressures caused by inertial forces to the retained groundmass and by hydrodynamic force and pore-water pressure build-up in the saturated cohesionless soils that often prevail at coastal areas. This pressure build-up both in the back-fill and the foundation soil may increase the lateral pressures to quay walls and generate liquefaction effects at the foundation soil. The aim of this study is to investigate the influence of liquefaction on the seismic response of a typical port gravity quay wall resting on a potentially liquefiable soil. The analyses were conducted, under effective stresses using OpenSees. Comparative results highlighted the effect of liquefaction in modifying the ground motion and the quay wall dynamic response. The main conclusion of the comparative numerical study in a typical gravity quay wall is that while the impact of the liquefaction on the amplitude of the acceleration of the wall is negligible compared to the non-liquefaction case, the effect on the permanent seaward horizontal and vertical displacements of the wall is very important, almost doubled, increasing in that way considerably the vulnerability of the wall.*

1 INTRODUCTION

Ports are critical facilities that represent major part of regional, national and international transportation facilities, sometimes located in areas susceptible to liquefaction. As quay walls are of the most important assets of a port, they might be strongly influenced by liquefaction hazards. They are earth retaining waterfront gravity structures, parallel to the shoreline that create sufficiently deep vertical front in order to allow the approach, berthing, mooring, operations and maintenance of ships and vessels. Block-type quay wall is the simplest type of gravity quay wall, which consists of concrete blocks constructed on a layer of gravel or crushed stone [1]. The examples of recent devastating earthquakes in 1995 Kobe, Japan [2], 1999 Kocaeli, Turkey [1], 2007 Niigata-Chuetsu Oki, Japan [3], 2010 Maule, Chile [4], 2011 Christchurch, New Zealand [5] among others, indicated that port waterfront gravity structures are particularly susceptible to ground shaking and ground failure, including liquefaction and lateral displacement, which may result in high economic losses. Therefore, the investigation of the seismic response of waterfront gravity quay walls has become a concern to the scientific community as well as the waterborne transportation industry.

The seismic response and vulnerability of waterfront quay walls has already been studied using numerical soil-structure interaction methods [6-14]. Pitilakis and Moutsakis [6] analysed the seismic behaviour of a gravity retaining quay wall and compared it with field observations. Kakderi and Pitilakis [7] proposed seismic fragility curves for typical monolithic gravity quay walls, neglecting possible damages due to liquefaction effects. In the framework of UPGRADE research project [8] seismic fragility curves are proposed for typical block-type gravity quay walls, considering possible friction and displacements between the interfaces of the construction blocks, again neglecting liquefaction-induced damages. Alielahi and Moghadam [9] investigated the influence of quay wall hunch on the seismic fragility, ignoring also soil liquefaction. Kamalzadeh and Pender [10] investigated the static and dynamic response of a gravity retaining wall for different Ricker wavelet excitations.

Among the vulnerability studies of waterfront gravity structures considering liquefaction, Ichii [11-12] and Miraei and Jafarian [13] proposed analytical seismic fragility curves for gravity-type quay walls, while Calabrese and Lai [14] developed fragility functions for blockwork wharves using artificial neural networks, considering different geometries, type of failure mechanism and the effect of liquefaction occurrence. All these studies do not extensively examine the effect of soil liquefaction on the seismic response of gravity quay walls and its surrounding soil.

In this context the herein work presents a numerical investigation of the effects of liquefaction on the seismic response of a typical port gravity quay wall resting on a liquefiable soil. The analyses are conducted, under effective stresses using OpenSees, with the direct approach, where the soil and the structure response is coupled. We compare the response of the wall for a number of strong ground excitations when liquefaction is not allowed to the case when it may occur. The results are presented and discussed in terms of acceleration time histories at different locations on the wall and the soil, as well as in terms of the residual seaward displacement and the permanent vertical displacement of the quay wall.

2 FRAMEWORK APPROACHES AND NUMERICAL MODELLING

A typical port quay wall system is used founded on the same soil profile prone to liquefaction under strong seismic excitations. The potential effect of the liquefaction in the global seismic response of the gravity quay wall is studied considering a coupled soil-structure system under effective stress conditions, where in a first step we artificially don't allow the liquefaction to happen while in the second we allow it.

2.1 Selection of the soil and structure typology

A typical gravity wall section of the Port of Thessaloniki has been selected. Based on the available geotechnical information, N_{SPT} values and laboratory data [15-16], we define a soil profile representative of the port area of Thessaloniki, Greece (Figure 1). The fundamental period of the soil profile, T_o, is equal to 0.71s. The high liquefaction potential of the subsoil layers is estimated according to EC8 guidelines [17]. The soil formations susceptible to liquefaction are located from -3.0m to -18.0m consisting mainly of silty/clayey sands and non-plastic silts (ML-SM, ML-CL, SC-SM) with low N_{SPT} values. Owing to the rather high liquefaction susceptibility of the port area, the soil profile refers to ground type S, in accordance to EC8 soil classification scheme. The height of the quay wall is equal to 14.0m. Figure 2 shows the geometry of the quay wall and its surrounding back-filled and mound gravel. The soil layers, the quay wall and its surrounding gravel characteristics are analytically described in the following.

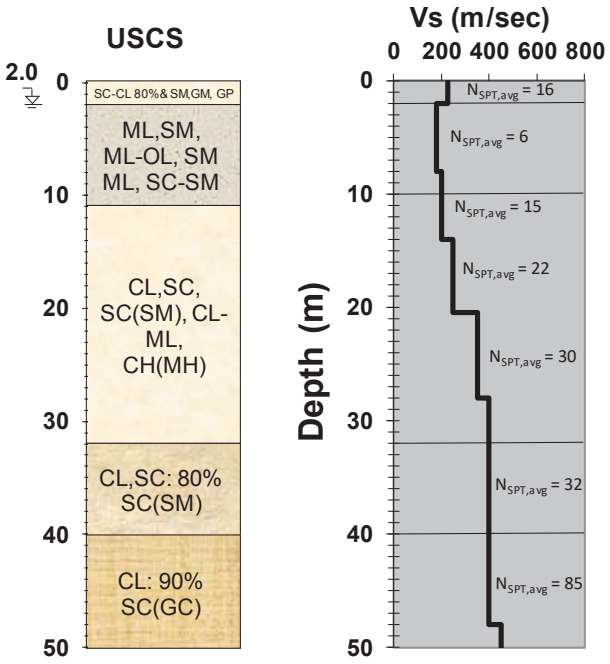

Figure 1: Representative soil profile with USCS classification as well as Vs profile and average N_{SPT} values.

2.2 Soil-structure modelling

Two-dimensional (2D) numerical simulation of the soil-structure system is conducted in OpenSees [18]. The soil grid adopted has a total length three times its depth to minimise wave reflections at the vertical boundaries. Thus, the dimensions of the soil model are 50.0m x 150.0m. Sufficiently dense discretization is achieved by using quadrilateral elements of 0.5m x 2.0m considering that the maximum frequency of interest is set to 10Hz, allowing an adequate number of elements to fit within the shortest wavelength of the propagating shear wave. Figure 3 illustrates the geometry of the finite element (FE) soil-structure model. The locations of the nodes at different sites of the soil model, namely A, B, C, D and FF (point at the free field surface), as well as at the top of the quay wall (W_T), used to capture the soil and quay wall seismic response are also shown.

The soil profile consists of different layers of cohesive and cohesionless soil materials (Figure 1), thus the soil model in OpenSees is divided into eight soil layers (Figure 3). Saturated unit weights are used for the soil below the ground water level (-2.0m), while nine-node

quadrilateral elements are used for the soil and the back-filled and mound gravel in the frame of effective stress analysis. Such elements are capable of simulating fluid-solid coupling during the earthquake excitation, based on Biot's theory of porous medium [19], as they have corner nodes with both displacement (u) and pore pressure (p) degrees of freedom and interior nodes with only two displacement degrees of freedom.

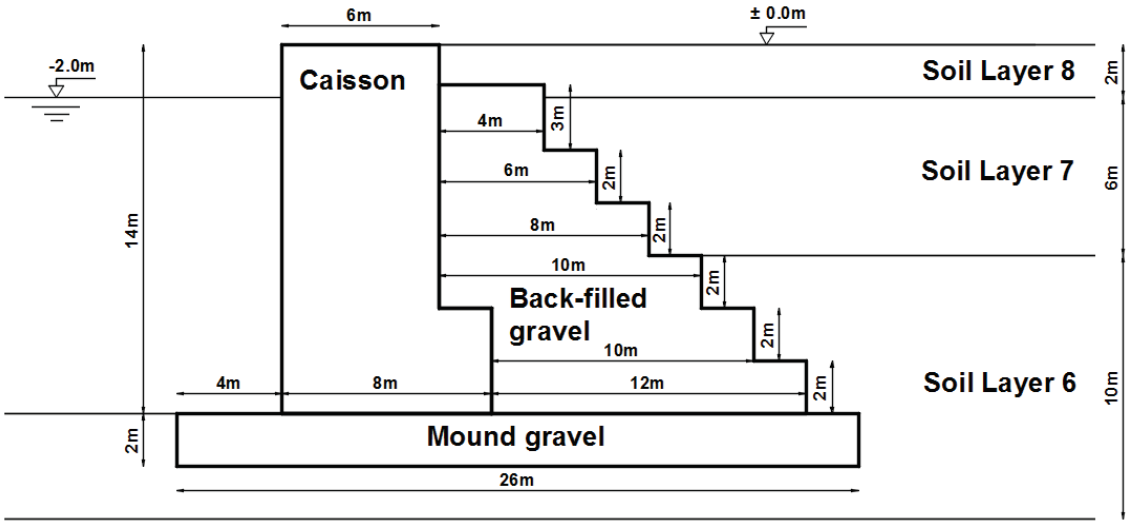

Figure 2: Geometry of the typical gravity quay wall and its surrounding back-filled and mound gravel.

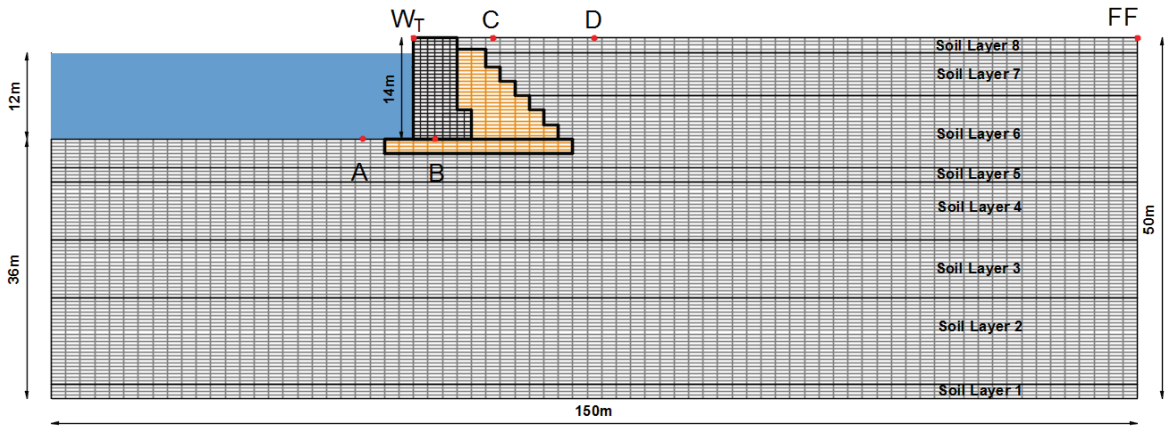

Figure 3: Geometry of the finite element soil-structure model along with the locations of the nodes used to capture the soil and quay wall seismic response.

The fully coupled (u-P) approach is applied, which can simulate permanent shear-strain accumulation in clean medium-dense cohesionless soils during liquefaction and dilation due to increased cyclic shear stiffness and strength. The constitutive model employed to describe the soil behaviour is based on Prevost's [20] multi-surface plasticity model, with some modifications by Yang [21]. During the application of the gravity load the material behaves in elastic range, while during the subsequent dynamic loading its response is elastic-plastic. To simulate the hysteretic behaviour of soil under cyclic loading, Prevost's [20] kinematic law is employed, therefore all yield surfaces correspond to stress space within the failure envelope [21-22] and comply with Masing loading-unloading-reloading criteria [23]. The cohesionless soil layers are simulated using the "PressureDependMultiYield02" elastic-plastic material in OpenSees. The yield function is assumed to follow the shape of the Drucker-Prager criterion and the yield surface is a function of cohesion and friction angle. Plasticity is expressed

through a non-associative plastic flow rule [22], capable of handling the contractive/dilative soil behaviour stimulated by shear loading to effectively depict the interaction between shear and volumetric responses. The cohesive soil layers are simulated with the "PressureIndependMultiYield" material in OpenSees, which describes an elastic-plastic material in which the volumetric stress-strain response is linear elastic and independent of the deviatoric response. This material simulates the monotonic or cyclic response of materials whose shear behaviour is insensitive to changes of the confinement pressure. The yield function is assumed to follow the Von Mises criterion and the yield surface is solely a function of the undrained shear strength. Plasticity, which exhibits only in the deviatoric stress-strain response, is defined via the multi yield surface plasticity model, with an associative plastic flow rule which considers that the incremental plastic strain vector is normal to the yield surface.

For each soil layer, the soil features are defined, namely the mass density (ρ), the shear wave velocity (V_s), the friction angle (φ) at the peak shear strength, the cohesion (c) and Poisson's ratio ν (taken equal to 0.35), while the reference low-strain shear (G_r) and bulk (B_r) moduli are computed. The mass density of the materials corresponds to the total mass densities, thus for the soil layers that overlay or underlay the groundwater table dry or saturated conditions should be reflected respectively. Table 1 summarizes the soil properties adopted for each soil layer. For soils susceptible to liquefaction, a set of parameters that describe and control the mechanism of the accumulation of completely plastic shear deformation caused by liquefaction, are also defined according to the proposed values of Yang et al. [24]. Regarding the gravel backfill, it is simulated employing the "PressureDependMultiYield02" material, where the mass density is set equal to 2.1 Mg/m^3 below the water table and 1.8 Mg/m^3 above the water table, while the friction angle φ, G_r and B_r are defined equal to 40^o, 189MPa and 567MPa respectively.

The quay wall is simulated using standard four-node plane strain quad elements 0.5m x 1.0m, with nodes that have only two translational degrees of freedom. It is noted that the quay wall is modelled as a monolithic component, neglecting the friction interfaces between the blocks forming the quay wall. The "*ElasticIsotropic"* material in OpenSees is used to model the quay wall, considering a Young's Modulus (E) equal to E=27000MPa, a mass density equal to ρ=2.4 Mg/m^3 and a Poisson's ratio equal to ν=0.2. No interface is considered between the quay wall and the surrounding soil material of the gravel backfill, while equal displacements are ensured between the quay wall and the backfill nodes.

Subsequently, the hydraulic boundaries of the model are also defined. As the ground water table is located at -2.0m depth, all the pore pressure nodes that lie above this level have their pore pressure degree of freedom fixed. This creates a water drainage path which allows the water to escape to the adjacent elements and ensures that no pore pressure is built up in the area above the groundwater table, thus it is maintained to zero. The same constrain is assigned to the nodes of the seabed which lie at the foot of the quay wall, as they are submerged beneath the water and to the backfill nodes which are in contact with the quay wall as well. The body of water and the dynamic effects it causes are incorporated into the model in a way that does not affect the effective stresses of the soil elements. The water forces are applied to the nodes of the seabed as vertical nodal masses. The water mass value for each of these nodes is derived by multiplying the half of the distance to adjacent nodes, the thickness of the elements this mass refers to, the depth of the water and the water's mass density. A similar process is followed to define the water forces applied at the vertical front face of the quay wall. In this case horizontal masses are assigned, calculated by applying a triangular distribution of the hydrostatic forces considering that the maximum depth is 12.0m.

Special boundary conditions are also assigned to ensure that free-field conditions exist at the lateral boundaries of the soil model and avoid the presence of wave reflections. In particu-

lar, the elements in the edge lateral columns of the mesh are given a significantly increased -practically infinite- thickness, so they appear to be adequately more massive than the rest of the elements in the interior of the mesh. In addition, periodic boundary conditions are achieved by bounding together the translational degrees of freedom for the nodes on either side of these lateral columns, so they perform equal displacements both in the horizontal and in the vertical direction. Finally, the soil grid is underlain by an elastic half-space, which stands for the finite rigidity of the underlying bedrock. A Lysmer and Kuhlemeyer [25] viscous damper is applied in the horizontal direction to the soil model base to account for the finite rigidity of the underlying half-space, setting a bedrock shear wave velocity equal to 750m/s and mass density equal to 2.2Mg/m^3. To define the Lysmer and Kuhlemeyer [25] dashpot, the viscous uniaxial material is used, which is described by the dashpot coefficient (c). The dashpot coefficient is calculated according to Joyner and Chen [26] by multiplying the underlying bedrock's mass density and shear wave velocity, as well as the base area of the soil to obtain the equivalent loading application throughout the site. To properly simulate the underlying elastic half-space necessitates that all the base nodes of the soil model are fixed against vertical translation only and left free to move in the horizontal direction while all are given equal horizontal displacements. Seismic energy dissipation during dynamic loading is accounted for by assigning mass and stiffness proportional Rayleigh damping with a damping ratio equal to 2.0%.

Layer Thickness (m)	Soil layer	Model	ρ (Mg/m^3)	G_r (MPa)	B_r (MPa)	φ (^{o})	c (kPa)
2m	8 (surface)	PDMY02	1.835	92.9	279.0	39	-
6m	7	PDMY02	1.886	61.1	183.0	32	-
10m	6	PDMY02	2.039	81.6	245.0	33.5	-
2m	5	PIMY	2.039	127.0	382.0	25	23
8m	4	PIMY	2.039	250.0	749.0	25	23
8m	3	PIMY	2.141	343.0	1030.0	25	25
12m	2	PIMY	2.141	343.0	1030.0	25	40
2m	1	PIMY	2.141	535.0	1610.0	20	50

Table 1: Soil properties adopted for the considered soil profile (PDMY02: PressureDependMultiYield02, PIMY: PressureIndependMultiYield).

3 NUMERICAL ANALYSIS

3.1 Seismic input motion

A representative set of 15 earthquake records is selected from the European Strong-Motion Database. They are all referring to rock type or stiff soils (ground types A and B according to EC8 soil classification scheme) with magnitude (M_w) and epicentral distance (R) between

$5.5<M_w<6.5$ and $0<R<45$km, respectively. They are covering a wide range of peak ground acceleration (PGA) from 0.13g to 0.51g. The selection criterion is the average acceleration spectra of the set to be of minimal "epsilon" [27] at the period range $0.00<T<2.00$sec with respect to the corresponding 5% damped median plus 0.5 standard deviations spectrum defined based on the ground motion prediction equation (GMPE) by Akkar and Bommer [28]. The optimization procedure is performed using REXEL [29], that allows obtaining combinations of accelerograms, which on average are compatible to the reference spectrum. The list of the selected records is presented in Table 2, while Figure 4 shows the 5% elastic response spectra of the selected earthquake records and their mean elastic response spectrum compared to the corresponding median plus 0.5 standard deviations of Akkar and Bommer [28] spectrum. The matching is satisfactory. Among the selected time histories it is worth to notice that the frequency content of the Kalamata and Umbria Marche 2 earthquake records (ID 414 and 594 respectively) is quite distinct compared to the other records (Figure 4), as they are characterized by long-period pulses unlike the other high-frequency records.

Earthquake Name	Date	M_w	Fault Mechanism	Epicentral Distance [km]	$PGA_{initial}$ [m/s^2]	$PGA_{corrected}$ [m/s^2]	EC8 Site class	Waveform ID
Umbria Marche (aftershock)	6/10/1997	5.5	normal	5	1.838	2.060	A	651
Valnerina	19/9/1979	5.8	normal	5	1.510	1.472	A	242
SE of Tirana	9/1/1988	5.9	thrust	7	4.037	3.826	A	3802
Lazio Abruzzo (aftershock)	11/5/1984	5.5	normal	15	1.411	1.373	A	990
Valnerina	19/9/1979	5.8	normal	5	2.012	2.060	A	242
Kozani	13/5/1995	6.5	normal	17	2.039	2.158	A	6115
Friuli (aftershock)	15/9/1976	6.0	thrust	12	1.339	1.373	A	149
Umbria Marche	26/9/1997	5.7	normal	23	1.645	1.668	A	763
Friuli (aftershock)	15/9/1976	6.0	thrust	14	2.586	2.649	B	134
Patras	14/7/1993	5.6	strike-slip	9	3.337	3.434	B	1932
Kalamata	13/9/1986	5.9	normal	11	2.670	2.747	B	414
Umbria Marche 2	26/9/1997	6.0	normal	11	5.138	5.592	B	594
Montenegro (aftershock)	24/5/1979	6.2	thrust	17	1.708	1.766	B	229
Kefallinia island	23/1/1992	5.6	thrust	14	2.223	2.060	B	6040
Ano Liosia	7/9/1999	6.0	normal	14	2.159	2.256	B	1714

Table 2: List of earthquake records used for the dynamic analyses.

These records are then filtered between 0.25 and 15 Hz, using a fourth-order bandpass Butterworth type filter. Baseline correction linear type is also applied. Table 2 presents also the values of $PGA_{corrected}$ obtained from the corrected accelerograms used for the analyses.

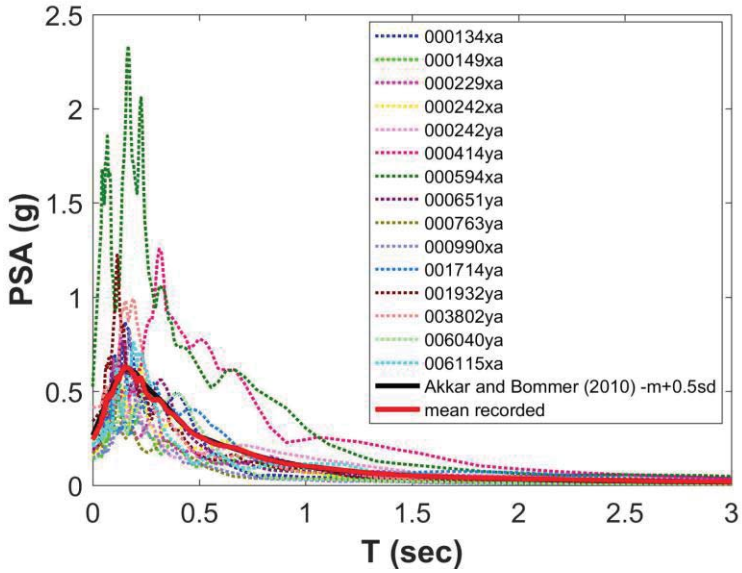

Figure 4: Elastic response spectra of the selected earthquake records and their mean elastic response spectrum in comparison with the corresponding median plus 0.5 standard deviations Akkar and Bommer [28] spectrum.

3.2 Comparative dynamic analysis

The effect of soil liquefaction on the seismic response of the typical gravity quay wall is illustrated below, conducting two sets of seismic analyses for the two conceptual modelling approaches using as input the earthquake records of Table 2. Layers of potential liquefaction are identified by the loss of effective confining stress (equal to zero) which is also verified by the corresponding stress-strain loops (e.g. at -15m depth at free field conditions as shown in Figure 5). Indicatively, Figure 5 presents the computed effective confinement profile and stress-strain hysteresis loops at specific depth for Kalamata earthquake motion (ID 414 record) for the two approaches, allowing or neglecting soil liquefaction.

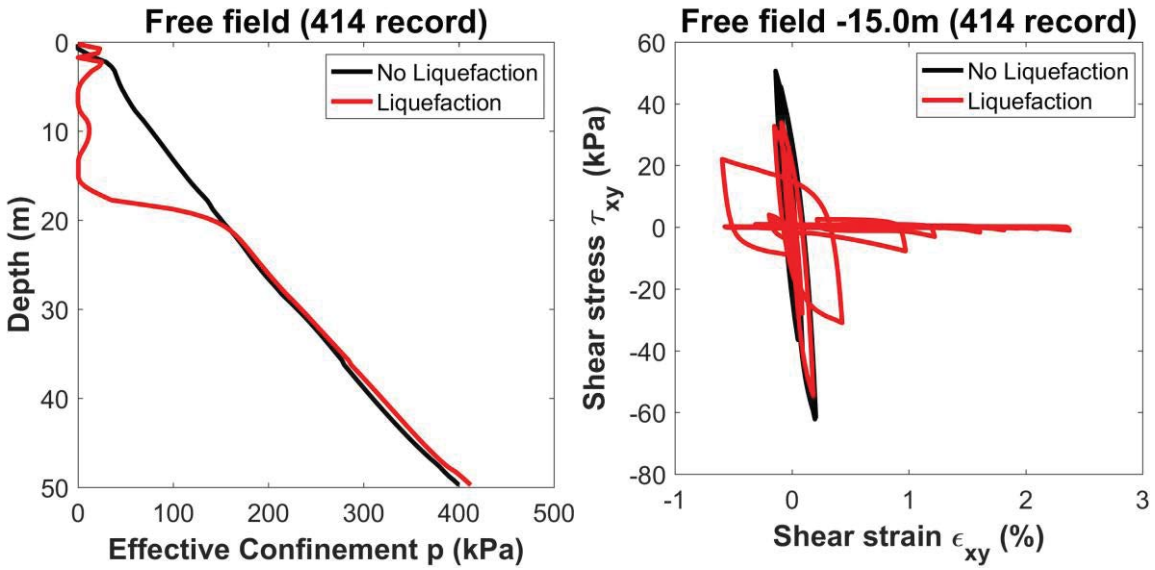

Figure 5: Effective confinement profile (left) and stress-strain hysteresis loops at -15.0m depth (right) for the ID 414 input motion at free-field conditions, for the liquefiable and the non-liquefiable cases.

For the case that we allow liquefaction to occur, the hysteresis loops corresponding to the time before the onset of liquefaction are smooth and are dominated by steeper slope, indicating greater values of the dynamic shear modulus which represents the shear stiffness of the soil, while after a specific point, a change in the pattern of the stress-strain loops is observed. Specifically, the circles are characterized by large shear strain amplitudes and adequately small shear stresses, leading to a radical decrease in the shear stiffness and accumulation of large shear strains (Figure 5).

The effect of liquefaction on the acceleration time histories and the frequency content of the motion at free field soil surface and on the quay wall is also examined. Indicatively, the acceleration time histories for the two considered approaches at the FF and the W_T for Kalamata (ID 414) and Ano Liosia (ID 1714) input motions, which are considered representative of the extreme and average response respectively, are presented in Figure 6 and Figure 7 respectively.

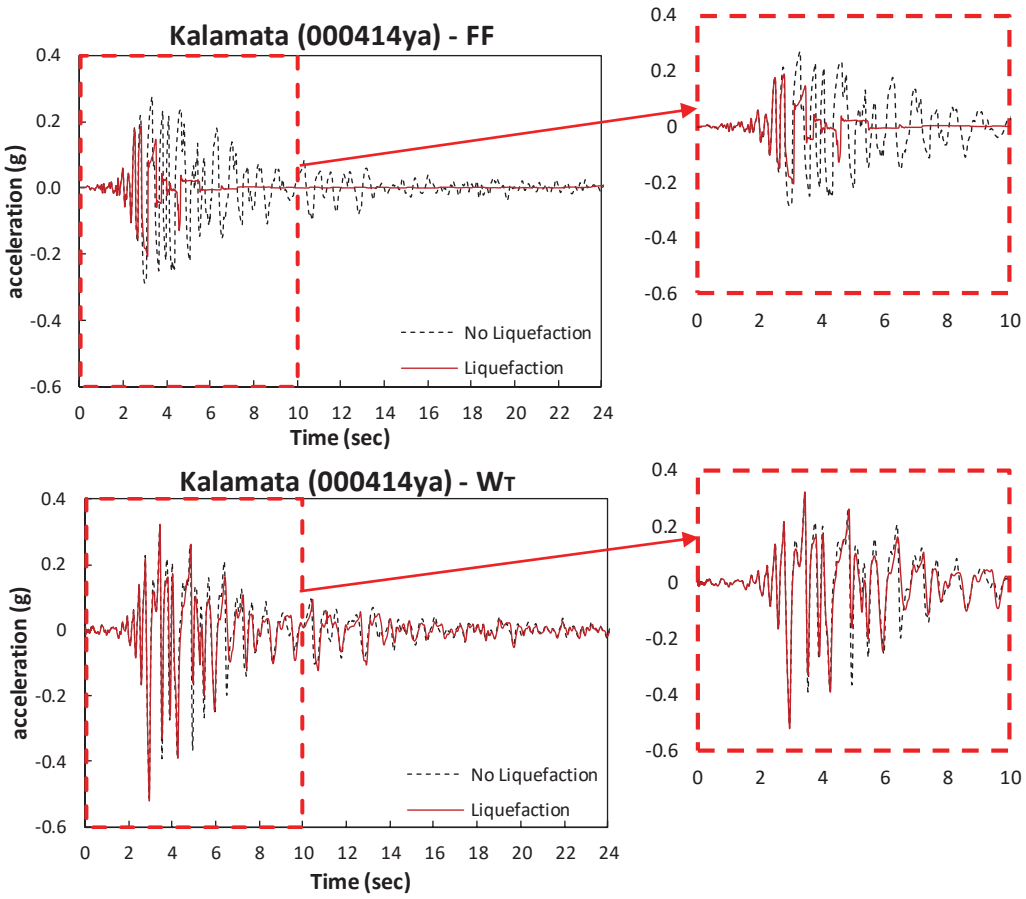

Figure 6: Comparison of the acceleration time histories computed at the free field conditions FF (top) and on the wall W_T (bottom) for the two approaches for Kalamata (ID 414) input motion.

Regarding the computed acceleration time history at the FF, as shown in Figure 6 (top) and Figure 7 (top) for Kalamata (ID 414) and Ano Liosia (ID 1714) input motions respectively, liquefaction apparition causes seismic energy dissipation and leads, as expected, to significant reduction in the strong ground motion duration. The amplitudes of the ground motion in the case where liquefaction occurs are decreased, compared to the corresponding values ignoring liquefaction. These trends are more pronounced for the lower-frequency Kalamata (ID 414) input motion while the Ano Liosia (ID 1714) input motion seems more representative of the average dynamic response.

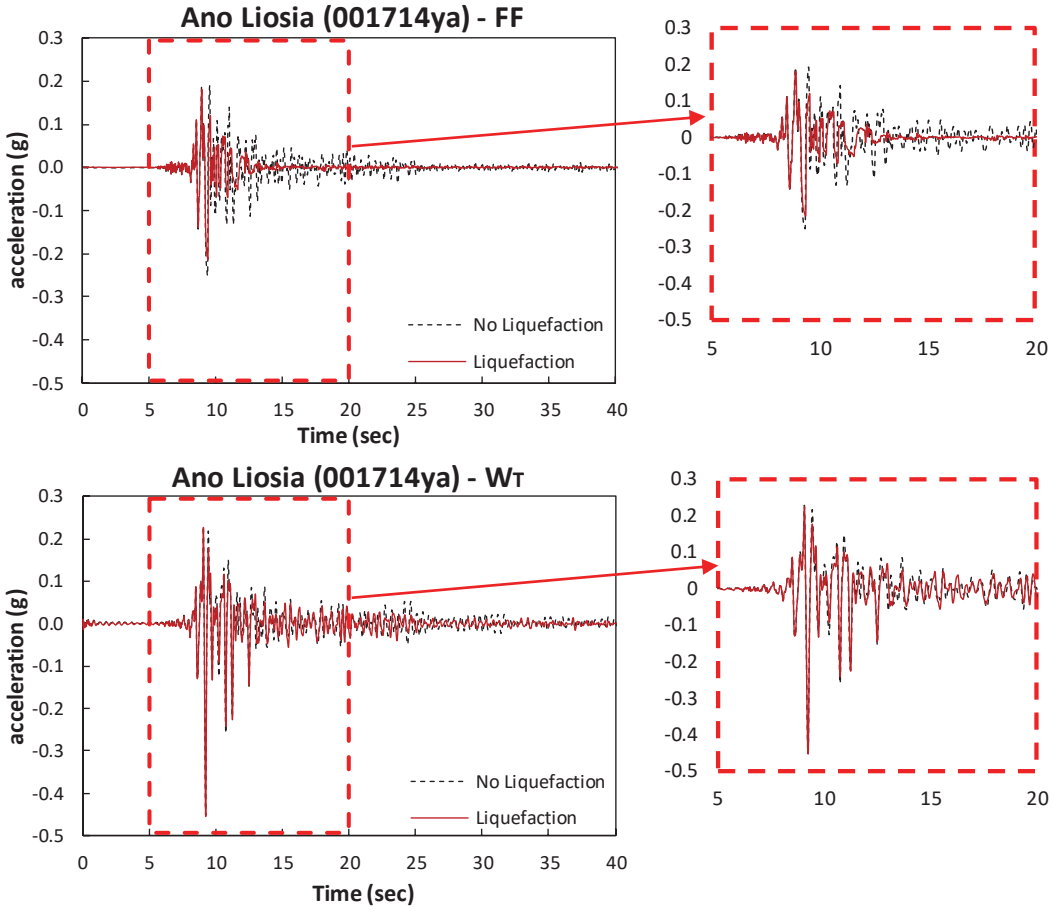

Figure 7: Comparison of the acceleration time histories computed at the free field conditions FF (top) and on the wall W_T (bottom) for the two approaches for Ano Liosia (ID 1714) input motion.

Contrary to the free field conditions it is observed (Figure 6 and Figure 7, bottom) that the liquefaction didn't alter the computed acceleration time histories on the top of the wall compared to the no-liquefaction case. Indicatively, computed acceleration time histories at different locations with the Kalamata (ID 414) and Ano Liosia records (ID 1714) used as rock input motion, are presented for the two approaches in Figure 8 and Figure 9. The reason of this phenomenon may be attributed to the oscillation of the rigid wall in a coupled system when receiving a rather similar seismic excitation at its base.

In Figure 10 we present the computed PGA values for all input motions used at the top of the wall (W_T) and at the different other locations i.e. FF, C and D. The computed residual seaward displacement and the permanent vertical displacement at the top of the quay wall are shown in Figure 11 for both approaches when allowing or restricting liquefaction. Moreover, to better understand the differences between the two approaches at the quay wall response in terms of displacements, the ratios of the permanent horizontal and vertical displacement values at the top of the wall (W_T) for the liquefiable case to the corresponding ones for the non-liquefiable case are also presented in Figure 12.

The main observation from the analyses of the PGA is that the computed values on the wall are getting large values independently of the presence or not of liquefaction and that the PGA values are progressively decreased with distance from the wall to the free field values (Figure 10 locations FF and D) due to the increase of the importance of liquefaction and non-

linear site effects. The closer we are to the wall the more the ground response is controlled by the oscillation of the wall itself. It should be also notified that the red points depict the results of the analysis for Umbria Marche 2 (ID 594) input motion where the analysis failed, and the results are presented only for completeness reasons. Moreover, for the liquefiable case at the FF (Figure 10, top-right) it is observed that for a PGA_{rock} value lower than approximately 0.2g there is still an amplification of the PGA relative to PGA_{rock}, while for PGA_{rock} values higher than 0.2g the PGA value of the seismic motion attenuates due to liquefaction. These observations are in accordance with the results of the study conducted from Lopez-Caballero and Modaressi Farahmand-Razavi [30].

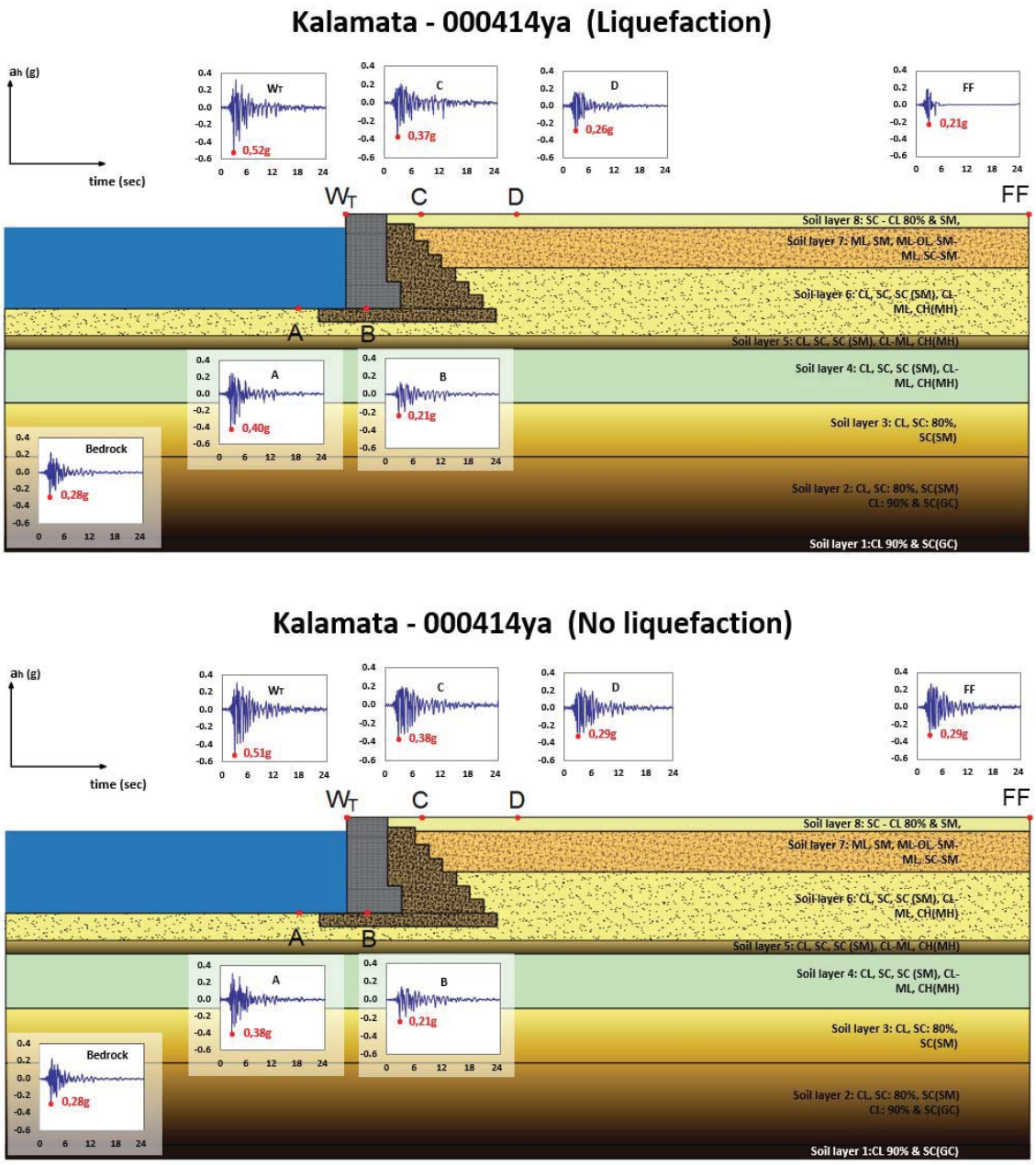

Figure 8: Acceleration time history response at the various sites of the model for Kalamata (ID 414) input motion allowing (top) or neglecting (bottom) liquefaction.

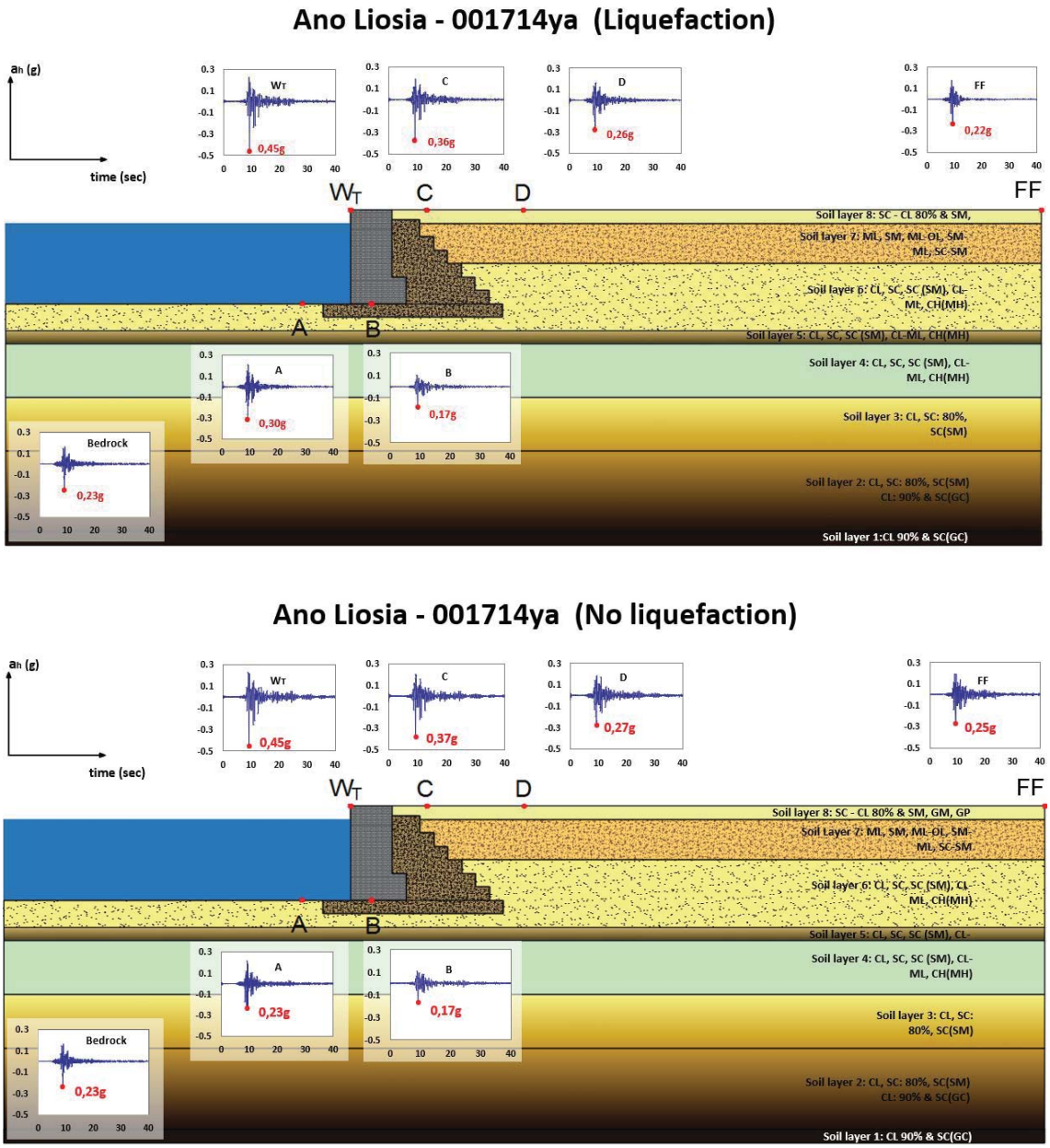

Figure 9: Acceleration time history response at the various sites of the model for Ano Liosia (ID 1714) input motion allowing (top) or neglecting (bottom) liquefaction.

Figure 11 presents the computed permanent horizontal and vertical displacements of the rigid wall, while in Figure 12 we present the ratio of the same displacements when considering the presence of liquefaction or not. It is clear that in the case of liquefaction the seaward permanent displacements of the wall are much higher, i.e. almost twice as high, compared to the non-liquefaction case, which nevertheless are not negligible. For example, for rock-basement excitations of 0.2g-0.3g the average value of the horizontal permanent displacement without liquefaction are of the order of 5 cm, and they are doubled in case liquefaction is considered. A similar trend is observed for the vertical displacements, where, however, the absolute and relative values are as expected lower compared to the horizontal displacements. More specifically, regarding the computed absolute displacement values, the permanent horizontal displacements vary from 2.3 cm to 60.3 cm when we consider soil liquefaction and from 1.9 cm to 31.9 cm when liquefaction is neglected, while the permanent vertical displacement val-

ues range between 2.1 cm and 17.8 cm for the liquefiable case compared to those of the non-liquefiable case that vary between 1.9 cm and 11.6 cm.

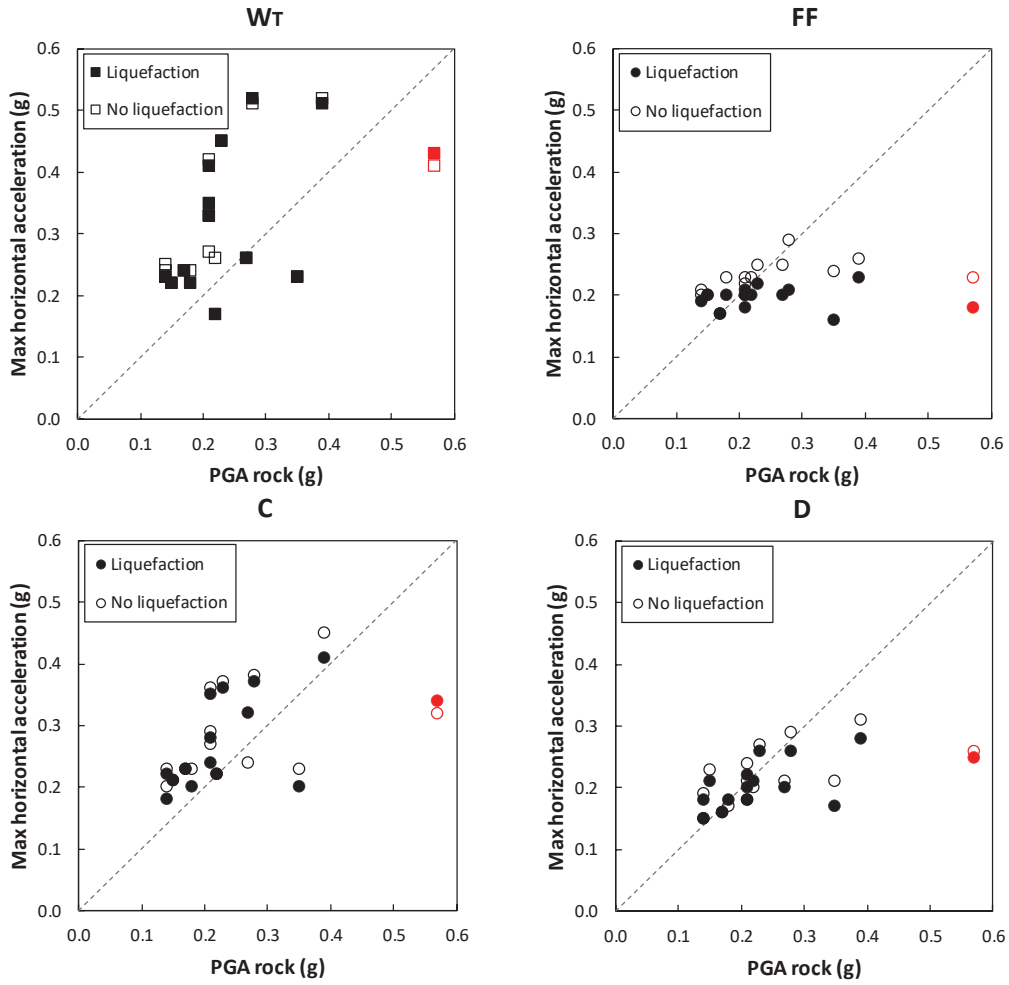

Figure 10: Maximum horizontal acceleration - PGA_{rock} pairs at different locations: W_T (top-left), FF (top-right), C (bottom-left) and D (bottom-right) for the two cases allowing (solid circles) or not liquefaction.

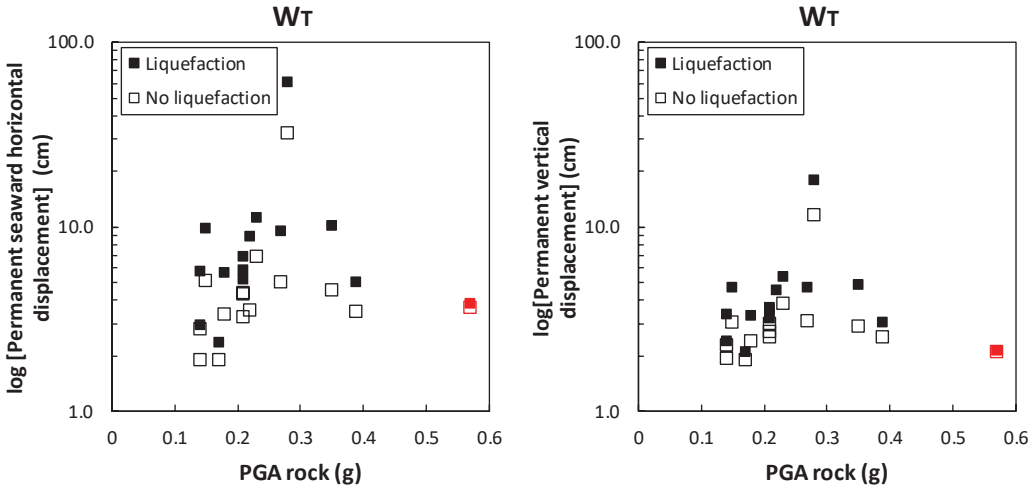

Figure 11: Permanent horizontal displacement (left) and permanent vertical displacement (right) variation with PGA_{rock} at the top of the wall (W_T) with (solid rectangles) and without liquefaction.

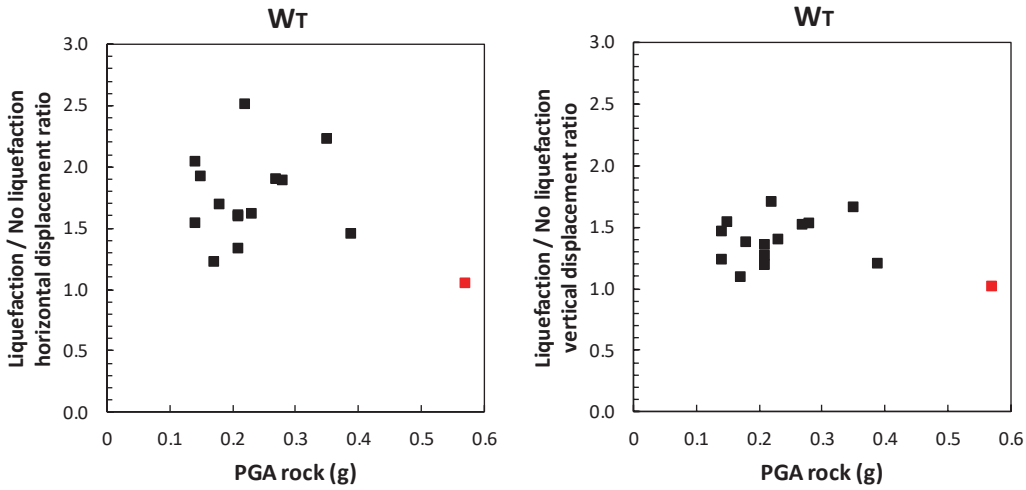

Figure 12: Ratios of the permanent horizontal (left) and vertical displacement (right) values computed at the top of the wall W_T for the liquefiable case to the corresponding ones for the non-liquefiable case.

According to PIANC [31], for gravity quay walls four damage states are defined (i.e. <1.5%, 1.5-5.0%, 5.0-10.0% and >15.0%) in terms of the normalized seaward displacement (horizontal displacements divided by the wall height), which is considered as an appropriate Damage Metric (DM) from the viewpoint of quay wall performance. In this study, the normalized seaward displacements vary from 0.23% to 6.03% when liquefaction is allowed and from 0.19% to 3.20% when liquefaction is neglected. Thus, for the liquefiable case the first three damage states could be reached, even without scaling of the records.

4 CONCLUSIONS

The influence of the liquefaction of the foundation soil on the seismic response of port gravity-type quay walls has been investigated for a typical structure of the Port of Thessaloniki. The numerical analysis has been conducted applying OpenSees with a set of 15 earthquake records having different amplitudes and frequency content, allowing or not liquefaction to occur. The main conclusion of the comparative study is that while the impact of the liquefaction on the amplitude of the acceleration of the wall is negligible compared to the non-liquefaction case, the effect on the permanent seaward horizontal and vertical displacements of the wall is very important, almost doubled, increasing in that way considerably the vulnerability of the wall. Further research is certainly needed to investigate and quantify the effects of liquefaction on the seismic response and vulnerability of a variety of port quay wall typologies and soil conditions, always prone to liquefaction under strong seismic ground motion excitations.

ACKNOWLEDGMENTS

This study was carried out in the framework of the ‘‘Resilient, system-wide seismic risk assessment of port facilities. Application to Thessaloniki Port system’’ RESPORTS project (http://resports.gr/), funded by the Hellenic Foundation for Research and Innovation (HFRI) and General Secretariat for Research and Technology (GSRT) under Grant Agreement No754.

REFERENCES

[1] H. Karakus, B.A. Ergin, I. Guler, K. Cihan, Y. Yuksel, Dynamic Response of Block type Quay Wall, *Proceedings of the 8th International Conference on Coastal and Port Engineering in Developing Countries*, IIT Madras, Chennai, India, 20-24 Feb, 2012.

[2] S.E. Chang (2000). Disasters and transport systems: loss, recovery and competition at the Port of Kobe after the 1995 earthquake, *J. Transp. Geogr.* 8(1), 53-65, 2000.

[3] R. Kayen, B. Collins, N. Abrahamson, S. Ashford, S.J. Brandenberg, L. Cluff, Investigation of the M6.6 Niigata-Chuetsu Oki, Japan, Earthquake of July 16, 2007, *US Department of the Interior & US Geological Survey*, Open File Report 1365, 2007.

[4] A.S. Elnashai, B. Gencturk, O.-S. Kwon, I.L. Al-Qadi, Y. Hashash, J.R Roesler, et al., The Maule (Chile) Earthquake of February 27, 2010: consequence assessment and case studies, *Mid-America Earthquake Center*, Research report 10-04, 2010.

[5] M. Cubrinovski, R.A. Green, L. Wotherspoon, Geotechnical Reconnaissance of the 2011 Christchurch, New Zealand Earthquake, v. 1, GEER Association Report 027, 2011.

[6] K. Pitilakis, A. Moutsakis, Seismic Analysis and Behaviour of Gravity Retaining Walls. The case of Kalamata harbour quaywall. *Journal of Soils and Foundations* 29(1), 1-17, 1989.

[7] K. Kakderi, K. Pitilakis, Seismic performance and reliability of port facilities – The case of Thessaloniki (Greece), *Proceedings of the 5th International Conf on Recent Advances in Geotechnical Earthquake Engineering and Soil Dynamics and Symposium*, 2010.

[8] UPGRADE Research project, Deliverable D8.2 Technical reports with the calculation results of the vulnerability of specific Greek port facilities, in Greek, 2015.

[9] H. Alielahi, M.R. Moghadam, Fragility Curves Evaluation for Broken-Back Block Quay Walls, *Journal of Earthquake Engineering* 21(1), 1-22, 2017.

[10] A. Kamalzadeh, M.J. Pender, Modelling the dynamic response of gravity retaining wall systems using OpenSees, *Earthquake Geotechnical Engineering for Protection and Development of Environment and Constructions*, ISBN: 978-0-367-14328-2, 2019.

[11] K. Ichii, Application of Performance-Based Seismic Design Concept for Caisson-Type Quay Walls, *PhD Dissertation*, Kyoto University, 2003.

[12] K. Ichii, Fragility Curves for Gravity-Type Quay Walls Based on Effective Stress Analyses. *Proceedings of the 13th World Conference on Earthquake Engineering*, 2004.

[13] M. Miraei, Y. Jafarian, Fragility curves for assessing the seismic vulnerability of gravity quay walls, *Proceedings of the 4th COMPDYN*, Kos island, Greece, 2013.

[14] A. Calabrese, C.G. Lai, Fragility functions of blockwork wharves using artificial neural networks, *Soil Dynamics and Earthquake Engineering* 52, 88-102, 2013.

[15] A. Anastasiadis, D. Raptakis, K. Pitilakis, Thessaloniki's detailed microzoning: subsurface structure as basis for site response analysis. *Pure and Applied Geophysics* 158(12), 2597-2633, 2001.

[16] K. Pitilakis, S. Argyroudis, S. Fotopoulou, S. Karafagka, K. Kakderi, J. Selva, Application of stress test concepts for port infrastructures against natural hazards. The case of Thessaloniki port in Greece, *Reliability Eng & System Safety* 184, 240-257, 2019.

[17] CEN, EN 1998-5. Eurocode 8: Design of structures for earthquake resistance - Part 5: Foundations, retaining structures and geotechnical aspects. *European Committee for Standardization*, Brussels, 2004

[18] S. Mazzoni S, McKenna F, Scott M.H., Fenves G.L. Open system for earthquake engineering simulation user command-language manual, *Pacific Earthquake Engineering Research Center*, University of California, Berkeley, 2009.

[19] M.A. Biot, Mechanics of deformation and acoustic propagation in porous media, *Journal of Applied Physics* 33(4), 1482-1498, 1962.

[20] J.H. Prévost, A simple plasticity theory for frictional cohesionless soils. *Soil Dynamics and Earthquake Engineering* 4, 9-17, 1985.

[21] Z. Yang, Numerical modelling of earthquake site response including dilation and liquefaction, *Ph.D. thesis*, Columbia University, New York, 2000.

[22] E. Parra, Numerical modelling of liquefaction and lateral ground deformation including cyclic mobility and dilation response in soil systems, *Ph.D. thesis*, Rensselaer Polytechnic Institute, Troy, NY, 1996.

[23] G. Masing, Eigenspannungen and verfertigung beim messing. *Proceedings of the 2nd International Congress for Applied Mechanics*, Zurich, Switzerland, 1926.

[24] Z. Yang, J. Lu, A. Elgamal, OpenSees Soil Models and Solid-Fluid Fully Coupled Elements. User's Manual, ver 1.0., University of California, San Diego, 2008.

[25] J. Lysmer, A.M. Kuhlemeyer, Finite dynamic model for infinite media. *Journal of the Engineering Mechanics Division ASCE* 95, 859-877, 1969.

[26] W.B. Joyner, A.T.F. Chen, Calculation of nonlinear ground response in earthquakes, *Bulletin of the Seismological Society of America* 65(5), 1315-1336, 1975.

[27] J.W. Baker, C.A. Cornell, A vector valued ground motion intensity measure consisting of spectral acceleration and epsilon. *Earthq Eng Struct Dyn*, 34(10), 1193-1217, 2005.

[28] S. Akkar, J.J. Bommer, Empirical equations for the prediction of PGA, PGV and spectral accelerations in Europe, the Mediterranean and the Middle East. *Seismological Research Letters*, 81:195-206, 2010.

[29] I. Iervolino, C. Galasso, E. Cosenza, REXEL: computer aided record selection for code-based seismic structural analysis, *Bull of Earthquake Engineering* 8(2), 339-362, 2010.

[30] F. Lopez-Caballero, A. Modaressi Farahmand-Razavi, Numerical simulation of liquefaction effects on seismic SSI. *Soil Dynamics and Earthquake Engineering* 28(2), 85-98, 2008.

[31] International Navigation Association – PIANC, Seismic design guidelines for port structures. Chairman: Iai S, Bakelma Publishers, Tokyo, 2001.

EURODYN 2020
XI International Conference on Structural Dynamics
M. Papadrakakis, M. Fragiadakis, C. Papadimitriou (eds.)
Athens, Greece, 23–26 November 2020

A 2.5 DIMENSIONAL INDIRECT TREFFTZ METHOD TO MODEL LINEAR ELASTIC SOILS

Hannes Englert[1], Fei Qu[2], and Gerhard Müller[2]

[1]Chair of Structural Mechanics, Technical University of Munich
Arcisstr. 21, 80333 Munich, Germany
e-mail: hannes.englert@tum.de

[2] Chair of Structural Mechanics, Technical University of Munich
Arcisstr. 21, 80333 Munich, Germany
e-mail: {fei.qu,gerhard.mueller}@tum.de

Keywords: Indirect Trefftz Method, Wave Based Method, 2.5 Dimensional Problems, Soil-structure Interaction

Abstract. *This contribution presents a 2.5-dimensional, frequency domain approach to model linear elastic soils, based on Indirect Trefftz Elements. 2.5-dimensional solution procedures allow a convenient way to model structures that are periodic in one direction.*
The solution of the problem is carried out in the frequency domain. One dimension is transformed to the wave number domain using a Fourier Transformation. The problem is solved for each wave number separately and the results are reproduced by superposing the different wave number solutions. For each wave number, Indirect Trefftz Elements are used to solve the differential equation governing the considered problem, allowing to model problems with boundaries of moderate complexity. With the help of a Helmholtz decomposition, the Lamé differential equation is split up in its irrotational and solenoidal parts, with each of the fields approximated by a truncated set of wave functions. The used wave functions inherently satisfy the governing equation of the problem. Inter-element continuity is enforced using a Galerkin approach.
Compared to conventional Finite Element Approaches the method incorporates the wave characteristics of the solution directly since the shape functions are chosen as a linear combination of propagating and evanescent waves. Inclusion of radiating boundary conditions is straightforward. The resulting systems of equations are smaller as compared to Finite Elements, which can reduce solving time for the soil model effectively. As a drawback, the method suffers from matrices that are fully populated and include complex entries.

1 INTRODUCTION

Vibrations introduced by heavy machines or railway lines are transported through the soil and affect systems in the vicinity as for example adjacent structures. Resulting oscillations may cause inconvenience or even damage to the exited systems. Densification in urban areas has lead to an additional awareness for this mechanism and the requirement to limit those effects became even more present. Since reduction measures are preferably planed during the design process, the demand for a proper prediction of vibrations and their propagation using numerical simulations has steadily increased.

Classical FEM approaches suffer from reflections at artificial boundaries since only areas of limited size can be modeled. Different approaches have been developed to deal with the infinite extensions of the soil in the context of numerical simulations. Extensions to the FEM include Transmitting Boundaries (TB) [1], Perfectly Matched Layers (PML) [2] and the Thin Layer Method (TLM) within others. Fontara [3] investigates two different formulations of PML in the frequency domain.

Besides, coupled Finite Element - Boundary Element methods (FEM-BEM) are widely used, to model the semi infinite system [4]. Francois [5] presents a 2.5 dimensional FEM-BEM procedure for systems with invariant geometry in one dimension. The approach uses Green's functions of a layered halfspace for the BEM model. This avoids the requirement to mesh the free surface.

Another approach, the Integral Transform Method (ITM) is based on available analytical solutions in the frequency domain, making use of the characteristics of the wave components of those solutions for negative frequencies [6]. Frühe [7] developed a solution for a halfspace with cylindrical or spherical inclusion using the ITM to couple the different analytical systems. Hackenberg and Dengler [8] enhanced the ITM approach with a FE procedure for 2.5 dimensional problems. The infinite extension of the problem is handled using analytical solutions in the context of the ITM whereas those parts requiring a finer resolution are described by the FEM. The degrees of freedom of the FE mesh along the common boundary with the ITM domain are transformed in the wave number domain to couple the two subsystems in a direct manner. Hackenberg [9] and later Freisinger [10] expanded the method for 3-dimensional problems and evaluated the insertion loss of different structures.

Different publications refer to Trefftz [11] like methods to solve bounded and unbounded problems. Jirousek [12] introduced Hybrid Trefftz FEM elements for various applications. Different authors [13] extended this idea for an application to 2-dimensional dynamic soil problems in the frequency domain and developed Hybrid-Trefftz displacement or stress elements. Moldovan [13] extended those elements to be applicable to biphasic media.

The Wave Based Method (WBM) belongs to the family of Indirect Trefftz methods and has originally been introduced by Desmet [14] for acoustic problems to cover the so called mid frequency gap, where pollution effects and increasing numerical effort prevent the applicability of traditional element-based procedures as the FEM. It is a deterministic prediction method based on the ideas of Trefftz using propagating and evanescent waves to set up the approximation space. The WBM is based on a rather coarse discretization of the problem domain, using convex subdomains, as shown in figure 1. The method was extended to plate in membrane and plate bending problems ([15, 16]). Later Klanner [17] showed an application of the WBM for thick plates. A summary of current extensions to the method is given in [18].

Huybrechs [19] investigates the numerical behavior of WBM and its approximation space and proposes an oversampled collocation method rather than a weighted residual method to solve

the problem. He also states, that the used function set rather resembles a frame than a basis in a mathematical sense. An overview of different Trefftz Methods, with focus on the used approximation space is given in [20].
This work aims to give an application of the WBM to 2.5 dimensional soil problems, described by the Lamé equation. The idea is to develop a more flexible solution procedure with respect to geometric restriction of methods like the ITM, that is always limited to simple geometries, with analytical solutions being available. Nevertheless the presented procedure can still handle radiating boundaries or infinite extensions straight away.

In the first chapter the theory of 2.5 dimensional problems is described. A Helmholtz de-

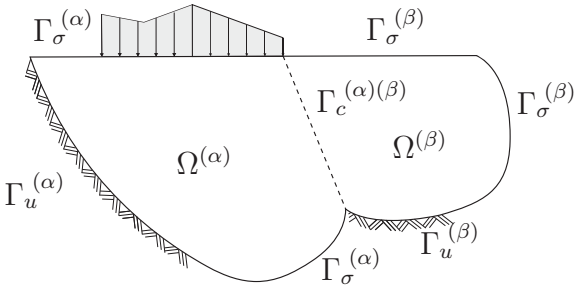

Figure 1: Concept of domain decomposition in the WBM

composition of the partial differential equation of the problem is given. The resulting three decoupled wave equations are used to define a suitable shape function approximation set in the frequency wave number domain (ω, k_x). After transformation the problem can be treated similar to conventional 2 dimensional approaches. In the next chapter the incorporation of the boundary residuals along real and artificial boundaries Γ, in the sense of a weighted residual approach is focused, followed by a short verification example and the conclusion.

2 2.5 DIMENSIONAL SOILS

The presented solution procedure handles systems with infinite extension in x-direction. Instead of solving the problem directly, a Fourier Transform (FT) of the considered system from time domain t to frequency domain ω and from the spatial coordinates x to the wave number domain k_x is carried out. Starting from a general 3-dimensional continua the governing equations are transformed in the frequency - wave number domain and solved for each frequency ω and wave number k_x separately. For the homogenous part of the resulting differential equation in the wave number frequency domain a Trefftz complete set of shape functions can be found, that spans the entire solution space and where each shape function itself inherently satisfies the underlying differential equation of the problem. A general shape function will be stated as $\mathrm{N}(x, y, z, t)$ in the following, here given in dependency of the time t and the spatial coordinates x, y and z. In a first step the FT with respect to time is carried out, defined by:

$$F(\omega) = \int_{-\infty}^{\infty} f(t) \cdot \mathrm{e}^{-\mathrm{i}\,\omega\, t}\, dt \tag{1}$$

The same procedure is repeated with respect to the spatial coordinate x:

$$F(k_x) = \int_{-\infty}^{\infty} f(x) \cdot \mathrm{e}^{-\mathrm{i}\, k_x\, x}\, dx \tag{2}$$

The transformed problem is solved using the shape functions $\hat{\mathrm{N}}(k_x, y, z, \omega)$, given in the k_x, y, z, ω domain. The same procedure is repeated for the inhomogeneous part of the differential equation. Therefore external loads are are also transformed to the k_x, y, z, ω domain, as shown in figure 2 for the spatial coordinate x.

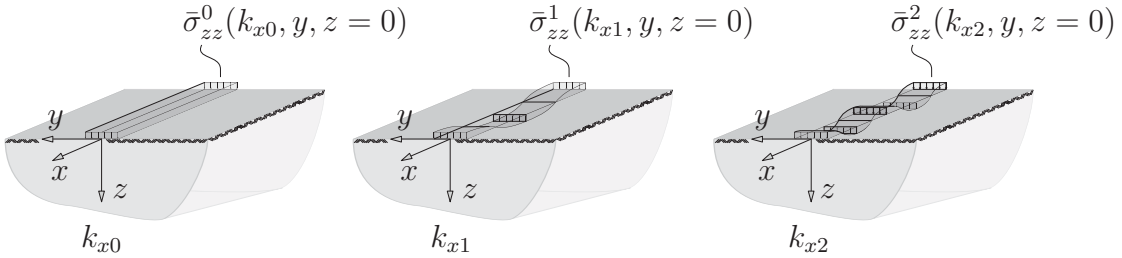

Figure 2: Concept of the Fourier Transform in x-direction for an external loading.

2.1 Governing Equations

The general problem is described by the Lamé Equation for 3-dimensional continua which is derived from the equilibrium,

$$\sigma^{ij}|_j + Q^i - \rho \ddot{u}^i = 0 \tag{3}$$

with the stress tensor σ^{ij}, internal volume forces Q^i and the inertia terms $\rho\ddot{u}^i$. Considering only the homogenous part of the equilibrium equation (3) and introducing the constitutive equation and the kinematic relations leads to the Lamé equation (4):

$$\mu u^i|^j_j + (\lambda + \mu) u^j|^i_j - \rho \ddot{u}^i = 0 \tag{4}$$

In the above equation a linear elastic, homogeneous, isotropic material descriptions has been used, with the Lamé constants λ and μ describing the material properties. Hysteretic damping effects are considered using a complex Young's modulus,

$$\underline{E} = E\left(1 + \mathrm{i}\,\mathrm{sgn}\left(\omega\right)\zeta\right) \tag{5}$$

with the imaginary unit $\mathrm{i} = \sqrt{-1}$ and the hysteretic damping ratio ζ.

2.2 Helmholtz Decomposition

The three coupled equations described by equation (4) can be transformed into linear independent equations using a Helmholtz decomposition. The solution of the Lamé equation can be written as the sum of a irrotational field given by the gradient of a scalar field Φ and a solenoidal field given by the rotation of a vector field $\mathbf{\Psi}$.

$$u^i = \Phi|^i + \Psi_l|_k \epsilon^{ikl} \tag{6}$$

This gives the following linearly independent wave equations.

$$\Phi|_j^j - \frac{1}{{c_p}^2}\ddot{\Phi} = 0 \qquad \text{with} \qquad c_p = \sqrt{\frac{\lambda + 2\mu}{\rho}} \tag{7}$$

$$\Psi_i|_j^j - \frac{1}{{c_s}^2}\ddot{\Psi}_i = 0 \qquad\qquad c_s = \sqrt{\frac{\mu}{\rho}}$$

Herein c_p denotes the compressional wave velocity and c_s the shear wave velocity respectively. The density of the soil is given by ρ. Applying the two-folded FT as mentioned in chapter 2 the wave equations can be written as Helmholtz equations

$$\left[-{k_x}^2 + {k_p}^2 + \frac{\partial^2}{\partial y^2} + \frac{\partial^2}{\partial z^2}\right]\hat{\Phi}(k_x, y, z, \omega) = 0 \tag{8}$$

$$\left[-{k_x}^2 + {k_s}^2 + \frac{\partial^2}{\partial y^2} + \frac{\partial^2}{\partial z^2}\right]\hat{\Psi}_1(k_x, y, z, \omega) = 0 \tag{9}$$

$$\left[-{k_x}^2 + {k_s}^2 + \frac{\partial^2}{\partial y^2} + \frac{\partial^2}{\partial z^2}\right]\hat{\Psi}_2(k_x, y, z, \omega) = 0 \tag{10}$$

with the wave numbers $k_p = \frac{\omega}{c_p}$ and $k_s = \frac{\omega}{c_s}$.

2.3 Boundary Conditions

The boundary is defined by either Dirichlet boundary conditions with prescribed displacements (equation (21)), Neumann boundary conditions with prescribed stress (equation (22)) or mixed Boundary Conditions (equations (23)).
The physical quantities in the cartesian reference system are recovered from the potentials $\hat{\Phi}$ and $\hat{\mathbf{\Psi}}$ using the following relations:

$$\hat{u}_x = \mathrm{i}\, k_x\hat{\Phi} - \frac{\partial}{\partial z}\hat{\Psi}_2 \tag{11}$$

$$\hat{u}_y = \frac{\partial}{\partial y}\hat{\Phi} + \frac{\partial}{\partial z}\hat{\Psi}_1 \tag{12}$$

$$\hat{u}_z = \frac{\partial}{\partial z}\hat{\Phi} - \frac{\partial}{\partial y}\hat{\Psi}_1 + \mathrm{i}\, k_x\hat{\Psi}_2 \tag{13}$$

and similar for the stress components:

$$\hat{\sigma}_{xx} = (2\mu + \lambda)\left(\mathrm{i}\, k_x\, \hat{u}_x\right) + \lambda\left(\frac{\partial}{\partial y}\hat{u}_y + \frac{\partial}{\partial z}\hat{u}_z\right) \qquad \hat{\sigma}_{xy} = 2\mu \cdot \left(\frac{1}{2}\frac{\partial}{\partial y}\hat{u}_x + \frac{1}{2}\mathrm{i}\, k_x\hat{u}_y\right) \tag{14}$$

$$\hat{\sigma}_{yy} = (2\mu + \lambda)\left(\frac{\partial}{\partial y}\hat{u}_y\right) + \lambda\left(\mathrm{i}\, k_x\, \hat{u}_x + \frac{\partial}{\partial z}\hat{u}_z\right) \qquad \hat{\sigma}_{yz} = 2\mu \cdot \left(\frac{1}{2}\frac{\partial}{\partial z}\hat{u}_y + \frac{1}{2}\frac{\partial}{\partial y}\hat{u}_z\right) \tag{15}$$

$$\hat{\sigma}_{zz} = (2\mu + \lambda)\left(\frac{\partial}{\partial z}\hat{u}_z\right) + \lambda\left(\mathrm{i}\, k_x\, \hat{u}_x + \frac{\partial}{\partial y}\hat{u}_y\right) \qquad \hat{\sigma}_{xz} = 2\mu \cdot \left(\frac{1}{2}\frac{\partial}{\partial z}\hat{u}_x + \frac{1}{2}\mathrm{i}\, k_x\hat{u}_z\right) \tag{16}$$

All used boundary conditions require the evaluation of displacements or stresses in normal or in plane direction, with the normal vector of the boundary $\mathbf{n} = n_i \cdot \mathbf{e}^{\,i}$ and two perpendicular in plane vectors $\mathbf{t}_1 = t_{1\,i} \cdot \mathbf{e}^{\,i}$ and $\mathbf{t}_2 = t_{2\,i} \cdot \mathbf{e}^{\,i}$. Finally the cartesian components are transformed to the normal and in-plane components using tensor calculus:

$$\sigma_n = n_i \cdot \sigma^{ij} \cdot n_j \qquad \sigma_{t_1} = n_i \cdot \sigma^{ij} \cdot t_{1\,j} \qquad \sigma_{t_2} = n_i \cdot \sigma^{ij} \cdot t_{2\,j} \tag{17}$$

$$u_n = n_i \cdot u^i \qquad u_{t_1} = t_{1\,i} \cdot u^i \qquad u_{t_2} = t_{2\,i} \cdot u^i \tag{18}$$

For the sake of conciseness, the relations from equation (11) to (18) are replaced by a differential operator $\mathcal{L}_u(\hat{\mathrm{N}})$ for the displacements or $\mathcal{L}_\sigma(\hat{\mathrm{N}})$ for the stresses respectively.

3 THE WAVE BASED METHOD

To solve the problem for each combination of frequency ω and wave number k_x the Wave Based Method (WBM) is used. A Trefftz complete basis of the partial differential equation (PDE) is employed. The approximation space is formed by a truncated set of wave functions. To ensure convergence a non-convex domain Ω has to be split up into multiple convex subdomains $\Omega = \Omega^{(\alpha)} \cup \Omega^{(\beta)}$ as shown in figure 1. Since the used shape functions fulfill the differential equation of the problem by definition, the total residual of the approximate solution results only of the accumulated errors along the boundaries.

3.1 Field Variable Expansion

The approximate solution is recaptured using a superposition of the shape functions $\hat{\Phi}_i$, $\hat{\Psi}_{i1}$ and $\hat{\Psi}_{i2}$ multiplied with the yet still unknown weighting factors c_i.

$$\hat{\mathbf{u}} = \sum_{i=1}^{I} \mathcal{L}_{\mathbf{u}}(\hat{\mathrm{N}}_i) \cdot c_i + \sum_{j=1}^{J} \hat{\mathbf{u}}_{p,j} \quad \text{with} \quad \mathcal{L}_{\mathbf{u}}(\hat{\mathrm{N}}) = \begin{pmatrix} \mathcal{L}_{u_x}(\hat{\mathrm{N}}) \\ \mathcal{L}_{u_y}(\hat{\mathrm{N}}) \\ \mathcal{L}_{u_z}(\hat{\mathrm{N}}) \end{pmatrix} \tag{19}$$

External loads can either be applied along the boundaries or as external volume loads. The later are included using particular solutions functions for an infinite domain. In equation (19), $\hat{\mathbf{u}}_{p,j}$ refers to the displacement field of the particular solution due to the external volume load j.
The shape functions are chosen in accordance with [15], applying a suitable truncation rule for the maximum of the integer values p_k respectively s_k with $k = 1 \ldots 4$. The used shape functions are listed in table 1, where $p_l = 1, 2, \ldots, P_{l,\max} \in \mathbb{N}^+$ and $p_m = 0, 1, \ldots, P_{m,\max} \in \mathbb{N}$ with $l = 1, 2$ and $m = 3, 4$ and similar rules applied for s_k.

The wave numbers k_1 and k_2 used for the shape functions are defined in equation (20) as the projected components of the physical wave numbers k_p and k_s to the y-z-plane.

$$k_1{}^2 = k_p{}^2 - k_x{}^2 \qquad k_2{}^2 = k_s{}^2 - k_x{}^2 \tag{20}$$

3.2 Incorporation of Boundary Residuals

A single shape function by itself violates the boundary conditions of the problem, resulting in a residual term along the boundaries. In theory, due to the completeness of the solution space, the residual term vanishes if an infinite number of shape functions is used. The occurring residual terms are given in equations (21) to (23) with the terms $\bar{(*)}(\mathbf{x})$ describing the non

Irrotational scalar field $\hat{\Phi}$			
set 1	$\hat{\Phi}_{p_1} = \sin(k_{p_{1y}}\, y) \cdot \mathrm{e}^{-\mathrm{i}\, k_{p_{1z}}\, z}$	$k_{p_{1y}} = \frac{p_1\, \pi}{L_y}$	$k_{p_{1z}} = \pm\sqrt{(k_1)^2 - (k_{p_{1y}})^2}$
	$\hat{\Phi}_{p_2} = \mathrm{e}^{-\mathrm{i}\, k_{p_{2y}}\, y} \cdot \sin(k_{p_{2z}}\, z)$	$k_{p_{2z}} = \frac{p_2\, \pi}{L_z}$	$k_{p_{2y}} = \pm\sqrt{(k_1)^2 - (k_{p_{2z}})^2}$
set 2	$\hat{\Phi}_{p_3} = \cos(k_{p_{3y}}\, y) \cdot \mathrm{e}^{-\mathrm{i}\, k_{p_{3z}}\, z}$	$k_{p_{3y}} = \frac{p_3\, \pi}{L_y}$	$k_{p_{3z}} = \pm\sqrt{(k_1)^2 - (k_{p_{3y}})^2}$
	$\hat{\Phi}_{p_4} = \mathrm{e}^{-\mathrm{i}\, k_{p_{4y}}\, y} \cdot \cos(k_{p_{4z}}\, z)$	$k_{p_{4z}} = \frac{p_4\, \pi}{L_z}$	$k_{p_{4y}} = \pm\sqrt{(k_1)^2 - (k_{p_{4z}})^2}$
Component $\hat{\Psi}_1$ of the solenoidal vector field			
set 1	$\hat{\Psi}_{1,s_1} = \cos(k_{s_{1y}}\, y) \cdot \mathrm{e}^{-\mathrm{i}\, k_{s_{1z}}\, z}$	$k_{s_{1y}} = \frac{s_1\, \pi}{L_y}$	$k_{s_{1z}} = \pm\sqrt{(k_2)^2 - (k_{s_{1y}})^2}$
	$\hat{\Psi}_{1,s_2} = \mathrm{e}^{-\mathrm{i}\, k_{s_{2y}}\, y} \cdot \cos(k_{s_{2z}}\, z)$	$k_{s_{2z}} = \frac{s_2\, \pi}{L_z}$	$k_{s_{2y}} = \pm\sqrt{(k_2)^2 - (k_{s_{2z}})^2}$
set 2	$\hat{\Psi}_{1,s_3} = \sin(k_{s_{3y}}\, y) \cdot \mathrm{e}^{-\mathrm{i}\, k_{s_{3z}}\, z}$	$k_{s_{3y}} = \frac{s_3\, \pi}{L_y}$	$k_{s_{3z}} = \pm\sqrt{(k_2)^2 - (k_{s_{3y}})^2}$
	$\hat{\Psi}_{1,s_4} = \mathrm{e}^{-\mathrm{i}\, k_{s_{4y}}\, y} \cdot \sin(k_{s_{4z}}\, z)$	$k_{s_{4z}} = \frac{s_4\, \pi}{L_z}$	$k_{s_{4y}} = \pm\sqrt{(k_2)^2 - (k_{s_{4z}})^2}$
Component $\hat{\Psi}_2$ of the solenoidal vector field			
set 1	$\hat{\Psi}_{2,s_1} = \cos(k_{s_{1y}}\, y) \cdot \mathrm{e}^{-\mathrm{i}\, k_{s_{1z}}\, z}$	$k_{s_{1y}} = \frac{s_1\, \pi}{L_y}$	$k_{s_{1z}} = \pm\sqrt{(k_2)^2 - (k_{s_{1y}})^2}$
	$\hat{\Psi}_{2,s_2} = \mathrm{e}^{-\mathrm{i}\, k_{s_{2y}}\, y} \cdot \cos(k_{s_{2z}}\, z)$	$k_{s_{2z}} = \frac{s_2\, \pi}{L_z}$	$k_{s_{2y}} = \pm\sqrt{(k_2)^2 - (k_{s_{2z}})^2}$
set 2	$\hat{\Psi}_{2,s_3} = \sin(k_{s_{3y}}\, y) \cdot \mathrm{e}^{-\mathrm{i}\, k_{s_{3z}}\, z}$	$k_{s_{3y}} = \frac{s_3\, \pi}{L_y}$	$k_{s_{3z}} = \pm\sqrt{(k_2)^2 - (k_{s_{3y}})^2}$
	$\hat{\Psi}_{2,s_4} = \mathrm{e}^{-\mathrm{i}\, k_{s_{4y}}\, y} \cdot \sin(k_{s_{4z}}\, z)$	$k_{s_{4z}} = \frac{s_4\, \pi}{L_z}$	$k_{s_{4y}} = \pm\sqrt{(k_2)^2 - (k_{s_{4z}})^2}$

Table 1: Shape functions

homogeneous part of the boundary condition.

$$\mathbf{R}_u^{(\alpha)}(\mathbf{x}) = \begin{cases} R_{u_n} &= \hat{u}_n(\mathbf{x}) - \bar{u}_n(\mathbf{x}) = 0 \\ R_{u_{t_1}} &= \hat{u}_{t_1}(\mathbf{x}) - \bar{u}_{t_1}(\mathbf{x}) = 0 \\ R_{u_{t_2}} &= \hat{u}_{t_2}(\mathbf{x}) - \bar{u}_{t_2}(\mathbf{x}) = 0 \end{cases} \quad \vee\, \mathbf{x} \in \Gamma_u \tag{21}$$

$$\mathbf{R}_\sigma^{(\alpha)}(\mathbf{x}) = \begin{cases} R_{\sigma_n} &= \hat{\sigma}_n(\mathbf{x}) - \bar{\sigma}_n(\mathbf{x}) = 0 \\ R_{\sigma_{t_1}} &= \hat{\sigma}_{t_1}(\mathbf{x}) - \bar{\sigma}_{t_1}(\mathbf{x}) = 0 \\ R_{\sigma_{t_2}} &= \hat{\sigma}_{t_2}(\mathbf{x}) - \bar{\sigma}_{t_2}(\mathbf{x}) = 0 \end{cases} \quad \vee\, \mathbf{x} \in \Gamma_\sigma \tag{22}$$

$$\mathbf{R}_{u\sigma}^{(\alpha)}(\mathbf{x}) = \begin{cases} R_{u_n} &= \hat{u}_n(\mathbf{x}) - \bar{u}_n(\mathbf{x}) = 0 \\ R_{\sigma_{t_1}} &= \hat{\sigma}_{t_1}(\mathbf{x}) - \bar{\sigma}_{t_1}(\mathbf{x}) = 0 \\ R_{\sigma_{t_2}} &= \hat{\sigma}_{t_2}(\mathbf{x}) - \bar{\sigma}_{t_2}(\mathbf{x}) = 0 \end{cases} \quad \vee\, \mathbf{x} \in \Gamma_{u\sigma} \tag{23}$$

For inter-element coupling the displacement field of element α is prescribed to element β and the stresses of element β to element α resulting in a additional residual term for each element.

3.3 Weighted Residual Formulation

By introducing the truncated set of wave functions as an approximate solution the residual terms along the boundaries do not disappear anymore, but can only be minimized in an integral sense, for example by using a weighted residual method. In the sense of a Galerkin procedure the same functions used for the approximation are used as weighting functions, denoted by $\delta(*)$.

$$\delta u_n = \sum_{i=1}^{K} \mathcal{L}_{u_n}(\mathbf{N}_i) \cdot \delta c_i \qquad \delta u_t = \dots \tag{24}$$

$$\delta \sigma_n = \sum_{i=1}^{K} \mathcal{L}_{\sigma_n}(\mathbf{N}_i) \cdot \delta c_i \qquad \delta \sigma_t = \dots \tag{25}$$

3.4 Solution and Post Processing

The weighted residual expression is evaluated along the complete boundary $\Gamma = \Gamma_\sigma \cup \Gamma_u \cup \Gamma_{u\sigma} \cup \Gamma_c$ and expressed in dependency of the defined boundary conditions as

$$-\int_{\Gamma_\sigma} \delta u_n \, R_{\sigma_n} + \delta u_{t_1} \, R_{\sigma_{t_1}} + \delta u_{t_2} \, R_{\sigma_{t_2}} \, d\Gamma_\sigma + \int_{\Gamma_u} \delta \sigma_n \, R_{u_n} + \delta \sigma_{t_1} \, R_{u_{t_1}} + \delta \sigma_{t_2} \, R_{u_{t_2}} \, d\Gamma_u \, ... = 0$$

which leads to the linear system of equations to be solved for the unknown contribution factors c_i:

$$\rightarrow \quad \delta \mathbf{c}^T \, (\mathbf{K}\,\mathbf{c} - \mathbf{f}) = 0 \tag{26}$$

The final physical values in the frequency-wave-number domain are reproduced using equation (19). After that an inverse FT with respect to time t and the spatial coordinate x is carried out in the sense of:

$$f(x,y,z,t) = \frac{1}{(2\pi)^2} \int_{-\infty}^{\infty} \int_{-\infty}^{\infty} \hat{F}(k_x,y,z,\omega) \cdot \mathrm{e}^{\mathrm{i}\,k_x x} \cdot \mathrm{e}^{\mathrm{i}\,\omega t} dk_x \, d\omega \tag{27}$$

4 NUMERICAL EXAMPLES

As a validation example a linear elastic homogenous soil is considered. The halfspace is loaded at the surface by a constant line loading. The calculated results are compared to a reference solution using the Fourier Transform (FT) of the load in spatial y-direction and the analytical response to each contribution in the wave number domain k_y. For the reference solution a repetition length of $B_y = 256\,[m]$ and $n = 4096$ Fourier terms are used. Due to comparability the example is solved for a uniform line loading with constants value in x-direction. An extension to different wave numbers k_x can be achieved using the procedure described in chapter 2. For the validation example a soil with the given parameters is used: elasticity modulus $E = 260 \cdot 10^5\,[\frac{N}{m^2}]$, Poisson ratio $\nu = 0.3$, density $\rho = 2000\,[\frac{kg}{m^3}]$ and hysteretic damping ratio $\zeta = 0.1$. The external loading at the halfspace surface is considered as an inhomogeneous Neumann boundary condition using equation (22) with constant value $\bar{\sigma}_n = 1[\frac{N}{m^2}]$.

The used decomposition for the WBM model is given in figure 3. Three coupled, convex subdomains are used to model the considered area. The chosen subdomains serve well to proof

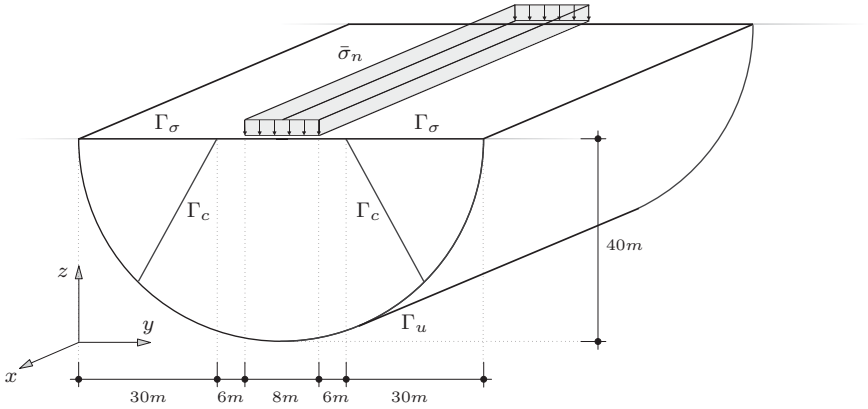

Figure 3: Validation example - Geometry and used decomposition into convex subdomains

inter-element continuity on the one hand side as well as the flexibility of the element boundary description on the other hand side. In this example, the dimensions of the modeled domain are chosen large enough that the effect of spurious reflections at the artificial exterior boundaries become small. Nevertheless they can not be neglected completely without further treatment. In the presented example this results in rather large relative errors for the left and right element at the surface. Figure 4 shows the results split up in real and imaginary part for a sample frequency

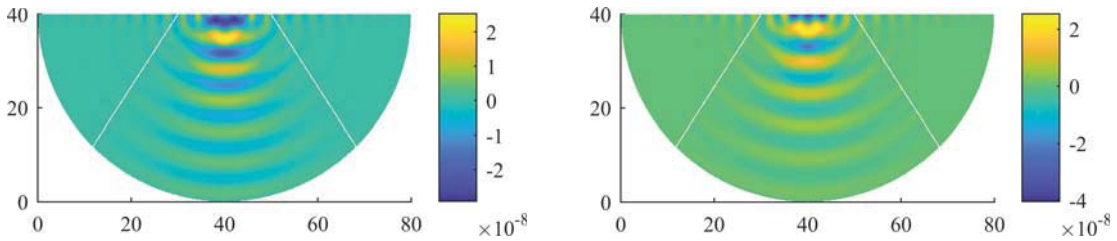

Figure 4: *(a)* Real part and *(b)* imaginary part of vertical displacements $u_z(x = 0)$ in $[m]$.

of $20\,[Hz]$. Figure 5 shows the results of the vertical displacement at the surface along a line $(x = 0, y, z = 40)$ for the given frequency of $20\,[Hz]$ comparing them against an ITM solution using the described FT of the load along the y-direction. Evaluating the relative error along the surface reveals the largest values at the beginning and end of the surface line load. This is not surprising due to the discontinuity of the boundary condition at exactly those positions.

5 CONCLUSION

The presented results show that the method can be adapted to model 2.5 dimensional soil problems and gives correct and precise results. Nevertheless the consideration of the semi infinite area should be included to avoid spurious reflections. This can be achieved by using a different set of shape functions for the exterior elements which is straight forward for the presented method. Furthermore special treatment of singularities as occurring at the beginning and end of the surface line load can enhance the numerical efficiency and convergence rate of the method significantly. Therefor particular solution functions for external loads as well as special

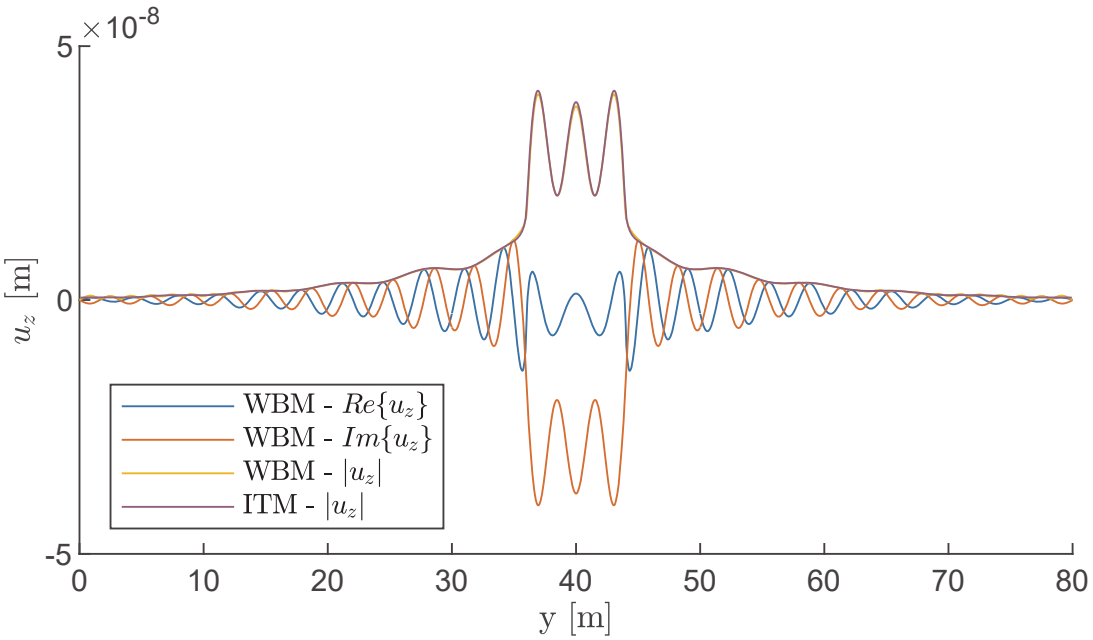

Figure 5: Vertical displacements u_z at surface $(z = 40, x = 0)$ for $20\,[Hz]$ *(yellow line)* and FT reference solution *(purple line)*

purpose functions for singularities due to the geometry of the problem should be developed in the future.

References

[1] E. Kausel, Local transmitting boundaries, Journal of Engineering Mechanics 114 (1988) 1011–1027.

[2] U. Basu, A. K. Chopra, Perfectly matched layers for time-harmonic elastodynamics of unbounded domains: Theory and finite-element implementation, Computer Methods in Applied Mechanics and Engineering 192 (2003) 1337–1375.

[3] I.-K. Fontara, W. Schepers, S. Savidis, F. Rackwitz, Finite element implementation of efficient absorbing layers for time harmonic elastodynamics of unbounded domains, Soil Dynamics and Earthquake Engineering 114 (2018) 625–638.

[4] P. Galvín, J. Domínguez, Analysis of ground motion due to moving surface loads induced by high-speed trains, Engineering Analysis with Boundary Elements 31 (2007) 931–941.

[5] S. François, M. Schevenels, P. Galvín, G. Lombaert, G. Degrande, A 2.5d coupled fe–be methodology for the dynamic interaction between longitudinally invariant structures and a layered halfspace, Computer Methods in Applied Mechanics and Engineering 199 (2010) 1536–1548.

[6] G. Müller, Ein Verfahren zur Erfassung der Fundament-Boden Wechselwirkung unter Einwirkung periodischer Lasten: Dissertation, Mitteilungen aus dem Institut für Bauingenieurwesen I, München, 1989.

[7] G. Frühe, Überlagerung von Grundlösungen in der Elastodynamik zur Behandlung der dynamischen Tunnel-Boden-Bauwerk-Interaktion, Shaker Verlag. Schriftenreihe des Lehrstuhls für Baumechanik, 2010.

[8] M. Hackenberg, M. Dengler, G. Müller, Implementation of the finite element method in the fourier-transformed domain and coupling with analytical solutions, Proceedings of the 9th International Conference on Structural Dynamics, EURODYN (2014).

[9] M. Hackenberg, A coupled integral transform method – finite element method approach to model the soil-structure-interaction, Schriftenreihe des Lehrstuhls für Baumechanik, 2017.

[10] J. Freisinger, G. Müller, Modellierung eines Halbraums mit sphärischem oder zylinderförmigem Hohlraum für dreidimensionale Boden-Bauwerk-Interaktion, Forschung im Ingenieurwesen 83 (2019) 31–42.

[11] E. Trefftz, Ein Gegenstück zum Ritzschen Verfahren, Proc. Second Int. Congress Appl. Mech. (1926) 131–137.

[12] J. Jirouseka, L. Guex, The hybrid-trefftz finite element model and its application to plate bending, International Journal for Numerical Methods in Engineering 23 (1986) 651–693.

[13] I. D. Moldovan, T. D. Cao, J. A. T. de Freitas, Hybrid-trefftz displacement finite elements for elastic unsaturated soils, International Journal of Computational Methods 11 (2014).

[14] W. Desmet, A wave based prediction technique for coupled vibro-acoustic analysis, 1998.

[15] Caroline Vanmaele, Development of a wave based prediction technique for the efficient analysis of low and mid frequency structural vibrations, 2007.

[16] C. Vanmaele, D. Vandepitte, W. Desmet, An efficient wave based prediction technique for plate bending vibrations, Computer Methods in Applied Mechanics and Engineering 196 (2007) 3178–3189.

[17] M. Klanner, K. Ellermann, Wave based method for the steady-state vibrations of thick plates, Journal of Sound and Vibration 345 (2015) 146–161.

[18] E. Deckers, O. Atak, L. Coox, R. D'Amico, H. Devriendt, S. Jonckheere, K. Koo, B. Pluymers, D. Vandepitte, W. Desmet, The wave based method: An overview of 15 years of research, Wave Motion 51 (2014) 550–565.

[19] D. Huybrechs, A.-E. Olteanu, An oversampled collocation approach of the wave based method for helmholtz problems, Wave Motion 87 (2019) 92–105.

[20] R. Hiptmair, A. Moiola, I. Perugia, A survey of trefftz methods for the helmholtz equation, in: B. e. a. Barrenechea (Ed.), Building Bridges, 2016, pp. 237–279.

EURODYN 2020
XI International Conference on Structural Dynamics
M. Papadrakakis, M. Fragiadakis, C. Papadimitriou (eds.)
Athens, Greece, 23–26 November 2020

MITIGATION OF GROUND VIBRATION FROM PILE DRIVING BY CIRCULAR ARRAYS OF RIGID BLOCKS PLACED ON THE GROUND SURFACE

Lars V. Andersen[1], **Peter Persson**[2], **and Andrew T. Peplow**[3]

[1] Department of Engineering, Aarhus University
Inge Lehmanns Gade 10, DK-8000 Aarhus C, Denmark
e-mail: lva@eng.au.dk

[2] Department of Construction Sciences, Lund University
P.O. Box 118, SE-221 00 Lund, Sweden
e-mail: peter.persson@construction.lth.se

[3] College of Natural and Health Sciences, Zayed University
P.O. Box 144534, Abu Dhabi, United Arab Emirates
e-mail: andrew.peplow@zu.ac.ae

Keywords: Ground Vibration, Pile Driving, Layered Soil, Insertion Loss, Wave Impedance.

Abstract. *Ground vibration associated with pile driving causes annoyance to inhabitants of the neighbouring environment and may possibly lead to damage on existing structures in the proximity of a construction site. Vibration mitigation near the source can reduce the problem. The paper investigates the effect of circular arrays of blocks, placed on the ground surface around the position at which the pile is driven. A semi-analytical model of a layered soil has been used for the analysis, and the blocks have been modelled as monolithic structures, accounting for the full structure–soil–structure interaction. Two different sites have been studied: a layered soil with three metres of soft sand over a half-space of till, and a five metres deep layer of soft clay overlying a half-space of lime. The block arrays consist of one to three concentric rings with radii 4, 8, and 12 m, respectively. The rings contain 6, 12, and 24 blocks, respectively, and the size of the blocks have been scaled such that each ring has the same total mass. The pile has not been modelled explicitly; instead vertical excitation has been applied in different depts over a circular area corresponding to the cross section of a pile. For the considered cases it has been found that an array of blocks, shaped as a "Stonehenge", may provide significant mitigation of the ground vibration level in a receiver zone placed 20–40 m from the pile. When a load is applied within the soft topsoil layer, the array provides an insertion loss in the order of 5–20 dB, depending on the size of the blocks and the configuration of the arrays. For loads applied deeper in the soil, within the stiffer half-space, the insertion loss is small and may in some situations be negative. However, this must be seen in the context that the transfer mobility in the reference state without the blocks, i.e. the greenfield, is low when the load is applied within the stiff half-space.*

1 INTRODUCTION

Environmental vibration from construction activities in urban environments causes annoyance to inhabitants. Long term exposure to noise and vibration may even lead to health problems [1,2], and excessive vibrations can be the cause of damage to structures. Hence, controlling the level of vibrations in the built environment is important.

Several ideas have been proposed for the mitigation of ground vibration from various sources. For rail-traffic-induced vibrations, concepts such as barriers, trenches and soil stiffening [3], [4], or heavy masses placed along the track [5] have been demonstrated to reduce the ground vibration levels in the shielded zones behind the barriers. Also, sheet pile walls in various configurations have been proposed for vibration screening [6–8]. However, installing such barriers will itself cause vibration during the driving of the individual piles.

As an alternative to the continuous barriers, wave impedance blocks (WIBs) placed on the ground surface or embedded within the soil can be used for the reduction of ground vibration [9–11]. Masoumi et al. [12] reported an experimental validation of the mitigation provided by such systems. WIBs – or another change in geometry or material – can be placed in a periodic array. Following the original idea of Mead [13], wave propagation in certain frequency bands can thereby be reduced significantly, theoretically leading to the presence of stop bands (or band gaps) with no propagation of energy. In this context, Persson et al. [14] suggested the reshaping of a landscape into an array of hills and/or valleys, while Andersen [15] analysed the effect of linear arrays of embedded WIBs using a two-dimensional model. The study was later extended to finite arrays in three-dimensions [16–18]. Also, simplified models were proposed for fast, preliminary analysis of WIB arrays placed on the ground surface [19,20].

Returning to the particular vibration problem related to installation of piles, a thorough study on the wave propagation via the soil and into buildings, including the effect on the structure and the occupants, was conducted by Athanasopoulos and Pelekis [21]. More recently, the vibratory sheet pile driving was studied by Deckner et al. [22–24]. The vibrations transmitted via the ground carry most of the energy in the frequency range relevant for whole-body vibrations, i.e. in the range 1–80 Hz. Further, buildings (or structural elements such as floors or walls) may resonate at the excitation frequencies involved in vibratory or impact pile driving [21].

A means of mitigating the ground vibrations from pile driving is therefore beneficial but demands that it can be realized at a low cost and without causing additional vibration. The use of WIBs placed on top of the ground could provide an efficient solution, by using a system of large construction waste-bags or other types of containers that can be filled with locally available material (excavated soil, recycled concrete, etc.), the work involved in establishing the vibration mitigation system would be minimal. Based on this idea, the authors previously proposed the introduction of a circular array of WIBs placed around a vibration source acting on the ground surface [25]. Different configurations of the array were tested, using a semi-analytical model. The main findings were that the WIB arrays provided an insertion loss (IL) of up to 20 dB in the vertical ground vibration levels, defined as the mean value in the zone 20–40 m away from the source. The effect was particularly pronounced at frequencies just above cut-on for wave propagation in soft topsoil, where the vibration levels peaked in the reference case without the WIBs. Also, an array with a configuration mimicking that of Stonehenge (with large blocks in the centre ring and gradually smaller blocks in the surrounding rings) was in many situations found to be more effective than arrays with block of equal size in all rings.

However, whereas Andersen et al. [25] concluded that the circular WIB arrays may be efficient for ground vibration mitigation related to surface sources, no analyses of buried sources or pile driving were performed. This paper, on the other hand, has focus on the IL related to vibrations generated by excitation at various depths below the ground surface. The frequency

range 0–80 Hz has been considered, as this is relevant for whole-body vibration and for the first eigenmodes of typical building elements and resonance in soil layers. To allow a direct comparison with the earlier findings, it has been chosen to use the same soil stratifications, i.e. 3 m of soft sand over a till half-space (Case 1), and 5 m of soft clay over a lime half-space (Case 2). However, compared to [25], only the "Stonehenge" configuration of the WIB array has been analysed in the paper. Ideally, to study the vibration from pile driving, a numerical model should account for the nonlinear response of the pile–soil system as proposed, for example, by Rooz et al. [26]. However, for a conceptual feasibility study of the suggested mitigation strategy, we propose the use of a simplified methodology. Hence, a linear viscoelastic model is used for the ground, and the pile is not modelled explicitly. Instead, vibration sources at various depths in the ground are considered. During the driving process, a pile will transfer energy to the soil, partly along the shaft, and partly at the tip. The proposed model allows a quantification of the IL that can be achieved for the contributions at each separate depth, but because of the simplified modelling approach it cannot be used for the assessment of the overall vibration levels.

The remaining parts of the paper are structured as follows. First, Section 2 describes the computational model. Then, Sections 3 and 4 provide the results and a discussion of the IL achieved in Cases 1 and 2, respectively. Finally, the main conclusions and suggestions for further research are given in Section 5.

2 SEMI-ANALYTICAL MODEL FOR THE SOIL AND RIGID BLOCKS

2.1 Transfer-matrix method for a layered ground with embedded sources

The analyses concern the vibration propagation into the far field, and in the case of man-made vibration due to pile driving, the cyclic shear strain magnitudes are small enough that a linear viscoelastic behaviour of the soil can be assumed. With wavelengths much longer than the characteristic grain size, a solid continuum model can be applied. The half-space $x_3 \leq 0$ is considered, assuming the ground surface and any internal interfaces to be horizontal. Given the linearity and horizontal invariance of the problem, the displacement in direction i at any point (x_1, x_2, x_3) and time t can be found as

$$u_i(x_1, x_2, x_3, t) = \int_{-\infty}^{0}\int_{-\infty}^{\infty}\int_{-\infty}^{\infty}\int_{-\infty}^{t} g_{ij}(x_1 - y_1, x_2 - y_2, x_3, y_3, t - \tau) \times p_j(y_1, y_2, y_3, \tau)\, \mathrm{d}\tau\, \mathrm{d}y_1\, \mathrm{d}y_2\, \mathrm{d}y_3, \qquad x_3 \leq 0\,, \quad (1)$$

where $g_{ij}(x_1 - y_1, x_2 - y_2, x_3, y_3, t - \tau)$ is the Green's function for the half-space, and $p_j(y_1, y_2, y_3, \tau)$ is the load applied at the position (y_1, y_2, y_3) and time τ.

The Green's function in the time–space domain cannot be found in closed form for a layered half-space. Instead, Eq. (1) is Fourier transformed into the frequency–horizontal wavenumber domain, arriving at the equation

$$\bar{U}_i(k_1, k_2, x_3, \omega) = \sum_{n=1}^{N_\mathrm{P}} \bar{G}_{ij}(k_1, k_2, x_3, y_{3n}, \omega)\, \bar{P}_j(k_1, k_2, y_{3n}, \omega). \quad (2)$$

$\bar{U}_i(k_1, k_2, x_3, \omega)$ is the triple Fourier transform of $u_i(x_1, x_2, x_3, t)$, while $\bar{P}_j(k_1, k_2, y_{3n}, \omega)$ is the triple Fourier transform of $p_j(y_1, y_2, y_3, \tau)$, and $\bar{G}_{ij}(k_1, k_2, x_3, y_3, \omega)$ is the triple Fourier transform of $g_{ij}(x_1 - y_1, x_2 - y_2, x_3, y_3, t - \tau)$. A discretization has been made in order to evaluate the contributions from a finite set of loads applied at the depths y_{3n}, $n = 1,2, \ldots, N_\mathrm{P}$. For each discrete depth that is not coinciding with an interface between two soil layers or the ground surface, an additional interface must be introduced in the model.

The material properties of each soil layer are defined in terms of the shear modulus G, Poisson's ratio ν, the mass density ρ, and the loss factor η. Thus, rate-independent hysteretic material damping is assumed, leading to a complex-valued dynamic stiffness of the soil. Next, for any combination of the source and receiver depths, x_3 and y_{3n}, the horizontal wavenumbers (k_1, k_2), and the angular frequency ω, an analytical solution for $\bar{G}_{ij}(k_1, k_2, x_3, y_{3n}, \omega)$ can be found by the layer transfer matrix-method proposed by Thomson [27] and Haskell [28]. The efficient implementation of Andersen and Clausen [29] has been used for the present analysis, augmented by the stabilization method proposed by Wang [30]. This allows a fast calculation of the response without necessitating a discretization over depth by the thin-layer method.

Once, $\bar{G}_{ij}(k_1, k_2, x_3, y_{3n}, \omega)$ and $\bar{P}_j(k_1, k_2, y_{3n}, \omega)$ have been evaluated for a given angular frequency, a double inverse Fourier transformation can be carried out with respect to k_1 and k_2 in order to obtain the solution in the frequency–space domain, $G_{ij}(x_1 - y_1, x_2 - y_2, x_3, y_3, \omega)$. In the present work, the load is assumed to be distributed uniformly over a circular horizontal area with a radius of $r_\mathrm{P} = 0.25$ m, corresponding to the cross section of the pile at a given depth. Hence, the load is axisymmetric. The same property applies to the Green's function, given the horizontal invariance of the stratification. This allows the double inverse Fourier transformation to be carried out in a semi-discrete manner with analytic transformation over the azimuth direction and discrete Fourier transformation in the radial direction. A discretization into 10 000 wavenumbers along the radial direction has been used, focussing on the range relevant to waves propagating in the layered medium, and Simpson integration has been applied for increased accuracy [29]. Since the frequency domain is considered in the present analyses, further inverse Fourier transformation into the time domain should not be carried out.

2.2 Rigid blocks interacting dynamically with the soil

An array with N_B rigid blocks is considered. The blocks are placed on the ground surface, and the dynamic soil–structure interaction (SSI) is modelled, discretizing the interface between each block and the soil into N_ssi points. The blocks have a rectangular footprint of 1 m × 2 m for the inner ring of the circular array, and smaller for the other rings. This footprint is discretized into 6 × 12 points. Around each of the SSI points, the traction is distributed uniformly over a circular area with the radius $r_\mathrm{ssi} = r_\mathrm{P} = 0.25$ m. Hence, the circular loaded areas have a small overlap, and a total of $N_\mathrm{SSI} = N_\mathrm{ssi} N_\mathrm{B} = 72 N_\mathrm{B}$ SSI points are present.

Unit loads will be applied, in turn, at a set of N_P source points. This adds N_P degrees of freedom (d.o.f.) to the problem. Thus, the model has $3N_\mathrm{P} + 3N_\mathrm{SSI}$ displacement d.o.f., leading to a global flexibility matrix $\mathbf{C}_\mathrm{SSI}(\omega)$, the elements of which are defined by the Green's function $G_{ij}(x_1 - y_1, x_2 - y_2, x_3, y_{3n}, \omega)$ that relates $U_i(x_1, x_2, x_3, y_{3n}, \omega_n)$ to $P_j(y_1, y_2, x_3, y_{3n}, \omega_n)$.

Since each rigid block has six d.o.f., $6N_B$ rigid-body modes exist for the array, in addition to the $3N_\mathrm{P}$ degrees of freedom associated with the source points. The relationship between the $3N_\mathrm{P} + 3N_\mathrm{SSI}$ d.o.f. and the $3N_\mathrm{P} + 6N_\mathrm{B}$ rigid-body modes is defined in terms of the matrix $\mathbf{U}_0$, and the dynamic stiffness matrix $\mathbf{D}_\mathrm{SSI}(\omega)$ for the reduced model can be found as

$$\mathbf{D}_\mathrm{SSI}(\omega) = \mathbf{U}_0^T \left(\mathbf{C}_\mathrm{SSI}(\omega)\right)^{-1} \mathbf{U}_0, \tag{3}$$

which has the dimensions $\left((3N_\mathrm{P} + 6N_\mathrm{B}) \times (3N_\mathrm{P} + 6N_\mathrm{B})\right)$. The displacement response at a set of receiver and observation points can finally be determined by postprocessing. Here, the donut-shaped area with inner radius 20 m and outer radius 40 m, centred at the load, is considered, using a pattern of nearly regular triangle with 0.5 m between the receiver points in the radial direction and approximately 1 m distance in the azimuthal direction. This provides 14 520 points in the receiver zone. Following the same discretization strategy, 4 921 observation points are present on the ground surface within the circular area inside the donut-shaped receiver zone.

2.3 Configurations of the rigid blocks and the loads

In the previous work by the authors [25], different configurations of circular WIB arrays were considered. Here, we shall only consider the so-called "Stonehenge" configuration. The WIBs are placed on the surface of the ground, forming one, two or three concentric rings. The radii are 4 m, 8 m, and 12 m, respectively, and the loads are applied at the centre of the rings at some depth below the ground surface. The reference point for each of the rigid blocks is placed at the centre of the rectangular base, i.e. in the centre of the SSI interface for each block. The number of blocks in Rings 1, 2 and 3 is 6, 12 and 24, respectively, as shown in Figure 1a.

The inner ring (Ring 1) serves as the reference in terms of block dimensions. As mentioned, the blocks in this ring have a rectangular footprint of the dimensions 1 m × 2 m. The shorter side length is in the radial direction, while the longer side length is tangential to the ring. Three different block heights are considered: 1 m, 2 m, and 3 m. The WIBs in Rings 2 and 3 are scaled uniformly in all directions, thus keeping the aspect ratio. The scaling factors $0.5^{1/3}$ and $0.5^{2/3}$ are used for the blocks in Rings 2 and 3, respectively, such that the total volume of the blocks in each ring will be the same. For example, with a height of 2 m and a mass density of 2 000 kg/m^3, corresponding to dense soil or granulated concrete, the mass of the blocks in Ring 1 is 4 000 kg each, while the individual blocks in Rings 2 and 3 have masses of 2 000 kg and 1 000 kg, respectively. Again, it is noted that such blocks could, for example, by realized by filling some type of containers with material that is already present at the construction site.

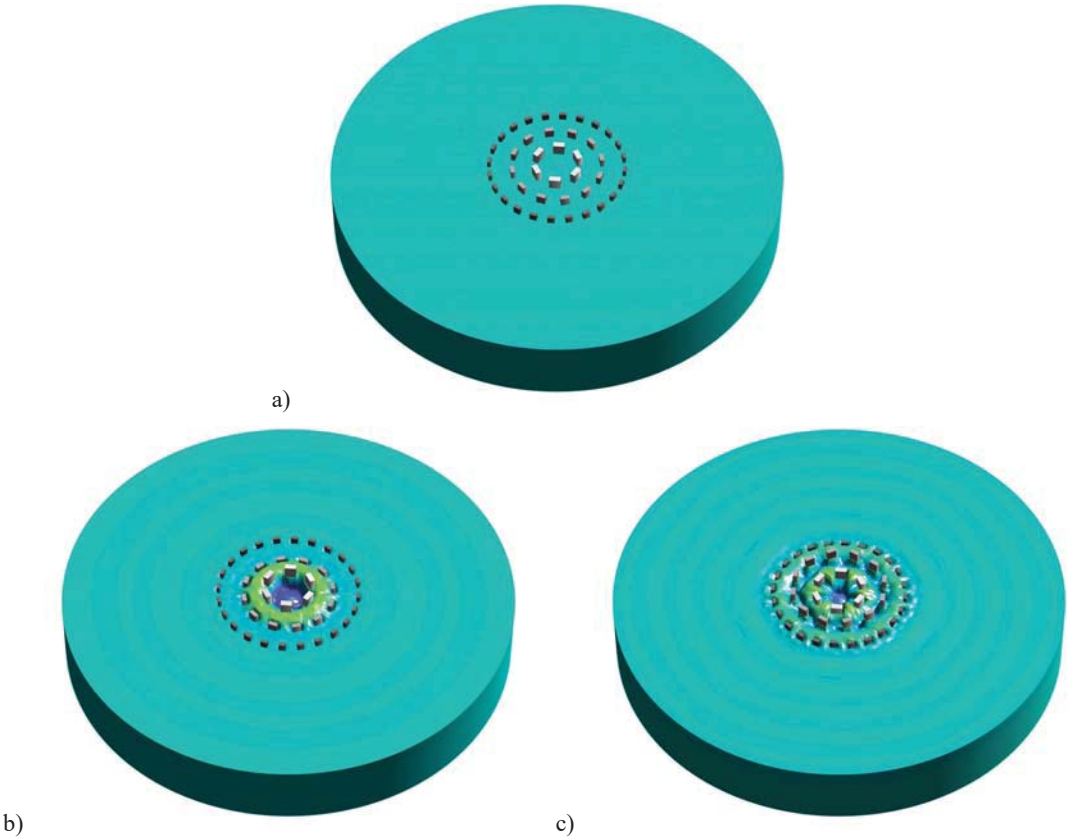

Figure 1: Model and example results: a) Configuration of the rigid blocks (WIBs) in the "Stonehenge" with three rings; b) ground vibration at 25 Hz; c) ground vibration at 30 Hz. The radii of the rings are 4 m, 8 m and 12 m, respectively, and the radius of the model is 40 m. The load is placed 2 m below the ground surface and applied vertically, uniformly distributed over a circular area with a radius of 0.25 m.

Figure 1b shows the ground displacement at 25 Hz due to a load applied 2 m below the ground surface and with three rings of WIBs placed in a "Stonehenge". The centre block height is 2 m, and the soil consists of 3 m of soft dry sand underlain by a till half-space (see Section 3, Table 1, for soil properties). Figure 1c shows the similar results at 30 Hz. At 25 Hz the displacement response is confined within the second ring, whereas large vibrations reach the third ring at 30 Hz. However, a clear effect is seen in the figure for both frequencies.

2.4 Insertion loss and transmission loss in the receiver zone

At any frequency, the vibration level in the receiver zone is influenced by 1) the source magnitude, geometry and position; 2) the transmission through the soil and any structures present within the close environment; and 3) the effect of the WIB array. A detailed discussion of the source is beyond the scope of the paper. However, assuming linear behaviour, the response scales linearly with the source magnitude. Further, as already mentioned, the load is applied uniformly on a circular area that could represent the cross section of a pile at a given depth.

Regarding the transmission of vibration through the soil, we assume that no obstacles or structures are present, except for the WIBs. The reference level (RL) for vibrations in the donut-shaped receiver zone is therefore taken as the level observed in the greenfield. In decibels, the RL for any point on the ground surface ($x_1, x_2, x_3 = 0$) and angular frequency ω is defined as

$$\mathrm{RL}_i^n(x_1, x_2, \omega) = 20\log_{10}\left(\left|U_i^{0n}(x_1, x_2, \omega)\right|\right) - 20\log_{10}(U_{\mathrm{ref}}). \tag{2}$$

Here $U_i^{0n}(x_1, x_2, \omega)$ is the ground surface displacement amplitude for a unit-magnitude (1 N) vertical distributed load applied around a source point at depth y_{3n}, and $U_{\mathrm{ref}} = 100$ pm. Only the vertical vibrations are considered. Thus, only $RL_3(x_1, x_2, \omega)$ is evaluated for the points within the receiver zone. Since a unit-magnitude load is applied, the RL may be regarded as a transfer mobility in dB for the layered ground.

The effect of a WIB array can be quantified in terms of an IL, defined as the difference in dB between the observed vibration levels before and after introducing the WIBs. Hence, a positive insertion loss implies a reduction in vibration level. For displacement component i, WIB configuration j, and pile (load) depth n, the IL is given as

$$\mathrm{IL}_i^{nj}(x_1, x_2, \omega) = 20\log_{10}\left(\left|U_i^{0n}(x_1, x_2, \omega)\right|\right) - 20\log_{10}\left(\left|U_i^{nj}(x_1, x_2, \omega)\right|\right), \tag{3}$$

where $U_i^{nj}(x_1, x_2, \omega)$ is the surface displacement amplitude obtained by applying the unit-magnitude load, i.e. the transfer mobility, after insertion of the WIB array. Again, only vertical vibration is considered, i.e. only $\mathrm{IL}_3^{nj}(x_1, x_2, \omega)$ is evaluated at the 3 780 receiver points.

To assess the importance of mitigation of ground vibration at a given frequency, it is necessary to study the RL and IL in combination. If the RL is high and the IL is low in a range of frequencies relevant to the generation of vibrations at the source, the received vibration level will be high. On the other hand, if the RL is low, a small (or even negative) IL can be tolerated, especially if the source level is also anticipated to be relatively low. This will form the basis for the discussion of the results presented in the following sections. As outlined in the introduction, two cases will be considered:

- Case 1: 3 m soft sand over a till half-space
- Case 2: 5 m soft clay over a lime half-space.

As a single measure of the RL and IL for different WIB arrays, the mean values of the RL and IL within the receiver zone will be used. The variation within the receiver zone is visualized by further calculating the 10% and 90% quantiles of the RL and IL.

3 CASE 1: 3 METRES OF SOFT DRY SAND OVER A HALF-SPACE OF TILL

The material properties for the soft sand layer and the underlying till half-space are given in Table 1. To examine the effect of the block height, three subcases are considered:

- Case 1.1: 1 m high blocks in Ring 1, and with either one, two or three rings
- Case 1.2: 2 m high blocks in Ring 1, and with either one, two or three rings
- Case 1.3: 3 m high blocks in Ring 1, and with either one, two or three rings.

It is noted that the blocks in Rings 2 and 3 will be smaller than those in Ring 1, as explained in Subsection 2.3 and shown in Figure 1a.

The blocks act as monolithic structures. The mass is proportional to the height, whereas the stiffness related to the soil–structure interaction is invariant to the block height. Hence, WIBs with different heights will resonate at different frequencies. This is even more pronounced for the pitch and rolling modes (or rocking) of the blocks, since a part of the rotational inertia scales with the cube of the height. Further, since the blocks in the Rings 1, 2 and 3 are not of the same size, the resonance frequencies will differ. The values are provided in Table 2, based on the static stiffness of the soil and the inertia of the blocks. It has been judged that the vertical vibration levels in the receiver zone are mainly influenced by the vertical motion (heave) of the blocks, their horizontal sliding, and their pitch rotation around the axis tangential to the perimeter of the ring. Hence, only the frequencies related to resonance in these modes are given.

An important observation can be made regarding the resonance frequencies in Table 2: they all lie in the frequency range 0–80 Hz, which is relevant to whole-body vibrations and building vibration. Further, this is the frequency range where most of the energy will be present in the excitation due to pile driving, and it may be expected that guided waves may be generated in the soft sand layer within this frequency range. The ratios between the resonance frequencies for the blocks and the cut-on frequencies for the layer waves can be expected to have an influence on the IL. Obviously, the mass of the WIBs will itself be important, since a heavier mass requires more energy to be moved.

The transfer mobility of the stratified soil, quantified in terms of the RL, depends strongly on whether the load is applied within the top layer of soft soil or within the underlying and much stiffer half-space. However, it has been found that the response is only marginally influenced by the relative depth of the load within the layer. Hence, to avoid an over-excessive number of figures, only two source points ($n = 2, 8$) will be considered, that is: $y_{3\,2} = -2$ m (which is inside the topsoil layer) and $y_{3\,8} = -8$ m (which is within the underlying half-space).

Soil layer (from top)	Shear modulus G [MPa]	Poisson's ratio ν [-]	Mass density ρ [kg/m^3]	Loss factor η [%]	Thickness h [m]
Sand, *soft, dry*	35.72	0.3330	1 553	4.50	3.0
Till (half-space)	500.0	0.3500	2 100	2.00	∞

Table 1: Soil properties for Case 1.

	Blocks in Ring 1			Blocks in Ring 2			Blocks in Ring 3		
	Heave	Sliding	Pitch	Heave	Sliding	Pitch	Heave	Sliding	Pitch
Case 1.1	34.8	30.0	24.6	42.4	36.9	31.7	52.6	46.0	37.2
Case 1.2	24.6	21.2	9.41	30.0	26.1	12.3	37.2	32.5	14.3
Case 1.3	20.1	17.3	5.21	24.5	21.3	6.84	30.3	26.6	7.90

Table 2: Resonance frequencies (in Hz) of the blocks in Case 1.

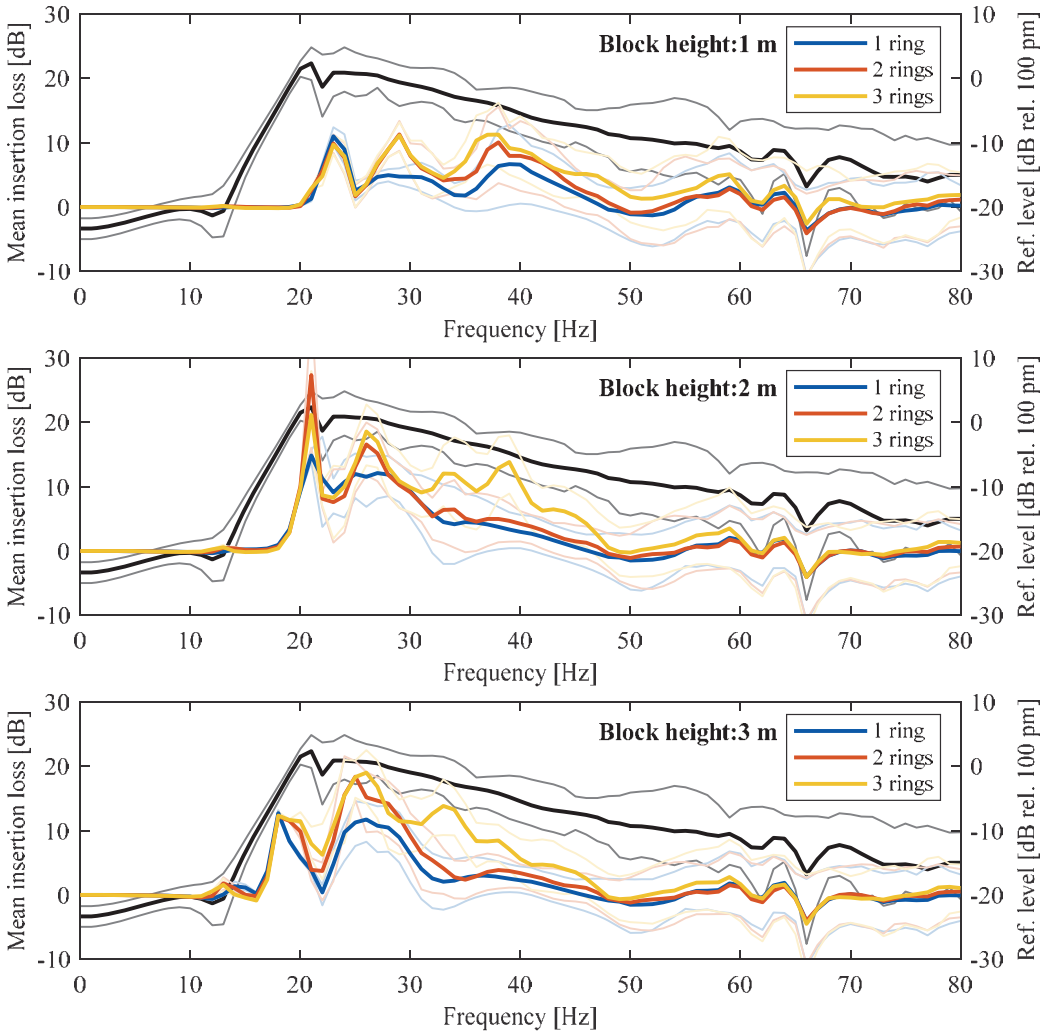

Figure 2: Mean ILs for the ground vibration within the donut-shaped surface area placed 20–40 m away from the centre of the load: Cases 1.1, 1.2, and 1.3, with the load acting 2 m below the ground. The black lines show the reference level of vibrations and the thin lines show the 10% and 90% quantiles of the respective quantities.

For the load depth of 2 m, Figure 2 shows the mean and the 10% and 90% quantiles of the RL (black lines) in Case 1. Further, the figure shows the mean and quantile values for the IL achieved with 1, 2 or 3 rings in the "Stonehenge" in Cases 1.1 (1 m high blocks in Ring 1), 1.2 (2 m high blocks in Ring 1), and 1.3 (3 m high blocks in Ring 1). For frequencies below 12.5 Hz, the RL is relatively small, about –22 dB rel. 100 pm. Then, within the interval 12.5–20 Hz, the RL increases to about 0 dB, indicating the presence of a cut-on frequency for wave propagation in the top layer at approximately 12.5 Hz. The shear wave velocity in the soft sand is about 150 m/s, which leads to a wavelength of 12 m at this frequency. Hence, the layer thickness matches with one quarter of a wavelength, which leads to resonance. From 20 Hz and up to 50 Hz, the RL decreases almost monotonously. This can be attributed to material dissipation and less constructive interference of waves. Beyond 50 Hz, where the shear wavelength becomes smaller than the layer thickness, the response varies differently.

For the various configurations of the WIB arrays, the IL peaks somewhere in the frequency range 18–38 Hz, with the exact position of the peak being dependent on the block height and

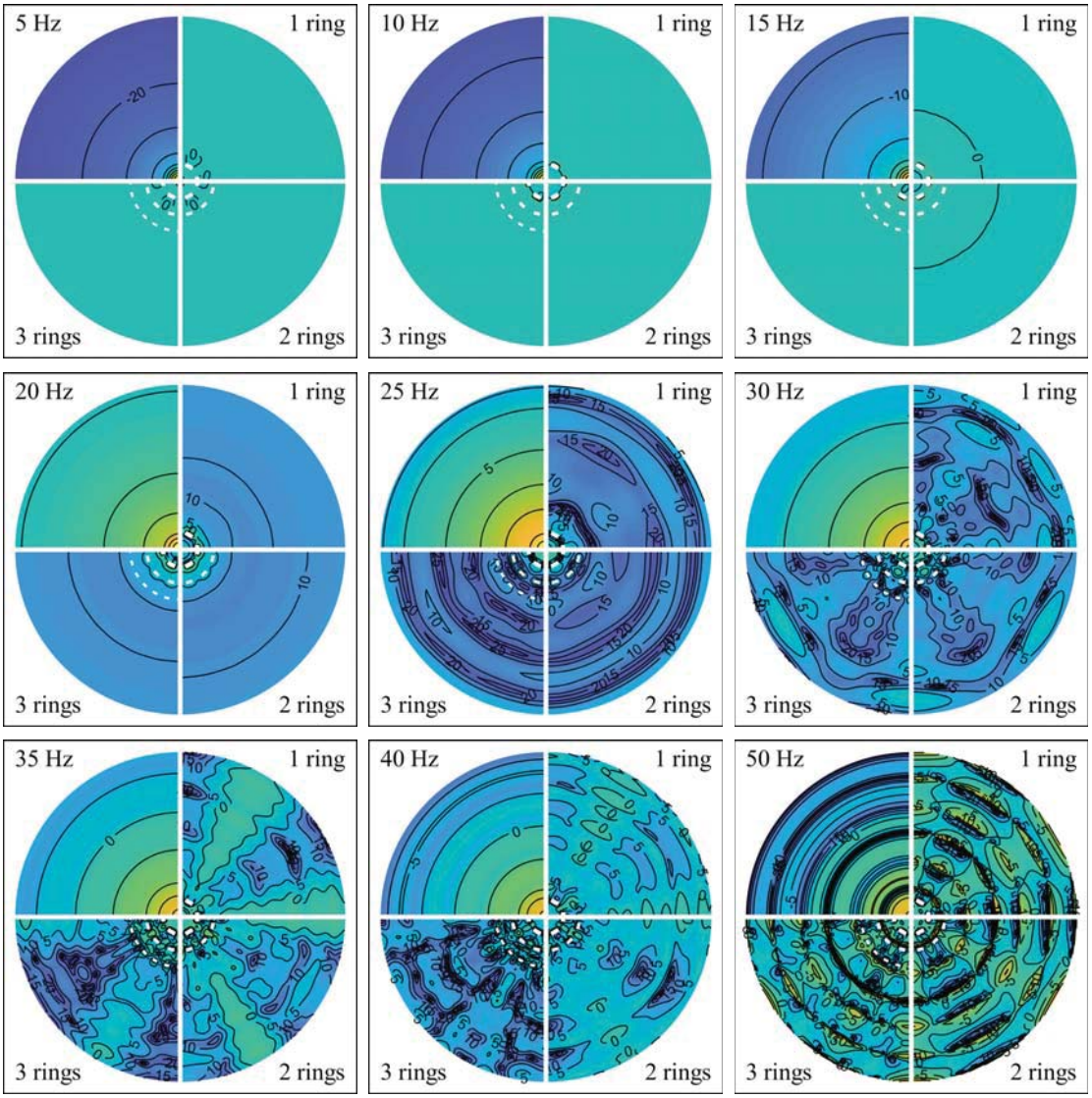

Figure 3: Contours of the reference vibration levels and ILs (in dB) for Case 1.2 with 1, 2, or 3 rings. The centre blocks are 2 m high and the vertical load is applied 2 m below the ground surface. Pale yellow/dark blue shades represent unfavourable/favourable values, respectively.

number of rings. In Case 1.1, with all three rings present, the IL is around 5–10 dB in the range 22–60 Hz, with some tips and dips. This configuration is more effective (providing higher IL than the other configurations) in the frequency range 35–80 Hz. The 1 m high blocks even provide a larger IL than the 2 or 3 m high blocks in the frequency range 45–60 Hz. However, a larger IL is obtained from 17 to 35 Hz in Cases 1.2 and 1.3. In most of the tested scenarios, the IL increases with the number of rings. As an exception, Case 1.2 is particularly effective around 21 Hz when only two rings are present. Also, in Cases 1.1 and 1.2, one ring of WIBs provides slightly higher IL than two or three rings around 23 Hz. Figure 3 shows the RL (top left quadrants of the subplots) and IL (remaining quadrants of the subplots) on the ground surface at nine selected frequencies for Case 1.2. The figure clearly shows that the array has limited effect for frequencies below 15–20 Hz. For frequencies higher than 25 Hz, the IL is subject to large variation within the receiver zone, which can also be seen from the quantile lines in Figure 2.

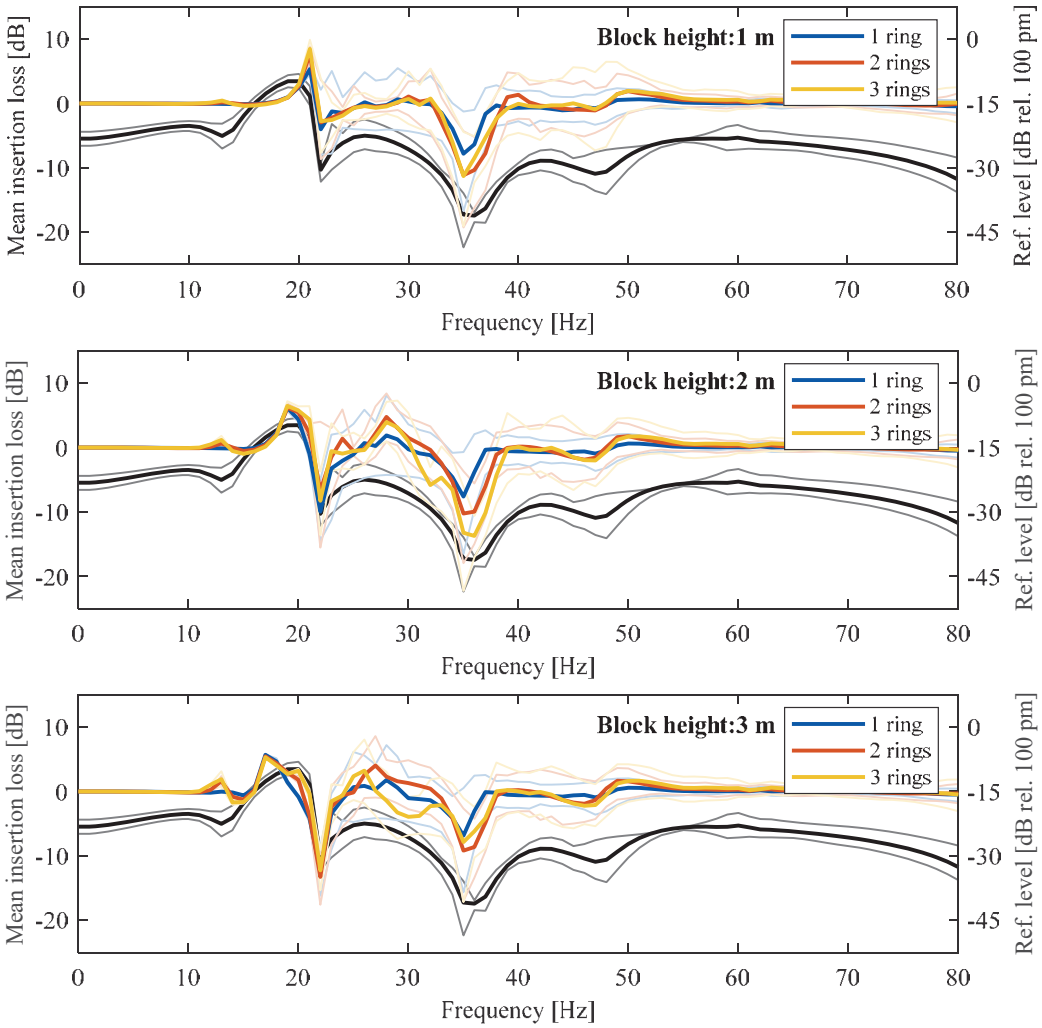

Figure 4: Mean ILs for the ground vibration within the donut-shaped surface area placed 20–40 m away from the centre of the load: Cases 1.1, 1.2, and 1.3 with the load acting 8 m below the ground. The black lines show the reference level of vibrations and the thin lines show the 10% and 90% quantiles of the respective quantities.

Figure 4 shows the mean and quantile values of the RL and IL in the receiver zone for Case 1 with the load applied at $y_{3\,8} = -8$ m. As an example of the local variations of the RL and IL within the receiver zone for this load depth, Figure 5 shows the results for Case 1.2, i.e. with a block height of 2 m in Ring 1. The WIB arrays have limited effect for frequencies below 15–20 Hz, similarly to the case with the load depth of 2 m. However, for the frequency range 12–55 Hz, the IL varies significantly and is, in some cases, negative, down to about –15 dB. The negative IL associated with the 2 and 3 m high blocks is more pronounced around 22 Hz, whereas the 1 and 2 m high blocks lead to lower IL around 35 Hz. However, with reference to Figure 2, this is where the higher IL is obtained when the load is applied at $y_{3\,2} = -2$ m.

Hence, a given configuration of the WIB array may provide a high IL in some frequency range when the load is applied at one depth, but it may be ineffective – or even amplify the ground vibration – in the same frequency range when the load is applied at another depth. A comparison of Figures 2 and 4 shows that the RL is about 20–30 dB lower when the load is applied at 8 m depth, compared to the load applied 2 m below the ground surface. This indicates

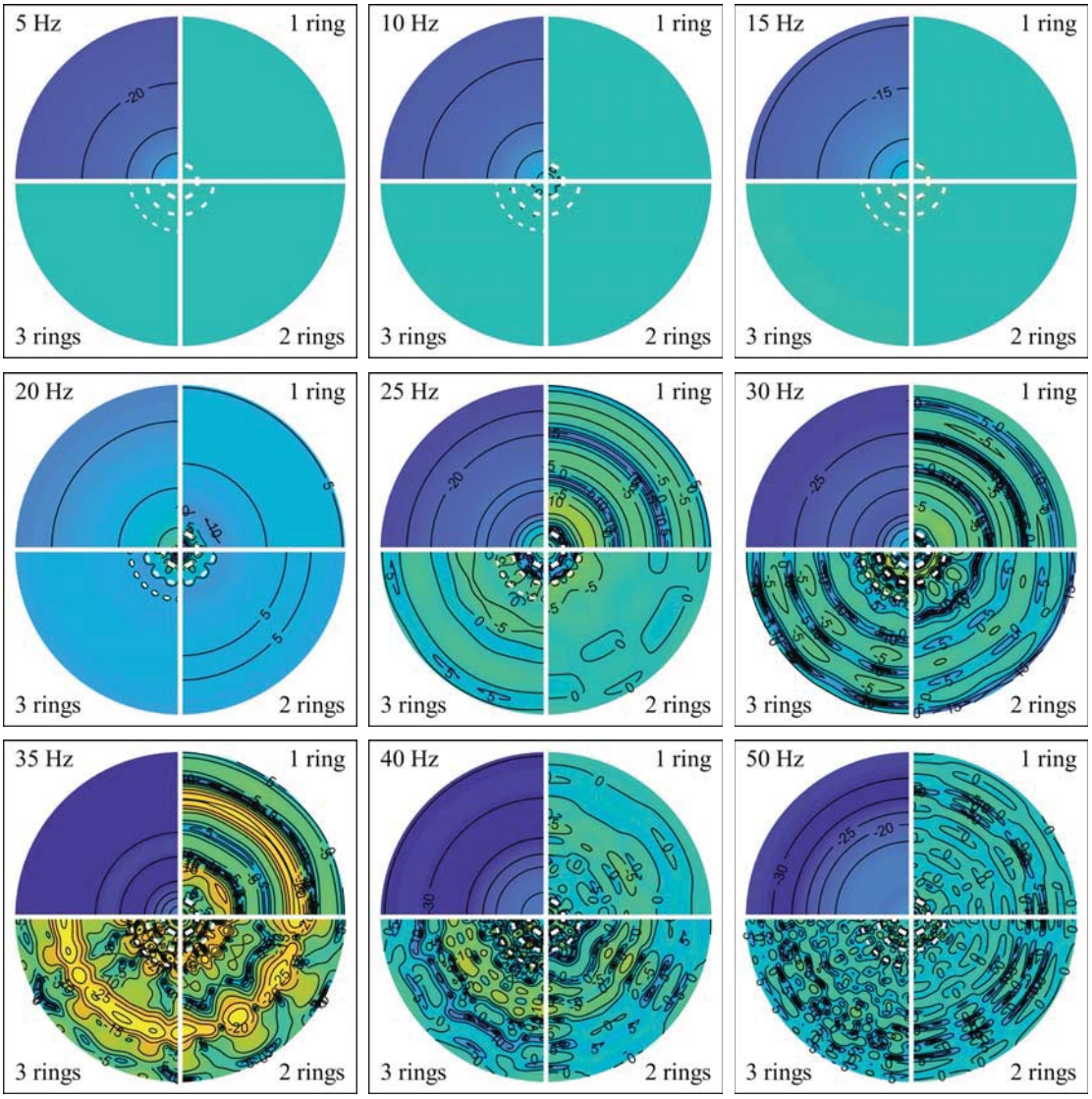

Figure 5: Contours of the reference vibration levels and ILs (in dB) for Case 1.2 with 1, 2, or 3 rings. The centre blocks are 2 m high and the vertical load is applied 8 m below the ground surface. Pale yellow/dark blue shades represent unfavourable/favourable values, respectively.

that the vibrations will not be trapped within, and guided by, the soft topsoil layer. In any case, the resulting vibration level in the receiver zone can be found as the RL minus the IL. Since the mean value of $\mathrm{RL}_3^8 - \mathrm{IL}_3^{8j}$ is well below zero for all considered frequencies, the poor performance of the WIB arrays for the deeper source has limited consequences for the overall quality of the mitigation technique. Instead, the WIB arrays imply a significant reduction of the vibration level when the load is applied within the soft top layer, exemplified by $y_{3\,2} = -2$ m. At these frequencies, the RL is around 0 dB. With reference to Table 2 and Figure 2, the larger values of IL_3^{2j} are present within the frequency range where the WIBs may resonate. Hence, depending on the soil stiffness, the WIBs can be designed to resonate in the frequency range for which a high IL is required. The size of the blocks and their the height relative to the footprint are design variables. To make adjustments on site, the height can be changed, e.g., by filling more soil or granulated concrete into containers, such as large construction waste-bags.

4 CASE 2: 5 METRES OF SOFT CLAY OVER A HALF-SPACE OF LIME

The site considered in Case 2 has a 5 m layer of soft wet clay underlain by a lime half-space. The material properties are given in Table 3, and it is noted that the clay is slightly softer than the sand considered in Case 1. Combined with the deeper top layer, this provides a lower cut-on frequency, around 7 Hz, compared to the cut-on frequency of 12.5 Hz in Case 1.

The resonance frequencies of the blocks within the WIB arrays can be found in Table 4. Notably, the resonance frequencies associated with the heave and pitch modes are higher than those in Case 1 (cf. Table 2), whereas the resonance frequencies related to sliding are lower. This can be explained by the soil deformation involved in the different modes of vibration. For the heave and pitch modes, the vertical motion of the SSI interfaces is important. Here, the impedance depends on the compressibility of the soil, which is low due to the high Poisson's ratio (0.4942) corresponding to nearly incompressible behaviour) compared to the Poisson's ratio in Case 1 (0.3330). On the other hand, the sliding mode is mainly influence by the shear stiffness, and since the shear modulus in Case 2 is about 10% lower than that in Case 1, the resonance frequency for the sliding mode can be expected to be lower as well.

Figure 6 shows the mean and quantile values of RL_3^2 and IL_3^{2j} (load placed at $y_{3\,2} = -2$ m) for Cases 2.1, 2.2, and 2.3, i.e. with block heights of 1 m, 2 m and 3 m, respectively, in Ring 1. Example results for the local variations within Case 2.3 are shown in Figure 7. Similarly, results for the load placed 8 m below the ground ($y_{3\,8} = -8$ m) are shown in Figure 8 and Figure 9.

For the load acting within the soft clay layer, 2 m below the ground surface, the reference vibration level within the receiver zone is small (about –45 dB) for frequencies below the cut-on frequency. A rapid increase in the RL can be seen from 7 Hz and up to about 14 Hz, where the TL has its maximum, around 7–8 dB. Beyond this peak, an almost linear monotonous decrease can be observed, reaching approximately –20 dB at 80 Hz.

The WIB arrays generally provide positive insertion loss when the load is placed at a depth of 2 m. With a block height of 1 m in Ring 1, the array delivers up to about 5–10 dB reduction in the vibration level within the receiver zone for the considered frequency range above 25 Hz. The effect of the second ring begins at around 30 Hz, and the third ring contributes to a further increase of the mean IL for frequencies above 35 Hz. The 2 m high blocks produce a mean IL comparable to that of the 1 m high blocks in most of the considered frequency range. As expected, a slight shift in the mean IL peaks towards lower frequencies can be seen. When the block height is further increase to 3 m, a significantly larger mean IL is obtained in the frequency range 18–25 Hz. The peak in the mean IL reaches 15 dB, independently of the number of rings in the array. However, the peak is slightly wider when two or three rings are present,

Soil layer (from top)	Shear modulus G [MPa]	Poisson's ratio ν [-]	Mass density ρ [kg/m^3]	Loss factor η [%]	Thickness h [m]
Clay, *soft, wet*	30.03	0.4942	1 694	4.50	5.0
Lime (half-space)	4 300	0.3500	2 100	2.00	∞

Table 3: Soil properties for Case 2.

	Blocks in Ring 1			Blocks in Ring 2			Blocks in Ring 3		
	Heave	Sliding	Pitch	Heave	Sliding	Pitch	Heave	Sliding	Pitch
Case 2.1	36.0	29.0	25.7	44.0	35.6	33.2	54.7	44.5	39.2
Case 2.2	25.4	20.5	9.85	31.1	25.2	12.9	38.7	31.4	15.0
Case 2.3	20.8	16.8	5.45	25.4	20.6	7.17	31.6	25.7	8.31

Table 4: Resonance frequencies (in Hz) of the blocks in Case 2.

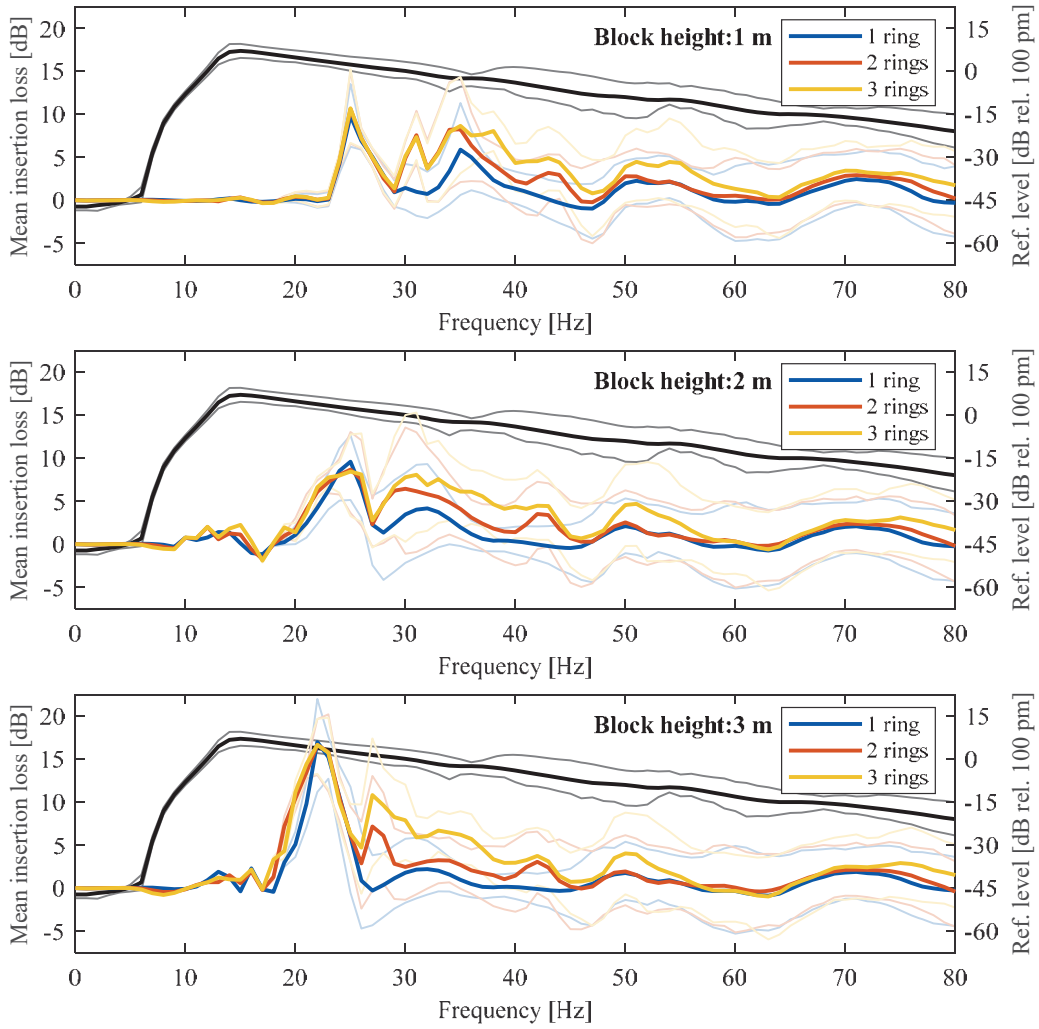

Figure 6: Mean ILs for the ground vibration within the donut-shaped surface area placed 20–40 m away from the centre of the load: Cases 2.1, 2.2, and 2.3 with the load acting 2 m below the ground. The black line shows the reference level of vibrations and the thin lines show the 10% and 90% quantiles of the respective quantities.

compared to the case with only one ring. For frequencies beyond 25 Hz, the ILs for Cases 2.1–2.3 are similar. Like it was found for Case 1, it can be observed that the WIB arrays have an effect in the frequency range where the WIBs may resonate.

The variations of the RL and IL produced by the 3 m high blocks (Case 2.3) are shown in Figure 7. Again, it is clearly seen that the effect of the WIB array is limited at low frequencies. The large IL observed around 18–25 Hz is also visible in this figure. However, even if the mean IL was previously found to reach nearly the same magnitude (15 dB), the subplots for the frequencies 20 and 25 Hz in Figure 7 show that the mean IL is the result of very different distributions for the array with only one ring versus the arrays with two or three rings. Especially, at 20 Hz the IL field is much more homogeneous and generally higher with two or three rings. This explains why the mean IL peak in Figure 6 is narrower for the array with one ring, and it also explains why the 10% and 90% quantile values are lower and higher, respectively, for one ring compared to two or three rings. Finally, at 30 Hz, zones with negative IL appear. A similar observation can be made for Case 1, with reference to Figure 3, where zones with negative IL

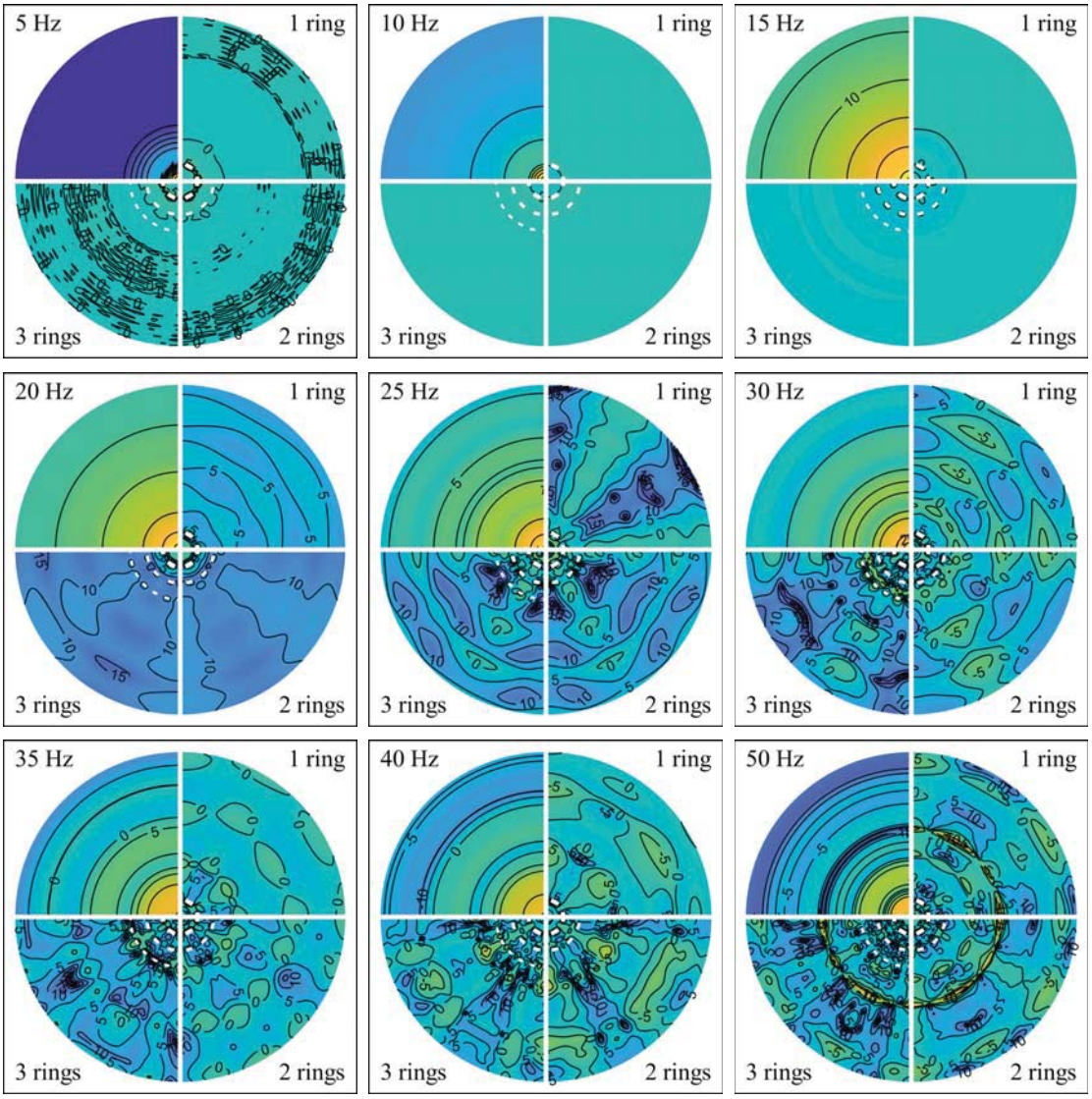

Figure 7: Contours of the reference vibration levels and ILs (in dB) for Case 2.3 with 1, 2, or 3 rings. The centre blocks are 3 m high and the vertical load is applied 2 m below the ground surface. Pale yellow/dark blue shades represent unfavourable/favourable values, respectively.

appear at 50 Hz. However, the mean IL is still positive at e.g. 50 Hz for both cases, when the load is applied 2 m below the ground surface (see Figures 2 and 4). For some higher frequencies, especially around 65 Hz in Case 1, a slightly negative mean IL is obtained. This should be seen in the context of the RL which is about 15–20 dB lower here compared to the maximum that occurs at around 20 Hz and 14 Hz in Cases 1 and 2, respectively. Further, the load spectra associated with pile driving can be expected to have less energy at higher frequencies.

Figure 8 shows the mean and quantile values of the RL and ILs in the receiver zone within Case 2, when the load is applied at 8 m depth. The RL is consistently below –35 dB rel. 100 pm in the entire frequency range relevant to whole-body vibration, i.e. up to 80 Hz. This is different when compared to Case 1, where an RL up to about –10 dB was obtained for frequencies slightly higher than the cut-on frequency of 12.5 Hz. A small local peak is also present in Case 2 for frequencies just above the cut-on frequency which is here around 7 Hz. However, this peak

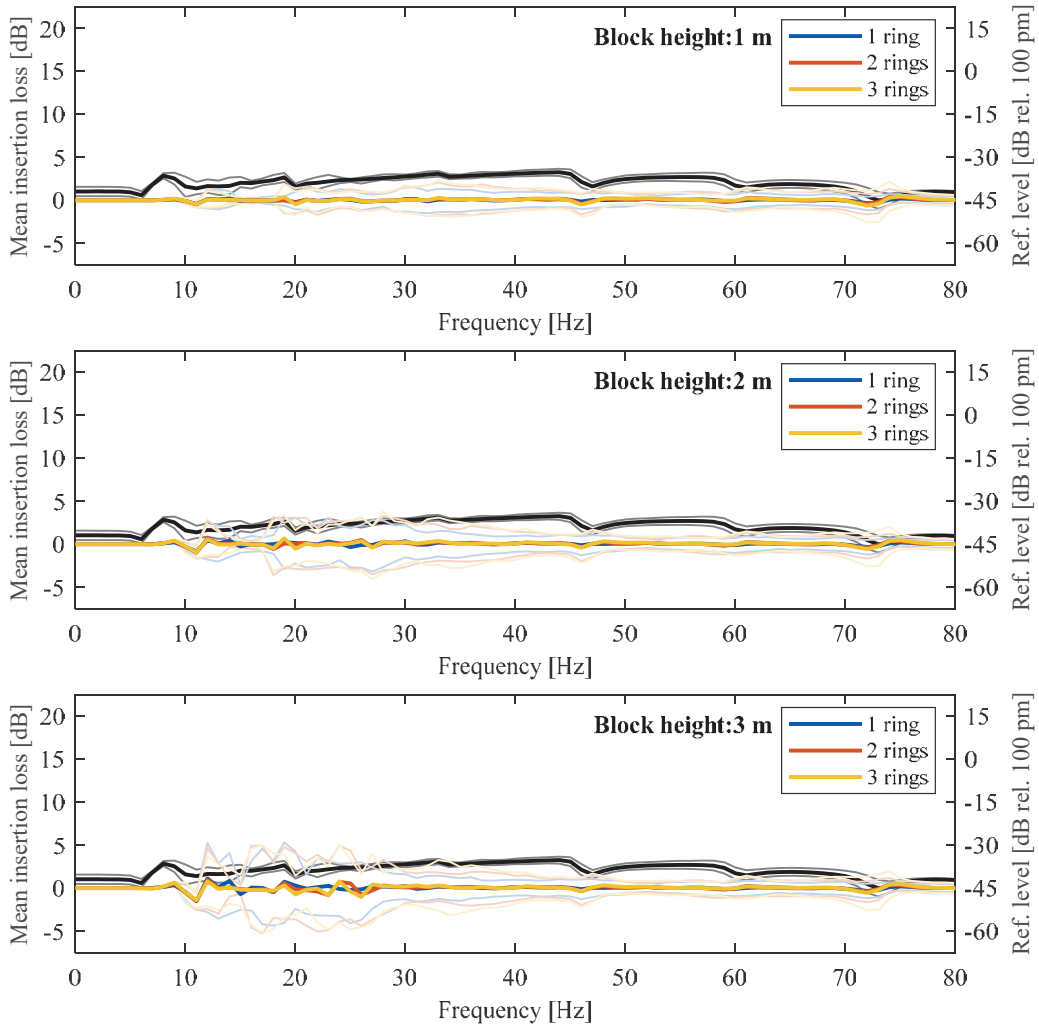

Figure 8: Mean ILs for the ground vibration within the donut-shaped surface area placed 20–40 m away from the centre of the load: Cases 2.1, 2.2, and 2.3 with the load acting 8 m below the ground. The black line shows the reference level of vibrations and the thin lines show the 10% and 90% quantiles of the respective quantities.

is much less pronounced, indicating that only a very small amount of the energy travelling within the ground enters the topsoil layer when the load is applied withing the lime half-space. This can be explained by the large impedance mismatch between the soft clay and the lime.

Compared to Case 1, more specifically by comparing Figures 4 and 8, it can be observed that the mean IL in Case 2 is nearly zero when the load is applied within the lime half-space, whereas some variation occurred in Case 1, when the load was applied within the till half-space. The very low impact of the WIB arrays on the IL can also be seen in Figure 9 which further shows that the number of rings has very limited influence. In Case 2 it is therefore even more pronounced, compared to Case 1, that the critical scenario will be related to loads applied within the soft topsoil. When the load acts within the deeper and stiffer soil, the transfer mobility to the ground surface is low.

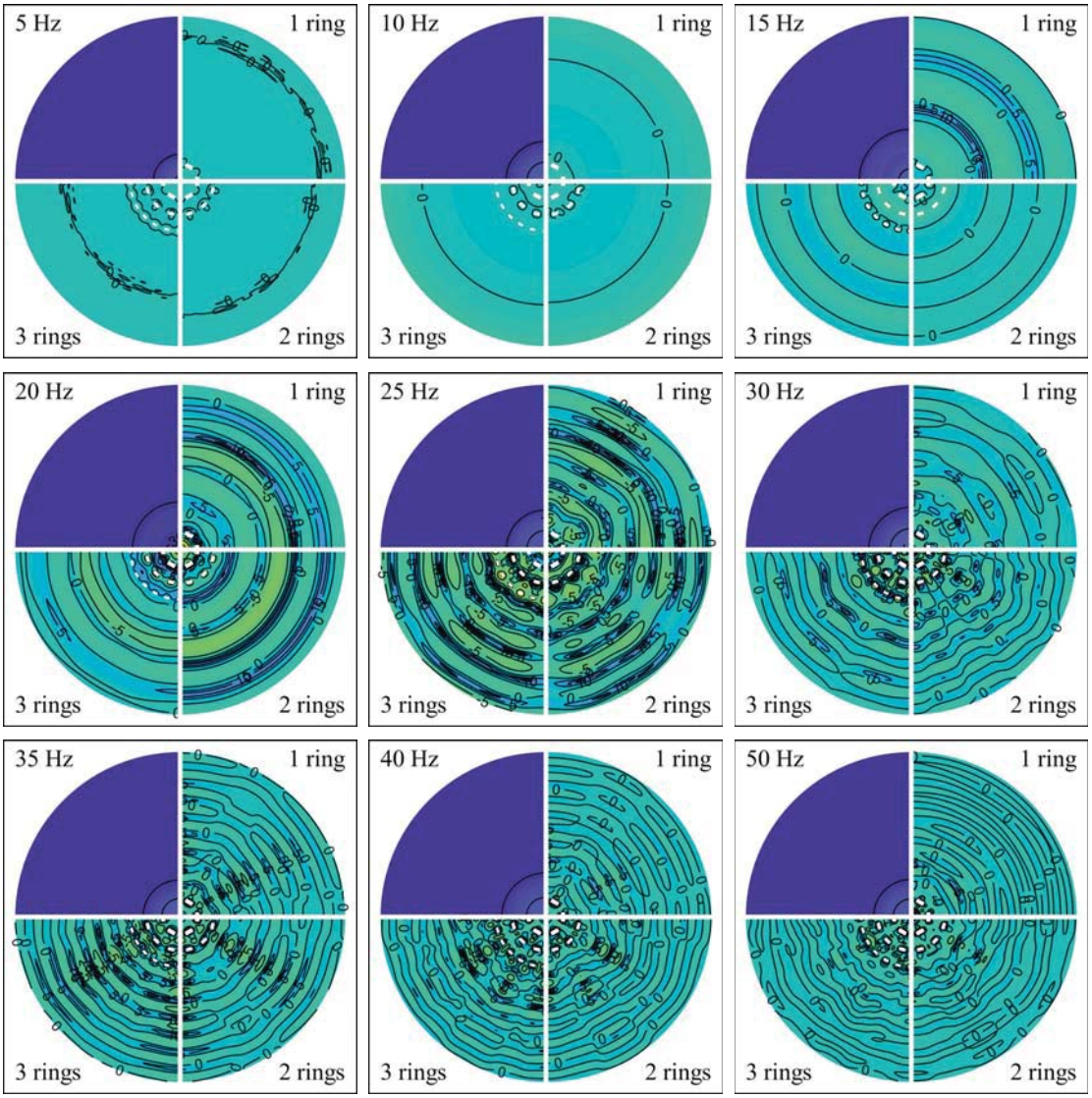

Figure 9: Contours of the reference vibration levels and ILs (in dB) for Case 2.3 with 1, 2, or 3 rings. The centre blocks are 3 m high and the vertical load is applied 8 m below the ground surface.
Pale yellow/dark blue shades represent unfavourable/favourable values, respectively.

5 CONCLUSIONS AND SUGGESTIONS FOR FURTHER RESEARCH

Based on a semi-analytical model of a layered soil, the insertion loss provided by circular arrays of monolithic blocks placed on the ground surface has been studied. It has been found that blocks placed in a so-called “Stonehenge” configuration effectively reduce the ground vibration level in a receiver zone 20–40 m away from the position at which a pile is driven into the soil. For two different cases, both of which consider a soft topsoil underlain by a stiffer half-space, an insertion loss of about 5–20 dB can be obtained by using blocks that could, on a construction site, be made from appropriate containers infilled with excavated soil or some heavy construction waste material. Adding more rings of wave impedance blocks to the array

will in most cases increase the insertion loss, but with an optimal tuning of the resonance frequencies, a significant reduction in the vibration level in the receiver zone can be achieved, even with a single ring of blocks, demonstrating the large mitigation potential of the solution.

In the present analyses, the pile has not been modelled explicitly. Instead, loads have been applied at different depths, in the soft topsoil or in the stiff half-space. When a pile is driven, forces will be transferred to the surrounding soil simultaneously along the shaft and the at the tip. Depending on the relative strengths of the soil down along the pile, the excitations produced along the shaft or at the tip may dominated. However, this cannot be modelled correctly by a simple viscoelastic model. Further research on the energy transfer mechanism between the pile and the soil is proposed in order to achieve more detailed quantification of the overall mitigation potential of circular block arrays.

Further, based on the observation that the block arrays are effective within the frequency range where the blocks may resonate, an optimization of the individual blocks is proposed for a future study. This can be combined with the optimization of the full array, focussed on placing the blocks on the ground such that the interference pattern of the scattered waves leads to an overall minimization of the transfer mobility within a selected receiver zone and for a given range of frequency.

Despite the shortcomings of the computational model, and knowing that a further potential for optimization exists, this study shows promise for an innovative technique where mitigation is placed *on* the ground surface which inhibits the transmission of vibration from *within* the body of the ground. Within the context of ground vibration, the method established here could be expected to apply to other scenarios with different source characteristics, i.e. different pile-driving methods. Developed further there could also be potential to study various source-types such as blasting or shock-vibration.

ACKNOWLEDGMENTS

The second author gratefully acknowledges the financial support from the Swedish Governmental Agency for Innovation Systems (Vinnova), grant ref. no. 2018-04159.

REFERENCES

[1] T. Münzel, F.P. Schmidt, S. Steven, J. Herzog, A. Daiber, M. Sørensen, Environmental Noise and the Cardiovascular System, J. Am. Coll. Cardiol. (2018). https://doi.org/10.1016/j.jacc.2017.12.015.

[2] T. Münzel, T. Gori, W. Babisch, M. Basner, Cardiovascular effects of environmental noise exposure, Eur. Heart J. (2014). https://doi.org/10.1093/eurheartj/ehu030.

[3] L. Andersen, S.R.K. Nielsen, Reduction of ground vibration by means of barriers or soil improvement along a railway track, Soil Dyn. Earthq. Eng. 25 (2005) 701–716.

[4] D.J. Thompson, J. Jiang, M.G.R. Toward, M.F.M. Hussein, E. Ntotsios, A. Dijckmans, P. Coulier, G. Lombaert, G. Degrande, Reducing railway-induced ground-borne vibration by using open trenches and soft-filled barriers, Soil Dyn. Earthq. Eng. 88 (2016) 45–59. https://doi.org/10.1016/j.soildyn.2016.05.009.

[5] A. Dijckmans, P. Coulier, J. Jiang, M.G.R. Toward, D.J. Thompson, G. Degrande, G. Lombaert, Mitigation of railway induced ground vibration by heavy masses next to the

track, Soil Dyn. Earthq. Eng. 75 (2015) 158–170. https://doi.org/10.1016/j.soildyn.2015.04.003.

[6] L. Andersen, A.H. Augustesen, Mitigation of traffic-induced ground vibration by inclined wave barriers – A three-dimensional numerical analysis, in: 16th Int. Congr. Sound Vib. 2009, ICSV 2009, 2009.

[7] L. Andersen, M. Liingaard, Vibration screening with sheet pile walls, in: H. Takemiya (Ed.), Environ. Vib. Predict. Monit. Mitig. Eval. (ISEV 2005), CRC Press, Taylor & Francis Group, London, Okayama, Japan, 20–22 September 2005, 2005: pp. 429–437.

[8] A. Dijckmans, A. Ekblad, A. Smekal, G. Degrande, G. Lombaert, Efficacy of a sheet pile wall as a wave barrier for railway induced ground vibration, Soil Dyn. Earthq. Eng. 84 (2016) 55–69. https://doi.org/10.1016/j.soildyn.2016.02.001.

[9] G.B. Warburton, J.D. Richardson, J.J. Webster, Forced Vibrations of Two Masses on an Elastic Half Space, J. Appl. Mech. 38 (1971) 148–156. https://doi.org/10.1115/1.3408735.

[10] G.B. Warburton, H.D. Richardson, J.J. Webster, Harmonic response of masses on an elastic half-space, J. Eng. Ind. Trans. ASME. 75 (1972) 158–170.

[11] A.T. Peplow, C.J.C. Jones, M. Petyt, Surface vibration propagation over a layered elastic half-space with an inclusion, Appl. Acoust. (1999). https://doi.org/10.1016/S0003-682X(98)00031-0.

[12] H. Masoumi, A. Van Leuven, S. Urbaniak, Mitigation of train induced vibrations by wave impeding blocks : numerical prediction and experimental validation, in: EURODYN 2014, 2014: pp. 863–870.

[13] D.J. Mead, Free wave propagation in periodically supported, infinite beams, J. Sound Vib. 11 (1970) 181–197. https://doi.org/10.1016/S0022-460X(70)80062-1.

[14] P. Persson, K. Persson, G. Sandberg, Reduction in ground vibrations by using shaped landscapes, Soil Dyn. Earthq. Eng. 60 (2014) 31–43.

[15] L.V. Andersen, Using periodicity to mitigate ground vibration, in: COMPDYN 2015 – 5th ECCOMAS Themat. Conf. Comput. Methods Struct. Dyn. Earthq. Eng., 2015.

[16] L.V. Andersen, P. Bucinskas, P. Persson, M. Muresan, L.-I. Muresan, I.-O. Paven, Mitigating ground vibration by periodic inclusions and surface structures, in: Proc. INTER-NOISE 2016 - 45th Int. Congr. Expo. Noise Control Eng. Towar. a Quieter Futur., 2016: pp. 7469–7480.

[17] L. V. Andersen, A. Peplow, P. Bucinskas, P. Persson, K. Persson, Variation in models for simple dynamic structure-soil-structure interaction problems, in: Procedia Eng., 2017: pp. 2306–2311.

[18] L.V. Andersen, A. Peplow, P. Bucinskas, Efficiency of nearly periodic structures for mitigation of ground vibration, in: 2017. https://doi.org/10.7712/120117.5439.18112.

[19] A. Peplow, L. Andersen, P. Bucinskas, Variations within simple models for structure-soil interaction, in: 24th Int. Congr. Sound Vib. ICSV 2017, 2017.

[20] A.T. Peplow, L.V. Andersen, P. Bucinskas, Environmental vibration reduction utilizing an array of mass scatterers, in: Procedia Eng., 2017. https://doi.org/10.1016/j.proeng.2017.09.359.

[21] G.A. Athanasopoulos, P.C. Pelekis, Ground vibrations from sheetpile driving in urban environment: Measurements, analysis and effects on buildings and occupants, Soil Dyn. Earthq. Eng. 19 (2000) 371–387. https://doi.org/10.1016/S0267-7261(00)00008-7.

[22] F. Deckner, K. Viking, S. Hintze, Aspects of ground vibrations due to pile and sheet pile driving, Electron. J. Geotech. Eng. 20 (2015) 11161–11176.

[23] F. Deckner, K. Viking, C. Guillemet, S. Hintze, Instrumentation system for ground vibration analysis during sheet pile driving, Geotech. Test. J. 38 (2015) 893–905. https://doi.org/10.1520/GTJ20140275.

[24] F. Deckner, K. Viking, S. Hintze, Wave Patterns in the Ground: Case Studies Related to Vibratory Sheet Pile Driving, Geotech. Geol. Eng. 35 (2017) 2863–2878. https://doi.org/10.1007/s10706-017-0285-x.

[25] L. V Andersen, A.T. Peplow, P. Persson, Mitigation of ground vibrations by circular arrays of rigid blocks, in: M. Papadrakakis, M. Fragiadakis (Eds.), Proc. 7th Int. Conf. Comput. Methods Struct. Dyn. Earthq. Eng. Vol. 2, National Technical University of Athens, Athens, 2019: pp. 3422–3447.

[26] A.F. Homayoun Rooz, A. Hamidi, A numerical model for continuous impact pile driving using ALE adaptive mesh method, Soil Dyn. Earthq. Eng. 118 (2019) 134–143. https://doi.org/10.1016/j.soildyn.2018.12.014.

[27] W.T. Thomson, Transmission of elastic waves through a stratified solid medium, J. Appl. Phys. 21 (1950) 89–93.

[28] N.A. Haskell, The dispersion of surface waves on multilayered media, Bull. Seismol. Soc. Am. 43 (1953) 17–34.

[29] L. Andersen, J. Clausen, Impedance of surface footings on layered ground, Comput. Struct. 86 (2008) 72–87.

[30] R. Wang, A simple orthonormalization method for stable and efficient computation of Green's functions, Bull. Seismol. Soc. Am. 89 (1999) 733–741.

EURODYN 2020
XI International Conference on Structural Dynamics
M. Papadrakakis, M. Fragiadakis, C. Papadimitriou (eds.)
Athens, Greece, 23–26 November 2020

TIME DOMAIN BEM-FEM COUPLING FOR SEISMIC SOIL-STRUCTURE INTERACTION ANALYSES CONCEIVED FOR AN ANSYS-MATLAB WORKFLOW

Francesca Taddei[1], Bettina Chocholaty[2], and Gerhard Müller[1]

[1]Chair of Structural Mechanics TUM Department of Civil, Geo and Environmental Engineering
Arcisstr. 21, 80333, Munich
e-mail: {francesca.taddei, gerhard.mueller}@tum.de

[2] Chair of Vibro-Acoustics of Vehicles and Machines TUM Department of Mechanical Engineering
Boltzmannstr. 15, 85748 Garching near Munich
e-mail: bettina.chocholaty@tum.de

Keywords: Soil-Structure Interaction, Boundary Element Method, Finite Element Method, BEM-FEM coupling, Time Domain.

Abstract. *In this contribution, we present the implementation of the coupling between the Finite Element Method (FEM) and the Boundary Element Method (BEM) in the time domain, for the analysis of the Soil-Structure Interaction (SSI) in the three dimensional space. The Boundary Element Method is based on the transient fundamental solutions for the half-space. The coupling between the BEM and the FEM is obtained using the soil's stiffness matrix and the soil reaction forces, which result from a convolution integral. The coupling is implemented linking the software MATLAB with the software ANSYS. The system of equations is solved in ANSYS and within the solution step MATLAB is activated to calculate the soil's stiffness matrix and the interaction forces at the interface between soil and structures at the current time step. Verification examples for static and dynamic cases are presented. A case study for a seismic excitation is presented to show the applicability of the proposed method.*

1 INTRODUCTION

The dynamic interplay between the buildings and the underlying soil is referred to as Soil-Structure Interaction (SSI). The soil acts both as a compliant support with a frequency-dependent flexibility and as a energy absorber, due to its infinite size. For certain combinations of buildings and soil, the SSI may lead to an amplification of the dynamic response w.r.t. the static response of the whole system, to a shift of the natural frequencies of the buildings and to a change in damping properties. Therefore, it is important to account for the dynamic behavior of the soil and its effect on the dynamic behaviour of the structures placed on it.. The main difficulty of simulating the SSI is related to the infinite size of the soil, for which the Sommerfeld radiation condition must be fulfilled.

Different methods exist to account for the SSI in seismic analysis of buildings, the most popular of which are the Finite Element Method (FEM), the Finite Difference Method (FDM) and the Boundary Element Method (BEM). A detailed state of the art can be found in [1].

For FEM the whole domain is discretised whereas in the BEM only the boundaries are divided into elements. Consequently, the dimension of the problem is reduced by one when using BEM. This leads to less necessary storage space. Moreover, the BEM can achieve higher accuracy for the results, since it uses fundamental solutions as weighting functions. These fundamental solutions fulfill exactly the boundary conditions.

Although research has been conducted on boundary elements since the 1960s, BEM is not as established as the FEM, mainly due to the fully populated system of equations generated by the BEM and the requirement of the existence of suitable fundamental solutions for the investigate soil systems (such as an homogeneous half space, a layered half space, etc...). Additionally, several commercial tools made the FEM user-friendly and versatile, while the BEM is rarely available as a ready-to-use black box. An extensive overview of the development of BEM can be found in [2].

The BEM for SSI can be used both in the Time Domain (TD) and in the Frequency Domain (FD), depending on the available fundamental solutions (also called Green's functions). The TD-BEM can be used for nonlinear problems and can lead to less computational effort for transient loads with a narrow frequencies spectrum. As a matter of fact, the transient fundamental solutions have a bounded support, while the FD fundamental solutions never vanish.

From general descriptions of the coupling of BEM and FEM for elastodynamics [3][4][5], the application to SSI problems was straightforward [6].

Further improvements of the BEM for SSI were achieved by using fundamental solutions for the half-space instead of the full space [7]. Depending on the given problem, the suitable fundamental solution can be chosen among the available ones [8] to optimize the computation. Several studies have been conducted on the topic of BEM for 2D- and 3D-structures in the time domain dealing with different issues, such as the choice of the suitable fundamental solutions (e.g. [9] and [10]) or the coupling of incompatible interfaces of BEM and FEM for 2D boundary elements ([11]).

Recently, Vasilev et al. [12] developed a hybrid computational tool, based on the FEM/BEM coupling. The hybrid numerical scheme is realized via the sub-structure approach, integrating the seismically active far-field geological media as a macro-finite element in the commercial program ANSYS. Here, they assume a plane strain state.

Galvin and Romero [13] developed a numerical tool *SSIFiBo* in MATLAB to study dynamic soil-structure interaction problems. The model is based on a three dimensional TD-BEM. This model allows computing structural forced-vibrations, as well as seismic responses.

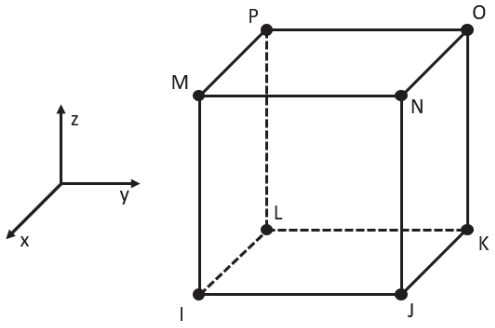

Figure 1: Notation of nodes for *SOLID185*, according to [18, p. 960]

Schepers [14] improved an existing customization of ANSYS [15] [16] [17] which allows FEM-BEM coupling of structures at the surface of an arbitrarily layered half-space, both in time and frequency domain.

In this work, we present the *Ssibefe* tool, a FEM-BEM coupling where the FEM subsystem (the building) is modeled using ANSYS and the BEM subsystem (the soil) is treated using MATLAB. The loading can be applied to the FEM elements and nodes and/or can be defined as a propagating transient plane wave in the soil with an arbitrary angle of incidence w.r.t the surface. Pre- and postprocessing is performed in ANSYS. The TD fundamental solutions for the homogenous half-space are taken from [8] and the procedure for the implementation is similar to the one described by [15], [16] and [17].

2 METHODS

2.1 MODELLING THE STRUCTURE WITH THE FINITE ELEMENT METHOD

The equation of motion for the structure reads:

$$\mathbf{M}\ddot{\mathbf{u}}(t) + \mathbf{C}\dot{\mathbf{u}}(t) + \mathbf{K}\mathbf{u}(t) = \mathbf{P}(t) + \mathbf{Q}(t), \tag{1}$$

where $\mathbf{M}$ is the mass matrix, $\mathbf{C}$ the damping matrix, $\mathbf{K}$ the stiffness matrix, $\mathbf{u}(t)$ the displacements and $\mathbf{P}(t)$ the external loading. All the aforementioned vectors and matrices can be determined as usual by means of classical FEM formulations. The key vector in this formulation is the vector $\mathbf{Q}(t)$, which contains the soil reactions at the interaction nodes. This is unknown and represents the influence of the soil as nodal forces, which result from the contact pressure at the soil–structure interface. This can be computed with the BEM formulation, described in section 2.2.

The analysis of the finite system is done with the commercial software *Ansys Mechanical APDL 2019 R2*. The structure is modelled by 3D solid elements, specifically the *SOLID185*-elements, which consist of 8 nodes [18]. The arrangement of the nodes is depicted in fig. 1.

2.2 MODELLING THE SOIL WITH THE BOUNDARY ELEMENT METHOD

2.2.1 Theoratical Background

At the heart of the TD-BEM used here lies the transient fundamental solutions for the 3D the half space subjected to a vertical or horizontal unit point load on the surface, that changes

in time as a Heaviside function (s. annex A). These satisfy the traction-free condition at the surfaces of the soil and the Sommerfeld radiation condition.

We start from the discretized form of the boundary integral formulation of the Lamé-Navier equation [19], in absence of body forces. At first the time dependency is not considered and will be treated separately in section 2.3. The displacements $\mathbf{w}^i$ at point i on the soil surface can be written as:

$$\mathbf{c}^i\mathbf{w}^i(\mathbf{x}^i) = \sum_{e=1}^{E}\sum_{n=1}^{N} \mathbf{q}_n^e \int_{S_e} \mathbf{N}_n \mathbf{g}(\mathbf{x},\mathbf{x}^i) dS - \sum_{e=1}^{E}\sum_{n=1}^{N} \mathbf{w}_n^e \int_{S_e} \mathbf{N}_n \mathbf{t}(\mathbf{x},\mathbf{x}^i) dS \tag{2}$$

with

$\mathbf{g}(\mathbf{x},\mathbf{x}^i)$: fundamental solution for the displacements evaluated at point $\mathbf{x}^i$ for loads at $\mathbf{x}$
$\mathbf{t}(\mathbf{x},\mathbf{x}^i)$: fundamental solution for the tractions evaluated at point $\mathbf{x}^i$ for loads at $\mathbf{x}$
$\mathbf{q}_n^e$: nodal forces at point $\mathbf{x}^i$
$\mathbf{w}_n^e$: nodal displacements at point $\mathbf{x}^i$
$\mathbf{N}_n$: shape functions of nodes at point $\mathbf{x}^i$
$\mathbf{c}^i$: geometrical coefficient, which is related to the the position of the load and contains unitary values at the soil surface for a smooth boundary
N, E, S_e: number of nodes per element, number of elements and area of each element respectively.

We assume constant tractions on each boundary element. Therefore, each boundary element has only one node at the centre of the bottom surface of the coupled finite element. The elements are pictured in fig. 2a. Here, the red circled nodes define the contributing coupling nodes.

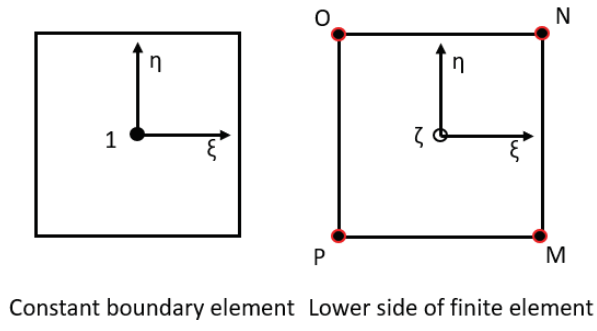

(a) Coupling nodes for constant shape functions.

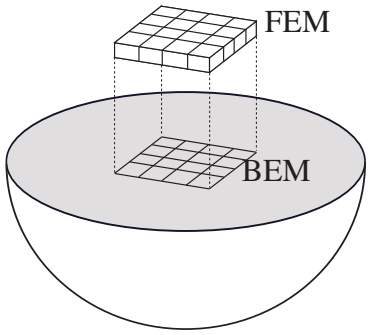

(b) Coupling surface.

Figure 2: Coupling between soil and structure.

We consider Heaviside-time-varying unit forces for each nodal component of displacements and tractions. If the load position is located inside the domain, the stresses $\mathbf{t}(\mathbf{x},\mathbf{x}^i)$ on the surface are equal to zero and only the first part of the right side of eq. (2) will be considered in further derivations, leading to the following expression for the the displacements:

$$\mathbf{c}^i\mathbf{w}^i(\mathbf{x}^i) = \sum_{e=1}^{E}\sum_{n=1}^{N} \mathbf{q}_n^e \Delta\mathbf{G}_n^e \tag{3}$$

where

$$\Delta\mathbf{G}_n^e = \int_{-1}^{1}\int_{-1}^{1} \mathbf{N}_n(\xi,\eta)\mathbf{g}(\mathbf{x},\mathbf{x}^i(\xi,\eta))J(\xi,\eta)d\xi d\eta \tag{4}$$

Here, $J(\xi, \eta)$ denotes the determinant of the Jacobian for the transformation of coordinates from the original Cartesian to a local element reference coordinate system.

To obtain the flexibility matrix of the soil, the integral in eq. (3) is evaluated $(E \cdot N)^2$ times. The integral is performed for all the interaction nodes as an observation point and with the loading position being located on every interaction node (collocation point method). This leads to a matrix $\mathcal{G}^{ji}$, where the rows j indicate the loading position information whereas the columns i indicate the observation position information. Once the unitary coefficients $\mathbf{c}^i$ are included in the system matrix, eq. (3) can be written in matrix form as:

$$\mathbf{w} = \mathcal{G}\mathbf{q} \tag{5}$$

The fundamental solution $\mathbf{g}(\mathbf{x}, \mathbf{x}^i)$ is a antisymmetrical second order tensor, originally defined in cylindrical coordinates, as described in annex A:

$$\mathbf{g}^{\text{cyl}} = \begin{bmatrix} g_{rr} & 0 & g_{rz} \\ 0 & g_{\phi\phi} & 0 \\ g_{zr} & 0 & g_{zz} \end{bmatrix} \tag{6}$$

with $g_{zr} = -g_{rz}$. The transformation from cylindrical to Cartesian coordinates is performed according to [15] (s. annex B).

Following the suggestions in [20], if the loading point $\mathbf{x}$ coincides with the observation point $\mathbf{x}^i$, a $1/r$-singularity occurs. This integration is solved using a transformation to polar coordinates according to [21] (s. annex C).

Summarizing, eq. (5) says that the interaction of the soil with any other elastic body at its surface can be represented by integrals over the contact surface and a force-displacement relationship can be established to built the stiffness or flexibility matrix of the soil.

The fundamental solutions depend on the dimensionless time τ which in turn depends on on the time t. The time dependency will be treated in the next section.

2.3 Time discretization

According to [15], for the application of the proposed method in the time domain, the displacement at the current time depends on the current contact pressures and on its history and is obtained with a convolution integral. For a Heaviside loading function, the second Duhamel integral is performed:

$$\begin{aligned} \mathbf{w}(t) &= \mathcal{G}(t) \otimes \mathbf{q}(t) \\ \mathbf{w}(t) &= \mathbf{q}(0)\mathcal{G}(t) + \int_0^t \mathcal{G}(t-\tau)\frac{d\mathbf{q}(\tau)}{d\tau}d\tau = \int_0^t \mathcal{G}(t-\tau)\frac{d\mathbf{q}(\tau)}{d\tau}d\tau. \end{aligned} \tag{7}$$

The transient fundamental solutions are captured in the matrix $\mathcal{G}(t)$

$$\mathcal{G}(t) = \begin{bmatrix} \mathcal{G}_{xx}(t) & \mathcal{G}_{xy}(t) & \mathcal{G}_{xz}(t) \\ \mathcal{G}_{yx}(t) & \mathcal{G}_{yy}(t) & \mathcal{G}_{yz}(t) \\ \mathcal{G}_{zx}(t) & \mathcal{G}_{zy}(t) & \mathcal{G}_{zz}(t) \end{bmatrix}. \tag{8}$$

The integral is split into intervals of the length Δt. By calculating the mean of the upper and lower value, the soil displacements for the time step $i+1$ can be deduced

$$\mathbf{w}^{i+1} = \frac{\mathcal{G}^{i+1} - \mathcal{G}^{i}}{2}\cancelto{0}{\mathbf{q}^0} + \frac{\mathcal{G}^{i+1} - \mathcal{G}^{i-1}}{2}\mathbf{q}^1 + \ldots + \frac{\mathcal{G}^{1} - \cancelto{0}{\mathcal{G}^0}}{2}\mathbf{q}^{i+1} \tag{9}$$

Subsequently, the flexibility of the soil is obtained after inserting the following abbreviations valid for constant time step duration for the whole simulation

$$\begin{aligned} \mathbf{F}^i &= \frac{1}{2}\left(\mathcal{G}^{i+1} - \mathcal{G}^{i-1}\right) \\ \mathbf{F}^{cur} &= \frac{1}{2}\mathcal{G}^1 = \frac{1}{2}\mathcal{G}(\Delta t) \end{aligned} \tag{10}$$

and considering the initial condition $\mathbf{q}^0 = 0$ and the relation $\mathcal{G}^0 = 0$, which results from causality, the deformations of the soil yield

$$\mathbf{w}^{i+1} = \underbrace{\mathbf{F}^i\mathbf{q}^1 + ... + \mathbf{F}^1\mathbf{q}^i}_{\mathbf{w}^{hist}} + \mathbf{F}^{cur}\mathbf{q}^{i+1} \tag{11}$$

If, additionally, a seismic excitation $\mathbf{s}$ occurs, one has to substitute the absolute displacements at the interaction nodes $\mathbf{w}^{i+1}$ with the relative displacements $(\mathbf{w}^{i+1} - \mathbf{s}^{i+1})$ to get

$$\mathbf{w}^{i+1} = \mathbf{w}^{hist} + \mathbf{F}^{cur}\mathbf{q}^{i+1} + \mathbf{s}^{i+1} \tag{12}$$

3 Implementation of the coupling

First, interaction nodes are defined, which are located at shared surfaces of the structure and the soil.

Fig. 2b shows the coupling surface between BEM and FEM for a square foundation. Since the numbering of the nodes is different for the BEM and the FEM subsytem, different letters identify different quantities:

- $\mathbf{u}_I$: displacements of the structure according to the nodal ordering of FEM at the interaction surface
- $\mathbf{v}$: displacements of the structure for nodal ordering of BEM at the interaction surface
- $\mathbf{w}$: displacements of the soil for nodal ordering of BEM at the interaction surface

The transformation matrices $\mathbf{T_u}$ and $\mathbf{T_q}$ help to couple the displacements of the two subsystems at the interface. These matrices are described in annex D.

From eq. (12), the soil's contact pressure can be computed as

$$\mathbf{q}^{i+1} = [\mathbf{F}^{cur}]^{-1}(\mathbf{w}^{i+1} - \mathbf{w}^{hist} - \mathbf{s}^{i+1}) \tag{13}$$

To satisfy compatibility at the interaction surface the structural displacements must equal the soil's displacement

$$\mathbf{w}^{i+1} = \mathbf{v}^{i+1} = \mathbf{T}_u\mathbf{u}_I^{i+1} \tag{14}$$

The soil reaction forces at the FEM nodes result from the combination of eq. (14) with eq. (15) as

$$\mathbf{Q}_I^{i+1} = \mathbf{T}_q\mathbf{q}^{i+1} = \underbrace{\mathbf{T}_q[\mathbf{F}^{cur}]^{-1}\mathbf{T}_u}_{\mathbf{K}_{soil}^{cur}}\mathbf{u}_I^{i+1} - \underbrace{\mathbf{T}_q[\mathbf{F}^{cur}]^{-1}\mathbf{w}^{hist}}_{\mathbf{Q}_I^{hist}} - \underbrace{\mathbf{T}_q[\mathbf{F}^{cur}]^{-1}\mathbf{s}^{i+1}}_{\mathbf{Q}_I^{seism}}, \tag{15}$$

where $\mathbf{K}_{soil}^{cur}$ is the soil's stiffness matrix.

Therefore, the equation of motion of the coupled problem becomes

$$\begin{bmatrix} \mathbf{M}_{RR} & \mathbf{M}_{RI} \\ \mathbf{M}_{IR} & \mathbf{M}_{II} \end{bmatrix} \begin{pmatrix} \ddot{\mathbf{u}}_R^{i+1} \\ \ddot{\mathbf{u}}_I^{i+1} \end{pmatrix} + \begin{bmatrix} \mathbf{C}_{RR} & \mathbf{C}_{RI} \\ \mathbf{C}_{IR} & \mathbf{C}_{II} \end{bmatrix} \begin{pmatrix} \dot{\mathbf{u}}_R^{i+1} \\ \dot{\mathbf{u}}_I^{i+1} \end{pmatrix} + \begin{bmatrix} \mathbf{K}_{RR} & \mathbf{K}_{RI} \\ \mathbf{K}_{IR} & \mathbf{K}_{II} + \mathbf{K}_{soil}^{cur} \end{bmatrix} \begin{pmatrix} \mathbf{u}_R^{i+1} \\ \mathbf{u}_I^{i+1} \end{pmatrix} = \begin{pmatrix} \mathbf{P}_R^{i+1} \\ \mathbf{P}_I^{i+1} \end{pmatrix} + \begin{pmatrix} 0 \\ \mathbf{Q}_I^{hist} + \mathbf{Q}_I^{seism} \end{pmatrix} \tag{16}$$

where I indicated the degrees of freedom (DOFs) at the interaction nodes, whereas the remaining DOFs are marked with R.

The flexibility matrix of the soil $\mathbf{F}^i$ in eq. (10) has to be calculated for every time step to deduce the quantity $\mathbf{w}^{hist}$.

The structural displacements $\mathbf{u}_I^i$ at the interaction nodes are computed by ANSYS at every time step and used to compute the soil reaction forces at $i+1$. The soil stiffness is added to the structure's stiffness through a user-defined super-element in ANSYS (element type *MATRIX50*) and the soil reactions are applied as external loads at the interaction nodes. The master DOFs of the soil super-element are the DOFs of the coupling nodes of the FEM-structure at the soil surface. With this configuration the system can be solved with usual solution routines in ANSYS. An overall calculation sequence for the proposed scheme is given in annex E.

It is to highlight, that, if the soil properties, the discretization of the elements at the interaction surface and the time step remain unchanged, a new analysis with different parameters and seismic and/or external loading can be carried out reusing the same flexibility matrix. This leads to a relevant reduction of computational time.

An interactive connection between MATLAB and ANSYS is created through the toolbox *aaS* (ANSYS as a Server) and the Mechanical APDL preprocessor and solver are accessed directly through MATLAB.

4 VERIFICATION

For the verification, we present the dynamic analysis of a rigid square foundation loaded with a Heaviside point load at its center. After the oscillation has decayed, the static displacement can be observed, so that also the static flexibility of the system can be compared to literature values. The results are compared to the ones found in [16], although we assume a Poisson's ratio $\nu = 0.25$ for the soil, while the reference results are computed with $\nu = 0.33$. As an additional reference, the static flexibility in different directions is compared to the reference values given in [22, p. 43].

As the results are normalized w.r.t. the quadratic foundation geometry and to the soil properties, the foundation side length a, the foundation thickness h, the shear modulus of the soil μ_s and the soil density ρ_s can be chosen arbitrarily. The Poisson's ratio is given ($\nu_s = 0.25$). The other problem parameters are given in tab. 1. In order to simplify the invetsigation, the Poisson's ratio of the foundation is set equal to 0, but could take any arbitrary value.

The vertical displacement u_z due to a vertical load P_z, the horizontal displacement u_x due to a horizontal load P_x, the rotation ϕ_y due to a moment around the y-axis M_y, the rotation ϕ_z due to a torsional moment M_z and finally the rotation ϕ_y due to a horizontal load P_x are examined. The loading starts at $\tau = \frac{tc_s}{a} = 1$. Two cases are investigated shown in fig. 4:

- massless foundation: the response follows the shape of the variation in time of the loading until it reaches a state of rest at $\approx \tau = 3$.

Table 1: Problem properties of the verification case.

Foundation density	massless foundation: $\rho_f = 0$
	massive foundation: $\rho_f = \frac{\rho_s}{h}\sqrt{\frac{a^2}{\pi}}$
Young's modulus of the foundation	$E_f \approx \mu_s * 10^{11}$
Poisson's ratio of the foundation	$\nu_f = 0$
Poisson's ratio of the soil	$\nu_s = 0.25$

- massive foundation: the foundation oscillated around the static response and, eventually, approaches the static solution at different times τ for the different directions of loading.

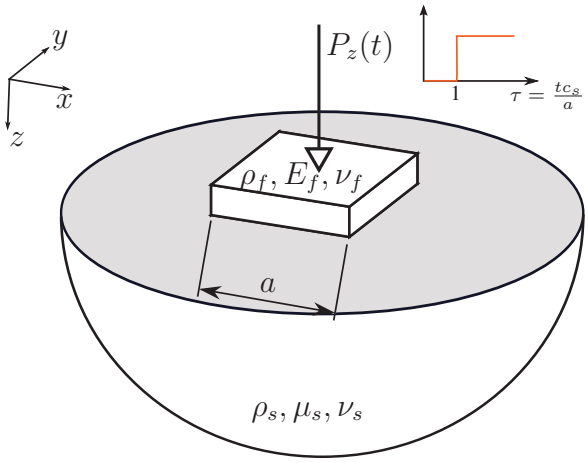

Figure 3: Verification case, shown for a vertical load.

The foundation and the soil surface are discretised with 8×8 elements with the side length $l = a/8$. The time step size is chosen as $\Delta t = 0.75l/c_s$, where $c_s = \sqrt{\frac{\mu_s}{\rho_s}}$ is the shear wave velocity of the soil.

The static flexibility is deduced from the displacements at rest. These are then compared in tab. 2 to the results from [16, pp. 107-111] and from the static stiffness values in [22, p. 43].

	$\frac{\mu_s a}{P_z}u_z$	$\frac{\mu_s a}{P_x}u_x$	$\frac{\mu_s a^3}{M_y}\phi_y$	$\frac{\mu_s a^3}{M_z}\phi_z$	$\frac{\mu_s a^2}{P_x}\phi_y$
Ssibefe	0.326	0.398	1.551	1.050	0.067
Bode [16]	0.2951	0.379	1.419	0.940	0.064
discrepancy [%]	1.11	1.05	1.09	1.12	1.05
Wolf [22]	0.319	0.380	1.5	0.964	-

Table 2: Static flexibility of a rigid, massless foundation on a homogeneous half-space.

As can be observed in tab. 2, the results are in good agreement. Nevertheless, small discrepancies especially between [16] and the results from *Ssibefe* occur for all modes, because of the different Poisson's ratios used. This is also confirmed in fig. 4a and fig. 4b, which show the transient displacements for the vertical and horizontal case respectively. Considering the different Poisson ratios, the different methods show a satisfying agreement.

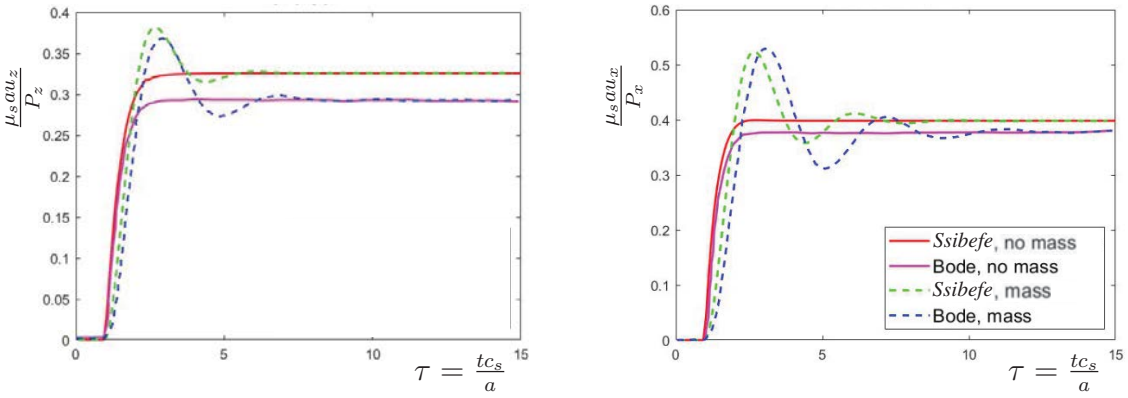

(a) Vertical displacement.

(b) Horizontal displacement.

Figure 4: Normalized displacements for a rigid square foundation subjected to a transient point load at the center in different directions.

5 SEISMIC APPLICATION OF THE *Ssibefe*

For the demonstration of the application of the *Ssibefe* for seismic problems, we present the dynamic analysis of an elastic cube of side length a resting on an elastic half space subjected to a seismic excitation resulting from an incident plane wave that propagates through the soil. Fig. 5 shows the investigated scenario.

Depending on the angle of incidence the wave, the direction of propagation and the time function, the seismic excitation at the interaction points $\mathbf{x}_I$ can be estimated according to eq. (17). The time function $s(t)$ of the plane wave can be chosen arbitrarily, from synthetic accelerogram to recorded data to analytical expressions. In this application, we assume a Ricker wavelet for the function $s(t)$, described by eq. (18) and plotted in fig. 6 for the specific loading parameters given in tab. 3.

$$\mathbf{s} = s\left(t - \frac{(\mathbf{x}_I - \mathbf{x}_0)^T \mathbf{n}}{c_{\text{ind}}}\right) \mathbf{s}_0 \tag{17}$$

$$s(t) = \left(1 - \pi^2 f_0^2 t^2\right) e^{\left(-\pi^2 f_0^2 t^2\right)} \tag{18}$$

The spectrum of the input is shown together with the output in fig. 9. In this application, the seismic wave propagates in the positive x-direction and the soil particles move along the x-axis, simulating a P-wave. The coordinates of the corner A of the building are $\mathbf{x} = [40\text{ m}, 5\text{ m}, 0\text{ m}]^T$ and the faces of the cubic building are oriented as the coordinate system.

The soil and structural properties are listed in tab. 5. The natural frequencies of the fixed-base cube are also given in tab. 4 for a better result interpretation. The element size is $l = 2.5$ m and the time step size is chosen equal to 0.025 s.

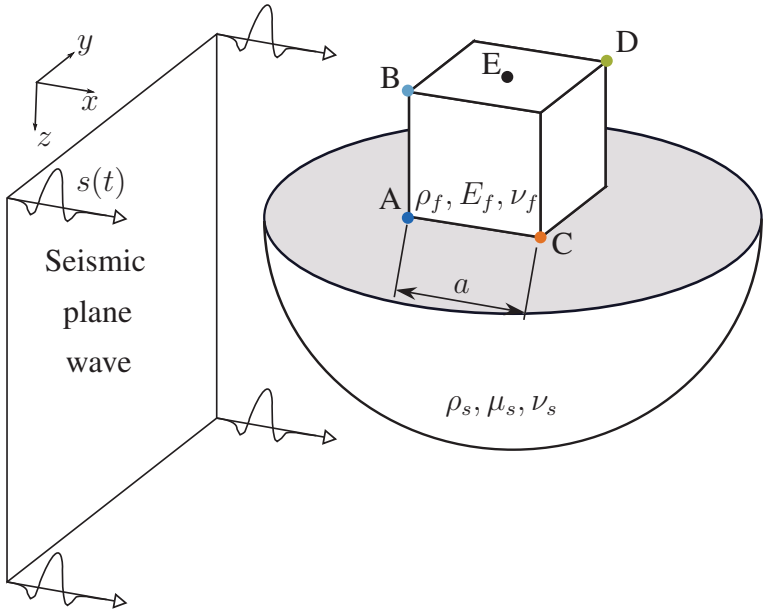

Figure 5: Building resting on an elastic half space subjected to a seismic excitation resulting from an incident plane wave that propagates through the soil.

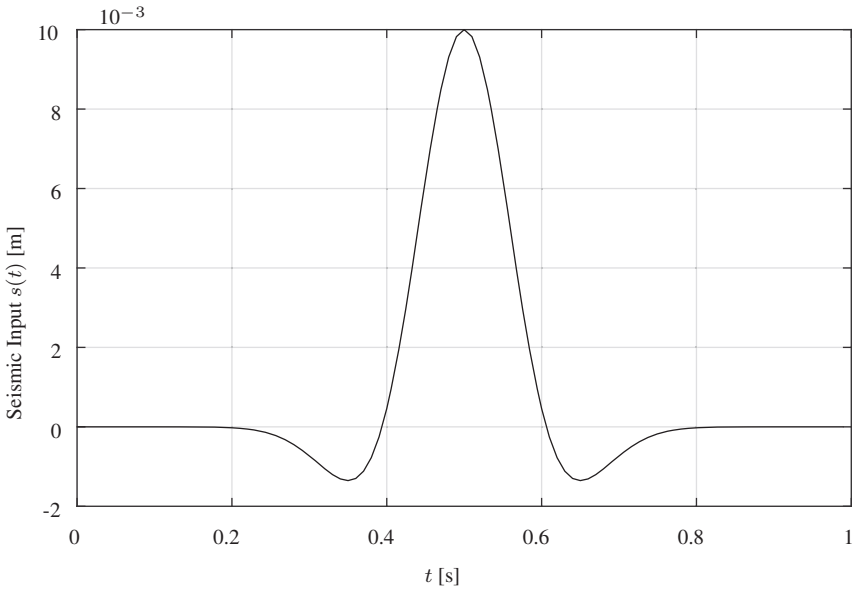

Figure 6: Time function of the seismic wave.

Table 3: Seismic load parameters.

Source position at $t = 0$	$\mathbf{x_0} = [0 \ 0 \ 0]^T$	[m]
Orientation of the wave	$\mathbf{n} = [1 \ 0 \ 0]^T$	[-]
Amplitude of the wave	$\mathbf{s}_0 = [0.01 \ 0 \ 0]^T$	[m]
Incident wave velocity	$c_{\text{ind}} = c_p = \sqrt{\frac{2\mu_s(1-\nu_s)}{1-2\nu_s}}$	[m/s]
Central frequency of the Ricker wavelet	$f_0 = 3$	[Hz]

Table 4: Soil and Structural properties.

μ_s	$40{\cdot}10^6$	[N/m^2]
ρ_s	2200	[Kg/m^3]
ν_s	0.25	[-]
a	40	[m]
E_f	$83{\cdot}10^6$	[N/m^2]
ρ_f	1000	[Kg/m^3]
ν_f	0.3	[-]

Table 5: Natural frequencies of the fixed-base building.

1. bending x, y	0.76750	[Hz]
1. torsion/bending	1.0436	[Hz]
1. axial	1.8322	[Hz]
2. bending x, y	2.0320	[Hz]
2. torsion/bending	2.5050	[Hz]
3. torsion/bending	3.0997	[Hz]
4. torsion/bending	3.1589	[Hz]
1. bending z	3.1680	[Hz]
2. axial/bending	3.5130	[Hz]

The results are compared to the ones obtained with the FEM/BEM coupling proposed by Bode [23], which runs on a ANSYS/FORTRAN Framework. The authors had the possibility to run the same identical example with both the existing framework [23] and the newly implemented *Ssibefe*. The only difference is the material damping in the soil, which we assumed equal to zero, while in Bode [23] it is small (0.1%) but not exactly zero. In the following discussion, only the horizontal displacements are shown, being those the largest. However, all the components of displacements and stresses can be computed.

Fig. 7 shows the horizontal displacements at the building base, at A and C. The delay of the wave arrival between the two points is correctly represented. Fig. 8 shows the horizontal displacements at the building top, at B and D and E. The spectra in fig. 9 show that the response at E is characterized by a natural frequency 0.6 Hz, which corresponds to the natural frequency of the 1st bending mode of the fixed-base building (0.76750 Hz) considering the influence of the soil. At the corners B and D also higher modes play an important role, as shown in fig. 9.

All the plots show good agreement between the reference results (Bode [23]) and the proposed results based on the *Ssibefe* tool. In general, there is a very slight difference of damping during the final oscillations, which leads to slightly different amplitudes and periods of oscillation. However, the difference can be neglected.

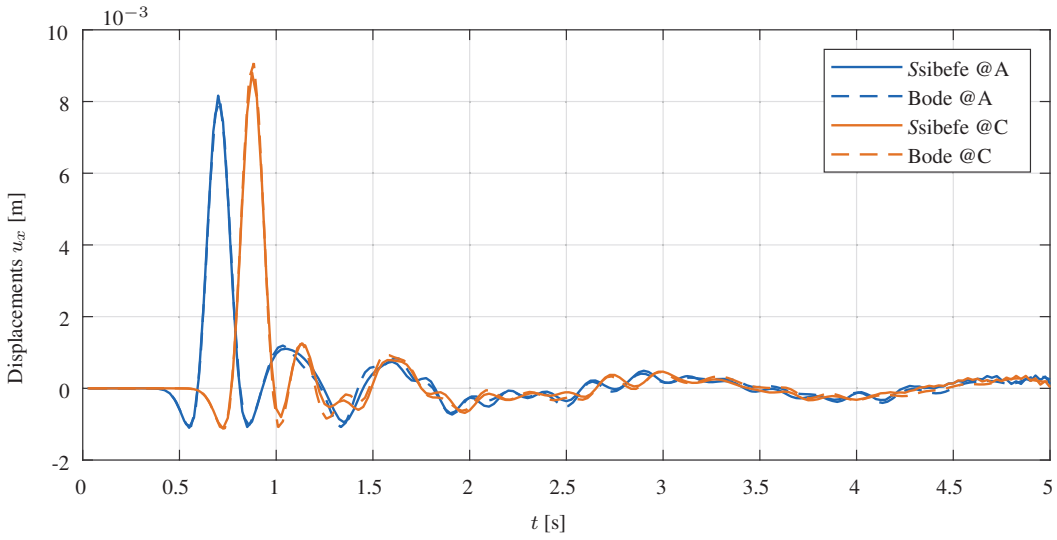

Figure 7: Horizontal displacements at the building base, at A and C.

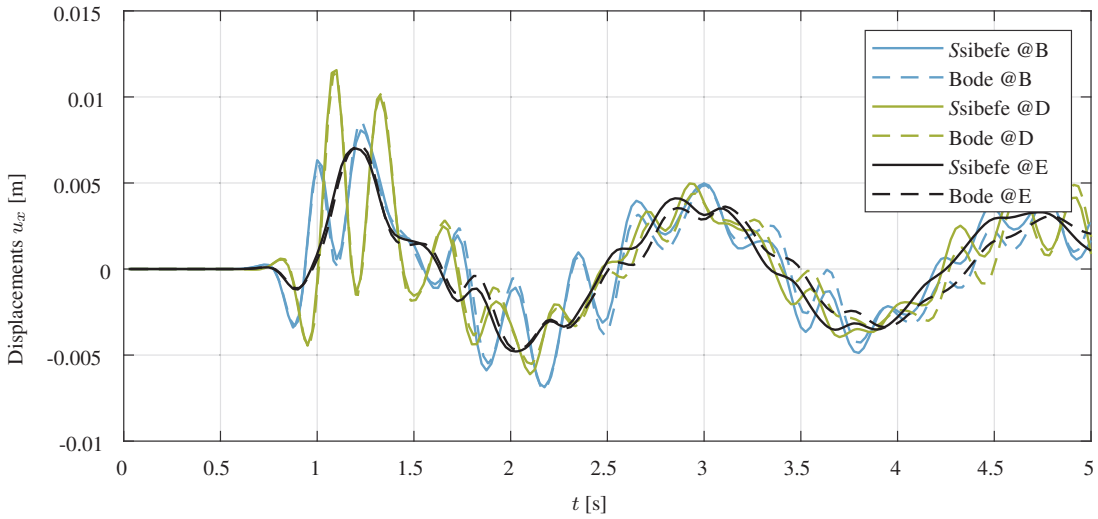

Figure 8: Horizontal displacements at the building top, at B and D and E.

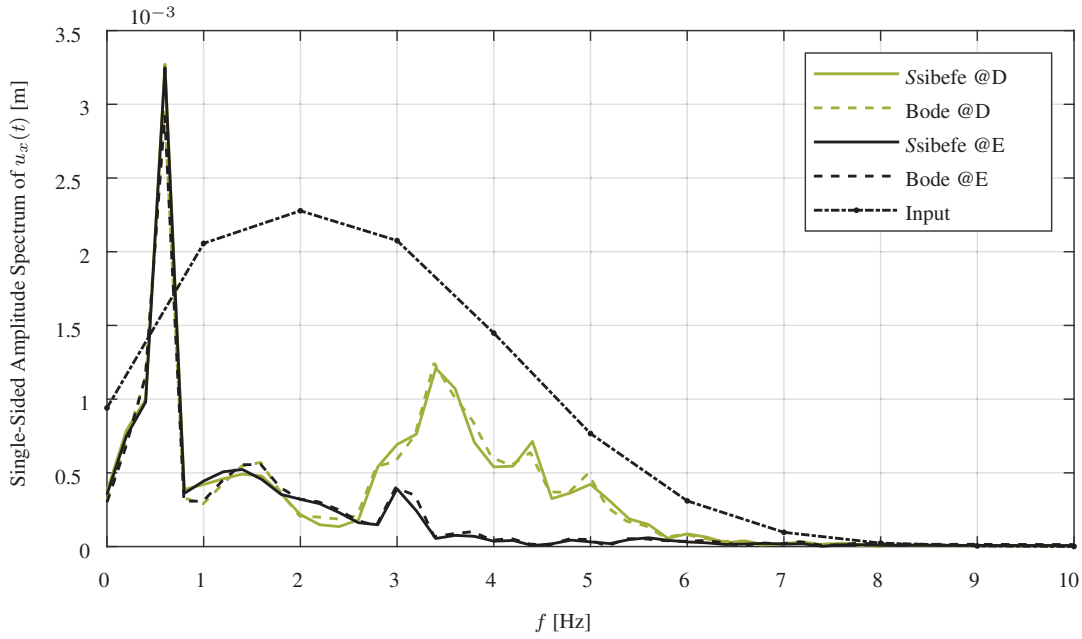

Figure 9: Spectra of the horizontal displacements at D and E, compared to the spectrum of the time function of the seismic wave.

6 CONCLUSIONS

In this contribution, we presented a new implementation of the coupling between the BEM and the FEM for soil-structure interaction problems, in the time domain. The developed computer tool *Ssibefe* is based on an interactive connection between MATLAB and ANSYS. The FEM part is generated through the ASNYS preprocessor, the soil reaction forces and the soil dynamic stiffness are computed with MATLAB functions based on the BEM formulation . The generated quantities are combined together into the coupled system of equations of the SSI system and the resulting system is solved with usual ASNYS solver routines. We presented the theoretical background of the methods and the time discretization approach. The tool can be used for both external loads on the structure and seimsic excitation. For the verification, we presented the dynamic analysis of a rigid square foundation loaded with a Heaviside point load at its center. The dynamic response as well as the static flexibility were compared to literature values, showing good agreement between the references and the results of the new implementation. Finally, we demonstrated the applicability of the *Ssibefe* tool for seismic problems, showing the dynamic analysis of an elastic cube of side length a resting on an elastic half space subjected to a seismic excitation resulting from an incident plane wave that propagates through the soil. The results match those from a reference software and show the potential of the proposed tool. Further developments of the *Ssibefe* tool will enable the consideration of layered soils, using fundamental solutions in the frequency domain, and additional forms of the seismic excitation.

REFERENCES

[1] N. Sharma, K. Dasgupta, and A. Dey, "A state-of-the-art review on seismic ssi studies on building structures," *Innovative Infrastructure Solutions*, vol. 3, no. 1, p. 22, 2018.

[2] P. Dineva, G. Manolis, and F. Wuttke, "Fundamental solutions in 3d elastodynamics for the bem: A review," *Engineering Analysis with Boundary Elements*, vol. 105, pp. 47–69, 2019.

[3] O. Zienkiewicz, D. Kelly, and P. Bettess, "The coupling of the finite element method and boundary solution procedures," *International journal for numerical methods in engineering*, vol. 11, no. 2, pp. 355–375, 1977.

[4] G. Beer, "Finite element, boundary element and coupled analysis of unbounded problems in elastostatics," *International Journal for Numerical Methods in Engineering*, vol. 19, no. 4, pp. 567–580, 1983.

[5] S. Ahmad and P. Banerjee, "Time-domain transient elastodynamic analysis of 3-d solids by bem," *International Journal for Numerical Methods in Engineering*, vol. 26, no. 8, pp. 1709–1728, 1988.

[6] D. Karabalis and D. Beskos, "Dynamic response of 3-d flexible foundations by time domain bem and fem," *International Journal of Soil Dynamics and Earthquake Engineering*, vol. 4, no. 2, pp. 91–101, 1985.

[7] C. Pekeris, "The seismic surface pulse," *Proceedings of the national academy of sciences of the United States of America*, vol. 41, no. 7, pp. 469–480, 1955.

[8] E. Kausel, *Fundamental Solutions in Elastodynamics: A Compendium*. Cambridge i.a.: Cambridge University Press, 2006.

[9] D. Rizos and D. Karabalis, "A time domain bem for 3-d elastodynamic analysis using the b-spline fundamental solutions," *Computational mechanics*, vol. 22, no. 1, pp. 108–115, 1998.

[10] D. Rizos, "A rigid surface boundary element for soil-structure interaction analysis in the direct time domain," *Computational Mechanics*, vol. 26, no. 6, pp. 582–591, 2000.

[11] I. Guzelbey, B. Kanber, and A. Erklig, "Coupling of finite and boundary element methods with incompatible interfaces," *Mathematical and Computational Applications*, vol. 10, no. 3, pp. 321–330, 2005.

[12] G. Vasilev, S. Parvanova, P. Dineva, and F. Wuttke, "Soil-structure interaction using bem-fem coupling through ansys software package," *Soil Dynamics and Earthquake Engineering*, vol. 70, pp. 104 – 117, 2015.

[13] P. Galvin and A. Romero, "A matlab toolbox for soil-structure interaction analysis with finite and boundary elements," *Soil Dynamics and Earthquake Engineering*, vol. 57, pp. 10 – 14, 2014.

[14] W. Schepers, "Fast 3d fem-bem coupling for dynamic soil-structure interaction," *Procedia engineering*, vol. 199, pp. 391–396, 2017.

[15] R. Hirschauer, *Kopplung von Finiten Elementen mit Rand-Elementen zur Berechnung der dynamischen Baugrund-Bauwerk-Interaktion*. PhD thesis, Technische Universität Berlin, 2001.

[16] C. Bode, *Numerisches Verfahren zur Berechnung von Baugrund-Bauwerk-Interaktionen im Zeitbereich mittels GREENnscher Funktionen für den Halbraum*. PhD thesis, Technische Universität Berlin, 2000.

[17] C. Bode, R. Hirschauer, and S. Savidis, "Soil–structure interaction in the time domain using halfspace green's functions," *Soil Dynamics and Earthquake Engineering*, vol. 22, no. 4, pp. 283–295, 2002.

[18] I. ANSYS, "Element reference," *ANSYS Mechanical APDL*, no. Release 15.0, 2013.

[19] A. Romero, D. López-Mendoza, and P. Galvin, "Bem-fem formulation in time domain for ssi analyses in layered soils," *Compdyn 2015*, 2015.

[20] G. Beer, I. Smith, and C. Duenser, *The boundary element method with programming: for engineers and scientists*. Wien: Springer Science & Business Media, 2010.

[21] L. Gaul, M. Kögl, and M. Wagner, *Boundary element methods for engineers and scientists: an introductory course with advanced topics*. Berlin i.a.: Springer Science & Business Media, 2003.

[22] J. Wolf, *Soil-structure-interaction analysis in time domain*. Englewood Cliffs: Prentice Hall, 1988.

[23] C. Bode, R. Hirschauer, and S. A. Savidis, "Soil-structure interaction in the time domain using halfspace green's functions," *Soil Dynamics and Earthquake Engineering*, vol. 22, no. 4, pp. 283 – 295, 2002.

Appendices

A Green's Functions

In this section the above mentioned fundamental solutions are shown [8, p.78-83].

A.1 Vertical load

$$r = \sqrt{x^2 + y^2} \quad \text{distance between loading and source point} \tag{A.1}$$

$$a^2 = \left(\frac{c_s}{c_p}\right)^2 = \frac{1-2\nu}{2(1-\nu)} \quad \text{ratio of s- and p-wave velocity} \tag{A.2}$$

$$\tau = \frac{t c_s}{r} \quad \text{dimensionless time} \tag{A.3}$$

$$H(t-t_0) = \left\{ \begin{array}{ll} 1 & t > t_0 \\ \frac{1}{2} & t = t_0 \\ 0 & t < t_0 \end{array} \right\} \text{Heaviside step function} \tag{A.4}$$

$$K(k) = \int_0^{\pi/2} \frac{d\theta}{\sqrt{1-k^2\sin(\theta)^2}} \quad \text{complete first elliptic integral} \tag{A.5}$$

$$\Pi(n,k) = \int_0^{\pi/2} \frac{d\theta}{(1+n\sin(\theta)^2)\sqrt{1-k^2\sin(\theta)^2}} \quad \text{complete third elliptic integral} \tag{A.6}$$

$$R(\xi^2) = (1-2\xi^2)^2 + 4\sqrt{\xi^2-1}\sqrt{\xi^2-a^2} = 0 \quad \text{Rayleigh function} \tag{A.7}$$

with $\xi = c_s/c$ a dimensionless wave slowness including the wave velocity c.

The Rayleigh function is further multiplied by $(1-2\xi^2)^2 + 4\sqrt{\xi^2-1}\sqrt{\xi^2-a^2}$ to obtain the bicubic equation

$$1 - 8\xi^2 + 8\xi^4(3-2a^2) - 16\xi^6(1-a^2) = 0 \tag{A.8}$$

For this equation the three roots $[\xi_1^2, \xi_2^2, \xi_3^2]$ are being calculated. The first two are non-physical values whereas $\xi_3 = c_s/c_r$ equals the ratio of shear and Rayleigh wave velocity. Due to considerations of real and complex roots of equation (A.8) the solutions of the half-space u_{zz} and u_{rz} are split into two domains ($\nu < 0.2631$ and $\nu > 0.2631$). Additionally, the numerical calculation of the first and third kind of the elliptic integral has to be implemented. This is done by adapting some parts but still applying the MATLAB code according to [8, pp. 250f.]. Further parameters are derived as follows

$$A_i = \frac{(1-2\xi_i^2)^2\sqrt{\|a^2-\xi_i^2\|}}{4(\xi_i^2-\xi_j^2)(\xi_i^2.-\xi_k^2)} \quad \xi_i \neq \xi_j \neq \xi_k \tag{A.9}$$

$$B_i = \frac{(1-2\xi_i^2)(1-\xi_i^2)}{(\xi_i^2-\xi_j^2)(\xi_i^2-\xi_k^2)} \quad \xi_i \neq \xi_j \neq \xi_k \tag{A.10}$$

$$k^2 = \frac{\tau^2 - a^2}{1-a^2} \tag{A.11}$$

$$n_i = \frac{1-a^2}{a^2-\xi_i^2} \tag{A.12}$$

$$C = \frac{(2\xi_3^2-1)^3}{1-4\xi_3^2+8(1-a^2)\xi_3^6} \tag{A.13}$$

$$Q_1(\tau) = 1 + 2z + \sqrt{z^2+z} \tag{A.14}$$

$$z = \frac{a^2-\xi_1^2}{\tau^2-a^2} \tag{A.15}$$

Important to notice is the fact that Q_1 should be replaced with $1/Q_1$ if $|Q_1| > 1$. With these definitions the displacements u_{zz} and u_{rz} can finally be obtained by

Case 1: $\nu < 0.2631$

$$u_{zz} = \frac{P(1-\nu)}{2\pi\mu r} \left\{ \begin{array}{ll} 0 & \tau < a \\ \frac{1}{2}\left[1 - \sum_{i=1}^{3} \frac{A_i}{\sqrt{\|\tau^2-\xi_i^2|}}\right] & a < \tau < 1 \\ 1 - \frac{A_3}{\sqrt{\xi_3^2-\tau^2}} H(\xi_3 - \tau) & \tau > 1 \end{array} \right\} \tag{A.16}$$

$$u_{rz} = \frac{P\tau}{8\pi^2\mu r} \left\{ \begin{array}{ll} 0 & \tau < a \\ \frac{1}{(1-a^2)^{3/2}} \left[2K(k) - \sum_{i=1}^{3} B_i \Pi(k^2 n_i, k)\right] & a < \tau < 1 \\ \frac{k^{-1}}{(1-a^2)^{3/2}} \left[2K(k^{-1}) - \sum_{i=1}^{3} B_i \Pi(n_i, k^{-1})\right] + \frac{2\pi C}{\sqrt{\tau^2-\xi_3^2}} H(\tau - \xi_3) & \tau > 1 \end{array} \right\} \tag{A.17}$$

Case 2: $\nu > 0.2631$

u_{rz} not available

$$u_{zz} = \frac{P(1-\nu)}{16\pi\mu r} \left\{ \begin{array}{ll} 0 & \tau < a \\ 8Re\left[\frac{(1-2\xi_1^2)^2(a^2-\xi_1^2)}{(\xi_1^2-\xi_2^2)(\xi_1^2-\xi_3^2)} \frac{1}{Q_1 - Q_1^{-1})}\right] + \frac{A_3}{\sqrt{\xi_3^2-\tau^2}} - 4 & a < \tau < 1 \\ \frac{2A_3}{\sqrt{\xi_3^2-\tau^2}} H(\xi_3 - \tau) - 8 & \tau > 1 \end{array} \right\} \tag{A.18}$$

A.2 Horizontal load

For a horizontal load the quantities u_{rx} and $u_{\theta x}$ are only known in case of the Poisson's ratio $\nu = 0.25$. Again some parameters have to be defined.

$$a_h = \frac{1}{3}\sqrt{3}, \quad \xi_1^2 = \frac{1}{4}, \quad \xi_2^2 = \frac{1}{4}(3-\sqrt{3}), \quad \xi_3^2 = \frac{1}{4}(3+\sqrt{3}) \tag{A.19}$$

$$C_1 = \frac{3}{4}\sqrt{3}, \quad C_2 = \frac{1}{8}\sqrt{6\sqrt{3}+10}, \quad C_3 = \frac{1}{8}\sqrt{6\sqrt{3}-10} \tag{A.20}$$

Subsequently, the displacements can be calculated

$$u_{rx} = \frac{P}{2\pi\mu r}\left\{\begin{array}{ll} 0 & \tau < a_h \\ \tau^2\left[\frac{C_1}{\sqrt{\tau^2-\xi_1^2}} - \frac{C_2}{\sqrt{\tau^2-\xi_2^2}} - \frac{C_3}{\sqrt{\xi_3^2-\tau^2}}\right] & a_h < \tau < 1 \\ 1 - \frac{2\tau^2 C_3}{\sqrt{xi_3^2-\tau^2}}[1-H(\tau-\xi_3)] & \tau > 1 \end{array}\right\} \tag{A.21}$$

$$u_{\theta x} = \frac{-3P}{8\pi\mu r}\left\{\begin{array}{ll} 0 & \tau < a_h \\ \left[\frac{1}{2} - \frac{4}{3}(C_1\sqrt{\tau^2-\xi_1^2} - C_2\sqrt{\tau^2-\xi_2^2} + C_3\sqrt{\xi_3^2-\tau^2})\right] & a_h < \tau < 1 \\ 1 - \frac{8}{3}C_3\sqrt{\xi_3^2-\tau^2}[1-H(\tau-\xi_3)] & \tau > 1 \end{array}\right\} \tag{A.22}$$

The above derived relations for the displacements due to horizontal and vertical loads are plotted while being scaled with the shear modulus μ and the distance r in the figures A.1 to A.4. For the later description via the tensor $\mathbf{g}$ according to [15], the quantities are written in a new notation, acconting for a changed coordinate system (the z-axis in the *Ssibefe* tool points downward while it was defined upward in [8]).

$$g_{zz} = u_{zz}, \quad g_{rz} = -u_{rz}, \quad g_{rr} = u_{rx}, \quad g_{\phi\phi} = -u_{\theta x}, \quad g_{zr} = u_{rz} \tag{A.23}$$

B Coordinate Transformation

The coordinate transformation

$$\mathbf{g}^{cart} = \mathbf{B}^T(\phi)\mathbf{g}^{cyl}\mathbf{B}(\phi) \tag{B.24}$$

can be accomplished by the rotation matrix

$$\mathbf{B}(\phi) = \begin{bmatrix} \cos(\phi) & \sin(\phi) & 0 \\ -\sin(\phi) & \cos(\phi) & 0 \\ 0 & 0 & 1 \end{bmatrix} \tag{B.25}$$

This leads to tab. B.1.

$g_{xx} = g_{rr}\cos^2(\phi) + g_{\phi\phi}\sin^2(\phi)$	$g_{xy} = (g_{rr} - g_{\phi\phi})\cos(\phi)\sin(\phi)$	$g_{xz} = g_{rz}\cos(\phi)$
$g_{yx} = g_{xy}$	$g_{yy} = g_{rr}\sin^2(\phi) + g_{\phi\phi}\cos^2(\phi)$	$g_{yz} = g_{rz}\sin(\phi)$
$g_{zx} = g_{zr}\cos(\phi) = -g_{xz}$	$g_{zy} = g_{zr}\sin(\phi) = -g_{yz}$	$g_{zz} = g_{zz}$

Table B.1: Green's functions in Cartesian coordinates.

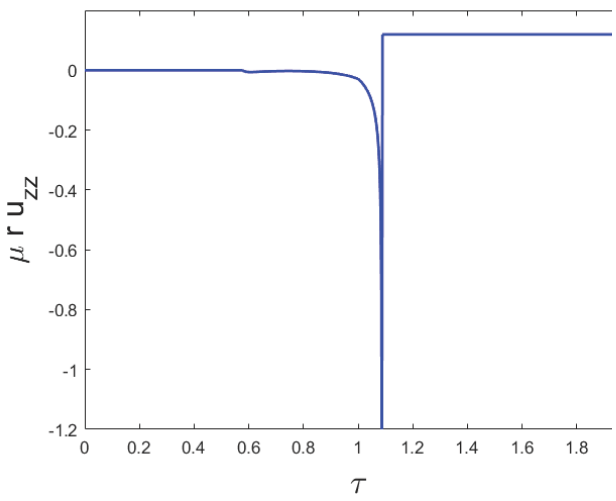

Figure A.1: Vertical displacement due to vertical load, $\nu = 0.25$.

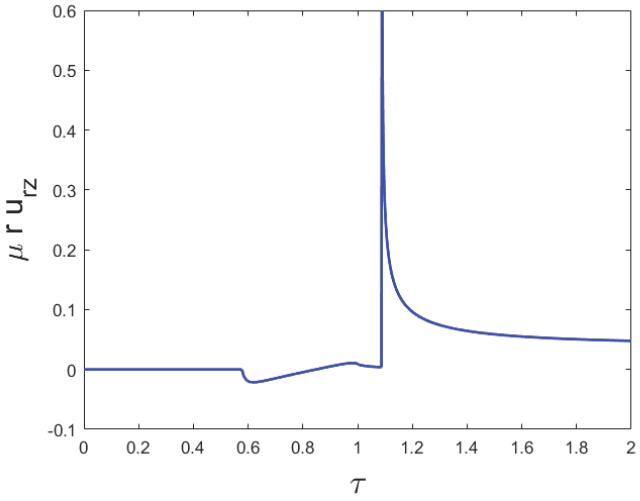

Figure A.2: Radial displacement due to vertical load, $\nu = 0.25$.

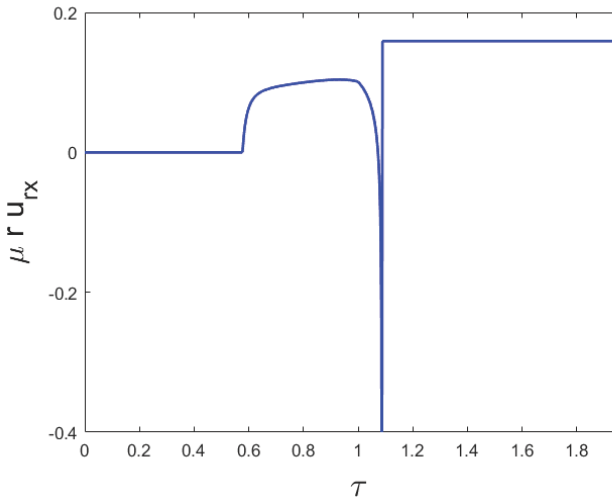

Figure A.3: Radial displacement due to horizontal load, $\nu = 0.25$.

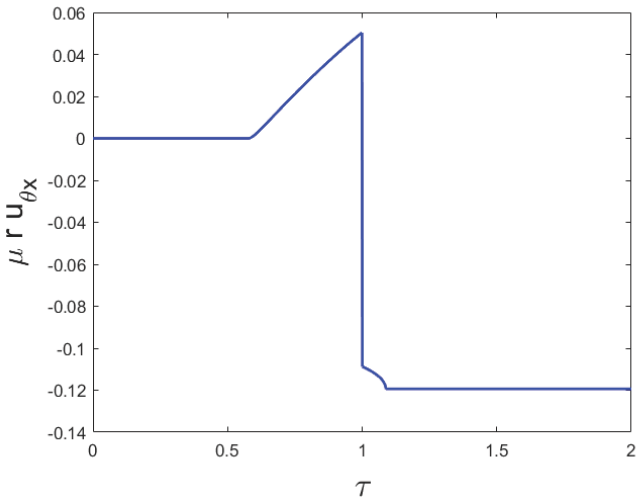

Figure A.4: Tangential displacement due to horizontal load, $\nu = 0.25$.

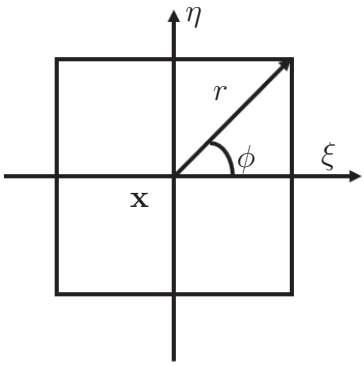

Figure C.1: Transformation to polar coordinates for constant boundary elements.

C Transformation to polar coordinates

To regularise the weak singularity of the integrand in eq. (4) a transformation to polar coordinates according to [21] can be used.

$$\Delta \mathbf{G}_n^e = \sum_{m=1}^{M} \sum_{k=1}^{K} \mathbf{N}_n(\xi_m, \eta_k) \mathbf{g}(r(\xi_m, \eta_k), \phi(\xi_m, \eta_k), t) J(\xi_m, \eta_k) W_m W_k \tag{C.1}$$

The coordinate system for constant elements is located in the centre of the element because the origin of the coordinate system should be at the loading node (see fig. C.1). The radius and the angle are adapted as follows

$$r(\xi, \eta) = \sqrt{\xi^2 + \eta^2} \qquad \phi(\xi, \eta) = atan2\left(\frac{\eta}{\xi}\right) \tag{C.2}$$

For the calculation of the Jacobian determinant changes of the partial derivatives occur

$$\begin{aligned} \frac{\partial r}{\partial \xi} &= \frac{\xi}{\sqrt{\xi^2 + \eta^2}} & \frac{\partial \phi}{\partial \xi} &= -\frac{\eta}{\xi^2 + \eta^2} \\ \frac{\partial r}{\partial \eta} &= \frac{\eta}{\sqrt{\xi^2 + \eta^2}} & \frac{\partial \phi}{\partial \eta} &= \frac{\xi}{\xi^2 + \eta^2} \end{aligned} \tag{C.3}$$

Except for these adaptations, formula (C.1) is valid for the constant elements as well. Since this regularisation approach led to the best results, it is used for all further calculations in this thesis.

D Transformation matrices from BEM to FEM

$$\mathbf{T}_u = \begin{bmatrix} [\mathbf{N}] & [\mathbf{0}] & [\mathbf{0}] \\ [\mathbf{0}] & [\mathbf{N}] & [\mathbf{0}] \\ [\mathbf{0}] & [\mathbf{0}] & [\mathbf{N}] \end{bmatrix} \tag{D.1}$$

with e.g.

$$\mathbf{N} = \begin{bmatrix} N_M & 0 & 0 & 0 & \dots \\ 0 & 0 & N_P & 0 & \dots \\ \dots & \dots & \dots & \dots & \dots \end{bmatrix} \tag{D.2}$$

$$\mathbf{T}_q = \mathbf{T}_u^T \mathbf{A} \tag{D.3}$$

with the matrix $\mathbf{A}$ which contains the element area as a diagonal matrix.

E Workflow of the *Ssibefe* tool

Figure E.1: Workflow of the *Ssibefe* tool.

EURODYN 2020
XI International Conference on Structural Dynamics
M. Papadrakakis, M. Fragiadakis, C. Papadimitriou (eds.)
Athens, Greece, 23–26 November 2020

EXPERIMENTAL IDENTIFICATION OF THE DYNAMIC BEHAVIOUR OF PILE-SOIL SYSTEM INSTALLED BY MEANS OF THREE DIFFERENT PILE-DRIVING TECHNIQUES

Athanasios Tsetas, Sergio S. Gómez, Apostolos Tsouvalas, Kees van Beek, Faraz S. Tehrani, Evangelos Kementzetzidis, Federico Pisanò, Ahmed Elkadi, Maxim Segeren, Timo Molenkamp, Andrei V. Metrikine

Faculty of Civil Engineering and Geosciences, Delft University of Technology,
Stevinweg 1, 2628 CN Delft, The Netherlands
e-mail: {A.Tsetas, s.sanchezgomez-1, A.Tsouvalas, C.vanBeek, F.Tehrani, E.Kementzetzidis, F.Pisano, A.S.K.Elkadi, M.L.A.Segeren, T.Molenkamp, A.Metrikine}@tudelft.nl

Keywords: Soil-structure interaction, pile driving, experimental testing, system identification, installation effects

Abstract. *A novel pile-driving technique, named Gentle Driving of Piles (GDP), that combines axial low-frequency and torsional high-frequency vibrations has been developed and tested recently. During the experimental campaign, several piles were installed onshore, making use of the GDP shaker. Besides those, a number of additional piles were installed using conventional pile-driving techniques, i.e. impact piling and axial vibratory driving. After the completion of the installation phase, the installed piles have been subjected to impact hammer tests with the following goals. First, the in–situ dynamic properties of the pile-soil system have been identified. Second, the post-installation soil state has been investigated, along with its evolution in time for each pile driving scenario. Preliminary analyses, of the data collected during the impact tests show dissimilar trends in the overall dynamic response between the piles installed with impact hammer and those installed with the axial and the GDP shakers.This observation suggests a difference in the post-installation dynamic behaviour of the pile-soil systems related to different pile-driving techniques. In this paper, a first attempt is made to identify the differences in the overall pile-soil dynamic behaviour of the piles installed by means of the three different pile-driving techniques.*

1 INTRODUCTION

The offshore wind industry plays a major role in the energy transition. Due to the sustainability targets set at international level, the installed capacity of offshore wind turbines is growing, leading to greater depths and distances to shore [7]. In that framework the foundations of offshore wind turbines are also affected by this consistent progression challenge. Monopiles are the most common foundations used for offshore wind turbines in shallow waters, like the North Sea [6]. Various alternative foundation concepts do exist, yet these substructures remain the most favorable choice due to simplicity of manufacture, ease of the installation procedure, robustness and proven reliability [1, 5].

Currently, impact pilling is the most common method for the installation of monopiles in the offshore environment [8]. However, the latter installation method engenders several issues that require further consideration. The major drawbacks are the high levels of noise generated during pile driving [9], which may be harmful for the aquatic species, and the large stresses developed at the pile head during hammer impact, that can reduce the structural life-time of the monopile due to fatigue [2]. Consequently, an alternative pile driving technique that can mitigate the noise emissions and does not peril the fatigue life of the structure, without compromise of the driving efficiency and the pile bearing capacity, has been a growing need. To that end, a novel pile-driving technique, named Gentle Driving of Piles (GDP), that aims to accomplish the stated objectives, has been recently developed. This technique is based on simultaneous application of low-frequency axial vibrations and high-frequency torsional vibrations at low amplitudes.

To test the novel pile driving technique, an experimental campaign was designed and executed in a site of medium to medium-dense sand. This experimental campaign encompassed the installation of several piles by means of three distinct pile driving techniques; namely, impact pilling, axial vibratory driving and GDP. Following the installation tests, that were concluded to be successful, further investigation was considered necessary to provide evidence that the bearing capacity and the dynamic properties of the pile-soil system have not been compromised and are within acceptable limits for operation. To this end, in the post-installation phase, lateral loading tests and impact tests with an instrumented hammer were conducted, in order to investigate further the effect of each installation method on the behaviour of the pile-soil system. More specifically, the response in operational conditions, the vibration characteristics and the temporal evolution of the dynamic properties of the pile-soil system are to be examined, in accordance with the aforementioned experimental tests. The present work is focused upon the instrumented hammer impact tests, in order to examine the dynamic behaviour of the installed piles in terms of prior- and post-loading response, temporal evolution of the system properties and influence of the respective installation method. At this point it was observed for the first time that the method of installation can have significant influence on the vibration characteristics of the system such as damping and dynamic stiffness.

This paper is structured as follows. In Section 2, the experimental tests and the identification procedure followed are described. Onwards, in Section 3 a collection of the most representative results are presented, along with some observations and relevant conclusions. In Section 4, the main conclusions accompanied by the research questions to be addressed in the near future are outlined.

2 EXPERIMENTAL TESTS AND IDENTIFICATION PROCEDURE

During the installation phase of the experimental campaign, several piles were installed by means of impact pilling, axial vibratory driving and GDP techniques. The dimensions of the

tests piles and the reaction pile are given in Table 1.

Pile Geometry	Test piles [m]	Reaction pile [m]
Length	10	10
Outer diameter	0.762	1.6
Wall thickness	0.0159	0.02

Table 1: Geometrical characteristics of the piles.

Evidently, since the main objective of the experimental campaign was the proof of concept of the GDP method, the majority of the piles were installed by means of the latter method. Furthermore, the rest of the piles in the experimental site were installed by impact and axial vibratory driving, the two conventional and currently most established installation methods [3]. The latter were mainly chosen to serve as reference cases, since they are vastly used in engineering applications and their features during and post-installation are considered to be known. The configuration of the installed piles is shown in Figure 1. The position of the 8 piles installed around the reaction pile is displayed, while the latter was used as a support for the post-installation lateral tests loading apparatus.

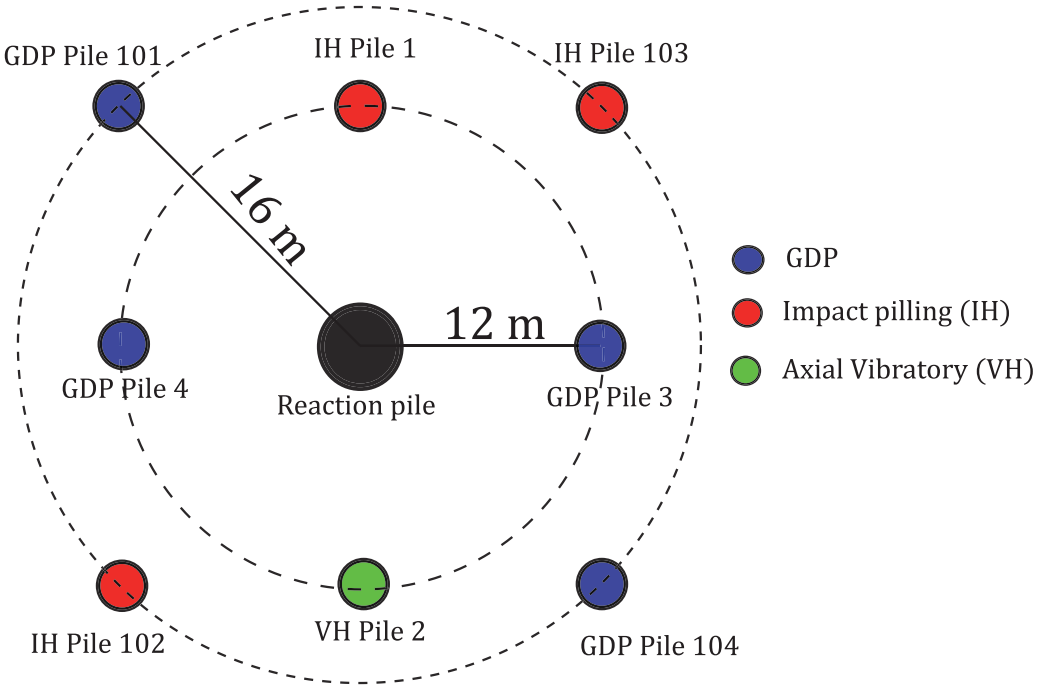

Figure 1: Pile layout

As already presented in Table 1, the test piles were 10 meters long, with final embedment depth of 8 meters. Accordingly, the height above the ground level was 2 meters, such that an adequate part of the pile could be used to mount the loading frame for the lateral loading tests.

2.1 Experimental set-up

In order to perform the impact hammer tests, 2 PCB tri-axial accelerometers and an instrumented impact hammer were used. The tests were performed on all the installed piles using the instrumentation set-up displayed in Figure 2.

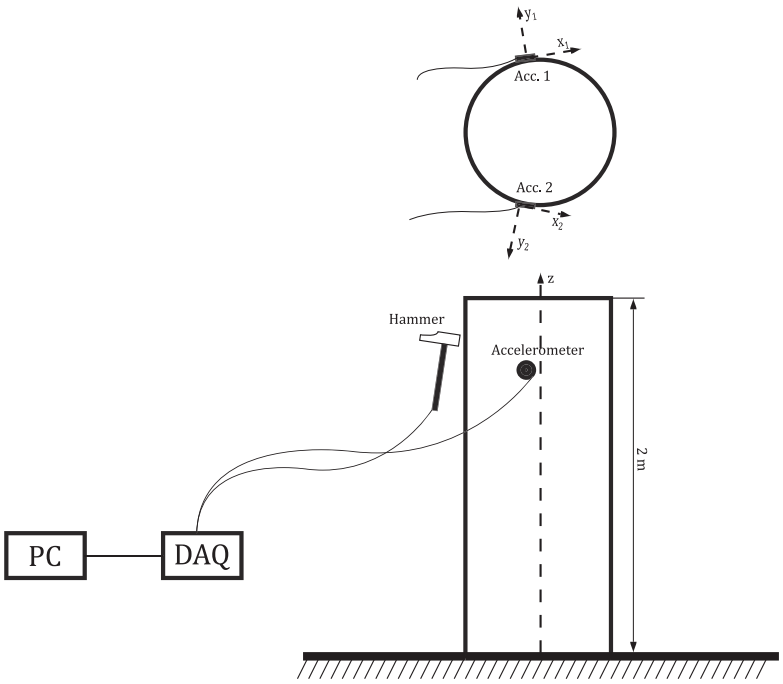

Figure 2: Experimental set-up and pile instrumentation

The instrumented hammer was used to excite the pile at two different locations and with different impact direction. First, the hammer was impacted horizontally, as shown in Figure 2 and at 1.5 meters above the ground surface. Each test was comprised of three distinct hits, in the same location and direction, in order to ensure the consistency of the measurements. In the same manner, hammer impact tests were repeated with an impact force applied along z-direction, at the top of the pile and in the same vertical line that the horizontal impacts were performed.

The accelerometers were mounted to the outer wall of the pile at the same height with the location of the horizontal hammer impacts, 1.5 meters from the ground surface. Acceleration data were registered in x, y and z directions simultaneously, with a sampling frequency that was set to 16 kHz for all tests.

During a period of two weeks, three hammer impact tests took place, one week apart from each other and in parallel with the lateral loading tests. The latter tests, conducted in parallel with the impact tests due to time constrains, were detrimental for the direct comparison of all the hammer tests, but did allow for a comparison of the installed piles in groups. Piles that were tested in analogous circumstances are grouped together and conclusions are drawn based on the features of each respective pile group.

In the present work two groups will be considered, one group including the four piles seen in Figure 1 at a radial distance of 16 meters from the reaction pile. These piles had been laterally loaded before the start of the impact hammer test, to mimic loading conditions similar to the ones encountered in offshore environments. This group was chosen on the basis that all piles had experienced lateral loading already and piles installed by two different techniques

comprise the first group, namely the impact-driven and the GDP piles. Thus, without drawing a conclusion with respect to the loading, the time evolution of the system properties and the effect of the installation method could be identified. The second group is comprised of two instrumented piles driven by axial vibratory driving and the GDP technique. At the first day of the hammer tests, both piles were not loaded, so a comparison was performed based on the data obtained from the testing on the first and last day of the experiments. In essence, the pre- and post-loading behaviours were compared, to showcase the effect of loading on the two piles driven with different techniques.

2.2 Identification procedure of the main system parameters

In this work, the half-power Band-width method (HPBW) is used to identify the main pile-soil system parameters. A natural frequency of the system can be obtained based on the location of a distinct peak in the acceleration frequency-response function (FRF) and its respective equivalent viscous damping ratio can be quantified accordingly.

The quality factor Q and the frequency ratio in resonance Ω_{res} of a damped system with viscous damping ratio ξ, are defined in a classical manner:

$$Q = \frac{\Delta\Omega_{\frac{1}{2}}}{\Omega_{\text{res}}} = \frac{\Omega^{+}_{\frac{1}{2}} - \Omega^{-}_{\frac{1}{2}}}{\Omega_{\text{res}}}; \quad \Omega_{\text{res}} = \sqrt{1-2\xi^2}, \tag{1}$$

in which $\Omega^{+}_{\frac{1}{2}}$ and $\Omega^{-}_{\frac{1}{2}}$ correspond to the frequencies at which the PSD function is half of the maximum value. A general expression for the damping ratio of a SDoF system can be obtained in terms of the quality factor, as follows [4]:

$$\xi = \frac{1}{\sqrt{2}}\sqrt{\frac{\sqrt{-Q^4+4Q^2+4}-2}{\sqrt{-Q^4+4Q^4+4}}} \tag{2}$$

Generally, for low-damped systems, it can be assumed that $Q << 1$. In these cases, the damping ratio can be approximated by the following expression:

$$\xi \approx \frac{1}{2}Q = \frac{\Delta\Omega_{\frac{1}{2}}}{2\Omega_{\text{res}}}. \tag{3}$$

This procedure is used in Section 3 to compute the selected natural frequencies and the equivalent damping ratios of the tested piles.

3 RESULTS

In the current section the power spectral density graphs (PSD) are presented for the selected 4 out of 8 piles, organized in a consistent manner as presented in subsection 2.1 to draw the relevant conclusions. The following graphs have been produced using the acceleration response measured along the y-direction of each sensor, during the lateral hammer impact tests, as shown in Figure 2. Each pair of simultaneous recordings for each hammer impact was averaged prior to signal analysis. Subsequently, the acceleration frequency-response functions from the 3 lateral hammer impacts per day were averaged. Finally, the averaged power spectral density S_{yy} of the pile-soil system at each day, for all responses and only lateral impacts, was obtained.

In Figure 3, the power spectral density for Pile IH-103, for each of the 3 testing days can be seen. Apparently, the PSD's of the three tests do not showcase significant deviation within the

testing period, while there exist some quite distinct peaks in the PSD of the system, which can be considered to correspond to resonant frequencies of the pile-soil system.

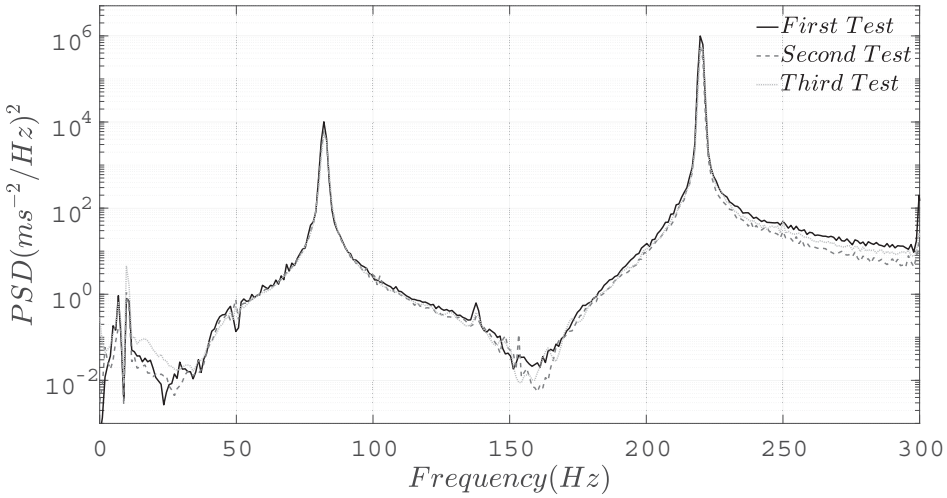

Figure 3: Power spectral density graphs for Pile IH-103 for all testing days

The PSD of the Pile GDP-101 can be seen in Figure 4. Similarly to Pile IH-103, Pile GDP-101 does not present significant alteration in its dynamic behaviour within the testing period.

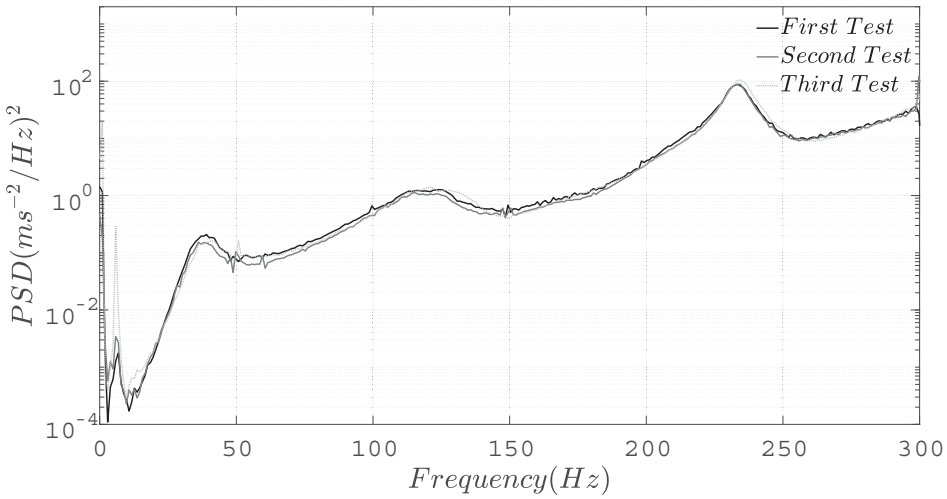

Figure 4: Power spectral density graphs for Pile GDP-101 for all testing days

To showcase the possible differences between the measured properties of the two systems, Figure 5 shows both PSDs of Pile IH-103 and Pile GDP-101, on the last testing day. It is evident that the responses of the two systems are quite dissimilar and though the time evolution of the properties of the two systems was shown to be insignificant in both cases. The difference in magnitude and mainly in the form of the PSDs is an indication of lower damping present in the pile-soil system of Pile IH-103. It needs to be noted that the piles have a structural dissimilarity. Specifically, all piles except the ones driven with impact piling, have a cap welded on the top of the pile, which was used to mount the axial vibratory and the GDP shaker. The effect of this

cap is not expected to be significant, but is still to be investigated. A final conclusion about the dynamic stiffness of the two systems can thus not be drawn at this stage. However, piles driven with the same installation method, all present identical behaviour. Thus, a consistent observation is made regarding the significant difference in the PSD magnitude and the damping ratio of the IH- and GDP-driven piles.

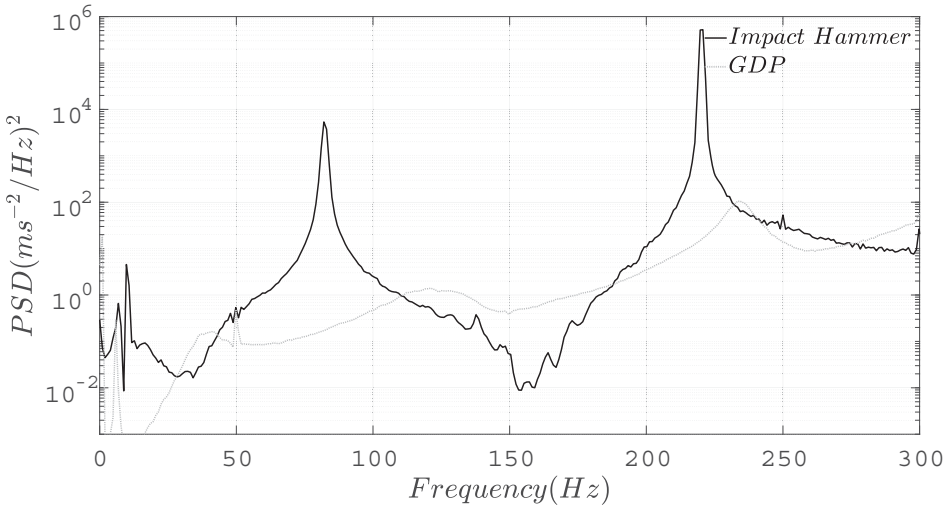

Figure 5: Power spectral density graphs for Pile IH-103 and Pile GDP-101 after the application of lateral loading

The HPBW method presented in Section 2.2 is used to quantify indicative vibration characteristics for Pile IH-103 and Pile GDP-101. In Figure 3, there are two distinct peaks observed in the same frequency and same amplitude for all the tests. Those two peaks are analyzed in Figure 3 and their corresponding natural frequencies ω_n and equivalent viscous damping ratios ζ_{eq} are presented in Fig. 6.

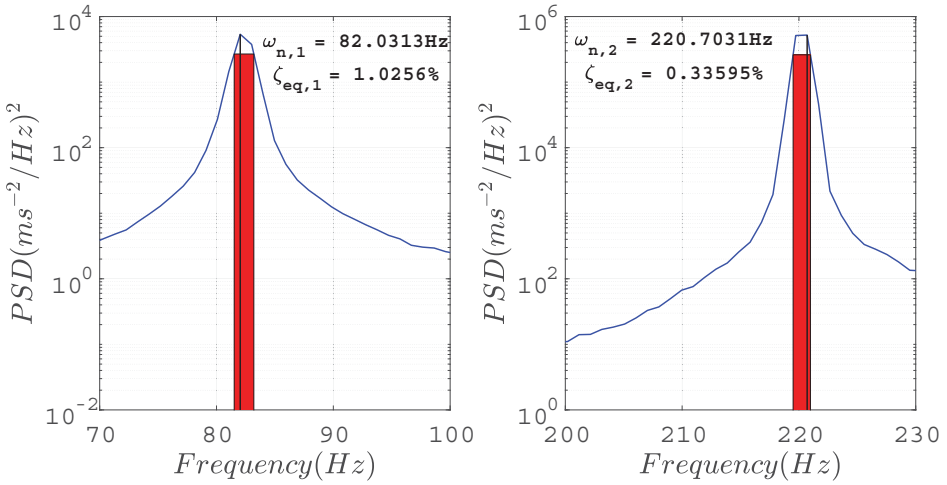

Figure 6: Identification of equivalent viscous damping ratio by the HBWM for Pile IH-103

In the same manner, for the PSDs presented in Figure 4 one peak can be clearly identified, that comprises also the fundamental frequency of the relevant time signal. Similarly to the IH-

103, the same identification procedure is followed and the respective natural frequency ω_n and equivalent viscous damping ratio ζ_n are given in Figure 7.

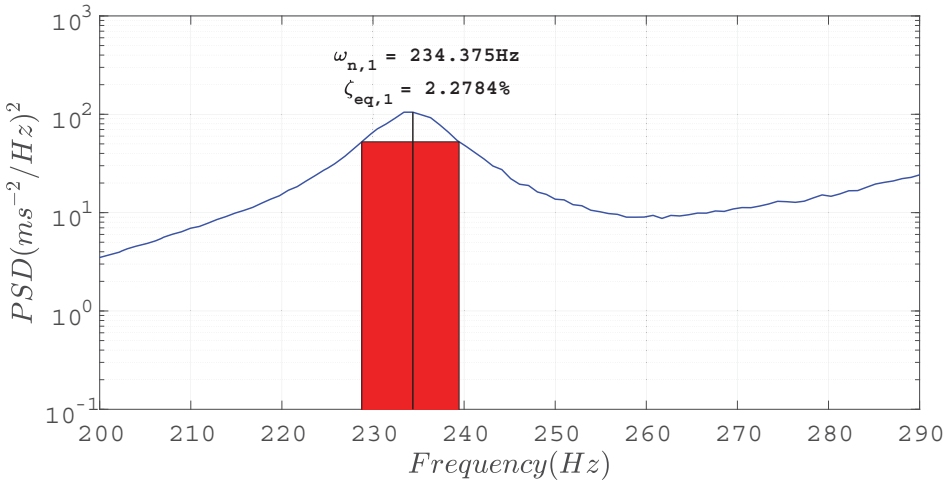

Figure 7: Identification of equivalent viscous damping ratio by the HBWM for Pile GDP-101

In continuation, the effect of the lateral loading is to be addressed by the PSDs of two piles, driven by axial vibratory and GDP techniques respectively. In Figure 8 the PSDs of Pile VH-2, installed with an axial vibratory hammer, are presented for the first and last day of the measurements, indicating prior and post-loading behaviour. The system characteristics, both in frequency and magnitude, indicate a decrease of dynamic stiffness after the application of lateral loading. As can be seen in Figure 8, the form of the PSD is preserved, but a shift to lower frequencies and an increase in magnitude take place, which both indicate a dynamic stiffness decrement. A multitude of reasons may have contributed to that observation, such as creation of a gap between the pile walls and the soil and degradation of the soil in the immediate vicinity of the pile.

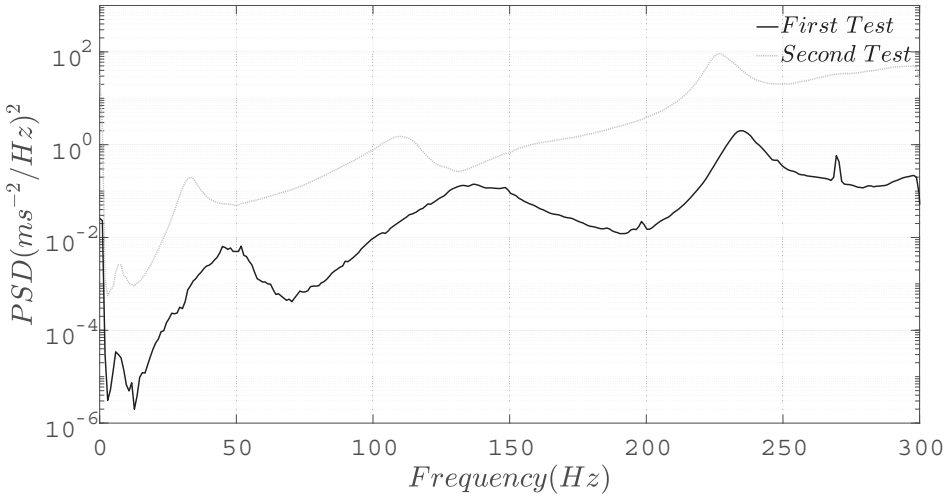

Figure 8: Power spectral density graphs for pile VH-2 in the first and last testing day

A qualitatively similar behaviour can be observed in Figure 9, which refers to Pile GDP-4.

Albeit, the shift of the PSD form with respect to the frequency is distinguished, no drop in the dynamic stiffness of the system, as was observed in the case of pile VH-2, is seen here.

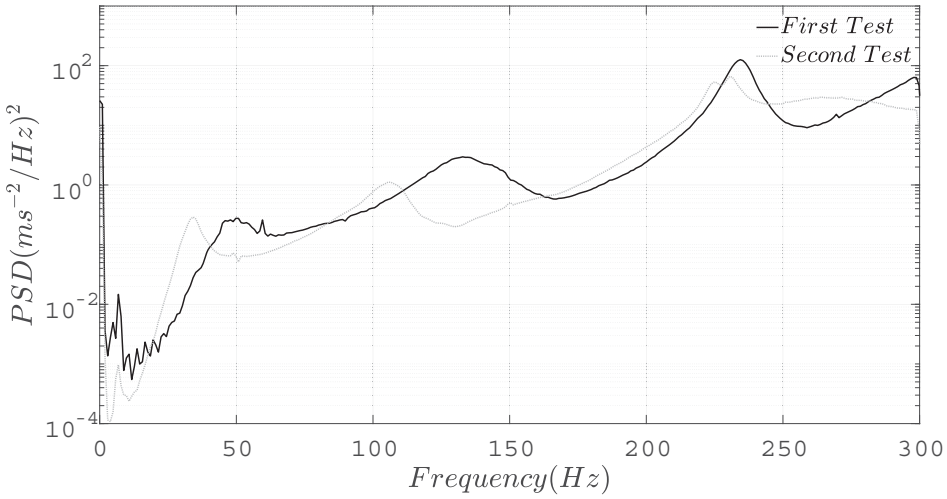

Figure 9: Power spectral density graphs for Pile GDP-4 in the first and last testing day

To investigate the latter observation, a PSD graph including both Pile VH-2 and Pile GDP-4 is presented in Figure 10. By inspection of this figure it can be inferred that the difference in pre- and post-loading behaviour is much greater in the Pile VH-2, compared to that of Pile GDP-4.

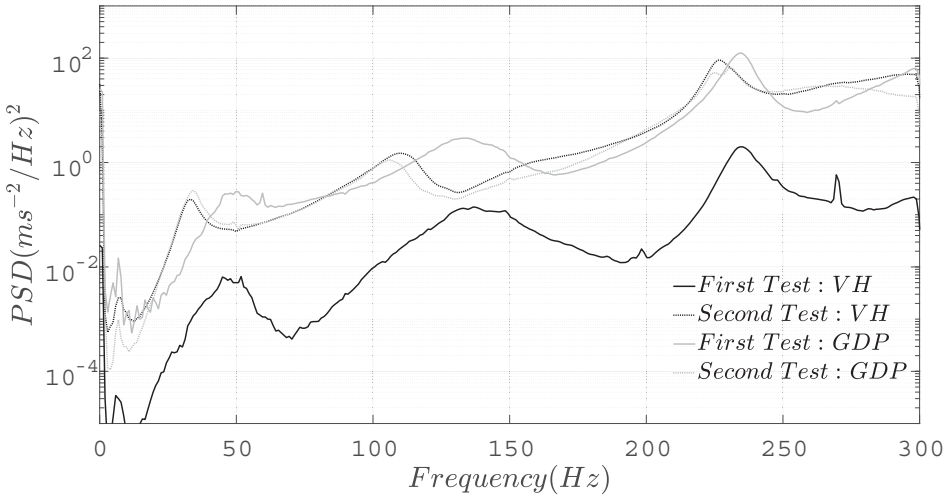

Figure 10: Power spectral density graphs for Pile VH-2 and Pile GDP-4 in the first and last testing day

4 CONCLUSIONS

To summarize, the work presented herein comprises a part of a test campaign, conducted in the context of investigating a novel pile driving method, namely the Gentle Driving of Piles (GDP). During the campaign, onshore installation of scaled piles by means of two conventional

pile driving methods, namely impact piling and axial vibratory driving and the novel GDP method was performed. The proof of concept was successfully accomplished indicating the potential of this novel method to fulfill the originally envisaged goals and motivations.

To realize these objectives, post-installation tests were conducted to examine the various aspects of the behaviour of the pile-soil system with respect to the reference cases of the conventional impact piling and axial vibratory driving. In this work, a part of the post-installation tests, namely impact tests with an instrumented hammer, is briefly discussed. Main objective of this work is to present a collection of selected results of these experimental tests, that can summarize and showcase the dominant trends observed in the majority of the data obtained. Final conclusions were not drawn, but mainly some indications, which will be used to guide a further investigation of the experimental data. A concise consideration of each respective case parameters, accompanied with numerical modeling and used in conjunction with all the available experimental results is intended with the aim to provide a better understanding of all the addressed techniques and predominantly of the GDP method.

5 Acknowledgements

This research is associated with the GDP project in the framework of the GROW joint research program. Funding from "Topsector Energiesubsidie van het Ministerie van Econsomische Zaken" under grant number TEHE117100 and financial/technical support from the following partners is gratefully acknowledged: Royal Boskalis Westminster N.V., CAPE Holland B.V., Deltares, Delft Offshore Turbine B.V., Delft University of Technology, ECN, Eneco Wind B.V., IHC IQIP B.V., SHL Offshore Contractors B.V., Shell Global Solutions International B.V., Sif Netherlands B.V., TNO, and Van Oord Offshore Wind Projects B.V.

References

[1] M Asgarpour. Assembly, transportation, installation and commissioning of offshore wind farms. In *Offshore Wind Farms*, pages 527–541. Elsevier, 2016.

[2] Jean Chung, Régis Wallerand, and Morgane Hélias-Brault. Pile fatigue assessment during driving. *Procedia Engineering*, 66:451–463, 2013.

[3] Ben C Gerwick Jr. *Construction of marine and offshore structures*. CRC press, 2007.

[4] Sergio Sanchez Gomez and AV Metrikine. The energy flow analysis as a tool for identification of damping in tall buildings subjected to wind: Contributions of the foundation and the building structure. *Journal of Vibration and Acoustics*, 141(1), 2019.

[5] K Lesny and W Richwien. Design, construction and installation of support structures for offshore wind energy systems. In *Wind Energy Systems*, pages 479–518. Elsevier, 2011.

[6] Rahmatallah Poudineh, Craig Brown, and Benjamin Foley. Global offshore wind market. In *Economics of Offshore Wind Power*, pages 15–31. Springer, 2017.

[7] S Rodrigues, C Restrepo, E Kontos, R Teixeira Pinto, and P Bauer. Trends of offshore wind projects. *Renewable and Sustainable Energy Reviews*, 49:1114–1135, 2015.

[8] Kurt Thomsen. *Offshore wind: a comprehensive guide to successful offshore wind farm installation*. Academic Press, 2014.

[9] Apostolos Tsouvalas and Andrei V Metrikine. Structure-borne wave radiation by impact and vibratory piling in offshore installations: From sound prediction to auditory damage. *Journal of Marine Science and Engineering*, 4(3):44, 2016.

EURODYN 2020
XI International Conference on Structural Dynamics
M. Papadrakakis, M. Fragiadakis, C. Papadimitriou (eds.)
Athens, Greece, 23–26 November 2020

DEVELOPMENT OF A METAMATERIAL PERIODIC FOUNDATION FOR SEISMIC PROTECTION

Ahmad SAOUD[1], **Ahmad OMAR**[2], **Diogo QUEIROS-CONDE**[2]

[1]Université Paris Nanterre
LEME LEME – Université Paris Nanterre Campus de Ville d'Avray 50, rue de Sèvres 92410 Ville d'Avray
ahmad.m.s3oud@gmail.com

[2]AZM University
ARCHIDES Lab Boulevard Fouad Chehab Tripoli, Lebanon
ahmad.omar.edu@gmail.com

[3] Université Paris Nanterre
LEME LEME – Université Paris Nanterre Campus de Ville d'Avray 50, rue de Sèvres 92410 Ville d'Avray
diogo.queiros-conde@parisnanterre.fr

Keywords: Periodic foundation, Metamaterial, Frequency band-gap, Attenuation, Seismic protection, Wave propagation.

Abstract. *One of the most recent and interesting research topics of structural seismic protection nowadays is the use of seismic metamaterials. The idea is based on the concept of phononic crystals or in another term the attenuation of propagating waves due to the periodic distribution of materials. There are different types of seismic metamaterials under study such as periodic void inclusion, periodic rigid inclusion, Metaforest that is considered as a natural seismic metamaterial and seismic isolation by using periodic foundation which is the subject and locus of this paper. Phononic crystals concept produces frequency band-gaps at different levels that are related to geometrical, physical and mechanical properties of arranged materials. Therefore, each propagating wave with a frequency within attenuation range will be blocked due to the local resonance phenomenon. The following research attempts to present the evolution of metamaterial periodic foundation system designed for seismic protection and the analysis of fundamental theory and methods of periodic materials. Finite element method is also employed and dynamic responses of a frame structure with periodic foundations are compared. Moreover, a parametric analysis is carried out to highlight on the influence of different geometrical, physical and mechanical parameters of the composite periodic foundation on the attenuation zone properties. In conclusion, this study proves that this seismic isolation concept has the potential to significantly reduce the seismic risk which in turn confirms the validity of the proposed metamaterial periodic foundation.*

1 INTRODUCTION

Natural disasters have been a threat to humanity with the support of industrial and urban evolutions that take place nowadays. One of the most significant catastrophes is a natural earthquake, taking into consideration its physical damages and human loss that it causes. Major research and studies have been implemented to discover the finest solutions to evade the chaos and crises left over by natural disasters, chiefly seismic ones. However, the most recent and interesting study is the propagating waves in periodic media that appeals to researchers' concern and generates approaches such as photonic crystals to alter the propagation of electromagnetic waves and phononic crystal for seismic protection. The end of 20th century witnessed the emergence of photonic crystals which comprise a periodic arrangement of materials with different dielectric properties that provide a dispersive medium to electromagnetic waves. Those materials highlight a frequency range called band gap, where electromagnetic waves cannot propagate. Photonic crystals' capability to manipulate electronic waves evokes suggestions to implement an analogous principle on propagating waves with different natures. Civil engineering researchers have applied that concept by changing scales on mechanical waves, such as sound waves or seismic waves which paves the route to broaden the notion of phononic crystal for seismic protection. The idea is based on the attenuation of propagating waves due to the periodic distribution of materials. There are different types of seismic metamaterials under study such as periodic void inclusion, periodic rigid inclusion, Metaforest (that is considered as a natural seismic metamaterial), and periodic foundation for seismic isolation which is the subject and locus of this paper. The addition of a flexible isolation system, such as rubber bearings, frictional/sliding bearings, and roller bearings, between the structure and the foundation, reduces the seismic effect on the structure and gives it a much lower fundamental frequency [12, 7, 3]. That system is the most prominent applied one in civil engineering for earthquake-resistant design to protect installations and buildings. The disadvantage of this strategy is that buildings usually have remarkably large horizontal displacements after an earthquake. To reduce those displacements, additional dampers are often required, which can lead to new problems [11, 9, 5]. Theoretically, researchers have proved the effectiveness of a phononic crystal in general and periodic foundation in particular to reach a new seismic isolation strategy.

This paper focuses on the development of metamaterial periodic foundation systems designed for seismic protection and the analysis of fundamental theory and methods of periodic materials. This research presents the design of a multidimensional composite periodic foundation for seismic isolation. It highlights on the influence of geometrical, phtysical and mechanical properties of periodic arrangements of materials on the band gaps properties. In addition, a study of the effectiveness of this approach at the strcutural scale will be shown.

2 Phononic Crystal

Phononic crystals are macroscopic materials blended with periodic distribution in one or many directions. Thus, they are able to block acoustic propagation in some directions and frequency ranges, by Bragg reflections or local resonance phenomenon of the periodic array's elements. Accordingly, the key of this concept is the frequency band gap.

2.1 Phononic Band Gap Structure

The aim of studies that treat the propagation of waves is to determine its behavior in terms of the relationship between the frequency and wave vector according to the other parameters in the medium of propagation. That relation is called a dispersion relation.

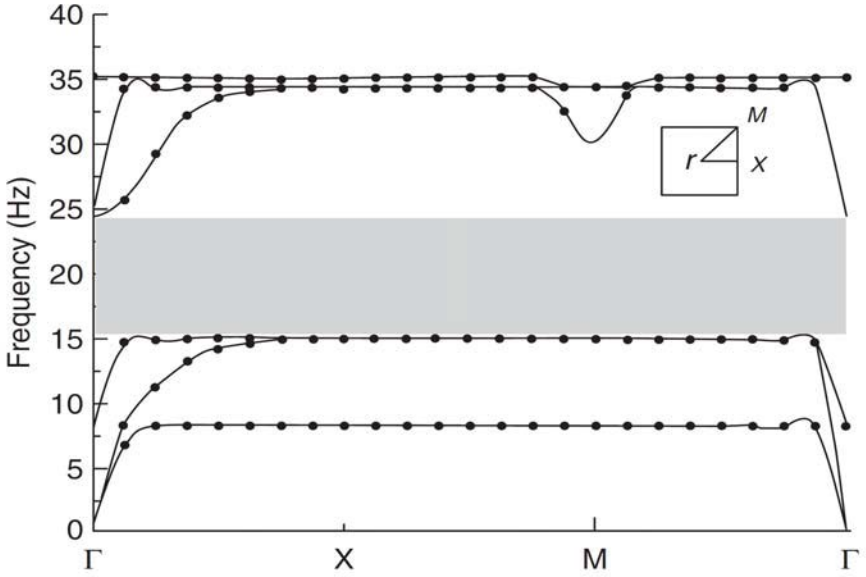

Figure 1: Dispersion relation between vectors and frequencies of waves [8].

Waves with frequencies that have no corresponding wave vector (K) on the abscissa cannot propagate in the periodic structure, since there are no corresponding modes which means these frequencies are inside the bandgap. The mechanism of forming the band gap is based on Bragg reflections due to the periodicity of crystal or the phenomenon of local resonance of resonators that are placed in protection systems.

2.2 Opening of Bandgap by Diffusion of Bragg

If the wavelengths (λ) of elastic waves are in the order of periodic structure's frequency, the bandgap is obtained due to Bragg reflection. You can distinguish between three different areas according to the value of the wavelength (λ) compared to the period of structure (a) [4].

- For $\lambda << a$: the wave propagates in a succession of media.
- For $\lambda >> a$: the wave is a little bit affected by structuring and it propagates in a homogeneous material.
- For $\lambda = a$: the wave is seriously affected by the periodicity of media. The propagation of waves is more complex than the previous cases.

2.3 Opening of Bandgap by Local Resonance

The appearance of bandgap of resonance is related to the fact that each resonator will trap a part of the energy of the transmitted wave, thus the stresses caused by the propagations of waves interact with the stresses of the resonance of resonators in anti-resonance frequency range, therefore the waves will be reflected. This association plays a key role in the presence or disappearance of a bandgap where wavelengths are far from the frequency of phononic Crystal [2].

3 Periodic Foundation and Theoretical Formulation

The two-dimensional (2D) periodic foundation consists of three materials with different geometrical, physical and mechanical properties of arranged materials. It consists of concrete plates

that have cylindrical or square steel inclusions surrounded by rubber, and they are periodically distributed in X and Y directions [6]. This type of foundation is a typical periodic foundation with local resonance. The basic idea of this new seismic isolation method is to replace the traditional solid foundation with the periodic foundation to reduce seismic risk.

3.1 Wave Equation

In a homogeneous medium, the equation of elastic wave propagation can be written in the form (Cheong et al [6]):

$$\rho\frac{\partial^2 u}{\partial t^2} = \nabla\cdot\left(\rho C_t^2\nabla u_i\right) + \nabla\cdot\left(\rho C_t^2\frac{\partial u}{\partial x_i}\right) + \frac{\partial}{\partial x_i}\left[\left(\rho C_l^2 - 2\rho C_t^2\right)\nabla\cdot u\right] \tag{1}$$

With i=1, 2, 3. For a 2D infinite system, the displacement vector $u_i = u(x, y)$ and the equation (1) will be:

$$\rho\frac{\partial^2 u}{\partial t^2} = \nabla_T\cdot\left(C_{44}\nabla_T u_i\right) + \nabla_T\cdot\left(C_{44}\frac{\partial u_T}{\partial x_i}\right) + \frac{\partial\left[\left(C_{11} - 2C_{44}\right)\nabla_T\cdot u_T\right]}{\partial x_i} \tag{2}$$

with $U_T = [u_x, u_y]$, $\nabla_T = \left[\frac{\partial}{\partial x}, \frac{\partial}{\partial x}\right]$,i=1,2

3.2 Periodic Boundary Conditions

The passage from one point of the array to another space of a mesh is translated by phase shift of $e^{i\overrightarrow{K_B}L}$. The calculation of the bandgaps of a periodic array is limited to the study of an elementary cell by applying periodic boundary conditions given by equation (4) below.

According to Bloch's theory [1], the solutions of the wave equation in the form of Floquet-Bloch can be written as:

$$u(r,t) = e^{i(k.r-wt)}.u_k\overrightarrow{r} \tag{3}$$

Where:
K: wave vector in the reciprocal space.
w: wave pulsation.
$u_k\overrightarrow{r}$ is on the same periodicity as the elastic parameters which is $u_k(r) = u_k(r + L)$
Thus,

$$u(r + L, t) = e^{i(k(r+L)-wt)}.u_k(r + L) = e^{ikL}.e^{i(k.r-wt)}.u_k(r) = u(r, t).e^{ikL} \tag{4}$$

4 Design and Development of Metamaterial Periodic Foundation

To apply phononic crystal concept for seismic protection, a bandgap in low frequency range (between 1 and 10Hz) should be found. Therefore, a local resonance phenomenon should be used in order to prevent seismic waves propagation in the sub-wavelnegth range [10].

4.1 Structure Configuration

The studied model is a 2D periodic foundation composed of a concrete matrix (a=1.4m) in which cylindrical steel inclusions (of radius r= 0,2m) are enrobed in rubber (of thickness e=0,2m). Each enrobed steel cylinder is considered as a resonator (figure 2), where every resonator absorbs the energy from wave at a frequency range located in the anti-resonance frequency range to reach an equilibrium between wave and resonators stresses, where the gap is observed

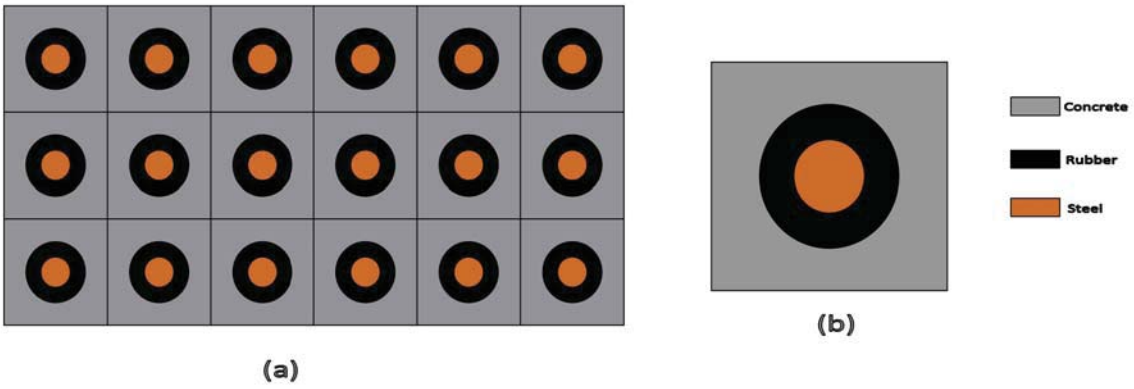

Figure 2: (a) plan (xy) section of periodic foundation, (b) plan (xy) section of the unit cell

4.2 Materials properties

The goal is to create a low frequency bandgap by using a local resonance phenomenon,which imposes the use of rubber material for the randall and steel or plumb material for the core, where the low rubber's elastic modulus and the high mass core allow this type of a resonator to resonate at low frequency

Materials	$\rho(Kg/m^3)$	E (GPa)	ν
Concrete	2450	28	0,3
Rubber	1300	$1{,}3 \cdot 10^{-4}$	0,463
Steel	7850	210	0,3
Plumb	11600	16,46	0,4

Table 1: Mechanical properties of used materials density ρ, elastic modulus E, Poisson's ratio ν.

4.3 Parametric Study

In this part, an elementary cell has been studied to determine the influence of the physical parameters (elastic modulus E, the density ρ and the Poisson's ratio ν) on the characteristics of the bandgap: the lower edge frequency (FEL), the upper edge frequency (UEF) and the width frequency deviation (FGW).

4.3.1 Numerical Model

The periodic structure is modeled with 2D plane deformation in Comsol Multiphysics software by implanting one cell. And, the finite element method is adopted to calculate structure's bandgap.

4.3.2 Boundary Conditions

The periodicity of the cells in the two directions (X, Y) are modelled by following Bloch's boundary conditions. The corresponding equations of Bloch's conditions are:

$$u_3 = u_1.e^{i.Kx.a}$$
$$v_3 = v_1.e^{i.Kx.a}$$
$$u_4 = u_2.e^{i.Ky.a}$$
$$v_4 = v_2.e^{i.Ky.a}$$

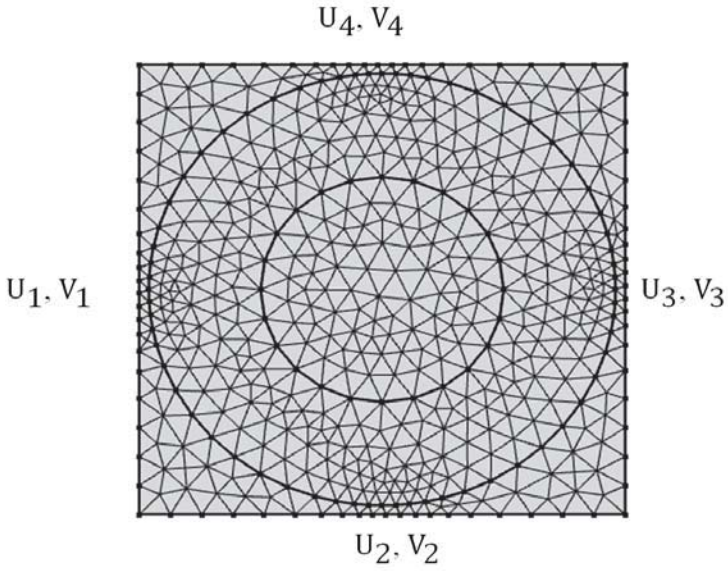

Figure 3: FE mesh and periodic conditions of a unit cell

4.3.3 Structure's Bands Calculation

The calculation of the dispersion curve is limited by the principal symmetric axes of the first Brillouin's zone. For every wave vector, the modes are calculated by using frequency analysis proposed by Comsol (figure 4).

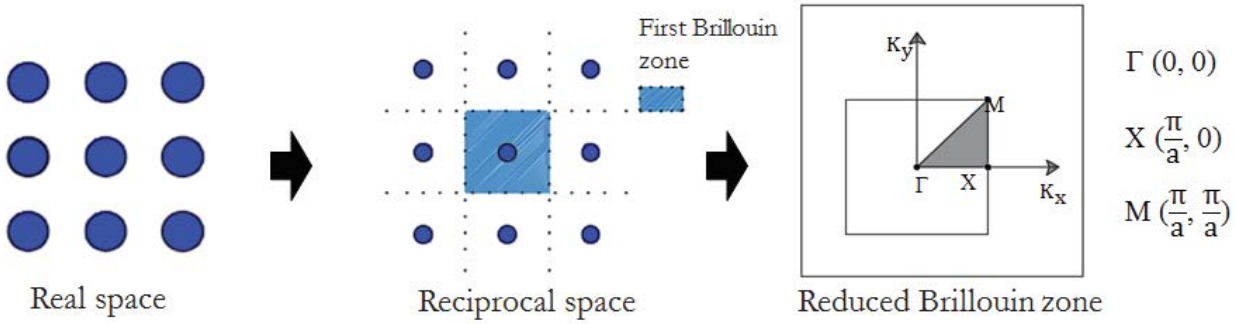

Figure 4: First irreducible Brillouin zone for a square periodic structure

Figure 5 shows the dispersion curve of model

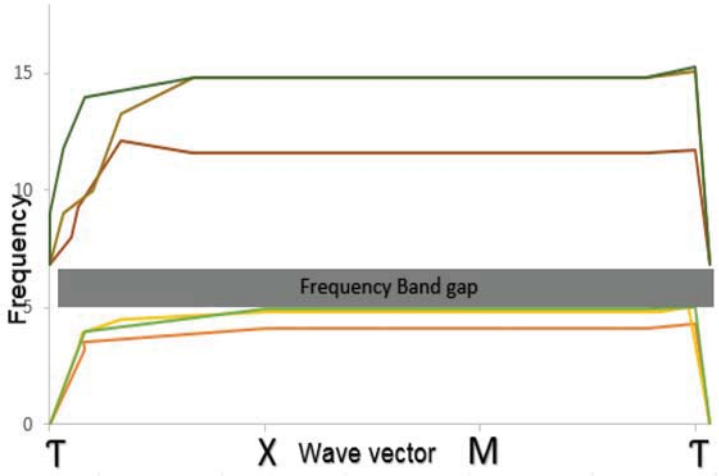

Figure 5: Dispersion cure of the periodic structure with reference properties

4.4 Results

The results indicate that the main physical parameters affecting the band gap properties are core density and rubber elastic modulus. The figures (6, 7) below show that LEF and UEF decrease and FGW increases when core density increases, and all characteristics of bandgap increase when rubber elastic modulus increases. These results demonstrate the important role of the low rubber elastic modulus on construction of periodic foundation with low frequency bandgap and the core density's effects to create low frequency bandgap.

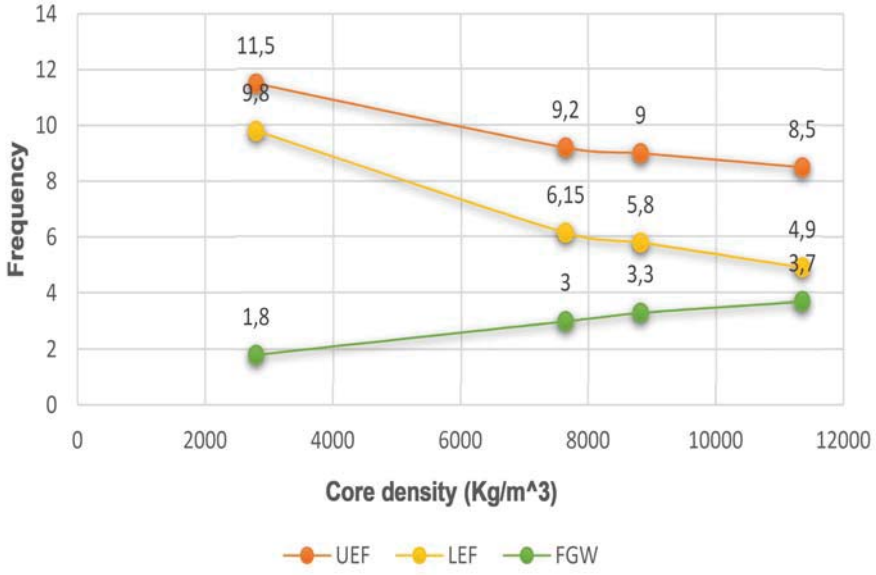

Figure 6: Core density Influence on bandgap's characteristics

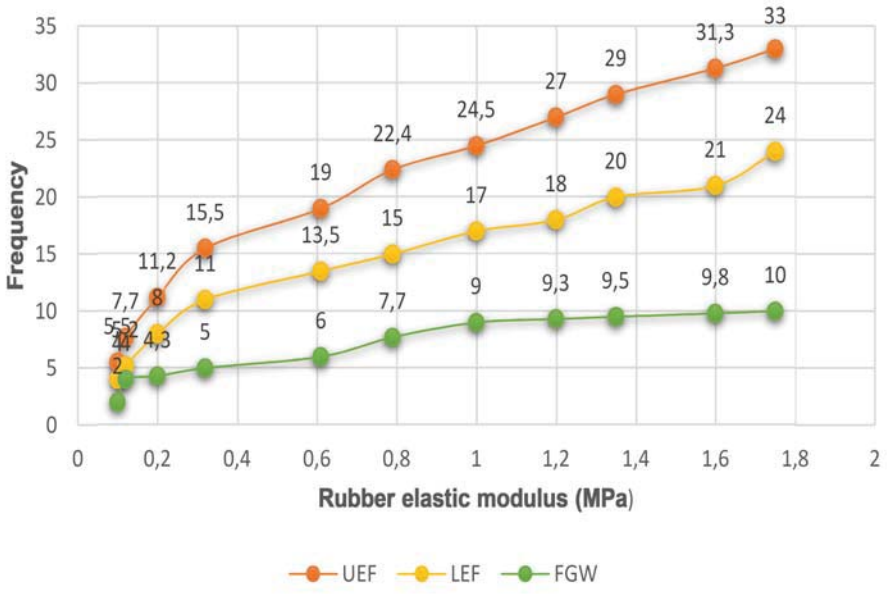

Figure 7: Rubber elastic modulus influence on bandgap's characteristics

5 Verification of the Effectiveness of a Metamaterial Periodic Foundation for Seismic Protection

In order to verify the effectiveness of periodic foundation, it is necessary to compare between the concrete base and periodic foundation. Thus, two models are built, one with a concrete base and the other with a periodic foundation. Both foundations have the same geometrical properties (3m*7 m*0.4m) and the same upperstructure which are composed of two storeys (3m*3.2m*2,9m).

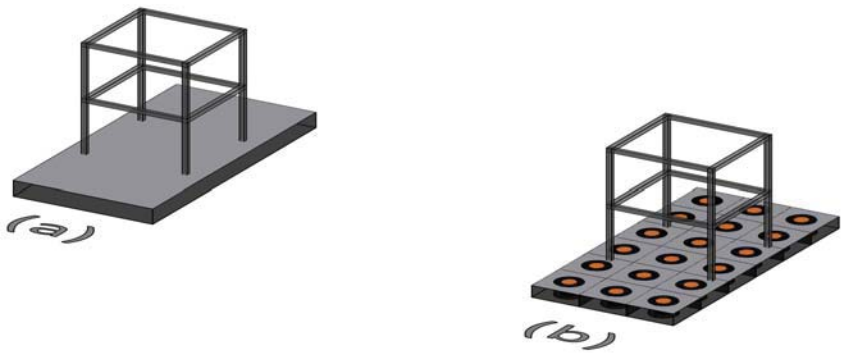

Figure 8: , Frame structure with (a) Concrete foundation (b) Periodic foundation,

The fundamental frequency of upperstructure is equal to 5.04 Hz, thus the cell's bandgap must cover its fundamental frequency. For this reason the following periodic foundation's cells properties (figure 9) have been adopted. These properties give a bandgap between [4.94; 6.8] Hz. Comsol Multiphysics software was used to create the finite element model adopted in this study with displacement conditions: zero displacement in the Z direction and 5cm of vibration amplitude with different frequencies in Y direction

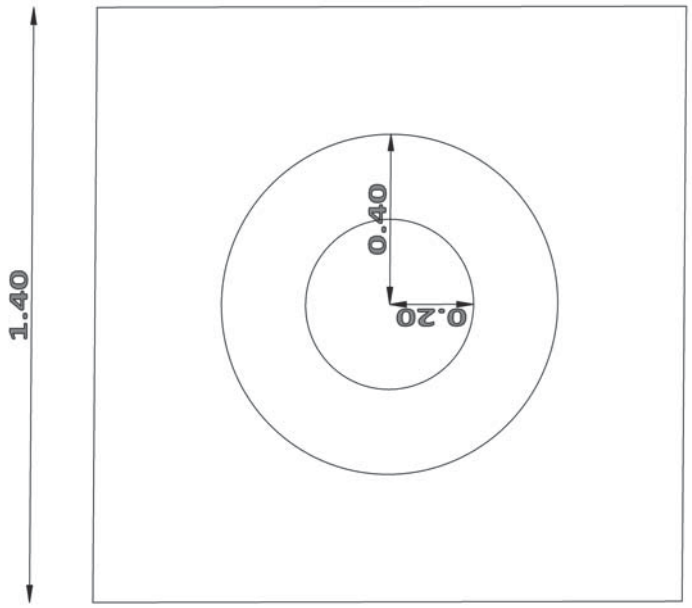

Figure 9: Dimension of periodic foundation's cell

5.1 Results and Analysis

The figure below shows the dynamic responses of the upperstructure and demonstrates the effectiveness of the periodic foundation in seismic isolation with reduction factor about 7 times inside the bandgap

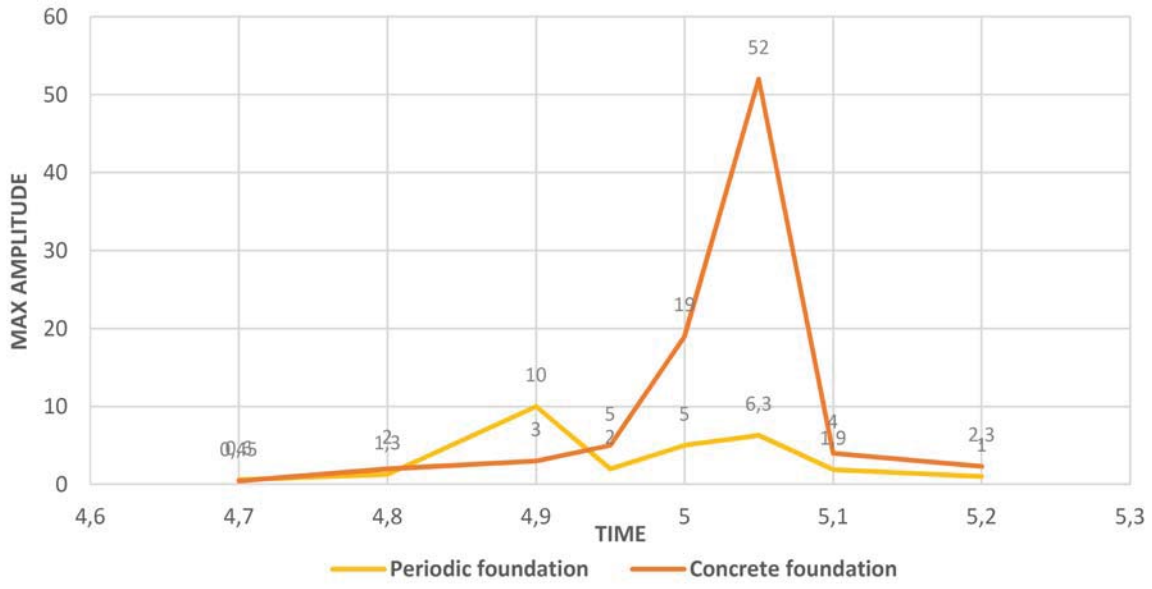

Figure 10: Relative displacement responses in Y direction for second story

6 CONCLUSIONS

The periodic distribution of materials provides itself with a new property, where it inhibits the propagation of elastic waves in the same directions and frequency ranges. These periodic materials are called phononic crystal. A big number of periodic structures is studied and all of these studies indicate the presence of bandgaps, where the waves cannot propagate.

In this paper, a periodic foundation based on local resonance phenomenon was investigated where the wavelengths of seismic waves are in order of a Kilometer. This research included a parametric study to determine the effect of the materials parameters on the bandgap which allowed us to deduce that the density of core and the elastic modulus of rubber are quite effective on bandgaps' characteristics. Moreover, a three-dimensional finite element structural model was used to validated the effectiveness of this periodic foundation approach in achieving its role as seismic attenuator in the desired frequency range [1 ; 10] Hz

REFERENCES

[1] Jia, G. and Shi, Z., "A new seismic isolation system and its feasibility study", Earthq Eng and Eng Vib, vol.9, no.1, (2010) 9: 75-82.

[2] Khelif, A. Achaoui, Y. Benchabane, S. Laude, V and Aoubiza, B., "Locally resonant surface acoustic wave band gaps in a two-dimensional phononic crystal of pillars on a surface", Phys. Rev. B 81, 214303 (2010).

[3] Sayani, P. J., Ryan, K. L. (2009). "Evaluation of approaches to characterize seismic isolation systems for design." Journal of Earthquake Engineering, 13(6), 835-851.

[4] Bernier, D., "Propriétés de superprisme des cristaux photoniques sur substrats SOI pour le démultiplexage en longueur d'onde", Thèse de doctorat - Université de Paris-Sud XI, Orsay, (Décembre 2008).

[5] Warn, G. P., Whittaker, A.S., and Constantinou, M. C. (2007). "Vertical stiffness of elastomeric and lead-rubber seismic isolation bearings." Journal of Structural Engineering-ASCE, 133(9), 1227-1236.

[6] Cheong, YK., Gorishnyy, T. and Thomas, EL, (2007), "Phononic Band Structures of Two-dimensional Hypersonic Phononic Crystals". Proceedings of the COMSOL Conference 2007. Boston

[7] Zhou, F. L., Tan, P., Xian, Q. L., Huang, X. Y., and Yang, Z. (2006). "Research and application of seismic isolation system for building structures." Journal of Architecture and Civil Engineering, 6(2), 1-8

[8] Chen Xiong, Zhifei Shi* and Hongjun Xiang "Attenuation of Building Vibration Using Periodic Foundations"

[9] Symans, M. D., Cofer, W. F., and Fridley, K. J. (2002). "Base isolation and supplemental damping systems for seismic protection of wood structures: Literature review." Earthquake Spectra, 18(3), 549-572

[10] Liu, Z., Zhang, X., Mao, Y., Zhu, Y. Y., Yang, Z., Chan, C. T. et Sheng, P., "Locally resonant sonic materials", Science, vol. 289, no. 5485, (2000), pp. 1734- 1736.

[11] Kelly, J. M. (1999). “The role of damping in seismic isolation.” Earthquake Engineering and Structural Dynamics, 28(1), 3-20

[12] Naeim, F., and Kelly, J. M. (1999). Design of seismic isolated structures: from theory to practice, John Wiley and Sons Inc., New York.

EURODYN 2020
XI International Conference on Structural Dynamics
M. Papadrakakis, M. Fragiadakis, C. Papadimitriou (eds.)
Athens, Greece, 23–26 November 2020

GENERATION OF ARTIFICIAL ACCELEROGRAMS CONSISTENT WITH EARTHQUAKE-INDUCED GROUND MOTIONS

Federica Genovese, Giuseppe Muscolino, Giovanni Biondi and Ernesto Cascone

Department of Engineering, University of Messina, Villaggio S. Agata, 98166 Messina, Italy.

e-mail: fedgenovese@unime.it, gmuscolino@unime.it, gbiondi@unime.it, ecascone@unime.it

Keywords: Artificial accelerograms, Fully non-stationary stochastic process, 1D Non-linear seismic site response analysis, Real ground motion records, Simulation.

Abstract. *Seismic response history analysis is the most significant approach for seismic analysis of structural and geotechnical systems, especially when nonlinearities are present. The main purpose of this analysis is the determination of the system response when it is subjected to a ground motion acceleration.*

Several approaches have been proposed to select the most appropriate seismic acceleration. The various approaches use, respectively: a) real accelerograms; b) synthetic accelerograms and c) artificial accelerograms. The artificial accelerograms for their versality are the most adopted. However, the main drawback of generated artificial accelerogram is the impossibility to take into account of both the time and frequency contents of real accelerograms when the spectrum compatibility is satisfied.

In this paper an alternative method is proposed. The proposed method requires the following steps: i) to select a target accelerogram; ii) to find a fully non-stationary model of earthquake ground acceleration such that the target accelerogram may be considered as one of its samples; iii) to evaluate the mean elastic spectrum of a set of generate fully non-stationary accelerogram samples; iv) to satisfy the compatibility of so determined elastic spectrum to elastic target response spectrum by means of an iterative procedure.

In order to quantify the influence of accelerogram models on the seismic response a non-liner geotechnical system is analysed. In particular, selected a target accelerogram recorded in a stiff soil, the response of a real soil deposit is evaluated assuming for the soil a non-linear one-dimensional (1D) model.

1 INTRODUCTION

A proper definition of the design seismic actions is a fundamental step in the dynamic analysis of structural and geotechnical systems as well as in dynamic soil-structure interaction problems. Seismic codes typically represent the earthquake-induced ground shaking in terms of pseudo-acceleration response spectrum. However, for strongly non-linear problems the use of the design response spectrum is improper and the selection of input motions to be used in non-linear dynamic analyses is required. In this framework, the increasing availability of strong motion records makes the use of *real accelerograms* an attractive option for a proper definition of the input motions [1] even if the results of the selection procedures are influenced by multiple sources of uncertainties related to the definition of the seismic hazard at the site of interest and to the criteria adopted to check the compatibility of the selected records with the frequency and energy content of a target motion expected at the site [2,3]. Despite different selection procedures have been proposed in the literature (e.g. [4,5,6]), depending on the characteristics of the expected target motion and on the adopted compatibility criteria, it may be impossible to select a suitable number of compatible accelerograms without applying large acceleration scale factors which distort the actual characteristics of selected motions leading to unrealistic inputs [2,3].

A suitable alternative for the definition of the input motion consist of sets of *synthetic accelerograms* obtained from seismological numerical models and accounting for site-to-source effects. The determination of the source parameters for previous earthquakes invariably carries a high degree of uncertainty, and the specification of these parameters to which the resulting ground motions can be highly sensitive for future earthquake scenarios can involve a significant degree of expert judgment [1].

Finally, *artificial accelerograms* generated using proper numerical procedures can be also adopted for engineering purposes. Traditionally, artificial accelerograms are generated to match a target response spectrum by obtaining a *power spectral density* (*PSD*) function from the target response spectrum and then to derive accelerogram samples as sinusoidal signals having random phase angles (see e.g. [7,8]). Recently it has been shown that the *artificial accelerograms* generated by applying the models proposed in the literature are not able to catch the up-crossing law of time axis, which is a measure of evolutionary frequency content of accelerograms in various seismological sites [9,10]. Moreover, it has been recognized that artificial accelerograms generated by applying stationary models, extensively adopted by International Seismic Codes, have an excessive number of cycles and consequently they possess unreasonably much higher energy content with respect to real ones [1,10].

In this vein, a new procedure for generating samples of a *fully non-stationary* zero-mean Gaussian process, having a target acceleration time-history as one of its own samples, is described in this paper. The procedure requires the following steps: i) select a target accelerogram; ii) find a *fully non-stationary* model of earthquake ground acceleration such that the target accelerogram may be considered as one of its samples; iii) generate a set of *fully non-stationary accelerogram* samples and evaluate their mean elastic response spectrum; iv) using an iterative procedure aimed to obtain the compatibility between this mean spectrum an that of the target accelerogram.

The reliability and the accuracy of the proposed procedure in generating sets of accelerograms with statistical characteristics similar to those of the target is also checked and discussed in the paper through a numerical application concerning 1D non-linear site response analysis. In this framework it is also shown that the proposed procedure is also able to catch both the time-varying amplitude and frequency content of the target accelerogram.

2 EVOLUTIONARY MODEL FOR EARTHQUAKE INDUCED GROUND ACCELERATION

According to the formulation recently proposed by the authors [9], the *fully non-stationary* model of earthquake ground acceleration is defined as the sum of zero-mean Gaussian *uniformly modulated* stochastic processes. Each *uniformly modulated* random process consists of the product of a positive deterministic *modulating function*, $a(t)$, and a stationary zero-mean Gaussian filtered sub-process, $X_k(t)$. The stochastic process so defined is able to catch simultaneously the time-varying intensity and the time-varying frequency content, although its component processes are individually *uniformly modulated*. Then, the *fully non-stationary* stochastic process $F_0(t)$, of time duration T_D, is here obtained by dividing the time interval $0 \div T_D$ in *n* contiguous time intervals of amplitude $\Delta T_k = t_k - t_{k-1}$ $(k = 1, 2 \cdots, n)$ and requiring that in each time interval the sub-process $X_k(t)$, possesses a unimodal *PSD* function, that is:

$$F_0(t) = \sum_{k=1}^{n} F_{0,k}(t) = a(t) \sum_{k=1}^{n} X_k(t)\, \mathbb{W}(t_{k-1}, t_k) \tag{1}$$

where $\mathbb{W}(t_{k-1}, t_k) = \mathbb{U}(t - t_k) - \mathbb{U}(t - t_{k-1})$ is the window function, with $\mathbb{U}(t)$ the unit step function. The one-sided *EPSD* function of the zero-mean Gaussian fully non-stationary process introduced in Eq.(1) results:

$$G_{F_0 F_0}(\omega, t) = \sum_{k=1}^{n} a^2(t)\, \mathbb{W}(t_{k-1}, t_k)\, G_{X_k}(\omega) \equiv \sum_{k=1}^{n} G_{X_k}(\omega, t) \tag{2}$$

Moreover, in the time interval $[t_{k-1}, t_k)$, the sub-process $X_k(t)$ is here characterised by the following one-sided *PSD* function:

$$G_{X_k}(\omega) = \beta_k^2 \left(\frac{\omega^2}{\omega^2 + \omega_{H,k}^2} \right) \left(\frac{\omega_{L,k}^4}{\omega^4 + \omega_{L,k}^4} \right) G_k^{(CP)}(\omega); \qquad k = 1, ..., n \tag{3}$$

where $\omega_{L,k}$ and $\omega_{H,k}$ are the *k*-th frequency control of the second order low pass and first order high pass Butterworth filters, respectively, $G_k^{(CP)}(\omega)$ is a unimodal one-sided *PSD* function, having unit area, which can be viewed as the linear combination of the displacement and velocity responses of a second-order oscillator subjected to two statistically independent Gaussian white noise processes [11]:

$$G_k^{(CP)}(\omega) = \frac{\rho_k}{\pi} \left(\frac{1}{\rho_k^2 + (\omega + \Omega_k)^2} + \frac{1}{\rho_k^2 + (\omega - \Omega_k)^2} \right); \qquad k = 1, ..., n \tag{4}$$

In equation (4) ρ_k and Ω_k are two free parameters. The first one is a circular frequency bandwidth, the second one is close enough to the predominant circular frequency of the *k*-th filtered stationary process. Finally, in Eq.(3) the coefficient β_k^2 is evaluated in such a way that the sub-process $X_k(t)$ possesses unit variance $\mathrm{E}\left\langle X_k^2(t) \right\rangle \equiv \sigma_{X_k}^2 = 1$. It is given in closed form solution as follows:

$$\beta_k^2 = \frac{2\, \bar{a}_k \bar{b}_k \left(\omega_{H,k}^4 + \omega_{L,k}^4 \right)}{\omega_{L,k}^3 \left(\bar{c}_k + \bar{d}_k + \bar{e}_k \right)} \tag{5}$$

where:

$$\begin{aligned}
\bar{a}_k &= \left(\rho_k^2+\Omega_k^2\right)^4 + 2\left(\rho_k^4 - 6\rho_k^2\Omega_k^2 + \Omega_k^4\right)\omega_{L,k}^4 + \omega_{L,k}^8;\\
\bar{b}_k &= \rho_k^4 + 2\rho_k^2\left(\Omega_k^2 - \omega_{H,k}^2\right) + \left(\Omega_k^2 + \omega_{H,k}^2\right)^2;\\
\bar{c}_k &= -2\,\bar{a}_k\,\rho_k\,\omega_{H,k}\,\omega_{L,k}\left(\rho_k^2 + \Omega_k^2 - \omega_{H,k}^2\right);\\
\bar{d}_k &= \left[\left(\rho_k^2+\Omega_k^2\right)^2\left(\rho_k^4 - 6\rho_k^2\Omega_k^2 + \Omega_k^4 + \omega_{L,k}^4\right) - \omega_{H,k}^2\left(\rho_k^2 - \Omega_k^2\right)\left(\left(\rho_k^2+\Omega_k^2\right)^2 + \omega_{L,k}^4\right)\right] \\
&\quad \times 2\omega_{L,k}\left(\omega_{H,k}^4 + \omega_{L,k}^4\right);\\
\bar{e}_k &= \sqrt{2}\,\bar{b}_k\,\rho_k\left\{\omega_{L,k}^2\left(\omega_{H,k}^2 - \omega_{L,k}^2\right)\left(\omega_{L,k}^4 + \rho_k^4 - 2\rho_k^2\Omega_k^2 - 3\Omega_k^4\right)\right. \\
&\quad \left. + \left(\omega_{H,k}^2 + \omega_{L,k}^2\right)\left[\rho_k^6 + \Omega_k^6 + 3\Omega_k^2\rho_k^2\left(\rho_k^2+\Omega_k^2\right) + \omega_{L,k}^4\left(\rho_k^2 - 3\Omega_k^2\right)\right]\right\}.
\end{aligned} \tag{6}$$

Scaling the *PSD* function (3) to have unit variance allows separating, in each time interval, the time variation in amplitude from the frequency content of the various segments of the stochastic process $F_0(t)$.

3 PARAMETERS ESTIMATION FROM A TARGET ACCELEROGRAM

The purpose of this section is to define a stochastic process $F_0(t)$ such that the target accelerogram, $\ddot{U}_g(t)$, may be considered as one of its samples. To do this the *modulating function* and the frequency content of the process $F_0(t)$ are estimated separately.

3.1 Estimation of modulating function

Let us consider a target accelerogram $\ddot{U}_g(t)$ of time duration T_D. To evaluate the *modulating function*, $a(t)$, the time interval $0 \div T_D$ is subdivided in three contiguous time intervals of amplitude $\Delta T_j = t_j - t_{j-1}$ $(j=1,2,3)$. The *modulating function* in the first time interval, $0 \le t < t_1$, is here assumed parabolically increasing from zero; while in the third time interval, $t_2 \le t \le T_D$, it is assumed exponentially decreasing. In the second time interval, $t_1 \le t < t_2$, a polynomial of *p*-th order to model the *modulating function* is adopted:

$$a(t) = \sum_{j=1}^{2} \bar{a}_j(t)\,\mathbb{W}(t_{j-1}, t_j) + a(t_2)\exp\left[\frac{(t-t_2)}{T_D - t_2}\ln\left(\frac{\left|\ddot{U}_g(T_D)\right|}{a(t_{n_a-1})}\right)\right]\mathbb{W}(t_2, t_3). \tag{7}$$

The parameter of the modulating function, $a(t)$, in the first two time intervals $[0, t_1)$,and $[t_1, t_2)$ are estimated by least-square fitting the expected energy of the fully non-stationary process to the energy of the target accelerogram. That is the following optimization problems is solved:

$$\begin{cases} \text{find } \alpha_1,\ \alpha_2,\cdots\ \alpha_p; \\ \text{minimising} \quad \int_{t_{j-1}}^{t_j}\left[E_{\ddot{U}_g}(t)-\int_{t_{j-1}}^{t}\left[a(t_{j-1})+\bar{a}_j(\tau)\right]^2 \mathrm{d}\tau\ \right]^2 \mathrm{d}t; \qquad j=1,2. \\ \text{such that} \quad \bar{a}_j(t)=\sum_{i=1}^{p}\alpha_i\,(t-t_{j-1})^i, \quad \bar{a}_j(t)\geq 0, \quad t_{j-1}\leq t<t_j; \end{cases} \tag{8}$$

where $a(0)=0$ and:

$$E_{\ddot{U}_g}(t)=\int_0^t \ddot{U}_{\mathrm{g}}^2(\tau)\,\mathrm{d}\tau \quad 0\leq t\leq T_D \tag{9}$$

is the cumulative energy function of the target accelerogram. Moreover, in the third time interval with $t\in[t_2,t_3\equiv T_D]$, the *modulating function* is approximated by an exponential decaying function whose coefficients are evaluated by imposing the continuity with the previous one and its decaying down to the absolute value, $\left|\ddot{U}_{\mathrm{g}}(T_D)\right|$, at the end of the target accelerogram:

$$a(t)=a(t_2)\exp\left[\frac{(t-t_2)}{T_D-t_2}\ln\left(\frac{\left|\ddot{U}_{\mathrm{g}}(T_D)\right|}{a(t_2)}\right)\right], \quad t_2\leq t\leq T_D. \tag{10}$$

3.2 Estimation of PSD function parameters

Since analysing the expected energy function of the fully non-stationary stochastic process $F_0(t)$, it is possible only to estimate the amplitude variation of the target accelerogram $\ddot{U}_{\mathrm{g}}(t)$, another criterion to estimate the variation of the frequency content of $F_0(t)$ must be established, such that $\ddot{U}_{\mathrm{g}}(t)$ may be considered as one of its samples. Once the time interval $0\div T_D$ is divided in *n* contiguous time intervals, this purpose is here achieved by capturing in the generic *k*-th time interval a group of seismic waves possessing the specific frequency distribution of the target accelerogram in the same time interval. To do this the spectral parameters, Ω_k, ρ_k, $\omega_{H,k}$ and $\omega_{L,k}$, appearing in Eq.(3), of the one-sided *PSD* function $G_{X_k}(\omega)$ of the stationary sub-process $X_k(t)$ must be appropriately estimated. In particular, the predominant circular frequency and the circular frequency bandwidth, are evaluated, respectively, as authors [9]:

$$\Omega_k\cong\frac{2\pi N_{0,k}^+}{\Delta T_k}; \quad \rho_k\simeq\frac{\pi N_{0,k}^+}{2\Delta T_k}\left[\pi-2\frac{N_{0,k}^+}{P_k}\right] \tag{11}$$

where N_0^+ and P_0 are the total number of *zero-level up-crossings* and the total number of *peaks* of target accelerogram. To complete the characterization of the one-sided *PSD* function $G_{X_k}(\omega)$, given in Eq.(3), the circular frequency control of two Butterworth filters $\omega_{H,k}$ and $\omega_{L,k}$ in all time intervals, $[t_{k-1},t_k)$, have to be estimated.

3.3 Fully non-stationary samples

Once the parameters characterizing the *fully-non stationary* zero-mean Gaussian process, $F_0(t)$, defined in Eq.(1), are estimated, it is easy to generate its samples in such a way that the selected target accelerogram can be considered as one of its own samples. Indeed, the *i*-th sample of the $F_0(t)$ stochastic process, containing in its set the target accelerogram $\ddot{U}_g(t)$, can be evaluated as:

$$F_0^{(i)}(t) = a(t)\sqrt{2\Delta\omega}\left[\sum_{r=1}^{m_N}\sin\left(r\,\Delta\omega t + \theta_r^{(i)}\right)\left(\sum_{k=1}^{n}\mathbb{W}(t_{k-1},t_k)\sqrt{G_{X_k}\left(r\,\Delta\omega\right)}\right)\right] \tag{12}$$

assuming a frequency increment $\Delta\omega = \omega_N / m_N = 0.1$, an upper cut-off circular frequency $\omega_N = 100$ rad/s, and the random phase angles, $\theta_r^{(i)}$, uniformly distributed over the interval $[0-2\pi)$. It follows $m_N = 1000$, and $\Delta t = \pi/(4\omega_N)$.

4 FULLY NON-STATIONARY SPECTRUM COMPATIBLE ARTIFICIAL ACCELEROGRAMS

In this section the *EPSD* of the fully non-stationary is modified to guaranty the spectrum compatibility of the sets of artificial accelerograms.
To reduce the gap between the elastic response spectrum of target accelerogram and the mean elastic response spectrum of artificial accelerograms an iterative procedure has to be implemented. The *EPSD* function (2) is rewritten as:

$$\begin{aligned}&\bar{G}_{F_0F_0}^{(j)}\left(\omega_k,t\right) = a^2(t)\bar{G}_0^{(j)}(\omega_k)\sum_{\ell=1}^{n}\mathbb{W}(t_{\ell-1},t_\ell)\,G_{X_\ell}\left(\omega_k\right);\\ &\bar{G}_{F_0F_0}^{(0)}\left(\omega_k,t\right) \equiv G_{F_0F_0}\left(\omega_k,t\right)\end{aligned} \tag{13}$$

In this equation $\bar{G}_0^{(j)}(\omega_k)$ is a corrective *PSD* function at the *j*-th iteration evaluated as follows [12]:

$$\bar{G}_{X_k}^{(j)}(\omega_k) = \bar{G}_{X_k}^{(j-1)}(\omega_k)\,\frac{S_e^{(T)}(\omega_\ell,\zeta_0)^2}{\bar{S}_e^{(j-1)}(\omega_\ell,\zeta_0)^2} \tag{14}$$

where $S_e^{(T)}(\omega_\ell,\zeta_0)$ is the elastic response spectrum of target accelerogram, $\bar{S}_e^{(j)}(\omega_\ell,\zeta_0)$ is the mean elastic response spectrum determined at the *j*-th iteration.

Notice that at first iteration it is assumed $\bar{G}_0^{(0)}(\omega_k) = 1$. Once the corrective *PSD* function is introduced, by using the original set of random phase angles, $\theta_r^{(i)}$, a new set of samples has to be calculated:

$$\bar{F}_0^{(i)}(t) = a(t)\sqrt{2\Delta\omega}\left[\sum_{r=1}^{m_N}\sin\left(r\,\Delta\omega t + \theta_r^{(i)}\right)\left(\sum_{\ell=1}^{n}\mathbb{W}(t_{\ell-1},t_k)\sqrt{\bar{G}_0^{(j)}(r\,\Delta\omega)G_{X_\ell}\left(r\,\Delta\omega\right)}\right)\right] \tag{15}$$

It has to be emphasized that the procedure should not be expected to be convergent at all selected control frequencies.

Moreover, it has been pointed out that it is not productive to iterate for more than about four cycles [12].
Obviously, by adopting the fully non-stationary process possessing, at the *j*-th iteration, the *EPSD* function (13), it is not possible to fully satisfy the energy content and the frequency content of target recorded accelerogram as well as the spectrum compatibility to its elastic response spectrum.
However, as will show in the next section, the proposed procedure furnishes a good compromise in satisfying these three aspects.

5 NUMERICAL APPLICATION

In order to highlight the reliability and the accuracy of the proposed procedure in generating sets of accelerograms with statistical characteristics similar to those of the target one, a numerical application concerning 1D non-linear site response analysis was used.
A comparison with the results obtained using a set of accelerograms generated using the stationary response spectrum compatible method [7] is also presented and discussed herein.

5.1 Target motion and site description

The target accelerogram consist of the N-S component of the ground motion recorded at Vasquez Rocks Park during the 1994 Northridge earthquake (M_w = 6.7). The recording stations is characterized by an average shear wave velocity in the upper 30 m equal to $V_{s,30}$ = 996 m/s and by a site-source distance R_{JB} = 23.1 km [13].
The ground motion, having an overall duration T_D = 36.6 s, was characterized by a peak ground acceleration a_{max} = 0.132 *g*, a *total* and *Arias intensity* equal to I_0 = 1.9 m^2/s^3 and I_A = 0.3 m/s, respectively, a significant strong motion duration (i.e. interval of time elapsed between the 5% and 95% of I_0) *SMD* = 7.3 s and a total number of *zero-level up-crossings* and of *peaks* equal to N_0^+= 196 and P_0 = 212, respectively.
The 1D site response analyses were carried out using the soil profile derived by [14] with reference to the port area of Tremestieri (Messina), located in the east cost of Sicily.
The shear wave velocity profile detected by a Cross Hole test in the upper 50 m, was interpolated using the following expression:

$$V_S(z) = V_{S0}\left(1+\alpha\frac{z}{H}\right)^m \tag{16}$$

with V_{S0} = 80 m/s, m = 0.5 and α = 50 and allowed to detect a seismic bedrock (V_s = 800 m/s) at a depth H = 99 m.
For this soil profile the average shear wave velocity is $\overline{V}_{S,H}$ =537 m/s and the fundamental period of elastic vibration is $T_{1,L}$ = 0.63 s.
For the site of interest, resonant column tests were also performed on soil samples retrieved at depths of 7, 13, 18.5 and 28.5 m.
The test results in terms of variation of the normalized shear modulus G/G_0 and of the damping ratio D with the shear strain amplitude γ, are plotted in Figure 1. The curves refer to effective vertical stresses σ_v' ranging from 100 to 300 kPa.

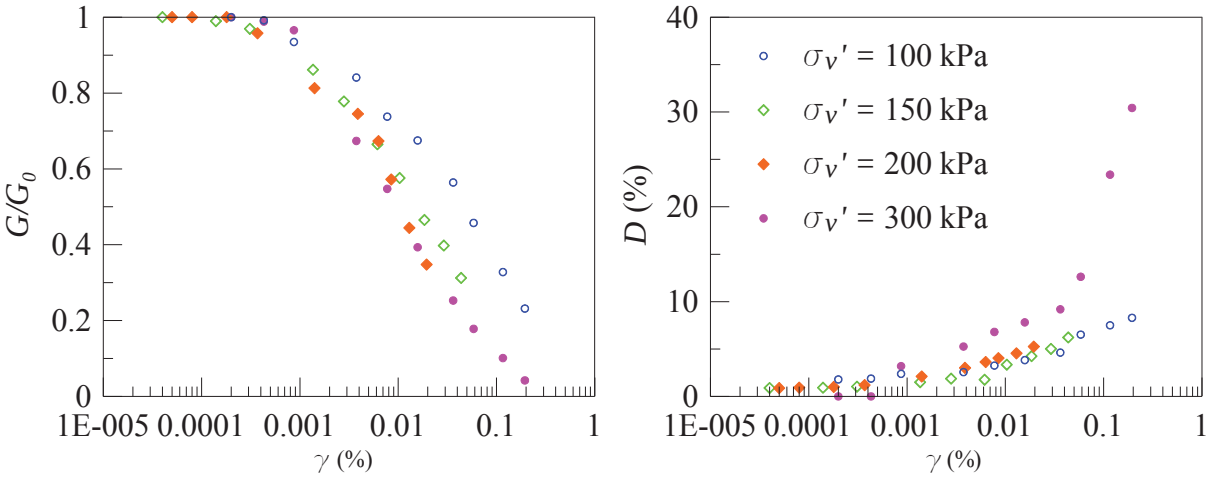

Figure 1: G/G0 – γ (a) and D – γ (b) curves evaluated or the site of interest.

5.2 Set of fully non-stationary accelerograms

Using the proposed procedure, a set of artificial accelerograms was generated using appropriate modulating and power spectral density functions which allowed to preserve the amplitude and the frequency content of the target motion.

To evaluate the *modulating function* $a(t)$, the time duration of the analysed accelerogram $0 \div T_D$, is divided in three time intervals, optimizing the choice of instants of passage from one time interval to adjacent ones (see e.g. [9]).

Figure 2 shows the absolute value of the target accelerogram together with the *modulating function* $a(t)$.

The parameters which characterise $a(t)$ are listed in Table 1, together with the values of the time instants t_1 and t_2, corresponding to the passage from one interval to another, the corresponding percentages of *total intensity* k_1% and k_2%, the order p of the polynomial in the second time interval, and the absolute value $|\ddot{U}_g(T_D)|$ at the end of the target accelerogram.

For the first two time-intervals, the polynomial coefficient α_i, obtained through the optimization procedure, are listed in Table 2.

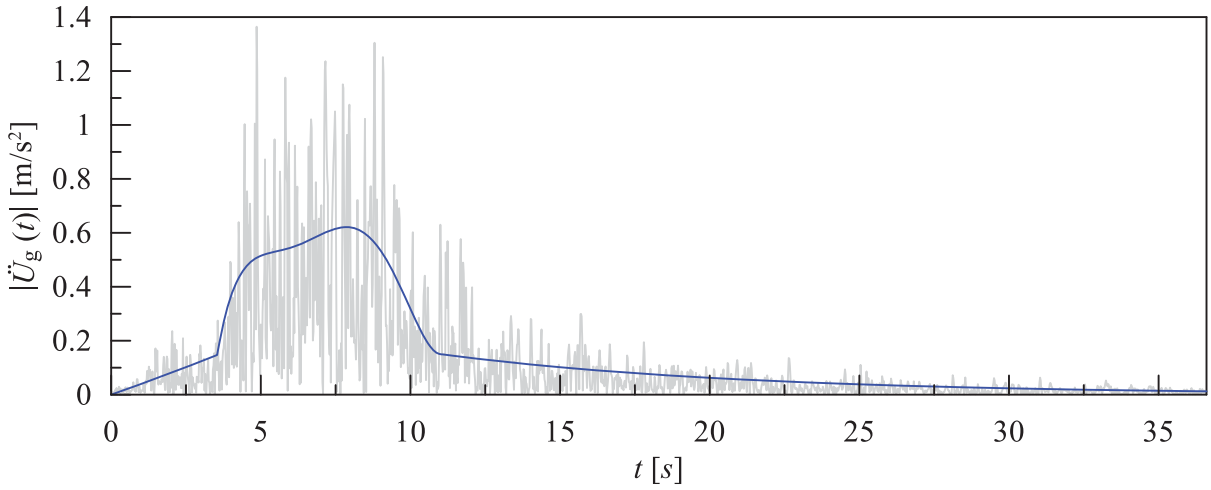

Figure 2: Absolute value of the analysed accelerograms and selected *modulating functions* $a(t)$.

t_1 [s]	t_2 [s]	k_1%	k_2%	p	$\lvert\ddot{U}_g(T_D)\rvert$ [m/s^2]
3.54	11.02	1	92	5	0.0123

Table 1: Parameters of the modulating function selected for the target accelerograms.

$0 \le t < t_1$		$t_1 \le t < t_2$				
α_1	α_2	α_1	α_2	α_3	α_4	α_5
0.039	$6.998 \cdot 10^{-4}$	0.641	-0.429	0.138	-0.020	$1.042 \cdot 10^{-3}$

Table 2: Polynomial coefficients [m/s^{i+2}] in the first two time-intervals of the modulating function.

The characterization of the *fully-non stationary* zero-mean Gaussian process $F_0(t)$ must be completed by estimating the predominant circular frequency Ω_k, and the bandwidth circular frequency ρ_k of the one-sided *PSD* function $G_{X_k}(\omega)$ of the stationary sub-process $X_k(t)$, according to Eq(11). As highlighted in [9], to obtain accurate results, the analysed accelerogram must be subdivided into many time intervals $\ddot{U}_{g,\ell}(t)$, each of which containing a number of *zero level up crossings* $N_{0,k}^+$ at least equal to one; consequently the target accelerogram is subdivided in 73 time intervals with a constant time step of 0.5 s. Through several numerical tests it was verified that the control frequencies of two Butterworth filters $\omega_{H,k}$ and $\omega_{L,k}$ can be assumed equal to $\omega_{H,k} = 0.1\,\Omega_k$ and $\omega_{L,k} = \Omega_k + 0.8\,\rho_k$, respectively. The parameters useful to the characterisation of the one-sided *PSD* function $G_{X_k}(\omega)$ are reported in Table 3.

time interval	N_0^+	P_0	Δt [s]	Ω_k [rad/s]	ρ_k [rad/s]	ω_H [rad/s]	ω_L [rad/s]	β^2
1	4	6	0.5	52.36	23.67	5.24	71.30	13.26
2	4	5	0.5	52.36	20.18	5.24	68.50	11.26
3	3	4	0.5	39.27	16.12	3.93	52.16	9.01
4	3	5	0.5	39.27	19.06	3.93	54.52	10.71
5	3	6	0.5	39.27	21.03	3.93	56.09	11.86
6	4	5	0.5	52.36	20.18	5.24	68.50	11.26
7	6	7	0.5	78.54	28.03	7.85	100.96	15.63
8	3	3	0.5	39.27	11.21	3.93	48.24	6.26
9	4	4	0.5	52.36	14.94	5.24	64.31	8.34
10	3	3	0.5	39.27	11.21	3.93	48.24	6.26
11	3	4	0.5	39.27	16.12	3.93	52.16	9.01
12	3	4	0.5	39.27	16.12	3.93	52.16	9.01
13	4	6	0.5	52.36	23.67	5.24	71.30	13.26
14	2	5	0.5	26.18	15.33	2.62	38.44	8.69
15	3	3	0.5	39.27	11.21	3.93	48.24	6.26
16	2	4	0.5	26.18	14.02	2.62	37.39	7.91
17	3	3	0.5	39.27	11.21	3.93	48.24	6.26
18	2	3	0.5	26.18	11.84	2.62	35.65	6.63
19	2	4	0.5	26.18	14.02	2.62	37.39	7.91
20	3	4	0.5	39.27	16.12	3.93	52.16	9.01
21	2	4	0.5	26.18	14.02	2.62	37.39	7.91
22	2	4	0.5	26.18	14.02	2.62	37.39	7.91
23	3	5	0.5	39.27	19.06	3.93	54.52	10.71
24	4	4	0.5	52.36	14.94	5.24	64.31	8.34
25	3	5	0.5	39.27	19.06	3.93	54.52	10.71
26	3	5	0.5	39.27	19.06	3.93	54.52	10.71

27	3	4	0.5	39.27	16.12	3.93	52.16	9.01
28	1	3	0.5	13.09	8.10	1.31	19.57	4.60
29	3	5	0.5	39.27	19.06	3.93	54.52	10.71
30	3	6	0.5	39.27	21.03	3.93	56.09	11.86
31	2	4	0.5	26.18	14.02	2.62	37.39	7.91
32	3	3	0.5	39.27	11.21	3.93	48.24	6.26
33	3	4	0.5	39.27	16.12	3.93	52.16	9.01
34	1	4	0.5	13.09	8.64	1.31	20.01	4.94
35	3	4	0.5	39.27	16.12	3.93	52.16	9.01
36	3	4	0.5	39.27	16.12	3.93	52.16	9.01
37	3	3	0.5	39.27	11.21	3.93	48.24	6.26
38	3	5	0.5	39.27	19.06	3.93	54.52	10.71
39	2	4	0.5	26.18	14.02	2.62	37.39	7.91
40	4	5	0.5	52.36	20.18	5.24	68.50	11.26
41	3	5	0.5	39.27	19.06	3.93	54.52	10.71
42	1	3	0.5	13.09	8.10	1.31	19.57	4.60
43	3	4	0.5	39.27	16.12	3.93	52.16	9.01
44	2	4	0.5	26.18	14.02	2.62	37.39	7.91
45	3	6	0.5	39.27	21.03	3.93	56.09	11.86
46	2	4	0.5	26.18	14.02	2.62	37.39	7.91
47	2	5	0.5	26.18	15.33	2.62	38.44	8.69
48	2	4	0.5	26.18	14.02	2.62	37.39	7.91
49	2	5	0.5	26.18	15.33	2.62	38.44	8.69
50	3	6	0.5	39.27	21.03	3.93	56.09	11.86
51	3	4	0.5	39.27	16.12	3.93	52.16	9.01
52	3	5	0.5	39.27	19.06	3.93	54.52	10.71
53	1	4	0.5	13.09	8.64	1.31	20.01	4.94
54	2	5	0.5	26.18	15.33	2.62	38.44	8.69
55	1	5	0.5	13.09	8.97	1.31	20.27	5.13
56	1	5	0.5	13.09	8.97	1.31	20.27	5.13
57	3	3	0.5	39.27	11.21	3.93	48.24	6.26
58	4	6	0.5	52.36	23.67	5.24	71.30	13.26
59	3	4	0.5	39.27	16.12	3.93	52.16	9.01
60	2	3	0.5	26.18	11.84	2.62	35.65	6.63
61	3	5	0.5	39.27	19.06	3.93	54.52	10.71
62	3	4	0.5	39.27	16.12	3.93	52.16	9.01
63	1	4	0.5	13.09	8.64	1.31	20.01	4.94
64	3	5	0.5	39.27	19.06	3.93	54.52	10.71
65	2	4	0.5	26.18	14.02	2.62	37.39	7.91
66	1	4	0.5	13.09	8.64	1.31	20.01	4.94
67	2	4	0.5	26.18	14.02	2.62	37.39	7.91
68	5	5	0.5	65.45	18.68	6.54	80.39	10.43
69	2	6	0.5	26.18	16.20	2.62	39.14	9.21
70	2	4	0.5	26.18	14.02	2.62	37.39	7.91
71	2	3	0.5	26.18	11.84	2.62	35.65	6.63
72	3	4	0.5	39.27	16.12	3.93	52.16	9.01
73	3	5	0.6	31.42	15.25	3.14	43.62	8.57

Table 3: Main parameters of the one-sided *PSD* functions in the time intervals analysed.

Once the parameters characterizing the *fully-non stationary* zero-mean Gaussian process, $F_0(t)$, are estimated, according to Eq.(12), it is easy to generate its samples in such a way that the selected target accelerogram can be considered as one of its own samples.

A more complete comparison can be performed by evaluating, for the analysed accelerogram, the cumulative energy function $E_{\ddot{U}_g}(t)$ and the cumulative *zero-level up-crossing*

function $N_0^+(t)$, which count the number of *zero-level up-crossing* until the time *t*. These two functions are compared, for the analysed accelerogram, with the corresponding mean value functions obtained by calculating the average of the results of the set of artificial accelerograms samples.

In particular, in Figure 3a the cumulative energy function of the analysed target accelerogram is compared to that obtained as the mean value of 50 samples. In the Figure 3a the cumulative energy function confidence intervals, evaluated as the mean values plus/minus the corresponding standard deviation, are also plotted.

In Figure 3b the cumulative *zero-level up-crossing* function of target accelerogram is compared with the mean value function of 50 samples and the *zero-level up-crossing* function confidence intervals. In Figures 3a and 3b, the shaded areas represent the envelope of the maximum and minimum values of the cumulative energy function and the cumulative *zero-level up-crossing* function of the 50 generated samples, respectively.

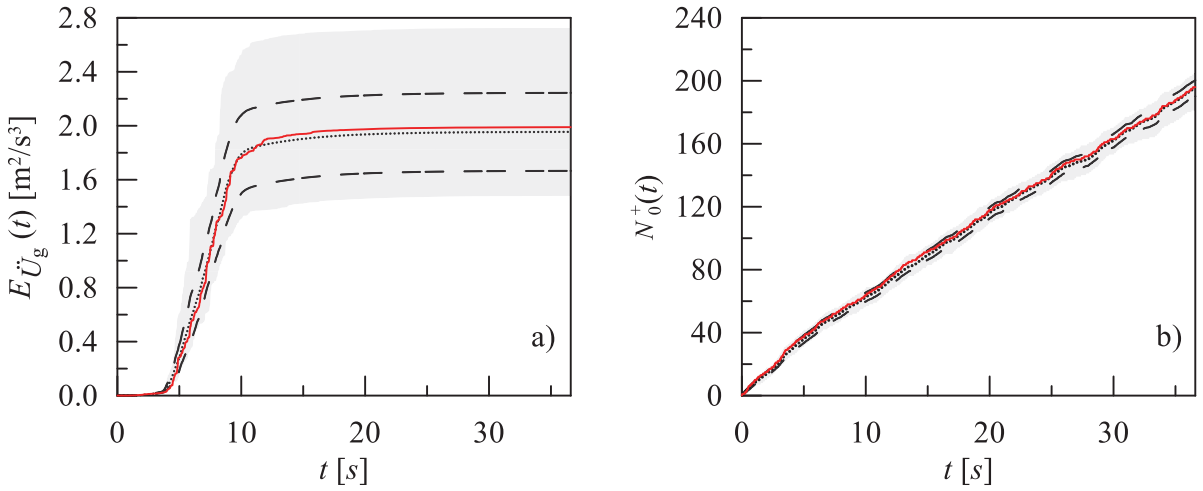

Figure 3: Comparison among the cumulative energy function a) and the cumulative zero-level up-crossing function b) of the selected accelerogram with statistics of the artificial ones: target function (red solid line); mean value function (black dotted line); mean value plus/minus standard deviation functions (black dashed lines); envelope of the maximum and minimum values of all samples (shaded area).

5.3 Set of Stationary accelerograms

A set of stationary spectrum compatible *artificial accelerograms* were also generated by applying the procedure proposed by [7]. According to this procedure the *PSD* function of the zero-mean Gaussian stationary process $G_{F_0F_0}^{(ST)}(\omega)$ is determined as follows:

$$G_{F_0F_0}^{(ST)}(\omega)=0, \quad 0\le\omega_\ell\le\omega_1;$$
$$G_{F_0F_0}^{(ST)}(\omega)=\frac{4\zeta_0}{\omega_\ell\pi-4\zeta_0\omega_{\ell-1}}\left[\left(\frac{S_e^{(T)}(\omega_\ell,\zeta_0)}{\eta_U(\omega_\ell,\zeta_0)}\right)^2-\Delta\omega\sum_{j=1}^{k-1}G_{F_0F_0}^{(ST)}(\omega_j)\right], \quad \omega_1<\omega_\ell\le\omega_N; \tag{17}$$

where $\omega_1\le 1\,(\text{rad/s})$ and ω_N (the cut off circular frequency) define the bounds of the existence domain of the *PSD* function $G_{F_0F_0}^{(ST)}(\omega)$, $\zeta_0=0.05$ is the damping ratio, $S_e^{(T)}(\omega_\ell,\zeta_0)$ is the target elastic pseudo-acceleration spectrum and $\eta_U(\omega_\ell,\zeta_0)$ is a peak factor

$$\eta_U(\omega_\ell,\zeta_0)=\sqrt{2\ln\left\{\frac{T_D\,\omega_\ell}{\pi}\left(-\ln 0.5\right)^{-1}\left[1-\exp\left[-q_U^{1.2}\sqrt{\pi\ln\left(\frac{T_D\,\omega_\ell}{\pi}\left(-\ln 0.5\right)^{-1}\right)}\right]\right]\right\}} \tag{18}$$

in which $q_U=0.246$ is the bandwidth factor. The samples of stationary Gaussian zero-mean process can be calculated by applying the following relationship:

$$\overline{\overline{F}}_0^{(i)}(t)=\sqrt{2\Delta\omega}\left[\sum_{r=1}^{m_N}\sin\left(r\,\Delta\omega t+\theta_r^{(i)}\right)\sqrt{G_{F_0F_0}^{(ST)}\left(r\,\Delta\omega\right)}\right] \tag{19}$$

5.4 Spectrum compatibility

To satisfy the spectrum compatibility between the mean elastic response spectrum of the 50 artificial fully non-stationary accelerograms and the elastic response spectrum of target accelerogram, the iterative procedure described in section 4 was applied.
In Figure 4a the average spectrum of the initial (*0*-th iteration) set of artificial accelerograms and of the samples generated after 4 iterations (*4*-th iteration), are compared with the target elastic pseudo acceleration response spectrum. In Figure 4b, the percentage deviation (*err*) between the target response spectrum and the mean of the response spectra generated by the *0*-th and *4*-th iterations are shown. The average spectrum of the set of artificial accelerograms generated by the stationary model and the correspondent deviation from the target response spectrum are also plotted in Figure 4a and in Figure 4b respectively.

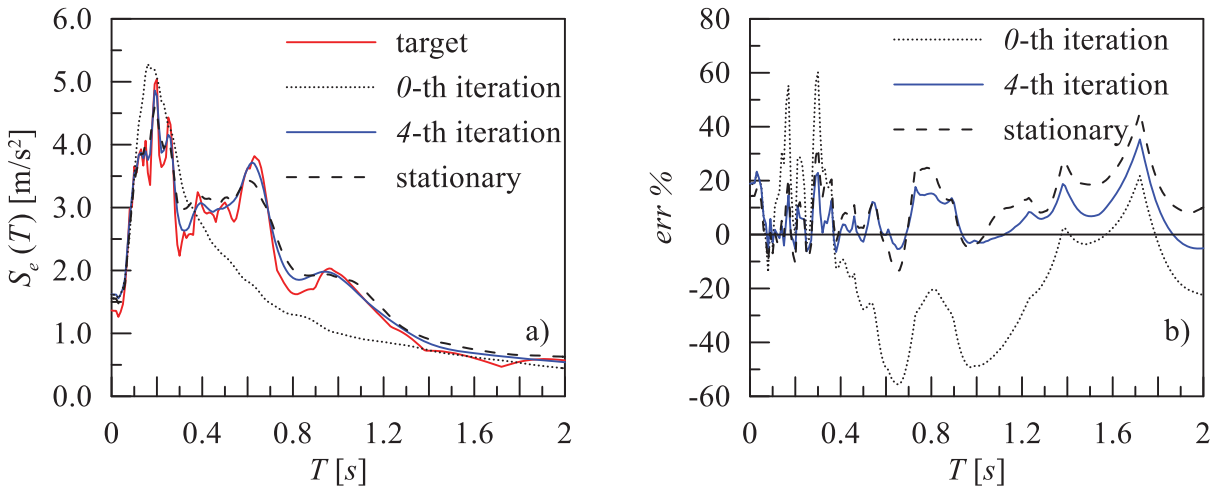

Figure 4: a) Target elastic response spectrum and mean elastic response spectra evaluated from 50 generated samples for the fully non-stationary model at the *0*-th and *4*-th iterations, and for stationary model; b) percentage errors among the target elastic response spectra and the mean ones.

In Figure 5 the time-history of the analysed target recorded accelerogram is compared with one sample of the fully non-stationary spectrum compatible accelerogram, $\overline{F}_0^{(i)}$, generate by means of Eq.(15), and one sample of the stationary spectrum compatible accelerogram $\overline{\overline{F}}_0^{(i)}$, generate by Eq.(19).

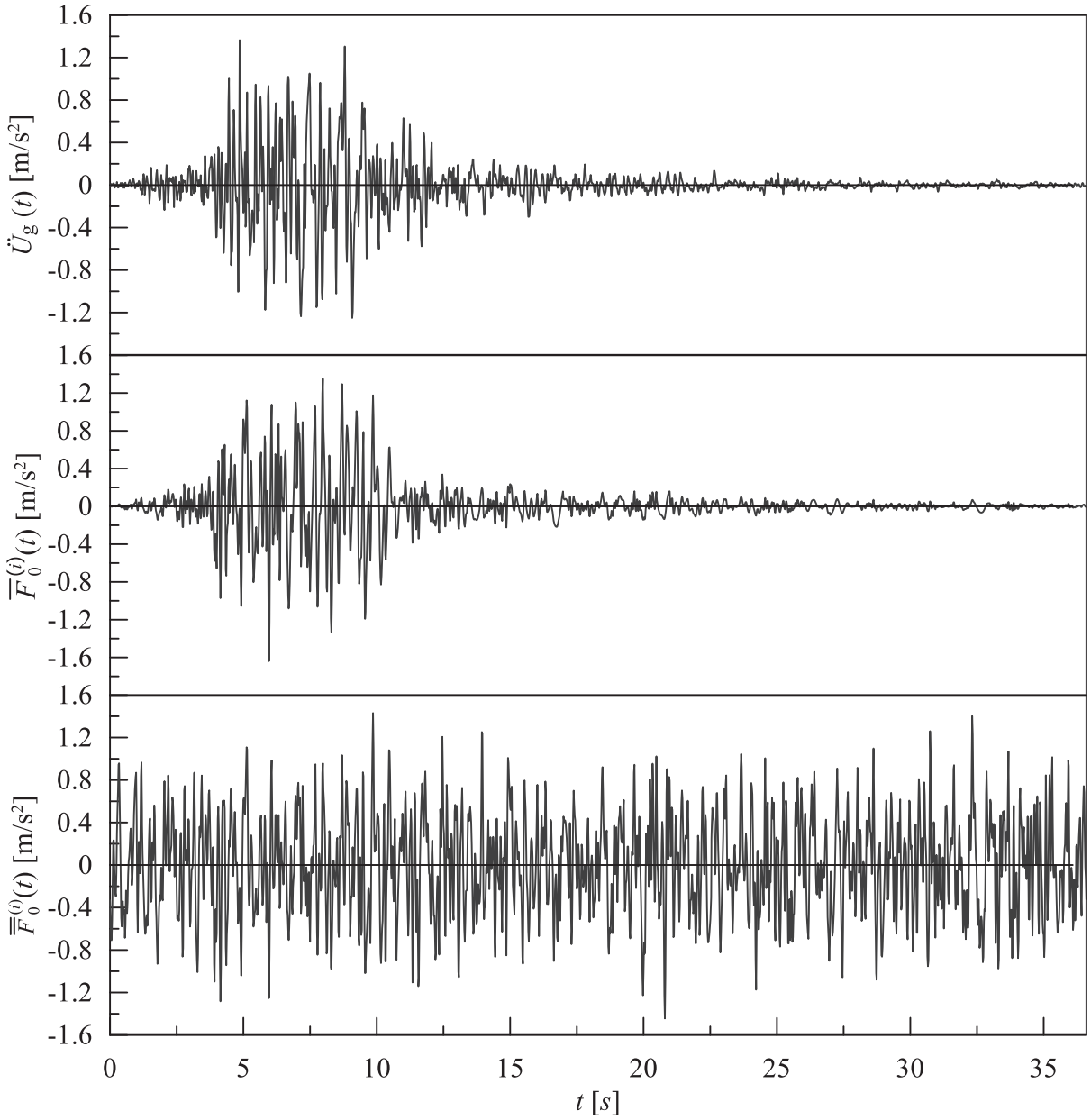

Figure 5: Comparison among the selected accelerogram and the corresponding *i*-th generated samples by the proposed fully non-stationary model $\overline{F}_0^{(i)}$ and the stationary model $\overline{\overline{F}}_0^{(i)}$.

The mean value of the cumulative *energy function* and the cumulative *zero level up crossing* function of the generated stationary samples are reported in Figure 6 with the corresponding functions obtained from the target and from the samples generated by applying the proposed fully non-stationary model.

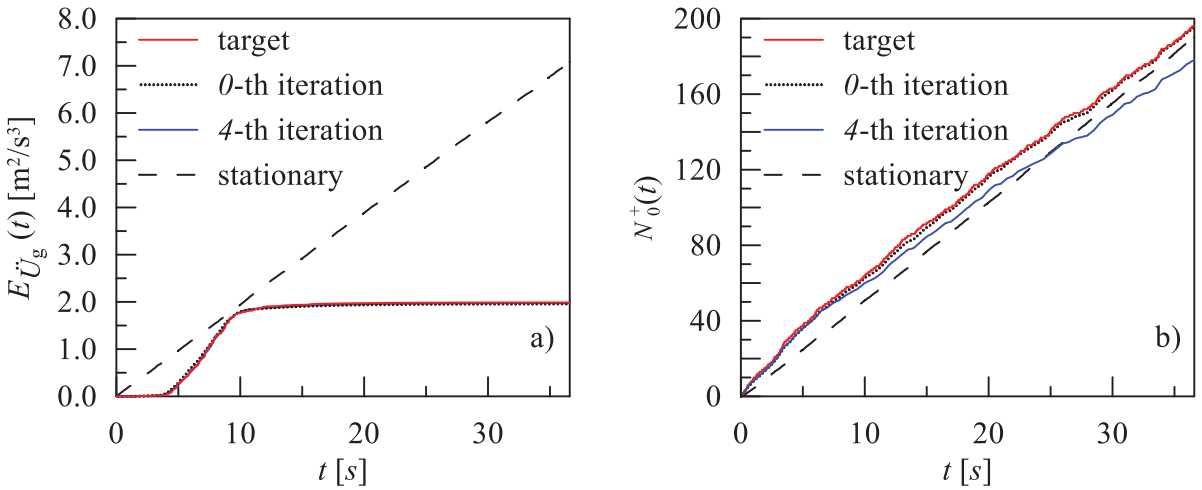

Figure 6: a) Comparison among the cumulative energy function of the target accelerogram and the mean cumulative energy functions of the fully non-stationary model, at the *0*-th and *4*-th iterations, and for stationary model; b) Comparison among the cumulative *zero level up crossing* function of the target accelerogram and the mean cumulative functions of the fully non-stationary model, at the *0*-th and *4*-th iterations, and for stationary model.

5.5 1D non-linear site response analyses

1D non-linear site response analyses were carried out through using the software Deepsoil vs. 6.1 [15]. The non-linear backbone formulation is described by the modified hyperbolic model MKZ developed by [16]. The hysteretic Re/Unloading Formulation, represented by the non-Masing model, is the MRDF-UIUC Pressure-Dependent Hyperbolic [17] model which leads to a simultaneous fit of modulus reduction and damping curves. In the analyses, the soil deposit is discretized in discrete 1 m layers having a soil unit weight γ = 19 kN/m^3 while the values V_b = 800 m/s and γ_b = 22 kN/m^3 are assigned to the shear wave velocity and unit weigh of the bedrock respectively.

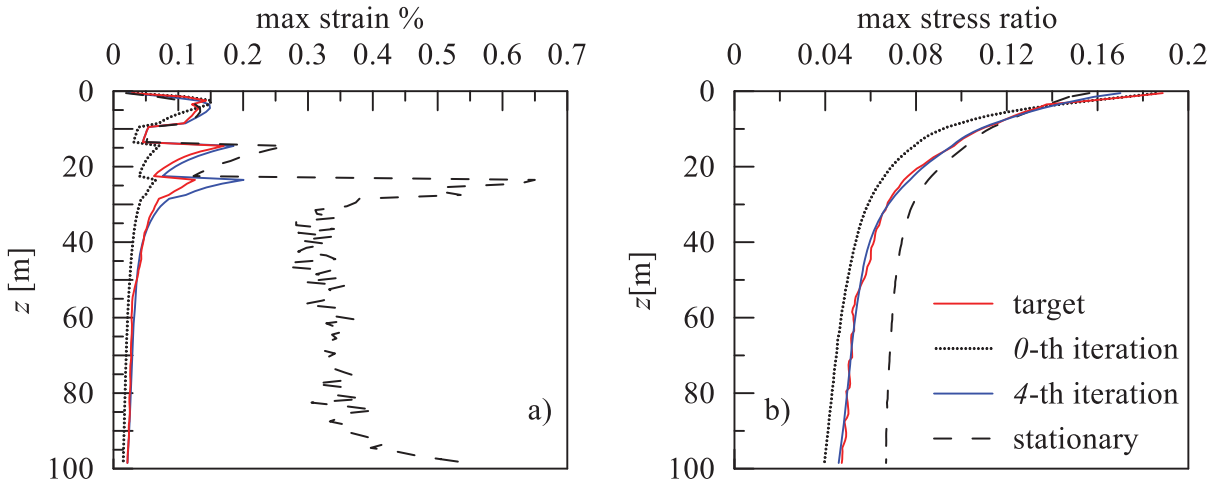

Figure 7: Profiles of peak shear strain (a) and peak stress ratio (b) computed for the target accelerogram (red line) and as the mean of the responses computed for each of the 50 spectrum-compatible stationary (dashed black line) and non-stationary (*0*-th and *4*-th iteration) artificial accelerograms.

The analysis results are presented in Figure 7 in terms of profiles of peak shear strains (Fig. 7a) and peak stress ratio (Fig. 7b) defined as the ratio between the peak shear stress, computed through the analysis, and the static effective vertical stress. Specifically, the Figure 7 shows the

profiles computed for the target accelerogram (continuous red line) and the profiles obtained as the mean of the responses computed for each of the 50 spectrum-compatible stationary (dashed black line) and non-stationary artificial accelerograms. In this latter case, the results refer to the average of the site responses computed for the initial (*0*-th iteration) set of artificial accelerograms and for the set obtained after *4* iterations of the procedure described in section 5.4 to achieve the spectral compatibility.
For both the peak strain and the peak stress ratio, it can be observed that, at all the depth (z), the response computed for the target accelerogram is in a good agreement with the average response predicted using the two sets (*0*-th and *4*-th iteration) of non-stationary accelerograms. Specifically, the effectiveness of the generation procedure described in this paper is clearly apparent from the comparison with the average response related to the set of spectrum-compatible non-stationary accelerograms (*4*-th iteration); in this case, differences between the average profile and the profile related to the target accelerogram less than 4% can be observed at all the depth with the only exception of the shallowest data ($z < 1$ m about) concerning the stress-ratio (Fig. 7b).
Conversely, larger differences are apparent between the profile related to the target accelerogram and the mean profile computed for the set of stationary spectrum-compatible accelerograms. These differences are more evident in terms of profile of peak strain (Fig. 7a) in the lower portion of the soil deposit. The differences in the computed profiles can be ascribed to the unreasonably much higher energy content which generally characterize artificial accelerograms generated by applying stationary models; as a consequence, these accelerograms are widely characterized by an excessive number of loading cycles in comparison with actual acceleration records [1] and by a very large strong motion duration (which is almost coincident with the total duration). These characteristics of the input motions lead to unacceptable errors in the prediction of the seismic response as a consequence of an overestimation of non-linear effects.
Accordingly, the need of procedures aimed to generate non-stationary ground motion to be used in non-linear seismic analysis is clearly apparent.

6 CONCLUSIONS

In this paper a procedure for generating fully non-stationary spectrum compatible artificial accelerograms has been proposed. In the procedure, the target accelerogram is subdivided in many contiguous time intervals in which appropriate unimodal Power Spectral density functions and modulating functions have been estimated to obtain cumulative energy and frequency content very close to the ones of the target accelerogram. To reduce the gap between the elastic response spectrum of the target accelerogram and the mean elastic response spectrum of fully non-stationary artificial accelerograms, an iterative procedure has been implemented.
A numerical application concerning 1D non-linear site response analysis showed that the use of artificial accelerograms generated by the proposed non-stationary spectrum compatible model leads to profiles of peak shear strain and peak stress ratio very close to that obtained using the target accelerogram as input motion. Contrary, the use of stationary accelerograms leads to results very far from those obtained using the target accelerogram as a consequence of a wrong estimate of the actual non-linear soil behaviour.
Finally, it has to be emphasised that the proposed method for generating fully non-stationary spectrum compatible accelerograms could represent a useful and promising tool in the analyses devoted to assess the seismic performance of structural and geotechnical systems through non-linear dynamic analyses.

REFERENCES

[1] Bommer, J.J., Acevedo, A.B. (2004). The use of real earthquake accelerograms as input to dynamic analysis. J. Earthquake Engineering, 8, Special issue, 1, pp. 43-91.

[2] Genovese F., Aliberti D., Biondi G., Cascone E. (2020). Influence of soil heterogeneity on the selection of input ground motion for 1D seismic response analysis. Springer Nature Switzerland AG 2020, F. Calvetti et al. (Eds.): VII CNRIG 2019, LNCE 40, pp. 694–704, 2020.

[3] Genovese, F., Aliberti, D., Biondi, G., Cascone, E. (2019). Geotechnical aspects affecting the selection of input motion for seismic site response analysis. 7th COMPDYN 2019, 24-26 June 2019, Crete, Greece, Vol. 1, pp. 151-161.

[4] Katsanos, E.I., Sextos, A.G., Manolis, G.D. (2010). Selection of earthquake ground motion records: A state-of-the-art review from a structural engineering perspective 2010. Soil Dynamics and Earthquake Engineering, Vol. 30 (4), pp. 157-169.

[5] Pagliaroli A, Lanzo G. Selection of real accelerograms for the seismic response analysis of the historical town of Nicastro (Southern Italy) during the March 1638 Calabria earthquake. Engineering Structures 2008; 30: 2211–2222.

[6] Genovese F, Aliberti D, Biondi G, Cascone E (2019). A procedure for the selection of input ground motion for 1D seismic response analysis. Proceedings of 7ICEGE 2019, Rome, Italy, p.p 2591–2598.

[7] Cacciola P, Colajanni P, Muscolino G. (2004). Combination of modal responses consistent with seismic input representation. Journal of Structural Engineering (ASCE); 130: 47-55.

[8] Cacciola P. (2010) A stochastic approach for generating spectrum-compatible fully non-stationary earthquakes. Computers and Structures;88: 889-901.

[9] Muscolino G., Genovese F., Biondi G., Cascone E. (2020). Generation of Fully Non-Stationary Random Processes Consistent with Target Seismic Accelerograms. Submitted to Soil Dynamics and Earthquake Engineering.

[10] Alderucci T, Muscolino G, Urso S (2019). Stochastic analysis of linear structural systems under spectrum and site intensity compatible fully non-stationary artificial accelerograms. Soil Dynamics and Earthquake Engineering. 2019; 126: paper e105762.

[11] Conte, J.P., Peng, B.-F. (1997). Fully nonstationary analytical earthquake ground-motion model. Journal of Engineering Mechanics (ASCE), 123(1), pp. 15-24.

[12] Vanmarcke, E.H., Gasparini, D.A. (1977). Simulated earthquake ground motions. Proceedings SMIRT-4 Conference, San Francisco, paper K1/9.

[13] Joyner WB, Boore DM (1981). Peak horizontal acceleration and velocity from strong motion records including records from the 1979 Imperial Valley, California, earthquake. Bulletin of the Seismological Society of America 1981; 71: 2011–2038.

[14] Genovese F. (2020). Influence of soil non-linear behaviour on the selection of input motion for dynamic geotechnical analysis. Challenges and Innovations in Geomechanics - Proceedings of the 16th International conference of IACMAG, 05-08, May 2021, Turin, Italy.

[15] Hashash Y.M.A., Musgrove M.I., Harmon J.A., Groholski D.R., Phillips C.A., & Park D. 2016. DEEPSOIL 6.1, User Manual.

[16] Matasovic N. 1993. Seismic response of composite horizontally-layered soil deposits, Ph.D. Thesis, Uni-versity of California, Los Angeles.

[17] Phillips, C. and Y. M. A. Hashash (2009). "Damping formulation for non-linear 1D site response analyses." *Soil Dynamics and Earthquake Engineering* 29(7): Pages 1143-1158.

EURODYN 2020
XI International Conference on Structural Dynamics
M. Papadrakakis, M. Fragiadakis, C. Papadimitriou (eds.)
Athens, Greece, 23–26 November 2020

FULL SCALE DYNAMIC TESTING OF WALL PANEL CONNECTIONS FOR PRECAST INDUSTRIAL BUILDINGS

Ilaria Venanzi[1], Laura Ierimonti[1], Filippo Ubertini[1], Annibale Luigi Materazzi[1], Leonardo Casali[2] and Giuseppe Paci[2]

[1]Department of Civil and Environmental Engineering, University of Perugia. Via G. Duranti, 93 - 06125 Perugia, Italy.
e-mail: {ilaria.venanzi,laura.ierimonti,filippo.ubertini,annibale.materazzi}@unipg.it

[2] Manini Prefabbricati spa
e-mail: {casali,pacig}@manini.it

Keywords: Precast Cladding Panels, Hammer-head strap connection, Earthquake resistant structures.

Abstract. *During the recent seismic events in Italy (such as L'Aquila 2009, Emilia 2012 and the 2016 Central Italy seismic sequence), several damages and collapses were observed in precast reinforced concrete industrial buildings. Although reliable seismic design criteria are nowadays available for precast frame structures, recent earthquakes showed that the optimal design of the cladding-to-structure connections is yet to be solved. Currently, in the seismic design practice of precast structures, the panels are modeled as additional masses, without any stiffness contribution. Then, the capacity displacement of the designed connection is compared with its demand displacement. This design practice does not correctly reflect the actual behavior of the connection because, due to the configuration of the anchorage devices that exert friction and blockage effects, a force exchange can occur between the panels and the supporting beams. This was demonstrated by the surveys carried out after the seismic events, reporting several damages to traditional anchorage systems. In the context presented above, the research work is aimed at investigating the seismic behavior of the first prototype of an innovative cladding-to-structure connection for precast industrial buildings. The innovative device is capable to guarantee higher robustness with respect to the devices currently available on the market, especially when friction forces on the sliding cart are significant and is able to avoid jamming of the cart. Full scale experimental tests are carried out on a prototype precast building equipped with cladding panels. The system is forced by a vibrodyne mounted on the roof and providing an in-plane sinusoidal force along the direction of the panel. Tests are repeated with two different types of connection between the wall panels and the structure: a traditional one and an innovative one, showing the superior performance of the new type of connection in reducing the load transfer and avoiding damage to the panel and the beam even at large excitation levels.*

usepackage float

1 INTRODUCTION

Precast reinforced concrete technology is a construction method which gained success especially in industrial constructions and commercial buildings, due to the need of large spans and plan dimensions. The 2012 Emilia-Romagna earthquake (central Italy) highlighted the seismic vulnerability of these structures in terms of direct and indirect losses [1], focusing the attention on damage prevention methodologies for prefabricated structures [2, 3].
In particular, precast buildings can experience collapses or serious damages in structural and nonstructural elements, expecially due to the lack of adequate beams-to-columns and cladding-to-structure connections [4], demostrating an insufficient safety level against seismic actions [5]. Indeed, connections should be able to absorb the relative displacements due to cyclic seismic loading in order to avoid damage for both vertical and horizontal panels [6, 7].
In this framework, the research work is aimed at investigating the in-plane anchorage performance of an innovative cladding-to-structure connection device. The new device has a joint capable of rotating along the two principal directions, as well as sliding along the vertical and horizontal direction. It follows that, during the seismic event, the connection can perform a rotational-translational motion. The idea is to effectively decouple the movement between the panel and the structural element, overcoming the major limitations associated with traditional anchorage systems, such as deformability, friction force and jamming of the cart.

2 THE CASE STUDY

The case study is a prototype single-story building (Figure 1) with plan dimensions of 10.2 x 14.6 m and with a height of 11.0 m. The frame is composed by reinforced concrete columns with a rectangular cross section, prestressed I-shaped beams along the shorter side of the structure, and U-shaped precast roof beams along the longer side. A reinforced concrete cladding

Figure 1: The full scale prototype building.

panel can be mounted on the structure and is connected to a reinforced concrete support beam.

The connection between the panel and the support beam is realized by 4 steel plates, two on each side of the support beam, equipped with a hole to house a central connection pivot. The support beam, integral with the wall panel and the principal beam as well, allows to measure the cladding-to-structure force exchange through the displacements transducers installed on the steel plates. A vibrodyne is installed on the rooftop, capable of inducing a sinusoidal force to the structure, as better detailed in the next section.
Two different types of hammer-head strap devices are used to connect the cladding panel to the support beam: a traditional hammer-head strap (Figure 2a) and a first prototype of an innovative device (Figure 2b).
The traditional connection is composed by: a hammer-head strap whose head is connected to the panel in a vertically oriented C-shaped steel channel; a bolt and a toothed washer connected to the support beam through an horizontally oriented C-shaped steel channel. The basic idea is that the panel and the structure are rigidly connected through the two blocks (channels). One of the limitations associated with the use of a traditional non-seismic connection concerns the significant amount of force exchange between the panel and the structure, due to the friction exerted in the anchorage components which can lead to a collapse mechanism. In order to improve the anchorage performance, the innovative connection has a rotating pin near the panel coinciding with the vertical bolt which allows rotation to take place around the vertical axis passing through the bolt (yellow dashed line in Fig. 2b). Furthermore, a sliding block is installed on the support beam that allows the sliding movement as indicated by the red arrow in Fig. 2b).

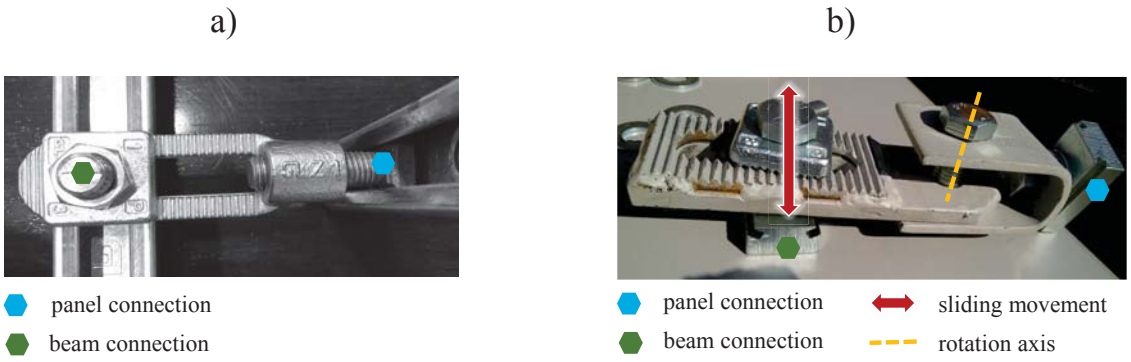

Figure 2: The tested connection devices: a) the traditional hammer-head strap; b) the first prototype of the innovative device.

3 EXPERIMENTAL SET-UP

The prototype building is instrumented with several types of sensors (Figure 3): n. 8 uniaxial piezoelectric accelerometers, model PCB393B12 with a sensitivity of 10 V/g, are located at the top of each column (A1-A8); n.2 accelerometrs (A9-A10) are installed on the support beam connecting the principal beam to the cladding panel; n. 2 accelerometers are positioned at the top of the cladding panel; n. 8 strain gauges are installed on the two faces of each steel plate (E1-E8 with reference to Figure 3) to measure the force exchange between the panel and the support beam. All the sensors are simultaneously acquired with the data acquisition (DAQ) system, model NIcDAQ9184, connected to the PC via Ethernet.

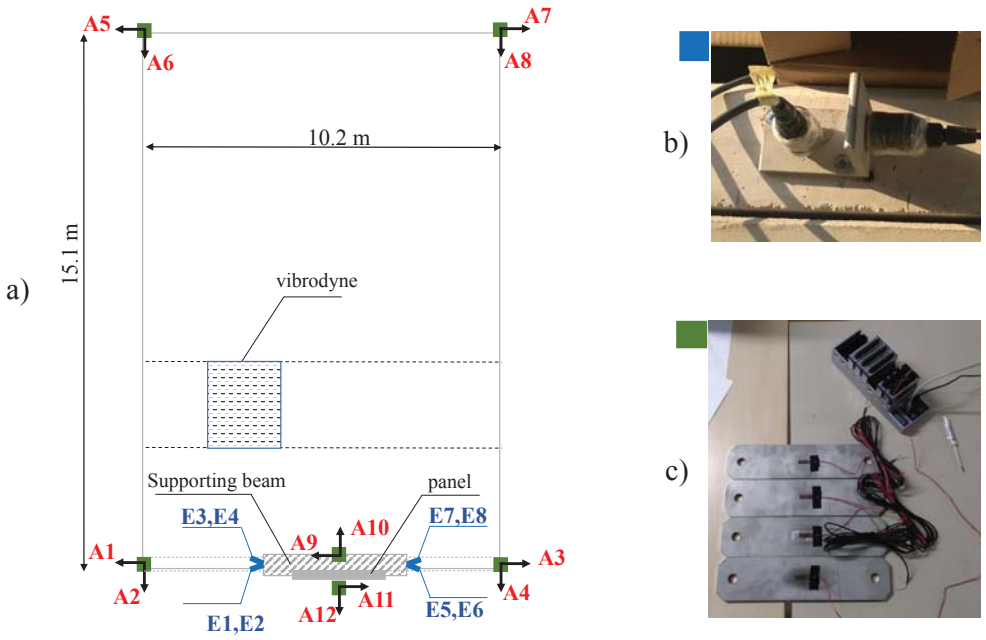

Figure 3: Sensors configuration: a) global configuration in plan; b) uniaxial accelerometers installed in two orthogonal directions; c) strain gauges installed in the steel plates to measure transmitted forces between cladding panel and structure.

The structure can be subjected to an harmonic force induced by a mechanical vibrodyne jointed to the rooftop in an eccentric position with respect to the geometric center of gravity. The vibrodyne is composed of two eccentric masses (70 Kg for each mass) whose movement induces the sinusoidal force in the horizontal direction.

4 PRELIMINARY ANALYSIS RESULTS

The experimental tests were carried out on July 3^{rd} and 5^{th}, 2019. The different configurations analyzed are:

- C1 - prototype building without the cladding panel.
- C2 - prototype building with the cladding panel connected through a traditional hammerhead strap connection.
- C3 - prototype building with the cladding panel connected through the innovative connection.

The response is measured by means of the accelerometers and displacement transducers as shown in Figure 3.

4.1 Ambient Vibration Test

In order to identify the structural dynamic properties of the prototype building, ambient vibration tests (AVTs) were carried out for the configurations C1 and C2, measuring micro tremors induced by ambient vibrations and daily activities. The data were recorded for a duration of 1 hour with a sampling frequency of 1652 Hz, which was down-sampled to 100 Hz. Figure 4 shows the normalized singular values (SV) of the spectral density matrix of all data

sets identified through the Frequency Domain Decomposition (FDD) approach with the indication of the first three principal vibration modes for configuration C1 (Figure 4a), configuration C2 (Figure 4b) and configuration C3 (Figure 4c). The vibration modes associated to the

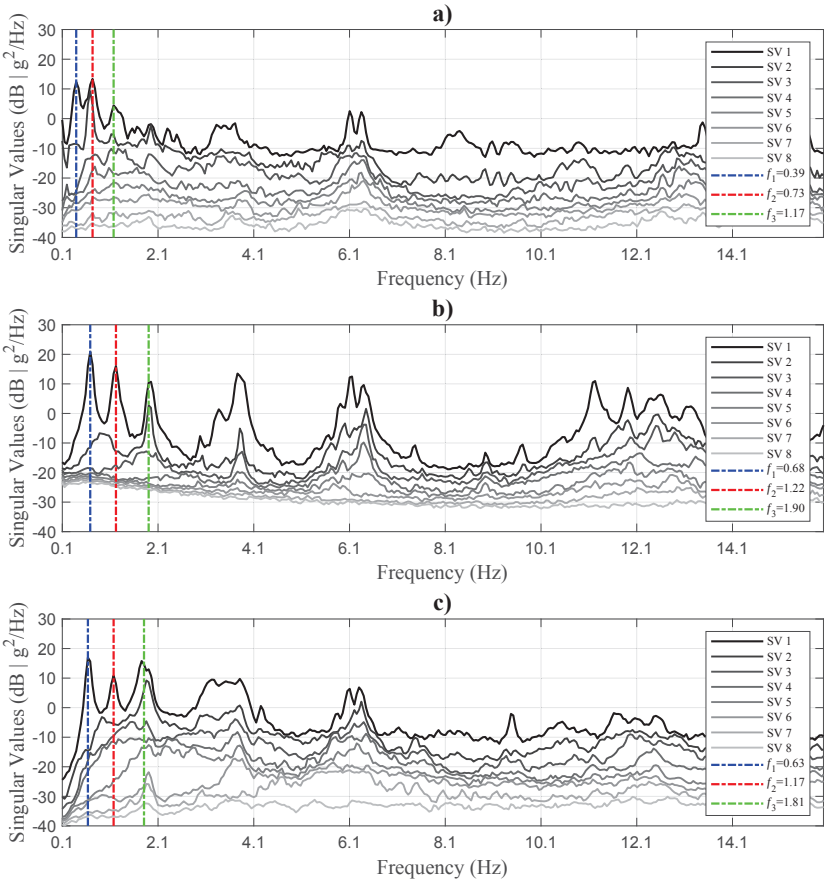

Figure 4: Singular values (SV) of the power spectral density matrix obtained from the AVT and identified resonant peaks of the first 3 modes: a) configuration C1, b) configuration C2, c) configuration C3.

first three principal vibration modes are presented in Figures 5-7. As regards configuration C1 (Figure 5), the first mode is flexural-torsional ($f_1 = 0.39$ Hz), the second is flexural-torsional ($f_2 = 0.73$ Hz) and the third one is purely torsional ($f_3 = 1.17$ Hz). As concerns configuration C2, from Figure 6 it can be observed that the first mode is flexural ($f_1 = 0.68$ Hz), the second is flexural-torsional ($f_2 = 1.22$ Hz) and the third is purely torsional ($f_3 = 1.90$ Hz). For further information, Figure 7 shows the first three principal vibration modes associated to configuration C3: the first flexural ($f_1 = 0.63$ Hz), the second flexural-torsional ($f_2 = 1.17$ Hz) and the third purely torsional ($f_3 = 1.81$ Hz). It is worth noticing that the different technologies used for the cladding-to-structure connection, i.e., configuration C2 vs configuration C3, does not significantly affect the evaluation of the principal vibration modes. Indeed, at low levels of vibrations the friction force exerted by the connection does not allow the sliding of the panel with a consequent similar dynamic behavior. In any case, slightly lower natural frequencies are observed using the innovative connection device, which is consistent with its mechanical behavior.

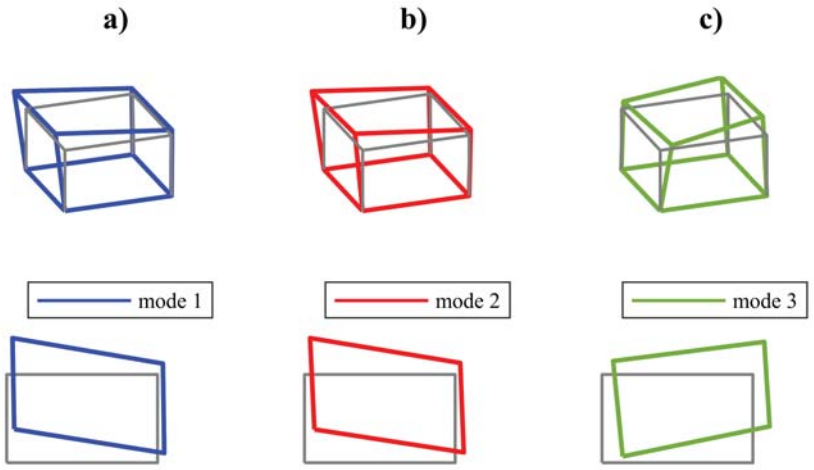

Figure 5: First three vibration modes obtained from the AVT for configuration C1.

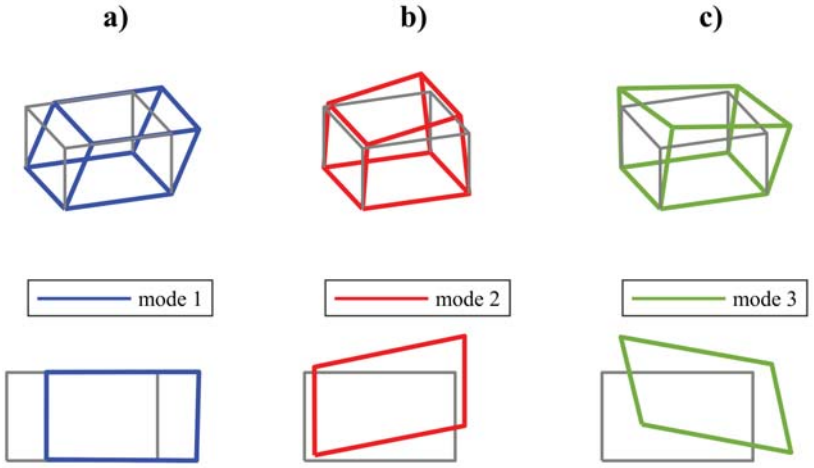

Figure 6: First three vibration modes obtained from the AVT for configuration C2.

4.2 Forced Vibration Tests

In this section some results of the forced vibration tests associated to configurations C1, C2 and C3 are presented. As an example, Figure 5 shows the horizontal lateral displacement evaluated for channels A1 and A2 for all the configurations. Displacement time histories were obtained by double integration of measured acceleration. In the case of configuration C1 (Figure 5a-b) the force induced by the vibrodyne has a maximum value of 3450 N. In the case of configuration C2 (Figure 5c-d) the force induced by vibrodyne has a maximum value of 8600 N, while in configuration C2 (Figure 5e-f) the maximum value corresponds to 5500 N.

The significant panel-to-structure force exchange reached with configuration C2 caused the partial damage of the traditional connection. This aspect is confirmed by analyzing Figure 6, which represents the mean value of the force measured during the tests by the strain gauges E1-E8 (Figure 3), suitably manipulated to reduce environmental effects (temperature and humidity)

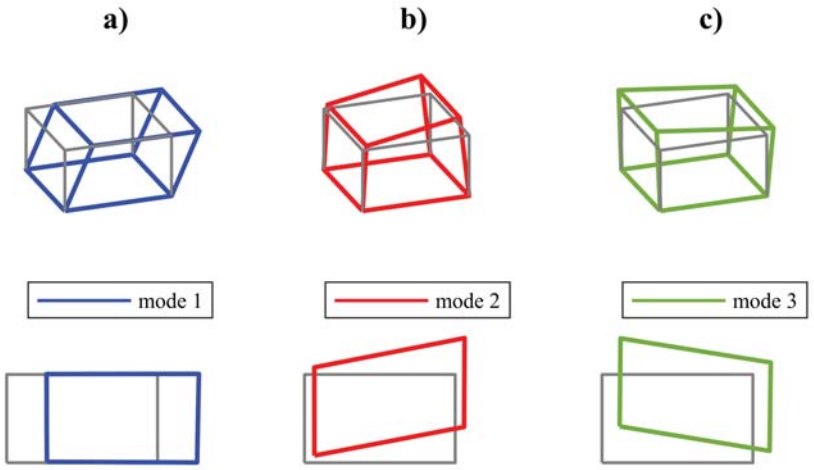

Figure 7: First three vibration modes obtained from the AVT for configuration C3.

and projected in the two main directions x and y. In particular, a Butterworth filter was used to clean up the signal. From the Figure it can be noted that the force exchange in the case of the traditional device is strongly higher (blue line) with respect to the case of the innovative device (red line).
Furthermore, Table 1 shows the maximum horizontal displacement (d) of the support beam and of the cladding panel corresponding to the maximum horizontal force provided by the vibrodyne considering configurations C2 and C3.
The experimental results confirm that force exchange between the panel and the structure due to the friction exerted between the anchorage components of the traditional connection device is not negligible, since it leads up to the connection collapse. Therefore, the reduced value of the cladding panel displacement associated to configuration C3 with respect to the support beam proves the superior performance of the new type of connection in reducing the load transfer and, consequently the in-plane movement of the panel, avoiding damages to the panel and the beam.
Results of forced vibration tests highlight the effectiveness of the first prototype of the innova-

Configuration	F_{max}	Support beam		Cladding panel	
	[N]	d_x [m]	d_y [m]	d_x [m]	d_y [m]
C2	8600	0.1954	0.1827	0.0479	0.0238
C3	5500	0.1390	0.0131	0.0018	0.0087

Table 1: Maximum horizontal displacement (d) of the support beam and of the cladding panel with the indication of the maximum horizontal force provided by the vibrodyne for C2 and C3 configuration.

tive device in improving the seismic behavior of the panel-to-structure connection for in-plane movement. Further prototypes, with optimized mechanical characteristics, will be tested considering both in-plane and out-of plane forces with the aim of improving robustness of the connection device against seismic loads.

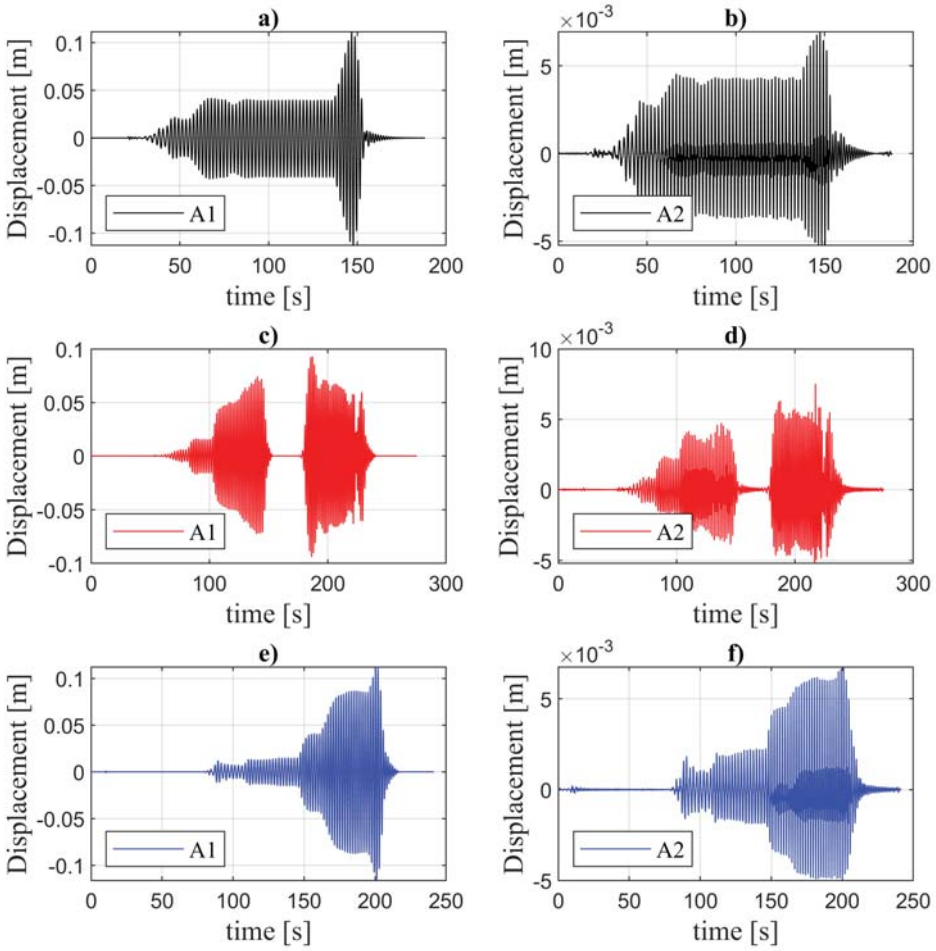

Figure 8: Horizontal displacements evaluated during the experimental tests: a) configuration C1 channel A1; b) configuration C1 channel A2; c) configuration C2 channel A1; d) configuration C2 channel A2; e) configuration C3 channel A1; f) configuration C3 channel A2.

5 CONCLUSIONS

The study has focused on the evaluation of the seismic behavior of the first prototype of an innovative connection between cladding panels and supporting structures. The main objective is to decouple the movement between the panel and the structure. For the purpose, a prototype building has been built and used to perform AVTs and forced vibration tests along the plane of the panel. The structural response has been measured by means of accelerometers and strain gauges. Both AVTs and force vibration tests were performed considering three different configurations: C1, C2 and C3. The anchorage performance of two types of systems (traditional vs innovative system) has been compared.

The effectiveness of the innovative device has been assessed by measuring the amount of force transmitted between the support beam and the cladding panel. On the one hand, the results of the experimental tests showed that the traditional device induces a not negligible force exchange between cladding panels and supporting beam. On the other hand, the first prototype of the innovative connection device considerably reduces the in-plane force transmission, decoupling

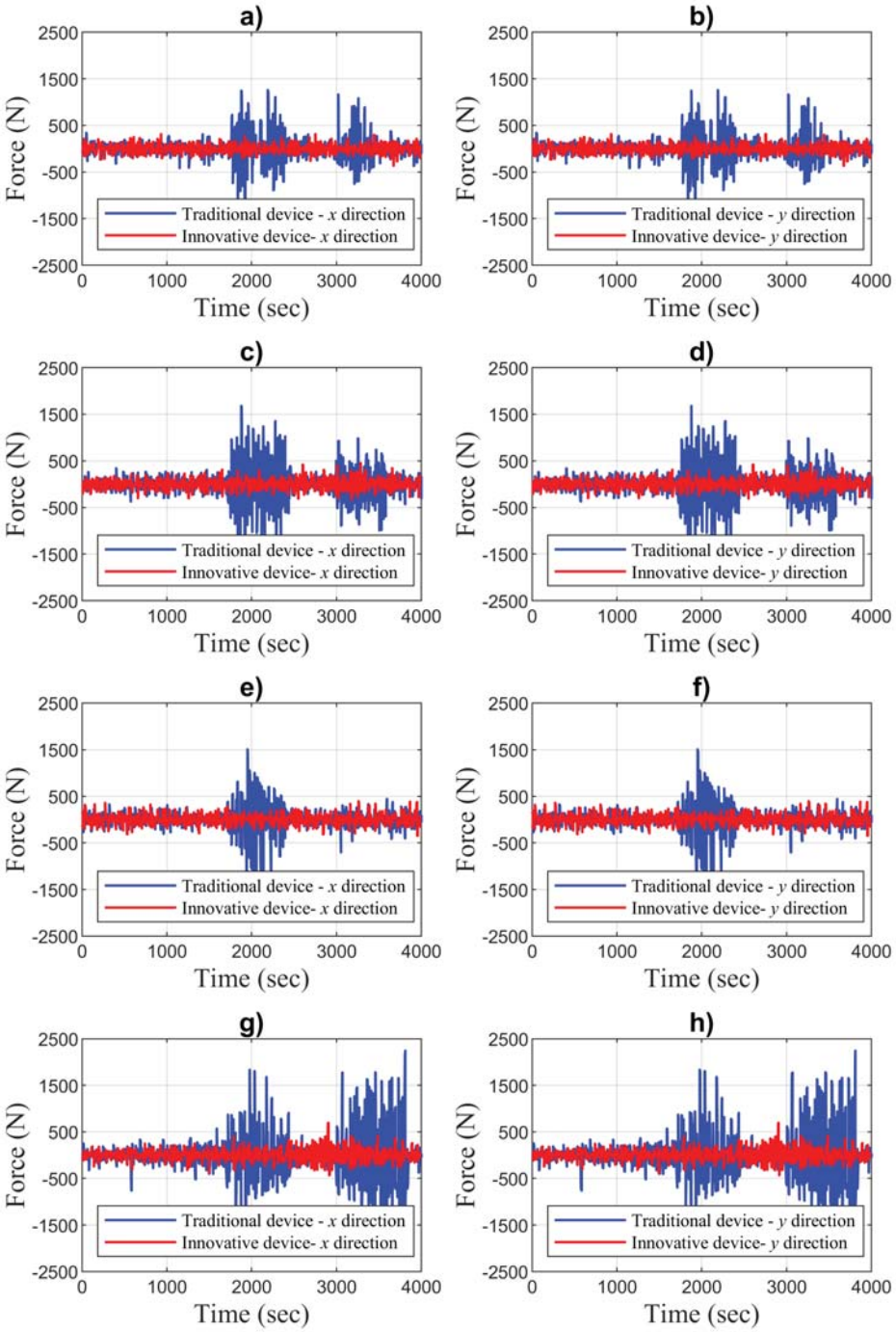

Figure 9: Panel-to-structure force exchange measured by the transducers for the traditional and innovative devices: a) Plate 1, *x* direction; b) Plate 1, *y* direction; c) Plate 2, *x* direction; d) Plate 2, *y* direction; e) Plate 3, *x* direction; f) Plate 3, *y* direction; g) Plate 4, *x* direction; h) Plate 4, *y* direction;.

more effectively the panel-structure movement. It follows that such a proposed design solution is promising towards an effective improvement of the seismic behavior of reinforced concrete precast structures, leading the way to further enhancements of the prototype device with the aim of considering both in-plane and out-of plane loads.

Ackowledgments

The Authors would like to acknowledge the support of the European social fund in the framework of POR FESR - Axis 8 - Seismic prevention and support for the recovery of the areas affected by the earthquake.

REFERENCES

[1] L. Liberatore, L. Sorrentino, D. Liberatore, L. D. Decanini, Failure of industrial structures induced by the Emilia (Italy) 2012 earthquakes, *Engineering Failure Analysis*, **34**, 629–647, 2013.

[2] L. Ierimonti, I. Venanzi, F. Ubertini, A.L. Materazzi, Vibration-based continuous monitoring for post-earthquake damage diagnosis of precast reinforced concrete buildings, *COMPDYN Proceedings*, **1**, 1032–1041, 2019.

[3] L. Ierimonti, I. Venanzi, F. Ubertini, A.L. Materazzi, Seismic damage assessment of precast reinforced concrete buildings based on monitoring data, *ANIDIS Proceedings*, In press, 2019.

[4] Safecladding Project – Improved fastening systems of cladding wall panels of precast buildings in seismic zones. Available at https: //cordis.europa.eu/project/rcn/104571/factsheet/en (accessed 20 January 2020).

[5] A. Belleri, B. Moaveni, I. Babuska, J.I. Restrepo, Damage assessment through structural identification of a three-story large-scale precast concrete structure. *Earthquake Engineering and Structural Dynamics*, **43**, 61–76, 2014.

[6] B. Zoubek, M. Fischinger,T. Isakovi Cyclic response of hammer-head strap cladding-to-structure connections used in RC precast building, *Engineering Structures*, **119**, 135–148, 2016.

[7] A. Belleri, M. Torquati, A. Marini, P. Riva, Horizontal cladding panels: in-plane seismic performance in precast concrete buildings. *Bulletin of Earthquake Engineering*, **14**, 1103–1129, 2016.

EURODYN 2020
XI International Conference on Structural Dynamics
M. Papadrakakis, M. Fragiadakis, C. Papadimitriou (eds.)
Athens, Greece, 23–26 November 2020

A GROUND MOTION MODEL FOR SEISMIC VULNERABILITY ASSESSMENT OF PROTOTYPE INDUSTRIAL PLANTS

C.Nardin[1], R.di Filippo[1], R.Endrizzi[1], I. Lanese[2], F.Paolacci[3], O.S.Bursi[1]

[1]University of Trento, Department of Civil, Environmental and Mechanical Engineering
via Mesiano 77, 38123 Trento, Italy
e-mail: chiara.nardin@unitn.it

[2] EUCENTRE Foundation
Via Adolfo Ferrata 1, 27100 Pavia, Italy

[3] Roma Tre University Department of Engineering
Via Vito Volterra 62, 00146 Rome, Italy

Keywords: Ground motion model, industrial plants, shaking table tests.

Abstract. *Relationships between seismic action, system response and relevant damage levels in industrial plants require a solid background both in experimental data, due to the high level of nonlinearity, and in knowledge of seismic input due to large uncertainty. Besides, risk and fragility analyses depend on the adoption of a huge number of seismic records usually not available in a site-specific analysis. In order to manage these issues and to gain knowledge on the definition of damage levels, limit states and performance for major-hazard industrial plant components, we present a possible approach and discuss results of an experimental campaign based on a real prototype industrial steel structure. The investigation of the seismic behaviour of the reference structure has been carried on through shaking table tests, focusing in particular on the structural or process-related interactions that can lead to serious secondary damages as leakage in piping systems or connections with tanks and cabinets. This has been possible thanks to the adoption of a ground motion model (GMM) able to generate a suite of synthetic time-histories records for specified site characteristic and earthquake scenarios. In fact, model parameters can be identified by matching the statistics of a target-recorded accelerogram to the ones of the model in terms of faulting mechanism, earthquake magnitude, source-to-site distance and site shear-wave velocity. Hence, the stochastic model, based both on these matched parameters and on filtered white-noise process, generates the ensemble of synthetic ground motions capable to capture the main features of real earthquake ground motions, including intensity, duration, spectral content and peak values. Finally, by means of the combination of a high-fidelity and a low-fidelity FE model as well as the stochastic input generated by a GMM, a seismic vulnerability assessment of both industrial components and the global structure can be carried out.*

INTRODUCTION

Between major natural hazard critical for industrial facilities, we can undeniably enlist seismic events. In fact, as well documented in literature - see [1]; [2]; [3] -, in these occurrence, industrial process plants have shown to be susceptible to experience significant damages both in primary structure and in secondary elements that usually constitute plant components and on which rely the operation of facilities.

Besides, as demonstrated by recent catastrophic events - like Tohoku earthquake in 2011 - and particularly stressed in the literature - see [4]; [5] - industrial facilities are especially vulnerable to those natural hazards which may trigger technological accidents: the so called NaTech events, i.e. Natural-Technological events. Therefore, there is a strong necessity to investigate interactions between primary structure and plant components, but also between the components among themselves, in order to avoid, as shown in previous references, serious consequences and critical secondary damages which, in addition to loss of production, also pose a danger to humans and the environment if hazardous substances are released due to leakages. In this perspective, the objective of the project SPIF, i.e. *Seismic Performance of Multi-Component Systems in Special Risk Industrial Facilities*, under the grant of European H2020 - SERA, *Seismology and Earthquake Engineering Research Infrastructure Alliance for Europe*, is to carry out a complete investigation of the seismic behaviour of industrial plants equipped with complex process technology by means of shaking table tests.

The case-test structure is a three-storey moment resisting steel frame with vertical and horizontal vessels and cabinets, arranged on the three levels and connected by pipes. The three levels are constructed as flexible diaphragm made of steel cross beams, partially covered with gratings. Tests are carried out without base isolation of the industrial structure. Furthermore, firmly anchored components are taken into account to compare their dynamic behavior and interactions with each other. Besides, the campaign structure is equipped with sensor systems integrated into the test structure itself for a rapid damage assessment.

Along with this line, the following paper focuses on the main aspects of investigation of seismic performances of a prototype steel-frame industrial plant, with a special focus on loss of containment (LoC) from bolted flange joints (BFJs), see [6], pipe bends and tee-joints, vessels' connections and anchorages. Therefore, seismic risk is evaluated through fragility curves analyses, according to [10] inside the framework of PBEE, [8].

In details, to take into account the variability of the seismic action and the high number of time histories needed, a GMM has been adopted, in order to generate a suite of synthetic time-histories records for specified site characteristic and earthquake scenarios, based on the results of a site-specific probabilistic seismic hazard analysis in severe seismic prone zone in Italy - PSHA, see [7].

Moreover, a faster-low (LF) and a refined high fidelity (HF) FE models are developed in order to represent the complexity of the experimental campaign with two different level of computational efforts and accuracy reproduced. The whole test campaigns provide then the necessary background to properly calibrate FE models. Therefore, in order to reduce the space of the GMM parameters, a global sensitivity analysis (GSA) over FE models is performed to assess the individual contributions of each input variables to the total variance of the model response. Finally, the LF model of the prototype industrial plant is adopted to perform a seismic fragility analysis with a cheaper computational effort demanded.

In sum, the paper is arranged into 6 main sections: the first section illustrates SPIF test structure, whilst the second one focuses on the characterization of the seismic input. The third

section presents the arrangement of the experimental campaign, in the fixed configuration. The fourth one deals with the description of the FE modelling of the primary structure and of the industrial components, such as pipes, bends and vessels. In the fifth section, we show the procedure in order to gain relevant seismic fragility curves both for components and the global system. In the last section, main conclusions are drawn and future developments are proposed.

THE SPIF STRUCTURE

The primary steel structure is a three storey moment resisting steel frame with flexible diaphragm made of crossbeams. The three dimensional primary steel structure is shown in Fig. (1). The ground-plan dimensions are 3.7 m x 3.7 m and the storey height is 3.1 m, which leads to a total height of 9.3 m. The rigid frame is simply supported on the reinforced concrete base plate and the crossbeams are hinged connected to the frame beams. In total four tanks are installed, two vertical tanks on the first level and two horizontal tanks on the second level. Furthermore one electrical cabinet is placed on the first level. Concerning piping system, the nominal pipe diameter is DN 100, with the exception of the suspended pipes on the third story that are DN 80. In addition, smaller single degree of freedom (SDOF) oscillators systems are installed on each of the three levels to investigate the structure component interaction for different periods in the linear and non-linear range.

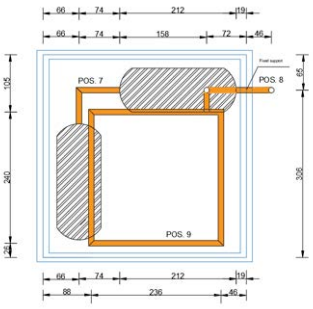

(a) Top view.

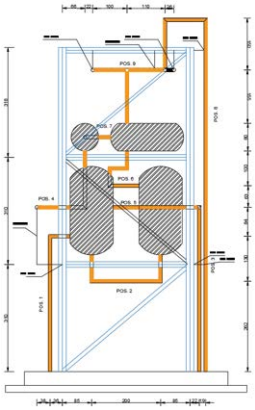

(b) Side view.

(c) 3D front view.

(d) 3D back view.

Figure 1: Representation with quote of the prototype industrial plant for SPIF project: (a) top, (b) side and (c)-(d) 3D front and back views.

Besides, the test structure is equipped with a complex system of sensors which includes FBG

fiber optics sensors, for LoC and leakage detection, strain-gauges, LVDT and accelerometer in strategical positions, as shown for example in Fig. (2).

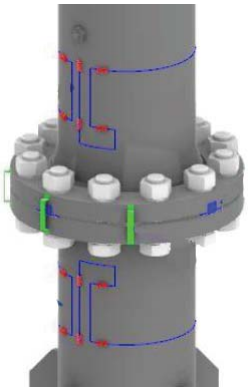

(a) FBG sensors.

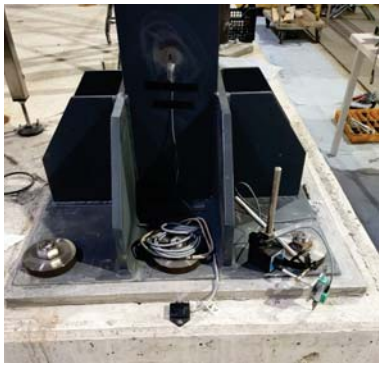

(b) Accelerometers at base joint.

Figure 2: Part of system's sensors applied to test structure: in more detail, (a) FBG sensors connected to flange susceptible to leakage phenomena, (b) disposition of accelerometer at base joint of the primary steel structure.

EXPERIMENTAL CAMPAIGN

Sequence and intensity levels of shaking table tests are performed so as to reach more severe damages or even collapses in components by passing from *fully operational* (OP) to *near collapse* (NC) limit states, or, as in case of major industrial plants, from *operating condition or design basis earthquake condition* (OBE) to *safe shutdown earthquake condition* (SSE). In particular, the first set of simulation tests are executed on the base isolated structure while the second set is run on the non-isolated configuration. In both configuration's setup, after tuning the shaking table, input signals are launched and then scaled with coefficient related to the probability of exceeding the seismic action, P_L, in T_L years other than the reference probability of exceedance P_{LR}, over the same T_L years, as reported in Tab. (2). In more details, according to

	Components EC8-4:(2.1.4)	**Buildings** EC8-4:(4.2.5)
Cl. I	0.8	0.8
Cl. II	1	1
Cl. III	1.2	1.2
Cl. IV	1.6	1.4

Table 1: Important class and coefficients according to EC8, Part 1 and Part 4.

the assumption during design phase of considering an importance factor γ_I equal to 1.0, it has been evaluated in Eq. (1) the ratio between the maximum allowed value of importance factor in case of components versus the assumed one, see Tab. (1): this ratio is then used as a scale factor in order to pass to a SLS *safe life limit state* for the structure and the equivalent OBE *operating condition or design basis earthquake condition* for pipe systems.

$$\gamma_I = \frac{1}{1.6} = 0.625 \tag{1}$$

Probability of Exceedance NTC18: 3.2.1			
OP	81	%	Fully Operational
DL	63	%	Damage Limit
SD	10	%	Significant Damage
NC	2.5	%	Near Collapse

Table 2: Probability of exceedance according to Italian Standards.

Then, according to EC8-Part 1: (2.1-4(P)Note), the value of the importance factor γ_I is obtained by the ratio between T_L and T_{LR}, i.e. time associated to the reference seismic action in order to achieve the same probability of exceedance in T_L years as in the T_{LR} years for which the reference seismic action is defined

$$\gamma_l = \left(\frac{T_{LR}}{T_L}\right)^{-1/k} with \quad k = 3 \tag{2}$$

as well as

$$\gamma_l = \left(\frac{P_L}{P_{LR}}\right)^{-1/k} with \quad k = 3 \tag{3}$$

again the needed factor with which multiply the reference seismic action. So, by referring to Italian codes in Tab. (2), importance factors for different limit states are evaluated and reported in Tab. (3), together with the reference peak ground acceleration of the spectra involved in the design phase. Main assumptions in order to evaluate proper spectra for the test structure were

	NC	**SD**	**DL**	**OP**	**units**
γ_I	1.000	0.625	0.541	0.498	[-]
a_{gR}	0.690	0.431	0.233	0.215	[g]
	SSE	**OBE**			

Table 3: Important coefficients and reference peak ground acceleration for different limit states.

in fact the following ones: · nominal life: 50 years; · soil type: C –T1; · damping: 5%; · peak ground acceleration: $a_{gR} = 0.69\,g$ and · importance class II.

Therefore, spectra-compatible accelerograms have been evaluated with a relative difference between matched and target spectra less than 10%. These accelerograms are assigned to both the configuration setup, i.e. structure with and without base isolation, with the 4 aforementioned different scale factors related to separated limit states.

Furthermore, for the isolated setup, natural records from PEER NGA-WEST2 database are selected, with the purpose of stressing the designed isolators. In particular, selection criteria were devoted to have a strong frequency content around the range of the working-isolated structure and to match the design spectrum. For this last point, it has been necessary to scale up the natural accelerogram selected with the first main issue, according to a scale factor derived as the ratio between maximum acceleration reached by the artificial seismic input and the natural one.

Then, in order to induce damage or collapse in previous analysed components, as, for example, leakage in selected flanges or collapse of vessel's footing, seismic records from ground

motion model are selected, thanks to the high variability of the ensemble site-characteristic generated. Hereafter, the main characteristics and peculiar aspects of the ground motion model are presented.

SEISMIC INPUT FROM GMM

Synthetic ground motions are employed in order to cover the range of IMs of interest and eventually obtain a sufficient large ensemble of time-histories for fragility curves analyses. Here, a synthetic ground motion model has been assumed in order to reproduce the spectral variability of recorded accelerograms. In particular, according to [9], with the purpose of calibrating the GMM for a specific geographical location and specific site characteristics, a PSHA deaggregation is performed. Along this line, in the assumption of far-field scenario, a severe seismic prone zone of central Italy is selected. Below, see Fig. (3), it is reported the main result of the probabilistic seismic hazard deaggregation analysis.

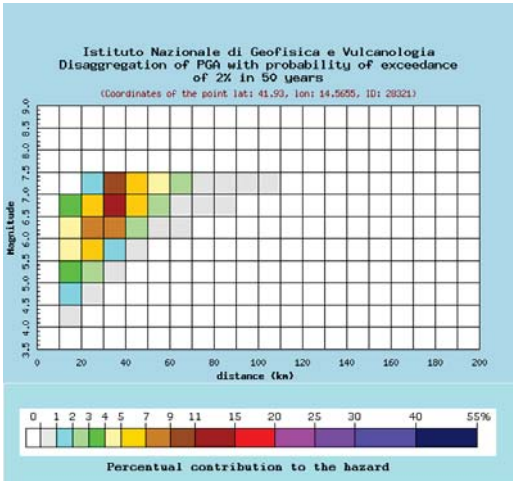

Figure 3: Probabilistic seismic hazard deaggregation analysis for Palmoli, Central Italy.

Moreover, the original recorded accelerograms are selected from the INGV site (http://www.ingv.it/) and ITACA - *Italian Accelerometric Archive* - Database, with the following criteria:

- fault to site distance $> 10\ km$;
- moment magnitude > 5.5;
- main shock seismic records only.

Besides, another core assumption, both in design of the structure and in selection of ground motions time histories, is correlated to the soil characteristics, that is assumed of type C according to European standards. Herein, in Tab. (4) compatible accelerograms are reported.

According to [11], GMM is defined in terms of a set of parameters based on ground motion properties with physical meaning, as reported in Tab. (4). The model is based on a modulated, filtered white-noise process and incorporates both temporal and spectral non-stationarities, as shown in Eq. (4)

$$a_g(t) = q(t,\alpha)\left[\frac{1}{\sigma_f(t)}\int_{-\infty}^{t} h(t-\tau,\lambda(\tau))\,\omega(\tau)d\tau\right] \tag{4}$$

	Earthquake Name	Station Name	$V_{S,30}[m/s]$	Distance fault-site $[km]$	Moment Magnitude $[M_w]$
1	IT-1979-0009-NORCIA	BVG	211	38	5,8
2	IT-1984-0004-LAZIO-ABRUZZO	CSN0	501	19,7	5,9
3	IT-1984-0004-LAZIO-ABRUZZO	PNT	325	26,8	5,9
4	IT-1984-0004-LAZIO-ABRUZZO	GRG2	187	49,1	5,9
5	IT-1984-0004-LAZIO-ABRUZZO	GRG1	192	49,1	5,9
6	IT-2009-0009-L-AQUILA	AVZ	199	35,1	5,5
7	IT-2009-0009-L-AQUILA	GSA	492	14,4	5,5
8	EMSC-20160824-CENTRAL-ITALY	TRE	353	45,3	6
9	EMSC-20160824-CENTRAL-ITALY	FOC	342	45,7	6

Table 4: Set of selected accelerograms from ITACA database.

where $\omega(\tau)$ is a white-noise process, while $\widehat{\alpha}$ is defined by means of

$$\widehat{\alpha} \, = \, arg \min_{\alpha} \left(\left| I_a \left(t_{45} \right) \, - \, \widehat{I}_a \left(t_{45} \right) \right| \, + \left| \left(t_{95} \right) \, - \, \widehat{I}_a \left(t_{95} \right) \right| \right) \tag{5}$$

It should be noticed that the modulating function $q(t, \alpha)$ completely defines the temporal characteristics of the process, whereas $h\left(t \, - \, \tau, \lambda(\tau)\right)$, denoting the impulse-response function IRF, and its time-varying parameters define the spectral characteristics of the process. In particular, IRF of a linear time-varying filter can be expressed as follows:

$$h\left(t \, - \, \tau, \lambda\left(\tau\right)\right) \, = \, f(\omega_f, \zeta_f) \tag{6}$$

where

$$\omega_f \, = \, \omega_{mid} \, + \, \omega'(t \, - \, t_{mid}) \tag{7}$$

Simulating process of GMM is then able to generate an ensemble of ground acceleration time-history similar to those illustrated in Tab. (4) for a given set of model parameters, as reported in Tab. (5).

Name	Distribution	Average Value	Units
I_a	Uniform	0,212	$[m/s]$
t_{mid}	Uniform	3,6	$[s]$
D_{5-95}	Uniform	8,8	$[s]$
ω_{mid}	Uniform	43,7	$[Hz]$
ζ_f	Uniform	0,25	$[-]$

Table 5: Distribution of stochastic GMM parameters.

Along this line, two main hyphotesis have been assumed: the first one is to consider parameters statistically independent; the second regards the choice of assuming uniform distributions in order to describe probability distribution of all the parameters, with the only exception of ω' that is assumed constant. Thus, in order to reduce the variability of the seismic input and to reduce the space of parameters, a set of 200 white-noises combining 200 accelerograms is performed on the LF model with a convergence check upon the third quartile of both spectral acceleration for $T_1 \, = 0.36 \, s$ and maximum displacement at top storey. Results are reported in Fig. (4) and Fig. (5) and indicate that at almost 100 of white-noises convergence is reached.

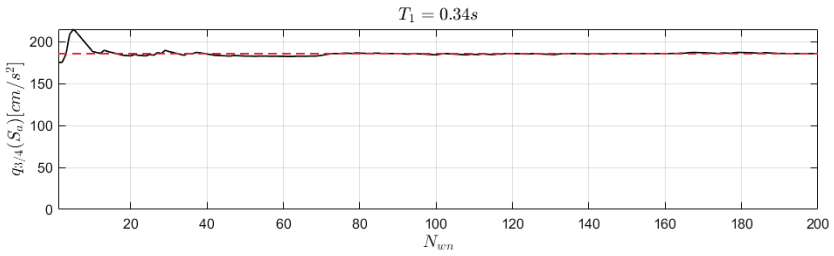

Figure 4: Check on number of white-noises N_{wn} at the third quartile for $S_a(T_1)$.

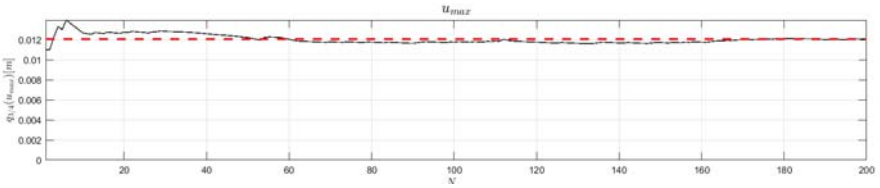

Figure 5: Check on number of white-noises N_{wn} at the third quartile for u_{max} at top storey.

THE FINITE ELEMENT MODEL

According to [9], one of the most important feature of a GMM is the possibility to study the structural response to earthquake with characteristics that are coherent with the site seismicity (e.g. fragility curves). The main disadvantage of this technique is the great number of non linear analysis necessary to take into account the variability of the seismic action. To overcome the numerical effort required in such procedure two model are needed.

First a low fidelity model (LF) that aims to reproduce the essential characteristics of the system with the smallest computational effort possible is developed. For our purposes this essential characteristics are: natural periods, base shear and behaviour of the major component such as tanks and piping system.

In a second phase an high fidelity model (HF) is introduced with the purpose to caught the behaviour of the structure in greater detail even with reference to the interaction between primary and secondary elements.

In the next section, only issues and principal techniques involved in the definition of LF and HF model of the isolators are discussed, while a general comment on the main differences between LF and HF model is briefly dwell.

Piping system

As can be seen in Fig. (1) the piping system is composed of straight pipes, bends, tee joint and BFJs. Since our purpose is to include in the model only the foundamental aspects of the structure, we firstly have to identify the most critical components for the LoC limit state. According to [14] there are only three possible failure modes for pipes: fracture due to excessive tensile loading, local buckling due to compressive action and low cycle fatigue. The first failure mode is prevent if the plastic deformation does not exceed the tensile strain limit ϵ_{Tu}, that the Author suggests to use a conservative value of 2%. Compressive failure is typical in pipe bends and the limit compression strain ϵ_{Cu} can be estimated from Eqn. (8)

$$\epsilon_{Cu} = 0.5 \cdot \left(\frac{t}{D}\right) - 0.0025 + 3000 \cdot \left(\frac{\sigma_h}{E}\right)^2 \tag{8}$$

Neglecting the effect of internal pressure, a value of 1% is found. Instead, the third failure

mode arises only if the component undergoes large plastic deformation several times. Thanks to results of preliminary analysis, it is possible to outline only two points (the nozzle in position 6 and the tee joint in position 5) with tension's value above yielding limit. To investigate the possibility of high stress level, those position are model with *shell finite elements*. It is important to notice LF model is an elastic one, since the structure is designed to remain elastic even under very high seismic shacking. In later analysis the elastic solution will be used as guide to choose significant ground motions to evaluate inelastic response of components. In conclusion, such level of deformation in pipes capable to induce failure seems to be unlikely. So, the weakest component for the LoC prevention are the BFJs. The model proposed by [15] is used to investigate the performance of the BFJs. This method is developed in the framework of the EN 1591-2009 and results in a linear domain like the one shown in Fig. (6). The BFJs are designed in accordance with EN 1591-2014 to ensure the performance level requested in two seismic condition:

- Operating condition basis earthquake **(OBE)**: it corresponds to an earthquake scenario, considering the seismic hazard of the site, that could reasonably affects the structure during his operating life time;
- Safe shut-down earthquake **(SSE)**: it corresponds to maximum ground motion for which some critical components of the plant must be designed to remain functional.

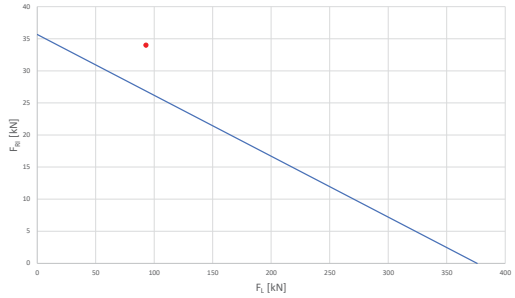

Figure 6: Example of leakage domain of the La Salandra model

To model the rest of the piping system in terms of mass and stiffness, several techniques are available. The easiest choice is to adopt beam element with reduced stiffness' value by means of flexibility factors. Codes provide an analytical formulation of these factors based on elasticity theory. Example of such factors, in the case of elbow element, are shown in equations below.

$$h = \frac{4 \cdot R \cdot e_n}{d_m^2} \tag{9}$$

$$k_B = \frac{1,65}{h} \tag{10}$$

In case of tee joint, no stiffness reduction is required. A more precise approach consist in the determination of flexibility factors for elbows derived from a FEA. In this case a FEM of pipe bends based on shell element is developed and moments are applied to one end. Then, by equating deflection of the FE model with an analogous system of beam deflection, it is possible to evaluate proper flexibility factors. According to [16] using this procedure flexibility factors

Flexibility factor		
Direction	UNI EN 13480-3	FEM
In plane	9.24	8.28
Out of plane	9.24	8.21

Table 6: Comparison between flexibility factor

Figure 7: FEM of a single elbow

for in plane and out of plane action can be found. The results of the two procedure are resumed in Tab. (6), while FE model employed is depicted in Fig. (7).

In this calculation, stiffening effects of pressure are neglected, since just few elbows are pressurized and with a negligible resultant effect caused by internal pressure.

The main hypothesis by referring to flexibility factor is that the ends of the elbow are free to ovalize. Thus, if this condition is not respected, a significant stiffening effect raise. In order to individuate those critical conditions, a parametric study is carried out with this scheme: a specimen made of two elbows (with direction specified in Tab. (7)) separated by a straight pipe is analysed. Several simulations are launched for increasing length of the central pipe from 200mm to 3000mm. During the simulation, two set of displacement are imposed to the specimen: a linear displacement parallel to the straight pipe and a rotation of one end. As a result mutual force to the imposed displacement are collected. For high length of central pipe, flexibility contribution for elbow is constant and the central pipe behaves like a beam with circular cross section. When the length of central pipe goes under a threshold value, a stiffening effect can be seen and also induce an error greater than 10%, compared to the equivalent beam behaviour. Thus, a cut-off length can be defined.

Bends scheme	Direction	L [mm]
L-R	Axial	450
	Bending	200
L-L	Axial	450
	Bending	300
L-U	Axial	450
	Bending	450

Table 7: Cut-off length

Looking at Tab. (7), it is possible to notice that in case of bending a cut-off length equal to $2,5D$ is adequate. This result are in good agreement with results of [16]. In the other cases, when forces are of primary importance, a greater value of $4D$ looks adequate.

FRAGILITY ASSESSMENT OF A STEEL STRUCTURE AND COMPONENTS

In this paragraph, a method for performing fragility assessment of components and structure is illustrated, based on the seismic response of the test structure on the LF model. In fact, by using outputs of the simulations, it is possible to evaluate fragility functions F_D defined as the conditional probability of an event - i.e. overpass a threshold for a certain damage state (D) - given the observation of an intensity measure (IM) which describes the seismic event, see [7] and [10].

$$F_D\left(im\right) \, = \, P\left[D \geq C_{LS} | IM \, = \, im\right] \tag{11}$$

So, it is clear the importance of the choice of both the intensity measure proper for the case-test and the definition of the damage state D and its class of limit state C_{LS}, seen as thresholds - [17].

The most popular procedure to compute fragility functions via time-history analysis can be summarized, according to [18] and [19], as follows:

- definition of a numerical model for the structure of interest, $y(t) \, = \, \mathcal{M}[\ddot{x}_g(t|IM \, = \, im); \theta_{\mathcal{M}(t)}]$ where $\mathcal{M}$ stands for the numerical model, $\theta_{\mathcal{M}}$ for a set of model parameters, and $\ddot{x}_g$ for the seismic input;
- selection of suitable IM and N ground motions of interest;
- selection of EDP of interest;
- definition of damage limit states D via EDP thresholds.

Given the N outcomes, it is common to assume a lognormal probability distribution for the random variable IM associated with the given damage state D. Then, the parameter of the lognormal can be estimated via the method of the maximum likelihood. However, one positive aspect of the likelihood function is that it can be written also for a generic probability density function $f(x;\theta)$, where θ is the set of parameter to be estimated. Thus, by dividing data into two groups, i.e. data that causes collapse and data that do not cause collapse, the likelihood function is given by:

$$\mathcal{L}\left(\theta\right) \, = \, \prod_{n=1}^{N} f\left(x;\theta\right)^{\overline{N}} \left[\, 1 \, - \, F\left(\overline{x};\theta\right)\right]^{\left(N \, - \, \overline{N}\right)} \tag{12}$$

or in logarithmic form

$$ln\mathcal{L}\left(\theta\right) \, = \, \sum_{n=1}^{N} f\left(x;\theta\right) \, + \, \left(N \, - \, \overline{N}\right) \left[\, 1 \, - \, F\left(\overline{x};\theta\right)\right] \tag{13}$$

and solution of the parameter can be found

$$\hat{\theta} \, = \, arg \min_{\theta} \left[-ln\mathcal{L}\left(\theta\right)\right] \tag{14}$$

CONCLUSIONS

In this paper, we investigate relationships between seismic action, system response and relevant damage levels in a prototype of an industrial plant. This has been possible by means of the development of a procedure that combines modeling of the industrial structure, in both primary and secondary elements, and selecting proper ground motion time histories for analyses. As a first step, we have defined a seismic scenario associated to a geographical site by means of a probabilistic seismic hazard analysis. Then, based on this analysis we provide an adequate seismic input employing a stochastic ground motion model calibrated against coherent natural seismic records. Successively, in order to select ideal signal causing desired damage in terms of limit states, a large set of synthetic time histories has been generated and assigned to a low fidelity finite element model. In particular, we focused on the modeling of secondary elements, such as elbows, tee-joints and bolted flange joints, i.e. critical elements within the steel structure. As a result, both the steel structure and relevant industrial components have been subjected to artificial spectrum-compatible and seismic records provided by a ground motion model. Thus targeted LS have been sought. Finally, we present the methodology to derive fragility curves based on the results of LF models.

ACKNOWLEDGEMENT

We wish to acknowledge the European Union's Horizon 2020 research and innovation programme under grant agreement No 730900 for funding project SPIF and EUCENTRE Fondation for access to the laboratory.

REFERENCES

[1] E. Cruz and D. Valdivia. *Performance of industrial facilities inthe chilean earthquake of 27 february 2010.* The Structural Design of Tall and Special Buildings, Vol. 20, pp. 83-101, 2011.

[2] M. Erdik and E. Uckan. *Earthquake Damage and Fragilities of Industrial Facilities*, Springer, pp. 3-13, 2014.

[3] E. Krausmann, V. Cozzani, E. Salzano, and E. Renni. *Industrial Accidents Triggered by Natural Hazards: An Emerging Risk Issue*, volume Vol.11. Natural Hazards and Earth System Sciences, 2011.

[4] M. Campedel. *Analysis of major industrial accidents triggered by natural events reported in the principal available chemical accident databases*, Technical report, JRC42281, Joint Research Centre Institute for the Protection and Security of the Citizen, Ispra, Italy, 2008. Report EUR 23391 EN - 2008.

[5] A. Cruz and N. Okada. *Consideration of Natural Hazards in the Design and Risk Management of Industrial Facilities*, Vol. 44(2):213-227 Natural Hazards, 2008.

[6] INDUSE2Safety. *Component Fragility Evaluation, Seismic Safety Assessment And Design Of Petrochemical Plants Under Design-Basis And Beyond-Design-Basis Accident Conditions*, RFS-CT-2014-00025, Work Package 4 – Deliverable D4.4.

[7] J. Baker. *Efficient Analytical Fragility Function Fitting Using Dynamic Structural Analysis*, Earthquake Spectra, 2015.

[8] T. Haukaas and A. Der Kiureghian. *Finite Element Reliabilityand Sensitivity Methods for Performance-Based Earthquake Engineering*, Technical report, PEER - Pacific Earthquake Engineering Research Center, 2004.

[9] S. Rezaeian and A. Der Kiureghian. *Stochastic Modeling and Simulation of Ground Motions for Performance-Based Earthquake Engineering*, Technical report, PEER - Pacific Earthquake Engineering Research Center, 2010.

[10] K. Porter, R. Kennedy, and R. Bachman. *Creating Fragility Function for Performance-Based Engineering*, Earthquake Spectra, 2007.

[11] S.Rezaeian and A. Der Kiureghian. *Simulation of synthetic ground motions for specified earthquake and site characteristics*, Earthquake Engineering and Structural Dynamics, (39):1155–1180, 2010.

[12] MATLAB. 9.5.0.1049112 (R2018b) Update 3. The MathWorks Inc., Natick, Massachusetts, 2018.

[13] Computer Structure, inc. *CSI Analysis Reference Manual*, November 2017.

[14] M. Vathi, S. Karamanos, I. Kapogiannis, and K. Spiliopoulos. *Performance criteria for liquid storage tanks and piping systems subjected to seismic loading*, Journal of Pressure Vessel Technology, 139, 05 2017

[15] V. La Salandra, R. di Filippo, O. Bursi, F. Paolacci, and S. Alessandri. *Cyclic response of enhanced bolted flange joints for piping systems*, PVP2016-63244.

[16] O. Kireev, D. Kireev, and A. Berkovsky. *Parametric study of flexibility factor for curved pipe and welding elbows*, 2013.

[17] H. Ebrahimian, F. Jalayer, A. Lucchini, F. Mollaioli, and G. Manfredi. *Preliminary ranking of alternative scalar and vector in-tensity measures of ground shaking*, Bulletin of Earthquake Engineering, 2015.

[18] K. Mackie and B. Stojadinovic. *Comparison of Incremental Dynamic, Cloud and Stripe Methods for Computing Probabilistic Seismic Demand Models*, ASCE: Proceedings of the 2005 Structures Congress, 2005.

[19] M. Broccardo. *Lecture notes: Principle for fragility function computation*, ETH Zürich: Probabilistic seismic risk analysis and management for civil systems, 2016.

EURODYN 2020
XI International Conference on Structural Dynamics
M. Papadrakakis, M. Fragiadakis, C. Papadimitriou (eds.)
Athens, Greece, 23–26 November 2020

SIMPLIFIED ESTIMATION OF DESIGN FAULT DISPLACEMENT FOR BURIED PIPELINES AT FAULT CROSSING

Vasileios E. Melissianos[1] and Dimitrios Vamvatsikos[2]

[1,2] Institute of Steel Structures, School of Civil Engineering, National Technical University of Athens
9, Iroon Polytechneiou str., GR-15780 Zografou Campus, Athens, Greece
e-mail: [1]melissia@mail.ntua.gr, [2]divamva@mail.ntua.gr

Keywords: pipeline – fault crossing, fault offset hazard, simplified expressions

Abstract. *A set of simplified expressions are derived for estimating the design fault displacement for pipelines crossing active faults by considering alternative scenarios, seismicity levels, and the pertinent uncertainties. Buried steel pipelines are an efficient and safe means of oil and gas onshore transportation and provide a direct link between extraction, processing, and consumption of fuel. Hazardous materials are transported via pipelines and consequently, any pipe failure may have devastating consequences. In case of crossing an active tectonic fault, the pipeline may be subject to significant deformations and strains threatening its integrity in the event of an earthquake. Its design hinges on a single value of the fault displacement magnitude, typically estimated as a specific "safe" percentile (e.g., 84%) from the surface displacement distribution given a "maximum" magnitude, estimated from regression models parameterized on fault characteristics. This single-scenario-based approach can lead to either conservative or unconservative designs as the actual level of safety is unknown. Instead, Probabilistic Fault Displacement Hazard Analysis (PFDHA) can provide a robust probabilistic basis to determine design values corresponding to specified return periods, at the cost of requiring extensive seismological data that may be unavailable for every single major or minor fault that a transmission or distribution pipeline crosses. Herein, logic tree aggregation is employed to cater to different levels of data completeness and provide design-level fault displacement values that incorporate all pertinent uncertainties.*

1 INTRODUCTION

Onshore buried pipelines transporting oil and gas are vulnerable to seismically-induced permanent ground displacements, such as those resulting from seismic fault activation. Tectonic fault offset is the primary cause of earthquake-related catastrophic pipe failures [1]. The structural performance of buried pipes under faulting has drawn the attention of numerous researchers over the last decades, carrying out experimental, analytical, and numerical studies (e.g. [2]–[5]). However, in the vast majority of studies, fault offset is considered to be deterministic (i.e. a few rather arbitrary values are considered) or is estimated via empirical expressions that relate fault characteristics (e.g. earthquake magnitude, fault geometry, rupture length, etc.), such as those published by Wells and Coppersmith [6]. In the case of typical structures, such as building and bridges, numerous design codes, standards or guidelines are available to estimate the seismic loading for a predefined level of design hazard, typically as the result of probabilistic seismic hazard analysis. Contrarily, for buried pipelines, a single fault displacement magnitude is considered as the worst-case scenario, consisting of a postulated occurrence of an earthquake with a specific magnitude at a specific location. Consequently, pertinent uncertainties are disregarded, resulting in a hazard-independent estimation with an unknown level of conservatism.

The environmental, social, and economic repercussions of a potential pipeline failure call for the employment of state-of-the-art methods for the estimation of fault offset magnitude and therefore the design of pipelines at fault crossings. To achieve parity with the design standards for buildings and bridges, at the very least an approach is needed to set the design fault displacement for a pipeline at a pre-defined hazard level. Hence, a better balance between safety, capital/maintenance costs, and environmental responsibility can be attained. The appropriate such method is the Probabilistic Fault Displacement Hazard Analysis (PFDHA) that was introduced by Youngs et al. [7] for the seismic hazard assessment of the planned nuclear waste repository at Yucca Mountain, Nevada, USA.

Transmission and distribution pipelines form an extensive network, covering areas that range from a few hundred thousand square meters to entire countries. When seismic areas are traversed, crossing major or minor tectonic faults is almost inevitable. These faults might be active or inactive, or even not mapped due to inactivity during the last thousands of years. In case of crossing a major fault, this will be probably fully mapped and recorded, allowing the implementation of a full probabilistic hazard analysis (PFDHA) to account for all geotechnical and seismological parameters of the crossing. On the other hand, designers are aware that the latter is not the case for minor faults, typically being poorly mapped and recorded resulting in a minimum or even zero data availability. The problem is regularly treated based on a blend of expert opinion, engineering assumptions, and the implementation of empirical regression equations to calculate/estimate the design fault displacement. Thus, the aforementioned drawbacks of the deterministic approach are inflated again in the design. The present study stands as the first step to develop a set of simplified expressions for the estimation of fault offset magnitude for pipe – fault crossings, in case there is insufficient data. The expressions are derived from the statistical processing of PFDHA results taking into account typical values of the pertinent seismological parameters of the European area.

2 FAULT DISPLACEMENT HAZARD

2.1 Probabilistic Fault Displacement Hazard Analysis

The basis of Probabilistic Fault Displacement Hazard Analysis (PFDHA) was originally established by Youngs et al. [7] and later modified/improved, for example in [8]–[11]. The outcome of PFDHA is the mean annual frequency (MAF) of exceeding fault displacement levels

at a site by considering the fault geometry, the fault slip rate, the distribution of earthquakes, and the pertinent aleatory and epistemic uncertainties. PFDHA has been applied for the pipeline – fault crossing problem by the authors in [12], adopting the "earthquake approach" that is derived from the classic Probabilistic Seismic Hazard Analysis [13]. The "principal faulting" of PFDHA is considered under the assumption that the pipeline crosses a main fault, while distributed faulting issues are neglected. The fault displacement hazard estimation depends, among others, on the fault event rate, the maximum earthquake magnitude, the surface rupture length (SRL), the position of the rupture along the fault trace, and the position of the pipeline crossing site.

PFDHA for pipe – fault crossing site is essentially an application of the total probability theorem:

$$\lambda_D(d) = v \sum_i P(D > d|m_i) P_M(m_i) \tag{1}$$

where v is the mean annual rate (seismic rate) of all earthquakes above a minimum earthquake magnitude of engineering significance, following a Poisson model of occurrences, $P_M(m_i)$ is the probability of magnitude M falling within the i-th bin characterized by m_i at its center and is estimated using the Gutenberg-Richter bounded recurrence law [14]. $P(D>d|m_i)$ is the probability that the fault displacement D exceeds a defined value d at the crossing site, given an earthquake of magnitude m_i has occurred. Eq. (1) is applied for both the average fault displacement (AD) and the maximum fault displacement (MD) options of PFDHA, each one associated with a different fault displacement prediction equation, similar to a ground motion prediction equation of classic PSHA.

2.2 Hazard uncertainty

The identification and quantification of uncertainties is an integral part of seismic hazard analysis as the hazard curve is sensitive to the parameters adopted in the analysis. Any uncertainty can be incorporated in PFDHA. Uncertainties are classified into two main categories, namely aleatory and epistemic. Aleatory uncertainties are related to the inherent variability of nature, e.g. randomness in earthquake magnitude, fault displacement, etc., and are handled through sampling. Epistemic uncertainties are related to the incomplete understanding of nature and in time can be reduced with better observations, e.g. ground motion prediction equations. These uncertainties lead to alternative hazard curves and are handled through logic trees [15] by creating different models for input parameters and assigning weight factors to the tree branches. Weight factors represent the relative belief of the engineer in alternative models, without necessarily being frequency-based probabilities [16]. It is noted that there is no evidence (recorded data) for favoring the AD or MD approach of PFDHA. Thus, this option is considered as an epistemic uncertainty and is assigned a weight factor equal to 0.50 in a logic tree formulation.

3 METHODOLOGY OUTLINE

3.1 Parameters

The aforementioned formulation of fault displacement hazard estimation requires the following key input parameters:

- Seismic rate v of all earthquakes above magnitude 4.50 (minimum earthquake magnitude of engineering significance)
- Fault type (strike-slip, normal, reverse)

- Maximum earthquake magnitude (M_{max})
- b-value of the Gutenberg-Richter Bounded Recurrence Law [14] (slope of the curve)
- Fault length (LF) in km
- Pipe – fault crossing point (XL) that is the ration of the location of the crossing point to the closet fault edge to the fault length with $0 < XL \leq 0.50$

Specifically, the seismic rate according to Eq. (1) is an external multiplier of the seismic hazard calculations that are carried out separately for each fault type. On the other hand, for reasons of practicality, parameters M_{max}, b, FL, and XL are treated as discrete variables and are assigned indicative realistic values as per Table 1.

Parameter	Values
M_{max}	4.65, 5.00, 5.35, 5.65, 6.00, 6.35, 6.65, 7.00, 7.35, 7.75, 8.25
b	0.70, 0.90, 1.10
LF	10, 20, 50, 100, 150, 200
XL	0.10, 0.20, 0.30, 0.40, 0.50

Table 1: Parameters considered in fault displacement hazard estimation.

The range of b-values of the Gutenberg-Richter Bounded Recurrence Law [14] is from 0.70 to 1.10 for stable and active regions in Europe (EU SERA project, http://www.sera-eu.org/en/home/). The range of M_{max} values is 4.50 to 8.50, discretized in 11 bins with the bin centers listed in Table 1. Wells and Coppersmith [6] provide expressions that relate fault characteristics along with the pertinent limitations regarding the applicability of the expressions. Thus, in the case of normal/reverse fault, the maximum considered fault length (LF) is 100km (discretized in 4 values), while in the case of strike-slip fault it is 200km (discretized in 6 values).

3.2 Knowledge levels

Application of the full PFDHA framework, as described so far, necessitates seismological and geotechnical data that are not always available, for example, in case of minor faults or faults considered to be inactive. To account for input data incompleteness, the aim is to formulate pertinent expressions for the estimation of the design fault displacement for different levels of data availability, as presented indicatively in Table 2.

	Parameters				
Level	fault type	b	M_{max}	LF	XL
A	✓	✓	✓	✓	✓
B	✓			✓	✓
C				✓	✓
D / D1	✓			✓	
D / D2	✓		✓		
E / E1				✓	
E / E2			✓		

Table 2: Indicative levels of data knowledge for the pipeline – fault crossing site with reducing data availability from Level A to Level E.

The available data at each level reflects the objective difficulties in gathering all the necessary data. Assuming a minor fault, the length can be estimated by analyzing satellite images and determining then the fault crossing point. However, this fault might have been inactive for

a long period, and consequently estimating the maximum earthquake magnitude and the *b*-value of Gutenberg-Richter Law might not be possible.

The present study stands as the first step towards formulating simplified expressions for the estimation of the design fault displacement for pipelines crossing faults. The seismic rate v in Eq. (1) is assumed to be $v = 1$, reflecting areas of roughly moderate seismicity, namely areas where an earthquake of magnitude above 4.50 is expected once a year on average. Levels A and B of Table 2 are examined for all fault types, taking into account all the parameters of Table 1.

3.3 Design fault displacement

The typical return period of $T = 475$ yrs is considered in the current version of EN1998-4:2006 [17]. Structures of higher importance than the typical one (namely significance factor equal to one) are designed with seismic loads that are increased by multiplying with significance (or performance) factors higher than 1.00. More return periods and equivalent probabilities of exceedance (PoE) in 50 yrs are considered hereinafter (Table 3). In more detail, a return period of $T = 225$ yrs refers to low importance infrastructure (e.g., minor pipelines not carrying fuel), while $T = 975$ yrs and $T = 2475$ yrs are reserved for significant structures or infrastructure.

T	PoE in 50 yrs	MAF
225 yrs	20%	0.0045
475 yrs	10%	0.0021
975 yrs	5%	0.0010
2475 yrs	2%	0.0004

Table 3: Return periods (*T*) considered and equivalent probabilities of exceedance (PoE) in 50 yrs and corresponding mean annual frequencies (MAF).

4 LEVEL A

Level A of data knowledge is the one that requires all available data, namely fault type, *b*-value, magnitude M_{max}, fault length (*LF*), crossing point (*XL*). Considering all values of Table 1 for strike-slip, normal, and reverse fault type, PFDHA (section 2) is performed for all possible combinations of parameter values. In case of a strike-slip fault, the number of fault displacement hazard curves produced is equal to (11 values of M_{max}) × (3 *b*-values) × (6 values of *LF*) × (5 values of *XL*) = 990, while in case of normal and reverse fault the number of hazard curves is equal to (11 values of M_{max}) × (3 *b*-values) × (4 values of *LF*) × (5 values of *XL*) = 660. Then, to identify the effect of each parameter on the hazard curve, the case of normal faulting is examined in Figure 1 where in each case a single parameter is varied, while the other three are kept constant. The "anchoring" central set of parameter values for this example is $M_{max} = 6.65$, $b\text{-value} = 0.90$, $LF = 50\text{km}$, and $XL = 0.30$. The effect of maximum earthquake magnitude is evaluated in Figure 1(a), where for low fault offsets the range of MAFs is roughly from 10^{-3} to 10^{-2}, while for very high offsets this range is 10 times higher. In general, the increase of M_{max} leads to lower MAFs, indicating that a higher magnitude earthquake is rarer. Then, the effect of the Gutenberg-Richter *b*-value is examined in Figure 1(b), where the hazard curves for varying *b*-values are almost parallel to one another. The increase of the *b*-value leads to lower MAFs since the *b*-value is the slope of the curve that provides the "expected" future earthquake magnitude. Thus, a higher *b*-value implies that more low magnitude events "will occur" for each large magnitude event and consequently the overall rate of large magnitude events becomes lower.

The displayed behavior of the hazard curves for varying fault length in Figure 1(c) may seem peculiar, as longer faults may seem to underproduce small displacements. However, one should bear in mind that all curves are calculated for the same seismic rate $v = 1.00$ meaning that one event with magnitude $M \geq 4.50$ is expected on average per year. Thus, taking, for example, a small offset value of $d = 0.10\text{m}$, $\lambda(0.10\text{m}) = 0.0184$ for $LF = 10\text{km}$, while $\lambda(0.10\text{m}) = 0.0032$ for $LF = 100\text{km}$. The reason is that contrary to peak ground acceleration (PGA) or spectral acceleration $S_a(T_1)$ wave-propagation effects that affect points outside the immediate fault rupture, a fault offset cannot be recorded outside the rupture itself. Thus, on a longer fault, the many small events that could produce such a low value of $d = 0.10\text{m}$ actually happen away from the crossing point, reducing the corresponding MAF. When larger fault offsets are considered, larger magnitudes automatically come into play, rupturing larger segments of the fault to produce more frequent larger offsets. Thus, a fault length of 10km will very rarely produce a displacement of $d = 2\text{m}$, having a MAF of $\lambda \approx 10^{-5}$ versus a MAF of $\lambda \approx 1.5 \times 10^{-4}$ for the 100km fault.

Finally, the effect of the crossing point location along the fault trace is examined in Figure 1(d). Youngs et al. [7] used normalized fault displacement data for the estimation of the conditional probability that the offset at a specific point will exceed a predefined value. The normalization is expressed as D/AD or D/MD where D is the fault offset, AD is the average fault displacement, and MD is the maximum fault displacement. Distributions of ratios D/AD and D/DD are expressed as a function of the crossing point x/LF (XL) with $f(D/AD$ or $D/MD|x/LF)$ being symmetric about a maximum value at $x/L = 0.50$. Thus, higher fault displacement is expected for values x/LF close to 0.50, as presented in Figure 1(d), where hazard curves for higher x/LF are parallelly "displaced" to lower MAFs.

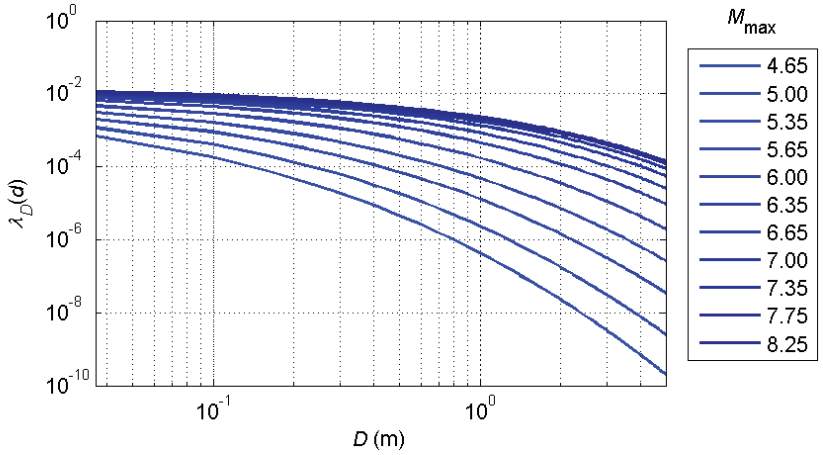

(a): varying magnitude M_{max}, b-value $= 0.90$, $LF = 50\text{km}$, and $XL = 0.30$

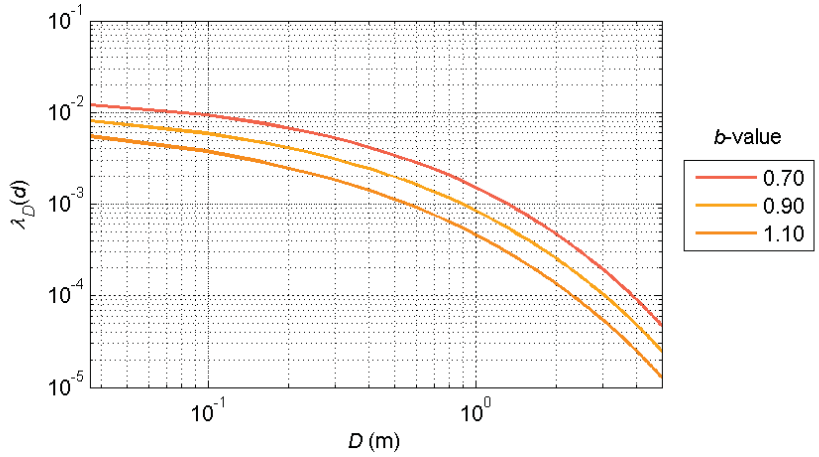

(b): $M_{\max} = 6.65$, varying b-value, $LF = 50$km, and $XL = 0.30$

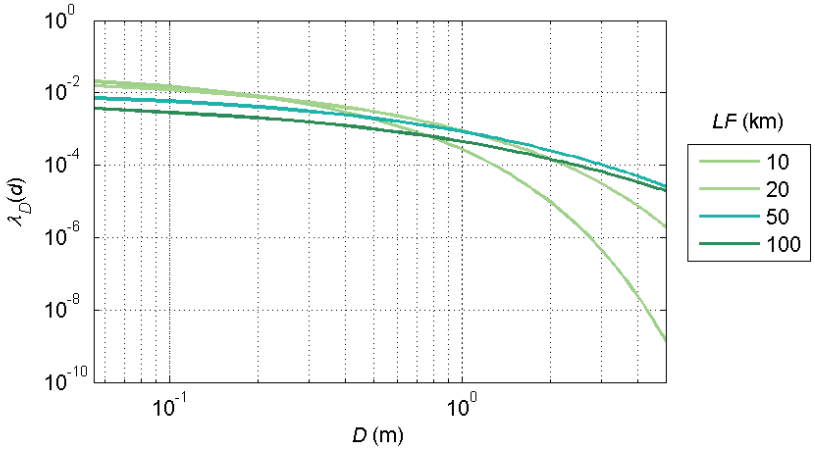

(c): $M_{\max} = 6.65$, b-value $= 0.90$, varying LF, and $XL = 0.30$

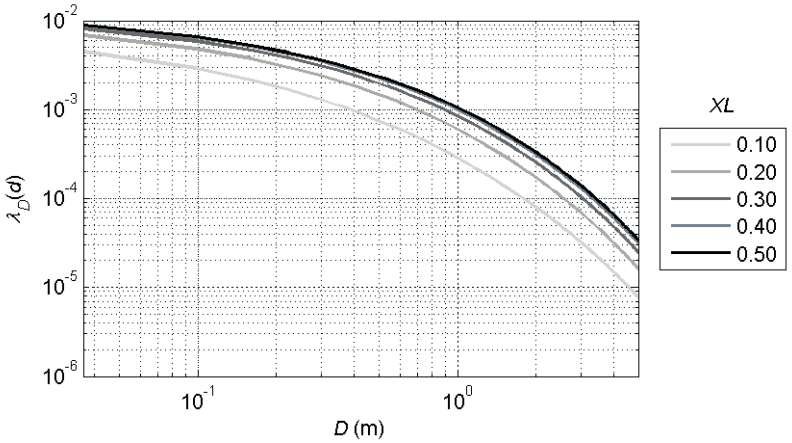

(d): $M_{\max} = 6.65$, b-value $= 0.90$, $LF = 50$km, and varying XL

Figure 1: Fault displacement hazard curves on pipeline crossing site.

5 LEVEL B

In knowledge Level B, the maximum earthquake magnitude ($M_{\max}$) and the b-value are unknown variables, as presented in Table 2. The logic tree of Figure 2 is formulated to handle the unknown variables by assigning pertinent weight factors to the tree branches. The weight factors for the b-value are listed in Table 4 and are selected based on expert opinion for European sites.

parameter value	weight factor w_b
0.70	0.1585
0.90	0.6830
1.10	0.1585

Table 4: Level B – weight factors for the parameter *b*-value of Gutenberg-Richter Law [14].

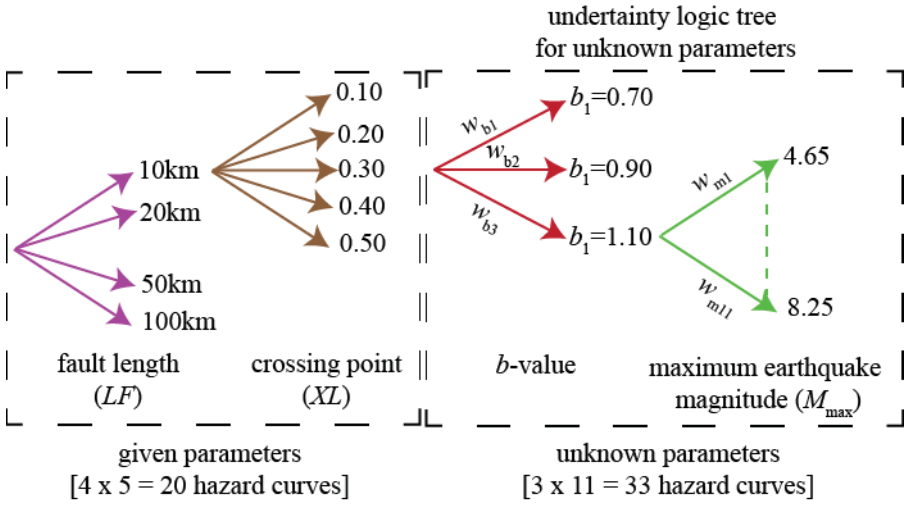

Figure 2: Logic tree formulation to handle unknown parameters in data knowledge Level B.

The weight factors for $M_{\max}$ are estimated based on the empirical expressions of Wells and Coppersmith [6]. The earthquake magnitude is normally distributed with respect to fault length (*LF*). The mean value of earthquake magnitude concerning *LF* and the corresponding standard deviation for each fault type are estimated after:

$$\text{Normal fault: } M_{mean} = 4.86 + 1.32\log_{10}(LF)\,,\sigma = 0.34 \tag{2}$$

$$\text{Reverse fault: } M_{mean} = 5.00 + 1.22\log_{10}(LF)\,,\sigma = 0.28 \tag{3}$$

$$\text{Strike-Slip fault: } M_{mean} = 5.16 + 1.12\log_{10}(LF)\,,\sigma = 0.28 \tag{4}$$

Thus, for every fault length considered, the mean earthquake magnitude is estimated using Eqs. (2)-(4). Then, the weight factor for each magnitude ($M_{\max}$) considered is evaluated as:

$$w_m = F(M_{\max}) = \Phi\left(\frac{M_{\max} - M_{mean}}{\sigma}\right) \tag{5}$$

In case of normal or reverse fault, following the procedure presented above along the logic tree of Figure 2 leads to the reduction of the total number of hazard curves (or combination of discrete parameter values) to consider from 660 to 20 [(4 values of *LF*) × (5 values of *XL*)], while in case of strike-slip fault the corresponding reduction is from 990 curves to 30 [(6 values of *LF*) × (5 values of *XL*)]. This reduction is simply achieved by summarizing the larger sample of hazard curves through the logic tree.

The next step in the process is to determine the fault offset values from each hazard curve that correspond to each return period of Table 3. The case of normal fault is illustrated in Figure 3, where the 20 hazard curves are plotted with solid lines and the 4 return periods under consideration are plotted with dashed horizontal lines. The grouping of hazard curves that is observed is related to the different fault lengths considered. In other words, the grouping of the

hazard curves is a combination of Figure 1(c) and Figure 1(d). The intersection of each horizontal line with a hazard curve provides a single point estimate of the fault offset, given the return period. Consequently, for each return period 20 fault offset values are estimated.

The fault displacement in meters with respect to fault length and crossing point can be estimated via the general function $d(LF, XL)$:

$$d(LF,XL) = p_{00} + p_{10}LF + p_{01}XL + p_{20}LF^2 + p_{11}(LF)(XL) + p_{02}XL^2 + p_{03}LF^3 + p_{21}(LF^2)(XL) + p_{12}(LF)(XL^2) \text{ (m)} \quad (6)$$

where p_{00}, p_{01}, …, p_{12} are the fitting coefficients. Evidently, to accommodate all observations on the relative significance of fault length (LF) and crossing point (XL), the length is captured with terms up to the third power, while for the crossing point, terms up to the second power are employed, including all interaction terms up to the third order. The resulting coefficients are listed in Table 5 for the normal fault, in Table 6 for the reverse fault, and in Table 7 for the strike-slip fault type. It is noted that Eq. (6) is applied for each return period of Table 3. Indicative results of the fitted surface for normal fault type and $T = 475$ yrs is shown in Figure 4. The root mean square error (RMSE), which is the standard deviation of the residuals (prediction errors), for each fitting is listed in Table 5 through Table 7, indicating that the error is at the order of a few centimeters, namely the data is very concentrated around the line of best fit. Finally, it is noted that the adjusted R-square is above 0.995 for all cases.

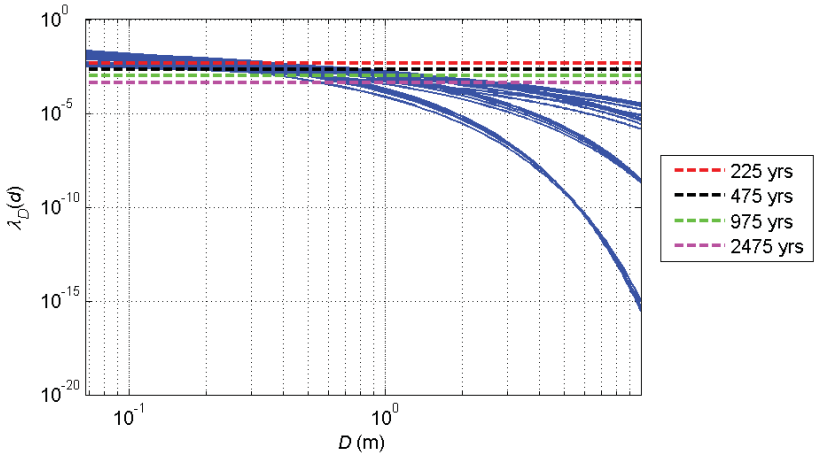

Figure 3: Normal fault: hazard curves (solid lines) of Level B and considered return periods (horizontal dashed lines).

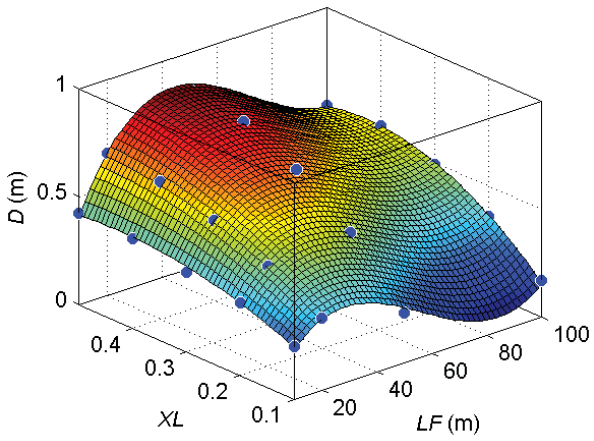

Figure 4: Normal fault: surface fitting for fault displacement values for $T = 475$ yrs.

Normal fault: coefficients for Eq. (6)											
T (yrs)	RMSE (m)	p_{00}	p_{10}	p_{01}	p_{20}	p_{11}	p_{02}	p_{30}	p_{21}	p_{12}	LF range (km)
225	0.007949	0.022940	0.008334	0.645058	-0.00031	0.029956	-0.84459	2.09E-06	-0.00021	-0.01306	10-100
475	0.014230	0.020385	0.015884	0.790144	-0.00049	0.064676	-1.39270	3.13E-06	-0.00041	-0.02287	10-100
975	0.022168	0.061270	0.024446	0.536158	-0.00066	0.113969	-1.30167	4.03E-06	-0.00054	-0.05946	10-100
2475	0.030221	0.111599	0.040342	-0.00829	-0.00090	0.181476	-0.78500	4.94E-06	-0.00061	-0.12243	10-100

Table 5: Normal fault: coefficients for estimating fault displacement in data knowledge Level B.

Reverse fault: coefficients for Eq. (6)											
T (yrs)	RMSE (m)	p_{00}	p_{10}	p_{01}	p_{20}	p_{11}	p_{02}	p_{30}	p_{21}	p_{12}	LF range (km)
225	0.011472	0.244408	-0.00727	1.731467	0	-0.00239	-1.66579	0	0	0	10-50
475	0.011735	0.369540	-0.00171	1.906638	-8.7E-05	0.008657	-1.55476	6.08E-07	-4.7E-05	-0.01238	10-100
975	0.018966	0.472529	0.00565	2.121767	-0.00020	0.017519	-1.41466	1.18E-06	-6.0E-05	-0.02203	10-100
2475	0.031966	0.645046	0.01593	2.063252	-0.00037	0.037789	-0.52237	2.04E-06	-6.7E-05	-0.04999	10-100

Table 6: Reverse fault: coefficients for estimating fault displacement in data knowledge Level B.

Strike-Slip fault: coefficients for Eq. (6)											
T (yrs)	RMSE (m)	p_{00}	p_{10}	p_{01}	p_{20}	p_{11}	p_{02}	p_{30}	p_{21}	p_{12}	LF range (km)
225	0.008359	0.013616	0.002373	0.653752	-6.8E-05	0.004795	-0.79558	0	0	0	10-50
475	0.027420	-0.001060	0.004466	0.868048	-8.1E-05	0.020072	-1.02385	2.68E-07	-7.5E-05	-0.00689	10-200
975	0.034403	-0.023590	0.007158	1.229490	-0.00010	0.047720	-1.86840	3.14E-07	-0.00013	-0.01972	10-200
2475	0.034899	0.076041	0.012777	0.593121	-0.00015	0.099034	-1.18712	3.77E-07	-0.00014	-0.07030	10-200

Table 7: Strike-slip fault: coefficients for estimating fault displacement in data knowledge Level B.

6 CONCLUSIONS

The estimation of design fault displacement for buried pipelines crossing active tectonic faults typically relies on regression equations, engineering assumptions, or expert opinion. Pipelines are structures of very high importance and consequently, it is deemed necessary to employ state-of-the-art probabilistic tools for the estimation of the design fault displacement. However, pipelines extend over hundreds or thousands of kilometers, crossing several major or minor, active, or potentially inactive tectonic faults. Thus, performing a full probabilistic hazard assessment of each fault crossing might not be possible or even desirable. Therefore, we presented a comprehensive first attempt to formulate simplified expressions for the calculation of the fault displacement.

The appropriate method for the seismic hazard assessment of fault is the Probabilistic Fault Displacement Hazard Analysis (PFDHA) that has been adjusted by the authors for buried pipeline – fault crossings. Considering a range of realistic values for the key input parameters of PFDHA, namely fault type, maximum earthquake magnitude, fault length, crossing point, and *b*-value for earthquake magnitude recurrence, analysis is carried out for all combinations of the input parameters. Results are then statistically processed by taking into account reduced levels of data knowledge, namely unknown parameters, to formulate simplified expressions that relate fault characteristics and fault offset, given the desired return period.

The developed simplified expressions are the first decisive step towards formulating a methodology for estimating the design fault displacement for pipeline – fault crossing considering different knowledge levels and with respect to the required return period. The proposed methodology aims at overcoming the typical drawbacks of the deterministic approach (regression equations, expert opinion, etc.), where pertinent uncertainties are disregarded, resulting in a hazard-independent estimation with an unknown level of conservatism.

7 ACKNOWLEDGMENTS

This research received funding from the European Union's HORIZON 2020 research and innovation programme under grant agreement No 821054, project: "HYPERION – Development of a Decision Support System for Improved Resilience & Sustainable Reconstruction of historic areas to cope with Climate Change & Extreme Events based on Novel Sensors and Modelling tools".

REFERENCES

[1] M.J. O'Rourke, J.X. Liu, *Seismic Design of Buried and Offshore Pipelines. Monograph MCEER-12-MN04*, Multidisciplinary Center for Earthquake Engineering Research, 2012.

[2] G.C. Sarvanis, S.A. Karamanos, Analytical model for the strain analysis of continuous buried pipelines in geohazard areas, *Engineering Structures* 152, 57-69, 2017.

[3] F.R. Rofooei, N.K.A. Attari, H.H. Jalali, New method of modeling the behavior of buried steel distribution pipes subjected to reverse faulting, *Journal of Pipeline Systems Engineering and Practice* 9(1), 1-13, 2018.

[4] H.E. Demirci, S. Bhattacharya, D. Karamitros, N. Alexander, Experimental and numerical modelling of buried pipelines crossing reverse faults, *Soil Dynamics and Earthquake Engineering* 114, 198-214, 2018.

[5] A. Tsatsis, M. Loli, G. Gazetas, Pipeline in dense sand subjected to tectonic deformation from normal or reverse faulting, *Soil Dynamics and Earthquake Engineering* 127, 105780, 2019.

[6] D.L. Wells, K.J. Coppersmith, New empirical relationships among magnitude, rupture length, rupture width, rupture area, and surface displacements, *Bulletin of the Seismological Society of America* 84(4), 974-1002, 1994.

[7] R.R. Youngs *et al.*, A methodology for probabilistic fault displacement hazard analysis (PFDHA), *Earthquake Spectra* 19(1), 191-219, 2003.

[8] R.E.S. Moss, Z.E. Ross, Probabilistic fault displacement hazard analysis for reverse faults, *Bulletin of the Seismological Society of America* 101(4), 542-1553, 2011.

[9] M.M. Angell, A.O.A. Geophysics, K. Hanson, R.R. Youngs, H. Abramson, Probabilistic fault displacement hazard assessment for flowlines and export pipelines, mad dog and Atlantis field developments, deepwater Gulf of Mexico, *Proceedings of the Annual Offshore Technology Conference*, 2579-2603, 2003.

[10] M.D. Petersen *et al.*, Fault displacement hazard for strike-slip faults, *Bulletin of the Seismological Society of America* 101(2), 805-825, 2011.

[11] R. Chen, M. D. Petersen, Probabilistic fault displacement hazards for the Southern San Andreas fault using scenarios and empirical slips, *Earthquake Spectra* 27(2), 293-313, 2011.

[12] V.E. Melissianos, D. Vamvatsikos, C.J. Gantes, Performance Assessment of Buried Pipelines at Fault Crossings, *Earthquake Spectra* 33(1), 201-218, 2017.

[13] C.A. Cornell, Engineering seismic risk analysis, *Bulletin of the Seismological Society of America* 58(5), 1583-1606, 1968.

[14] R. Gutenberg, C.F. Richter, Frequency of earthquakes in California, *Bulletin of the Seismological Society of America* 34, 185-188, 1944.

[15] J.J. Bommer, F. Scherbaum, The use and misuse of logic trees in probabilistic seismic hazard analysis, *Earthquake Spectra 2*4(4), 997-1009, 2008.

[16] N.A. Abrahamson, J.J. Bommer, Probability and uncertainty in seismic hazard analysis, *Earthquake Spectra* 21(2), 603-607, 2005.

[17] European Committee for Standardization (CEN), *EN 1998-4:2006, Eurocode 8 - Design of structures for earthquake resistance - Part 4: Silos, tanks and pipelines*, 2006.

EURODYN 2020
XI International Conference on Structural Dynamics
M. Papadrakakis, M. Fragiadakis, C. Papadimitriou (eds.)
Athens, Greece, 23–26 November 2020

INNOVATIVE DISSIPATIVE DEVICES WITH TENSEGRITY ARCHITECTURE AND SUPER ELASTIC BEHAVIOUR FOR THE SEISMIC PROTECTION OF STRUCTURES

N. Singh[1], A. Amendola[1], F. Santos [2], G. Benzoni[3] and F. Fraternali [1*]

[1]Dept. of Civil Engineering
University of Salerno
Salerno, Italy
e-mail: {snarinder, adamandola1, f.fraternali}@unisa.it

[2] FCT, Civil Engineering Department
Universidade NOVA de Lisboa, Portugal
e-mail: fpas@fct.unl.pt

[3] Dept. of Structural Engineering
University of California
San Diego, CA, USA
e-mail: gbenzoni@eng.ucsd.edu

Keywords: Seismic motions, Bracing systems, SMA, Energy dissipation devices.

Abstract. *The present paper deals with the design and the mechanical modeling of a seismic bracing system with tensegrity architecture, which operates as a lightweight mechanical amplifier for longitudinal displacements, efficiently limiting the inter-story drifts while dissipating energy. The proposed brace is based on a D-bar tensegrity structure with rhomboidal shape comprising Shape-Memory Alloy (SMA) tendons. The SMA tendons can develop austenitic-martensitic (solid to solid) phase transformations, which enable them to amplify the signals into wide super elastic hysteresis, while subjected to mechanical cycles, comprising strains up to ≈6-7%, with no residual deformations. The underlying concept of the proposed device is the use of SMA wire sections as the dissipating component, and some preliminary results have been presented in previous studies. Enhanced energy dissipation and re-centering capability of the current SMA-D-bar (SMAD) braces are illustrated by the seismic analysis of a benchmark structure. The efficiency of the designed bracing to minimize the seismic damage of the served structure paves the way for the development of advanced seismic energy dissipation systems incorporating tensegrity concepts and superelasticity.*

1 INTRODUCTION

Near field seismic vibrations are represented by pulses of short duration with extensive time periods with enormous peak ground speeds and accelerations [1]. Significant work in the field of seismic structure response control through passive energy dissipation devices (PEDs) has been outlined since previous two decades [2]. Which can be categorized into three different forms including semi-control, active and passive [3]. Passive control devices (passive energy dissipation devices (PEDD)) are considered to be the best in terms of efficiency, inexpensive and effective techniques to dissipate and eliminate the risk of seismic activity [4]- [6]. Permanent configuration of the energy dissipation devices in structure for the sole purpose of dissipation has been considered extremely effective which can dissipate significant seismic energy into other forms of energy thus reducing the risk of potential damage to the buildings [7]. Yet permanent devices are hard to fabricate and require a lot of resources to build them. In every field such as electrical, mechanical and civil engineering additive manufacturing has emerged as one of the basic and significant contributors. Due to its low cost and easy availability, the usability of the FDM (fused deposition modeling) has been enhanced since the last decade. Using the CAD (Computer Added Designs) packages, it has become possible to realize any pre-customized prototype and part with zero waste production technology [8]. To date, additive manufacturing has made a major contribution in the area of mechanical engineering. 3D printing has also shown its wide-spread use in the civil engineering sector. But very less research has been conducted in the field of additively manufactured seismic isolator. For civil / structural fields, this technology has been recognized far less. However, even after so much potential these technologies bring, these fields don't actually apply these technologies very often. Because most of the configurations were designed on site and in an industrial environment. But now several research works are being carried out to explore the effectiveness and feasibility of the additive manufacturing in civil engineering [9]- [12]. In present work an effort has been made to develop a tensegrity architecture based seismic isolator in which SMA wires were used as restitution elements and their response were observed in terms of amplification. Further, The main feature includes the use of additive manufacturing to prepare the linking components and the joints. The structure was developed using the commercial CAD program, and tested for prescribed motions that are expected to occur in structure during lateral force activity. Finally, the device was operated by implementing a customized NI based virtual interface. Furthermore, the presence of friction in joints can not be ruled out and the unaccounted dissipation of energy would also occur in joints. Which would also act as passive dissipation of energy in 3D printed bodies. In next sections, procedure for manufacturing such device has been discussed along with the testing and conclusions obtained from the research work.

2 MATERIALS AND METHODS

The main focus of this study was the development of an seismic bracing system with tensegrity architecture that could be helpful in seismic analysis of a structures . As mentioned in the previous section, the setup was intended to act as PED deviecs and SMA tendons were used as restitution elements. The dissipation of energy in buildings can be separated into two major categories, such as elastic dissipation and inelastic dissipation [13]. In this research work a system has been developed that relies on elastic dissipation mechanism such as PED devices. In Figure 1 various designs such as Diagonal 1(a) , Upper toggle 1(b), Chevron 1(c), Reverse toggle 1(d) and Scissor-jack 1(e) [14] have been shown.

The present study generalizes the Scissor-jack PED device shown in in Figure 1(e) bu de-

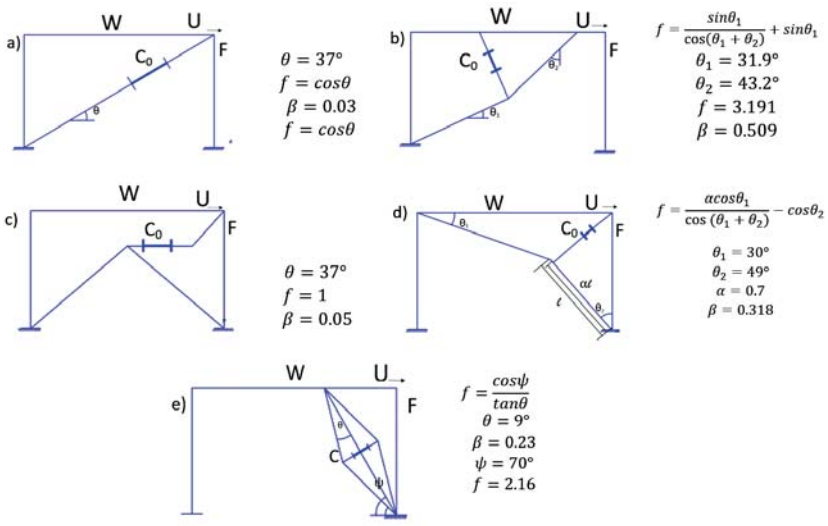

Figure 1: Different configurations of PED based systems [14]

signing a tensegrity structure with similar geometry, which is formed by a D-bar rhomboidal arrangement of four bars (blue solid elements in Fig. 2) connected each other through longitudinal and a transversal string/cable elements (red this elements in Fig. 2). This SMA-D-bar (SMAD) design allows the brace to produce stretching in the longitudinal string when it is loaded by a longitudinal force pointing upward, and, conversely, to produce stretching in the transverse string when it is loaded by a longitudinal force pointing upward (see also [15]).

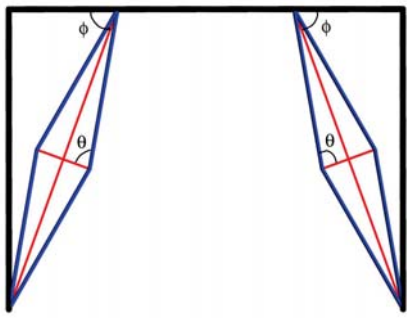

Figure 2: SMAD braces inserted into a frame structure

3 MECHANICAL MODELING

The SMAD bracing concept illustrated in Figure 2 is mechanically studied in terms of its displacement amplification and energy dissipation properties which could be very useful while assessing the seismic behavior of an earthquake-proof structure. The tensegrity-based SMAD brace is assumed to be in zero self-stress state while the structure has been assumed to be under zero external force P [15]. Because of the symmetry and loading condition of the SMAD brace, it is easy to observe that all the bars of such a structure bear an equivalent axial force N, which is assumed to be in compression. In addition, transverse SMA wires have been assumed to be carrying horizontal tensile force while vertical tensile forces are carried by the longitudinal SMAs. After assuming the forces in all the nodes, an equilibrium equation has been derived

(See Equation 1).

$$N = \frac{X}{cos\theta}, P = 2Xsin\theta - Y = Xtan\theta - Y \tag{1}$$

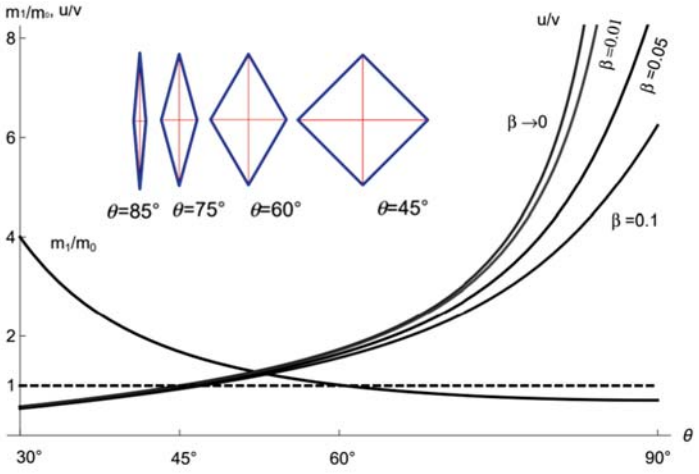

Figure 3: Displacement amplification response

When the bars acts as rigid bodies (since they feature axial stiffness much greater than the SMA wires), then the movement of SMAD brace can be described by Equation 2.

$$u/v = \left(\sqrt{4cos^2(\theta) - \beta(\beta - 4sin(\theta))} - 2cos(\theta)\right)/\beta \tag{2}$$

where *u, v and b* denote the longitudinal and the transverse displacements of the structure, and the length of the bars respectively. In the case where β approaches to 0, which shows nearly negligible movement of the brace from original position, Equation 2 converges to 'tan θ', where θ is angle of inclination. Figure 3 shows the various position of the SMAD braces at different angle of inclinations 'θ'. It has been observed that when θ approaches 90°, *u/v* ratio tends to achieve infinite values. Similarly at θ = 80° ratio becomes 5.67. Even at θ = 80° and β = 0.01, the *u/v* ratio experience a small change but with with substantially large value i.e., 5.26 (Fig. 3). In terms of the buckling load of the SMAD brace, it is useful to compare such a key mechanical parameter with that exhibited by a straight beam with length equal to the longitudinal size of the SMAD brace. Let us consider a SMAD brace with mass m_1 and straight beam with mass m_0, made of the same material, which feature the same buckling load. The analysis presented in Par. 3.3 of [16] allows us to conclude that such masses are related each other through the following equation

$$m_1/m_0 \; = \; (2\sin^5\theta)^{-\frac{1}{2}} \tag{3}$$

which gives $m_1/m_0 < 1$ for $\theta > 60.5$ degrees (Fig. 3). In particular, we observe that it results $m_1/m_0 \approx 0.73$ when $\theta = 80$ degrees (Fig. 3), which proves that tapered SMAD braces exhibit much higher buckling loads, over straight beams with equal mass. The mechanical modeling of the superelastic response of the SMA wires under stretching is given in Sect. 2.2 of Ref. [15], to which we refer the reader for details.

4 ANTI-SEISMIC BEHAVIOR

We wish now to study the seismic response of the SMAD-reinforced frame structure depicted in Fig. 2, by assuming the presence of hinged connections between the vertical columns and the horizontal beam, and at the basis of the columns. We let F denote the horizontal force acting on the frame, which is produced by a shaking excitation of the foundation structure, and let u_f denote the corresponding lateral displacement. As in [14], [15], the bars of the SMAD braces consist of TS 2×2×1/4' profiles, while the SMA strings are formed by strand comprising 12+6+1 SMA wires with 2mm diameter each [17]. The external frame has horizontal span of 2540 mm, and height of 1972 mm.The horizontal beam of the frame features a W8×21 profile, while the columns are made with W8×24 profiles [15]. Fig. 4 reports the F vs. u_F curves of frames reinforced with SMAD braces exhibiting different aspect angles ψ and θ, under of a dynamical displacement loading at the frequency of 4 Hz with maximum lateral displacement $u_F = 6$ mm. The results in Fig. 4 highlight the noticeable energy dissipation properties of the SMAD-reinforced brace, through superelastic response of the SMA strings/cables. Such a response does not induce appreciable permanent strains in the SMA cables [**?**], and therefore the SMAD-brace offers complete self-centering capabilities [18]- [19]. The additional results presented in Ref. [**?**] show that the non-invasive and self-centering SMAD braces feature energy dissipation capacity up to nearly 70% greater that that offerend by the schissor-jack device analyzed in [14].

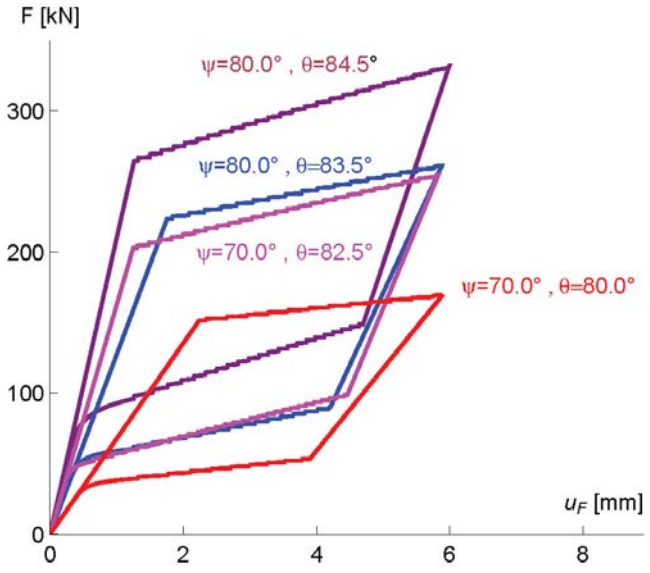

Figure 4: Force-displacement responses of a model frame reinforced with symmetrical SMAD braces.

5 CONCLUSIONS

The present paper has studied the seismic response of a tensegrity based bracing with superelastic tendons. This study showed that tensegrity inspires, light-weight bracings have a great potential in structural seismic protection. It can be clearly observed that compression efficiency of the proposed bracing is associated with a geometrical advantage, due to a metamaterial-type displacement amplification response. It has been shown that the proposed tensegrity bracing acts as a mechanical amplifier for longitudinal displacements, thus increasing the level of de-

formations experienced by the transverse SMA tendons, and the associated, superelastic energy dissipation. Based on the seismic vulnerability assessment it is possible to conclude that the proposed tensegrity-based bracings may successfully mitigate the earthquake induced damage in earthquake-proof structures, significantly reducing the probability of collapse under strong earthquakes [15]. Future work will include the experimental verification of the theoretical results presented in this work, to be conducted through structural identification procedures [20] on additively manufactured physical models of SMAD braces.

Acknowledgements

N.S., A.A. and F.F. acknowledge financial support from MIUR under the PRIN 2017 National Grant 'Multiscale Innovative Materials and Structures'(grant number 2017J4EAYB).

REFERENCES

[1] W-L. He, AK. Agrawal, Analytical model of ground motion pulses for the design and assessment of seismic protective systems, *Journal of Structural Engineering* 134, 1177-1188, 2008.

[2] FY .Cheng, H. Jiang, K. Lou, Smart structures: innovative systems for seismic response control, *CRC press* 2008.

[3] QL. Meng, MZ. Zhang, J. Ye, Fuzzy control strategy based on mode identification Used in semi-active control. *In Applied Mechanics and Materials*, 71, 3975-3982, 2011.

[4] DS. Saravanathiiban, Comparisons of Energy Dissipation in Structural Devices with Foundation Soil During Seismic Loading, *Doctoral dissertation, North Dakota State University*, 2010.

[5] P. Castaldo, Integrated seismic design of structure and control systems. *New York: Springer International Publishing*, 2014.

[6] M. Nath, Seismic design and performance of Yielding Shear Panel Device *Doctoral dissertation, Concordia University*.

[7] RD. Iacobucci, SA. Sheikh, O. Bayrak, Retrofit of square concrete columns with carbon fiber-reinforced polymer for seismic resistance. *Structural Journal*, 100(6), 785-94, 2003.

[8] C. Hu, Z. Sun , Y. Xiao, Q. Qin, Recent patents in additive manufacturing of continuous fiber reinforced composites. *Recent Patents on Mechanical Engineering*, 12(1), 25-36, 2019.

[9] SH. Huang ,P. Liu , A. Mokasdar, L. Hou, Additive manufacturing and its societal impact: a literature review, *The International Journal of Advanced Manufacturing Technology*, 67(5-8), 1191-1203, 2013.

[10] I. Gibson, DW. Rosen, B. Stucker, Additive manufacturing technologies, *New York: Springer*; 2014.

[11] S. Lim, RA. Buswell, TT. Le, SA . Austin, AG. Gibb, T. Thorpe, Developments in construction-scale additive manufacturing processes, *Automation in construction*, 21, 262-268, 2012.

[12] M. Moini, J. Olek, JP. Youngblood, B. Magee, PD. Zavattieri, Additive Manufacturing and Performance of Architectured Cement-Based Materials, *Advanced Materials*, 30(43), 1802123, 2018.

[13] AS. Whittaker, VV. Bertero, CL. Thompson, LJ. Alonso, Seismic testing of steel plate energy dissipation devices, *Earthquake Spectra*, 7(4), 563-604, 1991.

[14] AN. Sigaher, MC. Constantinou, Scissor-jack-damper energy dissipation system, *Earthquake Spectra*,19(1), 133–158, 2003.

[15] F. Fraternali, F. Santos, Mechanical modeling of superelastic tensegrity braces for earthquake-proof structures, *Extreme Mechanics Letters*, 33, 100578, 2019.

[16] RE. Skelton, MC. de Oliveira, Tensegrity Systems, *Springer*, 2010.

[17] V. Mercuri, Shape memory alloy strands: Conventional 3D FEM modeling and simplified models, *MSc Thesis, University of Pavia*, 2014.

[18] M. Dolce, R. Marnetto, Passive seismic devices based on shape memory alloys, *12th World Conference on Earthquake Engineering*, 1–8, 2000.

[19] Z. Xu, AK. Agrawal, WL. He, P. Tan, Performance of passive energy dissipation systems during near-field ground motion type pulses. *Engineering Structure*, 29(2), 224-236, 2007.

[20] F. Fabbrocino, I. Farina, and M. Modano, Loading noise effects on the system identification of composite structures by dynamic tests with vibrodyne, *Composites Part B-Engineering*, 115, 376-383, 2017.

EURODYN 2020
XI International Conference on Structural Dynamics
M. Papadrakakis, M. Fragiadakis, C. Papadimitriou (eds.)
Athens, Greece, 23–26 November 2020

EARTHQUAKE EFFECTS ON LOW PROFILE CONTAINER CRANE WITH SEISMIC ISOLATION DEVICE

L. Solazzi

Department of Mechanical and Industrial Engineering
University of Brescia
Via Branze, 38 - 25123 Brescia (Italy)
luigi.solazzi@unibs.it

Keywords: crane, lifting equipment, earthquake actions, dynamic behavior, anti-seismic device, seismic design, seismic performance.

Abstract. *The focus of this research is to evaluate and compare the mechanical behaviour of a big ship to shore low profile container crane subjected to earthquake actions, with and without anti-seismic device applied to it. For this purpose, a specific machine was designed considering different load and geometrical configurations. Subsequently, the earthquake actions were studied. The different acceleration spectrums were established by Italian standards. The anti –seismic device was chosen to limit the crane displacement to not compromise the crane performance due, for example, to the increase of the payload swinging effect. The numerical results show that, for each load and geometrical configurations assumed, the anti-seismic device has a positive effect, it reduces the maximum stress values (about 20%). The dynamical crane behaviour is practically unchanged with the isolation device adopted, it was observed a small reduction of the natural frequencies values and a little increase of the magnitude of the maximum displacement. These results are valid also in case of dynamic action applied to the crane due, for example, to the trolley and payload movement.*

1 INTRODUCTION

The scope of this research it to analyze the dynamical behavior of the ship to shore low profile container crane, which is the popular crane utilized in the port for moving containers from the quay to the ship and vice versa. In particular, the object of this study is to analyze the seismic effects on crane considering the introduction of the anti-seismic devices. The crane can be subjected to many different actions: dead load and inertia actions [1,2,3,4], moving payload and trolley [5,6], impulse loading [7], wind [8,9,10], earthquake [11,12]. The earthquake actions can be very dangerous, in fact, for example during Kobe earthquake (17/1/1995) [13,14] different cranes collapsed causing considerable damage also on the economic point of view. In this case, the principal failure modes for these structures are local or global buckling phenomena.

This topic is very important, and so in [15], for example, are collected some recommendations for design these machines. Several papers report studies on this phenomenon [16] both experimental [17] and especially on scaled model [18,19]. From these study, different solutions were proposed to avoid the damage caused by the earthquake, introducing a seismic isolation [20,21,22].

The purpose of this research is a feasibility study of the crane with and without the anti-seismic devices in order to promote (if there are positive benefits) the implementation of these components to the crane to increase the safety factor for the whole crane.

2 SHIP TO SHORE LOW PROFILE

The object of this research is a big ship to shore low profile container crane. The main characteristics and geometrical dimensions are reported in the table 1 and in the figure 1.

Maximum payload	45000 kg
Lifting speed (unloaded)	35 m/min
Lifting speed (loaded)	85 m/min
Beam translation	30 m/min
Trolley translation	170 m/min
Bridge sliding	40 m/min

Table 1: Main crane performance.

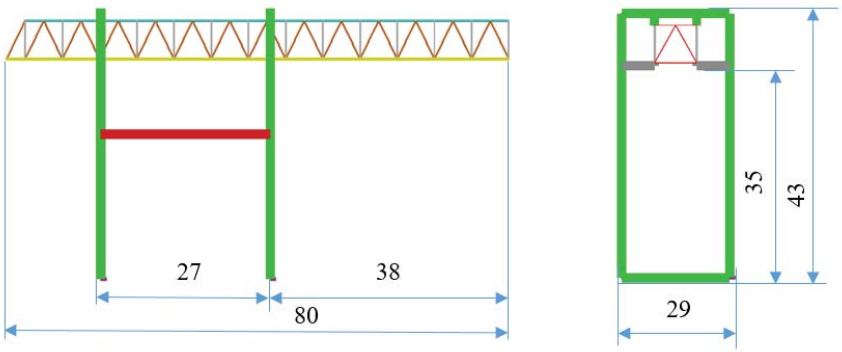

Figure 1: Main geometrical dimensions [m] for ship to shore low profile container crane.

2.1 Fem model

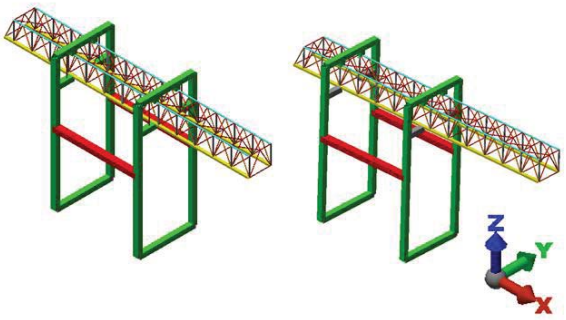

Figure 2 : Finite element crane model with the arm at sea side position and ground side position.

After preliminary analytical analyses, performed in order to design the main crane parts, a subsequent solid model and finite element analyses were carried out with the aim to study the crane mechanical behavior. Figure 2 shows the crane finite element model, which is composed of about 5000 quadratic beam elements and 8000 nodes.

The procedure adopted for dynamic analyses performed by finite element method technique (using Autodesk Simulation Software ®) is superposition modal method [23,24]. For this technique, the total mass involved for analyses is very important because it is correlated to the number of natural vibrational modes. Some standards adopt this value at least equal to 80% or more. In this research, the value adopted is equal to 90 % which corresponds about to the first 10 natural vibration modes.

2.2 Load conditions

The crane analyzed can assume different geometrical configurations and can be subjected to different load conditions. With the aim to analyze the machine, some of these configurations and actions were assumed as representative of the whole possibility of the working area and loads of the machine. They are:

1) arm completely out (sea side position) and unloaded structure;
2) arm completely out, sea side payload;
3) arm completely out, ground side payload;
4) arm in resting position, unloaded structure.

For each combination, three different analyses were performed. These analyses are:

a) linear static analysis;
b) modal analysis;
c) response spectrum analysis (assuming three different peak ground accelerations).

2.3 Response spectrum

The external actions induced by the earthquake were studied basing on the Italian Technical Standards 2008 (D.M. 14 Gennaio 2008), which are replaced by NTC 2018 (D. M. 17 Gennaio 2018) [25,26,27]; the acceleration spectrum is very similar to the Eurocode 8 Standard. Figure 3 shows an example of the accelerations spectra elaborated, which is equal for the two Italian standards adopted.

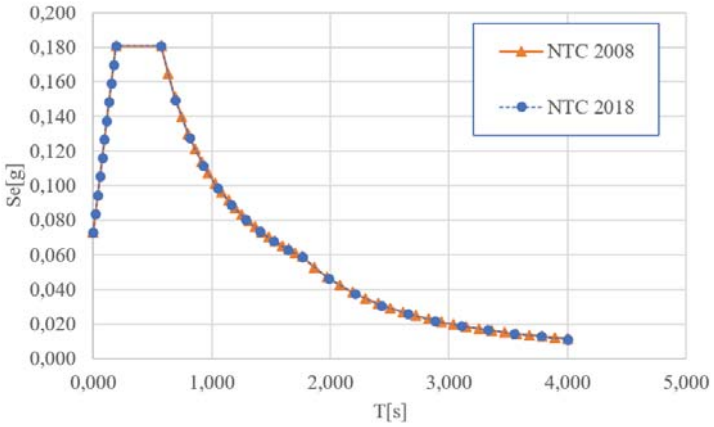

Figure 3: Comparison between acceleration spectra from NTC 2008 with that obtained by NTC 2018.

The earthquake analyses were performed considering three different "peak ground accelerations (PGA)", these values are PGA=0.15g, 0.2g and 0.35 g. In particular, the load spectra assumed refers to a very high earthquake action in specific South - Italian zone considering the structure life equal to 50 years.

.

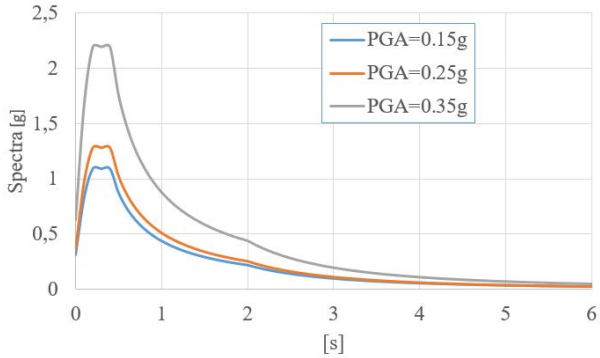

Figure 4: Three different load spectra applied to the ship to shore crane.

2.4 Results

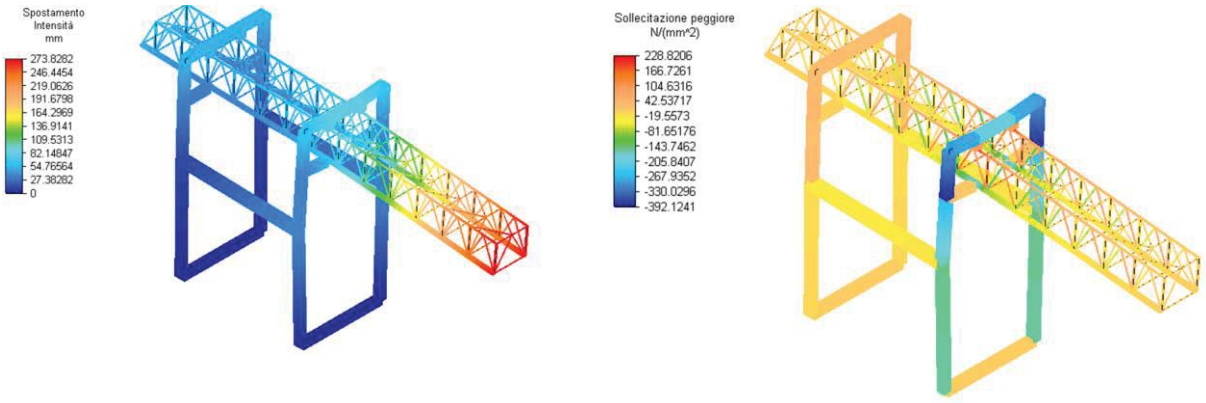

Figure 5: Stress and displacement in the second load condition (2,a).

Figure 5 shows the crane displacements and the stresses distribution in the second load condition, i.e. when the arm is positioned at sea side and the payload is applied at the end of the arm. The material assumed for crane design is a classical structural high strength steel (S460M or S460ML according to European standard EN 10025:2004) with the minimum yield strength equal to 460 MPa and tensile strength variable between 520 to 670 MPa. With this assumption, the safety factor is about 1.17, with respect to the yield strength and the ratio between the arm length and the maximum displacement that is about 300.

Table 2 shows the results from modal analyses for the same load condition. In particular, the table reports the first natural frequencies and the perceptual mass involved in the specific natural mode. The structure deformations are reported in the figure 6. The natural frequencies values are in agreement with the ones for this type of lifting machine [6,7,12].

Mode	Frequency [Hz]	%Mass X_direct.	%Mass Y_direct.	%Mass Z_direct.
1	0.213	0	50.51	0
2	0.409	0	49.05	0
3	0.416	99.29	0	0.09
4	1.07	0.33	0	33.59
5	1.18	0	0.03	0
6	2.64	0	0.01	0
7	3.97	0.01	0	48.34

Table 2: Main results from modal analyses in load condition 1,a).

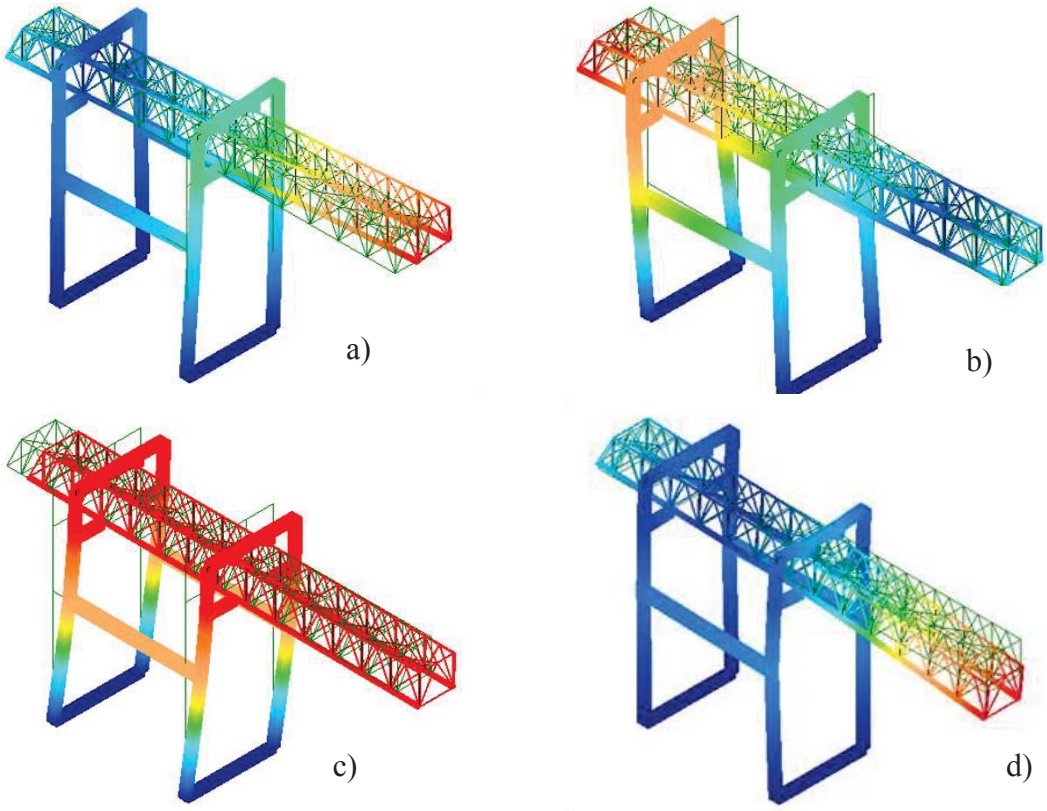

Figure 6: Crane displacement in corresponding of each vibration mode. a) 0.213 Hz, b) 0.409 Hz, c) 0.416 Hz) and d) 1.07 Hz.

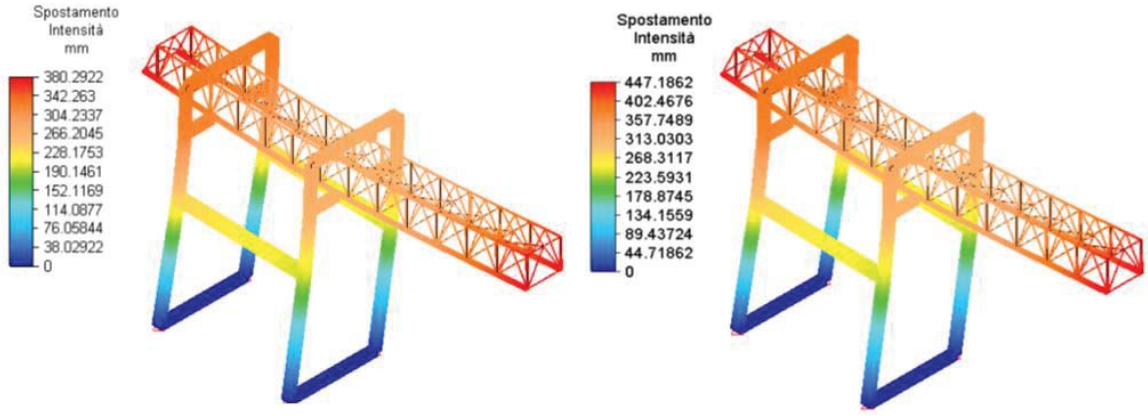

Figure 7: Crane displacements in the second load configuration assumed, subjected to PGA=0.15g and PGA=0.25g.

The modal results for other loads conditions are comparable with the previous reported. Figure 7 shows the displacement in the crane in the second load condition subjected to the load spectrum with PGA=0.15g. and with PGA=0.25g. It is important to underline that the crane trend deformation is obviously equal.

Table 3 reports the maximum displacement and the safety factor (respect to the yield strength) for the four load / geometrical conditions subjected to the static action and different earthquake magnitude.

	Load condition 1		Load condition 2		Load condition 3		Load condition 4	
PGA/Static	Max dis-placement [mm]	Safety factor	Max dis-placement [mm]	Safety factor	Max dis-placement [mm]	Safety factor	Max dis-placement [mm]	Safety factor
PGA=0.35g	902.6	0.56	764.2	0.54	750.7	0.54	828.1	0.61
PGA=0.25g	528.5	0.96	447.3	0.92	439.9	0.91	485.2	1.09
PGA=0.15g	449.3	1.15	380.5	1.09	373.9	1.08	412.4	1.22
STATIC	125.3	1.98	273.8	1.17	92.8	2.31	71.4	3.43

Table 3: Main results from static and earthquake analyses for different load conditions.

3 INTRODUCTION TO ANTI SEISMCI SYSTEM AND TECHNOLOGIES

As known, the anti-seismic system is a classical device mainly applied in the civil field; these components must dissipate the earthquake energy. In synthesis, the seismic isolation consists in decoupling the movement of the structure, usually only in horizontal plane, from that of the ground. This operation can be performed by inserting at the base an extremely flexible device and / or sliding ones or even rolling ones. With these components, the structure can move rigidly in the horizontal plane. The seismic dissipation consists in the insertion of several dampers in specific structure's points.

.

3.1 Choice criterion adopted

It is important to underline that the isolation device, adopted in order to reduce the stresses state magnitude on crane induced by earthquake, must not compromise the crane performance.

In another word, for example, it is important that the crane displacement isn't excessive to limit the increase of the pendulum load phenomenon, the time for load and unload the container, and so on. The finale product adopted (choose after several iterative analyses) consists of alternate layers of rubber and vulcanized reinforcement steel plate of limited thickness [28,29]. The commercial product reported in [30] can be applied to the cranes legs modifying the supports. The main parameter of this isolation device adopted is the horizontal stiffness, which is equal to 2kN/mm. This spring element was applied at the base of each crane leg.

After that the spring elements were included in the crane finite element model, the previous analyses were carried out again, in order to evaluate the seismic isolation device effects on the crane mechanical behaviour. The main results are reported in the table 4.

Table 4 shows the same results reported in the table 3 but in this case, the analyses consider the anti-seismic impact.

	Load condition 1		Load condition 2		Load condition 3		Load condition 4	
PGA/Static	Max displacement [mm]	Safety factor	Max displacement [mm]	Safety factor	Max displacement [mm]	Safety factor	Max displacement [mm]	Safety factor
PGA=0.35g	915.9	0.71	767.1	0.68	757.6	0.67	835.7	0.73
PGA=0.25g	536.7	1.20	450.3	1.10	443.9	1.14	489.7	1.24
PGA=0.15g	456.2	1.41	381.4	1.19	377.3	1.34	416.2	1.46
STATIC	125.8	1.98	274.5	1.21	92.8	2.31	72.1	3.49

Table 4: Main results from static and earthquake analyses for different load conditions.

4 INERTIA ACTIONS

As reported in the previous chapters, the implementation of the anti-seismic device reduces the maximum actions on the crane. Its effect is positive, in fact, it decreases the maximum stress values, avoid the possibility to make plastic hinge in the specific point of structure, reduce the overturning moment that can make the crane collapse and so on.

It is important to underline that the crane is subjected to many different inertia action induce by load and trolley movement as reported in the introduction paper. The maximum displacement and the payload oscillation must be limited in order to not increase, for example, the time for loading and unloading the container (for this specific crane). The choice of the anti-seismic device must take into account this phenomenon and so the apparatus adopted is a compromise between the positive effect (reduce the stress values) and the maximum crane displacement due to the trolley and payload movements.

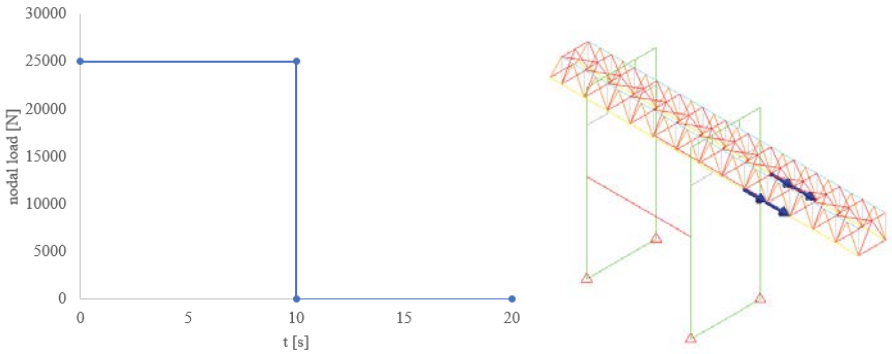

Figure 8: Trend of inertia action and schematic fem model.

This chapter reports the numerical results for the crane subjected to inertial action and compare the crane performance with and without the anti-seismic device applied to it. It is important to underline that, for this load condition reported, the main inertia actions are in the arm direction due to the trolley and the payload movements. For the study of this phenomenon, it was assumed that the inertia action is equal to 100000 N. This value corresponds to acceleration payload and trolley equal to a=2m/s2. The trend of this action is reported in figure 8 and it refers to start and stop the trolley movement.

Figure 9 reports the maximum crane displacement with and without the anti-seismic device.

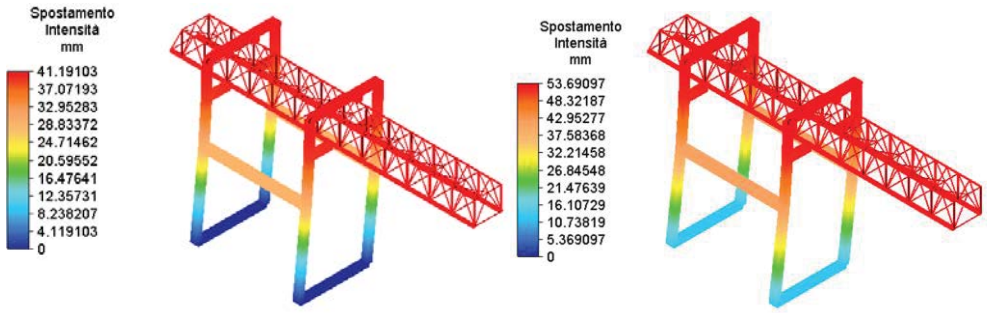

Figure 9: Maximum crane displacement a) without anti-seismic device and b) with it (in the static load applied).

Figure 10 shows the displacement trend in horizontal direction for crane with and without the anti-seismic device, subjected to the external action reported in figure 6.

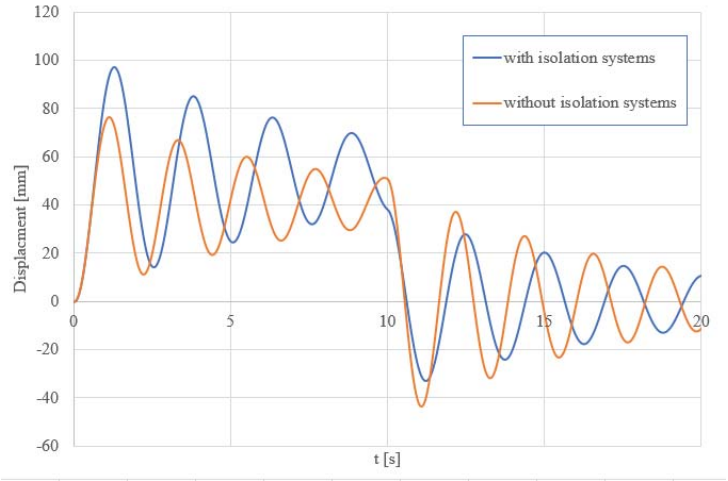

Figure 10: Crane displacement to the variable inertia action.

5 RESULTS

The main results of this research in order to evaluate the anti-seismic effects on the crane studied are reported in the previous tables and graphs and can be summarized with these points. The worst load condition is n°2 and corresponds to the arm at seaside position with payload (and trolley) applied at the end. With the minimum earthquake action (PGA=1.4), for all load conditions, the maximum stress value is near the material yield strength. The anti-seismic device reduces the maximum stress values and increases the safety factor about 20% especially in the case with the earthquake actions. In static load condition (for all configurations) the anti-seismic device shows a minimum and negligible effect. The variation in the natural frequencies values in the cases with and without isolation systems is negligible. In the

case of actions variable over time (like moving the payload), it is possible to observe an increase in the displacement value but this new trend can be easily taken into account to design the trolley movement control.

6 CONCLUSIONS

This research reports the main numerical results for a big ship to shore low profile crane with the seismic device applied at the crane base. The results of finite element analyses carried out show that the implementation of specific anti-seismic device caused a general lowering of the natural frequencies, that leads to maximum stress reduction and increase the displacements. However, the movements are not so high to prejudice the crane performance and usefulness of the isolation systems. With the specific isolation device implemented, the maximum displacements (for different geometrical and load conditions of crane) are comparable. It is very important to highlight that the final isolation system device chosen do not significantly increases the crane translation due to the inertial actions and so the crane performance in term of container movement per hour do not change. The different displacement trend can be easily implemented in the control system for the trolley movement in order to unchanged the crane productivity. The results of this feasibility study with the aim of implementing the isolation device to low profile container crane are encouraging. The research is still in progress in order to study both the crane mechanical behaviour subjected to earthquake with isolation device for different crane types, and the methodology adopted to choose the best isolation system device.

REFERENCES

[1] L. Solazzi, Experimental and analytical study on elevating working platform, *Procedia Engineering* 199, 2597-2602, 2017.

[2] L. Solazzi, N. Zrnic, Design a high capacity derrick crane considering the effects induced by load application and release, *Journal of Applied engineering Science* 15(1), 15-24, 2017.

[3] L. Solazzi, G. Incerti, C. Petrogalli, Estimation the dynamic effect in the lifting operations of a boom crane, *Proceedings - 28th European Conference on Modelling and Simulation,* ECMS 2014, 309-315, 2014.

[4] Z. A. Qiao, y. G. Sun, D. S. Dong, Research on Elastic Effect of the Frame Excited by Inertia Load of the Trolley, *8th Annual IEEE International Conference on Cyber Technology in Automation, Control and Intelligent Systems*, CYBER 2018, 10 April 2019, Article number 8688141, 867-872b, 2018.

[5] I. A. Lagerev, Research of dynamics of hydraulic loader crane in case of conjoint movement of sections, *Lecture Notes in Mechanical Engineering* 0, 2283-2293, 2019.

[6] L. Solazzi, M. Cima, Structural dynamics of big gantry crane subjected to different trolley move, *Journal of Physics: Conference Series* 164 (1), 24 July 2019, Article number 012046, 2019.

[7] L. Solazzi, C.Remino, G. Incerti, Overhead crane subjected to impulse loading, *Journal of Physics: Conference Series* 1264 (1), 24 July 2019, Article number 012045, 2019.

[8] H. Jiang, Y. Li, Dynamic Reliability Analysis of Tower Crane with Wind Loading, IOP *Conference Series: Materials Science and Engineering* 677(5), 2019.

[9] L. Solazzi, Stochastic wind loading applied to container crane, *FME Transaction* 46(3), 299-305, 2018.

[10] L. Solazzi, N. Zrnic, Numerical study of wind actions applied to a low profile container crane, *FME Transaction* 44(1), 29-35, 2016.

[11] P. Wang, L. Yu, W. Han, H. Tang, F. Yan, D. Zhao, Analysis on response of tower crane structures under random earthquake excitations, *Jixie Qiangdu /Journal of Mechan-ical Strength* 38 (1), 192-196, 2016.

[12] L. Solazzi, Ship to shore subjected to earthquake, *Procedia Engineering* 10, 2690-2695, 2011.

[13] M. A. Jordan, The 1995 Kobe Earthquake, *Liftech Consultants Inc*., 1995.

[14] V. Santiago-Fandiño, S. Sato, N. Maki, K. Iuchi, *The 2011 Japan Earthquake and Tsunami: Reconstruction and Restoration, Springer,* ISBN 978-3-319-58690-8, 2018.

[15] E. Soderberg, M. Jordan, Seismic response of jumbo container cranes and design recommendations to limit damage and prevent collapse, *Ports 2007: 30 Years of Sharing Ideas 1977-2007; Proceedings of the Eleventh Triennial International Conference*, 2007.

[16] G. Wang, Z. Li, D. Wang, J. Hu, Overview of test methods of seismic dynamic behavior of jumbo container cranes, *Wuhan Ligong Daxue Xuebao (Jiaotong Kexue Yu Gongcheng Ban)/Journal of Wuhan University of Technology (Transportation Science and Engineering)* 38(2), 267-272, 2014.

[17] L. D. Jacobs, R. DesRoches, R.T. Leon, Experimental study of the seismic response of container cranes, *Ports 2010: Building on the Past, Respecting the Future - Proceedings of the 12th Triannual International Conference*, 91-99, 2010.

[18] Y.L. Jin, X.K. Zhang, Experimental seismic analysis of a quayside container crane structure using a scaled model, *Proceedings of the Institution of Mechanical Engineers. Part I: Journal of Systems and Control Engineering* 227(8), 645-661, 2013.

[19] A. Yang, Y.P. Jin, Seismic shaking table tests of large quayside container crane, *Zhongguo Jixie Gongcheng/China Mechanical Engineering* 24(4), 437-444, 2013.

[20] N. Kobayashi, K.P. Hakamada, Parallel link type seismic isolator for tower crane, *Nihon Kikai Gakkai Ronbunshu, C Hen/Transactions of the Japan Society of Mechanical Engineers, Part C* 73(8), 2204-2210, 2007.

[21] K. Lu, W. Zhang, Z. Wu, H. Qiu, Anti-seismic device design for container crane and its model test, *Zhendong Ceshi Yu Zhenduan/Journal of Vibration, Measurement and Diagnosis* 31(4), 501-506, 2011.

[22] P. Zheng, Container crane seismic isolation device design method based on structural dynamics, *Applied Mechanics and Materials* 353-354, 1819-1825, 2013.

[23] H. Estrada, L.S. Lee, Introduction to Earthquake Engineering, *Taylor & Francis, CRC Press,* ISBN 9781498758260, 2017.

[24] F. Hejazi, K. Karimzadeh, Analysis Procedure for Earthquake Resistant Structures, *Springer Nature*, ISBN 9789811088384 2018.

[25] R. Landolfo, F. Mazzolani, D. Dubina, L. Simões da Silva, M. D'Aniello, Design of steel structures for buildings in seismic areas, *ECCS – European Convention for Constructional Steelwork*, ISBN (ECCS): 978-92-9147-138-6, 2017.

[26] F. Naeim, The seismic design handbook, 2 ed., *Springer Science + Business Media*, ISBN 978-1-4613-5681-3, 2001.

[27] G. P. Cimellaro, S. Marasco, Introduction to Dynamics of Structures and Earthquake Engineering, *Springer International Publishing*, ISBN 978-3-319-72540-6, 2018.

[28] J. M. Kelly, D. A. Konstantinidis, Mechanics of Rubber Bearings for Seismic and Vibration Isolation, *John Wiley & Sons*, ISBN 978-1-119-99401-5, 2011.

[29] D. Dong, J. Li, Y. Teng, Anti-Seismic Device Design for Container Crane and its Elastic-Plastic Time History Analysis, *Polish Maritime Research*, 22(s1), pp. 30-34, 2015.

[30] www.freyssinet.com

EURODYN 2020
XI International Conference on Structural Dynamics
M. Papadrakakis, M. Fragiadakis, C. Papadimitriou (eds.)
Athens, Greece, 23–26 November 2020

STEEL TRUSS BRIDGE WITH BUCKLING RESTRAINED DAMPER UNDER SEISMIC LOADING

Purevdorj Sosorburam[1] and Eiki Yamaguchi[2]

[1] Department of Civil Engineering, Kyushu Institute of Technology
Kitakyushu, Japan
e-mail: sosorburam.purevdorj277@mail.kyutech.jp

[2] Department of Civil Engineering, Kyushu Institute of Technology
Kitakyushu, Japan
yamaguch@civil.kyutech.ac.jp

Keywords: Steel Truss Bridge, Seismic Performance, Buckling Restrained Damper, Nonlinear Dynamic Analysis

Abstract. *The buckling restrained bracing (BRB) is widely used to improve the seismic behavior of a building. It is employed for a bridge as well, but the application is very limited. The BRB device may also be used as a damper rather than the structural component or the bracing, in which case the device is called a buckling restrained damper (BRD). Yet, such application has not been explored much. There are quite a few bridges designed according to the old seismic design codes in Japan. Their seismic resistance may not be satisfactory for the current seismic design codes. Against this background, the behavior of a steel truss bridge under a large seismic load is investigated by nonlinear dynamic finite element analysis. Some members are indeed found possibly damaged in the earthquake. Retrofitting is therefore needed. To this end, the application of the BRD is tried in the present study. A parametric study on the seismic behavior of the truss bridge with the BRD is conducted by changing the length and the cross-sectional area of the yielding core of the BRD, to this end. The FEA show that the BRD surely improves the seismic performance of the truss bridge and with some BRDs, all the members could stay intact. The points to note for the application of the BRD are also revealed.*

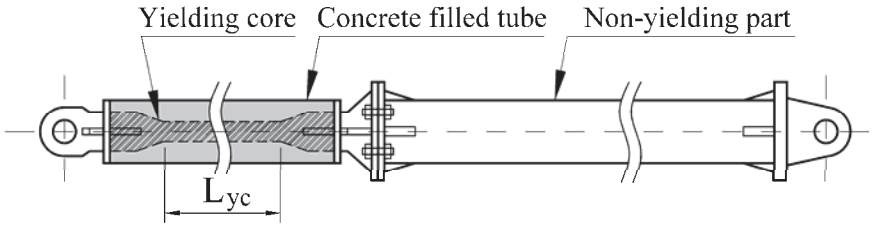

Figure 1: Buckling restrained damper (BRD).

1 INTRODUCTION

Many bridges were damaged by the earthquake in the past. The damage was investigated in the aftermath, and seismic design codes were upgraded whenever found necessary [1, 2]. It is noted that the 1995 Kobe Earthquake was the most influential in the revision of the Japanese seismic design codes.

New bridges are designed by the revised design codes. Existing bridges due to the old seismic design codes need be investigated to see if they satisfy the requirements of the revised seismic design codes. If the performance is not satisfactory, the bridge would be retrofitted.

There are various ways to improve seismic performance. One of the commonly employed methods is to install dampers. A typical type is a fluid viscous damper. For the building, the buckling restrained bracing (BRB) is getting popular [3]. It is basically a structural member, a bracing, and it undergoes plastic deformation in large seismic loading. Buckling is prevented by limiting the lateral displacement so that seismic energy is absorbed by the plastic deformation both in tension and compression. The application of the BRB to the bridge has been studied [4], yet it is still very limited.

The BRB device is not necessarily used just as a bracing; It could be used as a damper, which is then called a buckling restrained damper (BRD). In the present study, the application of the BRD is explored for retrofitting a truss bridge that does not satisfy the requirements of the current seismic design codes. A parametric study of the BRD is to be carried out to reveal its effectiveness on the seismic performance of the bridge.

The BRD is illustrated in Figure 1. Only a part of the BRD undergoes plastic deformation and absorbs seismic energy. This part is called the yielding core. The remaining part stays elastic and its deformation is small. In this study, the latter is assumed rigid. The length and the cross-sectional area of the yielding core are treated as parameters and several values are given to them. For all the analyses, ABAQUS [5]is used.

2 SAFETY EVALUATION

2.1 Safety evaluation

A simply supported steel truss bridge is dealt with in the present study. Figure 2 shows the truss with node numbers. The node numbers at the centers of the lateral members are neglected for the sake of clarity. The dimensions of the cross sections and the steel grades are given in Table 1. The yield strengths σ_y of SM490Y and SM400 are 355 N/mm^2 and 235 N/mm^2, respectively. Young's modulus E of the steel is 2.0×10^5 N/mm^2, Poison's ratio is 0.3 and the mass density is 7.85 t/m^3. Beyond the yield strength, the steel shows elastic-plastic behavior, which is modelled as the von Mises material with the kinematic hardening rule. The tangent stiffness beyond the yield strength in uniaxial tension is assumed E/100.

The truss bridge is supported by the hinge at Nodes 1 and 2, while Nodes 25 and 26 are supported by the roller so that these nodes can move in the longitudinal direction. The bridge

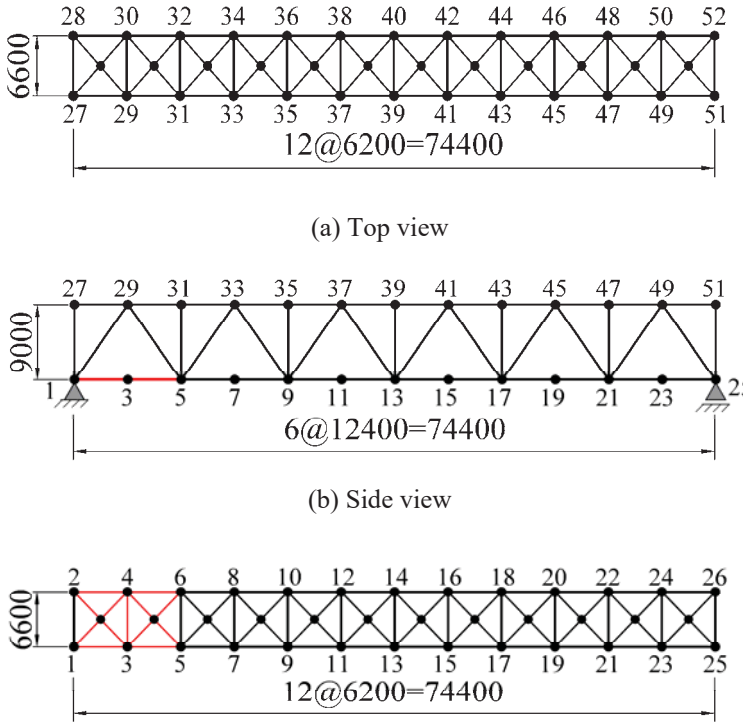

(a) Top view

(b) Side view

(c) Bottom view

Figure 2: Truss bridge model (mm).

has a reinforced concrete deck of 10.60 m in width and 200 mm in thickness on the upper chords.

The damage in the concrete deck wouldn't be so serious in general and the repair wouldn't be so difficult if any. The deck is therefore treated as an elastic body for the sake of simplicity. Young's modulus of the concrete is 2.1×10^4 N/mm^2, Poison's ratio is 0.2 and the mass density is 2.35 t/m^3.

Damping factors are 2% for the truss members and 3% for the concrete deck. Rayleigh damping is employed. 3-D beam elements B33 are used for the truss members, and shell elements S4R are for the concrete deck. In total, 1180 beam elements and 168 shell elements are employed for modelling the truss bridge.

2.2 Seismic performance

The seismic behavior of the truss bridge under seismic loading is obtained by the nonlinear dynamic analysis. The seismic loading recorded in the 2005 Niigata-Ken Chuetsu Earthquake (Figure 3) is applied in the longitudinal direction.

Following Specifications for Highway Steel Bridges [6], the safety is judged by the following equations:

$$R_t = \sigma/\sigma_y \quad \text{under tension} \tag{1}$$

$$R_c = \sigma/\sigma_{cr} \quad \text{under compression} \tag{2}$$

where σ is the induced axial normal stress and σ_{cr} is the compressive strength. The violation of the inequality (1) indicates that the member yields; the violation of the inequality (2) implies that local buckling takes place.

Table 1: Truss member

Members	Cross Section	Web (mm)	Flange (mm)	Steel Grade
1–5, 21–25, 2–6, 22–26		430 × 9	450 × 10	SM400
5–9, 17–21, 6–10, 18–22		412 × 22	450 × 19	SM490Y
9–17, 10–18		400 × 25	450 × 25	SM490Y
27–33, 45–51, 28–34, 46–52		518 × 14	450 × 16	SM490Y
33–37, 41–45, 34–38, 42–46		506 × 19	450 × 22	SM490Y
37–41, 38–42		502 × 21	450 × 24	SM490Y
1–29, 49–25, 2–30, 50–26		412 × 28	400 × 19	SM490Y
5–33, 45–21, 6–34, 46–22		418 × 22	400 × 16	SM400
9–37, 41–17, 10–38, 42–18		430 × 13	400 × 10	SM400
1–27, 2–28, 25–51, 26–52		430 × 13	400 × 10	SM400
29–5, 21–49, 30–6, 22–50		422 × 14	350 × 14	SM490Y
37–13, 13–41, 38–14, 14–42		430 × 11	350 × 10	SM400
33–9, 17–45, 34–10, 18–46		422 × 12	350 × 14	SM400
5–31, 6–32, etc.		422 × 12	350 × 14	SM400
25–52, 26–51, 1–28, 2–27		318 × 16	350 × 16	SM400
27–30, 28–29, etc.		138 × 10	350 × 14	SM400
1–4, 2–3, and etc.		180 × 10	200 × 10	SM400
27–28, 39–30, etc.		1068 × 10	350 × 16	SM400
1–2, 25–26		424 × 10	400 × 13	SM400
3–4, 5–6, etc.		230 × 10	250 × 10	SM400
5–32, 6–31, 21–48, etc.		140 × 16	250 × 10	SM400

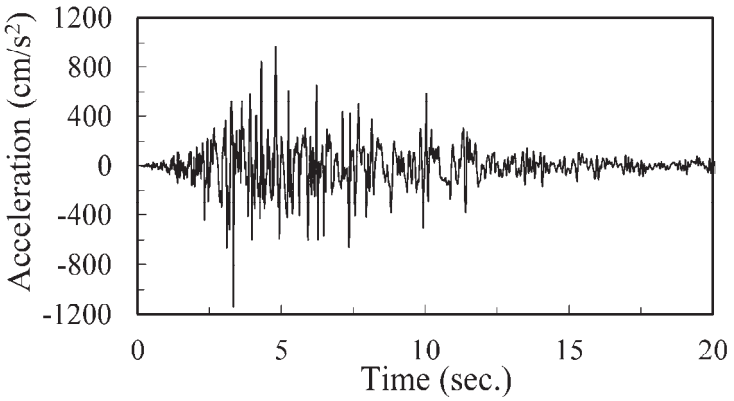

Figure 3: 2004 Niigata-Ken Chuetsu Earthquake.

The nonlinear dynamic analysis reveals that the members highlighted in red in Figure 2 would be possibly damaged, as the violation of Eq. (1) and/or Eq. (2) are/is found. The largest R_c is 1.21, which is observed in Members 1-3 and 2-4; the largest R_t is 1.07 which occurs also in Members 1-3 and 2-4.

3 INSTALLATION OF BRDS

3.1 BRD model and locations

For the yielding core of the BRD, LY225 is used. LY225 is a steel grade with Young's modulus 2.0×10^5 N/mm^2, Poisson's ratio 0.3 and the yield strength 225 N/mm^2. It exhibits the elastic-plastic behavior of the von Mises material with the kinematic hardening rule. The tangent stiffness beyond the yield strength in uniaxial tension is 3E/100.

The BRD is made in such a way that the buckling is prevented. Therefore, the yielding core is modeled by a single truss element T3D2.

Two BRDs are installed to the truss bridge near the lower chords possibly damaged. One end of one of the BRDs is set at the bridge abutment close to Node 1 and the other end is connected to Node 5. The other BRD is set between the bridge abutment close to Node 2 and Node 6.

3.2 Parametric study

To study the effective use of the BRD, a parametric study is conducted. Two parameters are considered, the length of the yielding core L_{yc} and the cross-sectional area of the yielding core A_{yc}. Specifically, the following values are considered herein:

$$L_{yc} = 1750,\quad 3500,\quad 7000,\quad 10500 \text{ mm}$$
$$A_{yc} = 5000,\quad 10000,\quad 20000,\quad 30000 \text{ mm}^2$$

The combination of these values results in 16 different BRDs. The BRD is named using the values of the parameters. For example, the BRD with L_{yc} = 1750 mm and A_{yc} = 5000 mm^2 is called BRD 1750-5000.

3.3 Effectiveness

The nonlinear dynamic analysis of the truss bridge with the BRD is conducted. It is found that the BRD surely improves the seismic performance of the bridge. The improvement of R_c

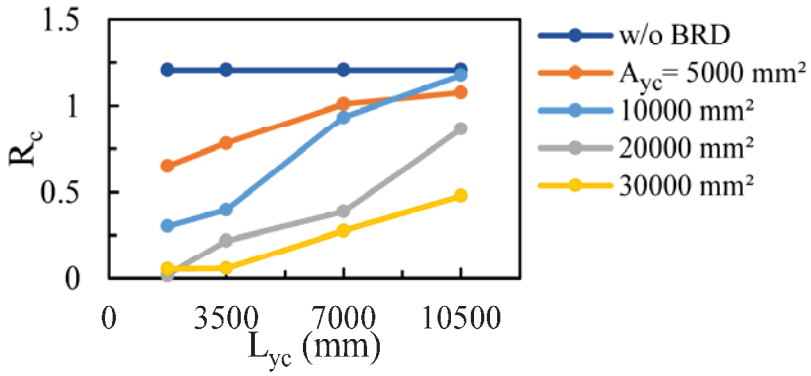

(a) Influence of L_{yc}

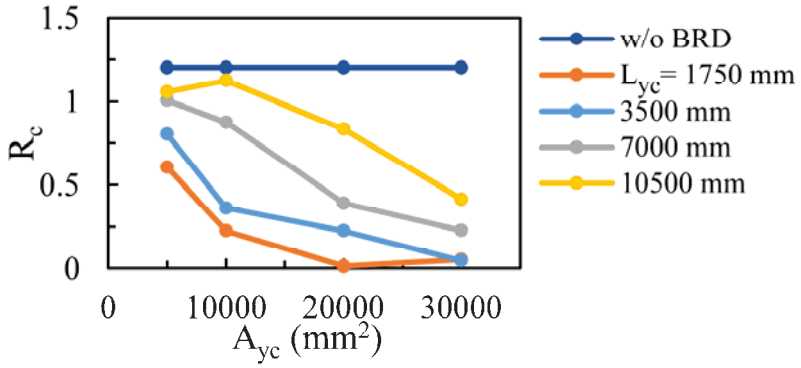

(b) Influence of A_{yc}

Figure 4: Effectiveness of BRD (Member 1-3).

is summarized in Figure 4. Through the parametric study, the following observations are made:

1. BRD is more effective with a shorter L_{yc};
2. BRD is more effective with a larger A_{yc};
3. The reduction in R_c is more pronounced than in R_t.

Obviously both parameters have a significant influence on the seismic performance of the truss bridge. However, the way they work is different.

Figures 5 and 6 show the time-history response with the BRDs. Figures 5 is the result with BRD 1750-5000, and Figures 6 is with BRD 10500-30000. In the former, the BRD is effective because it is short while the latter is effective because the cross-sectional area is large. In both figures, the stress in the truss member is the normal stress in the axial direction in the upper flange.

BRD 1750-5000 undergoes plastic deformation and absorbs seismic energy. Large strain occurs. The stress in Member 3-5, inside the BRD range, is reduced. The stress in Member 5-7, outside the BRD range, increases a little.

On the other hand, the strain in BRD 10500-30000 is small and the BRDs stay in an elastic state. Seismic energy is not absorbed at all. Yet the stress in Member 3-5 is reduced considerably, which is attributable to the large stiffness of the BRD. The significant increase in the stress in Member 5-7 is noted.

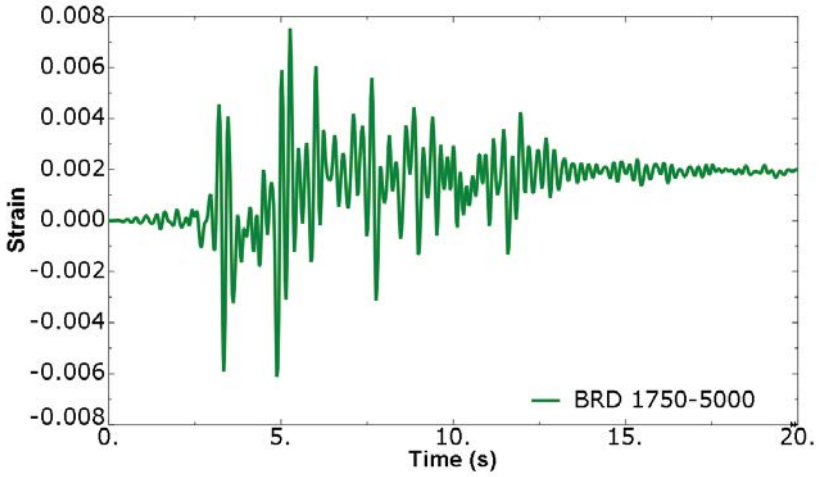

(a) Strain in yielding core

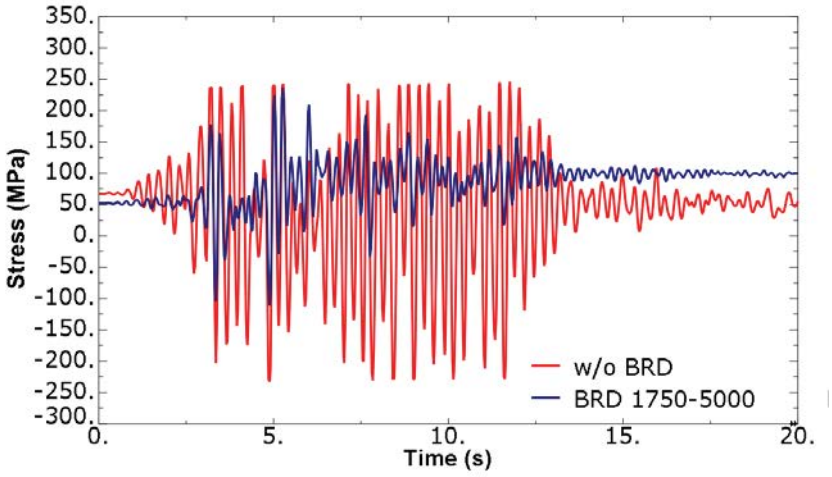

(b) Stress in Member 3-5

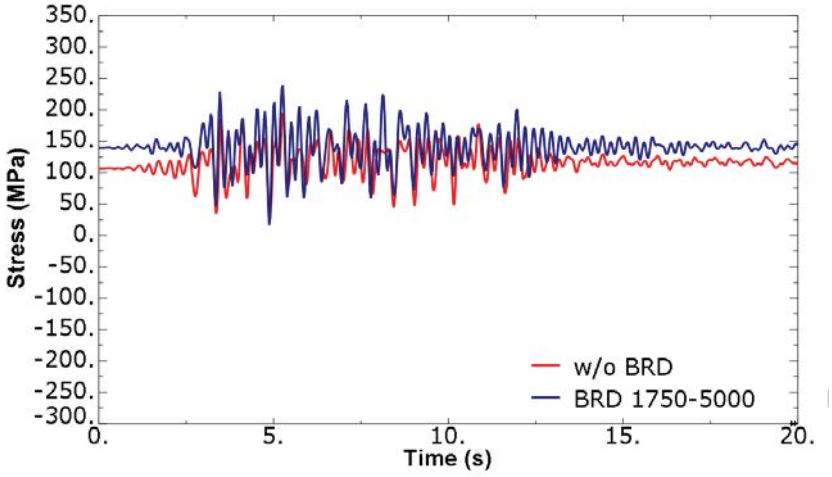

(c) Stress in Member 5-7

Figure 5: Seismic response with BRD 1750-5000.

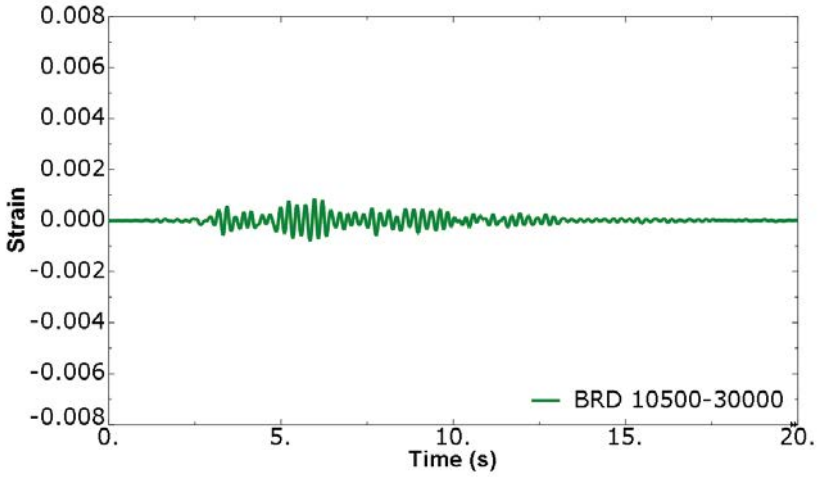

(a) Strain in yielding core

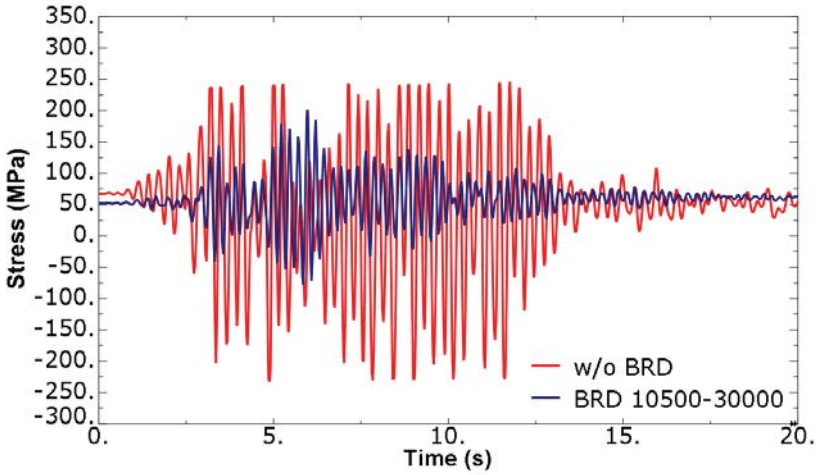

(b) Stress in Member 3-5

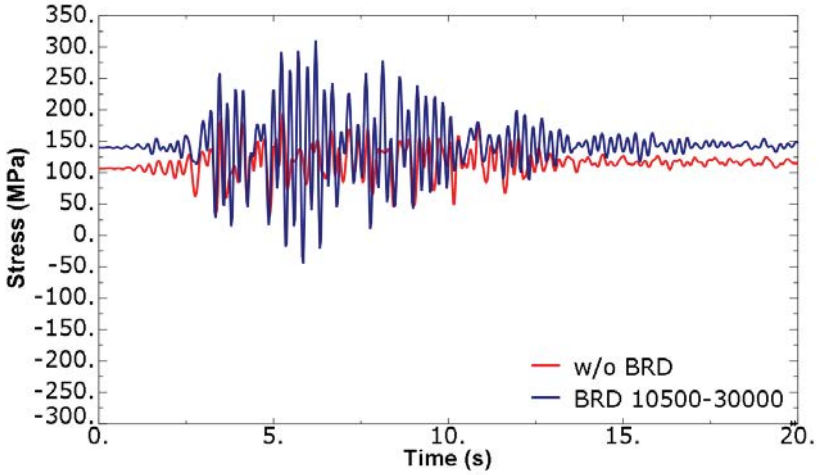

(c) Stress in Member 5-7

Figure 6: Seismic response with BRD 10500-30000.

Table 2: Seismic performance of truss bridge.

(a) R_c

		A_{yc} (mm^2)			
		5000	10000	20000	30000
L_{yc} (mm)	1750	Intact	Intact	Intact	Intact
	3500	Intact	Intact	Intact	Intact
	7000	Damaged	Intact	Intact	Intact
	10500	Damaged	Damaged	Intact	Intact

(b) R_t

		A_{yc} (mm^2)			
		5000	10000	20000	30000
L_{yc} (mm)	1750	Damaged	Damaged	Intact	Intact
	3500	Damaged	Damaged	Intact	Intact
	7000	Damaged	Damaged	Damaged	Intact
	10500	Damaged	Damaged	Damaged	Damaged

Summary of the seismic performance is given in Table 2. "Damaged" indicates that some members violate Eq. (1) and/or Eq. (2). "Intact" means all the members satisfy Eqs. (1) and (2): with some BRDs, no damage would occur in this truss bridge.

4 CONCLUDING REMARKS

The BRB device was applied to the truss bridge as a damper. The nonlinear dynamic analysis of the truss bridge has revealed that the BRD could improve the seismic performance considerably. It was found that with the shorter length and the larger cross-sectional area, the BRD works more effectively. With proper BRDs, the truss bridge could stay intact even under rather large seismic loading.

Both the length and the cross-sectional area influence the seismic performance of the bridge. A short yielding core absorbs seismic energy, but it may undergo large strain repeatedly; Low-cycle fatigue may take place. A larger cross-sectional area of the yielding core reduces the stress in the member inside the BRD range while the stress outside the BRD range increase noticeably. Those negative aspects must be taken into account carefully in the application of the BRD.

REFERENCES

[1] K. Kawashima, S. Unjoh, Seismic design of highway bridges, *Journal of Japan Association for Earthquake Engineering*, 4 (3), 283-297, 2004.

[2] J. Hoshikuma, Z. Guangfeng, Performance of seismic retrofitted highway bridges based on observation of damage due to the 2011 Great East Japan Earthquake, *Journal of JSCE*, 1, 343-352, 2013.T. Takeuchi, A. Wada, *Buckling Restrained Braces and Applications*, The Japan Society of Seismic Isolation, 2017.

[3] T. Usami, Z. Lu, H. Ge, A seismic upgrading method for steel arch bridges using buckling-restrained braces, *Earthquake Engineering & Structural Dynamics*, 34, 471-496, 2005.

[4] Dassault Systemes Simulia Corp., *User's Manual*, *ABAQUS Ver*. 6.13, 2013.

[5] Japan Road Association, *Specifications for Highway Bridges*, *Part II Steel Bridges and Steel Members*, 2017.

EURODYN 2020
XI International Conference on Structural Dynamics
M. Papadrakakis, M. Fragiadakis, C. Papadimitriou (eds.)
Athens, Greece, 23–26 November 2020

MONOTONIC AND CYCLIC BEHAVIOUR OF THE BEAM-TO-COLUMN JOINTS OF THE "FUTURE" MOCKUP

R. Tartaglia[1], **M. D'Aniello**[1], **and R. Landolfo**[1]

[1] Department of Structures for Engineering and Architecture, University of Naples Federico II
Via Forno Vecchio Naples Italy
e-mail: roberto.tartaglia@unina.it, mdaniel@unina.it, landolfo@unina.it

Keywords: Steel structures, Moment resisting, FE analyses, Joint.

Abstract. *The non-linear behavior of beam-to-column joints may significantly influence the seismic performance of steel moment resisting frames (MRFs). The current Eurocodes does not give detailed rules for seismic-resistant joints, but the next version of EN1998 will provide specific rules for pre-qualified joints whose background was matured within the RFCS research project "EQUALJOINTS". Recently the research project "FUTURE" has been approved within the "H2020-INFRAIA-01-2016-2017 Research Infrastructure for Earth-quake Hazard". In this project shake table tests will be carried out on a two-storey one bay MRF equipped with the beam-to-column joints prequalified according to EQUALJOINTS procedure, namely haunched joint, dog-bone and the extended stiffened joint. In this paper, the behaviour of joints under both monotonic and cyclic loads is investigated in order to verify the effectiveness of the design procedure. Parametric analyses were also carried out to investigate the influence of the finger shims on both non-linear behaviour of the joints. The results show that the design criteria are effective to guarantee the required performance of the joints and, despite the cumulative plastic deformation in the dissipative elements, the introduction of the finger shims are useful for the dismantling phase.*

1 INTRODUCTION

The seismic response of steel moment resisting frames (MRFs) is largely influenced by the behaviour of joints. At the current stage, EN1993-1-8 [1] does not give detailed rules for seismic-resistant joints. EN 1998-1 [2] allows using dissipative joints, provided that the design is supported by testing, which results in impractical solutions within the time and budget constraints of real-life projects. Even though the lack of analytical models to predict the joints behaviour to meet code requirements is more evident for dissipative beam-to-column connections, reliable design tools for non-dissipative connections are also necessary. These criticisms have been recently overcome for a set of bolted joints that were studied within the European research project "EQUALJOINTS" [5].

Steel MRFs are also sensitive to the combined effects of the coupling between vertical and horizontal components of earthquake ground motions [6-9]. Indeed, differently from far-field input, the combined components of strong earthquake motions may (i) change the axial forces in columns, (ii) increase bending moment and shear force demands in the connections, (iii) amplify plastic deformations, (iv) extend plastic hinge formations and (v) reduce the available ductility of dissipative zones.

Besides the joints and the effects induced by vertical ground motions (VGMs), also the design requirements of EC8 largely influence the response and the efficiency of steel MRFs. In particular, it is generally recognized that the drift limitations (i.e., damage limitation checks at serviceability limit state) often impose an increase of the lateral stiffness of MRF, hence the increase of beam and column sizes to satisfy such requirement typically results in significant design overstrength and non-economical solutions [9]. Indeed, EC8 compliant MRFs may be generally massive and expensive structures [10], due to the large consumption of steel. In addition, the larger are the beam-column shapes the more difficult and expensive is the manufacturing of the joints. Provided that the overall stability of the structure is guaranteed, the possibility to increase the drift limitations (e.g. from 0.75% up to 1.5% of the inter-storey height) can be beneficial to optimize the design and to improve the structural efficiency by reducing the design overstrength. This can be achieved through the application of special ductile claddings that are able to accommodate large interstorey drift ratios, higher than 1.5% [11]. The increase of lateral deformability may con-tribute to a greater sensitivity of the frames to P-Delta effects.

However, it is well recognized that the current EC8 provisions concerning the control of P-Delta effects is extremely conservative and excessively penalising for steel frames since it does not account for the material overstrength, the design over-strength and the hardening effects associated with redundancy and plastic redistribution [10].

In the light of the considerations discussed above concerning the criticisms of EC8, the European research project FUTURE (acronym of Full-scale experimental validation of steel moment frame with EU qualified joints and energy efficient claddings under Near fault seismic scenarios) has been recently financed. The main objectives of the project FUTURE are the investigation of seismic response of steel MRFs accounting for different types of prequalified beam-to-column joints as well as the role of ductile claddings under NF earthquakes. To this end, comprehensive shake table tests on specifically conceived mock-up have been planned. The mock-up is designed to be used in several experimental tests, after the substitution of damaged dissipative parts at the end of each them.

In this paper, the preliminary simulations to study

the influence of the finger shim plates on the monotonic and cyclic response of the beam-to-column joints of FUTURE mockup are presentented. This article is subdivided in three parts, as follows: in the first part some information about the project and the design of the

joints are reported; afterwards the modelling procedure is described. Finally, the results in terms of moment rotation curves and equivalent plastic deformations are reported.

2 THE FUTURE MOCKUP

The experimental mock-up is shown in Figure 1. The structure consists of a two storey steel MRF (5 m x 5 m) sub-structured from a reference archetype building. The mock-up is designed to detach and to replace easily all components that will experience plastic deformations, namely the column ends at the base level and the end portions of the beams with corresponding end-plate connections. The schematic view of reduced beam section (RBS), haunched (H) and extended stiffened (ES-E) are shown in Figure 2.

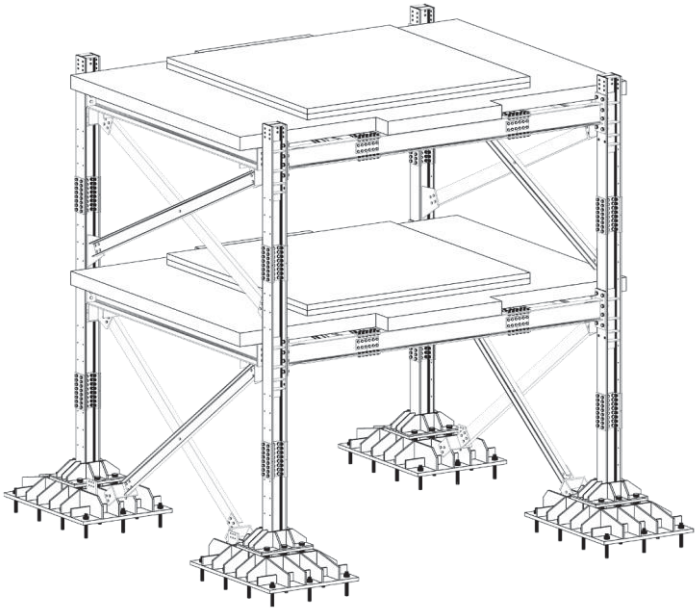

Figure 1: Experimental mock-up

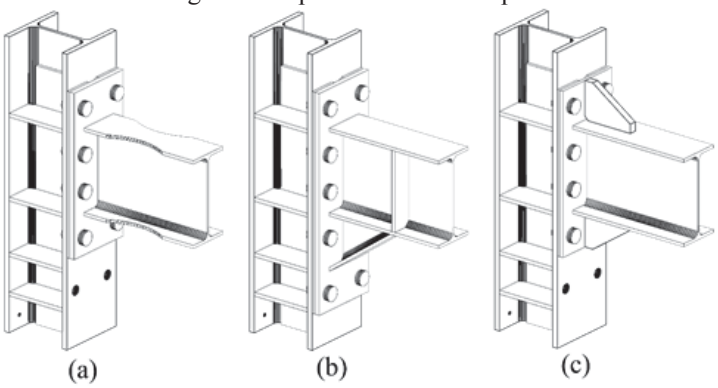

Figure 2: Investigated joints: a) Reduced beam section (RBS), b) Hunched (H) and c) Extended stiffened equal strength (ES-E)

3 THE INVESTIGATED BEAM-TO-COLUMN JOINTS

All investigated joints were designed according to the Equaljoints criteria [12]. In particular, the end-plate connections of haunched and RBS joints were designed as full-strength, namely to be stronger than the connected beam segment where plastic deformations are expected. ES joints were designed with equal strength connections, namely designed to guaran-

tee the contemporary yielding of both connection and beam. In addition, for all joint configurations the column web panel was de-signed to be stronger than the connected beam and connections in order to remain elastic during the whole experimental campaign. The capacity design requirements to obtain the required joint behaviour can be expressed by Eq. (1):

$$M_{wp,Rd} \geq M_{con,Rd} \geq M_{con,Ed} = \alpha \cdot (M_{B,Rd} + V_{B,Ed} \cdot s_h) \tag{1}$$

$$M_{wp,Rd} = V_{wp,Rd} \cdot z \tag{2}$$

In Equation 1, $M_{wp,Rd}$ is the flexural strength corresponding to the shear capacity of column web-panel (see Eq. (2), $V_{wp,Rd}$ is the column web shear resistance, z is the internal level arm, $M_{con,Rd}$ is the flexural strength of the connection zone, $M_{con,Ed}$ is the design bending moment at the column face, $M_{B,Rd}$ is the design bending strength of the beam, $V_{B,Ed}$ is shear force corresponding to the occurrence of the plastic hinge in the connected beam, s_h is the distance between the applied shear and the column face. α depends on the design performance level and it is given by $\gamma_{sh} \times \gamma_{ov}$ for the full strength joints, while equal to 1 for equal strength joints and to 0.8 for partial strength joints. (being γsh the hardening factor and γ_{ov} the ratio between the average and the characteristic yield stress of the steel) In the case of dissipative connections (i.e. equal and partial strength configurations), a further hierarchy criterion [12] was adopted in order to avoid the failure of the bolts, so that the design tensile strength of each bolt row should be larger than the strength of the connected plate accounting for both the random variability of its yield stress and the relevant strain hardening. This requirement is expressed by Eq. (3), being d the nominal bolt diameter, γ_{M0} and γ_{M2} the partial safety factors according to Eurocode 3.

$$t \leq \frac{0.42 \cdot d}{\sqrt{\gamma_{ov} \cdot \gamma_{sh}}} \cdot \sqrt{\frac{\gamma_{M0} \cdot f_{ub}}{\gamma_{M2} \cdot f_y}} \tag{3}$$

For each investigated joints two models were performed, namely one assumes the direct contact between the end-plate and the column flange and another con-siders the presence of finger shims that often are used for constructional reasons in the bolted beam-to-column joints (see Figure 3a).

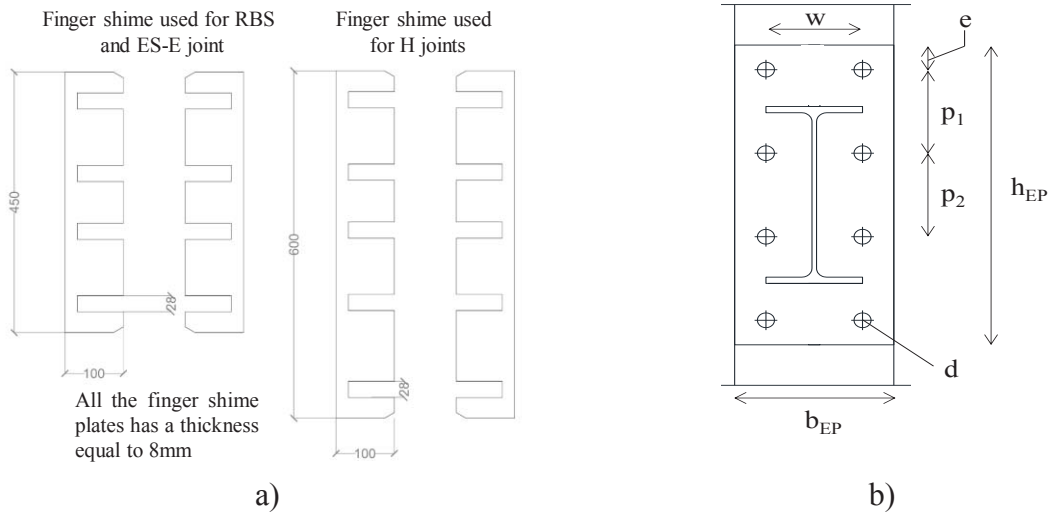

Figure 3: Geometric features of finger shims (a) and investigated connections (b).

The beam (IPE240A) and the column size (HEB200) are the same for all joint assemblies. Table 1 and Figure 3b reports the main geometrical features of all investigated joints. In addition, the rib introduced in the ES-E has a base of 135mm and a thickness of 15mm.

In the following, the results of both monotonic and cyclic analyses of each beam-to-column joint are reported in terms of moment rotation curves with also the distribution of the equivalent plastic deformation (PEEQ).

Joint Typologies	End plate			Bolts M16 grade 10.9				
	b_{EP}	h_{EP}	t_{EP}	d	e	p_1	p_2	w
	mm	mm	mm	mm	mm	mm	mm	mm
Reduced Beam section (RBS)	210	450	20	24	50	125	100	110
Hunched (H)	210	450	15	24	50	125	100	110
Extended stiffened joint (ES-E)	210	450	8	24	50	125	100	110

Table 1: Geometric features of the investigated joints

4 MODELLING ASSUMPTIONS

Finite element analyses (FEAs) were carried out using the finite element software ABAQUS 6.14 [13]; all details about the modelling procedure are reported in previous study of the Authors [14-17]. However, the main information about the modelling assumptions are summarized hereinafter.

All joints elements were discretized by C3D8I elements and a mesh sensitivity analyses was performed in order to choose the most appropriate mesh dimension (see Figure 4). The beam imperfections due to the mill tolerance allowed by EN 10034 (1993) were accounted for and applied to the model by scaling the deformed shape of associated buckling mode as shown in Tartaglia et al [15]. All assemblies are made by the European S355 steel with the exception of Grade 10.9 for the pre-loadable bolts. The stress-strain curves of the materials were obtained from coupon tests performed within the EQUALJOINTs research project. In the FE model, the Von Misses criteria and the combined (i.e. isotropic and kinematic) plastic hardening were assumed. The behaviour of bolts was modelled by multilinear force-displacement curve described by D'Aniello et al. [18]. To model the shank necking and the fracture in the threaded area the ductile damage was introduced in the model as proposed by Pavlovic et al [19]. The material of the welds was modelled by an elastic perfectly plastic constitutive law, with the yield stress equal to 460 MPa, which corresponds to an electrode grade A46 (as given by EN ISO 2560, 2009).

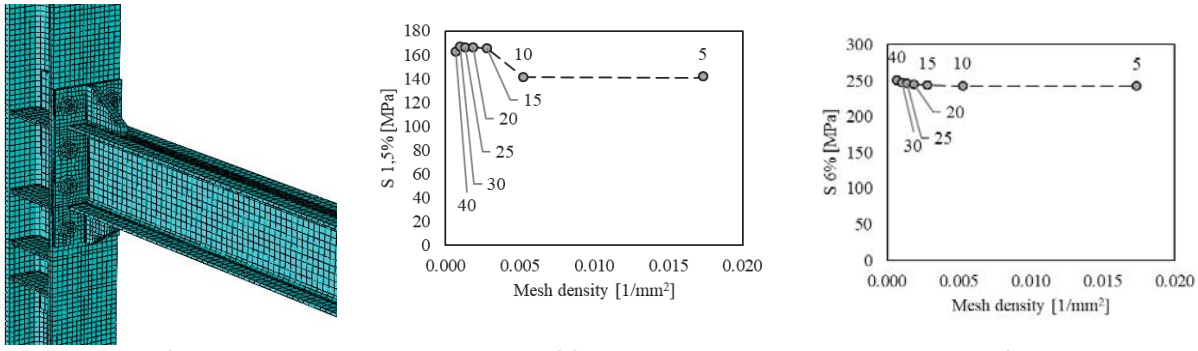

Figure 4: Example of the mesh on the ES-E joint Mesh (a) and mesh sensitivity analyses on the beam (b) and on the bolts (c).

5 RESULTS

5.1 Reduced beam section (RBS) joint

Figure 5 shows the results of both monotonic and cyclic analyses of RBS joints. The monotonic analyses were performed up to 10% of joint rotation while the AISC341 loading protocol was used for the cyclic simulations. Most of the plastic deformations are concentrated in the RBS section with the activation of a perfect plastic hinge leaving the connection almost elastic. However, some plastic deformation can be observed around the weld between the beam flange and the end-plate at a high level of imposed rotation (10%). The joints show a very ductile behaviour up to 6% of chord rotation with small decrease of resistance due to beam geometrical imperfections.

Comparing the results in terms of backbone curve no appreciable differences can be observed between the joints with and without finger shims. These considerations are also confirmed by the PEEQ distribution on both the investigated joints.

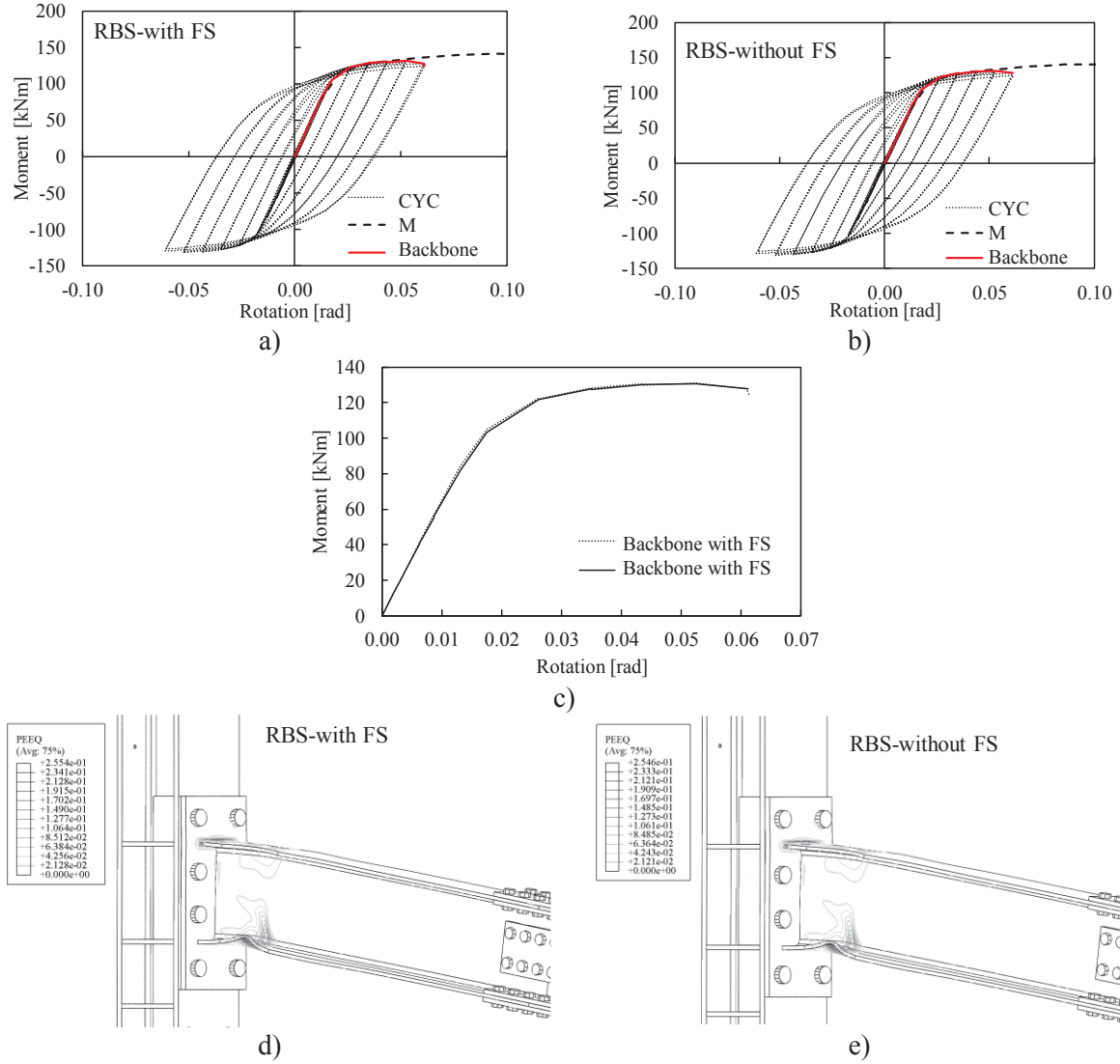

Figure 5: Monotonic and cyclic behaviour of RBS joints with and without finger shims.

5.2 Haunched joint

The results in terms of moment rotation curves and distribution of PEEQ for haunched joints with and without finger shims are summarized in Figure 6. As observed in the previous case also in haunched joints the plastic hinge forms at the extremity of the beam, leaving the connection and column web panel in elastic range. However, a larger reduction of resistance due to the beam flange local instability can be observed at 3.5% of rotation. The decrease of resistance is smaller than 20% at a 4% of rotation, hence these joints conform with both European and American requirements.

As in the previous case also for this type of connection no appreciable differences can be observed between the joints with and without the finger shims.

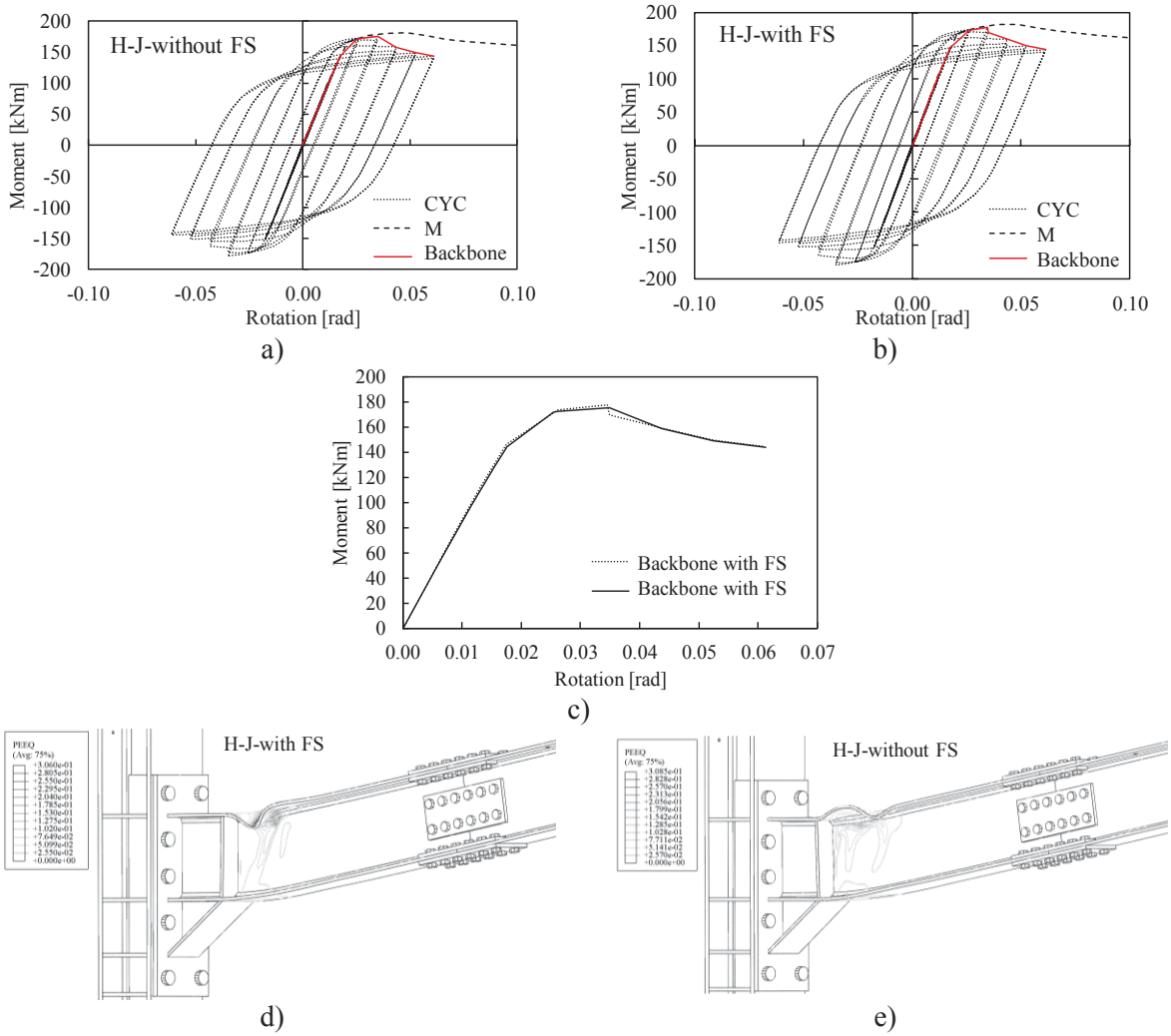

Figure 6: Monotonic and cyclic behaviour of haunched joints with and without finger shims

5.3 Extended stiffened equal strength (ES-E) Joint

Also the extended stiffened equal strength joints show a very ductile behaviour with plastic deformation in both beam and connection (see Figure 7).

Differently from the previous cases, the presence of finger shims gives some slight difference in terms of moment-rotation response curves, but negligible differences in terms of distribution of plastic deformations. The reason of such differences is mainly due to the longer

length of the bolt shanks in the joints with finger shims, which increases the deformability and the gap opening of the connection in its non-linear range.

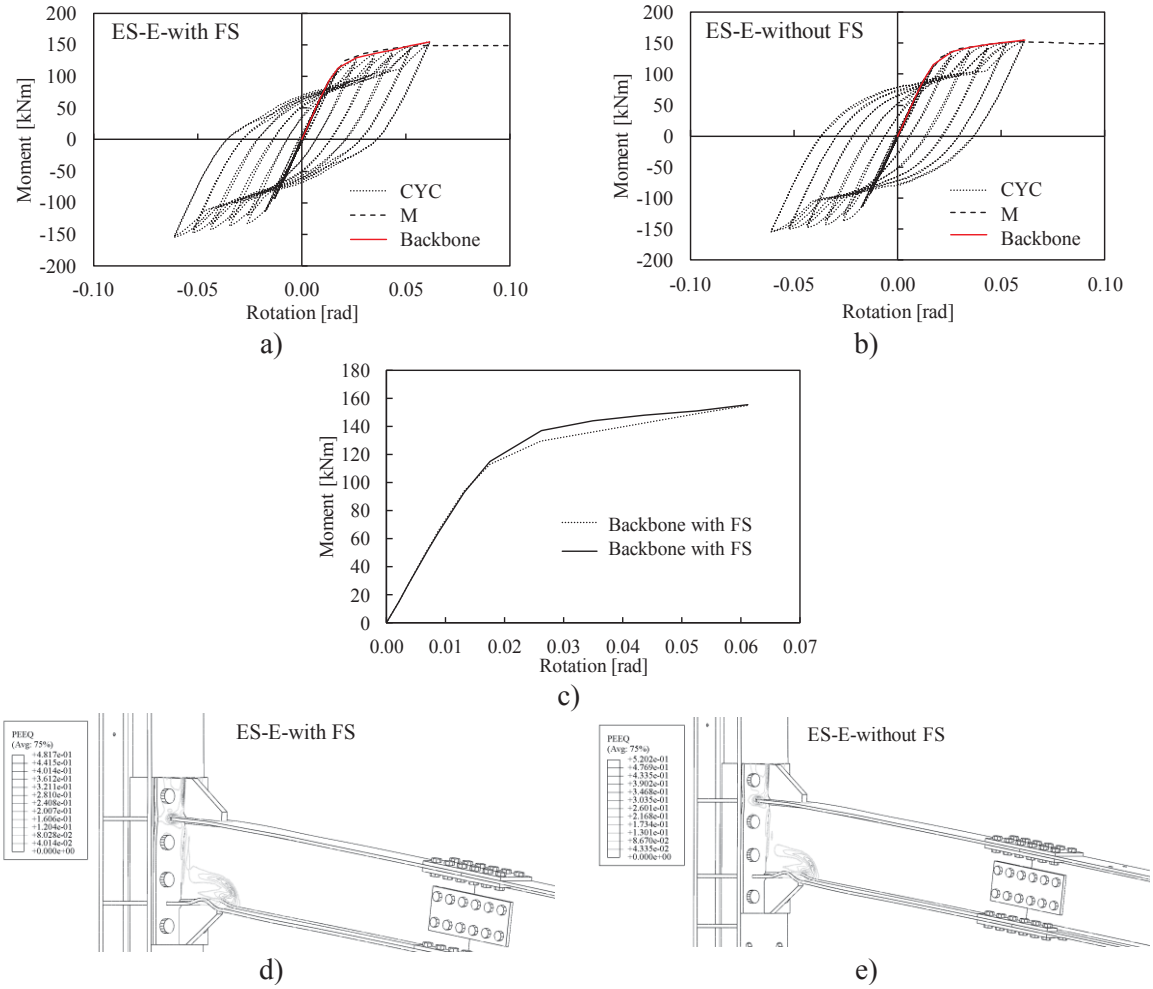

Figure 7: Monotonic and cyclic behaviour of ES-E joints with and without finger shims

6 CONCLUSIONS

The non-linear response and influence of finger-shim plates on three different beam-to-column joints configurations was investigated by means of finite element simulations. On the basis of the results, the following remarks can be pointed out:

- The bolted joint with reduced beam section ensures a very good ductile behaviour up to rotation of 6% without showing any resistance decrease. The performance of this type of joint is not influenced by finger shims.
- The haunched joint designed in accordance with the criteria developed within the Equaljoints research project allow to obtain a full rigid/full strength joint. The response is not affected by the introduction of the finger shim plates
- Differently from the previous cases, the influence of the finger shim plate can be observed for equal strength connection due to the larger deformability of the connection and some variation of the distribution of the contact forces when the connection opens. How-

ever, the presence of finger shims does not significantly modify the global performance of the joint.

REFERENCES

[1] EN 1993:1–8, Design of Steel Structures - Part 1–8: Design of Joints. CEN, 2005.

[2] EN 1998-1, Design of Structures for Earthquake Resistance - Part 1: General Rules, Seismic Actions and Rules for Buildings. CEN, 2005

[3] ANSI/AISC 358-16, Prequalified Connections for Special and Intermediate Steel Moment Frames for Seismic Applications, 2016.

[4] Building Standard Law of Japan (BSL).

[5] Landolfo R. European qualification of seismic resistant steel bolted beam-to-column joints: the Equaljoints project. *Proc. of 1st EU-Sino Workshop on Earthquake-resistance of Steel Structures Shanghai*, China, October 27, 2016.

[6] J.D. Goltz, The Northridge, California earthquake of January 17, 1994: general reconnaissance report, Report no. NCEER-94-0005. *Buffalo: National Centre for Earthquake Engineering Research*, 1994

[7] N.F.G. Youssef, D. Bonowitz, J.L. Gross, A survey of steel moment-resisting frame buildings affected by the 1994 Northridge earthquake, *Report no. NISTR 56254. Gaithersburg* (MD, USA),1995

[8] E. Watanabe, K. Sugiura, K. Nagata, Y. Kitane, Performances and damages to steel structures during 1995 Hyogoken–Nanbu earthquake, *Engineering Structures*, 20 (4–6), 282–90, 1998.

[9] L. Di Sarno, A.S. Elnashai, G. Manfredi, Assessment of RC columns subjected to horizontal and vertical ground motions recorded during the 2009 L'Aquila (Italy) earthquake, *Engineering Structures*, 33, 1514–1535, 2011.

[10] R. Tartaglia, M. D'Aniello, Di Lorenzo, A. De Martino, Influence of EC8 rules on p-delta effects on the design and response of steel MRF, *Ingegneria sismica*, 35 (3):104-120, 2018.

[11] R. Landofo R., Study of the seismic behavior of Knauf partition and façade walls based on the critical analysis of available experimental tests, Final report March 2013.

[12] M. D'Aniello, R. Tartaglia, S. Costanzo, R. Landolfo, Seismic design of extended stiffened end-plate joints in the framework of Eurocodes, *Journal of Constructional Steel Research*, 128, 512–527, 2017.

[13] Dassault (2014), Abaqus 6.14 - Abaqus Analysis User's Manual, Dassault Systèmes Simulia Corp.

[14] R. Tartaglia, M. D'Aniello, G.A. Rassati, J.A. Swanson, R. Landolfo, Full strength extended stiffened end-plate joints: AISC vs recent European design criteria. *Engineering Structures*, 159, 155–171, 2018.

[15] R. Tartaglia, M. D'Aniello, M. Zimbru, R. Landolfo, Finite element simulations on the ultimate response of extended stiffened end-plate joints, *Steel and Composite Structures, An International Journal*, 27(6), 727-745, 2018.

[16] R. Tartaglia, M. D'Aniello, R. Landolfo, The influence of rib stiffeners on the response of extended end-plate joints, *Journal of Constructional Steel Research*, 148, 669–690, 2018.

[17] R. Tartaglia, M. D'Aniello, G.A. Rassati, Proposal of AISC-compliant seismic design criteria for ductile partially-restrained end-plate bolted joints, *Journal of Constructional Steel Research,* 159, 364-383, 2019

[18] M. D'Aniello, D. Cassiano, R. Landolfo, Monotonic and cyclic inelastic tensile response of European preloadable GR10.9 bolt assemblies, *Journal of Constructional Steel Research*, 124: 77–90, 2016

[19] M. Pavlovic, C. Heistermann, M. Veljkovic, D. Pak, M. Feldmann, C. Rebelo, L.S. Da Silva, Connections in towers for wind converters. Part I: Evaluation of down-scaled experiments, *Journal of Constructional Steel Research* 115: 445-457, 2015.

EURODYN 2020
XI International Conference on Structural Dynamics
M. Papadrakakis, M. Fragiadakis, C. Papadimitriou (eds.)
Athens, Greece, 23–26 November 2020

DAMAGE-AVOIDANCE STEEL ROCKING FRAMES WITH BUCKLING-ENABLED COMPOSITE BRACING

Leena T. Kibriya[1], Christian Málaga-Chuquitaype[1], and Mohammad M. Kashani[2]

[1] Imperial College London, UK
{l.kibriya16, c.malaga}@imperial.ac.uk

[2] University of Southampton, UK
mehdi.kashani@soton.ac.uk

Keywords: Buckling-enabled bracing, Damage-avoidance, Rocking frame, Steel buildings

Abstract. *The severe social and economic impacts of recent earthquakes have inspired a growing interest in smart structural systems that offer immediate post-disaster occupancy. Post-tensioned rocking frames are emerging damage-avoiding seismic-resistant structures that employ rocking joints at member connections (to avoid major damage to primary structural elements) and unbonded post-tensioned strands (to provide self-centring capability). Nevertheless, currently available passive load-resisting systems to control the peak structural responses in steel rocking frames rely on sacrificial yielding components that accumulate damage during strong dynamic action. This results in a system with limited durability and a requirement for regular maintenance throughout the building's lifetime. By contrast, the recently proposed Buckling-Enabled Composite Bracing (BECB) elements can provide a thorough damage-avoidance solution by means of carefully controlled elastic buckling behaviour. In these systems, compression-only elements with circular-arc-shaped cross-sections are incorporated into steel rocking frames as lattice bracing in order to improve their dynamic performance. The proposed system has been shown to perform successfully under static loading and discrete sine-sweep ground motions for single-storey rocking frames. This further examines this innovative concept by performing numerical investigations on three-storey four-bay post-tensioned steel rocking buildings under real earthquake ground motions. The performances of conventional moment frames (MRFs) and their rocking frame counterparts (RFs) with and without BECB elements are compared through numerical simulations. Glass-fibre reinforced polymer (GFRP) is selected for the BECB elements. Static Pushover, Discrete Sine-sweep and Incremental Dynamic (IDA) analyses are performed to evaluate the buildings' performances. Damage measures investigated include maximum inter-storey drifts and floor accelerations. It is demonstrated that BECB members enhance the dynamic response of steel rocking frames by significantly reducing maximum storey drifts and accelerations.*

1 INTRODUCTION

In response to the severe socioeconomic impacts of earthquakes [1], rocking self-centring frames that employ elastic gap-opening mechanisms at the column-foundation and beam-column interfaces, have been proposed as damage-limiting alternatives. These systems utilize unbonded post-tensioned tendons to tie members together and re-centre the structure to its plumb position after strong ground motion. This configuration effectively prevents yielding of primary structural members, but can lead to large storey drifts and accelerations. Therefore, sacrificial elements that dissipate modest amounts of energy through yielding (damage) are typically provided to stabilize the rocking response.

Research devising methods of enhancing earthquake resilience for rocking structures has spanned over the last decade [2, 3, 4, 5, 6, 7, 8, 9, 10, 11]. Particularly for self-centring steel frames, the use of yielding thin steel plate infill walls [12, 13, 14], buckling-restrained braces [15], yielding seat angles [16, 17], short axial yielding devices [18], yielding web hourglass pins [19], or beam web/flange friction devices [20, 21, 22] have been explored. Although these technologies are very effective in reducing peak response quantities, they all comprise of sacrificial and/or replaceable components that accumulate damage during strong dynamic action. This results in a system with limited durability, and a requirement for frequent inspections and maintenance. Furthermore, in spite the inclusion of these technologies, the structures often experience permanent post-earthquake damage and require significant repair or replacement.

In contrast, the recently proposed buckling-enabled composite bracing (BECB) elements can provide a thoroughly damage-avoidance solution [23, 24]. In these systems, shell-like elements with GFRP material properties, are employed to improve the dynamic performance of rocking steel frames through their elastic buckling properties. A curvature in the cross-section is provided to increase the section's buckling capacity. Single-storey post-tensioned steel rocking frames with BECB have been shown to perform successfully under numerical testing to static displacement cycles and discrete sine-sweep ground motions [23], demonstrating reduced peak responses, greater lateral-load resistance, and no damage accumulation compared to systems without BECB.

This paper builds on this innovative concept by performing numerical investigations on three-storey post-tensioned steel rocking buildings. The performances of conventional moment frames (MRFs) and their rocking frame counterparts (RFs) with and without BECB elements are compared through numerical simulations. Numerically-generated frequency response functions (FRFs) are examined. Incremental Dynamic Analyses (IDA) are performed to evaluate the buildings' performances [25]. Multiple damage measures are investigated, including maximum inter-storey drifts and floor accelerations. It is demonstrated that BECB enhances the static and dynamic performance of rocking frames by significantly reducing the storey drifts and accelerations without any damage accumulation. This study forms a strong foundation towards the provision of truly damage-avoidance solutions and supplies the tools for further investigations into practical design methods.

2 PROPOSED STRUCTURES

The 3-storey steel moment-resisting frame (MRF) proposed by the Structural Control Committee of the American Society of Civil Engineers [26] for the SAC Steel Project was selected as the benchmark building herein. The structure's geometric and member details are presented in Figure 1. The building has a total height of 11.88 m, and width of 36.6 m. It represents a typical low-rise structure with an aspect ratio of 0.33. The beams are made of 248

MPa steel while 345 MPa steel is employed for the columns. The seismic mass of the first and second levels is 9.57×10^5 kg and the third level is 1.04×10^6 kg.

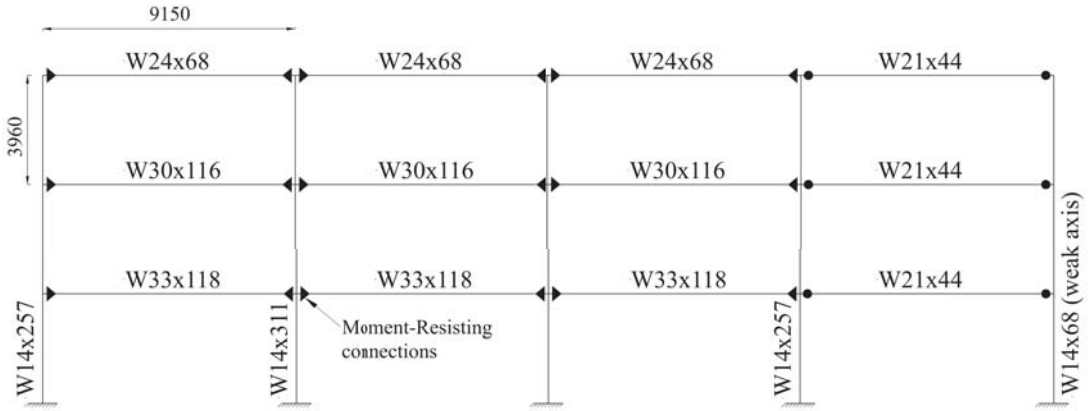

Figure 1: Three-storey, four-bay steel moment-resisting frame.

The rocking frame (RF) counterparts employed identical sections as the MRF with rocking connections at both the beam-column and column-foundation interfaces. To provide support for the BECB at ground level, a floor beam with section W33x118 was provided. A tendon cross section of 500 mm^2 was incorporated for the beams and columns. A view of the cross-section illustrating the geometric parameters of BECB member is presented in Figure 2 and the proposed configurations for the RF systems with BECB are presented in Figure 3.

For configuration 1, two sizes of BECB (8 elements in total) were incorporated in a single bay, including shorter members with dimensions of L (length) = 3.3 m, α (curvature) = 50◦, t (thickness) = 16 mm, r (radius) = 100 mm and longer members with L = 6.7 m, α = 50◦, t = 25 mm, r = 180 mm. For configuration 2 (C2), BECB elements were incorporated in two bays of the building. An isotropic elastic material with modulus 'E' of 18 GPa and Poisson's ratio 'μ' of 0.3 (GFRP) was used to simulate each BECB element in ABAQUS [27, 28] in order to obtain the respective buckling response.

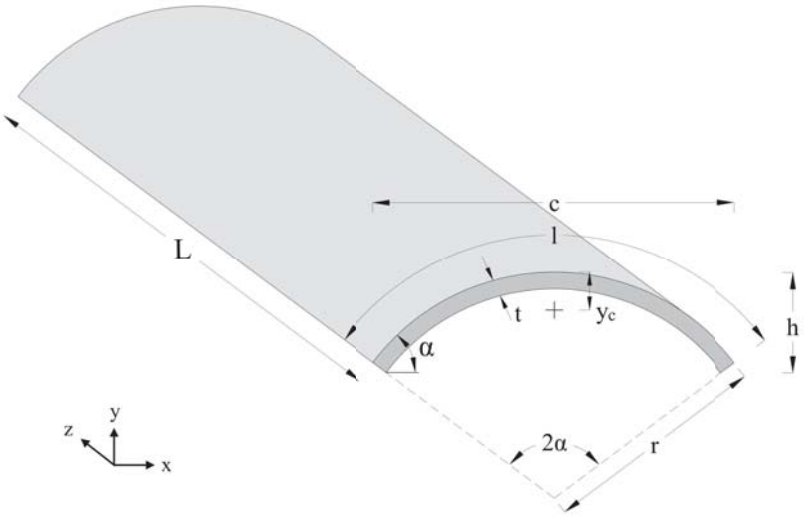

Figure 2: BECB element cross-section with geometric parameters.

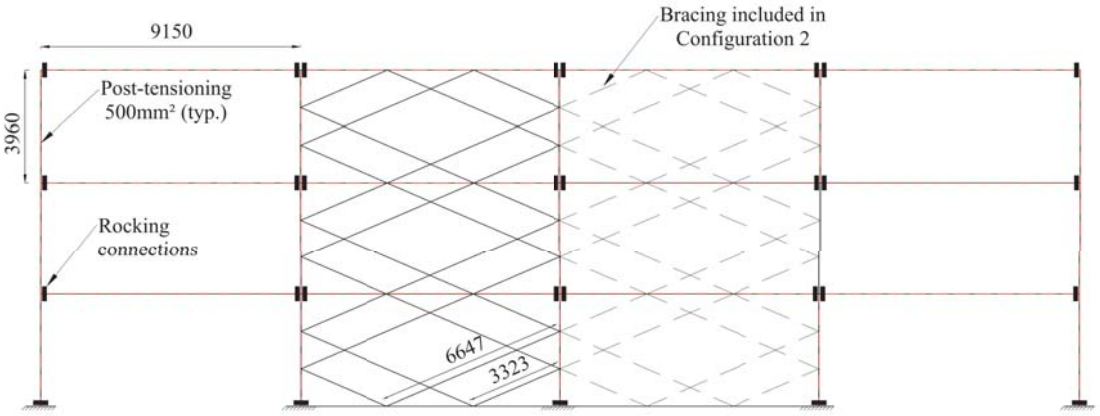

Figure 3: Three-storey, four-bay steel self-centring rocking frames with BECB in single and two bays (C2).

3 FINITE ELEMENT MODELLING

Four planar frames (MRF, RF, RF w/ BECB, and RF w/ BECB C2) with three-degrees-of-freedom per node were defined using the open source finite element framework OpenSees [29]. Force-based non-linear beam-column elements were used for beams and columns. A Steel01 material model was employed for the fibre sections with their respective yield strengths. Each section was discretized into 40 fibres and 2 force-based elements with 3 Gauss-Lobatto integration points per element. Geometric non-linearities were accounted for by means of a Corotational transformation. A constant stiffness proportional damping of 5% was specified for all models. All degrees of freedom for every structure were constrained at the foundation level to simulate a fixed base. Nodal masses were defined in the horizontal and vertical degrees of freedom, and lumped at the top of each column element. Beam gravity loads were applied as distributed loads along beam lengths.

The details of the rocking frames were simulated using the numerical modelling procedures proposed in [30]. The columns and tendons (beam and column) were modelled as continuous elements along the frame height and width. The post-tensioning tendons were modelled using Corotational Truss Elements with an initial stress uniaxial material (Steel02 material in OpenSees [29]). Zero-length gap elements (springs) were used to simulate the rocking surfaces. Elastic Perfectly Plastic material with no tension stiffness was defined for the gap element. The Lobatto integration scheme introduced in [31], was used to determine the distribution of the gap elements along member edges.

Elastic Bilinear uniaxial material was used to represent the pre to post-buckling behaviour of BECB. The MinMax uniaxial material [29] was used to define the failure envelope of the bracing members employing the fracture strain of GFRP [27]. Subsequently, the bracing members were represented as truss compression-only elements in the numerical models.

Static lateral loads were applied at the nodes assuming linear first-mode distribution. A displacement control strategy was used to perform the non-linear static analysis. Frequency response functions (FRFs) were generated using discrete sine-sweep input ground motions as originally proposed in [30]. MATLAB [32] was used to generate input harmonic base motions. Subsequently, Incremental dynamic analyses (IDA) were performed to evaluate the buildings' performances. The set of 22 far-field strong ground motion records from FEMA P695 (ATC-63) were selected for the analyses [33].

4 STATIC RESPONSE

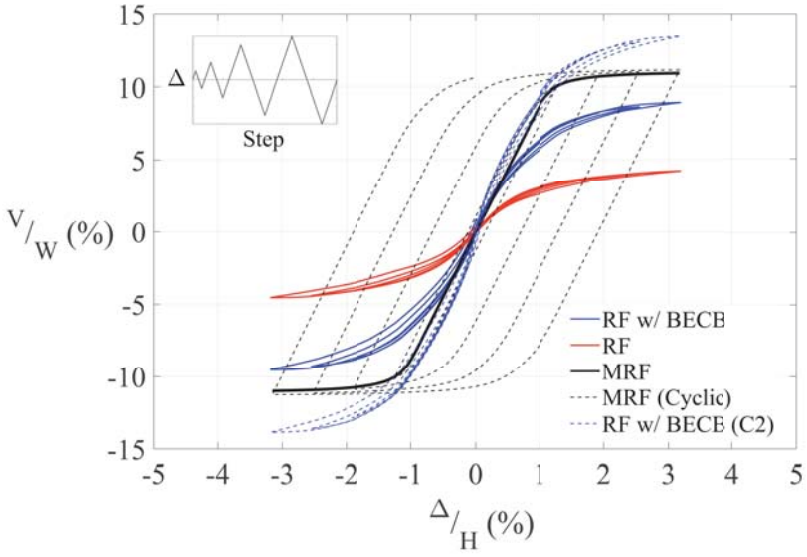

Figure 4: Static response comparison between moment-resisting frames (MRF) and rocking frames with and without BECB (RF w/BECB and RF w/BECB C2).

The results of the static analysis for the four buildings under consideration, are illustrated in Figure 4. This Figure plots the base shear 'V' against roof drift (Δ). The base shear 'V' was normalized using the total weight of each frame 'W'. Each frame configuration was subjected to a series of four horizontal cycles.

Figure 4 demonstrates that the bracing elements significantly increase the lateral load carrying capacity of both rocking frame configurations with BECB. The lateral resistance of the rocking frame without BECB (RF) was 55% lower than the moment-resisting frame (MRF). Rocking frame with BECB (RF w/BECB) exhibited a 30% increase in the lateral load resistance whereas configuration 2 showed a 63% increase compared to the RF. In comparison with the MRF, the lateral capacity of the RF w/BECB was 20% lower, whereas the RF w/BECB C2 was 15% higher. Additionally, Figure 4 demonstrates that all the RFs experienced zero residual drifts and damage accumulation, in contrast to the MRF.

5 FREQUENCY RESPONSE FUNCTIONS

A series of dynamic analyses were performed for low, medium, and high forcing amplitudes. The frequencies were normalized against the natural frequencies of the corresponding finite element models. The FRFs for all buildings are presented in terms of maximum storey accelerations in Figure 5. Moreover, the FRFs were utilized to identify the fundamental frequencies of the rocking building models using the maximum inflection points of the low-amplitude curves.

It can be observed from Figure 5 that the natural frequency of the MRF is 1 Hz, whereas the RF is 0.7 Hz. In comparison, the fundamental frequency of the RF w/ BECB and RF w/ BECB C2 are approximately 1.5 Hz and 2 Hz, respectively. Therefore, it is apparent that both configurations of the buckling-enabled braced frames are stiffer than their pure rocking frame counterpart. Contrary to the rocking structures, the fundamental frequency of the MRF is constant across all forcing amplitudes until yielding. It is also apparent that the RF has greater flexibility than its MRF counterpart, which is expected because of the increased storey displacements due to the gap-opening mechanisms and the absence of any lateral control device/mechanism.

Moreover, it can be observed that the maximum storey accelerations for the RF for high amplitude excitations is 55% greater than the MRF. The RF w/ BECB exhibited accelerations that were 25% higher than the MRF whereas the accelerations of RF w/ BECB C2 were very close (about 2-5% higher) to the MRF. Similarly, the RF w/ BECB showed a substantial reduction of upto 50% and the RF w/ BECB C2 of 35%, compared to the RF under medium to high amplitude excitations. Likewise, the maximum inter-storey drifts for RF were 40% higher than MRF. The RF w/ BECB 15% greater and RF w/ BECB C2 were 10% lower than MRF.

From the foregoing it is evident that steel rocking frames equipped with BECB result in significantly lower peak response quantities compared with systems without BECB and close to those exhibited by a conventional steel moment-resisting frame. Besides, BECB was also observed to enhance the overall stability of the rocking structure and numerical convergence during the analyses was achieved significantly quicker.

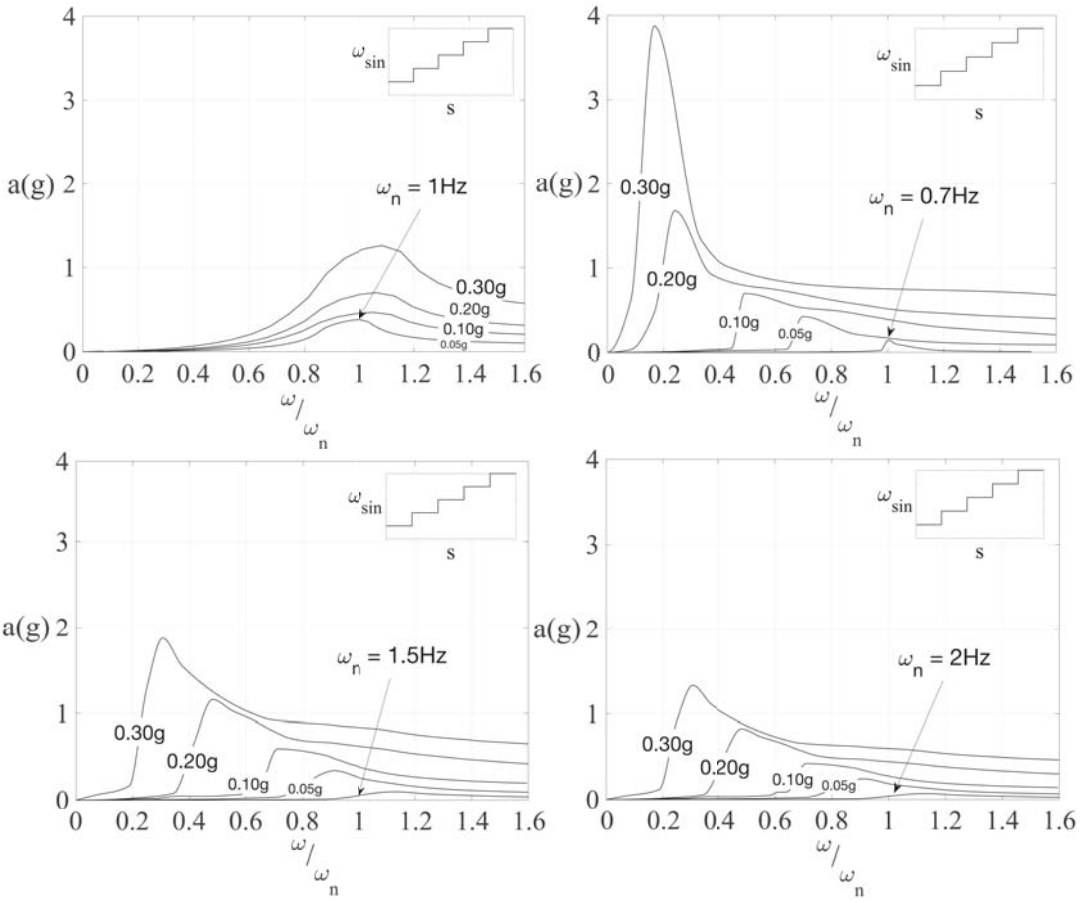

Figure 5: Frequency Response Functions (FRFs) for MRF (Top left), RF (Top right) RF w/ BECB (Bottom left), and RF w/BECB C2 (Bottom right).

6 INCREMENTAL DYNAMIC ANALYSIS

Previous sections have examined the static and dynamic behaviour of rocking steel frames equipped with BECB to conventional moment-resisting steel frames by subjecting them to idealized ground-motions. This section examines the effectiveness of the BECB by subjecting the buildings to a set of real earthquake records. To this end, the 22 far-field earthquake suite detailed in FEMA P695 and obtained from the Pacific Earthquake Engineering Research Center (PEER) database, were employed. The peak inter-storey drift ratio, was adopted as the damage measure (DM), while the spectral acceleration at the fundamental period of each re-

spective building, $Sa(T_1)$, was selected as the intensity measure (IM). The median (50^{th} percentile) IDA curves comparing the four buildings are presented in Figure 6.

It can be observed that the IDA curves of RF w/ BECB and RF w/ BECB C2 exhibited a higher elastic slope than the MRF, indicating a stiffer structure and hence lower relative displacements than MRF and RF. Likewise, the RF w/ BECB C2 remained in the elastic range for drifts of upto 4% whereas the elastic-plastic transition for the MRF was at the 2% ratio, with RF and RF w/BECB around 3%. Moreover, the MRF experienced softening after 2% drift and global collapse at approximately 10% drift. For the RF w/ BECB C2, softening was observed after yielding of the post-tensioning (at 4% drift) and this was followed by BECB fracture at 5% drift. Similarly, the RF w/ BECB building experienced first brace fracture at around 4% drift. The global collapse for RF w/ BECB C2 occurred at 7% drift. In contrast, the global collapse for the RF w/ BECB was at 5% and RF at 3%. It can also be observed that in the buildings with BECB, hardening occurred after BECB member buckling at 0.5% drift. The IDA curves of some records for the rocking frames displayed successive segments of softening and hardening behaviour (weaving) before final instability. This was more prominent for the RFs compared to other buildings.

In a practical setting, each building will be designed differently to satisfy similar demands and identical sections were used herein to allow a direct comparison of the structural responses. Furthermore, the proposed BECB system relies on controlled elastic buckling of GFRP members that do not accumulate plastic strains. Therefore, it is crucial that a compression-only response is ensured. A possible connection has been proposed in [23] between the BECB and the steel members. This was designed to allow a transfer of compressive forces during the lateral frame movement, causing the brace to buckle, while preventing tension stresses to be developed in the BECB. It is also important to mention that the proposed system is expected to remain elastic for typical recurrent lateral loads such as winds. Subsequently, the BECB members can be tuned to allow activation of the buckling response leading to a change in the dynamic behaviour only during periods of high demand.

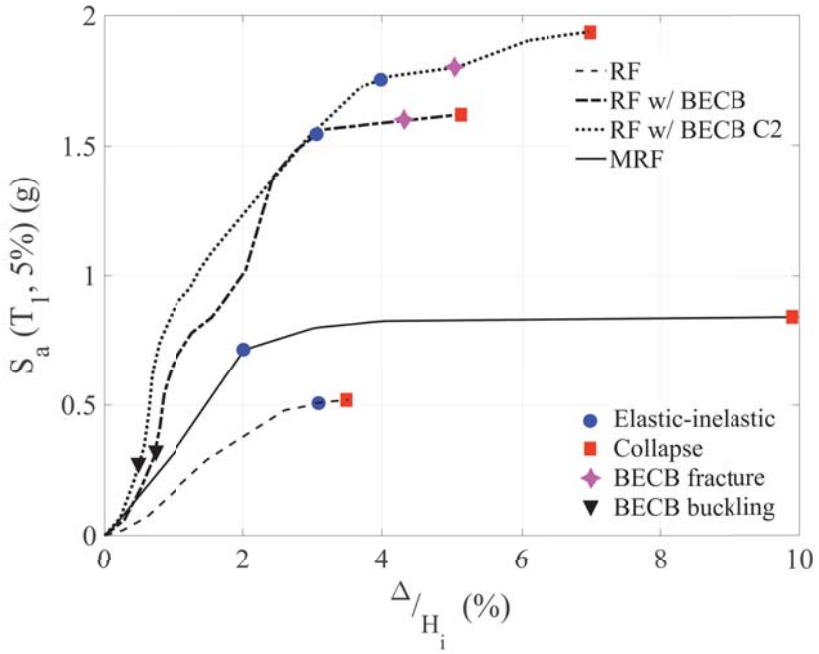

Figure 6 Summarized (50% fractile) IDA curves comparing the MRF, RF, RF w/BECB, and RF w/BECB C1 for 22 far-field earthquake records from FEMA P695 report.

7 CONCLUSIONS

Currently available lateral-load resisting systems for rocking frames comprise of replaceable yielding components that are damaged after strong motion leading to non-negligible maintenance costs and downtime. By applying the recoverable elastic buckling properties of the newly proposed bracing elements with circular-arc shaped cross-section this paper has demonstrated that a damage-avoidance rocking system can be achieved. The main research findings of this study are summarized below.

- In comparison with the moment-resisting frame, the lateral capacity of the rocking frame with BECB in two bays was 15% higher.
- Both configurations of the buckling-enabled braced frames were 1.5-2 times stiffer than their pure rocking frame and the moment-resisting frame buildings.
- The rocking frame with BECB in two bays exhibited maximum storey accelerations that were within 10% of the values experienced by the moment-resisting frame.
- The IDA curves of rocking frames with BECB displayed a greater elastic slope than the moment-resisting frame and pure rocking frame, indicating stiffer structures and hence lower relative displacements in the elastic range (for constant S_a).
- In the buildings with BECB, some hardening was observed after the initial BECB member buckling at an average of 0.5-1% drift ratios for the records considered.
- Both buildings with BECB remained elastic up to 3-4% drifts which are greater than the moment-resisting frame at 2% drift.
- The rocking frame with BECB employed in a single-bay experienced brace failure at 4% drift whereas the model with BECB in two bays exhibited the first brace fracture at 5% drift ratio.
- The pure rocking frame exhibited numerical non-convergence (collapse) at a drift ratio close to 4%. In contrast, the buildings with BECB collapsed at 5% and 7%, for each configuration respectively.
- The area between yielding and global instability was greater with the addition of BECB, compared to the pure rocking frame.

REFERENCES

[1] D. Kellenberg, A. Mobarak, The Economics of Natural Disasters, *Annual Review of Resource Economics* 3(1), 297–312, 2011.

[2] M. Priestley, S. Sritharan, J. Conley, S. Pampanin, Preliminary Results and Conclusions from the PRESSS Five-Story Precast Concrete Test Building, *PCI Journal* 44 (6), 42–67, 1999.

[3] Y.C. Kurama, R. Sause, S. Pessiki, L-w. Lu, Seismic Response Evaluation of Unbonded Post-Tensioned Precast Walls, *ACI Structural Journal* 99 (S66), 641–651, 2002.

[4] B.G. Morgen, Y.C. Kurama, A Friction Damper for Post-Tensioned Pre-Cast Concrete Moment Frames, *PCI Journal* 3189, 112 – 133, 2004.

[5] M.R. Eatherton, J. Hajjar, G.G. Deierlein, H. Krawinkler, S. Billington, X. Ma, Controlled rocking of steel-framed buildings with replaceable energy-dissipating fuses, *Proceedings of the 14th World Conference on Earthquake Engineering*, 2008.

[6] D. Roke, R. Sause, J. Ricles, N. Gonner, Design Concepts for Damage-Free Seismic-Resistant Self-Centering Steel Concentrically Braced Frames, *ASCE Structures Congress*, 2009.

[7] M.R. Eatherton, J. Hajjar, X. Ma, H. Krawinkler, G. Deierlein, Seismic design and behavior of steel frames with controlled rocking: part I-concepts and quasi-static subassembly testing, *ASCE Structures Congress* 1, 1534–1543, 2010.

[8] X. Ma, Seismic Design and Behavior of Self-Centering Braced Frame with Controlled Rocking and Energy Dissipating Fuses, *PhD Thesis*, Stanford University, 2010.

[9] T.L. Karavasilis, S. Kerawala, E. Hale, Hysteretic model for steel energy dissipation devices and evaluation of a minimal-damage seismic design approach for steel buildings, *Journal of Constructional Steel Research* 70, 358–367, 2012.

[10] L.L. Song, T. Guo, Y. Gu, Z.L. Cao, Experimental study of a self-centering pre-stressed concrete frame subassembly, *Engineering Structures* 88, 176–188, 2015.

[11] R. Thiers-Moggia, C. Málaga-Chuquitaype, Seismic protection of rocking structures with inerters, *Earthquake Engineering & Structural Dynamics* 48 (5), 528–547, 2019.

[12] P. Timler, C.E. Ventura, H. Prion, R. Anjam, Experimental and analytical studies of steel plate shear walls as applied to the design of tall buildings, *The Structural Design of Tall Buildings* 7 (3), 233–249, 1998.

[13] P.M. Clayton, J.W. Berman, L.N. Lowes, Subassembly testing and modelling of self-centering steel plate shear walls, *Engineering Structures* 56, 1848–1857, 2013.

[14] D.M. Dowden, R. Purba, M. Bruneau, Behavior of self-centering steel plate shear walls and design considerations, *Journal of Structural Engineering* 138, 11–21, 2011.

[15] L. Wiebe, Design of Controlled Rocking Steel Frames to Limit Higher Mode Effects, *PhD Thesis*, University of Toronto, 2010.

[16] J. Ricles, R. Sause, M. Garlock, C. Zhao, Posttensioned Seismic-Resistant Connections for Steel Frames, *Journal of Structural Engineering* 127 (2), 113–121, 2001.

[17] R. Sause, J.M. Ricles, M.M. Garlock, E. Vanmarcke, L-s. Peh, J. Liu, B. Shear, Self-Centering Seismic-Resistant Steel Frame Systems: Overview of Past and Current, *Precast Concrete*, 2010.

[18] C. Christopoulos, A. Filiatrault, C-M. Uang, B. Folz, Posttensioned Energy Dissipating Connections for Moment-Resisting Steel Frames, *Journal of Structural Engineering* 128 (9), 1111–1120, 2002.

[19] G. Vasdravellis, B. Uy, T.L. Karavasilis, Experimental validation of steel post-tensioned connections with web hourglass pins, *STESSA 2012: Proceedings of the 7th International Conference on Behaviour of Steel Structures in Seismic Areas* 139, 677–683, 2012.

[20] J. Iyama, C-y. Seo, J.M. Ricles, R. Sause, Self-centering MRFs with bottom flange friction devices under earthquake loading, *Journal of Constructional Steel Research* 65 (2), 314–325, 2008.

[21] H-J. Kim, C. Christopoulos, Friction Damped Posttensioned Self-Centering Steel Moment-Resisting Frames, *Journal of Structural Engineering* 134 (11), 1768–1779, 2008.

[22] Y-C. Lin, J.M. Ricles, R. Sause, C-y. Seo, Earthquake Simulations on a Self-Centering Steel Moment Resisting Frame with Web Friction Devices, *Structures Congress*, 2009.

[23] L.T. Kibriya, C. Málaga-Chuquitaype, M.M. Kashani, Buckling-enabled composite bracing for damage-avoidance rocking structures, *International Journal of Mechanical Sciences* 170, 1-22, 2020.

[24] L.T. Kibriya, C. Málaga-Chuquitaype, M.M. Kashani, Application of Buckling-Enabled Composite Bracing (BECB) to steel rocking Frames, *Proceedings of SECED: Earthquake Risk and Engineering Towards a Resilient World*, 2019

[25] D. Vamvatsikos, C.A. Cornell, Incremental dynamic analysis. *Earthquake Engineering and Structural Dynamics* 31 (3), 491-514, 2002.

[26] Y. Ohtori, R.E. Christenson, B.F. Spencer Jr, S.J. Dyke, Benchmark Control Problems for Seismically Excited Nonlinear Buildings, *Journal of engineering mechanics* 130 (4), 366-385, 2001.

[27] T. Sathishkumar, S. Satheeshkumar, J. Naveen, Glass fiber-reinforced polymer composites – A review, *Journal of Reinforced Plastics and Composites* 33 (13), 1258–1275, 2014.

[28] M. Smith, ABAQUS/Standard User's Manual Version 6.9, *Simulia*, 2009.

[29] F. McKenna, Object-oriented finite element programming: Frameworks for analysis, algorithms and parallel computing, *PhD Thesis*, University of California Berkeley, USA

[30] L.T. Kibriya, C. Málaga-Chuquitaype, M.M. Kashani, N. Alexander, Nonlinear dynamics of self-centring rocking steel frames using finite element models, *Soil Dynamics and Earthquake Engineering* 115, 826–837, 2018.

[31] H. Spieth, A. Carr, A. Murahidy, D. Arnolds, M. Davies, J. Mander, Modelling of post-tensioned precast reinforced concrete frame structures with rocking beam-column connections, *Proceedings of New Zealand Society of Earthquake Engineering Conference Canterbury*, 2004.

[32] I. MathWorks, Matlab: The language of technical computing, *MATLAB Primer*, Massachusetts, USA.

[33] FEMA, Quantification of Building Seismic Performance Factors, FEMA P695, Prepared by the Applied Technology Council (ATC), *Federal Emergency Management Council (FEMA)*, 2009.

EURODYN 2020
XI International Conference on Structural Dynamics
M. Papadrakakis, M. Fragiadakis, C. Papadimitriou (eds.)
Athens, Greece, 23–26 November 2020

OPTIMIZATION OF DISSIPATIVE REPLACEABLE LINK FRAMES BY ELASTIC HIGH STRENGTH STEEL COUPLING BEAMS

Marius Pinkawa[1], **Cristian Vulcu**[1,2], **Benno Hoffmeister**[1], **Markus Feldmann**[1]

[1] RWTH Aachen – Institute of Steel Construction / Center for Wind and Earthquake Engineering
Mies-van-der-Rohe Straße 1, Aachen, Germany
e-mail: m.pinkawa@stb.rwth-aachen.de

[2] Politehnica University of Timisoara – Department of Steel Structures and Structural Mechanics
Str. Ioan Curea Nr. 1, Timisoara, Romania
cristian.vulcu@upt.ro

Keywords: Seismic design, FUSEIS system, dual system, dissipative replaceable beam links, coupling beams

Abstract. *The Dissipative Replaceable Link Frame (DRLF) is an innovative lateral load resisting system, recently developed, investigated, and further optimized in the European research projects FUSEIS, MATCH, INNOSEIS and DISSIPABLE. The system consists of two strong columns, which are rigidly interconnected by several horizontal beams, forming a vertical VIERENDEEL beam. The interconnecting beams are attached by a bolted head plate connection, making them easily detachable. As they are separated from the slab, they do not take part in the gravity load bearing function. The dissipative beam links being the only intended spots of inelastic action and therefore energy dissipation, plus being easily exchangeable because of their bolted connection and missing participation in the gravity load bearing paths, act as exchangeable seismic fuses during a strong earthquake. After such an event, exchanging the beam links is foreseen to bring the structure back to its undamaged pre-earthquake stage quickly. However, Eurocode 8 demands on damage limitation affecting non-structural components – like e.g. partition walls – might represent a tough requirement on global lateral stiffness of the Link Frame systems. For high buildings, displacement verifications often govern the design, similar as known for conventional Moment Resisting Frames (MRF). In order to overcome this restriction, in this paper, a solution to increase lateral stiffness of Dissipative Replaceable Link Frames is investigated: Keeping the connections of the regular gravity frame hinged, strong elastic steel coupling beams are introduced, connecting two adjacent Link Frames. These coupling beams are not intended to dissipate energy, but instead should remain elastic, in order to keep the whole building easily repairable, by restricting seismic damage to the Dissipative Replaceable Links. Moreover, such additional source of lateral stiffness is able to improve re-centering capability to diminish accumulation of residual displacements during an earthquake and further to re-center the building when the seismic fuses are replaced. In this paper, preliminary conclusions on the concept and performance of this innovative system under development in the ongoing project DISSIPABLE are presented.*

1 INTRODUCTION

The Dissipative Replaceable Link Frame (DRLF) is an innovative lateral load resisting system, which was initially developed and investigated in the European research project "FUSEIS - dissipative devices for seismic-resistant steel frames" [1]. The objective of the FUSEIS project was to overcome the drawback of non-repairability of traditional systems such as Moment Resisting Frames (MRF), Concentrically Braced Frames (CBF) or Eccentrically Braced Frames (EBF). While such conventional systems perform well during strong seismic events due to dissipation of a large amount of energy, however, they are not economically repairable after the design basis earthquake has struck the structure. Thus, usually the only available option is the demolishing of the damaged building and replacing it by a new one. To overcome this issue, within the FUSEIS project several innovative systems have been developed, where the dissipative elements called fuses are the only source of energy dissipation and above all are easily replaceable after an earthquake.

One of the investigated systems was the formerly called FUSEIS-1 system (see [1], [2], [3]), which in this paper is called Dissipative Replaceable Link Frame (DRLF). It was further developed and investigated within the MATCH [4] and INNOSEIS [5] projects, and is further enhanced within the ongoing DISSIPABLE [6] project.

The DRLF system consists of two strong columns, which are rigidly interconnected by several beams, forming a vertical VIERENDEEL beam. In order to be easily detachable, these interconnecting beams – the Dissipative Replaceable Links (DRL) – are attached by a bolted head plate connection. As they are not coupled with the slab, consequently, they are not a part of the gravity load bearing frame. Optimally, inelastic action is foreseen to take place solely in the Dissipative Replaceable Links (DRL). When achieving this, they can act as exchangeable seismic fuses during a strong earthquake. Being the only source of energy dissipation by design, along with the missing participation in the gravity load bearing paths and moreover their detachable connection design, exchanging the Dissipative Replaceable Links is foreseen to bring the structure back to its undamaged pre-earthquake stage quickly, without the need of rebuilding the whole structure.

Eurocode 8 [7] demands on damage limitation affecting non-structural components – like e.g. partition walls – represent a tough requirement on global lateral stiffness of such Dissipative Replaceable Link Frame systems. For high buildings, displacement verifications often govern the design. In this case, usually partial-strength moment connections may be introduced to the gravity load bearing frames, in order to increase global stiffness. However, this may result in damage of the gravity frame connections, which are usually not feasibly repairable, finally pre-venting full exploitation of the potentially excellent energy dissipation capacity of such a system.

In this paper, an alternative solution of increasing lateral stiffness of Dissipative Replaceable Link Frame systems is investigated: Keeping the connections of the gravity frame hinged, strong elastic steel coupling beams are introduced, connecting two Dissipative Replaceable Link Frames. These coupling beams are not intended to dissipate energy, but instead should remain elastic, in order to keep the whole building easily repairable, by restricting seismic damage to the Dissipative Replaceable Link fuses only.

In the following, after a general introduction to the innovative concept of the Coupled Dissipative Replaceable Link Frame (CDRLF) system, two case studies of an 8-storey office building are presented. The first one, acting as 'reference system', is the already known Dissipative Replaceable Link Frame. Because the building is quite high, in total three bays with such frames were required, to comply with seismic requirements on stiffness. The second system, labelled as 'optimized system', introduced the concept of coupling beams. Consequently, only two bays

of DRLFs were needed. In a first step, the performance of both systems was assessed and compared via pushover analyses. Target displacements were derived based on the N2 method. Further on, for verification of the conclusions derived by the non-linear static analyses, dynamic time history analyses with seven recorded accelerograms have been conducted. The gain in performance achieved by the introduction of the coupling beams is discussed in terms of push-over curves, plastic mechanisms, inter-story drifts, residual displacements and repairability. It is demonstrated, how the optimized system is well able to comply with the foreseen performance targets.

2 DISSIPATIVE REPLACABLE LINK FRAMES

A schematic sketch of the Dissipative Replaceable Link Frame (DRLF) is shown in Figure 1, left panel. For high buildings, this type of system may have the issue of inherent flexibility, which is also a well-known issue for classical Moment Resisting Frames (MRF). Moreover, residual displacements may hinder the repairability performance target. In order to increase stiffness and re-centering capability, two of such frames might be connected by Coupling Beams, as shown in Figure 1, right panel. This combination results in the Coupled Dissipative Replaceable Link Frame (CDRLF). The lateral strength and stiffness of such a coupled frame is basically due to the frame action of the two single DRLFs as well as the Coupling Frame, which consists of the coupling beams and the strong columns, where the coupling beams are attached to. Thus, the internal strong columns contribute to both frames. The in total three frame actions act in series resulting in the global frame behavior (see Figure 2).

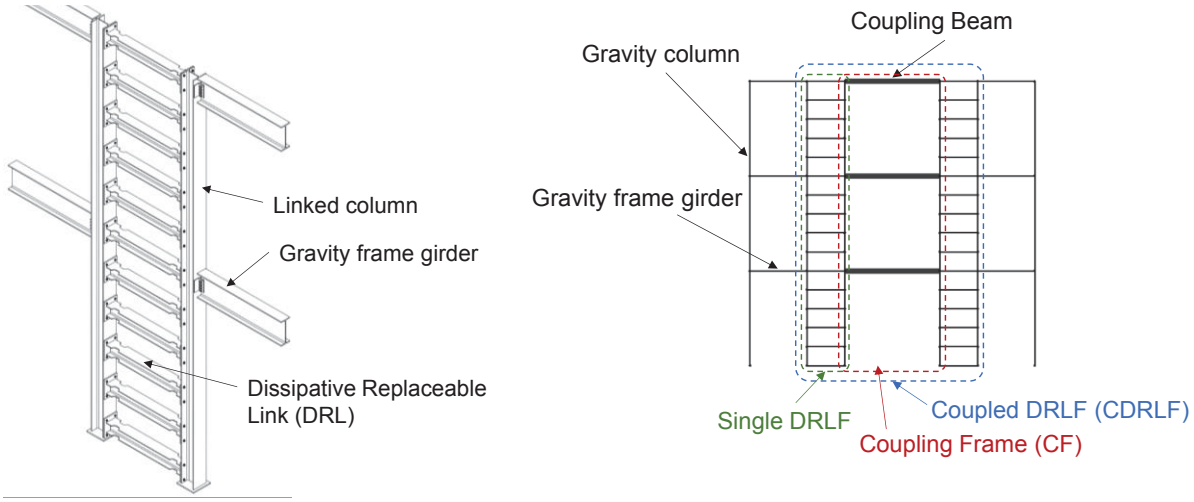

Dissipative Replaceable Link Frame (DRLF) Coupled Dissipative Replaceable Link Frame (CDRLF)

Figure 1: Single Dissipative Replaceable Link Frame (DRLF) (left) and two DRLFs coupled by elastic HSS Coupling Beams (CB) forming the Coupled Dissipative Link Frame (CDRLF) (right).

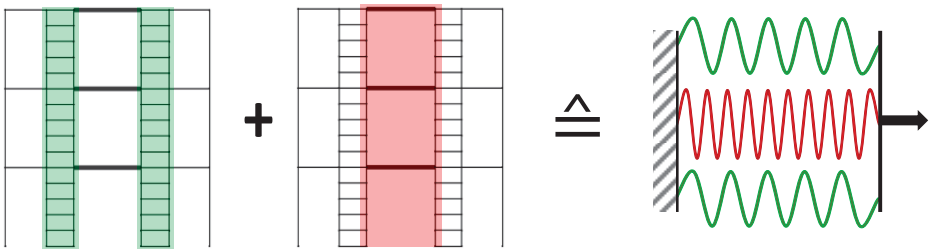

Figure 2: Two single Dissipative Replaceable Link Frames (DRLFs) and the Coupling Frame (CF) acting in series as resulting total lateral load resisting system.

The concept of coupling beams is a well-known one for linking two reinforced concrete shear walls. However, in this context, usually it are the coupling beams, which are foreseen to dissipate energy. See e.g. [8] for an innovative system of concrete shear walls connected via replaceable steel coupling beams. Contrary, in the scope of the research presented herein, the coupling beams need to remain elastic for the design basis earthquake (usually 10% in 50 years / 475 years return period). Therefore, the investigated innovative system could be best compared to dual frame systems, e.g. a combination of an EBF with a MRF, where the MRF is deemed to add stiffness and residual strength to the system, see e.g. [9].

Design equations for the DRLF have been developed in the FUSEIS [1] project and disseminated throughout the INNOSEIS [5] project. However, the coupling frame connecting two DRLF is a recently developed enhancement during the ongoing DISSIPABLE [6] project. Therefore, design equations and guidelines for the coupling frame are missing yet. For the time being, design verification by non-linear static (pushover) and/or response history analysis (RHA) is needed. Development of design guidelines is foreseen during the DISSIPABLE [6] project.

The coupling beams are suspected to high seismic strength demands. Moreover, once the beam links are plastified, the contribution of the Coupling Frame on the overall stiffness increases, further enlarging demands on coupling beams. Consequently, usually relatively high strength steels will be needed to be applied for these elements.

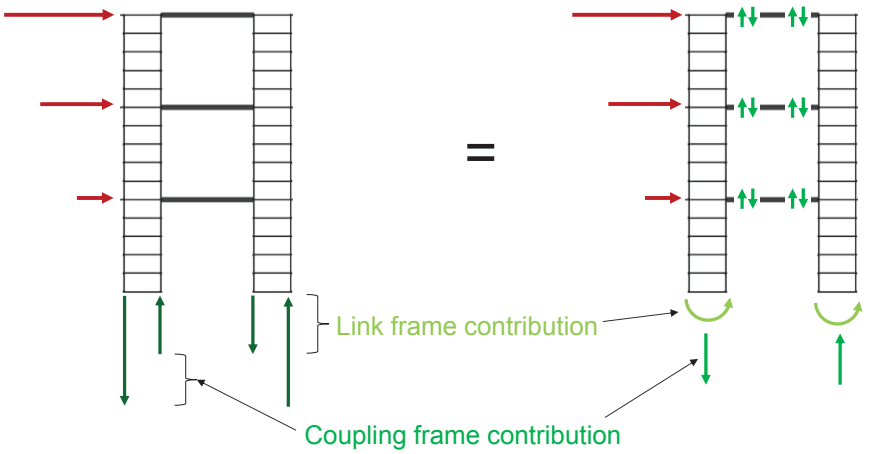

Figure 3: Load transfer and resistance contribution of the single DRLF and the CF.

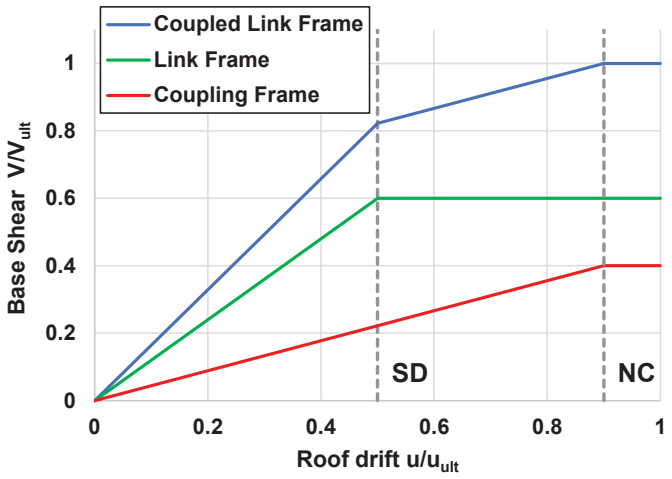

Figure 4: General behavior of the CDRLF and contribution of its single components.

The general design philosophy behind the CDRLF is summarized in Table 1. For frequent earthquakes, no damage shall occur to the overall lateral load resisting system. For the design basis earthquake, only the Dissipative Replaceable Links shall be damaged, while coupling beams are foreseen to remain elastic. Thus, the whole building results to be repairable, preventing its demolition. Only for very rare earthquakes, also the coupling beams are allowed to suffer damage, in order to prevent collapse of the building while sacrificing its reparability.

Possible design scenarios	10% in 10 yrs 95 yrs	10% in 50 yrs 475 yrs	2% in 50 yrs 2475 yrs
Performance target	No damage	Reparability	No collapse
Damage to dissipative links	No	Yes	Yes
Damage to coupling beams	No	No	Allowed
Reparability	---	Yes	No, if coupling beams damaged

Table 1: Design philosophy for the Coupled Dissipative Replaceable Link Frame (CDRLF).

3 CASE STUDY

To illustrate the concept of the CDRLF, in the following a typical 8-story office frame building has been designed in two different ways. In the first one, no coupling beams have been introduced, which rendered the system to be a DRLF. In the latter approach, the coupling frame effect was introduced, resulting in a CDRLF system.

The main dimensions of the initial situation used as starting point are shown in Figure 5. Firstly, the two designs have been conducted to satisfy seismic design requirements according to Eurocode 8 [7] regarding strength as well as stiffness. Table 2 shows an overview of the loads considered in design. Furthermore, the characteristics of the considered seismic action are summarized in Table 3.

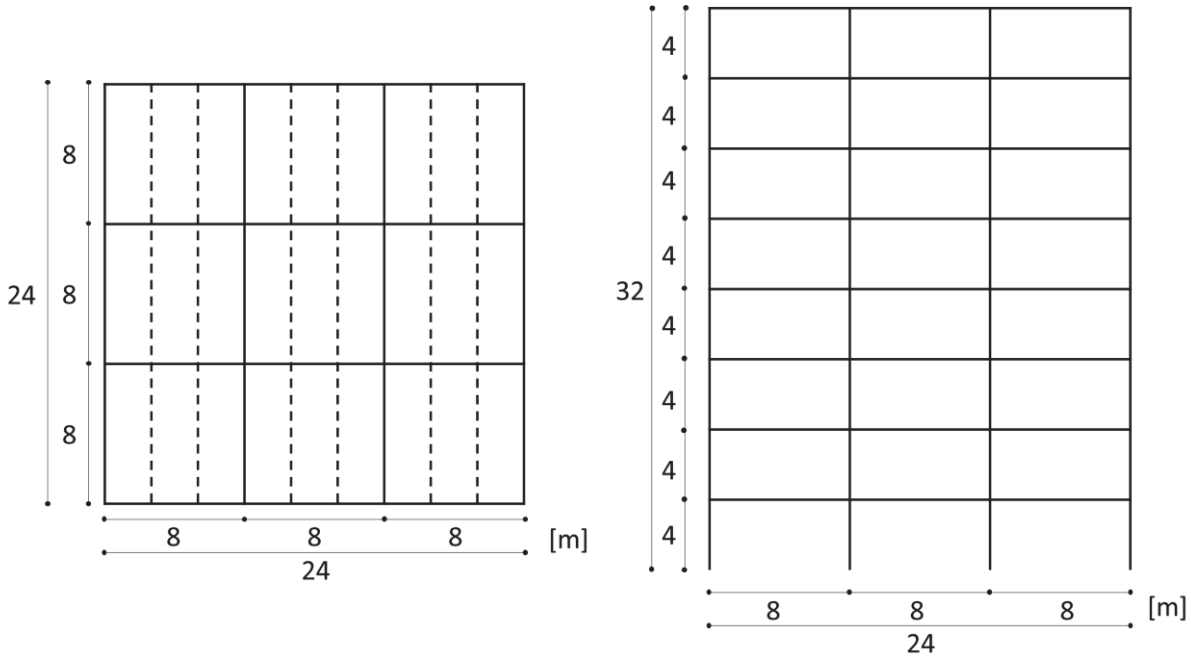

Figure 5: General floor plan and elevation of 8-story case study.

Design loads	Description	Load value
Dead loads	Composite slab and steel sheeting	2.75 kN/m²
Superimposed loads	Services, ceiling and raised floor	
	- intermediate floors	0.70 kN/ m²
	- top floor	1.00 kN/m²
	Perimeter walls	4.00 kN/m²
Live loads	Offices (Class B)	3.00 kN/m²
	Movable partitions	0.80 kN/m²

Table 2: Loading conditions used for design.

Seismic design action	Description
Peak ground acceleration	$\alpha_{gR} = 0.3g$
Importance factor (Class II)	$\gamma_I = 1.0$
Ground type	B ($S = 1.2$, $T_B = 0.15$ s, $T_C = 0.5$ s, $T_D = 2.0$ s)
Type of response spectrum	Type 1
Lower bound factor β	0.2
Behavior factor q	2.0 for the reference structural system 2.8 for the optimized structural system

Table 3: Seismic design action according to Eurocode 8.

Finally, the designs resulted in the following case study frames shown in Figure 6:

- Reference structural system: 2D frame with three Dissipative Replaceable Link Frames and pinned coupling beams (see Figure 6a), thus no coupling frame action;
- Optimized structural system: 2D frame with two Dissipative Replaceable Link Frames and two bays with coupling beams, for which alternating pinned/fixed connections were used (see Figure 6b); thus, the whole system is a Coupled Dissipative Replaceable Link Frame.

For a better understanding of the structural response, especially the influence and contribution of dissipative links and coupling beams, these two structural configurations were studied in detail by means of pushover and response history analyses.

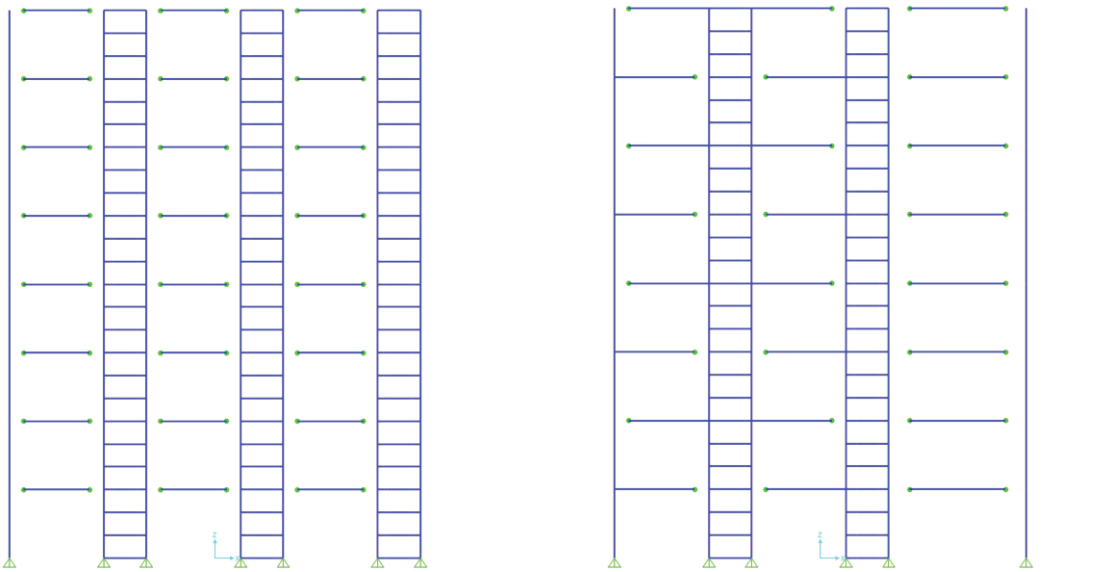

(a) Reference system – 3 × DRLFs (all coupling beam ends are pinned)

(b) Optimized system – 2 × DRLFs + 2 × CFs (coupling beam ends alternating pinned and fixed)

Figure 6: Case study frames: (a) reference system; (b) optimized system.

The general properties for the case study frames are summarized in Table 4. The design and analyses were performed with RSTAB 8 [10] and SAP2000 [11]. Based on the presence of the reinforced concrete slabs, a rigid diaphragm constraint was considered for the nodes of each floor. The masses were calculated automatically from the applied gravitational loading on the structure. The importance of the second order effect was evaluated through the value of the inter-story drift sensitivity coefficient θ [12]. The coefficient θ was computed for each level, and the maximum value was found between $0.1 < \theta \leq 0.2$. Consequently, second order effects were considered in an approximate way by multiplying the design values of the demands with the following factor: $\alpha = 1/(1-\theta)$.

The cross-sections used for the lateral force resisting system of the reference and optimized structural systems are presented in Table 5. The design of the lateral force resisting system was governed by the deformation limitation (corresponding to the serviceability limit state – SLS, and/or to the ultimate limit state – ULS). In case of the optimized system, the coupling beams were modeled with alternating pinned/fixed connections with the aim to increase their flexibility and to avoid the formation of plastic hinges at serviceability limit state (SLS), ultimate limit state (ULS) and as much as possible at near collapse (NC) seismic intensity level. Beside the pinned/fixed connection solution, the coupling beams corresponding to floors 1÷4 were realized with S460 steel grade (Table 5). Reduced beam sections (RBS) were considered for the dissipative links for both structural systems. The P-Delta effect of the seismic masses that was not attributed to the frame was considered by employing a leaning column. The maximum usable behavior factor q was 2.0 for the reference system and 2.8 for the optimized system. Larger behavior factors were not exploitable (i.e. not needed), because stiffness requirements did not allow for a further decrease of cross sections.

Structural system	Reference	Optimized
Stories	8 @ 4 m	8 @ 4 m
Bays	3 @ (5.5 + 2.5 m)	2 @ (5.5 + 2.5 m) & 1 @ 8 m
Column base connection	pinned	pinned
Coupling beam connections	pinned at both ends	fixed at one end, pinned at the other end

Table 4: General properties of the case studies.

	Reference system (T_1=2.75 sec.)		Optimized system (T_1=2.56 sec.)		
Floor	Links (S235)	Columns (S355)	Links (S235)	Coupling beams (S460 & S355)	Columns (S355)
8	HEA-200	HEB-450	HEA-200	HEB-400 (S355)	HEB-450
7	HEA-220	HEB-450	HEA-200	HEB-400 (S355)	HEB-450
6	HEA-220	HEB-450	HEA-200	HEB-400 (S355)	HEB-450
5	HEA-240	HEB-450	HEA-220	HEB-400 (S355)	HEB-450
4	HEA-240	HEB-450	HEA-240	HEB-400 (S460)	HEB-450
3	HEA-260	HEB-450	HEA-260	HEB-400 (S460)	HEB-450
2	HEA-260	HEB-450	HEA-280	HEB-400 (S460)	HEB-450
1	HEA-280	HEB-450	HEA-280	HEB-400 (S460)	HEB-450

Table 5: Cross-sections of elements for the reference and optimized system.

4 SEISMIC PERFORMANCE EVALUATION

The seismic performance was evaluated through: (i) nonlinear static analyses (pushover) using the N2 method [13]; and (ii) nonlinear dynamic analyses (time-history). Both types of analyses were performed using SAP2000 [11] and considering the 2D structural configurations illustrated in Figure 6. The N2 method [13] was used for determining the target displacements and the state of the two structural systems corresponding to the three seismic intensity levels. The response under a set of seven recorded accelerograms was evaluated through time-history analyses.

4.1 Nonlinear static analyses

The N2 method, developed by Fajfar [13] and comprised in Annex B of EN 1998-1 [7], can be used to verify the seismic performance of buildings designed by current methods (i.e. response spectrum analyses). The method combines the nonlinear static analysis of a multiple degrees of freedom system (MDOF) with an analysis based on the response spectrum of a single degree of freedom system (SDOF). The lateral story forces were assumed to be proportional to the 1st mode of vibration. Furthermore, the structural performance was evaluated for the limit states shown in Table 6, where "a_{gr}" is the reference peak ground acceleration of *0.3g*, and "a_g" represents the peak ground acceleration for a specific earthquake level.

Limit state	Return period, [years]	Probability of exceedance	a_g/a_{gr}	a_g/g
Damage Limitation (DL / SLS)	95	10% / 10 years	0.5	0.15
Significant Damage (SD / ULS)	475	10% / 50 years	1.0	0.30
Near Collapse (NC)	2475	2% / 50 years	1.7	0.51

Table 6: Limit states and corresponding scaling factors for the seismic input.

For beams subjected to flexure, based on FEMA 356 [14] and Annex B of EN 1998-3 [15], the following acceptance criteria were considered corresponding to the rotation at DL, SD and NC: $1{\cdot}\theta_y$, $6{\cdot}\theta_y$ and $8{\cdot}\theta_y$, where θ_y is the yield rotation. The damage state conditions of the plastic hinges associated to three limit states are similar in both codes, and it can be assumed that Immediate Occupancy (IO) corresponds to Damage Limitation (DL), Life Safety (LS) stands for Significant Damage (SD), and Collapse Prevention (CP) relates to Near Collapse (NC).

The plastic hinge definitions for the Dissipative Replaceable Links (see Table 7) were based on the parameters reported in [2].

Point	$M/M_{pl,RBS}$	$\theta/\theta_{pl,,RBS}$	Acceptance criteria	
A	0	0	Limit state	($\theta/\theta_{pl,RBS}$)
B	1	0	IO	15
C	1.27	40	LS	20
D	0.6	40	CP	35
E	0.6	45		

Table 7: Non-linear hinge parameters considered for the Dissipative Replaceable Links.

From the nonlinear static analyses, a pushover curve (capacity curve) was obtained for each structure. Further, using the N2 method [13], the target displacements (D_t) were obtained for the two structural systems corresponding to each of the three seismic intensity levels (i.e. SLS, ULS, NC). The obtained target displacement values are summarized in Table 8. As can be observed, very similar values were obtained for the two structures.

	Limit state	a_g/a_{gr}	Reference structure	Optimized structure
D_t [m]	DL / SLS	0.5	0.157	0.157
	SD / ULS	1.0	0.314	0.315
	NC	1.7	0.533	0.535

Table 8: Target displacements of reference and optimized structures.

The outcomes of the nonlinear static analyses are shown in terms of: (i) capacity curve (base shear force vs. top displacement); (ii) the state of the lateral load resisting frames corresponding to the three seismic intensity levels (SLS, ULS, NC), i.e. at the computed target displacements. It is to be noted that the target displacements are marked on each capacity curve. The outcomes are presented for the following configurations: (i) Reference structure (see Figure 7); (ii) Optimized structure (see Figure 8).

Based on the state of each structural configuration (plotted for the three seismic intensity levels – SLS, ULS and NC), the following observations can be made:

- at SLS – both structural configurations were characterized by an elastic response;
- at ULS – the reference structure was characterized by an elastic response, while plastic hinges developed in the dissipative links at the first five stories of the optimized structure;
- at NC – both structural systems evidenced plastic hinge development in the dissipative links, but the rotations did not reach the life safety or collapse prevention levels; in case of the optimized structure, the coupling beams did not develop plastic hinges.

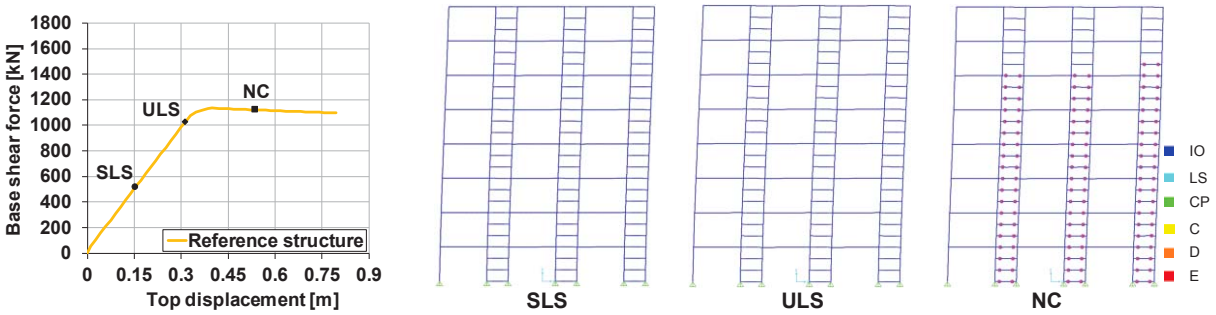

Figure 7: Reference structure: capacity curve and the state of the frame at the three seismic intensity levels – SLS, ULS, NC (i.e. a_g/a_{gr}=*0.5; 1.0; 1.7*).

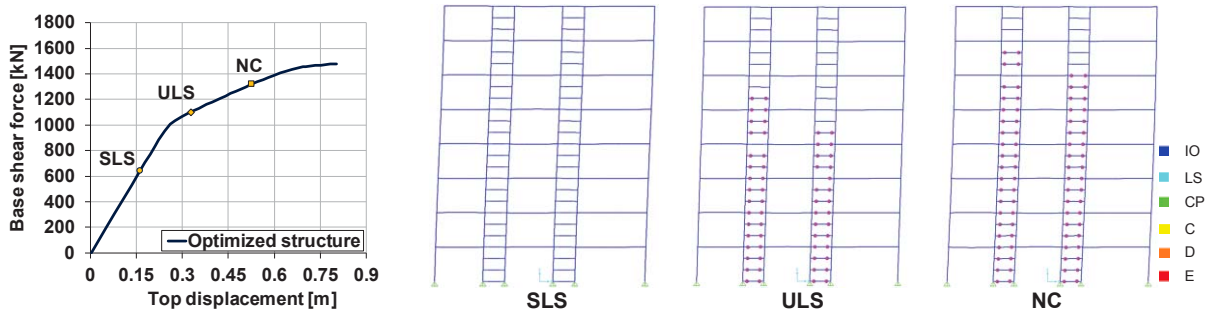

Figure 8: Optimized structure: capacity curve and the state of the frame at the three seismic intensity levels – SLS, ULS, NC (i.e. a_g/a_{gr}=*0.5; 1.0; 1.7*).

A comparison between the pushover curves of the two structural systems, i.e. reference and optimized, is shown in Figure 9a. As can be observed, the initial stiffness and the post-yield response of the two structural systems evidence some differences:

- The reference structure (for which the coupling beams were pinned at both ends) showed a relative lower initial stiffness. In the post yield region, the pushover curve was characterized by a horizontal tendency (i.e. large deformations with little decrease of force).
- In case of the optimized structure (for which the coupling beams were modeled with alternating pinned/fixed connections), the pushover curve evidenced a linear ascending tendency in the post yield region (i.e. capacity increases with the deformation).

The improved response of the optimized structures, i.e. bilinear shape with a linear ascending tendency in the post yield region, can be explained by examining the shape of the pushover curves of the two subsystems (i.e. coupling beam frames, dissipative link frames). Subsequently, the contribution of each of the two subsystems is illustrated in Figure 9b. Compared to the link-frame subsystems, the coupling beam frames are characterized by a linear-elastic response, with a lower stiffness and capacity. The linear-elastic response of coupling beam frames is therefore responsible for the linear ascending tendency in the post yield region of the optimized structural system and confirms the potential for improved performance and increased re-centering capacity.

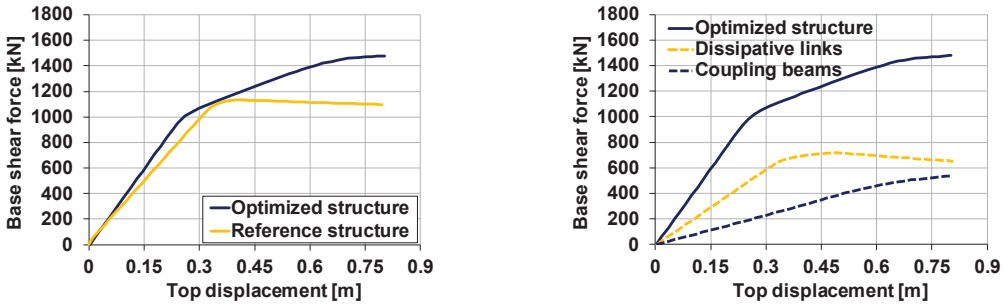

Figure 9: (a) Comparison between the pushover curves of the reference and optimized structural systems; (b) response/contribution of the dissipative link frames and coupling beam frames.

4.2 Nonlinear dynamic analyses

The two systems were further analyzed by means of dynamic time history analyses. A set of seven accelerograms matching the target spectrum has been chosen from the PEER NGA online ground motion database [16]. The scaling factors have been set such, that requirements according to the current draft of the revision of Eurocode 8 are met. These are as follows:

- Scaling factors not larger than *2.0*, nor smaller than *0.5*.
- The period range of interest has been set to $0.2 \cdot T_{1,min}$ to $1.5 \cdot T_{1,max}$, whereby $T_{1,min}$ and $T_{1,max}$ are the minimum and maximum fundamental periods of the considered frames.
- Within this period range, the ratio of mean to target spectrum should be within the range of *0.75* to *1.30*. Moreover, the average of this ratio over the considered period range should be larger than *0.95*. Also, for each individual spectrum the ratio should nowhere be below *0.5* within that range.
- Not more than two records of the same earthquake should be used.

The final suite of seven accelerograms is listed within Table 9. Each record can be correlated to the PEER data base with the Record Sequence Number (RSN). Figure 10 shows the target, mean and individual spectra along with a vertical line, indicating where the period range of interest begins. The first mode periods T_1 for the reference and optimized structure correspond to 2.75 s and 2.56 s, respectively. The 50%, 75% and 130% scaled target spectrum used for ground motion selection is also indicated in the figure.

#	RSN	Scale factor	R [km]	M	Earthquake name	Year	Station
1	6	1.11	6.1	6.95	Imperial Valley-02	1940	El Centro Array #9
2	15	1.95	38.7	7.36	Kern County	1952	Taft Lincoln School
3	20	1.32	26.9	6.5	Northern Calif-03	1954	Ferndale City Hall
4	30	1.65	9.6	6.19	Parkfield	1966	Cholame-Shandon #5
5	68	1.70	22.8	6.61	San Fernando	1971	Hollywood Stor FF
6	95	1.38	3.8	6.24	Managua Nicaragua-01	1972	Managua ESSO
7	96	1.85	4.7	5.2	Managua Nicaragua-02	1972	Managua ESSO

Table 9: Recorded acceleration time histories used for dynamic analyses.

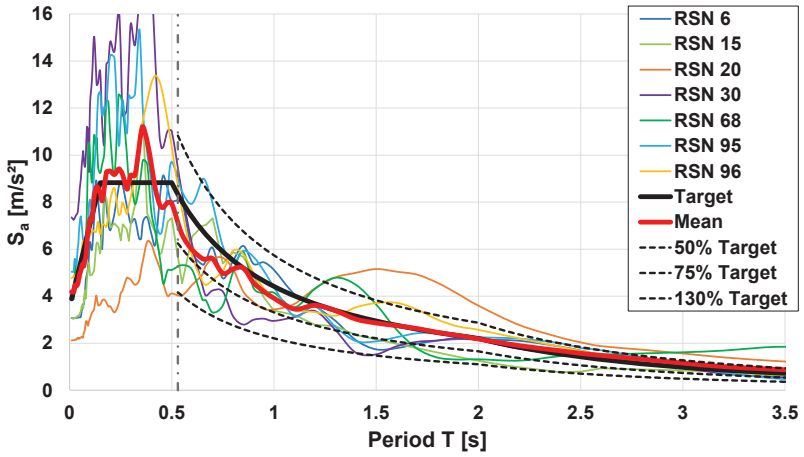

Figure 10: Elastic response spectra of mean and individual accelerograms compared to the target spectrum.

The outcomes of the time-history analyses are presented for both reference and optimized structural configuration in terms of: (i) comparison of the displacement at top floor; (ii) state of frame corresponding to the maximum displacement (i.e. scaled deformed shape with marked plastic hinges). Consecutively, the response under one of the seven accelerograms (i.e. *#5 – RSN 68*) at the three intensity levels (SLS, ULS and NC) is shown in Figure 11.

As can be observed, the time-history analyses evidenced the following:

- *at SLS (serviceability limit state – a_g/a_{gr}=0.5)*: ▪ plastic hinges did not develop in any of the two structural systems (reference or optimized); ▪ the comparison between displacements at top floor showed similar deformations – with slightly lower values corresponding to the optimized structure;
- *at ULS (ultimate limit state – a_g/a_{gr}=1.0)*: ▪ plastic hinges developed in the dissipative links (at seven out of eight stories) for both structural configurations; ▪ the comparison between displacements at top floor showed some differences, i.e. lower deformations corresponding to the optimized structure; ▪ the rotations within plastic hinges did not reach the life safety or collapse prevention levels;
- *at NC (near collapse – a_g/a_{gr}=1.7)*: ▪ a global plastic mechanism was evidenced with plastic hinges in the dissipative links for both structural systems; ▪ the comparison between displacements at top floor showed significant differences between the reference and optimized structure for five out of seven accelerograms which lead to residual deformations (i.e. *#1,3,5,6,7*); ▪ for both structural systems, the replaceable dissipative links did not evidence rotations corresponding to life safety or collapse prevention levels; ▪ the optimized structure evidenced plastic hinges in the coupling beams only for one out of seven accelerograms (i.e. *#3 – RSN 20*).

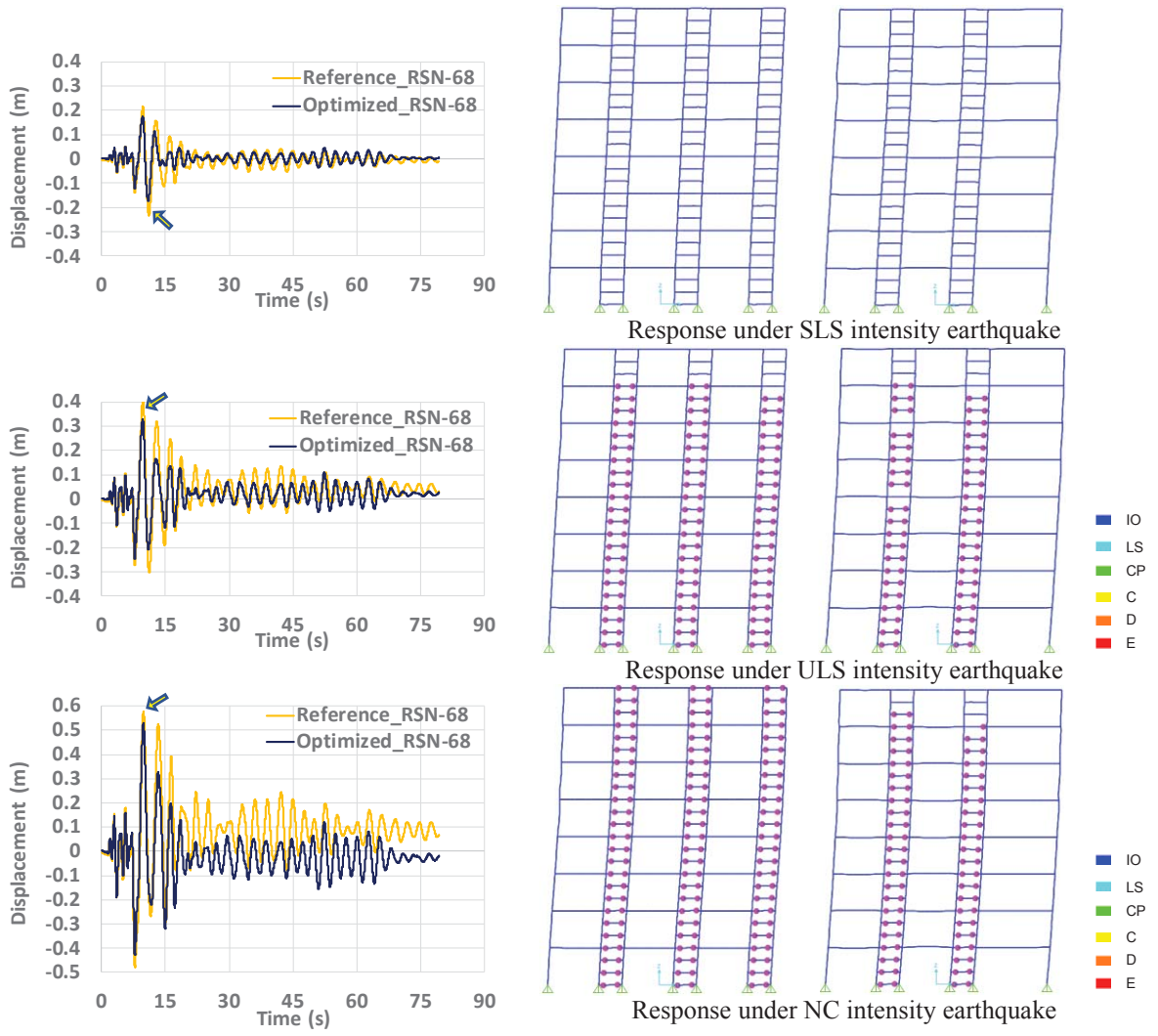

(a) Comparison of the response (b) Reference structure (c) Optimized structure

Figure 11: Outcomes of time-history analyses: (a) comparison of the response (top displacement vs. time); (b) & (c) state of reference and optimized structures.

The nonlinear dynamic analyses also allowed to evaluate the inter-story drifts corresponding to each: (i) structural configuration (reference / optimized); (ii) accelerogram (*#1 to #7*); (iii) seismic intensity level (SLS, ULS, NC).

Exemplarily, Figure 12 illustrates the inter-story drifts generated by one of the accelerograms (*#5 – RSN68*) within the two systems. In general, largest inter-story drifts occur at the mid-floors for the reference system, whereby the optimized system is characterized by larger drifts at the bottom and small ones at the top. Besides the lower floors, inter-story drifts tend to be less large for the optimized system compared to the reference structure.

The average of the maximum (+/-) inter-story drift values for the reference and optimized structures, corresponding to each seismic intensity level (SLS, ULS, NC), was computed from the outcomes of the set of seven selected accelerograms listed in Table 9. The average values summarized in Table 10 confirm the observations mentioned above regarding the minimum inter-story drifts also for other accelerograms. The maximum inter-story drifts occurred at 6^{th}÷7^{th} floor for the reference structure, respectively at 5^{th}÷6^{th} floor for the optimized structure.

In Figure 13 the average inter-story drifts between reference and optimized structure can be compared. Besides the first two floors, the optimized structure showed in general lower drifts. Moreover, the inter-story drift profile is more uniform throughout the height.

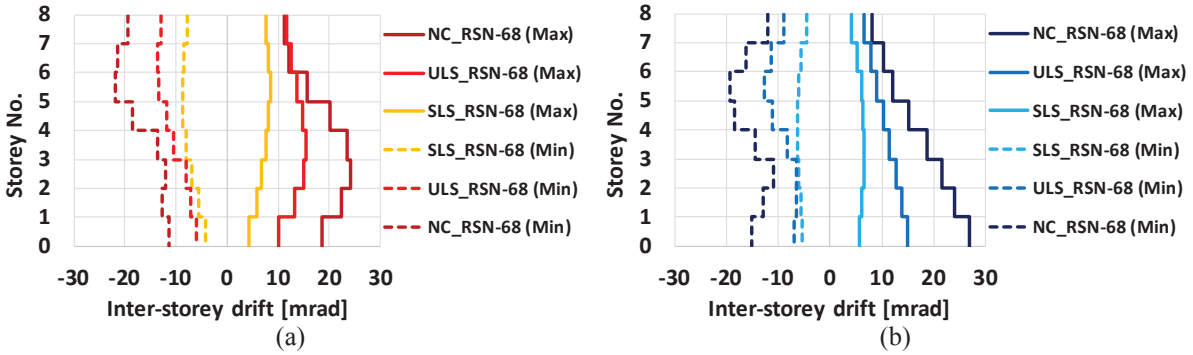

Figure 12: Inter-story drifts generated by *#5 – RSN68* within the corresponding structural systems: (a) reference structure; (b) optimized structure.

Story	Reference structure			Optimized structure			Ratio optimized/reference		
	SLS	ULS	NC	SLS	ULS	NC	SLS	ULS	NC
8	7.4	13.9	19.6	5.3	9.3	12.2	0.72	0.67	0.62
7	**7.7**	**14.5**	21.0	6.5	11.8	15.8	0.84	0.81	0.75
6	7.5	14.1	**21.5**	**7.1**	**13.2**	18.5	0.95	0.94	0.86
5	6.9	13.4	20.5	6.8	12.6	**18.6**	0.99	0.94	0.91
4	6.5	12.9	20.3	6.4	11.8	17.6	0.98	0.91	0.87
3	5.8	11.5	18.6	5.8	10.9	17.5	1.00	0.95	0.94
2	5.2	10.1	15.9	5.3	10.5	17.7	1.02	1.04	1.11
1	4.1	7.6	12.3	5.1	10.4	18.4	1.24	1.37	1.50

Table 10: Average of the maximum inter-story drifts [mrad] corresponding to the three seismic intensity levels (SLS, ULS, NC) and the two structural configurations (reference / optimized).

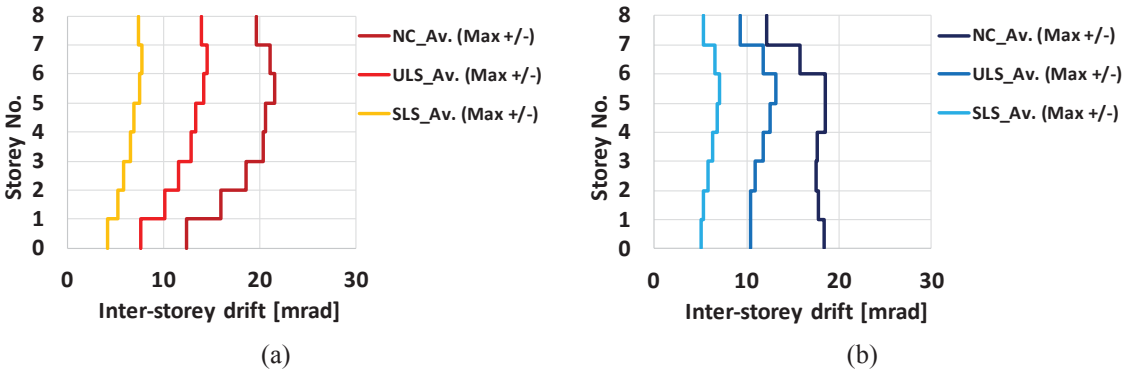

Figure 13: Average of the maximum (+/-) inter-story drifts corresponding to the three seismic intensity levels (SLS, ULS, NC) and the two structural configurations: (a) reference; (b) optimized.

The response of the two structural systems was evaluated by comparing the residual deformations. Figure 14 shows the residual deformation at the top floor corresponding to each of the seven accelerograms at NC intensity level for both structural configurations. As can be observed, the largest residual deformations were evidenced for *#3 – RSN 20*. Furthermore, for five out of seven accelerograms (*RSN 6 / 20 / 68 / 95 / 96*) the residual deformations of the optimized structure were approximately by two thirds lower compared to the reference structure.

Regarding the seismic performance and resilience of a structural system, some important aspects are represented by: (i) the possibility of structural repair; (ii) a low amount of residual deformations; (iii) the re-centering capability of the structure. Table 11: Reference vs. optimized structural configuration: fulfilment of resilience/seismic performance criteria shows an overview with regard to the fulfillment of the resilience and seismic performance criteria by the two structural systems (reference vs. optimized). Through the use of replaceable dissipative links, potentially both structural systems have the possibility to be repaired after a seismic event. In contrast to the reference structure (with relatively high residual deformations, and no re-centering capability), the optimized structural system fulfils all three criteria:

- *Structural repair* – through the use of replaceable dissipative devices;
- *Low residual deformations* – through the use of coupling beams of high strength steel and with alternating pinned/fixed connections (for an elastic response);
- *Re-centering capability* – by incorporating the two bays with coupling beams (of high strength steel and pinned/fixed connections) characterized by an elastic response, which will contribute to the structural re-centering during the replacement of the dissipative links.

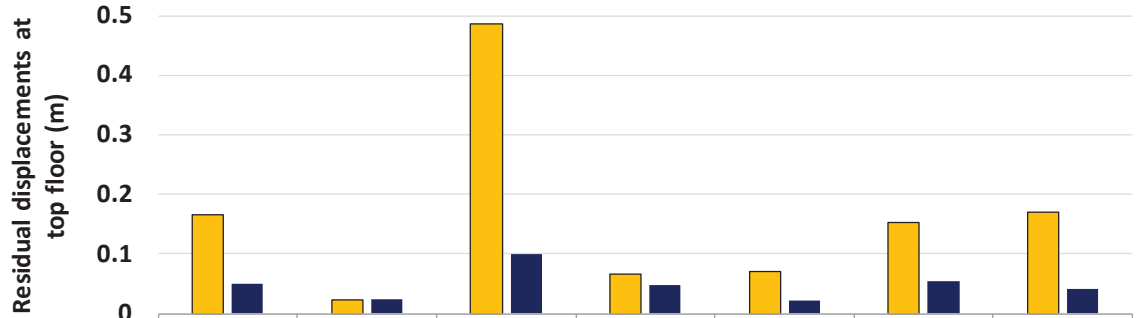

	RSN_06	RSN_15	RSN_20	RSN_30	RSN_68	RSN_95	RSN_96
Reference	0.166	0.024	0.485	0.066	0.070	0.152	0.171
Optimized	0.050	0.024	0.099	0.048	0.021	0.055	0.041

Figure 14: Reference vs. optimized structural system: residual displacements at the top floor corresponding to each of the seven accelerograms (NC seismic intensity level).

Performance criterion	Reference structure	Optimized structure
Structural repair	***Yes***: both structural systems are generally reparable through the use of Dissipative Replaceable Links (DRL)	
Low residual deformations	***No***: the reference structure is characterized by relatively high residual deformations	***Yes***: the optimized structural system is characterized by a significant reduction of residual deformations, resulting from the use of the two bays with pinned-fixed coupling beams
Re-centering capability	***No***: the reference structure does not possess any worth mentioning re-centering capability	***Yes***: the optimized structure contains two bays with pinned-fixed coupling beams that responded elastically, and therefore, would contribute to the re-centering of the structure during the replacement of the dissipative links

Table 11: Reference vs. optimized structural configuration: fulfilment of resilience/seismic performance criteria.

5 CONCLUSIONS

The preliminary investigations on the newly developed CDRLF system within this paper show its general feasibility and potential of enhancing the already known DRLF system regarding stiffness increase and improved re-centering capability for mid to high rise buildings. Thus, it renders an alternative to application of partial-strength joints to the gravity load bearing frame of a system with DRLFs, as conventionally done for introducing additional stiffness. Main conclusions derived from the investigated case study are as follows:

- The design philosophy was shown to work effectively for the considered case study. Damage to coupling beams was not triggered up to NC and beyond, while almost all of dissipative links showed plastic response.
- The optimized system, two DRLFs with 'one end fixed – the other end hinged' coupling beams, showed a significant improvement over the reference system with three DRLFs.
- The improvement consists of:
  - the decrease in needed amount of DRLF bays (two compared to three),
  - an improved global force displacement relationship (introduced hardening slope after damage to dissipative links),
  - lower inter-story drifts,
  - noteworthy re-centering capability and, thus,
  - much lower residual displacements.
- This optimization results in a system that fully complies with the envisaged performance targets, which is repairability by restricting damage to dissipative replaceable links only, limiting of residual displacements and providing re-centering capability by the coupling beams.
- To achieve the performance targets – widespread damage to dissipative links before damage to coupling beams is triggered – a balanced stiffness distribution between the two DRLFs and the coupling frames is necessary. The coupling frame needs to be stiff enough, to increase noteworthy overall stiffness, but on the same time flexible enough, to prevent attraction of too much force, once the DRLFs soften du to energy dissipation.
- The balance of the stiffness was achieved by introducing a hinge at one end of each coupling beam.
- Sophisticated static nonlinear (pushover) are needed to assure that the foreseen performance targets are met. Simple application of current seismic design equations for designing the CDRLF system does not necessarily guarantee a well performing structure. Therefore, simplified design equations especially for the coupling beams are needed to ease application of the CDRLF system in practice.
- The strength design of the coupling beams might be challenging, especially when both coupling beam ends are designed to be fixed. Thus, often coupling beams in high strength steel will be required, as the increase of section size would jeopardize the need of a balanced stiffness distribution between DRLFs and CFs.

Finally, it can be stated that the CDRLF system is currently under investigation within the ongoing DISSIPABLE project. The study presented in this research shows promising results. A testing campaign consisting of hybrid tests on a 2D frame as well as shaking table tests on a 3D structure is underway. Eventually, the project consortium will deliver design guidelines along with a worked example.

6 ACKNOWLEDGEMENTS

Research leading to the innovative design concept presented in this paper has received funding in the framework of following European research projects: FUSEIS ("Dissipative Devices for Seismic Resistant Steel Frames"), MATCH ("Material Choice for Seismic Resistant Structures"), INNOSEIS ("Valorization of Innovative Anti-Seismic Devices") and DISSIPABLE ("Fully Dissipative and Easily Repairable Devices for Resilient Buildings with Composite Steel-Concrete Structures"). The financial contribution of the Research Fund for Coal and Steel (RFCS) of the European Community is gratefully acknowledged.

The second author was supported by the Alexander von Humboldt Foundation through a Research Fellowship for Experienced Researchers, which is also gratefully acknowledged.

REFERENCES

[1] FUSEIS – Dissipative devices for seismic-resistant steel frames, Final Report, Grant Agreement RFSR-CT-2008-00032, 2011.

[2] G. Dougka, D. Dimakogianni, I. Vayas, Innovative energy dissipation systems (FUSEIS 1-1) — Experimental analysis. Journal of Constructional Steel Research 96 (2014) 69–80, http://dx.doi.org/10.1016/j.jcsr.2014.01.003.

[3] M. Pinkawa, B. Hoffmeister, S. Schaffrath, M. Feldmann, Seismic Design with FUSEIS Beam Links, *ANIDIS Conference, Pistoia, Italy*, 2017.

[4] MATCH – Material Choice for Seismic Resistant Structures, Final Report, Grant Agreement RFSR-CT-2013-00024, 2016.

[5] INNOSEIS – Valorization of Innovative Anti-Seismic Devices, Grant Agreement RFCS-2015-709434, 2017.

[6] DISSIPABLE – Fully Dissipative and Easily Repairable Devices for Resilient Buildings with Composite Steel-Concrete Structures, Grant Agreement RFCS-2017-800699, project ongoing (2018-2021).

[7] Eurocode 8: Design of structures for earthquake resistance – Part 1: General rules, seismic actions and rules for buildings; German version EN 1998-1:2004 + AC:2009.

[8] J. Xiaodong, W. Yandong, M. Qifeng, T. Okazaki, Cyclic Behavior of Replaceable Steel Coupling Beams, Journal of Structural Engineering, 2017, 143(2): 04016169.

[9] A. Ioan, A. Stratan, D. Dubina, M. Poljansek, F.J. Molina, F. Taucer, P. Pegon, G. Sabau, Experimental Validation of Re-centring Capability of Eccentrically Braced Frames with Removable Links, *Eng. Struct.*, Vol. 113, 2016, pp. 335-346, ISSN 0141-0296, https://doi.org/10.1016/j.engstruct.2016.01.038.

[10] RSTAB 8, Structural Analysis of General Frameworks, Dlubal Software GmbH, Tiefenbach, Germany, 2020.

[11] CSI Berkley, SAP2000 v21, Copyright Computers and Structures, 2019.

[12] R. Landolfo, F. Mazzolani, D. Dubina, L.S. da Silva, M. D'Aniello, Design of steel structures for buildings in seismic areas. ECCS – European Convention for Constructional Steelwork, ISBN (ECCS): 978-92-9147-138-6, DOI:10.1002/9783433609194, 2017.

[13] P. Fajfar, A nonlinear analysis method for performance-based seismic design, Earthquake Spectra, 16(3):573-92, 2000.

[14] FEMA 356, Prestandard and commentary for the seismic rehabilitation of buildings, Federal Emergency Management Agency, Washington (DC), 2000.

[15] Eurocode 8, Design of structures for earthquake resistance – Part 3: Assessment and retrofitting of buildings; German version EN 1998-3:2005 + AC:2010.

[16] T. D. Ancheta, et al., PEER NGA-West2 Database, PEER Report 2013/03, Pacific Earthquake Engineering Research Center, California, Berkeley, 2013.

EURODYN 2020
XI International Conference on Structural Dynamics
M. Papadrakakis, M. Fragiadakis, C. Papadimitriou (eds.)
Athens, Greece, 23–26 November 2020

USE OF HIGH-STRENGTH STEEL FOR MULTI-CRITERIA OPTIMIZATION OF DISSIPATIVE DEVICES

S. Caprili[1], **I. Panzera**[1], **and W. Salvatore**[1]

[1] Department of Civil and Industrial Engineering, University of Pisa,
Largo Lucio Lazzarino1, 56122, Italy
e-mail: ivanpanzera@gmail.com
{s.caprili,walter}@ing.unipi.it

Keywords: Energy dissipation, seismic dissipative device, High-Strength Steel, Optimization, Finite element analysis.

Abstract. *Among the various strategies for the seismic protection of buildings, the use of passive devices based on energy dissipation through the development of plastic deformations represents a valid, simple and economic solution. During seismic events, damage is concentrated in correspondence of the dissipative elements which are thought to be replaced in the post-seismic phase in order to fully recover the initial capacity of the device and, therefore, to restore the original building behaviour. In this context, the adoption of steel devices has relevant impact and advantages on the overall building performance. In the present study, the implementation of a steel dissipative and replaceable device using High-Strength Steels (HSS) for the non-dissipative components was deeply analyzed, and results are briefly presented. The improvement due to HSS adoption accounted for the direct/short-term economic aspects (i.e. cost of the device, weight) and the indirect/long-term ones (i.e. seismic risk performance) within a multi-criterial optimization procedure.*

1 INTRODUCTION

In the last decades, with the aim of preventing damages on structures due to seismic events, several passive protection devices were developed exploiting different energy dissipation strategies such as friction, viscous, viscoelastic or plastic [1],[2]. Concerning dissipative plastic devices, the adoption of steel systems progressively diffused thanks to their optimal mechanical performance, lightness, workability and application versatility. Steel components can be connected through "*dry*" systems to structural elements, e.g. using bolted joints, and this can provide relevant advantages in the post-seismic phase allowing the easy replacement of the damaged components and providing the fully-recovery of the initial capacity.
In the present study, a steel Dissipative and Replaceable Device (in the following called DRD) developed within the research project DISSIPABLE "*Fully dissipative and easily reparable device for resilient buildings with composite steel-concrete structures"* funded by the Research Fund for Coal and Steel of European Commission and actually ongoing, is presented and deeply analysed. DRD's conception was developed as improvement of the existing INERD^{TM} connections, already proposed by [3]-[4]. Figure 1a shows the geometric configuration of the DRD device. Two pairs of plates (external and internal) are connected to the steel frame and braces within the structural configuration; the transversal *pin*, located between the plates, is the dissipative component devoted to absorb the relative displacements of the plates, developing plastic deformations and then dissipating the seismic energy stored during the earthquake; as visible, the pin is designed to be replaced after damages.

Respect to the previous configuration of the INERD^{TM} system, additional transversal spacers between plates were added to avoid transversal deformation, observed during cyclic experimental tests [5] (Figure 1b). Another relevant aspect concerns the accumulation of ovalization of plates' holes, causing pinching phenomena on the hysteretic cycle resulting in the reduction of the dissipative capacity of the system (Figure 1c).

a) b) c)

Figure 1: a) Configuration of DRD device; b) lateral deformation of plates in the INERD^{TM} system [5]; c) typical hysteretic behaviour of the DRD device.

The present work, as suggested by the project's guidelines, deeply investigates the possible use of high-strength steels (HSS) for the DRD realization: the impact of HSS in terms of overall cost/benefits over the whole life-cycle of hypothetical structures equipped with DRDs, in terms of both of direct (i.e. fabrication, installation, working) and indirect (i.e. the expected annual losses due to the seismic risk) costs' reduction was considered. Several different mechanical configurations of the devices, defined by varying both material and geometry, were studied through a parametric numerical and economic analysis. The following decision variables were adopted to carry out a multi-criterial optimization analysis aiming to determine the optimal design solution.

- Material's *cost* for device fabrication.
- Device's *weight*: including diseconomies of manufacture, transport, installation and load on the structures.
- *Dissipative capacity* of the device, in terms of energy dissipation with respect to the stiffness of the device.

2 THE USE OF HIGH STRENGTH STEEL

In last decades, the use of HSS progressively increased for the manufacturing of structural components; several countries started to elaborate and adopt standard provisions including HSS in the structural design [6]. However, currently, the application of HSS for the seismic design is limited by existing seismic design codes and constructional practice. Mild Steel (MS) is typically preferred since presenting a higher ductility and a higher dissipative capacity [7]. Besides, if the use of HSS can effectively reduce elements' sections since provided by higher strength, deformability problems can affect steel structures, highly limiting – from a practical point of view – the employment of those grades. If properly used, HSS can guarantee several advantages to seismic constructions:

- *Economic advantages*: increasing the strength, it is possible to reduce sections and therefore the self-weight of structures as well as costs for material, transportation, fabrication, assembling, processing and welding, overall management.
- *Structural safety*: self-weight's reduction leads to reducing the seismic mass. Therefore, excellent toughness proprieties guarantee higher safety level.
- *Architectural advantages*: the reduction of elements' size enables special aesthetical and elegant structural solutions.
- *Sustainability advantages*: the employment of lower materials' quantity leads to a lower use of resources, energy consumption, to the reduction of CO_2 emissions and of waste material during the whole life of the structure.

On the other hand, the cost of HSS is usually higher than the one associated to MS grades, increasing with the increase of the yielding strength; however, the costs' increase is lower respect to the increase of the strength performance [8]. This means that, for a *static* design, the adoption of HSS can be preferred to MS, but, in the case of seismic design (or even in the case of fire design [8]), due to the more brittle behavior of HSS, the lower resistance to crack propagation [9] and the higher sensitivity towards heating induced by processing (flame cutting, welding, flame straightening, etc.), usually MS is preferred to HSS.

3 PARAMETRIC ANALYSIS

Taking into consideration the structural performance of DRD previously defined, HSS can be used for the non-dissipative components (i.e. plates and stiffeners). Increasing the strength capacity of the plates, it is expected to achieve lower accumulation of plastic ovalization phenomena with the following increase of the overall dissipative capacity of the device. The HSS implementation can be assessed in parallel to the possible reduction of plates' thickness, then decreasing the resulting weight and costs of the system.

3.1 Definition of parametric configurations' set

The geometrical configuration of the DRD device considered is shown in Figure 2. The pin, with a shaped circular section, is located within the holes of the plates with a gap of 1.0 mm.

For the pin, S235 steel grade was selected in order to provide optimal ductility performance; for the plates, five different steel grades and three different thickness combinations were otherwise considered (respectively equal to 30/20 mm, 30/15 mm and 25/15 mm for the external/internal plates), globally resulting in 5x3=15 different possible configurations.

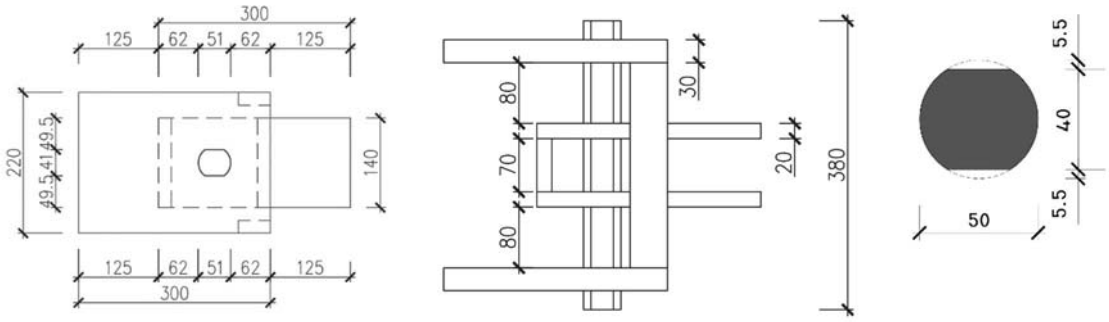

Figure 2: Geometrical configuration of the DRD.

Table 1 shows the five steel grades used for the plates, with indications concerning mechanical performance as suggested by EN10025-6-2004 [10] and estimated cost [€/kg], being f_y and f_u respectively the yielding and ultimate tensile strength, e_y and A the yielding and ultimate deformation. For the S235 used for the pin, the following values were adopted: f_y=215 MPa, f_u=360 MPa, A_g=0.40. In order to compare the results achieved by using HSS and ordinary MS, S355 steel grade was also considered. For the materials' cost estimation of Table 1 reference is made to [11], presenting the trend of the material cost (normalized to the one associated to S23) for each yielding stress of steel (Figure 3).

Steel grade	f_y [MPa]	e_y [-]	f_u [MPa]	A_g [-]	Cost [€/kg]	Weight [kg/m^3]
S355	355	0,0017	470	0,30	1,1549	7850
S500	500	0,0024	590	0,17	1,3434	7850
S620	620	0,0030	700	0,15	1,4994	7850
S690	690	0,0033	770	0,14	1,5904	7850
S890	890	0,0042	940	0,11	1,8504	7850

Table 1: Steel grades considered for optimization procedure.

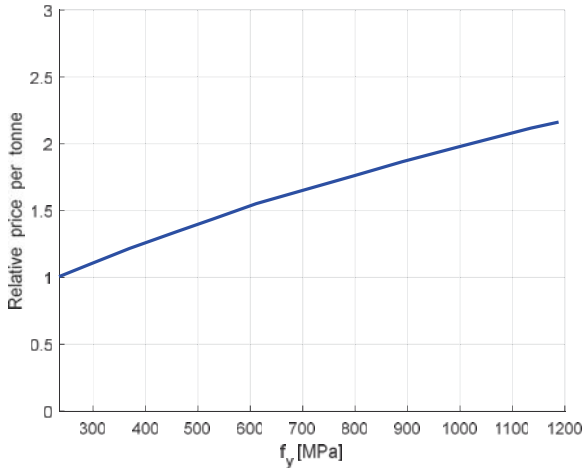

Figure 3: Steel material price vs yielding tension [11].

Cost vs yielding trend can be reliably approximated by equation (1), used for the evaluation of the costs presented in Table 1:

$$C(f_y) = 0.0013 \cdot f_y + 0{,}6934 \tag{1}$$

With the aim of assessing the practical application of the proposed solutions/combinations for the structural design, it was necessary to evaluate the connector-plate coupling as a "*pin*" connection, carrying out the resistance checks indicated by Eurocode 3 [12]. This highlighted that all the above-mentioned configurations satisfy all the requirements except for the bearing capacity of the internal plates, whose plasticization is therefore expected.

3.2 Numerical modelling of the DRD device

The numerical model of the DRD device was developed using the Finite Element (FE) software Abaqus® [13] basing on the model provided within the DISSIPABLE research project by the Instituto Superior Técnico (IST - Portugal), made available to the involved partners (Figure 4). Materials were represented through the used of elastic-plastic with isotropic-hardening law. A more refined mesh (cubic 4 mm sizes instead of 8 mm) was defined for the pin and the plates' portions close to it, providing better accuracy in the stress and strain distributions' calculation; element type selected was C3D4R. Contact between pin and plates was modelled as tangential "penalty" friction (with friction coefficient 0,45) and normal "hard" contact.

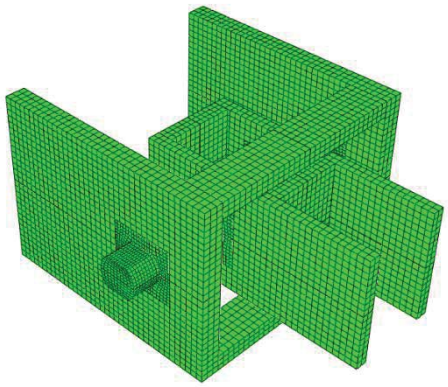

Figure 4: Numerical model of DRD developed with Abaqus ®.

3.3 Execution of numerical analyses and results

Each configuration was tested under cyclic loading condition using incremental imposed displacement according to the ECCS protocol [14]; 25 cycles were performed, whose amplification trend is presented in Figure 5a. In order to make each configuration easily comparable to the others, an equivalent yielding displacement (e_y) equal to 2.5 mm was assumed. The execution of preliminary monotonic pushover analyses showed that resulting capacity curves are not strictly affected by the variability of the steel grade adopted or by the internal plates' thickness and, as visible from Figure 5b, resulting differences are very small. Cyclic analysis was the performed using Abaqus/Standard.

Figure 6-shows the trend of the energy dissipated by the device for each considered configuration. Energy (E_n) was evaluated in correspondence of each n-th load step by means of equation (2), being F_n and δ_n respectively the force and the displacement associated to each n-th cycle.

$$E_n = E_{n-1} + \frac{1}{2} \cdot (F_n - F_{n-1}) \cdot (\delta_n - \delta_{n-1}) \quad (2)$$

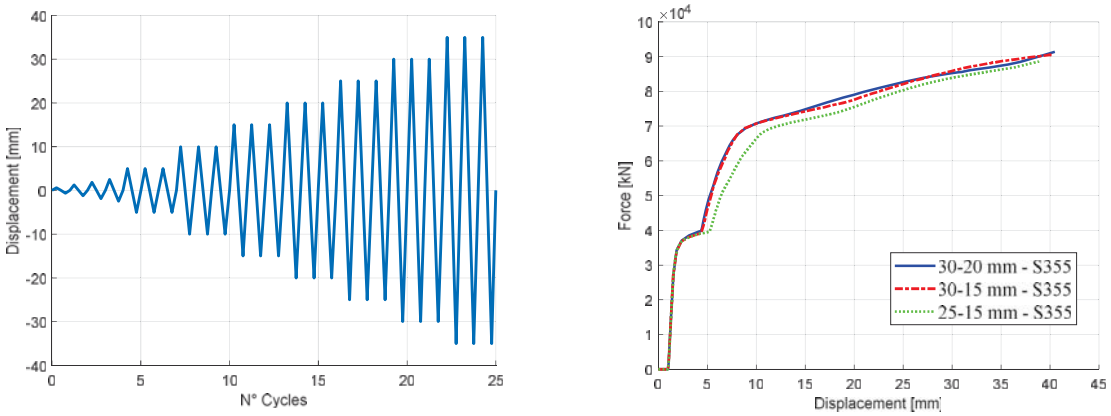

a) b)

Figure 5: a) Displacement history according to ECCS protocol; b) capacity curves for configurations with S355 and different thickness configurations (similar results for other steel grades were achieved)

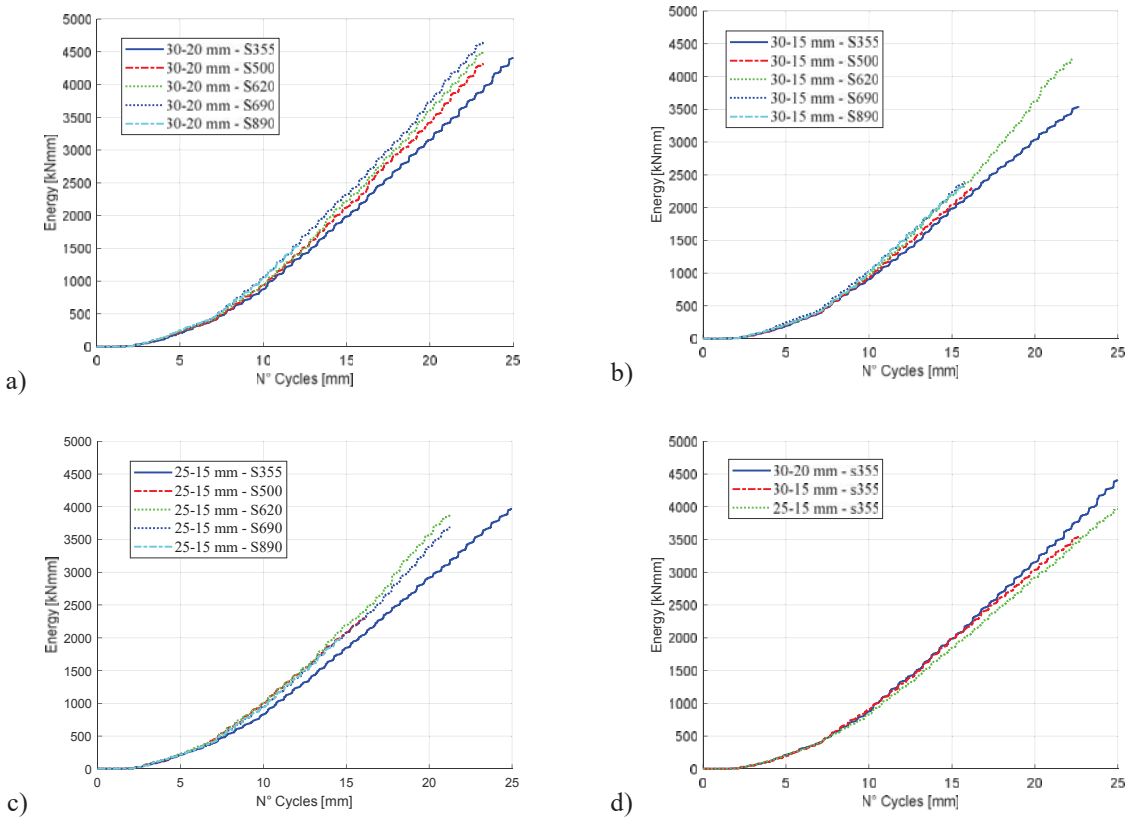

a) b)

c) d)

Figure 6: Accumulated energy vs N° cycles for different thickness combinations: a) 30-20 mm; b) 30-15 mm; c) 25-15 mm; d) comparison for S355.

It can be observed how the relative trend of the different curves remains proportional to the progress of the load cycles: higher HSS grades show better results in terms of dissipated energy

and reduction of the pinching effect. The optimization comparison is carried out in relation to the 12th cycle, achieved for all the configurations without numerical convergence errors.

The dissipative capacity shall be appropriately analysed in relation to the device' stiffness, proportional to the seismic input energy entering the structure. Analytical relationships available [3]-[15] allow to evaluate the device's stiffness according to the characteristics of the pin only; however, as can be observed by the numerical results, relevant differences in the stiffness occurred varying the thickness of the plates. For this reason, the value of the total energy accumulated by devices was divided by the average value of the stiffness developed (K_n) by the selected configuration, evaluated for each step according to equation (3):

$$K_n = \frac{(F_n - F_{n-1})}{(\delta_n - \delta_{n-1})} \tag{3}$$

The weight, cost (normalized according to the most expensive configuration), dissipated energy, maximum stiffness, energy/stiffness ratio for each configuration are presented in Table 2.

Configuration	W [kg]	Cost [-]	Energy [kNmm]	K_n [kNmm]	Energy / K_n
S355_30/20	54,8	0,64	1335,220	59,04	22,62
S500_30/20	54,8	0,74	1407,283	59,04	23,84
S620_30/20	54,8	0,82	1392,881	59,04	23,59
S690_30/20	54,8	0,87	1555,155	59,04	26,34
S890_30/20	54,8	1,00	1533,460	59,04	25,97
S355_30/15	51,4	0,60	1301,158	57,78	22,52
S500_30/15	51,4	0,69	1391,148	57,78	24,08
S620_30/15	51,4	0,77	1415,064	57,78	24,49
S690_30/15	51,4	0,81	1492,313	57,78	25,83
S890_30/15	51,4	0,93	1488,243	57,78	25,76
S355_25/15	46,6	0,54	1243,519	53,16	23,39
S500_25/15	46,6	0,62	1436,039	53,16	27,01
S620_25/15	46,6	0,69	1441,435	53,16	27,12
S690_25/15	46,6	0,73	1389,082	53,16	26,13
S890_25/15	46,6	0,84	1399,892	53,16	26,33

Table 2: Summary table on the optimization aspects for each configuration.

It is possible to observe how the configurations having of 25-15 mm thickness combination, although provided by lower dissipative capacity respect to the 30-15 mm ones (the best combination for energy optimization was S690_30/20), show the least stiffness and therefore allow to achieve the higher Energy / K_n ratio. S620_25/15 configuration turns out to be the best.

4 OPTIMIZATION PROCEDURE

In order to consider together the three performance aspects previously mentioned (i.e. weight-W, cost-C, energy/stiffness ratio-R) a multi-objective performance index (I) was defined as the weighted sum of the three quantities, linearly normalized as shown in Table 3 (0 – best, 1 – worst):

$$I_i = p_W \cdot W_i + p_C \cdot C_i + p_R \cdot R_i \tag{4}$$

The weights associated to each of the three involved parameters, namely p_W, p_C and p_R, are related to the importance of each aspect within the decision-making process of optimization. These weights can then vary in relation to several factors such as the typology of the structure, its function, the events expected during its whole life cycle, etc. For simplicity, two decisional

scenarios were considered: the first (corresponding to the index I_1) where equal importance is given to each optimization parameter (p_W, p_C, $p_R = 0.333$) and the second (corresponding to the index I_2) where the weight parameter has been neglected ($p_W = 0.0$, p_C, $p_R = 0.5$).

The normalized values for the quantities and the resulting indexes are reported in Table 3.

Configuration	W	C	R	I_1	I_2
S355_30/20	1	0,22	0,98	0,73	0,60
S500_30/20	1	0,43	0,71	0,71	0,57
S620_30/20	1	0,61	0,77	0,79	0,69
S690_30/20	1	0,72	0,17	0,63	0,44
S890_30/20	1	1,00	0,25	0,75	0,63
S355_30/15	0,59	0,13	1,00	0,57	0,57
S500_30/15	0,59	0,33	0,66	0,53	0,49
S620_30/15	0,59	0,50	0,57	0,55	0,54
S690_30/15	0,59	0,59	0,28	0,49	0,43
S890_30/15	0,59	0,85	0,30	0,58	0,57
S355_25/15	0	0,00	0,81	0,27	0,41
S500_25/15	**0**	0,17	**0,02**	0,06	0,10
S620_25/15	0	0,33	0,00	0,11	0,16
S690_25/15	0	0,41	0,21	0,21	0,31
S890_25/15	0	0,65	0,17	0,27	0,41

Table 3: Results of the optimization procedure.

Both for first (I_1) and second (I_2) scenario, configuration S500_25/15 is able to optimize the multi-objective index, being also the lightest solution and the one characterized by the lower resulting cost; this can be then considered as the best configuration. Differently, the configuration S355_25/15 is the one able to optimize the cost (and the weight) but showing the most disadvantageous dissipated energy/mean stiffness ratio. From Table 3, it can also be observed the value of R, which is progressively optimized by increasing the steel grade.

5 CONCLUSIONS

In the present study, the possibility of implementing a dissipative and replaceable device (DRD) with the use of high-strength steel (HSS) was considered using different combinations of thickness for the plates (i.e. the non-dissipative components of the device). The economic and performance aspects of the device, as the weight, the material's cost and the dissipative capacity were evaluated with the support of numerical analyses within an overall optimization procedure. Results clearly indicate that the adoption of HSS can increase the dissipative capacity without thereby increasing, necessarily, the stiffness of the system: this is particularly advantageous in combination to small thicknesses, for which the weight and cost of the device are then optimized.

ACKNOWLEDGMENTS

The present work has been developed within the framework of the European research project DISSIPABLE funded by the RFCS (European Union's Research Fund for Coal and Steel) – Grant Agreement no. RFCS2017-800699.

REFERENCES

[1] A. Christopoulos, C. Filiatrault, Principles of passive supplemental damping and seismic isolation, *IussPress,* Pavia , Italy, 2006.

[2] J. E. Martinez-Rueda, On the Evolution of Energy Dissipation, *Earthquake Spectra*, 18 (2), 309–346, 2002.

[3] P. Thanopoulos, I. Vayas, C. A. Castiglioni, L. Calado, A. Plumier, Behaviour of seismic resistant braced frames with innovative dissipative (INERD) connection, *Volume C:Proceedings Eurosteel 2005: 4th European Conference on Steel and Composite Structures*, Maastricht, The Netherlands, June 8 - 10, 2005..

[4] I. Vayas P. Thanopoulos: Innovative dissipative (INERD) pin connections for seismic resistant braced frames, *Steel Structures*, 5(5), 453 – 463, 2005.

[5] P. Thanopoulos, Αντισεισμική συμπεριφορά μεταλλικών φορέων με συστήματα απορρόφησης ενέργειας Παύλος Θανόπουλος Επιβλέπων: Ι . Βάγιας , Καθηγητής Ε . Μ . Π ., PhD Thesis, National Technical University of Athens, November 2006.

[6] H. Ban, G. Shi, A review of research on high-strength steel structures, *Proceedings of the Institution of Civil Engineers: Structures and Buildings*, 171(8), 625–641, 2018.

[7] J. Wang, G. Shi, Y. Shi, Experimental research on behavior of 460 MPa high strength steel I-section columns under cyclic loading, *Earthquake Engineering and Engineering Vibration* 13(4), 611–622, 2014.

[8] G. Q. Li, Y. B. Wang, S. W. Chen, The art of application of high-strength steel structures for buildings in seismic zones, *Advanced Steel Construction*, 11(4), 492–506, 2015.

[9] A. M. P. De Jesus, R. Matos, B. F. C. Fontoura, C. Rebelo, L. Simões Da Silva, M. Veljkovic, A comparison of the fatigue behavior between S355 and S690 steel grades, *Journal of Constructional Steel Research*, 79, 140–150, 2012.

[10] European Committee for Standardization (CEN), EN 10025, Hot rolled products of structural steels - Part 6: Technical delivery conditions for flat products of high yield strength structural steels in the quenched and tempered condition, 2009.

[11] P. Collin, B. Johansson, Bridges in high strength steel, *IABSE Symposium Report*, 92(4), 1–9, 1 January 2006.

[12] EN 1993-1, Eurocode 3: Design of steel structures - Part 1-8: Design of joints," *J. Constr. Steel Res.*, 54(2), 18–20, 2011.

[13] ABAQUS, "ABAQUS v. 6.14-2" Commercial FE Software and Documentation, Dassault Systèmes, Simulia Corporation, Providence, RI, USA, 2014.

[14] European Convention for Constructional Steelwork. Technical Committee 1, Structural Safety, and Loadings. Technical Working Group 1.3, "Seismic Design Recommended testing procedure for assessing the behaviour of structural steel elements under cyclic

loads", *European Convention for Constructional Steelwork*, 45, Brussels [Belgium], 1986.

[15] European Commission Research Programme of the Research Fund for Coal and Steel, INNOSEIS, Valorization of innovative anti-seismic devices, Work Package 4 – Deliverable 4 . 2 Volume on case studies for mid / high-rise buildings, 4 December 2017.

EURODYN 2020
XI International Conference on Structural Dynamics
M. Papadrakakis, M. Fragiadakis, C. Papadimitriou (eds.)
Athens, Greece, 23–26 November 2020

ENHANCED STRUCTURAL RESILIENCE THROUGH THE USE OF "LEAF-SPRING" COLUMNS AND REPLACEABLE DISSIPATIVE COMPONENTS

Cristian Vulcu[1,2], **Marius Pinkawa**[1], **Aurel Stratan**[2] and **Benno Hoffmeister**[1]

[1] RWTH Aachen / Institute of Steel Construction / Center for Wind and Earthquake Engineering
Mies-van-der-Rohe Str. 1, Aachen, Germany
{m.pinkawa, hoff}@stb.rwth-aachen.de

[2] Politehnica University of Timisoara / Department of Steel Structures and Structural Mechanics
Str. Ioan Curea Nr. 1, Timisoara, Romania
{cristian.vulcu, aurel.stratan}@upt.ro

Keywords: moment resisting frame; "*leaf-spring*" columns; re-centering capacity; replaceable dissipative component; full-strength/full-rigid joint; resilient and sustainable structural configuration; high strength steel;

Abstract. *The main challenges of the construction sector (at this point and in the coming decades) are: natural hazards, climate change, sustainability, competitiveness, technology take-up, in service performance, re-industrialization. Regarding natural hazards, the latest seismic events evidenced the need for more resilient earthquake-resistant structures. Justified by expensive repairs, downtime and/or building demolition – it has become a widely held belief that the ductility of a structure is not the final goal, and that preventing the loss of life is not sufficient for a modern structure. Consequently, the current study was launched with the aim of providing structural configurations and practical solutions for enhanced resilient and sustainable buildings and communities. In particular, the research aims at reducing the repair costs and downtime of a structure damaged by natural hazards (e.g. earthquakes) and, consequently, at providing a more rational design approach, with regard to sustainability. Both replaceable dissipative components and structural re-centering capabilities are addressed. In brief, the research activities consist in developing a set of bolted beam-to-column joints with replaceable dissipative components and investigating the applicability potential of innovative "leaf-spring" columns into building frames. The central idea of the current study is to combine and rigidly connect several columns in the shape of a "leaf-spring", and to benefit from the mechanical properties of such an innovative element. Primarily, the "leaf-spring" columns are aimed to provide the structure with re-centering capability and to improve the overall structural response. The current paper presents: (i) the aim, objectives and particularities of the current research; (ii) the outcomes of a case study (i.e. the design and seismic performance evaluation of standard vs. innovative structural configurations); (iii) a proposed solution for beam-to-column joints with replaceable components and for structural re-centering; (iv) the main conclusions and future research activities.*

1 INTRODUCTION

Advanced modern technologies have significantly pushed the development of our society. Yet, nature continues to offer proof of its unpredictable and destructive character. When subjected to natural hazards, buildings and other engineering structures should possess the ability to provide safety and stability. However, in the light of the latest seismic events, it has become clear that the current degree of seismic protection is unsatisfactory. This aspect was evidenced during recent earthquakes in: *Mexico* (*19.09.2017 - 7.1 M_w magnitude*), *Italy* (*24.08.2016 - 6.2 M_w*), *Nepal* (*25.04.2015 - 7.8 M_w*), *China* (*03.08.2014 - 6.3 M_w*), *Turkey* (*23.10.2011 - 7.2 M_w*), *Japan* (*11.03.2011 - 9.0 M_w*), *New Zealand* (*22.02.2011 - 6.2 M_w*), and *Chile* (*27.02.2010 - 8.8 M_w*). Under severe or even moderate earthquake activity, buildings have suffered extensive damage and even total collapse.

Buildings designed according to modern seismic codes are expected to exhibit a controlled ductile inelastic response during major earthquakes, implying extensive structural damage (see examples in Figure 1), along with, possibly substantial residual deformations. However, the structures might be difficult or uneconomical to repair due to the experienced damage and residual drifts and may need demolition and rebuilding.

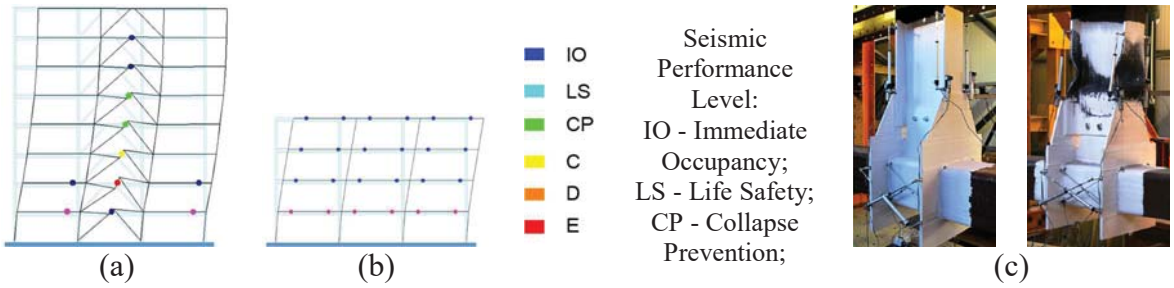

Figure 1: Examples of expected inelastic response of structural members: (a) dual eccentrically braced frame (D-EBF) with plastic hinges in shear links and beams; (b) moment resisting frame (MRF) with plastic hinges in beams; (c) beam-to-column joint (before and after test) with large plastic deformations in the dissipative zone [1]

The 2011 Christchurch (New Zealand) earthquake is a recent example of the necessity of more resilient earthquake resistant structural systems. Approximately 50% of the buildings in the central business district were declared unusable due to significant damage or due to proximity to dangerous and unsafe buildings, and nearly 1000 buildings were demolished [2]. The cost of rebuilding was estimated at $40 billion NZD (approx. 20% of New Zealand's GDP), without including the economic losses related to business downtime [2].

In order to reduce the structural damage caused by moderate to strong earthquakes, different strategies can be employed. The most sophisticated existing solutions are base isolation and the implementation of active and semi-active structural control [3]. Other strategies rely on supplementary damping through viscous, friction or yielding dampers. While some of these solutions are more efficient than others at reducing structural damage, all of them have the following disadvantages: specialized knowledge is required during design and erection; carefully carried out maintenance is needed; the initial cost is high. Another option implies a conventional structural design with replaceable dissipative members (easy to substitute after a moderate-to-strong earthquake), which will reduce the repair costs. An efficient system has to fulfil two requirements: (i) the inelastic deformation should occur only in removable elements; (ii) the damaged dissipative elements must be replaceable [15].

Self-centering systems, a relatively new concept, address the drawbacks of the conventional yielding systems, and have recently received much attention. A review is shown in [2]. Of sev-

eral practical applications, the following few are mentioned here: self-centering moment resisting frames (SC-MRFs) based on post-tensioned beam-to-column [4] and column base [5] connections, self-centering concentrically braced frames (SC-CBFs) [6], self-centering energy dissipative (SCED) bracing [7], steel self-centering devices (SSCDs) [8], and shape memory alloy self-centering buckling restrained braces (SC-BRBs) [9].

For a structure to be repairable, in addition to constraining the inelastic deformations to the removable dissipative members, any permanent (residual) drift needs to be eliminated, while providing a re-centering capability (in contrast to self-centering). Some of the most renowned removable dissipative component systems are: INERD connections [10], FUSEIS devices [11], buckling restrained braces (BRB) [12], steel plate shear walls (SPSW) [13], removable links in eccentrically braced frames (EBF) [14][15][16]. Beam-to-column joints with replaceable components were investigated as the following: (i) damage free joints with friction dampers [17]; (ii) joints with replaceable T-stub fuses [18][19] and yield-links [20][21][22][23][24][25][26].

Concepts as "re-centering capacity" and "removable dissipative element" were recently implemented in a dual structure, obtained by combining steel eccentrically braced frames (with removable bolted links) and moment resisting frames [27]. The easily replaceable bolted links provided the energy dissipation, while the more flexible, but still sufficiently stiff, moment resisting frames provided the necessary re-centering capability.

2 AIM AND OBJECTIVES OF THE CURRENT RESEARCH

The current research represents an attempt to face the challenges of the construction sector, and to respond to the vision documents from U.S. [28] and Europe [29]. Particularly, the current research has the aim to provide structural configurations and practical solutions for enhanced resilient and sustainable buildings and communities. The main objectives are:

- To look at the construction/deconstruction process from an open-minded perspective, and to propose solutions that provide enhanced resilience and sustainability, and that take into account also the concept of design for deconstruction;
- To develop a set of bolted beam-to-column joints with replaceable dissipative components;
- To investigate the applicability potential of "*leaf-spring*" columns in building frames;
- To investigate (experimentally and numerically) the behavior of joint assemblies with replaceable dissipative components undergoing large cyclic strains;
- To investigate the re-centering capability of frames equipped with "*leaf-spring*" columns;
- To provide a technical and economical comparison between a conventional, respectively a more resilient and sustainable structural system;
- To elaborate a set of design examples and to propose structural application schemes for the implementation of replaceable dissipative components and re-centering solutions.

3 CASE STUDY: STANDARD VS. INNOVATIVE STRUCTURAL SYSTEM

3.1 Structural configuration benchmark

For the development of a structural configuration benchmark, a representative 3D multi-story building configuration was selected. The following parameters were chosen considering as being representative for a 3D multi-story building located in a region with seismic hazard:

- Location: (a) Romania / Bucharest (Soft Soil); (b) Europe (Stiff Soil / Spectrum Type C)
- Building use: Office
- Structural type: Moment Resisting Frame (MRF)
- Number of stories: *4*

- Number of spans/bays: *3*
- Story height: *3.5 m*
- Span/bay length: *6.0 m*
- Outline of the slab: Exceeds the perimeter composed by the outer axes with *0.5 m*

The arrangement and dimensions of the structural configuration are illustrated in Figure 2. In particular, the floor layout with columns, main beams and secondary beams are shown in Figure 2a. Only the outer frames (illustrated in Figure 2b) act as lateral force resisting systems, while the internal structural system transfers the gravitational loading. Regarding the perimeter frames, only two of the three spans/bays are moment resisting. The obtained structural configuration is therefore symmetrical and has the same mechanical properties in both directions.

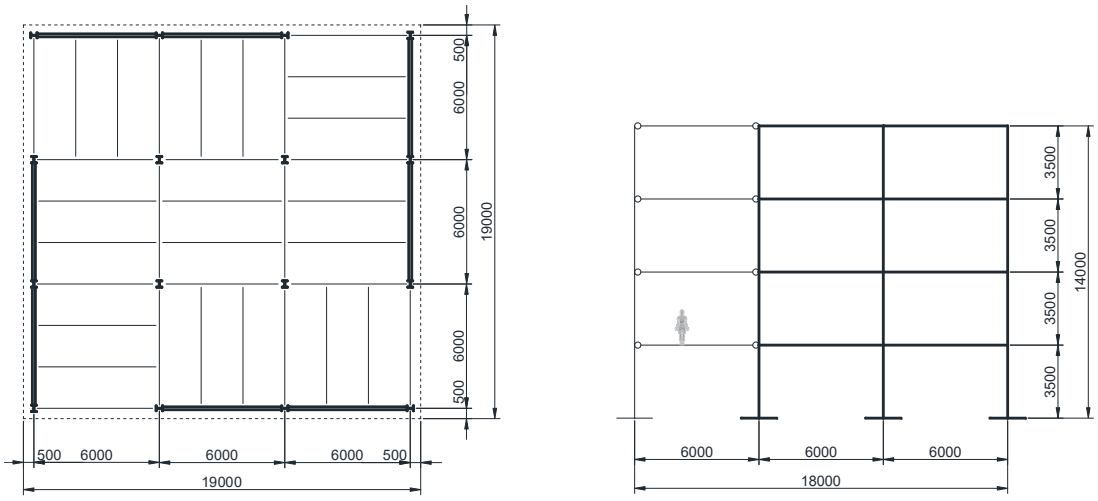

(a) (b)

Figure 2: Arrangement and dimensions (mm) of the structural configuration: (a) floor layout (with columns, main beams and secondary beams); (b) perimeter moment resisting frame

3.2 Characteristic values of actions

The *permanent actions* include the self-weight of the primary and supporting structure, as well as finishing elements connected with the structure:

- Uniform load acting on the slab: *5 kN/m²*
- Uniform load acting on the perimeter beams (from the glass façade): *3.5 kN/m*
- The weight of beams and columns is considered automatically within the analysis software

The *variable actions* acting on the slab, considering that the building is used for offices (category B), and including the equivalent load from partitioning walls, is:

- Uniform load acting on the slab at intermediate floors: *3.3 kN/m²*
- Uniform load acting on the slab at the top floor: *2.5 kN/m²*

The *seismic action* is defined for two soil conditions, and the following building data:

- Soil type (see the elastic and design spectra in Figure 3):
  - Soft soil (T_c*=1.6 sec.*): specific soil condition in Bucharest according to P100-2013 [31]
  - Stiff soil (T_c*=0.6 sec.*): soil type C according to EN 1998-1 [30]
- High seismic zone, considering a peak ground acceleration of: a_g*=0.3g*
- Importance of the building: office building, γ_I*=1.0 (→ a_g = 0.3×9.81 = 2.95 m/s²)*
- Behavior factor corresponding to moment resisting frames and high ductility class: *q=6.5*

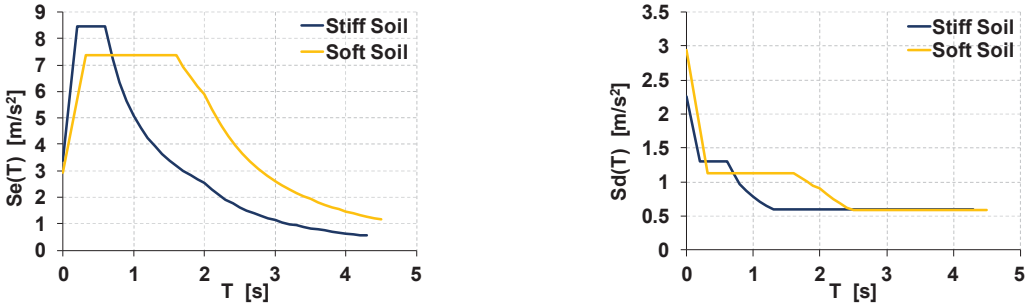

Figure 3: Soft & Stiff Soil: elastic and design spectrum for the horizontal components of the seismic action

3.3 Design of the standard structural configurations (MRF)

Two standard structural configurations were designed and analyzed with SAP2000 [32], i.e. one for soft and one for stiff soil. The structural configurations have a compact planar shape, the lateral force resisting system is placed symmetrically, and the reinforced concrete slab has a sufficient in plane stiffness in order to assure the diaphragm effect. The structural design was performed on 3D models (based on the layout illustrated in Figure 2), using a modal response spectrum analysis.

Based on the presence of the reinforced concrete slabs, a rigid diaphragm constraint was considered for the nodes of each floor. The outer columns were fully fixed at the base, and the connections between beam elements (fixed/pinned) were modelled according to the layout in Figure 2. The gravitational loads were applied on slabs (permanent and variable loads), and on the perimeter beams (permanent loads from the façade walls). The masses were calculated automatically from the applied gravitational loading on the structure. The beams were realized from S235 steel grade and the columns from S355 grade.

The modelling of global imperfections was performed based on the provisions from Section 5.3.2 of EN 1993-1-1 [33], i.e. through a system of equivalent lateral forces for each horizontal direction. The importance of the second order effects was evaluated through the value of the inter-story drift sensitivity coefficient (θ), which was determined according to Section 2.10 of [34], respectively Section 4.6.2.2(2) of P100-2013 [31]. The coefficient (θ) was computed for each level and each direction, and the maximum value was found between $0.1 < \theta \leq 0.2$. Consequently, the second-order effects were considered in an approximate way by multiplying the design values of the demands with the following factor: $\alpha = 1/(1-\theta)$.

The cross-section of elements for the lateral force resisting system of the standard designed structures (in Soft and Stiff Soil conditions) are presented in Table 1. The design of the lateral force resisting system was governed by the deformation limitation (corresponding to the serviceability limit state – SLS, and/or to the ultimate limit state – ULS).

Standard structure located in Soft Soil conditions (T_1=0.751 sec.)			Standard structure located in Stiff Soil conditions (T_1=0.977 sec.)		
Floor	Beam	Column	Floor	Beam	Column
4	IPE-600	HEB-600	4	IPE-500	HEB-500
3	IPE-600	HEB-600	3	IPE-550	HEB-500
2	IPE-750x137	HEB-600	2	IPE-550	HEB-500
1	IPE-750x137	HEB-600	1	IPE-550	HEB-500

Table 1: Cross-section of elements for the standard lateral force resisting system – Soft & Stiff Soil conditions.

3.4 Structural configurations with Leaf Spring Columns (LSC)

3.4.1. Description of the concept

The idea within the current research is to rigidly combine several columns in the shape of a ”*leaf-spring*”, and to benefit from the mechanical properties of such an innovative element. In contrast to a standard moment resisting frame (see Figure 4a), which does not possess any noteworthy re-centering capability, an innovative structural system is proposed as part of the current research (see Figure 4b). In particular, the structural configuration is composed of: (i) a Moment Resisting Frame (MRF) that acts as a lateral load resisting system and as a seismic energy dissipation system (through the development of plastic hinges in beams); (ii) an innovative Leaf Spring Column (LSC) that acts as a lateral load resisting element, which will suffer only elastic deformations and will provide the re-centering capability of the structure.

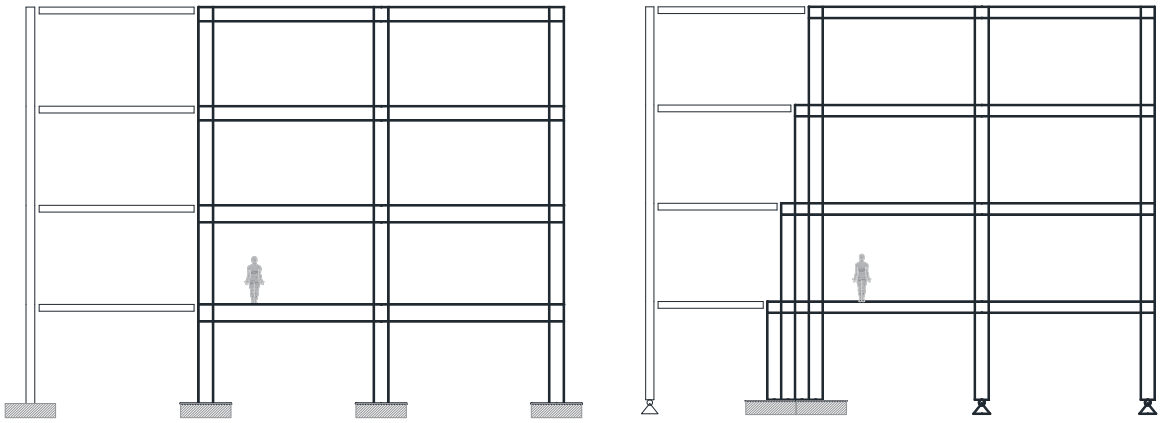

(a) [MRF] (b) [MRF+LSC]

Figure 4: Structural configuration: (a) standard moment resisting frame (MRF); (b) innovative structural system, i.e. a moment resisting frame equipped with a “*leaf-spring*” column (MRF+LSC)

3.4.2. Design of the innovative structural configurations (MRF+LSC)

The “*leaf-spring*” column (LSC) is intended to be realized by joining and connection of several steel profiles in a progressive manner (see Figure 4b). The individual profiles of the LSC are to be connected in such way as to prevent the relative displacement between each other, and to work as a unitary element. Ongoing finite element analyses are devoted to the investigation of the performance of LSC’s with bolted/welded connection between profiles.

Considering the standard moment resisting frames with 6.0 m span/bay (Figure 4a and Table 1) as a starting point (reference system), two structural configurations were developed and modelled using LSC’s and moment resisting bays (as illustrated in Figure 4b and Figure 5). An offset of 250 mm (half of the HEB-500 column height) was defined for the beams in MRF bays (for both standard and innovative structures). Also, the same input data was considered with regard to the material properties, geometry, loading conditions and combinations.

Compared to the designed reference structures (with standard MRF’s), the new structural system (see Figure 5) has been adapted regarding the following aspects:

- *LSC*: one “*leaf-spring*” column was used for each perimeter frame using HEB-500 profiles for the structure in Soft soil, and HEB-400 profiles for the structure in Stiff soil;
- *Secondary beams*: the secondary beams were arranged parallel to the main beams (see the perimeter MRF’s in Figure 5 and layout in Figure 17); this new arrangement has the aim

to allow the replacement of the dissipative main beams (which will be positioned with a certain gap below the slab);

- *Material for LSC's*: as the "*leaf-spring*" columns are to remain in the elastic range, the use of S700 high strength steel (HSS) was essential, and therefore in case of unavailable profiles of such steel grade, these would be realized from welded plates of equivalent thickness;
- *Beams from MRF bays*: the cross-section of the beams in the MRF bays could be decreased;
- *Base connections for columns*: the base connections of the MRF columns was considered as pinned based on the observation that a fixed connection would not result in noteworthy benefit, and that the presence of the LSC's prevents the development of bending moment at the other column bases;

An overview of the structural configuration is shown in Figure 5: (i) 3D view; (ii) perimeter lateral load resisting frame [LSC+MRF]; (iii) location of the LSC's; (iv) connections at column bases; (v) connections for secondary beams and main beams; (vi) secondary beams oriented parallel to the main beams (that are part of the perimeter frames).

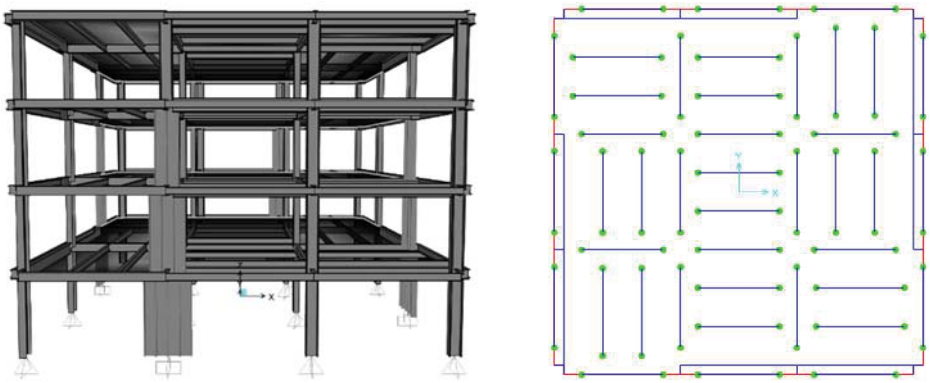

Figure 5: Proposed innovative structural configuration [MRF+LSC]: 3D view and floor layout (with connection characteristics for main and secondary beams)

The cross-section of elements for the lateral force resisting system of the designed innovative structures (in soft and stiff soil conditions) are presented in Table 2. As for the reference structure, the design of the lateral force resisting system was governed by the deformation limitation (corresponding to the serviceability limit state SLS, and/or the ultimate limit state ULS).

Innovative structure located in Soft Soil conditions (T_1=*0.711 sec.*)				Innovative structure located in Stiff Soil conditions (T_1=*0.966 sec.*)			
Floor	Beam	Column	LSC	Floor	Beam	Column	LSC
4	IPE-450	HEB-500	1 x (HEB-500)	4	IPE-400	HEB-400	1 x (HEB-400)
3	IPE-550	HEB-500	2 x (HEB-500)	3	IPE-450	HEB-400	2 x (HEB-400)
2	IPE-550	HEB-500	3 x (HEB-500)	2	IPE-450	HEB-400	3 x (HEB-400)
1	IPE-550	HEB-500	4 x (HEB-500)	1	IPE-450	HEB-400	4 x (HEB-400)

Table 2: Cross-section of elements for the innovative lateral force resisting system – Soft & Stiff Soil conditions.

3.4.3. Preliminary remarks regarding the use of LSC's

The particularities of standard moment resisting frames (i.e. design governed by deformation limitations, formation of plastic hinges in beams and at column bases) was confirmed during the design process of the two structural systems: standard [MRF] and innovative [MRF+LSC].

The state of a standard designed [MRF] system after a major seismic event would be characterized by large lateral deformations and yielded structural members (dissipative zones of the beams and the base of the columns). Such damages are usually very difficult to repair, making the demolition of the building and replacement by a new one the only available options.

The proposed innovative structural system (see Figure 4b and Figure 5), represents an important step forward towards the aim of providing structural configurations and practical solutions for enhanced resilient and sustainable buildings. From the design of the innovative structural system [MRF+LSC], the use of LSC's evidenced some advantages:

- It provided a change in the load transfer mechanism, i.e. compared to a standard [MRF] the lateral load was distributed among both LSC's and MRF bays;
- The LSC's acted like a "*leaf-spring*" – being characterized by elastic deformations (with a tendency to recover their initial un-deformed shape), and making them good candidates for providing structural re-centering capability;
- The use of LSC's and the change in the load transfer mechanism allowed reducing the cross section of beams and columns, as well as using pinned column base connections.

4 SEISMIC PERFORMANCE EVALUATION

The seismic performance was evaluated through: (i) nonlinear static analyses (pushover) using the N2 method [35]; and (ii) nonlinear dynamic analyses (time-history). Both types of analyses were performed using Sap2000 [31] and considering 3D structural configurations. However, for the current study the seismic action was applied only on "*x*" direction, and the deformations of the structure were blocked in "*y*" direction. Thus, 2D analyses were performed on the 3D structures that include two perimeter lateral load resisting frames on each direction.

4.1 Nonlinear static analyses

The N2 method, developed by Fajfar [35] and comprised in Annex B of EN 1998-1 [30], can be used to verify the seismic performances of buildings designed by current methods (i.e. spectral analysis). The method combines the nonlinear static analysis of a multiple degrees of freedom system (MDOF) with an analysis based on the response spectrum of a single degree of freedom system (SDOF). The lateral story forces were assumed to be proportional to the 1st mode of vibration. Furthermore, the structural performance was evaluated for the limit states shown in Table 3, where "a_{gr}" is the reference peak ground acceleration of *0.3g*, and "a_g" represents the peak ground acceleration for a specific earthquake level.

Limit state	Return period, [years]	Probability of exceedance	a_g/a_{gr}	a_g/g
Damage Limitation (DL / SLS)	95	10% / 10 years	0.5	0.15
Significant Damage (SD / ULS)	475	10% / 50 years	1.0	0.30
Near Collapse (NC)	2475	2% / 50 years	1.7	0.51

Table 3: Limit states and corresponding scaling factors for the seismic input.

For beams subjected to flexure, based on FEMA 356 [36] and Annex B of EN 1998-3 [37], the following acceptance criteria were considered corresponding to the rotation at DL, SD and NC: $1\theta_y$, $6\theta_y$ and $8\theta_y$, where θ_y is the yield rotation. The damage state condition of the plastic hinges (see the results of the structural analyses performed with Sap2000 [32]) associated to three limit states are similar in both codes, and it can be assumed that Immediate Occupancy

(IO) corresponds to Damage Limitation (DL), Life Safety (LS) stands for Significant Damage (SD), and Collapse Prevention (CP) relates to Near Collapse (NC).

From the nonlinear static analyses, a pushover curve (capacity curve) was obtained for each of the four structural configurations: (i) standard [MRF] in soft soil; (ii) innovative [MRF+LSC] in soft soil; (iii) standard [MRF] in stiff soil; and (iv) innovative [MRF+LSC] in stiff soil. Further, using the N2 method, the target displacements (D_t) were obtained for each of the four structural systems, and corresponding to the three seismic intensity levels (i.e. SLS, ULS, NC). Table 4 and Table 5 summarize the values of the computed target displacements corresponding to the standard and innovative structures located in soft and stiff soil, respectively.

	Limit state	a_g/a_{gr}	Standard structure: [**MRF**]	Innovative structure: [**MRF+LSC**]
	DL / SLS	0.5	0.09	0.09
D_t [m]	SD / ULS	1.0	0.17	0.19
	NC	1.7	0.30	0.32

Table 4: Target displacements of standard and innovative structures located in Soft Soil conditions

	Limit state	a_g/a_{gr}	Standard structure: [**MRF**]	Innovative structure: [**MRF+LSC**]
	DL / SLS	0.5	0.09	0.10
D_t [m]	SD / ULS	1.0	0.18	0.20
	NC	1.7	0.31	0.34

Table 5: Target displacements of standard and innovative structures located in Stiff Soil conditions

The outcomes of the nonlinear static analyses are shown in terms of: (i) capacity curve (base shear force vs. top displacement); (ii) the state of the perimeter lateral load resisting frame corresponding to the three seismic intensity levels – SLS, ULS, NC – i.e. at the computed target displacements. It is to be noted that the target displacements are marked on each capacity curve. The outcomes are presented for the following configurations:

- Figure 6 – Standard structure [MRF] located in Soft soil conditions;
- Figure 7 – Innovative structure [MRF+LSC] located in Soft soil conditions;
- Figure 8 – Standard structure [MRF] located in Stiff soil conditions;
- Figure 9 – Innovative structure [MRF+LSC] located in Stiff soil conditions.

Based on the state of each structural configuration (plotted for the three seismic intensity levels – SLS, ULS, and NC), the following observations can be made:

- at the SLS earthquake plastic hinges were developed in beams of both structural systems and soil conditions, but with rotations lower than the corresponding acceptance criteria;
- at ULS and NC earthquake plastic hinges developed in beams and at column bases for the standard MRF's (see Figure 6 and Figure 8), while for the innovative structures [MRF+LSC] – plastic hinges developed only in beams (see Figure 7 and Figure 9) as the column bases were pinned and only the LSC´s were considered with fixed connection; the plastic hinges from beams and/or columns did not reach rotations corresponding to life safety or collapse prevention criteria.

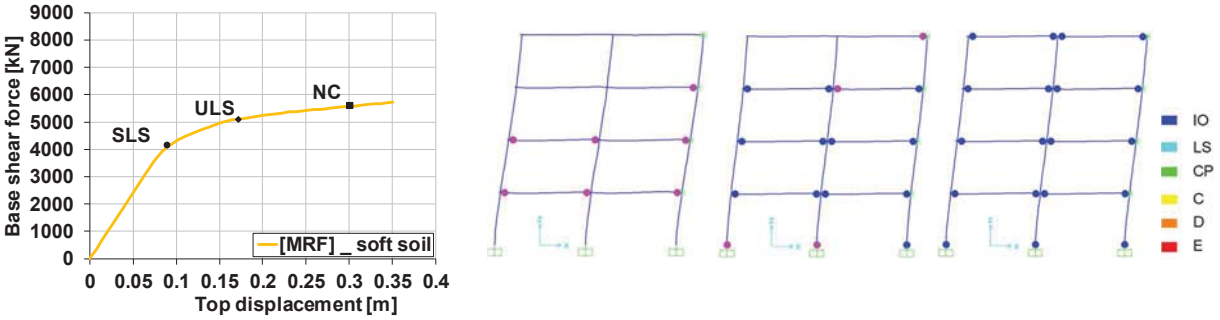

Figure 6: Standard structure located in Soft soil conditions: capacity curve (with marked target displacements) and the state of the perimeter lateral load resisting frame [MRF] at the three seismic intensity levels – SLS, ULS, NC (i.e. a_g/a_{gr}=*0.5; 1.0; 1.7*)

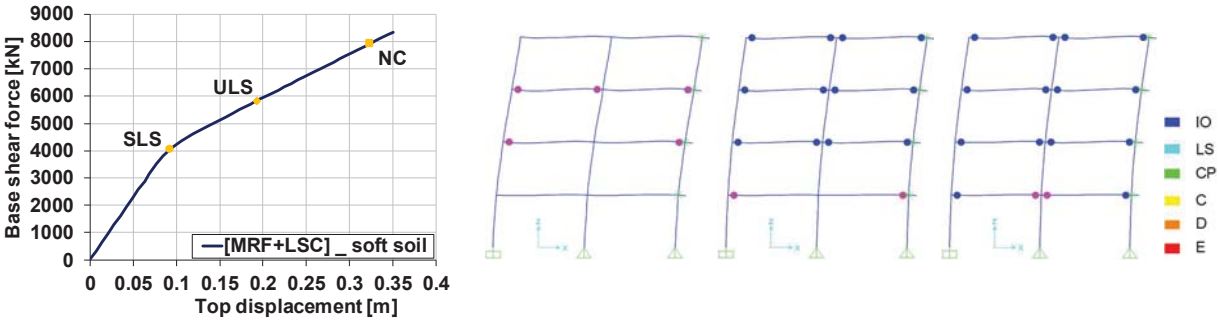

Figure 7: Innovative structure located in Soft soil conditions: capacity curve (with marked target displacements) and the state of the perimeter lateral load resisting frame [MRF+LSC] at the three seismic intensity levels – SLS, ULS, NC (i.e. a_g/a_{gr}=*0.5; 1.0; 1.7*)

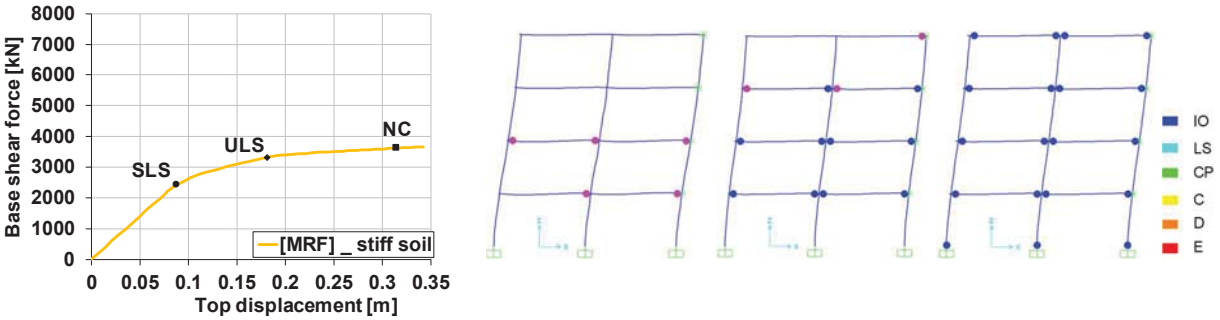

Figure 8: Standard structure located in Stiff soil conditions: capacity curve (with marked target displacements) and the state of the perimeter lateral load resisting frame [MRF] at the three seismic intensity levels – SLS, ULS, NC (i.e. a_g/a_{gr}=*0.5; 1.0; 1.7*)

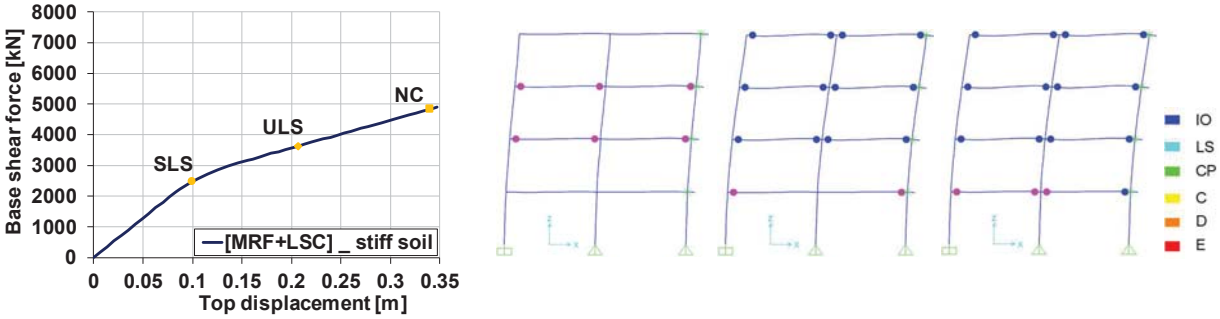

Figure 9: Innovative structure located in Stiff soil conditions: capacity curve (with marked target displacements) and the state of the perimeter lateral load resisting frame [MRF+LSC] at the three seismic intensity levels – SLS, ULS, NC (i.e. a_g/a_{gr}=*0.5; 1.0; 1.7*)

A comparison between the pushover curves of the two structural systems, i.e. standard [MRF] and innovative [MRF+LSC], designed for soft and stiff soil conditions – is shown in Figure 10. As can be observed, the initial stiffness of the two structural systems is similar, but the post-yield response is different:

- In case of the standard structure [MRF], the pushover curve is characterized by a relative horizontal tendency (i.e. large deformations with little increase of force).
- In case of the innovative structure [MRF+LSC], the pushover curve is characterized by a linear ascending tendency (where the capacity increases with the deformation).

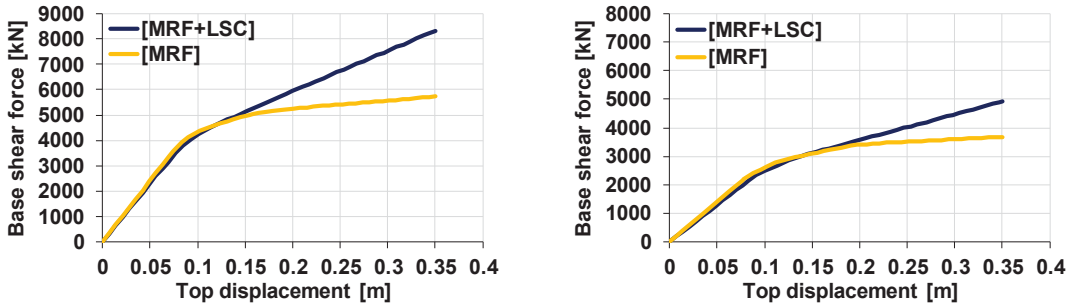

(a) (b)

Figure 10: Comparison between the pushover curves of the standard [MRF] and innovative [MRF+LSC] structural systems located in: (a) Soft soil conditions; (b) Stiff soil conditions

The improved response of the innovative structures, i.e. bilinear shape with a linear ascending tendency in the post yield region, can be explained by examining the shape of the pushover curves of the two subsystems (LSC's, MRF's with fixed columns). Subsequently, the contribution of each of the two subsystems is illustrated in Figure 11 for both soil conditions. Compared to the MRF subsystems, the LSC's are characterized by a linear-elastic response, with a lower stiffness and capacity (up to a *0.3 m* top displacement). The linear-elastic response of LSC's is therefore responsible for the linear ascending tendency in the post yield region of the [MRF+LSC] structural system and confirms the potential for the re-centering capacity.

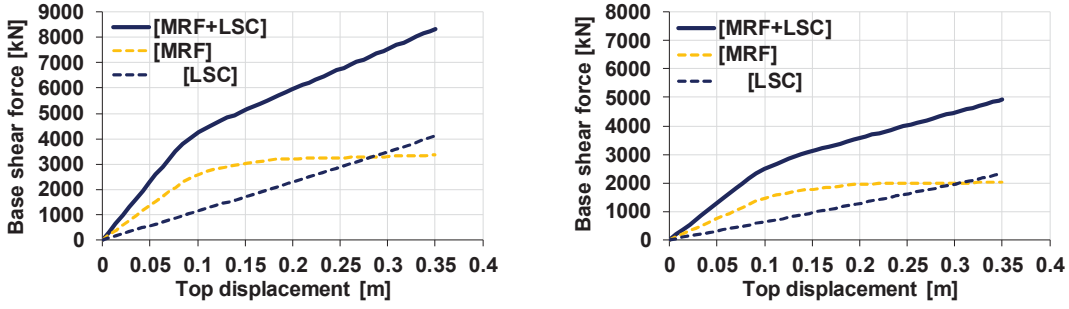

(a) (b)

Figure 11: Contribution of the two subsystems (MRF & LSC) corresponding to the innovative structure located in: (a) soft soil conditions; (b) stiff soil conditions

The linear-elastic response of the LSC's modeled using beam elements was checked also using a more advanced finite element modeling procedure, i.e. a pushover analyses were performed on an LSC modeled with shell elements using Abaqus (v2019) platform [38]. The comparison between the capacity curves from Sap2000 [32] and Abaqus (v2019) [38] was very close, and confirmed the modeling procedure used for the current structural configurations. Further numerical studies will be devoted for a more detailed investigation of LSC's.

4.2 Nonlinear dynamic analyses

For the nonlinear dynamic analyses, two sets of seven artificial accelerograms were adopted. The elastic response spectrum of the selected accelerograms is compared in Figure 12 with the corresponding target spectrum (for soft and stiff soil). For soft soil conditions the first mode period for the standard, respectively innovative structure corresponds to: $T_{1\text{-}st}=0.751$ *sec*; $T_{1\text{-}inno}=0.711$ *sec*. Regarding stiff soil, the first mode period for the standard, respectively innovative structure corresponds to: $T_{1\text{-}st}=0.977$ *sec*; $T_{1\text{-}inno}=0.966$ *sec*.

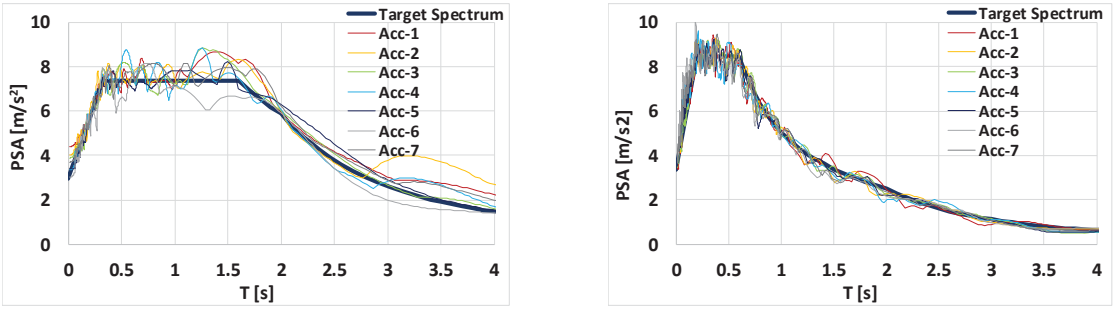

Figure 12: Elastic response spectrum of accelerograms compared to the target spectrum for Soft and Stiff Soil

The outcomes of the time-history analyses are presented for both standard and innovative structural configuration in terms of: (i) comparison of the displacement at top floor; (ii) state of frame corresponding to the maximum displacement (i.e. scaled deformed shape with marked plastic hinges). Consequently, the response under one of the most severe accelerograms (i.e. *Acc-7_soft*; *Acc-7_stiff*) at the three intensity levels - SLS (serviceability limit state - $a_g/a_{gr}=0.5$), ULS (ultimate limit state - $a_g/a_{gr}=1.0$), and NC (near collapse - $a_g/a_{gr}=1.7$) - is shown in:

- Figure 13 for standard [MRF] and innovative [MRF+LSC] structures designed for soft soil;
- Figure 14 for standard [MRF] and innovative [MRF+LSC] structures designed for stiff soil.

The time-history analyses under *Soft Soil* conditions (see Figure 13) evidenced the following:

- *at SLS (serviceability limit state – $a_g/a_{gr}=0.5$)*: ▪ plastic hinges did not develop in any of the two structural systems (standard or innovative); ▪ the comparison between displacements at top floor showed almost identical deformations;
- *at ULS (ultimate limit state – $a_g/a_{gr}=1.0$)*: ▪ plastic hinges developed in beams (at three out of four stories) for both structural configurations; ▪ plastic hinges developed at the column bases of the standard structure corresponding to only one accelerogram (i.e. *Acc-7,* see Figure 13); ▪ the comparison between displacements at top floor showed differences with some residual deformations corresponding to the standard structure [MRF];
- *at NC (near collapse – $a_g/a_{gr}=1.7$)*: ▪ a global plastic mechanism was evidenced with plastic hinges in beams and at column bases for the standard [MRF], and with plastic hinges in beams for the innovative structural system [MRF+LSC]; ▪ the comparison between displacements at top floor showed significant differences between standard and innovative structure for five out of seven accelerograms that caused the development of plastic hinges at column bases in the standard [MRF] and which lead to residual deformations (i.e. *Acc-2,3,4,5,7*); ▪ only one case with residual deformations was evidenced for the innovative structural system (i.e. *Acc-6*), however these were not generated by plastic hinges at column bases, but by the plastic hinges in beams (that are planned to be replaceable); ▪ for the standard structure [MRF], the beams at the first two stories developed plastic rotations in the range of 0.021÷0.025 rad (*Acc-2*; *Acc-7* – see Figure 13), that exceeded the life-safety criteria, and which was not observed for the innovative structure [MRF+LSC].

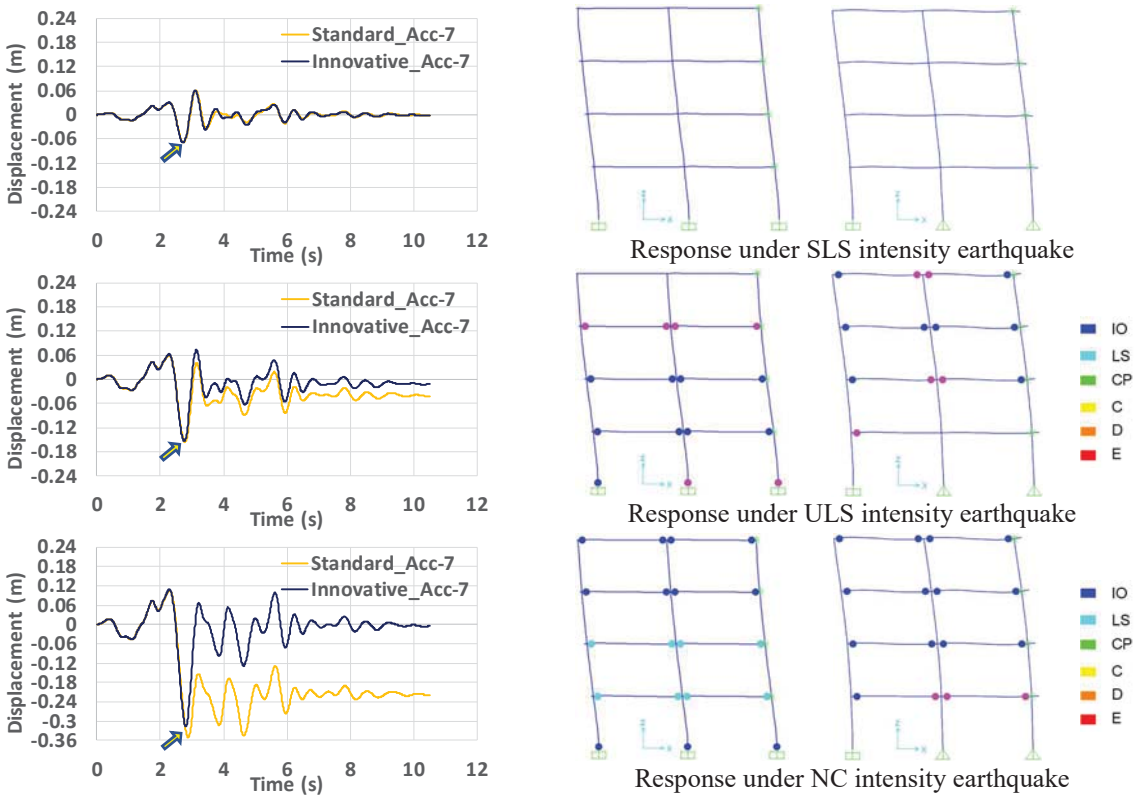

(a) Comparisson of the response (b) Standard structure (c) Innovative structure

Figure 13: Outcomes of time-history analyses for structures in Soft Soil conditions: (a) comparison of the response (top displacement vs. time); (b) & (c) state of standard [MRF] and innovative [MRF+LSC] structures

The time-history analyses under *Stiff Soil* conditions (see Figure 14) evidenced the following:

- *at SLS (serviceability limit state – a_g/a_{gr}=0.5)*: ▪ a minor plastic hinge developed in one beam corresponding to the innovative structure; ▪ the comparison between displacements at top floor showed almost identical deformations;
- *at ULS (ultimate limit state – a_g/a_{gr}=1.0)*: ▪ plastic hinges developed in beams (at three out of four stories) for both structural configurations, but the rotations did not reach the life safety (LS) level; ▪ no plastic hinges developed at the column bases; ▪ the comparison between displacements at top floor showed some differences, i.e. slightly lower deformations corresponding to the innovative structure;
- *at NC (near collapse – a_g/a_{gr}=1.7)*: ▪ a global plastic mechanism was evidenced in case of the standard structural system with plastic hinges in beams and at column bases, while in case of the innovative structure plastic hinges developed in all beams except at first floor; ▪ the comparison between displacements at top floor showed some differences, i.e. the innovative structure [MRF+LSC] evidenced lower deformations, but the differences were not in the same amount as observed for the structural system located in soft soil; ▪ the development of plastic hinges in beams and at column bases for the standard structure [MRF], respectively in beams for the innovative structure [MRF+LSC] lead to residual deformations, however with values lower than *5 cm*; ▪ the plastic hinges did not reach rotations corresponding to life safety in any of the two structural systems.

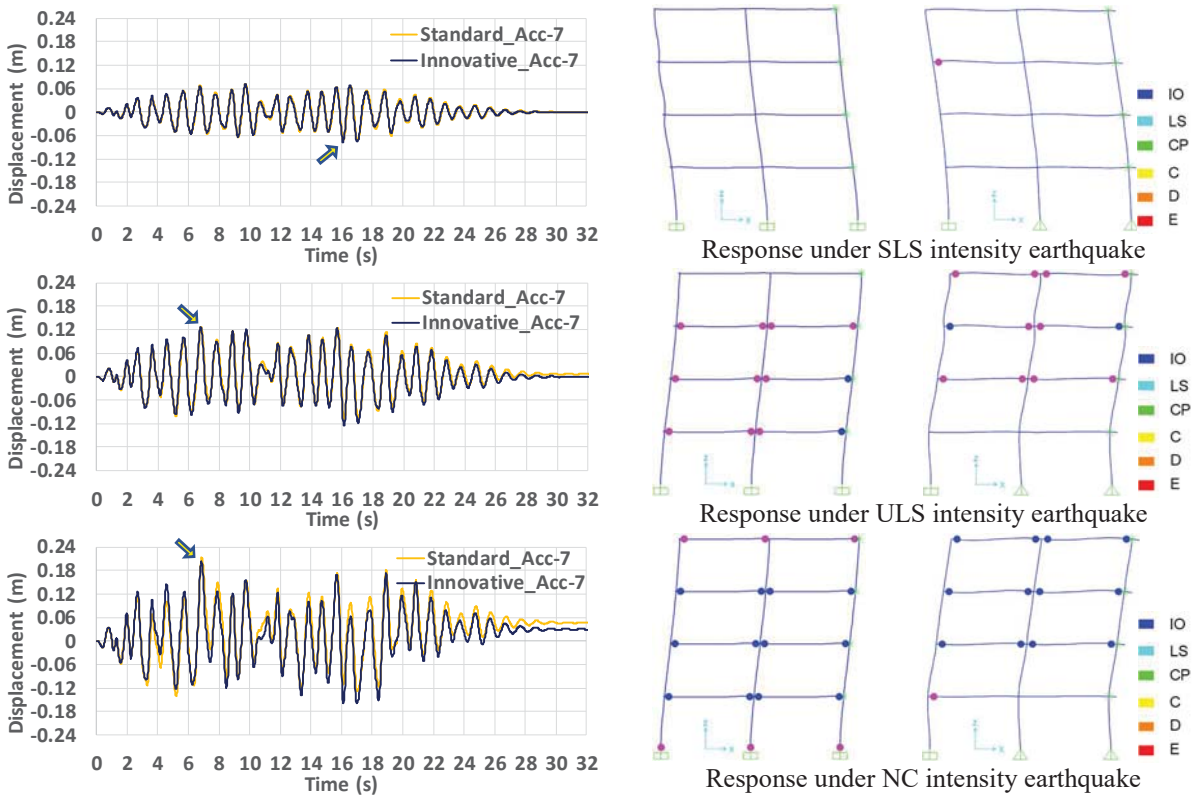

(a) Comparisson of the response (b) Standard structure (c) Innovative structure

Figure 14: Outcomes of time-history analyses for structures in Stiff Soil conditions: (a) comparison of the response (top displacement vs. time); (b) & (c) state of standard [MRF] and innovative [MRF+LSC] structures

The nonlinear dynamic analyses also allowed to evaluate the inter-story drifts corresponding to each: (i) structural configuration (standard / innovative); (ii) soil condition (soft / stiff); (iii) accelerogram (*Acc-1÷Acc-7*); (iv) seismic intensity level (SLS, ULS, NC). Figure 15 and Figure 16 illustrate the inter-story drifts generated by the two accelerograms (i.e. *"Acc-7_Soft", "Acc-7_Stiff"*) within the corresponding structural systems. The following observations can be made:

- the highest inter-story drift within the standard structure [MRF] occurred at the 2nd floor corresponding to both soil conditions and each of the three seismic intensity levels;
- the highest inter-story drift within the innovative structure [MRF+LSC] occurred at the 4th floor corresponding to both soil conditions and each of the three seismic intensity levels;
- the lowest inter-story drift was evidenced at the top floor for the standard structure [MRF], and at the 1st floor for the innovative structure [MRF+LSC];

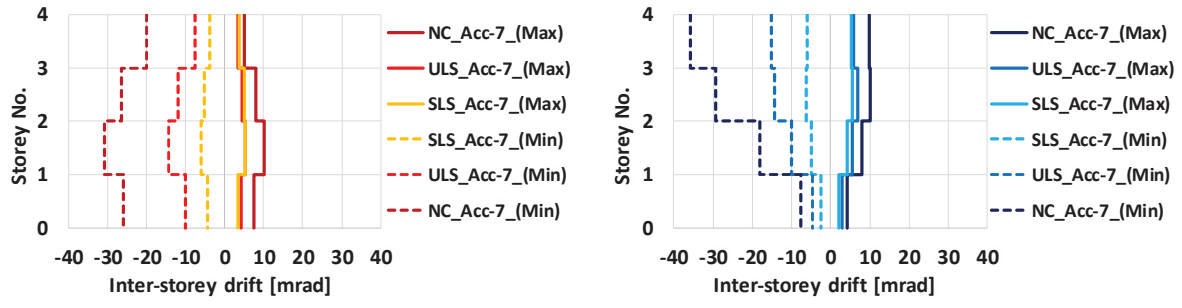

(a) (b)

Figure 15: Inter-story drifts generated by *"Acc-7_Soft"* within the corresponding structural systems: (a) standard structure [MRF]; (b) innovative structure [MRF+LSC]

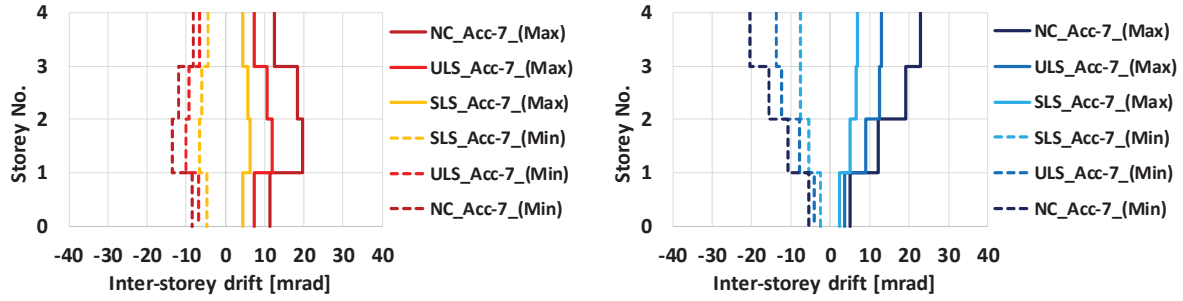

Figure 16: Inter-story drifts generated by *"Acc-7_Stiff"* within the corresponding structural systems: (a) standard structure [MRF]; (b) innovative structure [MRF+LSC]

An improved response of the innovative structures can be observed in Figure 15 and Figure 16 by comparison to the standard structures. In particular, the "*soft-story*" type of mechanism does not occur for the innovative structures, as the maximum (+/-) deformations occur at the top floor. Furthermore, the LSC's have a stiffening effect at the lower part of the structure.

The average of the maximum (+/-) inter-story drift values for the standard and innovative structures, corresponding to each seismic intensity level (SLS, ULS, NC), was computed from the outcomes of the two sets of seven accelerograms. The average values summarized in Table 6 for soft soil conditions and in Table 7 for stiff soil conditions, confirm the observations mentioned above also for other accelerograms.

Story	Standard structure [MRF]			Innovative structure [MRF+LSC]		
	SLS	ULS	NC	SLS	ULS	NC
4	3.6	6.5	13.4	5.4	**12.1**	**26.0**
3	4.8	9.7	19.4	**5.6**	11.6	21.7
2	**5.2**	**10.9**	**22.6**	4.3	8.2	13.8
1	3.7	7.3	18.1	2.2	3.9	6.2

Table 6: Average of the maximum inter-story drifts [mrad] corresponding to the three seismic intensity levels (SLS, ULS, NC) and the two structural configurations (standard / innovative) designed for Soft Soil conditions

Story	Standard structure [MRF]			Innovative structure [MRF+LSC]		
	SLS	ULS	NC	SLS	ULS	NC
4	4.4	7.3	11.1	**7.5**	**14.0**	**24.0**
3	6.1	10.6	16.7	7.5	13.2	19.6
2	**6.9**	**12.1**	**19.1**	5.4	9.1	12.8
1	4.6	7.6	11.9	2.5	4.2	5.8

Table 7: Average of the maximum inter-story drifts [mrad] corresponding to the three seismic intensity levels (SLS, ULS, NC) and the two structural configurations (standard / innovative) designed for Stiff Soil conditions

5 SOLUTION FOR THE REPLACEABLE DISSIPATIVE COMPONENTS

An efficient system has to fulfil two requirements: (i) the inelastic deformation should take place only in removable elements; (ii) the damaged dissipative elements must be replaceable. For a structure to be repairable, in addition to constraining the inelastic deformations to the removable dissipative members, any permanent (residual) drift needs to be eliminated, while providing a re-centering capability. As a result, the current study proposes the use of "*leaf-spring*" columns in order to prevent the formation of plastic hinges at the base of the columns,

and to provide the re-centering capability of the structure. In addition, the proposed solution for the replaceable dissipative components is illustrated in Figure 17, and consists of:

- Division of roles between frames, i.e. gravitational load resisting structure (the internal frames) / lateral load resisting structure (the perimeter frames);
- Rearrangement of secondary beams (see Figure 17a), i.e. with a parallel orientation to the main beams (i.e. those which are part of the lateral load resisting frame);
- Secondary beams from the façade are aimed to support the concrete slab and the façade elements (see Figure 17b);
- The replaceable dissipative components (i.e. the main beams) are to be decoupled from secondary beams and the concrete slab, and realized from two parts connected at mid span through a simple/continuous bolted connection (see Figure 17c).

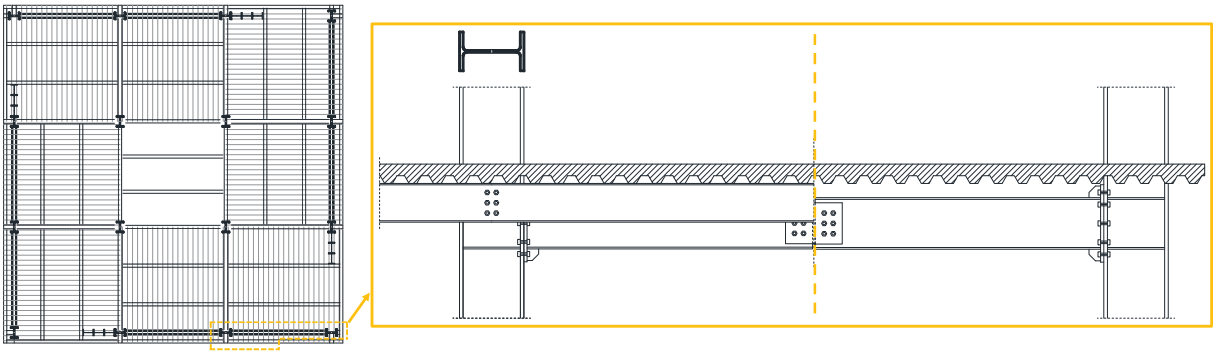

(a) (b) (c)

Figure 17: Proposed solution for the replaceable dissipative components: (a) floor layout – with arrangement of columns / main beams / secondary beams / steel deck for the concrete slab; (b) secondary beams from the façade; (c) replaceable dissipative components (main beams decoupled from secondary beams and concrete slab).

The proposed solution for replaceable dissipative components has the following advantages:

- The dissipative components (i.e. the main beams) are easy to inspect and to replace as these are manufactured from two parts that can be individually dismantled, and the weight is reduced to half;
- Even though the replacement of the dissipative beams might take some effort, it is much more favorable compared to demolishing the building and constructing a new one;
- The beam-to-column joints can be designed as full-strength/full-rigid joints and detailed based on existing connection solutions in seismic regions.

6 CONCLUSIONS

The current research represents an attempt to face the challenges of the construction sector and to respond to the two vision documents from U.S. [28] and Europe [29]. In particular, the research aims at reducing the repair costs and downtime of a structure hit by natural hazards (i.e. earthquakes), and consequently at a more rational design approach in the context of sustainability. Both replaceable dissipative components and structural re-centering capability are being addressed. In brief, the research activities consist in developing a set of bolted beam-to-column joints with replaceable dissipative components and investigating the applicability potential of innovative "*leaf-spring*" columns into building frames.

A structural configuration benchmark was developed for a 3D multi-story building. In a first stage, two standard structural configurations with perimeter moment resisting frames (MRF's) were designed for soft and stiff soil conditions (with a PGA of a_g=*0.3g*). Using the standard

structures [MRF] as reference, a set of innovative structural configurations [MRF+LSC] were developed and designed for the same loading and soil conditions. The inelastic response of the structures was evaluated through nonlinear static (pushover) and dynamic (time-history) analyses. A detailed description of the seismic performance was presented in Section 4.1 and 4.2. In brief, both structural systems evidenced an appropriate seismic performance, i.e.:

- *at SLS*: an elastic response of the standard [MRF] and innovative [MRF+LSC] structures;
- *at ULS*: plastic hinges developed in beams (at three out of four stories) for both structural configurations, but the rotations did not reach the life safety (LS) level;
- *at NC*: ▪ a global plastic mechanism was evidenced with plastic hinges in beams and at column bases for the standard [MRF], respectively with plastic hinges in beams for the innovative structural system [MRF+LSC]; ▪ for the standard structure [MRF] in soft soil conditions, some plastic hinges in beams reached rotations corresponding to life safety.

From the design and investigation of the two structural configurations, the soft soil conditions proved to be a more severe loading case and lead to: (i) higher cross-section of members; (ii) larger inter-story deformations and displacements at top floor; (iii) higher rotations in plastic hinges (i.e. life safety level was reached in some plastic hinges).

From the design and analyses of the innovative structural system [MRF+LSC], the use of LSC's evidenced some advantages and/or improvement of the structural response:

- It provided a change in the load transfer mechanism, i.e. compared to a standard MRF, the lateral load was distributed among both "*leaf-spring*" columns and MRF bays;
- The LSC's were characterized by a linear-elastic response, with a lower stiffness and capacity (up to a *0.3 m* top displacement) compared to the MRF subsystem;
- The use of LSC's and the change in the load transfer mechanism allowed to reduce the cross-section of beams and columns from the perimeter lateral load resisting frames, and to use pinned connections for the base of the columns;
- An improved response of the innovative structures, i.e. capacity curve with a linear ascending tendency in the post yield region;

A solution was proposed for beam-to-column joints with replaceable dissipative components (see Section 5), that will be further investigated along with the novel "*leaf-spring*" columns. Based on the outcomes of the current study, it can be stated that, compared to the standard structure [MRF] which does not possess any noteworthy re-centering capability, the innovative structural system [MRF+LSC] evidenced an improved seismic performance and increased resilience. The proposed structural system [MRF+LSC] and joining solution have the following advantages and/or improvement of the structural response:

- The [MRF] subsystem is the main lateral force resisting component (especially at the top floors) and the main seismic energy dissipation system – see pushover curve in Figure 11;
- The [LSC] subsystem is the secondary lateral force resisting component (see Figure 11) and provides (through its elastic response) the re-centering capability of the structure;
- The [LSC] subsystem: (i) contributes to the stiffening of the structure at the lower part; (ii) allows to use simple connections for the other columns and to reduce the cross-sections of beams and columns; (iii) prevents the formation of plastic hinges at column bases;
- The dissipative components (i.e. the main beams) are easy to inspect and to replace, as these are manufactured from two parts that can be individually dismantled and the weight is reduced to half;
- Even though the replacement of the dissipative beams might take some effort, it is much more favorable compared to demolishing the building and constructing a new one;

- The beam-to-column joints can be designed as full-strength/full-rigid joints, and detailed based on existing connection solutions in seismic regions.

Within the current study, the innovative structural configurations contained one LSC for each perimeter lateral load resisting frame. Consequently, two LSC's acted on each of the two main directions. This resulted in high demands and the necessity of using profiles of S700 high strength steel (eventually profiles manufactured from welded S700 plates of equivalent thickness). In order to keep the LSC's in the elastic range, but without using profiles of high strength steel, another solution would be to re-design the innovative structures by considering additional LSC's. Thus, the demands within LSC's and on the foundations would decrease.

The ongoing and future research activities are devoted to further investigate the proposed solution for structural re-centering ("*leaf-spring*" columns – LSC's) and replaceable dissipative components. Advanced finite element numerical simulations and eventually experimental investigations will be carried out. Structural analyses will be performed considering natural ground motion records, as well as building configurations with additional stories. A technical and economical comparison between the conventional and the more resilient and sustainable structural system (with replaceable components and re-centering capability) will be performed.

ACKNOWLEDGEMENTS

The first author was supported by the Alexander von Humboldt Foundation through a Research Fellowship for Experienced Researchers. This support and the hospitality provided by the Institute of Steel Construction / RWTH-Aachen University are gratefully acknowledged.

REFERENCES

[1] C. Vulcu, A. Stratan, A. Ciutina, D. Dubina, Beam-to-CFT High Strength Joints with External Diaphragm. I: Design and Experimental Validation. *J. Struct. Eng.*, 2017;143/5, DOI: 10.1061/(ASCE)ST.1943-541X.0001709. May-2017.

[2] N. Chancellor, M. Eatherton, D. Roke, T. Akbaş, Self-Centering Seismic Lateral Force Resisting Systems: High Performance Structures for the City of Tomorrow. *Buildings 2014*, 4(3), pp. 520–548; doi:10.3390/buildings4030520.

[3] F.Y. Cheng, H. Jiang, K. Lou, Smart Structures: Innovative Systems for Seismic Response Control. *CRC Press*; 2008.

[4] G. Herning, M.E. Garlock, E. Vanmarcke, Reliability-based evaluation of design and performance of steel self-centering moment frames. *J.Constr.SteelRes.* 2011;67:1495–1505.

[5] H. Chi, J. Liu, Seismic Behavior of Post-Tensioned Column Base for Steel Self-Centering Moment Resisting Frame. *J. Constr. Steel Res.* 2012;78:117–130.

[6] D. Roke, B. Jeffers, Parametric Study of Self-Centering Concentrically Braced Frame Systems with Friction-Based Energy Dissipation. In: Mazzolani, Herrera, editors. Stessa. London: Taylor & Francis Group; 2012. pp. 691–696.

[7] C. Christopoulos, R. Tremblay, H.-J. Kim, M. Lacerte, Self-Centering Energy Dissipative Bracing System for the Seismic Resistance of Structures: Development and Validation. *J. Struct. Eng.* 2008;134(96):1.

[8] A. Braconi, F. Morelli, W. Salvatore, Development, Design and Experimental Validation of a Steel Self-Centering Device (SSCD) for Seismic Protection of Buildings. *Bull. Earthq. Eng.* 2012;10:1915–1941.

[9] D.J. Miller, L.A. Fahnestock, M.R. Eatherton, Development and Experimental Validation of a Nickel–Titanium Shape Memory Alloy Self-Centering Buckling Restrained Brace. *Eng. Struct.* 2012;40: 288–298.

[10] A. Plumier, C. Doneux, C. Castiglioni, J. Brescianini, A. Crespi, S. Dell'Anna, et al., Two Innovations for Earthquake Resistant Design. INERD Project – Final Report; 2004.

[11] I. Vayas, Ph. Karydakis, D. Dimakogianni, G. Dougka, C. Castiglioni, A. Kanyilmaz, et al., FUSEIS Dissipative Devices for Seismic Resistant Steel Frames - Design Guide; 2012.

[12] S. Bordea, Dual Frame Systems of Buckling Restrained Braces. PhD Thesis, "Politehnica Timisoara University" Publishing House, ISBN: 978-606-554-059-0; 2010. 244pp.

[13] C. Neagu, Multi-Storey Building Frames Stiffened with Dissipative Shear Walls. PhD Th, "Politehnica Timisoara University" Publishing House, ISBN: 978-606-554-270-9; 2011.

[14] A. Stratan, D. Dubina, Bolted Links for Eccentrically Braced Steel Frames. In: Bijlaard FSK, Gres-nigt AM, van der Vegte GJ (Eds.), Proc. of 5th AISC/ECCS International Workshop "Connections in Steel Structures V: Behaviour, Strength & Design", June 3–5, Delft University of Technology, The Netherlands; 2004. p. 223–32.

[15] D. Dubina, A. Stratan, F. Dinu, Dual High-Strength Steel Eccentrically Braced Frames with Removable Links. *Earthquake Eng. Struct. Dynam.* 2008;37:1703–1720.

[16] N. Mansour, C. Christopoulos, R. Tremblay, Experimental validation of replaceable shear links for eccentrically braced steel frames. *J. Struct. Eng.* 2011;137(10):1141-1152.

[17] M. Latour, V. Piluso, G. Rizzano, Experimental Analysis and Design of Friction Joints Equipped with Sprayed Aluminium Dampers. 8th International Workshop on Connection in Steel Structures (Connections VIII), 24-26.05.2016, Boston USA.

[18] M. Latour, G. Rizzano, X-shaped T-stub Joints: Experimental Analysis and Design. 6th European Conference on Steel and Composite Structures (EUROSTEEL-2011), 31 August – 2 September 2011, Budapest, Hungary.

[19] L. Tong, Y. Chen, Y. Chen, C. Fang, Cyclic Behaviour of Beam-to-Column Joints with Cast Steel Connectors. *J. Const. Steel Res.*, Vol.116, 2016, pp.114-130, ISSN 0143-974X, https://doi.org/10.1016/j.jcsr.2015.09.005.

[20] C.-C. Chou, C.-C. Wu, C.-K. Jao, Y.-Y. Wang, Weakened and Strengthened Steel Moment Connections. 4th International Conference on Earthquake Engineering Taipei, Taiwan, October 12-13, 2006, paper no. 152.

[21] Y. Shen, C. Christopoulos, N. Mansour, R. Tremblay, Seismic Design and Performance of Steel Moment-Resisting Frames with Nonlinear Replaceable Links. *J. Struct. Eng.* 2011; 137(10), ASCE, ISSN 0733-9445/2011/10-1107–1117.

[22] C. Castiglioni, A. Drei, A. Kanyilmaz, L. Calado, I. Vayas, B. Hoffmeister, R. Gonçalves, Numerical and Experimental Results of FUSEIS Project. 15th World Conference on Earthquake Engineering, Lisbon, Portugal, 24-28.09.2012.

[23] X. Lin, Y. Hub, T. Okazakic, Study on Highly Elastic Seismic Structural System Based on Very High Strength Steel and Damage-Control Fuses. 8th European Conference on

Steel and Composite Structures (EUROSTEEL 2017), September 13–15, 2017, Copenhagen, Denmark. (*Wiley Online Library*). CE/Papers, doi: 10.1002/cepa.385.

[24] A.L. Zhang, S.H. Li, Z.Q. Jiang, H. Fang, C. Dou, Design Theory of Earthquake-Resilient Prefabricated Sinusoidal Corrugated Web Beam-Column Joint. *Eng. Struct.*, 2017;150:665-673, (https://doi.org/10.1016/j.engstruct.2017.07.088).

[25] C. Quan, W. Wang, T.-M, Chan, M. Khador, FE Modelling of Replaceable I-beam-to-CHS Column Joints under Cyclic Loads, *J. Const. Steel Res.*, V.138, 2017, 221-234, ISSN:0143-974X, https://doi.org/10.1016/j.jcsr.2017.07.012.

[26] SIMPSON: Strong-Tie. Strong Frame Design Guide. F-L-FS17 SIMPSON STRONG-TIE COMPANY INC, 2017.

[27] A. Ioan, A. Stratan, D. Dubina, M. Poljansek, F.J. Molina, F. Taucer, P. Pegon, G. Sabau, Experimental Validation of Re-centring Capability of Eccentrically Braced Frames with Removable Links, *Eng. Struct.*, Vol. 113, 2016, pp. 335-346, ISSN 0141-0296, https://doi.org/10.1016/j.engstruct.2016.01.038.

[28] S.J. Dyke, B. Stojadinovic, P. Arduino, M. Garlock, N. Luco, J.A. Ramirez, S. Yim, Vision 2020 for Earthquake Engineering Research; Report on an open-space technology workshop on future of earthquake engineering. 25-26.01.2010, St. Louis, Missouri, USA.

[29] European Construction Technology Platform (ECTP), Challenging and Changing Europe's Built Environment: A vision for a sustainable and competitive construction sector by 2030. February 25th, 2005. (www.ectp.org).

[30] CEN (European Committee for Standardization). "Eurocode 8: Design of structures for earthquake resistance – Part 1: General rules, seismic actions and rules for buildings." EN 1998-1-1, Brussels, Belgium, 2004.

[31] P100-1, "National seismic design code - Design provisions for buildings", Romania, 2013.

[32] CSI Berkley, SAP2000 v21, Copyright Computers and Structures, 2019.

[33] CEN (European Committee for Standardization). "Eurocode 3: Design of steel structures - Part 1-1: General rules and rules for buildings" EN 1993-1-1, Brussels, Belgium 2005.

[34] R. Landolfo, F. Mazzolani, D. Dubina, L.S. da Silva, M. D'Aniello, Design of steel structures for buildings in seismic areas. ECCS – European Convention for Constructional Steelwork, ISBN (ECCS): 978-92-9147-138-6, DOI:10.1002/9783433609194, 2017.

[35] P. Fajfar, A nonlinear analysis method for performance-based seismic design, *Earthquake Spectra*, 16(3):573-92, 2000.

[36] FEMA 356, Prestandard and commentary for the seismic rehabilitation of buildings, Federal Emergency Management Agency, Washington (DC), 2000.

[37] CEN (European Committee for Standardization). "Eurocode 8: Design of structures for earthquake resistance - Part 3: Assessment and retrofitting of buildings" EN 1998-3, 2005.

[38] Abaqus (v.2019) Analysis User's Manual I-V. Version 2019. USA: ABAQUS, Inc., Dassault Systèmes.

EURODYN 2020
XI International Conference on Structural Dynamics
M. Papadrakakis, M. Fragiadakis, C. Papadimitriou (eds.)
Athens, Greece, 23–26 November 2020

EXPERIMENTAL INVESTIGATION OF THE INFLUENCE OF TENSILE STRAIN ON THE CRACKING OF R/C VERTICAL STRUCTURAL ELEMENTS

Theodoros A. Chrysanidis[1], **Vassilis P. Panoskaltsis**[2]

[1] Demokritos University of Thrace
University Campus Xanthi-Kimmeria, Xanthi, 67100, Greece
e-mail: theodoros_gr@yahoo.com

[2] Demokritos University of Thrace
University Campus Xanthi-Kimmeria, Xanthi, 67100, Greece
vpanoska@civil.duth.gr

Keywords: Tensile strain, Cracking, Structural elements, Width

Abstract. *The main objective of this research is to study the phenomenon of cracking in the vertical structural elements of R/C constructions, in particular the columns and the walls, and more particularly in the extreme regions of the walls, namely the boundary columns. Various parameters of the phenomenon of cracking will be studied, e.g. load influence, tensile strain, etc. It has to be noted the fact that load application is a monotonic axial tensile loading that simulates the strain condition that takes place at the boundary edges of reinforced concrete seismic walls. Specifically, this type of loading simulates the tensile loading that takes place during the first semi-cycle of loading under seismic dynamic events. Experimental research takes place by the construction and use of a group of 4 experimental specimens subjected to different degrees of elongation. This test group examines the tensile parameter and how it affects the cracking. The test specimens in question are all reinforced with the same longitudinal reinforcement ratio (4.02%) and subjected to tensile degrees 10‰, 20‰, 30‰ and 50‰. Significant conclusions are reached on cracking, e.g. its extent, the size of the cracks, their positions, minimum crack width, maximum crack width, average crack width, number of cracks, etc.*

1 INTRODUCTION

Several international researchers have explored the phenomenon of cracking in reinforced concrete structures [1]–[23]. Although most of the given structures are typically reinforced in two directions, most studies carried out worldwide to investigate the behaviour of cracking have involved uniaxially tensiled reinforced concrete members with reinforcement in only one direction. To date there is not yet a widely established and accepted methodology for predicting cracking characteristics, e.g. crack widths and spacings between cracks [7], [9], [10], [23]–[26]. In addition, most of the existing research conducted has been strictly limited to the state of the stabilized crack pattern only and does not involve cracking behaviour and crack characteristics deep in the yield region [27], [28].

In the framework of the current study, an experimental program has been conducted involving reinforced concrete members detailed in two directions using longitudinal rebars and transverse reinforcement in the form of ties. This is a common construction practice used in at least the vast majority of concrete structures. As per the results outlined within this work, cracking behaviour and the crack characteristics are discussed. Useful conclusions concerning cracking under different degrees of elongation are derived. The experimental procedure of the current study has taken place in Aristotle University of Thessaloniki at the Laboratory of Strength of Materials but the result analysis has taken place in Democritus University of Thrace.

2 EXPERIMENTAL PROGRAM

2.1 Detailing of Test Specimens

The current experimental program consists of four test specimens. The thickness of each specimen is 7.5 cm and the length of the cross-section is 15 cm. The ratio between the length and the thickness of the cross-sectional area is equal to 2, which is a typical ratio for constructing reinforced concrete columns. The total height of the test specimen is equal to 90 cm. Each of the four specimens is subjected to a uniaxial central tensile loading. The main test element is between the metal plates and its height is 64 cm (Figure 1).

Table 1 shows the geometrical and detailing characteristics of all four specimens. All four segments tested here have been worked on in two directions through deformed bars in terms of reinforcement. The reinforcement of each specimen simulates a typical reinforcement found in the reinforced concrete columns of typical construction buildings or in the confined boundaries of reinforced concrete seismic walls. The construction scale used to simulate typical columns or typical confined boundaries was equal to 1:3, which is commonly used for research purposes worldwide [29], [30].

The number of longitudinal bars is equal to four. Each bar is placed at each corner of the column specimen and has a diameter of 12 mm. The longitudinal reinforcement ratio is equal to 4.02%. The transverse reinforcement consists of transverse ties placed along the height of the prism. The centre-to-centre distance between two ties is about 3.3 cm and the diameter of each tie is 4.2 mm. The only variable differentiating specimens from each other is the tensile strain. The nominal tensile strain takes values equal to 10.00%, 20.00%, 30.00% and 50.00%. It is well known that in real constructions, tensile strains up to 30.00% have been observed [31], [32]. Also, modern seismic and concrete codes have related provisions allowing large tensile strains for reinforcement bars [33]–[37]. These are the reasons why such large tensile strains were chosen to be applied to the elements. There is also, of course, the research interest itself, in examining what happens to cracking characteristics strained to such extents and their behaviour when such large strains are observed.

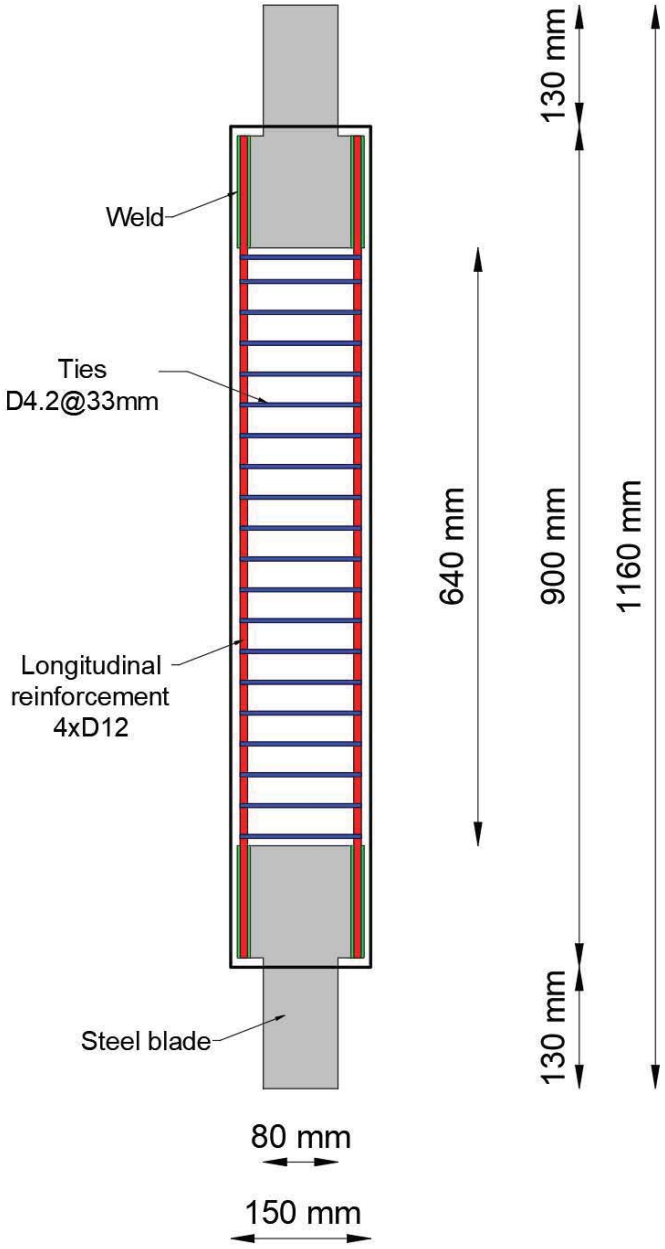

Figure 1: Vertical reinforcement layout for specimens.

N/A	Specimen name	Dimensions (cm)	Longitudinal reinforcement	Longitudinal reinforcement ratio [ρ_l] (%)	Transverse reinforcement	Nominal tensile strain (‰)
1	C-10	15x7.5x64	4xD12	4.02	D4.2@33 mm	10.00
2	C-20	15x7.5x64	4xD12	4.02	D4.2@33 mm	20.00
3	C-30	15x7.5x64	4xD12	4.02	D4.2@33 mm	30.00
4	C-50	15x7.5x64	4xD12	4.02	D4.2@33 mm	50.00

Table 1: Geometrical and detailed properties of element specimens

2.2 Loading Test Setup

A universal testing machine was used to apply the load. For example, for specimen C-20, the nominal degree of elongation is 20.00‰. Figure 2 displays the experimental configuration for imposing the tensile load. The rate of loading was slow, of the order of 4 mm/min, so no result was affected by the influence of the strain rate [38]–[40].

Figure 2: Loading test configuration.

3 RESULTS AND DISCUSSION

3.1 Experimental Findings

Figure 3 presents the change of tensile strain relative to the tensile load imposed on the test elements. It is obvious that specimens with a high nominal degree of elongation are subjected to high tensile strains too and vice versa. It is noted that the nominal degrees of tensile strain (10‰, 20‰, 30‰, 50‰) are slightly different from the residual actual tensile degrees, but these differences are small and negligible.

After conducting the experiments, different cracking formations and eventually cracking characteristics were noticed for each specimen. Figure 4 shows the state of each specimen after the end of the uniaxial tensile test. Cracks of small width are obvious for specimens with low degrees of tensile strain (10‰ and 20‰), while cracks of moderate and large width are present for specimens strained under larger degrees of elongation (30‰ and 50‰). It is apparent that the final cracking formation differs between the specimens, depending on the tensile strain they have sustained.

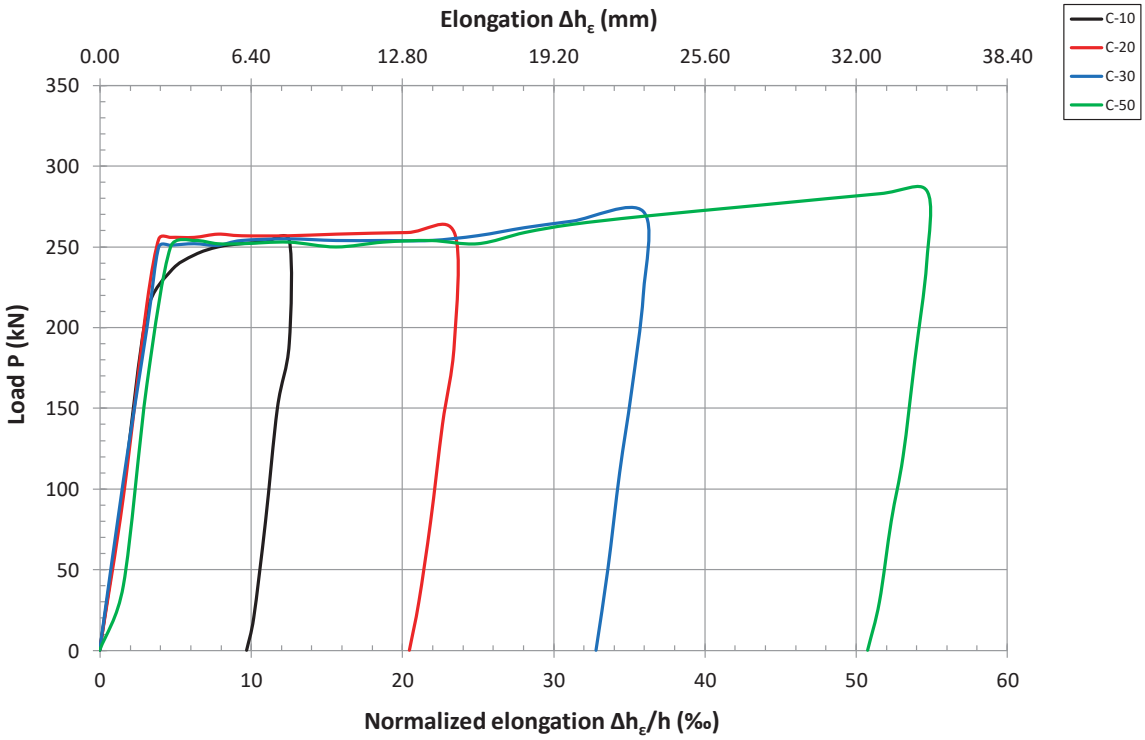

Figure 3: Diagram of tensile load versus elongation.

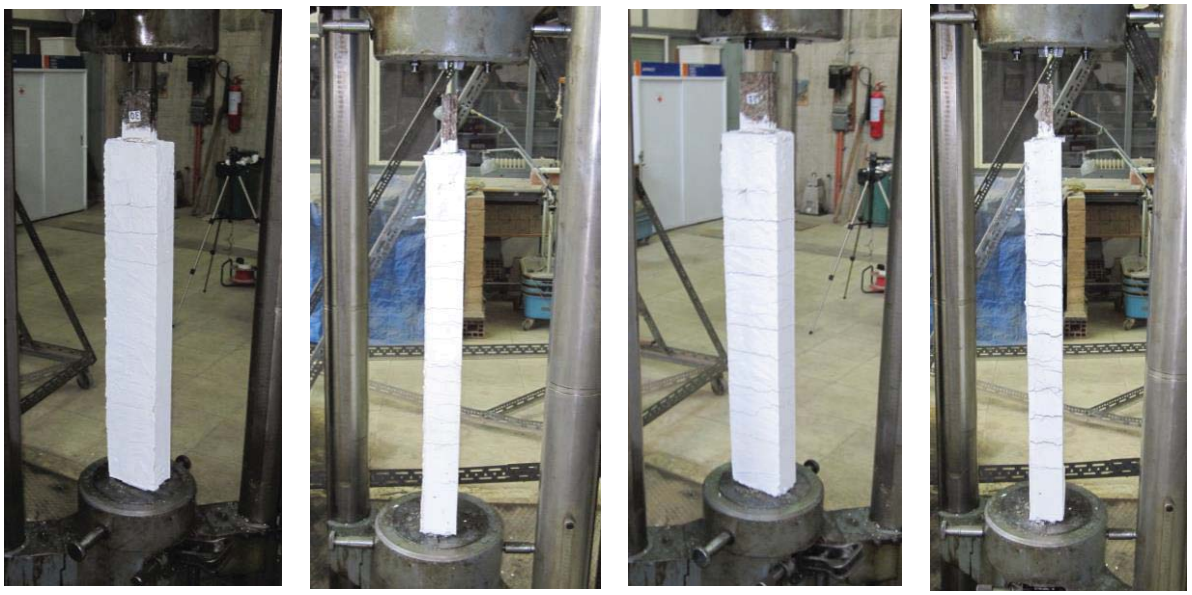

(a) **(b)** **(c)** **(d)**

Figure 4: Specimens after the uniaxial tensile test: (a) C-10, (b) C-20, (c) C-30, (d) C-50.

3.2 Analysis of Experimental Findings

The results of the analysis of the test findings for all segments are brought together in the following table and diagrams. Table 2 presents the width characteristics of the cracks. Figure 5 displays the variation of the crack width characteristics. Figure 6 – Figure 9 use bar charts to display the results for the same type of cracking characteristics, e.g. minimum width, average width, etc.

N/A	Specimen	Number of cracks [N]	Minimum crack width [W_{min}] (mm)	Maximum crack width [W_{max}] (mm)	Average crack width [W_{ave}] (mm)	W_{min}/W_{ave}	W_{max}/W_{ave}	W_{max}/W_{min}
1	C-10	5	0.6	1.5	1.100	0.55	1.36	2.50
2	C-20	9	0.5	2.0	1.256	0.40	1.59	4.00
3	C-30	10	1.0	2.9	1.810	0.55	1.60	2.90
4	C-50	11	2.1	3.8	3.064	0.69	1.24	1.81

Table 2: Crack width characteristics.

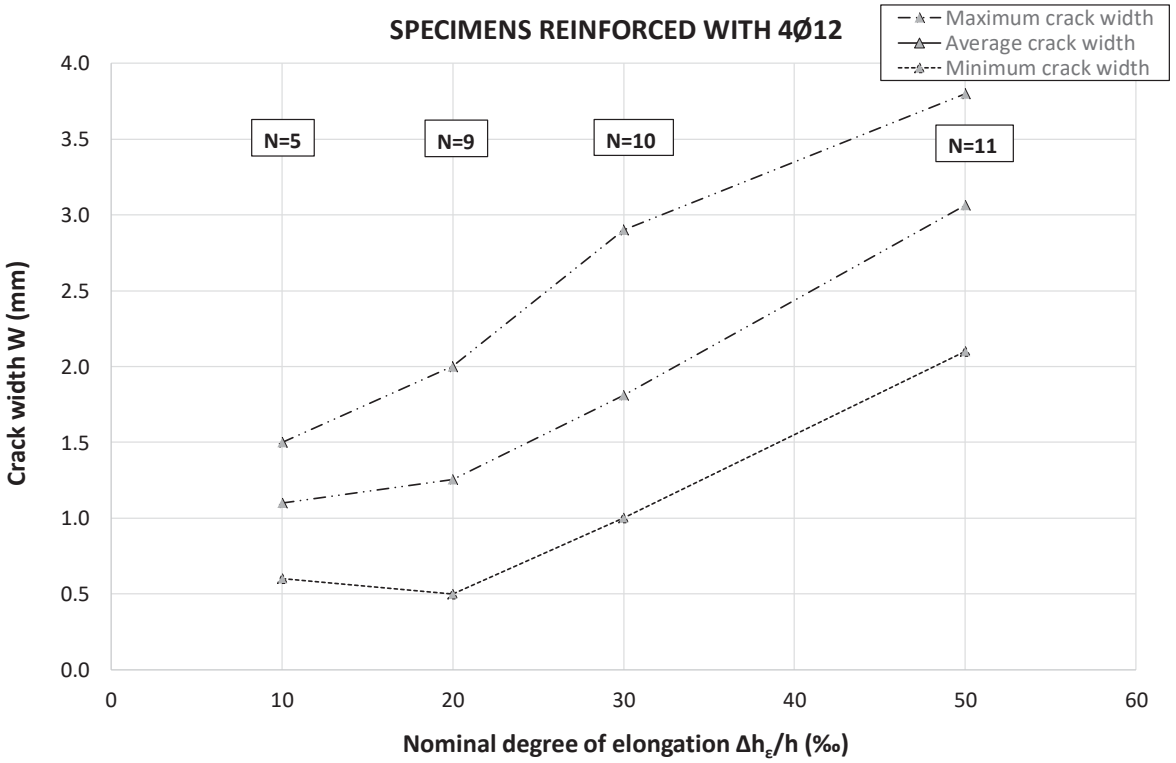

Figure 5: Change of crack width relative to the degree of elongation.

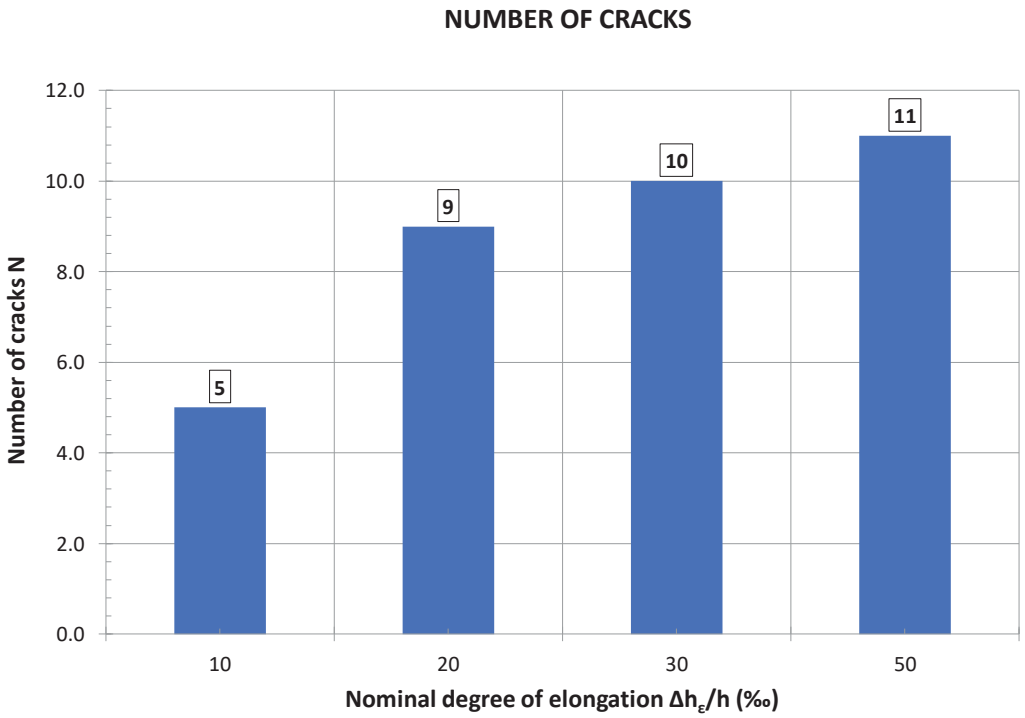

Figure 6: Bar chart of number of cracks regarding the degree of elongation.

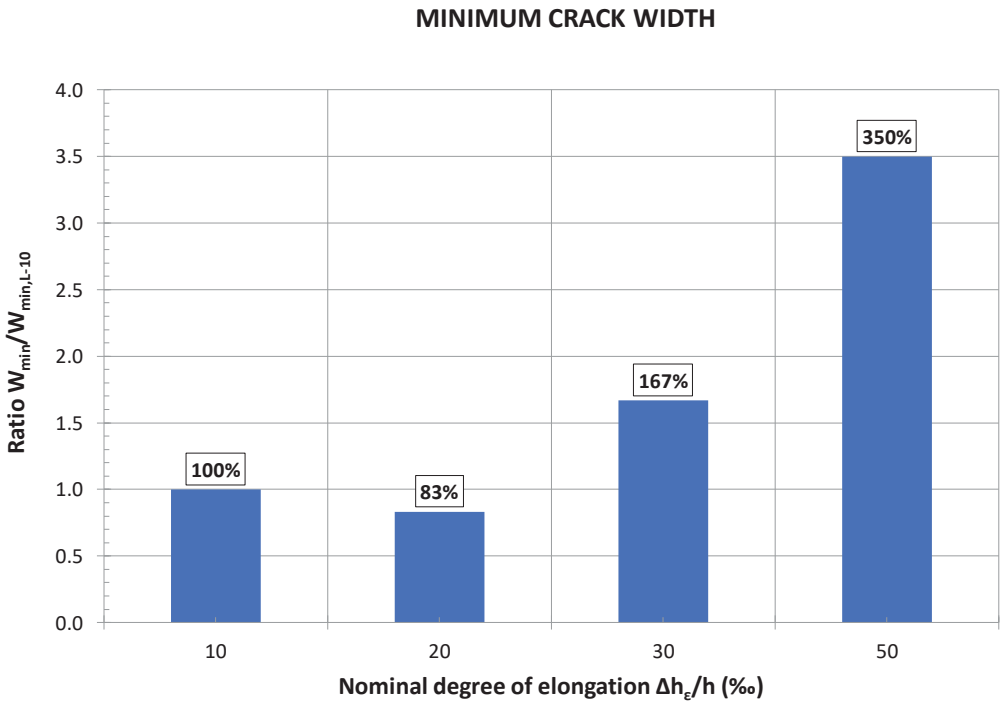

Figure 7: Bar chart of minimum crack width as a percentage of the minimum crack width of the reference specimen.

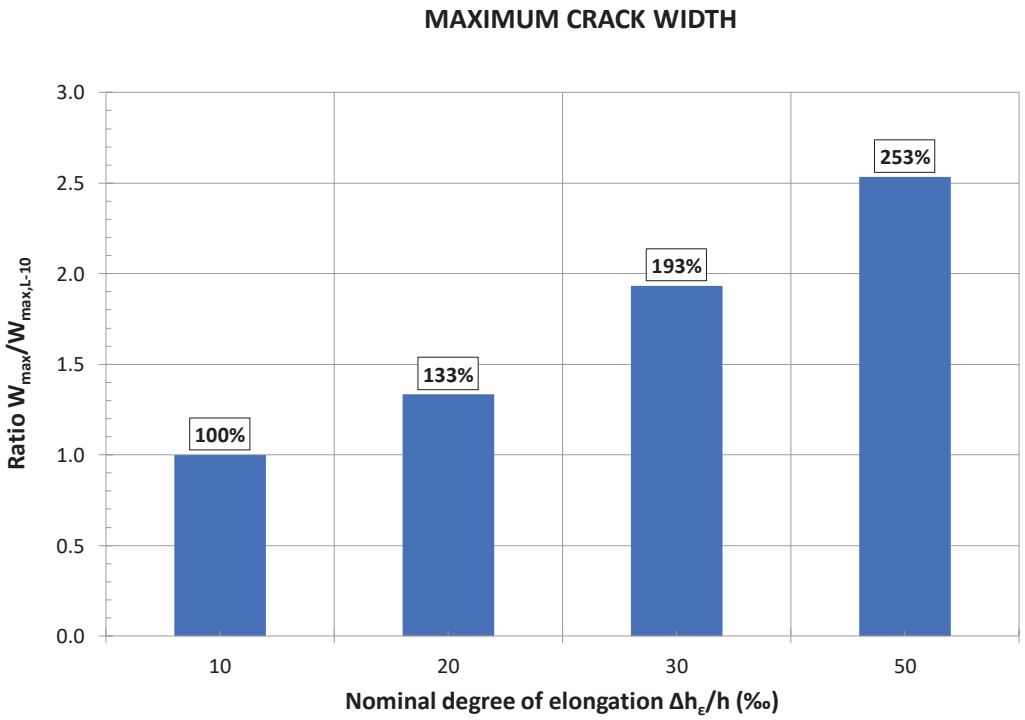

Figure 8: Bar chart of maximum crack width as a percentage of the maximum crack width of the reference.

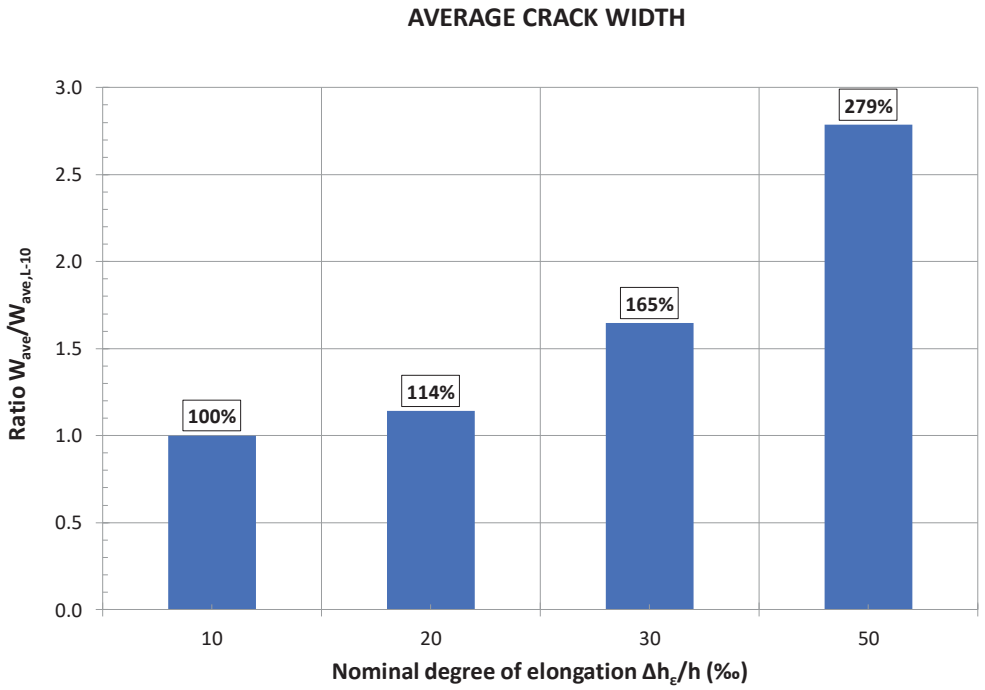

Figure 9: Bar chart of average crack width as a percentage of the average crack width of the reference specimen.

The experimental findings of the test elements were then analysed and evaluated:

1. Comparing the number of cracks formed with the tensile strain applied, it is obvious that the number of cracks formed increases with the increase of the degree of tensile strain applied (Table 2, Figure 6). For a better understanding of this phenomenon, more experiments concerning different longitudinal reinforcement ratios and arrangements of rebars need to be performed.
2. Comparing the crack width with the degree of elongation applied, it can be seen that the width becomes larger as the elongation degree sustained increases (Table 2, Figure 5). It is noteworthy that all types of crack width increase with the increment of the tensile degree – meaning the minimum, maximum and average crack width.
3. Specimen C-10 is characterized as the reference specimen. It is noticeable that although the normalized elongation (30‰) is three times greater for specimen C-30 compared to the elongation of the reference specimen (10‰), the increase of the minimum crack width is 1.67 times higher (167%). In all cases, the increase of their minimum crack width is smaller than the increase of the corresponding degree of elongation.
4. The increase of the average widths is smaller, too compared to the increase of normalized elongation, e.g., specimen C-30 displays a 165% increase in average crack width for a 300% elongation increase compared to the reference specimen.
5. The damage state of specimens indicates that cracks appear at or near to the tie positions (Figure 4). Thus, the presence of steel ties helps and promotes the disorganization of concrete around them.

4 CONCLUSIONS

This paper looks at four specimens to investigate cracking formation and behaviour in terms of the number of cracks and their width. The following conclusions are drawn:

1. The degree of tensile deformation holds a significant part in terms of the formation of cracks and their characteristics, e.g. the number of cracks formed and the width of cracks – whether considering the minimum, maximum or average value.
2. Higher degrees of elongation result in cracks with larger widths. Thus, the design of reinforced concrete structural components should take into account the degree of elongation because, as it is well known, large crack widths can lead to oxidization and deterioration of rebars and eventually affect structural safety.
3. The question arises of whether the longitudinal ratio or whether the arrangement of rebars plays an essential role, too. Further research is needed on the subject using test specimens with different longitudinal reinforcement ratios and arrangements. This will help to check the impact of the mechanical factor of reinforcement ratio has.

REFERENCES

[1] H. T. Hu and W. C. Schnobrich, “Nonlinear analysis of cracked reinforced concrete,” *ACI Structural Journal*, vol. 87, no. 2. pp. 199–207, 1990.

[2] Z. Shi, M. Suzuki, and M. Nakano, “Numerical Analysis of Multiple Discrete Cracks in Concrete Dams Using Extended Fictitious Crack Model,” *Journal of Structural*

Engineering, vol. 129, no. 3, pp. 324–336, 2003.

[3] C. Ouyang, E. Wollrab, S. M. Kulkarni, and S. P. Shah, "Prediction of Cracking Response of Reinforced Concrete Tensile Members," *Journal of Structural Engineering*, vol. 123, no. 1, pp. 70–78, 2002.

[4] K. A. Vu and M. G. Stewart, "Predicting the Likelihood and Extent of Reinforced Concrete Corrosion-Induced Cracking," *Journal of Structural Engineering*, vol. 131, no. 11, pp. 1681–1689, 2005.

[5] M. Lorrain, O. Maurel, and M. Seffo, "Cracking behavior of reinforced high-strength concrete tension ties," *ACI Structural Journal*, vol. 95, no. 5, pp. 626–635, 1998.

[6] S. L. Lee, M. A. Mansur, K. H. Tan, and K. Kasiraju, "Cracking Behavior of Concrete Tension Members Reinforced With Welded Wire Fabric.," *ACI Structural Journal*, vol. 84, no. 6. pp. 481–491, 1987.

[7] H. Marzouk, M. Hossin, and A. Hussein, "Crack width estimation for concrete plates," *ACI Structural Journal*, vol. 107, no. 3, pp. 282–290, 2010.

[8] C. H. Lu, W. L. Jin, and J. H. Mao, "Experimental Investigation of Corrosion-Induced Cover Cracking in Reinforced Concrete Structures," *Advanced Materials Research*, vol. 197–198, no. 4, pp. 1690–1693, 2011.

[9] S. K. Padmarajaiah and A. Ramaswamy, "Crack-width prediction for high-strength concrete fully and partially prestressed beam specimens containing steel fibers," *ACI Structural Journal*, vol. 98, no. 6, pp. 852–861, 2001.

[10] R. Gaetano and R. Filippo, "Cracking Response of RC Members Subjected to Uniaxial Tension," *Journal of Structural Engineering*, vol. 118, no. 5, pp. 1172–1190, 1992.

[11] H. Gesund and R. J. Frosh, "Another look at cracking and crack control in reinforced concrete. Paper by Robert J. Frosh," *ACI Structural Journal*, vol. 97, no. 2, p. 355, 2000.

[12] B. H. C. Chan, Y. K. Cheung, and Y. P. Huang, "C r a c k analysis o f reinforced concrete tension m e m b e r s," vol. 118, pp. 2118–2132, 1993.

[13] H. Mirzabozorg and M. Ghaemian, "Non-linear behavior of mass concrete in three-dimensional problems using a smeared crack approach," *Earthquake Engineering and Structural Dynamics*, vol. 34, no. 3, pp. 247–269, 2005.

[14] M. Byfield, "Control of cracking in reinforced concrete," *Structural Design from First Principles*, no. 105, pp. 271–288, 2018.

[15] B. P. Hughes and C. V. Cifuentes, "Comparison of Early-Age Crack Width Formulas for Reinforced Concrete.," *ACI Structural Journal*, vol. 85, no. 2. pp. 158–166, 1988.

[16] S. Yang and J. Chen, "Bond Slip and Crack Width Calculations of Tension Members.," *ACI Structural Journal*, vol. 85, no. 4. pp. 414–422, 1988.

[17] H. G. Sohn, Y. M. Lim, K. H. Yun, and G. H. Kim, "Monitoring crack changes in concrete structures," *Computer-Aided Civil and Infrastructure Engineering*, vol. 20, no. 1, pp. 52–61, 2005.

[18] M. M. Smadi and F. O. Slate, "Microcracking of high and normal strength concretes under short- and long-term loadings," *ACI Materials Journal*, vol. 86, no. 2. pp. 117–127, 1989.

[19] Y. H. Lee and K. Willam, “Mechanical properties of concrete in uniaxial compression,” *ACI Materials Journal*, vol. 94, no. 6, pp. 457–471, 1997.

[20] M. Aschheim and J. Browning, “Influence of Cracking on Equivalent SDOF Estimates of RC Frame Drift,” *Journal of Structural Engineering*, vol. 134, no. 3, pp. 511–517, 2008.

[21] G. Chen and G. Baker, “Influence of Bond Slip on Crack Spacing in Numerical Modeling of Reinforced Concrete,” *Journal of Structural Engineering*, vol. 129, no. 11, pp. 1514–1521, 2003.

[22] N. Ariyawardena, A. Ghali, and M. Elbadry, “Experimental study on thermal cracking in reinforced concrete members,” *ACI Structural Journal*, vol. 94, no. 4, pp. 432–441, 1997.

[23] Z. P. Bažant and B. H. Oh, “Spacing of Cracks in Reinforced Concrete,” *Journal of Structural Engineering*, vol. 109, no. 9, pp. 2066–2085, 2008.

[24] B. Bengt and L. Leroy, “Effects of Arrangement of Reinforcement on Crack Width and Spacing of Reinforced Concrete Members,” *ACI Journal Proceedings*, vol. 62, no. 11, pp. 1395–1420, 1965.

[25] Y. Goto, “Internal Cracks Formed in Concrete Around Deformed Tension Bars.,” *ACI Journal Proceedings*, vol. 68, no. 4, pp. 244–251, 1971.

[26] R. R. H. Zhu, W. Wanichakorn, T. T. C. Hsu, and J. Vogel, “Crack width prediction using compatibility-aided strut-and-tie model,” *ACI Structural Journal*, vol. 100, no. 4, pp. 413–421, 2003.

[27] Wood S. L., Wight J. K., and J. P. Moehle, “The 1985 Chile Earthquake, Observations on Earthquake Resistant Construction in Viña del Mar,” *Civil Engineering Studies*, vol. Structural, no. February 1987, p. 176 pp., 1987.

[28] M. Fintel, “Performance of Buildings With Shear Walls in Earthquakes of the Last Thirty Years,” *PCI Journal*, vol. 40, no. 3. pp. 62–80, 2014.

[29] G. G. Penelis and A. J. Kappos, *Earthquake-resistant Concrete Structures*. London, UK: E & F N SPON (Chapman & Hall), 1996.

[30] G. Penelis, K. Stylianidis, A. Kappos, and C. Ignatakis, *Reinforced Concrete Structures*. Thessaloniki, Greece: A.U.Th. Press, 1995.

[31] J. W. Wallace, “Behavior, design, and modeling of structural walls and coupling beams - Lessons from recent laboratory tests and earthquakes,” *International Journal of Concrete Structures and Materials*, vol. 6, no. 1, pp. 3–18, Mar. 2012.

[32] Y. H. Chai and S. K. Kunnath, “Minimum thickness for ductile RC structural walls,” *Engineering Structures*, vol. 27, no. 7, pp. 1052–1063, Jun. 2005.

[33] Standards New Zealand, “NZS 3101:2006, Concrete structures standard: Part 1 – The design of concrete structures,” Wellington, New Zealand, 2006.

[34] Canadian Standards Association, “CAN/CSA-A23.3-04, Design of Concrete Structures (Update No. 2 - July 2007),” Mississauga, Ontario, Canada, 2007.

[35] European Committee for Standardization, “EN 1998-1:2004, Eurocode 8: Design of structures for earthquake resistance - Part 1: General rules, seismic actions and rules for buildings,” Brussels, Belgium, 2004.

[36] Ministry of Environment Planning and Public Works, “Greek Code for the Design and Construction of Concrete Works,” Athens, Greece, 2000, p. . (In Greek).

[37] International Conference of Building Officials, “Uniform Building Code – Volume 2: Structural Engineering Design Provisions,” Whittier, California, USA, 1997.

[38] T. Chrysanidis, “Influence of elongation degree on transverse buckling of confined boundary regions of R/C seismic walls,” *Construction and Building Materials*, vol. 211, pp. 703–720, Jun. 2019.

[39] T. Chrysanidis and I. Tegos, “Axial and transverse strengthening of R/C circular columns: Conventional and new type of steel and hybrid jackets using high-strength mortar,” *Journal of Building Engineering*, vol. 30, no. January, p. 101236, 2020.

[40] T. A. Chrysanidis, “Evaluation of Out-of-Plane Response of R/C Structural Wall Boundary Edges Detailed with Maximum Code-Prescribed Longitudinal Reinforcement Ratio,” *International Journal of Concrete Structures and Materials*, vol. 14, no. 1. 2020.

EURODYN 2020
XI International Conference on Structural Dynamics
M. Papadrakakis, M. Fragiadakis, C. Papadimitriou (eds.)
Athens, Greece, 23–26 November 2020

EVALUATION OF CRACKING BEHAVIOR OF R/C VERTICAL COMPONENTS REINFORCED WITH VARYING LONGITUDINAL REINFORCEMENT RATIOS

Theodoros A. Chrysanidis[1], **Vassilis P. Panoskaltsis**[2]

[1] Demokritos University of Thrace
University Campus Xanthi-Kimmeria, Xanthi, 67100, Greece
e-mail: thchrysa@civil.duth.gr

[2] Demokritos University of Thrace
University Campus Xanthi-Kimmeria, Xanthi, 67100, Greece
vpanoska@civil.duth.gr

Keywords: Longitudinal ratio, Cracking, Spacing, Width

Abstract. *Cracking phenomenon in reinforced concrete members has troubled researchers and engineers worldwide due to the many mechanical parameters affecting this phenomenon. One such mechanical parameter is the longitudinal reinforcement ratio used for the detailing of vertical structural components in reinforced concrete structures. Although, the percentage of rebar content has been studied, it is the first time that cracking behavior is studied using varying ratios of rebars strained under a uniaxial tensile loading till a high degree of elongation found only at buildings sustained severe earthquake actions.*

This research is both experimental. For the experimental part, 8 test specimens in the form of R/C ties are used and strained using a monotonic uniaxial tensile loading simulating the tensile type of loading during the first cycle of dynamic seismic action. The first four test specimens are reinforced with longitudinal reinforcement ratio equal to 1.79% and the other four test specimens are reinforced with longitudinal reinforcement ratio equal to 3.19%. The test specimens are subjected to tensile degrees 10‰, 20‰, 30‰ and 50‰. Significant conclusions are reached concerning cracking behavior for different longitudinal ratios, e.g. number of cracks, crack width, crack spacing, etc.

1 INTRODUCTION

Cracking phenomenon and its characteristics has been explored by several researchers worldwide in reinforced concrete structures [1]–[23]. Although most of the given structures are typically reinforced in two directions, most studies carried out worldwide to investigate the behaviour of cracking have involved uniaxially tensiled reinforced concrete members with reinforcement in only one direction. To date there is not yet a widely established and accepted methodology for predicting cracking characteristics, e.g. crack widths and spacings between cracks [7], [9], [10], [23]–[26]. In addition, most of the existing research conducted has been strictly limited to the state of the stabilized crack pattern only and does not involve cracking behaviour and crack characteristics deep in the yield region [27], [28].

In the framework of the current study, an experimental program has been conducted involving reinforced concrete members detailed in two directions using longitudinal rebars and transverse reinforcement in the form of ties. The main aim of the present study is to investigate the influence of the longitudinal reinforcement ratio. As per the results outlined within this work, cracking behaviour and the crack characteristics are discussed. Useful conclusions concerning cracking under different longitudinal reinforcement ratios are derived. The experimental procedure of the current study has taken place in Aristotle University of Thessaloniki at the Laboratory of Strength of Materials and the result analysis has taken place in Democritus University of Thrace.

2 EXPERIMENTAL PROGRAM

2.1 Detailing of Test Specimens

The current experimental program consists of eight test specimens. The thickness of each specimen is 7.5 cm and the length of the cross-section is 15 cm. The ratio between the length and the thickness of the cross-sectional area is equal to 2, which is a typical ratio for constructing reinforced concrete columns. The total height of the test specimen is equal to 90 cm. Each of the eight specimens is subjected to a uniaxial central tensile loading. The main test element is between the metal plates and its height is 64 cm (Figure 1).

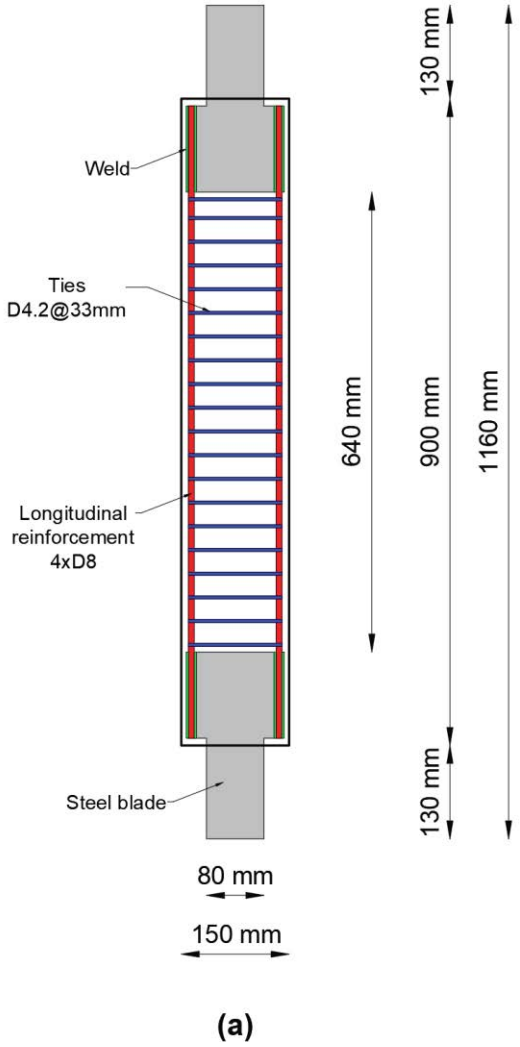

Figure 1: Vertical reinforcement layout for specimens reinforced with ratio equal to 1.79%.

Table 1 shows the geometrical and detailing characteristics of all eight specimens. There are two groups of test specimens. Each group consists of four test specimens. The reinforcement of each specimen simulates a typical reinforcement found in the reinforced concrete columns of typical construction buildings or in the confined boundaries of reinforced concrete seismic walls. The scale of construction used to simulate typical columns or typical confined boundaries was equal to 1:3, which is commonly used for research purposes worldwide [29], [30].

The number of longitudinal bars varies depending if the specimen belongs to the first group or the second group of test specimens. The longitudinal reinforcement ratio is equal to 1.79% for the first group of specimens and equal to 3.19% for the second group of specimens. The transverse reinforcement consists of transverse ties placed along the height of the prism. The axial distance between two ties is about 3.3 cm and the diameter of each tie is 4.2 mm. The only variable differentiating the two groups of specimens from each other is the longitudinal reinforcement ratio. The nominal tensile strain takes values equal to 10.00%, 20.00%, 30.00% and 50.00% for the four specimens of both groups. It is well known that in real constructions, tensile strains up to 30.00% have been observed [31], [32]. Also, modern seismic and concrete codes have related provisions allowing large tensile strains for reinforcement

bars [33]–[37]. These are the reasons why such large tensile strains were chosen to be applied to the elements. There is also, of course, the research interest itself, in examining what happens to cracking characteristics strained to such extents and their behaviour when such large strains are observed.

N/A	Specimen name	Length (cm)	Thickness (cm)	Effective height (cm)	Longitudinal reinforcement	Longitudinal reinforcement ratio [ρ_l] (%)	Transverse reinforcement	Nominal tensile strain (‰)
1	L-10	15	7.5	64	4xD8	1.79	D4.2@33 mm	2.75
2	L-20	15	7.5	64	4xD8	1.79	D4.2@33 mm	2.75
3	L-30	15	7.5	64	4xD8	1.79	D4.2@33 mm	2.75
4	L-50	15	7.5	64	4xD8	1.79	D4.2@33 mm	2.75
5	H-10	15	7.5	64	4xD8 + 2xD10	3.19	D4.2@33 mm	3.19
6	H-20	15	7.5	64	4xD8 + 2xD10	3.19	D4.2@33 mm	3.19
7	H-30	15	7.5	64	4xD8 + 2xD10	3.19	D4.2@33 mm	3.19
8	H-50	15	7.5	64	4xD8 + 2xD10	3.19	D4.2@33 mm	3.19

Table 1: Geometrical and detailed properties of prism specimens

2.2 Loading Test Setup

A universal testing machine was used to apply the load. For example, for specimen C-20, the nominal degree of elongation is 20.00‰. Figure 2 displays the experimental configuration for imposing the tensile load. The rate of loading was slow, of the order of 4 mm/min, so no result was affected by the influence of the strain rate [38]–[40].

Figure 2: Loading test configuration.

3 RESULTS AND DISCUSSION

3.1 Experimental Findings

Figure 3 presents the change of tensile strain relative to the tensile load imposed on the test elements for both groups of test specimens. It is obvious that specimens with a high longitudinal reinforcement ratio demand higher load values to be strained to the same degree of elongation compared to the specimens reinforced with low percentages of reinforcement.

After conducting the experiments, different cracking formations and eventually cracking characteristics were noticed for each specimen. Figure 4 shows the state of each specimen after the end of the uniaxial tensile test. Cracks of small width are obvious for specimens with low degrees of tensile strain (10‰ and 20‰), while cracks of moderate and large width are present for specimens strained under larger degrees of elongation (30‰ and 50‰). It is apparent that the final cracking formation differs between the specimens, depending on the tensile strain they have sustained.

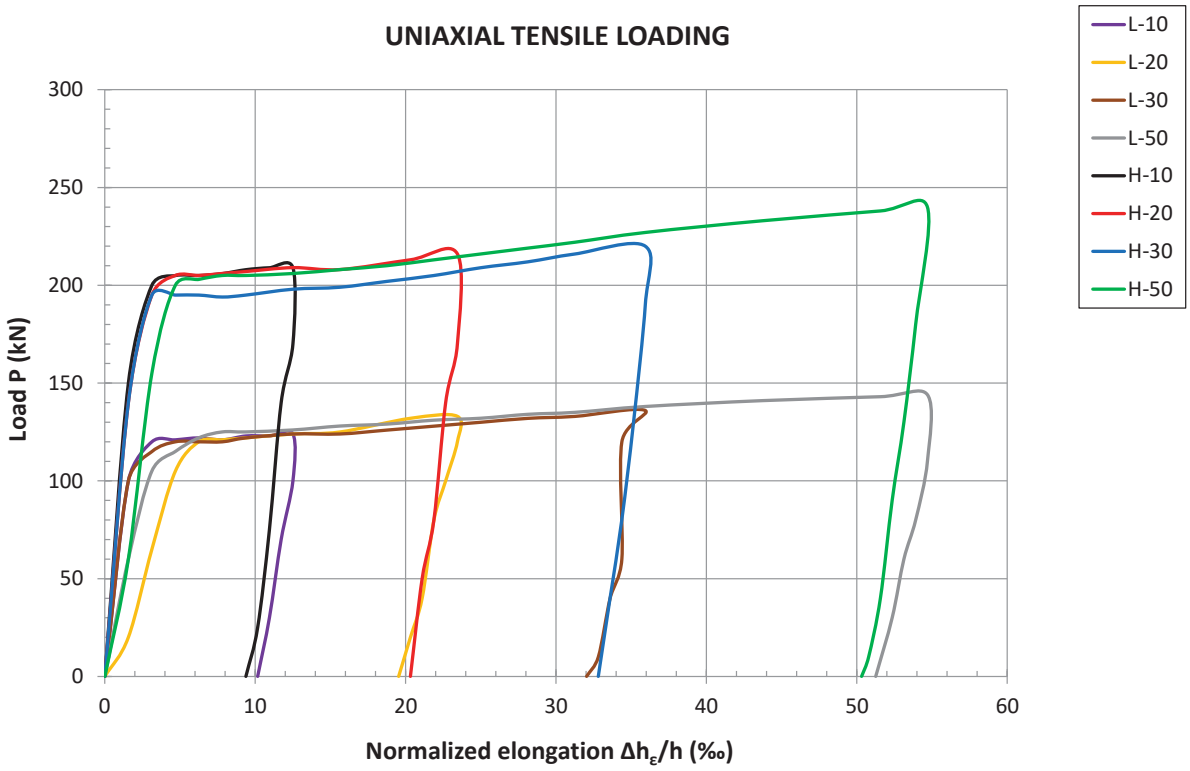

Figure 3: Diagram of tensile load versus elongation.

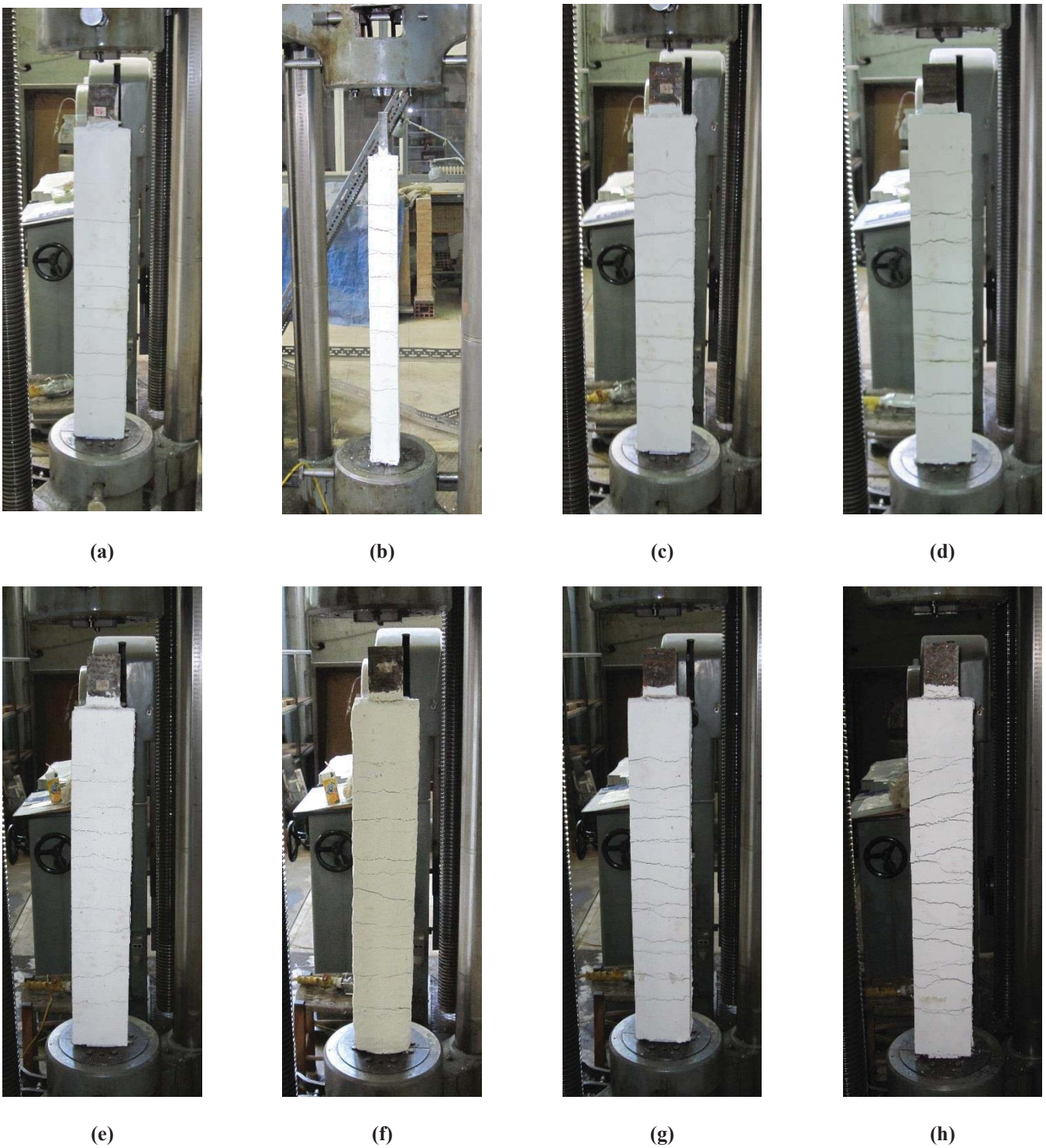

(a) **(b)** **(c)** **(d)**

(e) **(f)** **(g)** **(h)**

Figure 4: Specimens after the uniaxial tensile test: (a) L-10, (b) L-20, (c) L-30, (d) L-50, (e) H-10, (f) H-20, (g) H-30, (h) H-50.

3.2 Analysis of Experimental Findings

The results of the analysis of the test findings for all segments are brought together in the following table and diagrams. Table 2 presents the width characteristics of the cracks. Figure 5 displays the variation of the crack width characteristics for low-reinforced specimens, while

Figure 6 displays the same but this time for high-reinforced specimens. Figure 7 uses bar charts to display the number of cracks formed for both groups of test specimens, while Figure 8 uses, again, bar charts to display this time the results for the average crack width for low and high reinforcement specimens.

N/A	Specimen	Number of cracks [N]	Minimum crack width [W_{min}] (mm)	Maximum crack width [W_{max}] (mm)	Average crack width [W_{ave}] (mm)	W_{min}/W_{ave}	W_{max}/W_{ave}	W_{max}/W_{min}
1	L-10	9	0.2	1.5	0.844	0.24	1.78	7.50
2	L-20	9	1.2	2.3	1.678	0.72	1.37	1.92
3	L-30	9	1.4	3.1	2.311	0.61	1.34	2.21
4	L-50	9	1.9	6.7	3.811	0.50	1.76	3.53
5	H-10	11	0.2	1.0	0.655	0.31	1.53	5.00
6	H-20	12	0.2	1.5	1.050	0.19	1.43	7.50
7	H-30	13	0.6	2.0	1.354	0.44	1.48	3.33
8	H-50	13	0.8	3.2	2.277	0.35	1.41	4.00

Table 2: Crack width characteristics.

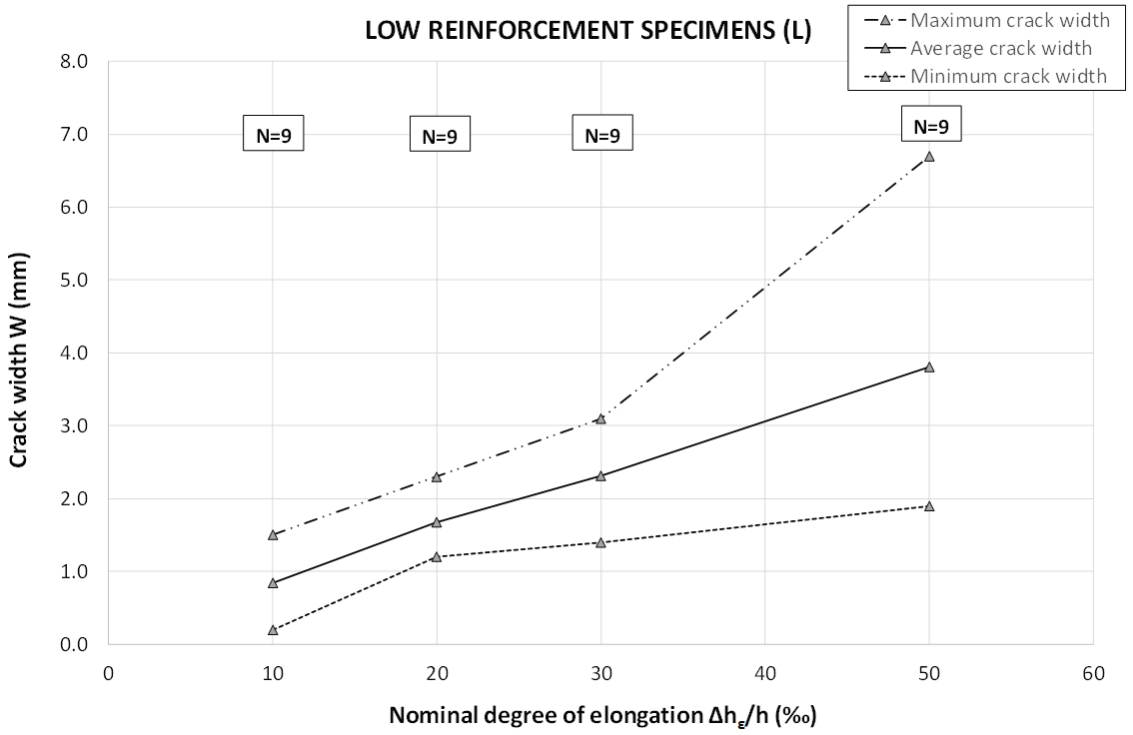

Figure 5: Change of crack width relative to the degree of elongation (low reinforcement specimens).

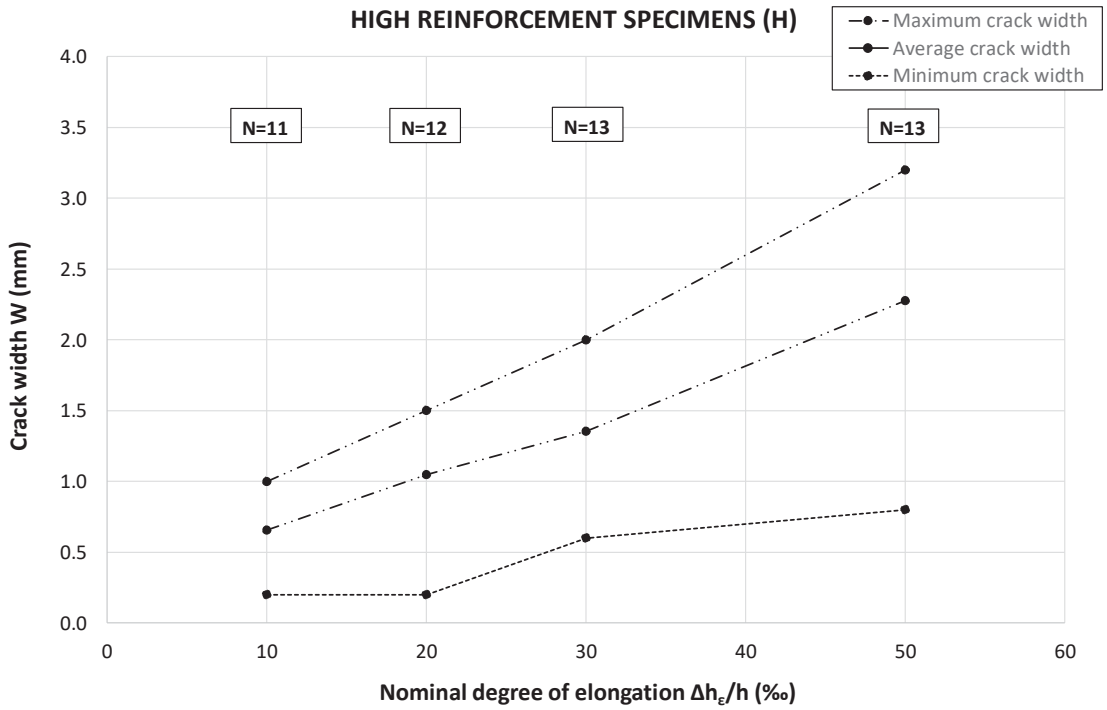

Figure 6: Change of crack width relative to the degree of elongation (high reinforcement specimens).

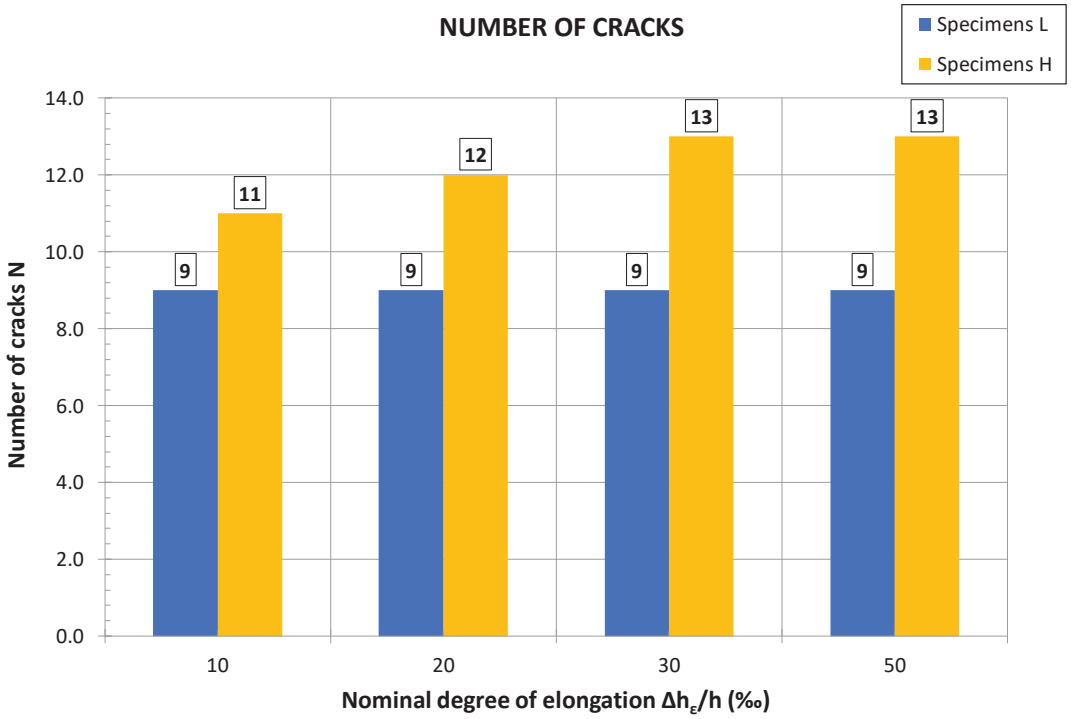

Figure 7: Bar chart of number of cracks regarding the degree of elongation.

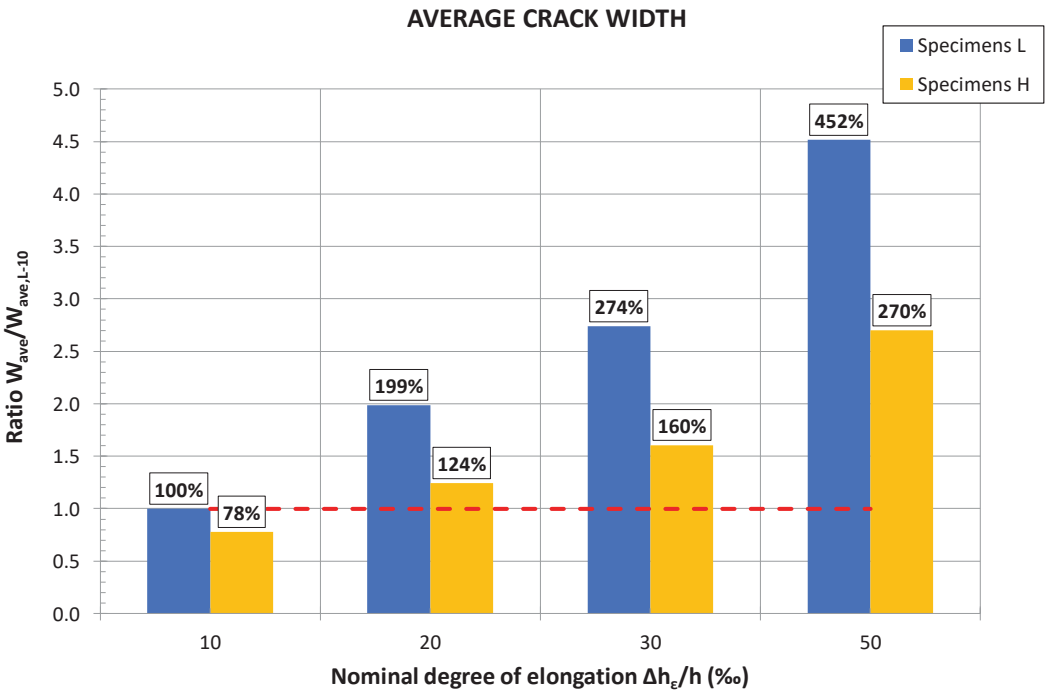

Figure 8: Bar chart of average crack width as a percentage of the average crack width of the reference specimen.

The analysis of the experimental findings of the tests conducted led to the following:

1. Comparing the number of cracks formed with the longitudinal reinforcement ratio used, it is obvious that the number of cracks formed increases with the increase of the longitudinal reinforcement ratio (Table 2, Figure 7). It seems that the presence of an increased percentage of rebars leads concrete to a larger disarrangement which results to an increased number of cracks formed throughout the height of the test specimens.
2. Comparing the average crack width with the percentage of longitudinal reinforcement utilized, it can be seen that the average width is larger for a smaller ratio of longitudinal reinforcement (Table 2, Figure 5).
3. Specimen L-10 is characterized as the reference specimen. It is noticeable that the normalized elongation (30‰) is three times greater for specimen L-30 compared to the elongation of the reference specimen (10‰) and the increase of the average crack width is 2.74 times higher (274%) compared to the average crack width of the reference specimen. In all cases, the increase of their average crack width follows closely the increase of the corresponding degree of elongation.
4. This is not true for the high reinforcement specimens. For the case of highly reinforced test specimens, it is obvious that although the normalized elongation (30‰) is three times greater for specimen H-30 compared to the elongation of the reference specimen (10‰), the increase of the average crack width is 1.60 times higher (160%). In all cases, the increase of their average crack width is smaller than the increase of the corresponding degree of elongation. This can be explained since the increment of the rebar content leads to an increment to the number of cracks

formed. Thus, a bigger number of cracks formed for the same tensile strain leads ultimately to smaller average crack width.

5. The damage state of specimens indicates that cracks appear at or near to the tie positions (Figure 4). Thus, the presence of steel ties helps and promotes the disorganization of concrete around them.

4 CONCLUSIONS

This paper looks at eight specimens to investigate cracking formation and behaviour in terms of the number of cracks and their average width. The following conclusions are drawn:

1. The degree of longitudinal reinforcement ratio used holds a significant part in terms of the formation of cracks and their characteristics, e.g. the number of cracks formed and the width of cracks.
2. Higher percentages of rebar ratio result in a higher number of cracks formed.
3. Higher longitudinal reinforcement ratios lead to smaller average crack widths. This fact should be taken into account when designing reinforced concrete structural elements since the width of cracks plays a crucial role to the duration of life of rebars.

REFERENCES

[1] H. T. Hu and W. C. Schnobrich, "Nonlinear analysis of cracked reinforced concrete," *ACI Structural Journal*, vol. 87, no. 2. pp. 199–207, 1990.

[2] Z. Shi, M. Suzuki, and M. Nakano, "Numerical Analysis of Multiple Discrete Cracks in Concrete Dams Using Extended Fictitious Crack Model," *Journal of Structural Engineering*, vol. 129, no. 3, pp. 324–336, 2003.

[3] C. Ouyang, E. Wollrab, S. M. Kulkarni, and S. P. Shah, "Prediction of Cracking Response of Reinforced Concrete Tensile Members," *Journal of Structural Engineering*, vol. 123, no. 1, pp. 70–78, 2002.

[4] K. A. Vu and M. G. Stewart, "Predicting the Likelihood and Extent of Reinforced Concrete Corrosion-Induced Cracking," *Journal of Structural Engineering*, vol. 131, no. 11, pp. 1681–1689, 2005.

[5] M. Lorrain, O. Maurel, and M. Seffo, "Cracking behavior of reinforced high-strength concrete tension ties," *ACI Structural Journal*, vol. 95, no. 5, pp. 626–635, 1998.

[6] S. L. Lee, M. A. Mansur, K. H. Tan, and K. Kasiraju, "Cracking Behavior of Concrete Tension Members Reinforced With Welded Wire Fabric.," *ACI Structural Journal*, vol. 84, no. 6. pp. 481–491, 1987.

[7] H. Marzouk, M. Hossin, and A. Hussein, "Crack width estimation for concrete plates," *ACI Structural Journal*, vol. 107, no. 3, pp. 282–290, 2010.

[8] C. H. Lu, W. L. Jin, and J. H. Mao, "Experimental Investigation of Corrosion-Induced Cover Cracking in Reinforced Concrete Structures," *Advanced Materials Research*, vol. 197–198, no. 4, pp. 1690–1693, 2011.

[9] S. K. Padmarajaiah and A. Ramaswamy, "Crack-width prediction for high-strength concrete fully and partially prestressed beam specimens containing steel fibers," *ACI*

Structural Journal, vol. 98, no. 6, pp. 852–861, 2001.

[10] R. Gaetano and R. Filippo, "Cracking Response of RC Members Subjected to Uniaxial Tension," *Journal of Structural Engineering*, vol. 118, no. 5, pp. 1172–1190, 1992.

[11] H. Gesund and R. J. Frosh, "Another look at cracking and crack control in reinforced concrete. Paper by Robert J. Frosh," *ACI Structural Journal*, vol. 97, no. 2, p. 355, 2000.

[12] B. H. C. Chan, Y. K. Cheung, and Y. P. Huang, "C r a c k analysis o f reinforced concrete tension m e m b e r s," vol. 118, pp. 2118–2132, 1993.

[13] H. Mirzabozorg and M. Ghaemian, "Non-linear behavior of mass concrete in three-dimensional problems using a smeared crack approach," *Earthquake Engineering and Structural Dynamics*, vol. 34, no. 3, pp. 247–269, 2005.

[14] M. Byfield, "Control of cracking in reinforced concrete," *Structural Design from First Principles*, no. 105, pp. 271–288, 2018.

[15] B. P. Hughes and C. V. Cifuentes, "Comparison of Early-Age Crack Width Formulas for Reinforced Concrete.," *ACI Structural Journal*, vol. 85, no. 2. pp. 158–166, 1988.

[16] S. Yang and J. Chen, "Bond Slip and Crack Width Calculations of Tension Members.," *ACI Structural Journal*, vol. 85, no. 4. pp. 414–422, 1988.

[17] H. G. Sohn, Y. M. Lim, K. H. Yun, and G. H. Kim, "Monitoring crack changes in concrete structures," *Computer-Aided Civil and Infrastructure Engineering*, vol. 20, no. 1, pp. 52–61, 2005.

[18] M. M. Smadi and F. O. Slate, "Microcracking of high and normal strength concretes under short- and long-term loadings," *ACI Materials Journal*, vol. 86, no. 2. pp. 117–127, 1989.

[19] Y. H. Lee and K. Willam, "Mechanical properties of concrete in uniaxial compression," *ACI Materials Journal*, vol. 94, no. 6, pp. 457–471, 1997.

[20] M. Aschheim and J. Browning, "Influence of Cracking on Equivalent SDOF Estimates of RC Frame Drift," *Journal of Structural Engineering*, vol. 134, no. 3, pp. 511–517, 2008.

[21] G. Chen and G. Baker, "Influence of Bond Slip on Crack Spacing in Numerical Modeling of Reinforced Concrete," *Journal of Structural Engineering*, vol. 129, no. 11, pp. 1514–1521, 2003.

[22] N. Ariyawardena, A. Ghali, and M. Elbadry, "Experimental study on thermal cracking in reinforced concrete members," *ACI Structural Journal*, vol. 94, no. 4, pp. 432–441, 1997.

[23] Z. P. Bažant and B. H. Oh, "Spacing of Cracks in Reinforced Concrete," *Journal of Structural Engineering*, vol. 109, no. 9, pp. 2066–2085, 2008.

[24] B. Bengt and L. Leroy, "Effects of Arrangement of Reinforcement on Crack Width and Spacing of Reinforced Concrete Members," *ACI Journal Proceedings*, vol. 62, no. 11, pp. 1395–1420, 1965.

[25] Y. Goto, "Internal Cracks Formed in Concrete Around Deformed Tension Bars.," *ACI Journal Proceedings*, vol. 68, no. 4, pp. 244–251, 1971.

[26] R. R. H. Zhu, W. Wanichakorn, T. T. C. Hsu, and J. Vogel, "Crack width prediction using compatibility-aided strut-and-tie model," *ACI Structural Journal*, vol. 100, no. 4, pp. 413–421, 2003.

[27] Wood S. L., Wight J. K., and J. P. Moehle, "The 1985 Chile Earthquake, Observations on Earthquake Resistant Construction in Viña del Mar," *Civil Engineering Studies*, vol. Structural, no. February 1987, p. 176 pp., 1987.

[28] M. Fintel, "Performance of Buildings With Shear Walls in Earthquakes of the Last Thirty Years," *PCI Journal*, vol. 40, no. 3. pp. 62–80, 2014.

[29] G. G. Penelis and A. J. Kappos, *Earthquake-resistant Concrete Structures*. London, UK: E & F N SPON (Chapman & Hall), 1996.

[30] G. Penelis, K. Stylianidis, A. Kappos, and C. Ignatakis, *Reinforced Concrete Structures*. Thessaloniki, Greece: A.U.Th. Press, 1995.

[31] J. W. Wallace, "Behavior, design, and modeling of structural walls and coupling beams - Lessons from recent laboratory tests and earthquakes," *International Journal of Concrete Structures and Materials*, vol. 6, no. 1, pp. 3–18, Mar. 2012.

[32] Y. H. Chai and S. K. Kunnath, "Minimum thickness for ductile RC structural walls," *Engineering Structures*, vol. 27, no. 7, pp. 1052–1063, Jun. 2005.

[33] Standards New Zealand, "NZS 3101:2006, Concrete structures standard: Part 1 – The design of concrete structures," Wellington, New Zealand, 2006.

[34] Canadian Standards Association, "CAN/CSA-A23.3-04, Design of Concrete Structures (Update No. 2 - July 2007)," Mississauga, Ontario, Canada, 2007.

[35] European Committee for Standardization, "EN 1998-1:2004, Eurocode 8: Design of structures for earthquake resistance - Part 1: General rules, seismic actions and rules for buildings," Brussels, Belgium, 2004.

[36] Ministry of Environment Planning and Public Works, "Greek Code for the Design and Construction of Concrete Works," Athens, Greece, 2000, p. . (In Greek).

[37] International Conference of Building Officials, "Uniform Building Code – Volume 2: Structural Engineering Design Provisions," Whittier, California, USA, 1997.

[38] T. Chrysanidis, "Influence of elongation degree on transverse buckling of confined boundary regions of R/C seismic walls," *Construction and Building Materials*, vol. 211, pp. 703–720, Jun. 2019.

[39] T. Chrysanidis and I. Tegos, "Axial and transverse strengthening of R/C circular columns: Conventional and new type of steel and hybrid jackets using high-strength mortar," *Journal of Building Engineering*, vol. 30, no. January, p. 101236, 2020.

[40] T. A. Chrysanidis, "Evaluation of Out-of-Plane Response of R/C Structural Wall Boundary Edges Detailed with Maximum Code-Prescribed Longitudinal Reinforcement Ratio," *International Journal of Concrete Structures and Materials*, vol. 14, no. 1. 2020.

EURODYN 2020
XI International Conference on Structural Dynamics
M. Papadrakakis, M. Fragiadakis, C. Papadimitriou (eds.)
Athens, Greece, 23–26 November 2020

GRAPHENE-RUBBER LAYERED COMPOSITES FOR SEISMIC ISOLATION

Maria Rosaria Marsico and Julián Mauricio Londoño Monsalve

University of Exeter

College of Engineering, Mathematics and Physical Sciences

North Park Road, EX4 4QF, Exeter, UK

m.r.marsico@exeter.ac.uk

j.londono-monsalve@exeter.ac.uk

Keywords: Seismic Isolation, Graphene Reinforced Elastomeric Isolators, Modal Analysis, Frequency Response Function.

Abstract. *In recent years, research has been conducted on the design and manufacture of lighter and low-cost seismic isolator devices. This include studies on elastomeric isolators made with alternative materials (e.g. glass or carbon fibre replacing steel sheets). Graphene-Reinforced Elastomeric Isolator (GREI) is proposed here to overcome the heavy weight and long manufacturing process of elastomeric isolators currently used.*
This manuscript presents an experimental dynamic analysis on rubber pads reinforced with a few layer graphene. Graphene deposition on rubber was achieved by a recently developed isopropyl alcohol assisted direct transfer method.
The experimental setup consisted of a single-degree-of-freedom mass-spring-damper system, with vertical load applied on tested specimens. Experimental modal analysis was performed and the mechanical properties essential to characterise the specimens were extracted from the measured frequency response function.
Results show that a few layer graphene transferred on a rubber pad increase vertical stiffness and damping of the graphene-rubber layered composite; this fosters the use of natural rubber in lieu of high damping rubber, saving the cost of reinforcing rubber with particulate fillers. Also, experimental results show that the mechanical properties of the graphene-rubber composite alter when varying the thickness of the graphene films transferred on rubber pads, stressing the sensitivity of the sample to the concentration of graphene.

1 INTRODUCTION

The concept of base isolation consists of interposing special devices such as elastomeric isolators between a structure and its foundation to decouple them. This layer gives the structure a fundamental frequency that is much lower than both its fixed-base frequency and the predominant frequency of the ground motion. Typical elastomeric isolators are made of alternate layers of steel and rubber and are used mainly in strategic and public buildings due to high cost of designing, production and installation. They are stiff vertically yet flexible horizontally and enable structures to survive potentially devastating seismic events. The primary weight in a steel-reinforced elastomeric isolator (SREI) is due to the reinforcing steel shims, which are used to provide the rubber-steel composite with high vertical stiffness. There is an on-going quest for new materials for elastomeric isolators which will result in highly efficient, ultra-lightweight and low-cost devices; this will extend the use of this technology to residential and commercial buildings, on a global scale.

Numerous studies have been conducted to investigate the dynamic behaviour of isolators reinforced with fibre sheets e.g. glass or carbon fibres (Fibre-Reinforced Elastomeric Isolators, FREI) [1-5]. However, aspects such as the design, the alignment and behaviour of the fibres, and the dependence of FREI to preloading history require further investigation.

An attractive alternative to using fibres to reinforce rubber is graphene. Graphene, a one-atom thick layer of carbon, is the strongest known material, which is also mechanically flexible. Many studies were conducted to determine the mechanical properties, electrical conductivity, gas permeability and thermal stability of this material; however, there are only a few works that incorporate graphene into elastomers. For instance, Prud'Homme et al. demonstrates the prominent potential of graphene in improving the mechanical properties of elastomers; Wu observed that graphene can be used to tune the vulcanization kinetics of rubbers [6-7].

The idea behind this research is to reinforce pure rubber with a few layer graphene and to create Graphene-Reinforced Elastomeric Isolator (GREI). This research also aims at exploiting the properties of graphene to enhance the damping of the graphene-rubber compound. Additional damping in the graphene-rubber compound will open the possibility of using pure rubber in lieu of high damping rubber; this will lead to save costs for reinforcing rubber with special particles and further reducing the cost of the devices. The dynamic response of square and circular graphene-rubber specimens with applied vertical load is investigated and experimental results are discussed.

2 SPECIMENS AND EXPERIMENTAL SETUP

In order to study the influence of the first shape factor, which is a dimensionless measure of the aspect ratio of the single layer of the elastomer, we have manufactured two sets of samples, with circular and square geometries.

Set 1 consists of three specimens. Specimen 1.1 is made of a square pure rubber pad 47 mm side and 15 mm thick; Specimen 1.2 is made of a square rubber pad 47 mm side and 15 mm thick with a circular thick layer of graphene on the top with diameter of 38 mm; and Specimen 1.3 is made of a square rubber pad 47 mm side and 15 mm thick with a circular thin layer of graphene on the top with diameter of 38 mm (Figure 1a).

Set 2 consists of two specimens made with nine circular pads of rubber each with diameter 47 mm and thickness 1.5 mm. Specimen 2.1 is made of nine pads of pure rubber bonded together using a cold vulcanizing agent. Specimen 2.2 is made of nine pads of rubber alternated to eight circular thin layers of graphene with diameter 38 mm (Figure 1b-c). Set 1 samples are

confined to two 72x72mm square steel plates 3 mm thick, while Set 2 samples are confined to two circular steel plates 3 mm thick with 72 mm diameter.

Graphene deposition on rubber was achieved by an isopropyl alcohol assisted direct transfer method [8]. To vary the thickness of the graphene films on rubber, multiple transfers of graphene films were used (i.e. 3 transfers for the thin films and 6 transfers for the thick films). The elastomer used in the samples is natural rubber with hardness 70° Shore A Degree, measured experimentally using a RS Pro digital durometer. The total height of the specimens is assumed equal to the thickness of the rubber that is 15 mm for Set 1 and 13.5 mm for Set 2 samples. Indeed, the thickness of a few layer graphene transferred on top of the rubber pad is negligible (a ten-layer graphene film is ~ 4.61 nm).

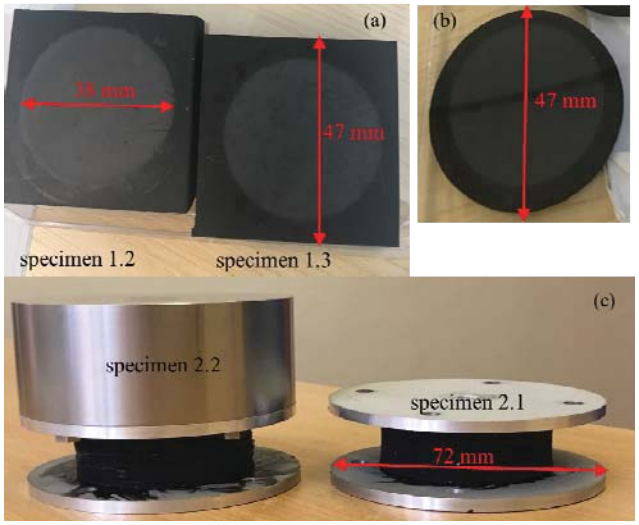

Figure 1: (a) Specimens 1.2 and 1.3 made of a square rubber pad 15 mm thick. (b) Circular sample 1.5 mm thick rubber pad with a few layer graphene on top. (c) Specimen 2.2 made of nine circular rubber pads with 1 kg applied vertical load; Specimen 2.1 made of nine circular rubber pads.

The experimental setup is shown in Figure 2 and can be seen as a single-degree-of-freedom (SDOF) mass-spring-damper system. A vertical SignalForce Shaker V20 applies dynamic loading to the bottom of the specimen. A load cell is attached to the bottom steel plate of each specimen to measure the vertical forces effectively transmitted from the shaker; gravity loads are applied on the specimens in the form of a solid stainless steel cylinder bolted to the upper steel plate (1 kg and 2 kg at a time). Two accelerometers were used to record accelerations at the top of the added mass (i.e. stainless steel cylinder) and at the bottom of the lower steel plate respectively. LABVIEW software was used to acquire and process experimental data.

Experimental modal analysis was performed and the dynamics of the system and the mechanical properties essential to characterize the specimens were extracted from the measured Frequency Response Function (FRF).

Vibration tests were also performed on one of the 3 mm steel plates alone to define its natural frequency and ultimately to assess any dynamic interaction with the dynamic behaviour of the graphene-rubber compound.

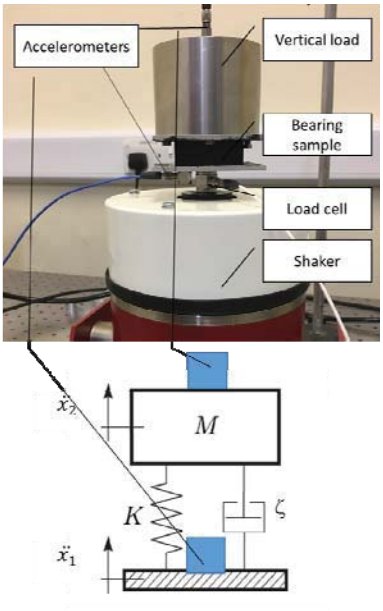

Figure 2: Experimental setup at the Dynamics Laboratory of the University of Exeter and corresponding SDOF mass-spring-damper system.

3 ANALYSIS

The natural frequency and damping of the specimens were initially estimated from the FRF using the peak-picking and half-power bandwidth methods. The vertical natural frequency of the three specimens is plotted in Figure 3, also showing that for exciting frequencies less than 250 Hz (i.e. a frequency ratio less than 0.7) the dynamic response of the specimens is disturbed by the dynamic response of the confining steel plates. FRFs show that the vertical natural frequency of the two specimens 1.2 and 1.3 made of a rubber pad and a few layer graphene on top (either thin or thick) is higher than the natural frequency of the specimen made of pure rubber (specimen 1.1). This result proves that specimens 1.2 and 1.3 are stiffer vertically than specimen 1.1, and that the increase in vertical stiffness is likely due to the added layers of graphene.

The damping ratios of the specimens 1.2 and 1.3 are higher (0.73% and 17% respectively) than that of the specimen 1.1. Such an increase in damping ratio is beneficial to base isolation systems, which typically employ high damping rubber elastomeric isolators (in which rubber is reinforced with particulate fillers) to provide additional damping. It follows that any increase in damping in the graphene-rubber compound (such as in specimens 1.2 and 1.3) would enable using low damping natural rubber and save the costs associated with filling rubber.

The natural frequency of the specimen made of nine rubber pads (specimen 2.1) was found to be higher than the frequency of the specimen made of rubber pads alternated with eight layers of graphene (specimen 2.2). Vertical natural frequency of Set 2 samples with vertical load 1 kg are depicted in Figure 4, also showing the transmissibility. As the natural frequency is lower in specimen 2.2 than in specimen 2.1, the vertical stiffness calculated experimentally is also lower in the graphene-reinforced rubber specimen compared to that in the specimen made of rubber pads only. Besides that, experimental results indicate a lower damping factor of the specimen reinforced with graphene compared to the damping factor of the specimen made of rubber pads only. Such a decrease of vertical frequency, vertical stiffness and damping factor in the specimen reinforced with graphene is likely due to an excessive quantity of

graphene present in the specimen 2.2, provoking loss of adhesion between layers of graphene-reinforced rubber and unexpected inner behaviour between the graphene particles.

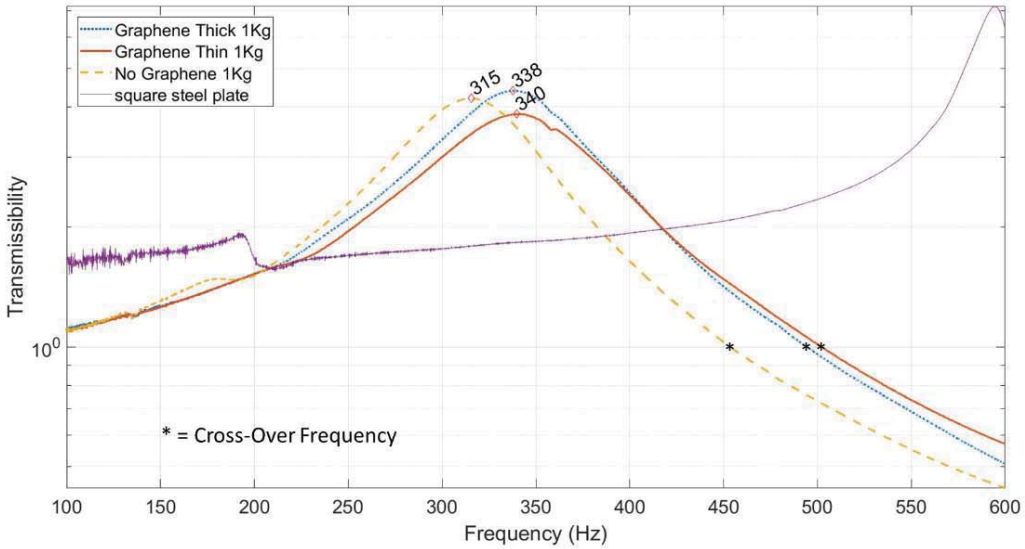

Figure 3: Set 1 samples with vertical load 1 kg: transmissibility and cross-over frequency at transmissibility T =1.

Research studies also demonstrated that strength in graphene-elastomer nanocomposite is sensitive to preparation techniques. It follows that the preparation of Set 2 specimens and their peculiar geometry (alternated layers of rubber and graphene) may have produced microstructural changes weakening the specimens and affecting their mechanical properties.

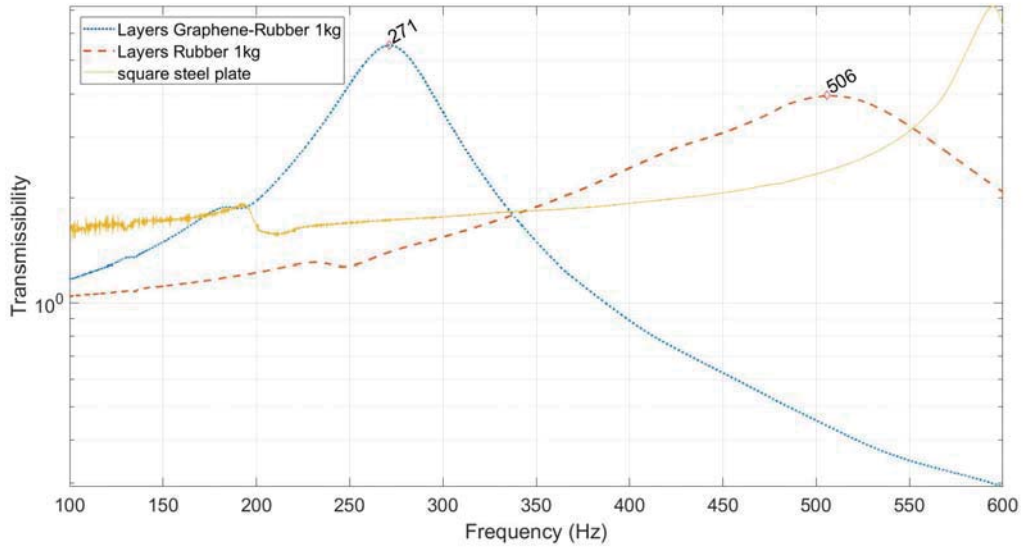

Figure 4: Transmissibility of Set 2 samples with vertical load 1 kg.

4 CONCLUSIONS

Experimental results show that by adding a few layer graphene the vertical stiffness and damping of Set 1 samples increase. In particular, the vertical stiffness increases by 15.7% when a thin layer of graphene is added on the top of a 15 mm thick rubber pad, and by 14.5% when a thick layer of graphene is added. It follows that a few layer graphene is a viable and low-cost alternative to reinforce elastomeric isolators and to replace heavy steel reinforcing

shims. Experimental results also show that a few layer graphene transferred on top of the specimen enhance the damping. They show an increase of 17.7% in the damping of the composite rubber-thin layer of graphene, and of 0.7% in the composite rubber-thick layer of graphene; hence natural rubber can be used in lieu of high damping rubber, saving the cost of reinforcing rubber with particulate fillers.

Results point out that an excessive concentration of graphene is detrimental to the mechanical properties of the samples, e.g. specimen 1.2 (with a thick layer of graphene) has lower vertical frequency and damping than specimen 1.3 (with a thin layer of graphene).

Unwanted behaviour of the rubber pad due to high concentration of graphene is evident from the experimental results on Set 2 samples too. The specimen made with nine rubber pads alternated with eight layers of graphene exhibits lower vertical stiffness and damping factor than the specimen made of nine rubber pads only. Eight layers of graphene worsen the performance of the rubber, although it is likely that less layers would enhance its mechanical properties, as it has seen in the response of specimen 1.3 with a thin layer of graphene on top. These results lay the foundation for expanding this research into seismic metamaterials and for investigating the optimal quantity of graphene to be transferred homogenously on the rubber pad that would enhance its mechanical properties.

REFERENCES

[1] A. Strauss, Experimental investigations of fiber and steel reinforced elastomeric bearings: Shear modulus and damping coefficient, *Engineering Structures*, 75, 402-413, 2014.

[2] P. M. Osgooei, et al., Experimental and finite element study on the lateral response of modified rectangular fiber-reinforced elastomeric isolators (MR-FREIs), *Engineering Structures*, 85, 293-303, 2015.

[3] M. R. Marsico, et al., Tension Buckling in Rubber Bearings affected by Cavitation, *Engineering Structures*, 56, 656-663, 2013.

[4] P. Angeli, G. Russo, A. Paschini, Carbon fiber-reinforced rectangular isolators with compressible elastomer: Analytical solution for compression and bending, *International Journal of Solids and Structures*, 50(22): 3519-3527, 2013.

[5] A. E. Javid, J. Kelly; J. L. Sackman, United States Patent, US5904010A, 1999.

[6] R. K. Prud'Homme, B. Ozbas, I. Aksay, R. Register, D. Adamson, Functional Graphenerubber nanocomposites, United States Patent, US7745528B2, 2010.

[7] J. Wu, et al., Vulcanization kinetics of graphene/natural rubber nanocomposites, *Polymer*, 54, 3314-3323. 10.1016/j.polymer.2013.04.044, 2013.

[8] D. W. Shin, et al., A New Facile Route to Flexible and Semi‐Transparent Electrodes Based on Water Exfoliated Graphene and their Single‐Electrode Triboelectric Nanogenerator, *Advanced Materials*, 30, 1802953. 10.1002/adma.201802953, 2018.

EURODYN 2020
XI International Conference on Structural Dynamics
M. Papadrakakis, M. Fragiadakis, C. Papadimitriou (eds.)
Athens, Greece, 23–26 November 2020

CYCLIC PERFORMANCE OF WIND TURBINE TOWER WITH CONCRETE-FILLED DOUBLE SKIN STEEL TUBE SECTION UNDER TORSION

Yu-Hang WANG [1], Shu-Qi WANG [1], Guo-Bing LU [1] and Ji-Ke Tan [1]*

[1] School of Civil Engineering, Chongqing University, Chongqing 400045, China
e-mail: wangyuhang@cqu.edu.cn, 1105216095@qq.com, luguobing@cqu.edu.cn, tjk23@sina.com
* Corresponding author: tjk23@sina.com (J.K. TAN).

Keywords: Concrete-filled double skin steel tube, cyclic performance, hysteretic behaviour, pure torsion

Abstract. *In order to investigate the cyclic performance of concrete-filled double skin steel tube columns (CFDST), tests of six CFDST specimens subject to cyclic pure torsion loading were carried out. Parameters being investigated include various section type, hollow ratios and steel ratios. Failure mode, ductility, hysteretic behaviour, bearing capacity and energy dissipation capacity were analysed. The experimental results show that the CFDST exhibit good cyclic performance, torsional bearding capacity and good energy dissipation. Besides, simplified calculation model was proposed to predict the ultimate torsion of CFDST, and good agreement between the proposed simplified calculation model and design methods proposed by Huang-Hong are achieved for the calculated results of the yield torsion of specimens. A finite element analysis (FEA) model was established to investigate the behaviour of CFDST, the results of FEA model were agreed well with test results in terms of the torsional moment (T) versus rotation angle (θ) curves.*

1 INTRODUCTION

Wind energy is a kind of clean renewable energy, wind power generation is the most widely used and the fastest-growing new energy generation technology. As a main load carrying structure in the wind turbine, the tower not only supports the weight of necelle and rotor, but also bears the wind load and dynamic load. Therefore, the tower plays an important role in the stable operation of the whole machine. Considering the principle of concrete-filled double skin steel tube (CFDST), a new type of CFDST composite tower for wind power tower structure is proposed in this paper, as shown in Figure 1. The upper part is a steel tower, and the lower part is the CFDST composite tower which is connected by the bolts. The inner and outer steel plates of CFDST composite tower are connected to the concrete by the studs to enhance the connection between steel plates and concrete.

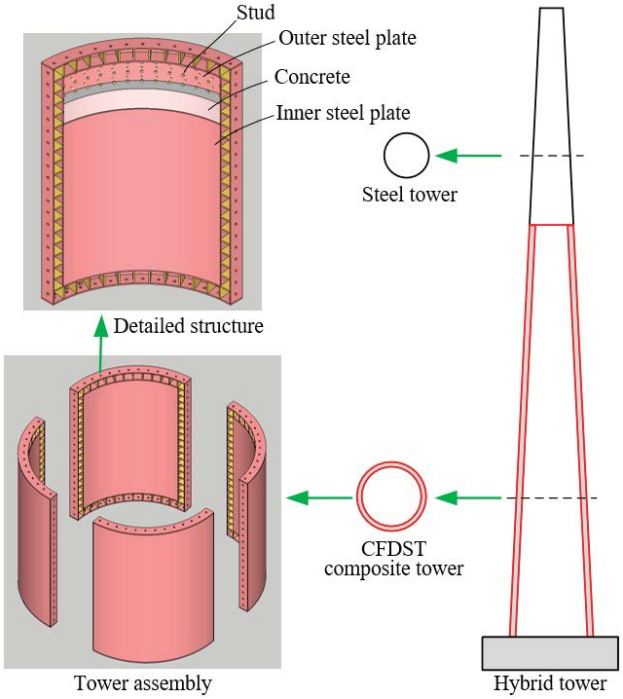

Figure 1: Schematic diagram of CFDST composite tower

In recent years, the overall reliability analysis and the axial compression test of components for the CFDST composite tower at the bottom has been carried out in literature [1]-[3]. The influence of different section number and diameter ratio of upper and lower sections on bearing capacity was obtained. It was pointed out that CFDST composite tower at the bottom was more suitable for high-power wind turbine. Han et al. [4]-[6] carried out axial compression and eccentric compression tests of CFDST columns by taking the ratio of diameter to thickness of steel tube, hollow rate, ratio of length to thickness and eccentricity as main parameters, and proposed practical calculation methods of bearing capacity for CFDST columns under axial compression and eccentric compression. Huang et al. [7]-[8] conducted an experimental study on the monotone torsional behaviour of four CFDST columns with square section and six CFDST columns with circular section, considering the steel content and hollow rate as the main parameters. The test results showed that the CFDST columns has good ductility and high bearing capacity.

However, there are few studies on the mechanical properties of CFDST columns and CFDST composite tower under cyclic torsional load. Therefore, through carrying out quasi-

static tests, this paper studies the cyclic performance of CFDST columns under torsion load. It provides reference for the research on torsional resistance and engineering design of CFDST composite tower.

2 EXPERIMENTAL INVESTIGATION

2.1 Specimens

Six specimens were designed to investigate the cyclic performance of CFDST under torque load, including two square section CFDST short columns, two CFDST rectangular section short columns and two circular section CFDST short columns. Parameters of specimens were hollow ratio and section type. All steel tubes were seamless steel tubes. The geometric dimensions of specimens are shown in Figure 2.

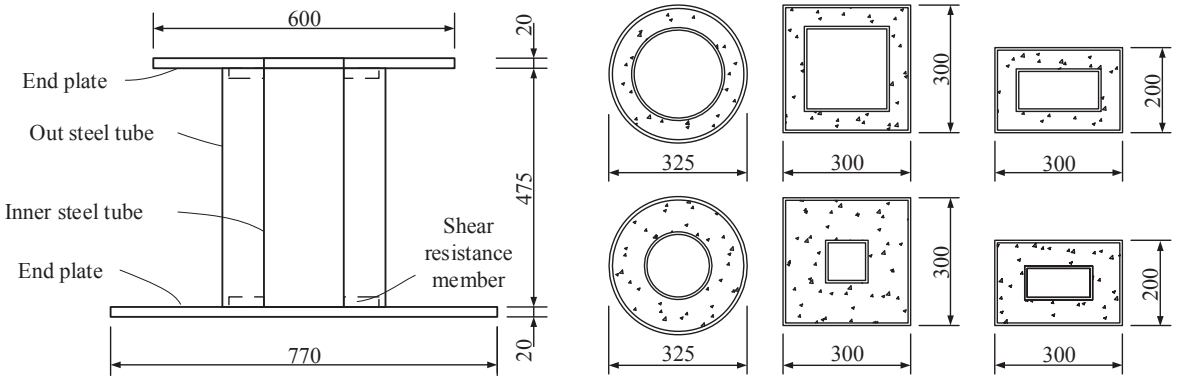

Figure 2: Geometric dimension of specimens

The steel tubes of specimens were welded on the end plates. In order to ensure sandwich concrete bearing torque load, four shear components were welded on the end plates. The sandwich concrete was poured into the space between outer steel tube and inner steel tube through the reserved holes in the upper end plate. The cubic concrete compressive strength f_{cu} are shown in Table 1. Mechanical properties of steel tubes (f_{yo}-yield strength of outer steel tube, f_{uo}-tensile strength of outer steel tube, E_{so}-Young's modulus of outer steel tube, f_{yi}-yield strength of outer steel tube, f_{ui}-tensile strength of outer steel tube, E_{si}-Young's modulus of outer steel tube) are shown in Table 2.

No.	1	2	3	4	5	6	7	8	9	Average
f_{cu} (MPa)	37.51	44.10	41.60	41.96	45.16	45.24	43.2	39.91	40.36	42.1

Table 1: Mechanical properties of sandwich concrete

No.	Outer tube (mm)	Inner tube (mm)	f_{yo} (MPa)	f_{uo} (MPa)	E_{so} (GPa)	f_{yi} (MPa)	f_{ui} (MPa)	E_{si} (GPa)
CC-T1	ϕ325×8.15	ϕ159×4.34	317.07	506.41	210	329.02	475.46	233
CC-T2	ϕ325×8.15	ϕ219×6.30	317.07	506.41	210	361.27	481.87	206
RR-T1	300×200×4.60	160×80×3.80	232.71	388.78	205	353.33	430.33	216
RR-T2	300×200×4.60	200×100×3.88	232.71	388.78	205	406.33	479.33	239
SS-T1	300×300×5.34	100×100×3.54	352	508.57	197	310.67	371.67	228
SS-T2	300×300×5.34	200×200×3.54	352	508.57	197	283	403.67	232

Table 2: Mechanical properties of steel tubes

2.2 Test setup

A test setup was designed to apply cyclic torque load to CFDST columns. As shown in Figure 3, the test setup was mainly composed of top girder, steel base, actuator and rigid link. The upper and lower end plate of CFDST specimens were respectively connected with the top girder and the steel base through the high-strength bolts, and pretension was applied on the high-strength bolts to ensure that no relative sliding occurred between the end plates of specimens and test setup. The rigid link was used to fix the top end of specimens. One end of the rigid link is connected with the middle part of the top girder through a universal hinge and the other end is hinged with the base. Cyclic torque load on CFDST specimens was applied through the top girder by actuator.

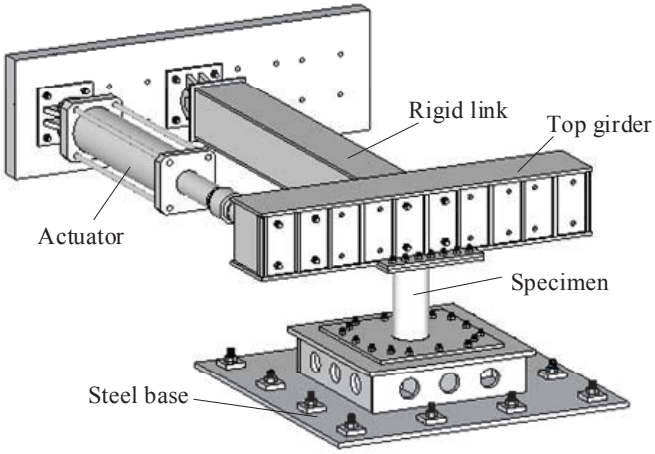

Figure 3: Test setup

2.3 Test results and analysis

The typical failure mode of CFDST specimens with three section types are shown in Figure 4. For circular section CFDST specimens, when the cyclic pure torsional load was applied, the maximum circumferential shear stress (τ) of sandwich concrete of circular section CFDST specimens initially occurred on the outer edge. When the maximum shear stress or the maximum tensile stress reached the concrete tensile strength, the sandwich concrete cracked. Outer and inner steel tube of CFDST specimens can be regarded as a circular thin-walled steel tube. Under cyclic pure torsional load, the maximum principal tensile stress (σ_1) and the maximum principal compressive stress (σ_3) of hollow thin-walled steel tube element along the directions of 45 ˚ and 135 ˚, as shown in Figure 5. Generally, the hollow thin-walled steel tube under cyclic pure torsional load was more easily buckling to inside of section than buckling to outside of section. Buckling of outer steel tube of CFDST specimens was constrained by sandwich concrete, and the material strength of the outer steel tube can be fully utilized. The constraint effect of sandwich concrete on inner steel tube was weakness, and the inner steel tube of CFDST specimens under cyclic torque load was prone to occur local buckling.

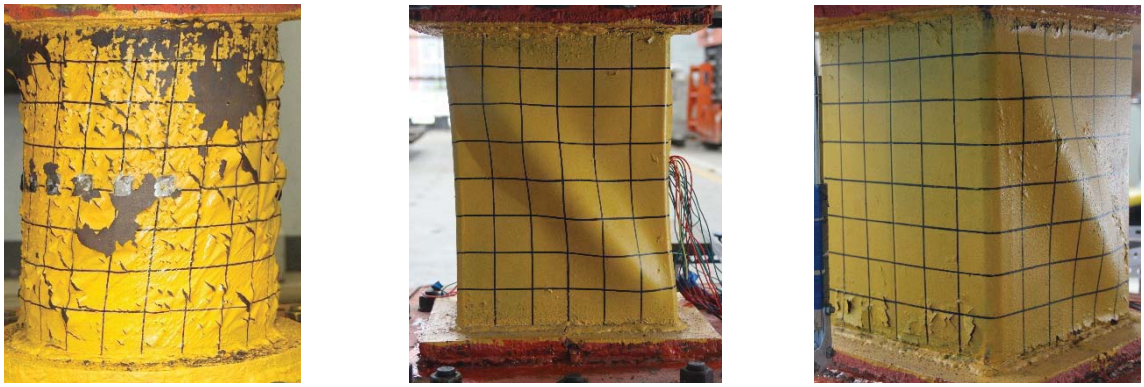

(a) Circular section (b) Rectangular section (c) Square section

Figure 4: Local buckling of specimens

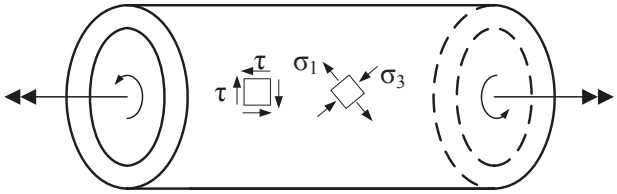

Figure 5: Stress diagram of circular section CFDST specimens

For square and rectangular section CFDST specimens, the maximum circumferential shear stress (τ) and the maximum principal stress (σ_1, σ_3) of the square and rectangular section CFDST columns appear initially at the middle of long edge. When the maximum shear stress or the maximum tensile stress reaches the tensile strength of sandwich concrete, cracks appeared on sandwich concrete. Under cyclic pure torsional load, the maximum principal tensile stress (σ_1) and the maximum principal compressive stress (σ_3) of hollow thin-walled steel tube element along the directions of 45 ˚ and 135 ˚, as shown in Figure 6. Generally, the hollow thin-walled steel tube with square or rectangular section under cyclic pure torsion was more easily buckling to inside the section. Because of the sandwich concrete constrained the buckling deformation of outer steel tube of CFDST columns with square or rectangular section, the strength of outer steel tube can be fully utilized. Obviously, the sandwich concrete of CFDST columns with square or rectangular section had limited constraint effect on inner steel tube.

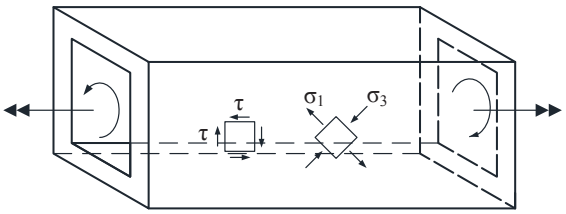

Figure 6: Stress diagram of CFDST with square and rectangular section

The torsional moment versus rotation angle hysteresis loops of CFDST columns with circular, square and rectangular section were in plump shapes, as shown in Figure 7. It means that the CFDST columns have a perfect behavior under cyclic pure torque load. There is no significant decline in the torsional moment versus rotation angle skeleton curves of circular section CFDST columns, as shown in Figure 8(a). The torsional moment versus rotation angle

skeleton curves of square and rectangular section CFDST columns declined significantly after the peak torsional capacity appeared, as shown in Figures 8(b) and (c). The key mechanical characteristic data of torsional moment versus rotation angle skeleton curves of CFDST column specimens were extracted, as shown in Table 3. The yield point of specimens can be defined according to literature [9]. The rotational ductility coefficient μ_θ is the ratio of the ultimate torsional angle θ_u to the yield rotation angle θ_y, which is an important index to measure the inelastic deformation capacity of members. The performance of CFDST columns improved with the increase of the value of μ_θ. T_p is the peak value of the torsional moment. The ultimate torsional angle θ_u refers to the maximum torsion angle subjected to a load larger than 85% of the ultimate bearing capacity or the torsion angle at the end of the test. The overall performance of CFDST columns with circular section under cyclic pure torsion load was better than CFDST columns with square and rectangular section.

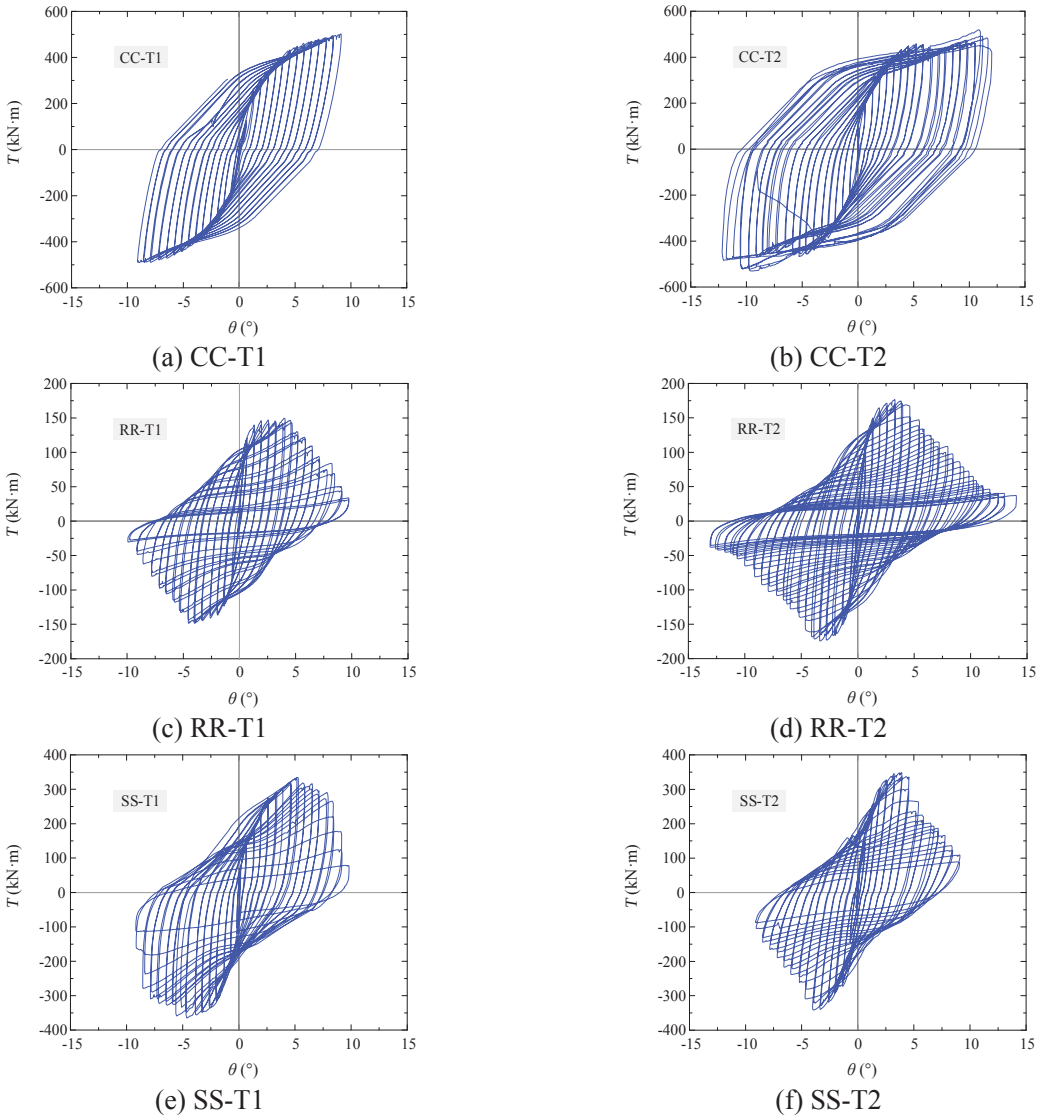

(a) CC-T1 (b) CC-T2

(c) RR-T1 (d) RR-T2

(e) SS-T1 (f) SS-T2

Figure 7: Torsion moment-rotation angle hysteresis loops curves

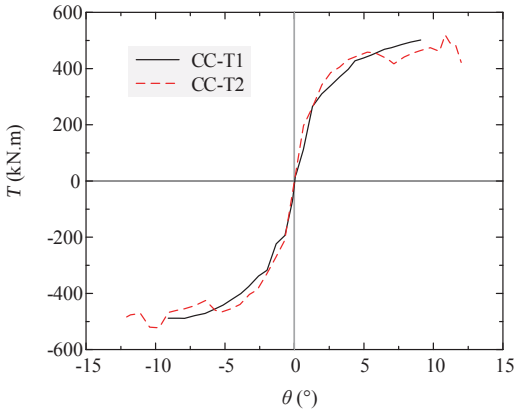

(a) Circular section

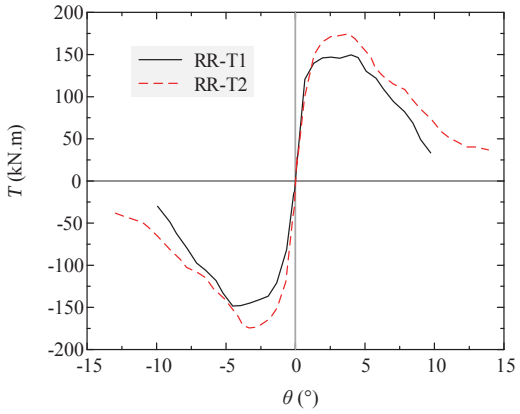

(b) Rectangular section

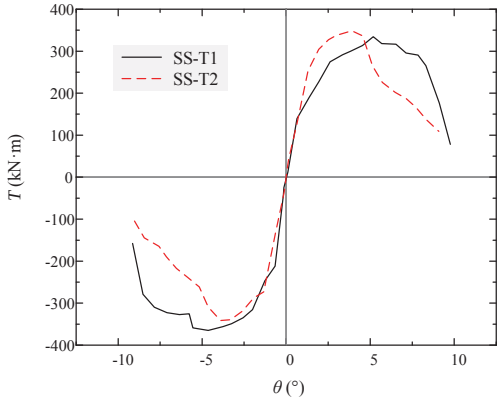

(c) Square section

Figure 8: Skeleton curves of specimens

No.	T_y (kN·m)		θ_y (°)		T_p (kN·m)		θ_u (°)		μ_θ	
	+	-	+	-	+	-	+	-	+	-
CC-T1	333.45	-343.29	2.46	-2.70	501.68	-489.19	9.09	-9.08	3.70	3.36
CC-T2	394.17	-395.76	2.88	-2.98	519.74	-522.48	11.87	-12.07	4.12	4.05
RR-T1	126.37	-113.70	0.87	-1.22	149.57	-148.47	5.34	-5.45	6.14	4.47
RR-T2	135.61	-132.56	1.17	-0.97	174.61	-174.44	5.33	-4.71	4.56	4.86
SS-T1	284.31	-338.39	3.03	-2.76	334.62	-364.98	7.95	-7.82	2.62	2.83
SS-T2	291.02	-280.70	1.78	-1.65	348.65	-341.36	4.88	-4.84	2.74	2.93

Table 3: Characteristic parameters of skeleton curves

3 FEA MODEL AND ANALYSIS

3.1 FEA model

A “shell-solid” finite element analysis (FEA) model was established to investigate the behaviour of CFDST columns under pure torsion. In this model, both the steel tubes were discretized by 4-node thin shell elements, and sandwiched concrete was discretized by 8-node brick elements. The element meshes for circular, square, rectangular section and boundary

conditions are shown in Figure 9. The contract property between steel tubes and sandwiched concrete was considered. In normal direction, hard contract is applied, and in the tangential direction penalty friction formulation is adopted. The friction coefficient for the FEA model is 0.6.

In order to simulate cyclic strengthen behaviour of steel tubes under cyclic torsion, the Ramberg-Osgood constitutive relation curve of structural steel Q235B under cyclic load in reference [10], E=2.06×10^{5}Mpa, K=1.065, n=0.104, as following:

$$x=y+(y/K)^{1/n} \tag{1}$$

$$x=\varepsilon/\varepsilon_y \tag{2}$$

$$y=\sigma/\sigma_y \tag{3}$$

The stress-strain relation presented by Han et al. [11] was used to simulate the plastic behaviour of core concrete in CFDST under cyclic torsion, is shown as following:

$$\begin{aligned} y &= 2x - x^2 && (x \le 1) \\ y &= \frac{x}{\beta_0 \cdot (x-1)^{\eta} + x} && (x > 1) \end{aligned} \tag{4}$$

Where:

$$x = \varepsilon / \varepsilon_0 \quad , \quad y = \sigma / \sigma_0$$

$$\sigma_0 = f_c'$$

$$\varepsilon_0 = \varepsilon_c + 800 \cdot \xi^{0.2} \cdot 10^{-6}$$

$$\varepsilon = (1300 + 12.5 f_c') \cdot 10^{-6}$$

$$\eta = \begin{cases} 2 & (\text{CFST with circular section}) \\ 1.6 + 1.5 / x & (\text{CFST with square section}) \end{cases}$$

$$\beta_0 = \begin{cases} \left(2.36 \times 10^{-5}\right)^{\left[0.25+(\xi-0.5)^7\right]} \cdot (f_c')^{0.5} \times 0.5 \ge 0.12 & (\text{CFST with circular section}) \\ \dfrac{(f_c')^{0.1}}{1.2\sqrt{1+\xi}} & (\text{CFST with square section}) \end{cases}$$

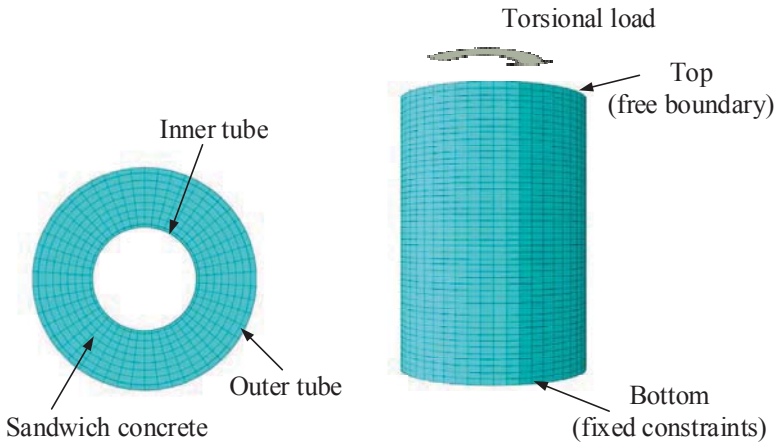

(a) Mesh of circular section

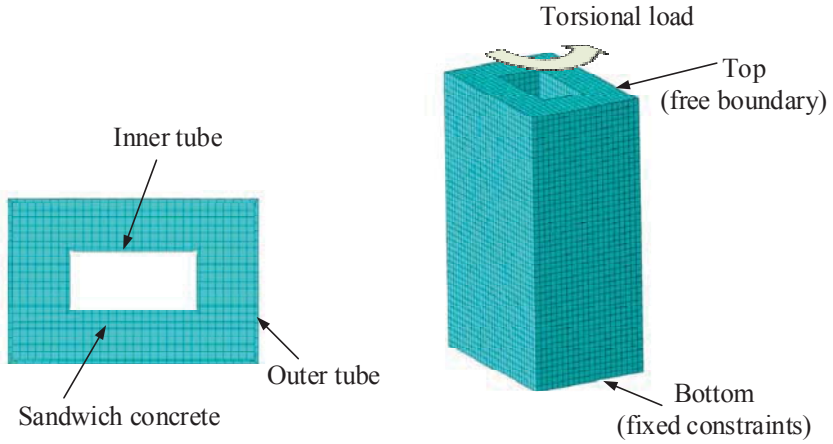

(b) Mesh of circular section

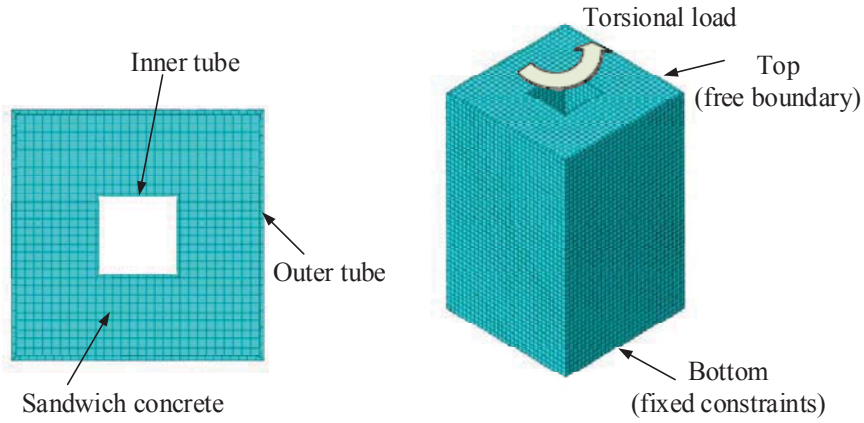

(c) Mesh of circular section

Figure 9: Element mesh and boundary conditions

3.2 Analysis and discussion

The measured torsional moment (T) versus rotation angle (θ) skeleton curves are compared with the result calculated from the FEA model, as shown in Figure 10. It can be found that, the calculated results obtained from FEA model were in good agreement with test result from initial loading to peak loading stage. The elastic stiffness predicted by FEA model and test results of CFDST with rectangular section are in good agreement, generally. Due to the space between bolt and bolt hole wall and larger torsional moment, the elastic stiffness predicted by FEA model with circular and square section were larger than test results. The peak torsional moment predicted by FEA model (T_{uc}) are compared with the measured results (T_{ue}) in Table 4. In this paper, on the torsional moment (T) versus rotation angle (θ) curves calculated by the FEA model, the torsional moment corresponding to the measured peak displacement was taken as peak torsion moment.

3.3 Typical failure mode

Figure 11 shows the predicted typical failure modes of inner steel tubes of CFDST columns subjected to pure torsion. It can be seen that the failure modes of inner steel tube predicted by FEA model and test result are in good agreement, respectively. Inward local buckling was obvious for the inner steel tubes of rectangular and square CFDST columns, while no obvious buckling occurred on inner steel tube of circular CFDST columns. Figure 12

shows that the shear stress of sandwiched concrete of CFDST columns distributed Symmetrical.

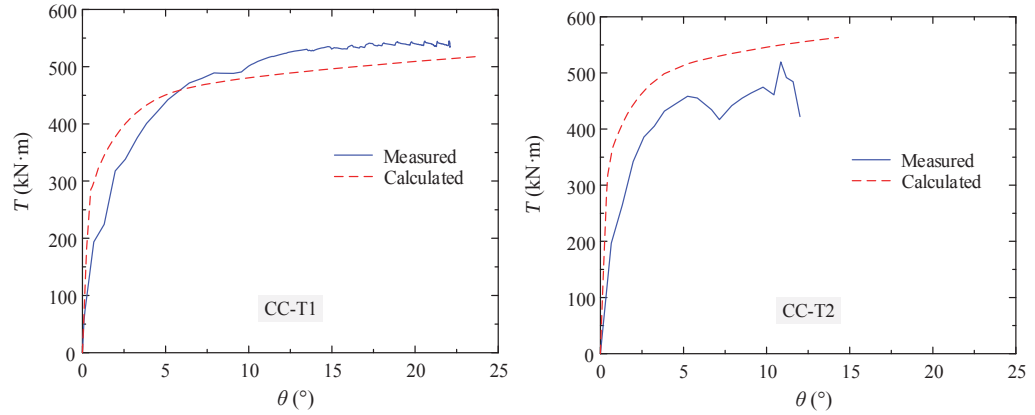

(a) Circular section

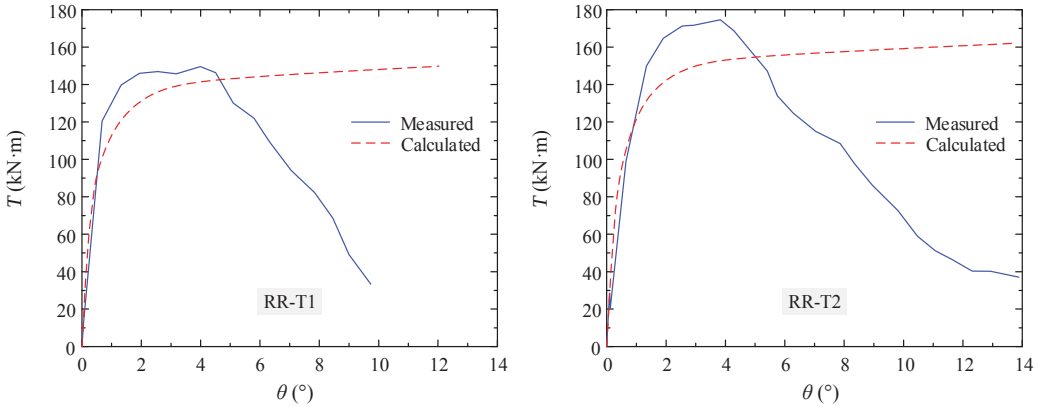

(b) Rectangular section

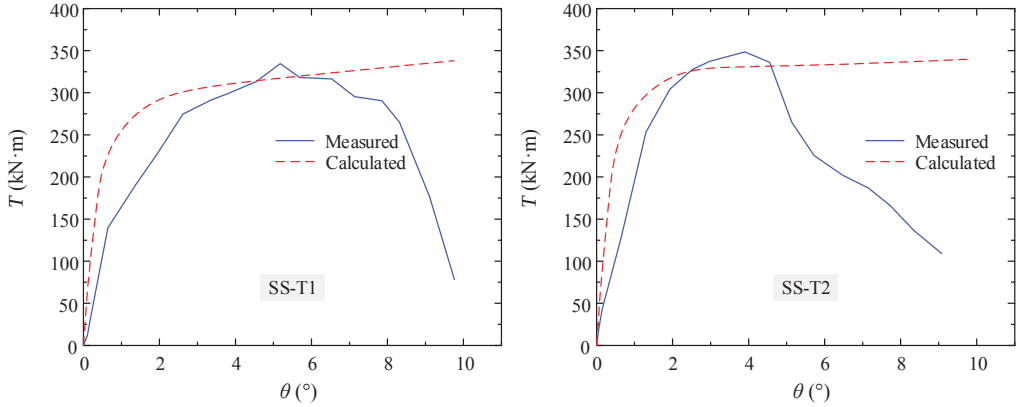

(c) Square section

Figure 10: Comparison of test curves and FEA curves

No.	Out tube	Inner tube	f_{yo} (MPa)	f_{yi} (MPa)	f_{cu} (MPa)	T_{ue} (kN·m)	T_{uc} (kN·m)	T_{ue}/ T_{uc}
CC-T1	φ325×8.15	φ159×4.34	317	329	42	501	480	0.95
CC-T2	φ325×8.15	φ219×6.3	317	361	42	519	550	1.05
RR-T1	300×200×4.6	160×80×3.8	233	353	42	149	141	0.94
RR-T2	300×200×4.6	200×100×3.8	233	406	42	174	152	0.87
SS-T1	300×300×5.34	100×100×3.54	352	310	42	334	316	0.94
SS-T2	300×300×5.34	200×200×3.54	352	283	42	348	331	0.94

Mean	0.95
COV	0.05

Table 4: Comparison of test results and FEA results

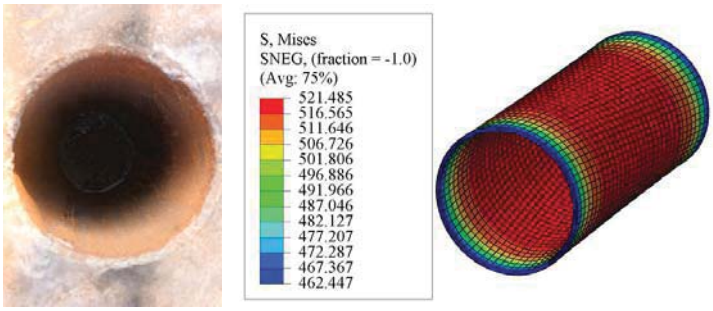

(a) Circular section

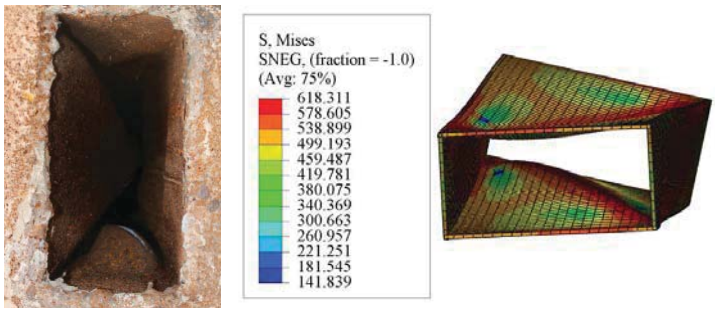

(b) Rectangular section

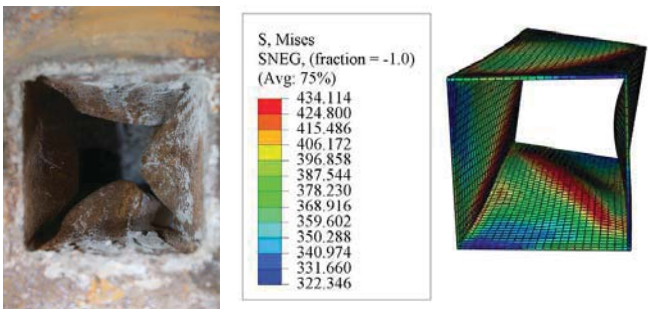

(c) Square section

Figure 11: Comparison of damage modes between test and FEM results (inner tubes unite: MPa)

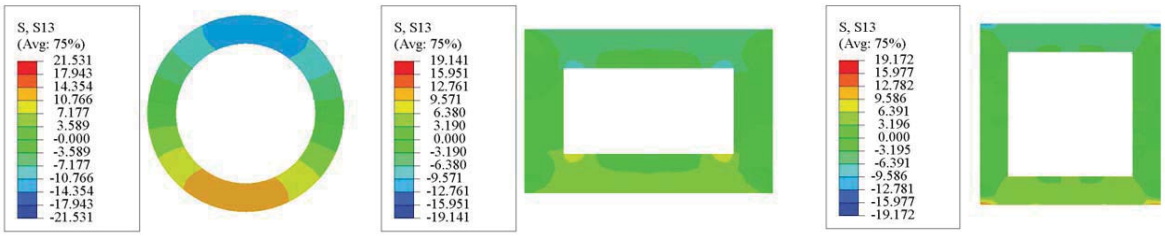

Figure 12: Distributions of shear stress of sandwiched concrete (unite: MPa)

4 DESIGN METHOD

The torsional bearing capacity of CFDST columns were mainly provided by sandwich concrete, inner steel tube and outer steel tube [12]. It is assumed that the design method of torsional bearing capacity of CFDST members as following:

$$T_{uc}=T_c+T_{so}+T_{si} \tag{5}$$

Where, T_c, T_{so} and T_{si} are torsional moment carried by sandwich concrete, outer steel tube and inner steel tube, respectively.

The sandwich concrete can be considered as plain concrete. The design method of the torsional bearing capacity of sandwich concrete can be calculated by the torsional bearing capacity formula of plain concrete. Because of outer steel tube and inner steel tube have a confined effect on the sandwich concrete, regardless of the reduction of the tensile strength of the concrete, the design method of the torsional bearing capacity of sandwich concrete is as follows:

$$T_c=f_t W_t \tag{6}$$

For square section

$$W_t=b_h^2\cdot(3h_h-b_h)/6-(b_h-2t_w)^2\cdot(3h_w-(b_h-2t_w))/6 \tag{7}$$

For circular section

$$W_t=\pi(d_o^3-d_i^3)/12 \tag{8}$$

Due to the confined effect caused by sandwich concrete, it is assumed the steel tubes under torque load can fully developed plasticity, and the outer steel tube and the inner steel tube are thin-walled closed-section steel tubes. The design method of torsional bearing capacity of the outer steel tube and the inner steel tube are as follows:

$$T_{so}=2A_0t_o\tau_{oyv} \tag{9}$$

$$T_{si}=2A_0t_i\tau_{iyv} \tag{10}$$

Where, $\tau_{oyv}=0.58f_{oyv}$ and $\tau_{iyv}=0.58f_{iyv}$ are shear strength of outer steel tube and inner steel tube, respectively. t_o and t_i are wall thickness of outer steel tube and inner steel tube. A_0 is the area enclosed by centre line of wall thickness of steel tube.

The calculated result and the test results in literature [12] are compared in Table 5. It can be found that, the calculated result is in good agreement with test result. Also, the calculated results are more conservative and safety.

Section type	No.	T_{ue} (kN·m)	T_{uc} (kN·m)	T_{uc}/T_{ue}	Section type	No.	T_{ue} (kN·m)	T_{uc} (kN·m)	T_{uc}/T_{ue}
Circular section	CO1I1	24.6	23.5	0.95	Square section	SO4I3	34.8	30.9	0.88
	CO1I2	33.2	29.8	0.89		SO5I3-1	44.4	38.3	0.86
	CO2I1	32.3	31.7	0.98		SO5I3-2	47.0	38.3	0.81
	CO2I2	42.1	38.0	0.90		SO6I3	48.8	45.6	0.93
	CO3I1	48.8	44.0	0.90					
	CO3I2	54.3	50.3	0.92					
Mean				0.92					0.87
COV				0.032					0.04

Table 5: Test result and simplified model result

The constitutive relationship of structural steel under cyclic load was studied by Shi et al [10]. The results show that the cyclic load can increase the strength of steel by nearly 20% in the range of common strain.

The yield load calculated by theoretical formula is compared with test results in Table 6. It can be found that, generally good agreement is obtained between the calculated results and test results. In Table 6, T_{ye} is the average value of absolute value of positive and negative yield load. Tensile strength of sandwich concrete can be calculated by $f_t=0.395f_{cu}^{0.55}$.

No.	D (B×H)×t_{so} (mm)	d (b×h)×t_{si} (mm)	f_{syo} (MPa)	f_{syi} (MPa)	f_{cu} (MPa)	T_{ye} (kN·m)	T_{uc} (kN·m)	T_{uc}/ T_{ue}
CC-T1	ϕ 325×8.15	ϕ 159×4.34	317	329	42.1	338	341	1.00
CC-T2	ϕ 325×8.15	ϕ 219×6.3	317	361	42.1	394	411	1.04
RR-T1	300×200×4.6	160×80×3.8	232	353	42.1	120	153	0.99
RR-T2	300×200×4.6	200×100×3.8	232	406	42.1	134	170	1.02
SS-T1	300×300×5.34	100×100×3.54	352	310	42.1	311	311	0.85
SS-T2	300×300×5.34	200×200×3.54	352	283	42.1	285	354	1.04
Mean								0.99
COV								0.06

Table 6: Test result and simplified model result

5 CONCLUSION

In this paper, six concrete-filled double skin steel tube (CFDST) specimens subject to cyclic pure torsion loading were tested. The cyclic performance of CFDST columns was investigated. The main conclusions can be obtained as follows:

(1) The sandwich concrete had a significant impact on the CFDST columns under torsion load and the sandwich concrete changed the failure mode of outer steel tubes of CFDST columns.

(2) The overall performance of circular section CFDST columns under cyclic pure torsion loading was better than square and rectangular section CFDST columns.

(3) A “shell-solid” finite element analysis (FEA) model was established, and the validated FEA model can accurately simulate the behaviour of CFDST columns.

(4) A simplified theoretical model and design method were proposed to calculate the torsional bearing capacity of CFDST columns under pure torsion loading, the experimental and finite element comparative analysis results show that the simplified theoretical design method can predict the torsion capacity of CFDST columns effectively.

ACKNOWLEDGEMENTS

The research is supported by the Project of Fok Ying Tung Education Foundation (171066), National Natural Science Foundation of China (51890902) and Chongqing Science and Technology Bureau (cstc2019jcyj-zdxm0099).

REFERENCES

[1] Liu YX. Research on key technology of wind power tower design for steel-concrete composite structure. *Harbin Institute of Technology*, 2016. (in Chinese)

[2] Song SH. Strength and stability analysis of hybrid tower of wind turbine based on finite element analysis. *Qingdao University*,2017. (in Chinese)

[3] Yi JH, Han TH. Reliability Analysis on Wind Turbine Tower Structures with Composite Section. *Journal of the Korean Society of Hazard Mitigation*, 2016, 16(4): 185-194.

[4] Yang YF, Han LH. Concrete-filled double-skin tubular columns under fire. *Magazine of Concrete Research*. 2008, 60(3):211~222.

[5] Tao Z, Han LH, Huang H. Mechanical behavior of concrete-filled double skin steel tubular columns. *China Civil Engineering Journal.* 2004,37(10):41-51. (in Chinese)

[6] Tao Z, Han LH, Huang H. Concrete-filled double skin steel tubular columns with square section under eccentric loads. *China Civil Engineering Journal.* 2003,36(2):34-51. (in Chinese)

[7] Huang H, Yang J, Zhang AG, Chen MC. Pure torsion behaviors of concrete filled double-skin (CHS inner and SHS outer) steel tubes. *Journal of Guangxi University :Nat Sci Ed.* 2012,37(4):678-682. (in Chinese)

[8] Huang BJ. Research on behavior of concrete filled double-skin steel tubular columns subjected to pure torsion. *East China Jiaotong University*.2012. (in Chinese)

[9] Zhou XH, Liu JP. Performance and design of steel tube confined concrete column, *Science Press*, Beijing, 2010.

[10] Shi Y, Wang M, Wang Y. Experimental and Constitutive Model Study of Structural Steel Under Cyclic Loading. *Steel Construction*, 2011, 67(8):1185-1197.

[11] Han LH, Yao GH, Zhao XL. Tests and calculations for hollow structural steel (HSS) stub columns filled with self-consolidating concrete (SCC). *Journal of Constructional Steel Research*, 2005, 61(9):1241-1269.

[12] Huang H, Han LH, Zhao XL. Investigation on concrete filled double skin steel tubes (CFDSTs) under pure torsion. *Journal of Constructional Steel Research*, 2013, 90(Complete):221-234.

EURODYN 2020
XI International Conference on Structural Dynamics
M. Papadrakakis, M. Fragiadakis, C. Papadimitriou (eds.)
Athens, Greece, 23—25 November 2020

THE ST. SILVESTRO BELFRY IN L'AQUILA: FROM THE REHABILITATION WORKS TO THE ACTUAL PERFORMANCE IN TERMS OF DYNAMIC PROPERTIES AND FRAGILITY FUNCTIONS ESTIMATION

Ilaria Capanna[1], Riccardo Cirella[1], and Angelo Aloisio[1] and Rocco Alaggio[2] and Franco Di Fabio[2] and Massimo Fragiacomo[2]

[1]Universita degli Studi dell'Aquila
Department of Civil, Construction-Architectural and Environmental Engineering (DICEAA), Via G. Gronchi, 18, L'Aquila, Italy
e-mail: {ilaria.capanna,riccardo.cirella,angelo.aloisio1}@graduate.univaq.it

[2] Universita degli Studi dell'Aquila
Department of Civil, Construction-Architectural and Environmental Engineering (DICEAA), Via G. Gronchi, 18, L'Aquila, Italy
e-mail: {rocco.alaggio, franco.difabio, massimo.fragiacomo}@univaq.it

Keywords: Masonry tower, Operational modal analysis, Model updating, Fragility functions.

Abstract. *Masonry towers are widespread ancient constructions, located even in seismic zone. The assessment of their seismic capacity is a required task owing to the vulnerability and predisposition to suffer damage. Slender structures are also involved in peculiar dynamic behavior, like torsional mode shapes and acceleration amplification at height. The accuracy of the seismic response prediction depends by the knowledge of geometry, masonry properties and constraint boundary conditions, frequently uncertain. The authors investigated the seismic behavior of a tower, the St.Silvestro belfry in L'Aquila (Italy). The St.Silvestro complex was hit by the 2009 earthquake. The rehabilitation works was finalized to mitigate the vulnerabilities of the masonry complex. The results of operational modal lead to the updating of a finite element model, in terms of dynamic properties. The seismic performance of the belfry are assessed in terms of probability of collapse and revealed through fragility curves.*

1 INTRODUCTION

Masonry towers (MTs) are cultural buildings disseminated in urban contest, even in areas with high seismic hazard, isolated or included in the clustered buildings. In ancient times, MTs were conceived to withstand only gravity loads. Their vulnerability under horizontal loads is ascribed to the brittleness of the masonry and the geometric configuration. The poor quality of the masonry combined with the specific vertical configuration yields considerable tensional state at the basement, seismic amplification at height and dynamic phenomena which are uncommon for ordinary masonry constructions. Furthermore the geometric irregularities could worse the damage patterns and surrounding buildings could modify the seismic response, reducing the slenderness. Nevertheless, the induced damages by seismic events provide information about their dynamic behavior. Generally, the most frequent response of the steam of MTs is exhibited in local mechanisms, like overturning. While the upper part of the tower is involved in the rotation and sliding of the pillars, causing cracks in the arches, due to the lack of tie rods or hooping ties, slender pillars and roof too heavy and/or thrusting. Nevertheless, several structural configurations could modify the failure modes, worsening a damage pattern or causing specific cracks. The analysis could include the whole of the structural parameters to foresee a realistic response, on which the protection measures could evaluated. A strategy to reduce the uncertainties of the unknown parameters is a deep investigation, through a complete diagnostic and a critical analysis. Unfortunately, the knowledge is not feasible owing to the lack of historical data and the impossibility of invasive and destructive test. But a meaningful strategy to foresee a realistic structural response is the development a synergic integration between numerical and experimental analysis. To this aim, Operational Modal Analysis (OMA) is a powerful method that allows the investigation of modal parameters in a non-invasive way. The authors performed several studies on the seismic behavior of a masonry tower, the St.Silvestro belfry. The operational modal analysis and the numerical modeling are performed. In this paper the actual dynamic response of the belfry is investigated through the OMA. After that, the seismic performance, in terms and the derivation of fragility curves, are evaluated on a refined finite element model of the structure.

2 THE INVESTIGATED CASE STUDY: ST.SILVESTRO BELFRY IN L'AQUILA

2.1 Description of the building

St.Silvestro complex is a monumental building, situated in L'Aquila (Italy), built between XIII and XIV century, during the dominance of the king Federico II. The interior is divided in three naves of which the length of the central is twice of the lateral ones. Ogival arches separate the naves and support a masonry wall with a thickness of 80 cm and a height of 5 meters. The symmetric facade has a large Gothic window. While, the belfry is located in the right side of the church façade and it is as long as the lateral nave. It presents a rectangular plan with 5.5 and 6.9 meters per sides. The height of the tower is 33 m. A steel staircase arrives at the bell cell, characterized by slender masonry piers and large windows. The thickness of the masonry changes in correspondence with each wall: 1.05, 1.20, 1.40 and 1.60 m. The complex was built in local masonry [1], with irregular units arranged in irregular texture, namely "Apparecchio Aquilano".

Figure 1: Panoramic view of St.Silvestro church.

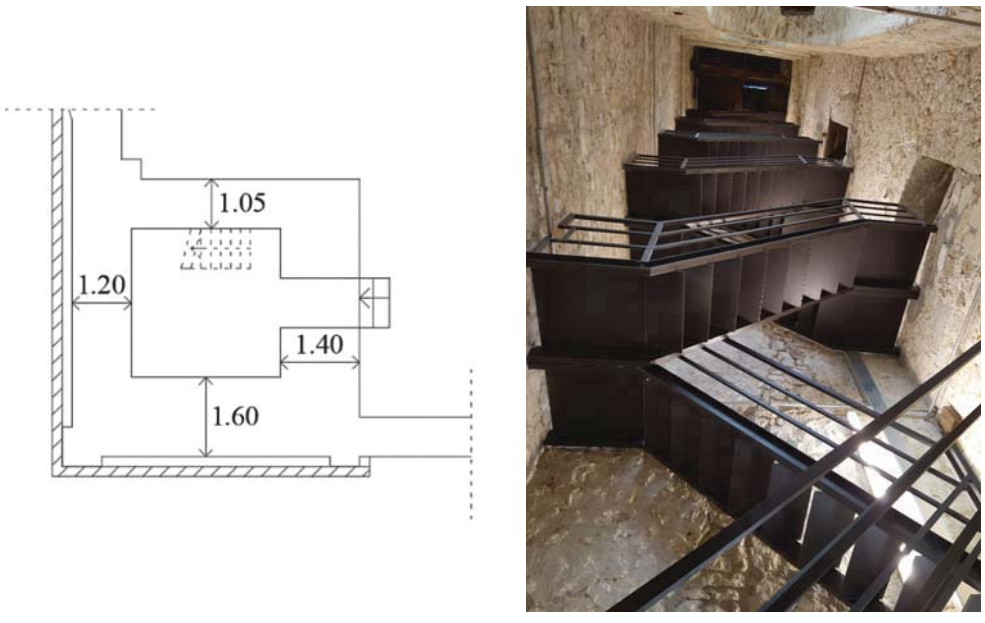

(a) (b)

Figure 2: Cross-section of the masonry tower (a) and the detail of the steel staircase inside the bell tower (b).

2.2 Suffered damage and underwent restorations

During the earthquakes swarm in 2009, the bell tower exhibited a local response. In particular, the visible damage pattern identified two overturning mechanism, like marked in red in Fig.3. The first mechanism involved the entire MT in a composed overturning around a cylindrical hinge located at the basement.

Figure 3: Crack scenario and schematisation of collapse mechanisms of the bell tower after the earthquakes (from the Fine Art Authority on-line site).

The second mechanism involved the upper part of the belfry in an overturning around a cylindrical hinge located at the gutter of the church (at 10.20 meters from the basement). These kinds of seismic response are a peculiar dynamic behavior of historical buildings. In fact, the lack of connection wall-to-wall and floor-to-wall is the main structural feature that induces a local response, as out of plane mechanism of the walls. Monumental buildings are often characterized by poor quality of masonry due to decay and arrangement over time, leading to a local collapse, even earlier to exhibit a out of plane response.

Based on the surveyed damage, the restoration of the St.Silvestro belfry focused on the repair of damage, closing the cracks by horizontal stone connections and injections. Whereas the reinforcement was finalized to assign a box-like behavior. Inserted steel rods avoided the out of plane response, recovering the lack of connection. From a visual inspection, it is noted that the position of the steel rods is close to an old installation in wood realized in a past restoration. In fact, due to high seismic risk of L'Aquila, the use of the wood pervaded noble and poor buildings as anti-seismic timber devices [2].
Moreover, the reinforcement ensured the enhancement of the mechanical properties of the masonry thanks grout injections, respecting the architectural criteria.

3 APPRAISAL OF THE ACTUAL PERFORMANCE OF THE BELFRY

3.1 In situ dynamic investigation

The appraisal of the performance of monumental buildings, including masonry towers, requires a deep knowledge of the structural system, in order to achieve a high level of accuracy. The recourse to specific test ensures the characterization of the building. Non destructive test, like visual and non invasive inspections, are not always able to grasp the unknown parameters. For example, the reliability of the thermal camera is related to the thermal equilibrium of the wall. Whereas destructive test could be compromise the architectural value of the component of the building. Others methods rely on the identification of the dynamic properties of the structure in its in-situ condition whether the architectural value of monumental buildings or the utilization of the infrastructure requires non destructive test methods. A powerful on site dynamic investigation is the Operational Modal Analysis (OMA) technique. Among the algorithms in time domain, the Stochastic Subspace Identification (SSI) method is used for the estimate of modal parameters from Output Only measurements. The SSI method is classified as Covariance-Driven Stochastic Identification (Cov-SSI) and Data-Driven Stochatsic Subspace Identification (DD-SSI), that was generalized to a reference-based version (SSI-cov/ref) by Peeters and De Roeck [3].
The dynamic campaign on St.Silvestro belfry was performed on December 2019, in order to investigate the structure response under ambient vibration measurements. The setup of the campaign involved 10 biaxial accelerometers, of which 2 accelerometers provided a reference location [4], while the other 7 were placed in the inferior levels in several measurement points, as displayed in the layout depicted in Fig.4. The data were sampled at a rate of 250 Hz. The cut-off frequency of the anti-aliasing filter was set to 20 Hz. The number of samples was set to N=720000, which resulted in a measurement time of 1 hour. Data from multi-setup measurements, with 4 setups, were then merged following the approach recalled in [5]. Two modes arise from the stabilization diagram and revealed translation shapes, as reported in Fig.5.

3.2 Numerical modelling

The dynamic response of the St.Silvestro belfry is evaluated also through a numerical analysis. Two different structural models were adopted. A model, with bi-dimensional finite elements, was developed aimed to reproduce the refinement behavior of the belfry, used for the model updating. An equivalent frame model, with a one-dimensional finite element, was performed to overtake the computational burden of non-linear analysis. The finite elements consisted of four frames, with an equivalent section with each wall, resorting to lumped plasticity [6]. A rigid-perfectly plastic behavior with final brittle failure was assigned to all plastic hinges. The whole structure has been assumed fixed to the foundation, considering the soil-structure as

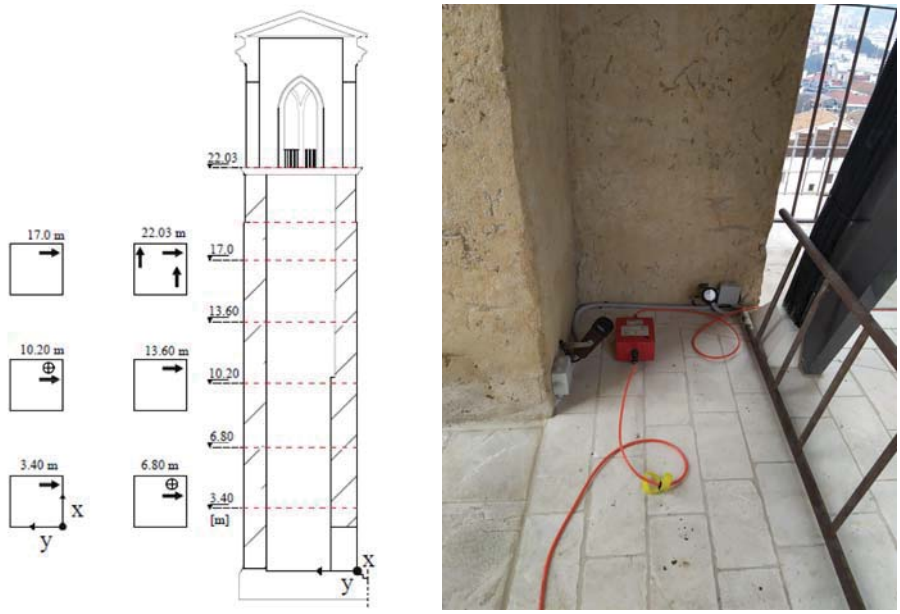

Figure 4: Experimental setup, showing the position of the accelerometers along the height of the tower. On the right: a sensor placed on the the top of the bell tower, at the height of 22,03 m.

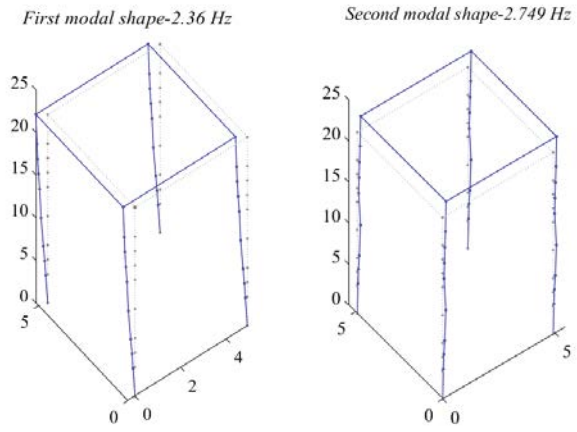

(a) (b)

Figure 5: First two experimental mode shapes deriving from OMA.

negligible. The neighboring church was included in the model by non-linear springs. The mechanical parameters of the reinforced masonry are assigned starting from the value reported in the Italian Standard Code[7] for unreinforced masonry, as reported in Table 1, and applying the corrective factor for the restoration measure carried out.

Table 1: Mechanical parameters of irregular stone masonry.

Unreinforced masonry	f_m [MPa]	τ_0 [MPa]	E [MPa]	G [MPa]	γ [Mpa]
Irregular stone masonry	2	0.043	1230	410	21

Starting from numerical results, the model updating was carried out.

3.3 Model updating of modal properties

The model updating aims to correct the finite element model by processing the results from dynamic test on the structure. To measure the distance between the estimated modal parameters and the numerical ones, the following objective function is used [8]:

$$C = \sum_{i=1}^{M} \gamma_i \left(\frac{\omega_i^m - \omega_i^c}{\omega_i^m} \right)^2 + \beta \sum_{i=1}^{M} (1 - diag(MAC(\Phi_i^m, \Phi_i^c))) \tag{1}$$

where the apex $(*)^m$ indicates a measured variable, the apex $(*)^c$ a calculated variable, Φ_i is the mode shape vector, M is the number of modes, MAC is the modal assurance criterion [9], while γ_i and β are weighting factors. The weighting factors are set equal to one.

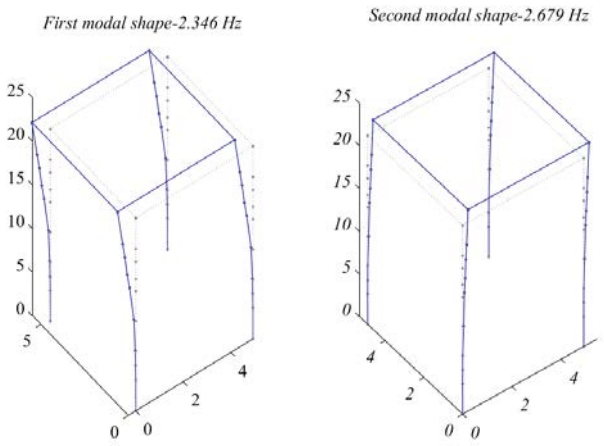

Figure 6: (a) First mode shape from model updating; (b) Second mode shape from model updating

The model updating was performed with the aim to detect the elastic modulus E of the masonry. According to the Italian Guidelines, an acceptable range for the modulus E value was investigated. The optimization led to a value of E for the walls in x direction equal to 3540 MPa, while the modulus for the y direction was identified to be equal to 3360 MPa [10]. The evaluated MAC takes the value equal to 0.78 for the first mode and to 0.88 for the second one, ensuring a consistent correspondence. The other values are negligible.

3.4 Derivation of fragility functions

The seismic performance of the belfry, after the restoration, are estimated through fragility function. The probability of collapse of the structure is evaluated, for four limit states of interest, as a function of ground motion intensity measure, IM [11], which, in this paper, is the PGA itself. The occurrence or non occurrence of collapse is defined by the exceeding of a given displacement, for a given set of ground motion and dynamic structural analysis results. A lognormal cumulative distribution function is used for fitting the fragility function based on data collected from non linear dynamic analysis [11]:

$$P(C|IM = x) = \Phi\left(\frac{ln(x/\theta)}{\beta}\right) \tag{2}$$

where $P(C|IM = x)$ is the probability that a ground motion with $IM = x$ will cause the structure to collapse; Φ is the standard normal cumulative distribution function (CDF); θ is the median of the fragility function (the IM level with 50% probability of collapse); and β is the standard deviation of ln IM (sometimes referred to as the dispersion of IM). Since the truncated incremental analysis was carried out, an alternative procedure [11] to estimate the parameters θ and β is followed, obtained by varying the parameters until a certain likelihood function is maximized. Specifically, the parameters are obtained by maximizing the logarithm of the following likelihood function:

$$\{\hat{\theta}, \hat{\beta}\} = argmax_{\hat{\theta},\hat{\beta}} \sum_{j=1}^{m} \left[ln\Phi\left(\frac{ln(IM_i/\theta)}{\beta}\right)\right] + [n-m]\, ln\left[1 - \Phi\left(\frac{ln(IM_{max}/\theta)}{\beta}\right)\right] \tag{3}$$

where $\hat{}$ denotes an estimated parameter, $\Phi()$ the standard normal distribution PDF, n the number of ground motion used in the analysis, m the number of m ground motions that caused collapse at IM levels lower than IM_{max}, $\Phi()$ the standard normal distribution CDF. The parameters of Eq.(3) are estimated for each of the earthquake recordings. The resulting two parameters of the fragility function, representative of all considered seismic scenarios, are obtained taking the mean of all the couples of parameters estimated from each truncated incremental dynamic analysis. Fig.7 shows the obtained fragility functions, for the x direction, that reveals the high-

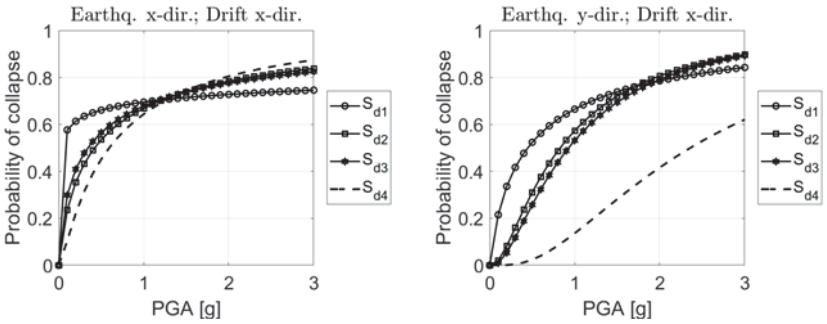

(a) (b)

Figure 7: Fragility curves of the numerical model of the masonry tower.

est value of probability of collapse due to the significant drifts in its direction of application. The in-homogeneous structural characteristics, in terms of the mechanical parameters and horizontal restrains, gives rise to the different probabilities of collapse. In detail, the restoration

works foresaw a different improvement of the mechanical property of the masonry, assigning different value of the elastic modulus and the strength resistance of the masonry. In addition, the horizontal constraint provided by the church is not the same between the two direction due to the different stiffness and connection of the adjacent masonries. Nevertheless, a further deep characterization is required in order to grasp the boundary conditions accurately.

4 FINAL REMARKS

A procedure for a reliable assessment of seismic response of a masonry tower is performed. The case study investigated is St.Silvestro belfry, located in the centre of L'Aquila and damaged by 2009 earthquake. By discussing the restoration works, the numerical and operational modal results, the paper aims at offering a reliable approach to obtain the seismic response with its confidence intervals. The prediction of the seismic performance of masonry towers is an tricky task, owing to the lack of the building knowledge. In order to overcome the uncertainties, an integrated approach between numerical and experimental analysis is a powerful procedure, as discussed in this paper. The experimental campaign has investigated the modal parameters of the St.Silvestro belfry. In particular OMA has allowed the evaluation of frequencies and modal shapes, taking into account the influences of neighboring construction, else uncertain. The model updating has founded the correspondence between the experimental data and numerical results. After that, the correct actual modal behavior is assessed. Furthermore the numerical model has yielded the seismic behavior in terms of fragility functions. Hence the integrated approach is capable to predict the seismic performance and the damage during the service condition or future earthquakes accurately, on which monitoring and retrofitting could be designed.

5 ACKNOWLEDGEMENTS

The geometric survey and additional information of the monumental complex of St.Silvestro were found on the online site of Fine Art Authority.

REFERENCES

[1] A. Borri, G. Cangi, M. Caraboni, A. Giancarlo, F. Menghini, L. Procacci, R. Vetturini, Sisma del 6 aprile 2009 in abruzzo e bbcc: il caso della chiesa di s. silvestro a l'aquila, bollettino ingegneri (4-2010) (2010) 3–24.

[2] A. Aloisio, M. Fragiacomo, G. D'Alò, Traditional tf masonries in the city centre of l'aquila–the baraccato aquilano, International Journal of Architectural Heritage (2019) 1–18.

[3] B. Peeters, G. De Roeck, Reference-based stochastic subspace identification for output-only modal analysis, Mechanical systems and signal processing 13 (6) (1999) 855–878.

[4] M. Döhler, L. Mevel, Subspace-based fault detection robust to changes in the noise covariances, Automatica 49 (9) (2013) 2734–2743.

[5] M. Döhler, E. Reynders, F. Magalhaes, L. Mevel, G. De Roeck, A. Cunha, Pre-and post-identification merging for multi-setup oma with covariance-driven ssi, in: Dynamics of Bridges, Volume 5, Springer, 2011, pp. 57–70.

[6] L. Pasticier, C. Amadio, M. Fragiacomo, Non-linear seismic analysis and vulnerability evaluation of a masonry building by means of the sap2000 v. 10 code, Earthquake engineering & structural dynamics 37 (3) (2008) 467–485.

[7] . Ministerial Decree n.7, Instructions for the application of the updating "Technical codes for constructions", M.D. 17/01/2018 (In Italian), 2019.

[8] M. Friswell, J. E. Mottershead, Finite element model updating in structural dynamics, Vol. 38, Springer Science & Business Media, 2013.

[9] R. J. Allemang, D. L. Brown, A correlation coefficient for modal vector analysis, in: Proceedings of the 1st international modal analysis conference, Vol. 1, SEM Orlando, 1982, pp. 110–116.

[10] M. Pastor, M. Binda, T. Harčarik, Modal assurance criterion, Procedia Engineering 48 (2012) 543–548.

[11] J. W. Baker, Efficient analytical fragility function fitting using dynamic structural analysis, Earthquake Spectra 31 (1) (2015) 579–599.

List of Figures

1 Panoramic view of St.Silvestro church. 3
2 Cross-section of the masonry tower (a) and the detail of the steel staircase inside the bell tower (b). 3
3 Crack scenario and schematisation of collapse mechanisms of the bell tower after the earthquakes (from the Fine Art Authority on-line site). 4
4 Experimental setup, showing the position of the accelerometers along the height of the tower. On the right: a sensor placed on the the top of the bell tower, at the height of 22,03 m. 6
5 First two experimental mode shapes deriving from OMA. 6
6 (a) First mode shape from model updating; (b) Second mode shape from model updating 7
7 Fragility curves of the numerical model of the masonry tower. 8

List of Tables

1 Mechanical parameters of irregular stone masonry. 7

EURODYN 2020
XI International Conference on Structural Dynamics
M. Papadrakakis, M. Fragiadakis, C. Papadimitriou (eds.)
Athens, Greece, 23–26 November 2020

OUT-OF-PLANE SHAKING TABLE TESTS ON DUTCH BUILDING PRODUCTS

A.J. Bronkhorst, C.P.W. Geurts

TNO
Structural Dynamics
Delft
e-mail: okke.bronkhorst@tno.nl

Keywords: Shaking table tests, one-way bending, unreinforced masonry, timber frame supported straw block wall

Abstract.

A shaking table experiment was performed to study the influence of several building products on the out-of-plane behavior of load-bearing walls in one-way bending. The products that were investigated are a high-strength mortar (Remix/Strating), a mortar-less dry-stacked masonry system (ClickBrick), a renovation anchor tie system (Fischer), and compressed straw blocks supported by a timber frame (Straw Blocks). The results obtained for the specimen with these products were compared to tests performed on two cavity wall specimen (R1 and R2) constructed from materials typically applied in Dutch masonry buildings. The results show that the test specimen with the ClickBrick dry-stacked system and the specimen with the Fischer renovation anchor have a larger flexibility than specimen R1 and R2. The Remix/Strating specimen with high-strength mortar displayed linear elastic behavior up to larger peak table accelerations than specimen R1 and R2, suggesting an improvement in the damage resistance. The Straw Blocks specimen could not be tested up to failure due to the limitations of the table; linear elastic behavior was observed until PTA = 1.2 g in the ground floor configuration and PTA = 0.7 g in the first floor configuration.

1 INTRODUCTION

Gas extraction in the province of Groningen in the North of the Netherlands has resulted in induced earthquakes in this region. The strongest event was the Huizinge earthquake (16th of August 2012) with a magnitude $M_w = 3.6$. The largest PGA level measured in this event was about 0.1 g. Although the magnitude of these earthquakes is relatively low, there is a risk for the building stock [1] because a large portion of the buildings in this region consist of unreinforced masonry (URM) and was not designed for seismic loads.

Until recently, little was known about the seismic performance of Dutch URM buildings. An extensive testing campaign by EUCentre and the TU Delft [2] on some typical Groningen buildings and building components has provided a better understanding on the performance of the more earthquake-prone buildings. This campaign has provided a basis for assessment of the existing building stock. Still, relatively little is known about the seismic performance of other (new) building products used in Dutch construction. Companies active in the construction industry wish to have a better understanding of the performance of their products under earthquake loading.

Various studies on the effect of earthquakes on masonry buildings, e.g. [3-6], found that damage to and failure of these buildings often has to do with the out-of-plane behavior of the load-bearing walls. Depending on the boundary conditions, different failure patterns can occur. Figure 1 shows two types of failure patterns that are often observed in buildings. The pattern in Figure 1 (left) is known as one-way bending failure. This is common in long walls or walls without support on both sides. The pattern in Figure 1 (right) is two-way bending failure, which occurs in walls where all sides are supported.

The out-of-plane behavior of masonry walls has been studied quite extensively. Doherty [7] performed shaking table tests on URM wall specimen to study the rocking and collapse behavior of a one-way spanning wall. Vaculik [8] studied the dynamic behavior of half-scale walls in two-way bending; an extensive shaking table test program was performed on 5 specimen in which the changes in properties (effective stiffness, natural frequency and damping) were monitored in detail. A detailed study of the influence of the top and bottom boundary condition was made by Dazio [9]. The results of this study showed that besides the slenderness and overburden load, the boundary conditions play an important role in the out-of-plane behavior of masonry walls.

Relatively few studies have been performed on the out-of-plane behavior of cavity walls. As part of the testing campaign by EUCentre [2], Graziotti et al [10] performed shaking table tests on the one-way bending behavior of cavity walls. They investigated the influence of the number of anchor ties, and made a comparison with the out-of-plane behavior a single leaf wall. They found that for all cavity walls the horizontal displacements of the inner and outer leaf were the same, even for the specimen with a small number of ties (2 ties/m^2).

To obtain a better understanding of the seismic performance of some building products applied in the Netherlands, an experimental shaking table test campaign was performed. The one-way out-of-plane bending behavior of various load-bearing walls including those building products was investigated with a similar experiment setup as developed by Graziotti et al [10].

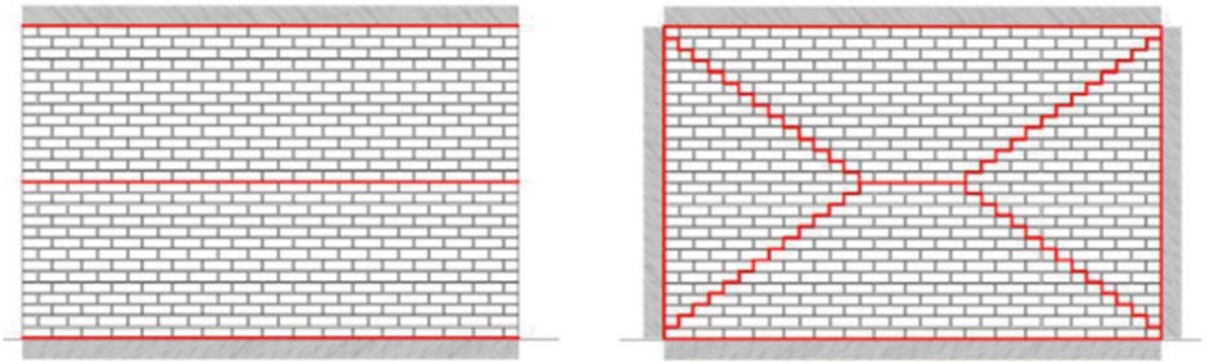

Figure 1: Damage patterns for (left) one-way bending and (right) two-way bending, after Graziotti et al. [7].

Five different cavity wall specimen and one wall specimen of compressed straw blocks supported by a timber frame were tested. Two cavity wall specimen (R1 and R2) were constructed from materials typically applied in Dutch masonry buildings. The products applied in the other specimen are a high-strength mortar (Remix/Strating), a dry-stacked masonry system (Click-Brick), a renovation anchor tie system (Fischer), and compressed straw block system supported by a timber frame (Straw Blocks).

Chapter 2 explains the setup of the shaking table experiment, and describes the various test specimen that were tested. Chapter 3 presents and discusses some of the results obtained for the various wall specimen. Chapter 4 gives the conclusions of this work.

2 EXPERIMENT

This chapter describes the setup of the experiment, the applied signals and the procedure. More detailed information can be found in [11-14].

2.1 Test setup

The tests were carried out on a uniaxial shaking table shown in Figure 2. The table has an area of 2 m x 3 m and a weight of 3.5 ton. The hydraulic actuator is controlled with the Moog test software package Integrated Test Suite.

Figure 2 shows the setup of the experiment. A triangular support frame (A) was placed behind the test specimen to support the top boundary condition. The natural frequency of the support frame is 25 Hz, to ensure an acceleration signal at the top of the specimen similar to the table acceleration in the frequency range of interest (0 – 20 Hz). A steel beam (B) is placed on top of the test specimen; the beam is connected with a hinge to the support frame. On both sides of the test specimen a beam (C) extends from the support frame. This beam catches the top beam (B) when the test specimen fails. The top beam (B) is pulled down with a predefined force by means of a spring construction (D) on both sides of the specimen. The force exerted by the springs represents the building mass on top of the wall. The applied force was dependent on the test configuration and the specimen, par. 2.5 specifies the applied forces. The aluminum frame (E) is used for laser sensors to measure the displacements of the test specimen during the tests. A similar frame is placed on the inside of the test specimen.

Figure 2: Overview photo of the test set-up with some components highlighted: the support frame (A), the upper beam (B), the support structure for the upper beam (C), the prestressing structure (D) and the laser frame (E).

2.2 Test specimen

A total of 6 different wall specimen were tested; 5 specimen were URM cavity walls, one specimen was a straw block wall supported by a timber frame. Figure 3 shows pictures of one of the cavity wall specimen and of the straw block timber frame specimen. All test specimen were constructed on a concrete block (1.47 m wide, 0.4 m deep and 0.2 m high). The global dimensions and weight (excluding concrete block) of the test specimen are given in Table 1. The cavity between inner and outer leaf was 80 mm for all cavity wall specimen.

The load-bearing inner leaf of the 5 cavity wall specimen was built with white calcium silicate (CS16) bricks in stretcher bond and Remix/Sakrete mortar (adhesive strength 0.45 N/mm^2). The calcium silicate stone is 214 mm wide, 102 mm deep and 72 mm high. All cavity wall specimen had an inner leaf of 32 layers with six and a half stretchers per layer.

Two cavity wall specimen were made of materials typically applied in Dutch masonry buildings, these specimen are referred to as Reference 1 and 2 (R1 and R2). Specimen R1 had an outer leaf of solid clay bricks (2.1 kg per brick). The outer leaf of specimen R2, consisted of perforated clay bricks (1.7 kg per brick). Both solid and perforated brick are 209 mm wide, 99 mm deep and 50 mm high. The outer leaves of specimen R1 and R2 consisted of 43 brick layers, with six and a half stretchers per layer. The Remix BM2 M5 mortar (adhesive strength 0.2 N/mm^2) was used in the outer leaves of both specimen. The inner and outer leaf of R1 and R2 were connected by L-shaped anchor ties (4.3 anchors per m^2) of type UNI-L (32512).

Figure 3: Front view and side view of one of the URM cavity wall specimen (top) and of the straw block timber frame specimen (bottom).

Test specimen	Description	Dimensions [m]	Mass [kg]
Reference 1 (R1)	URM cavity wall - solid brick outer leaf	2.68 x 1.46 x 0.28	1390
Reference 2 (R2)	URM cavity wall - perf. brick outer leaf	2.68 x 1.47 x 0.28	1318
Fischer	URM cavity wall - renovation anchor ties	2.68 x 1.46 x 0.28	1296
Remix/Strating	URM cavity wall - high-strength mortar	2.67 x 1.47 x 0.28	1397
ClickBrick	URM cavity wall - dry-stacked masonry	2.67 x 1.47 x 0.28	1160
Straw Blocks	Straw single wall - timber frame support	2.70 x 1.40 x 0.40	193

Table 1: Description, dimensions (height, width and thickness) and mass (excluding concrete base) of the test specimen.

The Fischer test specimen was constructed of the same materials as specimen R2, except for the anchor ties. The inner and outer leaf of this specimen were connected by Fischer renovation anchors, type VBS-8x225 A4. These anchors were inserted after construction of the cavity wall without the UNI-L anchor ties.

The Remix/Strating specimen was also constructed of the same materials as specimen R2, except for the mortar in the outer leaf. The outer leaf was built with a high-strength Remix/Sakrete mortar, with an adhesive strength of 0.5 N/mm^2.

The ClickBrick specimen had an outer leaf of ClickBrick stones. These perforated stones (240 mm wide, 100 mm high and 90 mm deep) are stacked dry; the stones are interconnected by means of metal clips. The top 3 of the 27 layers of stones were also glued together with a sealant. The inner and outer leaf were also connected with the UNI-L anchor ties.

The Straw Blocks specimen consisted of compressed straw blocks, supported by a wooden frame. The test specimen consisted of two elements of 0.7 meter wide. The two elements are connected by means of rods across the width of the test piece. At the bottom of the element, the wooden frame is attached to the concrete block by means of four M16 bolts.

2.3 Instrumentation

Figure 4 shows the sensor positions on the test specimen. Acceleration measurements (blue squares) were performed on the concrete block (a1) and the top beam (a32). Accelerations were also measured at 3 positions over the height on the inner (a32 – a35) and outer leaf (a29 – a31) of the specimen. Displacements of the test specimen relative to the shaking table were measured with lasers at the indicated positions d17 – d27 (yellow rectangles) in Figure 4. All sensors were sampled with a frequency of 500 Hz. The data was filtered with an eight-order Butterworth filter with a lowpass frequency of 50 Hz.

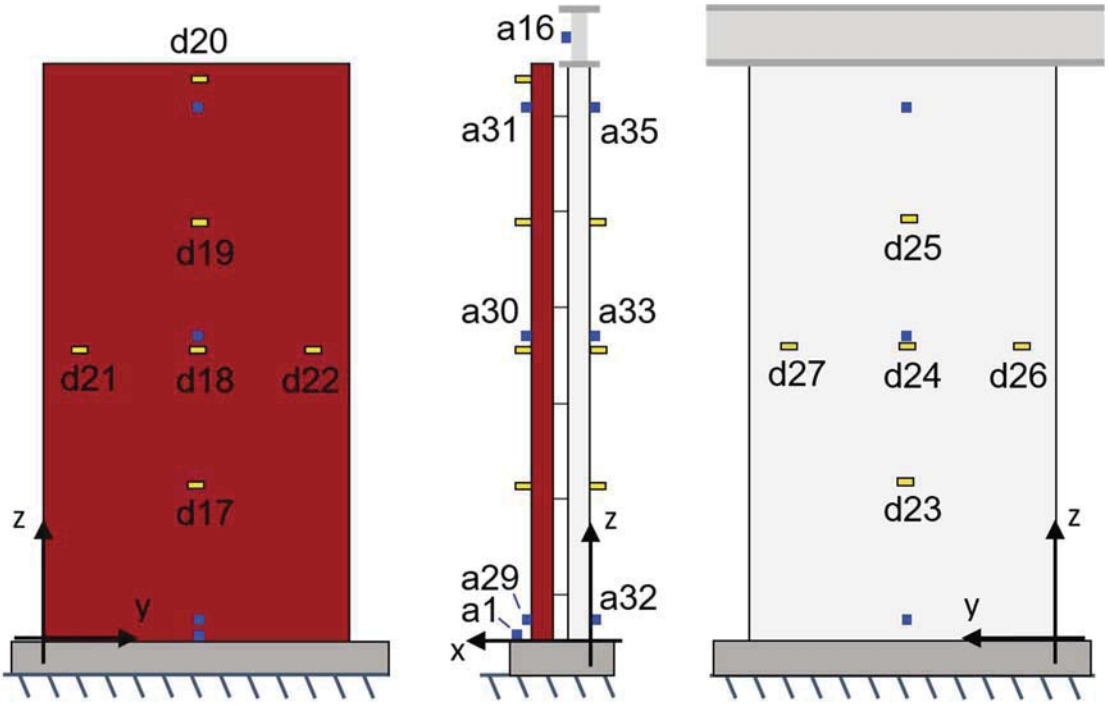

Figure 4: Schematic representation of the front, side and rear view of the test specimen with lasers (yellow) and accelerometers (blue) on the outer leaf (red) and the inner leaf (white), the concrete block and the top beam.

2.4 Signals

Figure 5 shows the earthquake signals applied in this experiment. These signals were also used in shaking table tests on masonry cavity walls by Graziotti et al. [10]. Graziotti et al. [10] [15] selected the Gr-1 signal based on research by Crowley et al. [16] on representative signals for Groningen earthquakes. The Gr-2 signal was created by Graziotti et al. [15] using the finite element package TREMURI for a 2-storey building; the Gr-1 signal was imposed at the level of the foundation of the building model and the Gr-2 signal was registered at the first floor.

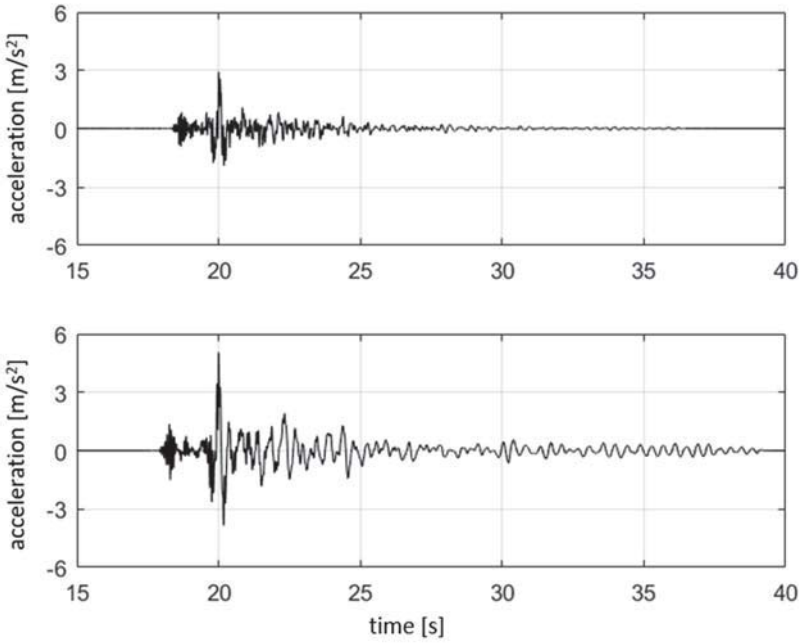

Figure 5: The earthquake signals applied in the shaking table tests (top) Gr-1 and (bottom) Gr-2. The presented signals represent the SF = 100% signals.

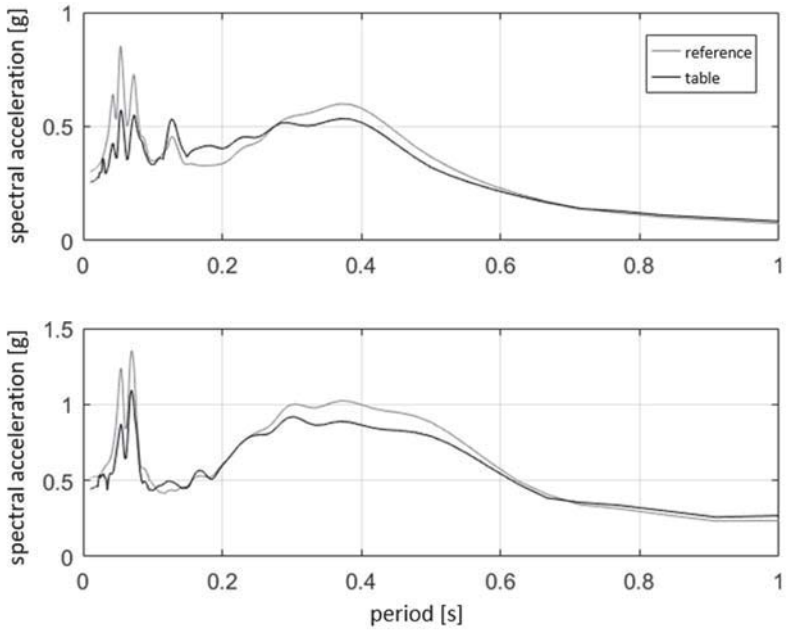

Figure 6: The response spectra (determined with 5% damping) of test signal (top) Gr-1 and (bottom) Gr-2. The presented spectra represent the SF = 100% spectra.

Figure 6 shows the desired (reference) and realized (table) response spectra of the Gr-1 and Gr-2 100% signals. For periods between 0.02 s and 1 s, the maximum difference between the reference and the table spectrum was 30%.

2.5 Test sequence

The tests on each specimen were performed in two phases, with two different test configurations:

1. Ground floor configuration
   An overburden load was applied to the top of the test specimen that is representative for a wall element on the ground floor of a 2-storey building (19 kN for the cavity wall specimen and 6.3 kN for the Straw Blocks specimen). In this configuration, the Gr-1 signal was simulated on the table.
2. First floor configuration
   The overburden load was reduced to a representative load for a wall element on the first floor of a 2-storey building (9 kN for the cavity wall specimen and 3 kN for the Straw Blocks specimen). In this configuration, the Gr-2 signal was simulated on the table.

In both configurations, the peak table acceleration (PTA) of the signal simulated on the table was gradually increased. The applied increase is indicated with a scaling factor (SF), with SF = 100% corresponding with the signals presented in Figure 5. Several tests were performed at each scaling factor. Table 2 gives the average PTA over all tests performed at a certain scaling; between brackets the standard deviation is specified.

Damage inspections were performed at regular intervals throughout the test program. In each inspection the specimen were examined visually; pictures were taken of both sides of the test specimen.

To prevent damage to the instrumentation, the lasers and acceleration sensors were removed when relative displacements larger than 1 cm were measured.

		R1	**R2**	**Fischer**	**Remix/ Strating**	**ClickBrick**	**Straw Blocks***
Signal	SF	PTA [g]	PTA [g]	PTA [g]	PTA [g]	PTA [g]	PTA [g]
Ground floor configuration							
Inspection 0 and hammer test							
Gr-1	20%	0.054 (+/-0.004)	0.053 (+/- 0.003)	0.050 (+/- 0.003)	0.050 (+/- 0.003)	0.051 (+/- 0.001)	0.052 (+/- 0.004)
Gr-1	40%	0.095 (+/- 0.001)	0.098 (+/- 0.004)	0.094 (+/- 0.003)	0.099 (+/- 0.007)	0.097 (+/- 0.002)	0.098 (+/- 0.005)
Inspection 1 and hammer test							
Gr-1	60%	0.141 (+/- 0.004)	0.153 (+/- 0.009)	0.148 (+/- 0.001)	0.153 (+/- 0.021)	0.143 (+/- 0.004)	0.157 (+/- 0.009)
Gr-1	80%	0.188 (+/- 0.001)	0.195 (+/- 0.003)	0.193 (+/- 0.005)	0.191 (+/- 0.008)	0.189 (+/- 0.004)	0.208 (+/- 0.010)
Inspection 2 and hammer test							
Gr-1	100%	0.245 (+/- 0.002)	0.239 (+/- 0.009)	0.260 (+/- 0.005)	0.247 (+/- 0.008)	0.239 (+/- 0.004)	0.270 (+/- 0.004)
Gr-1	140%	0.370 (+/- 0.019)	0.332 (+/- 0.022)	0.362 (+/- 0.021)	0.339 (+/- 0.008)	0.333 (+/- 0.014)	0.352 (+/- 0.013)
Inspection 3 and hammer test							
Gr-1	200%	0.467 (+/- 0.004)	0.460 (+/- 0.014)	0.509 (+/- 0.010)	0.480 (+/- 0.010)	0.487 (+/- 0.011)	0.499 (+/- 0.008)
Inspection 4 and hammer test							
Gr-1	250%	0.561 (+/- 0.012)	0.580 (+/- 0.005)	-	0.593 (+/- 0.001)	0.591 (+/- 0.011)	0.598 (+/- 0.015)
Inspection 5 and hammer test							
Gr-1	300%	0.710	-	-	-	-	0.713 (+/- 0.010)
Inspection 6							
First floor configuration							
Hammer tests							
Gr-2	20%	0.100 (+/-0.004)	0.106 (+/-0.002)	0.108 (+/-0.002)	0.100 (+/-0.001)	0.105 (+/-0.001)	0.109 (+/-0.003)
Gr-2	40%	0.198 (+/-0.001)	0.194 (+/-0.006)	0.191 (+/-0.003)	0.190 (+/-0.002)	0.193 (+/-0.004)	0.199 (+/-0.004)
Inspection 7 and hammer test							
Gr-2	70%	0.324 (+/-0.001)	0.323 (+/-0.002)	0.315 (+/-0.006)	0.320 (+/-0.011)	0.319 (+/-0.002)	0.326 (+/-0.003)
Gr-2	100%	0.429 (+/-0.008)	0.435 (+/-0.006)	0.426 (+/-0.005)	0.421 (+/-0.004)	0.435 (+/-0.006)	0.446 (+/-0.004)
Inspection 8 and hammer test							
Gr-2	130%	0.505 (+/-0.001)	0.540 (+/-0.009)	0.538 (+/-0.010)	0.529 (+/-0.012)	0.547 (+/-0.004)	0.548 (+/-0.002)
Inspection 9 and hammer test							
Gr-2	150%	0.697 (+/-0.134)	0.610 (+/-0.008)	-	0.596 (+/-0.011)	0.597 (+/-0.001)	0.608 (+/-0.002)
Inspection 10 and hammer test							
Gr-2	170%	-	0.693 (+/-0.07)	-	0.754 (+/-0.065)	-	0.687 (+/-0.016)
Inspection 11 and hammer tests							
Gr-2		-	0.593	-	-	-	-

Table 2: Overview of tests on the wall specimen with signal Gr-1 and Gr-2 at different scales (SF). Several tests were performed at each intensity scale; the average PTA and standard deviation (between brackets) are specified.
* Additional ground floor configuration tests were performed on the Straw Blocks specimen up to SF = 500%.
Additional information on the test programs can be found in [11-14].

3 RESULTS AND DISCUSSION

This chapter presents and discusses results on the peak displacements measured on the inner and outer leaf of the specimen and the regular damage inspections performed in-between signal tests. Other results obtained on the changes in the effective stiffness and the natural frequency with increasing shaking intensity can be found in [11-14].

3.1 Ground floor configuration results

Figure 7 shows the measured maximum and minimum displacement in the middle of the inner and outer leaf of the test specimen against the peak table acceleration (PTA). A trend line (black dotted line) is fitted on the measured data for which PTA $\leqslant$ 0.2 g. This trend line is used to assess at which PTA the peak displacements in the middle of the specimen exceed this linear trend, which is an indication for changes in the properties of the specimen.

Figure 7(a) shows that for specimen R1 the peak displacement is larger than this linear trend for PTA > 0.4 g. Although this non-linear behavior can be an indication for damage accumulation in the specimen, no damage was observed in the inspections until test SF = 300% (PTA = 0.71 g). Note that the peak displacement that occurred during the test with SF = 300% is not plotted in Figure 7(a), because it was greater than the measurement range of the lasers.

Figure 7(b) shows the peak displacements of specimen R2. For peak table accelerations up to 0.4 g, the linear trend observed between peak displacements and PTA has the same slope as that observed for specimen R1. For PTA > 0.4 g, the peak displacements observed in specimen R2 remain relatively close to the linear trend. This indicates smaller changes in the properties of specimen R2, and suggests less damage accumulation than in specimen R1. No damage was observed in the ground floor configuration inspections performed on this specimen.

The peak displacements of the Fischer specimen, shown in Figure 7(c), follow a linear trend up to a PTA = 0.5 g. For a given PTA, the measured peak displacements are about a factor 2 greater than those observed for specimen R1 and R2. This suggests the out-of-plane bending stiffness of the Fischer specimen is smaller than that of R1 and R2. This could be the result of the more flexible connection between the inner and outer leaf due to the rubber plug applied in the renovation anchor. Because of the large displacements, the ground floor configuration tests on this specimen were stopped after the tests performed at a PTA = 0.5 g (SF = 200%).

Figure 7(d) shows the peak displacements of the Remix/Strating specimen with increasing PTA. The minimum and maximum displacement follow a linear trend up to a PTA = 0.6 g. This linear trend has the same slope as the trends observed for test specimen R1 and R2.

The peak displacements of the ClickBrick specimen, shown in Figure 7(e), follow a linear trend up to a PTA = 0.5 g. For PTA > 0.3 g, the peak displacements of the outer leaf are slightly (~0.3 mm) larger those of the inner leaf. This is probably due to the greater flexibility of the outer leaf, which mainly gets its stiffness from the clip elements between the dry-stacked stones.

The results of the Straw Blocks specimen are shown in Figure 7(f). Because of the linear elastic behavior of the specimen for the tests up to SF = 300%, additional tests were performed up to SF = 500% (not specified in Table 2, see [14] for detailed information). Figure 7(f) shows the peak displacements follow a linear trend up to PTA = 1.2 g. The slope of this trend is smaller than the slopes observed for specimen R1 and R2.

Apart from specimen R1, no visual damage was observed in the damage inspections performed in the ground floor configuration setup. Figure 8 shows no damage was observed on the outer leaf of specimen R1 up to inspection 5; after the test at SF = 300% a crack was observed near the middle of the R1 specimen, see Figure 8(c).

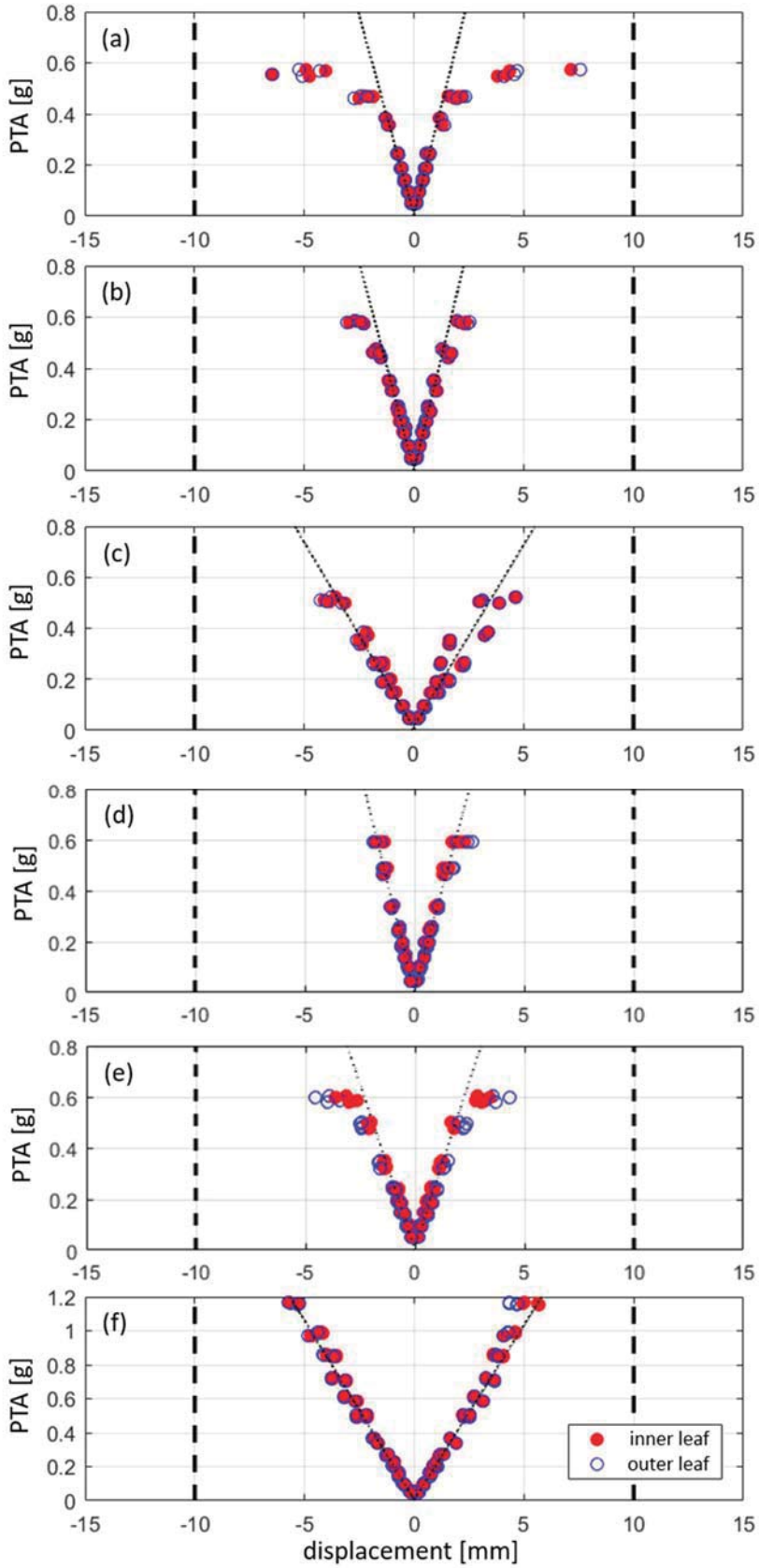

Figure 7: Peak displacement middle test specimen versus peak table acceleration (PTA) for Gr-1 signals: (a) R1, (b) R2, (c) Fischer, (d), Remix/Strating, (e) ClickBrick, and (f) Straw Blocks. The black broken line indicates the measurement range of the lasers; the black dotted line is a fitted line on the data with PTA $\leqslant$ 0.2 g.

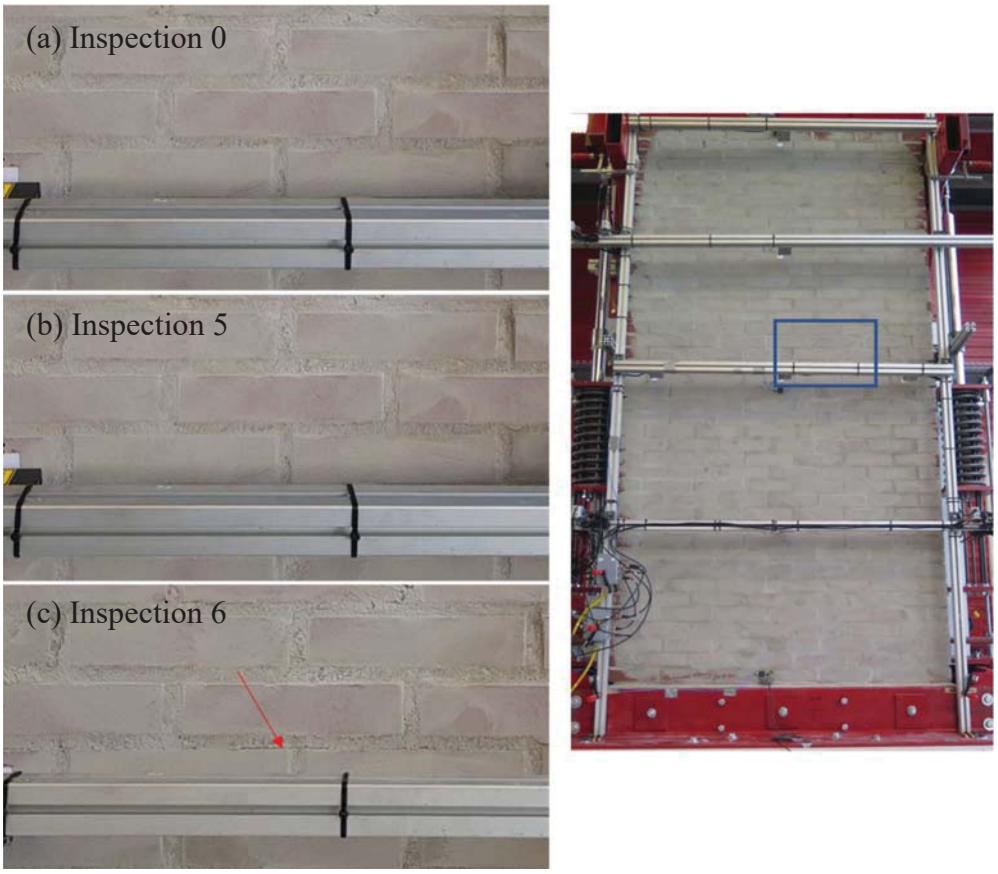

Figure 8: Pictures of the specified zone on specimen R1 (blue frame) in subsequent damage inspections: (a) inspection 0, (b) inspection 5, and (c) inspection 6. The red arrow indicates observed damage (hairline fracture).

3.2 First floor results

Figure 9(a) shows the measured maximum and minimum displacement in the middle of test specimen R1. Up to a peak table acceleration (PTA) of 0.2 g, the peak displacements of specimen R1 follow a linear trend with PTA. For a PTA > 0.2, the peak displacements are larger than this linear trend. In the tests with a PTA = 0.4 g (SF = 100%), a crack formed in the outer leaf at about ¾ of the height of the specimen ($z / h \approx 0.75$). Figure 10(c) shows a picture of the crack (top red arrow) that was observed in damage inspection 8 after this test. In addition to this new crack, the original crack had visibly increased (bottom red arrow), as can also be seen in Figure 10(c). The specimen failed in the third test at SF = 150%. The results of these tests are not presented in Figure 9(a) because the peak displacements exceeded the measurement range of the lasers.

The peak displacements measured on specimen R2 follow a linear trend up to 0.3 g. From a PTA = 0.4 g the peak displacements become slightly larger than this trend; in the tests with a PTA = 0.6 g, the peak displacements increase sharply. The first damage was observed in the inspection after this test, see Figure 10(e). The results of the tests at SF = 170% (PTA ≈ 0.7 g) are not shown because the displacements were larger than the measurement range of the lasers. After two tests at 170%, another damage inspection was carried out. In addition to an increase in the original crack formation at $z / h \approx 0.6$, a new crack was created at $z / h \approx 0.75$. The specimen failed after the third test at 170%.

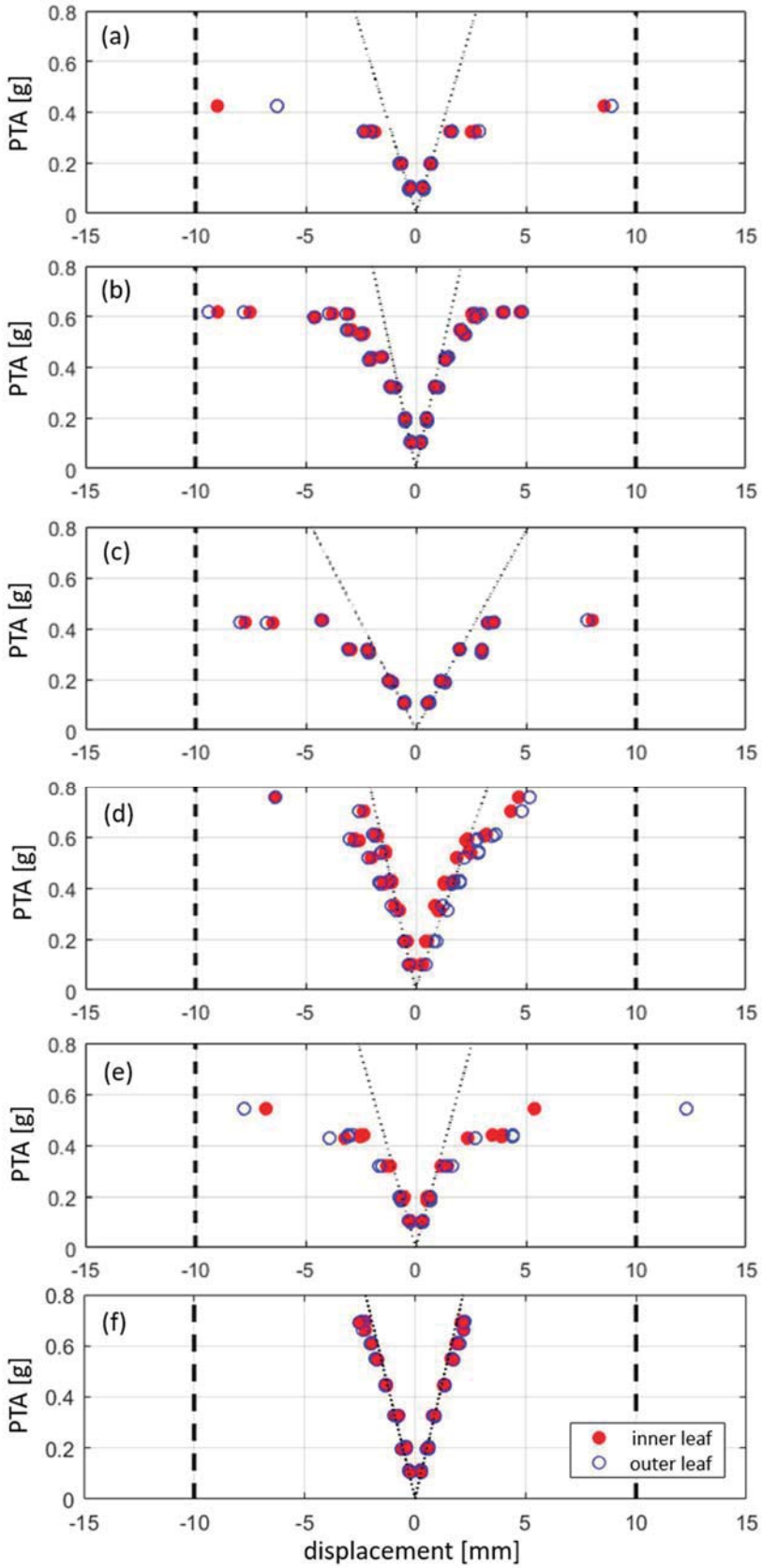

Figure 9: Peak displacement middle test specimen versus peak table acceleration (PTA) for Gr-2 signals: (a) R1, (b) R2, (c) Fischer, (d), Remix/Strating, (e) ClickBrick, and (f) Straw Blocks. The black broken line indicates the measurement range of the lasers; the black dotted line is a fitted line on the data with PTA $\leqslant$ 0.2 g.

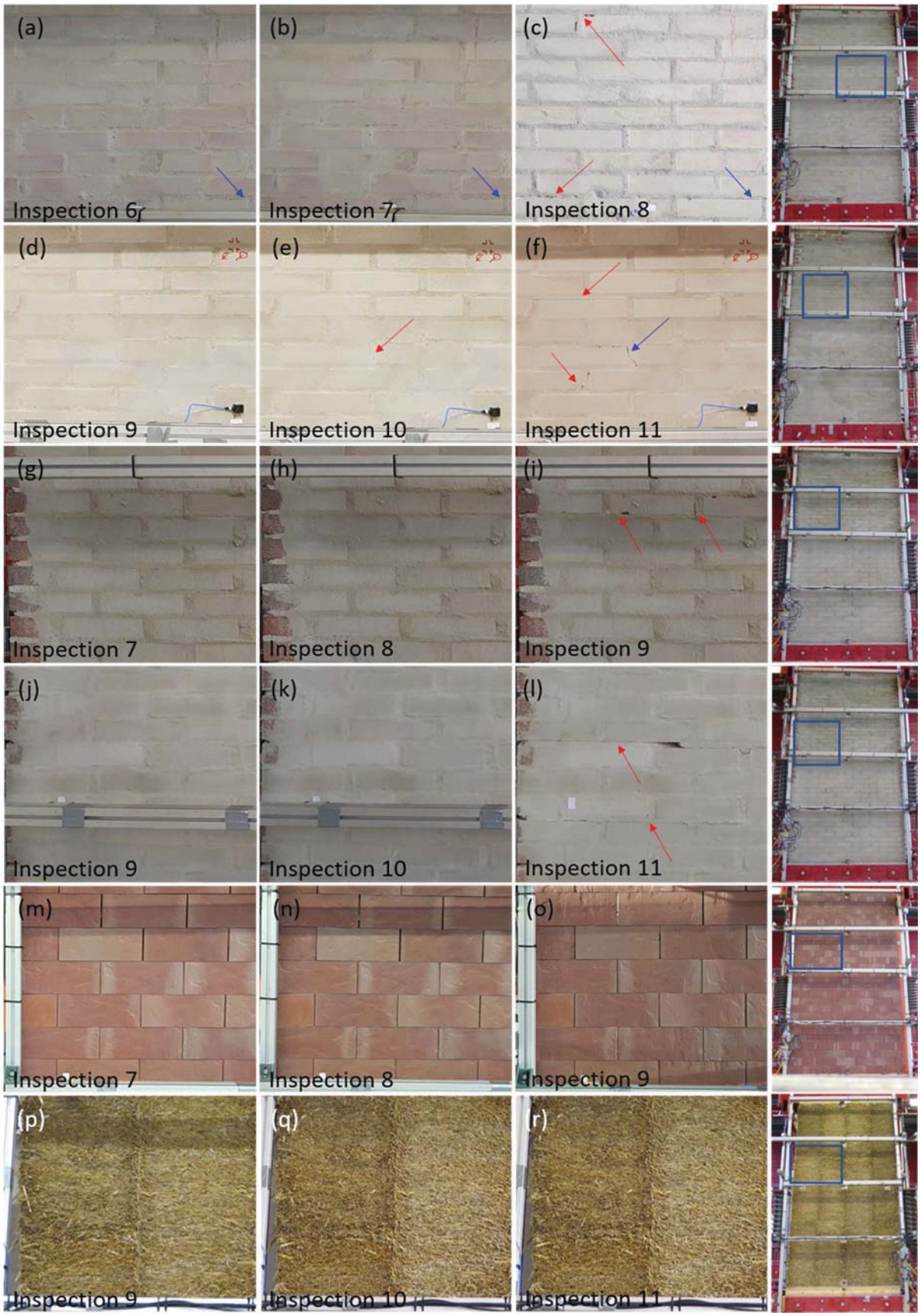

Figure 10: Pictures taken of the indicated zones in subsequent inspections on specimen (a-c) R1, (d-f) R2, (g-i) Fischer, (j-l) Remix/Strating, (m-o) ClickBrick and (p-r) Straw Blocks in the specified inspections. The red arrow indicates observed new damage, the blue arrow indicates damage also observed in an earlier inspection.

Figure 9(c) shows the peak displacements of the Fischer specimen with increasing PTA. The minimum and maximum displacement follow a linear trend up to a PTA = 0.2 g. In the tests with PTA = 0.4 (SF = 100%), a clear increase in peak displacement can be seen. However, no damage was observed in inspection 8 after these tests. Damage was observed after the first test with SF = 130%; damage inspection 9 was performed immediately after this test. Figure 10(i) shows cracking at z / h ≈ 0.75, indicated with red arrows. The Fischer specimen failed in the third test with SF = 130%.

The peak displacements of the Remix/Strating specimen are shown in Figure 9(d). The minimum and maximum displacement follow a linear trend up to a PTA ≈ 0.5 g. The peak displacements deviate from the linear trend from a PTA = 0.6 g. Visual damage was observed after the third test at SF = 170%; Figure 10(l) shows cracks at z / h ≈ 0.5 and z/h ≈ 0.6. The Remix/Strating specimen failed in the subsequent test at SF = 170%. The results of the Remix/Strating specimen indicate that the application of the high-strength mortar in the outer leaf increases the damage resistance.

Figure 9(e) shows the peak displacements of the ClickBrick specimen. The minimum and maximum displacement follow a linear trend up to a PTA ≈ 0.3 g. From a PTA ≈ 0.4 g, a clear increase in peak displacement is seen. However, no visual damage was observed in any of the inspections on the ClickBrick specimen. The test specimen failed in the third test at SF = 150%.

Figure 9(f) shows the peak displacements of the Straw Blocks specimen with increasing PTA. The minimum and maximum displacement follow a linear trend until the last test at SF = 170% (PTA = 0.7 g). The Straw Blocks test specimen showed no damage after completion of the tests in the first floor configuration.

4 CONCLUSION

This paper presented some of the results of an experimental study on the out-of-plane one-way bending behavior of load-bearing walls with various building products. Products that were investigated are a high-strength mortar (Remix/Strating), a mortar-less dry-stacked masonry system (ClickBrick), a renovation anchor tie system (Fischer), and a compressed straw block system (Straw Blocks). The results obtained for the specimen with these products were compared to tests performed on two cavity wall specimen (R1 and R2) constructed from materials typically applied in Dutch masonry buildings.

At shaking intensities with PTA < 0.4 g (ground floor configuration) both reference specimen R1 (solid brick outer leaf)) and R2 (perforated outer leaf) had the same linear elastic peak displacement response in the middle of the specimen. For larger PTA, specimen R1 displayed significantly larger peak displacements than R2. This indicates smaller changes in the properties of specimen R2, and suggests less damage accumulation.

The peak displacements of the Fischer specimen (renovation anchor) were about a factor 2 greater than those observed for specimen R1 and R2. This indicates the out-of-plane bending stiffness of the Fischer specimen is smaller than that of R1 and R2. The rubber plug applied in the renovation anchor might result in a more flexible connection between the inner and outer leaf, resulting in a lower out-of-plane bending stiffness.

The Remix/Strating specimen displayed linear elastic behavior up to a PTA ≈ 0.5 g in the first floor configuration. This result indicates an improvement of the damage resistance of the cavity wall compared to specimen R1 and R2, due to the high strength mortar applied in the outer leaf.

The peak displacements of the outer leaf of the ClickBrick specimen were slightly larger those of the inner leaf. This is probably due to the greater flexibility of the outer leaf, because

of the flexible clip elements between the dry-stacked stones. Although the specimen exhibited significant non-linear behavior from a PTA of 0.4 g in the first floor configuration, no damage was observed in the damage inspections up to failure.

The Straw Blocks specimen could not be tested up to failure due to the limitations of the table; linear elastic behavior was observed until a PTA = 1.2 g in the ground floor configuration and a PTA = 0.7 g in the first floor configuration.

For future work it is recommended to investigate the influence of specimen and record-to-record variability on the findings of the current study.

ACKNOWLEDGEMENTS

This work is part of the research project “Beoordelingskader voor herstel en versterking bij aardbevingen” which was performed by TNO in cooperation with Strating, Remix Droge Mortel, FeNB2, Fischer, Straw Blocks Systems, Wienerberger, BuildinG, and EPI-Kenniscentrum. The research is supported by the TKI Deltatechnologie.

REFERENCES

[1] J. van Elk, A. Mar-Or, L. Geurtsen, J. Uilenreef, D. Doornhof, Seimic hazard and risk assessment Groningen Field update for production profile GTS – raming 2019, NAM, 2019.

[2] F. Graziotti, A. Penna, G. Magenes, A comprehensive in situ and laboratory testing program supporting seismic risk analysis of URM buildings subjected to induced earthquakes, Bulletin of Earthquake Engineering, 2018.

[3] D. Dizhur, J.M. Ingham, L. Moon, M. Griffith, A. Schultz, I. Senaldi, G. Magenes, J. Dickie, S. Lissel, J. Centeno, C. Ventura, J. Leiti, P. Lourenco, Performance of masonry buildings and churches in the 22 February 2011 Christchurch earthquake, Bulletin of the New Zealand Society for Earthquake Engineering, 44, 4, 279-297, 2011.

[4] D. Dizhur, J. Campbell, A. Schultz, and J.M. Ingham, Observations from the 2010/2011 Canterbury earthquakes and subsequent experimental pull-out test program of wall-to-diaphragm adhesive anchor connections, Journal of the Structural Engineering Society of New Zealand, 26(1), April 2013.

[5] NZSEE, The seismic assessment of existing buildings – Technical guidelines for engineering consultants, Section C8 – Unreinforced Masonry Buildings, 2017.

[6] J.M. Ingham, M.C. Griffith, The performance of unreinforced masonry buildings in the 2010/2011 Canterbury earthquake swarm, Report to the Royal Commission of Inquiry into Building Failure Caused by the Canterbury Earthquake, http://canterbury.royalcommission.govt.nz/documents-by-key/20110920.46, 2011.

[7] K.T. Doherty, An investigation of the weak links in the seismic load path of unreinforced masonry buildings, PhD thesis, University of Ade-laide, 2000.

[8] J. Vaculik, Unreinforced masonry walls subjected to out-of-plane seismic actions, PhD thesis, University of Adelaide, 2012.

[9] A. Dazio, The effect of the boundary conditions on the out-of-plane behavior of unreinforced masonry walls, WCEE 14, Beijing, 2008.

[10] F. Graziotti, U. Tomassetti, A. Penna, G. Magenes, Out-of-plane shaking table tests on URM single leaf and cavity walls, Engineering Structures 125, 455-470, 2016.

[11] A.J. Bronkhorst, S.A. Verdenius, Triltafeltesten uit-het-vlak wandelementen: Fischer proefstuk en Referentie proefstukken, TNO 2019 R10923, 2019.

[12] A.J. Bronkhorst, S.A. Verdenius, Triltafeltesten uit-het-vlak wandelementen: ClickBrick proefstuk en Referentie proefstukken, TNO 2019 R10932, 2019.

[13] A.J. Bronkhorst, S.A. Verdenius, Triltafeltesten uit-het-vlak wandelementen: Remix/Strating proefstuk en Referentie proefstukken, TNO 2019 R10933, 2019.

[14] A.J. Bronkhorst, S.A. Verdenius, Triltafeltesten uit-het-vlak wandelementen: Straw Blocks proefstuk en Referentie proefstukken, TNO 2019 R10934, 2019.

[15] F. Graziotti, U. Tomassetti, A. Rossi, S. Kallioras, M. Mandirola, E. Cenja, A. Penna, G. Magenes, Experimental campaign on cavity-wall systems representative of the Groningen building stock, EUC318/2015U, EUCENTRE, Pavia, Italy, 2015.

[16] H. Crowley, J. Bommer, R. Pinho, Selection of records for nonlinear dynamic analysis of Groningen buildings, version 1.0, 13th May 2015.

EURODYN 2020
XI International Conference on Structural Dynamics
M. Papadrakakis, M. Fragiadakis, C. Papadimitriou (eds.)
Athens, Greece, 23–26 November 2020

AN EXPERIMENTAL STUDY ON THE RELATIONSHIP BETWEEN EARTHQUAKE DAMAGE AND THE NATURAL FREQUENCY OF WOODEN HOUSE

Kazuhiro Hayashi [1], Ariyoshi Yamada [2] and Yoshiyuki Komiya[2]

[1] Toyohashi University of Technology
1-1 Hibarigaoka, Tempaku-cho, Toyohashi, Aichi, Japan
e-mail: hayashi@ace.tut.ac.jp

[2] Hakusan Corporation
J Tower 10F, 1-1 Nikko-cho, Fuchu, Tokyo, Japan
{yamadaa, yoshiyuki.komiya}@hakusan.co.jp

Keywords: E-defense, High seismic grade, Primary natural frequency, Amplitude dependent, Damage evaluation

Abstract. *The 1995 Kobe earthquake and the 2011 Tohoku megathrust earthquake caused catastrophic consequences to a large number of wooden houses. A quick damage evaluation of houses in a disaster-stricken area is important to avoid confusion after an earthquake. In recent years, several methods have been examined to monitor aseismic performance of wooden houses, aiming at detecting damage by measuring changes in the dynamic characteristics of buildings before and after an earthquake, such as natural periods.*

In 2019, a shaking table test of a full-scale wooden house was conducted at E-Defense, NIED. The test specimen was a frame-type three-story wooden house (Japanese seismic grade index: 3). In the three directional shaking table test, the main excitation consisted of six JMA Kobe waves and four JR Takatori waves at different amplitudes. The maximum horizontal acceleration of each of the excitations ranged from 1.79 m/s2 to 14.43 m/s2. In the experiment, damage to the specimen gradually increased at each shaking. Eventually, the maximum story drift angle of the first story reached 1/19.

The authors examined the relationship between earthquake-induced damage and the reduction of natural frequency by microtremor measurement. In the experiment, the natural frequency of the wooden houses showed an insignificant decrease within the maximum story drift angle of 1/300 or less. A significant reduction of the primary natural frequency occurred after the drift angle exceeded 1/50 and the house was damaged to some extent. Even in the ultimate state where the maximum story drift angle exceeded 1/20, the primary natural frequency was 60% or larger than the original state.

1 INTRODUCTION

The 1995 Kobe earthquake [1] and the 2011 Tohoku earthquake [2] caused catastrophic consequences to many wooden houses. A quick damage evaluation of houses in a disaster-stricken area is important to minimize confusion after an earthquake. In recent years, several methods have been examined to monitor aseismic performance of wooden houses, aimed at detecting damage by measuring changes in the dynamic characteristics of buildings before and after an earthquake, such as natural periods [3, 4].

In this paper, the authors examined the relationship between earthquake-induced damage and the reduction of natural frequency by microtremor measurement based on the experimental results of a shaking table test of a full-scale wooden house.

2 E-DEFENSE SHAKING TABLE TEST

E-Defense of NIED (National Research Institute for Earth Science and Disaster Resilience, Japan) is the world's biggest shaking table (15m x 20m), and can precisely reproduce three-dimensional ground motion, such as that recorded at the Kobe Earthquake, with a test model of 1,200 tf on the shaking table.

2.1 Specimen

In 2019, a shaking table test of full-scale wooden houses was conducted at E-Defense. Two 3-story wooden houses were used for the test (see Figure 1): an adopted Post and Beam (P&B) structure, and a Shear-Wall (SW) structure. Both were built following the generic construction methods of Japanese Grade-3 index buildings (these seismic performances are 1.5 times the required level of the Japanese design code). The house's outer wall, interior, kitchen, bathroom, furniture and fixtures were prepared for the test, in addition to its structural members. This paper only discusses the P&B specimen. As shown in Figure 2, the base-isolation system was installed under the RC footing of the P&B specimen.

Figure 2 shows a plan view of each floor. As shown in Figure 2, seismographs and micrometers were placed on the 1st and 3rd floor.

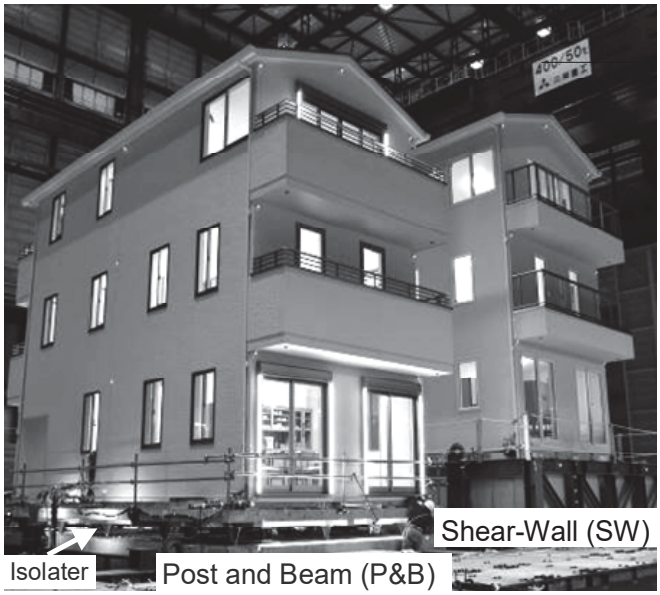

Figure 1: Two 3-story wooden houses.

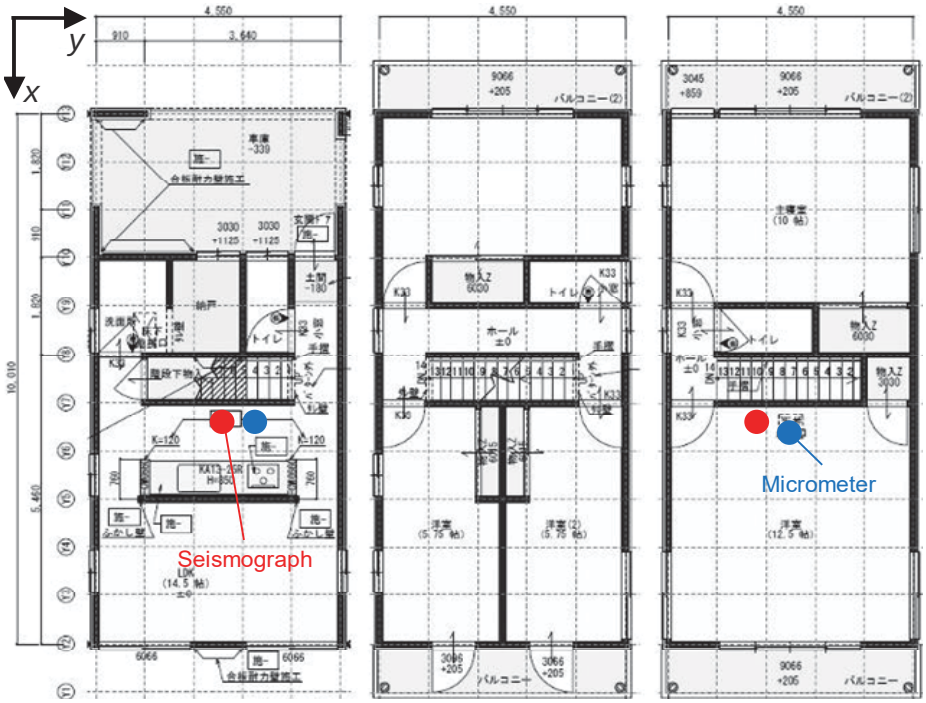

(a) 1st Floor (b) 2nd Floor (c) 3rd Floor

Figure 2: Plan view of P&B specimen.

2.2 Input waves

The shaking table test was programmed to impose gradually progressive damage to the wooden houses using input waves of gradually increasing amplitude. A total of six JMA Kobe waves (see Figure 3) of different amplitudes and four JR Takatori waves (see Figure 4) were used. The maximum horizontal acceleration of each main excitation ranged between 1.79 m/s^2 to 14.43 m/s^2. Table 1 shows the maximum acceleration for each excitation.

In the excitation I to VI, the base-isolation system was functioning. The device was then removed, and the footing of specimen was fixed to the shaking table.

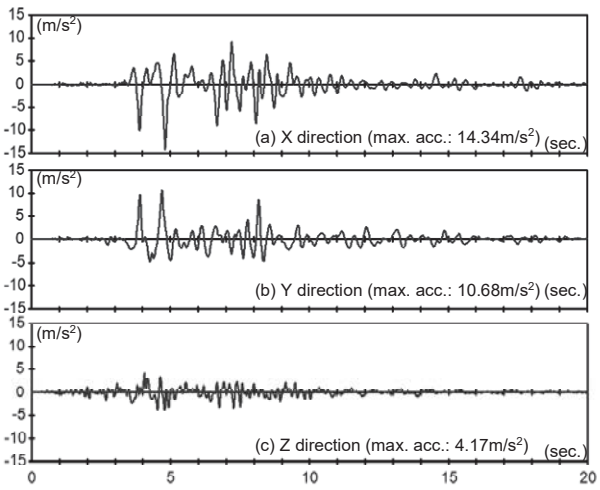

Figure 3: JMA Kobe Wave 100% (Excitation IX).

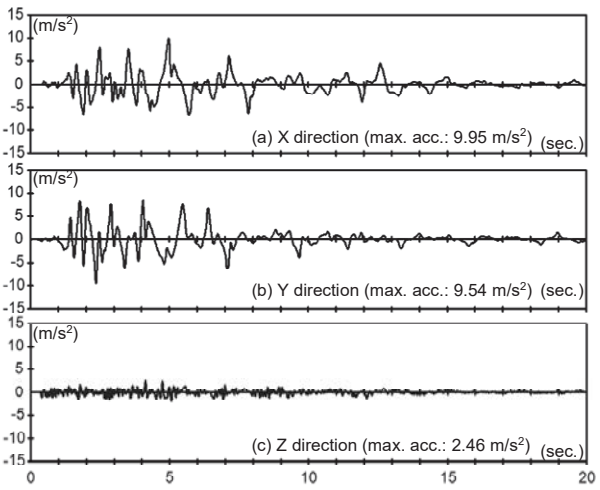

Figure 4: JR Takatori Wave 100% (Excitation X).

Table 1: Example of the construction of one table.

Excitation Number	Input Wave	Maximum Acceleration (m/s^2)			Footing	Maximum Story Drift Angle (1st story)		Microtremor Measurement
		X dir.	Y dir.	Z dir.		X dir.	Y dir.	
I	JMA Kobe 25%	2.21	1.90	0.87	Base isolation	1 / 1,250	1 / 1,111	(1) Original
II	JMA Kobe 50%	5.15	4.24	1.94		1 / 833	1 / 909	
III	JR Takatori 25%	1.87	1.79	0.38		1 / 1,250	1 / 1,250	
IV	JR Takatori 50%	4.10	4.16	0.90		1 / 769	1 / 588	(2) After Excitation IV
V	JMA Kobe 100%	14.43	11.02	4.15		1 / 588	1 / 400	
VI	JR Takatori 100%	962	9.19	2.56		1 / 400	1 / 313	
VII	JMA Kobe 25%	2.22	1.90	0.78	Fixed	1 / 769	1 / 526	(3) After Excitation VI
VIII	JMA Kobe 50%	5.06	4.28	1.82		1 / 145	1 / 128	
IX	JMA Kobe 100%	14.34	10.68	4.17		1 / 27	1 / 49	
X	JR Takatori 100%	9.95	9.54	2.46		1 / 19	1 / 36	(4) After Excitation X

2.3 Microtremor measurement

As shown in Table 1, microtremor measurements were taken four times. The first measurement (1) was performed before Excitation I. At this time, the specimen was non-damage (original condition). The second measurement (2) was after Excitation IV, and the third measurement (3) was after Excitation VI. Thus far, the specimen was a base-isolation system. The last measurement (4) was conducted after all the shaking table tests. This measurement results included the damage to the specimen that occurred after the footing was fixed to the shaking table.

2.4 Damage to the wooden house

In Table 1, the maximum story drift angle (SDA) of the test specimen (1st story) during the main excitation is shown. Until excitation IV (JMA Kobe 25%, 50%, and JR Takatori 25%, 50%), the maximum story drift angle was 1/500 or less, indicating an elastic behaviour. In excitation VI (JR Takatori 100%), the maximum story drift angle exceeded 1/400. The interior wall cloths were partially cracked, although the degree level of plasticization was not high. The base-isolation system of the specimen was functioning normally. In excitation IX and X (JMA Kobe 100% and JR Takatori 100%), the maximum story drift angle exceeded 1/50, and significant damage occurred, as shown in Figure 5.

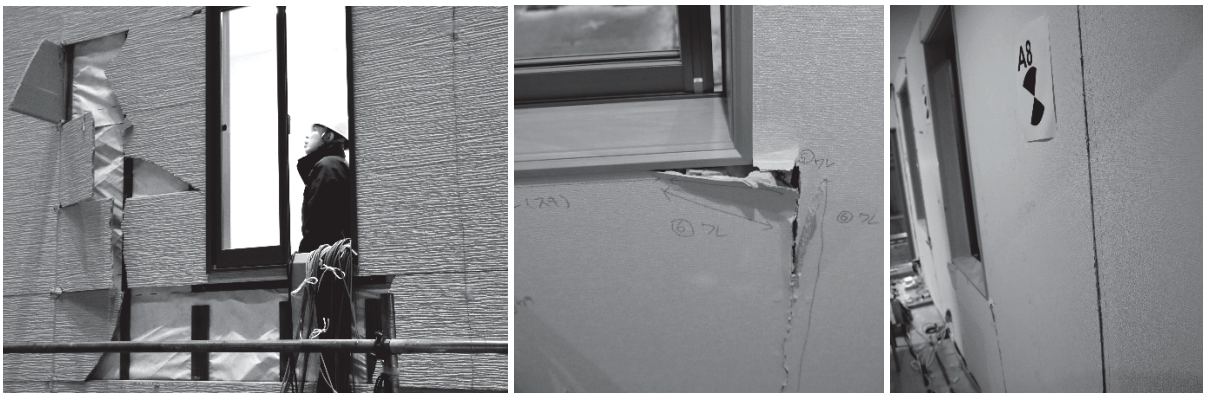

Figure 5: Damage of test specimen.

3 RESULTS OF MICROTREMOR MEASUREMENT

Figures 6 and 7 show the transfer function between 3rd floor acceleration response and 1st floor. Figure 6 is the *X* direction (the long side of the test specimen), and Figure 7 the *Y* direction (the short side). Red lines show the microtremor measurement (1), blue lines show the measurement (3), and purple lines show the measurement (4). In a non-damage condition (the original), the natural frequencies (the peak amplitude of the transfer function) of the test specimen were: *X* direction, 6.18 Hz, *Y* direction, 4.81 Hz. After Excitation VI, when the maximum story drift angle reached 1/400 to 1/313, the natural frequencies changed to 5.86 Hz (95% of the original) and 4.71 Hz (98%). In this range, the variations of natural frequencies were small, even though the test specimen (wooden house) was damaged. After Excitation X when the maximum story drift angle exceeded 1/50, the natural frequencies decreased to 3.86 Hz (62% and 80% of the original).

Figures 8 show the natural frequency - the maximum story drift angle relationship. In the experiment, the natural frequency of the wooden houses showed an insignificant decrease within the maximum story drift angle of 1/300 or less.

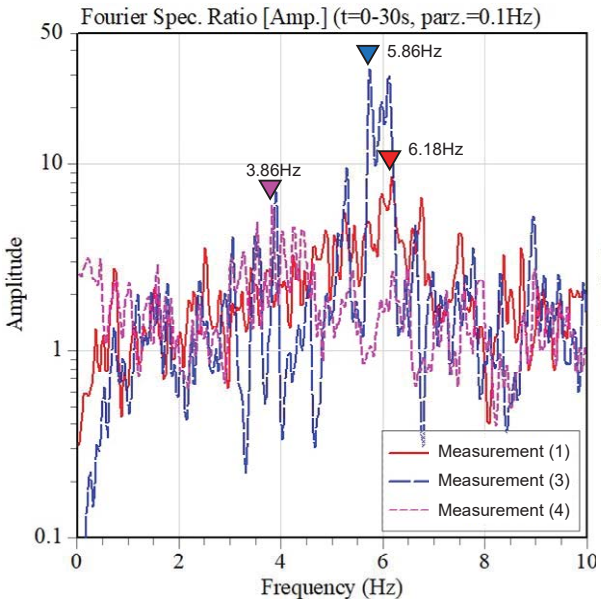

Figure 6: Transfer function of *X* direction.

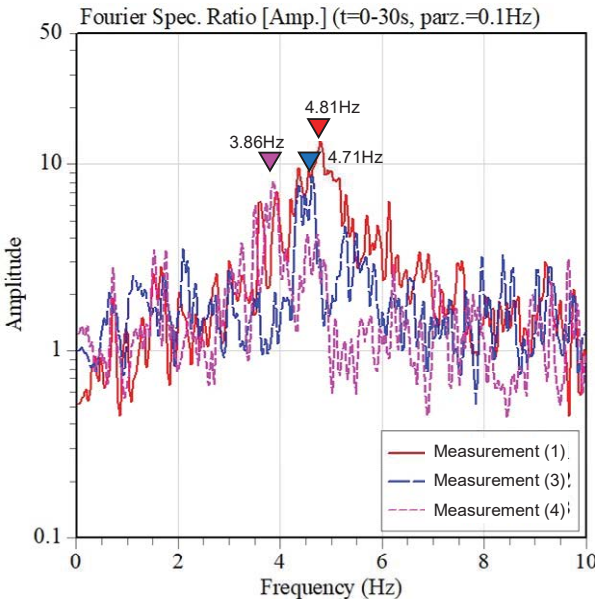

Figure 7: Transfer function of *Y* direction.

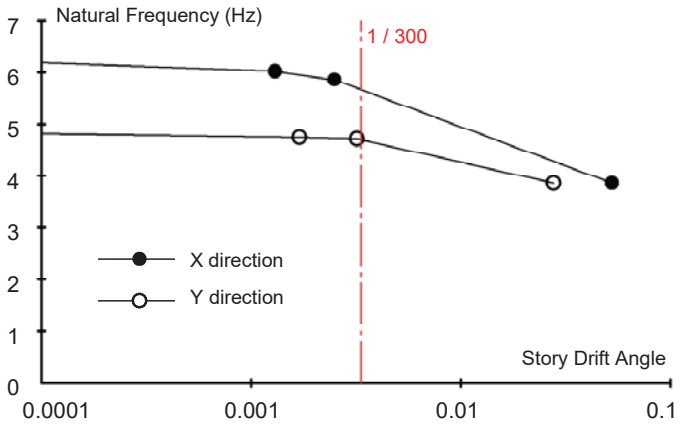

Figure 8: Natural Frequency - Maximum Story Drift Angle Relationship.

4 CONCLUSIONS

This paper examined the relationship between earthquake-induced damage and the reduction of natural frequency by microtremor measurement based on a shaking table test of a full-scale wooden houses conducted at E-Defense, NIED. The excitation consisted of six JMA Kobe waves and four JR Takatori waves at different amplitudes. In the experiment, damage to the specimen gradually increased at each shaking. Eventually, the maximum story drift angle of the first story reached 1/19.

The natural frequency of the wooden houses showed an insignificant decrease within the maximum story drift angle of 1/300 or less. A significant reduction of the primary natural frequency occurred after the drift angle exceeded 1/50, and the house was damaged to some extent. Even in the ultimate state where the maximum story drift angle exceeded 1/20, the primary natural frequency was 60% or larger than the original state.

ACKNOWLEDGEMENTS

The present work is partially supported by Tokyo Metropolitan Resilience Project of National Research Institute for Earth Science and Disaster Resilience (NIED). The authors are also grateful to Associate Professor Takuya Nagae of Nagoya University, Dr. Takahito Inoue and Dr. Takehiro Takahashi of NIED for their valuable assistance throughout this project.

REFERENCES

[1] Editorial Committee for the Report on the Hanshin-Awaji Earthquake Disaster, *Report on the 1995 Hanshin-Awaji Earthquake disaster*, 1998. (in Japanese)

[2] Joint Editorial Committee for the Report on the Great East Japan Earthquake Disaster, *Report on the 2011 Great East Japan Earthquake disaster*, 2015. (in Japanese)

[3] A. Sone, S. Yamamoto and A. Masuda, "Identification of dynamic characteristics of structure and its change by using wavelet analysis of records of microtremor and response of structure on ordinary condition and during strong shock," *Journal of Structural and Construction Engineering (Transactions of AIJ)*, Vol. 61, No.490, pp.65-72, 1996.12. (in Japanese)

[4] S. Saito, M. Sugino and Y. Hayashi, "Evaluation of deformation dependency of primary natural frequency decrease rate of low-rise houses by microtremor measurement: on Japanese conventional wooden, light-gauge steel, and traditional wooden structure," *Journal of Structural and Construction Engineering (Transactions of AIJ)*, Vol. 84, No.757, pp.343-350, 2019.03. (in Japanese)

[5] C. Yenidogan, T. Nagae, R. Nishi, T. Takahashi, Y. L. Chung, J. Chen, K. Shinagawa, Y. Kawamata, S. Yamada, H. Kashiwa, K. Hayashi, T. Inoue, M. Furuta, T. Oyokawa, S. Hirano, T. Iizuka, Y. Niitsu, S. Uwadan, S. Takeuchi, H. Waki, S. Shimoda, K. Suzuki, K. Anahara, A. Suganuma, I. Nakamura, "E-Defense test on functionality of three-story residential houses including underground pipe lines (Metropolitan resilience PJ) Part.5-22," *Summaries of Technical Papers of Annual Meeting, AIJ*, Structures-III, pp.634-668, 2019.09. (in Japanese)

EURODYN 2020
XI International Conference on Structural Dynamics
M. Papadrakakis, M. Fragiadakis, C. Papadimitriou (eds.)
Athens, Greece, 23–26 November 2020

PERFORMANCE OF A LINEAR SOLUTION FOR APPROXIMATING NONLINEAR RESPONSE OF REINFORCED CONCRETE STRUCTURES SUBJECTED TO EARTHQUAKE SHAKING

Kevin Kariuki[1], Tarjei Heen[1], Lars Halvor Kaasa[1], and Amir M. Kaynia [2,3]

[1]Dr. Ing. A. Aas-Jakobsen
Lilleakerveien 4a, 0283 Oslo, Norway
e-mail: {kka,the,lhk}@aaj.no

[2] Department of Structural Engineering, Norwegian University of Science and Technology, Richard Birkelandsvei 1a, 7491 Trondheim, Norway
e-mail: amir.kaynia@ntnu.no

[3] Norwegian Geotechnical Institute, P.O- Box 3930 Ullevaal Stadion, 0806 Oslo, Norway
e-mail: amir.m.kaynia@ngi.no

Keywords: Seismic analysis, Nonlinear analysis, Suspension bridges, Concrete pylons.

Abstract. *Nonlinear Time History Analyses (NTHA) are generally regarded as the most accurate way of predicting the dynamic response of a structure to a given seismic ground motion. However, these types of analyses are computationally demanding and require proper software. The aim of this paper is to investigate the feasibility and accuracy of an Equivalent Linear analysis (ELA) where material nonlinearity is accounted for through an iterative procedure with the use of secant stiffnesses. The method is applied to one of the pylons of a major suspension bridge recently designed in Chile. For comparative purposes, two models are created in the open-source framework OpenSees: 1) a full nonlinear fiber model where nonlinear material behaviour is accounted for through distributed plasticity, and 2) an elastic model where the element flexural stiffnesses are updated using the ELA method. The analyses are carried out for seven earthquake time histories. The results show that the ELA is able to reproduce the maximum forces in the structure with a satisfactory accuracy. However, the method is not able to capture regaining of stiffness once cracks are closed due to cyclic responses.*
For further verification, several pushover analyses are also conducted on both models with the inertial forces extracted from the most unfavourable time-steps in the nonlinear time domain analysis. The pushover analysis verifies that the ELA method is capable of predicting the structural response up to the point of yielding of the steel reinforcement or crushing of the concrete. Nevertheless, the method is fairly accurate in identifying possible plastic hinges, and to some degree, assessing the ductility of the structure.

1 INTRODUCTION

Large suspension bridges are particularly susceptible to earthquake excitation due to their slender configurations. When built in seismic active areas, earthquake induced forces often become the most prominent design criteria, thus accurately capturing this effect during design calculations are of top priority. This is no exception for the Chacao Bridge, which upon completion will connect the island of Chiloé to the Chilean mainland. The suspension bridge spans approximately 2750 meters, divided into two main spans of 1155 and 1055 meters supported by three pylons. The Norwegian consultant company Aas-Jakobsen participated in the international design team tasked with designing the bridge. One of the firm's task was design of the bridge pylons. The northern and southern pylons consist of two pylon legs connected by three girders, all of which are made from hollow Reinforced Concrete (RC) sections. With the bridge located in one of the most seismic active regions in the world, namely the subduction zone between the Nazca Plate and the South American Plate [1, 2], a complete time history analysis (THA) was deemed necessary to predict the structures response to a seismic event. The analysis was carried out in RM-Bridge [3] with seven ground motion records corresponding to a seismic event with a return period of 1030-years (Maximum Probable Earthquake) [4].

Although widely recognised as an accurate way of capturing the behaviour of structures subjected to cyclic dynamic forces [5], running a full NTHA on large structures such as the Chacao Bridge quickly becomes a momentous task and convergence is not guaranteed. If, however, the sections of the structure are expected to exceed their elastic domain during an seismic event, the forces resulting from an THA may be too conservative since the ductile behaviour of the structure is not captured [6].

To cope with the issue of overestimating forces when designing the Chacao Bridge pylons, an iterative procedure was proposed, hereby referred to as the ELA. First, the nonlinear moment-curvature relation was calculated for each section in the Finite Element (FE) model. Then, a series of elastic THAs was carried out using the same ground motion record. Following each analysis, the largest absolutes moment for each section was obtained and used together with the appropriate moment curvature relation to determine the secant stiffness of that section. A new elastic model with updated stiffness properties was then established. When the flexural stiffnesses of the sections converge after a number of THAs, the nonlinear material response of the structure is considered approximately captured. The final iteration with converged stiffness properties will therefore in principal have the same resulting forces as those following a full NTHA. An elastic analysis with secant stiffnesses is allowed by the AASHTO Seismic Design Manual, as long as the distribution of forces are verified to be consistent with expected nonlinear behaviour [7]. The use of cracked stiffness properties is also recommended by the Eurocode 8 when performing a linear elastic analyses [8]. However, it appears that little attention has been paid to investigate the consistency between the two methods. A comparative study was therefore conducted using the South Pylon of the Chacao Bridge. A FE model with linear elastic elements was developed in OpenSees [9], onto which the ELA could be conducted. A second model with nonlinear material properties was used as a baseline. Finally, multiple pushover analyses were performed for further verification of the methods capabilities.

2 MODEL DESCRIPTION

2.1 OpenSees Model

The FE model of the South Pylon in this study was established in the open source software framework OpenSees [9]. The geometry and material properties of the models were based on

the RM-Bridge model previously created by Aas-Jakobsen during the design of the Chacao Bridge with minor modifications. The suspension cables were simplified as springs at the top of each pylon leg. Additionally, the foundation SSI-matrices were simplified by neglecting off-diagonal terms and modelling the remaining parts as linear springs.
For the comparative purpose of this study, two models were established; a model with nonlinear material properties using the fiber section functionality provided in OpenSees and a linear elastic model. The nonlinear fiber model utilized the built-in material models *Concrete02* [10] and *Steel02* [11] for the concrete and reinforcement fibers, respectively. The moment-curvature relations used in the ELA were obtained with the same material models. The chosen material parameters are summarized in Tables 1 and 2.

Parameter	Symbol	Value
Expected maximum compressive strength	f_{pc}	58.5 MPa
Initial modulus of elasticity	E_{cm}	32.1 GPa
Strain at maximum compressive strength	ε_{c0}	3.64 ‰
Ultimate compressive strength	f_{pcu}	49 MPa
Ultimate compressive strain	ε_{cu}	5 ‰
Expected tensile strength	f_t	4.05 MPa
Tensile softening stiffness	E_{ts}	4.41 MPa
Ratio between unloading and initial slope	λ	0.5

Table 1: *Concrete02* material parameters.

Parameter	Symbol	Value
Expected yield strength	f_y	470 MPa
Young's modulus	E_s	200 GPa
Yield strain	ε_y	2.35 ‰
Strain hardening ratio	b	0.06
Isotropic hardening parameter	a_1	0
Isotropic hardening parameter	a_2	1
Isotropic hardening parameter	a_3	0
Isotropic hardening parameter	a_4	1
Asymptote parameter	R_0	0.20
Asymptote parameter	cR_1	0.925
Asymptote parameter	cR_2	0.15

Table 2: *Steel02* material parameters.

P-Δ transformation was applied in order to capture nonlinear geometry effects, with the pylon carrying gravity loads from the bridge deck in addition to its self weight resulting in severe compression forces. Damping was included as Rayleigh damping, with a chosen target damping ratio of 5 % for the two fundamental modes in the longitudinal and transverse directions of the bridge.

2.2 Model verification

As the discretization of the fiber section is important for the performance of both the full nonlinear analysis and the ELA method, a study on discretization was conducted to decide on the appropriate average size of the concrete fibers in the pylon. The study was performed by calculating the moment-curvature diagrams for representative sections along the pylon with varying axial forces. The results revealed that a mesh consisting of 25×10 concrete fibers per side of each pylon leg element was sufficiently accurate without restricting the efficiency of the analyses, as seen in Figure 1.

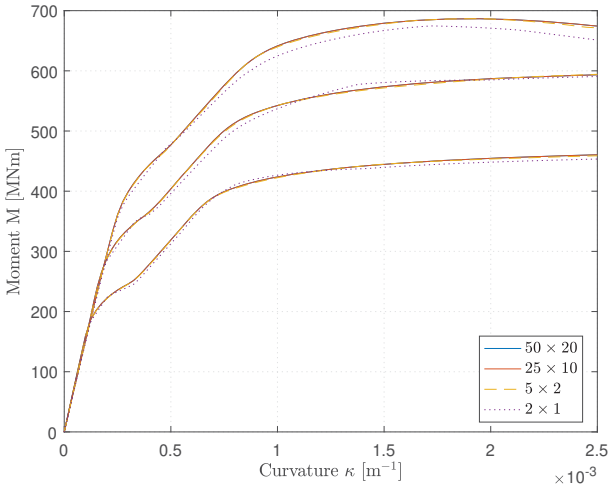

Figure 1: Moment-curvature relations for different meshing and axial load.

The modal properties of the two models were compared to verify that their initial stiffnesses and therefore initial dynamic properties would be similar. The mean deviation of modal periods for the first 20 modes is 1.26%, with a maximum deviation of 2.15% in mode number 20. This was deemed sufficiently accurate to assume similar initial behaviour between the models under both static and dynamic loading.

3 ANALYSIS PROCEDURE

3.1 Equivalent Linear Analysis

The algorithm for the ELA was developed using a combination of the THA solver in OpenSees and MATLAB for post-processing data. The method is largely based on nonlinear moment-curvature relations for the RC sections, so these are initially computed by performing a section response analysis for each fiber section in OpenSees. Since this relation depends on axial force, seen in Figure 2a, a series of different scaling of the gravity load was applied so that each element had a number of moment-curvature diagrams associated with it. The stiffness properties of the initial linear elastic elements were taken as the slope of the tangent at the origin for the corresponding moment-curvature relations with unit gravity load. A full transient THA was then conducted in OpenSees using the the linear elastic model and Newmark's constant average acceleration method as time-stepping scheme. The selected ground motion was applied in both horizontal directions with a time step of 0.01 seconds. Data regarding forces, acceleration and displacements was recorded during the analysis and upon completion written to text files. MATLAB was then invoked to post process the results. For each element, MATLAB scripts obtained the maximum moment about both principle axes along with the corresponding axial forces. The

updated stiffness about each axis was then obtained by finding the intersection point between the moment and the appropriate moment-curvature relation, as shown in Figure 2b. By making use of the relation

$$EI = \frac{M}{\kappa} \tag{1}$$

where M and κ is the moment and curvature about the section axis, the secant stiffness was taken as the slope of a line going through the origin and the intersection point. Since the axial load changes for each iteration during the procedure, the intersection point was linearly interpolated between existing curves, enveloping moment-curvature relations so to avoid recomputing these for each iteration.

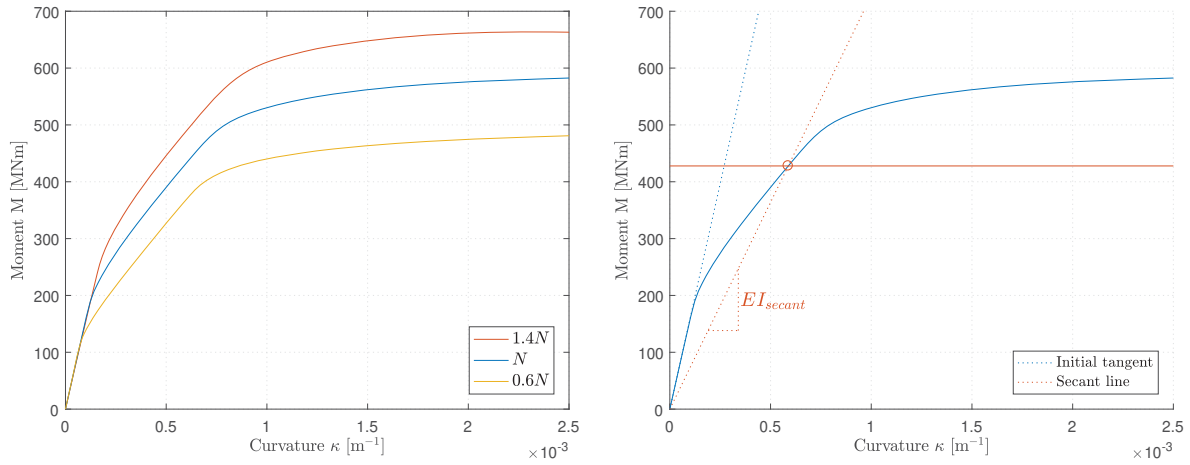

(a) Effect of compressive load for M-κ relation.

(b) Secant line in M-κ relation.

Figure 2: Determination of secant line using moment.

The updated stiffness for each element was taken as the mean between the newly acquired and previous value, to ensure smoothness during the scheme. A new linear elastic model with updated stiffness properties was then created. If the newly obtained stiffness values differed significantly from the previous ones, another iteration was initiated using the updated model. The iterations continue until the change in all element stiffnesses falls below a given convergence threshold.

3.2 Pushover Analysis

The pushover analyses were conducted with inertial forces as basis for the load distribution. For each critical element, e.g. base elements in the pylon legs or cross-beams, the total acceleration in each node was retrieved for the time-step where the maximum bending moment appeared for that element. The different total acceleration profiles were then multiplied with the mass matrix to obtain the inertial forces which were set as the load level for load factor $\lambda = 1$. The obtained distributions were then scaled from $\lambda = 0$ until the solution failed to converge. This procedure was conducted on both the full nonlinear model, as well as the one using the ELA iteration scheme.

4 ANALYSIS RESULTS

4.1 THA

The results from the time history analyses show that in general the ELA method was able to capture maximum bending moments in critical sections of the pylon. Table 3 summarizes the maximum forces in selected elements of the pylon, averaged over all seven ground motions for both the initial elastic model and the reduced stiffness model obtained through ELA. The average reduction ratios from the initial stiffness of the elements are also included in the table. The moments are normalized by the bending moment values following the NTHA by using the formula

$$M^* = \frac{M}{M_{fiber}} \tag{2}$$

Element	Ratio	$M^*_{y,initial}$	$M^*_{y,final}$	$M_{y,fiber}$ [MNm]
4101	0.63	1.12	1.06	338
4103	0.80	1.11	1.03	274
4106	0.99	1.10	0.96	187
4112	0.99	1.04	1.21	92
4115	0.82	1.10	1.11	192
4120	1.00	1.04	1.03	53
4501	0.31	1.27	1.03	185
4701	0.35	1.13	1.01	137

Table 3: Summary of average normalized bending moments about the bridges transverse axis.

Figure 3 and 4 plot the displacement and moment response histories of the full nonlinear fiber model, the initial elastic model and the converged model using the ELA for one of the input ground motions. The maximum bending moment response for each model is highlighted in the plot. Figure 5 shows the maximum absolute value of the bending moments at the base of the pylon normalized against the bending moment response of the fiber section model, with the average values across all seven ground motions plotted at the bottom.

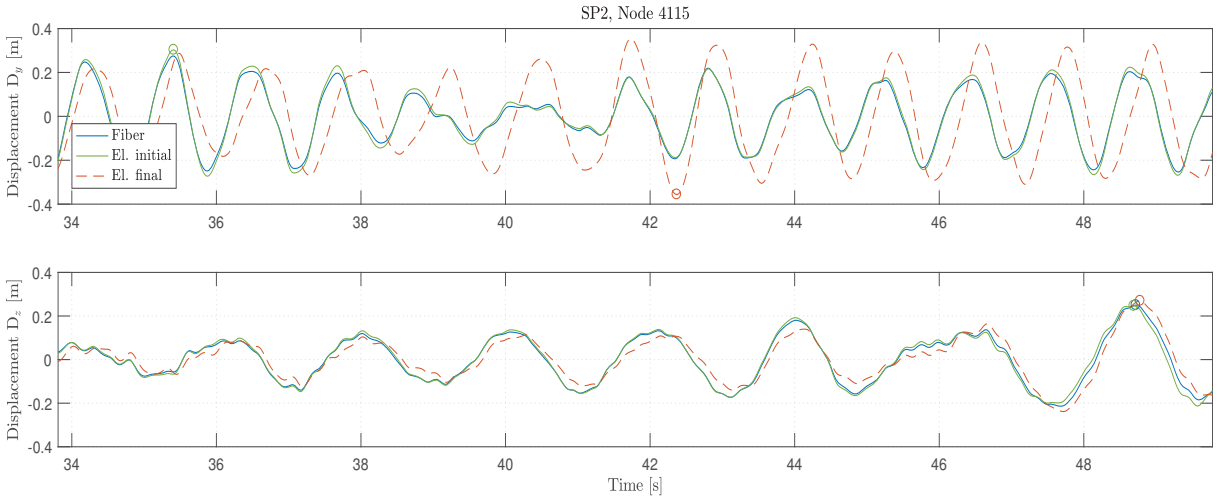

Figure 3: Displacement response history of upper part of pylon.

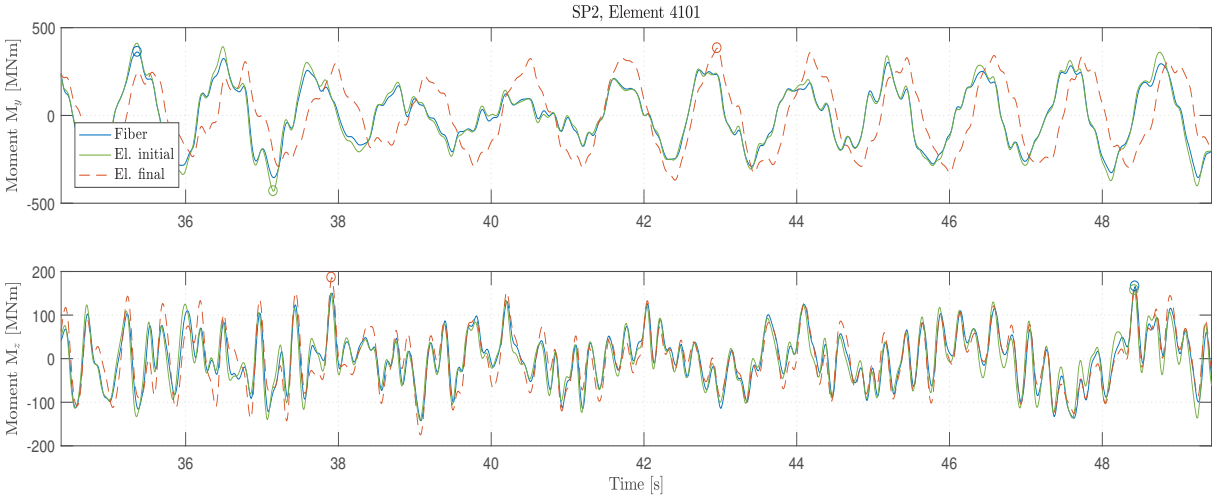

Figure 4: Moment response history in base of pylon.

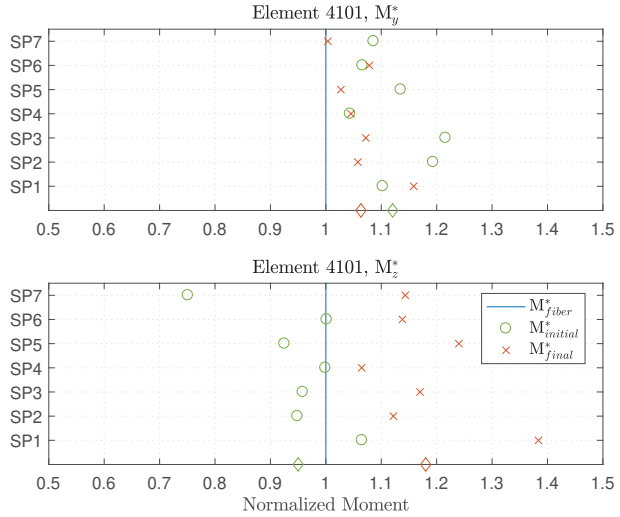

Figure 5: Moment response history of element 4101.

When studying the time histories for the various input ground motions, it is clear that in the ELA performed well in approximating the bending moments in the pylon. From Table 3, the largest deviation between the final iteration of the ELA and the full nonlinear model was 21%, which occurs in element 4112. A possible reason for the deviation in this element is the combination of low bending moment levels and large deflections in this particular area of the pylon. This in turn means that the forces and therefore reduction ratios are largely governed by the stiffness of the remaining elements of the pylon and consequentially second order geometrical effects plays a significant role. This effect can also be seen in the bottom part of Figure 5, where the M_z values appear quite spurious, and are in general larger for the final iteration of the model based on the ELA than the model with initial stiffnesses. This is a general trend in areas with small bending moments and can be attributed to second order geometrical effects.

For the remaining elements listed in the table, the largest deviations were in the range of 1-11%, which from an engineering point of view is acceptable for an approximate method. For the displacement time histories, the model using the ELA was slightly shifted in its response compared to the model with initial stiffnesses and the full nonlinear model. This is is explained

by the fact that the stiffness of the various elements in the ELA model are based on the largest forces throughout the response history. The ELA model also does not include closing of cracks which in sum yields a lower stiffness and therefore larger, phase-shifted displacements.

4.2 Pushover analysis

The pushover analyses conducted in this study served as a foundation for verifying the results from the THAs, as well as a separate examination for comparing the response of structures using the ELA and nonlinear material models. Figure 6 plots the load-displacement pushover curve for the analysis L1, while Figure 7 plots the moment distributions for load factor $\lambda = 1$ and $\lambda = 1.5$ where the latter is the load factor where the model using the ELA failed to converge. Analysis L1 corresponds to the inertial force level and distribution which yields the largest bending moments at the base of the western pylon leg, that is, element 4101. The results for the base and upper part of the pylon are summarized in Table 4.

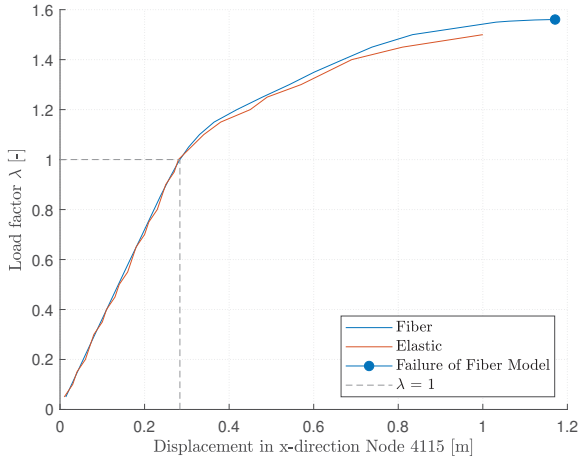

Figure 6: Force-displacement pushover curve for analysis L1.

When transient and cyclic effects are excluded, the pushover analyses shows the ELAs ability of accurately approximating the nonlinear model during static analysis. The various pushover analyses conducted demonstrate that the ELA performed well both up to the load level retrieved from the THAs and beyond. For design purposes, pushover analyses performed on models with the ELA method can be used to predict the location of possible plastic hinges. It can also be implemented to control safety factors for given load levels from transient analyses.

Element	Ratio $\lambda = 1$	$M^*_{\lambda=1}$	Ratio $\lambda = 1.5$	$M^*_{\lambda=1.5}$
4101	0.95	0.99	0.47	1.03
4201	0.95	1.00	0.47	1.04
4115	0.92	1.02	0.47	1.05
4215	0.93	1.01	0.31	1.04

Table 4: Summary of critical element for pushover analysis L1.

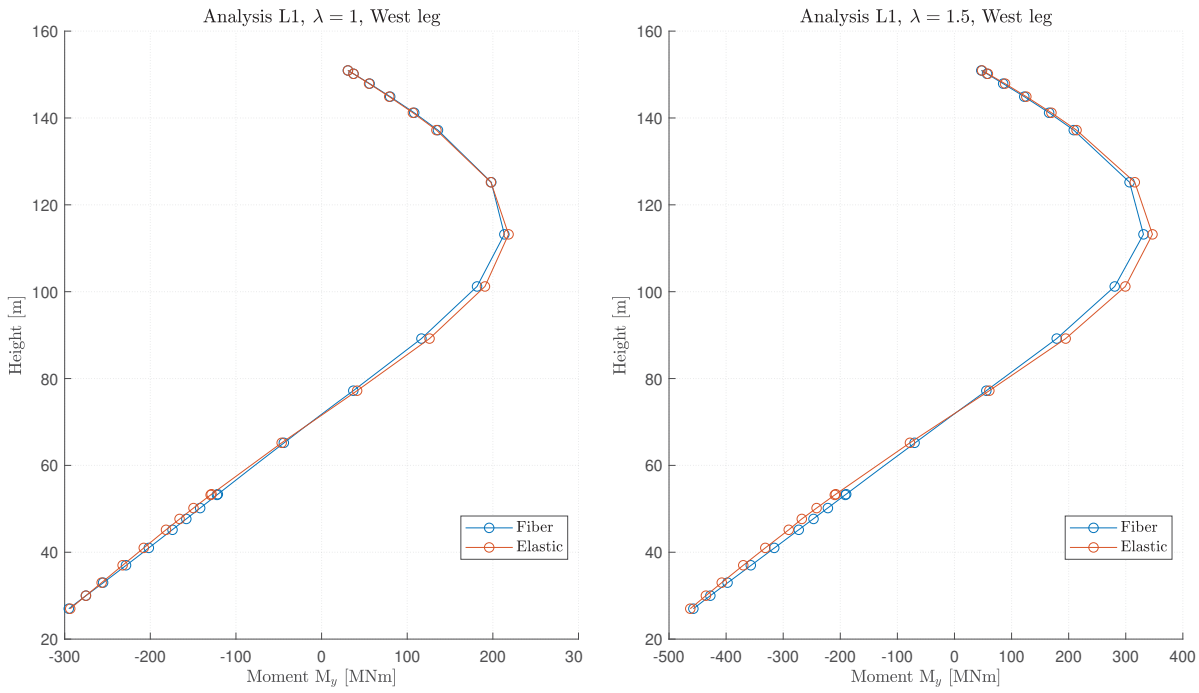

(a) (b)

Figure 7: Moment distribution in the pylon legs for analysis L1.

5 CONCLUSION

The goal of this study has been to assess if the the secant stiffness can provide a reasonable approximation to the nonlinear material behavior of structures. By assessing the forces succeeding ELAs and comparing these to the forces following full NTHAs, several remarks can be made. For the majority of elements the approximation of forces is satisfactory, especially for those enduring large moments during the THA. There are however anomalies where the ELA increases the gap between responses which may be rooted in the shortcomings of the method. Unlike a full NTHA, the ELA is not able to take effects such as cyclic degradation, closing of cracks and dissipation of energy due to cracking of the concrete into consideration. Further, since the stiffness reduction developments occur independent of each other during each iteration, information regarding interaction between elements is lost.The consequence of this is an overall softer structure, with certain unpredictable properties. Rather than using the stiffness values obtained following the ELA, it is proposed to use these as guidelines for creating new ones. By selecting stiffnesses enveloped by the initial and reduced values, more towards the latter, overestimation of stiffness reduction is counteracted. The resulting structure will then inherit a realistic crack distribution. The quality of the nonlinear approximation was confirmed by pushover analyses, where the ELA was capable of accurately producing similar bending moment and deflection patterns as the nonlinear fiber model. When reaching load levels where post-yield capacity was expected, the ELA produced bending moments with slightly higher values in the elements experiencing the largest stiffness reductions. This is due to how the ELA obtains secant stiffnesses for moments close to the section's ultimate capacity.

Overall, the ELA has proven to be a valid alternative to a full nonlinear analysis. The method is also code-compliant as it satisfies the requirements from both Eurocode 8 and the AASHTO Guide Specifications for LRFD Seismic Bridge Design with regards to providing results that are consistent with expected nonlinear material behaviour.

6 ACKNOWLEDGMENTS

This paper is partly based on the MSc thesis of the first two authors in the Department of Structural Engineering at the Norwegian University of Science & Technology (NTNU) [12]. These authors would like to thank Aas-Jakobsen for providing the neccecary resources for preparing this paper, as well as their general support for this study.

REFERENCES

[1] S.E. Barrientos. Earthquakes in Chile. *Geological Society Special Publication*, 01 2007.

[2] J. R. Elliott, E. Hussain, V. Silva, M. Villar-Vega, R. Amey, and G. Rauscher. Contrasting Seismic Risk for Santiago, Chile, from Near-field and Distant Earthquake Sources. In *AGU Fall Meeting Abstracts*, volume 2018, pages G13A–03, December 2018.

[3] RM Bridge. *Connect Edition*. Benteley Systems Incorporated, Exton, Pennsylvania, 2019.

[4] Aas-Jakobsen, SYSTRA, Hyundai Engineering & Construction, and OAS. *Dynamic Impedances and Foundation Input Motions*. Report CHB-SAJ-DGN-DOC-GB-0223, 2018. Not publicly available.

[5] Enrico Spacone, Filip C Filippou, and Fabio F Taucer. Fibre beam–column model for non-linear analysis of r/c frames: Part i. formulation. *Earthquake Engineering & Structural Dynamics*, 25(7):711–725, 1996.

[6] A.K. Chopra. *Dynamics of Structures: Theory and Applications to Earthquake Engineering*. Civil Engineering and Engineering Mechanics Series. Prentice Hall, 2012.

[7] American Association of State Highway, Transportation Officials. Subcommittee on Bridges, and Structures. *AASHTO Guide Specifications for LRFD Seismic Bridge Design*. American Association of State Highway and Transportation Officials, 2011.

[8] Standard Norge. *Eurocode 8: Design of structures for earthquake resistance - Part 1: General rules, seismic action and rules for buildings*. NS-EN 1998-1:2004+A1:2013+NA:2014, 2014.

[9] Frank McKenna, Silvia Mazzoni, Michael H. Scott, and Gregory L. Fenves. Opensees command language manual. *Open System for Earthquake Engineering Simulation*, 2006.

[10] Yassin MH Mohd. Nonlinear analysis of prestressed concrete structures under monotonic and cyclic loads. *PhD Thesis*, 1995.

[11] Filip Filippou, A D'Ambrisi, and A Issa. Effects of reinforcement slip on hysteretic behavior of reinforced concrete frame members. *ACI Structural Journal*, 96, 05 1999.

[12] Tarjei Heen and Kevin W. Kariuki. Investigative study on method for approximating non-linear material behavior in reinforced concrete structures subjected to seismic ground motions. *Master's thesis, Norwegian University of Science & Technology*, 2019.

EURODYN 2020
XI International Conference on Structural Dynamics
M. Papadrakakis, M. Fragiadakis, C. Papadimitriou (eds.)
Athens, Greece, 23–26 November 2020

BEHAVIOUR OF REINFORCED CONCRETE STRANDS DURING TENSION TEST INSPECTED WITH DIC

Haukur J. Eiriksson[1], **Bjarni Bessason**[1]

[1] Faculty of Civil and Environmental Engineering, University of Iceland
Hjardarhagi 2-6, 107 Reykjavik, Iceland
H.J. Eiriksson: e-mail: haukurj@hi.is, B.Bessason: bb@hi.is

Keywords: Reinforced concrete strands, bond slip, free length, DIC

Abstract. *Knowledge about the plastic behaviour of steel bars in reinforced concrete (RC) structures is important, especially for seismic design. The paper presents the results of experimental tests where the main aim was to observe the plastic deformations, interaction and bond-slip of reinforcement bars inside concrete strands. In standard tests of reinforcement bars the gauge length is 5d (i.e. five times the diameter of the bar). The tests on the concrete strands revealed that a length of 5d is not representative for the actual section length of the reinforcement bar, which develops free length inside the tested concrete strands that is longer than 5d.*

1 INTRODUCTION

Destructive testing of RC elements includes the risk of damaging conventional meters and sensors that are directly connected to the specimens. A non-contact optical technique known as Digital Image Correlation (DIC) is an alternative method where this risk is not a problem. The main principle of the DIC-method is to use camera and take continuously photos with short time interval of the test specimen during the loading of the test specimen. Digital image correlation technique is then used to match a selected facet on pictures taken of the surface of the test specimen before and after each load step, i.e. between pictures in the series, and thus follow the deformations throughout the entire test. The method can detect deformations anywhere on the surface of the specimen which is facing the camera. Meaning that "meters" can be located afterwards anywhere on the test specimen's surface, which is very convenient for crack development in concrete and necking in reinforcement bars in long test specimens.

The DIC technology has been applied for more than three decades. It was originally proposed by a group of researchers at the University of South Carolina, USA, early in the 1980s [1, 2]. Since then the method has been developed and refined and the algorithms have been improved [3, 4]. Improvements in digital camera technology in recent decades, e.g. higher resolution, have facilitated improvements in DIC analysis. The accuracy of the DIC analysis depends on the resolution of the camera used, the distance from camera to specimen, and by the fines and details of the pattern on the surface of the test specimen. The quality of the processing algorithms and software used to correlate the images is also very important.

The knowledge of how plastic deformations develop and how interaction and bond-slip of reinforcement bars inside concrete elements develop under seismic action is essential for rational and economical seismic design of RC structures. Number of experimental and analytical studies of bond slip in RC elements exists in the literature [5, 6, 7]. Some more recent studies have used the DIC technique in investigating bond slip [8, 9].

In this paper the results of experimental tests using DIC technique are presented where the main aim was to study the plastic deformations, interaction and bond-slip of reinforcement bars inside concrete strands. Prior to the testing of the strands, novel uniaxial DIC tests were done on long unboned reinforcement bars, i.e. bars without concrete confinement, in order to get basic information on both longitudinal and lateral plastic deformations of long ribbed steel bars [10]. The test results of the long steel bars help to explain the observed behaviour of the bond slip in the RC strands.

2 TEST SPECIMENS AND TEST SETUP

2.1 Reinforcement bars

Prior to the testing of the concrete strands, tests were made on eight reinforcement bars alone (i.e. not inside concrete) with the same length as the bars inside the concrete strands [10]. Six of the bars had thickenings at the ends and two of them were without thickenings (Table 1).

The reinforcement bars had a characteristic yield strength of min 500MPa and a strain at max stress of min 7.5% according to class C in Eurocode 2 [11]. The bars had two rows of transverse ribs and two longitudinal ribs. All the bars fulfilled the demands concerning strength, strain and geometry according to Eurocode 2 [11] and EN 10080:2005 [13].

The reinforcement bars were washed with hydrochloric acid (HCl), primed with a thin layer of matte white spray paint and finally marked manually with a black pen (Fig. 1).

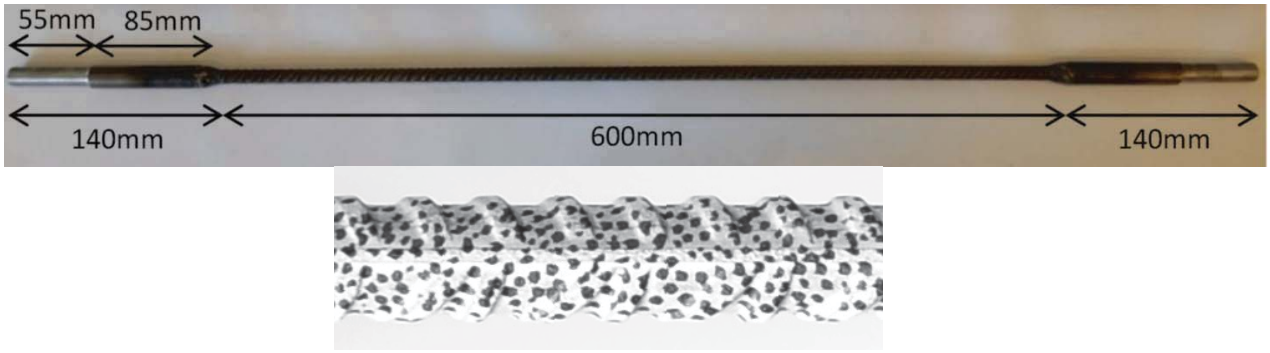

Figure 1: (a) Reinforcement bar (10mm) with thickenings at both ends that were used in two of the concrete strand test specimens. (b) The surface of the bars that were tested alone (Table 1) were dotted with black dots for the DIC analysis.

Test and bar no.	Diameter (mm)	Free length (mm)	Resolution of pictures (pixels/mm)	(mm/pixel)	Remarks
2.1, 2.2, 2.3, 2.4	10	775	9.01	0.111	Thickening at the ends
3.1, 3.2	10	775	7.43	0.135	Thickening at the ends
4.1, 4.2	10	775	7.43	0.135	No thickenings

Table 1: Overview of the reinforcement bars tested alone (i.e. not inside concrete), where the bars are numbered with the test number followed by a running number. The free length is the visible part of the bars between the grips of the testing machine.

2.2 Concrete strands

Tests were made on four concrete strands with a dimension of 100x100x740mm with one 10mm ribbed reinforcement bar located at the centre (Fig. 2, Table 2). The reinforcement ratio is 0.79%. The concrete had a cylinder compressive strength of 32MPa and an axial tensile strength of 23MPa. The concrete strands were primed and dotted the same way as the reinforcement bars (Fig. 2)

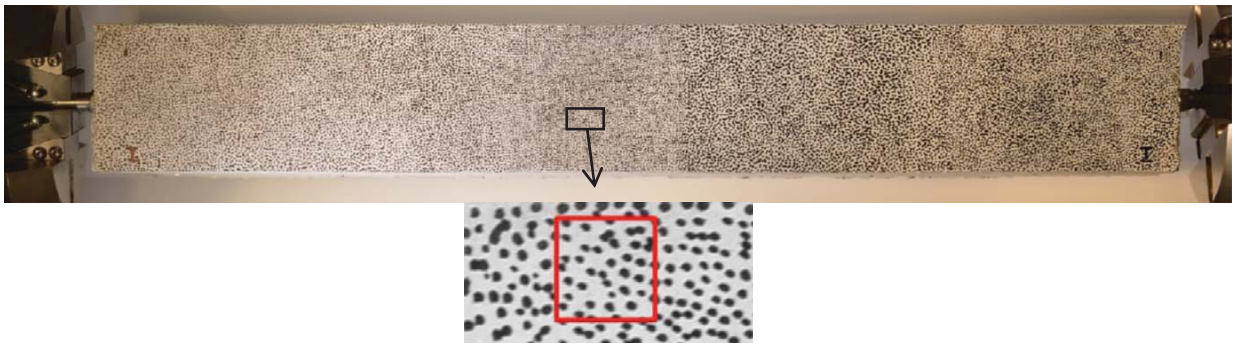

Figure 2: Concrete strand with ribbed reinforcement bar at centre (the test specimen on the picture is located vertically in the testing machine, but is here shown horizontally). The side that is facing the camera is dotted with black dots for the DIC analysis. The size of the dots can be seen inside the red box which is 10x10mm at size.

Concrete strand no.	Width (mm)	Length (mm)	Bar diam. (mm)	Resolution of pictures (pixels/mm)	(mm/pixel)	Remarks
1, 2, 3, 4	100x100	740	10	8.78	0.114	Bar in strands 1 & 2 had thickening at the ends

Table 2: Overview of the concrete strands tested.

Two of the concrete test specimens (strands 3 and 4) had a normal reinforcement bar, but the other two (strands 1 and 2) were equipped with bar with thickenings at the ends. The thickenings secured that the in-elastic behavior of the bars took place inside the concrete, as the stress in the thickenings was in the elastic state during the test. The thickenings consist of steel rods with a 16mm diameter that were welded to the reinforcement bars (end to end). The diameter was reduced to 14mm on the outermost 55mm so they fitted into the grips of the testing machine (Fig. 1).

2.3 Test setup, hardware and software

All tests (i.e. bars alone and the concrete strands) were executed in an Instron testing machine with a capacity of 500kN. A 500kN load cell was used to measure the applied load. The test setup for the concrete strands is shown on Fig. 3 and the test setup for the reinforcement bars alone was identical. The tests were executed in a displacement controlled mode at a speed of 0,1mm/sec. The elastic stress rate in the bars (in tests for bar alone) was within given limits in EN ISO 6892-1:2009 [12]. Pictures were taken with one second interval, but not all the pictures were though used in the DIC analysis. The number of pictures used in each DIC analysis was in the range 164-203. One camera with 36-megapixel resolution was used in the tests. A monitor showing the jack load was located close to the specimen and visible on all photos and was used for synchronisation of the load with the DIC analysis.

In DIC analysis "subsets", each including a different random pattern, are defined and tracked as the specimen moves and deforms. The displacement of the centre of each subset is given in the output results. The size of the subsets must be defined in harmony with the resolution of the pictures and the applied pattern, where several dots are needed inside each subset. Generally, the size of the subsets in this study was in the range of 1.0×1.0mm to 3.4×3.4 mm for the reinforcement bars and 13.8×13.8mm for the concrete strands. The software DaVis 8 from LaVision [14] was used in the DIC analysis.

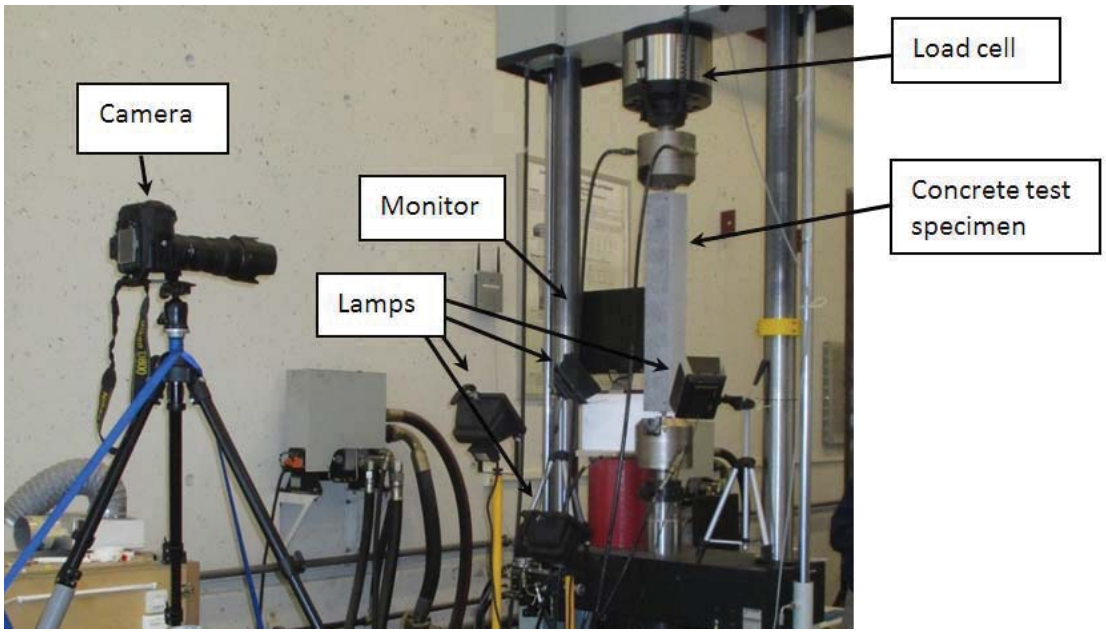

Figure 3: Test setup with one camera on a tripod, four lamps and a monitor.

3 TEST RESULTS

3.1 Test of reinforcement bars

The standard uniaxial stress-strain curves for steel bars are based on laboratory tests of bars with 5d gauge length, where d is the diameter of the steel bar [11, 12]. Because the DIC analysis is executed after the test, the location of the gauge segment can be decided after the test, symmetric about the neck. The gauge length can also be different from 5d. In the test series of 170-600 mm long reinforcement bars the following gauge lengths were used: 1d, 3d, 5d and 10d [10]. The stress-strain curves for these gauge lengths were identical all the way to the max stress, but after that the segment including the neck dominated the strain development. As both the uniaxial and lateral strain was measured, the Poisson's ratio could be determined. The Poisson's ratio increased rapidly during the yielding phase to 0.44-0.49 and was constant all the way to rupture. The bars developed a yielding plateau where the yielding propagated from one end of the bar to the other (Lüder's behaviour [15]) on approximately 1d long segment at a time.

In Fig. 4 strain-vs-picture (corresponds to strain-vs-time) and stress-vs-picture curves for twelve 50mm long side-by-side segments are shown. Note that the stress-vs-picture curve is scaled down by 5000 in order to fit into the graph. The outermost segments (segment 1 and 12) included the welding at the thickenings. The following notes 1-5 are marked on the graph on Fig. 4:

1. Up to picture no. 20 the bar is in the elastic range.
2. Between pictures no. 20-40 the stress-curve has a bending shape that begins at approximately 400MPa. The bending shape is a result of yielding in segments 1 and 12 in the bar at the welds (i.e. the strain on the vertical axis increases rapidly in segments 1 and 12). The heat from the execution of the welds resulted in lower yield stress in the bar at the welds and in a different yield behaviour (bend shape instead of a yielding plateau).
3. Between pictures no. 40-75 the stress-curve is horizontal, i.e. yielding plateau. The yielding strain can be observed as vertical jump in the strain curves beginning with segment 2. When segment 2 stops yielding segment 3 takes over and so in continues in a numeric order to the last segment 11[10]. I.e. the yielding-front propagates from one end of the bar to the other, known as Lüder's behaviour [15].
4. Between pictures 75-155 the whole bar goes through a strain hardening process.
5. Between pictures 155-164 necking occurs in segment 1, i.e. the bar fails at the weld in segment 1. All the bars with thickenings failed in the bar at the weld.

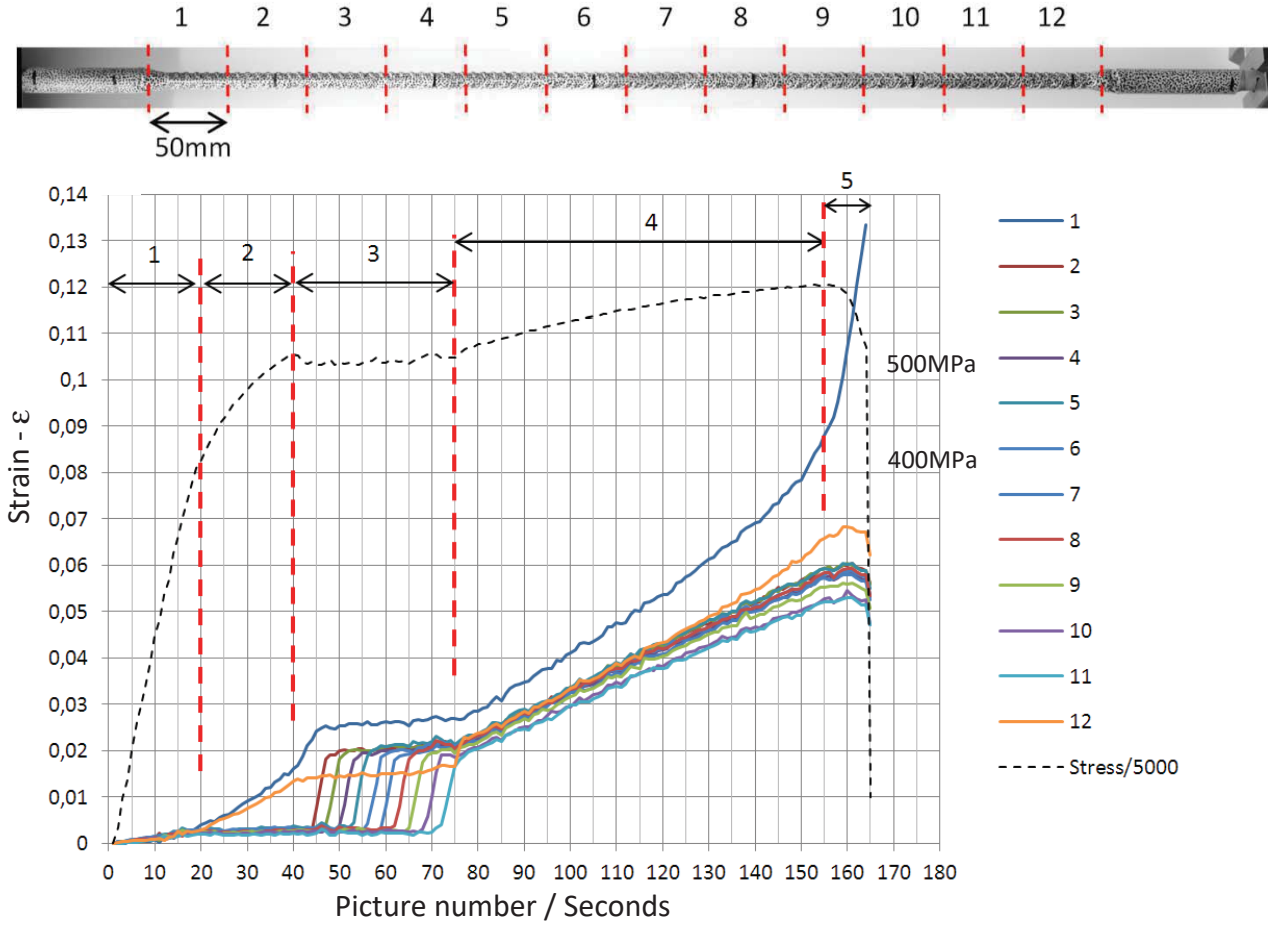

Figure 4: The strain development in twelve 50mm long side by side segments numbered 1-12 as a function of the picture number for reinforcement bar no. 2.1 with thickening at the ends. The segments including a weld are number 1 and 12. The stress in the bar is also shown as a function of the picture number scaled down by 5000 in order to fit into the graph.

Classical stress-strain diagrams for each segment are shown on Fig. 5 and as before segments 1 and 12 show different behaviour from the other segments.

The graph on Fig. 6 shows a stress-strain curve for bar 2.1 that is with thickening at the ends and for bar 4.1 that is without thickenings. Both curves are for gauge segments that includes the neck. The stress-strain curves for all the other bars included in the test (Table 1) are identical to the ones shown on Fig. 6. The heat from execution of the weld is affecting the stress-strain behaviour in the segments including the weld, but not the other segments, as can be seen on the strain-curves for all twelve segments for bar 2.1 on Fig. 4 and on the stress-strain curves on Fig. 5. Firstly, it affects the yielding behaviour as the curve starts bending at approximately 400MPa, instead of following a straight line to the yielding plateau, like segments 2-11 for bar 2.1 on Fig. 5. Secondly, the stress-strain curves are much shorter, so both the max stress and the failure occurred much earlier/at lower strain, in the segments including the weld than the others not including a weld. As can be seen on the graph on Fig. 6 the strain at max stress is though fulfilling the demand of 7.5% elongation for reinforcement bar in class C [11]. Segment 1 on Fig. 4 and Fig. 5 is the same as the one used to present bar 2.1 on Fig. 6 (shown as blue curve on all the graphs). The strain curves for the other segments not including a weld (i.e. segments 2-11) only reached 5-6% strain when segment 1, that included the neck, failed (Fig. 4 and 5).

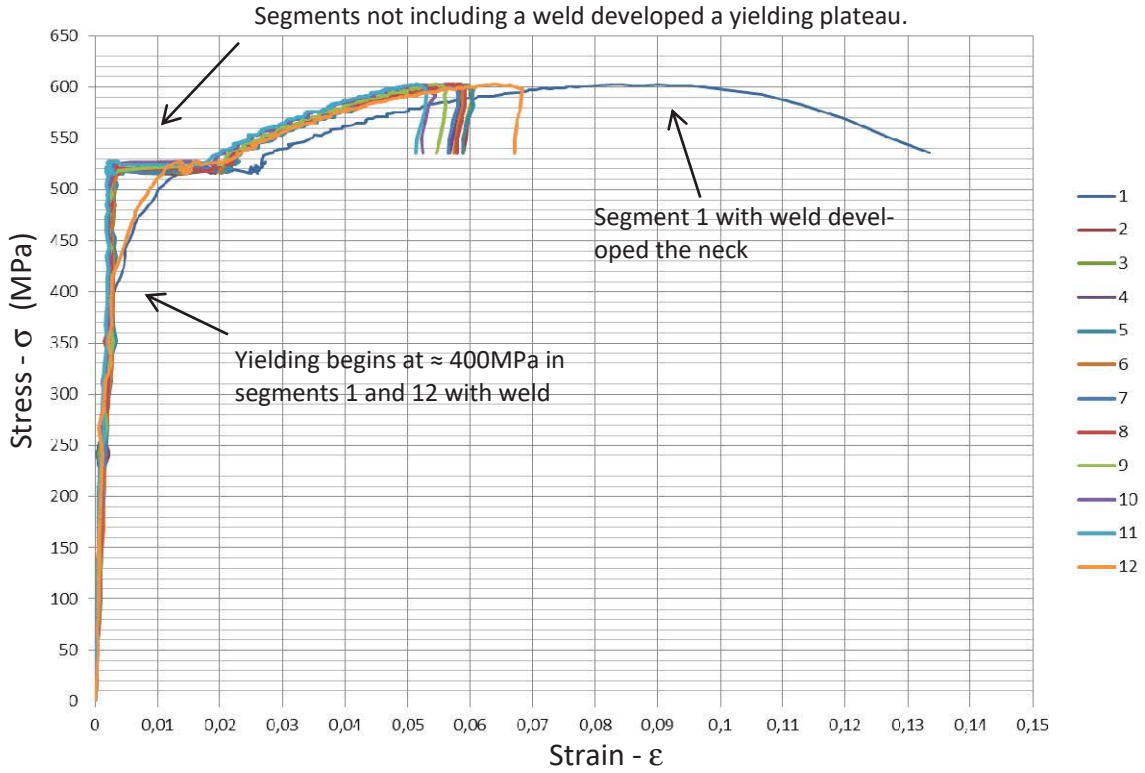

Figure 5: The stress curve and the twelve strain curves in bar 2.1 on graph 4 are here shown together as stress-strain curves. The segment including the neck finished the stress-strain development while the other segments stopped. Segments 1 and 12 including a weld started yielding at app. 400MPa and had a curved shape and a small yielding plateau, while the other segments not including a weld developed a yielding plateau.

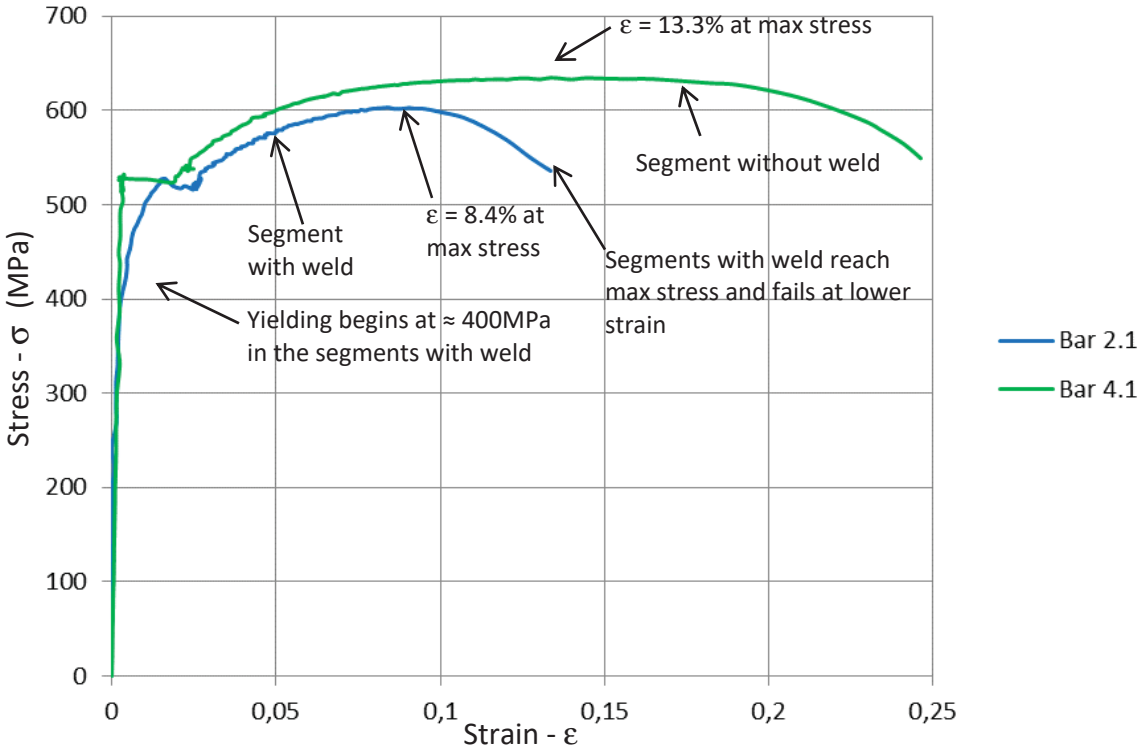

Figure 6: Stress-strain curves for bar 2.1 with thickenings and bar 4.1 without thickenings, where both gauge segments included the neck. The heat from the execution of the welding affects the stress-strain behaviour of the segment including the weld.

3.2 Test of concrete strands

The development of the crack widths and the strain across the cracks was determined on the surface of the test specimens facing the camera. The gauge length was decided to be 50mm as for the reinforcement bars, i.e. five times the diameter of the reinforcement bar inside the concrete. As the DIC analysis was performed after the test the gauge segments could be located with the crack in the centre. Eleven points on each side of the crack were used to determine an average crack width and average strain (Fig. 7).

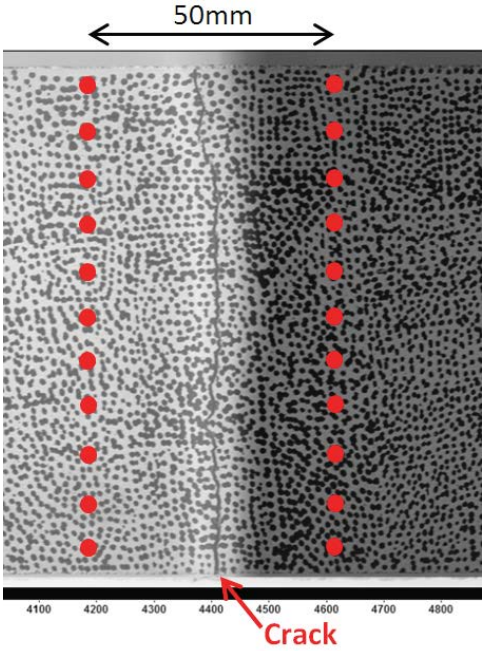

Figure 7: Eleven points on each side of the crack (red dots) were used to determine average values for the crack width and the strain across the crack.

Concrete strand no. 1 was the only specimen that developed two cracks (Fig. 8). No other damage was observed in the concrete. The reinforcement bar ruptured inside the concrete strand at the welding at top, which was confirmed by smashing the concrete with a hammer after the test. The outstanding part of the bar/thickening moved 15mm out of the concrete at the top, but no movement of the bar/thickening at the bottom was observed.
Concrete strand no. 2 developed one crack (Fig. 8). No other damage was observed in the concrete. The reinforcement bar ruptured inside the concrete strand at the welding at top, which became obvious after the test when the bar that was inside the smaller concrete part was easily pulled out of the concrete with bare hands (Fig.8). No movement of the outstanding part of the bars/thickenings was observed.
Concrete strand no. 3 developed one crack (Fig. 8). As expected in strands with reinforcement without thickening at the ends, damage of the concrete at top and bottom was observed. The top of the concrete strand splitted and punching failure was observed at both end surfaces. The bar ruptured at the top, outside the concrete.
Concrete strand no. 4 developed one crack (Fig. 8). As expected in strands with reinforcement without thickening at the ends, damage of the concrete at top and bottom was observed in form of punching failure at both end surfaces. The bar ruptured at the top, outside the concrete.

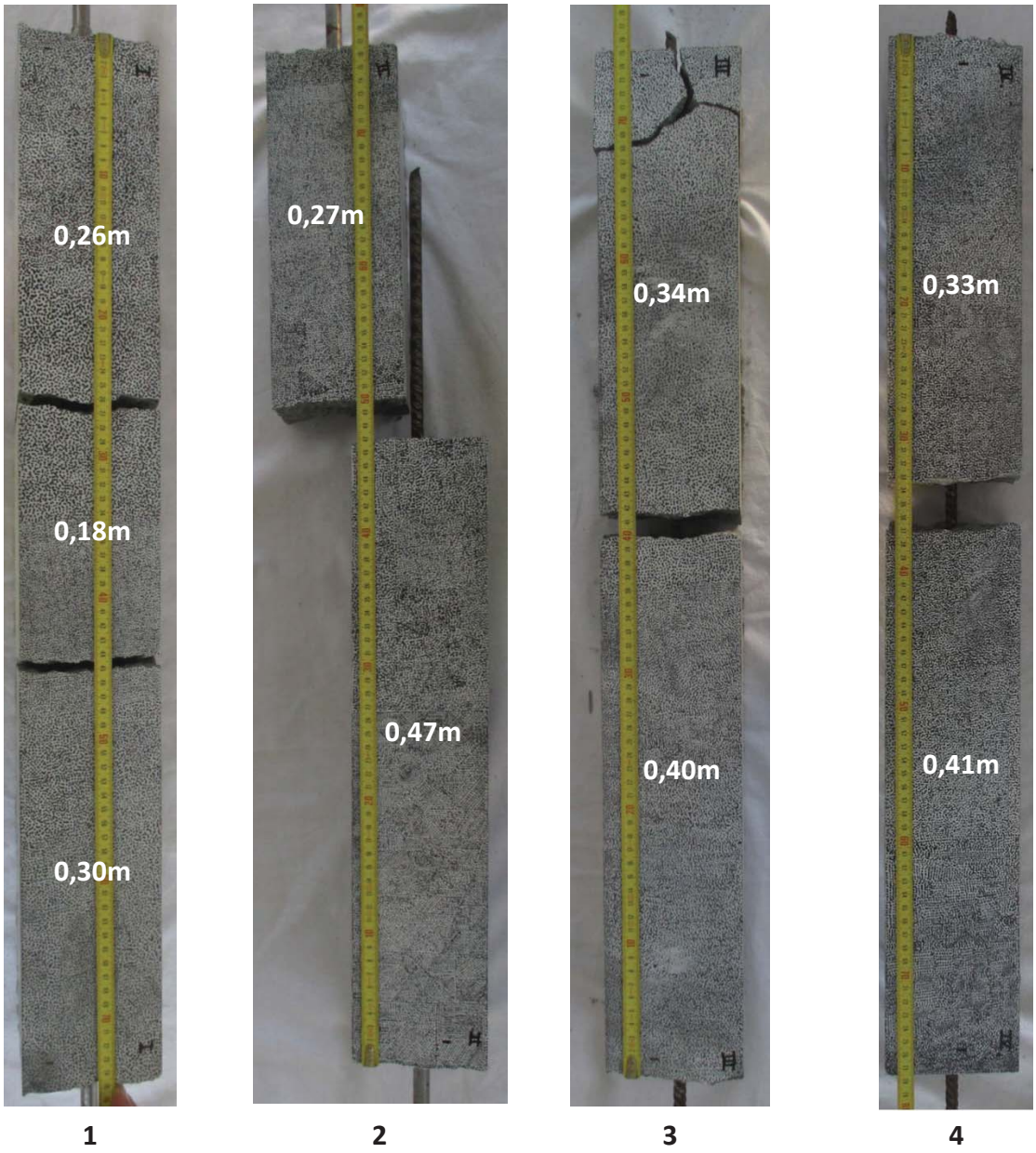

Figure 8: Side view of all four concrete strands after the test, facing the same way as during the test. Test specimen 1 and 2 developed no failures at the ends as the reinforcement had thickenings at the ends. The reinforcement ruptured inside the concrete. Test specimen 3 and 4 had no thickenings in the reinforcement and therefore they developed some failure at the ends. The reinforcement ruptured outside the concrete.

The development of the crack width (w in mm) and the applied axial jack force (P in kN) in the four concrete strands as a function of the displacement of the jack (u in mm) is shown in Fig. 9. In all cases the cracks opened simultaneously with the load drop in the force and in the case of concrete strand 1 there occurred two load drops, one for each crack. As can be seen on the development of the cracks in concrete strand 1 and 2, where the bars have thickening at the ends, the curves show a very steady increase of the crack width, compared with concrete strand 3 and 4 (Fig. 9). The reason is that all the yielding elongation in the bar in strands 1 and 2 happens inside the concrete, while the elongation of the bar outside the concrete is not contributing to the crack width in strands 3 and 4. The curves for the crack width in strands 3 and 4 are therefore not as steady.

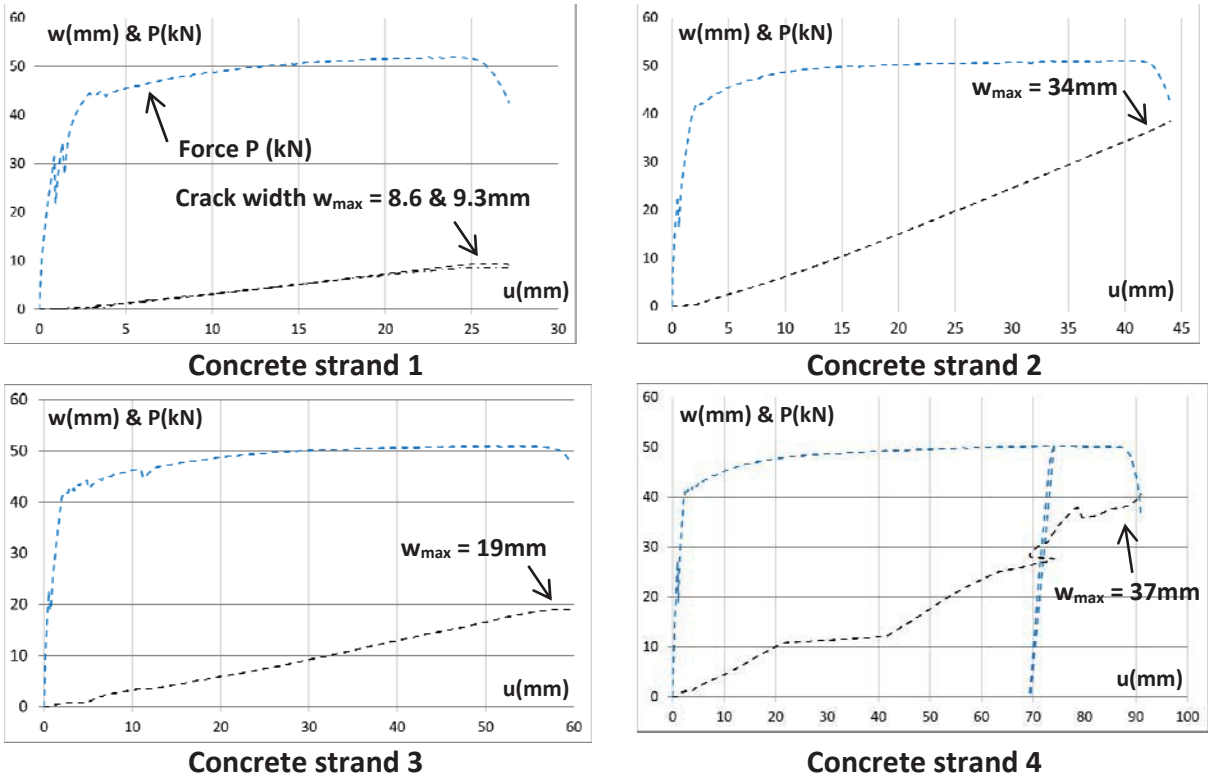

Figure 9: The development of the crack width (w in mm) in the four concrete strands as a function of the displacement of the jack (u in mm). The force in the jack (P in kN) is also on the graph.

In concrete strand 1 the crack width in both cracks starts descending at the same time the force starts descending. The reason is that the bar ruptured in the top weld and the outstanding part of the bar/thickening moved out of the concrete. That is not the case in concrete strand 2 as the crack width continues to increase during the descending part of the force (necking in the bar). The reason is that the necking of the bar occurred completely inside the concrete and contributed to the crack width.

As discussed earlier, another study of the reinforcement bars revealed a development of a yielding plateau where the yielding propagated from one end of the bar to the other. This was then followed by a strain hardening of the whole bar. It was also revealed that the stress-strain curves for gauge lengths in the range of 1d to 10d were identical all the way to the max stress [10]. These findings are important for the understanding of the behaviour of the bars inside the concrete together with the findings in this test, that gauge segments including a weld show different behaviour in the strain development, yield stress and max stress.

In concrete strand 1 and 2 the welds played a bigger role than anticipated in the beginning. The cracks occurred in some distance from the end of the concrete strand as expected, at the end of the transfer zone where the bond between the concrete and the reinforcement bar have transferred sufficient part of the tension force to the concrete, able to over win the tension strength in the concrete and create a crack. In the crack zone the reinforcement bar carries the whole force alone and there is the biggest stress in the bar. The bar starts yielding and because of the Poisson's ratio, which increases during the yielding phase to a value in the range of 0.44 to 0.49 [10], the bar also develops lateral contraction, affecting the bond between the bar and the concrete. The yielding of the bar propagated away from the crack in both directions and reached the weld at top in concrete strands 1 and 2 which failed. This became evident in the case of concrete strand 2 that the yielding is propagating along the bar all the way to the weld which failed and the reinforcement bar could after the test easily be pulled out of the top

concrete part with bare hands (Fig. 8). The bottom part of concrete strand 2 was cut into seven pieces whereof six of them were 50mm in length (Fig. 10). The bond between the reinforcement and the concrete was checked with a hammer. The reinforcement bar inside the two concrete pieces closest to the crack was very loose inside the concrete, while the third one had more resistance. The reinforcement bar inside the fourth piece barely moved when it was hit hard with the hammer and then not at all in concrete pieces number five and six. This indicates that the bar didn't yield all the way to the end of the bottom part of concrete strand 2. The length of the reinforcement bar belonging to the top part of concrete strand 2 (which was easily pulled out of the concrete with bare hands) is 200mm (Fig. 8) and if assumed that the reinforcement was loose inside concrete pieces no. 1 and 2 on Fig. 10 the total size of the free length is 300mm, i.e. 30d.

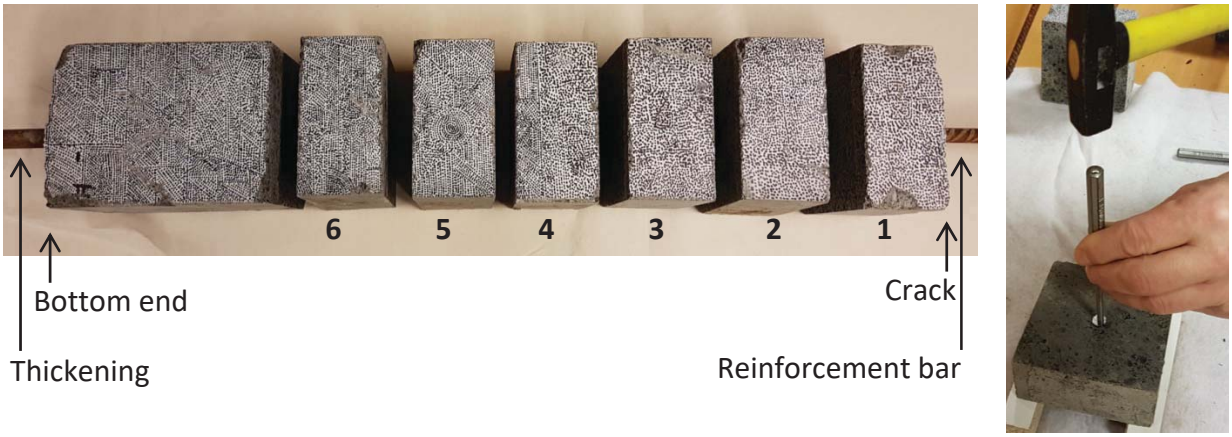

Figure 10: The bottom part of concrete strand 2 (see Fig. 8) was cut into seven pieces for comparison of the bond between the reinforcement and the concrete. The reinforcement in the two concrete pieces closest to crack where loose inside the concrete, but the resistance in the bar increased with the distance away from the crack. The resistance was checked with a hammer.

This simple test indicates that the reinforcement bars lose the bond to the concrete when the longitudinal strain together with the lateral strain increases. This also becomes evident when size of the crack widths is studied.

Concrete strands 1 and 2 have welds in the bars at the thickenings and the strain at max stress in the reinforcement bars is in the range of 8.4-13.3% according to the graph on Fig. 6, depending on whether the yielding occurs in a segment with or without a weld. When the yielding occurs along a long section, like described above, the total elongation of the bar is somewhere in the above-mentioned range, but is most likely closer to the latter value because the weld is only a small part of the total length of the bar that is yielding. Concrete strand 2 had a crack width of 34mm (Fig. 9) and by using the measured free length of 300mm, it results in a strain of 11.3%. By using that strain value for concrete strand 1, also having reinforcement bar with a weld that failed, it results in a free length of app. 8d for both cracks.

Concrete strands 3 and 4 had reinforcement bar without thickenings/welds and the strain can be assumed to be close to the latter strain value mentioned above, i.e. 13.3%. For a standard gauge length of 5d (50mm) it would result in a crack width of 6.7mm. Concrete strand 3 had a crack width of 19mm demanding a free length of 14d and app. 28d is needed for the 37mm crack width in concrete strand 4.

4 DISCUSSION AND CONCLUSIONS

In standard tests of reinforcement bars the gauge length is 5d, but the tests presented in this paper on concrete strands with one 10mm reinforcement bar in the centre, revealed that the free length of the reinforcement bars inside the concrete strands was in the range of 8d-30d. As the whole bar is active along the free length (not only in the vicinity of the neck) and the stress-strain behaviour of the reinforcement bars is the same up to max stress, even though the free length becomes larger than 5d, it results in a large plastic elongation in the uniaxial direction together with a lateral contraction of the bar of the size of 44-49% of the longitudinal strain. The ribs lose its grip on the concrete and the reinforcement bar becomes free inside the concrete. The actual free length becomes longer than 5d resulting in longer elongation of the bar (in mm) avoiding premature rupture of the reinforcement bar during earthquakes.

REFERENCES

[1] W.H. Peters, W.F. Ranson. Digital imaging techniques in experimental stress analysis. *Opt Eng*. 21(3), 427-431, 1982

[2] M.A Sutton, W.J. Wolters, W. H. Peters, W. F. Ranson, S. R. McNeill. Determination of displacements using and improved digital correlation method. *Image Vis Comput*. 1(3), 133-139, 1983.

[3] H. Lu, P.D. Cary. Deformation measurements by Digital Image Correlation: Implementation of as second-order displacement gradient. *Exp Mech*.40(4), 393-400, 2000.

[4] B. Pan. Two-dimensional digital image correlation for in-plane displacement and strain measurements: A review. *Meas Sci Technol*. 20(6), 1-17, 2009

[5] M. Obata, M. Inoue, Y. Goto, The failure mechanism and the pull-out strength of a bond-type anchor near a free edge. *Mechanics of materials*, *28*(1-4), 113-122, 1998.

[6] B.M. Luccioni, D.E. López, R.F. Danesi. Bond-slip in reinforced concrete elements. *Journal of structural engineering*, *131*(11), 1690-1698, 2005

[7] J. Melo, C. Fernandes, H. Varum, H. Rodrigues, A. Costa, A. Arêde. Numerical modelling of the cyclic behavior of RC elements built with plain reinforcing bars. *Engineering structures*, *33*(2), 273-286, 2011.

[8] H.C. Biscaia, N. Franco, C. Chastre. Development of a simple bond-slip model for joints monitored with the DIC technique. *Archives of Civil and Mechanical Engineering*, *18*(4), 1535-1546, 2018

[9] H.C. Biscaia, N. Franco, C. Chastre. Stainless steel bonded to concrete: an experimental assessment using the DIC technique. *International Journal of Concrete Structures and Materials*, *12*(1), 9. 2018

[10] H.J. Eiriksson, B. Bessason, R. Unnthorsson, Uniaxial and lateral strain behaviour of ribbed reinforcement bars inspected with digital image correlation, *Structural Concrete*, 19, 1992-2004, Doi: 10.1002/suco.201800042, 2018

[11] Eurocode 2: Design of Concrete Structures – Part 1-1: General rules and rules for buildings, European Committee for Standardization; 2004.

[12] EN ISO 6892-1:2009. Metallic materials – Tensile testing – Part 1: Method of test at room temperature, 2009.

[13] EN 10080:2005. Steel for the Reinforcement of Concrete – Weldable Reinforcing Steel – General. European Committee for Standardization; 2005.

[14] LaVision. DaVis 8, Data Acquisition and Visualization software, LaVision GmbH, Anna-Vandenhoeck-Ring, D-37081 Goettingen, www.lavision.de. 2015.

[15] J. C. Fisher, H. C. Rogers. Propagation of Lüder's band in steel wires, *ACTA Metallurgica*, 4, 180-185. 1956.

EURODYN 2020
XI International Conference on Structural Dynamics
M. Papadrakakis, M. Fragiadakis, C. Papadimitriou (eds.)
Athens, Greece, 23–26 November 2020

REVIEW OF SITE EFFECT MODELING METHODS CONSIDERING EXPERIMENTAL GEOPHYSICAL DATA

Rita Abou-Jaoude[1,2], Nisrine Makhoul[3], Jean-Alain Fleurisson[1], Alexandrine Gesret[1]

[1]MINES ParisTech, Centre de Géosciences
35 Rue Saint Honoré, 77300 Fontainebleau, France
e-mail: {rita.abou_jaoude, jean-alain.fleurisson, alexandrine.gesret}@mines-paristech.fr

[2] University of Balamand
Al Kurah, North of Lebanon, Lebanon
e-mail: rita.abou_jaoude@mines-paristech.fr

[3] Notre Dame University-Louaize
Zouk-Mosbeh, Keserwan, Lebanon
e-mail: nmakhoul@ndu.edu.lb

Keywords: Site effects, Amplification, Experimental studies, Numerical analysis, H/V, MASW.

Abstract. *It is well known that seismic waves are affected by the geological nature of the different layers in which they propagate close to the surface. The various structural and topographic elements cause the incident signal to be reflected, refracted, or diffracted. As a result, the combination of those different waves modifies the spatial, spectral, and temporal characteristics of the wavefield. These phenomena are called site effects. Especially amplifications of the ground motion acceleration is observed, which may induce failure of the structures located on the surface, as well as slope instabilities. The spatial variability of the ground motion can be very significant over small distances, because of the changes in the geometry and the soil conditions. During the last years, many research works have been conducted through numerical simulations on simplified slope geometries in order to identify the effect of geological, topographic and input signal parameters on the amplification of the amplitude of seismic waves. However, the predictions resulting from the numerical simulations are often different from the field observations. So, this paper firstly presents an in-depth literature review about available methods to model site effects and their implications. Secondly, it also focused on results of existing works that benefit from experimental data in the analytical modeling; more especially works considering geophysical data obtained through H/V and MASW experiments are examined.*

1 INTRODUCTION

An earthquake is known by the shaking of the Earth surface, which may cause severe structural destruction and deaths. Energy is suddenly released in the Earth's lithosphere, creating seismic waves, that propagate to reach the surface.
During their journey to the surface, the seismic waves face different kinds of effects, that can modify the spatial, spectral and temporal characteristics of the signal such as its direction, amplitude, duration and frequency content ..., and therefore affect the ground motion. Those effects depend mainly on the complexity of the source mechanism, the path followed by the seismic waves and site effects close to the surface.
Speaking of site effects, seismic waves are affected by the geological structure of the soil in which they propagate. For example, when a seismic wave arrives at an alluvial basin, its propagation velocity decreases while the amplitude of its signal increases. As the geometry and conditions of a sedimentary layer vary over short distances, it means that the seismic signal may vary over small surfaces.
Despite all the harm and risks caused by such phenomena, it has been difficult so far to study the slope stability during dynamic events. In many research studies numerical simulations have been performed on simplified slope geometries (2D models), to identify the effect of geological, topographic and input signal parameters, on the amplification of the amplitude of seismic waves [1, 2, 3, 4, 5, 6]. Few studies have used more realistic geological and geomorphological site conditions (3D models) to compute ground motion amplifications due to surface topography [7, 8, 9].

Therefore, this paper presents an in-depth literature review about available methods to model site effect and its implications. It also focused on results of existing works that benefit from experimental data in the analytical modeling; more especially works considering geophysical data obtained through H/V and MASW experiments we analyzed.

2 SITE EFFECTS

During major historical earthquakes, different aspects of damages have been observed in various locations for the same event. The waves behavior and characteristics, and therefore the distribution of damage, were mainly controlled by the type of soil in which the seismic waves propagate. This phenomenon is commonly called as site effects.
Seismic site effects are related to the alteration of the seismic waves when they propagate close to the surface; seismic waves are trapped in sediment layers (softer layers), they are reflected and refracted on all the borders, edges, slopes and the bottom of sedimentary basin until they dissipate all their energy. That is why infrastructures such as buildings, bridges may be damaged due to the important spatial variability of the ground motion over very small distances.
Many observations around the world have shown that the amplification of a signal could reach 10 times the initial signal amplitude due to similar effects, and it mainly depends on the velocity contrast between the layers and the geometry of the basin [10]. Reflections and refractions also happen when seismic waves reach hills and mountains, which may induce failure of structures situated on the surface or slope instabilities.
Generally, two site effects are considered: the ones due to the geological nature of the soil and those due to the topography.

2.1 Geological site effects

Geological site effects caught the attention of researchers [11, 12, 13, 14] since the Mexico earthquake in 1985, when this large earthquake struck Mexico City with a moment magnitude of 8. Even though its epicenter was located along the Pacific Coast (more than 350 km far from Mexico-City), the city suffered major damage due to the large earthquake magnitude and its geological conditions, which consists of the ancient lake beds that Mexico City sits on. As usually observed, the acceleration amplitude strongly decreased with the distance from the epicenter (from 150 $\mathrm{cm/s^2}$ recorded at a station very close to the epicenter, to 18 $\mathrm{cm/s^2}$ at a station situated at 200 km from the epicenter), but locally increased a lot up to 170 $\mathrm{cm/s^2}$ when the seismic waves reached the alluvial deposit on which Mexico City has been founded: seismic waves have been trapped and they reached the resonance frequency of the site [15]. This was the first time where seismic site effects have been evidenced. Furthermore, a large number of the cities hit by earthquakes were damaged according to the geological and lithological nature of the soil, where they are constructed.

2.2 Topographical site effects

Different observations carried out in the past showed that seismic ground motion is affected by the variation of the site's topography. This hypothesis was presented by Levret et al. (1986) [16] to explain the damages observed in the village of Rognes in France located on a hill, during the Lambesc's earthquake in 1909. Other examples also show that damages were more severe on the crest of hills than on its bottom: San Fernando earthquake in 1971 [17], Whitter Narrow's earthquake (California) in 1987 [18], Chichi earthquake (Taiwan) in 1989, Northridge's earthquake (California) in 1994 [19, 20], Salvador earthquake in 2001, Sichuan earthquake (China) in 2008. One of the first topographic site effects was reported by Spudich et al. (1996) [20] who analyzed signals recorded in several seismological stations installed along Mount Tarzana slope in Los Angeles. They noticed high amplification of the seismic motion, caused by the Northridge earthquake aftershocks, between the crest and the bottom of the hill. Since then, many experimental studies [21, 22, 23, 24, 25, 26, 27, 28, 29, 20, 30, 31] were conducted to better understand the topographic site response. 2D & 3D numerical simulations [17, 32, 33, 34] showed a 30 to 100% increase in the amplification of the ground motion for frequencies between 2 and 5 Hz. There are many explanations for the causes of topographic site effects, and what may affect the wave:

- The interference between the slope of the hill and the incident angle of the wave, especially the SV waves [18, 29].
- The interference between the incident wave and the diffracted waves [29].
- The wave ray path along the topographic surface [35].

2.3 Site effects assessments

Site effects can be generally detected by the three following characteristics:

- The amplification of the ground in the subsurface layers.
- The resonant frequency.

- The length of the seismic ground motion.

Different approaches were developed over the years and three are frequently used to evaluate seismic site effects:

- The Horizontal to Vertical Spectral Ratio using Microtremors recordings at a single station (ambient noise) MHVSR [36], detailed in section 3.
- The Horizontal to Vertical Spectral Ratio using Earthquake data EHVSR [37], detailed in section 3.4.
- The Classical Spectral Ratio CSR [38], detailed in section 4.

The definition for each of the methods and their respective limitations are introduced in the following sections.

3 THE SINGLE STATION MHVSR ANALYSIS APPROACH

Ambient noise or microtremors were first investigated by Omori in 1908 [39] and caught the attention of Japanese researchers, especially after 1950. Measurement of microtremors was used to estimate geological conditions and mechanical properties of the subsurface materials. The application of microtremors was first proposed by Kanai & Tanaka in 1961 [40]. After that, several research investigations were conducted to evaluate its capacity in assessing the ground motion characteristics and the site response of sediment deposit [41, 42, 15, 43, 44].
The ambient noise is a mixture of various wave types, most of the time generated by sources located at the surface of the Earth or at the bottom of the sea. In other words, ambient noise is a constant vibration created by the combination of low-frequency $<$1Hz and 1Hz (ocean, meteorology, wind, etc...), and high-frequency $>$1Hz (human activities, machinery, etc...).

3.1 Nakamura method

To better understand whether microtremors are composed of body waves or surface waves, a series of theoretical and numerical studies were conducted by Nogoshi and Igarashi. Based on the theoretical HVSR of Rayleigh waves founded by Suzuki in 1933 [45] and the numerical analysis of Ohta in 1963 [46], Nogoshi and Igarashi concluded in a sequence of articles [47, 48], that a microtremor is caused by Rayleigh waves. This clarifies why they did not initiate the famous Nakamura method, also known as the horizontal to the vertical spectral ratio of microtremors MHVSR. Despite that some article are citing them as founders of the Nakamura method [49, 50, 51, 52], they did not describe the characteristics and the basics of the MHVSR technique. The confusion may be caused by the fact that the original papers of the japanese researcher Nakamura were published in Japanese [53]. The MHVSR method estimates the amplification, and the resonant frequency of the surface layer [54, 36] as explained by the Japanese researcher Yutaka Nakamura.

3.2 Empirical development and amplification estimation

The Japanese researcher Y. Nakamura tried to estimate the horizontal amplification of the ground motion by computing the ratio between the horizontal spectra of microtremors measured on soft soil (f) and bedrock (b) sites (base ground) H_f/H_b. Then he decided to use the vertical

components instead of horizontal ones V_f/V_b to eliminate as much as possible the peaks caused by Rayleigh waves, and, therefore, to point out the effect of shear waves. After this procedure, he defined the spectral amplitude ratio as the ratio between horizontal-motion spectral ratio and vertical-motion spectral ratio, both on-site and on bedrock

$$\frac{H_f/H_b}{V_f/V_b} \tag{1}$$

Based on different observations [36, 55, 56, 57], $H_b/V_b \simeq 1$, this means that the Nakamura method makes it possible to derive an estimation of the amplification characteristics and resonant frequency by only using either earthquake motion records HVSR or microtremors HVSR of the measurements at the ground surface [36][53].
After comparison with the results of different surveys and data, Nakamura obtained the following relationships between the averaged thickness and the averaged shear wave velocity of the subsurface layer (V_s) and the base ground (bedrock) (V_{sb}):

$$V_s = \frac{V_{sb}}{A} \tag{2}$$

$$h = \frac{V_{sb}}{4AF} \tag{3}$$

with A the peak amplification factor that occurs at or close to the resonant frequency F.

From equations 2 and 3, we obtain:

$$F_n = n(\frac{V_s}{4h}) \tag{4}$$

where n is an index designating the n^{th} mode of oscillation [58]. When n=0, we obtain the resonant frequency f_0 for the fundamental mode over a 1D medium.

Based on Molnar et al. (2018) [52], the microtremor HVSR was developed for several purposes such as:

- Identifying the presence of stiff layers.
- Estimating the depth of soil thickness h through the peak amplitude when assuming the value of V_s (equation 2) [44, 59, 60, 61].
- Identifying the lateral heterogeneities in the subsoil when the H/V curves present some peculiar shapes [62, 63, 64, 65].

3.3 Field data Collection

The MHVSR single station methodology is considered as a non-invasive and inexpensive easy method to apply for seismic site characterization. On the other hand, the field data collection of ambient noise should follow some rules to get more stable MHVSR and more precise curve peaks. Some of these rules consist of:

- Using a three-component velocimeter,

- Leveling the velocimeter on the surface, where the conditions represent a natural, free field ground characteristic,
- Placing the feet of the sensor directly onto the soft soil (vegetation should be removed),
- Protecting the sensor from direct wind [66],
- Collecting data on natural ground surfaces better than on surfaces constructed by man (pavement), which may alter the peak of the MHVSR [67] or over underground cavities (should be avoided otherwise it is recommended to take multiple recordings at different times),
- Conducting the recordings early in the morning, to minimize noise from human activities, and for enough duration (the lower frequency required, the greater the recording time and the larger time window should be) [68].

The data collected can be analyzed using the Geopsy software package (`www.geopsy.org`), according to the SESAME project recommendations, that standardized the H/V method [52].

3.4 H/V using earthquake data EHVSR

During the Field observations performed by [27, 29, 69], the horizontal component of the seismic ground motion was much more amplified than the vertical components. Sometimes, even the polarization of the seismic ground motion could be considered. For example, during the experimental studies on the hill in Tarzana California, the horizontal component perpendicular to the hill slope was more amplified than the parallel one [20, 70].
Thus, for this method, it is considered that only the horizontal component of the motion (SH waves) are affected by site effects at least for low frequencies. Therefore, the vertical components are considered as the reference of the ground motion. The fact that the EHVSR method does not require a reference station represents an advantage.
The experimental results issued by both H/V spectral ratio methods (EHVSR and MHVSR), present good agreements [71, 72, 73].

3.5 Interpretations and limitations of H/V

The H/V method has been mostly used until now to study the effects due to sediment-filled-valleys, and rarely used in determining the topographic site effects even if it produces satisfactory results. This technique allows the determination of the fundamental resonance frequency of the subsurface, but does not allow the determination of the level of amplification on a large band of frequencies.
Normally, with the absence of shear wave velocity inversions with depth, the plot of the H/V curves presents sharp clear peaks when the structure of the subsoil is flat (1D), and an amplitude equal to or higher than 1 in the entire frequency domain except around $2f_0$ (presence of Rayleigh waves). As mentioned in the previous paragraph, the sensitivity of the horizontal components to the geological and topographical changes in the medium, is greater than for the vertical ones. Therefore, the detachment of the horizontal and vertical components, having stratigraphic origins, is illustrated in the Fourier Spectra of the three components with an eye-shape [67] (black arrow in figure 1).
The latter helps us understand that narrow H/V peaks are artificial and not natural, or of anthropic origins, because they are not characterized by spectral eye-shapes [61]. Acquiring the

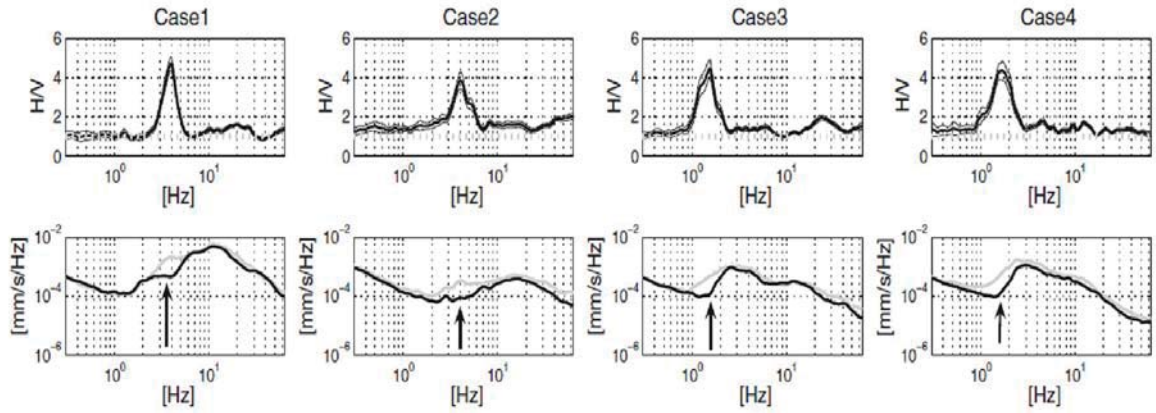

Figure 1: First row shows average H/V curves with the standard deviation with respect to the average. Second row shows average spectra (Z → black, EW → gray solid line, NS → gray dotted line). Stratigraphic columns are, for each site, from top to bottom: 1) Silt/igneous bedrock; 2) gravel/sedimentary bedrock; 3) clay/igneous bedrock; 4) clay/igneous bedrock [67].

data is a simple task, but the interpretation of their H/V curves poses several challenges at different levels. The peculiarity in the shape of H/V curves, such as broad peaks and plateau-like shapes and even amplitudes lower than 1, usually indicates a shear wave velocity inversion due the presence of cavities, stiff soil layer over softer soil, artificial soil, lateral heterogeneities, lateral sediment thickness variation (2D & 3D structures) and anthropic layers. An example is given in figure 2, of two H/V plots representing the different behavior of the curves depending on the site chosen to acquire the measurements.

Therefore, it is not wise to estimate a preliminary fundamental frequency just by applying the H/V technique. The application of complementary active or passive geophysical methods such as the multichannel analysis of surface waves (MASW), helps to avoid misinterpretations of the soil fundamental frequency [65, 61] and better evaluate the site effects.

Here are some examples on what could affect the H/V curves:
(1) Numerical simulations of microtremors on actual sedimentary basins (e.g. Santa Clara, Grenoble, Switzerland, Japan) were conducted, and the results showed a difference between the H/V peak frequency in a 3D velocity structure model and the fundamental frequency in a 1D velocity structure model. For 2D & 3D structures, the peak frequencies of the H/V curves are $\pm$ equal to 20 to 40% of the theoretical 1D resonant frequency (Equation 4) [75, 63, 64].
(2) In 2009, Castellaro and Mulgari [67] found that recording ambient vibrations with sensors placed on a concrete layer or asphalt, affects the H/V curves and alters the amplitude. This is in contradiction with the Site EffectS assessment using AMbient Excitations (SESAME) European project (`http://sesame-fp5.obs.ujf-grenoble.fr/index.htm`) recommendations [66]. The SESAME project present guidelines and recommend procedures for field data acquisition (ambient noise), processing and interpretation of the results using the H/V spectral ratio technique, and allows the measurement of ambient noise on artificial surfaces.

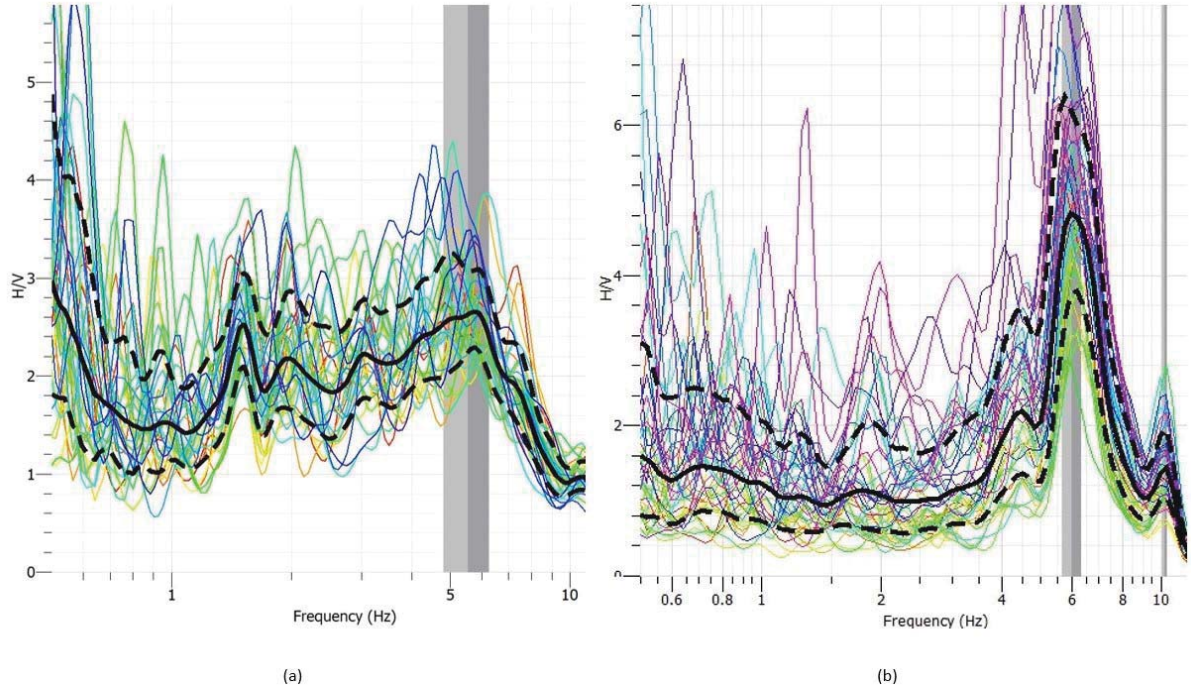

Figure 2: H/V preliminary results from recordings on two particular sites of Byblos in Lebanon. Colored plots refer to different profiles estimated for the different time windows, the black plot represents their average and the dashed ones represent the standard deviation with respect to the average. The grey area represents the averaged peak frequency and its standard deviation. (a) Ambient noise was recorded at a site laying on an anthropic layer with a moderate inclination of the subsoil (data recorded during our experimental/geophysical field mission in 2019). (b) Ambient noise was recorded at a site after the excavation of the anthropic layer. The Geopsy software was used to compute the H/V and to plot the curves [74].

4 THE CLASSICAL SPECTRAL RATIO

In addition to the microtremor HVSR and earthquake HVSR methods, we can distinguish another approach for the evaluation of site effects: The classical spectral ratio CSR [38].
This method consists in the calculation of the ratio between ground motion Fourier spectra recorded at a given site and at reference site . A seismic recording on a site i is represented in the frequency domain by:

$$S_i(f) = O(f) * P_i(f) * H_i(f) * I_i(f) \tag{5}$$

where O(f) represents the seismic source effect, P_i(f) the propagation path effects, H_i(f) the modification of the signal due to the characteristics of the soil on the subsurface, I_i(f) the response of the recording instruments and f is the frequency.
This equation shows all the effects that influence a seismic signal, that is why it becomes difficult, to separate site effects from other effects when the signal is recorded near the source. The spectral ratio of the different seismic signals recorded at two different sites (the study and the so called reference sites respectively) for the same seismic event, allows eliminating the seismic source effect, the propagation path effect and the response of the recording instruments as the distance between the site of study and the reference site is negligible compared to the epicenter

distance. The only remaining effect is the site effects:

$$\frac{S_{is}(f)}{S_{ir}(f)} = \frac{H_{if}(f)}{H_{ir}(f)} \tag{6}$$

where S_i is the Fourier transform of the signal recorded on the site of study and S_r is the Fourier transform of the signal recorded on the reference site.

This method presents some constraints:
(1) The necessity to find a reference site that is not affected by site effects. According to Chavez-Garcia et al.(1996) [37] and Lebrun et al. (1999) [71], the reference site station should be on the same geological layer (because, in this case, the same geological nature of the soil won't influence the amplification), and at a minimum distance of one wavelength from the topography. However, Sanchez-Sesma et Campillo (1991) [76] suggested choosing the reference site on the ground base (bedrock) that does not present any variation in topography and that is situated at a minimum distance of two times the horizontal dimension of the hill. Other studies [77, 57, 55] recommended choosing the reference site where the HVSR is close to unity at all frequencies. This kind of site reference could be hard to find, so we must select the best possible reference station [37].
(2) The source and the propagation path should be the same for the site being studied and the reference site, which is possible when the epicenter of the event is far enough from both stations (larger than five times the distance between the two stations).

These are the reasons why the CSR method is not very practical to perform, but it is still used in the evaluation of topographic site effects [77, 37, 71].

5 MULTICHANNEL ANALYSIS OF SURFACE WAVES (MASW)

Since a surface wave is frequency-dependent, the Multichanel Analysis of Surface Waves (MASW) method is based on the study of the dispersion of surface waves [78]. This technique is widely used to construct the subsurface Vs profile, obtained by inversion of surface-wave dispersion curves [79]. Two MASW techniques are used: active and passive [80], it depends on how the surface waves are generated. The passive MASW is based on measurements of ambient noise, whereas the active technique is based on generating surface waves using a sledgehammer or any other active seismic sources [81] and a linear receiver array of geophones, collecting data in a roll-along mode. The penetration depth of surface waves is usually limited at 30 m, because of frequency (wavelength) limitations, but this can varies with the site and type of active source used. The MASW data can be analyzed for example with the GEOPSY package (`www.geopsy.org`) using built-in tools to extract the dispersion curve (DC) and invert them.

For the deeper layers of the soil, when investigating is required, the microtremor array methods (MAM) can be used to resolve phase velocities of the lower frequency band (deeper part of the Vs profile) depending on the bandwidth of sources, resonant sensor frequency and the largest inter-station distances of the array. The successful results from (MAM) producing reliable dispersion curves have been accepted as an indirect proof for the assumption of surface wave predominance [49].

6 DISCUSSION AND CONCLUSIONS

This paper presents an in-depth literature review about available methods to model site effects and their implications. It presents results of existing works that benefit from experimental data in the analytical modeling and focuses on geophysical works obtained through H/V and MASW experiments.

It was noted that, microtremor recordings are a very good, easy and inexpensive technique for the estimation of site characteristics (resonant frequency and amplification thickness). Different studies showed a good agreement between numerical and experimental calculations, especially in urban zones. Therefore, it can be used to obtain a map of the fundamental resonant frequency of a city, in microzonation studies, especially in low seismic areas [82, 50, 83], and in the evaluation of site response. Even if the H/V method using ambient noise is considered easier, its application for the evaluation of topographic effects is still limited. Lebrun et al. (1999) [71] obtained consistent results with HVSR and CSR at low frequencies. Therefore, he confirmed the suggestion of Lermo et Chavez- Garcia (1993) [56] and Chavez-Garcia et al. (1996) [37], that it is possible to evaluate topographic site effects with the HVSR technique [84, 85]. Nevertheless, in this case, more experiments and 3D numerical modeling should be conducted to confirm their conclusions.
The application of multichannel analysis of surface waves (MASW) [78] is a powerful active source method for obtaining phase velocities for the high-frequency band. Thus, the dispersion curves obtained are used to provide Vs profiles that contain information on shallow sedimentary structures in a cost-effective and time-efficient manner.
Both the multichannel and single station methods have, when used alone, more limitations in comparison to their combined use. This is why the main goal is to combine the H/V spectral ratio from ambient noise (HVSR method) with the MASW technique to obtain reliable shear-wave velocity profiles of the subsurface down to bedrock. This combination allows deriving quantitative information on S-wave velocity sections for the study site. A similar combination of techniques is reported in the seismological literature by Scherbaum et al.(2003) [86] and Zor et al.(2010) [87].

The understanding and the usage of these different approaches, is still very important in the research domain to better evaluate experimentally and numerically the site effects. The implementation of these methods is in progress on the experimental site of Byblos in Lebanon. The purpose of the ongoing research work is to perform a careful comparison between results from numerical modeling of site effects and field observations and recordings on this experimental site. For this purpose, site investigations will allow acquiring the geological and seismic data necessary for the simulations and also to perform a microzoning on the site; semi-permanent equipment will be installed to record ground motions. The coherence of recorded signals will be evaluated using the Multichannel Analysis of Surface Waves and H/V ratio. Then, building a realistic model using the acquired experimental data, and a real topographic profile chosen from the Byblos region and conducting a numerical study using the Flac 2D/3D software, will allow comparing results from the numerical simulations with instrumental data. Combining experimental and numerical data for real sites instead of using simple parameters and geometries, makes this review and the research work in progress interesting, because the results will be more realistic in terms of spatial distribution of the soil movement, as well as the consequences in terms of amplification factors, slope stability, and building vulnerability.

7 ACKNOWLEDGMENTS

We are grateful to the following academic institutions: MINES-Paristech PSL University, Centre de Géosciences, Balamand University and Notre Dame University for supporting this research work, and to the SAFAR program (Campus France) for funding the first year of the PhD thesis.

REFERENCES

[1] P. Mozco, A. Rovelli, P. Labak, and L. Malagnini, "Seismic response of the geologic structure underlying the Roman Colosseum and a 2-D resonance of a sediment valley," *Annals of Geophysics*, vol. 38, no. 5-6, 1995.

[2] C. Bourdeau, *Effets de site et mouvements de versant en zones sismiques : apport de la modélisation numérique*. phdthesis, École Nationale Supérieure des Mines de Paris, July 2005.

[3] A. Pagliaroli, G. Lanzo, and B. D'Elia, "Numerical evaluation of topographic effects at the nicastro ridge in southern italy," vol. 15, no. 3, pp. 404–432. Publisher: Taylor & Francis.

[4] H. T. Nguyen, *Évaluation des effets de site topographiques dans les pentes soumises à des sollicitations dynamiques par simulations numériques*. phdthesis, Ecole Nationale Supérieure des Mines de Paris, Dec. 2015.

[5] L. Lenti and S. Martino, "The interaction of seismic waves with step-like slopes and its influence on landslide movements," *Engineering Geology*, vol. 126, pp. 19–36, Feb. 2012.

[6] Z. Zhang, *Dynamic slope stability and geomorphological site effects : Numerical simulations and back analysis*. phdthesis, PSL Research University, Dec. 2018.

[7] S.-J. Lee, D. Komatitsch, B.-S. Huang, and J. Tromp, "Effects of Topography on Seismic-Wave Propagation: An Example from Northern TaiwanEffects of Topography on Seismic-Wave Propagation: An Example from Northern Taiwan," *Bulletin of the Seismological Society of America*, vol. 99, pp. 314–325, Feb. 2009. Publisher: GeoScienceWorld.

[8] E. Chaljub, P. Moczo, S. Tsuno, P.-Y. Bard, J. Kristek, M. Käser, M. Stupazzini, and M. Kristekova, "Quantitative Comparison of Four Numerical Predictions of 3D Ground Motion in the Grenoble Valley, FranceQuantitative Comparison of Four Numerical Predictions of 3D Ground Motion in the Grenoble Valley," *Bulletin of the Seismological Society of America*, vol. 100, pp. 1427–1455, Aug. 2010.

[9] E. Maufroy, V. M. Cruz-Atienza, and S. Gaffet, "A Robust Method for Assessing 3-D Topographic Site Effects: A Case Study at the LSBB Underground Laboratory, France," *Earthquake Spectra*, vol. 28, pp. 1097–1115, Aug. 2012.

[10] J. F. Semblat, M. Kham, E. Parara, P. Y. Bard, K. Pitilakis, K. Makra, and D. Raptakis, "Seismic wave amplification: Basin geometry vs soil layering," *Soil Dynamics and Earthquake Engineering*, vol. 25, pp. 529–538, Aug. 2005.

[11] A. M. Chandler, "Building damage in Mexico City earthquake," *Nature*, vol. 320, pp. 497–501, Apr. 1986.

[12] J. G. Anderson, P. Bodin, J. N. Brune, J. Prince, S. K. Singh, R. Quaas, and M. Onate, "Strong ground motion from the Michoacan, Mexico, earthquake," *Science*, vol. 233, no. 4768, pp. 1043–1049, 1986. Publisher: American Association for the Advancement of Science.

[13] C. L. Dufka, "The Mexico City Earthquake Disaster," *Social Casework*, vol. 69, pp. 162–170, Mar. 1988.

[14] P.-Y. Bard, M. Campillo, F. J. Chávez-Garcia, and F. Sánchez-Sesma, "The Mexico Earthquake of September 19, 1985—A Theoretical Investigation of Large- and Small-scale Amplification Effects in the Mexico City Valley," *Earthquake Spectra*, vol. 4, pp. 609–633, Aug. 1988.

[15] S. Singh, E. Mena, and R. Castro, "Some aspects of source characteristics of the 19 September Michoacan earthquake and ground amplification in and near Mexico City from strong ground motions data," *Bull. Seism. Soc. Am*, vol. 78, no. 2, p. 451, 1988.

[16] A. Levret, C. Loup, and X. Goula, "The Provence earthquake of 11th June 1909 (France). A new assessment of near field effects," *Modern Approaches in Geophysics*, pp. 383–399, 1988.

[17] D. M. Boore, "The effect of simple topography on seismic waves: Implications for the accelerations recorded at Pacoima Dam, San Fernando Valley, California," *Bulletin of the Seismological Society of America*, vol. 63, pp. 1603–1609, Oct. 1973.

[18] H. Kawase and K. Aki, "Topography effect at the critical SV-wave incidence: Possible explanation of damage pattern by the Whittier Narrows, California, earthquake of 1 October 1987," *Bulletin of the Seismological Society of America*, vol. 80, pp. 1–22, Feb. 1990.

[19] S. A. Ashford and N. Sitar, *Seismic response of steep natural slopes*. Earthquake Engineering Research Center, University of California, 1994.

[20] P. Spudich, M. Hellweg, and W. H. K. Lee, "Directional topographic site response at Tarzana observed in aftershocks of the 1994 Northridge, California, earthquake: Implications for mainshock motions," *Bulletin of the Seismological Society of America*, vol. 86, pp. S193–S208, Feb. 1996.

[21] D. M. Boore, "A note on the effect of simple topography on seismic SH waves," *Bulletin of the Seismological Society of America*, vol. 62, pp. 275–284, Feb. 1972.

[22] L. L. Davis and L. R. West, "Observed effects of topography on ground motion," *Bulletin of the Seismological Society of America*, vol. 63, pp. 283–298, Feb. 1973.

[23] A. M. Rogers, L. J. Katz, and T. J. Bennett, "Topographic effects on ground motion for incident P waves: A model study," *Bulletin of the Seismological Society of America*, vol. 64, pp. 437–456, Apr. 1974.

[24] W. D. Smith, "The Application of Finite Element Analysis to Body Wave Propagation Problems," *Geophysical Journal International*, vol. 42, pp. 747–768, Aug. 1975.

[25] L. B. Sills, "Scattering of horizontally-polarized shear waves by surface irregularities," *Geophysical Journal International*, vol. 54, pp. 319–348, Aug. 1978.

[26] D. W. Griffiths and G. A. Bollinger, "The effect of Appalachian Mountain topography on seismic waves," *Bulletin of the Seismological Society of America*, vol. 69, pp. 1081–1105, Aug. 1979.

[27] B. E. Tucker, J. L. King, D. Hatzfeld, and I. L. Nersesov, "Observations of hard-rock site effects," *Bulletin of the Seismological Society of America*, vol. 74, pp. 121–136, Feb. 1984.

[28] S. H. Hartzell, D. L. Carver, and K. W. King, "Initial investigation of site and topographic effects at Robinwood Ridge, California," *Bulletin of the Seismological Society of America*, vol. 84, pp. 1336–1349, Oct. 1994.

[29] H. Pedersen, B. L. Brun, D. Hatzfeld, M. Campillo, and P.-Y. Bard, "Ground-motion amplitude across ridges," *Bulletin of the Seismological Society of America*, vol. 84, no. 6, pp. 1786–1800.

[30] S. Chaillat, M. Bonnet, and J.-F. Semblat, "A Fast Multipole Method formulation for 3D elastodynamics in the frequency domain," *Comptes Rendus Mécanique*, vol. 335, pp. 714–719, Nov. 2007.

[31] S. Chaillat, M. Bonnet, and J.-F. Semblat, "A multi-level fast multipole BEM for 3-D elastodynamics in the frequency domain," *Computer Methods in Applied Mechanics and Engineering*, vol. 197, pp. 4233–4249, Sept. 2008.

[32] P.-Y. Bard, "Diffracted waves and displacement field over two-dimensional elevated topographies," *Geophysical Journal International*, vol. 71, pp. 731–760, Dec. 1982.

[33] M. Bouchon, C. A. Schultz, and M. N. Toksöz, "Effect of three-dimensional topography on seismic motion," *Journal of Geophysical Research: Solid Earth*, vol. 101, no. B3, pp. 5835–5846, 1996.

[34] S. A. Ashford, N. Sitar, J. Lysmer, and N. Deng, "Topographic effects on the seismic response of steep slopes," *Bulletin of the Seismological Society of America*, vol. 87, pp. 701–709, June 1997.

[35] F. J. Sánchez-Sesma, "Elementary solutions for response of a wedge-shaped medium to incident SH and SV waves," *Bulletin of the Seismological Society of America*, vol. 80, pp. 737–742, June 1990.

[36] Y. Nakamura, "A method for dynamic characteristics estimation of surface layers using microtremor on the surface," *RTRI report*, vol. 4, pp. 18–27, 1988.

[37] F. J. Chávez-García, L. R. Sánchez, and D. Hatzfeld, "Topographic site effects and HVSR. A comparison between observations and theory," *Bulletin of the Seismological Society of America*, vol. 86, pp. 1559–1573, Oct. 1996.

[38] R. D. Borcherdt, "Effects of local geology on ground motion near San Francisco Bay," *Bulletin of the Seismological Society of America*, vol. 60, pp. 29–61, Feb. 1970.

[39] F. Omori, "Note on the Destructive Earthquakes in the Shinanogawa Valley and those along the Japan Sea Coast," *Tokyo Sugaku-Buturigakkwai Kizi Dai 2 Ki*, vol. 4, no. 15, pp. 288–293, 1908.

[40] K. Kanai and T. Tanaka, "On microtremors VIII," *Bulletin of the Earthquake research institute*, vol. 39, pp. 97–115, 1961.

[41] Y. Ohta, H. Kagami, N. Goto, and K. Kudo, "Observation of 1- to 5-second microtremors and their application to earthquake engineering. Part I. Comparison with longperiod accelerations at the Tokachi-Oki earthquake of 1968.," *Bull. Seism. Soc. Am.*, vol. 68, pp. 767–79, 1978.

[42] H. Kagami, S. Okada, K. Shiono, M. Oner, M. Dravinski, and A. K. Mal, "Observation of 1- to 5-second microtremors and their application to earthquake engineering. Part III. A two-dimensional study of site effects in the San Fernando Valley," *Bulletin of the Seismological Society of America*, vol. 76, pp. 1801–1812, Dec. 1986.

[43] H. Yamanaka, M. Dravinsky, and H. Kagami, "Continuous measurments of microtremors on sediments and basement in Los Angeles, California," *Bull. Seism. Soc. Am.*, vol. 86, pp. 1595–1609, 1993.

[44] M. I.-v. Seht and J. Wohlenberg, "Microtremor measurements used to map thickness of soft sediments," *Bulletin of the Seismological Society of America*, vol. 89, pp. 250–259, Feb. 1999.

[45] T. Suzuki, "Amplitude of Rayleigh Waves on the Surface of a Stratified Medium," *Bulletin of the Earthquake Research Institute, Tokyo Imperial University*, vol. 11, pp. 187–195, June 1933.

[46] Y. Ohta, "On the phase velocity and amplitude distribution of Rayleigh type waves in stratified double layer (in case of $\lambda \neq \mu$)," *Zisin*, vol. 2, no. 16, pp. 12–25, 1963.

[47] M. Nogoshi and T. Igarashi, "On the propagation characteristics of microtremors," *J. Seism. Soc. Japan*, vol. 23, pp. 264–280, 1970.

[48] M. Nogoshi and T. Igarashi, "On the amplitude characteristics of microtremor (part 2): Journal of the Seismological Society of Japan," 1971.

[49] P.-Y. Bard and others, "Microtremor measurements: a tool for site effect estimation," *The effects of surface geology on seismic motion*, vol. 3, pp. 1251–1279, 1999. Publisher: Balkema, Rotterdam.

[50] B. Lebrun, D. Hatzfeld, and P. Y. Bard, "Site Effect Study in Urban Area: Experimental Results in Grenoble (France)," in *Earthquake Microzoning* (A. Roca and C. Oliveira, eds.), Pageoph Topical Volumes, pp. 2543–2557, Basel: Birkhäuser, 2002.

[51] B.-C. Sylvette, C. Cécile, B. Pierre-Yves, C. Fabrice, M. Peter, K. Jozef, and D. Fäh, "H/V ratio: a tool for site effects evaluation. Results from 1-D noise simulations," *Geophysical Journal International*, vol. 167, pp. 827–837, Nov. 2006.

[52] S. Molnar, J. F. Cassidy, S. Castellaro, C. Cornou, H. Crow, J. A. Hunter, S. Matsushima, F. J. Sánchez-Sesma, and A. Yong, "Application of Microtremor Horizontal-to-Vertical Spectral Ratio (MHVSR) Analysis for Site Characterization: State of the Art," *Surveys in Geophysics*, vol. 39, pp. 613–631, July 2018.

[53] Y. Nakamura, "What Is the Nakamura Method?," *Seismological Research Letters*, vol. 90, pp. 1437–1443, July 2019.

[54] Y. Nakamura and A. Saito, "Estimation of Amplification Characteristics of Surface Ground and PGA Using Strong Motion Records in Japan," in *Proc. 17th JSCE Earthquake Engineering Symposium*, pp. 25–28, 1983.

[55] Y. Nakamura, "Research and development of intelligent earthquake disaster prevention systems UrEDAS and HERAS," *Proc. Japan Soc. Civil Eng*, vol. 1996, no. 531, pp. 1–33, 1996.

[56] J. Lermo and F. J. Chávez-García, "Site effect evaluation using spectral ratios with only one station," *Bulletin of the Seismological Society of America*, vol. 83, pp. 1574–1594, Oct. 1993.

[57] C. Lachet, D. Hatzfeld, P.-Y. Bard, N. Theodulidis, C. Papaioannou, and A. Savvaidis, "Site effects and microzonation in the city of Thessaloniki (Greece) comparison of different approaches," *Bulletin of the Seismological Society of America*, vol. 86, pp. 1692–1703, Dec. 1996.

[58] N. A. Haskell, "Crustal reflection of plane SH waves," *Journal of Geophysical Research (1896-1977)*, vol. 65, no. 12, pp. 4147–4150, 1960.

[59] K.-G. Hinzen, B. Weber, and F. Scherbaum, "On the resolution of h/v measurements to determine sediment thickness, a case study across a normal fault in the lower rhine embayment, germany," *Journal of Earthquake Engineering*, vol. 08, pp. 909–926, Nov. 2004.

[60] A. Gosar and A. Lenart, "Mapping the thickness of sediments in the Ljubljana Moor basin (Slovenia) using microtremors," *Bulletin of Earthquake Engineering*, vol. 8, pp. 501–518, June 2010.

[61] S. Castellaro, "The complementarity of H/V and dispersion curvesH/V and dispersion curves," *Geophysics*, vol. 81, pp. T323–T338, Nov. 2016. Publisher: GeoScienceWorld.

[62] H. Uebayashi, "Extrapolation of Irregular Subsurface Structures Using the Horizontal-to-Vertical Spectral Ratio of Long-Period Microtremors," *Bulletin of the Seismological Society of America*, vol. 93, pp. 570–582, Apr. 2003. Publisher: GeoScienceWorld.

[63] P. Guéguen, C. Cornou, S. Garambois, and J. Banton, "On the Limitation of the H/V Spectral Ratio Using Seismic Noise as an Exploration Tool: Application to the Grenoble Valley (France), a Small Apex Ratio Basin," *Pure and Applied Geophysics*, vol. 164, pp. 115–134, Jan. 2007.

[64] S. Özalaybey, E. Zor, S. Ergintav, and M. C. Tapırdamaz, "Investigation of 3-D basin structures in the İzmit Bay area (Turkey) by single-station microtremor and gravimetric methods," *Geophysical Journal International*, vol. 186, pp. 883–894, Aug. 2011. Publisher: Oxford Academic.

[65] A. Macau, B. Benjumea, A. Gabàs, S. Figueras, and M. Vilà, "The Effect of Shallow Quaternary Deposits on the Shape of the H/V Spectral Ratio," *Surveys in Geophysics*, vol. 36, pp. 185–208, Jan. 2015.

[66] J.-L. Chatelain, B. Guillier, F. Cara, A.-M. Duval, K. Atakan, P.-Y. Bard, and The WP02 SESAME team, "Evaluation of the influence of experimental conditions on H/V results from ambient noise recordings," *Bulletin of Earthquake Engineering*, vol. 6, pp. 33–74, Feb. 2008.

[67] S. Castellaro and F. Mulargia, "The Effect of Velocity Inversions on H/V," *Pure and Applied Geophysics*, vol. 166, pp. 567–592, Apr. 2009.

[68] P.-Y. Bard, C. Acerra, G. Aguacil, A. Anastasiadis, K. Atakan, R. Azzara, R. Basili, E. Bertrand, B. Bettig, F. Blarel, S. Bonnefoy-Claudet, B. Paola, A. Borges, M. Sørensen, L. Bourjot, H. Cadet, F. Cara, A. Caserta, J.-L. Chatelain, and S. Zacharopoulos, "Guidelines for the implementation of the H/V spectral ratio technique on ambient vibrations measurements, processing and interpretation," *Bulletin of Earthquake Engineering*, vol. 6, pp. 1–2, Mar. 2008.

[69] S. Gaffet, G. Cultrera, M. Dietrich, F. Courboulex, F. Marra, M. Bouchon, A. Caserta, C. Cornou, A. Deschamps, and J.-P. Glot, "A site effect study in the Verchiano valley during the 1997 Umbria-Marche (Central Italy) earthquakes," *Journal of seismology*, vol. 4, no. 4, pp. 525–541, 2000. Publisher: Springer.

[70] V. Graizer, "Low-velocity zone and topography as a source of site amplification effect on Tarzana hill, California," *Soil Dynamics and Earthquake Engineering*, vol. 29, no. 2, pp. 324–332, 2009. Publisher: Elsevier.

[71] B. LeBrun, D. Hatzfeld, P. Y. Bard, and M. Bouchon, "Experimental study of the ground motion on a large scale topographic hill at Kitherion (Greece)," *Journal of Seismology*, vol. 3, no. 1, pp. 1–15, 1999. Publisher: Springer.

[72] S. Molnar and J. F. Cassidy, "A comparison of site response techniques using weak-motion earthquakes and microtremors," *Earthquake spectra*, vol. 22, no. 1, pp. 169–188, 2006.

[73] B. Hassani, A. Yong, G. M. Atkinson, T. Feng, and L. Meng, "Comparison of Site Dominant Frequency from Earthquake and Microseismic Data in CaliforniaComparison of Site Dominant Frequency from Earthquake and Microseismic Data in California," *Bulletin of the Seismological Society of America*, vol. 109, pp. 1034–1040, June 2019. Publisher: GeoScienceWorld.

[74] N. Makhoul and J. Harb, "Dynamic properties of Byblos municipality building with soil-structure interaction using geophysical methods," *Procedia Engineering*, vol. 199, pp. 206–211, Jan. 2017.

[75] B. Guillier, C. Cornou, J. Kristek, P. Moczo, S. Bonnefoy-Claudet, P. Y. Bard, and D. Fäh, "Simulation of seismic ambient vibrations: does the H/V provide quantitative information in 2D-3D structures," in *Third international symposium on the effects of surface geology on seismic motion Grenoble, France*, vol. 30, 2006.

[76] F. J. Sánchez-Sesma and M. Campillo, "Diffraction of P, SV, and Rayleigh waves by topographic features: A boundary integral formulation," *Bulletin of the Seismological Society of America*, vol. 81, no. 6, pp. 2234–2253, 1991. Publisher: The Seismological Society of America.

[77] J. Lermo and F. J. Chávez-García, "Are microtremors useful in site response evaluation?," *Bulletin of the Seismological Society of America*, vol. 84, pp. 1350–1364, Oct. 1994.

[78] C. B. Park, R. D. Miller, and J. Xia, "Multichannel analysis of surface waves," *Geophysics*, vol. 64, no. 3, pp. 800–808, 1999. Publisher: Society of Exploration Geophysicists.

[79] J. Xia, R. D. Miller, and C. B. Park, "Estimation of near-surface shear-wave velocity by inversion of Rayleigh waves," *Geophysics*, vol. 64, no. 3, pp. 691–700, 1999. Publisher: Society of Exploration Geophysicists.

[80] C. B. Park, R. D. Miller, J. Xia, and J. Ivanov, "Multichannel analysis of surface waves (MASW)—active and passive methods," *The Leading Edge*, vol. 26, no. 1, pp. 60–64, 2007. Publisher: Society of Exploration Geophysicists.

[81] C. B. Park, R. D. Miller, N. Rydén, J. Xia, and J. Ivanov, "Combined use of active and passive surface waves," *Journal of Environmental and Engineering Geophysics*, vol. 10, no. 3, pp. 323–334, 2005. Publisher: GeoScienceWorld.

[82] P. Theves-Costa, L. Matias, and P. Bard, "Seismic behaviour estimation of thin alluvium layers using microtremors recordings," *Soil Dynamics and Earthquake Engineering*, vol. 15, pp. 201–209, 1996.

[83] M. Mirzaoglu and . Dýkmen, "Application of microtremors to seismic microzoning procedure," *Journal of the Balkan Geophysical Society*, vol. 6, pp. 143–156, Aug. 2003.

[84] A. Pagliaroli, K. Pitilakis, F. J. Chávez-García, D. Raptakis, P. Apostolidis, O.-J. Ktenidou, M. Manakou, and G. Lanzo, "Experimental study of topographic effects using explosions and microtremors recordings," in *Fourth International Conference on Earthquake Geotechnical Engineering, Thessaloniki, Greece*, 2007.

[85] F. Panzera, G. Lombardo, and R. Rigano, "Evidence of topographic effects through the analysis of ambient noise measurements," *Seismological Research Letters*, vol. 82, no. 3, pp. 413–419, 2011. Publisher: Seismological Society of America.

[86] F. Scherbaum, K.-G. Hinzen, and M. Ohrnberger, "Determination of shallow shear wave velocity profiles in the Cologne, Germany area using ambient vibrations," *Geophysical Journal International*, vol. 152, no. 3, pp. 597–612, 2003. Publisher: Blackwell Publishing Ltd Oxford, UK.

[87] E. Zor, S. Özalaybey, A. Karaaslan, M. C. Tapırdamaz, S. . Özalaybey, A. Tarancıoğlu, and B. Erkan, "Shear wave velocity structure of the İzmit Bay area (Turkey) estimated from active–passive array surface wave and single-station microtremor methods," *Geophysical Journal International*, vol. 182, pp. 1603–1618, Sept. 2010. Publisher: Oxford Academic.

EURODYN 2020
XI International Conference on Structural Dynamics
M. Papadrakakis, M. Fragiadakis, C. Papadimitriou (eds.)
Athens, Greece, 23–26 November 2020

HYBRID COLLAPSE TEST OF STEEL COLUMNS WITH NONLINEAR FRAME SUBSTRUCTURING AND FORCE REDISTRIBUTION

Konstantinos A. Skalomenos[1,2], Masahiro Kurata[2], Yoshiki Ikeda[2]

[1]Department of Civil Engineering, University of Birmingham
Edgbaston, B15 2TT, Birmingham, United Kingdom
e-mail: k.skalomenos@bham.ac.uk

[2]Disaster Prevention Research Institute, Kyoto University
Gokasho, Uji, 611-0011, Kyoto, Japan

Keywords: Steel MRFs, Pushover analysis, Hybrid test, Steel tubular columns, Collapse

Abstract. *A hybrid test method that uses the nonlinear static (pushover) analysis to examine the static force-deformation response of building structures is presented. The ultimate performance of the columns at the base of steel moment-resisting-frames (MRFs) is evaluated experimentally considering force redistribution due to the failures of panel zones and beams. The test method combines static sub-structuring techniques and finite element analysis methods. The behavior of the steel MRF is simulated by the finite element analysis program ABAQUS, while the first story column is physically tested online. Three actuators are used to simulate the physical continuity between the analytical and experimental substructures by controlling the axial load, the drift angle, and the bending moment distribution along the column length. A square tubular steel column was tested as a part of a five-storey five-bay steel MRF. The frame was deformed to a roof drift equal to 12% using pushover analysis that incorporates a novel mixed force/displacement controlling algorithm. The measured storey drift for the tested column was almost 30.0%. The test system ensured realistic loading and boundary conditions to the column sub-structure, which was tested in full interaction with the MRFs until global frame collapse. The frame deformed in a collapse mechanism that involved the first two storeys.*

1 INTRODUCTION

In recent years, steel is becoming an increasingly popular construction material [1]. The benefits and reason for the increase in popularity include the speed of erection, reliability of components and high strength to weight ratio thus allowing smaller foundations. As a high-performance structural type, steel moment-resisting-frames (MRFs) usually constitute the main earthquake or wind resistant mechanism in multi-storey buildings [1]. In seismic design, the large inherent ductility of steel MRFs allows engineers to adopt larger behavior factors q (or reduction factors R) compared to other structural types, and potentially, steel MRFs can withstand multiple damages in members and connections when they are subjected to intense single or multiple hazard events. Nevertheless, the sudden failure of individual components increases force demands to the adjacent elements and leads to a significant internal force redistribution, which is not intended in the inelastic design.

When the columns of the first storey are design to be fixed to the foundation beam, they exhibit multiple failures such as yielding, local buckling, and fracture. Although evaluating the ultimate behavior of columns experimentally has been the main research topic for many years in the field [2-5], this has been mostly done by treating the column as an individual member with a given length. However, as far as the inelastic behavior of the framed structure is concerned in the preliminary design stage, local failures occurred in the column itself or in the neighboring components, such as beams, panel zones and connections [6] (Figure 1a) can define new loading boundaries to the original tested column length. As shown in Figure 1b, the moment at the top of the column subassembly which is initially considered to be zero (inflection point) in cantilever column tests can take positive or negative values depending on the failure level and failure sequences occurred in the column and the remaining structure.

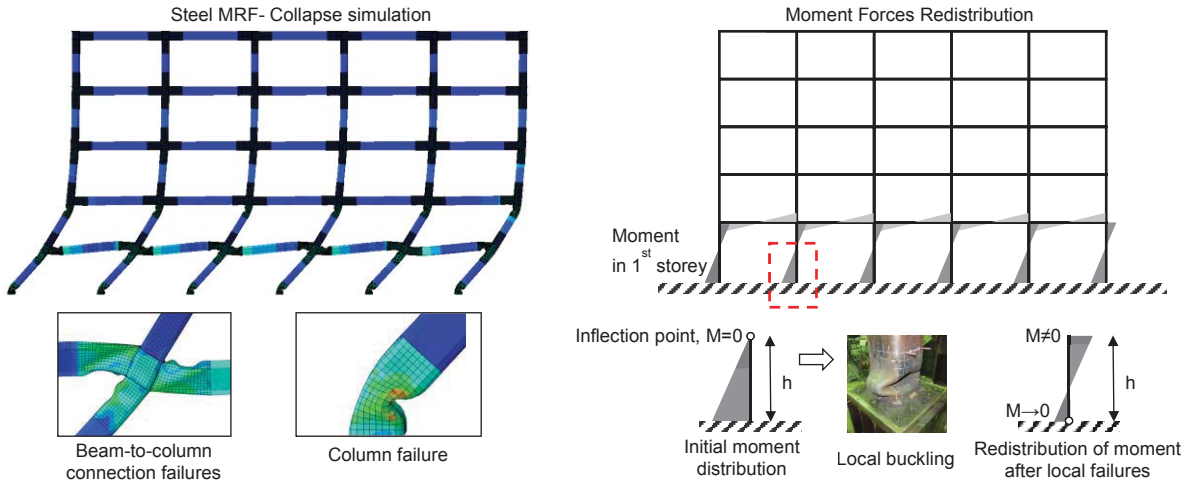

Figure 1: (a) Collapse simulation of a 5-storey 5-bay steel framed structure, local buckling failures in beams and columns [6]; (b) moment redistribution in columns at base after local buckling in beams and columns.

This paper develops an experimental platform for conducting column tests transferring the pragmatic loads and deformation demands to the column boundaries considering the inelastic behavior of the whole framed structure. To achieve this scope, a substructure-based hybrid test environment is developed for subjecting column specimens to collapse by performing in parallel an advanced inelastic static pushover analysis to building structure. The test method considers online updating of the model based on the experimental information. The redistribution of

force and ductility demands induced by the failures of the peripheral to the column building members is imposed by incorporating an appropriate number of loading jacks linked online to a finite element analysis performed in ABAQUS [7].

A square tubular column is physically tested to evaluate the proposed test platform. Three actuators that control the axial load, the moment at the column base and top, and the lateral deformations are used to simulate the physical continuity between the analysis frame and the test column. A MATLAB [8] user-subroutine interferes on the main control program and ABAQUS [7] to impose the target drift angle and loads to the column quasi-statically. The ultimate capacity of the column sub-structure is evaluated up to almost 30% storey drift, which corresponds to a roof drift equal to 12%. The test method is reasonable, and a smooth operation is achieved. By using the proposed test method, columns can be tested under various frame design parameters, and the collapse behavior of the column sub-structure and frame can be clarified with reasonable accuracy.

2 BUILDING STRUCTURE

The structure considered in this study is a moment-resisting-frame (MRF) of a prototype five-storey, five-bay steel office building designed based on the Japanese seismic design code [9, 10]. It has a rectangular floor plan with aspect ratio equal to 1.70. The longitudinal dimension L_X has length 32.0 m and five bays, while the transverse dimension L_Y has length 18.6m and three bays. In Figure 2a, the structural system of a typical floor plan is presented while in Figure 2b the elevation of the building is shown. The total building's height is 20.50 m. The structural system illustrated in Figure 2a consists of three planar moment resisting frames (MRFs) along the X axis and two planar MRFs along the Y axis. The building has square tube column sections (width×thickness: 500×22 in mm) and H beam sections (height×width×web thickness×flange thickness: 600×250×12×19 for the first three storeys and H-600×250×12×22 for the last two storeys). Grade of steels BCP325 and SN490B were adopted for columns and beams, respectively. The ultimate strength design of the building was achieved through a characteristic factor $D_s = 0.25$ (i.e., behavior factor $q = 4.0$), while the allowable strength and drift limitation requirement of 1 / 200 was satisfied for a base shear coefficient $C_0 = 0.20$. The period of the building is 0.94 sec along the X axis and 0.90 sec along the Y axis. A full description of the building can be found in [6].

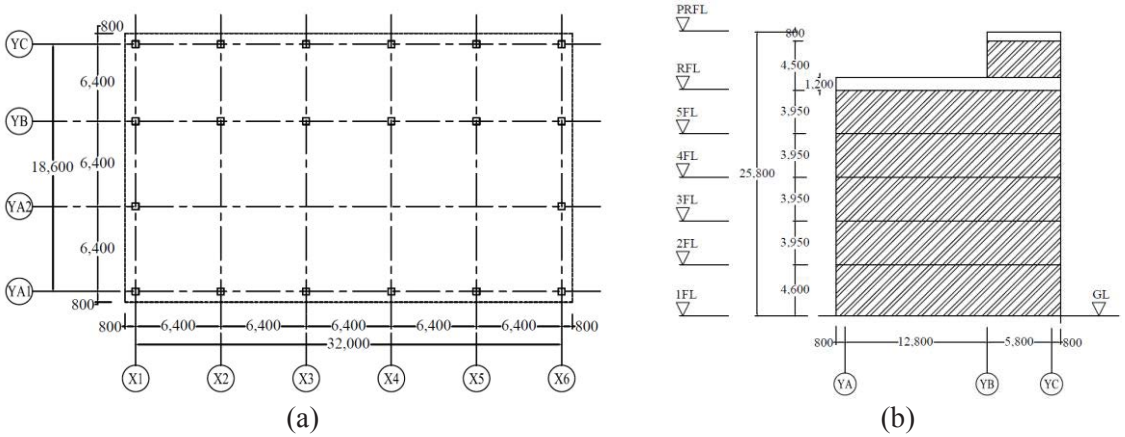

(a) (b)

Figure 2: (a) Plan view of the building; and (b) side view of the building.

3 ONLINE TEST METHOD

3.1 Concept

The concept of the test method is illustrated in Figure 3a and b. One plane steel MRF of the three along the X direction shown in Figure 1 is considered. The steel MRF is divided into two parts: (a) the analytical; and (b) the experimental substructure. The experimental substructures are the column at the building base while the rest structure consists the analytical substructure. The numerical model is created with the aid of the FEA software ABAQUS [7], which can capture with fair accuracy the non-linear behavior of frame components with ultimate failure that of local buckling. Details of the FEA model are given in a following subsection. The test of the column specimen is to acquire accurate information about the restoring forces and column stiffness. The restoring forces are applied to the numerical substructure to reproduce the restraint of the first story column.

In Figure 3b, the rotation and the moment at the column base are denoted by the letters θ_i and M_i, respectively. In the proposed on-line test method, the column bases are excluded from the frame model and replace by a non-linear rotational spring with constant $K_{rot,i}$. The column height is considered equal to the clear mid-height of the first storey. The axial force reaction and the moment of the column top, as obtained from the FEA for a given θ_i, are imposed to the column substructure by means of three jacks. The on-line test is conducted in many steps i. At each loading step, the restoring moment of the column substructure is measured experimentally (M_i) and is used along the corresponding θ_i to predict the spring constant $K_{rot,i+1}$ of the following step i+1 in the numerical model to reproduce the actual column restraint. The next analysis step is performed with the updated model. At the i+1 analysis step, the difference between the experimental and numerical M_i at the previous analysis step i, is imposed as external pseudo moment to compensate the over- or under-estimation of the column restraint. A restart procedure featured by the FEA is repeatedly used to accommodate the restored information of the hybrid test at each step operated by MATLAB main program developed in [11, 12].

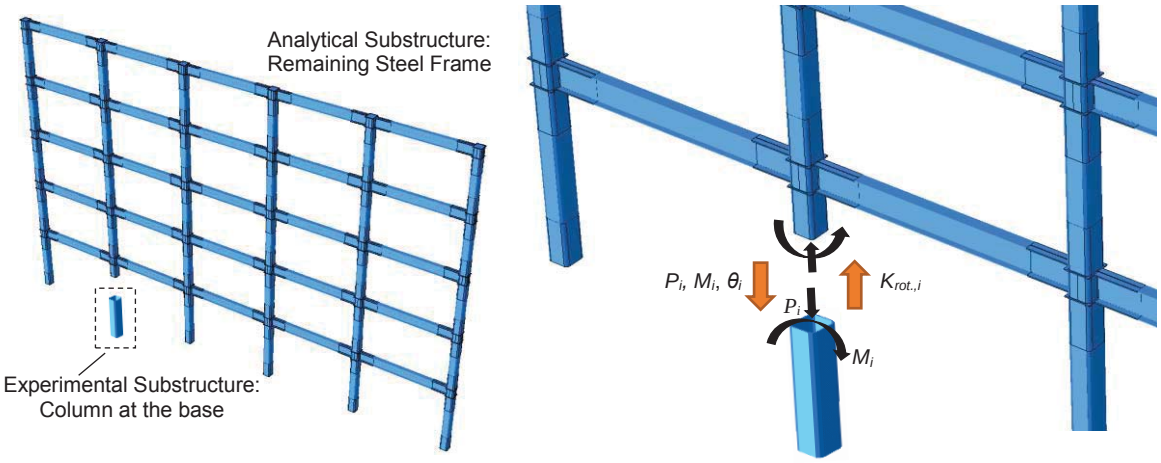

Figure 3 (a) Sub-structuring concept; (b) On-line update of column-frame boundary conditions.

3.2 Finite Element Model of the Analytical Substructure

The plane frame shown in Figure 3a was modelled by the finite element analysis software ABAQUS [7] using the fishbone sub-structuring technique [13]. The overall view and modelling details of the fishbone model is shown in Figure 4. The model developed is a mixed shell/beam element model that combines the powerful nonlinear S4R shell elements with beam-column elements. Shell elements were used in the critical regions of the building, such as beam-column connections, where strong geometrical nonlinearities (e.g., local buckling) are expected to take place. Beam-column elements were used for the remaining length of the beams and columns, which tend to remain mostly elastic. The inelastic behavior of column at the base is simulated through a non-linear moment-rotation spring. The spring constant is calculated using the experimental data at each restart analysis step, as discussed in the previous section.

For sufficiently small strains, steel is modeled as a linear elastic isotropic material with density ρ=7850 kg/m^3, modulus of elasticity E=205 GPa and Poisson ratio ν=0.3. For large strain analysis, the constitutive model used for steel includes pressure-independent plasticity with kinematic hardening. A strain hardening equal to 1.0% of the modulus of elasticity was assigned.

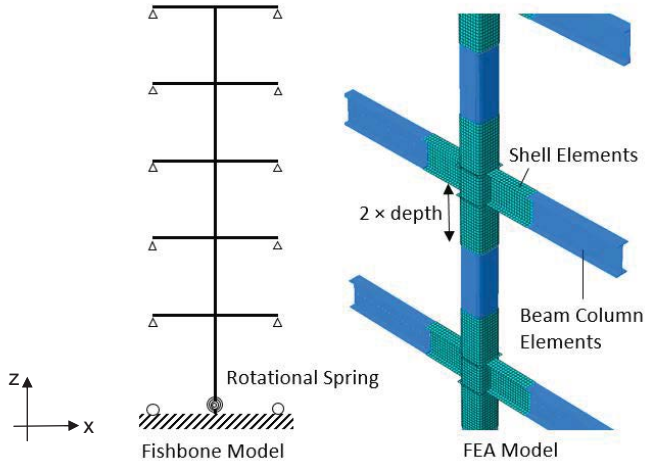

Figure 4 Fishbone model in ABAQUS [7].

3.3 Analysis

Static pushover analysis has been widely used in earthquake engineering and design of buildings, such as in the Capacity Spectrum Method (CSM) [14]. In general, pushover analysis is used for seismic evaluation of existing buildings and design verification for new construction in order to identify damage states and their correlation with the amplitude of the seismic ground motion. Among the advantages of the pushover analysis method are that it is simple, fast and provides all the capacity points of a structure until collapse [15, 16].

The force distribution that is applied to the structure in each increment of the static pushover collapse test is updated according to the first eigenmode of the structure. This eigenmode is calculated with the use of a shifted block Lanczos algorithm, similar to that developed and described in detail in [7, 17]. However, it is recognized that static analysis with force-control cannot be used to trace the descending branch of the structural response at large deformations. For the above reason, in this study the restart analysis is used only with general static analysis

with mixed force and displacement control. A full description of the inelastic pushover analysis platform used in present hybrid test can be found in [6].

3.4 Loading System and Test Substructure

Three hydraulic jacks ensure physical continuity between the analytical and experimental substructures by controlling axial loads, moments and column drifts. The test set-up is illustrated in Figure 5. One jack is placed vertically to impose the axial load (Jack 1: force control), while the other two are placed horizontally to apply the column rotations (Jack 2: displacement control) and moment at the column top (Jack 3: load control). The L-shaped element was designed to be as rigid as possible.

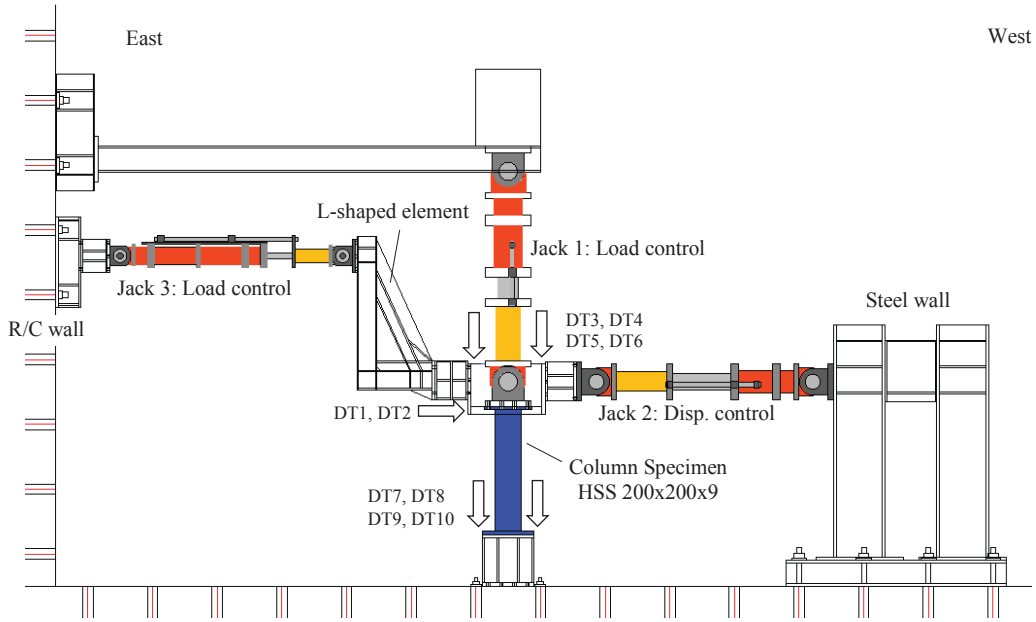

Figure 5 Test set-up for the online hybrid test.

Floor	Elastic Modulus [GPa]	Yield Stress (YS) [MPa]	Ultimate Stress (US) [MPa]	Stress at US	Elongation (%)
Flange	193	345	527	15.04	34.4
Corner	172	502	585	5.56	13.8

Table 1: Properties of column based on the coupon test results.

Linear displacement traducers (DT1 to DT10) were used to measure the rotation of the column top and basement as well as lateral story drifts. The column specimen had a square hollow structural steel (HSS) section with 200 mm width d, 9 mm thickness t and corner curvature r = 3.5t. The clear height of the column was equal to 802 mm while its total height measured from the column bottom to the middle point of the pin end of the vertical jack was equal to 1,030 mm. The column specimen was fabricated from a plate of conventional Japanese SN490 steel to realize equivalent behavior to BCP325 column in a small scale. Coupon tests were performed and material properties such as, elastic modulus, yield stress (YS), ultimate stress (US), strain measured at US, and rapture elongation are shown in Table 1.

4 TEST RESULTS

4.1 Overall Behavior

Figure 6 shows the hybrid static pushover collapse test. In Figure 6a the analytical substructures are illustrated at its both initial position and final position. The fishbone frame model deforms in a collapse mechanism that involves the first two stories. This collapse mechanism is identical with the one introduced in Figure 1a where the whole framed building was considered. The behavior of the column at base was investigated experimentally and the information was transferred to the analytical substructure through the hybrid simulation. In the fishbone frame model, active plastic hinge were formed at the column just below the panel zone of the second storey level and at the beam ends of the first storey. Figure 6b illustrates the overall view of the ultimate column deformation as controlled by the three jacks during the hybrid test. The progress of local buckling at the tested column is highlighted in Figure 6c.

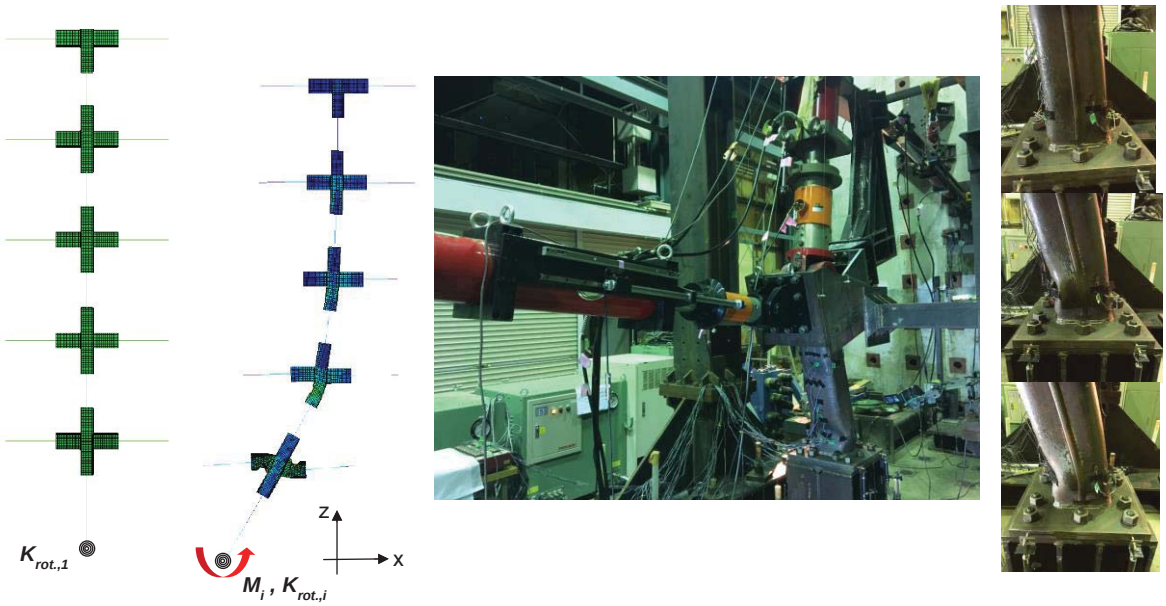

(a) (b) (c)

Figure 6 (a) Collapse simulation in Abaqus [7]; (b) column deformation controlled by the hybrid test set-up; (c) progress of local buckling during the test.

Figure 7a shows the pushover curve for building as obtained during the hybrid test. The period T of the fishbone frame model was 0.98 sec. The mode shape was [1.00; 2.13; 2.92; 3.54; 4.66] while the load proportion factor (LPF) during the test was [1.00; 1.78; 2.45; 2.97; 3.93]. The curve is presented in the typical fashion: total lateral force on the building (base shear force) normalized by the weight of the fishbone frame model on the vertical axis versus roof drift on the horizontal axis. The weight of the fishbone model W is equal to the total building's weight divided by three (number of the seismic resistant frames) and then divided by five for distributing equally the weight to the six columns. The building is seen to have an over-strength of more than 2 relative to its design base shear of 0.26W [7]. The pushover curve reaches 0.62W at a roof drift of 0.05 radians and then descends. The descending branch drops more steeply after reaching a roof drift of 0.07. Figure 7b shows the bending moment at the column base M_b against the roof drift. The M_b is normalized by the plastic moment of the square tubular column. The maximum $M_{b,max}$ was found to be 225 kNm at a roof drift of 0.06 radians. The calculated plastic moment M_p of the section is 155.60 kNm based on the flange yield stress (Table 1).

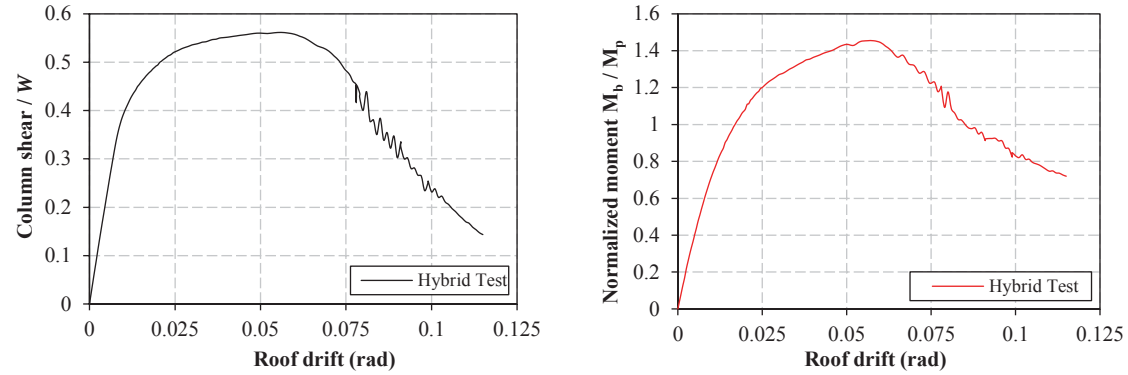

(a) (b)

Figure 7 (a) Pushover curve; (b) Bending moment at column base.

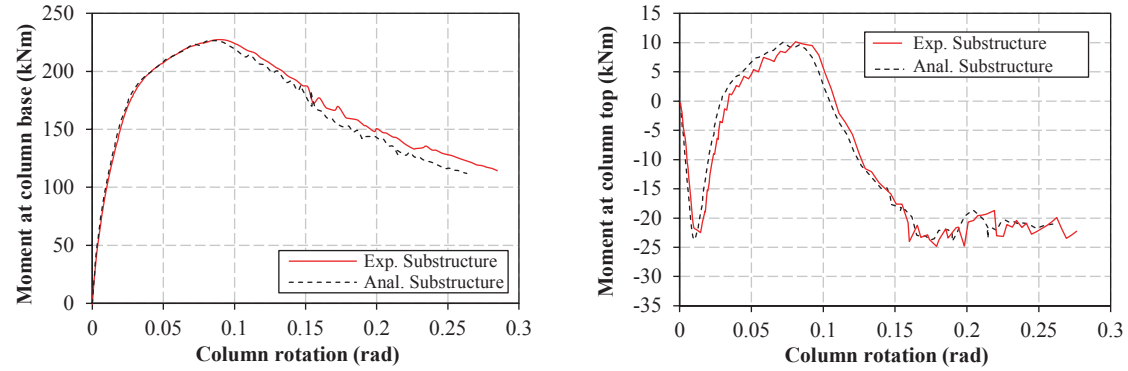

(a) (b)

Figure 7 Hybrid test consistency: (a) bending moment at column base M_b – column rotation; and (b) bending moment at column top M_t – column rotation.

4.2 Loading control

Figure 7a compares the bending moment at column base M_b – column rotation relationship between analytical and experimental substructures, while Figure 7b compares the bending moment at column top M_t – column rotation relationship in the same format. Based on these figures one can observe that the proposed hybrid simulation was successful in updating the analytical substructure based on the experimental values and vice versa. The moment distribution along the tested column was kept almost the same as the one determined in finite element analysis. All the jacks were synchronized accurately and effectively imposed the bending moments and rotations to the column specimen up to the very end of test. The variation of the bending moment at column top maintains the correct column curvature (single or double) as determined in frame analysis. The maximum $M_{t,max}$ was almost equal to -25 kNm, a value that corresponds to 11% of the maximum bending moment at column base ($M_{b,max}$ = 225 kNm).

5 CONCLUSIONS

A hybrid test method which uses the nonlinear adaptive static (pushover) analysis to evaluate the static force-deformation response of structures until collapse is presented. The method was validated on a five-storey five-bay steel moment-resisting frame (MRF) designed based on the Japanese seismic design code. Main conclusions of the present study are as follows:

- The hybrid test method uses finite element modelling methods for members and materials. Failures related to strength and stiffness reduction, such as shear inelastic deformation of panel zones and local buckling of beams, are captured with fairly accuracy. The load distribution transferred to the experimental substructure is updated accounting for the stiffness reduction.
- The analytical substructure is simplified further by adopting the fishbone modelling methods in order to reduce the computational time. The test system appears to ensure accurate loading and boundary conditions to the column test substructure. Overall, the fishbone model deformed in a similar way with the full five-storey five-bay MRF model. A collapse mechanism that involved the first two stories was observed.
- For the test substructure, a square tubular column located at the first storey of the frame was examined. The frame was deformed up to a 12% roof drift. The measured storey drift for the tested column was almost 30.0%. The maximum bending moment applied at column top was almost equal to -25 kNm, which is 11% of the maximum moment of the column ($M_{b,max}$ = 225 kNm).
- The building is seen to have an reserved capacity of more than 2 against its design base shear of 0.26W at the ultimate strength design. The pushover curve reaches 0.62W at a roof drift of 0.05 radians and then descends. The descending branch drops more steeply after reaching a roof drift of 0.07.

ACHNOWLEDGEMENTS

This work was supported by the New Exploratory Research Grant (2019H-04 / 3604835687) awarded to the first author by the Disaster Prevention Research Institute (DPRI). The authors are tankful to Nippon Steel Corporation for providing the column specimen. The authors are also grateful to Mr. Shingo Hamauzu, postgraduate of Kyoto University, and technicians of Structures Lab in DPRI for their valuable assistance. The research travel fund at University of Birmingham for conference attendance is gratefully acknowledged.

REFERENCES

[1] American Institute of Steel Construction (AISC), Structural Steel: An Industry Overview. AISC. 2018

[2] H. Krawinkler, Cyclic loading histories for seismic experimentation on structural components, *Earthquake Spectra* 12(1), 1996.

[3] J. Fogarty, S. El-Tawil, Collapse resistance of steel columns under combined axial and lateral loading, *Journal of Structural Engineering*, 142(1):04015091, ASCE, 2016.

[4] J. Cravero, A. Elkady, DG. Lignos, Experimental evaluation and numerical modeling of wide-flange steel columns subjected to constant and variable axial load coupled with lateral drift demands, *Journal of Structural Engineering*, 146(3): 04019222, ASCE, 2020.

[5] KA. Skalomenos, K. Hayashi, R. Nishi, H. Inamasu, M. Nakashima, Experimental behavior of concrete-filled steel tube columns using ultra-high strength steel, *Journal of Structural Engineering* 142(9), 04016057, ASCE, 2016.

[6] KA. Skalomenos, G. Papazafeiropoulos G, A computational method for performing nonlinear adaptive pushover analysis of structures through ABAQUS simulation, *paper ID*

19194 in Proceedings of 7th COMPDYN International Conference on Computational Methods in Structural Dynamics and Earthquake Engineering, 2019.

[7] ABAQUS, Analysis User's Manual version 6.14, Dassault Systems, 2016.

[8] MathWorks, Inc. MATLAB R2016a. Natick, MA: MathWorks, Inc., 2016.

[9] BSL, Building standard law, 2000 [in Japanese].

[10] BCJ, Structural provisions for building structures. Tokyo: Building Center of Japan, 1997 [in Japanese].

[11] KA. Skalomenos, M. Kurata, M. Nakashima M, On-line hybrid test method for evaluating the performance of structural details to failure, *Earthquake Engineering and Structural Dynamics* 47(3), 555-572, 2018.

[12] KA. Skalomenos, M. Nakashima, M. Kurata, Seismic capacity quantification of gusset-plate connections to fracture for ductility-based design, *Journal of Structural Engineering of*, 144(10): 04018195, ASCE, 2018.

[13] N. Luco, Y. Mori, Y. Funahashi, CA. Cornell, M. Nakashima, Evaluation of predictors of non-linear seismic demands using 'fishbone' models of SMRF buildings, *Earthquake Engineering and Structural Dynamics* 32, 2267-2288, 2003.

[14] SA. Freeman, Review of the development of the capacity spectrum method. *ISET Journal of Earthquake Technology*, 41(1), 1-13, 2004.

[15] AK. Chopra, RK. Goel, A modal pushover analysis procedure for estimating seismic demands for buildings. *Earthquake Engineering and Structural Dynamics*, 31, 561–582, 2002.

[16] P. Panyakapo, Cyclic pushover analysis procedure to estimate seismic demands for buildings. *Engineering Structures*, 66, 10-23, 2014.

[17] RG. Grimes, JG. Lewis, HD. Simon, A shifted block Lanczos algorithm for solving sparse symmetric generalized eigenproblems, *SIAM Journal on Matrix Analysis and Applications* 15(1), 228-272, 1994.

EURODYN 2020
XI International Conference on Structural Dynamics
M. Papadrakakis, M. Fragiadakis, C. Papadimitriou (eds.)
Athens, Greece, 23–26 November 2020

FRF-BASED MODAL TESTING OF HORIZONTALLY SWAYING STRUCTURES USING OCXO SYNCHRONISED WIRELESS ACCELERAMETERS FOR SIMULTANEOUS FORCE AND VIBRATION RESPONSE MEASUREMENTS

Wai Kei Ao[1], **and Aleksandar Pavic**[1]

[1]University of Exeter
College of Engineering, Mathematics and Physical Sciences
Kay Building, North Park Road, Exeter, EX4 4QF, UK
e-mail: wka203@exeter.ac.uk, a.pavic@exeter.ac.uk

Keywords: Force vibration, frequency response function (FRF), OCXO high-precision synchronised wireless accelerometers, modal analysis

Abstract. *This paper describes an experimental validation of a novel FRF-based modal testing system designed to measure experimentally sway modes of tall timber and other building structures. The test uses a set of synchronised electrodynamic shakers and oven-controlled crystal oscillator (OCXO) high-precision synchronised wireless accelerometers for simultaneous force and response measurements. This modal testing system makes no use of cables or radio-waves to connect all accelerometers simultaneously with the multi-channel data acquisition system but provides a perfect synchronised measurement of a practically unlimited number of force and response channels. The system will be used to to estimate experimentally sway modes of as-built tall timber buildings. Therefore, the aim of this paper is to demonstrate the feasibility of the OCXO-based system in high-rise building FRF measurements. Two nominally identical FRF-based modal testing exercises were carried out on a 15-tonne laboratory-based test floor structure supported by 4 columns in order to measure its horizontal 'swaying' modes of vibration using: (1) a well-established and quality assured 'wired' system based on a 20-channel spectrum analyser, and (2) OCXO-based wireless system. It was shown that the two methodologies produce almost identical modal testing results and that the OCXO-based method is robust and reliable for field utilisation on high-rise buildings.*

1 INTRODUCTION

High-rise buildings dominate the skylines of many cities in the world, which have decided to go 'up' rather than 'out' to cope with transportation and other challenges facing their growing population. Vibration serviceability due to wind-induced lateral sway has become the de-facto governing design criterion for economically designed novel high-rise buildings above 50 m, dictating the size, shape and therefore cost of such structures. Damping ratios and natural frequencies of key modes of vibration that can be excited by wind are key modal parameters which are used in design to size the structure and predict wind-induced sway vibrations of tall buildings in service.

However, recent practice shows that damping and natural frequencies of tall buildings are also quite unreliable parameters to assume in design. Underestimation of the fundamental natural frequency of up to 50 % by the finite element model (FEM) relative to its experimental counterpart is common. The situation with damping ratios is similar or worse due to uncertainties in the values of modal damping ratios measured in as-built buildings. Natural frequencies and damping ratios in as-built tall building structures are essentially non-linear and amplitude dependent. To an extent where is currently not known, therefore, the traditional output-only ambient vibration testing (AVT) or ambient vibration survey (AVS) methods for their estimation based only on measured responses to unmeasured ambient excitation which vary with time are naturally producing estimates of modal parameters which vary from one block of data to another.

A standard input-output modal test (MT) or experimental modal analysis (EMA) where both the excitation force and the corresponding dynamic response are measured with the aim of experimentally estimating a structure's frequency response function (FRF) is a much more powerful tool to deal with structural non-linearities and uncertain modal parameters such as the natural frequency and damping. For many decades, EMA has traditionally dominated aerospace and automotive sectors, whereas AVT has been very much used in experimental dynamic testing of large civil engineering structures. This despite the fact that AVT generally has in principle inferior performance as to its quality of modal parameters relative to EMA.

The key reason for this situation are practical difficulties in exciting a tall building with a measurable force, causing a measurable response without damaging the building at the point of excitation. If this problem is overcome the next logistical complication is measuring such responses simultaneously throughout the building needed to estimate experimentally mode shapes and complete the set of four modal properties: natural frequencies, modal damping ratios, modal masses and mode shapes. Therefore, MT based on FRFs in tall buildings are practically non-existent in literature.

This paper describes novel FRF-based MT of sway modes of a large 15-tonne laboratory structure using a set of synchronised electrodynamic shakers and OCXO high-precision synchronised wireless accelerometers for simultaneous force and response measurements. This MT system makes no use of cables or radio-waves to connect response accelerometers simultaneously with the multi-channel data acquisition system and provides perfect synchronous measurement of practically unlimited number of force and response channels. The system will be used to estimate sway modes via FRF-based MT of as-built tall timber buildings.

This paper has five sections. After the introduction in Section 1, the test structure is described in Section 2. Section 3 describes the novel FRF-based modal testing set-up for the horizontal sway modes of the test structure. Section 4 then describes the results of the modal testing and their interpretation. Finally, Section 5 provides conclusions.

2 TEST STRUCTURE

The test structure was a reconfigurable floor panel weighing approximately 15 tonnes, with approximate dimensions 7.5 m×5 m, as shown in Figure 1a. The test structure was placed indoors in the laboratory of Vibration Engineering Section, University of Exeter, UK. This was one of five possible configurations of the test structure which can be re-configured into two full-scale footbridges spanning 15 m and three floor panels with a surface area of around 40-50 m^2 [2]. The floor plate structure made of 12 sandwich plate systems (SPS) panels was supported by of two main girders (UB 457×191×82 mm) and two secondary beams (UB 305×165×40 mm). M22 countersunk bolts were used to inter-connect the SPS panels with each other through steel strips (SP02 200×2279×12 mm) running under the panels, as shown in Figure 1d, and make them acting as a continuous plate supported by four edge beams (SB01 UC 203×203×46 mm), as shown in Figure 1c. Figure 1b shows the support detail used to transfer the loading from the floor panel to the column (SC01 UC 203×203×46 mm). The size and shape of this structure made it a perfect test bed to try the new wireless FRF-based modal testing technique to measure its sway modes of vibration.

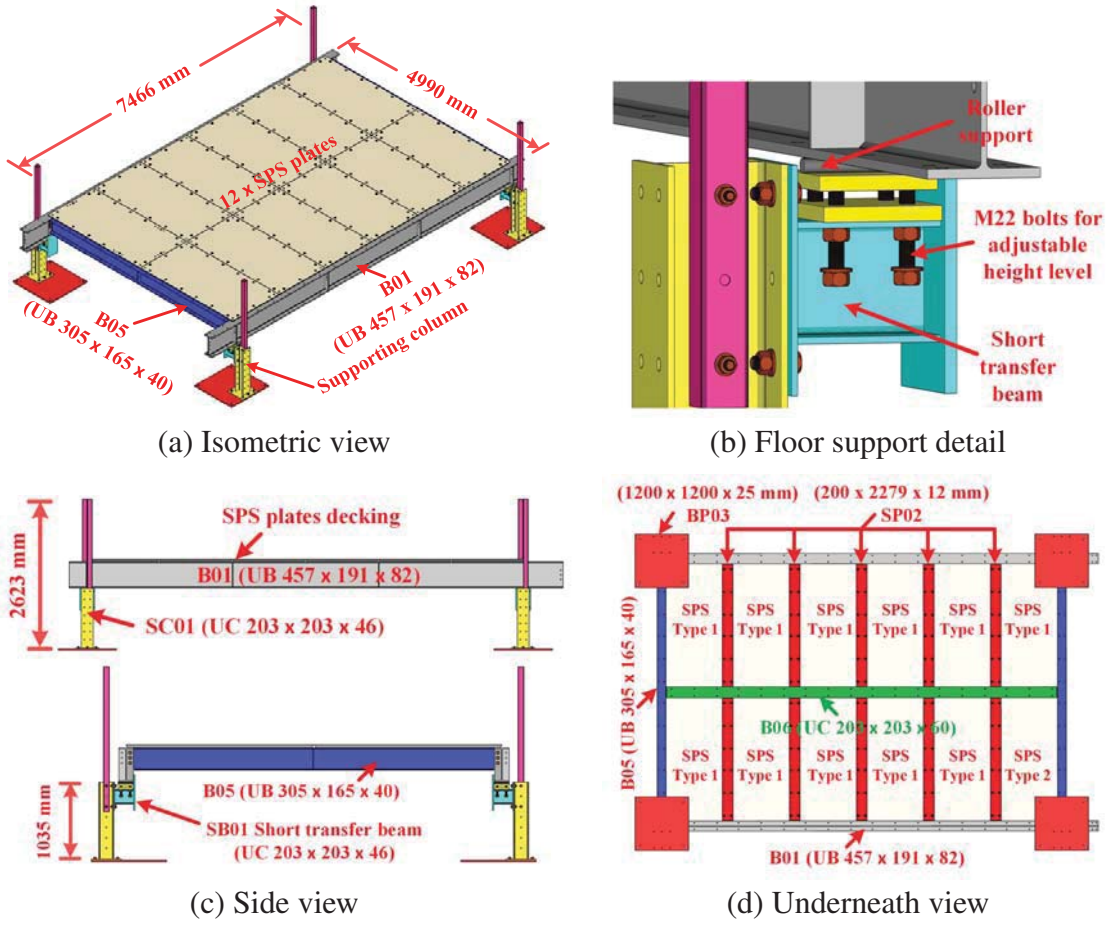

(a) Isometric view

(b) Floor support detail

(c) Side view

(d) Underneath view

Figure 1: Reconfigurable test-bed floor panel structure

3 MODAL TESTING SETUP

The main purpose of this modal testing exercise was to prove the feasibility of the novel modal testing system which had to satisfy the following requirements:

1. Fast in-situ setting up; this was facilitated by using wireless accelerometers;

2. Suitable for modal testing to estimate horizontal sway modes; facilitated by electrodynamic shakers able to generate a full range of measurable excitation forces in the horizontal direction with sufficiently low frequency content, and

3. Ability to measure as precisely as possible modal damping ratios and investigate nonlinear behaviour; this was facilitated by SIMO (single-input multi-output) FRF-measurement and modal testing strategy.

The significant novelty of the wireless system was that both the force and acceleration responses were recorded simultaneously using oven controlled crystal oscillator (OCXO) technology [3] for synchronisation of otherwise disconnected channels for acquiring the excitation force (by measuring acceleration of the known shaker moving mass) and the corresponding structural response. The use of this high-precision OCXO-synchronized data acquisition system meant that there was no need for any wired or wireless radio (GPS, Wi-Fi, UWB, GMS, 3G/4G/5G, etc.) connection while acquiring fully synchronised force and structural response data enabling FRF estimation.

The key reason for the above requirements is that the system had to be deployable in fully operational tall timber buildings, so as little as possible disruption and safety considerations dictated the need for a system which is fast to set-up and does not need wires running across floor levels which are notorious time consuming to setup and potentially unsafe due to tripping hazard.

3.1 Test grid and setup

Figure 2 shows the test grid featuring 15 test points (TPs) used in the modal testing. At each TP Honeywell QA750 force balanced accelerometers were placed to measure positive acceleration in the positive x direction, as shown in Figure 2. Moreover, two APS Dynamics Inc. shakers (Model 400) were positioned both at TP11 (denoted with two magenta triangles), to excite the structure horizontally in the x direction at a single degree of freedom. Therefore, for the purpose of the FRF estimation, TP11 was chosen as a reference point.

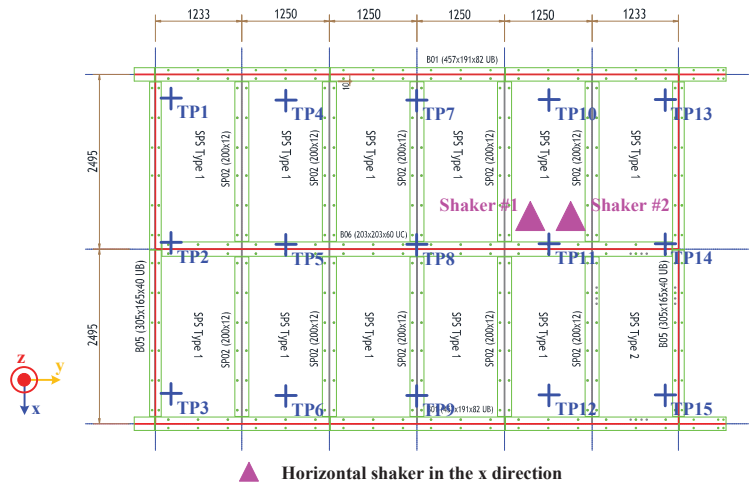

Figure 2: Test grid. Two horizontal shakers were positioned at TP11

Figure 3a shows the test structure instrumented in the VES laboratory. The five yellow boxes are the OCXO-synchronised data loggers. Up to four horizontally positioned QA750 sensors, as shown in Figure 3b, were connected to the data logger.

(a) Photo of the test structure

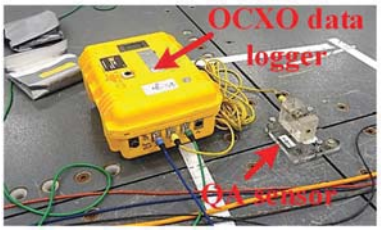

(b) Photo of data logger (yellow box) with acceleration sensor

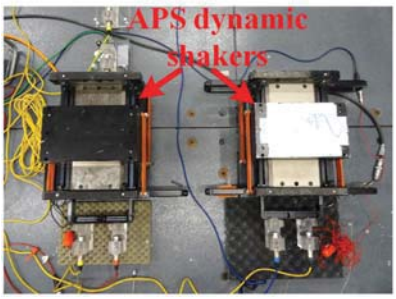

(c) Photo of two APS shakers

Figure 3: Photo of the test structure and equipment

Due to the limited number of the OCXO data loggers and accelerometers not all 15 test points and two shakers were possible to instrument with accelerometers at the same time. Therefore, the modal testing using the OCXO-based system was divided into acquiring two sets of FRF-data. The first set covered two shakers and 12 test points (TP1-12), and the second set covered again two shakers and the remaining three test points (TP13-15).

After finishing the OCXO-based input-output measurements, a well established and quality assured standard FRF-measurement method was used with the wired accelerometers in the measurement chain where the data acquisition and processing were done by a 20-channel Data Physics DP730 spectrum analyser (SA). This was done to obtain nominally identical FRF data for validation of the FRFs measured using the OCXO data loggers. Only excitation and response measurements pertinent to the x-direction (Figure 2) were carried out.

3.2 Methodology for measuring FRF data wirelessly

Figure 4 shows the block diagram representing the methodology of the OCXO and SA systems.

To run and control the 'wireless' FRF measurement using OCXO data loggers, a minimum wired system featuring SA was part of the measurement chain. This was done for two reasons:

1. To make use of the SA's ability to generate and post-process input-output data for a range of very useful excitation forcing functions traditionally used in FRF measurements (random, chirp, stepped sine and swept since, etc.), and

2. To quality assure OCXO-based FRF measurements considering that the OCXO data are not being monitored during the modal testing. Therefore, to check how the modal test

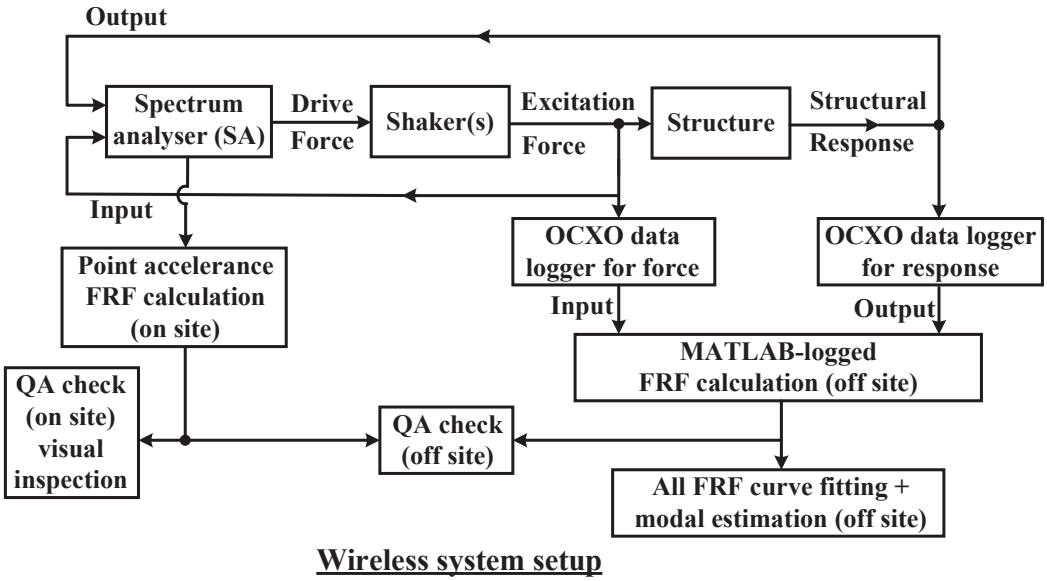

Figure 4: FRF-based modal testing scheme combining the 'wireless' OCXO-based measurement of FRFs across the whole structure with the limited 'wired' SA-based point-accelerance FRF measurement

was progressing a minimum wiring was used to measure only the point-accelerance FRF at TP11 using the SA in parallel with the OCXO system.

Such traditional SA-based FRF measurement was instantaneously available for visual inspection to determine if sufficient quality FRF data was being obtained and how many averages were used. The key underlying assumption was that the nominally identical OCXO-based FRF data, calculated using a different set of accelerometers just for the FRF point accelerance measurement, would - after post processing - produce the same FRF data as the SA-based counterpart. A key purpose of this testing exercise was to check if such assumption was correct. Normally, in point-accelerance FRF measurements pertinent to the building sway modes, the excitation shaker(s) and the data acquisition centre are very close towards the top of the building so there is no need for long wiring across several floor levels.

Therefore, at the reference test point, each of the two shakers had two sensors: one connected to the SA (wired) and the other to the OCXO data logger (wireless) (Figure 3c). In particular, one yellow OCXO box near TP11 and collecting the response data from that point and shakers acted as a 'master clock' for other OCXO boxes facilitating response measurements at other response points. This 'master clock' was then used synchronise other 'slave clocks' at the other locations. After the OCXO time synchronisation, each yellow box would have the same time clock a negligible delay of less than one micro-second was expected and the structural input-output measurement could start.

3.3 Methodology for measuring FRF data using wired system

Figure 5 shows photo of wired accelerometers at all 15 TPs featuring six 4-channel extension reels, external signal conditioners and DP730 spectrum analyser.

It can be seen that all connection cables and extension reel cables had to pass over the structure to the standard 20-channel SA-based data acquisition system. In a real building situation, cables from extension reels would run across many floors and over many floor levels making

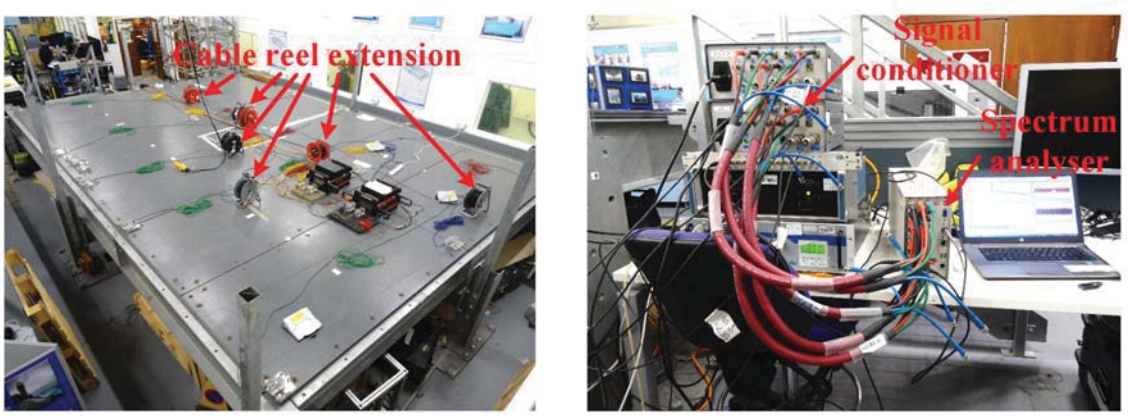

(a) Photo of modal testing (b) Photo of data acquisition system

Figure 5: Modal testing setup up using a standard 'wired' SA-based setup

their safe installation in an operational building time consuming and overall management quite challenging from health and safety as well as efficiency points of view. Figure 6 shows a standard 'wired' FRF measurement setup.

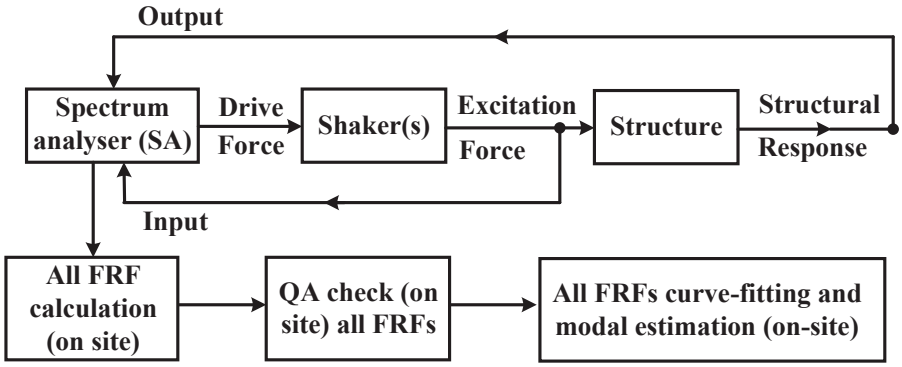

Wired system setup

Figure 6: FRF-based modal testing scheme based on the standard 'wired' setup featuring SA-based measurement of all FRFs

4 FORCE AND ACCELERATION RESPONSE DATA PROCESSING, FRF CALCULATION AND CURVE FITTING, AND ESTIMATION OF MODAL PROPERTIES

Figure 7 shows two raw data sample histories (sample number on the horizontal axis and voltage amplitude on the vertical axis) pertinent to the acceleration of the shaker armature. These two sets of data were recorded using two accelerometers connected side by side to the shaker armature (Figure 3c), so they represent nominally the same information. However, the blue trace was acquired using the OCXO data logger, and the red trace using the SA data acquisition. Although the two traces are nominally identical there is an unknown time shift between them. Strictly speaking, the duration of the time shift is not needed considering that the OCXO boxes were all synchronised. However, as the OCXO system was new there was a need to validate it against the SA data which were treated as a 'gold' standard. For that, at the end of the random excitation driven by a signal from the SA, the shaker mass was moved

manually to create a clear 'reference event' which was then used to determine exactly the time delay between the OXCO and SA data. This was found to be consistent across all comparable sets of OCXO- and SA-recorded data pertinent to the point mobility measurements enhancing confidence in the OXCO-recorded data. This delay was used to shift all OXCO-recorded data to look like the SA-recorded data to enable easier visual comparison.

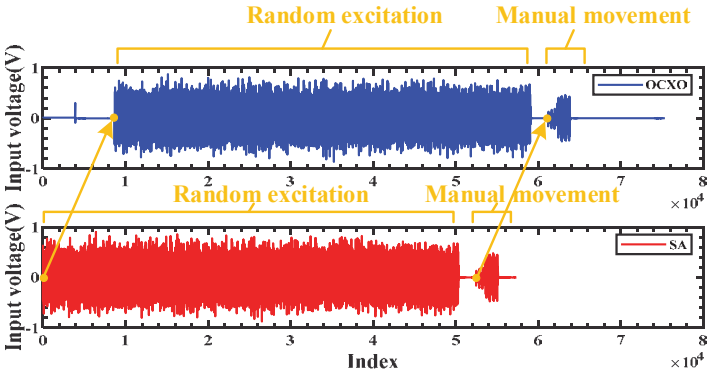

Figure 7: Comparison of the raw OCXO- and SA-recorded data pertinent to the shaker force measured by measuring acceleration of the known armature mass

Figure 8 provides a visual comparison of such two sets of data. It can be seen that the two sets of data are very much identical for practical purposes which validated the OCXO-recoded data.

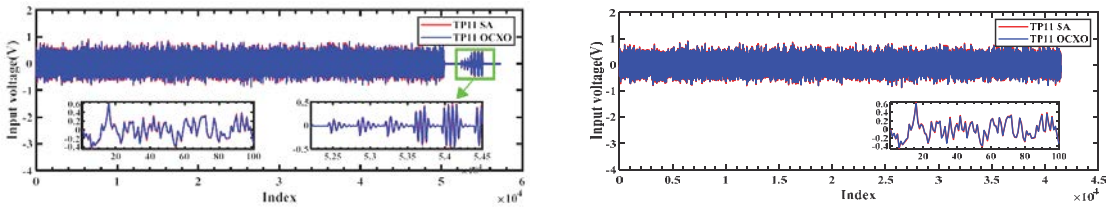

(a) Voltage time history showing the manual mass movement

(b) Voltage time history after removing the manual movement

Figure 8: The raw OCXO- and SA-recorded voltage data pertinent to the shaker force, plotted one above the other

The raw data was then converted into a time history and scaled. Figure 9 shows examples of the random excitation and response, using the two data acquisition systems.

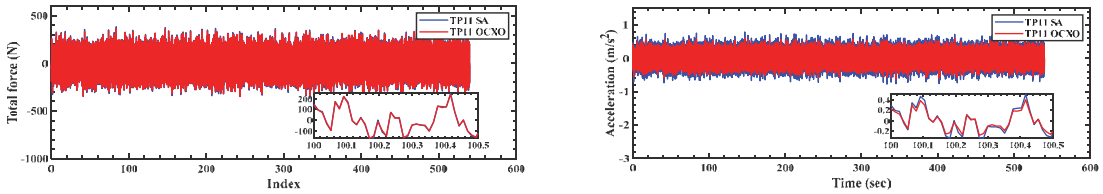

(a) Total input force

(b) Acceleration at reference point

Figure 9: Examples of total random excitation force (input) and the relevant acceleration at the refer-ence test point TP11

It can be seen that the two sets of overlaid time histories are very much identical with some negligible discrepancies appearing on the acceleration response data.

The FRF was calculated between the total input force and all measured acceleration responses at 15 test points. The total input force from the two simultaneously running shakers was obtained by simple summing of the two shaker random forces measured as each shaker was driven by the same random force signal generated by the SA, part of single-input multiple-output (SIMO) modal testing process. Therefore, in total, 15 FRFs were measured. In total, 4096 data blocks of 53 s duration were acquired. FRFs were estimated using 75 % overlap of the data blocks and a total of 100 averages in conjunction with the Hanning windowing. This yielded a frequency resolution of 0.01875 Hz.

Figure 10 shows the point-accelerance FRF measured at TP11 for the first 12 TPs (FRF set 1) and the remaining 3 TPs (set 2).

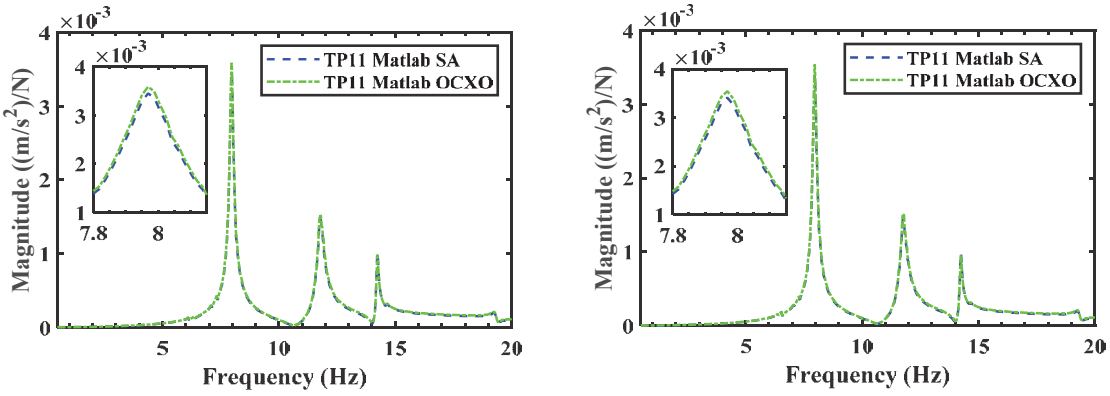

(a) Set 1 reference FRF (b) Set 2 reference FRF

Figure 10: Point-accelerance FRF magnitudes for FRF sets 1 and 2

Although measured at different times, assuming that the structure is linear and time-invariant those two reference FRFs should, of course, be identical, as they clearly very nearly are.

In addition, it can also be seen in Figure 10 that the SA- and OCXO-based measurements were consistent and for practical purposes identical. Therefore, the OCXO high-precision synchronised wireless system was proven to be of sufficient quality to carry out reliable FRF measurements. Using the 15 OCXO-measured FRFs, Figure 11 shows their magnitudes and phases, and the curve fitting results for the first three sway modes of vibration measured.

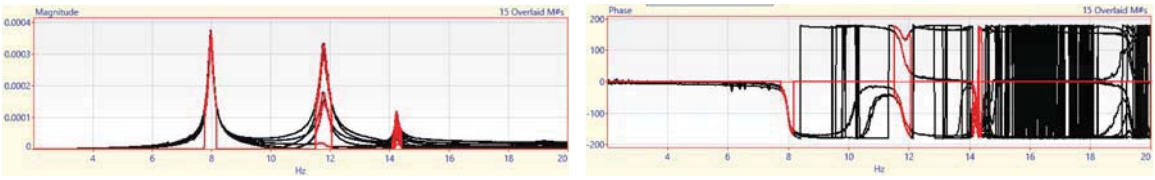

(a) FRF magnitude (b) FRF phase

Figure 11: All measured FRF magnitudes and phases (black traces), including the curve-fitting results (red traces)

FRF and curve-fitting data in Figure 11 indicates good quality of the data and fitting. The

curve-fitting used that the SIMO polynomial fitting ([4]). The lowest three modes identified in Figure 11 are shown in Figure 12.

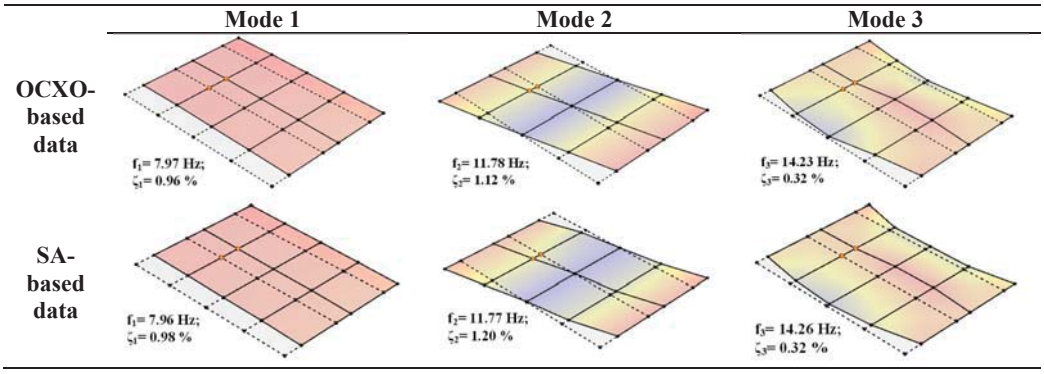

Figure 12: First three horizontal sway modes

The first mode at around 7.96 Hz is a clear sway in the x-direction, whereas the second mode at around 11.78 Hz is an antisymmetric twisting of the floor plate. The third mode at around 14.23 Hz implies an in-plane motion of the middle line engaging the 'strip' connection between the SPS plates in the horizontal direction. All three modes are logical for this type of structure.

Table 1 summarises the modal properties of the structure using OCXO and SA systems. The relative errors of the natural frequencies and modal damping ratios were calculated and are also presented in Table 1.

Mode number	OCXO		Spectrum analyser		Relative error		MAC value
	Modal frequency (Hz)	Modal damping (%)	Modal frequency (Hz)	Modal damping (%)	Frequency (%)	Damping (%)	
1	7.97	0.96	7.96	0.98	0.17	2.25	0.994
2	11.78	1.12	11.77	1.20	0.08	6.29	0.976
3	14.23	0.32	14.26	0.32	0.19	2.91	0.957

Table 1: Comparison of OCXO and SA-based modal properties

The natural frequency error is smaller than 0.2 %, whereas the damping ratio has the maximum error of approximately 6 %. The table also gives the modal assurance criterion (MAC) value ([5]). The MAC calculation is used to compare the level of similarity of the two sets of mode shapes. For each pair of the SA- and OCXO-estimated mode shapes the MAC is almost 1, which means that the identified mode shapes are very similar, indeed. In conclusion, the SA- and OCXO-based data acquisition methods produced almost identical modal testing results validating the described OCXO-based 'wireless' methodology for the FRF data gathering.

Finally, Figure 13 shows measured and regenerated (using modal data for the first four estimated modes) point mobility FRFs at TP11 - for SA- and OCXO-based data acquisition systems.

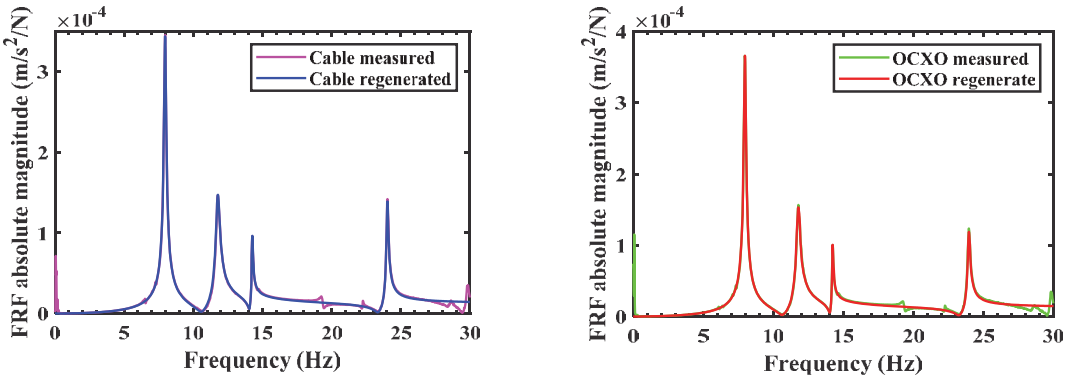

(a) SA-based (b) OCXO-based

Figure 13: Point mobility FRFs at TP11 – Left: SA-based measured and regenerated; Right: - OCXO-based measured and regenerated

It can be seen that the measured and regenerated FRFs are very close indeed, validating again the OCXO-based approach.

5 CONCLUSIONS

This paper proposes a new methodology of using OCXO high-precision synchronised wireless accelerometers for FRF measurements. The aim was to demonstrate the feasibility of the OCXO-based system for use in high-rise building FRF measurement. Therefore, two nominally identical FRF-based modal tests were carried out on a 15-tonne laboratory-based test floor in order to measure its horizontal 'swaying' modes of vibration using:

1. A well-established and quality assured 'wired' system based on a 20-channel spectrum analyser, and;

2. OCXO-based wireless system.

It was shown that the two methodologies produce almost identical modal testing results and that the OCXO-based method is efficient robust and reliable for field utilisation on high-rise buildings.

Acknowledgement

The authors would like to acknowledge financial support of the EU and UK Forestry Commission funded project The Dynamic Response of Tall Timber Buildings under Service Load (Dyna-TTB) supported under the umbrella of ERA-NET Cofund ForestValue.

REFERENCES

[1] Dynamic Response of Tall Timber Buildings under Service Load, *Available at: https://www.dynattb.com*, Accessed 2020-02-20.

[2] Emma J. Hudson, Paul Reynolds Design and Construction of a Reconfigurable Pedestrian Structure, *Experimental Techniques: a publication for the practicing engineer*, 2016.

[3] James Mark WilliamBrownjohn, Siu-Kui Au, Yichen Zhu, Zhen Sun, Binbin Li, James Bassitt, Emma Hudson, Hongbin Sun, Bayesian operational modal analysis of Jiangyin Yangtze River Bridge, *Mechanical Systems and Signal Processing*, **110**, 210–230, 2018.

[4] ME'SCOPE, Vibrant Technology, Inc., *Available at: https://www.vibetech.com*, Accessed 2020-03-29.

[5] Ewins D.J., Modal Testing Theory and Practice, *Research Studies Press LTD*, 1984.

EURODYN 2020
XI International Conference on Structural Dynamics
M. Papadrakakis, M. Fragiadakis, C. Papadimitriou (eds.)
Athens, Greece, 23–26 November 2020

TESTING OF ADDITIVELY MANUFACTURED SMALL SCALE RC SPECIMENS FOR STATISTICAL VALIDATION OF STRUCTURAL MODELS IN EARTHQUAKE ENGINEERING

Lorenzo Del Giudice[1], Rafal Wrobel[2], Christian Leinenbach[2], and Michalis F. Vassiliou[1]

[1] IBK, ETH Zurich
Stefano-Franscini-Platz 5, CH-8093 Zurich
e-mail: {delgiudice, vassiliou}@ibk.baug.ethz.ch

[2] Empa, Swiss Laboratories for Materials Science and Technology
Überlandstrasse 129, CH-8600 Dübendorf
{rafal.wrobel, christian.leinenbach}@empa.ch

Keywords: Model Validation, Physical Modelling, 3D printing, Additive Manufacturing, Reinforced Concrete, Centrifuge Modelling, Small Scale Testing

Abstract. *This paper claims that a major source of error in Seismic Analysis of Structures is the assumptions used to scale up from component- to system-level behavior. It also claims that validation of numerical models should be performed statistically. As a statistical validation requires multiple virgin specimens, the paper suggests the use of a 3D printer to construct the reinforcement of microRC specimens (1:40) to be tested in a geotechnical centrifuge. It presents some first tests on gypsum-based microconcrete, additively manufactured rebars with diameters as low as 0.35mm, and small scale RC beams. The properties observed seem to resemble the ones of full scale RC components. Given the material properties, Opensees is able to accurately capture the behavior of the microbeam.*

1 INTRODUCTION

Structural models blatantly fail to blindly predict the response of shake table tests. This paper claims that the problem sources from the uncertainty/error introduced to scale up from the component-level cyclic to the system -level dynamic behavior of the problem. It also claims that the appropriate way to validate models in Earthquake Engineering is to perform multiple tests on virgin specimens under different ground motions, and to demand that the model predict the Cumulative Distribution Function (CDF) of the maxima of the response quantity of interest. Then manufacturing the virgin specimens becomes the constraint. Therefore, this paper suggests, that the specimens be constructed at a small scale (1:40) using an additive manufacturing technology to fabricate and place the reinforcement. A geotechnical centrifuge should be used to preserve similitude of stresses.

2 STATEMENT OF THE PROBLEM

Time history analysis is considered as the state of the art in modeling of the seismic response of RC structures. Its most widespread validation procedure is the test of predicting the response of an RC structure tested on a shaking table. However, blind prediction contests show that the contestants fail in predicting the response of the tested specimens with reasonable accuracy, even for structures much simpler than the ones constructed in practice, and even when the structural properties and measured excitation are given to the contestants [1].

For example, the simple RC model shown in Figure 1 (left) was tested on the shaking table of UCSD in 2010 under 6 ground motions [2-3]. A total of 41 expert teams (17 from professional practice and 24 from the academia) were invited to predict the response. The measured response and the prediction for the maximum top displacement are indicatively shown in Figure 1 (middle). There is a large dispersion of the numerical results and many predictions grossly underestimate or overestimate displacements. Interestingly, after the test series of the six earthquakes the column did not appear to have failed. However, only 14 out of 41 contestants predicted non-failure, while the rest predicted failure. Within the group that predicted failure, there was a large dispersion related to the mode of failure (Figure 1, right).

Panagiotou et al. 2010 [4] tested a full-scale 7-story building slice with a rectangular wall (Figure 2, left) under 4 ground motions. 21 teams were invited to predict the response. Indicative results for the absolute maximum displacement for the last excitation are shown in Figure 2 (right) (Panagiotou, Personal Communication). Again there is a large dispersion among the contestants and most of them fail to predict the response with a reasonable accuracy. In the context of post-Galileo science, the above indicative results directly question current analysis and design methods.

In order to track the main source of the error, one can break down the sources of error and uncertainty at 3 levels: Material, Component, and System Level. Given the behavior at each level, the engineer makes certain (good or bad) assumptions to level-up. For example, for given material properties in cyclic loading we use the beam theory and a set of assumptions for the interaction of rebars and concrete to reach the component level cyclic behavior.

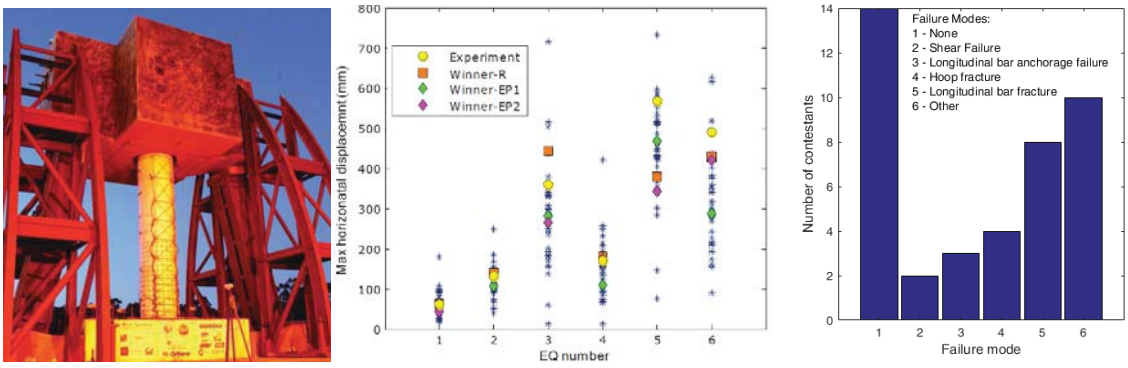

Figure 1. Left: Bridge column tested in UCSD [2]. Middle: Maximum top displacements predicted by the blind prediction contest contestants [3]. Right: Number of predictions for each of the six suggested failure modes [3]

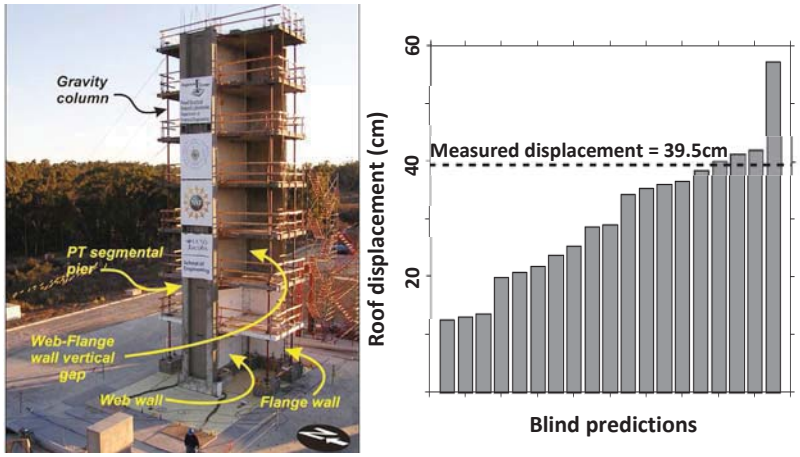

Figure 2. Left: Building slice tested on UCSD[5]. Right: Predictions of blind prediction contest (courtesy of Marios Panagiotou).

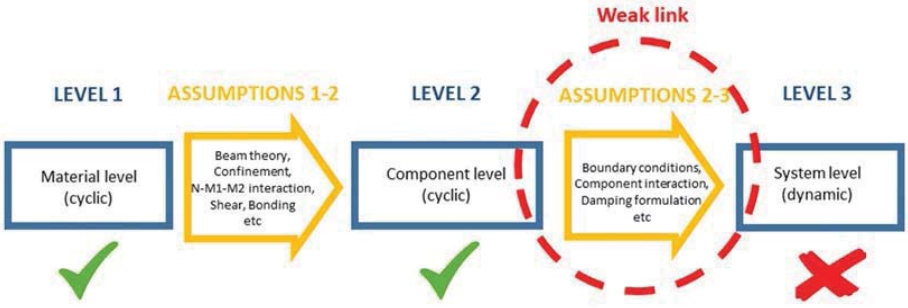

Figure 3. Schematic representation of material to component to system level transition.

Then, using another set of assumptions (boundary conditions, interaction of components, damping model, numerical integration scheme) we reach the system level. Moreover, one should discriminate between quasi static and dynamic behavior. Contrary to blind prediction of system-level dynamic behavior, predicting the component-level cyclic behavior has been proven a more successful process [6-7-8]. Therefore, it is reasonable to assume that the main source of error is the assumptions that earthquake engineers do to scale up from component-level cyclic to system-level dynamic behavior.

This is in accordance with Bradley (2013) [9]: He claims that current uncertainty propagation methods usually focus on the first two levels of modelling, while it is often the transition from component to system level that induces the largest error (Figure 3). Apart from very insightfully

illustrating the above problem and identifying its solution "as a key research area in the coming years" Bradley (2013) [9] does not seem to offer a way of addressing it - and to our knowledge such a way has not been offered in the literature.

It is worth mentioning that there is currently no consensus on fundamental issues of structural modelling: Important figures of Earthquake Engineering disagree on conceptual issues like fiber vs lumped plasticity, or how damping should be modelled. This paper claims that this disagreement sources from the lack of a large database of full scale dynamic tests to serve as a validation benchmark.

3 THE CONCEPT OF STATISTICAL VALIDATION

Bachmann et al. (2018, 2019) [10-11] claimed that the conventional validation test of reproducing the experimentally obtained response to a particular ground motion with acceptable accuracy is too strict of a validation test for structural models. The Earthquake Engineering design problem involves predicting the statistics of the response to an ensemble of ground motions characterizing a given seismic hazard; not to a single ground motion. This is a weaker model validation test that requires that the structural model only be unbiased and introduce less uncertainty than the uncertainty of the excitation itself. Bachmann et al. (2018, 2019) [10-11] applied this weaker (but sufficient) validation procedure on the 1963 Housner dynamic response model of an uplifting structure (Figure 4, left). They performed 600 shaking table tests using a well-defined and repeatable uplifting structure as well as 600 numerical simulations of these tests, and compared both the individual test responses and the statistical aggregates of these responses focused on predicting limit states such as overturning or maximum tilt angle (Figure 4). They showed that the 1963 Housner model passes the weak validation test (Figure 4, right) even though it fails the strong validation test (Figure 4, middle). In other words, in this case the motion-to-motion variability is more important than the accuracy of the structural model. Therefore, the model is good enough for the scope of Earthquake Engineering.

It is worth noting that the concept of comparing seismic analysis methods in terms of the statistics of the response to sets of ground motions rather than in terms of individual responses is not something novel in Earthquake Engineering. It can be seen in Chapter 23 of the 4th edition of Chopra's Structural Dynamics textbook [12]. However, up to now it involved comparisons between different analysis methods (usually a more approximate against a more refined, taken as benchmark); not between an analysis method and experimental tests.

The optimal validation procedure question extends beyond Earthquake and Structural Engineering. Roy and Oberkampf (2011) [13] describe a comprehensive framework for verification, validation, and uncertainty quantification in scientific computing that resembles the method proposed herein.

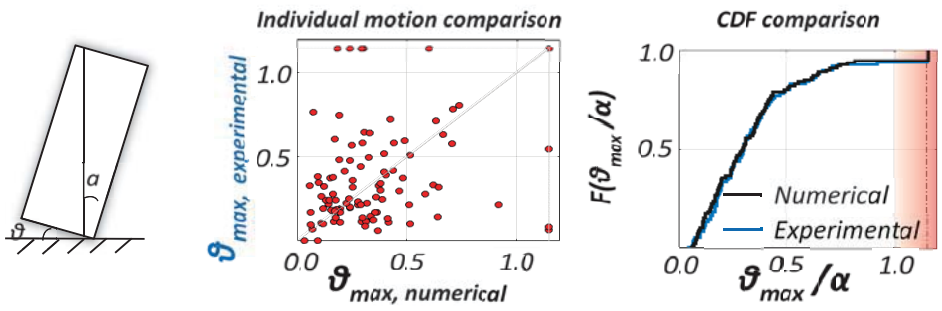

Figure 4. Left: Uplifting oscillator; Middle: Comparison of the maximum rotation obtained experimentally and numerically: Individual motion comparison; Right: CDF Comparison. Adapted from Bachmann et al. (2018).

Extending this statistical validation method to more realistic structures is not trivial: Since testing of RC specimens, involves damaging them, one would need multiple virgin specimens. This is cost- and time-wise not viable in full scale, and this is the reason why researchers only perform comparisons between individual excitations.

4 TESTING OF MICROSPECIMENS

To address the above contradiction, we restrict the problem from the statistical validation of the whole numerical modelling procedure (which is impossible) to the statistical validation of the assumptions to scale up from component-level to system level dynamic response. The latter can be performed with multiple virgin small-scale models (say 1:40 scale) in a centrifuge. Then constructing multiple specimens at such a scale becomes the constraint.

As geotechnical engineers often need to describe Soil Structure Interaction problems, they have used reduced-scale models of piles and walls, although using different materials. Knappett et al. (2011) [14] developed a micro-concrete (concrete with small-scale aggregates and gypsum instead of cement) for use in geotechnical centrifuge. They present experimental results on tests on 1:40 scaled RC beams and slabs made of microconcrete and steel wires as reinforcement. The modes of failure between model and prototype scales coincide, and the quantitative comparison of strength and ductility is relatively good, even if seen from the potentially stricter point of view of a structural engineer. Strength is better captured than the moment-curvature relationship and stiffness, but we have reasons to believe that the actual situation is better than described by Knappet et al. 2011 [14]: They compared the experimental M-κ relations they obtained, to analytical solutions using cracked cross section analysis. However, based on Panagiotakos and Fardis (2001) [15] and Priestley et al. (2007) [16] suggestions, such an analysis would be too stiff. Thus, the apparent extra flexibility is not a product of the scaled model, but of the equations that Knappet et al. 2011 [14] used to predict the prototype behavior. If one uses the stiffnesses provided by Priestley et al. (2007) [16] the curves match much better.

The micro-concrete that was developed was subsequently used to study a rocking isolated RC bridge pier at a 1:40 scale [17]. However there were three limitations: (a) The accuracy in positioning of the handmade micro-reinforcement, as well as the diameter of the stirrups (they were larger than what proper scaling would suggest). (b) The construction time: It took 8 hours of quasi-watchmaker's work and many failed specimens for a single column. (c) It was practically impossible to build frames, as there were difficulties in positioning the rebars in the joints at a 1:40 scale by hand.

This paper suggests that the problem of manufacturing and placing the reinforcement can be solved by using a metal 3D printer. Then, the construction of multiple specimens for a statistical validation of numerical models is time-wise feasible. Moreover, the method allows for the experimental study of a plethora of structural engineering problems that was impossible till now, namely SSI, pounding between adjacent buildings, or between a bridge and the abutment.

In order to avoid scale phenomena, it is necessary to perform the material and component level cyclic tests, at the model scale, namely 1:40. This paper presents some first experimental results of compression and tension strength of microconcrete, 3D printed steel reinforcement of 0.50 mm nominal diameter (without considering the ribs), and 4 point bending tests on microRC beams.

5 TESTING OF MICROCONCRETE IN TENSION AND COMPRESSION

Microconcrete comprises a mixture of plaster, sand and water. In this work, Saint-Gobain Hartform 1 gypsum based plaster was used. Perth silica sand with d50 = 0.23 mm was used as a model aggregate. Figure 5 compares a typical aggregate size distribution scaled down 40 times

to the distribution of the used sand. The ratio of the water/plaster/sand ratio of the mixture was 0.4/1/1.

Cylindrical specimens of size 50 by 112 mm were constructed and tested in compression (Figure 6, left) after 20 days. The deformation was applied at a rate of 0.5 mm/min. The results are shown in Figure 6, right. In the future, smaller models, as close to 1:40, will be constructed to study any scale effect and to take it into account in the numerical model validation procedure.

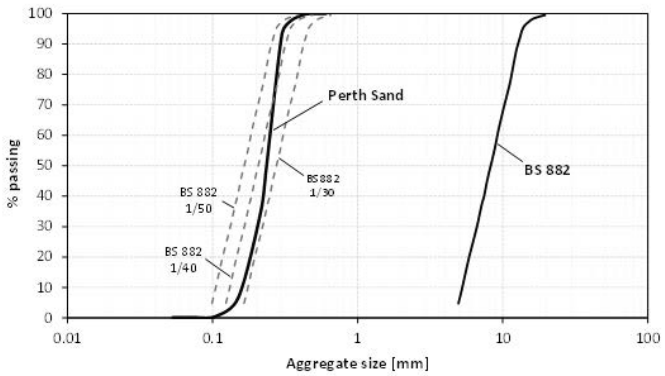

Figure 5. Scaling of typical aggregate size.

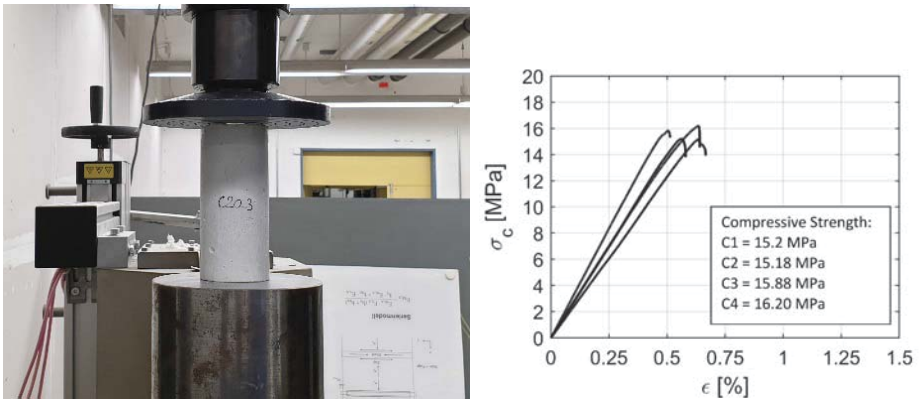

Figure 6. Left: Compression test setup. b) Stress-Strain curves.

Figure 7. Four point bending test setup.

Unreinforced 12.5x12.5x80 mm and 40x40x160 mm size rectangular beams were also constructed and tested in 4 point bending after 20 days (Figure 7). Figure 8 shows their force-deformation diagram as well as the tension strength of the unreinforced concrete. The maximum flexural strength is larger for the small specimens, this is in agreement with the well known size effect.

6 TESTING OF 3D PRINTED MICRO REINFORCEMENT IN TENSION

The 3D reinforcements were produced by Laser powder Bed Fusion (LPBF) technology using a Sisma Mysint100 equipped with a fiber laser of wavelength 1061 nm and a laser spot size 55 μm. The material used for manufacturing reinforcement was gas atomized 316l stainless steel powder provided by Oerlikon Metco. The tested reinforcement had a diameter of 0.35 mm for the stirrups and 0.50 mm for the rebars (1:40 scaled models of Φ14 and Φ20). Printing the rebars in a way that their bonding with concrete is similar to one of the prototype models is not trivial and will be a subject of future research. Due to some limitations in the size of the working chamber and appearance of high residual stress during the LPBF process, manufacturing the ribs of the reinforcement in 1:40 scale is problematic.

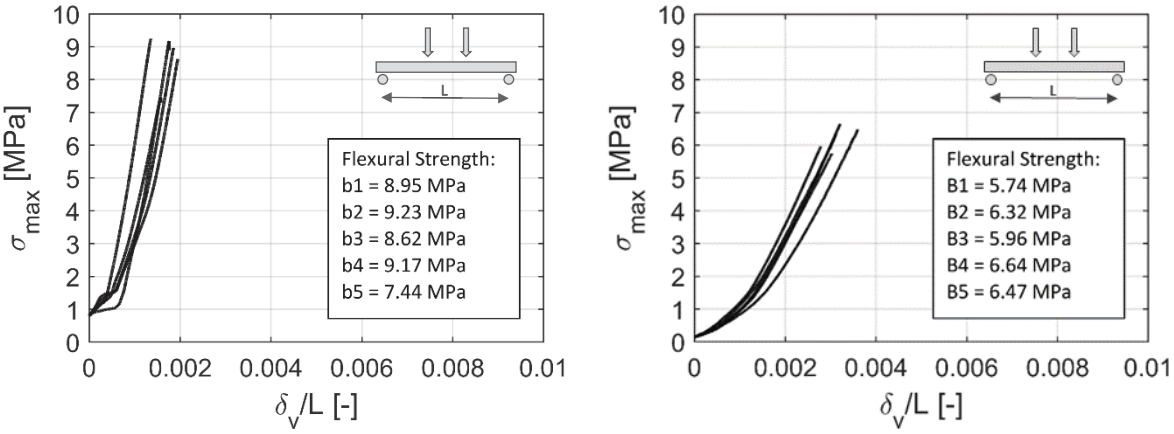

Figure 8. Maximum tension stress in the beam (σmax) vs normalized deflection in the middle (δv) normalized with respect to the beam spam between the supports (L) Left: Four point bending test results 12.5x12.5x80 mm beam. Right: b) Four point bending test results 40x40x160 mm beam.

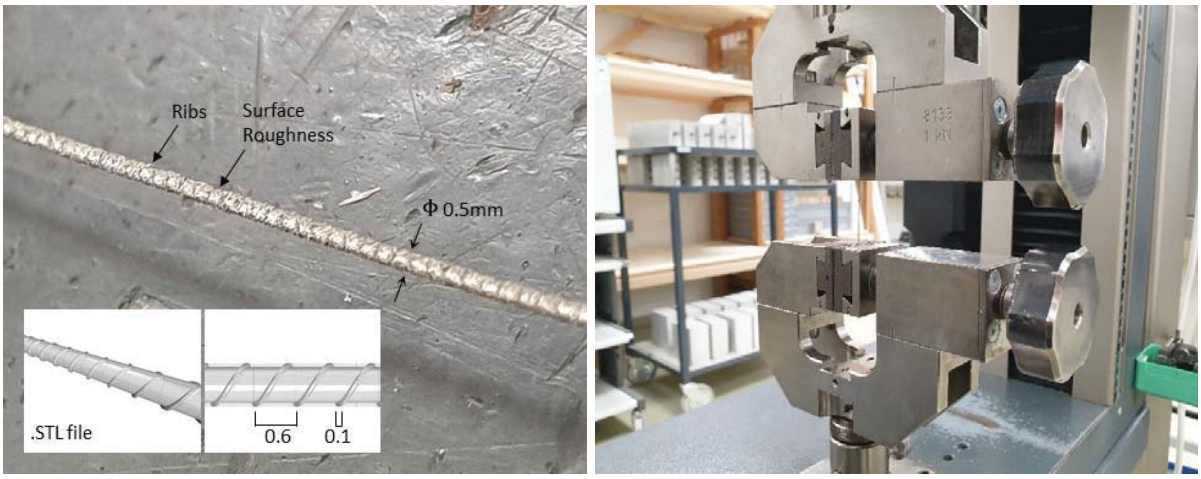

Figure 9. Left: .STL file and printed rebar. Right: Uniaxial tension test setup.

The minimum feature size of LPBF parts is around 200 μm (i.e. of 10 mm in the prototype scale). The ribs would have a size on the order of 1 mm in the prototype scale. However, the LPBF process results in a rough surface anyways with Ra values of 15-20 μm. For many technical applications, post processing steps reducing surface roughness (e.g. grinding, polishing) are required. In our case, we did not apply this process, as roughness is a target property. Moreover, an attempt to print ribs was made. Figure 9, left shows the STL file that was used for printing the parts as well as a photo of the rebar surface in the as-manufactured state.

Some of the rebars were tested in tension in order to assess the yielding and maximum strength of the printed rebars. The tests were performed with a Zwick Universal Testing Machine equipped with a 1 kN load cell. The initial gap between the clamping jaws was 30 mm which increased at a rate of 0.1 mm/min.

5 specimens were tested. Figure 10 left shows the results of the tension tests for all 5 tested specimens. The yield strength of the rebars was defined imposing a conventional 0.01 offset of the initial linear part of the curves. The average yield and maximum strength of the specimens were fy = 400.7 MPa and ft,max = 454.5 MPa. Casati et al. (2016) [18]on (10 mm × 10 mm × 75 mm) specimens had shown a yield strength of the 3D printed 316L stainless steel of 500-600 MPa meaning that the 0.5 mm diameter rebars were weaker: Any defects as well as the surface roughness will have a more pronounced effect in small-scale specimens. Hence there is a scale effect that needs further investigation. The Young modulus was 75 GPa, which is substantially lower than the 180 GPa value reported by Casati et al. (2016) [18], showing that more research is needed on the field to understand why.

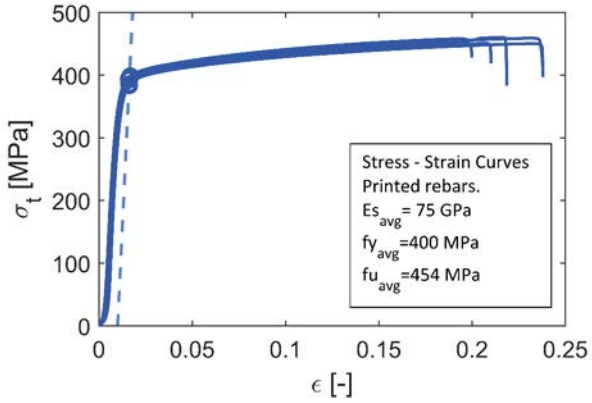

Figure 10. Tension tests of printed rebars.

7 FOUR POINT BENDING TESTS OF MICROREINFORCED CONCRETE BEAMS

Three model beams were manufactured and tested to determine their bending properties. The beams were designed to represent a 1/40 scale beam with 0.50 m by 0.50 m cross section and 3.2 m length, featuring 6 Φ20 longitudinal rebars and Φ14 shear reinforcement with 10cm spacing, all in the prototype scale. This translated in the model scale into 80 mm long beams with a cross section of 12.5 mm by 12.5 mm, Φ0.50 longitudinal rebars, and Φ0.35 stirrups spaced at 2.5 mm. The entire reinforcement cage, i.e. rebars and stirrups, was printed with the desired layout. Figure 11 shows the reinforcement cage detail, as well as the cross section layout.

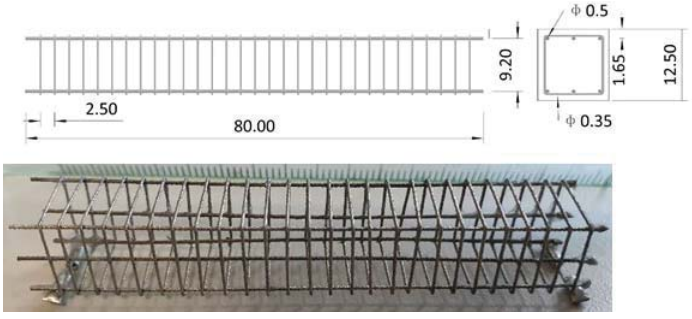

Figure 11. Reinforcement details and 3D printed cage.

The reinforcement was carefully placed into the mold, making sure that the 1.65 mm cover was respected. Subsequently the microconcrete was casted. The specimens were left for 2 days in the molds which were then removed. The unmolded specimens cured for other 18 days for a total of 20 curing days before testing.

The test setup consisted of a four point bending test with a support span of 60 mm and a loading span, i.e. the spacing of the loading pins, of 20 mm (Figure 12a). The applied loading rate was 0.1 mm/min to ensure static testing conditions. Figure 12 (b-d) shows the moment-vertical displacement plot, at the middle of the beams.

The average moment capacity was 3220 Nmm. Moreover, we noticed that after a first quasi-linear branch the curves become jagged at about 2'000 Nmm, this region corresponds to the crack onset within the loading span. A visual inspection during the tests has indeed shown that the first cracks appeared when the first peak of the curves were observed.

A visual inspection of the specimens after the tests has shown that the printed rebars fractured. Hence, the bonding strength created by the surface roughness and the printed details was enough to prevent debonding.

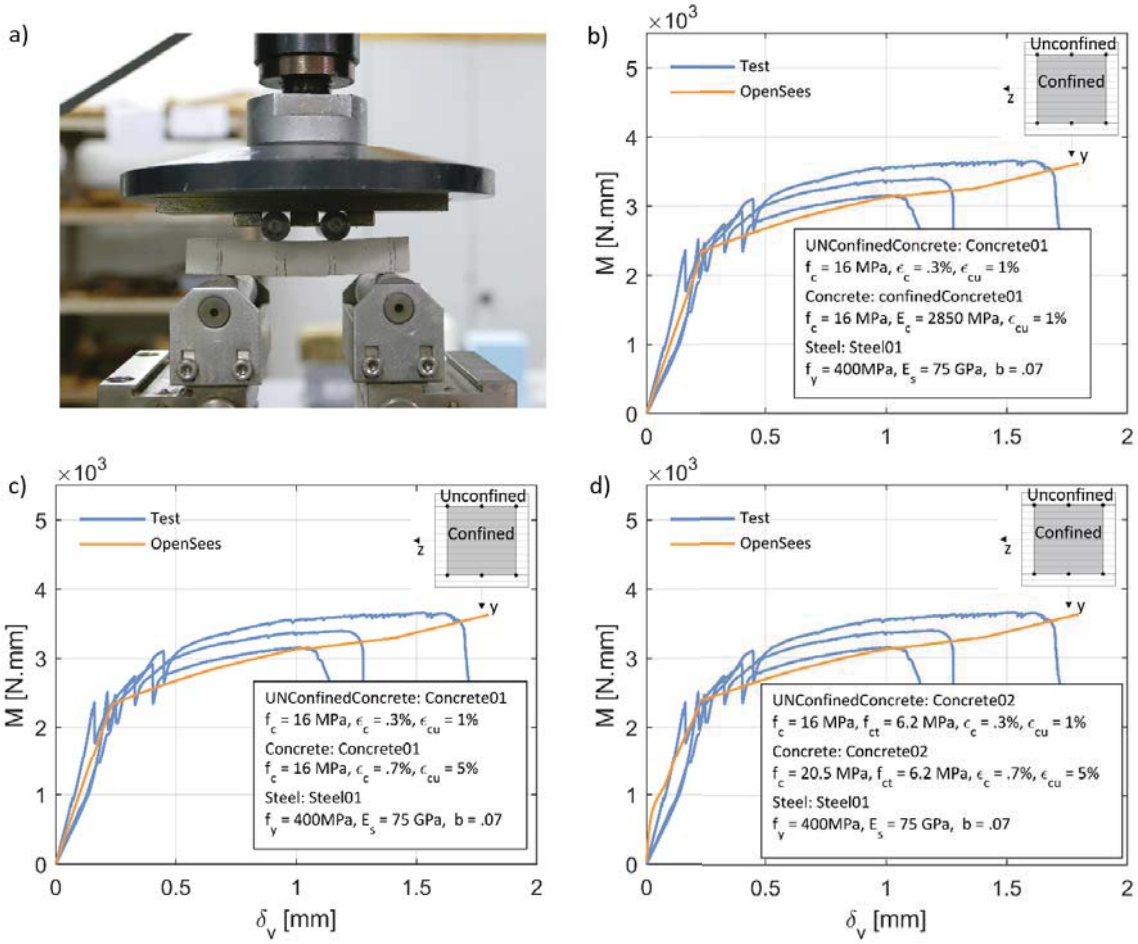

Figure 12. Comparison between experimental results and OpenSees simulation using fiber model.

Numerical models of the four point bending test were developed in OpenSees and the results compared against the experimental curves. The beam was modelled using a displacement-based element with non linear fiber section. The section was divided into three types of fibers, i.e. confined concrete (in the area enclosed by the rebars), unconfined concrete (concrete cover), and steel (longitudinal rebars). Steel was modelled with Steel01 material with fy=400 MPa,

Es=75 GPa, and 7% hardening. Different concrete modelling options were tried (Figure 12(b-d). Concrete01 has zero tension strength, while Concrete02 behaves linear-softening behavior in tension. ConfinedConcrete01 computes the confined concrete properties automatically based on the transverse reinforcement. In all cases, we used the results of the compression and bending tests to characterise the unconfined concrete. When confined properties were needed as an input, the Mander et al. (1988) [19] model was used. Figure 12 (b–d) shows the comparison between experimental results and the OpenSees analyses. The numerical results seem to be in good agreement with the experimental ones, which indicates that the fundamental assumptions valid for reinforced concrete elements, such as perfect bonding between steel and concrete and plane cross sections, apply for the micro-reinforced concrete beams.

8 CONCLUSIONS

Additive manufacturing is a promising technology for the automated construction of the reinforcement cages of small scale RC specimens. The tested members show a behavior, which is close to full scale RC structural members – with the exception of concrete tension strength, that needs to be reduced. Therefore, it seems feasible to use the proposed methodology to construct small scale models of full structures with the aim of testing them on a shake table inside a geotechnical centrifuge. The shake table tests datasets can be used by the Earthquake Engineering community to statistically validate the assumptions that it usually does to scale up from component-level cyclic to system-level dynamic behavior, namely boundary conditions, interaction of components, conceptual formulation of damping, and participation of slabs. Further investigations on materials and component at small scale are required.

REFERENCES

[1] P. Fajfar, Analysis in seismic provisions for buildings: past, present and future, in *European Conference on Earthquake Engineering Thessaloniki, Greece*, 2018, pp. 1–49.

[2] M. Schoettler, J. Restrepo, G. Guerrini, and D. E. Duck, A full-scale, single-column bridge bent tested by shake-table excitation, 2012.

[3] V. Terzic, M. J. Schoettler, J. I. Restrepo, and S. A. Mahin, Concrete column blind prediction contest 2010: outcomes and observations, *PEER Report*, vol. 1, pp. 1–145, 2015.

[4] M. Panagiotou and J. I. Restrepo, Displacement-based method of analysis for regular reinforced-concrete wall buildings: Application to a full-scale 7-story building slice tested at UC–San Diego, *Journal of Structural Engineering*, vol. 137, no. 6, pp. 677–690, 2011.

[5] M. Panagiotou, J. I. Restrepo, and J. P. Conte, Shake-table test of a full-scale 7-story building slice. Phase I: Rectangular wall, *Journal of Structural Engineering*, vol. 137, no. 6, pp. 691–704, 2011.

[6] M. Trüb, Numerical modeling of high performance fiber reinforced cementitious composites, *IBK Bericht*, vol. 333, 2011.

[7] Collapse Prevention Center [2011]. [Online]. Available: http://www.collapse-prevention.net/download/Competition/RC_Frame/RC_Frame_ Competition.htm. [Accessed: 29-Sep-2019].

[8] X. Lin and X. Lu, Numerical models to predict the collapse behavior of RC columns and frames, *The Open Civil Engineering Journal*, vol. 11, no. 1, 2017.

[9] B. A. Bradley, A critical examination of seismic response uncertainty analysis in earthquake engineering, *Earthquake engineering & structural dynamics*, vol. 42, no. 11, pp. 1717–1729, 2013.

[10] J. A. Bachmann, M. Strand, M. F. Vassiliou, M. Broccardo, and B. Stojadinović, Is rocking motion predictable?, *Earthquake Engineering & Structural Dynamics*, vol. 47, no. 2, pp. 535–552, Feb. 2018, doi: 10.1002/eqe.2978.

[11] J. Bachmann, M. Strand, M. F. Vassiliou, M. Broccardo, and B. Stojadinovic, Modelling of rocking structures: Are our models good enough?, in *2nd International Conference on Natural Hazards & Infrastructure (ICONHIC 2019)*, 2019.

[12] A. K. Chopra, *Dynamics of structures: theory and applications to earthquake engineering*, 4th ed. Prentice Hall: Pearson, 2012.

[13] C. J. Roy and W. L. Oberkampf, A comprehensive framework for verification, validation, and uncertainty quantification in scientific computing, *Computer methods in applied mechanics and engineering*, vol. 200, no. 25–28, pp. 2131–2144, 2011.

[14] J. A. Knappett, C. Reid, S. Kinmond, and K. O'Reilly, Small-scale modeling of reinforced concrete structural elements for use in a geotechnical centrifuge, *Journal of Structural Engineering*, vol. 137, no. 11, pp. 1263–1271, 2011.

[15] T. B. Panagiotakos and M. N. Fardis, Deformations of reinforced concrete members at yielding and ultimate, *Structural Journal*, vol. 98, no. 2, pp. 135–148, 2001.

[16] M. J. N. Priestley, G. M. Calvi, and M. J. Kowalsky, *Displacement-based seismic design of structures*. IUSS press, 2007.

[17] M. Loli, J. A. Knappett, M. J. Brown, I. Anastasopoulos, and G. Gazetas, Centrifuge modeling of rocking-isolated inelastic RC bridge piers, *Earthquake engineering & structural dynamics*, vol. 43, no. 15, pp. 2341–2359, 2014.

[18] R. Casati, J. Lemke, and M. Vedani, Microstructure and fracture behavior of 316L austenitic stainless steel produced by selective laser melting, *Journal of Materials Science & Technology*, vol. 32, no. 8, pp. 738–744, 2016.

[19] J. B. Mander, M. J. N. Priestley, and R. Park, Theoretical stress-strain model for confined concrete, *Journal of structural engineering*, vol. 114, no. 8, pp. 1804–1826, 1988.

EURODYN 2020
XI International Conference on Structural Dynamics
M. Papadrakakis, M. Fragiadakis, C. Papadimitriou (eds.)
Athens, Greece, 23–26 November 2020

MEASUREMENT OF SOIL STRAINS UNDER EARTHQUAKE LOADING

Xiaoyu Guan[1], **Gopal S.P. Madabhushi**[1], **and Mark Talesnick**[2]

[1]Schofield Centre, Department of Engineering, University of Cambridge
address
e-mail: {xg257, mspg1}@cam.ac.uk

[2] Faculty of Civil and Environmental Engineering, Israel Institute of Technology
address
e-mail: talesnik@technion.ac.il

Keywords: Soil strain, Direct measurement, New device, Centrifuge tests, Earthquake loading.

Abstract. *A new device has been developed for the direct measurement of soil strains under earthquake loading in centrifuge testing. The main body of the device is a potentiometer used to measure soil deformation directly. Two MEMS accelerometers are attached to either end of the device to obtain soil deformation as a semi-direct measurement method. Two different centrifuge models, a level sand bed and a slope, were prepared with dry sands to achieve small and large soil deformation, respectively. A series of model earthquake motions were applied to the centrifuge models. The strains obtained with the new devices are compared with the indirect measurement of Piezo-electric accelerometers. It is found that this new direct method to measure soil strain could be applicable for medium to large soil deformation, that is, in the case of relatively strong earthquakes.*

1 INTRODUCTION

Soil deformation induced by earthquakes can cause damage to structures and even pose a threat to human life. An important parameter in seismic analyses is soil strain. However, obtaining accurate measurements of strain remains challenging. Currently, the most widely-used measurement methods in geotechnics can be classified into two types, sensor-based and image-based methods.

Sensor-based methods generally involve two kinds of sensors, displacement measurement sensors (e.g., LVDTs, LDTs, laser displacement sensors and FBG sensors) and acceleration measurement sensors (e.g., MEMS and Piezo-electric accelerometers). However, most widely used displacement measurement sensors, such as LVDTs, LDTs and laser displacement sensors, are placed outside the soil mass and are used to measure the movement of the soil adjacent to the boundary [2, 4, 6], and thus their measurements are likely to suffer from boundary effects. To measure soil deformation within soil, FBG sensors came into use [13]. However, data processing for such sensors involves assumptions about parameters in calculation of displacements. Furthermore, these FBG sensors are costly and too delicate to be deployed widely under strong earthquake loading. In contrast, unlike displacement measurement sensors, acceleration measurement sensors can be placed within soil and indirectly provide displacements through double integration for strain calculation [14]. The problem of acceleration measurement sensors is that the numerical errors induced by integration in data processing may affect the accuracy of the results.

Image processing techniques comprise two methods, the Computerized X-ray tomography (CT) [10] and Particle Image Velocimetry (PIV) [11, 12]. Although the CT method can measure internal deformation, some intrusive marking may be required, disturbing the soil models that are being tested. In the PIV technique, soil deformations are defined across transparent surfaces, and thus the results suffer from boundary effects. Moreover, in dynamic tests costly high-speed cameras are necessary, making this technique expensive to apply.

This paper presents a new device developed to obtain soil strain within soil directly based on measurements of relative displacements of soil columns. The performance of this device is evaluated in comparison with a common method using dynamic centrifuge testing which is currently the most advanced experimental method available. The applicability of the new device is discussed based on the results in soil deformation analyses.

2 METHODOLOGY

A new device-based method and a common method used in this research are introduced. The detailed calculation process of soil characteristics, including shear stress, strain, shear moduli and damping, is demonstrated. Information on model preparation, testing programs, and signal processing is provided.

2.1 New device-based method

A new device (Figure1(a)) is used to obtain dynamic strains in this research. The device is comprised of two kinds of instruments, a potentiometer and two MEMS accelerometers. The potentiometer is used for direct measurement of displacements between the two aluminium plates. The two accelerometers are used for measurement of accelerations of either plate. With these accelerations, the displacements between the two plates can also be calculated via double integration. In this research, the displacements are caused by the horizontal and shear deformation of the small column confined by the two plates attached to the device during seismic

loading. In Figure 1(b), a unit volume is used to explain the principle of the calculation of strains. Since the measured or calculated relative displacements are applied to a soil column with realistic dimensions, those displacements should be normalised by their real lengths. Such normalised displacements also represent linear strains ε_{xx}. Thus, shear strains can be obtained from

$$\gamma = \varepsilon_{xx1} - \varepsilon_{xx2} \tag{1}$$

where ε_{xx1} and ε_{xx2} are the linear strains at the top and bottom surface of the soil block, respectively.

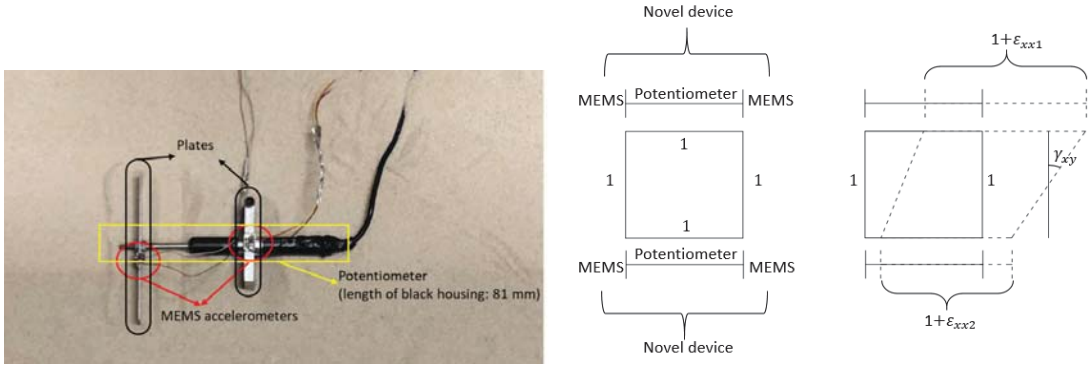

(a) A view of a new device. (b) Measurement principle.

Figure 1: New device for direct strain measurement.

2.2 Absolute acceleration-based method.

Two different equations are available for estimating shear strain. The shear strain at the mid-point between two adjacent accelerometers can be expressed as

$$\gamma = \frac{\Delta u}{\Delta z} \tag{2}$$

where Δu is the difference of displacements obtained from the records of the two accelerometers, and Δz is the difference of the two depths at which the two accelerometers are placed. For the case of a vertical array of accelerometers, Zeghal et al. [15] derived the shear strains γ_i at the depth of Δz_i, as

$$\gamma_i\left(z_i\right) = \frac{1}{\Delta z_{i-1} + \Delta z_i}\left[\left(u_{i+1} - u_i\right)\frac{\Delta z_{i-1}}{\Delta z_i} + \left(u_i - u_{i-1}\right)\frac{\Delta z_i}{\Delta z_{i-1}}\right]\left(i = 2, 3, 4\cdots\right) \tag{3}$$

where the subscript i is the number of the accelerometers.

Shear stress can be calculated based on absolute accelerations. Applying the classic beam theory, Brennan et al. [1] derived an equation to obtain the shear stress τ at the depth z_i, written as

$$\tau\left(z_i\right) = \frac{1}{2}\,\rho\,\frac{\left[\ddot{u}_i {z_i}^2 + \ddot{u}_i z_i\left(z_i - 2z_1\right)\right]}{\left(z_i - z_1\right)} \tag{4}$$

where ρ is the density of the sand.

2.3 Mohr's circle of strains

Mohr's circles of strains aim to present relationship between the normal strains and half of the shear strains of the unit volume. Two points, $(\varepsilon_{yy}, \gamma_{yx}/2)$ and $(\varepsilon_{xx}, -\gamma_{xy}/2)$, are needed to plot Mohr's circles. In this research, the normal strains perpendicular to the moving direction of the shaft of the potentiometer are assumed to be zero (i.e., $\varepsilon_{yy} = 0$ under plane strain condition). Thus, with the linear strains obtained from the new device and the shear strains obtained based on the absolute accelerations, the Mohr's circles of strains can be plotted.

2.4 Shear modulus and damping

Shear stress-strain loops are plotted with the calculated shear stress and strain from the absolute accelerations. The ratio of the magnitude of stress to the magnitude of strain is regarded as the shear modulus [1]. The obtained shear moduli G are normalised by small-strain moduli G_{max} which were obtained with an air hammer developed by Ghosh and Madabhushi [3], following the expression

$$G_{max} = \rho \, {v_s}^2 \tag{5}$$

where v_s is the velocity of the shear wave created by the air hammer. The equivalent damping ratios D can be obtained from these loops, following the equation

$$D = \frac{W}{2\pi \, W_e} \tag{6}$$

where W is the total energy dissipation during each loop and W_e is the energy dissipation in the equivalent elastic system. Specifically, W equals to area of each loop, while W_e equals to the area bounded by the representative line segment in the calculation of G and the strain axis.

2.5 Model preparation and test program

The preparation of a level sand bed model and a slope model at an angle of 30° were conducted with an automatic sand pouring machine [7], using dry Hostun sand. The maximum and minimum void ratios of the sand are 1.01 and 0.555 respectively, and the specific gravity of the sand grains is 2.65 [8]. Some 1-g shanking table tests were conducted under different seismic motions, but the new device was unable to capture the soil movement, indicating that the new device lacks high sensitivity. For this reason, the two models were both prepared with loose sand whose relative densities were 33% and 36% respectively. Both models were tested at 50-g level in the Turner Beam Centrifuge at Cambridge University. The instrumental layouts of the two models are illustrated in Figure 2. Table 1 shows the properties of the earthquakes for both tests. This research focuses on the single sinusoidal signals with the main driving frequencies ranging from 0.8 Hz to 1.2 Hz over 10 cycles.

2.6 Signal processing

The key to obtaining correct strain is appropriate signal filtering. Under-filtered signals, especially those involving low-frequency components, result in significant errors during integration of the accelerations. Such errors cause invalid shear stress-strain loops and as a result to inaccuracies in the determination of shear moduli and damping ratios. On the other hand, over-filtering, producing perfectly smooth stress-strain loops, damages part of the real signal. The signal filtering in this research is based on plots of fast Fourier transform (FFT). A band-pass filter with a frequency range of 0.4 Hz to 5 Hz was employed for EQ4 in Test-1.

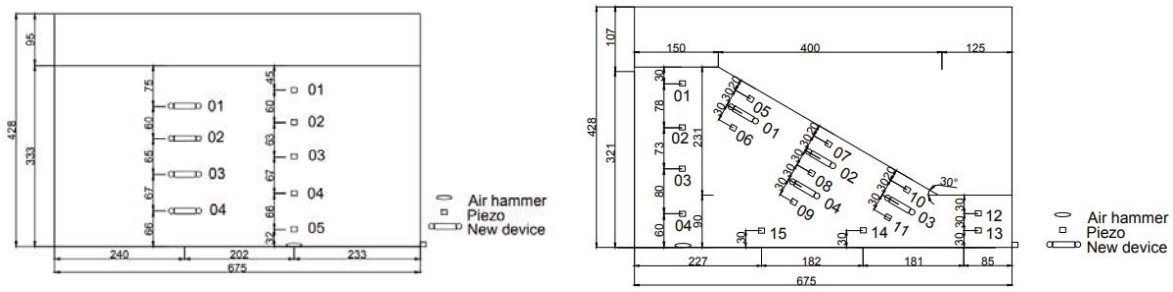

(a) (b)

Figure 2: Instrumental layout of: (a) level sand bed model (b) slope model.

Test-1 (level sand)			Test-2 (slope)		
EQ no.	Frequency (Hz)	Max. acc. (g)	EQ no.	Frequency (Hz)	Max. acc. (g)
EQ1	1	0.04	EQ1	1	0.06
EQ2	1	0.21	EQ2	1	0.26
EQ3	0.8	0.14	EQ3	0.8	0.20
EQ4	1.2	0.25	EQ4	1.2	0.34
EQ7	2.6	0.27	EQ5	2.6	0.38

Table 1: Experimental programs of both tests in prototype-scale.

3 DYNAMIC STRAINS IN THE LEVEL SAND BED

3.1 Absolute acceleration based results

The five Piezo-electric accelerometers recorded the absolute accelerations at different elevations in the sand, as shown in Figure 3(a). The amplitudes of accelerations increased with decreasing depth, i.e. amplification, indicating smaller stiffness at smaller depths. The acceleration amplification ratio is defined as the ratio of the average peak accelerations in two horizontal directions to the average peak acceleration of the input signal. Figure 3(c) displays the variation of the ratios with depth for four earthquakes, suggesting that the magnitudes of the earthquakes had marginal effect on the amplification ratios.

The corresponding absolute displacements (Figure 3(b)) were obtained by double integration of the absolute accelerations. Only the cyclic displacements are displayed, since Piezo-electric accelerometers do not respond to the low-frequency components well. The displacements became larger at smaller depths, that is, the larger soil deformation occurred in the shallower layers.

3.2 New device-based results

The accelerations measured by the MEMS accelerometers represent the movement of the two plates of the new device. The relative accelerations, that is, the difference between the two sets of the accelerations, are shown in Figure 4(a). Similar to the variation of the absolute accelerations, the relative accelerations increased towards the sand surface. The comparison between the measured and integrated relative displacements is presented in Figure 4(b). The accelerometers captured the soil movement, while the potentiometers failed to record useful movement, indicating that the potentiometers may lack sensitivity for small deformation measurement. Thus, the data obtained from MEMS accelerometers are focused on for the following

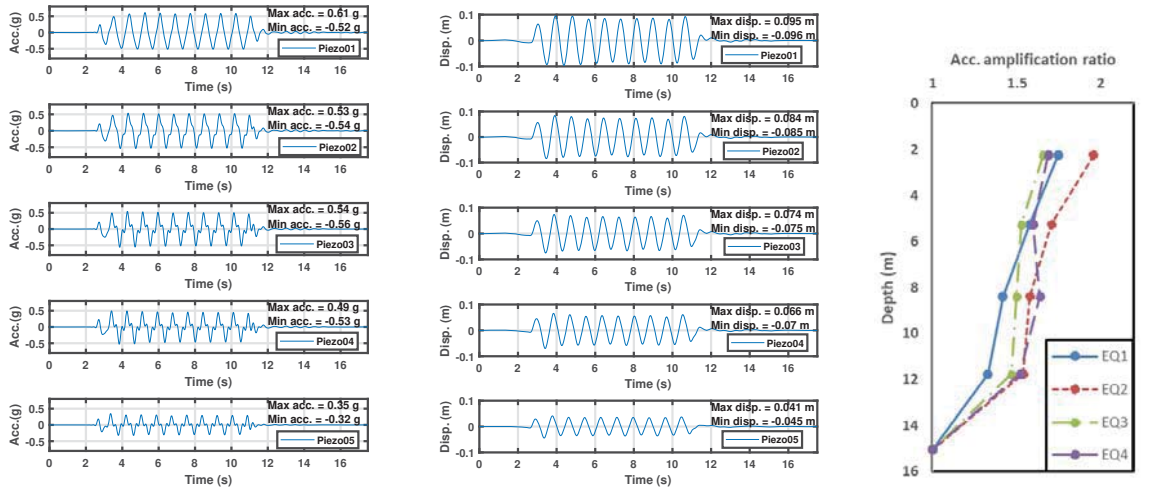

(a) Absolute acceleration records. (b) Absolute displacement records. (c) Amplification ratios.

Figure 3: Dynamic response of sand during EQ4 in Test-1.

analyses of Test-1.

A comparison between the absolute acceleration- and relative acceleration-based shear strains is shown in Figure 4(c). The dynamic shear strains from the MEMS accelerometers are generally smaller than those from the Piezo-electric accelerometers. Furthermore, the difference was larger at the larger depth (11.7 m). This is possibly because of the friction between the shaft and the housing, preventing the plates from moving freely with the soil.

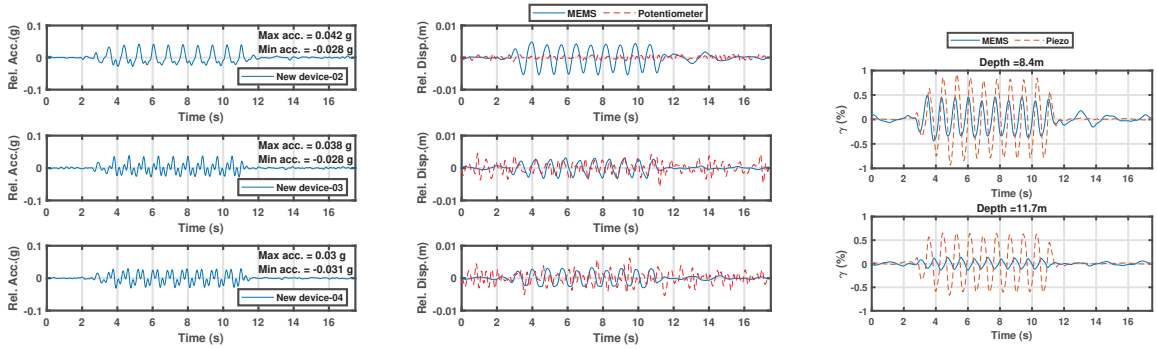

(a) (b) (c)

Figure 4: Results of dynamic analysis of the level sand bed subjected to EQ4: (a)relative acceleration histories from MEMS acceleometers (b)comparison between calculated displacements from MEMS accelerometers and measured displacements from potentiometers (c)comparison between shear strains from MEMS accelerometers and those from Piezo-electric accelerometers.

3.3 Shear modulus and damping

To plot normalised shear modulus degradation curve, an air hammer test at 50-g level was conducted to obtain G_{max} and the corresponding shear moduli in the test were obtained with the accelerations measured by the Piezo-electric accelerometers. The shear modulus curves based on two empirical equations proposed by Hardin and Drnevich [5], and Oztoprak and

Bolton [9] are presented for comparisons with the shear moduli obtained in this test. Figure 5(a) shows the experimental results are within the boundary of the two empirical curves and are generally closer to the curve of Oztoprak and Bolton [9]. These results seem to form a trend line, consistent with the empirical curves. Regarding the damping ratios, Figure 5(b) shows that the experimental results are generally above the empirical curve of Hardin and Drnevich [5], suggesting higher level of damping in the sand.

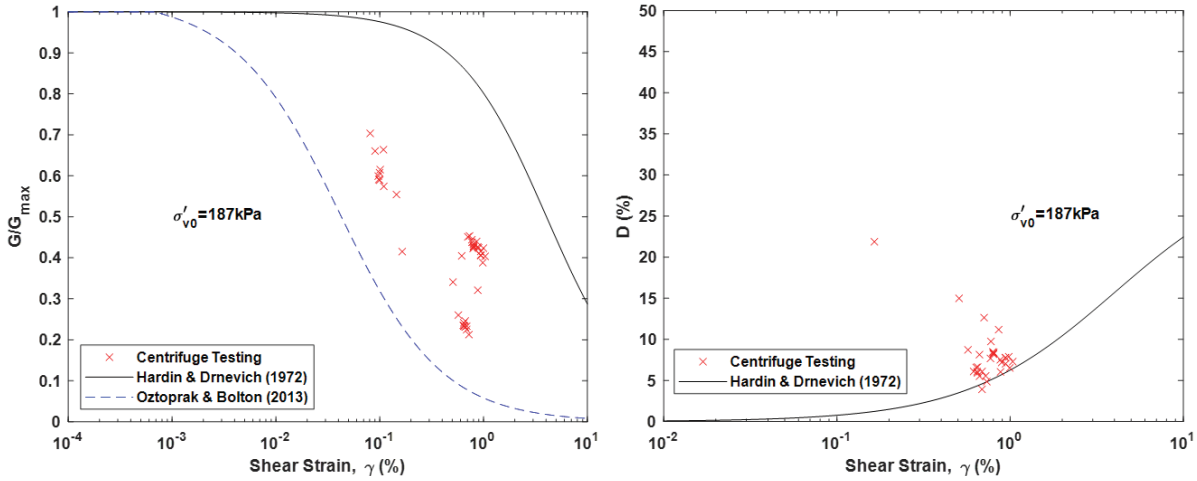

(a) Shear modulus degradation curve. (b) Damping curve.

Figure 5: Variation of shear modulus and damping with strain.

4 DYNAMIC STRAINS IN THE SLOPE MODEL

The dynamic response of a level soil bed subjected to the strong earthquake EQ4 has been analysed with the data obtained in Test-1, but the response of the potentiometers indicates low sensitivity. Therefore, a slope model, in which larger soil deformation tends to occur, was tested, and the results are presented and discussed.

4.1 Absolute acceleration based results

Table 2 shows that the accelerations at the slope crest (see Piezo-05 and -06) were larger than other locations around the slope. The difference between the peak +ve and –ve accelerations decreased, indicating soil sliding along the slope. Furthermore, the difference became smaller from the crest to the base.

Piezo no.	Depth in the slope (m)	Max. acc. (g)	Min. acc. (g)
05	1	0.41	-0.58
06	4	0.46	-0.59
07	1	0.28	-0.39
08	4	0.36	-0.42
10	1	0.38	-0.41

Table 2: Absolute accelerations around the slope during EQ4 in Test-2.

4.2 New device-based results

Following the same procedure of analyses of Test-1, the relative displacements measured by potentiometers and those calculated from accelerations are shown in Figure 6(a). The displacements agree with each other well. However, the relative displacements from accelerations are slightly different from those measured directly. Such a discrepancy could result from signal filtering, as the measured accelerations were filtered more than the measured displacements. Moreover, the noise may have different phases, that is, the calculated displacements can be larger or smaller than the measured ones. In addition, the linear strains were larger at the deeper layer than at the shallower layer of the mid-slope (Figure 6(b)). This could indicate the existence of slip plane.

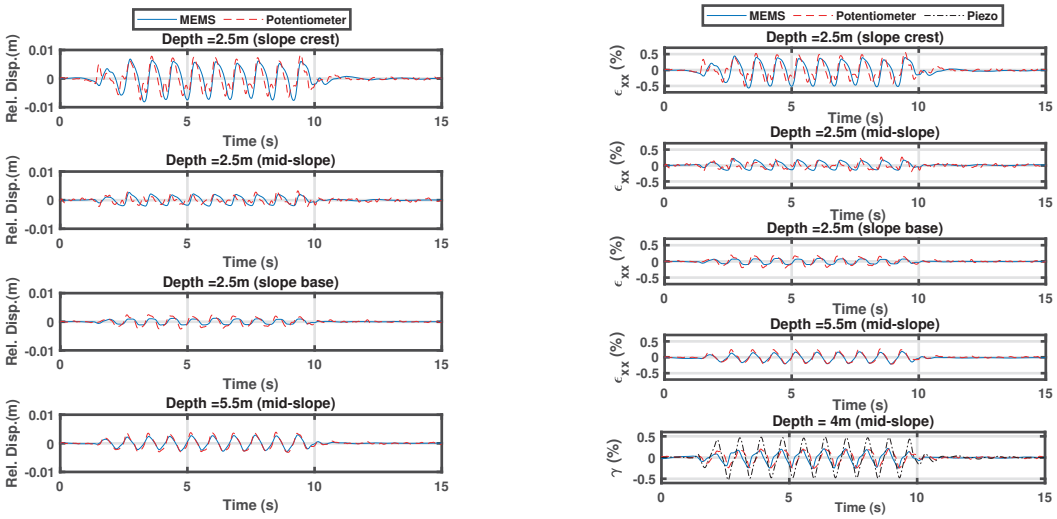

(a) Comparison of relative displacements.

(b) Comparison of cyclic strains.

Figure 6: Result comparisons based on the various measurement methods during EQ4 in Test-2.

The potentiometers producing satisfactory relative displacement time-histories, the corresponding cyclic shear strains are compared with those calculated based on the absolute accelerations in Figure 6(b). As expected, the shear strains from relative accelerations and relative displacements show a good match. However, the cyclic strains based on the measurements of the Piezo-electric accelerometers are approximately 1.5 times larger than those based on the measurements of the new devices. The friction between the shaft and the housing of the potentiometer could be the primary reason. Additionally, the numerical errors could also cause the discrepancy.

4.3 Mohr's circles of strains

The maximum cyclic linear strains and maximum shear strains during the same cycle were used for Mohr's circles (Figure 7). Generally, the radii of circles at each location decreased with the number of cycles, indicating increasing soil stiffness. Additionally, the largest radii were seen at the slope crest (Figure 7(a)), while the smallest radii were observed at the mid-slope near the surface (Figure 7(b)). This indicates that larger soil deformation occurred at the crest, where confining pressures were relatively small.

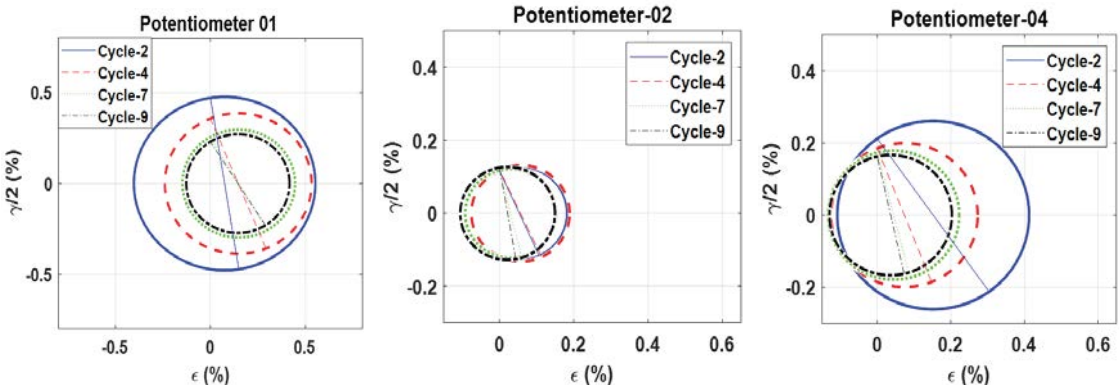

(a) (b) (c)

Figure 7: Mohr's circles of strains.

5 CONCLUSIONS

This research has developed and tested a new device to measure soil deformation and verify the applicability of the new device. Two dynamic centrifuge tests were conducted on a level sand model and a slope model, respectively. Four new devices were used to measure soil strains directly based on a new principle. The results obtained with this new direct measurement method were compared with those obtained with a commonly-used indirect measurement method.

This research shows that the accelerations measured in the sand in both tests increased towards the sand surface, but the magnitudes of the earthquakes had a negligible impact on such acceleration amplification. This confirms that soil deformation is larger where confining stress is smaller. It was also found that the shear moduli calculated in the tests are generally within the boundary of the two empirical equations proposed by Hardin and Drnevich [5], and Oztoprak and Bolton [9], respectively. Specifically, those shear moduli fall closer to the curve presented by Oztoprak and Bolton [9]. For damping ratios, they fall generally above the empirical curve presented by Hardin and Drnevich [5]. This curve may be more applicable to the strain range from 0.15% to 1% under similar site conditions, as the experimental damping ratios are closer to it within this range. Another major finding is observed in the results obtained in Test-2 where the larger soil deformation was simulated, that is, the displacement records of the potentiometers show a good agreement with the calculated displacement histories based on the records of the MEMS accelerometers. It is, therefore, concluded that the new device could be applicable for large soil deformation.

However, it should be noted that the discrepancy between the results obtained from the new measurement methods and those obtained from the widely-employed method proposed by Brennan et al. [1] is still clear. As indicated by the experimental results in this research, the friction between the housing and shaft tends to affect the data significantly. Thus, more efforts should be made to reduce or even eliminate the friction in future research. Despite the discrepancy, this research undoubtedly provides some valuable evidence that this new measurement device can provide valid results with further improvement.

References

[1] A. Brennan, N. Thusyanthan, and S. Madabhushi. Evaluation of shear modulus and damping in dynamic centrifuge tests. *Journal of Geotechnical and Geoenvironmental Engineer-*

ing, 131(12):1488–1497, 2005.

[2] A. Elgamal, M. Zeghal, V. Taboada, and R. Dobry. Analysis of site liquefaction and lateral spreading using centrifuge testing records. *Soils and Foundations*, 36(2):111–121, 1996.

[3] B. Ghosh and S. Madabhushi. An efficient tool for measuring shear wave velocity in the centrifuge. In *Proceedings of the international conference on physical modelling in geotechnics*, pages 119–124. AA Balkema, 2002.

[4] S. Goto, F. Tatsuoka, S. Shibuya, Y. Kim, and T. Sato. A simple gauge for local small strain measurements in the laboratory. *Soils and foundations*, 31(1):169–180, 1991.

[5] B. O. Hardin and V. P. Drnevich. Shear modulus and damping in soils: design equations and curves. *Journal of Soil Mechanics & Foundations Div*, 98(sm7), 1972.

[6] Y. M. Hashash, S. Dashti, M. I. Romero, M. Ghayoomi, and M. Musgrove. Evaluation of 1-d seismic site response modeling of sand using centrifuge experiments. *Soil Dynamics and Earthquake Engineering*, 78:19–31, 2015.

[7] S. Madabhushi, N. Houghton, and S. Haigh. A new automatic sand pourer for model preparation at university of cambridge. In *Proceedings of the 6th International Conference on Physical Modelling in Geotechnics*, pages 217–222. Taylor & Francis Group, London, UK, 2006.

[8] H. Mitrani. *Liquefaction remediation techniques for existing buildings*. PhD thesis, University of Cambridge, 2006.

[9] S. Oztoprak and M. Bolton. Stiffness of sands through a laboratory test database. *Géotechnique*, 63(1):54–70, 2013.

[10] B. Shi, Y. Murakami, Z. Wu, J. Chen, and H. Inyang. Monitoring of internal failure evolution in soils using computerization x-ray tomography. *Engineering Geology*, 54(3-4):321–328, 1999.

[11] S. A. Stanier, J. Blaber, W. A. Take, and D. White. Improved image-based deformation measurement for geotechnical applications. *Canadian Geotechnical Journal*, 53(5):727–739, 2015.

[12] D. White, W. Take, and M. Bolton. Soil deformation measurement using particle image velocimetry (piv) and photogrammetry. *Geotechnique*, 53(7):619–631, 2003.

[13] D. Xu, L. Borana, and J. Yin. Measurement of small strain behavior of a local soil by fiber bragg grating-based local displacement transducers. *Acta Geotechnica*, 9(6):935–943, 2014.

[14] M. Zeghal. Lotung site: downhole seismic data analysis. *Rep. Electric Power Research Institute*, 1993.

[15] M. Zeghal, A. Elgamal, H. Tang, and J. Stepp. Lotung downhole array. ii: Evaluation of soil nonlinear properties. *Journal of geotechnical engineering*, 121(4):363–378, 1995.

EURODYN 2020
XI International Conference on Structural Dynamics
M. Papadrakakis, M. Fragiadakis, C. Papadimitriou (eds.)
Athens, Greece, 23–26 November 2020

STRUCTURAL PROPERTIES OF UNREINFORCED MASONRY WALLS CONSIDERING CONSTRUCTION QUALITIES

Dong-Hyeon Shin[1], **and Hyung-Joon Kim**[2]

[1] University of Seoul
Engineering 1 Bldg, University of Seoul 163 Seoulsiripdaero, Dongdaemun-gu, Seoul 02504 KOREA

[2] University of Seoul
Arch & Civil Eng'g Bldg, University of Seoul 163 Seoulsiripdaero, Dongdaemun-gu, Seoul 02504 KOREA
hyungjoonkim@uos.ac.kr

Keywords: unreinforced masonry walls, diagonal tension tests, construction quality, non-structural component, bed-joints, head-joints

Abstract. *Non-structural unreinforced masonry (URM) walls are generally consisted of cement bricks and mortar used for joint material. Bricks in masonry works should be completely glued on bed and head-joints with sufficient thickness. In typical masonry construction, variation of thickness and recess of bed and head-joints is inevitable and they are important physical parameters that can be used in determining the construction quality of masonry works. Thus, it is necessarily required to investigate the influence of construction quality on the structural properties of an URM wall. As preliminary investigations, this study experimentally evaluates the effects of construction quality to the diagonal tension behavior of a masonry unit. The effects are discussed with selected test parameters, thicknesses and recesses of joints which can be considered to be critical quantities to erection time related to the construction quality of the test specimens. Test results present that the failure modes of the specimens are considerably dependent upon the construction qualities and their strength and elastic modulus increase in the specimen with better construction quality presenting the smaller recess and the larger thickness of the bed and head-joints.*

1 INTRODUCTION

Unreinforced masonry (URM) walls used as a non-structural element in building construction have been commonly implemented for architectural space zoning. The lessons learned from historical earthquakes have demonstrated that non-structural URM walls can be vulnerable to even low intensity of seismic attacks resulting in free structural damage to a building structure. Under cyclic loading, they suffer fatal failures classified into toe compression failure, rocking, bed-joint sliding, diagonal cracking and overturning failures. Thus, current seismic design codes, such as AIK [1] and ASCE [2], prescribe the design requirements for non-structural URM walls in order that their seismic performance improves and, in turn, the seismic damage is limited under even severe ground motion shaking.

A nonstructural URM wall consists of concrete bricks laminated by mortar without any reinforcements for structural integrity. Thin layer glue-mortar is applied to the perimeter sides of a brick to make bed and head-joints in the horizontal and vertical directions of a wall, respectively. Bricks in a masonry unit are manufactured with relatively excellent quality control. However, although construction specifications [3] for masonry works recommend that bed and head-joints of sufficient thickness (usually larger than 10 mm) be installed, the quality of in-situ mortar bed and head-joint works is still hardly controlled in a construction site. The construction quality of mortar joint works can be quantitively represented by their thickness and recess which will be chosen as test parameters for this study.

In order to assess the structural behavior of an URM wall resulting from such complicate material composition, the structural properties of a masonry unit first need to be precisely evaluated. This is carried out by compressive tests of prisms and diagonal tension tests of masonry units. This study investigates the influence of the thickness and recess of mortar joints on the structural properties which can be obtained from diagonal tension tests of a masonry unit. To do this, specimens for diagonal tension tests of masonry units were prepared with three construction qualities, "*Good*", "*Fair*" and "*Poor*" which can be classified by masonry piling time correlated with apparent physical test parameters, the thickness and recess of mortar joints. The testing parameters are statistically analyzed according to the construction qualities. Also, test results of the masonry unit specimens manufactured with different construction quality are discussed in terms of their strength and elastic modulus. This *pilot* test program intends to demonstrate the relation between the structural properties and the construction quality of masonry walls which can become basis information on the seismic evaluation of existing and new masonry building structures.

2 DESCRIPTION OF TEST SPECIMENS

The structural behavior of a non-structural URM wall mainly depends on the properties of masonry units affected by the construction quality which is influenced by a lot of factors including the workmanship of skilled laborers, working environments, working temperatures, working space, etc. All of factors related to construction quality of masonry works are closely represented by a masonry piling time. It was known throughout interview with skilled laborers that they are capable of piling only about 120 bricks in carrying out masonry works according to very strict working manual while they can pile more than 200 bricks under the allowance of poor construction quality. This study considers a masonry piling time as the main factor which can determine the construction qualities of masonry works.

Figure 1 shows the shapes and dimensions of specimens for diagonal tension test specimens according to ASTM [4]. The masonry unit specimens with 390 mm width, 392 mm height and 90 mm thickness were made with a total 12 cement bricks which were piled to 6 layers. The dimensions of each brick are 190 mm × 90 mm × 57 mm. According to general

construction specifications for masonry works, the thickness t_{bj} of both bed and head-joints is planned to be larger than 10 mm and straight head-joints are avoided. Note that during construction of the specimens, a value of t_{bj} for each specimen would be changed and would also have spatial variation within an individual specimen. A total of 30 specimens was prepared and 10 specimens were constructed with each construction quality classified into "*Good*", "*Fair*" and "*Poor*" which are dependent upon the masonry piling time *T*. Table 1 summaring the statistics of *T*s shows that mean values of *T*s increase for the specimens with better construction quality. Regardless of the construction qualities, the coefficients of variation COVs are similar. This means that all specimens categorized into the same construction quality maintain the similar degree of variation of masonry piling times.

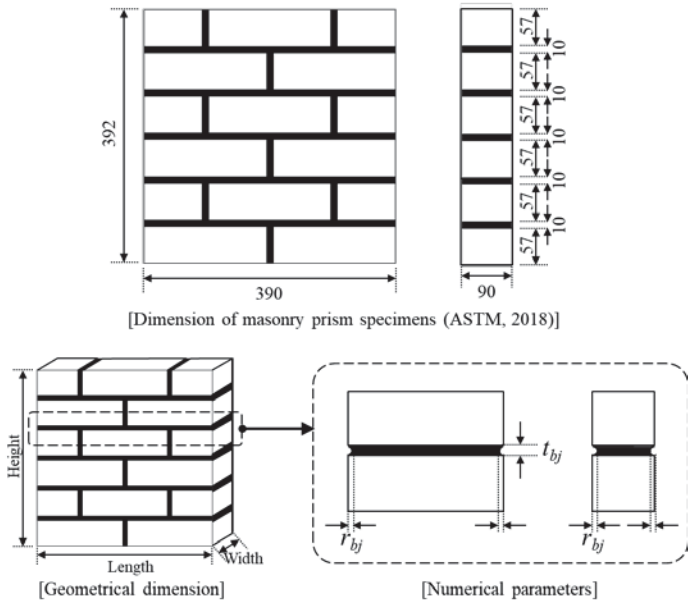

Measurement of masonry prism specimen

Specimen	G04	Quality	Good	
Measurement location	Front view		Rear view	

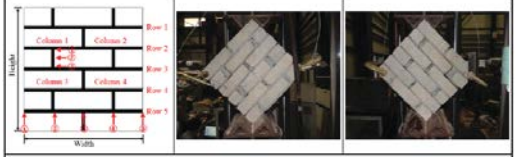

Geometrical dimension of specimens				
Length, mm	390	Height, mm	380	THK., mm	90.45

r_{bj} – row

–	①	②	③	④	⑤
row 1	-3.13	-1.98	-7.07	-4.54	-8.75
row 2	-2.66	-4.08	-3.98	-6.59	-6.25
row 3	-4.40	-3.58	-8.49	-4.74	-3.09
row 4	-25.04	-9.21	-5.24	-5.42	-16.54
row 5	-7.79	-1.47	-1.37	-0.99	-2.78

t_{bj} – row

–	①	②	③	④	⑤
row 1	8.41	7.40	8.10	8.92	9.18
row 2	9.95	11.24	8.87	9.24	8.82
row 3	10.61	9.66	8.35	6.43	6.14
row 4	9.79	9.89	9.35	8.60	8.15
row 5	6.28	9.09	9.18	8.51	7.26

Figure 1: Dimension of specimens and numerical parameters representing masonry construction qualities

	Good	Fair	Poor
Mean, *T*, sec	231	113	105
Standard deviation, sec	19.4	12.4	9.2
Coefficient of variation, COV, %	8.4	8.6	8.7

Table 1: Statistical information for construction time of masonry unit specimens

Values of *T*s are considered as the main index of construction quality in manufacturing the specimens. More physical parameters are required to verify the relation between construction quality (represented by masonry piling time *T*) and the structural properties of the masonry unit specimens. This study considers the thickness t_{bj} of both bed and head-joints and their recess r_{bj} from the brick surface as the apparent testing parameters, shown in Figure 1. Values of t_{bj} and r_{bj} of all the specimen were examined after curing. For each specimen, a total of 37 measurements (12 at head joints and 25 at bed joints) was measured using a digital Vernier caliper.

The distributions of t_{bj} and r_{bj} values measured at the bed and head-joints in the specimens are found in Figures 2 and 3. Regardless of types of joints, the larger t_{bj} values and the smaller absolute values of r_{bj} are founded at the masonry unit specimens erected with better construc-

tion quality. A mean of t_{bj} values is the smallest at the head-joints for the *Poor* specimens while the corresponding mean values for the *Good* and *Fair* specimens are relatively close to 10 mm which is the planned joint thickness. Values of t_{bj} larger than 10 mm are found in the head-joint for some *Good* specimens. Mortar filling in bed-joints is better than in head-joints, which magnifies the variation of r_{bj} values measured in head-joints.

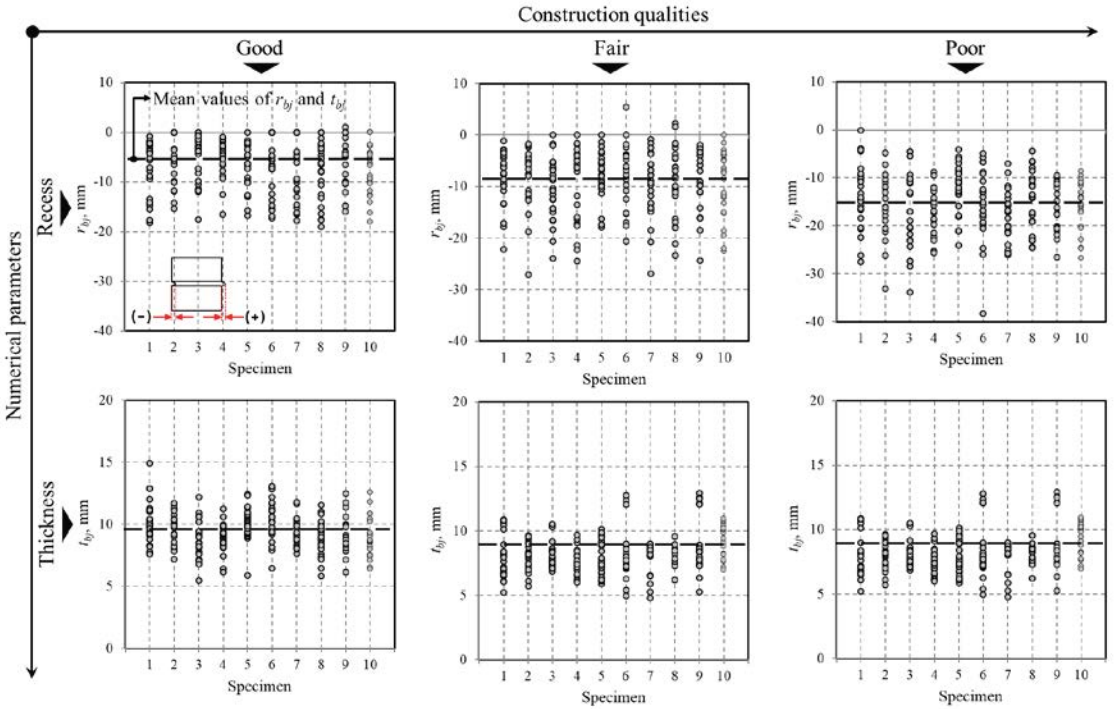

Figure 2: Distribution of numerical parameters measured at bed-joints in specimens

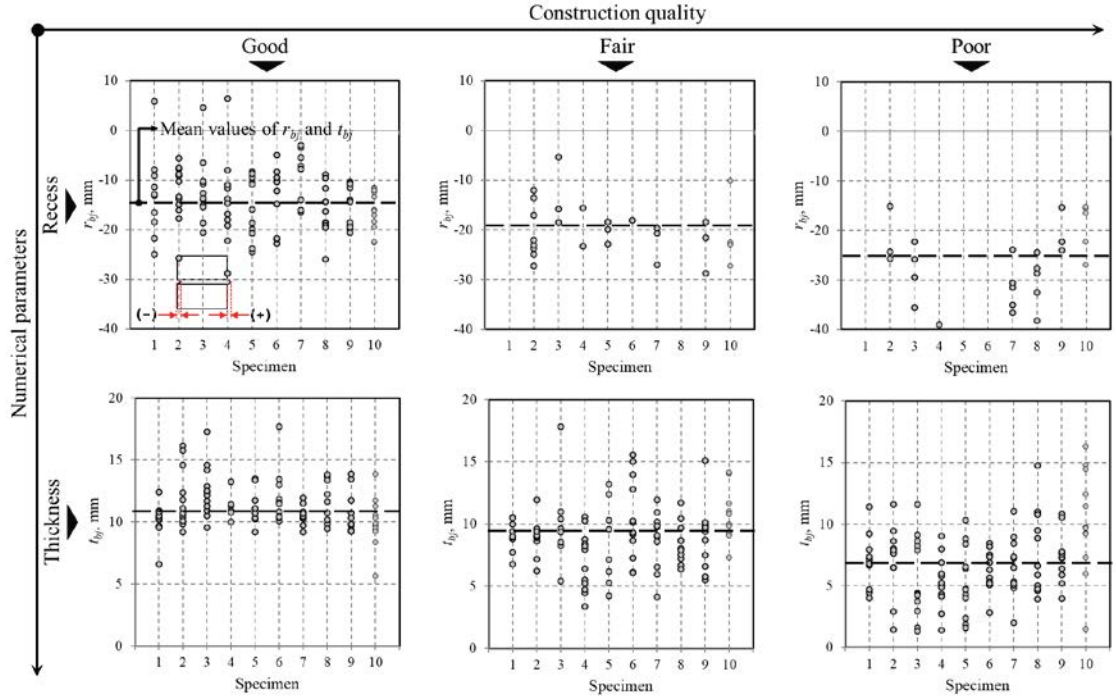

Figure 3: Distribution of numerical parameters measured at head-joints in specimens

Statistical spatial variations of t_{bj} and r_{bj} values measured at both of the bed and head-joints in the specimens were investigated and summarized in Figure 4. Expected values of r_{bj} measured at the bed-joints are the smallest at their center and are increased at the edges while those of t_{bj} are relatively constant along a joint line. Unlike the bed-joints, means of r_{bj} values measured at the head-joints of the *Good* specimens are the largest at their center. For the *Fair* and *Poor* specimens, means of r_{bj} values at the head-joints are smaller as the distance from the bottom bed-joint is increased. Again, the largest spatial variation of both t_{bj} and r_{bj} values is also observed at the *Poor* specimens even if there is still some degree of spatial distribution in the *Good* specimens.

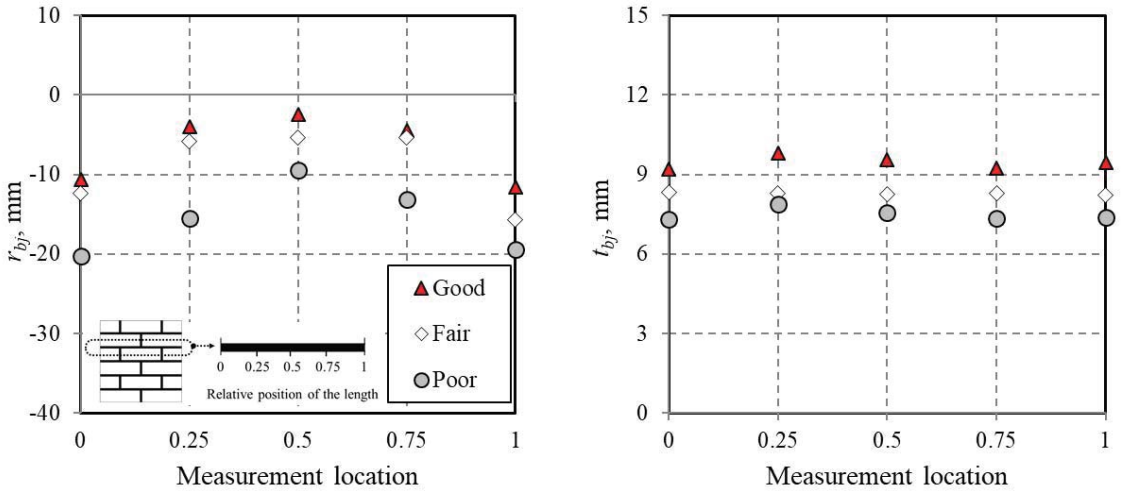

(a) Bed-joints

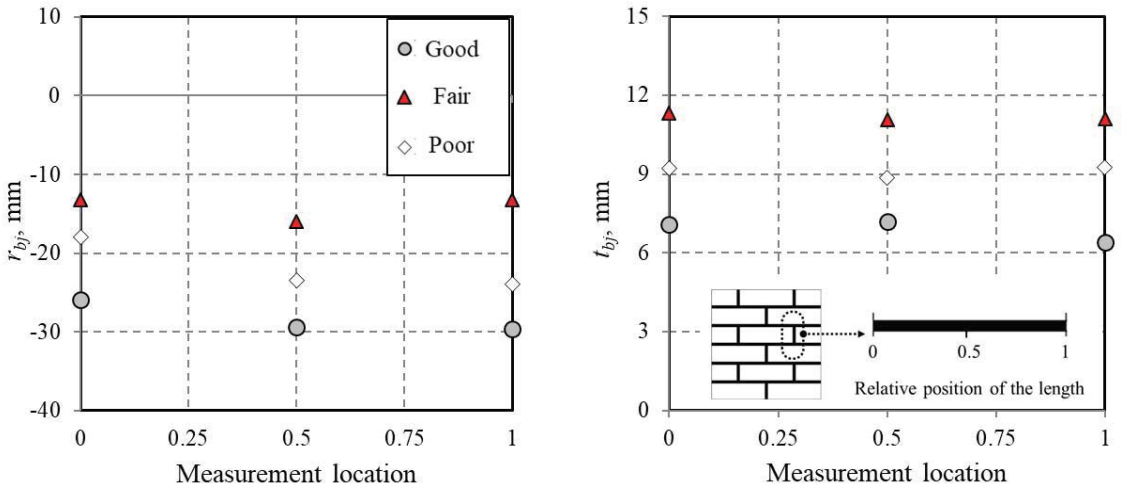

(b) Head-joints

Figure 4: Mean numerical parameters at measurement locations

3 EFFECTS OF CONSTRUCTION QUALITY ON DIAGONAL TENSION BEHAVIOR OF TEST SPECIMENS

Diagonal tension tests were carried out with the Universal Testing Machine with 500 kN capacity. Figure 5 presents crack patterns observed at the end of each test. Also, the failure

modes relied on the construction quality of the specimens are shown in the figure. In the *Good* specimens, cracks parallel to the loading direction developed along bed and head-joints alternately. A few cracks were also found in bricks. Similar crack pattern was observed in the *Fair* specimens. However, for the *Poor* specimens most of cracks were developed along one of bed-joints where is relatively short of filling mortar. Compared to the *Good* and *Fair* specimens, the total travelling length of cracks in the *Poor* specimens was shortened, which causes a brittle mode.

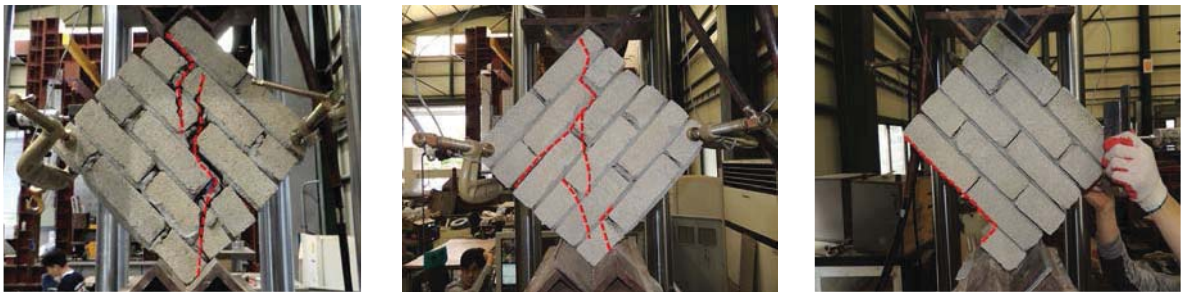

(a) *Good* specimen (b) *Fair* specimen (c) *Poor* specimen

Figure 5: Dominant failure modes of masonry unit specimens according to construction quality

Diagonal tension tests are typically performed to find out the direct shear stress and modulus which are important structural properties used for the seismic evaluation of a non-structural URM wall. Figure 6 contains measured shear stresses, τ_m at the maximum applied loads and shear modulus, G_m of the specimens. In this figure, solid parallelograms represent their mean values of the *Good*, *Fair*, and *Poor* specimens. The mean values of τ_m are, respectively, 0.56, 0.44 and 0.35 MPa for the *Good*, *Fair*, and *Poor* specimens, which demonstrates their dependence on the construction quality. The normalized means of τ_m values to that of the *Good* specimens, $\tau_{m(good)}$ are 0.79 and 0.63 for the *Fair* and *Poor* specimens, respectively. Note that even the mean of τ_m measured at the *Poor* specimens is still larger than the codified shear strength of 0.2 MPa [5] which is close to the smallest shear stress in the *Poor* specimen. The correlation of shear modulus with construction quality of masonry unit are similar to that of shear stress. The normalized means of G_m values to that of the *Good* specimens, $G_{m(good)}$ are *0.80* and *0.57* for the Fair and Poor specimens, respectively.

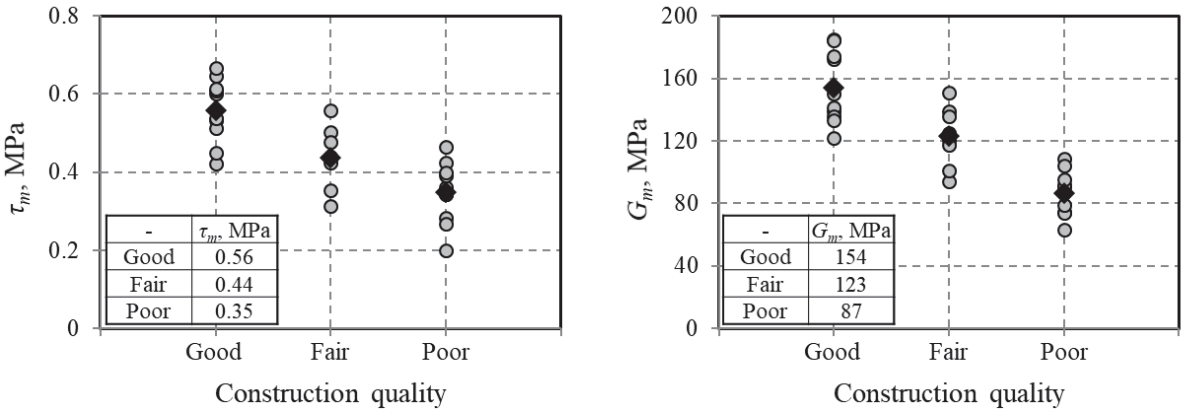

(a) Distribution of shear stress, τ_m (b) Distribution of shear modulus, G_m

Figure 6: Distributions of mechanical properties of masonry unit specimens

The normalized τ_m and G_m values are further analyzed to investigate effects of combination of the parameters, t_{bj} and r_{bj}, in detail. To do this, a normalized net mortar filling area factor, Λ defined as a ratio a net mortar filling area, $(A_{bj} - t_{bj} \times r_{bj})$ to the total joint area A_{bj} is introduced. Figure 7 shows the relations between the normalized τ_m and G_m, and Λ values for each type of joints in the all specimens. Linear correlation is clearly presented in the bed-joints rather than the head-joints. This is due to a factor that Λ values of the head-joints are not correlated with the construction quality, as shown in the figure where some of the *Poor* specimens have the head-joints with mortar-filling area that is larger than the corresponding of the *Good* and *Fair* specimens. In the bed-joints, Λ values increase for the specimens constructed with better quality. Most of the normalized τ_m and G_m values can be conservatively estimated using a linear equation established by considering one standard deviation from a trend line shown as a solid line in the figure.

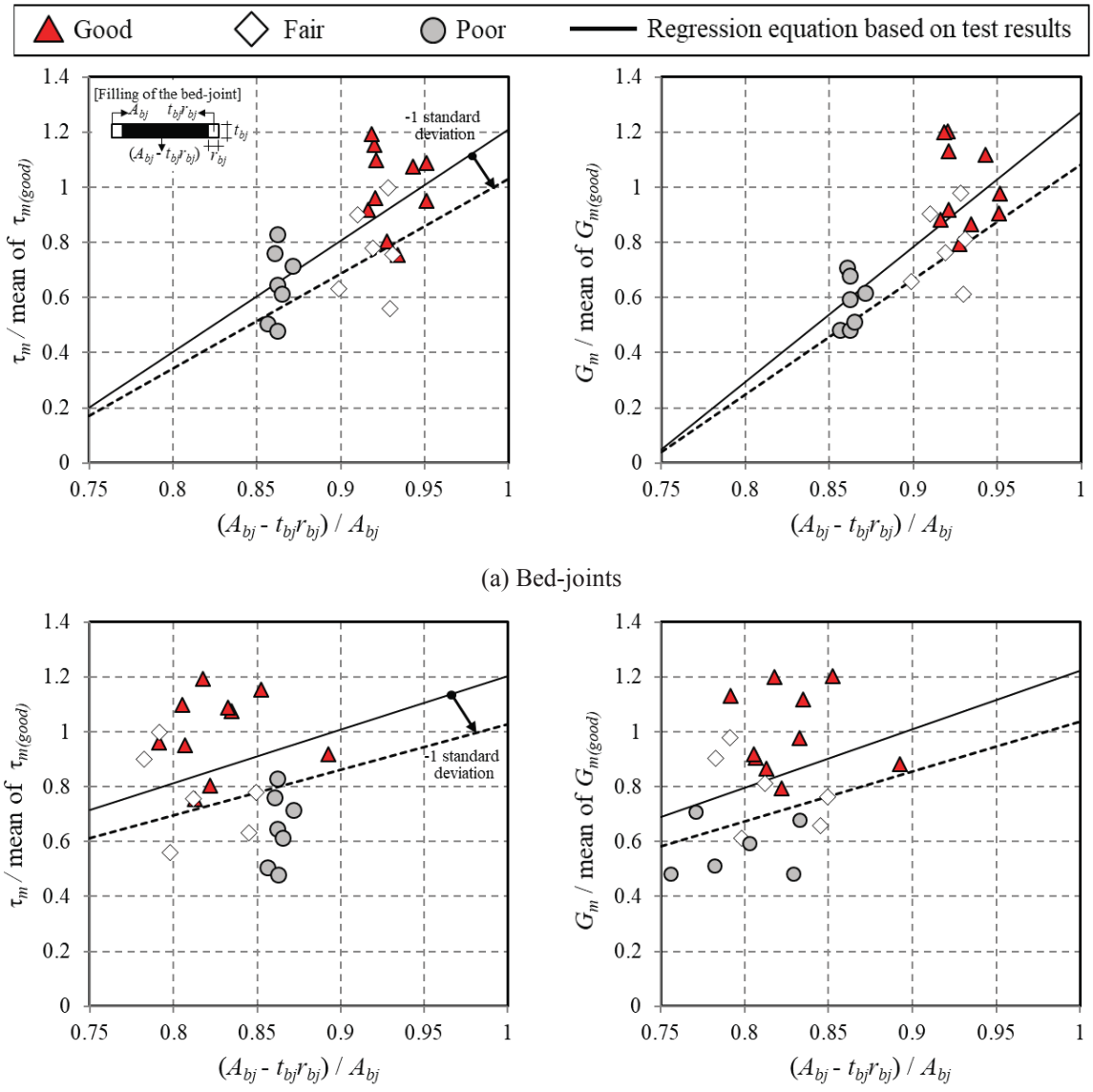

(a) Bed-joints

(b) Head-joints

Figure 7: Relation between numerical parameters and filling of the bed and head joints measured at unit specimen

4 CONCLUSIONS

This study is carried out diagonal tension tests of masonry units manufactured with construction qualities of "*Good*", "*Fair*" and "*Poor*" that can be differentiated by the thickness and recess of mortar joints. The effects of construction quality on the structural properties of the specimens are investigated. This *pilot* test program intends to provide basic information on the influence of construction qualities on the seismic capacities of nonstructural URM walls.

A total of 30 specimens with 390 mm width, 392 mm height and 90 mm thickness was prepared. Of them, 10 specimens were constructed with each construction quality classified into "*Good*", "*Fair*" and "*Poor*". This study considers the thickness t_{bj} and the depth of recess r_{bj} as parameters representing construction qualities. The largest t_{bj} values and the smallest absolute values of r_{bj} were founded in the *Good* specimens while a mean of t_{bj} values was the smallest at the head-joints for the *Poor* specimens. In statistical spatial variations of t_{bj} and r_{bj} values, the largest spatial variation of both t_{bj} and r_{bj} values was also observed at the *Poor* specimens.

The *Good* and *Fair* specimen's cracks developed into bed and head-joints alternately. In the *Poor* specimens, most of cracks were developed and propagated on a single bed-joint, which causes a brittle failure mode. The mean shear stresses are, respectively, 0.56, 0.44 and 0.35 MPa for the *Good*, *Fair*, and *Poor* specimens. Similar to the mean shear stresses, the correlation of shear modulus with construction quality is presented. There exists the linear correlation between normalized shear stress and modulus and a normalized net mortar filling area factor in the bed-joints. The normalized shear stress and modulus are increased with the increase in mortar filling area of the specimens.

ACKNOEWLEDGEMENT

This research was supported by a grant (20AUDP-C146352-03) from the Architecture & Urban Development Research Program funded by the Ministry of Land, Infrastructure and Transport of the Korean Government.

REFERENCES

[1] Architectural Institute of Korea (AIK), *Seismic Building Design Code and Commentary (Korean Building Code), KDS 41 17 00*, Architectural Institute of Korea, Seoul, Korea, 2019.

[2] American Society of Civil Engineers (ASCE), *Minimum Design Loads and Associated Criteria for Buildings and Other Structures, ASCE/SEI 7-16*, American Society of Civil Engineers, Virginia, U.S.A, 2016.

[3] Ministry of Land Infrastructure, and Transport (MLIT), *Korean Construction Specification, KCS 41 34 01, Masonry Construction*, Ministry of Land Infrastructure, and Transport, Korea Construction Standard Center, Korea, 2016.

[4] American Society of Testing and Materials, *Standard Test Method for Diagonal Tension (Shear) in Masonry Assemblages, ASTM E519 / E519M-15*, ASTM International, West Conshohocken, PA, U.S.A, 2015.

[5] American Society of Civil Engineers (ASCE), *Seismic Evaluation and Retrofit of Existing Buildings, ASCE/SEI 41-06*, American Society of Civil Engineers, Virginia, U.S.A., 2006.

EURODYN 2020
XI International Conference on Structural Dynamics
M. Papadrakakis, M. Fragiadakis, C. Papadimitriou (eds.)
Athens, Greece, 23–26 November 2020

DIRECT OBSERVATION OF BOND FAILURE OF FATIGUE PULL-OUT TEST WITH LIQUID WATER BY USING DIC

Ahmed Okeil[1], Koji Matsumoto[2], and Kohei Nagai[3]

[1] Penta-Ocean Construction Co., Ltd.
Tokyo, Japan.
E-mail: ahmed.atia@mail.penta-ocean.co.jp & okeil@iis.u-tokyo.ac.jp

[2] Hokkaido University
Sapporo, Japan.
km312@eng.hokudai.ac.jp

[3] Institute of Industrial Science
The University of Tokyo
Tokyo, Japan.
nagai325@iis.u-tokyo.ac.jp

Keywords: Local bond, Fatigue, Pull-out failure, Deformed bar, Image processing

Abstract: *A part of reinforced concrete structures are always subjected to dynamic repeated loading and simultaneously subjected to liquid water from an external source such as rains. These structures, especially the old ones, have numerous surface cracks that allow water to penetrate concrete and reach steel-concrete interface and subsequently affect the bond between concrete and steel bars. Against this issue, a fatigue pull-out test was carried out with supplying of water to investigate experimentally the bond behavior between the concrete and a deformed bar by using digital image correlation technique (DIC).A fatigue pull-out test was applied to a deformed steel bar which was embedded in a concrete specimen. The specimen had a trapezoidal "window," which allows full continues observation and measurements of concrete or cement paste displacements and subsequently strains by recording high-resolution digital video which was later analyzed by DIC software. The experiment focuses on the failure mechanism of the deformed bar from the concrete and the mechanism of the sludge's formation in the vicinity of the deformed bar. The results show that the actual deformations of concrete in case of fatigue test were captured well in both positive and negative direction of loading by using the DIC technique and they matched the past results. Also, the experimental results show that the pull-out failure of the deformed bar occurred due to the failure inside the concrete, not through the interface between the concrete and the deformed bar.*

1 INTRODUCTION

The combination of concrete, which has high durability in compression; and reinforcement that is ductile in tension, is used in civil engineering structures to ensure high strength with sufficient deformations to resist disaster. The load transform from the deck or slab in the superstructure to the foundations in substructure occurs due to the bond between the concrete and the embedded reinforcement bars. The mechanical behavior between the reinforcement lugs and the surrounding concrete at the steel-concrete interface is primarily responsible for acquiring high bond. Thus, several types of research have studied the global and local bond behavior between the concrete and the reinforcement bars for the static cases, and as a result, several bond models have been established [1, 2, 3, 4]. Also, local cracks at the reinforcement lugs scale and the influence of deformations patterns around the steel-concrete interface have been investigated experimentally [5, 6, 7].

Meanwhile, most of the civil engineering structures are subjected to dynamic loads, especially fatigue loads, resulting in severe localized bond damage and significant movement between the rebar and the surrounding concrete comparing to static loads. Extensive studies have been performed on both material and structural level to understand the bond behavior between the concrete and the rebar under fatigue loads [8, 9, 10, 11]. It was reported that fatigue loads always cause micro-cracks that affect stress distribution around the rebar, followed by cracks propagation, and finally leading to fracture of the rebar.

However, in real situations, civil engineering structures are also exposed to liquid water from an external source such as rains, and that case is considered being the worst scenario to affect the durability and thus the serviceability of the structures. Against this issue, recently, researches have been carried out on the fatigue properties of reinforced concrete elements, such as slab decks and beams, focusing on the effect of external liquid water. It was revealed that the fatigue life of RC beams in seawater is significantly reduced compared with that in the air [12, 13]. Also, it was found that the pull-out failure of deformed bars unaccompanied by macro cracking is produced by the complex action of external liquid water and fatigue by the conversion of the matrix in the vicinity of the deformed bar into sludge [14, 15].

Recently, some new techniques such as digital image correlation (hereafter referred to DIC) have been introduced to investigate deeply the material properties and analyze the surface deformations of concrete material [16, 17, 18]. Direct observation and clear measurements of the deformations near the concrete-steel interface at the local level became available by using that technique. Few studies on that technique have shown the applicability of using such a technique in standard pull-out tests in which one deformed bar is embedded centrally in concrete specimens [19]. Also, the DIC technique was used to investigate the local bond behavior and the local cracking phenomena in case of axial tension tests of reinforced concrete beams [20]. The results showed the high ability of the DIC technique to identify the shear transfer zone around the concrete-steel interface and clarify the local opening-sliding behavior between the concrete and the deformed bars.

Against this substance, there was a need to imply one of the most advanced methods to investigate the bond degradation behavior in reinforced concrete members, which are subjected to dynamic repeated loads. In this study, the fatigue pull-out test of a deformed bar from a massive concrete specimen was carried out with the presence of external liquid water. For the first time, in the case of fatigue experiments, a powerful experimental procedure for monitoring and examining local deformations between ribs of deformed bar and concrete has been proposed by using the DIC technique. This experiment improves our understanding regarding the local bond degradation behavior between the concrete and the deformed bars; and the mechanism, which governs that behavior.

2 EXPERIMENTAL PROGRAM

2.1 Material Properties

Ordinary Portland Cement (OPC) was used as the main binder for concrete. The water to cement ratio (w/c) was 60 % by weight, and the maximum size of the coarse aggregate was 20 mm. Also, fine aggregates and high-performance air entraining (AE) water reducing agents were used for the mixture. The concrete compressive strength was measured based on a standard cylinder with dimensions of 100 mm X 200 mm. Details of the concrete mix proportions and its strength are given in Table 1.

A deformed screw-shaped type of reinforcement rebar was used for this experiment. This type was used because of having a flat surface on its two sides, which is useful for attaching the steel strain gauges for local strain measurements. Also, this type was used to avert a possible reduction in the area of rebar at locations of strain gauges. The type of rebar was D25 in compliance with the JIS standard. The properties of the reinforcement are listed in Table 2.

W/C (%)	Water (kg/m^3)	Cement (kg/m^3)	Sand (kg/m^3)	Gravel (kg/m^3)	AE (gm)	Slump (cm)	Air content (%)	f_c (MPa)
60	190	315	810	1008	1.1	9.5	4.5	28

Table 1: Mix proportions and fresh properties of concrete

Type	Diameter (mm)	Area (cm^2)	Weight (kg/m)	Yield strength (MPa)	Modulus of Elasticity (MPa)
D25	25.4	5.067	3.98	490	190,000

Table 2: Material properties of reinforcement bar

2.2 Specimen

Figure 1 shows the set-up of the experiment that was arranged according to a typical fatigue pull-out test. The test specimen was almost a cuboidal concrete with dimensions of 300 mm x 300 mm x 250 mm. A single screw-shaped deformed bar was placed at the center of the concrete specimen. A single screw-shaped deformed bar was placed at the center of the concrete specimen. The dimensions of the specimen were selected to be small as much as possible; so that the specimen could be easily handled, but at the same time large enough to include an opening for the direct observation purpose. As the purpose of this study is to investigate the bond behavior between the deformed bar and the surrounding concrete, therefore, direct monitoring and observation of the interface between the deformed bar and the concrete were needed. Thus the formwork of the specimen was not filled with concrete material; instead, a cubic opening was formed during the set-up of the form by using a 'Polyurethane Foam' material, as shown in figure 2. This 'opening' may affect the stress distribution at the interface between the concrete and the rebar due to the unsymmetrical of the specimen. Meanwhile, the opening allows for close and continuous monitoring and observation of the deformations in the concrete. It was found that the height of the 'opening' should be around one-fifth of the total height of the specimen to reduce as much as possible the stress disturbance around the rebar while allowing appropriate lighting and subsequently monitoring of the desired area inside the opening [19]. Also, the formwork was designed to include four aluminum tubes to make four voids inside the concrete, as shown in figure 3. These voids were used later to fix the specimen to the base plate of the machine by PC rods and anchors. The setting was considered accurately to avoid any vibration or displacement of the specimen while applying the fatigue load to the deformed bar.

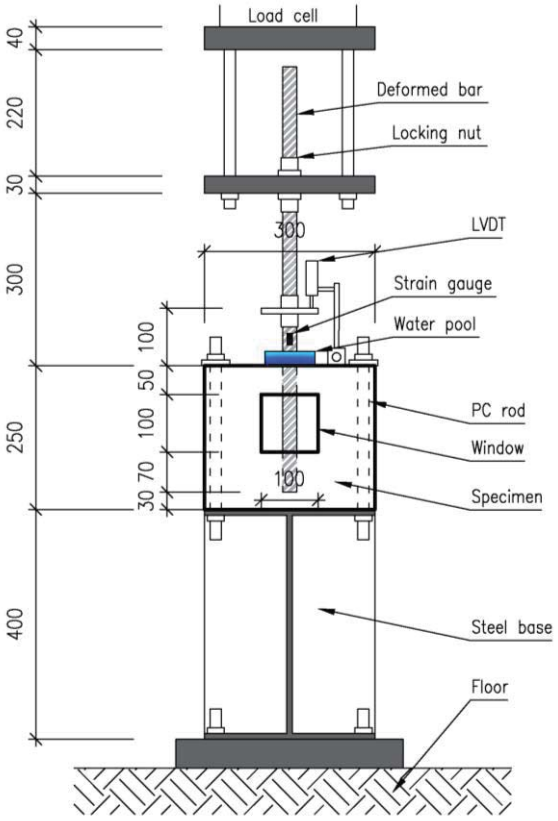

Figure 1: The set-up of the experiment (units: mm).

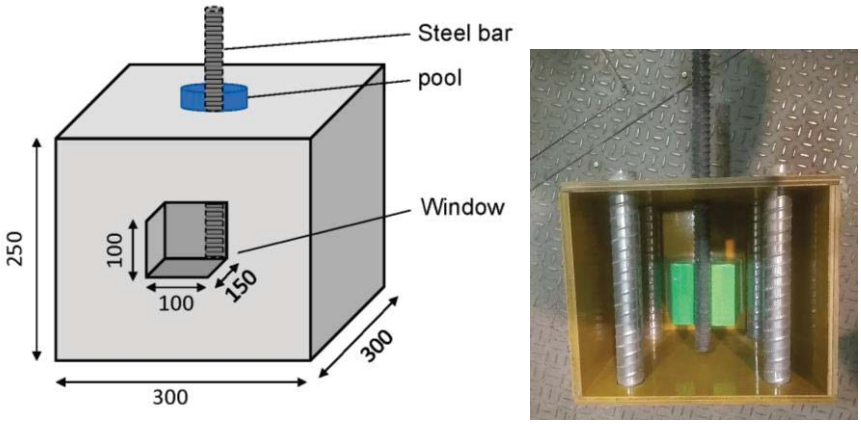

Figure 2: Lay-out of the test specimen (units: mm).

2.3 Mixing, casting and curing

The rebar was placed horizontally with arranging it at the center of the formwork, and it was settled above the foam piece. Lubricating oil was applied to all sides of the formwork for easy separation of the concrete from the formwork. Concrete was poured carefully from the top and segregation of the coarse aggregate was avoided. A needle vibrator was used to compact the concrete during the casting. After twenty-four hours of casting, the formwork was removed, and the specimen was cured by being covered with wet a cloth since formwork removing until the day before the test to avoid the drying shrinkage cracks.

2.4 Technical requirements

The purpose of this experiment is to study the local bond behavior between the concrete and the rebar in case of applying fatigue load with the supplying of liquid water. Therefore, there was a need to visualize and monitor the local bond interaction zone under the combined effect of fatigue load and water supply inside the concrete. Regarding that purpose, digital image correlation (DIC) analysis was used to obtain local deformations, such as displacements, from a high-resolution video that recorded during the experiments (GOM Correlate [20]). Before running the DIC analysis, images had to be extracted from the video with the same parameters; the software FFmpeg was used for that process [21]. GOM correlate can clearly identify areas of a measurement image which contains sufficient image information for analysis, and then identify the same areas in other images. These areas called "square facets," and the software recognizes them by their stochastic pattern structure, and the facets must have a unique gray level distribution which can be clearly identified by the software.

For the crack propagation purpose, and to investigate the contact surface between concrete and the deformed bar, the surface of the concrete was not sprayed before doing the test. Meanwhile, after the hardening of the concrete, the smooth outer layer of the concrete around the deformed bar inside the opening was removed and polished by using a handheld power tool called "disc grinder," as shown in figure 3. This step helps in achieving the required surface state similar to DIC analysis requirements. After removing this layer, aggregates could be seen, and this helps in tracking the crack propagation and observing how is the process of crack propagation through aggregates.

A high-resolution video camera (4k) was used for recording the loading process during the test. The resolution of the camera (i.e., the number of pixels per area in an image) is 3840 pixels × 2160 pixels, to catch very local deformations inside the opening.

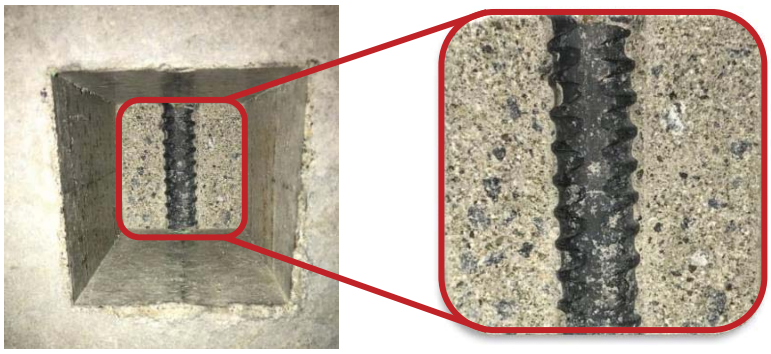

Figure 3: Removing surface layer of concrete inside the window

2.5 Test procedure

The testing apparatus for the fatigue pull-out test is shown in figure 4. Before testing, the specimen was arranged at the top of the steel base of the fatigue machine. The base of the steel frame was specially designed for that purpose and according to the dimensions of the specimen. The specimen was fixed with the steel base by using four steel anchors and four PC rods that were put inside the voids of the specimen. The deformed bar of the specimen was fixed with the jack load of the machine by steel nuts. To ensure the eccentricity of the rebar inside the specimen during the loading, two strain gauges were attached to both sides of the deformed bar outside the specimen. A liquid water pool was prepared at the top surface of the specimen by a circular plastic sheet that was attached to the specimen, as shown in figure 5. The specimen was tested vertically. A high-resolution video camera (4k) was used in front of the specimen window for recording during the test. To eliminate interruptions from surround-

ing light, a powerful LED light source was utilized to illuminate the sample and let only the reflected light go through the camera lens. The elongation and slip of the deformed bar were obtained from the relative displacement between the top surface of the specimen and the deformed rebar. For that purpose, linear variable displacement transducer (LVDT) was used at the top surface of the concrete, as shown in figure 4.

The dynamic load was applied automatically by the fatigue machine and monitored from load cell readings, which were displayed through the data logger. The capacity of the fatigue machine is 200 kN, and the magnitude of the applied load was about (± 50 kN), which was equivalent to 40 % of the rebar yield point, and low stress repeated reversal loading was used. The frequency of the loading was 1.0 Hz.

Figure 4: Testing apparatus of the experiment

Figure 5: Water pool at the top surface of the specimen

3 RESULTS AND DISCUSSIONS

Figure 6 shows the load versus pull-out displacement relationship for the concrete specimen with a deformed bar. The load was interrupted at (0 – 100 – 1000 – 3000 – 7000 and 10000) cycles during the loading process to check manually the pull-out behavior of the deformed bar and to check the cracks' status inside the window. These cracks were hard to be seen by naked eyes. The pull-out failure occurred after almost 10147 cycles. It was seen that air bubbles were generated from the beginning of the loading process, the water at the top surface of the specimen became cloudy, and then the pull-out of the deformed bar occurred. The failure occurred by the deformed bar being smoothly pulled out from the concrete specimen, unlike the failure of the static pull-out test in which the cone shape failure occurred at the surface of the concrete.

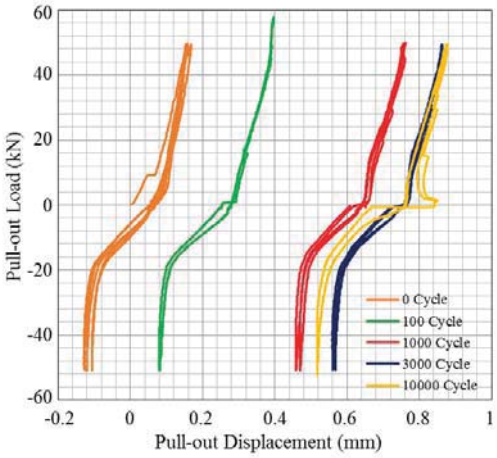

Figure 6: Pull-out load - pull-out displacement relationship

3.1 Deformations inside concrete by DIC

Image correlation software (GOM) was used to process the recorded data and derive the displacement and strain fields from the consecutive photographs that were extracted from video during the test. The local deformations, obtained from DIC analysis, were based on analysis of videos at (0 – 100 – 1000 – 3000 – 7000 and 10000) cycles. Figure 7 shows the contours of major principal strains (e1) at (0 – 100 – 1000 – 3000 – 7000 and 10000) cycles respectively. Each figure shows two deformation types in principal directions, one is at +50 kN, another one is at -50 kN. The local cracks, which were produced, have very tight widths which were hard to be seen by naked eyes. Therefore, calculated strains in the vicinity of the already formed crack have relatively large values (in the order of 1 %) because they are derived from displacements in the order of the crack width. It is clear that the local deformations are developed and increase gradually in both directions at each load level.

As explained before, a theoretically schematic diagram for deformations of concrete around the reinforcing bar, after the formation of internal cracks, was established by Goto [7] (as shown in Figure 8). According to his theory, as the tension in the steel bar increases, the concrete around the deformed bar presents the appearance of a comb. This complicated behavior of the concrete-steel interface was captured well by using the DIC technique in case of fatigue test in both positive and negative loading direction. Internal cracks form in concrete around the deformed bar at angle of about 60° to the bar axis. The actual deformations of concrete around the surface of the deformed bar were observed and measured during the loading process and they well matched the schematic diagram of Goto.

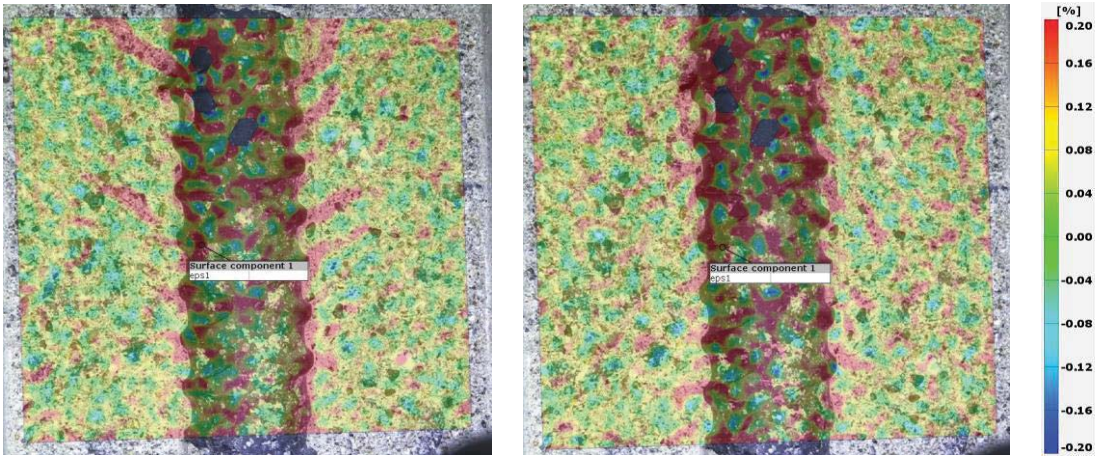

(a) Major principal strain e1 at 100 cycles (+50 & -50 kN)

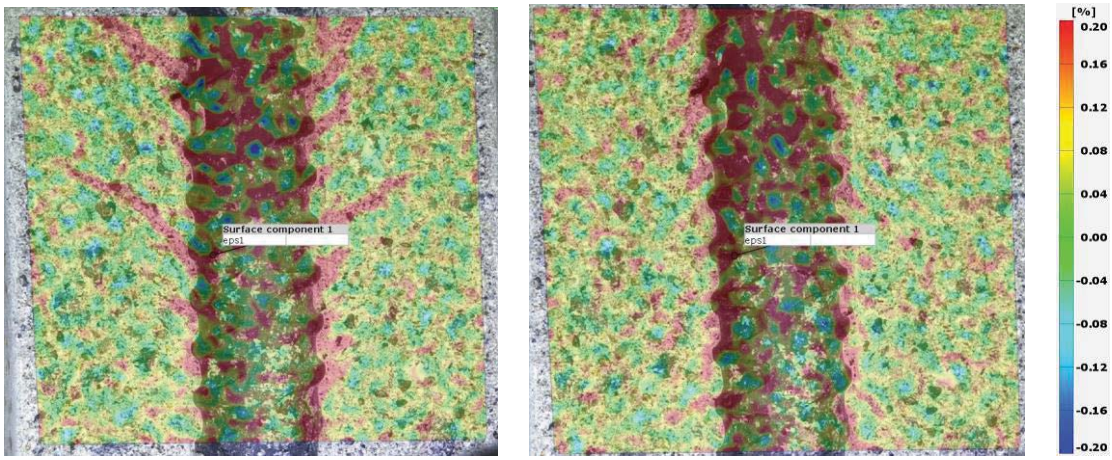

(b) Major principal strain e1 at 1000 cycles (+50 & -50 kN)

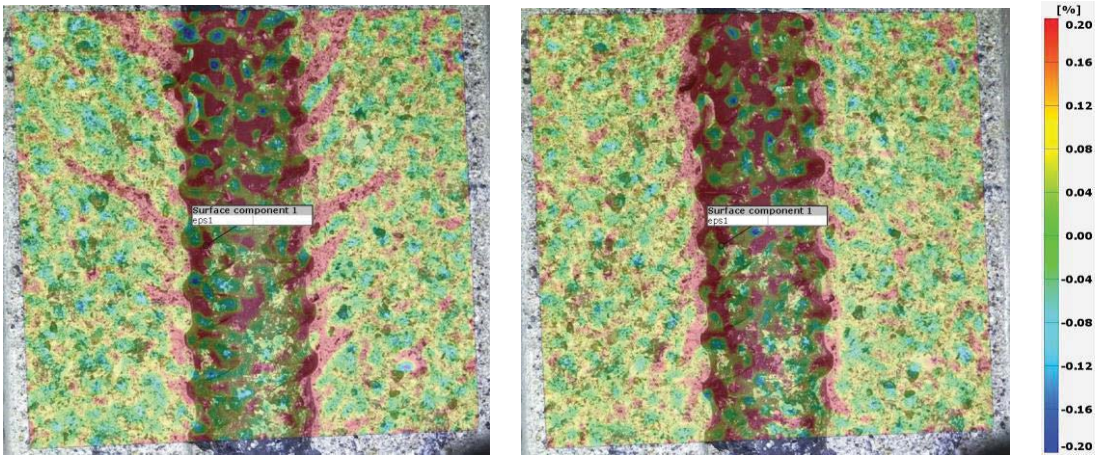

(c) Major principal strain e1 at 3000 cycles (+50 & -50 kN)

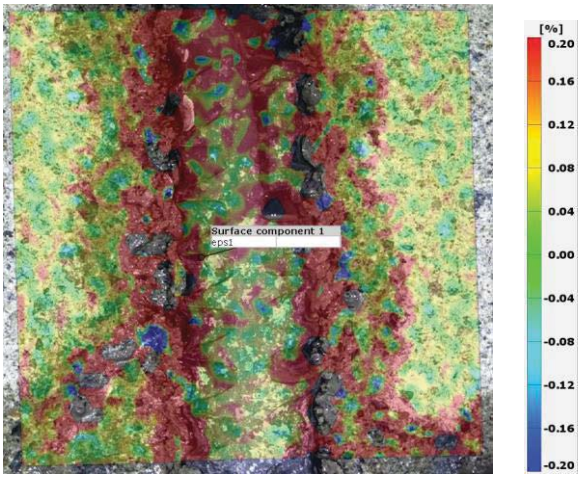

(d) Major principal strain e1 at 10000 cycles

Figure 7: Major principal strain e1 at different loading cycles

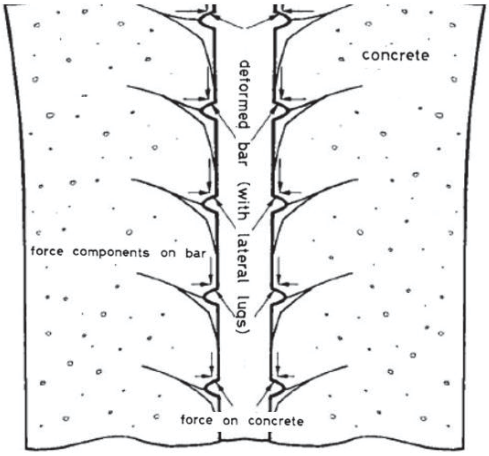

Figure 8: Schematic diagram of local deformation in concrete around the rebar (Goto, 1976)

3.2 Failure Mechanism and Sludge Formation

As mentioned above, the pull-out failure occurred after 10147 cycles. It was noticed that air bubbles were generated from the beginning of the loading process, the water at the top surface of the specimen became cloudy, and then the pull-out of the deformed bar occurred. Through continuous visual observation for the recorded video, it was found that the pull-out of the rebar occurred because the failure was developed inside the concrete surface (refer to Figure 9), not through the contact surface between the concrete and the deformed bar. Also, by visual observation at the top surface of the specimen and through the window inside the specimen, it was found that the concrete was converted to sludge around the ribs of the deformed bar, as shown in Figure 9 & 10. Also, the cone failure shape associated with macro cracks which are normally produced in the static pull-out test was not observed. The failure occurred by the deformed bar being smoothly pulled out from the concrete specimen. Therefore, it is thought that there is a convoluted interaction between the water ingress and the fatigue load that produced this type of failure.

Figure 9: Failure surface between the concrete and the rebar

From above visual observations, it is considered that when fatigue pull-out load is applied with external liquid water simultaneously, the pull-out failure of the deformed bar is occurred because of the conversion of the surrounding concrete to sludge, which is a different failure mechanism from the static test. Figure 11 shows the failure mechanism of the deformed bar associated with sludge formation. It is shown that in the vicinity of the deformed bar, the bearing force from the rib of the rebar is applied in one direction during a one-sided fatigue load, causing high stress in that direction in front of the rib. Meanwhile, with the repeated reversal load, the direction of the bearing force produced from the rib changes to the opposite direction causing high stress in opposite direction at the same zone within a distance almost (2-5 mm). Therefore, fine cracks are produced in opposite directions in the concrete in front of the ribs. As the ingress of liquid water increases, the pull-out strength becomes less than the applied load, and the granulation occurs around the deformed bar, then the formation of the sludge gradually progresses deeper. After that, significant pull-out failure occurs to the deformed bar from the concrete.

Figure 10: Sludge formation at the top surface of the specimen after dried

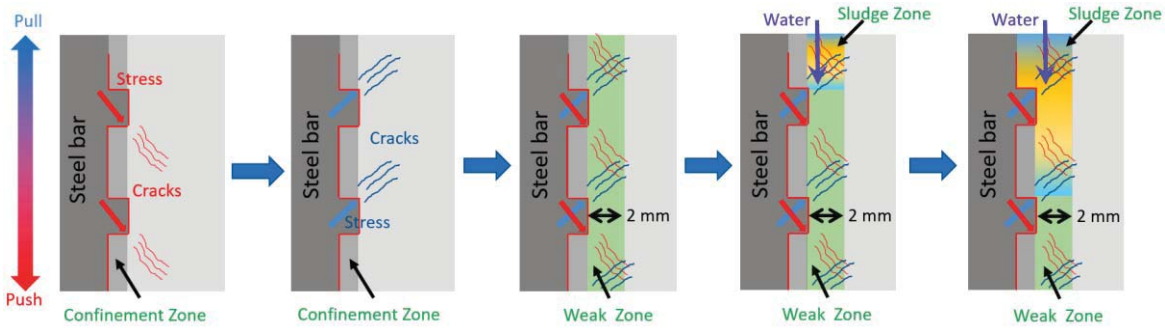

Figure 11: Failure mechanism of deformed bar with a conversion to sludge under pull-out

4 CONCLUSION

This paper presents an experimental study of the fatigue pull-out test of a deformed bar, which was embedded in a concrete specimen with the presence of external liquid water. For direct monitoring and observation purpose of the interface between the rebar and the concrete, the specimen had an opening, which was formed during casting. DIC analysis was used to visualize local deformations at the concrete-steel interface inside the window. The following conclusions have been drawn from this work:

1. The actual deformations of concrete in case of fatigue test are captured well in both positive and negative directions of loading by using the DIC technique, and they matched the past results. Internal cracks form in concrete around the deformed bar at an angle of about 60° to the bar axis.
2. The pull-out of the deformed bar occurs because the failure is developed inside the concrete surface, not through the contact surface between the concrete and the deformed bar.
3. When fatigue pull-out load is applied with external liquid water simultaneously, the pull-out failure of the deformed bar occurs due to the conversion of the surrounding concrete to sludge, which is a different failure mechanism from the static test.
4. A schematic diagram has been established to explain the failure mechanism of the deformed bar associated with sludge formation from the beginning of the load applying until the failure of the deformed bar.

REFERENCES

[1] H. Shima, L. L. Chou, and H. Okamura, Micro and macro models for bond in reinforced concrete, *Journal of the Faculty of Engineering*, 39(2), 133-194, 1987.

[2] R. Eligehausen, E. P. Popov, and V. V. Bertero, Local bond stress-slip relationships of deformed bars under generalized excitations, *University of California, Report no. UCB/EERC-83/23 of the National Science Foundation*, 1983.

[3] L.A. Lutz and P. Gergely, Mechanics of bond and slip of deformed bars in concrete, *ACI Journal*, 64(11), 711-721, 1967.

[4] B. S. Hamad, Bond strength improvement of reinforcing bars with specially designed rib geometries, *ACI structural journal*, 92(1), 3-13, 1995.

[5] B. B. Broms, Technique for investigation of internal cracks in reinforced concrete members, *ACI Journal*, 62(l), 35-44, 1965.

[6] D. Watstein, and R. G. Mathey, Width of Cracks in Concrete at the Surface of Reinforcing Steel Evaluated by Means of Tensile Bond Specimens, *ACI Journal*, 56(1), 47-56, 1959.

[7] Y. Goto, Cracks formed in concrete around deformed tension bars, *ACI Journal*, 68(4), 244-251, 1971.

[8] T. Ralejs, and T. Kutti, Fatigue strength of plain, ordinary, and lightweight concrete, *Journal Proceedings*, 76(5), 1979.

[9] H. Jan Ove, Fatigue of concrete by constant and variable amplitude loading, *Special Publication* 75, 71-110, 1982.

[10] O. B. Hwan, Fatigue life distributions of concrete for various stress levels, *Materials Journal*, 88(2), 122-128, 1991.

[11] G. Mallet, Fatigue of Reinforced Concrete, *HMSO, Department of Transport, Transport and Road Research Laboratory, London,* 1991.

[12] S. Matsui, Effect of Water on Fatigue Strength of RC Slabs of Road Bridges under Moving Loads, *Proceedings of Japan Concrete Institute*, 9(2), 627-632, 1987. (in Japanese)

[13] H. Roper, and G.B. Hetherington, Fatigue of Reinforced Concrete Beams in Air, Chloride Solution, and Sea Water, *International Concrete Abstracts Portal*, 75, 307-330, 1982.

[14] N. Chijiwa, H.T. Mai, M. Iwanami, T. Saito, and A. Yamana, Rapid Degradation of Concrete Anchorage Performance by Liquid Water, *Journal of Advanced Concrete Technology*, 13, 438-448, 2015.

[15] K. Matsumoto, H. Yamaguchi, and K. Nagai, Fatigue pull-out failure of deformed bars in concrete under the effect of liquid water. *Cement and Concrete Composites*, 91, 198-208, 2018.

[16] D. Corr, M. Accardi, L. Graham-Brady, and S. Shah, Digital image correlation analysis of interfacial de-bonding properties and fracture behavior in concrete, *Engineering Fracture Mechanics*, 74(1), 109-121, 2007.

[17] J. Kozicki, and J. Tejchman, Experimental investigations of strain localization in concrete using Digital Image Correlation (DIC) technique, *Archives of Hydro-Engineering and Environmental Mechanics*, 54(1), 3-24, 2007.

[18] S.G. Shah, and J.M Chandra Kishen, Determination of fracture parameters of concrete interfaces using DIC, *Fracture Mechanics of Concrete and Concrete Structures*, 1208-1215, 2010.

[19] O. Leibovich, A. N. Dancygier, and D. Z. Yankelevsky, An Innovative Experimental Procedure to Study Local Rebar-Concrete Bond by Direct Observations and Measurements, *Experimental Mechanics*, 56(5), 673-682, 2016.

[20] A. Okeil, K. Matsumoto, and K. Nagai, Investigation on Local Bond Behavior in Concrete and Cement Paste around a Deformed Bar by Using DIC Technique, *Cement and Concrete Composites*, 109, 103540, 2020.

[21] GOM Correlate, Inspection and Testing Guide, 2016 available at: http://www.gom.com/index.html. (Accessed August 2014).

[22] F. Bellard, M. Niedermayer, FFmpeg, 2012. http://ffmpeg.org.

EURODYN 2020
XI International Conference on Structural Dynamics
M. Papadrakakis, M. Fragiadakis, C. Papadimitriou (eds.)
Athens, Greece, 23–26 November 2020

SHAKE TABLE TEST FOR SEISMIC PERFORMANCE EVALUATION ACCORDING TO ANCHORING INTERVAL OF SUPPORT ELEMENTS PANEL SYSTEM

Jaehan Park[1], Haeyong Park[2], and Sanghoon Oh[2]

[1] Doctoral course, Department of Architectural Engineering in the Graduate School, Pusan National University, Busan, Republic of Korea
e-mail: jaehan0523@pusan.ac.kr

[2] Senior Researcher, Seismic Research and Test Center, Pusan National University, Busan, Republic of Korea
e-mail: haeyong@pusan.ac.kr

[3] Professor, School of Urban, Architecture and Civil Engineering, Pusan National University, Busan, Republic of Korea
e-mail: osh@pusan.ac.kr

Keywords: Cladding, Support Elements, Seismic Performance Evaluation, Shake Table Test, In-plane displacement

Abstract. *In this study, the seismic performance evaluation is performed for the connection method each support elements and the anchoring interval of support elements panel system among several types of cladding system. The anchoring of the general support elements panel system is installed at intervals of 1,000mm. In order to grasp the problem, the concrete filled channel is installed in the test frame. It is implemented to realize the site situation. The specimens consist of 6 types according to the connection method and the anchoring method. In the experiment, the shake table test was carried out in the in-plane direction for 6 specimens, including the construction examples using the steel frame. Because the experiment considered in-plane direction displacement depending on the sensitivity of the cladding. After each seismic simulation test, damage is visually inspected, and used as a basis for evaluating seismic performance. The maximum response drift angle of test frame was measured at 4% rad. The damage type was defined by performance levels, in order to compare the observed damage by visual inspection according to the measured response drift angle. Finally, the fragility analysis of support elements panel system was conducted based on the previous seismic performance evaluation data.*

1 INTRODUCTION

1.1 Background

In the event of an earthquake, nonstructural components, directly or indirectly, cause damage to building and structures. This involves damage to equipment as well as damage to life and property caused by self-damage, that is falling of nonstructural components. Although the damage to these nonstructural components is considered secondary and tertiary damage, it is likely to develop into large-scale damage, and hence, must be secured against earthquakes. Some nonstructural components (ceilings, water tanks) have been used dynamic analysis. However, exterior materials such as curtain walls and masonry are difficult to secure by dynamic analysis. Therefore, in this study, shake table test are performed in the in-plane direction on six variables including construction cases using a test frame to evaluate the seismic performance and fragility of support elements.

1.2 Scope and purpose

To conduct the test on support elements, the system that attaches the external finishing materials such as metal and stone to the square steel pipe is mainly used. Vertical and horizontal members are welded together using 1.6mm thick square steel pipe. In this experiment, shake table tests were carried out on a total of six specimens using these connecting methods as variables. The experiment aims to compare the seismic performance of the support elements panel system according to the experimental variables for the same seismic wave. The experiment is carried out by calculating the acceleration spectrum of this experiment considering the domestic standard KDS 41 17 00 for RRS of ICC ES AC156, which is a shake table test method for nonstructural components. The experiment is conducted by generating an artificial earthquake wave according to the method presented in AC156. The seismic performance comparison based on the test results is estimated by conducting damage assessment through visual inspection. Performance level and damage items should be defined for visual inspection. In this study, damages to the support elements panel system are defined by referring to the transmission items based on the performance level and performance target level of the nonstructural components in ASCE 41-17, and the type of earthquake damage presented in FEMA E-74

1.3 Test specimens

The main experimental variables is the method of connecting the vertical and horizontal members of the support elements and the method of anchoring the structure of the support elements. In general, the support elements to be bonded by spot welding or line welding is set as the control group, and the support elements with a no welding connection is set as the experimental group. Each connecting method is shown in Figure 1. Chemical anchors and set anchors are used to anchor the support elements to the structure, and the difference between the two can be seen in Figure 2. To compare the behavior characteristics of each experimental variable under the same earthquake condition, six specimens were arranged in three rows using the front and rear elevations of the test frame, as shown in Figure 3. In this case, concrete-filled c-beams were pre-installed in the test frame before the test specimens were installed to fasten the anchorages of the support elements. Based on the anchorage-fastening conditions (chemical anchor construction or set anchor construction), each specimen was installed as close as possible to the actual construction. According to the installation conditions, all the specimens were set to resist horizontal external force in the in-plane direction.

Specimen name	Steel truss		Metal panel				Fastener anchoring method
	Member Section (mm×mm×mm)	Welding detail	Width (mm)	Height (mm)	Thickness (mm)	Connection detail	
LPC	50×50×1.6	Line	1,400	600	1.6	Piece	Chemical
NPC		No				Piece	Chemical
NCC		No				Clip	Chemical
LPS		Line				Piece	Set
SPS		Spot				Piece	Set
SPC		Spot				Piece	Chemical

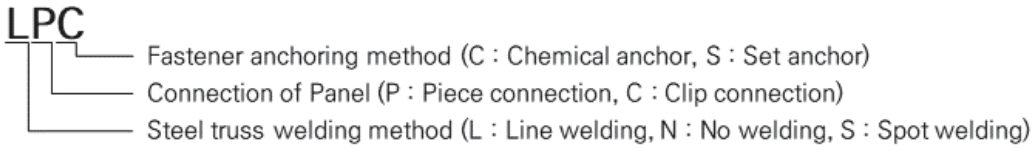

Table 1: Specimen information

(a) Line welding

(b) Spot welding

(c) No welding detail

Figure 1: Details of support elements connection method

(a) Chemical anchor

(b) Set anchor

Figure 2: Anchorage detail

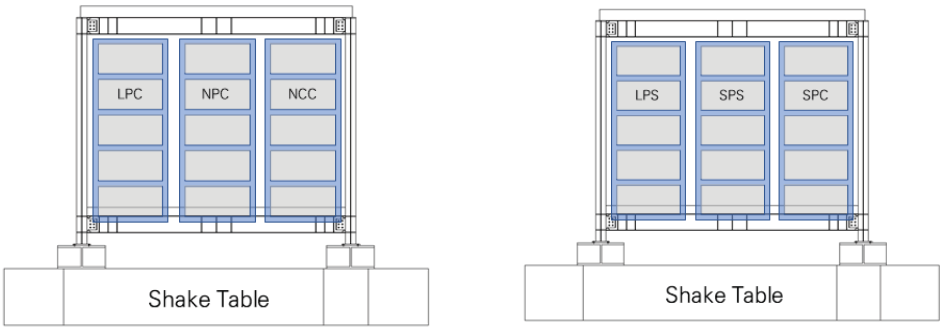

(a) Front (b) Rear

Figure 3: Specimen installation

2 EXPERIMENT INFORMATION

2.1 Test frame

The test frame is a single-story unit frame with a long span of 4.5m (in the direction of the weak axis of the column), short span of 4m (strong axis of the column), and a height of 3.5m. A concrete slab is installed on the upper and lower parts (upper: 200mm; lower: 150mm). In this experiment, the deformation capacity as well as the acceleration resistance capability of the exterior material are examined. Therefore, the frame is weakly placed in the excitation direction so that the frame can be deformed. The state of the test frame is as shown in Figure 4.

(a) Front of test frame (b) Inside of specimen

Figure 4: The state of test frame

2.2 Test method

The shake table test uses an artificial seismic wave that meets the conditions of the ICC ES AC156: 2010 response spectrum. The prepared Required Response Spectrum (RRS) is as shown in Figure 5 and the seismic parameters are as shown in Table 2. The prepared RRS is a response spectrum for nonstructural components corresponding to domestic design seismic force (recurrence period: about 1,000 years). The shake table test was carried out by increasing the artificial seismic wave by adjusting the scale factor based on the acceleration value of the response spectrum shown in Table 2.

Building Code	Test Criteria	S_{DS}*(g)	z/h*	Horizontal	
				A_{FLX-H}(g)	A_{RIG-H}(g)
KDS 41 17 00	ICC ES AC156	0.55	1.00	0.88	0.66

*S_{DS}: Spectral response acceleration at short period, z/h: Height factor ratio

When, $A_{FLX-H} = S_{DS}\left(1 + 2\frac{z}{h}\right)$, $A_{RIG-H} = 0.4S_{DS}\left(1 + 2\frac{z}{h}\right)$

Table 2: Parameters for the required response spectrum

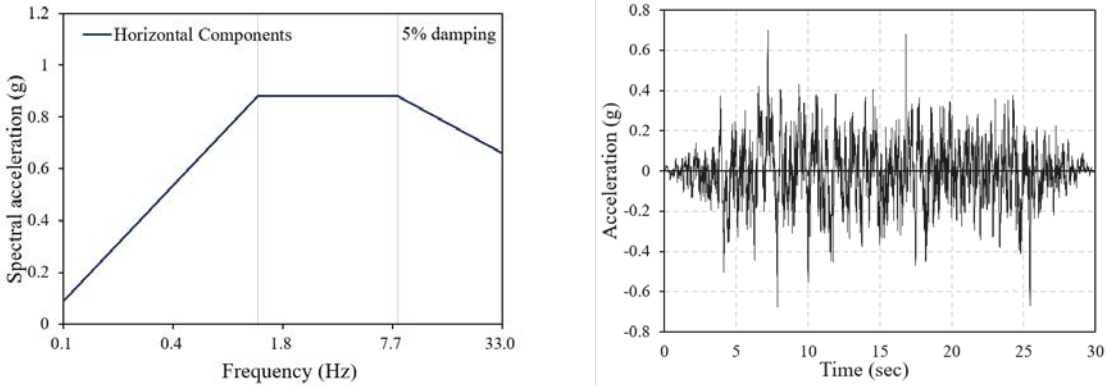

(a) Required response spectrum (5% damping) (b) Acceleration-time history

Figure 5: Input wave information

2.3 Definitions of available damage

In the case of the domestic standard (KDS 41 17 00), it is difficult to objectively evaluate and compare the performance of nonstructural components by the experimental results because there is no example of damage according to the performance level of nonstructural components, including the support elements panel system. Therefore, this study defines the acceptable damage of cladding for each performance level by referring to the performance levels of the nonstructural components of the cladding presented in ASCE 41-17. To carry out objective damage assessment and performance comparison, damage to the enclosure system is defined as shown in Table 3.

Division		Acceptable damage			Unacceptable damage
		Operational	Position Retention	Life Safety	
Support elements panel system	Panels	- Cracks in sealant - Loosening - Slight damage to joint piece	- Partial breakage - Plastic deformation - Joint piece falling below 1/2 of the unit - Tearing of joint edge	- Joint separation (Do not dislodge) - Major plastic deformation - Joint piece falling above 1/2 of the unit	- Fall out - Dislodged
	Support elements	- creation of dust - slight damage	- Welding crack of fastener - Loosening of fastener's nut - Plastic deformation of fastener - Welding crack of support elements connection	- Partial break of anchor - Partial welding break of fastener - Major deformation of support elements - Deflection of support elements - Partial break of support elements connection	- Complete Breakage of anchor - Complete Breakage of fastener - Fall out of support elements

Table 3: Definition of acceptable damage of cladding

2.4 Sensor installation

To analyze the response of the specimen, accelerometer and wire LVDTs were installed at the main points of the specimen. The items to observe are the acceleration response and story drift of the upper and lower test frames. According to the test method of uniaxial excitation, the uniaxial accelerometer was attached to the upper and lower parts of the test frame, and the wire LVDTs were installed in four places of the upper and lower column members on one side of the test frame as shown in Figure 6. The relative displacement of the shake table and the test specimen was measured with wire LVDTs.

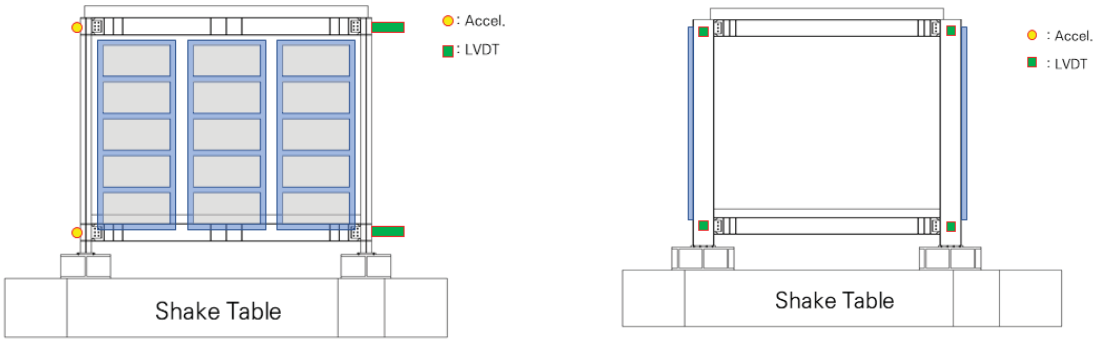

(a) Front (b) Right side

Figure 6: Sensor installation

3 SEISMIC PERFORMANCE EVALUATION

3.1 Test result

1) acceleration response

The AC156 used as a reference for this experiment requires that the output data satisfy the following two requirements for the input data after the shake table test is completed.

(1) Test Response Spectrum (TRS) should enclose the RRS.

(2) The peak in response acceleration-time history should satisfy more than 90% of ZPA (Zero Period Acceleration).

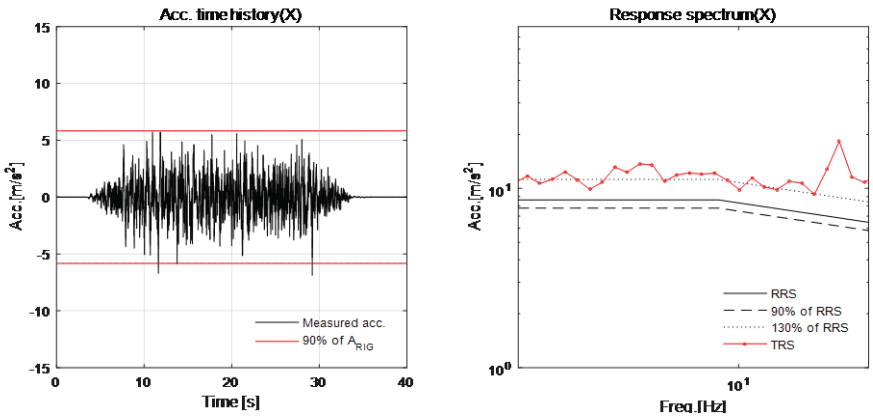

Figure 7: Acceleration time history, TRS and RRS (Step 3)

2) Story drift

To calculate the story drift, the displacement of the specimens was calculated using the average of the front displacement and the rear displacement, and each displacement was calculated using the displacement of the upper part of the test frame and the displacement of the lower part of the test frame. Table 4 shows the displacement of the front part and the rear part. The calculated maximum story drift angle of each test frame was more than 0.1%rad in step 2 (EQ 80%) and more than 0.2%rad in step 3 (EQ 100%). This means that the test frame in which the test specimens were installed underwent deformation above the maximum allowable story drift angle (0.2%rad, seismic level 2) of the structure specified in KDS 41 17 00.

Step	Peak relative displacement(mm)		Story drift (mm)	Story drift angle (radian)
	Front side column	Rear side column		
1	14.62	14.70	14.66	0.0042
2	41.18	40.68	40.93	0.0116
3	72.32	68.32	70.32	0.0201
4	96.66	86.12	91.39	0.0259
5	123.28	104.38	113.83	0.0325
6	140.54	119.80	130.17	0.0371
7	163.78	130.24	147.01	0.0412
8	164.80	129.04	146.92	0.0404

Table 4: Displacement response

3.2 Visual inspection

Visual inspection before the experiment confirmed that structural damage did not occur. The main types of damages that occurred after each test at each excitation stage are as follows.

1. Welding crack and plastic deformation of fastener
2. Complete breakage of fasteners

Table 5 shows the damage to the test specimens at each step according to the performance levels defined in Table 3. In addition, the symbols for each damage location are defined as shown in Figure 8, and the locations of the damages listed in Table 5 and Table 6 can be confirmed by referring to them.

In summary, the failure modes of all specimens were determined by anchoring forces at anchorage and fasteners, nut loosening, and fastener-welding break. After damage of the anchorage and the fastener, the damage of the support elements and the panels was slight as the horizontal external force was not sufficiently transmitted to the panel and the support elements. However, compared with the case where the support elements were connected by spot welding or line welding, the specimens with no welding method showed relatively little damage compared to the fastener, and no complete failure of the fastener was observed until the final step.

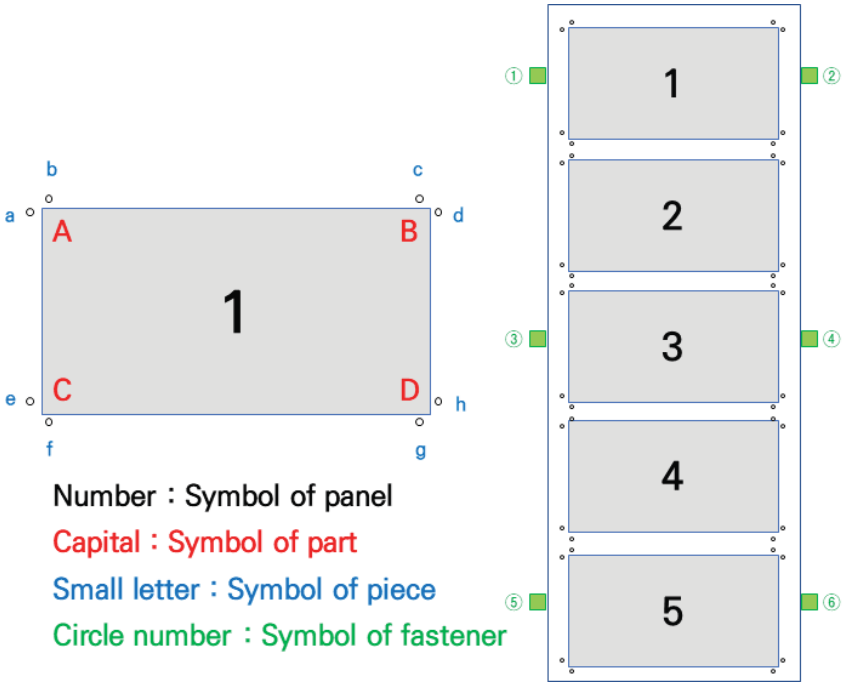

Figure 8: Definition of damage location

	LPC		NPC		NCC	
	Support elements	Panels	Support elements	Panels	Support elements	Panels
50	(No damage)	(No damage)	(No damage)	(No damage)	(No damage)	(No damage)
80	Welding crack of fastener (④)	(No damage)	(No damage)	(No damage)	Loosening of fastener's nut (①)	(No damage)
100	Welding crack of fastener (①) Partly welding break of fastener (②, ⑤)	(No damage)	Slight damage of fastener (①, ③, ④)	(No damage)	(No damage)	(No damage)
120	Major deformation of fastener (②) Plastic deformation of fastener (③) Welding crack of fastener (⑥)	(No damage)	Loosening of fastener's nut (④) Plastic deformation of fastener (⑤)	(No damage)	(No damage)	Loosening (5-a)
140	Partly welding break of fastener (①) **Complete breakage of fastener (②)**	(No damage)	Plastic deformation of fastener (①, ②, ⑥)	Loosening (3-f)	(No damage)	(No damage)
160	Major deformation of fastener and Partly welding break of fastener (④, ⑥)	(No damage)	Major deformation of fastener (①, ②, ⑤, ⑥) Plastic deformation of fastener (③)	Loosening (2-a)	(No damage)	Joint separation (almost clip)
180		(No damage)	Major deformation of fastener (③) Plastic deformation of fastener (④)	(No damage)	Major deformation of fastener (②)	(No damage)

Table 5: Damage measurement table for each specimen

	SPC		SPS		LPS	
	Support elements	Panels	Support elements	Panels	Support elements	Panels
50	Welding crack of fastener (⑤)	(No damage)	Welding crack of fastener (⑤)	(No damage)	(No damage)	(No damage)
80	Welding crack of fastener (①) Loosening of fastener's nut (③) Partly welding break of fastener (⑥)	Loosening (5-g)	(No damage)	(No damage)	Slight damage of fastener (⑥)	(No damage)
100	Welding crack of fastener (②) Partly welding break of fastener (⑤)	(No damage)	Partly welding break of fastener (①, ⑤) Loosening of fastener's nut (⑥)	(No damage)	Welding crack of fastener (①) Partly welding break of fastener (②) Loosening of fastener's nut (③) Plastic deformation of fastener (④, ⑤, ⑥)	(No damage)
120	Partly welding break of fastener (①, ②) Welding crack of fastener (④) **Complete breakage of anchor (③)** **Complete breakage of fastener (⑥)**	(No damage)	Loosening of fastener's nut (②, ③) Partly welding break of fastener (④)	(No damage)	Partly welding break of fastener (①)	(No damage)
140	**Complete breakage of fastener (④)** Partly welding break of fastener (⑤)	(No damage)	Partly welding break of fastener (⑤)	(No damage)	**Complete breakage of fastener (①)**	(No damage)
160	**Complete breakage of fastener (②, ③, ⑥)**	(No damage)	Major deformation of fastener (②, ③, ⑥) **Complete breakage of fastener (⑤)**	(No damage)	**Complete breakage of fastener (②, ⑥)**	Loosening (4-c)
180	-	(No damage)	-	(No damage)	**Complete breakage of fastener (①)**	(No damage)

Table 6: Damage measurement table for each specimen

3.3 Fragility evaluation

In this study, the support elements panel system was analyzed for fragility by considering the story drift angle. The fragility function is the probability of exceeding the occurrence of damage corresponding to each performance level, depending on the influence factor. Figure 9 shows the seismic fragility curve for each specimen. This is the result of fragility curves using the mean of story drift angles and the natural logarithmic standard deviation. This fragility curve is a function of the fragility of the subject, and hence, if any of the variables do not match the subject, and hence, if any of the variables do not match the subject, there is an unreliable disadvantage.

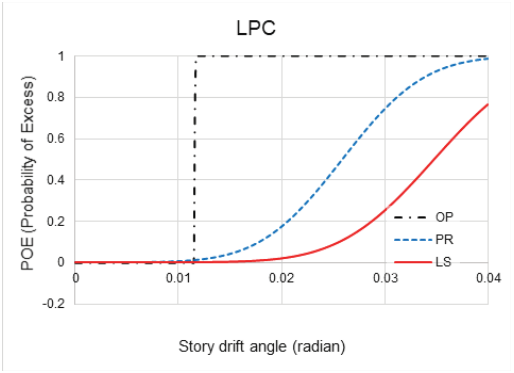

(a) LPC

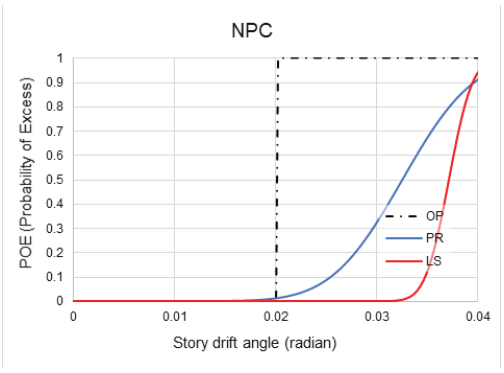

(b) NPC

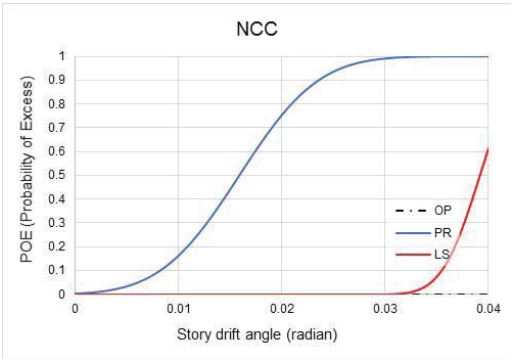

(c) NCC

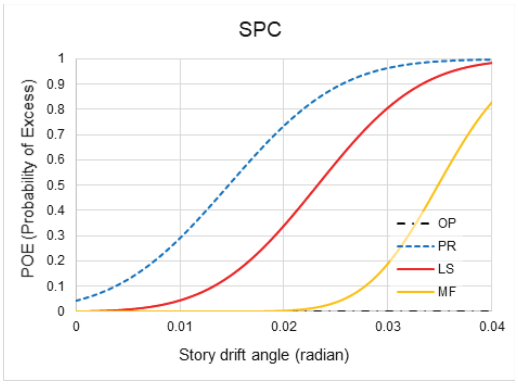

(d) SPC

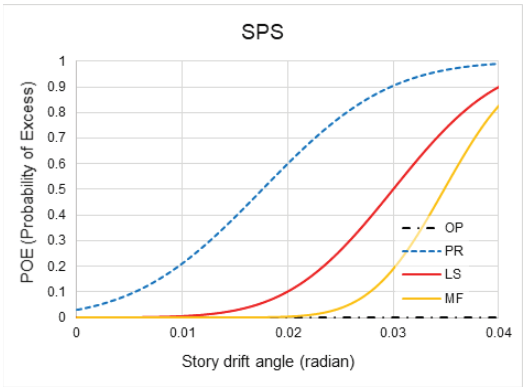

(e) SPS

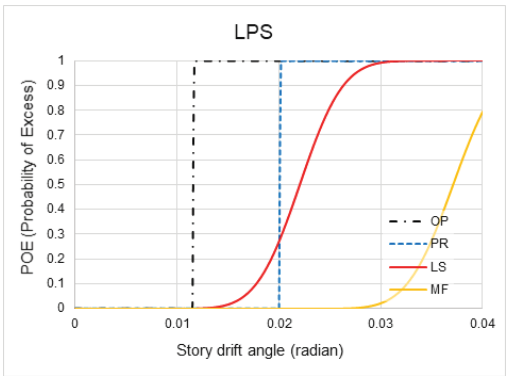

(f) LPS

Figure 9: Fragility curve

4 CONCLUSION

In most cases, the anchoring interval of support elements is constructed in units of 1,000mm, and the anchorage is constructed by chemical anchor or set anchor. To understand this problem, concrete-filled c-beams were installed at intervals of 1,000mm, and the experiment was implemented to realize the site situation. In all six specimens classified in this experiment, the failure mode was determined by anchor fall-out, loosening of fastener, and fastener-welding failure. In the case of the support elements using the welding method, the support elements themselves could be damaged owing to the complete failure of the anchorage. On the contrary, in the case of the support elements not using the welding method, complete failure of the fastener was not observed until the final excitation caused by the plastic deformation of the fasteners. Therefore, dropping the support element was found to be a better method for ensuring safety.

ACKNOWLEDGMENTS

This research was supported by a grant(20AUDP-C146352-03) from Architecture & Urban Development Research Program funded by Ministry of Land, Infrastructure and Transport of Korean government.

REFERENCES

[1] American Society of Civil Engineers. "Minimum design loads and associated criteria for buildings and other structures." American society of civil engineers, 2017.

[2] FEMA. "FEMA E-74 Reducing the risks of nonstructural earthquake damage—A practical guide." (2011).

[3] ICC Evaluation Service. "AC 156 acceptance criteria for seismic certification by shake table testing of nonstrucutral components." *ICC Evaluation Service* (2010).

[4] Choi, Kyung Suk, et al. "A Study on Evaluation of Floor Response Spectrum for Seismic Design of Non-Structural Components." *Journal of the Earthquake Engineering Society of Korea* 17.6 (2013): 279-291.

[5] Mohebbi, Saeed, et al. "Experiments on seismic behaviour of steel sheathed cold-formed steel shear walls cladded by gypsum and fiber cement boards." *Thin-Walled Structures* 104 (2016): 238-247.

[6] Oh, Sang Hoon, Jong Won Park, and Hae Yong Park. "Shake Table Test on Seismic Performance Evaluation of the Bolted Connection Type Paneling System with Exterior Finish Material." *Journal of the Earthquake Engineering Society of Korea* 22.1 (2018): 23-32.

[7] Huang, Baofeng, Wensheng Lu, and Khalid M. Mosalam. "Shaking table testing of granite cladding with undercut bolt anchorage." *Engineering Structures* 171 (2018): 488-499.

EURODYN 2020
XI International Conference on Structural Dynamics
M. Papadrakakis, M. Fragiadakis, C. Papadimitriou (eds.)
Athens, Greece, 23–26 November 2020

SHAKING TABLE TEST FOR EVALUATION OF SEISMIC PERFORMANCE ACCORDING TO EDGE CLEARANCE OF GLAZING CURTAIN WALL SYSTEM

Yang, Jung Woo[1]· Park, Hae Yong[2]· Oh, Sang Hoon[3]

[1]Master candidate, Department of Architectural Engineering in the Graduate School, Pusan National University
Busan, Republic of Korea
E-mail: jjangwoo7@Pusan.ac.kr

[2] Senior Researcher, Seismic Research and Test Center, Pusan National University
Busan, Republic of Korea
E-mail: haeyong@pusan.ac.kr

[3] Professor, School of Urban, Architecture and Civil Engineering, Pusan National University
Busan, Republic of Korea
E-mail: osh@pusan.ac.kr

Keywords: Shaking table test, Edge clearance, Glazing curtain wall system, Seismic performance, Damage assessment

Abstract. *In this paper, shaking table tests was conducted to evaluate the seismic performance according to the edge clearance of the glazing curtain wall system. Most tests on glazing curtain wall systems in Korea have been carried out by assessing airtightness and water-tightness to determine the stability in the out-plane direction. However, in the case of an earthquake, the stability in the in-plane direction is also important for glazing curtain wall systems. Therefore, the in-plane seismic performance of glazing curtain wall system is evaluated by calculating the edge clearance using the domestic seismic design standard (KDS 41 17 00:2019, 18.3.4) and applying the results as the experimental variables. The acceleration spectrum used in the experiment was derived by considering ICC ES AC-156, the foreign shaking table test method for non-structural elements, and KDS 41 17 00:2019. The excitation was gradually increased by adjusting the acceleration scale of the artificial seismic waves. The purpose of this experiment is to evaluate the seismic performance of glazing curtain wall systems in terms of the edge clearance for the same earthquake. To evaluate the seismic performance corresponding to the test results, a damage assessment was conducted through a visual inspection. After the experiment, the damage limits for each performance level of the glazing curtain wall were newly defined, and the requirements for the relative displacement of the glazing curtain wall systems Korea were verified.*

1. INTRODUCTION

The Po-hang earthquake damaged to nonstructural elements of buildings such as exteriors and glass, with three times more cost than for structural elements. Nonstructural elements are connected to the main structural members of buildings and perform specific functions within the building, but they do not support external loads. This results in a loss of function for the building and the damage of important facilities and equipment is linked to the 2nd and 3rd damages, so the possibility of large-scale damage is high[3]. Although glazing curtain walls are commonly used in modern buildings such as high-rises buildings due to their light weight and beauty, the seismic design criteria in Korea(KDS 41 17 00: 2019) do not clearly dictate seismic design. In addition, the relative displacement requirements for "18.3.4 curtain walls, stores and partition wall glass" are based on the those of ASCE 7-10 in the United States[1], but there are no shaking table test. Since studies that validate the domestic relative displacement criteria are needed.

Therefore, in this Study, based on the RRS of ICC ES AC-156, a foreign shaking table test method, the acceleration spectrum of this experiment considering the domestic standard (KDS 41 17 00: 2019) was derived first, and artificial seismic waves were generated and applied to the experiment according to the method proposed in AC-156[4]. By conducting shaking table tests in the in-plane direction, the glass standards (KDS 41 17 00 18.3.4) used in the current domestic curtain wall were verified, and the damage limit level is defined for the glazing curtain wall suitable for domestic use.

2. SEISMIC DESIGN CRITERIA FOR GLAZING CURTAIN WALL SYSYTEM

2.1 The current national standard

Curtain walls are classified as non-structural elements in building standards (KBC 2016) and they are designed to withstand the equivalent static loads and relative displacements. Glass is light in weight but is also brittle, and it is classified as a displacement-sensitive element rather than acceleration-sensitive. Domestic relative displacement criteria for nonstructural elements are based on the contents of ASCE 7-10 in the United States[1]. The relative displacement due to earthquakes, which nonstructural elements should accommodate, can be obtained as follows.

$$\begin{gathered} D_{pI} = D_p I_E \\ D_p = \delta_{xA} - \delta_{yA} \\ \text{only}, D_p \le (X - Y)\frac{\Delta_{aA}}{h_{sx}} \end{gathered} \tag{1}$$

In case of I_E is importance factor of the non-structural element. In the domestic standard, the importance factor of a curtain wall is not clearly defined. However, in the US, FEMA E-74 clearly defines ER (engineered required) requirements for exterior wall components such as glazed exterior wall systems[3]. It means I_E=1.5 that requires seismic design in domestic standard. In addition, h_{sx} is the height used to define the allowable story drift, δ_{xA} and δ_{yA} are displacement in x or y of A-phase vertical position on the floor displacement of x story. X and Y are respectively height from the underside of the structure to the upper attachment point x and the lower attachment point y. Δ_{aA} refers to the allowable story drift of the structure. The domestic standard (KDS 41 17 00 18.3.4) also sets out the relative displacement requirements for the glass used in the curtain wall, and also based on ASCE 7-10[1,6].

$$\Delta_{fallout} \ge 1.25 D_{pI} \;\; Only, \Delta_{fallout} \ge 13mm \tag{2}$$

Here, $\Delta_{fallout}$ refers to the relative displacement of the glass falling off the curtain wall, the front of the store, the partition wall through the experiment or analysis. However, if there is sufficient clearance between the glass and the frame and the contact between the glass and the frame does not occur at the required relative displacement, the following equation may be used.

$$D_{clear} \geq 1.25 D_{PI}$$
$$D_{clear} = 2c_1\left(1 + \frac{h_p c_2}{b_p c_1}\right) \quad (3)$$

In the case of a rectangular glazing frame

In this case, D_{clear} refers to the relative displacement of the frame in which the contact between the glass and the frame occurs, and it is defined for the height of the glass. $h_p$and $b_p$are the height and the width of rectangular glazing panels, respectively, and c_1 and c_2 mean average clearance values between glass and frame that of horizontal clearance on the left and right sides and vertical clearances on the upper and lower surfaces, respectively.

2.2 Staged damage assessment according to the performance level

In the case of non-structural elements that are subject to seismic design under current national standards, structural safety and functionality should be maintained even after an earthquake. In particular, glass installed in curtain walls should be able to sufficiently accommodate the relative displacement that occurs. For the evaluations, electrical, electronic and communication equipment can be evaluated quantitatively or qualitatively using standard methods, but most nonstructural elements are evaluated using qualitative assessments, such as visual inspections. Moreso, the criteria for damage according to the performance level of non-structural elements are not clear, so it is necessary to clarify the criteria and classification for seismic performance. For example, the international standard FEMA E-74 classifies damage types of non-structural elements caused by earthquakes into Functional Loss (FL), Property Loss (PL), and Life Safety (LS)[3]. In case of ASCE 41-13 damages of nonstructural elements are classified into four stages: Operational (N-A), Position Retention (N-B), Life Safety (N-C), and Not Considered (N-D)[2]. “A Shake Table Test for Seismic Performance Evaluation of Bolted Joint Panel Systems with External Finishing Materials,” was suggest definition of damage for paneling system according to performance level considering ASCE 41-13[5].

The purpose of this study is not just to identify the type of damage of nonstructural elements, but to derive the clear criteria for damage to glazing curtain walls that can be reflected into future seismic performance assessments. Therefore, to clearly define damages considering the performance level of the glazing curtain wall system, the definition of damage of nonstructural elements in ASCE 41-13 and “A Shake Table Test for Seismic Performance Evaluation of Bolted Joint Panel Systems with External Finishing Materials,” are referred to. Damage by performance level of nonstructural components presented in ASCE 41-13 and paper is shown in Table1 and Table 2.

Table 1 Nonstructural performance levels and illustrative damage-Glazing component

	Nonstructural Performance Levels		
Component Group	Operational(N-A)	Position Retention(N-B)	Life Safety(N-C)
Glazing	• No cracked or broken panes.	• Some cracked panes; none broken. • Limited loss of weather-tightness	• Extensively cracked glass with potential loss of weather-tightness and security. • Overhead panes do not shatter of fall

Table 2 Definition of damage for paneling systems according to the performance level

Performance target for a paneling system		
Operational (OP)	Position Retention (PR)	Life Safety (LS)
• Crack in the sealing • Damage of a joint piece	• Partial fracture of a stone panel • Minute weld crack in the truss • Plastic deformation of a metal panel • Silicone rubber tear • Minute deformation of a fastener	• Large deformation of the truss • Large crack or separation in the truss connection • Truss connection fracture • Large deformation or fall of a fastener • Panel fall

3. EXPERIMENTAL DESIGN AND METHOD

3.1 Experimental design

Tests of glazing curtain wall systems in Korea, have performed only static experiments on displacement and wind tunnel tests in the out-plane directions. Therefore, shaking table tests were conducted to evaluate the dynamic seismic performance of a glazing curtain wall by measuring the end clearance and to verify the relative displacement requirements of glass used for curtain wall in the current national standard. In addition, due to the characteristics of the non-structural elements called curtain walls, they cannot stand on the shaking table. So glazing curtain wall systems are installed on the test frame and Uniaxial excitation was performed only in in-plane direction.

The test frame is a one-story unit frame with a height of 3.5m, 4.5m long span and 4m short span and a concrete slab with a thickness of 200mm and 150mm on the upper and lower parts of the frame, respectively is installed. Flanges of girder and flanges of column are consist of full penetration welds, and girder webs and column flanges are bolted through shear tabs. In addition, the weld access holes shape at the end of the beam web is made up of a quarter circle. According to the test frame, all column members behave in a rigid or weak axis depending on the direction of excitation. Therefore, the structure in these experiments was set up a weak axis to occur sufficient deformation. In the case of the installation, the joining jig was first installed on the shaking table, and the test frame was mounted on the test jig. Detailed test frame drawings and weights of the test frame are shown in Table 3 and Figure 1.

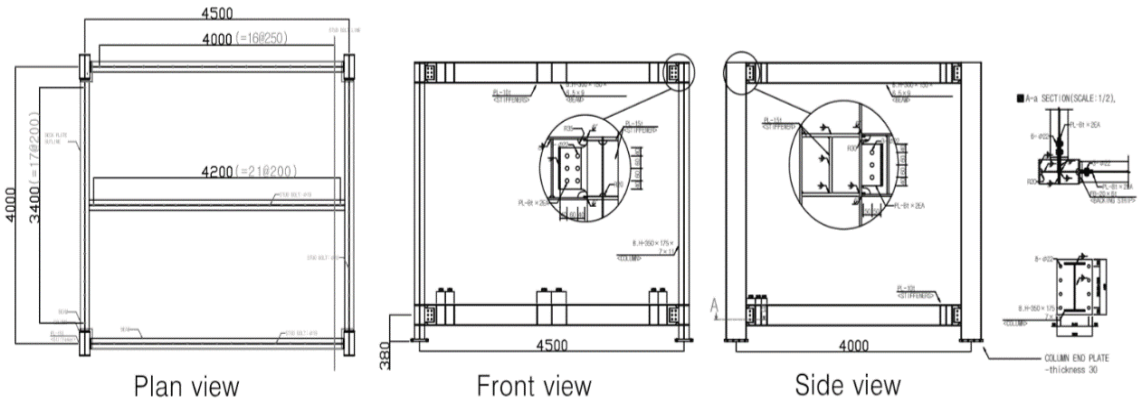

Figure 1 Test frame schematic

Table 3 Test frame specifications

Part of Test Frame		Dimension(mm)			Weight(kN·f)
		Width		Thickness	
		X-direction	Y-direction		
Slab	Upper part	4500	4000	200	86.4
	Lower part	4500	4000	150	64.8
Girder	Upper part	H-300x150x6.5x9 (SS400)			7.2
	Lower part	H-300x150x6.5x9 (SS400)			5.7
Column		H-350x175x7x11 (SS400)			7.2

The test subjects are glazing curtain wall system that composed of mullions, transoms and glass commonly used in Korea. Experimental variable is the edge clearance (b) and support depth (c) of the glazing panel shown in Fig. 1. Control specimen is satisfied requirement that specified in the Korean Architectural Structural Standards (KDS 41 17 00: 2019, 18.3.4). So edge clearance was set to 10mm (edge clearance + support depth = 25 mm). Because contact between the glass and the frame does not occur due to sufficient clearance between the glass and the frame. Comparison group is consisted of 5mm specimens with edge clearance that did not satisfy this condition and 15mm and 20mm specimens with deeper end clearance than the condition. Total subject included 4 specimens. Specification and the drawings of the control specimen are shown in Table 4 and Figure 2. In order to compare the behavior of each test variable under the same earthquake experience, four specimens were arranged in two rows using the front and rear of the test frame. According to the installation conditions, all specimens were set to resist the horizontal external force in the in-plane direction.

Table 4 Specimen specifications

Specimen Name	Clearance D_{clear}	Dimension(mm)			Location
		Width	Height	Thickness	
D05	5	2,000	3,650	150	Rear left
D10	10				Rear right
D15	15				Front left
D20	20				Front right

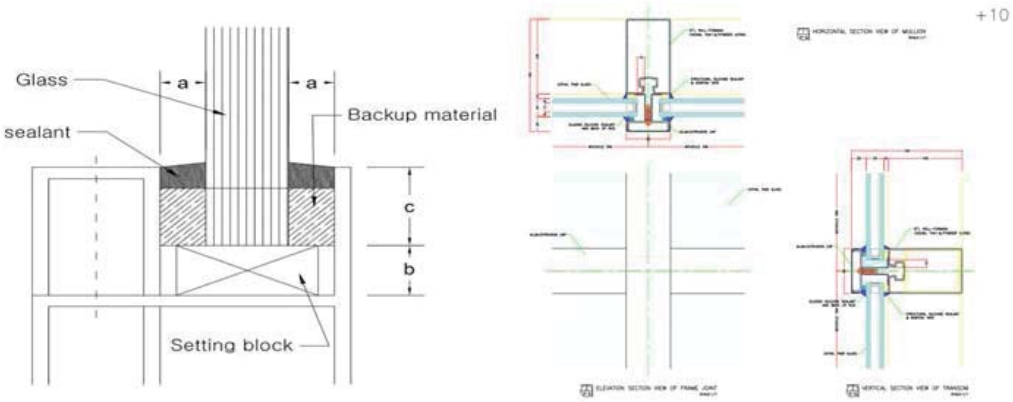

Figure 2 Detailed drawing of control specimen

3.2 Experimental method

The seismic performance evaluation of the glazing curtain wall can be carried out by conducting the shaking table test in AC-156 and the dynamic test in AAMA 501.6[4,7]. Therefore, in this study, the acceleration spectrum considering the national standard (KDS 41 17 00: 2019) is consulted for the RRS of ICC ES AC-156: 2010, and Artificial seismic waves generated according to the method proposed in AC-156 were used in the experiment. The excitation method was gradually increasing excited by adjusting the acceleration scale of the artificial seismic wave, and excites only in horizontal dimension (left and right directions). The required response spectrum (RRS) of the seismic wave used in the shaking table test is applied by a seismic parameter according to the set conditions (Effective ground acceleration(S): 0.22g, Ground condition: S_3) that is assumed according to the domestic building design standard. Therefore, the prepared RRS is the response spectrum for nonstructural elements corresponding to the design earthquake force that return period of 1000 year in domestic standard. The prepared RRS is shown in Figure3 and Seismic parameter is shown in Table 5.

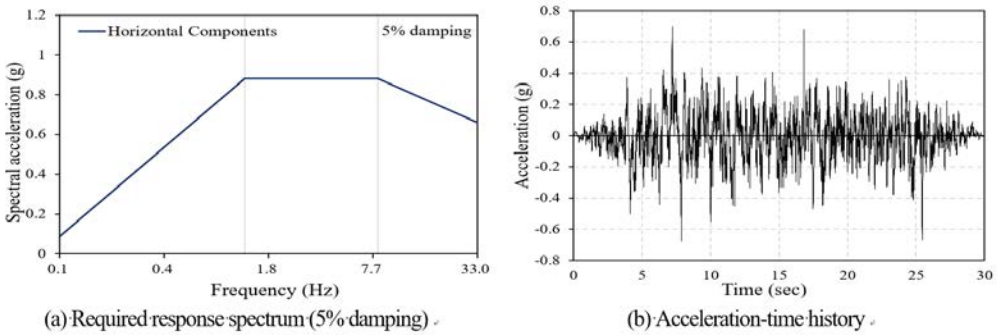

Figure 3 Input wave information

Table 5 Parameters for the required response spectrum

Building Code	Test Criteria	S_{DS}* (g)	z/h*	Horizontal	
				A_{FLX-H} (g)	A_{RIG-H} (g)
KDS 41 17 00	ICC-ES AC156	0.55	1.00	0.88	0.66

* S_{DS} : Spectral response acceleration for a short period, z/h : Height factor ratio

In here, $A_{FLX-H} = S_{DS}\left(1 + 2\frac{z}{h}\right)$, $A_{RIG-H} = 0.4S_{DS}\left(1 + 2\frac{z}{h}\right)$

3.3 Experimental procedure and sensor measurement plan

Shaking table test follows the sequence shown in Table 6. Pre-test inspection was performed with a visually inspection of the state of external deformation and damage, installation position and state of the accelerometer and displacement gauge measuring device, and etc. After the pre-test inspection, resonance search test is performed to evaluate the suitability of the test response spectrum or to analyze the test frame deformation. The maximum amplitude of the random wave for resonance detection was 0.05g and the frequency range was 1.0Hz ~ 50.0Hz. A seismic simulation test was performed by creating an acceleration time history using the defined response spectrum. The oscillation duration of the acceleration time history is 30 seconds and the amplitude of the seismic duration is 20 seconds. The experiment was carried out incrementally in the left and right (X) directions of the test frame by adjusting the acceleration scale using the prepared artificial earthquake wave. At this time, the acceleration scale was excited with 50%, 80%, and 100% of the reference earthquake wave (EQ), and then

the acceleration scale was increased by 20% intervals. Finally, after the seismic performance test at each stage as in the pre-experimental test, the structural deformation and damage state were visually inspected and recorded. The termination conditions are as follows.

1. When the next excitation level cannot be performed due to equipment limit
2. Hazardous structural damage occurs such as excessive plastic deformation of the test frame
3. Serious damage has occurred in specimen, and it is judged that next test would not be meaningful.

Table 6 Test procedure

Step	Test Name	Test Method	Remarks
1	Pre-test inspection	· Visual inspection	-
	Resonance search test	· Random wave (Dir. = X)	· Amp : 0.05 g · Freq. : 1.0Hz~50.0Hz
	Seismic simulation test (EQ 50%)	· 1 axial time history test	· S_{DS} : 0.275 g · ZPA : 0.33 g
	Post-test inspection	· Visual inspection	-
2	Resonance search test	· Random wave (Dir. = X)	· Amp : 0.05 g · Freq. : 1.0Hz~50.0Hz
	Seismic simulation test (EQ 80%)	· 1 axial time history test	· S_{DS} : 0.44 g · ZPA : 0.528 g
	Post-inspection	· Visual inspection	-
3	Resonance search test	· Random wave (Dir. = X)	· Amp : 0.05 g · Freq. : 1.0Hz~50.0Hz
	Seismic simulation test (EQ 100%)	· 1 axial time history test	· S_{DS} : 0.55 g · ZPA : 0.66 g
	Post-inspection	· Visual inspection	-
4	Resonance search test	· Random wave (Dir. = X)	· Amp : 0.05 g · Freq. : 1.0Hz~50.0Hz
	Seismic simulation test (EQ 120%)	· 1 axial time history test	· S_{DS} : 0.66 g · ZPA : 0.792 g
	Post-inspection	· Visual inspection	-
5	Resonance search test	· Random wave (Dir. = X)	· Amp : 0.05 g · Freq. : 1.0Hz~50.0Hz
	Seismic simulation test (EQ 140%)	· 1 axial time history test	· S_{DS} : 0.77 g · ZPA : 0.924 g
	Post-inspection	· Visual inspection	-
6 7	• • •	• • •	• • •
8	Resonance search test	· Random wave (Dir. = X)	· Amp : 0.05 g · Freq. : 1.0Hz~50.0Hz
	Seismic simulation test (EQ 200%)	· 1 axial time history test	· S_{DS} : 1.1 g · ZPA : 1.32 g
	Post-inspection	· Visual inspection	-

In order to analyze the response of the specimen, the accelerometer and the displacement gauge (wire LVDT) were installed at the main points of the specimen. The items to be observed are the acceleration of the table base and the upper and lower parts of the test frame, and the relative displacement of the test frame. A single-axis accelerometer was attached to the table base and the upper and lower parts of the test frame according to the uniaxial excitation test method, and the wire LVDT was installed at the top and the bottom of the post member on one side of the test frame. The location and orientation of the sensors are shown in Table 7 and Figure 5.

Table 7 Sensor location and orientation

Description	Location	Sensor Name	Dir.*	Sensor		
				Model	Serial	Cal. date
A1	Table base	acc 1	X	8315A030D0TA00	5039210	2019.04.22.
A2	Bottom of test frame	acc 2	X	3711B1130G	5141	2019.05.07.
A3	Top of test frame	acc 3	X	3711B1130G	5145	2019.05.07.
D1	Bottom of front side column	lvdt 1	X	DP-1000E	BDH120417	2019.04.09.
D2	Top of front side column	lvdt 2	X	DP-1000E	BDH120418	2019.05.06.
D3	Bottom of rear side column	lvdt 3	X	DP-1000E	BDH120440	2018.10.04.
D4	Top of rear side column	lvdt 4	X	DP-1000E	BDH130605	2019.04.09.

* X: Longitudinal

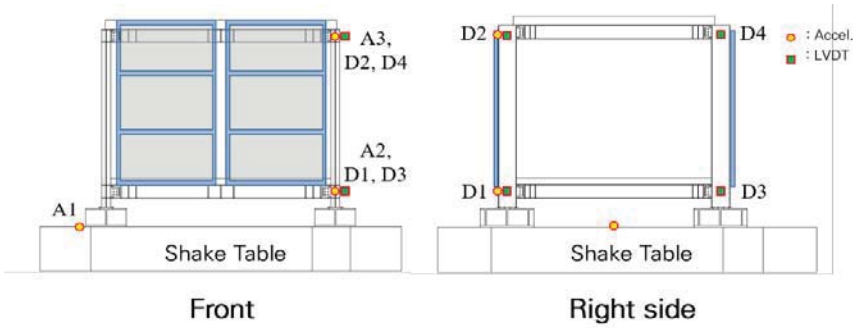

Figure 4 Sensor location

4. EXPERIMENTAL RESULTS

4.1 Resonant frequency

The resonance of the test frame was determined by calculating the transfer function of the response acceleration at the upper and lower positions of the test frame with respect to the acceleration input from the table base. The transfer function (T_{ab}) is calculated by the cross power spectral density (P_{aa}) of the input and output signals relative to the power spectral

density (P_{ba}) of the input signal. In order to improve the accuracy of the resonance analysis, each signal has applied a Symmetric Hamming Window.

$$T_{ab}(f) = \frac{P_{ba}(f)}{P_{aa}(f)} \quad (4)$$

Resonance test results are shown in Table 8, The natural frequency is expressed by the transfer function of the upper response acceleration (A3 / A1) of the test frame for each table base and the transfer function of the upper response acceleration (A3 / A2) of the lower test frame. The Table 8 shows that the resonant frequency of test frame decreased by 10% when going from step2 to step 3.

Table 8 Resonance search test summary

Step	Resonant Frequency(A3/A1) (Hz), df = 0.125 Hz	Resonant Frequency(A3/A2) (Hz), df = 0.125 Hz
1 (S_{DS} = 0.275 g)	2.50	2.50
2 (S_{DS} = 0.44 g)	2.50	2.50
3 (S_{DS} = 0.55 g)	2.25	2.25
4 (S_{DS} = 0.66 g)	2.25	2.25
5 (S_{DS} = 0.77 g)	2.25	2.25
6 (S_{DS} = 0.88 g)	2.25	2.25
7 (S_{DS} = 0.99 g)	2.25	2.25
8 (S_{DS} = 1.1 g)	2.25	2.25

4.2 Acceleration response

AC-156, the reference standard, requires that the output data of the seismic test based on the verification test result meet the following two conditions for the input data.

1. TRS (Test Response Spectrum) should enclose RRS (Required Response Spectrum)
2. Peak value in response acceleration-time history should satisfy more than 90% of ZPA.

The seismic test results of all stages planned in this experiment were found to satisfy the above conditions. Figures 5 and 6 shows the acceleration-time history graphs of Step 1 with the smallest magnitude and Step 8 with the largest magnitude.

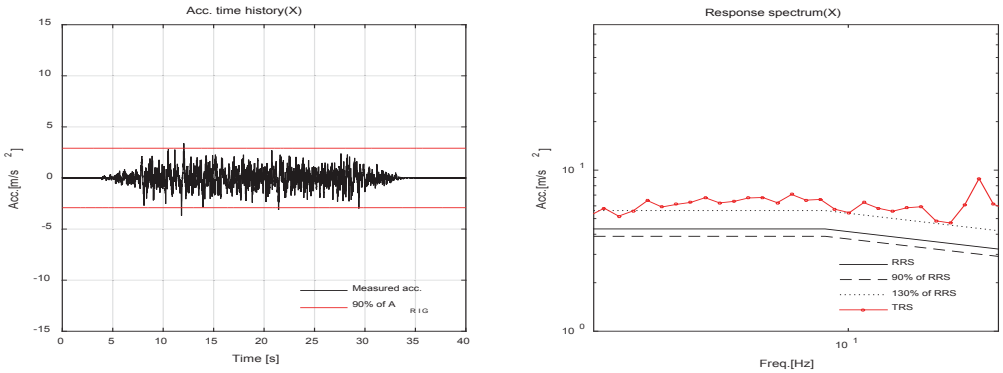

Figure 5 Acceleration time history, TRS and RRS (Step 1, SDS = 0.275 g)

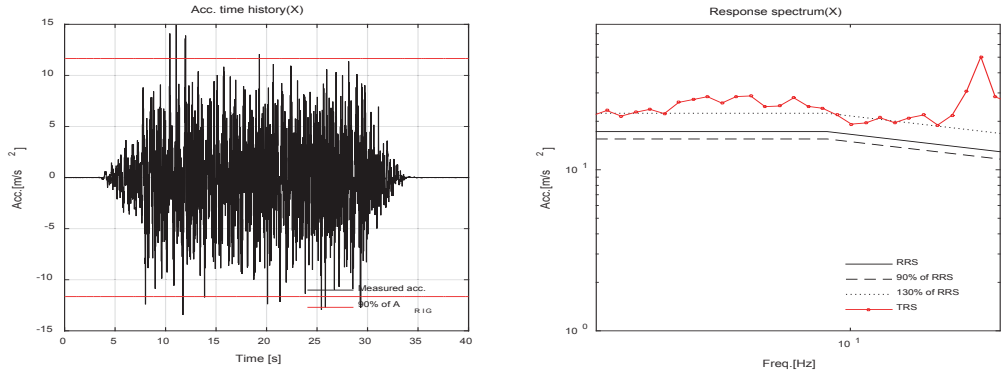

Figure 6 Acceleration time history, TRS and RRS (Step 8, SDS = 1.1 g)

4.3 Story drift angle

To calculate the Story drift angle, the measured front displacement (δ_{front}) and rear displacement (δ_{back}) of the test frame are used, as shown in the Figures 7 and 8. Each displacement was calculated using the displacement difference between the upper part of the experimental structure and the lower part of the test frame according to time history, and Table 9 shows displacement response of test frame. The maximum story drift angle of the test frame was 0.01 rad or more at Step 2(EQ 80%) and 0.02 rad or more at Step 3(EQ 100%). This means that the test frame on which the specimens was installed has been subjected to deformation exceeding seismic level 2 specified in the KDS 41 17 00: 2019.

$$\theta_{front} = \frac{\delta_{front}}{h} \qquad \theta_{back} = \frac{\delta_{back}}{h}$$

$$\theta_{frame} = \frac{\theta_{front} + \theta_{back}}{2}$$

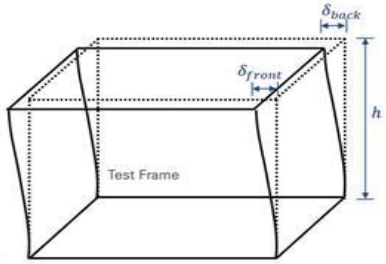

Figure 7 Method to calculate the drift angle

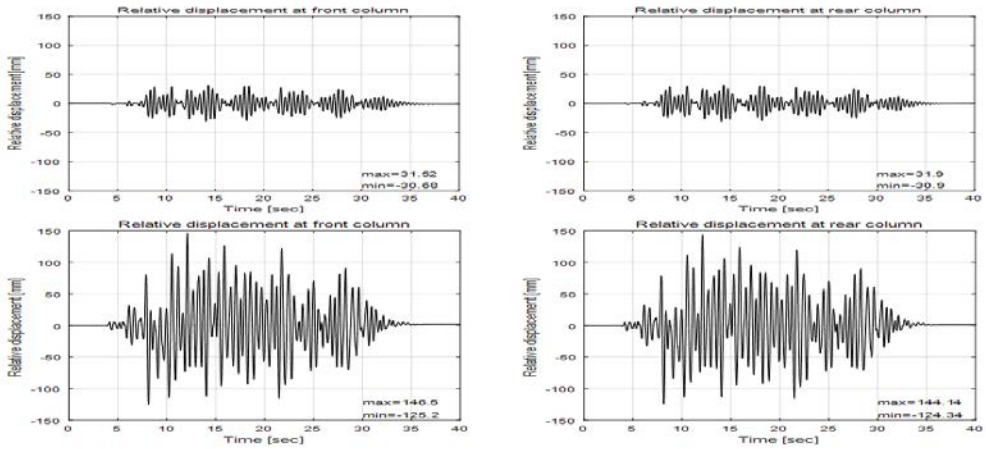

Figure. 8 Relative displacements between the upper and lower of the test frame over time history (Step 1 and 8)

Table 9 Displacement response

Step	Peak relative displacement (mm)		Story drift angle (radian)
	Front side column, δ_{front}	Rear side column, δ_{back}	
1 (EQ 50%)	31.52	31.90	0.0090
2 (EQ 80%)	62.38	61.46	0.0177
3 (EQ 100%)	80.14	78.08	0.0225
4 (EQ 120%)	96.14	95.58	0.0274
5 (EQ 140%)	112.58	110.80	0.0319
6 (EQ 160%)	129.54	127.18	0.0367
7 (EQ 180%)	142.12	139.14	0.0402
8 (EQ 200%)	146.50	144.14	0.0415

4.4 Damage assessment of specimens by excitation steps

The damage of the test specimen according to the story drift angle for each step is summarized in the table as follows.

Table 10 Damage condition according to the test steps

Step	Story drift Angle (radian)	D05	D10	D15	D20
Step 1 (EQ50%)	0.0090	No damage			
Step 2 (EQ80%)	0.0177	No damage			
Step 3 (EQ100%)	0.0225	 Slip of the fastener	No damage	 Minor crack in the silicone	 Minor crack in the silicone
Step 4 (EQ120%)	0.0274	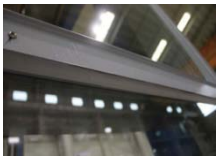 Minor crack in the silicone	 Minor crack in the silicone and minor slip of the fastener	 Expansion of the silicone crack	 Expansion the silicone crack

Step 5 (EQ140%)	0.0319	 Expansion the silicone crack and deformation of the fastener	 Expansion of silicone crack and slip of the fastener	 Expansion of silicone crack and minor slip of the fastener	 Expansion of the silicone crack
Step 6 (EQ160%)	0.0367	 Expansion of silicone crack	 Expansion of silicone crack	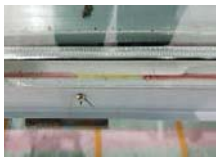 Expansion of silicone crack	 Deformation of the fastener
Step 7 (EQ180%)	0.0402	 Partial cracking of the glass	 Partial cracking of the glass	 Partial cracking of the glass	 Partial cracking of the glass
Step 8 (EQ200%)	0.0415	 Plastic deformation of the grid elements	 Plastic deformation of the grid elements	 Joint separation of the fastener	 Joint separation of the fastener

In case of the specimen that do not satisfy edge clearance requirements of the domestic standard (KDS 41 17 00: 2019 18.3.4), damages such as cracks in the sealing material are occurred after deformation of the fastener. However in case of specimens that satisfying or excessively satisfying the criteria, the deformation and slip of the fastener appeared after cracking and expansion of the sealing material. Step 7 (EQ180%) showed partial breakage at the glass edges in all specimens. In particular, in the case of D05 specimens that do not satisfy the criteria and D15 specimens that were excessively satisfied, noticeable cracks appeared at the edges of the glazing panel. In Step 8 (EQ200%), joint fastener separation and plastic deformation of the grid elements were observed in all specimens, but there was no overall breakage or dropping of the glass in any of the specimens during the excitation step.

4.5 Definition of damage limit by performance level of glazing curtain wall

In order to compare the degree of damage in the glazing curtain wall, the damage limits for each performance level of the glazing curtain wall were defined considering ASCE 41-13 and domestic papers. The operational level is the level of damage that maintains the functionality of the curtain wall without replacement of the sub-parts, and the damage level of the Position Retention was defined as that of sub-parts needing replacement or repair, such as major cracking in the silicone, partial crack of the glass, or the damage that is clearly identified with the naked eye. In addition, damage requiring immediate evacuation of people, such as falling glass debris, overall cracks in the glazing panels, and excessive failure of the cover pieces, were defined as damages to safety levels. None of the three phases allowed damage that could cause serious hazard, such as falling of glazing panels, collapse of the grid elements.

Table 11 Definition of damage glazing curtain wall system by performance level

Classification		Acceptable damage states (Minor failure)		Acceptable damage states (Major Failure)
		Operational (OP)	Position Retention (PR)	Life Safety (LS)
Glazing Curtain Wall System	Glazing	- Minor Crack of the sealing material	- Major Expansion of silicone cracks - Partial cracks in the glazing panel	- Total cracks in the glazing panel - Falling of glass debris
	Grid element	- Loosening of the cover pieces	- a few cover pieces failed - Minor plastic deformation of the grid elements - Minor Plastic deformation of the fasteners and bolts	- Excessive failure of the cover piece - Excessive plastic deformation of the grid element - Excessive plastic deformation of the fasteners and bolts

5. CONCLUSIONS

In this study, shaking table test is conducted of glazing curtain wall system with reference to the RRS presented by ICC ES AC156. After conducting this experiment, the damages of each specimen was assessed through a visual inspection for each step, and the results are shown in the data above. In addition, in order to evaluate the results of this experiment, we suggested damages of the glazing curtain wall system that considered performance levels by referring domestic research and international standards such as ASCE 7-10 and ASCE 41-13. The types of damage occur alone or in combination and have been shown sealing material cracks, fastener and grid element movement, and glass breakage. Figure 9 shows the results of the damage assessment of glazing curtain wall system by performance level and also indicated acceptable story drift angle of domestic steel structure. The conclusions are as follows.

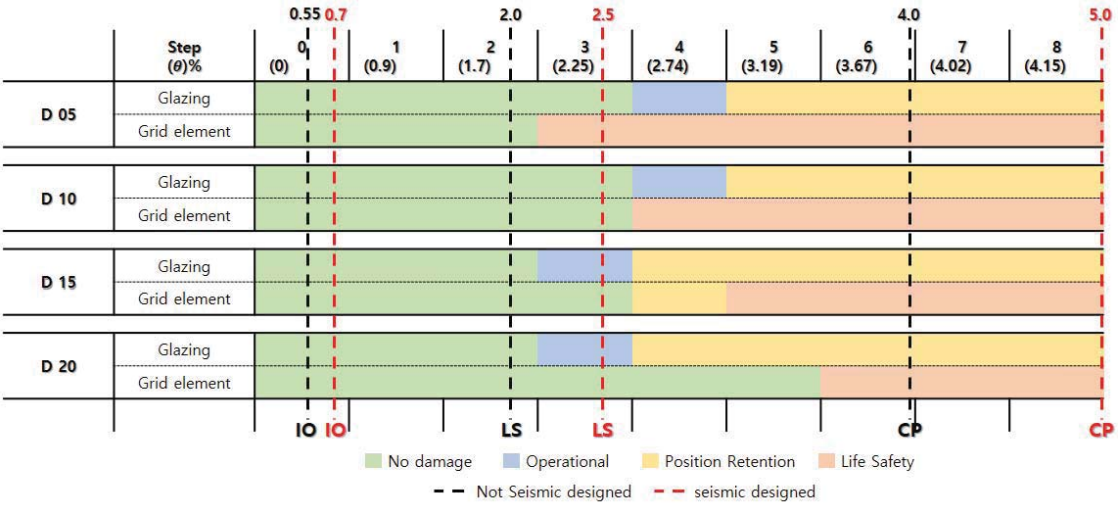

Figure 9 Damage assessment of glazing curtain wall system by performance level

1) Damage occurred simultaneously or individually on glazing and grid elements. In addition, as the end clearance widened, silicon material damage occurred from the initial step, whereas, damage to the grid element occurred at a larger story drift angle.

2) The damage occurred for the first time in all specimens in Step 3(2.25% of story drift angel) except for the D10 specimen. Specimen(D05), which failed to meet the domestic structural standard (KDS 41 17 00: 2019, 18.3.4), the damage pattern of Life Safety level, such as a slip or deformation of the fastener was shown before damages of Operational and Position Retention level. However, in the case of specimens satisfying the criteria(D15, D20), damages

including the slip of the fastener is occurred after the sealing material cracked

3) In the case of the D05 specimen with insufficient end clearance, damage to the life safety level occurred before reaching the life safety story drift angle of 2.5% of the steel structure designed as a seismic category 1 was shown. In addition all of the specimens which had sufficient end clearance were subject to damage that satisfied the criteria. Therefore, the current relative displacement requirement(KDS 41 17 00: 2019, 18.3.4) for curtain wall glass are suitable, but some research is required for 13mm, which is the minimum edge clearance in criteria.

4) The story drift angle at the final excitation stage(Step 8) was about 4% rad, and unacceptable damage such as a drop of the glazing panel and collapse of grid elements did not occur, but all specimens were showed partial breakage of the glazing panel at Step 7 (EQ180%). In last Step (EQ200%), excessive plastic deformation of the grid elements and separation of the fasteners are occurred.

5) Since all specimens had partial cracking in glazing panel at the edges, measures were expected to be needed to prevent the edges from colliding with the curtain wall structure and glazing. In addition, in the case of the hidden-bar type of curtain wall, failure in the structural sealing material is directly related to drop out of the glazing panel. Therefore, it is necessary to study the damage limit of hidden bar type curtain wall that considered the performance level.

ACKNOWLEDGMENTS

This research was supported by a grant(20AUDP-C146352-03) from the Architecture & Urban Development Research Program funded by Ministry of Land, Infrastructure and Transport of the Korean government.

REFERENCES

[1] ASCE. Minimum Design loads for building and other structures. American Society of Civil Engineers. Standards ASCE/SEI 7-10. c2010

[2] ASCE. Seismic Evaluation and Retrofit of Existing Buildings. American Society of Civil Engineers. Standards ASCE/SEI 41-13. c2013

[3] Federal Emergency Management Agency. Reducing the risks of Nonstructural Earthquake Damage. FEMA E-74. FEMA. c2012

[4] ICC-ES. Acceptance Criteria for Seismic Certification by Shake table Testing of Nonstructural Components. c2010

[5] Oh Sang Hoon, Park Jong Won, Park Hae Yong. Earthquake Engineering Society of Korea. Shake Table Test on Seismic Performance Evaluation of the Bolted Connection Type paneling System with Exterior Finish Material. c2018

[6] Architectural Institute of Korea. Korea Building Code and Commentary. KBC2016. c2016

[7] American Architectural Manufactures Association (AAMA). Recommended Dynamic Test method for determining the Seismic Drift Causing Glass Fallout from a Wall Systems. Publication NO. AAMA 501.6-09. c2009

[8] Baofeng Huang, Shiming Chen, Wensheng Lu, Khalid M. Mosalam. Soil Dynamics and Earthquake Engineering, Seismic demand and experimental evaluation of the nonstructural building curtain wall: A review. c2017

[9] Carolina Aiello, Nicola Caterino, Giuseppe Maddaloni, Antonio Bonati, Annalisa Franco, Anotonio Occhiuzzi. Construction and Building Materials. Experimental and numerical investigation of cyclic response of a glass curtain wall for seismic performance assessment. c2018

EURODYN 2020
XI International Conference on Structural Dynamics
M. Papadrakakis, M. Fragiadakis, C. Papadimitriou (eds.)
Athens, Greece, 23–26 November 2020

EXPERIMENTAL SEISMIC ASSESSMENT AND PROTECTION OF MUSEUM ARTEFACTS

M. Fragiadakis[1], L. DiSarno[2], A. Saetta[3], M.G. Castellano[4], I. Rocca[3], S. Diamantopoulos[1], V. Crozet[5], I. Politopoulos[5], T. Chaudat[5], S. Vasic[5], I.E. Bal[7], E. Smyrou[7], I. Psycharis[1], T.C. Hutchinson[6], L. Berto[3],

[1] School of Civil Engineering, National Technical University of Athens
Iroon Polytechniou 9, 15780, Athens, Greece
mfrag@mail.ntua.gr; {sdiamadop, ipsych}@central.ntua.gr

[2] University of Sannio, Benevento, Italy
University of Liverpool, UK
ldisarno@unisannio.it

[3] Department of Architectural Construction, University IUAV
30135 Venice, Italy
{saetta, lberto}@iuav.it; roccairene1@libero.it

[4] Research & Development Supervisor, FIP mec srl
Via Scapacchiò 41 - 35030 Selvazzano Dentro (PD) – Italy
maria.gabriella.castellano@fipmec.it

[5] DEN-Service d'études mécaniques et thermiques (SEMT)
CEA, Université Paris-Saclay, F-91191 Gi4f-sur-Yvette, France
{vincent.crozet, ioannis.politopoulos, thierry.chaudat, sandra.vasic}@cea.fr

[6] Department of Structural Engineering, University of California
San Diego, 9500 Gilman Dr., MC 008, La Jolla, CA 92093-0085
tahutchinson@ucsd.edu

[7] Research Centre for Built Environment NoorderRuimte Hanze University of Applied Sciences Groningen, The Netherlands
{i.e.bal, e.smyrou}@pl.hanze.nl

Keywords: artefacts, museum, statues, busts, rocking, base isolation, shaking-table, shape memory alloy, seismic loading, earthquake

Abstract. *Earthquakes are a major threat to monuments and to museums and their valuable contents worldwide. The protection of cultural heritage structures and also of museums and their treasures against earthquakes is hence a top priority. The paper will present large scale shaking table tests on cultural heritage assets and will emphasize on the use computing models in tandem with experimental testing. More specifically, the paper will present an extensive*

experimental campaign on the seismic response of artefacts, with emphasis on statues and busts. The tests have been carried out in the framework of SEREME project (Seismic Resilience of Museum Contents) at the AZALEE seismic simulator of CEA in Saclay, Paris under the auspices of the EC funded SERA project. The aim is to understand the seismic response of statues and busts and then develop novel and cost-effective risk mitigation schemes for improving the seismic resilience of museum valuable contents. The study is focused on the investigation of the seismic response of two real-scale marble roman statues and three busts of three roman emperors standing on pedestals of different types and size. Both non-isolated and seismically isolated artefacts are considered, while two new and highly efficient base isolation systems, tailored to art objects, have been tested. The first isolator is a pendulum-based system, while the second utilizes Shape Memory Alloy wires. Specifically tailored, numerical models of varying complexity, for single and two-block rocking systems, were developed for the needs of this study and are also assessed against the experimental results.

1 INTRODUCTION

Earthquake actions pose an immense threat to museums and their contents. For example, during the recent earthquakes on 21 July 2017 and 24 March 2020, in the island of Kos (Greece) and in Zagreb (Croatia), respectively, severe and widespread damage were reported in the archaeological museums of the cities. The earthquakes extensively damaged the sculpture exhibition, where many artefacts were dislocated, leaned against the walls, or overturned. In the case of heavy and slender sculptures, the overturning mechanism, apart from damaging the sculptures themselves, poses a serious threat to other standing exhibits in the gallery and the visitors. It is, therefore, of paramount importance to rely on methods and tools for characterizing the seismic risk of museum artefacts and, where necessary, proposing cost-efficient protective measures.

The study of the seismic behaviour of museum assets and the investigation of novel and cost-effective risk mitigation schemes for improving the seismic resilience of European museums has received little attention in the past. The H2020-SERA project Seismic Resilience of Museum contEnts (SEREME) aims to fill this gap through extensive shake table tests on real-scale busts and statues. The aim of this large experimental campaign is to understand the seismic response of statues and busts and then develop novel and cost-effective risk mitigation schemes for improving the seismic resilience of museum valuable contents. The study focuses on the investigation of the seismic response of two real-scale marble roman statues and three busts of roman emperors standing on pedestals of different types and size. Both isolated and non-isolated artefacts are considered, while two new and highly efficient base isolation systems, tailored to art objects, are tested dynamically under seismic scenarios. The tested isolators include a pendulum-based system and devices with Shape Memory Alloy (SMA) wires. Furthermore, the importance of the hosting building is examined. Specifically tailored, numerical models of varying complexity, for single and two-block rocking systems, will developed for the needs of this study and will be assessed with the aid of the experimental results of the SEREME campaign.

The study of the seismic vulnerability of museum artefacts, especially of slender, human-formed statues, is related to the research on the dynamic response of rocking rigid blocks. The dynamic characteristics of the hosting structures are also important. This is evident from the fact that, on many occasions, damage to the structure was reported leaving the exhibits intact and vice-versa. Although the problem is coupled, it can be studied looking separately at the structure and its contents, provided that the contents are not attached to the building. The seismic response of building contents is a topic of growing interest, since it is directly related to seismic loss assessment and earthquake community resilience. Building contents can be

either attached to the structure, or may consist of objects that are simply standing. Museum exhibits belong generally to the latter category, while free-standing components are often studied as rocking objects. The response of the latter components is sensitive to acceleration and velocity-based quantities and also their geometry. Today, there is lack of standards, while the existing approaches in the literature are general in concept and do not sufficiently address the mechanisms of the variety of rocking objects. The reliability of such analytical approaches has also been scarcely validated with extensive testing, such as shake experiments.

Common structural analysis and design methods require the assessment of stress resultants and displacement-based quantities. Additionally, the three-dimensional rocking response has not received the interest it deserves. On the other hand, building contents, in most cases, consist of objects that are freestanding. There are recent works in which the seismic response of freestanding contents is investigated [1, 2, 3]. Museum exhibits belong to the latter category and the freestanding components are often studied as rocking objects, hence their response is sensitive to acceleration and velocity-based quantities. Geometrical properties of the artefacts also have significant effects on the dynamics and earthquake response of the components. Additionally, when freestanding components are placed on a pedestal, made either from marble or steel, their dynamic response is more difficult to be predicted with simplified methods.

The seminal analytical work carried out on the seismic response of rocking objects in the 60's [4] stimulated several quantitative studies that have focused primarily on numerical solutions [5, 6, 7, 8]. Recently, however, Purvance et al. [9] carried out extensive experimental and numerical studies in order to investigate the overturning response of symmetric and asymmetric blocks with both simple and complex basal contact conditions and also proposed block overturning fragilities. Similarly, ready-to-use fragility curves were proposed by Konstantinidis and Makris [10] through a comprehensive experimental program on full-scale freestanding laboratory equipment located on several floor levels. The latter studies, however, focused primarily on the behaviour of single blocks. Dual block systems were first studied numerically by Psycharis [11], while the recent experimental work of Wittich and Hutchinson [12] studied asymmetric free-standing component configurations. It is worth noting that, for rocking rigid objects, such as artefacts, the response, at least in terms of overturning motion, is size-dependent, thus the scaling of the specimens is not possible and the experimental tests should be based on full-scale specimens.

Nowadays, considering the huge earthquake losses registered in the recent earthquakes, especially in the Mediterranean region, it is also deemed imperative to propose viable and cost-effective seismic protection measures for free-standing statues and busts. Podany [13] discussed a range of retrofitting measures based on the best practice followed by the J. Paul Getty Museum in Los Angeles, in California, where a newly developed base isolation device has been employed. Past research on the seismic protection of art objects using isolators, includes primarily several analytical-numerical investigations (e.g. [14, 15]), while to our knowledge only few experimental studies can be found in literature. However, the effectiveness of the use of seismic isolators for light weight components should be further investigated to characterize thresholds for accelerations and horizontal displacements for an adequate seismic protection of the artefacts.

The H2020-SERA SEREME project aims to fill the experimental gaps highlighted above and to include comprehensive shake-table tests of several configuration of free-standing and base isolated statues and busts. The freestanding artefacts are installed either directly on the marble floor, or on a pedestal. The objective of the campaign was to give insight on the seismic behaviour of statues and busts as well as to evaluate the effectiveness of two different seismic risk mitigation systems. A total of 5 pairs of real scale marble artefacts were tested, 3 busts installed on marble pedestals and 2 statues. Seven different testing arrangements (also

termed “Configurations”) were considered during this experimental campaign and more than 400 seismic tests were performed. Two innovative base isolation devices were utilized as retrofitting remedies. The first system is a combination of friction pendulum isolators [16], a system designed for light components. The second system is a newly developed device utilizing shape memory alloy wires in the horizontal plane. The isolation devices tested are patented systems, namely ISOLART® PENDULUM &ISOLART® SMA, which are manufactured by the Italian company FIP Mec, a member of the User Team. In order to obtain a direct evaluation of the isolator effectiveness, for each test configuration, pairs of two similar artefacts were tested together in an isolated and a non-isolated arrangement. The shake-table tests were carried out considering uniaxial, biaxial and triaxial earthquake loadings at increasing amplitudes. In order to evaluate the influence of the frequency content and the directionality of the seismic excitation, 13 different waveforms were applied to the shake table (8 uni-directional motions, 3 bi-directional motions and 2 tri-directional motions). Regarding the instrumentation, the artefacts motions were recorded using accelerometers, gyroscopic and displacement sensors.

2 MUSEUM CONTENTS TESTED

The experimental campaign of SEREME focused on the investigation of the seismic behaviour of real-scale marble statues and busts standing on pedestals. The case study statues and busts were selected with different geometry and weights; they are replicas of ancient roman emperors. Five busts of roman emperors were utilized: two of emperor Traiano, two of Augusto and one of Tito. Furthermore, four statues were also purchased, two standing on a low height marble pedestal (quoted as “Figura Femminile”) and two simple female form statues (quoted as “Fanciulla”). Since all specimens are made from solid marble, the average weight of the busts is 250-300kg, while that of the statues was 500-600kg. The replicas of the same statue/bust have approximately the same geometry, but they are not perfectly identical (Figure 1). The seismic response of a display case was also examined.

(a) (b)

Figure 1. Components used for the shake table tests: (a) Busts and display case, (b) female statues.

The busts are placed on a pedestal which is used to bring the specimens to the eye-level of the visitor. Three different pedestal types were identified and then adopted for the experimental tests: (i) solid pedestal, with dimensions 45×45×100 cm, (ii) hollow pedestal, with dimensions 35×35×100 cm, and (iii) modern type metallic pedestals that were provided by the Italian manufacturer Fallani. The traditional, hollow and solid, pedestals were made of concrete which has a specific weight close to that of marble. To reproduce realistic conditions for

in-situ friction, on the upper and the lower face of the pedestals, 3 cm thick marble plates were installed. Solid pedestals have large weights (nearly 500kg) and they also employ large bases, thus these pedestals are not prone to uplift. On the other hand, hollow pedestals are slender with weight 226kg and have a base with smaller width equal to 35c. Furthermore, its centre of gravity is much higher compared to the solid case. The metallic pedestal has a large square base with side equal to 85 cm and it weighs only 85 kg.

In order to simulate the floor of museums, where typically busts and statues are hosted, the non-isolated specimens were placed on a marble floor surface. The marble has thickness equal to 3 cm and it is positioned on stiff wood also 3 cm thick. Both marble and wood were directly bolted on the shake table. All specimens are placed on top of the marble floor and pedestal without any connection material. In the case of isolated specimens, the isolator was bolted on the table with the aid of specific holders that adjusts the holes of the table to the holes of the device. For the SMA isolators, marble plates were glued on the upper surface of the isolator, while the specimens are simply standing.

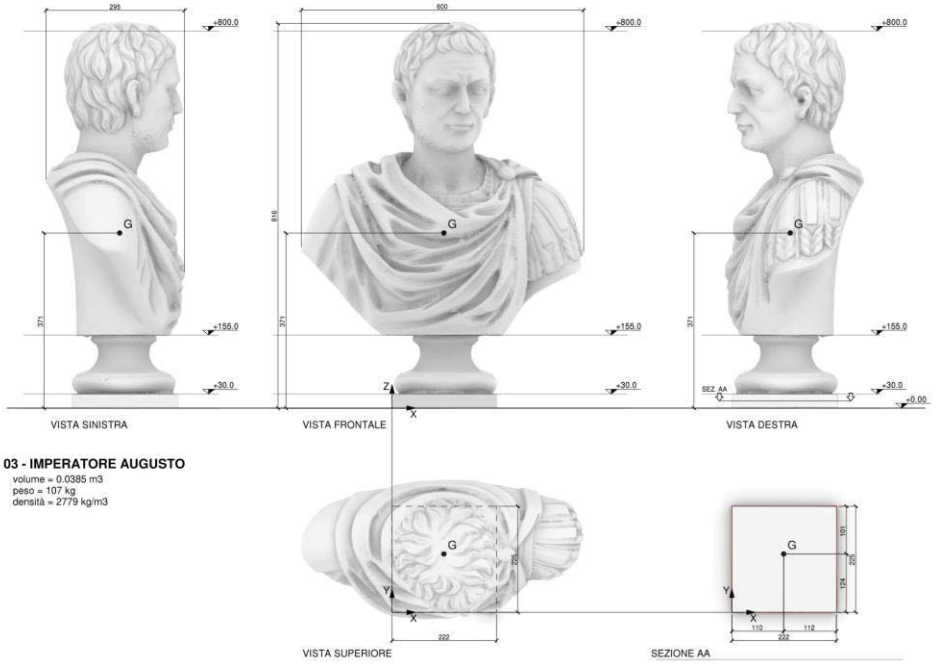

Figure 2. (a) Geometric properties of the Emperor August bust.

The static friction coefficient was measured for the marble-marble interface with inclined tests. The inclined tests were repeated 10 times in order to determine the mean friction angle. For the plate-plate marble interface the mean friction coefficient μ was found equal to 0.79, while for the bust-plate interface it was found equal to 0.39. The values of the friction coefficient for plate-plate interface that were derived experimentally comply with those provided in the literature. Conversely, the friction marble-plate interface was found unexpectedly low. However, both mean values were also verified during the shake table tests where sliding was observed approximately at peak ground acceleration (PGA) values close to the ones measured (the condition to have friction is PGA>μg). To increase the friction coefficient, where necessary, a thin layer of a rubber material was glued at the bottom of the busts. The friction coefficient at the interface of the marble floor and the bottom of the statues was found sufficiently high and thus no measures were required.

Laser scanning was carried out by a joint research team before moving them the artefacts from the vendor to CEA. Digitalization with laser scanning provides the geometrical properties of the specimens. The purpose of laser scanning is two-fold: (i) it provides a finite element (FE) mesh of the geometry of the artefacts that can be used to perform numerical simulations, and (ii) it allows the calculation of fundamental properties of the components, such as the centre of mass (CM), the total mass, the rotational moments of inertia and the distance of the CM from the pivot points. Furthermore, the laser scanning verified that the specimens are made from solid marble through calculating the ratio of the scanned volume over the measured weight of each specimen. Example of laser scanning information obtained are shown in Figure 2 for the bust of Emperor August.

Two different base isolator technologies were adopted (Figure 3): a friction pendulum isolator and an innovative device with shape memory alloy (SMA) wires. The tested seismic isolator systems were manufactured by the Italian company FIP Mec srl: the selected isolators are marketed as ISOLART® SMA and ISOLART® PENDULUM, respectively. ISOLART® PENDULUM, is similar to common pendulum isolators used for structures, but it consists of different materials and it has been designed specifically for low-mass structures such as objects of art. The main difference between the two isolation devices is the range of mass of the objects to seismically isolate. For ordinary friction pendulum bearings, the friction can be large because of low vertical pressure. To overcome the problem, an increase of the vertical force, or a decrease of the friction coefficient is required. For this purpose, the friction pendulum was used to isolate several artefacts together which are standing on a heavy steel plate, thus increasing the vertical force (Figure 3a). Therefore, three pendulum isolators were employed to isolate a floor on which a group of artefacts (2 or 3 artefacts) was installed. The installation of the ISOLART® PENDULUM devices is shown in Figure 3a.

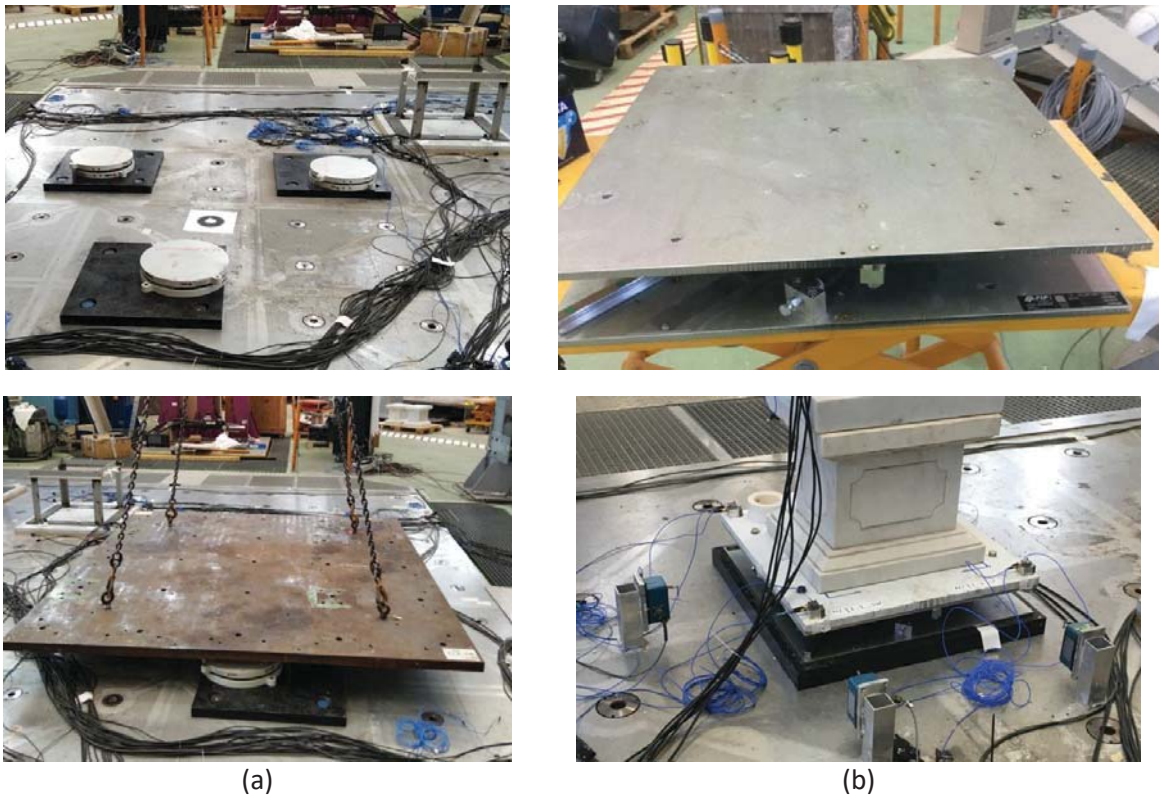

(a) (b)

Figure 3 Tested isolation systems: (a) friction pendulum isolator, (b) SMA isolator.

ISOLART® SMA, i.e. the SMA-based isolator, is a novel isolator based on SMA wires that are effective in limiting the horizontal displacements of the device. ISOLART® SMA is a patented isolation system which takes advantage of the super-elastic properties of SMA wires, i.e. their capacity to have a stress-induced non-linear behaviour similar to elasto-plastic behaviour up to high deformations (about 7%) and unload to zero displacement. As shown Figure 3b, the SMA isolator can be used to isolate a single specimen each time, which is a significant advantage. Although all SMA isolators adopted have the same dimensions, the properties of the SMA may differ. Three different types of SMA isolators were tested.

Due to the large variety of specimens, pedestals and isolators, seven different Configurations were analysed experimentally using the 6-DOFs shake table AZALEE. The seven testing configurations were designed taking into consideration the limited testing time available and also the needs of the project. The tests of each configuration lasted approximately 2, or 3 days. Configuration 1, was sub-divided into five sub-configurations, shown in Figure 4 up to Figure 8 and considers only the SMA isolators. The caption of each figure explains the properties of the tested configuration. In order obtain a direct comparison between the isolated and the non-isolated case, the sub-configurations compare pairs of two similar artefacts tested side-by-side in an isolated and a non-isolated arrangement. Instead of testing simultaneously more than a pair of specimens, single pairs were considered every time. This practice offered speed during the tests, while it also allowed to focus on one tested pair every time. In configurations I.4 and I.5 a display case was tested, first isolated and then non-isolated.

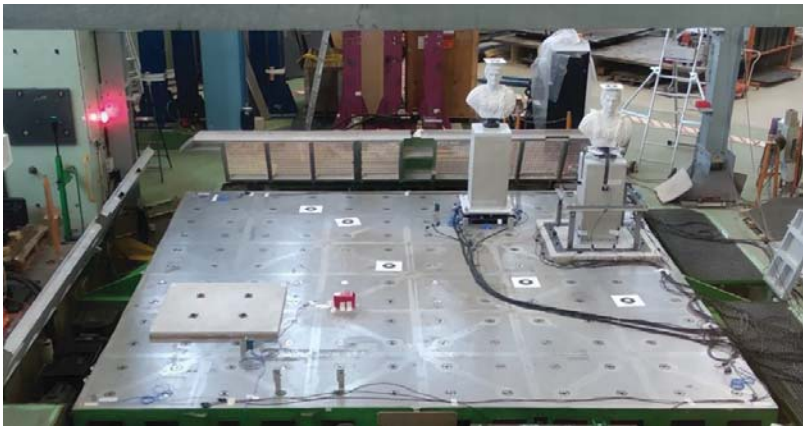

Figure 4. Configuration I-1: Traiano bust on solid pedestal; on marble and on SMA isolator

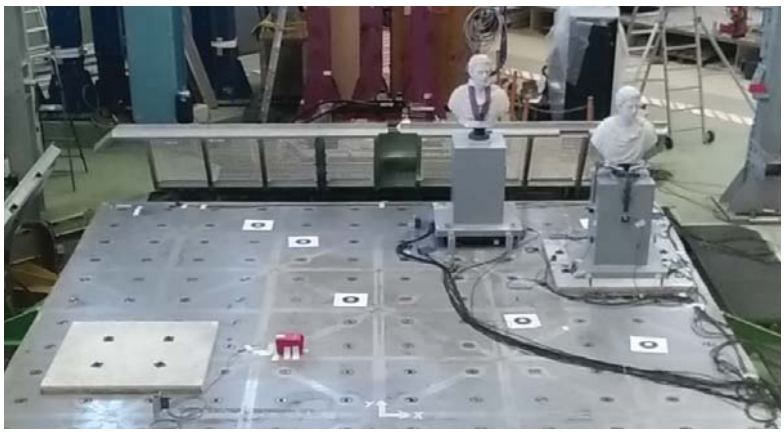

Figure 5: Configuration I-2: Traiano bust on steel metallic pedestal; on marble and on SMA isolator.

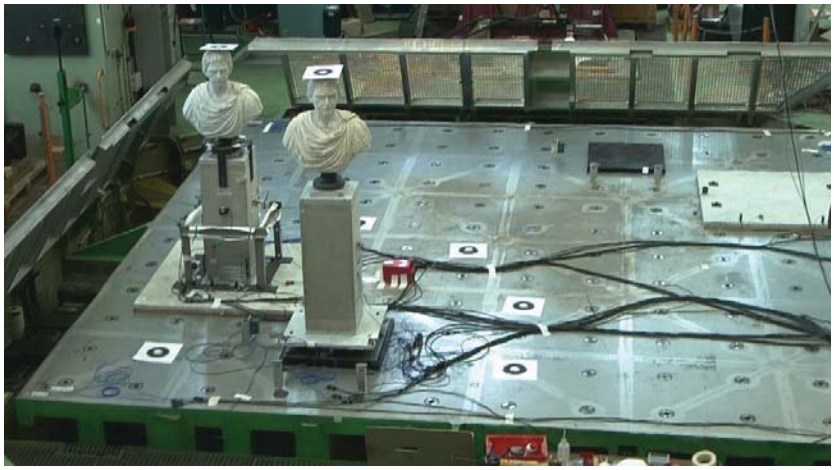

Figure 6: Configuration I-3: Augusto bust on hollow pedestal; on marble and on SMA isolator.

Figure 7: Configuration I-4: Female statue (Figura femminile) standing on the ground pedestal and non-isolated display case and isolated display case (SMA isolator)

Figure 8: Configuration I-5: Female statue (Fanciulla) standing on the ground pedestal and non-isolated display case and non-isolated display case

Figure 9: Configuration II: Non-isolated vs isolated statues (friction pendulum system). The pairs of specimens compared are: (i) Traiano bust on solid pedestal, (ii) Fanciulla and (iii) Figura femminile.

Figure 10: Configuration III: Non-isolated vs isolated statues (friction pendulum system). The pairs of specimens compared are: (i) Tito bust on metallic pedestal, (ii) Augusto bust on solid pedestal, and (iii) Traiano bust on hollow pedestal.

Configurations II and III are shown in Figure 9 and Figure 10, respectively. These two configurations test the friction pendulum as seismic isolator. In Figure 9, the two female statues and one bust were positioned on top of the friction pendulum isolators. The specimens were positioned on the steel plate in way that the centre of mass of the specimens approximately coincides with the centre of mass of the plate. Configuration III (Figure 10) compares simultaneously the three different types of pedestals. Since only five busts were available, for the metallic pedestals only the non-isolated case was considered. Furthermore, the upper face of the metallic pedestals was reinforced with an 8mm thick steel plate which considerable improved the performance of the system compared to Configuration I.2 (Figure 5).

3 NUMERICAL SIMULATIONS

Due to the complex geometry of museum exhibits and the uncertainties of the problem, the numerical simulation of artefacts and museum exhibit systems presents significant difficulties. Complex simulations should be repeated for each exhibit, or for groups of exhibits with similar geometrical characteristics. Moreover, despite the great value of museum exhibits, in practice all decisions about their safety are taken by museum curators, who have empirical knowledge, e.g. experience of past earthquakes, but no technical background to perform sophisticated computer simulations.

Specimen	Standing conditions	Rocking Acceleration (g)		Overturning (mm/s)	
		$a_{rock,B,x}$	$a_{rock,B,Y}$	$v_{cr,X}$	$v_{cr,Y}$
Figura Femminile with pedestal		0.244	0.207	0.446	0.344
Fanciulla		0.296	0.226	0.382	0.289
Emperor Traiano	Bust only	0.240	0.236	0.297	0.308
	Bust on solid pedestal	0.330	0.331	0.423	0.424
	Bust on hollow pedestal	0.207	0.208	0.280	0.281
	Bust on steel pedestal	0.293	0.292		
Emperor Tito	Bust only	0.283	0.254	0.262	0.309
Emperor Augusto	Bust on solid pedestal	0.283	0.253	0.257	0.304
	Bust on hollow pedestal	0.220	0.216	0.294	0.29
	Bust on steel pedestal	0.318	0.310		

Table 1 Peak ground acceleration that initiate rocking and overturning velocity estimates.

The possible methods of analysis are either simplified calculations based on first principles, or advanced methods of analysis, e.g. analyses using FE modelling, or the discrete element method (DEM). Simplifications are based on simplifying the geometry to one or two rectangular, rigid bodies. These are basic geometric calculations that do not require engineering knowledge, but give useful information such as the maximum ground acceleration for which the system will slide or will engage into a rocking motion. When laser scanning information is available, these calculations are more accurate and, despite their simplicity, they are very important and helpful. Table 1 shows the peak ground acceleration values that initiate rocking for each of the specimen considered. In the case of busts standing on a pedestal, the two bodies are, crudely, assumed to behave as a single body. Table 1 also shows the velocity that triggers overturning motion according to the relationship proposed by Ishiyama [17]. This is a conservative lower bound estimation, as opposed to the rocking initiation acceleration which is exact.

Laser scanning was adopted for determining the geometric characteristics of the busts and of the statues that were tested. The scanning provides FE models that allow to perform simulations, but with increased CPU requirements. Furthermore, the accuracy of the scanning is very high and results to very fine and detailed finite element models which do not offer more accuracy but they require excessive memory and CPU resources. It is, therefore, necessary to also have simple models for the seismic response prediction.

The FE method offers several advantages concerning the accuracy, but there are also difficulties in utilizing the analytical simulation approach. The surface-to-surface interaction between the upper surface of the pedestal and the lower surface of the bust requires knowledge of the friction coefficient and the damping ratio, while damping of the motion due to rocking impacts cannot be introduced in a straightforward manner. Also, the FE method is more realistic if the bodies have some flexibility. Introducing the flexibility and the real modulus of elasticity of the artefacts will increase the CPU time, thus making prohibitive a large number of simulations. On the other hand, the Discrete Element Method (DEM) assumes that the objects are rigid and consequently can be adopted with reduced computational costs. For the interaction between the surfaces, appropriately calibrated springs should be introduced in the model. Psycharis et al. [18] have described the numerical model for the simulation of a multi-drum ancient column which is subjected to natural ground motion records. The column consists of eight rigid bodies, the upper placed on the top of the lower. In this work the 3DEC software has been used for the simulation of a problem that has similarities to the problem at hand.

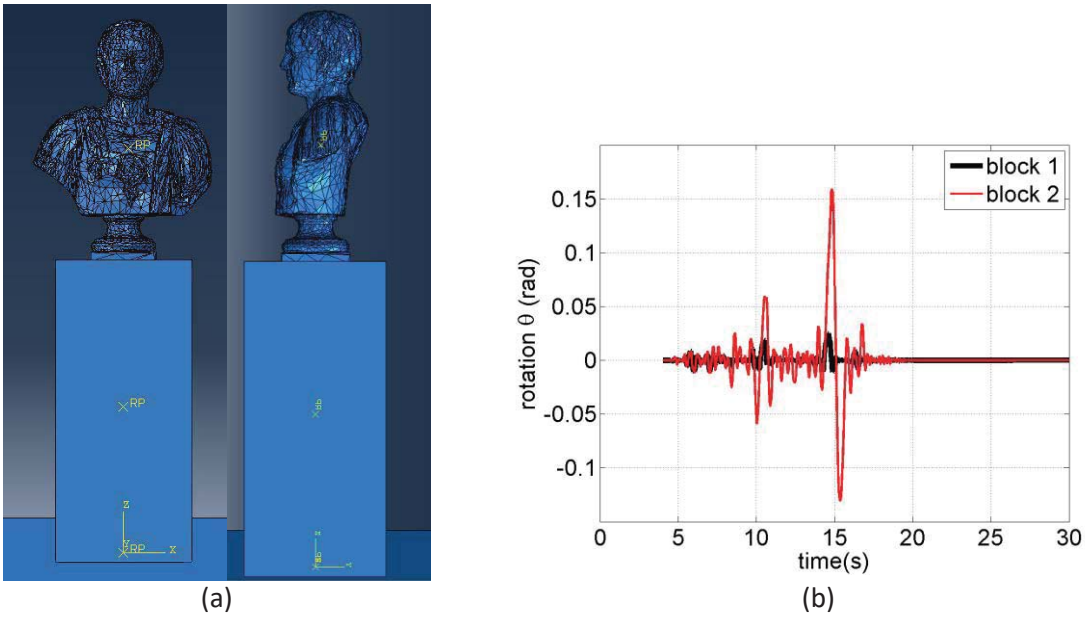

Figure 11. (a) Finite Element model (pedestal-bust), (b) response time history.

Models that consider either two-block assemblies (pedestal-bust) or freestanding, symmetric or asymmetric, rocking blocks (a freestanding statue or a bust that rocks on a pedestal in rest) are a possible alternative to the costly FEM and DEM simulations. Such simple models are typically limited to one-direction simulations and hence the procedure should be repeated for both the longitudinal and the transverse direction due to the asymmetry of the specimens. A simplified approach is offered by using the equation of motion proposed by Housner [4]. A possible way to handle the equations of Housner [4] has been proposed by Diamantopoulos and Fragiadakis [8]. For the two-block case and for simplicity reasons the work of Psycharis [11] can be adopted. Vlachos et al. [19] presented a first attempt to extend the two-block problem in case of asymmetric upper block when the pedestal is symmetric.

4 TEST SETUP

To evaluate the influence of frequency content of the excitation, as well as the directionality of the seismic input, five different earthquake ground motions were adopted in this experimental study. The ground motion records and their properties are shown in Table 2. The records were applied in different combinations every time, i.e. first the X-component was applied alone, the Y component afterwards and then the X and Y components were applied simultaneously.

Earthquake	Date	Mw	Station	Distance hypocentral	Soil category	PGA (g)
Emilia, Italy	29.05.2012	6.0	T0800	14.4	C* (EC8)	L: 0.33 T: 0.25 V: 0.33
Athens, Greece	07.09.1999	5,9	Syntagma Metro B	10.0	Stiff soil	L: 0.109, T: 0.086, V: 0.087
L'Aquila, Italy	06.04.2009	6.3	Aterno river-AQA	< 2km	Stiff soil	L: 0.45, T: 0.39, V: 0.37
Kalamata, Greece	09/13/1986	6.2	Nomarchia	5.0	Stiff soil	L: 0.22, T: 0.29

Kobe, Japan	1/16/1995	6.9	Takatori, Japan	22.2 (< 1.5 km)	C* (EC8)	L: 0.068
Emilia, Italy – first storey	29.05.2012	6.0	T0800	14.4	C* (EC8)	L: 0.37

Table 2 Ground motion records used for the testing campaign.

The record combinations adopted are listed in Table 3. For each record combination, the ground motion amplitude was gradually scaled up. In general, the target intensity levels considered were: 0.15g, 0.20g, 0.25g, 0.35g, 0.40g and 0.50g. For simulations where simultaneously two, or three, components were considered, a uniform scaling factor was adopted for all record components considered, while the target acceleration refers either to the X-, or the Y-component. When both X and Y are present, it refers to the X-component. For the Takatori and the Kalamata records, the maximum permissible scaling factor is controlled by the maximum allowable displacement of the shake table that cannot exceed 10cm. As expected, differences between target PGA and the PGA measured as input to the shake table were observed. On average 25-40 shake table runs were performed for each of the seven tested configurations.

ID	Record	Components	Target PGA
1	Emilia	X	0.15, 0.25, 0.35, 0.40, 0.50
2	Emilia	Y	0.15, 0.25, 0.35, 0.40, 0.50
3	Emilia	XYZ	0.15, 0.25, 0.35, 0.40, 0.50
4	Emilia	XY	0.15, 0.25, 0.35, 0.40, 0.50
5	Emilia	Y (first floor)	0.15, 0.25, 0.35, 0.40, 0.50
6	Emilia	YZ (first floor)	0.15, 0.25, 0.35, 0.40, 0.50
7	Syntagma	X	0.15, 0.25, 0.35, 0.40, 0.50
8	Takatori	Y applied on X	0.10, 0.15
9	Takatori	YZ applied on X	0.10, 0.13, 0.2, 0.24
10	Takatori	Y	0.10, 0.18, 0.2, 0.24
11	L'Aquila	X	0.15, 0.25, 0.35, 0.40, 0.50
12	L'Aquila	XYZ	0.15, 0.25, 0.35, 0.40, 0.50
13	Kalamata	X	0.15, 0.20, 0.25, 0.30

Table 3 Record combinations.

Apart from five naturally recorded ground motions, the acceleration response history of the first floor of the museum was considered. The museum is the Archaeological museum of Pella in Greece. This is a new reinforced concrete building. The building was modelled with OpenSees software and it was subjected to the five ground motion records of Table 2. Since it is a two storey RC building with many shear walls, it is a quite stiff structure (Tx =0.17s, Ty =0.14s) and hence large amplifications were observed at the stories. Among the various floor acceleration histories, the first storey of the Emilia 2012 (Italy) response acceleration was adopted for the tests.

5 OBSERVATIONS AND PRELIMINARY RESULTS

A vast amount of data was obtained during the experimental campaign that lasted approximately two months. The User Team is currently working on post-processing the experimental data. However, very interesting observations were made during the campaign. Due to the protection measures no major damage on the specimens occurred, while the most typical damage type observed is the failure at the corners of the specimens. This damage is shown in Figure 12 for both the bust and the statues. This type of damage happened practically to all busts of Configuration I.1-I.5, while the damage of statue show in Figure 12b happened once. Since a large number of tests had to be repeated, the marble bases of the busts were replaced, while

for the statue the failed wedge shown in Figure 12b was repaired by gluing it back and retesting the statue isolated. No damage occurred at the pedestals. The metallic modern pedestals when tested in Configuration I.2, exhibited some mild bending of their upper face, where the bust was standing. The lateral bending due to the selfweight of the bust affected the dynamic response. In order to mitigate this effect, in Configuration III, an 8mm thick plate was used to reinforce the pedestal.

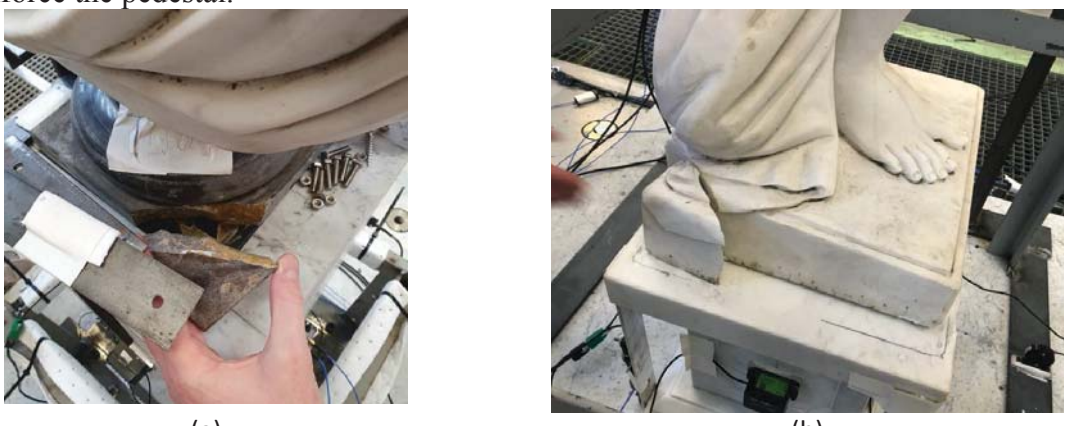

(a) (b)

Figure 12. Typical damage at the base of the specimens: (a) bust, (b) base of the statue.

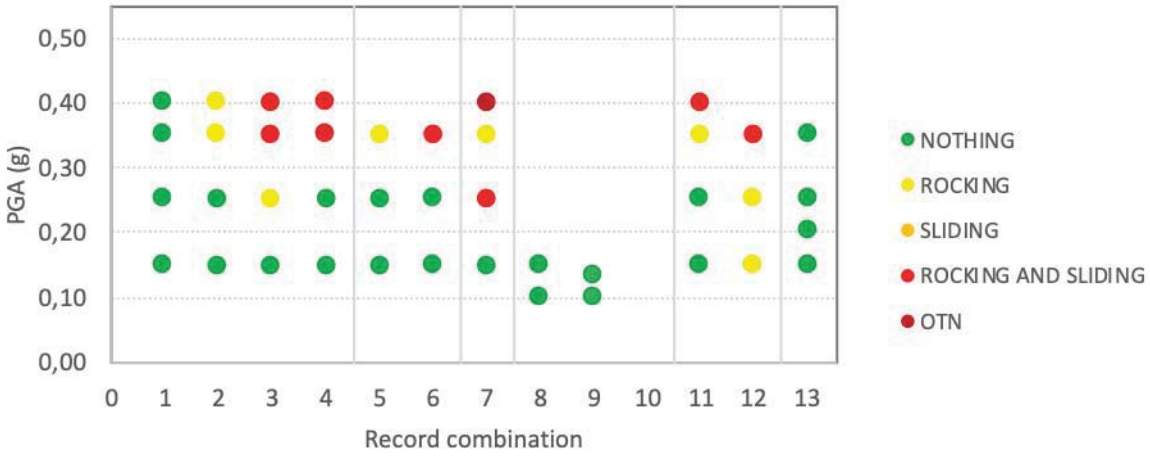

Figure 13. Response of the non-isolated bust of Configuration I.1.

Figure 13 summarizes the response of the non-isolated bust in Configuration I.1 where the bust of emperor Traiano was positioned on top of the solid pedestal. The solid pedestal, due to its massive geometry, never uplifted and hence only rocking of the bust was observed. As expected from the PGA values of Table 1, no uplift occurred for PGA values below 0.20g. Note that the accelerations of Figure 13 are the theoretical predictions; the latter differ, sometimes considerably, from the values recorded on the shake table. Comparing record combinations 1 and 2 to combinations 3 and 4, it is evident that the bidirectional ground shaking is more severe for the bust, since overturning was observed at much lower accelerations for the Emilia earthquake. This observation also holds for the L'Aquila record (combinations 11 and 12). The Takatori and Kalamata ground motions have a low recorded PGA and have a large frequency content. These records were scaled but they were not critical for the busts, as opposed to the Syntagma ground motion which was severe.

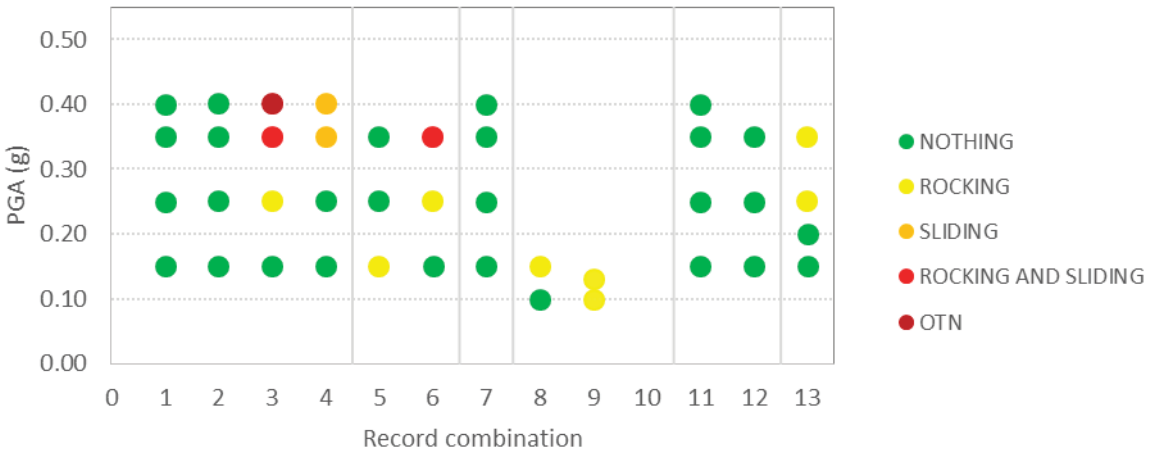

Figure 14. Response of the SMA-isolated bust of Configuration I.1.

Different observations hold also for the SMA isolated specimen. As show in Figure 14, the specimen was safe for most ground motion levels, practically for most ground motions. The Emilia XYZ ground motion produced sliding and rocking that threatened the bust for a PGA of 0.40g. This is attributed to the large vertical acceleration component. This was also seen for the first-floor response when a vertical component is present. Interestingly, rocking was observed also for the Takatori and the Kalamata ground motions.

Important findings were obtained from the experimental campaign and are briefly summarized as follows:

- For high excitation intensity tests, the non-isolated artefacts are prone to show a complex rocking and sliding behaviour. The impact induced by the rocking motion can be a source of damage to the base of the busts, especially at the corner points of the base of the bust.
- The response of the busts on the solid and the on the hollow pedestal is substantially different. The uplift of the hollow pedestal was always small and difficult to identify visually. However, it is clear that it considerably affected the seismic response. Whether the bust is safer on the solid, or on the hollow pedestal is a topic that deserves further research; the tests have shown that the safety depends also on the ground motion frequency content.
- Tests where the friction coefficient between the bust and the pedestal was low, i.e. when friction coefficients vary between 0.20 and 0.30, revealed that sliding is a beneficial response mode for the bust. If the sliding motion of the rigid object is controlled, then some sliding is desirable.
- In most of the cases, the considered mitigation methods have been effective in the prevention of the rocking/sliding behaviour of the artefacts. As a result, these mitigation methods improved significantly the seismic behaviour of the artefacts. Especially the friction-pendulum system was very efficient in practically all tests. Some attention is required in the case of high vertical component. Although the vertical earthquakes considered were very strong, some attention is required in this respect.
- The metallic pedestals, due to their geometry, did not uplift and hence they were equally efficient as the solid ones, provided that they can fully support the weight of the artwork.

- The response of the statues was well predicted and with no surprises. When the input acceleration was below the rocking initiation threshold, the statues performed some high frequency oscillation.
- The base of some of the statues was not fully flat, due to structural imperfections. This lack of planarity affected the response and threatened the safety of the statues. This issue has been also reported in previous research in the literature.
- The simplified calculations, summarized in Table 2, are very important and useful. Such information should be always advised when taking seismic protection measures for artefacts.

6 CONCLUSIONS

The project presents an extensive experimental campaign on the seismic response of artefacts, with emphasis on statues and busts. The tests took place in the framework of SEREME project (Seismic Resilience of Museum Contents) at the AZALEE seismic simulator of CEA in Saclay, Paris under the auspices of the SERA project. The campaign aims to help us understand the seismic behaviour of the selected statues and busts and then to develop novel and cost-effective risk mitigation schemes for improving the seismic resilience of valuable objects hosted in European museums. Two real-scale marble (replicas are usually made from gypsum) roman statues and three busts of three roman emperors standing on three pedestals of different types and size are investigated concerning their response under seismic loading. The artefacts are considered either isolated or non-isolated. In the latter case, two new and highly efficient base isolation systems, tailored to art objects, are tested. The efficiency and the effectiveness of the isolators are of the main interest for the authors. The first isolator is a pendulum-based system, while the second utilizes Shape Memory Alloy wires. Different configurations were considered for examining all cases. The importance of the hosting building is also examined, i.e. building type, stiffness and story that hosts the artefacts. Specifically tailored, numerical models of varying complexity and Finite Element models for single and two-block rocking systems were developed for the needs of this study and are also assessed against the experimental results.

REFERENCES

[1] L. Berto, T. Favaretto, A. Saetta, Seismic risk mitigation technique for art objects: experimental evaluation and numerical modeling of double concave curved surface sliders. *Bulletin of Earthquake Engineering*, 11(5): 1817-1840, 2013.

[2] A. Chiozzi, M. Simoni, A. Tralli, Base isolation of heavy non-structural monolithic objects at the top of a masonry monumental construction, *Materials and Structures*, 49(6): 2113-2130, 2015.

[3] L. Di Sarno, G. Magliulo ,D. D'Angela, E. Cosenza, Experimental assessment of the seismic performance of hospital cabinets using shake table testing, *Earthquake Eng. Struct. Dyn*., 48(1), 103–123, 2017.

[4] WG. Housner, The behaviour of inverted pendulum structures during earthquake, *Bulletin of the Seismological Society of America*, 53: 403-417, 1963.

[5] E. Voyagaki, I.N. Psycharis, G. Mylonakis, Rocking response and overturning criteria for free standing rigid blocks to single - lobe pulses, *Soil Dynamics and Earthquake Engineering*, 46:85-95, 2013.

[6] J. Zhang, N. Makris, Rocking response of free-standing blocks under cycloidal pulses, *Journal of Engineering Mechanics*, 127: 473-483, 2001.

[7] E. Dimitrakopoulos, E. Fung, Closed-form rocking overturning conditions for a family of pulse ground motions, *Proceedings of the Royal Society of London A: Mathematical, Physical and Engineering Sciences*, 472:20160662, 2016.

[8] S. Diamantopoulos, M. Fragiadakis, Seismic response assessment of rocking systems using single degree-of-freedom oscillators, *Earthquake Eng. Struct. Dyn*., 48(7), 689–708, 2019.

[9] M.D. Purvance, A. Anooshehpoor, J.N. Brune, Free-standing block overturning fragilities: numerical simulation and experimental validation, *Earthquake Eng. Struct. Dyn.*, 37(5):791–808, 2008.

[10] D. Konstantinidis, N. Makris, Experimental and analytical studies on the response of freestanding laboratory equipment to earthquake shaking, *Earthquake Eng. Struct. Dyn.*, 38(6):827–848, 2009.

[11] I.N. Psycharis, Dynamic behaviour of rocking two-block assemblies, *Earthquake Eng. Struct. Dyn.*, 19: 555–575, 1990.

[12] C.E. Wittich, T.C. Hutchinson, Shake table tests of unattached, asymmetric, dual-body systems, *Earthquake Eng. Struct. Dyn.*, 46(9): 1391–1410, 2017.

[13] J. Podany, An overview of Seismic Damage Mitigation for Museums, *International Symposium on Advances of Protection Devices for Museum Exhibits*, Beijing & Shanghai, China, April 13-15, 2015.

[14] I. Psycharis, M. Fragiadakis, I. Stefanou, Seismic reliability assessment of classical columns subjected to near source ground motions, *Earthquake Eng. Struct. Dyn.*, 42(14): 2061-2079, 2013.

[15] I. Calio, M. Marletta, Passive control of the seismic rocking response of art objects, *Engineering Structures*, 25(8): 1009-1018, 2003.

[16] A. Contento, A. Di Egidio, On the use of base isolation for the protection of rigid bodies placed on a multi-storey frame under seismic excitation, *Engineering Structures*, 62–63: 1–10, 2014

[17] M.G. Castellano, A.E. Pigouni, L. Marcolin, S. Infanti, S. Baggio, L. Berto, P. Faccio, I. Rocca, A. Saetta, Testing of the seismic isolation system for the bust of Francesco I d'Este in Modena, Italy, *Proceedings of 10th international conference on Structural Analysis of Historical Constructions (SAHC 2016)*, Leuven, Belgium, September 13-15, 2016.

[18] YY. Ishiyama, Motions of rigid bodies and criteria for overturning by earthquake excitations, *Earthquake Eng. Struct. Dyn.*, 10(5):635–650, 1982.

[19] N. Vlachos, S. Diamantopoulos, M. Fragiadakis, Seismic response assessment of artefacts freestanding on a solid pedestal. *4th Hellenic National Conference on Earthquake Engineering and Technical Seismology*, Athens, 5-7 September, 2019.

EURODYN 2020
XI International Conference on Structural Dynamics
M. Papadrakakis, M. Fragiadakis, C. Papadimitriou (eds.)
Athens, Greece, 23–26 November 2020

A MACHINE LEARNING APPROACH TO NONLINEAR RESPONSE ANALYSIS OF STRUCTURES

Panagiotis Georgakis[1], Manolis Georgioudakis[2], and Michalis Fragiadakis[2]

[1] School of Civil Engineering
National Technical University of Athens
GR 15780, Zografou Campus
e-mail: pgeorgakis@hotmail.com

[2] School of Civil Engineering
National Technical University of Athens
GR 15780, Zografou Campus
{geoem, mfrag}@mail.ntua.gr

Keywords: nonlinear response history analysis, machine learning

Abstract. *Nonlinear response history analysis (NRHA) is the most accurate seismic performance assessment method but it can be computationally intensive when it is applied to multi degree of freedom (DOF) structural systems. Machine learning techniques have gained increasing interest in engineering fields and can consist a powerful tool for reliable predictions with their ability to quickly and accurately identify trends or patterns through experimental or artificially generated data. In this study, we propose a robust machine learning pipeline to estimate the nonlinear response analysis of multi-DOF systems in terms of their maximum displacement/ductility aiming to eliminate the computational cost of the NRHA analysis. A pulse extraction process is used to quantify the wavelet parameters of a ground motion records which, along with the material parameters of the structural system consist the training data set. It is shown that adequate predictions were obtained through the validation of various benchmark structures which can act as a reference tool for an engineer in practice.*

1 INTRODUCTION

Nonlinear response history analysis (NRHA) is the most realistic seismic performance assessment tool of structures which requires the use of recorded acceleration time-histories as input into numerical simulations. Evidently, it can be computationally intensive when it is applied to multi degree-of-freedom (DOF) structural systems, particularly when dealing with parametric studies or/and incremental dynamic analyses. Different techniques have been proposed in the literature to reduce the computational cost of such analyses e.g. record simplification, record down-sampling, modified inverse Fourier transform, to name a few.

Machine learning (ML) techniques are constantly gaining increasing interest in engineering fields [1] and can consist a promising tool for reliable predictions with their ability to quickly and accurately identify trends or patterns through experimental or artificially generated data. In this study, we propose a robust machine learning pipeline to estimate the nonlinear response analysis of multi-DOF systems in terms of their maximum displacement/ductility aiming to eliminate the computational cost of the NRHA analysis. A pulse extraction process is used [2] to quantify the wavelet parameters of a ground motion records which, along with the material parameters of the structural system consist an adequate training data set. The applicability and efficiency of the proposed approach is demonstrated first in a single-DOF oscillator that is used as a benchmark example. A comparison study between various ML regression models, is followed by, in order to choose the efficient ML technique that will be used for the training process. It is shown that adequate predictions were obtained through the validation of various single-DOF benchmark structures which can act as a reference tool for an engineer in practice.

2 PULSE EXTRACTION OF NEAR-FIELD GROUND MOTIONS

Near-field ground motion records are characterized by dominant pulses in the ground velocity time histories, as well as high frequency content in acceleration time histories, especially at sites located in the forward direction of the fault rupture (directivity effects) [3]. The investigation of the ability to compose a near-field ground motion record with its pulse simulations [4] is a topic of great interest in the research community. Many researchers have proposed mathematical models for the representation of near-field ground motions mainly based on underlying wavelets. Among them, the model proposed by Mavroeidis and Papageorgiou (M&P) [2] introduced one of the most important pulse representation methods, that consists a mathematical representation of ground motion movements relying on designing a complex wavelet (based on Gabor wavelet). Gabor wavelet is characterized by four principal parameters (A, f_p, γ, ν), the most important of them is the pulse frequency f_p the calculation of which is based on the convolution spectrum. The analytical expression of the Gabor wavelet is given as follows:

$$f(t) = Ae^{-(2\pi\frac{f_p}{\gamma})^2 t^2} \cos(2\pi f_p t + \nu)$$

where:

A: is the amplitude
f_p: is the prevailing frequency
γ: is the oscillatory character ($\gamma > 1$)
ν: is the phase angle

However, this wavelet has a significant disadvantage, due to the existence of the exponential component that prevents the development of closed solutions for the response of single-stage

systems. To this end, M&P improved this model by allowing the development of closed solutions for estimating response spectra and determining spectral characteristics in Fourier form. This improved wavelet has the same parameters as the Gabor wavelet [5] and its analytical expression is given as follows:

$$f(t) = 0.5A\left[1 + \cos\left(2\pi\frac{f_p t}{\gamma}\right)\right]\cos(2\pi f_p t + \nu)$$

Natural ground motion records may consist of more than one discrete pulses. The pulse extraction process adopted in this study combines the use of the wavelet by M&P for the efficient representation of directional pulses along with the determination of each wavelet parameters. This process allows the identification and the output of all pulses located in the range of medium and high periods. If all extracted pulses are superimposed, a simulation of the entire ground motion can be produced (
Figure 1). The characteristics of the wavelets are determined by their optimal adjustment (maximum correlation) in the velocity response spectrum of each ground motion record.

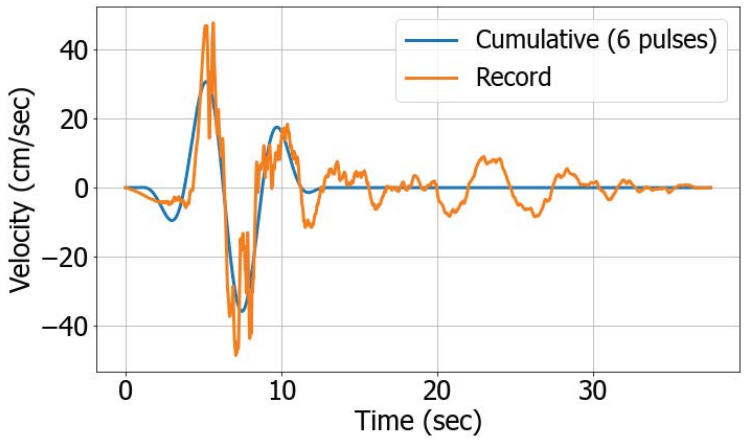

Figure 1: Cumulative velocity (6 pulses representation) of a ground motion record.

3 CASE STUDY: BILINEAR OSCILLATOR

The efficiency of the proposed approach is demonstrated in a single-DOF oscillator described by a hysteretic material model (uniaxial bilinear material with kinematic hardening) defined with four material parameters (fundamental period T, damping ratio ζ, yield force F_y and hardening ratio k). A database was generated consisting of 387 near-field ground motions records (distance from the rapture < 60 km), obtained from the Next Generation Attenuation for Western US (NGA-West2) (PEER 2017) [6]. The material parameters of the single-SDOF oscillator were adopted to artificially create a dataset using a range of values as shown in Table 1. For each ground motion of the database a total of 625 nonlinear history response analysis were conducted and the maximum displacement (u_{max}) along with maximum force ($F_{s,max}$) of the SDOF oscillator are obtained creating the dataset of outcomes.

Variable	Lower Bound	Upper Bound	Step
T [s]	0.1	0.9	0.1
ζ	0.01	0.1	0.01
F_y [% of SDOF mass]	0.1	0.9	0.1
k	0.1	0.9	0.1

Table 1: Lower, upper bound and step values for SDOF bilinear oscillator.

In order to avoid the nonlinear response analysis for a given ground motion record, two machine learning models are trained. The parameters of six pulses that represent each record along with the parameters of the bilinear material model consist the input data, while u_{max} and $F_{s,max}$ consist the output data of the two ML models, respectively. Each ML model is treated as a regression problem. A final subset of 337 records from the database with their corresponding pulse extraction parameters, were used for the training process of each ML model. The rest of 50 records were used to evaluate the performance of each ML model.

Choosing the proper machine learning algorithm for predicting purposes is not always a straightforward procedure, mainly depending on the inherent characteristics of the problem to solve. Thus, for each ML model a comparison study was elaborated between four regression ML algorithms (linear regression, extreme gradient boosting regressor – XGBoost, random forest regressor and bagging regressor). The root mean square error (RMSE), i.e. error between the tested (u_{max} / $F_{s,max}$) and predicted value ($\hat{u}_{max}$ / $\hat{F}_{s,max}$), as well as the mean absolute error (MAE) ware adopted as measures of performance of the machine learning algorithms. Table 2 shows the RMSE value of each of the four machine learning algorithms. It is shown that all of the four algorithms exhibit more or less the same performance with the random forest regressor to perform best in both cases. The tested vs predicted values of each machine learning algorithm are depicted in scatter plots of Figure 2.

	RMSE		MAE	
Model	u_{max}	$F_{s,max}$	u_{max}	$F_{s,max}$
Linear Regression	7.73E-04	8.93E-02	4.30E-04	5.80E-02
XGBoost	8.20E-04	5.66E-02	4.29E-04	4.46E-02
Random Forest	7.67E-04	5.63E-02	4.65E-04	4.22E-02
Bagging	8.55E-04	5.82E-02	5.12E-04	4.24E-02

Table 2: RMSE of the four machine learning algorithms.

The XGBoost regressor was selected as a compromise between the performance and the robustness of the algorithm, in order to further investigate the importance of each feature of the ML models. Figure 3 shows the ten most important features of the XGBoost regressor with its score. It is clearly shown the first three pulses amplitudes (A_1, A_2 and A_3), as well as F_y have an important role in the predictive performance of both ML models. The performance of each machine learning algorithm by fine tuning the number of the most important features is shown in Figure 4. It is shown that XGBoost outperforms the other three algorithms in all cases. In addition, it is worth noticed that the performance of linear regression model remains relatively stable even though the number of important features are high, because of the inability to represent the inherent nature of the problem due to its nonlinearity.

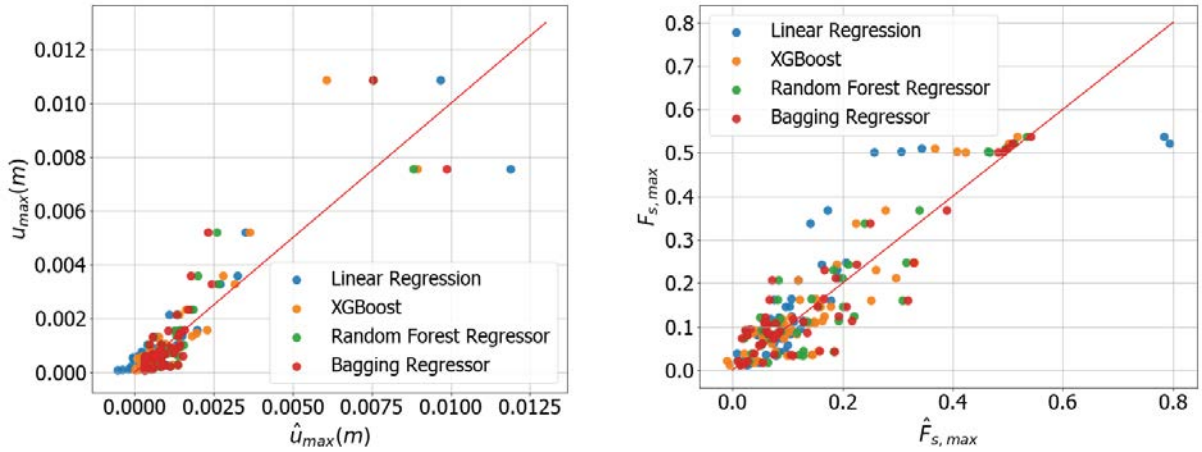

(a) (b)

Figure 2: Scatter plots of various ML algorithms for (a) u_{max} and (b) F_{smax} model.

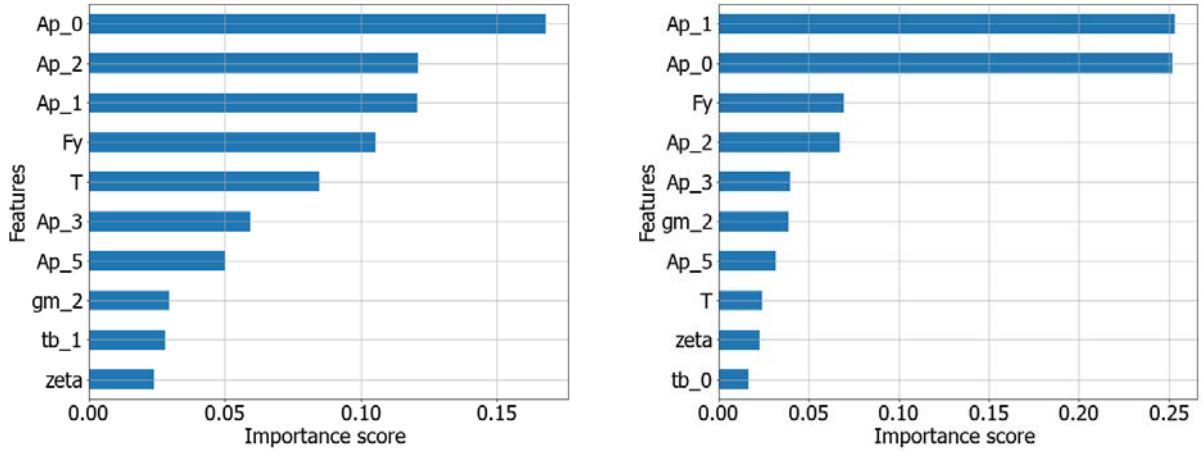

(a) (b)

Figure 3: Comparison of the feature importance for XGBoost regressor for (a) u_{max} and (b) F_{smax} model.

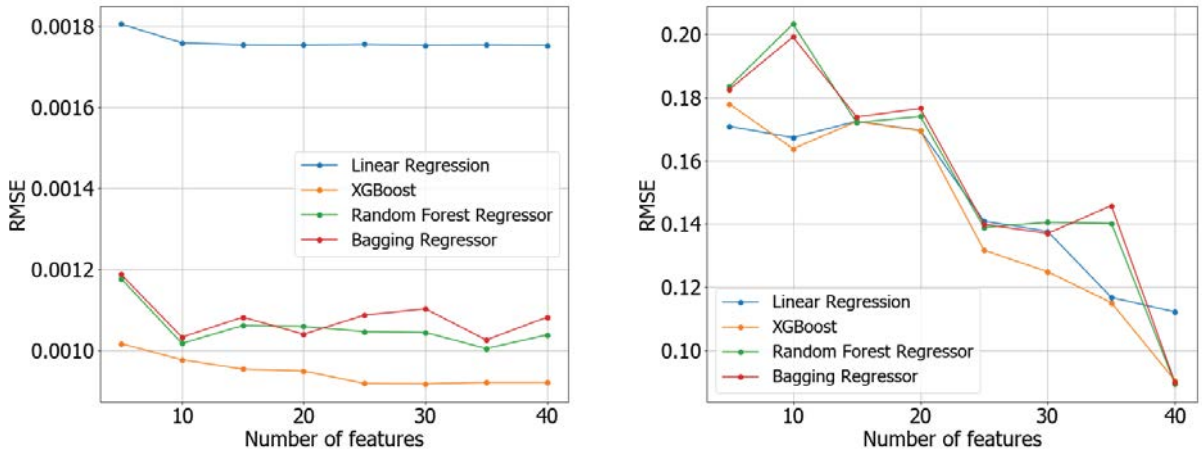

(a) (b)

Figure 4: Comparison of number of features vs RMSE of various ML algorithms for (a) u_{max} and (b) F_{smax} model.

4 CONCLUSIONS

We propose a robust machine learning pipeline to estimate the nonlinear response analysis of multi-DOF systems in terms of their maximum displacement/ductility aiming to eliminate the computational cost of the NRHA analysis. A pulse extraction process is used to quantify the wavelet parameters of a ground motion records which, along with the material parameters of the structural system consist an adequate training data set. The applicability and efficiency of the proposed approach is demonstrated first in a single-DOF oscillator that is used as a benchmark example. A comparison study between various ML regression models shown that XGBoost regressor can be selected as a compromise between the performance and the robustness. It is shown that the performance of linear regression model remains relatively stable even though the number of important features of the ML regression models are high, due to the inability in representation of the nonlinear inherent nature of the problem.

REFERENCES

[1] H. Salehia and R. Burgueñoa, Emerging artificial intelligence methods in structural engineering, *Engineering Structures*, **171**, 170–189, 2018.

[2] G.P. Mavroeidis and A.S. Papageorgiou, A Mathematical Representation of Near-Fault Ground Motions, *Bulletin of the Seismological Society of America*, **93**(3), 1099–1131, 2003

[3] V. Kardoutsou, I. Taflampas and I.N. Psycharis, A New Pulse Indicator for the Classification of Ground Motions, *Bulletin of the Seismological Society of America*, **107**(3), 1356–1364, 2017.

[4] C. Repapis, P. Mimoglou, V. Dimakopoulou, I.N. Psycharis, I.M. Taflampas, Efficient strong motion duration of pulse ‐ like records for nonlinear structural analyses, *Earthquake Engineering and Structural Dynamics*, **49**(5), 479–497, 2020.

[5] D. Gabor. Theory of communication. *Journal of the Institution of Electrical Engineers – Part III: Radio and Communication Engineering*, **93**(26), 429–457, 1946.

[6] PEER (Pacific Earthquake Engineering Research Center). 2017. “Shallow crustal earthquakes in active tectonic regimes.” Accessed August, 2020. http://ngawest2.berkeley.edu.

EURODYN 2020
XI International Conference on Structural Dynamics
M. Papadrakakis, M. Fragiadakis, C. Papadimitriou (eds.)
Athens, Greece, 23–26 November 2020

IDENTIFICATION OF A STOCHASTIC PROCESS MODELING THE STIFFNESS OF THE VOCAL FOLDS FOR A VOICE PRODUCTION MODEL REPRESENTED BY A NEURAL NETWORK

E. Cataldo [1], C. Soize [2], R. L. Silva [1] and J. M. M. da Silva [1]

[1]Universidade Federal Fluminense, Telecommunications Engineering Departament and Graduate program in Telecommunications Engineering,
Rua Mário Santos Braga, S/N, Centro, Niteroi, RJ, CEP: 24020-140, Brazil
e-mail:{ecataldo,rlima,jmarcos}@id.uff.br

[2] Université Gustave Eiffel, Laboratoire Modelisation et Simulation Multi Echelle, MSME UMR 8208 CNRS, 5 Bd Descartes, 77454 Marne-La-Vallée, France
e-mail: christian.soize@univ-eiffel.fr

Keywords: Stochastic modeling, Identification of stochastic processes, voice production, mechanical models, jitter

Abstract. *The aim of this paper is to use Artificial Neural Networks (ANNs) to solve a nonlinear inverse stochastic problem to identify a random process related to the stiffness of the vocal folds in a voice production model. The identification will be performed using the power spectral density function associated with the random process, which has two control parameters. For each pair of these parameters, realizations of the glottal signal are generated. This acoustic pressure signal is obtained just after the air passing through the vocal folds, which is filtered and amplified by the vocal tract generating the voice. As the stiffness of the vocal folds model is taken as a stochastic process, jitter phenomenon, characterized by the deviations of the glottal time interval in relation to a mean value, is present in each realization of the glottal signal. For each glottal signal obtained a set of measures can be extracted and this set is used as the input for an ANN constructed to solve the corresponding inverse problem.*

1 INTRODUCTION

The phonatory system is one of the most important sensory structures and, therefore, it is one of the main agents of the language. The voice has a fundamental importance in the transmission of knowledge, feelings and emotions. Over the years, researchers have had interests in some aspects of the human voice due to its peculiarities and actions in society

The phonation occurs when the glottis closes (adduction) and a column of air, expelled from the lungs, forces passing through the vocal folds. Then, pulses of air are produced forming a (quasi-)periodic acoustic pressure signal called the glottal signal, which goes into the vocal tract (portion that goes from the glottis up to the mouth), where it is filtered, amplified, and finally radiated by the mouth generating the sound we hear.

The glottal signal is not exactly periodic due to small deviations in relation to a mean value of the glottal time interval called jitter. This random phenomenon has practical applications as the identification of pathologies from the vocal folds, identification of voice aging, voice recognition, speaker recognition and other [1, 2, 3]. There are different objective ways to measure jitter as, for example, the absolute jitter and the local jitter. In general, values of local jitter between 0.1% and 1.04% indicate normal voice, that is, a voice that is not symptomatic of a pathology [4].

In this work, it is taken into account a simplified mechanical one-mass-spring-damper model for the generation of jitter, which considers the unification of two deterministic models named Qureshi model [5] and Gomes Model [6], and the stiffness is modelled as a stochastic process. Then, an artificial neural network (ANN) is trained to substitute the non-linear mapping from voice features to some control parameters of the numerical model. Random realizations of voice signals are obtained from the model and features are extracted from each realization. The features are used as inputs for the ANN and the corresponding inverse stochastic process is solved; that is, the stochastic model of the stiffness is identified using two control parameters of its power spectral density.

2 UNIFIED STOCHASTIC MODEL

The idea is to construct a stochastic model for the vocal folds based on the source-filter theory, where the source, the glottal signal, is obtained through a mathematical/mechanical model. However, before discussing the stochastic model, the corresponding deterministic model, also original, is constructed based on two other models from the literature, named: the Qureshi model [5] and the Gomes model [6]. Both models generate the glottal signal, the source, and the final idea is to consider the best characteristics of each model to construct the proposed unified deterministic model.

The sketch considered for the unified model is the one proposed by Qureshi and reproduced in Fig. 1: The movement of each vocal fold is given by a rotary motion about its support point

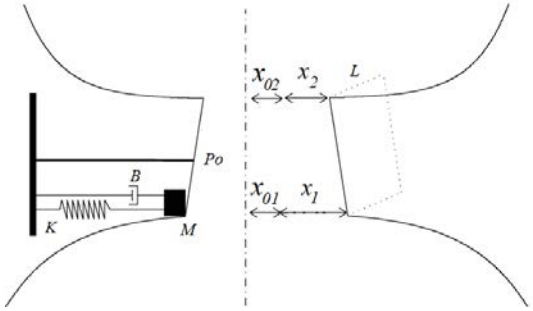

Figure 1: Sketch of the Qureshi model.

P_0. A single mass-spring system with mass M, spring constant K, and damper, with damping constant B, is attached to the glottis at its entrance. The model is assumed to be symmetric about its central line so that the left side of the vocal fold is the same as its right one. The glottal entry displacement is represented by $x_1(t)$, while $x_2(t)$ corresponds to the glottal exit displacement. The vertical component of the fulcrum point divides the glottis in two parts that are assumed to have the same length. The characteristic of a nonlinear damping is introduced in the model, according to the Gomes model, and the equation of the motion for a single vocal fold is described by

$$M\ddot{x_1}(t) + B(1 + \eta\, x_1^2(t))\, \dot{x}_1(t) + K(t)\, x_1(t) = P_g(t)\,. \tag{1}$$

The mean glottal pressure P_g is given by

$$P_g(t) = \frac{2\tau P_{sub}\dot{x}_1(t)}{K_t(x_0 + x_1(t))}\,, \tag{2}$$

where P_{sub} is the subglottal pressure, τ is the glottal time delay, x_0 is the mean position of oscillation of the vocal folds in the middle of the glottis, η is the nonlinear coefficient damping, and k_t is the coefficient of transglottal pressure.

Considering x_{01} and x_{02} the rest position, pre-phonation, of the vocal folds in the glottal input and output, respectively, L the width of the vocal folds, and $x_2(t) = -r(x_1(t) - x_0)$, according to [7], the glottal flow $u_g(t)$ is given by Eq. 3:

$$u_g(t) = \sqrt{\frac{2P_{sub}(t)}{k_t\,\rho}} A_{out}(t)\,, \tag{3}$$

where ρ is the air density and $A_{out}(t)$ is given by Eq. 4:

$$A_{out}(t) = \begin{cases} 2L(x_{02} + x_2(t))\,, & x_2(t) > -x_{02} \\ 2Lx_{02}\,, & \text{otherwise}\,. \end{cases} \tag{4}$$

After generating $u_g(t)$, the convolution with the filter (vocal tract) should be performed to produce the sound we hear. However, this work is concentrated in the glottal signal. The next step is the construction of the stochastic model of the vocal folds based upon the unified deterministic model proposed here.

The objective is to vary the frequency of the voice signal. As the mass is fixed, the stiffness is considered as a stochastic process following some ideas proposed by [8] with the corresponding changes, because the model created here does not consider the coupling between the vocal tract and the vocal folds.

Let E be the mathematical expectation. The stochastic process $K(t)$, indexed by $\mathbb{R}$, is constructed according to the properties defined as follows.

1. For all t, $0 < k_0 \leq K(t)$, where k_0 is a positive constant independent of t.

2. $K(t)$ is a non-Gaussian stationary stochastic process such that $E\{K(t)^2\} < +\infty$ for all t (second-order stochastic process), for which its mean function (that is independent of t) is written as $E\{K(t)\} = \underline{K} > k_0 > 0$, and which is assumed to be mean-square continuous in order to guaranty the existence of a power spectral measure.

A representation of the stochastic process K is chosen as described by

$$K(t) = K_0 + (\underline{K} - K_0)(\bar{z} + Z(t))^2, \tag{5}$$

where $\{Z(t), t \in \mathbb{R}\}$ is a second-order Gaussian stochastic process, centered, mean-square continuous, stationary and ergodic, physically realizable, and $\bar{z}$ is a constant such that for all real t, $E\{(\bar{z}+Z(t))^2\} = 1$, $E[K(t)] = \underline{K}$, and $E\{(\bar{z}+Z(t))^4\} < +\infty$, because $E\{K^2(t)\} < +\infty$. Then, $Z(t)$ can be seen as the response of a linear filter such that $Z(t) = (h * N_\infty)(t)$, where N_∞ is the centered Gaussian white noise with power spectral density $S_{N_\infty} = \frac{1}{2\pi}$ and where the frequency response function of the filter is the Fourier transform given by Eq. 6:

$$\widehat{h}(\omega) = (\mathcal{F}\{h\})(\omega) = a/(i\omega + b)\,. \tag{6}$$

The stochastic process $Z(t)$ can be obtained solving the linear Itô stochastic differential equation that is written as Eq. 7:

$$dY(t) = -b\,Y(t)\,dt + a\,dW(t)\ \ ,\ \ t > 0\,, \tag{7}$$

with initial condition $Y(0) = 0$ and where W is the normalized Wiener stochastic process with real value, indexed by $[0, +\infty]$. When $t_0 \to +\infty$, the stochastic process $\{Y(t), t > t_0\}$ goes asymptotically to the stationary stochastic process Z. Taking a sufficiently large value of t_0, Eq. (7) is used to generate realizations of the stochastic process $Z(t)$. Following Eq. (1), and considering the displacement of the vocal folds as a stochastic process, $x_1(t)$ becomes $X_1(t)$, and the dynamics of the vocal folds is then given by the stochastic differential equation Eq. 8:

$$M\ddot{X}_1(t) + B\,(1 + \eta\,X_1^2(t))\,\dot{X}_1(t) + K(t)\,X_1(t) = P_g(t)\ . \tag{8}$$

All the other equations related to the unified deterministic model should be rewritten substituting $x_1(t)$ and $x_2(t)$ by $X_1(t)$ and $X_2(t)$, respectively. With these modifications, the voice signals generated will indicate the presence of jitter and to quantify its level present in each voice signal, some measures are calculated.

2.1 MEASURES

For each glottal signal, measures will be extracted. They are: four jitter measures, HNR (harmonic richness fator), dH12 (difference between the first and second harmonics), mean and standard variation of the fundamental frequency, the 10 first hamonics and two time measures relating the opening time and the closing time of the vocal folds with the total glottal interval.

Jitter measures and frequency measures will be discriminated in the following.

2.1.1 Jitter measures

First of all, four jitter measures are considered: absolute jitter, relative jitter, jitter rap and jitter ppq5, defined in the following.

- Absolute Jitter (Jit_{abs}): it is the cycle-to-cycle variation of the fundamental frequency, i.e, the average absolute difference between consecutive periods, in seconds, given by

$$Jit_{abs} = \frac{\sum_{i=1}^{N-1} |T_{i+1} - T_i|}{N-1}, \tag{9}$$

  in which T_i is the time interval of each complete glottal cycle and where N is the number of intervals considered.

- Relative Jitter (Jit_{rel}): it is the average absolute difference between consecutive glottal intervals, divided by the average period, and given by

$$Jit_{rel} = \frac{Jit_{abs}}{\frac{\sum_{i=1}^{N} |T_i|}{N}}. \tag{10}$$

  In general, relative jitter values between 0.1% and 1.04% are considered as normal voices indicator, without pathological characteristics.

- Rap Jitter (Jit_{Rap}): is the three point period perturbation quotient jitter.It is computed as the average absolute difference between a period and the average of it and its two closest neighbors divided by the average period.

- PPQ5 Jitter (Jit_{PPPQ5}): is the five point period perturbation quotient jitter. It is computed as the average absolute difference between a period and the average of it and its four closest neighbors divided by the average period.

2.2 Frequency measures

First is $H1 - -H2$ or $dH12$ which is the difference of the first and second harmonics of the glottal frequency spectrum waveform in decibel. Another similar parameter is harmonic richness factor (HRF), which is defined as the ratio between the sums of the amplitudes of harmonics above the fundamental frequency and the magnitude of the fundamental frequency or the first harmonic in decibels. It is shown by the Eq. 11:

$$HRF = \frac{\sum_{r \geq 2} H_R}{H_1} \tag{11}$$

Here H_R represents the magnitude of the rth harmonic.
The third measure considered is the magnitude of the first 10 harmonics.

3 SIMULATIONS

In this section, simulations with the stochastic model proposed are performed. The variation of the parameter a, from Eq. 7, is considered. All the other parameters will be fixed and their values are given in Tab. 1.

Parameters	Values
M	$0.476\,g$
B	$100\,Nsm^{-1}$
η	5000
Pm	$800\,Pa$
Kt	1.1
τ	$0.001\,s$
x_0	$0.01\,cm$
x_{01}	$0.001\,cm$
x_{02}	$0.001\,cm$
ρ	$1.15 \times 10^{-2}\,kgm^{-3}$
L	$1.4\,cm$
b	1000000
k_0	$200\,Nm^{-1}$

Table 1: List of parameters and their values.

For the simulations, it is important to perform a convergence analysis, mainly for the solution of the Itô stochastic differential equation used to generate realizations of $K(t)$. Then, asymptotically stationary and ergodic solutions have been considered and, the mean value and the second moment of $K(t)$ have been estimated by

$$E\{K(n)\} = \lim_{n\to+\infty} \overline{K}(n) \quad , \quad \overline{K}(n) = \frac{1}{n}\sum_{i=0}^{n} K(i)\,; \tag{12}$$

$$E\{K^2(n)\} = \lim_{n\to+\infty} \overline{K}^2(n) \quad , \quad \overline{K}^2(n) = \frac{1}{n}\sum_{i=0}^{n} K^2(i)\,. \tag{13}$$

Figure 2 show three cases of glottal signals considering different levels of jitter, taking into account different values of a, showing that it is possible to generate the phenomenon with the model proposed.

Table 2 shows different values of jitter, and two corresponding measures, considering different values for a, in the the case of normal voices, without pathological characteristics (the first two values of a) and also three cases of voices with pathological characteristics (the last three values of a).

The glottal interval, that is, the total time of a complete glottal cycle, is a random variable and its inverse, $F_0 = \frac{1}{T}$, is the random variable called the fundamental frequency.

4 INVERSE PROBLEM WITH AN ARTIFICAL NEURAL NETWORK

The methodology proposed uses Artificial Neural Networks (ANN) to map from the features extracted of the glottal signal to the two parameters of the power spectral density.

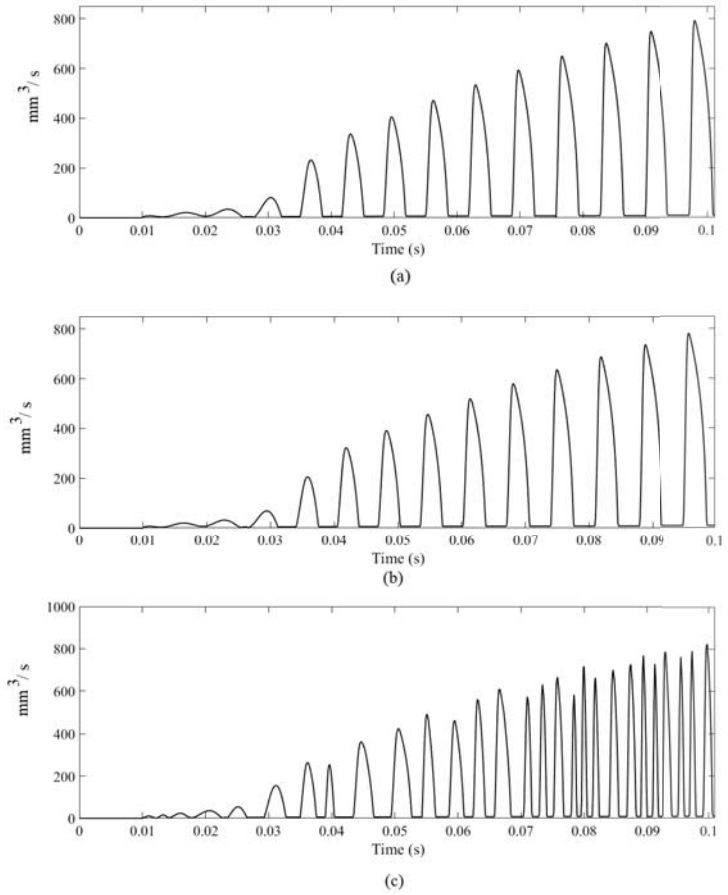

Figure 2: (a) Glottal signal without jitter $a = 0$, (b) Glottal signal with $Jit_{loc} = 0.5\%$ and (c) Glottal signal with $Jit_{loc} = 6.13\%$.

The stochastic process $U_g(t)$, the glottal signal, is represented in this work as a non-linear mapping of a vector $[a, b]$ through the stochastic model presented. To invert this mapping, using ANNs, it is required to extract a vector of features from $U_g(t)$ for which the ANN can learn to estimate the random vector $[a, b]$, according to Eq. 6.

The inputs of the constructed neural network, corresponding to the features extracted from the glottal signal, will then be: (i) the mean value of the fundamental frequency; (ii) the standard deviation of the fundamental frequency, (iii) dH_{12}, HRF, the four measures of Jitter (Absolute, Local, Rap and PPQ5), the values of the first **ten** harmonics and two time coefficients called $Open_1$, defined as the ratio between the opening time interval of the vocal folds and the total glottal interval, and $Open_2$ defined as the ratio between the closing time interval of the vocal folds and the total glottal interval. There are 22 parameters to be considered for the ANN. Clearly, some of these parameters give redundant information.

The methodology applied to solve the inverse problem can be divided in two parts: the first part consists in producing a training set for the ANN, by solving the direct problem; i.e, given a and b, parameters from the spectral density of the stochastic process related to the stiffness K, it is possible to generate realizations of the glottal signal and to extract all the parameters. The second part corresponds to the inverse problem; i.e, given the features extracted from the glottal signal, values from a and b are obtained.

The methodology is described in the following:

a	*Absolute Jitter*	*Local Jitter*
160	2.27×10^{-5}	0.34%
200	3.25×10^{-5}	0.50%
500	1.72×10^{-4}	2.70%
700	1.88×10^{-4}	3.00%
1000	3.78×10^{-4}	6.13%

Table 2: Absolute and local *jitter for voices without pathological characteristics and also with pathological characteristics.*

1. A set is created containing 10000 realizations of the pair (a, b) and the mathematical/mechanical model of the vocal folds is used to generate the glottal pulse; that is, 10000 realizations of the glottal pulse are obtained. For each realization, the set of features are extracted.

2. An artificial neural network is created, from the last item, in order to obtain more realizations of the glottal signal. The ANN created is a A feedforward multi-layer perceptron (MLP) network and the Levenberg-Marquardt optimization algorithm is used during learning phase. It solves the direct problem and uses 70% of the realizations for training, 15% for testing and 15% for validation. With the ANN created 30000 realizations are obtained and this is used for the extension of the results of the corresponding mechanical model. The inputs a and b are normalized because the scale of these values are very different. Considering $\mathbf{x}$ the vector containg the values x_i corresponding to the input (a or b).

3. It is important to normalize the inputs because the scale of their values are much different. The idea is to normalize all the values inside the interval $[-1, 1]$. Considering min_x and max_x the minimum and the maximum of the range of the parameter x, the values of x normalized, denoted by x_{norm} is given by Eq. 14:

$$\mathbf{x_{norm}} = \frac{(x - min_x)(2)}{max_x - min_x} - 1\,. \tag{14}$$

4. Then, an ANN is constructed for solving the corresponding inverse stochastic problema. Again, a feedforward multi-layer perceptron (MLP) network is constructed and the Levenberg-Marquardt optimization algorithm is used during learning phase. The training set of realizations is divided in three parts: 70% of the realizations are used for training, 15% for testing the network performance during training and 15% for the validation check. As the scale of the input/output parameters of the ANN are very different, a normalization is performed in all the inputs so that any realization of the training set lies between -1 and 1. The 30000 realizations of the vector of features were used as input to obtain 30000 realizations of the output; that is, realizations of pair (a, b).

   All the simulations were performed using the Matlab® Neural Networks Toolbox.

5 RESULTS

An example will be presented at first.

1. The values of a and b obtained were such that the variation of a was from 50 up to 4500, with step 10, and the variation of b was from 100000 to 1500000, with step 2000. These

values were considered as inputs for the ANN created to solve the direct problem; that is, after having been obtained values with the corresponding mechanical model. With this extension, more values of the features of the glottal signal could be obtained and it is very important to train the ANN.

2. Then, a new ANN was created to solve the corresponding inverse problema. The values obtained from the last item were used as inputs for this new ANN.

3. A confusion matriz was constructed and shown in Fig. 3:

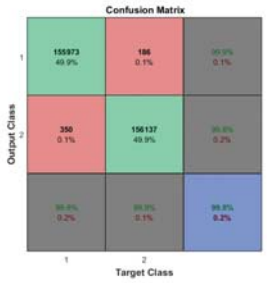

Figure 3: Confusion matrix.

4. Some tests were performed with specific values. The Tab. 3 shows some results:

position	$(\mathbf{a}, \mathbf{b})desired$	$(\mathbf{a}, \mathbf{b})obtained$
200	$(50, 498000)$	$(70, 498750)$
1000	$(50, 696000)$	$(70, 699900)$
5000	$(120, 284000)$	$(120, 277940)$
20000	$(330, 842000)$	$(330, 841890)$

Table 3: Absolute and local *jitter for voices without pathological characteristics and also with pathological characteristics.*

In the following, an experimental case is performed.

An audio produced by a woman, of a vowel /a/, is used. At first, using an inverse filtering method (the so-called IAIF) the corresponding glottal signal is obtained. Then, features of the glottal signal are obtained and submitted to the ANN created previously. And the results obtained are in the following: $a = 450$ and $b = 1500000$.

More examples are necessary and clearly there are still some limitations because the experimental signal can give parameters far from the ones trained by the ANN.

6 CONCLUSIONS

A stochastic model to generate voiced sounds with jitter has been proposed based on the unification of two deterministic models from the literature and considering one parameter as a stochastic process, the stiffness of the vocal folds. Two control parameters have been considered for the corresponding power spectral density and they were identified through an Artificial Neural Network created for solving the corresponding inverse stochastic problem.

Considering simulated data, the ANN solved the problem in a very satisfactory way and the challenge is to use this idea to experimental data. An example is presented with experimental data showing that it is possible to do it.

It is important to note that the features extracted from the experimental data should be near the range covered by the ANN and sometimes it can not be possible. Then, the next challenge is to upgrade the model and the ANN, and also the algorithm, to create conditions for identifying parameters corresponding to more general experimental data.

7 ACKNOWLEDGMENTS

This work was supported by CNPq.

8 CONFLICT OF INTEREST STATEMENT

The authors disclose any financial and personal relationships with other people or organisations that could inappropriately influence their work.

REFERENCES

[1] K. A. Wilcox, Y. Horii, Age and Changes in vocal jitter, *Journal of Gerontology*, **35(2)**, 194–198, 1980.

[2] L. Li, H. Saigusa, Y. Hakazawa, A pathological study of bamboo nodule of the vocal fold, *Journal of Voice*, **24(6)**, 738–741, 2010.

[3] L. Mendonza, M. Vellasco, E. Cataldo, M. B. Silva, A. A. Apolinario, Classification of Vocal Aging Using Parameters Extracted From the Glottal Signal, *Journal of Voice*, **21(2)**, 157–68, 2014.

[4] D. Wong, R. M. Ito, B. N. Cox, I. R. Titze, Observation of perturbations in a lumped-element model of the vocal folds with application to some pathological cases, *The Journal of the Acoustical Society of America*, **89(1)**, 383–394, 1991.

[5] T. M. Qureshi, A one-mass physical model of the vocal folds with seesaw-like oscillations, *Archives of acoustics*, **36(1)**, 15–27, 2011.

[6] K. G. Lourenço, Modelagem, análise matemática e validação experimental in vitro da fonação. PhD Thesis, Universidade de Brasília, Brazil, 2013.

[7] I. R. Titze, The physics of small-amplitude oscillation of the vocal folds, *Journal of the accoustical society of America*, **83**, 1536–1552, 1988.

[8] E. Cataldo, C. Soize, Stochastic mechanical model of vocal folds for producing jitter and for identifying pathologies through real voices, *Journal of Biomechanics*, **74**, 126–133, 2018.

[9] P. Alku, Glottal wave analysis with Pitch Synchronous Iterative Adaptive Inverse Filtering, *Speech Communication*, **11 (2)(3)**, 109–118, 1992.

EURODYN 2020
XI International Conference on Structural Dynamics
M. Papadrakakis, M. Fragiadakis, C. Papadimitriou (eds.)
Athens, Greece, 23–26 November 2020

AIRSHIP GUST RESPONSE PROBABILISTIC MODEL CONSTRUCTION

F. Poirion[1] **and G. Mortchelewicz**[1]

[1]ONERA, Université Paris Saclay
poirion@onera.fr, guy.mortchelewicz@onera.fr

Keywords: Airship, Gust, Probabilistic surrogate, Karhunen Loeve.

Abstract. *In the context of random environment, time-domain simulation of structural responses is often necessary when the structure is nonlinear, but not only : when the structure is linear and the excitation modelled as a non-stationnary non-Gaussian process, Monte Carlo approaches are necessary to identify the probabilistic distribution of the output. In this paper we use a stochastic model developped for non-stationnary and non- Gaussian random processes. It is based on an empirical Karhunen-Loeve expansion of the process constructed from an available data basis. We study the particular case of linear structures: the Monte Carlo becomes particularely simple: one needs only to consider the construction of a low number of responses, corresponding to the deterministic eigen functions of the Karhunen-Loeve expansion, hence avoiding high number of calls to industrial codes. The KL expansion of the response is then obtained directly using these responses and the system output probabilistic characterization can be constructed through Monte Carlo simulation of the KL output model. This approach is used in order to quantify the effect of gusts on a future airship using a database obtained during a winter storm from which a model of vertical gusts isconstructed. Response comparisons for realistic and gusts and the one prescribed by national regulation requirements will be shown.*

1 INTRODUCTION

There exists today a new interest in airship exploitation as appears a need for a safe and sustainable solution that can deliver heavy cargo or personnel to remote communities that have no infrastructures. For instance the Flying Whales start-up has launched a 60 ton capacity airship project which size is unusual: 150 m long, 60 m large and 40 m height.

Figure 1: Flying Whale LCA60T airship project. Source: Flying Whales

New regulations had to be specified in order to certify such modern airships and among them was introduced one dedicated to gust. In the TAR (Transport Airship Regulation) the gust is modeled as an harmonic excitation and the question which arises is how will the airship response to real gusts, which exist within a turbulent wind field, compare to the regulation gust response. Real gusts are random phenomena which can be modeled as non-stationary and non-Gaussian processes. Therefore one needs to characterize the output of the airship to this random excitation. Airship is modeled as a coupled aerodynamic/structure system and due to the very low Mach number involved in airship flight the use of a linearized aerodynamic code is entirely justified. Nevertheless the response characterization goes through a complete Monte-Carlo approach since the input is non-stationary and non-Gaussian which can render the methodology numerically very expensive for high dimension structural models. We show that when the input process can be represented by its Karhunen Loeve expansion, the linearity of the numerical code allows to construct directly the Karhunen Loeve expansion of the response which can be used to generate samples used for constructing various estimators of the response. An illustration will be given on a simplified airship model which will be subject to real gusts identified in given wind measures.

2 PROBABILISTIC MODEL CONSTRUCTION OF OBSERVED SAMPLE PATHS

Three dimensional wind data are relatively scarce and existing gust databases contain insufficient samples in order to be relevant in a Monte Carlo procedure. An enrichment method will therefore be used in order to generate supplementary synthetic samples. This method, based on Karhunen Loeve expansion of stochastic process, is described in [10, 7]. We shall briefly recall the main ingredients.

Karhunen-Loève (KL) expansion provides a suitable framework for modeling a non-stationary scalar random process $X(t,\omega)$:

$$\forall t \in \mathcal{D},\ X(t) = \lim_{N\to+\infty} \sum_{\alpha=1}^{N} \sqrt{\lambda_\alpha}\, \xi_\alpha\, \phi_\alpha(t), \tag{1}$$

in which $\xi_1, \xi_2, \ldots, \xi_\alpha, \ldots$ are uncorrelated random variables given by

$$\xi_\alpha = \frac{1}{\sqrt{\lambda_\alpha}} \int_{\mathcal{D}} < X(t), \phi_\alpha(t) > dt, \tag{2}$$

where the λ_α and $\phi_\alpha(t)$ are the solutions of the integral equation

$$\int_{\mathcal{D}} R_X(t,t')\phi(t')dt' = \lambda\phi(t), \tag{3}$$

and where the limit in (1) is taken in the space $L^2(\Omega, \mathbb{R})$.

Let be given $\mathcal{N}$ measures $\{X^{(l)}(t_i)\ ;\ i = 1, ..., N\}\ ;\ l = 1, \mathcal{N}$ of a random phenomenon sample path. The first step to the KL expansion construction is to estimate the empirical autocorrelation of the underlying process X:

$$R(t_i, t_j) = \frac{1}{\mathcal{N}} \sum_{l=1}^{\mathcal{N}} X^{(l)}(t_i) X^{(l)}(t_j) \tag{4}$$

Solving the discretized eigenvalue problem (3) yields the λ_α and $\phi_\alpha(t_i)$, for $\alpha, i = 1, N$.

The second step is to construct the samples $\xi_\alpha^{(l)}$ using relation (2) which gives an explicit relation :

$$\xi_\alpha^{(l)} = \frac{1}{\sqrt{\lambda_\alpha}} \sum_{i=1}^{N} X^{(l)}(t_i)\phi_\alpha(t_i)\Delta t\ ;\ l = 1, \mathcal{N}\ ;\ \alpha = 1, N \tag{5}$$

where Δt is the sampling time step.

In order to be able to use the KL expansion for simulating the random process X, the last step is to identify the distribution of the random vector $\xi = (\xi_1, ..., \xi_N)$, which in the general case is not Gaussian. This multivariate distribution will be approximated by a Gaussian kernel density estimator :

$$\hat{f}_{\mathcal{N},h}(x) = \frac{1}{\mathcal{N} h^N (2\pi)^{N/2}} \sum_{\ell=1}^{\mathcal{N}} \exp \frac{(x - \xi^{(\ell)})^T (x - \xi^{(\ell)})}{2h^2} \tag{6}$$

where $\xi^{(\ell)}, \ell = 1, \mathcal{N}$ are the observed samples of random variable ξ.

Details on kernel density estimators construction can be found in the following references [3, 9, 8].

Simulation of a multivariate random variable ξ described by the kernel density (6) is straightforward:

- generate a random integer J uniformly distributed on $\{1, 2, ..., \mathcal{N}\}$
- generate a $\mathcal{N}$-dimensional normalized Gaussian random variable $\mathcal{G}$
- construct the sample $\xi = \xi^{(J)} + h \times \mathcal{G}$.

In practice, the approximation due to truncation of the KL expansion is evaluated considering the total energy $\int_{[0,T]} E(X(t)^2)dt$ of the process : $\int_{[0,T]} R_X(t,t)dt = \sum_\alpha \lambda_\alpha$, the relative error ϵ being then defined by:

$$\epsilon = \sum_{\alpha=1}^{N_T} \lambda_\alpha \; / \; \sum_{\alpha=1}^{\infty} \lambda_\alpha = \sum_{\alpha=1}^{N_T} \lambda_\alpha \; / \; \int_{[0,T]} R_X(t,t)dt \tag{7}$$

Numerically, the total energy can be determined from the empirical autocorrelation function of the N trajectories:

$$\int_{[0,T]} R_X(t,t)dt = \sum_{i=1}^{N} R_X(t_i,t_i)\Delta t_i$$

Finally one has to characterize the response of a system to a random excitation modeled as a KL expansion:

$$X(t,\omega) = \sum_{\alpha=1}^{M} \sqrt{\lambda_\alpha}\, \xi_\alpha(\omega)\, \phi_\alpha(t) \quad \rightarrow \quad H \quad \rightarrow \quad Y(t,\omega)$$

When the system is linear it is possible to use the input expression linearity to construct directly a probabilistic model of the system output.

3 RESPONSE OF A LINEAR DYNAMICAL SYSTEM TO KL EXCITATION

There exist many real-life systems which are described using industrial linear codes: in structures, aeronautics, etc. The use of such linear approximations of real structures and systems are still today mandatory in the conception phase or for optimization because high fidelity models are too CPU intensive. This is particularly true for probabilistic analysis based on Monte Carlo approaches. Even in the case of linear systems, there exist no analytic methods to characterize the system output when the excitation is modeled through a non-Gaussian non-stationary process. One has to go through numerical simulations in order to construct various statistical estimators.

Consider a linear system described through a differential equation

$$Y'(t) = A(t)Y(t) + X(t) \; ; \; Y(0) = Y_0 \; ; \; t \in [0,T]. \tag{8}$$

It is well known that its solution can be written

$$Y(t) = H(t,0)Y_0 + \int_0^t H(t,s)X(s)ds \tag{9}$$

where H is the resolvent matrix. Function H is the impulse response function and represents the linear system. It is generally obtained using an industrial code (Nastran, Marc, ...) and its derivation can be computationally expensive for high dimension models such as the ones encountered in aeronautics. When X is a general second order stochastic process defined on

a given probability space $(\Omega, \mathcal{T}, P)$, Monte Carlo approaches have to be used in order to construct statistical estimators of Y, and, even in a linear context, Monte Carlo based probabilistic analysis can become non practical for some applications. When X is approximated through a truncated KL expansion denoting $m_X(t)$ its expectation, relation (9) can be written,

$$Y(t,\omega) = H(t,0)Y_0 + \int_0^t H(t,s)m_X(s)ds + \sum_{\alpha=1}^{N} \sqrt{\lambda_\alpha}\xi_\alpha \int_0^t H(t,s)\phi_\alpha(s)ds, \ ; \ t \in [0,T] \quad (10)$$

The output characterization necessitates only $N+2$ calls of the linear codes, whith N generally less than 100 in order to construct the N deterministic response functions $\psi_\alpha(t) = \int_0^t H(t,s)\phi_\alpha(s)ds$, the initial condition and the mean excitation response. The probabilistic analysis is then achieved generating random linear combinations of these N functions.

4 AIRSHIP AEROELASTIC MODEL

The illustrations given in the following involve an airship model of dimensions $150 \times 60 \times 44$ meters and a weight of 60 tons. The cruise flight altitude is 1000 meter at a speed of 100 km/h. A crude finite element model, sufficiently meaningful for the aeroelastic illustration is used and is represented on figure 2.

The coupled system airship/aerodynamic forces is modeled using the code CAPRI [4, 5] which uses a linearized aerodynamic model based on the doublet lattice method [1]. The use of a linearized model is totally justified for an airship due to the very low Mach number involved: Mach 0.086. The aerodynamic force due to a gust is given in the frequency domain by the relation:

$$\hat{F}(\omega) = T(\omega) \times \frac{\hat{W}(M,\omega)}{V} \quad (11)$$

where V is the airship speed, $\hat{W}(M,\omega)$ the Fourier transform of a gust and $T(\omega)$ the transfer function calculated by the CAPRI code for a set of frequency values. Using a rational approximation of the transfer function allows to build a time domain representation of the force, solving a differential equation [6]. What is considered for certification is the charge factor defined by:

$$N(t) = \frac{F(t)}{Mg}, \quad (12)$$

where M is the airship mass and g the standard gravity.

5 GUST MODELS

The transportation airship requirements imply that the airship structure integrity should not be affected when the airship encounters an isolated gust defined by the following expression

$$v_g = \frac{V_g}{2}(1 + \cos(\pi \frac{x - x_g}{L_g})) \text{ for } |x - x_g| \leq L_g \quad (13)$$

where v_g is the gust speed at the point of coordinate x, x_g is the coordinate of the gust center, V_g is the maximal gust speed located at point x_g, L_g is the gust half length.

Such a gust is of course not representative of real gusts as it will be shown later on. Therefore it is interesting to compare the real gust and the regulation gust effects on the structure. First

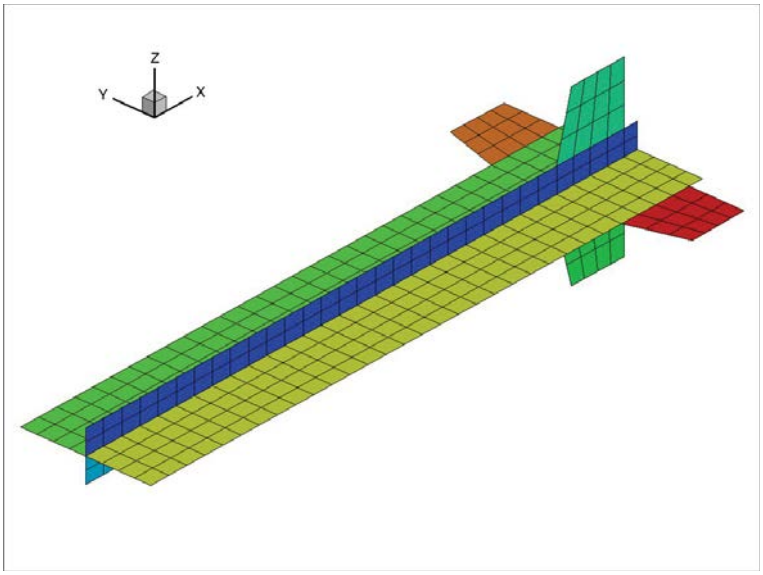

Figure 2: Airship finite element model

it is necessary to define what is a gust: a gust is a short-term wind speed variation within a turbulent wind field. There exist several methods to detect gusts in a wind time history [2], in this application we shall consider what is called the *velocity increment* method: a moving window of length T is shifted along the wind time history $W(t)$ and a gust of amplitude V_g is detected when $W(T) - W(0) = V_g$. There exist several public wind databases available, here

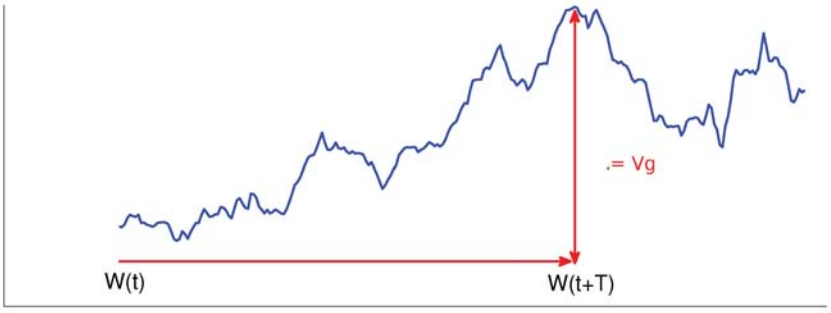

Figure 3: Velocity increment gust detection

we shall use a wind data obtained in a FINO offshore research platform [1] located in the North sea during a winter storm. The three components of the wind have been recorded during three days. Figure 4 shows the longitudinal and vertical component of the wind time history. This last component will be used in order to detect gusts.

6 NUMERICAL ILLUSTRATION

The transportation airship requirements fix the maximum gust speed V_g to 7.6 m/s for an airship speed equal to 100 km/h. The gust half length L_g is chosen equal to 75 m (the airship

[1]FINO: Research platforms in the North Sea and in the Baltic Sea, GL-Windenergie, Hamburg (http://www.fino-offshore.de)

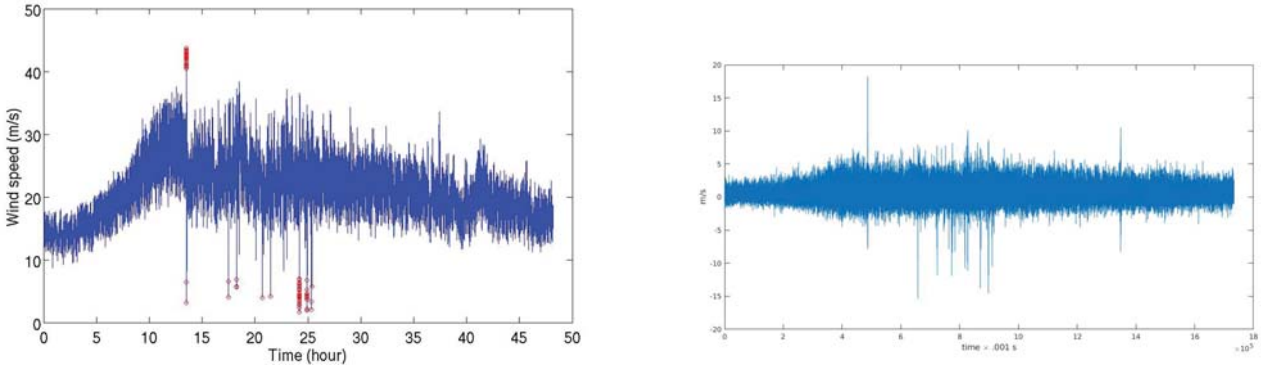

Figure 4: Horizontal and vertical wind time history

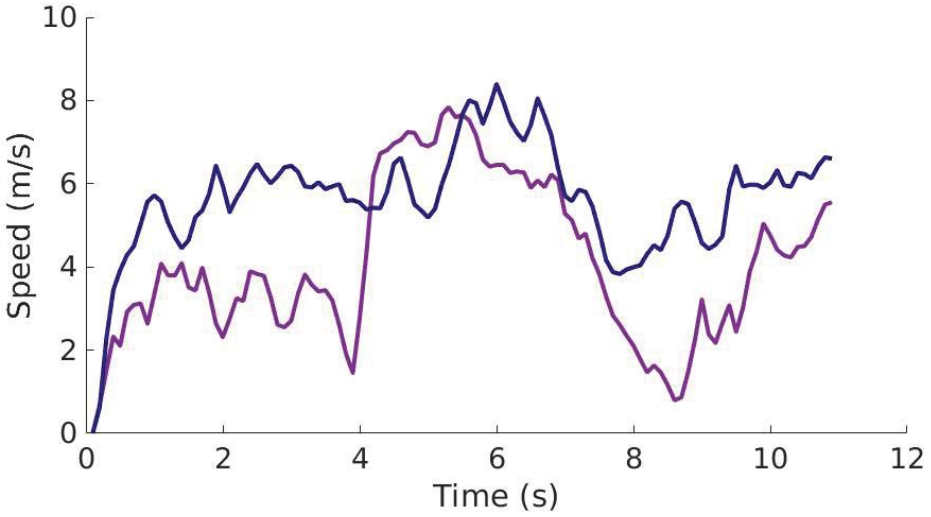

Figure 5: Two detected gusts

length being equal to 150 m). In a first stage we shall detect gusts characterized by the above values of V_g and L_g in the recorded vertical wind time history. Thirty nine gusts are detected and figure 5 shows two of them. Figure 6 compares the mean real gust and the TAR prescribed gust.

6.1 Input simulation

In a second stage the Karhunen Loeve stochastic model of the vertical gusts is constructed using the thirty nine gusts in the database. Thirty four terms are kept in the expansion. Using this model, 5000 gust sample paths are generated, each leading to the calculation of the corresponding charge factor. Figure 7 shows the mean charge factor as well the $\pm\sigma$ dispersion due to the generated gusts compared to the charge factor due to the TAR requirement gust, figure 8 gives the mean number of crossings of the charge factor for different levels.

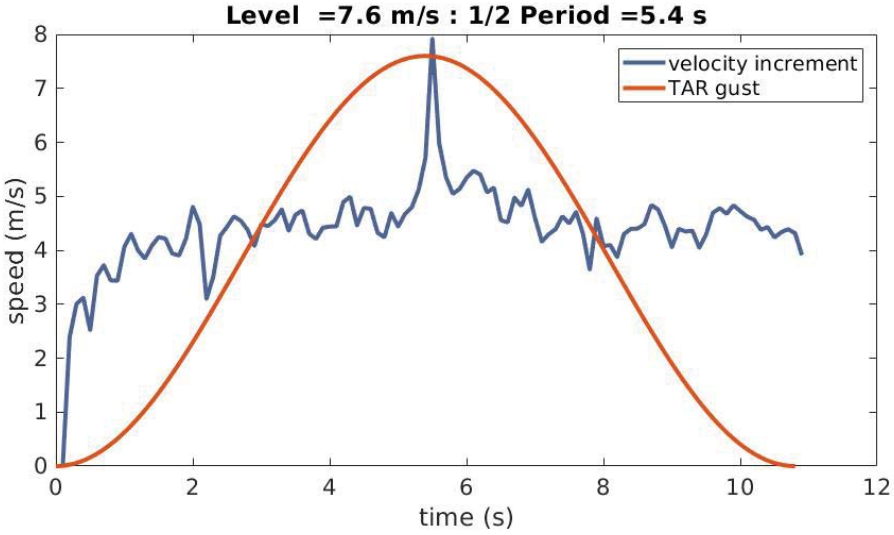

Figure 6: Mean gusts

6.2 Output simulation

We construct now the image of the gust Karhunen Loeve expansion by the linear aeroelastic operator: the input of the operator is the expansion eigen functions and the mean gust. The initial condition in equation 8 is 0. Relation 10 yields the Karhunen Loeve expansion of the random charge factor which can be used to generate additional responses in order to construct various statistical estimates. Again, 5000 simulated responses of the charge factor are generated using the KL image expansion and the same estimators as above are constructed. Figure 9 shows the mean charge factor as well the $\pm\sigma$ dispersion due to the simulated charge factor and, of course, the result is the same as the one shown on figure 7. Figure 10 shows the mean number of crossings of the charge factor for different levels calculated using the input stochastic model or the output stochastic model: the results are identical.

7 CONCLUSION

We have shown in this paper that when a linear system is excited by a stochastic process represented by its Karhunen Loeve expansion, one could directly construct the Karhunen Loeve expansion of any system output, allowing its use for direct Monte Carlo characterization. An illustration has been given related to the identification of an airship response to wind gusts. The gust are represented by a Karhunen Loeve expansion constructed from a database containing turbulent wind time history measures. Results haves shown in particular the important output (charge factor) scattering compared to the one obtained using the transport air requirements.

REFERENCES

[1] E. Albano and W. Rodden. A doublet lattice method for calculating lift distributions on surfaces in subsonic flows. *AIAA Journal*, 7(2):279–285, Feb 1969. Errata vol 7, no. 11 Nov. 1969.

[2] E. Branlard. Wind energy: On the statistics of gusts and their propagation through a wind farm. *ECN-Wind-Memo-09*, 2009.

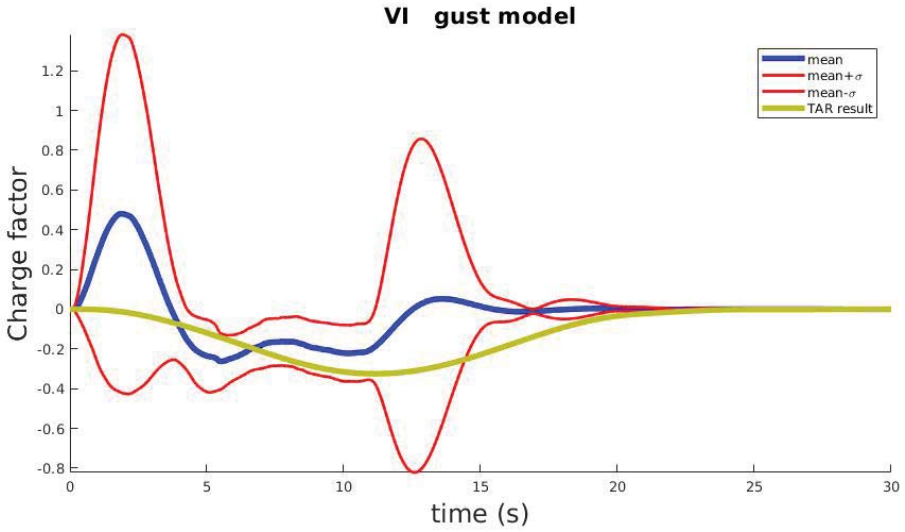

Figure 7: Mean charge factor

[3] L. Devroye and L. Györfi. *Nonparametric density estimation : the L_1 view*. John Wiley, New York, 1985.

[4] G. Mortchéléwicz. Prediction of aircraft transonic aeroelasticity by the linearised Euler equations. In *41th Israel annual conference Aerospace Science*, february 2001.

[5] G. Mortchéléwicz. CAPRI user guide. techreport RT 1/16459, ONERA, 2009.

[6] F. Poirion. On some stochastic methods applied to aeroservoelasticity. *Aerospace Science and Technology*, 4:pp 201–214, 2000.

[7] F. Poirion and I. Zentner. Stochastic model construction of observed random phenomena. *Probabilistic Engineering Mechanics*, 36:63–71, 2014. doi 10.1016/j.probengmech.2014.03.005.

[8] D. W. Scott. *Multivariate Density Estimation: Theory, Practice, and Visualization*. 1992.

[9] B.W. Silverman. *Density Estimation for Statistics and Data Analysis*. Chapman & Hall, 1986.

[10] I. Zentner and F. Poirion. Enrichment of seismic ground motion data basis using Karhunen-Loève expansion. *Earthquake Engineering and Structural Dynamics*, 41(14):1945–1957, 2012.

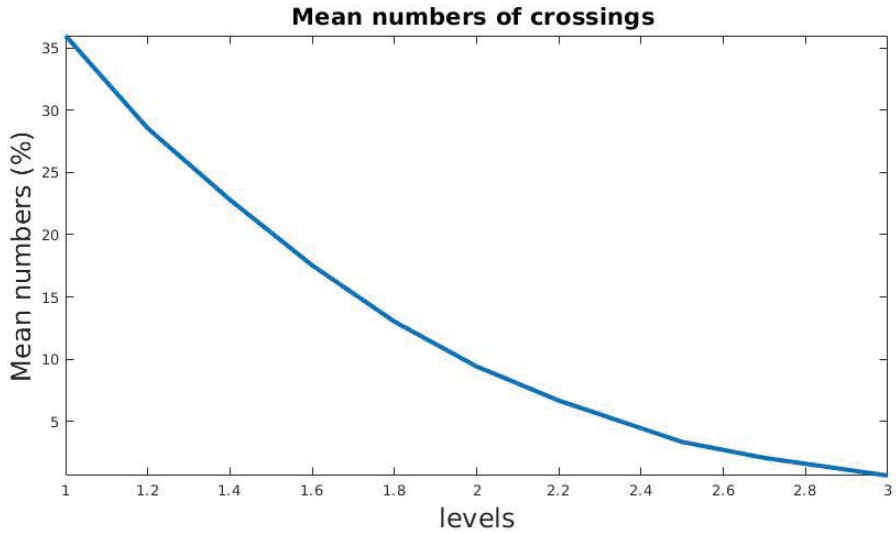

Figure 8: Mean number of crossings

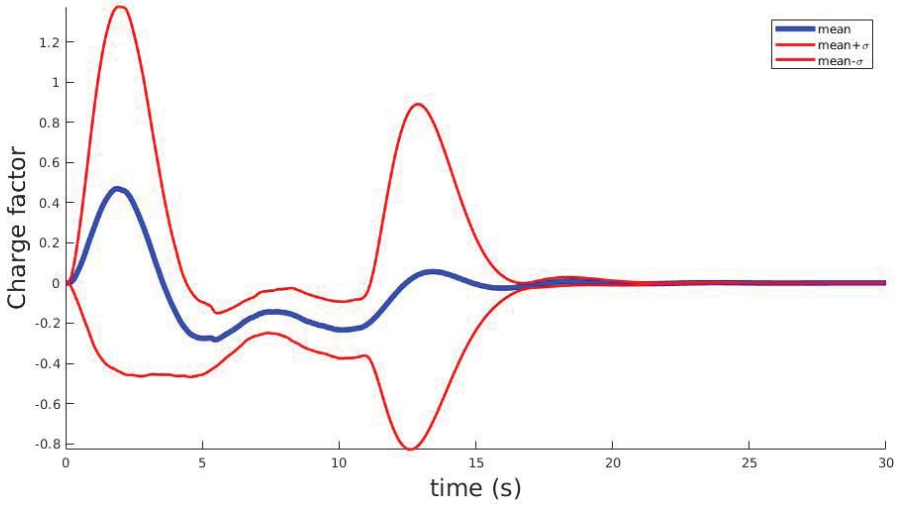

Figure 9: Mean charge factor

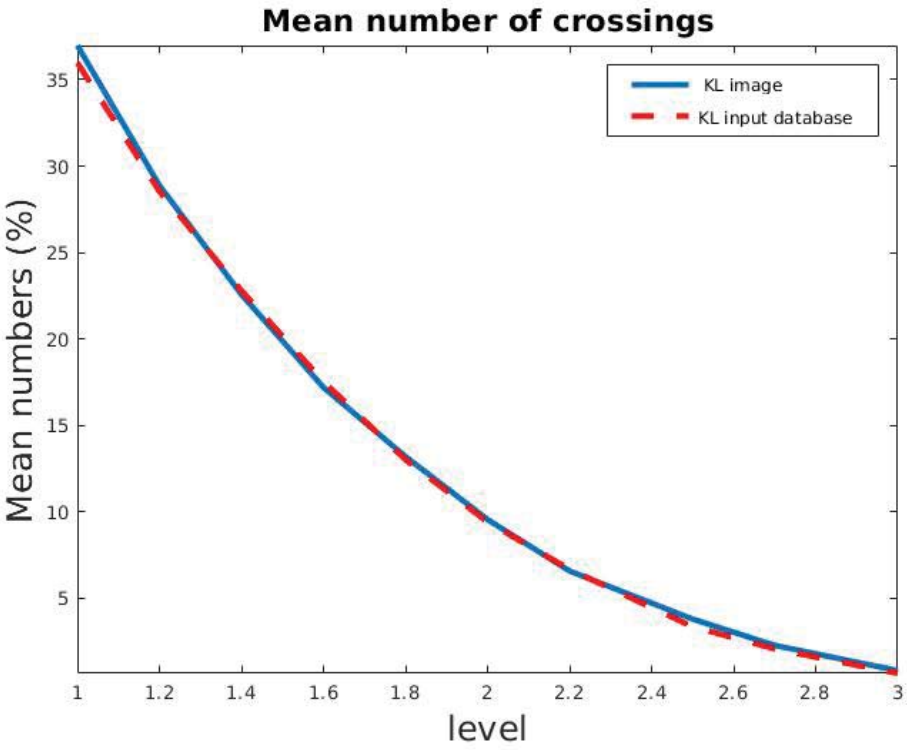

Figure 10: Mean number of crossings

EURODYN 2020
XI International Conference on Structural Dynamics
M. Papadrakakis, M. Fragiadakis, C. Papadimitriou (eds.)
Athens, Greece, 23–26 November 2020

STATE-OF-THE-ART REVIEW OF MACHINE LEARNING APPLICATIONS TO GEOTECHNICAL EARTHQUAKE ENGINEERING PROBLEMS

Z. Achmet[1], **L. Di Sarno**[1,2]

[1] Department of Engineering
University of Sannio, Benevento, Italy
e-mail: zeinepach@gmail.com, disarno@unina.it

[2] School of Engineering, Department of Civil Engineering and Industrial Design
University of Liverpool, Liverpool, UK
disarno@unina.it

Keywords: Machine Learning, Earthquake Engineering, Geotechnical Engineering

Abstract. *In recent years there has been a proliferation in the availability of information generated across a range of engineering disciplines. Artificial intelligence techniques such as machine learning have found a wide range of applications as computationally efficient tools to reveal underlying trends in large and complex data sets. This state-of-the-art review discusses recent advances in the application of machine learning to geotechnical earthquake engineering problems. Such algorithms as Gaussian process regression, support vector machines, artificial neural networks, decision trees, random forests and their applications to this field are reviewed. Particular attention will be paid to machine learning applications for earthquake-induced soil liquefaction potential prediction, inelastic response spectra prediction, site-specific spectral acceleration prediction, dynamic soil-structure interaction, slope stability evaluation, shallow and deep foundation capacity prediction, soil and shear strength prediction. The training data set, the machine learning model configuration, the training, and the evaluation process, as well as the generalization capacity of each model, will be examined. The performance of different methods will be compared, and future research challenges will be discussed.*

1 INTRODUCTION

In recent years machine learning (ML) methods as computationally efficient tools to reveal underlying trends in complex problems have found a wide range of applications in many engineering fields. Since the late 1980s techniques like artificial neural networks (ANN) have been applied successfully to many civil engineering problems including geotechnical engineering. The applications of ANNs in civil engineering between 1989 and 2000 are discussed in Adeli's [1] literature review paper. Pre-2001 applications of ANNs to geotechnical engineering are reviewed in detail by Shahin et al. [2], while pre-2010 applications can be found in the review of Shahin et al. [3].

The purpose of this paper is to discuss recent advances in the application of machine learning techniques to geotechnical and geotechnical aspects of earthquake engineering fields. Among the many available ML algorithms in the literature, the ANNs and the support vector machines (SVM) were the most common in these fields. Besides these algorithms, applications of the Gaussian process regression (GPR), decision tree, and random forest algorithms are also included in this review. In order to facilitate the understanding of the ML applications, a brief description of the algorithms, as well as the ML model evaluation methods are given in the next section.

The geotechnical and geotechnical earthquake engineering problems are very complex in their nature and many assumptions are introduced in order to model them with traditional methods. The availability of experimental data, or even in some cases data from finite element analysis, has made the application of ML methods more and more popular in recent years enabling the use of these data as a tool. Many applications can be found in the literature, such as ANN based constitutive models, foundation capacity prediction, soil liquefaction potential prediction and applications to soil structure interaction. In this study, uniaxial compressive strength prediction using ANNs and SVMs, pile capacity prediction models using GPR, SVM and ANNs, shallow foundation capacity prediction using ANN and SVM, soil shear strength prediction, earthquake-induced soil liquefaction potential using SVM, decision tree and random forest, SVM and GPR applications for slope stability prediction, ANN and SVM applications to dynamic soil structure interaction, and applications of ANNs to site specific seismic analysis and inelastic response spectrum prediction are reviewed.

2 THEORETICAL BACKGROUND

Machine learning (ML) is the scientific study of algorithms and statistical models that computer systems use to perform a specific task without using explicit instructions, relying instead on patterns and inference. It is a subset of artificial intelligence. Machine learning algorithms build a mathematical model based on sample data, known as "training data", in order to make predictions or decisions without being explicitly programmed to perform the task [4],[5].

Machine learning algorithms are often categorized as *supervised* and *unsupervised*. In supervised learning, each training example is a pair consisting of an input feature and a desired output and the algorithm analyzes the training data and produces an inferred function, which can be used for mapping new examples [6]. In unsupervised learning, the training data has only the input values and the algorithm identifies commonalities in the data and reacts based on the presence or absence of such commonalities in each new piece of data.

The supervised learning method is used for *classification* and *regression* problems. In classification problems, the outputs are restricted to a limited set of values (a category or a group). Regression problems are named for their continuous outputs, meaning that they may have any value within a range.

There are plenty of algorithms for either task. In this section, the artificial neural networks, support vector machines, Gaussian process regression algorithm, decision trees and random forests, as well as their performance evaluation are briefly discussed.

2.1 Artificial neural networks

The artificial neural network is a computing technique designed to simulate the human brain's method of problem solving. The similarity between the ANNs and the human brain is that they both acquire skills in processing data and finding solutions through training [7]. Artificial neural networks consist of simple computing units "artificial neurons", and each unit is connected to the other units via weight connectors. These units calculate the weighted sum of the inputs and determine the output using an activation function. A schematic representation of an ANN with multiple inputs and a single neuron in the hidden layer (the layer between the input and output layer) is shown in Figure 1. The illustrated ANN has n input features X_1 to X_n and their connections with the unit in the hidden layer is the feature multiplied with its weight w_i and added bias b_i. The single unit in the hidden layer sums all the weighted inputs, applies an activation function f to the sum and passes the output α to the next layer. In this case, the next layer is the output unit Y and it provides the prediction of the ANN for the output value.

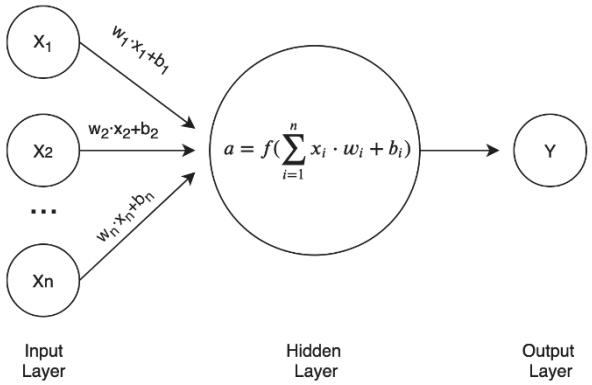

Figure 1: Artificial neural network with single neuron and multiple inputs.

The process of calibrating the values of the weights and biases of the ANN to predict the desired output correctly is called training. In the case of supervised learning, the learning algorithm will adapt the weights and biases depending on the error between the predicted output and the real output. The optimal ANN for a given training set is obtained by minimizing the loss function using an optimization algorithm.

2.2 Support vector machines

Support vector machines (SVM) are supervised learning models for classification and regression. For the binary classification case, the basic idea of a SVM is to find the optimal hyper-plane, i.e. decision surface, for linearly separable patterns, extend to linearly inseparable patterns by transforming the original data to map into new space with the kernel function and

use the SVM algorithm for pattern recognition. Support vectors are the data points that lie closest to the decision surface, and which have direct bearing on the optimal location of the decision surface.

Support vector machines maximize the margin around the separating hyperplane. The decision function is fully specified by the support vectors which are usually a small subset of the training samples. This becomes a quadratic programming problem that can be solved by standard methods. Similar to ANNs, the inputs of an SVM are input-output training pairs and the output is a set of weights *w*, one for each feature, whose linear combination predicts the value of the output. The important difference compared to ANNs is that SVMs use the optimization of maximizing the margin to reduce the number of weights that are non-zero to just a few that correspond to the support vectors.

The optimal separating hyper-plane of an SVM for a binary classification problem is illustrated in Figure 2. Anything on or above the hyper-plane $w \cdot x - b = 1$ is of one class with label 1. Accordingly, anything on or above the hyper-plane $w \cdot x - b = -1$ is of the other class with label -1. The data points on these hyper-planes are the support vectors, while the geometrical distance between them is $\frac{2}{\|w\|}$. The hyper-plane $w \cdot x - b = 0$ is the median of them and it is the optimal separating hyper-plane. The parameter $\frac{b}{\|w\|}$ determines the offset of the hyperplane from the origin.

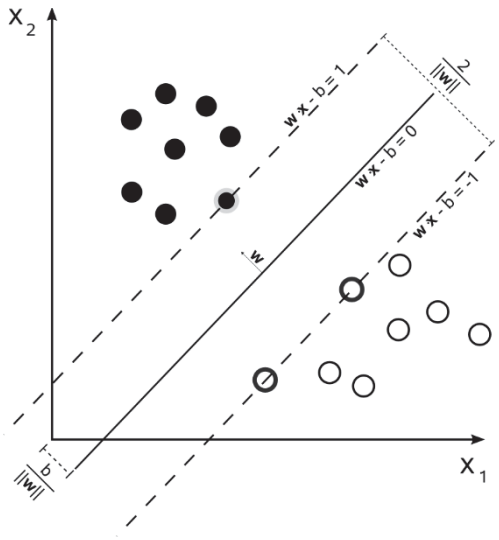

Figure 2: Optimal separating hyper-plane for binary classification.

Support vector machines for regression (SVR) use the same principles as the SVM for classification with only a few minor differences. In the case of regression, a margin of tolerance is set in approximation to the SVM which would have already requested it from the problem. The algorithm in this case is more complicated. However, the main idea is the same: to minimize the error, individualizing the hyperplane which maximizes the margin, keeping in mind that part of the error is tolerated. Details for the mathematical formulation of SVMs and SVRs are discussed by Christianini and Shawe-Taylor [8].

2.3 Gaussian process regression

In probability theory and statistics, a Gaussian process is a stochastic process (a collection of random variables indexed by time or space), such that every finite collection of those random variables has a multivariate normal distribution, i.e. every finite linear combination of them is normally distributed. The distribution of a Gaussian process is the joint distribution of all those random variables.

A machine learning algorithm that involves a Gaussian process uses lazy learning and a measure of similarity between points (the kernel function) to predict the value for an unseen point from training data. In a training set where x_i are the input features and y_i is the output, a Gaussian process regression model addresses the question of predicting the value of a response variable y_{new} given the new input vector x_{new} and the training data. The prediction is not just an estimation for that point but also has uncertainty information. It is a one-dimensional Gaussian distribution. The mathematical formulation of the GPR algorithm can be found in Rasmussen and Williams [9].

2.4 Decision trees and random forest

Decision trees build classification or regression models in the form of a tree structure. It breaks down a data set into smaller and smaller subsets while at the same time an associated decision tree is incrementally developed. The final result is a tree with decision nodes and leaf nodes. A decision node has two or more branches. Leaf nodes represent a classification or a decision. The topmost decision node in a tree, which corresponds to the best predictor, is called the root node. Decision trees can handle both categorical and numerical data.

The random forest is an algorithm consisting of many decision trees used for both classification and regression problems. It uses bagging and feature randomness when building each individual tree to try to create an uncorrelated forest of tree whose prediction by committee is more accurate than of an individual tree.

2.5 Bias and variance of machine learning models

How satisfactory the performance of an ML model depends on its predictions and how well it generalizes on an unseen data set. The bias variance trade-off is a way of analyzing the expected generalization error of a learning algorithm, with respect to a particular problem as a sum of three terms, the bias, the variance, and a quantity called the irreducible error, resulting from noise in the problem itself. It can be applied to all forms of supervised learning [10].

The bias is an error from erroneous assumptions in the learning algorithm. In other words, it is the difference between the average prediction of the model and the correct target value. Models with high bias pay very little attention to the training data and oversimplifies the model. It always leads to high error with training and test data. The variance is an error from sensitivity to small fluctuations in the training set. High variance can cause an algorithm to model random noise in the training data rather than the intended output. Models with high variance pay a lot of attention to training data and do not generalize with unseen data. As a result, such models perform very well on training data but have high error rates on test data.

In supervised learning underfitting happens when a model is unable to capture the underlying pattern in the data. Such models usually have high bias and low variance. Conversely,

overfitting happens when a model captures the noise along with the underlying pattern which occurs when trained with a noisy data set. These models have low bias and high variance.

2.6 Evaluation of machine learning models

To obtain a model that generalizes well on unseen data, there is a need to minimize the total error finding a good balance between bias and variance. Hence, there is a need to find a way to accurately measure the prediction error of the model. A common approach is using the data itself to estimate the prediction error.

The simplest technique for this approach is the holdout set method, splitting the data initially into two groups. One group is used to train the model and the second group is used to measure the model's error after training. Another commonly used approach is the cross-validation method which works by splitting the data into sets of *n* folds. The training and error estimation process is repeated *n* times. Each time *n-1* groups are combined and used to train the model. The group that was not used in the training is used to estimate the prediction error. The final error of the ML model is the average of the *n* calculated errors.

3 UNIAXIAL COMPRESSIVE STRENGTH PREDICTION

Cevik et al. [11] used the results of laboratory experiments as training data and developed an ANN model to estimate the uniaxial compressive strength of some clay-bearing rocks selected from Turkey, giving an emphasis on assessing the role of slake durability indices and clay contents. They performed X-ray diffraction analyses, slake durability index tests and the uniaxial compressive strength test on selected samples from Soma and Eskisehir regions. Then, they developed ANN based constitutive models for clay-bearing rocks based on the experimental data. The input features of the ANN model were the origin of the rocks, two/four cycle slake durability indices and the clay contents, while the output was the uniaxial compressive strength. They used 80% of the training data for training and 20% for testing. Their study showed that the ANN method had quite satisfying accuracy compared to other models.

Ceryan et al. [12] developed an ANN model to predict the uniaxial compressive strength of carbonate rocks. They collected 56 groups of block samples from the Tasonu Quarry in Trabzon, Turkey and performed X-ray diffraction analyses, and test such as, specific density, unit weight, porosity, P-wave velocity, slake durability, aggregate impact value and uniaxial compressive strength. They used all possible regression technique in order to select the input features for the ANN model. They used the total porosity and the P-wave velocity in the solid part of the sample as input features for the ANN, while the output was the uniaxial compressive strength. They used 80% of the training data for training and 20% for testing. They compared the results of the ANN model with multiple linear regression model and they concluded that the ANN model was capable of modeling the uniaxial compressive strength.

Tinoco et al. [13] proposed a SVM model to predict the uniaxial compressive strength of jet grouting columns. The training data set included 472 data points collected from different columns constructed in different places with different soil properties. The uniaxial compressive strength of each sample was obtained from an unconfined compression test with sample strain instrumentation. The proposed model had 9 input features, which were the relation between the mixture porosity and the volumetric content of cement, the age of mixture, the percentage of clay, the jet grouting method, inverse of the dry density of soil cement mixture, the void ratio, the cement content, the water content and the water cement ratio. To assess the generalization

capacity of their model they used 20-fold cross-validation method, which had an acceptable final error.

4 PILE CAPACITY PREDICTION

Pal and Deswal [14] developed a GPR model to predict the load-bearing capacity of piles and compared its results with an SVM model and empirically derived relationships. They used a data set which was derived from actual pile-driving records in cohesion less soil to train both models. Out of a total of 94 data points, they used 59 for training and 35 for testing. The results of this data set indicated that the GPR algorithm had improved performance compared with SVM and empirical relationships. Additionally, they used another data set consisting of 38 pieces of data to validate the performance of the GPR model.

Samui and Kim [15] developed a least square SVM and multivariate adaptive regression spline (MARS) to predict the lateral load capacity of pile foundations. They use the pile diameter, pile embedment depth, load eccentricity and undrained shear strength of the soil as input features for their models. Their data set had 41 data points, and they used 31 of them for training and the remaining data points for testing. They concluded that the developed models outperform the other available methods.

Kordjazi et al. [16] developed three SVM models with different kernel functions to predict the ultimate axial load-carrying capacity of piles based on cone penetration test (CPT) data. They used a data set consisting of 108 data points obtained from the literature. They used the type of static pile load test, pile material, method of installation, pile tip (closed or open), embedded length, pile-soil contact perimeter, cross sectional area of the pile tip, average cone tip resistance along the embedded length of the pile, average sleeve friction, and the average cone tip resistance beneath the pile tip as input features of the SVM model. The ultimate load bearing capacity of the pile was the single output variable. They used 83 data points for training and 25 for testing. They concluded that the SVM model with the radial basis kernel function and the Pearson VII kernel function had the best results. They compared the performance of the SVM model with CPT-based methods for determining the pile capacity. The comparison showed that the SVM models provide more accurate pile capacity prediction.

Momeni et al. [17] proposed an ANN model to estimate the axial load bearing capacity of piles. In order to create the training data, they performed 36 pile driving analyzer tests at various sites in Indonesia. The tested piles were reinforced and pre-stressed concrete piles with varying lengths and diameters and most of the tests were conducted in cohesionless soils. To represent the soil characteristics, the results of soil penetrations tests (SPT) were collected. The average SPT values along the pile shaft and tip, the pile length, the pile area and the pile set were used as input features. The output variables of the ANN were the shaft, tip and the ultimate bearing capacity of the pile. Their study indicated that the ANN model results were in a close agreement with those obtained from high strain dynamic pile testing.

Moayedi and Rezaei [18] developed an ANN model to predict the ultimate uplift capacity of under-reamed piles embedded in dry cohesionless soil. The training data, which had 432 data points, was obtained from small-scale laboratory work from a previous study. The input features of the ANN model were the base diameter, the angle of the enlarged base, the shaft diameter, and the embedment ratio, while the singe output of their model was the ultimate uplift resistance. The results of the ANN model they proposed showed that it can be applied to precisely predict the experimental results.

5 SHALLOW FOUNDATION CAPACITY PREDICTION

Ziaee et al. [19] proposed an ANN model to predict the bearing capacity of shallow foundations on rock masses using as training data a comprehensive database of rock socket, centrifuge rock socket, plate load, and large-scaled footing load test results. The database included the results of experiments on circular and square footings of different sizes on various types of rock masses. They used 85% of the data set for training and 15% for testing. The input features of the ANN model were the rock mass rating, the unconfined compressive strength of rock, the ratio of joint spacing to foundation width, and the angle of internal friction of the rock mass. The output was the ultimate bearing capacity of the foundation. Their study concluded that the ANN model had notably better performance than the traditional equations.

Moayedi and Hayati [20] used various ML algorithms such as feed forward neural network, radial basis neural network, SVM, tree regression fitting model and adaptive neuro-fuzzy inference system to predict the ultimate bearing capacity of strip footing near a slope. The training data were obtained from extensive finite element modeling of a shallow strip footing located near a homogenous sandy slope. The input features of the ML models were the soil type, the slope angle, the setback ratio and the applied load on the footing and the single output of the models was the settlement of the footing. The comparison of the models showed that the feed forward neural network had the most accurate results.

6 SOIL SHEAR STENGTH PREDICTION

Pham et al. [21] developed four ML methods to predict the shear strength of soft soils and compared their results. The methods they used were ANN, particle swarm optimization – adaptive neuro-fuzzy inference system, genetic algorithm - adaptive neuro-fuzzy inference system, and SVR. They used case studies of 188 plastic clay soil samples collected from Nhat Tan and Cua Dai bridge projects in Vietnam as training data. The input features of the models were the moisture content, clay content, liquid limit, and the plastic limit and the single output feature was the shear strength of the soil. They concluded that out of the four models the particle swarm optimization – adaptive neuro-fuzzy inference system performed best.

7 SOIL LIQUEFACTION POTENTIAL PREDICTION

Samui et al. [22] proposed two SVM models for classification based on actual shear wave velocity data in order to evaluate the seismic-liquefaction potential. The training data included information of soil characteristics and earthquake parameters. Out of 186 available data points, they used 130 for training and 56 for testing the SVM models. For the soil characteristics based SVM model the input features where the effective vertical stress, the soil type, the shear wave velocity, the peak horizontal acceleration, and the earthquake magnitude. For the shear wave velocity based model the input features were the shear wave velocity, the peak horizontal acceleration and the magnitude. For both cases the output of the models was whether liquefaction occurs or not. Their study indicated that the shear wave velocity based SVM model was sufficiently capable to predict the liquefaction potential.

Samui [23] developed a SVM model for classification in order to predict soil liquefaction based on actual CPT data from the 1999 Chi-Chi, Taiwan earthquake. He used the cone resistance, cyclic stress ratio, local friction, pore pressure, total stress, effective stress, peak ground surface acceleration and earthquake magnitude as input features. The proposed model had 100% prediction accuracy. Furthermore, he simplified the model using only two input

parameters, the cone resistance and the peak ground surface acceleration. The second model had 89% prediction accuracy. He concluded that the SVM model was a robust method for classifying liquefaction potential.

Lee and Chern [24] developed an SVM for classification using as input features the earthquake magnitude, total overburden pressure, effective overburden pressure, cone resistance from CPT, and peak ground acceleration. They trained the model with a data set which had 466 field liquefaction performance records and CPT measurement. They used the cross-validation method to evaluate the performance of the model. They compared the SVM with an ANN model and concluded the SVM model had more accurate results.

Ardakani and Kohestani [25] proposed a decision tree for classification based on CPT data to predict the seismic liquefaction potential. The training data they used consisted of a total of 109 cases, 78 of them used for training and 31 for testing. The input features of the decision tree were the cone resistance, total vertical stress, total effective stress, mean grain size, normalized peak ground surface acceleration, cyclic stress ratio, and the earthquake magnitude. The overall classification accuracy of the decision tree was 98%.

Kohestani et al. [26] developed two random forest models based on CPT data to evaluate the seismic liquefaction potential of soil. The random forest models were trained and validated using 226 field records of liquefaction performance and CPT measurements. The input features for the first model were the normalized cone tip resistance, soil type index, vertical effective stress, and the seismic cyclic stress ratio adjusted to an earthquake magnitude of 7.5, while for the second model inputs were the cone tip resistance, sleeve friction ratio, effective vertical stress, total vertical stress, maximum horizontal ground surface acceleration, and the earthquake magnitude. The models were compared to ANN and SVM models using the same input features found in the literature.

8 SLOPE STABILITY

Samui and Kothari [27] investigated the capability of a least square SVM (LSSVM) model to perform slope stability analysis. They developed two LSSVM models, one regression model to predict the factor of safety of the slope and one classification model to predict the stability status. Their training data consisted of 46 case studies of slopes, 32 used for training and 14 for testing. The input features of the models were the unit weight, cohesion, angle of internal friction, slope angle, height and the pore water pressure coefficient. They concluded that the proposed LSSVM was a robust model for slope stability analysis.

Kang et al [28] developed a probabilistic stability evaluation method for slopes based on GPR and Latin hypercube sampling. Their analysis was composed of three parts. Firstly, they used the Latin hypercube sampling technique to generate samples for constructing the response surface. Then, based on those samples they used the GPR model to establish the response surface to approximate the limit state function. Finally, they performed Monte Carlo simulation via the GPR response surface to estimate the system failure probability of slopes. They examined five case samples to verify the effectiveness of the methodology. The results of their study showed that the system reliability analysis they proposed could accurately setermine the system failure probability with a relatively small number of deterministic slope stability analyses.

9 SOIL STRUCTURE INTERACTION

Farfani et al. [29] proposed ANN and SVM models for dynamic analysis of soil-pile-structure (SPS) systems based on experimental data, which was produced by carrying out a series of centrifuge tests on SPS systems. The experiments included several configurations of SPS systems as well as a large number of real buildings with earthquake motions recorded inside them and at their nearby free-field ground surface. ANN and SVM models were developed to predict the maximum acceleration of the superstructure at the head of the column (SSA) and of the pile heads using as input parameters the peak base acceleration, amplitude factor of the earthquake record, length of column, mass on column and number of piles. The training data had a total of 70 data points, 45 of them used for training and the rest for testing the networks. Since the number of data points was relatively low, they created two ANN and two SVM models each having one output parameter (SSA or PHA). They performed finite element analysis to compare the ANN and SVM results. Furthermore, they extended their study creating ANN and SVM models in order to estimate the period of a structure based on recorded data taken from previous studies. The data included the soil-structure-interaction effects on 57 buildings, having various structural systems from different sites and under different earthquakes. The input features of these models were the maximum horizontal acceleration, the effective height of the building, embedment depth of the foundation, shear wave velocity of the soil, hysteretic damping of the soil and the radii of an equivalent circular foundation having a moment of inertia or a surface equal to the real foundation. The ratio of the fundamental periods of the building for fixed base and flexible base was the output. The results of their study showed that ML methods can be used for solving the complex problem of seismic response of structures in much less time compared to finite element modeling with acceptable accuracy if the necessary data is available.

10 SITE-SPECIFIC SEISMIC ANALYSIS

Kamatchi et al. [30] developed an ANN based methodology to predict site-specific acceleration values. In order to create the data for training they generated strong ground motions at bedrock level for a chosen site in Delhi, India due to earthquakes considered to originate from the central seismic gap of the Himalayan belt using necessary geological and geotechnical data and they performed one-dimensional equivalent linear site response analyses to calculate the surface level ground motions and response spectrums. Out of 49815 data points in their data set, 35000 data points were used for training and 14815 for testing. The input features of the ANN model were the moment magnitude of the earthquake, the shear wave velocity model of the soil, the depth of the soil stratum, the damping ratio and the vibration period of the SDOF oscillator. The output of the ANN was the average spectral acceleration at the surface. The trained ANN was validated using borehole log data of an actual soil site and two different buildings. The comparison showed that the ANN had a tolerable error.

11 INELASTIC RESPONSE SPECTRUM PREDICTION

Bojorquez et al. [31] proposed an ANN to estimate the inelastic response spectrum for earthquake acceleration records. Fifty earthquake ground motions taken from the NGA database and recorded at sites with different types of soils were used to train the proposed ANN model. They used 42 data points for training and 8 for testing the results of the trained network. In their study, they used the moment magnitude, fault mechanism, Joyner-Boore distance, the

shear-wave velocity above site depth of 30 m, the fundamental period of the structure, and the system ductility as input values of the ANN. The output of the ANN was the pseudo-spectral acceleration at first mode of acceleration. Even though they used a relatively small data set for the training, the results of the trained network had acceptable agreement with the actual response spectrum.

12 CONCLUSION REMARKS

In this study, the post-2010 applications of machine learning techniques to geotechnical earthquake engineering have been reviewed. Particular attention was given to uniaxial compressive strength prediction, pile and shallow foundation capacity prediction, soil shear strength prediction, prediction of the earthquake-induced soil liquefaction potential, slope stability prediction, dynamic soil structure interaction problems, site specific seismic analysis, and inelastic response spectrum prediction. It was observed that the artificial neural networks and support vector machines were the most commonly applied algorithms of the options available which shows their superior performance in complex problems compared to other algorithms. Also, the number of applications to soil constitutive models, to foundation capacity prediction, and soil liquefaction is greater than the applications to geotechnical earthquake engineering problems like dynamic soil structure interaction and site-specific seismic analysis. Future studies could include more applications to this field to consider not only the complex nature of soils, but also the complexity of earthquake characteristics.

Machine learning techniques have several advantages in simulating the complex behavior of most geotechnical and geotechnical earthquake engineering problems compared with the conventional methods. In most traditional mathematical models, the problem is simplified, or several assumptions are made, and the structure of the model is assumed in advance. Whereas, machine learning algorithms, as a data driven approach, rely on the training data to determine the structure and the parameters of the model without simplifying the problem or incorporating any assumptions. This requires the use of an adequate amount of data in order to develop a machine learning model which generalizes well. In most of the reviewed studies the training data was quite small, and the trained algorithm was able to make accurate predictions for specific input feature ranges. Hence, the already developed machine learning models could be updated to provide better results by adding new training examples in the data set and larger data sets could be used in future studies.

Despite the success of machine learning techniques in modeling complex geotechnical earthquake engineering problems, they suffer from some shortcomings, like model robustness, transparency and knowledge extraction, and uncertainties. The epistemic and aleatory uncertainties in machine learning models can be addressed by applying a probabilistic approach, such as Gaussian process regression algorithm or probabilistic deep learning methods. Furthermore, more robust models can be achieved by using larger data sets and deep learning techniques, like deep neural networks which use numerous hidden layers, each providing a different interpretation to the data it processes. In this way, critical features of the input data can be identified, and hidden patterns in highly complex problems can be found, providing better predictions. Improvements in these areas will greatly enhance the performance of machine learning applications to geotechnical earthquake engineering and other civil engineering problems.

ACKNOWLEDGEMENTS

This work was supported by the Horizon 2020 Programme of the European Commission under the MSCA-RISE-2015-691213-EXCHANGE-Risk Grant (Experimental and Computational Hybrid Assessment of NG Pipelines Exposed to Seismic Hazard, www.exhance-risk.eu). This support is gratefully acknowledged.

REFERENCES

[1] H. Adeli, Neural networks in civil engineering: 1989-2000, *Computer-Aided Civil and Infrastructure Engineering* 16, 126–142, 2001.

[2] M.A. Shahin, M.B. Jaksa, H.R. Maier, Artificial neural network applications in geotechnical engineering, *Australian Geomechanics* 36, 49–62, 2001.

[3] M.A. Shahin, M.B. Jaksa, H.R. Maier, Recent advances and future challenges for artificial neural systems in geotechnical engineering applications, *Advances in Artificial Neural Systems* 2009, 1–9, 2009.

[4] J.R. Koza, F.H. Bennett, D. Andre, M.A. Keane, Automated design of both the topology and sizing of analog electrical circuits using genetic programming, *Artificial Intelligence in Design* 96, 151–170, 1996.

[5] C.M. Bishop, Pattern Recognition and Machine Learning, *Springer*, ISBN: 9780387310732, 2006.

[6] S.J. Russell and P. Norvig, Artificial Intelligence: A Modern Approach, *Prentice Hall*, ISBN: 9780136042594, 2010.

[7] S. Haykin, Neural Networks and Learning Machines, *Pearson Education, Inc*., ISBN: 9780131471399, 2009.

[8] N. Christianini, J. Shawe-Taylor, An Introduction to Support Vector Machines and Other Kernel-Based Methods, *Cambridge University Press*, ISBN: 9780521780193, 2000.

[9] C.E. Rasmussen, C.K. Williams, Gaussian Processes for Machine Learning, *The MIT Press,* ISBN: 9780262182539, 2006.

[10] C. Sammut and G.I. Webb, Bias-Variance-Covariance Decomposition, in Encyclopedia of Machine Learning, *Springer*, ISBN: 9780387301648, 2011.

[11] A. Cevik, E.A. Sezer, A.F. Cabalar, C. Gokceoglu, Modeling of the uniaxial compressive strength of some clay-bearing rocks using neural network, *Applied Soft Computing Journal* 11, 2587–2594, 2011.

[12] N. Ceryan, U. Okkan, A. Kesimal, Prediction of unconfined compressive strength of carbonate rocks using artificial neural networks, *Environmental Earth Sciences* 68, 807–819, 2013.

[13] J. Tinoco, A. Gomes Correia, P. Cortez, Support vector machines applied to uniaxial compressive strength prediction of jet grouting columns, *Computers and Geotechnics* 55, 132–140, 2014.

[14] M. Pal, S. Deswal, Modelling pile capacity using Gaussian process regression, *Computers and Geotechnics* 37, 942–947, 2010.

[15] P. Samui, D. Kim, Least square support vector machine and multivariate adaptive regression spline for modeling lateral load capacity of piles, *Neural Computing and*

Applications 23, 1123–1127, 2013.

[16] A. Kordjazi, F.P. Nejad, M.B. Jaksa, Computers and geotechnics prediction of ultimate axial load-carrying capacity of piles using a support vector machine based on CPT data, *Computers and Geotechnics* 55, 91–102, 2014.

[17] E. Momeni, R. Nazir, D.J. Armaghani, H. Maizir, Application of artificial neural network for predicting shaft and tip resistances of concrete piles, *Earth Sciences Research Journal* 19, 85–93, 2015.

[18] H. Moayedi and A. Rezaei, An artificial neural network approach for under-reamed piles subjected to uplift forces in dry sand, *Neural Computing and Applications* 31, 327–336, 2019.

[19] S.A. Ziaee, E. Sadrossadat, A.H. Alavi, D. Mohammadzadeh Shadmehri, Explicit formulation of bearing capacity of shallow foundations on rock masses using artificial neural networks: application and supplementary studies, *Environmental Earth Sciences* 73, 3417–3431, 2015.

[20] H. Moayedi, S. Hayati, Modelling and optimization of ultimate bearing capacity of strip footing near a slope by soft computing methods, *Applied Soft Computing Journal* 66, 208–219, 2018.

[21] B.T. Pham, L.H. Son, T.A. Hoang, D.M. Nguyen, D. Tien Bui, Prediction of shear strength of soft soil using machine learning methods, *Catena* 166, 181–191, 2018.

[22] P. Samui, D. Kim, and T.G. Sitharam, Support vector machine for evaluating seismic-liquefaction potential using shear wave velocity, *Journal of Applied Geophysics* 73, 8–15, 2011.

[23] P. Samui, Liquefaction prediction using support vector machine model based on cone penetration data, *Frontiers of Architecture and Civil Engineering in China* 7, 72–82, 2013.

[24] C.Y. Lee, S.G. Chern, Application of a support vector machine for liquefaction assessment, *Journal of Marine Science and Technology* 21, 318–324, 2013.

[25] A. Ardakani and V.R. Kohestani, Evaluation of liquefaction potential based on CPT results using C4.5 decision tree, *Journal of Artificial Intelligence and Data Mining* 3, 85–92, 2015.

[26] V.R. Kohestani, M. Hassanlourad, and A. Ardakani, Evaluation of liquefaction potential based on CPT data using random forest, *Natural Hazards* 79, 1079–1089, 2015.

[27] P. Samui, D.P. Kothari, Utilization of a least square support vector machine (LSSVM) for slope stability analysis, *Scientia Iranica* 18, 53–58, 2011.

[28] F. Kang, S. Han, R. Salgado, and J. Li, System probabilistic stability analysis of soil slopes using Gaussian process regression with Latin hypercube sampling, *Computers and Geotechnics* 63, 13–25, 2015.

[29] H.A. Farfani, F. Behnamfar, A. Fathollahi, Dynamic analysis of soil-structure interaction using the neural networks and the support vector machines, *Expert Systems with Applications* 42, 8971–8981, 2015.

[30] P. Kamatchi, J. Rajasankar, G.V. Ramana, A.K. Nagpal, A neural network based methodology to predict site-specific spectral acceleration values, *Earthquake*

Engineering and Engineering Vibration 9, 459–472, 2010.

[31] E. Bojórquez, J. Bojórquez, S.E. Ruiz, A. Reyes-Salazar, Prediction of inelastic response spectra using artificial neural networks, *Mathematical Problems in Engineering* 2012, 2012.

EURODYN 2020
XI International Conference on Structural Dynamics
M. Papadrakakis, M. Fragiadakis, C. Papadimitriou (eds.)
Athens, Greece, 23–26 November 2020

RELIABILITY ASSESSMENT OF THE DYNAMIC BEHAVIOR OF HIGH-SPEED RAILWAY BRIDGES USING FIRST ORDER RELIABILITY METHOD

Reza Allahvirdizadeh[1], Andreas Andersson[2], and Raid Karoumi[3]

[1]Division of Structural Engineering and Bridges, KTH Royal Institute of Technology, Stockholm, Sweden
e-mail: reza.allahvirdizadeh@byv.kth.se

[2] Division of Structural Engineering and Bridges, KTH Royal Institute of Technology, Stockholm, Sweden
Swedish Transport Administration, Solna, Sweden
e-mail: andreas.andersson@byv.kth.se

[3]Division of Structural Engineering and Bridges, KTH Royal Institute of Technology, Stockholm, Sweden
e-mail: raid.karoumi@byv.kth.se

Keywords: High-speed railway bridges, Bridge dynamics, Structural reliability, First order reliability methods, Running safety, Serviceability limit state.

Abstract. *The operational speed of the trains is intended to be significantly increased forthcoming; which consequently questions the safety level of the current design concepts concerning different performance limits. Thus, the reliability of the simply supported single-span bridges is assessed in the current article adopting the first-order reliability method (FORM) approach. In this regard, the dynamic response of the aimed bridges is investigated under the passage of a series of moving loads using available closed-form solutions in the literature. Hereof, axle load, car body/train configuration, flexural rigidity, damping, mass and model uncertainties are considered as random variables; while train-track-bridge interactions are neglected and the procedure is repeated for a wide range of span lengths and train velocities. Then, the safety index corresponding to each case is evaluated by considering running safety as the limit state function; where, the bridge deck vertical acceleration is taken as the capacity of the system. The outcomes are presented as average probability of exceeding the limit state versus train speed and categorized based on span lengths.*

1 INTRODUCTION

Former studies have shown that ballast instability is the dominant design criteria of high-speed railway bridges in comparison to the contact loss or excessive deflections. The latter statement is particularly validated for short to medium span bridges using numerical simulations [1, 2]. It was observed that this phenomenon may occur at high vertical accelerations leading the interlock between grains to be lost or the lateral resistance of sleeper to be reduced. Its possibility of occurrence significantly increases under resonance conditions; which may occur due to high speed and repeated action of the axle loads [3].

In this regard, Zacher and Baeßler [4] conducted a shaking table test; in which they observed that the lateral resistance of the sleeper was significantly reduced at vertical accelerations about 7 m/s^2. The obtained outcomes revealed that the proposed vertical acceleration limit in EN-1990-A2 [5], i.e. 3.5 m/s^2 for ballasted tracks comply with a safety factor of 2. Therefore, further researches particularly reliability assessments may be conducted to evaluate the achieved safety level by following current regulations. Those investigations may lead to more reliable design thresholds.

Generally, probability of failure/violation (p_f) of limit state (performance) function can be estimated by calculating reliability integral as follows [6]:

$$p_f = P[R - S \leq 0] = P[G(\mathbf{X}) \leq 0] = \int ... \int_{G(X)\leq 0} f_X(\mathbf{x}) d\mathbf{x} \tag{1}$$

Where, $G(\mathbf{X})$ is the limit state function (safety margin) representing capacity (resistance - R) minus demand (load effects - S) and $f_X(\mathbf{x})$ is the joint probability density function of all random (basic) variables.

The aforesaid integration cannot be calculated in real (complicated) problems; in which contributing random variables present an n-dimensional hyperspace. Thus, practical solutions have been developed to either numerically evaluate the integral (such as Monte Carlo simulations) or approximate it (e.g. First Order Reliability Method - FORM). The current article adopted FORM to evaluate the probability of ballast instability in simply supported bridges under the passage of high-speed trains.

Within the FORM method, the safety level is expressed as a *reliability index* (β); which is the shortest distance from the origin to the desired limit state function (see Figure 1). Then, the probability of failure can be estimated as Eq. 2:

$$p_f \approx \Phi(-\beta) \tag{2}$$

Where Φ is the standard Normal (Gaussian) distribution function.

Generally, FORM considers the linear approximation of the limit state function using Taylor series expansion around the most probable point (MPP) or checking point (shown as u^* in Figure 1); which its surrounding area has the highest contribution on the failure probability. Detailed information regarding FORM can be found in [6, 7]. Therefore, its outcome would depend on the used formulation defining failure surface; which is contrary to invariant problem. Thus, considered random variables and consequently, the limit state function should be transformed to standard Normal space using Hasofer-Lind transformation (Eq. 3).

$$U_i = \frac{X_i - \mu_{X_i}}{\sigma_{X_i}} \tag{3}$$

Where, X_i is the basic random variable with first two moments of μ_{X_i} and σ_{X_i} and U_i is the transformed random variable.

Furthermore, the obtained direction cosines ($\boldsymbol{\alpha}$) can be used as a sensitivity of the transformed limit state function to the random variables. In this study, the omission sensitivity factor (γ_i) is employed in addition to the direction cosines; which presents the relative importance of the random variable on reliability index if it was considered as deterministic. It is defined as the ratio of the reliability index when the i^{th} random variable is deterministic (β_i^f) to the reliability index when all variables are stochastic [8]. For independent random variables it would be as follows:

$$\gamma_i = \frac{\beta_i^f}{\beta} = \frac{1}{\sqrt{1-\alpha_i^2}} \tag{4}$$

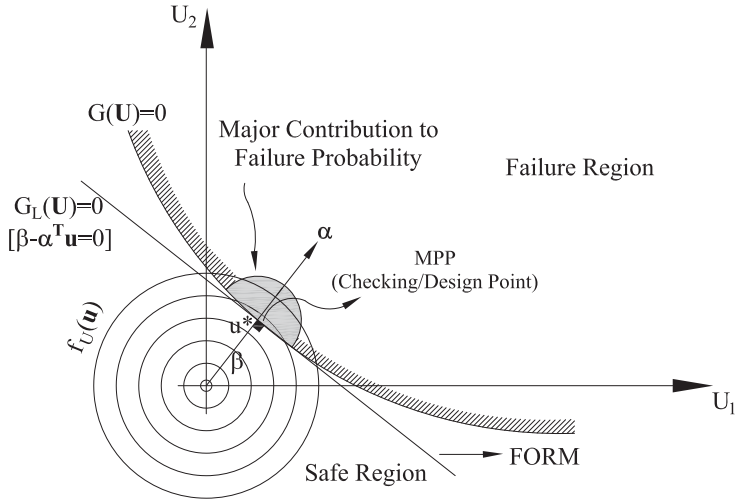

Figure 1: Schematic concept of the FORM [6, 7]

2 CONSIDERED ANALYTICAL SOLUTION

Detailed investigation of the dynamic behavior of railway bridges can be achieved by modeling bridge structure, boundary conditions (soil-structure interaction - SSI), ballast, track, rail, train and their interactions (train-track-bridge interaction - TTBI). Schematic view of such a general model is shown in Figure 2a. In spite of providing detailed insight regarding dynamic response, the general model requires considering many random variables; which significantly increases computational costs of reliability evaluations. Furthermore, the probability characteristics of interaction- and boundary condition related variables are not well exploited. Thus, a simplified model including passage of a series of moving loads along a simply supported beam is taken into account here (see Figure 2b).

A close-form solution has been previously presented by [9, 10] to calculate beam deflection under such loading scenario. Therefore, the second derivative of the proposed solution is derived here to estimate the vertical acceleration of the bridge. Those equations are presented in Eqs. (5) to (10).

$$\ddot{u}(t) = \sum_{n=1}^{\infty} \ddot{q}_n(t)\phi_n(x) = \sum_{n=1}^{\infty} \ddot{q}_n(t)\sin(\frac{n\pi x}{L}) \tag{5}$$

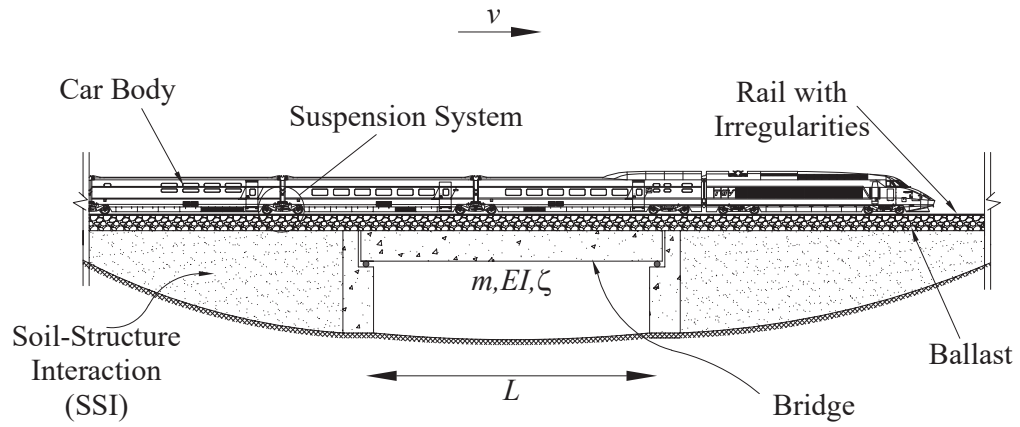

(a) General model with TTBI

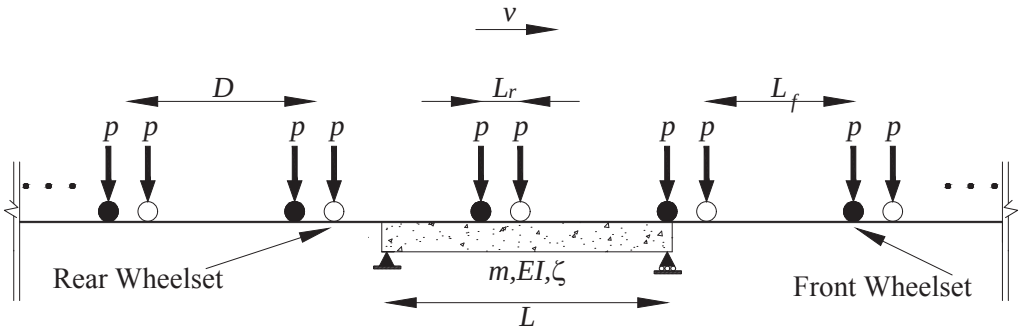

(b) Simplified adopted model

Figure 2: General modeling of railway bridge under passage of trains versus simplified adopted load model

$$\ddot{q}_n(t) = \frac{2pL^3}{EI\pi^4}[P_n(v,t) + P_n(v,t - L_f/v)] \tag{6}$$

$$\begin{aligned} p_1 &= 1 - {S_n}^2, \quad p_2 = 2\xi_n S_n, \quad p_3 = -\xi_n \omega_n \\ p_4 &= \frac{S_n(2{\xi_n}^2 + {S_n}^2 - 1)}{\sqrt{1 - {\xi_n}^2}}, \quad t_k = \frac{(k-1)D}{v} \end{aligned} \tag{7}$$

$$P_n(v,t) = \frac{1}{n^4}\sum_{k=1}^{N}\frac{1}{{p_1}^2 + {p_2}^2}\left[A(t-t_k).H(t-t_k) + (-1)^{n+1}A(t-t_k-\frac{L}{v}).H(t-t_k-\frac{L}{v})\right] \tag{8}$$

$$\begin{aligned} \alpha_1 = -p_1{\Omega_n}^2, \quad \alpha_2 = p_2{\Omega_n}^2, \quad \alpha_3 &= p_2{p_3}^2 + 2p_3p_4\omega_{dn} - p_2{\omega_{dn}}^2 \\ \alpha_4 &= {p_3}^2p_4 - 2p_2p_3\omega_{dn} - p_4{\omega_{dn}}^2 \end{aligned} \tag{9}$$

$$A(t) = \alpha_1 \sin\Omega_n t + \alpha_2 \cos\Omega_n t + e^{p_3 t}\left[\alpha_3 \cos\omega_{dn} t + \alpha_4 \sin\omega_{dn} t\right] \tag{10}$$

Where, $\ddot{u}(t)$ is the deck acceleration, $\ddot{q}_n(t)$ is the generalized coordinate, $\phi_n(x)$ is the mode shape of the n^{th} mode of vibration, L is the span length of the beam, p is the axle load, EI is the flexural rigidity of the beam, v is the speed of the train, L_f is the distance between the front and rear wheelsets subsystems in each car body, $S_n = n\pi v/\omega_n L$ is the speed parameter corresponding to the n^{th} mode of vibration, ξ_n is the damping ratio of the n^{th} mode of vibration, D is the distance between front to front or rear to rear wheelsets in subsequent car bodies, N is the number of car bodies, $H(t)$ is the Heaviside function, $\Omega_n = S_n\omega_n$ is the exciting frequency implied by the moving load and $\omega_{dn} = \omega_n\sqrt{1-\xi_n^2}$ is the damped frequency of the n^{th} mode of vibration.

It is worthwhile noting that only the first mode of vibration is considered here for the sake of simplification. Such consideration imposes some errors particularly at off-resonance speeds; however, it results in accurate enough predictions for resonance speeds. Therefore, considering only one mode of vibration may not generally affect the safety of the bridge.

Additionally, it has been previously observed that spreading axle loads through the track structure (rails, sleepers and ballast) significantly reduces the bridge response particularly for the short span ones [11]. Therefore, a reduction coefficient is multiplied by the obtained response from the aforementioned analytical solution; which is obtained by fitting the presented relationship in Eq. 11 to the graphically proposed reduction factor in [12].

$$R(\lambda) = \begin{cases} 0.14 & ,\lambda \leq 1.5 \\ -0.00011\lambda^4 + 0.0053\lambda^3 - 0.083\lambda^2 + 0.57\lambda - 0.54 & ,1.5 < \lambda < 8.0 \\ 1.0 & ,\lambda \geq 8.0 \end{cases} \tag{11}$$

Where, $\lambda = v/f_1$ is the wavelength.

2.1 Verification of analytical solution

A previously presented example by Yang et al. [9] is taken into account to verify the adopted analytical solution. For this objective, mid-span acceleration of a simply supported beam with $L = 20$ m, $I = 2.81$ m^4, $E = 29.43$ GPa and $m = 34088$ kg/m under passage of a train with $N = 5$, $L_f = 18$ m, $L_r = 6$ m, $p = 215.6$ kN and $v = 122.4$ km/h is calculated. The considered speed corresponds to the resonance speed of the bridge. Additionally, two cases, i.e. without damping and $\xi = 2.5\%$ is taken into account. The obtained analytical accelerations are compared with those resulted from numerical evaluations in Figure 5; which, a promising agreement can be distinguished. It is worthwhile noting that the numerical calculations are conducted using Newmark's average acceleration method; however, reduction factor due to load distributions is neglected for the comparison objectives.

3 BASIC VARIABLES AND LIMIT STATE FUNCTION

As mentioned, the current article aims at evaluating the probability of ballast instability under passage of high-speed trains. Thus, the performance function regarding this limit state would be as follows:

$$G(\mathbf{X}) = a_{limit} - |a_{max}(\mathbf{X})|(1+\chi_m) \tag{12}$$
$$\mathbf{X} = (N, D, p, v, L, E, I, A_d, A_b, \rho_d, \rho_b, \xi, \chi_m)$$

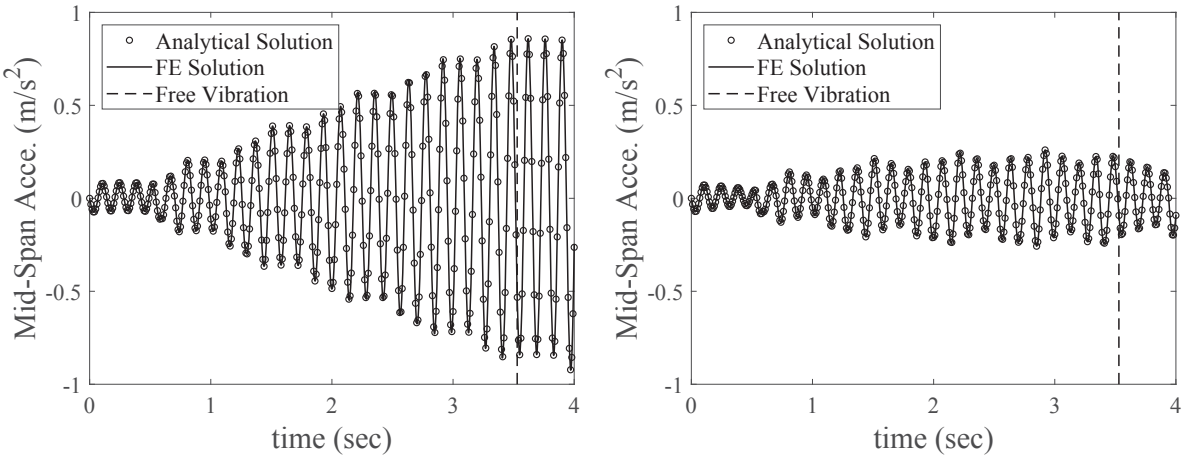

(a) Without damping (b) $\xi = 2.5\%$

Figure 3: Verification of analytical solution with numerical method by comparing mid-span acceleration

Where, a_{limit} is the vertical acceleration initiating ballast instability, E is the modulus of elasticity of deck, I is the moment of inertia of deck, A_c is the deck area, A_b is the ballast area, ρ_d is the mass density of deck, ρ_b is the mass density of ballast, ξ is the damping ratio and χ_m is the model uncertainty. It is worthwhile noting that ballast has much lower modulus of elasticity than the deck [1]; which led its contribution in stiffness to be neglected.

As previously mentioned, only few shaking table tests have been conducted to determine the vertical acceleration leading ballast instability [4]. Thus, a triangular probability distribution is considered for a_{limit}; which its mode equals to experimentally captured value, i.e. 0.7g. Furthermore, a possible variation of 0.1g is taken into account based on authors' judgment to define its boundaries.

Regarding the applied loads, it is hardly possible to collect information corresponding to the variability of parameters in commercial trains. Thus, proposed load models in Annex E of Eurocode [13] are applied here. Hence, the uncertainty on moving loads would be a function of constant axle load (p_{axle}) and occupancy rate (α in %). By assuming the full passenger capacity of each car body as 65 and average weight of each passenger as 70 kg, the moving load can be calculated as Eq. 13; which is developed in kN units.

$$p = p_{axle} + 0.225\alpha \tag{13}$$

In order to select practically reasonable geometrical values (i.e. span length, moment of inertia and deck/ballast area) 62 single span and single track bridges in Sweden are surveyed. Detailed information about them can be found in [14]. The span length of the desired bridges varies between [5-30]m. Therefore, evaluations are conducted within this range for deterministic span lengths with a resolution of 5m.

The distribution of span length, moment of inertia, deck and ballast areas in addition to their linear correlations are depicted in Figure 4. A strong correlation between span length, moment of inertia and deck area is evident; while as expected, the ballast area seems to be independent on span length. Hence, a conditional probability for the moment of inertia and deck area is assigned (see Figures 5a and 5b); which, the parameters are extracted by regression analysis and fitting lower and upper boundaries. On the other

hand, the shown scatter plot of the ballast area (see Figure 5c) reveals that they mostly vary around mean value regardless of the span length. Due to extracting distributions from a limited database, a triangular probability distribution is adopted for the all geometrical random variables.

It is well-known that the response of the bridges is highly dependent on the damping ratio particularly around resonant speed. Additionally, the contribution of several factors makes damping measurement a tedious task; which may result in scattered outcomes. Therefore, the proposed lower bound in [12] is taken here as the mean value of the damping ratio.

Discussed simplifications and existing lack of knowledge on different aspects of the problem deviate the predicted responses by the adopted solution from corresponding real values. Thus, a model uncertainty (χ_m) is applied to the limit state function; which should be obtained from comparison of the experimentally captured values with those resulted from the numerical model. However, the lack of such information led to propose a model based on the authors' judgment. In this regard, a Gaussian probability density function with zero mean and a standard deviation of 20% is taken into account.

Considering all, the assigned parameters for the variables are reported in Table 1.

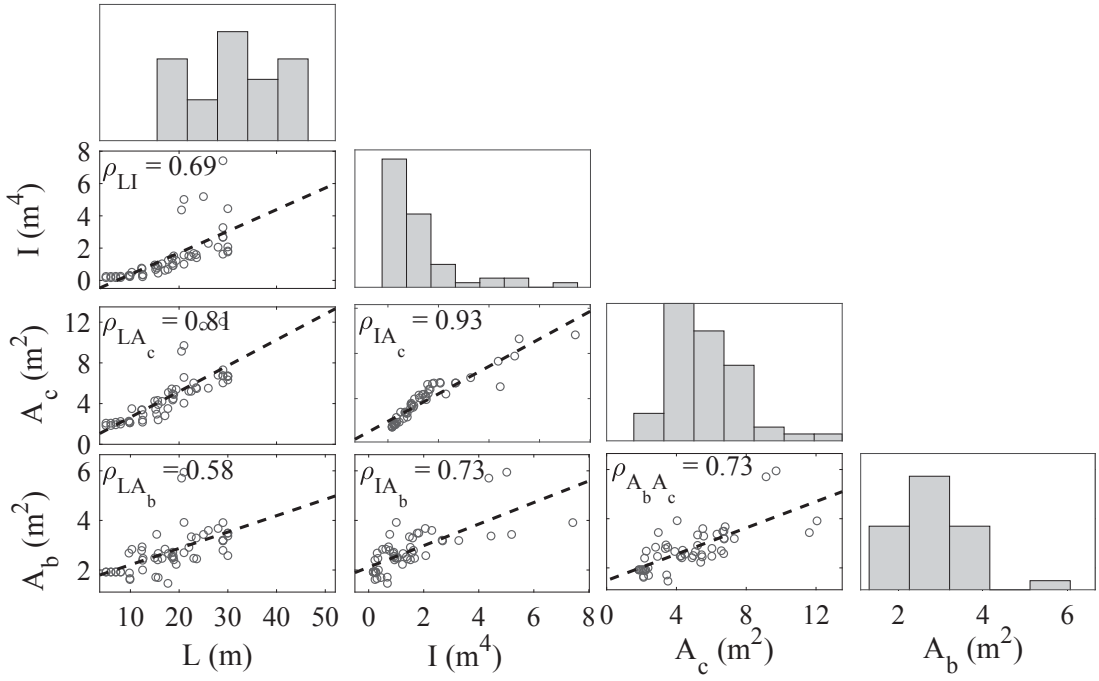

Figure 4: Correlation between span length, deck moment of inertia, deck area and ballast area

4 RESULTS AND DISCUSSION

Initially, the considered bridges are assessed following deterministic approaches. For this objective, the speed of passing trains swept between 100 km/h up to 400 km/h; while the average values are assigned for each variable. The analyses are repeated by changing each variable to mean plus/minus one standard deviation; while other variables remained constant. Hence, the train speed leading the vertical acceleration to surpass 3.5 m/s^2 is extracted (see for instance Figure 6). The obtained deterministic operating train speeds are reported in Table 2.

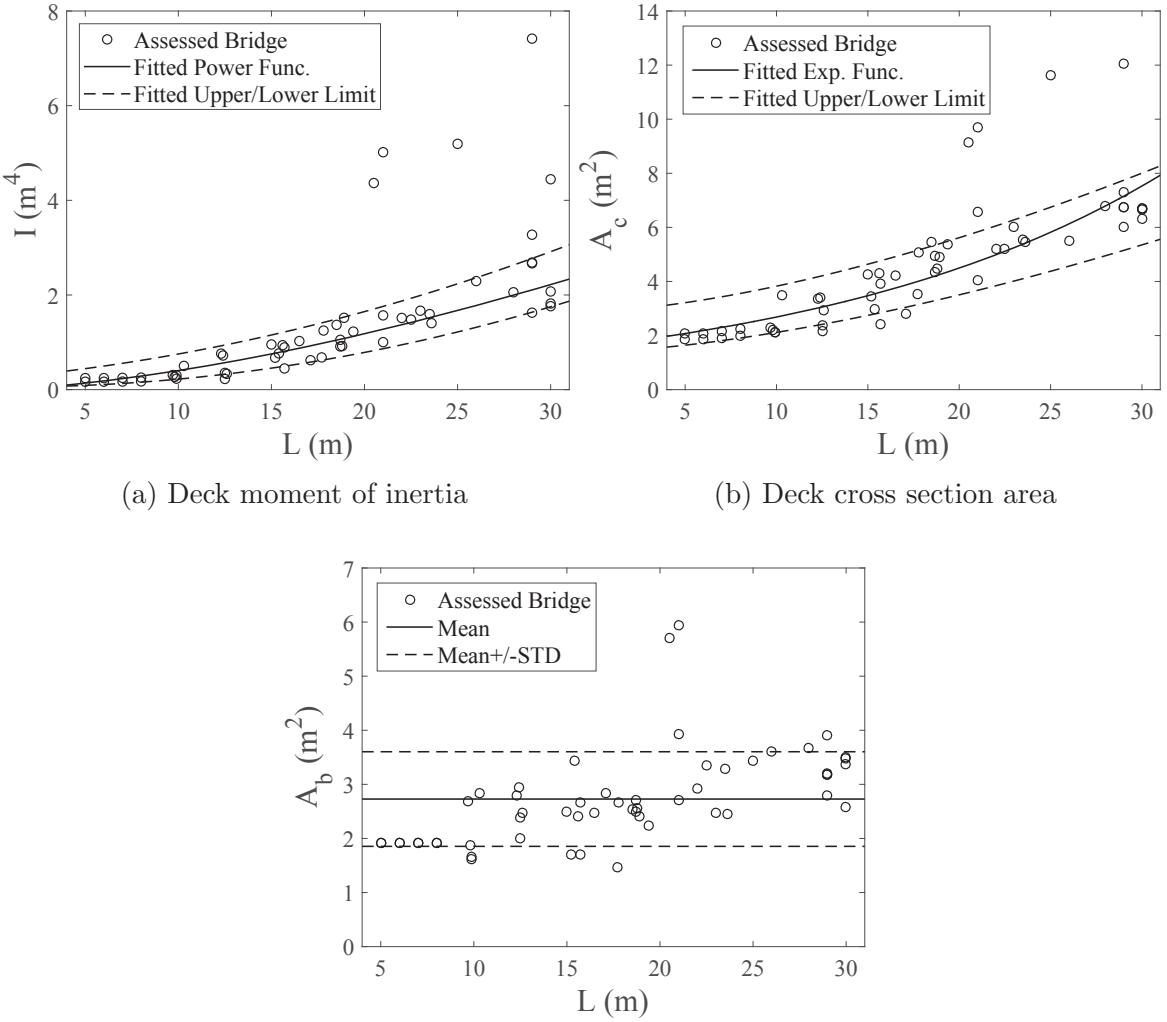

(a) Deck moment of inertia

(b) Deck cross section area

(c) Ballast area

Figure 5: Distribution function for deck moment of inertia, deck cross section area and ballast area as a function of span length

Then, the reliability of the developed limit state function is assessed using FORM. In this regard, UQLab toolbox [16] is employed to conduct the analyses and extract the corresponding probability of violence. For this objective, the span length of the bridge is assumed as a deterministic parameter varying in the desired range and properties of the other parameters are adopted as those tabulated in Table 1. Then, the reliability of each bridge is assessed for all considered trains with different configurations; while a speed resolution of 2 km/h is taken into account. Since the probability of violation is calculated at discrete points; then, the average exceeding (failure) probability ($p_{f,ave}$) can be calculated using Eq. 14 [18].

$$p_{f,ave} = \int_{v_l}^{v_u} P(a_{deck}(v) > a_{limit}) f_v(v) dv \approx \frac{1}{n} \sum_{i=1}^{n} P(a_{deck}(v_i) > a_{limit}) \tag{14}$$

Where, n is the number of discrete evaluations.

Variable	Unit	Dist.	Mean/Mode Min.	STD/Bound. Max.	Ref.
a_{limit}	m/s^2	Triangular	7.0	[6.0-8.0]	-
N	-	Uniform (Integer)	11	18	[13]
D	m	Uniform	18	27	[13]
L_r	m	Uniform	2.5	3.5	[13]
p_{axle}	kN	Deterministic	170	-	[13]
α	%	Uniform	0	100	-
v	km/h	Deterministic	100	400	-
L	m	Deterministic	5	30	-
E	GPa	Truncated Gaussian [a]	29.7	3.5	[15]
I	m^4	Triangular [b]	M_I	[LB_I-UB_I]	-
A_c	m^2	Triangular [c]	M_{A_c}	[LB_{A_c}-UB_{A_c}]	-
A_b	m^2	Triangular	2.7	[1.85-3.6]	-
ρ_c	kg/m^3	Lognormal [d]	7.82	0.04	[1]
ρ_b	kg/m^3	Uniform	1500	2100	[1]
ξ	%	Lognormal [e]	μ_ξ	σ_ξ	[1, 12]
χ_m	%	Gaussian	0	20	-

[a] The mean value is obtained from $5015\sqrt{f'_c}$ [MPa] and considering C35 as typical concrete class in bridges. A COV of equaling 12% is also considered. Due to controlled construction conditions of the railway bridges, the assigned probability distribution is truncated for values deviated more than two standard deviation from the mean value.
[b] The mode is obtained from regression analysis between span length and moment of inertia in the surveyed bridges; which equals as $M_I = 0.011(L^{1.55})$. Furthermore, the lower and upper bounds would obtain from $\mathrm{LB}_I = 0.002L^2 - 0.004L + 0.06$ and $\mathrm{UB}_I = 0.00185L^2 + 0.034L + 0.23$, respectively.
[c] The mode is obtained from regression analysis between span length and cross section area; which equals as $M_{A_c} = 1.6\exp(0.052L)$. Since cross section area is highly correlated to the moment of inertia; therefore, boundaries are obtained from $\mathrm{LB}_{A_c} = 1.781M_I + 1.4$ and $\mathrm{UB}_{A_c} = 2.3M_I + 2.9$, respectively.
[d] Reported mean and standard deviation correspond to 2500 kg/m^3 and 100 kg/m^3 mean and standard deviation in physical space, respectively.
[e] The mean value of the damping in normal space is obtained from $1.5 + 0.07(20 - L)$ [12] for bridges with less than 20 m span length and equals to 1.5% [12] for others. It is needed to be transformed to logarithmic space. Furthermore, the standard deviation of the lognormal distribution should be obtained by considering aforesaid mean and standard deviation of 0.3% in physical space.

Table 1: Considered variables and their stochastic/deterministic properties

The aforesaid probabilities are required to be compared by an appropriate target reliability index. Regarding the nature of the problem, it can be inferred both as serviceability (SLS) or ultimate (ULS) limit states. The former corresponds to the maintenance and tamping of the ballast; however, the later can be considered as severe cases in which ballast instability may lead to derailment. Hence, $\beta = 3.1$ ($p_f \approx 10^{-3}$) is considered as the target reliability [17, 18].

Then, the average probability of exceeding vertical limit acceleration versus train speed is illustrated in Figure 7. Only outcomes corresponding to 5m and 30m span lengths are presented here for the sake of brevity; while, the extracted operating speeds for all bridges

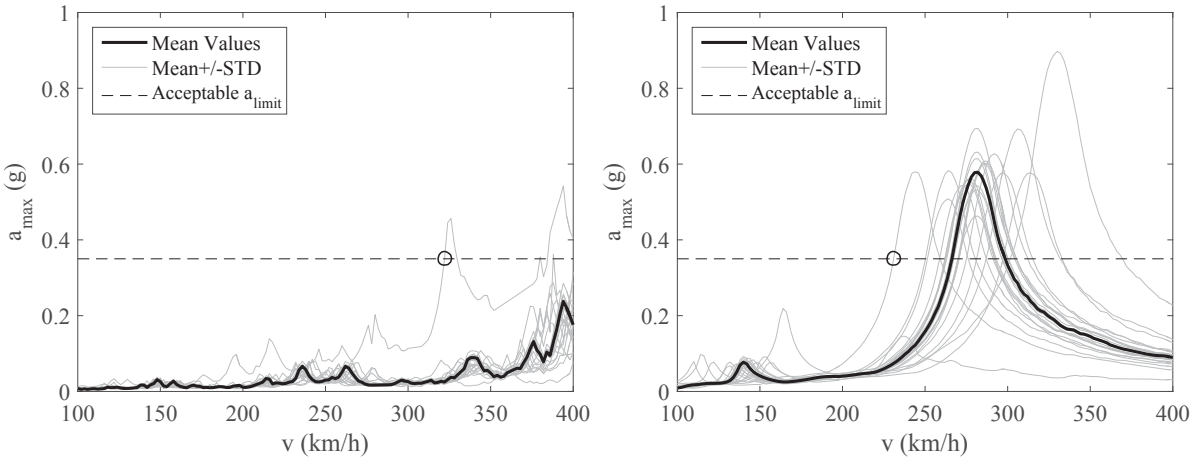

(a) L = 5m (b) L = 30m

Figure 6: Deterministic running safety assessment of the considered bridges

are reported in Table 2. As can be seen, the conventional deterministic approach does not lead at a constant safety level; which may result in designs with ambiguous capacity. Furthermore, it can be inferred from those safety indices that the conventional design method does not satisfy the desired safety level ($p_f = 10^{-3}$). The latter statement is particularly true for bridges with larger span lengths. Such lower safety may arise from several factors. Most importantly, shorter span bridges have generally higher frequencies. Thus, higher train speeds are required to observe the resonance phenomenon. In addition, the distribution of loads on track structure significantly reduces the response of bridges with shorter span lengths; while its influence would be negligible for larger span lengths.

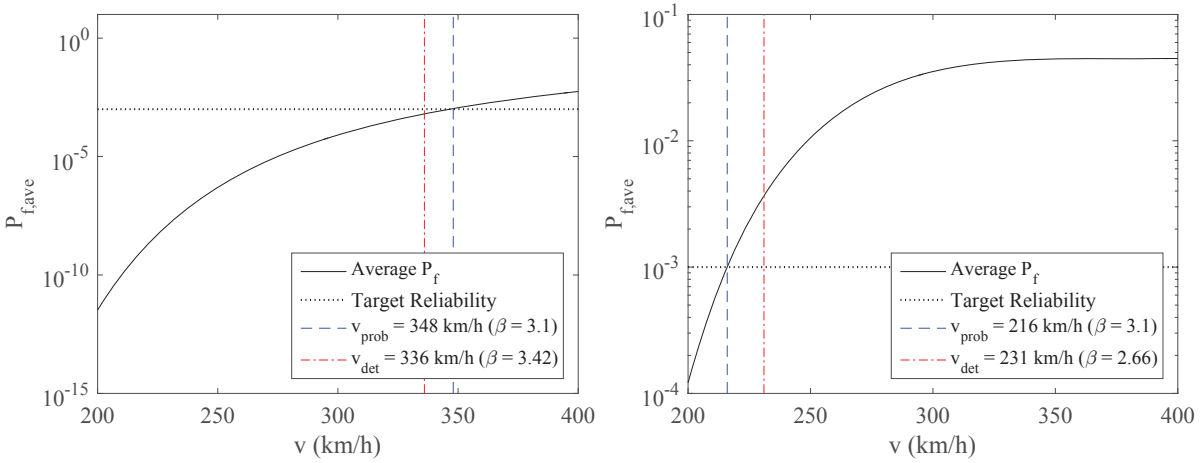

(a) L = 5m (b) L = 30m

Figure 7: Reliability-based assessment of the considered bridges

Finally, the sensitivity of the reliability evaluations to the considered random variables is assessed using both direction cosines and omission sensitivity factor (see Figure 8). As can be seen, the response is most sensitive to variations on car-body length, modulus

L (m)	v_{prob} (km/h)	v_{det} (km/h)	β_{det}
5	348	322.0	3.42
10	230	315.5	1.97
15	250	284.0	2.37
20	170	215.0	2.01
25	148	186.0	2.27
30	216	231.0	2.66

Table 2: Comparison between reliability-based assessment versus deterministic evaluation

of elasticity and deck moment of inertia. It is worthwhile to note that deck/ballast cross section area and their mass densities are also relatively important; which leads the reliability level to be sensitive on their combination, i.e. mass of the bridge.

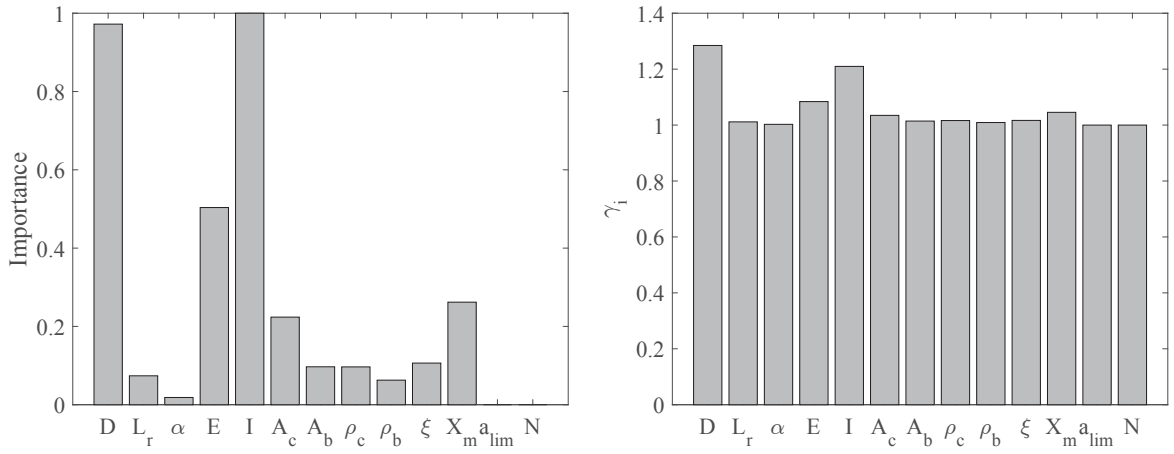

(a) Sensitivity from direction cosines

(b) Omission sensitivity

Figure 8: Sensitivity of the reliability evaluations to the considered random variables

5 CONCLUSIONS

- An existing closed-form solution is adopted to evaluate the reliability of simply supported single span high-speed railway bridges using FORM. It was noted that the conventional deterministic dynamic assessments result in bridges which do not satisfy desired target reliability level ($\beta = 3.1$).

- Despite applying a safety factor of 2.0 for the vertical acceleration limit, the conventional design method does not lead to a constant safety level on bridges with different span lengths.

- Reliability of the bridges are mostly sensitive to the car-body length, modulus of elasticity and deck moment of inertia. Moreover, the mass of the bridge would be a function of deck cross section area, ballast area, concrete mass density and ballast mass density. Thus, by considering their importance the assessed reliability would be considerably sensitive to their combination, i.e. mass of the bridge.

REFERENCES

[1] Rocha J.M., Probabilistic Methodologies For the Safety Assessment of Short Span Railway Bridges For High-Speed Traffic, PhD Dissertation, University of Porto, 2015.

[2] Arvidsson T., Train-Track-Bridge Interaction for the Analysis of Railway Bridges and Train Running Safety, PhD Dissertation, KTH Royal Institute of Technology, 2018.

[3] Frýba L., A Rough Assessment of Railway Bridges For High Speed Trains, *Engineering Structures*, **23**, 548–556, 2001.

[4] Zacher M., Baeßler M., Dynamic Behaviour of Ballast on Railway Bridges, in Dynamics of High-Speed Railway Bridges, *Taylor & Francis*, 2009.

[5] CEN, EN 1991-A2, Eurocode 0: Basis of Structural Design - Annex A2: Applications for Bridges, European Committee for Standardization, 2005.

[6] Melchers R.E., Beck A.T., Structural Reliability Analysis And Prediction, *Wiley*, ISBN: 978-1-119-26599-3, 2018.

[7] Sørensen J.D., Notes in Structural Reliability Theory And Risk Analysis, Department of Civil Engineering, Aalborg University, 2011.

[8] Madsen H., Omission Sensitivity Factors, *Structural Safety*, **5**, 35–45, 1988.

[9] Yang Y.B., Yau J.D., Hsu L.C., Vibration of Simple Beams Due to Trains Moving at High Speeds, *Engineering Structures*, **19**(11), 936–944, 1997.

[10] Yang Y.B., Yau J.D., Wu Y.S., Vehicle-Bridge Interaction Dynamics With Applications to High-Speed Railways, *World Scientific*, ISBN: 981-238-847-8, 2004.

[11] Jin Z., Huang B., Ren J., Pei S., Reduction of Vehicle-Induced Vibration of Railway Bridges due to Distribution of Axle Loads Through Track, *Shock and Vibration*, Article ID 2431980, 2018.

[12] ERRI D 214/RP 9, Rail Bridges for Speeds > 200 km/h, Final Report Part A: Synthesis of the Results of D 214 Research, European Rail Research Institute, 1999.

[13] CEN, EN 1991-2, Eurocode 1: Actions on Structures - Part 2: Traffic Loads on Bridges, European Committee for Standardization, 2003.

[14] Museros P., Andersson A., Marti V., Karoumi R., Dynamic Behaviour of Bridges Under Critical Articulated Trains: Signature and Bogie Factor Applied to the Review of Some Regulations Included in EN 1991-2, Submitted to *Journal of Rail and Rapid Transit*, 2020 (Under Review).

[15] Wiśniewski D.F., Safety Formats For the Assessment of Concrete Bridges with Special Focus on Precast Concrete, PhD Dissertation, University of Minho, 2007.

[16] Marelli S., Sudret B., *UQLab: A Framework for Uncertainty Quantification in MATLAB*, In the 2nd International Conference on Vulnerability and Risk Analysis and Management (ICVRAM 2014), University of Liverpool, UK, 2014.

[17] JCSS, Probabilistic Model Code, 12th Draft, *JCSS-Joint Committee on Structural Safety*, ISBN: 978-3-909386-79-6.

[18] Hirzinger B., Adam C., Oberguggenberger M., Salcher P., Approaches for Predicting the Probability of Failure of Bridges Subjected to High-Speed Trains, *Probabilistic Engineering Mechanics*, **59**, 103021, 2020.

EURODYN 2020
XI International Conference on Structural Dynamics
M. Papadrakakis, M. Fragiadakis, C. Papadimitriou (eds.)
Athens, Greece, 23–26 November 2020

RESPONSE OF ELASTIC SHOCK OSCILLATORS AND ELASTO-PLASTIC OSCILLATORS, WHITELY EXCITED, FROM ENERGY BALANCE AND STOCHASTIC ANALYSES

Laurent B. Borsoi[1], **Philippe Piteau**[2]

[1] LTB-Conseils
19 route de la Plage, 50740, Carolles, France
e-mail: laurent.borsoi@orange.fr

[2] Den-Service d'études mécaniques et thermiques (SEMT), CEA, Université Paris-Saclay,
F-91191, Gif-Sur-Yvette, France
e-mail: philippe.piteau@cea.fr

Keywords: Oscillator, Elasto-Plastic, Shock, White Noise, Energy Balance, Diffusion Process, Stochastic Variational Inequality

Abstract. *This paper deals with mechanical nonlinear oscillators, of mass-spring type, subjected to white noise excitation. First, a remarkable property is noted: the energy, per time unit, injected into the oscillator by the external force depends only on the white PSD level (directly), and the oscillator mass (inversely). So, different oscillators, whatever their nonlinearities and dissipation mechanisms, receive, and consequently dissipate, the same energy rate from the white noise provided they have the same mass. It is discussed how this simple energy balance, eventually connected to additional conjectures, gives information about the dynamics of oscillators of two classes, (i) the elastic shock oscillators (ESO), and (ii) the elasto-plastic oscillators (EPO), both including different subclasses (for the symmetry of stops or the type of plasticity). But relevant theories are needed to go further. The paper focuses on two items linked to stochastic diffusion processes. Concerning ESO with undamped stops, the theory leads, via the Fokker-Planck equation, to an analytical expression for the probability density function (PDF) of the oscillator in the phase space. Quantities of interest (like Rice frequency, impact frequency or distribution) may then be deduced under closed-form, even for totally asymmetric ESO. Concerning (perfectly) EPO, a completely new approach has appeared for a decade, based on stochastic variational inequality (SVI). The infinitesimal generator proper to the diffusion is degenerated and works in the special phase space defined from the EPO velocity and its elastic displacement. Joint PDF can be numerically determined through heavy computations, as illustrated by an example using finite differences. Finally, the paper comments the "white noise of engineers", the PSD of which is realizable since truncated in frequency, which justifies some assumptions and simplifies the plastic-elastic transitions for EPO, as well as the stop contact phases for ESO.*

1 INTRODUCTION

The starting point for apprehending mechanical vibration relies ordinarily on the single oscillator made of a lumped mass, a linear spring and a viscous dashpot. Indeed, this 1-DOF model evidences, without too much mathematics, basic physical concepts of linear vibration such as free or forced response, resonance, etc. Moreover, it even represents sometimes "reality" with sufficient accuracy, i.e. at the first order filter. At last, it gives birth to more advanced concepts, such as response spectrum or transfer function, that found many linear analyses of multi-DOF structures, in various fields: seismic, shock, random vibration, etc. Moving from linear to nonlinear vibration is never a straight forward extrapolation, but constitutes a *giant* step as the superposition principle is lost and no general theory exists. Consequently, the nonlinear vibration issues must be solved on a case-by-case basis. Nevertheless, the 1-DOF approach remains a good starting point, despite two major differences with the linear case: (i) the multiplication of 1-DOF models according to the nonlinearity; (ii) the dramatic challenging task for the multi-DOF extensions.

This paper deals with such 1-DOF approach. For keeping a certain degree of generality, it considers nonlinear single oscillators of two distinct classes, (i) the elastic shock oscillator (ESO), and (ii) the elasto-plastic oscillator (EPO), both subjected to white noise excitation.

Firstly, these cases, although a priori academic, are emblematic of real situations in mechanical or civil engineering. ESO under white noise might be associated to flow induced vibration (FIV) of components excited by turbulence, and whose supports have gaps, which is common in industrial facility to cope with thermal expansion. EPO under white noise might be associated to structures or components seismically shaken, that experience plastic excursions, the quantification of which is needed, notably in the margin studies with beyond design earthquakes.

Secondly, ESO and EPO present well-marked and very different nonlinearities that may be considered as two extreme cases, without and with "memory". But thirdly, the white noise excitation is rather universal; it does not depend on the oscillator response as any additive external force, but injects energy into the oscillator independently of its rigidity or damping, which is really a remarkable property.

Schematically, the paper aims at understanding and quantifying some features of the dynamics of ESO and EPO, whitely excited, by following two opposite ways. The first one, very simple, is based on the elementary energy balance mentioned above, eventually connected to additional conjectures. The second one, quite complicated in comparison and more mathematical, uses results produced by the theory of stochastic diffusion processes. The amount of information naturally grows with the degree of sophistication of analyses. But it is always interesting - and it is one of the paper's goals - to stress how very simple analyses can provide pertinent results, especially for extracting orders in magnitude.

2 ENERGY INJECTED BY A WHITE NOISE

The energy injected, per time unit, into the oscillator by the external force f(t) - in other words, the inserted mechanical power - may be heuristically calculated by considering an approximated or "truncated" white noise with time step Δt. In this modeling, the continuous force f(t) is a step piecewise function, build from the discretized values $f(t_k)$ of the force at time $t_k=k\times\Delta t$, $k\in\mathbb{Z}$: $f(t)=\sum_k f(t_k)\times\left(H(t-t_k)-H(t-t_{k+1})\right)$, where H is the Heaviside function and $f(t_k)$ a randomly distributed variable with zero mean and finite variance, all values being independent one from each other. By construction, the force value $f(t_k)$ and the oscillator velocity $\dot{x}(t_k)$ are independent variables, but $f(t_k)$ and the oscillator velocity

$\dot{x}(t_k + \Delta t)$ at the end of the time step are linked through the impulse generated by the force f(t) constant during the time step Δt. If this later is small enough for ensuring first order developments, we have (with m the oscillator lumped mass):

$$\Delta\dot{x}_k(\Delta t) = \dot{x}(t_k + \Delta t) - \dot{x}(t_k) = \frac{f(t_k).\Delta t}{m} \tag{1}$$

In fact, the impulse is linear on the time interval Δt: $\Delta\dot{x}_k(\tau) = f(t_k).\tau/m$, $\tau \in [0, \Delta t)$. The mathematical expectation of the instantaneous injected power is thus:

$$P_f = \langle p_f(t) \rangle = \frac{1}{\Delta t}\left\langle \int_0^{\Delta t} f(t_k).\Delta\dot{x}_k(\tau).d\tau \right\rangle = \frac{\Delta t}{2.m}\left\langle f(t_k)^2 \right\rangle \tag{2}$$

Let F_0 the level of the power spectral density (PSD) of the mathematical white noise expressed in negative and positive pulsations ω, ranging from -∞ to +∞ and, so, leading to an infinite variance. The "physical" white noise f(t), as build above, has a finite variance since Δt is finite: $\langle f(t)^2 \rangle = \langle f(t_k)^2 \rangle$. Its PSD can be easily deduced from the auto-correlation function, $R_{ff}(\tau) = \langle f(t).f(t+\tau) \rangle$; we have [3]: $S_{ff}(\omega) = \frac{\Delta t}{2\pi}.\langle f(t_k)^2 \rangle.\left(\frac{\sin(\omega\Delta t/2)}{\omega\Delta t/2}\right)^2$. By assimilating the mathematical PSD level to the zero-pulsation value of the physical PSD, $S_{ff}(0) = F_0$, we can get the following expression: $\int_{-\infty}^{+\infty} S_{ff}(\omega).d\omega = 2.F_0.\frac{2\pi}{2\Delta t} = \langle f(t)^2 \rangle = \langle f(t_k)^2 \rangle$, in which we recognize the Shannon cut-off pulsation: $\omega_c = 2\pi/2\Delta t$. So, Eq.(2) gives for the averaged power injected by f(t):

$$P_f = \langle p_f(t) \rangle = \frac{\Delta t}{2.m}\langle f(t_k)^2 \rangle = \frac{\pi.F_0}{m} \tag{3}$$

The energy rate injected by the white force f(t) is directly proportional to the PSD level and inversely proportional to the oscillator mass. No other characteristic acts in Eq.(3). Therefore, all the oscillators of the same mass, subjected to white noises of the same intensity, receive the same amount of energy, whatever their stiffnesses, dissipation mechanisms, and/or non-linearities of all kind (with or without a memory effect). Consequently, on the only condition that (at least) one dissipation mechanism exists, and works without any saturation, all the oscillators will dissipate the same energy rate and exhibit stationary responses (removing the initial transient part if the oscillator is at rest when the white noise applies).

3 DAMPED ELASTIC OSCILLATOR

Let us first consider a simple elastic oscillator made of the mass m, the elastic spring k_0, the viscous dashpot c_0 (always positive), submitted to a centered white noise force of intensity F_0 (PSD level). Thus, the mass motion satisfies the following time-history dynamic equation: $m.\ddot{x}(t) + c_0.\dot{x}(t) + k_0.x(t) = f(t)$. The differential energy dissipated by the dashpot at time t is: $dE_d(t) = c_0.\dot{x}(t).dx = c_0.\dot{x}(t)^2.dt$; hence the instantaneous dissipated power: $p_d(t) = c_0.\dot{x}(t)^2$; therefore, in average:

$$P_d = \langle p_d(t) \rangle = c_0.\langle \dot{x}(t)^2 \rangle = c_0.\sigma_{\dot{x}}^2 \tag{4}$$

Moreover, the injected power (precisely, its mathematical expectation) is strictly equal to the dissipated power (idem) for stationary processes since the vibratory energy (kinetic + potential elastic) is time independent: $\langle E_v(t)\rangle = \langle m.\dot{x}(t)^2/2 + k_0.x(t)^2/2\rangle = ct.$ Equalizing Eq.(4) to Eq.(3) produces the well-known formula for the velocity variance:

$$\sigma_{\dot{x}}^2 = \frac{\pi.F_0}{m.c_0} \tag{5}$$

Conjecturing the Rice pulsation, defined as: $\omega_{Ri} = \sigma_{\dot{x}} / \sigma_x$, is here equal to the oscillator eigen-pulsation, $\omega_0 = \sqrt{k_0 / m}$, we deduce from Eq.(5):

$$\sigma_x^2 = \frac{\pi.F_0}{m.c_0.\omega_{Ri}^2} = \frac{\pi.F_0}{k_0.c_0} \tag{6}$$

which is effectively the right expression for the displacement variance of an elastic oscillator whitely excited. In addition, it is recalled that the oscillator response is Gaussian.

4 ELASTIC SHOCK OSCILLATOR (ESO)

ESO model is presented Figure 1-a. ESO are "without memory" in the sense that the current state of the oscillator in the phase space (displacement-velocity) is sufficient to determine the internal force that applies on the mass. A typical behavior law in terms of force-displacement relationship is shown Figure 1-b. We consider as ESO sub-classes:

- the elastic symmetric shock oscillator (ESSO), with two symmetrical stops in compression, and consequently an odd behavior law for positive and negative displacements of the mass;
- the elastic asymmetric shock oscillator (EASO), e.g. with one stop on only one side, the behavior remaining linear in the opposite direction.

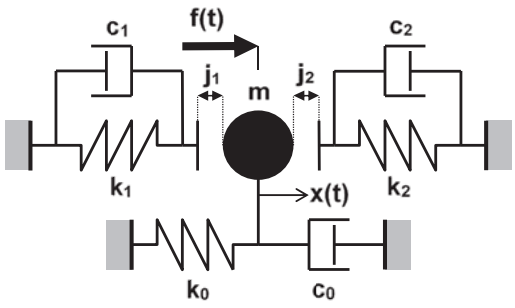

(a) ESO Model

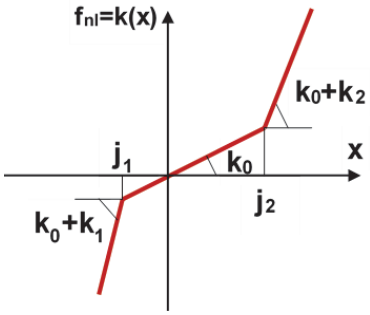

(b) Load-Displacement Law

Figure 1: Elastic Shock Oscillator (ESO)

4.1 ESO Response from Energy Balance

First, we consider ESSO, taking $j_1=j_2$ for the gap size, $k_1=k_2>>k_0$ for the stop stiffness, and $c_1=c_2=0$ for undamped stops (see Fig.1-a). So, the only dissipative component remains the viscous dashpot c_0 that is permanently acting; therefore, Eq.(5) still holds, which permits to get the *accurate* velocity variance that is independent of the stop characteristics (gap, rigidity).

The gap system is intuitively "bordered" by two extreme cases concerning the gap size: infinite (open gaps) or zero (closed gaps), that both produce a linear behavior. So, it can be conjectured that the actual Rice pulsation lies in the range: $\omega_0 \le \omega_{Ri} \le \omega_1 \simeq \sqrt{k_1 / m}$.

Let σ_{x0} the standard deviation in displacement obtained from Eq.(6), and attached to the associated linear oscillator (ALO) that corresponds to ESO with open gaps. The reduced gap, $j^*=j_1/\sigma_{x0}$, informs, at least qualitatively, about the occurrence of impacts knowing the ALO response is Gaussian. So, for "high" values of the reduced gap ($j^* \ge 3$), the impact frequency almost coincides with the ALO crossing rate [1-4]; for the right stop (idem for the left one): $f_j \simeq f_0.\exp(-j^{*2}/2)$; moreover, the Rice frequency is (quasi) the ALO one: $f_{Ri} \cong f_0 = \omega_0/2\pi$. But of course, the ALO predictions are no longer quantitative for lower reduced gaps.

Nevertheless, it appears that the impact peak values may be correctly estimated. The ESO joint PDF in the phase space is unknown (see § 4.2). But, we may conjecture: (i) the stationary PDF can be splitted according to the uncorrelated variables that are the displacement and velocity: $p(x,\dot{x}) = p_x(x).p_{\dot{x}}(\dot{x})$; (ii) the velocity part $p_{\dot{x}}(\dot{x})$, whose standard deviation is known via Eq.(5), is Gaussian. Common developments, e.g. [3,4], then permit to establish that the positive crossing velocity ($\dot{x}_a^+$) of any threshold (a) follows a Rayleigh distribution:

$$p_c(\dot{x}_a^+) = \frac{\dot{x}_a^+}{\sigma_{\dot{x}}^2}.\exp\left\{-\frac{\dot{x}_a^{+2}}{2.\sigma_{\dot{x}}^2}\right\} \quad ; \quad \left\langle \dot{x}_a^+ \right\rangle = \sqrt{\frac{\pi}{2}}.\sigma_{\dot{x}} \quad ; \quad \left\langle \dot{x}_a^{+2} \right\rangle = 2.\sigma_{\dot{x}}^2 \tag{7}$$

On the other hand, we can assume that, during each phase of stop contact, the impact peak value F_{max}, developed in the stop, depends at the 1st order on the impact velocity (velocity just at the contact start). This is equivalent to "forget" the white noise and dashpot, anticipating a quasi-zero mean effect. Hence the energy balance: $F_{max}^2 / 2.k_1 + k_0.j_1.(x_{max} - j_1) = m.\dot{x}_{j1}^{+2}/2$, with $F_{max} = k_1.(x_{max} - j_1)$. From Eq.(7), $\sigma_{\dot{x}0} = \omega_0.\sigma_{x0}$, $F_{max}^2 + 2.k_0.j_1.F_{max} \approx (F_{max} + k_0.j_1)^2$, we obtain the following approximation:

$$\frac{\langle F_{max} \rangle}{k_0.\sigma_{x0}} \simeq \sqrt{\frac{\pi}{2}}.\sqrt{\alpha} - j^* \quad \text{with} \quad \alpha = \frac{k_1}{k_0} \tag{8}$$

which will be proven to be excellent (see § 4.2).

4.2 ESO Response from Stochastic Diffusion Process

The ESO response to a white excitation constitutes a stochastic diffusion process (a class of Markov process) when described in the phase space displacement-velocity. Thus, the joint PDF, that is time dependent $p_t(x,\dot{x})$ given the initial conditions (e.g. ESO at rest when suddenly excited), satisfies a partial derivatives equation (PDE), the Fokker-Planck equation (also named forward Kolmogorov eq.), that is hereafter derived for ESO with undamped stops, k(x) being the nonlinear rigidity (see [1-5]):

$$\frac{\partial p_t(x,\dot{x})}{\partial t} = -\frac{\partial[\dot{x}.p_t(x,\dot{x})]}{\partial x} - \frac{\partial[(-k(x).m^{-1} - c_0.\dot{x}.m^{-1}).p_t(x,\dot{x})]}{\partial \dot{x}} + \pi F_0.m^{-2}.\frac{\partial^2 p_t(x,\dot{x})}{\partial \dot{x}^2} \tag{9}$$

The left term $\partial p/\partial t$ vanishes in stationary regime. Then, Eq.(9) has a "simple" analytical solution under the form, $p=C.\exp(-\gamma.E_v)$, where E_v is the ESO vibratory energy (elastic potential U(x) + kinetics $m.\dot{x}^2/2$), and C and γ two constants [5]:

$$p(x,\dot{x}) = \frac{1}{2\pi.\sigma_{x0}.\sigma_{\dot{x}0}.A}.\exp\left\{-\frac{1}{2.\sigma_{x0}^2}.\frac{2.U(x)}{k_0} - \frac{\dot{x}^2}{2.\sigma_{\dot{x}0}^2}\right\} \tag{10}$$

In Eq.(10), σ_{x0} and $\sigma_{\dot{x}0}$ represent the ALO standard deviations, respectively in displacement and velocity (see Eq.(6) & (5)). First, we note that the PDF properties, conjectured in the previous section, are verified. The constant A (or $C = 1/2\pi.\sigma_{x0}.\sigma_{\dot{x}0}.A$) is for the PDF normalization: $\int_{-\infty}^{+\infty}\int_{-\infty}^{+\infty} p(x,\dot{x}).dx.d\dot{x} = 1$, and is given in Appendix A for ESSO and EASO. Trivial calculations using the above PDF give birth to closed-form formula for certain quantities of interest [5-6]. Let us quote:

Crossing Rate. By applying the well-known Rice formula, $\nu_a^+ = \int_0^{+\infty} \dot{x}.p(a,\dot{x}).d\dot{x}$, we obtain:

$$\nu_a^+ = \nu_0^+.\exp\left\{-\frac{1}{2.\sigma_{x0}^2}.\frac{2.U(a)}{k_0}\right\} \quad \text{with} \quad \nu_0^+ = \frac{f_0}{A} \tag{11}$$

Impact Frequency. Using Eq.(11), and distinguishing the left stop (subscript 1) and the right one (subscript 2), we have:

$$\nu_{j1} = \nu_0^+.\exp(-j_1^{*2}/2) \quad ; \quad \nu_{j2} = \nu_0^+.\exp(-j_2^{*2}/2) \tag{12}$$

Rice Frequency. For ESSO (see Appendix A for the G value and EASO).

$$f_{Ri} = \frac{1}{2\pi}.\sqrt{\frac{\sigma_{\dot{x}}^2}{\sigma_x^2}} = f_0.\sqrt{\frac{A}{G}} \tag{13}$$

The reduced frequencies (ν_0^+ / f_0) & (f_{Ri} / f_0) are shown Figure 2-a for ESSO having different ratios of rigidity $\alpha = k_1/k_0$.

Peak penetration PDF. Under a "narrow band assumption": one single peak of x(t) per stop contact, of amplitude (a), we get the conditional PDF: $p(a \mid a \geq j_2) = -(\partial\nu_a^+ / \partial a) / \nu_{j2}^+$. Noting, $\zeta_2^* = (a - j_2)/j_2$, the reduced penetration of the right stop, we then deduce the PDF:

$$p(\zeta_2^*) = j_2^{*2}\left(\zeta_2^*.(1+\alpha_2)+1\right).\exp\left\{-\frac{j_2^{*2}}{2}\left(\zeta_2^{*2}.(1+\alpha_2)+2.\zeta_2^*\right)\right\} \tag{14}$$

This simplified expression agrees with more rigorous ones derived from filtered white noise, [5], see section 6. It stands also for the left stop with $\zeta_1^* = (|a| - j_1)/j_1$.

Impact Mean Force. This quantity may be derived from previous Eq.(14). We get for the right stop (similar formula for the left stop):

$$\frac{\langle F_{max,2}\rangle}{k_0.\sigma_{x0}} = \sqrt{\frac{\pi}{2}}.\frac{\alpha_2}{\sqrt{1+\alpha_2}}.\exp\left(\frac{j_2^{*2}}{2.(1+\alpha_2)}\right).\operatorname{erfc}\left(\frac{j_2^*}{\sqrt{2.(1+\alpha_2)}}\right) \tag{15}$$

Eq.(8), "made by hand", appears to be a first order development of Eq.(15) in j*. So, at the zero order, the (reduced) mean impact force does not depend on the gap size, but only on the stop rigidity (via α), and it slightly decreases by opening the gaps, as illustrated Figure 2-b.

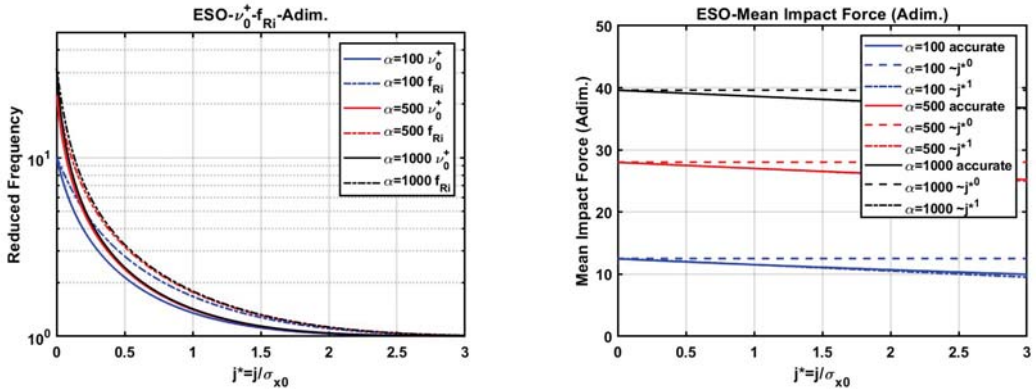

(a) Zero Crossing Rate & Rice Frequency (b) Mean Impact Force

Figure 2: Results for Elastic Shock Oscillator (ESO)

5 ELASTO-PLASTIC OSCILLATOR (EPO)

EPO model is schematized Figure 3-a where the dotted arrow stands for the elasto-plastic restoring force. EPO totally differ from ESO through the softening rigidity (ESO has hardening one) and the memory effect embedded in the plastic drift that may be viewed as a hidden internal variable. Indeed, at time t, the EPO displacement, $x(t)=x_p(t)+z(t)$, comprises a plastic part $x_p(t)$, and an elastic one, here named z(t), to avoid confusion with the elastic limit x_e present in the force-displacement relationship. Thus, the current displacement x(t) is not sufficient to determine the internal force that applies on the mass (the oscillator past response, via x_p, is required). The type of plasticity, encapsulated in the behavior law, pilots different subclasses (see Fig.3); we consider here:

- the elastic-perfectly-plastic oscillator (EPPO), with a zero plastic slope and a symmetrical plasticity in tension and compression (Fig. 3-b);
- the elastic-unilaterally-plastic oscillator (EUPO), with a plasticity only in tension (and a zero-plastic slope; Fig. 3-c);
- the elastic-kinematically-plastic oscillator (EKPO), with a non-zero plastic slope and a kinematic plasticity, i.e. the elastic range stays constant and equal to the initial one, whatever the plastic drift (Fig. 3-d).

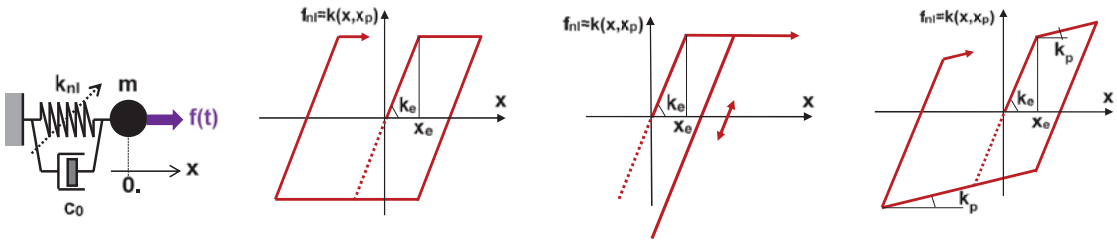

(a) EPO Model (b) EPPO Law (c) EUPO Law (d) EKPO Law

Figure 3: Elasto-Plastic Oscillator (EPO)

5.1 EPO Response from Energy Balance

The elastic part of the EPO displacement is bounded, by construction, to the elastic limit(s). Consequently, it is often adequate to reduce the EPO dynamics to the quantification of the plastic drift which dramatically depends on the plasticity model that is operated.

EUPO. Considering, first, an EUPO with plasticity only in tension, zero plastic slope (Fig.3-c), and no viscous damping. The only dissipative mechanism in this system is the work made by the plastic force, $f_e = k_e.x_e$, during the plastic drift, $x_p(t)$, that is always growing in the positive direction. We get from the energy balance:

$$\frac{\pi.F_0}{m} = f_e.\left\langle \dot{x}_p^+ \right\rangle \tag{16}$$

where we recognize, in the last right term, the plastic growing average rate, including both the plastic phases, $z(t)=x_e$, and the elastic ones, $z(t)<x_e$, $dx_p(t)/dt=0$.

Let the EUPO at rest and virgin at time 0, $z(0)=0$, $x_p(0)=0$, when suddenly excited. The plastic growing rate, extracted from Eq.(16), gives a solid information about the oscillator displacement at time t: $x(t) \simeq x_p(t) \simeq \left\langle \dot{x}_p^+ \right\rangle.t$, provided the time t is large enough to count a lot of plastic events while erasing the initial elastic phase (before the 1st plasticity). Note that the plastic excursions are unavoidable, whatever the plastic force level (f_e), the detail of which (parameters x_e, k_e) doesn't matter. Now, if the EUPO is viscously damped, Eq.(16) is changed into (the decomposition of the plastic rate is explained hereafter):

$$\frac{\pi.F_0}{m} = c_0.\left\langle \dot{x}^2 \right\rangle + f_e.\left\langle \dot{x}_p^+ \right\rangle = c_0.\left\langle \dot{x}^2 \right\rangle + f_e.\nu_p^+.\left\langle \delta_p^+ \right\rangle \tag{17}$$

with two dissipation mechanisms in competition according to the reduced elastic limit, $x_e^*=x_e/\sigma_{x0}$, σ_{x0} being the standard deviation of the ALO that is equivalent to EPO with infinite elastic limit. Just like ESO, for "high" values, $x_e^* \geq 3$, the plasticity frequency almost coincides with the ALO crossing rate of the elastic limit: $\nu_p^+ \simeq f_0.\exp(-x_e^{*2}/2)$; moreover, the oscillator velocity, at the entry in plasticity, follows the Rayleigh distribution of Eq.(7), which permits to estimate the mean plastic drift through a crude energy balance:

$$\left\langle \dot{x}_e^{+2} \right\rangle = 2.\sigma_{\dot{x}0}^2 \Rightarrow k_e.x_e.\left\langle \delta_p^+ \right\rangle \simeq \frac{1}{2}m.\left\langle \dot{x}_e^{+2} \right\rangle \Rightarrow \left\langle \delta_p^+ \right\rangle \simeq \frac{\sigma_{\dot{x}0}^2}{\omega_0^2.x_e} = \frac{\sigma_{x0}}{x_e^*} \tag{18}$$

For lower values, $x_e^*<3$, more advanced analyses are necessary. Nevertheless, rough orders of magnitude might be conjectured from the oscillator conditions at each plasticity exit (at time τ_n): $z(\tau_n) = x_e$, $\dot{x}(\tau_n) = 0$. So,

$$\left\langle \dot{x}^2 \right\rangle = \left\langle \dot{x}_p^2 \right\rangle + \left\langle \dot{z}^2 \right\rangle \sim (\omega_0.x_e)^2/2 \tag{19}$$

to be inserted in Eq.(17). EUPO is a special case where the knowledge of the global plastic rate, through the energy balance, gives directly a pertinent information about the plastic drift which is constantly growing. This is no longer the case for EPPO and EKPO.

EPPO. In the elastic-perfectly-plastic oscillator (Fig.3-b), the plasticity occurs in tension or compression in a symmetrical way, with identical plastic parameters, except for the signs; for example, undamped EPPO leads to an energy balance similar to Eq.(16):

$$\begin{gathered} \frac{\pi.F_0}{m} = +f_e.\left\langle \dot{x}_p^+ \right\rangle - f_e.\left\langle \dot{x}_p^- \right\rangle = 2.f_e.\left\langle \dot{x}_p^+ \right\rangle \\ \text{with } \left\langle \dot{x}_p^+ \right\rangle = \nu_p^+.\left\langle \delta_p^+ \right\rangle;\ \left\langle \dot{x}_p^- \right\rangle = \nu_p^-.\left\langle \delta_p^- \right\rangle;\ \nu_p^- = \nu_p^+;\ \left\langle \delta_p^- \right\rangle = -\left\langle \delta_p^+ \right\rangle \end{gathered} \tag{20}$$

Consequently, the mathematical expectation of the plastic drift, viewed as a stochastic process, is always zero, whatever the time t. This is a correct, but poor information for people generally interested in the maximum displacement reached during the period of observation (0,T), or, in other words, in the demanded ductility: $\mu_T = \max_{0\le t\le T} |x(t)| / x_e$. In fact, the plastic drift is similar to a *Brownian motion*: its average is zero, but its variance linearly grows with the time. This has been demonstrated for damped EPPO, first heuristically (e.g. see [9]), then mathematically [13]. The knowledge of this growing rate permits, using the central limit theorem, to determine the demanded ductility in a probabilistic way [9]. Unfortunately, this requires additional ingredients out of the scope of the only Eq.(20), that can nevertheless be used as discussed in section 5.2.

EKPO. The introduction of a non-zero plastic slope k_p (Fig.3-d), even very weak, dramatically changes the plastic drift with respect to EPPO. Let the EKPO initially at rest (and virgin); the kinematic plasticity (with a constant elastic range) makes the oscillator to continuously experience plastic excursions, but the plastic drift will have a zero mean, and a finite variance, *time invariant* once the stationary regime reached (e.g. see [11]). Determining this variance, and more generally the EKPO dynamics, requires additional ingredients that only detailed analyses can provide. But analyses, "at the zero order" or "by hand", are always interesting for the understanding. Such a primitive analysis could be reduced to:

$$\frac{\pi.F_0}{m} \approx f_e.\left\langle\left|\dot{x}_p\right|\right\rangle;\ \left\langle\left|\dot{x}_p\right|\right\rangle = \nu_p.\left\langle\left|\delta_p\right|\right\rangle;\ \left\langle\delta_p^2\right\rangle \simeq 2.\left\langle\left|\delta_p\right|\right\rangle^2;\ \left\langle x_p^2(t)\right\rangle \sim \left\langle\delta_p^2\right\rangle / 2.A \qquad (21)$$

The 1st relation is the energy balance for an undamped EKPO with a moderate plastic slope, in such a way f_e is taken constant. The 2nd one is the decomposition of the average (absolute) plastic rate into the plastic frequency and the mean absolute plastic jump. The 3rd one supposes an exponential law for the plastic jumps, which is roughly verified in most cases, the velocity being Rayleigh distributed at the entry in plasticity [11]. The 4th one is specific to EKPO. Omitting the subscript p, we can write the nth plastic jump: $x_{n+1} = x_n + \delta_n$. By taking the mathematical expectation of this relation, squared, we obtain for the stationary regime, $\left\langle\delta_n^2\right\rangle + 2\left\langle x_n.\delta_n\right\rangle = 0$, where the 2nd term must be negative. At the 1st order, given the EKPO plastic law, and reinforced by time-history simulations, we have, in mean, $\delta_n = -A.x_n$, with A constant, which explains the 4th relation. Shortly, Eq.(21) says that the knowledge of ν_p and A suffices to get, in order of magnitude, the plastic variance from the energy balance, and consequently the demanded ductility, the plastic drift being Gaussian. How these two parameters, ν_p and A, could be conjectured cannot be detailed here.

5.2 EPPO Response from Stochastic Diffusion Process

Following the seminal paper [7] by Karnopp & Sharton, a lot of works (e.g. see [8-12]) has been made using the conditional probability devoted to the ALO, and exposed in Appendix B. Such use is clear: first, the EPPO behaves linearly and elastically between two plastic excursions, and, secondly, the initial conditions of *each* elastic phase are driven by the plasticity exit and are known: $z(0) = \pm x_e$; $\dot{z}(0) = 0$ (with a time reset). The joint PDF $p_t(z,\dot{z})$, whose expression is analytical, permits to obtain relevant statistics at the first ALO crossing of the elastic barriers ±xe, i.e. when the EPPO enters again in plasticity.

Among these statistics, a key factor is the probability P_1 that the next plasticity occurs immediately, on the opposite elastic barrier, after a half-cycle corresponding roughly to the ALO semi-period ($T_0/2$). Indeed, plasticity occurs by "clumps" in EPPO, made of a succession of

elementary plastic events, of alternate sign, spaced in time by about $T_0/2$. The probability P_1 directly pilots the clump size <N>, i.e. the average number of successive cascaded plastic excursions; it also takes place in the net plastic increment finally obtained at the end of the clump, after an algebraic summation of successive plastic shifts [9] (see after for α & β):

$$\langle N\rangle = \sum_{1}^{\infty} N.p(N) = \frac{1}{1-P_1}\ ;\ \left\langle \delta_p^c \right\rangle = 0\ ;\ \left\langle (\delta_p^c)^2 \right\rangle = 2.\left(\alpha^2 + \frac{P_1}{1-P_1^2}\beta^2 - \frac{P_1}{1+P_1}\alpha\beta \right) \qquad (22)$$

Time-history simulations, as well as the use of the joint PDF $p_t(z,\dot{z})$, show that the velocity distribution, at the entry in plasticity, follows rather well a Rayleigh distribution like Eq.(7) (but with unknown $\sigma_{\dot{x}}$). Consequently, from a crude energy balance (where the average effect of white noise and viscous damping would be zero), each elementary plastic jump follows an exponential law, the parameters of which are α for the *first* jump in the clump, and β for *all* the others *in* the clump; hence Eq.(22-right) that represents the variance of an *idealized* plastic jump modeling the "clump". Moreover, by construction, the plastic clump frequency is:

$$\nu_p^c = \frac{2.\nu_p^+}{\langle N\rangle} = 2.\nu_p^+.(1-P_1) \qquad (23)$$

By assuming the independency of two successive clumps, the growing rate of the *"Brownian"* plastic variance is $\nu_p^c.\left\langle (\delta_p^c)^2 \right\rangle$. Therefore, invoking the central limit theorem, the plastic displacement, at time t, of an EPPO initially virgin is normally distributed with zero mean and variance: $\sigma_{xp}^2(t) = \nu_p^c.t.\left\langle (\delta_p^c)^2 \right\rangle$. On the other hand, the EPPO is said "collapsed" if the demanded ductility, μ_T, exceeds the allowable one, μ, during the period (0,T). A simple development, based on the reflexion principle proper to the (true) Brownian motion, leads to estimate the EPPO collapse probability P_C as (see [9]):

$$P_C(\mu,T) = 1-\left(1-P(\mu,T)\right)^2 \text{ with } P(\mu,T) = 2.\int_{\mu.x_e}^{+\infty} \frac{1}{\sqrt{2\pi}.\sigma_{xp}(T)}.\exp\left(-x_p^2/2.\sigma_{xp}^2(T)\right).dx_p \qquad (24)$$

This *"Brownian"* approach, that requires the determination of four parameters: P_1, α, β, ν_p^c, may be simplified, using Eq.(20) and supposing $\alpha \approx \beta \approx \left\langle \delta_p^+ \right\rangle$:

$$\nu_p^c.\left\langle (\delta_p^c)^2 \right\rangle = \frac{4.\left\langle \dot{x}_p^+ \right\rangle.\beta}{1+P_1} \qquad (25)$$

This formula shows how the global plastic rate extracted from the energy balance must be married with the plastic parameters P_1 and β related to plasticity in the clump; (see also [17]).

5.3 EPPO from Stochastic Variational Inequality (SVI)

This section summarizes, without any mathematical rigor, the new ideas emerging for a decade to characterize the EPPO dynamics. Readers are invited to consult the references [13-15], for more details, especially for the mathematical foundations. For clarification, the previous notations are completed as follows: y(t) is the oscillator velocity, Z the elastic limit ($Z \equiv x_e$), w(t) a Wiener process, the time derivative of which produces the forcing white noise; in addition, all the force terms are referred to a unit mass (m=1).

SVI. EPPO satisfies the following usual equations in the time domain:

$$\begin{gathered}\text{elastic phase: } \ddot{z}+c_0.\dot{z}+k_0.z=\dot{w}(t) \;\; ; \text{ plastic phase: } \dot{y}+c_0.y\pm k_0.Z=\dot{w}(t)\\ \text{with: } \; z(t)=x(t)-x_p(t) \;\; ; \;\; y(t)=\dot{x}(t)\end{gathered} \tag{26}$$

In fact, the whole may be encapsulated into the stochastic variational inequality (SVI):

$$\forall t, \forall|\varphi|\le Z,\; dy(t)=-\big(c_0.y(t)+k_0.z(t)\big).dt+dw(t) \;\; ; \;\; \big(dz(t)-y(t).dt\big).\big(\varphi-z(t)\big)\ge 0 \tag{27}$$

in which x(t) no longer appears explicitly. This formulation permits, in a mathematically well-founded and rigorous way, to derive a PDE involving the couple (z(t),y(t)) with the non-standard boundary conditions attached to the plastic saturation: z(t)=±Z. Particularly, the infinitesimal generator, proper to the diffusion process, can be determined using Ito's lemma. This generator is given in Appendix C, while the concept, and its current use, are briefly reported hereafter.

Diffusion Generator. The pair made of the elastic displacement, $z(t)\equiv z_t$, and the oscillator velocity, $y(t)\equiv y_t$, constitutes a Markov process of diffusion in R^2. This process may be described thanks a set (Ω) of continuous functions, $\phi(z,y)$: $R^2\to R$, of sufficient regularity. The operator, $T_t(\phi):\Omega\to\Omega$, is thus defined as follows: $T_t\phi(z_s,y_s)=\big\langle\phi(z_{t+s},y_{t+s})\,|\,(z_s,y_s)\big\rangle$; in words, for each location z(s),y(s) in the phase space at time s, it gives the mathematical expectation of the function ϕ at time t+s, i.e. after a delay of t. This operator forms a semi-group; noting z for z_0, y for y_0: $T_{t+s}\phi(z,y)=T_t(T_s\phi(z,y))=(T_t\circ T_s)\phi(z,y)$; $T_0\phi(z,y)=\phi(z,y)$, from which the infinitesimal generator L is defined: $L\phi(z,y)=\lim_{t\to 0}(T_t\phi(z,y)-\phi(z,y))/t$. This concept is classic for Markov process, but the generator has here an unusual form (see App. C), and, moreover, it will be operated in an original way.

Generator Use. The derivation, $\partial(T_t\phi)/\partial t=T_tL\phi=LT_t\phi$, can be easily proved, at least heuristically. Noting for clarity, $T_t\phi(z,y)=v_\phi(t,z,y)$, so: $\partial v_\phi(t,z,y)/\partial t-Lv_\phi(t,z,y)=0$.

The Laplace transform of v_ϕ is: $u_{\lambda,\phi}(z,y)=\int_o^{+\infty}e^{-\lambda t}.v_\phi(t,z,y).dt$. Integrating by parts and using the previous relation, $\partial v_\phi/\partial t=Lv_\phi$, we get: $\lambda.u_{\lambda,\phi}(z,y)=\phi(z,y)+\int_o^{\infty}e^{-\lambda t}.Lv_\phi(t,z,y).dt$, that finally gives, as the generator L is time independent (in invariant model):

$$\lambda.u_{\lambda,\phi}(z,y)-Lu_{\lambda,\phi}(z,y)=\phi(z,y) \tag{28}$$

The final value theorem for the Laplace transform F(λ) of the function f(t) specifies that: $\int_0^{\infty}e^{-\lambda t}.\partial_t f(t).dt=\lambda.F(\lambda)-f(0^+)\;\Rightarrow\;\lim_{\lambda\to 0}\lambda.F(\lambda)=f(+\infty)$. Applying here this theorem:

$$\lim_{\lambda\to 0}\lambda.u_{\lambda,\phi}(z,y)=\lim_{t\to\infty}v_\phi(t,z,y)=\lim_{t\to\infty}\big\langle\phi\big(z(t),y(t)\big)\big\rangle=\int m(z,y).\phi(z,y).dz.dy \tag{29}$$

in which m(z,y) stands for the stationary probability density function (PDF) of the pair (z,y). It is worth noting that the initial conditions (z, y, at time 0) are "dissolved" in this formulation since: $\forall(z,y),\lim_{\lambda\to 0}\lambda.u_{\lambda,\phi}(z,y)=\int m(z,y).\phi(z,y).dz.dy=\text{constant}$.

PDF computation. For the computation, the PDF m(z,y) is approximated by a decomposition on a set of given basis functions, $g^i(z,y)$: $m(z,y)\simeq\sum_i m_i.g^i(z,y)$, where m_i are the unknown scalars to be determined. The computation process is thus clear:

(a) Choice of a "sufficient small" λ.

(b) For each i, resolution in $u_{i,\lambda}$ of Eq.(28): $\lambda u_{i,\lambda}(z,y) - L u_{i,\lambda}(z,y) = g^i(z,y)$, which provides according to Eq.(29): $\lambda.u_{i,\lambda} \simeq \int \sum_j m_j.g^j(z,y).g^i(z,y).dz,dy \simeq \sum_j m_j.G_{ij}$.

(c) Inversion of the system: $\left[G_{ij}\right]\left\{m_j\right\} = \left\{\lambda.u_{i,\lambda}\right\}$, where $G_{ij} = \int g^i(z,y).g^j(z,y).dz.dy$.

Finite Difference. The previous step (b) is solved by a finite difference method on a limited grid, from -Z to +Z for the elastic displacement z (which is self-obvious), from -Y to +Y for the oscillator velocity y (see Fig.4-a). Y is large enough to ensure a Neuman condition on the border $\partial u/\partial y=0$. The L operator (App. C) is discretized in a symmetrical, but very common way. For example, noting i and j the subscripts respectively attached to z and y, we have for the terms involving derivatives with respect to y:

$$(L_y u)_{i,j} \triangleq \frac{a_{22}}{2}\frac{u_{i,j+1} - 2u_{i,j} + u_{i,j-1}}{\Delta y^2} - \max(0, b_{i,j})\frac{u_{i,j+1} - u_{i,j}}{\Delta y} - \min(0, b_{i,j})\frac{u_{i,j} - u_{i,j-1}}{\Delta y} \qquad (30)$$

with $b_{i,j} = (c_0 y_j + k_0 z_i)$; see [16] for details. Figure 4-b shows an example of PDF, m(z,y), obtained with the grid of Fig.4-a (ξ_0=4%, x_e*=1). We particularly notice the PDF profile on the elastic barriers: z=+x_e, y≥0 ; z=-x_e, y≤0 . This PDF is coherent with Monte-Carlo results, but the precision and convergence rate cannot be discussed here.

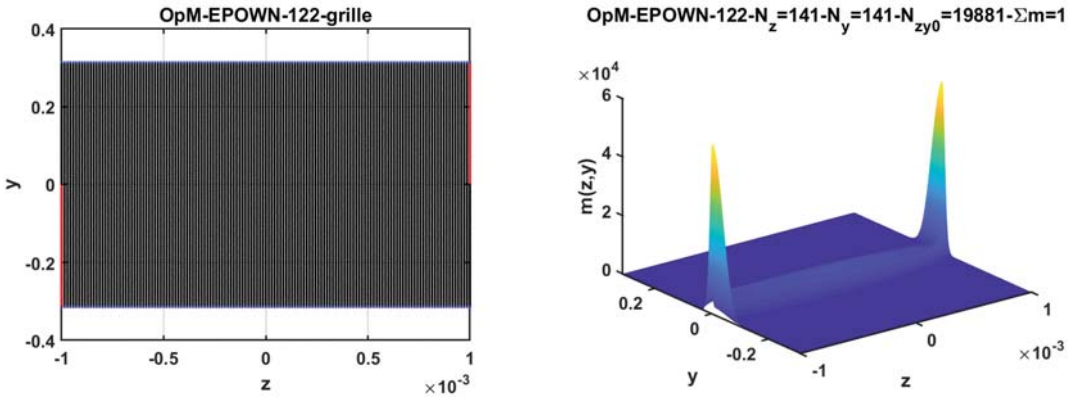

(a) Finite Difference Grid (b) Stationary PDF m(z,y)

Figure 4: Example of PDF Computation for EPO, from SVI theory

6 "WHITE NOISE OF ENGINEER"

White noise is nowadays defined as the time derivative (in the sense of distribution) of Wiener process, which permits mathematically-well-founded developments. But degenerating the mathematical white noise F_0, the variance of which is infinite, into a physically-realizable process $S_{ff}(\omega)$ remains a necessity for engineers which face the real world. This transformation is generally without great consequence provided the cut-off frequency (~1/2.Δt) is large enough compared to the oscillator characteristic frequencies. Furthermore, engineers are most of the time interested in quantities at macro-or-meso-scale, by nature filtered or averaged. Nevertheless, we should be aware about the specificity of white noise, as well as the eventual impact of the cut-off frequency. Indeed, the convergence of certain quantities, as the time step Δt decreases, can be affected or "polluted" by micro-peaks-or-oscillations taking place in the oscillator trajectory. The purpose of this section is just to illustrate such phenomena.

Concerning ESO, Figure 5-a presents an example of peak penetration PDF obtained from Eq.(14), under "a narrow band assumption" (NBA). Analytical PDF got from filtered white noise (FWN) are also indicated, following [5] with a first order filter of eigen-pulsation, $\Omega=\Omega^*\times\omega_{j0}$ (ω_{j0} being the ESO pulsation with closed gaps). We see on Fig. 5-a how the PDF slightly differ as Ω^* increases, while producing very close mean values. The NBA assumption, "one single peak per stop contact", is so justified, as the more as it produces simple expressions such as Eq.(14) & (15).

Concerning EPO, Figure 5-b presents the crossing frequency $\nu_e(t)$ of the elastic limit x_e for an EUPO coming out of plasticity ($x=x_e$) at t=0. It has been obtained from the Rice formula: $\nu_e(t)=\int_0^{+\infty}\dot{x}.p_t(x_e,\dot{x}).d\dot{x}$, applied to the conditional probability reported in Appendix B. By definition, $\nu_e(t).dt$ is the probability of crossing during the differential time interval [t,t+dt). For short durations, this probability may be integrated [17]. We see on Fig. 5-b two contributions. The "bump", on the right part of the dotted blue line, corresponds to the crossing probability, roughly a period later (T_0=0.1 s). But we see also, on the left part, the asymptotic increase of the PDF towards t=0. Physically, it corresponds to a return in plasticity, just after the exit, due to a noise impulse, all the more possible as the elastic restoring force is weak and the noise intensity strong. The integral of this PDF portion tends to 1 (probability almost surely) for "true" white noise, for which the border between plasticity and elasticity becomes fuzzy in time. The plastic-elastic border is more and more net as the white noise is truncated in frequency. But this illustrates how simulations, especially in the time domain, may be delicate when involving white noises, and the necessity of "adequate" quantities to make comparisons or convergence tests.

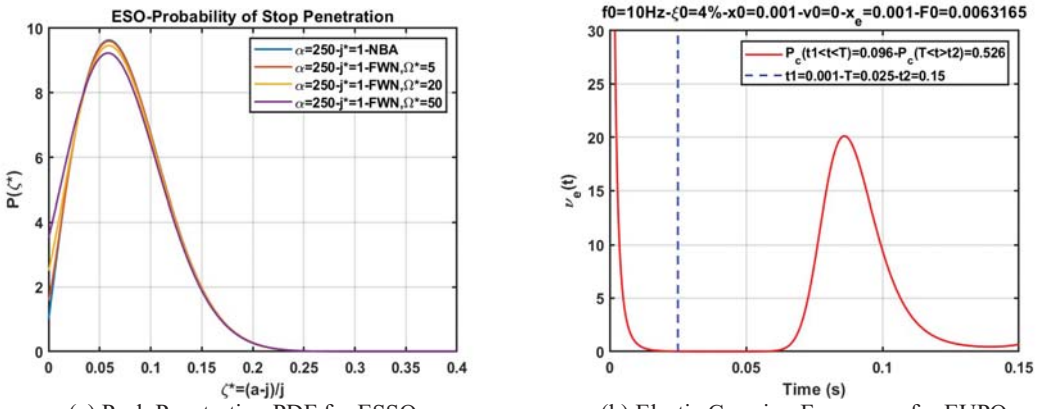

(a) Peak Penetration PDF for ESSO (b) Elastic Crossing Frequency for EUPO

Figure 5: Two Illustrations for the "White Noise of Engineer" (Band-Limited)

7 CONCLUSION

This paper treated of the response of nonlinear single oscillators submitted to white noise excitations. The oscillators were, on the one hand, the elastic shock oscillators (ESO), with symmetrical or asymmetrical stops (resp. ESSO & EASO), and, on the other hand, the elasto-plastic oscillators (EPO), with different types of plasticity: perfect, unidirectional or kinematic (resp. EPPO, EUPO & EKPO). The subject is very broad, and the purpose of the paper was just to illustrate the following points:

- A white external force injects the same energy rate into all the oscillators having the same mass, whatever their non-linearities and dissipation mechanisms. Thus, a simple energy

balance provides a first level of information about the oscillators' dynamics, that can even be very quantitative in some cases (EUPO, ESO) with the help of additional conjectures.

- The next step is to build and feed the dynamics on nonlinear oscillators from the ones of the associated linear oscillators (ALO), the theory of which is well mastered. This "old" and common way is always source of improvements (e.g. [17] for EPO).
- The "ultimate" step is evidently to use relevant theories concerning the stochastic diffusion processes, such as Fokker-Planck equation (used here for ESO), or stochastic variational inequality (SVI, used here for EPPO). In most cases, these theories result in numerical computations (e.g. [6] for ESO with damped stops) that can serve of references, just like Monte-Carlo simulations. But special care must be done to the white noise specificity.
- Finally, analytical results devoted to nonlinear single oscillators, whitely excited, could appear of only academic interest, while Monte-Carlo simulations can now be easily operated. But the authors' opinion is that 1-DOF results, especially with closed-forms, exceed the academic sphere by providing tendencies that could be useful for engineers. Figure 2-b is such an example: it was not a priori evident that opening the gaps in ESO let quasi-unchanged the mean impact force. The change of plastic behavior, from "Brownian" for EPPO, to stationary for EKPO, is another example.

An engineer must have clear ideas. And this is the *set* of analyses, from the simplest (e.g. 1-DOF with energy balance) to the most complex (e.g. based on sophisticated finite-element models), that should forge his mind in the clarification and hierarchization of the involved physical phenomena he has to cope with.

REFERENCES

[1] Y.K. Lin: Probabilistic Theory of Structural Dynamics. Robert E. Krieger Publishing Company, Reprint 1996.

[2] P. Krée, C. Soize: Mécanique aléatoire. Dunod, Paris, 1983.

[3] R.J. Gibert: Vibrations des structures. Interactions avec les fluides. Sources d'excitation aléatoires. Paris. Editions Eyrolles, 1988.

[4] A. Preumont: Vibrations aléatoires et analyse spectrale. Presses Polytechniques et Universitaires Romandes, 1990.

[5] P. Guihot: Analyse de la réponse de structures non linéaires sollicitées par des sources d'excitation aléatoires - Application au comportement des lignes de tuyauteries sous l'effet d'un séisme. PhD Thesis, Université de Paris VI, 1990.

[6] L. Borsoi, P. Piteau, X. Delaune, J. Antunes: Shock Oscillator Response by Fokker-Planck Equation to Analyze a Loosely Supported Tube Subjected to Turbulence and Fluid-Elastic Forces. IX Int. Conf. on Structural Dynamics, Porto; (EURODYN 2014).

[7] D. Karnopp, T.D. Scharton: Plastic deformation in random vibration. The Journal of the Acoustical Society of America, 39 (1966), 1154-61.

[8] E.H. Vanmarcke, D. Veneziano: Probabilistic seismic response of simple inelastic systems. 5th World Conference on Earthquake Engineering, Rome, March 1973.

[9] L. Borsoi, P. Labbé : Approche probabiliste de la ruine d'un oscillateur élasto-plastique sous séisme. 2ème colloque national de l'AFPS, St-Rémy-Les-Chevreuses, avril 1989.

[10] O. Ditlevsen, L. Bognar: Plastic displacement distributions of the Gaussian white noise excited elasto-plastic oscillator. Probabilistic Engineering Mechanics 8 (1993) 209-231.

[11] C. Feau: Les méthodes probabilistes en mécanique sismique. Applications aux calculs de tuyauteries fissurées. PhD Thesis CEA-Université d'Evry, 2003.

[12] C. Feau: Probabilistic response of an elastic perfectly plastic oscillator under Gaussian white noise. Probabilistic Engineering Mechanics 23 (2008) 36-44.

[13] L. Mertz: Inéquations variationnelles stochastiques et applications aux vibrations de structure mécaniques. PhD Thesis, Université Pierre et Marie Curie, 2 décembre 2011.

[14] A. Bensoussan, L. Mertz, O. Pironneau, J. Turi: An Ultra Weak Finite-Element Method as an Alternative to a Monté-Carlo Method for an Elasto-Plastic Problem with Noise. SIAM Journal Numerical Analysis, Vol.47 (5), (2009), pp 3374-3396.

[15] A. Bensoussan, J. Turi: Degenerate Dirichlet Problems Related to the Invariant Measure of Elasto-Plastic Oscillators. Applied Mathematics & Optimization (2008) 58 (1), 1-27.

[16] L. Mertz, G. Stadler, J. Wylie: A Feynman-Kac formula approach for computing expectations and threshold crossing probabilities of non-smooth stochastic dynamical systems. Physica D, 397 (2019) 25-38.

[17] L. Borsoi: Plastic drift of single oscillators whitely excited, using the random points theory by Stratonovitch. To be submitted.

APPENDIX A: RESULTS FOR ELASTIC SHOCK OSCILLATOR (ESO)

ESSO: elastic symmetric shock oscillator. EASO: elastic asymmetric shock oscillator.

Subscripts 1, 2 are respectively for the left and right stop (Fig.1-a); j is the gap size (j≥0); j* the reduced gap size, e.g. $j_1^* = j_1 / \sigma_{x0}$ (σ_{x0} is the ALO standard deviation); α the ratio of the stop stiffness over the permanent one, e.g. $\alpha_1 = k_1 / k_0$. The subscripts are omitted for ESSO : $j = j_1 = j_2$, $\alpha = \alpha_1 = \alpha_2$, except for the stop rigidity noted k_1.

Constant A: $A = \dfrac{A_1 + A_2}{2}$ for EASO, with (idem for A_2):

$$A_1 = \operatorname{erf}\left(\frac{j_1^*}{\sqrt{2}}\right) + \frac{1}{\sqrt{1+\alpha_1}}.\exp\left(\frac{-j_1^{*2}.\alpha_1}{2.(1+\alpha_1)}\right).\operatorname{erfc}\left(\frac{j_1^*}{\sqrt{2.(1+\alpha_1)}}\right) \qquad \text{(A-1)}$$

For ESSO: $A = A_1 = A_2$.

Mean displacement: for EASO, $E(x) = \dfrac{\sigma_{x0}}{\sqrt{2\pi}.A}.(H_1 - H_2)$, with (idem for H_2):

$$H_1(j_1^*, \alpha_1) = \left\{ \frac{\alpha_1}{1+\alpha_1}.\exp\left(\frac{-j_1^{*2}}{2}\right) - \frac{\alpha_1}{(1+\alpha_1)^{3/2}}.j_1^*.\sqrt{\frac{\pi}{2}}.\operatorname{erfc}\left(\frac{j_1^*}{\sqrt{2.(1+\alpha_1)}}\right).\exp\left(\frac{-j_1^{*2}}{2}\frac{\alpha_1}{1+\alpha_1}\right)\right\} \qquad \text{(A-2)}$$

For ESSO, E(x)=0 (the mean displacement is obviously zero).

Standard deviation: $\sigma_x^2 = \dfrac{\sigma_{x0}^2}{A}.\left\{\dfrac{g(j_1^*, \alpha_1) + g(j_2^*, \alpha_2)}{2}\right\} - \left[E(x)\right]^2$, with:

$$g(j^*,\alpha)=\left\{\begin{array}{l}\operatorname{erf}\left(\frac{j^*}{\sqrt{2}}\right)-\sqrt{\frac{2}{\pi}}.j^*.\frac{\alpha^2}{(1+\alpha)^2}.\exp\left(\frac{-j^{*2}}{2}\right)+\\ \operatorname{erfc}\left(\frac{j^*}{\sqrt{2.(1+\alpha)}}\right).\frac{1}{(1+\alpha)^{3/2}}.\left(1+j^{*2}.\frac{\alpha^2}{(1+\alpha)}\right).\exp\left(\frac{-j^{*2}}{2}\frac{\alpha}{1+\alpha}\right)\end{array}\right\} \qquad \text{(A-3)}$$

For ESSO: $\sigma_x^2=\sigma_{x0}^2\frac{G}{A}$, with $G=g(j^*,\alpha)$; G is noted in uppercase to distinguish ESSO.

APPENDIX B: CONDITIONAL PROBABILITY FOR A LINEAR OSCILLATOR [7,9]

$x_0,\dot{x}_0$: initial conditions at time t=0. F_0: white noise intensity (PSD for -∞<ω<+∞).

$$p(x,\dot{x},t\mid x_0,\dot{x}_0)=\frac{1}{2\pi.\sigma_{x(t)}.\sigma_{\dot{x}(t)}.\sqrt{1-\rho_t^2}}.$$
$$\exp\left\{\frac{-1}{2.(1-\rho_t^2)}.\left[\frac{(x-C_t)^2}{\sigma_{x(t)}^2}-\frac{2\rho_t(x-C_t)(\dot{x}-\dot{C}_t)}{\sigma_{x(t)}.\sigma_{\dot{x}(t)}}+\frac{(\dot{x}-\dot{C}_t)^2}{\sigma_{\dot{x}(t)}^2}\right]\right\} \qquad \text{(B-1)}$$

1st order terms: $C_t=x_0.g(t)+\dot{x}_0.h(t)$; $\dot{C}_t=x_0.\dot{g}(t)+\dot{x}_0.\dot{h}(t)$, with (B-2)

$$g(t)=e^{-\xi_0.\omega_0.t}.\left(\frac{\xi_0.\sin(\omega_d.t)}{\sqrt{1-\xi_0^2}}+\cos(\omega_d.t)\right);\ h(t)=e^{-\xi_0.\omega_0.t}.\frac{\sin(\omega_d.t)}{\omega_d}\ ;\ \omega_d^2=\omega_0^2.(1-\xi_0^2)$$

2st order terms: $\sigma_x^2(t)=\frac{2\pi.F_0}{m^2}.I_1(t)$; $\sigma_{\dot{x}}^2(t)=\frac{2\pi.F_0}{m^2}.I_2(t)$; $\rho_t=\frac{\pi.F_0.h^2(t)}{m^2.\sigma_{x(t)}.\sigma_{\dot{x}(t)}}$ (B-3)

$$I_1(t)=\frac{1}{\omega_d^2}.\left\{e^{-2.\xi_0.\omega_0.t}\left(-\frac{1}{4.\xi_0.\omega_0}+\frac{\xi_0}{4.\omega_0}.\cos(2\omega_d.t)-\frac{\sqrt{1-\xi_0^2}}{4.\omega_0}.\sin(2\omega_d.t)\right)+\frac{1-\xi_0^2}{4.\xi_0.\omega_0}\right\}$$

$$I_2(t)=\frac{e^{-2.\xi_0.\omega_0.t}}{\omega_d}\left\{-\frac{1}{4\xi_0.\sqrt{1-\xi_0^2}}+\frac{\xi_0}{4\sqrt{1-\xi_0^2}}\cos(2\omega_d.t)+\frac{1}{4}.\sin(2\omega_d.t)\right\}+\frac{1}{4\xi_0.\omega_0}$$

APPENDIX C: INFINITESIMAL GENERATOR FOR EPPO

$$L\phi=\lim_{t\to 0}\frac{\langle\phi(z_t,y_t)\rangle-\phi(z,y)}{t}=\left\{\begin{array}{l}L\phi\triangleq\frac{a_{22}}{2}\frac{\partial^2\phi}{\partial y^2}-(c_0y+k_0z)\frac{\partial\phi}{\partial y}+y\frac{\partial\phi}{\partial z},\ \text{if } |z|<Z\\ L_+\phi\triangleq\frac{a_{22}}{2}\frac{\partial^2\phi}{\partial y^2}-(c_0y+k_0Z)\frac{\partial\phi}{\partial y}+\min(0,y)\frac{\partial\phi}{\partial z},\ \text{if } z=+Z\\ L_-\phi\triangleq\frac{a_{22}}{2}\frac{\partial^2\phi}{\partial y^2}-(c_0y-k_0Z)\frac{\partial\phi}{\partial y}+\max(0,y)\frac{\partial\phi}{\partial z},\ \text{if } z=-Z\end{array}\right.$$

with $a_{22}=\frac{2\pi.F_0}{m^2}$; c_0 and k_0 stands here for $c_0.m^{-1}$ and $k_0.m^{-1}$. (C-1)

EURODYN 2020
XI International Conference on Structural Dynamics
M. Papadrakakis, M. Fragiadakis, C. Papadimitriou (eds.)
Athens, Greece, 23–26 November 2020

EFFICIENT ESTIMATION OF THE SKEWNESS OF THE RESPONSE OF A WAVE-EXCITED OSCILLATOR

Margaux Geuzaine[1] **and Vincent Denoël**[2]

[1]Structural and Stochastic Dynamics, University of Liège, Belgium
Allée de la Découverte, Liège, B-4000
e-mail: {mgeuzaine,v.denoël}@uliege.be

[2] F.R.S-FNRS, National Fund for Scientific Research, Belgium
Rue d'Egmont, 8, B-1000 Bruxelles

Keywords: multiple timescales, spectral analysis, inertial loading, skewness, variance, wave loading.

Abstract. *The Multiple Timescale Spectral Analysis is a framework relying on the existence of well-separated timescales in the dynamic response of structures to generalize for higher-order statistics the famous background/resonant decomposition, widely applied by the wind engineering community to compute the variance of the response of SDOF structures or of each modal response of MDOF structures. This fast spectral analysis method mainly concerns the statistics of the response of onshore structures subjected to a buffeting wind loading whose characteristic frequency is typically lower than the natural frequencies of the structures concerned. By contrast, when dealing with wave-loaded floating offshore structures, the roles of the slow and fast timescales are likely to be interchanged and the method is extended further in this paper to compute rapidly the variances and the skewnesses of modal responses of such structures responding in the inertial regime as well, since these statistics are necessary to consider the influence of the non-Gaussianity of the loading.*

1 INTRODUCTION

The stochastic surge response of a floating structure is governed by a nonlinear differential equation. The nature of this equation is such that the basic input of the problem, the water particle velocity which is commonly assumed to be a Gaussian random process, results in a non Gaussian surge response [10]. As a consequence, the extreme value response might substantially differ from the results predicted with a Gaussian model, which would be based on the variance of the response only [11, 8]. A typical model developed in marine engineering is based on the cubic translation and the evaluation of higher statistical moments [16]. There are two approaches to the solution of this type of problem.

The first approach relies on the generation of samples of the problem input (the wave velocity) and the numerical solution of the problem based on appropriate time marching algorithms. In order to reduce the influence of the sampling and because of the coexistence of several timescales in the problem, namely the slow dynamics of the oscillator and the fast inertial wave loading, it is necessary to model very long signals with very short time steps. This makes this first method computationally intense although straightforward as to its practical implementation.[1],[7],[9]

The second approach consists in a spectral analysis and its higher order extensions [17, 10]. Although the strict equivalence between time and frequency domains vanishes as soon as the problem at hand features some nonlinearities, it is still possible to find relatively accurate estimates of the solution of the problem when the nonlinearities are limited [12]. The use of Volterra and Wiener series is one such approach [15, 13]. In a spectral approach, the variance of the response is obtained as a result of the integral of the power spectral density, while the third (and higher) moments are obtained by integration of the bispectrum (and higher spectra, respectively). Because of the existence of the several timescales in the response, the numerical integration of these spectra might be intense too. However, it is possible to take advantage of the specific form of the spectra and proceed to their Multiple Timescale Spectral Analysis [5]. This method consists in taking advantage of the known local shape of either factor of the spectra (either related to the load, either to the structural filter) and provide approximations of the integral. This method is known to be approximately two orders of magnitude (100 times) faster than a standard numerical integration. It founds its roots in the small correlation expansion [14] and has been being applied in wind engineering since the introduction of the famous background/resonant decomposition [2]. The Multiple Timescale Spectral Analysis generalizes several other similar approximations which provide a simple and rapid evaluation of the statistics of the structural response (covariance [3], third moment [4]) in linear or slightly nonlinear systems [6].

In this paper, the Multiple Timescale Spectral Analysis is specialized to the case of a single-degree-of-freedom system subject to a stochastic loading distributed over its resonant and inertial regimes, i.e. with a main loading frequency band above the natural frequency of the structure. This configuration is typical of the surge response of floating structures and would be typically tackled by means of a numerical integration of the spectra. Instead, we suggest to decompose the response, at second and third orders, as a sum of a resonant and an inertial components. Numerical validations demonstrate the accuracy of the proposed approximate, while being significantly faster.

2 FORMULATION OF THE PROBLEM

2.1 Governing equations

The force exerted by random waves on an oscillating point-like structure, which is undoubtedly small compared to the wavelength of waves, can be expressed according to the Morison equation by the sum of an inertial loading component

$$f_m(t) = k_m \dot{u}(t) \tag{1}$$

resulting from a linear transformation, as the overhead dot denotes partial differentiation in time t, of $u(t)$, the fluctuations of the water velocity around the constant current speed u_c, and a drag, or viscous, loading component

$$f_d(t) = k_d \left|u_c + u(t)\right| \left(u_c + u(t)\right) \tag{2}$$

depending on a nonlinear function of the water velocity, i.e. the sum of the current and the waves speeds. For the sake of simplicity in this short paper, the influence of the movement of the structure itself on the loading is considered as negligible. The coefficients k_m and k_d are related to geometric and hydrodynamic properties through:

$$k_m = c_m \rho_w v_w \quad \text{and} \quad k_d = c_d \rho_w a_w / 2 \tag{3}$$

where ρ_w is the water density, c_m is the inertia coefficient, c_d is the drag coefficient and a_w is the cross-sectional area of v_w, the volume of the submerged part of the structure.

The surge response of a single degree-of-freedom structure subjected to such a one-dimensional Morison-type force is therefore governed by the nonlinear second order differential equation

$$m\ddot{x}(t) + c\dot{x}(t) + kx(t) = f_m(t) + f_d(t) \tag{4}$$

where $x(t)$ is the displacement, k is the stiffness, c is the viscosity and m is the effective mass of the structure, i.e. the mass of the structure plus the added mass of fluid accelerating with the structure, as represented in Figure 1. Because of the memoryless nonlinearity included in the drag loading component, the response of the structure is expected to be non-Gaussian, even if the only input of the dynamical system, the random process $u(t)$, is supposed to be zero-mean, Gaussian, stationary and thus fully defined by its power spectral density $S_u(\omega)$.

The developments presented next are valid no matter the analytical or experimental definition selected for this power spectral density (PSD) but, in order to illustrate the results in a simple manner, the structure is assumed to be located at the still-water level in deep water. In this specific case, the application of the Linear Airy Wave Theory gives

$$S_u(\omega) = \omega^2 S_h(\omega) \tag{5}$$

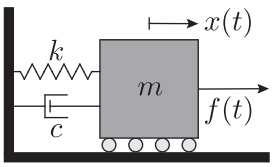

Figure 1: Typical single degree-of-freedom system

and it has been decided then to model the power spectral density $S_h(\omega)$ of the wave elevation process $h(t)$ by the two-sided Pierson-Moskovitz spectrum

$$S_h(\omega) = \frac{5}{32}\frac{\omega_h^4}{|\omega|^5} h_s^2 \mathrm{e}^{-\frac{5}{4}\left(\frac{\omega_h}{\omega}\right)^4} \tag{6}$$

with two parameters, h_s and ω_h, known as the significant wave height and the circular frequency corresponding to the peak of the spectrum of the wave elevation process. By cancelling the derivative of the PSD of the water velocity fluctuations, its own peak circular frequency, ω_u, is found to be equal to

$$\omega_u = \sqrt[4]{\frac{5}{3}}\omega_h \tag{7}$$

The power spectral densities employed in this paper are two-sided and their integration over the circular frequencies ω, from $-\infty$ to ∞, provides the variance of the associated process. Consequently, the variance of the water elevation process and the variance of the water velocity process are respectively given by

$$\sigma_h^2 = \left(\frac{h_s}{4}\right)^2 \quad \text{and} \quad \sigma_u^2 = \sqrt{\frac{3\pi}{4}}\omega_u^2\sigma_h^2 \tag{8}$$

2.2 Dimensionless formulation

A dimensionless formulation of this problem can be written by introducing a characteristic time t_r, a characteristic response x_r and a characteristic wave particle velocity u_r. Defining the dimensionless time $\tilde{t} = t/t_r$, the dimensionless displacement $\tilde{x}\left(\tilde{t}\right) = x\left[t\left(\tilde{t}\right)\right]/x_r$ and the dimensionless water velocity $\tilde{u}\left(\tilde{t}\right) = u\left[t\left(\tilde{t}\right)\right]/u_r$, Equation (4) becomes

$$\frac{m}{kt_r^2}\tilde{x}'' + \frac{c}{kt_r}\tilde{x}' + \tilde{x} = \frac{k_m u_r}{kx_r t_r}\tilde{u}' + \frac{k_d u_c^2}{kx_r}\left|1 + \frac{u_r}{u_c}\tilde{u}\right|\left(1 + \frac{u_r}{u_c}\tilde{u}\right) \tag{9}$$

after a divison by kx_r. The coefficient in front of the dimensionless drag loading component is set to unity by equalizing the characteristic elastic force kx_r to the force of the current $k_d u_c^2$. It is also chosen to define the reference time t_r as the inverse of $\omega_0 = \sqrt{k/m}$, the natural frequency of the system, in order to obtain a unitary coefficient in front of the highest order derivative. Lastly, the reference speed u_r is chosen as σ_u, the standard deviation of the water velocity process $u(t)$, and the presence of the turbulence intensity of waves, $\lambda_u = \sigma_u/u_c$, is hence revealed in the dimensionless formulation of the equation of motion

$$\tilde{x}'' + 2\xi_s\tilde{x}' + \tilde{x} = \kappa_u\lambda_u\tilde{u}' + |1 + \lambda_u\tilde{u}|\,(1 + \lambda_u\tilde{u}) \tag{10}$$

where the symbol $'$ denotes differentiation with respect to the new independent coordinate $\tilde{t}$. Besides,

$$\xi_s = \frac{c}{2m\omega_0} \quad \text{and} \quad \kappa_u = \frac{k_m\omega_0}{k_d u_c} \tag{11}$$

are respectively the structural damping ratio and the loading ratio. Similarly, Equation (5) is rewritten dimensionlessly as

$$S_{\tilde{u}}(\tilde{\omega}) = \sqrt{\frac{3}{\pi}}\frac{\varepsilon_u^2}{|\tilde{\omega}|^3}\mathrm{e}^{-\frac{3}{4}\left(\frac{\varepsilon_u}{\tilde{\omega}}\right)^4} \tag{12}$$

where $\tilde{\omega} = \omega t_r$ is the nondimensional circular frequency and $\varepsilon_u = \omega_u/\omega_0$ is the frequency ratio. The integration property of power spectral densities holds true for the nondimensional processes and can be applied to the rescaled water velocity process, $\tilde{u}(\tilde{t})$, to demonstrate that this input is now characterized by a unit variance, $\sigma^2_{\tilde{u}} = 1$, regardless the value of the frequency ratio ε_u. Interestingly enough, Equation (11) can be rearranged to introduce κ_c, the Keulegan-Carpenter number, that theoretically describes the relative importance of the drag loading component over the inertial loading component. It effectively plays this role in the equation of motion as it appears in the denominator of the loading ratio

$$\kappa_u = \frac{\varepsilon_u}{\kappa_c} \tag{13}$$

According to the Vashy-Buckingham theorem, the problem described in Equation (10) and Equation (12) is actually ruled by a set of four dimensionless numbers, $\{\xi_s, \lambda_u, \varepsilon_u, \kappa_u\}$. In wind engineering applications, where a very similar equation is encountered, these four parameters are typically all small and this property allows to simplify the governing equation. The inertial loading component is directly discarded and the absolute value is not needed anymore in the drag loading component since its argument is always positive. The expansion of the governing equation consequently yields

$$\tilde{x}'' + 2\xi_s\tilde{x}' + \tilde{x} = 1 + 2\lambda_u\tilde{u} + \lambda_u^2\tilde{u}^2 \tag{14}$$

in which the third term is at least one order of magnitude below the second because of the smallness of the turbulence intensity of wind, as detailed in [6]. In marine engineering applications, the structural damping ratio is usually still a small number, ranging between 10^{-3} and 10^{-1}, but the turbulence intensity of waves can reach values up to 2 or more. In addition, the loading ratio and the frequency ratio may take values above one, in the range $[10^0; 10^3]$, when wave-loaded structures are compliant in surge, as floating offshore wind turbines or floating bridges.

3 MULTIPLE TIMESCALE SPECTRAL ANALYSIS

Since the homogenous part of the dynamic system at hand (10) is linear, it is fully characterized by its frequency response function

$$H(\tilde{\omega}) = \frac{1}{1 - \tilde{\omega}^2 + 2i\xi\tilde{\omega}} \tag{15}$$

The PSD of the response thus takes the canonical form

$$S_{\tilde{x}}(\tilde{\omega}) = S_{\tilde{f}}(\tilde{\omega})\, K_s(\tilde{\omega}) \tag{16}$$

where the kernel function is, at second order,

$$K_s(\tilde{\omega}) \equiv |H(\tilde{\omega})|^2 = \frac{1}{\left(1 - \tilde{\omega}^2\right)^2 + 4\xi^2\tilde{\omega}^2}. \tag{17}$$

and, similarly, the bispectrum of the response is given by

$$B_{\tilde{x}}(\tilde{\omega}_1, \tilde{\omega}_2) = B_{\tilde{f}}(\tilde{\omega}_1, \tilde{\omega}_2)\, K_b(\tilde{\omega}_1, \tilde{\omega}_2) \tag{18}$$

where $B_{\tilde{f}}(\tilde{\omega}_1, \tilde{\omega}_2)$ represents the bispectrum of the loading. At third order, the kernel reads [4]

$$K_b(\tilde{\omega}_1, \tilde{\omega}_2) \equiv H(\tilde{\omega}_1)\, H(\tilde{\omega}_2)\, H(-\tilde{\omega}_1 - \tilde{\omega}_2) \tag{19}$$

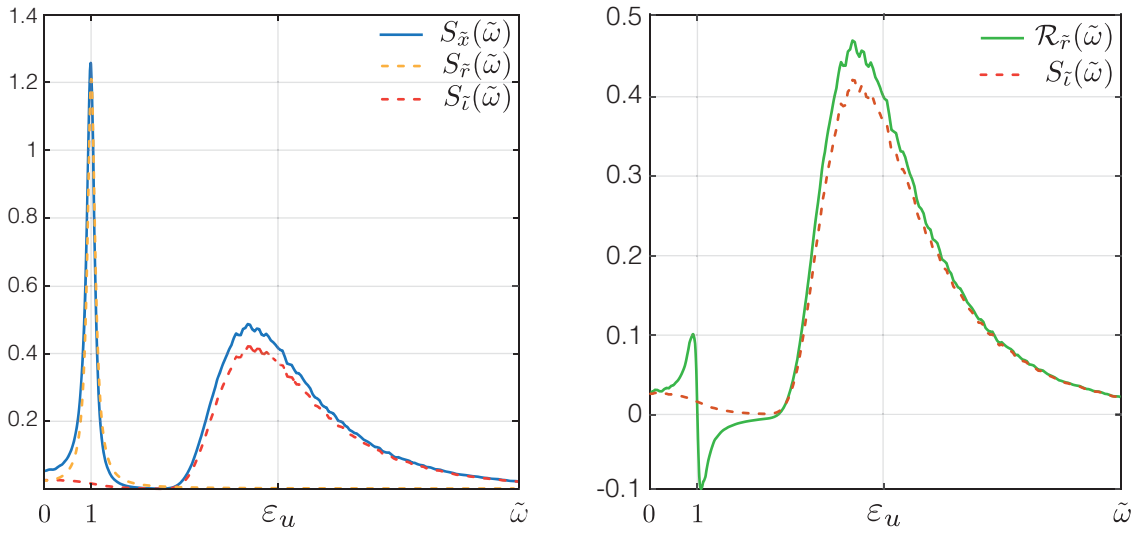

Figure 2: Typical shape of the PSD of the response (symmetrical, represented for $\tilde{\omega} \geq 0$) Numerical values: $\kappa_u = 10$; $\lambda_u = 1$; $\varepsilon_u = 5$ and $\xi = 10^{-1}$.

In a spectral approach, the statistical moments of the response are obtained by the (heavy) integration of the corresponding spectra, in particular

$$m_{2,\tilde{x}} = \int_{\mathbb{R}} S_{\tilde{x}}\left(\tilde{\omega}\right) \mathrm{d}\tilde{\omega} \qquad \text{and} \qquad m_{3,\tilde{x}} = \iint_{\mathbb{R}^2} B_{\tilde{x}}\left(\tilde{\omega}_1, \tilde{\omega}_2\right) \mathrm{d}\tilde{\omega}_1 \mathrm{d}\tilde{\omega}_2 \tag{20}$$

for the second and third moments. The Multiple Timescale Spectral Analysis aims at approximating these integrals with just a few operations [5], while providing at the same time a clear understanding of the different sources of contribution to the integral. Once statistical moments are determined, the skewness coefficient

$$\gamma_{\tilde{x}} = \frac{m_{3,\tilde{x}}}{m_{2,\tilde{x}}^{3/2}} \tag{21}$$

can be computed and used together with the peak factor model.

3.1 Second central moment of the response

As shown in Figure 2, when the frequency ratio ε_u is greater than one, the PSD of the response basically features:
- two resonant peaks having a width of ord (ξ) and being centered in $\tilde{\omega} = \pm 1$;
- two inertial peaks reaching their maximum value when $|\tilde{\omega}| = \text{ord}\left(\varepsilon_u\right)$ and spreading over the frequencies whose absolute value is above a given fraction ζ of the frequency ratio, $|\tilde{\omega}| > \zeta\varepsilon_u$;
- a flat background region in the vicinity of the origin.

As a first step, the introduction of the strained coordinates $\tilde{\omega} = \xi\tilde{\eta} \pm 1$, with $\tilde{\eta} = \text{ord}\left(1\right)$ at most, into Equation (16) allows to focus on the resonant peaks of the PSD of the response and the Taylor series expansion of the kernel function for small damping ratios yields

$$K_s\left(\xi\tilde{\eta} \pm 1\right) \simeq \frac{1}{4\xi^2}\left(\frac{1}{\left(\tilde{\eta}^2+1\right)} \mp \frac{\left(\tilde{\eta}^2+2\right)}{\left(\tilde{\eta}^2+1\right)^2}\xi\tilde{\eta} + \text{ord}\left(\xi^2\right)\right) \tag{22}$$

Likewise, the PSD of the loading is also expanded in Taylor series and reads

$$S_{\tilde{f}}\left(\xi\tilde{\eta}\pm 1\right) \;\simeq\; S_{\tilde{f}}\left(\pm 1\right) + S_{\tilde{f}}^{(1)}\left(\pm 1\right)\xi\tilde{\eta} + \text{ord}\left(\xi^2\right) \tag{23}$$

where the superscript (i) indicates the i-th derivative with respect to the dimensionless circular frequency $\tilde{\omega}$. While it seems reasonable to truncate Equation (22) at leading order on account that $\xi \ll 1$, it is necessary to check that the PSD of the loading is almost constant on the interval of interest, or more formally that

$$S_{\tilde{f}}^{(1)}\left(\pm 1\right) \;\leq\; \text{ord}\left(S_{\tilde{f}}\left(\pm 1\right)\right) \tag{24}$$

to be allowed to neglect higher order terms in Equation (23). If this condition is fulfilled, the PSD of the response is approximately equal to

$$S_{\tilde{r}}\left(\tilde{\omega}\right) \;=\; \frac{S_{\tilde{f}}\left(1\right)}{4\xi^2}\left(\frac{\xi^2}{\left(\left(\tilde{\omega}+1\right)^2+\xi^2\right)} + \frac{\xi^2}{\left(\left(\tilde{\omega}-1\right)^2+\xi^2\right)}\right) \tag{25}$$

in the regions spanned by the strained coordinates $\tilde{\omega} = \xi\tilde{\eta} \pm 1$, since the PSD of the loading is symmetric. This local approximation is represented by the yellow dashed line in Figure 2. The resonant component of the variance is eventually given by

$$m_{2,\tilde{r}} \;=\; \int_{\mathbb{R}} S_{\tilde{r}}\left(\tilde{\omega}\right)\mathrm{d}\tilde{\omega} = \frac{\pi}{2\xi}S_{\tilde{f}}\left(1\right). \tag{26}$$

Applying the procedure recommended in [5], the subtraction of $S_{\tilde{r}}\left(\tilde{\omega}\right)$ from the PSD of the response $S_{\tilde{x}}\left(\tilde{\omega}\right)$ provides a first residual with only two inertial peaks

$$\mathcal{R}_{\tilde{r}}\left(\tilde{\omega}\right) \;=\; S_{\tilde{x}}\left(\tilde{\omega}\right) - S_{\tilde{r}}\left(\tilde{\omega}\right) = S_{\tilde{f}}\left(\tilde{\omega}\right)\mathcal{K}_s\left(\tilde{\omega}\right) \tag{27}$$

in which

$$\mathcal{K}_s\left(\tilde{\omega}\right) \;=\; \left|H\left(\tilde{\omega}\right)\right|^2 - \frac{S_{\tilde{r}}\left(\tilde{\omega}\right)}{S_{\tilde{f}}\left(\tilde{\omega}\right)} \tag{28}$$

is the residual kernel function. A new coordinate stretching, $\tilde{\omega} = \left(\zeta\tilde{\eta}\pm 1\right)/\epsilon_u$ with $\epsilon_u = {}^1\!/_{\varepsilon_u} \ll 1$ and $\tilde{\eta} = \text{ord}\left(1\right)$ at most again, is then injected into Equation (27) to zoom on the inertial peaks. The Taylor series expansion of the residual kernel function for small values of ϵ_u yields

$$\mathcal{K}_s\left(\left(\zeta\tilde{\eta}\pm 1\right)/\epsilon_u\right) \;\simeq\; \frac{\epsilon_u^4}{\left(1\pm\zeta\tilde{\eta}\right)^4} - \frac{S_{\tilde{f}}\left(1\right)}{S_{\tilde{f}}\left(\left(\zeta\tilde{\eta}\pm 1\right)/\epsilon_u\right)}\frac{\epsilon_u^2}{\left(1\pm\zeta\tilde{\eta}\right)^2} \tag{29}$$

at leading order and the second term, coming from the approximations of the resonant peaks, can be discarded if

$$\frac{S_{\tilde{f}}\left(1\right)}{S_{\tilde{f}}\left(\left(\zeta\tilde{\eta}\pm 1\right)/\epsilon_u\right)} \;\leq\; \text{ord}\left(\epsilon_u^3\right) \tag{30}$$

in the interval of interest. However, even though the residual is correctly fitted by

$$S_{\tilde{\imath}}\left(\tilde{\omega}\right) \;=\; \frac{S_{\tilde{f}}\left(\tilde{\omega}\right)}{\tilde{\omega}^4} \tag{31}$$

in the regions spanned by the stretched coordinates $\tilde{\omega} = \xi\tilde{\eta} \pm 1$, this is not an appropriate local approximation, in the sense of the Multiple Timescale Spectral Analysis, because it is not always integrable near $\tilde{\omega} = 0$, regardless of the definition of the PSD of the loading. Considering, instead, the $(0, 4)$ Padé approximant

$$\mathcal{P}\,(0,4)\,[\mathcal{K}_s\,(\tilde{\omega})] = \frac{1}{1/\mathcal{K}_s\,(0) + \tilde{\omega}^4} \tag{32}$$

for the residual kernel, the local approximation

$$S_{\tilde{\imath}}\,(\tilde{\omega}) \;\; = \;\; \frac{S_{\tilde{f}}\,(\tilde{\omega})}{1/\mathcal{K}_s\,(0) + \tilde{\omega}^4} \tag{33}$$

of the residual is now integrable near $\tilde{\omega} = 0$ and matches the residual in the background region as well. The integrand is ultimately made totally independent from structural characteristics, such as the natural frequency of the system, by observing that $S_{\tilde{p}}\,(1) \simeq S_{\tilde{p}}\,(0)$, since $\varepsilon_u \gg 1$, and is represented by an orange dashed line in Figure 2. At the end, the mainly inertial, partly background, component of the variance of the response is given by

$$m_{2,\tilde{\imath}} \;\; = \;\; \int\limits_{\mathbb{R}} \frac{S_{\tilde{f}}\,(\tilde{\omega})}{2 + \tilde{\omega}^4} \mathrm{d}\tilde{\omega}. \tag{34}$$

and the variance of the response is approximated by the sum of the resonant and inertial contributions as

$$m_{2,\mathrm{mtsa}} \;\; = \;\; \frac{\pi}{2\xi} S_{\tilde{f}}\,(1) + \int\limits_{\mathbb{R}} \frac{S_{\tilde{f}}\,(\tilde{\omega})}{2 + \tilde{\omega}^4} \mathrm{d}\tilde{\omega}. \tag{35}$$

This approximation seems less advantageous, at first glance, than its equivalent background/resonant decomposition, since the inertial component is still expressed by means of an integral. Nevertheless, it is noticed that this integral only involves the loading and can be established, even maybe in closed-form, a priori, for a given PSD of loading.

3.2 Third central moment of the response

As shown in Figure 3, when the frequency ratio is greater than one, the bispectrum of the response exhibits essentially:
- six background bi-resonant peaks on an area of ord (ξ^2), centered in $(\pm 1, 0)$, $(\pm 1, 0)$ and $\pm\,(1, -1)$;
- six bi-resonant inertial peaks on an area of ord (ξ^2), centered in $\pm\,(1, -2)$, $\pm\,(2, -1)$ and $\pm\,(1, 1)$;
- six bi-background inertial triangular basins located between the background bi-resonant peaks and the bi-resonant inertial peaks;
- six resonant bi-inertial pairs of peaks, centered in $\pm\,(\varepsilon_u, 0)$, $\pm\,(0, \varepsilon_u)$ and $\pm\,(\varepsilon_u, -\varepsilon_u)$.

Focusing first on the region where $\tilde{\omega}_1$ and $\tilde{\omega}_2$ are both of ord (1), it appears quite clearly that the bispectrum of the response behaves locally as

$$B_{\tilde{r}}\,(\tilde{\omega}_1, \tilde{\omega}_2) \;\; = \;\; \Re\left[B_{\tilde{f}}\,(0,0)\right] K_b\,(\tilde{\omega}_1, \tilde{\omega}_2) \tag{36}$$

because the bispectrum of the loading is almost constant in this zone and its imaginary part is equal to zero. In addition, the third order kernel decreases fast enough along $\tilde{\omega}_1$ and $\tilde{\omega}_2$ for the

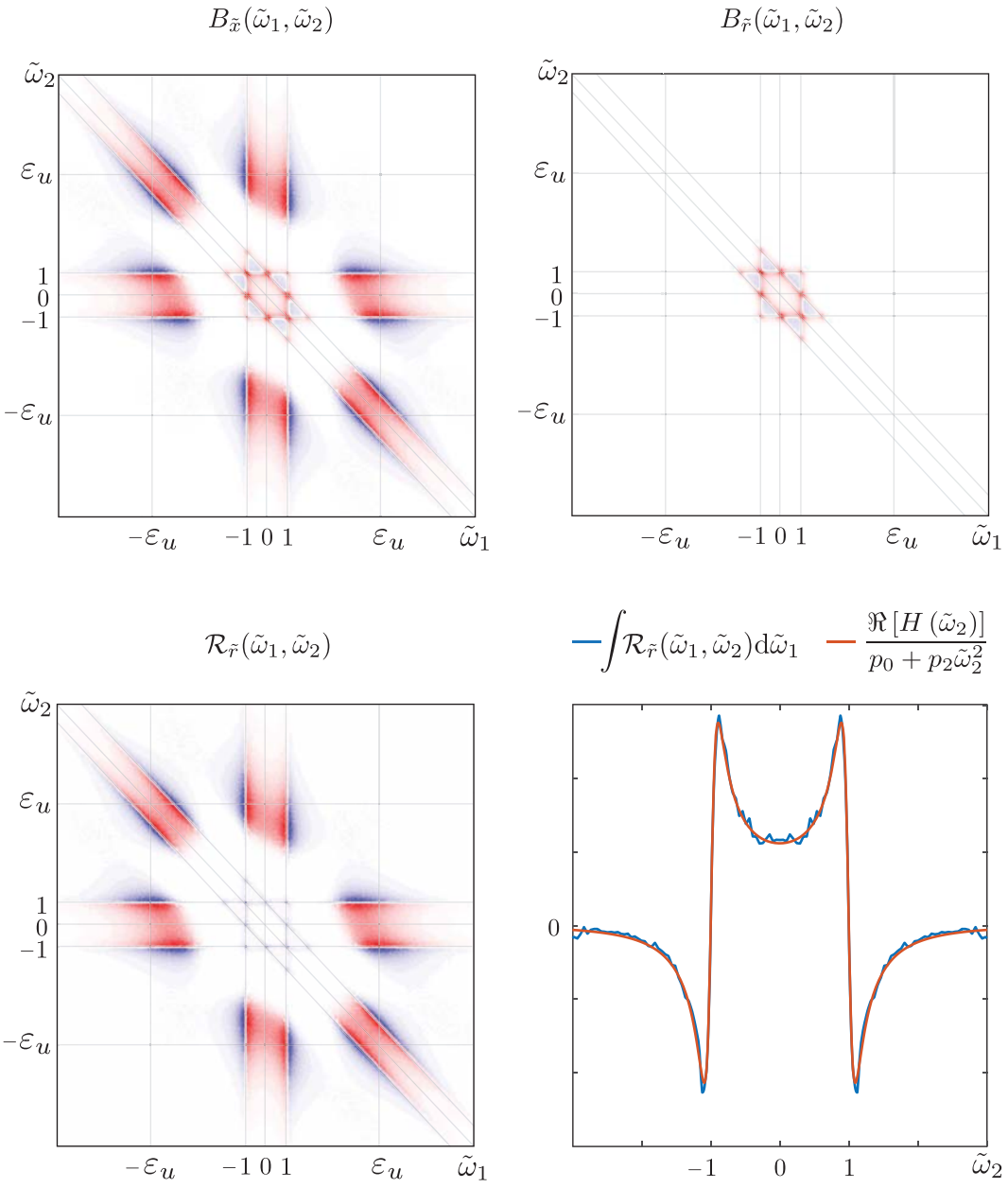

Figure 3: Typical shape of the bispectrum of the response $B_{\tilde{x}}(\tilde{\omega}_1, \tilde{\omega}_2)$. Numerical values: $\kappa_u = 10$; $\lambda_u = 1$; $\varepsilon_u = 5$ and $\xi = 10^{-1}$.

approximation presented in Equation (36) to be local and integrable, as required by the multiple timescale spectral analysis. Its double integration gives a simple and rapid estimation of the component of the third central moment of the response in the vicinity of the origin

$$m_{3,\tilde{o}} \quad = \quad \frac{8\pi^2}{3\left(1+8\xi^2\right)}\Re\left[B_{\tilde{f}}\left(0,0\right)\right] \tag{37}$$

which corresponds to the area under the six background bi-resonant peaks, the six bi-resonant inertial peaks and the six bi-background inertial triangular basins.

Then, the subtraction of $B_{\tilde{r}}\left(\tilde{\omega}_1,\tilde{\omega}_2\right)$ from the bispectrum of the response provides a first residual

$$\mathcal{R}_{\tilde{r}}\left(\tilde{\omega}_1,\tilde{\omega}_2\right) \quad = \quad \mathcal{B}_{\tilde{f}}\left(\tilde{\omega}_1,\tilde{\omega}_2\right)K_b\left(\tilde{\omega}_1,\tilde{\omega}_2\right) \tag{38}$$

where

$$\mathcal{B}_{\tilde{f}}\left(\tilde{\omega}_1,\tilde{\omega}_2\right) \quad = \quad B_{\tilde{f}}\left(\tilde{\omega}_1,\tilde{\omega}_2\right) - \Re\left[B_{\tilde{f}}\left(0,0\right)\right] \tag{39}$$

and a new coordinate stretching, $\tilde{\omega}_1 = \tilde{\eta}_1/\epsilon_u$ and $\tilde{\omega}_2 = \tilde{\eta}_2$ with $\tilde{\eta}_1$ and $\tilde{\eta}_2$ of ord (1), is injected into Equation (38) in order to zoom on one of the resonant bi-inertial pair of peaks. The leading order term of the Taylor series expansion of the third order kernel for small values of ϵ_u corresponds to

$$K_b\left(\tilde{\omega}_1,\tilde{\omega}_2\right) \quad \simeq \quad K_s\left(\tilde{\omega}_1\right)\Re\left[H\left(\tilde{\omega}_2\right)\right] \tag{40}$$

where we recover the second order kernel and the real part of the frequency response function. Interestingly enough, each of those two distinguished functions depends on only one coordinate in the intervals of interest. In order to ensure the integrability of the local approximation near $\tilde{\omega}_1 = 0$ and $\tilde{\omega}_2 = \pm 1$, respectively, the second order kernel is approximated by a $(0,4)$ Padé approximant, similarly to what was done before with the inertial component of the PSD of the response,

$$\mathcal{P}\left(0,4\right)\left[K_s\left(\tilde{\omega}_1\right)\right] \quad = \quad \frac{1}{1+\tilde{\omega_1}^4} \tag{41}$$

and the real part of the frequency response function, on the contrary, cannot be simplified on account that the damping ratio is a small number. In addition, the variations of the bispectrum of the loading along $\tilde{\omega}_1$ and along $\tilde{\omega}_2$ have both to be taken into account. The first ones are indeed required to get a local approximation that resembles the residual while the second ones are needed to obtain a non-zero result for the resonant bi-inertial component of the third central moment of the response, since

$$\int_{\mathbb{R}} \Re\left[H\left(\tilde{\omega}_2\right)\right]\mathrm{d}\tilde{\omega}_2 \quad = \quad 0 \tag{42}$$

However, the number of points where the bispectrum has to be evaluated is drastically reduced by using a $(0,2)$ Padé approximant to fit correctly the integral of the residual along $\tilde{\omega}_1$ when $\tilde{\omega}_2$ is of ord (1). It reads

$$\mathcal{P}\left(0,2\right)\left[\int_{\mathbb{R}} \frac{\mathcal{B}_{\tilde{f}}\left(\tilde{\omega}_1,\tilde{\omega}_2\right)}{1+\tilde{\omega_1}^4}\mathrm{d}\tilde{\omega}_1\right] \quad = \quad \frac{1}{p_0+p_2\tilde{\omega}_2^2} \tag{43}$$

in which

$$p_0 = \int_{\mathbb{R}} \frac{\mathcal{B}_{\tilde{f}}\left(\tilde{\omega}_1, 0\right)}{1+\tilde{\omega_1}^4} \mathrm{d}\tilde{\omega}_1 \quad \text{and} \quad p_2 = \int_{\mathbb{R}} \frac{\mathcal{B}_{\tilde{f}}^{(0,2)}\left(\tilde{\omega}_1, 0\right)}{1+\tilde{\omega_1}^4} \mathrm{d}\tilde{\omega}_1 \tag{44}$$

where the superscript (i,j) indicates the (i,j)-th derivative with respect to $\tilde{\omega}_1$ and $\tilde{\omega}_2$. It is worth to note that the Padé approximant is entirely independant from the structural characteristics again. The resonant bi-inertial component of the third central moment of the response is finally given by

$$m_{3,\tilde{\imath}} = \int_{\mathbb{R}} \frac{\Re\left[H\left(\tilde{\omega}_2\right)\right]}{p_0 + p_2 \tilde{\omega}_2^2} \mathrm{d}\tilde{\omega}_2$$

and the third moment of the response approximately corresponds to

$$m_{3,\mathrm{mtsa}} \;=\; m_{3,\tilde{o}} + m_{3,\tilde{\imath}} \tag{45}$$

3.3 Numerical validation

The mathematical developments presented in Sections 3.1 and 3.2 are now validated by comparing the results obtained with the multiple timescale spectral analysis to the results coming from Monte Carlo simulations.

First, the PSD of the dimensionless water velocity fluctuations, $S_{\tilde{u}}\left(\tilde{\omega}\right)$, is computed according to Equation (12) for a given set of dimensionless numbers. A time-history of wave velocity fluctuations, $\tilde{u}\left(\tilde{t}\right)$, is then generated by computing the inverse Fourier transform of

$$U\left(\tilde{\omega}_i\right) \;=\; \sqrt{S_{\tilde{u}}\left(\tilde{\omega}_i\right) N \tilde{\omega}_s} \mathrm{e}^{\mathrm{j}\,\theta_i} \tag{46}$$

where $N = 10^8$ is the number of elements, $\tilde{\omega}_s = 20\ \varepsilon_u$ is the sampling circular frequency and θ_i is a phase angle randomly drawn from a uniform distribution in the interval $[0, 2\pi[$. At this point, it is already possible to check that the frequency content of the wave velocity signal is correctly represented by superimposing its PSD on the theoretical one. Figure 4 shows the very good agreement between them. Then, a loading sample is obtained by calculating

$$\tilde{f} \;=\; \kappa_u \lambda_u \tilde{u}' + \left|1 + \lambda_u \tilde{u}\right| \left(1 + \lambda_u \tilde{u}\right). \tag{47}$$

It is used differently in the time domain analysis and in the Multiple Timescale Spectral Analysis.

In time domain, the loading sample enters into the equation of motion which is hence solved numerically to obtain the evolution of the displacement of the structure in time, $\tilde{x}\left(\tilde{t}\right)$. To do so, the finite difference method with an explicit scheme has been chosen here but any other time marching algorithm would obviously provide almost exactly the same results. At the end, the second and third central moments of the response are respectively given by

$$m_{2,\tilde{x}} \;=\; \mathbb{E}\left[\left(\tilde{x}\left(\tilde{t}\right) - \mathbb{E}\left[\tilde{x}\left(\tilde{t}\right)\right]\right)^2\right] \tag{48}$$

$$m_{3,\tilde{x}} \;=\; \mathbb{E}\left[\left(\tilde{x}\left(\tilde{t}\right) - \mathbb{E}\left[\tilde{x}\left(\tilde{t}\right)\right]\right)^3\right] \tag{49}$$

where the operator $\mathbb{E}\left[.\right]$ stands for the mathematical expectation, computed over the samples.

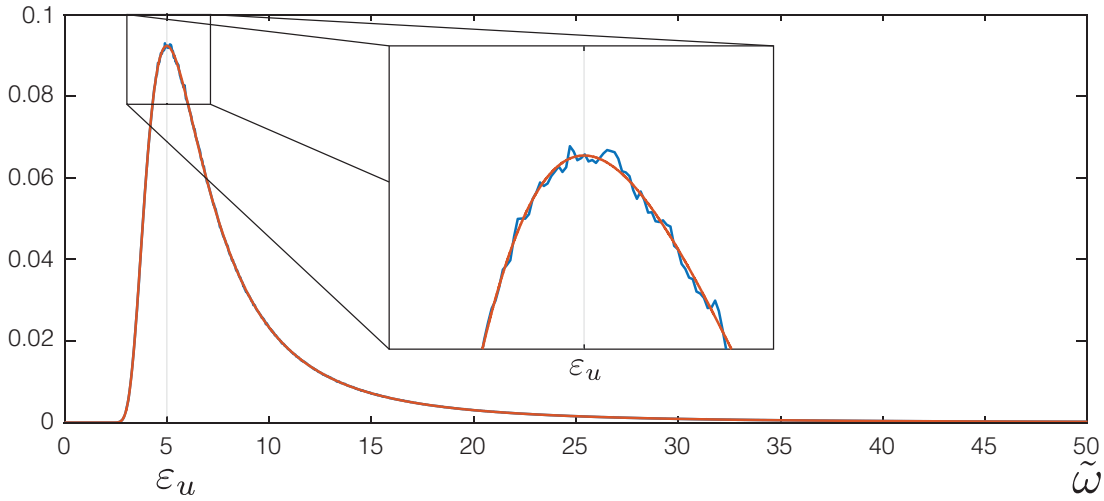

Figure 4: Typical shape of the power spectral density of the water velocity fluctuations.

In the spectral approach, we start by determining the power spectral density and the bispectrum associated to the loading sample. From there on, we just follow the steps detailed in Sections 3.1 and 3.2 to obtain the resonant and the inertial components of the second and third central moments of the response. Since we have kept the same set of dimensionless numbers throughout the whole paper, the local approximations and the first residual of the power spectral density and of the bispectrum of the response are respectively shown in Figure 2 and Figure 3.

The numerical results are summarized in Table 1 together with the computational time required in both cases. The second and third central moments of the response are computed much more rapidly with the Multiple Timescale Spectral Analysis and are very close to the references obtained with Monte Carlo simulations.

$S_{\tilde{f}}(1)$	$m_{2,\tilde{x}}$	$m_{2,\tilde{r}}$	$m_{2,\tilde{\imath}}$	$m_{2,\text{mtsa}}$	t_{time}	t_{mtsa}
0.05	3.58	0.76	2.60	3.36	5 s	0.1 s
$B_{\tilde{f}}(0,0)$	$m_{3,\tilde{x}}$	$m_{3,\tilde{o}}$	$m_{3,\tilde{\imath}}$	$m_{3,\text{mtsa}}$	$\gamma_{\tilde{x}}$	γ_{mtsa}
$8 \cdot 10^{-3}$	0.93	0.20	0.68	0.88	0.137	0.143

Table 1: Numerical values: $\kappa_u = 10$; $\lambda_u = 1$; $\varepsilon_u = 5$ and $\xi = 10^{-1}$

4 CONCLUSIONS

The background/resonant decomposition (which is widely applied in wind engineering) is a particular application of the Multiple Timescale Spectral Analysis where the natural frequency of the oscillator is larger than the frequency content of the loading. In this paper, we have specialized the concept to the companion problem, where the natural frequency of the oscillator is smaller than the characteristic frequency of the loading, as is typical in floating structures considered in marine engineering. Instead of the heavy numerical integration of the power spectral density and bispectrum of the structural response, the proposed methodology is able to determine the statistical moments of the response as a sum of two components. These two components correspond to a resonant contribution and an inertial contribution. The same decomposition is used for both the second and third orders. The resonant contribution takes a very similar shape as the well known existing approximations. Conversely to the companion problem though, the inertial contribution requires the evaluation of an integral, which is however

less cumbersome than in the formal numerical integration of the spectra since it involves the loading only.

The proposed methodology has been benchmarked against Monte Carlo simulations. It shows a significant CPU saving while offering a very competitive accuracy. It will certainly serve as a major cornerstone of a multi degree-of-freedom model, where the response of a structure in its modal basis will be computed as a linear combination of modal (single degree-of-freedom) responses.

ACKNOWLEDGEMENTS

The work of the first author is supported by a FRIA grant from the F.R.S-FNRS, the Belgian Fund for Scientific Research.

References

[1] R Adrezin, P Bar-Avi, and Haym Benaroya. Dynamic response of compliant offshore structures. *Journal of aerospace engineering*, 9(4):114–131, 1996.

[2] Alan Garnett Davenport. The application of statistical concepts to the wind loading of structures. *Proceedings of the Institution of Civil Engineers*, 19(4):449–472, 1961.

[3] Vincent Denoël. Estimation of modal correlation coefficients from background and resonant responses. *Structural Engineering and Mechanics: an International Journal*, 32(6): 725–740, 2009.

[4] Vincent Denoël. On the background and biresonant components of the random response of single degree-of-freedom systems under non-gaussian random loading. *Engineering structures*, 33(8):2271–2283, 2011.

[5] Vincent Denoël. Multiple timescale spectral analysis. *Probabilistic Engineering Mechanics*, 39:69–86, 2015.

[6] Vincent Denoël and Luigi Carassale. Response of an oscillator to a random quadratic velocity-feedback loading. *Journal of Wind Engineering and Industrial Aerodynamics*, 147:330–344, 2015.

[7] Ahmed A Elshafey, Mahmoud R Haddara, and H Marzouk. Dynamic response of offshore jacket structures under random loads. *Marine Structures*, 22(3):504–521, 2009.

[8] Mircea Grigoriu. Crossings of non-gaussian translation processes. *Journal of Engineering Mechanics*, 110(4):610–620, 1984.

[9] Zhiyu Jiang, Xiangqian Zhu, and Weifei Hu. Modeling and analysis of offshore floating wind turbines. In *Advanced Wind Turbine Technology*, pages 247–280. Springer, 2018.

[10] A Kareem and J Zhao. Analysis of non-gaussian surge response of tension leg platforms under wind loads. 1994.

[11] Dae Kun Kwon and Ahsan Kareem. Peak factors for non-gaussian load effects revisited. *Journal of Structural Engineering*, 137(12):1611–1619, 2011.

[12] YM Low. Frequency domain analysis of a tension leg platform with statistical linearization of the tendon restoring forces. *Marine Structures*, 22(3):480–503, 2009.

[13] Martin Schetzen. The volterra and wiener theories of nonlinear systems. 1980.

[14] Rouslan L Stratonovich. *Topics in the theory of random noise*, volume 2. CRC Press, 1967.

[15] SR Winterstein, TC Ude, and T Marthinsen. Volterra models of ocean structures: Extreme and fatigue reliability. *Journal of Engineering Mechanics*, 120(6):1369–1385, 1994.

[16] Steven R Winterstein and Tina Kashef. Moment-based load and response models with wind engineering applications. *J. Sol. Energy Eng.*, 122(3):122–128, 2000.

[17] Tokuo Yamamoto. Moored floating breakwater response to regular and irregular waves. *Applied Ocean Research*, 3(1):27–36, 1981.

EURODYN 2020
XI International Conference on Structural Dynamics
M. Papadrakakis, M. Fragiadakis, C. Papadimitriou (eds.)
Athens, Greece, 23–26 November 2020

EXTREME DYNAMIC RESPONSE OF EXTENDED BRIDGE STRUCTURES SUBJECTED TO INHOMOGENEOUS ENVIRONMENTAL LOADING

Bernt J. Leira[1] **and Jian Dai**[1]

[1] Department of Marine Technology, NTNU
MTS, Otto Nilsens vei 10, Trondheim, Norway
e-mail: {bernt.leira,jian.dai}@ntnu.no

Keywords: Inhomogeneous, Loads, Extreme, Response

Abstract. *For structures with large extensions in the horizontal plane (such as bridges with ultra-long spans), it is very likely that the characteristics of the environmental processes (such as wind, waves and earthquakes pressure) will exhibit inhomogeneous features across the structure. It is accordingly important to know how these features will affect the extreme dynamic response level of such bridges. In particular, the question arises whether application of simplified homogeneous load models will imply an under-prediction or an over-prediction of the extreme dynamic response. It will be also be of significant interest to identify the most "dangerous" load pattern for the case of inhomogeneous models and to compute the associated relative probability that this particular pattern may occur.*

These effects are investigated first by analysis of a simplified and "generic" case study of an extended line structure subjected to dynamic wave loading of the homogeneous versus the inhomogeneous type. A "forward calculation" is applied in order to study the extreme response level corresponding to these two load categories. It is next demonstrated how an inverse algorithm is able to identify the most critical inhomogeneous load pattern and the associated probability that this will occur (for given statistical models of the load parameters).

A numerical study of the hydroelastic response of a 4.6 km long fjord crossing floating bridge subjected to inhomogenous versus homogeneous stochastic wave loads is subsequently carried out. The bridge has a straight-line shape and is supported by 35 pontoons along its full length. To restrain the transverse motion in the horizontal plane, four clusters of deep water mooring lines are applied in order to strengthen the transverse stiffness of the bridge.

1 INTRODUCTION

The question arises whether inhomogeneous loading can lead to higher dynamic response levels than homogenous loading. Furthermore, there might be particular inhomogeneous load patterns that could possibly create significant amplification effects due to "modal resonance" phenomena. These features are presently illustrated in relation to a simplistic structural model and an "inverse" algorithm is applied in order to identify critical load patterns.

The effects of inhomogeneous wave loading are subsequently illustrated in connection with dynamic response of a floating bridge with an ultra-long span. Such and similar bridge concepts are presently being considered for crossing of extremely wide fjords along the West Coast of Norway, see e.g. [1, 2, 3, 4, 5, 6].

2 INHOMOGENEOUS LOADING: A GENERIC CASE STUDY

A simplified and "generic" case study of an extended line structure subjected to a deterministic dynamic wave loading of the homogeneous versus the inhomogeneous type is first considered. A "forward calculation" is applied in order to study the extreme response level corresponding to these two load categories. It is next demonstrated how an inverse algorithm is able to identify the most critical inhomogeneous load pattern and the associated probability that this will occur (for given statistical models of the load parameters). The findings from this simplified example are then summarized, and consequences for analysis and design of extended structures with more complex dynamic behaviour are discussed.

2.1 Forward modeling

A straight bridge structure of length L which is subjected to long-crested regular waves propagating at an angle θ is first analysed. Initially, the load pattern is uniformly distributed in space (with magnitudes q), see Figure 1 for an illustration. The line structure is taken to be simply supported at both ends, and the main bridge girder is supported by three pontoons at the three interior quarter points (i.e. at x = -L/4, 0 and +L/4). The bending stiffness of the bridge girder is EI, the cross-section area is A, the mass per unit length is m and the structural damping per unit length is c. The three pontoons all have the same mass (M_i = M for i = 1,2,3, which also includes hydrodynamic added mass in the direction transverse to the bridge axis), and with the same hydrodynamic damping (C_i = C for i = 1,2,3 also in the transverse direction)

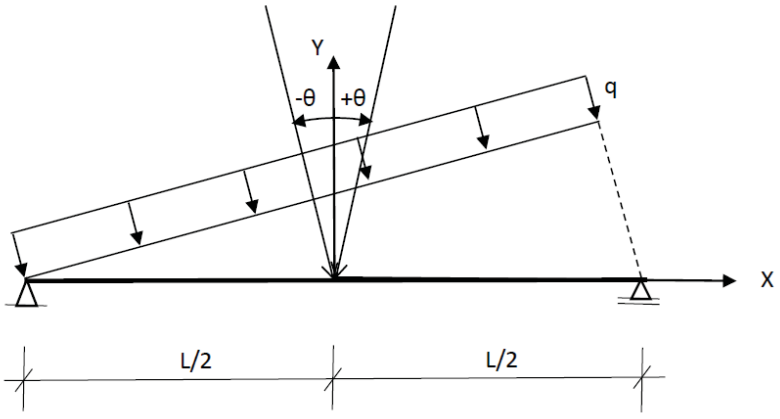

Figure 1. Line structure subjected to uniform load patterns with harmonic time variation.

The lateral dynamic response (strong-axis bending moment) of the line structure for the present loading is computed by application of the mechanical transfer functions for the relevant natural modes. Here, it is assumed that the first three horizontal modes are the relevant ones. These correspond respectively one, two and three sinusoidal half-waves. The lateral displacement is then expressed as follows:

$$\mathrm{v}(x,\theta,\omega,t)=\left[\sum_{j=1}^{3}\left[Q_j\cdot\cos(\theta\ )\right]\cdot\left|H_j(\omega)\right|\cdot\varphi_j(x)\right] \tag{1}$$

where $\varphi_j(x) = \sin(j\pi x/L+j\pi/2)$ is mode-shape number j (for j=1,2 and 3), $|H_j(\omega)|$ is the modulus of the frequency transfer function for mode number j. The modal load which corresponds to the distributed load q is expressed as:

$$Q_j=q\sum_{l=1}^{3}\cos\left(\omega t+k\cdot\sin(\theta_k)\cdot x_l\right)\cdot\varphi_j(x_l)\ \text{ for }\ \ \mathrm{j}=1,2,3;\ \text{and } l=1,2,3 \tag{2}$$

where the three x-coordinates of the pontoons are given as $x_1 = -L/4$, $x_2 = 0$ and $x_3 = +L/4$; $k = 2\pi/\lambda$ is the wave number corresponding to the frequency ω, as given by the wave length λ, which is obtained from the dispersion relationship for deep water (i.e. $\lambda = \omega^2/g$). The wave period is here taken as T = 10 seconds, implying a frequency of $2\pi/T=2\pi/10$.

The model mass, damping and stiffness properties of the line structure are expressed in terms of integrals involving the square of the mode shape functions and the corresponding curvatures:

$$\begin{aligned}
M_j &= M=\int_0^L m\cdot\varphi_j^2(x)\,dx+\sum_{l=1}^{3}M_P(\omega)\cdot\varphi_j^2(x_l)=\frac{mL}{2}+M_P(\omega)\cdot\sum_{l=1}^{3}\sin^2\left(\frac{j\pi\cdot x_l}{L}\right)=\frac{mL}{2}+2\cdot M_P(\omega)\\
C_j &= C=\int_0^L c\cdot\varphi^2(x)\,dx+\sum_{l=1}^{3}C_P(\omega)\cdot\varphi_j^2(x_l)=\frac{cL}{2}+C_P(\omega)\cdot\sum_{l=1}^{3}\sin^2\left(\frac{j\pi\cdot x_l}{L}\right)=\frac{cL}{2}+2\cdot C_P(\omega)\\
K_j &= \int_0^L EI\cdot\left(\frac{d^2\varphi_j(x)}{dx^2}\right)^2dx=\frac{EI\cdot L}{2}\cdot\left(\frac{j\pi}{L}\right)^4=\frac{(j\pi)^4\,EI}{2L^3}
\end{aligned} \tag{3}$$

where $M_P(\omega)$ is the pontoon mass (including hydrodynamic added mass) and $C_P(\omega)$ is the corresponding hydrodynamic damping in the lateral direction of the bridge.

Based on the model mass and stiffness, the corresponding natural frequencies for the three modes are obtained as:

$$\omega_j=\sqrt{\frac{K_j}{M_j}}=\left(\frac{j\pi}{L}\right)^2\cdot\sqrt{\frac{EI}{m+\dfrac{4\cdot M_P(\omega)}{L}}} \tag{4}$$

Furthermore, based on the modal properties, the modulus and phase angle for each of the three modes are then given as:

$$\left|H_j(\omega)\right| = \frac{1}{K_j\left[\left(1-\beta_j^2\right)^2 + \left(2\lambda_j\beta_j\right)^2\right]^{\frac{1}{2}}} \qquad \varepsilon_j(\omega) = \text{Arctan}\left[\frac{2\lambda_j\beta_j}{\left(1-\beta_j^2\right)}\right] \qquad (5)$$

where the frequency ratio for each mode is expressed as $\beta_j = \omega/\omega_j$ and the damping ratio is $\lambda_j = C_j/2M_j\omega_j$

The load frequency is next specialized to be $\omega = 0.9\cdot\omega_1$, and the three different load frequency ratios then become :

$$\beta_j = \left\lfloor \frac{0.9\omega_1}{\omega_j} \right\rfloor = \left\lfloor \frac{0.9}{j^2} \right\rfloor \qquad (6)$$

The damping ratios the three different modes are equal to $\lambda_1 = 1\%$, $\lambda_2 = 1.5\%$ and $\lambda_3 = 5\%$. The resulting simplified expression for the lateral displacement is then obtained as:

$$\text{v}(x,\theta,\omega,t) = \sum_{j=1}^{3}\left[Q_j\cdot\cos(\theta)\right]\cdot\left|H_j(\omega)\right|\cdot\varphi_j(x)\cdot\cos\left(\omega t-\varepsilon_j\right) \qquad (7)$$

The ratios between the values of the three mechanical transfer functions are approximately the following: $H_3(\omega)/H_1(\omega) = 19$ and $H_2(\omega)/H_1(\omega) = 500$. This implies that if the modal loads Q_j were identical, mode 2 would have a much higher influence on the displacement response than the other two mode shapes (and in particular mode 1).

The strong axis bending moment of the line structure is obtained from the curvature along the bridge accordingly and becomes:

$$M(x,\theta,\omega,t) = EI\cdot\sum_{j=1}^{3}\left[Q_j\cdot\cos(\theta)\right]\cdot\left|H_j(\omega)\right|\cdot\left(\frac{j\pi}{L}\right)^2\cdot\varphi_j(x)\cdot\cos\left(\omega t-\varepsilon_j\right) \qquad (8)$$

where EI is the corresponding bending stiffness of the bridge girder (for strong axis bending), The corresponding bending stresses are then obtained by dividing with the bending resistance of the girder.

Clearly, an important issue is at which cross-section along the line structure that the maximum bending moment will occur. This location will change for different combinations of the two direction parameters. However, the location can in all cases be seen to occur within the interval -L/3 to 0. Here, the quarter point (i.e. at x = –L/4) is selected for the purpose of illustration. The bending moment as a function of time and the direction angle of the incoming load is shown in Figure 2. It is seen that there are two positive maxima (both with magnitudes around 6.7) at times t slightly above t = 0 and slightly above t =10 sec. The corresponding value of the wave direction angle is around 0.7 radians in both cases. There is a single negative maximum (with the same magnitude as the positive maxima) at time t = 5 sec, which also occurs for a wave direction angle of around 0.7 radians.

The probability that the dynamic bending moment exceeds a given value (at a given cross-section, which preferably is the one with the highest bending moment along the line structure) can now be obtained by introducing a joint probability density function for the two basic variables t and θ. Denoting this density function by $f_{t,\theta}(t,\theta)$, the probability of exceeding a given

value of the bending moment can then be evaluated by integrating across the area in the (t,θ)-plane for which the given value of the bending moment is exceeded.

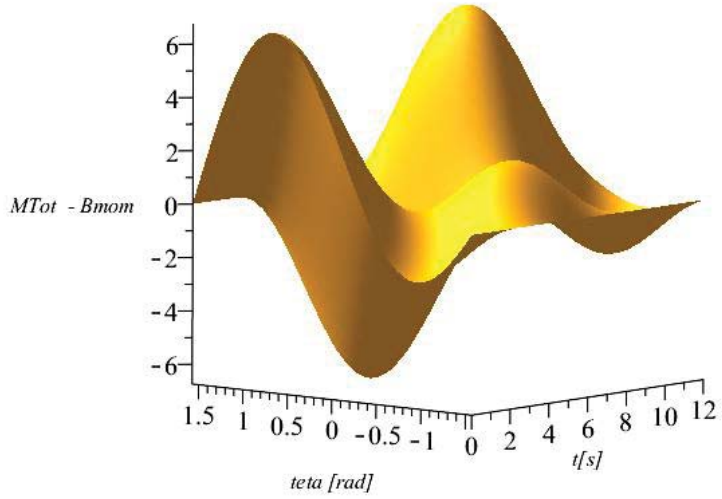

Figure 2. Normalized bending moment diagram of line structure for cross-section at x=-L/4, homogeneous loading. Normalization factor is EI/qL^3.

The subdomain which gives the maximum contribution to this integral will depend on the shape of the probability density function. For illustration purposes, we first apply a uniform joint density function with constant value in the rectangle bounded by the lines t=0., t=10 sec and $\theta = -\pi/2$, $\theta = +\pi/2$. The maximum contribution to the integral is then due to the regions close to the boundaries at t=0 and t=10 sec. In general, the probability of exceeding the specified bending moment value can then be evaluated by means of Monte Carlo simulation or FORM/SORM techniques, [7, 8]. The latter also provides direct information about the critical combination of time and wave direction. However, since time is strictly not a random variable as it runs sequentially through all the values from 0 to 10 seconds (and of course through subsequent load periods if such are given), calculation of this probability boils down to a one-dimensional formulation at the "critical" time, for which the load direction becomes the only remaining basic variable. This implies that the probability of being in the "exceedance region" can be calculated by application of the cumulative distribution function of the direction variable. For a uniform probability distribution in the range from $-\pi/2$ to $+\pi/2$, the cumulative distribution function for a given angle is just the cumulative angle divided by the length of the total interval (i.e. π).

The following probabilities are obtained for a selection of four different bending moment magnitudes: (i) a normalized bending moment value of 4 gives a probability of 0.35 (corresponding to the direction interval from around 0. rad to 1.1 rad) (ii) a normalized bending moment value of 5 gives a probability of 0.24 (corresponding to the direction interval from around 0.25 rad to 1.0 rad) (iii) a normalized bending moment value of 6 gives a probability of 0.17 (corresponding to the direction interval from around 0.4 rad to 0.9 rad) (iv) a normalized bending moment value of 6.7 gives a probability of 0.0068 (corresponding to the direction interval from around 0.64 rad to 0.67 rad). If the load direction is e.g. is instead parabolically distributed (i.e. $f_\theta = 1.9\cdot(0.5-\theta/\pi)*(0.5+\theta/\pi) = 1.9\cdot(0.25-(\theta/\pi)^2)$, the probabilities for the four cases instead become somewhat higher: (i)0.44 (ii)0.30 (iii)0.20 and (iv)0.012.

Subsequently, the case of *inhomogeneous loading* is addressed. A linear variation from zero to a maximum load intensity value is introduced for the load pattern. By requiring that the mean load intensity is the same as the constant value for the homogeneous case, the maximum intensity of the load components will be 2*q. This case is illustrated in Figure 3.

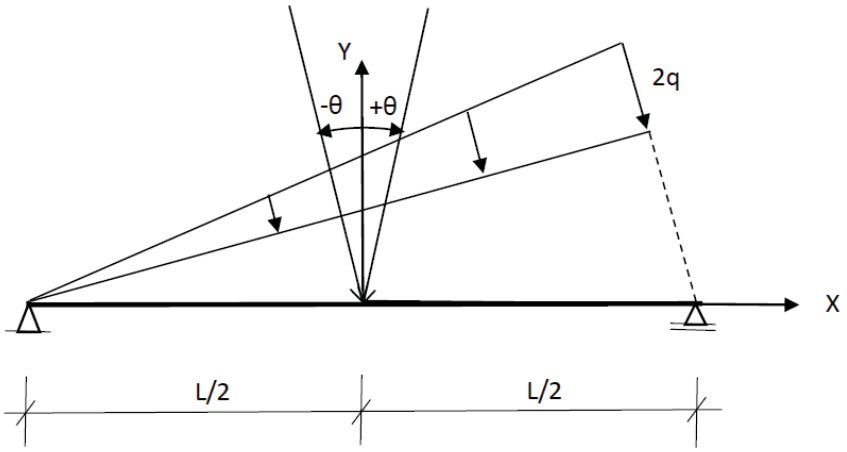

Figure 3. Line structure subjected to a non-homogeneous load pattern (linear variation) with harmonic time variation.

The modal loads for this case are obtained by introducing corresponding load factors, $f(x_l)$ at each pontoon:

$$Q_j = q\sum_{l=1}^{3}\cos\left(\omega t + k\cdot\sin\left(\theta_k\right)\cdot x_l - \varepsilon_j\right)\cdot f\left(x_l\right)\cdot\varphi_j\left(x_l\right) \qquad \text{for } j=1,2,3; \text{ and } l=1,2,3 \qquad (9)$$

where $f(x_1) = 0.25$, $f(x_2) = 0.5$ and $f(x_3) = 0.75$. For the present load pattern, the normalized bending moment for the cross-section at x = -L/4 is shown in Figure 4. It is seen that there is now a maximum negative peak at t = 0 and a maximum positive peak with a magnitude of 17 at around t=7.5 seconds.

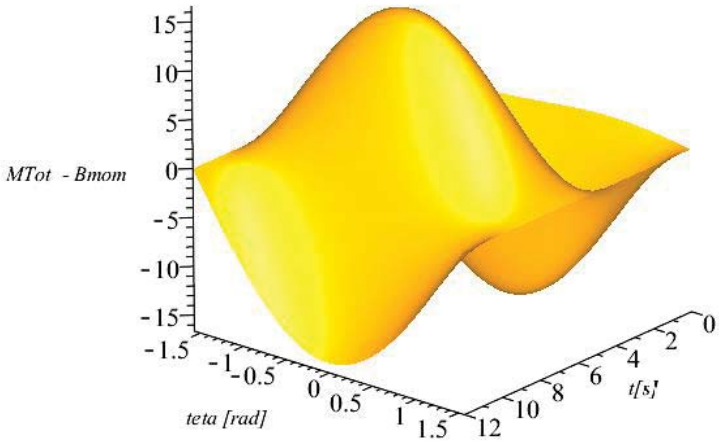

Figure 4. Normalized bending moment diagram of line structure for cross-section at x=-L/4, non-homogeneous loading. Normalization factor is EI/qL^3.

For the present case, five different magnitudes of the bending moment are considered and the corresponding direction intervals with associated probabilities are determined. These are as follows: (i) a normalized bending moment value of 12 gives a probability of 0.51(corresponding to the direction interval from around -0.8 rad to +0.8 rad) (ii) a normalized bending moment value of 14 gives a probability of 0.45 (corresponding to the direction interval from around -0.7 rad to 0.7 rad) (iii) a normalized bending moment value of 6 gives a probability of 0.32 (corresponding to the direction interval from around -0.5 rad to 0.5 rad) (iv) a normalized bending moment value of 16 gives a probability of 0.13 (corresponding to the direction interval from around -0.2 rad to 0.2 rad) (v) a value of 17 gives a probability of 0.0063 (corresponding to the direction interval from around -0.01 rad to 0.01 rad). If the load direction is e.g. parabolically distributed (i.e. $f_\theta = 1.9\cdot(\theta/\pi-0.5)*(\theta/\pi+0.5) = 1.9\cdot(\theta/\pi)2-0.25$), the probabilities for the five cases instead become: (i)0.70 (ii)0.62 (iii)0.46 (iv)0.19 and (v) 0.0096, i.e. somewhat higher than for the uniformly distributed case.

More complex load patterns (and also with different frequencies for different directions) could easily be constructed in order to represent various types of environmental loading. However, the main point to be made here is that non-homogenous loading may lead to amplification for some of the modal loads and accordingly give rise to higher dynamic response levels. Furthermore, for unidirectional loading the critical angle may change for different load patterns.

2.2 Inverse analysis

The question is next whether it is possible to find the most critical combination of the load parameters for a given cross-section along the line structure by a more efficient procedure without having to calculate the response for all combinations of time and direction values (or even more complex combinations for cases where more than two parameters are involved).

Here, it is considered whether this can be achieved by means of FORM/SORM techniques by application of uniform joint probability density function of the two parameters as input to the analysis. These techniques are usually based on the so-called Rosenblatt transformation which converts the uniformly distributed basic variables into normalized Gaussian variables (with zero mean values and unit variance). Subsequently, a search is performed in the normalized plane to identify the "critical" point on the failure surface (i.e. the surface for which the mechanical limit state function is zero, i.e. implying that the response bending moment is equal to the specified value of the bending moment). This is referred to as the "design point", see e.g. [7,8] for a more detailed description of the procedure.

This approach is here illustrated for both the homogenous and non-homogeneous load cases. For the former, the design point in the normalized Gaussian plane has the following coordinates for the four different cases: (i) (1.1,0.35) (ii) (1.25,0.41) (iii) (1.46,0.55) and (iv) (1.9,0.56). By transforming back to the physical parameter space, these point corresponds to the following time-direction angle combinations: (i) (8.6sec, 0.43rad) (ii) (8.9sec, 0.5rad) (iii) (9.3sec, 0.66rad) and (iv) (9.7sec, 0.67rad).

The main purpose of this analysis is to identify the most likely "parameter combination point", which here corresponds to a specific combination of time and direction. However, as a side product the probability of failure of the line structure (i.e. the probability that the bending moment will exceed the specified value) for the case of uniformly distributed load parameters can also be found based on the design point coordinates in the normalized plane. This is based on the relationship $\Phi(-\beta) = p_f$, where $\beta = u_2$, with u_2 denoting the design point coordinate for the normalized direction variable and with p_f denoting the probability of failure (i.e. the probability of exceeding the specified value of the bending moment).

By including only the load direction as a random variable, the design point for the corresponding "normalized variable" will change slightly. Essentially, it will be the point on the failure surface which is closest to the origin purely along the u_2 coordinate axis. Hence, the second point of the relevant direction interval is generally not identified. Accordingly, the estimated failure probabilities will be too high as compared to those obtained from the forward analysis. The following probabilities are now obtained for the four different cases: (i) p_f=0.36 (ii) p_f=0.34 (iii) p_f=0.29 (iv) p_f =0.28. It is seen that these probabilities are on the high side as compared to those obtained from the forward modeling, especially for the lowest probabilities. More correct probability values could be obtained as part of the inverse analysis by application of more refined methods such as Monte Carlo simulation techniques. For high dimensions, this would require that sufficiently accurate but numerically efficient response analysis methods are applied e.g. by application of surrogate models (response surface techniques).

For the non-homogenous load case, transformation of the design points in the normalized Gaussian line to the "physical load direction line" give the following coordinates for the five different cases: (i) (θ=-/+0.8) (ii) (θ=-/+0.7) (iii) (θ=-/+0.5) (iv) (θ=-/+0.2) and (v) (θ=-/+0.01). Here, the -/+ sign indicates that one of these points will be identified depending on whether the search algorithm starts at a positive or negative value. Again, it is seen that this is just one of the points that were identified based on the forward analysis. However, for this case the relevant points are symmetric around the origin. Applying only one of these points will imply an overestimation of the failure probabilities. The following values are obtained for the five different cases: (i) p_f=0.75 (ii) p_f=0.72 (iii) p_f=0.66 (iv) p_f =0.56 and (v) p_f =0.50. It is seen that these are on the high side compared to those from the forward analysis, especially for the smallest probabilities. If both of the "design points" are identified from the analysis, the correct values for the failure probabilities will be obtained.

Based on more exact information about the joint probability density function (pdf) of the load direction parameter, this will generally result in much more peaked shape than the uniform model. Accordingly, the most likely load parameter combination to result in failure of the structure will also change (relative to the case with uniformly distributed variables). This was also demonstrated in connection with the forward modelling by application of a parabolic density function for the load direction angle.

Furthermore, inclusion of additional random variables which represent physical properties of the structure and the environment are generally required in order to provide a more realistic description. By repeating the analysis for these cases, the coordinates of the most critical load combination point and the failure probability will change once more.

3 DYNAMIC RESPONSE TO INHOMOGENOUS WAVE LOAD FOR AN ULTRA-LONG FLOATING BRIDGE

In order to illustrate the effects of inhomogeneous loading on the dynamic response of a structure with an ultra-long span, the floating bridge shown in Figures 5 (graphical illustration) and Figure 6 (system layout) is considered. Such bridges are relevant e.g. for very wide lake or fjord crossings. The present structure is quite similar to a concept which is proposed for crossing of the Bjørnafjord at the west coast of Norway [3].

The hydroelastic responses of the 4.6 km long straight, side-anchored floating pontoon bridge subjected to wave loads is investigated. The vertical stiffness of the bridge is provided by 35 evenly spaced pontoons along the bridge girder. The transverse motion of the bridge is restrained by clusters of mooring lines tethered at four pontoons. Owing to the very large span and hydrological topology across the Bjørnafjord, inhomogeneity in the wave field exists. Various effects of inhomogeneous wave conditions on the hydroelastic responses of the float-

ing bridge are also examined. These include the inhomogeneity in wave direction, significant wave height, peak period as well as the coherence and correlation of waves at different locations along the entire length of the floating bridge. For the purpose of comparison, the bridge responses under homogeneous wave load cases are also studied. In addition, the effects of wave load components and short-crestedness are presented and discussed.

Figure 5. Graphical display of straight floating bridge design concept, [2]

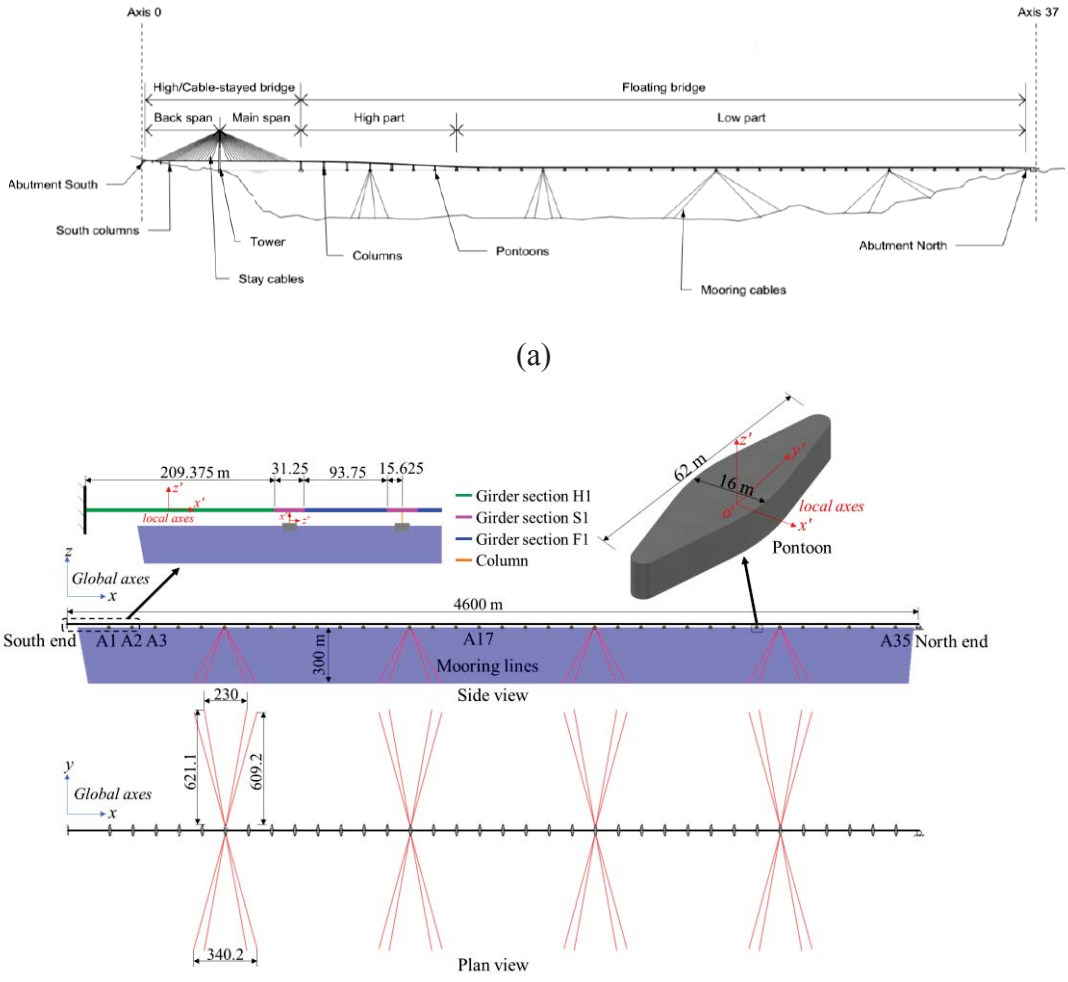

Figure 6. Straight floating bridge: (a) design concept and (b) idealised model, [3, 4, 6].

3.1 Structural model

The bridge structure is represented by beam elements with discrete pontoons, and the wave loading is of a stochastic nature such that spectral densities are applied in order to characterize the frequency distribution of the wave energy. Furthermore, directional spreading functions provide information about the directional distribution of the wave energy. For inhomogeneous loading, these quantities will generally vary as functions of the coordinates in the horizontal plane.

In order to focus on the wave load effect on the floating bridge section, this study employs an idealised, generic floating bridge model based on the low part of the design concept. As illustrated in Fig. 1(b), the simplified floating bridge, 4.6 km long and 18 m elevated above the water surface, is resting on 35 evenly spaced pontoons (which are referred to by their location as A1 to A35) and held in position by four mooring clusters. The water depth is set to 300 m and assumed to be constant across the entire bridge length. In view of the overall dimensions of the bridge, the girders and columns are reasonably modelled as Euler-Bernoulli beams and the mooring lines are represented by using bar elements submerged beneath the water surface. The pontoons are regarded as rigid bodies interacting with water. The connection between mooring lines and the pontoons in the conceptual design is provided on the side wall of the moored pontoon. The mooring line is terminated just above the chain stopper. The boundary conditions of the bridge model are given in Table 1.

Boundary	Translation			Rotation		
	x	y	z	R_x	R_y	R_z
South end	fixed	fixed	fixed	fixed	fixed	fixed
North end	free	fixed	fixed	fixed	fixed	free

Table 4. Boundary conditions

Note that the translational degree of freedom of the bridge girder along the x-axis at the North end is released to allow for axial deformation due to thermal effects. All the applied parameters are based on the independent feasibility studies of the straight floating bridge concept by Multiconsult and DNV GL [2, 3].

3.2 Load representation and load cases

A full stochastic wave load model is applied for the present dynamic response analysis. Accordingly, the basis for computation of random wave loads and associated dynamic response is provided by the wave spectral densities at the locations at the different pontoons. These spectral densities are generally parameterized by the significant wave height and the peak period. Phase information about wave elevation at the different pontoons is provided by the cross-spectral densities.

Table 2 lists the design wave load cases specified in the design basis [1] with a principal wave direction in the sector of 225°-315°. Note that a common practice in an engineering design is to apply the worst wave condition to the entire bridge structure. In view of this, inhomogeneous wave load cases may be reasonably established by scaling up the significant wave heights H_s and peak periods T_p measured at the three DWRs such that the highest inhomogeneous H_s and T_p are equal to the homogeneous wave characteristics listed in Table 2. Due to the lack of further information, the wave inhomogeneity between the DWRs is assumed to vary in a linear manner.

Return period	Wind waves			Swell		
	H_s	T_p	θ_p	H_s	T_p	θ_p
1-year	1.30 m	4.6 s	225°-315°	0.26 m	20 s	300°
100-year	2.40 m	5.9 s	225°-315°	0.40 m	20 s	300°

Table 2. Design homogeneous wave conditions [1]

Three inhomogeneous wave conditions are also considered, see [1]. The first two are the 1-year and 100-year inhomogeneous wave conditions established based on field measurement data. Due to availability of data, only wind waves are represented for these conditions. The waves corresponding to these two conditions exhibit a relatively large spatial variation in θ_p with a minor inhomogeneity in H_s and a constant T_p. Examining these two wave conditions is expected to reveal the effect of inhomogeneity in relation to wave direction on the bridge responses. The third condition describes a different pattern of 100-year inhomogeneous waves established based on wave conditions at another measurement site. A compared with the first two conditions, θ_p remains unchanged in condition 3. A much larger inhomogeneity in H_s and T_p is present and its effect may be revealed by comparing with the corresponding homogeneous conditions. Furthermore, inhomogeneous swell with a longer T_p that may give excitation to the lower order vibration modes of the floating bridge is also accounted for in condition 3.

Number	Description			
	Return period	Wind sea condition	Swell condition	Wave correlation
LC1.1a	1-year	H_s = 1.3 m, T_p = 4.6 s, θ_p = 288°	-	Fully correlated
LC1.1b		H_s = 1.23 m, T_p = 4.6 s, θ_p = 288°	-	Fully correlated
LC1.2		H_s = 1.3 m, T_p = 4.6 s, θ_p = 288°	-	Uncorrelated
LC1.3		condition 1	-	Fully correlated
LC1.4		condition 1	-	Uncorrelated
LC2.1a	100-year	H_s = 2.4 m, T_p = 5.9 s, θ_p = 288°	-	Fully correlated
LC2.1b		H_s = 2.27 m, T_p = 5.9 s, θ_p = 288°	-	Fully correlated
LC2.2		H_s = 2.4 m, T_p = 5.9 s, θ_p = 288°	-	Uncorrelated
LC2.3		condition 2	-	Fully correlated
LC2.4		condition 2	-	Uncorrelated
LC3.1a	100-year	H_s = 2.4 m, T_p = 5.9 s, θ_p = 288°	H_s = 0.4 m, T_p = 20 s, θ_p = 300°	Fully correlated
LC3.1b		H_s = 2.27 m, T_p = 5.9 s, θ_p = 288°	H_s = 0.24 m, T_p = 20 s, θ_p = 300°	Fully correlated
LC3.2		H_s = 2.4 m, T_p = 5.9 s, θ_p = 288°	H_s = 0.4 m, T_p = 20 s, θ_p = 300°	Uncorrelated
LC3.3		condition 3	condition 3	Fully correlated
LC3.4		condition 3	condition 3	Uncorrelated

*Load cases with grey shadow correspond to homogeneous wave conditions

Table 3. Load cases and descriptions

Table 3 summarises the wave load cases to be examined in this study. There are three main load cases (LCs), namely LC1, LC2 and LC3 that correspond to the wave conditions listed in Table 2. Each LC is comprised of three inhomogeneous wave load cases and one homogeneous wave load case that serves as a basis for comparison with the inhomogeneous wave load cases. The homogeneous wave load cases (LC1.1, LC2.1 and LC3.1) are further categorised into sub-cases a and b. Case a is defined by using the parameters listed in the design basis [1] and Table 5, whereas the H_s in case b is scaled down to match the average H_s in an inhomogeneous wave condition. The latter describes a sea state with the same wave energy as in the inhomogeneous wave load case provided that T_p remains unchanged.

Time domain sample functions of the sea elevation are generated by summation of the various harmonic components and Monte Carlo simulation of the relevant random phase angles. If the unidirectional wave spectrum, directional distribution and random phase angles of the wave components are identical at all pontoons, the described wave conditions along the full length of the floating bridge are homogeneous. Otherwise, the wave conditions are inhomogeneous. Furthermore, if the phase angle in an inhomogeneous wave field for arbitrary pontoon numbers i and j are taken to be same, the wave conditions along the entire length of the bridge are fully coherent and correlated. On the other hand, if the phase angles are completely random at various pontoon locations, the corresponding wave conditions are incoherent as well as uncorrelated, i.e. they are statistically independent (in the case of Gaussian processes).

In all case studies, five independent wave realisations of each load case are used to reduce the variations in the stochastic results. In addition to the wave inhomogeneities described in Table 3, this study also investigates the effect of short-crestedness of wind waves.

3.3 Dynamic response to inhomogeneous versus homogeneous loading

LC1: Load case with 1-year return period

To reveal the effect of wave short-crestedness on the bridge responses, Figure 7 plots the standard deviation of the weak axis bending moment M_y due to unidirectional long-crested waves for comparison with short-crested waves. As it can be seen, short-crested waves result in a much larger M_y along the full length of the bridge for both homogeneous and inhomogeneous wave load cases. The differences are up to 176% for homogeneous waves and 129% for inhomogeneous waves. This implies that oblique wave components in short-crested waves significantly augment the weak axis bending moment of the girder when compared with long-crested waves in a near beam sea condition.

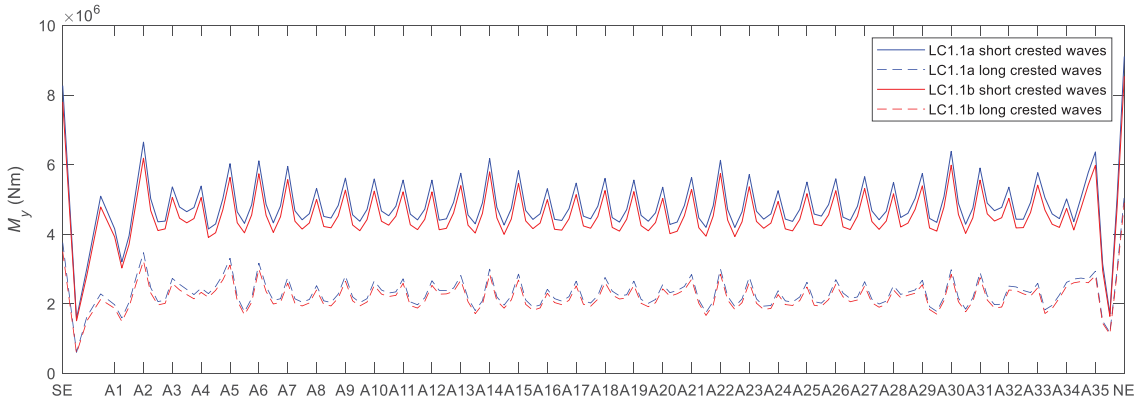

(a)

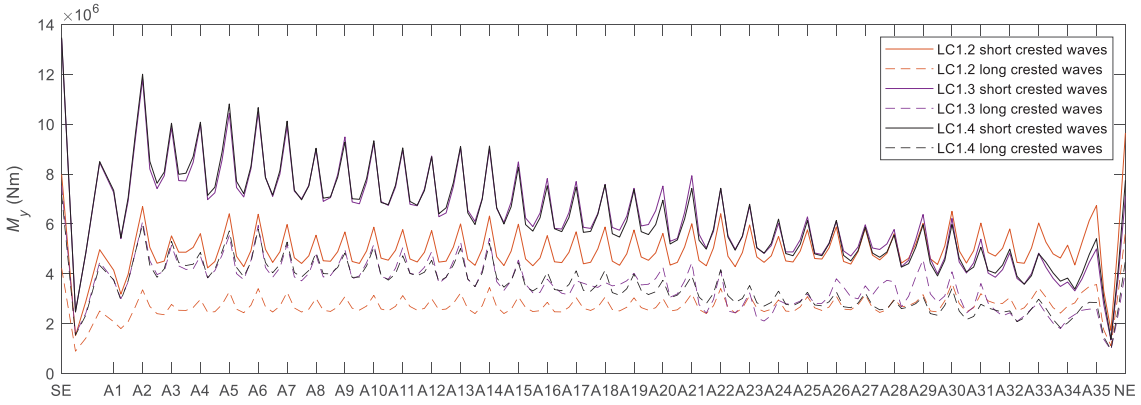

(b)

Figure 7. Effect of wave short-crestedness and wave inhomogeneity on standard deviation of weak axis bending moment under 1-year wave load cases (LC1): (a) homogeneous waves and (b) inhomogeneous waves.

LC2 and LC3: Load cases with 100-year return period

Figure 8 compares the standard deviation of M_y for LC2 and LC3. The comparison of homogeneous wave load cases shows that the results for LC2.1a and LC3.1a are very close to each other. This reveals that the inclusion of swell has a negligible effect on M_y. The comparison with inhomogeneous wave load cases (see Fig. 8(b)) shows that near the south end, more higher order vibration modes are excited by wind waves in LC3 than LC2 and the excitation level is lower. Moving from A10 to A27, the increase in T_p results in a change from higher order modes to lower order modes being excited by the wind waves. In addition, an increase in the extent of excitation of modes by wind waves is also observed, due to the combined effect of increasing T_p and H_s. The swell also excited M_y responses near the period of 20 s. However, no resonance is expected and thus swell has a limited effect on the dynamic M_y responses.

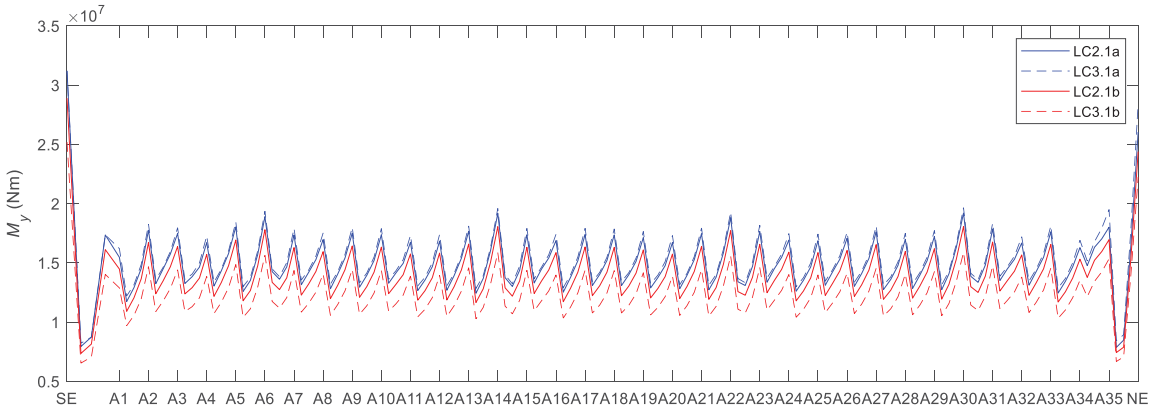

(a)

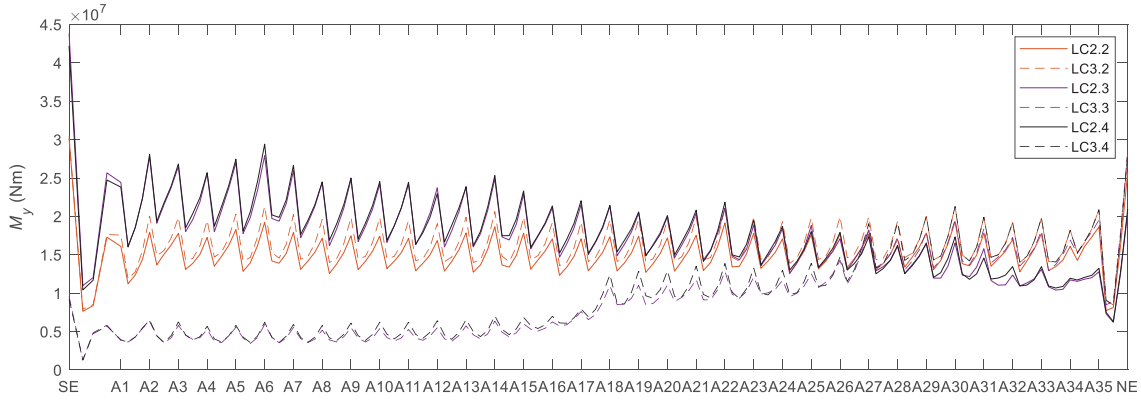

(b)

Figure 8. Standard deviation of weak axis bending moment under 100-year wave load cases (LC2 and LC3): (a) homogeneous waves and (b) inhomogeneous waves.

3.4 Extreme bridge response and accumulated fatigue damage

The extreme values of the bridge responses for a given (stationary) sea state are basically expressed as a product of the standard deviation and an amplification factor. The value of the amplification factor depends on the statistical nature of the response processes (i.e. Gaussian or non-Gaussian) and the length of the time period being considered. Accordingly, the ratios between the extreme values of the bending moments for the different load cases are also mainly the same as for the standard deviations. For fatigue damage accumulation, the effects are even stronger since the "standard deviation effect" is exponentiated to a power higher than one (and since the mean value essentially does not enter the picture). The effects of inhomogeneous versus homogeneous load representations in relation to design of the bridge structure are clearly of high importance.

4 CONCLUSIONS

The present paper has addressed the question of whether inhomogeneous load patterns can give rise to higher dynamic response levels than homogenous loading. This is shown to be the case, both for a simplistic model of a straight-line bridge, and subsequently for a more comprehensive and realistic model of a floating bridge with an ultra-long span. An important task will then clearly be to identify possible critical inhomogeneous load patterns and the corresponding probability associated with the event that this pattern will occur. This has been illustrated for the simplistic structural model. An ultra-long-span floating bridge structure is also analysed with to compare homogeneous and inhomogeneous load cases of different kinds.

As a general observation, it is found that the challenge associated with inhomogeneous load patterns is that they can easily can give rise to "modal resonance" phenomena, which occurs when the spatial load pattern more or less coincides with the mode shape. An inverse scheme for identification of such critical load patterns was outlined. The probability that such patterns may create critical extreme response levels is also quantified as part of the algorithm. As part of future developments, application of the outlined inverse scheme to large and complex bridge structural models is aimed at. It is anticipated that this may require utilization of reduced order models and surrogate models (also referred to as digital twins) in order to develop numerically efficient schemes.

Acknowledgment

Parts of this work was supported by the Research Council of Norway through the project 268403/O80 Design and Verification of Large Floating Coastal Structures – Environmental description, structural loads, responses and mooring system.

REFERENCES

[1] Statens Vegvesen, SBJ-32-C3-SVV-90-BA-002 Design basis Bjørnafjorden rev E. Statens Vegvesen, Norway, 2018.

[2] Xiang X, Løken A. Hydroelastic analysis and validation of an end-anchored floating bridge under wave and current loads. Proceedings of the 38th International Conference on Ocean, Offshore and Arctic Engineering, Glasgow, 9-14 June, 2019.

[3] Multiconsult. SBJ-31-C3-MUL-22-RE-100-0 – Analysis and design (Base Case). Multiconsult AS, Oslo, Norway; 2017.

[4] DNV GL. SBJ-31-C3-DNV-62-RE-018-0 Bjørnafjorden side anchored floating bridge - independent global analyses. DNV GL, Oslo, Norway; 2018.

[5] Viuff T, Leira BJ, Xiang X, Øiseth O. Effects of wave directionality on extreme response for a long end-anchored floating bridge. *Applied Ocean Research* 2019;90:101843.

[6] J. Dai, B.J. Leira, T. Moan, M. Kvittem, Inhomogeneous Wave Loading", Accepted for publication in *Journal of Marine Structures,* March 14, 2020.

[7] Madsen, H.; Krenk, S. and Lind, N.C. (1986):"Methods of structural safety", Prentice-Hall, Englewood Cliffs, New Jersey.

[8] Melchers, R. E. (1999):"Structural Reliability Analysis and Prediction", John Wiley & Sons, Chichester, UK.

EURODYN 2020
XI International Conference on Structural Dynamics
M. Papadrakakis, M. Fragiadakis, C. Papadimitriou (eds.)
Athens, Greece, 23–26 November 2020

UNCERTAINTY ABOUT ENVIRONMENTAL VIBRATION TESTS: A CASE STUDY

A. Di Primio[1], N.Fiorini[2], D. Spina[2], C. Valente[1], M. Vasta[1]

[1]University "G. D'Annunzio", Department of Engineering and Geology
viale Pindaro Pescara
e-mail: alice.diprimio@unich.it, claudio.valente@unich.it, marcello.vasta@unich.it

[2]Department of Civil Protection, Presidency of the Council of Ministers,
Via Vitorchiano 2, Rome
e-mail: daniele.spina@protezionecivile.it, noemi.fiorini@protezionecivile.it

Keywords: Environmental vibration tests, uncertainty, masonry vaults, modal parameters.

Abstract. *Environmental vibration tests are useful tools for the evaluation of real structures, since they can be carried out during the structure operating conditions. As drawback, the low intensity level of the vibrations makes it difficult to identify precisely the modal parameters of the structure. The objective of the work is to study the uncertainty related to the identification of modal parameters of masonry structures subjected to environmental vibrations. The work deals with experimental records derived from a masonry barrel vault that is conceived as a sequence of arches according to its cross sectional behavior. Two different structural configurations are considered: the vault in its original configuration and the vault in its retrofitted configuration according to current design concepts. Two symmetric arches for each vault configuration are analyzed and the relevant dynamic response monitored. The modal parameters (frequencies, mode shapes and damping ratios) are estimated using operational modal analysis techniques. Four different records, for each structural configurations, are processed to investigate the stationary of the estimates. The results indicate that even though the modal parameters are quite different between the two configurations the related uncertainty are similar in contrast to the common assumptions that the retrofitted configuration should be less dispersive than the original one. As concerns the individual modal parameters it is confirmed that the frequencies present the lower uncertainties whereas the damping ratios are endowed with the higher uncertainties. In any case the uncertainty level does not hide the general pattern of the damping ratios. The imprecision in the mode shapes identification, measured through the MAC index, shows unexpectedly stable and accurate estimates.*

1 INTRODUCTION

In the last decades the need for an effective seismic protection and vulnerability reduction of the cultural heritage determined a growing interest in structural monitoring as a knowledge-based assessment tool to quantify the uncertainties in the structural performances [1]. One of the main purposes of structural monitoring is to observe the structural response to loads and environmental influences over a period of time in order to reduce the uncertainties in the assessment of the actual structural conditions [2]. Different are the fields where uncertainty plays an important role and towards researchers turned their attention: variability of external actions, data dispersion due to measurement inaccuracies, modeling errors related to numerical approximations, changes in material properties [3, 4].

In this paper, the uncertainty related to the structural dynamic response in terms of modal parameters is analyzed. Environmental vibration tests were performed on purpose and Operational Modal Analysis (OMA) was used to identify frequencies, damping, and mode shapes [5]. OMA is a very powerful tool to estimate the modal parameters of a structure when subjected to environmental loads, that is when no measurement of the input is available [6, 7]; of course the quality of the estimates depends also on the choice of the parameters of the particular identification process adopted [8]. One disadvantage of OMA, is its inability in providing the modal masses. Therefore, in the estimation of modal parameters, the mode shapes cannot be mass normalized. Methods for the estimation of the mode shapes scaling factors were proposed and suggestions provided to overcome this limitation [9,10].

Environmental vibration tests are often resorted to in those cases in which the structure under investigation should remain in its full operational conditions. In this instance, because of the small amplitude of the vibrations, it is conceivable that the uncertainties in the modal parameters estimates could affect the stationary of the results. The paper aims at providing a contribution to this problem through the investigation of the peculiar case study of masonry arches. The entity by which uncertainty affects the results is assessed under different circumstances that involve the comparisons among different arches, different structural schemes and different field records.

2 THE ANALYZED STRUCTURE AND THE MONITORING SYSTEM

The analyzed structure is the barrel vault depicted in Figure 1. The vault is about 11.0 m long and 4.3 m large with an approximate circular shape of radius 2.5 m [11]. The vault cross section develops uniformly along the longitudinal axis and the two terminal gables are detached from the vault so that they do not affect significantly the vault behavior at the boundaries. The vault rests on squat thick walls that turn out to be very rigid as compared to the vault. The filling material is quite loose and act essentially as an added mass without providing further stiffness. This vault was damaged in occasion of the l'Aquila earthquake in 2009 and the described configuration pertains to this damaged vault in its original (*O*) state. In 2018 the same vault was subjected to important retrofitting works aimed at moving the fundamental frequencies towards less sensitive ranges to the seismic action. This was obtained by using a lighter filling material cemented with mortar; inserting fiberglass strips glued at the vault extrados; adding transversal masonry stiffeners and perimetral steel curbs. This vault configuration pertains to the vault in its retrofitted (*R*) state.

As concern the monitoring system, a large testing campaign was carried out. The paper reports only the part of the overall campaign functional to the present investigation.

Since the main vault deformation takes place in the transversal direction and in consideration of the uniform longitudinally behavior, it was decided to monitor the vault as it was con-

stituted by a sequence of arches. Two different arches were monitored and analyzed. For comparison purposes these arch sections were taken symmetrically placed with respect to the vault centerline and labelled arch *l* (left) and arch *r* (right), Figure 1.

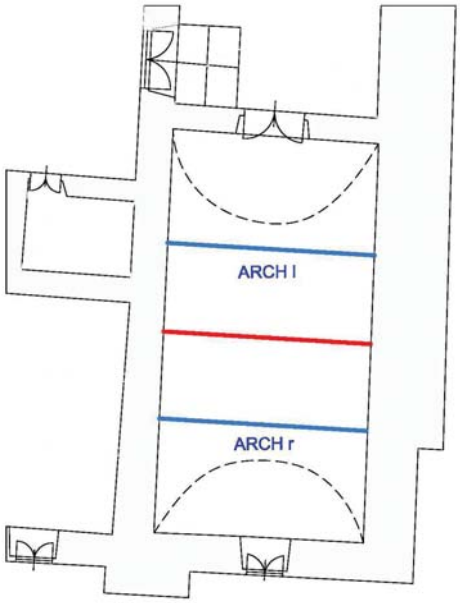

Figure 1. Plan view of the vault: centreline in red; arch *l* and arch r in blue.

Piezoelectric single axis accelerometers were employed (PCB 393A03 by Piezotronics) which are voltage mode output sensors characterized by a 1000 mV/g sensitivity, a ±5g full-scale and a frequency range from 0.5 to 2000Hz with a 5% error. Each accelerometer was connected, by means of shielded cables, to a 24-channels data logger (LMS-SCADAS) mobile hardware with a 24-bit A/D board for a dynamic range of 150 dB. The accelerometers were magnetically fixed to proper metal plates bolted at the intrados of the vault. All the measurement chain was managed by a notebook, Figure 2.

Five measurement points per arch were considered: one at key, two at the arches base and two at the kidneys. Each measurement point comprised a couple of sensors oriented in such a way to record tangential and radial accelerations, as shown in Figure 2, for a total of 10 accelerometers per arch.

Figure 2. Typical biaxial accelerometer and system management equipment.

3 MODAL PARAMETER IDENTIFICATION

In the ambient vibration tests, it is unfeasible to measure the ambient excitation so that the output response of the structure is the only information available to be processed for identification purposes. This circumstance is referred to as Operational Modal Analysis (OMA). A variety of commercial system identification packages exists. In the present case, the LMS TestLab software by Siemens was used since it is licensed together with the monitoring system adopted. TestLab embodies the PolyMAX algorithm [12] to estimate the modal parameters according to a frequency domain processing of the recorder signals.

In the case of OMA, the input spectra are replaced by the assumption that the input is a white noise, i.e. it has a constant power spectrum, independent on frequency. Under this hypothesis output spectra can be modelled with the same expression of the Frequency Response Functions (FRF). The theoretical formulation of the algorithm can be found in [12]. Hereafter, a brief description of the method, functional to the subject of the paper, is given. "PolyMAX", is a polyreference version of the least-squares complex frequency-domain (LSCF) method and makes use of the so-called right matrix-fraction model. One main benefit of the polyreference method is that very closely spaced poles can be effectively separated.

The PolyMAX method is based on two main steps each of which makes use of a least squares solution. In the first step, a stabilisation diagram is constructed via frequency response functions; in this step, frequency and damping ratios are estimated. In the second step, the mode shapes are found, starting from the user selection of the stable poles in the stabilization diagram. The stabilization diagram allows to distinguish the real structural modes from the numerical ones; a mode is defined "stable" if its frequency and damping do not vary as the model order increases.

Frequencies, damping ratios and modal shapes, identified with the above procedure, are used to discuss the uncertainty related to the modal properties of the masonry vault.

4 RESULTS

All the identification process was repeated twice according to the two different *O* and *R* structural configurations. In both cases, the data collected in a basic time window of 3600s were processed and modal parameters identified (frequencies, damping ratios and mode shapes).

In order to evaluate the stationarity of the results, 3 further time windows were processed. These time windows were obtained by segmentation of the basic one as reported in Table 1:

Time window label	Time window duration (s)	Time segment (s)
T - Total duration	3600	0 – 3600
I - Initial segment	1800	0 – 1800
C - Central segment	1800	900 – 2700
F - Final segment	1800	1800 – 3600

Table 1: Basic signal segmentation

In line with the concepts of interval arithmetic, numbers are expressed as intervals bounded by the minimum and maximum $I = [min, max]$ values attained by the set of the identified ordinary crisp quantities [14].

For the present purposes, an alternative more expressive representation is given by the use of the central value or midpoint C and of the radius Δ of the interval:

$$I = [C \pm \Delta] \qquad \text{where:} \quad C = (max + min)/2; \quad \Delta = (max - min)/2 \tag{1}$$

In equation (1) C can be intended as the "mean" value and Δ as the entity of "imprecision or uncertainty" of the estimates. As compared to Δ, that provides an absolute value, the relative uncertainty U can be evaluated by the ratio: $U = \Delta / C$.

In Figure 3 and 4 the identified frequencies are reported respectively for the O and the R configuration separately for the arch l, Figures 3a and 4a, and the arch r, Figures 3b and 4b. Each figure shows the identified frequencies subdivided per mode and per time window.

The inspection of the figures allows to state that the identified frequencies are highly stable regardless the time window or the mode considered. This feature is shared also by both configurations O or R and the relevant arches l or r. This result confirms that any arch of the vault can be used equivalently for monitoring purposes.

The above applies with the exception of mode 3 configuration O, arch l, time segments I and C. In this case it was not possible to identify any valid frequency. This aspect is nonetheless to be considered positive; in fact, or the frequencies are accurately identified or they are not at all. A further positive aspect is that this defect does not influence the remaining identification with special regard to the adjacent time segments.

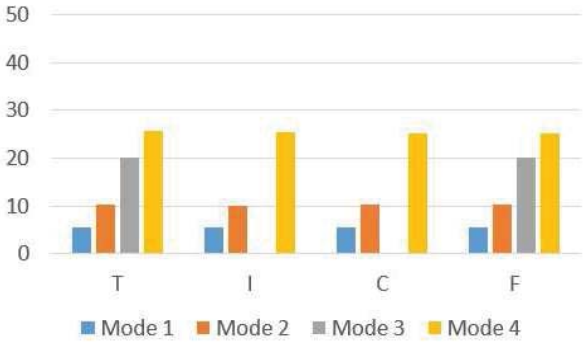

Figure 3a. Frequencies (Hz): config O, arch l

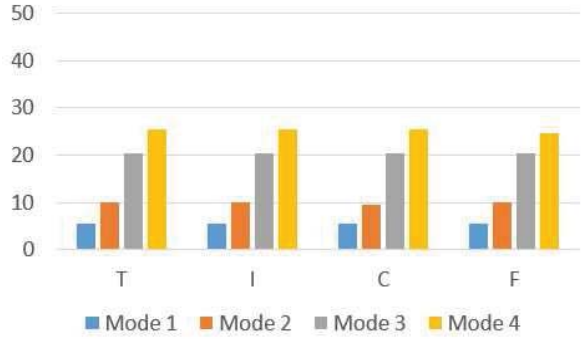

Figure 3b. Frequencies (Hz): config O, arch r

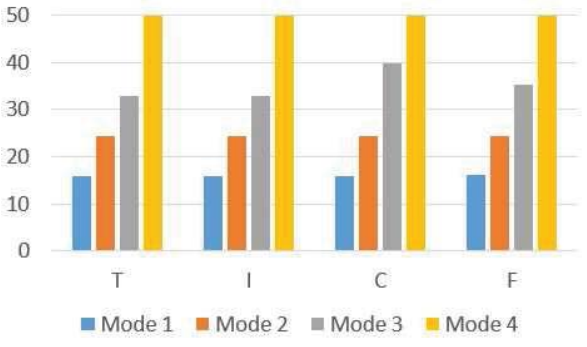

Figure 4a. Frequencies (Hz): config R, arch l

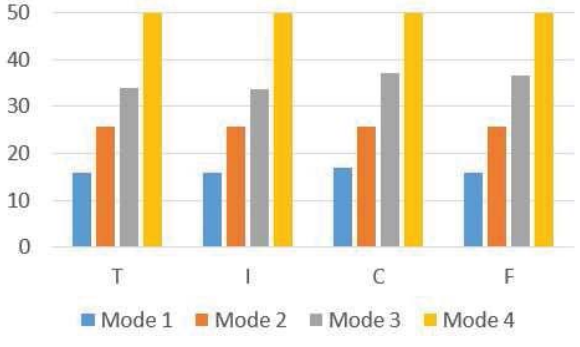

Figure 4b. Frequencies (Hz): config R, arch r

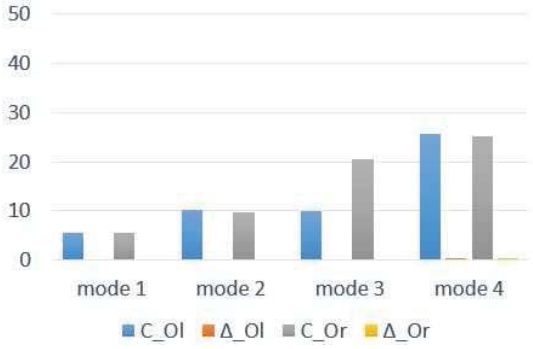

Figure 5. Frequency uncertainty: config O

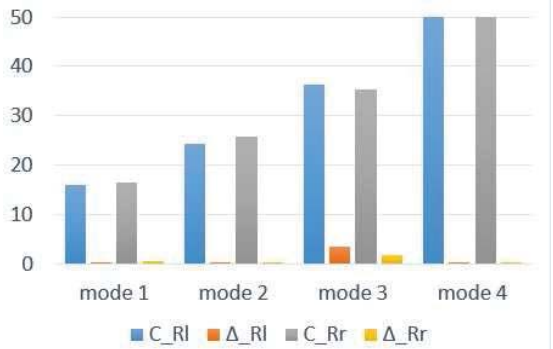

Figure 6. Frequency uncertainty: config R

The uncertainty level Δ against the central value C of the estimated frequencies is shown in Figures 5 and 6 where it is possible to appreciate the strong stationarity of the estimates.

As a conclusion, it is possible to substantiates the common assumption that frequencies can be identified with high accuracy and negligible uncertainties at least in the field of civil structures where the interested frequencies are usually the lower ones.

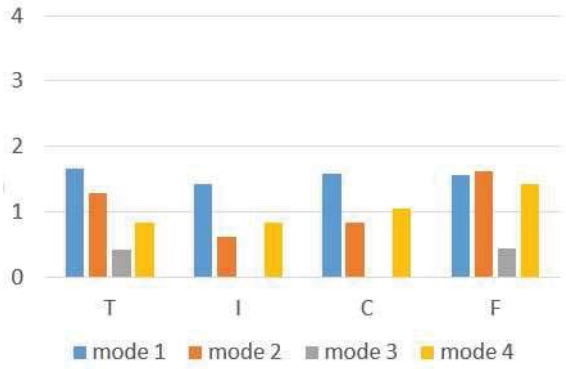

Figure 7a damping (%), config *O*, arch *l*

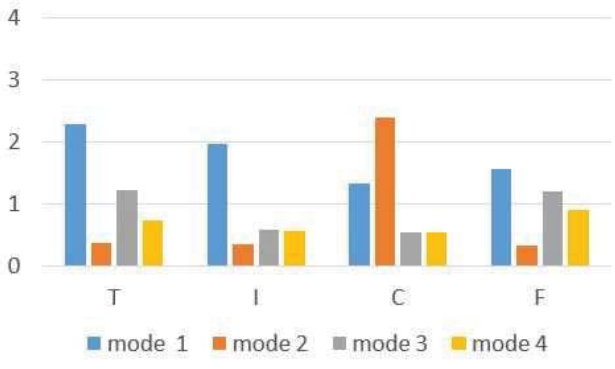

Figure 7b damping (%), config *O*, arch *r*

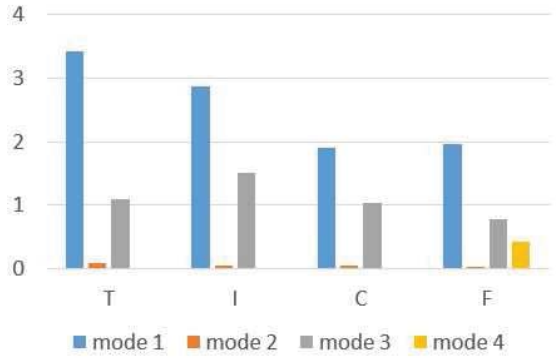

Figure 8a damping (%), config *R*, arch *l*

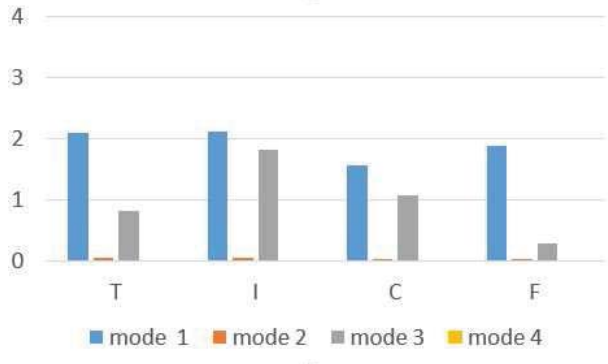

Figure 8b damping (%), config *R*, arch *r*

In general terms it can be stated that the fundamental damping model, i.e. the way in which the damping smears over the modes, is similar for the two arches, *l* and *r*, of the same *O* or *R* configuration with only small uncertainty. This similarity makes it possible to choose any arch as an equivalent candidate for monitoring.

It is observed a systematic prevalence of the damping values of mode 1 compared to the other modes for both configurations. This aspect is markedly evident for the *R* configuration. In addition to the above, it is also observed that the damping (energy dissipation) is distributed over all the modes for the *O* configuration, whereas it is concentrated in the first and third modes for the R configuration. As if it were all the modes of configuration *O* contribute on an equal level in energy dissipation; whereas for the configuration *R* as if it were modes 2 and 4 relate to a rigid body motion that does not produce (hysteretic) damping. This result is coherent with the hypothesis that the modes 2 and 4 would displace rigidly as a consequence of the deformation of the support walls of the vault.

The absolute value of the damping, referred to the first and third mode of both *R* and *O* configurations, happens to be greater for *R* than for *O*. This result is unexpected if one consider the common reasonable assumption that energy dissipation should be higher for "loose" structures (*O*) than for "tied" ones (*R*).

The Figures 9 and 10 refer to the configuration *O* and configuration *R* respectively. Each figure reports the central values *C* and the uncertainties *Δ* evaluated for arch *l* and arch *r* in correspondence with the four identified vibration modes. It is observed a good agreement between the trend of the *C* values in the two cases of arch *l* and arch *r*.

Both configurations *O* and *R* show negligible uncertainty with respect to the first fundamental mode shape. In the other cases, the uncertainty on damping does not show a defined trend. The uncertainties *Δ* remain always a relatively small fraction of *C*. In a couple of cases involving arch *r* of both configurations *Δ* attains values close to *C* displaying large dispersion of the identified values.

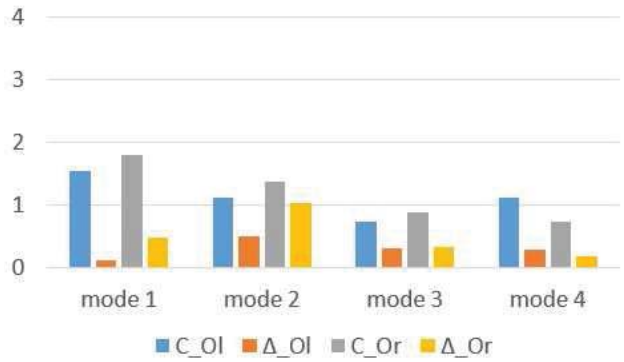

Figure 9 Damping uncertainty: config *O*

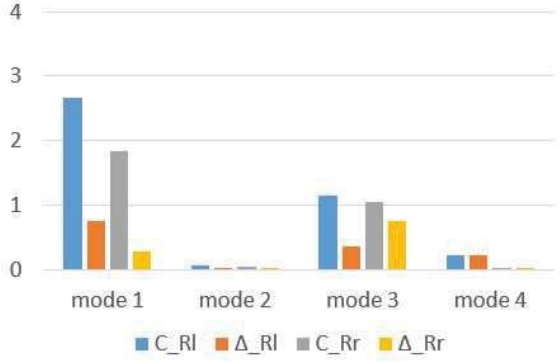

Figure 10 Damping uncertainty: config *R*

In order to get a homogeneous presentation of the results, the comparison among the mode shapes was carried out by means of the Modal Assurance Criterion (MAC) [14,15].

Presently, the advantage related to the use of the MAC index is that it allows to express the level of correlation between two mode shapes by just one number. In this way, it is possible to apply the equation (1) to quantify the uncertainty *Δ* also in the case of the mode shapes. The MAC is defined as (being $()^T$ the transpose operator):

$$MAC(\phi_{Sn}, \phi_{Sm}) = \frac{\left|\phi_{Sn}^T \cdot \phi_{Sm}\right|^2}{(\phi_{Sn}^T \cdot \phi_{Sn})(\phi_{Sm}^T \cdot \phi_{Sm})} \qquad (2)$$

and takes values in the range [0, 1] where 0 means no consistency and 1 means perfect matching. In equation (2) ϕ_{Sn} is the mode shape of order *S* identified using the time segment *n* and ϕ_{Sm} is the mode shape of the same order *S* but identified using the time segment *m*. So, for example, ϕ_{2C} is the mode shape *S* = *2* relative to the time segment *n* = C.

In the present case, the Modal Phase Collinearity (MPC) was used to quantify the degree of complexity of the identified mode shapes. It was found that in all examined cases MPC takes on values close to 100% that demonstrate perfect collinearity or monophase behavior. Consistently real evaluated mode shapes were used in the computations.

Ultimately, for each mode shape, the MAC indices were computed for the cases I, C and F against the common reference T as shown in Table 2.

T against all time segments	T-I	T-C	T-F

Table2: Couples of time segments for MAC computation.

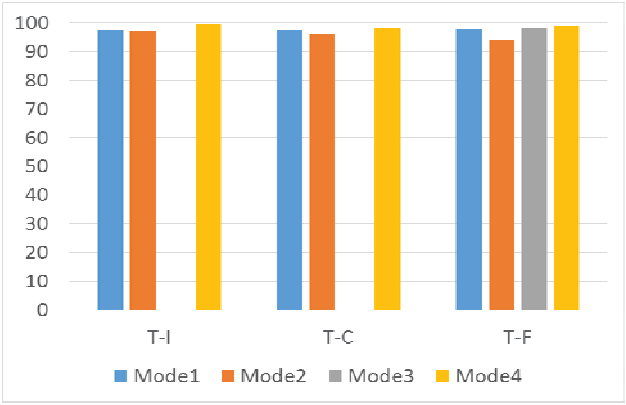

Figure 11a. MAC (%): Config *O*, Arch *l*.

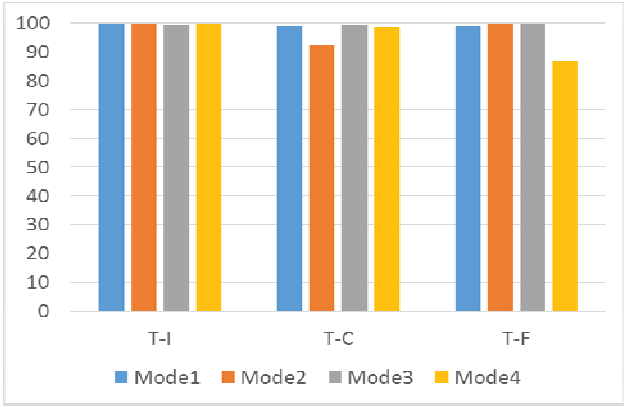

Figure 11b. MAC (%:) Config. *O*, Arch *r*.

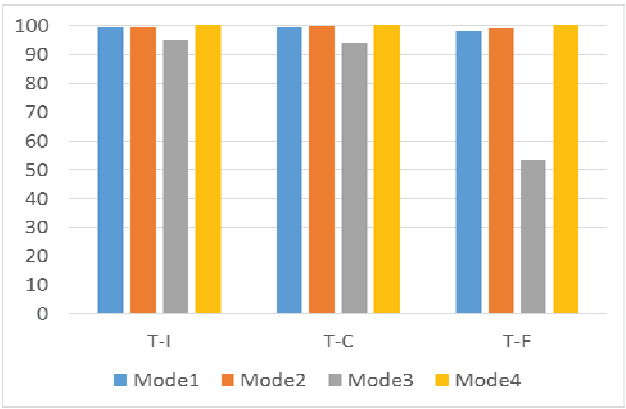

Figure 12a. MAC (%): Config. *R*; Arch *l*.

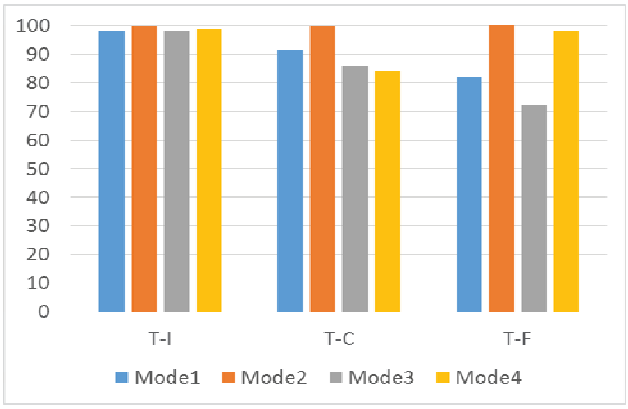

Figure 12b. MAC (%): Config. *R*; Arch *r*.

The results are illustrated in Figures 11 to 14 that are organized in the same format used to discuss the uncertainty relevant to frequencies and damping ratios. The histograms show the MAC values for the various combinations of the time segments, Table 2. The higher the MAC values are the lower the spread of the identified values is. That can be rephrased as: the more the similitude among the mode shapes is the lower the uncertainty is.

By the inspection of Figures 11 to 12 the following general comments can be dawn. The histograms are relatively similar; this statement applies whatever the structural configuration (*O* or *R*) and the measurement arch (*l* or *r*) are. The dispersion of the MAC values does not increase significantly as the mode shape order increases, except for the configuration *R* arch *r*. This was somewhat surprising considering that the *R* configuration should have a more regular behavior.

A more detailed inspection of the figures shows that the mode shape 3 is the hardest to be precisely identified. This happens especially in correspondence of the time segment F as clearly evidenced in Figure 12a; apart configuration *O*, arch *l*, time segments I and C where it is not detected at all (see also Figures 3a and 7a).

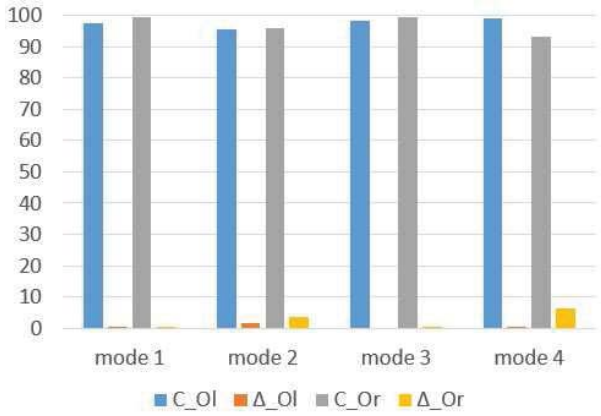

Figure 13. MAC uncertainty: Config *O*

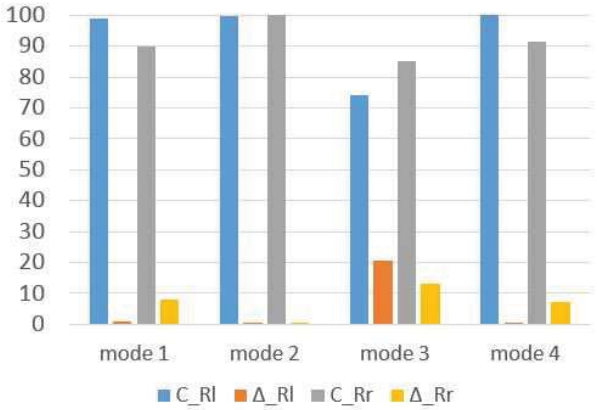

Figure 14. MAC uncertainty: Config *R*

The Figures 13 and 14 refer to the configuration *O* and configuration *R* respectively. Each figure reports the central values *C* and the uncertainties *Δ* evaluated for arch *l* and arch *r* in correspondence with the four identified vibration modes.

From the figures it is observed a *C* value greater than 90% for all the considered cases except for mode 3 where *C* is slightly below 80%. In any case a negligible uncertainty *Δ* lower than 10% with the only exception of mode shape 3 where *Δ* is of the order of 20%.

However, it is confirmed that any of the two arches *l* or *r* can be equivalently adopted for monitoring purposes even if with there exist some scatter of the results yet within acceptable uncertainty margins.

A summary of the relative uncertainty is given in Table 3 where the *U* values are listed, mode by mode, for frequencies, damping ratios and mode shapes.

Config	U_{freq}				U_{damp}				U_{MAC}			
/mode	O_l	O_r	R_l	R_r	O_l	O_r	R_l	R_r	O_l	O_r	R_l	R_r
1	0	1	1	3	7	27	29	15	0	0	1	9
2	1	3	0	0	45	76	46	29	2	4	0	0
3	-	0	1	5	-	38	32	72	-	7	28	15
4	1	1	0	0	27	25	97	54	1	0	0	8

Table 3: Relative uncertainty *U* (%) of the modal parameters: Config *O*, *R*, arches *l*, *r*.

In the inspection of the table it should be remembered that mode 3 was the hardest to identify as highlighted by the absence of any valid frequency in the O_l configuration and by the large scatter in the U_{MAC} case. Apart this aspect, the listed values show very low and negligible uncertainty in the U_{freq} case; the same can be said for the U_{MAC} case where the uncertainty is generally small, but not always entirely insignificant. The U_{damp} in turn is affected by high and dispersed uncertainty.

Whichever be the case, the dispersion of the *U* values does not show well defined trend and can be considered randomly distributed for all the modal parameters. This occurs for both configurations *O* and *R* and the arch *l* or *r* considered. The uncertainty level is roughly the same for the two configurations. This last finding contrasts the common assumption that a retrofitted "tied" structure should be less dispersive than the original "loose" one.

6 CONCLUSIONS

The work is devoted to the study of the uncertainty in the identification of the modal parameters of vaulted masonry structures. Only the transversal behavior of the vault was considered so that the dynamic response was monitored according to two arches symmetrically placed with respect to the central line of the vault.

Environmental tests were performed and the recorded signals processed to identify frequencies, damping ratios and mode shapes. To this end, the entire recorded signals was partitioned in sub time segments to control the stationarity of the identified quantities among the different time segments. The uncertainty was quantified in line with the concept of interval numbers characterized by the central value and the radius (uncertainty) of the interested range of values. The mode shapes needed to be processed to be represented by scalar quantities. To this end the MAC index of each mode shape obtained from the single sub time segment respect to the mode shape of the entire recorded signal was used. The measurements campaign and the identification process were repeated twice for two different vault configurations: the vault as it was in its original state and after retrofit interventions.

The results indicate that the uncertainty relevant to the two configurations is similar in contrast to the conventional assumption that the retrofitted "tied" configuration should be less dispersive than the original "loose" one. The results indicate also that the two arches, according to which the vault was monitored, showed very similar behavior so that any arch of the vault can be equivalently adopted for monitoring purposes within acceptable uncertainty margins. As concerns the individual modal parameters it is confirmed that the frequencies present negligible uncertainties whereas the damping ratios are endowed with the higher uncertainties. As a final result it can be said that the dispersion of the estimates of the modal parameters do not increase significantly as the mode order increases.

7 REFERENCES

[1] F. Lorenzoni, F. Casarin, M. Caldon, K. Islami, C. Modena, Uncertainty quantification in structural health monitoring: Applications on cultural heritage buildings, *Mechanical Systems and Signal Processing*,66-67, 268-281, January 2016.

[2] S. Marwitz , V. Zabel, Relations between the quality of identified modal parameters and measured data obtained by structural monitoring, *Proceedings of Isma2018 and USD 2018,* Leuven, 3747-3758, 2018.

[3] X. Lin, Z. Zong, J. Niu, Finite element model validation of bridge based on structural health monitoring-Part II: Uncertainty propagation and model validation, *ScienceDirect*, *Elsevier*, 279-289, 2015.

[4] S. W. Doebling, F. M. Hemez, Overview of Uncertainty Assessment for Structural Health Monitoring, *Proceedings of the 3rd International Workshop on Structural Health Monitoring*, California, 2-15, September 17-19, 2001.

[5] A. Di Primio, N. Fiorini, D. Spina, C. Valente, M. Vasta, Monitoring of a strengthened barrel vault. *Proceedings of the 7th ECCOMAS Thematic Conference on Computational Methods in Structural Dynamics and Earthquake Engineering*, Crete, 19124-19143, 24–26 June 2019.

[6] L. Zhang, R. Brincker, P. Andersen, An Overview of Operational Modal Analysis: Major Development and Issues, *Proceedings of the 1st IOMAC Conference*, Denmark, 2005.

[7] B. Peeters, G. De Roeck, Stochastic System Identification for Operational Modal Analysis: A Review, *Journal of Dynamic Systems, Measurement and Control*, 123,659-667, 2001.

[8] V. Analysis - a Case Study, *Proceedings of the IMAC XXXIV: a Conference and Exposition on Structural Dynamics* Zabel, F. Magalh˜aes, C. Bucher, The Influence of Parameter Choice in Operational Modal, Orlando, 2016.
[9] G. Acunzo, N. Fiorini, F. Mori, D. Spina, Modal mass estimation from ambient vibrations measurement: A method for civil buildings, *Mechanical Systems and Signal Processing*, 98, 580-593, 2018.
[10] J. Cara, Computing the modal mass from the state space model in combined experimental operational modal analysis, *Journal of Sound Vibrations*, 370, 94–110, 2016.
[11] A. Di Primio, N. Fiorini, D. Spina, C. Valente, Monitoring and damage assessment of the Bussi castle vaulted system, *Proceedings of the 10th International Masonry Conference*, Milan, 2-11, July 9-11, 2018.
[12] B. Peeters, H. Van der Auweraer. PolyMAX: a revolution in Operational Modal Analysis, *Proceedings of the 1st IOMAC*, Copenaghen, Denmark, 2005.
[13] W. Heylen, S. Lammens, P. Sas, Modal Analysis Theory and Testing, K.U.Leuven, Belgium, 1997.
[14] R.E. Moore, Interval Analysis, *Prentice-Hall, Englewood Cliffs*, New Jersey, 1966.
[15] R.J. Allemang, The Modal Assurance Criterion (MAC): Twenty Years of Use and Abuse, *Journal of Sound and Vibration*. **37**(8), 14-21, 2003.
[16] P. Vacher, B. Jacquier, A. Bucharles, Extensions of the MAC criterion to complex modes, *Proceedings of ISMA2010 including USD2010*, Leuven, September 2010.

EURODYN 2020
XI International Conference on Structural Dynamics
M. Papadrakakis, M. Fragiadakis, C. Papadimitriou (eds.)
Athens, Greece, 23–26 November 2020

RESPONSE OF NONLINEAR SECONDARY OSCILLATORS IN CASCADE TO RANDOM EXCITATION

Stavros Kasinos[1], Eleni Chatzi[2], and Christian Málaga-Chuquitaype[3]

[1]Imperial College London
Department of Aeronautics, London, UK
e-mail: s.kasinos@gmail.com

[2]ETH Zurich
Department of Civil, Environmental and Geomatic Engineering, Zurich, Switzerland
e-mail: chatzi@ibk.baug.ethz.ch

[3]Imperial College London
Department of Civil and Environmental Engineering, London, UK
e-mail: c.malaga@imperial.ac.uk

Keywords: Earthquake, Extreme events, Nonlinear secondary oscillator, Stochastic excitation.

Abstract. *The paper deals with the steady-state stationary response of single-degree-of-freedom nonlinear secondary oscillators in stochastically driven linear primary structures. Equations governing the primary-secondary dynamic interaction are presented, followed by a concise exposition of a two-degree-of-freedom system assembly with dimensionless coefficients. Stochastic forcing is successively modelled as monochromatic, white noise, and filtered white noise process, representing extreme forms of narrow-band and wide-band excitations, as well as an intermediate case, characterised by the Clough-Penzien stationary power spectrum, commonly adopted in earthquake engineering applications. A decomposition-synthesis approach is presented in order to analytically approximate the response of the secondary system in cascade, by quantifying the statistics to individual forcing components, and synthesising the results to obtain the response of an equivalent linear secondary system. Demonstrated to the case of a Duffing secondary oscillator, and compared with pertinent Monte-Carlo simulations, the derived formulas permit accurate and efficient quantification of the secondary system's response as a function of the design input parameters of the system assembly and the excitation.*

1 INTRODUCTION

For a plethora of structural systems encountered in engineering it is essential to specify their reliability under environmental loading conditions. Examples include missile and aircraft vibration due to atmospheric turbulence, the vibration of buildings and bridges due to earthquakes and wind, vehicle vibration due to ground and track surface irregularities, and the motion of ships and offshore structures due to wave excitation. Environmental loads are random by nature and comprise the dominant source of uncertainty for such systems. For this reason, numerous efforts have been devoted to the development of methods for the response quantification and analysis of dynamical systems subjected to random excitations.

Previous research endeavours mostly deal with primary systems, that is, load-bearing structures, modelled either as linear or weakly nonlinear, and driven by an excitation of idealised form, including broadband white noise and filtered white noise, characterised by various spectral shapes [1]. However, much research effort is still needed to provide efficient and accurate tools for estimating the response of nonlinear secondary systems subjected to random loads. Secondary structures, also referred to as subsystems, are defined as the auxiliary mechanical, electrical and electronic components and contents that are not part of the primary load-bearing structure, arising in modern engineering applications [2]. It is now well established that their reliability in the face of an extreme environmental event is essential as their damage can influence the operational continuity of the primary structure, leading to loss of life, injury, direct and indirect economic loss.

In this paper, the stochastic response of nonlinear single-degree-of-freedom secondary oscillators, in randomly excited linear primary building structures, is investigated. The full primary-secondary dynamic interaction is considered first and simplified equations are derived for a reduced two-degree-of-freedom system assembly with dimensionless coefficients. Stochastic forcing is then successively modelled as monochromatic, white noise and filtered white noise process. The first two, characterised by diametrically opposed spectral properties, represent extreme scenarios of a narrow-band and wide-band excitation, while the latter represents the intermediate case of the Clough-Penzien [3] stationary power spectrum, commonly adopted in earthquake engineering applications. A decomposition-synthesis approach is then presented in order to analytically approximate the stochastic response of the secondary system, with an application to a secondary Duffing oscillator. Based on the premise that the secondary structure is driven in a one-way interaction, the idea is to decouple the subsystems under the cascade analysis approximation [4], decompose the driving acceleration at the oscillator's position of attachment to individual components, separately quantify the response statistics, and synthesise the results to obtain the response of an equivalent linear secondary system. The resulting analytical approximation formulas fully characterise the response probability density functions under the excitation types considered, permit accurate and efficient quantification, and directly relate the statistical response parameters to the design input parameters of the primary-secondary system assembly and the excitation.

2 PRIMARY-SECONDARY SYSTEM VIBRATION

Consider the case of a dynamical system consisting of a single-degree-of-freedom (SDoF) secondary (S) oscillator attached to a multi-degree-of-freedom (MDoF) primary (P) structure. The P system represents herein a multi-storey building, while the S oscillator describes an attachment, whose performance is potentially critical to the overall resilience.

The differential equation governing the response of the combined system when subjected to

seismic excitation, assumed at rest for $t \leq 0$, reads:

$$\mathbf{M} \cdot \ddot{\mathbf{u}}(t) + \mathbf{C} \cdot \dot{\mathbf{u}}(t) + \mathbf{F}_r(\mathbf{u}(\mathbf{t})) = -\mathbf{M} \cdot \boldsymbol{\tau}\, \ddot{u}_{\mathrm{g}}(t)\,, \tag{1}$$

satisfying the initial conditions $\mathbf{u}(0) = \mathbf{0}_{n+1}$ and $\dot{\mathbf{u}}(0) = \mathbf{0}_{n+1}$, where $\mathbf{u}\,(t) = \left\{ \mathbf{u}_{\mathrm{p}}^{\top}\,(t) \,\middle|\, u_{\mathrm{s}}\,(t) \right\}^{\top}$ is the partitioned array collecting the $n+1$ DoFs relative to the ground, in which $\mathbf{u}_{\mathrm{p}}\,(t) = \{u_{\mathrm{p}1}\,(t), \ldots, u_{\mathrm{p}n}\,(t)\}^{\top}$ is the vector listing the n dynamically significant DoFs of the P structure, the superscripted $\top$ being the transpose operator; $u_{\mathrm{s}}(t)$ is the translational DoF of the S oscillator; $\boldsymbol{\tau} = \left\{ \boldsymbol{\tau}_{\mathrm{pg}}^{\top} \,\middle|\, 1 \right\}^{\top}$ is a partitioned array where $\boldsymbol{\tau}_{\mathrm{pg}}$ is the $(n \times 1)$ vector of seismic incidence; $\ddot{u}_g(t)$ is the unidirectional horizontal component of the ground acceleration, the overdot denoting differentiation with respect to the time t. Furthermore, $\mathbf{M}$ and $\mathbf{C}$ are the mass and damping matrices, partitioned as:

$$\mathbf{M} = \left[\begin{array}{c|c} \mathbf{M}_{\mathrm{p}} & \mathbf{0}_n \\ \hline \mathbf{0}_n^{\top} & m_{\mathrm{s}} \end{array}\right] \;; \quad \mathbf{C} = \left[\begin{array}{c|c} \mathbf{C}_{\mathrm{p}} + c_{\mathrm{s}}\, \boldsymbol{\tau}_{\mathrm{ps}} \boldsymbol{\tau}_{\mathrm{ps}}^{\top} & -c_{\mathrm{s}}\, \boldsymbol{\tau}_{\mathrm{ps}} \\ \hline -c_{\mathrm{s}}\, \boldsymbol{\tau}_{\mathrm{ps}}^{\top} & c_{\mathrm{s}} \end{array}\right], \tag{2}$$

where $\mathbf{M}_{\mathrm{p}}$ and $\mathbf{C}_{\mathrm{p}}$ are the mass and damping matrices of P, while m_{s} and c_{s} the associated coefficients for S; $\mathbf{0}_n$ being a zero vector of dimensions $(n \times 1)$; $\boldsymbol{\tau}_{\mathrm{ps}}$ is the $(n \times 1)$ incidence vector of the feedback action of S on P; and $\mathbf{F}_r(\mathbf{u})$ is a nonlinear restoring force that depends on the state of the system.

It has long been recognised that conventional methods can be cumbersome for the analysis of combined systems, owing to each subsystem's characteristics and dissimilarities between them, as well as impractical for design purposes, since, the P structure needs to be reanalysed for every change introduced on S. Even, if the combined system is linear,

$$\mathbf{F}_r(\mathbf{u}(t)) = \mathbf{F}_{r,lin}(\mathbf{u}(t)) = \left[\begin{array}{c|c} \mathbf{K}_{\mathrm{p}} + k_{\mathrm{s}}\, \boldsymbol{\tau}_{\mathrm{ps}} \boldsymbol{\tau}_{\mathrm{ps}}^{\top} & -k_{\mathrm{s}}\, \boldsymbol{\tau}_{\mathrm{ps}} \\ \hline -k_{\mathrm{s}}\, \boldsymbol{\tau}_{\mathrm{ps}}^{\top} & k_{\mathrm{s}} \end{array}\right] \cdot \left[\begin{array}{c} \mathbf{u}_{\mathrm{p}}(t) \\ \hline u_{\mathrm{s}}(t) \end{array}\right], \tag{3}$$

$\mathbf{K}_{\mathrm{p}}$ and k_{s} being the stiffness matrix and stiffness coefficient for P and S, the necessary and sufficient Caughey-O'Kelly condition $\mathbf{K} \cdot \mathbf{M}^{-1} \cdot \mathbf{C} = \mathbf{C} \cdot \mathbf{M}^{-1} \cdot \mathbf{K}$ [5] will, in general, not be satisfied and therefore classical modal analysis is inadmissible. However, recent advances on the decoupling of linear systems permit decoupling of Eq. (1) by the method of phase synchronisation through solution of the quadratic eigenvalue problem $(\mathbf{M} \cdot \lambda^2 + \mathbf{C} \cdot \lambda + \mathbf{K}) \cdot \mathbf{v} = 0$ [6–8].

2.1 Reduced primary-secondary system assembly

Let us now consider the case of a nonlinear S oscillator attached to a P system, as depicted in Figure 1, the latter assumed to be linear and classically damped. This assumption is not unduly restrictive, as critical infrastructure are often designed to respond within their linear-elastic regime and the survivability of internal equipment is in question. Furthermore, we separately consider P and therefore uniformly distributed energy dissipation is routinely assumed. The objective here is to formulate the system of differential equations in a simplified form, and pave the way for quantifying the S system's response under stochastic excitation in the next section.

Denoting $u_{\mathrm{s}}^{\mathrm{p}}(t)$ as the translational DoF of the S oscillator relative to the motion of the P structure, the equation of motion of P, can be conveniently expressed as:

$$\mathbf{M}_{\mathrm{p}} \cdot \ddot{\mathbf{u}}_{\mathrm{p}}(t) + \mathbf{C}_{\mathrm{p}} \cdot \dot{\mathbf{u}}_{\mathrm{p}}(t) + \mathbf{K}_{\mathrm{p}} \cdot \mathbf{u}_{\mathrm{p}}(t) = -\mathbf{M}_{\mathrm{p}} \cdot \boldsymbol{\tau}_{\mathrm{pg}} \ddot{u}_{\mathrm{g}}(t) - \boldsymbol{\tau}_{\mathrm{ps}}\, m_{\mathrm{s}} \left(\ddot{u}_{\mathrm{s}}^{\mathrm{p}}(t) + \boldsymbol{\tau}_{\mathrm{ps}}^{\top} \ddot{\mathbf{u}}_{\mathrm{p}}(t) + \ddot{u}_{\mathrm{g}}(t) \right) . \tag{4}$$

Furthermore, we denote $\ddot{\mathbf{u}}_{\mathrm{p}}^{(\mathrm{a})}(t) = \ddot{\mathbf{u}}_{\mathrm{p}}(t) + \boldsymbol{\tau}_{\mathrm{pg}} \cdot \ddot{u}_{\mathrm{g}}(t)$ as the vector listing the absolute accelerations of the P DoFs; $\ddot{u}_{\mathrm{ps}}^{(\mathrm{a})}(t) = \boldsymbol{\tau}_{\mathrm{ps}}^{\top} \cdot \ddot{\mathbf{u}}_{\mathrm{p}}^{(\mathrm{a})}(t)$ as the absolute acceleration of the P structure at the location of the S oscillator; and $\ddot{u}_{\mathrm{s}}^{(\mathrm{a})}(t) = \ddot{u}_{\mathrm{s}}^{\mathrm{p}}(t) + \ddot{u}_{\mathrm{ps}}^{(\mathrm{a})}(t)$ as the absolute acceleration of the S mass.

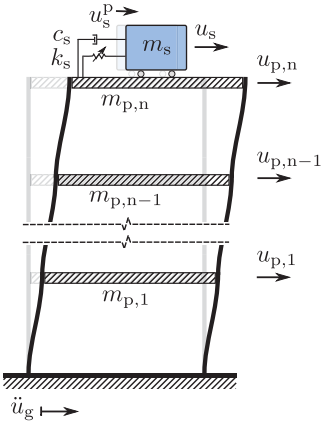

Figure 1: Combined linear P nonlinear S system.

2.1.1 Modal transformation

Aiming at reducing the dimensions of the P-S combined dynamic system, the equations of motion of the P structure are projected onto the reduced modal subspace. Accordingly, a solution to the real-valued eigenproblem $\mathbf{M}_{\mathrm{p}} \cdot \boldsymbol{\Phi}_{\mathrm{p}} \cdot \boldsymbol{\Omega}_{\mathrm{p}}^2 = \mathbf{K}_{\mathrm{p}} \cdot \boldsymbol{\Phi}_{\mathrm{p}}$ is sought, where $\boldsymbol{\Phi}_{\mathrm{p}} = \left[\boldsymbol{\phi}_{\mathrm{p1}}, \ldots \boldsymbol{\phi}_{\mathrm{p}n}\right]$ is the $(n \times n)$ modal matrix, whose columns are the n modal shapes of the P structure, and $\boldsymbol{\Omega}_{\mathrm{p}} = \mathrm{diag}\left\{\omega_{\mathrm{p1}}, \ldots, \omega_{\mathrm{p}n}\right\}$ is the diagonal spectral matrix listing the associated modal circular frequencies in ascending order. If the P-S dynamic interaction has its largest effects on the ith mode of vibration of the P structure, the following transformation can be adopted:

$$\mathbf{u}_{\mathrm{p}}(t) \approx \boldsymbol{\phi}_{\mathrm{p}i}\, q_{\mathrm{p}i}(t)\,, \tag{5}$$

where $q_{\mathrm{p}i}(t)$ is the ith modal coordinate of the P structure corresponding to the largest modal participation factor. Without loss of generality, the modal shape $\boldsymbol{\phi}_{\mathrm{p}i}$ can be normalised such that the largest horizontal displacement is set equal to 1.

Upon substitution of Eq. (5) in Eq. (4), pre-multiplication of the result by $\boldsymbol{\phi}_{\mathrm{p}i}^{\top}$ and further manipulations, one obtains:

$$\ddot{u}_{\mathrm{ps}i}(t) + 2\,\zeta_{\mathrm{p}i}\,\omega_{\mathrm{p}i}\,\dot{u}_{\mathrm{ps}i}(t) + \omega_{\mathrm{p}i}^2\,u_{\mathrm{ps}i}(t) = -\phi_{\mathrm{ps}i}\left(\beta_i\,\ddot{u}_{\mathrm{g}}(t) + \gamma_i\,\ddot{u}_{\mathrm{s}i}^{(\mathrm{a})}(t)\right)\,, \tag{6}$$

where $u_{\mathrm{ps}i}(0) = 0$ and $\dot{u}_{\mathrm{ps}i}(0) = 0$, and where $u_{\mathrm{ps}i}(t) = \phi_{\mathrm{ps}i}\,q_{\mathrm{p}i}(t)$ denotes the contribution of the ith mode of vibration to the seismic response of the P structure at the position of the S oscillator, $\phi_{\mathrm{ps}i} = \boldsymbol{\tau}_{\mathrm{ps}}^{\top} \cdot \boldsymbol{\phi}_{\mathrm{p}i}$ being the corresponding modal displacement; $\ddot{u}_{\mathrm{s}i}^{(\mathrm{a})}(t) = \ddot{u}_{\mathrm{s}}^{\mathrm{p}}(t) + \ddot{u}_{\mathrm{ps}i}(t) + \ddot{u}_{\mathrm{g}}(t)$ is the absolute acceleration of the S mass, considering for the P structure only the contribution of the ith mode of vibration; $\zeta_{\mathrm{p}i}$ and $\omega_{\mathrm{p}i}$ are the ith modal values of equivalent viscous damping ratio and circular frequency of the P modal oscillator, respectively; $\beta_i = \widetilde{m}_{\mathrm{p}i}^{-1}\,\boldsymbol{\phi}_{\mathrm{p}i}^{\top} \cdot \mathbf{M}_{\mathrm{p}} \cdot \boldsymbol{\tau}_{\mathrm{pg}}$ is the ith dimensionless modal factor for the seismic input, with $\widetilde{m}_{\mathrm{p}i} =$

$\boldsymbol{\phi}_{\mathrm{p}i}^{\top} \cdot \mathbf{M}_{\mathrm{p}} \cdot \boldsymbol{\phi}_{\mathrm{p}i}$ being the ith modal mass for the P structure; similarly, $\gamma_i = \widetilde{m}_{\mathrm{p}i}^{-1}\, \phi_{\mathrm{ps}i}\, m_{\mathrm{s}}$ is the ith dimensionless modal factor for the S feedback on the P structure.

In what follows, for the sake of simplifying the notation, the generalised P coordinate $u_{\mathrm{ps}i}(t)$ is replaced with $u_{\mathrm{p}}(t)$, and the modal index i is dropped in all the other quantities in Eq. (6) resulting to:

$$\ddot{u}_{\mathrm{p}}(t) + 2\,\zeta_{\mathrm{p}}\,\omega_{\mathrm{p}}\,\dot{u}_{\mathrm{p}}(t) + \omega_{\mathrm{p}}^2\,u_{\mathrm{p}}(t) = -\phi_{\mathrm{ps}}\left(\beta\,\ddot{u}_{\mathrm{g}}(t) + \gamma\left(\ddot{u}_{\mathrm{g}}(t) + \ddot{u}_{\mathrm{p}}(t) + \ddot{u}_{\mathrm{s}}^{\mathrm{p}}(t)\right)\right)\,. \tag{7}$$

It is clear that the contribution of higher modes can be included in the procedure, if needed. Notably, setting $\gamma = 0$ decouples Eq. (7) from the equation governing the seismic response of the S oscillator, leading to the so-called 'cascade approximation', where the P-S dynamic interaction is neglected. It is worth noting here that the condition $\gamma = 0$ does not imply a massless S system, but merely the fact that the feedback action of S on P is negligible. Furthermore, in the special case where P is a SDoF oscillator, i.e. $n = 1$, then, $\phi_{\mathrm{ps}} = \beta = 1$ and $\gamma = m_{\mathrm{s}}/m_{\mathrm{p}}$.

2.1.2 Duffing secondary oscillator

Without loss of generality, the simplest case of a SDoF S Duffing oscillator, extensively studied in the literature, is considered next. Dynamic equilibrium of the mass m_{s} in the horizontal direction gives:

$$\ddot{u}_{\mathrm{s}}^{\mathrm{p}}(t) + 2\,\zeta_{\mathrm{s}}\,\omega_{\mathrm{s}}\,\dot{u}_{\mathrm{s}}^{\mathrm{p}}(t) + \omega_{\mathrm{s}}^2\left(u_{\mathrm{s}}^{\mathrm{p}}(t) + \lambda\,\left(u_{\mathrm{s}}^{\mathrm{p}}(t)\right)^3\right) = -\ddot{u}_{\mathrm{p}}^{(\mathrm{a})}(t)\,, \tag{8}$$

where $u_{\mathrm{s}}^{\mathrm{p}}(0) = 0$ and $\dot{u}_{\mathrm{s}}^{\mathrm{p}}(0) = 0$, $u_{\mathrm{s}}^{\mathrm{p}}(t)$ being the displacement of the S oscillator relative to the P structure at its point of attachment; ζ_{s} and $\omega_{\mathrm{s}} = \sqrt{k_{\mathrm{s}}/m_{\mathrm{s}}}$ are the viscous damping ratio and natural circular frequency of S in its elastic range, k_{s} being its elastic stiffness; λ is a constant, for $\lambda = 0$ the restoring force reduces to the linear one, while $\lambda < 0$ and $\lambda > 0$ represent softening and hardening phases, respectively; $\ddot{u}_{\mathrm{p}}^{(\mathrm{a})}(t) = \ddot{u}_{\mathrm{p}}(t) + \ddot{u}_{\mathrm{g}}(t)$ is the absolute horizontal acceleration of P at the position of S, in which $\ddot{u}_{\mathrm{p}}(t)$ satisfies Eq. (7).

3 STOCHASTIC FORCING MODEL

Consider a ground acceleration $\ddot{u}_{\mathrm{g}}(t)$, successively modelled as monochromatic, white noise, and filtered white noise stationary Gaussian process. The monochromatic and white noise excitations, characterised by diametrically opposed properties, represent herein the extreme forms of narrow-band and wide-band processes, respectively, while the coloured noise represents an intermediate case, characterised by a modified Kanai-Tajimi (KT) power spectrum (Kanai [9]; Tajimi [10]) suggested by Clough and Penzien (CP) [3], commonly used in earthquake engineering applications. Their power spectral density (PSD) functions are, respectively, given by:

$$S_{\ddot{u}_{\mathrm{g}}}(\omega) = \alpha\,\delta\left(|\omega| - \omega_0\right)\,;\quad S_{\ddot{u}_{\mathrm{g}}}(\omega) = S_0\,;\quad S_{\ddot{u}_{\mathrm{g}}}(\omega) = S_0 \cdot H_k(\omega) \cdot H_c(\omega)\,, \tag{9}$$

for $-\infty < \omega < \infty$, where α is the strength of the unit impulse $\delta(\cdot)$ and ω_0 is the arrival frequency; S_0 represents a constant PSD level due to white noise; and $H_k(\omega)$ and $H_c(\omega)$ represent the KT and CP filters, respectively, given by:

$$H_k(\omega) = \frac{1 + 4\,\zeta_g^2\,(\omega/\omega_g)^2}{\left(1 - (\omega/\omega_g)^2\right)^2 + 4\,\zeta_g^2\,(\omega/\omega_g)^2}\,;\quad H_c(\omega) = \frac{(\omega/\omega_f)^4}{\left(1 - (\omega/\omega_f)^2\right)^2 + 4\,\zeta_f^2\,(\omega/\omega_f)^2}\,, \tag{10}$$

where ω_g and ζ_g are the frequency and damping ratio of the soil layer, respectively, and the parameters ω_f and ζ_f control the CP filter's characteristics.

In the CP model, $H_k(\omega)$ attenuates the frequency content for $\omega > \omega_g$ as $\omega \to \infty$, and amplifies the frequencies in the vicinity of $\omega = \omega_g$. $H_c(\omega)$ is then introduced to eliminate the low-frequency content, thus assuring finite power for the ground displacement.

4 RESPONSE QUANTIFICATION OF NONLINEAR SECONDARY OSCILLATOR

In §2 simplified equations were presented for the dynamic interaction of the P-S system. In this section a decomposition-synthesis (DS) approach is presented for the analysis of linear and equivalent linear S systems. The purpose is the quantification, through analytical approximations, of the response of the nonlinear S to stochastic excitation, with indicative application to an S Duffing oscillator subjected to the excitation considered in §3. The basic idea is to decouple P and S, separately quantify the response statistics to individual forcing components, and synthesise the results to obtain the response of an equivalent linear S oscillator.

4.1 Primary structure

To apply the DS method, we first assume that the S oscillator is essentially driven in a one-way interaction. On setting $\gamma = 0$, Eq. (7) and (8) decouple and can sequentially be considered. We emphasise that this is desirable as different S can be considered for the same P configuration.

Next, we proceed with quantification of the probabilistic structure of $\ddot{u}_{\mathrm{p}}^{(\mathrm{a})}$, which constitutes the driving acceleration of the S oscillator. We decompose this in two terms:

$$\ddot{u}_{\mathrm{p}}^{(\mathrm{a})}(t) = \ddot{u}_{\mathrm{p}}(t) + \ddot{u}_{\mathrm{g}}(t)\,, \tag{11}$$

and since both $\ddot{u}_{\mathrm{p}}(t)$ and $\ddot{u}_{\mathrm{g}}(t)$ are stationary and Gaussian distributed, $\ddot{u}_{\mathrm{p}}^{(\mathrm{a})}(t)$ will also be so. The autocorrelation function of the process $\ddot{u}_{\mathrm{p}}^{(\mathrm{a})}(t)$ may be expressed in terms of the autocorelation and cross-correlation functions of $\ddot{u}_{\mathrm{p}}(t)$ and $\ddot{u}_{\mathrm{g}}(t)$, and therefore one can obtain the PSD of $\ddot{u}_{\mathrm{p}}^{(\mathrm{a})}(t)$ as:

$$S_{\ddot{u}_{\mathrm{p}}^{(\mathrm{a})}}(\omega) = S_{\ddot{u}_{\mathrm{p}}}(\omega) + S_{\ddot{u}_{\mathrm{g}}}(\omega) + 2\,\mathbb{R}\mathrm{e}\{S_{\ddot{u}_{\mathrm{p}}\ddot{u}_{\mathrm{g}}}(\omega)\}\,, \tag{12}$$

where $S_{\ddot{u}_{\mathrm{p}}}(\omega)$, the response PSD of $\ddot{u}_{\mathrm{p}}(t)$, is related to the excitation through,

$$S_{\ddot{u}_{\mathrm{p}}}(\omega) = \omega^4 S_{u_{\mathrm{p}}}(\omega)\,; \quad S_{u_{\mathrm{p}}}(\omega) = |H_{\mathrm{p}}(\omega)|^2\, S_{\ddot{u}_{\mathrm{g}}}(\omega)\,, \tag{13}$$

in which $H_{\mathrm{p}}(\omega)$ is the frequency response function (FRF), given by:

$$H_{\mathrm{p}}(\omega) = \frac{\phi_{\mathrm{ps}}\,\beta}{\omega^2 - 2\,i\,\zeta_{\mathrm{p}}\omega_{\mathrm{p}}\,\omega - \omega_{\mathrm{p}}^2}\,. \tag{14}$$

Furthermore, the last term in Eq. (12) can be interpreted as the sum of the cross-spectral density functions $S_{\ddot{u}_{\mathrm{p}}\ddot{u}_{\mathrm{g}}}(\omega)$ and $S_{\ddot{u}_{\mathrm{g}}\ddot{u}_{\mathrm{p}}}(\omega)$, where $S_{\ddot{u}_{\mathrm{p}}\ddot{u}_{\mathrm{g}}}(\omega) = S^*_{\ddot{u}_{\mathrm{g}}\ddot{u}_{\mathrm{p}}}(\omega)$, in which $*$ denotes conjugation, and:

$$S_{\ddot{u}_{\mathrm{p}}\ddot{u}_{\mathrm{g}}}(\omega) = -\omega^2 S_{u_{\mathrm{p}}\ddot{u}_{\mathrm{g}}}(\omega)\,; \quad S_{u_{\mathrm{p}}\ddot{u}_{\mathrm{g}}}(\omega) = H_{\mathrm{p}}(\omega) S_{\ddot{u}_{\mathrm{g}}}(\omega)\,. \tag{15}$$

Notably, Eq. (12) expresses the PSD of the driving acceleration for S to individual components, simplifying manipulation. Furthermore, it permits the direct generation of floor acceleration time series ensembles corresponding to specified ground excitation spectral shapes,

through standard stochastic forcing simulation methods [11], for the numerical analysis of the nonlinear S.

The process variance of $\ddot{u}_{\mathrm{p}}^{(\mathrm{a})}(t)$, fully characterising the zero mean ($\mu_{\ddot{u}_{\mathrm{p}}^{(\mathrm{a})}} = \mu_{\ddot{u}_{\mathrm{p}}} + \mu_{\ddot{u}_{\mathrm{g}}} = 0$) Gaussian (absolute acceleration) response of P, can thus be readily obtained as:

$$\sigma^2_{\ddot{u}_{\mathrm{p}}^{(\mathrm{a})}} = \int_{-\infty}^{\infty} S_{\ddot{u}_{\mathrm{p}}^{(\mathrm{a})}}(\omega)\,\mathrm{d}\omega = \sigma^2_{\ddot{u}_{\mathrm{p}}} + \sigma^2_{\ddot{u}_{\mathrm{g}}} + 2\,\sigma_{\ddot{u}_{\mathrm{p}}\ddot{u}_{\mathrm{g}}}\,, \tag{16}$$

where $\sigma^2_{\ddot{u}_{\mathrm{p}}}$, $\sigma^2_{\ddot{u}_{\mathrm{g}}}$ and $\sigma_{\ddot{u}_{\mathrm{p}}\ddot{u}_{\mathrm{g}}}$ are the variances and covariance of the underlying processes, respectively, given by:

$$\sigma^2_{\ddot{u}_{\mathrm{p}}} = \int_{-\infty}^{\infty} S_{\ddot{u}_{\mathrm{p}}}(\omega)\,\mathrm{d}\omega\,; \quad \sigma^2_{\ddot{u}_{\mathrm{g}}} = \int_{-\infty}^{\infty} S_{\ddot{u}_{\mathrm{g}}}(\omega)\,\mathrm{d}\omega\,; \quad \sigma_{\ddot{u}_{\mathrm{p}}\ddot{u}_{\mathrm{g}}} = \int_{-\infty}^{\infty} \mathbb{R}\mathrm{e}\{S_{\ddot{u}_{\mathrm{p}}\ddot{u}_{\mathrm{g}}}(\omega)\}\,\mathrm{d}\omega\,. \tag{17}$$

4.2 Secondary oscillator

To estimate the response of the S oscillator, system nonlinearities can be important and to this end an appropriate quantification scheme needs to be employed. Herein the statistical linearisation approach [1] is adopted.

Accordingly, the nonlinear Duffing oscillator's Eq. (8) is replaced with a linear one:

$$\ddot{u}_{\mathrm{s}}^{\mathrm{p}}(t) + 2\,\zeta_{\mathrm{s}}\,\omega_{\mathrm{s}}\,\dot{u}_{\mathrm{s}}^{\mathrm{p}}(t) + \omega^2_{\mathrm{eq}} u_{\mathrm{s}}^{\mathrm{p}}(t) = -\ddot{u}_{\mathrm{p}}^{(\mathrm{a})}(t)\,, \tag{18}$$

where ω_{eq} represents the natural frequency of the equivalent linear system.

Minimising the mean square of the error $\varepsilon = \omega_{\mathrm{s}}^2\left(u_{\mathrm{s}}^{\mathrm{p}}(t) + \lambda\,\left(u_{\mathrm{s}}^{\mathrm{p}}(t)\right)^3\right) - \omega^2_{\mathrm{eq}} u_{\mathrm{s}}^{\mathrm{p}}(t)$ with respect to ω^2_{eq}, one obtains:

$$\omega^2_{\mathrm{eq}} = \omega_{\mathrm{s}}^2\left(1 + 3\,\lambda\,\sigma^2_{u_{\mathrm{s}}^{\mathrm{p}}}\right)\,. \tag{19}$$

The response statistics can then be obtained through the following spectral relationships:

$$\sigma^2_{u_{\mathrm{s}}^{\mathrm{p}}} = \int_{-\infty}^{\infty} S_{u_{\mathrm{s}}^{\mathrm{p}}}(\omega)\,\mathrm{d}\omega\,; \quad \sigma^2_{\dot{u}_{\mathrm{s}}^{\mathrm{p}}} = \int_{-\infty}^{\infty} S_{\dot{u}_{\mathrm{s}}^{\mathrm{p}}}(\omega)\,\mathrm{d}\omega\,; \quad \sigma^2_{\ddot{u}_{\mathrm{s}}^{\mathrm{p}}} = \int_{-\infty}^{\infty} S_{\ddot{u}_{\mathrm{s}}^{\mathrm{p}}}(\omega)\,\mathrm{d}\omega\,, \tag{20}$$

where the PSD functions $S_{u_{\mathrm{s}}^{\mathrm{p}}}(\omega)$, $S_{\dot{u}_{\mathrm{s}}^{\mathrm{p}}}(\omega)$ and $S_{\ddot{u}_{\mathrm{s}}^{\mathrm{p}}}(\omega)$ take the form:

$$S_{u_{\mathrm{s}}^{\mathrm{p}}}(\omega) = |H_{\mathrm{s}}(\omega)|^2\, S_{\ddot{u}_{\mathrm{p}}^{(\mathrm{a})}}(\omega)\,; \quad S_{\dot{u}_{\mathrm{s}}^{\mathrm{p}}}(\omega) = \omega^2 S_{u_{\mathrm{s}}^{\mathrm{p}}}(\omega)\,; \quad S_{\ddot{u}_{\mathrm{s}}^{\mathrm{p}}}(\omega) = \omega^4 S_{u_{\mathrm{s}}^{\mathrm{p}}}(\omega)\,, \tag{21}$$

in which $H_{\mathrm{s}}(\omega)$ is the FRF of the equivalent linear system in Eq. (18), given by:

$$H_{\mathrm{s}}(\omega) = \frac{1}{\omega^2 - 2\,i\,\zeta_{\mathrm{s}}\,\omega_{\mathrm{s}}\,\omega - \omega^2_{\mathrm{eq}}}\,. \tag{22}$$

We note that we deliberately avoid the matrix notation in the previous, emphasising the asynchronous response evaluation of the two subsystems, and enabling the adoption of alternative linearisation techniques for the S system such as, for instance, a higher order linearisation [12].

4.2.1 Monochromatic excitation

We next proceed with the evaluation of the random vibration integrals in Eq. (20). To this end the decomposed form of individual components, simplifies manipulation of the integrals which are conveniently computed analytically by utilising the general formula in [13], for the three

types of excitation considered. We note that solution of the integrals corresponding to the P structure's response falls beyond the scope of this work.

The monochromatic excitation is first considered. In this case, the response PSD retains similar form to the PSD of the excitation in Eq. (9), that is, an impulse whose strength depends on the parameters of the P-S system assembly. The displacement and velocity response variance then reads:

$$\sigma^2_{u^{\mathrm{p}}_{\mathrm{s}}} = \frac{2\,\alpha}{\mathcal{C}^m_1} + \frac{2\,\alpha\,\beta\,\omega_0^2\,\phi_{\mathrm{ps}}\,\mathcal{C}^m_2}{\mathcal{C}^m_1\,\mathcal{C}^m_3}\,; \quad \sigma^2_{\dot{u}^{\mathrm{p}}_{\mathrm{s}}} = \omega_0^2\,\sigma^2_{u^{\mathrm{p}}_{\mathrm{s}}}\,, \tag{23}$$

where $\mathcal{C}^m_1$ - $\mathcal{C}^m_3$ are a set of coefficients provided in Appendix A.

Notably, the same approach can be used for the acceleration response of the S oscillator although the analytical formulas will not be provided herein.

4.2.2 White noise excitation

For the white noise excitation, the response is given by:

$$\sigma^2_{u^{\mathrm{p}}_{\mathrm{s}}} = \frac{\pi S_0}{2\,\zeta_{\mathrm{s}}\,\omega^2_{\mathrm{eq}}\,\omega_{\mathrm{s}}} + \frac{\pi S_0\,\beta\,\phi_{\mathrm{ps}}\,\mathcal{C}^w_1}{2\,\zeta_{\mathrm{p}}\,\zeta_{\mathrm{s}}\,\omega_{\mathrm{s}}\,\mathcal{C}^w_2}\,; \quad \sigma^2_{\dot{u}^{\mathrm{p}}_{\mathrm{s}}} = \frac{\pi S_0}{2\,\zeta_{\mathrm{s}}\,\omega_{\mathrm{s}}} + \frac{\pi S_0\,\beta\,\phi_{\mathrm{ps}}\,(\mathcal{C}^w_3 + \mathcal{C}^w_4)}{2\,\zeta_{\mathrm{p}}\,\zeta_{\mathrm{s}}\,\omega_{\mathrm{s}}\,\mathcal{C}^w_2}\,, \tag{24}$$

where the associated coefficients $\mathcal{C}^w_1$ - $\mathcal{C}^w_4$ are likewise reported in Appendix A.

Evidently, the first term in Eq. (23) and (24) solely depends on the ground excitation while the second term also depends on the P system's parameters. On setting $\phi_{\mathrm{ps}} = 0$, the latter vanishes corresponding to an S oscillator mounted at ground level.

4.2.3 Filtered white noise excitation

The details of the analysis for the filtered white noise excitation characterised by the Clough-Penzien spectrum are lengthy, and therefore only the case where $\phi_{\mathrm{ps}} = 0$ will be provided herein. In this case the variance of the response reads:

$$\sigma^2_{u^{\mathrm{p}}_{\mathrm{s}}} = \frac{\pi S_0\,\omega_{\mathrm{g}}^2\,(\mathcal{C}^f_1 + \mathcal{C}^f_2 + \mathcal{C}^f_3 + \mathcal{C}^f_4)}{\mathcal{C}^f_5}\,; \quad \sigma^2_{\dot{u}^{\mathrm{p}}_{\mathrm{s}}} = \frac{\pi S_0\,\omega_{\mathrm{g}}^2\,(\mathcal{C}^f_6 + \mathcal{C}^f_7 + \mathcal{C}^f_8 + \mathcal{C}^f_9)}{\mathcal{C}^f_5}\,, \tag{25}$$

where the coefficients $\mathcal{C}^f_1$ - $\mathcal{C}^f_9$ are given in Appendix A.

On combining Eq. (19) with Eq. (23), (24) and (25), the resulting algebraic equations can be solved numerically for ω_{eq} and therefore $\sigma^2_{u^{\mathrm{p}}_{\mathrm{s}}}$ and $\sigma^2_{\dot{u}^{\mathrm{p}}_{\mathrm{s}}}$ can be evaluated from the above expressions.

4.3 Numerical investigations

Figure 2 presents spectra of the response variance of the Duffing S oscillator, for the three excitation types considered, as a function of the parameter $\lambda > 0$, and for $\phi_{\mathrm{ps}} = \{0, 0.5, 1\}$, the latter representing an oscillator mounted at ground level, at an intermediate height, and at roof level, respectively. The analytical derived expressions for the statistical linearisation procedure have been used for this purpose, and are compared with the stationary response value of the nonlinear system in Eq. (8), numerically computed via pertinent Monte Carlo simulations. The analysis has been carried out using the following reference values: $\alpha = 0.3$ and $\omega_0 = 10\,\mathrm{rad/s}$ (monochromatic excitation); $S_0 = 0.003\,\mathrm{m^2/s^3}$ (white noise); $S_0 = 0.003\,\mathrm{m^2/s^3}$, $\omega_g = 10\,\mathrm{rad/s}$, $\zeta_g = 0.4$, $\omega_f = 1\,\mathrm{rad/s}$ and $\zeta_f = 0.6$ (filtered white noise [11]); and $\beta = 1.3$,

$\omega_\mathrm{p} = 14.76$, $\omega_\mathrm{s} = 1.4\,\omega_\mathrm{p}$, $\zeta_\mathrm{p} = 0.05$ and $\zeta_\mathrm{s} = 0.02$ (for the P-S system assembly [4]). In this plot, $\sigma^{2*}_{u^\mathrm{p}_\mathrm{s}}$ and $\sigma^{2*}_{\dot{u}^\mathrm{p}_\mathrm{s}}$ denote the displacement and velocity response variances, normalised by the associated peak variances in the linear case, at roof level (i.e. $\lambda = 0$ and $\phi_\mathrm{ps} = 1$).

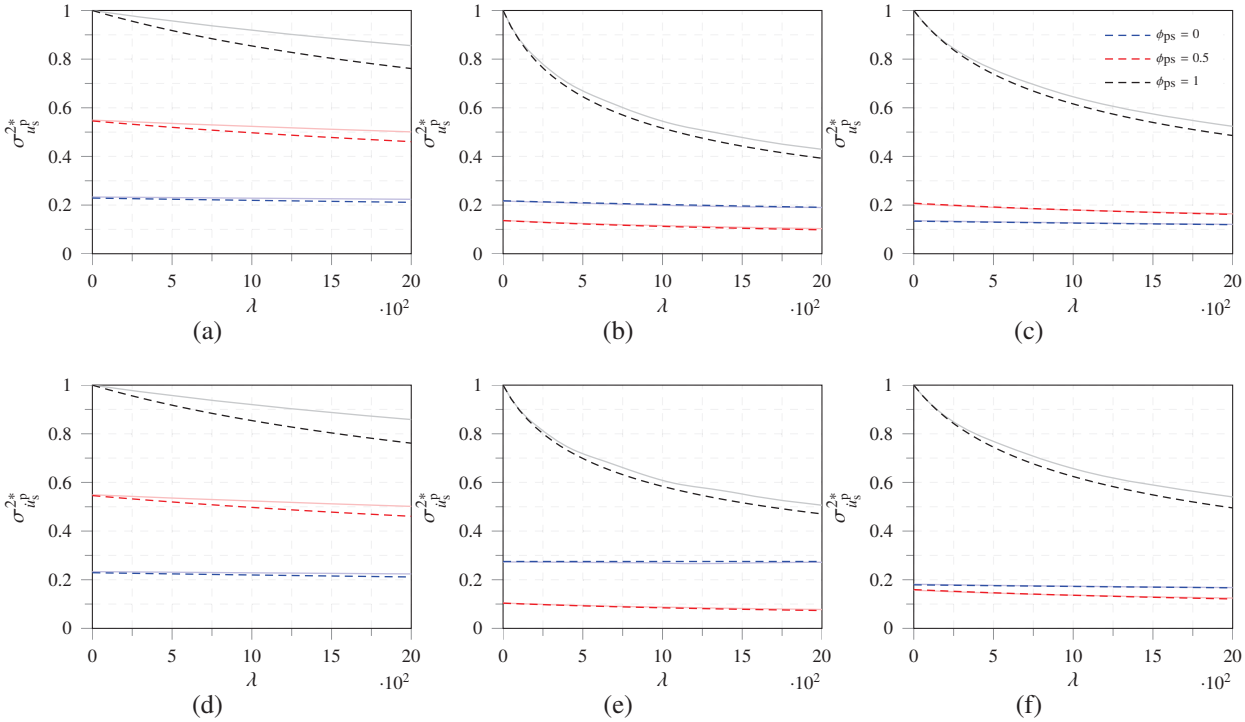

Figure 2: Variation of the secondary Duffing oscillator's mean square displacement (top) and velocity (bottom) response with λ and ϕ_ps. Comparison of statistical linearisation (dashed lines) and Monte Carlo simulation (solid lines) for: (a, d) monochromatic ($\alpha = 0.3$, $\omega_0 = 10\,\mathrm{rad/s}$); (b, e) white noise ($S_0 = 0.003\,\mathrm{m^2/s^3}$); and (c, f) filtered white noise ($S_0 = 0.003\,\mathrm{m^2/s^3}$, $\omega_g = 10\,\mathrm{rad/s}$, $\zeta_g = 0.4$, $\omega_f = 1\,\mathrm{rad/s}$, $\zeta_f = 0.6$) excitation. Reference parameters: $\beta = 1.3$, $\omega_\mathrm{p} = 14.76$, $\omega_\mathrm{s} = 1.4\,\omega_\mathrm{p}$, $\zeta_\mathrm{p} = 0.05$, $\zeta_\mathrm{s} = 0.02$.

Overall, the response variances (i.e. the areas under the associated PSD curves), are finite, and are smooth functions of the parameter λ. The statistical linearisation provides a good approximation of the nonlinear response for the cases considered. As expected, the effectiveness of the approximation deteriorates with λ, that is, at higher nonlinearity levels. We note that the validity of the derived expressions has been further confirmed through Monte Carlo simulations carried out directly on the equivalent linear system.

An interesting observation is that the response variance does not always increase with ϕ_ps (i.e. lower spectral ordinates are shown in Figures 2(b) and 2(e) for $\phi_\mathrm{ps} = 0.5$ when compared to $\phi_\mathrm{ps} = 0$). This is an important consequence of Eq. (16), which implies that even though $\sigma^2_{\ddot{u}_\mathrm{p}}$ will always increase with ϕ_ps (due to the amplified motions on the P structure), $\sigma^2_{\ddot{u}^{(\mathrm{a})}_\mathrm{p}}$ may or may not, as it also depends on the covariance of processes $\ddot{u}_\mathrm{p}$ and $\ddot{u}_\mathrm{g}$. Consequently, the response variance of S may or may not increase with ϕ_ps.

Finally, even though the application of the statistical linearisation procedure is straightforward, it cannot account for the existence of higher harmonics, such as the case of white noise and filtered white noise excitation, and therefore alternative quantification schemes need to be sought to achieve further improvements in accuracy.

5 CONCLUSIONS

The steady-state stationary response quantification and analysis of nonlinear secondary oscillators in randomly driven linear primary building structures, has been addressed. By utilising a modal coordinate transformation, simplified equations posed as a reduced two-degree-of-freedom system with dimensionless coefficients, have been derived for the primary-secondary system assembly.

Three different types of stochastic excitation spectra have been considered: monochromatic excitation, representative of the extreme scenario of a narrow-band process; white noise excitation, the extreme form of a wide-band process; and the intermediate case of filtered white noise characterised by the Clough-Penzien power spectrum, commonly used in earthquake engineering applications. A decomposition-synthesis approach has been presented for the analysis of linear and equivalent linear secondary systems, whereby the stochastic response of the nonlinear secondary system is analytically approximated, with an application to a secondary Duffing oscillator. In this approach, the secondary system is first decoupled from the primary structure under the cascade analysis approximation. The stochastic forcing delivered to the secondary system is decomposed as the sum of individual forcing components, the response statistics are separately quantified using spectral relationships, and are pieced-together to construct the overall response of an equivalent linear secondary system.

Decomposition of the power spectral density of the driving acceleration at the oscillator's position, simplifies the manipulation of the random vibration integrals and enhances the understanding on the physical meaning of the response. It further facilitates the direct generation of floor acceleration time series ensembles for the numerical analysis of nonlinear secondary systems. The resulting analytical expressions, derived herein for the secondary Duffing oscillator under the three types of excitation considered, approximate the response probability density functions and permit the accurate and efficient quantification, expressing the statistical parameters of the response as a function of the corresponding design input parameters of the system assembly and the excitation. Future work will involve the inclusion of the contribution of higher modes, and extensions to other types of nonlinear oscillators and multi-degree-of-freedom secondary systems using alternative statistical quantification schemes.

APPENDIX A. COEFFICIENTS

The coefficients $\mathcal{C}_1^m$ - $\mathcal{C}_3^m$ for the monochromatic excitation (§ 4.2.1) are:

$$\mathcal{C}_1^m = 4\,\zeta_\mathrm{s}^2\,\omega_0^2\,\omega_\mathrm{s}^2 + \left(\omega_0^2 - \omega_\mathrm{eq}^2\right)^2\,; \tag{26a}$$

$$\mathcal{C}_2^m = \omega_0^2\,(\beta\,\phi_\mathrm{ps} - 2) + 2\,\omega_\mathrm{p}^2\,; \tag{26b}$$

$$\mathcal{C}_3^m = \left(4\,\zeta_\mathrm{p}^2 - 2\right)\omega_0^2\,\omega_\mathrm{p}^2 + \omega_0^4 + \omega_\mathrm{p}^4\,. \tag{26c}$$

The coefficients $\mathcal{C}_1^w$ - $\mathcal{C}_4^w$ for the white noise excitation (§ 4.2.2) are:

$$\mathcal{C}_1^w = \zeta_\mathrm{p}\,\omega_\mathrm{eq}^2(\beta\,\phi_\mathrm{ps} - 2) + \beta\,\zeta_\mathrm{s}\,\omega_\mathrm{p}\,\omega_\mathrm{s}\,\phi_\mathrm{ps} + 2\,\zeta_\mathrm{p}\omega_\mathrm{p}^2\,; \tag{27a}$$

$$\mathcal{C}_2^w = 2\,\omega_\mathrm{eq}^2\,\omega_\mathrm{p}\left(\left(2\,\zeta_\mathrm{p}^2 - 1\right)\omega_\mathrm{p} + 2\,\zeta_\mathrm{p}\,\zeta_\mathrm{s}\,\omega_\mathrm{s}\right) + \omega_\mathrm{p}^2\left(4\,\zeta_\mathrm{p}\,\zeta_\mathrm{s}\,\omega_\mathrm{p}\,\omega_\mathrm{s} + 4\,\zeta_\mathrm{s}^2\omega_\mathrm{s}^2 + \omega_\mathrm{p}^2\right) + \omega_\mathrm{eq}^4\,; \tag{27b}$$

$$\mathcal{C}_3^w = \zeta_\mathrm{s}\,\omega_\mathrm{p}\,\omega_\mathrm{s}\left(4\,\zeta_\mathrm{p}^2\omega_\mathrm{eq}^2(\beta\,\phi_\mathrm{ps} - 2) + \beta\,\omega_\mathrm{p}^2\phi_\mathrm{ps}\right)\,; \tag{27c}$$

$$\mathcal{C}_4^w = \zeta_\mathrm{p}\left(4\,\zeta_\mathrm{s}^2\omega_\mathrm{p}^2\omega_\mathrm{s}^2(\beta\,\phi_\mathrm{ps} - 2) + \omega_\mathrm{eq}^4(\beta\,\phi_\mathrm{ps} - 2) + 2\,\omega_\mathrm{eq}^2\omega_\mathrm{p}^2\right)\,. \tag{27d}$$

The coefficients $\mathcal{C}_1^f$ - $\mathcal{C}_9^f$ for the filtered white noise excitation (§ 4.2.3) are:

$$\mathcal{C}_1^f = 4\,\zeta_\mathrm{f}^3\,\omega_\mathrm{eq}^2\,\omega_\mathrm{f}^2\,\omega_\mathrm{g}^2\left(4\,\zeta_\mathrm{g}^3\,\omega_\mathrm{eq}^2 + 4\,\zeta_\mathrm{g}^2\,\zeta_\mathrm{s}\,\omega_\mathrm{g}\,\omega_\mathrm{s} + \zeta_\mathrm{g}\,\omega_\mathrm{g}^2 + \zeta_\mathrm{s}\,\omega_\mathrm{g}\,\omega_\mathrm{s}\right)\,; \tag{28a}$$

$$\begin{aligned}\mathcal{C}_2^f =& 4\,\zeta_{\rm f}^2\,\omega_{\rm f}\,\omega_{\rm g}\left(4\,\zeta_{\rm g}^3\,\omega_{\rm eq}^2+4\,\zeta_{\rm g}^2\,\zeta_{\rm s}\,\omega_{\rm g}\,\omega_{\rm s}+\zeta_{\rm g}\,\omega_{\rm g}^2+\zeta_{\rm s}\,\omega_{\rm g}\,\omega_{\rm s}\right)\left(\zeta_{\rm g}\,\omega_{\rm eq}^2\left(\omega_{\rm f}^2+\omega_{\rm g}^2\right)\right.\\ &\left.+\,\zeta_{\rm s}\,\omega_{\rm g}\,\omega_{\rm s}\left(\omega_{\rm eq}^2+\omega_{\rm f}^2\right)\right);\end{aligned} \tag{28b}$$

$$\begin{aligned}\mathcal{C}_3^f =& \zeta_{\rm f}(16\,\zeta_{\rm g}^5\,\omega_{\rm eq}^4\,\omega_{\rm f}^2\,\omega_{\rm g}^2+16\,\zeta_{\rm g}^4\,\zeta_{\rm s}\,\omega_{\rm eq}^2\,\omega_{\rm f}^2\,\omega_{\rm g}(\omega_{\rm eq}^2+\omega_{\rm f}^2+2\,\omega_{\rm g}^2)\omega_{\rm s}\\ &+\zeta_{\rm s}\,\omega_{\rm g}^3\,\omega_{\rm s}((\,\omega_{\rm eq}^2-\omega_{\rm f}^2)^2+4\,\zeta_{\rm s}^2\,\omega_{\rm f}^2\,\omega_{\rm s}^2)+4\,\zeta_{\rm g}^3(\omega_{\rm eq}^2\,\omega_{\rm f}^2\,\omega_{\rm g}^4+\omega_{\rm eq}^4(\omega_{\rm f}^2-\omega_{\rm g}^2)^2\\ &+4\,\zeta_{\rm s}^2\,\omega_{\rm f}^2\,\omega_{\rm g}^2(2\,\omega_{\rm eq}^2+\,\omega_{\rm f}^2+\omega_{\rm g}^2)\omega_{\rm s}^2)+\zeta_{\rm g}\,\omega_{\rm g}^2(\,\omega_{\rm eq}^2(\omega_{\rm f}^2-\omega_{\rm g}^2)^2+\\ &4\,\zeta_{\rm s}^2(2\,\omega_{\rm f}^2\,\omega_{\rm g}^2+\omega_{\rm eq}^2\,(\omega_{\rm f}^2+\omega_{\rm g}^2))\omega_{\rm s}^2)+4\,\zeta_{\rm g}^2\,\zeta_{\rm s}\,\omega_{\rm g}^3\,\omega_{\rm s}(\omega_{\rm eq}^4+\omega_{\rm eq}^2\,\omega_{\rm g}^2\\ &+\omega_{\rm f}^2(\omega_{\rm f}^2+\omega_{\rm g}^2+4\,\zeta_{\rm s}^2\,\omega_{\rm s}^2)));\end{aligned} \tag{28c}$$

$$\begin{aligned}\mathcal{C}_4^f =& \zeta_{\rm g}\,\zeta_{\rm s}\,\omega_{\rm f}(4\,\zeta_{\rm g}^2\,\omega_{\rm f}^2+\omega_{\rm g}^2)\,\omega_{\rm s}(\omega_{\rm eq}^4+2\,\omega_{\rm eq}^2\,\omega_{\rm g}((-1+2\,\zeta_{\rm g}^2)\omega_{\rm g}+2\,\zeta_{\rm g}\,\zeta_{\rm s}\,\omega_{\rm s})\\ &+\omega_{\rm g}^2(\omega_{\rm g}^2+4\,\zeta_{\rm g}\,\zeta_{\rm s}\,\omega_{\rm g}\,\omega_{\rm s}+4\,\zeta_{\rm s}^2\,\omega_{\rm s}^2));\end{aligned} \tag{28d}$$

$$\begin{aligned}\mathcal{C}_5^f =& 2\,\zeta_{\rm f}\,\zeta_{\rm g}\,\zeta_{\rm s}(\omega_{\rm f}^4+4\,\zeta_{\rm f}\,\zeta_{\rm g}\,\omega_{\rm f}^3\,\omega_{\rm g}+2(-1+2\,\zeta_{\rm f}^2+2\,\zeta_{\rm g}^2)\omega_{\rm f}^2\,\omega_{\rm g}^2\\ &+4\,\zeta_{\rm f}\,\zeta_{\rm g}\,\omega_{\rm f}\,\omega_{\rm g}^3+\omega_{\rm g}^4)\omega_{\rm s}\,(\omega_{\rm eq}^4+2\,\omega_{\rm eq}^2\,\omega_{\rm f}((-1+2\,\zeta_{\rm f}^2)\omega_{\rm f}+2\,\zeta_{\rm f}\,\zeta_{\rm s}\,\omega_{\rm s})\\ &+\omega_{\rm f}^2(\omega_{\rm f}^2+4\,\zeta_{\rm f}\,\zeta_{\rm s}\,\omega_{\rm f}\,\omega_{\rm s}+4\,\zeta_{\rm s}^2\,\omega_{\rm s}^2))(\omega_{\rm eq}^4+2\,\omega_{\rm eq}^2\,\omega_{\rm g}((-1+2\,\zeta_{\rm g}^2)\omega_{\rm g}+2\,\zeta_{\rm g}\,\zeta_{\rm s}\,\omega_{\rm s})\\ &+\omega_{\rm g}^2(\omega_{\rm g}^2+4\,\zeta_{\rm g}\,\zeta_{\rm s}\,\omega_{\rm g}\,\omega_{\rm s}+4\,\zeta_{\rm s}^2\,\omega_{\rm s}^2));\end{aligned} \tag{28e}$$

$$\begin{aligned}\mathcal{C}_6^f =& 4\,\zeta_{\rm f}^2\,\omega_{\rm f}\,\omega_{\rm g}(\zeta_{\rm g}\omega_{\rm eq}^2+\zeta_{\rm s}\,\omega_{\rm g}\,\omega_{\rm s})(\zeta_{\rm g}\,\omega_{\rm eq}^2\,\omega_{\rm g}^2(\omega_{\rm f}^2\,+\omega_{\rm g}^2)+16\,\zeta_{\rm g}^4\,\zeta_{\rm s}\,\omega_{\rm eq}^2\,\omega_{\rm f}^2\,\omega_{\rm g}\,\omega_{\rm s}\\ &+\zeta_{\rm s}(\omega_{\rm eq}^2+\omega_{\rm f}^2)\omega_{\rm g}^3\,\omega_{\rm s}+4\,\zeta_{\rm g}^2\,\zeta_{\rm s}(\omega_{\rm eq}^2+\omega_{\rm f}^2)\omega_{\rm g}^3\,\omega_{\rm s}\\ &+4\,\zeta_{\rm g}^3(\omega_{\rm eq}^4(\omega_{\rm f}^2+\omega_{\rm g}^2)+4\,\zeta_{\rm s}^2\omega_{\rm f}^2\,\omega_{\rm g}^2\,\omega_{\rm s}^2));\end{aligned} \tag{28f}$$

$$\begin{aligned}\mathcal{C}_7^f =& \zeta_{\rm f}(\zeta_{\rm g}\,\omega_{\rm eq}^4(4\,\zeta_{\rm g}^2\,\omega_{\rm eq}^2+\,\omega_{\rm g}^2)(\omega_{\rm f}^4+2(-1+2\,\zeta_{\rm g}^2)\omega_{\rm f}^2\omega_{\rm g}^2+\omega_{\rm g}^4)+\,\zeta_{\rm s}\,\omega_{\rm g}(32\,\zeta_{\rm g}^4\,\omega_{\rm eq}^4\,\omega_{\rm f}^4\\ &+4\,\zeta_{\rm g}^2(1+4\zeta_{\rm g}^2)\omega_{\rm eq}^2\,\omega_{\rm f}^2(\omega_{\rm eq}^2+\,\omega_{\rm f}^2)\omega_{\rm g}^2+((1+4\,\zeta_{\rm g}^2)\omega_{\rm eq}^4-2\,\omega_{\rm eq}^2\,\omega_{\rm f}^2\\ &+(1+4\,\zeta_{\rm g}^2)\omega_{\rm f}^4)\omega_{\rm g}^4)\omega_{\rm s}+4\,\zeta_{\rm g}\,\zeta_{\rm s}^2\,\omega_{\rm f}^2\,\omega_{\rm g}^2(4\,\zeta_{\rm g}^2(1+4\,\zeta_{\rm g}^2)\omega_{\rm eq}^2\,\omega_{\rm f}^2+((2+4\,\zeta_{\rm g}^2)\omega_{\rm eq}^2\\ &+(1+8\,\zeta_{\rm g}^2)\omega_{\rm f}^2)\omega_{\rm g}^2+\omega_{\rm g}^4)\,\omega_{\rm s}^2+4\,\zeta_{\rm s}^3\,\omega_{\rm f}^2\,\omega_{\rm g}^3(16\,\zeta_{\rm g}^4\,\omega_{\rm f}^2+\,\omega_{\rm g}^2+4\,\zeta_{\rm g}^2\,\omega_{\rm g}^2)\omega_{\rm s}^3);\end{aligned} \tag{28g}$$

$$\begin{aligned}\mathcal{C}_8^f =& \zeta_{\rm g}\,\zeta_{\rm s}\,\omega_{\rm f}^3(4\,\zeta_{\rm g}^2\,\omega_{\rm f}^2+\,\omega_{\rm g}^2)\omega_{\rm s}(\omega_{\rm eq}^4+2\,\omega_{\rm eq}^2\,\omega_{\rm g}(-\omega_{\rm g}+2\,\zeta_{\rm g}^2\,\omega_{\rm g}+2\,\zeta_{\rm g}\,\zeta_{\rm s}\,\omega_{\rm s})\\ &+\omega_{\rm g}^2(\omega_{\rm g}^2+4\,\zeta_{\rm g}\,\zeta_{\rm s}\,\omega_{\rm g}\,\omega_{\rm s}+4\,\zeta_{\rm s}^2\,\omega_{\rm s}^2));\end{aligned} \tag{28h}$$

$$\begin{aligned}\mathcal{C}_9^f =& 4\,\zeta_{\rm f}^3\,\omega_{\rm eq}^2\,\omega_{\rm f}^2\,\omega_{\rm g}^2(\zeta_{\rm g}\,\omega_{\rm eq}^2\,\omega_{\rm g}^2+16\,\zeta_{\rm g}^4\,\zeta_{\rm s}\,\omega_{\rm eq}^2\,\omega_{\rm g}\,\omega_{\rm s}+\zeta_{\rm s}\,\omega_{\rm g}^3\,\omega_{\rm s}+4\,\zeta_{\rm g}^2\,\zeta_{\rm s}\,\omega_{\rm g}^3\,\omega_{\rm s}\\ &+4\,\zeta_{\rm g}^3(\omega_{\rm eq}^4+4\,\zeta_{\rm s}^2\,\omega_{\rm g}^2\,\omega_{\rm s}^2)).\end{aligned} \tag{28i}$$

References

[1] J. Roberts and P. Spanos. *Random vibration and statistical linearisation*. Dover, 2003.

[2] S. Kasinos. *Seismic response analysis of linear and nonlinear secondary structures*. PhD thesis, 2018.

[3] R. W. Clough and J. Penzien. *Dynamics of structures*. McGraw-Hill, 1975.

[4] S. Kasinos, M. Lombardo, N. Makris and A. Palmeri. Dynamic response analysis of nonlinear secondary oscillators to idealised seismic pulses. *Earthquake Engineering and Structural Dynamics*, 2020.

[5] T. Caughey and M. O'Kelly. Classical normal modes in damped linear dynamic systems. *Journal of Applied Mechanics*, **32**, 583–588, 1965.

[6] F. Ma, M. Morzfeld and A. Imam. The decoupling of damped linear systems in free or forced vibration. *Journal of Sound and Vibration*, **329**, 3182–3202, 2010.

[7] M. Morzfeld, F. Ma and B. Parlett. The transformation of second-order linear systems into independent equations. *SIAM Journal on Applied Mathematics*, **71**, 1026–1043, 2011.

[8] D. Kawano, R. Salsa , F. Ma and M. Morzfeld. A canonical form of the equation of motion of linear dynamical systems. *Proceedings of the Royal Society A*, **474**, 2018.

[9] K. Kanai. Semi-empirical formula for the seismic characteristics of the ground. *Bulletin of Earthquake Research Institute*. University of Tokyo, 1957.

[10] H. Tajimi. A statistical method for determining the maximum response of a building structure during an earthquake. *Proceedings of the second World conference on earthquake engineering*, 1960.

[11] S. Kasinos and F. Ma. Stochastic response quantification of fixed-base and base-isolated rigid-plastic blocks. *3rd International Conference on Uncertainty Quantification in Computational Sciences and Engineering*, 2019.

[12] R. Iyengar. Higher order linearization in non-linear random vibration. *International Journal of Non-Linear Mechanics*, **23**, 385–391, 1988.

[13] P. Spanos. An approach to calculating random vibration integrals. *Journal of Applied Mechanics*, **54**, 409–413, 1987.

EURODYN 2020
XI International Conference on Structural Dynamics
M. Papadrakakis, M. Fragiadakis, C. Papadimitriou (eds.)
Athens, Greece, 23–26 November 2020

EFFECTS OF MECHANICAL UNCERTAINTIES ON DYNAMIC PROPERTIES OF CROSS-LAMINATED TIMBER FLOORS

Marija Milojević [1], Marija Nefovska-Danilović [1], Stana Živanović [2] and Miroslav Marjanović [1]

[1] University of Belgrade, Faculty of Civil Engineering
Bulevar kralja Aleksandra 73
{mmilojevic, marija, mmarjanovic}@grf.bg.ac.rs

[2] University of Exeter, College of Engineering, Mathematics and Physical Sciences
North Park Road, Exeter, EX4 4QF
e-mail: S.Zivanovic@exeter.ac.uk

Keywords: CLT floors, Dynamic properties, Uncertainty quantification, Monte Carlo simulation, Finite element modeling

Abstract. *This paper investigates the effects of material properties (mass density, elastic and shear moduli) on dynamic properties of simply-supported CLT floors (natural frequencies, mode shapes and modal mass). Uncertainty quantification analysis has been carried out based on Monte Carlo simulations by varying material properties. Numerical modelling and analysis of the investigated CLT floors has been performed using finite element models in Abaqus CAE. The results show that uncertain mechanical parameters having significant influence on the dynamic properties are mass density, elastic modulus E_L, and shear moduli G_{LT} and G_{RT}, where L, T and R denote longitudinal, tangential and radial direction, respectively.*

1 INTRODUCTION

Recent technological advances and new construction techniques have led to the development of a natural composite material called cross-laminated timber (CLT). CLT is a multilayer composite, composed of several thin wooden layers bonded together in a crosswise manner. It has outstanding structural strength, stiffness and aesthetic properties, a high level of prefabrication, fire resistance and fast construction speed. Therefore, CLT is not only environmentally highly sustainable but also cost- and performance-competitive in comparison with the conventional mineral-based building materials (concrete and masonry) providing low carbon footprint and comfortable living conditions. This has been validated on many large-span residential, public and commercial floors in multistorey buildings in Europe and North America in the past decade [1-2]. An important aspect when designing CLT floors is the comfort criteria for vibrations. Due to low floor mass and high stiffness-to-weight ratio, human activities may cause vibration serviceability issues, such as annoyance to human occupants in buildings and malfunction of vibration sensitive equipment. Consequently, accurate and reliable prediction of dynamic properties of CLT floors is of great importance. However, there exists a limited research regarding vibration performance of CLT floors [3-6].

Main sources of uncertainties in timber floors related to their vibration performance are: (i) variability of mechanical properties of the wood as orthotropic material, (ii) pedestrian dynamic load and, (iii) boundary conditions. Item (i) is associated with a great variety of wood species used as a base material in civil engineering, leading to the variety of bulk material properties of wood [7]. In addition, the used material species may differ layer-wise, increasing the uncertainty related to the vibration performance of composite floor structure.

Effect of the variability of material properties on the modal and vibroacoustic properties of a conventional wooden floor have been studied by Persson et al. [8] and Persson & Floden [9]. They employed probabilistic analysis based on Monte Carlo (MC) simulations. Qian et al. [10] developed a stochastic finite element prediction tool to quantify the variability of mechanical properties of a CLT floor slab. The results of the performed studies indicate that the variability of mechanical properties of wood material can have a large impact on the natural frequencies and acoustic performance of the investigated wooden floors.

Mechanical material properties of CLT are differently regulated in technical approvals [11, 12], which might lead to significant differences between the actual mechanical properties and those defined in the design guidelines and recommendations. Material properties depend on the strength class of CLT as well as the strength class of the base material. For example, the values of shear moduli (G_{LT} and G_{LR}, see Fig. 1b) range from 600-690 N/mm^2, while the characteristic rolling shear modulus G_{RT} ranges from 50 to 60 N/mm^2, [11]. Poisson's ratios depend on the moisture level and they are usually adopted on the basis of experimental measurements for hardwoods and softwoods. Consequently, this can lead to inaccurate and unreliable prediction of the dynamic properties of CLT floors.

This paper aims to investigate the effects of the variability of material properties in terms of mass density, elastic/shear moduli and Poisson's ratios on dynamic properties of CLT floors (natural frequencies, mode shapes and modal mass). Uncertainty quantification analysis has been carried out using Monte Carlo simulations, by sampling selected material properties of CLT after the preliminary sensitivity analysis. Numerical modelling and analysis of the investigated CLT floors have been performed using finite element (FE) models in Abaqus CAE [12] and automated by making use of Python scripting. After this introductory section, Section 2 elaborates the computation of dynamic properties of selected CLT panel. In Section 3, preliminary sensitivity analysis, along with the uncertainty quantification analysis, has been carried out. Based on the performed analyses, conclusions have been derived in Section 4.

2 DYNAMIC PROPERTIES OF CLT FLOOR

2.1 Numerical model

Layout and dimensions of an analyzed 5-layer CLT floor panel are presented in Fig. 1a. FE-based numerical model of the CLT floor has been created by using Abaqus CAE software package [13]. The finite element mesh consists of 625 S4R shell elements (quadrilateral 4-node shell element with reduced integration and assigned composite section). Each layer (k) of CLT panel exhibits elastic orthotropic material behavior defined as:

$$\begin{Bmatrix} \varepsilon_L \\ \varepsilon_T \\ \varepsilon_R \\ \gamma_{TR} \\ \gamma_{LR} \\ \gamma_{LT} \end{Bmatrix}^{(k)} = \begin{bmatrix} 1/E_L & -\nu_{TL}/E_T & -\nu_{RL}/E_R & 0 & 0 & 0 \\ -\nu_{LT}/E_L & 1/E_T & -\nu_{RT}/E_R & 0 & 0 & 0 \\ -\nu_{LR}/E_L & -\nu_{TR}/E_T & 1/E_R & 0 & 0 & 0 \\ 0 & 0 & 0 & 1/G_{TR} & 0 & 0 \\ 0 & 0 & 0 & 0 & 1/G_{LR} & 0 \\ 0 & 0 & 0 & 0 & 0 & 1/G_{LT} \end{bmatrix}^{(k)} \begin{Bmatrix} \sigma_L \\ \sigma_T \\ \sigma_R \\ \tau_{TR} \\ \tau_{LR} \\ \tau_{LT} \end{Bmatrix}^{(k)} \quad (1)$$

In Eq. (1), E_L, E_T and E_R are elastic moduli in longitudinal (L), transverse (T) and radial direction (R), respectively, ν_{ij} are the Poisson's ratios, and G_{ij} are the shear moduli of the orthotropic material (Fig. 1b). The above are the 9 independent material coefficients for an orthotropic material. Assuming the same material behavior in the R and T direction, i.e. $E_R = E_T$, $G_{LR} = G_{LT}$, resulted in the total number of 7 elastic constants of a single layer of CLT panel. Material properties of the CLT layers for C24 timber class used as the initial (mean) values in the analysis are given in Table 1.

ρ (kg/m^3)	E_L (MPa)	$E_R = E_T$ (MPa)	$G_{LR} = G_{LT}$ (MPa)	G_{RT} (MPa)	ν_{LT}	ν_{LR}	ν_{RT}
450	11000	370	690	69	0.49	0.39	0.64

Table 1. Material properties for C24 timber class of CLT panels

Since the CLT panel is made of several orthotropic layers, which material axes are oriented by angles 0° and 90° with respect to the global (laminate) coordinates, the constitutive relations (1) must be transformed from the local (material) coordinate system to the global coordinate system using the well-known transformation matrix.

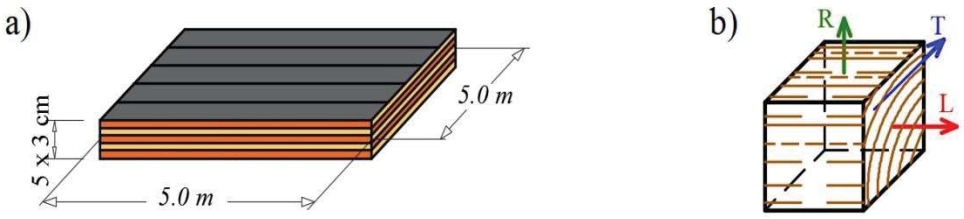

Figure 1. Layout of a 5-layer CLT floor

Simply supported boundary conditions have been assigned to the floor edges by constraining the displacements in X and Z direction (for the edges parallel to x-axis), and displacements in Y and Z direction (for the edges parallel to y-axis).

2.2 FE modal analysis

Dynamic properties of the first five bending and the first shear vibration modes have been calculated based on the material properties data given in Table 1. Natural frequencies and modal

masses that correspond to unity scaled mode shapes are presented in Table 2. The six vibration modes are shown in Fig. 2.

Mode No.	Mode type	Natural frequency f (Hz)	Modal mass m (kg)
1	1st bending	14.78	426.17
2	2nd bending	30.01	423.85
3	3rd bending	45.47	425.25
4	4th bending	54.66	419.62
5	5th bending	56.87	420.69
12	1st shear	123.99	844.46

Table 2. Dynamic properties of the CLT floor

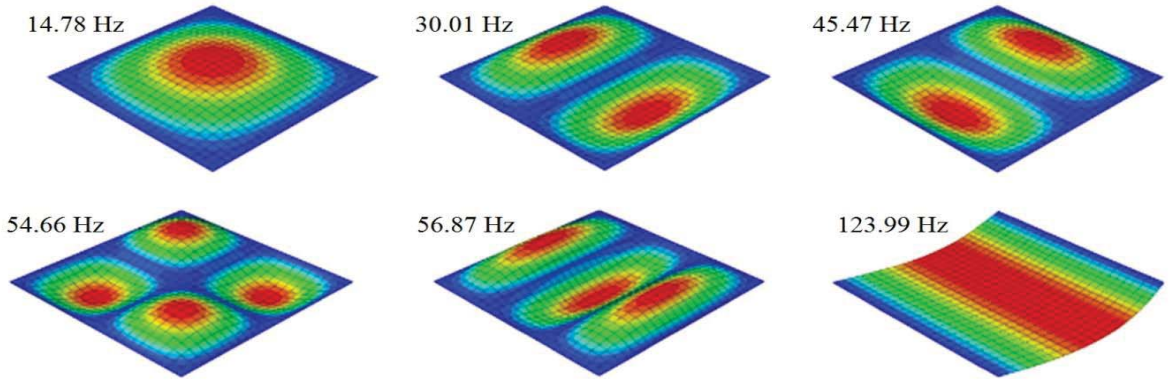

Figure 2. Mode shapes of the CLT floor

3 INFLUENCE OF MECHANICAL PROPERTIES

3.1 Preliminary sensitivity analysis

A preliminary sensitivity analysis has been carried out to ascertain the influence of the material parameters on the dynamic properties of CLT floor. For this purpose, elastic and shear moduli and mass density of the CLT panel have been increased and decreased by 20%, in comparison to the mean values given in Table 1. The results are presented in Figs. 3-6 in terms of relative change Δ with respect to the reference (mean) values. Natural frequencies and modal masses for all modes are found to be equally affected by the variability of the mass density ρ. Natural frequencies are most affected by the change of the longitudinal elastic modulus E_L, while the effect of elastic moduli E_R and E_T is found to be negligible. Shear modulus G_{LT} has the strongest impact on the dynamic properties of the first shear mode shape, while the first five bending modes are found to be less affected. Influence of the shear modulus G_{LR} and Poisson's ratios is negligible. Elastic and shear moduli, as well as the Poisson's ratios have insignificant influence on the modal masses of the first five bending modes. However, decrease of the shear modulus G_{LT} resulted in the change of the first shear mode shape and consequently the change of the corresponding modal mass for 75%, Fig. 7.

As a result of the sensitivity analysis, only four material parameters: mass density, elastic modulus E_L, and shear moduli G_{LT} and G_{RT} have been selected as uncertain parameters for further uncertainty quantification analysis.

As expected, 20% increase in CLT mass density resulted in the 20% increase in modal mass and around 9% decrease in frequency. The analogous trend was detected when mass density was reduced by 20% (see Fig. 3 for details).

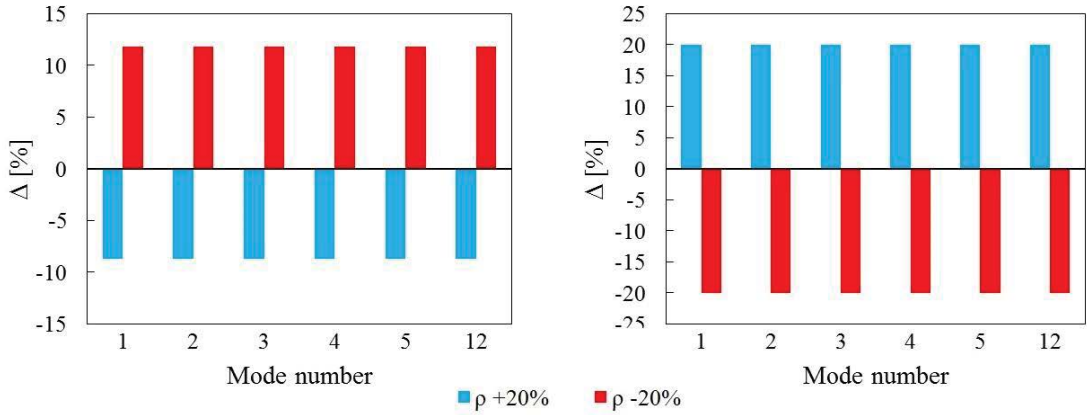

Figure 3. Influence of mass density on natural frequencies (left) and modal masses (right)

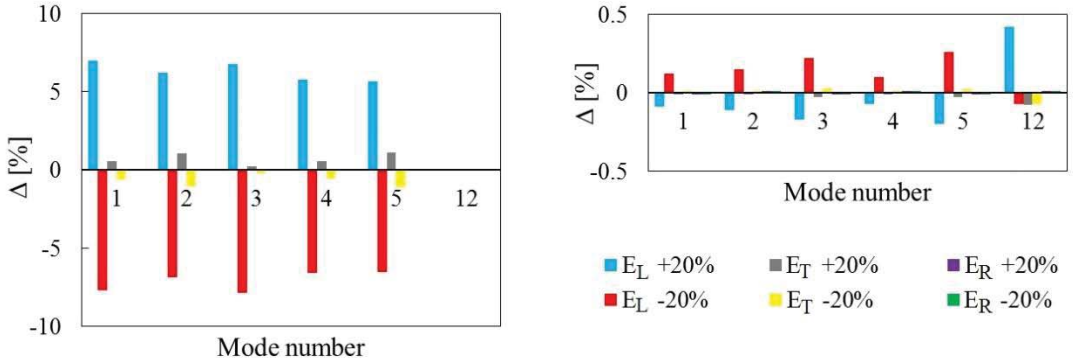

Figure 4. Influence of elastic moduli on natural frequencies (left) and modal masses (right)

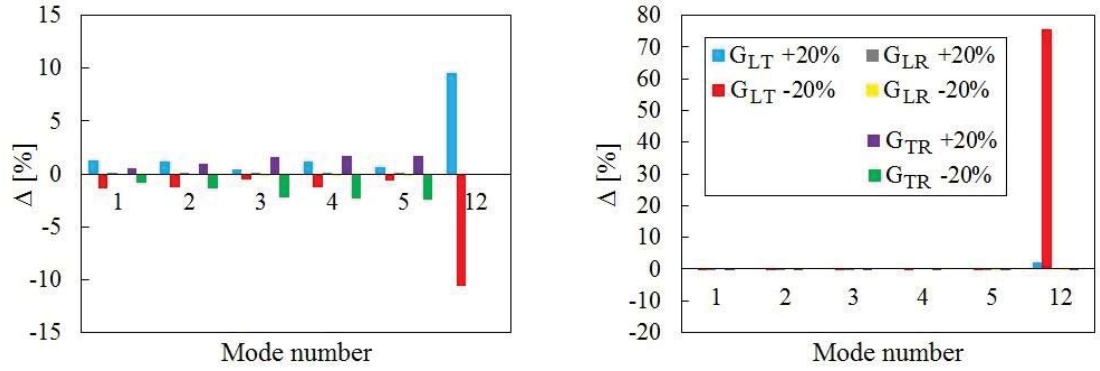

Figure 5. Influence of shear moduli on natural frequencies (left) and modal masses (right)

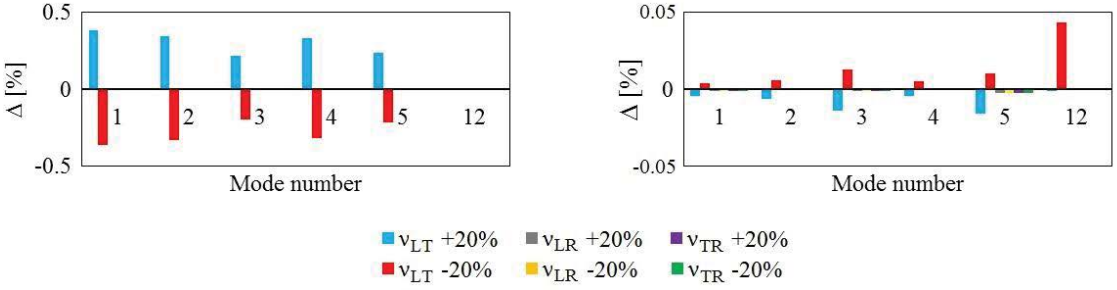

Figure 6. Influence of Poisson's ratios on natural frequencies (left) and modal masses (right)

3.2 Uncertainty quantification analysis

Properties of the four uncertain mechanical parameters of the CLT floor are given in Table 3. Mean values are those used in the initial FE analysis (Table 1). It is assumed that the parameters follow normal distribution, while the coefficient of variation (COV) is assumed to be 10%, based on the recommendations given in [9]. Latin hypercube sampling technique (ref?) has been applied first to generate samples for the four uncertain parameters used to perform 10,000 MC simulations.

Mechanical parameter	Distribution	Mean value	COV (%)
Elastic modulus E_L	Normal	11000	10
Shear modulus G_{LT}	Normal	690	10
Shear modulus G_{RT}	Normal	69	10
Mass density ρ	Normal	450	10

Table 3. Statistical properties of the four uncertain mechanical parameters

Generation of Abaqus input files with different set of mechanical parameters has been carried out using Python scripting. After completing modal analysis in the FE model, the natural frequencies, modal masses and unity scaled mode shapes have been automatically read from the output files created by Abaqus and statistically analyzed.

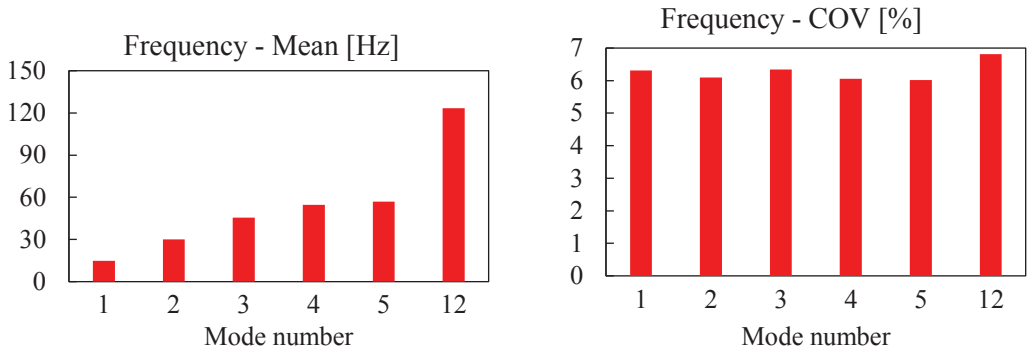

Figure 7. Statistical properties of natural frequencies

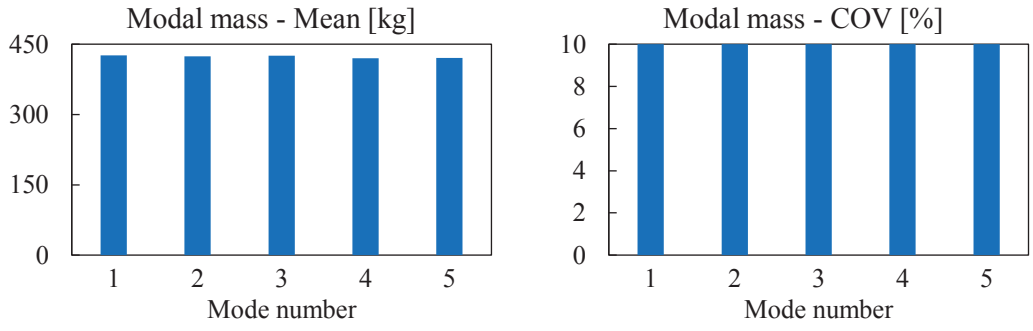

Figure 8. Statistical properties of modal masses

The results presented in Figs. 7-8 show that COV of 10% for the four input mechanical parameters resulted in the COVs of 6.31%, 6.10%, 6.34%, 6.06% and 6.02% for the natural frequencies of the first five bending modes, respectively, and 6.81% for the first shear mode. The results for natural frequencies follow lognormal distribution. Variations of input parameters resulted in the COV of 10% for modal masses of the first five bending modes, following

the normal distribution and maintaining the nature of the mode shapes. However, variation of input parameters qualitatively changed the first shear mode shape. Consequently, variation of the corresponding modal mass cannot be described either by normal or lognormal distribution, as shown in Fig. 9b.

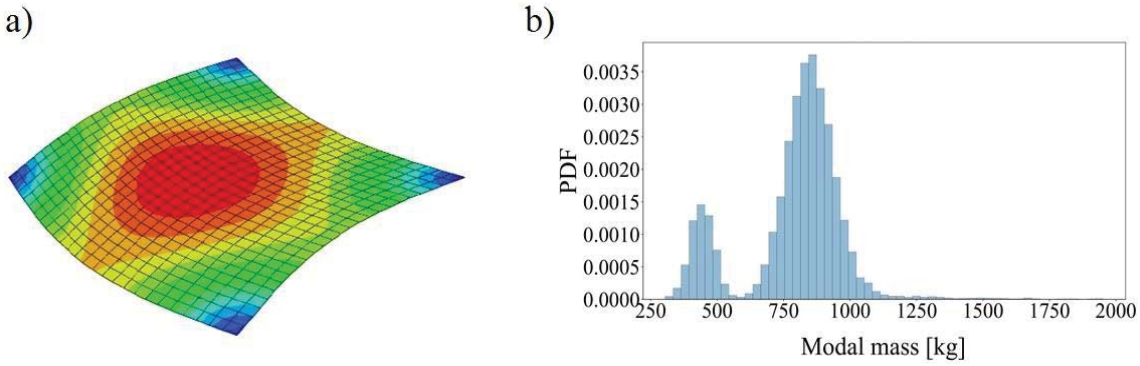

Figure 9. (a) First shear mode shape obtained when G_{LT} modulus is decreased by 20%; (b) variation of the modal mass of the first shear mode

4 CONCLUSIONS

MC-based uncertainty quantification analysis of simply supported CLT floor has been performed in the paper to ascertain the influence of mechanical properties on the dynamic properties (natural frequencies, modal masses and mode shapes) of CLT floor. The following conclusions have been derived:

- The preliminary sensitivity analysis demonstrated that uncertain mechanical parameters having significant influence on the dynamic properties are mass density, elastic modulus E_L, and shear moduli G_{LT} and G_{RT}. In addition, 20% decrease of shear modulus G_{LT} resulted in the decrease of natural frequency of the first shear mode by 10.56% and increase of the modal mass by 75.80% due to the change of corresponding mode shape.
- Uncertainty of mechanical parameters of CLT floor has a significant influence on the natural frequencies. COV of 10% resulted in the COVs of approximately 6% for the natural frequencies of the first five bending modes, and 10% for the corresponding modal masses. The results for natural frequencies follow lognormal distribution, while modal masses for the first five bending modes follow the normal distribution.
- COV of 10% in the input mechanical parameters resulted in the COV of 6.81% for the natural frequency of the first shear mode and the qualitative change of the shear mode shape. Consequently, corresponding modal mass could not be described by either Normal or lognormal distribution.

ACKNOWLEDGMENTS

The financial support of the Ministry of Education, Science and Technological Development of the Republic of Serbia and the Science Fund of the Republic of Serbia, is acknowledged.

REFERENCES

[1] I. Danzig, Tall Wood in Canada: Feasibility Study, Technical Guide, and Wood Innovation and Design Centre, *19. Internationales Holzbau - Forum*, 2013.

[2] A. Ringhofer, G. Schickhofer, Timber in Town - Current examples for residential buildings in CLT and tasks for the future, *Graz University of Technology*, Graz, Austria, 2013.

[3] A. Thiel, CLT and floor vibrations: A comparison of design methods, *International Council for Research and Innovation in Building and Construction Working Commission W18 - Timber Structures CIB-W18*, Karlsruhe, Germany, 2013.

[4] L. Hu, Y.H. Chui, CLT Handbook – Chapter 7: Vibration performance of CLT floors, US edition, ISBN: 978-0-86488-554-8, 2013.

[5] E. Ussher, K. Arjomandi, J. Weckendorf, I. Smith, Predicting effects of design variables on modal responses of CLT floors, *Structures*, 11, 40-48, 2017.

[6] E. Ussher, K. Arjomandi, J. Weckendorf, I. Smith, Prediction of motion responses of cross-laminated-timber slabs, *Structures*, 11, 49-61, 2017.

[7] S. J. Pang, G. Y. Jeong, Effects of combinations of lamina grade and thickness, and span-to-depth ratios on bending properties of cross-laminated timber (CLT) floor, *Construction and Building Materials*, 222, 142-151, 2019.

[8] P. Persson, C. Frier, L. Pedersen, L.V. Andersen, L. Manuel, Influence of uncertain parameters on modal properties of wood floors, *Proceedings of the 7th International Conference on Structural Engineering, Mechanics and Computation*, Cape Town, South Africa, 2019.

[9] P. Persson, O. Floden, Effect of material parameter variability on vibroacoustic response of wood floors, *Applied Acoustics*, 146, 38-79, 2019.

[10] C. Qian, S. Menard, D. Bard, J. Negreira, Development of a vibroacoustic stochastic finite element prediction tool for a CLT floor, *Applied Sciences*, 9(6), 1106, 2019.

[11] R. Brandner, D. Flatscher, A. Ringhofer, G. Schickhofer, A. Thiel, Cross Laminated Timber (CLT): overview and development, *European Journal of Wood and Wood Products*, 74(3), 331-351, 2016.

[12] M. Wallner-Novak, I. Koppelhuber, K. Pock, Cross-laminated timber structural design: Basic design and engineering principles according to Eurocode, *pro:Holz Austria*, ISBN: 978-3-902926-03-6, 2014.

[13] Abaqus, User manual. Version 6.9, Providence, RI, USA: DS SIMULIA Corp, 2009.

EURODYN 2020
XI International Conference on Structural Dynamics
M. Papadrakakis, M. Fragiadakis, C. Papadimitriou (eds.)
Athens, Greece, 23–26 November 2020

MODEL UNCERTAINTIES IN NLFEAs OF RC SYSTEMS UNDER CYCLIC LOADS

Paolo Castaldo[1], **Diego Gino**[1], **Guglielmo Amendola**[1] **and Elena Miceli**[1]

[1] Politecnico di Torino
Corso Duca degli Abruzzi 24, Turin, Italy
e-mail: {paolo.castaldo@polito.it, diego.gino@polito.it, guglielmo.amendola@polito.it, elena.miceli@studenti.polito.it}

Keywords: NLFEAs; model uncertainties; reinforced concrete structures; cyclic loads

Abstract. *This work is focused on the resistance model uncertainties in non-linear finite element analyses (NLFEAs) for reinforced concrete structures under cyclic loading conditions. In detail, different walls experimentally tested are numerically reproduced by means of appropriate plane stress finite elements (FE) structural models within different assumptions and numerical codes. After that, the values of the global resistances computed through numerical simulations are compared to the experimental outcomes to evaluate the influence of the different assumptions on the mechanical behaviour of reinforced concrete members subjected to cyclic loads.*

1 INTRODUCTION

The adoption of non-linear finite element analyses (NLFEAs) for structural design and assessment of structures and infrastructures is one of the main innovation in civil engineering in the last decades. Such kind of instruments are able to reproduce with accuracy the mechanical behaviour of reinforced concrete (RC) structures. In order to allow the correct use of NLFEAs from designers and analysts, several guidelines and recommendations for NLFEAs have been developed [1]-[2] to assess the safety and resilience of infrastructure systems [3]-[4]. Moreover, several applications are reported in the literature with examples of appropriate procedures devoted to calibrate and interpret the outcomes from NLFE models [5]-[6]. Over the years, different methodologies denoted as "safety formats" for NLFEAs have been proposed by several researchers [7]-[8] and international codes [9]-[10] as well as their applications have been discussed by [11]-[13]. In the mentioned above methods, the aleatory uncertainties associated to material properties and the epistemic uncertainties related to the numerical definition of the structural model need to be properly treated in order to derive reliability-based values of the global structural responses [14]-[18]. Concerning the materials uncertainty, the corresponding variability is well known and reported in the scientific literature, whereas the resistance model uncertainty associated with NLFEAs needs to be investigated due to the possible different modelling hypotheses that can be assumed by engineers and analysts to model some physical phenomena without a perfect knowledge. For this reason and especially within seismic field, an appropriate evaluation of the resistance model uncertainties for NLFEAs of RC structures is still necessary with the aim to account for their influence in presence of cyclic loads. In detail, different assumptions can be performed regarding the parameters that govern the equilibrium, kinematic compatibility and constitutive equations in cyclic loading configurations according to scientific literature and numerical codes. In the present study, the cyclic responses of ten experimental tests on shear walls known from the literature [19]-[21] are compared to the related numerical outcomes derived from appropriate 2D NLFEAs. In detail, a multitude of NLFEAs are developed for each experimental test in order to investigate the effect of each assumption on the global resistance of each structural element. This comparison is herein based on the definition of different eighteen plausible structural models combing different types of numerical code with different mechanical constitutive laws for the reinforced concrete elements in cyclic loading configurations.

2 UNCERTAINTIES WITHIN SAFETY FORMATS FOR NLFEAS

Commonly, both epistemic and aleatory uncertainties influence structural engineering problems [14]. Focusing on the epistemic uncertainties, all the choices performed to define a specific numerical model (i.e., modelling hypotheses) as well as all the assumptions concerning auxiliary non-physical parameters [14] belong to this group of uncertainties.

The global safety formats for NLFEAs proposed by codes [9],[22] and [23]-[24], allow to evaluate the design structural resistance R_d as follows:

$$R_d = \frac{R_{rep}}{\gamma_R \gamma_{Rd}} \tag{1}$$

where

- R_{rep} = representative value of the global structural resistance (i.e., the peak resistance value with reference to cyclic analyses) estimated using NLFEAs;

- γ_R = global resistance partial safety factor which covers the inherent randomness of the material properties;
- γ_{Rd} = resistance model uncertainty partial safety factor that covers all the epistemic uncertainties related to the different assumptions within the model definition.

With specific reference to NLFEAs on RC structural systems under cyclic loads (e.g., the case of earthquake engineering), they may present significantly higher levels of modelling uncertainties if compared to the static loading configurations. In compliance with [14],[25] the resistance model uncertainty random variable ϑ can be expressed as:

$$\vartheta = \frac{R_{Exp}}{R_{NLFEA}} \tag{2}$$

where:

- R_{Exp} = global structural resistance from experimental investigation;
- R_{NLFEA} = global structural resistance from NLFEAs.

3 NLFE MODELLING ASSUMPTIONS AND OUTCOMES FROM NUMERICAL SIMULATIONS

3.1 Characterization and differentiation of the numerical models

As discussed in the previous sections, several modelling hypotheses may be adopted when plane stress NLFEAs are carried out to analyse the seismic response of reinforced concrete structural systems under cyclic loading. Two numerical codes [26]-[27], denoted as numerical code A and B anonymously, are employed to model numerically the experimental tests of [19]-[21] using four-nodes iso-parametric quadrilateral plane stress finite elements having linear interpolant shape functions and 2x2 Gauss integration points. A calibration process of the mesh size has been developed for each experimental test and numerical. The non-linear system of equation is solved by means of the standard Newton-Raphson method [2]. For each load step, the maximum number of iterations has been set equal to 200 adopting the displacement norm convergence criteria with a tolerance set equal to 2%.

A non-linear curve with compression softening and reduction of the compressive strength due to transversal cracking has been used for the concrete behaviour in compression. In detail, the law of [28] is adopted in order to model the mono-axial concrete compressive behaviour both in confined and unconfined zones.

The shear behaviour of concrete has been reproduced associating a constant value to the shear retention factor with the purpose to model the mechanism of aggregate interlock in cyclic response of the shear walls [29]. The un-loading/re-loading process is characterized by a linear relation secant to the origin with reference to both compressive and tensile concrete response [26]-[27]. The uniaxial model for concrete behaviour is extended to plane stress configuration in line with [30]. The smeared cracking with fixed crack direction model has been adopted in order reproduce cracked state concrete [31]. The reinforcement has been modelled by means of a tri-linear constitutive law with cyclic damaging process modelled in compliance to the suggestion of [32]. The reinforcements have been modelled by means of discrete reinforcement with the assumption of perfect bond.

The tensile concrete strength as well as the Young's modulus are derived from the experimental compressive strength in compliance with [33].

An additional discrimination between the modelling hypotheses has been specified with reference to both the concrete tensile response and the shear stiffness of concrete in cracked configuration. As regards the concrete tensile response, the "tension stiffening effect" cannot be neglected. In this way, in addition to the elastic-brittle and to the elastic-plastic model, a third law "LTS (i.e., linear tension softening)" is herein assumed [14]. The first two hypotheses are conceived as lower and upper bounds for tensile response of concrete. The LTS law has been calibrated through an iterative procedure with the aim to best fit each experimental test with the use of a specific numerical code.

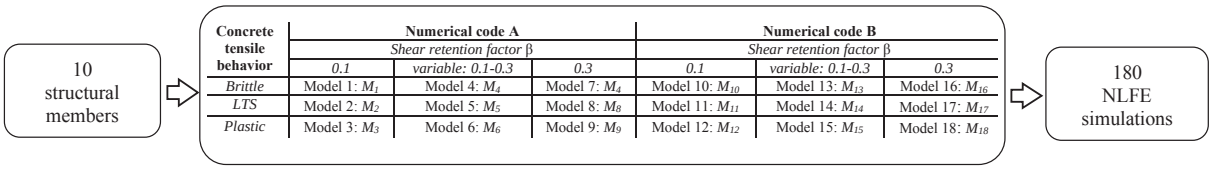

Figure 1: Summary of the 18 modelling hypotheses.

With reference to the shear stiffness, the shear retention factor β, that relates the shear stiffness of concrete after and before cracking, is assumed equal to 0.1 or to 0.3 [34]-[35] or properly calibrated for each numerical code and tensile behaviour and experimental test. In fact, in the third case, an iterative process is used to define the most appropriate value of β within the interval 0.1-0.3 [34]-[35]. Altogether, combining the the three different concrete tensile behaviours with the three different values of shear retention factor and the two numerical codes, 18 different modelling hypotheses (i.e., structural models M_j with $j=1,\ldots,18$ representative of the epistemic uncertainties) derive, as reported in Figure 1.

3.2 Experimental tests and numerical outcomes

The numerical and experimental results of [19]-[21], expressed in terms of lateral load vs displacement diagrams, are herein compared.

The experimental investigation of [19] focus on six reinforced concrete walls designed in pairs in order to have equal percentage of bending reinforcement but different percentage of shear reinforcement. In this study, only 3 walls are taken into consideration denoted respectively as SW4, SW6, SW8. In detail, they have the following geometrical characteristics: 1.20 m high, 0.6 m wide, 0.06 m thick and stiffened by a 0.2 m x 0.25 m inferior beam, and by a 0.2 m x 0.15 m superior beam useful to spread the applied horizontal load. All the walls are subjected to the same load history as showed in Figures 2-4. The tests have been performed in displacement control from 2 mm up to failure, performing two complete cycles with a 2 mm increment each time. The compressive strength of concrete is within the range 36.9 to 45.8 MPa in the different tests, whereas the flexural reinforcement remains constant in the web differently to the shear reinforcement and the vertical reinforcement that vary in the boundary elements. The numerical outcomes from the simulations expressed in terms of peak global structural resistance are presented in Table 1. The outcomes from NLFEAs are reported in Figures 2-4 (a)-(f) with reference to the several modeling hypotheses.

In general, the minimum values of the peak lateral loads are obtained adopting the elastic-brittle constitutive law for concrete tensile behavior, while the numerical models with plastic constitutive law always overestimate both the peak load and stiffness. It can also be observed that the best results are achieved with a shear retention factor equal or close to 0.1 for the tests SW6 and SW8. The simulations generally overestimate the global structural resistance, but underestimate the ductility because many simulations fail before if compared to the experimental results.

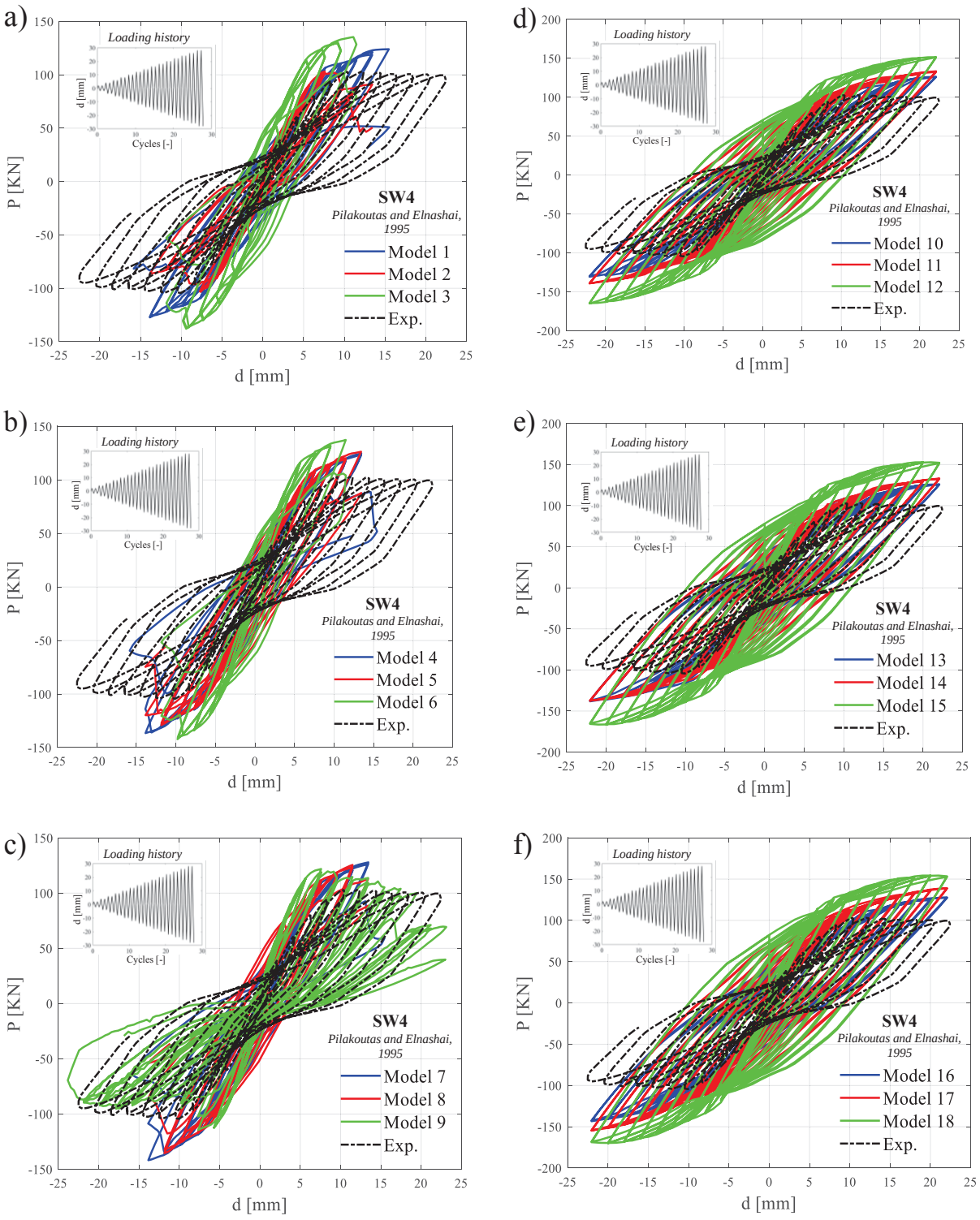

Figure 2: Comparison between NLFEAs and experimental tests expressed as load vs displacement curves - SW4 of [19]; (a-c) Numerical code A, (d-f) Numerical code B.

Figure 2-4 (a-c) and (d-f) show how the dependence of the results on the numerical code choice (numerical code A and B, respectively): in Figure 2-4 (a-c) the numerical models fail before the end of the experimental load history, while in Figure 2-4 (d-f) the simulations reach

the end of the analysis but overestimate the resistance, especially, for the Models 12, 15 and 18. The failure mode consists of the yielding of the main reinforcements and of the crushing of concrete in the boundary compressed element on the opposite side.

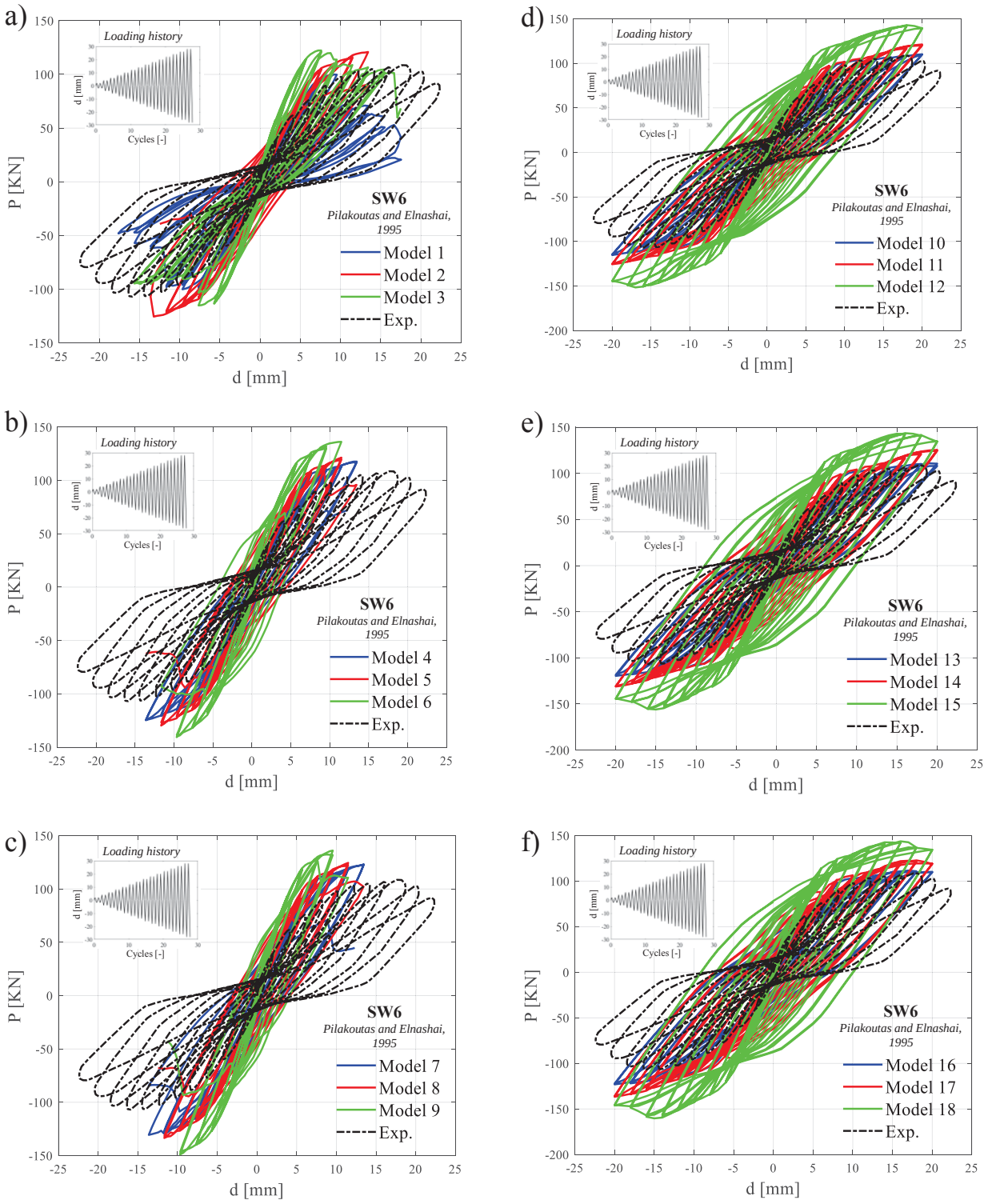

Figure 3: Comparison between NLFEAs and experimental tests expressed as load vs displacement curves – SW6 of [19]; (a-c) Numerical code A, (d-f) Numerical code B.

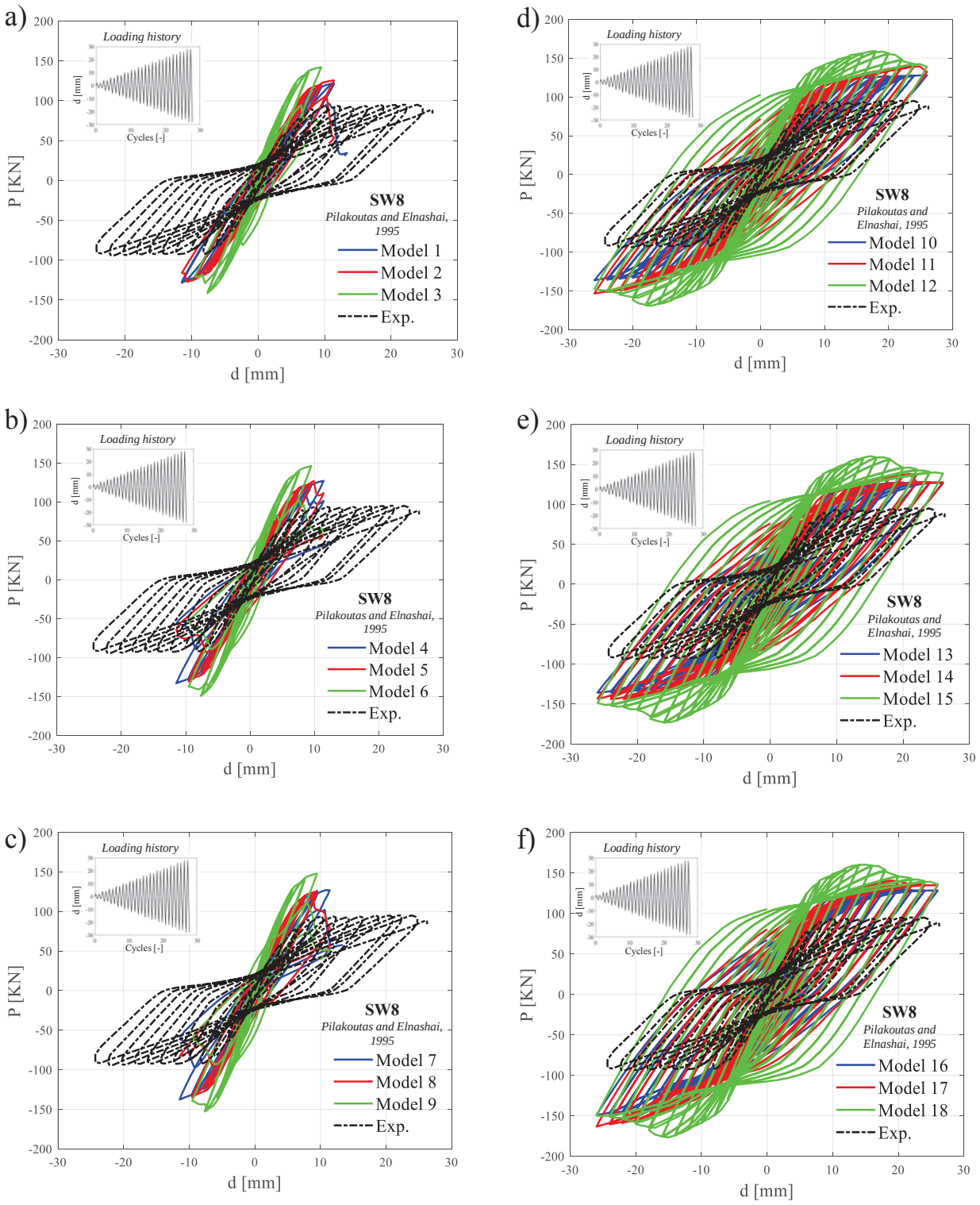

Figure 4: Comparison between NLFEAs and experimental tests expressed as load vs displacement curves – SW8 of [19]; (a-c) Numerical code A, (d-f) Numerical code B.

Exp. Test	R_{Exp} kN	R_{M1} kN	R_{M2} kN	R_{M3} kN	R_{M4} kN	R_{M5} kN	R_{M6} kN	R_{M7} kN	R_{M8} kN	R_{M9} kN
SW4	103.0	124.0	103.4	135.4	124.9	126.4	137.4	127.8	125.5	121.8
SW6	108.6	100.1	120.8	122.2	117.6	121.3	134.3	123.0	124.5	136.0
SW8	95.1	128.5	127.3	142.2	133.0	130.9	149.1	137.7	135.2	152.8
Exp. Test	R_{Exp} kN	R_{M10} kN	R_{M11} kN	R_{M12} kN	R_{M13} kN	R_{M14} kN	R_{M15} kN	R_{M16} kN	R_{M17} kN	R_{M18} kN
SW4	103.0	126.3	133.5	151.6	125.8	133.1	152.8	127.8	139.1	154.3
SW6	108.6	110.3	121.3	142.9	110.8	125.4	142.7	111.6	122.7	143.7
SW8	95.1	128.0	139.4	159.2	127.8	137.7	160.4	131.9	140.8	160.5

Table 1: Peak resistances from both the experimental tests R_{EXP} [19] and NLFEAs R_{NLFEA} for the different modelling hypotheses.

The experimental tests of [20] concern four identical walls of dimensions 1300x650x65mm, that are constrained inferiorly by a beam of section 200x300mm which simulates a stiff foundation. At the top there is a stiff beam to uniformly transmit the imposed displacement on the top of the wall. The flexural reinforcement is represented by ϕ8/100mm in the web, while the distance is reduced to 70mm in the boundary elements. The shear reinforcement is composed of ϕ6.25/260mm over the entire width of the wall and of additional stirrups of ϕ4/130mm in the boundary elements. The shear walls denoted as SW31, SW32 and SW33 are herein considered for the modelling uncertainty investigation. The experimental tests present a load history composed of four or five cycles with displacements of a few millimeters and then of a monotonic displacement increase up to failure. The compressive strength of concrete varies in the range 35-53 MPa in the different tests. The numerically computed peak global structural resistances are listed in Table 2. Figures 5-7 (a)-(f) show that the models related to elastic-plastic model for the tensile response of concrete (i.e., Models 3, 6, 9, 12, 15, 18) overestimate both the resistance and stiffness, while models having the assumption of elastic-brittle or linear tension softening in tension have more or less the same behavior with a stiffness similar to the actual one in the cyclic phase. In general, an underestimation of the resistance is recognized. It can be also noted that the more the shear retention factor increases (up to the value 0.3), the more the dissipated energy increases too.

Exp. Test	R_{Exp} kN	R_{M1} kN	R_{M2} kN	R_{M3} kN	R_{M4} kN	R_{M5} kN	R_{M6} kN	R_{M7} kN	R_{M8} kN	R_{M9} kN
SW31	115.9	111.9	120.8	160.2	121.3	133.3	168.9	127.7	139.3	174.4
SW32	111.0	110.3	114.8	142.8	114.9	118.3	142.7	119.1	131.1	144.3
SW33	111.5	107.2	111.5	129.8	110.4	114.0	139.4	113.8	117.6	143.8
Exp. Test	R_{Exp} kN	R_{M10} kN	R_{M11} kN	R_{M12} kN	R_{M13} kN	R_{M14} kN	R_{M15} kN	R_{M16} kN	R_{M17} kN	R_{M18} kN
SW31	115.9	87.8	117.5	139.8	98.0	127.2	147.6	98.9	131.8	151.2
SW32	111.0	93.7	101.6	129.4	93.9	101.9	129.5	99.4	102.2	129.7
SW33	111.5	94.6	96.0	118.7	95.2	101.1	122.8	95.7	98.8	126.9

Table 2: Peak resistances from both the experimental tests R_{EXP} [20] and NLFEAs R_{NLFEA} for the different modelling hypotheses.

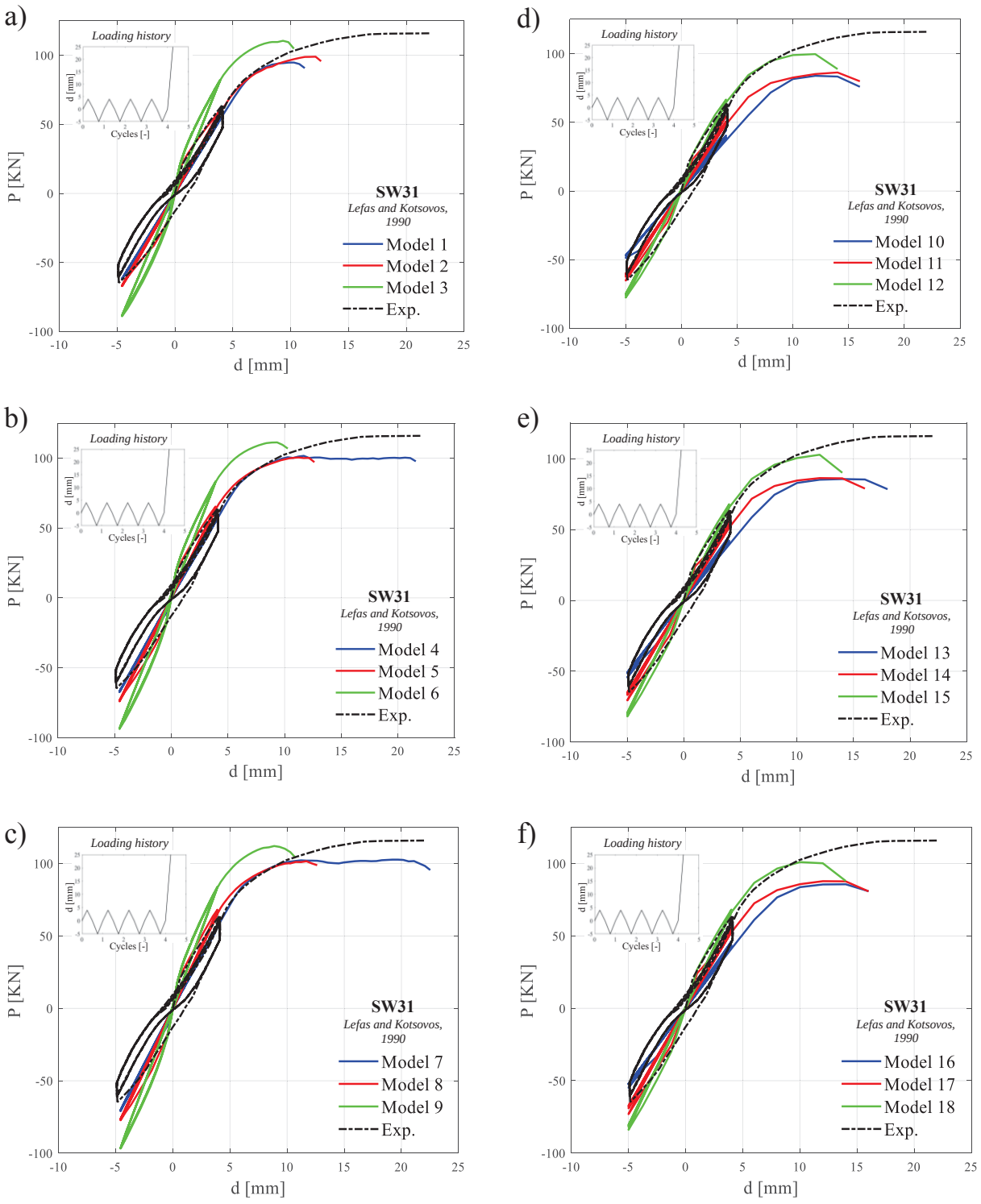

Figure 5: Comparison between NLFEAs and experimental tests expressed as load vs displacement curves – SW31 of [20]; (a-c) Numerical code A, (d-f) Numerical code B.

The failure mode is reached through the yielding of the tensile reinforcements and crushing of concrete located at the bottom of the boundary elements. Some simulations do not reach

the ultimate experimental displacement but fail upon reaching the maximum load or for a slightly greater displacement than the one achieved in the cyclic phase.

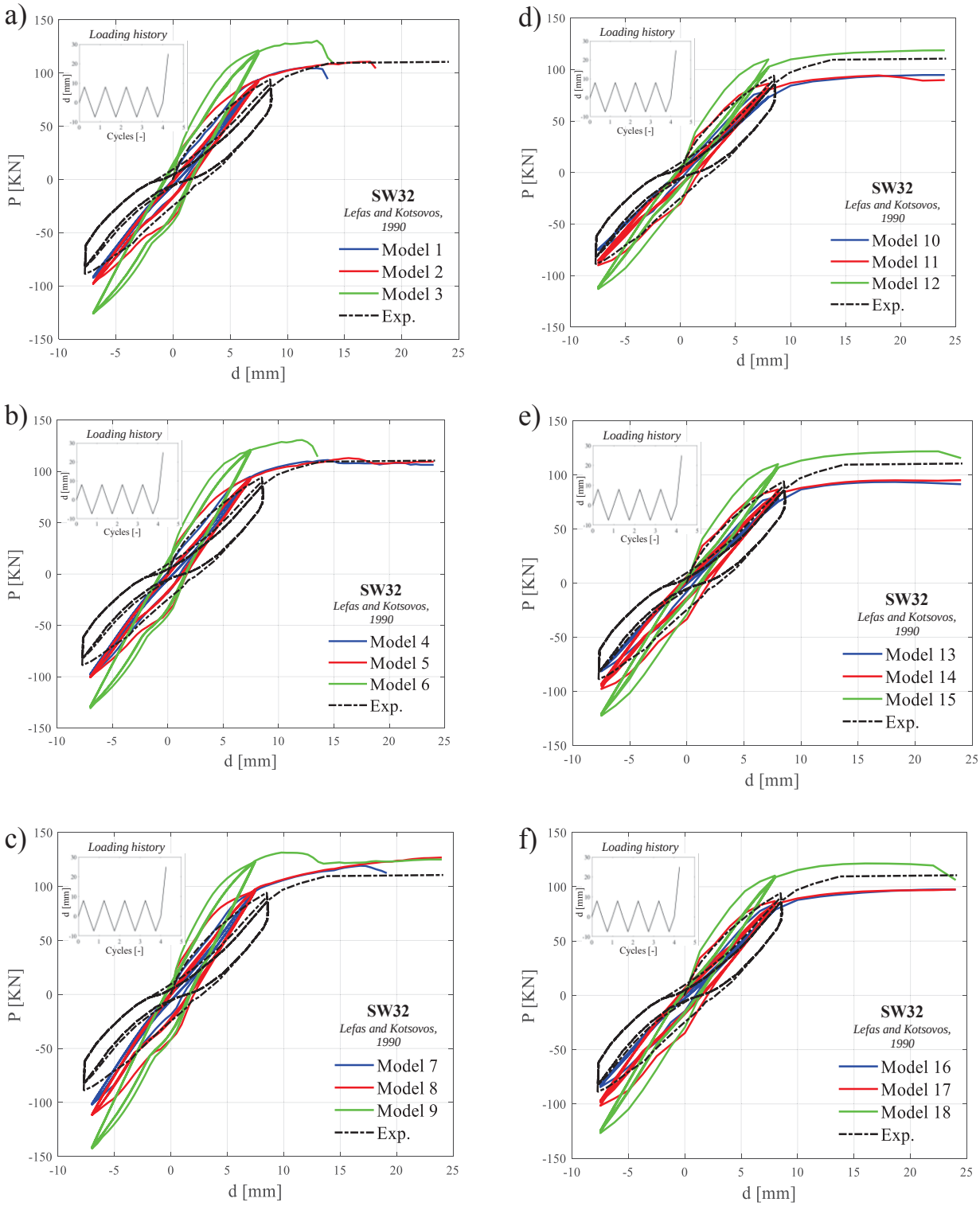

Figure 6: Comparison between NLFEAs and experimental tests expressed as load vs displacement curves – SW32 of [20]; (a-c) Numerical code A, (d-f) Numerical code B.

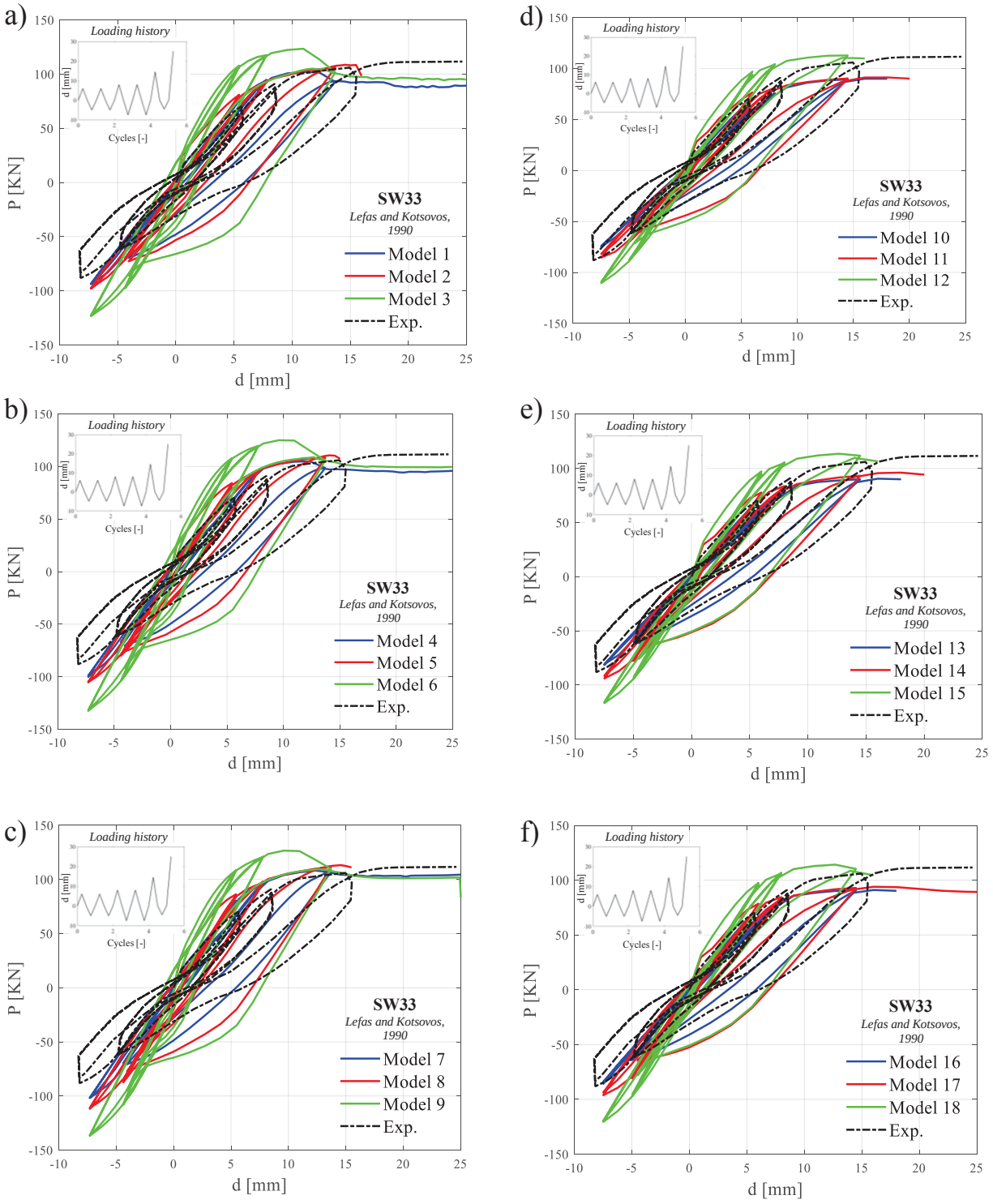

Figure 7: Comparison between NLFEAs and experimental tests expressed as load vs displacement curves – SW33 of [20]; (a-c) Numerical code A, (d-f) Numerical code B.

The laboratory tests of [21] investigate RC walls subjected to a in-plane quasi-static cyclic loading. In detail, four specimens (WSH2, WSH3, WHS4, WSH6) are considered and reproduced by means of numerical simulations. The walls have same geometry (i.e., 4.03 m high, 2 m wide and 0.15 m thick) and are fixed at the base through a beam integral with the support-

ing surface of section 0.6 m high and 0.7 wide and protruding 0.4 m from the two sides of the wall, while at the top there is a 0.4 m thick and 0.92 m high beam with a taper to favourite the connection with the wall. On this beam the axial load is provided and the cyclic loading history is applied by means of actuators located at a distance of 0.39 m from the upper edge. The walls are all reinforced with ϕ6/150 mm located horizontally along the entire width of the wall. They differs in the percentage of flexural reinforcement and in the percentage of shear reinforcement in the boundary element as well as for the value of the applied axial load. The WSH2 wall has flexural reinforcements of 6ϕ10, spaced at 75 mm in the boundary elements, and of 24ϕ6 in the web spaced at 125 mm (symmetrically starting from the outside to the center). The shear reinforcement consists of ϕ6/150 mm across the entire width, as mentioned above, and of stirrups ϕ6/75mm that enclose the ϕ10s and of a ϕ4.2 hoop that binds the two central ϕ10s. The specimen WSH3 is reinforced with 6ϕ12 on the boundary elements spaced at 100 mm, and with 22ϕ8 in the web spaced at 125 mm, and has a shear reinforcement identical to the WSH2. The wall WSH4 differs from the WSH3 concerning the shear reinforcement composed of ϕ6/150 mm across the entire width and of ϕ6/150 mm in the boundary element. The specimenWSH6 has the same bending reinforcement of the previous one with a higher reinforcement percentage in the boundary element. There are ϕ6/50 mm closed stirrups around the four lateral flexural bars, and another closed stirrup of 4.2/50 mm which encloses the four inners ϕ12. The compressive strength of concrete and axial load are similar for WSH2, WSH3 and WSH4 with values of 40.5, 39.2 and 40.9 MPa and 691, 686 and 695 kN, respectively. While WSH6 has a higher compressive strength equal to 45.6 MPa and an axial load of 1476 kN. The loading history is in line with the standard protocol by [36].

Exp. Test	R_{Exp}	R_{M1}	R_{M2}	R_{M3}	R_{M4}	R_{M5}	R_{M6}	R_{M7}	R_{M8}	R_{M9}
	kN	kN	kN	kN	kN	kN	kN	kN	kN	kN
WSH2	359.0	378.3	363.2	512.0	386.0	369.4	521.6	436.6	407.5	562.5
WSH3	454.0	441.4	443.6	604.8	454.0	448.9	659.5	549.1	474.3	674.2
WHS4	443.0	450.8	448.9	508.5	467.6	450.7	525.9	484.2	523.8	567.7
WSH6	597.0	633.9	624.4	732.7	665.2	658.3	744.8	689.0	678.2	794.9
Exp. Test	R_{Exp}	R_{M10}	R_{M11}	R_{M12}	R_{M13}	R_{M14}	R_{M15}	R_{M16}	R_{M17}	R_{M18}
	kN	kN	kN	kN	kN	kN	kN	kN	kN	kN
WSH2	359.0	376.9	410.1	493.8	367.7	413.7	489.9	389.6	410.3	488.6
WSH3	454.0	481.6	532.7	603.6	500.1	542.2	617.0	483.1	532.4	607.3
WHS4	443.0	404.8	441.5	474.4	423.3	442.1	481.0	435.5	457.8	483.5
WSH6	597.0	617.7	661.6	739.5	624.8	664.4	758.2	638.6	673.4	768.9

Table 3: Peak resistances from both the experimental tests R_{EXP} [21] and NLFEAs R_{NLFEA} for the different modelling hypotheses.

At each displacement level the wall has been subjected to two full cycles. The results of numerical simulations expressed as peak global structural resistance are presented in Table 3. Figures 8-11 (a)-(f) show that assuming the tensile behaviour of the concrete brittle or LTS reproduces efficiently the actual behaviour, while the models with concrete tensile behaviour perfectly plastic overestimate both the resistance and stiffness.

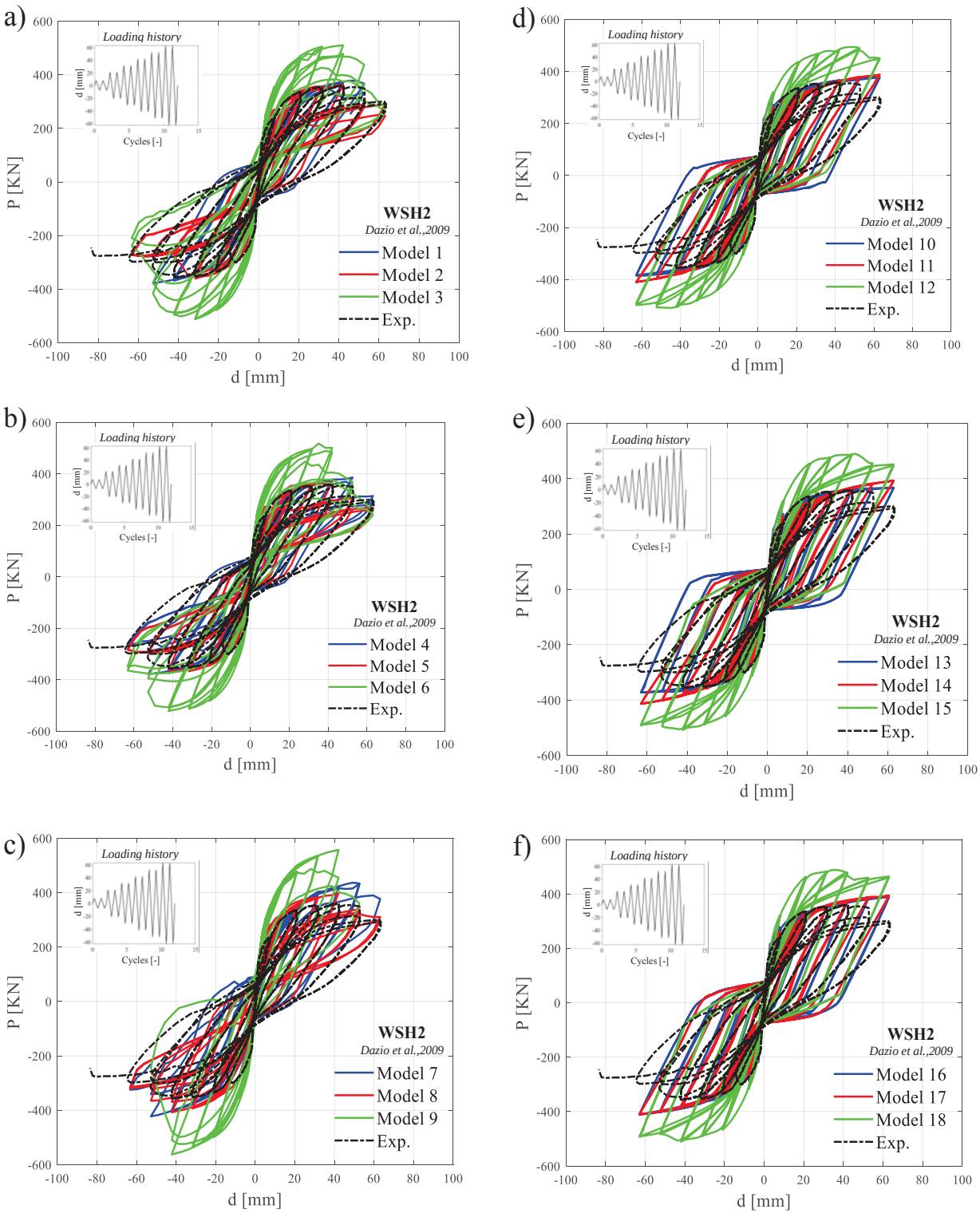

Figure 8: Comparison between NLFEAs and experimental tests expressed as load vs displacement curves – WSH2 of [21]; (a-c) Numerical code A, (d-f) Numerical code B.

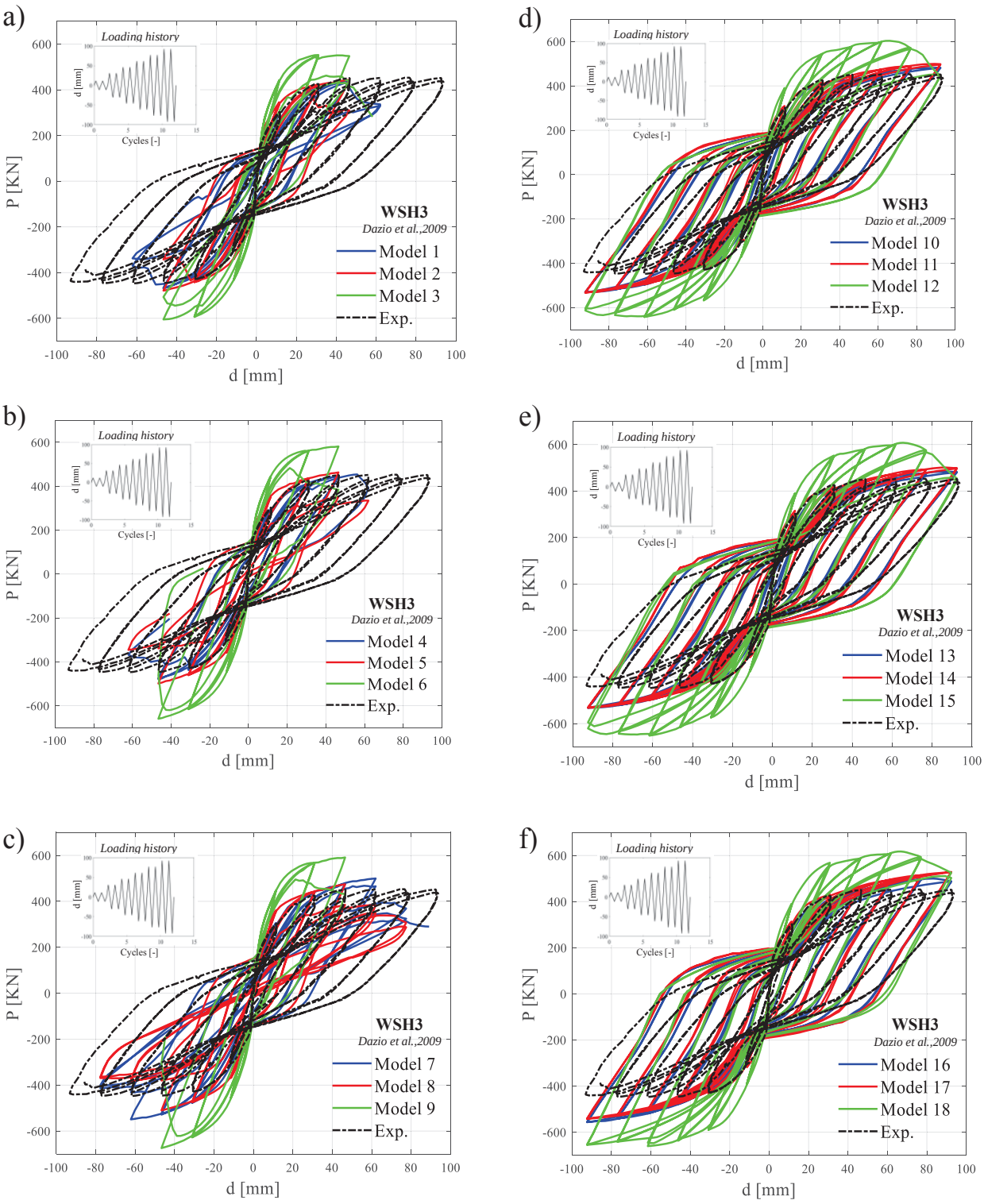

Figure 9: Comparison between NLFEAs and experimental tests expressed as load vs displacement curves – WSH3 of [21]; (a-c) Numerical code A, (d-f) Numerical code B.

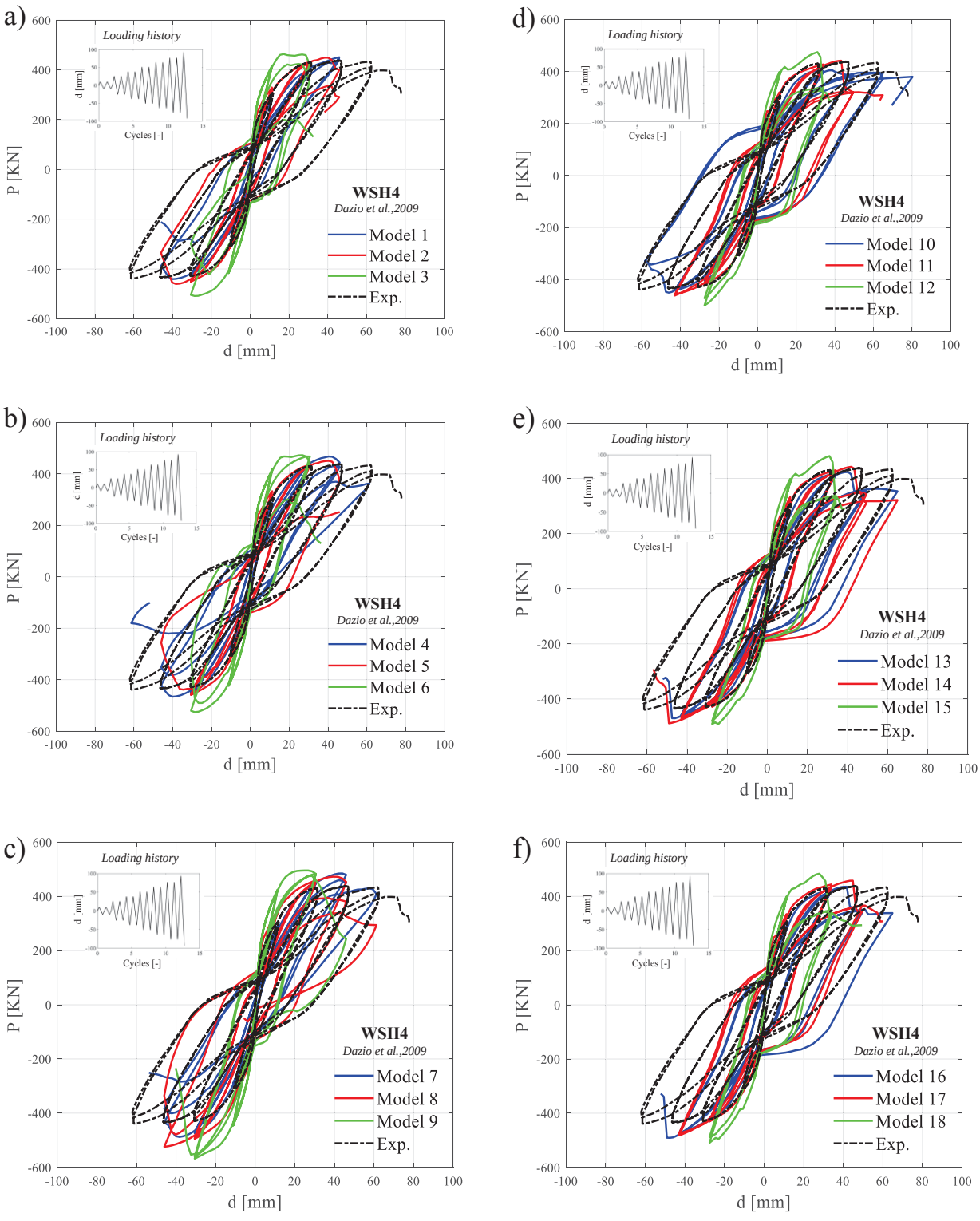

Figure 10: Comparison between NLFEAs and experimental tests expressed as load vs displacement curves – WSH4 of [21]; (a-c) Numerical code A, (d-f) Numerical code B.

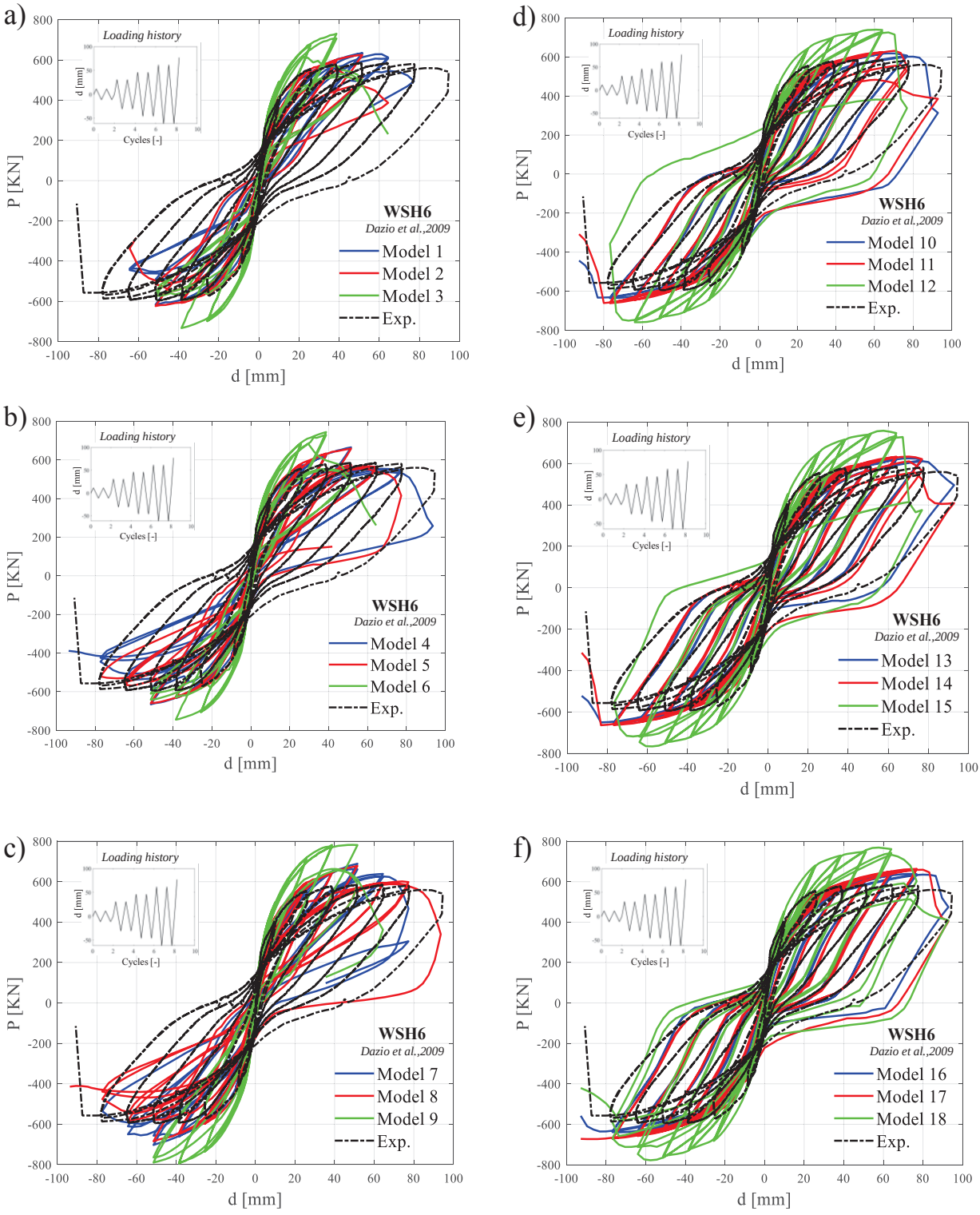

Figure 11: Comparison between NLFEAs and experimental tests expressed as load vs displacement curves – WSH6 of [21]; (a-c) Numerical code A, (d-f) Numerical code B.

4 DISCUSSION

The results deriving from the abovementioned 180 non-linear FE simulations can be used in order to quantify the resistance model uncertainties in plane stress NLFEAs of RC structures under cyclic loads. These results show the several difficulties in reproducing the actual failure behaviour of structural members. The outcomes in terms of ratio $\vartheta = R_{Exp}/R_{NLFEA}$ reported in Table 4 demonstrate that the two extreme hypotheses regarding concrete tensile behaviour (i.e., elastic-brittle and elastic-plastic) do not represent in all the cases the bound limits concerning the experimental peak of resistance.

Exp.	M_1	M_2	M_3	M_4	M_5	M_6	M_7	M_8	M_9
Test	-	-	-	-	-	-	-	-	-
SW4	0.83	1.00	0.76	0.82	0.81	0.75	0.81	0.82	0.85
SW6	1.08	0.90	0.89	0.92	0.90	0.81	0.88	0.87	0.80
SW8	0.74	0.75	0.67	0.72	0.73	0.64	0.69	0.70	0.62
SW31	1.04	0.96	0.72	0.96	0.87	0.69	0.91	0.83	0.66
SW32	1.01	0.97	0.78	0.97	0.94	0.78	0.93	0.85	0.77
SW33	1.04	1.00	0.86	1.01	0.98	0.80	0.98	0.95	0.78
WSH2	0.95	0.99	0.70	0.93	0.97	0.69	0.82	0.88	0.64
WSH3	1.03	1.02	0.75	1.00	1.01	0.69	0.83	0.96	0.67
WHS4	0.98	0.99	0.87	0.95	0.98	0.84	0.91	0.85	0.78
WSH6	0.94	0.96	0.81	0.90	0.91	0.80	0.87	0.88	0.75
Mean	0.96	0.95	0.78	0.92	0.91	0.75	0.86	0.86	0.73
CoV	10%	8%	9%	9%	9%	8%	9%	8%	10%

Exp.	M_{10}	M_{11}	M_{12}	M_{13}	M_{14}	M_{15}	M_{16}	M_{17}	M_{18}
Test	-	-	-	-	-	-	-	-	-
SW4	0.82	0.77	0.68	0.82	0.77	0.67	0.81	0.74	0.67
SW6	0.98	0.90	0.76	0.98	0.87	0.76	0.97	0.88	0.76
SW8	0.74	0.68	0.60	0.74	0.69	0.59	0.72	0.68	0.59
SW31	1.32	0.99	0.83	1.18	0.91	0.79	1.17	0.88	0.77
SW32	1.18	1.09	0.86	1.18	1.09	0.86	1.12	1.09	0.86
SW33	1.18	1.16	0.94	1.17	1.10	0.91	1.16	1.13	0.88
WSH2	0.95	0.88	0.73	0.98	0.87	0.73	0.92	0.87	0.73
WSH3	0.94	0.85	0.75	0.91	0.84	0.74	0.94	0.85	0.75
WHS4	1.09	1.00	0.93	1.05	1.00	0.92	1.02	0.97	0.92
WSH6	0.97	0.90	0.81	0.96	0.90	0.79	0.93	0.89	0.78
Mean	1.02	0.92	0.79	1.00	0.90	0.78	0.98	0.90	0.77
CoV	16%	15%	13%	14%	14%	13%	14%	15%	12%

Table 4: $\vartheta = R_{Exp}/R_{NLFEA}$ for all the modelling hypotheses and related mean values and coefficient of variations (CoV).

These results highlight the effectiveness of the different assumptions to reproduce the cyclic response of the structural members. In fact, the differences between the experimental and the numerically predicted resistances may be significantly high: unsafe values up to 0.64 are obtained for the shear walls SW8 and WSH2. It means that the finite element models are not always able to reproduce the experimental behaviour accurately but sometimes overestimate the peak resistances of the walls under specific hypotheses leading to unsafe estimations. This issue is a crucial aspect in relation to safety verifications for seismic analyses. With reference

to each numerical model M_j, Table 4 also reports the mean value and coefficient of variation (CoV). The lowest unsafe bias is achieved for model M_6 and M_9 as well as concerning models M_{10} to M_{18} the highest dispersion are recognised. In particular, a substantial difference can be noted between Numerical code A and B. In fact, the numerical code A seems to provide slightly unsafe bias factors with respect to the numerical code B (in average, 0.85 against 0.90, respectively). Concerning the coefficient of variation, the numerical code A presents a lower level of dispersion of the data with respect to the numerical code B (in average, 9% against 14%, respectively). These results can be useful to develop statistical and probabilistic analyses [37]-[42] to interpret and treat the model uncertainty variable θ. Moreover, it is also highlighted that the choice of the type of software to solve a specific structural problem is relevant. More details may be found in [43].

5 CONCLUSIONS

The present investigation is devoted to quantify the resistance model uncertainties when the global structural resistance of RC structural systems under cyclic loads is estimated through plane non-linear finite element method analyses. A set of experimental tests concerning different walls subject of cyclic shear actions have been numerically simulated by means of 180 NLFEAs combining two different numerical codes, three different constitutive laws for the tension behaviour of concrete and three different shear retention factors. It can be observed that when the tensile behaviour for concrete is assumed perfectly plastic, a greater overestimation of the structural resistance always derives as well as the shear retention factor varies the amplitude of the cycle, and therefore influences the dissipated energy. However, in terms of resistance, a shear retention factor assumed close to 0.1 is the one that allows to obtain the best results with respect to the experimental outcomes. The average bias factor between the different modelling hypotheses is quantified as 0.88 with an average coefficient of variation of 11%.

ACKNOWLEDGEMENTS

This work is part of the collaborative activity developed by the authors within the framework of the Commission 3 – Task Group 3.1: "Reliability and safety evaluation: full-probabilistic and semi-probabilistic methods for existing structures" of the International Federation for Structural Concrete (*fib*).

This work is also part of the collaborative activity developed by the authors within the framework of the WP 11 – Task 11.4 – ReLUIS.

REFERENCES

[1] B. Belletti, C. Damoni, MAN Hendriks, Development of guidelines for nonlinear finite element analyses of existing reinforced and prestressed beams. *European Journal of Environmental and Civil Engineering*, 15(9): 1361-1384, 2011.

[2] *fib* Bulletin N°45, Practitioner's guide to finite element modelling of reinforced concrete structures – State of the art report. Lausanne, 2008.

[3] Troisi R., Alfano G. 2019. Towns as Safety Organizational Fields: An Institutional Framework in Times of Emergency. *Sustainability*, 11: 7025, 2019, doi:10.3390/su11247025.

[4] Troisi R., Alfano G. 2020. Firms'crimes and land use in Italy. An exploratory data anlysis. New Metropolitan Perspectives, International Symposium – 4th edition, 27-30 May 2020, pp 10.

[5] D. La Mazza, L. Giordano, P. Castaldo, D. Gino, Assessment of the efficiency of seismic design for structural robustness of rc structures , *Ingegneria Sismica*, 34(3-4): 63-77, 2017.

[6] D. Gino, G. Bertagnoli, G. Mancini, Effect of endogenous deformations on composite bridges. Recent Progress in Steel and Composite Structures - *Proceedings of the 13th International Conference on Metal Structures, ICMS 2016*, 15-17 June 2016, Zielona Gora, Poland, pp. 287-298, 2016.

[7] DL. Allaix, VI. Carbone, G. Mancini G. Global safety format for non-linear analysis of reinforced concrete structures. *Structural Concrete,*14(1): 29-42, 2013.

[8] H. Shlune, K. Gylltoft, M. Plos, Safety format for non-linear analysis of concrete structures. *Magazine of Concrete Research,* 64(7): 563-574, 2012.

[9] CEN EN 1992-2 Eurocode 2 Design of concrete structures, Part 2: concrete bridges. *CEN 2005*. Brussels.

[10] *fib* Model Code for Concrete Structures 2010. Lausanne. 2013.

[11] P. Castaldo, D. Gino, G. Mancini, Safety formats for non-linear analysis of reinforced concrete structures: discussion, comparison and proposals. *Engineering Structures*, 193,136-153, 2019.

[12] M. Blomfors, M. Engen, M. Plos, Evaluation of safety formats for non-linear finite element analyses of statically indeterminate concrete structures subjected to different load paths. *Structural Concrete*, 17(1): 44-51, 2016.

[13] V. Cervenka, Reliability-based non-linear analysis according to fib Model Code 2010. *Structural Concrete*. 14(1): 19-28, 2013.

[14] P. Castaldo, D. Gino, G. Bertagnoli, G. Mancini, Partial safety factor for resistance model uncertainties in 2D non-linear finite element analysis of reinforced concrete structures. *Engineering Structures,* 176:746-762, 2018.

[15] P. Castaldo, D. Gino, VI. Carbone, G. Mancini, Framework for definition of design formulations from empirical and semi-empirical resistance models, *Structural Concrete*, 19(4): 980-987, 2018.

[16] D. Gino, P. Castaldo, G. Bertagnoli, L. Giordano, G. Mancini, Partial factor methods for existing structures according to *fib* Bulletin 80: Assessment of an existing prestressed concrete bridge. *Structural Concrete*, 31: 15-31, 2020. https://doi.org/10.1002/suco.201900231

[17] Castaldo P., Alfano G. Seismic reliability-based design of hardening and softening structures isolated by double concave sliding devices, *Soil Dynamics and Earthquake Engineering*, 129: 105930, 2020.

[18] AD. Kiureghian, O. Ditlevsen, Aleatory or epistemic? Does it matter?,M *Structural Safety,* 31: 105-112, 2009.

[19] K. Pilakoutas, A. Einashai, Cyclic Behaviour of Reinforced Concrete Cantilever Walls, Part I : Experimental Results, *ACI Structural Journal*, no.92-S25, 1995.

[20] ID. Lefas, MD. Kotsovos, Strength and deformation characteristics of reinforced concrete walls under load reversals. *ACI Structural Journal,* no.87-S74, 1990.

[21] A. Dazio, K. Beyer, H. Bachmann, Quasi-static cyclic tests and plastic hinge analysis of RC structural walls. *Engineering Structures* 31: 1556-1571, 2009.

[22] *fib* Model Code for Concrete Structures 2010. 2013. Lausanne.

[23] M. Blomfors, M. Engen, M. Plos, Evaluation of safety formats for non-linear finite element analyses of statically indeterminate concrete structures subjected to different load paths. *Structural Concrete*, 17(1): 44-51, 2016.

[24] V. Cervenka, Reliability-based non-linear analysis according to fib Model Code 2010. *Structural Concrete*. 14(1): 19-28, 2013.

[25] M. Holický, J.V. Retief, M. Sikora, Assessment of model uncertainties for structural resistance. *Probabilistic Engineering Mechanics.* 45: 188-197, 2016.

[26] ATENA 2D v5. 2014. *Cervenka Consulting s.r.o*. Prague. Czech Republic.

[27] DIANA FEA BV 2018. Delftechpark 19a 2628 XJ Delft. The Netherlands.

[28] M. Saatcioglu, S.R. Razvi, Strength and ductility of confined concrete. *Journal of Structural engineering,* 118(6):1590–1607, 1992.

[29] B. Belletti, M. Scolari, F. Vecchi, PARC_CL 2.0 crack model for NLFEA of reinforced concrete structures under cyclic loadings. *Computer and Structures,* 191: 165-179, 2017.

[30] H.B. Kupfer, H.K. Gerstle, Behavior of Concrete under Biaxial Stresses. *Journal Engineering Mechanics Division,* 99(4), 1973.

[31] H.R. Riggs, G.H. Powell, Rough crack model for analysis of concrete. *J. Eng. Mech. Div. ASCE*, 112(5): 448-464, 1986.

[32] M. Menegotto, E. Pinto, Method of analysis for cyclically loaded reinforced concrete plane frames including changes in geometry and non-elastic behavior of elements under combined normal force and bending, *Proceedings, IABSE Symposium*. Lisbon, Portugal, 1973.

[33] EN 1992-1-1. Eurocode 2 – Design of concrete structures. Part 1-1: general rules and rules for buildings. CEN 2014. Brussels.

[34] D.L. Araújo, L.C. Carmo, F.G.T. Nunes, R.D.T. Filho, Computational modelling of steel fibre reinforced Concrete beams subjected to shear. *IBRACON Structures and Materials Journal*, vol. 3, n1, 2010.

[35] E. Fehiling, T. Bullo, Ultimate load capacity of reinforcement steel fibre concrete deep beams subjected to shear. *Finite elements in Civil Engineering Applications*, Hendriks & Rots, 2002.

[36] R. Park, Ductility evaluation from laboratory and analytical testing. In: *Proceedings of the 9th world conference on earthquake engineering*. Vol. III, 1988.

[37] Garzillo C., Troisi R. Le decisioni dell'EMA nel campo delle medicine umane. In EMA e le relazioni con le Big Pharma - I profili organizzativi della filiera del farmaco, G. Giappichelli, 85-133, 2015.

[38] Golzio L. E., Troisi R. The value of interdisciplinary research: a model of interdisciplinarity between legal re-search and research in organizations. *Journal For Development And Leadership*, 2: 23-38, 2013.

[39] Nese A.; Troisi R. Corruption among mayors: evidence from Italian Court of Cassation judgments, *Trends In Organized Crime*, 1-26, 2018. DOI:10.1007/s12117-018-9349-4.

[40] Troisi R., Golzio, L. E. Legal studies and organization theory: a possible cooperation. *Manageable cooperation* - European Academy of Management: 16th EURAM Conference, Paris, 1-2, 1-4 June 2016.

[41] Troisi R., Guida V. Is the Appointee Procedure a Real Selection or a Mere Political Exchange? The Case of the Italian Health-Care Chief Executive Officers. *Journal of Entrepreneurial and Organizational Diversity*, 7 (2): 19-38, 2018, DOI:10.5947/jeod.2018.008.

[42] Troisi R. Le risorse umane nelle BCC: lavoro e motivazioni al lavoro. In Progetto aree bianche. Il sistema del credito cooperativo in Campania, 1: 399-417, 2012.

[43] Castaldo, P., Gino, D., Bertagnoli, G. & Mancini, G. Resistance model uncertainty in non-linear finite ele-ment analyses of cyclically loaded reinforced concrete systems, *Engineering Structures*, 211: 110496, 2020, https://doi.org/10.1016/j.engstruct.2020.110496.

EURODYN 2020
XI International Conference on Structural Dynamics
M. Papadrakakis, M. Fragiadakis, C. Papadimitriou (eds.)
Athens, Greece, 23–26 November 2020

UNCERTAINTIES IN WIND-INDUCED LOADS ON HYPERBOLIC PARABOLOID ROOFS: WIND-TUNNEL TESTS AND ANALYTICAL MODELS

Fabio Rizzo and Vincenzo Sepe

Department of Engineering and Geology, University "G. D'Annunzio"
Viale Pindaro 42, 65127 Pescara, Italy
{fabio.rizzo, vincenzo.sepe}@unich.it

Keywords: wind-tunnel tests, hyperbolic paraboloid roof, wind loads, pressure coefficients, experimental uncertainties.

Abstract. *The design coefficients provided by a wind-tunnel campaign on in-scale models, e.g. the pressure coefficients discussed in this paper, are always affected by physiological and unavoidable uncertainties. On the other hand, wind-induced loads at the real scale (e.g. peak pressure coefficients) may be provided, with a prescribed confidence level, by analytical models that include stochastic characteristics of the wind field (mean values, standard deviation, skewness, kurtosis) obtained by wind-tunnel tests. Based on aerodynamic tests on hyperbolic paraboloid models in the boundary layer wind-tunnel of the CRIACIV (Italy), this paper discusses a typical example of experimental uncertainties, i.e. the asymmetries measured for geometries and wind directions nominally symmetric, and investigates their effects on peak pressure coefficients provided by analytical models. To this aim, experimental peak pressure coefficients and their analytical prediction are compared for symmetrical geometries under wind flow direction parallel to the symmetry axis, and it is noted that asymmetries shown by experimental tests may be reduced by appropriate analytical models, that can therefore contribute to filter out the effects of experimental uncertainties for design purposes.*

1 INTRODUCTION

Although computational fluid dynamics (CFD) has become more and more accurate and reliable in the last years, and can therefore be an invaluable tool in the preliminary design stage, wind tunnel tests on in-scale models are still the more reliable way to get the wind-induced loads for structures with a complex shape.

Wind-tunnel tests, however, are always affected by several uncertainties, due to the measurements chain, to the scaling of the real building at the model size, to the geometrical details of the model and to its mechanical characteristics. The design coefficients provided by a wind-tunnel campaign, e.g. the pressure coefficients discussed in this paper, are therefore also affected by physiological and unavoidable uncertainties; this is the case, for example, of nominally symmetric and symmetrically loaded models for which wind-tunnel tests turn out instead asymmetric pressure fields.

As shown by the scientific literature, on the other hand, a sound prediction of wind-induced loads at the real scale may benefit of analytical models (e.g. [1][2][3]) able to provide, for example, average or peak pressure coefficients with a prescribed confidence level. To this aim, analytical models may use the stochastic characteristics of the wind field (mean values, standard deviation, skewness, kurtosis) obtained by wind-tunnel tests. This point has been addressed in a recent paper of the writers [4].

This paper is based on experimental results on hyperbolic paraboloid models tested in the boundary layer wind-tunnel of the CRIACIV (Italy) [4-9] and is part of a wider research that also deals with non-structural aspects of the design [10,11]. The paper discusses a typical example of experimental uncertainties, i.e. the asymmetries measured for geometries and wind directions nominally symmetric, and investigates their effects on peak pressure coefficients provided by two of the analytical models discussed in [4], i.e. the classical Davenport model and the modified Hermite model discussed in [1].

2 WIND-TUNNEL TESTS

Aerodynamic tests on a large set of hyperbolic paraboloid roofs were described in previous papers of the writers [5-9]. Wooden in-scale models with 16 different geometries and 16 different wind angles were tested in the boundary layer wind tunnel of CRIACIV (Interuniversity Research Center on Building Aerodynamics and Wind Engineering), in Italy.

In particular, this paper is focused on results obtained by wind tunnel test on roofs with square and rectangular plan and eight different geometries are discussed here.

The models represent closed buildings, e.g. as those of sports halls, and this paper discusses the aerodynamic pressure field recorded on the roof surfaces. Due to the stiffness of the models, that can be considered as rigid, roof displacements and therefore aeroelastic effects are not considered; this is an usual step in the preliminary design of this kind of structures.

2.1 The sample square and rectangular models

Figure 1 describes the geometries discussed in Sect. 2.2 and Sect. 3.

The eight geometries considered here are denoted by three letters that refer to the model plan shape (square, S, or rectangular, R), to the model height (higher, H, or lower, L), and to the roof curvature (with smaller curvature or flatter, F, or higher curvature, C), respectively.

As reported in fig. 2, the roof surface consists of 89 and 95 elementary regions for the square and rectangular plan, respectively. Pressure time-histories were recorded (details in [6]) for about 30 seconds with an acquisition frequency of about 250 Hz for several angles of inci-

dence of wind. To explore situations nominally symmetric, only the wind directions 0° and 90° are discussed be' ›w, as shown in fig. 1.

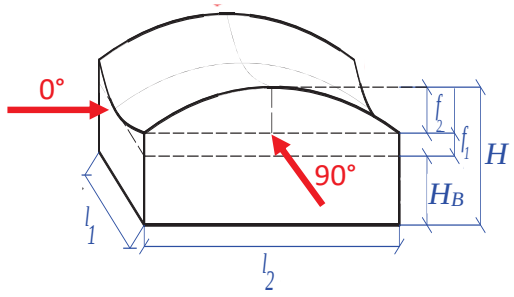

model	l_1 [cm]	l_2 [cm]	f_1 [cm]	f_2 [cm]	H [cm]	H_B [cm]
SLF	80	80	2.67	5.33	21.33	13.33
SHF	80	80	2.67	5.33	34.66	26.66
SLC	80	80	4.44	8.89	26.66	13.33
SHC	80	80	4.44	8.89	39.99	26.66
RLF	40	80	2.67	5.33	21.33	13.33
RHF	40	80	2.67	5.33	34.66	26.66
RLC	40	80	4.44	8.89	26.66	13.33
RHC	40	80	4.44	8.89	39.99	26.66

Figure 1: The eight sample models

2.2 Pressure coefficients

For the pressure tap of each elementary region of the roof, the measured pressure time-history *p(t)* is described by non-dimensional pressure coefficients $c_p(t)$, defined as

$$c_p(t) = \frac{p(t) - p_0}{\frac{1}{2}\rho V_m^2} \tag{1}$$

where ρ denotes the air density and V_m and p_0 the mean speed at the roof level and the static pressure of undisturbed flow, respectively. Positive and negative values of c_p represent pressure larger than p_0 and suction, respectively.

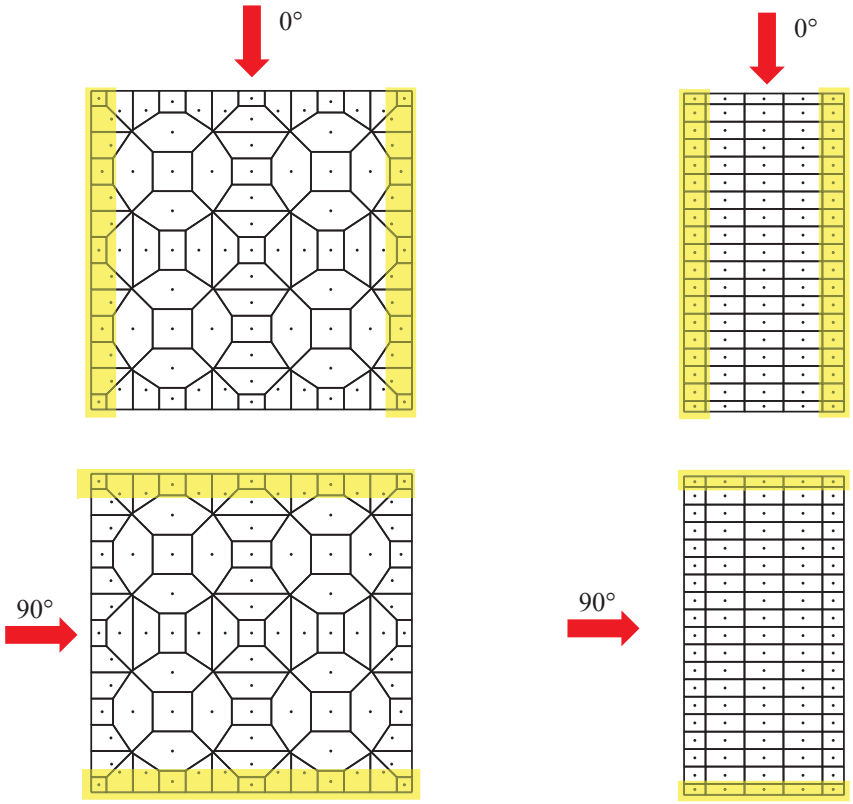

Figure 2: Map of the pressure taps for square and rectangular plans. The two alignments of pressure taps on the left and right edges of the roof with respect to the mean wind speed are highlighted in yellow

For each wind direction along a symmetry axis (angle 0° and 90°), Figure 2 reports the two alignments of pressure taps (highlighted in yellow) on the left and right edges of the roof with respect to wind direction, whose measured pressure coefficients will be compared to each other to discuss asymmetries shown by experimental tests.

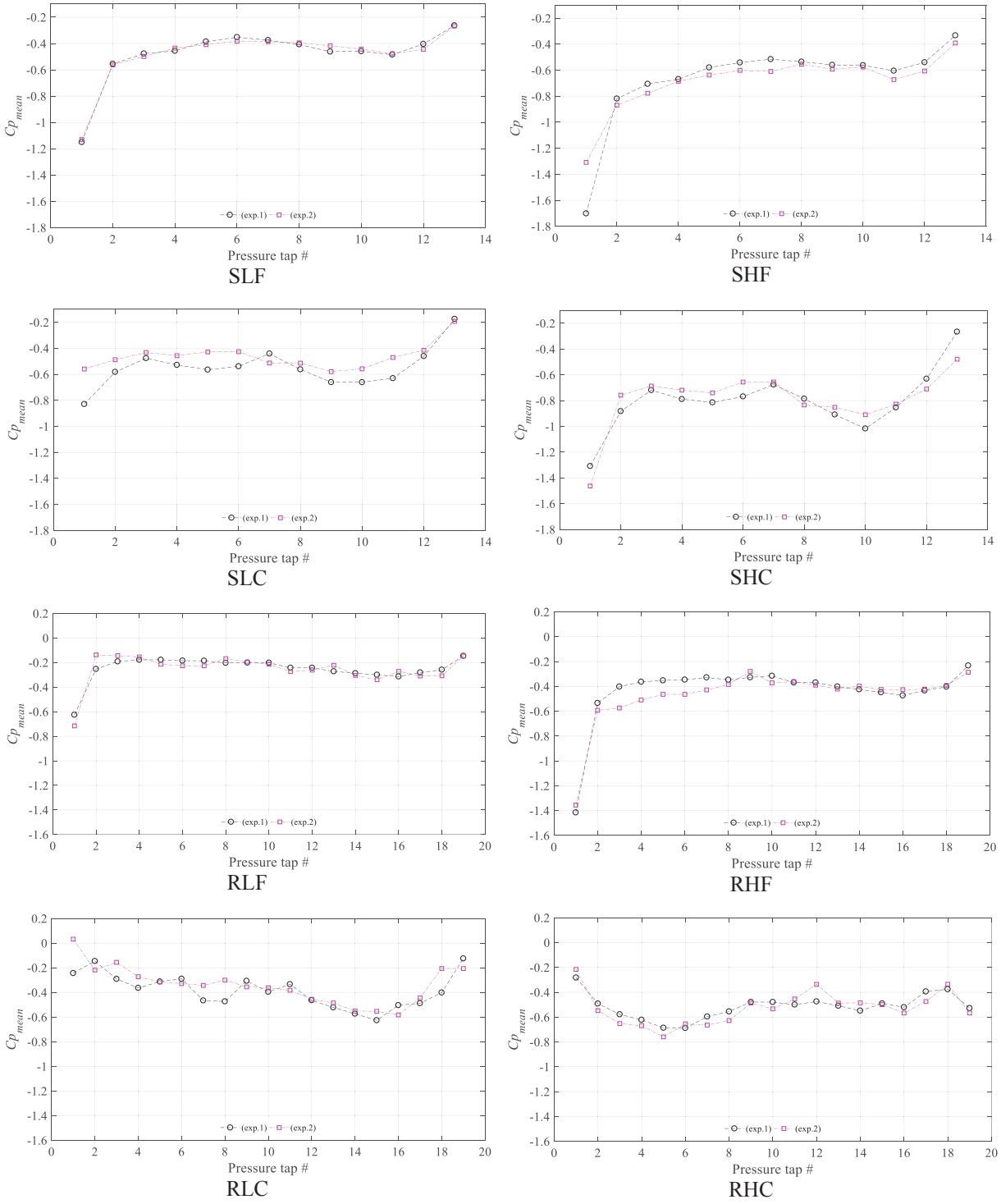

Figure 3: mean value $c_{p,mean}$ of the experimental c_p for the eight models in fig. 1 and $\theta = 0°$, measured by the pressure taps along the roof sides on the left (black curve) and on the right (red curve) of the wind direction.

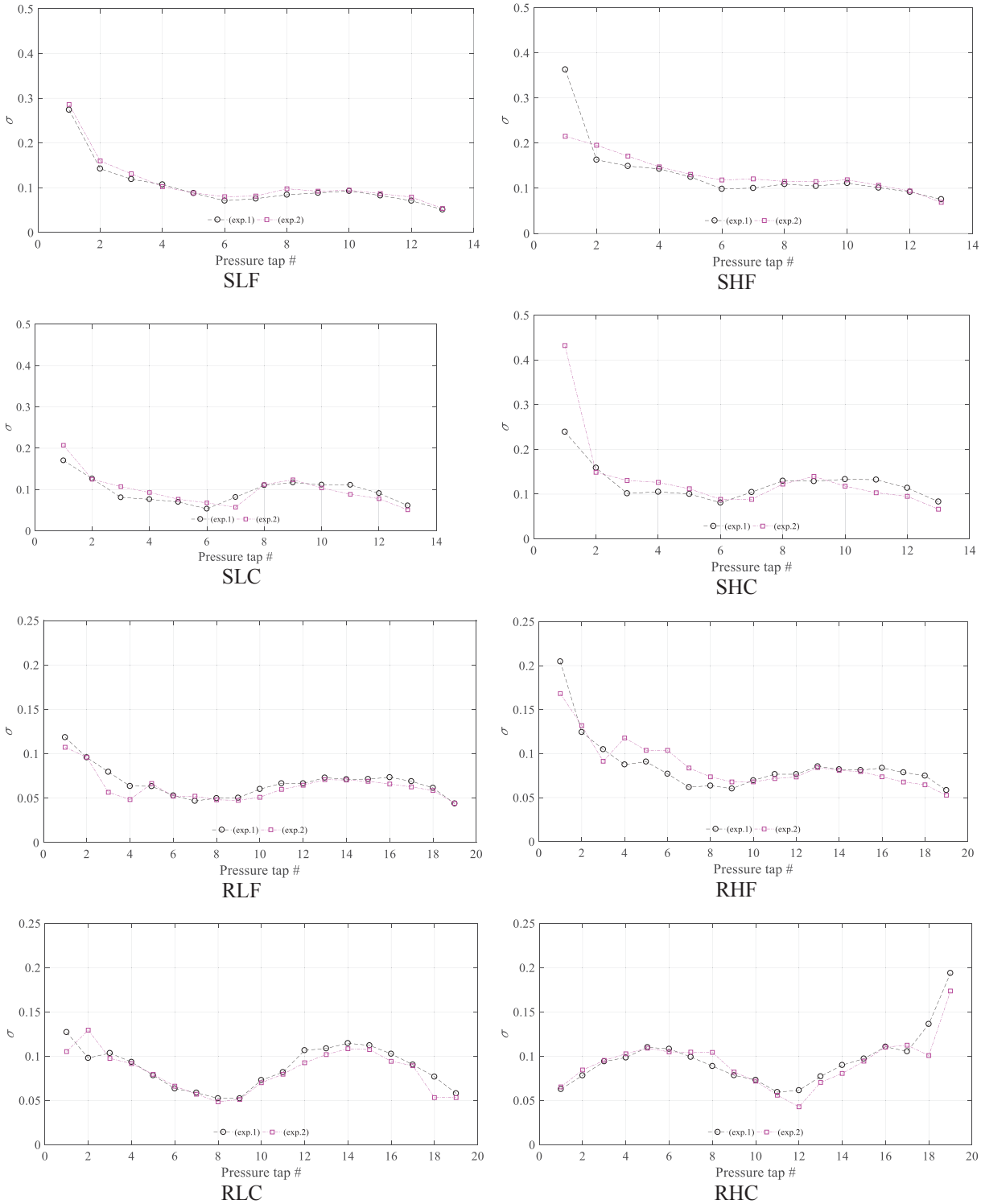

Figure 4: standard deviation σ_{cp} of the experimental c_p for the eight models in fig. 1 and $\theta = 0°$, measured by the pressure taps along the roof sides on the left (black curve) and on the right (red curve) of the wind direction.

3 EXPERIMENTAL AND ANALYTICAL PEAK PRESSURE COEFFICIENTS

Fig. 3 and 4 report the mean $c_{p,mean}$ and the standard deviation σ_{cp}, respectively, of the experimental c_p for the eight models in fig. 1 and $\theta = 0°$, measured by the pressure taps along the roof sides on the left and on the right of the wind direction.

It can be observed that for $\theta = 0°$ the differences between the mean $c_{p,mean}$ of the experimental pressure coefficients (fig. 3) measured by the pressure taps along the two sides of the roof are almost negligible for low curvature roofs (SLF, SHF, RLF, RHF). This can easily be explained once considered that for $\theta = 0°$ the wind flow impacts on the hogging curvature of the model and it is confined by the across-wind sagging curvature, and this implies small detachment regions. As also expected, on the other hand, for more curved models (SLC, SHC, RLC, RHC) the differences become more relevant, because of more pronounced detachment regions of the flow due to the larger curvature.

A similar trend has been observed for the standard deviations σ_{cp} of the experimental pressure coefficients (fig. 4).

The behavior becomes quite different for wind angle $\theta = 90°$, when the flow impacts the models on their highest wall, with a consequent detachment of the flow for a large part of the roof. In this case, as shown by results for square models reported in fig. 5 and 6 ($c_{p,mean}$ and σ_{cp}, respectively), the differences between the two alignments of pressure taps are still negligible for the lower model with smaller curvature (SLF). They are instead significantly larger for more curved ones, as shown by both $c_{p,mean}$ and σ_{cp} for SLC and SHC, and also for the highest model with smaller curvature (SHF), where significant differences of σ_{cp} have been found.

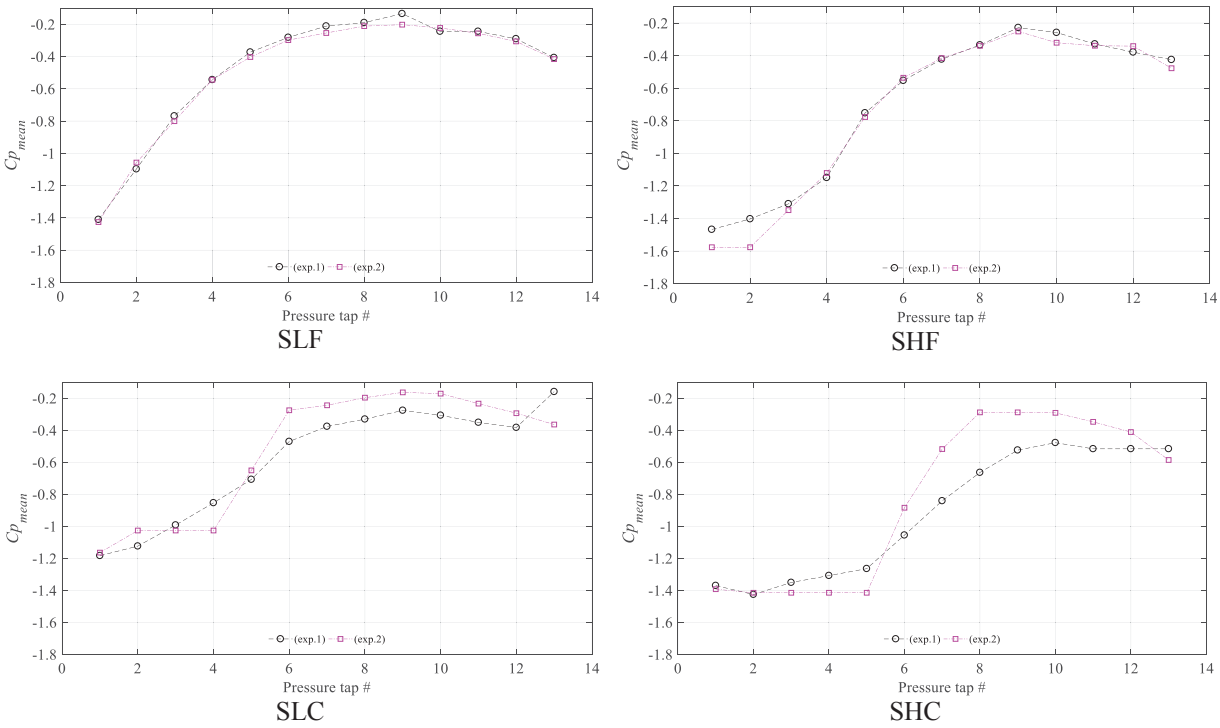

Figure 5: mean value $c_{p,mean}$ of the experimental c_p for the four square models in fig. 1 and $\theta = 90°$, measured by the pressure taps along the roof sides on the left (black curve) and on the right (red curve) of the wind direction.

Due to the experimentally observed non-symmetric behavior already discussed with reference to $c_{p,mean}$ and σ_{cp}, the differences between minimum (suction) values of c_p along the two alignments of pressure taps follow a similar trend or they are even more large, as shown for example by the extreme values in fig. 7 for square models and $\theta = 0°$.

The difference is even more evident for the experimental values of the peak factor g corresponding to the minimum values of c_p (i.e. suction), reported in fig. 8.

Peak factor g is defined as

$$c_p^{\min} = c_{p,\text{mean}} - g\ \sigma_{cp} \tag{2}$$

where for each pressure tap $c_{p,\text{mean}}$, σ_{cp} and $c_p^{\min}$ are the mean, the standard deviation and the minimum value of the c_p time history recorded in wind-tunnel tests, respectively.

On the other hand, for the sample cases discussed here also maximum values of c_p are almost always negative (suction) and smaller in absolute value than minima, and therefore they have no practical relevance to design purpose and are no further discussed below.

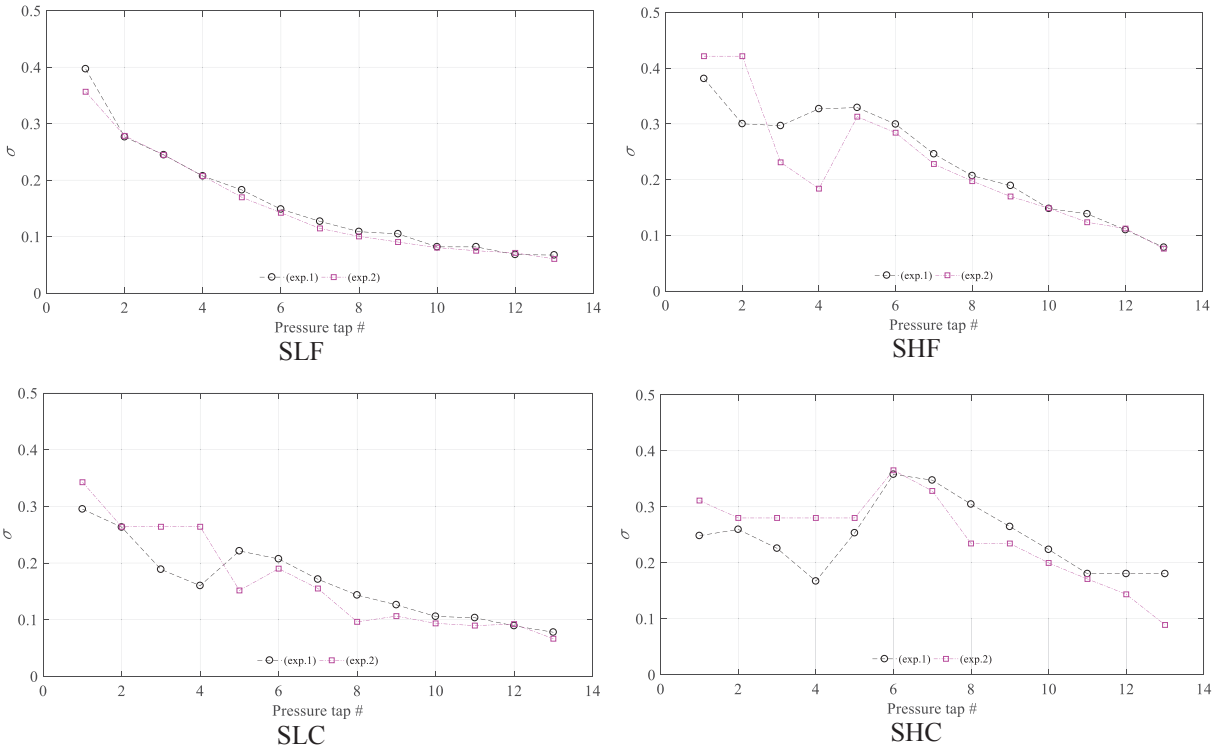

Figure 6: standard deviation σ_{cp} of the experimental c_p for the four square models in fig. 1 and $\theta = 90°$, measured by the pressure taps along the roof sides on the left (black curve) and on the right (red curve) of the wind direction.

Figures 7 also show for square models and $\theta = 0°$ the minimum values of c_p evaluated according to the classical Davenport model and to the analytical modified Hermite model [1]. Similarly, fig. 8 also show for square models and $\theta = 0°$ the peak factor g evaluated according to the classical Davenport model and to the modified Hermite model [1]. As expected, the Davenport peak factor assume almost constant values around 3.5.

It can be observed that, when compared to experimental results, the analytical models generally reduce the differences between the extreme values $c_p^{\min}$ of the two alignments of pressure taps. This is not true for the peak factor g evaluated according to the analytical modified Hermite model [1], which keeps maintaining significant differences between taps expected to have a symmetric behavior. In the authors' opinion, however, this difference should be reduced by evaluating g from the minimum expected values of c_p according to a soundly based statistical procedure (e.g. Cook and Mayne [12]), instead of assuming the minimum recorded values $c_p^{\min}$ as done here, and this will be investigated in future research.

Although differences between the two alignments are not negligible, however, the average value of $c_p^{\min}$ provided by the modified Hermite model [1] for pressure taps nominally symmetric is closer, with respect to the estimation provided by the Davenport model, to the aver-

age of their recorded extreme suction values. This can be explained by considering that in the Davenport model g turns out to be almost constant, while a recent research [4] shows that for this kind of geometries g may have quite large variations.

All in all, therefore, and according to these results for symmetrical geometries under wind flow direction parallel to the symmetry axis, asymmetries shown by experimental tests may be reduced by appropriate analytical models, that can therefore contribute to filter out the effects of these and others experimental uncertainties for design purposes.

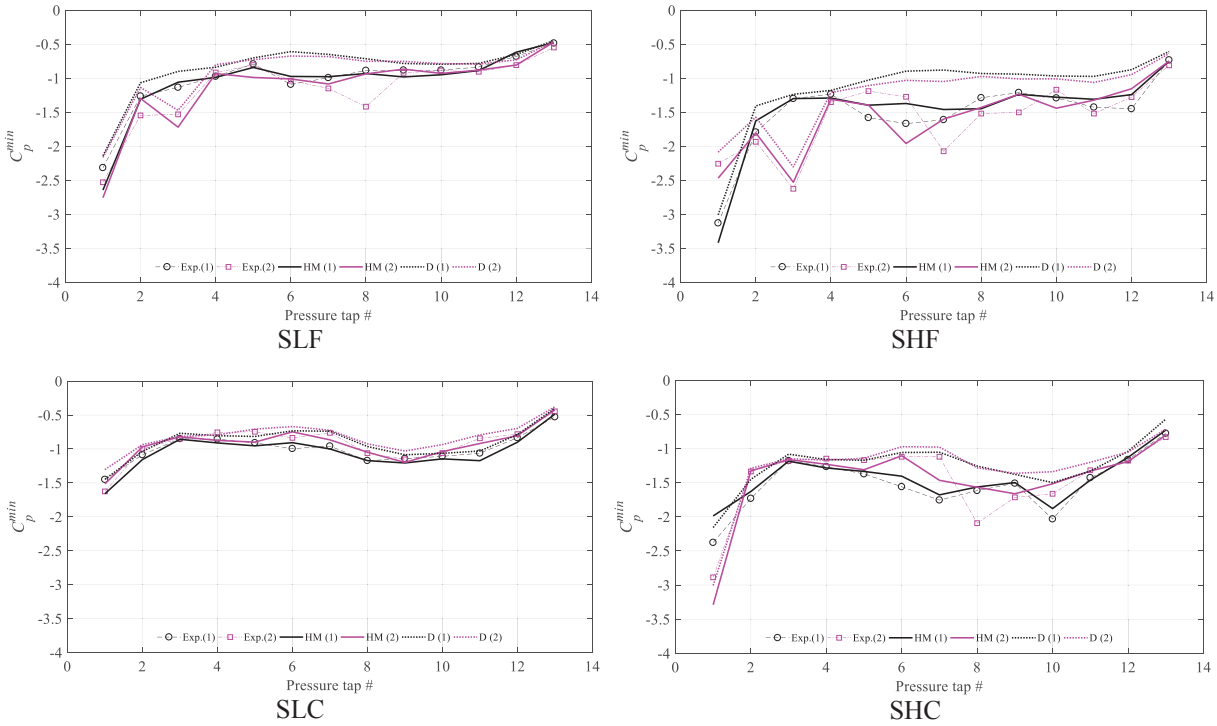

Figure 7: minimum value c_p^{min} of the experimental c_p for the four square models in fig. 1 and $\theta = 0°$, measured by the pressure taps on the left (broken black curve) and on the right (broken red curve) of the wind direction; peak values of c_p obtained with analytical models (Davenport and modified Hermite [1]) are also shown (dotted and continuous lines, respectively).

4 CONCLUSIONS

- Based on experimental results on hyperbolic paraboloid models tested in the boundary layer wind-tunnel of the CRIACIV (Italy) [4-9], this paper shows that experimental values of pressure coefficients are affected by physiological uncertainties, as the asymmetries measured for geometries and wind directions nominally symmetric.
- Although the results reported require further investigation, they suggest that technical codes should include asymmetrical load conditions also in case of nominally symmetric geometries and wind directions.
- Experimental peak pressure coefficients and their prediction given by two analytical models are compared for symmetrical geometries under wind flow direction parallel to the symmetry axis, and it is noted that asymmetries shown by experimental tests may be reduced by appropriate analytical models, that can therefore contribute to filter out the effects of experimental uncertainties for design purposes.

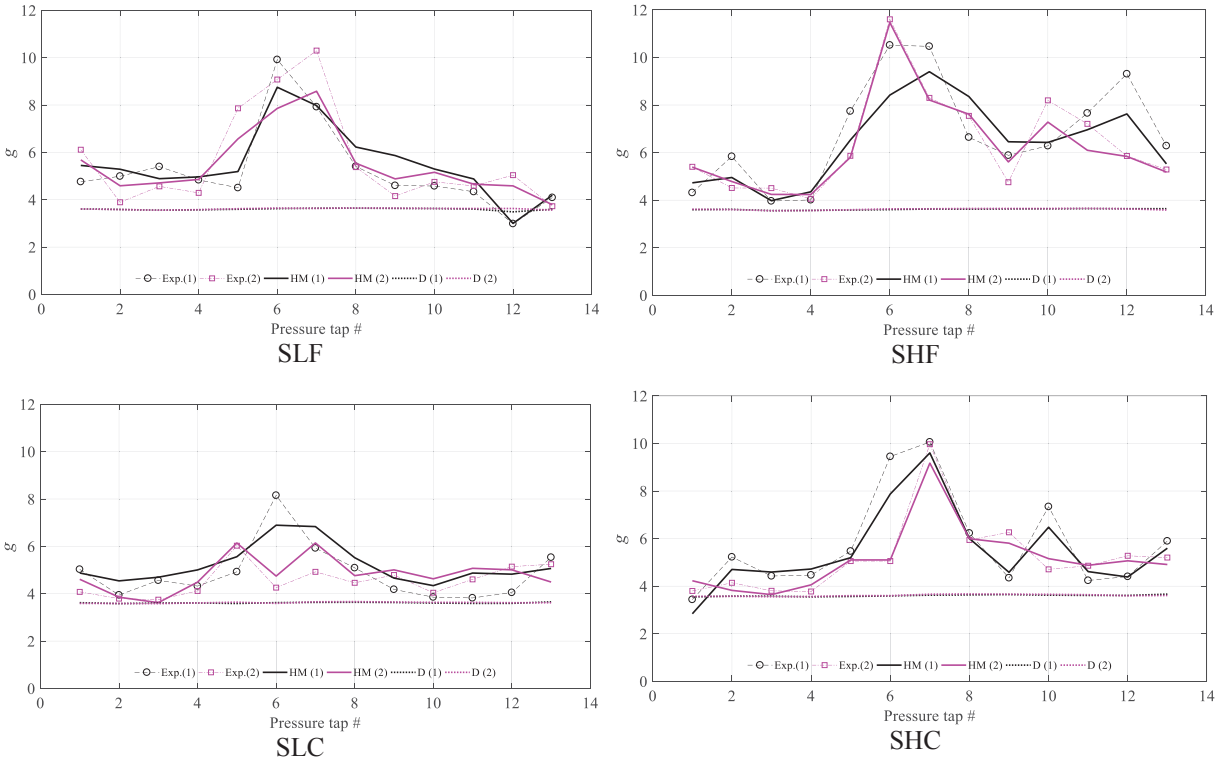

Figure 8: peak factor g for the minimum values (suction) of the experimental c_p for the four square models in fig. 1 and $\theta = 0°$, measured by the pressure taps along the roof sides on the left (broken black curve) and on the right (broken red curve) of the wind direction; peak factor g obtained with analytical models (Davenport and modified Hermite [1]) are also shown (dotted and continuous lines, respectively).

ACKNOWLEDGMENTS

The financial support of University ‘‘G. D’Annunzio” of Chieti-Pescara is acknowledged by the authors. Authors would like to thanks Professor Michele Barbato, UC-Davis University, California, USA, for sharing his expertise about the peak factors statistics and their prediction through analytical models.

REFERENCES

[1] D. Kwon, A. Kareem, Peak factors for non-Gaussian load effects revisited. *J Struct Eng,* 137(12):1611–1619, 2011.

[2] M. F. Huang, W. Lou, C. M. Chan, N. Lin, X. Pan, Peak distributions and peak factors of wind-induced pressure processes on tall buildings. *J Eng Mech* 139(12):1744–56, 2013.

[3] M. Liu, X. Chen, Q. Yang, Estimation of peak factor of non-Gaussian wind pressures by improved moment-based Hermite model, *Journal of Engineering Mechanics,* 143(7), 06017006-1-9, 2017.

[4] F. Rizzo, M. Barbato, V. Sepe, Peak factor statistics of wind effects for hyperbolic paraboloid roofs, *Engineering Structures*, 173, 313-330, 2018.

[5] F. Rizzo, V. Sepe, M. Vasta, Correlation structure of wind-tunnel pressure fields for a hyperbolic paraboloid roof, *XXIII Conference of the Italian Association of Theoretical and Applied Mechanics (AIMETA 2017)*, Salerno, Italy, September 4-7, 2017.

[6] F. Rizzo, P. D'Asdia, M. Lazzari, L. Procino, Wind action evaluation on tension roofs of hyperbolic paraboloid shape. *Engineering Structures*, 33 (2), 445-461, 2011.

[7] F. Rizzo, P. D'Asdia, F. Ricciardelli, G. Bartoli, Characterization of pressure coefficients on hyperbolic paraboloid roofs. *Journal of Wind Engineering & Industrial Aerodynamics*, 102, 61–71, 2012.

[8] F. Rizzo, V. Sepe, Static loads to simulate dynamic effects of wind on hyperbolic paraboloid roofs with square plan. *Journal of Wind Engineering & Industrial Aerodynamics*, 137-146, 2015.

[9] F. Rizzo, F. Ricciardelli, Design pressure coefficients for circular and elliptical plan structures with hyperbolic paraboloid roof. *Engineering Structures*, 139, 153-169, 2017.

[10] F. Rizzo, P. Zazzini, Improving the acoustical properties of an elliptical plan space with a cable net membrane roof, *Journal of Acoustics Australia*, 44, 449-456, (11-16-2016) ISSN: 08146039, DOI: 10.1007/s40857-016-0072-5, 2016

[11] F. Rizzo, P. Zazzini, Shape dependence of acoustic performances in buildings with a Hyperbolic Paraboloid cable net membrane roof. *Journal of Acoustics Australia*, 45 (2), (01-01-2017) 421–443, ISSN: 08146039, DOI: 10.1007/s40857-017-0092-9, 2017

[12] N.J. Cook, Mayne, J.R., A novel working approach to the assessment of wind loads for equivalent static design, *J. Wind Eng. Ind. Aerod.*, 4(2), 149-164. https://doi.org/10.1016/0167-6105(79)90043-6, 1979.

EURODYN 2020
XI International Conference on Structural Dynamics
M. Papadrakakis, M. Fragiadakis, C. Papadimitriou (eds.)
Athens, Greece, 23–26 November 2020

BAYESIAN MODEL UPDATING FOR EXISTING SEISMI-ISOLATED BRIDGES USING OBSERVED ACCELERATION RESPONSE DATA

Masaru Kitahara[1], **Matteo Broggi**[1], **and Michael Beer**[1]

[1] Institute for Risk and Reliability, Leibniz Universität Hannover
Callinstr. 34, 30167 Hannover, Germany
e-mail: {masaru.kitahara, broggi, beer}@irz.uni-hannover.de

Keywords: Bayesian model updating, Bhattacharyya distance, uncertainty quantification, ageing existing bridge, time-series data

Abstract. *In ageing existing bridges, the deterioration of the members cannot be ignored and the model parameters should be carefully estimated in time through observation data from the structures. On seismic-isolated bridges, the post-yield stiffness of rubber bearings is a particularly critical parameter, since it affects the structural behavior against huge earthquakes. Additionally, its characteristic can be captured using available seismic response data. In this study, a seismic-isolated bridge pier is modelled as a two degree of freedom lumped mass system and its uncertain model parameters are estimated based on time-histories of the acceleration response through Bayesian model updating. The Bhattacharyya distance is used as a comprehensive uncertainty quantification (UQ) metric to capture multiple uncertainty sources from both model predictions and observation data. A sequential procedure is proposed to prevent the so-called "dimensional curse" due to very high dimensional time-series data in model updating. In this procedure, the Bhattacharyya distance is calculated for each predefined time segment and their root mean square is adopted as the UQ metric. The results demonstrate that the proposed framework can successfully update model parameters including the post-yield stiffness of the rubber bearing through seismic response data. Furthermore, the calibrated model can represent wholly the probability distribution of the target time-series observation.*

1 INTRODUCTION

Over the past decades, seismic isolation has been considered as an attractive technology to mitigate the risk of seismic damages on highway bridges [1-3]. Seismic isolation aims to shift the natural frequency of a structure away from the dominant frequency of earthquakes and to provide additional damping capacity in order to reduce seismic loadings on the structure. Among various types of isolation systems, rubber bearings have been widely used [3].

On the other hand, it is well known that the structural property of rubber bearings is varied due to aging deterioration. Long-term deterioration characteristics of natural rubber bearings were studied based on accelerated thermal oxidation tests [4], and decrease in the rupture strain and increase in the stiffness of bearings were also reported [5, 6]. Moreover, Onodera et al. [7] showed that deteriorated bearings increase the response of reinforced concrete (RC) piers at lower seismic intensity compared to bearings without deterioration based on incremental dynamic analysis. Hence, current model parameters of deteriorated bearings need to be carefully estimated through available seismic response data to compute seismic reliability of the bridges with deteriorated bearings in order to prevent their failure in future earthquakes.

Bayesian model updating [8, 9] is a powerful tool successfully employed to estimate model parameters through observation data. It has been widely accepted that uncertainties should be appropriately considered in model updating; thus, uncertainty quantification (UQ) metrics are significant to comprehensively and quantitatively measure the difference between model predictions and observation data. As an alternative to the classical Euclidian distance, the Bhattacharyya distance was proposed as a potential UQ metric capable of capturing a higher level of statistical information [10]. Bi et al. [11] developed an approximate Bayesian computation model updating framework, where the Bhattacharyya distance was fully embedded. The accuracy and efficiency of the framework were demonstrated through a three degree of freedom (DOF) spring-mass system example and a modal analysis of an airframe structure. Nevertheless, modal responses were used as the target output features in these examples and applicability for time-series responses, such as seismic responses, still needs to be investigated.

In this study, a sequential procedure is proposed to prevent the so-called "dimensional curse" due to very high dimensional time-series data in model updating. In this sequential procedure, the Bhattacharyya distance is calculated for each predefined time segment and their root mean square (RMS) is adopted as the UQ metric. In this context, the applicability and usefulness of the proposed method is examined updating model parameters of existing seismic-isolated bridges including the post-yield stiffness of rubber bearings through seismic response data.

2 MODEL DESCRIPTIONS

The target bridge, used in this study, is a seismic-isolated bridge designed based on the design specifications of highway bridges and manual on bearings for highway bridges by Japan Road Association [12, 13]. The seismic-isolated bridge pier is modelled as a 2-DOF lumped mass system, as shown in Figure 1(a), and descriptions of the bridge are also detailed in Table 1. Force-displacement relationships of the rubber bearing and RC pier are described by hysteresis loops using bi-linear model and stiffness degradation bi-linear model (so-called Takeda model) [14], respectively. The ultimate strength of the pier is idealized as same as its yield strength; thus, the pier has no post-yield stiffness. In addition, Rayleigh damping is assumed in which damping ratios of the bearings and pier are given as 0% and 2%, respectively.

Dynamic response analysis of the 2-DOF system is conducted by Newmark β method ($\gamma = 1/2$ and $\beta = 1/4$) with the time step $\Delta t = 0.001$sec. NS component of JR Takatori record during the 1995 Kobe earthquake is selected as the input ground motion and time-histories of the acceleration response at the superstructure is shown in Figure 1(b).

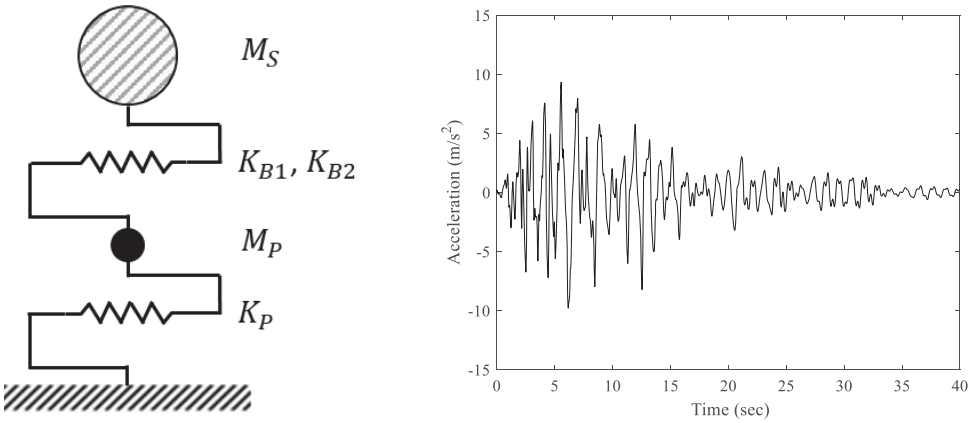

(a) 2-DOF lumped mass system (b) Time-histories of the acceleration response at the superstructure

Figure 1: 2-DOF lumped mass system and its time-histories of the acceleration response.

Model parameter		Characteristic value
Superstructure	Mass M_S (ton)	604.0
Rubber bearing	Yield strength (kN)	1118
	Yield stiffness K_{B1} (kN/m)	40000
	Post-yield stiffness K_{B2} (kN/m)	6000
RC pier	Mass M_P (ton)	346.2
	Yield strength (kN)	3374
	Yield displacement (m)	0.0306
	Ultimate displacement (m)	0.251
	Yield stiffness K_P (kN/m)	110100

Table 1: Descriptions of the target bridge.

3 THEORIES AND METHODS

3.1 Bhattacharyya distance-based UQ metric

The numerical model with n input parameters and m output features can be expressed as:

$$\mathbf{y} = f(\mathbf{x}) \tag{1}$$

where $\mathbf{x} = [x_1, x_2, \cdots, x_n]^T$ and $\mathbf{y} = [y_1, y_2, \cdots, y_m]^T$ are the input and output vectors, respectively. The function can be either a structural analysis (e.g. dynamic response analysis of the target bridge, in which model parameters listed in Table 1 are the input parameters and time-histories of the acceleration response are the output features) or a meta-model.

In Bayesian model updating, some of the input parameters are considered as uncertain parameters while the remaining parameters are treated as deterministic parameters. Then, randomly sampled values of the parameters are used to calculate the corresponding output features. Suppose the sample size is N_{sim}, model predictions $\mathbf{Y}_{sim} \in \mathbb{R}^{N_{sim} \times m}$ are obtained as:

$$\mathbf{Y}_{sim} = [\mathbf{y}_1, \mathbf{y}_2, \cdots, \mathbf{y}_m], \ \ \mathbf{y}_i = \left[y_{1i}, y_{2i}, \cdots, y_{N_{sim}i}\right]^T, \ \forall i = 1, \cdots, m \tag{2}$$

In addition to model predictions, observed features are required as the target of model updating. Suppose the number of observations is N_{obs}, observation data $\mathbf{Y}_{obs} \in \mathbb{R}^{N_{obs} \times m}$ have a similar structure as Equation (1), where only the number of rows is changed.

After getting model predictions and observation data, the UQ metric can be defined to capture the discrepancy between them. The classical Euclidian distance metric is expressed as:

$$d_E(\mathbf{Y}_{obs}, \mathbf{Y}_{sim}) = \sqrt{(\overline{\mathbf{Y}}_{obs} - \overline{\mathbf{Y}}_{sim})(\overline{\mathbf{Y}}_{obs} - \overline{\mathbf{Y}}_{sim})^T} \tag{3}$$

where $\overline{\mathbf{Y}}_{\blacksquare}$ is the row vector of means of the features. The Euclidian distance only considers the effect of the mean, thus a more comprehensive distance accounting for a higher level of statistical information is required. The Mahalanobis distance can consider the effect of the variance and covariance, while it cannot take into account the difference in the distribution shapes.

The Bhattacharyya distance is hence proposed herein to measure the degree of overlap between distributions of two random variables and is expressed as:

$$d_B(\mathbf{Y}_{obs}, \mathbf{Y}_{sim}) = -\log\left[\int_{\mathbb{X}} \sqrt{p_{obs}(y)p_{sim}(y)}dy\right] \tag{4}$$

where $p_{\blacksquare}(x)$ is the probability density function (PDF) of the sample; $\mathbb{X}$ is the m-dimensional space, implying $\int_{\mathbb{X}} \blacksquare dx$ is the integration performed over the whole output space. Despite the advantage on uncertainty characterization, the direct calculation of Equation (4) is impractical because precise estimation of the PDF is generally unavailable, especially when the amount of observation data is limited. Hence, an approximate Bhattacharyya distance based on probability mass functions (PMFs) of discrete distributions is introduced as:

$$d_B(\mathbf{Y}_{obs}, \mathbf{Y}_{sim}) = -\log\left\{\sum_{i_m=1}^{n_{bin}} \cdots \sum_{i_1=1}^{n_{bin}} \sqrt{p_{obs}(b_{i_1,i_2,\cdots,i_m})p_{sim}(b_{i_1,i_2,\cdots,i_m})}\right\} \tag{5}$$

where $p_{\blacksquare}(b_{i_1,i_2,\cdots,i_m})$ is the PMF value of the bin $b_{i_1,i_2,\cdots,i_m}$. Bins are generated as a grid within the lower and upper bounds of all values of model predictions and observation data. More detailed information of the binning algorithm can be referred to Ref. [11].

More attention is paid that the grid is created in a m-dimensional space; thus, it is difficult to directly employ the Bhattacharyya distance using very high dimensional time-series data as the output features (due to so-called "curse of dimensionality"). To overcome this issue, a sequential procedure is proposed as following:

1) Define the common short time segment Δt_0 of both $\mathbf{Y}_{obs}$ and $\mathbf{Y}_{sim}$, and take RMS of them for each time segment.
2) Use the RMS of each time segment $\mathrm{RMS}_{\mathbf{Y}_{obs}i}$ and $\mathrm{RMS}_{\mathbf{Y}_{sim}i}$, $\forall i = 1, \cdots, k(= m \cdot \Delta t/\Delta t_0)$ independently to calculate the Bhattacharyya distance.
3) Again, take RMS of the set of the Bhattacharyya distance $\mathbf{d}_B = [d_{B1}, d_{B2}, \cdots, d_{Bk}]$ and employ it as an alternative UQ metric.

The principle of the time segment Δt_0 in step 1) is that a smaller Δt_0 leads to employing more detail information from the time-series data, while it leads to larger computational burden for the calculation of the UQ metric. Note that, an advantage to take RSM of $\mathbf{Y}_{obs}$ and $\mathbf{Y}_{sim}$ in step 1) is simplicity to address the different time resolutions in model predictions and observation data.

3.2 Bayesian model updating

The Bayesian model updating framework is based on the Bayes' theorem [8]:

$$P(\mathbf{X}|\mathbf{Y}_{obs}) = \frac{P_L(\mathbf{Y}_{obs}|\mathbf{X})P(\mathbf{X})}{P(\mathbf{Y}_{obs})} \tag{6}$$

where $P(\mathbf{X})$ is the prior distribution representing the initial knowledge about the input parameters, $P(\mathbf{X}|\mathbf{Y}_{obs})$ is the posterior distribution representing the updated knowledge based on observation data, $P(\mathbf{Y}_{obs})$ is the normalized factor ensuring the posterior distribution integrates to one, and $P_L(\mathbf{Y}_{obs}|\mathbf{X})$ is the likelihood function, theoretically defined as the probability of observation data conditional to each instance of the inputs.

The likelihood function is theoretically expressed as:

$$P_L(\mathbf{Y}_{obs}|\mathbf{X}) = \prod_{i=1}^{N_{obs}} P(\boldsymbol{y_i}|\mathbf{X}) \tag{7}$$

where $P(\boldsymbol{y_i}|\mathbf{X})$ is the probability distribution of ith observation data conditional to the corresponding instance of the inputs. However, the direct calculation of Equation (7) is generally unrealistic for practical applications because precise estimation of $P(\boldsymbol{y_i}|\mathbf{X})$ requires large number of simulated features. Hence, an approximate likelihood function based on the Bhattacharyya distance is defined as:

$$P_L(\mathbf{Y}_{obs}|\mathbf{X}) \propto exp\left\{-\frac{d_B(\mathbf{Y}_{obs}, \mathbf{Y}_{sim})^2}{\varepsilon^2}\right\} \tag{8}$$

where ε is the so-called width factor controlling the centralization of the posterior distribution. This likelihood function is based on the approximate Bayesian computation [15], in which any types of statistics can be used to measure the difference between model predictions and observation data in the kernel, and the Gaussian kernel is adopted in this study. Combining with the Bhattacharyya distance, the new likelihood function is capable of capturing comprehensive uncertainty information from both model predictions and observation data.

In addition, the normalized factor $P(\mathbf{Y}_{obs})$, also known as evidence, is also a non-trivial component as the direct integration of $P(\mathbf{X}|\mathbf{Y}_{obs})$ over the whole sample space. Thus, the TMCMC algorithm [16] is proposed in this study by introducing a series of intermediate PDFs of the inputs, which gradually converge to the posterior distribution, and thus avoiding the direct calculation of the integral.

4 CASE STUDY ON THE SEISMIC-ISOLATED BRIDGE PIER MODEL

4.1 Problem descriptions

The case study is performed on the 2-DOF system shown in Figure 1(a). The post-yield stiffness of the bearing K_{B2} as well as the initial stiffness of the bearing and pier K_{B1}, K_R are assigned as uncertain parameters while the remaining parameters are fixed constants with characteristic values listed in Table 1. Time-histories of the acceleration response at the superstructure against JR Takatori record are taken as the output features whose uncertainty are driven by the uncertain parameters. Both aleatory and epistemic uncertainties are included by modeling the uncertain parameters as independent Gaussian random variables, where distribution coefficients, which are multiplied by the characteristic values, are not fixed but unknowns lying within given intervals. The intervals of means μ and standard deviations σ associated to the uncertain parameters are detailed in Table 2.

Observation data $\mathbf{Y}_{obs}$ are simulated by assigning target values of the distribution coefficients, which are defined based on Adachi [17], shown in the last column of Table 2. Based on these target values, 100 random samples of the input parameters are generated and subsequently 100 observation samples are obtained by evaluating the model. The duration time of JR Takatori

record is 40sec and consequently the output features have 40,000 dimensions; thus, the direct calculation of the Bhattacharyya distance is apparently impossible and the proposed sequential procedure is required. In this study, the short time segment is set as $\Delta t_0 = 1$sec.

The purpose of the case study is to demonstrate the Bhattacharyya distance as a universal UQ metric in Bayesian model updating based on time-series data to calibrate the uncertainty distribution characteristics of the input parameters. In particular, the case study focuses on updating the post-yield stiffness of the bearing, which cannot be captured by modal responses, using seismic response data.

Parameter	Uncertainty characteristic	Target value of epistemic input
K_P	Gaussian, $\mu_1 \in [0.5, 1.5]$, $\sigma_1 \in [0.0, 0.15]$	$\mu_1 = 1.0$, $\sigma_1 = 0.07$
K_{B1}	Gaussian, $\mu_2 \in [0.5, 1.5]$, $\sigma_2 \in [0.0, 0.15]$	$\mu_2 = 1.0$, $\sigma_2 = 0.07$
K_{B2}	Gaussian, $\mu_3 \in [0.5, 1.5]$, $\sigma_3 \in [0.0, 0.15]$	$\mu_3 = 1.0$, $\sigma_3 = 0.07$

Table 2: Uncertainty properties of the input parameters.

4.2 Updating results

The Bayesian model updating is performed using the TMCMC algorithm [12]. Prior distributions of all uncertain parameters are set to be uniform distribution within the pre-defined intervals listed in Table 2.

The posterior distributions of the parameters calibrated by the Bhattacharyya distance metric are obtained, as shown in Figure 2. The diagonal subfigures illustrate the histograms of the posterior distributions and the other subfigures show the scatters of the posterior samples. It can be seen that all of the uncertain distribution parameters are significantly updated compared with their prior uniform distributions and accurately converge to their target values.

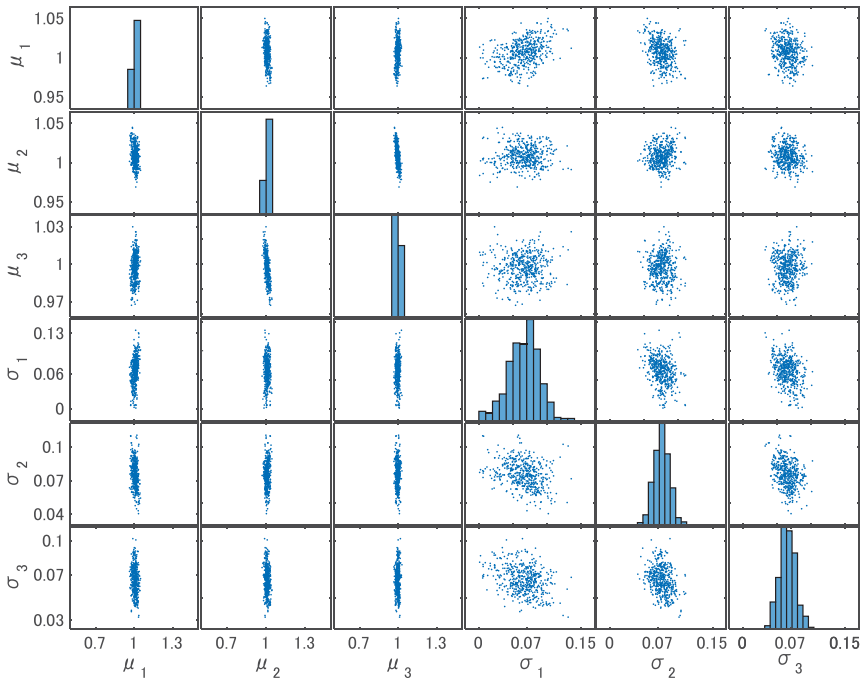

Figure 2: Posterior distributions of the uncertainty distribution characteristics.

Figure 3 illustrates the comparison between the target and updated scatters and histograms of the arbitrary selected RSM of the time-histories. Here, $\mathrm{ACC}_{\mathrm{RSMi}}$ denotes the RSM of the time-histories of the acceleration response corresponding to the ith time segment. Distribution properties of all RSMs of the time-histories are precisely updated to be identical with the target distributions, implying the proposed UQ metric, as the RSM of the set of the Bhattacharyya distance, has the capability to recreate wholly the distribution of the target time-histories.

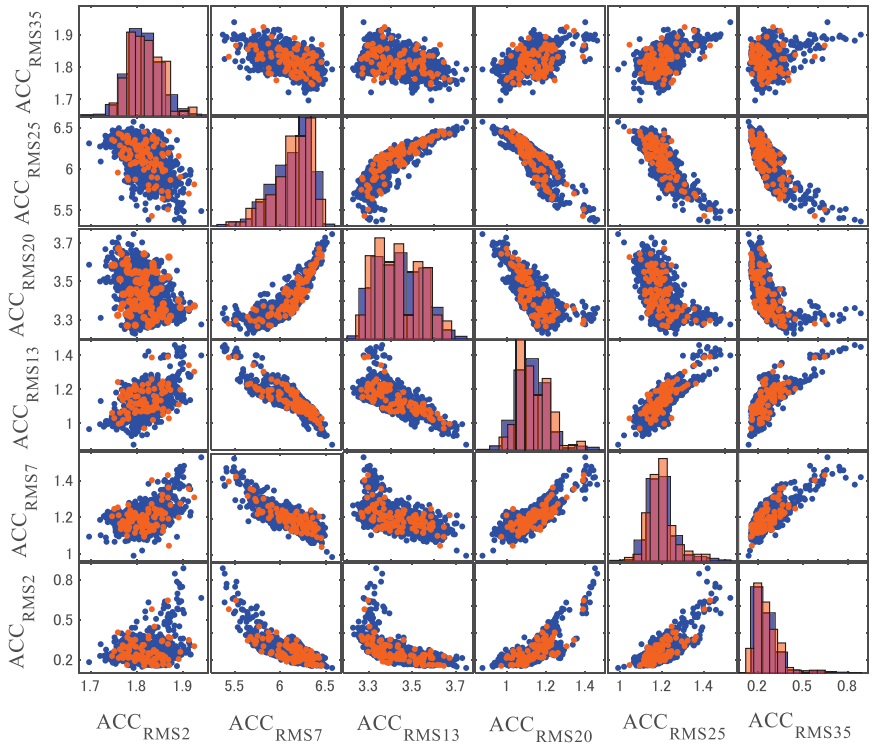

Figure 3: The target scatters (in orange) and updated output scatters (in blue).

Finally, updated values of the uncertain parameters are obtained by evaluating means of the posterior distributions, as detailed in Table 3. Percentage errors compared with the target values are also given in parentheses. The means have quite high updating precisions with errors less than 1%, while the standard deviations has relatively large errors more than 6%. Nevertheless, the final updated distributions of the outputs coincide well with the target distributions, as shown in Figure 3, demonstrating that the Bhattacharyya distance has successfully captured comprehensive uncertainty information from both model predictions and observation data.

Input	Target value	Updated value
μ_1	1.0	$1.0069(0.7\%)$
μ_2	1.0	$1.0081(0.8\%)$
μ_3	1.0	$0.9972(-0.3\%)$
σ_1	0.07	$0.0654(-6.6\%)$
σ_2	0.07	$0.0754(7.7\%)$
σ_3	0.07	$0.0654(-6.6\%)$

Table 3: Updated results of the uncertain parameters.

5 CONCLUSIONS

The Bhattacharyya distance is proposed as a comprehensive uncertainty quantification metric and a sequential procedure is introduced for its application for high dimensional time-series data. The proposed metric is utilized in Bayesian model updating and demonstrated through seismic-isolated bridge pier model example. Model parameters including the post-yield stiffness of the rubber bearing, which cannot be captured by modal responses, are successfully updated using seismic response data. Moreover, the proposed uncertainty quantification metric can handle rather than input parameters, but their uncertainty distribution characteristics, such as the calibrated model can represent the probability distribution of the time-series outputs as same as the multiple observations. As mentioned in Section 3.1, the selection of the predefined time segment Δt_0will affect the updating results and its computational burden, thus the investigation of the suitable value for the time segment should be addressed in the future work.

REFERENCES

[1] M. Abe, J. Yoshida, Y. Fujino, Multiaxial Behaviors of Laminated Rubber Bearings and Their Modeling. I: Experimental Study, *Journal of Structural Engineering*, 130(11), 19-32, 2004.

[2] IG. Buckle, RL. Mayes, Seismic Isolation: History, Application, and Performance – A World View, *Earthquake Spectra*, 6(2), 161-201, 1990.

[3] A. Rahman Bhuiyan, M. Shahria Alam, Seismic performance assessment of highway bridges equipped with superelastic shape memory alloy-based rubber isolation bearing, *Engineering Structures,* 49, 396-407, 2013.

[4] Y. Itoh, H.S. Gu, Prediction of aging characteristics in natural rubber bearings used in bridges, *Journal of Bridge Engineering*, 14(2), 122-128, 2009.

[5] K. Hayashi, Y. Adachi, K. Komoto, H. Yamamoto, A. Igarashi, J. Dang, T. Higashide, Experimental verification for remaining performance of lead rubber bearings with aging deterioration, *Journal of JSCE (A1)*, 70(4), 1032-1042, 2014.

[6] M. Shinohara, J. Hoshikuma, Experimental evaluation of property of lead rubber bearing damaged due to earthquake, *Journal of JSCE (A1)*, 71(4), 587-599, 2015.

[7] M. Onodera, H. Matsuzaki, M. Suzuki, Effect of deteriorated isolators on the seismic response of reinforced concrete columns with isolator, *Journal of JSCE (A1)*, 71(4), 737-748, 2015.

[8] J.L. Beck, L.S. Katafygiotis, Updating models and their uncertainties. I: Bayesian statistical framework, *Journal of engineering Mechanics*, 124(4), 455-461, 1998.

[9] L.S. Katafygiotis, J.L. Beck, Updating models and their uncertainties. II: Model identifiability, *Journal of engineering Mechanics*, 124(4), 463-467, 1998.

[10] S. Bi, S. Prabhu, S. Cogan, S. Atamturktur, Uncertainty Quantification Metrics with Varying Statistical Information in Model Calibration and Validation, *AIAA Journal*, 55, 3570-3583, 2017.

[11] S. Bi, M. Broggi, M. Beer, The role of the Bhattacharyya distance in stochastic model updating, *Mechanical Systems and Signal Processing*, 117, 437-452, 2019.

[12] Japan Road Association, *Design specifications of highway bridges V Seismic design (2012 English version)*, Maruzen, 2016.

[13] Japan Road Association, *Manual on bearings for highway bridges*, Tokyo, Maruzen, 2004 (In Japanese).

[14] T. Takeda, M.A. Sozen, N.N. Nielsen, Reinforced concrete response to simulated earthquakes, *Journal of the Structural Division*, 96(12), 2557-2573, 1970.

[15] C. Safta, K. Sargsyan, H.N. Najm, K. Chowdhary, B. Debusschere, L.P. Swiler, M.S. Eldred, Probabilistic Methods for Sensitivity Analysis and Calibration in the NASA Challenge Problem. *Journal of Aerospace Information Systems,* 12, 219–234, 2015.

[16] J. Cheng, Y.C. Chen, Transitional Markov Chain Monte Carlo Method for Bayesian Model Updating, Model Class Selection, and Model Averaging, *Journal of engineering Mechanics*, 133(7), 916-832, 2007.

[17] Y. Adachi, *Reliability analysis and limit state design method of isolated bridges under extreme ground motions*, Doctoral thesis, Kyoto University, Japan, 2002 (In Japanese).

EURODYN 2020
XI International Conference on Structural Dynamics
M. Papadrakakis, M. Fragiadakis, C. Papadimitriou (eds.)
Athens, Greece, 23–26 November 2020

NONLINEAR SYSTEM IDENTIFICATION OF CORRODED REINFORCED CONCRETE STRUCTURES BASED ON SEISMIC RESPONSE DATA

Shaghayegh Abtahi[1], Zhenning Liu[2], and Yong Li[3]

[1] University of Alberta, Department of Civil and Environmental Engineering, Donadeo Innovation Centre for Engineering, 9211-116 St., Edmonton, Canada; abtahi1@ualberta.ca

[2] University of Alberta, Department of Civil and Environmental Engineering, Donadeo Innovation Centre for Engineering, 9211-116 St., Edmonton, Canada; zliu6@ualberta.ca

[3] University of Alberta, Department of Civil and Environmental Engineering, Donadeo Innovation Centre for Engineering, 9211-116 St., Edmonton, Canada; yong9@ualberta.ca

Keywords: Fiber Beam-Column Element with Bond-Slip, Steel corrosion, Unscented Kalman Filter, Model Updating

Abstract. *This paper proposes an innovative methodology to estimate the mechanical properties of corroded reinforced concrete (RC) structures based on recorded seismic response data. The essential idea of this approach is to combine the recursive Bayesian inference method with advanced finite element (FE) modeling strategies to estimate the corrosion-affected model parameters. Specifically, in the advanced FE model for corroded RC structures, the effect of corrosion in steel reinforcements (e.g., deteriorated bond-slip) are taken into account. The corrosion-affected model parameters are estimated by minimizing the model-predicted response and the measured response for an instrumented structure during an earthquake through recursive Bayesian inference (i.e., unscented Kalman filter). In this study, simulated seismic response data with additive noise is used for two application examples to demonstrate the proposed methodology with a focus on the deteriorated bond-slip only. The first application example considered consists of a statically tested column with real corrosion. An FE model is developed for this column with validation based on the static test and used to simulate seismic response data for demonstration purposes. The second application example considers an uncorroded bridge column which was tested on a shake-table. The FE model developed for this column is validated based on the shake-table test data and used to simulate the seismic response data for a corroded column where artificial corrosion is assumed. The successful estimation of the model parameters for corroded columns shows that the proposed methodology can potentially be used to identify the unknown mechanical properties of real-world corroded RC structures using recorded seismic response data.*

1 INTRODUCTION

Aging reinforced concrete (RC) structures are under high risk of deteriorations, such as corrosion in aggressive environments. Understanding the seismic performance of these corroded RC structures is one of the major requirements in the field of structural engineering, which assists the decision-making for aged RC structures. To this end, a twofold study is required: first, a computationally efficient finite element (FE) modeling approach, which is able to capture all the aspects of corrosion-induced structural properties; second, a nonlinear FE model updating (FEMU) methodology, which can automatically adjust the nonlinear behavior of the structure based on the measured response.

To quantify the effect of corrosion on the structural performance, several studies have focused on the corrosion-affected behavior of RC structures considering the steel mass loss ratio as a measure of corrosion level [1,2]. However, the common assumption in these studies is perfect bonding between reinforcing steel and the surrounding concrete (i.e., identical axial strain for rebars and concrete). In order to investigate the true performance of corroded RC structures, the corroded bond-slip behavior is required to be incorporated in nonlinear FE modeling, such as implied in [3–5]. In this study, the innovative fiber beam-column element with bond-slip that is developed by [6], enhanced and implemented recently in *OpenSees* [7] by the authors [5], is employed. This element introduces additional degrees of freedom for steel movement to account for the relative slip between steel rebars and the surrounding concrete, in which an explicit bond-slip relationship is considered. Hence, the effect of corrosion on bonding properties can be integrated into the bond-slip model used in the FE model for corroded structures. In this study, the corroded bond-slip behavior is implemented by combining the commonly used bond-slip model for uncorroded structures proposed by Eligehausen et al. [8] with the corrosion model for bonding properties per [3].

In order to develop a nonlinear FE model, which is able to predict accurately the measured structural response, a nonlinear FEMU approach is required. Several studies have proposed different techniques for nonlinear FEMU, including Bayesian inference or stochastic filtering methods, such as extended Kalman filter (EKF) and unscented Kalman filter (UKF). Some recent studies have applied EKF to nonlinear FEMU problems using simulated seismic response data (e.g., [9]); however, this approach has limited capability when applied to highly nonlinear problems because it is based on Taylor series expansion for linearization in first-order approximation of statistics. By contrast, the UKF, another stochastic filtering method based on the Kalman filter, uses the unscented transform for more accurate estimation of the first-order and second-order statistics (i.e., mean, covariance) [10]. The broad use of this method in the literature (e.g., [11–13]) indicates its robustness to solve nonlinear FEMU problems. However, to the best knowledge of the authors, the aforementioned stochastic filtering methods have not been utilized for system identification of corroded structures (e.g., health condition assessment of aged structures). The research work presented here consists of the first of its kind in the literature.

This study focuses on the identification of corroded bonding properties in RC columns using simulated seismic data with various noise levels. For this purpose, two experimental RC columns are considered: a statically tested RC column with real corrosion [14] and a shake-table tested RC bridge pier column with no corrosion [15]. The nonlinear FE model for these two columns are both validated and used to simulate seismic response data based on two columns with artificial corrosion for nonlinear FEMU. These two application examples demonstrate the capability of Bayesian inference to estimate the corroded bond-slip properties in aged RC structures after a brief description of stochastic inference method (i.e., UKF) used in this study.

2 CORROSION MODEL FOR BOND-SLIP

The rebar corrosion in aged RC structures influences the bond-slip behavior and reduces the contribution of steel rebars due to diminished composite action between steel and concrete. To account for such effect, this study proposes a corroded bond-slip model, which employs the bond-slip behavior for uncorroded RC structures developed by Eligehausen et al. [8] and the corrosion-induced modification factors for bonding properties [3], denoted as Kivell model. In this model, the maximum bonding stress, t_1^c, and the residual bonding, t_3^c, are both related to the corrosion level K, which is defined as the percentage of reinforcement mass loss ratio. The corroded properties t_1^c and t_3^c are defined according to Eq. (1) and Eq. (2), respectively.

$$\frac{t_1^c}{t_1^0} = \begin{cases} 1.2e^{-0.076K} \le 1.0 & K > 3\% \\ 1.0 & K \le 3\% \end{cases} \tag{1}$$

$$\frac{t_3^c}{t_1^c} = \begin{cases} 0.26 + 0.13K & 0 \le K < 3\% \\ 0.65 & 3\% \le K < 13\% \\ 0.65 - 0.06(K - 13) & 13\% \le K < 20\% \\ 0.23 & K \ge 20\% \end{cases} \tag{2}$$

In addition to the corrosion-induced reduction in the above properties for the bond-slip model, the cumulative damage factors are used in cyclic behavior to characterize the corrosion-affected degradation in the hysterical behavior. Readers of interest are referred to [3] for details. Such a corroded bond-slip model is implemented in *OpenSees* by the authors [5].

3 FE MODEL VALIDATION OF RC COLUMNS

The two RC columns considered in this study are both modeled through a newly developed fiber beam-column element with bond-slip in *OpenSees* by the authors [5] and validated based on the experimental data. Both validated nonlinear FE models will be used later in this study to simulate seismic response data after introducing artificial corrosion to the bonding.

3.1 Corroded RC column

The first RC column considered in this study is a corroded RC column tested under the static cyclic loading, denoted as Meda column [14], which is corroded so that the mass loss ratio of the longitudinal reinforcement (i.e., corrosion level) is equal to 20%. Figure 1(a) represents the geometry and section details for this column. The column is modeled with the newly developed fiber beam-column element with bond-slip in *OpenSees*, and the corroded bond-slip model mentioned earlier is used to consider the degraded bond-slip properties. Additionally, for the purpose of model validation, the other corrosion effects for the tested column are also taken into account, including the corresponding concrete cover spalling due to volumetric expansion of steel because of corrosion products, the reduced strength of concrete according to [16,17], rebar cross-section area reduction as well as the steel strength reduction caused by pitting corrosion [18]. The same loading protocol as the experiment is used to simulate the cyclic load-deflection curve of the corroded column in the experimental test. To emphasize the importance of corroded bond-slip, the case with perfect bonding but all other corrosion effects is also considered here for comparison. Figure 1(b) shows the resultant force-drift ratio hysteresis for the perfect bonding case by the gray solid curve, the corroded bonding case by the black solid curve, and experimental results by the dashed black curve. The FE model predictions with corroded bonding are in good agreement with the experi-

mental results until reaching the deformation level of about 2.0% drift ratio. It is worth mentioning that the pinching behavior (or less energy dissipation) is captured well comparing to the perfect bonding case, since this effect is dominated by bond-slip. However, the strength degradation at large deformation levels is not captured due to buckling of the reinforcement [14], while the effect of buckling are beyond the scope of this study.

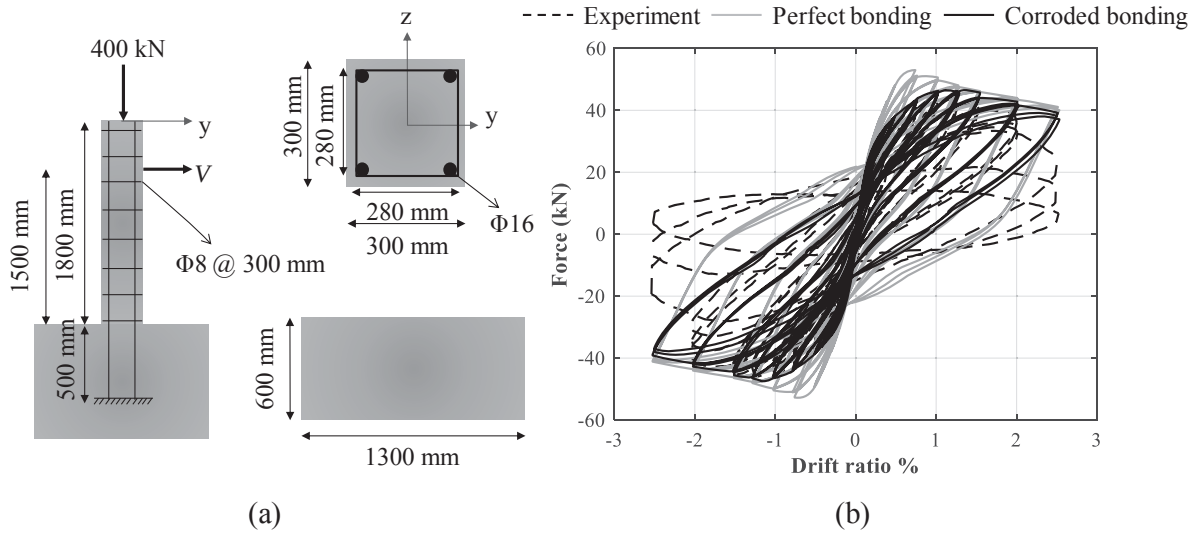

Figure 1: Meda column: (a) geometry and section details, and (b) force-drift ratio hysteresis comparison between FE and experimental prediction

3.2 Uncorroded RC column

The uncorroded RC column considered here is a RC bridge column tested under earthquake loading on the shake table at the University of California, San Diego in 2010, denoted as UCSD column [15]. Figure 2(a) describes the geometry and section details. This column is subjected to a sequence of 10 earthquake ground motions, and the first one: Loma Prieta ground motion recorded at Agnew State Hospital with a moment magnitude of 6.9, is considered. Similar to the previous column, it is modeled by the newly developed fiber beam-column element with bond-slip in *OpenSees*. The time-history of the top drift ratio is plotted in Figure 2(b) for the RC column with perfect bonding in comparison with the experimental results. Additionally, Figure 2(c) describes the top drift ratio time-history for the RC column with imperfect bonding (i.e., uncorroded normal bonding) compared to the experimental results. As indicated, the response of the model with imperfect bonding is in a proper correlation with the experiment compared to the model with perfect bonding, which implies the importance of bond-slip in the prediction accuracy of nonlinear FE models for RC columns.

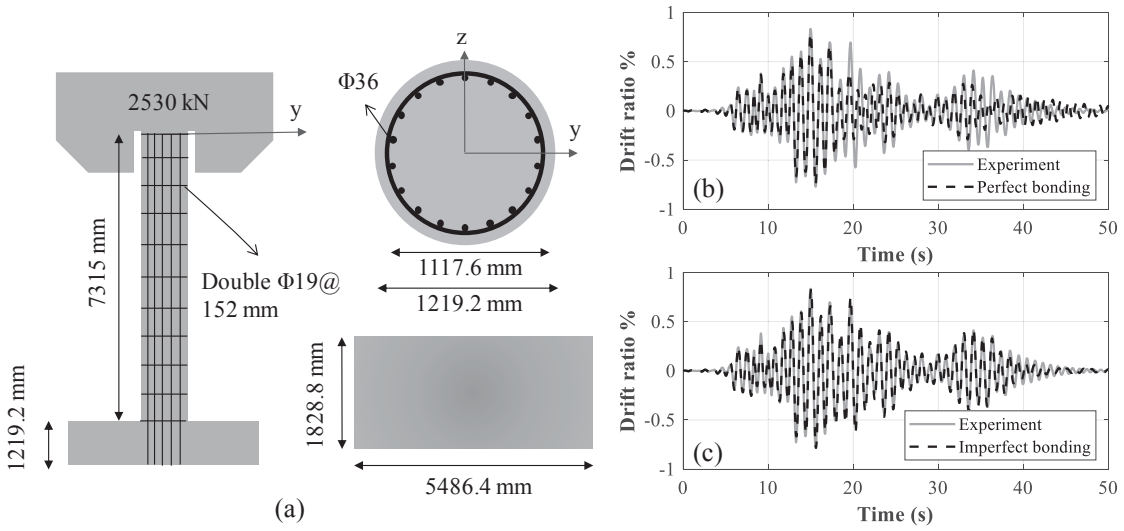

Figure 2: UCSD column: (a) geometry and section details, (b) top drift ratio time-history comparison between FE prediction with perfect bonding and experiment, and (c) top drift ratio time-history comparison between FE prediction with imperfect bonding and experiment

4 STOCHASTIC INFERENCE FOR PARAMETER ESTIMATION

Direct measurements of the corroded bonding properties are challenging and thus the accurate modeling parameters are not readily available. Such uncertainties in the FE modeling aspects can compromise the predictability of the model and in turn bias the residual performance evaluation of aged RC structures with corrosion. As such, reliable estimation of the parameters is needed for better simulation and for damage/condition assessment. Nonlinear parameter estimation using stochastic inference, such as UKF [10], can be integrated with nonlinear FE modeling to identify such uncertain modeling aspects by performing nonlinear FEMU, if other measurements are available. Such a strategy is briefly summarized as follows.

The unobservable time-invariant vector $\boldsymbol{x}$, containing unknown/uncertain FE model parameters, is represented as a random walk process in UKF (i.e., a linear state-transition equation); see Eq. (3):

$$\boldsymbol{x}_k = \boldsymbol{x}_{k-1} + \boldsymbol{w}_{k-1} \tag{3}$$

where the subscript k and $k-1$ denote the current and previous analysis steps, respectively; $\boldsymbol{w}$ is additive zero-mean white Gaussian noise (AWGN) with a diagonal covariance matrix $\boldsymbol{Q}$. The measurement (observation) vector of the system response, $\boldsymbol{y}$, is related to the unobservable vector, $\boldsymbol{x}$, through the nonlinear FE model prediction through the measurement equation, as shown in Eq. (4). In this equation, a prediction error vector $\boldsymbol{v}$, which is a zero-mean white Gaussian noise vector with a known covariance matrix $\boldsymbol{R}$, is used to model the inherent model uncertainty and the measurement noise in $\boldsymbol{y}$.

$$\boldsymbol{y}_k = \boldsymbol{h}_k(\boldsymbol{x}_k, \ddot{u}^g_{1:k}) + \boldsymbol{v}_k \tag{4}$$

Here, $\boldsymbol{h}_k(\boldsymbol{x}_k, \ddot{u}^g_{1:k})$ represents the simulated structure response at analysis step k. It is evaluated by analyzing the nonlinear FE model with the current model parameter vector $\boldsymbol{x}_k$, subjected to the earthquake ground motion acceleration series until the current time step.

By defining the state-transition and measurement equations, stochastic inference (e.g., UKF) can be utilized to estimate the posterior mean vector $\boldsymbol{\mu}_k^{\boldsymbol{xx}}$ and the corresponding covariance matrix $\boldsymbol{P}_k^{\boldsymbol{xx}}$ of $\boldsymbol{x}_k$ recursively when more observations are available as time evolves. This

is to incorporate the information obtained from experimental observations in a Bayesian framework at time step k. Compared with other Bayesian methodologies, Kalman filter-based approach allows efficient updating through the Kalman gain matrix, which is introduced as a weight measure based on the difference between the prediction ($\boldsymbol{h}_k(\boldsymbol{x}_k, \ddot{u}^g_{1:k})$) and observation (measurement) $\boldsymbol{y}_k$. The Kalman gain is calculated by the cross-covariance matrix between $\boldsymbol{x}_k$ and $\boldsymbol{y}_k$, $\boldsymbol{P}_k^{xy}$, and the covariance matrix of $\boldsymbol{y}_k$, $\boldsymbol{P}_k^{yy}$. By applying UKF, the values of $\boldsymbol{P}_k^{xy}$ and $\boldsymbol{P}_k^{yy}$ are estimated by unscented transform, in which a series of sigma points (SPs) are deterministically defined by $\boldsymbol{P}_k^{xx}$ and $\boldsymbol{\mu}_k^{xx}$ and the nonlinear FE model is evaluated as these SPs. Readers of interest are referred to [11,19] for details.

5 NONLINEAR FINITE ELEMENT MODEL UPDATING

The validated FE models for the two RC columns (i.e., Meda column and UCSD column) are used here to demonstrate the potential in estimating corrosion-affected parameters by a nonlinear FEMU strategy, integrating stochastic filtering and efficient FE modeling for corroded RC structures. For this purpose, the bonding properties of these two columns, t_1 and t_3, are assumed to be degraded due to artificial corrosion. Both of these columns are subjected to earthquake excitations, which are chosen purposely to have a short duration in order to save computational cost but without loss of generality. For the Meda column, the Loma Prieta earthquake recorded at Agnew State Hospital station is selected from the Next-Generation Attenuation ground motion database [20]. This ground motion is so scaled to reach the ductility demand (i.e., deformation demand with respect to the yield deformation) of 2.0 for the Meda column. The ground motion selected for the UCSD column is the Kobe earthquake (1995) recorded at the Takatori station [20]. This ground motion is scaled so that the ductility demand of 8.0 is reached for the UCSD column, where significant nonlinearity is involved in this column. The nonlinear FEMU strategy is employed to identify corroded t_1 and t_3 for these columns with different corrosion levels in the column and different noise levels in the measurements (e.g., the displacement at the top of the column used in this study).

5.1 FEMU of Meda column with different corrosion levels

To investigate the capability of the proposed methodology for identifying the corrosion-affected bonding properties, this study considers two levels of corrosion for the Meda column: 16% mass loss ratio as a medium level, and 24% mass loss ratio as a high level. The corrosion level corresponds to the age of the column and is dependent on the cover concrete, environmental conditions, etc. [1,18]. For the Meda column with a relatively small thickness in concrete cover, 16% and 24% corrosion levels represent the age of the column to be about 25 and 40 years in medium corrosion intensity situation, respectively. The effect of corrosion on the bonding properties (i.e., t_1 and t_3) is focused in this study. For 16% corrosion level, the ratios of the corroded to uncorroded values for t_1 and t_3 are equal to 0.33 and 0.48, respectively, per the Kivell model [3]. Similarly, the corroded to uncorroded ratios for t_1 and t_3 are 0.24 and 0.14 for the Meda column with 24% corrosion level.

Since no experimental observations are available, seismic simulation data, which are generated through the nonlinear FE model for the Meda column with corroded bond-slip, i.e., degraded t_1 and t_3 (denoted as the true parameters), are used. Note that in this section, accurate measurement from high precision sensors is assumed, and thus no noise is considered. In this study, only one observation is used, i.e., the time-history of the top drift ratio of the column subjected to the earthquake ground motion. Using the observations, the corroded bonding parameters considered here will be estimated through UKF.

In UKF, the initial guess for the bonding properties are assumed to be those for the uncorroded case. Figure 3(a) shows the time-history of the drift ratio of the Meda column with 16% corrosion level based on the initial set of parameters (i.e., before updating) with comparison to the observation. The observation is presented as true finite element analysis (FEA) and the initial response is denoted as initial FEA. By using the aforementioned UKF, the corroded bonding properties (t_1 and t_3) are updated. Figure 3(b) demonstrates the FE prediction of the same column after updating with comparison to the observation. Comparing Figure 3(a) and (b) indicates the FE prediction is improved significantly, and a near-perfect correlation is achieved using the updated model parameters. For more details, the updating histories for t_1 and t_3, are presented in Figure 4(a) and (b), respectively, in addition to their 95% confidence intervals (CI). The first parameter (t_1) is converged to the true value in the very beginning and the uncertainty in this parameter estimation decreases significantly since it is corresponding to the stiffness and yield stress of the bonding behavior. On the other hand, the second parameter (i.e., t_3) is converged later as expected but with only a slight reduction in the uncertainty. The reason lies in the fact that this parameter is to be influential after the bond yielding.

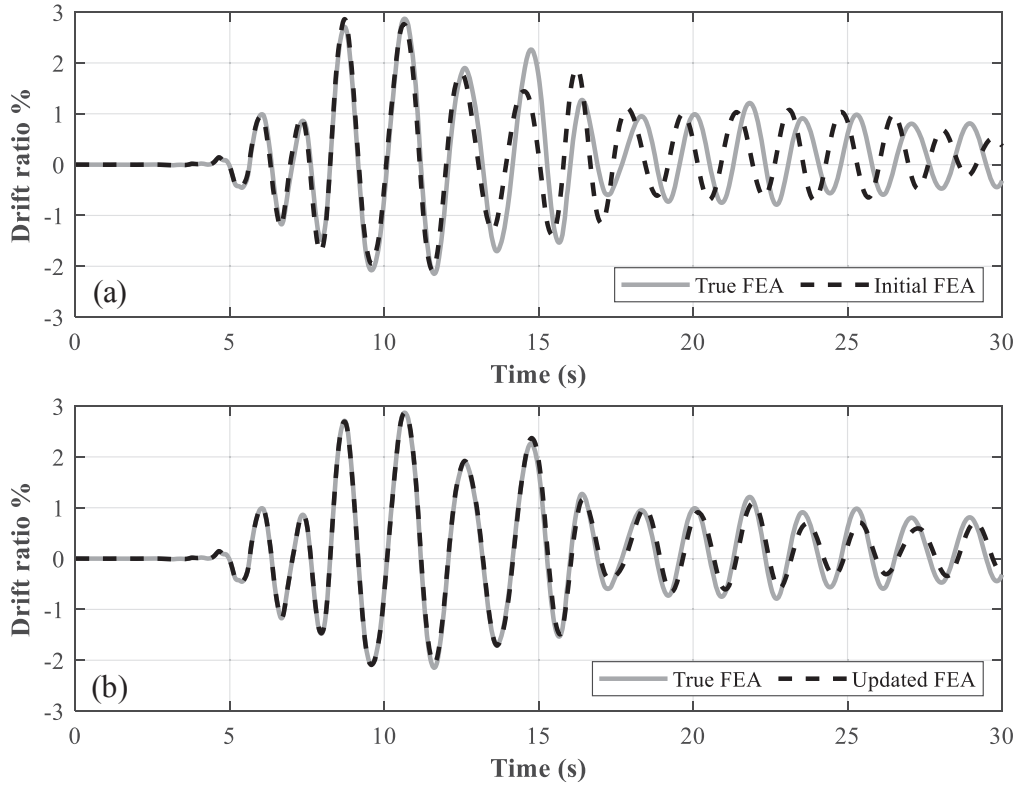

Figure 3: Time-history of drift ratio for Meda column with 16% corrosion level and zero noise in the observation: (a) before and (b) after updating

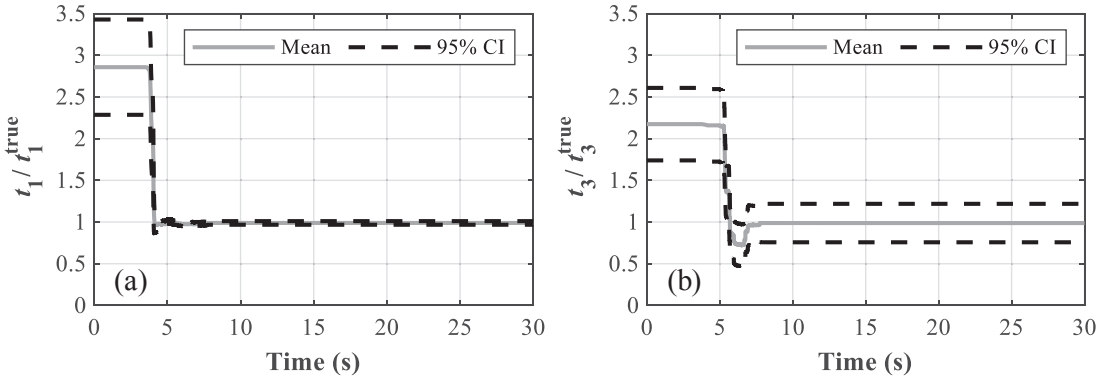

Figure 4: Updating history for (a) t_1 and (b) t_3 for Meda column with 16% corrosion level and zero noise in the observation

Similarly, the Meda column with a high-level corrosion is studied. Figure 5(a) and (b) show the time histories of the top drift ratio predicted from the FE model based on the bonding properties before and after updating in comparison with the observation (i.e., true FEA results). The comparison shows that nonlinear FEMU has led to a notable improvement in the FE prediction for this column with a high corrosion level as well. Therefore, it can be concluded that the proposed FEMU approach is also able to capture the effect of corrosion on the bonding properties in different levels. Similar to the previous case, the updating histories of t_1 and t_3 are presented in Figure 6(a) and (b), respectively. Note that in this case, due to the high level of corrosion, the bond yielding occurs at the earlier time step than the previous case and hence, t_3 would be updated earlier as well, and the associated uncertainty is reduced more.

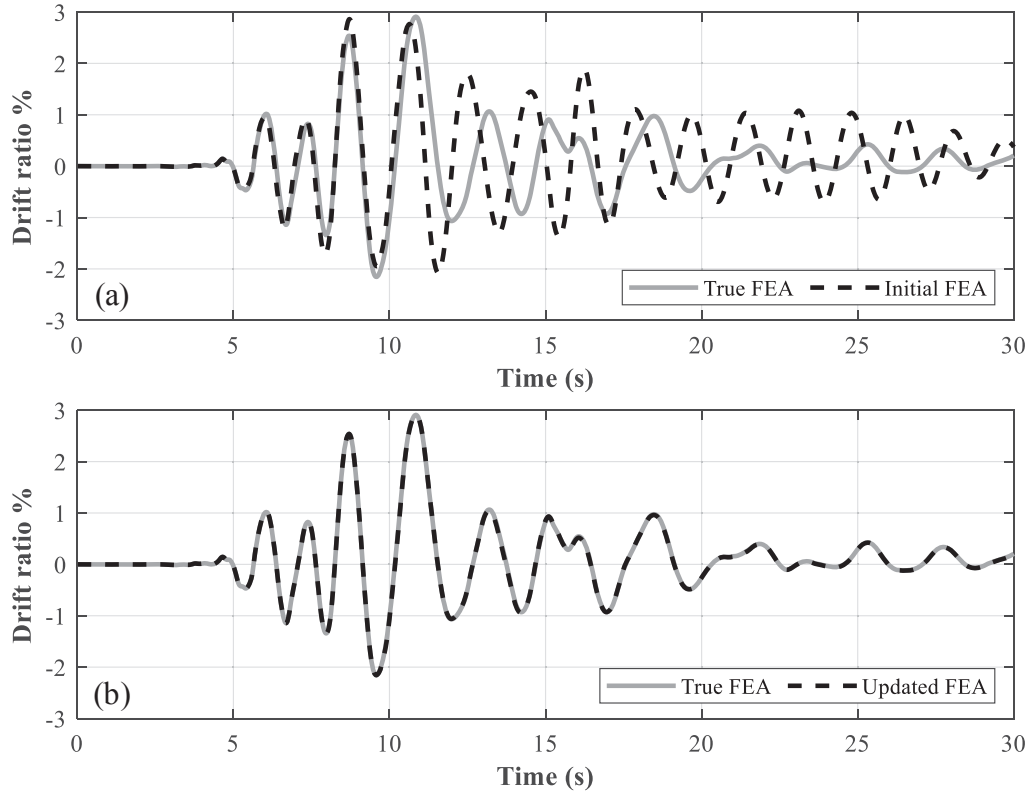

Figure 5: Time-history of drift ratio for Meda column with 24% corrosion level and zero noise in the observation: (a) before and (b) after updating

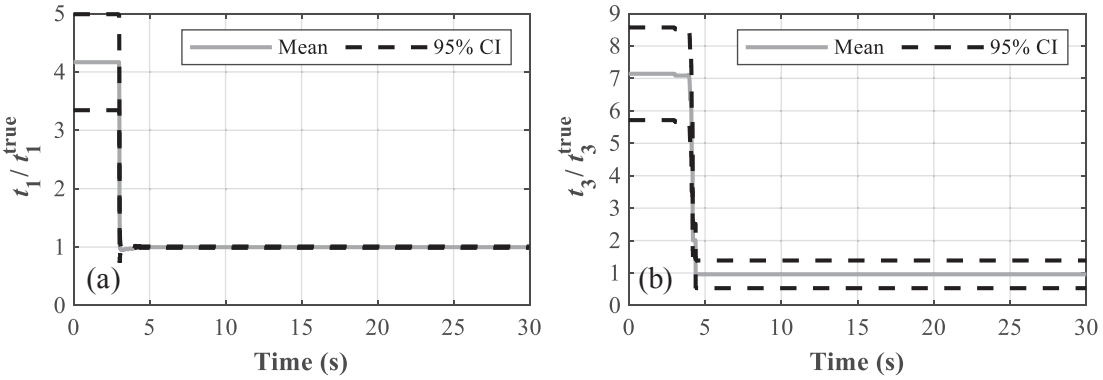

Figure 6: Updating history for (a) t_1 and (b) t_3 for Meda column with 24% corrosion level and zero noise in the observation

5.2 FEMU of Meda column with different noise levels

In the previous section, the observations are assumed to be noise-free. However, in reality, the observations are typically involved with various levels of noise, which may pollute the measurements and thus affect the updating process. To show the robustness of the proposed methodology for corrosion-affected parameter estimation in RC structures, this section considers the polluted observation with different levels of noise. As such, a medium and a high level of AWGN, with a standard deviation of 2% and 5% of the maximum response (i.e., maximum displacement), respectively, are considered here to contaminate the prediction from the true FE model defined earlier for the Meda column with 16% corrosion level. Figure 7(a) and (b) show the comparison between the time-histories of top drift ratio before and after updating based on the observation with 2% noise, for the Meda column under the effect of 16% corrosion level. In addition, Figure 8(a) and (b) present the updating histories of t_1 and t_3 corresponding to this case. The comparison reveals the employed methodology is able to update the parameters so that the FE prediction is in a good agreement with the observation, even though a low-level measurement noise (2%) exists. However, the estimation for t_3 is more challenging when noise comes into play.

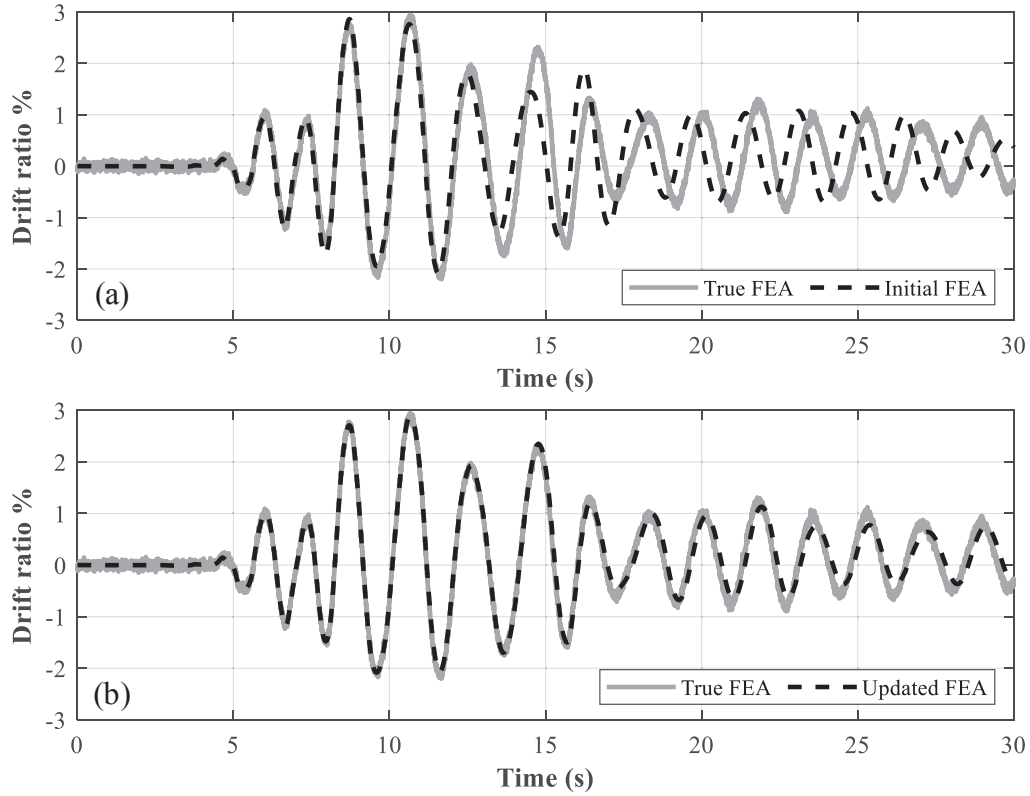

Figure 7: Time-history of drift ratio for Meda column with 16% corrosion level and 2% noise in the observation: (a) before and (b) after updating

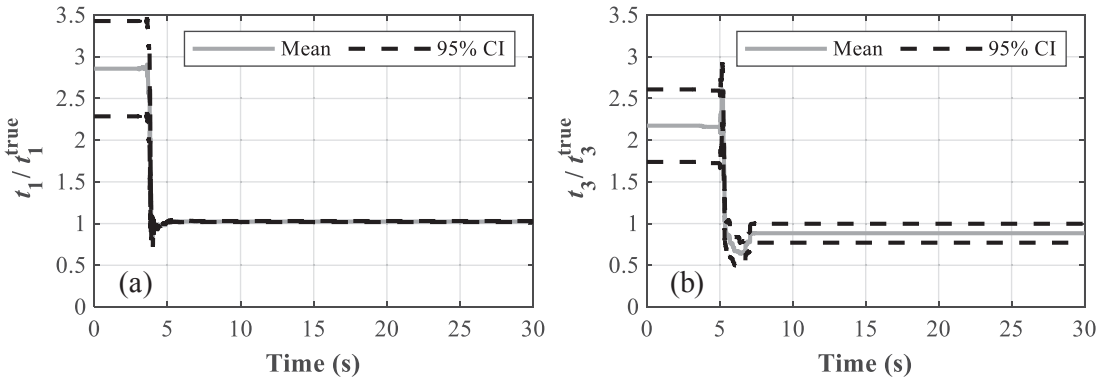

Figure 8: Updating history for (a) t_1 and (b) t_3 for Meda column with 16% corrosion level and 2% noise in the observation

The higher level of noise (i.e., 5% AWGN) is considered here. The nonlinear FE model is updated through UKF, and the predicted responses before and after updating are illustrated in Figure 9(a) and (b), respectively. Similar to the previous cases, the updating histories of t_1 and t_3 are displayed in Figure 10(a) and (b). The demonstrated results of this case reaffirm UKF is able to update the corroded bonding properties properly, even when a relatively high level of noise (5%) exists. Note that according to Figure 10(b), similar to Figure 8(b), the final values of t_3 are different from the true value. This difference mainly stems from the additive noise considered for these two cases, which affects the accuracy of the updating results. However, the global behavior of the column is not significantly sensitive to this parameter (i.e., t_3) and hence, the drift ratio time-history is still in a good agreement with the true FE results.

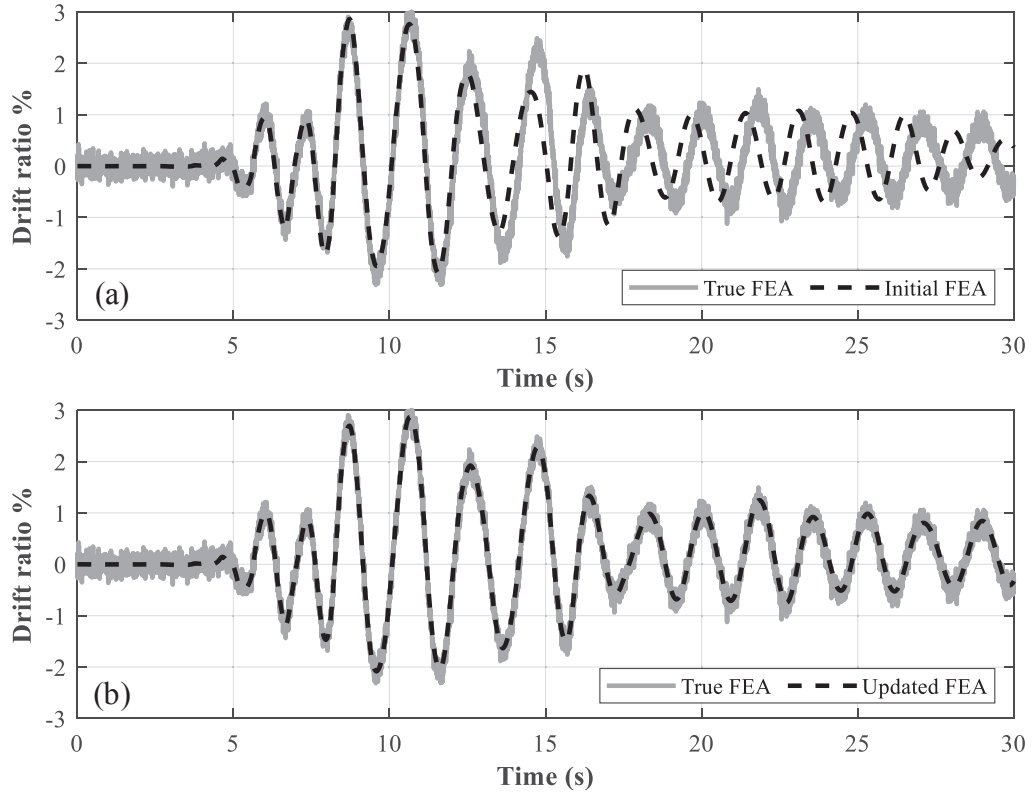

Figure 9: Time-history of drift ratio for Meda column with 16% corrosion level and 5% noise in the observation: (a) before and (b) after updating

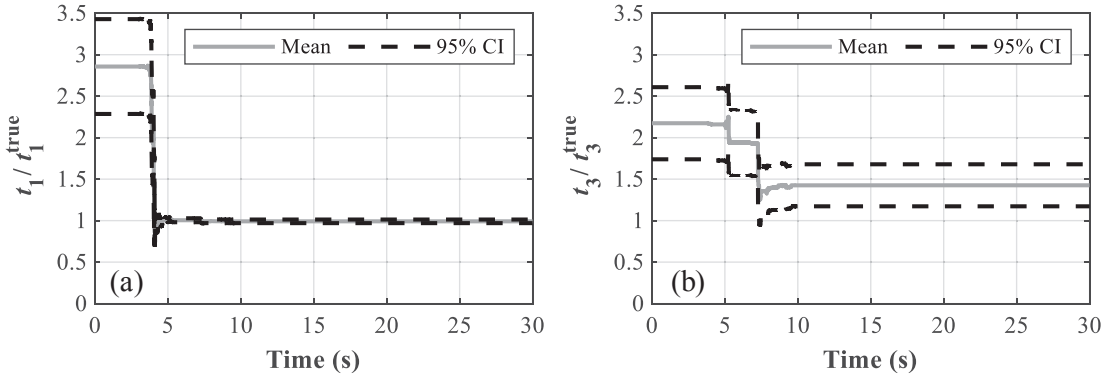

Figure 10: Updating history for (a) t_1 and (b) t_3 for Meda column with 16% corrosion level and 5% noise in the observation

5.3 FEMU of UCSD column under high-intensity excitation

In addition to the Meda column, UCSD column with artificial corrosion (16% corrosion level) is also considered. The ratio of corroded to uncorroded t_1 equals to 0.33, and the ratio of corroded to uncorroded t_3 equals to 0.63, per [3]. This developed RC column with these parameter values is assumed to be true FE and used to generate observations during the selected earthquake with a high seismic ductility demand. Figure 11(a) and (b) display the time-histories of the top drift ratio before and after updating with comparison to the observation, respectively. In addition, the updating histories for t_1 and t_3 are shown in Figure 12(a) and (b). According to Figure 11, the updated response is in a better correlation with the observation than the initial FEA responses. Note for the UCSD column with 16% of corrosion, the bond-

slip behavior stays in a range that the residual stress (i.e., t_3) does not play a significant role and then, the parameter is not altered in the updating process but the uncertainty is reduced due to the relative strong excitation.

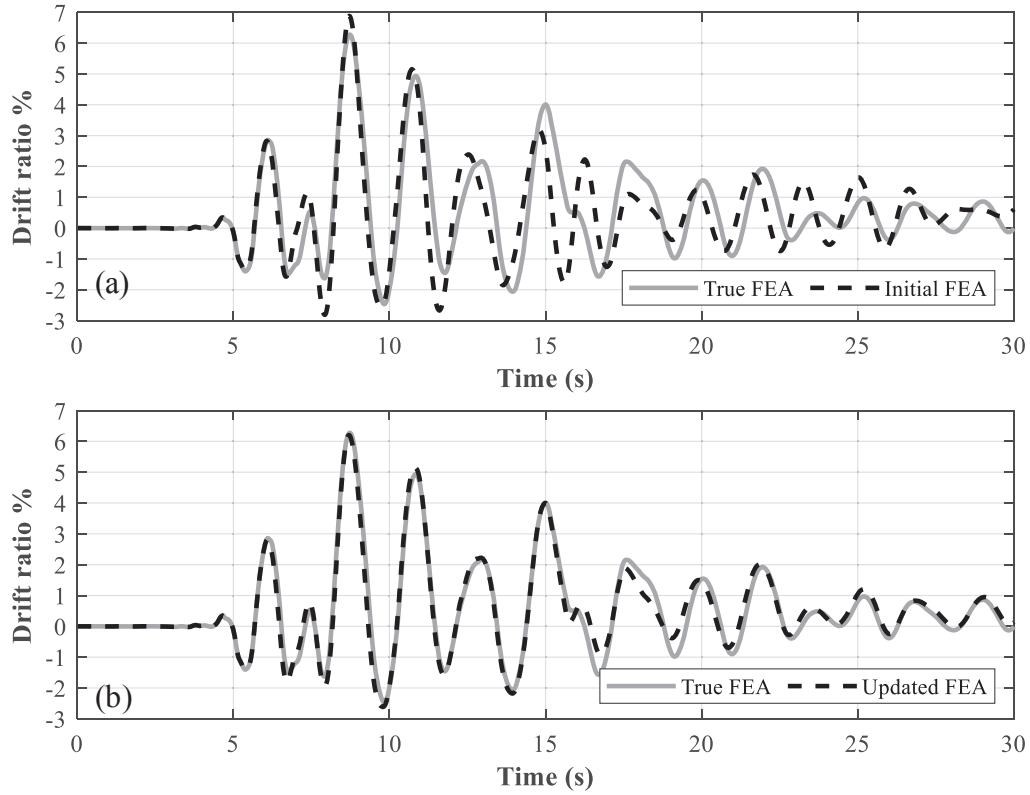

Figure 11: Time-history of drift ratio for UCSD column with 16% corrosion level and zero noise in the observation: (a) before and (b) after updating

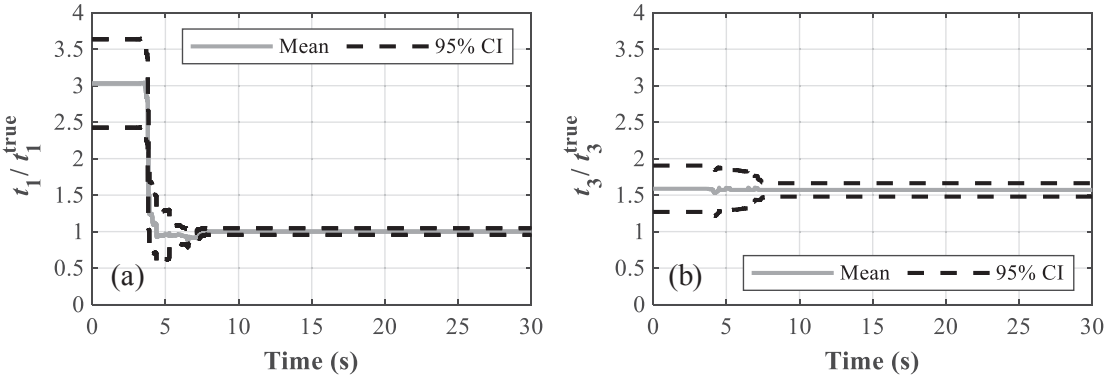

Figure 12: Updating history for (a) t_1 and (b) t_3 for UCSD column with 16% corrosion level and zero noise in the observation

6 CONCLUSIONS

This study proposes integrating stochastic filtering, such as the unscented Kalman filtering (UKF) strategy, with nonlinear FE model for corroded concrete structures, to estimate the corroded bond-slip properties based on global response observations (i.e., displacement history). To this end, a newly developed fiber beam-column element with bond-slip is used to model two RC columns. The FE models of the two considered RC columns are validated based on

the available experimental data. However, the measured responses utilized for parameter estimation in this study are simulated data from the nonlinear FE model of the RC columns with artificial corrosion. Different levels of corrosion and noise are considered. The presented study shows that the proposed methodology can successfully estimate the corroded bond-slip properties and significantly improve the model prediction accuracy. It indicates that the methodology adopted in this study is promising to be used for condition assessment of aged RC structures based on recorded seismic response data.

REFERENCES

[1] KAT. Vu, MG. Stewart, Structural reliability of concrete bridges including improved chloride-induced corrosion models, *Structural Safety* 22, 313-33, 2000.

[2] J. Ghosh, JE. Padgett, Aging considerations in the development of time-dependent seismic fragility curves, *Journal of Structural Engineering* 136, 1497-1511, 2010.

[3] A. Kivell, A. Palermo, A. Scott, Complete model of corrosion-degraded cyclic bond performance in reinforced concrete, *Journal of Structural Engineering* 141, 4014222, 2015.

[4] NS. Vu, B. Yu, B. Li, Prediction of strength and drift capacity of corroded reinforced concrete columns, *Construction and Building Materials* 115, 304-318, 2016.

[5] S. Abtahi, Y. Li, Nonlinear behavior of reinforced concrete structures considering bond-slip under corrosion, *Proceedings of the 17th World Conference on Earthquake Engineering*, Sendai, Japan, 2020.

[6] E. Spacone, S. Limkatanyu, Responses of reinforced concrete members including bond-slip effects, *ACI Structural Journal* 97, 831-839, 2000.

[7] S. Mazzoni, F. McKenna, MH. Scott, GL. Fenves, B. Jeremic, Open system for earthquake engineering simulation: User Command Manual, *Pacific Earthquake Engineering Research Center*, Berkeley, California, USA, 2006.

[8] R. Eligehausen, E. Popov, VV. Bertero, Local bond stress-slip relationships of deformed bars under generalized excitations: Experimental results and analytical model, *EERC Report 83-23*, Earthquake Engineering Research Center, University of California, Berkeley, California, USA, 1983.

[9] H. Ebrahimian, R. Astroza, JP. Conte, Extended Kalman filter for material parameter estimation in nonlinear structural finite element models using direct differentiation method, *Earthquake Engineering and Structural Dynamics* 44, 1495-1522, 2015.

[10] EA. Wan, R. Van Der Merwe, The unscented Kalman filter for nonlinear estimation, *Proceedings of IEEE 2000 Adaptive Systems for Signal Processing, Communications, and Control Symposium (Cat. No. 00EX373)*, pages 153-158, 2000.

[11] R. Astroza, H. Ebrahimian, Y. Li, JP. Conte, Bayesian nonlinear structural FE model and seismic input identification for damage assessment of civil structures, *Mechanical Systems and Signal Processing* 93, 661-687, 2017.

[12] R. Astroza, N. Barrientos, Y. Li, EIS. Flores, Z. Liu, Bayesian updating of complex nonlinear FE models with high-dimensional parameter space using heterogeneous

measurements and a batch-recursive approach, *Engineering Structures* 201, 109724, 2019.

[13] Z. Liu, Y. Li, R. Astroza, Parameter estimation of a shake-table tested bridge column with bond-slip effect using stochastic inference, *Proceedings of CSCE Annual Conference*, Saskatoon, Saskatchewan, Canada, 2020.

[14] A. Meda, S. Mostosi, Z. Rinaldi, P. Riva, Experimental evaluation of the corrosion influence on the cyclic behaviour of RC columns, *Engineering Structures* 76, 112-123, 2014.

[15] M. Schoettler, J. Restrepo, G. Guerrini, DE. Duck DE, francesco carrea, A full-scale, single-column bridge bent tested by shake-table excitation, *https://DatacenterhubOrg/Resources/7268*, 2012.

[16] JB. Mander, MJN. Priestley, R. Park, Theoretical stress-strain model for confined concrete, *Journal of Structural Engineering* 114, 1804-1826, 1988.

[17] D. Coronelli, P. Gambarova, Structural assessment of corroded reinforced concrete beams: modeling guidelines, *Journal of Structural Engineering* 130, 1214-1224, 2004.

[18] MG. Stewart, DV. Rosowsky, Time-dependent reliability of deteriorating reinforced concrete bridge decks, *Structural Safety* 20, 91-109, 1998.

[19] R. Astroza, H. Ebrahimian, JP. Conte, Material parameter identification in distributed plasticity FE models of frame-type structures using nonlinear stochastic filtering, *Journal of Engineering Mechanics* 141, 4014149, 2015.

[20] B. Chiou, R. Darragh, N. Gregor, W. Silva, NGA project strong-motion database, *Earthquake Spectra* 24(1), 23-44, 2008.

EURODYN 2020
XI International Conference on Structural Dynamics
M. Papadrakakis, M. Fragiadakis, C. Papadimitriou (eds.)
Athens, Greece, 23–26 November 2020

DAMAGE DETECTION OF JOINING TECHNOLOGIES FOR PRINTED CONTROLLER BOARDS IN AUTOMOBILES

Moritz Hülsebrock[1], Maximilian Herrnberger[2], Heiko Atzrodt[3], and Roland Lichtinger[2]

[1]Technische Universität Darmstadt
Magdalenenstr. 4, 64289 Darnstadt
e-mail: moritz.huelsebrock@sam.tu-darmstadt.de

[2] BMW AG
Taunusstr. 41, 80807 München
e-mail: {maximilian.herrnberger, roland.lichtinger}@bmw.de

[3] Fraunhofer LBF
Bartningstr. 47, 64289 Darmstadt
e-mail: heiko.atzrodt@lbf.fraunhofer.de

Keywords: Bayesian Model Updating,Transitional MCMC, Parametric Model Order Reduction, Structural Health Monitoring, Printed Circuit Board

Abstract. *The reliable design of power electronics for automobiles is one of the major challenges in the advancing electrification of the powertrain. The printed controller boards (PCB) in particular are affected by the demanding operating conditions. The objective of this ongoing investigation is to analyze the effect of different joining technologies between the PCB and the casing on the reliability. Therefore, a structural health monitoring (SHM) concept is presented based on a Bayesian model updating framework that monitors changes in the stiffness of the joint connection. To cope with the computational challenges associated with the approach, parametric model order reduction is applied. The concept is validated by a generic use case where one of the joints has a sudden loss of stiffness.*

1 INTRODUCTION

The advancing electrification of the powertrain in automobiles introduces new components and hence new challenges for a reliable design. One of those components is the Power Electronical Unit (PEU) that transforms the direct current (DC) from the battery to an alternating current (AC) for the electric motor. The power electronic operates in demanding environments resulting in a challenging task for a reliable design. Depending on the component, different stressors come into play - e.g. high temperatures, temperature cycling, humidity, dust or vibration can endanger safe operation [1]. Due to their complex design and uneven mass distribution, vibrations are the main stressors for printed circuit boards (PCBs) [2]. The present work illustrates the current state of an ongoing investigation analyzing the effect on the reliability of different joining technologies connecting the PCB to the casing. The goal of the investigation is to replicate stresses on the PCB in an automobile on a test rig and analyze the effect of different joining technologies on the vibration behavior and derive the change in reliability from it. The power electronics and especially the PCB are crucial components where failure can lead to serve accidents. Therefore, a structural health monitoring (SHM) strategy for the experiment as well as later applications in the automobile is presented that monitors changes in the vibration behavior due to loosening of bolt connections between the PCB and the casing. SHM strategies have been used for a long time for monitoring structures like bridges [3, 4] or skyscrapers [5]. Due to the advancements in sensor technology and signal processing in recent years, those strategies are applied to other engineering structures like milling machines [6] and composite structures [7]. SHM methods can be divided into two groups: model based and feature based methodes [8]. *Model-based methods* correlate the observational signatures of abnormal structures with analytical or quantitative models to detect the damage parameters [8]. Common methods are autoregressive and moving average (ARMA) model [9], hidden Markov model (HMM) [10] or artifical neural network (ANN). In contrast to that, *Feature-based methods* are based on a two step process. The first step is the extraction of features (e.g. eigenfrequencies, mode shape, damping rations) and the second one is the interpretation of these features. The interpretation is usually performed by classical model updating algorithms [11–13]. Structural model updating methods are essentially a process of adjusting uncertain parameters of a finite element model by comparing it to measurement data. For the application of SHM classical deterministic gradient-based model updating methods have a disadvantage to probabilistic methods because of their tendency to converge into local minima. Probabilistic methods are based on stochastic simulation algorithms such as Markov Chain Monte Carlo (MCMC) [14] and Transitional MCMC [15, 16]. Model updating algorithms involve a moderate to very large number of FE reanalyses. For complex systems that easily involve hundreds of thousands of degree-of-freedom (DOF), the computational effort is too high for time-critical operations. Therefore, different approaches are used to reduce the analysis time ranging from the use of model order reduction techniques [17], surrogate models [18], and code parallelization [19,20]. Most often component mode synthesis (CMS) techniques [17], e.g. Craig-Bampton, are applied to carry out system analysis in a reduced space and to decrease the computational effort that arises from the variation of uncertain parameters [21, 22]. In the usual workflow, the structures under consideration are separated into substructures [3] and reassembled allowing the alteration linearly depended system parameters like stiffness, density or thickness of shell elements. To decrease the computational effort the reassembled system matrix can be further reduced [3, 23], avoiding the re-assembly of the reduced system matrices from the original matrices. This leads to solving the eigenproblem of the reduced-order model being the only time consuming analysis step.

Within this work, the development of the real-time capable parametric model of the test rig and a generic use case are presented. The use case includes the data acquisition from a time-domain simulation model, signal processing, modal parameter extraction by an operational modal analysis, data clustering and mode matching by a k-Means algorithm as well as the implementation of Bayesian SHM approach to monitor changes in the stiffness of the joint parameter.

2 STRUCTURAL HEALTH MONITORING USING MODAL CHARACTERISTICS

This paper presents details of the application of a Bayesian probabilistic framework that allows online SHM to monitor stiffness changes in the mounting of a PCB in an automobile by analyzing modal data (eigenfrequencies and modeshapes) from ambient vibration. The identified modal parameters are clustered by a k-Means algorithm [24] to enable a classification based on multiple previous measurements, therefore taking uncertainties into account and allowing a framework of inference in the presence of incomplete data [25]. The evaluation of the Bayesian framework is carried out by the so-called Transitional Markov Chain Monte Carlo (TMCMC) algorithm [15].

2.1 Bayesian formulation

The Bayesian model updating framework is based on the Bayes' Theorem, which is formulated in [26]. Adjusted to structural model updating, the Bayes' Theorem [12, 27] is described by

$$P(\theta|D,M) = \frac{P(D|\theta,M)P(\theta|M)}{p(D|M)}, \tag{1}$$

where M denotes the model class, D denotes the experimental data, which consists of the measured modal properties of the structure under consideration, and θ describes the parameter vector of the unknown, adjustable model parameters. The posterior distribution $P(\theta|D,M)$ expresses the conditional probability of θ on the prior probability $P(\theta|M)$ and the experimental data. The likelihood function $P(D|\theta,M)$ is a measure of agreement between the measured data D and the model out for a given data set θ.

The formulation of the likelihood function using modal data is derived in [25]. The experimental data obtain by an operational modal analyses algorithm is assumed to consist of N_s sets, $D = [\omega_{1,j}...\omega_{N_m,j}, \Phi_{1,j}\ ...\ \Phi_{1,N_m}]_{j=1}^{N_s}$ composed of N_m modal frequencies ω_r and N_m incomplete mode shape vectors $\Phi_r \in \Re_0^N$, where N_0 is the number of measured DOFs. The likelihood function can be written as

$$P(D|\theta,M) = c\,exp\left(-\frac{1}{2}\sum_{r=1}^{N_m} J_r(\theta)\right), \tag{2}$$

where $J_r(\theta)$ is given by

$$J_r(\theta) = \sum_{j=1}^{N_s}\left[\left(\frac{1-\omega_{r,j}^2/\hat{\omega}_r^2}{\epsilon}\right)^2 + (1-\frac{|\hat{\Phi}_r^T\Phi_{r,j}|^2}{(\hat{\Phi}_r^T\hat{\Phi}_r)^2})\Big/\delta_r^2\right]. \tag{3}$$

Here, $\hat{\omega}_r$ and $\hat{\Phi}_r$ denote the model eigenfrequenies and mode shapes respectively, while ϵ_r and δ_r denote the variance of the prediction error of the r-th eigenfrequency and mode shape.

2.2 Parametric model order reduction

One of the major drawbacks of the Bayesian model updating is the need for many iterations of solving the eigenvalue problem. For large FE-models, the computational effort might become infeasible. Therefore, a parametric model order reduction is performed. The mass and stiffness matrices of the substructures are exported individually and reassembled afterwards. The assembled system matrices here denoted as $\mathbf{M}_a$ and $\mathbf{K}_a$ can be represented by

$$\mathbf{M}_a = \sum_{i=1}^{N} \mathbf{M}_i^S \tag{4}$$

$$\mathbf{K}_a = \sum_{i=1}^{N} \mathbf{K}_i^S. \tag{5}$$

Calculating the transformation matrix (e.g. by modal model order reduction or Craig-Bampton reduction) of the assembled matrices the system can be reduced by

$$\mathbf{M}_{a,r} = \mathbf{T}^T \mathbf{M} \mathbf{T} = \mathbf{T}^T \left(\sum_{i=1}^{N} \mathbf{M}_i^S \right) \mathbf{T} \tag{6}$$

$$\mathbf{K}_{a,r} = \mathbf{T}^T \mathbf{K} \mathbf{T} = \mathbf{T}^T \left(\sum_{i=1}^{N} \mathbf{K}_i^S \right) \mathbf{T}$$

while maintaining the possibility of changing linearly dependent parameters of all subsystems. The parameterized system matrices can be describe as

$$\mathbf{M}_{a,r}(\theta) = \mathbf{M}_{a,r}^0 + \sum_{i=1}^{N_\theta} \mathbf{M}_{i,r}^S \theta_i \tag{7}$$

$$\mathbf{K}_{a,r}(\theta) = \mathbf{K}_{a,r}^0 + \sum_{i=1}^{N_\theta} \mathbf{K}_{i,r}^S \theta_i.$$

where $\mathbf{M}_{a,r}^0$, $\mathbf{K}_{a,r}^0$, $\mathbf{M}_{i,r}^S$, $\mathbf{K}_{i,r}^S$ are constant matrices independent of θ_i.

3 VIRTUAL PCB TEST RIG

The purpose of the virtual PCB test rig is to demonstrate the interaction between the different parts of the SHM concept and show the capabilities of the presented parametric model order reduction technique.

The FE simulation tool is used for developing the FE-model of the PCB. The model is constructed based on the design of the PCB that later will be used on the real test rig. For the PCB FR-4 material properties [28] are assumed. The capacitors are modeled as rigid mass points that are attached to the PCB by solder. The joint between the PCB and the casing is modeled by a spring element assuming the stiffness of a screw joint. For the simulation, three nodes are selected as sensors, highlighted in Fig. 1 by the red circles. The sensors are used for determining the modal parameters by an output only modal analyses algorithm.

The model is exported to the commercial numerical computing environment by an interface application. To test the capabilities of the presented model order reduction technique, the first 15 eigenfrequencies of the full and reduced model are compared for changing stiffness of one of the spring elements. The number of retained modes are 50, 70, 150, and 200 modes. Fig. 2 shows the fractional error for the first 15 eigenfrequencies for the case that the stiffness of one

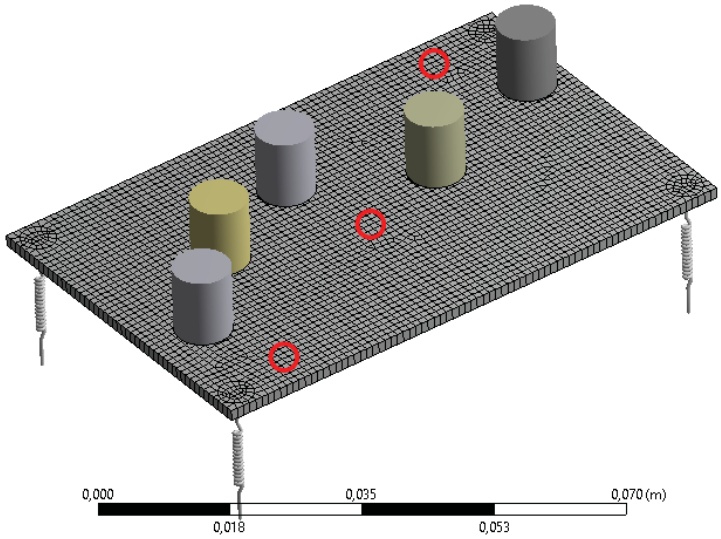

Figure 1: ANSYS model of the PCB with five capacitors. The joint to the casing is modeled by four spring elements. The sensor positions are highlighted by red circles.

spring element is multiplied by $\theta = 0.01$, hence showcasing a server change in stiffness of one of the screw joints. Even for a relatively small amount of retained modes the reduction shows only small errors. For the further analyses, 70 modes are used.

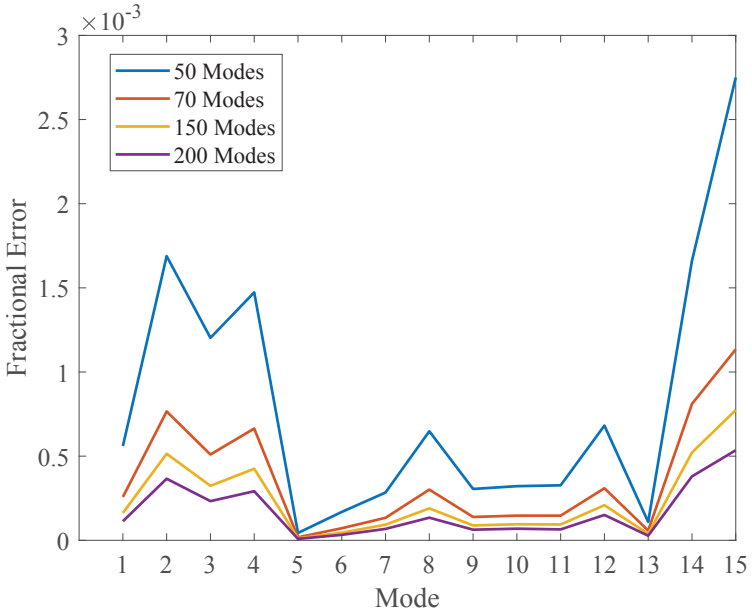

Figure 2: Fractional Error of the first 15 modes with different amount of retained modes for the model reduction.

The measurement data for the model updating and monitoring of the system is obtained by a Simulink model of the PCB that is excited by band limited white noise. The time signal of the three sensors is filtered by a 6th order Bessel filter with a cut-off frequency at 3 kHz to model the behavior of an analog acceleration sensor. The data acquisition is completed by rate transition block modeling the A/D converter. After each simulation (simulation time 50s), the digitized time data is analyzed by an automated operational modal analysis algorithm using k-Means clustering [24]. With the assumed sensor positioning the algorithm is able to consistently

identify 13 eigenfrequencies in the range from 20 Hz to 3 kHz. After each simulation, the new set of modal parameters is added to the data set used for model updating. To minimize the effect of uncertainties in the identification, the last 100 identified modal parameters are stored in the data set for model updating. A sudden loss of stiffness in one of the screws after five simulation steps is used to showcase the capabilities of the utilized Bayesian model updating framework. The starting values for the prior distribution are assumed to be normal distributed with $\mu(\theta) = 1$ and $\sigma(\theta) = 0.2$. The results in Fig. 3 show that the algorithm is capable of correctly identifying the damaged screw from the change in the vibration behavior. Due to of the data from previous measurements in the data set, a time delay in the identification is visible.

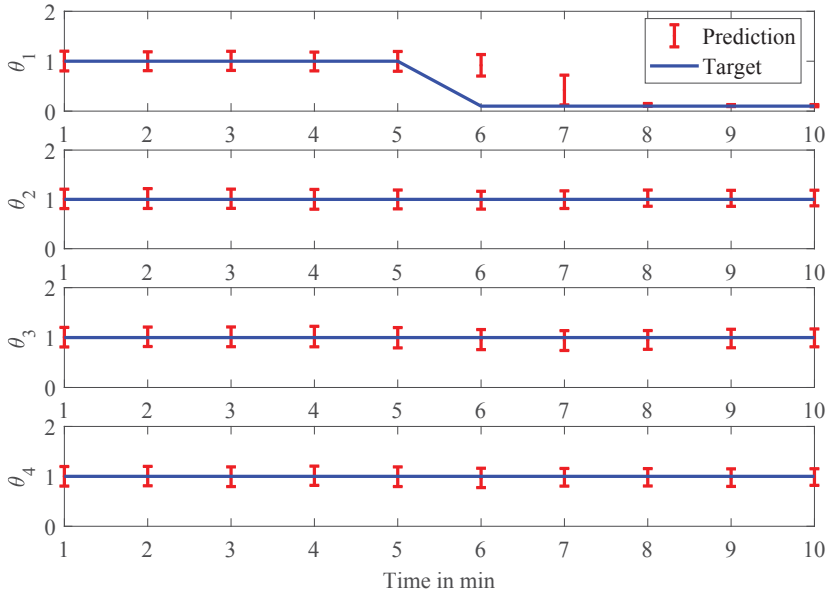

Figure 3: Test case to validate the used Bayesian model updating framework interacting with the SHM concept, showcasing a sudden stiffness loss in one of the screw joints after five time steps

Furthermore, the results show that the algorithm is only able to converge for the changed stiffness. This can be explained by the small sensitivity of the modal parameters due to the high stiffness of the joint connection.

4 Conclusion

In this paper, a SHM concept for a PCB test rig is presented and validated for a generic test case. The SHM is built around a Bayesian model updating framework that uses a parametric model order reduced model of the PCB test rig. The model reduction approach allows alteration of linear dependent parameters with high accuracy even for a small number of retained modes. The simulated test case shows that changes in stiffness of screw joints between the PCB and the casing can be correctly identified if the changes are big enough. The presented concept allows the efficient simulation of complex mechanical system and monitor changes in the model parameters. Further investigation have to be done towards the uncertainty in the measurement data and the model.

REFERENCES

[1] Johannes Falck, Christian Felgemacher, Andreja Rojko, Marco Liserre, and Peter Zacharias. Reliability of power electronic systems: An industry perspective. *IEEE Industrial Electronics Magazine*, 12(2):24–35, 2018.

[2] JS Karppinen, J Li, and M Paulasto-Krockel. The effects of concurrent power and vibration loads on the reliability of board-level interconnections in power electronic assemblies. *IEEE Transactions on Device and Materials Reliability*, 13(1):167–176, 2012.

[3] Costas Papadimitriou and Dimitra-Christina Papadioti. Component mode synthesis techniques for finite element model updating. *Computers & structures*, 126:15–28, 2013.

[4] Tyler Harms, Sahra Sedigh, and Filippo Bastianini. Structural health monitoring of bridges using wireless sensor networks. *IEEE Instrumentation & Measurement Magazine*, 13(6):14–18, 2010.

[5] Qiusheng Li, Yinghou He, Kang Zhou, Xuliang Han, Yuncheng He, and Zhenru Shu. Structural health monitoring for a 600 m high skyscraper. *The Structural Design of Tall and Special Buildings*, 27(12):e1490, 2018.

[6] D Goyal and BS Pabla. The vibration monitoring methods and signal processing techniques for structural health monitoring: a review. *Archives of Computational Methods in Engineering*, 23(4):585–594, 2016.

[7] Xinlin P Qing, Shawn J Beard, Amrita Kumar, Teng K Ooi, and Fu-Kuo Chang. Built-in sensor network for structural health monitoring of composite structure. *Journal of Intelligent Material Systems and Structures*, 18(1):39–49, 2007.

[8] Lihui Wang and Robert X Gao. *Condition Monitoring and Control for Intelligent Manufacturing*. Springer-Verlag London Limited, 2006.

[9] E Peter Carden and James MW Brownjohn. Arma modelled time-series classification for structural health monitoring of civil infrastructure. *Mechanical systems and signal processing*, 22(2):295–314, 2008.

[10] Abdenour Soualhi, Hubert Razik, Guy Clerc, and Dinh Dong Doan. Prognosis of bearing failures using hidden markov models and the adaptive neuro-fuzzy inference system. *IEEE Transactions on Industrial Electronics*, 61(6):2864–2874, 2013.

[11] John E Mottershead, Michael Link, and Michael I Friswell. The sensitivity method in finite element model updating: a tutorial. *Mechanical systems and signal processing*, 25(7):2275–2296, 2011.

[12] James L Beck and Lambros S Katafygiotis. Updating models and their uncertainties. i: Bayesian statistical framework. *Journal of Engineering Mechanics*, 124(4):455–461, 1998.

[13] Yves Govers and Michael Link. Stochastic model updating covariance matrix adjustment from uncertain experimental modal data. *Mechanical Systems and Signal Processing*, 24(3):696–706, 2010.

[14] Nicholas Metropolis, Arianna W Rosenbluth, Marshall N Rosenbluth, Augusta H Teller, and Edward Teller. Equation of state calculations by fast computing machines. *The journal of chemical physics*, 21(6):1087–1092, 1953.

[15] Jianye Ching and Yi-Chu Chen. Transitional markov chain monte carlo method for bayesian model updating, model class selection, and model averaging. *Journal of engineering mechanics*, 133(7):816–832, 2007.

[16] Wolfgang Betz, Iason Papaioannou, and Daniel Straub. Transitional markov chain monte carlo: observations and improvements. *Journal of Engineering Mechanics*, 142(5):04016016, 2016.

[17] Roy R Craig Jr and Mervyn CC Bampton. Coupling of substructures for dynamic analyses. *AIAA journal*, 6(7):1313–1319, 1968.

[18] Seung-Seop Jin and Hyung-Jo Jung. Sequential surrogate modeling for efficient finite element model updating. *Computers & structures*, 168:30–45, 2016.

[19] Panagiotis E Hadjidoukas, Panagiotis Angelikopoulos, Costas Papadimitriou, and Petros Koumoutsakos. π4u: A high performance computing framework for bayesian uncertainty quantification of complex models. *Journal of Computational Physics*, 284:1–21, 2015.

[20] Broggi M. Calvi A. Goller, B and G.I. Schüeller. A stochastic model updating technique for complex aerospace structures. *Finite Elements in Analysis and Design*, 47:739–752, 2011.

[21] Etienne Balmes. Parametric families of reduced finite element models. theory and applications. *Mechanical Systems and Signal Processing*, 10(4):381–394, 1996.

[22] HJ Pradlwarter, GI Schuëller, and GS Szekely. Random eigenvalue problems for large systems. *Computers & Structures*, 80(27-30):2415–2424, 2002.

[23] Christoph Tamm and Sara Perfetto. Design and optimization of mechatronic systems using a holistic and parametric simulation approach. *IFAC-PapersOnLine*, 52(15):271–276, 2019.

[24] Eugen Neu, Frank Janser, Akbar A Khatibi, and Adrian C Orifici. Fully automated operational modal analysis using multi-stage clustering. *Mechanical Systems and Signal Processing*, 84:308–323, 2017.

[25] Michael W Vanik, James L Beck, and SK2000 Au. Bayesian probabilistic approach to structural health monitoring. *Journal of Engineering Mechanics*, 126(7):738–745, 2000.

[26] Thomas Bayes. Lii. an essay towards solving a problem in the doctrine of chances. by the late rev. mr. bayes, frs communicated by mr. price, in a letter to john canton, amfr s. *Philosophical transactions of the Royal Society of London*, (53):370–418, 1763.

[27] Lambros S Katafygiotis and Jim L Beck. Updating models and their uncertainties. ii: Model identifiability. *Journal of Engineering Mechanics*, 124(4):463–467, 1998.

[28] Elena Zukowski, Thomas Kimpel, Daniel Kraetschmer, and Andreas Roessle. Efficient modeling of printed circuit boards structures for dynamic simulations. In *2015 16th International Conference on Thermal, Mechanical and Multi-Physics Simulation and Experiments in Microelectronics and Microsystems*, pages 1–5. IEEE, 2015.

EURODYN 2020
XI International Conference on Structural Dynamics
M. Papadrakakis, M. Fragiadakis, C. Papadimitriou (eds.)
Athens, Greece, 23–26 November 2020

REAL-TIME BAYESIAN PARAMETER, STATE AND INPUT ESTIMATION USING OUTPUT-ONLY VIBRATION MEASUREMENTS

Daniz Teymouri[1], Omid Sedehi[1], Lambros S. Katafygiotis[1], Costas Papadimitriou[2]

[1] Department of Civil and Environmental Engineering, Hong Kong University of Science and Technology
Hong Kong, China
Emails: dteymouri@connect.ust.hk, osedehi@connect.ust.hk, katafygiotis.lambros@gmail.com

[2] Department of Mechanical Engineering, University of Thessaly
Volos, Greece
Email: costasp@uth.gr

Keywords: Bayesian learning, Real-time estimation, Structural identification, Noise characterization, Response predictions.

Abstract. *This paper presents a new sequential Bayesian method for the real-time estimation of state, input, parameters, and noise characteristics in dynamical systems using output-only measurements. It is an extension of the method developed by the authors for the joint input-state estimation in linear time-invariant systems* [1], [2]. *This method is built upon the Taylor series expansion of the state-space model and conjugate prior distributions, where the noise characteristics are described using Gaussian distributions and their covariance matrices are assumed to follow inverse Wishart distributions. When the Bayes rule is applied, explicit formulations for the posterior distributions are obtained, which allows efficient and real-time computations. The application of this method to a simple numerical example is demonstrated, which confirms its efficacy in handling this coupled estimation problem. It is observed that this method delivers accurate estimations for the state, input, model parameters, and noise covariance matrices when the results are compared with the actual values. Moreover, the proposed method has the potential to mitigate the low-frequency errors commonly produced in estimations of input forces and displacement responses when only acceleration responses are measured.*

1 INTRODUCTION

Kalman Filter (KF) is a well-established tool in the context of real-time estimation, which provides an efficient estimation of the dynamic response for linear time-invariant (LTI) systems. However, the performance of KF can be deteriorated in the absence of knowledge about the external input forces and system properties. Moreover, the KF is inapplicable when the system has nonlinearity in terms of material properties and geometric changes. This has motivated investigators to develop methods to estimate the system state, input forces, and dynamical parameters in real-time and simultaneously. However, the nonlinear nature of the joint

parameter-state estimation problems requires approximating the state-space formulations. Thus, Extended Kalman Filter (EKF) and Unscented Kalman Filter (UKF) have been developed to cope with this difficulty [3], [4]. While the EKF simplifies the formulation through the first-order Tylor series expansion, the UKF treats the nonlinearity in parameters through a numerical method offering exact solutions up to third order. However, this superior accuracy comes at the expense of additional computational cost. Furthermore, when the noise characteristics are non-Gaussian, these methods often appear to be inadequate, which has brought about the development of particle filters [5], [6]. However, using these filters is not desirable in practice mainly due to the high computational cost associated with the sampling over the parameters space.

The joint input-state estimation in LTI systems is another type of real-time estimation problem first addressed in [7]. Later, Hsieh [8] proposed the so-called two-stage recursive method, and Gillijns & De Moor [9] proved the optimality of this filter in the unbiased minimum variance (UMV) sense. Lourens et al. [10] implemented this filter for modally-reduced dynamical models, enhancing its computational efficiency. Another approach is Augmented Kalman Filter (AKF) introduced in [11], which applies the original KF to estimate an augmented vector of state and input. However, the displacement responses and input forces obtained using these filters are often observed to be contaminated with spurious low-frequency drift components arisen from the double integration over noisy acceleration response measurements. Eftekhar Azam et al. [12] developed Dual Kalman Filter (DKF) for the simultaneous estimation of state and input in LTI systems and have demonstrated the important role of the input covariance matrix in mitigating the drifts. Moreover, Naets et al. [13] prescribed using dummy displacement/strain measurements to reduce these drift in estimations. Nevertheless, these methods require the selection of regularization parameters, which is not always a trivial task. In the published literature, L-curve methods have been suggested for fine-tuning of the input and noise covariance matrices [12]. However, these methods hinder the capability of these methods to offer real-time and automated estimation, as they often require user interference and offline calibration.

In general, the performance of Kalman-type filters is reliant on the initial values of the parameters, and inappropriate choices of the noise covariance matrices can deteriorate the accuracy up to a great extent. Thus, several adaptive methods have been suggested for updating the process and measurement noise in real-time. These methods can be categorized into four groups, namely Bayesian, maximum likelihood, correlation, and covariance-matching methods [14], [15]. Recently, a sequential Bayesian method is developed for the real-time estimation of input, state, and noise covariance matrices [1], [2]. It is observed that this method can considerably mitigate the low-frequency drifts from the estimations of input and displacement responses [1], [2].

The simultaneous estimation of state, input, and parameters has led to an emerging type of real-time methods. Naets et al. [16] have developed a method for the coupled estimation of state, input, and parameters using a model reduction technique paired with the EKF. The UKF has been applied to this coupled estimation problem in Lei et al. [17]. The combination of UKF and DKF has appeared in Dertimanis et al. [18] as an efficient method to treat this joint estimation problem.

This paper aims to address the coupled estimation of the state, input, system parameters, as well as noise parameters using sparse output-only measurements. It follows the same line as the sequential Bayesian method presented in [1], [2] developing a new framework for the coupled estimation problems. It uses the first-order Taylor series expansion to simplify the formulations and proposes a new efficient algorithm. Details of this method will appear in the future, and in this paper, the proposed method is examined using a linear single-degree-of-

freedom (SDOF) system. The paper will continue with Section 2, briefly introducing the method. In Section 3, a numerical example is employed to test and verify the method, and in the end, conclusions are drawn.

2 PROBLEM STATEMENT

A state-space stochastic representation of dynamical systems can be obtained in discrete-time based on the second law of motion and the zero-order hold assumption for the input, which yield [1]:

$$\mathbf{z}_k = \mathbf{A}(\boldsymbol{\theta}_{k-1})\mathbf{z}_{k-1} + \mathbf{B}(\boldsymbol{\theta}_{k-1})\mathbf{p}_{k-1} + \mathbf{v}_k^z \quad , \quad \mathbf{v}_k^z \sim N(\mathbf{0}, \mathbf{Q}_k^z) \tag{1}$$

where $\mathbf{z}_k \in \mathbb{R}^{2N_{DOF}}$ is the state vector at discrete time $t_k = k\Delta t,\ k = \{0,1,2,...,n\}$, containing displacement and velocity responses at N_{DOF} degrees-of-freedom (DOF) sampled at Δt; $\mathbf{p}_k \in \mathbb{R}^{N_I}$ is a vector consisting of N_I unknown external forces; $\mathbf{v}_k^z \in \mathbb{R}^{2N_{DOF}}$ is the process noise considered to be white and Gaussian; $\mathbf{A}(\boldsymbol{\theta}_{k-1}) = \mathbf{e}^{\mathbf{A}_c(\boldsymbol{\theta}_{k-1})\Delta t}$ and $\mathbf{B}(\boldsymbol{\theta}_{k-1}) = \left(\mathbf{A}(\boldsymbol{\theta}_{k-1}) - \mathbf{I}\right)\mathbf{A}_c(\boldsymbol{\theta}_{k-1})^{-1}\mathbf{B}_c(\boldsymbol{\theta}_{k-1})$ are the system and input-to-state matrices for the discrete-time formulation and explained in terms of their continuous-time counterparts given as

$$\mathbf{A}_c(\boldsymbol{\theta}_{k-1}) = \begin{bmatrix} \mathbf{0} & \mathbf{I} \\ -\mathbf{M}^{-1}\mathbf{K}(\boldsymbol{\theta}_{k-1}) & -\mathbf{M}^{-1}\mathbf{C}(\boldsymbol{\theta}_{k-1}) \end{bmatrix},\ \mathbf{B}_c(\boldsymbol{\theta}_{k-1}) = \begin{bmatrix} \mathbf{0} \\ \mathbf{M}^{-1}\mathbf{S}_p \end{bmatrix} \tag{2}$$

where $\mathbf{M} \in \mathbb{R}^{N_{DOF} \times N_{DOF}}$, $\mathbf{C}(\boldsymbol{\theta}_{k-1}) \in \mathbb{R}^{N_{DOF} \times N_{DOF}}$, and $\mathbf{K}(\boldsymbol{\theta}_{k-1}) \in \mathbb{R}^{N_{DOF} \times N_{DOF}}$ are the mass, damping, and stiffness matrices, respectively; $\boldsymbol{\theta}_k \in \mathbb{R}^{N_\theta}$ is a vector of unknown parameters; $\mathbf{S}_p \in \mathbb{R}^{N_{DOF} \times N_I}$ is a matrix specifying the spatial distribution of external forces acting on the system of interest. This state-space representation is nonlinear-in-parameters even if the stiffness and damping matrices are explained as a linear of function of the unknown parameters $\boldsymbol{\theta}_k$. Moreover, the parameters are regarded as time-variant whose variation between consecutive time instances can be described using the so-called random walk model:

$$\boldsymbol{\theta}_k = \boldsymbol{\theta}_{k-1} + \mathbf{v}_k^\theta \quad , \quad \mathbf{v}_k^\theta \sim N\left(\mathbf{0}, \mathbf{Q}_k^\theta\right) \tag{3}$$

where $\mathbf{v}_k^\theta \in \mathbb{R}^{N_\theta}$ characterizes the variation over each interval considered to be white, zero-mean, and Gaussian having the covariance matrix $\mathbf{Q}_k^\theta \in \mathbb{R}^{N_\theta \times N_\theta}$.

Let $\mathbf{d}_k \in \mathbb{R}^{N_0}$ be a vector of response quantities of interest observed at the discrete time t_k. It can be proved that this dynamical response can be written in terms of the system state, input, parameters, as well as the measurement noise leading to the following observation model [1]:

$$\mathbf{d}_k = \mathbf{G}(\boldsymbol{\theta}_k)\mathbf{z}_k + \mathbf{J}(\boldsymbol{\theta}_k)\mathbf{p}_k + \mathbf{w}_k \quad , \quad \mathbf{w}_k \sim N(\mathbf{0}, \mathbf{R}_k) \tag{4}$$

where $\mathbf{G}(\boldsymbol{\theta}_k) \in \mathbb{R}^{N_0 \times N_s}$ and $\mathbf{J}(\boldsymbol{\theta}_k) \in \mathbb{R}^{N_0 \times N_I}$ are the output influence and the direct transmission matrices, respectively, which can be found in [1]; $\mathbf{w}_k \in \mathbb{R}^{N_o}$ is the measurement noise vector modeled as Gaussian white processes with zero-mean and unknown covariance matrix $\mathbf{R}_k \in \mathbb{R}^{N_0 \times N_0}$, respectively.

We state that the problem lies in the real-time estimation of the state, input, parameters, as well as the noise characteristics based on sparse output-only measurements. We address this

problem using the foregoing state-space representation and through a novel sequential Bayesian approach. The presented approach is an extension of the method developed recently by the authors, particularly for the joint estimation of input and state in LTI systems [1], [2]. Of course, the mathematical formulation of this method is skipped in view of this paper's length. However, the method used here consists of five major steps, namely constructing prior distributions, jointly estimating parameters-input-state, estimating cross-covariance matrices, identifying noise characteristics, and making predictions for the next time step. In the derivation of this method, linear Taylor series expansions are employed to simplify both the observation and process models. Moreover, this method benefits from conjugate prior distributions, which allows producing closed-form expressions for the posterior distributions, which reduces the computational burden as well. This implementation includes using Gaussian distribution for the additive noise components as stated earlier, as well as adopting Inverse Wishart distributions for the noise covariance matrices. Further details about this method to be disclosed in the future, and in the remainder, we demonstrate this method by using a simple numerical example.

3 ILLUSTRATIVE EXAMPLE

Figure 1 shows a single degree-of-freedom (SDOF) spring-mass-damper system selected to demonstrate the proposed method. For ease of comparison, the system properties are set to be the same as the example presented in [18], wherein $M = 30\text{kg}$, $C = 700\text{N.s/m}$ and $K = 40\text{MN/m}$. The modal frequency and modal damping ratio for the SDOF system with the above-mentioned properties are 184 Hz and 0.01, respectively. The discrete-time acceleration response of this system is sampled at $\Delta t = 0.001s$ and considered as the measured quantity. This artificial response is generated when the system is subjected to zero-mean Gaussian white input process having 200N standard deviation. The measurement noise is modeled by a zero-mean Gaussian process with the standard deviation of 1% root-mean-square of the noise-free response and added on top of the acceleration response. Note that the zero-order hold assumption is employed when the discrete-time response is created.

The stiffness of the spring $K \equiv \theta$ and the applied force are considered to be unknown. The problem is to estimate and update the input, state, stiffness, and noise parameters in real-time using acceleration-only measurements.

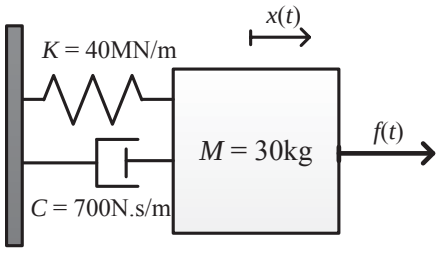

Figure 1: SDOF spring-mass-damper system considered for testing the method

The initial value for the parameters is selected to be $\theta_{0|0}$=0.8K=32MN/m. The input and parameter variances are both set to 100. The initial covariance matrix of the state is considered to be diagonal having elements of order 10^3. The estimation period is considered 200s, aiming to ensure the stability and accuracy of the method.

Figure 2 presents the estimation of stiffness. It is observed that within the first 10s, the estimation reaches to a satisfactory threshold varying around the actual value. The variation of the stiffness identified decreases as the time goes by, which is attributed to the convergence of

the noise covariance matrices. Moreover, the estimation of the applied force is displayed in Figure 3. For comparison, two windows each 1s long are enlarged, indicating the accuracy of the method in estimating the input. To shed light on the misfit between the actual and estimated input, the errors are plotted in Figure 4 in both time and frequency domains. In Figure 4(a), it is evident that the large errors appearing in the beginning swiftly decrease and reach to a stationary process with much smaller amplitude. This error process is transformed to the frequency-domain in Figure 4(b), showing that relatively large errors around the system's natural frequency. We believe this issue is attributed to the variation of identified stiffness. Another notable observation is the mitigation of low-frequency drifts up to a great extent.

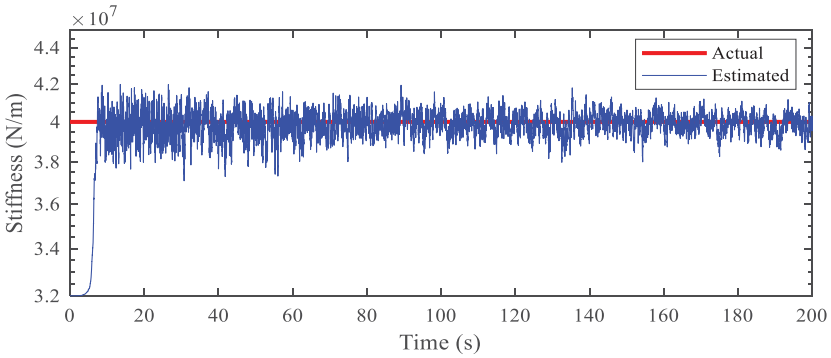

Figure 2: Identification of the stiffness using the proposed method

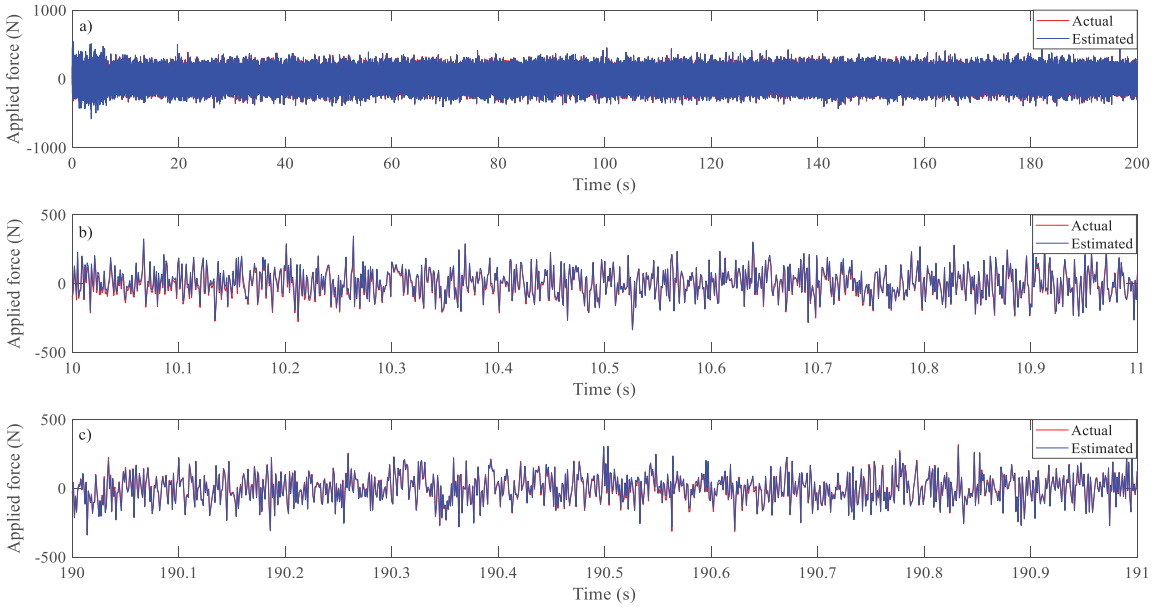

Figure 3: Estimation of input force over different intervals

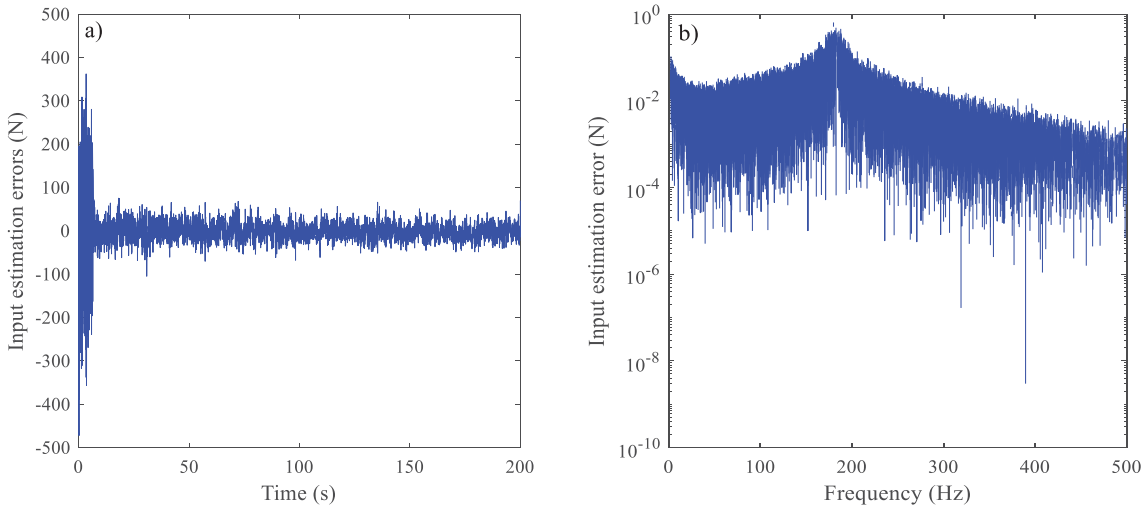

Figure 4: Input estimation errors presented in time and frequency domains

Figure 5 shows the time-history displacement response estimated using the proposed method. When these estimations are compared with the actual values, it is observed that the proposed method delivers accurate estimations and particularly free of significant low-frequency errors. This conclusion is reinforced when we zoom into different segments of the response, e.g. intervals [10-11s] and [190-191s]. It is to be noted that similar observations are made for the velocity and acceleration responses, which confirms the validity of the method. However, they are not presented here for brevity.

Figure 6 indicates the real-time estimation of the process noise covariance matrix and the stiffness variance. As shown, these variances converge and reach to stationary settings as time passes, putting emphasis on the stability of the estimators.

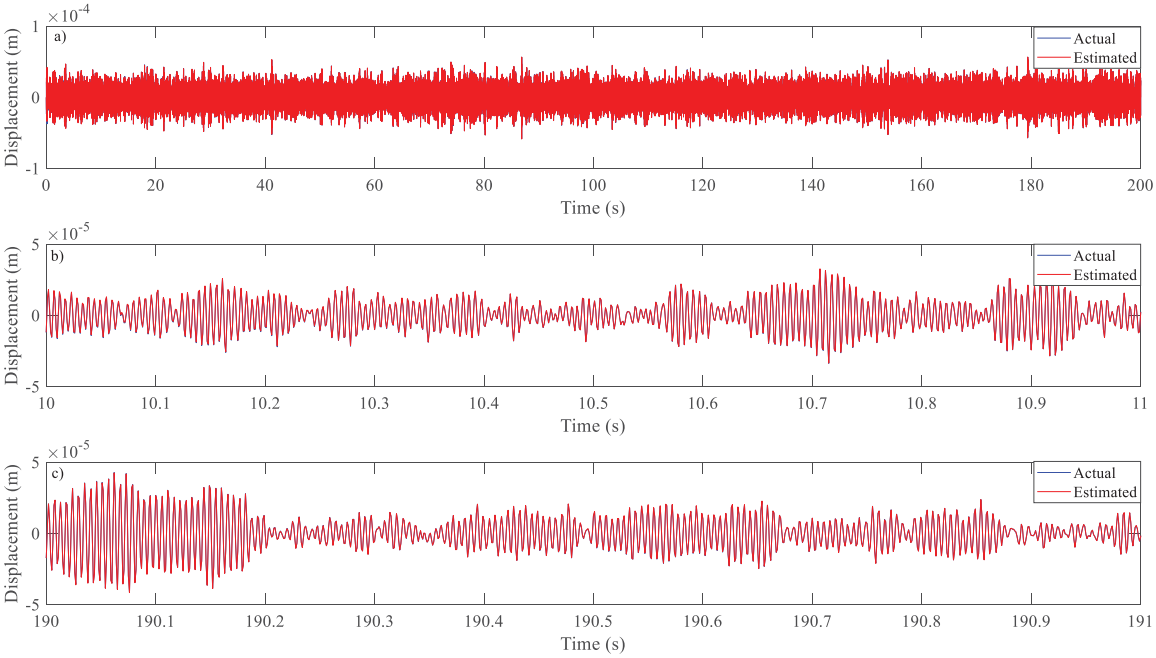

Figure 5: Estimation of the displacement response using the proposed method

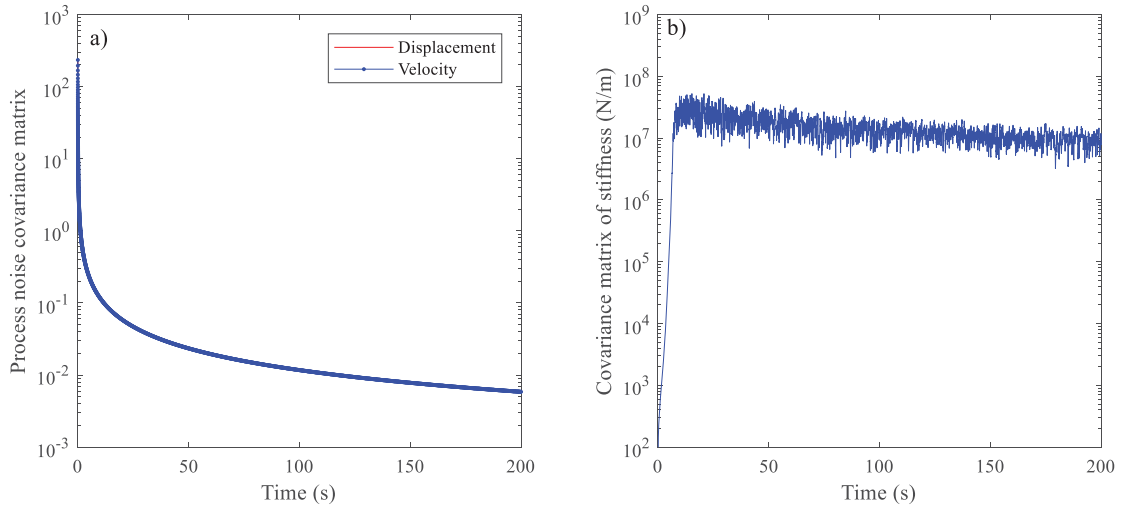

Figure 6: Real-time estimation of noise covariance matrices (a) process noise covariance matrix (b) variance of the stiffness

4 CONCLUSIONS

A new sequential Bayesian method is introduced for the coupled estimation of state, input, parameters, as well as noise covariance matrices using response-only measurements. This method is examined and tested using a simple numerical example. The convergence of the estimations to the actual values is demonstrated, and the stability of the estimations is verified using a basic numerical example. It is also observed that the proposed filter is capable of mitigating the adverse effect of using noisy acceleration responses, and corrects inappropriate choice of noise covariance made at the beginning, delivering highly accurate estimations. More examples to appear in the future aiming to lend further validity and verification to the method presented herein.

5 AKNOWLEDGEMENT

Financial support from the Hong Kong Research Grants Council under project No. 16234816, 16212918, and 16211019 is gratefully acknowledged.

REFERENCES

[1] O. Sedehi, C. Papadimitriou, D. Teymouri, and L. S. Katafygiotis, “Sequential Bayesian estimation of state and input in dynamical systems using output-only measurements,” *Mech. Syst. Signal Process.*, vol. 131, 2019.

[2] D. Teymouri, O. Sedehi, L. S. Katafygiotis, and C. Papadimitriou, “A New Online Bayesian Approach for the Joint Estimation of State and Input Forces using Response - only Measurements,” in *13th International Conference on Applications of Statistics and Probability in Civil Engineering, ICASP13*, 2019, pp. 1–7.

[3] H. Ebrahimian, R. Astroza, and J. P. Conte, “Extended Kalman filter for material

parameter estimation in nonlinear structural finite element models using direct differentiation method," *J. Int. Assoc. Earthq. Eng.*, vol. 44, no. 44, pp. 1495–1522, 2015.

[4] E. N. Chatzi and A. W. Smyth, "The unscented Kalman filter and particle filter methods for nonlinear structural system identification with non-collocated heterogeneous sensing," *Struct. Control Heal. Monit.*, vol. 16, no. 1, pp. 99–123, 2009.

[5] J. Ching, J. L. Beck, and K. A. Porter, "Bayesian state and parameter estimation of uncertain dynamical systems," *Probabilistic Eng. Mech.*, vol. 21, no. 1, pp. 81–96, 2006.

[6] S. Eftekhar Azam and S. Mariani, "Dual estimation of partially observed nonlinear structural systems: A particle filter approach," *Mech. Res. Commun.*, vol. 46, pp. 54–61, 2012.

[7] P. K. Kitanidis, "Unbiased minimum-variance linear state estimation," *Automatica*, vol. 23, no. 6, pp. 775–778, 1987.

[8] C.-S. Hsieh, "Robust Two-Stage Kalman Filters for Systems with Unknown Inputs," *IEEE Trans. Automat. Contr.*, vol. 45, no. 12, pp. 2347–2378, 2000.

[9] S. Gillijns and B. De Moor, "Unbiased minimum-variance input and state estimation for linear discrete-time systems with direct feedthrough," *Automatica*, vol. 43, no. 5, pp. 934–937, 2007.

[10] E. Lourens, C. Papadimitriou, S. Gillijns, E. Reynders, G. De Roeck, and G. Lombaert, "Joint input-response estimation for structural systems based on reduced-order models and vibration data from a limited number of sensors," *Mech. Syst. Signal Process.*, vol. 29, pp. 310–327, 2012.

[11] E. Lourens, E. Reynders, G. De Roeck, G. Degrande, and G. Lombaert, "An augmented Kalman filter for force identification in structural dynamics," *Mech. Syst. Signal Process.*, vol. 27, no. 1, pp. 446–460, 2012.

[12] S. Eftekhar Azam, E. Chatzi, and C. Papadimitriou, "A dual kalman filter approach for state estimation via output only acceleration measurements," *Mech. Syst. Signal Process.*, no. 60–61, pp. 866–886, 2015.

[13] F. Naets, J. Cuadrado, and W. Desmet, "Stable force identification in structural dynamics using Kalman filtering and dummy-measurements," *Mech. Syst. Signal Process.*, vol. 50–51, pp. 235–248, 2015.

[14] V. A. Bavdekar, A. P. Deshpande, and S. C. Patwardhan, "Identification of process and measurement noise covariance for state and parameter estimation using extended Kalman filter," *J. Process Control*, vol. 21, no. 4, pp. 585–601, 2011.

[15] M. Song, R. Astroza, H. Ebrahimian, B. Moaveni, and C. Papadimitriou, "Nonlinear Model Updating Using Recursive and Batch Bayesian Methods."

[16] F. Naets, J. Croes, and W. Desmet, "An online coupled state/input/parameter estimation approach for structural dynamics," *Comput. Methods Appl. Mech. Eng.*, vol. 283, pp. 1167–1188, 2015.

[17] Y. Lei, D. Xia, K. Erazo, and S. Nagarajaiah, "A novel unscented Kalman filter for recursive state-input-system identification of nonlinear systems," *Mech. Syst. Signal Process.*, vol. 127, pp. 120–135, 2019.

[18] V. K. Dertimanis, E. N. Chatzi, S. Eftekhar Azam, and C. Papadimitriou, "Input-state-parameter estimation of structural systems from limited output information," *Mech. Syst. Signal Process.*, vol. 126, pp. 711–746, 2019.

EURODYN 2020
XI International Conference on Structural Dynamics
M. Papadrakakis, M. Fragiadakis, C. Papadimitriou (eds.)
Athens, Greece, 23–26 November 2020

HIERARCHICAL BAYESIAN UNCERTAINTY QUANTIFICATION OF DYNAMICAL MODELS UTILIZING MODAL STATISTICAL INFORMATION

Omid Sedehi[1], Costas Papadimitriou[2], and Lambros S. Katafygiotis[1]

[1] Department of Civil and Environmental Engineering, Kong University of Science and Technology, Hong Kong, SAR of China
{sedehi.omid, katafygiotis.lambros}@gmail.com

[2] Department of Mechanical Engineering, University of Thessaly, Volos, Greece
costasp@uth.gr

Keywords: Bayesian learning, Hierarchical modeling, System identification, Uncertainty quantification, Model inference.

Abstract. *Updating dynamical models based on experimental modal information has become an important topic in structural health monitoring. This paper revisits this significant problem and develops a new two-stage hierarchical Bayesian framework, aiming to improve the quantification of uncertainty. This framework employs the Bayesian FFT approach to identify the modal parameters along with their identification uncertainty, and then, it utilizes this modal information to update the stiffness matrix. It can quantify the variability of both modal and structural parameters over multiple data sets while characterizing their identification uncertainty as well. This framework also proposes a new basis to assign optimal and appropriate weights for modal features. It weights different modal parameters based on the sum of identification uncertainty and the ensemble variability such that more uncertain parameters will be assigned smaller weights. As a result, a coherent quantification of uncertainty is attained by following Bayesian probability logic. Ultimately, experimental data from a shear building structure is used for demonstrating the proposed framework.*

1 INTRODUCTION

Bayesian statistical framework [1] has become central in structural health monitoring (SHM) since it provides a rigorous mathematical tool to quantify uncertainties. This framework has been developed further to tackle various problems visited in SHM, including the methods seasoned for updating dynamical models based on experimental modal information. Two decades ago, Vanik et al. [2] have first developed a Bayesian framework for updating stiffness parameters by comparing and matching experimental and analytical modal properties. Beck et al. [3] have used this framework to address damage detection in a probabilistic fashion. However, the original formulations [2] require matching the analytical and experimental dynamical modes. Yuen et al. [4] have introduced an efficient Bayesian formulation to handle

this problem without imposing any mode matching concept. This study establishes a Gaussian distribution to provide an explicit relationship between the structural and modal parameters and to avoid solving the eigenvalue problems. Christodoulou and Papadimitriou [5] have demonstrated that the weighting of modal features plays a crucial role in obtaining the most probable values of structural parameters accurately. They have also proposed a Bayesian method to calibrate the weights. Goller et al. [6] have introduced an evidence-based approach for the calibration of the weights. Au and Zhang [7] have developed a two-stage approach, which first identifies the modal parameters and their uncertainties using the Bayesian FFT approach [8], [9] and then updates the structural parameters accordingly. Behmanesh et al. [10] have proposed a hierarchical Bayesian method to account for the variability of structural parameters. The computing technique used in [10] is a Gibbs sampling method associated with the Metropolis-Hasting algorithm. However, this computational method appears to be inefficient as the number of parameters grows. For globally identifiable problems, an asymptotic approximation of the likelihood function can drastically reduce the computational cost and provides theoretical insights as to the separation of identification uncertainty and variability [11]. In the original framework, the data sets correspond to statistically independent experiments. However, this assumption can be relaxed by breaking a long time-history data set into multiple segments and capturing the variability through the same approach [12]. An extension of this framework to Bayesian operational modal analysis has recently appeared in [13]. These studies show that the hierarchical Bayesian framework provides robust uncertainties.

In this study, we develop a two-stage hierarchical Bayesian framework for model inference problems. In the first stage, the modal information is obtained from the Bayesian FFT method [8], [9], and in the second stage, this information is employed to update the stiffness parameters using a method similar to [4]. This development benefits from the hierarchical Bayesian framework presented in [11], [13].

2 HIERARCHICAL BAYESIAN FRAMEWORK

2.1 Problem statement

Let $M(\boldsymbol{\theta}) \in \boldsymbol{M}$ be a linear dynamical model, selected from a class of models $\boldsymbol{M}$ and described mathematically as a function of free parameters $\boldsymbol{\theta} \in \mathbb{R}^{N_\theta}$. These parameters are assumed herein to characterize the uncertainty associated with the stiffness matrix. The so-called substructure approach is convenient to express the stiffness and mass matrices in terms of the substructures' stiffness/mass matrices giving:

$$\mathbf{K}(\boldsymbol{\theta}) = \sum_{p=1}^{N_\theta} \theta_p \mathbf{K}_p \quad ; \quad \mathbf{M} = \sum_{p=1}^{N_\theta} \mathbf{M}_p \tag{1}$$

where $\mathbf{K}(\boldsymbol{\theta})$ and $\mathbf{M} \in \mathbb{R}^{N_{DOF} \times N_{DOF}}$ are the global stiffness and mass matrices, respectively; $\mathbf{K}_p$ and $\mathbf{M}_p \in \mathbb{R}^{N_{DOF} \times N_{DOF}}$ are the stiffness and mass matrices of the pth substructure. Note that the structural model is assumed to have N_{DOF} degrees-of-freedom (DOFs). This parameterization is advantageous since it provides a linear relationship between the global stiffness matrix and the unknown parameters. In this study, the mass matrix is considered to be known and computed from architectural and structural drawings. On the contrary, the parameters of the stiffness matrix should be updated based on the vibration measurements.

The primary goal is to calibrate the stiffness parameters and their uncertainty using N_D time-history data sets collected in the full data set $\mathbf{D} = \{D_s, s = 1,2,...,N_D\}$ while $D_s = \{\mathbf{y}_{j,s} \triangleq \mathbf{y}_s(j\Delta t) \in \mathbb{R}^{N_o}, j = 0,1,2,...,N-1\}$ is a particular sequence of response-only

measurement obtained at N_o DOFs and Δt intervals. Updating the model directly based on vibration responses, as proposed in [11], is non-trivial and difficult, mainly due to the fact that the input loading is not known. Consequently, it is preferred to identify the modal features first and then use them for inferring the stiffness parameters. This paper follows a similar approach by establishing a two-stage hierarchical Bayesian framework. In the first stage, the modal frequencies and mode shapes are inferred using the Bayesian FFT approach. In the second stage, the stiffness parameters are updated by comparing the identified and analytical modal parameters.

2.2 Hierarchical prior distribution

Let $\boldsymbol{\omega}^2=[\omega_1^2 \ ... \ \omega_{N_m}^2]^T$ and $\boldsymbol{\Phi}=[\boldsymbol{\phi}_1^T \ ... \ \boldsymbol{\phi}_{N_m}^T]^T$ be the experimental modal frequencies and mode shape vectors, respectively, where each pair $\{\omega_i^2 \in \mathbb{R}^1, \boldsymbol{\phi}_i \in \mathbb{R}^{N_0}\}$ corresponds to the ith dynamical mode when N_m modes are observed. Likewise, the modal parameters of the structural model $M(\boldsymbol{\theta}) \in \boldsymbol{M}$ can be expressed as $\boldsymbol{\varpi}^2=[\varpi_1^2 \ ... \ \varpi_{N_m}^2]^T$ and $\boldsymbol{\Psi}=[\boldsymbol{\psi}_1^T \ ... \ \boldsymbol{\psi}_{N_m}^T]^T$, where similarly the pair $\{\varpi_i^2 \in \mathbb{R}^1, \boldsymbol{\psi}_i \in \mathbb{R}^{N_{DOF}}\}$ is modal frequency and mode shape vector of the ith dynamic mode. Of course, the analytical modal parameters vary with stiffness parameters. The statistical relationship between the analytical modal parameters and the stiffness parameters is described as [4]:

$$p(\boldsymbol{\varpi}_s^2, \boldsymbol{\Psi}_s \,|\, \boldsymbol{\theta}_s, \sigma_\varepsilon^2) = \prod_{i=1}^{N_m} N\left(\mathbf{K}(\boldsymbol{\theta}_s)\boldsymbol{\psi}_{i,s} \,|\, \varpi_{i,s}^2 \mathbf{M}\boldsymbol{\psi}_{i,s}, \sigma_\varepsilon^2 \mathbf{I}_{N_{DOF}}\right) \tag{2}$$

where σ_ε^2 is the prediction error variance reflecting how accurate the Eigen equation is satisfied. Note that the subscript s represents that one parameter correspond to the data set D_s. Thus, the stiffness parameters are variable over different data sets. This variability is considered using a hyper Gaussian distribution imposed over the stiffness parameters giving:

$$p(\boldsymbol{\theta}_s \,|\, \boldsymbol{\mu}_{\boldsymbol{\theta}}, \boldsymbol{\Sigma}_{\boldsymbol{\theta}\boldsymbol{\theta}}) = N(\boldsymbol{\theta}_s \,|\, \boldsymbol{\mu}_{\boldsymbol{\theta}}, \boldsymbol{\Sigma}_{\boldsymbol{\theta}}) \tag{3}$$

where $\boldsymbol{\mu}_{\boldsymbol{\theta}} \in \mathbb{R}^{N_{\boldsymbol{\theta}}}$ and $\boldsymbol{\Sigma}_{\boldsymbol{\theta}} \in \mathbb{R}^{N_{\boldsymbol{\theta}} \times N_{\boldsymbol{\theta}}}$ are the hyper mean vector and covariance matrix, respectively. Likewise, the modal features $\{\boldsymbol{\omega}^2, \boldsymbol{\Phi}, \boldsymbol{\varpi}^2, \boldsymbol{\Psi}\}$ are specific to each experiment (data set) and modeled as statistically independent. The discrepancy between the experimental and analytical modal parameters describing each experiment can be written as

$$\begin{bmatrix} \boldsymbol{\omega}_s^2 \\ \boldsymbol{\Phi}_s \end{bmatrix} = \begin{bmatrix} \boldsymbol{\varpi}_s^2 \\ \boldsymbol{\Gamma}_s \boldsymbol{\Psi}_s \end{bmatrix} + \begin{bmatrix} \boldsymbol{\varepsilon}_{\boldsymbol{\omega}_s} \\ \boldsymbol{\varepsilon}_{\boldsymbol{\Phi}_s} \end{bmatrix} \tag{4}$$

where $\boldsymbol{\Gamma}_s \in \mathbb{R}^{N_m N_o \times N_m N_{DOF}}$ is a known selection matrix, which specifies the observed DOFs, and $[\boldsymbol{\varepsilon}_{\boldsymbol{\omega}_s}^T \quad \boldsymbol{\varepsilon}_{\boldsymbol{\Phi}_s}^T]^T$ is the prediction error vector described through a class of maximum-entropy probability distribution given as

$$\boldsymbol{\varepsilon}_{\boldsymbol{\omega}_s^2} \underset{i.i.d.}{\sim} N\left(\mathbf{0}, \boldsymbol{\Sigma}_{\boldsymbol{\omega}^2}\right) \quad ; \quad \boldsymbol{\varepsilon}_{\boldsymbol{\Phi}_s} \underset{i.i.d.}{\sim} N\left(\mathbf{0}, \boldsymbol{\Sigma}_{\boldsymbol{\Phi}}\right) \tag{5}$$

where $\boldsymbol{\Sigma}_{\boldsymbol{\omega}^2} \in \mathbb{R}^{N_m \times N_m}$ and $\boldsymbol{\Sigma}_{\boldsymbol{\Phi}} \in \mathbb{R}^{N_o N_m \times N_o N_m}$ are the covariance matrices of the modal frequencies and mode shape vectors, respectively. These parameters are to be inferred from the data as well. Having considered this statistical model, the probability distribution of the experimental modal parameters conditional on the analytical ones can be written as

$$p(\boldsymbol{\omega}_s^2, \boldsymbol{\Phi}_s \,|\, \boldsymbol{\varpi}_s, \boldsymbol{\Psi}_s, \boldsymbol{\Sigma}_{\boldsymbol{\omega}^2}, \boldsymbol{\Sigma}_{\boldsymbol{\Phi}}) = N\left(\boldsymbol{\omega}_s^2 \,|\, \boldsymbol{\varpi}_s^2, \boldsymbol{\Sigma}_{\boldsymbol{\omega}^2}\right) N\left(\boldsymbol{\Phi}_s \,|\, \boldsymbol{\Gamma}_s \boldsymbol{\Psi}_s, \boldsymbol{\Sigma}_{\boldsymbol{\Phi}}\right) \tag{6}$$

Figure 1 shows the hierarchical structure of the proposed probabilistic model. The conditional dependence of parameters is shown by the arrows, and the unknown parameters are

shown using the white circles. Each time-history data is shown by a gray circle. For brevity, the parameters having common realizations over data sets are collected into a hyper-parameters set $\varphi = \{\boldsymbol{\mu}_{\boldsymbol{\theta}}, \boldsymbol{\Sigma}_{\boldsymbol{\theta}}, \boldsymbol{\Sigma}_{\boldsymbol{\omega}^2}, \boldsymbol{\Sigma}_{\boldsymbol{\Phi}}, \sigma_{\varepsilon}^2\}$, and the data-set-specific parameters are collected into $\delta = \{\boldsymbol{\omega}_s^2, \boldsymbol{\Phi}_s, \boldsymbol{\varpi}_s^2, \boldsymbol{\Psi}_s, \boldsymbol{\theta}_s\}_{s=1}^{N_D}$. Therefore, the joint prior distribution of all parameters can be written as

$$p(\delta,\varphi) = p(\varphi)\prod_{s=1}^{N_D} p(\boldsymbol{\omega}_s^2, \boldsymbol{\Phi}_s \mid \boldsymbol{\varpi}_s^2, \boldsymbol{\Psi}_s, \boldsymbol{\Sigma}_{\boldsymbol{\omega}^2}, \boldsymbol{\Sigma}_{\boldsymbol{\Phi}})\, p(\boldsymbol{\varpi}_s, \boldsymbol{\Psi}_s \mid \boldsymbol{\theta}_s, \sigma_{\varepsilon}^2)\, p(\boldsymbol{\theta}_s \mid \boldsymbol{\mu}_{\boldsymbol{\theta}}, \boldsymbol{\Sigma}_{\boldsymbol{\theta}}) \tag{7}$$

where $p(\delta,\varphi)$ is the joint prior distribution and $p(\varphi)$ is the prior distribution of the hyper-parameters considered to uniform. It is notable that only the experimental modal parameters have a direct relationship with the measured responses. This relationship is described by the likelihood function, which will be discussed in the next section.

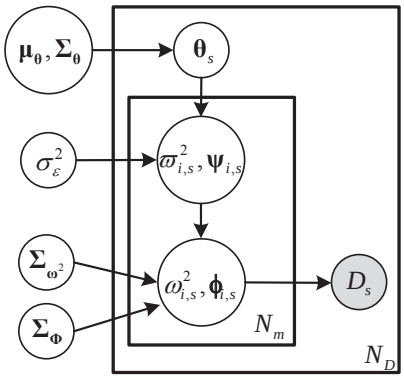

Figure 1: An overview of the hierarchical probabilistic model used for two-stage Bayesian model inference

2.3 Bayesian formulation

Given that the vibration responses are statistically independent, the Bayes' rule gives the joint posterior distribution of all parameters as

$$p(\delta,\varphi \mid \mathbf{D}) \propto \prod_{s=1}^{N_D} p(D_s \mid \boldsymbol{\omega}_s^2, \boldsymbol{\Phi}_s)\, p(\boldsymbol{\omega}_s^2, \boldsymbol{\Phi}_s \mid \boldsymbol{\varpi}_s^2, \boldsymbol{\Psi}_s, \boldsymbol{\Sigma}_{\boldsymbol{\omega}^2}, \boldsymbol{\Sigma}_{\boldsymbol{\Phi}})\, p(\boldsymbol{\varpi}_s, \boldsymbol{\Psi}_s \mid \boldsymbol{\theta}_s, \sigma_{\varepsilon}^2)\, p(\boldsymbol{\theta}_s \mid \boldsymbol{\mu}_{\boldsymbol{\theta}}, \boldsymbol{\Sigma}_{\boldsymbol{\theta}}) \tag{8}$$

where $p(\delta,\varphi \mid \mathbf{D})$ is the joint posterior distribution of all parameters, $p(D_s \mid \boldsymbol{\omega}_s^2, \boldsymbol{\Phi}_s)$ is the likelihood function of the data set D_s. It worth noting that, in derivation of this equation, the prior joint distribution is replaced from Eq. (7). The likelihood function connects the experimental modal parameters to the vibration responses. The Bayesian FFT approach [8], [9] provides a rigorous method to simplify the likelihood function by the following Gaussian distribution [13]:

$$p(D_s \mid \boldsymbol{\omega}_s^2, \boldsymbol{\Phi}_s) \propto N\left(\boldsymbol{\omega}_s^2 \middle| \hat{\boldsymbol{\omega}}_s^2, \hat{\boldsymbol{\Sigma}}_{\boldsymbol{\omega}_s^2}\right) N\left(\boldsymbol{\Phi}_s \middle| \hat{\boldsymbol{\Phi}}_s, \hat{\boldsymbol{\Sigma}}_{\boldsymbol{\Phi}_s}\right) \tag{9}$$

where $\hat{\boldsymbol{\Sigma}}_{\boldsymbol{\omega}_s^2}$ and $\hat{\boldsymbol{\Sigma}}_{\boldsymbol{\Phi}_s}$ are the covariance matrices showing how confident we are in the identified modal frequency and mode shapes, respectively. We refer to this data-driven uncertainty as identification uncertainty. The parameters $\hat{\boldsymbol{\omega}}_s^2$ and $\hat{\boldsymbol{\Phi}}_s$ are the most probable values (MPVs) of the modal parameters. The reader can refer to [13] for a detailed derivation of this approximate likelihood function. When this simplification is introduced into Eq. (8), it is possible to marginalize the experimental modal features explicitly. After simplification, we will arrive at

$$p(\{\boldsymbol{\varpi}_s^2,\boldsymbol{\Psi}_s,\boldsymbol{\theta}_s\}_{s=1}^{N_D},\varphi\,|\,\mathbf{D}) \propto \prod_{s=1}^{N_D} N\left(\boldsymbol{\varpi}_s^2\middle|\boldsymbol{\varpi}_s^2,\boldsymbol{\Sigma}_{\boldsymbol{\omega}^2}+\hat{\boldsymbol{\Sigma}}_{\boldsymbol{\omega}_s^2}\right) N\left(\boldsymbol{\Gamma}_s\boldsymbol{\Psi}_s\middle|\hat{\boldsymbol{\Phi}}_s,\boldsymbol{\Sigma}_{\boldsymbol{\Phi}}+\hat{\boldsymbol{\Sigma}}_{\boldsymbol{\Phi}_s}\right) \times \prod_{s=1}^{N_D}\left[N\left(\boldsymbol{\theta}_s\,|\,\boldsymbol{\mu}_{\boldsymbol{\theta}},\boldsymbol{\Sigma}_{\boldsymbol{\theta}}\right)\prod_{i=1}^{N_m} N\left(\mathbf{K}(\boldsymbol{\theta}_s)\boldsymbol{\psi}_{i,s}\,|\,\varpi_{i,s}^2\mathbf{M}\boldsymbol{\psi}_{i,s},\sigma_\varepsilon^2\mathbf{I}_{N_{DOF}}\right)\right] \tag{10}$$

where $p(\{\boldsymbol{\varpi}_s^2,\boldsymbol{\Psi}_s,\boldsymbol{\theta}_s\}_{s=1}^{N_D},\varphi\,|\,\mathbf{D})$ is the joint distribution of remaining parameters. Note that the procedure followed here for the marginalization is similar to the approach presented in [14]. This joint distribution can be used directly to compute the MPVs. Since the stiffness parameters are globally identifiable, it is however desirable to approximate the expressions relying on the stiffness parameters and the analytical modal features using another Laplace approximation. This set of parameters is essentially $\eta=\{\{\boldsymbol{\varpi}_s^2,\boldsymbol{\Psi}_s,\boldsymbol{\theta}_s\}_{s=1}^{N_D},\boldsymbol{\Sigma}_{\boldsymbol{\omega}^2},\boldsymbol{\Sigma}_{\boldsymbol{\Phi}},\sigma_\varepsilon^2\}$. For this purpose, we first explain that Eq. (10) can be rewritten as

$$p(\{\boldsymbol{\varpi}_s^2,\boldsymbol{\Psi}_s,\boldsymbol{\theta}_s\}_{s=1}^{N_D},\varphi\,|\,\mathbf{D}) \propto \prod_{s=1}^{N_D}\left[N\left(\boldsymbol{\theta}_s\,|\,\boldsymbol{\mu}_{\boldsymbol{\theta}},\boldsymbol{\Sigma}_{\boldsymbol{\theta}}\right)\exp\left(-J(\eta)\right)\right] \tag{11}$$

where $J(\eta)$ is the negative logarithm of the expressions summarized from the LHS of Eq. (10) given as

$$J(\eta)=\frac{1}{2}\sum_{s=1}^{N_D}\left[\ln\left|\boldsymbol{\Sigma}_{\boldsymbol{\omega}^2}+\hat{\boldsymbol{\Sigma}}_{\boldsymbol{\omega}_s^2}\right|+\ln\left|\boldsymbol{\Sigma}_{\boldsymbol{\Phi}}+\hat{\boldsymbol{\Sigma}}_{\boldsymbol{\Phi}_s}\right|+\left(\boldsymbol{\varpi}_s^2-\hat{\boldsymbol{\omega}}_s^2\right)^T\left(\boldsymbol{\Sigma}_{\boldsymbol{\omega}^2}+\hat{\boldsymbol{\Sigma}}_{\boldsymbol{\omega}_s^2}\right)^{-1}\left(\boldsymbol{\varpi}_s^2-\hat{\boldsymbol{\omega}}_s^2\right)\right] + \frac{1}{2}\sum_{s=1}^{N_D}\left[\left(\boldsymbol{\Gamma}_s\boldsymbol{\Psi}_s-\gamma_{i.s}\hat{\boldsymbol{\Phi}}_s\right)^T\left(\boldsymbol{\Sigma}_{\boldsymbol{\Phi}}+\hat{\boldsymbol{\Sigma}}_{\boldsymbol{\Phi}_s}\right)^{-1}\left(\boldsymbol{\Gamma}_s\boldsymbol{\Psi}_s-\gamma_{i.s}\hat{\boldsymbol{\Phi}}_s\right)+\sum_{i=1}^{N_m}\sigma_\varepsilon^{-2}\boldsymbol{\psi}_{i,s}^T\left(\mathbf{K}(\boldsymbol{\theta}_s)-\varpi_{i,s}^2\mathbf{M}\right)^2\boldsymbol{\psi}_{i,s}\right] \tag{12}$$

where |.| denotes the matrix determinant. This particular treatment of parameters allows separating the identification of η and $\{\boldsymbol{\mu}_{\boldsymbol{\theta}},\boldsymbol{\Sigma}_{\boldsymbol{\theta}}\}$. Later, it will be shown that this strategy is beneficial for separating different type of uncertainties.

It is worth to highlight that, when calculating the MPV, the mode shape vectors should be optimized subjected to the unit-norm constrain. This can be accomplished through the Lagrange multiplier approach using a method like [15]. Imposing this constraint requires the minimization of the following objective function:

$$J(\eta,\{\chi_{i,s},\lambda_{i,s}\}_{i=1\,s=1}^{N_m\,N_D})=J(\eta)+\frac{1}{2}\sum_{s=1}^{N_D}\sum_{i=1}^{N_m}\left[\chi_{i,s}\left(1-\boldsymbol{\psi}_{i,s}^T\boldsymbol{\psi}_{i,s}\right)+\lambda_{i,s}\left(\boldsymbol{\psi}_{i,s}^T\mathbf{T}_{i,s}^T\mathbf{T}_{i,s}\boldsymbol{\psi}_{i,s}-\gamma_{i,s}^2\right)\right] \tag{13}$$

where $\chi_{i,s}$ and $\lambda_{i,s}$ are the Lagrange multipliers should be identified as well. The minimization of this function yields the MPVs. Moreover, the exponential function in the RHS of Eq. (11) can be approximated by a Gaussian distribution centered at the MPVs. The covariance matrix of this distribution is equal to the inverse of the Hessian matrix of $J(\eta)$ evaluated at the MPVs. This approximation simplifies Eq. (11) into

$$p(\{\boldsymbol{\theta}_s\}_{s=1}^{N_D},\boldsymbol{\mu}_{\boldsymbol{\theta}},\boldsymbol{\Sigma}_{\boldsymbol{\theta}}\,|\,\mathbf{D}) \propto \prod_{s=1}^{N_D} N\left(\boldsymbol{\theta}_s\middle|\boldsymbol{\mu}_{\boldsymbol{\theta}},\boldsymbol{\Sigma}_{\boldsymbol{\theta}}\right)N\left(\boldsymbol{\theta}_s\middle|\hat{\boldsymbol{\theta}}_s,\hat{\boldsymbol{\Sigma}}_{\boldsymbol{\theta}_s}\right) \tag{14}$$

where $\hat{\boldsymbol{\theta}}_s$ and $\hat{\boldsymbol{\Sigma}}_{\boldsymbol{\theta}_s}$ are the MPV and identification uncertainty of the stiffness parameters obtained from data set D_s, respectively. In [11], it is proved that marginalization of $\boldsymbol{\theta}_s$'s provides:

$$p(\boldsymbol{\mu}_{\boldsymbol{\theta}},\boldsymbol{\Sigma}_{\boldsymbol{\theta}}\,|\,\mathbf{D}) \propto \prod_{s=1}^{N_D} N\left(\boldsymbol{\mu}_{\boldsymbol{\theta}}\middle|\hat{\boldsymbol{\theta}}_s,\boldsymbol{\Sigma}_{\boldsymbol{\theta}}+\hat{\boldsymbol{\Sigma}}_{\boldsymbol{\theta}_s}\right) \tag{15}$$

where $p(\boldsymbol{\mu}_{\boldsymbol{\theta}}, \boldsymbol{\Sigma}_{\boldsymbol{\theta}} \mid \mathbf{D})$ is the marginal posterior distribution of the hyper-parameters characterizing the stiffness parameters. In a special case when $\hat{\boldsymbol{\Sigma}}_{\boldsymbol{\theta}_s}$'s are fairly constant, the MPVs of the hyper-parameters are obtained [12]:

$$\hat{\boldsymbol{\mu}}_{\boldsymbol{\theta}} = \frac{1}{N_D}\sum_{s=1}^{N_D}\hat{\boldsymbol{\theta}}_s \tag{16}$$

$$\hat{\boldsymbol{\Sigma}}_{\boldsymbol{\theta}} = \frac{1}{N_D}\sum_{s=1}^{N_D}(\hat{\boldsymbol{\theta}}_s - \hat{\boldsymbol{\mu}}_{\boldsymbol{\theta}})(\hat{\boldsymbol{\theta}}_s - \hat{\boldsymbol{\mu}}_{\boldsymbol{\theta}})^T - \frac{1}{N_D}\sum_{s=1}^{N_D}\hat{\boldsymbol{\Sigma}}_{\boldsymbol{\theta}_s} \tag{17}$$

where $\hat{\boldsymbol{\mu}}_{\boldsymbol{\theta}}$ and $\hat{\boldsymbol{\Sigma}}_{\boldsymbol{\theta}}$ are the MPVs. These equations also reveal that the MPV of the hyper mean vector is the average of realizations obtained from different data sets. Moreover, the MPV of the hyper covariance matrix is determined as the difference of the ensemble covariance matrix computed from different realizations and the mean of identification uncertainties.

3 EXPERIMENTAL EXAMPLE

A three-story shear building small-scale structure is used for verifying the proposed framework shown in Figure 2(a). The acceleration time-history responses of the three floors were measured when subjected to N_D = 40 independent white Gaussian base excitations. The averaged singular value spectrum is plotted in Figure 2(b). Based on this figure, three resonant bands can be selected as [3.2–5.2 Hz], [12.0–14.0 Hz], and [17.5–19.5 Hz] for applying the Bayesian FFT approach. For each data set, the modal frequencies and mode shape vectors are thus obtained along with their identification uncertainty.

Figure 2(c) shows the dynamical model considered to describe the structure. It is a simple shear frame whose columns have unknown stiffness. The mass matrix is considered to be known and concentrated on each floor. Thus, there exist three unknown stiffness parameters to be identified from each data set, and their hyper-parameters should be inferred from multiple data sets. The modal statistical information obtained is then used for updating the modal and stiffness parameters. Table 1 presents the MPVs and the total uncertainty comprising both identification uncertainty and the variability. Table 2 presents both the identification uncertainty and the ensemble variability. These results demonstrate the proposed hierarchical framework in terms of the separation of the different sources of uncertainty and providing uncertainties robust to the variability induced by the modeling errors.

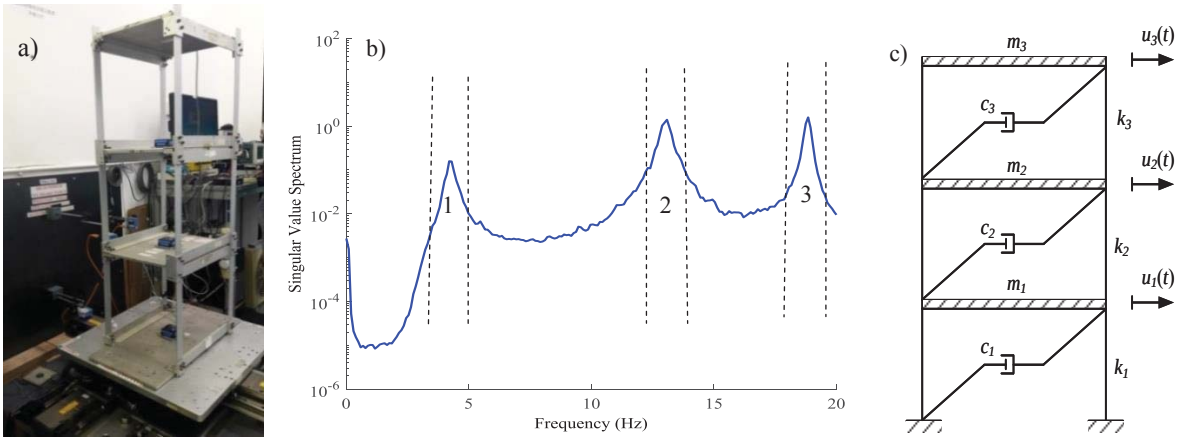

Figure 2: Small-scale structure tested on a shaking table b) Averaged singular value spectrum obtained from the three measured acceleration responses

Table 1: MPV and uncertainties computed for the modal frequencies and mode shape components

Analytical parameters	Averaged MPVs	Total uncertainty (S.D.)
ϖ_1 (rad/s)	27.43	0.0435
ψ_{11}	0.395	0.0010
ψ_{21}	0.602	0.0015
ψ_{31}	0.694	0.0017
ϖ_2 (rad/s)	81.96	0.0374
ψ_{12}	0.7499	0.0055
ψ_{22}	0.12612	0.0010
ψ_{32}	-0.6494	0.0047
ϖ_3 (rad/s)	118.28	0.0469
ψ_{13}	-0.481	3.2e-05
ψ_{23}	0.727	4.9e-05
ψ_{33}	-0.489	3.3e-05

Table 2: Quantification of the uncertainty using the sampling and asymptotic approximation approaches

Stiffness parameters	Hyper mean MPV (KN/m)	Standard deviation (KN/m)	
		Identification uncertainty*	Ensemble variability**
K_1	17.827	2.14e-06	0.454
K_2	24.368	1.19e-05	0.134
K_3	26.287	6.68e-06	0.132

* Averaged over realizations obtained from each data set

** Computed based on the MPV of the hyper covariance matrices

4 CONCLUSIONS

A hierarchical Bayesian modeling framework was developed to update dynamical models based on modal statistical information. This framework is coherent and consistent in terms of using Bayesian probability logic. It employs the Bayesian FFT approach for modal inference and updates the stiffness parameters based on the modal statistical information. This framework weights modal features based on their total uncertainty composed of the identification uncertainty and their variability across different data sets. It delivers the promise to quantify the variability induced due to modeling errors through efficient asymptotic approximations. This achievement is important since the variability often predominantly exceeds the identification uncertainty obtained using a Bayesian non-hierarchical probabilistic framework.

5 ACKNOWLEDGMENTS

Financial support from the Hong Kong Research Grants Council under project No. 16212918 and 16211019 is gratefully acknowledged.

REFERENCES

[1] J. L. Beck and L. S. Katafygiotis, "Updating models and their uncertainties. I: Bayesian statistical framework," *J. Eng. Mech.*, vol. 124, no. 4, pp. 455–461, Apr. 1998.

[2] M. W. Vanik, J. L. Beck, and S. K. Au, "Bayesian Probabilistic Approach to Structural Health Monitoring," *J. Eng. Mech.*, vol. 126, no. 7, pp. 738–745, Jul. 2000.
[3] J. L. Beck, S.-K. Au, and M. W. Vanik, "Monitoring Structural Health Using a Probabilistic Measure," *Comput. Civ. Infrastruct. Eng.*, vol. 16, no. 1, pp. 1–11, Jan. 2001.
[4] K.-V. Yuen, J. L. Beck, and L. S. Katafygiotis, "Efficient model updating and health monitoring methodology using incomplete modal data without mode matching," *Struct. Control Heal. Monit.*, vol. 13, no. 1, pp. 91–107, Jan. 2006.
[5] K. Christodoulou and C. Papadimitriou, "Structural identification based on optimally weighted modal residuals," *Mech. Syst. Signal Process.*, vol. 21, no. 1, pp. 4–23, 2007.
[6] B. Goller, J. L. Beck, and G. I. Schuëller, "Evidence-Based Identification of Weighting Factors in Bayesian Model Updating Using Modal Data," *J. Eng. Mech.*, vol. 138, no. 5, pp. 430–440, 2012.
[7] F. L. Zhang and S. K. Au, "Fundamental two-stage formulation for Bayesian system identification, Part II: Application to ambient vibration data," *Mech. Syst. Signal Process.*, vol. 66–67, pp. 43–61, 2016.
[8] K.-V. Yuen and L. S. Katafygiotis, "Bayesian fast Fourier transform approach for modal updating using ambient data," *Adv. Struct. Eng.*, vol. 6, no. 2, pp. 81–95, 2003.
[9] S. Au, F. Zhang, and Y. Ni, "Bayesian operational modal analysis: Theory, computation, practice," *Comput. Struct.*, vol. 126, pp. 3–14, Sep. 2013.
[10] I. Behmanesh, B. Moaveni, G. Lombaert, and C. Papadimitriou, "Hierarchical Bayesian model updating for structural identification," *Mech. Syst. Signal Process.*, vol. 64–65, pp. 360–376, 2015.
[11] O. Sedehi, C. Papadimitriou, and L. S. Katafygiotis, "Probabilistic hierarchical Bayesian framework for time-domain model updating and robust predictions," *Mech. Syst. Signal Process.*, vol. 123, pp. 648–673, May 2019.
[12] O. Sedehi, C. Papadimitriou, and L. S. Katafygiotis, "Data-driven uncertainty quantification and propagation in structural dynamics through a hierarchical Bayesian framework," *Probabilistic Eng. Mech.*, vol. 60, no. January, p. 103047, Apr. 2020.
[13] O. Sedehi, L. S. Katafygiotis, and C. Papadimitriou, "Hierarchical Bayesian operational modal analysis: Theory and computations," *Mech. Syst. Signal Process.*, vol. 140, p. 106663, Jun. 2020.
[14] O. Sedehi, L. S. Katafygiotis, and C. Papadimitriou, "A Time-Domain Hierarchical Bayesian Approach for model updating," in *16th European Conference on Earthquake Engineering (16ECEE)*, 2018.
[15] W. J. Yan and L. S. Katafygiotis, "A novel Bayesian approach for structural model updating utilizing statistical modal information from multiple setups," *Struct. Saf.*, vol. 52, no. PB, pp. 260–271, 2015.

EURODYN 2020
XI International Conference on Structural Dynamics
M. Papadrakakis, M. Fragiadakis, C. Papadimitriou (eds.)
Athens, Greece, 23–26 November 2020

RISK-TARGETED MAPS FOR ALICANTE PROVINCE (SPAIN)

A. Kharazian[1], S. Molina[2], J. Galiana-Merino[3], N. Agea-Medina[4]

[1] Multidisciplinary Institute for Environmental Studies "Ramon Margalef" (IMEM) University of Alicante, Spain
alireza.kharazian@ua.es

[2] Multidisciplinary Institute for Environmental Studies "Ramon Margalef" (IMEM) Dept. Earth Sciences and Environment - Faculty of Sciences University of Alicante, Spain
sergio.molina@gcloud.ua.es

[3] University Institute of Physics Applied to Sciences and Technologies Dept. Physics, Systems Engineering, and Signal Theory, Polytechnic School University of Alicante, Spain
jj.galiana@ua.es

[4] Multidisciplinary Institute for Environmental Studies "Ramon Margalef" (IMEM) University of Alicante, Spain
noelia.agea@ua.es

Keywords: seismic hazard, earthquake engineering, collapse probability, risk targeting, Alicante

Abstract. *The areas with higher seismic risks in Spain are located in the South and South-East of Spain. For instance, the recent seismic hazard analysis performed in the Alicante and Elche have obtained a PGA of 200 cm/sec^2 approximately in the region and indicated that the highest contribution to the seismic hazard comes from the seismicity due to the Crevillente and the Bajo Segura faults. Many studies have demonstrated that the design of structures in the region through the use of "uniform hazard" principle, does not guarantee that the collapse risk in the region is uniform as well, i.e., even in those regions with similar PGAs corresponding to the same mean return period, the seismic risk in terms of failure probability will be significantly different. A new approach called "risk targeting" has already been adopted by new generations of seismic codes and associated research, where the parameters are specified to ensure a tool for the design of buildings with a probability of collapse alike or at least harmonized throughout the area concerned. Consequently, in this study, we will focus on the evaluation of the collapse probability of the buildings and then developing the risk-targeted maps of the Alicante. Finally, the preliminary obtained results will be discussed.*

1 INTRODUCTION

Seismic assessment and structural designs are continually evolving, as evidenced by the rapid development of new procedures illustrated by the Pacific Earthquake Engineering Research Center (PEER); performance-based earthquake engineering framework [1]. Numerous studies aimed to integrate the principle of probability into seismic performance evaluation, taking into account the uncertainties related not only to seismic input but also to structural properties, capacity and model [2, 3, 4, and 5]. In order to estimate the seismic demand at a specific location, the vast majority of the Earthquake Design Codes rely on a seismically defined return period (for example, 10% in 50 years) of intensity measures. The decision to design the structure in accordance with a "uniform hazard" level is based on the idea that a process like this leads to the same annual probability of collapse as anywhere, in the buildings. Nevertheless, this fact happens only if the collapse probability of the structure will be a certain value that is infeasible in real cases. Recently, multiple studies have demonstrated that a design-based earthquake determined on a uniform hazard theory does not necessarily lead to the design of structures with a consistent risk of collapse in different areas. These inconsistencies are due to the different shape of the hazard curve for different regions and uncertainties in failure capacity of structures [6] arising from a set of factors, such as different material properties, differences in design, and among others. Hence, a structure can collapse for a different ground motion with what it was designed for. Moreover, as the shape of the hazard curve depends on the site location, even the buildings designed for the same ground motion will have different values of collapse probability.

Based on the work by [6], it would be more consistent to use "uniform risk" assumption in which the design ground motion is estimated to provide a constant level of risk. This algorithm was used to present the risk-targeted maximum considered earthquake (MCER) ground motion (ASCE7-10) [7]. Accordingly, using the proposed method, Douglas et al. [8] presented a risk-targeted seismic design map for France. In the study by [9], various parameters involved in developing risk-targeted design maps are analyzed and maps for Europe developed using SHARE seismic hazard results (www.share-eu.org). The risk-targeted map of Romania was developed by [10], using the hazard model of SHARE. [11] applied site- and structure specific fragility curves to estimate the risk-targeted design ground motion. [12] addressed some research results relating to the risk of failure in residential and industrial construction, in compliance with the Italian code. They showed that seismic structural reliability tends to decrease with increasing seismic hazard to the building site, despite the homogeneous return period of excess of seismic design ground motion. [13] presented a review of the state of the art of this technique, highlighting efforts to constrain better some of the input parameters. In addition, they discussed the problems in the practical implementation of this approach and the alternative forward paths. [14] have performed the probabilistic seismic hazard analysis and a risk-targeted map for Tehran provided based on the hazard curves achieved. [15] presented a risk-targeted seismic design map for Iran, considering the seismic hazard models from the EMME14 project [16] and STD-2800 [17]. Recently, [18] performed a review and comparison among the existing approaches with regard to the implementation of uniform-risk concepts in the performance-based design of structures. Among these, one based on the use of risk-targeted behavior factors (RTBFs) has been recently considered for the development of future versions of Eurocode 8 [19]. [20] demonstrated the effects of the RTBF approach being applied to the concept of risk-targeted maps for Italy.

In this study, using the updated seismic hazard in the regions of Alicante and Elche [21] and employment of generic fragility curves, the distribution of the risk-targeted ground motion has

been estimated for these areas. This study aims at evaluating the relevant peak ground accelerations for a given target annual collapse probability and different collapse probability for a given peak ground acceleration which corresponds to a specific mean return period of seismic action.

2 SEISMIC HAZARD MODEL

The seismic hazard map of Spain was recently updated after the events occurred in the Murcia region, such as the 1999 earthquake in Mula (Mw=4.7), 2002 in Bullas (Mw=5.0), 2005 in La Paca (Mw=4.8) or the destructive Lorca earthquake occurred in 2011 (Mw= 5.2) with catastrophic consequences in Lorca town despite being a relatively small event. None of those events were included in the seismic hazard map published under the framework of the current Spanish seismic code NCSE-02. For example, the PGA at rock for a 0.1 probability of exceedance in 50 years was 0.14 g and 0.15 g for Alicante and Elche respectively (according to NCSE-02) and it has been increased to 0.18 g and 0.20g with the updated of the seismic hazard map [21].

In this work, we have carried out a specific analysis of the seismic hazard map in both municipalities using the Spanish seismic catalog updated until 2018. The computation was done using the seismic zones proposed by IGN-UPM Working Group and updating the activity rate and beta values of the zone within the influence area of both cities (150 km). The software R-CRISIS [22, 23] was used to compute the seismic hazard map in terms of PGA for a probability of exceedance in 50 years (Figure 1).

As we can see, the seismic hazard results have slightly increased regarding previous studies.

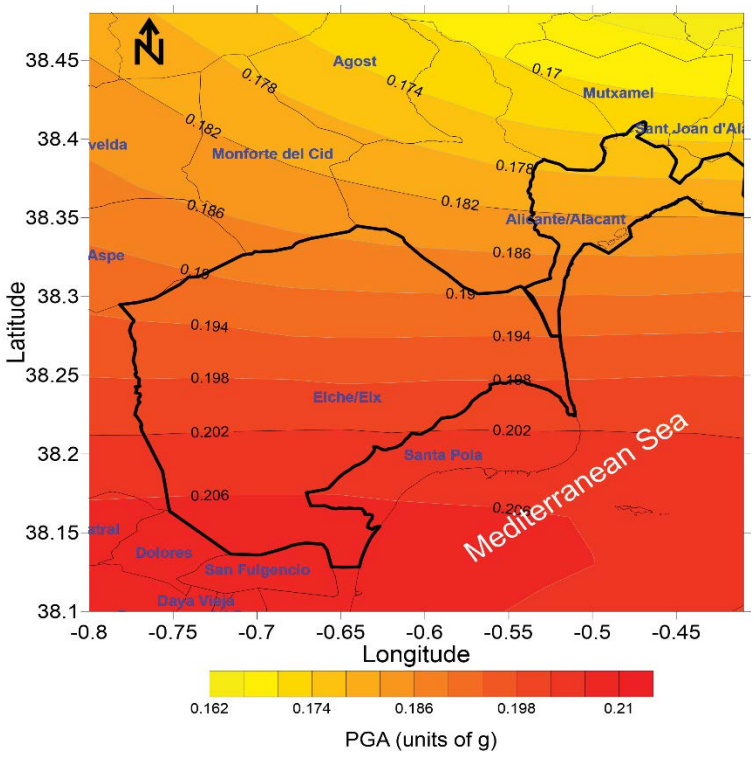

Figure 1: Seismic hazard map (PGA at rock) for the municipalities of Elche and Alicante for 0.1 exceedance probability in 50 years.

Therefore, we have chosen two sites (one in each municipality) as representatives of the PSHA values in the urban areas. Figure 2 represents the seismic hazard curves of PGA in terms of annual probability of exceedance and probability of exceedance in 50 years which will be used for the calculation of the risk-targeted hazard.

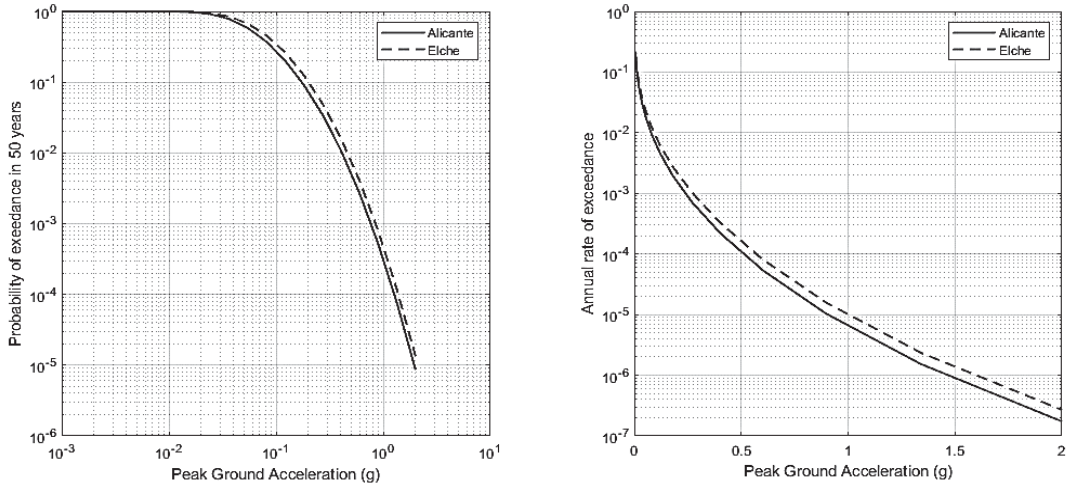

Figure 2: Seismic hazard curves for Alicante and Elche.

3 CALCULATION OF RISK-TARGETED MAP

In order to perform a risk-targeted analysis, it is necessary to develop the fragility curve corresponds to the structures under study. Considering that in this approach, the fragility curves should cover the vulnerability of a large range of different building typologies and on the other hand, developing these curves are too expensive for a specific building class and location, the generic collapse fragility curves will be used for all building classes in the desired area. It should be noted that the provided curve must be sufficiently generic to capture all possible vulnerabilities [8]. The fragility function is conditional upon the values of ground motion design and outlines the conditional probability of exceeding a limit state, which hereinafter is the collapse of a structure, for a given design ground motion with a specific mean return period (RP). In this study, the 475-year mean return period was implemented (i.e., 10% probability of exceedance in 50 years), since it is the most widely accepted value in Europe. The fragility functions are presented as lognormal distributions with two parameters: the median value of PGA and the logarithmic standard deviation of PGA (β). Hence, one can say, in order to develop a generic fragility curve for risk-targeted analysis, it is necessary to define the parameters of Pc|gm, and β. The latter (Pc|gm) is the conditional probability of collapse under the design ground motion with 475-year return period and the former (β) is taking into consideration several sources of uncertainty in the collapse capacity, such as the record-to-record variability, the uncertainty in the collapse definition, and, ideally other sources such as human error, that even the most advanced numerical models cannot accommodate [9].

Regarding with logarithmic standard deviation of the fragility functions, there are significant different values proposed by other researches. As an example, Luco et al. [6], used a β value of 0.8, while Douglas et al. [8] suggested value of 0.5. the β value of 0.6 was considered in the study by [9], while Vanzi et al. [24] used a value of 0.2. It is important to note that, using the higher values of β more than 0.8, provides a low probability of collapse even in highly seismic regions, which seems an unrealistic scenario. On the other hand, assuming low values of β (e.g.,

less than 0.2), leads to more steep collapse fragility curves that could provide 100% probability of collapse even at low ground motion levels. The estimation of Pc|gm, needs the design and evaluation of a large number of structures and a wide range of hazard levels. As stated earlier in this study, the probability of collapse corresponds to the peak ground acceleration of the hazard curve with a mean return period of 475 years. Several studies suggest different values of Pc|gm. For instance, Douglas et al. [8] suggested a Pc|gm value of 10^{-5}, while Silva et al. [9] used a value of 10^{-3}. Ulrich et al. [25] proposed a value of 10^{-7} for low, frequent design ground motion levels and 10^{-5} for higher and rarer design ground motion in their study. However, Silva et al. [9], believe this range of probability of collapse (i.e., 10^{-7} to 10^{-5}) is too extremely low for ordinary structures. Luco et al. [6], have selected 10% probability of collapse under MCE, which corresponds to the probability of collapse at 475-year ground motion ranging from 10^{-2} to 10^{-3} [9]. Fajfar and Dolšek [26] have computed the value of Pc|gm in the range of 10^{-4} to 10^{-5} and Vanzi et al. [24] used the value of 1.3×10^{-6} for the probability of collapse under gravity loads.

According to the PBEE method and using the seismic hazard curve and collapse fragility function the annual collapse rate of a structure, λ_c is determined using the following classic convolution products given by [27]:

$$\lambda_c = -\int_0^{+\infty} F(s).\frac{dG(s)}{ds}ds \tag{1}$$

Where F(s) is the fragility function (conditional probability of collapse for a given ground motion) and G(s) is the hazard curve. The integration in equation (1) does not have a closed-form solution [28], therefore an iterative process is required for calculation of annual collapse rate. As suggested by [9, 28] the annual failure probability will be computed by dividing both the fragility curve and the seismic hazard curve into a large number of segments and then numerically integration the distribution. Based on the Poisson assumption, the annual collapse rate is converted into the annual probability of collapse. It should be noted that since we are targeting the very low values, there is a negligible difference between the values of the annual probability of collapse P_c and the annual collapse rate (i.e., mean annual frequency of collapse, MAF). Since, the main objective of the risk-targeted analysis is the estimation of ground motion consistent with the target risk (i.e., accepted annual P_c), it is necessary to define an acceptable level of seismic risk, which can be expressed as annual collapse probability. Hence, in the iterative process, the value of design ground motion changes in each step until reaching the desired value of annual collapse probability. The obtained design ground motion at the final step will be the risk-targeted ground motion. Based on the study by [6], for each seismic site, the risk coefficient is calculated by dividing the obtained former value and the uniform hazard ground motion. Finally, the values of risk-targeted design ground motion are created by multiplying this coefficient to the current seismic design ground motion maps. Regarding with acceptable annual probability of collapse, there are different suggestions from other researches and seismic codes. For example, ASCE 2010 [7], proposed value of 2.0×10^{-4} for the United States. Douglas et al. [8], suggested using the value of 1.0×10^{-5} as a reasonable value. In the work by Silva et al. [9], the value of 5.0×10^{-5} established as an acceptable annual probability of collapse.

In order to investigate the effect of these parameters on the annual probability of collapse, a simple sensitivity analysis has been performed. In this analysis, different combinations of values for β and Pc|gm are considered (i.e., β = 0.5, 0.6, 0.7, and, 0.8 and Pc|gm = 10^{-2} … 10^{-5}). Then values of P_c (annual probability of collapse) will be calculated by developing the generic fragility curves and the computational approach described above. Figure 3a and 3b show the

relation of the annual probability of collapse with the parameters of Pc|gm, and β for Alicante and Elche, respectively.

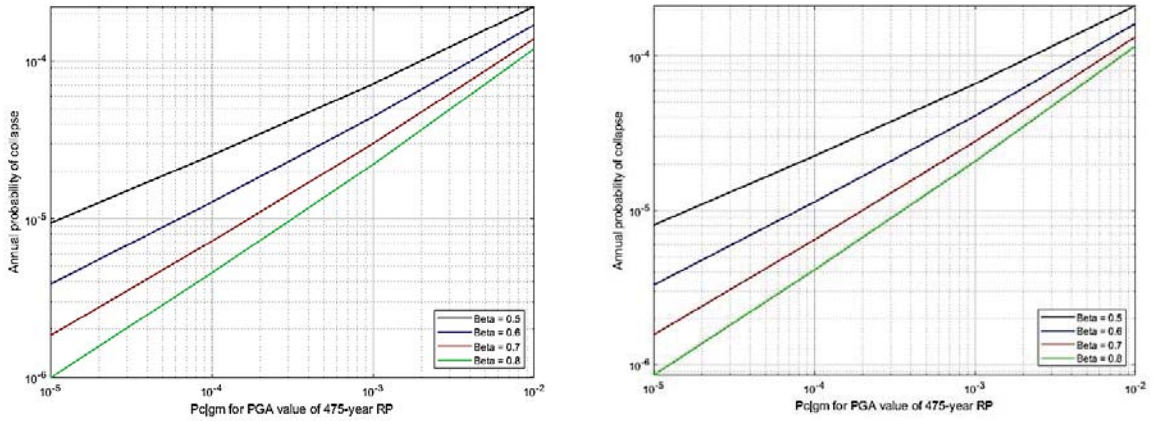

(a) Alicante (b) Elche

Figure 3: Relation of annual probability of collapse with Pc|gm, and β

As shown in Figure 3, for both sites, the annual probability of collapse converges to a certain value when the conditional probability of collapse for a given design ground motion with a 475-year return period rises up to 10^{-2}. According to the analysis, in this study, we considered the values of 0.7, 10^{-2}, and 10^{-4} for β, Pc|gm, and P_c, respectively. Moreover, in the following sections for risk targeting analysis, the values proposed by other researches such as [6, 9] will be considered for a better comparison of the obtained results.

4 RESULTS FOR ALICANTE AND ELCHE

In this section, the risk-targeted maps for Alicante and Elche are built with the combination of target annual collapse probabilities and standard deviations suggested by [6, 9] as well as the ones assumed in this study. In order to evaluate the effect of two main input parameters, namely the standard deviation β and the probability of collapse for a given design ground motion with a 475-year mean return period (defining the fragility function) a series of maps were generated.

The first two tables (i.e., Table 1 and Table 2) show the annual probability of collapse for Alicante and Elche, Respectively. These values are corresponding to the PGA with a mean return period of 475 years. The standard deviation is considered as 0.6, 0.7, and 0.8 while the Pc|gm was taken as 0.1 and 0.001.

	β = 0.6	**β = 0.7**	**β = 0.8**
Pc|gm = 0.1	8.090×10^{-4}	8.054×10^{-4}	8.264×10^{-4}
Pc|gm = 0.001	4.421×10^{-5}	2.990×10^{-5}	2.207×10^{-5}

Table 1: Annual probability of collapse for the PGA corresponding to a mean return period of 475 years in Alicante

	β = 0.6	**β = 0.7**	**β = 0.8**
Pc|gm = 0.1	8.081×10^{-4}	8.077×10^{-4}	8.319×10^{-4}
Pc|gm = 0.001	4.089×10^{-5}	2.788×10^{-5}	2.071×10^{-5}

Table 2: Annual probability of collapse for the PGA corresponding to a mean return period of 475 years in Elche

Table 1 and Table 2 show the distinctive values of the annual probability of collapse. In the case of the Pc|gm = 0.001, Alicante has the highest probability of collapse, whereas in the case of Pc|gm = 0.1, the largest collapse probability is observed in Elche. Based on the seismic hazard map of the Alicante and Elche (Figure 1), it should be concluded that Elche has the highest collapse probability, but as it was observed above, using different values of Pc|gm in this approach, may lead to opposite results. A similar observation has been reported in the works by [9, 10] in which reveals some questions about this approach.

The four maps shown in Figure 4, represent the risk-targeted ground motions for the municipality of Elche corresponding to the annual collapse probability of 2×10^{-4}. The PGAs were calculated for $\beta = 0.6$ and 0.8 and using Pc|gm = 0.1 and 0.001.

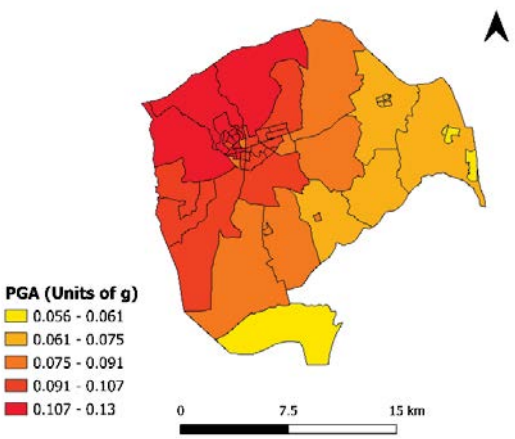

(a) Uniform risk-targeted map for target collapse probability 2×10^{-4}, $\beta = 0.6$, and Pc|gm = 10^{-3}

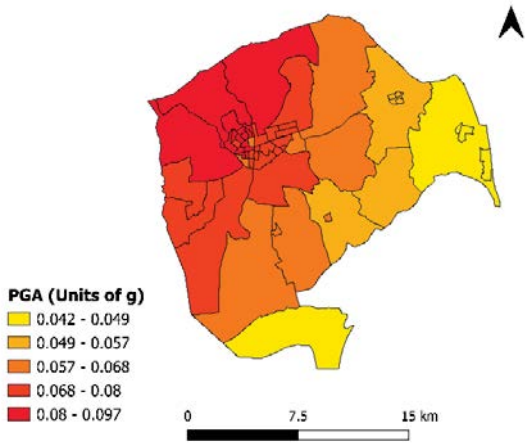

(b) Uniform risk-targeted map for target collapse probability 2×10^{-4}, $\beta = 0.8$, and Pc|gm = 10^{-3}

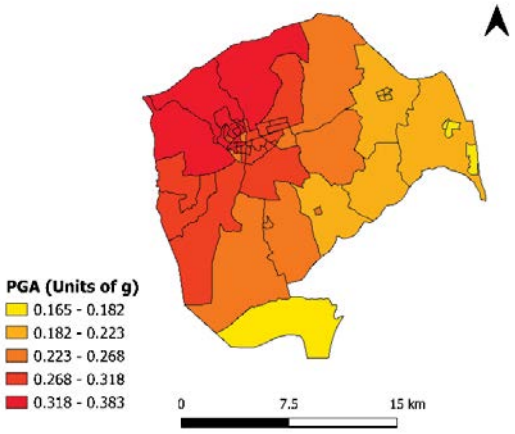

(c) Uniform risk-targeted map for target collapse probability 2×10^{-4}, $\beta = 0.6$, and Pc|gm = 10^{-1}

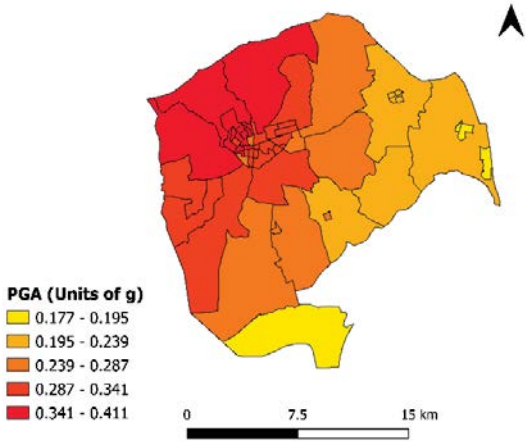

(d) Uniform risk-targeted map for target collapse probability 2×10^{-4}, $\beta = 0.8$, and Pc|gm = 10^{-1} (Elche)

Figure 4: Risk-targeted ground motion maps for Elche

A comparison between Figure 4a and Figure 4b, indicates the larger values of β, results in the lower risk-targeted ground motion (almost 20% reduction). On the contrary, Figure 4c and Figure 4d show an increase of 7% by increasing the value of β. The risk-targeted ground motions in the Figure 4a and Figure 4c, show that for a given value of acceptable collapse probability and standard deviation, the ground motion level leads to larger values by increasing the

value of Pc|gm. A comparison between Figure 4b and Figure 4d displays the same trend as mentioned before.

Finally, assuming $\beta = 0.7$ and $Pc|gm = 10^{-2}$ and target annual collapse probability of 10^{-4}, the risk-targeted ground motion maps for municipalities of Alicante and Elche are shown in Figure 5.

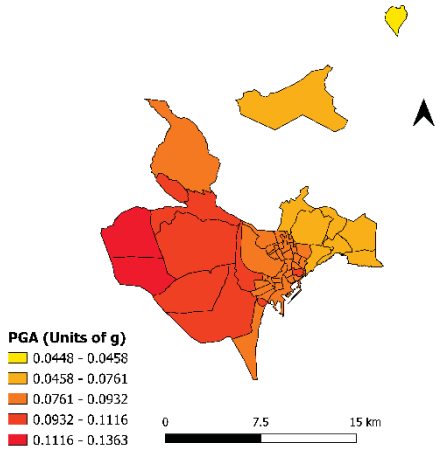

(a) Uniform hazard map for Alicante corresponding to 10% Probability of exceedance in 50 years

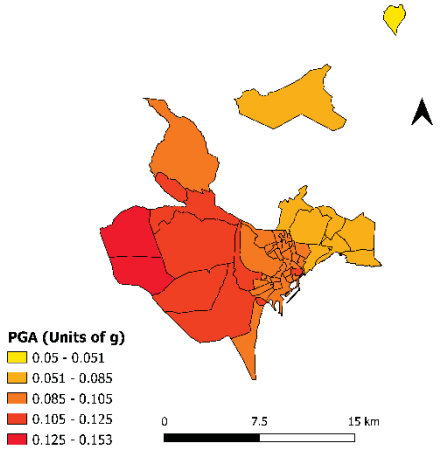

(b) Uniform risk-targeted map for target collapse probability 10^{-4}, $\beta = 0.7$, and $Pc|gm = 10^{-2}$ (Alicante)

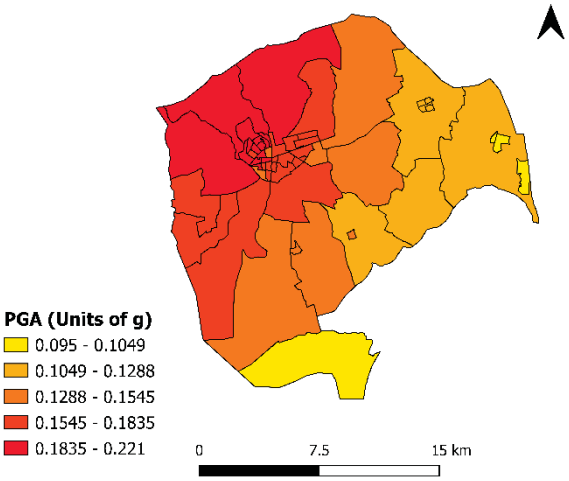

(c) Uniform hazard map for Elche corresponding to 10% Probability of exceedance in 50 years

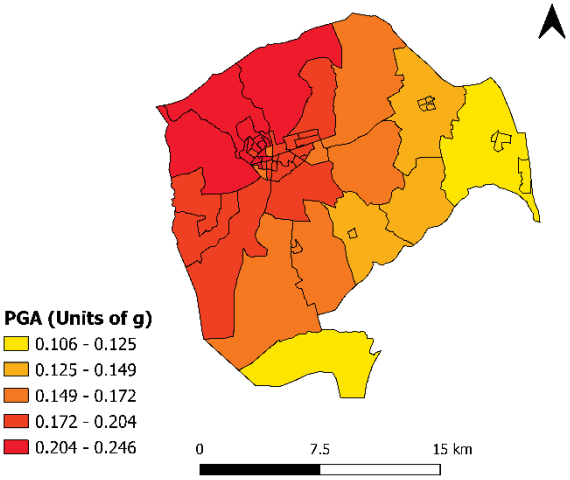

(d) Uniform risk-targeted map for target collapse probability 10^{-4}, $\beta = 0.7$, and $Pc|gm = 10^{-2}$ (Elche)

Figure 5: Uniform ground motion maps for Alicante (a and b) and Elche (c and d)

According to Figure 5a and Figure 5b, the risk-targeted ground motion in the municipality of Alicante varies between 0.05g and 0.153g with an average value of 0.098g indicating an almost 11% increase in the ground motion level. Figure 5c and Figure 5d show that the risk-targeted acceleration in the municipality of Elche changes from 0.106g to 0.246g with the average value of 0.162g representing 10% increase approximately. Clearly, the results of risk-targeted maps would be considerably different by variation of Pc|gm threshold in which considered in this study.

5 CONCLUSIONS

In this study, risk-targeted maps are developed for municipalities of Alicante and Elche based on the updated seismic hazard map of Spain [21]. The annual probability of collapse was calculated by using the convolution product between seismic hazard and fragility function. The relevant parameters suggested by [6, 9] and the results of the sensitivity analysis were also used to establish the generic fragility curves. Furthermore, by considering an acceptable collapse probability and the approach explained earlier in previous sections, the risk-targeted ground motion maps revealed. The results highlight the preliminary conclusions as follow:

- The influence of standard deviation on the annual probability of collapse is relevant, but no clear trends are observed.
- The influence of Pc|gm on annual collapse probability is significant.
- Given that these parameters (i.e., acceptable collapse probability, standard deviation, and distribution of collapse) can allocate different values proposed in the past works, different risk-targeted maps will be obtained for the considered regions in this study.
- Based on the assumed parameters and obtained results, it can be shown with some minor changes to the uniform hazard maps (up to 10%), the uniform risk of collapse will be achieved in the municipalities of Alicante and Elche.

Based on the obtained results, it is clear that risk-targeted seismic maps need to be created for the other municipalities and in the more extended work for Spain.

6 ACKNOWLEDGMENTS

The study has received funding from the European Union's Horizon 2020 research and innovation program under grant agreement No 821046, the Ministerio de Economía, Industria y Competitividad through research project CGL2016-77688-R, the Generalitat Valenciana through the research project AICO/2016/098 with the collaboration and funding provided by Elche and Alicante municipalities.

REFERENCES

[1] Porter KA (2003) An overview of PEER's performance-based earthquake engineering methodology. In: Proceedings of ninth international conference on applications of statistics and probability in civil engineering.

[2] Dolšek M (2009) Incremental dynamic analysis with consideration of modeling uncertainties. Earthq Eng Struct Dyn 38(6):805–825.

[3] Liel AB, Haselton CB, Deierlein GG, Baker JW (2009) Incorporating modeling uncertainties in the assessment of seismic collapse risk of buildings. Struct Saf 31(2):197–211. https ://doi.org/10.1016/j.strus afe.2008.06.002

[4] Tubaldi E, Barbato M, Dall'Asta A (2011) Influence of model parameter uncertainty on seismic transverse response and vulnerability of steel–concrete composite bridges with dual load path. J Struct Eng 138(3):363–374.

[5] Fib (2012) Probabilistic performance-based seismic design, bulletin 68, International federation of structural concrete, Lausanne, CH.

[6] Luco N, Ellingwood B, Hamburger RO, Hopper JD, Kimball JK, Kircher CA (2007) Risk targeted versus currents seismic design maps for the conterminous United States. In: Proceedings of the 2007 Structural Engineers Association of California (SEAOC) Convention, Lake Tahoe, CA.

[7] American Society of Civil Engineers (ASCE), 2010. Minimum Design Loads for Buildings and Other Structures (ASCE 7-10), Reston, VA.

[8] Douglas J, Ulrich T, Negulescu C (2013) Risk-targeted seismic design maps for mainland France. Nat Hazards 65(3):1999– 2013. https://doi.org/10.1007/s11069-012-0460-6

[9] Silva V, Crowley H, Bazzurro P (2016) Exploring risk-targeted hazard maps for Europe. Earthquake Spectra 32(2):1165–1186. https://doi.org/10.1193/112514EQS 198M

[10] Vacareanu R, Pavel F, Craciun I, Coliba V, Arion C, Aldea A, Neagu C (2018) Risk-targeted maps for Romania. J Seismol 22:407–417. https://doi.org/10.1007/s10950-017-9713-x

[11] Spillatura A (2018) "From record selection to risk targeted spectra for risk-based assessment and design," Ph.D. Thesis, Dipartimento di Costruzionie Infrastrutture, Istituto Universitario degliStudi Superiori (IUSS), Pavia, Italy

[12] Iervolino I, Spillatura A, Bazzurro P (2018) Seismic reliability of code conforming Italian buildings. J Earthq Eng 22:5–27. https://doi.org/10.1080/13632469.2018.1540372

[13] Douglas J., Gkimprixis A. (2018) Risk Targeting in Seismic Design Codes: The State of the Art, Outstanding Issues and Possible Paths Forward. In: Vacareanu R., Ionescu C. (eds) Seismic Hazard and Risk Assessment. Springer Natural Hazards. Springer, Cham. https://doi.org/10.1007/978-3-319-74724-8_14

[14] Zaman M, Ghayamghamian MR (2019) Bull Earthq Eng. https://doi.org/10.1007/s10518-019-00625-0

[15] Taherian, A.R., Kalantari, A. Risk-targeted seismic design maps for Iran. J Seismol 23, 1299–1311 (2019). https://doi.org/10.1007/s10950-019-09867-6

[16] Danciu L et al (2017) The 2014 earthquake model of the Middle East: seismogenic sources. Bull Earthq Eng:1–32

[17] BHRC (2014) Iranian code of practice for seismic resistant design of buildings, Standard 2800, 4th edn. Building and Housing Research Center, Tehran

[18] Gkimprixis A, Tubaldi E, Douglas J (2019) Comparison of methods to develop risk targeted seismic design maps. Bull Earthq Eng 17:3727–3752. https://doi.org/10.1007/s10518-019-00629-w

[19] EN 1998-1 cEN, Eurocode 8 – Design for Structures for Earthquake Resistance, Part 1: General Rules, Seismic Actions and Rules for Buildings, European committee for Standardization (cEN), Brussels, Belgium, December 2004.

[20] Douglas, J., Gkimprixis, A., & Tubaldi, E. (2019). Derivation of risk-targeted maps for Italy based on a simplified approach. Derivation of risk-targeted maps for Italy based on a simplified approach, XVIII Convegno ANIDIS L'ingegneria Sismica in Italia : Ascoli Piceno, 15-19 settembre 2019 2-9.

[21] IGN-UPM Working group (2017). Actualización de Mapas de Peligrosidad Sísmica de España 2012. Instituto Geográfico Nacional, Universidad Politécnica de Madrid. Centro Nacional de Información Geográfica, 267 pp. (in Spanish).

[22] Ordaz, M., Martinelli, F., D'Amico, V., & Meletti, C. (2013). CRISIS2008: A flexi-ble tool to perform probabilistic seismic hazard assessment. Seismological Re-search Letters, Vol. 84, No. 3, pp. 495-504, DOI: 10.1785/0220120067.

[23] Ordaz, M., Martinelli, F., Aguilar, A., Arboleda, J., Meletti, C., & D'Amico, V. (2017). R-CRISIS. Program and platform for computing seismic hazard. http://www.r-crisis.com/

[24] Vanzi I, Marano GC, Monti G, Nuti C (2015) A synthetic formulation for the Italian seismic hazard and code implications for the seismic risk. Soil Dyn Earthq Eng 77:111–122

[25] Ulrich, T., Negulescu, C., and Douglas, J., 2014. Fragility curves for risk-targeted seismic design maps, Bulletin of Earthquake Engineering 12, 1479–1491

[26] Fajfar, P., and Dolšek, M, 2012. A practice-oriented estimation of the failure probability of building structures, Earthq Eng Struct Dynam 41, 531–547

[27] Kennedy RP (2011) Performance-goal based (risk informed) approach for establishing the SSE site specific response spectrum for future nuclear power plants. Nucl Eng Des 241(3):648–656. https://doi.org/10.1016/j.nucengdes.2010.08.001

[28] Eads L, Miranda E, Krawinkler H, Lignos DG (2013) An efficient method for estimating the collapse risk of structures in seismic regions. Earthq Eng Struct Dyn 42:25–41. https://doi.org/10.1002/eqe.2191

EURODYN 2020
XI International Conference on Structural Dynamics
M. Papadrakakis, M. Fragiadakis, C. Papadimitriou (eds.)
Athens, Greece, 23–26 November 2020

EFFECT OF MODELLING ASSUMPTIONS ON THE SEISMIC PERFORMANCE ASSESSMENT OF THIN REINFORCED CONCRETE WALL BUILDINGS

Orlando D. Arroyo[1], Dirsa M. Feliciano[1], Julián Carrillo[2], and José I. Colombo[3]

[1] Department of Infrastructure and Sustainability, Universidad de La Sabana. Campus Universitario Puente del Común, Chia, Colombia. e-mail: {orlando.arroyo,dirsafeag}@unisabana.edu.co

[2] Department of Civil Engineering, Universidad Militar Nueva Granada, Colombia. Carrera 11 N°101-80, Bogotá, Colombia, e-mail: wilmer.carrillo@umng.edu.co

[3] Department of Civil Engineering, Universidad Diego Portales. Vergara 210, Santiago, Chile. e-mail: jose.colombo@udp.cl

Abstract. *The increasing demand for housing in emerging countries has driven the construction of a significant number of buildings using thin reinforced concrete (RC) walls with a single layer of reinforcement. Studies in Latin America have found buildings using walls as thin as 80 mm and as height as 7 stories. The advantage of this structural system relies on its economy and its construction speed; however, different concerns emerge about the seismic performance of buildings using this system. These relate to the possible lack of ductility, the scarcity of information about their behavior during earthquakes, and the absence of design guidelines supported by experimental research. Contributing to these needs, researchers have conducted several studies, most of them focused on experimental campaigns to assess the seismic behavior of thin RC walls. Despite these efforts, there is still need of more information about buildings constructed with this structural system, particularly about their analytical modelling. This research investigated the effect that different modelling assumptions have on the seismic performance assessment of buildings with thin RC walls. A six-story building constructed in Bogotá, Colombia using 100 mm walls reinforced with welded-wire mesh (WWM), was modelled in OpenSees using the shear flexure interaction multiple line vertical element model, with different assumptions for damping and steel behavior. In terms of damping, two Rayleigh damping schemes were used, one considering the initial stiffness and other with the current stiffness. For steel modeling, the material properties obtained from experimental testing were used for two approaches, one that considered buckling and other where it was ignored. For further comparison, models with deformed bars instead of WWM were created. The seismic performance of the different models was evaluated through incremental dynamic analyses, using the FEMA P-695 ground motion suite. From these analyses, the interstory drift ratios, steel and concrete strains were recorded, which served as input for the development of seismic fragility functions. The results show that modelling parameters exert and influence at the different seismic performance levels, particularly on the collapse fragility of the WWM building. At the MCE level, the collapse probability observed for the WWM model with bar buckling was 14.8% higher than the model without buckling. This percentage was 7.4% for the model with damping proportional to the current stiffness compared to the model that used the initial stiffness. All things considered, the findings suggest that the modelling parameters have an influence on the analytical response of thin RC wall buildings.*

1 INTRODUCTION

In recent years, housing demand in Latin America has increased considerably. To supply this demand, an important number of low and mid-height buildings with thin reinforced concrete (RC) walls have been constructed in seismic prone countries like Venezuela, Mexico, Chile, Peru and Colombia [1–5]. The advantage of this structural system relies on its speed of construction and its economy. In Colombia, RC walls as thin as 80 mm have been used [6], using one layer of web reinforcement with welded-wire mesh (WWM) reinforcement or deformed bars (DB). The latter type of reinforcement has higher adoption because it allows a higher construction speed, and WWM with limited ductility capacity [7] are currently being using for projects in major cities like Medellín and Bogotá.

Several of the described buildings do not fulfill seismic requirements of major design codes like the ACI 318 [8], therefore local codes in some countries have included special provisions for buildings with thin RC walls to reflect on the awareness of housing demands. For instance, the Mexican Metropolitan Code [9] allows buildings of up to two stories with structural walls of 100 mm thickness. Similarly, the Chilean code [10] allows the use of ordinary RC walls for structures up to five stories if they are designed with a strength reduction factor equivalent to that of masonry structures. For such walls, a single or double layer of web reinforcement may be used, and the minimum wall thickness is 100 mm. In other countries like Colombia, whose local code shares many similarities with the ACI 318 [11], it does not include specific clauses for these type of buildings, and designers are following the RC wall building provisions.

Different concerns emerge about the seismic performance of buildings with thin RC walls, especially for those reinforced with WWM. These relate to the absence of design guidelines supported by experimental research, the scarcity of information about their behavior during earthquakes, and the possible lack of ductility. With these needs in mind, researchers have investigated the behavior of thin RC walls by both analytical and experimental means.

Some experimental campaigns have been carried to assess the seismic behavior of thin RC walls with different configurations, such as walls with different thickness and lap splicing [12], walls constructed with lightweight and low-strength concrete [13], and walls reinforced with welded-wire mesh [14]. Other tests have been conducted to compare the dynamic and quasi-static behavior of thin RC walls [15], to propose shear strength and hysteretic response rules [16], and to evaluate their out-of-plane behavior [17]. Moreover, equations have been proposed to estimate their shear strength [18] and numerical models have been proposed to simulate their seismic behavior [19,20]. Also, nonlinear three-dimensional analysis of typical Peruvian RC thin wall buildings have been conducted [18], and fragility function have been calculated for one-story houses reinforced with WWM in Perú [21] and for typical Chilean two-story houses [22].

Regardless of the described efforts, there is still need of more analytical information about the seismic behavior of thin RC walls that can provide guidance about the best practices for their usage as a structural system. In particular, there is need to understand the effect which different modelling assumptions have on the assessment of their seismic performance.

Contributing to these needs, this research investigates the seismic performance of a six-story thin RC wall building located in Bogotá, Colombia. This building was designed per the Colombian NSR-10 [23]. First, this article describes the building structural configuration and then, a section of the building is selected for developing nonlinear model in OpenSees [24], using the shear-flexure interaction multiple line vertical element (SFI-MVLEM) [25] model for the thin RC walls. The base model considers Rayleigh damping proportional to the building initial stiffness and does not include bar buckling. A second model was created that considers bar buckling.

A third model considers Rayleigh damping proportional to the current stiffness. These models are subjected to incremental dynamic analyses (IDA) [26] using the far field suite of the FEMA P-695 [27], which served as input information for the development of seismic fragility functions.

2 DESCRIPTION OF THE CASE STUDY BUILDING

A six-story building constructed in Bogotá, the capital city of Colombia, is taken as case study. This building was part of a survey conducted by the Colombian Earthquake Engineering Research network (CEER) in four major cities in Colombia.

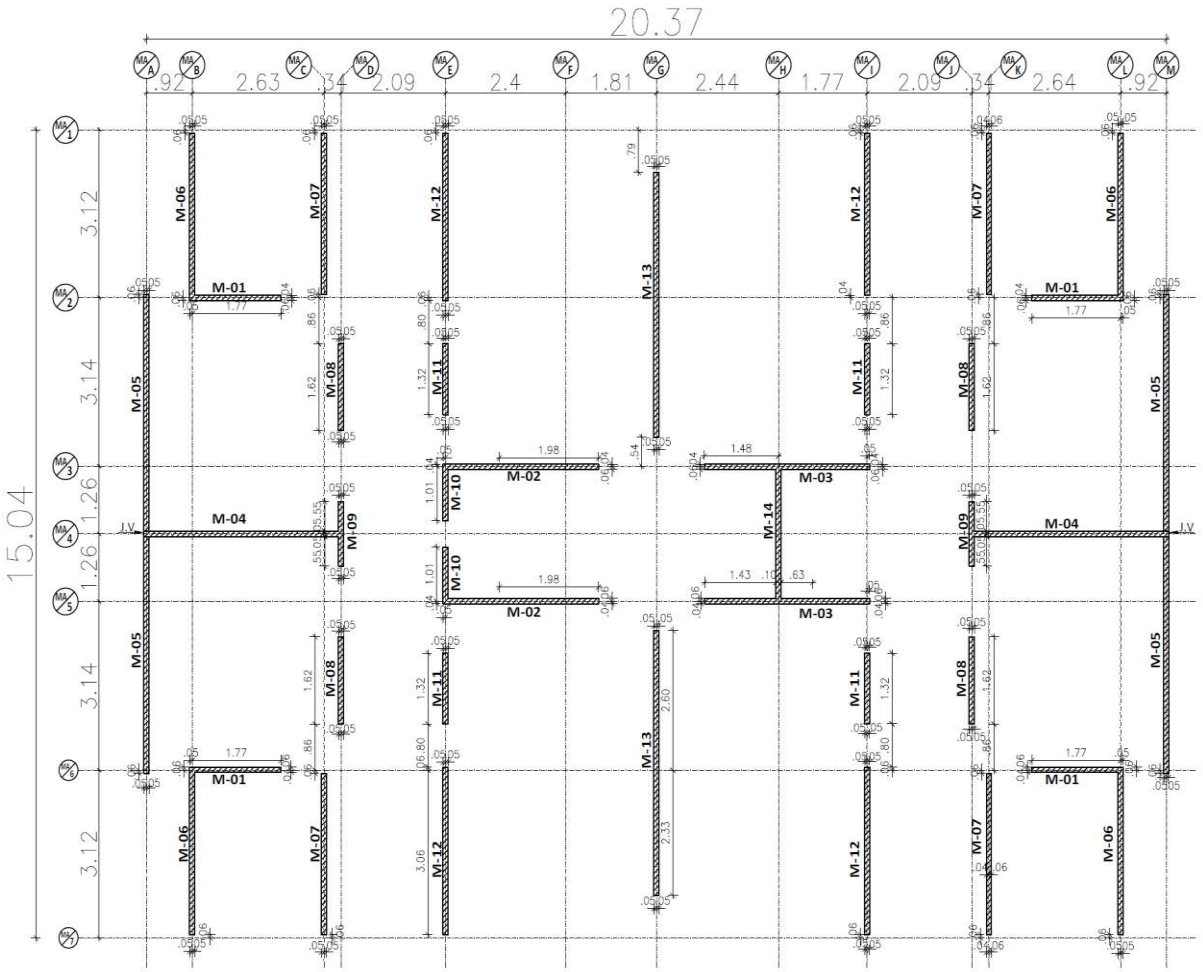

Figure 1: Plan configuration of a six-story building located in Bogotá, Colombia. Dimensions are in m.

The building has identical stories, which have a plan distribution (Figure 1) with a 4:3 aspect ratio and a free inter-story height of 2.45m. The building was designed according to the Colombian design code (NSR-10) for a design acceleration Sa = 0.5625g, with a structural system that uses 100 mm walls reinforced with a single steel mesh in the center of the wall. These walls are also used to separate habitational spaces. As stated by the structural drawings, the mesh used for wall reinforcement has 6.5 mm diameter bars with a separation of 150 mm in both directions, which are the equivalent of a vertical reinforcement ratio $\rho = 0.0023$ and a horizontal reinforcement ratio $\rho_h = 0.0023$. According to the ETABS model obtained by CEER, the fundamental period of the building is 0.36s, a value within the limits observed for this type of buildings. This elastic model was used to calculate the axial loads of each one of the building walls.

3 DESCRIPTION OF THE NONLINEAR MODELS

The seismic performance evaluation of this building is conducted considering a section in the X direction (Figure 2) of the building, which is comprised of four walls. This direction was selected because it represents the weakest building direction, as the larger number of walls have their main orientation in the Y direction. The four selected walls are a major part of the building lateral force resisting system in the X direction used for this study.

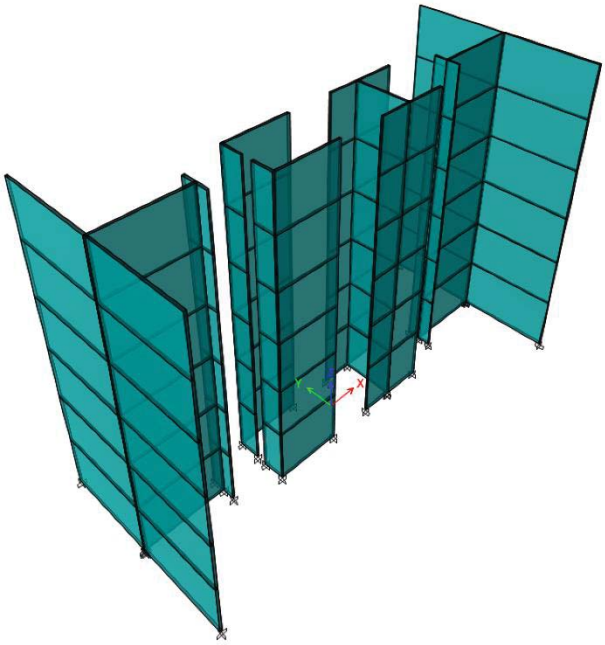

Figure 2: Building section used for nonlinear analyses.

The nonlinear response of this section is assessed using an OpenSees model. The shear-flexure interaction multiple vertical line element (SFI-MVLEM) [25] is used to model the behavior of the walls, using six panels for the inner walls and eight panels for the outer walls. As the walls are reinforced with a single layer of reinforcement without confinement, the concrete is modeled as unconfined using the ConcreteCM material, with $f'_c = 21$ MPa, and a strain at peak concrete strength $e_c = 0.002$. For the model with welded-wire mesh, the steel properties are obtained from the tests by Carrillo et al. [7], which report an elastic modulus $E = 210GPa$, a yielding stress $f_y = 621MPa$, an ultimate stress $f_u = 687MPa$ and an ultimate strain $e_u = 0.0155$. This last property is the cause of major concerns about the potential lack of ductility of these walls, as well as their seismic performance [7]. For the model with deformed bars, material properties $E_s = 210GPa$, $f_y = 420MPa$, $f_u = 630MPa$ and an ultimate strain $e_u = 0.15$. Both steel types are modelled using the Hysteretic material in OpenSees, in combination with the MinMax material to account for the fracture after exceeding the ultimate strain. For both models, the foundation is modeled as rigid, and the gravity loads for the model are calculated based on the expected loads and using the combination 1.05 D + 0.25 L. Rayleigh damping was applied to the model, with 2.5% damping to the first and third mode of the structure.

A base model considers damping proportional to the building initial stiffness and does not include bar buckling. A second model was created that considers bar buckling and a third model considers Rayleigh damping proportional to the current stiffness. Hereinafter these models will be referred as the Damping1, Buckling and DampingC models.

These models were subjected to incremental dynamic analysis using the 44 ground motions of the FEMA P-695 suite [27]. For the models with WWM, the ground motions were scaled to 0.25, 0.5, 1.0, 1.5 and 2.0 times the design acceleration of the building. For the model with DB, two additional factors of 3.0 and 3.5 were included. The concrete stress, inter-story drifts, roof drifts and steel strain were recorded during the dynamic analyses. Several failure modes were considered based on these results. Crushing of the unconfined concrete was assumed to occur at an e = 0.004 strain. Steel failure was considered due to fracture when the recorded strain exceeded the ultimate strain.

Four damage levels were defined for the DB and WWM based on the inter-story drifts. The limits for the slight, moderate and extensive damage were set based on the recommendations by Carrillo and Alcocer [28]. For the collapse limit, it was defined at 0.4% based on the findings reported by the same authors. This limit was set to 5% for the model with DB (Table 1).

Damage level	Deformed bars	Welded-wire mesh
Slight	0.15%	0.10%
Moderate	0.40%	0.25%
Extensive	0.65%	0.35%
Collapse	1.00%	0.40%

Table 1: Limits for the drifts in the DB and WWM models

4 SEISMIC PERFORMANCE RESULTS

The results of the incremental dynamic analyses were used to calculate the fragility functions at the four damage levels described in table 1. For each damage level the probability of exceeding a given damage level was computed as the number of times that the observed drift was higher than the limit, divided by the number of ground motions (44). The results were fitted to a log normal distribution. The distribution parameters for the WWM and DB models are reported in Tables 2 and 3, and the corresponding functions for the buildings are shown in Figures 3 and 4.

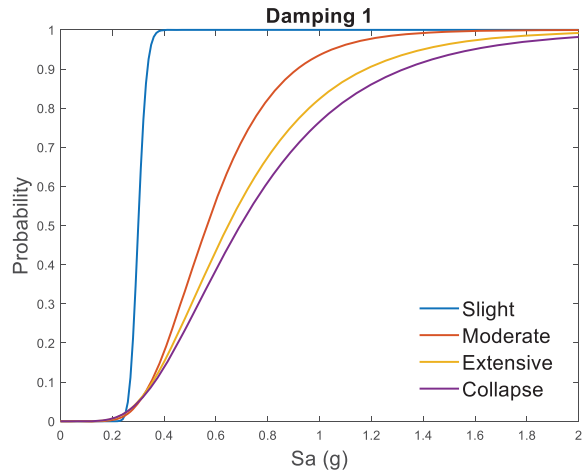

(a)

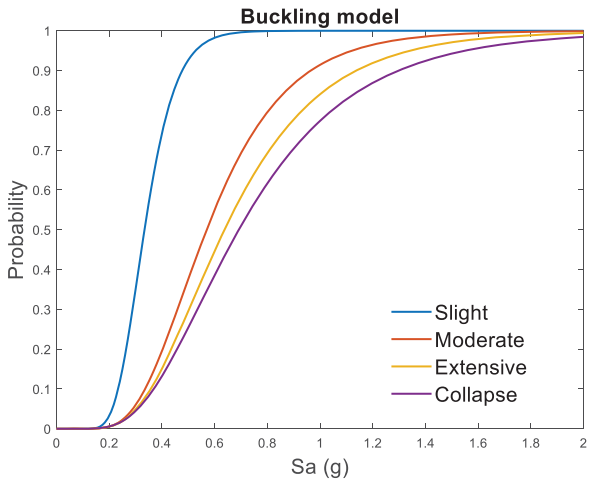

(b)

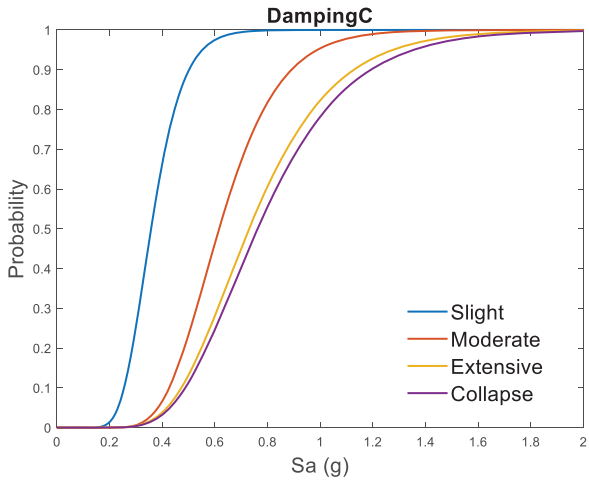

(c)

Figure 3: Fragility functions for the building with welded-wire mesh considering the (a) Damping1, (b) Buckling and (c) DampingC models

Damage level	Damping 1		Buckling		DampingC	
	Θ	β	Θ	β	Θ	β
Slight	0.300	0.087	0.334	0.278	0.358	0.264
Moderate	0.565	0.376	0.569	0.412	0.617	0.288
Extensive	0.647	0.468	0.637	0.452	0.731	0.339
Collapse	0.694	0.506	0.692	0.491	0.763	0.349

Table 2: Fitted lognormal parameters for the buildings with WWM

The results from Figure 3 show that the modelling assumptions exert an influence on the observed seismic response during the analyses of the buildings. At the maximum credible earthquake (Sa = 0.84g) level, the collapse probability observed for the Damping1, Buckling and DampingC models were 61.4%, 70.4% and 65.9%, respectively. Compared to the Damping1 model, the Buckling and DampingC models are 14.8% and 7.4% higher; however, the three values are significantly higher than the 10% limit that is expected for buildings designed according to modern design codes. Steel fracture was the dominant failure mode observed for the three models, demonstrating that despite the modelling scheme used for damping and steel, the use of WWM for thin RC results in buildings with seismic performance that falls below what is expected for code compliant buildings.

Table 2 allows several observations. The comparison between the Damping1 and Buckling model shows that both modelling hypothesis lead to similar median values for the moderate, extensive and collapse levels. In contrast, the median for the slight level is 10% higher for the Buckling model, suggesting that including buckling exerts an influence at lower performance states. The comparison of β values shows that these are larger for the Buckling model at the slight and moderate levels and similar for the extensive and collapse levels. A possible explanation for this behavior is that the drift limits for the extensive and collapse levels are similar for the buildings with WWM, and in the case of collapse, the fracture and not the buckling of steel control this limit.

The results of for the DampingC model show that this modelling assumption leads to less variability in the seismic response, as evidenced by the β values, which are smaller for at the

moderate, extensive and collapse levels. In contrast, the Θ values are higher when this scheme is used to simulate the seismic response. Figure 4 shows the fitted fragility functions for the three modelling assumptions at the collapse level, showing that the DampingC model has smaller probabilities than the Damping1 and Buckling models for smaller intensity earthquakes.

On the other hand, for earthquakes with larger intensities, this model has higher collapse probabilities. Although there may be several reasons that contribute, it is likely that at these earthquakes the stiffness matrix may have reduced significantly, causing a reduction in the overall damping. This consequence of using the damping proportional to the current matrix stiffness has been discussed before by Charney [29].

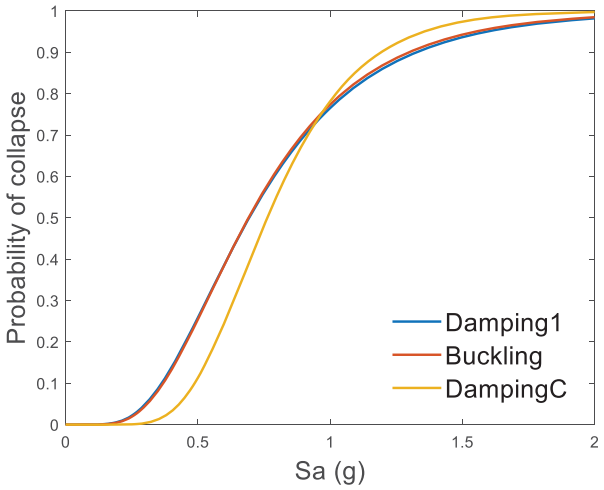

Figure 4: Collapse fragility of the WWM buildings for the three modelling assumptions

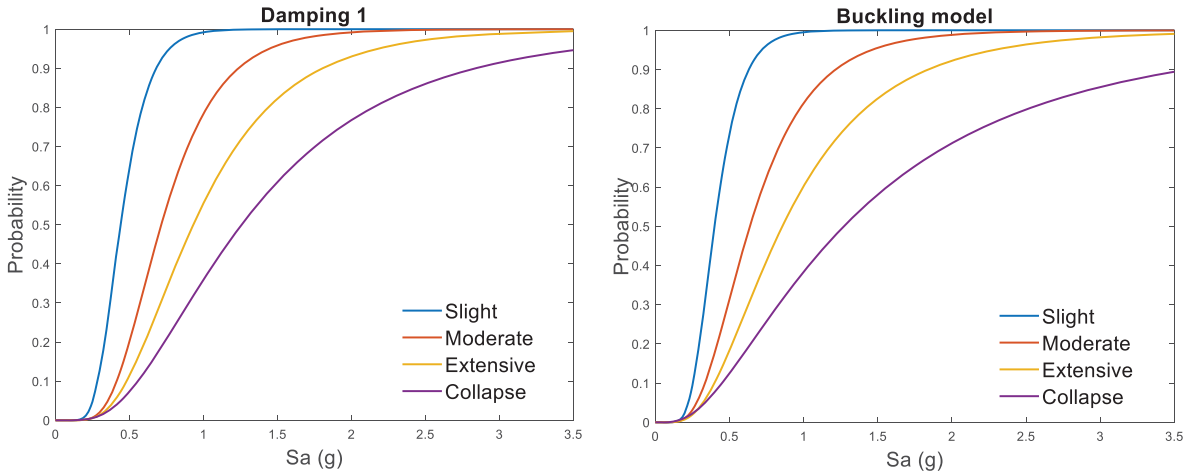

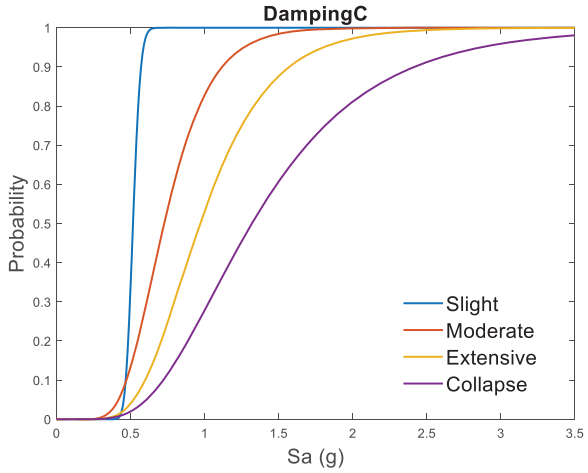

(c)

Figure 5: Fragility functions for the building with deformed bars considering the (a) Damping1, (b) Buckling and (c) DampingC models

Damage level	Damping 1		Buckling		DampingC	
	Θ	β	Θ	β	Θ	β
Slight	0.441	0.340	0.400	0.356	0.516	0.078
Moderate	0.715	0.427	0.638	0.503	0.727	0.337
Extensive	0.932	0.516	0.857	0.597	0.970	0.377
Collapse	1.258	0.635	1.272	0.811	1.319	0.472

Table 3: Fitted lognormal parameters for the buildings with DB

The results for the models with deformed bars show that the modelling assumption also exert an influence for this type of building, particularly in the variability parameters. At the slight damage level, the Θ parameter varies from 0.4g for the Buckling model to 0.516g for the DampingC model, a 29% difference. However, the coefficients of variations at this level are 77%, 89% and 15% for the Damping1, Buckling and DampingC models. This smaller variation of the DampingC model is evidenced by the steep function in Figure 5c.

At the moderate and extensive damage levels, the Damping1 and DampingC models had similar Θ parameters, although the DampingC model had lesser variability in the response, as evidence by the smaller value for β (Table 3). At these performance levels, the Buckling model had significantly higher variability than the Damping1 and DampingC model, with β values that are up to 49% and 58% for the moderate and extensive levels.

The comparison of the three modelling assumptions at the collapse level (Figure 6) shows that the DampingC model exhibits a similar trend to the one observed for the buildings with WWM. Compared to the Damping1 and Buckling models, this modelling scheme produces smaller probabilities at lower acceleration levels, and bigger probabilities for higher acceleration values. In contrast with the models with WWM, where the Damping1 and Buckling models showed identical performance, Figure 6 also shows that the inclusion of bar buckling with deformed bars has an impact on the collapse of the building. This model showed the opposite behavior of the DampingC model, with higher probabilities for lower accelerations and smaller ones for higher accelerations.

At the maximum credible earthquake, the models with Damping1 and Buckling showed a 20.4% probability of collapse and the DampingC model an 18.2% probability, which double the 10% target value of modern design codes. Although unacceptable, these probabilities are significantly smaller than those observed for the buildings with WWM, further supporting the fact that the lack of ductility of the WWM severely hinders the seismic performance, and that this type of structural system should be limited in seismic prone regions.

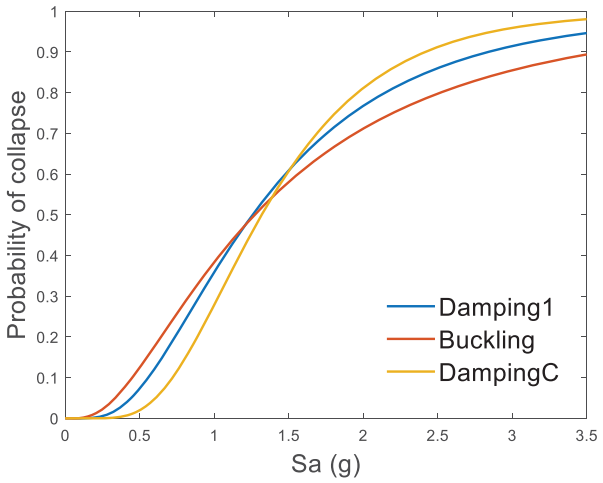

Figure 6: Collapse fragility of the DB buildings for the three modelling assumptions

6 Conclusions

This paper investigated the effect that different modelling assumptions have on the seismic assessment of thin RC wall buildings reinforced with a single layer of reinforcement. For this purpose, a six-story building constructed using this system was modelled in OpenSees considering two Rayleigh damping schemes, one proportional to the initial stiffness matrix and other proportional to the current stiffness matrix. Two approaches were used to model the behavior of the reinforcing steel, one that ignores the bar buckling and other that includes it. Although this building was constructed using welded-wire mesh (WWM) as reinforcement, a model with deformed bars (DB) was also created for the sake of further comparisons. All models were subjected to incremental dynamic analyses and the results were used to calculate the seismic fragility functions at four different damage levels. The findings of this paper support several conclusions:

The use of the current stiffness matrix for the damping produces seismic fragility functions with the smallest level of variation. At the collapse level, when compared to the models with damping proportional to the initial stiffness and bar buckling, this modelling scheme produced smaller probabilities for lower acceleration levels, and bigger probabilities for higher accelerations. This behavior occurred for both type of steel reinforcement (WWM and DB) and it was result of the reduction in damping for larger accelerations, where the building damage reduces the stiffness component of the damping.

For the buildings with WWM, the models with stiffness proportional to initial stiffness and with bar buckling showed similar results at the slight and moderate damage levels, and identical behavior at the extensive and collapse performance levels. This suggests that the inclusion of bar buckling affects the behavior for small to medium accelerations, but for larger ones, the lack of ductility of the WWM becomes a governing factor and these performance limits are

controlled by the steel fracture and not its buckling. In contrast, for the buildings with DB, the additional ductility of the steel allows bar buckling to exert an influence and this modelling scheme produces smaller probabilities for larger accelerations.

In terms of seismic performance at the maximum credible earthquake, the building with WWM had collapse probabilities of 61.4%, 70.4% and 65.9% for the models with initial damping, bar buckling and current damping. For the building with DB, the corresponding values were 20.4%, 20.4% and 18.2%. For both types of reinforcement, these probabilities are higher than the 10% limit that is expected for buildings designed according to modern design codes, particularly those of the WWM buildings. These findings support the idea that the use of RC thin walls for mid-rise buildings should be limited for seismic prone areas, regardless of the type of reinforcement used.

7 References

[1] Mejía L, Ortiz J, Osorio L. World Housing Encyclopedia. Earthquake Engineering Research Institute and International Association for Earthquake n.d. http://db.world-housing.net/building/109/.

[2] Carrillo J, Alcocer SM, Uribe R. Prediction of shear performance of concrete walls for housing. XVII Natl. Congr. Earthq. Eng., Puebla, Mexico: 2009.

[3] Muñoz A, Delgado R, Peña C. Seismic performance of limited ductility shear–wall buildings. Universidad Católica de Lima, 2006.

[4] Yañez D. Linear seismic analysis of tunnel form buildings. Universidad de los Andes, 2006.

[5] Santa María H, Hube MA, Rivera F, Yepes-Estrada C, Valcárcel JA. Development of national and local exposure models of residential structures in Chile. Nat Hazards 2017;86:55–79. doi:10.1007/s11069-016-2518-3.

[6] Sanchez J, Arteta CA. Statistical characterization of thin reinforced concrete wall buildings for high seismic hazard regions. VIII Natl. Congr. Earthq. Eng., Barranquilla, Colombia: 2017.

[7] Carrillo J, Diaz C, Arteta CA. Tensile mechanical properties of the electro-welded wire meshes available in Bogotá, Colombia. Constr Build Mater 2019;195:352–62. doi:10.1016/J.CONBUILDMAT.2018.11.096.

[8] ACI Committee 318. 318-14 Building code requirements for structural concrete and commentary. vol. 11. American Concrete Institute Farmington Hills, MI; 2014. doi:10.2748/tmj/1232376167.

[9] NTCS-2004. Additional technical standards for earthquake resistant design. Construction Regulations for the Federal District. Gaceta Oficial del Departamento del Distrito Federal; 2004.

[10] Ministry of Housing and Urbanism M. DS 60, Reinforced Concrete – Design and Calculations Requirements, replacing D.S. N 118 2010. Santiago, Chile: 2010.

[11] Arroyo O, Barros J, Ramos L. Comparison of the Reinforced-Concrete Seismic Provisions of the Design Codes of the United States, Colombia, and Ecuador for Low-Rise Frames. Earthq Spectra 2018;34:441–58. doi:10.1193/102116EQS178EP.

[12] Quiroz LG, Maruyama Y, Zavala C. Cyclic behavior of thin RC Peruvian shear walls: Full-scale experimental investigation and numerical simulation. Eng Struct 2013;52:153–67. doi:10.1016/j.engstruct.2013.02.033.

[13] Almeida J, Prodan O, Rosso A, Beyer K. Tests on thin reinforced concrete walls subjected to in-plane and out-of-plane cyclic loading. Earthq Spectra 2017;33:323–45. doi:10.1193/101915EQS154DP.

[14] Carrillo J, Lizarazo JM, Bonett R. Effect of lightweight and low-strength concrete on seismic performance of thin lightly-reinforced shear walls. Eng Struct 2015;93:61–9. doi:10.1016/j.engstruct.2015.03.022.
[15] Carrillo J, Alcocer SM. Experimental investigation on dynamic and quasi-static behavior of low-rise reinforced concrete walls. Earthq Eng Struct Dyn 2013;42:635–52. doi:10.1002/eqe.2234.
[16] Rosso A, Almeida JP, Beyer K. Stability of thin reinforced concrete walls under cyclic loads: state-of-the-art and new experimental findings. Bull Earthq Eng 2016;14:455–84. doi:10.1007/s10518-015-9827-x.
[17] Luna BN, Rivera JP, Whittaker AS. Seismic behavior of low-aspect-ratio reinforced concrete shear walls. ACI Struct J 2015;112:593–603. doi:10.14359/51687709.
[18] Carrillo J, Alcocer SM. Shear strength of reinforced concrete walls for seismic design of low-rise housing. ACI Struct J 2013;110:415–25.
[19] Rosso A, Almeida JP, Beyer K. Numerical simulation with fibre beam-column models of thin RC column behaviour under cyclic tension-compression, Santiago, Chile: 2017.
[20] Carrillo J, Alcocer SM. Strength degradation model for low-rise reinforced concrete walls derived from dynamic and quasi-static tests. Earthq Spectra 2015;31:197–214. doi:10.1193/011713EQS008M.
[21] Quiroz LG, Maruyama Y. SEISMIC PERFORMANCE OF THIN RC WALLS REINFORCED WITH ELECTRO-WELDED WIRE MESH IN LIMA , PERU 2013;2:101–10.
[22] Hube MA, Santa María H, Arroyo O, Vargas A, Almeida J, López M. Seismic performance of squat thin reinforced concrete walls for low-rise constructions. Earthq Spectra 2020.
[23] Sismica AC de I. Reglamento Colombiano de Construcción Sismo Resistente NSR-10. 2010.
[24] Mazzoni S, McKenna F, Scott MH, Fenves GL. OpenSees command language manual. Pacific Earthq Eng Res Cent 2006:451.
[25] Kolozvari K, Tran TA, Orakcal K, Wallace JW. Cyclic shear-flexure interaction in reinforced concrete structural Walls - Modeling and validation. NCEE 2014 - 10th U.S. Natl. Conf. Earthq. Eng. Front. Earthq. Eng., vol. 141, 2014, p. 04014136. doi:10.4231/D3ZS2KD5B.
[26] Vamvatsikos D, Cornell CA. Applied incremental dynamic analysis. Earthq Spectra 2004;20:523–53. doi:10.1193/1.1737737.
[27] Federal Emergency Management Agency (FEMA). Quantification of building seismic performance factors FEMA P-695. 2009.
[28] Carrillo J, Alcocer SM. Acceptance limits for performance-based seismic design of RC walls for low-rise housing. Earthq Eng Struct Dyn 2012:n/a-n/a. doi:10.1002/eqe.2186.
[29] Charney FA. Unintended Consequences of Modeling Damping in Structures. J Struct Eng 2008;134:581–92. doi:10.1061/(ASCE)0733-9445(2008)134:4(581).

EURODYN 2020
XI International Conference on Structural Dynamics
M. Papadrakakis, M. Fragiadakis, C. Papadimitriou (eds.)
Athens, Greece, 23–26 November 2020

SENSITIVITY OF SPECIAL STEEL MOMENT FRAMES TO THE INFLUENCE OF COLUMN-BASE HYSTERETIC BEHAVIOR INCLUDING GRAVITY FRAMING SYSTEM

Pablo Torres-Rodas[1], Francisco Flores[2,3], Bryam X Astudillo[2] and Sebastian Pozo[2]

[1]Universidad San Francisco de Quito
Diego de Robles
e-mail: patorresr@usfq.edu.ec

[2]Universidad de Cuenca
Avenida Doce de Abril
{francisco.flores, bryam.astudilloc, sebastian.pozo}@ucuenca.edu.ec

[3]Universidad del Azuay
Avenida Veinte y Cuatro de Mayo
fflores@uazuay.edu.ec

Keywords: Steel Moment Frame, Probability of Collapse, Base Connections, Gravity Framing

Abstract. *Special Steel Moment Frames (SMFs) are one of the most common lateral-load resisting systems. Hysteretic energy in these systems is dissipated by the development of plastic hinges at the end of the beams. In order to guarantee the desired collapse mechanism, columns, beam-column, and column base connections are sized employing the capacity design-criteria. Recent research on column base plates indicates that these connections pose high deformation capacity and may be used as part of the dissipative energy system. These findings have motivated studies to evaluate a possible strong-column weak-base connection criterion, implying a reduction on the base demands and, consequently, a nonlinear incursion of these connections. The implication is a potential reduction of connection costs at similar building performance. However, these studies have neglected the influence of the gravity system on the seismic performance of the SMFs analyzed. Consequently, a study that includes the profound influence of gravity system while investigates the consequences of seismic demands reduction of base plates has not been conducted. Against this backdrop, this research presents a parametric study conducted on an 8-story SMF, which evaluates the probability of collapse considering three different levels of base connection strength while including the gravity system. Results indicate that gravity systems tend to enforce the building to deform on the first mode of shape even at large floor displacements while base rotations are increased significantly. The design implication is that base-connections should be kept designed to carry the plastic capacity of the column.*

1 INTRODUCTION

Steel Moment Frames (SMFs) are one of the preferred lateral-load resisting systems by the construction industry due to their high deformation capacity as well as architectural versatility. Because of this, these systems have been extensively studied over the last decades. Early studies on the topic started to understand their modes of response under gravity loads. Formal requirements for lateral forces started officially after the 1906 San Francisco earthquake, although seismic provisions were not mandated until 1948. Before the 1994 Northridge earthquake, it was assumed that SMFs are ductile without special detailing. However, this assumption was challenged by the way how the buildings performed during this earthquake. In a post-earthquake evaluation, brittle failure was observed in the connections. Extensively experimental programs were conducted after that aimed to develop ductile behavior in the connections. These investigations ended up in notably design guidelines for new and existing SMFs (e.g., FEMA 355 [1]).

Typically, the SMFs consist of an assembly of beams and column elements rigidly connected between them. Because of this, the main components are beams, columns, beam-column connections, and column base connections. As mentioned before, special attention has been given to beam-column connections. Although, in a less degree compared to beam-column connections, column base connections have been studied during the last years through experimental and numerical investigations. Two types of base connections have been used in the context of US construction practice: i) for low-to-midrise buildings exposed base plates are preferred. These connections consist of a steel column welded to a base plate, which is anchor to the foundation; ii) on the other hand, for high-rise buildings, embedded base connections are the norm. This detail consists of a steel column embedded in a concrete foundation.

Recent experimental studies conducted on column base connections (i.e., exposed and embedded type) indicate that these connections have high deformation capacity with desirable hysteretic properties [2–5]. Furthermore, other experimental programs conducted on columns [6,7] suggest that these members, especially when subjected to axial load, may have limited ductility due to local phenomena such as local and lateral-torsional buckling. This background suggests that the current design criteria for column base connections (i.e., design them to remain elastic) may be unjustified, considering that this approach is protecting the more ductile component (i.e., base connection over column member). This criterion of strong base connection – weak column may be attributed to the sparse information about the dissipative properties of column base connections, and to the intuitive idea that connections are less ductile than component members. Besides, the construction of strong base connections implies a significant extra cost. For instance, when an exposed base plate is specified, thicker base plates and a large number of anchor bolts are required to satisfy the demands (based on capacity design principles). If an embedded base connection is detailed (e.g., in the case of mid-rise or tall buildings), the embedded depth may be significant.

Falborski et al., 2020 [8] conducted a parametric study to investigate the effect of base connection strength, flexibility, and deformation capacity on the probability of collapse of four SMFs (i.e., 4-story, 8-story, 12-story, and 20-story). Four levels of column base connection strength were considered in this study. The first level (the lowest one in terms of strength) corresponds to a base connection designed for reduced seismic loads (i.e., R=8). Two intermediate levels of strength include designing the base connection for R=3 and Ω_o=3. Finally, the strong base criteria, which implies designing the connection for the fully plastified and strained hardened attached column. Each of these strength levels is associated with a rotational stiffness calculated by methods developed by Kanvinde et al., 2012 [9] for the exposed base plates and Torres-Rodas et al., 2017 [10] for the embedded details. The hysteretic characteristics of the

connections were considered based on the recommendations of Torres-Rodas et al., 2016 [11] (for exposed base plates), and Torres-Rodas et al., 2018 [12] (for embedded base connections). The main finding of this investigation was that similar performance (i.e., acceptable probability of collapse) for all the SMFs might be obtained by designing the base connections for the strength level corresponding to demands computed with over-strength seismic loads (i.e., Ω_o =3) rather than for $1.1R_yM_p$ of the attached column. The key design implication was that the base connections must be detailed to accommodate rotations of 0.05 rad in order to use over-strength seismic load combinations. However, it is important to mention that this study did not include the effect of the gravity framing system on the response of the SMFs which were analyzed.

The influence of gravity framing system on the seismic performance of SMFs have been reported in the past. Gupta and Krawinkler [13] addressed the response of SMFs at different seismic hazard levels using four models. Two of them included the gravity system. The results of this study indicate that significant improvement in the response of the SMFs may be achieved at large inter-story drifts when the gravity system is included. These authors defined gravity connections with a simple rotational spring in which the peak strength was reached at 0.02 rad and 0.01 rad for the positive and the negative moments, respectively. Other studies [14] predicted the influence of gravity system on the seismic performance of SMFs through the definition of a confidence factor, which indicates whether the structure satisfies the collapse prevention criteria at the Maximum Considered Earthquake (MCE). Flores et al. 2014 [15] investigated the effect of the gravity framing system on the probability of collapse of SMFs with the use of FEMAp695 methodology. These authors analyzed three SMFs (2-story, 4-story, and 8-story) in their study. The influence of two main parameters was investigated, i.e., the stiffness of the gravity columns and the strength of gravity-beam connections. Results indicate that gravity framing system deeply influences the seismic performance by reducing the probability of collapse. The reviewed studies consider idealized boundary conditions, i.e., either pinned or fixed-bases in their analyses.

In summary, studies conducted on SMFs to examine the influence of gravity framing systems typically have been carried out considering idealized boundary conditions (i.e., fixed or pinned bases), neglecting the potential benefit of base-connections as energy dissipative mechanisms. On the other hand, studies (e.g. [8,16]) carried out on the topic to assess the influence hysteretic behavior of column base connections on the seismic response of SMFs neglected the beneficial effect of the gravity system. This backdrop motives the present investigation to examine the interrelation between the column base connection strength, stiffness, and deformation capacity with the seismic performance of SMFs (by using FEMAp695 methodology) incorporating the beneficial effect of gravity columns and gravity beam-column connections, seeking to explore the consequences of using a strong-column weak-base connection criterion that leverages the hysteretic properties of these connections.

This paper starts by describing in this introductory section the studies conducted on the topic in the past. Subsequently, the methodology employed in the current investigation is described, detailing the 8-story SMF model used herein. Sophisticated nonlinear time history analysis was conducted on the 8-story SMF model to investigate the effect of column base connection strength, flexibility and deformation capacity accompanied by gravity framing system on its seismic performance expressed in terms of its probability of collapse at MCE level. Results from the simulations are discussed, and potential implications for design are presented.

2 METHODOLOGY OF ANALYSIS

The scientific basis of this research consists of a series of Nonlinear Time History (NTH) analysis conducted on an 8-story archetype frame complemented by Nonlinear Static Pushover

(NSP) analysis. The 8-story SMF analyzed herein belongs to the NEHRP project [17] and was designed assuming a Response Coefficient Factor $R=C_d=8$ and site class "D" conditions under the seismic design category D_{max}. Fig. 1 illustrates its characteristics (plan view, elevation, and member size). The height of the frame is 31.8m and consists of three-bay frames located at the perimeter of the building plan. The bay width is 6.00m. The height of the first story is 4.50m, while the height of the rest of the stories is 3.90m. A dead load of 4.78 kN/m^2 was applied on all the floors, while an unreduced live load of 2.38 kN/m^2 was applied on all floors except on the roof, where a live load of 0.95 kN /m^2 was applied. A perimeter load of 1.20 kN/m^2 was assigned to simulated cladding. Beam-column connections were detailed as Reduced Beam Section (RBS) connections based on AISC 341 [18] recommendations.

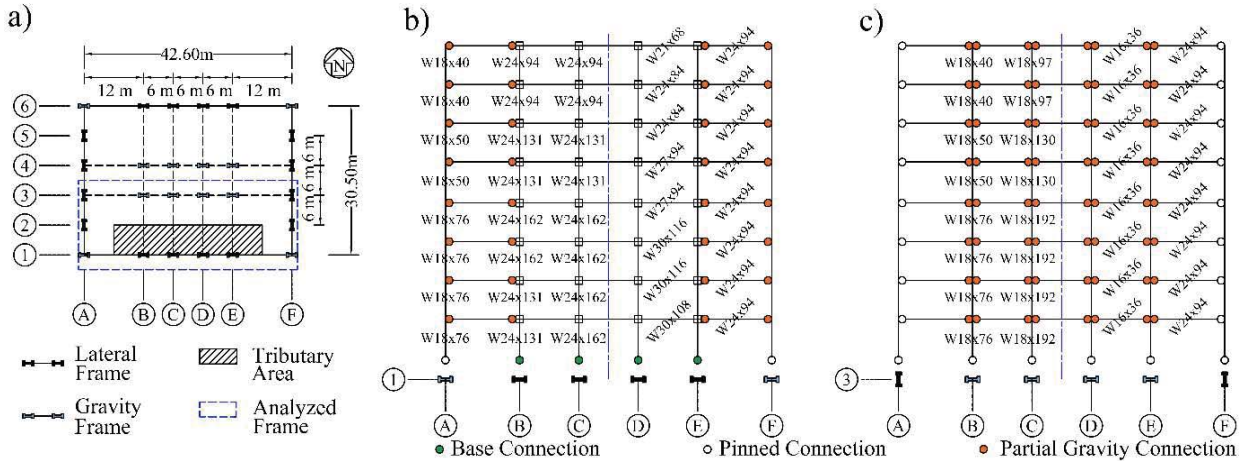

Figure 1: 8-story SMF. a) Plan view. b) Elevation view axis 1. c) Elevation view axis 3.

The beams and columns are modeled as linear-elastic elements with the plasticity concentrated at their ends. For beam elements, nonlinear rotational springs are placed at the RBS locations, while in the columns, rotational springs are located at their ends. These nonlinear rotational springs are aimed to capture the hysteretic response of the connections. The hysteretic model employed is the well-known Ibarra-Medina-Krawinkler (IMK) model, which consists of a tri-linear backbone curve with kinematic strain hardening and monotonic deterioration, supplemented with rules to capture cyclic strength and stiffness deterioration [19]. This model inherits an important limitation from uniaxial plasticity formulations, i.e., it cannot capture moment-axial load interaction. Because of it, this phenomenon is represented in an approximate manner. First, the gravity load is considered as an average value of the axial load to be presented in the NTH analysis [20,21]. Next, a reduced bending strength may be calculated with the interaction equations from AISC [22]. This reduced strength is used in the rotational springs at the end of the columns. Panel zone is modeled as a hinged parallelogram assembly by rigid elements with a nonlinear spring at one of the corners to represent shear distortions in the panel zone. The properties of these springs (i.e., for beam-column connections and panel zone) are computed based on the recommendations [13,21].

The column base connection for this SMF was detailed as an embedded base connection. Its hysteretic response was capture by the model proposed by [12] for embedded base connections. This model has a trilinear backbone curve similar to the IMK models, supplemented by rules aimed to capture the hysteretic response as well as modes of deterioration found in column base connections. The backbone curve of the models is defined by the following parameters: the moment at first yield, initial rotational stiffness, maximum moment (i.e., peak strength), and

rotation of the connection associated with its peak strength. These parameters were estimated from analytical models available in the literature. For instance, the maximum connection strength (i.e., M_{peak}) was calculated by Grilli and Kanvinde 2016 [23]. Besides, these authors showed that the moment at first yield might be considered as 70% of M_{peak}, which is the criteria considered herein. The rotational stiffness of these connections was calculated by the method proposed by Torres-Rodas et al. (2017) [10], which consists of calculating the flexibility of the connection by aggregating the deformations within the components (Fig. 2a).

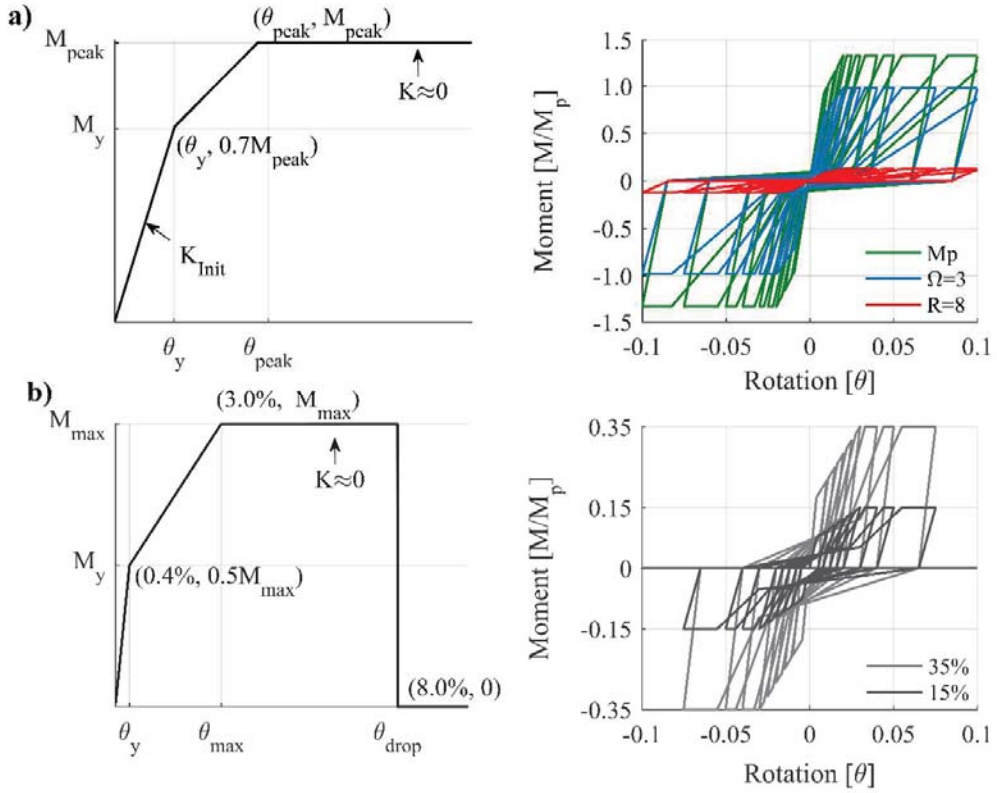

Figure 2: Hysteretic models for a) Base base connection. b) PR gravity connection.

As per Falborski et al., 2020 [8], three different levels of column base connection strength are considered in this paper (for the parametric analysis) which consist of a connection design to resist: i) $1.1R_yM_p$ of the attached column which corresponds to the capacity design criteria; ii) Over-strength seismic loads, i.e., Ω_o =3; and iii) Reduced seismic loads, i.e., R=8. It is anticipated based on previous work ([24,25]) that the first level of strength (i.e., capacity design criteria) will not allow the development of inelastic rotations while the last one will imply large inelastic rotations for which the connections must be properly detailed. The flexural capacity of each base connection strength level is provided in Table 1.

Strength Level	**Moment Strength**	
	Int (kN.m)	**Ext** (kN.m)
$R=8$	309.04	292.35
$\Omega=3$	1167.36	2309.99
$1.1R_yM_p$	2612.09	3276.38
Fixed-Base	-	-

Table 1: Base Connection Strength Levels

The gravity framing system is included as part of the lateral-load resisting system in the simulations, as shown in Fig. 1c. Gravity beam and column sizes were obtained through a typical design based on ASCE 7 [26] and AISC 360 [22]. The gravity connections are considered as partially restrained (PR) connections [15,27]. The main characteristic of these connections is that their capacity is lower than the plastic capacity (i.e., M_p) of the beam, which ranges from 15-35% of M_p [28]. The model developed by Elkady and Lignos 2015 [27] is used to capture the influence of PR connections in the seismic performance of SMFs. The effects of column base hysteretic behavior and the gravity framing system on the seismic performance of SMFs are considered parametrically, while four cases are presented for all the archetype frames. The first case corresponds to the models without any gravity framing. The second case consists of analyzing only the influence of gravity columns, neglecting the effect of gravity connections. This is performed by an approach proposed by Flores et a., 2015 [15] by concentrating all the gravity columns in a lumped elastic column pinned at the base and attached to the SMFs, as illustrated in Fig. 1. The last two cases include the effect of gravity system beams using a rotational spring aimed to capture the hysteretic response of PR connections. Two main parameters defined this spring, i.e., the strength and initial stiffness (Fig. 2b). In this paper, two values of PR strength are considered. The first value represents 15% of the beam M_p, while the second one a 35% of M_p of the beam. Table 2 summarizes the details and define an appropriate notation for all models analyzed herein.

Notation	**Column Base Strength Level**
$R = 8$	$R = 8$
$\Omega = 3$	$\Omega = 3$
Mp	$1.1R_yM_p$
Fix	Fixed-Base
Notation	**Gravity System Strength Level**
Non	No gravity system
00%	Only gravity columns (or partial connections 00%)
15%	15%Mp
35%	30%Mp

Table 2: Models Analyzed in this study

Two types of analyses are carried out in this paper. These analyses are 1) Nonlinear Time History (NTH) analysis, and 2) Nonlinear Static Pushover (NSP) analysis. The NTH analysis is conducted on the archetype frame to parametrically investigate the effects of column base strength, rotational stiffness, and ductility accompanied by the beneficial influence of gravity columns, and PR connections strength on 1) the probability of collapse of SMFs at MCE level, and 2) the seismic performance (i.e., inter-story drift ratios) at the Maximum Considered Earthquake (i.e., 2 % probability of exceedance in 50 years). The SMF analyzed herein is first simulated with idealized boundary conditions (i.e., fixed base) without considering the influence of the gravity framing following current design practice. Next, it is analyzed considering three different levels of base connection strength (i.e., R=8, Ω_o=3, and $1.1R_yM_p$), and three different values of PR connection strength (i.e., 0%, 15%, and 30% of M_p) in the presence of gravity columns.

The software OpenSees is used for all the simulations since it has been extensively verified for NTH simulations [29]. A collapse assessment relative to each of the models simulated was conducted following the FEMAp695 methodology. Sideways collapse is defined by FEMAp695 (2010) when the IDA curves become flat (or typically with a slope less than 20%), or when the inter-story drift ratios reach a value of 10% from which the structure is extremely unlikely (if not impossible) to recover [30,31]. In this manner, the median collapse capacity of each of the simulations may be obtained once 22 out of 44 ground motions produce sideways collapse. This median collapse capacity is compared with the site-hazard (i.e., probability of exceedance of 2% in 50 years) to compute the collapse margin ratio (CMR). This CMR is adjusted with the spectral shape factor (which considers the spectral shape of rare earthquakes in California) to obtain the adjusted collapse margin ratio (ACMR). Finally, the probability of collapse can be computed with the ACMR. This metric of performance is used to evaluate the safety of the archetype frame and to understand their sensitivity to variations in column base connection strength with the inclusion of the gravity framing system (varying PR connections strength).

In addition to IDA simulations, this study presents the results of the NTH analysis conducted on the archetype frame to assess the effect of column base strength, and stiffness accompanied by gravity framing in the inter-story drift ratios at MCE level of shaking (i.e., probability of exceedance of 2% in 50 years). For this purpose, the suite of ground motions from FEMAp695 methodology is considered too severe [32]. A suite of 40 ground motions selected by Medina and Krawinkler [33] is scaled up to MCE-level of shaking, assuming soil type D, which is representative of the Los Angeles basin.

Apart from the NTH analysis, a Nonlinear Static Pushover (NSP) analysis is conducted on the models to supplement the information obtained from the NTH analysis. The NSP analysis generates "pushover curves," which provides general insights on frame response (e.g., collapse mechanism) and structural properties. Two structural properties may be obtained from NSP analysis; 1) system overstrength, 2) period-based ductility. The next section discusses the results of the NTH and NSP analysis on the models conducted in this investigation and possible implications in design.

3 DISCUSSION OF RESULTS

This section summarizes the results obtained from the NTH and NSP analysis described in the previous section conducted on the 8-story SMF with possible implications in design. Fig. 3 summarizes the results from NSP analysis. Fig. 3a illustrates the effect of base connection strength and gravity framing on the pushover curve. Each color of Fig. 3a represents the results of a model analyzed for different connection strength levels while each inset contains different curves that highlight the influence of PR gravity beam-column connections for a specific base connection strength. Fig. 3a indicates that an increase in base connection strength entails an increase in the system overstrength as well as in the period-base ductility. The same trend is observed when the strength of PR beam-column gravity connections is increased. In general, the overall frame behavior is improved with the inclusion of gravity framing while increasing base connection strength.

Fig. 3b illustrates the building deformed shape under different base connections and PR beam-column connections strength. Similar to Fig. 3a each color represents a different base connection strength level. As a general trend, a decrease in base connection strength tends to concentrate deformations on the first floor. The more impacting case is the one corresponding to R=8, where a soft story is formed when gravity framing is not included. Even though base flexibility tends to concentrate deformations at first-floor gravity framing counteracts this effect by linearizing the inter-story drift ratios along with the height of the frame.

The yielding mechanisms are presented for two cases of analysis: 1) R=8–Non and 2) R=8–35% and shown in Fig. 3c. In the first case, the point P1 represent the RBS connection yielding on the second floor. Then the point P2 represents the yielding on the base connection. P3 shows that RBS connections reach the deterioration on a drift of 0.75%, and P4 represents the top column yielding of the second floor, causing the highest deterioration on the structure's capacity. The addition of the gravity system keeps constant the P1 and P2 yielding events but increases the ductility of the system. The deterioration on RBS connection is reached on point P3' on a drift of 1.45%, which duplicates the drift reached without the gravity system. The next yielding point P4' occurs when the partial connection of the gravity system reaches the threshold of $0.8V_{max}$. Moreover, this model, which includes gravity framing, does not present the weak-story mechanism that led the R=8–Non model to the fragile behavior.

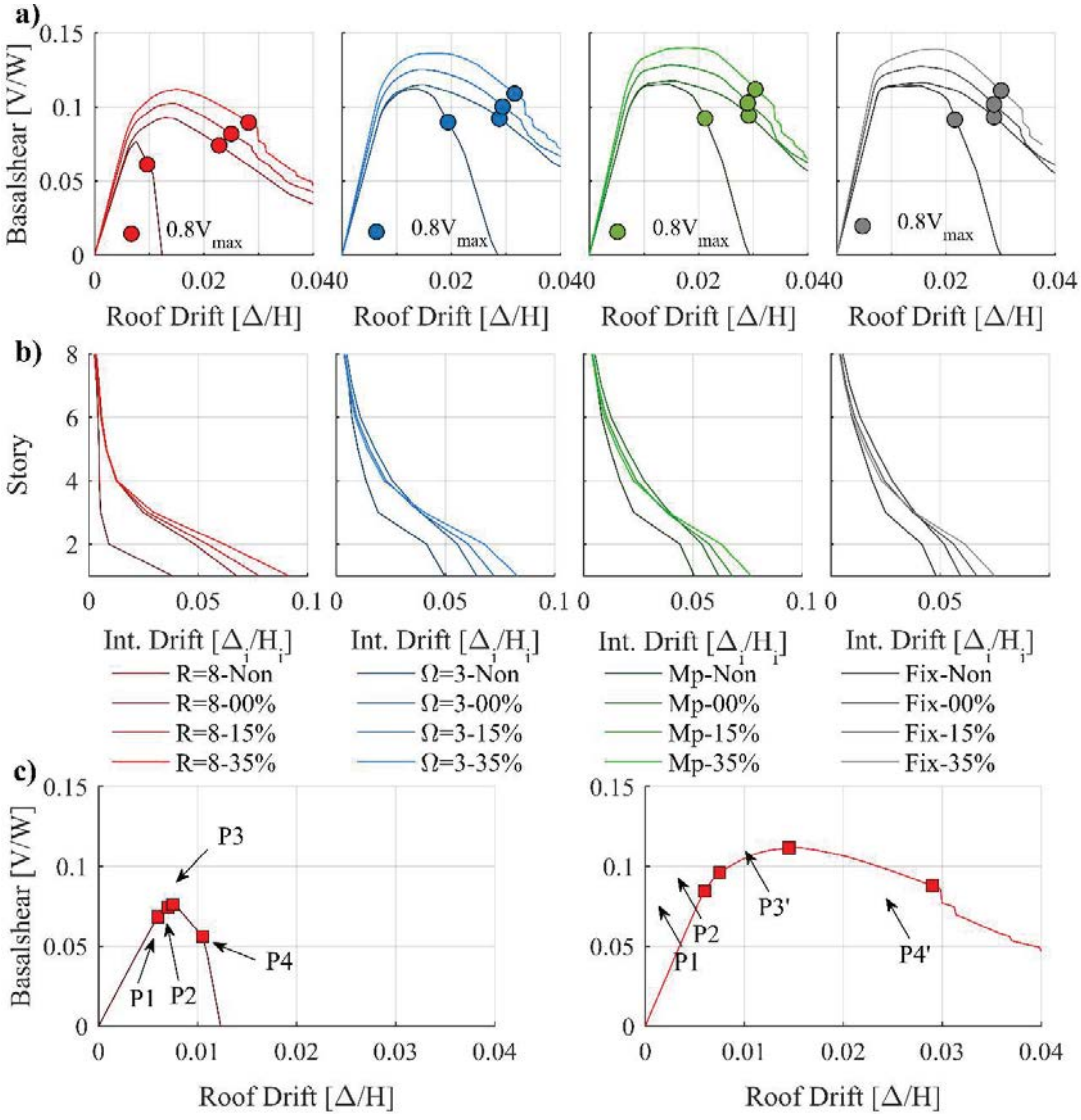

Figure 3: Results from static analysis. a) Pushover: R=8, Ω_o=3, $1.1R_yM_p$, and Fixed-Base. b) Inter-story drift profile: R=8, Ω_o=3, $1.1R_yM_p$, and Fixed-Base. c) Yielding Mechanism for two models: R=8-Non, and R=8-35%.

Fig. 4 summarizes the NTH results conducted on the 8-story SMF. Fig. 4a presents the Collapse Margin Ratio (CMR) for each connection strength level while in each inner inset, the influence of PR connections is illustrated. In other words, each color set corresponds to a

connection strength level (i.e., R=8, Ω_o=3, 1.1R_yM_p, Fixed-Base.) while each tone color represents a PR connection strength. As per Fig. 4a and 4b, there are no significant differences between the collapse probability or the CMR value between the models Ω_o=3, 1.1R_yM_p, and Fixed-base. However, the case R=8 presents an unacceptable performance in terms of collapse probability when the gravity system is not included. As a general trend, a decrease in base connection strength entails an increase of probability of collapse while the inclusion of the gravity system always improves the system behavior even if only the gravity columns continuum stiffness (i.e., Col.) is included. The former may be attributed to the fact that a decrease of base connection strength entails an increase of base flexibility, which drops the inflection point of first story columns moment diagrams. This results in an increment of stresses at the top of the fist story columns, which may give rise to a soft story.

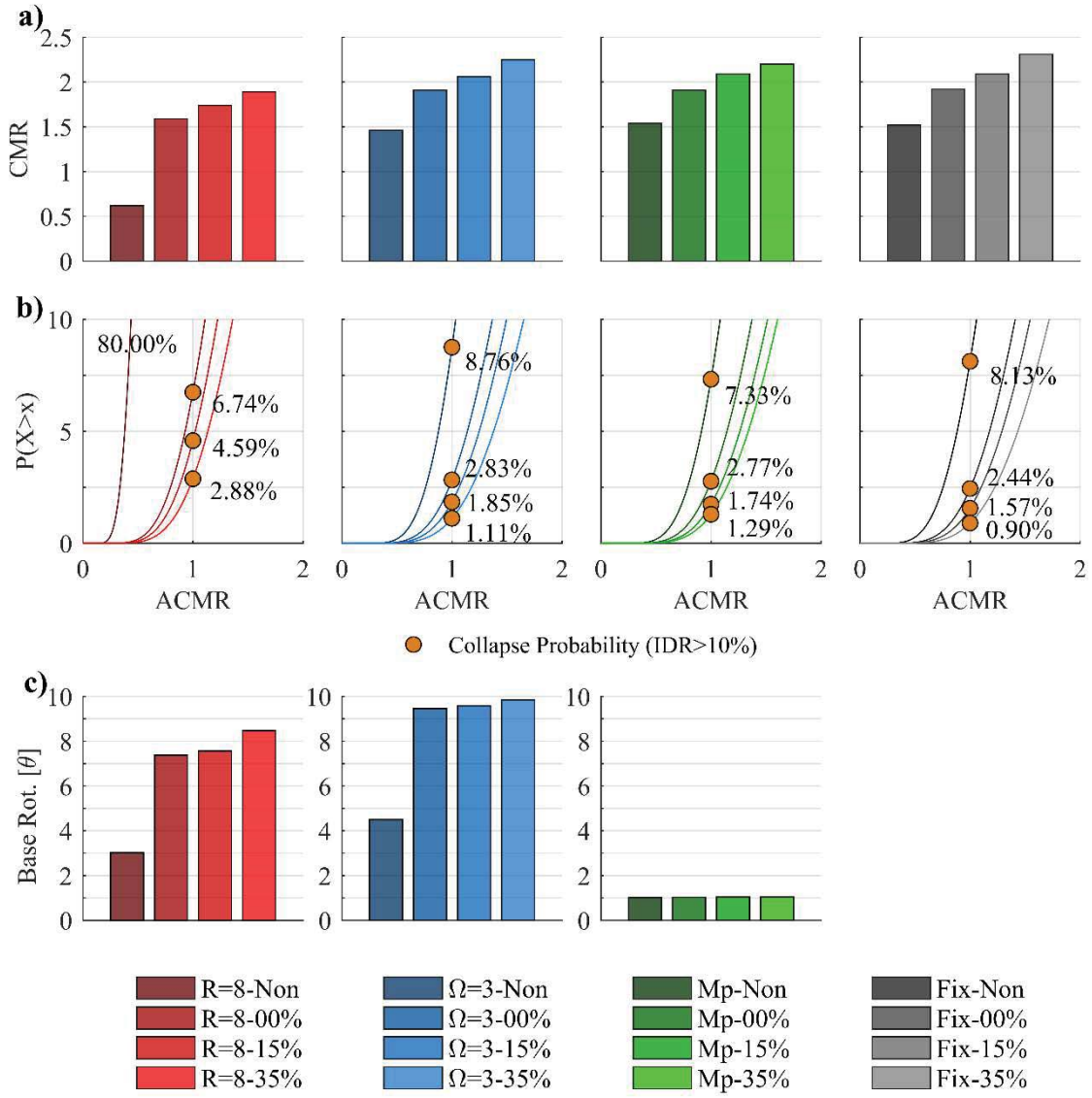

Figure 4: Collapse analysis. a) Collapse margin ratio: R=8, Ω_o=3, M_p, and Fixed-Base. b) Probability of collapse: R=8, Ω_o=3, 1.1R_yMp, and Fixed-Base. c) Median base rotation: R=8, Ω_o=3, and 1.1R_yMp.

Fig.4c presents the median of the base connection rotations obtained from NTH analysis on the verge of structural collapse for each column base connection strength varying PR beam-column connection strength. As expected, when the connection is designed for carrying a moment corresponding to $1.1R_yM_p$, rotations are less than 1% implying elastic behavior. In general, rotations are increased when base connection strength is reduced. A closer inspection of Fig. 4c reveals interesting results. The addition of the gravity system presents a singular effect in the base connection rotations, which are significantly increased. This may be explained due to the fact that the gravity system tends to enforce the building to deform in the first shape mode. Consequently, this phenomenon avoids the formation of soft-story mechanisms decreasing the system probability of collapse while implying a significant increment in base rotation demands. These results imply that although the gravity system counteracts the detrimental effect of base flexibility (in the probability of collapse of the 8-story SMF), it would require connections detailed to hold rotations in the order of 10%.

At first glance, results from IDA (Fig. 4b) indicate that base connection strength could be reduced (even for the case R=8), and similar performance can be achieved compared with the strong base criteria when the gravity system is included. However, an inspection of base rotations indicates that this conclusion cannot be stated unless base connections are properly detailed to hold rotations in the order of 10%.

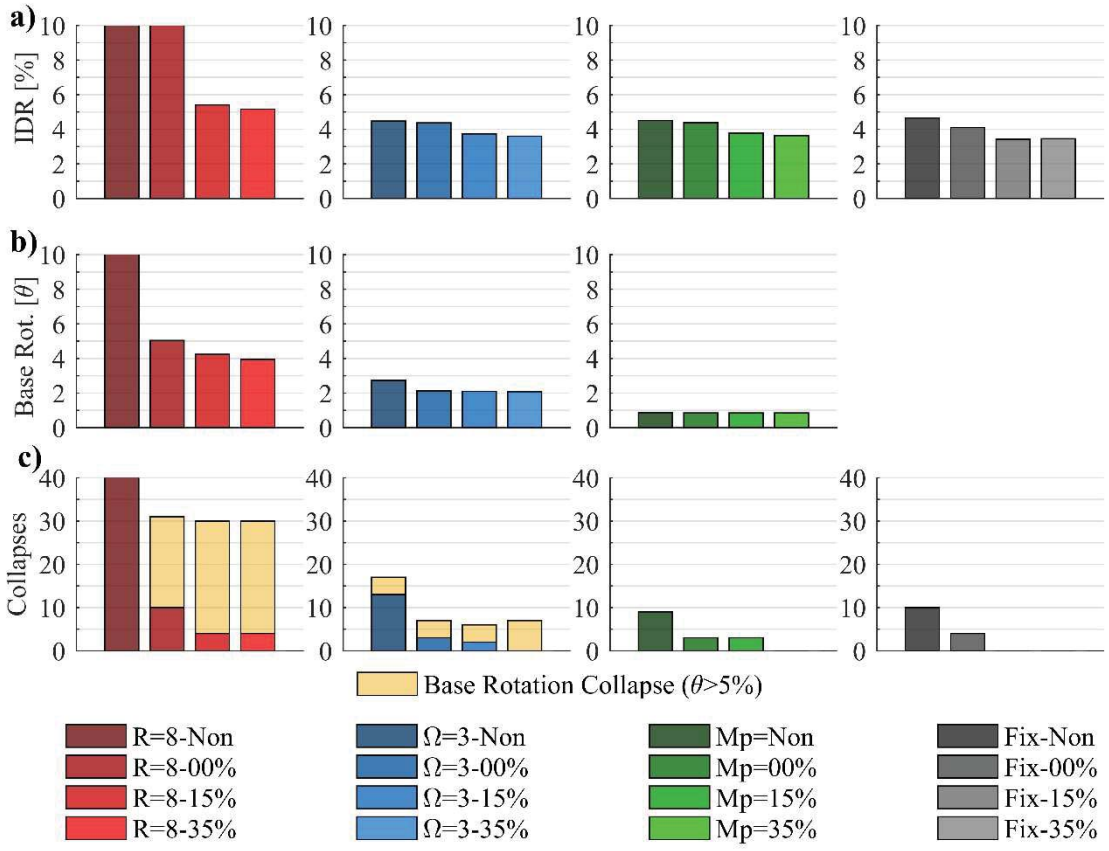

Figure 5: NTH analysis at MCE level of shaking. a) Inter-story drift ratios: R=8, Ω_o=3, $1.1R_yM_p$, and Fixed-Base. b) Median column base rotations: R=8, Ω_o=3, and $1.1R_yM_p$. c) The number of Sidesway Collapses in the SMF: R=8, Ω_o=3, $1.1R_yM_p$, and Fixed-Base.

The seismic performance of the SMF at MCE level of shaking was conducted in order to explore the effect of base connection behavior in the presence of gravity framing on the inter-story drift ratios. As per Fig. 5a, the cases Ω_o=3, $1.1R_yM_p$, and Fixed-Base leads to similar results even for different values of PR connection strength except for the case R=8 that presents the highest drifts. Specifically, the simulations conducted on the case R=8 presents drifts superior to 10% when gravity framing was neglected and when only the stiffness of gravity columns was included. On the other hand, considering the hysteresis of PR gravity connections entails a significant reduction of drifts, which highlights the effect of these gravity-connections in the overall system behavior. Fig. 5b shows the median base rotations for each simulation. Base rotations ranging from 1% for the strongest base to 10% for the weakest one are reported. In contrast to collapse assessment, at the MCE level of shaking, the gravity framing tends to reduce these rotations. This is explained because the effect of gravity framing is maximum at large deformations (at the verge of collapse), while its influence is minor at smaller deformations. Finally, Fig. 5c presents the number of sidesway collapses in the analyzed frame versus the number of connection failures. It is defined that a connection will fail beyond a 5% base rotation threshold [2-5]. As expected, the inclusion of the gravity system reduces the number of building collapses significantly. However, it is important to indicate that for all the cases corresponding to R=8, although the gravity system reduces the number of collapses, the number of base connection failures (i.e., rotations exceeding 5%) is high. From a design point of view, this will imply detailing column base connections for significant rotation capacity. On the other hand, base connections designed for Ω_o=3 and $1.1R_yM_p$ show a similar number of sidesway collapses even though the gravity system is excluded from the analysis. However, a closer inspection of the cases corresponding to Ω_o=3 strength level reveals a high number of connection failures (i.e., rotations beyond 5%), implying that connections need to be detailed to hold these significant levels of base rotations.

4 CONCLUSIONS

This paper investigates parametrically the effect of base connection strength, rotational stiffness, and deformation capacity incorporating the effect of gravity framing system on the seismic performance of an 8-story SMF. The scientific basis of this research consists of a series of NTH simulations conducted on the frame. Three levels of base connection strength are considered in this study (i.e., R=8, Ωo=3, and $1.1R_yM_p$), while the influence of gravity framing and PR gravity connections strength is included in each case analyzed giving a total of 16 mathematical models. In all models, sophisticated NTH analysis is conducted, which is supplemented by NSP. The NTH analysis is aimed to investigate the influence of base connection behavior accompanied by gravity framing on 1) probability of collapse of the SMF following the methodology described at FEMAp695; 2) inter-story drift ratios at MCE level.

Results from NTH analysis indicate that a reduction of base connection strength is accompanied by an increment on base-connection flexibility. This phenomenon tends to drop the inflection point of the moment diagram from the first story columns leading to a soft story mechanism. Specifically, when the gravity system is neglected, the model corresponding to base strength level R=8 presents unacceptable performance (i.e., probability of collapse in the order of 80%) while stronger base connections are on the verge of the 10% threshold. Inclusion of gravity framing in general decreases the probability of collapse to values less than 5%. Even the cases analyzed for the weak base connection criteria (i.e., R=8) present acceptable performance when the effect of the gravity system is considered. This may be attributed to the fact that gravity columns tend to enforce the SMF to deform on the first mode of shape, reducing stress concentrations on the first story.

Interestingly, when the gravity system is included, the median rotations at the base increase significantly except for the case where base connections are detailed by the capacity designed criterion. For this latter case, base rotations are less than 1% implying purely linear elastic behavior. On the other hand, a reduction in base connection strength entails a significant increase in base rotations. The implications might be important. If base connection strength is reduced, it must be detailed to hold rotations close to 10%. Up to this point, there are no guidelines to achieve this ductile behavior. Therefore, from the author's analysis base connections must be kept design based on capacity design principles or another collapse criteria should be proposed to consider a base connection failure limite state (i.e., base connection rotation < 5.0%).

This study is subjected to several limitations. First, only one archetype frame is analyzed. It is recommended to investigate further the effect of base connection behavior accompanied by gravity framing with different frames varying in height and plan view. Other limitations from this study that might be described are the bias due to ground motion effects, including the effects of vertical acceleration components, and assumptions related to the models such as concentrated plasticity models vs. distributed plasticity models. However, the results of this study must be understood as the first parametric investigation aimed to evaluate the impact of base connection behavior in the presence of the gravity framing system on the seismic performance of SMFs.

REFERENCES

[1] FEMA 355, State of the Art Report on Connection Performance, 2000.

[2] J. Tryon, Simple Models for Estimating the Rotational Stiffness of Steel Column-to-Footing Connections, (2016). https://www.semanticscholar.org/paper/Simple-Models-for-Estimating-the-Rotational-of-Tryon/6ed12ed24b5c84c28cb7b21c52c863ee8aa2855c.

[3] N. Barnwell, Experimental Testing of Shallow embedded Connections Between Steel Columns and Concrete Footings, (2015). https://scholarsarchive.byu.edu/etd/4428/.

[4] I. Gomez, G. Deierlein, A. Kanvinde, Exposed Column Base Connections Subjected to Axial Compression and Flexure, 2010. https://datacenterhub.org/resources/1239.

[5] C.A. Trautner, T. Hutchinson, P.R. Grosser, J.F. Silva, Investigation of Steel Column–Baseplate Connection Details Incorporating Ductile Anchors, Journal of Structural Engineering. 143 (2017) 04017074. https://doi.org/10.1061/(ASCE)ST.1943-541X.0001759.

[6] J. Newell, C.-M. Uang, Cyclic Behavior of Steel Columns with Combined Axial Load and Drift Demands, Department of Structural Engineering, University of California, San Diego, La Jolla, California, 2006.

[7] A. Elkady, D.G. Lignos, Full-Scale Testing of Deep Wide-Flange Steel Columns under Multiaxis Cyclic Loading: Loading Sequence, Boundary Effects, and Lateral Stability Bracing Force Demands, Journal of Structural Engineering. 144 (2018) 04017189. https://doi.org/10.1061/(ASCE)ST.1943-541X.0001937.

[8] T. Falborski, P. Torres-Rodas, F. Zareian, A. Kanvinde, Effect of base-connection strength and ductility on the seismic performance of steel moment frames, (2020).

[9] A.M. Kanvinde, D.A. Grilli, F. Zareian, Rotational Stiffness of Exposed Column Base Connections: Experiments and Analytical Models, Journal of Structural Engineering. 138 (2012) 549–560. https://doi.org/10.1061/(ASCE)ST.1943-541X.0000495.

[10] P.T. Rodas, F. Zareian, A. Kanvinde, Rotational Stiffness of Deeply Embedded Column–Base Connections, Journal of Structural Engineering. 143 (2017) 04017064. https://doi.org/10.1061/(ASCE)ST.1943-541X.0001789.

[11] P.T. Rodas, F. Zareian, A. Kanvinde, Hysteretic Model for Exposed Column–Base Connections, Journal of Structural Engineering. 142 (2016) 04016137. https://doi.org/10.1061/(ASCE)ST.1943-541X.0001602.
[12] P. Torres-Rodas, F. Zareian, A. Kanvinde, A hysteretic model for the rotational response of embedded column base connections, Soil Dynamics and Earthquake Engineering. 115 (2018) 55–65. https://doi.org/10.1016/j.soildyn.2018.08.015.
[13] A. Gupta, H. Krawinkler, Prediction of seismic demands for SMRFs with ductile connections and elements, SAC Steel Project, 1999.
[14] K. Lee, D.A. Foutch, Performance Evaluation of Damaged Steel Frame Buildings Subjected to Seismic Loads, Journal of Structural Engineering. 130 (2004) 588–599. https://doi.org/10.1061/(ASCE)0733-9445(2004)130:4(588).
[15] F.X. Flores, F.A. Charney, D. Lopez-Garcia, Influence of the gravity framing system on the collapse performance of special steel moment frames, Journal of Constructional Steel Research. 101 (2014) 351–362. https://doi.org/10.1016/j.jcsr.2014.05.020.
[16] Y. Cui, F. Wang, S. Yamada, Effect of Column Base Behavior on Seismic Performance of Multi-Story Steel Moment Resisting Frames, International Journal of Structural Stability and Dynamics. 19 (2019) 1940007. https://doi.org/10.1142/S0219455419400078.
[17] NIST, Evaluation of the FEMA P-695 Methodology for Quantification of Building Seismic Performance Factors, National Institute of Standards and Technology, Gaithersburg, MD, 2010.
[18] AISC, Prequalified Connections for Special and Intermediate Steel Moment Frames for Seismic Applications, (2010).
[19] D. Lignos, Sidesway Collapse of Deteriorating Structural Systems Under Seismic Excitations, (2008).
[20] A. Hartloper, D. Lignos, Updates to the ASCE-41-13 provisions for the nonlinear modeling of steel wide-flange columns for performance-based earthquake engineering, Ce/Papers. 1 (2017) 3072–3081. https://doi.org/10.1002/cepa.359.
[21] NIST, Guidelines for nonlinear structural analysis and design of buildings. part IIa - steel moment frames, National Institute of Standards and Technology, Gaithersburg, MD, 2017. https://doi.org/10.6028/NIST.GCR.17-917-46v2.
[22] AISC, Specification for Structural Steel Buildings, (2016).
[23] D. Grilli, A. Kanvinde, TENSILE STRENGTH OF EMBEDDED ANCHOR GROUPS: TESTS AND STRENGTH MODELS, Charles Pankow Foundation, 2015.
[24] P. Torres-Rodas, F. Zareian, A. Kanvinde, Seismic Demands in Column Base Connections of Steel Moment Frames, Earthquake Spectra. 34 (2018) 1383–1403. https://doi.org/10.1193/062317EQS127M.
[25] P. Torres-Rodas, J. Fayaz, F. Zareian, Strength resistance factors for seismic design of exposed based plate connections in special steel moment resisting frames, Earthquake Spectra. 36 (2020) 537–553. https://doi.org/10.1177/8755293019891714.
[26] ASCE 7, ed., Minimum design loads and associated criteria for buildings and other structures, American Society of Civil Engineers, Reston, Virginia, 2017.
[27] A. Elkady, D.G. Lignos, Effect of gravity framing on the overstrength and collapse capacity of steel frame buildings with perimeter special moment frames: EFFECT OF GRAVITY FRAMING ON STEEL BUILDINGS WITH PERIMETER SMF, Earthquake Engineering & Structural Dynamics. 44 (2015) 1289–1307. https://doi.org/10.1002/eqe.2519.
[28] J. Liu, A. Astaneh-Asl, Moment–Rotation Parameters for Composite Shear Tab Connections, Journal of Structural Engineering. 130 (2004) 1371–1380. https://doi.org/10.1061/(ASCE)0733-9445(2004)130:9(1371).

[29] S. Mazzoni, F. McKenna, M.H. Scott, G.L. Fenves, OpenSees Command Language Manual, (2006).
[30] A. Kanvinde, Micromechanical Simulation of Earthquake Induced Fractures in Steel Structures, Blume Earhquake Engineering Center, Stanford, California, 2004.
[31] D. Vamvatsikos, C.A. Cornell, Applied incremental dynamic analysis, Earthquake Spectra. 20 (2004) 523–553. https://doi.org/10.1193/1.1737737.
[32] F. Zareian, A. Kanvinde, Effect of Column-Base Flexibility on the Seismic Response and Safety of Steel Moment-Resisting Frames, Earthquake Spectra. 29 (2013) 1537–1559. https://doi.org/10.1193/030512EQS062M.
[33] R. Medina, H. Krawinkler, Seismic Demands for Nondeteriorating Frame Structures and their Dependence on Ground Motions, The John A. Blume Earthquake Engineering Center, Stanford, California, 2003.

EURODYN 2020
XI International Conference on Structural Dynamics
M. Papadrakakis, M. Fragiadakis, C. Papadimitriou (eds.)
Athens, Greece, 23–26 November 2020

A MULTI-OBJECTIVE OPTIMAL PARAMETER DESIGN PROCEDURE FOR SLIDE BRIDGE BEARINGS UNDER SEISMIC EXCITATION BASED ON A DETERMINISTIC-STOCHASTIC MODELING APPROACH

X. He[1], **A. Igarashi**[2]

[1] Department of Urban Management, Kyoto University
Nishikyo-ku, Kyoto 615-8530, JAPAN
he.xinhao.25u@st.kyoto-u.ac.jp

[2] Disaster Prevention Research Institute, Kyoto University
Gokasho, Uji-shi, Kyoto 611-0011, JAPAN
igarashi.akira.7m@kyoto-u.ac.jp

Keywords: Slide bridge bearings, Multi-objective optimization, Seismic excitations, Stochastic-deterministic approach, Seismic performance assessment

Abstract. *In the process of seismic performance-based design of bridges with slide bearings, there exist intrinsic tradeoffs between minimization of bearing displacement and that of the pier response in selecting bearing parameters for strong earthquake events. However, difficulty in determining the optimal parameters of the bearings that satisfy the two objectives arises, in conjunction with considerable computational resource requirement for nonlinear time-history analysis. In order to find the solutions of the multi-objective optimization problem that reduce the computational cost, a procedure that utilizes the stochastic structural response of equivalent linear systems is proposed. To obtain the performance indices, seismic load is modeled as a stationary random process, whose characteristics are determined for the standard design ground motions specified by the Japanese design code, and the nonlinear behavior of the slide bearings is modeled as equivalent-linear elements using the stochastic linearization technique. As the result, a set of optimal parameter candidates is obtained as the Pareto-front solutions in the multi-objective function space. As the next step, the search of the optimal parameters is conducted by performing nonlinear time-history analysis only for the Pareto-front solution parameter sets to save the computational requirement. As a numerical example, the proposed method is applied to bridges with two types of slide bearings: the uplifting sliding shoe (UPSS) consisting of multiple sliding surfaces, and functionally discrete bearings (FDB) in which friction bearings and elastomeric bearings set in parallel are combined. It is demonstrated that the seismic performance of the bridge for the case of the design parameters obtained by the proposed procedure is almost equivalent to the one with the optimal parameters found by the conventional exhaustive search approach.*

1 INTRODUCTION

The bridge bearing with seismic functionality is recognized as a key component to facilitate the required seismic performance. With the use of these devices, elongation of the natural period and providing supplementary energy dissipation capability are achieved so that both the bearing and pier responses are minimized under strong earthquakes. In addition, a better serviceability that includes the control of ambient vibration and the thermal elongation problem of the girders can be achieved in regular maintenance and management.

Recently, some unconventional bridge bearings have been proposed to provide more flexible and feasible options for seismic performance enhancement of bridges. The uplifting slide shoe (UPSS) bearing [1, 2] is a new type of bearing consisting of multiple sliding surfaces, as shown in Fig. 1(a). The mechanism of UPSS is characterized by sliding actions on different sliding surfaces. The horizontal sliding surface of UPSS is to accommodate the thermal effects and small vibration of continuous girders, while the inclined sliding surface is to provide extra restoring force to effectively mitigate the excessive horizontal displacement response of the girders under strong earthquake events. The functionally discrete bearing (FDB) system [3] is a combination of elastomeric bearings and sliding bearings to separately provide restoring force and energy dissipation ability, as shown in Fig. 1(b). Unlike the conventional rubber bearings, this system allows required period elongation of the structural systems and the energy dissipation performance.

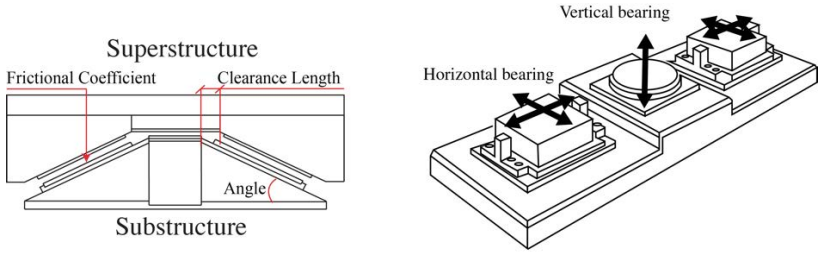

(a) UPSS (b) FDB

Figure 1: Schematics of UPSS and FDB.

In the process of the seismic performance-based design of bridges with either of these types of bearings, there exist intrinsic tradeoffs between minimization of bearing displacement and that of pier response in selecting bearing parameters for strong earthquake events. However, difficulty in determining the optimal parameters of these devices arises. Conventional exhaustive search method requires numerous computational resources to perform the nonlinear time-history analysis for many cases of the slide bearing parameters to determine the corresponding optimal design, since all of the possible parameter combinations are of a large number, whereas only a small number of the parameter combinations satisfy the optimal design criteria. On the other hand, the objective function of the optimization problem is usually unknown due to the complexity of nonlinear time-history analysis. Therefore, a fast search algorithm to determine the optimal parameter selection is required.

The optimal design of structures can be achieved by different approaches according to previous studies. Feng et al. [4] derived the optimal parameters for the tall building with mega substructure configuration under white-noise excitations by minimizing the mean square of the responses of interest. A series solution of the H_∞ optimization problem and a closed-form algebraic solution of the H_2 optimization problem for the dynamic vibration absorber attached to linear systems were given by Asami et al. [5]. The optimal design of the unconventional tuned mass damper to individually minimize the response quantity of interest was investigated in Refs. [6, 7]. Specifically, Hoang and Fujino [6] investigated the optimal parameter design of rubber

bearings for seismic response mitigation of a long-span truss bridge in Japan. Under the consideration of nonlinear structural elements, optimal parameter design of nonlinear base isolation systems was investigated by Reggio [8] and De Domenico [9] based on stochastic dynamic analysis. In addition, a performance-based optimization procedure for nonlinear structures subjected to random seismic excitation is proposed by Xu and Spencer [10] to deal with optimal parameter design for competing performance objectives.

In this study, a deterministic-stochastic approach is proposed to achieve the multi-objective design of slide bearings under seismic excitation. To obtain the performance indices, seismic load is modeled as a stationary random process and the nonlinear behavior of the slide bearings is modeled as equivalent-linear elements using the stochastic linearization technique. As the result, a set of optimal parameter candidates is obtained as the Pareto-front solutions in the multi-objective function space. As the next step, the search of the optimal parameters is conducted by performing nonlinear time-history analysis only for the set of the Pareto-front solution parameter sets to save the computational requirement. As a numerical example, the proposed method is applied to optimal parameter selection of UPSS and FDB in a girder bridge. It is demonstrated that the seismic performance of the bridge for the case of the design parameters obtained by the proposed procedure is almost equivalent to the one with the optimal parameters found by the conventional exhaustive search approach.

2 MODELING

A bridge with a straight girder supported by single columns with UPSS or FDB is studied. The dynamic behavior of the bridge in the longitudinal direction is simplified as a lumped-mass model with two horizontal degrees of freedom (DOF), as shown in Fig. 2.

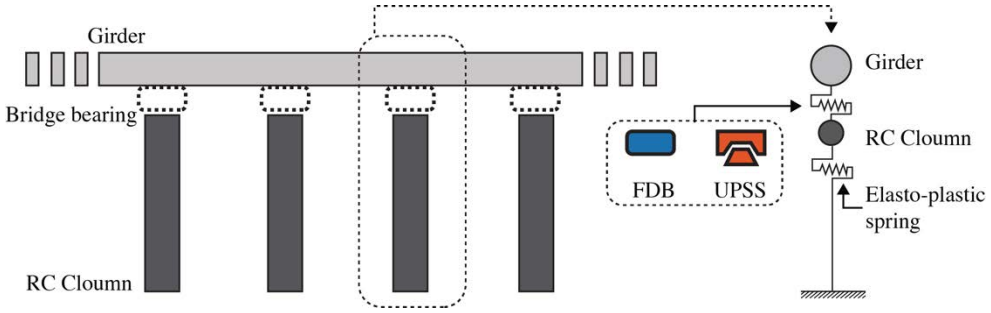

Figure 2: Bridge model with application of UPSS or FDB

2.1 Equation of motion

The governing equation of the system is given as:

$$\boldsymbol{M}\ddot{\boldsymbol{u}} + \boldsymbol{g}(\boldsymbol{u}, \dot{\boldsymbol{u}}) = -\boldsymbol{\tau}\ddot{u}_g \tag{1}$$

where $\boldsymbol{M} = \mathrm{diag}(m_1, m_2)$, m_1 and m_2 are the masses of the pier and girder, respectively; $\boldsymbol{u} = [u_1 \quad u_2]^T$ is the vector of the nodal displacements and $\dot{\boldsymbol{u}} = [\dot{u}_1 \quad \dot{u}_2]^T$ is the vector of the nodal velocities; $\boldsymbol{g}(\boldsymbol{u}, \dot{\boldsymbol{u}})$ is the reaction force vector, which can be linear or nonlinear; $\ddot{u}_g$ is the ground acceleration; $\boldsymbol{\tau} = [1 \quad 1]^T$ is the excitation vector to couple the input and the structural DOFs.

The mechanical behavior of UPSS and the superstructure can be simplified as a point mass sliding on three sliding surfaces, as shown in Fig. 3. Based on the dynamic equilibrium condition, the restoring force of UPSS is expressed as:

$$f_2 = \begin{cases} \mu m_2 g \ \mathrm{sgn}(\dot{u}_b), & -L < u_b < L \\ N \sin\theta \ \mathrm{sgn}(u_b) + \mu N \cos\theta \ \mathrm{sgn}(\dot{u}_b), & (u_b < -L) \text{ or } (u_b > L) \end{cases} \quad (2)$$

where $N = m_2 g \cos\theta$ is the resistant force of the inclined sliding surface, and g is the gravitational acceleration; μ is the friction coefficient of sliding interface; θ is the inclined angle of the inclined sliding surfaces from the horizontal direction; L is the distance of the clearance length from the neutral position of the horizontal sliding surface to the beginning of the inclined sliding surface; u_b is the relative displacement of the bearing with respect to the pier; and $\mathrm{sgn}(\cdot)$ is the signum function.

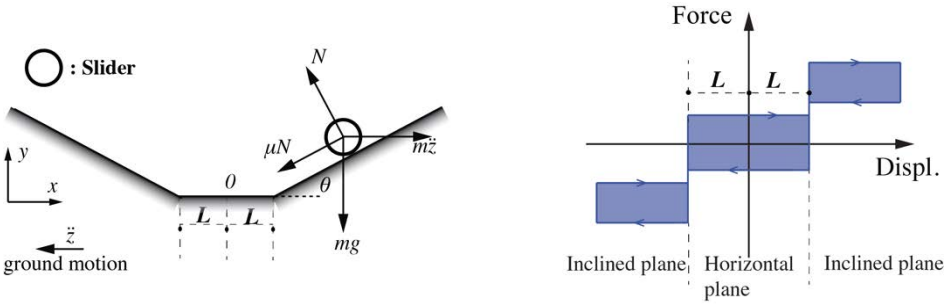

Figure 3: Mechanism of UPSS

Since FDB is a combination of rubber bearings and slide bearings, the mechanical behavior of FDB is expressed as the sum of that of the two types of bearings, as shown in Fig. 4. The sliding bearing is represented by the Coulomb friction model, and the rubber bearing is represented by an elastic linear spring. The restoring force of FDB is expressed as:

$$f_b = k_b u_b + \mu m_2 g \ \mathrm{sgn}(\dot{u}_b) \quad (3)$$

where $k_b = m_2(2\pi/T_b)^2$ is the stiffness of the rubber bearing, and T_b is the specified natural period when the superstructure is in the fixed bearing condition.

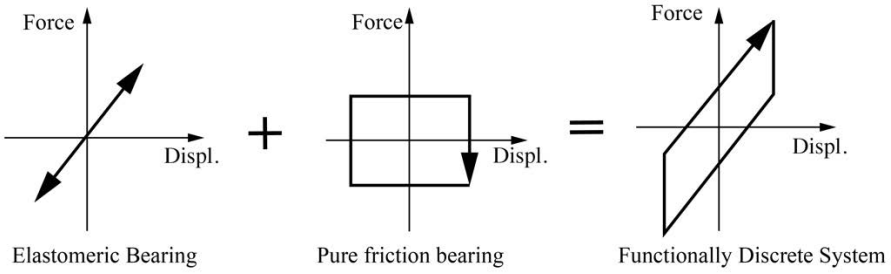

Figure 4: Mechanism of FDB

The behavior of the RC pier supporting the bridge bearing is represented by the Clough's degrading stiffness model in the nonlinear time-history analysis. The initial stiffness of the RC pier is specified so that the elastic period for the fixed bearing condition is 0.5 sec, and the yielding strength is 0.66g lateral force.

2.2 Stochastic representation of seismic excitations

The ground motion is assumed to be represented by the modified Kanai-Tajimi model [11, 12]. In the time domain, this model can be expressed in a state-space form as Eq. (4).

$$\dot{\boldsymbol{x}}_f = \boldsymbol{A}_f \boldsymbol{x}_f + \boldsymbol{B}_f w(t) \quad (4)$$

$$p(t) = \boldsymbol{C}_f \boldsymbol{x}_f$$

where,

$$\boldsymbol{x}_f = \begin{bmatrix} u_f \\ \dot{u}_f \\ u_g \\ \dot{u}_g \end{bmatrix};\ \boldsymbol{A}_f = \begin{bmatrix} 0 & 1 & 0 & 0 \\ -\omega_f^2 & -2\zeta_f\omega_f & \omega_g^2 & 2\zeta_g\omega_g \\ 0 & 0 & 0 & 1 \\ 0 & 0 & -\omega_g^2 & -2\zeta_g\omega_g \end{bmatrix};\ \boldsymbol{B}_f = \begin{bmatrix} 0 \\ 0 \\ 0 \\ 1 \end{bmatrix};\ \boldsymbol{C}_f^T = \begin{bmatrix} -\omega_f^2 \\ -2\zeta_f\omega_f \\ \omega_g^2 \\ 2\zeta_g\omega_g \end{bmatrix}$$

in which $w(t)$ is the bedrock Gaussian white-noise process; ω_g and ζ_g are the fundamental circular frequency and damping ratio, respectively, of the surface soil layer in the Kanai-Tajimi model; ω_f and ζ_f are the parameters of the second filter suggested by Clough and Penzien.

The peak ground acceleration (PGA) is related to the spectral intensity of the white-noise [9] as Eq. (5):

$$S_w = \frac{0.141\zeta_g \ddot{u}_{g0}^2}{\omega_g\sqrt{1+4\zeta_g^2}} \tag{5}$$

The parameters of the modified K-T model are determined by the PSD of the standard design ground motions in the Japanese design code through the least-square method.

2.3 Stochastic response of MDOF structures

The above equation of motion can be substituted into an equivalent linearized form, if $\boldsymbol{g}(\boldsymbol{u}, \dot{\boldsymbol{u}})$ satisfies some smoothness requirement and the input is a zero-mean stationary Gaussian process so as to minimize the mean square error between the linearized counterpart and the original nonlinear system [13], as shown in Eq. (6):

$$\boldsymbol{M}\ddot{\boldsymbol{u}} + \left(\boldsymbol{C} + \boldsymbol{C}_{eq}\right)\dot{\boldsymbol{u}} + \left(\boldsymbol{K} + \boldsymbol{K}_{eq}\right)\boldsymbol{u} = -\boldsymbol{\tau}\ddot{u}_g \tag{6}$$

where $\boldsymbol{C}$ and $\boldsymbol{K}$ are the damping matrix and stiffness matrix for linear elements, respectively; $\boldsymbol{C}_{eq}$ and $\boldsymbol{K}_{eq}$ are the equivalent linearized damping and stiffness matrices for nonlinear elements, respectively.

Then the governing equation can be rewritten into a state-space form as:

$$\begin{aligned} \dot{\boldsymbol{x}}_s &= \boldsymbol{A}_s\boldsymbol{x}_s + \boldsymbol{B}_s w(t) \\ \boldsymbol{y}_s &= \boldsymbol{C}_s\boldsymbol{x}_s + \boldsymbol{D}_s w(t) \end{aligned} \tag{7}$$

where $\boldsymbol{x}_s = [\boldsymbol{u}^T \quad \dot{\boldsymbol{u}}^T]^T$ is the state vector, $\boldsymbol{y}_s$ is the response vector, and

$$\boldsymbol{A}_s = \begin{bmatrix} \boldsymbol{0}_{N\times N} & \boldsymbol{I}_{N\times N} \\ -\boldsymbol{M}^{-1}\left(\boldsymbol{K} + \boldsymbol{K}_{eq}\right) & -\boldsymbol{M}^{-1}\left(\boldsymbol{C} + \boldsymbol{C}_{eq}\right) \end{bmatrix}, \qquad \boldsymbol{B}_s = \begin{bmatrix} \boldsymbol{0}_{N\times 1} \\ \boldsymbol{M}^{-1}\boldsymbol{\tau} \end{bmatrix}$$

the matrices $\boldsymbol{C}_s$ and $\boldsymbol{D}_s$ are the response matrices, which are determined by the specified outputs.

Combined with the ground motion model, the state of the combined system can be expressed as Eq. (8):

$$\begin{aligned} \dot{\boldsymbol{x}}_a &= \boldsymbol{A}_a\boldsymbol{x}_a + \boldsymbol{B}_a w(t) \\ \boldsymbol{y}_s &= \boldsymbol{C}_a\boldsymbol{x}_a \end{aligned} \tag{8}$$

where $\boldsymbol{x}_a = \left[\boldsymbol{x}_s^T \quad \boldsymbol{x}_f^T\right]^T$ is the augmented state-space vector collecting displacement and velocities of both the system and the filter variables, and

$$\boldsymbol{A}_a = \begin{bmatrix} \boldsymbol{A}_s & \boldsymbol{B}_s\boldsymbol{C}_f \\ \boldsymbol{0}_{r\times 2N} & \boldsymbol{A}_f \end{bmatrix}, \qquad \boldsymbol{B}_a = \begin{bmatrix} \boldsymbol{0}_{2N\times 1} \\ \boldsymbol{B}_f \end{bmatrix}, \qquad \boldsymbol{C}_a = \begin{bmatrix} \boldsymbol{C}_s & \boldsymbol{D}_s\boldsymbol{C}_f \end{bmatrix}$$

in which $r = 4$ is the size of the filter equation describing the modified K-T model.

The second order moment of the stochastic structural response is considered as the performance objective, which is defined as $\boldsymbol{\Gamma}_{\boldsymbol{x}_a} = E[(\boldsymbol{x}_a - \boldsymbol{\mu}_a)(\boldsymbol{x}_a - \boldsymbol{\mu}_a)^T]$, where $\boldsymbol{\mu}_a$ is the expected value vector and $E[\cdot]$ denotes the expectation operator. In stationary cases, the covariance matrix is a constant matrix. With the assumption of a zero-mean Gaussian process as input and zero-mean initial conditions, the covariance of the structural response $\boldsymbol{\Gamma}_{\boldsymbol{x}_a} = E[\boldsymbol{x}_a\boldsymbol{x}_a^T]$ is governed by the following Lyapunov equation: $\boldsymbol{A}_a\boldsymbol{\Gamma}_{\boldsymbol{x}_a} + \boldsymbol{\Gamma}_{\boldsymbol{x}_a}\boldsymbol{A}_a^T + 2\pi\boldsymbol{B}_a S_w \boldsymbol{B}_a^T = 0$. Note that the solution of the above equation is implicit, since the determination of linearized coefficients is dependent on the corresponding second-order moment responses which are unknown. Hence, an iterative procedure should be performed until the convergence is reached by initializing the procedure with a linear system.

2.4 Stochastic linearization

If the structural responses are assumed to be stationary random processes, the equivalent linearized damping and stiffness can be determined through the stochastic linearization technique [13] as Eq. (9).

$$K_{eq}^{(i,j)} = E\left[\frac{\partial g_i}{\partial u_j}\right], \qquad C_{eq}^{(i,j)} = E\left[\frac{\partial g_i}{\partial \dot{u}_j}\right] \tag{9}$$

Since the inclined surfaces of UPSS are responsible for controlling the excessive horizontal response under strong earthquakes, only the action of UPSS sliding on the inclined surfaces is considered here. The restoring force of UPSS in the horizontal direction can be simplified as Eq. (10).

$$f_b = N\sin\theta\,\mathrm{sgn}(u_b) + \mu N\cos\theta\,\mathrm{sgn}(\dot{u}_b) \tag{10}$$

where the same definition applies to the symbols as mentioned above.

Hence, the stochastic linearization coefficients for UPSS can be solved by Eq. (11).

$$\begin{aligned} K_{eq}^{(b,b)} &= E\left[\frac{\partial f_b}{\partial u_b}\right] = N\sin\theta\,E\left[\frac{\partial \mathrm{sgn}(u_b)}{\partial u_b}\right] = N\sin\theta\,E[2\delta(u_b)] = N\sin\theta\sqrt{\frac{2}{\pi}}\frac{1}{\sigma_{u_b}} \\ C_{eq}^{(b,b)} &= E\left[\frac{\partial f_b}{\partial \dot{u}_b}\right] = \mu N\cos\theta\,E\left[\frac{\partial \mathrm{sgn}(\dot{u}_b)}{\partial \dot{u}_b}\right] = \mu N\cos\theta\sqrt{\frac{2}{\pi}}\frac{1}{\sigma_{\dot{u}_b}} \end{aligned} \tag{11}$$

where $\delta(\cdot)$ denotes Dirac delta function.

Similarly, the stochastic linearization coefficients for FDB can be solved by Eq. (12).

$$K_{eq}^{(b,b)} = k_b, \qquad C_{eq}^{(b,b)} = \mu m_2 g\sqrt{\frac{2}{\pi}}\frac{1}{\sigma_{\dot{u}_b}} \tag{12}$$

2.5 Stochastic and deterministic modeling analysis

The constraint conditions for parameter selection and the structural information for the stochastic analysis are listed in the Table I. Since minimization of the pier response is considered

to be one of the optimization objectives, the stiffness and damping properties of the bridge pier are assumed to be constant in the stochastic analysis. On the other hand, the structural information for the nonlinear time-history analysis (NTHA) is presented in the Table II.

Mass ratio m_2/m_1		3.0
Pier	Natural period T_1	0.5 (sec)
	Damping ratio ξ_1	0.02
Elastomeric bearing	Natural period T_b	1.0~2.0 (sec)
	Damping ratio ξ_b	0.03
Friction coefficient μ		0.05~0.15
UPSS inclined angle θ		5 ~30 (°)

Table I: Design variables and structural parameters for stochastic analysis

Mass of girder m_2	900 (ton)
Mass of RC bridge pier m_1	300 (ton)
Initial natural period of RC pier $T_{0,1}$	0.5 (sec)
Yield strength of RC pier	0.66g
Clearance of UPSS L	0.03 (m)

Table II: Structural parameters for NTHA

3 MULTI-OBJECTIVE DESIGN

3.1 Pareto-front solutions

Since minimization of both the bearing and bridge pier responses is a multi-objective optimization problem, the Pareto-front solution is introduced in the form of the ε-Constraint method. This method is to minimize the pier response for a given bearing displacement demand as expressed by Eq. (13).

$$\begin{aligned} &\min J_I(\boldsymbol{x}) \\ \text{Subjected to:} \quad &J_{II}(\boldsymbol{x}) < \varepsilon_m, \qquad m = 1,2,3,\dots,M \\ &\boldsymbol{x}_{lb} < \boldsymbol{x} < \boldsymbol{x}_{ub} \end{aligned} \tag{13}$$

where the performance objectives J_I and J_{II} are the second-order moment of the displacement response of the bridge pier and that of the bearing, respectively; ε_m is the constraint condition in terms of the bearing response; $\boldsymbol{x}_{lb}$ and $\boldsymbol{x}_{ub}$ are the lower and upper bounds of the design variable vector, as shown in Table I.

3.2 Procedure for optimal parameter selection

The procedure to determine the optimal design is given as follows and as Fig. 5:

I. Determine the parameters of the modified K-T model for a given standard ground motion accelerogram of the design code. The PSD corresponding to the ground motion accelerogram is firstly determined by the Welch's method, and then the paramters of the modified K-T model are determined by the least square method.
II. Compute the second-order moment of the structural responses for all possible parameter combinations through the stochastic dynamic analysis.
III. Select a set of optimal parameter candidates through the Pareto solutions of the all stochastic responses. The constraint condition (ε_m) of the Pareto-front is ranging from the minimum bearing displacement to the maximum bearing displacment responses (σ_{u_b}).
IV. Search the optimal design for the given bearing displacement demand by performing nonlinear time-history analysis only using the set of the optimal parameter candidates obtained in the previous step.

Since the selected optimal parameter candidates are a subset of all possible parameter combinations, the computational resources are considerably reduced in comparison with the conventional exhaustive search approach.

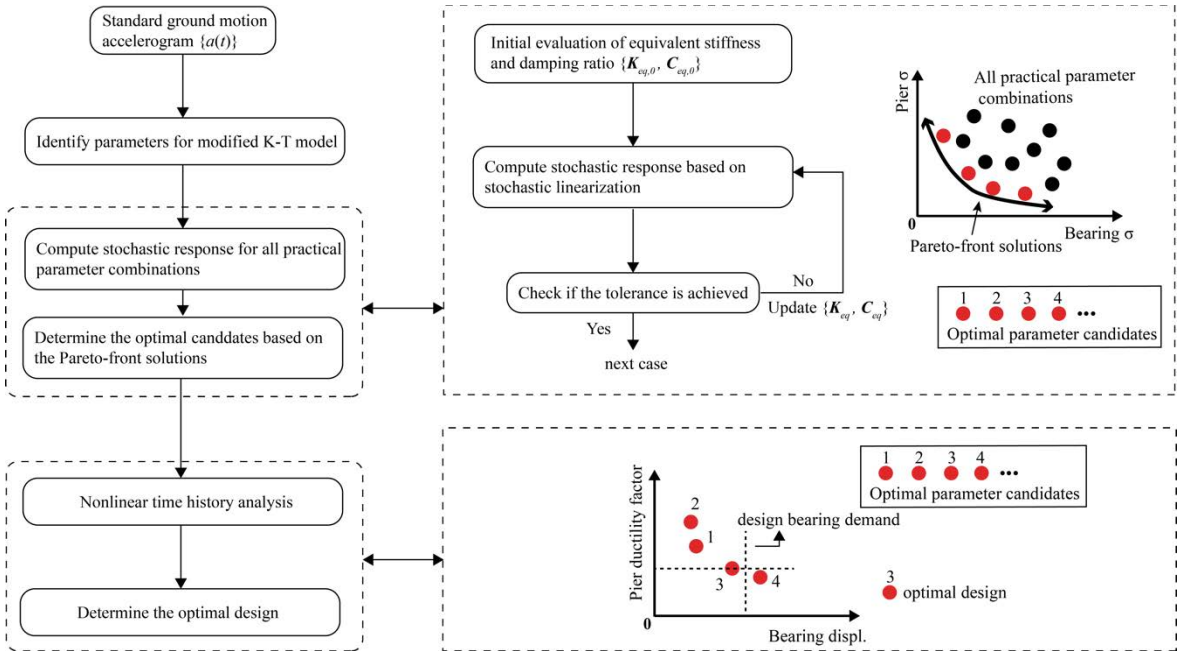

Figure 5: Flowchart of the proposed procedure

3.3 Numerical example

An example of determination of the optimal parameters for UPSS and FDB is presented. The corresponding structural parameters are given in section 2.

The standard ground motion II-I-2 provided in the Japanese Highway Bridges Design Specification [14] is used in this example. The corresponding accelerogram and PSD of the standard ground motion are shown in Fig. 6. As indicated by this figure, PSD of the modified K-T model determined by the least-square method shows a good agreement with that of the standard ground motion.

Then, the optimal parameter candidates of the bearings are determined based on the Pareto solutions of the stochastic dynamic response of all possible parameter combinations, as shown in Fig. 7.

Finally, the optimal design is searched by performing the nonlinear time-history analysis using the limited set of the Pareto solution parameters (optimal parameter candidates). For all possible bearing displacement demands, the maximum pier response ductility factors obtained by the proposed procedure are plotted in the Fig. 8 with red dots. As indicated by this figure, the seismic performance of the bridge for the case of the optimal design shown by red dots are close to that obtained by the conventional exhaustive search approach indicated by black dots.

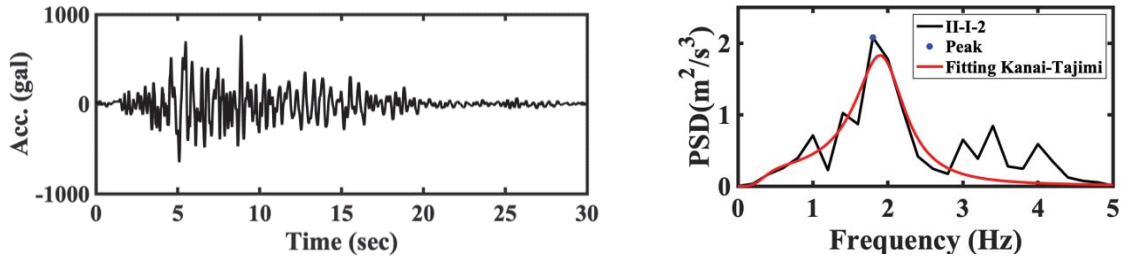

(a) Time history of acceleration (b) PSD

Figure 6: Standard ground motion

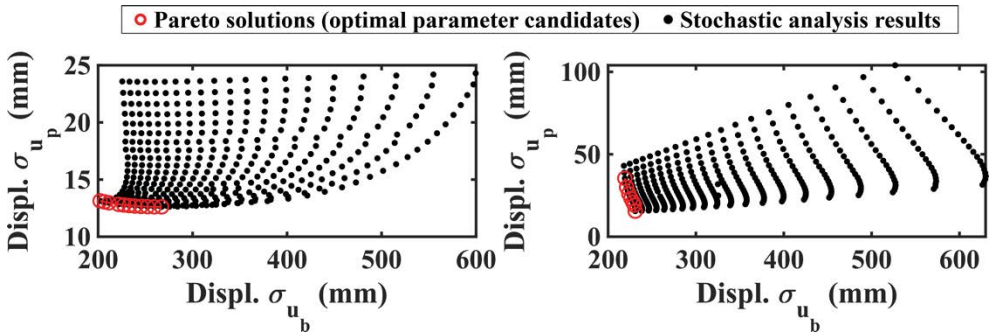

(a) Cases of UPSS (b) Cases of FDB

Figure 7: Pareto solutions of stochastic analysis

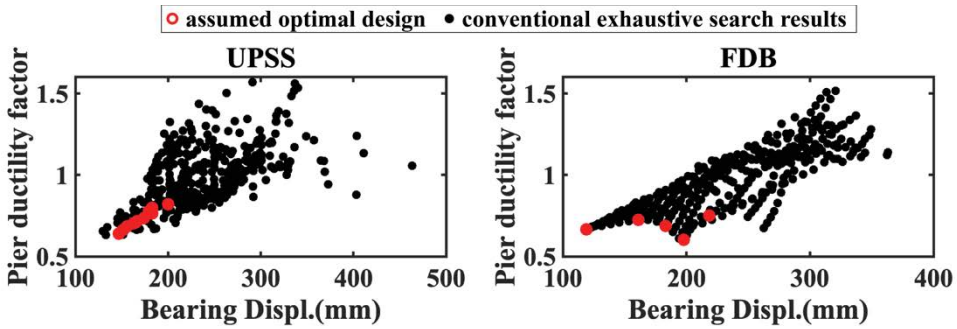

(a) Cases of UPSS (b) Cases of FDB

Figure 8: Comparison with conventional exhaustive search

More specifically, for a given bearing displacement demand (200mm), the optimal design for UPSS is determined as $\mu = 0.11$, $\theta = 5°$ and that for FDB is $\mu = 0.15$, $T_b = 1.45$ sec. The corresponding seismic responses of the bridge are shown in Fig. 9.

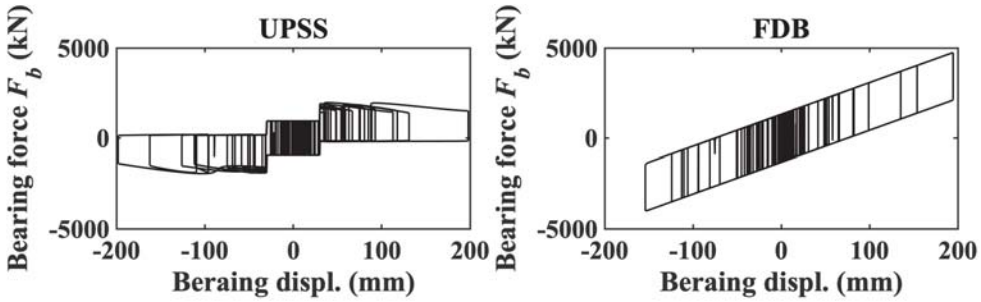

(a) Bearing response, UPSS (b) Bearing response, FDB

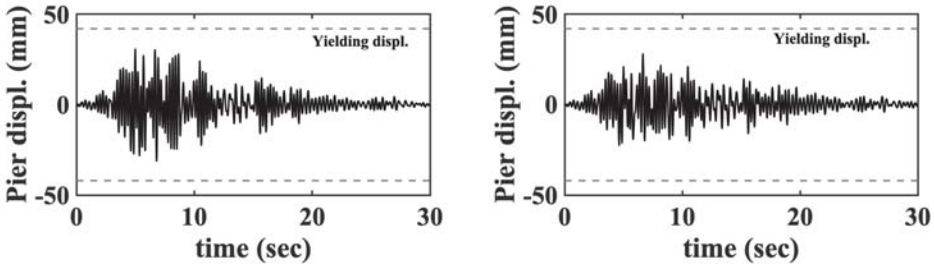

(c) RC pier response, UPSS (d) RC pier response, FDB

Figure 9: Bridge response for the optimal parameters

4 EFFECTIVENESS

To validate the effectiveness of the proposed procedure compared with the conventional exhaustive search approach, the definition of assessment error is firstly given. In the ideal situation, the assumed Pareto solutions perfectly match with the exact Pareto solutions obtained by the conventional exhaustive search. However, errors appear, if the minimum pier response obtained from the proposed procedure is higher than the minimum value obtained by the conventional exhaustive search, for a given bearing displacement demand, as shown in Fig. 10. Thus, the amount of assessment error is defined as:

$$\text{error} = \frac{\Delta d}{D} \times 100\% \tag{14}$$

where Δd is the difference between the two minimum pier responses obtained from the two approaches, and D denotes the difference between the maximum and minimum pier responses obtained by the conventional exhaustive search for the given bearing displacement demand.

The results for UPSS and FDB under 18 standard ground motions covering three different soil conditions and two earthquake source types are shown in Fig. 11, where the horizontal axis is normalized by the maximum and minimum bearing displacements of each case. As indicated by this figure, error of each ground motion case shows different precision depending on the characteristics of the ground motion. The mean error over most of the bearing displacement range is lower than 4% for UPSS and is approximately 11.5% for FDB, while the mean error tends to rise when the bearing displacement demand is in lower level.

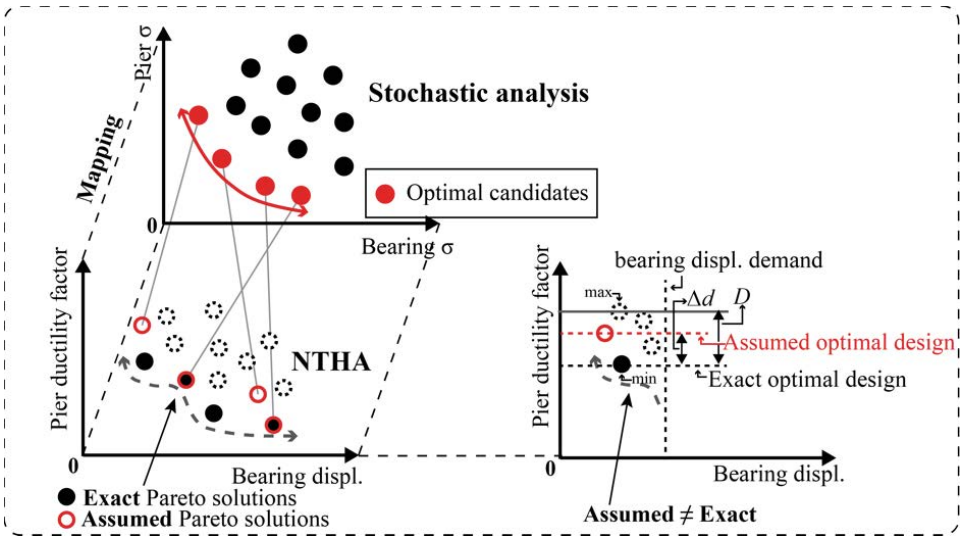

Figure 10: Illustration of assessment error

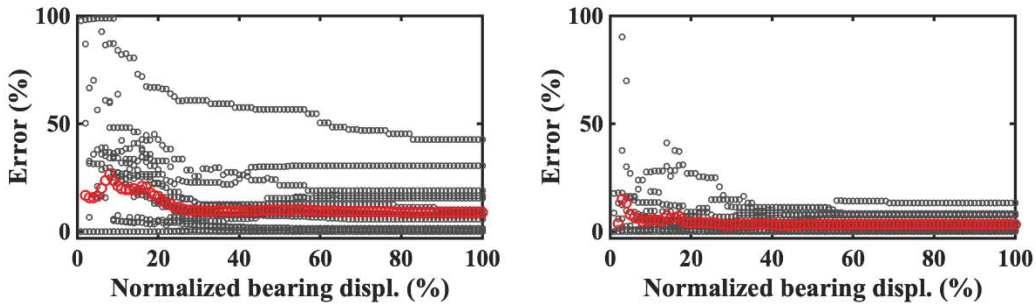

(a) Cases of FDB (b) Cases of UPSS

Figure 11: Assessment error of the proposed method (18 standard ground motions in Japanese design code)

5 CONCLUSIONS

For the seismic design of bridges with unconventional slide bridge bearings, a stochastic-deterministic approach to determine bearing parameters is proposed to achieve the multi-objective optimal design that minimizes the bearing displacement as well as the pier response to save the computational requirement. A numerical example is given for the optimal design of slide bearings of two types, namely UPSS and FDB, under strong ground motions. It is demonstrated that the seismic performance of the bridge for the case of the design parameters obtained by the proposed procedure is almost equivalent to the one with the optimal parameters found by the conventional exhaustive search approach.

REFERENCES

[1] M. Y. Fakhouri, A. Igarashi, Multiple‐slider surfaces bearing for seismic retrofitting of frame structures with soft first stories. *Earthquake Engineering & Structural Dynamics*, 42(1), 145-161, 2013.

[2] M. Y. Fakhouri, A. Igarashi, Dynamic response control of multi-story structures by isolators with multiple plane sliding surfaces: A parametric study. *Engineering Structures*, 34, 81-94, 2012.

[3] Functionality discrete bearing system. Retrieved from https://hanshin-exp.co.jp/company/skill/library/mainte/22105.html

[4] M. Q. Feng, A. Mita, Vibration control of tall buildings using mega subconfiguration. *Journal of engineering mechanics*, 121(10), 1082-1088, 1995.

[5] T. Asami, O. Nishihara, A. M. Baz, Analytical solutions to H_∞ and H_2 optimization of dynamic vibration absorbers attached to damped linear systems. *Journal of vibration and acoustics*, 124(2), 284-295, 2002.

[6] N. Hoang, Y. Fujino, P. Warnitchai, Optimal tuned mass damper for seismic applications and practical design formulas. *Engineering Structures*, 30(3), 707-715, 2008.

[7] A. Reggio, M. D. Angelis, Optimal energy‐based seismic design of non‐conventional Tuned Mass Damper (TMD) implemented via inter‐story isolation. *Earthquake Engineering & Structural Dynamics*, 44(10), 1623-1642, 2015.

[8] A. Reggio, M. De Angelis, Optimal design of an equipment isolation system with nonlinear hysteretic behaviour. *Earthquake Engineering & Structural Dynamics*, 42(13), 1907-1930, 2013.

[9] D. De Domenico, G. Ricciardi, Optimal design and seismic performance of tuned mass damper inerter (TMDI) for structures with nonlinear base isolation systems. *Earthquake Engineering & Structural Dynamics*, 47(12), 2539-2560, 2018.

[10] Jiaqi Xu, Billie F. Spencer Jr, and Xilin Lu, Performance-based optimization of nonlinear structures subject to stochastic dynamic loading. *Engineering Structures*, 134: 334-345, 2017.

[11] K. Kanai, Semi-empirical formula for the seismic characteristics of the ground. *Bulletin of the earthquake research institute*, 35, 309-325, 1957.

[12] R. W. Clough, J. Penzien, Dynamics of Structures. *Computers and Structures, Inc., Berkeley, Calif*, 2003.

[13] T. S. Atalik, S. Utku, Stochastic linearization of multi-degree-of-freedom non-linear systems. *Earthquake Engineering & Structural Dynamics*, 4(4), 411-420, 1976.

[14] Japan road association: Design specification for highway bridges · Part V, Seismic design. *Maruzen*, 2017.

EURODYN 2020
XI International Conference on Structural Dynamics
M. Papadrakakis, M. Fragiadakis, C. Papadimitriou (eds.)
Athens, Greece, 23–26 November 2020

PARAMETRIC ANALYSIS AND COMPARISON OF MODELS USED IN THE ANALYSIS OF STEEL STRUCTURES

Bryam Astudillo[1*], Sebastian Pozo[1], and Francisco Flores[1, 2]

[1] Department of Civil Engineering, Universidad de Cuenca
Av. 12 de Abril s/n, Cuenca, Ecuador
{bryam.astudilloc; sebastian.pozo; francisco.flores}@ucuenca.edu.ec

[2] Department of Civil Engineering, Universidad del Azuay
Av. 24 de Mayo 7-77, Cuenca, Ecuador
fflores@uazuay.edu.ec

Keywords: Nonlinear analysis, performance-based engineering, collapse assessment.

Abstract. *Performance-based seismic engineering has been gaining acceptance in the last decade. This philosophy seeks to ensure that a structure satisfies specific behavioral requirements for a given event. There are different guides and methodologies to evaluate structural performance, but conceptually they do not keep much difference. In order to perform an evaluation a mathematical model is required; however. However, the idealizations to represent the behavior of structural elements can vary significantly, giving rise to models with different degrees of complexity in their implementation or computational costs. Furthermore, the wide range of approaches, such as lumped or distributed plasticity and their calibration, can generate different results. To this, it must be added that not always a robust model is the best option for a performance analysis since it would not be practical to implement.*

This paper compares the pertinence of different modeling approaches to conduct a performance analysis on an 8-story building with Steel Special Moment Frames under different seismic intensity levels. Moreover, this article establishes the influence of various parameters (i.e., hysteretic detailing, Rayleigh damping, axial-moment interaction) within mathematical models on the overall response of the structure. For the purpose, FEMA P-695 methodology, as well as the ASCE 7-16 maximum-drifts requirements were used to run a sensitivity analysis between models aiming to warn of inappropriate practices.

Within the findings, it can be emphasized that the secondary stiffness (in-cycle deterioration) of the element is the parameters that influence the most in the collapse response as opposed to cyclic degradation. Also, it must be noted that adding a smother yielding transition causes a higher seismic performance, which could be unconservative within an evaluation. Furthermore, the analyses illustrate how misusing an initial-stiffness proportional Rayleigh damping produces unrealistic performance values. Additional comments are made on the methodologies used to account for axial-moment interaction in lumped-plasticity models.

1 INTRODUCTION

Performance-based seismic engineering has been gaining acceptance in the last decade. This philosophy seeks to ensure that a structure can satisfy certain behavioral requirements established for a given event. In the case of the design basis earthquake intensity (DBE) and maximum considered earthquake (MCE), the event corresponds to an earthquake with 10% and 2% probability of exceedance in 50 years, respectively. There are different guides and methodologies to evaluate the performance of the structure, but conceptually they do differ from each other.

FEMA P695 [1] allows calculating the probability of collapse depending on the intensity of the earthquake, but this implies carrying out more complex analyses and assuming that the modeling of the elements is appropriate up to collapse levels. The FEMA P695 methodology is consistent with the objectives of collapse prevention by establishing a probability of collapse less than 10% for an earthquake with a return period of 2475 years (i.e. MCE). On the other hand, there are simpler procedures that establish the performance acceptance criteria for an assigned earthquake intensity. For example, ASCE7-16 [2] establishes that, at the global level, the average inter-story drift should not exceed 2% for DBE and 4% for MCE intensity. Also, ASCE7-16 states that for MCE there should not be more than one unacceptable result (e.g. collapse) in a set of 11 earthquakes.

For the evaluation of the structure's performance, it is needed a mathematical model that can simulate its behavior. However, the idealizations to represent the behavior of structural elements can vary significantly giving rise to models with different degrees of complexity in their implementation or computational costs and even generate diverse results. The NIST modeling guides [3] differentiate three main modeling approaches: 1) concentrated plasticity, 2) distributed plasticity and 3) continuous models with finite elements. Similarly, there are different damping idealizations with variations in their implementation (e.g. Rayleigh damping). It is also important to consider that not always a robust model is the best option for a performance analysis since its use would not be practical for complex methodologies. Thus, selecting the appropriate mathematical model becomes relevant, as well as knowing the sensitivity of the performance response to the selection of a certain modeling approach and the calibration of its parameters.

Some investigations compare the effect of different modeling approaches at the element level [4] but not the structure's performance at a global level. The purpose of this research is to compare the relevance of different models to accomplish performance analysis of an 8-story building with Steel Special Moment Frames (SSMF) as the lateral system. In addition, this article establishes the influence of various parameters within mathematical models on the overall response of the structure. This research analyzes three main modeling parameters. The first one is related to the constitutive law used on concentrated and distributed plasticity models. The second is related to the damping assignation on distributed plasticity models. And finally, the coupled axial-flexural moment modeling is assessed for concentrated plasticity models.

1.1 Background

The concentrated plasticity technique is currently the most used approach for modeling SSMF. This approach calibrates the element's behavior with phenomenological criteria. Therefore, based on experimental results [5,6] the response of a structural element (e.g. beams and columns) subjected to static or dynamic loads can be simulated. One of the first approaches to perform nonlinear analysis was introduced decades ago assuming an elastic perfectly plastic hysteretic behavior for beams and columns [7,8]. With the advances in

computational resources, further studies had implemented more features such as hardening, deterioration, and cyclic degradation. A more detailed review of articles is presented in appendix A of FEMA P-440A [9]. It should be noted that models with abrupt transitions are oriented to mark each stage of the behavior of the element (cracking, yielding, etc.) and it can be more practical. However, there are models with a smooth transition of stiffness which is meant to 1) to represent the progressive yielding of the element and 2) to alleviate the numerical procedures near the yielding points. Previous research has shown that for floor accelerations, these models with smoother transitions of stiffness shown slightly lower acceleration demands than models with abrupt transitions [10]. The Ibarra-Medina-Krawinkler model (IMK) [11] and their later modifications (ModIMK) [5,12] are the reference hysteretic model that includes strength and stiffness deterioration properties to simulate the response of SSMF.

The limitation of the lumped plasticity approach is that very specific zones are assigned for the element's yielding. Furthermore, given its formulation, it does not allow to consider the interaction of the axial-moment (P-M) load and, therefore the calibration is performed for a given axial force. To take into consideration the effect of the axial load on the capacity of the section, the flexural capacity has to be reduced based on an imposed axial load before the dynamic analyses are executed. The moment capacity under an axial load follows the interaction equations presented in AISC 360 [13]; however, there are different strategies to calculate the axial load to be considered in the equations.

On the other hand, the distributed-plasticity approach requires to define the behavior of the section at each integration point. This is achieved by 1) explicit modeling the section using fibers that have been assigned a stress-strain relationship (material constitutive) or 2) with the calibration of the moment-curvature response of a predetermined section. The advantage of fiber modeling is that it does not require an extensive process of calibration based on experimentation because the response is integrated throughout the section itself. This approach also allows capturing the axial-moment interaction automatically during the analysis. In general, the main problem of the distributed plasticity approach are the concentration of deformations, the loss of objectivity and the difficulty to represent material softening. To deal with this problem, solutions have been proposed from several authors, ranging from modifying the behavior at the section level, applying the material-regularization technique [14,15] up to variations of the formulations [16–18].

There are two main formulations for distributed plasticity, 1) force-based and 2) displacement-based. The main difference is that the first one determines the forces of the sections performing static equilibrium. This results in a constant axial force and a linear distribution of moments in the absence of distributed forces [19]. The second approach interpolates the deformations of the sections, resulting in constant axial-deformation and the linear distribution of the curvature along with the element [20]. The last requires a greater discretization of the element than the force-based formulation to obtain the same level of accuracy [21]. The force-controlled formulation using fibers will be used in this study to simulate distributed-plasticity.

In addition to the simulation of elements' behavior, damping can also influence a seismic response of a building. Rayleigh damping is the most common technique to simulate damping. It is a type of equivalent viscous damping that facilitates the resolution of the differential equation of motion in the linear range by making the damping matrix classic or diagonalizable as well as the mass and rigidity matrix. Some complications come once the structure has entered the non-linear range [22]. This happens because the proportionality coefficients become time-variant as well as the stiffness matrix. In the case of concentrated plasticity models, Rayleigh damping is considered with a time-invariant stiffness matrix by excluding damping in the rotational springs that contained the nonlinear properties [23]. This solution prevents the generation of unreal damping forces that cause underestimation of displacements, overestima-

tion of efforts and underestimation of the collapse potential of the building. However, in distributed plasticity models, damping assignment considering a stiffness matrix proportional only to the elastic elements is not possible because all elements are able to capture inelastic behavior to their constitutive law.

2 METHODOLOGY

The building to be analyzed was taken from the ATC 76-1 project [24] within the 2RSA group. This 8-story and 3-bay building was designed for a D_{max} category (maximum spectral acceleration of 1.0, and a one-second acceleration of 0.6) [1]. The height of the first floor is 15ft and 13ft for the rest of the floors, and the length of each span is 20ft. The lateral system consists of steel special moment frames (SSMF). The beams have RBS pre-qualified connections type defined by parameters a, b and c (0.625bf, 0.750db and 0.25bf respectively). The element sections are shown in Table 1.

Story	Elevation [in.]	Beam	Exterior Col.	Interior Col.	Doubler Plate Size [in]	
					Exterior Col.	Interior Col.
1	166.55	W30X108	W24X131	W24X162	1/16	9/16
2	322.55	W30X116	W24X131	W24X162	1/16	3/8
3	478.55	W30X116	W24X131	W24X162	1/16	11/16
4	634.55	W27X94	W24X131	W24X162	0	3/8
5	790.55	W27X94	W24X131	W24X131	0	9/16
6	946.55	W24X84	W24X131	W24X131	0	7/16
7	1102.55	W24X84	W24X94	W24X94	0	9/16
8	1258.55	W21X68	W24X94	W24X94	0	5/16

Table 1: Sections and geometry

Initially, FEMA P-695 methodology was used for the performance evaluation of the structure using different modeling approaches. It is a tool to determine the performance factors of earthquake-resistant systems. However, this methodology specifies that it can also be used to demonstrate the correct performance to the collapse of structures designed under the requirements of ASCE 7. For these analyses, it was considered that the structure collapsed once it reached an inter-story drift of 10%. At this drift deformation, it is assumed that the elements are no longer able to resist gravity loads due to P-Δ effects and the results of modeling are no longer reliable.

The nonlinear models were developed with the specifications provided in the next section. Their behavior was validated through a series of checks [25]. Among them, the verification of the hysteretic behavior, modal analysis, yielding sequence, ductility and over-resistance, damping assignment.

The earthquakes selected for the evaluation have been obtained from the Far-Field set corresponding to the methodology and scaled to the period C_uT_a according to the design spectrum. Finally, a dynamic incremental analysis (IDA) was performed for each model until a 50% of collapses is obtained in order to calculate the Collapse Margin Ratio (CMR). This CMR value is adjusted by a spectral shape factor (SSF) that is a function of the period ductility and design category, resulting in the Adjusted Collapse Margin Ratio (ACMR). This SSF modification takes into account the effect of the frequency content of the series of earthquakes.

To obtain the probability of collapse at other intensity levels, a logarithmic adjustment was made according to the methodology. The uncertainty parameter (β_{TOT}) that represents the ad-

justment deviation is defined in terms of four sources of uncertainty due to 1) the variability between records (β_{RTR}) as a function of ductility, 2) design requirements (β_{DR}), 3) experimental data (β_{TD}) and 4) model quality (β_{MDL}). β_{DR} and β_{TD} are not dependent on the model, while β_{MDL} is subjective to the qualitative criterion proposed by the designer. Once the adjustment is made, the probability of collapse of the structure for the MCE is calculated, contrasting with the design objective (probability of collapse less than 10% under this intensity).

On the other hand, a comparison was made with simpler analyses to perform the evaluation, which do not imply subjecting the models to intensities of collapse. This evaluated the global performance of the structure under DBE and MCE with maximum inter-story drifts of 2% and 4% respectively as the limit criteria as described in ASCE 7-16. It should be emphasized that under MCE intensity, according to this criterion, it is not allowed more than one collapse for a set of 11 earthquakes.

3 MATHEMATICAL MODELS

The two-dimension models were developed in OpenSees [26]. To include the effects of geometric nonlinearity, all the gravity system loads were concentrated in a leaning column that does not add rigidity to the structure. Masses and loads are shown in Table 2. The splices of the columns were not modeled and the contribution of slab and gravity columns were neglected. The behavior of the beam-column connection was simulated using the theory developed by Krawinkler [27] which consists of simulating the shear through a rotational spring with trilinear behavior. In effect, the panel-zone is modeled by eight rigid elements connected in three corners by pinned joints and with the rotational spring calibrated to represent the shear at the fourth corner. Hysteretic material within OpenSees was used for this spring.

Story	Mass	Load over the tributary area [ksi]	Load over leaning column [ksi]
1	2.16779	250.8	586.5
2-7	2.15148	248.1	582.8
8	1.90950	216.1	521.4

Table 2: Masses and loads

The behavior of beams and columns was represented trough the concentrated and distributed plasticity approaches with different modeling assumptions. To evaluate the importance of detailing the hysteretic behavior, a concentrated-plasticity model was chosen and it was subjected to changes in the uniaxial material of the plastic hinges. The evaluated behaviors are 1) elastoplastic behavior with hardening (PM-BM) using uniaxial material Steel01, 2) hardening with a smooth transition (PM-SBM) using Steel02, 3) hardening, deterioration and cyclic degradation of stiffness (PM-DM) and 4) hardening and deterioration post hardening, but without cyclic degradation (PM-HM) using uniaxial material Bilin. The calibration of the springs used in the concentrated plasticity models was based on the experimentation and regressions proposed in [5,12]. Likewise, Steel01 and Steel 02 were used in the steel constitutive curve (Steel ASTM A992) for the fibers of the distributed plasticity models with the force-controlled formulation giving raise to the models described later. In the case of fibers, calibration was done at the material level (not the element).

Additionally, Rayleigh damping was used. It was proportional to the mass and proportional to the stiffness (initial or tangential, depending on the model) with a target damping of 2.5% and constant coefficients based on the fundamental period of the structure (T_1), and $0.2T_1$. The influence of damping was analyzed in the distributed plasticity models (as nonlinear ele-

ments can not be excluded). The models that were used presented 1) elastoplastic behavior with hardening and damping proportional to the initial stiffness (FM-BM-I), 2) hardening with smoothed transition and damping proportional to the initial stiffness (FM-SBM-I) and variations of damping proportional to the tangential stiffness giving 3) FM-BM-T and 4) FM-SBM-T.

The models used to compare the moment-axial force interactions are one model with distributed plasticity in the columns (PM-FM), which implicitly accounts for P-M interaction, and two models of concentrated plasticity, which do not include the interaction. Thus, for the concentrated-plasticity models, each uses a different technique to reduce the moment capacity to deal with this disadvantage. In the evaluation guide of the FEMA P695 [24], they suggest that the axial load for each element is calculated considering the gravity loads plus half the maximum load due to lateral forces. More recent studies show that the constant gravity load has a greater influence than the transitory loads resulting from the dynamic effects [28]; therefore, the behavior of the element can be predicted by the relationship between the gravity load and the effective yield stress P_g/P_{ye} only [3,6]. These two techniques give rise to models PM-BM-F and PM-BM respectively.

In addition to the already mentioned models, a simpler model was developed that includes nonlinearities at the beams and the base of the columns only. In summary, for the parametric study, 11 models were developed as shown in Table 3.

Plasticity	Model	Hyst. Behavior	Damping	P-M interaction
Concentrated	PM-BM-F	Steel01	Only elastic elements (rotational springs were excluded)	FEMA
	PM-DM	Bilin		NIST
	PM-HM	Bilin w/o degrad.		
	PM-BM	Steel01		
	PM-SBM	Steel02		
	SM	Steel01		
Distributed	FM-BM-I	Steel01	β proportional to K_{ini}	Implicit
	FM-SBM-I	Steel02		
	FM-BM-T	Steel01	β proportional to K_{tg}	
	FM-SBM-T	Steel02		
Mixed	PM-FM	Steel01	β proportional to K_{tg} excluding springs.	Implicit

Table 3: Model summary

4 RESULTS AND DISCUSSIONS

First, the influence of the hysteretic behavior, damping and forces interaction is compared in nonlinear static and dynamic analysis to point out certain characteristics. In the case of dynamic analysis, the 1st story drift is shown because it presented the greatest differences. Similarly, the models are compared in the calculation of the CMR, which allows quantifying the collapse performance of the structure. Then, models are evaluated using the FEMA P-695 adjusted fragility curves and collapse probability. Finally, the global performance-based on inter-story drifts is compared with the intensities of DBE and MCE among all models.

It should be noted that all models have similar initial stiffness as expected, giving fundamental periods close to the reference value of 2.29 seconds.

4.1 Influence of hysteretic behavior

In Figure 1 the behavior of a beam hinge under the compared assumptions is shown. In terms of energy, it could be inferred that the PM-DM model will limit the dissipation by hysteresis of the structural element more than the other models, which would cause a more premature collapse in the structure. Likewise, among the models that only show hardening, the model with smoothed transition would also cause a lower dissipation capacity compared to the model with abrupt transitions, however, the responses show that this softened transition model makes the structure to have a better performance.

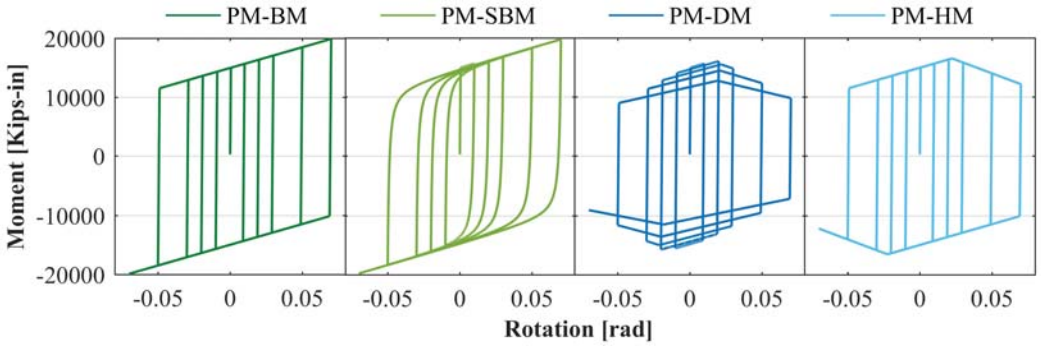

Figure 1 Hysteretic behavior of a beam under the compared assumptions

It is observed in Figure 2 that the smoothed transition has no major influence on the static analysis, however, the inclusion deterioration does cause a decrease in the ductility of the structure due to the drop in stiffness. In this figure, it can also be noticed the influence of the P-Delta effect, since, without it, the model with hardening would never have shown a decrease of the basal shear as seen after the roof drift is approximately 2%. The degradation characteristics are not observable in the analysis performed since a monotonic load analysis was carried out.

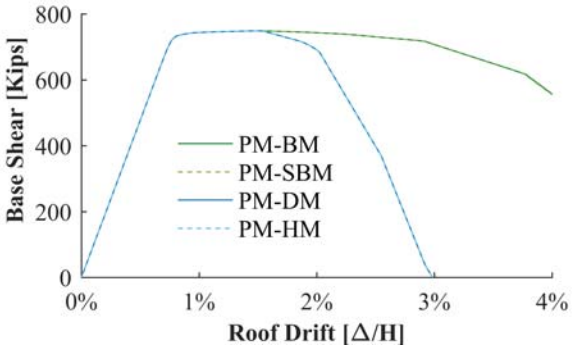

Figure 2 Non-linear static analysis for models with different hysteretic behavior

On the other hand, in the dynamic analysis (Figure 3a) the smoothing effect causes smaller residual drifts than the PM-BM model due to the Bauschinger effect on the reload-rigidity. Also, it is observed that the parameter that has the greatest effect is deterioration causing the structure to have the maximum drifts. Regarding the inclusion of the cyclic degradation of the

element, it increases, even more, the drifts that the structure reaches. However, this last parameter has less impact than deterioration.

The CMR values (Figure 3b) are congruent with the analysis of the dynamic response presented above. With these values, it can be established that the use of a smoother hysteretic curve improves the seismic performance which could be non-conservative from the design point of view. Similarly, the inclusion of cyclic degradation does not have a great effect on the building performance because CMRs among the models that include the backbone curve is very close. Again, it can be observed that the parameter that significantly decreases the performance of the structure is the in-cycle deterioration of the elements.

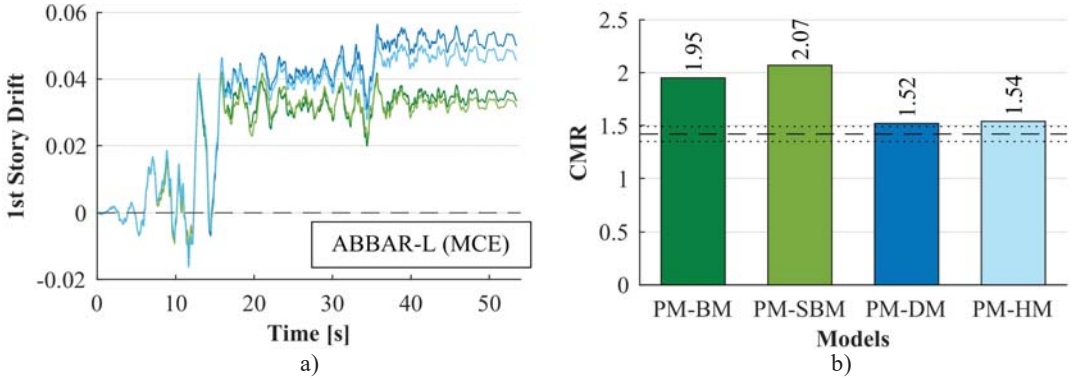

Figure 3 a) Non-linear dynamic analysis and b) CMR for models with different hysteretic behavior

4.2 Influence of material constitutive and damping in distributed-plasticity models

Figure 4a shows the material constitutive law assigned to each fiber of the distributed-plasticity elements. This represents the steel properties, with the difference in the stress-strain yielding transition.

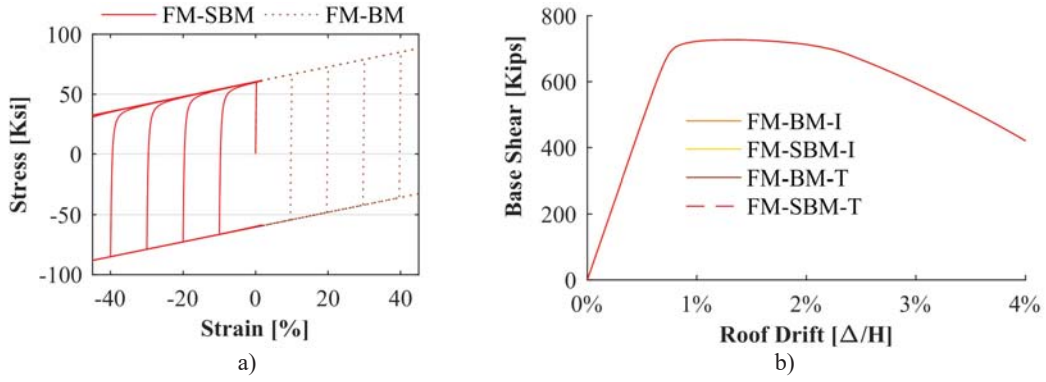

Figure 4 a) Stress-Strain relationship of steel and b) Non-linear static analysis in distributed models

As in the models of concentrated plasticity, the effect of the stiffness transition (transition of the stress-strain curve in this case) does not influence the response of the building in the nonlinear static analysis presented in Figure 4b.

In the nonlinear dynamic analysis presented in Figure 5a, it is observed that models with softened transition produce lower drifts, just as in the concentrated-plasticity case. Now for the same hysteretic behavior, comparing the damping assignment, it is observed that the damping proportional to the initial stiffness causes smaller drifts. This is because the structures is over-damped because the stiffness of the structure decreases when yielding occurs. From this analysis, it can be said that the least conservative approach of the cases presented is to use a model with hardening and smoothed transition and apply Rayleigh damping proportional to the initial rigidity. It should also be pointed out that applying Rayleigh damping proportional to tangential stiffness causes the analyses to have greater convergence problems. At this point, for more complex prototypes, the implementation of this feature in the model should be evaluated whether it is worth or not to increase the computational cost of the analysis depending on the errors this will cause.

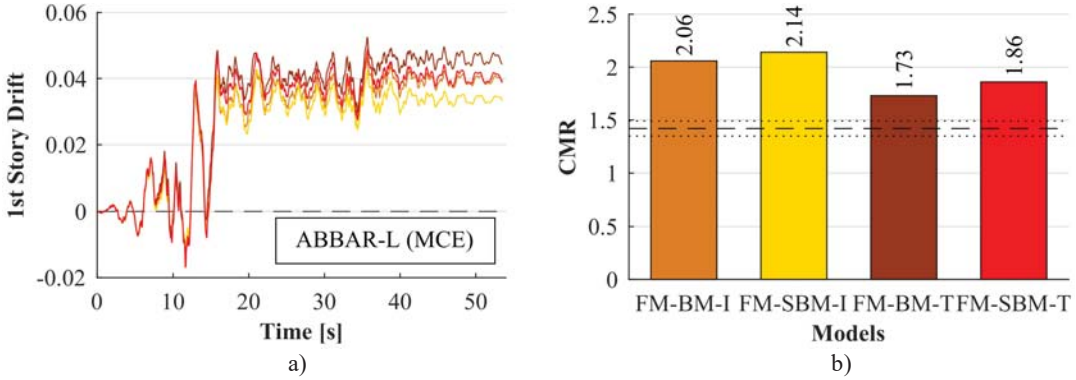

Figure 5 a) Non-linear dynamic analysis and b) CMR for models with different damping assumptions

The collapse analysis presented in Figure 5b confirms that the most conservative case (out of the four cases) is the FM-BM-T model, however, the CMR value is still far from the reference value (PM-DM). This higher CMR value is interpreted as a better performance of the building, however, this is because none of these models of distributed plasticity considers the deterioration of the elements due to the incompatibility in their force-based formulation using fibers as covered in [29].

4.3 Influence of P-M interaction

For this comparison, all models were chosen to have an elastoplastic hysteretic behavior with hardening as shown in Figure 6. In this figure, it is also shown the reductions that have been made to one of the columns.

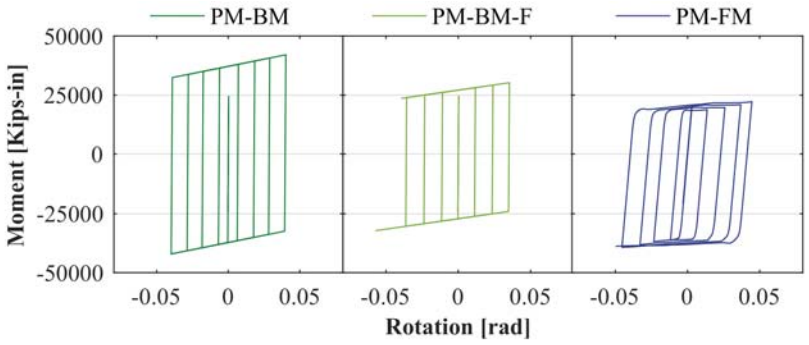

Figure 6 Hysteretic behavior of a base column under different P-M interaction considerations

The methodologies adopted for concentrated plasticity do not consider the asymmetric behavior of the element (i.e. compression or tension) neither the variation of axial forces along the time. It is also observed that PM-FM response shows a lower flexural capacity when the column is under compression loads.

For the non-linear static analysis (Figure 7), it is observed that the FEMA-type reduction method (based on gravity and lateral loads) underestimates the structure's ductility due to its more conservative reductions. In contrast, the NIST-type reduction (based only on gravity loads) slightly overestimates the over-strength and ductility to the model that does consider the interaction automatically.

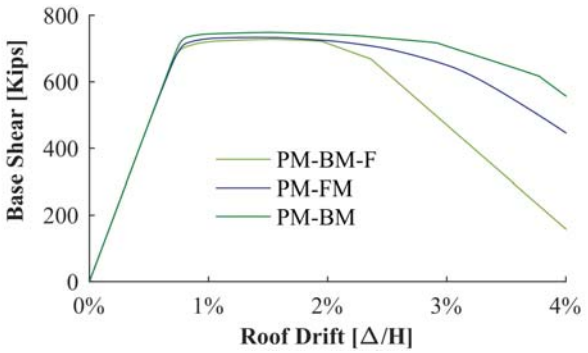

Figure 7 Non-linear static analysis under different P-M interaction considerations

This same trend can be observed in the dynamic analysis presented in Figure 8a where the FEMA type reduction causes greater drifts than the mixed plasticity model while the NIST type reduction can give non-conservative values. The CMR values are presented in Figure 8b, where it is seen that the response of the structure, even at collapse intensities, falls between the two methodologies when the axial-moment interaction is included by the fiber model.

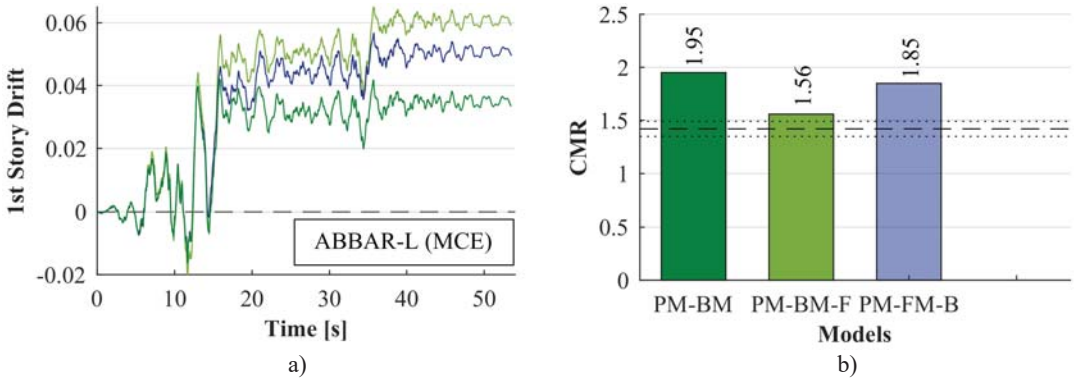

a) b)

Figure 8 a) Non-linear dynamic analysis and b) CMR values under different P-M interaction considerations

4.4 Collapse performance evaluation according to FEMA P-695

Results of the fundamental period and ductility of each model are presented in Table 4. It can be seen that the periods are similar to the value of the reference model (2.29sec). Concerning to ductility, the model with deterioration is the one that represents lower ductility and agrees with the original reference model. Also, the corresponding SSF and β_{TOT} values according to FEMA methodology P695 are shown. Uncertainty, $\beta_{TOT,}$ remains similar for all models due to their high ductility.

Model	Period	Ductility	SSF	β_{TOT}
PM-BM-F	2.284	3.74	1.38	0.5
PM-DM	2.283	2.99	1.32	0.4992
PM-HM	2.283	2.99	1.32	0.4992
PM-BM	2.283	5.30	1.47	0.5
PM-SBM	2.280	5.29	1.47	0.5
SM	2.281	-	1.61	0.5
FM-BM-I	2. 282	4.39	1.42	0.5
FM-SBM-I	2. 282	4.39	1.42	0.5
FM-BM-T	2. 282	4.39	1.42	0.5
FM-SBM-T	2.282	4.39	1.42	0.5
PM-FM-B	2.284	4.75	1.44	0.5

Table 4: Fundamental period, ductility, SSF, and β_{TOT} summary

One of the differences in performing the analysis of collapses following the FEMA P695 methodology is the use of the SSF factor. This factor modifies the CMR leading to a better performance of the structure. In Figure 9a the fragility curve for the most complex model (PM-DM) and the effect of the SSF is observed. The solid line represents the fragility curve considering the modification of the CMR while the dashed line represents the adjustment with the original CMR.

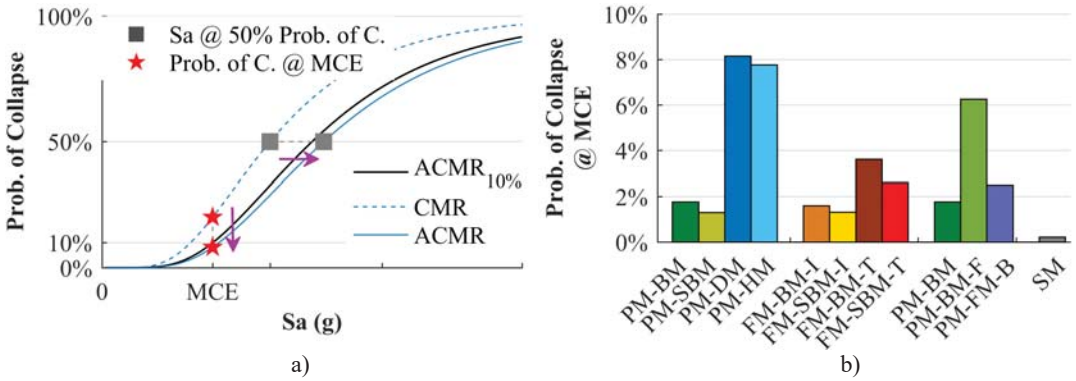

Figure 9 a) Fragility curve for PM-DM and b) Summary of collapse probabilities for all models

It is observed that when displacing the acceleration necessary to produce 50% of collapses, the probability of collapse for the acceleration corresponding to the MCE decreases. The black line represents the reference curve with the values presented in FEMA P695 for collapse evaluation; in other words, for an uncertainty value of 0.5, the fragility curve that generates a probability of collapse of 10% at the MCE. Given this reference, it is observed that the adjustment parameter of the CMR can cause a model to go from not fulfilling the collapse objective to satisfactorily fulfill. For example, the PM-DM goes from a probability of collapse of 20.12% to 8.15%.

Figure 9b shows a summary of the collapse probabilities obtained for each model. It is observed that models with high values of probability of collapse are those that consider the in-cycle deterioration (backbone curve) of the elements (i.e. PM-DM and PM-HM). Also, it is seen that for this structure, excluding the strength and stiffness cyclic degradation will cause an error of less than 5% to evaluate the probability of collapse. Additionally, comparing the models with different stiffness transition, it is seen that the smooth transition cause to reduce the probability of collapse around 20%, for concentrated plasticity as for distributed plasticity approaches.

Analyzing damping assignation in the models with distributed plasticity, it is seen that using the initial stiffness may cause a reduction of up to 50% in the collapse probability in comparison with tangent stiffness. Thus, more caution should be taken to the assumptions regarding damping.

About the techniques to account for P-M interaction in lumped plasticity models, by using the momentum capacity reduction in columns based on gravity loads, the model overestimates the building performance in relation to the mixed plasticity model. In contrast, it can be seen that reducing the capacity in accordance with axial forces including gravity and lateral forces, almost duplicates the probability of collapse, which could be very conservative. Congruently, the probability of collapse of the distributed plasticity model, FM-BM-T, relies on between the lumped plasticity models that had the same assumptions.

Also, the probability of collapse was calculated for the simplified model. It produced negligible values of collapse probability, so its use in this methodology is not recommended in contrast to what research has shown in the evaluation of floor acceleration [10].

4.5 Performance evaluation according to ASCE 7-16.

In ASCE 7-16, the SSF factor is not considered which causes more conservative results. This is consistent with the lower complexity of the process. For MCE-level analyses, the ref-

erence inter-story drift may not exceed 4% drifts. Additionally, no more than one out of 11 earthquakes might give an unacceptable result (i.e. collapse). For the prototype used, all the models generate at least one collapse to the MCE, so 1.2 times the median drift was used as a reference value for the evaluation.

It can be observed in Figure 10a that, for the MCE intensity, the median values of the maximum inter-story drifts are similar between the models; however, they present a different distribution of drifts in the upper quartiles. For example, concentrated plasticity models with deterioration and distributed plasticity models with tangential damping do not satisfy the maximum number collapses that are allowed despite satisfying the limiting condition of inter-story drifts of 4%. This shows that conducting performance analysis without including these modeling characteristics can lead to erroneous decisions, overestimating the performance of the structure. In the case of the model with FEMA reduction, it also exceeds the maximum limit of allowed collapses, however, this is only due to the excessive reduction of the moment-capacity of the columns. Regarding the simplified model, this has a decent prediction of the median drift, which could serve as a rapid approach for the iterative design of the building to meet performance limits.

Similarly, Figure 10b shows the distribution of the maximum inter-story drifts under the DBE level. In this case, the models, besides having similar medians, inter-story drifts present a similar distribution. The analyzed parameters do not present major influence to this intensity, even the simplest model can simulate the behavior as the other models do. One of the characteristics that should be noted in the models is that they all show a collapse, except for those that use softened hysteretic behavior with damping proportional to the initial stiffness. Furthermore, all models agree that the building does not meet the performance objectives at the design level by exceeding the 2% target-drift in more than half of the analyses.

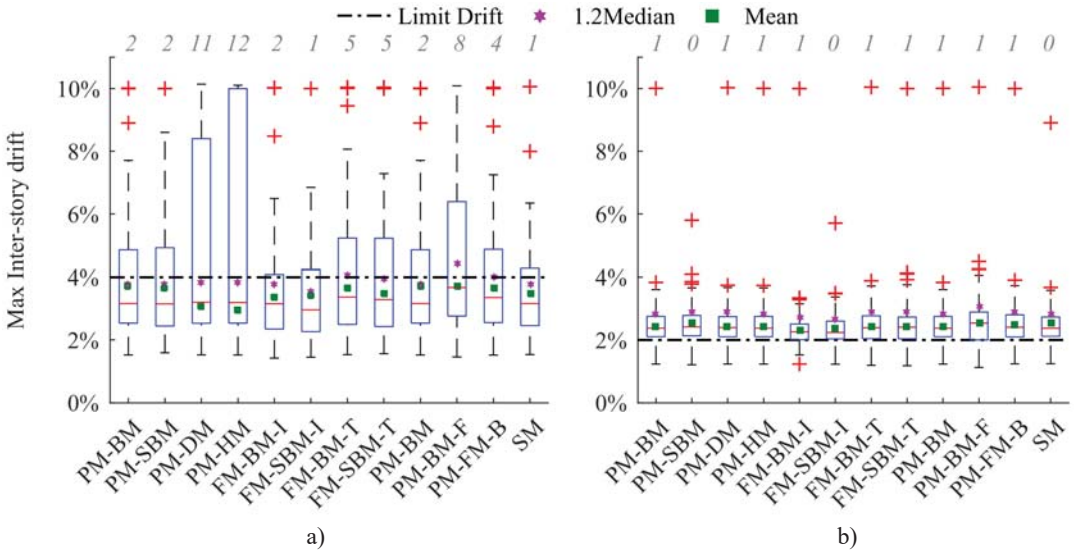

Figure 10 Maximum inter-story drifts distribution under a) MCE level and b) DBE

5 CONCLUSIONS

- In the models with concentrated and distributed plasticity, it was observed that using non-smoothed curves for the collapse analysis can be reflected in a lower seismic performance of the structure, which would be conservative.
- The inclusion of the cyclic degradation of the structural elements does not cause greater variations in the performance of the structure, so not considering them in the analyzes would avoid the complexity of the calibration without losing greater objectivity in the study. In fact, the main characteristic of the hysteretic curves for collapse prediction is the inclusion of in-cycle deterioration. Not including this behavior could overestimate the performance of the structure, which would not be a good practice.
- Assigning proportional damping to the initial stiffness generates a false better performance of the structure under collapse; however, this is due to the overdamping that is generated when the structure enters the non-linear range. Therefore, caution should be used in the assignation of damping, especially in distributed plasticity where nonlinear elements can not be excluded.
- The probability of collapse in lumped-plasticity models showed to be sensitive to the method used to reduce the flexural capacity. Reduction based on gravity loads underestimates the collapse probability in comparison with models that accounted for the P-M interaction. In contrast, the reduction based on gravity and lateral loads overestimate the collapse probability. Thus, future research should be made to recommend using a weighted average between the two techniques or some other method to include the axial-moment interaction in the concentrated plasticity models to evaluate the performance of the structure.
- The spectral form factor has a great influence on the probability of a structure collapse. Using this value to adjust the CMR can cause a model to go from not meeting performance objectives to fully satisfying them.
- For the performance evaluation under MCE, it is recommended to use the models that include deterioration, since, although models without this characteristic can give similar results in terms of the median drift, the number of collapses produced can be underestimated.
- Despite the influences of the parameters in the CMR values, it must be pointed out that, to evaluate the behavior of the structure under design performance levels, these have no greater impact. For design intensities, even a simplified model can approximate the performance evaluation response at maximum inter-story drifts. It should also be evaluated in terms of residual drifts.
- The results and conclusions correspond specifically to the presented 8-story building; however, it is necessary to carry out the same study on more prototypes to generalize the influence of modeling in the performance evaluation of structures.

REFERENCES

[1] FEMA P-695, QUANTIFICATION OF BUILDING SEISMIC PERFORMANCE FACTORS., Federal Emergency Management Agency, 2009.

[2] ASCE 7, Minimum Design Loads and Associated Criteria for Buildings and Other Structures, American Society of Civil Engineers, Reston, VA., 2016.
[3] ATC, Guidelines for nonlinear structural analysis and design of buildings. part IIa - steel moment frames, National Institute of Standards and Technology, Gaithersburg, MD, 2017. https://doi.org/10.6028/NIST.GCR.17-917-46v2.
[4] R.-Y. Wu, C.P. Pantelides, Concentrated and Distributed Plasticity Models for Seismic Repair of Damaged RC Bridge Columns, J. Compos. Constr. 22 (2018) 04018044. https://doi.org/10.1061/(ASCE)CC.1943-5614.0000879.
[5] D.G. Lignos, H. Krawinkler, Deterioration Modeling of Steel Components in Support of Collapse Prediction of Steel Moment Frames under Earthquake Loading, J. Struct. Eng. 137 (2011) 1291–1302. https://doi.org/10.1061/(ASCE)ST.1943-541X.0000376.
[6] A. Hartloper, D. Lignos, Updates to the ASCE-41-13 provisions for the nonlinear modeling of steel wide-flange columns for performance-based earthquake engineering, Ce/Papers. 1 (2017) 3072–3081. https://doi.org/10.1002/cepa.359.
[7] G.V. Berg, D.A. DaDeppo, Dynamic analysis of elasto-plastic structures, (1959).
[8] J. Penzien, Dynamic response of elasto-plastic frames, Trans. Am. Soc. Civ. Eng. 127 (1960) 1–13.
[9] FEMA P-440A, Effects of Strength and Stiffness Degradation on Seismic Response, Federal Emergency Management Agency, 2009.
[10] Francisco X. Flores, B.X. Astudillo, D.V. Barrera, R.A. Jerves, I.L. Martinez, S.P. Pozo, Level of Detail Required to Model Special Steel Moment Frames to Evaluate Floor Accelerations in Nonstructural Components, in: Struct. Congr. 2019, 2019: pp. 426–437. https://doi.org/10.1061/9780784482230.040.
[11] L.F. Ibarra, R.A. Medina, H. Krawinkler, Hysteretic models that incorporate strength and stiffness deterioration, Earthq. Eng. Struct. Dyn. 34 (2005) 1489–1511. https://doi.org/10.1002/eqe.495.
[12] D.G. Lignos, H. Krawinkler, A Database in Support of Modeling of Component Deterioration for Collapse Prediction of Steel Frame Structures, in: Struct. Eng. Res. Front., American Society of Civil Engineers, Long Beach, California, United States, 2007: pp. 1–12. https://doi.org/10.1061/40944(249)31.
[13] AISC 360, Specification for Structural Steel Buildings, American Institute for Steel Construction., Chicago, Ill., 2016.
[14] J. Coleman, E. Spacone, Localization Issues in Force-Based Frame Elements, J. Struct. Eng. 127 (2001) 1257–1265. https://doi.org/10.1061/(ASCE)0733-9445(2001)127:11(1257).
[15] D. Addessi, V. Ciampi, A regularized force-based beam element with a damage–plastic section constitutive law, Int. J. Numer. Methods Eng. 70 (2007) 610–629. https://doi.org/10.1002/nme.1911.
[16] M.H. Scott, G.L. Fenves, Plastic Hinge Integration Methods for Force-Based Beam–Column Elements, J. Struct. Eng. 132 (2006) 244–252. https://doi.org/10.1061/(ASCE)0733-9445(2006)132:2(244).
[17] C.-L. Lee, F.C. Filippou, Efficient Beam-Column Element with Variable Inelastic End Zones, J. Struct. Eng. 135 (2009) 1310–1319. https://doi.org/10.1061/(ASCE)ST.1943-541X.0000064.
[18] P. Sideris, M. Salehi, A Gradient Inelastic Flexibility-Based Frame Element Formulation, J. Eng. Mech. 142 (2016) 04016039. https://doi.org/10.1061/(ASCE)EM.1943-7889.0001083.
[19] E. Spacone, F.C. Filippou, F.F. Taucer, FIBRE BEAM-COLUMN MODEL FOR NONLINEAR ANALYSIS OF R/C FRAMES: PART I. FORMULATION, Earthq. Eng.

Struct. Dyn. 25 (1996) 711–725. https://doi.org/10.1002/(SICI)1096-9845(199607)25:7<711::AID-EQE576>3.0.CO;2-9.
[20] T. Hughes, The Finite Element Method, Linear Static Dyn. Finite Elem. Anal. (1987).
[21] A. Neuenhofer, F.C. Filippou, Evaluation of Nonlinear Frame Finite-Element Models, J. Struct. Eng. 123 (1997) 958–966. https://doi.org/10.1061/(ASCE)0733-9445(1997)123:7(958).
[22] F.A. Charney, Unintended Consequences of Modeling Damping in Structures, J. Struct. Eng. 134 (2008) 581–592. https://doi.org/10.1061/(ASCE)0733-9445(2008)134:4(581).
[23] F. Zareian, R.A. Medina, A practical method for proper modeling of structural damping in inelastic plane structural systems, Comput. Struct. 88 (2010) 45–53. https://doi.org/10.1016/j.compstruc.2009.08.001.
[24] NIST, Evaluation of the FEMA P-695 Methodology for Quantification of Building Seismic Performance Factors, National Institute of Standards and Technology, USA, 2010.
[25] F. Flores, F. Charney, S. Pozo, B. Astudillo, Structural Behavior Checks Prior Performing Non linear Dynamic Analysis, in: 2018.
[26] S. Mazzoni, F. McKenna, M.H. Scott, G.L. Fenves, OpenSees command language manual, Pac. Earthq. Eng. Res. PEER Cent. 264 (2006).
[27] A. Gupta, H. Krawinkler, Seismic demands for the performance evaluation of steel moment resisting frame structures, (1998).
[28] Y. Suzuki, D. Lignos, Large scale collapse experiments of wide flange steel beam-columns, in: 2015.
[29] S. Pozo, B. Astudillo, E. Samaniego, F. Flores, Objective Phenomenological Constitutive Law for Collapse Analyses in Distributed Plasticity Steel Frame Models, J. Struct. Eng. (submitted). (2020).

EURODYN 2020
XI International Conference on Structural Dynamics
M. Papadrakakis, M. Fragiadakis, C. Papadimitriou (eds.)
Athens, Greece, 23–26 November 2020

DYNAMIC RESPONSE OF EXISTING STEEL FRAMES WITH MASONRY INFILLS UNDER MULTIPLE EARTHQUAKES

Luigi Di Sarno[1], Jing-Ren Wu[1], Fernando Gutiérrez-Urzúa[2], Fabio Freddi[2], Mario D'Aniello[3], Oh-Sung Kwon[4], Stathis Bousias[5] and Matjaž Dolšek[6]

[1] Department of Civil Engineering and Industrial Design, University of Liverpool
The Quadrangle, Brownlow Hill, Liverpool, United Kingdom
e-mail: {luigi.di-sarno,jingren.wu}@liverpool.ac.uk

[2] Department of Civil, Environment and Geomatic Engineering, University College London
Gower Street, London, United Kingdom
{f.freddi,f.urzua}@ucl.ac.uk

[3] Department of Structures for Engineering and Architecture, University of Naples Federico II
Corso Umberto I 40, Naples, Italy
mdaniel@unina.it

[4] Department of Civil and Mineral Engineering, University of Toronto
27 King's College Cir, ON M5S, Toronto, Canada
os.kown@utoronto.ca

[5] Structures Laboratory (STRULAB), Civil Engineering Department, University of Patras
University Campus, 26504 Rio Achaia, Patras, Greece
sbousias@upatras.gr

[6] Faculty of Civil and Geodetic Engineering, University of Ljubljana
Kongresni trg 12, 1000, Ljubljana, Slovenia
matjaz.dolsek@fgg.uni-lj.si

Keywords: Existing steel frames, Masonry infills, Multiple earthquakes, Dynamic analysis

Abstract. *Existing steel moment-resisting frames in several seismic regions worldwide are often characterised by high vulnerability to earthquakes due to insufficient local and/or global ductility. Therefore, it is of paramount importance to assess their response under strong motions and provide cost-effective retrofitting remedies. However, the current code-based assessment framework utilized in Europe for assessing existing structures is inadequate and requires improvement, especially to account for the contribution of masonry infills as they significantly influence the seismic response of steel buildings. To this end, the H2020-INFRAIA-SERA project HITFRAMES (i.e., HybrId Testing of an Existing Steel Frame with Infills under Multiple EarthquakeS) aims at experimental evaluation of a case study building representative of non-seismically designed European steel frames. This paper presents the dynamic response analyses of the case study building and serves as a theoretical prediction of the experimental results*

for HITFRAMES. The case study building is analysed as a bare, an infilled and a retrofitted frame with buckling restrained braces (BRBs), respectively. It is subjected to the natural seismic sequence recorded during the 2016-2017 Central Italy earthquakes. The modal properties of the case study building are determined first, followed by the investigation of its non-linear dynamic response. The dynamic tests are performed with the earthquake records scaled to different intensity levels to simulate the structural performance under different limit states according to Eurocode 8-Part 3. The impact of masonry infills and BRB-retrofit is also investigated by comparing the response of models with different configurations. It can be concluded that appropriately-designed BRBs are effective in protecting steel frames from experiencing critical damage during earthquakes and reducing significantly the transient and residual drift.

1 INTRODUCTION

It has now been widely recognised in modern seismic codes that the inelastic behaviour of structural systems plays an important role in their seismic response during earthquakes. However, numerous existing buildings in current earthquake-prone areas in Europe were constructed before the seismic provisions of Eurocode 8 or complied with low seismic resistance. Such buildings are often characterised by insufficient ductile design and low energy dissipation capacity, hence high vulnerability to earthquakes. Therefore, it is necessary to develop an advanced framework of the assessment of existing buildings, which further leads to an optimised retrofit solution.

Previous research has been done on the seismic performance of existing steel frames [1][2][3], which is a popular topic in the context of assessing existing buildings. Typical damage on existing steel frames after strong ground motions include significant yielding on columns, especially at beam-column connections, cracks or partial collapse of cladding and masonry infills, and large residual drifts that leave the building little residual strength to carry vertical loading. It is also found that the seismic performance of the steel building was greatly affected by the presence of the infill walls. Existing research in literature shows that masonry infills considerably increase the lateral stiffness and strength of buildings and at the same time cause much higher localised stress at the contact areas between the corners of infills and the framed system, normally the beam-column connections [4][5][6]. Moreover, the presence of infills may lead to even higher vulnerability of existing building to collapse in moderate and strong earthquakes, as it increases the possibility of soft storey mechanisms at lower floors, eventually resulting in the collapse of the entire building.

However, despite large effort has been put into the study of seismic behaviour of infilled structures, most research was carried out on reinforced concrete buildings and there is a lack of studies on steel building with infills. Besides, most of the popular numerical models of masonry infill walls (e.g. single strut model) were developed and calibrated for reinforced concrete buildings, which naturally leads to the question that whether those models of infills are appropriate in the case of steel buildings, which are usually more flexible compared to reinforced concrete buildings. To this end, the H2020-SERA project 'Hybrid Testing of an Existing Steel Frame with Infills under Multiple Earthquakes' (HITFRAMES) aims at performing pseudo-dynamic tests on a typical existing steel frame model and providing insights on the seismic behaviour of existing steel building with infills. The project also involves assessment of the retrofit technique that uses buckling restrained braces (BRBs), which are efficient energy dissipation devices that are capable of withstanding both tension and compression in an almost symmetrical way [7][8][9].

This paper presents the theoretical estimation of the structural response of a two-storey steel moment-resisting frame under multiple earthquakes. The steel frame was designed to sustain only gravity loads with similar deficiencies found in the previously-mentioned steel building in Amatrice, hence is considered not safe under moderate and strong earthquakes and requires retrofit. The steel frame was modelled in OpenSees [10] as a bare, an infilled and a retrofitted frame with BRBs, respectively, so that the response with different configurations of the steel frame model can be compared. Firstly, the seismic response of the steel frame under the unscaled record of selected earthquake sequence will be investigated, so that some moderate damage are expected without global collapse. Then a scaling factor of 3.0 will be applied to the record of earthquake sequence in order to cause more significant damage on the structure. This paper also presents comparison of the peak and residual inter-storey drifts of different models to investigate the effects of infills and effectiveness of the BRBs. Besides, to predict the performance of the steel frame during laboratory tests and to assess the capability of the designed

BRB system, i.e. to what extent it can protect the steel frame and masonry infills and improve the overall resistance of the steel building to strong earthquakes, the behaviour of columns, masonry infills and BRBs will be examined individually.

Apart from the time history analysis, pushover analysis has already been performed according to the procedure in Eurocode 8-Part 3 [11] as a preliminary assessment of the steel frame and the results are provided in two previous papers [12][13].

2 THE 'HITFRAMES' PROJECT

A brief description of the HITFRAMES project will be provided here; the main aims of the project include:

- Develop reliable methods for assessing seismic performance of existing steel frames with infills under multiple earthquakes;
- Develop appropriate design procedures of BRBs that account for the contribution of masonry infills;
- Perform fragility analysis of existing steel frames with infills and retrofitted with BRBs under multiple earthquakes.

To achieve the above goals, a case study steel frame, which consists of three bays and two storeys and is referred to as the *prototype* frame hereafter, was designed to be a representative of existing steel buildings. The steel frame was designed for gravity loadings only and is characterised by weak column-strong beam seismic behaviour and soft storey mechanism. Then a two-storey one-bay sub-structure of the prototype frame was scaled down by a factor of 0.75 and was tested in the Structures Lab of University of Patras, Greece. The scaled sub-structure is referred to as the *test* frame hereafter.

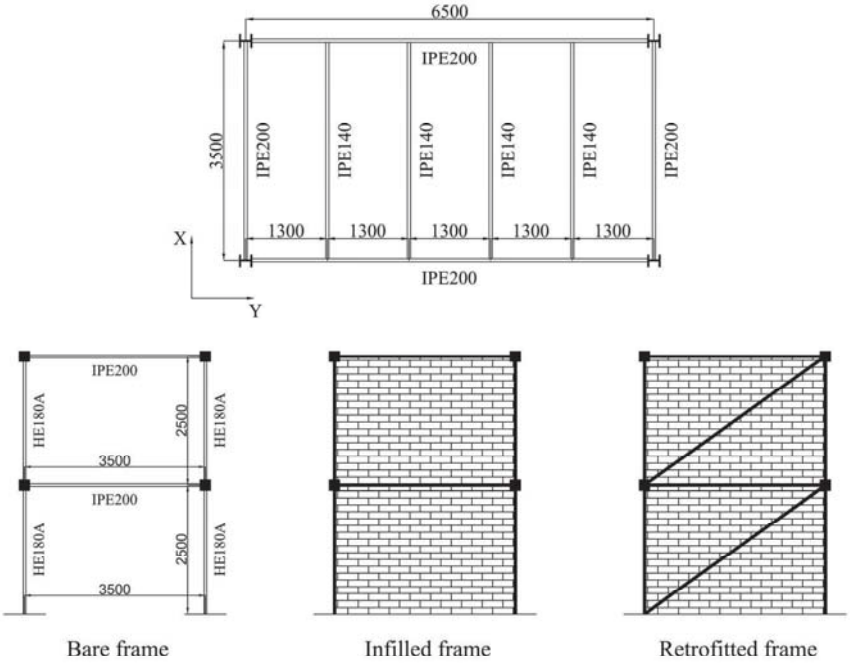

Figure 1: Plan view (top) and side view (bottom) of the test frame with different configurations (unit: mm).

The geometric properties of the test frame are provided in Figure 1. The steel profiles after scaling are IPE200, IPE140 and HE180A respectively for external beams, internal beams and columns. The steel grade is S355 (f_y = 355MPa) for all beams and columns. Besides, the

composite slab consists of 250mm-thick concrete slab poured on 1.25mm-thick corrugated steel sheet (SYMDECK 73). Furthermore, all external beams are connected to columns through full penetration welding, and fully rigid beam column connections are considered in this study. It is worth noting that stiffeners were placed at all beam-column connections and column base connections. Figure 2 demonstrates the position of stiffeners. Finally, the BRB consists of a BRAD damper and an elastic steel bracing, which are connected in series to each other. The BRAD damper has a hysteretic behaviour with an ultimate strength of 210kN at 20mm displacement. The BRB will be installed externally to the framed structure and attached to the flange of columns with specially designed connection systems.

Figure 2: Stiffeners at beam column connection and column base.

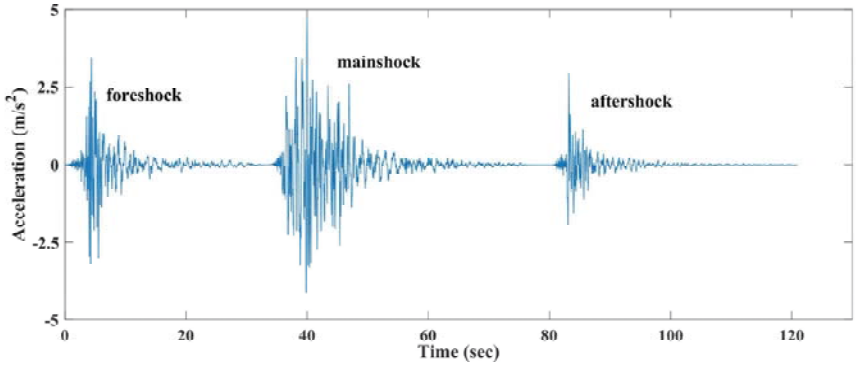

Figure 3: Acceleration history of the selected ground motion sequence.

Event	Date	M_w	R_{epi} (km)	PGA
foreshock	24/08/2016	6.0	15.3	0.35
mainshock	30/10/2016	6.5	4.6	0.48
aftershock	26/10/2016	5.4	9.4	0.30

Table 1: Summary of records of the selected earthquake sequence used in this study.

To facilitate the tests in laboratory, a series of earthquakes records have been selected to form an earthquake sequence. Figure 3 shows the acceleration history of the earthquake sequence, which includes a foreshock with peak ground acceleration (PGA) of 0.35g, a mainshock with PGA of 0.48g and an aftershock with PGA of 0.30g. Their information is also summarised

in Table 1. Those records are able to reflect the moderate-to-high seismicity in some areas of the Southern Europe based on their PGAs.

3 NUMERICAL MODELLING IN OPENSEES

Similar to what has been done in [13], the test steel frame was built in the finite element software OpenSees [7] considering three different configurations:

- Case A: bare frame (only beams and columns are included)
- Case B: infilled frame (bare frame + masonry infills)
- Case C: retrofitted frame (bare frame + masonry infills + BRBs)

For finite element modelling of the test frame, beams and columns are modelled with lumped and distributed plasticity, respectively. Each beam consists of an elastic element with modulus of elasticity 210GPa, plus two end plastic hinges to represent the lumped plasticity. The property of the plastic hinges is determined based on the moment-rotation relationship suggested in [14]. The plastic hinges are further modified based on the proposal in [15] to ensure more accurate overall lateral stiffness. The property of beam plastic hinges is shown in Figure 4. It should be noted that only the beam plastic hinges in X direction (test direction) are considered in the model. On the other hand, all columns are modelled using fibre-elements with ten integration points. The columns have the same modulus of elasticity as the elastic elements in beams and with 2% post-yield strain hardening.

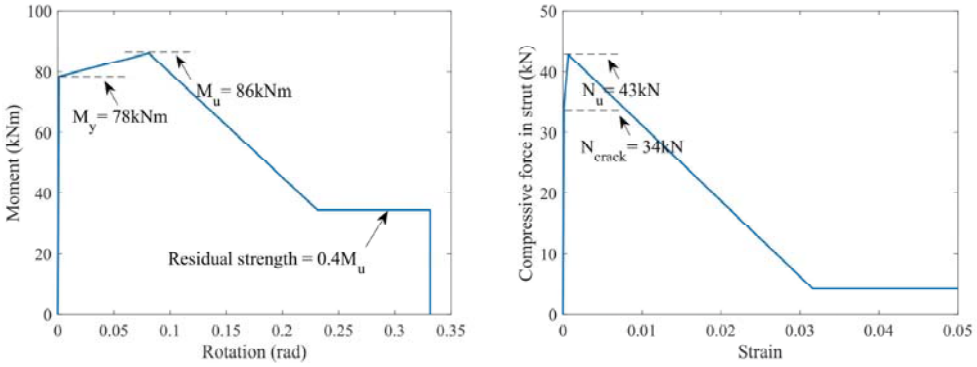

Figure 4: Backbone curve of the beam plastic hinges (left) and the infill struts (right).

In terms of the modelling of masonry infills, there are several alternatives available in literature ([4][5][16][17][18] among others), however, most of the widely-used models were developed for reinforced concrete buildings and their reliability of being applied in steel frames, which are normally more flexible than concrete buildings, is not examined. In this case study, the single-strut model adapted from the one used by Mohammad [16] and Liberatore and Decanini [18] is temporally adopted, and its property will be adjusted in the future according to the test results. A detailed discussion on the modelling of infills is provided in [13]. Figure 4 shows the backbone curve of infill struts in the compressive range, while in the tensile range, zero-strength is assumed.

4 MODAL ANALYSIS

Modal analyses are firstly performed on all the three cases in the X direction (see Figure 1). Table 2 summarises the periods and associated mode shapes and modal masses of the first and second mode. By comparing the results from Case A and B, it is clear that both the fundamental and second periods are decreased by more than 80% due to the presence of infills, which

considerably reduces the natural periods by contributing significantly to the lateral stiffness. In terms of the effective mass in each mode, the infills slightly increase the modal mass of the first mode and consequently decrease the mass participated in the second mode.

Case	1st mode			2nd mode		
	period (sec)	mode shape	modal mass	period (sec)	mode shape	modal mass
Case A	0.71	0.4552 1.000	87.1%	0.25	-1.8674 1.0000	12.9%
Case B	0.12 (-83%)	0.5644 1.000	92.5% (+6%)	0.05 (-82%)	-1.5043 1.000	7.5% (-42%)
Case C	0.12 (-83%)	0.5585 1.000	92.3% (+6%)	0.05 (-82%)	-1.5224 1.000	7.7% (-40%)

Table 2: Modal properties of the case study steel frame in the test direction.

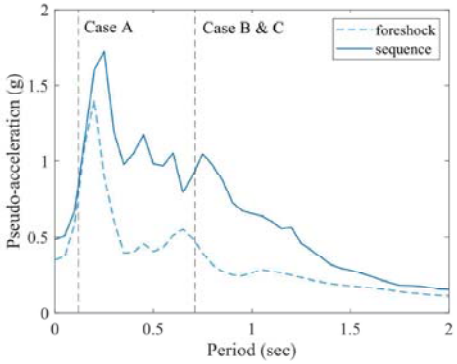

Figure 5: Elastic response spectrum of the foreshock and entire sequence in Table 1.

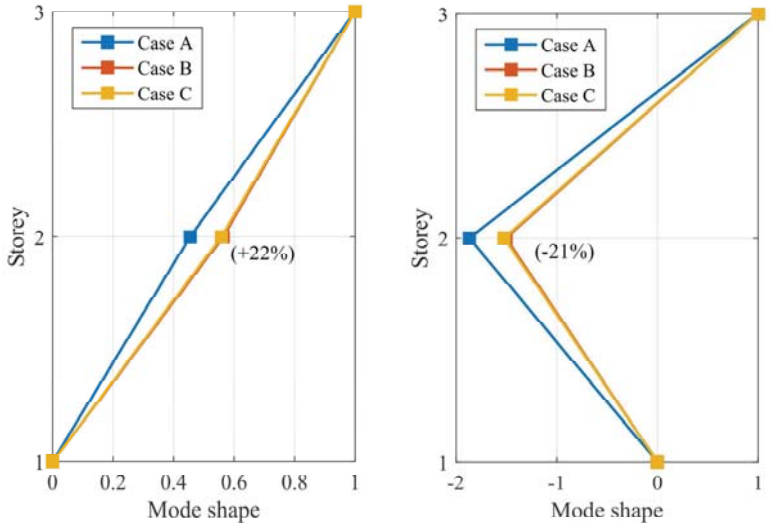

Figure 6: Normalised mode shape for the first mode (left) and the second mode (right).

Figure 5 shows the elastic response spectrum of the foreshock and entire sequence selected in Table 1. It is found that the spectral acceleration with respect to the entire sequence is much higher than the one associated with the foreshock, except in the range of period from 0.1 to 0.15 sec, where small differences between the two spectra are observed. It should be noted that the fundamental periods of the infilled and retrofitted frame are within the above range. However, when the infilled frame is damaged, its natural periods will be longer, hence will experience higher seismic loading during the whole sequence than during the foreshock only.

Figure 6 shows the normalised mode shape of the first and second mode from all three cases. Since in all cases the fundamental mode dominates the structural behaviour, it is evident that the infilled frame is more likely to possess the soft storey mechanism as the infills will concentrate the deformation to the lower storey in this case. By comparing Case B and C, it is found that attaching BRBs to the test frame barely affects its modal properties at the initial state. However, as found in [13], the infilled frame in Case B may not able to maintain its initial modal properties during earthquakes and its natural periods and mode shapes may experience great changes due to the failure of masonry infills.

5 TIME HISTORY ANALYSIS

This section presents the results of time history analysis performed on the finite element model of the test frame. The inter-storey drifts and residual drifts of different models will be compared to investigate the effects of infills and effectiveness of the BRBs. The behaviour of columns, masonry infills and BRBs will also be presented individually in the following sections. The assessment of the test frame will be carried out with the help of inter-storey drift limits in Table 3 proposed by ASCE41-06 [19], which are adapted to comply to the limit states in EC8-3 [11], i.e. Damage Limitation (DL), Significant Damage (SD) and Near Collapse (NC) limit state.

DL	SD	NC
0.7%	2.5%	5.0%

Table 3: Inter-storey drift ratio limits adapted to the limit states in EC8-3.

5.1 Structural response under unscaled earthquake sequence

The response of the test frame with the three different configurations are compared in Figure 7 in terms of their first and second storey drift. The effects of infills is evident as the amplitudes in Figure 7 are reduced by more than 50% when the infills are present. It is also found that the current zero-acceleration periods, which were introduced to simulate the time interval between two earthquakes, are not long enough for the bare frame to rest due to the large vibration amplitudes and relatively low damping ratio of steel frames (3% damping assumed for the test frame). However, it is adequate to calm down the infilled and retrofitted frame, therefore, quite long periods of low-amplitude vibration are expected when the infilled frame is tested in the laboratory.

By comparing the first and second floor drifts, it can be concluded from Figure 7 that for the bare frame, the roof displacement are equally distributed to the first and second storey, which is consistent with its first mode shape in Figure 6. For the infilled and retrofitted frame, the drift of the second floor is considerably smaller than that of the first floor, indicating concentration of lateral displacement on the first floor (soft-storey mechanism), where more evident damage may be observed. Besides, Figure 7 also shows that the bare frame experienced large residual drift on both floors after the second earthquake, which has the largest PGA as indicated in Table

1. On the other hand, the residual drifts of the infilled and retrofitted frame are very small and can be neglected. The peak and residual drifts are summarised in Table 4. Finally, it seems that the BRBs do not have significant effects on the overall structural behaviour when they are installed on the infilled frame, although it tends to slightly reduce the storey drift. Since it is found from previous discussion that the first-floor slab (also the top of ground floor) suffers the critical lateral displacement in Case B and C, the response of columns, infills and BRBs on the ground floor will be presented hereafter.

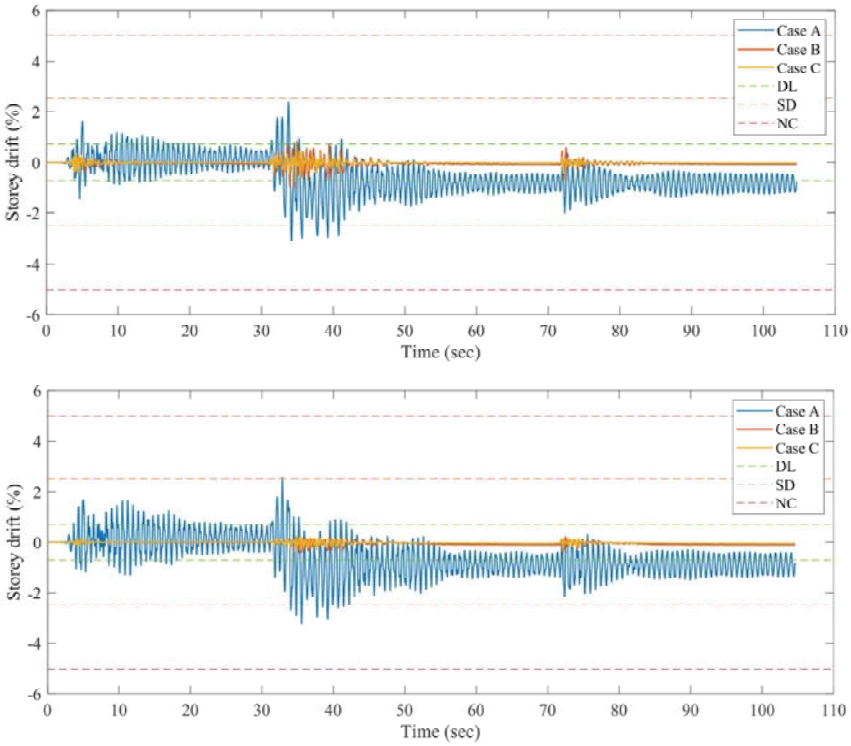

Figure 7: Response of the case study frame in terms of the first (top) and second (bottom) floor drift under unscaled earthquake sequence.

		GM1		GM2		GM3	
		Peak	Residual	Peak	Residual	Peak	Residual
Case A	1F	1.6	0.13	3.1	0.83	2.0	0.84
	2F	1.7	0.15	3.2	0.89	2.1	0.88
Case B	1F	0.5	0.05	1.1	0.08	0.8	0.07
	2F	0.1	0.00	0.4	0.11	0.4	0.11
Case C	1F	0.5	0.05	0.9	0.07	0.5	0.08
	2F	0.2	0.01	0.2	0.03	0.1	0.03

Table 4 Peak and residual drifts (%) of the case study frame under unscaled earthquake sequence.

Figure 8 presents the moment-rotation behaviour at the base of columns on the two sides of the test frame. It is found that the columns in the bare frame reached a maximum rotation of more than twice the yield rotation θ_y, while in the infilled and retrofitted frame, the maximum column base rotation was around θ_y and $0.5\theta_y$, respectively. It is also noticed that the BRB

caused slight differences between the behaviour of columns on its two sides, probably due to the higher axial load in the left-side column in Figure 1 as a result of the orientation of the BRB. Furthermore, the response of masonry infills with and without BRBs is presented in Figure 9, which shows the axial force-displacement diagram of the two struts forming the same masonry wall but in opposite directions. As expected, the designed BRBs reduced the displacement of masonry infills both in tension and in compression, however, it failed to protect the infills from cracking and experiencing degrading of stiffness. Figure 10 shows the behaviour of the BRBs adopted for the retrofit of the case study frame. It is clearly demonstrated that the BRBs are only slightly yield and have not fully developed their full post-yield strength and displacement capacity.

It can be concluded that in the case of unscaled earthquake sequence, the BRBs were barely activated, therefore, they only contributed to the lateral stiffness and strength of the structure and hardly improved the overall energy dissipation capability. The columns were well protected from yielding by infills and BRBs, and the structure were verified safe at significant damage limit state according to Table 3, and the retrofitted frame was close to satisfying the damage limitation limit state.

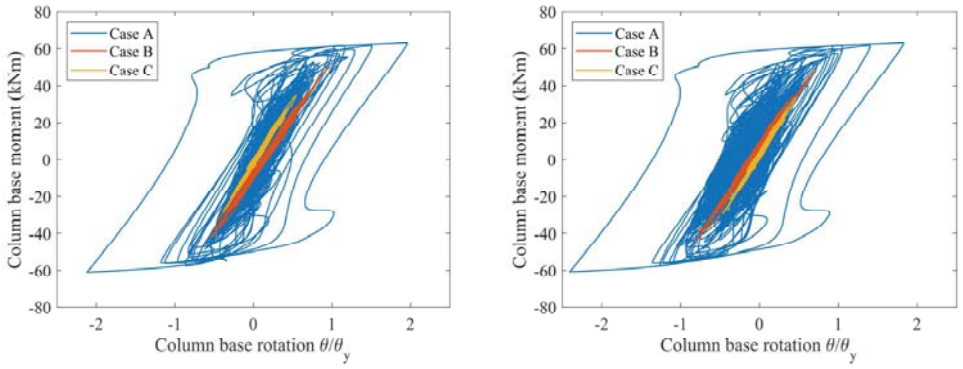

Figure 8: Moment-rotation response of ground floor columns in Figure 2.

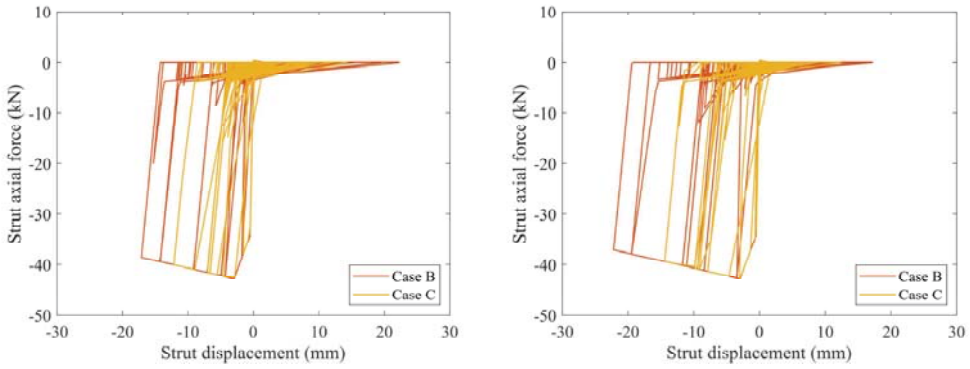

Figure 9: Force-displacement diagram of masonry infill struts on the ground floor in opposite directions.

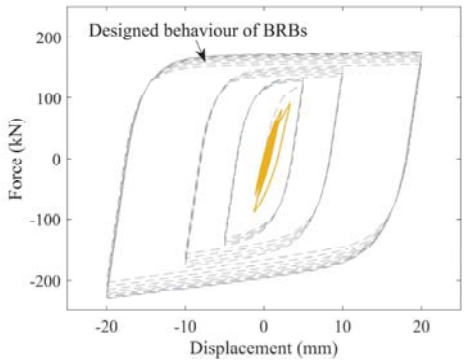

Figure 10: Cyclic behaviour of BRB in Case C.

5.2 Structural response under scaled earthquake sequence

The results obtained with the scaled earthquake sequence are presented in this section in a similar manner to what have been done for the unscaled earthquake sequence. It should be noted that the bare frame in Case A were not involved in this part of assessment as it is by nature not able to survive such strong earthquakes. Generally speaking, the test frame experienced much more severe damage when it was under the scaled earthquake sequence, which meets the expectation of significantly damaging the infilled frame in the lab so that more information of the seismic behaviour of the steel frame can be collected for further study. Figure 11 shows the inter-storey drift of the frame in Case B and C. It is clear that the infilled frame experienced increasing residual drifts up to 2.4% after each earthquake on both storey when there was no protection from BRBs, and the first storey suffered a peak drift of nearly 6% during the second earthquake. Besides, it is also clearly demonstrated in Figure 11 that the BRBs in Case C effectively reduced both the peak drift of the steel frame by around 50% and in most cases reduced the residual drift by a large amount as well, as indicated in Table 5.

Figure 12 shows the response of columns. It is found that under the strong earthquakes, the columns in the infilled frame were significantly yielded and suffered large deformation at the column bases (approximately $5\theta_y$). However, the rotation of column in the retrofitted frame was reduced to around $2\theta_y$. Figure 13 and 14 shows the cyclic response of infill struts and BRBs, respectively. It can be anticipated from Figure 13 that severe damage or even partial collapse may occur on the infill walls without BRBs' protection, as one of the struts is approaching its residual strength, which is around 4kN. However, when the BRBs were included, the infills experienced 50% smaller peak displacement in both tension and compression, although cracks and stiffness degradation were still observed. This is not a surprise as the BRBs adopted failed to prevent the infills from cracking under the previous unscaled earthquake sequence. The behaviour of BRB in Figure 14 suggests that the BRB was activated during the earthquake sequence with a shift of equilibrium position to around 0.01mm. It also experienced a larger displacement than its ultimate limit, which occurred during the second earthquake component, indicating that in reality the BRB was probably unable to dissipate energy anymore after it was broken.

In conclusion, when a scaling factor of 3 was applied to the previous earthquake sequence, the BRBs on the ground floor were clearly activated and contributed to the energy dissipation capability through its cyclic behaviour. The columns were protected with maximum base rotation being reduced by more than 50%, and the retrofitted frame were eventually verified safe at the near collapse limit state according to Table 3.

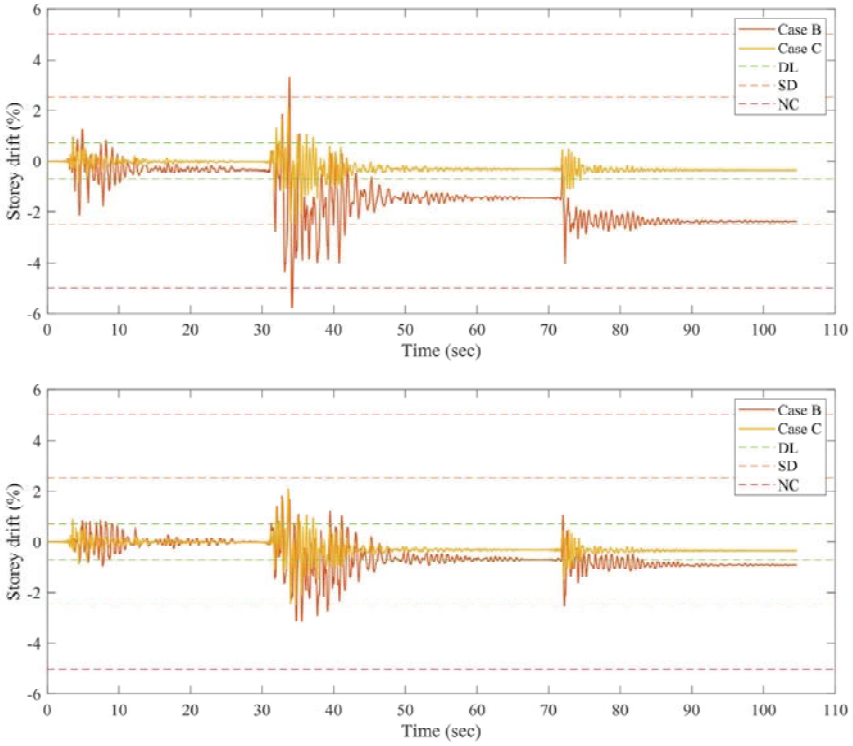

Figure 11: Response of the case study frame in terms of the first (top) and second (bottom) floor drift under scaled earthquake sequence.

		GM1		GM2		GM3	
		Peak	Residual	Peak	Residual	Peak	Residual
Case B	1F	2.1	0.35	5.8	1.47	4.0	2.38
	2F	0.9	0.00	3.1	0.70	2.5	0.90
Case C	1F	0.9	0.01	2.5	0.32	1.5	0.34
	2F	0.7	0.02	1.8	0.16	1.5	0.18

Table 5: Peak and residual drifts (%) of the case study frame under scaled earthquake sequence.

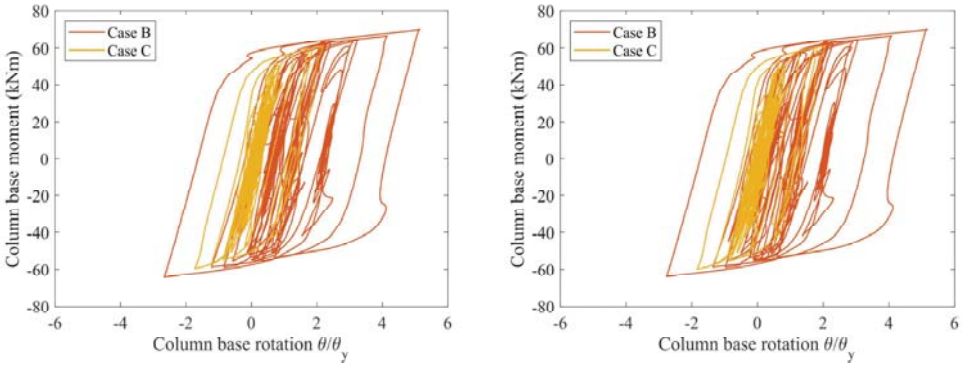

Figure 12: Moment-rotation response of ground floor columns in Figure 2.

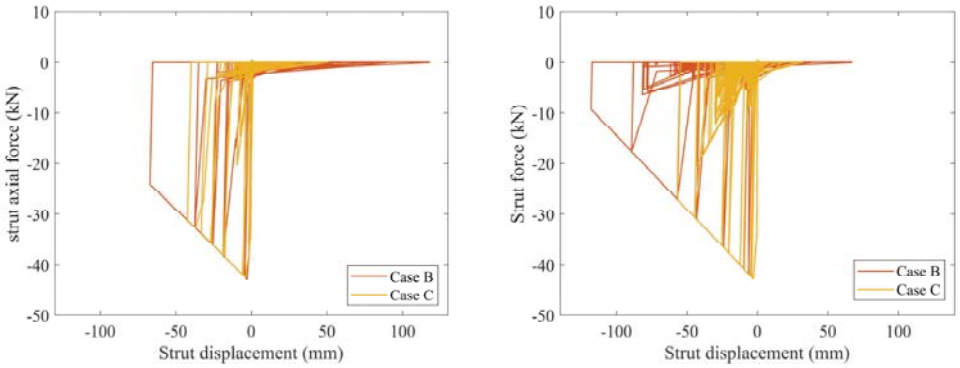

Figure 13: Force-displacement diagram of masonry infill struts on the ground floor in opposite directions.

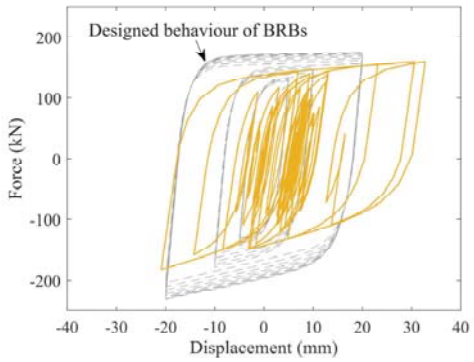

Figure 14: Cyclic behaviour of BRB in Case C.

6 CONCLUSIONS

This paper presented the results of preliminary dynamic analysis carried out on a 2-storey case study steel frame designed for the experimental tests of the HITFRAMES project. The steel frame was designed to be a representative of existing steel frames in Southern Europe. Dynamic analysis was performed on the steel frame in different configurations, including the bare frame, the infilled frame and the infilled frame retrofitted with BRBs. The analysis was done as a preparatory work for the experimental tests.

Three earthquakes were selected in this study to form an earthquake sequence. The unscaled record of the entire sequence was applied to the steel frame in the first part of analysis. In the second part, the record was scaled by a factor 3.0 and then applied to the steel frame. The inter-storey drifts of both floors were examined as well as the response of column, masonry infills and BRBs, in order to assess the capability of the designed BRB system of protecting the steel frame and masonry infills. It is found that under the unscaled earthquake sequence record, the BRB were barely activated, although it helped reduce the deformation of both columns and masonry infills by around 50% and eliminated yielding in columns. When the intensity of input earthquake record was increased by a factor of 3.0, it is concluded that the BRBs were significantly damaged and exceeded its maximum deformation capacity. The column base rotation was reduced by nearly 50% due to the protection of BRBs and yielding in column was considered to be minimised. This protection is also reflected by the dramatic reduction in the transient and residual drift, where the former was decreased by around 50% and the latter was reduced to a negligible level.

A major limitation in this study is that the flexibility of beam-column connections were not accounted for in either the strong or weak axis of columns, although the column panel zones (along the strong axis) do not play an important role in this study, since the tests will be performed along the weak axis of columns. The column base connections were not considered, either. These limitations may significantly affect the results of the real tests, which will be updated in the model calibration based on the test results.

7 ACKNOWLEDGEMENTS

The financial support from Seismic Engineering Research Infrastructure for HITFRAMES (SERA) Project, funded within the H2020-INFRAIA-2016-2017 Framework Program of the European Commission under grant agreement No.730900 is greatly appreciated. Any opinions, findings and conclusions, or recommendations expressed in this paper are those of the authors and do not necessarily reflect those of SERA sponsors.

REFERENCES

[1] L. Di Sarno, F, Paolacci, A.G. Sextos, Seismic performance assessment of existing steel buildings: a case study, *Key Engineering Materials* 763, 1067-1076, 2018.

[2] L. Di Sarno, A.S. Elnashai, Bracing systems for seismic retrofitting of steel frames, *Journal of Constructional Steel Research* 65(2), 452-465, 2009.

[3] J. Ruiz-García, J.C. Negrete-Manriquez, Evaluation of drift demands in existing steel frames under as-recorded far-field and near-fault mainshock–aftershock seismic sequences, *Engineering Structures* 33(2), 621-634, 2010.

[4] M. Dolšek, P. Fajfar, The effect of masonry infills on the seismic response of a four-storey reinforced concrete frame - a deterministic assessment, *Engineering Structures* 30(7), 1991-2001, 2008.

[5] G. Uva, D. Raffaele, F. Porco, A. Fiore, On the role of equivalent strut models in the seismic assessment of infilled RC buildings, *Engineering Structures* 42, 83-94, 2012.

[6] M. Dolšek, P. Fajfar, Simplified non-linear seismic analysis of infilled reinforced concrete frames, *Earthquake engineering & structural dynamics* 34(1), 49-66, 2005.

[7] L. Di Sarno and G. Manfredi, Seismic retrofitting with buckling restrained braces: Application to an existing non-ductile RC framed building, *Soil Dynamics and Earthquake Engineering* 30(11), 1279–1297, 2010.

[8] L. Di Sarno and G. Manfredi, Experimental tests on full-scale RC unretrofitted frame and retrofitted with buckling restrained braces, *Earthquake Engineering and Structural Dynamics* 41(2), 315-333, 2012.

[9] F. Freddi, L. Ragni, E. Tubaldi and A. Dall'Asta, Probabilistic Performance Assessment of Low-Ductility RC Frames Retrofitted With Dissipative Braces, *Earthquake Engineering and Structural Dynamics* 42, 993-1011, 2013.

[10] S. Mazzoni, F. McKenna, M.H. Scott, G.L. Fenves, OpenSees command language manual, Pacific Earthquake Engineering Research (PEER) Centre, 264, 2006.

[11] British Standards Institution, BS EN 1998-3:2005, Eurocode 8. Design of structures for earthquake resistance - Part 3: Assessment and retrofitting of buildings, London: BSI; 2005.

[12] L. Di Sarno, J.R. Wu, M. D'Aniello, S. Costanzo, R. Landolfo, O.S. Kwon, F. Freddi, Assessment of existing steel frames with infills under multiple earthquakes, *Proceedings of COMPDYN 2019, 7th International Conference on Computational Methods in Structural Dynamics and Earthquake Engineering*, 2019.

[13] L. Di Sarno, F. Gutiérrez-Urzúa, F. Freddi, M. D'Aniello, R. Landolfo, O.S. Kwon, S. Bousias, M. Dolšek, J.R. Wu, M.G. Castellano, Pseudo-dynamic testing of existing steel frames with masonry infills: assessment and retrofitting with BRBs, *Proceedings of ANIDIS 2019, XVII Convegno ANIDIS - L'Ingegneria Sismica in Italia*, 2019.

[14] D.G. Lignos and H. Krawinkler, Deterioration modeling of steel components in support of collapse prediction of steel moment fames under earthquake loading, *Journal of structural engineering* 137(11), 1291–1302, 2011.

[15] F. Zareian, and R.A. Medina, A practical method for proper modeling of structural damping in inelastic plane structural systems, *Computers and structures* 88(1-2), 45-53, 2010.

[16] N. Mohammad, L. Liberatore, F. Mollaioli, and S. Tesfamariam, Modelling of masonry infilled RC frames subjected to cyclic loads: State of the art review and modelling with OpenSees, *Engineering Structures* 150, 599–621, 2017.

[17] M.N. Fardis, and T.B. Panagiotakos, Seismic design and response of bare and masonry-infilled reinforced concrete buildings. Part II: Infilled structures, *Journal of Earthquake Engineering* 1(3), 475–503, 1997.

[18] L. Liberatore, and L.D. Decanini, Effect of infills on the seismic response of high-rise RC buildings designed as bare according to Eurocode 8, *Ingegneria sismica* 3, 7-23, 2011.

[19] American Society of Civil Engineering, ASCE41-06. Seismic rehabilitation of existing buildings, Reston, Virginia, 2005.

EURODYN 2020
XI International Conference on Structural Dynamics
M. Papadrakakis, M. Fragiadakis, C. Papadimitriou (eds.)
Athens, Greece, 23–26 November 2020

SEISMIC RESILIENCE ASSESSMENT FOR THE G7 HIGHWAY BRIDGE IN GREECE

Akrivi Chatzidaki[1], Konstantinos Bakalis[2], and Dimitrios Vamvatsikos[1]

[1] National Technical University of Athens
Heroon Polytechniou 9, 15780 Zografou, Greece
{cakrivi, divamva}@central.ntua.gr

[2] EPFL ENAC IIC RESSLAB
GC B3 505 (Bâtiment GC), Station 18, CH-1015 Lausanne
konstantinos.bakalis@epfl.ch

Keywords: resilience assessment, road infrastructure, seismic risk assessment, bridges

Abstract. *The seismic risk is assessed for two twin bridges, one per direction, forming the G7 branch of the Egnatia Odos highway in Greece. These are structurally independent horizontally-curved cantilevered-deck three-span reinforced concrete structures with a monolithic pier-to-deck connection that have been designed circa 2004 according to Greek and European standards. The aim is to develop a tool for pre-event risk assessment and rapid post-event inspection of critical road infrastructure by combining hazard, vulnerability and sensor information (where available) to predict the resulting consequences. To enhance the assessment resolution, a component-based approach is followed, allowing us to evaluate damage scenarios for individual critical components (i.e., piers and bearings) and propagate them to the system-level performance. Consequences are quantified in terms of repair losses, downtime, and traffic capacity losses, the latter identified as the number of closed lanes and the allowable speed limit for the open ones. This allows tracing back the consequences after an event to individual bridge components to help road operators establish bridge inspection prioritization protocols and manage associated incidents, facilitating the rapid assessment of the state of the bridge and optimal recovery to full functionality.*

1 INTRODUCTION

Road operators nowadays face the challenge of efficient maintenance and operation of road infrastructure networks as well as the rapid inspection in case of natural hazard events. To this effect, significant effort has been invested in quantifying risk and resilience for interdependent road networks. Risk assessment focuses on estimating the probability of undesirable/extreme event occurrence and on the quantification of the associated consequences, such as monetary loss, downtime etc. (e.g., Kappos et al. [1]). Resilience goes a step further to assess the follow-up to a failure, attempting to quantify the system's ability to recover after a catastrophic event. Thus, resilience incorporates the dimension of time to measure the ability of the entire system to retain and recover functionality after a potential event, considering either a single or multiple hazards. For example, conceptual views of infrastructure resilience have been discussed by Cimellaro et al. [2], Argyroudis at al. [3], and Ouyang et al. [4], while Kilanitis and Sextos [5] and Costa [6] have offered focus on road networks under seismic hazard. Still, the definition and application of a practical multi-hazard approach on any realistic infrastructure system remains a challenge.

In response, the PANOPTIS project integrates multi-hazard resilience assessment of highway networks with real-time sensor information to offer a holistic tool for pre-event assessment and rapid post-event inspection of critical road infrastructure under multiple hazards. It is a decision support tool that helps road operators efficiently inspect, maintain and safely operate existing road networks and mitigate the risks. In PANOPTIS two types of sensors are employed, namely (i) sensors providing information on the hazard, such as seismographs, and (ii) sensors providing information on the response of the structure, such as accelerometers. The near-real-time sensor integration has formed the basis of our approach, necessitating focusing on multiple hazard and damage/loss scenarios to accommodate rapid damage and consequence identification. To this extent, an enhanced resolution is adopted for the highway assets, allowing tracing back potential consequences to individual components with more ease, facilitating the rapid inspection after a potentially damaging natural hazard event. This paper presents the framework for resilience assessment of highway assets within the PANOPTIS project, using the G7 bridge of Egnatia Odos in Greece as the case study that is subjected to the seismic hazard.

2 RISK AND RESILIENCE ASSESSMENT FRAMEWORK FOR THE HIGHWAY BRIDGE

Seismic risk assessment according to the PBEE framework [7] requires convolving the seismic hazard with the vulnerability to quantify risk. Vulnerability functions are probabilistic distributions of losses given the Intensity Measure (IM) of interest. They translate the physical damage into monetary loss, repair time, downtime, traffic capacity reduction etc. Vulnerability functions can either be derived empirically based on data from past catastrophic events or they can be analytically computed by combining fragility with the associated consequence functions. The consequence functions are probabilistic distributions of losses given a level of damage that are usually derived empirically. In PANOPTIS two approaches can be followed for vulnerability assessment, termed system-only and component-based. System-only approaches are the norm and employ classic system-level fragility curves, such as the ones of HAZUS-MH [8], which are combined with the corresponding cumulative consequences to the asset for the given damage state. On the contrary, the component-based approach of FEMA P-58 [9] involves employing component-based fragility curves that provide the probability of a component violating the limit states of interest given the component's Engineering Demand

Parameter(s) EDP(s). These are convolved with the losses/consequences implied by each component to generate high-resolution vulnerability functions. Herein the component-based approach is followed as it allows identifying potential consequences of individual bridge components with more ease, since a general rating of "moderate damage" on the bridge would be quite vague in contrast to "moderate damage state on the bearings", which would more efficiently help road operators to establish prioritization protocols and facilitate rapid inspection.

Resilience assessment requires also the definition of the system's recovery function. For instance, Cimellaro et al. [10] proposed adopting a linear, trigonometric or exponential recovery function depending on the response of the system and the stakeholder/owner/operator. Even more complicated shapes have been proposed, such as by Miles and Chang [11] or Zhang et al. [12]. In our case, functionality is quantified in terms of the traffic capacity of the system. Starting at 100% capacity, the event causes a drop to a lower capacity level (fewer cars allowed through) due to reduction in the allowable speed limit and/or potential lane closure that is required for inspection and damage fixing. All such restrictions are lifted and the full traffic capacity of the bridge is assumed to be restored only when all damages are fixed, thus he "bathtub" recovery function of Figure 1 is adopted.

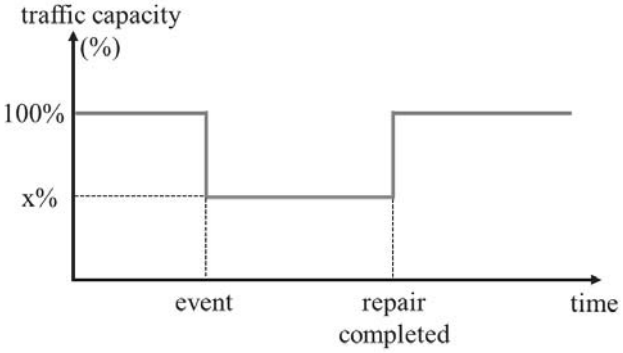

Figure 1: "Bathtub" recovery function, showing that the traffic capacity is reduced in a catastrophic event and is restored to 100% when the repair actions are completed.

3 CASE-STUDY BRIDGE

The G7 bridge is located at the Metsovo-Panagia section of Egnatia Odos in Greece (Figure 2a and b). It consists of two structurally independent twin bridges, each of them carrying one traffic direction of two lanes resulting in four lanes for both directions. The bridge was designed circa 2004 and built in 2009 following the cantilever method of construction with in-situ concreting. Each of the twin bridges has three spans of 75+120+75m resulting in 270m total length. The longitudinal axis of the bridges is curved in both horizontal and vertical plane. The deck is a prestressed single-cell concrete box girder with its depth varying from 2.75m close to the abutments to 7.25m at the piers, that is monolithically connected to the two piers (M1 and M2) of 41.70m and 49.50 height, respectively. The cross section of both piers is hollow rectangular of in-situ cast concrete with 7.35x4.0m external dimensions and 0.75m width. The piers are appropriately oriented so that deformation in the transverse bridge direction leads to bending around their strong-axis, while deformation in the longitudinal bridge direction leads to weak-axis bending for the piers. They are founded within the rock via concrete shafts of 10m diameter and 15m height. The deck is supported via two pot-bearings at each abutment that allow the horizontal deck movements in both longitudinal and transverse bridge directions while a third bearing is added in the middle, having a transverse shear key to eventually restrict transverse bridge displacement.

(a) location of the G7 bridge (b) G7 bridge of the Egnatia Odos highway

Figure 2: G7 bridge of the Egnatia Odos highway in Greece.

4 UNDERSTANDING THE BRIDGE BEHAVIOR

The bridge may displace longitudinally, transversally or even vertically. Due to the monolithic deck-to-pier connections such displacements become of importance at the abutments, where the deck rests on bearings.

4.1 Bridge behavior in the longitudinal direction

In the longitudinal bridge direction, the expansion joint shown by green color in Figure 3 prevents the deck from hitting the abutment. Potential deck movement during normal bridge operation can be attributed to expansion/contraction caused by temperature changes, concrete creep, or as a result of braking especially of heavy vehicles, such as trucks. During earthquakes the expansion joint is expected to prevent the deck hitting the ballast wall. Its opening is 0.53m and is composed of steel beams. If bridge-to-deck deformation exceeds the value of approximately 0.5·0.53m, the steel longitudinal "beams" that form the structure of the joint are expected to sustain considerable damage thus requiring repair or even replacement. For higher relative deformations exceeding the gap of 0.53m, the deck is expected to hit the upper part of the ballast wall (indicated by mustard color in Figure 3) thus causing significant damage. It should be noted that the continuity of the backwall is interrupted at the sacrificial joint (shown by cyan color in Figure 3), thus in this case potential damages are limited to the upper part of the ballast wall and to the approach slab (also shown in mustard color) that is monolithically connected to it. In this case, steel plates are typically placed as a temporary measure to bridge the damaged parts until they are repaired. In case of extensive deck-to-abutment deformation, which is not expected to occur for the design level earthquake, the deck can further move up to a limit of approximately ±1.50m when it might either hit the ballast wall (see the distance indicated in red in Figure 3) or fall from the pedestal, which results in deck unseating (see distance indicated in magenta color in Figure 3). Of course, in this case the bearings will also be damaged due to extensive deformations beyond their capacity. It should be noted that even if deck unseating happens, this would not result in collapse since the deck is monolithically connected to the piers. Still it is an unlikely situation that would require considerable

repair actions. The abutments are founded on solid rock thus they are not assumed to be vulnerable to the seismic action.

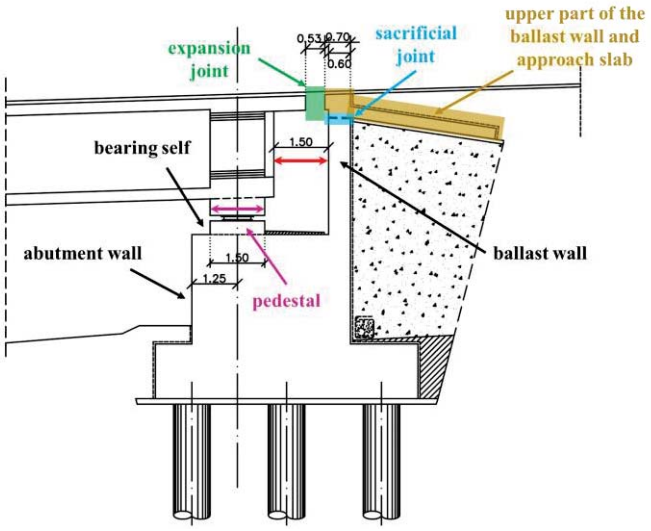

Figure 3: Support conditions of the deck in the longitudinal bridge direction, showing the expansion joint in green, the sacrificial joint in cyan, the upper part of the ballast wall, the pedestal in magenta and the approach plate in mustard color and the deck-to-abutment displacement thresholds that indicate deck hitting the ballast wall in red or deck unseating in magenta.

4.2 Bridge behavior in the transverse direction

The structural system of the bridge is designed and constructed so that the bridge mainly deforms in the longitudinal direction during earthquakes. However, it is also important to identify potential damages caused by transverse deck-to-abutment deformations. As presented in Figure 4, the shear key of the middle bearing (indicated in red color) restricts the transverse deck displacement up to the load of 250tn. If this load is exceeded, the shear key is expected to break thus letting the deck to move freely since pot bearings (shown in blue) enable such movements. If the deck-to-abutment deformation exceeds ±0.05m the deck is expected to hit the elastomeric bearings placed at the safety walls (shown in green color in Figure 4) which restrict further movements and partially alleviate impact. The safety walls of the G7 case act as transverse stoppers, hence they have an increased width of 0.75m. Overall, the bridge is designed so that in the design earthquake the shear key does not break, while in stronger earthquakes it can break thus in this case safety walls restrain further movement, until their eventual shear failure.

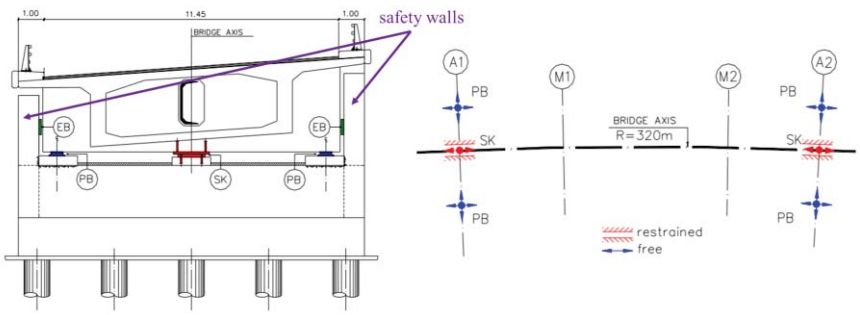

Figure 4: Support conditions of the deck in transverse bridge direction showing the elastomeric bearing (EB, green color), pot bearings (PB, blue color) and the bearing with the shear key acting in transverse bridge direction (SK, red color) (adapted from [13]).

4.3 Vertical bride displacements

Overall the deck is designed not to uplift during the design earthquake, however higher intensity events can very well cause uplift, immediately resulting to damage in the bearings.

5 DEFINITION OF CRITICAL BRIDGE COMPONENTS

After having elaborated on the bridge behavior in potential longitudinal, transverse and vertical displacements, the critical bridge components that might sustain damage during earthquakes can be identified along with the associated limit states and consequences. The critical components considered for the G7 bridge of Egnatia Odos are the piers, bearings, abutments, ballast walls, safety walls, pedestals, the deck and the expansion joints. Regarding the piers, they are critical components that may experience damage due to longitudinal or transverse bridge displacements. The response of the piers is discretized in the four limit-states of Stefanidou [14], thus associated thresholds are calculated based on the proposed closed-form equations. For the other components of the bridge, the limit states are derived based on the manufacturer's data as well as discussions with professional bridge engineers.

The consequences associated to each damage state are quantified based on expert opinion in terms of repair cost, repair time and the standard procedures the road operators follow until damages are repaired. These relate to the number of lanes that should be closed and/or the maximum allowable speed of the vehicles in remaining open ones.

6 RISK AND RESILIENCE ASSESSMENT

6.1 Non-linear modeling

A three-dimensional (3D) reduced-order model of the bridge was developed by [15] on the OpenSees platform [16], as shown in Figure 5. Due to its computational efficiency, it is also employed for our purposes. The deck is assumed to remain elastic thus it is modeled using linear elastic beam-column elements following the central axis of the deck. Rigid elements are added on both sides to carefully capture the double curvature of the bridge. Force-based beam-column elements discretized into longitudinal steel and concrete fibers are used for modeling the piers, with appropriate stress-strain laws to represent the confined core concrete, the unconfined concrete of the cover and the steel rebars. The effect of confinement is calculated on the basis of the Mander et al. model [17]. Rigid elements of zero mass are used for connecting the deck with the bearings, the latter being modeled via a set of one-dimensional springs to model the restraints imposed upon the deck ends by the bearings, the backwalls and the sidewalls. They allow a longitudinal deck-abutment gap-opening displacement of up to 1.50m, until unseating occurs, while they also simulate the sequential failure of the deck and backwall top and eventual contact of deck and backwall after a gap closing displacement of 1.5m. The shear key of the middle bearings is introduced via a hysteretic spring fracturing at the load of 250tn, also accounting for contact with the side walls of the abutment if the shear key collapses. The bridge is founded on the bedrock via deep foundations thus the piers are assumed to be fixed. The fundamental period of the bridge vibrates at T_1 = 1.65sec and is the longitudinal-direction-dominant one, while the second eigen-period is the transverse-direction-dominant one with T_2 = 1.54sec.

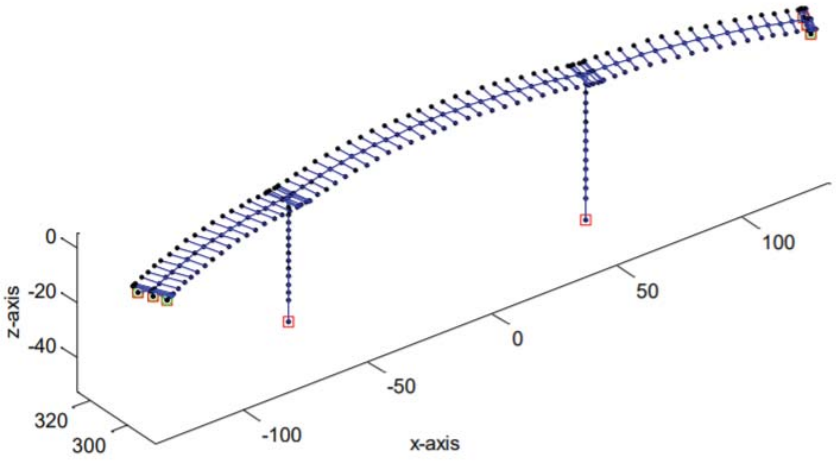

Figure 5: 3D reduced-order model of the G7 bridge [15].

6.2 Site-specific seismic hazard assessment

The G7 bridge is located in an earthquake prone area thus it is important to consider the site-specific seismic hazard during the analysis. The state-of-the-art average spectral acceleration, *AvgSa*, ([18]-[20]) is adopted as the IM:

$$AvgSa(T_{Ri}) = \left(\prod_{i=1}^{n} Sa(T_{Ri}) \right)^{1/n} \tag{1}$$

It is the geometric mean of *n* spectral acceleration ordinates, *Sa*, at periods T_{Ri}. Each *Sa* ordinate is the geometric mean of the 5%-damped spectral acceleration from the two horizontal components of each ground motion. The periods, T_{Ri}, are equally spaced in [0.3s, 3.0s] with an increment of 0.1s. The seismic hazard is assessed on the basis of probabilistic seismic hazard analysis (PSHA), using the OpenQuake software [21], by employing the area source model of the SHARE project [22] and the ground motion prediction equation proposed by Boore and Atkinson [23]. The resulting seismic hazard curve is presented in Figure 6b in terms of the *AvgSa* and the mean annual frequency, *MAF*, of exceeding it. The *AvgSa* with 20%, 10% and 2% probabilities exceedance in 50 years are also shown in the same Figure.

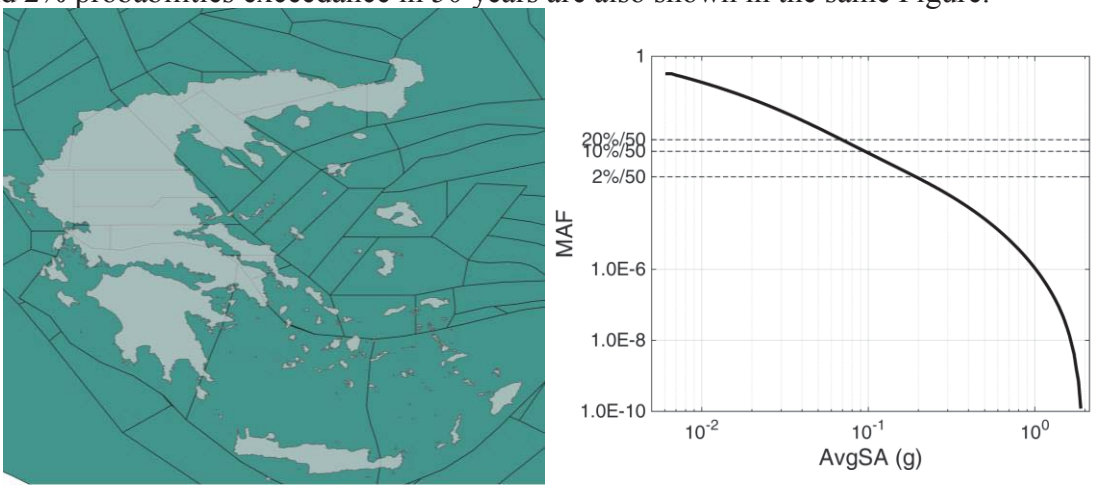

(a) (b)

Figure 6: Site-specific seismic hazard assessment using the area source model of the SHARE project that is presented in (a). The resulting seismic hazard curve is shown in (b).

For each hazard level, a set of 30 ground motion records is selected that is compatible to the site-specific seismic hazard based on the Conditional Spectrum ([24], [25]). This bridge is not expected to sustain considerable damage under the design level earthquake, thus three additional set of records are selected for *AvgSa* equal to 0.5, 1.0 and 1.5g.

6.3 Non-linear dynamic analyses

The non-linear model of the bridge is subjected to nonlinear dynamic analyses using the 6 sets of CS-compatible ground motion records. Both horizontal components of each ground motion are applied on the 3D model of the bridge, after being appropriately scaled to match the level of *AvgSa* for the given set. Therefore, the analysis results are grouped in the six stripes of Figure 7 (multi-stripe analysis, MSA), where each point represents an AvgSa-EDP pair, the latter being the response parameter of interest. The EDPs are appropriately selected to adequately characterize the response of the critical bridge components that may sustain damage and whose performance defines damage states. For instance, in Figure 7a the maximum drift ratio of the M1 pier is presented, that is the square root of sum of squares (srss) of pier drifts in the longitudinal and transverse directions, while in Figure 7b the maximum gap closure of the left abutment is shown.

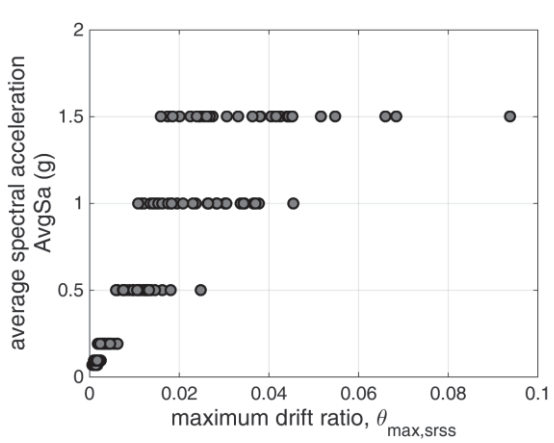

(c) *AvgSa* versus maximum srss drift ratio for the M1 pier

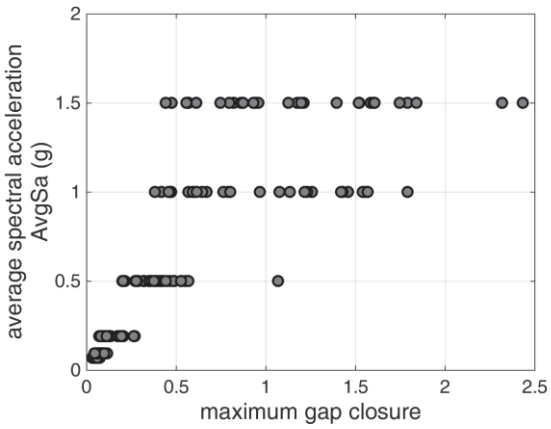

(d) *AvgSa* versus maximum gap closure for the left abutment

Figure 7: Multi-stripe analysis results. For each of the six stripes, the bridge is subjected to a set of 30 hazard-consistent CS-compatible ground motion records.

6.4 RESILIENCE ASSESSMENT OUTPUTS

For each level of the IM, multiple damage and associated consequence scenarios are defined by randomly sampling the corresponding distributions in the pre-event phase of PANOPTIS based on the MSA results. In each case, the time-to-recover is computed by adding the time needed for repairing the damages associated with each individual component, assuming that they are tackled in series. For simplification purposes, we assume perfect correlation in the demand and the capacities of the two twin bridges. This means that both of them are expected to sustain the exact same damage level, thus for example in both bridges we might close one out of the two lanes if needed. Of course, this simplification is not exactly the case and a non-perfect correlation in the seismic capacities should be taken into account.

Our main metric of functionality is the theoretical traffic capacity, without regard to the actual traffic loads. This is a demand-agnostic view of the system functionality, as obviously the full capacity of the road is not necessarily used at all times of the day, or all days of a year. Still, it remains a useful metric that does not require traffic load estimates for current and fu-

ture use, allowing us to offer an objective "timeless" comparison of the damaged and undamaged states of the bridge. Specifically, the traffic capacity of any bridge state is estimated as $TC = MaxSpeed \cdot NOL$, i.e., as the product of the speed limit, *MaxSpeed*, multiplied by the number of open lanes, *NOL*. Consequently, the traffic capacity reduction, *R*, can be quantified as

$$R = \left(TC_{pre} - TC_{post}\right) / TC_{pre} \tag{2}$$

where TC_{pre} and TC_{post} are the pre- and post-even capacities, respectively. For the former, the undamaged state of the bridge stipulates a 90km/h speed limit with 2 lanes of traffic for each twin bridge. The mean annual frequency of exceeding each value of *R* is presented in Figure 8a), while the 16, 50 and 84% quantiles given the intensity in terms of are presented in Figure 8b). Evidently, no loss of functionality is observed for intensities lower than 0.2g, or mean annual frequencies higher than $2 \cdot 10^{-4}$. In other words, loss of even the lowest possible value of functionality happen with a return period larger than $1/(2 \cdot 10^{-4}) = 5000$yrs. On the other hand, when such an event occurs, the capacity loss is steep, with functionality losses of up to 30% occurring with only slightly higher return periods, typically owing to bearing and/or expansion joint damages.

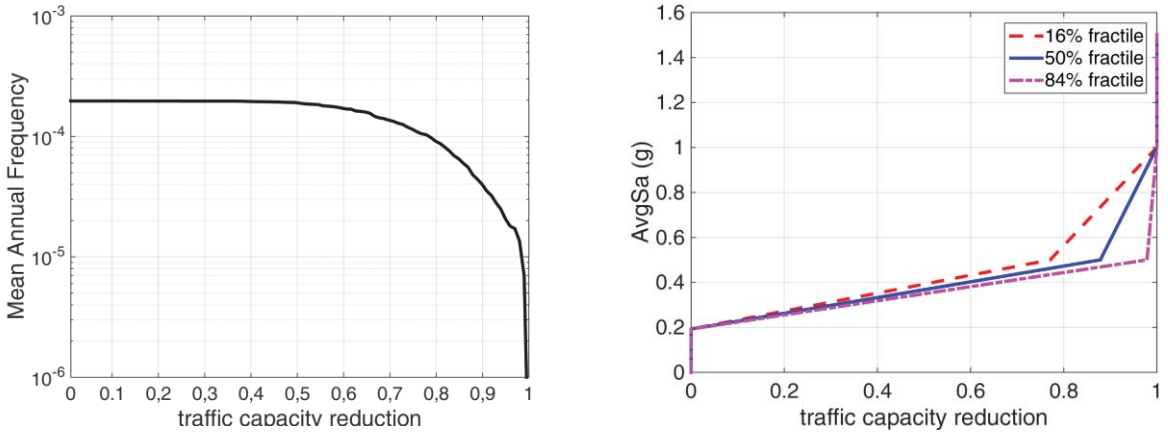

(a) (b)

Figure 8: (a) Mean annual frequency of exceeding traffic capacity reduction values and (b) 16, 50 and 84% quantiles of the traffic capacity reduction given the *AvgSa*.

7 CONCLUSIONS

A methodology is presented for modeling the structure and data dependencies for the resilience assessment of a highway bridge within the PANOPTIS project. This approach can be applied for each individual highway/road infrastructure asset and the combined results can be used for the resilience assessment of the entire interconnected system. The proposed framework is quite straightforward, still the toughest part is the definition of the limit states on a component basis and the quantification of the associated consequences in a consistent way for all components. This challenge requires the assistance of engineers specialized in the design and construction of similar structures as well as of road operators experienced in road maintenance, repair and rehabilitation after potential damaging events. Once the required limit states and consequences are defined, the proposed methodology can be implemented for the resilience assessment of a given highway asset.

8 ACKNOWLEDGEMENT

The first author gratefully acknowledges the financial support provided by the Eugenides Foundation in Greece. Financial support has also been provided by the Innovation and Networks Executive Agency (INEA) under the powers delegated by the European Commission through the Horizon 2020 program "PANOPTIS–Development of a decision support system for increasing the resilience of transportation infrastructure based on combined use of terrestrial and airborne sensors and advanced modelling tools", Grant Agreement number 769129. The authors would also like to acknowledge Dr. Panagiotis Panetsos, Egnatia Odos company and Chris Giannelos for helping us define the damage states and the associated consequences.

9 REFERENCES

[1] A. Kappos, A. Sextos, S. Stefanidou, G. Mylonakis, M. Pitsiava, G. Sergiadis, Seismic risk of inter-urban transportation networks, *Procedia Economics and Finance*, 18, 263-270, 2014.

[2] G.P. Cimellaro, A.M. Reinhorn, M. Bruneau, Framework for analytical quantification of disaster resilience, *Engineering structures*, 32, 3639-3649, 2010.

[3] S.A. Argyroudis, S.A. Mitoulis, M.G. Winter, A.M. Kaynia, Fragility of transport assets exposed to multiple hazards: state-of-the-art review toward infrastructural resilience, *Reliability Engineering and System Safety*, 191, 106567, 2019.

[4] M. Ouyang, L. Dueñas-Osorio, X. Min, A three-stage resilience analysis framework for urban infrastructure systems, *Structural safety*, 36-37, 23-31, 2012.

[5] I. Kilanitis, A. Sextos, Integrated seismic risk and resilience assessment of roadway networks in earthquake prone areas, *Bulletin of earthquake engineering*, 17, 181-210, 2019.

[6] C.Q. Costa, Impact of earthquakes due to disruption in transportation networks using open tools and datasets, PhD thesis, University of Pavia, Italy, 2018.

[7] C.A. Cornell, H. Krawinkler, Progress and challenges in seismic performance assessment, *PEER Center News 2000*, 3, 1-4, 2000.

[8] National Institute of Building Sciences and Federal Emergency Management Agency (NIBS and FEMA), Multi-hazard loss estimation methodology, Earthquake model, HAZUS-MH Technical Manual, Federal Emergency Management Agency, Washington, D.C., 2003.

[9] FEMA P58-1, Seismic performance assessment of buildings: 1–Methodology, *Applied Technology Council for the Federal Emergency Management Agency*, 2012.

[10] G.P. Cimellaro, A.M. Reinhorn, M. Bruneau, Quantification of seismic resilience, *Proceedings of the 8th US National conference on Earthquake Engineering*, 2006.

[11] S.B. Miles, S.E. Chang, Modeling community recovery from earthquakes, *Earthquake Spectra* 22(2), 439-458, 2006.

[12] W. Zhang, N. Wang, C. Nicholson, Resilience-based post-disaster recovery strategies for road-bridge networks, *Structure and Infrastructure Engineering*, *13*(11), 1404-1413, 2017.

[13] C. Giannelos, D. Vamvatsikos, Simplified seismic performance assessment over the lifetime of a highway bridge subject to pier reinforcement corrosion, *Proceedings of the*

COMPDYN2011 Conference on Computational Methods in Structural Dynamics and Earthquake Engineering, Corfu, Greece, 2011.

[14] S. Stefanidou, Specific fragility curves for as built and retrofitted bridges, PhD Thesis (in greek). Aristotle University of Thessaloniki, 2015.

[15] D. Vamvatsikos, I. Sigalas, Seismic performance evaluation of a horizontally curved highway bridge using incremental dynamic analysis in 3D, *Proceedings of the 4th European Workshop on the seismic behaviour of irregular and complex structures*, Thessaloniki, Greece, 2005.

[16] S. Mazzoni, F. McKenna, M. Scott, G. Fenves, Open system for earthquake engineering simulation: OpenSees command language manual, University of California, Berkeley, CA, 2000.

[17] B.J. Mander, J.M. Priestley, R. Park, Theoretical stress-strain model for confined concrete, *Journal of Structural Engineering* 114, 1804-1826, 1988.

[18] P. Cordova, G. Deierlein, S.F. Mehanny, C.A. Cornell, Development of a two-parameter seismic intensity measure and probabilistic assessment procedure, *The Second U.S.-Japan Workshop on Performance-Based Earthquake Engineering Methodology for Reinforced Concrete Building Structures*, Sapporo, Hokkaido, Japan, 2001.

[19] D. Vamvatsikos, C.A. Cornell, Developing efficient scalar and vector intensity measures for IDA capacity estimation by incorporating elastic spectral shape information, *Earthquake Engineering and Structural Dynamics* 34, 1573-1600, 2005.

[20] A.K. Kazantzi, D. Vamvatsikos, Intensity measure selection for vulnerability studies of building classes, *Earthquake Engineering and Structural Dynamics* 44, 2677-2694, 2015.

[21] D. Monelli, M. Pagani, G. Weatherill, V. Silva, H. Crowley, The hazard component of OpenQuake: the calculation engine of the Global Earthquake Model, *15th World Conference on Earthquake Engineering*, Lisbon, Portugal, 2012.

[22] D. Giardini et al., Seismic Hazard Harmonization in Europe (SHARE): *Online Data Resource*, 2013.

[23] D.M. Boore, G.M. Atkinson, Ground-motion prediction equations for the average horizontal component of PGA, PGV, and 5%-damped PSA at sectral periods between 0.01 s and 10.0 s, *Earthquake Spectra*, 24, 99-138, 2008.

[24] T. Lin, C.B. Haselton, J.W. Baker, Conditional spectrum-based ground motion selection. Part I: Hazard consistency for risk-based assessments, *Earthquake Engineering and Structural Dynamics* 42, 1847-1865, 2013.

[25] M. Kohrangi, P. Bazzurro, D. Vamvatsikos, A. Spillatura, Conditional spectrum-based ground motion record selection using average spectral acceleration, *Earthquake Engineering and Structural Dynamics* 46, 1667-1685, 2017.

EURODYN 2020
XI International Conference on Structural Dynamics
M. Papadrakakis, M. Fragiadakis, C. Papadimitriou (eds.)
Athens, Greece, 23–26 November 2020

LIMITATIONS OF EUROCODE 8 DUAL DUCTILITY CLASS APPROACH IN SEISMIC DESIGN OF RC HIGH-RISE BUILDINGS

Jelena R. Pejovic[1], Nina N. Serdar[2], and Radenko R. Pejovic[2]

[1] University of Montenegro
Faculty of Civil Engineering
Montenegro
e-mail: jelenapej@ucg.ac.me

[2] University of Montenegro
Faculty of Civil Engineering
Montenegro
ninas@ucg.ac.me, radenko@ucg.ac.me

Keywords: Eurocode 8, ductility class, high-rise buildings, shear force

Abstract. *The paper contains a discussion of limitations of dual ductility class approach in seismic design of reinforced concrete (RC) high-rise buildings designed according to Eurocode 8. An extensive study is performed in order to examine the applicability of Eurocode 8 provisions related to ductility classes for seismic design of RC walls in high-rise buildings. As representative buildings, 20-storey, 30-storey and 40-storey RC high-rise buildings with core wall structural system are selected. For the purposes of the conducted study, nonlinear time-history analyses are performed for 60 ground motion records with a wide range of magnitudes, distances to source and various soil types. Design seismic shear forces obtained by Eurocode 8 for medium and high ductility classes are analyzed and compared with the real shear forces obtained by nonlinear time-history analyses. The current Eurocode 8 provisions for calculating seismic design shear forces in RC walls yields significantly incorrect results when it is applied to RC walls of high-rise buildings. The results derived in this study indicate that RC high-rise buildings should be designed according Eurocode 8 provisions specified for medium ductility class, taking into consideration the weakness of the existing procedure for calculating design shear force. The need of introducing a single ductility class for RC high-rise buildings is pointed out.*

1 INTRODUCTION

Over the past decades, the construction of high-rise buildings in seismically active areas has become an everyday design trend, which is mainly due to growing urbanisation, rapid growth of cities, and concentration of material resources in urban environments. This is why comprehensive seismic studies of RC high-rise buildings have to be conducted for earthquake-prone areas. Given the sensitivity of high-rise buildings to horizontal loads (earthquake and wind loads), special attention should be paid to seismic analysis of RC high-rise buildings. Even in conditions where the horizontal wind load is relevant for design, which typically occurs for higher RC buildings, approximately 250 m in height, it is not entirely adequate to neglect seismic analysis [1]. High-rise buildings have frequency response range that is much wider than in the case of lower buildings. The wide frequency range of actual earthquake records can induce very complex seismic responses of high-rise RC buildings [2]. Due to the specific behavior of high-rise buildings exposed to seismic effects, the provisions of existing seismic design codes (such as Eurocode 8 EN1998-1 [3]) are usually not sufficient to design seismically resistant RC high-rise buildings. EN1998-1[3] does not define restrictions in terms of number of storeys, but it is the fact that number of storeys has the influence on seismic behavior, and so most commonly existing provisions of EN1998-1 [3] are inadequate and need to be revised for RC high-rise buildings. The most recent studies have shown that modifications and improvements to Eurocode 8 procedures are required [4]–[7]. Rutenberg and Nsieri [4] has shown that the Eurocode 8 procedure for calculating design shear force is conservative for DCH walls and gives lower value of magnification factor ε for DCM walls. Kappos and Antoniadis [5] proposed modified shear force design Eurocode 8 envelope for dual system of walls. Antoniou et al. [6] in their research concluded that Eurocode 8 overestimates the post-elastic amplification of shear walls. Antoniou et al. [7] have shown that actual moments exceed the linear design Eurocode 8 envelope over most of the wall height for mid-rise wall-frame structures.

In the literature, there is a lack of research on this topic with regard to the RC high-rise buildings. In this study, RC high-rise buildings with core wall structural system and three characteristic heights: 20-storey, 30-storey and 40-storey are analysed in order to examine the limitations of EN1998-1 [3] dual ductility class approach in seismic design of RC high-rise buildings

2 DESCRIPTION OF SELECTED REPRESENTATIVE RC HIGH-RISE BUILDINGS

A three representative RC high-rise buildings with core wall structural system, 20-storey, 30-storey and 40-storey high, designed according to Eurocode 8 provisions for two different ductility class (high and medium) are examined. The considered structures are 36x32m in size at the base, with spans in the X direction of 10x8x8x10m and spans in the Y direction of 10x6x6x10m (Figure 1). RC core is 16 x 12 m in size at the base and is located in the central part of the buildings. It consists of three characteristic complex cross section walls (U and I cross-sectional shapes) connected in the X direction of structure by coupling beams. In the area between the central RC core and the perimeter of the structure there is no structural elements. RC frames were formed in the circumferential planes. Vertical structural members are connected with a floor flat slab. The dimensions of the individual structural elements differ for different storey numbers and they are determined in accordance with the requirements defined in Eurocode 2 EN1992-1-1 [8] and EN1998-1 [3]. The main characteristic of the considered RC high-rise structures are shown in the Table 1.

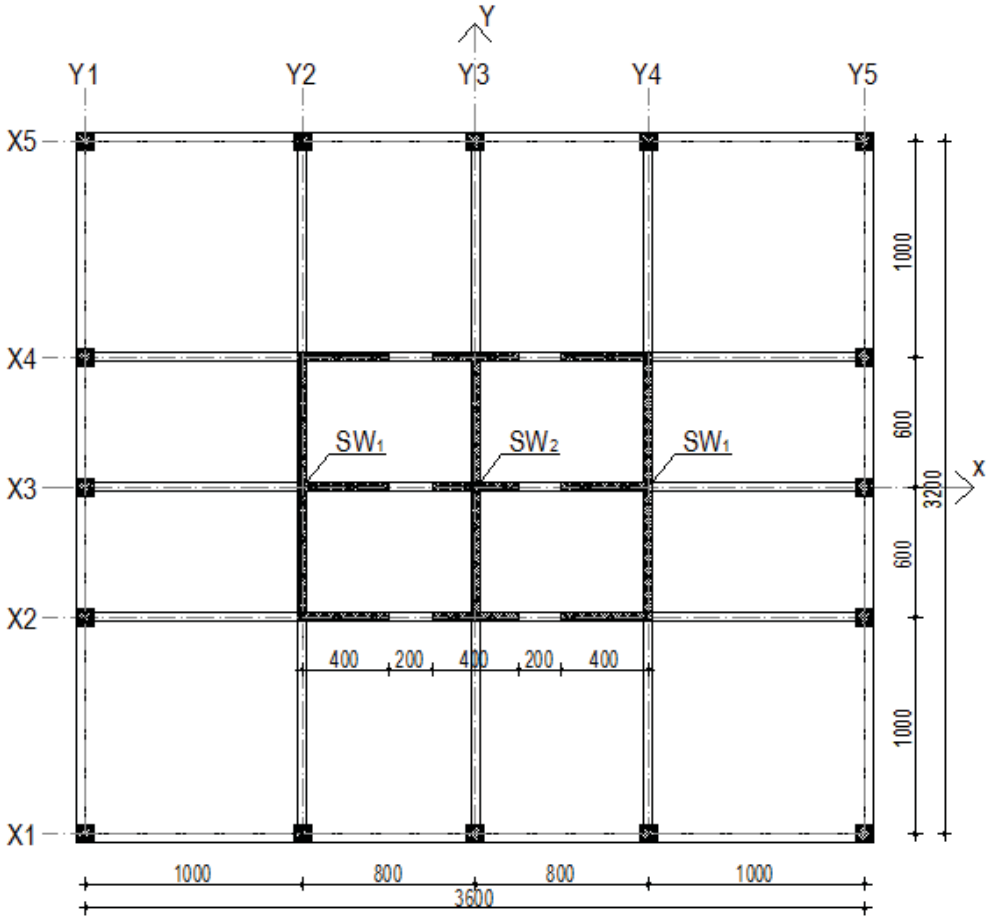

Figure 1: Base plan view of the representative buildings.

Features	20-storey	30-storey	40-storey
Total height (m)	60	90	120
Storey height (m)	3	3	3
Storey RC slab thickness (m)	0.20m	0.20m	0.20m
RC beams (m)	0.40x0.65	0.40x0.65	0.40x0.65
RC columns (m)	0.80x0.80	0.80x0.80	0.90x0.90
Core walls thickness (m)	1-5 storey: 0.30 6-20 storey: 0.20	1-5 storey: 0.40 6-30 storey: 0.30	1-10 storey: 0.55 11-40 storey: 0.45
Coupling beams in X direction (m)	1-5 storey: 0.3x0.8 6-20 storey: 0.2x0.8	1-5 storey: 0.4x0.8 6-30 storey: 0.3x0.8	1-10 storey: 0.55x0.8 11-40 storey: 0.45x0.8
Concrete f_{ck} (f_{cm}) (MPa)	35(43)	45(53)	55(63)
Reinforcement f_{yk}(f_{ym}) (MPa)	500(575)	500(575)	500(575)
Modulus of elasticity E_{cm} (MPa)	34000	36000	38000

Table 1: The main characteristic of the considered RC high-rise structures.

3 SEISMIC DESIGN OF REPRESENTATIVE BUILDINGS ACCORDING TO EN1998-1

Seismic design of the representative RC high-rise buildings is done according to Eurocode 2 EN1992-1-1 [8] and Eurocode 8 EN1998-1 [3]. The considered buildings are designed for two ductility classes defined in EN 1998-1: high ductility class (DCH) and medium ductility

class (DCM). For defining seismic load, the design response spectrum type 1 (magnitude of surface wave M_S>5.5) with adopted value of design peak horizontal acceleration 0.37g is used. The structural system of the considered buildings is a ductile wall system in both horizontal directions according to the classification in EN1998-1 [3]. Considering the structural system and the regularity achieved, the adopted values of the behavior factors for the DCM ductility class is 3.6, and for the DCH class is 5.4.

The ETABS2013 [9] was used for linear seismic analysis of considered buildings. 3D linear models are constructed in ETABS2013 [9]. 50% of the uncracked flexural and shear stiffness is considered in linear analysis according to EN1998-1 [3]. The storey slabs are modeled as rigid diaphragms in the horizontal plane. The vertical structural system is modeled with absolute supports at the foundation level. The structures of the selected buildings are regular in base and over the height. In addition to lateral stability and rigidity, the structures of the buildings under consideration also have adequate torsional resistance and rigidity. On the each storey and in the both considered X and Y directions, the structural eccentricity e_o and the torsional radius r satisfy the conditions defined in EN1998-1 [3].

The total seismic forces for the two horizontal orthogonal directions were calculated by multi-modal response spectrum analysis, which is quite appropriate given the influence of higher modes on RC high-rise buildings. The results from linear multi-modal response spectrum analysis are shown in Table 2.

Number of storeys			20	30	40
Total base shear force for in Y direction for DCM (kN)			18503	24331	32454
Total base shear force for in X direction for DCM (kN)			16348	23266	32340
Total base shear force for in Y direction for DCH (kN)			15376	21322	29441
Total base shear force for in X direction for DCH (kN)			14946	21385	29989
Periods in Y direction (sec)	Mode	1	1.652	2.880	4.097
		2	0.389	0.623	0.858
		3	0.181	0.270	0.355
Periods in X direction (sec)	Mode	1	1.641	2.597	3.511
		2	0.480	0.702	0.880
		3	0.250	0.347	0.423
Mass participation factors in Y direction (%)	Mode	1	64.26	63.53	63.24
		2	20.32	19.43	18.94
		3	7.04	7.05	7.05
Sum of mass part.factors in Y direction (%)			94.85	93.58	92.88
Mass participation factors in X direction (%)	Mode	1	69.36	67.70	66.08
		2	15.96	17.40	18.78
		3	5.49	5.23	5.68
Sum of mass part.factors in X direction (%)			93.64	93.11	93.18

Table 2: The linear multi-modal response spectrum analysis results.

The analysis of the calculated seismic and gravitational effects obtained in the structural elements revealed that the total seismic force is dominantly accepted by RC walls of the core. For this reason, RC core was subjected to further detailed calculations and designing according to the relevant EN1998-1 [3] provisions and subsequently RC core walls were also analysed using nonlinear time-history analyses. The serviceability limit state according to EN1998-1 [3] has been checked and it was found that it provisions are satisfied. All the provisions of the EN1998-1 [3] regulations regarding the dimensioning and reinforcement detailing

of ductile walls of the ductility classes DCM and DCH were applied. Certain walls of RC core, since they represent complex sections of walls, composed of connected rectangular segments, were treated as integral parts consisting of webs in the direction in which the seismic shear force acts, with flanges normal to them. This is also in accordance with the rules defined in EN1998-1 [3]. The considered positions of integral shear walls (complex cross sections of U and I, SW1 and SW2) are shown in Figure 1.

The design values of the walls bending moments were obtained from the EN1998-1 [3] bending moments envelope for a seismic design situation. The design shear force along the height of the walls were determined using the corresponding values of the shear force magnification factor ε for the individual ductility classes. All requirements related to dimension acquisition (height of critical zone, minimum wall thickness, thickness and length of boundary elements) and reinforcement detailing for vertical and horizontal reinforcement (stirrups) of the boundary elements in critical zones and areas outside critical zones, as well as requirements related to vertical and horizontal web reinforcement are fulfilled.

4 NONLINEAR TIME-HISTORY ANALYSIS

The nonlinear spatial model of the RC core walls was made. The PERFORM-3D software [10] was used for the nonlinear time-history analysis. The core walls are modeled using nonlinear vertical fiber elements representing the expected behavior of the concrete and reinforcing steel [11]. The area and location of reinforcement within the cross-section, as well as concrete properties, were defined using individual fibers forming the cross-section of the wall. The shear behavior is modeled as elastic. Stress-strain relationship for unconfined concrete, confined concrete, and reinforcement, compliant with recommendations given in Eurocode 8 [3], were adopted. The data of the European strong-motion database [12] were used as database of ground motions. Sixty seismic records were selected. Out of these records 25 were recorded in rock, which corresponds to the type A soil according to EN1998-1 [3]. The remaining thirty-five records were recorded on stiff soil, which corresponds to the type B soil according to EN1998-1 [3]. Magnitude values for selected records range between 5.1 and 7.0, while distances to source vary from 5 to 70 km. The basic criterion used in this paper for the selection of ground motions is that the mean value of their response spectra be compatible with the corresponding target spectrum in a wider range of periods. The elastic spectrum from EN1998-1 [3] was selected as the target spectrum for the return period of 475 years, with the design ground acceleration amounting to 0.37g. The mean squared error method (MSE) is selected for ground motions scaling [13]. Figures 2 and 3 show: response spectra of selected ground motions scaled by MSE method for the intensity level of 10%/50, the mean spectrum and relevant target spectra (Eurocodes 8 elastic spectra) for the intensity level of 10%/50 and the mean spectrum for the intensity level of 2%/50, for certain soil types.

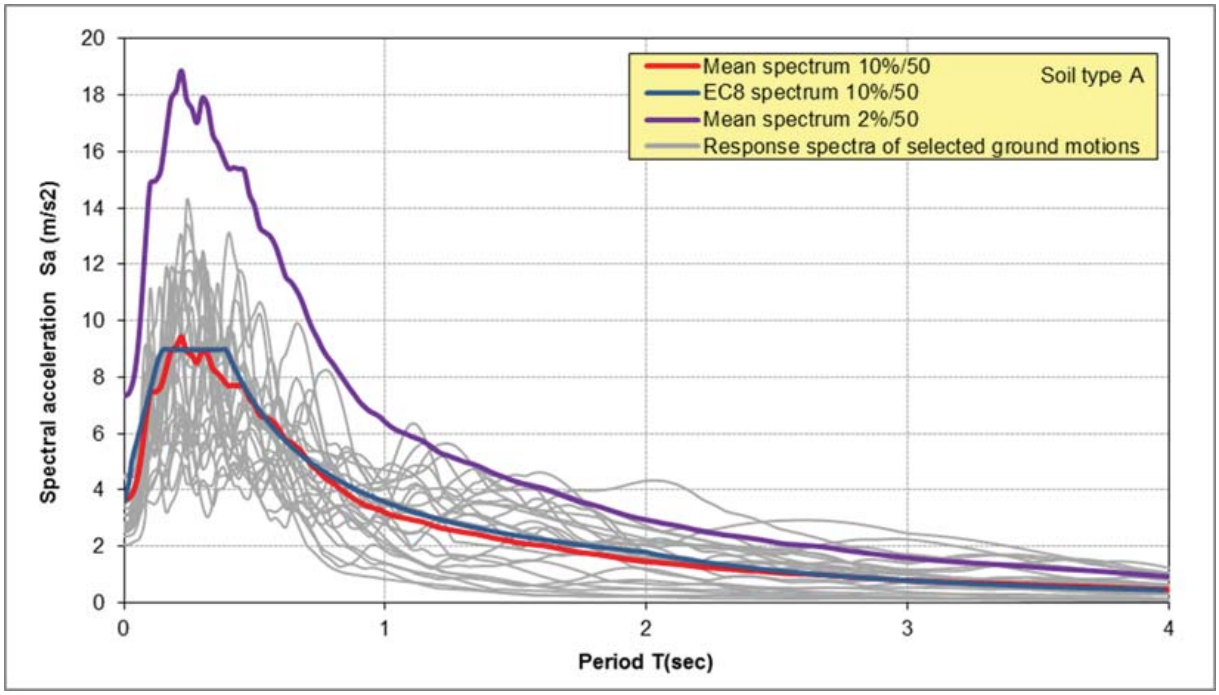

Figure 2: Characteristic response spectra of the selected ground motions for soil type A.

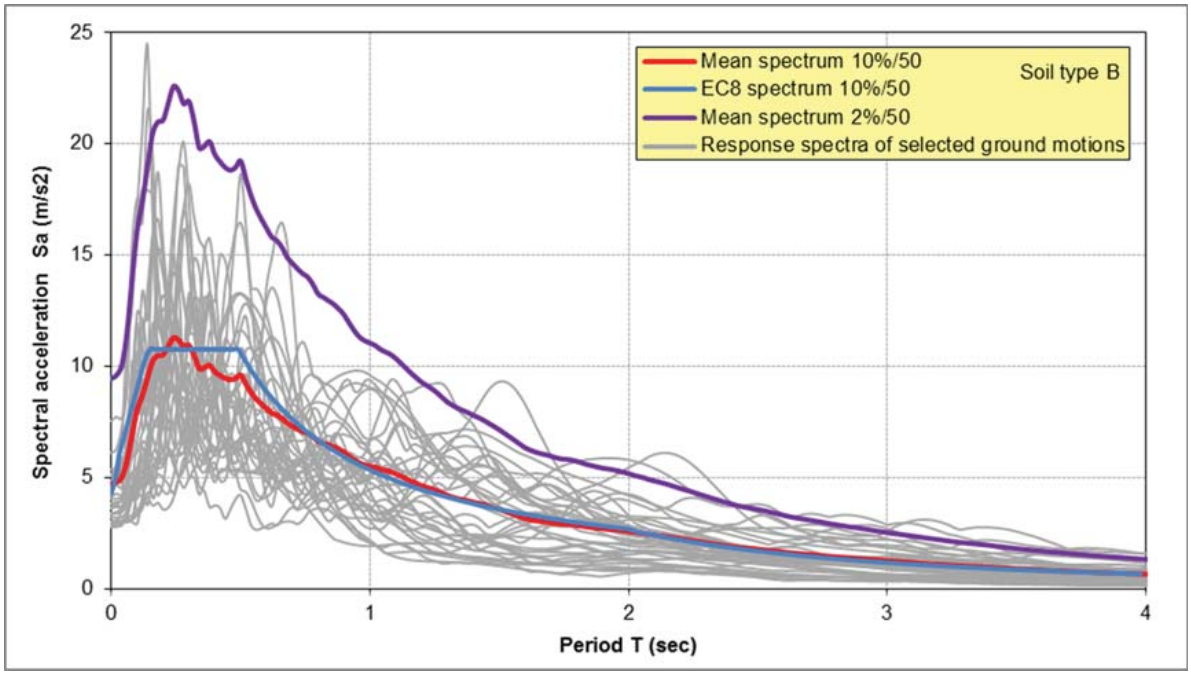

Figure 3: Characteristic response spectra of the selected ground motions for soil type B.

5 ANALYSIS RESULTS

The considered buildings are designed for two ductility classes defined in EN 1998-1: high ductility class (DCH) and medium ductility class (DCM). During the design of representative RC high-rise buildings for specific ductility classes in accordance with EN1998-1 [3], certain specificities were observed. Firstly, it has been observed that for RC high-rise buildings, characterized by higher values of the fundamental periods, the values of design spectrum for fun-

damental mode $S_d(T_1)$ are very low (less then the lower boundary of the horizontal project spectrum β defined in EN1998-1 [3]). For this reason, the total seismic forces in linear analysis for DCH and DCM buildings do not differ much (see Table 2). It is interesting to notice that for lateral force method of analysis, which is not advisable for RC high-rise buildings due to the influence of higher modes, the values of the total seismic forces for the individual ductility classes would be identical.

Further, due to the high values of the design shear forces in DCH walls, obtained by existing EN1998-1 [3] procedure, it is practically impossible to satisfy demand regarding diagonal compression failure of the web due to shear in the web $V_{Rd,max}$ [3]. The design shear force V_{Ed}, according to rules from EN1998-1 [3], must be less than shear resistance controlled by diagonal compression in the web $V_{Rd,max}$ [3]. Outside the critical region, this shear resistance is calculated as in EN 1992-1 [8] for monotone loads, while in the critical region, 40% of the value outside of critical region is proposed by EN1998-1 [3]. This EN1998-1 [3] rule is based on experimental research done by Biskinis et al. [14]. Biskinis et al. [14] has shown that the cyclic load significantly reduces this resistance and that the shear resistance $V_{Rd,max}$, is averages 40% of the value defined in EN 1992-1 [8]. These differences are very large and for this reason stated reduction of $V_{Rd,max}$ is included in EN 1998-1 only for DCH walls in the critical area. This large reduction of the design shear resistance $V_{Rd,max}$, applied together with the shear magnification, might be prohibitive for the usage of DCH RC ductile walls. Fulfillment of shear control would only be possible with unrealistically large wall thicknesses. This limitation is noted by previous studies even for lower buildings and for this reason, the DCM walls are not included in EN1998-1 [3] by this provision, while the above-mentioned experimental findings are not confirmed with the more experimental tests [15]. Due to the inability to the fulfilment of this EN1998-1 [3] provision for DCH RC walls with the realistic wall thickness, the considered representative RC high-rise buildings are designed to fulfil all the EN1998-1 [3] provisions except demand regarding diagonal compression failure.

In Figure 4, characteristic seismic shear force diagrams in wall (SW_1) in Y direction for three representative buildings are shown: V'_{Ed} – seismic shear forces obtained by multi-modal response spectrum analysis according to EN1998-1 [3], V_{Ed} – design seismic shear forces obtained by EN1998-1 [3], and $V_{Rd,max}$ - the shear resistance controlled by diagonal compression in the web. It is easy to notice that in critical regions of the wall for the DCH ductility class, the shear resistance $V_{Rd,\,max}$ is significantly less than the design shear force V_{Ed}, while for the ductility class DCM the design shear forces satisfy the condition that they are less than shear resistance.

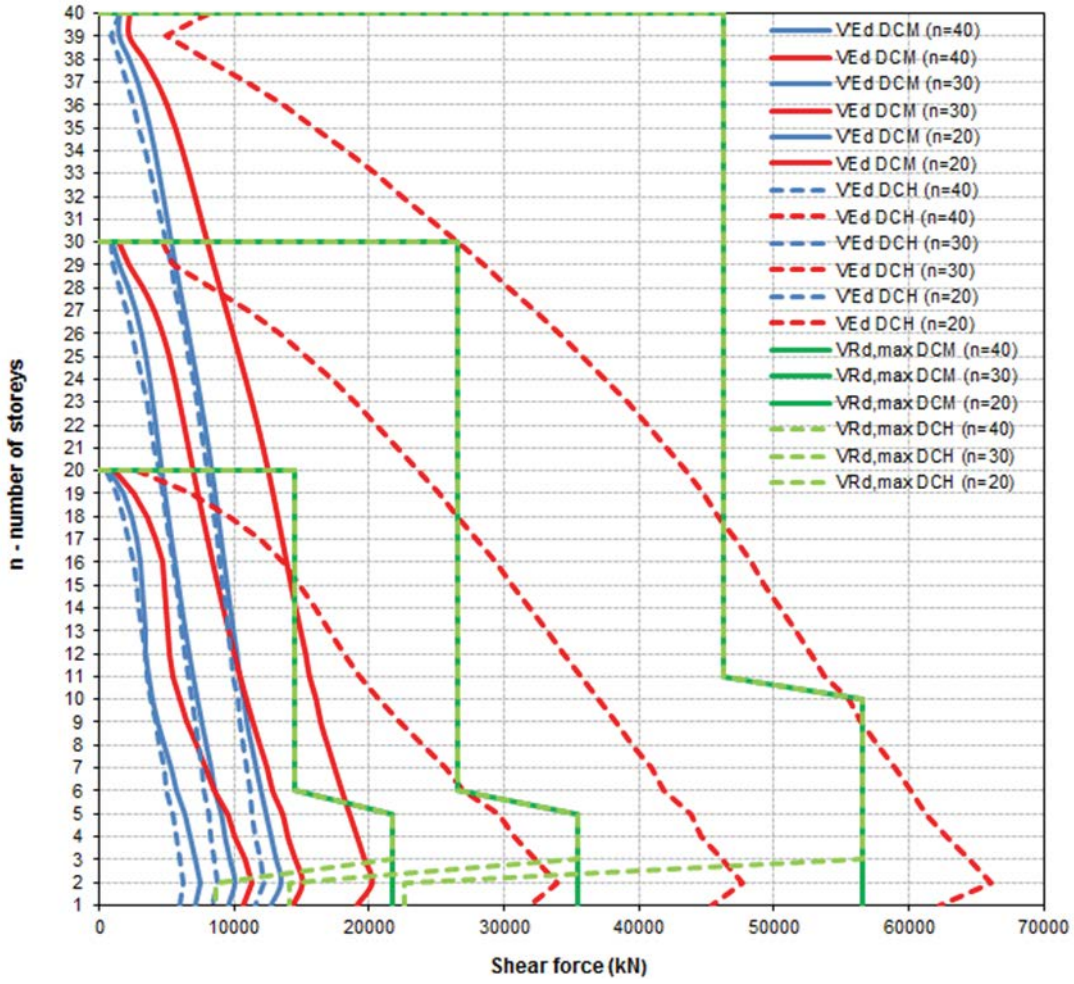

Figure 4: The characteristic seismic shear force diagrams in wall SW_1.

Figure 4 also shows that the shear forces along the wall height obtained by linear analysis V'_{Ed} do not differ much for the ductility classes DCM and DCH. These two facts, i.e. similar values of shear forces from linear analysis for individual ductility classes and inability to meet shear control in the case of DCH class, clearly indicate that RC high-rise buildings should be designed for DCM ductility class for the current state of EN1998-1 [3].

Furthermore, Figure 5 shows the characteristic values of the base shear forces of wall SW1 for the Y direction for DCM and DCH buildings. In addition to the shear forces V'_{Ed}, V_{Ed} i $V_{Rd,max}$ at the base of the wall, the values of the shear forces obtained from nonlinear time-historey analysis V_{na} are shown. V_{na} is the mean value of seismic shear forces obtained by using the 60 selected ground motions.

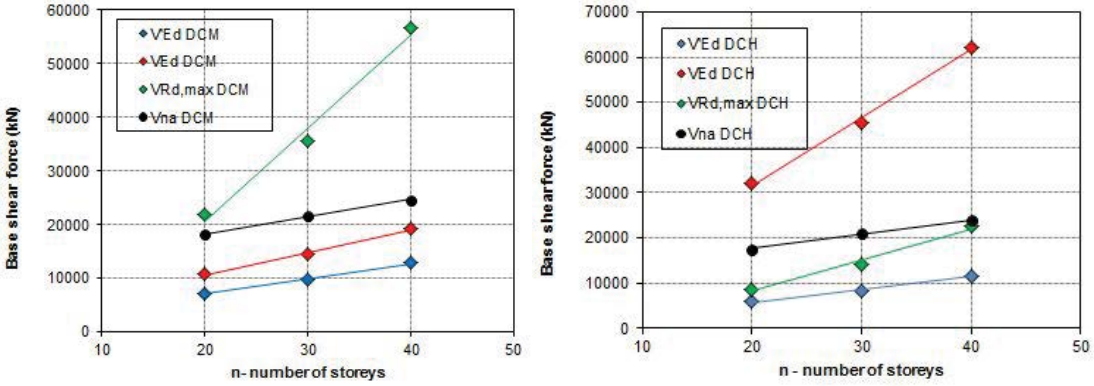

Figure 5: The characteristic base seismic shear forces in wall SW_1.

From the Figure 5, it can be seen that for the DCM ductility class, the shear forces obtained from the nonlinear time-history analysis V_{na} are higher than the designed ones, indicating that it is not appropriate to use a constant value of the magnification factor of 1.5 for the DCM ductility class. This imposes the need to calculate the increase factor ε in the same way as in the case of the DCH ductility class. On the other hand, for the DCH ductility class, the shear force values V_{na} differ significantly from the design values, which, unlike DCM shear forces, are overestimated or much larger than the actual forces that occur in the walls during an earthquake. It can be concluded that the correction of seismic design forces calculation for RC high-rise buildings in EN1998-1 [3] is required.

Also the high level of normal compressive force in the walls of high-rise RC buildings can be a limiting factor when designing high ductility class. For this reason, an analysis of the feasibility of achieving the required displacement ductility was performed for the three representative buildings designed for the DCM and DCH ductility classes. Given that for high-rise RC buildings characterized by values of fundamental vibration periods greater than 0.7s, the principle of equal displacements applies, the behavior factor is equal to displacement ductility factor [16]. The results of nonlinear time-history analyzes in buildings with a fundamental period greater than about 0.7s, showed that the maximum displacements in the elasto-plastic system are approximately equal to those in an elastic system that has the same initial stiffness but has no limited bearing capacity [17]. For the purposes of this analysis, the calculation of displacement ductility factors was done using the recommendations given by [16]. Paulay and Priestley [16] derived displacement ductility factors for RC vertical cantilever elements. The displacement ductility factor depending on the curvature ductility factor is calculated using the equation 1:

$$\mu_\Delta = 1 + 3 \cdot (\mu_\varphi - 1) \cdot \frac{L_p}{L} \cdot \left(1 - 0.5 \cdot \frac{L_p}{L}\right) \tag{1}$$

Where: μ_φ is curvature ductility factor, L_p plastic hinge length, L wall height. The theoretical background for derivation of the expression for the displacement ductility factor has been discussed in the literature [16]. The length of the plastic hinge is also determined by [16] as follows (equation 2):

$$L_p = 0.2 \cdot D_w + 0.044 \cdot h_e \tag{2}$$

Where: D_w wall cross-section thickness and h_e effective wall height equal to the height of the cantilever wall with the horizontal force at the top of the wall and the same value of moment and shear force at the fixed end as in the case of the actual wall.

For the three considered representative RC high-rise buildings using the XTRACT [18] software, cross-sections of the walls at the location of the plastic hinge were analyzed and moment-curvature dependencies for the plastic hinge were derived. The curvature ductility factors were determined using the derived dependencies. Based on derived curvature ductility factors for individual representative RC high-rise buildings, designed for both ductility classes, displacement ductility factors were calculated, which at the same time represent behavior factors q. Figure 6 shows the derived behavior factors for individual representative RC high-rise buildings.

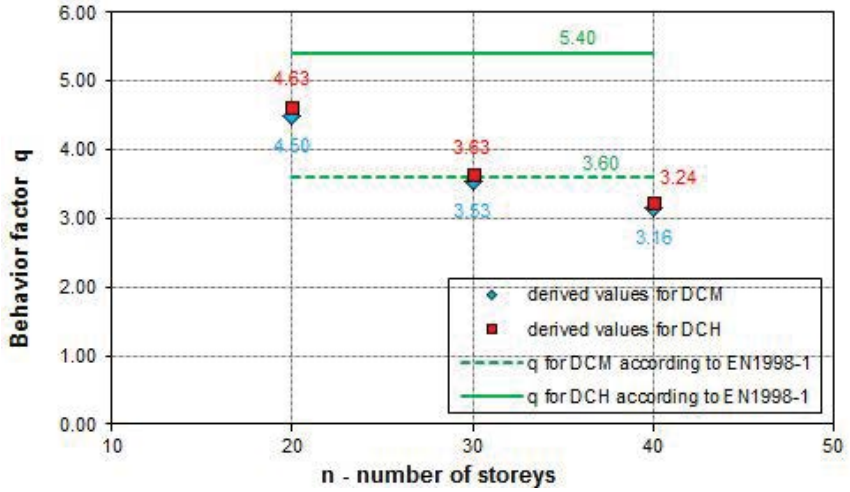

Figure 6: The derived behavior factors.

From the Figure 6, the limitations in terms of the behavior factors values for RC high-rise buildings can be noticed. The highest behavior factor is obtained for the case of a 20-story representative building due to the least normal compression force in the wall and therefore the highest curvature ductility in plastic hinge cross section and the corresponding displacement ductility. For reasons of maximum values of normal compression force in wall of 40-storey building, the smallest behavior factor is obtained. For all three buildings designed for the DCH ductility class, smaller behavior factors, than the value defined by EN1998-1 [3], were derived. Buildings designed for DCM have satisfactory values of derived behavior factors, that is, greater or approximately the same value as those for the DCM class according to EN1998-1 [3]. Exception is a 40-story building that has a slightly lower value. These results also indicate the limitation of the application of the DCH ductility class to the design of RC high-rise buildings in accordance with EN1998-1 [3]. The presence of higher normal compression forces in the RC walls of high-rise buildings is a limiting factor when considering the DCH ductility classes. With the increase in number of storeys, the possibility of achieving an appropriate value of displacement ductility, characteristic for the DCH ductility class, decreases. Therefore RC high-rise buildings should be designed with DCM ductility class, wherein there are wider possibilities for defining the behavior factor q for the DCM ductility class. This range can be defined depending on different parameters (for example: number of storeys, structural system, etc.).

6 CONCLUSIONS

In analysis of seismic design of representative high-rise buildings for DCM and DCH ductility classes, in accordance with Eurocode 8, the following conclusions were pointed out:

- The conducted analysis has shown that total seismic base shear forces for considered ductility classes (DCM and DCH) differs only 5-15%. This occurs because the values of design spectrum for fundamental mode $S_d(T_1)$ of high-rise buildings are very low, less than values related to lower bound factor for the horizontal design spectrum β (defined in Eurocode 8). Therefore, the influence of behaviour factor q on design spectrum for fundamental mode is negligible. The seismic base shear forces of the first mode for DCM and DCH ductility class have the same value while shear forces for higher modes differ slightly. There is a need to introduce a unique ductility class for RC high-rise buildings.
- Due to the high design shear forces in DCH walls, it is practically impossible to satisfy demand regarding diagonal compression failure of the web due to shear in the web. Large reduction of the shear resistance of DCH wall controlled by diagonal compression, applied together with magnification of shear forces with current Eurocode 8 procedure, limits the design of DCH ductile walls. Fulfillment of shear control would only be possible with unrealistically large wall thicknesses.
- From the analysis of the possibility of achieving the required displacement ductility for the DCH class, it is concluded that the presence of higher normal compression forces is a limiting factor when applying the DCH ductility class. With increasing number of stories, the ability to achieve the appropriate value of displacement ductility, characteristic for the DCH ductility class, decreases. Such results indicate the limitation of the application of the DCH ductility class to the design of RC high-rise buildings in accordance with Eurocode 8.
- All these facts clearly indicate that RC high-rise buildings should be designed according Eurocode 8 provisions specified for medium ductility class, taking into consideration the weakness of the existing procedure for calculating design shear force. The need of introducing a single medium ductility class for RC high-rise buildings is pointed out.

REFERENCES

[1] Ji J, Elnashai A.S, Kuchma D.A, An analytical framework for seismic fragility analysis of RC high-rise buildings, *Engineering Structures* 29 (2007) 3197–3209. doi:10.1016/j.engstruct.2007.08.026, 2007.

[2] Brownjohn JMW, Lateral loading and response for a tall building in the non-seismic doldrums, *Engineering Structures* 2005 27(12):1801-12, 2005.

[3] EN1998-1 Eurocode 8 – Design of structures for earthquake resistance. Part 1: General rules, seismic actions and rules for buildings. European standard EN 1998-1, *European Committee for Standardization*, Brussels, 2004.

[4] Rutenberg A, Nsieri E., The seismic shear demand in ductile cantilever wall systems and the EC8 provisions, *Bull Earthq Eng* 2006;4:1–21. doi:10.1007/s10518-005-5407-9, 2006.

[5] Kappos AJ, Antoniadis P. A, contribution to seismic shear design of R/C walls in dual structures, *Bull Earthq Eng* 2007;5:443–66. doi:10.1007/s10518-007-9041-6, 2007.

[6] Antoniou, K., Tsionis, G. and Fardis, M.N., Inelastic Shears in Ductile RC Walls of Mid-Rise Wall-Frame Buildings and Comparison to Eurocode 8, *Bulletin of Earthquake Engineering*, 13(2015) , 841–869, doi:10.1007/s10518-014-9641-x, 2015.

[7] Antoniou, K., Tsionis, G. and Fardis, M.N., Evaluation of Eurocode 8 Rules for Wall Shear Demands in Wall-Frame RC Buildings, Proceedings of the Second European Conference on Earthquake Engineering and Seismology, Istanbul, Turkey, 2014.

[8] EN 1992-1-1 Eurocode 2: Design of Concrete Structures - Part 1-1: General Rules and Rules for Buildings, European Committee for Standardization, Brussels, 2004.

[9] ETABS2013, Integrated Analysis, Design and Drafting of Buildings Systems, CSI Computers and Structures Inc., 2013.

[10] PERFORM3D, CSI Computers and Structures Inc. PERFORM 3D nonlinear analysis and performance assessment for 3D structures, 2006.

[11] Powell GH. PERFORM 3D detailed example of a tall shear wall building by Dr. Graham H. Powell. Nonlinear modeling, analysis and performance assessment for earthquake loads. Berkeley: CSI Computers & Structures Inc., 2007.

[12] Ambraseys N, Smit P, Sigbjornsson R, Suhadolc P, Margaris B. Internet-site for European strong-motion data. Eur Comm Dir XII, Environ Clim Program 2002. http://www.isesd.cv.ic.ac.uk, 2002.

[13] PEER Pacific Earthquake Engineering Research Center. Technical report for the peer ground motion database web application. Berkeley, 2010.

[14] Biskinis D.E., Roupakias G.K. and Fardis M.N., Degradation of shear strength of RC members with inelastic cyclic displacements, *ACI Structural Journal 101*, No.6, 2004.

[15] Fardis MN, Carvalho EAA, Ezio F, Pinto P, Plumier A. Designers' guide to EN 1998-1 and EN 1998-5 Eurocode 8 : design of structures for earthquake resistance : general rules, seismic actions, design rules for buildings, foundations and retaining structures. London: London : Thomas Telford, 2005.

[16] Paulay T., Priestley N., Seismic design of reinforced concrete and masonry buildings. Wiley, New York, 1992.

[17] Janković S., Osnove seizmičkog planiranja i projektovanja za inženjere arhitekture i građevine, Građevinski fakultet u Podgorici, Univerzitet Crne Gore, AMG Knjiga, 2014

[18] XTRACT, Cross Section Analysis Software for Structural Engineers. Imbsen Software systems, 2001.

EURODYN 2020
XI International Conference on Structural Dynamics
M. Papadrakakis, M. Fragiadakis, C. Papadimitriou (eds.)
Athens, Greece, 23–26 November 2020

SEISMIC PERFORMANCE AND RESILIENCE QUANTIFICATION OF A ROCKING BRIDGE FRAME

Anastasios I. Giouvanidis[1*] **and You Dong**[1]

[1]Department of Civil and Environmental Engineering, The Hong Kong Polytechnic University
Hung Hom, Hong Kong
e-mail: agiouv@polyu.edu.hk, you.dong@polyu.edu.hk

Keywords: rocking, analytical dynamics, fragility, seismic loss, resilience.

Abstract. *Conventionally designed bridges, i.e. when the column is monolithically connected with the ground (fixed-base), sustain considerable damage at the column ends after severe earthquakes. Seismic damage often determines whether or not the bridge remains functional after an earthquake event. Rocking isolation, on the other hand, allows structural components to uplift and pivot; thus, in principle, it relieves the structure from excessive deformations and damage. However, rocking isolation is still rarely applied in engineering practice, mainly due to the lack of thorough understanding of its dynamic (seismic) performance and its post-earthquake financial benefits. This paper redirects our attention to the main benefits of rocking design, and conducts a thorough seismic loss assessment adopting two different rocking bridge configurations in terms of their post-earthquake economic losses and resilience. In particular, this work extends the well-established performance-based earthquake engineering framework to evaluate the seismic losses of the examined rocking structures accumulated following severe seismic events and quantify their post-earthquake resilience. The analysis reveals the considerably mitigated seismic losses and the remarkable post-earthquake resilience that a rocking bridge offers when carefully designed. In particular, even a slight modification of the slenderness of the structure leads to a substantial enhancement of its seismic performance; reinforcing its potential as an alternative seismic design paradigm for bridges. The above findings illustrate the considerable financial benefits of such innovative seismic-resistant structural systems, which can serve as an efficient seismic design paradigm for future bridge engineering applications.*

1 INTRODUCTION

Conventional bridge seismic design provides the necessary strength and ductility to the structure to withstand seismic forces and avoid collapse. Such a design concept, though, accepts the "*prize*" of sustainable seismic damage after severe earthquakes. Seismic damage is an important measure that often determines whether or not a bridge remains operational following a seismic event. Rocking design, on the other hand, relieves the structure from seismic damage by allowing structural components to uplift and pivot during an earthquake. After the Chilean earthquake in 1960, the seminal work of Housner [1] revealed the benefits of rocking design and triggered a thorough investigation on the seismic performance [2, 3, 4, 5, 6, 7, 8, 9, 10, 11, 12] of various rocking structural systems [13, 14, 15, 16, 17, 18].

The mechanical configuration of the single-column frame of Fig. 1, where the column is monolithically connected with the footing (or base) while the column-base system can detach from the ground when subjected to a ground motion, is particularly attractive for bridge design. Various studies have experimentally and/or numerically investigated its seismic performance highlighting: (i) the mitigated seismic forces that are transmitted to the column of the structure; and (ii) the negligible seismic damage and small residual displacements that the rocking structure sustains [19, 20, 21, 22, 23, 24]. On the other hand, the analytical studies that focus on the potential post-earthquake financial benefits of rocking structures still remain scarce. Modelling the structural system of Fig. 1 as a two degree-of-freedom oscillator, Giouvanidis and Dong [25] compared the seismic performance of a (single-column) rocking versus a conventionally designed (fixed-base) bridge. That study revealed the remarkable post-earthquake financial benefits that a rocking bridge offers when carefully designed.

This research is motivated by the lack of analytical studies that thoroughly quantify the post-earthquake financial benefits of a rocking bridge. In particular, it extends the well-established performance-based earthquake engineering framework to investigate the seismic performance of two rocking bridge configurations and to unveil the influence of design parameters (i.e. slenderness) on their functionality and resilience in the aftermath of severe seismic hazard scenarios. In this context, this research study: (i) redirects our attention to the main benefits of rocking design (e.g. seismic loss, post-earthquake resilience); and (ii) paves the way for a more holistic seismic assessment framework of single-column rocking bridges.

2 ANALYTICAL MODELLING OF A ROCKING BRIDGE FRAME

Fig. 1 illustrates the examined single-column rocking bridge frame. Assuming rigid ground conditions and no sliding at the rocking interface allow the structure to uplift and pivot during an earthquake exhibiting planar rocking motion. When the rocking structure of Fig. 1 remains in full contact with the ground, it behaves as a single degree-of-freedom system. Thus, its motion is captured by the deformation of the column u. After rocking commences, the motion of the rocking structure is captured by both the deformation of the column u and the rocking rotation ϕ of the base [26, 27].

Consider the rocking oscillator of Fig. 1 with a concentrated mass m at height h. The column has a total mass of m_c and elastic stiffness of EI uniformly distributed along its length. The rigid base has mass m_b and width $2b$. For simplicity, assume the lumped mass m creates no moment of inertia, while the rigid base creates moment of inertia with respect to its center of mass equal to $I_{m_b} = (1/3)\, m_b b^2$. The equations of motion of the rocking oscillator

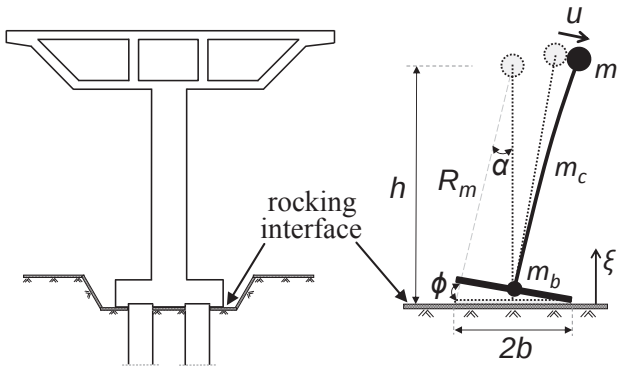

Figure 1: Typical single-column rocking bridge frame (left) modelled as a two degree-of-freedom oscillator (right)

can be derived using the general form of the Lagrange's equation:

$$\frac{d}{dt}\left(\frac{\partial L}{\partial \dot{u}}\right) - \frac{\partial L}{\partial u} = Q, \qquad \frac{d}{dt}\left(\frac{\partial L}{\partial \dot{\phi}}\right) - \frac{\partial L}{\partial \phi} = 0 \tag{1}$$

where $L = T - V$, with T the kinetic energy, V the potential energy and Q the generalized force, whose mathematical derivations are for brevity omitted herein (see [25] for more details). While the oscillator of Fig. 1 exhibits planar rocking, the equations that describe its motion become [25]:

$$\begin{array}{l} \left(m+\frac{33}{140}m_c\right)\ddot{u} + \left(m+\frac{11}{40}m_c\right)h\ddot{\phi} = \\ -C\dot{u} - \frac{3EI}{h^3}u + \left[\left(m+\frac{33}{140}m_c\right)u - sgn\left(\phi\right)\left(m+\frac{3}{8}m_c\right)b\right]\dot{\phi}^2 \\ -\ddot{u}_g\left(m+\frac{3}{8}m_c\right)\cos\phi + g\left(m+\frac{3}{8}m_c\right)\sin\phi \end{array} \tag{2}$$

$$\begin{array}{l} \left(m+\frac{11}{40}m_c\right)h\ddot{u} + \left[\begin{array}{l}\left(I_{m_b}+m_b b^2\right)+m\left(h^2+b^2\right)+mu^2 - sgn\left(\phi\right)2mbu \\ +m_c\left(\frac{1}{3}h^2+b^2\right)+\frac{33}{140}m_c u^2 - sgn\left(\phi\right)\frac{3}{4}m_c bu\end{array}\right]\ddot{\phi} = \\ \quad -\left(2m+\frac{33}{70}m_c\right)u\dot{u}\dot{\phi} + sgn\left(\phi\right)\left(2m+\frac{3}{4}m_c\right)b\dot{u}\dot{\phi} \\ \quad +\ddot{u}_g\left[\begin{array}{l}-sgn\left(\phi\right)\left(m+m_b+m_c\right)b\sin\phi \\ -\left(m+\frac{1}{2}m_c\right)h\cos\phi + \left(m+\frac{3}{8}m_c\right)u\sin\phi\end{array}\right] \\ \quad +g\left[\begin{array}{l}-sgn\left(\phi\right)\left(m+m_b+m_c\right)b\cos\phi \\ +\left(m+\frac{1}{2}m_c\right)h\sin\phi + \left(m+\frac{3}{8}m_c\right)u\cos\phi\end{array}\right] \end{array} \tag{3}$$

whereas when it remains in full contact with the ground, the pertinent equation of motion becomes:

$$\left(m+\frac{33}{140}m_c\right)\ddot{u} = -C\dot{u} - \frac{3EI}{h^3}u - \ddot{u}_g\left(m+\frac{3}{8}m_c\right) \tag{4}$$

where C is the damping coefficient responsible for the energy loss while the structure vibrates, $sgn\left(\phi\right)$ is the signum function of the rocking rotation ϕ and $\ddot{u}_g\left(t\right)$, g denote the ground and the gravitational acceleration, respectively.

Rocking initiates when the overturning moment due to the external forces exceeds the restoring moment of the structural system. Hence, uplift occurs when [25]:

$$\pm h\frac{m+\frac{11}{40}m_c}{m+\frac{33}{140}m_c}\left[\begin{array}{l}C\dot{u}+\frac{3EI}{h^3}u \\ +\ddot{u}_g\left(m+\frac{3}{8}m_c\right)\end{array}\right] \mp \ddot{u}_g\left(m+\frac{1}{2}m_c\right)h - g\left[\begin{array}{l}\left(m+m_b+m_c\right)b \\ \mp\left(m+\frac{3}{8}m_c\right)u\end{array}\right] > 0 \tag{5}$$

where the upper sign denotes clockwise rotations and the lower sign counter-clockwise rotations.

During rocking, the smooth motion of the structure is interrupted by nonsmooth events (i.e. impacts) when $\phi = 0$ and kinetic energy is lost. Following [28, 29], this study assumes totally inelastic impacts, where the rocking oscillator remains in full contact with the ground after each impact and uplifts when the condition of Eq. (5) is met. Under these assumptions, the sole post-impact unknown is the flexural velocity $\dot{u}^+$. Conservation of angular momentum gives [25]:

$$\dot{u}^+ = \dot{u}^- + \frac{I_{m_b} - m_b b^2 + m_c\left(-b^2 + \frac{1}{3}h^2 + \frac{33}{140}u^2\right) + m\left(-b^2 + h^2 + u^2\right)}{\left(m + \frac{11}{40}m_c\right)h}\dot{\phi}^- \tag{6}$$

where $\dot{u}^-$ and $\dot{\phi}^-$ denote the pre-impact flexural and angular velocity, respectively.

3 RESILIENCE-BASED EARTHQUAKE ENGINEERING ASSESSMENT OF THE EXAMINED ROCKING BRIDGE FRAMES

To evaluate the seismic performance of a structural system, the Pacific Earthquake Engineering Research (PEER) Center proposed the *performance-based earthquake engineering* (PBEE) framework [30, 31]. The PBEE analysis allows for a quantitative assessement of the seismic performance of a structural system in terms of engineering parameters, such as the expected seismic loss accumulated in the aftermath of an earthquake. The PBEE framework encompasses four steps: hazard analysis, structural analysis, damage analysis and loss analysis. The

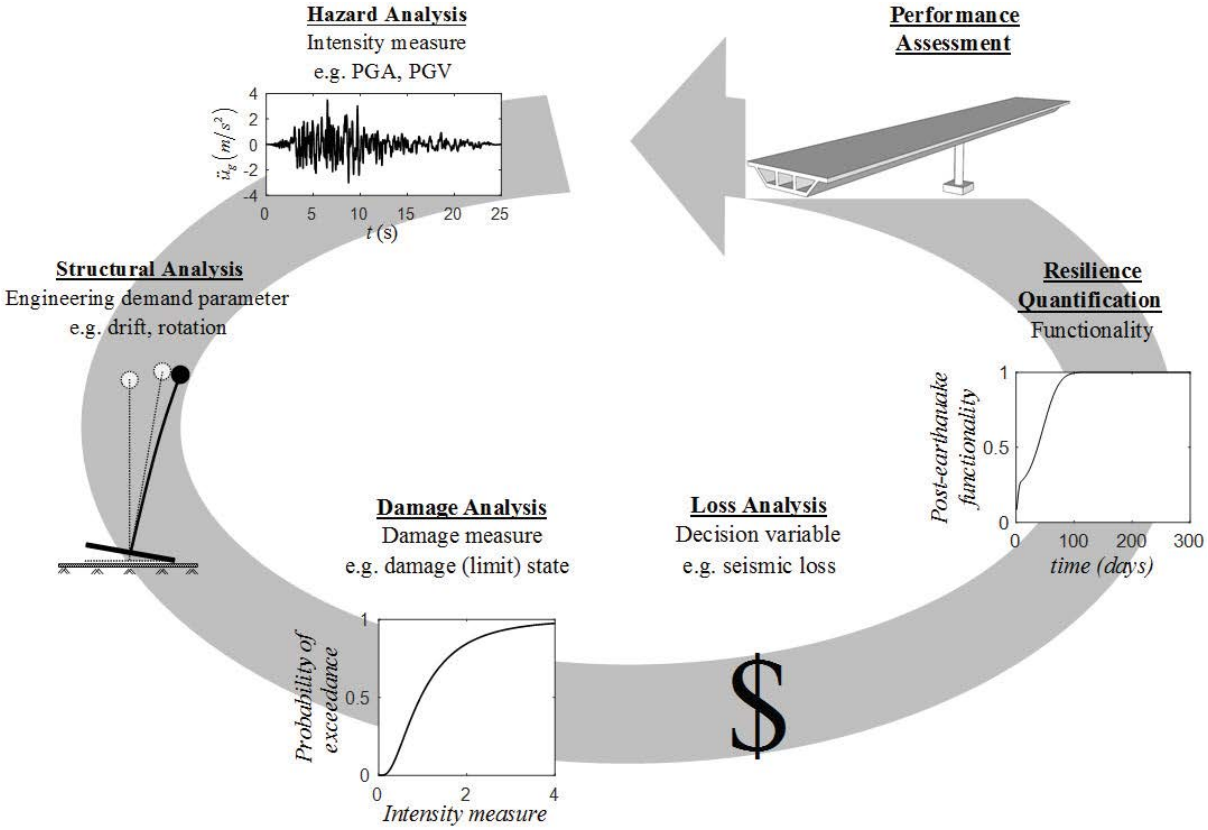

Figure 2: Resilience-based earthquake engineering framework

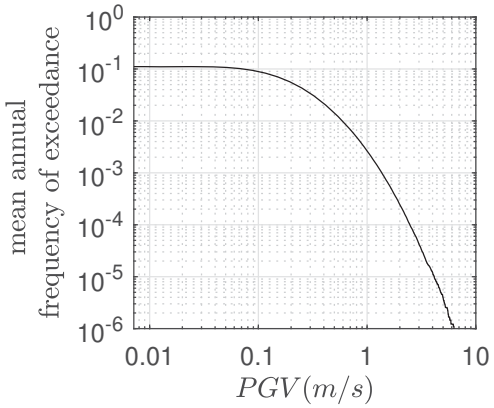

Figure 3: Hazard curve (in logarithmic scale) for the area of focus after conducting the probabilistic seismic hazard analysis

PBEE framework, though, does not incorporate the post-earthquake functionality and resilience of the structure, which are also important indicators of its seismic performance. On the other hand, the *resilience-based earthquake engineering* (RBEE) framework of Fig. 2 focuses on mitigating the earthquake-induced risks to enable rapid recovery of the structure in the aftermath of severe earthquakes [32]. Therefore, the RBEE appears to be a more holistic approach and it is considered as an extension of the PBEE in the design process (Fig. 2).

3.1 Hazard Analysis

To perform the probabilistic seismic hazard analysis (PSHA), this section assumes that the examined rocking bridge frames are located in California laying on a strike-slip fault. The minimum and maximum moment magnitudes M_w are taken as 5.5 and 8, respectively, while the shear wave velocity is $V_{s,30} = 480$ m/s. The Joyner-Boore distance is $R_{JB} = 5$ km. The intensity measure (IM) considered herein is the peak ground velocity (PGV) as it was shown to be the most critical for overturning various rocking configurations [33, 34]. To connect the earthquake events that are likely to appear in the examined area (i.e. California) with their annual frequency of exceedance, the Gutenberg-Richter recurrence law is adopted [35, 36]:

$$\log_{10}\lambda_M = 3.94 - 0.89 \cdot M \tag{7}$$

where λ_M is the frequency of the earthquakes with magnitudes greater than M. Fig. 3 plots the hazard curve (in logarithmic scale) that provides the mean annual frequency of exceedance λ_M of every earthquake that is likely to occur in the area of focus.

3.2 Structural Analysis

This section investigates the seismic response of two single-column rocking bridge frames (Fig. 1). Each frame is part of a two-span (box-girder) bridge of total length L = 60 m and width W = 10 m. Assume the lumped mass m is located at height h = 8 m, while the total mass of the column and of the base is $m_c = 0.25m$ and $m_b = 0.15m$, respectively. The two rocking bridge frames have different slenderness α and subsequently different base-width $2b$, while they have the same height h. Consider one rocking frame with base-width $2b$ = 3 m and slenderness $\alpha = 0.18$ rad $= \pi/17$ (i.e. $\alpha < \pi/15$ [37]), and another with base-width $2b$ = 4.6 m and slenderness $\alpha = 0.28$ rad $= \pi/11$ (i.e. $\pi/15 < \alpha < \pi/10$ [37]). Both structural

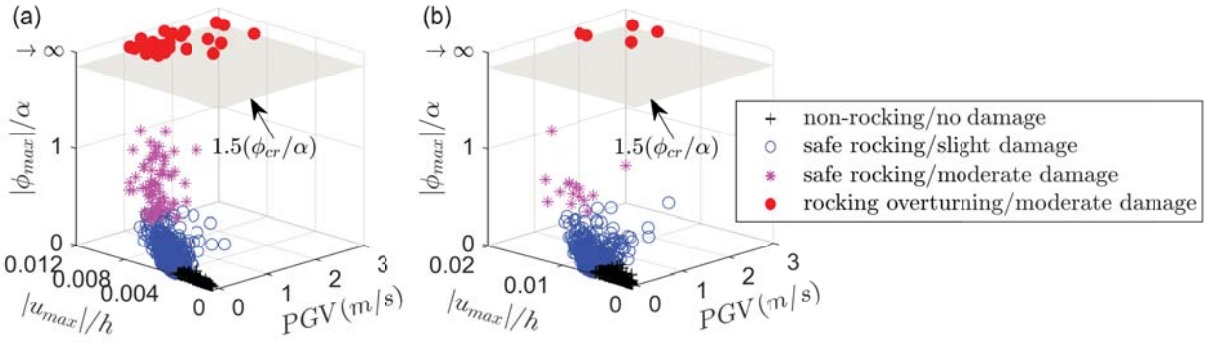

Figure 4: Seismic response analysis of a rocking bridge frame with slenderness (a) α = 0.18 rad and (b) α = 0.28 rad (Fig. 1)

configurations have identical natural frequency $\omega_n = 8p$, where $p = \sqrt{g/R_m} \simeq 1.1$ rad/sec is the frequency parameter of both rocking oscillators, and R_m is the diagonal distance of the lumped mass from the pivot points (Fig. 1). In addition, the analysis assumes a constant damping ratio $\zeta = 5\%$ when the examined rocking bridge frames exhibit rocking motion and a reduced damping ratio when they remain in full contact with the ground (see e.g. [27] for further details).

To perform the structural analysis, appropriate engineering demand parameters (EDPs) which describe the motion of the two examined structural systems need first to be defined. This work adopts as EDPs: (i) the absolute maximum flexural deformation $|u_{max}|$ normalized with respect to the height h; and (ii) the absolute peak rocking rotation $|\phi_{\max}|$ normalized with respect to the slenderness α (Fig. 1).

$$EDP_1 = \frac{|u_{\max}|}{h}, \qquad EDP_2 = \frac{|\phi_{\max}|}{\alpha} \tag{8}$$

For consistency, each rocking bridge frame is subjected to a series of strong ground motions adopted from the Pacific Earthquake Engineering Research (PEER) Center [38]. The adopted ground motions consist of two horizontal components and one vertical. Both horizontal components are used separately, while the vertical component is ignored. To induce higher levels of demand, a scale factor of 1, 1.25 and 1.5 is, respectively, assigned to the accelerograms of the adopted database. Therefore, 960 response-history analyses are conducted for each of the examined structural systems.

Fig. 4 illustrates the structural response of both rocking bridge frames with respect to the adopted IM. Fig. 4 reveals that increasing the slenderness of the structure considerably mitigates the rocking response $|\phi_{\max}|/\alpha$. However, note that, increase of the slenderness leads also to an increase of the structural deformation $|u_{max}|/h$ and, subsequently, potentially higher levels of damage. In addition, Fig. 4 shows that when the rotation $|\phi_{\max}|/\alpha$ exceeds 1.5 times the critical rotation ϕ_{cr}/α [27], the structure becomes dynamically unstable and overturns.

3.3 Damage Analysis

The seismic response of the rocking bridge frame of Fig. 1 is related to the damage occurred at the structure through appropriate damage measures. This work assumes that damage is occurred only at the column of the structure due to seismic forces [39]; all other kinds of damage are ignored. When excessive damage occurs, the structure collapses and subsequently

Damage limit state	Capacity limit	Response mode	Damage description
LS1	$\frac{\lvert u_{\max}\rvert}{h} = \frac{u_{cr}}{h}$	Rocking initiation	*Slight* concrete cracking and spalling at the column. Onset of yielding of the reinforcing bars. Column in operational condition (damage requires no more than cosmetic repair)
LS2	$\frac{\lvert \phi_{\max}\rvert}{\alpha} = 0.35$	Safe rocking	*Moderate* concrete cracking and spalling at the column. Damage to the exposed reinforcing bars. Minimal residual displacements. Column is still operational. Damage at the pivot points and the abutments due to rocking motion (column is structurally sound, damage is repairable)
LS3	$\frac{\lvert \phi_{\max}\rvert}{\alpha} = 1.5\left(\frac{\phi_{cr}}{\alpha}\right)$	Rocking overturning	*Moderate* concrete cracking and spalling at the column. Damage to the exposed reinforcing bars. Minimal residual displacements. Column is still operational. Damage at the pivot points and the abutments due to rocking motion (column is structurally sound, damage is repairable, the column-base system can be reused after the applied repair methods, the whole bridge needs to be reconstructed)

Table 1: Damage limit states of the rocking bridge frame of Fig. 1 [25].

the bridge needs to be reconstructed. In addition, when excessive rocking rotation occurs, the rocking bridge might overturn, thus, reconstruction of the the bridge is again required. To define the levels of the expected damage accumulated at the examined rocking bridge frames, this work adopts the pertinent damage limits states proposed in Giouvanidis and Dong [25]. Table 1 illustrates the adopted damage limit states, where u_{cr}/h is the critical deformation of the column when rocking initiates (i.e. when the condition of Eq. (5) is met).

This section employs the fragility function fitting method [40] to calculate the probability of the examined structures to exceed the certain limit values that correspond to each damage limit state. The fitting methodology to calculate the probability of exceedance can be estimated following the *maximum likelihood estimation* (MLE) approach [40]. In general, the MLE method calculates the fragility function parameters for which the assumed lognormal distribution attains the highest likelihood of producing the observed data. Fig. 5 plots the fragility curves for both rocking bridge frames (i.e. with slenderness $\alpha = 0.18$ rad and $\alpha = 0.28$ rad respectively). Note from Fig. 5 that, indeed, increase of the slenderness of the structure considerably decreases its probability of exceeding the certain damage limit states of Table 1.

3.4 Loss Analysis

The structural damage of the rocking bridge frames accumulated in the aftermath of a seismic event, investigated in Section 3.3, is related to the seismic loss through decision variables, e.g. the seismic (repair) loss. The seismic loss is defined as the sum of the seismic consequences

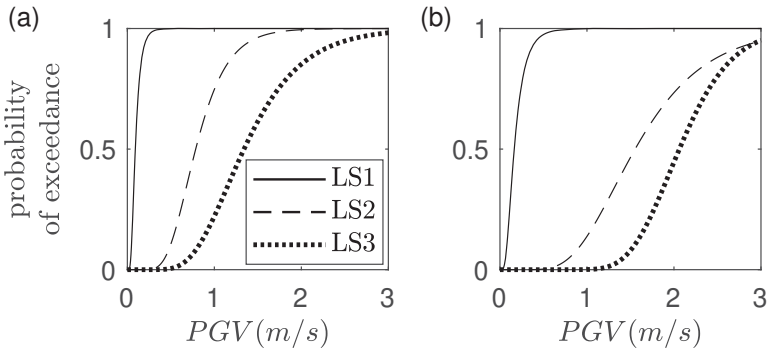

Figure 5: Fragility curves of a rocking bridge frame with slenderness (a) α = 0.18 rad, (b) α = 0.28 rad (Fig. 1) with respect to the adopted intensity measure

(e.g. damage and subsequently repair cost) weighted with their probability of occurrence. The expected seismic loss under the given IM can be expressed as [41]:

$$E\left(l\right) = \sum_{i=1}^{n} C_i \cdot P_{LSi|IM} \tag{9}$$

where C_i represents the seismic consequences, e.g. the repair costs associated with the given damage limit state i, and $P_{LSi|IM}$ is the conditional probability of the structure to be at the given damage limit state. The consequences of a seismic event C_i are quantified in monetary values and expressed as the summation of the direct and indirect costs accumulated after an earthquake event. This work considers only the direct costs, which are associated with the reconstruction expenses and are directly related to the level of structural damage. Therefore, the seismic consequence C_i associated with a given damage limit state is assumed proportional to the reconstruction cost of the rocking bridge [42, 43, 41]:

$$C_i = RCR_i \cdot c_{rec} \cdot W \cdot L \tag{10}$$

where W and L are the bridge width and length respectively. c_{rec} is the reconstruction cost (per square meter), which is translated into 2,306 $\$/m^2$ in present monetary values [44]. RCR_i is the repair cost ratio that corresponds to each damage limit state. The repair cost ratios are expressed as a percentage of the reconstruction cost of the bridge, and they differ from damage limit state to damage limit state; the more severe the damage, the larger the repair cost ratio. Table 2 presents the pertinent repair cost ratio values for each damage limit state of the rocking bridge frame of Fig. 1 [45, 25].

To assess the expected seismic losses of the examined rocking structures, this study considers nine different seismic hazard scenarios. These scenarios correspond to seismic events with T_R = 40, 72, 125, 225, 475, 975, 1,485, 2,475 and 4,975-year return period, which translate into a probability of 71%, 50%, 33%, 20%, 10%, 5%, 3%, 2% and 1%, respectively, that at least one such event will occur in the next 50 years in the area of focus. The hazard curve of Fig. 3 provides the intensities in terms of PGV values that correspond to the adopted seismic hazard scenarios, i.e. 0.37, 0.51, 0.65, 0.83, 1.08, 1.36, 1.53, 1.76 and 2.11 m/s, respectively.

Fig. 6 presents a comparison of the two rocking bridge structures in terms of the expected seismic loss accumulated after the considered seismic hazard scenarios normalized with respect to their construction cost. Note that, even though the two rocking structures have slightly different geometry (i.e. due to the different base-width $2b$), for simplicity, this work assumes that

Damage limit state	Repair cost ratio [45]	Repair methods description	Downtime (days) [45, 46]	
			Mean	Standard deviation
LS1	0.03	Repair slight concrete cracking/spalling at the column (epoxy injection, patch with concrete, etc.)	0.6	0.6
LS2	0.08	Repair moderate concrete cracking/spalling at the column, repair damaged reiforcing bars (patch with concrete, reinforce and recast, etc.). Repair damage at the pivot points and the abutments	2.5	2.7
LS3	1	Repair moderate concrete cracking/spalling at the column, repair damaged reiforcing bars (patch with concrete, reinforce and recast, etc.). Repair damage at the pivot points and the abutments. Reuse the column-base system after the applied repair methods. Reconstruction of the whole bridge	46	22

Table 2: Repair cost ratio and downtime values for each damage limit state of the rocking bridge frame of Fig. 1 [25].

they have the same construction cost (i.e. 2,306 $\$/m^2$ [44]). Fig. 6 unveils that even a slight modification of the slenderness of the rocking frame can lead to a drastic decrease of the seismic losses. Note that, even under a severe seismic event (i.e. with $T_R = 4{,}975$-year return period and 1% probability of occurrence in the next 50 years), the rocking bridge with larger slenderness yields seismic losses equivalent to 50% of the construction cost of the bridge; a considerable post-earthquake financial benefit. For all the remaining seismic hazard scenarios examined herein, the pertinent seismic losses are less than 25% of the construction cost of the bridge. A further decrease on the expected seismic losses can be achieved by enhancing further its seismic performance, thus, decreasing its seismic fragility (Fig. 5), via the use of e.g. additional re-centering and/or energy dissipation capacity; increasing in that way, though, its construction cost. However, such an analysis is beyond the scope of the present study.

3.5 Resilience quantification

Resilience, as a performance indicator, quantifies the recovery (or restoration) functions of a structural system following a seismic event. In general, after an earthquake, repair methods are applied to the damaged structure and its functionality starts enhancing. The expected (dimensionless) time-variant functionality $Q(t)$ can be expressed as [47]:

$$Q(t) = \sum_{i=1}^{n} FR_i(t) \cdot P_{LSi|IM} \tag{11}$$

where $P_{LSi|IM}$ is the conditional probability of the structure to be at the given damage limit state, and $FR_i(t)$ denotes the functionality restoration process of the structure for each damage limit state. This study models the functionality restoration process of the examined rocking

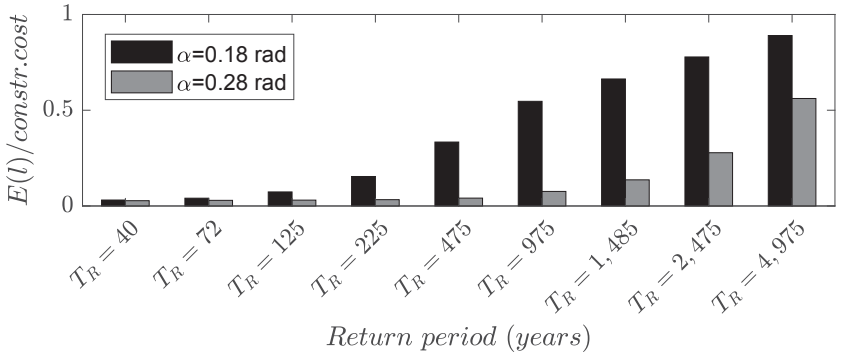

Figure 6: Expected seismic loss normalized with respect to the construction cost of the examined rocking bridges in the aftermath of various seismic hazard scenarios

structures as a normal cumulative distribution function corresponding to each damage limit state i [48, 45]:

$$FR_i(t) = \frac{1}{2}\left[1 + erf\left(\frac{t-\mu_{d_i}}{\sqrt{2}\sigma_{d_i}}\right)\right] \tag{12}$$

where μ_{d_i} and σ_{d_i} represent the mean and standard deviation, respectively, of the time during which the bridge is under restoration (i.e. downtime). HAZUS [45] proposed appropriate mean and standard deviation values of downtime (in days) for conventionally designed (fixed-base) bridges. To estimate the downtime values for rocking bridges, Mantawy et al. [46] experimentally compared the seismic performance of a rocking versus a conventionally designed (fixed-base) bridge. That study showed that the construction time of the rocking bridge is (on average) 5 times lower than the construction time of the fixed-base bridge. In other words, the downtime of the rocking structure is considered as 1/5 of the downtime of the fixed-base structure. Following [46], Table 2 presents the pertinent mean and standard deviation values of downtime for the rocking structures of Fig. 1 [25]. The resilience of the rocking structure of Fig. 1 under the investigated time-interval (i.e. Δt = 365 days) can be expressed as [49]:

$$R = \frac{1}{\Delta t}\int_{t_0}^{t_0+\Delta t} Q(t)\,dt \tag{13}$$

where t_0 indicates the time-instant the seismic event occurs.

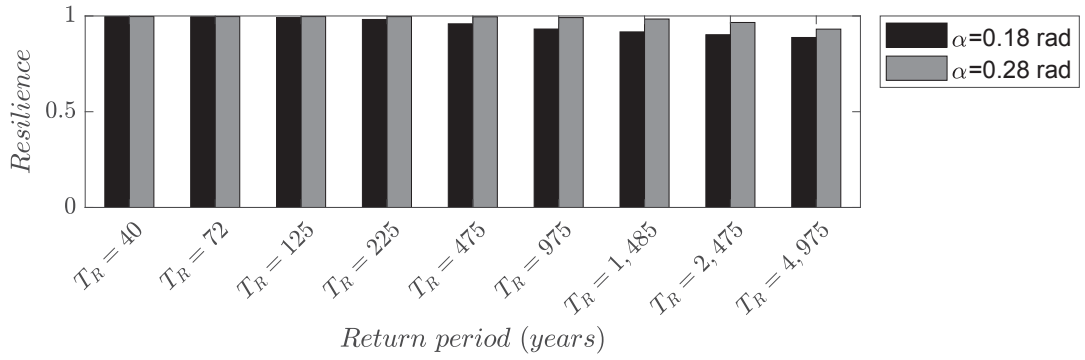

Figure 7: Resilience of the examined rocking bridges when subjected to different seismic hazard scenarios under the investigated time-interval of Δt = 365 days

Fig. 7 quantifies the resilience of the examined rocking bridge structures; the closer to unity the more resilient the structure. Specifically, Fig. 7 illustrates that both rocking bridges show remarkable resilience in the aftermath of severe earthquake events under the investigated time-interval Δt. However, the rocking bridge with larger slenderness exhibits (slightly) enhanced resilience after all the examined seismic hazard scenarios. Note that, its resilience starts deteriorating only when a maximum considered earthquake occurs (i.e. with $T_R = 2{,}475$-year return period and 2% probability of occurrence in the next 50 years). In sum, Figs 6, 7 reveal the remarkable post-earthquake financial benefits (i.e. decreased seismic losses and increased resilience) that a rocking bridge offers when carefully designed.

4 CONCLUSIONS

This work investigates the seismic performance of two rocking bridge frames, which are particularly attractive for bridge design. For the purposes of the present analysis, this work extends the well-established performance-based earthquake engineering (PBEE) framework to compare the two rocking structures in terms of their seismic fragility and the accumulated seismic losses in the aftermath of extreme hazard scenarios. In addition, it extends the PBEE approach to quantify their post-earthquake resilience adopting a more holistic resilience-based earthquake engineering framework.

The analysis reveals the considerably mitigated seismic losses that a rocking bridge offers when carefully designed. In particular, this study shows that a slight modification of the slenderness of the structure can lead to a drastic decrease of its post-earthquake financial losses. Further, results show that even under an extreme seismic hazard event, i.e. with 1% probability of occurrence in the next 50 years and $T_R = 4{,}975$-year return period, the rocking bridge frame with larger slenderness yields financial losses equivalent to 50% of the construction cost of the bridge; a considerable post-earthquake financial benefit. Importantly, this paper also unveils the remarkable post-earthquake resilience of the examined rocking bridge structures. Specifically, modifying the slenderness of a rocking bridge enhances its resilience against various seismic hazard scenarios. Importantly, when a rocking bridge is carefully designed, it sustains its resilience at the highest level till a maximum considered earthquake occurs (i.e. with $T_R = 2{,}475$-year return period and 2% probability of occurrence in the next 50 years). The above findings redirect our attention to the considerable post-earthquake financial benefits of rocking isolation, which can serve as an efficient seismic isolation technique for future bridge engineering applications.

REFERENCES

[1] G.W. Housner, The behavior of inverted pendulum structures during earthquakes, *Bulletin of the Seismological Society of America*, **53**(2), 403–417 (1963).

[2] E.G. Dimitrakopoulos, M.J. DeJong, Revisiting the rocking block: Closed-form solutions and similarity laws, *Proceedings of the Royal Society A: Mathematical, Physical and Engineering Science*, **468**(2144), 2294–2318 (2012).

[3] E.G. Dimitrakopoulos, M.J. DeJong, Overturning of retrofitted rocking structures under pulse-type excitations, *Journal of Engineering Mechanics*, **138**(8), 963–972 (2012).

[4] M.J. DeJong, E.G. Dimitrakopoulos, Dynamically equivalent rocking structures, *Earthquake Engineering & Structural Dynamics*, **43**(10), 1543–1563 (2014).

[5] R. Truniger, M.F. Vassiliou, B. Stojadinovic, An analytical model of a deformable cantilever structure rocking on a rigid surface: experimental validation, *Earthquake Engineering & Structural Dynamics*, **44**(15), 2795–2815 (2015).

[6] A.I. Giouvanidis, E.G. Dimitrakopoulos, *The role of the prestressed tendons on the seismic performance of hybrid rocking bridge bents*, Proceedings of the VII European Congress on Computational Methods in Applied Sciences and Engineering (ECCOMAS), Paper ID 8340, June 5-10, Crete Island, Greece, (2016).

[7] E.G. Dimitrakopoulos, E.D.W. Fung, Closed-form rocking overturning conditions for a family of pulse ground motions, *Proceedings of the Royal Society A: Mathematical, Physical and Engineering Science*, **472**(2196), 20160662 (2016).

[8] M.F. Vassiliou, S. Burger, M. Egger, J.A. Bachmann, M. Broccardo, B. Stojadinovic, The three-dimensional behavior of inverted pendulum cylindrical structures during earthquakes, *Earthquake Engineering & Structural Dynamics*, **46**(14), 2261–2280 (2017).

[9] J.A. Bachmann, M. Strand, M.F. Vassiliou, M. Broccardo, B. Stojadinovic, Is rocking motion predictable?, *Earthquake Engineering & Structural Dynamics*, **47**(2), 535–552 (2018).

[10] M.F. Vassiliou, Seismic response of a wobbling 3D frame, *Earthquake Engineering & Structural Dynamics*, **47**(5), 1212–1228 (2017).

[11] J.A. Bachmann, M.F. Vassiliou, B. Stojadinovic, Rolling and rocking of rigid uplifting structures, *Earthquake Engineering & Structural Dynamics*, **48**(14), 1556–1574 (2019).

[12] M.N. Reggiani, M.F. Vassiliou, Displacement-based analysis and design of rocking structures, *Earthquake Engineering & Structural Dynamics*, **48**(14), 1613–1629 (2019).

[13] J.A. Bachmann, M.F. Vassiliou, B. Stojadinovic, Dynamics of rocking podium structures, *Earthquake Engineering & Structural Dynamics*, **46**(14), 2499–2517 (2017).

[14] A.I. Giouvanidis, *Non-smooth seismic response analysis of the rocking frame*, MPhil Thesis, The Hong Kong University of Science and Technology, Hong Kong (2015).

[15] E.G. Dimitrakopoulos, A.I. Giouvanidis, Seismic response analysis of the planar rocking frame, *Journal of Engineering Mechanics*, **141**(7), 04015003 (2015).

[16] A.I. Giouvanidis, E.G. Dimitrakopoulos, Seismic performance of rocking frames with flag-shaped hysteretic behavior, *Journal of Engineering Mechanics*, **143**(5), 04017008 (2017).

[17] A.I. Giouvanidis, M. Fragiadakis, E.G. Dimitrakopoulos, *Vulnerability assessment of flag-shaped hysteretic rocking bridge bents*, Proceedings of the 6th ECCOMAS Thematic Conference on Computational Methods in Structural Dynamics and Earthquake Engineering (COMPDYN), Paper ID 18339, June 15-17, Rhodes Island, Greece, (2017).

[18] A.I. Giouvanidis, *Seismic response analysis of rocking structures: Hybrid behavior, contact phenomenon and critical earthquake characteristics*, PhD Thesis, The Hong Kong University of Science and Technology, Hong Kong (2018).

[19] D. Marriott, S. Pampanin, A. Palermo, Quasi-static and pseudo-dynamic testing of unbonded post-tensioned rocking bridge piers with external replaceable dissipaters, *Earthquake Engineering & Structural Dynamics*, **38**(3), 331–354 (2009).

[20] W. Trono, G. Jen, M. Panagiotou, M. Schoettler, C.P. Ostertag, Seismic response of a damage-resistant recentering posttensioned-hyfrc bridge column, *Journal of Bridge Engineering*, **20**(7), 04014096 (2014).

[21] M. Panagiotou, W. Trono, G. Jen, P. Kumar, C.P. Ostertag, Experimental seismic response of hybrid fiber-reinforced concrete bridge columns with novel longitudinal reinforcement detailing, *Journal of Bridge Engineering*, **20**(7), 04014090 (2014).

[22] G. Antonellis, M. Panagiotou, Seismic response of bridges with rocking foundations compared to fixed-base bridges at a near-fault site, *Journal of Bridge Engineering*, **19**(5), 04014007 (2014).

[23] A. Agalianos, A. Psychari, M.F. Vassiliou, B. Stojadinovic, I. Anastasopoulos, Comparative assessment of two rocking isolation techniques for a motorway overpass bridge, *Frontiers in Built Environment*, **3**, 47 (2017).

[24] A.S. Saad, D.H. Sanders, I.G. Buckle, Experimental evaluation of bridge column foundation rocking behavior, *Journal of Bridge Engineering*, **23**(11), 04018088 (2018).

[25] A.I. Giouvanidis, Y. Dong, Seismic loss and resilience assessment of single-column rocking bridges, *Bulletin of Earthquake Engineering*, DOI: 10.1007/s10518-020-00865-5, (2020).

[26] S. Acikgoz, M.J. DeJong, The interaction of elasticity and rocking in flexible structures allowed to uplift, *Earthquake Engineering & Structural Dynamics*, **41**(15), 2177–2194 (2012).

[27] M.F. Vassiliou, R. Truniger, B. Stojadinovic, An analytical model of a deformable cantilever structure rocking on a rigid surface: development and verification, *Earthquake Engineering & Structural Dynamics*, **44**(15), 2775–2794 (2015).

[28] A.I. Giouvanidis, E.G. Dimitrakopoulos, Nonsmooth dynamic analysis of sticking impacts in rocking structures, *Bulletin of Earthquake Engineering*, **15**(5), 2273–2304 (2017).

[29] J. Zhang, Y. Xie, G. Wu, Seismic responses of bridges with rocking column-foundation: A dimensionless regression analysis, *Earthquake Engineering & Structural Dynamics*, **48**(1), 152–170 (2019).

[30] P. Fajfar, H. Krawinkler, *Seismic design methodologies for the next generation of codes*, Taylor & Francis (1997).

[31] J. Moehle, G.G. Deierlein, *A framework methodology for performance-based earthquake engineering*, Proceedings of the 13th World Conference on Earthquake Engineering, Paper No 679. Vancouver, B.C., Canada (2004).

[32] G.P. Cimellaro, C. Renschler, M. Bruneau, *Introduction to resilience-based design (RBD)*, In: Computational Methods, Seismic Protection, Hybrid Testing and Resilience in Earthquake Engineering, pp. 151–183. Springer (2015).

[33] E.G. Dimitrakopoulos, T.S. Paraskeva, Dimensionless fragility curves for rocking response to near-fault excitations, *Earthquake Engineering & Structural Dynamics*, **44**(12), 2015–2033 (2015).

[34] A.I. Giouvanidis, E.G. Dimitrakopoulos, Rocking amplification and strong-motion duration, *Earthquake Engineering & Structural Dynamics*, **47**(10), 2094–2116 (2018).

[35] B. Gutenberg, C.F. Richter, Frequency of earthquakes in California, *Bulletin of the Seismological Society of America*, **34**(4), 185–188 (1944).

[36] USGS: *Earthquake probabilities in the San Francisco Bay region: 2002-2031*, Tech. Rep. 03-214, Working Group on California Earthquake Probabilities, United States Geological Survey (2003).

[37] Y. Xie, J. Zhang, R. DesRoches, J.E. Padgett, Seismic fragilities of single-column highway bridges with rocking column-footing, *Earthquake Engineering & Structural Dynamics*, **48**(7), 843–864 (2019).

[38] J.W. Baker, T. Lin, S.K. Shahi, N. Jayaram, *New ground motion selection procedures and selected motions for the peer transportation research program*, Tech. Rep. PEER Report 2011/3, Pacific Earthquake Engineering Research Center, University of California, Berkeley, CA (2011).

[39] W.K. Lee, S.L. Billington, Performance-based earthquake engineering assessment of a self-centering, post-tensioned concrete bridge system, *Earthquake Engineering & Structural Dynamics*, **40**(8), 887–902 (2011).

[40] J.W. Baker, Efficient analytical fragility function fitting using dynamic structural analysis, *Earthquake Spectra*, **31**(1), 579–599 (2015).

[41] Y. Dong, D.M. Frangopol, D. Saydam, Time-variant sustainability assessment of seismically vulnerable bridges subjected to multiple hazards, *Earthquake Engineering & Structural Dynamics*, **42**(10), 1451–1467 (2013).

[42] J.B. Mander, *Fragility curve development for assessing the seismic vulnerability of highway bridges*, Tech. rep., University at Buffalo (1999).

[43] A. Decò, P. Bocchini, D.M. Frangopol, A probabilistic approach for the prediction of seismic resilience of bridges, *Earthquake Engineering & Structural Dynamics*, **42**(10), 1469–1487 (2013).

[44] Y. Zheng, Y. Dong, Y. Li, Resilience and life-cycle performance of smart bridges with shape memory alloy (SMA)-cable-based bearings, *Construction and Building Materials*, **158**, 389–400 (2018).

[45] HAZUS-MH: *Multi-hazard loss estimation methodology - earthquake model (technical manual)*, Tech. Rep. MH MR5, Federal Emergency Management Agency, Washington (2010).

[46] I.M. Mantawy, T. Thonstad, D.H. Sanders, J.F. Stanton, M.O. Eberhard, Seismic performance of precast, pretensioned, and cast-in-place bridges: Shake table test comparison, *Journal of Bridge Engineering*, **21**(10), 04016071 (2016).

[47] Y. Dong, D.M. Frangopol, Risk and resilience assessment of bridges under mainshock and aftershocks incorporating uncertainties, *Engineering Structures*, **83**, 198–208 (2015).

[48] ATC: *Earthquake damage evaluation data for California*, Tech. Rep. ATC-13, Applied Technology Council, Redwood City, CA (1985).

[49] G.P. Cimellaro, A.M. Reinhorn, M. Bruneau, Framework for analytical quantification of disaster resilience, *Engineering Structures*, **32**(11), 3639–3649 (2010).

EURODYN 2020
XI International Conference on Structural Dynamics
M. Papadrakakis, M. Fragiadakis, C. Papadimitriou (eds.)
Athens, Greece, 23–26 November 2020

MODIFIED INTENSITY MEASURES TO IMPROVE ACCURACY IN FRAGILITY ANALYSIS

M. Ciano[1*], M. Gioffrè[1], K. Thiele[2], and M. Grigoriu[3]

[1]Dept. of Civil and Environmental Engineering, Univ. of Perugia
Via G. Duranti 93, 06125 Perugia, Italy
e-mail: {matteo.ciano,massimiliano.gioffre}@unipg.it

[2] Dept. of Civil Engineering, TU Braunschweig
Beethovenstraße 51, 38106 Braunschweig, Germany
e-mail: k.thiele@stahlbau.tu-braunschweig.de

[3] Dept. of Civil and Environmental Engineering, Cornell University
Ithaca, NY 14853, USA
e-mail: mdg12@cornell.edu

Keywords: Seismic intensity measures, Modified seismic intensity measures, Fragility analysis, Fragility cureves, Earthquake engineering, Complex mdof structural systems.

Abstract. *Seismic performance of structural systems is assessed by performing fragility analysis. Generally, downstream of this analysis, fragility curves are estimated in order to obtain the structural system performance. Seismic fragilities are the probability that the structural response of a system overcomes specified limit states for given seismic intensity measure. The most widespread procedure to estimate seismic fragility curves is based on scaling seismic accelerograms by a reference intensity measure (e.g. single/multiple ordinates of the pseudo-acceleration response spectrum or peak ground acceleration). Recently, it was shown that this methodology gives limited if any information on the structural seismic performance when the dependence between the intensity measure and the system demand parameter of interest (e.g. max inter-story displacement) is weak. This paper presents a general algorithm to improve the accuracy in fragilities estimation when the dependence between the intensity measure and the demand parameter is weak and the widely used method in Performance-Based Earthquake Engineering does not give accurate results. The proposed algorithm is based on a linear transformation of samples of a given intensity measure, which improves the correlation with a set of demand parameters. Fragility curves are obtained using the transformed intensity measure samples and compared with those estimated with the standard approach. The effectiveness of the proposed algorithm is demonstrated for an actual multi-degree of freedom structural system.*

1 INTRODUCTION

Seismic fragilities are the probability that the structural response of a system overcomes specified limit states for given seismic intensity measure (IMs). Performance-Based Earthquake Engineering (PBEE) ambition is to evaluate structural efficiency by fragility analysis. The Federal Emergency Management Agency (FEMA) recommends to estimate the seismic fragility curve by an approach based on scaling the seismic accelerograms with a reference intensity measure IM [1]. This method is widely applied because it is simple and, together with Monte Carlo simulation, it overcomes the problem of the limited number of natural recorded ground motions available for fragility analysis.

Two groups of IMs are usually used to define the seismic fragilities: (i) functional of samples of seismic ground acceleration process $A(t)$, such as peak ground acceleration (PGA); (ii) functional of filtered version of samples of $A(t)$, e.g. single/multiple ordinates of pseudo-acceleration response spectrum $S_a(T)$ for different structural system periods T [2, 3, 4]. In particular, the IMs in the second group, that are widely used to define the fragilities, depend on the system demand parameter D (e.g. max inter-story displacement) on which the analysis is based [5, 6, 7, 8].

The usefulness of this procedures [1] based on scaled seismic ground motion acceleration is indisputable, but it was shown that this methodology gives limited if any information on the structural seismic performance when the dependence between the IM and D is weak [9]. Moreover, the dependence between these two variables (i.e. IM and D) depends on the seismic direction, the intensity measure and the demand parameter considered [10, 11]. In particular, assumed an IM, the dependence can vary significantly with different seismic directions. For example, the fragilities defined as function of $S_a(T)$ for nonlinear single degree of freedom (SDOF) system to a seismic acceleration process $A(t)$ have large uncertainties when D and $S_a(T)$ are weakly correlated. Furthermore, the fragilities defined as function of multiple ordinates of $S_a(T)$ experience poor improvements if compared to the case of single ordinate of $S_a(T)$. It was demonstrated that the dependence between IMs and various system demand parameters, D, is weak for nonlinear system and also for complex multi-degree of freedom (MDOF) linear structures [9, 10, 11]. This issue can be avoided by defining the fragilities as functions of parameters of the law of $A(t)$. This approach was first introduced in [12] and used in [13, 14, 15] to estimate fragility surfaces. However, this approach requires a high computational cost.

This paper presents a general approach to improve the accuracy in fragilities estimation when the dependence between the intensity measure IM and the demand parameter D is weak and the widely used method in Performance-Based Earthquake Engineering [1] does not give accurate results. This general method is based on a modified version of the current intensity measure approach. In particular, once an IM is chosen it is mapped in a suitable space where D and the IM are correlated. The proposed algorithm is based on a linear transformation of samples of a given IM, which improves the correlation with a set of demand parameters. Fragility curves are obtained using the transformed IM samples and compared with those estimated with the standard approach. An actual multi-degree of freedom structural system, a school building in Norcia, Italy, is considered as case study.

Finally, the effectiveness of the proposed approach is demonstrated by comparing the fragility estimates obtained with a chosen seismic intensity measure and the its modified version.

2 BACKGROUND

Let I be the set of demand parameters which yield a structural failure. The fragility can be defined as

$$\begin{aligned} P_f(\xi) &= P(D \in I \subset \mathbb{R} | IM = \xi) \\ &= E[1(D \in I | IM = \xi)] = \int_I f_{D|IM}(x|\xi)\, dx \end{aligned} \tag{1}$$

i.e. the probability that a structural system enters a damage state given a ground motion with scalar/vector intensity measure $IM = \xi$, where $1(\cdot)$ and $f_{D|IM}(\cdot|\xi)$ are the indicator function and probability density function (PDF) of the conditional variable $D|(IM = \xi)$, respectively. The fragility in (1) is usually estimated from the structural response to scaled seismic time histories, $a(t)$ of the stochastic process $A(t)$ [16], and its accuracy depends on the scaling procedure, the sample size and the IMs properties.

When D and IM are strongly dependent, the random variable $D|IM$ has small variance, i.e. $f_{D|IM}(\cdot|\xi)$ is concentrated about its mean value. On the contrary, when D and IM are weakly dependent the random variable $D|IM$ has large variance. In the limit, $f_{D|IM}(\cdot|\xi)$ becomes a δ-function or D and $D|IM$ have the same PDF when D and $D|IM$ are perfectly correlated or independent, respectively [9]. In the latter case, the fragility in (1) does not depend on ξ. Within this context, especially if (1) is estimated by the commonly used method [1], it is crucial to quantify the dependence between the demand parameter D and various IM definitions to implicitly determine whether or not fragilities, defined as function of the commonly used IMs, can provide useful information for PBEE of actual complex multi-degree of freedom (MDOF) linear and nonlinear structural systems. If the dependence between D and IM is strong, the fragility $P_f(\xi)$ gives accurate information [10, 11]. The opposite holds when the dependence between D and IM is weak. Several statistical tools can be used to investigate the dependence between the random variables D and IM, which includes correlation coefficients, copula models and multivariate extreme value theory [9]. In this work the correlation coefficient is used to quantify the dependence between D and IM.

The IMs used in PBEE to scale seismic acceleration ground motion are divided into three broad categories: (i) non-structures-specific scalar IMs; (ii) structures-specific scalar IMs; (iii) vector-valued IMs. A complete classification of the most known IMs in literature is reported in [6]. In this work, two version of IMs are considered to estimate the fragilities

$$IM_1 = PGA \tag{2}$$

$$IM_2 = S_a(T_1, \zeta_1) \tag{3}$$

where T_1 is the first period of the MDOF structural system with associated damping ratios ζ_1. It is worth noting that the two IMs in Equations (2) and (3) are the most widely used in literature [6].

3 THE MODIFIED INTENSITY MEASURE (IM^*)

Let $X(t)$ be the response vector-valued process of an arbitrary MDOF structural system to the ground acceleration $A(t)$. The demand parameter is defined as

$$D^{(j)} = \max_{0 \le t \le \tau} |h(X(t))|, \quad j = 1, \ldots, m \tag{4}$$

where τ is the time length of $A(t)$, while $h(\cdot)$ is a function mapping the response $X(t)$ into the j-th system demand parameter (e.g. maximum displacement/acceleration) and m is the number of demand parameters of interest. The dependence between the random variables $D^{(j)}$, $j = 1, \dots, m$, and IM is a measure to quantify the accuracy in the estimation of $P_f(\xi)$ [11]. When this dependence is weak the widely used method in PBEE [1] does not give accurate results. To overcome this issue it is proposed to replace samples of a chosen standard intensity measure IM with a suitable linear transformation that modifies the dependence with the selected demand parameters samples. In particular, for each n_s samples, $a_i(t)$, $i = 1, \dots, n_s$, of the random process $A(t)$ the corrisponding IM and $D^{(j)}$ are evaluated, i.e. im_i and $d_i^{(j)}$, $i = 1, \dots, n_s$. For each of these samples, the z-scores $z(d_i^{(j)})$ and $z(im_i)$, $i = 1, \dots, n_s$, of the standardized random variables

$$z(D^{(j)}) = \frac{D^{(j)} - E[D^{(j)}]}{\sigma(D^{(j)})}\,, \quad j = 1, \dots, m \tag{5}$$

$$z(IM) = \frac{IM - E[IM]}{\sigma(IM)} \tag{6}$$

are computed, respectively. It is worth noting that if the random variables defined in Equations (5) and (6) are linearly dependent, the correlation coefficient is equal to one and the scatter plots of pairs of samples $z(d_i^{(j)})$ and $z(im_i)$ describe straight line. Given the demand parameter $D^{(j)}$, for each pair of samples $z(d_i^{(j)})$ and $z(im_i)$ it is possible to evaluate the distance from perfect correlation

$$e_i^{(j)} = |z(d_i^{(j)}) - z(im_i)|\,, \quad i = 1, \dots, n_s, \quad j = 1, \dots, m \tag{7}$$

and estimate the average distance of the j demand parameters

$$\bar{e}_i = \frac{1}{m} \sum_{j=1}^{m} e_i^{(j)}\,, \quad i = 1, \dots, n_s\,. \tag{8}$$

The samples obtained with Equation (8) can be considered as realizations of a random variable $\bar{E}$. The linear transformation

$$im_i^* = [z(im_i) + \bar{e}_i]\sigma(IM) + E[IM]\,, \quad i = 1, \dots, n_s \tag{9}$$

gives samples that can be considered the realizations of a new intensity measure IM^*.

The procedure reported above describes a general algorithm that can be used to transform any intensity measure IM (e.g. Eqs (2) and (3)) into samples of its modified version, IM^*. It is worth noting that for $m = 1$ (i.e. one demand parameter), the correlation estimated from the n_s samples of D and IM^* is exactly one. When $m > 1$ it is not possible to have perfect correlation, but the correlation between $D^{(j)}$ and IM^* is significantly higher than the one estimated from samples of $D^{(j)}$ and IM.

It follows that the IM^* samples obtained with Equation (9) can be used to scale the ground acceleration records to build fragility curves that give more accurate information on the structural system performance when compared with the standard intensity measures.

4 CASE STUDY

The procedure described in the previous Section is used to build fragility curves of a structural system of a school in Norcia (Italy) that was affected by the 2016 earthquake sequence.

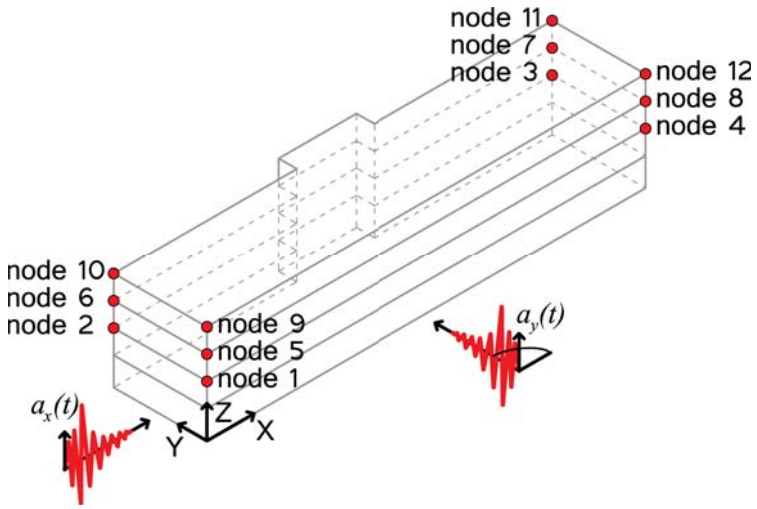

Figure 1: Seismic directions used in the analyses and reference node locations.

The structural system consists of a reinforced concrete frame (RCF) on four floors with a dissipative bracing system, made of Buckling-Restrained Axial Dampers (BRAD), and inverse beams foundation. The RCF and foundation are modeled with classical beam elements, while the BRAD elements are modeled with the constitutive law described in [17]. The obtained numerical model details on the school building and the model modal parameters are reported in [10].

Linear analyses are performed to evaluate the structural response. In this work the maximum absolute inter-story displacement in the y-direction D_{dy} (Fig. 1) is considered as demand parameter in the fragility analysis. It is well known that the maximum inter-story drift is correlated with different damage states [18] and, in general, it gives information for the performance-based seismic assessment.

The strong event recorded in Norcia on October 30th, 2016 is used to calibrate the stochastic non-stationary process $\boldsymbol{A}(t)$. Structural analyses are developed for each samples of the process $\boldsymbol{A}(t) = \{A_x(t); A_y(t)\}$, i.e. $\boldsymbol{A}(t)$ is a two-varied stochastic process, that acts in x and y global-directions of the finite element numerical model (FEM) (Figure 1). The non-stationary model described in [19, 20] is used to generate samples $a_x(t)$ and $a_y(t)$ of $A_x(t)$ and $A_y(t)$, respectively. The probabilistic model used for $\boldsymbol{A}(t)$ is calibrated with actual time histories recorded at the school base during the October 30th, 2016 earthquake.

The demand parameter D_{dy} is obtained by a three-step Monte Carlo algorithm: (i) n_s ground motion acceleration time series $a_n(t)$ of the process $A_n(t)$, $n = x, y$, are generated using the method proposed in [19]; (ii) linear time domain numerical dynamic structural analyses are used to obtain response samples $\boldsymbol{x}(t)$ of $\boldsymbol{X}(t)$ assuming proportional damping ratio $\zeta = 5\%$; (iii) n_s samples of the random vector $D_{dy} = \{D_y^{(1)}, D_y^{(2)}, \ldots, D_y^{(m)}\}$ are computed using Equation (4). In this case study the interstorey drifts in y-direction at the $m = 12$ node positions shown in Figure 1 are selected as demand parameters.

4.1 Improving dependence between D and IM

In this section, first scatter plots and the correlation between the random variables $D_y^{(j)}$ and the two IMs in Equations (2) and (3) are investigated. Second the dependence is improved

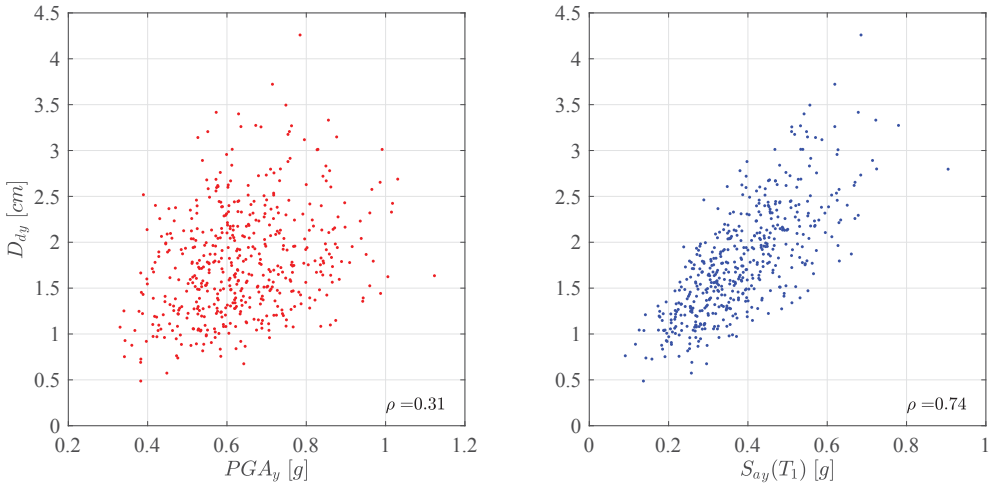

Figure 2: Scatter plots of $n_s = 500$ samples of (PGA_y, D_{dy}) and $(S_{ay}(T_1), D_{dy})$ at node #12.

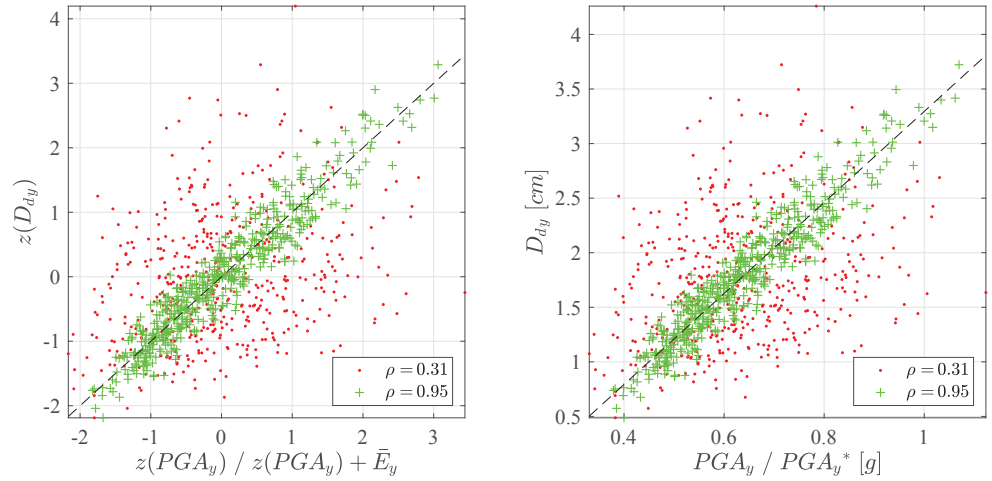

Figure 3: Scatter plots of $n_s = 500$ samples at node #12: $(z(PGA_y), z(D_{dy}))$ red dots, $(z(PGA_y)+\bar{E}_y, z(D_{dy}))$ green crosses (left panel); (PGA_y, D_{dy}) red dots, $(PGA_y{}^*, D_{dy})$ green crosses (right panel).

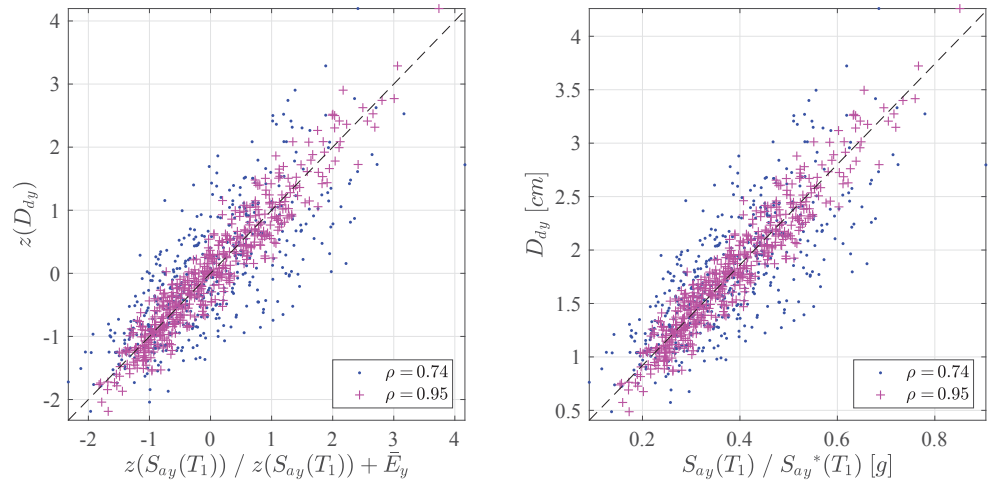

Figure 4: Scatter plots of $n_s = 500$ samples at node #12: $(z(S_{ay}(T_1)), z(D_{dy}))$ blue dots, $(z(S_{ay}(T_1)) + \bar{E}_y, z(D_{dy}))$ magenta crosses (left panel); $(S_{ay}(T_1), D_{dy})$ blue dots, $(S_{ay}{}^*(T_1), D_{dy})$ magenta crosses (right panel).

with the procedure described in Section 3.

Figure 2 shows scatter plots of $ns = 500$ samples of the seismic drift in y-direction $D_{dy} = D_y^{(j)}$, $j = 12$, (Fig. 1), against the two intensity measures IM_{ly}, $l = 1, 2$ (Eq. (2)-((3)) estimated from samples of $A_y(t)$ from left to right, respectively, together with the estimated correlation coefficient ρ. Damping ratio $\zeta_1 = 5\%$ is assumed for IM_{2y}. The results presented in the left panel of Figure 2 demonstrate that the peak ground acceleration in the y-direction, $PGA_y = IM_{1y}$, represents an unsatisfactory intensity measure given the low value of the correlation coefficient, $\rho = 0.31$, between D_{dy} and IM_{1y}. The fragility estimated using this IM would provide poor information on the seismic structural performance. In the present case, the same holds for $IM_{2y} = S_{ay}(T_1)$ since the conditional random variable $D_{dy}|IM_{2y}$ has large variance (i.e. D_{dy} and IM_{2y} are low correlated). In general, when using the intensity measure in Equation (3), it was demonstrated that IM_{2n}, $n = x, y$, can be both strongly and weakly correlated with the demand parameter depending on the selected structural response of interest and the earthquake direction [11].

The initial correlation between the chosen m demand parameters and the IMs described above can be improved using the procedure presented in Section 3. Samples of the demand parameters and the two intensity measures in Figure 2 are first transformed into their standardized versions using Equations (5) and (6) and the distance from perfect correlation is evaluated by Equation (7) for each of the m demand parameters. Then, the n_s average distances are evaluated using Equation (8) and collected in the vector $\bar{E}_y$ that is used to correct the samples of $z(IM_{ly})$, $l = 1, 2$. The last step is to evaluate samples of the modified intensity measure IM^* using Equation (9).

Figures 3 and 4 show the obtained results for the intensity measures $IM_{1y} = PGA_y$ and $IM_{2y} = S_{ay}(T_1)$, respectively. In particular the left panels report the scatter plots and the correlation coefficients before and after the correction in the standardized space, i.e. ($z(IM_{ly})$, $z(D_{dy})$), and ($z(IM_{ly}) + \bar{E}_y$, $z(D_{dy})$), $l = 1, 2$, respectively. The right panels report the scatter plots of the same samples (before and after the correction) linearly transformed back into their original space by Equation (9), i.e. (IM_{ly}, D_{dy}), and ($IM_{ly}{}^*$, D_{dy}), $l = 1, 2$, respectively. In these figures the scatter plots with $IM_{1y} = PGA_y$ are red dots and green crosses, before and after the correction, respectively, while those with $IM_{2y} = S_{ay}(T_1)$ are blue dots (before) and magenta crosses (after).

The two figures demonstrate the ability of the proposed algorithm to improve the correlation between the selected demand parameters and intensity measures. This will result into an improved accuracy in the fragility curves.

Is interesting to note that the linear transformation of the intensity measure samples obtained in this case study does not significantly change the intensity measures first four statistical moments. Figures 5-6 show the probability density functions (PDFs) and the first four statistical moments estimated from samples of the original intensity measures IM_{ly}, $l = 1, 2$ (left panels) and their modified versions $IM_{ly}{}^*$ (right panels). In particular, Figure 5 shows the results for $IM_{1y} = PGA_y$, while Figure 6 refers to $IM_{2y} = S_{ay}(T_1)$.

4.2 Estimation of fragility curves

The seismic fragility analysis, as also recommended by FEMA, is commonly based on a four-steps algorithm consisting of scaling seismic accelerograms by a reference IM. In particular, in this paper the following steps are considered

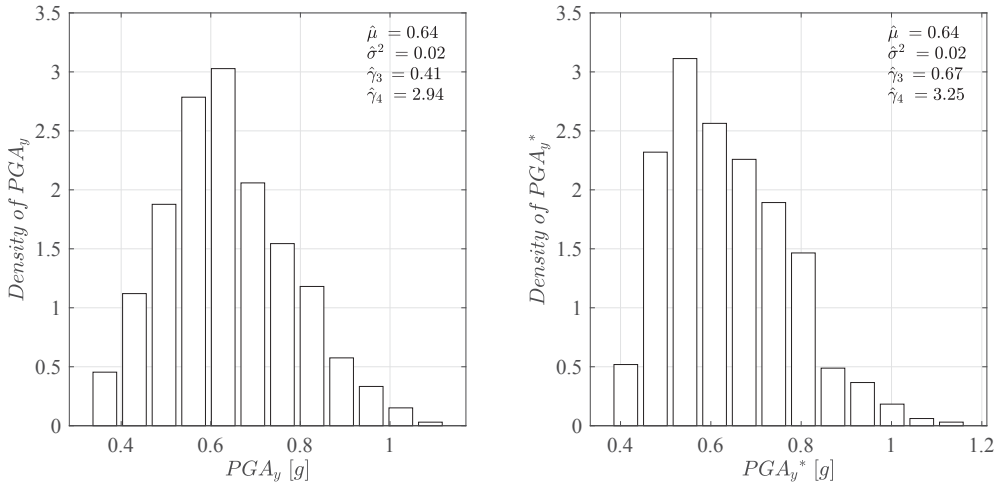

Figure 5: Estimated PDF for $n_s = 500$ samples of PGA_y (left panel) and $PGA_y{}^*$ (right panel).

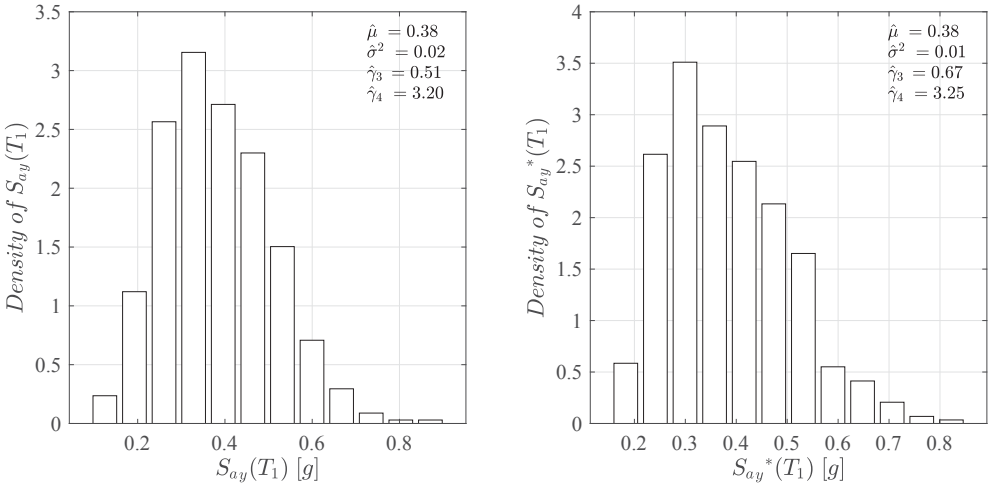

Figure 6: Estimated PDF for $n_s = 500$ samples of $S_{ay}(T_1)$ (left panel) and $S_{ay}{}^*(T_1)$ (right panel).

1. selection of a finite set of intensity measures $\{\xi_k\}$, $k = 1, \ldots, N$;
2. generation of $n_s = 500$ independent samples $a_{n,i}(t)$, $i = 1, \ldots, n_s$ of $A_n(t)$, $n = x, y$ using the method reported in [19];
3. for each of the values $\{\xi_k\}$ scale the n_s acceleration records, $a_{n,i}(t)$, in order to have the intensity level $IM_{ly} = \xi_k$, $\xi_k > 0$, $l = 1, 2$;
4. for each of the values $\{\xi_k\}$ estimate fragility as

$$\hat{P}_f(\xi_k) = \sum_{i=1}^{n_s} 1(d_{k,i} \in I)/n_s \tag{10}$$

where $1(\cdot)$ is the indicator function and $d_{k,i}$, $i = 1, \ldots, n_s$, are samples of the demand parameters computed for each intensity level ξ_k by linear dynamic analysis. The previous four-steps

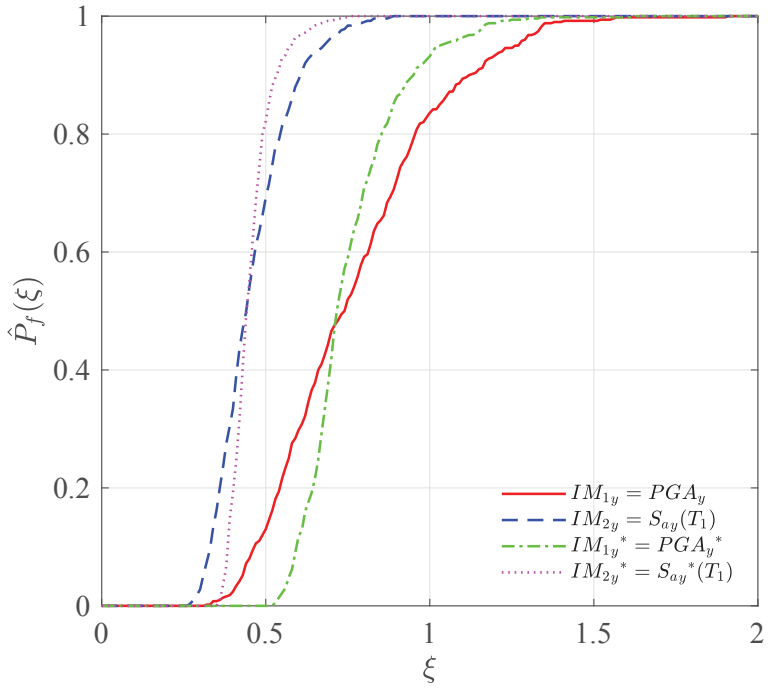

Figure 7: Fragilities against intensity level ξ for different definitions of IMs and its modified version IMs^* at node $\#12$, seismic drifts D_{dy} for limit state $\bar{D}_{d_y} = 2cm$.

algorithm is used to estimate fragility curves using both samples of the original and the transformed intensity measures.

Figure 7 reports the obtained fragility curves of the inter-storey drift at node $\#12$ for limit state $\bar{D}_{d_y} = 2cm$. It is worth noting that the fragility curves obtained with the modified intensity measures (dash-dotted green and dotted magenta lines) are steeper than those estimated using the original intensity measures (continuous red and dashed blue lines). This is consistent with the lower variability (i.e. lower variance) of the conditional random variable $D|IM^*$.

5 CONCLUSION

In Performance-Based Earthquake Engineering the seismic fragilities are commonly estimated by the classical approach based on scaling the seismic accelerograms with a reference intensity measure (IM). For this method, a strong dependence is required between the demand parameter D of the structural system, on which the fragility analysis is based, and the IM used for scaling, in order to have accurate fragility curves. The approach provides limited if any information on the seismic performance of the structural system for weak dependence between D and IM.

The work presented in this paper proposed a general approach to improve the accuracy in fragilities estimation when the dependence between the intensity measure IM and the demand parameter D is weak and the widely used method in Performance-Based Earthquake Engineering does not give accurate results. In particular, samples of any chosen intensity measure IM are linearly transformed in order to improve the correlation with a set of selected demand parameters. The new samples can be considered as realizations of a modified intensity measure IM^* and used to scale the ground acceleration records to build fragility curves that give more

accurate information on the structural system performance when compared with the standard intensity measures.

The effectiveness of the proposed method in improving the fragility curves accuracy was demonstrated on an actual multi-degree of freedom structural system of a school building in Norcia (central Italy). The results demonstrate the effectiveness of the modified seismic intensity measure in fragility analysis. Work is in progress to investigate the accuracy of fragilities based on modified intensity measures in nonlinear structural systems.

REFERENCES

[1] FEMA. Seismic performance assessment of buildings: Vol. 1–methodology. *Applied Technology Council for the Federal Emergency Management Agency, CA, USA*, 2012.

[2] J. M. O'connor and B. R. Ellingwood. Site-dependent models of earthquake ground motion. *Earthquake Engineering & Structural Dynamics*, 21(7):573–589, 1992.

[3] D. Lopez Garcia and T. T. Soong. Sliding fragility of block-type non-structural components. part 1: Unrestrained components. *Earthquake Engineering & Structural Dynamics*, 32(1):111–129, 2003.

[4] G. Sevieri, A. De Falco, and G. Marmo. Shedding light on the effect of uncertainties in the seismic fragility analysis of existing concrete dams. *Infrastructures*, 5(3):22, 2020.

[5] N. S. Kwong, A. K. Chopra, and R. K. McGuire. A framework for the evaluation of ground motion selection and modification procedures. *Earthquake Engineering & Structural Dynamics*, 44(5):795–815, 2014.

[6] H. Ebrahimian, F. Jalayer, A. Lucchini, F. Mollaioli, and G. Manfredi. Preliminary ranking of alternative scalar and vector intensity measures of ground shaking. *Bulletin of Earthquake Engineering*, 13(10):2805–2840, 2015.

[7] N. S. Kwong, A. K. Chopra, and R. K. McGuire. Evaluation of ground motion selection and modification procedures using synthetic ground motions. *Earthquake Engineering & Structural Dynamics*, 44(11):1841–1861, 2015.

[8] N. S. Kwong, A. K. Chopra, and R. K. McGuire. A ground motion selection procedure for enforcing hazard consistency and estimating seismic demand hazard curves. *Earthquake Engineering & Structural Dynamics*, 44(14):2467–2487, 2015.

[9] M. Grigoriu. Do seismic intensity measures (IMs) measure up? *Probabilistic Engineering Mechanics*, 46:80 – 93, 2016.

[10] M. Ciano, M. Gioffrè, and M. Grigoriu. On the accuracy of seismic fragilities for actual non-linear MDOF systems. In *Proceedings of the 8th International Conference on Computational Stochastic Mechanics (CSM 8)*, pages 121–130, 2018.

[11] M. Ciano, M. Gioffrè, and M. Grigoriu. The role of intensity measures on the accuracy of seismic fragilities. *Probabilistic Engineering Mechanics*, 60:103041, 2020.

[12] C. Kafali and M. Grigoriu. Seismic fragility analysis: Application to simple linear and nonlinear systems. *Earthquake Engineering & Structural Dynamics*, 36(13):1885–1900, 2007.

[13] A. Radu. A framework for earthquake risk engineering. *Procedia engineering*, 199:3576–3581, 2017.

[14] A. Radu and M. Grigoriu. An earthquake-source-based metric for seismic fragility analysis. *Bulletin of Earthquake Engineering*, 16(9):3771–3789, 2018.

[15] M. Ciano, M. Gioffré, and M. Grigoriu. Seismic performance detection by fragility analysis: a comparison between standard and alternative approaches. In *Proceedings of the XVIII ANIDIS Conference Seismic engineering in Italy: Ascoli Piceno, 15-19 September*, pages 226–234. Pisa University Press, 2019.

[16] J. W. Baker. Conditional mean spectrum: Tool for ground-motion selection. *Journal of Structural Engineering*, 137(3):322–331, 2010.

[17] Y.-K. Wen. Method for random vibration of hysteretic systems. *Journal of the engineering mechanics division*, 102(2):249–263, 1976.

[18] J. Ruiz-García and E. Miranda. Probabilistic estimation of residual drift demands for seismic assessment of multi-story framed buildings. *Engineering Structures*, 32(1):11–20, 2010.

[19] M. Grigoriu, S. E. Ruiz, and E. Rosenblueth. The mexico earthquake of september 19, 1985 — nonstationary models of seismic ground acceleration. *Earthquake Spectra*, 4(3):551–568, 1988.

[20] M. Ciano, M. Gioffrè, V. Gusella, and M. Grigoriu. Modeling and simulation of nonstationary thunderstorm outflows. In *Conference of the Italian Association for Wind Engineering*, pages 222–233. Springer, 2018.

EURODYN 2020
XI International Conference on Structural Dynamics
M. Papadrakakis, M. Fragiadakis, C. Papadimitriou (eds.)
Athens, Greece, 23–26 November 2020

OPTIMAL VISCOUS DAMPER PLACEMENT TO PREVENT POUNDING OF ADJACENT BUILDINGS

Huseyin Cetin[1], Baki Ozturk*[2], and Ersin Aydin[1]

[1] Nigde Omer Halisdemir University
Dept.of Civil Engineering, Nigde, Turkey
e-mail: eaydin@ohu.edu.tr, henainsaat@hotmail.com

*[2] Hacettepe University
Dept.of Civil Engineering, Ankara, Turkey
e-mail: bakiozturk@hacettepe.edu.tr

Keywords: Pounding, optimal dampers, adjacent buildings, viscous dampers, seismic effects.

Abstract. *Structural pounding is prevalent in general during earthquake shaking for adjacent structures in earthquake prone cities. In this study, the prevention of pounding effect is targeted by the optimal placement of viscous damping elements within the adjacent buildings. One of the important reasons of the pounding phenomenon is the out of phase vibrations of adjacent structures. A couple of adjacent structures which have different heights are modeled as shear buildings to set the proposed method. The relative displacement, defined as the extraction of horizontal displacements of adjacent structures at the top level of the shorter building, are chosen as the objective function to be minimized. In addition, reduction of relative displacement of the buildings and the effects of various vibration characteristics of each building is investigated based on transfer functions. Equations of motion of a structure, which are uncoupled when each structure is considered alone, become coupled when damping elements are placed in between the adjacent structures. The first mode response of the structures is considered while the transfer function response is derived. Optimal designs are determined for different total damping levels and different vibration characteristics of adjacent structures. The results of numerical analyses reveal that optimal designs effectively decrease the relative displacements between adjacent structures. Optimal designs are compared with the uniform design and without damper cases. The numerical analyses show that the proposed optimal damper design method in this study is vigorously effective for the prevention of pounding of adjacent buildings.*

1 INTRODUCTION

In this study, the prevention of pounding effect is targeted by the optimal placement of viscous damping elements within the adjacent buildings. If the viscous damper's (VDs) phase of relative acceleration is the same with the phase of the main structure's velocity, maximum energy dissipation is executed by damping forces. Therefore, VDs manufacture damping forces proportional to damping coefficient and relative velocity between neighboring stories at the same elevation level [1-3]. Analytical models of different impacts have been developed to define the structural response of adjacent structures during an earthquake [4-7]. Stavroulakis and Abdalla [8] derived optimality conditions by minimizing potential energy of adjacent structures. Jeng et al. [9] proposed a method called Spectral Difference Method and Double Difference Combination rule based on random vibration theory. In order to prevent pounding, Lin [10] developed a statistical method of the mean and standard deviation of the separation distance of adjacent buildings based on the random vibration theory. Valles and Reinhorn [11] studied pounding problem based on the radius of pseudo energy. Zhang and Xu [12] calculated optimal values of viscoelastic dampers to reduce the maximum seismic response under random seismic response. Zhu and Xu [13] and Zhu et al.[14] derived analytical formulas to find optimal parameters of Maxwell model defined for fluid dampers used to link two adjacent structures. Aldemir and Aydin [15] proposed an active control algorithm for adjacent structures. Kasai et al. [16] proposed a method, called the "spectral difference (SPD) method" based on spectral approach. Previous studies have shown that VDs placed between adjacent buildings are very effective in reduction of pounding cases.

The most important reason for pounding of adjacent buildings is their motions at different phases. In this study, to counterwork the pounding of two adjacent buildings, the allocation of VDs which are optimally placed between them is suggested. In this optimal design, one of the gradian based optimization algorithms, which is called Steepest Direction Search Algorithm (SDSA) [17], is applied considering the optimal condition to find optimum viscous damper quantities and their settlement to adjoining shear buildings. The relative displacement of top floor of the shorter building and middle floor of the taller building is considered as an objective function to be minimized in frequency domain. The behaviors of two adjacent buildings having different heights are evaluated with and without viscous dampers. Therefore, the reduction of relative transfer function displacement (U_R) between the top floor of shorter building and middle floor of taller building is monitored to detect the effectiveness of optimally designed VDs for prevention and reduction of pounding of adjacent shear buildings. This proposed design method is tested under El Centro (NS) ground motion record as well.

2 FORMULATION OF THE PROBLEM

As shown in Figure 1, s number of stories for shorter shear building A on the left side and n number of stories for taller shear building B on the right side are considered. In Figure 1, k_{As} and k_{Bn} are stiffnesses of the i^{th} floor of the buildings A and B. In the same way, m_{As} and m_{Bn} are the floor masses, respectively. The c_{As} and c_{Bn} , which are at the i^{th} floor for the buildings A and B, represent the structural damping coefficients proportional to floor masses. The c_{ads}^{A} and c_{adn}^{B} denote the added viscous dampers for prevention of pounding between the adjacent buildings A and B.

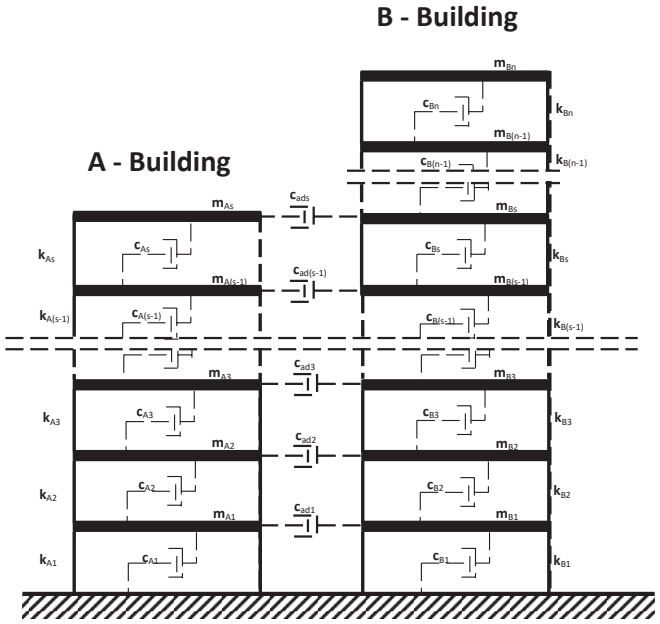

Figure 1: Adjacent buildings A and B with added viscous dampers.

The equation of motion of the shear buildings A and B can be separately expressed as follows.

$$\boldsymbol{M}_A\ddot{\boldsymbol{y}}_A(t) + \boldsymbol{C}_A\dot{\boldsymbol{y}}_A(t) + \boldsymbol{K}_A\boldsymbol{y}_A(t) = \boldsymbol{M}_A\boldsymbol{r}_A\ddot{y}_g(t) \tag{1}$$

$$\boldsymbol{M}_B\ddot{\boldsymbol{y}}_B(t) + \boldsymbol{C}_B\dot{\boldsymbol{y}}_B(t) + \boldsymbol{K}_B\boldsymbol{u}_B(t) = \boldsymbol{M}_B\boldsymbol{r}_B\ddot{y}_g(t) \tag{2}$$

In these equations, $\boldsymbol{M}_A$, $\boldsymbol{M}_B$, $\boldsymbol{C}_A$, $\boldsymbol{C}_B$, $\boldsymbol{K}_A$, $\boldsymbol{K}_B$ represent mass, structural damping and stiffness coefficient matrices of the buildings A and B, respectively. $\boldsymbol{y}_A(t)$ and $\boldsymbol{y}_B(t)$ denote displacement vectors of the buildings A and B, and over-dots show the derivatives according to time. $\ddot{y}_g(t)$ is the horizontal ground acceleration. $\boldsymbol{r}_A$ and $\boldsymbol{r}_B$ are influence vectors which consist of ones and zeros for the buildings A and B. The adjacent shear buildings A and B are modeled with added viscous dampers which are located between them. The equation of motion of the combined system can be written as follows.

$$\boldsymbol{M}\ddot{\boldsymbol{y}}(t) + \boldsymbol{C}\dot{\boldsymbol{y}}(t) + \boldsymbol{K}\boldsymbol{y}(t) = \boldsymbol{M}\boldsymbol{r}\ddot{y}_g(t) \tag{3}$$

$\boldsymbol{M}$, $\boldsymbol{C}$, $\boldsymbol{K}$ indicate mass, damping and stiffness matrices of the system composed of adjacent buildings A and B. $\boldsymbol{y}(t)$ is the system displacement vector. The system influence vector can be defined as $\boldsymbol{r}$ ={1,1,..,1}. $\boldsymbol{M}$, $\boldsymbol{C}$, $\boldsymbol{K}$ can be detailed further as follows.

$$\boldsymbol{M} = \begin{bmatrix} \boldsymbol{M}_A & \boldsymbol{0} \\ \boldsymbol{0} & \boldsymbol{M}_B \end{bmatrix} \tag{4}$$

$$\boldsymbol{K} = \begin{bmatrix} \boldsymbol{K}_A & \boldsymbol{0} \\ \boldsymbol{0} & \boldsymbol{K}_B \end{bmatrix} \tag{5}$$

$$\boldsymbol{C} = \begin{bmatrix} \boldsymbol{C}_A & \boldsymbol{0} \\ \boldsymbol{0} & \boldsymbol{C}_B \end{bmatrix} + \boldsymbol{C}_{ad} \tag{6}$$

in which $\boldsymbol{0}$ is the null vector and the added matrix $\boldsymbol{C}_{ad}$ placed between adjacent buildings A and B can be defined as follows.

$$\boldsymbol{C}_{ad} = \begin{bmatrix} \boldsymbol{C}_{ad}^{A} & \boldsymbol{C}_{ad}^{B} \\ \boldsymbol{C}_{ad}^{B} & \boldsymbol{C}_{ad}^{A} \end{bmatrix} \tag{7}$$

where, $\boldsymbol{C}_{ad}^{A} = -\boldsymbol{C}_{ad}^{B}$.

The Fourier transform of system equation for the adjacent buildings can be expressed as follows.

$$(\boldsymbol{K} + i\omega\boldsymbol{C} - \omega^2\boldsymbol{M})\boldsymbol{Y}(\omega) = -\boldsymbol{M}\,\boldsymbol{r}\,\ddot{Y}_g(\omega) \tag{8}$$

In this equation, $\boldsymbol{Y}(\omega)$ is the Fourier transform of displacement vector $(\boldsymbol{t})$, and $\ddot{Y}_g(\omega)$ is the Fourier transform of horizontal ground acceleration $\ddot{y}_g(t)$. $i = \sqrt{-1}$ denotes the imaginary unit.

The floor displacement transfer function $\boldsymbol{U}_D(\omega)$ of the adjacent buildings can be expressed as follows.

$$\boldsymbol{U}_D(\omega) = -(\boldsymbol{K} + i\omega\boldsymbol{C} - \omega^2\boldsymbol{M})^{-1}\boldsymbol{M}\boldsymbol{r} \tag{9}$$

3 DEFINITION OF THE OPTIMIZATION PROBLEM

The k^{th} value of relative displacement transfer function of the s^{th} floor level, which is also the objective function to be minimized, can be defined as,

$$U_{Rk}(\omega) = |U_{Ds}(\omega)| - |U_{Dn}(\omega)| \tag{10}$$

The objective function of the problem can be minimized using the SDSA method [17] considering optimal conditions. It gives the optimum damping distribution and the transfer function gives the value of the peak displacement. There are an active total of dampers and one passive constraint as many as the number of design variables in each damper. Active and passive restrictions on the total of the dampers added can be written as follows.

$$\sum_{i=1}^{n} \bar{c}_{adi} = W \tag{11}$$

$$0 < c_{adi} < \bar{c}_{adi} \qquad (i=1,\ldots,n) \tag{12}$$

W, $\bar{c}_{ad}$ are an upper limit value given for the sum of the damping coefficients of the dampers and the given upper limit value for the damping coefficient of each damper, respectively. Lagrangian (L) functional under the selected objective function and constraints is given as,

$$L(\bar{c}_{ad}, \lambda, \mu, \nu) = U_{Rk}(\omega) + \lambda(\sum_i^n \bar{c}_{ad} - W) + \sum_{i=1}^n \mu_i(0 - c_{adi}) + \sum_{i=1}^n \nu_i(c_{adi} - \bar{c}_{ad}) \quad (13)$$

In this equation, n is the number of design variables, and $\mu = \mu_i$ and $\nu = \nu_i$ are the Lagrange multipliers.

Taking into consideration the optimum damping criteria for relative displacement at the top of the structures, the damping coefficients of Lagrangian functional L ($\mu = 0$, $\nu = 0$) are taken according to c_{adi} (i = 1, ..., n) and λ without the upper and lower constraints in order to minimize the objective function of the problem,

$$U_{R,j} + \lambda = 0 \quad (j = 1, \dots, n) \; 0 < c_{adj} < \bar{c}_{adj} \quad (14)$$

Here, the expression $(.)_{,j}$ shows the partial derivatives with respect to c_{adj}. It should be considered that the damping coefficients cannot be negative in the dampers added. There is no physical significance of the damping coefficients to be zero. If the upper and lower constraints of the damping coefficients are active, the equation above should be corrected as follows,

$$U_{R,j} + \lambda \geq 0 \qquad c_{adj} = 0 \quad (15)$$

$$U_{R,j} + \lambda \leq 0 \qquad c_{adj} = \bar{c}_{adj} \quad (16)$$

4 NUMERICAL EXAMPLE

In order to understand the efficiency of the proposed method, four story and eight story adjacent buildings system with and without VDs, which is shown in Figure 2, is considered as an example. The floor masses and stiffness for building A are $m_{As} = 3.2 \times 10^4$kg and $k_{As} = 1 \times 10^7$kg for *s*=1,…,4. The floor masses and stiffness for building B are $m_{Bn} = 3.2 \times 10^4$kg and $k_{Bn} = 10 \times 10^7$kg for *n*=1, 2…, 8. The natural damping ratios of the first modes of shear buildings A and B are $\xi_{A1} = \xi_{B1} = 0.02$. The natural frequencies for the first modes of buildings A and B are $\omega_{A1} = 6.1$ rad/s and $\omega_{B1} = 30.60$ rad/s, respectively. Figure 3 depicts variation of the 4th floor absolute displacement transfer function $|U_{D4}|$ with respect to excitation frequency for the buildings A and B in the case of without control. The structural damping is taken as proportional to mass matrix. The ratio of periods of buildings A and B for the first modes is $\frac{T_{A1}}{T_{B1}} = 1.68$. Total quantity of the VDs inserted to adjacent buildings is $\bar{c}_{ad} = 20x\ 10^4$ Ns/m.

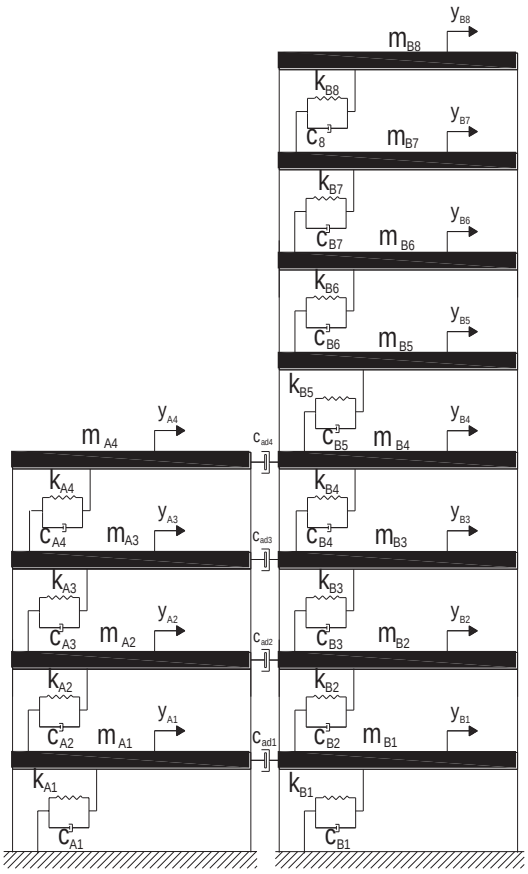

Figure 2: Four story and eight story adjacent buildings with viscous dampers.

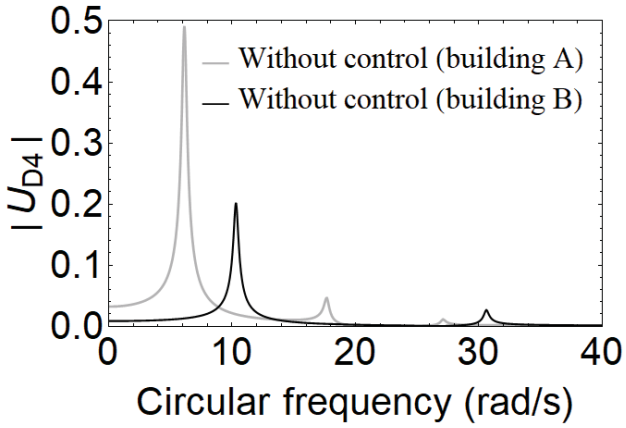

Figure 3: Variation of the 4th floor absolute displacement transfer function $|U_{D4}|$ with respect to excitation frequency for the buildings A and B in the case of without control.

The optimum distribution of damping is calculated in 300 steps by using the Steepest Direction Search Algorithm (SDSA) with respect to the 4th floor relative displacement transfer function $U_{R4}(\omega)$. Figure 4 shows the distribution of VD between adjacent buildings. As shown in Figure 4, VD is totally focused on the top floor of the four-story building A in the adjacent building system. Figure 5 demonstrates the reduction of the objective function $U_{R4}(\omega)$ according to redesign step number. After execution of optimum VD distribution, the variation of the objective function $U_{R4}(\omega)$ considering the excitation frequency and time his-

tory of the 4th floor relative displacement (RD) between the adjacent buildings are shown in Figures 6 and 7, respectively. It can be observed that the proposed method is very effective in descending the relative response between adjacent buildings A and B.

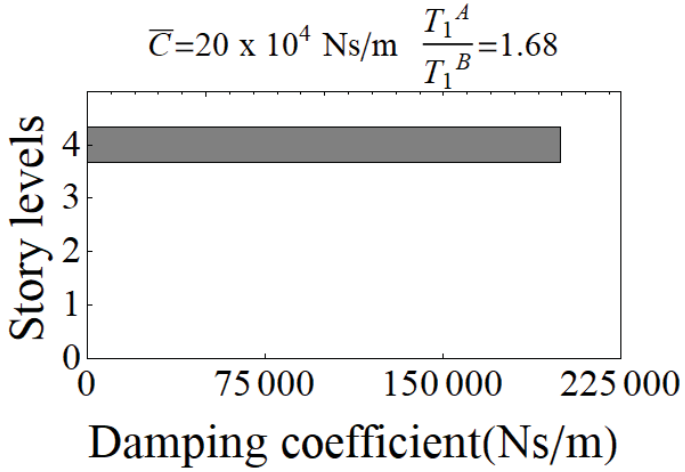

Figure 4: Optimal distribution of the VD with respect to relative displacement between the adjacent buildings

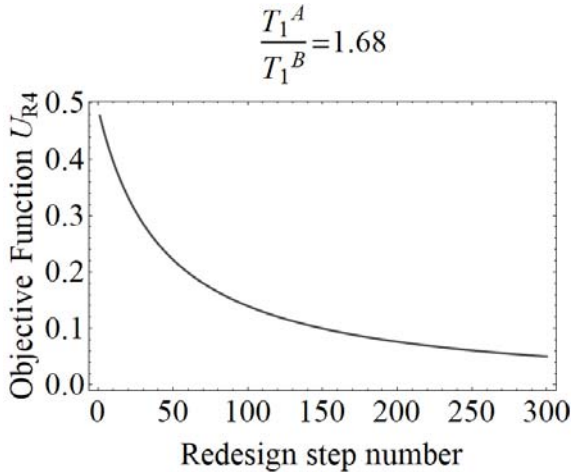

Figure 5: Reduction of the objective function $U_{R4}(\omega)$ according to redesign step number.

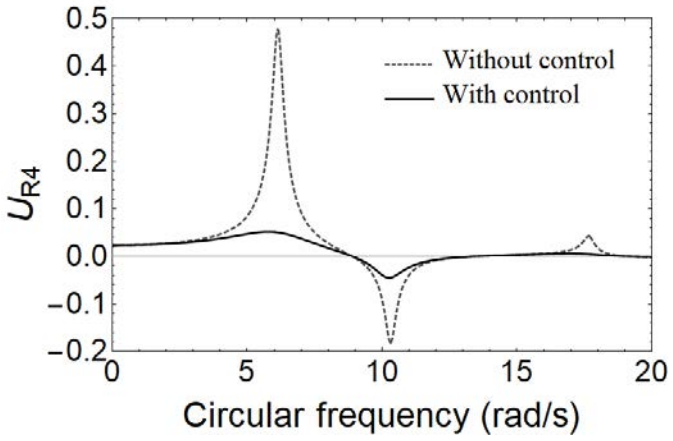

Figure 6: The variation of objective function $U_{R4}(\omega)$ considering the excitation frequency

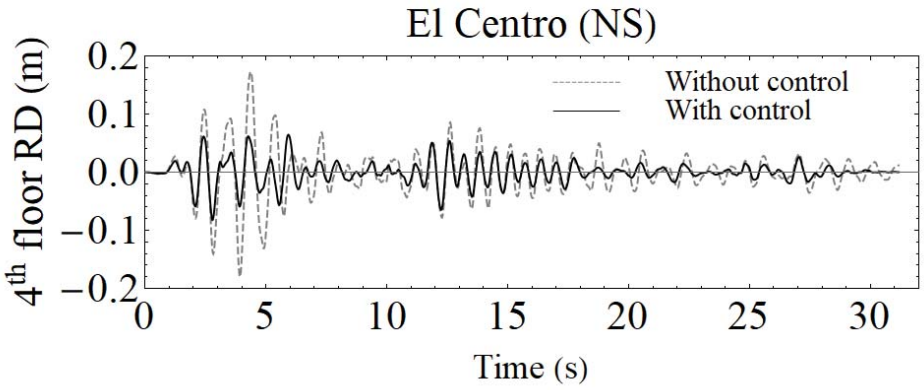

Figure 7: Time history of the 4th floor relative displacement (RD) between the adjacent buildings

5 CONCLUSION

In this study, the following conclusions can be obtained.

(1) In order to overcome pounding between the adjacent buildings, the optimal distribution of VDs has been studied using the SDSA. Optimization results have shown that the most suitable VD location in between the adjacent buildings A and B is at the top floor of building A.

(2) Comparison of the structural behavior of adjacent buildings with and without VDs is provided. It is shown that enhancing the VD capacity is very effective in decreasing the amplitude of relative displacement of the adjacent buildings and dissipating the energy of the system as well. In this study, VD location focused on the top floor of shorter building A.

(3) Considering the decrease in pounding of the adjacent buildings, the proposed method is quite effective. The objective function $\boldsymbol{U_{R4}(\omega)}$, which relies on the excitation frequency, is reduced. It is also effective in the mitigation of relative displacement between the adjacent buildings which can be observed in time history analysis.

REFERENCES

[1] H. Cetin, E. Aydin, A New Tuned Mass Damper Design Method based on Transfer Functions. *KSCE Journal of Civil Engineering*, 2, 89-120, 2019.

[2] H. Cetin, E. Aydin, B. Ozturk, Optimal design and distribution of viscous dampers for shear building structures under seismic excitations. *Frontiers in Built Environment, Frontiers*, 5, 1-13, 2019.

[3] TT. Soong, G.F. Dargush, Passive energy dissipation systems in structural engineering, John Wiley& Sons Ltd., Chichester, UK, and New York NY, pp. 227- 317, 1997.

[4] SA. Anagnastopoulos, Pounding of buildings in series during earthquakes. *Earthquake Engineering and Structural Dynamics*, 16:3, 443-456, 1988.

[5] E. Aydin, B. Ozturk, L. Yesil, Application of Viscous Dampers for Prevention of Pounding Effect in Adjacent Buildings, *14th European Conference on Earthquake Engineering*, Ohrid, 2010.

[6] E. Aydin, B. Ozturk, M. Dikmen, Optimal Damper Placement to Prevent Pounding of Adjacent Structures Considering a Target Damping Ratio and Relative Displacement, *Omer Halisdemir University Journal of Engineering Sciences*, 6:2, 581-592, 2017.

[7] E. Aydin, B. Ozturk, H. Cetin, T. Simsek, Application of Viscous Dampers for Prevention of Pounding in Adjacent Reinforced Concrete Buildings, *16th World Conference on Earthquake Engineering*, Santiago, Chile, 2017.

[8] GE. Stavroulakis, K.A. Abdalla, Contact between adjacent structures. *Journal of Structural Engineering*, 2838-2850, 1991.

[9] V. Jeng, V., K. Kasai, B.F, Maison, A spectral difference method to estimate building separations to avoid pounding. *Earthquake Spectra*. 8:2, 201-223, 1992.

[10] JH. Lin, Seperation distance to avoid seismic pounding of adjacent buildings. *Earthquake Engineering and Structural Dynamics*. 26, 395-403, 1997.

[11] RE. Valles, AM, Reinhorn, Evaluation, prevention and mitigation of pounding effects in building structures, *Report No NCEER-97-0001, National Centre for Earthquake Engineering Res.*, State University of New York, Buffalo, NY, 1997.

[12] WS. Zhang, YL. Xu, Dynamic characteristics and seismic response of adjacent buildings linked by discrete dampers. *Earthquake Engineering and Structural Dynamics*, 28, 1163-1185, 1999.

[13] HP. Zhu, YL. Xu, Optimum parameters of Maxwell model defined damper used to link adjacent structures. *Journal of Sound and Vibration*, 279, 253-274, 2005.

[14] HP. Zhu, Y. Wen, H. Iemura, A study on interaction control for seismic response of parallel structures. *Computers and Structures*, 79, 231-242, 2001.

[15] U. Aldemir, E. Aydin, An active control algorithm to prevent the pounding of adjacent structures, *Vibration Problems ICOVP*, Istanbul, 2005.

[16] K. Kasai, AR. Jagiasi, V. Jeng, Inelastic vibration phase theory for seismic pounding mitigation. *Journal of Structural Engineering*, 122, 1136-1146, 1996.

[17] I. Takewaki, Optimal Damper Placement For Planar Building Frames Using Transfer Functions. *Struct.Mult.-Disp.Optim*., 20, 280-287, 2000.

EURODYN 2020
XI International Conference on Structural Dynamics
M. Papadrakakis, M. Fragiadakis, C. Papadimitriou (eds.)
Athens, Greece, 23–26 November 2020

SEISMIC RELIABILITY-BASED DESIGN OF STRUCTURES EQUIPPED WITH DFPS

P. Castaldo[1] and G. Alfano[2]

[1] Department of Structural, Geotechnical and Building Engineering (DISEG), Politecnico di Torino
Turin, Italy
e-mail: paolo.castaldo@polito.it

[2] Department of Political and Communication Sciences, University of Salerno, Via Giovanni Paolo 132, 84084 Salerno, Italy
e-mail: galfano@unisa.it

Keywords: seismic isolation, double friction pendulum bearing, seismic reliability-based design, ductility demand, behaviour factor, post-yield hardening/softening stiffness.

Abstract. *This work deals with seismic reliability-based design (SRBD) for softening and hardening structures equipped with double friction pendulum system (DFPS) isolators. The isolated system is represented by means of an equivalent 3dof model having a softening/hardening post-yield slope for the superstructure and velocity-dependent rules for the two surfaces of the DFP devices. The yielding characteristics of the superstructures are defined in compliance with the seismic hazard of L'Aquila site (Italy) and with NTC18 assuming ordinary characteristics. Considering several natural seismic records and the relevant random variables, incremental dynamic analyses are carried out for assessing the seismic fragility and the seismic reliability of these systems. Finally, seismic reliability-based design (SRBD) curves for these systems are proposed.*

1 INTRODUCTION

Sliding pendulum bearings are more and more used to isolate buildings and infrastructures in seismic zone [1]-[3] and have been studied by many researchers (e.g., [4]-[5]) in order to ensure appropriate safety and resilience levels to infrastructure systems [6]-[7]. Probabilistic analyses together with reliability-based investigations have also been developed by [8]-[9] as well as reliability and reliability-based optimization analyses for base-isolated systems have been discussed in [10]-[11]. Adopting the friction coefficient in addition to the earthquake characteristics as the main aleatory uncertainties, seismic reliability and life-cycle cost analyses of 3D base-isolated reinforced concrete (RC) structures have been commented in [12]-[13]. Referring to elastic systems isolated through single FPS, the seismic reliability-based design (SRBD) approach in general terms has been presented in [14]. In the literature articles [15] and [16], two different optimization approaches are proposed for systems equipped with FPS: in [15], with the purpose to minimize the superstructure displacement demand, the influence of the system properties and of the soil conditions on the optimal friction coefficients is examined; in [16], the ratio peak ground acceleration/velocity is assumed as the relevant parameter to determine the optimal friction coefficients. The studies [17]-[19] investigated the seismic performance of bridges or structures equipped with DFPS (doubleFPS) or FPS providing [19] useful relationships to assess the seismic response of structures isolated by frictional isolators and highlighting that the principal benefit of the DFPS bearing in comparison to the singleFP is the capacity to accommodate larger displacements.

With regard to the design of base-isolated systems when they respond inelastically, seismic code provisions [20]-[24] prescribe low values for the strength reduction factor [20],[24] or behavior factor [21]-[22] to avoid non linear dynamic amplification phenomena (e.g., partial resonance) [25]. In detail, NTC18 [22], the Japanese building code [23] and Eurocode 8 [21] state 1.5 as maximum value, without specifying a distinction between the ductility and overstrength factor term. A behavior factor equal to 0.375 times the value for corresponding fixed-base structures and no larger than 2 is prescribed in ASCE 7 [20].

This study describes the seismic reliability-based design (SRBD) for softening and hardening structural systems equipped with DFPS devices and located in L'Aquila (Italy). The isolated system is represented by means of an equivalent 3-degree-of-freedom (3dof) model having a softening/hardening post-yield slope for the superstructure and velocity-dependent rules for the two surfaces of the DFP devices [4]. In this way, a wide parametric analysis is developed investigating the influence of different elastic and inelastic structural system properties of the superstructure and of the DFPS for increasing behavior factors [20]-[23]. In addition, the investigation is carried out assuming the both friction coefficients of the two surfaces of the DFPS and the characteristics of the ground motions as the main aleatory uncertainties. In detail, the both friction coefficients are modelled by means of appropriate Gaussian probability density functions (PDFs) and, the Latin Hypercube Sampling (LHS) method [26]-[27] is employed to generate the input data. After that, several incremental dynamic analyses (IDAs) are developed for increasing seismic intensity levels in compliance with the site seismic hazard to assess the seismic fragility curves and, successively, the seismic reliability curves. Finally, SRBD curves for the two surfaces of the DFPS devices are provided as design relationships. The results herein presented allow a comparison with the outcomes when single-FPS are employed [28],[29] in order to highlight the potential advantages of the DFPS and recommend reliable values of the displacement demands to the DFPS bearings.

2 EQUATIONS OF MOTION FOR NON-LINEAR STRCTURAL SYSTEMS WITH DFPS

The equivalent system depicted in Figure 1 is a 3dof system presents a dof for the superstructure behaviour and two dofs for the responses of the two surfaces of the DFPS. This equivalent system has been adopted to model the mechanical nonlinearities of the superstructure and of the DFPS [30].

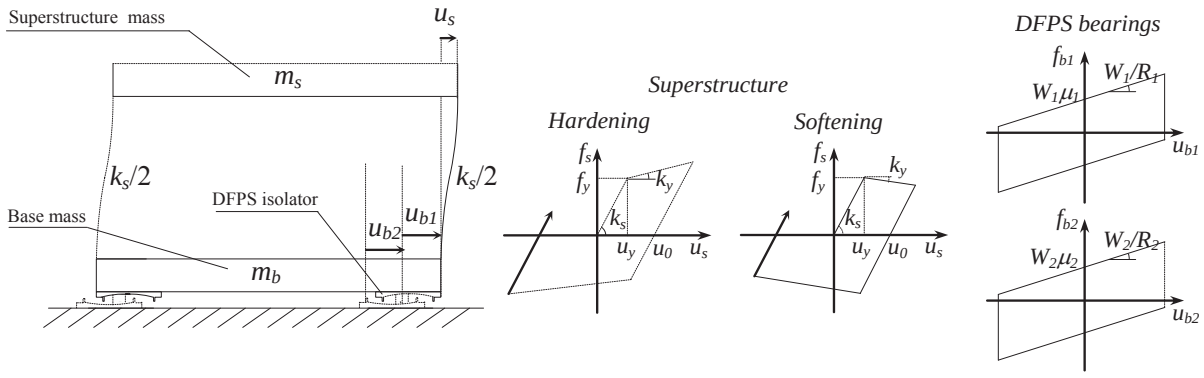

Figure 1: 3dof model with the constitutive laws.

Regarding the free body diagram of the DFPS, the bearing restoring forces of the DFPS apply:

$$f_{b,1} = \frac{W_1}{R_1} u_{b,1} + \mu_{d,1} W_1 \operatorname{sgn}\left(\dot{u}_{b,1}\right) \tag{1a}$$

$$f_{b,2} = \frac{W_2}{R_2} u_{b,2} + \mu_{d,2} W_2 \operatorname{sgn}\left(\dot{u}_{b,2}\right) \tag{1b}$$

where $W_1 = \left(m_b + m_s\right) g$ denotes the weight on the upper surface (surface 1) of the isolator, $W_2 = \left(m_b + m_s + m_d\right) g$ is the weight on the lower surface (surface 2) of the isolator, g is the gravity constant, R_1 and R_2 are the curvature radii of the two surfaces of the isolator, $u_{b,1}$ represents the displacement of the surface 1 with respect to the slider, $u_{b,2}$ is the slider displacement with respect to the ground, $\mu_{d,1}$ and $\mu_{d,2}$ denote the sliding friction coefficients of the two surfaces and sgn is the signum function of the sliding velocity for each surface. In this work, the surface 1 presents higher values of both the friction coefficient and the radius of curvature. Precisely, $\mu_{d,1}$ is chosen as $4\mu_{d,2}$ and $R_1=2R_2$ [30].

Along each surface, the friction coefficient applies [4]-[5]:

$$\mu_{d,i} = f_{\max,i} - \left(f_{\max,i} - f_{\min,i}\right) \exp\left(-\alpha \dot{u}_{b,i}\right) \quad \text{for } i = 1,2 \tag{2}$$

where $f_{\max,i}$ and $f_{\min,i}$ are, respectively, the friction coefficients at high and very low sliding velocities of the i-th surface. The values of 30 and 3 are assumed, respectively, for α and $f_{\max,i} / f_{\min,i}$ for each sliding surface [15],[28].

The hardening or softening behaviour of the superstructure is modelled herein through a bilinear constitutive law. In this way, the response is elastic if Eqn.(3) is verified and the restoring force $f_{s,i}$ is expressed according to Eqn.(4):

$$\left|u_{s,i}-u_{0,i-1}\right|<y\left(u_{s,i}\right) \tag{3}$$

$$f_{s,i}\left(u_{s,i}\right)=k_s\left(u_{s,i}-u_{0,i-1}\right) \tag{4}$$

where $f_{s,i}$ denotes the restoring force at time instant i, $u_{s,i}$ represents the superstructure deformation at the same instant, $u_{0,i-1}$ is the maximum inelastic response at time instant $(i-1)$ and k_s is the superstructure elastic stiffness. The term $y(u_{s,i})$ is the yielding function depending on the displacement as explained in [31]. Defining u_y as the yield displacement, whose yield force is f_y, H or S denotes the ratio of the hardening or softening post-yield stiffness over the elastic stiffness [32]-[33], evaluated as:

$$H=S=\frac{k_y}{k_s} \tag{5}$$

The superstructure response is in plastic phase if Eqn.(6) is verified and the restoring force can be calculated through Eqn.(7):

$$\left|u_{s,i}-u_{0,i-1}\right|\geq y(u_{s,i}) \tag{6}$$

$$f_{s,i}\left(u_s\right)=k_s(u_{s,i}-y(u_{s,i}))\,\mathrm{sgn}(u_{s,i}-u_{0,i-1}) \tag{7}$$

Therefore, the equations of motion that govern the inelastic response of the equivalent 3dof system to the seismic input $\ddot{u}_g(t)$, without any viscous dissipative capacities for the DFPS, are:

$$m_s\ddot{u}_s+(m_s+m_b)\ddot{u}_{b,1}+(m_s+m_b+m_d)\ddot{u}_{b,2}+\frac{W_2}{R_2}u_{b,2}+W_2\mu_2\,\mathrm{sgn}\left(\dot{u}_{b,2}\right)=-(m_s+m_b+m_d)\ddot{u}_g$$

$$m_s\ddot{u}_s+(m_s+m_b)\ddot{u}_{b,1}+(m_s+m_b)\ddot{u}_{b,2}+(m_s+m_b)\frac{g}{R_1}u_{b,1}+(m_s+m_b)g\mu_1\,\mathrm{sgn}\left(\dot{u}_{b,1}\right)=-(m_s+m_b)\ddot{u}_g$$

$$m_s\ddot{u}_s+m_s\ddot{u}_{b,1}+m_s\ddot{u}_{b,2}+c_s\dot{u}_s+f_{s,i}(u_s)=-m_s\ddot{u}_g \tag{8a,b,c}$$

where m_s, m_b and m_d represent respectively the mass of the superstructure, of the isolation level and of the slider, c_s is the superstructure viscous damping factor. Dividing Eqn.(8a) by $m_s+m_b+m_d$ as well as Eqn.(8b) by m_b+m_s and Eqn.(8c) by m_s, defining the mass ratios as $\gamma_s=m_s/(m_s+m_b+m_d)$, $\gamma_b=m_b/(m_s+m_b+m_d)$ and $\gamma_d=m_d/(m_s+m_b+m_d)$ [34], the isolation $\omega_{b,i}=\sqrt{g/R_i}$ and structural $\omega_s=\sqrt{k_s/m_s}$ circular frequency, the structural damping ratio $\xi_s=c_s/2m_s\omega_s$, the non-dimensional equations become as follows:

$$\gamma_s \ddot{u}_s + (\gamma_s + \gamma_b)\ddot{u}_{b,1} + \ddot{u}_{b,2} + \omega_{b,2}^2 u_{b,2} + g\mu_2 \operatorname{sgn}\left(\dot{u}_{b,2}\right) = -\ddot{u}_g$$
$$\gamma_s \ddot{u}_s + (\gamma_s + \gamma_b)\ddot{u}_{b,1} + (\gamma_s + \gamma_b)\ddot{u}_{b,2} + (\gamma_s + \gamma_b)\omega_{b,1}^2 u_{b,1} + (\gamma_s + \gamma_b) g\mu_1 \operatorname{sgn}\left(\dot{u}_{b,1}\right) = -(\gamma_s + \gamma_b)\ddot{u}_g$$
$$\ddot{u}_s + \ddot{u}_{b,1} + \ddot{u}_{b,2} + 2\omega_s \xi_s \dot{u}_s + a_s(u_s) = -\ddot{u}_g \tag{9a,b,c}$$

where $a_s\left(u_s\right) = f_s\left(u_s\right)/m_s$ denotes the dimensionless superstructure force proportional to the elastic stiffness k_s if the response is elastic or depends on the yielding condition if the system responds inelastically. Note that the elastic vibration period of the isolation system provided by the DFPS devices depends on which surfaces are moving during the earthquake [19]. In detail, if only one surface slides, the isolation period depends only on the radius of curvature of that surface R_i and the bearing behaves like a simple FPS [14], whereas when the both surfaces slide, the isolation effective period applies [19]:

$$T_b = 2\pi\sqrt{\frac{R_1 + R_2}{g}} \tag{10}$$

It follows that the seismic isolation degree [35], expressed as the variable isolation period over the structural period of vibration, is not a constant during an earthquake event. Moreover, when the both surfaces slide simultaneously the restoring force of the DFPS isolator can be evaluated as $\mu_e W_1$ neglecting the mass of the slider [30], where μ_e is the effective sliding coefficient given by:

$$\mu_e = \frac{\mu_{d,1}R_1 + \mu_{d,2}R_2}{R_1 + R_2} \tag{11}$$

Regards the inelastic behavior of the superstructure [36]-[37], Eqn.s (12)-(13) define, respectively, the inelastic capacities in terms of behavior factor, q, and displacement ductility, μ, defined, respectively, as:

$$q = \frac{f_{s,el}}{f_y} = \frac{u_{s,el}}{u_y} \tag{12}$$

$$\mu = \frac{u_{\mathrm{s,max}}}{u_y} \tag{13}$$

where $f_{s,el}$ and $u_{s,el}$ represent the peak response values, respectively, in terms of strength and displacement when the superstructure responds elastically during a ground motion, whereas $u_{\mathrm{s,max}} = \left|u_s(t)\right|_{\max}$ denotes the peak inelastic response in terms of displacement. The terms u_y and f_y are, respectively, the yielding displacement and strength. More details may be found in [30].

3 INCREMENTAL DYNAMIC ANALYSES

This section describes the results achieved from the incremental dynamic analyses (IDAs) of the system in Figure 1 within a wide parametric analysis, considering several structural parameters and as Italian site: L'Aquila (42°38'49''N and 13°42'25''E and a soil class B). In detail, the responses of the superstructure, of the DFPS are investigated for increasing intensity measure (*IM*) levels and shown in the following figures adopting 30 real ground motions,

which have also been used in previous studies by the authors [28],[29],[30], to describe the aleatory uncertainty on the seismic input denoted as record-to-record variability. The *IM* is herein chosen as the spectral displacement at the effective isolated period $S_D(T_b)$.

Elastic and inelastic properties of the isolated superstructure

Within the parametric analysis, the following deterministic parameters are taken into account: the isolation degree I_d with respect to the equivalent effective isolated period of Eq.(10) = 2, 4, 6 and 8; the equivalent effective isolation period T_b of Eq.(10) = 3s, 4s, 5s and 6s; the mass ratios: γ_s = 0.6 and 0.8, γ_d = 0.001, and so γ_b = 0.399 and 0.199; the behaviour factor q = 1.1, 1.2, 1.3, 1.4, 1.5, 1.6, 1.7, 1.8, 1.9 and 2, according to [20]-[23], and the post-yield softening or hardening stiffness ratio S or H = 0.03 [38]-[39]. Combing all these properties, 768 equivalent inelastic 3dof systems derive. The isolation damping ratio ξ_b is assumed equal to 0% whereas, superstructure damping ratio ξ_s equal to 2%.

Neglected the inelastic properties and considering only the elastic ones, 32 different 3dof systems derive (with the different values of I_d, of T_b and of the mass ratios). Assuming $\mu_{d,1}$ and $\mu_{d,2}$ equal to 4% and 1%, respectively, and a ratio equal to 2 between R_1 and R_2 [30], for 32 elastic 3dof elastic systems, it has been possible to evaluate the average elastic responses, in Matlab-Simulink [40], to the 30 records scaled to the *IM* value of the life safety limit state for L'Aquila: the $IM = S_D(T_b)$ applies 0.311 m for T_b=3, 4, 5 s and 0.26 m for T_b =6 s [22]. In this way, the yielding characteristics of the 768 inelastic 3dof systems have been computed in terms of the average values of both yield strength and yield displacement (i.e., $f_{y,\text{average}}$ and $u_{y,\text{average}}$) divided by the increasing values of q, as expressed by Eqn.(14):

$$u_{y,average} = \frac{f_{y,average}}{k_s} = \frac{f_{s,el,average}}{k_s q} = \frac{u_{s,el,average}}{q} \tag{14}$$

Incremental dynamic analysis (IDA) curves

This sub-section deals with the responses of the 768 equivalent 3dof hardening and softening systems, considering the aleatory uncertainties of the sliding friction coefficients through 15 sampled couples, to the 30 seismic inputs scaled to the increasing $IM = S_D(T_b)$, varying in the range from 0 m to 0.45 m. Specifically, for each *IM* level and parameter combination, 450 numerical non-linear analyses have been developed. The isolated non-linear hardening and softening systems are modelled in Matlab-Simulink [40], by employing the Runge-Kutta-Fehlberg integration algorithm to solve Eqn.(9) and determine the responses of the superstructure and of the DFPS bearings.

For each softening structural system, the collapse condition assumed within the numerical analyses is reached when the response of the superstructure is equal to zero. For the other systems as well as for the isolation devices any limitation is not considered.

Form the results of the non-linear incremental dynamic analyses, it has been possible to estimate the collapsed system cases together with the displacement ductility demand μ for the superstructure and the displacements for the DFPS (i.e., peak value for each one of the two surfaces "$u_{b,1}$ and $u_{b,2}$" and peak value of their sum computed at each time instant "u_b"). These response parameters are denoted as the engineering demand parameters (EDPs) and their peak

values have been fitted by means of lognormal distributions [12]-[15],[28],[41],[42] at each *IM* level. In detail, for each lognormal distribution, through the maximum likelihood estimation (MLE) technique [43]-[47], the mean, $\mu_{\ln}(EDP)$, and the standard deviation, $\sigma_{\ln}(EDP)$, have been computed as well as the 50th, 84th and 16th percentile.

It is also important to specify that neither other aleatory uncertainties not epistemic uncertainties have been herein considered [48]-[49].

Figures 2-3 depict the IDA curves for hardening structures. The results related to I_d =2 and 8, T_b =3s and 6s and γ_s equal to 0.6 are herein illustrated.

Fig. 2 depicts the IDA curves of the isolation level EDP $u_{b,\max}$, which is the peak value of the sum of $u_{b,1}$ and $u_{b,2}$ in each time instant. The lognormal mean of $u_{b,\max}$ is higher by increasing T_b and I_d. Moreover, the increase of q causes a slight decrease of $u_{b,\max}$, especially for higher values of I_d. The results are consistent with the ones achieved in [29] considering a single concave sliding device.

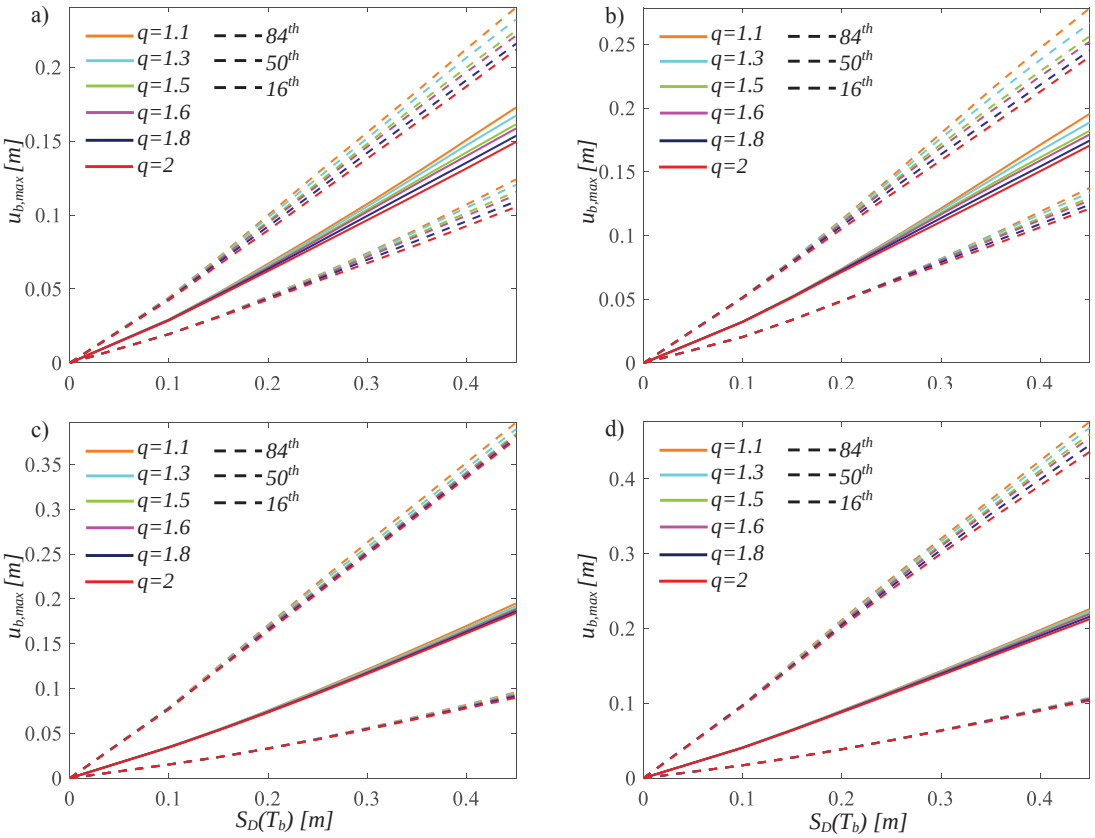

Figure 2: IDA curves of the isolation level with γ_s =0.6 for I_d=2, T_b=3 s, H=0.03 (a), I_d=2, T_b=6 s, H=0.03 (b), I_d=8, T_b=3 s, H=0.03 (c), I_d=8, T_b=6 s, H=0.03 (d).

Fig. 3 depicts the IDA results for the EDP μ. The corresponding statistical parameters are strongly influenced by the variation of q. In fact, an its increase leads to a very high displacement ductility demand μ. In addition, $\mu_{\ln}(\mu)$ highly decreases by decreasing T_b but is higher for lower values of I_d, especially for high values of T_b.

The IDA results of the isolation level and of the superstructure for the softening behavior are not reported because the influence of the data related to the dynamic collapses has been taken

into account within the assessment of the seismic fragility, as discussed in the next section, together with the description of the influence of the other structural properties (i.e., γ_s, q and S) on both the DFPS and the softening superstructures.

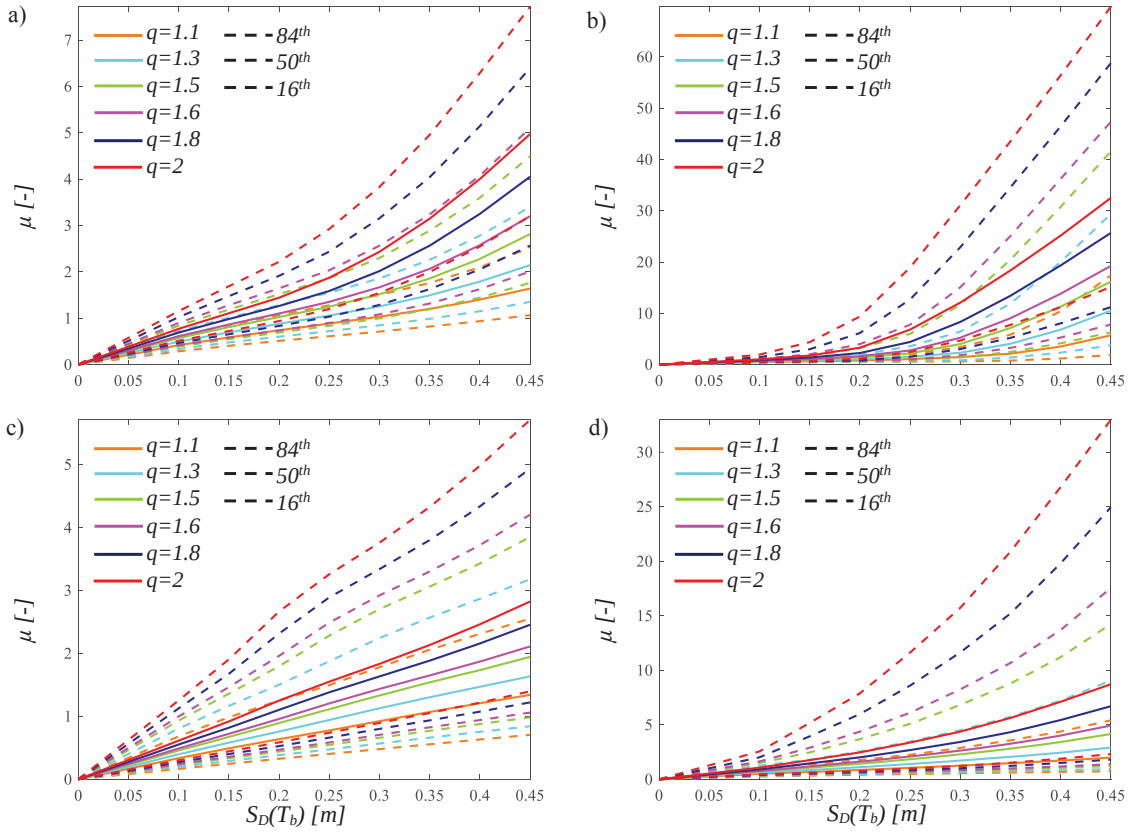

Figure 3: IDA curves of the superstructure with γ_s=0.6 for I_d=2, T_b=3 s, H=0.03 (a), I_d=2, T_b=6 s, H=0.03 (b), I_d=8, T_b=3 s, H=0.03 (c), I_d=8, T_b=6 s, H=0.03 (d).

4 SEISMIC FRAGILITY CURVES

The definition of the limit states with respect to the EDP is necessary to reach the fragility assessment. In detail, different thresholds, respectively, in terms of the radius in plan for each surface of the DFPS isolator, $r_1[m]$ and $r_2[m]$, and of the displacement ductility for the superstructure, $\mu[-]$, have been selected. In this way, the probabilities P_f exceeding the different limit states at each *IM* level, have been numerically computed. Tables 1-2 report, respectively, the failure probabilities in 50 years [50] and the corresponding thresholds, related to the *LS*s provided by the codes [21]-[22]: the failure probability in 50 years [13],[50] associated to the collapse limit state [22] for the DFPS; whereas, the failure probability in 50 years [13],[50] associated to the life safety *LS* [22] for the superstructure in compliance with the design.

For each structural system of the 768 equivalent 3dof systems, the probabilities P_f exceeding the different limit states at each *IM* level, are numerically computed and successively fitted through lognormal distributions [14] with a R-square value higher than 0.8. For the softening systems, the number of both the collapse cases has been considered to estimate the seismic fragility through the total probability theorem [29],[51], as follows:

$$P_{SL}(IM = im) = (1 - F_{EDP|IM=im}(LS_{EDP})) \cdot \frac{N_{not-collapse}}{N} + 1 \cdot \left(1 - \frac{N_{not-collapse}}{N}\right) \quad (15)$$

where N is the overall number of analyses at each IM level, and $N_{not-collapse}$ is the number of numerical simulations without any collapse.

Figures 6-8 depict the fragility curves for increasing IM regarding both softening and hardening structures. Precisely, the curves related to the different structural properties and only to some limit state thresholds ($LS_{r,4}$ and $LS_{\mu,3}$) and to I_d=8 and T_b=3s, are illustrated.

Generally, the seismic fragility is lower for increasing the corresponding limit state threshold and is the highest for the post-yield softening behavior.

Figure 4 illustrates the fragility curves regarding the overall response of isolation level for hardening models.

Figures 6-7 depict the fragility curves of the two surfaces of DFPS for the softening systems.

For the all limit states, P_f decreases slightly for increasing γ_s. Then, especially for high limit state thresholds, the fragility increases by increasing T_b, I_d and decreasing q. Note that the probability exceeding a limit state is quite low for the single surface, with a lower probability for the surface 2 characterized by a lower friction coefficient with a lower radius of curvature, in compliance with the IDA results. Obviously, higher values are achieved for the softening behaviour.

The fragility curves for the nonlinear superstructures are shown in Figures 5 (hardening) and 8 (softening). The exceeding probabilities are slightly lower as γ_s decreases but highly increase for increasing values of q. Conversely, lower values of T_b for fixed I_d lead to an increase of the seismic fragility because a decrease of the period T_s means a decrease of the correlated yielding displacement as well as lower values of T_b for fixed I_d lead to higher values of the seismic fragility. In fact, the coupling between I_d and T_b influences T_s and the associated yielding displacement and so, as also discussed in [28]-[29], with reference to systems with low T_s, the ensuing dynamic amplification can negatively affect the superstructure responses increasing the seismic fragility.

	$LS_{r,1}$	$LS_{r,2}$	$LS_{r,3}$	$LS_{r,4}$	$LS_{r,5}$	$LS_{r,6}$	$LS_{r,7}$	$LS_{r,8}$	$LS_{r,9}$	$LS_{r,10}$
r_i *[m] for i =1,2*	0.05	0.1	0.15	0.2	0.25	0.3	0.35	0.4	0.45	0.5
p_f=1.5·10^{-3} in 50 years										

Table 1: Limit state thresholds for the two surfaces of the DFPS with the associated exceeding probability.

	$LS_{\mu,1}$	$LS_{\mu,2}$	$LS_{\mu,3}$	$LS_{\mu,4}$	$LS_{\mu,5}$	$LS_{\mu,6}$	$LS_{\mu,7}$	$LS_{\mu,8}$	$LS_{\mu,9}$	$LS_{\mu,10}$
μ *[-]*	1	2	3	4	5	6	7	8	9	10
p_f=2.2·10^{-2} in 50 years										

Table 2: Limit state thresholds in terms of μ with the associated exceeding probability.

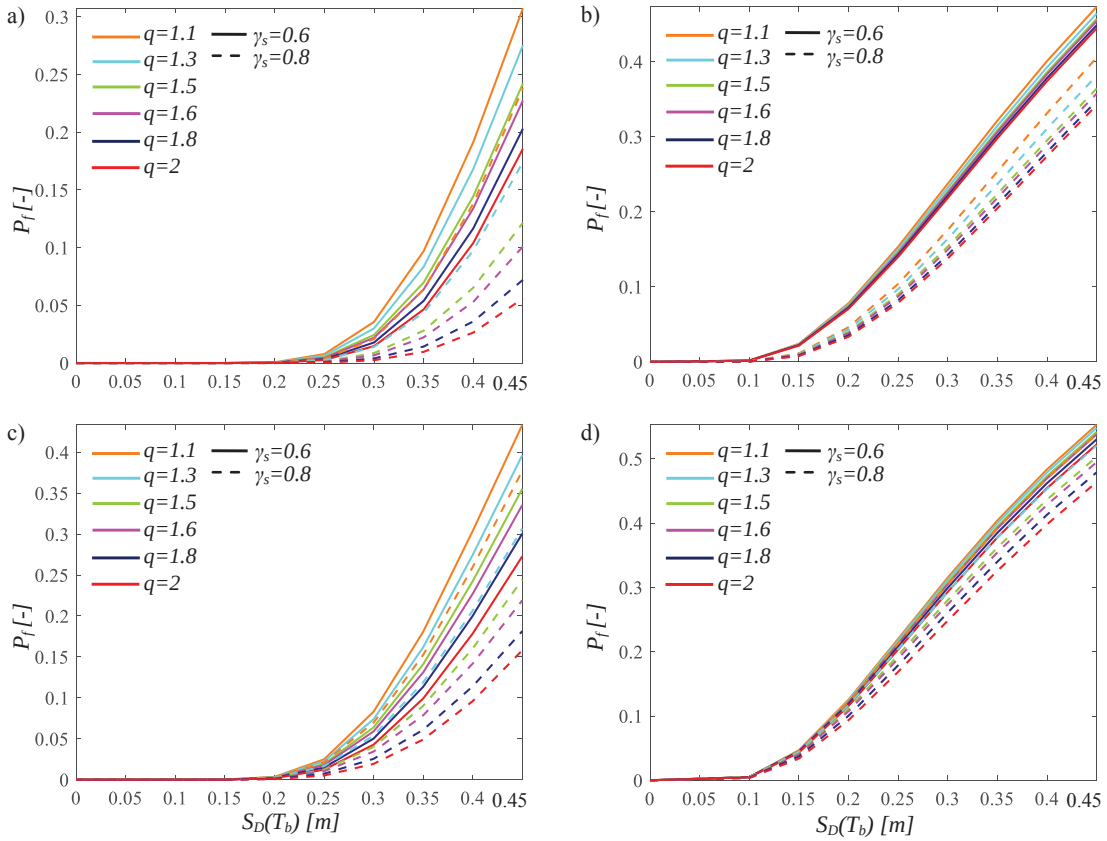

Figure 4: Seismic fragility of the isolation level corresponding to $LS_{r,4}$=0.2 m, for I_d=2, T_b=3 s, H=0.03 (a), I_d=2

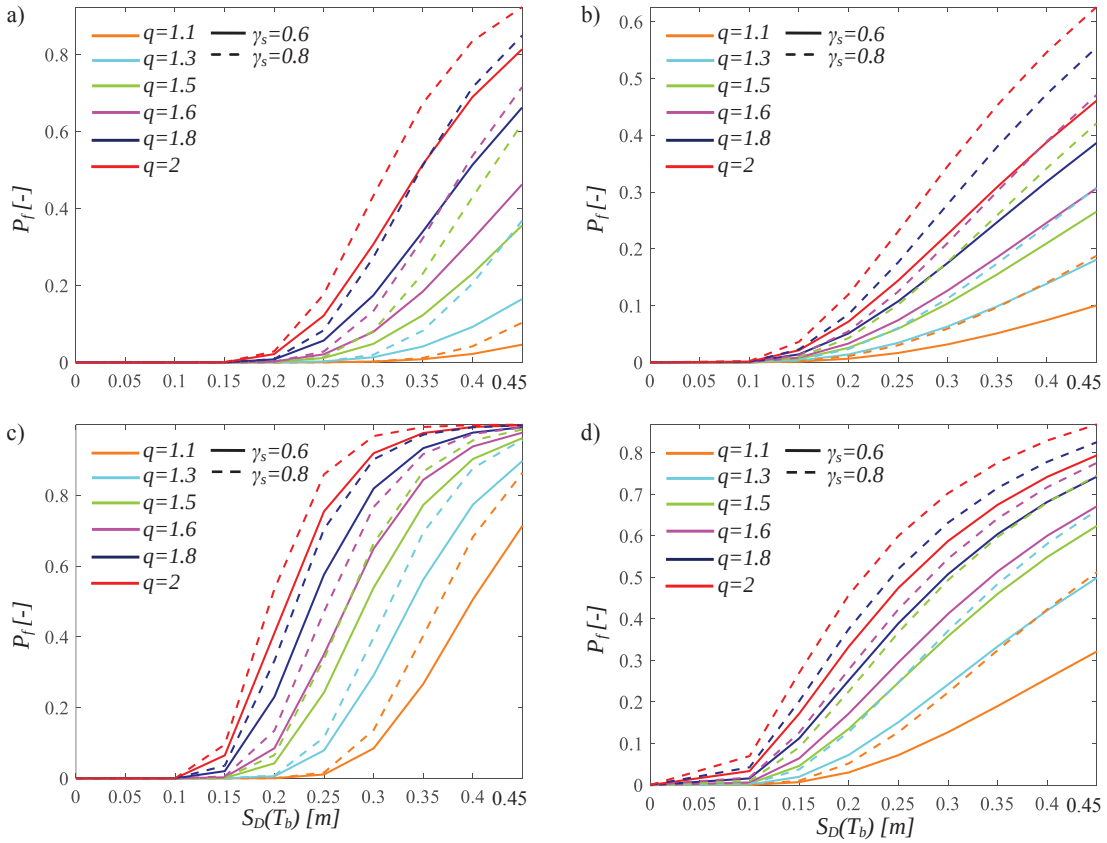

Figure 5: Seismic fragility of the superstructure corresponding to $LS_{\mu,3}$=3, for I_d=2, T_b=3 s, H=0.03 (a), I_d=2 and T_b=6 s, H=0.03 (b), I_d=8 and T_b=3 s, H=0.03 (c), I_d=8 and T_b=6 s, H=0.03 (d).

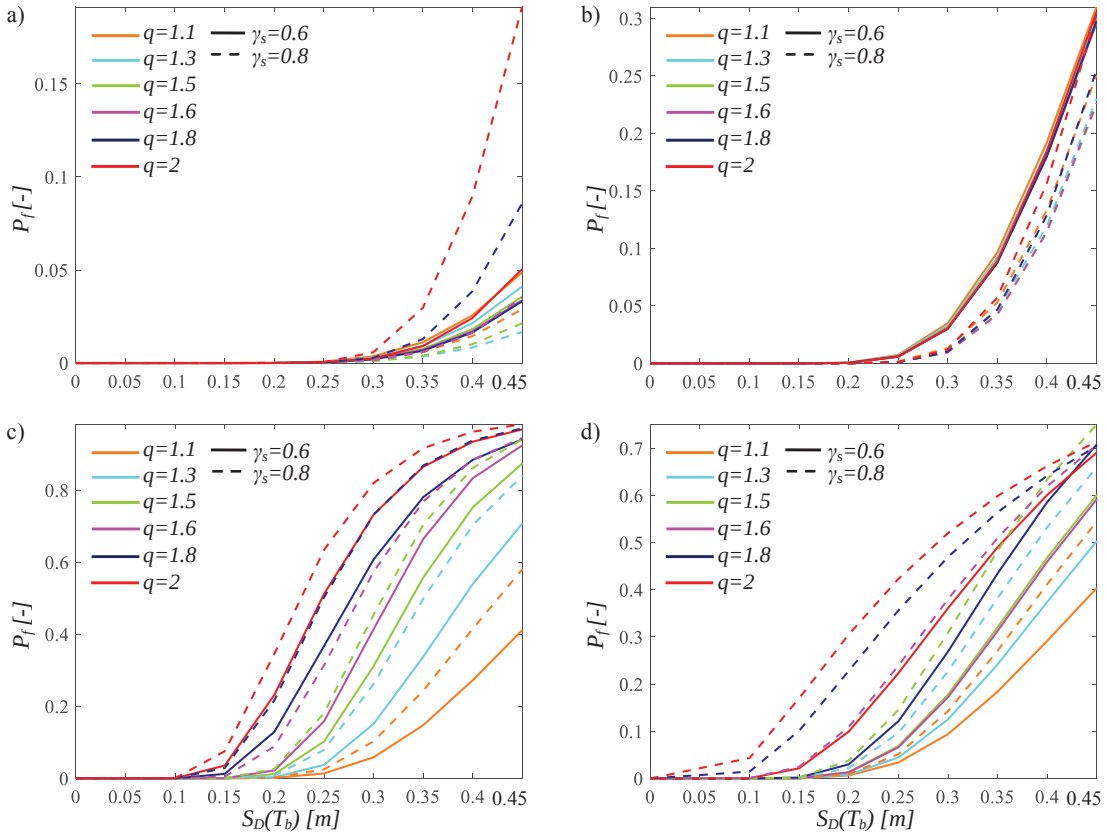

Figure 6: Seismic fragility of the sliding surface 1 corresponding to $LS_{r,4}$=0.2 m, for I_d=2, T_b=3 s, S=0.03 (a),

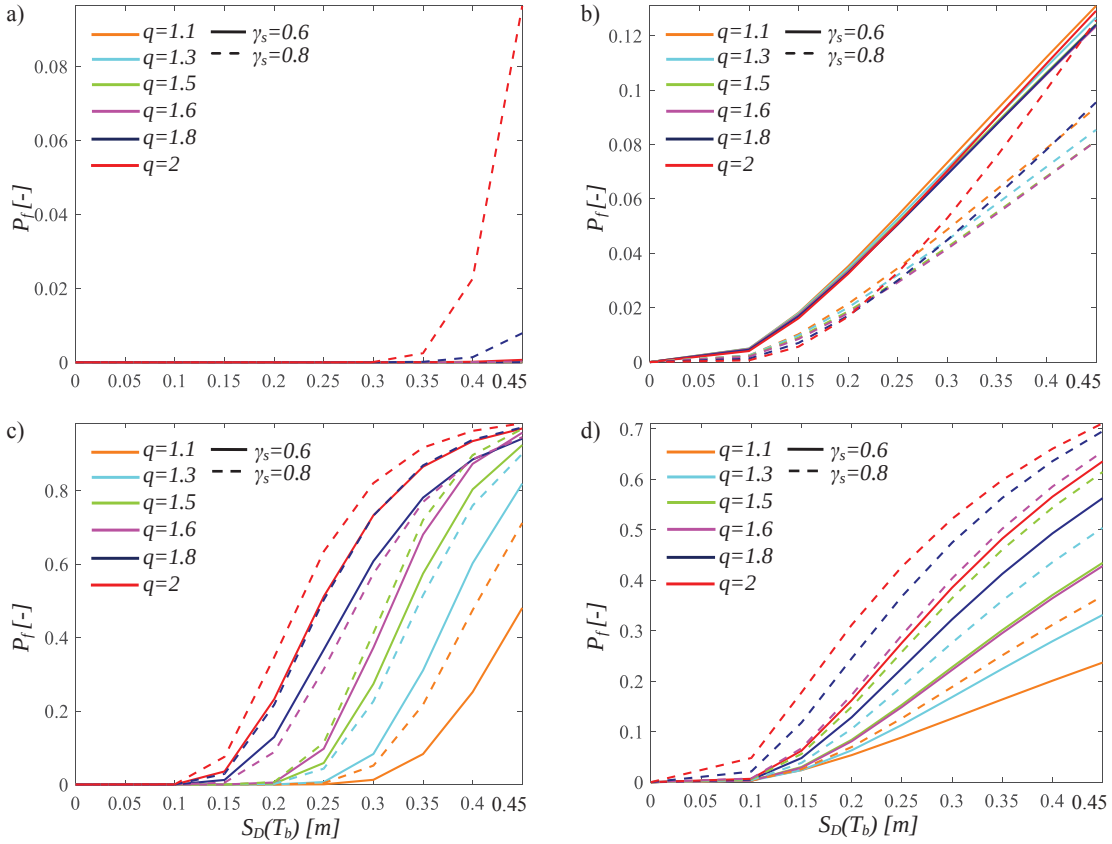

Figure 7: Seismic fragility of the sliding surface 2 corresponding to $LS_{r,4}$=0.2 m, for I_d=2, T_b=3 s, S=0.03 (a), I_d=2 and T_b=6 s, S=0.03 (b), I_d=8 and T_b=3 s, S=0.03 (c), I_d=8 and T_b=6 s, S=0.03 (d).

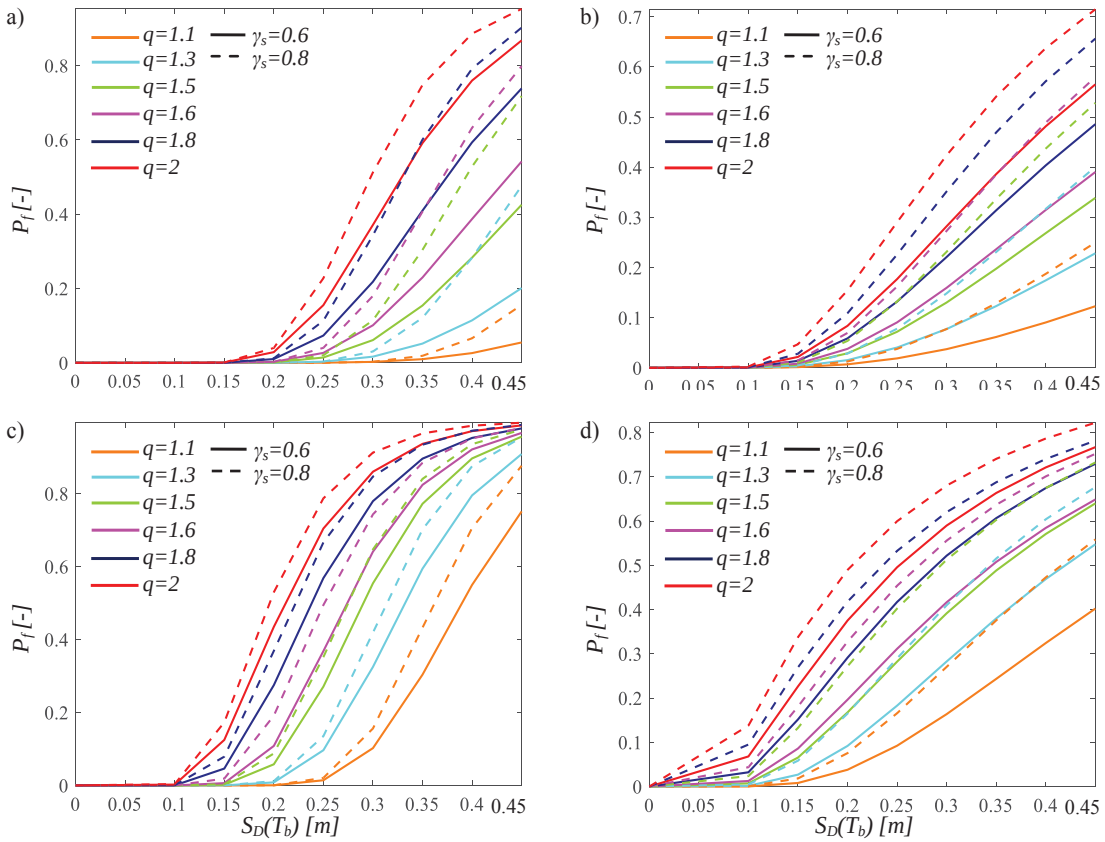

Figure 8: Seismic fragility of the superstructure corresponding to $LS_{\mu,3}=3$, for I_d=2, T_b=3 s, S=0.03 (a), I_d=2 and T_b=6 s, S=0.03 (b), I_d=8 and T_b=3 s, S=0.03 (c), I_d=8 and T_b=6 s, S=0.03 (d).

5 SEISMIC RELIABILITY-BASED DESIGN CURVES FOR DFPS

This section illustrates the results of the seismic reliability assessment for all the equivalent softening or hardening structures isolated by DFPS within their lifetime of 50 years. This assessment is composed of the following two steps: (i) computation of the convolution integral between the seismic fragility curves and the seismic hazard curves, expressed in terms of the same $IM=S_D(T_b)$ [22],[29], to assess the mean annual rates exceeding the limit states; (ii) assessment of the probabilities exceeding the limit states in 50 years through the homogenous Poisson model.

As regards the DFPS isolators, the seismic reliability curves can be seen as the SRBD curves to design the dimensions in plan of each surface and the overall dimension of these devices depending on the expected reliability target and of the structural properties. Figures 9-10 show, respectively, the linear regressions, representative of the seismic reliability of the overall dimension of the isolation level, in the semi-logarithmic space for hardening and softening structures. The R-square value is higher than 0.8. The figures demonstrate that the seismic reliability of the isolation level decreases for the softening behavior in comparison to the hardening case. The increasing direction of the structural parameter q is denoted by means of the arrow in the figures. As for hardening models, these curves demonstrate that an exceeding probability of $P_f=1.5\cdot10^{-3}$ (corresponding to the collapse limit state in 50 years) [50]-[52] requires a global dimension ranging from about 0.3 m to about 1 m depending on the structural characteristics. Instead, for softening superstructures, higher values are required.

Figures 11-22 show the seismic reliability curves for the hardening and softening superstructures highlighting the great influence of the behavior factor as well as the great contribution of the hardening properties in comparison to the softening ones.

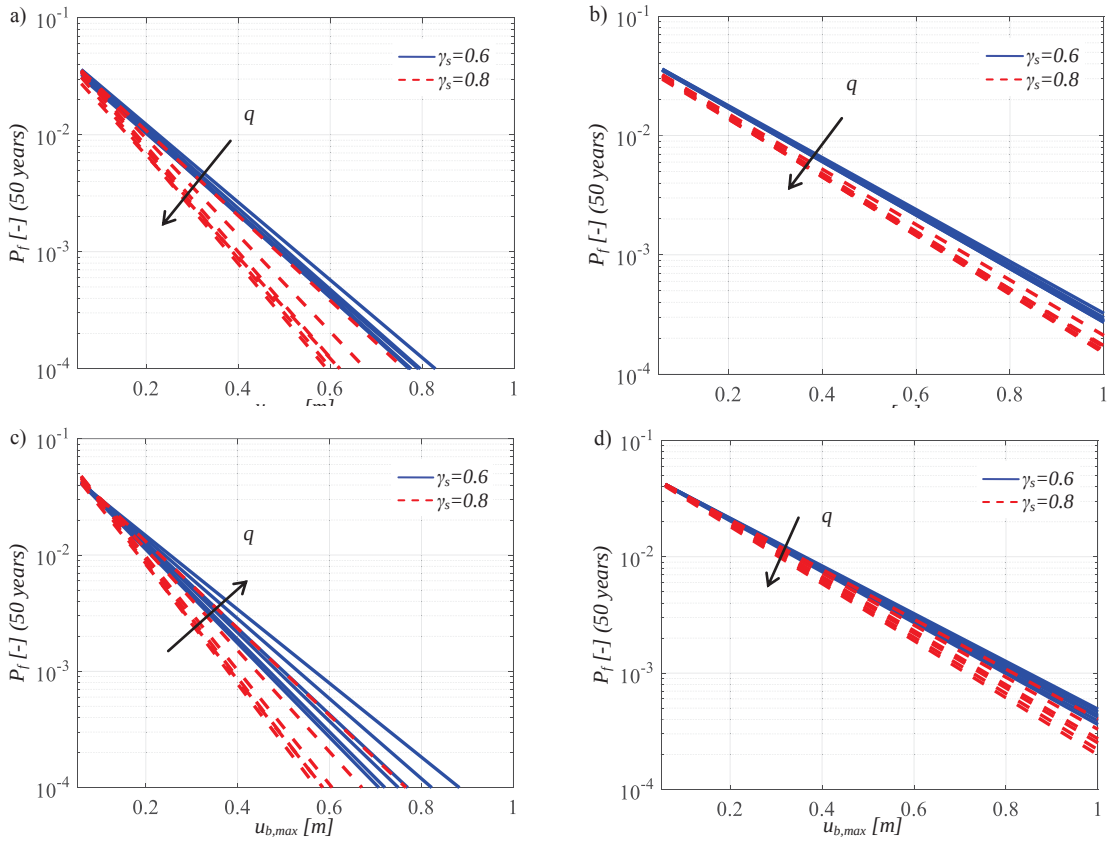

Figure 9: Seismic reliability of the isolation level related to I_d=2, T_b=3 s, H=0.03 (a), I_d=2 and T_b=6 s, H=0.03 (b), I_d=8 and T_b=3 s, H=0.03 (c), I_d=8 and T_b=6 s, H=0.03 (d).

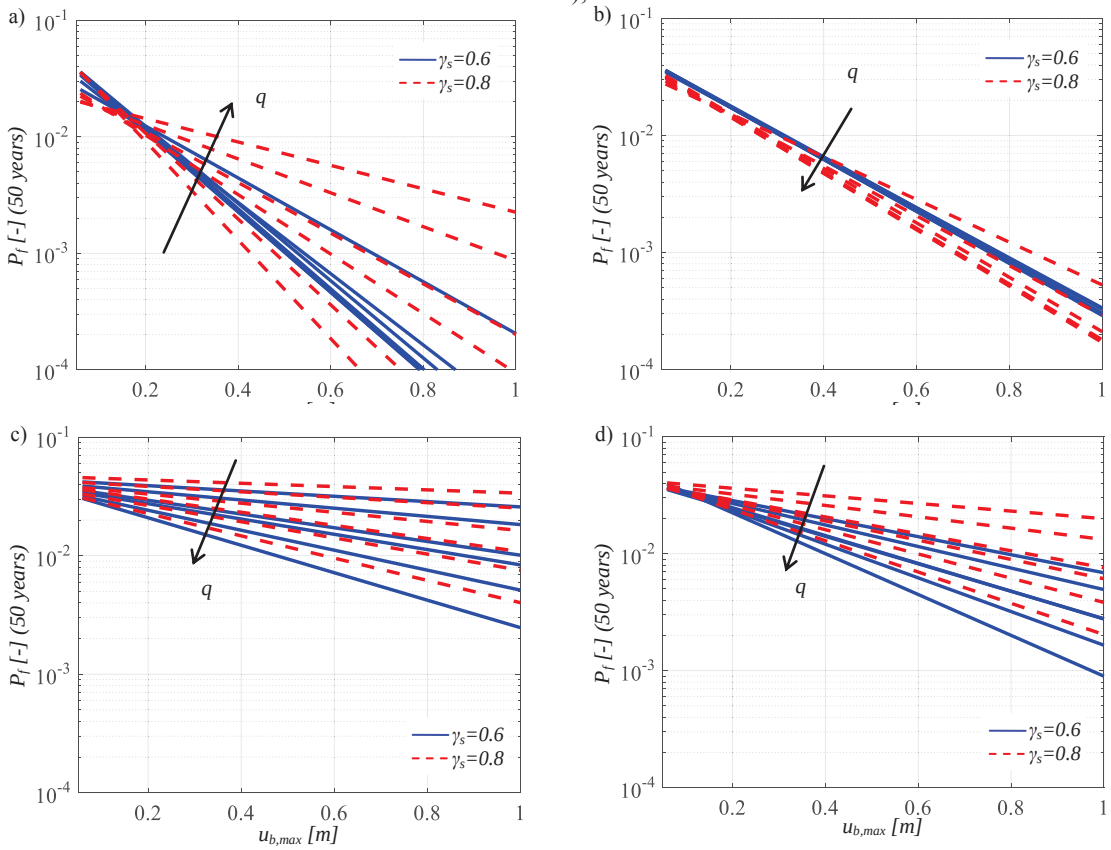

Figure 10: Seismic reliability of the isolation level related to I_d=2, T_b=3 s, S=0.03 (a), I_d=2 and T_b=6 s, S=0.03 (b), I_d=8 and T_b=3 s, S=0.03 (c), I_d=8 and T_b=6 s, S=0.03 (d).

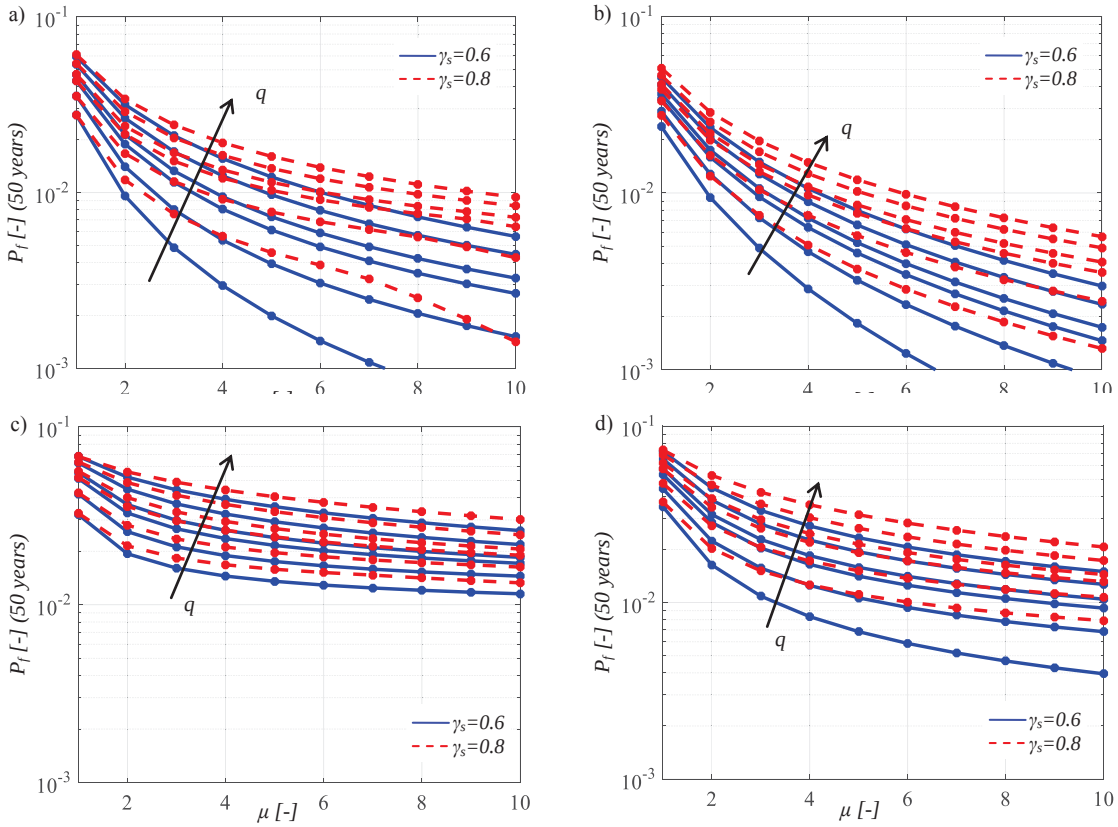

Figure 11: Seismic reliability of the superstructure corresponding to I_d=2, T_b=3 s, H=0.03 (a), I_d=2 and T_b=6 s, H=0.03 (b), I_d=8 and T_b=3 s, H=0.03 (c), I_d=8 and T_b=6 s, H=0.03 (d).

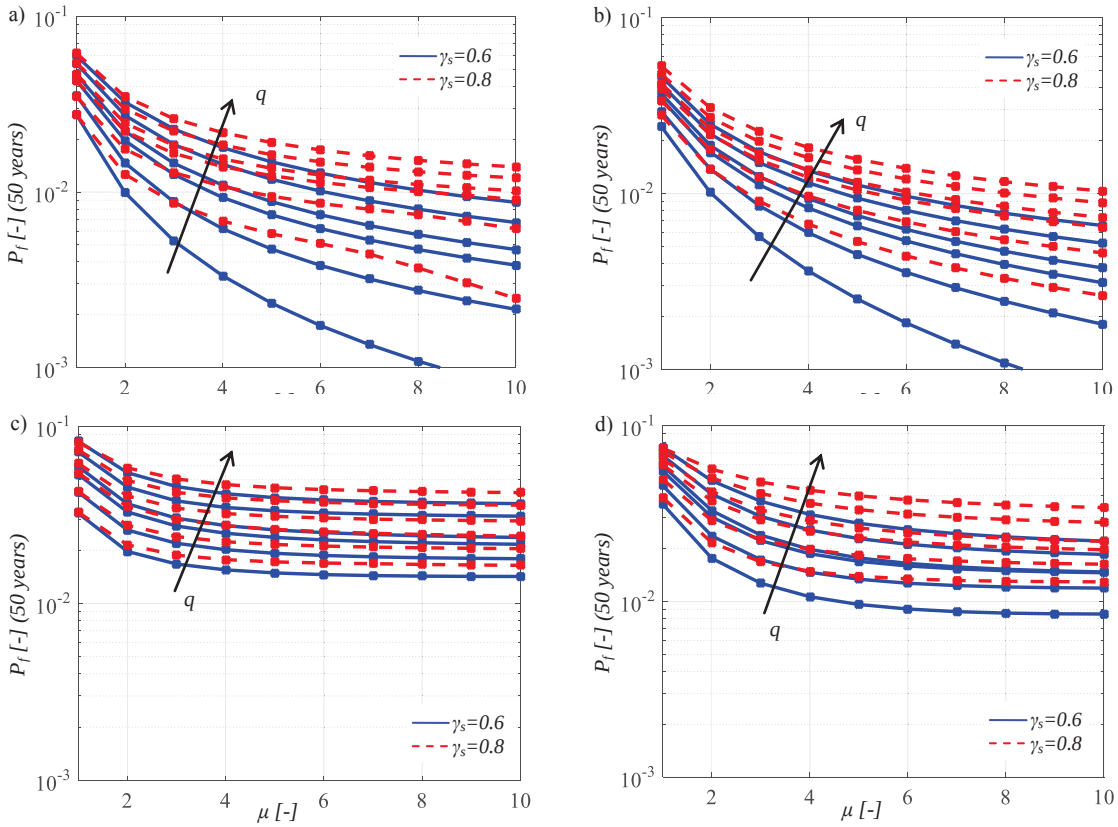

Figure 12: Seismic reliability of the superstructure corresponding to I_d=2, T_b=3 s, S=0.03 (a), I_d=2 and T_b=6 s, S=0.03 (b), I_d=8 and T_b=3 s, S=0.03 (c), I_d=8 and T_b=6 s, S=0.03 (d).

6 CONCLUSIONS

This study focuses on the seismic reliability-based response of hardening and softening structures isolated with double concave sliding isolators. A wide investigation is presented considering different elastic and inelastic mechanical properties and assuming the friction coefficients together with the characteristics of the seismic ground motions as random variables. Adopting an equivalent 3dof system with non-linear velocity-dependent rules for the two surfaces of the DFPS, incremental dynamic analyses are carried out for several natural seismic records, different behavior factors and post-yield stiffness ratios. Then, the seismic fragility curves are derived for each engineering demand parameters of interest for these systems: peak values of the response of the superstructure, of the upper surface and of the lower surface of the DFPS. Successively, assuming a lifetime of 50 years and the seismic hazard of L'Aquila (Italian site), seismic reliability-based design curves are derived for the DFPS. The results have highlighted the great influence of the behavior factor as well as the negative effects of the post-yield stiffness also regarding the seismic reliability of the superstructure.

REFERENCES

[1] C. Christopoulos, A. Filiatrault, Principles of Passive Supplemental Damping and Seismic Isolation. IUSS Press: Pavia, Italy, 2006.

[2] VA. Zayas, SS. Low, SA. Mahin, A simple pendulum technique for achieving seismic isolation. *Earthquake Spectra* 1990; 6:317–33.

[3] L. Su, G. Ahmadi , IG. Tadjbakhsh, Comparative study of base isolation systems. *Journal of Engineering Mechanic* 1989; 115:1976–92.

[4] A. Mokha , MC. Constantinou, AM. Reinhorn, Teflon Bearings in Base Isolation. I: Testing. *J. Struct. Eng.* 1990; 116(2): 438-454.

[5] MC. Constantinou, A. Mokha, AM. Reinhorn, Teflon Bearings in Base Isolation. II: Modeling. *J. Struct. Eng*. 1990; 116(2):455-474.

[6] Troisi R., Alfano G. 2019. Towns as Safety Organizational Fields: An Institutional Framework in Times of Emergency. *Sustainability*, 11: 7025, 2019, doi:10.3390/su11247025.

[7] Troisi R., Alfano G. 2020. Firms'crimes and land use in Italy. An exploratory data anlysis. New Metropolitan Perspectives, International Symposium – 4th edition, 27-30 May 2020, pp 10.

[8] BM. Ayyub, RH. McCuen, Probability, statistics, and reliability for engineers. 2nd ed. NY: CRC Press; 2002.

[9] YK. Lin, GQ. Cai, Probabilistic structural dynamics—advanced theory and applications. NY: McGraw-Hill; 1995.

[10] J. Chen, W. Liu, Y. Peng, J. Li, Stochastic seismic response and reliability analysis of base-isolated structures. *J Earthquake Eng* 2007;11:903–24.

[11] SK. Mishra, BK. Roy, S. Chakraborty, Reliability-based-design-optimization of base isolated buildings considering stochastic system parameters subjected to random earth-

quakes. *Int J Mech Sci* 2013;75:123–33.

[12] P. Castaldo, B. Palazzo, P. Della Vecchia, (2014) Seismic reliability analysis of base-isolated structures with friction pendulum system, EESMS 2014 - 2014 IEEE Workshop on Environmental, Energy and Structural Monitoring Systems, Proceedings, 6923276, 114-119.

[13] P. Castaldo, B. Palazzo, P. Della Vecchia, Life-cycle cost and seismic reliability analysis of 3D systems equipped with FPS for different isolation degrees, *Engineering Structures*, 2016, 125:349–363, http://dx.doi.org/10.1016/j.engstruct.2016.06.056.

[14] P. Castaldo, G. Amendola, B. Palazzo , Seismic fragility and reliability of structures isolated by friction pendulum devices: Seismic reliability-based design (SRBD), *Earthquake Engineering and Structural Dynamics*, 2017, 46(3); 425–446, DOI: 10.1002/eqe.2798.

[15] P. Castaldo, M. Ripani, Optimal design of friction pendulum system properties for isolated structures considering different soil conditions, *Soil Dynamics and Earthquake Engineering*, 2016, 90:74–87, DOI: 10.1016/j.soildyn.2016.08.025.

[16] P. Castaldo, E. Tubaldi, Influence of ground motion characteristics on the optimal single concave sliding bearing properties for base-isolated structures. *Soil Dynamics and Earthquake Engineering*, 2018, 104: 346–364.

[17] YS. Kim, CB. Yun, Seismic response characteristics of bridges using double concave friction pendulum bearings with tri-linear behavior. *Engin. Struct*. 29, 2007, 3082-3093.

[18] P. Castaldo, M. Ripani, R. Lo Piore, Influence of soil conditions on the optimal sliding friction coefficient for isolated bridges. *Soil Dynamics and Earthquake Engineering*, 2018, 111:131–148, https://doi.org/10.1016/j.soildyn.2018.04.056.

[19] CS. Tsai , TC. Chiang, BJ. Chen, Experimental evaluation of piecewise exact solution for predicting seismic responses of spherical sliding type isolated structures. *Earthquake Engineeering and Structural Dynamics*, 2005;34:1027-1046 DOI: 10.1002/equ.430.

[20] Structural Engineering Institute. Minimum design loads for buildings and other structures. Amer. Society of Civil Engineers, 2010.

[21] European Committee for Standardization. Eurocode 8-Design of Structures for Earthquake Resistance. Part 1: General Rules, Seismic Actions and Rules for Buildings, Brussels, 2004.

[22] NTC18. Norme tecniche per le costruzioni. Gazzetta Ufficiale del 20.02.18, DM 17.01.18, Ministero delle Infrastrutture.

[23] Japanese Ministry of Land, Infrastructure and Transport, Notification No. 2009–2000, Tech. Standard for Structural Specif.s and Calculation of Seismically Isolated Buildings 2000.

[24] Quantification of Building Seismic Performance Factors, FEMA P695 / June 2009.

[25] A. Occhiuzzi, D. Veneziano and J. Van Dyck, Seismic design of base isolated structures, Savidis (Ed.), Balkema, Rotterdam, NL.

[26] MD. Mckey, WJ. Conover, RJ. Beckman, A comparison of three methods for selecting values of input variables in the analysis from a computer code. Technometrics 1979;21:239-45.

[27] D. Celarec, M. Dolšek, The impact of modelling uncertainties on the seismic performance assessment of reinforced concrete frame buildings. *Engineering Structures* 2013;52:340–354.

[28] P. Castaldo, B. Palazzo, T. Ferrentino T., Seismic reliability-based ductility demand evaluation for inelastic base-isolated structures with friction pendulum devices, *Earthquake Engineering and Structural Dynamics*, 2017, 46(8): 1245-1266, DOI: 10.1002/eqe.2854.

[29] P. Castaldo, B. Palazzo, G. Alfano, MF. Palumbo, Seismic reliability-based ductility demand for hardening and softening structures isolated by friction pendulum bearings, 2018, *Structural Control and Health Monitoring*, e2256. https://doi.org/10.1002/stc.2256.

[30] Castaldo P., Alfano G. Seismic reliability-based design of hardening and softening structures isolated by double concave sliding devices, *Soil Dynamics and Earthquake Engineering*, 129: 105930, 2020.

[31] HK. Hong, CS. Liu, Internal symmetry in bilinear elastoplasticity, International Journal of Non-Linear Mechanics, 1999, 34:279–288.

[32] GD. Hatzigeorgiou, Ductility demand spectra for multiple near- and far-fault earthquakes. *Soil Dynamics and Earthquake Engineering* 2010;30 170-183.

[33] GD. Hatzigeorgiou, GA. Papagiannopoulos, DE. Beskos, Evaluation of maximum seismic displacements of SDOF systems form their residual deformation. *Engineering Structures* 2011;33 3422-3431.

[34] F. Naeim, KM. Kelly, Design of Seismic Isolated Structures: From Theory to Practice. John Wiley & Sons, Inc.; 1999.

[35] B. Palazzo, Seismic Behavior of base-isolated Buildings. Proc. International Meeting on earthquake Protection of Buildings, Ancona, 1991.

[36] A. Gupta, H. Krawinkler, Seismic demands for performance evaluation of steel moment resisting frame structures. The John A. Blume Earth. Eng. Center report No. 132, June 1999.

[37] C. Adam, LF. Ibarra, H. Krawinkler, Evaluation of P-Delta effects in non-deteriorating MDOF structures from equivalent SDOF systems. *13th Word Conference on Earthquake Engineering*, Vancouver, B.C., Canada 2004, Paper No. 3407.

[38] GD. Hatzigeorgiou, Ductility demand spectra for multiple near- and far-fault earthquakes. *Soil Dynamics and Earthquake Engineering* 2010;30 170-183.

[39] C. Adam, LF. Ibarra, H. Krawinkler, Evaluation of P-Delta effects in non-deteriorating MDOF structures from equivalent SDOF systems. *13th Word Conference on Earthquake Engineering*, Vancouver, B.C., Canada, 2004, Paper No. 3407.

[40] Math Works Inc. MATLAB-High Performance Numeric Computation and Visualization Software. User's Guide. Natick: MA, USA, 1997.

[41] H. Aslani, E. Miranda, Probability-based seismic response analysis. *Engineering Structures* 2005; **27**(8): 1151-1163.

[42] KL. Ryan, AK. Chopra, Estimation of Seismic Demands on Isolators Based on Nonlinear Analysis. *J. Struct. Eng.*, 130(3), 392–402, 2004.

[43] Garzillo C., Troisi R. Le decisioni dell'EMA nel campo delle medicine umane. In EMA e le relazioni con le Big Pharma - I profili organizzativi della filiera del farmaco, G. Giappichelli, 85-133, 2015.

[44] Golzio L. E., Troisi R. The value of interdisciplinary research: a model of interdisciplinarity between legal re-search and research in organizations. *Journal For Development And Leadership*, 2: 23-38, 2013.

[45] Nese A.; Troisi R. Corruption among mayors: evidence from Italian Court of Cassation judgments, *Trends In Organized Crime*, 1-26, 2018. DOI:10.1007/s12117-018-9349-4.

[46] Troisi R., Golzio, L. E. Legal studies and organization theory: a possible cooperation. *Manageable cooperation* - European Academy of Management: 16th EURAM Conference, Paris, 1-2, 1-4 June 2016.

[47] Troisi R., Guida V. Is the Appointee Procedure a Real Selection or a Mere Political Exchange? The Case of the Italian Health-Care Chief Executive Officers. *Journal of Entrepreneurial and Organizational Diversity*, 7 (2): 19-38, 2018, DOI:10.5947/jeod.2018.008.

[48] Castaldo, P., Gino, D., Bertagnoli, G. & Mancini, G. Resistance model uncertainty in non-linear finite ele-ment analyses of cyclically loaded reinforced concrete systems, *Engineering Structures*, 211: 110496, 2020, https://doi.org/10.1016/j.engstruct.2020.110496.

[49] P. Castaldo, D. Gino, G. Mancini, Safety formats for non-linear analysis of reinforced concrete structures: discussion, comparison and proposals. *Engineering Structures*, 193,136-153, 2019.

[50] RD. Bertero, VV. Bertero, Performance-based seismic engineering: the need for a reliable conceptual comprehensive approach. *Earthquake Engineering and Structural Dynamics,* 2002;31:627–652 (DOI: 10.1002/eqe.146).

[51] P. Bazzurro, CA. Cornell, N. Shome, JE. Carballo, Three proposals for characterizing MDOF nonlinear seismic response. *Journal of Structural Engineering*, 1998, 124(11), 1281-1289.

[52] CEN – European Committee for Standardization. Eurocode 0: Basis of Structural Design. Final draft. Brussels, 2006.

EURODYN 2020
XI International Conference on Structural Dynamics
M. Papadrakakis, M. Fragiadakis, C. Papadimitriou (eds.)
Athens, Greece, 23–26 November 2020

GLOBAL AND LOCAL PERFORMANCE LEVELS ON THE PROBABILISTIC EVALUATION OF THE STRUCTURAL POUNDING EFFECT BETWEEN ADJACENT RC STRUCTURES

Maria G. Flegga[1], **Maria J. Favvata**[2]

[1] University of Patras, Civil Engineering Department
Rio Patras 26504, Greece
mariaflegga@upnet.gr

[2] University of Patras, Civil Engineering Department
Rio Patras 26504, Greece
mfavvata@upatras.gr

Keywords: reinforced concrete frame, pounding effect, fragility curves, local engineering demands, performance levels, Eurocode 8, nonlinear dynamic analyses

Abstract. *In this study the seismic performance of a real multistory RC frame structure against pounding with an adjacent shorter and stiffer structure is evaluated based on probabilistic assessment methods. The examined pounding case is between an 8-story RC frame and a 3-story rigid barrier (very stiff structure) with equal story heights (floor-to-floor interaction). Three different initial gap distances (d_g) between the adjacent structures are considered. The seismic performance of the 8-story structure without the pounding effect is also included for comparison reasons. The probabilistic evaluation of the pounding effect is performed through fragility curves in terms of global and local engineering demand parameters (EDPs) as a function of the intensity measure (IM). For this purpose, linear and bilinear regression models in log-log space have been considered to define the relationship between the examined EDPs and IMs. The commonly used intensity measures (IMs) of peak ground acceleration, PGA and that of spectral acceleration corresponding to the fundamental period of the examined structure, Sa($T_{1,8\text{-story}}$) are adopted. Displacement and rotation EDPs that could control the global state of the structure are examined at different performance levels. However, the most critical issue in earthquake-induced interaction between adjacent structures is the local responses of the columns at the pounding side. Thus, three local performance levels in terms of ductility capacity of the external columns at each story level of the 8-story frame have also been incorporated in the probabilistic assessment of the pounding problem. The results of this study indicate that the probability of pounding between the examined structures is increased as the separation gap distance d_g decreases. The fragility curves of the 8-story frame are significantly influenced due to the structural pounding effect. The probability of damage at columns seems to be an important parameter that has to be further investigated. Different types of global and local performance levels altered the intensity values for the seismic hazard of the structural pounding.*

1 INTRODUCTION

Field observations after numerous destructive earthquakes all over the world indicate that pounding is frequently observed when strong earthquakes strike big cities and densely populated urban areas. In these events it has been proved that the interaction between adjacent buildings results in local damages at the pounding area of the structures while there are cases where the seismic pounding has been identified as a primary cause for the initiation of collapses. In this view, the problem of earthquake induced pounding between adjacent buildings has received substantial attention over the last two to three decades [e.g. 1-14]. In the beginning these studies were based on the response of pairs or sets of colliding single degree of freedom systems in earthquake excitations [1]. However, results about the influence of the structural pounding on the seismic response of real multistory reinforced concrete structures based on inelastic time-history analyses have also been reported (e.g. [4], [5], [8], [9], [13], [14]). It is noted here that Karayannis and Favvata [4] for the first time, examined the influence of the structural pounding problem on the ductility requirements and the overall seismic response of reinforced concrete structures with unequal heights designed according to the Eurocodes 2 and 8. Since then an extensive work in this field, revealed that the local ductility demands of the columns in the pounding area of the tall structure are critically increased due to the interaction with an adjacent shorter and stiffer structure, at the floors above the highest contact story level. Furthermore, results have clearly shown that in situations of potential pounding, neglecting its possible local effects leads to non-conservative building design or assessment that may become critical in some cases [11, 13].

On the other hand, the typical measure that modern codes specify against structural pounding is the provision for sufficient separation between the adjacent buildings [15-17]. However, the estimation of the separation gap distances between the structures is not directly incorporated with the seismic hazard level and the local capacities of the structural members that may suffer the pounding effect. As properly pointed out by Barbato and Tubaldi [18] the minimum gap distance prescribed by the current seismic design codes is based on a uniform-hazard response spectrum that corresponds to an ultimate design limit state. In this way the structural pounding is related only with the ultimate design seismic performance of the building and thus the evaluated gap separation is not appropriately correlated with other levels of seismic demand. Abdel Raheem [10] studied the pounding effect on the global response of structures at different levels of seismic hazard in order to establish mitigation solution using rubber shock absorber devices. In this study [10], the design codes limitations for the evaluation of the gap size between adjacent structures are presented and the need for adequate characterization of the correlation between displacement responses of nonlinear systems is stressed. In this research direction, a deterministic seismic assessment of the inter-story pounding effect at different levels of seismic demand is presented by Favvata [13]. For the examined interaction cases, the minimum required gap distances between adjacent RC structures have been evaluated taking also into account the local capacities of the columns that suffer the inter-story pounding effect.

Nevertheless, this study is focused on the probabilistic seismic assessment procedures that have been used so far for the evaluation of the pounding risk between adjacent structures [18-30]. Penzien [19] presented an analytical procedure to evaluate the separation distance that is required between two buildings to avoid seismic pounding. The procedure is based on equivalent linearization of non-linear hysteretic behavior. Based on the reliability methods and random vibration theory, Hong et al. [20] presented a procedure to evaluate the required separation distance with or without considering possible uncertainty in structural properties. Another numerical simulation approach to estimate the seismic pounding risk of adjacent buildings separated by a minimum code-specified separation distance during a certain period

has been presented by Lin and Weng [21]. The overall pounding probability of adjacent buildings was evaluated by combining the results of the seismic hazard analyses and the relations of peak ground acceleration and the conditional pounding probability. Lopez-Garcia and Soong [22] examined the accuracy of the Double Difference Combination (DDC) rule in predicting the separation necessary to prevent seismic pounding between linear structural systems. Furthermore, in 2009 the same authors [23] evaluated the accuracy of four different criteria to calculate the necessary separation against seismic pounding between nonlinear hysteretic structural systems. Tubaldi and Barbato [25], proposed a reliability-based procedure to evaluate the level of safety corresponding to a given value of the separation distance between adjacent buildings. The proposed procedure is used to estimate a) the probability of pounding between linear single-degree-of-freedom systems and b) the reliability of the design code's formula to define building separation distances.

In 2013, Tubaldi et al. [26] presented a probabilistic seismic demand model (PSDM) for pounding risk assessment suitable for use within modern performance-based design frameworks. For the purposes of their study, the case of two adjacent buildings modeled as single-degree-of-freedom systems with linear and nonlinear hysteretic behavior was considered and parametrically evaluated. An innovative reliability-based methodology for the design of the separation distance between adjacent buildings is proposed by Barbato and Tubaldi [18]. Several different buildings modeled as linear elastic single-degree-of-freedom (SDOF) and multi-degree-of-freedom systems, as well as SDOF nonlinear hysteretic systems are examined. The proposed methodology provides consistent safety levels for different building properties and different seismic hazard conditions.

Another probabilistic investigation of the structural pounding using a simplified two degree-of-freedom structural model was recently presented by Chase et al. [27]. In this study an attempt to include the column’s nonlinear behavior was presented. In Tubaldi et al [28, 29] linear and bilinear probabilistic seismic demand models PSDMs are proposed for the assessment of the pounding risk. Parameters such as, the seismic intensity measure IM and the model describing the EDP statistics given the IM are discussed and evaluated. Linear single-degree-of-freedom (SDOF) systems and nonlinear hysteretic multi-degree-of-freedom (MDOF) systems are considered. Finally, Naeej et al [30] presented a probabilistic evaluation of the separation distance between adjacent structures with equal heights by using bilinear elastoplastic SDOF systems. For this purpose, numerical models with varying structural models have been generated using a robust Monte-Carlo simulation.

The above review of the literature indicates that the probabilistic evaluation of the pounding problem is still in an early state of knowledge. Lack of relation attempts between the seismic performances of a real structure with the probabilistic assessment of the pounding effect still exists and more limitations are identified. So far, SDOF and/or MDOF linear elastic systems, as well SDOF nonlinear systems have been used. In most of the cases, the peak relative displacement between the adjacent structures has been examined as key parameter of the pounding risk, while the case of floor-to-floor pounding type has been considered.

Based on the above discussion, in this study a probabilistic assessment of the seismic pounding between adjacent structures at different global and local performance levels is attempted. The IDA method [31] has been employed to estimate the seismic global and local demand parameters of a multistory RC frame structure due to the pounding effect. The computer program Drain-2dx and the Matlab programming tool are used for the needs of this study.

2 EXAMINED POUNDING CASE

In this study the seismic performance of a real RC frame structure against pounding with an adjacent shorter and stiff structure is evaluated based on probabilistic assessment methods. The examined pounding case is an interaction case between an 8-story RC frame and a 3-story rigid barrier (very stiff structure). The story levels of the two adjacent structures have the same height so that collisions may occur between the story diaphragms and consequently between the story masses (floor-to-floor pounding type). The top level of the potential contact point of the adjacent structures is located at the 4th floor level of the 8-story frame. The assumption of using a rigid 3-story structure has been adopted in order the overall assessment of the pounding effect to be engaged only on the global and local responses of the 8-story frame. In a future study the characteristics of both adjacent structures could be the main topic under concern. In Eurocode 8 the minimum gap distance separation is defined at the top level of the potential contact point of the adjacent structures based on either the maximum relative displacement of both structures (using the Square Root of Sum of Squares – SRSS rule) or the maximum plastic displacement of the one building. For the examined interaction case according to the Eurocode 8 a minimum gap distance of 9.0 cm between the 8-story frame structure and the 3-story rigid barrier is required in order to prevent the pounding at the 4th floor level. In order to incorporate the separation gap distance between the two structures, as a key parameter of this study three different initial gap distances (d_g) are considered, namely $d_g = 0.0$ cm (structures in contact from the beginning), $d_g = 4.5$ cm and $d_g = 9.0$ cm (Eurocode's requirement). The seismic performance of the 8-story structure without the pounding effect is also included for comparison reasons.

3 DESIGN OF 8-STORY RC FRAME STRUCTURE

The 8-story frame structure was designed according to Eurocodes 2 and 8, meeting the Ductility Capacity Medium (DCM) criteria of the codes. The seismic behavior factor for the frame was q=3.75. The mass was taken equal to M=(G+0.3Q)/g (where G gravity loads and Q live loads) and the design base shear force was equal to V=(0.3g/q)M. Reduced values of member moments of inertia (I_{ef}) were considered in the design to account for the cracking; for beams $I_{ef}=0.5I_g$ (where I_g the moment of inertia of the gross section) and for the columns $I_{ef}=0.9I_g$. Critical for the dimensioning of the columns proved to be in most cases the code provision, regarding the axial load ratio limitation $v_d \leq 0.65$ and in a few cases (columns of the upper stories) the code minimum dimensions requirements. Structure geometry and reinforcement of the columns of the 8-story RC frame structure are shown in Figure 1.

4 STRUCTURAL MODELLING

In this work, the computer program package Drain-2dx is used. The finite element mesh for the 8-story RC frame structure utilizes an one-dimensional element for each structural member, while two types of one-dimensional beam-column elements were used. For the simulation of the beams the common lumped plasticity model has been employed. This element considers the inelastic behavior concentrated in zero-length "plastic hinges" at the element's ends. For the columns of the structure a special purpose element of "distributed plasticity" type accounting for the spread of inelastic behavior both over the cross-sections and along the deformable region of the member length is adopted. More details can be found in Favvata [13]. Collisions are simulated using contact elements that become active when the corresponding nodes come into contact. The response of the contact element is described by: a) the negative direction of the X-axis that represents the condition that the buildings move away from each other and b) the positive direction of the X-axis that simulates the actual behavior of the structures in case there is a small gap distance (d_g) between them. It is possible that the structures move one towards the

other, but the displacements are small, and the existing gap is not covered. In this case the contact element remains non-active and the buildings continue to vibrate independently. In the case that the structures move one towards the other and the displacements bridge the existing gap or the structures are in contact from the beginning then the contact element responds as a spring with almost infinite stiffness [13].

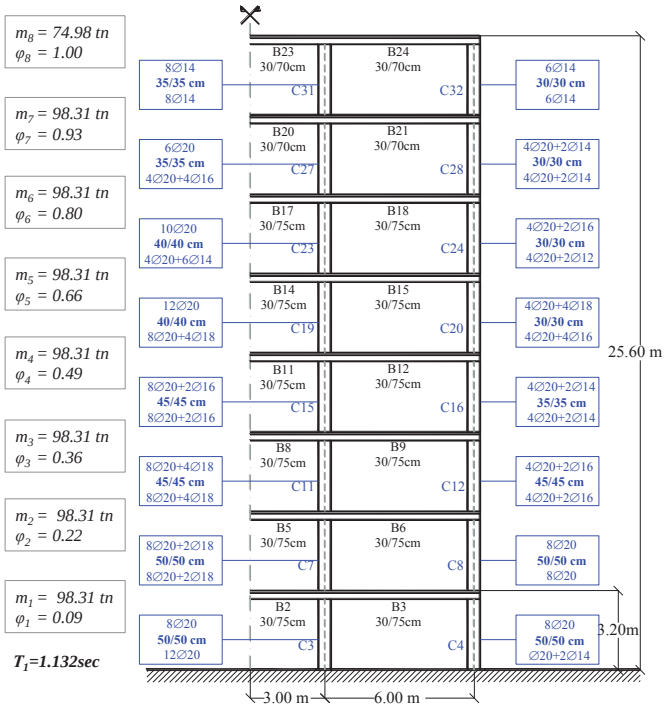

Figure 1: Examined 8-story RC frame structure.

5 KEY ASSUMPTIONS FOR THE PROBABILISTIC ASSESMENT OF THE POUNDING EFFECT

5.1 Probabilistic seismic demand model

A probabilistic seismic demand model is a mathematical relation between the structural response and the earthquake intensity measure (IM) [32]. The structural response is described through engineer demand parameters (EDPs) representing the global or the local responses of a structural system such as maximum interstory drift, moments, curvature, e.tc. On the other hand, the intensity measures (IMs) refer to ground motion characteristics that may be structural independed (PGA, PGV e.tc.) or structural depended ($Sa(T_1)$, $Sv(T_1)$ e.tc.). In order to develop the probabilistic seismic demand model (PSDM), EDP|IM pairs should be generated through nonlinear dynamic analysis. Statistical process of EDP|IM pairs synthesizes the PSDM. The mathematical representation of median structural demand response $\widehat{EDP}$ and the IM can be approximated by a two parameters power law model [33, 34]:

$$\widehat{EDP}|IM = a\, IM^b \tag{1}$$

The coefficients α and b are calculated through linear regression analysis of logarithm of IM and EDP, so the equation (1) is transformed to the following expression:

$$ln\,\widehat{EDP}|IM = b\, ln\, IM + ln\, a + \varepsilon|IM \tag{2}$$

where, ε|IM is the random error with mean zero and variance σ^2.

The structural response demand is assumed to follow lognormal distribution [33] with logarithm standard deviation $\beta_{EDP|IM}$ which is calculated by the following equation:

$$\beta_{EDP|IM} = \sqrt{\frac{\sum_{i=1}^{n}\left(ln\, EDP_i|IM - ln\,\widehat{EDP}|IM\right)^2}{n-2}} \quad (3)$$

The mathematical representation of the PSDM leads to a closed form solution that permits the definition of the fragility curves [34]. Each fragility curve describes, the probability a EDP to exceed the capacity $\hat{C}$ for a given IM and can be calculated as:

$$G_{EDP|IM}(C|IM) = P[EDP|IM \geq C|IM] = \Phi\left(\frac{ln\,\widehat{EDP}|IM - ln\,\hat{C}}{\beta_{EDP|IM}}\right) \quad (4)$$

$\Phi(.)$ denotes the standard normal cumulative function, $\hat{C}$ the median value of the capacity and $\beta_{EDP|IM}$ the logarithm standard deviation (eq. 3).

Nevertheless, it has also been shown that linear representation of PSDM is not always accurate to describe the structural response for entire range of IM [35-37]. Therefore, the adoption of a bilinear regression model especially for local EDPs seems to be more valid to capture the nonlinear behaviour of the structural members. The bilinear regression model can be described by the following expression:

$$ln\,\widehat{EDP}|IM = (a_1 + b_1\, ln\, IM)(1 - H_1) + [ln\, EDP|IM^* + b_2(ln\, IM - ln\, IM^*)]H_1 + \varepsilon|IM \quad (5)$$

The coefficients α_1, b_1 and b_2 are defined through linear regression analysis and determine the slope of the two linear branches. H_1 is a dummy variable which is equal to $H_1 = 0$ for $IM \leq IM^*$ and $H_1 = 1$ for $IM > IM^*$. Finally, the parameter IM^* is the intersection of two linear branches, while $ln\, EDP|IM^*$ is the value of the EDP at the intersection point.

5.2 Examined EDPs and IMs

The incremental dynamic analysis (IDA) method [31] has been used to define the seismic demands of the 8-story structure due to the pounding effect. In this way the necessary EDPs sample are accomplished as a function of the intensity measure (IM) that has been selected for the assessment. For this purpose, four different EDPs are evaluated: a) maximum interstory drift (IDR_{max}), b) maximum top drift (TDR_{max}), c) rotational demands θ of the columns of the 8-story frame and d) maximum curvature ductility demands $\mu_{\varphi,max}$ of the external columns at the pounding side of the frame.

The commonly used intensity measures (IMs) of peak ground acceleration (PGA) and that of spectral acceleration corresponding to the fundamental period of the 8-story frame Sa ($T_{1,8\text{-story}}$) are considered in this study. Both components of seven different seismic excitations (totally 14 records) extracted from the PEER's database [40] are used with each IM to be scaled in the range of 0.005g to 1.4g. Thus, a total number of 1348 inelastic dynamic analyses have been performed. The characteristics of the seismic excitations are presented in Table 1.

In this study, the global EDPs of IDR_{max} and TDR_{max} seem to conform better with the linear regression model. Figure 2 shows the median structural response of the RC frame in terms of IDR_{max} and TDR_{max} for linear PSDM and for the examined cases of "without pounding effect" and "d_g = 0.0 cm". On the other hand the local demand of maximum curvature ductility $\mu_{\varphi,max}$ seems to be expressed more accurate through a bilinear model. In Figure 3 the PSDMs of the external column C20 as a function of the two IMs by using linear and bilinear regression model are presented for all the examined pounding cases. As breakpoint of the bilinear demand models

is considered the $\mu_{\varphi,max} = 1.0$ that represents the transition from linear ($\mu_\varphi \leq 1.0$) to nonlinear behaviour ($\mu_\varphi > 1.0$).

	Seismic excitations	*Italy Arienzo, 1980*	*Italy Auletta, 1980*	*Chi-Chi Taiwan06, 1999*	*Denali-Alaska, 2002*	*Loma Prieta, 1989*	*Chi-Chi Taiwan04 1999*	*San Fernando, 1971*
PGA (m/sec^2)	component FN	0.268	0.615	0.073	0.869	1.090	0.096	0.153
	component FP	0.405	0.655	0.070	0.975	0.509	0.075	0.181
$Sa_{,T1}$ (m/sec^2)	component FN	0.282	0.545	0.073	1.447	0.704	0.136	0.114
	component FP	0.322	0.458	0.052	0.411	0.654	0.099	0.213
Duration, t (s)		24	34	42	60	25	60	14
Mw		6.9	6.9	6.3	7.9	6.9	6.2	6.6
R [km]		52.9	9.6	83.4	50.9	63.1	116.2	89.7

Table 1: Main characteristics of the seismic excitations

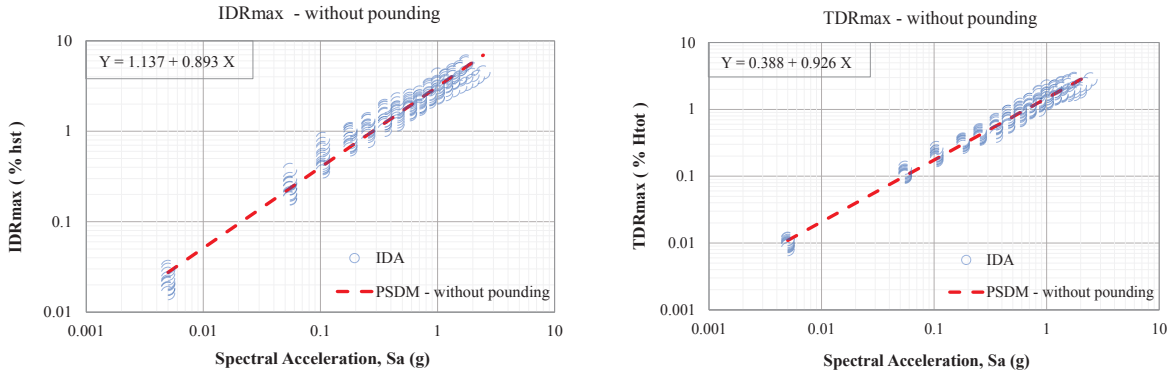

(a) without pounding effect

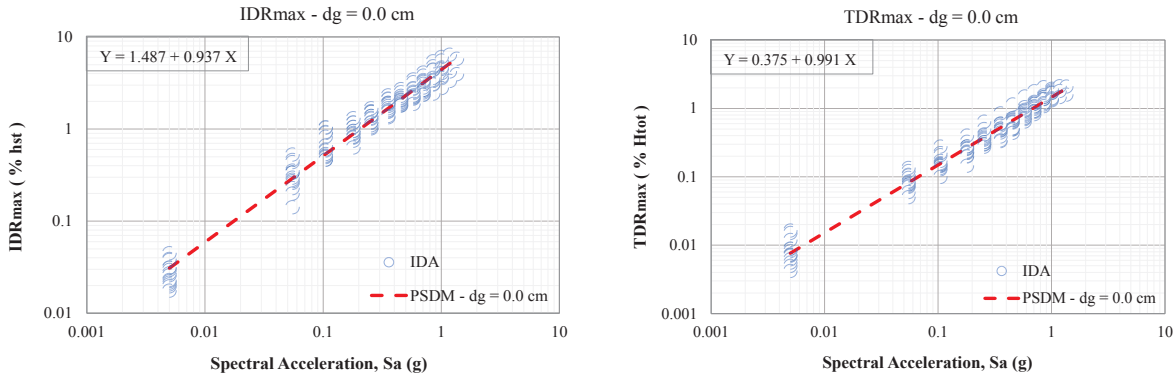

(b) initial gap distance dg = 0.0 cm

Figure 2: Linear PSDMs in log-log space for the global EDPs of maximum interstory drift IDRmax and maximum top drift TDRmax, as a function of Sa.

Furthermore, in the probabilistic methods the selection of the IM should verify the criteria of efficiency and sufficiency [38]. An efficienct IM reduces the variation in estimation of the

structural demand for a give IM. The efficiency can be quantified by using the logarithm standard deviation $\beta_{EDP|IM}$. A sufficient IM indicates that it is conditionally independed of ground motion characteristic such as Magnitude (M_w) and source-to-source distance (R) [38], [39]. Adopting a sufficient IM avoids potentially biased in the calculation of the fragility curves. The sufficient of an IM is quantified through linear regression analysis of the residuals $\varepsilon|IM$ from PSDM and M_w or R through corresponding p-value. A small p-value (less than a cut-off value of 0.05) indicates that regression is statistically significant and the IM is insufficient. The IMs of this study have also been evaluated in terms of sufficiency and efficiency and indicative results are presented in Table 2, for global EDPs. For all the examined cases of this study, it has been observed that the dispersion of the regression models is lower in the case of Sa than in the case of the PGA. Figure 4 displays the variation of dispersion of the examined IMs for linear PSDM (LPSDM) and bilinear regression PSDM (BPSDM) for the local EDP of $\mu_{\varphi,max}$ of column C20. It is observed that the dispersion in the elastic range is significant lower than the inelastic one. Both IMs exhibite lower dispersion at the first branch of BPSDM while the nonlinear behaviour of the structural member tends to reduce the efficiency of the model.

On the other hand, Figure 5 shows p-values of bilinear PSDMs of PGA and Sa for the examined pounding cases. The results show that the null hypothesis for the significance of the regression cannot be rejected in the case of Sa. The p-values corresponding to PGA are lower than the cut-off value of 0.05 indicating that is statistically depended of ground morion characteristics.

5.3 Examined performance levels - PLs

The probabilistic evaluation of the pounding effect is performed through fragility curves in terms of EDP|IM. Each fragility curve represents the probability of exceeding a particular performance level (PL) that corresponds to a specific value of EDP as a function of the IM. Thus, the fragility curves of this study are developed based on different structural global and local performance levels. In this direction, the next four global performance levels are chosen to be examined for the IDR_{max} and TDR_{max} demand parameters [41]:

(i) the level of immediate occupancy (IO) that corresponds to a maximum interstory drift equal to 1% of the story height (h_{st}) (ATC-40: IO level; 1% drift),
(ii) the level of life safety (LS) that corresponds to a maximum interstory drift equal to 1.5% of the story height (h_{st}) (ATC-40: LS level; 1.5% drift),
(iii) the level of collapse prevention (CP) that corresponds to a maximum interstory drift equal to 2.5% of the story height (h_{st}) (ATC-40: CP level; 2.5% drift) and
(iv) top drift equal to 1% of the total height of the structure (H_{tot}).

Assuming that the most critical column controls the global state of the structure two more structural performance levels in terms of rotational criteria are also examined: (a) Significant Damage (SD) level when the rotation at any column exceeds the 75% of the ultimate rotation θ_u , and (b) Near Collapse (NC) level when the rotation at any column exceeds the ultimate rotation θ_u . The ultimate rotation (θ_u) of the critical each time column of the structure is evaluated based on the recommendations of Eurocode 8 - part3 [42].

Finally, the local curvature ductility capacities ($\mu_{\varphi\text{-}PL}$) of the external columns of the 8-story RC frame have been estimated for three different performance levels (PL) of near collapse (NC), significant damage (SD) and damage limitation (DL) (Eurocode 8-part3, [42]).

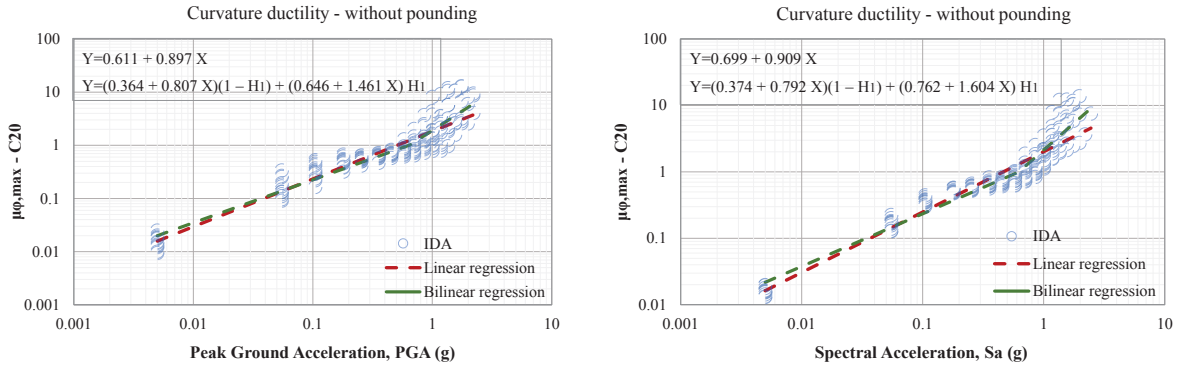

(a1)

(a2)

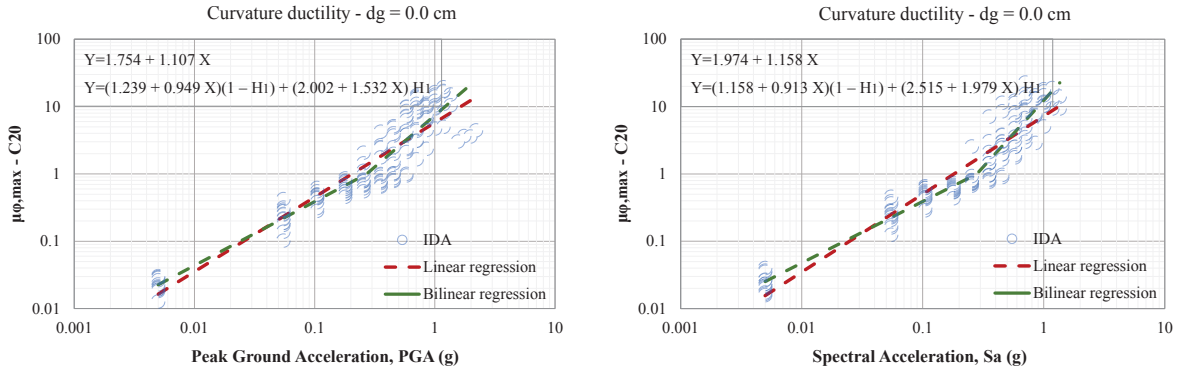

(b1)

(b2)

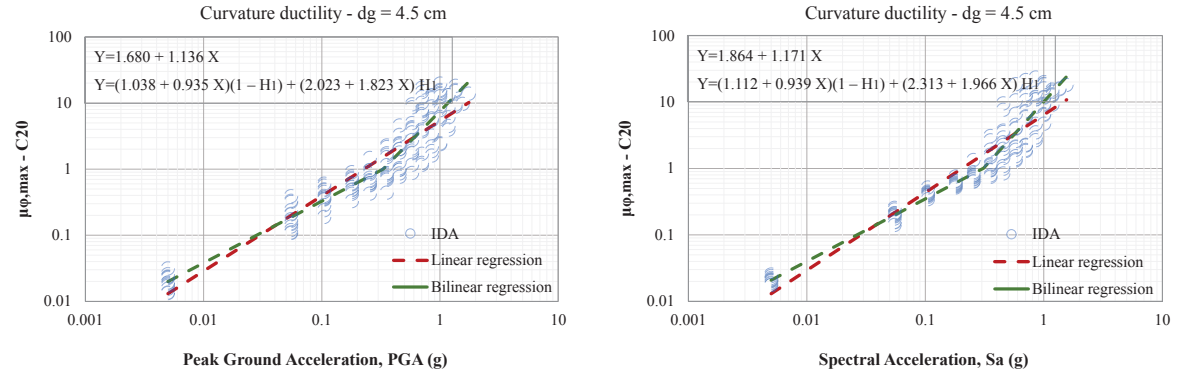

(c1)

(c2)

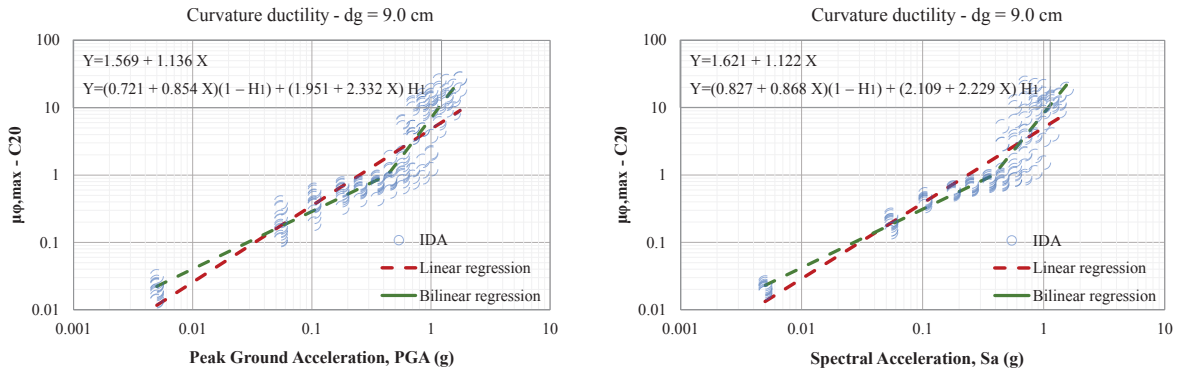

(d1)

(d2)

Figure 3: Comparison of linear and bilinear PSDMs in log-log space for the local EDP of the maximum curvature ductility $\mu_{\varphi,max}$ of the column C20 of the RC frame. Results are taken for both IMs (PGA and Sa) and for all the examined pounding cases: (a) without pounding effect, (b) initial gap distance dg = 0.0 cm, (c) initial gap distance dg = 4.5 cm, (d) initial gap distance dg = 9.0 cm.

EDPs	*IDR max*						*TDR$_{MAX}$*					
IMs	PGA	Sa	PGA	Sa	PGA	Sa	PGA	Sa	PGA	Sa	PGA	Sa
	Efficiency $\beta_{EDP\|IM}$		Sufficiency Mw p-value		Sufficiency R p-value		Efficiency $\beta_{EDP\|IM}$		Sufficiency Mw p-value		Sufficiency R p-value	
without pounding	0.284	0.219	0.000	0.398	0.000	0.565	0.313	0.157	0.000	0.919	0.000	0.209
dg=0.0cm	0.280	0.243	0.023	0.529	0.001	0.093	0.330	0.245	0.000	0.686	0.000	0.760
dg=4.5cm	0.291	0.225	0.000	0.046	0.000	0.581	0.322	0.151	0.000	0.175	0.000	0.522
dg=9.0cm	0.289	0.214	0.000	0.246	0.000	0.995	0.326	0.141	0.000	0.389	0.000	0.561

Table 2: Efficiency and sufficiency of the examined IMs.

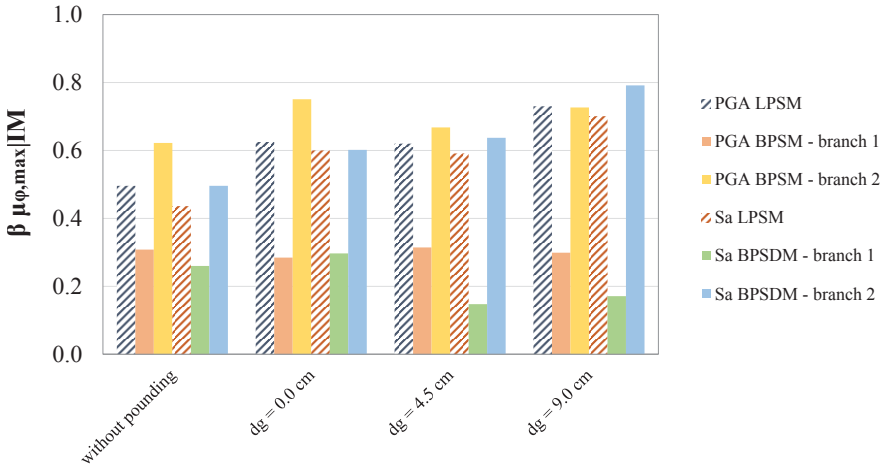

Figure 4: Dispersion of linear and bilinear regression model for the local EDP $\mu_{\varphi,max}$ of the column C20 as a function of PGA and Sa.

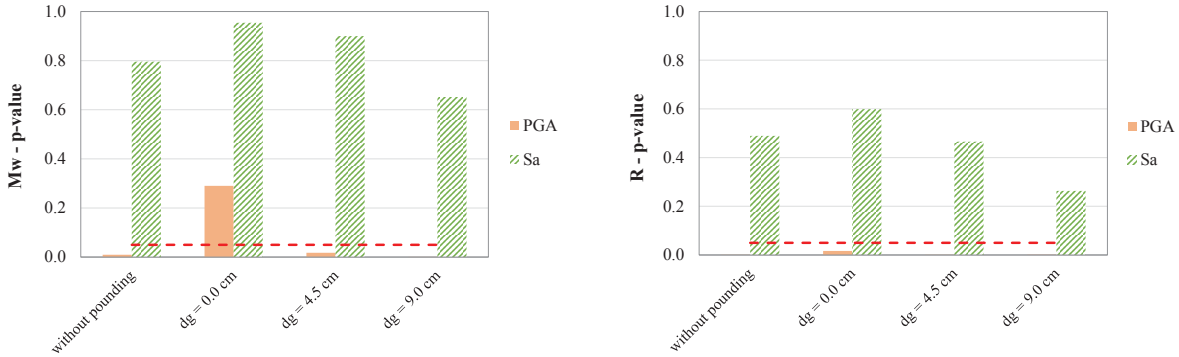

Figure 5: Evaluation of p-value for the bilinear regression model of the local EDP $\mu_{\varphi,max}$ of the column C20.

6 RESULTS

In Figure 6, the probability of exceeding a pre-defined displacement the floor level of the 8-story building that layes at the top level of the contact point with the 3-story rigid structure is evaluated. As pre-defined displacement limit is considered the initial gap distance d_g between the adjacent structures. The examined interaction cases are: $d_g = 0.0$ cm, $d_g = 4.5$ cm, $d_g = 9.0$cm and $d_g = 50$ cm (without pounding). It can be observed that the 8-story frame is more vulnerable

to pounding with the adjacent shorter and stiffer structure as smaller the initial separation gap distance between them is. Thus, considering a probability of pounding between the examined structures equal to 60%, an earthquake intensity of 0.25g is critical when $d_g = 4.5$ cm, while in case of $d_g = 9.0$ cm the critical IM value is 0.55g.

A different approach provides that for an earthquake intensity of Sa=0.3g the probability of pounding between the examined structures is about 80% for $d_g = 4.5$ cm while in case of d_g=9.0cm this probability is less than 10%.

In Figure 7 the fragility curves of the 8-story frame in terms of maximum interstory drift (IDR_{max}) are presented for all the examined interaction cases: (a) without pounding effect, (b) initial gap distance $d_g = 0.0$ cm, (c) initial gap distance $d_g = 4.5$ cm, (d) initial gap distance d_g=9.0 cm. Each fragility curve represents the probability that a particular performance level (PL) of IDR_{max} is exceeded as a function of the IM (PGA or Sa). In this study, three global performance levels have been chosen to be examined for the IDR_{max} demand parameter (section-5.3). It can be observed that the more exigent the performance level (PL) is, the fragility curves move towards greater values of IM. Moreover, in all the examined cases, the dispersion of the $IDR_{max}|IM$ values is reduced when the intensity measure Sa is used instead of the PGA. Similar observations also hold when the probability of exceeding a particular performance level (PL) of the maximum top drift (TDR_{max}) in the 8-story frame as a function of the IM, is estimated. Thus, in Figures 8 and 9 the effect of the pounding on the fragility curves of $IDR_{max}|Sa$, and $TDR_{max}|Sa$, are presented and discussed.

Figure 8 shows that in the case of earthquake-induced pounding, the 8-story frame has exhibited the same probability of exceeding a particular performance level (PL) of the maximum interstory drift (IDR_{max} - $\%h_{st}$), at a lower value of Sa in comparison to the case without the pounding effect. The probability for the 8-story frame to exceed a specific PL of IDR_{max} at the same Sa value is increased due to the pounding effect as the initial gap distance between the adjacent structure is decreased. Indicative results for Sa = 0.3g and Sa = 0.6g are pointed in Figure 8d. Moreover, the results of this study show that even in low values of earthquake intensity measures (e.g. Sa < 0.2g) the effect of the pounding between the two adjacent structures is depicted on the fragility curves of the 8-story frame in terms of $IDR_{max}|IM$.

On the other hand, the pounding effect is depicted on the fragility curves of the 8-story frame in terms of $TDR_{max}|IM$ when the value of the IM is greater than 0.6g (see Fig. 9).

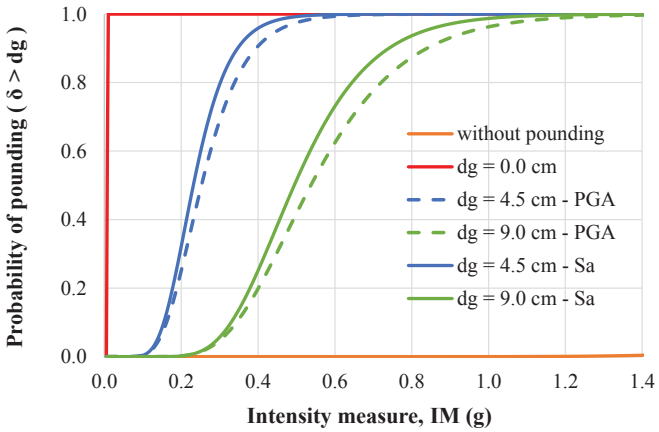

Figure 6: Probability of pounding the 8-story frame with the 3-story rigid barrier structure for initial gap distance (d_g) equal to: $d_g = 0.0$ cm, $d_g = 4.5$ cm, $d_g = 9.0$ cm and $d_g = 50.0$ cm (without pounding).

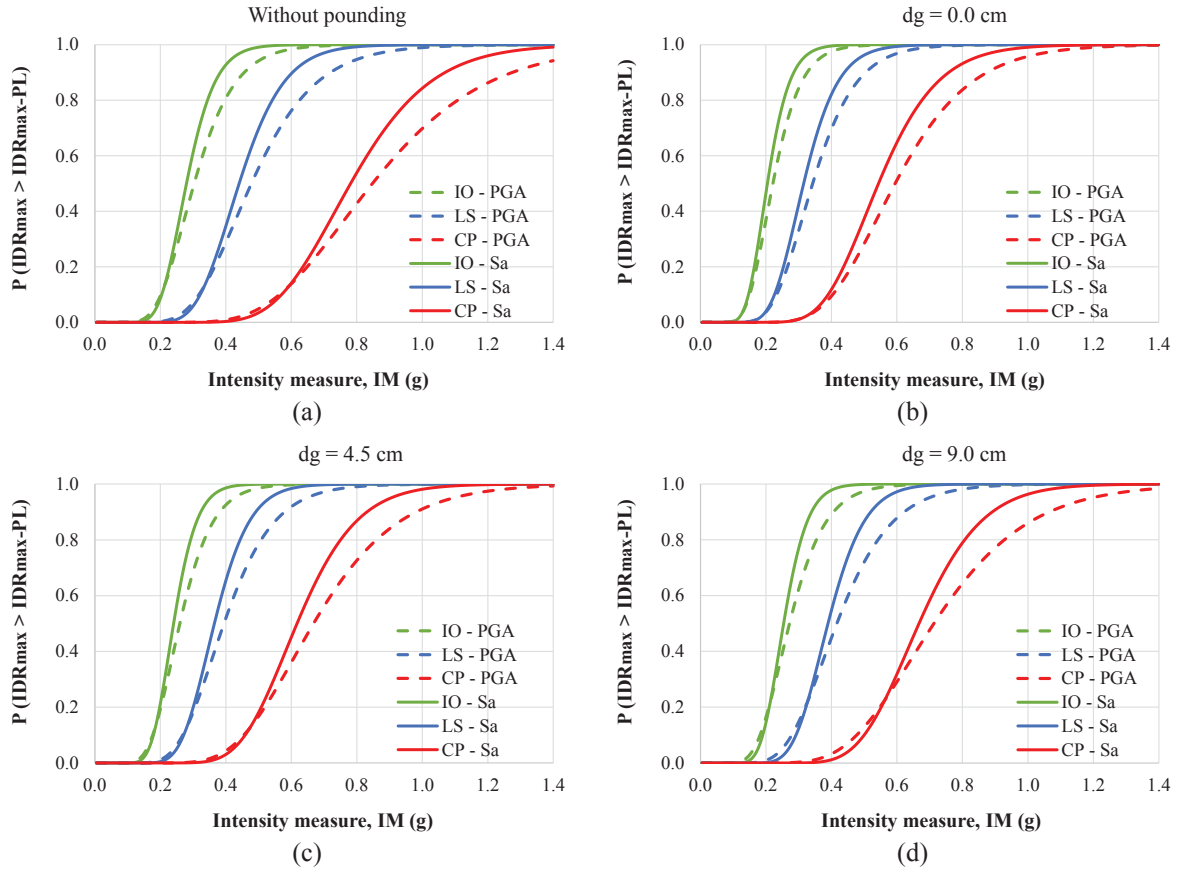

Figure 7: Probability of exceeding a particular performance level (PL) of the maximum interstory drift (IDR_{max} -%h_{st}) the 8-story frame as a function of the IM. Influence of the PL. Results are taken for intensity measure PGA and Sa. Fragility curves: (a) without pounding effect, (b) initial gap distance d_g = 0.0 cm, (c) initial gap distance d_g = 4.5 cm, (d) initial gap distance d_g = 9.0 cm.

Beneficial seems to be the influence of the pounding between the adjacent structures on the fragility curves of the 8-story frame in terms of $TDR_{max}|Sa$, when the two structures are in contact from the beginning d_g = 0.0 cm and Sa > 0.6g. As it can be observed in Figure 9, the 8-story frame has exhibited the same probability of exceeding the 1% of TDR_{max}, at a greater value of Sa due to the pounding effect (d_g = 0.0 cm).

The fragility curves of the 8-story frame that describe the probability of exceeding two different performance levels in terms of rotation at any column of the structure as a function of PGA and Sa, are presented in Figure 10. The examined performance levels are: (a) Significant Damage (SD) when the rotation θ at any column exceeds the 75% of the ultimate rotation θ_u, and (b) Near Collapse (NC) when the rotation at any column exceeds the ultimate rotation θ_u. The ultimate rotation (θ_u) of the critical each time column of the structure is evaluated based on the recommendations of Eurocode 8-part3. It can be observed that, the fragility curves of the 8-story frame in terms of θ|IM move towards a lower value of IM due to the interaction with the adjacent shorter and stiffer structure when compared with the fragility curves without pounding effect. Furthermore, the results in Figure 10 show that in the case of considering the two adjacent structures in contact from the beginning (d_g = 0.0 cm) the probability of exceeding the rotation limit that corresponds to a particular PL any column of the frame is significantly

increased due to the pounding, under the same value of IM, in comparison to the case of free vibration.

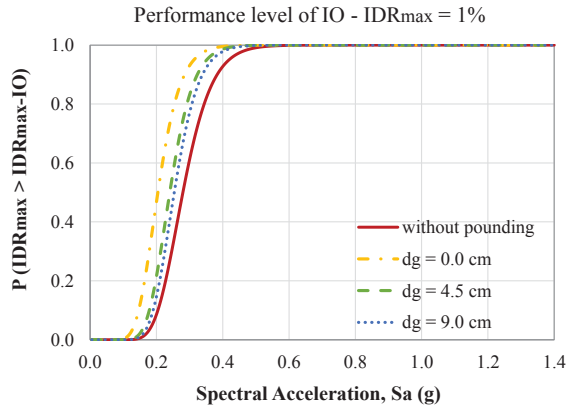

(a)

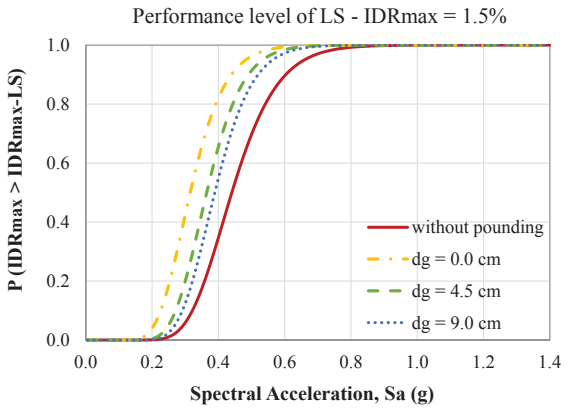

(b)

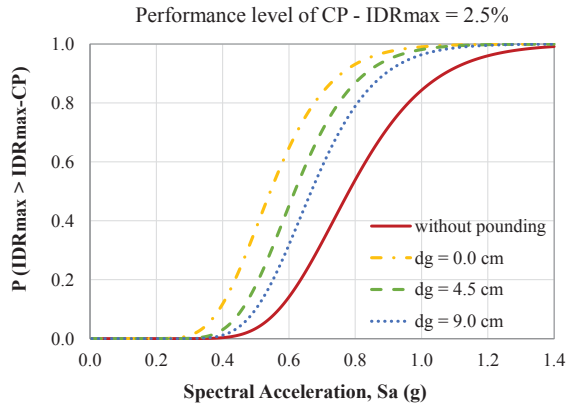

(c)

Sa	PL	P(IDR$_{max}$ > IDR$_{max}$-PL) Without pounding	d_g = 0.0 [cm]	d_g = 4.5 [cm]	d_g = 9.0 [cm]
0.3g	IO	61%	93%	83%	77%
	LS	6%	42%	20%	12%
	CP	0%	1%	0%	0%
0.6g	CP	14%	65%	45%	32%

(d)

Figure 8: Influence of the pounding effect on the probability of the 8-story frame to exceed a particular performance levels (PL) in terms of maximum interstory drift (IDR$_{max}$ -%h$_{st}$) as a function of the Sa. Fragility curves: (i) without pounding effect, (ii) d_g = 0.0 cm, (iii) d_g = 4.5 cm, (iv) d_g = 9.0 cm.

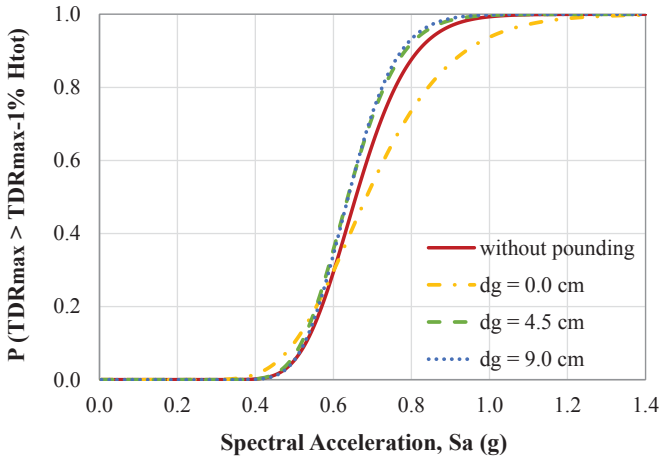

Figure 9: Influence of the pounding effect on the probability of exceeding the performance level (PL) of 1% maximum top drift (TDR$_{max}$- % H$_{tot}$) the 8-story frame as a function of the Sa. Fragility curves: (i) without pounding effect, (ii) d_g = 0.0 cm, (iii) d_g = 4.5 cm, (iv) d_g = 9.0 cm.

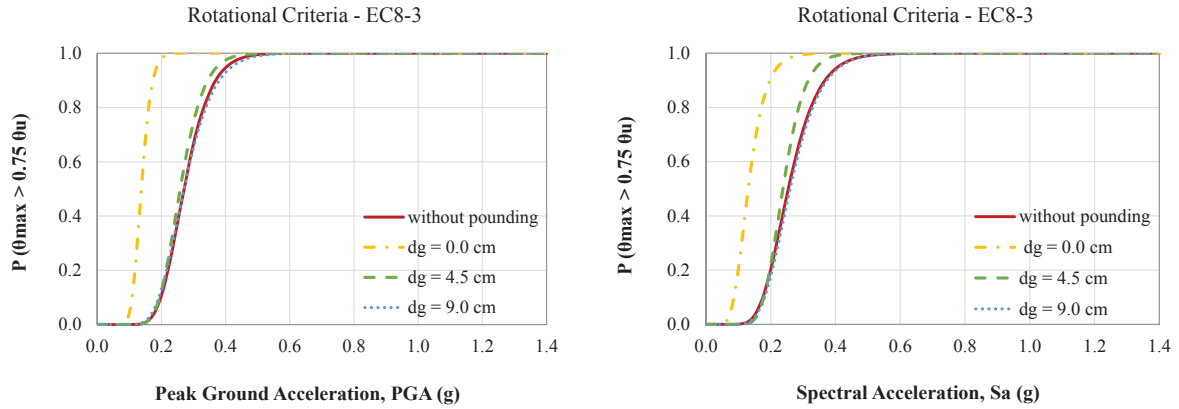

(a) Performance level of Significant Damage (SD)

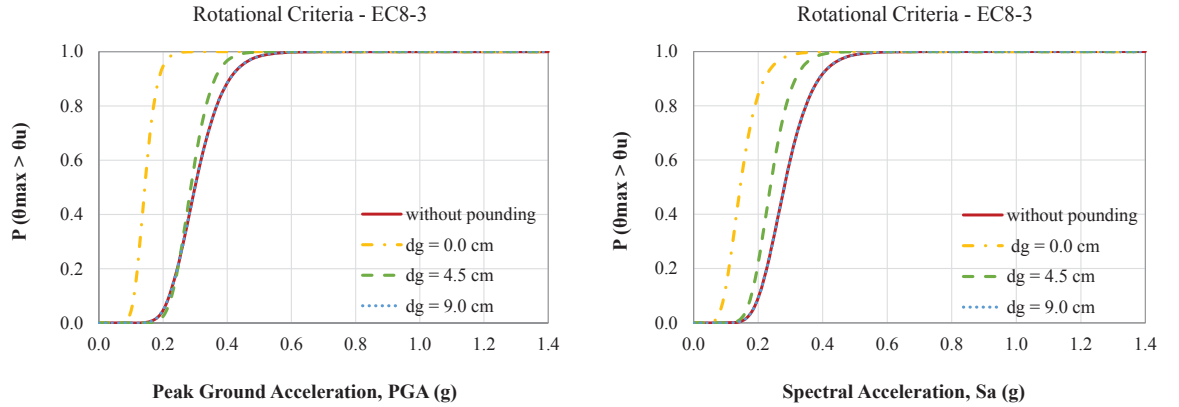

(b) Performance level of Near Collapse (NC)

Figure 10: Influence of the pounding effect on the fragility curves of the 8-story frame at two different performance levels (PL) in terms of rotation θ requirements at any column of the frame as a function of the PGA and Sa. Fragility curves: (i) without pounding effect, (ii) d_g = 0.0 cm, (iii) d_g = 4.5 cm, (iv) d_g = 9.0 cm.

For example, in Figure 10b, for Sa = 0.2g the corresponding fragility curve indicates a probability value of 84% to exceed the rotation limit state of NC any column of the 8-story frame structure when d_g = 0.0 cm, while in the case without the pounding effect the corresponding probability is less than 10%. Also, the results in Figure 10 show that, for IM values greater than 0.4g the vulnerability of the frame is critical in terms of rotational demands of columns, since the examined performance levels have been exceeded, while the study of the pounding effect seems meaningless. Nevertheless, the results in Figure 11, indicate that this observation may lead to conservative solutions, as it is discussed below.

In this study, the local ductility requirements of the columns of the 8-story structure have also been incorporated in the probabilistic assessment of the pounding effect. For this purpose, fragility curves at each floor level of the 8-story frame in terms of maximum curvature ductility $\mu_{\varphi,max}$ of the external columns at the pounding side have been developed as a function of PGA and Sa. For each column the probability of exceeding the limit states of Near Collapse (NC), Significant Damage (SD) and Damage Limitation (DL) (Eurocode 8 - part3) is evaluated. Therefore, in Figure 11, indicative results about the influence of the pounding effect on the fragility curves in terms of $\mu_{\varphi,max}|Sa$ are presented. Based on these results it can be observed that for the examined 8-story RC frame structure with and without pounding problems critical is the local response of the columns at the top floor levels (C28 and C32). The fragility curves of these columns (C28 and C32) shift towards lower values of IM due to the pounding effect.

Vital seems to be the effect of the pounding on the local responses of the columns of the 5th and 6th floor level (C20 and C24) as it is demonstrated in Figure 11a. These columns are just above the top level of the contact point of the adjacent structures. The effect of the pounding on the fragility curves $\mu_{\varphi,max}|Sa$ of these columns at the performance level of DL can be evaluated within an earthquake intensity range of 0.2g to 1.0g. Similarly, in the cases of SD and NC performance levels the corresponding critical range is 0.2g to 1.4g. Moreover, when the separation gap distance between the structures is decreased the fragility curves shift towards to a lower value of IM. These observations contrast with the comments that have been deduced based on the results of Figure 10. Figure 11 illustrates that the pounding effect can be evaluated for intensity values greater than the 0.4g when the local ductility demands of the columns are considered.

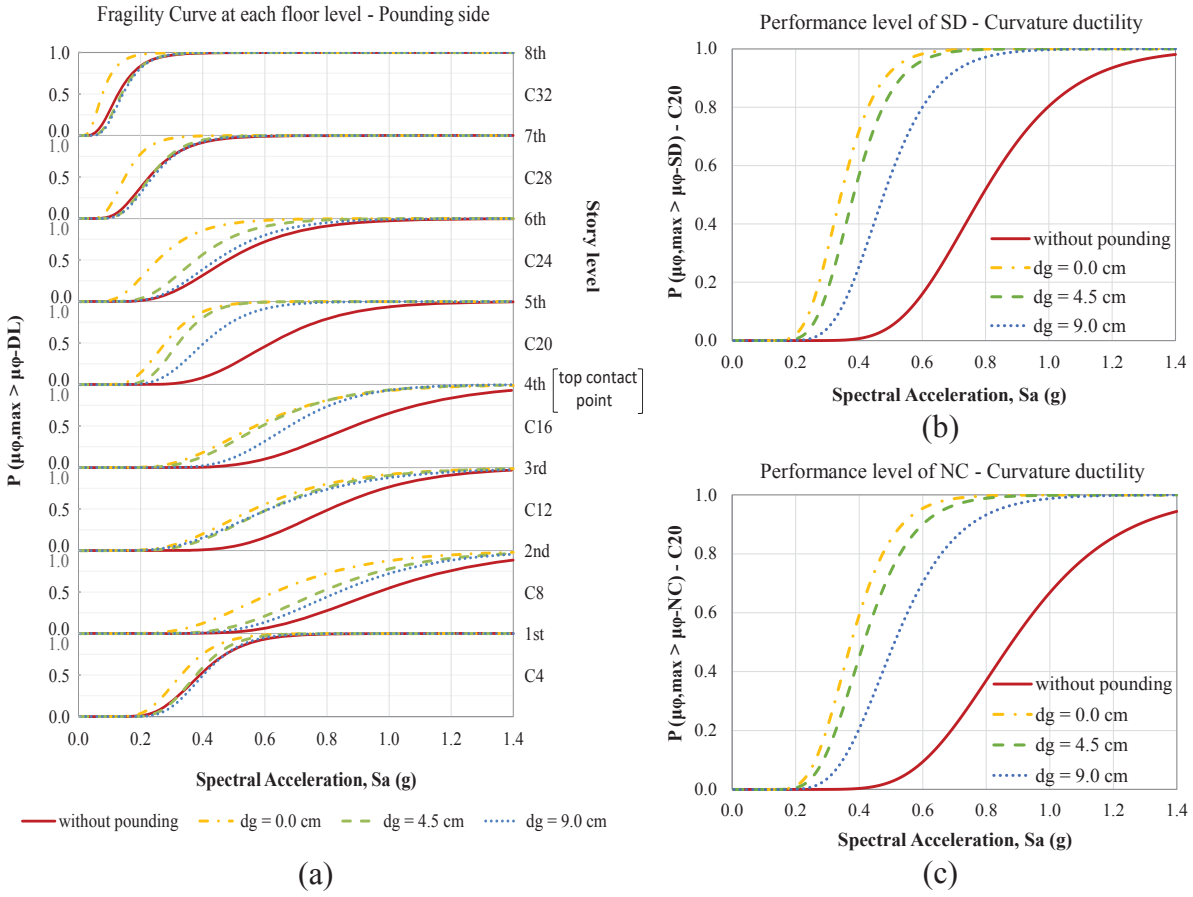

Figure 11: Influence of the pounding effect on the probability to exceed a particular performance level (PL) in terms of maximum curvature ductility $\mu_{\varphi,max}$, the external columns of the 8-story frame at the pounding side as a function of the Sa. Fragility curves: (i) without pounding effect, (ii) d_g = 0cm, (iii) d_g = 4.5cm, (iv) d_g = 9.0 cm.

Furthermore, it can be observed that for an earthquake intensity equal to 0.4g the probability of the external column C20 to exceed the curvature capacity at the performance level of DL is 48% when d_g = 9.0 cm. This probability is increased to 80 % for initial gap distance between the adjacent structures equal to 4.5 cm and to 88% for d_g = 0.0 cm. Similarly, for Sa=0.4g the probabilities of exceeding the rotation capacity at the level of SD the column C20 is 25%, 56% and 72% for d_g = 9.0 cm, d_g = 4.5 cm and d_g = 0.0 cm, respectively. In the case of NC these probabilities are decreased to the values of 20%, 45%, 59% for d_g = 9.0 cm, d_g = 4.5 cm and

d_g=0.0 cm, respectively. In all the examined cases of "without pounding effect" the column's response is elastic one (probability equal to zero) for Sa = 0.4g.

7 CONCLUSIONS

Based on the results of this study the following concluding remarks are noted:

- The 8-story frame is more vulnerable to pounding with the adjacent 3-story rigid structure as smaller the initial separation distance (d_g) between them is.
- The probability for the 8-story frame to exceed a specific global or local performance level at the same value of intensity measure (IM) is increased due to the pounding effect.
- The more exigent the performance level is, the fragility curves move towards greater values of intensity measure (IM).
- For the 8-story frame, the probability of damage due to the pounding effect can be gauged through the fragility curves at different global performance levels of IDR_{max} even for values of earthquake intensity less than 0.2g.
- For the examined global performance level of TDR_{max} the probability of damage due to the pounding effect can be evaluated only for values of earthquake intensity greater than 0.6g and only for d_g = 0.0 cm.
- The probability of damage due to the pounding effect for the global performance levels in terms of the local EDP rotation θ can also be assessed even for values of earthquake intensity less than 0.2g. Nevertheless, in this study for IM values greater than 0.4g the vulnerability of the frame is critical due to the increased rotational demands of columns.
- Finally, in case of incorporating the local performance levels of curvature ductility, the probability of damage due to the pounding effect is depicted in a wide range of earthquake intensity values and for all the examined d_g.

REFERENCES

[1] S. A. Anagnostopoulos, Pounding of buildings in series during earthquakes, *Earthquake Engineering and Structural Dynamics*, 16, 443-456, 1988.

[2] Papadrakakis, M., Mouzakis, H., Plevris, N., Bitzarakis, S., A Lagrange multiplier solution method for pounding of buildings during earthquakes, *Earthquake Engineering and Structural Dynamics* 20, 981-998, 1991.

[3] S.A. Anagnostopoulos, K.V. Spiliopoulos, An investigation of earthquake induced pounding between adjacent buildings, *Earthquake Engineering and Structural Dynamics* 21, 289-302, 1992.

[4] C.G. Karayannis, M.J. Favvata, Earthquake-induced interaction between adjacent reinforced concrete structures with non-equal heights, *Earthquake Engineering and Structural Dynamics* 34, 1-20, 2005a.

[5] C.G. Karayannis, M.J. Favvata, Inter-story pounding between multistory reinforced concrete structures, *Structural Engineering and Mechanics* 20(5), 505-526, 2005b.

[6] R. Jankowski, Assessment of damage due to earthquake-induced pounding between the main building and the stairway tower, *Key Engineering Materials* 347, 339-344, 2007.

[7] G.L. Cole, R.P. Dhakal, F.M. Turner, Building pounding damage observed in the 2011 Christchurch earthquake, *Earthquake Engineering and Structural Dynamics* 41 (5), 893-913, 2012.

[8] D.R. Pant, A.C. Wijeyewickrema, Structural performance of a base-isolated reinforced concrete building subjected to seismic pounding, *Earthquake Engineering and Structural Dynamics* 41 (12), 1709-1716, 2012.

[9] S. Efraimiadou, G.D. Hatzigeorgiou, D.E. Beskos, Structural pounding between adjacent buildings subjected to strong ground motions: Part I: The effect of different structures arrangement, *Earthquake Engineering and Structural Dynamics* 42 (10), 1509-1528, 2013.

[10] S.E. Abdel Raheem, Mitigation measures for earthquake induced pounding effsects on seismic performance of adjacent buildings, *Bulletin of Earthquake Engineering*, 12 (4), 1705-1724, 2014.

[11] M.J. Favvata, Interaction of adjacent multistory RC frames at significant damage and near collapse limit states, *WIT Transactions on The Built Environment* 152, 47-59, 2015.

[12] R. Jankowski, Pounding between inelastic three-storey buildings under seismic excitations, *Key Engineering Materials* 665, 121-124, 2016.

[13] M.J. Favvata, Minimum required separation gap for adjacent RC frames with potential interstory seismic pounding, *Engineering Structures* 152, 643-659, 2017.

[14] S.E. Abdel Raheem, M.Y.M. Fooly, A.G.A. Abdel Shafy, A.M. Taha, Y.A. Abbas, M.M.S. Abdel Latif, Numerical simulation of potential seismic pounding among adjacent buildings in series, *Bulletin of Earthquake Engineering* 17(1), 439-471, 2019.

[15] ACI Committee 318, Building Code Requirements for Structural Concrete (ACI 318-95) and Commentary (ACI 318R-95), American Concrete Institute, Detroit, 1995.

[16] Eurocode 2, Design of Concrete Structures. Part 1.1: General Rules and Rules for Buildings. European Committee for Standardization, Brussels, EN 1992-1-1, 2004.

[17] Eurocode 8, Design of Structures for Earthquake Resistance. Part1: General Rules, Seismic Actions and Rules for Buildings. European Committee for Standardization, Brussels, EN 1998-1, 2004.

[18] M. Barbato, E. Tubaldi, A probabilistic performance-based approach for mitigating the seismic pounding risk between adjacent buildings, *Earthquake Engineering and Structural Dynamics* 42 (8), 1203-1219, 2013.

[19] J. Penzien, Evaluation of building separation distance required to prevent pounding during strong earthquakes, *Earthquake Engineering and Structural Dynamics* 26 (8), 849-858, 1997.

[20] H.P. Hong, S.S. Wang, P. Hong, Critical building separation distance in reducing pounding risk under earthquake excitation, *Structural Safety* 25 (3), 287-303, 2003.

[21] J.H. Lin, C.C. Weng, Probability analysis of seismic pounding of adjacent buildings, *Earthquake Engineering and Structural Dynamics* 30, 1539-1557, 2001.

[22] D. Lopez-Garcia, T.T. Soong, Assessment of the separation necessary to prevent seismic pounding between linear structural systems, *Probabilistic Engineering Mechanics* 24, 210-223, 2009.

[23] D. Lopez-Garcia, T.T. Soong, Evaluation of current criteria in predicting the separation necessary to prevent seismic pounding between nonlinear hysteretic structural systems, *Engineering Structures* 31(5), 1217-1229, 2009.

[24] E. Tubaldi, M. Barbato, S. Ghazizadeh, A probabilistic performance-based risk assessment approach for seismic pounding with efficient application to linear systems, *Structural Safety* 36-37, 14-22, 2012.

[25] E. Tubaldi, M. Barbato, Stochastic analysis of the risk of seismic pounding between adjacent buildings, *Computational Methods in Stochastic Dynamics* 2, 309-326, 2013.

[26] E. Tubaldi, F. Freddi, M. Barbato, Probabilistic seismic demand and fragility assessment for evaluating the separation distance between adjacent buildings, *Proceedings of the 11st International Conference on Structural Safety and Reliability*, 2013.

[27] J.G. Chase, F. Boyer, G. Labrosse, G.A. MacRae, G.W. Rodgers, Probabilistic risk analysis of structural impact in seismic events for linear, *Earthquake Engineering and Structural Dynamics* 43(80), 1565-1580, 2014.

[28] E. Tubaldi, F. Freddi, M. Barbato, Probabilistic seismic demand model for pounding risk assessment, *Earthquake Engineering and Structural Dynamics* 45 (11), 1743-1758, 2016.

[29] E. Tubaldi, F. Freddi, M. Barbato, Assessment of seismic-induced pounding risk based on probabilistic demand models, *Proceedings of the 16th World Conference on Earthquake Engineering*, 2017.

[30] M. Naeej, J.V. Amiri, S.G. Jalali, Probabilistic evaluation of separation distance between two adjacent structures, *Structural Engineering and Mechanics* 67 (5), 427-437, 2018.

[31] D. Vamvatsikos, C. Cornell, Incremental Dynamic Analysis, *Earthquake Engineering and Structural Dynamics* 31, 491-514, 2002.

[32] K. Mackie, B. Stojadinovic, Comparison of Incremental Dynamic, Cloud, and Stripe Methods for Computing Probabilistic Seismic Demand Models, *Structures Congress 2005: Metropolis and Beyond*, 1-11, 2005.

[33] N. Shome, Probabilistic seismic demand analysis of nonlinear structures, *Report No. RMS-35*, Department of Civil Engineering, Stanford University, 1999.

[34] C. Cornell, F. Jalayer, R. Hamburger, D. Foutch, Probabilistic Basis for 2000 SAC Federal Emergency Management Agency Steel Moment Frame Guidelines, *Journal of Structural Engineering-ASCE* 28(4), 526-533, 2002.

[35] S. Ramamoorthy, P. Gardoni, J. Bracci, Probabilistic Demand Models and Fragility Curves for Reinforced Concrete Frames, *Journal of Structural Engineering-ASCE* 132(10), 1563-1572, 2006.

[36] J.W. Bai, P. Gardoni, M.B.D. Hueste, Story-specific demand models and seismic fragility estimates for multi-story buildings, *Structural Safety* 33(1), 96-107, 2011.

[37] K. Mackie, B. Stojadinovic, Seismic Demands for Performance-Based Design of Bridges, *Pacific Earthquake Engineering Research Center*, Report, 2003.

[38] N. Luco, C. Cornell, Structure-Specific Scalar Intensity Measures for Near-Source and Ordinary Earthquake Ground Motions, *Earthquake Spectra* 23(2), 357-392, 2007.

[39] J. Padgett, B. Nielson, R. DesRoches, Selection of optimal intensity measures in probabilistic seismic demand models of highway bridge portfolios, *Earthquake Engineering and Structural Dynamics* 37, 711-725, 2008.

[40] PEER Ground Motion Database, http://peer.berkeley.edu/peer_ground_motion_database, 2011.

[41] Applied Technology Council (ATC), Seismic evaluation and retrofit of concrete buildings. Volumes 1 and 2, Report no. ATC-40, Redwood City (CA), 1996.

[42] Eurocode 8, Design of Structures for Earthquake Resistance. Part 3: Assessment and Retrofitting of Buildings. European Committee for Standardization, Brussels, EN 1998-3, 2005.

[43] V. Prakash, G.H. Powell, S. Gampbell, DRAIN-2DX Base Program Description and User's Guide, *UCB/SEMM Report No. 17/93*, University of California, 1993.

EURODYN 2020
XI International Conference on Structural Dynamics
M. Papadrakakis, M. Fragiadakis, C. Papadimitriou (eds.)
Athens, Greece, 23–26 November 2020

FRAGILITY CURVES FOR RC FRAMED BUILDINGS SUBJECTED TO EARTHQUAKE-INDUCED LANDSLIDE: COMPARISON BETWEEN 2D AND 3D STRUCTURAL MODELS

Giacomo Miluccio, Fulvio Parisi, and Edoardo Cosenza

Department of Structures for Engineering and Architecture, University of Naples Federico II
Via Claudio 21, 80125 Naples, Italy
e-mail: {giacomo.miluccio, fulvio.parisi, cosenza}@unina.it

Keywords: Earthquake-induced landslides, RC framed buildings, Cumulative damage, Fragility analysis.

Abstract. *Earthquake-induced landslides are strongly dangerous secondary events of earthquakes, which every year cause huge losses around the world. In this paper, the structures at the toe of slopes subjected to the impact of landslides were considered. A probabilistic procedure developed in another paper is applied to two-story reinforced concrete building without infill walls. A method to evaluate cumulative damage to structures due to earthquake shaking and landslide impact was implemented through MATLAB. The variability in landslide-related loading, in terms of extension in plan and impact angle, was considered. A 2D frame was taken out from a 3D model and sequential response analysis was carried out on both models through OpenSees. Uncertainties were modelled through probability distributions of primary variables that mostly influence structural response, allowing the derivation of fragility curves via simulation. The probability of collapse was investigated under varying peak ground acceleration and impact velocity, which were considered as intensity measures for earthquake shaking and landslide impact, respectively.*

1 INTRODUCTION

Earthquake shaking can produce a number of secondary events such as tsunamis, fires, explosions, and landslides. The latter events are characterized by high destructive potential and can be distinguished in two categories according to their velocity: slow-moving landslides and flow-type landslides. The former mostly affect buildings located upstream of the slopes, as their structural response is influenced by differential settlements induced at the base of the structure [2]–[5]. By contrast, flow-type landslides are characterized by very high velocities and the damages to the structures are caused by their impact on building façades. Therefore, most of damage affects buildings located downstream of the slopes. Recent studies investigated the fragility of 2D structures impacted by flow-type landslides [6], associating structural damage with the velocity of the flow (v) that was assumed as intensity measure (IM) [7].

In this paper, the fragility of a reinforced concrete (RC) framed building located downstream of the slope and subjected to earthquake-induced landslide is discussed. Cumulative damage due to the seismic action and landslide impact was assessed through the proposed methodology. Furthermore, a 2D frame taken out from a 3D model was taken into account in order to compare its fragility curves to those obtained for the entire 3D model.

2 MODELING ASSUMPTIONS

The case study considered herein concerns a structure designed for gravity loads only, according to design criteria in force in Italy before 1971 [8]. The structural model adopted consists of two spans of equal length and two storeys with same height. A rigid diaphragm was assumed at each floor level, whereas the structure was considered fixed at the base. All columns have a square section, whereas the beams are characterized by a rectangular cross section. Infill walls were not considered in the capacity model, so the structure is totally bare, as shown in Figure 1 and 2. The 2D frame is located on the perimeter of the building, as highlighted by the red box in Figure 1.

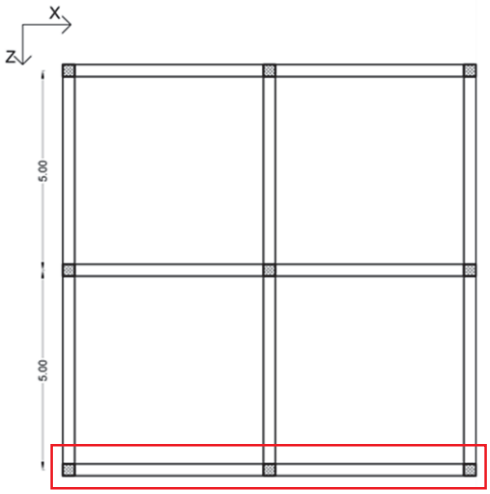

Figure 1. Building plan (dimensions in meters).

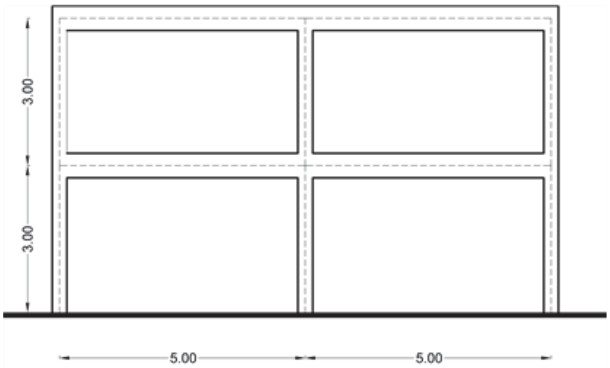

Figure 2. Building elevation (dimensions in meters).

Modelling criteria for seismic actions, landslide load and structural system, as well as the methodology adopted, are described in detail in the papers by Miluccio et al. [9] and Parisi et al. [6]. Figure 3 shows the landslide loads assumed, whereas Figure 4 represents the sequential analysis adopted to account for cumulative damage due to earthquake shaking and landslide impact. All analyses were carried out through OpenSees software [10].

The intensity of seismic shaking was measured through the peak ground motion (PGA), which is an IM well correlated with both damage to low-period structures and occurrence of earthquake-induced landslides (see e.g. [1], [11]).

It was assumed that the landslide velocity has a constant maximum value over a time span sufficiently long to cause the out-of-plane collapse of infill walls and subsequent impact on columns along both X and Z global axes.

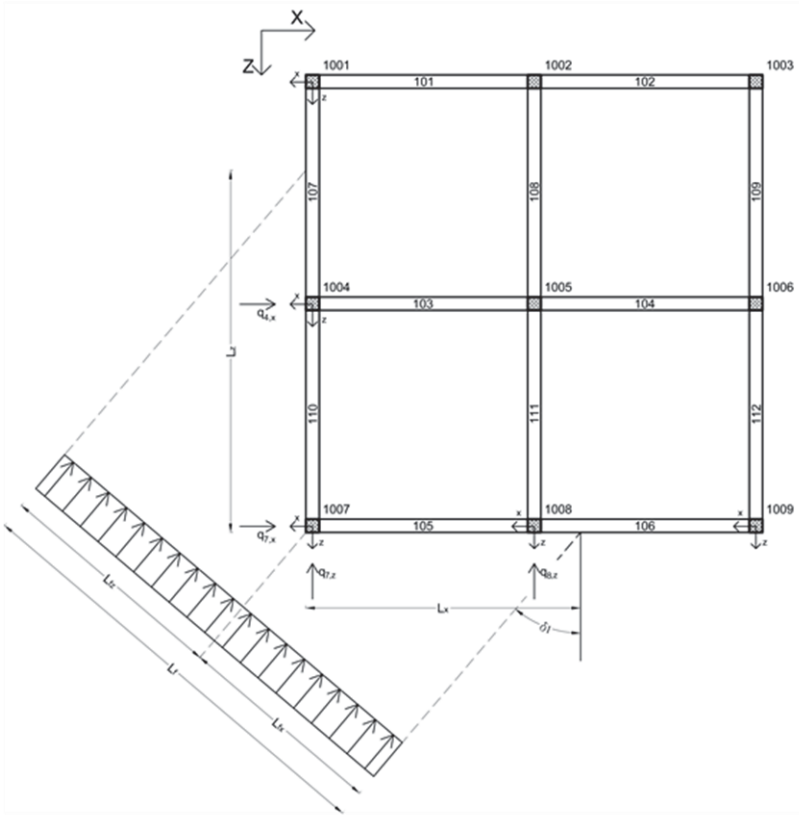

Figure 3. General scheme for diagonal landslide impact.

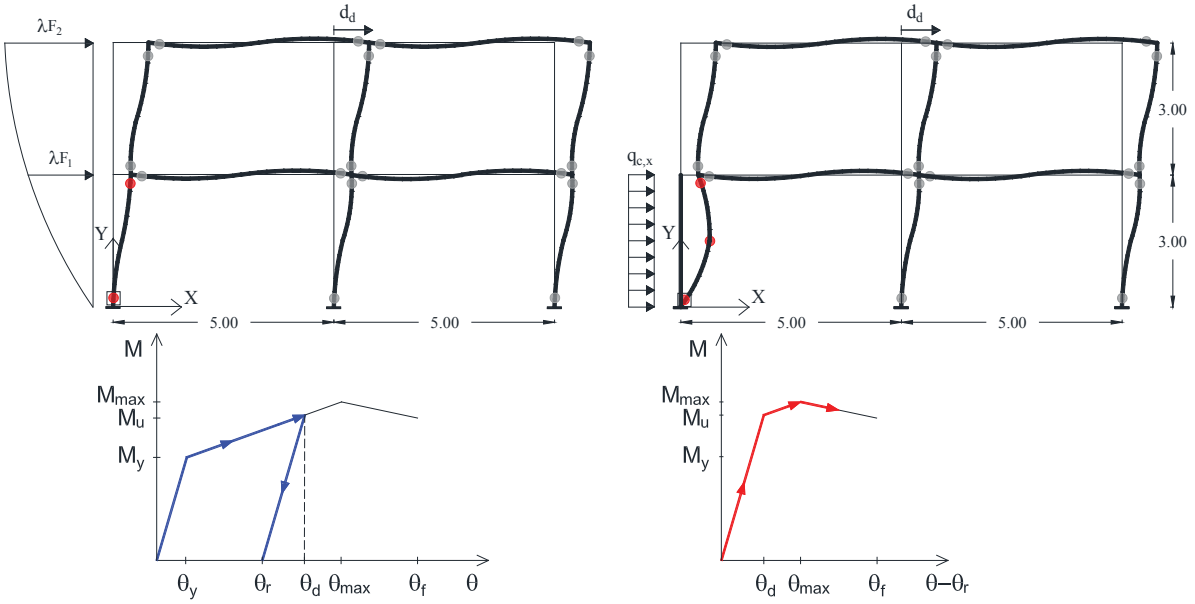

Figure 4. Sequential nonlinear modelling and analysis: (a) earthquake ground shaking; (b) landslide impact.

3 SENSITIVITY ANALYSIS

Sensitivity analysis was carried out in order to evaluate the influence of the earthquake parameters (PGA and ϑ) and landslide parameters (L_f and δ) on the structural response. A PGA equal to $0.1g$, $0.2g$ and $0.3g$ with an angle ϑ equal to 0°, 30° and 45° was assumed for the 3D model, whereas, in order to define landslide, three values of extension on plan L_f and angle δ were assumed. The L_f was defined equal to: d_b, $\sqrt{2}L$ and H_{col}, whereas the angle δ is equal to 0°, 30° and 45°. Where H_{col} is the section width of columns; L stands for the on-centre distance between consecutive columns (along either the X-axis or Z-axis of the building plan) and d_b is the diagonal of building plan. As regards the 2D frame, a value of ϑ equal to 0° and δ equal to 45° was assumed, considering different valued of PGA and L_f in order to define the level of damage linked to the seismic shaking and the different structural response linked to the involvement of a variable number of columns impacted by the landslide. Therefore, 81 loading scenarios were obtained for the 3D model and 9 scenarios for the two-dimensional model.

$PGA = 0.1g, 0.2g, 0.3g$ $\vartheta = 0°, 30°, 45°$		
	L_f [m]	δ
1	$\sqrt{2}H_{col}$	30°
2	$\sqrt{2}H_{col}$	45°
3	$\sqrt{2}H_{col}$	0°
4	$\sqrt{2}L$	30°
5	$\sqrt{2}L$	45°
6	$\sqrt{2}L$	0°
7	d_b	30°
8	d_b	45°
9	d_b	0°

Table 1. Loading scenarios for sensitivity analysis.

Due to the large amount of results, the scenario that underlines the difference in structural response in the case of 3D or 2D modelling was chosen.

Figure 3 shows the deformed shape of structure in the collapse condition and is characterized by a PGA equal to 0.2*g*. In both models, the plastic rotation demand in the plastic hinges is about 40% of total capacity. A soft-storey mechanism was developed and light red colour in Figure 3a represents the damage in the plastic hinges at the head and toe of the columns on the first level. That damage is typical of buildings designed for gravity loads only subjected to seismic shaking. Following the seismic action, the response of the structure impacted by the landslide was assessed, considering the cumulated damage. An extension of the landslide equal to d_b was defined, determining, in the 2D model, an impact of the landslide on the all columns of the first level. In the 3D model, the elements that does not impacted by the landslide help the entire structure to undergo much smaller displacements when load increases. That aspect is underlined in Figures 3a and 3b, by the difference between the deformation of the structure due to the seismic shaking (black dashed line) and landslide impact (blue solid line). In the 3D model the displacements induced by landslide are very small, with a shear collapse of the elements involved into landslide impact, whereas, the 2D structure exhibits much larger displacements, leading the elements to express a flexural type behaviour, with a collapse of the plastic hinges and reaching their ultimate rotation.

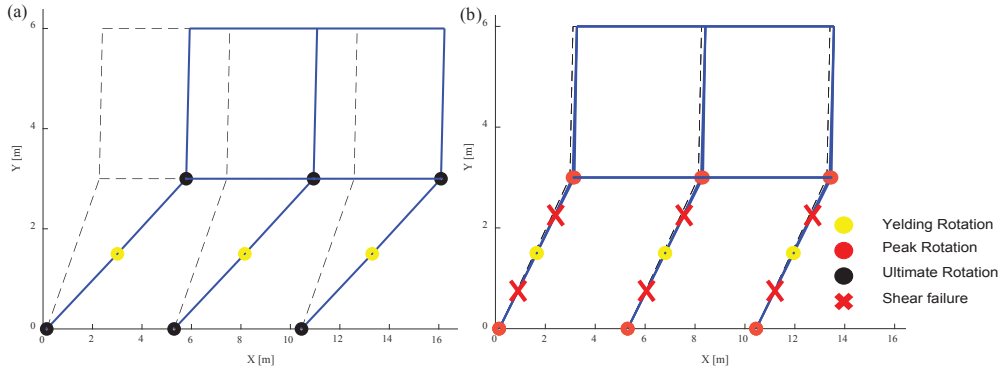

Figure 5. Near-collapse deformed shapes along X-axis considering cumulative damage under PGA = 0.2g, $\vartheta = 0°$, $\delta = 45°$ and $L_f = d_b$: (a) 2D Model; (b) 3D Model.

4 FRAGILITY ANALYSIS

The Monte Carlo procedure was implemented in the MATLAB® software [12] in order to carry out the fragility analysis. A number of 10^3 models was defined, assuming appropriate probability distributions regarding loads, geometries and materials [6]. For each realization, the procedure described in [9] was adopted for both 3D and 2D models.

The IMs defined, PGA and *v*, were assumed to range from: 0 to 0.6*g* with a step of 0.025*g* and 0 to 10 m/s with step of 1 m/s, respectively. The probability of collapse P_f was defined as the probability of reaching the ultimate rotation in the first plastic hinge of the columns at the first level, given a fixed value of PGA and *v*. P_f was assessed as the ratio between the number of cases that collapse to the number of total cases ($N_{sim} = 10^3$). Finally, the probability points obtained were fitted by a log-normal distribution [13].

The results obtained for the two models (3D and 2D) were showed in Figure 6 and in table 2, where the median values of the PGA (μ), the logarithmic standard deviation (β) and the distribution coefficient (R^2) are indicated. The fragility curves were extrapolated from the two sets of curves described above. It can be noted that for low speeds, the fragility of the 2D

model is slightly less than fragility of 3D model. As the speed increases, i.e. the damage linked to the landslide impact increases, the 2D structure has a much higher fragility than the three-dimensional model. In that case (i.e. medium-high value of v), PGA median values of 2D and 3D model are about 0.06g and 0.13g, respectively, for v = 7 m/s, whereas when v is equal to 10 m/s the median value of PGA for 2D model is 10 times smaller than 3D model. For v = 7 m/s there is an intersection between the curves of 2D and 3D models. When PGA has lower values, the damages linked to the landslide impact are higher and the two-dimensional model has a bigger fragility than the 3D one, whereas, with increasing PGA, the 3D model has a higher curve than the two-dimensional model, presenting a greater fragility towards the seismic shaking.

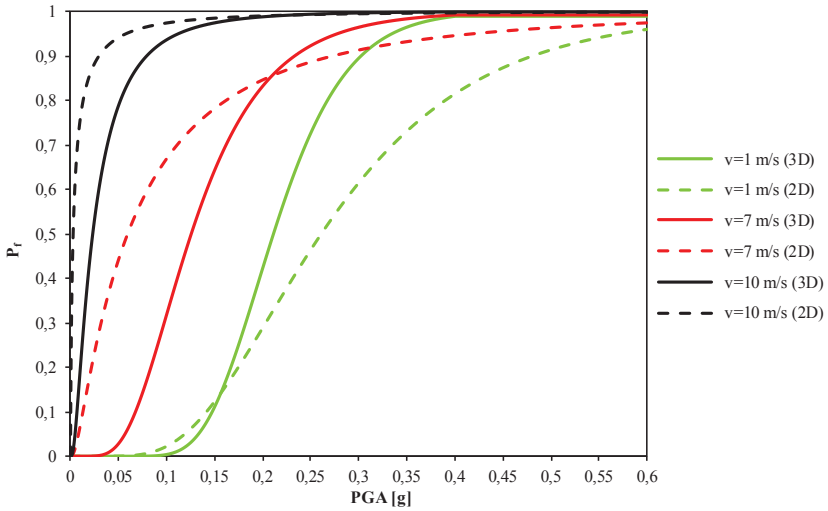

Figure 6. Fragility curves considering cumulative damage due to earthquake ground shaking and landslide impact: 3D Model (solid lines) and 2D Model (dash lines).

	3D Model			2D Model		
v [m/s]	μ [g]	β	R^2	μ [g]	β	R^2
1	0.21	0.28	0.98	0.26	0.48	0.98
7	0.13	0.48	0.79	0.06	1.19	0.89
10	0.02	0.96	0.92	0.003	1,85	0.71

Table 2. Parameters and coefficients of determination of log-normal fragility curves.

5 CONCLUSIONS

The main goal of this study was the fragility assessment of RC framed buildings subjected to seismically-induced landslides, comparing the response of a 3D model with respect to a two-dimensional one. A sequential nonlinear analysis was implemented in order to consider the cumulated damage induced by seismic shaking and subsequently by the impact of the landslide. The rotation of the plastic hinges was considered as an engineering demand parameter.

The sensitivity analysis showed a totally different behaviour with regards to the two different models. By adopting a 3D model of the structure, the failure of columns was related with their shear collapse and appears to be concentrated in the elements impacted by the landslide.

In the case of a 2D model, the flexural collapse of the elements was reached, with a more distributed damage and the triggering of a soft storey mechanism for the global structure.

The fragility analysis showed a significant increasing in the vulnerability for the 2D structure in the case of medium-high velocities, whereas, for lower velocities, where the damage by earthquake shaking is predominant, the 3D structure has a greater vulnerability.

The study, whether the structure is taken through a three-dimensional model or through a simplified 2D model, shows a significant increase in the fragility considering the cumulative damage when landslide with medium-high velocities occurs.

ACKNOWLEDGEMENTS

This study was carried out in the framework of GRISIS research project (Gestione dei Rischi e Sicurezza delle Infrastrutture a Scala regionale) funded by Regione Campania.

REFERENCES

[1] X. Wang, G. Nieand, D. Wang, Relationships between ground motion parameters and landslides induced by Wenchuan earthquake, *Earthquake Science*, 23(3), 233-242, 2010.

[2] S.D. Fotopoulouand, K.D. Pitilakis, Vulnerability assessment of reinforced concrete buildings subjected to seismically triggered slow-moving earth slides, *Landslides*, 10(5), 563-582, 2013.

[3] S.D. Fotopoulouand, K.D. Pitilakis. Fragility curves for reinforced concrete buildings to seismically triggered slow-moving slides, *Soil Dynamics and Earthquake Engineering*, 48, 143-161, 2013.

[4] S.D. Fotopoulouand, K.D. Pitilakis, Probabilistic assessment of the vulnerability of reinforced concrete buildings subjected to earthquake induced landslides, *Bulletin of Earthquake Engineering*, 15, 5191-5215, 2017.

[5] S.D. Fotopoulouand, K.D. Pitilakis, Vulnerability assessment of reinforced concrete buildings at precarious slopes subjected to combined ground shaking and earthquake induced landslide, *Soil Dynamics and Earthquake Engineering*, 93, 84-98, 2017.

[6] F. Parisi, G. Sabella, Flow-type landslide fragility of reinforced concrete framed buildings, *Engineering Structures*, 131, 28-43, 2017.

[7] O. Mavrouli, S. Fotopoulou, KD. Pitilakis, G. Zuccaro, J. Corominas, A. Santo, F. Cacace, D. De Gre-gorio, G. Di Crescenzo, E. Foerster, T. Ulrich, Vulnerability assessment for reinforced concrete buildings exposed to landslides, *Bulletin of Engineering Geology and the Environment*, 73(2), 265-289, 2014.

[8] G. Manfredi, A. Masi, R. Pinho, GM. Verderame, M. Vona, Valutazione degli edifici esistenti in cemento armato, *IUSS Press*, 2007 [in Italian].

[9] G. Miluccio, F. Parisi, E. Cosenza, Impact of cumulative damage on fragility of RC framed buildings subjected to earthquake-induced landslides, *XI International Conference on Structural Dynamics, Eurodyn,* 2020.

[10] F. McKenna, G.L. Fenves, M.H. Scott, OpenSees: Open system for earthquake engineering simulation. California: Pacific Earthquake Engineering Research Center, University of California Berkeley, 2004. Available at http://opensees.berkeley.edu.B.

[11] Y. Jafarian, A. Lashgari, M. Miraei, Multivariate fragility functions for seismic landslide hazard assessment, *Journal of Earthquake Engineering*, DOI: 10.1080/13632469.2018.1528909, 2018.

[12] MATLAB and Statistics Toolbox Release R2018a. The MathWorks Inc., Natick, Massachusetts.

[13] K. Porter, R. Kennedy, R. Bachman, Creating fragility functions for performance-based earthquake engineering, *Earthquake Spectra*, 23(2), 471-489, 2007.

EURODYN 2020
XI International Conference on Structural Dynamics
M. Papadrakakis, M. Fragiadakis, C. Papadimitriou (eds.)
Athens, Greece, 23–26 November 2020

IMPACT OF CUMULATIVE DAMAGE ON FRAGILITY OF RC FRAMED BUILDINGS SUBJECTED TO EARTHQUAKE-INDUCED LANDSLIDES

Giacomo Miluccio, Fulvio Parisi, and Edoardo Cosenza

Department of Structures for Engineering and Architecture, University of Naples Federico II
Via Claudio 21, 80125 Naples, Italy
e-mail: {giacomo.miluccio, fulvio.parisi, cosenza}@unina.it

Keywords: Earthquake-induced landslides, RC framed buildings, Cumulative damage, Fragility analysis.

Abstract. *Numerical studies and field missions have shown that seismically-induced slides and rock falls are secondary events of earthquakes with very high destructive potential. In many cases, the loss induced by the landslide phenomenon has significantly exceeded the impact of earthquake shaking. Recent studies proposed fragility models for 2D reinforced concrete (RC) framed buildings on the crest of the slope subjected to slow-moving landslide. In this paper, a new fragility model is proposed for RC framed buildings located downstream of the slope, and hence subjected to landslide impact loading. A two-storey structure, which was designed only to gravity loads, was selected as case study. According to Monte Carlo simulation method, one thousand realizations of the structure were randomly generated by considering uncertainties on both landslide parameters and structural properties. The peak ground acceleration was chosen as intensity measure (IM) for earthquake ground shaking, whereas the landslide impact velocity was selected as landslide IM. The novelty of this paper includes the consideration of (i) the uncertainty on landslide width and impact angle, and (ii) damage accumulation due to earthquake shaking and landslide impact. Both the generation of random load-capacity models and post-processing of analysis results were performed in Matlab, whereas sequential structural analyses were carried out with OpenSees. The inter-storey drift ratio was assumed as engineering demand parameter and two limit states were assumed, producing as many fragility curves of the structure.*

1 INTRODUCTION

Many secondary events are induced by ground shaking: fires, explosion, tsunami and landslides. In the literature, studies about damages due to earthquake-induced events were studied. Wang et al. [1] outlined huge damages to structural systems due to landslides produced by the 2008 Wenchuan earthquake in China. Many studies were carried out to develop fragility models for 2D reinforced concrete (RC) framed buildings on the crest of the slope (e.g. [2]–[5][3]). Damages were related to vertical and horizontal differential displacements of foundation soil. In the case of slow-moving earthquake-induced landslides, the peak ground displacement can be considered as intensity measure (IM), which can be correlated with peak ground acceleration (PGA) [6]. Actually, landslide-related settlements at base of the structure are the main cause of building collapse. More recent studies investigated the fragility of 2D structural models located downstream of the slope [7], in order to evaluate the behaviour of the structure impacted by landslide. In that case, flow-type landslides were considered, so structural damage was associated with impact velocity of the debris flow, which was then assumed as IM of fragility models.

In this study, a 3D structural model at the base of the slope was considered in order to define the fragility of RC framed buildings to fast-moving earthquake-induced landslides. Accordingly, ground shaking intensity was measured through PGA, whereas the impact velocity was chosen as IM for the landslide. Cumulative damage due to the sequence of earthquake shaking and landslide impact is simulated, considering the variability of both width and direction of the landslide in the building plan.

2 MODELLING OF LOADS AND STRUCTURE

2.1 Assumptions

The case-study building was assumed to be designed for gravity loads only, according to past Italian codes in force before 1971 [8][5]. The structural system is composed of two storeys and two bays per storey, with the same height and span respectively. Each floor system was modelled as a rigid diaphragm. Columns and beams were modelled with squared and rectangular cross sections. A rigid basement was considered at the base of buildings and soil-structure interaction was not taken into account. Infill walls were not considered in the capacity model of the structure, resulting in a bare framed system as shown in Figures 1 and 2.

The inelastic behaviour of frame elements was modelled in accordance to the lumped plasticity approach. Flexural-shear interaction and axial load-biaxial bending moment interaction were defined in line with Eurocode 8 (EC8) – Part 3 [10] and models available in the literature [11]–[12]. In addition to plastic hinges at element ends, a third plastic hinge was assigned to mid cross sections of first-storey columns, hence accounting for potential damage induced by the landslide impact.

Gravity loads were uniformly distributed over beams according to their tributary floor areas. PGA was chosen as IM for ground shaking, also because of its potential use in modelling the landslide occurrence conditioned upon earthquake intensity (e.g. [1] and [13][13]). Seismic performance assessment was carried out in terms of displacements according to EC8 [10]. The displacement capacity was derived through a nonlinear static (pushover) analysis of the structure, under varying incidence angle (ϑ) of seismic actions with respect to the global X-axis of building plan.

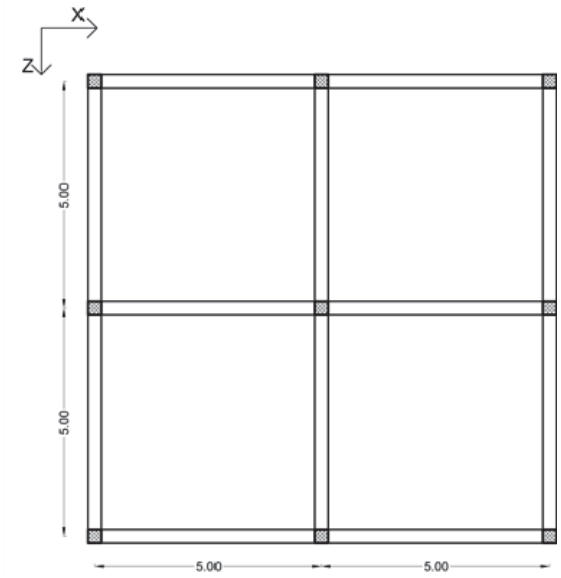

Figure 1. Building plan (dimensions in meters).

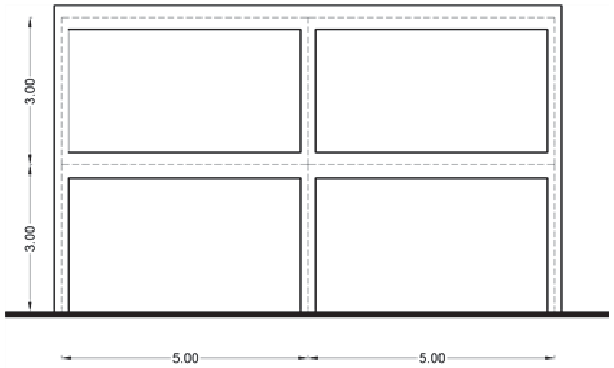

Figure 2. Building elevation (dimensions in meters).

The impact velocity of soil mass was chosen as IM for the landslide, according to many studies in the literature that define a relationship between structural damages and intensity of rapid landslides [14]. Impact loading was simulated through lateral pressures defined as sum of hydrostatic pressures and kinetic pressures, which are linearly and uniformly distributed over the height of columns, respectively. The earth-flow height was assumed between 0.5 and 1.5 times the inter-story eight. Therefore, the components of pressure along the axis of building plan were defined as follows:

$$p_{dx}(z_s) = \rho g(D - z_s) + \rho v^2 \cos^2 \delta \tag{1}$$

$$p_{dz}(z_s) = \rho g(D - z_s) + \rho v^2 \sin^2 \delta \tag{2}$$

where g = acceleration of gravity; D = flow depth; ρ = flow density; z_s = height of generic soil layer from the sliding surface of the flow; v = impact flow velocity; δ = angle between flow direction and perpendicular axis of impacted building façade ($\delta = 0$ in case of perpendicular impact). A variable size of the landslide in plan was considered. According to Parisi et al. [7], a uniform pressure distribution per unit length (p_{eq}) was defined to be applied on columns:

$$q_x = p_{eq} b_c \cos\delta \tag{3}$$

$$q_z = p_{eq} b_c \sin\delta \tag{4}$$

where b_c and h_c indicate the dimensions of column cross section along the X- and Z-axis of the building plan. Thus, landslide-related loading was modelled as uniformly distributed pressures both in plan and over the height of columns (Fig. 3).

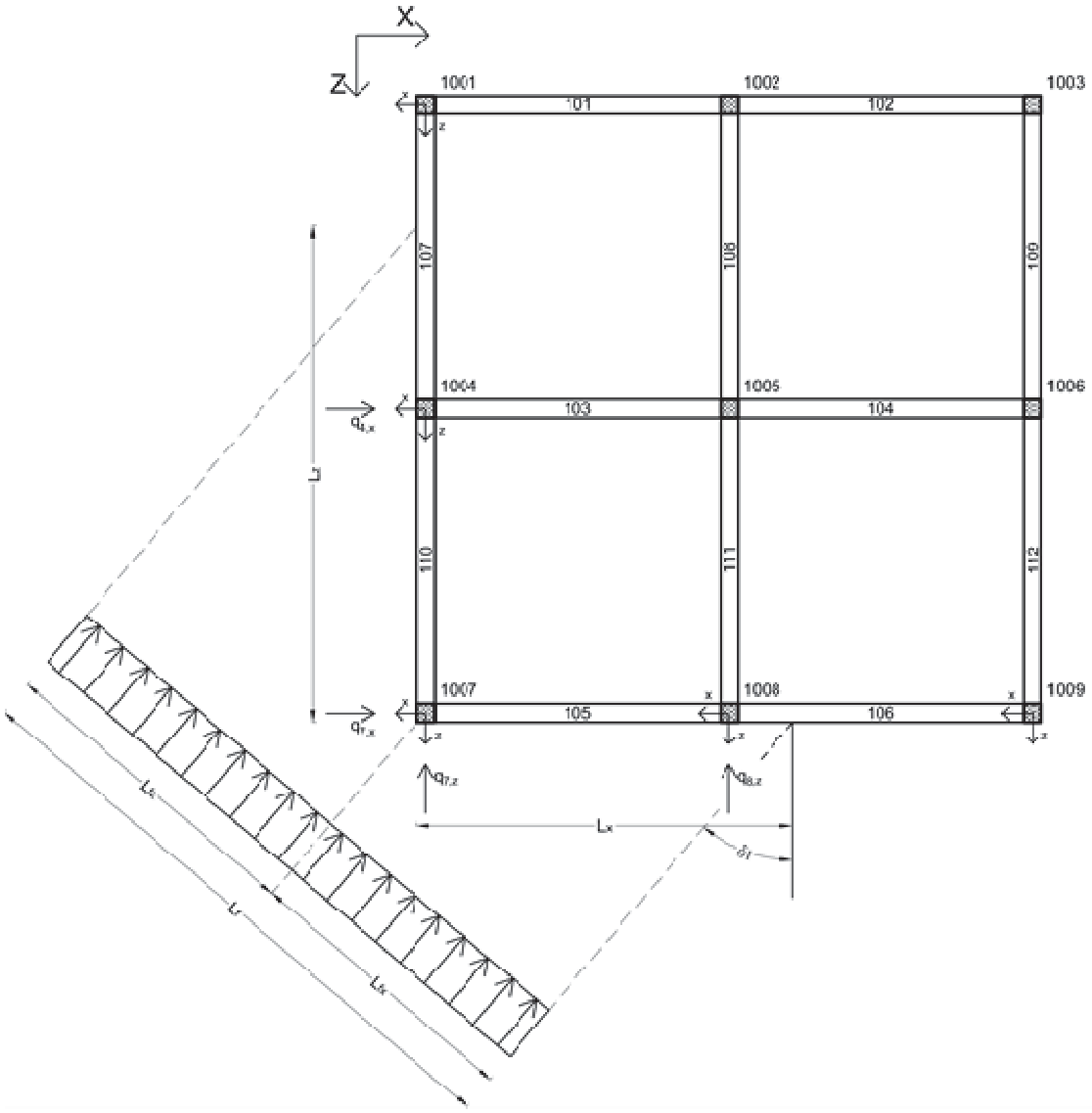

Figure 3. General scheme for diagonal landslide impact.

2.2 Procedure

An eigenvalue analysis was carried out with OpenSees® [15] to evaluate modal shapes and vibration periods of the elastic structure. The building symmetry produces the same first two modal shapes and periods along global axes. An inelastic model was developed in OpenSees® [15] according to the lumped plasticity approach and pushover analysis with displacement control was carried out to assess the effects of earthquake ground shaking on the building

structure. The N2 method was used to evaluate seismic displacement demand, considering the worst lateral force profile among those provided by EC8 - Part 3 [10][9]. Accordingly, the inelastic capacity of building was defined in terms of displacements, assuming structural collapse to be associated with the first occurrence of maximum chord rotation in a plastic hinge. In case displacement demand did not reach capacity, a degraded capacity model was defined to consider cumulative damage due to subsequent landslide impact. This was consistent with the assumption that landslide impact follows seismic shaking, hence allowing a sequential analysis. To that aim, a non-degrading stiffness model was adopted to define the unloading branch of moment-rotation diagrams of plastic hinges. A nonlinear static analysis with force control was then carried out to simulate landslide impact on the building façade. Figures 4a and 4b show the sequence of structural analyses performed for earthquake shaking and landslide impact.

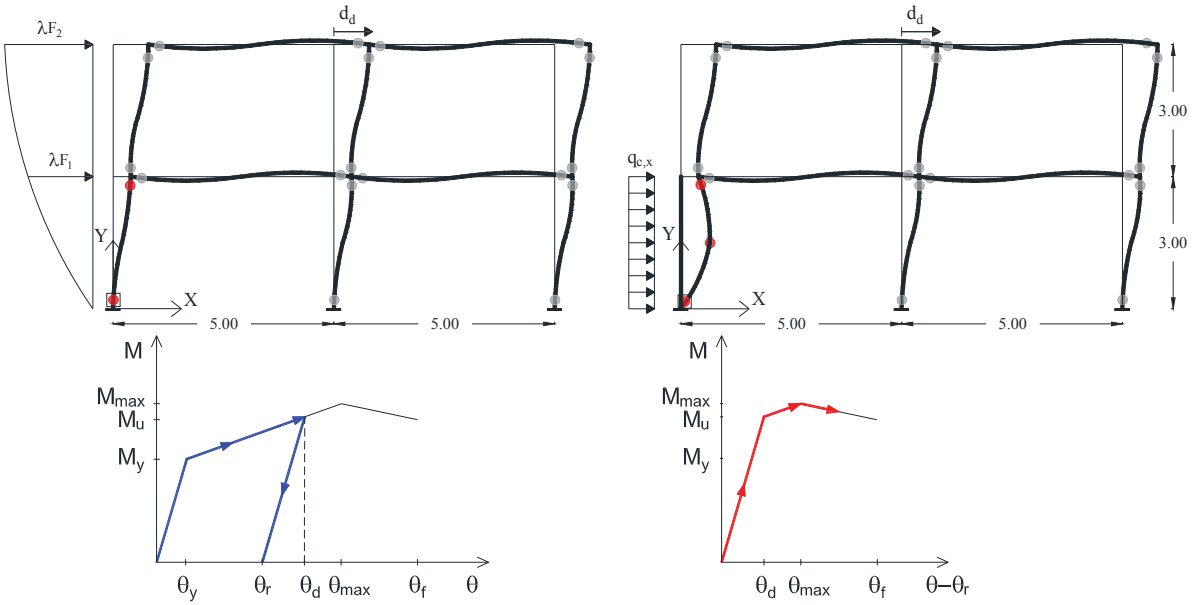

Figure 4. Sequential nonlinear modelling and analysis: (a) earthquake ground shaking; (b) landslide impact.

3 SENSITIVITY ANALYSIS

3.1 Methodology

The case-study building was parametrically analysed to investigate the influence of earthquake and landslide parameters on structural response. PGA was set to 0.1g, 0.2g and 0.3g, whereas the incidence angle of seismic action (ϑ) was assumed to be 0°, 30°and 45°. In terms of landslide parameters, three values of landslide width (L_f) and three values of landslide impact angle (δ) were considered. L_f was set to $\sqrt{2}H_{col}$, $\sqrt{2}L$ and d_b, where: H_{col} is the sectional width of columns; L stands for the on-centre distance between consecutive columns (along either the X-axis or Z-axis of the building plan); and d_b is the diagonal of building plan. δ was assumed to be 0°, 30° and 45°. By contrast, the height of landslide mass was set constant and equal to 3 m, i.e. the inter-storey height of the structure. Considering the variability of parameters indicate above, 81 scenarios were defined as shown in Table 1.

$PGA = 0.1g, 0.2g, 0.3g$ $\vartheta = 0°, 30°, 45°$		
	L_f [m]	δ
1	$\sqrt{2}H_{col}$	30°
2	$\sqrt{2}H_{col}$	45°
3	$\sqrt{2}H_{col}$	0°
4	$\sqrt{2}L$	30°
5	$\sqrt{2}L$	45°
6	$\sqrt{2}L$	0°
7	d_b	30°
8	d_b	45°
9	d_b	0°

Table 1. Definition of loading scenarios for sensitivity analysis.

For each scenario, the procedure described in Section 2.2 was adopted. Analysis results in terms of demand-capacity ratio (DCR), collapse velocity (i.e. the landslide velocity that leads the structure to collapse), and near-collapse deformed shape of the structure, are discussed below.

3.2 Discussion of results

The first set of sensitivity analyses were carried out to evaluate the variability of collapse velocity (v_c). Due to the huge number of scenarios and analysis results, only the output for scenarios with $\vartheta = 30°$ are described later on.

As the case-study building was designed only to gravity loads, its collapse mechanism can be governed by brittle shear failure of columns under lateral loading. Therefore, the influence of shear failure was investigated by assuming two different capacity models: (i) model with consideration of shear failure in columns of pre-damaged structure, namely the structure previously damaged under seismic ground motion; (ii) model without consideration of shear failure. In model (ii), the elements can suffer only a flexural failure, which was assumed to occur when chord rotation demand reached the maximum rotation capacity of plastic hinges.

Figures 5a and5b show the collapse velocity versus the landslide width under varying scenario in terms of landslide angle and PGA, for models (i) and (ii) respectively. In Figure 5a, the collapse velocity ranges between 7 and 8 m/s, showing a minor influence of damage due to earthquake shaking. The ground motion intensity causing structural collapse was $PGA_c = 0.3g$, as outlined by a horizontal line with $v_c = 0$ m/s. The collapse velocity drops when the landslide width is equal to the diagonal size of building plan, because more elements are involved in the collapse mechanism. Moreover, the scenario with frontal landslide impact (i.e. $\delta = 0°$) is characterized by the lowest values of collapse velocity.

Focusing on Figure 5b, the maximum velocity that the structure was able to withstand (with the smallest landslide width) is approximately equal to 15 m/s. In that case, if shear failure is not considered in the capacity model of the structure, columns develops a flexural behaviour up to the maximum chord rotation capacity (θ_{max}).

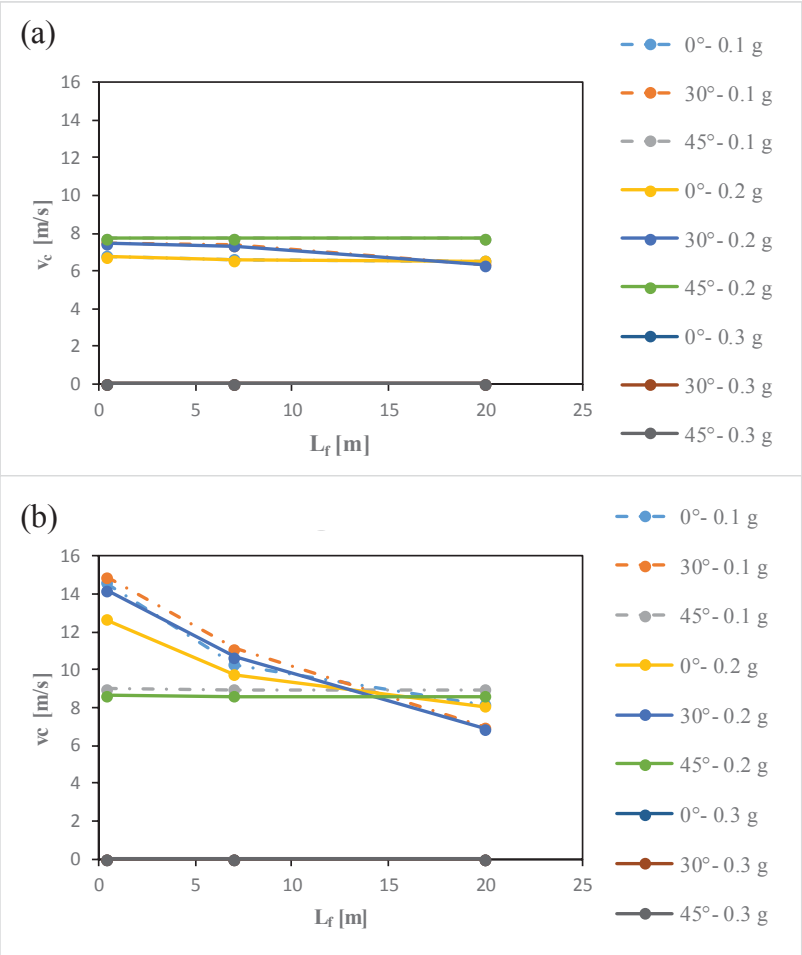

Figure 5. Influence of landslide width and impact angle on collapse velocity: (a) model with consideration of shear failure; (b) model without consideration of shear failure.

Moreover, the influence of damage due to earthquake shaking is more significant than that observed in Figure 5a. If shear failure of columns is considered, a limited number of columns are involved in the collapse mechanism, showing very low values of chord rotation. Conversely, if columns are assumed to develop their full flexural capacity and hence larger chord rotations (Fig. 5b), the influence of shaking-related damage increases.

Figures 6a–f show DCRs in first-floor columns under varying PGA and ϑ. Figures 6a, 6c and 6e are related to PGA = 0.1g, whereas the others to PGA = 0.2g. This motivates DCRs approximately equal to 50% in case of PGA = 0.2g, which are very higher than those predicted under the lowest PGA level. Scenarios with PGA = 0.2g produced very high levels of plastic rotation demand in columns, resulting in evenly distributed damage throughout the structure. This played a key role in nonlinear response of pre-damaged structure to subsequent landslide impact on perimeter columns.

Structural response to earthquake shaking is graphically represented by near-collapse deformed shapes in Figures 7a–f. Red-tagged plastic hinges outline the attainment of ultimate chord rotation, and hence element failure. The direction of seismic shaking has major influence, as evidenced by comparison between Figures 7a–b, 7c–d and 7e–f, which are respectively related to ϑ = 0°, ϑ = 30° and ϑ = 45°. Figures 6b, 6d and 6f show that DCRs increase by 10% when the earthquake shaking angle increases from 0° to 30° and 45°. In all cases, the structure suffered a soft-story mechanism as typical collapse mechanism of structure designed for gravity loads only without seismic detailing.

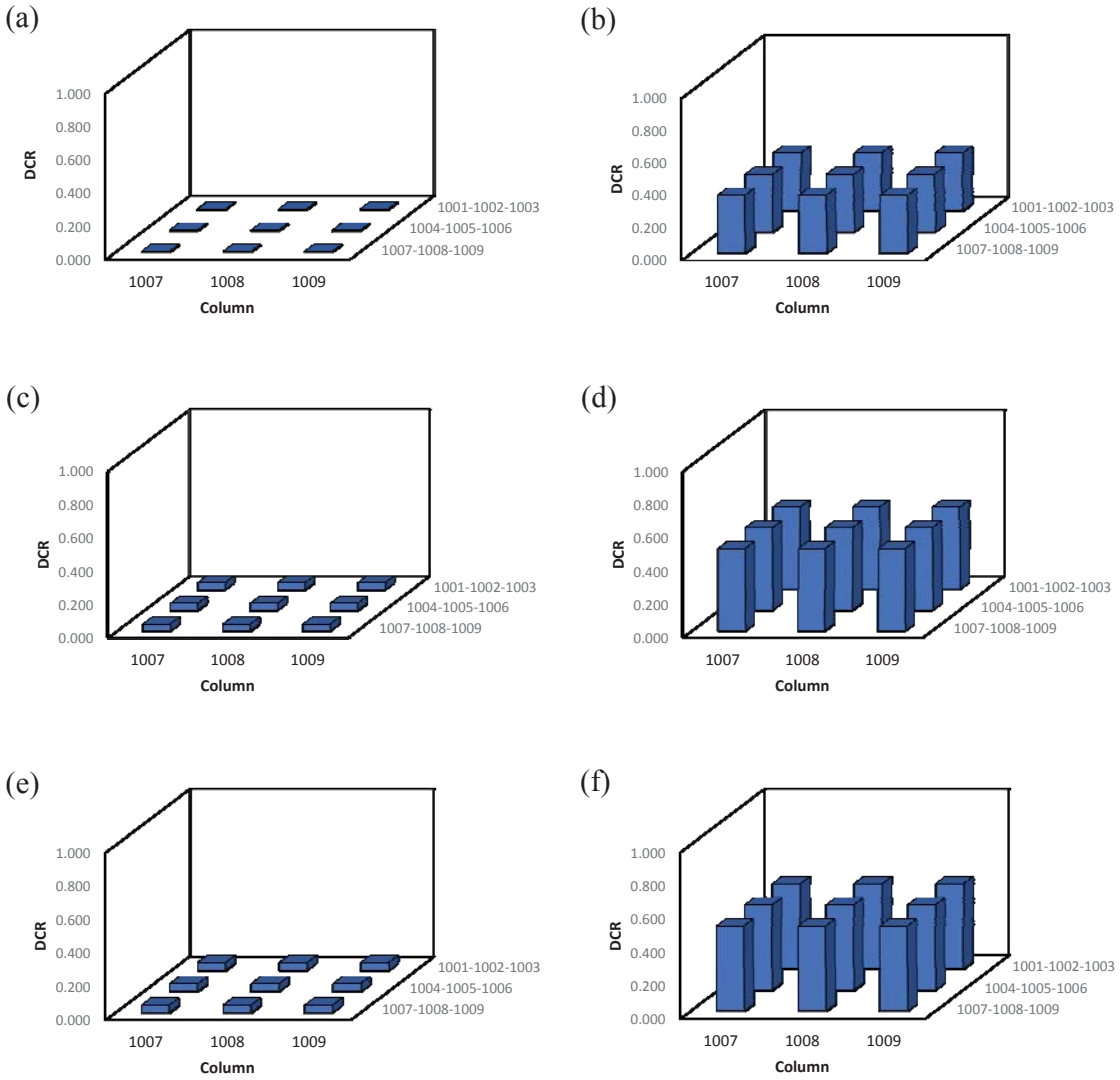

Figure 6. DCR for first-floor columns under varying PGA and ϑ: (a) PGA = 0.1g – ϑ = 0°; (b) PGA = 0.2g – ϑ = 0°; (c) PGA = 0.1g – ϑ = 30°; (d) PGA = 0.2g – ϑ = 30°; (e) PGA = 0.1g – ϑ = 45°; (f) PGA = 0.2g – ϑ = 45°.

It is noted that lateral displacements were amplified to better show collapse mechanisms. According to the procedure described in Section 2.2, a nonlinear static analysis with force control was run to simulate landslide impact on building façade considering shaking pre-damage predicted through seismic pushover analysis. DCRs are depicted in Figures 8a and 8b for capacity models neglecting and considering shear column failure, respectively. For the sake of brevity, analysis results shown in those figures are related to a selected scenario, i.e. the loading case defined by $\vartheta = 30°$, $\delta = 30°$ and $L_f = d_b$.

If Figure 8a is considered, the huge value of landslide width (L_f equal to the diagonal of the building plan) and the angle of landslide flow produced a collapse mechanism involving all columns located at the first floor level. Thus, plastic hinges reached the maximum chord rotation capacity and a soft-storey mechanism developed. By contrast, the inclusion of shear column failure in the capacity model induced a strongly different collapse mechanism, which mostly involved only the perimeter columns impacted by the landslide. In that case, structural collapse was reached under low levels of plastic rotation demand as a consequence of high shear force levels. Moreover, when PGA = 0.1g, damage due to earthquake shaking was very slight, with no influence on structural behaviour.

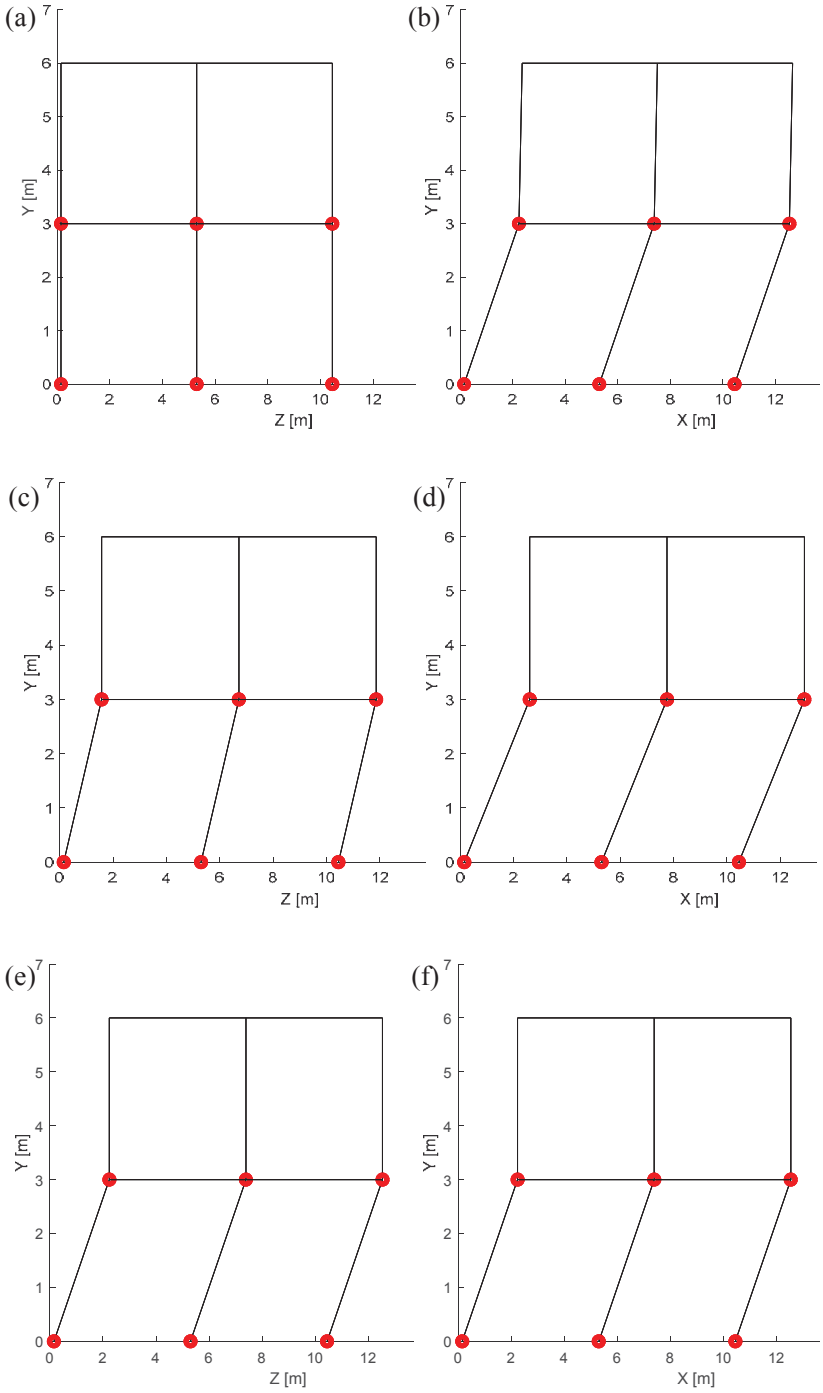

Figure 7. Near-collapse deformed shapes along Z- and X-axis due to earthquake shaking under PGA = 0.2g and different ϑ values: (a) Z-axis – $\vartheta = 0°$; (b) X-axis – $\vartheta = 0°$; (c) Z-axis – $\vartheta = 30°$; (d) X-axis – $\vartheta = 30°$; (e) Z-axis – $\vartheta = 45°$; (f) X-axis – $\vartheta = 45°$.

The DCR distribution in Figure 8b is described by near-collapse deformed shapes in Figure 9a–d, which schematically represent near-collapse deformed shapes due to cumulative damage after seismic shaking and landslide impact under PGA ranging from 0.1g to 0.2g. Dashed black lines indicate displacements due to earthquake shaking only, whereas solid blue lines represent final displacements after landslide impact. The latter produced the achievement of shear failure in columns, resulting in a soft-storey mechanism.

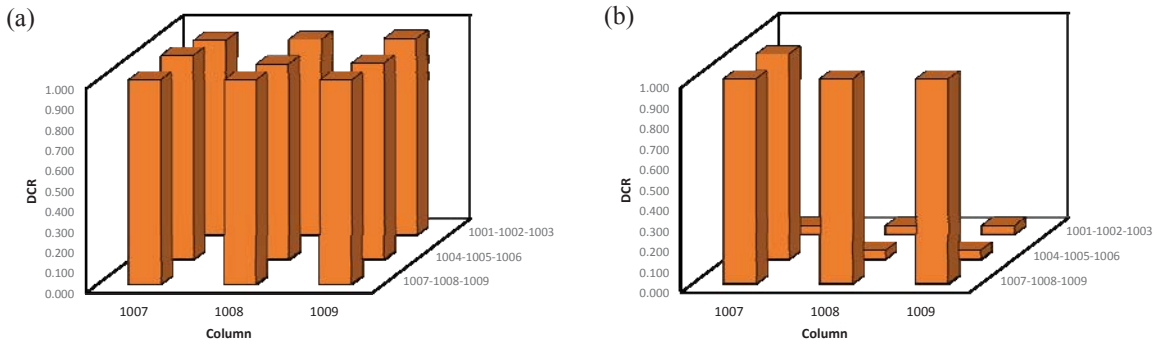

Figure 8. Cumulative DCR for first-floor columns under PGA = 0.1g, $\vartheta = 30°$, $\delta = 30°$ and $L_f = d_b$: model without consideration of shear column failure; (b) model with consideration of shear column failure.

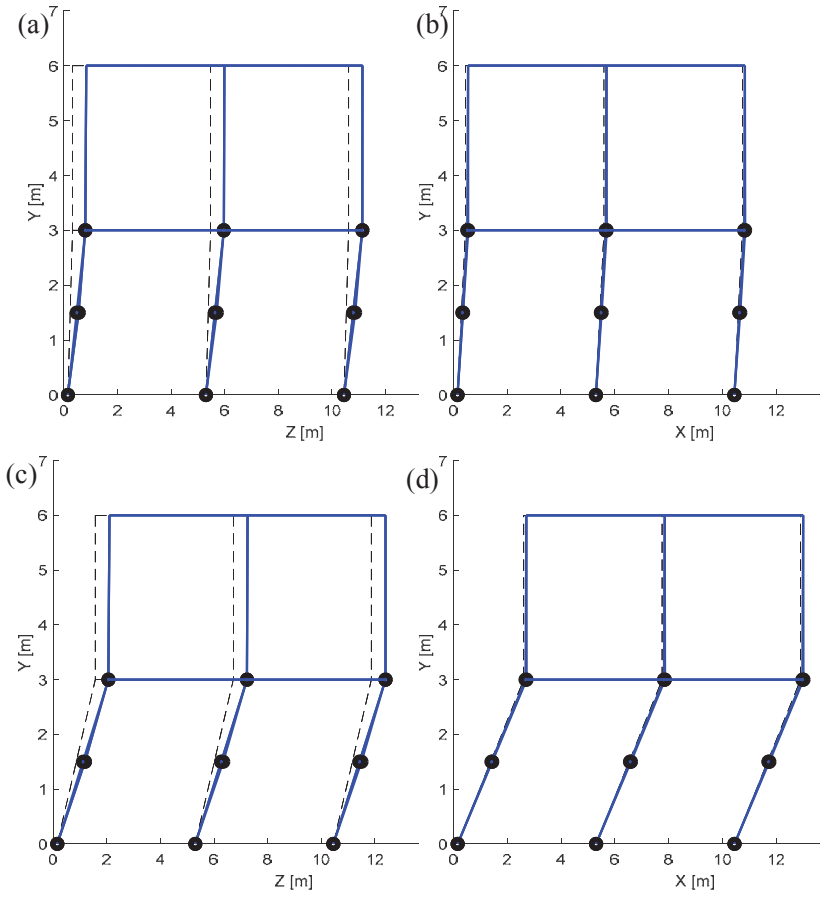

Figure 9. Near-collapse deformed shapes along Z- and X-axis considering shear column failure and cumulative damage under $\vartheta = 30°$, $\delta = 30°$, $L_f = d_b$: (a,b) PGA = 0.1g; (c,d) PGA = 0.2g (dashed black lines indicate displacements due to earthquake shaking; solid blue lines indicate total displacements after landslide impact).

4 FRAGILITY ANALYSIS

4.1 Methodology

The fragility analysis of the case-study building was carried out following the procedure summarised in Figure 10. Uncertainties in materials, geometry, loads and capacity model were defined through random variables with continuous probability distributions used in a previous study [7].

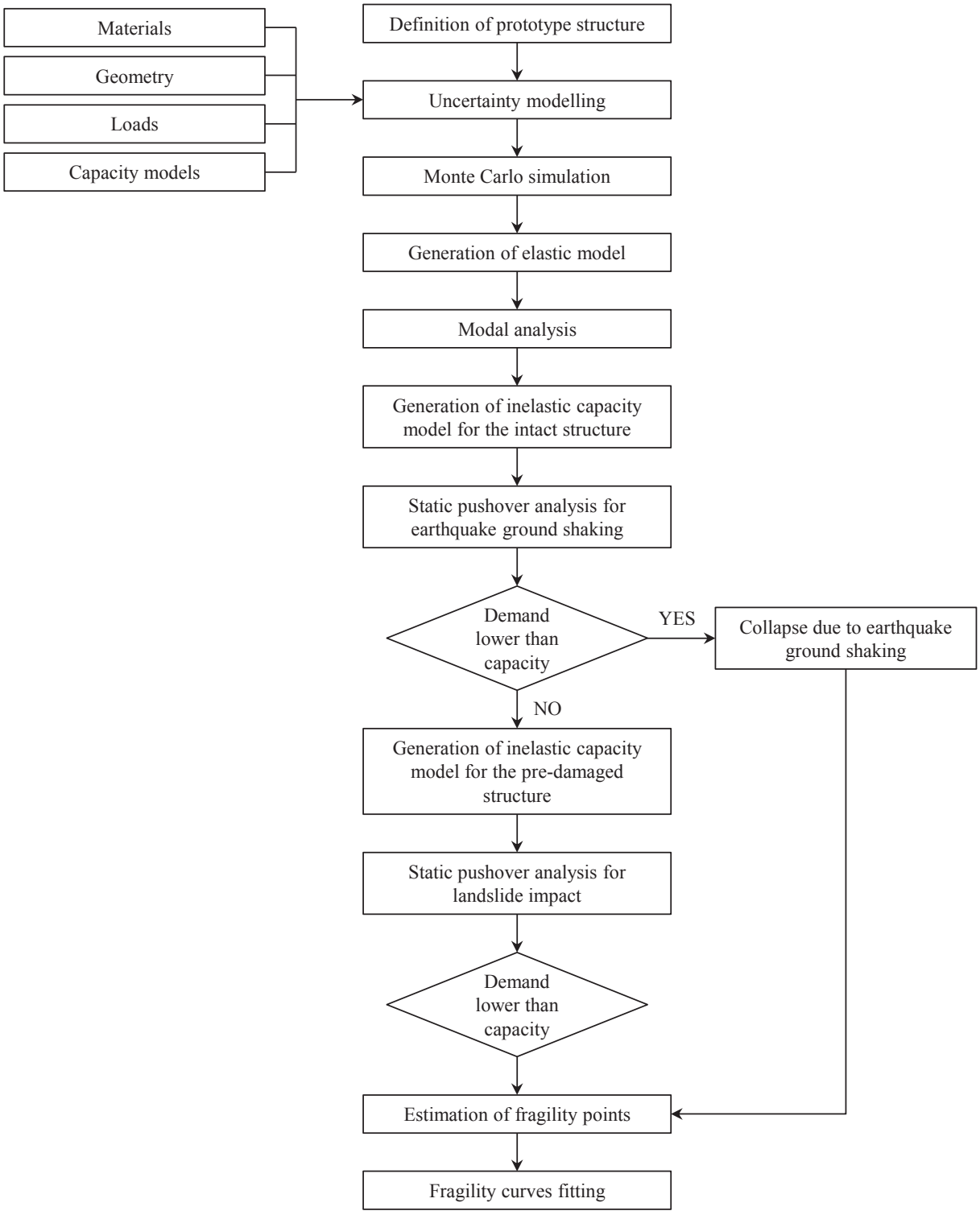

Figure 10. Flowchart of earthquake-induced landslide fragility analysis.

OpenSees® [15] and MATLAB® [16] software packages were used to automatically perform 10^3 random generations of load-capacity models and nonlinear sequential analyses. The fragility procedure was implemented through the Monte Carlo simulation method, considering the uncertainty modelling discussed above. For each realization, the sequential nonlinear analysis described in Section 2.2 was applied, assuming PGA ranging from 0.05g to 0.4g with step equal to 0.025g.

The impact velocity v of landslide was assumed to range from 0 to 10 m/s with step equal to 1 m/s. Damage associated only with earthquake shaking is related to the case of $v = 0$, whereas landslide impact with the maximum selected velocity always caused collapse of columns.

A biaxial interaction model [12][12] was used considering a degraded behaviour of plastic hinges in each direction to account for pre-damage due to earthquake shaking. A corner column was considered as the element in the worst condition of loading (impact in all cases) and capacity (lowest axial load).

The collapse fragility P_f (i.e. the conditional probability of exceeding the ultimate rotation in a plastic hinge of a first-floor column given PGA and v) was evaluated as the ratio between the number of collapse cases and the total number of simulations ($N_{sim} = 10^3$). A lognormal distribution function was fitted to fragility points in order to derive fragility curves for each velocity and PGA level [17].

In line with previous sensitivity analysis, fragility curves were derived for both capacity models considered in this study, highlighting the role of shear column failure on the vulnerability of the case-study building structure.

4.2 Discussion of results

The two sets of fragility curves are shown in Figures 11a and 11b, considering or not the shear failure of columns, respectively. Table 2 outlines the median PGA (μ), logarithmic standard deviation (β) and coefficient of determination (R^2) of fragility curves. Over all cases, R^2 reached very high values ranging between 0.85 and 0.99.

If shear failure of columns is considered (Fig. 11a), fragility curves can be grouped according to three ranges of impact velocity:

(i) v = 1–5 m/s, which are low velocity levels where structural vulnerability is mostly associated with earthquake shaking; in that case, the median PGA causing collapse is approximately 0.2g.

(ii) v = 6–7 m/s, which are medium velocity levels where structural vulnerability depends on both earthquake shaking and landslide impact, reducing the median collapse PGA to approximately 0.15g.

(iii) v = 8–10 m/s, which are high velocity levels where structural vulnerability is mostly associated with landslide impact on building façade, resulting in a median PGA equal to about 0.04g.

Dealing with the second set of fragility curves related to capacity models neglecting shear column failure (Fig. 11b), the vulnerability depends on two ranges of impact velocity as follows:

(i) v = 1–7 m/s, which are low-medium velocity levels where structural vulnerability is mostly associated with earthquake shaking, highlighting a median PGA approximately equal to 0.2g;

(ii) v = 8–10 m/s, which are high velocity levels where structural vulnerability depends on both earthquake shaking and landslide impact, resulting in a median PGA equal to 0.17g.

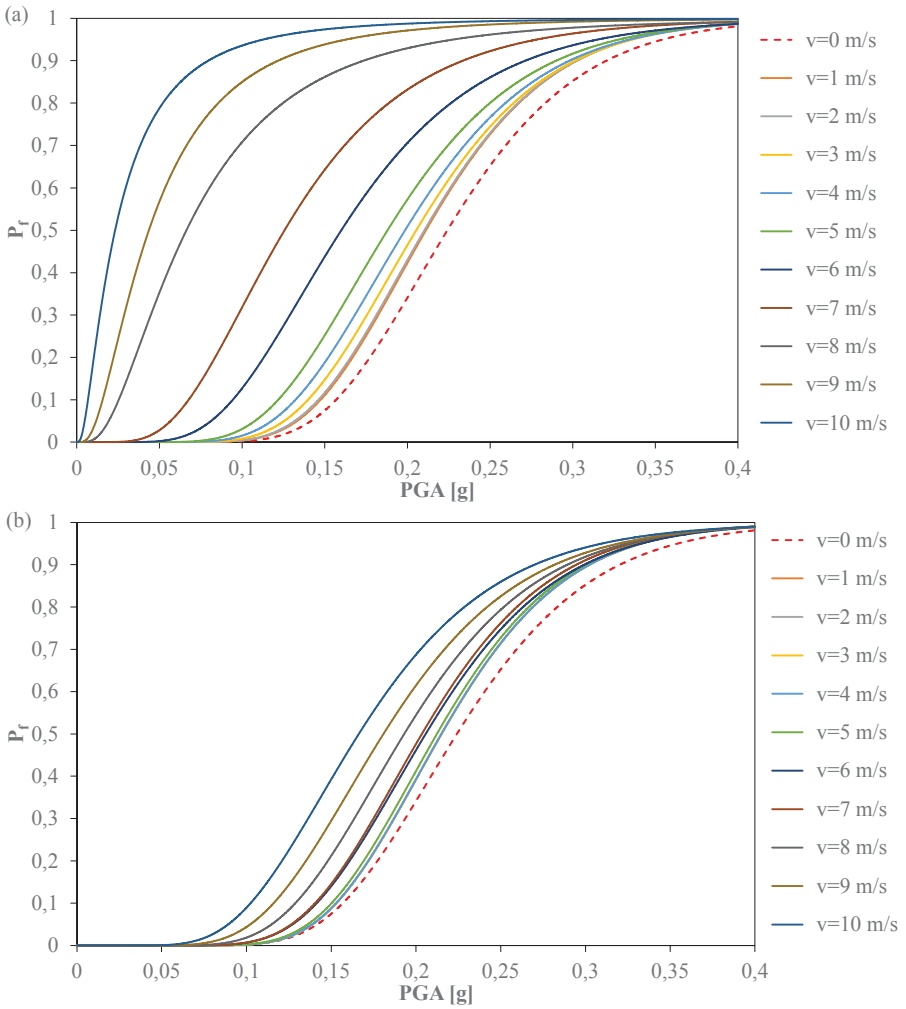

Figure 11. Fragility curves considering cumulative damage due to earthquake ground shaking and landslide impact: (a) model considering shear column failure; (b) model neglecting shear column failur.

	Model with shear failure			Model w/o shear failure		
v [m/s]	μ [g]	β	R^2	μ [g]	β	R^2
0	0.22	0.28	0.98	0.22	0.28	0.98
1	0.21	0.28	0.98	0.22	0.27	0.98
2	0.21	0.28	0.98	0.22	0.27	0.98
3	0.20	0.30	0.98	0.22	0.27	0.98
4	0.20	0.32	0.95	0.22	0.27	0.98
5	0.19	0.34	0.92	0.21	0.27	0.98
6	0.16	0.41	0.85	0.21	0.29	0.97
7	0.13	0.48	0.79	0.20	0.29	0.97
8	0.07	0.75	0.85	0.18	0.32	0.92
9	0.04	0.80	0.87	0.18	0.35	0.93
10	0.02	0.96	0.92	0.17	0.38	0.91

Table 2. Parameters and coefficients of determination of lognormal fragility curves.

5 CONCLUSIONS

The primary goal of this study was the fragility assessment of RC framed buildings subjected to earthquake-induced landslide hazard. To assess the effects of ground shaking and subsequent landslide impact, a computational strategy based on sequential nonlinear analysis of structural response was set up and implemented. The chord rotation of plastic hinges was assumed as engineering demand parameter measuring the structural response to sequential loading. This allowed the evaluation of cumulative damage due to earthquake actions and lateral pressures acting at the ground floor of the building. Uncertainties were modelled and propagated according to standard Monte Carlo simulation, accounting for diagonal impact and variable size of the landslide in plan.

Sensitivity analysis results underline the influence of width and impact angle of the landslide on structural response under varying ground shaking intensity. As landslide width increases, a growing number of columns are involved in the collapse mechanism of the structure. For the case-study building, sensitivity analysis evidenced upper bound capacity levels for ground shaking and landslide impact, which were respectively associated with $PGA_{max} = 0.4g$ and $v_{max} = 10$ m/s. Those limit values were then considered later in fragility analysis. Sensitivity analysis highlighted a totally different behaviour modes of the structure, depending on whether shear failure of columns is considered or not. In the former case, the structure experienced local collapse of columns, whereas in the other a soft-story mechanism was observed. As far as collapse velocity is concerned, the capacity model including shear failure reached collapse at $v_c = 6–7$ m/s, whereas collapse velocities $v_c > 14$ m/s were found when shear failure was not taken in due consideration.

Fragility analysis highlighted a significant vulnerability increase when landslide impact with medium-high velocity is expected. Therefore, the seismic risk of structures located in landslide-prone areas should be assessed with a multi-hazard approach to account for cumulative damage due to earthquake shaking and subsequent landslide movements.

Future developments of this study will include the analysis of 3D structural models with masonry infill walls, considering potential benefits from seismic design rules and detailing.

ACKNOWLEDGEMENTS

This study was carried out in the framework of GRISIS research project (Gestione dei Rischi e Sicurezza delle Infrastrutture a Scala regionale) funded by Regione Campania.

REFERENCES

[1] X. Wang, G. Nieand, D. Wang, Relationships between ground motion parameters and landslides induced by Wenchuan earthquake, *Earthquake Science*, 23(3), 233-242, 2010.

[2] S.D. Fotopoulouand, K.D. Pitilakis, Vulnerability assessment of reinforced concrete buildings subjected to seismically triggered slow-moving earth slides, *Landslides*, 10(5), 563-582, 2013.

[3] S.D. Fotopoulouand, K.D. Pitilakis. Fragility curves for reinforced concrete buildings to seismically triggered slow-moving slides, *Soil Dynamics and Earthquake Engineering*, 48, 143-161, 2013.

[4] S.D. Fotopoulouand, K.D. Pitilakis, Probabilistic assessment of the vulnerability of reinforced concrete buildings subjected to earthquake induced landslides, *Bulletin of Earthquake Engineering*, 15, 5191-5215, 2017.

[5] S.D. Fotopoulouand, K.D. Pitilakis, Vulnerability assessment of reinforced concrete buildings at precarious slopes subjected to combined ground shaking and earthquake induced landslide, *Soil Dynamics and Earthquake Engineering*, 93, 84-98, 2017.

[6] E.M. Rathje, G. Saygili, Probabilistic assessment of earthquake-induced sliding displacements of natural slopes, *Bulletin of New Zealand Society for Earthquake Engineering*, 42(1), 18-27, 2009.

[7] F. Parisi, G. Sabella, Flow-type landslide fragility of reinforced concrete framed buildings, *Engineering Structures*, 131, 28-43, 2017.

[8] G. Manfredi, A. Masi, R. Pinho, GM. Verderame, M. Vona, Valutazione degli edifici esistenti in cemento armato, *IUSS Press*, 2007 [in Italian].

[9] G. Miluccio, F. Parisi, E. Cosenza, Fragility curves for RC framed buildings subjected to earthquake-induced landslide: comparison between 2d and 3d structural models, *XI International Conference on Structural Dynamics, Eurodyn,* 2020.

[10] EN 1998-3:2004, Eurocode 8: Design of structures for earthquake resistance – Part 1: General rules, seismic actions and rules for buildings, *Comité Européen de Normalisation*.

[11] D. Biskinis, G.K. Roupakias, M.N. Fardis, Degradation of shear strength of reinforced concrete members with inelastic cyclic displacements, *ACI Structural Journal*, 101(6), 773-783, 2004.

[12] M. Di Ludovico, G.M. Verderame, A. Prota, G. Manfredi, E. Cosenza, Experimental behaviour of nonconforming RC columns with plain bars under constant axial load and biaxial bending, *Journal of Structural Engineering*, 139(6), 897-914, 2013.

[13] Y. Jafarian, A. Lashgari, M. Miraei, Multivariate fragility functions for seismic landslide hazard assessment, *Journal of Earthquake Engineering*, DOI: 10.1080/13632469.2018.1528909, 2018.

[14] O. Mavrouli, S. Fotopoulou, KD. Pitilakis, G. Zuccaro, J. Corominas, A. Santo, F. Cacace, D. De Gre-gorio, G. Di Crescenzo, E. Foerster, T. Ulrich, Vulnerability assessment for reinforced concrete buildings exposed to landslides, *Bulletin of Engineering Geology and the Environment*, 73(2), 265-289, 2014.

[15] F. McKenna, G.L. Fenves, M.H. Scott, OpenSees: Open system for earthquake engineering simulation. California: Pacific Earthquake Engineering Research Center, University of California Berkeley, 2004. Available at http://opensees.berkeley.edu.B.

[16] MATLAB and Statistics Toolbox Release R2018a. The MathWorks Inc., Natick, Massachusetts.

[17] K. Porter, R. Kennedy, R. Bachman, Creating fragility functions for performance-based earthquake engineering, *Earthquake Spectra*, 23(2), 471-489, 2007.

EURODYN 2020
XI International Conference on Structural Dynamics
M. Papadrakakis, M. Fragiadakis, C. Papadimitriou (eds.)
Athens, Greece, 23–26 November 2020

PARAMETER INVESTIGATION OF RELAXED UNCERTAIN POWER SPECTRA FOR STOCHASTIC DYNAMIC SYSTEMS

Marco Behrendt[1,2], Marius Bittner[1], Liam Comerford[2], Matteo Broggi[1] and Michael Beer[1,2,3]

[1]Institute for Risk and Reliability, Leibniz University Hannover, Germany
e-mail: {behrendt, bittner, broggi, beer}@irz.uni-hannover.de

[2]Institute for Risk and Uncertainty, University of Liverpool, United Kingdom
e-mail: l.comerford@liverpool.ac.uk

[3]Department of Structural Engineering, Tongji University, Shanghai, P.R. China

Keywords: Power Spectral Density, Stochastic Dynamics, Stochastic Process, Spectral Representation, Uncertainty Quantification.

Abstract. In structural dynamics the considerations of statistical uncertainties are imperative to ensure a realistic modelling of loading and material parameter setup. It is well known that any deterministic analysis only constitutes a narrow result for the given input parameters. Because of aleatoric or epistemic uncertainties, many factors must be considered either in certain interval margins or with subjective probabilities. Especially in the case of seismic ground motion, due to significant uncertainties, a reliable prediction of future event characteristics is important in designing safe structures.

This work attends to the well known statistical procedure of simulating time histories of a mechanical model under an artificially generated earthquake loading, which is modelled by a stochastic process. The stochastic processes in this work are throughout synthesized using the Spectral Representation Method (SRM). A key aspect of this procedure is the estimation of the Power Spectrum Density (PSD). The PSD determines dominant frequencies and their magnitude of influence on the stochastic process and in nature on the earthquake signals. There are numerous methods to estimate the PSD from source data, however, the amount of data available is seldom enough to do this accurately and reliably. To address this issue, the authors suggest that the PSD model itself could be defined as a random vector in the frequency domain, thereby encompassing a range of possible valid PSD models for a given data set. For a stationary process, the random dimension of said model would be dependent upon its frequency discretisation.

On a simple mechanical system, artificially generated stochastic processes with the novel described underlying power spectra are analysed utilizing a Monte Carlo simulation. A reliability statement of the mechanical system in the form of a first-passage problem is defined to acquire a probability of failure which is used alongside first- and second-order moments of the system's output as reasonable benchmark values.

1 INTRODUCTION

Many problems in engineering sciences are subject to random vibrations and thus lead to stochastic dynamic problems, for example, where environmental processes have an influence. These examples could be high-rise buildings, bridges or critical infrastructure subjected to earthquake, wind loads, or offshore platforms excited by waves. Because of the structural complexity, incomplete information of the system as well as hardly predictable natural processes, aleatory and epistemic uncertainties exist. Therefore, for these aforementioned facilities often a direct application of safety codes of civil engineering practice is not possible, which demands detailed time analyses and simulations to ensure a robust design [1]. To determine the influence of environmental processes on structures by running simulations, it is necessary to record these influences and apply them to a model with a system excitation/response process [2]. For this purpose, e.g. different earthquake ground motions are recorded and utilised for system analysis. However, these real data records are often already subjected to uncertainties. These uncertainties can arise due to various reasons, such as a limited amount of samples, damaged sensors, device failure, perhaps due to the environmental process itself, sensor threshold limitations and measurement errors. Additionally, the sensor could capture the data incorrectly, e.g. extreme features or other causes such as sensor maintenance, bandwidth limitation or data acquisition restrictions could lead to poor quality of the data records. For this reason, the real data records must be represented in an appropriate manner and the uncertainties mitigated as much as possible [3].

Since stochastic dynamics have been studied very efficiently in recent decades, different models have been developed to describe seismic ground motion. One of these tools to capture information of phenomena involving random fluctuations in time and space is the Power Spectral Density (PSD), which is widely used in the modelling of stochastic processes, especially in applications such as earthquake, wind and ocean engineering [4, 5, 6]. In earthquake engineering, for example, the use of the PSD dates back to Housner [7] or Kanai [8]. At least in the linear case considered in this work, a relationship between the system response can be derived with an elegant relationship between the power spectra of the input data and that of the output data [9]. Nonetheless, the available information of the probabilistic models for the input is often not enough to directly assess the resulting randomness of a structural response. For seismic ground motions with critical peaks, the structural response is generally non-linear and a direct relation of the probabilistic input models to the probabilistic output is not available. For this purpose the Monte Carlo simulation (MC) will be applied. It has been shown that for complex non-linear relations MC can compute probabilistic characteristics of the response. [10]

For the development of a load model that uses such a random excitation process, the following applies: The more real data sets are available, the better, since the numerical results are statistically more accurate for a large amount of data. In addition, it is useful if the underlying physics is understood well in order to make further assumptions. Because both cases are often not satisfied, other approaches must be found to develop a load model that represents the data in the best possible way [3]. In the context of a First-Passage reliability statement that requires for assessment the actual excitation of a mechanical model, the main focus of the method to mimic the seismic ground motion is to accurately represent the underlying stochastic information of the process. For the purpose of this work, the Spectral Representation Method (SRM) seems to be the most suited. In this

procedure, different processes with a specified PSD are generated. For standard cases this method generates a stationary homogeneous process, see e.g. [11, 12].

When estimating the PSD from multiple real data records by averaging their periodograms, it is assumed that the process defined by the records may be represented by a single PSD. When dealing with real data, the uncertainty introduced by this assumption could be significant and at the very least, an attempt should be made to quantify it. In this work, an approach is pursued where the single discrete frequencies are treated as probability density functions, which leads to a subjective probabilistic model. Therefore meaningful statistical variables of the ensemble are extracted. Based on these variables a probability density function for each single frequency is calculated.

This work is organised as follows: An explanation in which form the environmental processes are available and how a power spectrum density is estimated from a stochastic process is presented in section 2. Section 3 describes how the novel relaxed power spectral density is developed using subjective probabilities. In section 4 the First-Passage reliability measure is introduced. To validate the model a numerical example and a comparison of different approaches is given in 5. The final conclusion is given in section 6.

2 STOCHASTIC PROCESSES REPRESENTATION AND POWER SPECTRUM ESTIMATION

Given a real-valued stationary process $X(t)$. For each of these processes exist a corresponding orthogonal process $Z(\omega)$. Thus, $X(t)$ can than be written in the form

$$X(t) = \int_0^\infty e^{i\omega t} dZ(\omega), \tag{1}$$

where $Z(\omega)$ has the following properties:

$$\begin{aligned} E(\left|dZ^2(\omega)\right|) &= 4S_X(\omega)d\omega \\ E(dZ(\omega)) &= 0. \end{aligned} \tag{2}$$

In Eq. 2, $S_X(\omega)$ describes the two-sided power spectrum of the stationary process $X(t)$, see [13]. To generate a stationary stochastic process, the following model, first formulated by Shinozuka, is considered in this work [12]:

$$X(t) = \sum_{n=0}^{N-1} \sqrt{4S_X(\omega_n)\Delta\omega}\cos(\omega_n t + \varphi_n(\theta)), \tag{3}$$

where

$$\begin{aligned} \omega_n &= n\Delta\omega, \quad n = 0, 1, 2, \ldots, N-1 \\ \Delta\omega &= \frac{\omega_u}{N} \end{aligned} \tag{4}$$

with $N \to \infty$ and $\varphi_n(\theta)$ as $n_\varphi = N$ uniform distributed phase angles in the range $[0, 2\pi]$. This method is commonly referred to as the Spectral Representation Method (SRM). For the power spectrum density $S_X(\omega)$ the filtered noise power spectrum

$$S_X(\omega) = \frac{1 + a\omega^2}{(\omega_p^2 - \omega^2)^2 + (2\zeta\omega\omega_p)^2} \tag{5}$$

is used with $a = 5$ and $\zeta = 0.25$ as shape parameters and $\omega_p = 10$ rad/s as peak frequency [14]. The power spectrum S_X with the given parameters is depicted in Fig. 1.

To transform a stochastic process from time domain to frequency domain, the discrete Fourier transform is applied. A frequently used estimator of the power spectrum is the periodogram [15] which can be understood as the squared absolute value of the discrete Fourier transform of the time signal $x(t)$:

$$\hat{S}_X(\omega_k) = \lim_{T\to\infty} \frac{2\Delta T}{T} \left| \sum_{t=0}^{T-1} x_t e^{-2\pi i k t/T} \right|^2 \tag{6}$$

In this equation, T is the number of data points, t describes the data point index in the record, k is the integer frequency for $\omega_k = \frac{2\pi k}{T_0}$ and T_0 is the total length of the record. In Fig. 1, the power spectrum is given and the corresponding generated stochastic process is depicted.

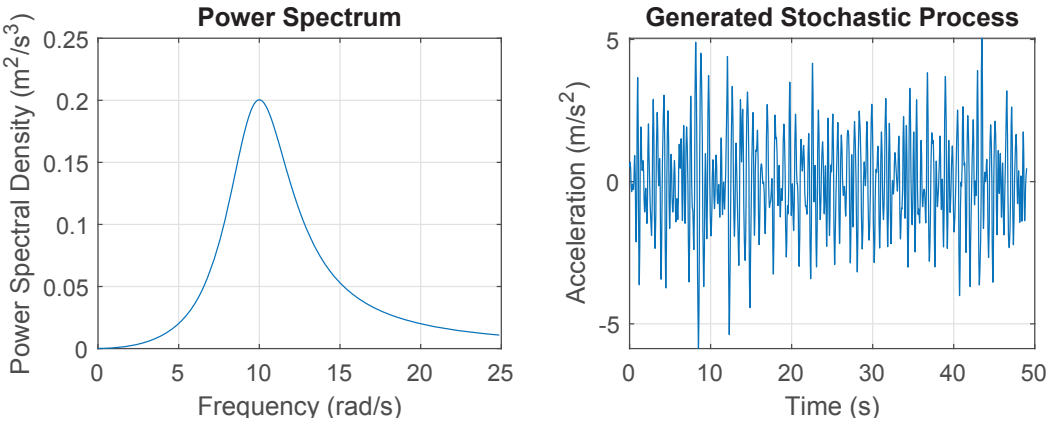

Figure 1: Example for the filtered noise power spectrum (left) and a generated stochastic process (right)

3 RELAXED POWER SPECTRUM

Uncertainties occur in the data records and in the estimation process. To account for these uncertainties, a relaxed model of a power spectrum is developed. The term "relaxed" means, that instead of a single power spectrum an ensemble of power spectra is utilised to determine a probability density function for each frequency. Although the individual power spectra in the ensemble show the same characteristics and shape, there is still variance among them, see Fig. 2. In order to determine a representative power spectrum for the ensemble, a relaxed spectrum represented by a uniform distribution or truncated normal distribution can be utilised.

For both approaches, first the ensemble of power spectra has to be estimated from an ensemble of simulated stochastic processes or real data records from seismic ground motions. Therefore, the periodogram (Eq. 6) is utilised. The ensemble can be seen as a set of different power spectra with cardinality R, i.e. ensemble $= \{\hat{S}_{X_i}\}, i = 1, 2, ..., R$. Here, R is determined by the number of available power spectra estimated either from real seismic ground motions or from artificially created stochastic processes. Each PSD in the set can be evaluated and yield a value $s_{i,\omega_n} = \hat{S}_{X_i}(\omega_n)$.

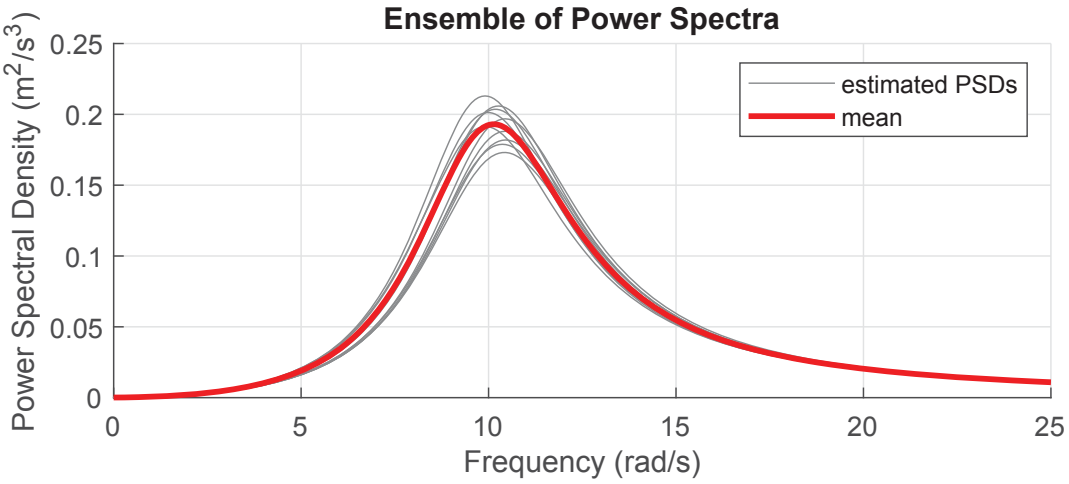

Figure 2: Ensemble of power spectra

3.1 Relaxed power spectrum utilising a uniform distribution

For the development of the relaxed power spectrum with a uniform distribution, the maximum and minimum for the power spectral density s_{i,ω_n} for each frequency ω_n of the ensemble is determined. These values are then used as the upper and lower bound for the uniform distribution.

$$f_{U,\omega_n}(s; a_{\omega_n}, b_{\omega_n}) = \begin{cases} \frac{1}{b_{\omega_n} - a_{\omega_n}} & \text{for } a_{\omega_n} \leq s \leq b_{\omega_n}, \\ 0 & \text{for } s \notin [a_{\omega_n}; b_{\omega_n}] \end{cases} \tag{7}$$

where a_{ω_n} and b_{ω_n} describe the minimum and maximum value of the power spectral density for each frequency:

$$a_{\omega_n} = \min[s_{\omega_n}], \quad b_{\omega_n} = \max[s_{\omega_n}] \tag{8}$$

For instance, the resulting relaxed power spectrum is depicted in Fig. 3 (left).

3.2 Relaxed power spectrum utilising a truncated normal distribution

Based on the ensemble of power spectra, given in the preceding section, mean (Eq. 9) and standard deviation (Eq. 10) are calculated for each frequency.

$$\mu_{\omega_n} = \frac{1}{R} \sum_{i=1}^{R} s_{i,\omega_n} \tag{9}$$

$$\sigma_{\omega_n} = \sqrt{\frac{1}{R} \sum_{i=1}^{R} \left(s_{i,\omega_n} - \mu_{\omega_n} \right)^2} \tag{10}$$

with $\omega_n = n\Delta\omega, n = 0, 1, 2, \ldots, N-1$ and R the ensemble's cardinality. By extracting these statistical information from the ensemble, a truncated normal distribution (Eq. 11) is used to calculate the relaxed power spectrum. The probability density function is given by

$$f_{TN,\omega_n}(s; \mu_{\omega_n}, \sigma_{\omega_n}, a = 0, b = \infty) = \frac{1}{\sigma_{\omega_n}} \frac{\phi(\frac{s-\mu_{\omega_n}}{\sigma_{\omega_n}})}{\Phi(\frac{b-\mu_{\omega_n}}{\sigma_{\omega_n}}) - \Phi(\frac{a-\mu_{\omega_n}}{\sigma_{\omega_n}})}, \tag{11}$$

where $a = 0$ and $b = \infty$ defines the interval, $\phi(\xi) = \frac{1}{\sqrt{2\pi}} \exp\left(-\frac{1}{2}\xi^2\right)$ is the standard normal distribution and $\Phi(s) = \frac{1}{2}\left(1 + \mathrm{erf}(s/\sqrt{2})\right)$ is the corresponding cumulative distribution function. As negative values are not possible in terms of power spectra, the interval $[0; \infty]$ is defined beforehand.

The resulting relaxed power spectrum for the ensemble using a truncated normal distribution is depicted in Fig. 3 (right).

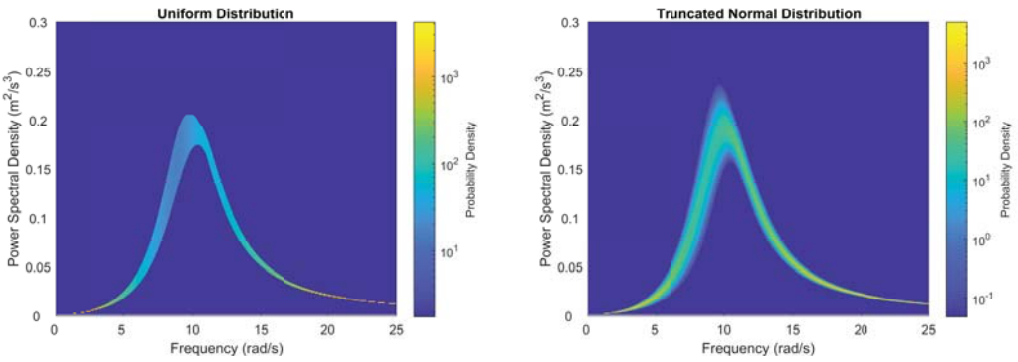

Figure 3: Relaxed power spectrum with probability density functions for each frequency derived from the ensemble given in Fig. 2; Uniform distribution (left); Truncated normal distribution (right)

3.3 Relaxed Spectral Representation Method

With the previous definitions in Eq. 7 and Eq. 11 a new formulation for the SRM in Eq. 3 can be given. This shall be called the Relaxed Spectral Representation Method (RSRM):

$$X(t,\theta) = \sum_{n=0}^{N-1} \sqrt{4 S_{X,\omega_n}(\theta)\Delta\omega}\, \cos(\omega_n t + \varphi_n(\theta)), \tag{12}$$

where $S_{X,\omega_n}(\theta)$ denotes that corresponding to each ω_n a distribution function according to either Eq. 7 or Eq. 11 is defined, which using a sample technique, such as inverse sampling, yields the PSD value. This leads likewise as for $\varphi_n(\theta), n_\varphi$ to a number of n_S new random distributions, which are now distinctively for each ω_n defined, i.e. $S_{X,\omega_n}(\theta), n_S$. The extension is not ideal due to the large number of random variables. However, for a first accurate approximation this approach was chosen. For instance, the probability density functions for the frequencies 5 rad/s, 10 rad/s and 15 rad/s for both, uniform and truncated normal distributed relaxed power spectrum, are depicted in Fig. 4.

4 FIRST-PASSAGE RELIABILITY PROBLEM

In the introduction, a referral to the safety of critical infrastructure and high-rise buildings under the influence of environmental processes such as earthquakes has been given. In practice, this safety of structures is approached by defining the structure's reliability. An application-specific problem related to seismic reliability could be: "Under a particular earthquake loading, does the structure exceed a certain critical displacement?" To tackle this problem a well defined mechanical model is proposed with which simulations are carried out. The simulation outputs are analysed to identify the first exceedances of a pre-defined critical displacement. These first time exceedances can be counted as

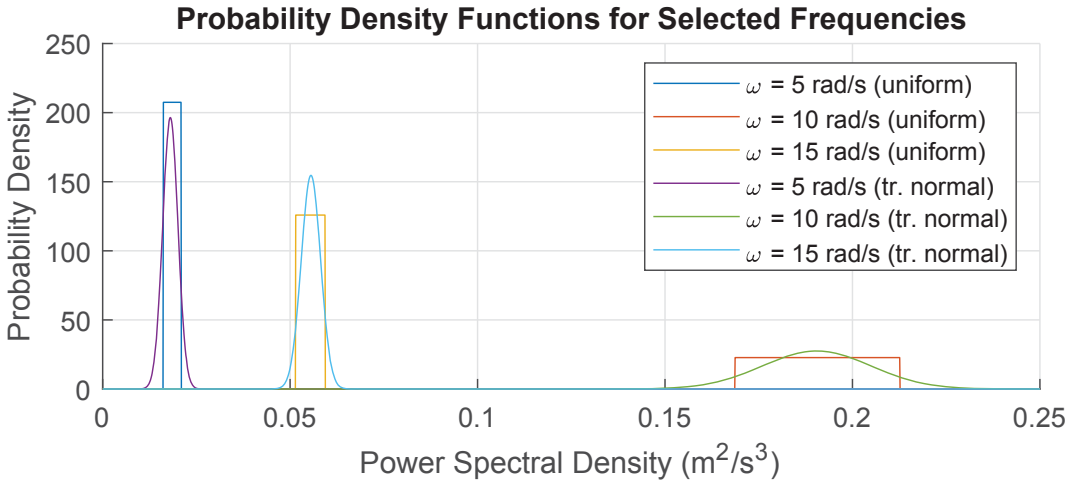

Figure 4: Probability density functions for selected frequencies

failure events. Such an approach is common for hysteretic structures subjected to seismic excitation where a failure can occur due to e.g. cumulative plastic deformations. All these assumptions regarding the occurrence of a failure can be gathered under the term First-Passage Reliability Problem [16]. Note that the exact time of exceedance is not of interest in the analysis of this work.

Since seismic excitation is a natural phenomenon that inhibits a stochastic nature, no exact statement about the occurrence of these failures can be given. To estimate the probability of an exceedance a Monte Carlo simulation can be applied. The estimated probability of exceedance is then called the probability of failure and denoted by p_f.

4.1 Probability of failure

First a relation between a critical value and the systems response is defined. Let

$$g(\boldsymbol{\theta}) = C_{crit} - D(\boldsymbol{\theta}) \tag{13}$$

be the performance function, sometimes also referred to as limit state function, where C_{crit} is a pre-defined capacity value that may or may not be exceeded by a systems demand $D(\boldsymbol{\theta})$. The vector $\boldsymbol{\theta} = (\theta_1, \theta_2, ..., \theta_{n_\theta})$ is composed of all random parameters affecting the system. This may include physical properties as well as random modelling parameters used to simulate e.g. a forced excitation. All probability density functions (PDFs) in $\boldsymbol{\theta}$ are known and the random dimension is n_θ (i.e. the total number of Random Variables). With this mathematical threshold description of a failure the performance function Eq. 13 can be used to describe a corresponding failure region F by a relational description for the value of $g(\boldsymbol{\theta})$:

$$\begin{aligned} g(\boldsymbol{\theta}) \leq 0 \rightarrow \boldsymbol{\theta} \in F \\ g(\boldsymbol{\theta}) > 0 \rightarrow \boldsymbol{\theta} \notin F. \end{aligned} \tag{14}$$

The probability of failure for any arbitrary multivariate probability distribution function $f_{\boldsymbol{\Theta}}(\boldsymbol{\theta})$ is then calculated by following integral over the whole failure domain F

$$p_f = \int_F f_{\boldsymbol{\Theta}}(\boldsymbol{\theta}) d\boldsymbol{\theta}, \tag{15}$$

since the exact failure domain is usually unknown, by using the indicator function $\mathcal{I}(\boldsymbol{\theta})$ with $\mathcal{I}(\boldsymbol{\theta}) = 1$ if $\boldsymbol{\theta} \in F$ and 0 otherwise, the above integral can be expanded on the whole domain and rewritten to

$$p_f = \int_{-\infty}^{+\infty} \mathcal{I}(\boldsymbol{\theta}) f_{\boldsymbol{\Theta}}(\boldsymbol{\theta}) d\boldsymbol{\theta} = E[\mathcal{I}(\boldsymbol{\theta})]. \tag{16}$$

4.2 Monte Carlo simulation

The expression in Eq. 16 allows the Monte Carlo (MC) estimation of p_f to be

$$\hat{p}_f = \frac{1}{N_{MC}} \sum_{i=1}^{N_{MC}} \mathcal{I}(\theta_{i,n_\theta}) \tag{17}$$

where N_{MC} indicates the number of Monte Carlo samples used. For each $\boldsymbol{\theta}_i$ a deterministic analysis with n_θ random inputs is carried out. This estimators variance and the corresponding coefficient of variation are

$$\mathrm{Var}[\hat{p_f}] = \frac{\hat{p_f} - \hat{p_f}^2}{N_{MC}}, \quad \nu_{p_f} = \frac{\sqrt{\mathrm{Var}[\hat{p_f}]}}{\hat{p_f}}. \tag{18}$$

All derivations in this section, with a focus on a high dimensional random space, can be revisited in [17].

5 NUMERICAL EXAMPLE

With the two novel descriptions of the underlying PSDs, several Monte Carlo simulations (MCS) are carried out to investigate the effect of the now different stochastic processes and their influence on a specific exemplary reliability problem by comparing the MCS estimated probability of failure. Variance and coefficient of variation are tracked for different numbers of MC samples.

5.1 Model

A simple Single Degree-of-Freedom (SDOF) linear oscillator in the form

$$m\ddot{\boldsymbol{x}}(t) + c\dot{\boldsymbol{x}}(t) + k\boldsymbol{x}(t) = \boldsymbol{F}(\boldsymbol{\theta}, t), \tag{19}$$

with mass $m = 50$ kg, spring constant $k = 1922$ N/m and damping coefficient $c = 37.2$ kg/s is introduced. $\boldsymbol{x}, \dot{\boldsymbol{x}}, \ddot{\boldsymbol{x}}$ are displacements, velocities and accelerations of the system. The forcing term on the right hand side $\boldsymbol{F}(\boldsymbol{\theta}, t)$ is modelled by the stochastic process as introduced in section 2 utilizing the novel random relaxed spectra as given in section 3. Above equation is solved using an explicit Runge-Kutta scheme according to [18]. The capacity within the performance function C_{crit} is chosen to be 0.0055 m. The demand D is the maximum absolute displacement of the system through the whole time domain and given as

$$g(\boldsymbol{\theta}) = 0.0055 - \max_{t \in [0, T_E]} \left[|\boldsymbol{x}(\boldsymbol{\theta}, t)| \right]. \tag{20}$$

Note that since the right hand side of Eq. 19 contains a random input, the systems output $\boldsymbol{x}(\boldsymbol{\theta})$ becomes random as well. The exact time t of an exceedance is not of interest here but an exceedance is only counted once in a certain time interval $[0, T_E]$. All values and

parameters were chosen in order to generate a relatively small probability of failure which is $p_f < 0.01$.

The random dimension n_θ present in the model (Eq. 19) highly affects the MCS efficiency and therefore needs a careful consideration. In Eq. 3 random phase angles are introduced to create shifted harmonics. In order to prevent repeating behaviour of the stochastic process due to the restricted number of harmonic terms N a sufficiently large number n_φ of summands, containing random phase angles, corresponding to the simulation time need to be chosen. This relationship was chosen to be

$$n_\varphi \geq \lceil \frac{T_E \omega_u}{2\pi} \rceil \tag{21}$$

where $\omega_u = 25$ rad/s is the so called cut-off frequency in Eq. 4 and T_E is the total simulation time given to be 49 s. This results in $n_\varphi = 195$ uniform distributed phase angles.

5.2 Random distributions and random dimension

Because of the summation of the SRM and RSRM in e.g. Eq. 12 for each random phase angle a random PSD value according to $S_{X,\omega_n}(\theta)$ is sampled. This results in $n_\varphi = n_S$ and $n_\theta = n_\varphi + n_S = 390$ random distributions. For the further analysis three different cases will be explored.

- Case 1: SRM with $\varphi_{1,2,\dots,n_\varphi} \sim U([0, 2\pi])$
- Case 2: RSRM-U with $\varphi_{1,2,\dots,n_\varphi} \sim U([0, 2\pi])$ and $S_{X,\omega_{1,2,\dots,n_S}} \sim f_U(s, a_{\omega_n}, b_{\omega_n})$
- Case 3: RSRM-TN with $\varphi_{1,2,\dots,n_\varphi} \sim U([0, 2\pi])$ and $S_{X,\omega_{1,2,\dots,n_S}} \sim f_{TN,\omega_n}(s; \mu_{\omega_n}, \sigma_{\omega_n}, a = 0, b = \infty)$

Note that for all three cases the same set $\{\varphi_n(\theta)\}$ of random phase angles has been used. The increase of the total random dimension n_θ is not the ultimate goal of this work, on the contrary with further experiments the total number of used random distributions in this model shall be reduced. But as for now to mimic the given crisp PSD function this approach has been used.
Exemplary results for the stochastic process of Eq. 12 and the underlying PSD, $S_{X,\omega_n}(\theta)$ in Case 2 and Case 3 can be seen in Fig. 5. Since the bounds are chosen reasonably small, only a 5 s stochastic process is shown to make differences visible.

5.3 Results & discussion

For all cases different number of MC samples N_{MC} are sampled to estimate p_f. For instance, the results of one MC simulation solving Eq. 19 in each case are shown in Fig. 6. For the full-time history of the system's response, the difference between the three cases is not directly visible. It is obvious that no forcing signal $\boldsymbol{F}(\boldsymbol{\theta}, t)$ for this simulation is able to deflect the system into reaching the capacity C_{crit}. Further analyses with large numbers of MC samples have been carried out and p_f was estimated. These results are gathered in Tab. 1 and calculated according to Eq. 18. Case 1 is the classic SRM - Spectral Representation Method, Case 2 the RSRM-U, Relaxed Spectral Representation Method using uniform distributions for the PSD and Case 3 RSRM-TN using the truncated normal distributions. From these results in Tab. 1 the assumption could be made that p_f and

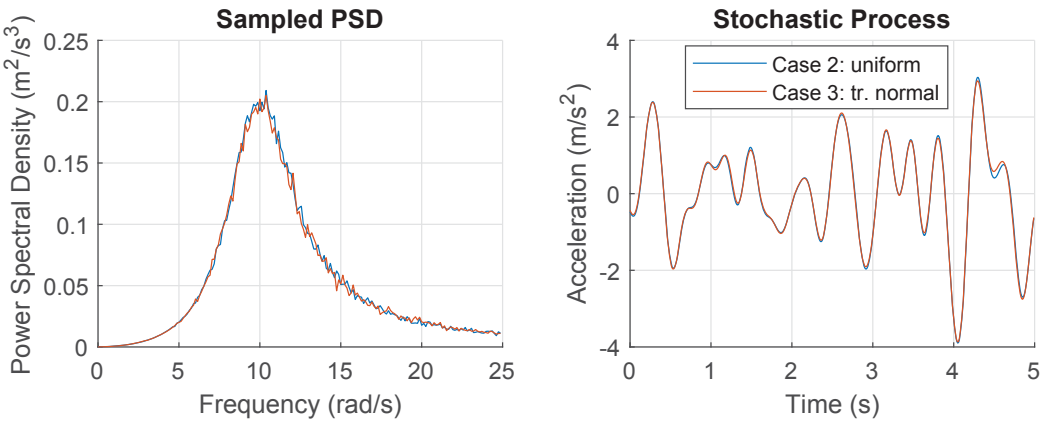

Figure 5: Example for two generated power spectral densities (left) and the corresponding stochastic processes in a time window of 5 s (right)

ν_{p_f} are independent from the case and therefore of the underlying presented random PSD function. Evidence could be that the differences between all results have a magnitude smaller than 10^{-3}. Though, when a detailed relation is shown as in Fig. 7 differences especially in the amplitude can be spotted. The results given in Tab. 1 and Fig. 6 are to be explained due to a considerate definition of the random PSD values. Boundaries and model parameters were carefully chosen.

In Tab. 1 it can be seen that the p_f does not change significantly when using the RSRM instead of SRM. The goal of this paper was to establish a random definition of the stochastic processes underlying PSD function. The reliability measure as well as first- and second-order moments were chosen to be measured in order to prove that no significant model changes were imposed from the RSRM towards the model versus the SRM influence on the model. This would mean that the induced aleatoric uncertainty by adding new random distributions to describe the PSD is not unnecessarily increased. However, if a few model parameters are changed, e.g. the simulation time T_E or the random dimensions

Table 1: Simulation results for the presented cases with a different number of MC samples N_{MC}.

Method	N_{MC}	$\sqrt{\mathrm{Var}[x]}$ (m)	E[x] (m)	max[$\lvert x\rvert$] (m)	ν_{p_f}	p_f
Case 1 SRM	$2.5 \cdot 10^5$	$1.9 \cdot 10^{-7}$	$-7.9 \cdot 10^{-9}$	0.0074	0.0204	0.0095
	$5.0 \cdot 10^5$	$1.9 \cdot 10^{-7}$	$3.0 \cdot 10^{-9}$	0.0072	0.0145	0.0095
	$7.5 \cdot 10^5$	$1.9 \cdot 10^{-7}$	$5.9 \cdot 10^{-9}$	0.0074	0.0120	0.0092
	$1.0 \cdot 10^6$	$1.9 \cdot 10^{-7}$	$2.2 \cdot 10^{-10}$	0.0075	0.0102	0.0095
Case 2 RSRM-U	$2.5 \cdot 10^5$	$1.9 \cdot 10^{-7}$	$-8.0 \cdot 10^{-9}$	0.0074	0.0204	0.0095
	$5.0 \cdot 10^5$	$1.9 \cdot 10^{-7}$	$2.9 \cdot 10^{-9}$	0.0072	0.0145	0.0094
	$7.5 \cdot 10^5$	$1.9 \cdot 10^{-7}$	$5.9 \cdot 10^{-9}$	0.0074	0.0119	0.0093
	$1.0 \cdot 10^6$	$1.9 \cdot 10^{-7}$	$1.7 \cdot 10^{-10}$	0.0075	0.0103	0.0094
Case 3 RSRM-TN	$2.5 \cdot 10^5$	$1.9 \cdot 10^{-7}$	$-7.9 \cdot 10^{-9}$	0.0074	0.0204	0.0095
	$5.0 \cdot 10^5$	$1.9 \cdot 10^{-7}$	$2.9 \cdot 10^{-9}$	0.0072	0.0146	0.0093
	$7.5 \cdot 10^5$	$1.9 \cdot 10^{-7}$	$6.0 \cdot 10^{-9}$	0.0074	0.0119	0.0093
	$1.0 \cdot 10^6$	$1.9 \cdot 10^{-7}$	$1.6 \cdot 10^{-10}$	0.0075	0.0102	0.0095

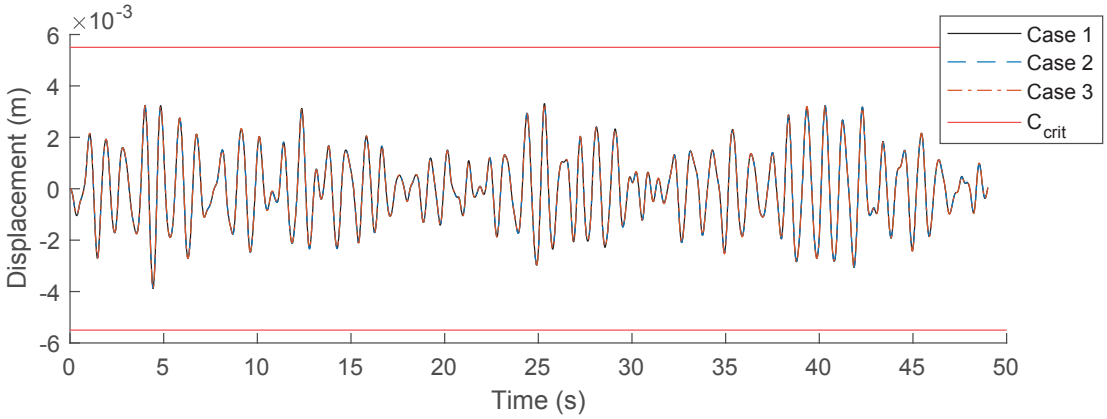

Figure 6: One MC full system response for all cases.

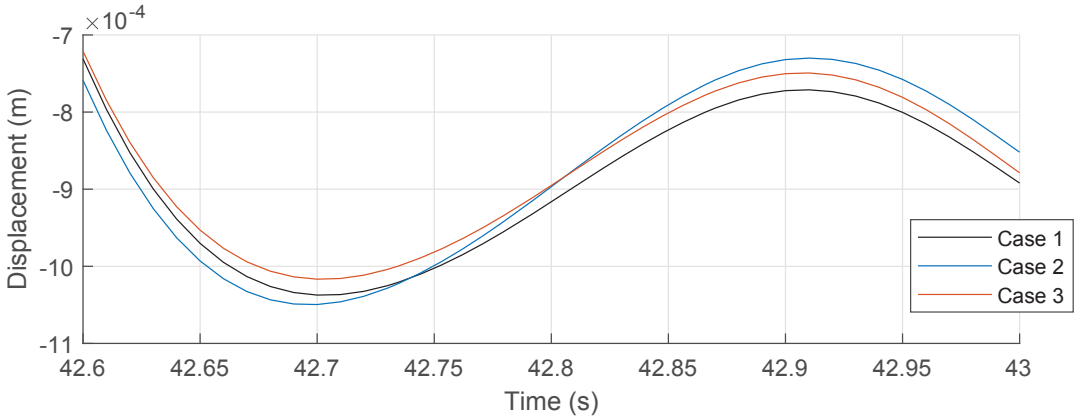

Figure 7: System response for all cases in $t \in [42.6s, 43.0s]$

n_φ, n_S that affect the number of summands, as in Eq. 21 or Eq. 12 a huge variation in results can be observed. This leaves the task open to diminish the epistemic uncertainty of the RSRM in combination with a mechanical system.
For all MC simulations the calculation time was monitored. As measured a respective number $t_{sim} = \frac{\text{simT}}{N_{MC}}$, where simT is the machine's needed calculation time, of how long the calculation took per single sample was calculated. As average over all different MC simulations this delivered following results: SRM= 3.896 ms/sample, RSRM-U= 4.172 ms/sample, RSRM-TN= 4.119 ms/sample. Since from the formulation of the SRM a summation needs to be carried out, which is realised in a for loop an additional sampling for each summand does not significant increase the calculation time.

6 CONCLUSION

In this work, a novel representation of the power spectral density function was presented. Instead of using discrete values for the power spectral density for each frequency, statistical information from an ensemble of power spectra can be extracted and a corresponding probability distribution function can be calculated. In this way, the power spectral density is "relaxed" as the previous discrete values are now treated as probability functions. Therefore, not only one value for a specific frequency is possible, but a range of values with different probabilities. It has been shown, that the developed relaxed power

spectra are usable for producing non-ergodic process realisations immediately applicable for Monte Carlo simulation analyses.

The relaxed power spectrum offers several advantages compared to the traditional power spectral density. Due to the sensor limitations mentioned in section 1 and the estimation of power spectra, the excitation and response of simulations are subject to uncertainties. Therefore, a single discrete value as solution is unlikely to be true and reliable. The relaxed spectrum is more robust as it is able to capture these uncertainties. A range of possible excitations with different probabilities are then known, yielding various plausible solutions. Especially in the case that a high amount of real data records are available, an approach with subjective probabilities is useful to calculate a relaxed power spectrum, since it is possible to obtain reliable statistical informations of the ensemble. The same holds for artificially generated stochastic processes as an unlimited number can be generated.

For the development of the proposed relaxed power spectrum a crucial point is the choice of the utilised probability density function. Here, a uniform distribution and a truncated normal distribution are used, for comparison purposes. It has been shown, that the selection of the PDF has not a big influence to the simulated displacement of a single Degree-of-Freedom model with a First-Passage problem. The two models show very similar results, also in comparison with the traditional spectral representation method. It can be deduced that the relaxation of the models is a valid method to take uncertainties into account. In order to confirm these results other investigations with more complex structures, e.g. non-linear finite element simulations, must be carried out.

Furthermore, there is also a need to understand the influence of the model parameters and how they affect the underlying system. Since it was observed that even small changes in these parameters caused a large variation in the results, this must be investigated in order to make the relaxed models applicable to any structure with a different set of parameters.

Finally the ultimate goal is to reduce the total number of used random distributions. In this work an approach has been chosen to simulate stochastic processes as close to a target precise PSD as possible. This took a careful parameter setting. In future work the possibilities of decreasing the random dimension will be targeted. Additionally, synergies with the Stochastic Harmonic Function representation will be explored.

7 ACKNOWLEDGEMENT

Part of this work was funded by the German Research Foundation (Grants BE 2570/4-1 and CO 1849/1-1) as part of the project 'Uncertainty modelling in power spectrum estimation of environmental processes with applications in high-rise building performance evaluation'.

REFERENCES

[1] G. I. Schuëller. On the treatment of uncertainties in structural mechanics and analysis. Computers & Structures, 85:235–243, 03 2007.

[2] L. Comerford, I. A. Kougioumtzoglou, and M. Beer. An artificial neural network approach for stochastic process power spectrum estimation subject to missing data. Structural Safety, 52:150–160, 2015.

[3] L. Comerford, H. A. Jensen, F. Mayorga, M. Beer, and I. A. Kougioumtzoglou. Compressive sensing with an adaptive wavelet basis for structural system response and reliability analysis under missing data. Computers & Structures, 182:26–40, 2017.

[4] A. Powell and S. H. Crandall. Random Vibration. The Technology Press of the Massachusetts Institute of Technology, Cambridge, 1958.

[5] Y.-K. Lin and G.-Q. Cai. Probabilistic structural dynamics: advanced theory and applications. McGraw-Hill New York, 1995.

[6] J. Li and J. Chen. Stochastic dynamics of structures. John Wiley & Sons, 2009.

[7] G. W. Housner. Characteristics of strong-motion earthquakes. Bulletin of the Seismological Society of America, 37(1):19–31, 1947.

[8] K. Kanai. Semi-empirical formula for the seismic characteristics of the ground. Bulletin of the earthquake research institute, 35:309–325, 1957.

[9] J. Chen, W. Sun, J. Li, and J. Xu. Stochastic harmonic function representation of stochastic processes. Journal of Applied Mechanics, 80(1):011001, 2013.

[10] G. I. Schuëller. Efficient monte carlo simulation procedures in structural uncertainty and reliability analysis - recent advances. Structural Engineering and Mechanics, 32(1):1–20, 2009.

[11] M. Shinozuka and C.-M. Jan. Digital simulation of random processes and its applications. Journal of Sound and Vibration, 25(1):111 – 128, 1972.

[12] M. Shinozuka and G. Deodatis. Simulation of stochastic processes by spectral representation. Applied Mechanics Reviews, 44(4):191–204, 1991.

[13] L. Comerford, I. A. Kougioumtzoglou, and M. Beer. Compressive sensing based stochastic process power spectrum estimation subject to missing data. Probabilistic Engineering Mechanics, 44:66–76, 2016.

[14] M. Beer and P. D. Spanos. A neural network approach for simulating stationary stochastic processes. Structural Engineering and Mechanics, 32(1):71–94, 2009.

[15] D. E. Newland. An introduction to random vibrations, spectral & wavelet analysis. Courier Corporation, 2012.

[16] H. J. Pradlwarter and G. I. Schueller. Exceedance Probabilities of MDOF-Systems Under Stochastic Excitation. Applied Mechanics Reviews, 50(11S):S168–S173, 11 1997.

[17] P. S. Koutsourelakis, H. J. Pradlwarter, and G. I. Schuëller. Reliability of structures in high dimensions, part i: algorithms and applications. Probabilistic Engineering Mechanics, 19(4):409 – 417, 2004.

[18] L. F. Shampine and M. W. Reichelt. The matlab ode suite. SIAM Journal on Scientific Computing, 18(1):1–22, 1997.

EURODYN 2020
XI International Conference on Structural Dynamics
M. Papadrakakis, M. Fragiadakis, C. Papadimitriou (eds.)
Athens, Greece, 23–26 November 2020

AN APPLICATION OF GENERATIVE ADVERSARIAL NETWORKS IN STRUCTURAL HEALTH MONITORING

G. Tsialiamanis[1], E. Chatzi[2], N. Dervilis[1], D. J. Wagg[1], K. Worden[1]

[1]Dynamics Research Group, Department of Mechanical Engineering, University of Sheffield, Mappin Street, Sheffield S1 3JD

[2] ETH Zurich, Institute of Structural Engineering
Stefano-Franscini-Platz 5, 8093 Zurich

Keywords: Structural health monitoring, machine learning, neural networks, generative adversarial networks, GANs

Abstract. *In the current work, the use of generative adversarial networks (GANs) in a simulated structural health monitoring (SHM) application is studied. A specific type of GAN is considered, aiming at a disentangled representation of underlying features and clusters of data through some latent variables. This idea could prove useful in SHM, since explanation of how damage mechanisms or environmental conditions affect a structure may be exploited in order to monitor structures more effectively. In a simulated mass-spring example, different damage cases are introduced by reducing the stiffness of specific springs and different damage levels by applying different extents of stiffness reduction. The GAN implementation proves able to capture different damage cases through its categorical latent variables, as well as the damage extent within its continuous latent variables. The results demonstrate that the latent variables are indeed capturing the effect of damage in the structure and can be exploited for the purpose of condition assessment.*

1 Introduction

Modern societies extensively rely on structural elements. Everyday activities depend on structures like bridges, engines, power generators etc. Malfunction or damage of these critical systems may lead to delays in transportation, power shutdowns or even injury or death of individuals. Avoiding such failures and guaranteeing safe operation and efficient performance is therefore a matter of critical importance. *Structural Health Monitoring* (SHM) offers a tool to this end. SHM is employed to ensure operability and safety of structures and to avoid consequences of failure. Many different approaches have been proposed in the context of SHM, but all of them can be categorised according to the hierarchical structure proposed by Rytter [1] and extended in [2]:

1. Is there damage (*existence*)?
2. Where is the damage in the system (*location*)?
3. What kind of damage is present (*type/classification*)?
4. How severe is the damage (*extent/severity*)?
5. How much useful (safe) life remains (*prognosis*)?

Ascending in Rytter's hierarchy makes the task at hand more difficult than the one in the previous step. Detecting if damage exists requires definition of the normal condition of a structure and divergence from that is an indication of damage and has to be examined. The second step of localising damage, requires further knowledge about the behaviour of a structure and how damage in various areas may affect the structural response. Moreover, defining the type of damage is a task that requires further understanding of the structural behaviour and of the manner in which different types of damage affect observed features of the structure. Finally, the two last steps in the hierarchy, demand understanding of the damage mechanism in order to define its severity and to further predict the useful life of the structure under the specific damage case. Although some data driven methods would promise to do this without really understanding the mechanism as long as sufficient instances of failure are recorded.

It is straightforward that dealing with these tasks involves acquiring and processing data in order to infer results about the condition of a structure. Taking into account the progress made in the disciplines of data analysis and *machine learning* (ML), diverse methods from these fields have been exploited for the purposes of SHM [2]. Regarding the first step in the aforementioned hierarchy, ML has been used to perform outlier detection using autoencoders to explain data corresponding to the normal condition of a structure [3]. Autoencoders were chosen because they are able to explain data belonging to an arbitrary manifold. For damage classification or localisation, ML classifiers have been used [4], yielding quite good accuracy. The main drawback of these methods is that data from damage states is required to perform their tasks. Oftentimes however, data from damaged states are absent, or only limited samples are available. Furthermore, to perform tasks further up in Rytter's hierarchy, understanding of the underlying physics of structures and damage mechanisms is needed.

Trying to understand the underlying physics within such a context, one may attempt to study a black box model that is performing well on a task related to the underlying mechanism of the problem. A representative example of such a case is a model trained on patient data [5] that was able to predict schizophrenia with adequate precision. It is clear then that it may be worth

spending some time studying the model in an attempt to understand better how schizophrenia works and which symptoms indicate its existence. The same scheme may be applied on structures with models trained on identifying damage location/type. A black-box model like a neural network [6] may be exploited to understand the way some type of damage affects a structure.

A specific type of black-box model that is targeted to capturing the physics of a specific problem, is the generative model. More specifically, Generative Adversarial Networks (GANs) [7] and Variational Autoencoders (VAEs) [8] are neural networks that learn how to generate data that look like reality. It is believed that, by studying these types of neural networks and the way they produce data, further understanding of the underlying problems may be achieved. In the current work, a specific type of GAN is used, the infoGAN [9]. This specific type of network achieves a disentanglement in the latent feature space of the data which may have great benefits in an SHM application. The use of such networks is considered in the task of classifying data from structures and also in defining latent variables that explain the extent of damage in the data or the variation of a parameter affecting the behaviour of the structure.

2 Generative Adversarial Networks (GANs)

2.1 Vanilla GANs

The traditional scheme followed in ML is the training of a model to perform classification [6] or regression [10]. To extend this to images, convolutional neural networks were developed [11] yielding superior performance in the two mentioned tasks. Recently, a new type of neural network has emerged, the *Generative Adversarial Network* [7]. The goal of this new scheme is to generate images that resemble reality, which is achieved via use of *two* neural networks. The first one is termed the *generator* and produces "fake" images given a latent vector. The second network is the *discriminator*, which tries to identify whether an image is fake (generated by the generator) or real (coming from the available dataset). Through training both of these networks, improve in reaching their objective and finally, the generator, provided with some latent vector, can generate images that appear to be real. More intuitively, this means that the generator maps a latent vector distribution into a distribution or a manifold of the real data. The layout of the basic (vanilla) GAN can be seen in Figure 1.

The generator is a multi-layer perceptron (MLP) that takes as input a latent noise vector $\mathbf{z}$ coming from a probability distribution $p_z(\mathbf{z})$ and maps it into a vector (or an image) $G(\mathbf{z})$ of dimension equal to the dimension of the training samples. The discriminator is another MLP that takes as inputs, vectors (or images) $\mathbf{x}$, and outputs the probability of the sample being real, $P(\mathbf{x} = real) = D(\mathbf{x})$. The training of D is carried out by maximising the probability that it assigns the correct label ("real" or "fake") to the samples. At the same time, the training of the generator, G, is accomplished by trying to minimise the probability that the discriminator classifies the generated samples as fake, i.e. minimisation of $log(1 - D(G(z)))$. Following from [7], the objective function can be interpreted as a two player minmax game given by,

$$\min_G \max_D V(D,G) = \mathbb{E}_{\mathbf{x}\sim p_{data}(\mathbf{x})}[\log D(\mathbf{x})] + \mathbb{E}_{\mathbf{z}\sim p_z(\mathbf{z})}[\log 1 - D(G(\mathbf{z}))] \tag{1}$$

Training of such a network is performed in two steps per epoch. During the first step, random samples are created by the generator and they are concatenated with a batch of real samples from the dataset. The resulting training batch is used to train the discriminator for one epoch by

back-propagating the error of the output. The target label for the real samples is 1 and for the generated ones is 0. The right-hand side of equation (1) is set in this step as the objective function and its **maximisation** is attempted. Consequently, the two networks are clipped together, as in Fig 1, and random samples of the latent vector are generated in order to create random generated samples. These samples are fed into the whole GAN and the target outputs are labels of 1. The weights of the discriminator's connections are considered as constants during the second training phase and the error is back-propagated in order to train the generator. This latter time, the objective function is comprised exclusively from the second term of the right-hand side of equation (1) and its **minimisation** is sought. Following this training scheme, during the first step the discriminator learns to distinguish between real and generated images and the generator to generate images that the discriminator classifies as real.

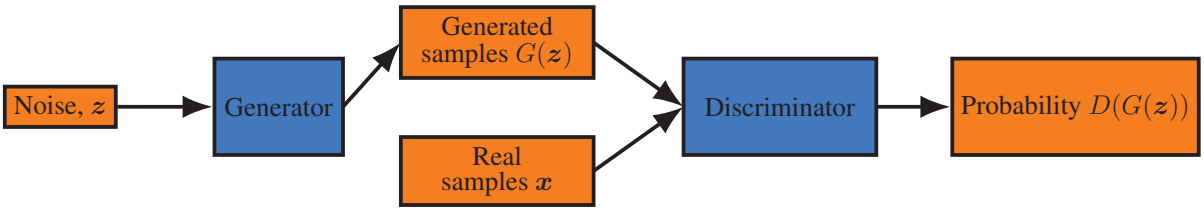

Figure 1: Vanilla GAN layout.

The most straightforward application of GANs is to generate artificial data to augment a dataset. Training neural networks is highly dependent on the size of the available dataset. The rule-of-thumb for training neural networks that generalise well [12], specifies that for each trainable weight of the neural network, 10 training samples are needed. Acquiring data is difficult and some times even expensive. Labelled images are hard to be obtained and their manual labeling costs. In cases of image datasets, augmentation can also be achieved by rotation of the pictures or colour change etc. In SHM though, the securing of data from structures in different damage cases or under different environmental conditions is expensive or even impossible; the samples are usually limited and augmentation is not that easy. For this purpose, GANs can be used to increase the size of a dataset and may even serve as interpolators. Especially for deep networks and even more for deep convolutional neural networks, where the number of trainable parameters is huge, augmentation of available dataset size could yield an efficient way to increase the generalisation performance of models [13].

Another use of GANs is found in filling gaps in pictures [14, 15]. In this case, GANs trained on a dataset are able to use pictures with missing pixels and generate a complete picture by replacing missing pixels with something that fits well in the gap. This is a great example of how this type of model may assist in repairing corrupted datasets. At the same time, these results are encouraging the perspective that GANs achieve a better linkage of data to the driving physics (or semantics) than traditional neural networks, since they are able repair corrupted data that they have never seen before.

Furthermore, GANs are applied in image processing [16, 17, 18]. This application is also an impressive usage of GANs, since they are able to capture through their latent variables, specific features of the data. Afterwards, the users are able to manipulate the latent vectors and use the generator to produce images, whose characteristics fit custom needs. A similar approach in the current work is followed and an attempt is performed to capture in the latent code the extent and type of damage in a structure. The ability to describe such features through a latent vector

and generate data corresponding to specific damage cases or to the extent of damage would be beneficial for the purposes of SHM, since further progress related to the fourth and fifth steps in Rytter's hierarchy could be achieved.

2.2 Information Maximising Generative Adversarial Nets

According to the classic formulation of GANs described, the latent variables used as inputs in the generator do not encapsulate any specific features from the data. This is because no restriction is imposed during training that every variable would describe a specific feature, resulting in latent noise variables that correspond to entangled features or combinations of features. In order to improve performance regarding the representation of disentangled features by the latent variables, a slightly different architecture and training scheme is followed in [9], called *Information Maximising Generative Adversarial Nets* (InfoGAN).

The procedure followed to enforce this disentanglement will be described below. At first, the latent vector is divided into two parts, the latent noise $\mathbf{z}$ and the latent code $\mathbf{c}$. The noise part $\mathbf{z}$ is used to model noise that may be present in the data, while the latent code $\mathbf{c}$ is used to represent interpretable features of the data. Following [9], the output of the generator becomes $G(\mathbf{z}, \mathbf{c})$. In order for the latent code $\mathbf{c}$ to have a meaning, there should be high mutual information between the code $\mathbf{c}$ and the generator distribution $G(\mathbf{z}, \mathbf{c})$, i.e. $I(\mathbf{c}; G(\mathbf{z}, \mathbf{c}))$. The term $I(c; G(\mathbf{z}, \mathbf{c}))$ represents the amount of information learnt from knowledge of $G(\mathbf{z}, \mathbf{c})$ about $\mathbf{c}$ and can be calculated using two entropy terms from,

$$I(\mathbf{c}; G(\mathbf{z}, \mathbf{c})) = H(\mathbf{c}) - H(\mathbf{c}|G(\mathbf{z}, \mathbf{c})) = H(G(\mathbf{z}, \mathbf{c})) - H(G(\mathbf{z}, \mathbf{c})|\mathbf{c}) \tag{2}$$

where $H(\mathbf{x})$ and $H(\mathbf{x}|\mathbf{y})$ are the entropy of the random variable $\mathbf{x}$ and the conditional entropy of $\mathbf{x}$ given $\mathbf{y}$, respectively.

Trying to get further insight into equation (2), one realizes the reduction of uncertainty about $\mathbf{c}$ when $G(\mathbf{z}, \mathbf{c})$ is observed. If the two variables are completely independent, then the term is equal to zero. So for the maximisation of (2), given $\mathbf{x} \sim P_G(x)$, $P_G(\mathbf{c}|\mathbf{x})$ should have small entropy. Trying to maximise this term, enforces a deterministic relationship between the two variables. To include this quantity in the optimisation process, the following modification is made in the cost functions from equation (1),

$$\min_G \max_D V_1(D, G) = \min_G \max_D V(D, G) - \lambda I(\mathbf{c}; G(\mathbf{z}, \mathbf{c})) \tag{3}$$

In practice though, maximisation of $I(\mathbf{c}; G(\mathbf{z}, \mathbf{c}))$ is non-trivial, as one has no access to the

posterior $P_G(\mathbf{c}|\mathbf{x})$. To avoid maximising it directly, an auxiliary distribution $Q(\mathbf{c}|\mathbf{x})$ is defined,

$$
\begin{aligned}
I(\mathbf{c}; G(\mathbf{z}, \mathbf{c})) &= H(\mathbf{c}) - H(\mathbf{c}|G(\mathbf{z}, \mathbf{c})) = \\
&\mathbb{E}_{\mathbf{x}\sim G(\mathbf{z},\mathbf{c})}[\mathbb{E}_{\mathbf{c}\sim P(\mathbf{c}|\mathbf{x})}[\log P(\mathbf{c}|\mathbf{x})]] + H(\mathbf{c}) = \\
&\mathbb{E}_{\mathbf{x}\sim G(\mathbf{z},\mathbf{c})}[\mathbb{E}_{\mathbf{c}\sim P(\mathbf{c}|\mathbf{x})}[\log \frac{P(\mathbf{c}|\mathbf{x})}{Q(\mathbf{c}|\mathbf{x})} Q(\mathbf{c}|\mathbf{x}))]] + H(\mathbf{c}) = \\
&\mathbb{E}_{\mathbf{x}\sim G(\mathbf{z},\mathbf{c})}[\mathbb{E}_{\mathbf{c}\sim P(\mathbf{c}|\mathbf{x})}[\log \frac{P(\mathbf{c}|\mathbf{x})}{Q(\mathbf{c}|\mathbf{x})}] - \mathbb{E}_{\mathbf{c}\sim P(\mathbf{c}|\mathbf{x})}[\log Q(\mathbf{c}|\mathbf{x}))]] \\
&+ H(\mathbf{c}) = \\
&\mathbb{E}_{\mathbf{x}\sim G(\mathbf{z},\mathbf{c})}[\underbrace{D_{KL}(P(\cdot|\mathbf{x})||Q(\cdot|\mathbf{c}))}_{\geq 0} - \mathbb{E}_{\mathbf{c}\sim P(\mathbf{c}|\mathbf{x})}[\log Q(\mathbf{c}|\mathbf{x}))]] \\
&+ H(\mathbf{c}) \\
&\geq \mathbb{E}_{\mathbf{x}\sim G(\mathbf{z},\mathbf{c})}[\mathbb{E}_{\mathbf{c}\sim P(\mathbf{c}|\mathbf{x})}[\log Q(\mathbf{c}|\mathbf{x})]] + H(\mathbf{c})
\end{aligned}
\tag{4}
$$

The technique of maximising the lower bound of the mutual information is called Variational Information Maximisation [19]. In equation (4) the quantity to be maximised is the first term of the final formula, since $H(\mathbf{c})$ is a constant and has an analytical form and a common distribution is chosen for $\mathbf{c}$. To avoid sampling from the posterior in the inner expectation of the expression in equation (4), the **Lemma 5.1** of [9] is used; according to which, for random variables X, Y and functions $f(x, y)$ under suitable regularity conditions it applies that: $\mathbb{E}_{x\sim X, y\sim Y|x}[f(x,y)] = \mathbb{E}_{x\sim X, y\sim Y|x, x\sim X|y}[f(x,y)]$. Following this result a variational lower bound, $L_1(G, Q)$, of the mutual information $I(\mathbf{c}; G(\mathbf{z}, \mathbf{c}))$ is defined,

$$
\begin{aligned}
L_1(G, Q) &= \mathbb{E}_{\mathbf{x}\sim G(\mathbf{z},\mathbf{c})}[\mathbb{E}_{\mathbf{c}\sim P(\mathbf{c}|\mathbf{x})}[\log Q(\mathbf{c}|\mathbf{x})]] = \\
&\mathbb{E}_{\mathbf{c}\sim P(\mathbf{c}), \mathbf{x}\sim G(\mathbf{z},\mathbf{c})}[\log Q(\mathbf{c}|\mathbf{x})] + H(\mathbf{c}) \leq I(\mathbf{c}; G(\mathbf{z}, \mathbf{c}))
\end{aligned}
\tag{5}
$$

In equation (5), the quantity to be maximised is the log-probability of the auxiliary distribution Q. In practice Q is modeled using a neural network. The newly-defined neural network is part of the discriminator network of the vanilla GAN. By defining the neural network Q, maximisation of the quantity in equation (5) is performed by back-propagating its error.

In the categorical case, in order to maximise $\log Q(\mathbf{c}|\mathbf{x})$ by training Q, the output is given by a softmax function and the categorical-crossentropy loss function gives the desired results. In the case of a continuous code $\mathbf{c}$, a maximum likelihood estimation (MLE) scheme has to be followed. The outputs of the neural network are two for each continuous code c_i; one for the mean value of the code and one for the variance. Afterwards, the loss function to be maximised is the mean log probability of all the outputs corresponding to the continuous code inputs. Assuming that $\mathbf{c}$ comes from a Gaussian distribution and that the variables c_i are independent, the loss function is

given by,

$$\log[Q(\mathbf{c}|\mathbf{x})] = \log[\prod_{i=1}^{n_c} P(c_i)] = \sum_{i=1}^{n_c} \log P(c_i) = \\ \sum_{i=1}^{n_c} [-\frac{1}{2}\log(2\pi\sigma_i^2) - \frac{(c_i-\mu_i)^2}{\sigma_i^2}] \propto \sum_{i=1}^{n_c} [-\log(\sigma_i) - \frac{(c_i-\mu_i)^2}{\sigma_i^2}] \tag{6}$$

In equation (6), c_i corresponds to the input value in the neural network and μ_i, σ_i are the mean and variance of each distribution of the code c_i. An overview of the network architecture of the infoGAN is shown in Fig 2. It becomes clear that the logic behind this architecture is that a sample is generated by the generator; it should look real, so that the discriminator classifies it as real and the parameters of the code **c** that were used to generate it should be as distinguishable as possible by the auxiliary neural network Q. Following this scheme, the infoGAN is expected to generate samples belonging to different classes (or manifolds) using different categorical codes $\mathbf{c}_{cat}$ and to explain the variability of features within the classes, using the continuous code $\mathbf{c}_{cont}$. Also, some random noise is added via **z** because as usual, noise in the data exists and should be modelled.

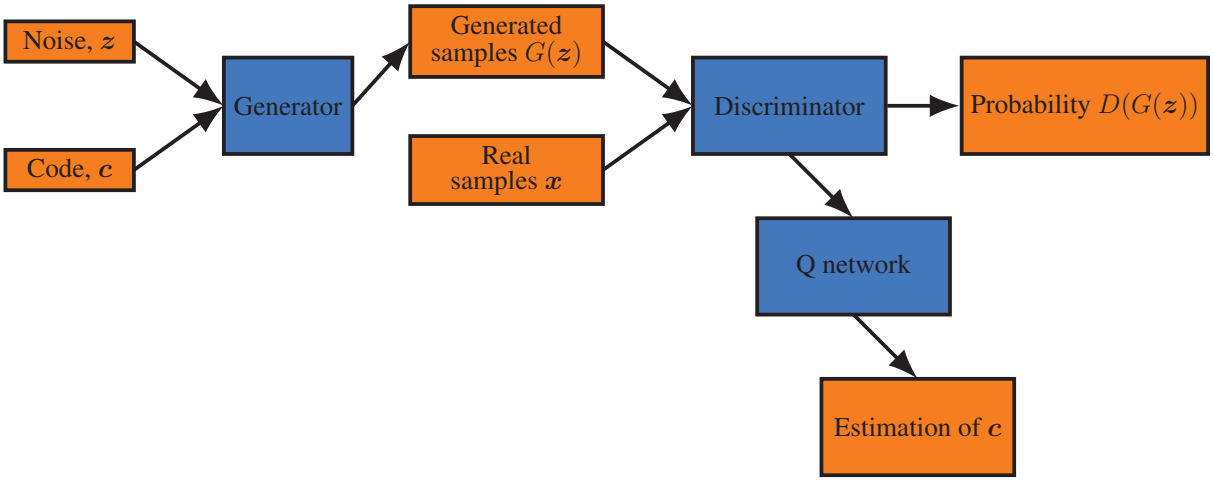

Figure 2: InfoGAN layout.

3 Application on simulated data

3.1 Simulation description

For the application of GANs to structural data, a simple simulated linear six-degree-of-freedom lumped mass system is examined. The masses of the system were all equal to one, the stifness of the undamaged states of the springs equal to 10^4 and a diagonal damping matrix was assumed with its elements equal to 25. The system was simulated using a fourth-order Runge-Kutta integration scheme. The excitation was a white noise signal applied on the first mass. In order to introduce different levels of damage in the structure, stiffness reductions were applied on springs 1-2, 2-3, 3-4 and 4-5. The reducted stifnesses came from normal distributions with mean values of 80% of the initial values of the system and variance equal to 4.5% of the initial stiffness of each spring.

In each simulation the *transmissibilities* between masses 1-2, 2-3, 3-4 and 4-5 were calculated, concatenated and considered as the samples representing each simulation. The normal condition concatenated transmissibilities are shown in Figure 4. Transmissibilities are a useful tool in monitoring real structures, where one has no knowledge about the input excitation to a dynamical system, in order to calculate the *frequency response function* (FRF). The sampling frequency of the simulation was $200Hz$; each transmissibility consists of 512 spectral lines and noise with variance equal to 5% of the transmissibility's variance was added to each one of them. In order to visualise the data, a *principal component analysis* (PCA) [20] was performed on the data and the first three principal components were plotted. In Figure 5 each batch/manifold of points corresponds to a different damage case. Moreover, through the gradual colour transition, the different damage levels are shown. A yellow colour represents points with low damage level (5-7.5% stiffness reduction) and dark red points correspond to higher damage levels (32-35%).

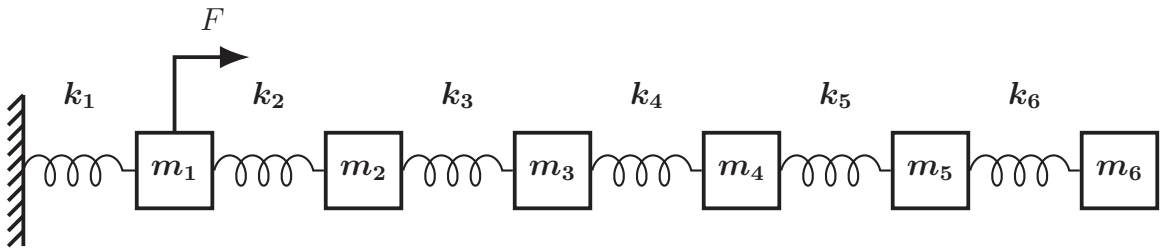

Figure 3: Mass-spring system.

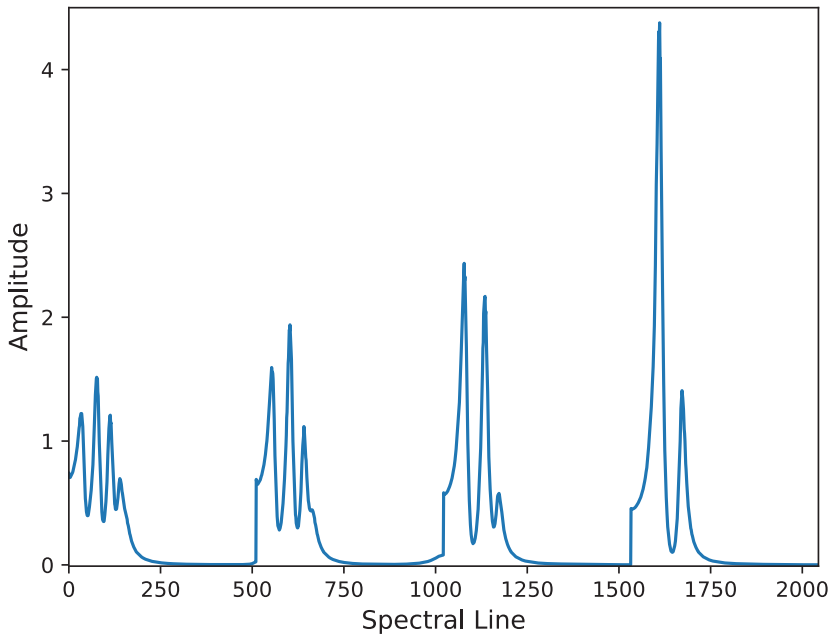

Figure 4: Normal condition concatenated transmissibilities.

Each damage case affects the transmissibilities in a different way. To be able to judge the results of the GANs to be trained consequently, an illustration of influence of that stiffness reduction on the transmissibilities is offered in Figure 6. Each different colour line corresponds to different

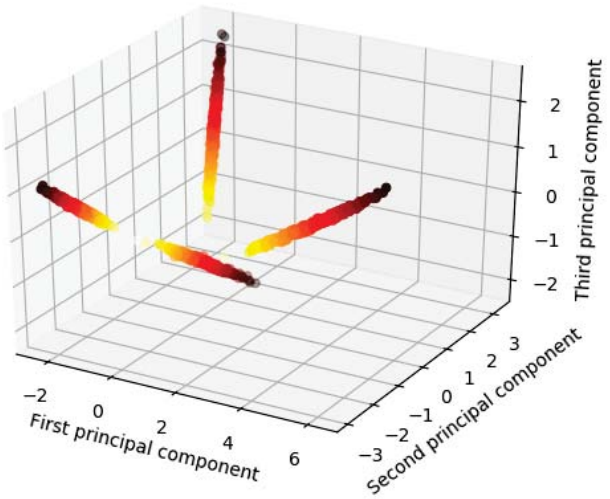

Figure 5: First three principal components of simulated transmissibilities. Gradual colour change from yellow to dark red represents lower to higher damage levels respectively.

damage level and the "movement" of the diagram as the damage extent increases is depicted. Damage induced in different springs causes similar effects to the one shown in Figure 6, but in different areas of the diagram.

3.2 InfoGAN training

The infoGAN was trained on the five first principal components of the data (explaining 99% of the variance) in order to reduce both training time and trainable parameters of the networks. Since the PCA transformation is linear, the infoGAN training is not considered to be assisted by it in any way other than the dimensionality reduction. In the input layer of the generator, two latent variables z_i sampled from a Gaussian distribution $z \sim N(0, 1)$ were used because noise is present in the data. Four categorical variables $c_{i,cat}$ sampled with equal probability were also used, since there are four different damage cases and one continuous c_{cont}, sampled also from a Gaussian distribution similar to the previous one. The expected result is that the generator should be able to generate samples corresponding to the different damage cases by altering the categorical variables and also corresponding to the damage extent by varying the continuous latent variable.

The discriminator was chosen to be a neural network with two hidden layers comprising 60 and 30 nodes and an output layer. The generator was also defined as a neural network with two hidden layers of 100 and 15 nodes and an output layer with five nodes. The ideal size of the networks is not considered to be the object of the current work, therefore, choosing the best architecture is not examined and was simply performed by trying different architectures manually and selecting the ones that had satisfying results in terms of the value of the loss function. The networks were initialised several times and the one with the lowest value for the loss function was kept. In contrast to vanilla GANs, where the value of the objective function oscillates during training, the value of the regularisation term in the loss function of infoGANs (4) gets lower by training and selection of the network with the lowest value of the cost function is a legitimate

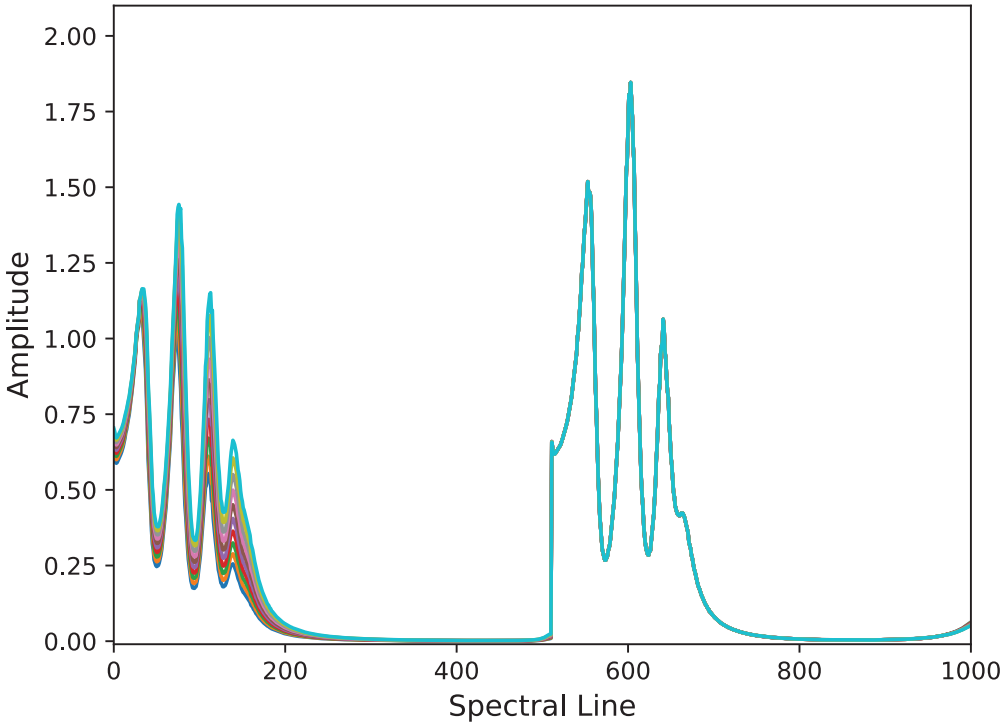

Figure 6: First damage case samples, focused on the first transmissibility, which is affected by the damage. Different colours reflect gradually increasing damage level, from cyan (no damage) to blue (highest damage level).

strategy.

Having trained the generator, random samples are generated and studied. For each categorical variable, 1000 samples were generated varying the continuous c_{cont} in the interval $[-2.0, 2.0]$ and generating random values for the latent noise vector $\mathbf{z}$. In Figure 7. It is clear that the generated points are quite close to the areas of the original points. It is also clear that each categorical variable forces the generated points to belong to different clusters of the data, as long as the manifolds of these clusters are not connected.

3.3 Classification and regression using GANs

In order to exploit the results of training a GAN, apart from generating artificial data, two more use cases are examined. The first one is classification of the data and the second one is a regression scheme; both in an unsupervised manner. The algorithm so far required minimal supervision for the results above. The only supervised part of the algorithm was the definition of the number of noise, categorical and continuous variables in the latent space.

For the classification process, random samples are generated in the principal component space for each categorical variable separately. Subsequently, for each sample in the original dataset the closest generated point is sought in terms of the Euclidean distance between the points. The class assigned to the sample from the dataset is the class of the categorical variable that was used to generate the closest point to the sample. Following this procedure for every point in

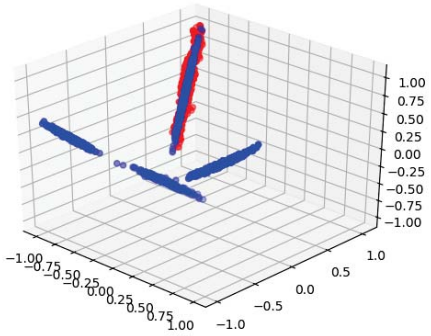

(a) First categorical variable.

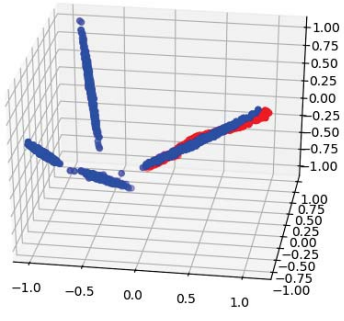

(b) Second categorical variable.

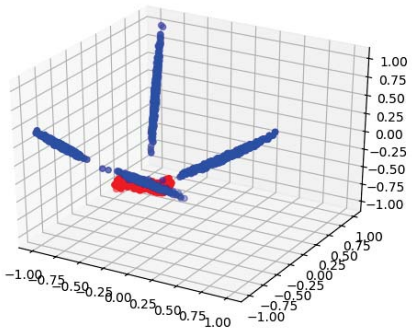

(c) Third categorical variable.

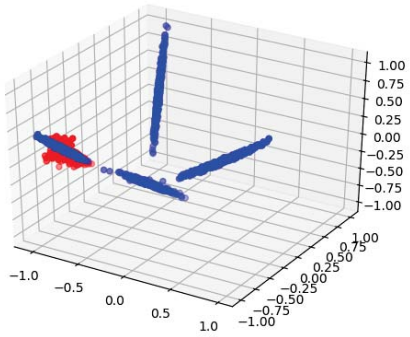

(d) Fourth categorical variable.

Figure 7: Generated points (red) and original points (blue) using different categorical variables.

the dataset, the result of the classification is shown in Figure 8a. Each colour corresponds to a different cluster assigned by the algorithm. The classification is perfect, as each point is classified correctly. In order to contrast performance against a more trivial unsupervised classification algorithm, a K-means clustering algorithm [21] is also applied on the same dataset and the results are shown in Figure 8b. It is clear that there are some misclassified points using the K-means algorithm.

Regarding the regression scheme, the captured variance from the continuous variable is examined. In order to illustrate what the continuous variable has captured, more samples were generated this time with the noise latent variables z considered constant and equal to zero. Again for each categorical variable, several samples were generated by using different values for the continuous variable in the interval $[-3.0, 3.0]$. The results are shown in Figure 10. The variable has captured some of the physics, explaining how the extent of damage affects the transmissibilities but the fit is not perfect. By generating samples in the principal component space and transforming them back to the original space, the effect of varying the continuous and the categorical code can be illustrated. In Figure 9 the transmissibilities generated the way mentioned above are shown for the categorical variable that corresponds to the first damage case. It is clear that the continuous variable has the same effect on the diagram as the same "movement" occurs as in the one with

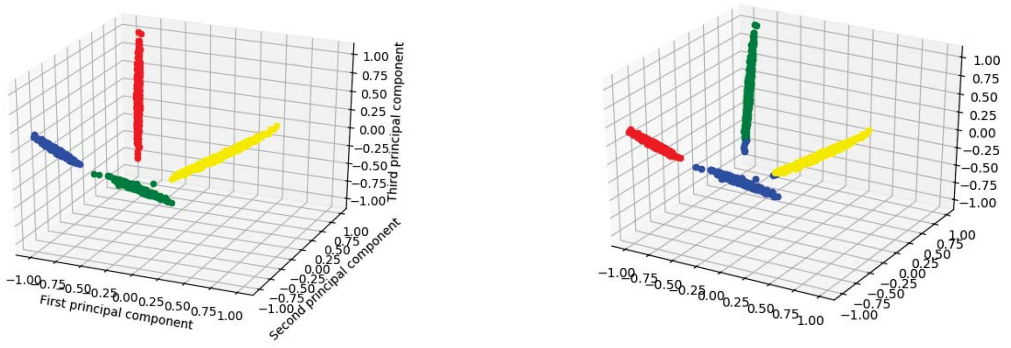

(a) (b)

Figure 8: Results of the classification procedure using the GAN generator (left) and a K-means algorithm (right).

different damage extents in Figure 6. Similar behaviour is observed with the rest of the damage cases.

4 Conclusions

Summarising, this work demonstrates that there exist certain benefits in using GANs, and more specifically infoGANs, in SHM. Using simulated data, it was illustrated that an infoGAN with only prior knowledge of the number of different states of the structure is able to fit latent variables in the distribution of the real data. Being trained on the data, the algorithm could be used to classify the samples according to the categorical variables defined and at the same time to produce artificial samples in a desired class. Furthermore, the continuous variable was able to capture an underlying varying feature of the data, that of the extent of damage. As before, samples could be generated by altering the continuous variable, while keeping the categorical variable constant. This way, the effect of the level of damage was observed on the generated *transmissibilities*. It could be stated that the infoGAN is imitating the damage mechanism through the continuous code variables and such a scheme could be followed with a view to understanding how damage mechanisms affect specific structures.

Since the GAN is an artificial intelligence algorithm, the results it yields should be evaluated in this context. In artificial intelligence, the goal is for algorithms to perform as good as human intelligence would and if possible, outperform it. In the case of classifying points in a feature space, human-like behaviour is quite similar to the way infoGANs cluster data. A human examining this data, in order for two batches of points to belong in different clusters, their manifolds should be disjoint. The infoGAN exhibits a similar behaviour, as for it to generate points using different categorical variables, the real points should belong in two unconnected manifolds. Under this assumption, the algorithm's performance is quite good, since it classifies points the same way a human would and can moreover perform it in multidimensional spaces, which humans usually are not able to perceive and process.

Focusing on SHM and damage detection, if damage occurs gradually, the points representing the status of the structure smoothly moves in space as a function of the damage extent. In this case the infoGAN algorithm should be able to capture this change through a continuous latent

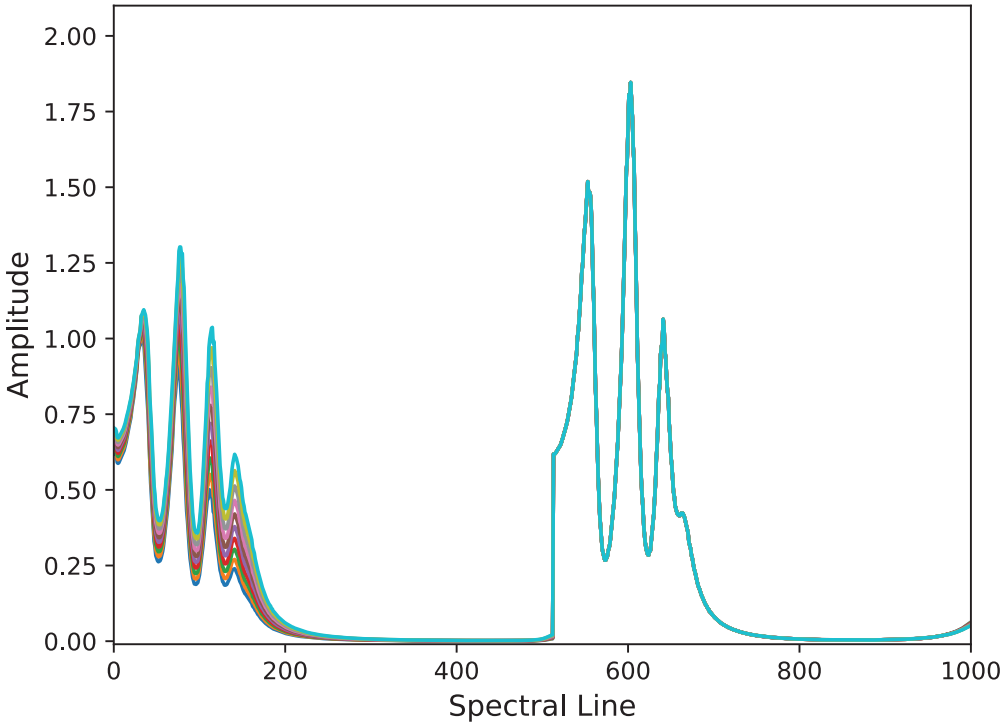

Figure 9: Generated samples, using a single categorical variable, corresponding to the first damage case and varying the continuous variable, focused on the first transmissibility, which is affected by the damage. Different colours reflect gradually increasing damage level, from cyan (lower damage level) to blue (higher damage level).

variable. If damage occurs suddenly, the infoGAN might be able to capture it as a different cluster through its categorical variables. At the same time, generation of artificial data for different clusters or values of underlying variables as damage extent is possible. In cases of continuous monitoring of structures, some varying environmental conditions in the acquired data may be captured. In this case, the infoGAN should also be able to capture the variation of the parameters in its continuous variables. This observation points out a potential use of infoGANs in large databases in order to define trends and different clusters of data caused either by damage or benign changing environmental conditions.

Acknowledgements

The authors would like to acknowledge the support of the European Union (EU). G.T is supported by funding from the EU's Horizon 2020 research and innovation programme under the Marie Sklodowska-Curie grant agreement DyVirt (764547). The authors also gratefully acknowledge the support of the UK Engineering and Physical Sciences Research Council (EPSRC) through grant references EP/R003645/1, EP/R004900/1 and EP/S001565/1.

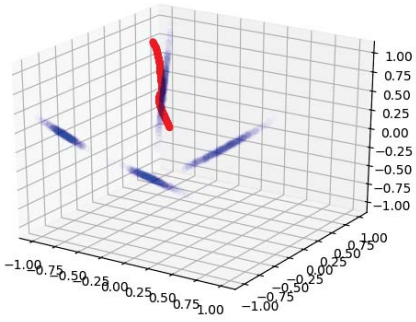

(a) First categorical variable.

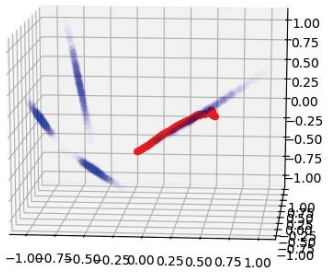

(b) Second categorical variable.

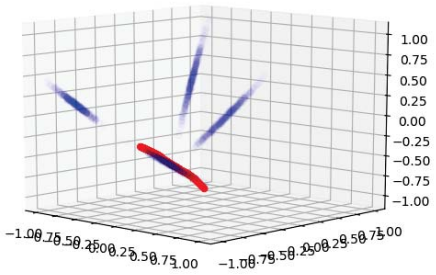

(c) Third categorical variable.

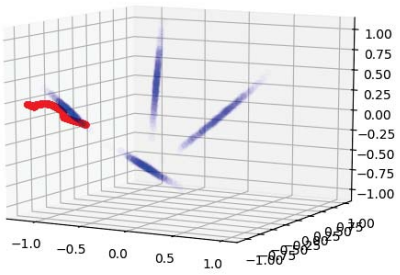

(d) Fourth categorical variable.

Figure 10: Generated points (red) and original points (blue) using different categorical variables, constant noise variable equal to zero and varying the continuous code variable in the interval $[-3.0, 3.0]$.

REFERENCES

[1] A. Rytter, Vibrational based inspection of civil engineering structures, Ph.D. thesis (1993).

[2] C. R. Farrar, K. Worden, Structural Health Monitoring: A Machine Learning Perspective, John Wiley & Sons, 2012.

[3] K. Worden, Structural fault detection using a novelty measure, Journal of Sound and Vibration 201 (1) (1997) 85–101.

[4] G. Manson, K. Worden, D. Allman, Experimental validation of a structural health monitoring methodology: Part III. Damage location on an aircraft wing, Journal of Sound and Vibration 259 (2) (2003) 365–385.

[5] R. Miotto, L. Li, B. A. Kidd, J. T. Dudley, Deep patient: An unsupervised representation to predict the future of patients from the electronic health records, Scientific Reports 6 (1) (May 2016).

[6] C. M. Bishop, Neural Networks for Pattern Recognition, Oxford University Press, Inc., New York, NY, USA, 1995.

[7] I. Goodfellow, J. Pouget-Abadie, M. Mirza, B. Xu, D. Warde-Farley, S. Ozair, A. Courville, Y. Bengio, Generative adversarial nets, in: Advances in neural information processing systems, 2014, pp. 2672–2680.

[8] D. P. Kingma, M. Welling, et al., An introduction to variational autoencoders, Foundations and Trends in Machine Learning 12 (4) (2019) 307–392.

[9] X. Chen, Y. Duan, R. Houthooft, J. Schulman, I. Sutskever, P. Abbeel, Infogan: Interpretable representation learning by information maximizing generative adversarial nets, in: Advances in Neural Information Processing Systems, 2016, pp. 2172–2180.

[10] D. F. Specht, A general regression neural network, IEEE transactions on neural networks 2 (6) (1991) 568–576.

[11] A. Krizhevsky, I. Sutskever, G. E. Hinton, Imagenet classification with deep convolutional neural networks, in: Advances in Neural Information Processing Systems, 2012, pp. 1097–1105.

[12] L. Tarassenko, Guide to Neural Computing Applications, Elsevier, 1998.

[13] M. Frid-Adar, I. Diamant, E. Klang, M. Amitai, J. Goldberger, H. Greenspan, GAN-based synthetic medical image augmentation for increased cnn performance in liver lesion classification, Neurocomputing 321 (2018) 321–331.

[14] D. Pathak, P. Krahenbuhl, J. Donahue, T. Darrell, A. A. Efros, Context encoders: Feature learning by inpainting, in: Proceedings of the IEEE conference on computer vision and pattern recognition, 2016, pp. 2536–2544.

[15] Y. Li, S. Liu, J. Yang, M.-H. Yang, Generative face completion, in: Proceedings of the IEEE Conference on Computer Vision and Pattern Recognition, 2017, pp. 3911–3919.

[16] G. Perarnau, J. Van De Weijer, B. Raducanu, J. M. Álvarez, Invertible conditional GANs for image editing, arXiv preprint arXiv:1611.06355 (2016).

[17] A. Brock, T. Lim, J. M. Ritchie, N. Weston, Neural photo editing with introspective adversarial networks, arXiv preprint arXiv:1609.07093 (2016).

[18] H. Zhang, V. Sindagi, V. M. Patel, Image de-raining using a conditional generative adversarial network, IEEE transactions on circuits and systems for video technology (2019).

[19] D. Barber, F. V. Agakov, The IM algorithm: a variational approach to information maximization, in: Advances in Neural Information Processing Systems, 2003, p. None.

[20] K. Pearson, LIII. on lines and planes of closest fit to systems of points in space, The London, Edinburgh, and Dublin Philosophical Magazine and Journal of Science 2 (11) (1901) 559–572.

[21] J. MacQueen, et al., Some methods for classification and analysis of multivariate observations, in: Proceedings of the fifth Berkeley Symposium on Mathematical Statistics and Probability, Vol. 1, Oakland, CA, USA, 1967, pp. 281–297.

EURODYN 2020
XI International Conference on Structural Dynamics
M. Papadrakakis, M. Fragiadakis, C. Papadimitriou (eds.)
Athens, Greece, 23–26 November 2020

A NEAT APPROACH TO STRUCTURAL HEALTH MONITORING

G. Tsialiamanis[1], **D. J. Wagg**[1], **N. Dervilis**[1], **K. Worden**[1]

[1]Dynamics Research Group, Department of Mechanical Engineering, University of Sheffield,
Mappin Street, Sheffield S1 3JD

Keywords: Structural health monitoring, machine learning, neural networks, neuroevolution of augmenting topologies (NEAT).

Abstract. *In the current paper, an application of the neuroevolution of augmenting topologies (NEAT) algorithm is considered in a structural health monitoring (SHM) application. The algorithm is a variation of genetic algorithms, applied in neural networks, and has the goal of optimising both the topology and the weights and biases of a neural network model. The algorithm is applied here to an SHM problem instead of using feedforward neural networks. The algorithm is called to search for the best-fitting topology in the task, which would otherwise be sought through experimenting with the size and number of the layers of the neural network. Having used the algorithm, the accuracy is found to be close to the one achieved using classically trained neural networks. Another aspect of the application is that subnetworks were defined for every damage case of the problem, whose topologies are much simpler than a fully-connected feedforward neural network. These subnetworks define classification submodels that may be used in different combinations, building models for a subset of damage cases and input features.*

1 Introduction

Structures are essential elements of human everyday life. From living in houses to moving from one place to another, structures play a key role in activities that are vital for everyone and monitoring them is required in order to make sure that they operate in the way in which they were designed. A malfunctioning structure could cause various problems. A building that has been damaged endangers the lives of those that live within it. Malfunctioning wind turbines may produce reduced electrical energy or even collapse, having as a result huge economic costs. A damaged bridge that requires stopping traffic on it, results in huge delays and even bigger financial damage to people who need to cross the bridge as part of their business. Taking into account the potential consequences of failure of structures, the need to monitor them emerges.

The discipline of acquiring data from structures through sensors, processing them and inferring results about the health state of the structure is called *structural health monitoring* (SHM). There are several approaches to monitoring structures but the most dominant use *data-driven* or *machine learning* (ML) methods [1], in order to infer results about the data. The models created are, in general, black-box models that rely on existing data acquired from a structure. There are several tasks that such a model may be called on to perform; a hierarchical way of classifying these tasks is given by Rytter in [2]:

1. Is there damage (*existence*)?
2. Where is the damage in the system (*location*)?
3. What kind of damage is present (*type/classification*)?
4. How severe is the damage (*extent/severity*)?
5. How much useful (safe) life remains (*prognosis*)?

The first two tasks are the most simple ones and in the context of machine learning, they have been dealt with using quite simple approaches. In [3], Mahalanobis distances were calculated between the baseline condition of a structure and the condition that is tested for the existence of damage. More complicated and more robust approaches for detecting the existence of damage are given in [4]. Another novelty measure that indicates existence of damage is given in [5]; it is defined using autoencoders in order to describe the manifold to which the data of the normal condition of the structure belong. If some testing data belong to the same manifold, the samples are considered as healthy; otherwise, it is considered that damage exists in the structure and it should be examined. Regarding the second level of Rytter's hierarchy; in [6], neural networks have been used to localise damage in an aircraft wing. The neural network was trained to classify damage into nine location different classes, according to features that were extracted from sensors placed on the wing.

Neural networks are machine learning algorithms that can approximate any arbitrary function [7], that explains the relationship between some input and some output values. For this reason, they have been widely used in the context of SHM and in many other disciplines including natural language processing, computer vision, etc. A major drawback of neural networks is that they require large training datasets in order to generalise well on unseen data. Moreover, selecting their architecture involves hyperparameters that have to be tuned by the user with a view to creating a model that fits the training data and generalises well on testing data.

In the current work, an approach to avoid selecting the exact architecture of a neural network for

an SHM problem is studied. This approach is called *neuroevolution of augmenting topologies* (NEAT) [8]. According to this approach, a genetic algorithm scheme is followed to train the neural network weights and at the same time create its topology from scratch [9]. The mainstream approach of training a feed-forward neural network requires trying different numbers and sizes for the hidden layers. In the end, the neural network that performs best on the task that they were trained for is used. This may be considered a brute force search for the best architecture and sometimes may take a lot of time. In addition, the architectures that are tested through this approach follow a specific pattern and more complicated approaches are not considered. The algorithm is tested here on experimental data with the task of localising/classifying damage on a structure.

2 Training neural networks using genetic algorithms

2.1 Genetic algorithms

Genetic algorithms are widely used in many scientific disciplines; they are a means of optimisation of given objective functions, as explained in [10]. In engineering, such algorithms have been used in order to optimise the design of whole structures [11], according to a quantity of interest, or even to select the model that best describes some acquired data [12].

Genetic algorithms draw inspiration from the natural selection scheme that exists in nature; individuals - structures, models or whichever entity is set to be optimised - are initially born with random characteristics. Afterwards, their strength is calculated through a fitness function that reflects the quantity whose optimisation is sought. In every generation, individuals that do better according to the fitness function, survive, while the rest die. One of the most important aspects of a genetic algorithm is the creation of offspring. Couples of individuals that have survived, create offspring that inherit characteristics from both their parents and have a probability of a mutation in their characteristics. Following this framework, the population moves towards the areas in the parameter space that generate more appropriate values regarding the fitness function and through creation of offspring through mutation, the space is further explored. The individuals may be points in an n-dimensional space representing parameters of a model, or even whole structures. There are many variations on the described genetic algorithm but they all, more or less, follow this scheme.

One of the main reasons that genetic algorithms are chosen as an optimisation tool is that the quantities that are being optimised or minimised may be a function without a specific formula. A quite common way of optimising function parameter values is using gradient descent [13], a requirement of which is having a formula that needs to be minimised or maximised and also, the formula should be differentiable. Quite often, the quantity that needs to be optimised may be a discrete one, such as the accuracy of a model in terms of number of correct decisions.

Another aspect that makes genetic algorithms powerful, is that they are thought to be exploring the parameter space to a greater extent than other methods, including gradient descent. An ideal solution to the problem of finding the optimal value for some quantities of interest, would be an exhaustive search in the whole parameter space. Through this kind of search, finding the optimal solution/global minimum or maximum is ensured, but in most cases it is computationally intractable. In contrast, a gradient-descent search, will follow a single path in the parameter space that depends on the initial value of the parameters and on the gradient of the objective function on each point during search and may hit a local minimum. Using a genetic algorithm, discrete points in the parameter space are chosen and the ones that do better in optimising the

objective function survive. The population slowly moves towards the areas in space that optimise the objective function, but at the same time explores a bigger part of the space than the gradient descent, since mutations create many different points in space rather than following a single path. This property is also the reason that a genetic algorithm is less likely to get stuck in local minima/maxima.

In the context of neural networks, where gradient descent through backpropagation is the most common way of training, tuning the trainable parameters may be alternatively performed using a genetic algorithm [14]. Using this approach, local minima may be avoided and also the loss function does not need to be differentiable. According to this framework of training, the neural network still has a fixed architecture. This idea may not allow finding the optimal solution, since the optimal network architectures vary according to the task for which they are used. Since the topology/architecture of the network also affects its functionality, exploring the space of topologies along with the space of parameters would be convenient and so a different scheme is proposed in [8] -the neuroevolution of augmenting topologies.

2.2 Neuroevolution of augmenting topologies (NEAT)

Following the aforementioned approach, the architecture of the network is not predefined. To avoid a predefined topology and force the algorithm to search for the one that performs best in some task, an augmenting topology scheme is followed. Again, the general genetic algorithm is used, as random individual neural networks are generated. The initial state of networks is considered to be a totally unconnected network with some input and output nodes. The first population is formed by creating random connections between these nodes. A fitness function is defined and performance of each network is evaluated in every generation. Consequently, the procedures of genetic encoding, mutation and crossover between networks have to be defined.

2.2.1 Genetic encoding

In order to perform the operations needed for the evolution of the population, an encoding of each individual neural network is needed. This encoding is referred to as the *genome* or *genotype*, and the network it corresponds to is the *phenotype*, in parallel with human DNA being an encoding and the phenotype being the way this encoding is translated into human characteristics. For the purposes of the algorithm, the genome will be a list with the connections, called *genes*, that have been defined in the network with a chronological order. The list will increase in length as generations pass, since new connections will be defined due to mutations or crossover.

By defining a chronological order or *historical marking* as mentioned in [8], a global naming for every mutation that has happened is achieved. Since mutations will be happening at random within the population, it is plausible that the same mutation may occur more than once. In such a case, the genes that correspond to the same connection in the networks, should be identified as so. During crossover, if a historical marking exists in both parents, it should be inherited to the offspring. An example of a genome and its phenotype is shown in Figure 1, where the encoding of a network is shown. Using the historical markings, encoding of the same connection in many different genes, is avoided.

In: 1 Out: 5 Weight: 0.7 Bias: 0.3 Enabled Hist. marking: 1	In: 2 Out: 5 Weight: -0.5 Bias: 0.12 Enabled Hist. marking: 3	In: 3 Out: 4 Weight: -0.17 Bias: 0.92 Enabled Hist. marking: 5	In: 5 Out: 4 Weight: 1.22 Bias: 0.83 Enabled Hist. marking: 6

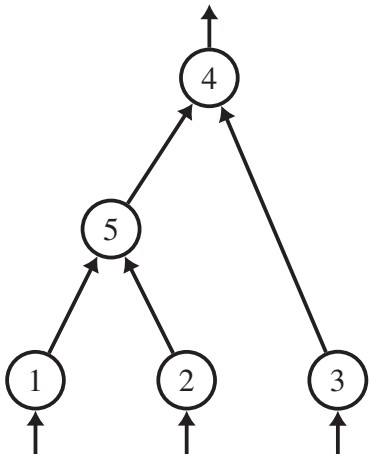

Figure 1: Example of a genome and the corresponding *phenotype* [8].

2.2.2 Mutation

One of the basic operations of a genetic algorithm is the mutation of individuals; this allows further exploration of the parameter space. In the case of NEAT, mutations should be able to explore both the network topology space and the parameter space of the networks. In order to explore the parameter space of the networks, mutations are allowed in the weights and biases of the connections and the activation and aggregative functions of nodes.

Mutations of the weights and biases are quite trivial. At the end of every generation, offspring have a probability of mutating a weight or a bias term from their connections. The mutations are simply changes in the values of the variables. The most common way of defining the new value is through sampling from a normal distribution with mean value μ equal to the current value of the parameter and a variance σ^2 that is defined by the user. This scheme introduces four hyper-parameters in the algorithm that the user has to define; the probabilities of a weight (p_w) or a bias mutation (p_b) and the power of the mutations or the variances (σ_w^2 and σ_b^2) of the distributions used to define the mutated value. Small values assigned to these hyper-parameters will result in a more thorough search in the parameter space, but also probably in a slower convergence of the algorithm.

The first mutation that applies to the topology of the networks is the *add connection* mutation; a connection is added between two nodes that so far have not been connected. Nodes and their IDs are shared amongst every individual in the population. Every network though has different connections defined in between the nodes and through this mutation type, new connections are defined within the mutated individual. The weight of the new connection is sampled from a random distribution and a historical marking is assigned to it. The opposite mutation should also be considered, the *disable connection*. This type of mutation, straightforwardly disables an existing connection in an individual. An example of how an add connection mutation is encoded

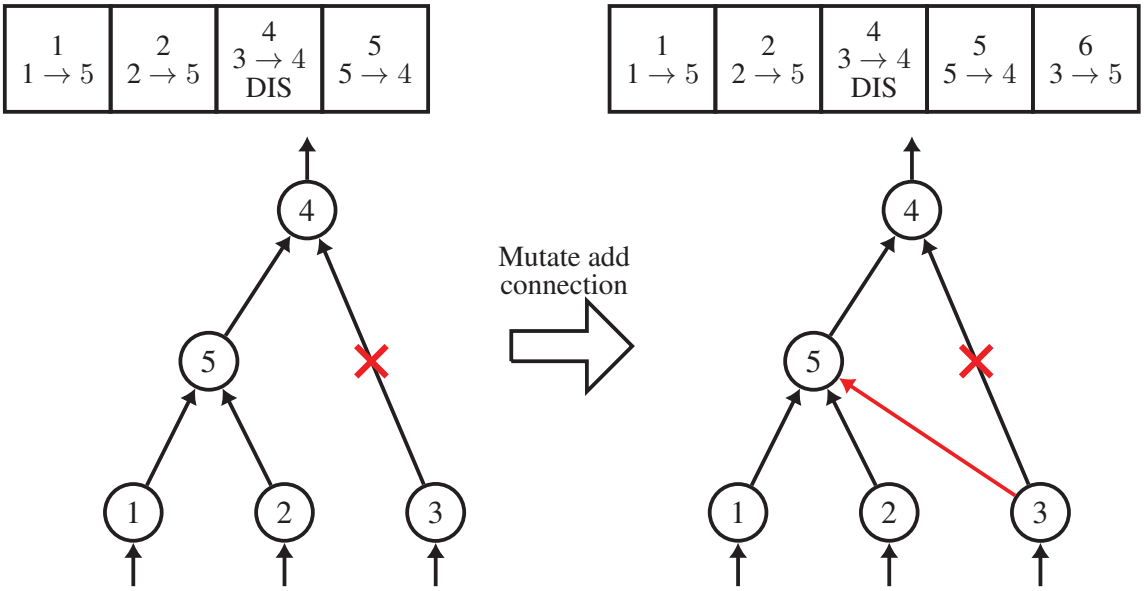

Figure 2: Example of an *add connection* mutation and the corresponding genome change [8].

is shown in Figure 2, where also a disabled connection is shown.

The second mutation regarding the topology is the *add node*, where a new node that did not exist so far is introduced. The way that such a node is added is by splitting an existing connection into two and placing a node between the two new ones. The old connection is disabled and the two new ones are added to the genome of the individual. The connection leading to the new node has a weight of 1 and the second one has weight equal to the weight of the old connection. The new node has a new ID and it is available in every individual to be connected through *add connection* mutations with other nodes. An example of the *add node* mutation is shown in Figure 3.

2.2.3 Crossover

Finally, the crossover operation is needed to completely define the genetic algorithm procedure. The crossover is performed using the genetic encoding of the networks. The genomes of the parents are placed in parallel according to the historical marking of each gene in the genomes. If a gene with a specific historical marking exists only within the genome of one parent, it is directly inherited to the offspring. If a gene with the same historical marking exists in both parents, it is inherited to the child by the most fit parent. An example is shown in Figure 4.

3 Application on experimental data

3.1 Experiment description

In order to test the algorithm, an experimental setup is considered [6]. The experiment is that of simulating damage on an aircraft wing. The wing was set in the laboratory and was excited with white noise using a shaker attached to its bottom surface. Sensors were placed on it as shown in Figure 5. The experiments were performed using the wing in both damaged and undamaged states. The damaged states were simulated by removal of one out of nine different wing panels. The panels that correspond to a different damage case are each shown in Figure 6.

The quantities that were recorded during the experiments with the damaged wing, were the

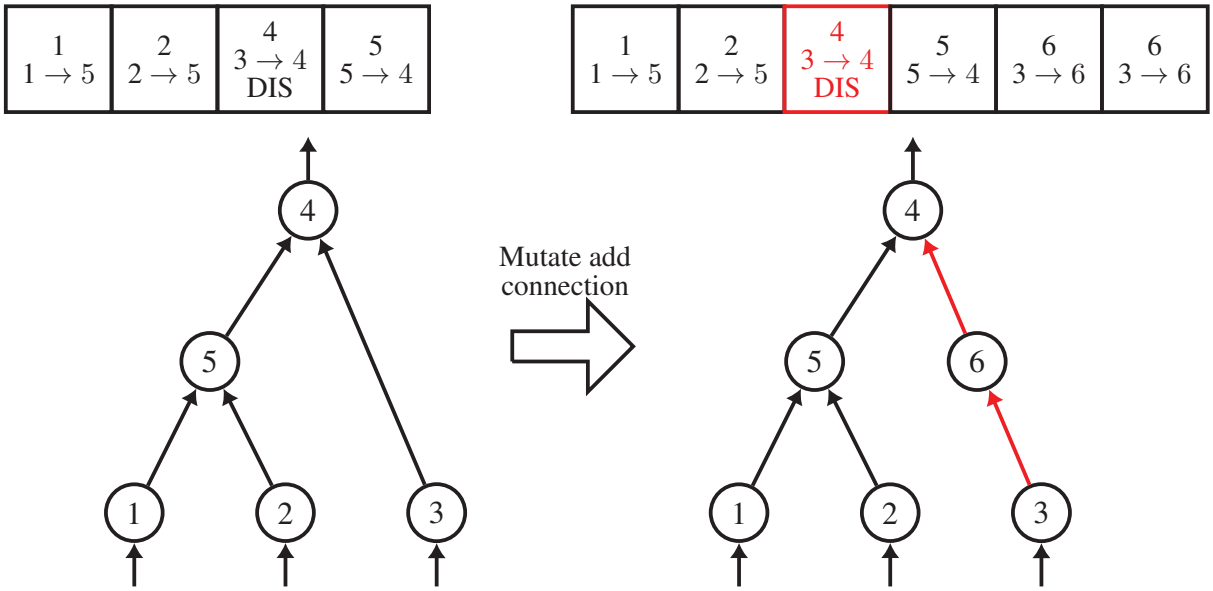

Figure 3: Example of an *add node* mutation and the corresponding genome change [8].

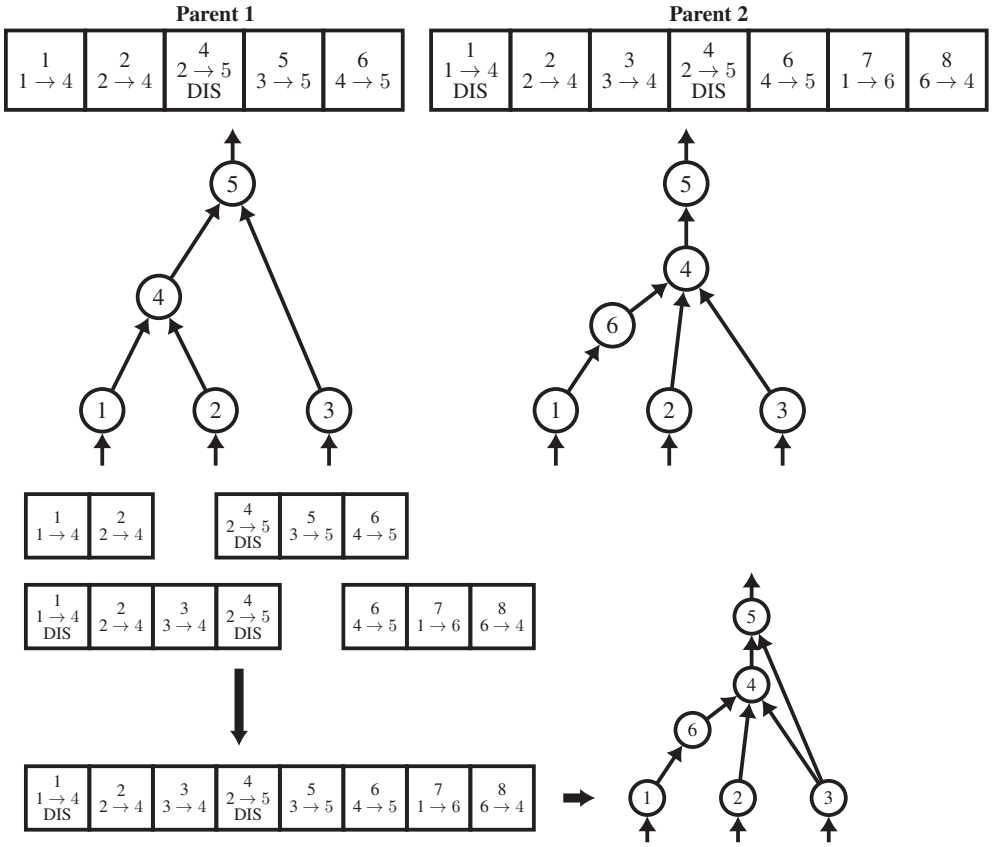

Figure 4: Crossover process given two parents and their genomes [8].

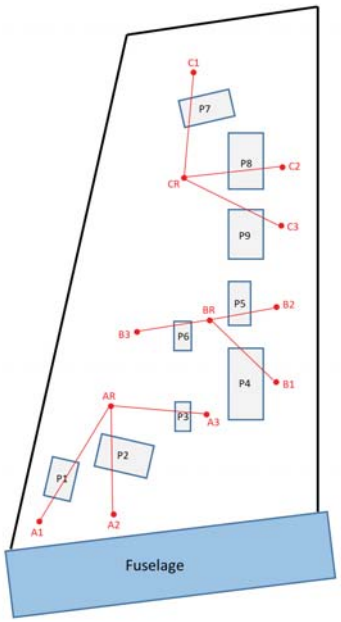

Figure 5: Configuration of sensors placed on the GNAT wing [6].

transmissibilities between two sensors. Transmissibilities are a quite useful feature, since knowledge about the excitation force is not required, in contrast to the case of a *frequency response function* (FRF). The transmissibilities were recorded between sensors AR and A1, A2 and A3 and similarly between the rest of the sets shown in Figure 5. This procedure resulted in nine different transmissibilities that were available for both the undamaged and the damaged states. Subsequently, intervals within the transmissibilities that were more sensitive to damage were identified "by eye"; this resulted in 72 different intervals and for each one of them, novelty indices were calculated between the normal condition transmissibilities and the testing cases. The novelty indices were calculated using the Mahalanobis distance,

$$D_{\zeta}^2 = (\mathbf{x}_{\imath} - \overline{\mathbf{x}})^T S^{-1} (\mathbf{x}_{\imath} - \overline{\mathbf{x}}) \tag{1}$$

where $\mathbf{x}_{\imath}$ is the sample whose Mahalanobis distance is calculated, $\overline{\mathbf{x}}$ is the mean vector of the observations and S^{-1} is the covariance matrix of the observations.

The type of model that was selected to classify the data was a neural network taking as inputs the values of the novelty indices and as output one out of nine classes of damage. In order to further reduce the feature space, a genetic algorithm was used to select the best subset of features out of the 72 novelty indices [15]; this resulted in nine novelty indices. The neural network was selected to be a feedforward neural network with one input layer, a hidden layer and a decision/output layer. The best size for the hidden layer was selected according to the performance of the networks in the validation set after having tried different sizes. The optimal network had nine nodes in the hidden layer and the its accuracy is shown in the confusion matrix in Table 1. The total accuracy was 98.14% on the testing set.

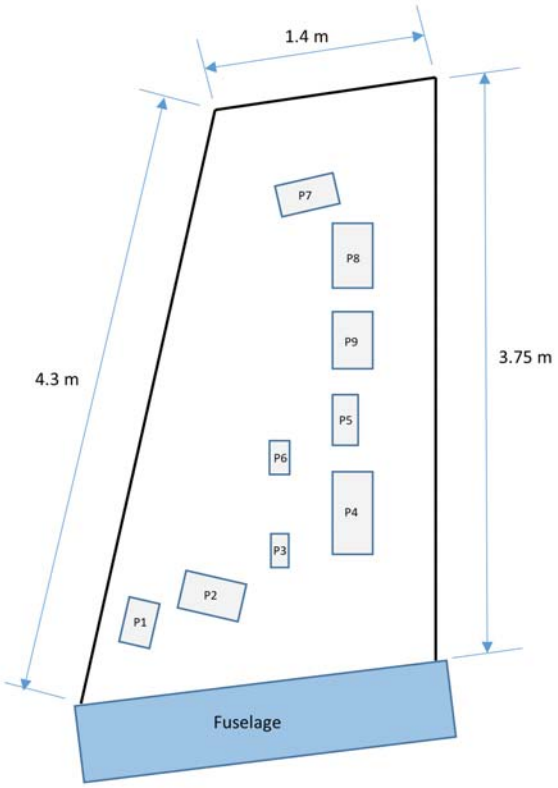

Figure 6: Schematic drawing of wing panels removed to simulate the nine damage cases [6].

Predicted panel	1	2	3	4	5	6	7	8	9
Missing panel 1	65	0	0	0	0	0	0	0	1
Missing panel 2	0	65	0	1	0	0	0	0	0
Missing panel 3	1	0	62	0	0	1	0	1	1
Missing panel 4	0	0	0	66	0	0	0	0	0
Missing panel 5	0	0	0	0	66	0	0	0	0
Missing panel 6	0	3	0	0	0	62	0	1	0
Missing panel 7	0	0	0	0	0	0	66	0	0
Missing panel 8	1	0	0	0	0	0	0	65	0
Missing panel 9	0	0	0	0	0	0	0	0	66

Table 1: Confusion Matrix of neural network classifier, test set, total accuracy: 98.14% [15].

Predicted panel	1	2	3	4	5	6	7	8	9
Missing panel 1	63	1	0	0	0	0	0	0	2
Missing panel 2	0	62	0	1	0	0	0	0	3
Missing panel 3	0	1	61	2	0	0	0	0	2
Missing panel 4	1	0	0	65	0	0	0	0	0
Missing panel 5	0	0	0	0	66	0	0	0	0
Missing panel 6	1	1	1	0	1	61	0	0	1
Missing panel 7	0	0	0	0	0	2	63	0	1
Missing panel 8	1	0	0	0	0	0	0	65	0
Missing panel 9	1	0	0	0	0	2	0	0	63

Table 2: Confusion Matrix of fittest NEAT individual, test set, total accuracy: 95.79%.

3.2 NEAT training

Taking into account the time needed to select the optimal size for the hidden layer, as well as the fact that the neural network selected had a restricted architecture since it was a feedforward one, application of NEAT was attempted on the same problem. By applying NEAT in this problem, a different topology for the network is expected and maybe a more interpretable model. The exact datasets were used in order to facilitate comparison between the two algorithms.

The population for NEAT was chosen to be a 500-neural network population with a *rectifier* or *relu* activation function on their nodes. The probabilities of mutating a weight or a bias term were both 0.7 and the mutate power was 0.1 in both cases. Moreover, the probabilities of adding a new connection or a new node were both 0.5 and the probability of deleting a connection was 0.05. The fitness function was set to be the accuracy of predictions given by a softmax function σ,

$$\sigma(\mathbf{x})_i = \frac{\exp(x_i)}{\sum_j \exp(x_j)} \tag{2}$$

applied on the values of the output nodes of each network, using this function on the output of the networks, the algorithm allows their interpretation as probabilities.

3.3 Results and splitting into subnetworks

Having trained the population, after 3216 generations and about a day of training, the fitness of the "strongest" individual had been stable for many generations and so it was considered to have converged. The confusion matrix for the fittest individual on the testing set is shown in Table 2. The accuracy is slightly lower than the accuracy of the original work where feedforward networks were used.

It is worth isolating the sub-networks that describe how each output node is activated. This is done by looking for paths from every input node to each output node separately. Doing so, the subnetworks that are found for every damage class are shown in Figure 7. Connections with green colour represent positive weights while the ones in red correspond to negative weights. It is particularly interesting that subnetworks whose structure is quite simple have been created. For example the subnetwork corresponding to panel 9, is affected only by input features 3, 7 and

Predicted panel	1	2
Missing panel 1	64	2
Missing panel 2	0	66

Table 3: Confusion Matrix regarding classifying cases of missing panels 1 and 2 using the respective subnetworks, accuracy = 98.48%.

8. This separation could result in further insight into the physics of the problem, as it is more interpretable than a fully connected neural network.

Another aspect of this approach is that these subnetworks could be combined and used as a modular classification model for a subset of damage cases. For example, one may be interested in creating a classifier that would be able to distinguish between the classes of missing panel 1 or missing panel 2. The procedure to be followed is to use the subnetworks of the two cases and assign a label to the sample according to which subnetwork generated a greater value on its output node. By applying this algorithm for the case of damage cases 1 and 2, the confusion matrix for the testing data is shown in Table 3. It is also worth noting that using this approach, the values of the input features that are needed are those of features 1, 2, 3, 4, 5, 6, 8, since they are the subset of input features that are used by the two subnetworks.

4 Conclusions

An alternative approach to training neural networks for SHM was presented, that of augmenting topologies. The algorithm used does not have a specific topology for the neural network that is going to be trained, but is searching for an optimal one using a genetic algorithm. Following this approach, the size and architecture of the network to be used does not have to be predefined. Even though selection of a topology is avoided, new training hyperparameters have to be defined, for example the probabilities of the creation of a new node or a new connection in the population of neural networks.

The results of the classification task in the SHM example described, reveal that the accuracy of the fittest individual was close to the accuracy of a feedforward neural network trained using backpropagation. The training time, taking into account recent advances in hardware used in applying backpropagation in neural networks, is much larger for the NEAT algorithm. The training time for NEAT could be lower if a parallelisation scheme was followed, which was not used in the current work.

Although there are some disadvantages in applying such an algorithm, some advantages emerged; the first is that the fitness function may be a discrete quantity that could not be used as a cost function in a feedforward neural network. Furthermore, the isolation of subnetworks presented, generated quite simple sub-models for each damage case, whose extraction is not applicable in a feedforward neural network. The use of such subnetworks for classification of a subset of damage cases was also shown to be possible. These modular models used a subset of features which may prove useful in cases that some features may not available. In such cases, inference may still be made for subsets of damage cases.

Finally, more simple or more complex architectures that are not achievable by using a mainstream feedforward network are considered. The approach of augmenting topologies allows a greater variety of networks to be tested for the task at hand. In many problems, this may result in models that achieve greater accuracy compared to other neural networks. The algorithm has also the

potential of allowing recurrent connections that may also fit the underlying physics of a problem and approximate better the real relationship between inputs and outputs.

Acknowledgements

The authors would like to acknowledge the support of the European Union (EU). G.T is supported by funding from the EU's Horizon 2020 research and innovation programme under the Marie Sklodowska-Curie grant agreement DyVirt (764547). The authors also gratefully acknowledge the support of the UK Engineering and Physical Sciences Research Council (EPSRC) through grant references EP/R003645/1, EP/R004900/1 and EP/S001565/1.

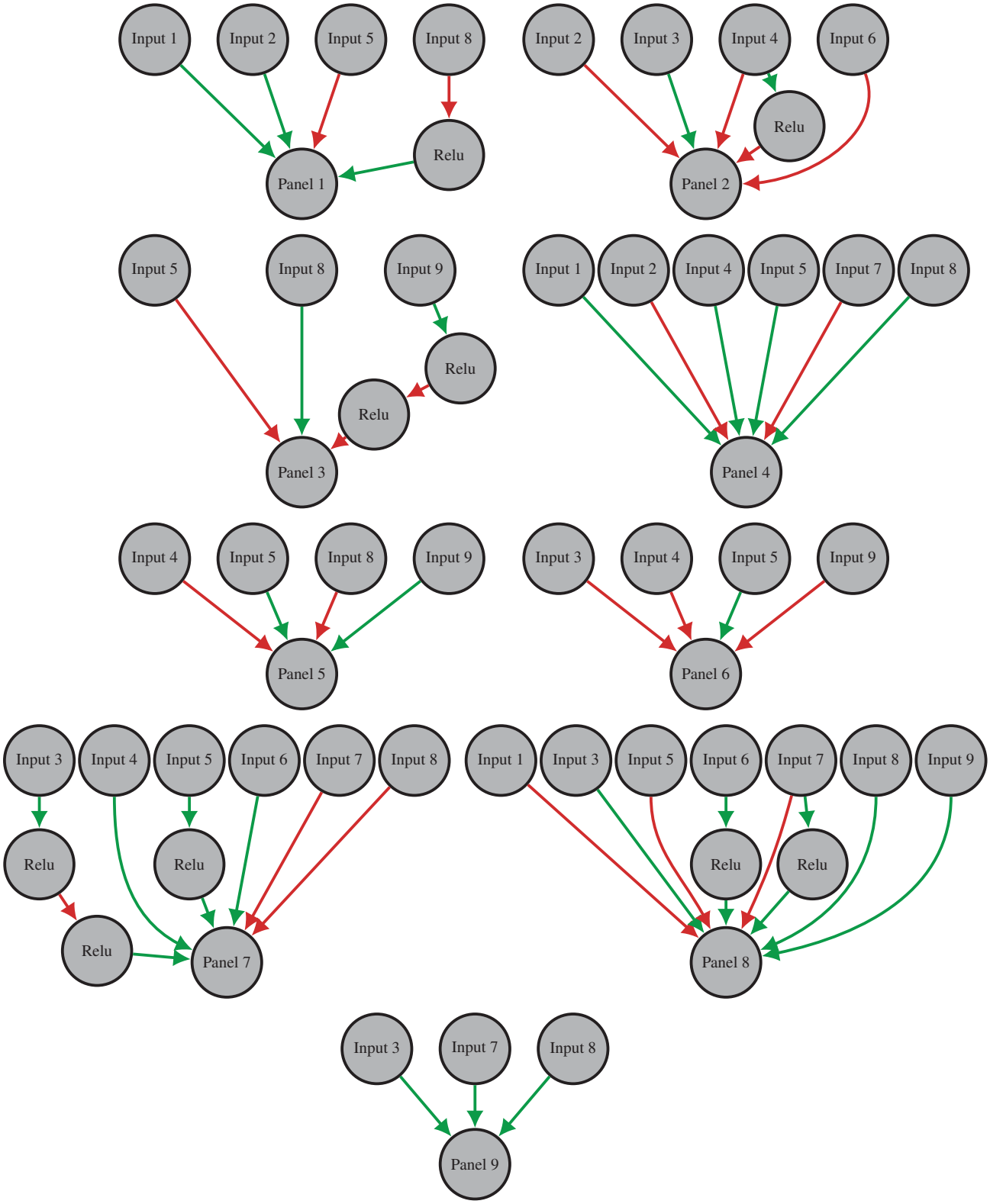

Figure 7: Subnetworks for each damage case.

REFERENCES

[1] C. R. Farrar, K. Worden, Structural Health Monitoring: A Machine Learning Perspective, John Wiley & Sons, 2012.

[2] A. Rytter, Vibrational based inspection of civil engineering structures, Ph.D. thesis (1993).

[3] E. Papatheou, G. Manson, R. J. Barthorpe, K. Worden, The use of pseudo-faults for novelty detection in SHM, Journal of Sound and Vibration 329 (12) (2010) 2349–2366.

[4] N. Dervilis, I. Antoniadou, R. J. Barthorpe, E. J. Cross, K. Worden, Robust methods for outlier detection and regression for SHM applications, International Journal of Sustainable Materials and Structural Systems 2 (1/2) (2016).

[5] K. Worden, Structural fault detection using a novelty measure, Journal of Sound and Vibration 201 (1) (1997) 85–101.

[6] G. Manson, K. Worden, D. Allman, Experimental validation of a structural health monitoring methodology: Part III. Damage location on an aircraft wing, Journal of Sound and Vibration 259 (2) (2003) 365–385.

[7] G. Cybenko, Approximation by superpositions of a sigmoidal function, Mathematics of Control, Signals, and Systems 2 (4) (1989) 303–314.

[8] K. O. Stanley, R. Miikkulainen, Evolving neural networks through augmenting topologies, Evolutionary Computation 10 (2) (2002) 99–127.

[9] M. Mitchell, An introduction to genetic algorithms, MIT press, 1998.

[10] D. Whitley, A genetic algorithm tutorial, Statistics and Computing 4 (2) (1994) 65–85.

[11] V. K. Koumousis, P. G. Georgiou, Genetic algorithms in discrete optimization of steel truss roofs, Journal of Computing in Civil Engineering 8 (3) (1994) 309–325.

[12] A. B. Abdessalem, N. Dervilis, D. Wagg, K. Worden, Model selection and parameter estimation in structural dynamics using approximate Bayesian computation, Mechanical Systems and Signal Processing 99 (2018) 306–325.

[13] S. Ruder, An overview of gradient descent optimization algorithms, arXiv preprint arXiv:1609.04747 (2016).

[14] D. J. Montana, L. Davis, Training feedforward neural networks using genetic algorithms., in: IJCAI, Vol. 89, 1989, pp. 762–767.

[15] K. Worden, G. Manson, G. Hilson, S. Pierce, Genetic optimisation of a neural damage locator, Journal of Sound and Vibration 309 (3-5) (2008) 529–544.

EURODYN 2020
XI International Conference on Structural Dynamics
M. Papadrakakis, M. Fragiadakis, C. Papadimitriou (eds.)
Athens, Greece, 23–26 November 2020

A PROBABILISTIC APPROACH TOWARDS UNCERTAINTY QUANTIFICATION IN JOINED STRUCTURES

A. Muraleedharan, R.J. Barthorpe, K. Worden

Dynamics Research Group, Department of Mechanical Engineering, University of Sheffield
Mappin Street, Sheffield S1 3JD, UK
e-mail: a.muraleedharan, r.j.barthorpe, k.worden@sheffield.ac.uk

Keywords: Joints, connections, structural dynamics, validation, calibration, uncertainty, probabilistic methods.

Abstract. *Computer models are inevitable in the present world, and the past few years have witnessed significant improvements in modelling capabilities. Most of the critical engineering structures in the real world exhibit complex behaviour and are often made up of constitutive subsystems or components. In most of the cases, performance or test data at system level might not be adequately available to perform a full-scale validation and hence the predictions from such a model cannot be relied upon in taking crucial decisions. A straightforward approach is to validate the individual subsystems or components and establish confidence in those respective models. Although various components can be modelled reasonably accurately, the prediction of the overall response of a structure also depends on the interaction between various components; developing and validating such a full-scale model is not an easy job. In this regard, it could be narrated that the connections or joints between the components are equally important as the components themselves and need to be modelled as accurately as needed, and the respective models validated. This paper discusses an approach to deal with system-level responses, where the components, as well as the joints between them are treated as separate subsystems. An isolated model has been employed to validate the model for the joint separately and a probabilistic approach is adopted to propagate various parameters and associated uncertainties through the respective models to predict the overall response. This approach is demonstrated through a generic problem, where two different subsystems are connected together to form a full system.*

1 INTRODUCTION

The process of developing any computational model starts with a concept. The concept depends on the understanding of the underlying physics of the process, which paves the way to fit a mathematical model to the concept. This mathematical model defines how different parameters affect the process. In order to solve this mathematical model, a numerical strategy is adopted (e.g. a computer code) and it is this computer code that usually predicts the required response. It is an important step to make sure that the model is good enough for purpose, and that is where verification, calibration and validation come into the picture. Figure 1 shows various stages in the development of a numerical model and where verification, calibration and validation come in.

It is through verification that one confirms the ability of the numerical strategy to accurately represent the underlying mathematical equation. There are different methods of verification that exist depending on the type of the code, and this is still an active topic of research [1, 2, 3]. Even when the code is verified and is proven to give accurate results based on the mathematical model, the parameters of the mathematical model might require calibration or fine tuning. It is through calibration that one can update the parameters so that the mathematical model predicts the responses with accuracy. This process involves comparing the output from the model with real or experimental data to confirm that the parameters are tuned well [4, 5]. Calibration updates the mathematical model based on the experimental results, but the ability of the model to perform well in different settings can be realised only if the concept in the beginning was right; this is established through validation. Model validation refers to the process of determining the degree to which a model (and its associated data) is an accurate representation of the real world from the perspective of the intended use of the model [3].

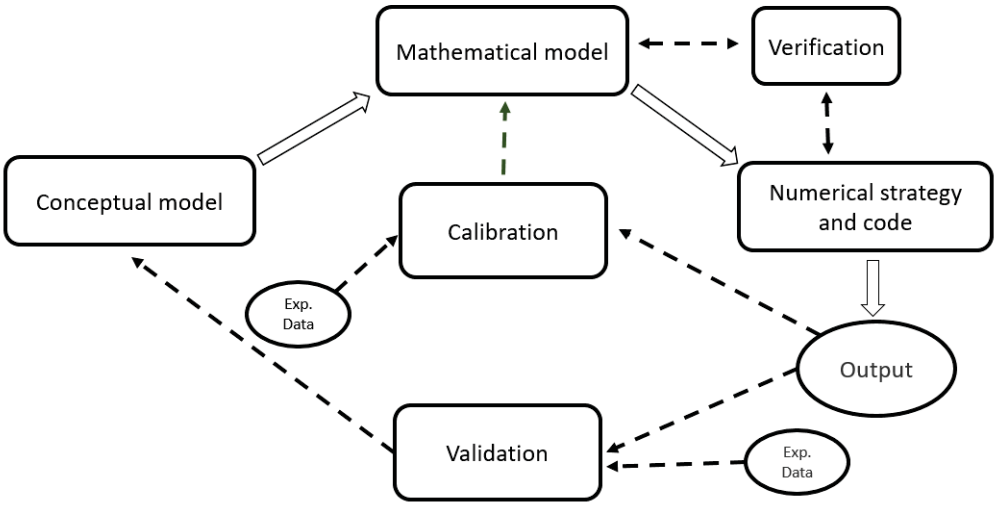

Figure 1: Stages in development of a numerical model.

Both validation and calibration require performance or test data. In practice, many engineering structures are impractical to test to obtain these data and in such situations, it may not be possible to calibrate or validate a model. This paper discusses such situations were a structure cannot be tested, but the substructures or components can be tested. In such cases where the component or subsystem-level models can be calibrated and validated, these can be used to have

better predictions at the system level. This situation also depends on the interaction between the components and in the physical sense, these interactions are determined by the joints. This fact makes it important to know more about joints, and the way joints influence structural responses.

The initial part of the paper reviews methods to apply calibration of parameters through subsystem-level models before focusing on joints. The primary aim is to present an approach to deal with connected systems and on how to address the joints in such systems. The interaction of a joint, and ways of addressing the joints in a system are also discussed. The paper adheres to a probabilistic framework, and hence applications of Bayesian statistics can be found linked to some key concepts. An example problem on a simple connected setup is employed to discus the key concepts and methodologies presented.

2 SUBSYSTEM-LEVEL MODELS

2.1 Concept

Due to the practical difficulties in testing entire structures, calibration and validation data cannot always be obtained for models (system-level models) representing many engineering structures. Nevertheless, simpler parts of the same structure (subsystems) or individual components may be tested independently and the data thus obtained can be used to calibrate and validate the respective subsystem-level or component-level models. A component-level model is a subsystem-level model where the subsystem is reduced to just one component. This process of validating the subsystem-level models does not directly validate the system-level models, but the inferences from the validation exercises at such lower levels, can be used to improve the system-level model and thus to obtain better predictions of the behaviour of the overall structure through these improved system-level models. One way to improve the system-level model is through updating the parameters in the system-level models through observations of the subsystem-level models which employ the same parameters. Integrating the calibration and validation process in the subsystem-level models facilitates the use of better-calibrated parameters in the system-level models, which results in better predictions [6].

This process of obtaining better-calibrated parameters is realised through a probabilistic approach where updated parameters from individual subsystem-level models are further updated according to the respective validation results. This process improves the results and is particularly applicable in situations where there are multiple subsystem-level models to calibrate for the same parameter. To better understand the process, let a system-level model, H, be assumed for a system S such that the model predicts a response Y_S, from an input X_S. It can be expressed as

$$Y_S = H(X_S, \theta_S) \tag{1}$$

where θ_S represents the parameters that define the model. Furthermore, assume that this system is formed of two subsystems. Let G_1 and G_2 be subsystem-level models that represent subsystems S_1 and S_2 of the structure being represented by H,

$$Y_{S_1} = G_1(X_{S_1}, \theta_1, \theta_2) \tag{2}$$

$$Y_{S_2} = G_2(X_{S_2}, \theta_2) \tag{3}$$

Here, θ_1 and θ_2 are subsets of θ_S and θ_S may have other parameters which are not addressed by either of the subsystems,

$$\theta_S = \{\theta_1, \theta_2, \theta_3, ...\theta_n\} \tag{4}$$

This vector may be represented as,

$$\theta_S = \{\theta_1, \theta_2, \theta_{extra}\} \tag{5}$$

where the additional parameters are represented as $\theta_{extra} = \{\theta_3, \ldots \theta_n\}$.

If data for calibration (D_1^c and D_2^c) and validation (D_1^v and D_2^v) are available at the subsystem levels S_1 and S_2 respectively, models G_1 and G_2 can be calibrated for the parameters and validated. Once the calibrated distributions of the parameters, θ_1 and θ_2, are obtained from both the models, the result of validation can be applied to and propagated through the system-level model H to obtain a better prediction Y_s. This process is explained below and a graphical representation of the problem is illustrated in Figure 2. A probabilistic graphical modelling framework [7, 8] enables better control over the process and the changes in response predictions can be updated in real time through additional calibration and validation data. In this paper, graphical models are not employed, but graphical representations are illustrated for better understanding of the model interactions.

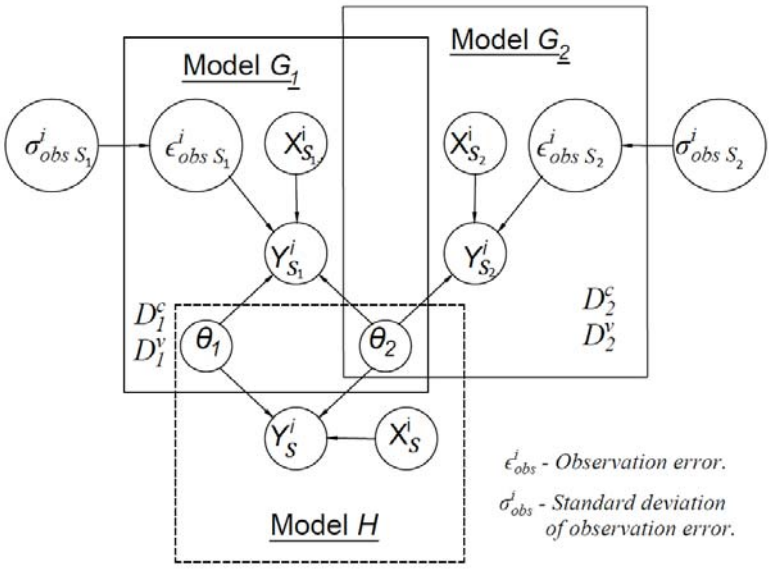

Figure 2: Graphical representation of the system and subsystem-level model interaction.

2.2 Calibration

Let $p(\theta_1)$ and $p(\theta_2)$ be the prior distributions of the parameters θ_1 and θ_2 respectively. D_1^c and D_2^c refer to the calibration data for the models G_1 and G_2 respectively. From the calibration data, posterior distributions of θ_1 and θ_2, $p(\theta_1|D_1^c)$, $p(\theta_2|D_1^c)$ and $p(\theta_2|D_2^c)$ can be obtained through a Bayesian approach [4]. The posterior of a parameter θ of a model G with calibration data D^c and a prior $p(\theta)$ can be obtained using the following relation,

$$p(\theta|D^c, G) = \frac{P(D^c|\theta, G)p(\theta)}{\int P(D^c|\theta, G)p(\theta)d\theta} \tag{6}$$

$P(D^c|\theta, G)$ is the likelihood function of θ and can be expressed as,

$$P(D^c|\theta, G) \propto \prod_{i=1}^{n} \frac{1}{\sigma\sqrt{2\pi}} e^{-\frac{(Y_i - G(X_i, \theta_i)^2)}{2\sigma^2}} \tag{7}$$

where σ is the standard deviation of the observation errors. Here, θ_1 can be calibrated through G_1 and θ_2 through either G_1 or G_2 or through both G_1 and G_2 together at once. In situations where both the subsystem-level models G_1 and G_2 are considered together, the likelihood function $P(D_1^c, D_2^c|\theta_2, G_1, G_2)$ is given by (assuming independence between the models),

$$P(D_1^c, D_2^c|\theta_2, G_1, G_2) \propto (\prod_{i=1}^{n} \frac{1}{\sigma\sqrt{2\pi}} e^{-\frac{(Y_i - G_1(X_i,\theta_i)^2)}{2\sigma^2}})(\prod_{j=1}^{n} \frac{1}{\sigma\sqrt{2\pi}} e^{-\frac{(Y_j - G_2(X_j,\theta_j)^2)}{2\sigma^2}}) \tag{8}$$

2.3 Validation

Once the process of calibration is completed, the individual subsystem-level models can be validated from the available validation data D_1^v and D_2^v corresponding to G_1 and G_2 respectively [9, 10, 11]. An integral aspect of any validation process lies in having a validation metric. Different validation metrics are discussed in various parts of literature [2, 12]. The use of a Bayes factor B [11] as a validation metric finds application in such problems. The Bayes factor represents the likelihood ratio, and in cases where there is only a single model $G(\theta)$, it can be used to represent the ratio of likelihood of observing the data with null (G) and alternate hypotheses ($G^{'}$),

$$B = \frac{P(D^v|G)}{P(D^v|G^{'})} = \frac{\frac{P(G|D^v p(D^v)}{P(G)}}{\frac{P(G^{'}|D^v p(D^v)}{P(G^{'})}} = \frac{P(G|D^v)P(P(G^{'})}{P(G^{'}|D^v)P(G)} \tag{9}$$

The Bayes factor gives a measure on the probability of a model to be validated. The probability of a model G being valid based on available validation data D^v, represented as $P(G|D^v)$ can be obtained from the equation,

$$P(G|D^v) = \frac{B}{B+1} \tag{10}$$

It is obvious from the equation that a Bayes factor equal to one ($B = 1$) corresponds to equal probabilities for the model to be valid and not to be valid. In a generic approach, the model which corresponds to the highest Bayes factor might be more probable and be selected, but [6] proposes a method where all models are selected based on their respective probabilities of being valid, to update the already calibrated parameters. Once the probabilities of subsystem-level models G_1 and G_2 being valid ($P(G|D_1^v)$ and $P(G|D_2^v)$) are determined as above, the probabilities corresponding to the respective models not being valid ($P(G^{'}|D_1^v)$ and $P(G^{'}|D_2^v)$) can also be obtained. Assuming independence between the models, $P(G^{'}|D_1^v) = 1 - P(G|D_1^v)$ and $P(G^{'}|D_2^v) = 1 - P(G|D_2^v)$.

This approach can also be used to find the probabilities that both the models are valid, only one of the models is valid or both the models are not valid [6]. The literature [6] also proposes to include the prior distribution weighted accordingly with the probability of both the models being invalid. This strategy makes complete sense, as no posteriors can be relied on in cases where the models are invalid. For example, here, θ_1 exists only in the subsystem-level model G_1 and hence the only applicable factors would be $P(G_1|D_1^v)$ and its compliment $P(G_1^{'}|D_1^v)$; the prior $p(\theta_1)$ shall be weighted according to $P(G_1^{'}|D_1^v)$.

2.4 Isolated models

In the current discussion, the number of subsystem-level models is limited to two in which one can obtain calibration and validation data. Through these models, G_1 and G_2, and the

associated test data, one could propagate updated and probabilistically-weighted parameters through the model H to facilitate better predictions. But still, the model H, involves other parameters that were not addressed with the subsystem-level models. These situations also arise in real life situations where all the subsystems or components of a structure cannot be tested thus compromising the reliability of the predictions. It is in this context that the importance of isolated models shall be discussed. In order to calibrate a parameter associated to a system or subsystem-level model, an isolated model, specifically designed to address the case can be used. These isolated models shall represent structures which are feasible for testing, and more importantly shall involve the parameters which need to be updated. In this case, one can employ an isolated model G_3 representing a simple structure which can be tested. Let the model be mathematically represented as,

$$Y_3 = G_3(X_3, \theta_3) \tag{11}$$

where X_3 and Y_3 refer to input and output respectively. This model and the associated calibration and validation data D_3^c and D_3^v can be used to obtain a reliable distribution for θ_3, represented as $p(\theta_3|D_3^c, D_3^v)$ using the methods described before.

While the approach discussed above remains a good way of propagating parameters through the system-level models, the validation at the system level still remains a problem. This approach considers the system-level model as an independent model from the subsystem-level models and the focus lies on calibrating the parameters that define the model through subsystem-level models or isolated models. The advantage of such isolated models is that the models and associated structures need not be a part of the structure under consideration. While considering the subsystem-level models as representing real parts of the structure is advisable, isolated models can be used to fill the gap in missing parameters through subsystem-models. A proper metric [2, 12] to evaluate the degree of validation that can be achieved through validating subsystem-level models of different degrees of similarity and assessing the similarity in the role of the subsystems in the full system itself remains a hurdle at present, which demands expert knowledge and critical engineering judgements in proceeding with such assumptions.

2.5 Interaction function

It is important to approach the problem in a way that directs one towards a validated model at the system level. Apart from calibration and validation of the subsystem-level models as a means of obtaining calibrated parameters, it has to be such that these models directly form a part of the overall system or the system-level model and interact within the model towards obtaining target quantities. This interaction between different subsystem-level models in a structural engineering scenario is not easy to generalise and can be specific to a particular problem. These interactions can be defined using an interaction function which governs how the different subsystem-level models compile to a system-level model.

Looking back at the previously-defined system S represented by system-level model H, formed of two subsystems S_1 and S_2 represented by subsystem-level models G_1 and G_2, the interaction function f_H shall determine the interaction between models G_1 and G_2,

$$H = f_H(G_1(\theta_1, \theta_2), G_2(\theta_2), \theta_{extra}) \tag{12}$$

Here, once G_1 and G_2 are validated, they contribute towards more reliable predictions with the model H. The extra parameters may not be calibrated and the part of the system-level model H which is not validated is limited to the interaction function. Calibration of some or all of the additional parameters θ_{extra} may be performed through isolated models (such as G_3)

as described above, and propagated through this system-level model. There could be situations where the subsystems are represented by more than one model; in such a case, multiple models can be used for updating the same parameters, but the most valid model representing the subsystem's role in the model shall be the one selected. A Bayesian hypothesis selection approach [11] can be adopted to select the best model in these situations. Again, a Bayes factor can be used to select between models. To select between two models G_3 and G_4, with respective validation data D_3^v and D_4^v, the Bayes factor between G_3 and G_4 can be obtained as in equation (13). A Bayes factor greater than one favours the model G_3, and less than one favours the model G_4, where,

$$B = \frac{P(D_3^v|G_3)}{P(D_4^v|G_4)} = \frac{\frac{P(G_3|D_3^v p(D_3^v)}{P(G_3)}}{\frac{P(G_4|D_4^v p(D_4^v)}{P(G_4)}} = \frac{P(G_3|D_3^v)P(P(G_4)}{P(G_4|D_4^v)P(G_3)} \tag{13}$$

3 JOINTS

Any structure (system level) could be divided into subsystem-level components and an approach to predict system-level responses through subsystem-level inferences is described above. However, real structures are more complex. Although the components form the structure, the interaction between the components is as important as the components. These interactions between the connected components within a structure are governed by the joints. In a system-level model representing a full structure, it is an obvious need to find parameters that define any joints involved; however, these joint specific parameters may not be existent in the subsystem-level models that could be validated. Moreover, any possibility to validate the modelling concepts related to the joints are also lost. It is in this context that it becomes a necessity to calibrate for the joint-specific parameters and to validate the joint-specific models through an appropriate method. An effective approach to deal with the above aspects of joints is through treating joints as a separate subsystem. The role of this subsystem in a full system is to connect components or other subsystems together in the required configuration, and a model representing this subsystem - the joint model - shall be good enough to address this role. Thus, the system-level model will be a combination of the subsystem-level models and the joint models that determines how the subsystems shall interact within the full structure.

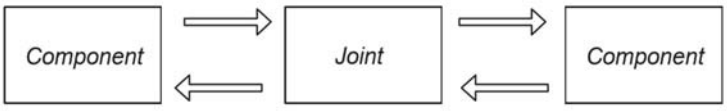

Figure 3: Interaction of a joint with components.

In many cases, as it might not be practical enough to test the components in connection, joint models will often be isolated models of simpler test structures (connected structures) with the same type of joint, which could be tested. It is also an obvious fact that a joint does not exist on its own, but only co-exists with the components it connects together. Therefore, in any exercise to calibrate or validate a joint model in a structure through isolated structures, care must be taken to select or design the test-joint, so that it should effectively address major parameters that define the joint and in a way that it closely matches the purpose of the joint in the full structure.

A joint, apart from having its own general properties (such as the Young's modulus and Poisson's ratio of weld material in case of the welded joint), might also possess properties that

are dependent on the components it connects, and even properties specific for the particular combination of the components being connected (such as thickness of a component). With an isolated model as described above, most of the physics, which are general for a particular type of a joint, can be characterised and the associated parameters updated and propagated through any system level models as in the previous sections. While the calibration and validation of isolated models enhances the results, the system-level model shall also be capable of including the uncertainties arising from any properties which were not validated through the joint model or either of the subsystem models. These parameters come into the system-level model as new elements - additional parameters θ_{extra} as explained in the previous sections.

A well-selected isolated model for the joint which can closely represent the functioning of the joint in the structure, can be integrated into the system-level model through the interaction function. The joint model has a significant role in determining the interaction between the components and it is very important to include such validated models of joints in the interaction function. The primary function of any joint model is to address how the joint influences various degrees of freedom between the components and the effect of various physical and geometrical parameters on this influence. An isolated joint model which can address this effects on a similar, simpler structure can be projected on to a different scenario of connecting different structures (the actual components or subsystems) thorough a proper interaction function and with help of any extra parameters that might be necessary to define the specific interaction. Suppose the joint model is represented by J,

$$Y_J = J(X_J, \theta_J) \tag{14}$$

where Y_J is the response to an input X_J and θ_J represent the parameters that define the joint model. If this joint model can be calibrated for the parameters θ_J and also validated, it could then be used to in the interaction function together with the other subsystem-level models to obtain the system-level model H,

$$H = f_H(G_1(\theta_1, \theta_2), G_2(\theta_2), J(\theta_J), \theta_{extra}) \tag{15}$$

Here, θ_{extra} includes additional parameters required to define the joint in the full-structure, as well as any other parameters that may be required to define the full-structure through the system-level model. If all subsystems and joints in a full structure are considered such that there are no additional parameters involved in defining a system-level model, the system responses and uncertainties can be quantified with better accuracy; however, in a real structure where tests are not possible in the connected configuration, such scenarios of not requiring any additional parameters are unlikely.

4 EXAMPLE CONNECTED SYSTEM

4.1 Problem description

In order to demonstrate the approach to deal with a connected system, an example problem is introduced. In this setting, the full structure is a 3-DOF spring-mass-damper system fixed onto a beam. The beam is hinged at one end and supported at the other end through a spring as shown in Figure 4a. The 3-DOF spring-mass-damper system is shown in Figure 4b.

The target quantity here is the acceleration of the top mass of the 3-DOF system, in the connected configuration when the beam is subjected to a random vibration at point A (midpoint of the beam) as shown in Figure 4a. It has to be assumed here that one cannot test the full

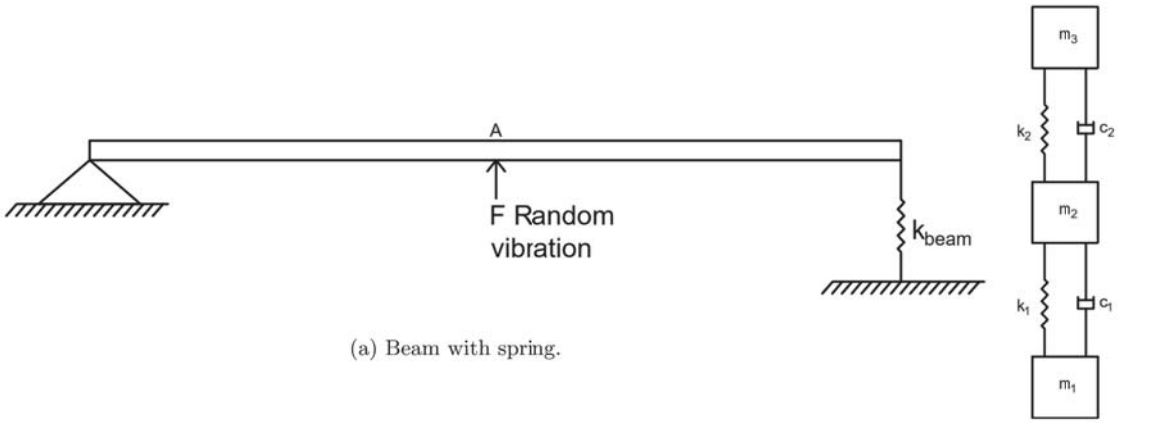

(a) Beam with spring.

(b) 3-DOF system.

Figure 4: Subsystems to be connected.

structure and hence no calibration or validation data are available at the system level. The 3-DOF spring-mass-damper system shown in Figure 4b forms one of the subsystems, S_1 and the Beam with spring in Figure 4a forms the second subsystem S_2.This example problem has been inspired by a similar model and validation exercise presented in [13]. Test data are assumed to be available at the subsystems levels, which make it possible to carry out the calibration and validation operations at the subsystem levels for individual subsystem-level models. These exercises can be carried out using the methods described before using a Bayesian approach [4, 11, 6]. In order to predict reliably the response quantity of interest - the acceleration at the top mass - one has to use the validation and calibration results from the subsystem level. As described in the previous section, this also involves having a reliable joint model, so that the interaction between the two subsystems can be realised. The following sections explain how this could be realised in the context of this example.A similar problem is discussed in

Tables 1 and 2 show various parameter values considered in this example. The parameters related to the beam were assumed deterministic to reduce the computational costs associated, while the parameters associated with the 3-DOF system are assumed random. The role of these parameters will be more evident in the following sections.

Parameter	Value
E - Modulus of Elasticity	210 Gpa
ν - Poissons ratio	0.3
ρ - Density	2700 kg/m^3
L - Length	0.5 m
b - cross sectional breadth	0.01 m
h - cross sectional height	0.01 m
k_{beam} - stiffness of spring	$10^5 N/m$

Table 1: Parameters governing the beam in Figure 4.

4.2 Joint as a subsystem

Here, apart from considering the 3-DOF system and the beam-with-spring as subsystems, one needs to address the joint as a separate subsystem. In this particular example, it is assumed

Parameter	Mean	Standard deviation
$k_1 = k_2$	10000 N/m	200 N/m
$c_1 = c_2$	0.3 Ns/m	0.03 Ns/m
k_j - prior	8000 N/m	800 N/m
c_j	0.3 Ns/m	0.03 Ns/m
α	350 mm	4 mm
k_s	$10^6 N/m$	$10^4 N/m$
k_p	3000 N/m	150 N/m

Table 2: Parameters governing 3-DOF system and joint.

that the 3-DOF system is being connected to the beam, but to simplify the problem the connection is being represented with a spring and a damper. This might be a debatable and simplest representation of a connection by itself, but as the focus is not on modelling, this simplicity helps a lot in highlighting the specific approach that is being demonstrated. Even in this simplest representation, one needs an isolated system to calibrate for the parameters of the joint; as mentioned earlier, the joint cannot exists on its own. Therefore, any tests can only be performed on a connected system and by reducing the complexity of this isolated connected system, the joint-model can be validated more reliably. This test can be achieved through isolated connected systems where the connected components have well-validated models by themselves and the calibration and validation operations limit specifically to the introduced joint. Here in this example, an isolated model with the same joint as used in the full structure (represented by a spring and damper) connecting two sample masses - which are perfectly calibrated - is used. The parameters of the joint (k_j and c_j) can be calibrated and also this model, which predicts the dynamic behaviour of systems connected by the particular joint can also be validated. Figure 5 illustrates the isolated connected system used for calibration and validation (of the isolated model) of the joint model.

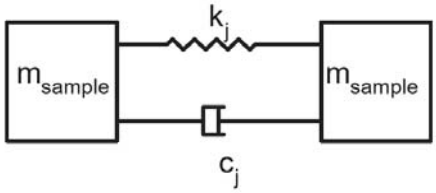

Figure 5: Isolated setup for validating joint model.

Since calibration and validation operations are possible on the subsystem models S_1 and S_2, three different validated and calibrated models will be available in this case. The calibration and validation of these models is not exercised here, as the paper focuses on a different aspect. However, interested readers are referred to [4, 11, 6, 9] to strengthen their knowledge in Bayesian calibration and validation procedures. Here, it is assumed that perfectly-validated models exist for both S_1 and S_2 and all the associated parameters in those subsystem-level models are calibrated. Furthermore, the isolated model for the joint is also calibrated for the respective parameters k_j and c_j, and this model is validated.

4.3 Subsystem-level models

Adhering to the convention adopted in the earlier sections, let the subsystem level models be G_1 and G_2 respectively for the subsystems S_1 and S_2. The model representing the isolated joint model is denoted J. The model G_1 predicts the acceleration of the mass m_3 when a force F_1 excites the mass m_1; is represented mathematically using the dynamic equation (16). $[m]$, $[c]$, $[k]$, and $[F]$ in the following equations represents the mass, damping, stiffness and force matrices respectively,

$$[m]_{S_1}[\ddot{X}] + [c]_{S_1}[\dot{X}] + [k]_{S_1}[X] = [F]_{S_1} \tag{16}$$

The force F_1 being a time series, the acceleration, velocity and displacement of all the masses at any point in time can be calculated from the above model described in (16) through a valid time integration scheme [14, 15]. Similarly regarding the model for the beam with spring, S_2, it is a finite element model with beam elements and does not consider any out of the plane degrees of freedom. This model is also realised using the dynamic equation, where the mass and stiffness matrix of the beam are developed [16] with a damping of 2% assumed. This subsystem model G_2, predicts the responses (acceleration, velocity and displacement) at every node in the finite element model on application of a force, which here is random,

$$[m]_{S_2}[\ddot{X}] + [c]_{S_2}[\dot{X}] + [k]_{S_2}[X] = [F]_{S_2} \tag{17}$$

The isolated joint model, which is also calibrated and validated, connects two masses and is capable of representing the interaction between them in a dynamic context. The joint itself is composed of the spring and damper, but it determines how the masses interact with each other. Further-more, in the system-level model, the same joint determines how S_1 (3-DOF system) and S_2 (beam with spring) interact,

$$[m]_J[\ddot{X}] + [c]_J[\dot{X}] + [k]_J[X] = [F]_J \tag{18}$$

4.4 Integrating subsystem-level models

Having validated models of the two subsystems, and also a validated model representing a similar joint, it is required to predict the response at the system level through the system-level model. As explained in the previous sections, the system level model H can be realised through an interaction function as described before,

$$H = f_H(G_1(\theta_{S_1}), G_2(\theta_{S_2}), J(\theta_J), \theta_{extra}) \tag{19}$$

This interaction function here is a code or scheme that decides how the 3-DOF system S_1, is joined to the Beam S_2, through the joint J. It is easy to imagine in this simpler example, on what the interaction function is intended to do. There exists a validated joint model which can represent the interaction between two connected components. In the isolated condition, the components it connects are purposefully limited to a simpler entity (two calibrated masses here) to make the calibration and validation process feasible. However, it is the same joint that exists in the full structure, connecting more complex subsystems (S_1 and S_2 in this example). When the same isolated joint model is modified by replacing one of the sample masses with S_1 and the other with S_2, the full structure shall be defined. The interaction function is intended to do exactly the same task of integrating these models together in the required configuration demanded by the specific problem.

While the above described process seems trivial, it must be noted that the model-integration process may not be completed without extra parameters that define many specific criteria and properties of the joint. Although the isolated joint model represented the interaction between the two sample masses perfectly, when joining S_1 and S_2, it needs additional parameters that define further specifications of the joint. This is often the case in real engineering where a particular joint may not be fully replicated using simpler connected systems. Although a good part of the joint can be represented through the simpler isolated connections, there exist certain aspects which are to be addressed in the real connection which were not present in such isolated models.

In this isolated joint model, it represents the connecting of two nodal masses, and it does not have any parameters that define any point of connection, simply because it was not needed. But when the same joint connects the beam and the 3-DOF systems together, there exists a need to define where and how they are connected together, which mass is being connected together with the beam and at what point in the beam is it going to be connected. Therefore, the interaction function shall address these qualities of the joint and this demands more parameters that can define such qualities.

In this particular example, a new parameter α, which defines the distance from the hinged end of the beam to where the 3-DOF system (S_1) is connected is introduced as an additional parameter. Another parameter β which can take values 1, 2 or 3 defines the index of mass to be connected. Furthermore, an effect on stiffness and damping values is also considered. This latter takes into account the effect of the substructures on the joint. In the real world, the connection is influenced also by the components being connected and as the components change, the effect will be witnessed in the interaction due to their influence on joint characteristics. The additional stiffness and damping parameters are represented as k_p and k_s. Figure 6 gives a pictorial representation of how the subsystem-level models get integrated with the isolated joint model through extra parameters. Note that additional parameters, which were absent in the isolated model are required to define the connection.

The interaction function f_H, generates the system-level model from the subsystem-level models, in this case by generating new mass, stiffness and damping matrices. The parameters of the joint, the parameter α which define the location of the joint in the beam, β which defines the location of joint in the 3-DOF system, the additional stiffness parameters k_p and k_s, all influence the formation of the new matrices. Here, β is a constant, assuming the mass being connected is always the bottom mass m_1, but the other parameters are expected to be uncertain and a Gaussian distribution is assumed. The interaction function determines the indices of various elements in the matrices in the system-level model, according to the parameters. Equation (20) represents the stiffness matrix in the system level model, by concatenating the stiffness matrix of the 3-DOF system to the stiffness matrix of the beam through the joint in generic form,

$$[m]_S[\ddot{X}] + [c]_S[\dot{X}] + [k]_S[X] = [F]_S \tag{20}$$

In a system-level model thus obtained, a good part of it is validated as all the subsystem-level models are validated. A model for the same joint is also validated fully in an isolated connection set-up. Employing the same validated models in the system-level models improves the reliability of the predicted responses and the part of the system not validated is limited to the function which defines how the different models interact. Although this aspect of the system relies on expert knowledge, the possibility to validate the constituent subsystem-level models is a decent achievement in most engineering problems. It is also very important to make

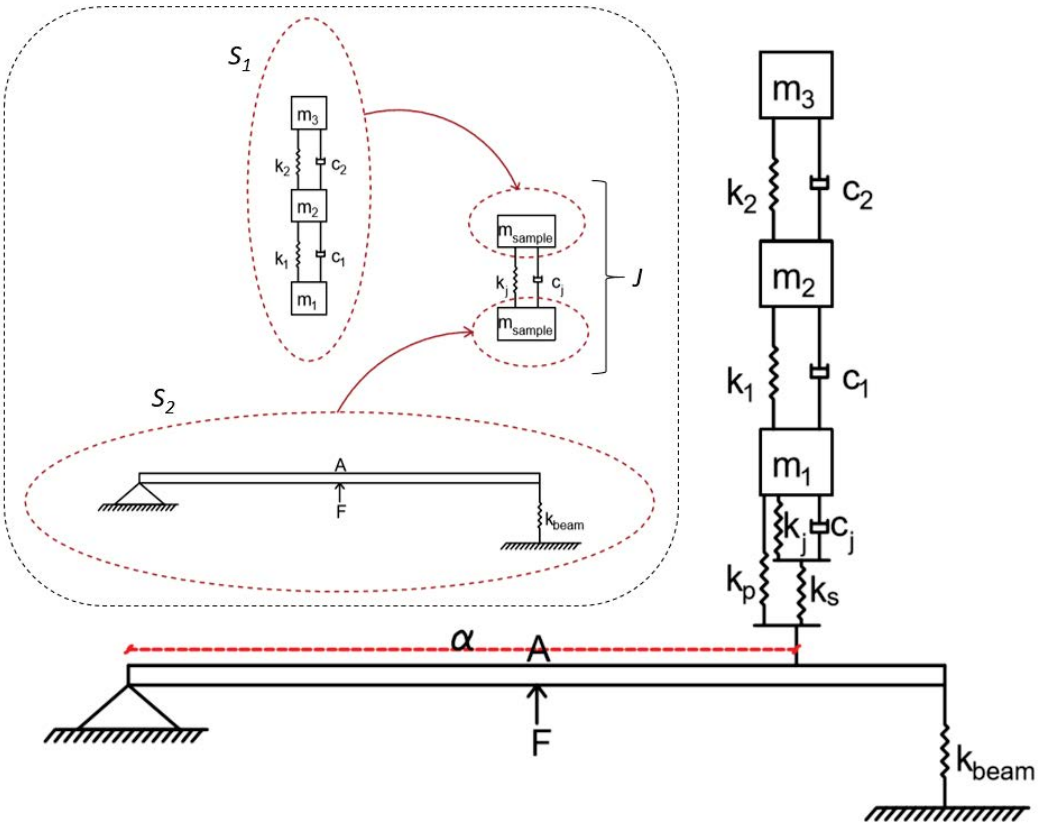

Figure 6: Interaction between subsystem level models.

sure that the additional parameters are addressed properly and the uncertainties related to these parameters are considered while predicting the target quantities.

4.5 System-level model

Figure 7 shows the graphical representation of the current problem. As one can clearly interpret, the system-level model share most of the parameters from the subsystem-level models G_1 and G_2, and the isolated joint model J. Furthermore, the system-level model H itself was developed through integrating the subsystem-level models G_1, G_2 and J with the additional parameters. The models G_1, G_2 and J have associated calibration data through which the parameters can be updated, and also these subsystem-level models can be validated.

The validation results from the subsystem-level model, apart from influencing the updating of parameters, will also play a major role in improving the reliability of predictions at the system level. A good part of the interaction is defined through the isolated joint model, which when validated, improves the confidence further. As discussed before in the paper, if there are more subsystem-level models, which might not be used in the formation of the system level model, but help in calibrating the parameters, they can be included in the graph network so that the parameters can be better calibrated.

4.6 Calibration of the joint model

Once again stressing that the point of this paper is not intended to demonstrate the calibration and validation exercises, but to propose an approach to deal with the joints, the subsystem

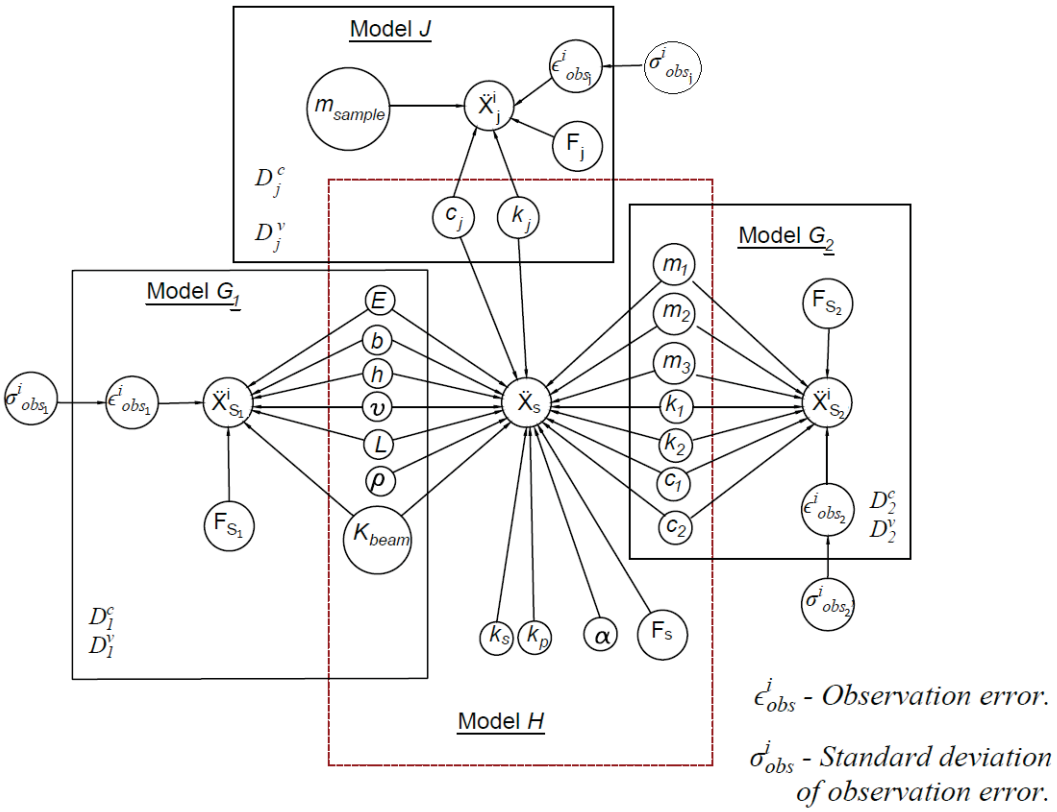

Figure 7: Graphical representation of the problem.

models, as well as the isolated joint models are assumed to be validated. Furthermore, all the parameters defining both subsystems are assumed calibrated. However, to demonstrate the purpose of considering the joint as a separate subsystem, the stiffness at the joint k_J is assumed not to be calibrated. This parameter needs to be calibrated through the isolated joint model.

The prior value of k_J is given in Table 2. In a scheme where the joints are not considered, it will be this prior value that would be propagated through the system-level model. Since the joint is being treated as a separate subsystem, the model for the joint can be calibrated (and validated - for this problem it is assumed that the model is validated). Here, the model J is calibrated for k_J from the calibration data D^c_j which in this case is the natural frequency of the the isolated connected system.

The posterior of the joint parameter $p(k_j|D^c_j, J)$ is given by,

$$p(k_j|D^c_j, J) = \frac{p(D^c_j|k_j, J)p(k_j)}{\int p(D^c_j|k_j, J)p(k_j)dk_j} \tag{21}$$

and as in equation (7), the likelihood function can be expressed as,

$$p(D^c_j|k_j, J) \propto \prod_{i=1}^{n} \frac{1}{\sigma\sqrt{2\pi}} e^{-\frac{(\omega^i - J(m,k^i_j)^2)}{2\sigma^2}} \tag{22}$$

The posterior of k_j was obtained through a Metropolis-Hastings MCMC algorithm and the updated k_J values are shown in Figure 8. The red dashed line corresponds to the prior and the blue one corresponds to the posterior distribution of k_J.

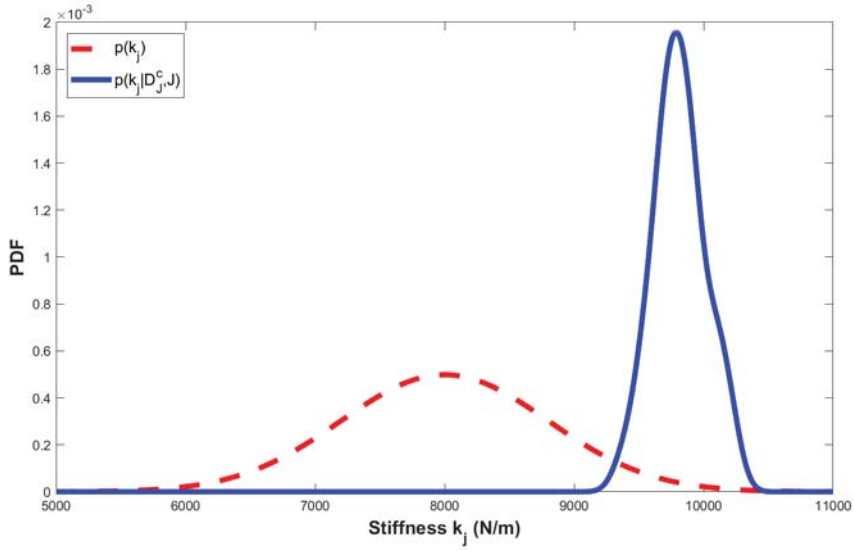

Figure 8: Joint parameter k_j before and after calibration (by considering an isolated joint model).

4.7 System-level responses: some numerical results

In this particular example, three different cases of the system-level models are considered to demonstrate the approach of considering joints as separate sub-systems and in considering extra parameters that might be needed to define a connected system. In the first case, it is assumed that no extra parameters are required to define the connected system, or all the parameters were identified and calibrated through the isolated joint model. The case is realised through system-level model H_1. In the second case, it is assumed that the extra parameters k_p and k_s are considered, while α is assumed to be constant. Model H_2 represents the second case. In the third case, all the three extra parameters and associated uncertainties are considered and the model H represents this case. The models H_1 and H_2 in terms of the interaction function is represented below.

$$H_1 = f_{H1}(G_1(\theta_{S1}), G_2(\theta_{S2}), J(\theta_J)) \tag{23}$$

$$H_2 = f_{H2}(G_1(\theta_{S1}), G_2(\theta_{S2}), J(\theta_J), k_p, k_s) \tag{24}$$

The results (the maximum acceleration at the third mass) shown in Figure 9 are obtained by considering the system level model H_1 corresponding to Case 1. The black line corresponds to the value of acceleration considering the posterior distribution of k_j, $p(k_j|D_j^c, J)$ and the red dotted line corresponds to the same acceleration when k_j is not calibrated through an isolated model. Figure 10 compares the results when the joint parameter k_j is calibrated through an isolated model and when it is not, in case of considering all the additional parameters and the associated uncertainties, i.e. through the model H. Both these figures show the importance of calibrating the joint parameters. In the absence of an isolated model to calibrate for the parameter k_j, one could only go with the prior assumptions and hence affect the predictions.

It also needs to be noted that the system-level models might require additional parameters to define the connection properly, represented in this example through k_p, k_s and α. Here k_p and k_s are the additional stiffness parameters representing the complexity at the connection, and α is assumed so as to account for the uncertainty in the location of the connection. Although these

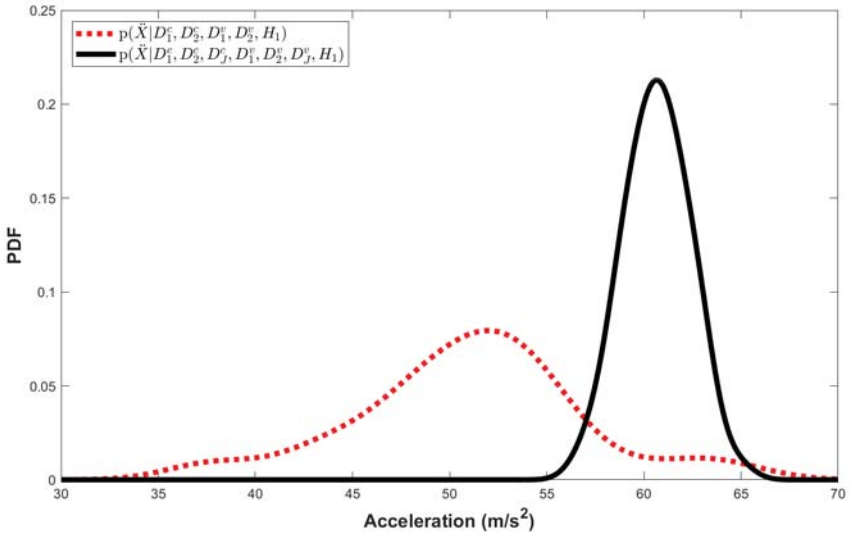

Figure 9: Acceleration of 3^{rd} mass before and after calibration of joint parameter k_j (Additional joint parameters k_p, k_s and α not considered : System-level model H_1).

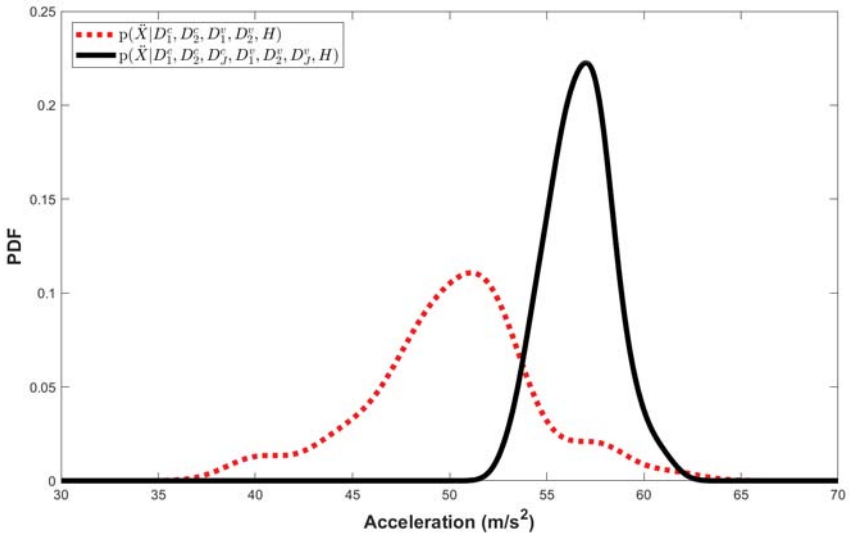

Figure 10: Acceleration of 3^{rd} mass before and after calibration of joint parameter k_j (Additional joint parameters k_p, k_s and α considered) : System-level model H).

parameters were not able to be calibrated through any subsystem-level models, they need to be considered with due importance; any models should have provisions to take this into account. Figure 11 illustrates the comparison between responses (maximum acceleration at the third mass) under various considerations, 1) Through model H_1, when no additional parameters are considered, 2) through model H_2, when no the extra parameters k_p and k_s are considered while α is assumed to be constant and 3) through model H where k_p and k_s are considered as well as the uncertainty in exact location is considered through α.

The red dotted line corresponds to the case when no additional parameters are considered while the blue dashed line represents the response when k_p and k_s are considered. The black line corresponds to the system-level model H where all extra parameters and uncertainties assumed

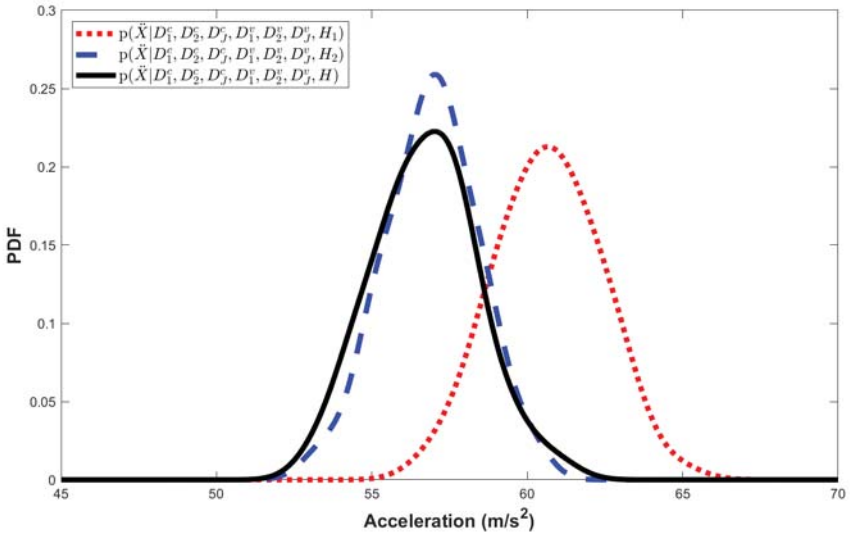

Figure 11: Acceleration of 3^{rd} mass : sensitivity to additional parameters k_p, k_s and α.

in this example are considered. The effect of additional parameters can be evidently noticed from these. In a real engineering problem, the magnitudes of different additional parameters might be different but might play very important roles in determining the total responses and should be considered with due importance.

5 SUMMARY

As this approach to deal with connected systems focuses on uncertainties related to the underlying mathematical model, the process of verification at full system level is not discussed. It has to be specifically noted that any numerical code shall be subjected to a suitable verification methodology that aligns well with the particular problem. To summarise the overall approach, the steps involved in predicting the response of a full structure can be listed as follows; this assumes that the full structure cannot be tested or performance data cannot be collected, while the constituent subsystems can be tested.

1. Identify and select the relevant subsystem-level models. More than one model can be selected if they increase reliability in calibrated results at a later stage.
2. Obtain calibration and validation data for all the considered subsystem-level models.
3. Identify the types of joints that connect various subsystems in the full structure.
4. Select isolated connected specimens with the same type of joints, which can be tested.
5. Develop suitable joint models to represent the joint interaction in the isolated set-ups.
6. Obtain calibration and validation data for the joint models.
7. Perform calibration exercises on all available models.
8. Validate the subsystem and joint models.
9. Update the calibrated parameters in each model with the result of validation.

10. Select the most valid subsystem-level models (in case of multiple models) for use in the system-level model.

11. Select the most valid joint models to be used in the system-level model.

12. Formulate the interaction function that can integrate the subsystem-level models to form the system-level model. (Expert knowledge and engineering judgments are demanded at this stage.)

13. Identify the additional parameters required to define the system-level model. (Those parameters that were not addressed at subsystem level.)

14. Use expert knowledge to address the uncertainties in these parameters.

15. Propagate all the parameters through the developed system-level model to predict the results.

6 CONCLUSION

A general approach to deal with predicting responses of connected structures, more reliably through inferences from testing their parts or components, was discussed in this paper. This approach helps in calibrating the parameters through subsystem-level models and validating the subsystem-level models including the joints. Considering the joints in a system as a separate subsystem enables one to calibrate and validate the joints through isolated models; this was found to be promising in situations where system-level data are not available for calibration and validation. The interactions of the validated subsystem-level models are defined through interaction functions to obtain the system-level model. This approach ensures that the constituent models and their interactions (defined by joints) are validated. The fact that an isolated model may not be able to address all the parameters that define a particular connection between particular components and the necessity to include these additional parameters in the system-level model was also dealt with in the paper. Such an approach enables better prediction and better quantification of uncertainties in the predicted responses.

In future, the authors are aligned to work on these approach in real structural engineering problems and to quantify the improvements in reliability of results with respect to other existing methods. The future works are expected to develop and demonstrate more clearly, various strategies regarding validation of joint models.

7 ACKNOWLEDGEMENT

This project is supported by funding from the EU's Horizon 2020 research and innovation programme under the Marie Skłodowska-Curie grant agreement number 764547 (DyVirt ETN).

REFERENCES

[1] American Society of Mechanical Engineers. *Standard for Verification and Validation in Computational Fluid Dynamics and Heat Transfer: An American National Standard*. American Society of Mechanical Engineers, 2009.

[2] P.J. Roache. *Fundamentals of Verification and Validation*. hermosa publ., 2009.

[3] L.E. Schwer. An overview of the ptc 60/v&v 10: guide for verification and validation in computational solid mechanics. *Engineering with Computers*, 23(4):245–252, 2007.

[4] M.C. Kennedy and A. O'Hagan. Bayesian calibration of computer models. *Journal of the Royal Statistical Society: Series B (Statistical Methodology)*, 63(3):425–464, 2001.

[5] W.L. Oberkampf, S.M. DeLand, B.M. Rutherford, K.V. Diegert, and K.F. Alvin. Error and uncertainty in modeling and simulation. *Reliability Engineering & System Safety*, 75(3):333–357, 2002.

[6] S. Sankararaman and S. Mahadevan. Integration of model verification, validation, and calibration for uncertainty quantification in engineering systems. *Reliability Engineering & System Safety*, 138:194–209, 2015.

[7] D. Koller and N. Friedman. *Probabilistic Graphical Models: Principles and Techniques*. MIT press, 2009.

[8] L.E. Sucar. *Probabilistic Graphical Models: Principles and Applications*. Springer, 2015.

[9] X. Jiang and S. Mahadevan. Bayesian inference method for model validation and confidence extrapolation. *Journal of Applied Statistics*, 36(6):659–677, 2009.

[10] X. Jiang and S. Mahadevan. Bayesian validation assessment of multivariate computational models. *Journal of Applied Statistics*, 35(1):49–65, 2008.

[11] R. Rebba, S. Huang, Y. Liu, and S. Mahadevan. Statistical validation of simulation models. *International Journal of Materials and Product Technology*, 25(1-3):164–181, 2006.

[12] K. Dvurecenska, S. Graham, E. Patelli, and E.A. Patterson. A probabilistic metric for the validation of computational models. *Royal Society Open Science*, 5(11):180687, 2018.

[13] J.R. Red-Horse and T.L. Paez. Sandia national laboratories validation workshop: structural dynamics application. *Computer Methods in Applied Mechanics and Engineering*, 197(29-32):2578–2584, 2008.

[14] M.A. Dokainish and K. Subbaraj. A survey of direct time-integration methods in computational structural dynamics—i. explicit methods. *Computers & Structures*, 32(6):1371–1386, 1989.

[15] K. Subbaraj and M.A. Dokainish. A survey of direct time-integration methods in computational structural dynamics—ii. implicit methods. *Computers & Structures*, 32(6):1387–1401, 1989.

[16] H. Benaroya, M. Nagurka, and S. Han. *Mechanical Vibration: Analysis, Uncertainties, and Control*. CRC Press, 2017.

EURODYN 2020
XI International Conference on Structural Dynamics
M. Papadrakakis, M. Fragiadakis, C. Papadimitriou (eds.)
Athens, Greece, 23–26 November 2020

ON THE USE OF NONLINEAR NORMAL MODES FOR NONLINEAR REDUCED ORDER MODELLING

Thomas E. Simpson[1], **Nikolaos Dervilis**[2], **and Eleni Chatzi**[1]

[1]Institute of Structural Engineering, Department of Civil, Environmental and Geomatic Engineering, ETH Zürich
Stefano-Franscini Platz 5, 8093, Zürich, Switzerland
e-mail: simpson,chatzi@ibk.baug.ethz.ch

[2] Dynamics Research Group, Department of Mechanical Engineering, University of Sheffield.
Sheffield S1 3JD, UK.
e-mail: n.dervilis@sheffield.ac.uk

Keywords: NNMs, ROMs, Autoencoders, Dynamics

Abstract. *In many areas of engineering, nonlinear numerical analysis is playing an increasingly important role in supporting the design and monitoring of structures. Whilst increasing computer resources have made such formerly prohibitive analyses possible, certain use cases such as uncertainty quantification and real time high-precision simulation remain computationally challenging. This motivates the development of reduced order modelling methods, which can reduce the computational toll of simulations relying on mechanistic principles. The majority of existing reduced order modelling techniques involve projection onto linear bases. Such methods are well established for linear systems but when considering nonlinear systems their application becomes more difficult. Targeted schemes for nonlinear systems are available, which involve the use of multiple linear reduction bases or the enrichment of traditional bases. These methods are however generally limited to weakly nonlinear systems. In this work, nonlinear normal modes (NNMs) are demonstrated as a possible invertible reduction basis for nonlinear systems. The extraction of NNMs from output only data using machine learning methods is demonstrated and a novel NNM-based reduced order modelling scheme introduced. The method is demonstrated on a simulated example of a nonlinear 20 degree-of-freedom (DOF) system.*

1 INTRODUCTION

The utilisation of nonlinear finite element simulations for dynamic problems has become more common in recent years as a result of increasing computational power rendering possible analyses that were previously prohibitively expensive. However, increasing interest in uncertainty quantification and digital twins once again raises the issue of computational resources. As such, the development of efficient metamodelling schemes for nonlinear dynamical systems is necessary. Meta-models are models which approximate a full-order or high-resolution model to some degree of accuracy, whilst greatly decreasing the cost of evaluation.

Reduction of FE models was initially considered with regards to the reduction of linear elastic models in the 1960s and techniques such as the Craig-Bampton and MacNeal-Rubin methods [1][2], are well developed and widely used for the reduction of linear FE models. These methods largely make use of linear normal modes as a reduced basis on which the systems' equations of motion are projected. Normal modes form a very efficient reduction basis for linear systems due to their orthogonality and the ability to target certain frequency regions of interest. When considering nonlinear systems however, these linear methods are not appropriate, as the concept of linear normal modes no longer holds. The most common method for the reduction of weakly nonlinear FE models adopts Proper Orthogonal Decomposition (POD), wherein a dynamic simulation of the system is carried out with "snapshots" of the response field extracted at various time intervals. These snapshots are used to construct an optimal linear reduction basis using singular value decomposition [3]. Related recent work explores the extension of the traditional reduction approach by inclusion of higher order enrichments, such as mode shape derivatives [4].

An alternative to this reduction approach is offered by a theory which extends the concept of normal modes to nonlinear systems, the so-called nonlinear normal modes (NNMs). Several different formulations of NNMs exist with the Shaw-Pierre modes being considered in this work, which build on the fundamental work of Rosenberg [5]. As a result of their ability to form a nonlinear manifold, these NNMs can provide a very efficient reduction basis for nonlinear systems [6]. Furthermore, they should be generally valid over the whole phase space of a system and not require multiple, energy dependent reduction bases as in the case of linear methods. In the following work, NNMs are used as basis to construct a reduced order model of a nonlinear system. Autoencoder neural networks are used to extract these NNMs, a recurrent neural network (RNN) is then used to create a regression approximating the overall system, making use of the extracted NNMs as a basis.

The layout of this paper is as follows. Section 2 introduces the theoretical background of nonlinear normal modes along with the process of their extraction. Section 3 describes autoencoder neural networks, their architecture and common usage. Section 4 then discusses the conceptual framework of the reduced order modelling procedure used herein. Section 5 discusses the regression problem in the reduced order model and briefly introduces the long short term memory (LSTM) neural network used. Section 6 gives a demonstration of the reduced order modelling method in practice, the nonlinear MDOF system approximated is described along with greater details on the implementation of the ROM on this system. Finally section 7 contains the conclusions and further work considerations.

2 Nonlinear Normal Modes

2.1 Shaw-Pierre Manifolds

Shaw and Pierre first proposed their theory of non-linear normal modes in 1993. They defined a NNM as being a "a motion which takes place on a two dimensional invariant manifold in phase space". More simply put, this means that in a Shaw-Pierre NNM the motion of each point in the system could be given as a function of the displacement and velocity of a single point in the system. This function if plotted in phase space, would form a surface which is the manifold they refer to. In the case of the linear system, the manifold would be a flat plane. Nonlinearities in a system cause curvature of this manifold. This curvature results in the amplitude dependence of mode shapes observed in nonlinear systems [7].

The calculation of these NNMs however is rather challenging, the assumption of the normal mode forming an invariant manifold is represented in equation 1. In this equation x_i and $\dot{x}_i$ are the displacement and velocity of the ith coordinate in the response whilst u_i and v_i represent the displacement and velocity of the ith transformed coordinate in the NNM. It can be seen that velocity and displacement of each of the coordinates in the NNM's can be described as a function of a displacement velocity pair of a single coordinate. These are linked by the functions f_i and g_i. This relationship is then substituted into the equation of motion which results in a new formulation of the equations of motion, which are unfortunately at least as difficult to solve as the original case. The solution here is to assume a power series solution for the functions $f_1 \cdots f_n$ and $g_1 \cdots g_n$. This then allows for analytical solution for some cases and numerical solutions for the general case.

$$\begin{bmatrix} x_1 \\ \dot{x}_1 \\ x_2 \\ \dot{x}_2 \\ \vdots \\ x_n \\ \dot{x}_n \end{bmatrix} = \begin{bmatrix} u_1 \\ v_1 \\ u_2 \\ v_2 \\ \vdots \\ u_n \\ v_n \end{bmatrix} = \begin{bmatrix} u_1 \\ v_1 \\ f_2(u_1, v_1) \\ g_2(u_1, v_1) \\ \vdots \\ f_n(u_1, v_1) \\ g_n(u_1, v_1) \end{bmatrix} \tag{1}$$

2.2 Output Only Extraction

Some previous work examined the use of machine learning methods to extract NNMs from output only data of nonlinear systems in a manner similar to how singular value decomposition can be used for principal orthogonal decomposition. The work of Worden and Green [8] made use of the representation of NNMs as truncated polynomial series as defined in the Shaw-Pierre paper. Having assumed the form of these polynomials, the coefficients were inferred through an optimisation procedure wherein statistical independence up to a given order of correlation was also maximised. In addition, in the work of Dervilis et al, [9], various machine learning methods drawn from the field of manifold learning were demonstrated for the extraction of NNMs. Both these methods were illustrated on systems of few degrees of freedom for both simulated datasets and an experimental 4 DOF nonlinear dataset from Los Alamos national laboratory [10].

3 Autoencoder Neural Networks

Autoencoder neural networks are a specialised type of neural network often used for dimensionality reduction or de-noising problems [11]. They are constructed, as illustrated in Figure 1,

as a deep neural network architecture with a so-called "bottleneck" layer in which the number of nodes is reduced; in the case of this example to one. The key concept of their operation involves setting the cost function of the network such that the output attempts to re-create the inputs as closely as possible. By the inclusion of the bottleneck layer which forces the data through a lower dimensional feature space, a near optimal reduction of the data onto the feature space dimension can be achieved. The hidden layers in the network allow for a nonlinear transform of the input coordinates before the bottleneck layer. The nature of an autoencoder is such that it simultaneously learns both the encoding operation to transform from the physical to latent space, and the decoding operation whereby the latent variables are returned to the physical space.

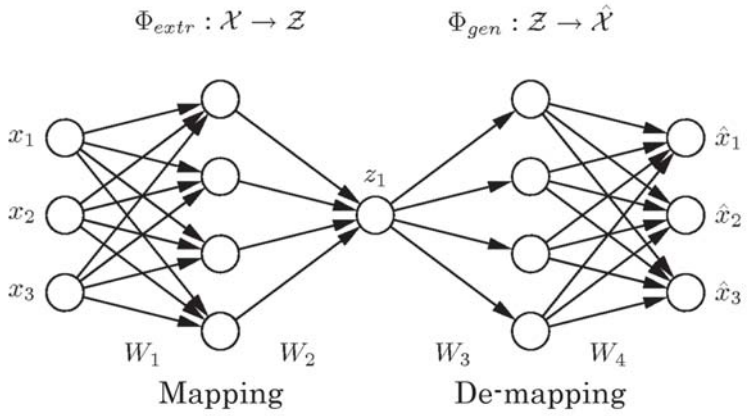

Figure 1: Architecture of an AANN with input/output dimension of 3 and a bottleneck dimension of 2.

Autoencoders have previously been used in similar applications in which it is desired that a model for a system be constructed on a lower dimensional "manifold", whereby it is believed that high dimensional data can be well described as existing on a lower dimensional space [12]. In the case of nonlinear structural dynamics it is thought that the NNMs could correspond to this lower dimensional manifold on which the majority of the high dimensional data can be represented. The same way that a high dimensional linear finite element model can often be represented on a far lower number of mode shapes. The encoding of an autoencoder is the function through which the high dimensional input data can be transformed to the lower dimensional manifold or NNM space, whilst the decoder can provide the inverse operation.

4 Model Order Reduction with Autoencoders

The first step of the model order reduction method used herein involves generating training data from the system of interest. This pertains to creating simulation time histories for the model of both the forcing and response of the system at all DOFs. Having generated time histories, the autoencoder can be used to compress the dimensionality down to a reduced number of latent variables or NNMs. These are extracted from the displacement time histories of the data with a number of NNMs retained, which balances reduction in the dimensionality of the system with accuracy of reconstruction of the full field response, as shown in Figure 2. In this process the cost function used is described by Equation 2, which can be seen as the mean squared error of

reconstruction between the original time series and those after compression.

$$\ell(\hat{x}) = \frac{1}{N}\sum_{i=1}^{N}(x_i - \hat{x_i})^2 \tag{2}$$

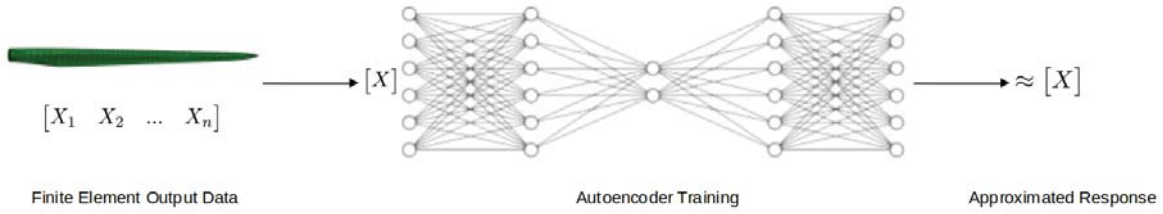

Figure 2: 1st step of ROM; a reduced number of NNMs are extracted from output only dataset

As opposed to projection based reduction methods, whereby the original equations of motion can be projected on to the reduced coordinate set and solved through conventional means, the method developed herein uses a statistical regression to allow for future simulations of the system. The regression model is trained which predicts the response of the system within the NNMs based on a given forcing time history, as illustrated in Figure 3. The regression model is trained based on the forcing time histories used for the simulation, F, and the corresponding NNMs are extracted by the encoder, Y.

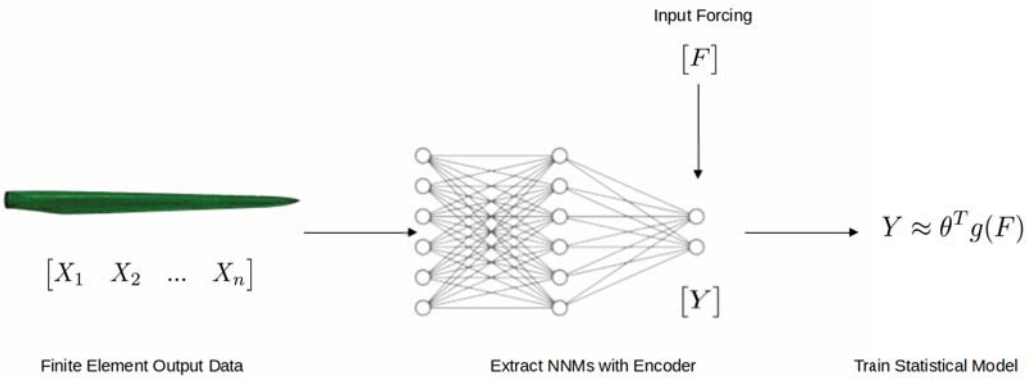

Figure 3: 2nd step of the ROM; a regression model is trained which predicts response in the retained NNMs based on forcing histories.

The final step in the metamodelling process is to predict the system response to a new forcing time history. As illustrated in Figure 4, the trained regression model is used to predict the response of the system within the NNMs, having predicted this response, Y_{pred}, the full field response, X_{pred}, can be recovered by using the decoding portion of the autoencoder.

5 LSTM Neural Networks

In constructing the meta-model, a statistical regression model must be used which can predict new time histories of the latent variables based on forcing time histories. The time series nature of the data would encourage the use of a method including an auto-regressive element. The nonlinear nature of the system would further require a nonlinear regression method to accurately

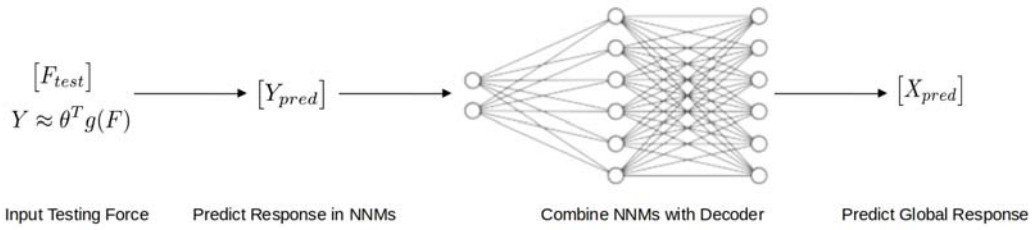

Figure 4: 3rd step of the ROM; the response in the NNMs is predicted for new forcing histories and the full response is reconstructed through the decoder

represent the nonlinear dynamics. In this case it was decided to use a neural network regression architecture, the advantages of neural networks being the scalability and ability to perform MIMO regression.

Recurrent neural networks (RNNs) are a class of networks developed specifically for dealing with sequence data such as time series [13]. The core of an RNN is not dissimilar from that of an ARX model. A basic RNN consists of a unit which receives as input exogenous variables along with a hidden state value which is propagated from the previous time step. Based on these inputs a new value of the hidden state is calculated using a conventional neural network layer, i.e. through multiplication with a weight matrix and then application of an activation function. The output at each time step can then be calculated through an additional layer or layers which act upon the hidden state of the RNN. The hidden state of the RNN can preserve some context information about the previous states and inputs. In contrast to an ARX method however, it is not necessary to state apriori, how many previous values of input and outputs should be considered. This means that theoretically, RNNs can be very powerful at learning relationships between time series with long term dependencies, however, in practice it was found that when training an RNN using back propagation through time, the process suffered from vanishing gradients. As a result of this, a conventional RNN struggles to propagate errors back through many time steps and hence fails to learn long term dependencies [14]. This motivated the development of more advanced RNN cells, such as the long short term (LSTM) cell [15].

Much of the significant work with RNNs has been achieved making use of LSTM cells. These have found very wide use in the field of natural language processing (NLP) [16] as well as time series forecasting [17]. In the area of mechanical systems however, the use of LSTM networks is less prevalent with a limited amount of work applying them to traditional system identification problems [18]. They have proven themselves however, to be capable of learning long term nonlinear relationships in NLP tasks and hence have significant potential as a useful regression framework for nonlinear time series.

6 Case Study

We verify applicability of the proposed method on a 20 degree-of-freedom mass, spring, damping system. The system was considered to be comprised of 20 masses in a chain, with linear spring, linear damping and nonlinear spring elements between each mass, as demonstrated in Figure 5. The nonlinearity of the non-linear spring elements is of the cubic type. Forcing was applied to this system in two locations, at the first and final masses in the chain. All the parameters are assumed uniform across all degrees of freedom and the underlying linear system is proportionally damped; the parameters are defined as follows: $M_i = 0.1\,kg$, $K_l = 100\,N/m$, $C_l = 0.1\,kg/s$, $K_{nl} = 2500\,N/m^3$.

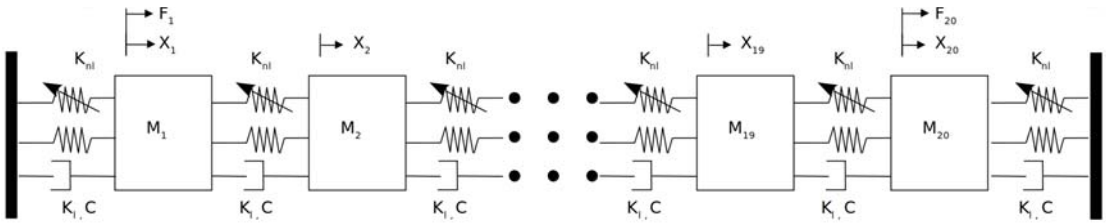

Figure 5: The simulated 20 DOF system including cubic nonlinear spring elements between each mass.

Time series simulations of this system were carried out using a 4th order Runge-Kutta fixed step integration scheme. A sampling frequency of 100 Hz was used for the simulation with a total time series length of 1000s. The forcing applied at masses 1 and 20 comprises realisations of a constant amplitude Gaussian white noise input, which had been low pass filtered with a cut-off frequency of 8 Hz. Figure 6 shows the multicoherence between the input forcing and the outputs of the system both for the underlying linear system and the nonlinear system tested. The nonlinear system shows considerably more incoherence with the input than the linear system, this demonstrates the considerable nonlinearity of the response. For both systems the region of interest is principally at frequencies below 8 Hz. In both cases the response begins to become completely incoherent at higher frequencies it is thought that this is largely an artifact of the processing, since the forcing contains very little energy at higher frequencies both the input and output in this region is very small making the coherence value very sensitive to numerical and processing errors.

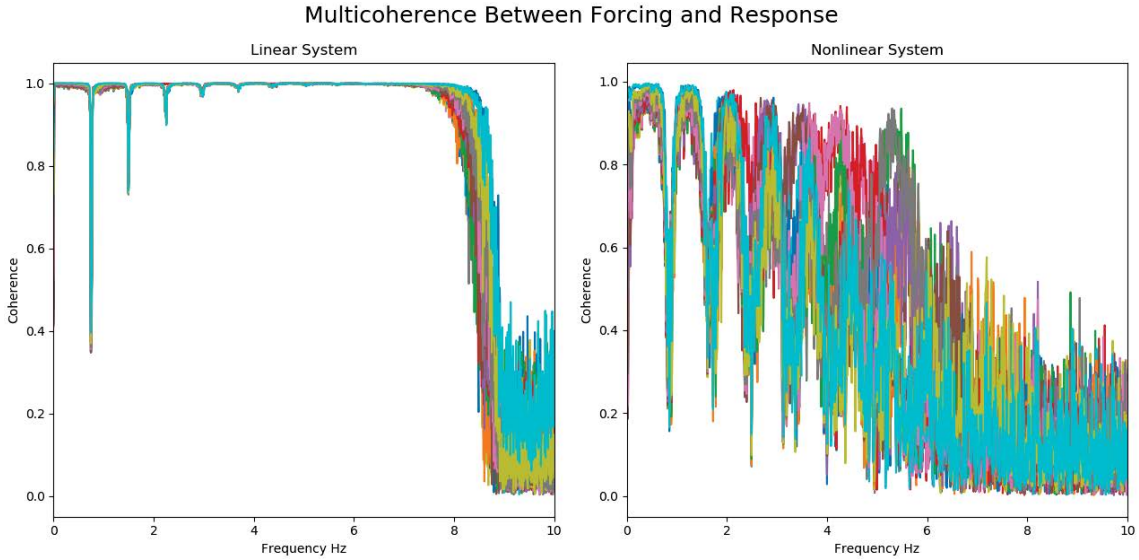

Figure 6: Multicoherence of the signal

Figure 7 demonstrates the comparative magnitude of the restoring force in the linear and nonlinear spring elements of the system a the 10^{th} DOF. The magnitude of the nonlinear restoring force can be seen to be considerable regularly exceeding that of the linear elements. As such it can be considered that the system considered differs significantly from the underlying linear system. The remaining DOFs also demonstrated similar behaviour.

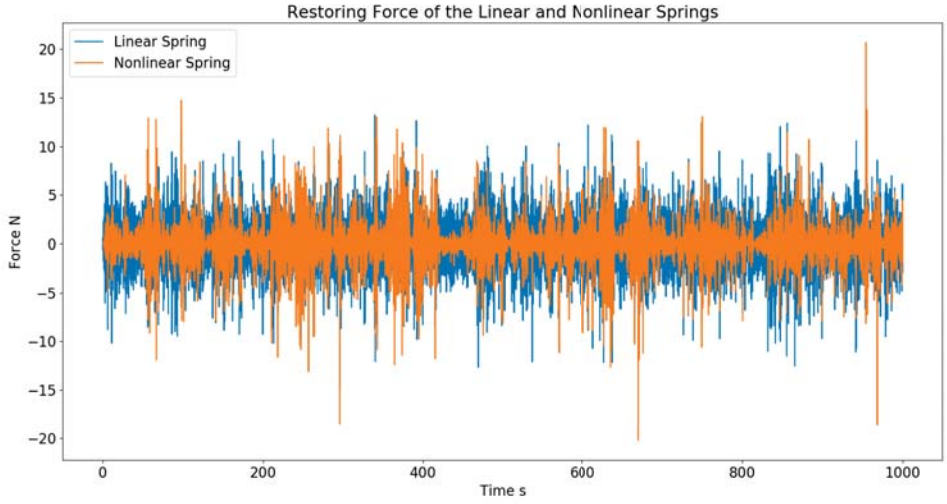

Figure 7: Restoring Force time History of the Linear and Nonlinear Spring Elements at the 10^{th} DOF

6.1 NNM Extraction

A 5 layer autoencoder is used for the extraction of NNMs from the output data. The encoder receives as input the 20 dimensional data corresponding to the displacement time histories at each of the 20 masses. The encoder portion consists of a hidden layer containing 20 nodes with a linear activation function, followed by a second 20-node layer with a hyperbolic tangent activation function. These layers were followed by the bottleneck layer consisting of 10 nodes. The decoder portion of the autoencoder mirrors the encoder in reverse, passing through a 20 node hidden layer with a hyperbolic tangent activation to a 20 node layer with a linear activation to the 20 dimensional output layer.

For the training of the autoencoder, a training dataset consisting of the first 50 % of the time histories was used corresponding to the first 500 s. The second 50 % of the time histories were used as a testing dataset. It is noteworthy that the resulting training and testing loss values were similar, indicating that the NNMs captured were generalisable over the whole dataset. Figure 8 shows the full order response along with the response reconstructed with 10 retained NNMs for the 1st DOF in the model.

It is worth noting, that in previous studies involving output only extraction of NNMs using machine learning, that a key justification in referring to the extracted components as NNMs, is that the components be statistically independent. This statistical independence is considered to be analogous to the modal invariance property of theoretical NNMs [8][7] and the orthogonality property of linear modes. Figure 9 presents the correlation matrix of the NNMs extracted by the autoencoder used herein. The non-zero off diagonal elements of this matrix imply significant correlation between the extracted components which implies that these are rather NNM-like quantities and do not comply with the strict definition of NNMs.

6.2 Response Prediction in the Latent Space

The response prediction in the NNMs involves a non-linear multivariate time series forecasting problem. This problem proved to be the most challenging aspect of the ROM process. Various regression architectures were attempted including polynomial NARX, Gaussian pro-

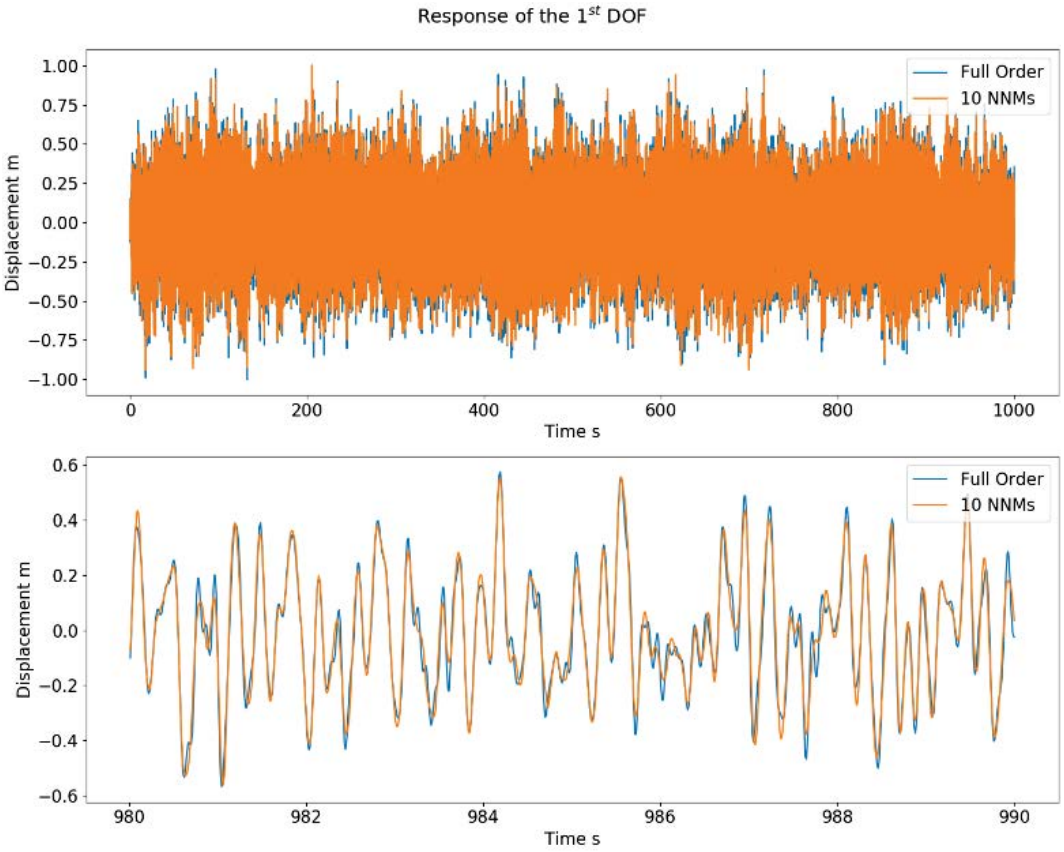

Figure 8: Reconstruction of the response at the 1st DOF with 10 retained NNMs

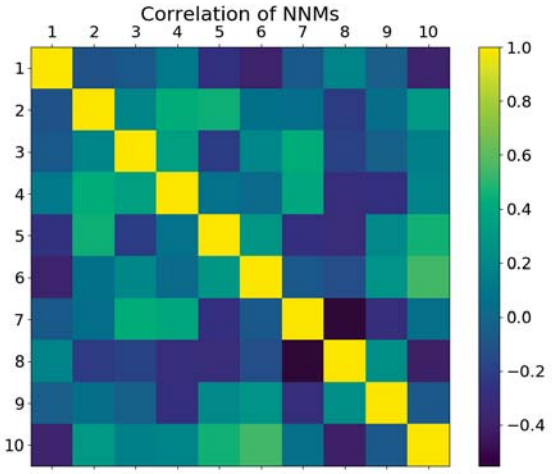

Figure 9: Correlation between the 10 extracted NNMs

cess NARX and recurrent neural net-works (RNN). Finally, a long short term (LSTM) neural network [15], a type of RNN with improved long term memory characteristics, was used for this process. The regression was setup as an autoregressive process. This implies that the input for the prediction model at each time step includes not only the current and previous values of the forcing, but also previous values of the output. In training a prediction error was used,

meaning that for each time step the ground truth values of the previous system outputs were given. During the testing stage however, a simulation error was used, meaning that the outputs predicted by the model at previous steps were subsequently fed to the model as inputs at a next time instant. The LSTM network used 64 hidden cells with 100 previous input and output values also fed as inputs to the network. The training data was assumed as the first 60% of the time histories with predictions made on the next 1000 points corresponding to 10s, the exogenous inputs for this prediction were taken as the next 1000 points of forcing time history, which were not used in the training process. Initial states used for the first model prediction, were taken from the final "true" values in the training dataset.

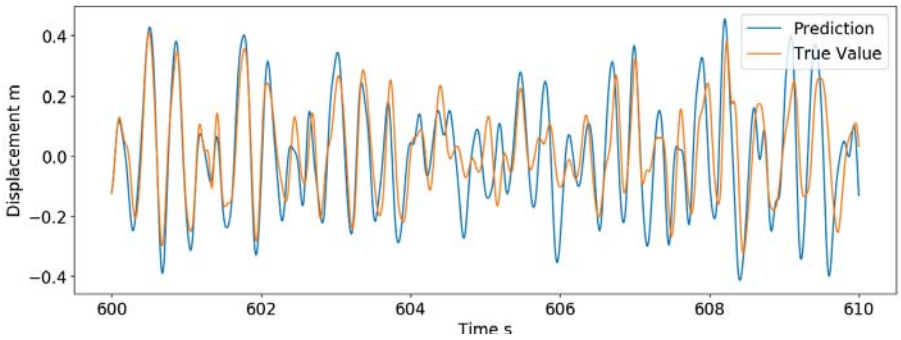

Figure 10: The respone prediction in the latent space for the 1st NNM

Figure 10 compares the prediction of the response in one of the NNMs using the LSTM regression to the "true value". The latter is the value obtained when the physical coordinate time series is passed through the encoder section of the autoencoder. The prediction performs well initially but diverges somewhat over time, it is noteworthy however that the prediction does not become unstable. Similar performance was obtained for all of the 10 NNMs predicted.

6.3 Response Prediction in the Physical Space

Upon availability of the response predictions of the system in the NNM variables, the full response prediction can be determined by simply passing the predicted NNM time histories through the decoder portion of the autoencoder. The decoder combines the NNMs so as to recreate the response in the physical space and is hence analogous to the nonlinear super-position discussed by Shaw and Pierre.

Figure 7 compares the true and predicted values of the response simulated for 1000 timesteps between the ground truth and the model predicted values. For these predictions, the testing dataset lies outside of the training dataset both in the case of the autoencoder training and the regression model training. The predictions shown include both the 1st and 10th DOF predictions, in both cases, the prediction performance is initially quite good with performance decreasing with in-creasing simulation time. Whilst the performance does degrade over time, the predictions still remain stable and of a similar magnitude and frequency as the true values. The mean squared error values for each of the predictions shown below were 0.025 and 0.048 respectively. These two examples are indicative of the performance of the method across all 20 degrees of freedom of the system.

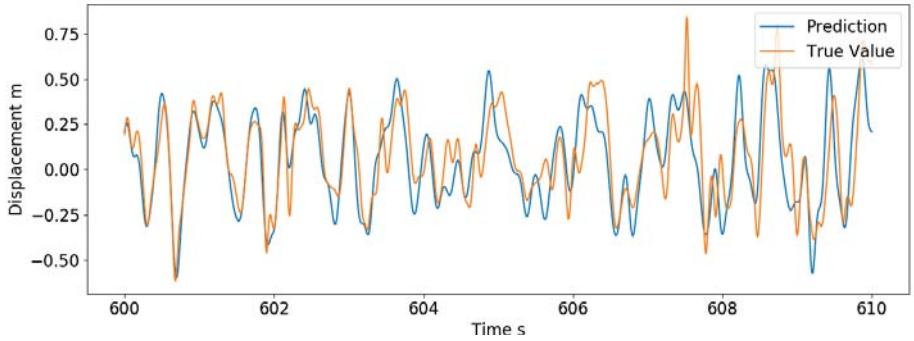

(a)

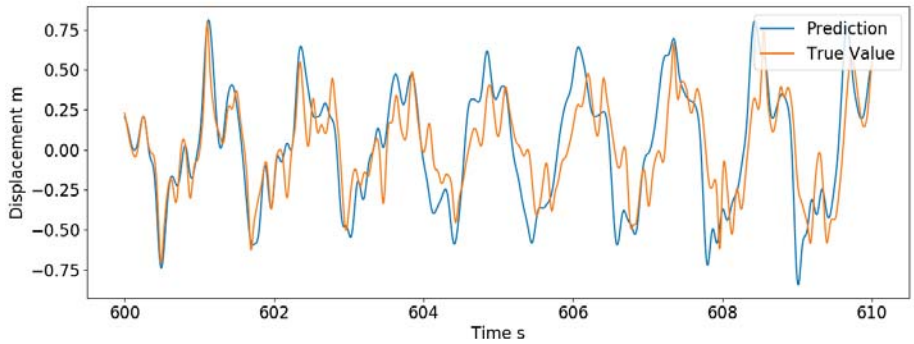

(b)

Figure 11: The final response prediction for both the 1st (a) and 10th (b) DOF for a new force history input

7 Conclusions

A novel reduced order modelling method was demonstrated, which relies exclusively on input and output data from nonlinear structural systems to allow for time series predictions under arbitrary dynamic forcing. The method makes use of nonlinear normal modes as an efficient reduction basis for nonlinear dynamical systems. It was discussed how these NNMs can be extracted using machine learning methods in an invertible manner and a predictive model was created using an LSTM neural network. The modelling procedure was demonstrated on a 20 DOF nonlinear system featuring cubic nonlinearities. Despite shortcomings in the reconstruction accuracy, which is understandable for this high order of nonlinearity, the proposed method shows considerable promise.

The demonstrated method does offer numerous advantages. It does not assume any a priori form of the nonlinearity considered and hence may be generally applicable to multiple systems. Secondly, due to the nonlinear nature of the NNMs, they should, if sufficient training data is used, be generally valid over the whole state trajectory of a system, as opposed to previous methods based on linear projections.

Future development will concentrate on improving the performance of the regression problem in order to increase the accuracy of the model predictions. In addition, it will be investigated how the amplitude range of the forcing affects the modelling technique and to whether the model can generalise well to broad ranges of input amplitude. Further to this, the method will be tested on larger scale problems, such as finite element simulations of nonlinear elements

or jointed systems. It is also thought that the method may demonstrate greater advantages when applied to larger models, due to a greater number of redundant degrees of freedom. Finally, it is worth noting that variational autoencoders [19] can be considered to enforce statistical independence of the extracted components, hence improving predictive capability.

Acknowledgements

This work was carried out as part of the ITN project DyVirt and has received funding from the European Union's Horizon 2020 research and innovation programme under the Marie Skłodowska-Curie grant agreement No 764547

References

[1] Roy Craig and Mervyn Bampton. Coupling of Substructures for Dynamic Analyses. *AIAA Journal, American Institute of Aeronautics and Astronautics*, 6(7):1313–1319, 1968.

[2] D De Klerk, D J Rixen, and S N Voormeeren. General Framework for Dynamic Substructuring: History, Review, and Classification of Techniques. 2008.

[3] Kevin Carlberg and Charbel Farhat. A Proper Orthogonal Decomposition-Based Augmented Conjugate Gradient Algorithm for Nearby Problems. Technical report, 2009.

[4] Long Wu and Paolo Tiso. Nonlinear model order reduction for flexible multibody dynamics: a modal derivatives approach. *Multibody Syst Dyn*, 36:405–425, 2016.

[5] R M Rosenberg. The Normal Modes of Nonlinear n-Degree-of-Freedom Systems. *Journal of Applied Mechanics*, 29(1):7–14, 1962.

[6] George Haller and Sten Ponsioen. Nonlinear normal modes and spectral submanifolds: existence, uniqueness and use in model reduction. *Nonlinear Dynamics*, 86:1493–1534, 2016.

[7] S W Shaw and C Pierre. Normal Modes for Non-Linear Vibratory Systems. *Journal of Sound and Vibration*, 164(1):85–124, jun 1993.

[8] K Worden and P L Green. A machine learning approach to nonlinear modal analysis. *Mechanical Systems and Signal Processing*, 84B:34–53, 2016.

[9] N. Dervilis, T.E. Simpson, D.J. Wagg, and K. Worden. Nonlinear modal analysis via non-parametric machine learning tools. *Strain*, 55(1), 2019.

[10] Elói Figueiredo, Gyuhae Park, Joaquim Figueiras, Charles Farrar, and Keith Worden. Structural Health Monitoring Algorithm Comparisons Using Standard Data Sets. Technical report, Los Alamos National Laboratory, 2009.

[11] G. E. Hinton and R. R. Salakhutdinov. Reducing the dimensionality of data with neural networks. *Science*, 313(5786):504–507, jul 2006.

[12] Youngjoon Yoo, Sangdoo Yun, Hyung Jin Chang, Yiannis Demiris, and Jin Young Choi. Variational Autoencoded Regression: High Dimensional Regression of Visual Data on Complex Manifold. Technical report, 2017.

[13] David E Ruineihart, Geoffrey E Hint, and Ronald J Williams. LEARNING INTERNAL REPRESENTATIONS BY ERROR PROPAGATION two. Technical report, 1985.

[14] Yoshua Bengio, Patrice Simard, and Paolo Frasconi. Learning Long-Term Dependencies with Gradient Descent is Difficult. *IEEE Transactions on Neural Networks*, 5(2):157–166, 1994.

[15] Sepp Hochreiter and Jürgen Schmidhuber. Long Short-Term Memory. *Neural Computation*, 9(8):1735–1780, nov 1997.

[16] Martin Sundermeyer, Ralf Schlüter, and Hermann Ney. LSTM Neural Networks for Language Modeling. Technical report.

[17] Andre Gensler, Janosch Henze, Bernhard Sick, and Nils Raabe. Deep Learning for solar power forecasting - An approach using AutoEncoder and LSTM Neural Networks. In *2016 IEEE International Conference on Systems, Man, and Cybernetics, SMC 2016 - Conference Proceedings*, pages 2858–2865. Institute of Electrical and Electronics Engineers Inc., feb 2017.

[18] Yu Wang. A new concept using LSTM Neural Networks for dynamic system identification. In *Proceedings of the American Control Conference*, pages 5324–5329. Institute of Electrical and Electronics Engineers Inc., jun 2017.

[19] Diederik P. Kingma and Max Welling. Auto-encoding variational bayes. In *2nd International Conference on Learning Representations, ICLR 2014 - Conference Track Proceedings*. International Conference on Learning Representations, ICLR, dec 2014.

EURODYN 2020
XI International Conference on Structural Dynamics
M. Papadrakakis, M. Fragiadakis, C. Papadimitriou (eds.)
Athens, Greece, 23–26 November 2020

KALMAN-BASED COUPLED RESPONSE-INPUT ESTIMATION DURING ENVIRONMENTAL TESTS ON THE BOX ASSEMBLY WITH REMOVABLE COMPONENT STRUCTURE

S. Vettori[1,2], E. Di Lorenzo[1], B. Peeters[1], E. Chatzi[2]

[1]Siemens Digital Industries Software
Interleuvenlaan 68, 3000, Leuven, Belgium
e-mail: {silvia.vettori,emilio.dilorenzo,bart.peeters}@siemens.com

[2] Institute of Structural Engineering, ETH Zürich
Stefano-Franscini-Platz 5, CH-8093 Zürich
e-mail: chatzi@ibk.baug.ethz.ch

Keywords: Virtual Sensing, Kalman Filter, Response Estimation, Environmental Testing, Boundary Condition Challenge.

Abstract. *Environmental tests are conventional procedures conducted to verify whether a spacecraft and all its components can stand the random excitations to which they are subjected throughout their operational life. In this framework, the Boundary Condition Challenge (BCC) aims at the establishment of new testing practices that allow to improve the poor operational environment representation currently achieved during environmental tests. The challenge focuses on the Box Assembly with Removable Component (BARC), a mock-up which is currently studied by several research institutes. The BARC has been subject to a measurement campaign carried-out at Siemens Industry Software, during which it has been placed on a modal shaker of comparable size and excited along its vertical axis. In order to improve service response replication during these tests, Virtual Sensing (VS) techniques, such as Kalman-type filters, can be used for estimating the complete response field from a limited number of measured responses. Moreover, by jointly estimating states and inputs, the unmeasured loads applied to the system can also be inferred. This work proposes the use of a combination of strain and acceleration observations to enhance the estimation of the mentioned unmeasured inputs.*

1 INTRODUCTION

Environmental testing is a standard procedure in spacecraft engineering used for verifying the resistance of the system and all its components to the random excitations to which they are subjected throughout their operational life. During these tests, the spacecraft is mounted on a shaker testing facility of comparable size and excited with the purpose of replicating its in-service structural response. Limitations in the adopted vibration control strategies and difficulties in reproducing realistic boundary conditions, can give rise to a poor operational environment representation, leading to undesired issues, e.g. over- or under testing, errors in failure modes and time to failure estimation or even damage.

In this framework, a collaboration between Kansas City National Security Campus (managed by Honeywell Federal Manufacturing & Tecnology) and Sandia National Laboratories introduced the Boundary Condition Challenge (BCC) [1], [2] [3]. The goal of the BCC is to improve the in-service environment replication at a component level during environmental tests. The challenge makes use of a simple demonstrator known as the "Box Assembly with Removable Component" (BARC).

Virtual Sensing (VS) techniques such as Kalman-type filters [4], can be used for environmental testing applications to combine information from simulated models and test data with the purpose of estimating the quantities of interest, e.g. the complete strain field on the tested component or/and the inputs provided to the structure by the shaker [5] [6]. In this view, the Augmented Kalman Filter (AKF) [7] has been employed in [8], on strain data acquired during a measurement campaign performed by exciting the BARC via a monoaxial electrodynamic shaker. The mentioned work shows that a good response reconstruction can be achieved. At the same time, the absence of acceleration data among the observations used in the AKF [9] [10] and the test boundary conditions uncertainties, strongly affect the input estimation results.

This work proposes the use of a combined set of strain and acceleration observations to be employed in the AKF. A comparison with results obtained by using strain observations only is hereby provided. It is shown how the addition of acceleration measurements contributes to enhance the input estimation results. Boundary conditions uncertainties, which still influence the estimation outcome, will be object of future investigations.

2 VIRTUAL SENSING FOR ENVIRONMENTAL TESTS ON THE BARC

In order to improve the currently adopted environmental testing procedures, a full comparison between operational and test component responses, both when the sole component or the entire assembly are tested, must be available. In this sense, VS techniques can be used to expand the information pertaining to the system's response, i.e., to infer response at locations that are hard to instrument or even to yield the full field response of the tested structure. Additionally, joint input-state estimation techniques can be used for estimating inputs applied to the system, given that they are not usually measured during environmental tests.

2.1 Test campaign

Virtual Sensing techniques have been employed on data acquired during the test campaign described in detail in [8]. The BARC, object of the mentioned tests and shown in Figure 1, is made up of two units: the upper one plays the role of the component under test, while the lower one, addressed as "subassembly", represents a general fixture used to attach the component on the shaker during tests.

Figure 2a shows the complete setup adopted during the mentioned test campaign, while

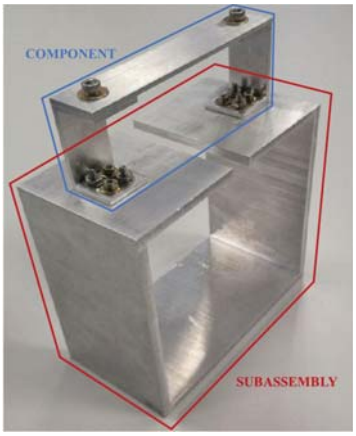

Figure 1: The Box Assembly with Removable Component

detailed focus on the sensors and BARC's connection to the shaker is provided in Figure 2b. Several excitation signals with different amplitude levels have been used during tests, such as single sines, sine sweeps and random signals.

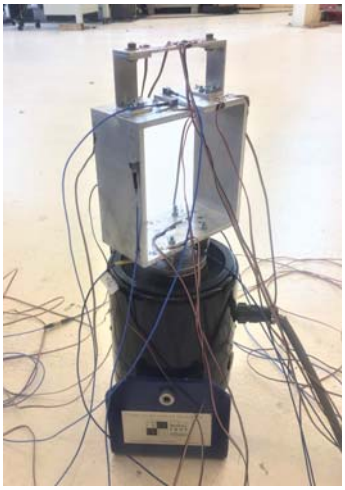

(a) BARC mounted on a monoaxial electrodynamic shaker

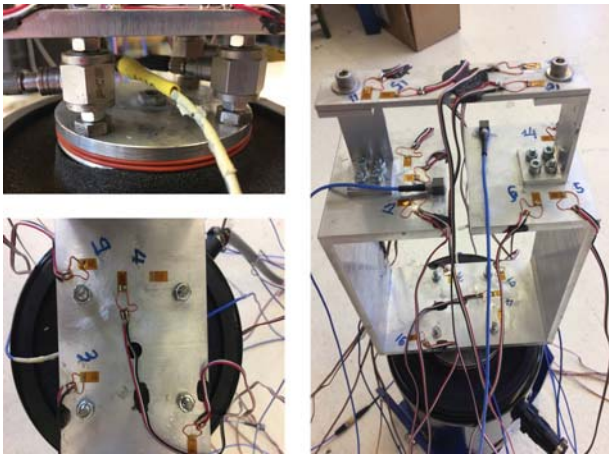

(b) Detailed view of sensors and BARC's attachment on the shaker

Figure 2: Test setup

2.2 Virtual Sensing: objectives and adopted procedures

Kalman-based strategies are well known tools for input-state-response estimation and can be therefore adopted for environmental testing applications, such as the BARC case study. Their working principle consists in combining a discrete-time state space representation of the system with observations measured at a limited number of locations on the structure with the purpose of inferring the states of the system at each time step, as well as the unknown input. From the estimated states, the responses at unmeasured locations can be derived.

In [8], the estimation of the quantities of interest via the AKF during a test run performed using a pseudo random signal (0.3 V RMS level) was proposed. Indeed, random signals repre-

sent the type of excitation adopted during environmental tests.
The state-space matrices of the system are usually retrieved by making use of a validated simulation model which can well represent the physical system and the boundary conditions to which it is subjected during tests. A Reduced Order Model (ROM) is usually built in order to reduce the computational effort derived by models large dimensions. For the hereby described application, a Model Order Reduction (MOR) technique, as described in [11], has been applied. According to this method, the dynamic behavior of the BARC can be formulated as a superposition of modal contributions and the adopted reduction basis includes the normal modes of the system in the frequency range of interests and a set of Residual Inertia-Relief Attachment (RIRA) modes, one for each unknown input to be estimated. More details about how this procedure has been implemented for the BARC case can be found in [8].

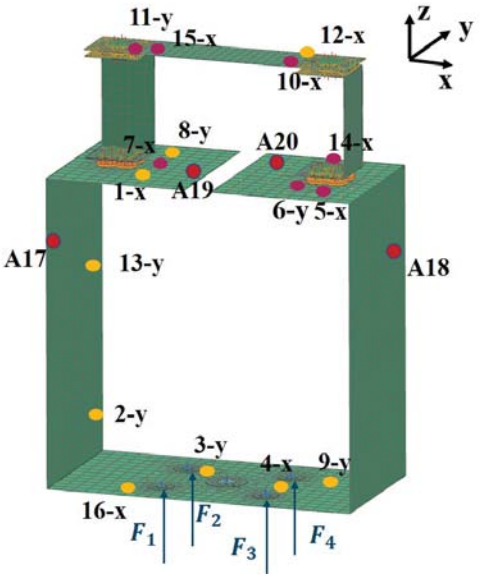

Figure 3: Sensors map: accelerometers (red), measured (yellow) and unmeasured (magenta) strain sensors locations

Figure 3 shows the test sensors (sixteen monoaxial strain gages and four triaxial accelerometers) locations and directions obtained by applying an existing Optimal Sensor Placement (OSP) strategy [12] [13]. Moreover, the four inputs to be estimated are reported. Figure 2b shows that a monoaxial force cell has been placed between the BARC and the shaker at each bolted connection, i.e., at each input location, in order to measure the applied forces in Z direction. These quantities were indeed used as references for the estimation.
Only a reduced subset of nine strains has been included in the set of observations used in the AKF, the remaining ones have been used as reference quantities to check the validity of the response estimation. The measured locations have been chosen in order to focus on response estimation at the component level and to guarantee that measurements collocated with the applied forces could be included. Indeed, collocated measurements allow for a more accurate reconstruction of the inputs [14].
The observability requirements for the reduced sensor set have been checked by ensuring that the condition number of the observability matrix [8] for the reduced set is of the same order of magnitude as the one obtained in the full sensor set, which is guaranteed by the OSP adopted

stategy.

3 INPUT-STATE-RESPONSE ESTIMATION USING THE AKF

3.1 Strain-based Virtual Sensing for environmental testing: results and limitations

As pointed out in [8], the AKF provides a good response estimation, except for the poor reconstruction of high frequency components magnitude on the sensor measuring in y direction. This model gap is well compensated for measured signals in x direction, such as sensor 10, because higher measured response levels were detected for all the sensors measuring in x direction with respect to the ones measuring in y direction.
On the contrary, as shown in Figure 5, input estimation fails to provide good results. The imprecise estimation of the four vertical forces can be explained by the presence of strong boundary conditions uncertainties. As reported in Figure 5 (right), the measured forces are not characterized by flat PSDs. The BARC was indeed exhibiting modal deformations at its several natural frequencies during tests, thus affecting the quantities measured by the force cells. Moreover, according to the natural frequency and the corresponding mode shape, the four force cells were differently influenced, thus resulting in four different PSD shapes. Additionally, the boundary conditions used in the model introduce a strong approximation of the test configuration. In this respect, including the shaker in the model and modeling its interaction with the BARC represents another additional development.

3.2 Virtual Sensing using a fusion of strain and acceleration sensors

This Section reports on the results obtained by applying the AKF for jointly estimating inputs and responses using an observations set that contains both strain and acceleration measurements. Figure 4 illustrates the response estimation of strain sensors 10 and 11 when acceleration sensors A17, A18, A19, A20 shown in Figure 3 are included in the measured quantities. A comparison with the results obtained in the case of strains-only observations is also offered. Moreover, Table 1 reports the RMSE values of the estimated responses with respect to their measured time histories. It is possible to conclude that a good agreement is obtained between the two resulting estimated quantities for both sensors 10 and 11.

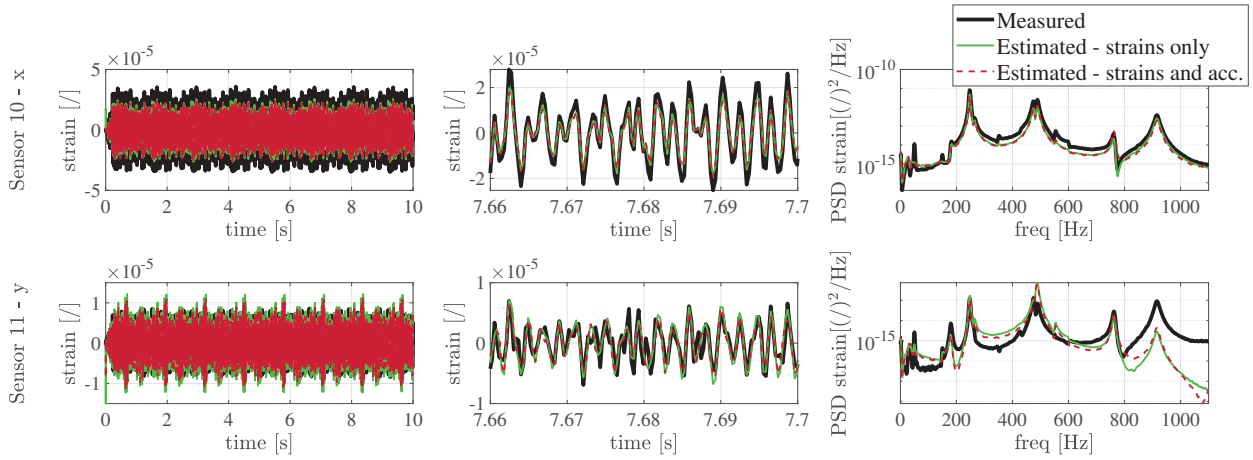

Figure 4: Time history (left), detailed time history (middle) and PSD (right) of strain responses of sensors 10 and 11.

	Sensor 10 - x	Sensor 11 - y
Strains only	3.98×10^{-6}	2.83×10^{-6}
Strains and accelerations	4.11×10^{-6}	2.81×10^{-6}

Table 1: RMSE values of the estimated responses of sensors 10 and 11 with respect to their measured time histories.

Figure 5 proposes a comparison between the input estimation results obtained in the strains-only case and the ones achieved in case the combined set of strains and accelerations is used. This plot indicates that the introduction of a direct feedthrough, i.e., a non-zero output-input matrix in the observation equation of the state-space model, allows for an overall better force estimation. In particular, Figure 5 (right) shows that including accelerations allows to detect PSDs peaks, e.g. at around 250, 550 and 760 Hz, that are not identified when using only strains. Moreover, from Figure 5 (left) it is possible to notice that the force amplitude better matches the actually measured one, with the exception of input 1, which is overestimated.

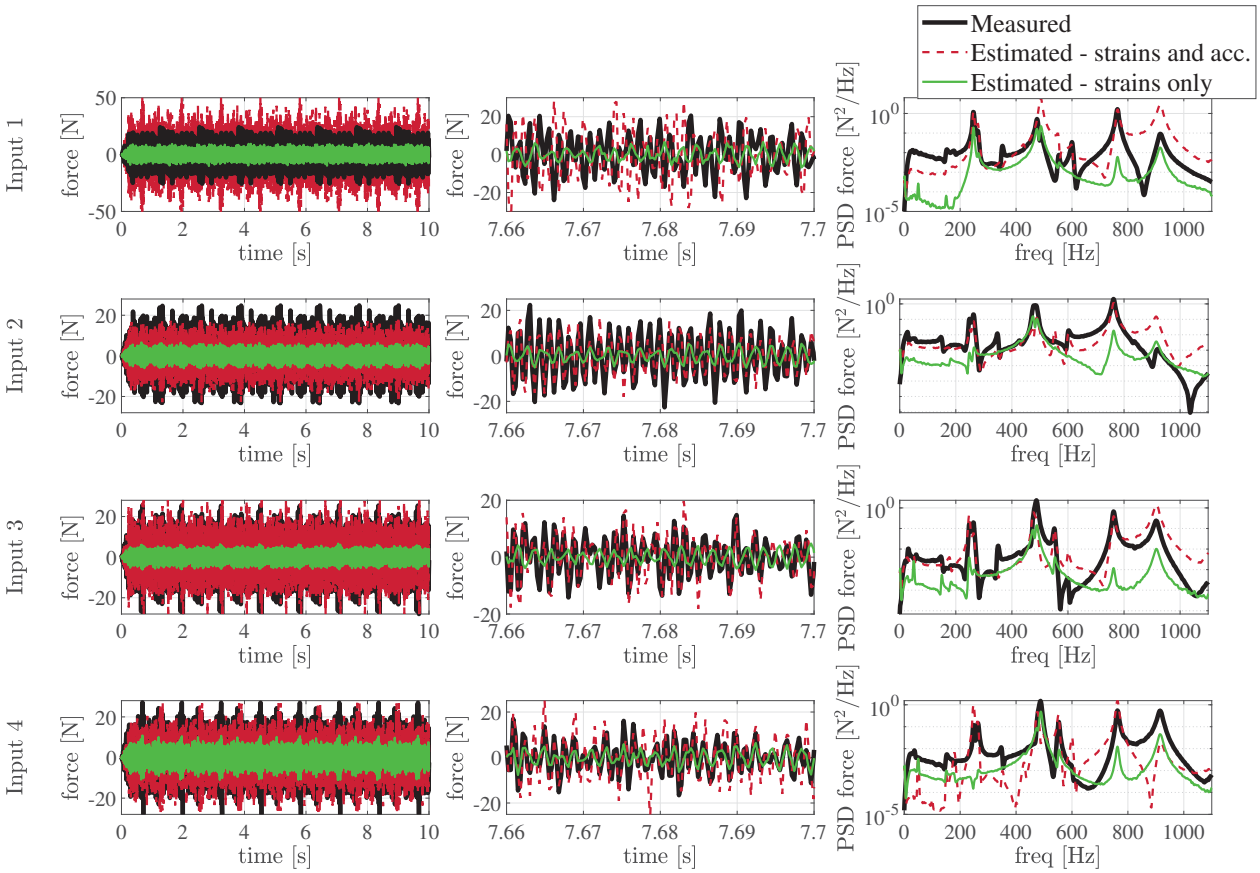

Figure 5: Time history (left), detailed time history (middle) and PSD (right) of input 1, input 2, input 3 and input 4.

Table 2 shows the RMSE values of the four estimated inputs with respect to their measured time histories. The RMSEs comparison for inputs 2 and 3 demonstrates the enhancement achieved by introducing acceleration observations. On the contrary, the RMSE values associated with inputs 1 and 4 show an increase with respect to the values obtained in the strains-only

case. The RMSE related to input 1 is indeed effect of the previously mentioned overestimation, which can be explained by the poor reproduction of the test boundary conditions in the model. Indeed, this issue can negatively influence the terms relating input 1 and the acceleration observations in the output-input matrix of the system's state-space model. Likewise, also the RMSE increase for input 4, visible in some overestimated peaks in Figure 5 (input 4, center), can be attributed to the boundary conditions uncertainties.

	Input 1	Input 2	Input 3	Input 4
Strains only	8.1	7.1	8.7	4.8
Strains and accelerations	17.7	6.9	8.2	8.9

Table 2: RMSE values of the estimated inputs with respect to their measured time histories.

4 CONCLUSIONS

An enhancement of the AKF application to environmental tests on the BARC has been proposed in this paper. A previously presented work [8] already discussed the potential of the AKF for both input and state estimation on this simple hardware demonstrator. Limitations of the application of the algorithm to strains-only data have been pointed out. The present work has reported the results obtained by employing the AKF on an observations set including strain and acceleration measurements. It is shown that the introduction of accelerations, even if non-collocated with the unknown inputs, improves the global result in terms of input estimation. On the contrary, no differences are detected in terms of component response estimation. However, uncertainties affecting the test boundary conditions and their approximated representation in the simulation model still influence the estimation results. In this sense, a further improvement could consist in including the shaker in the simulation model in order to take into account its interaction with the BARC.

5 ACKNOWLEDGEMENTS

The author gratefully acknowledge the European Commission for its support of the Marie Sklodowska Curie program through the ITN DyVirt project (GA 764547).

REFERENCES

[1] William Larsen, Jason R Blough, James P DeClerck, Charles D VanKarsen, David E Soine, and Richard Jones. Initial modal results and operating data acquisition of shock/vibration fixture. In *Topics in Modal Analysis & Testing, Volume 9*, pages 363–370. Springer, 2019.

[2] Umberto Musella, Mariano Alvarez Blanco, Davide Mastrodicasa, Giovanni Monco, Manzato Simone, Bart Peeters, Emiliano Mucchi, Patrick Guillaume, et al. Combining test and simulation to tackle the challenges derived from boundary conditions mismatches in environmental testing. In *Sensors and Instrumentation, Aircraft/Aerospace, Energy Harvesting & Dynamic Environments Testing, Volume 7*, pages 259–269. Springer, 2020.

[3] Daniel P Rohe, Scott Smith, Matthew RW Brake, James DeClerck, Mariano Alvarez Blanco, Tyler F Schoenherr, and Troy J Skousen. Testing summary for the box assembly

with removable component structure. In *Sensors and Instrumentation, Aircraft/Aerospace, Energy Harvesting & Dynamic Environments Testing, Volume 7*, pages 167–177. Springer, 2020.

[4] Saeed Eftekhar Azam, Eleni Chatzi, Costas Papadimitriou, and Andrew Smyth. Experimental validation of the kalman-type filters for online and real-time state and input estimation. *Journal of vibration and control*, 23(15):2494–2519, 2017.

[5] Costas Papadimitriou, Claus-Peter Fritzen, Peter Kraemer, and Evangelos Ntotsios. Fatigue predictions in entire body of metallic structures from a limited number of vibration sensors using kalman filtering. *Structural Control and Health Monitoring*, 18(5):554–573, 2011.

[6] Vasilis K Dertimanis, EN Chatzi, S Eftekhar Azam, and Costas Papadimitriou. Input-state-parameter estimation of structural systems from limited output information. *Mechanical Systems and Signal Processing*, 126:711–746, 2019.

[7] E Lourens, Edwin Reynders, Guido De Roeck, Geert Degrande, and Geert Lombaert. An augmented kalman filter for force identification in structural dynamics. *Mechanical Systems and Signal Processing*, 27:446–460, 2012.

[8] Silvia Vettori, Emilio Di Lorenzo, Roberta Cumbo, Umberto Musella, Tommaso Tamarozzi, Bart Peeters, and Eleni Chatzi. Kalman-based virtual sensing for improvement of service response replication in environmental tests. In *Proceedings of 38th International Modal Analysis Conference (IMAC38), Houston, TX, US*, 2019.

[9] Kristof Maes, E Lourens, Katrien Van Nimmen, Edwin Reynders, Guido De Roeck, and Geert Lombaert. Design of sensor networks for instantaneous inversion of modally reduced order models in structural dynamics. *Mechanical Systems and Signal Processing*, 52:628–644, 2015.

[10] Øyvind Wiig Petersen, Ole Øiseth, and Eliz-Mari Lourens. Estimation of the dynamic response of a slender suspension bridge using measured acceleration data. *Procedia engineering*, 199:3047–3052, 2017.

[11] Roy R Craig Jr. A review of time-domain and frequency-domain component mode synthesis method. 1985.

[12] R Cumbo, T Tamarozzi, K Janssens, and W Desmet. Kalman-based load identification and full-field estimation analysis on industrial test case. *Mechanical Systems and Signal Processing*, 117:771–785, 2019.

[13] Tommaso Tamarozzi, Enrico Risaliti, Ward Rottiers, Wim Desmet, et al. Noise, ill-conditioning and sensor placement analysis for force estimation through virtual sensing. In *In International Conference on Noise and Vibration Engineering (ISMA2016),*, pages 1741–1756. KATHOLIEKE UNIV LEUVEN, DEPT WERKTUIGKUNDE, 2016.

[14] Kristof Maes, Katrien Van Nimmen, E Lourens, A Rezayat, P Guillaume, Guido De Roeck, and Geert Lombaert. Verification of joint input-state estimation for force identification by means of in situ measurements on a footbridge. *Mechanical Systems and Signal Processing*, 75:245–260, 2016.

EURODYN 2020
XI International Conference on Structural Dynamics
M. Papadrakakis, M. Fragiadakis, C. Papadimitriou (eds.)
Athens, Greece, 23–26 November 2020

COMPUTATIONALLY EFFICIENT HIERARCHICAL BAYESIAN MODELING FRAMEWORK FOR LEARNING EMBEDDED MODEL UNCERTAINTIES

Xinyu Jia[1], Omid Sedehi[2], Costas Papadimitriou[1] and Lambros S. Katafygiotis[2]

[1] Department of Mechanical Engineering, University of Thessaly, Volos, Greece
e-mail: {jia, costasp@uth.gr}

[2]Department of Civil and Environmental Engineering, The Hong Kong University of Science and Technology, Hong Kong, China
osedehi@connect.ust.hk, katafygiotis.lambros@gmail.com

Keywords: Hierarchical Bayesian modeling; uncertainty propagation; model updating; structural dynamics; structural reliability; model reduction.

Abstract. *A hierarchical Bayesian modeling (HBM) framework has recently been developed for estimating the uncertainties in the parameters of physics-based models of systems, as well as propagating these uncertainties to estimate the uncertainty in output quantities of interest. According to the framework, uncertainties due to model error are embedded into the model parameters by assigning a parameterized probability distribution and inferring the hyper-parameters of this distribution using multiple sets of experimental data. Herein the framework is extended to properly account for the uncertainty in the prediction error model. The error term is modeled by a Normal distribution with hyper parameters to be estimated by the multiple sets of data. This generalization allow making consistent uncertainty propagation for response quantities of interest. New asymptotic approximations for estimating the uncertainties in the hyper-parameters, as well as propagating these uncertainties to model parameters and observed and unobserved output quantities of interest are developed. The proposed framework provide realistic account of model uncertainties that are insensitive to large number of data sets, avoiding severe underestimation of uncertainty arising from conventional Bayesian learning techniques. Problems drawn from structural dynamics applications are used to demonstrate the effectiveness of the proposed framework.*

1 INTRODUCTION

Bayesian tools can rationally integrate data and physics-based models in order to select the most appropriate models among alternative competing ones, estimate the parameters of these models and their uncertainties, as well as propagating uncertainties to predict important quantities of interest in operation and safety of structural systems [1]. Despite significant advances in the development of Bayesian inference tools for uncertainty quantification and propagation (UQP) in structural dynamics, some challenges still exist and need to be resolved. For example, due to the redundant information carried in the data, the classical Bayesian framework often underestimates the uncertainty, resulting in an inherent reduction of the parameter uncertainty as the number of data increases. More importantly, standard Bayesian procedures do not properly take into account the uncertainty in the parameters due to variability in experimental data, environmental conditions, material properties, manufacturing process, assembling process, and nonlinear mechanisms activated under different loading conditions. Therefore, a better account of the uncertainty is to embed uncertainties within the model by introducing a hierarchy in the model parameters [2].

In this work, a computational efficient HBM framework [3, 4] is further developed and applied to model updating, uncertainty calibration and propagation for linear structural dynamics models using multiple modal data sets. Novel computing tools, based on asymptotic approximations [5] and sampling algorithms [6], are incorporated for parameter inference and uncertainty propagation within the HBM framework. A remarkable feature of this framework lies in the capability to account for identification precision, prediction error, as well as model error, environmental and operational variabilities, offering realistic uncertainties as evidenced in the application. A spring-mass chain model with simulated, noise contaminated, multiple measured modal data sets is used to demonstrate the effectiveness of the proposed approach.

The presentation in this paper is organized as follows. In Section 2, the comprehensive HBM framework based on modal data is proposed. The effectiveness of the proposed method is demonstrated using a 10 degrees of freedom (DoF) spring-mass chain system in Section 3. Section 4 reports the conclusions of this study.

2 PROPOSED COMPUTATIONAL EFFICIENT HBM FRAMEWORK

Let $D=\{D_i,\ i=1,2,\ldots,N_D\}$ be the measured full data sets from the structure comprising N_D independent experiments. Each data set $D_i=\left\{\hat{\lambda}_{r,i},\phi_{r,i}\in R^{N_0},r=1,2,\ldots,m\right\}$ denotes the *i-th* experiment and consists of the square of modal frequencies $\hat{\lambda}_{r,i}$ and mode shapes $\phi_{r,i}$ at N_0 measured degrees of freedoms (DOFs), where m is the number of the observed modes [7]. For each experiment, the modal properties have been obtained by modal estimation techniques using available input-output or output-only vibration measurements. Consider a parameterized class of structural models *M* that is used to predict the squares of the modal frequencies $\lambda_r(\boldsymbol{\theta})$ and mode shapes $\phi_r(\boldsymbol{\theta})$, where $\boldsymbol{\theta}$ is the model parameter set. Herein, uncertainties are embedded into the model parameters by assigning the Gaussian prior probability density function (PDF)

$$p(\boldsymbol{\theta})=N(\boldsymbol{\theta}|\mu_{\boldsymbol{\theta}},\Sigma_{\boldsymbol{\theta\theta}}) \tag{1}$$

for $\boldsymbol{\theta}$ with hyper mean $\mu_{\boldsymbol{\theta}}$ and hyper covariance matrix $\Sigma_{\boldsymbol{\theta\theta}}$ to be estimated using the multiple datasets..

The discrepancy between the *i*-th predicted modal properties and the *i*-th measured data set is quantified based on the prediction error equations, given as follows:

$$\begin{aligned}
&\hat{\lambda}_{r,i} = \lambda_{r,i}(\boldsymbol{\theta}_i) + \hat{\lambda}_{r,i}\ e_r, \\
&\underline{\hat{\phi}}_{r,i} = \beta_{r,i}(\boldsymbol{\theta}_i)\underline{\phi}_{r,i}(\boldsymbol{\theta}_i) + \left\|\underline{\hat{\phi}}_{r,i}\right\|\ \underline{\varepsilon}_r, \\
&\beta_{r,i}(\boldsymbol{\theta}_i) = \frac{\underline{\hat{\phi}}_{r,i}^T \underline{\phi}_{r,i}(\boldsymbol{\theta}_i)}{\underline{\phi}_{r,i}^T(\boldsymbol{\theta}_i)\underline{\phi}_{r,i}(\boldsymbol{\theta}_i)}
\end{aligned} \tag{2}$$

where e_r and $\underline{\varepsilon}_r$ are respectively the prediction errors for the modal frequency and the mode shape components of the *r*-th mode. The prediction errors are then modeled by zero-mean Gaussian variables $e_r \sim N(e_r \mid 0, \sigma^2)$ and $\underline{\varepsilon}_r \sim N(\underline{\varepsilon}_r \mid \underline{0}, \Sigma)$, with covariance matrix $\Sigma = \sigma^2 I$. The standard deviation σ is the hyperparameter to be estimated using the multiple datasets.

According to Bayes rules, the joint posterior distribution of all parameters is built as follows [3]:

$$p(\{\boldsymbol{\theta}_i\}_{i=1}^{N_D}, \Sigma, \boldsymbol{\mu}_{\boldsymbol{\theta}}, \boldsymbol{\Sigma}_{\boldsymbol{\theta}\boldsymbol{\theta}} \mid D) \propto p(\boldsymbol{\mu}_{\boldsymbol{\theta}}, \boldsymbol{\Sigma}_{\boldsymbol{\theta}\boldsymbol{\theta}}) \prod_{i=1}^{N_D} \left[p(\mathrm{D}_i \mid \boldsymbol{\theta}_i, \Sigma)\, \mathrm{N}(\boldsymbol{\theta}_i \mid \boldsymbol{\mu}_{\boldsymbol{\theta}}, \boldsymbol{\Sigma}_{\boldsymbol{\theta}\boldsymbol{\theta}}) \right] \tag{3}$$

where the individual likelihood function $p(\mathrm{D}_i \mid \boldsymbol{\theta}_i, \boldsymbol{\Sigma}_i)$ can be derived based on Eq. (2) as:

$$p(D_i \mid \boldsymbol{\theta}_i, \boldsymbol{\Sigma}) \propto \frac{1}{(\sigma)^{(N_0+1)m}} \exp\left[-\frac{1}{2\sigma^2}\left(J_1(\boldsymbol{\theta}_i) + J_2(\boldsymbol{\theta}_i) \right) \right] \tag{4}$$

where

$$\begin{aligned}
J_1(\boldsymbol{\theta}_i) &= \sum_{r=1}^{m} \frac{\left(\hat{\lambda}_{r,i} - \lambda_{r,i}(\boldsymbol{\theta}_i) \right)^2}{\left(\hat{\lambda}_{r,i} \right)^2} \\
J_2(\boldsymbol{\theta}_i) &= \sum_{r=1}^{m} \frac{\left\| \underline{\hat{\phi}}_{r,i} - \beta_{r,i}(\boldsymbol{\theta}_i)\underline{\phi}_{r,i}(\boldsymbol{\theta}_i) \right\|^2}{\left\| \underline{\hat{\phi}}_{r,i} \right\|^2}
\end{aligned} \tag{5}$$

By using the Taylor expansion for $L\left(\boldsymbol{\theta}_i, \sigma^2\right) = -\ln p(\mathrm{D}_i \mid \boldsymbol{\theta}_i, \Sigma)$, it can be shown that the likelihood function can be approximated by a normal distribution (valid for large number of data) as:

$$p(\mathrm{D}_i \mid \boldsymbol{\theta}_i, \Sigma) \propto N\left(\sigma^2 \mid \hat{\sigma}^2, \frac{2\hat{\sigma}^4}{m\left(N_0 + 1\right)} \right) N\left(\boldsymbol{\theta}_i \mid \hat{\boldsymbol{\theta}}_i, 2\hat{\sigma}^2 \left[H\left(\hat{\boldsymbol{\theta}}_i\right) \right]^{-1} \right) \tag{6}$$

where $\hat{\boldsymbol{\theta}}_i$ and $\hat{\sigma}^2$ are computed by minimizing $L\left(\boldsymbol{\theta}_i, \sigma^2\right)$, and $H\left(\hat{\boldsymbol{\theta}}_i\right) = \dfrac{\partial^2 \left(J_1(\boldsymbol{\theta}_i) + J_2(\boldsymbol{\theta}_i) \right)}{\partial \boldsymbol{\theta}_i \partial \boldsymbol{\theta}_i^T}$ is the hessian matrix evaluated at $\hat{\boldsymbol{\theta}}_i$. By solving the marginalization integrals over the model parameters, one can derive the marginal distribution of the hyper-parameters $\boldsymbol{\theta}_i$ as:

$$p(\Sigma,\boldsymbol{\mu}_{\boldsymbol{\theta}},\boldsymbol{\Sigma}_{\boldsymbol{\theta\theta}}\,|\,\mathrm{D}) \propto p(\boldsymbol{\mu}_{\boldsymbol{\theta}},\boldsymbol{\Sigma}_{\boldsymbol{\theta\theta}})\,p(\Sigma)$$
$$\prod_{i=1}^{N_D}\left[N\left(\sigma^2\,|\,\hat{\sigma}^2,\frac{2\hat{\sigma}^4}{m(N_0+1)}\right)N(\boldsymbol{\mu}_{\boldsymbol{\theta}}\,|\,\hat{\boldsymbol{\theta}}_i,\boldsymbol{\Sigma}_{\boldsymbol{\theta\theta}}+2\hat{\sigma}^2*\left[H\left(\hat{\boldsymbol{\theta}}_i\right)\right]^{-1})\right] \tag{7}$$

Then the posterior PDF of model parameters can be computed as:

$$p(\boldsymbol{\theta}\,|\,\mathrm{D}) = \int_{\boldsymbol{\mu}_{\boldsymbol{\theta}}}\int_{\boldsymbol{\Sigma}_{\boldsymbol{\theta\theta}}}\int_{\Sigma} p(\boldsymbol{\theta}\,|\,\Sigma,\boldsymbol{\mu}_{\boldsymbol{\theta}},\boldsymbol{\Sigma}_{\boldsymbol{\theta\theta}})\,p(\Sigma,\boldsymbol{\mu}_{\boldsymbol{\theta}},\boldsymbol{\Sigma}_{\boldsymbol{\theta\theta}}\,|\,\mathrm{D})\;d\boldsymbol{\mu}_{\boldsymbol{\theta}}d\boldsymbol{\Sigma}_{\boldsymbol{\theta\theta}}d\Sigma$$
$$\approx \frac{1}{N_s}\sum_{i=1}^{N_s} N(\boldsymbol{\theta}\,|\,\boldsymbol{\mu}_{\boldsymbol{\theta}}{}^{(i)},\boldsymbol{\Sigma}_{\boldsymbol{\theta\theta}}{}^{(i)}) \tag{8}$$

where N_s is the number of the samples. The TMCMC algorithm [8] is used in this work to generate samples from the PDF in Eq. (7). Samples of the modal parameters are generated from Eq. (8) by noting that the PDF is a mixture of normal distributions. It should be noted that the sampling approaches no longer involve model runs. The model parameter uncertainty can be propagated for predicting the quantity of interest (QoI) W (modal properties, displacements, acceleration, etc) as:

$$p(W\,|\,D) \approx \frac{1}{N_s}\sum_{m=1}^{N_s} p\left(W\,|\,\boldsymbol{\theta}^{(m)},\Sigma^{(m)}\right) \tag{9}$$

3 APPLICATION

A 10-DoF spring-mass chain system fixed at one end (base) and free at the other end. The system can be used to simulate the response of a 10-story shear building. The system is excited at the base. The nominal spring stiffness and mass values for each link are 1.8kN/m and 1kg, respectively. The damping ratio for each mode is assumed to be 0.02. Three (3) model parameters are introduced for the stiffness. The first parameter multiplies the nominal stiffness values of the stories 1-3, the second parameters multiplies the stiffness values of stories 4-6, and the third parameter multiplies the stiffness values of the stories 7-10. 40 data sets based on modal data (modal frequencies and modal shapes) are simulated, which represent the measured data. Simulated datasets for the modal properties are generated by from the prior model for the model parameters using as mean the nominal values of the model parameters and as covariance matrix a diagonal one with standard deviation equal to 2% of the mean. A 2% modeling error is also added to the simulated square root of the modal frequencies and the modeshapes to account for measurement noise.

The proposed HBM is then applied for parameter estimations and model predictions. BASIS [9] is used to draw the posterior distribution of the parameters. Only the first five modes are identified, and 5 sensors located in the stories 1, 3, 5, 7, 9 are considered. The posterior distribution of hyper parameters is shown in Fig. 1. It can be seen that a non-zero peak value is obtained of the hyper variance, this is due to the existence of the variability over the multiple data sets. The PDF of the prediction error calculated based on Eq. (7) is shown in Fig. 2, which is essential for further predicting output QoI. Fig. 3 shows the uncertainty bounds of the model parameters along with the error bars obtained from individual data set. It is noted that the uncertainty bounds decrease as the number of data sets increases. However, it will tend to a non-zero value which represents the variability of the data sets. Therefore, the HBM framework can consider the variability of the multiple data sets, and also give a reason-

able uncertainty bounds unlike the classical Bayesian approach.

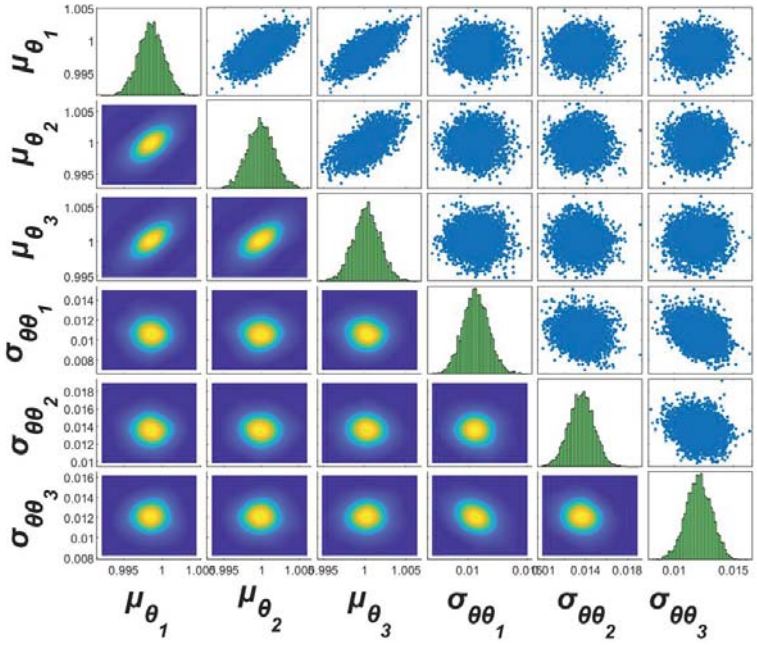

Fig. 1 Posterior distribution of hyper parameters

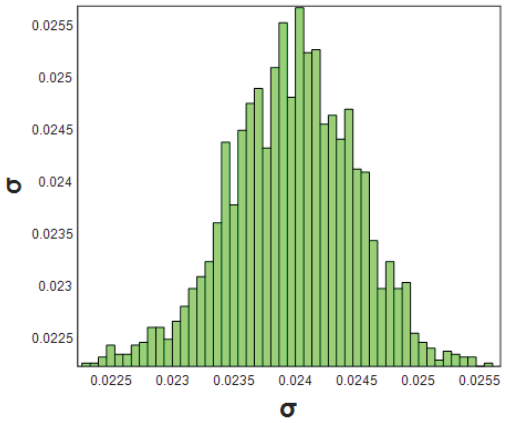

Fig. 2 PDF of prediction error

The uncertainty estimated for the model parameters is then propagated for predicting the uncertainty in the acceleration. Two cases are considered. In the first one the prediction error in the modal properties is not taken into account and the uncertainty is due to the structural model parameter uncertainty. In the second case, the prediction error uncertainty in the modal properties is also considered. As shown in Fig. 4(a), the uncertainty bound of the acceleration is non-zero when the prediction error is not included in the uncertainty propagation. Due to a larger variability over the data sets, one can get a larger uncertainty bound of the estimated model parameters such that a realistic uncertainty bound of the acceleration is obtained even if the prediction error is not considered. Fig. 4(b) shows the propagated acceleration by considering the prediction error. It can be observed that a much larger uncertainty is obtained compared to the case for which the prediction error is not considered.

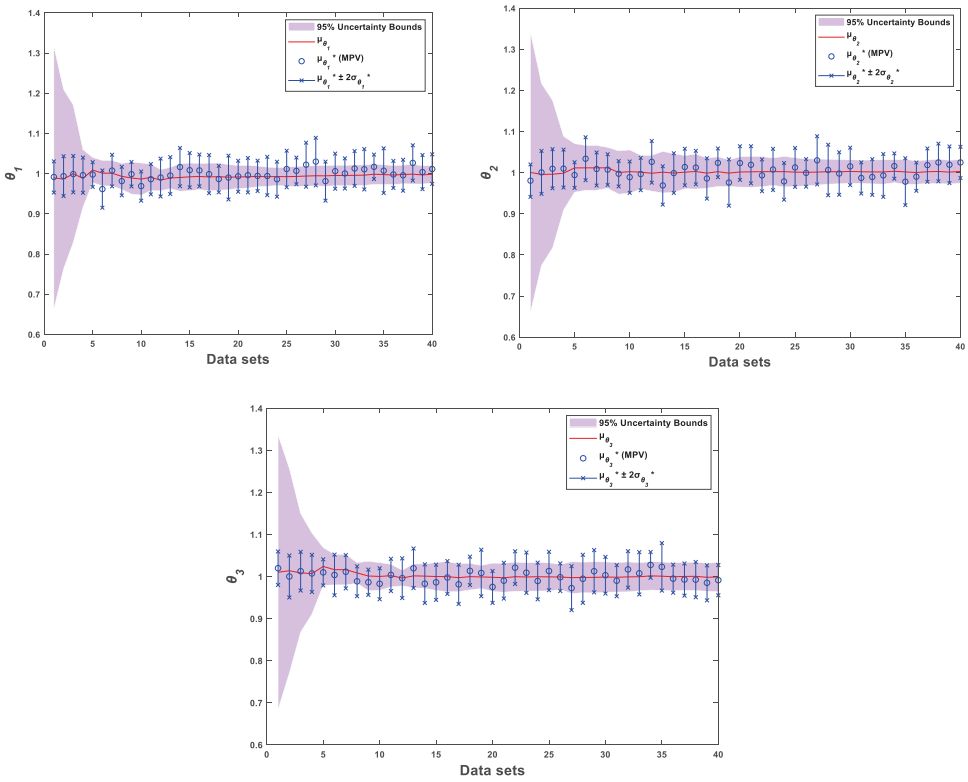

Fig. 3 Posterior PDF of $\boldsymbol{\theta}$'s in comparison with the realizations of individual data sets shown by error bars

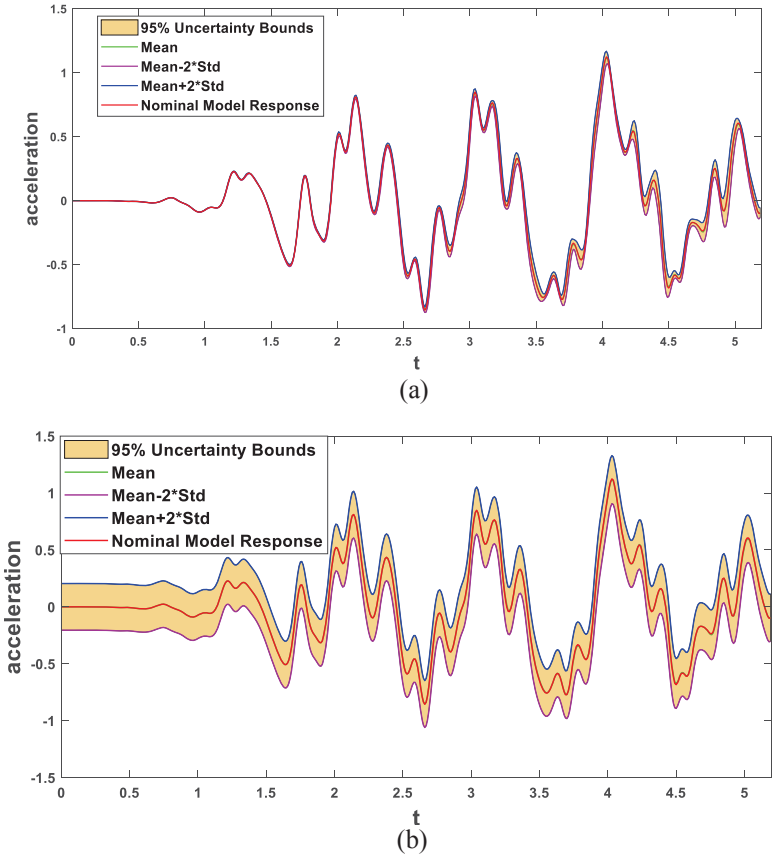

Fig. 4 Predicted accelerations (a) without prediction error and (b) with prediction error

4 CONCLUSIONS

A computational efficient HBM based on multiple modal data sets is proposed in this paper to estimate the structural model parameters and the prediction error parameters. Uncertainties are embedded into the model parameters and also the prediction errors by assigning normal distributions to these parameters and model errors with hyper parameters, the mean and covariance matrices of the normal distributions. Asymptotic approximations are used to estimate the hyper parameters and propagate uncertainty in output QoI. The effectiveness of the proposed formulation has been demonstrated by a spring-mass chain model. The proposed HBM framework properly accounts for the uncertainty due to variability in experimental data, environmental conditions, modeling assumptions and nonlinear mechanisms activated under different loading conditions. The HBM framework can predict the output QoI with reasonable accuracy, producing reliable uncertainty bounds.

The framework can be integrated with sampling methods for computing system reliability using the identified model uncertainties. For complex large-scale models, the excessive computational cost involved in the framework can be substantially alleviated using model reduction or surrogate techniques[10]. The proposed HBM framework applied herein to linear structural systems and multiple sets of modal properties measurements can also be extended to non-linear structural systems given multiple sets of response time histories measurements.

Acknowledgment: This project has received funding from the European Union's Horizon 2020 research and innovation programme under the Marie Skłodowska-Curie grant agreement No 764547.

REFERENCES

[1] C. Papadimitriou, Bayesian uncertainty quantification and propagation (UQ+ P): state-of-the-art tools for linear and nonlinear structural dynamics models, *Identification Methods for Structural Health Monitoring, Springer* 137-170, 2016.

[2] I. Behmanesh, B. Moaveni, G. Lombaert, C. Papadimitriou, Hierarchical Bayesian model updating for structural identification, *Mechanical Systems and Signal Processing* 64, 360-376, 2015.

[3] O. Sedehi, C. Papadimitriou, L.S. Katafygiotis, Probabilistic hierarchical Bayesian framework for time-domain model updating and robust predictions, *Mechanical Systems and Signal Processing* 123, 648-673, 2019.

[4] M. Song, B. Moaveni, C. Papadimitriou, A. Stavridis, Accounting for amplitude of excitation in model updating through a hierarchical Bayesian approach: Application to a two-story reinforced concrete building, *Mechanical Systems and Signal Processing* 123, 68-83, 2019.

[5] G. Ballesteros, P. Angelikopoulos, C. Papadimitriou, P. Koumoutsakos, Bayesian hierarchical models for uncertainty quantification in structural dynamics, *Vulnerability, uncertainty, and risk: Quantification, mitigation, and management* 162, 1615-1624, 2014.

[6] S. Wu, P. Angelikopoulos, J.L. Beck, P. Koumoutsakos, Hierarchical Stochastic Model in Bayesian Inference for Engineering Applications: Theoretical Implications and Efficient Approximation, *ASCE-ASME Journal of Risk and Uncertainty in Engineering Systems, Part B: Mechanical Engineering* 5, 011006, 2019.

[7] H. Jensen, C. Papadimitriou, Bayesian Finite Element Model Updating, Sub-structure Coupling for Dynamic Analysis: Application to Complex Simulation-Based Problems Involving Uncertainty, *Springer International Publishing* 179-227, 2019.

[8] J. Ching, Y.-C. Chen, Transitional Markov chain Monte Carlo method for Bayesian model updating, model class selection, and model averaging, *Journal of Engineering Mechanics*, 133, 816-832, 2007.

[9] S. Wu, P. Angelikopoulos, C. Papadimitriou, P. Koumoutsakos, Bayesian annealed sequential importance sampling: an unbiased version of transitional Markov chain Monte Carlo, *ASCE-ASME Journal of Risk and Uncertainty in Engineering Systems, Part B: Mechanical Engineering* 4, 011008, 2018.

[10] H. Jensen, C. Papadimitriou, Sub-structure Coupling for Dynamic Analysis, 2019.

EURODYN 2020
XI International Conference on Structural Dynamics
M. Papadrakakis, M. Fragiadakis, C. Papadimitriou (eds.)
Athens, Greece, 23–26 November 2020

ON THE IMPLEMENTATION OF ADAPTIVE INVERSE CONTROL TO VIRTUAL TRANSFER SYSTEMS

Thomas Simpson, Vasilis K. Dertimanis, and Eleni N. Chatzi

Chair of Structural Mechanics & Monitoring, Institute of Structural Engineering, ETH Zurich
Stefano-Franscini-Platz 3, 8093 Zurich, Switzerland
e-mail: {simpson,v.derti,chatzi}@ibk.baug.ethz.ch

Keywords: Hybrid Testing, Transfer System, Adaptive Inverse Control, Digital Twins.

Abstract. *The potential of real-time hybrid simulation (RTHS) has been increasingly explored over the last twenty years, bringing numerous methods into focus, both from a scientific and a technological perspective. In contrast to other forms of hybrid simulation, such as pseudo-dynamic substructuring, RTHS poses significant challenges in both its numerical and experimental counterparts, mainly due to the hard real-time constraints that must be met during each execution of the associated control loop.*

As far as the numerical substructure is concerned, the time step of the numerical integration scheme should conform to the step of the real time control loop. This is quite demanding for substructures of increasing complexity and usually necessitates the introduction of a reduced order model [1]. The numerical substructure is linked to the physical one through a transfer system, which brings additional complexity into the loop, as it is characterized by its own dynamics. Here, issues involving the accurate reproduction of the control signal, the elimination of the inherited time delay, the control-structure interaction and the rejection of all disturbance sources, are still subject to intensive research.

Among other considerations, the application of adaptive inverse control (AIC) methods [2] has shown quite good performance in terms of accurate time-series reproduction. In this study, we explore further the effectiveness of AIC via its implementation to a recently published virtual RTHS benchmark problem [3]. In specific, we adopt a filtered-X AIC framework and we report on its effectiveness in modelling the control plant (e.g. transfer system and physical substructure) under representative input signals, partitioning schemes and parametric uncertainties. Our assessment shows a high degree of efficacy and robustness for the proposed AIC architecture and suggests further investigation, mainly in actual RTHS tests.

1 INTRODUCTION

The Digital Twin is a concept of considerable interest in a multitude of industries currently. The essence of the concept is the assimilation of models with data to create an overall system model. This model should, within an operational range of interest, be able to predict system behaviour sufficiently accurately to inform key decisions in both design, operation and maintenance [4]. Digital Twins have arisen as more and more engineering components are designed and monitored through computational models. However, several instances still exist whereby numerical models are insufficient; notably in highly nonlinear regions such as joints between components [5]. Hence the need for the incorporation of physical models in the Digital Twin framework. Hybrid simulation provides a method through which physical models can be dynamically coupled with numerical models and can hence be seen as an important addition to achieve the required fidelity of a Digital Twin.

Hybrid simulation involves the creation of coupled dynamic tests in which a computer is coupled to a physical component in a dynamic testing rig. The system is then solved as a whole by intergrating the numerical system, calculating predicted forces at the interface between the structures and applying this to the physical system. The response of the physical system is then measured and fed back into the equations in the numerical system [6]. The "gold standard" of hybrid simulation is real time hybrid simulation (RTHS) wherein real time implies that the time scales of the numerical and physical system are the same; this allows for tests which incorporate rate dependent nonlinearities in the physical component and are hence more representative of the true system.

When considering the real time aspect, the issue of actuator control becomes very important in hybrid simulation. The dynamics of the actuation system can have very significant effects on the reproduction of the reference signal from the equations of motion, and that which is actually applied by the actuator. This results in two key control issues when implementing a RTHS scheme, namely, (i) the accurate reproduction (through the transfer system) of the reference signal that corresponds to the common boundaries between the experimental and the numerical substructure; and (ii) the suppression of the time delay, which is inevitably introduced by the transfer system (actuators, A/D-D/A converters, etc.). The first issue is a typical control problem, while the second is a problem of prediction.

In this work, a benchmark virtual RTHS is considered, as developed by Silva et al. [3] for the purpose of comparing various control schemes, this benchmark system virtually models both the numerical and physical substructures along with the dynamics of the actuation system. The problem of then developing a controller for the reduction of actuator delay and error can then be considered in isolation. This study discusses such a control strategy and introduces an alternative framework for the effective reproduction of reference signals, which is based exclusively on adaptive signal processing and requires no prior knowledge about the dynamics of the transfer system, the specimen and their interaction. The controller used is based on the filtered-X algorithm [7] for adaptive tracking control which has been widely used in signal processing [8] and previously applied to the problem of control in hybrid simulation [2].

2 THE vRTHS BENCHMARK PROBLEM

The RTHS case study considered herein pertains to the recently published virtual benchmark problem of Silva *et. al* [3]. In specific, we focus on the control plant part of the vRTHS paradigm, a layout of which is displayed in Fig. 1. Table 2 shows the numerical values of the parameters, some of which are considered as uncertain that follow the Gaussian distribution

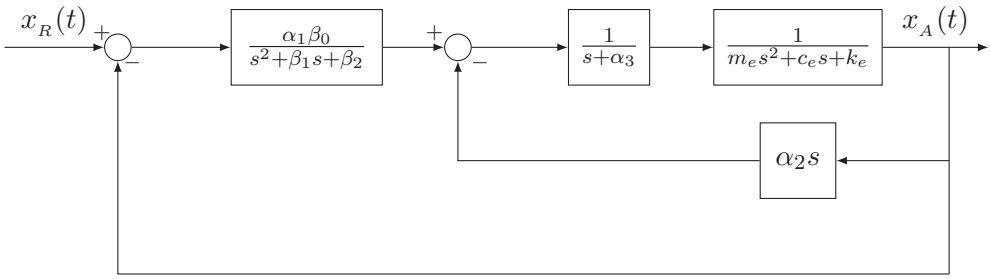

Figure 1: Layout of the control plant (transfer system plus experimental substructure). From left to right, the transfer functions on the upper correspond to the valve, actuator and experimental substructure dynamics, respectively, while the transfer function on the inner feedback loop corresponds to the control-structure interaction dynamics. The signals $x_{_R}(t)$ and $x_{_A}(t)$ refer to the reference and the achieved response of the experimental substructure, respectively. Adapted from [3].

with the indicated mean and standard deviation.

Parameter	**Component**	**Nominal value**	**St. dev.**	**Units**
$\alpha_1\beta_0$	Servo-valve	2.13×10^{13}	-	m Pa/s
α_2	Actuator	4.23×10^{6}	-	m Pa
α_3	Actuator	3.3	1.3	1/s
β_1	Servo-valve	425	3.3	-
β_2	Servo-valve	10×10^{4}	3.31×10^{3}	1/s
m_e	Exp. sub.	29.1	-	kg
c_e	Exp. sub.	114.6	-	kg/s
k_e	Exp. sub.	1.19×10^{6}	5×10^{4}	N/m

Table 1: Parameter values for the control plant of Fig. 1. From [3].

By applying block diagram algebra on the closed loops of Fig. 1, the transfer function between the reference and the achieved signals, $x_R(t)$ and $x_A(t)$, respectively, is given by [3]

$$G(s) = \frac{B_0}{A_5 s^5 + A_4 s^4 + A_3 s^3 + A_2 s^2 + A_1 s + A_0} \tag{1}$$

for

$$\begin{aligned}
B_0 &= \alpha_1\beta_0 A_0 = k_e\alpha_3\beta_2 + \alpha_1\beta_0 \\
A_1 &= k_e\alpha_3\beta_1 + (k_e + c_3\alpha_3 + \alpha_2)\beta_2 \\
A_2 &= k_e\alpha_3 + (k_e + c_3\alpha_3 + \alpha_2)\beta_1 + (c_e + m_e\alpha_3)\beta_2 \\
A_3 &= (k_e + c_3\alpha_3 + \alpha_2) + (c_e + m_e\alpha_3)\beta_1 + m_e\beta_2 \\
A_4 &= c_e + m_e\alpha_3 + m_e\beta_1 \\
A_5 &= m_e
\end{aligned} \tag{2}$$

In discretizing Eq. 1 the zero-order hold scheme is applied for $T_s = 1$ ms, leading to a nominal digital transfer function of the form

$$G(z) = \frac{C_1 z^{-1} + C_2 z^{-2} + C_3 z^{-3} + C_4 z^{-4} + C_5 z^{-5}}{1 + D_1 z^{-1} + D_2 z^{-2} + D_3 z^{-3} + D_4 z^{-4} + D_5 z^{-5}} \tag{3}$$

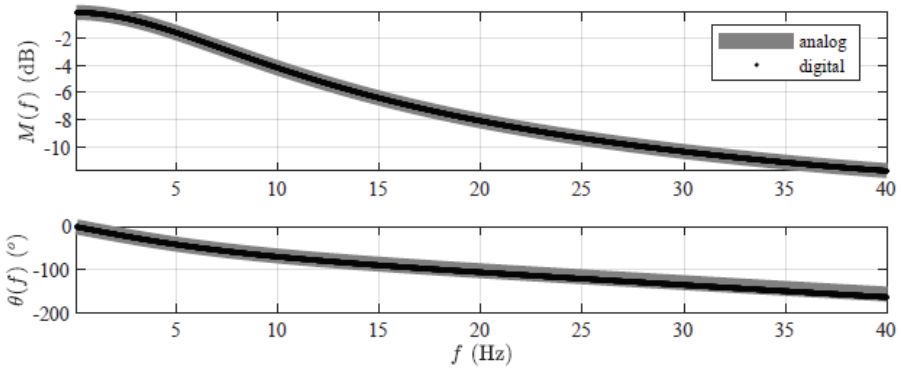

Figure 2: Frequency response of the analog ($G(s)$) and digital ($G(z)$) nominal transfer functions.

with parameters shown in Tab. 2. Notice that $G(z)$ is characterized by unit delay: this is attributed to the fact that the transfer function of the experimental substructure (see Fig. 1) has displacement as output. In the case of velocity, or acceleration control, this transfer function has to be modified accordingly, leading to corresponding zero-delay digital equivalents. In the case of the displacement, the close resemblance between $G(s)$ and $G(z)$ is confirmed in Figure 2, where the frequency response of both transfer functions is plotted.

Numerator		**Denominator**	
Coefficients	**Roots**	**Coefficients**	**Roots**
$C_1 = 5.637 \times 10^{-6}$	-21.347	$D_1 = -4.383$	0.953
$C_2 = 1.349 \times 10^{-4}$	-2.149	$D_2 = \ \ 7.878$	$0.905 \pm 0.406j$
$C_3 = 3.174 \times 10^{-4}$	-0.403	$D_3 = -7.239$	$0.810 \pm 0.190j$
$C_4 = 1.169 \times 10^{-4}$	-0.041	$D_4 = \ \ 3.394$	
$C_5 = 4.226 \times 10^{-6}$	0	$D_5 = -0.649$	

Table 2: Numerator and denominator coefficients for the nominal digital control plant.

Table 2 shows further the roots of the numerator and denominator polynomials, from where it is deduced that the control plant is of nonminimum phase. By applying the theory of two-sided $\mathcal{Z}$-transform, $G^{-1}(z)$ can be expanded to either a causal, but unstable series, or to a noncausual, but stable one. The former expansion is obviously unacceptable, as it would lead to control plant instability. The latter is acceptable, yet this would mean that the inverse controller would be a predictor. This behaviour is typical for plants having nonminimum phase features [7]. In such cases, the best practice is to attempt adapting the controller (see next section) to delayed responses of the control plant. To demonstrate how this is accomplished, assume that $G^{-1}(z)$ can be expanded to a convergent (i.e., stable) series as

$$G^{-1}(z) = \cdots + g_2 z^{-2} + g_1 z^{-1} + g_0 + g_{-1} z^1 + g_{-2} z^2 + g_{-3} z^3 + \ldots \tag{4}$$

If the g_{-i} terms are negligible, then one can discard the noncasual part of the expansion and obtain a casual, stable inverse transfer function. Since, however, this is usually not the case, a delay term is added to the signal path, and an inverse filter of the form

$$z^{-\Delta} G^{-1}(z) = z^{-\Delta}\big(\cdots + g_2 z^{-2} + g_1 z^{-1} + g_0 + g_{-1} z^1 + g_{-2} z^2 + g_{-3} z^3 + \ldots\big) \tag{5}$$

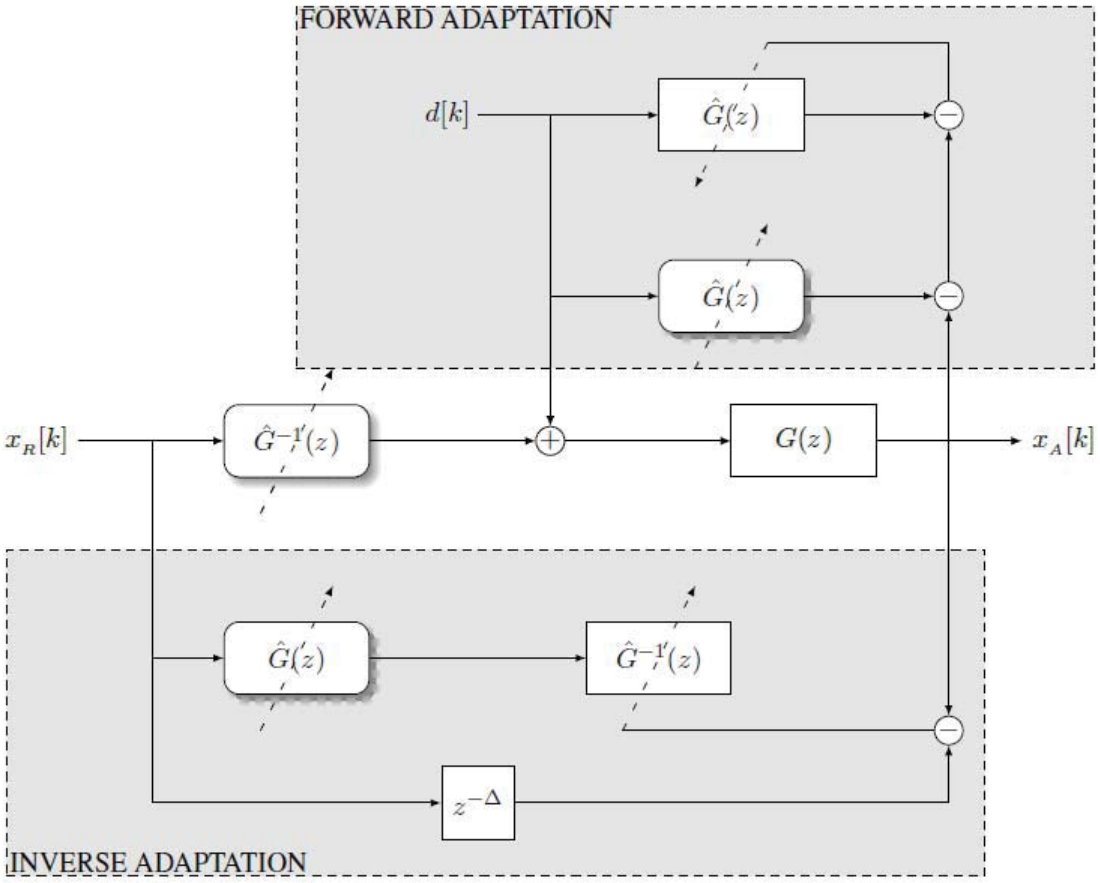

Figure 3: Graphical representation of the adaptive inverse control process. The hat symbol denotes estimate and the shadowed boxes indicate copies of the respective forward/inverse adaptive filters. $d[k]$ is the dither signal.

is estimated online, allowing for more terms of the expansion to be included, using the adaptive scheme that is outlined next.

3 ADAPTIVE INVERSE CONTROL

Our strategy for adapting an inverse controller to the control plant of Fig. 1 is based on the work of Dertimanis *et. al* [2] and it is sketched in Fig. 3. It consists of two successive stages that are implemented in real-time:

- The *forward adaptation* stage, where a finite impulse response (FIR) estimate of the $G(z)$, $\hat{G}(z)$, is estimated.

- The *inverse adaptation* stage, where a FIR estimate of $G^{-1}(z)$, $\hat{G}^{-1}(z)$, is made.

When both stages have been successfully executed and convergence has been achieved, the controller can immediately accept any reference signal for reproduction through the transfer system.

3.1 Forward adaptation

In view of Fig. 3, the adaptive identification of the control plant is achieved though the use of a "dither" signal, $d[k]$. Notice that in this stage the weights of the FIR filter that pertain to the inverse controller are zero, thus, the reference signal $x_R[k]$ does not reach the control plant.

If simultaneous estimation of forward and inverse filters is selected, then, as Fig. 3 illustrates, the plant is excited by both the reference and the dither signals, while forward adaptation is performed using only the dither one. In any case, the dither signal is usually a realization of a zero-mean Gaussian white noise process (see the discussion on the effects of training signals in Dertimanis *et. al* [9], in order to excite all modes of the control plant up to the Nyquist rate.

The adaptation is carried out using the decorrelated LMS method [10], which combines improved convergence properties and low computational complexity. At each step, the adaptive filter's output is calculated as

$$\hat{x}_{_A}[k] = \mathbf{g}^T[k]\mathbf{d}[k] \tag{6}$$

where $\mathbf{g}^T[k]$ are the filter coefficients, $\mathbf{g}^T[k] = \begin{bmatrix} g[k,0] & c[k,1] & \dots & c[k,n_g] \end{bmatrix}^T$, $\mathbf{x}[k] = \begin{bmatrix} d[k] & d[k-1] & \dots & d[k-n_g] \end{bmatrix}$ and n_g is the order of the filter. The coefficients are updated by

$$\mathbf{g}[k+1] = \mathbf{g}[k] + \mu[k]\mathbf{g}[k] \tag{7}$$

for a step size $\mu[k]$

$$\mu[k] = \frac{\rho e[k]}{\mathbf{d}^T[k]\mathbf{s}[k]} \tag{8}$$

In Eq. 8, ρ is a trimming factor, $e[k] = x_{_A}[k] - \hat{x}_{_A}[k]$ is the error between the measured and the predicted signal and $\mathbf{s}[k]$ is the filter gradient, updated by

$$\mathbf{s}[k] = \mathbf{d}[k] - \alpha[k]\mathbf{d}[k-1] \tag{9}$$

with $a[k]$ denoting the decorrelation coefficient

$$a[k] = \frac{\mathbf{d}^T[k]\mathbf{d}[k-1]}{\mathbf{d}^T[k-1]\mathbf{d}[k-1]} \tag{10}$$

3.2 Inverse adaptation

The inverse adaptation process, which can be initiated before full convergence of the forward adaptation has been achieved, is shown at the lower part of Fig. 3. It utilizes a copy of $\hat{G}(z)$ just before the inverse adaption process and attempts to minimize the overall system error, e.g. the difference between a delayed version of the reference signal and the response of the control plant. Adaptation is succeeded using the discrete cosine transform-least mean square (DCT-LMS) filter [11], which consists of the orthogonalization, the power normalization and the filtering steps. In the former, the input vector is transformed by the DCT as

$$w[k,i] = \sum_{\ell=0}^{n_{g_I}-1} Q_{n_{g_I}}(k,\ell)u[k-\ell], \;\; i = 0,1,\dots,n_{g_I}-1 \tag{11}$$

with n_{g_I} being the order of the inverse filter and $Q_{n_{g_I}}(k,\ell)$ the DCT coefficients, which can be calculated a priori offline from

$$Q_{n_{g_I}}(k,\ell) = \sqrt{\frac{2}{n_{g_I}}} K_k cos\left(\frac{k(\ell+1/2)\pi}{n_{g_I}}\right), \;\; k,\ell = 0,1,\dots,n_{g_I}-1 \tag{12}$$

for

$$K_k = \begin{cases} \frac{1}{\sqrt{2}}, & k = 0 \\ 1, & k \neq 0 \end{cases} \tag{13}$$

The transformed values are accordingly normalized by the square root of their power via

$$v[k,i] = \frac{w[k,i]}{\sqrt{P[k,i]+\epsilon}}, \;\; i = 0,1,\ldots,n_{g_I} \tag{14}$$

where ϵ is a small constant and

$$P[k,i] = P[k-1,i] + (1-\gamma)w^2[k,i], \;\; i = 0,1,\ldots,n_{g_I} \tag{15}$$

and the power update factor $\gamma \in (0,1]$. The inverse filter weights are updated according to

$$g_I[k+1,i] = g_I[k,i] + \mu e[k] v[k,i], \;\; i = 0,1,\ldots,n_{g_I} \tag{16}$$

where $e[k]$ is the overall system error.

4 IMPLEMENTATION

To validate and assess our control framework, we adopt a realization of the vRTHS problem that pertains to the first partitioning case explained in Silva *et. al* [3, Tab. 01]. To reduce high demands on the discretization process and the associated sampling rates, our simulations are performed at a sampling period $T_s = 1$ ms, and thus Eq. 1 is sampled at this rate. The reference signal corresponds to the displacement at the boundary between the numerical and the "experimental" substructure. During the training phase, it is selected as a zero-mean Gaussian white noise of variance 10^{-7}, modulated through a low-pass filter with a cut–of frequency at 250 Hz, while the dither signal is also zero-mean Gaussian white noise of the same variance.

Our implementation proceeds via the following steps:

- Assign values for the standard parameters and obtain realizations of the uncertain ones [3, Tab. 02].
- Perform forward adaptation for extracting a FIR estimate of the control plant.
- Upon successful convergence of the forward adaptation path, we lock the weights and we switch to the inverse adaptation path.
- Finally, when the inverse adaptation path has converged to a FIR estimate of the control plant's inverse, we again lock the weights of the inverse and we switch the reference signal to the one intended for RTHS. The time-series of this signal are obtained from conducting simulations via the original distributed software code of Silva *et. al* [3]

It is further mentioned that, after initial investigations, the orders for the forward and inverse FIR models are kept constant and equal to $n_g = 300$ and $n_{g_I} = 200$, respectively, while the reference signal's delay is set to $\Delta = 100$.

Indicative results for one occurrence of the aforementioned steps are expanded over Figs 4–7. Focusing on the top plot of the first, one can clearly observe the underlying adaptation procedure. The adaptive modeling step of the control plant evolves over the first 15–20 s (although convergence has been achieved already from the first 1-3 s), in which the reference signal (in black) is significantly larger than the achieved one (in red): this is due to the fact that herein only the dither signal is involved to the adaptation process. Accordingly, the inverse adaptation does not show any chattering and/or instabilities, while again convergence is achieved relatively

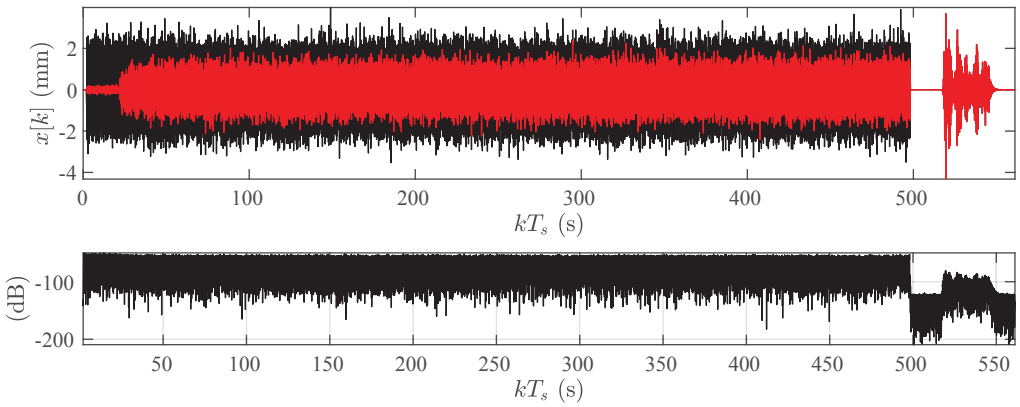

Figure 4: Top: evolution of the adaptive inverse control process for a single realization of the uncertain parameters. Bottom: overall adaptation error.

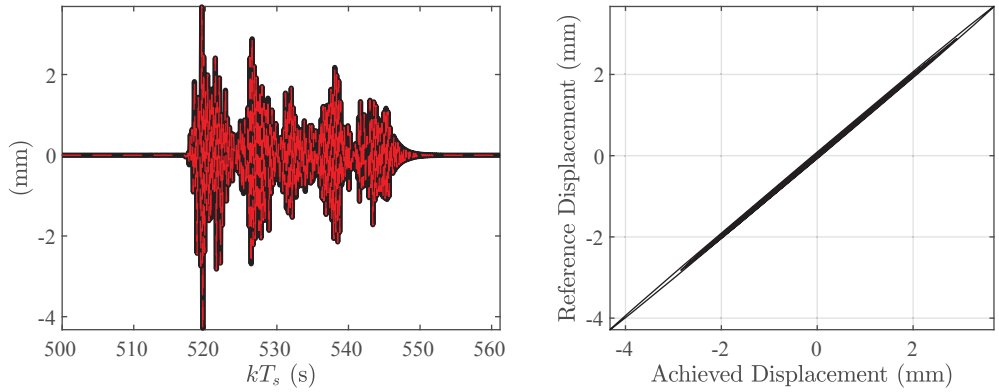

Figure 5: Left: zoom of Fig. 4 at the part of the simulation where the RTHS displacement is applied. Right: Synchonization plot between the reference and the achieved signals.

early (around 50 s the overall error does not essentially reduce anymore. Perhaps a proper adjustment of the DCT-LMS parameters can speed up convergence). When the adaptive inverse controller is properly adapted to the control plant, the execution of the desired reference signal follows after a short pause. The quality in the reproduction of the desired displacement is depicted in Fig. 5, from where an excellent synchronization plot between the (delayed) reference and achieved signals can be observed.

In terms of FIR models, Fig. 6 displays the resulted forward and inverse filters. The former succeeds in accurately reproducing the digital impulse response of the control plant (e.g. the inverse $\mathcal{Z}$-transform of Eq. 3) at the selected order, rendering the adopted deconvolution algorithm quite successful. Regarding the resulted shape of the inverse filter, with low-valued leading weights, significant ones at the middle and negligible trailing values, essentially explains the effects of Eq. 5 to the process. The convolution of the two resembles a digital impulse, as illustrated in Fig. 7, where the impulse response of the cascaded forward and inverse FIR models is plotted. Notice that, while the digital impulse does not reach unity, the reproduction of the reference signal is almost perfect. This is merely due to the flat amplitude of the corresponding frequency response function at 0 db, over a wide frequency range that reaches up to 100 Hz (the effective band of most hydraulic actuators used in structural testing).

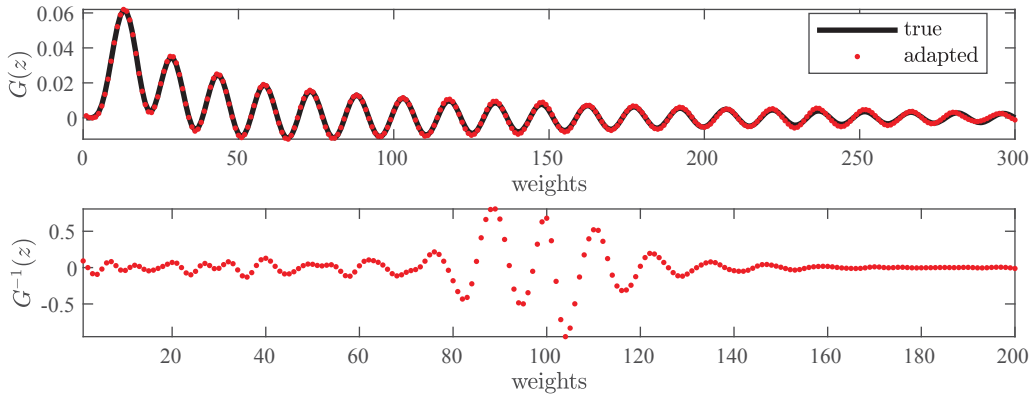

Figure 6: Top: true digital impulse response (continuous black curve) of the control plant and adapted FIR model (red dotted curve). Bottom: adapted FIR model for the inverse of the control plant.

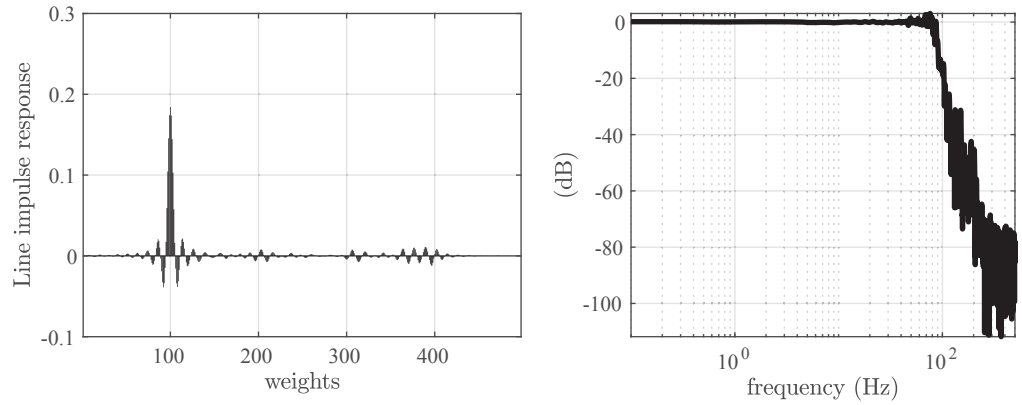

Figure 7: Left: Impulse response of the cascaded forward and inverse FIR models. Right: amplitude of the associated frequency response function.

5 CONCLUSIONS

Adaptive inverse control offers many advantages, compared to conventional control methodologies. Among others, it requires no prior model for the control plant, it is exclusively based on digital signal processing (thus it is fast), while it retains certain stability and robustness features, due to the FIR filters involved. This comes at the cost of somehow increased model orders, the computational cost of which is, nevertheless very small (in the orders of μs in processors with typical specifications). In this respect, our methodology showed quite satisfactory results and we aim at further investigating its capabilities, by testing its efficacy within the RTHS loop.

6 ACKNOWLEDGEMENTS

The authors have received funding from the European Union's Horizon 2020 research and innovation programme under the Marie Skłodowska-Curie grant agreement No. 764547.

REFERENCES

[1] T. Simpson, D. Giagopoulos, V.K. Dertimanis, , and E.N. Chatzi. On Dynamic Substructuring of Systems with Localised Nonlinearities. In *Proceedings of IMAC XXXVIII*, Houston, USA, 2020.

[2] V.K. Dertimanis, H.P. Mouzakis, and I.N. Psycharis. On the acceleration-based adaptive inverse control of shaking tables. *Earthquake Engineering & Structural Dynamics*, 44(9):1329–1350, 2015.

[3] C.E. Silva, D. Gomez, A. Maghareh, S.J. Dyke, and B.F. Spencer Jr. Benchmark control problem for real-time hybrid simulation. *Mechanical Systems & Signal Processing*, 135:#106381, 2020.

[4] K. Worden, E.J. Cross, P. Gardner, R.J. Barthorpe, and D.J. Wagg. On digital twins , mirrors and virtualisations. *Imac-Xxxvii*, 2019.

[5] D. Wagg. The Digital Twin for Engineering Applications. Technical report, The University of Sheffield, 2018.

[6] P. Benson Shing. Real-Time Hybrid Testing Techniques. pages 259–292. Springer, Vienna, 2008.

[7] B. Widrow and E. Wallach. *Adaptive Inverse Control: a Signal Processing Approach*. John Wiley & Sons Ltd., New York, USA, 2007.

[8] Quanzhen Huang, Xiaojin Zhu, Zhiyuan Gao, Shouwei Gao, and Enyu Jiang. Analysis and implementation of improved multi-input multi-output filtered-X least mean square algorithm for active structural vibration control. *Structural Control and Health Monitoring*, 2013.

[9] V.K. Dertimanis, H.P. Mouzakis, and I.N. Psycharis. Real–Time Shaking Table Adaptive Modeling under Acceleration Control: Effects of Training Signals and Specimen Dynamics. In *Proceedings of the Sixth World Conference on Structural Control and Monitoring*, Barcelona, Spain, 2014.

[10] G.-O. Glentis, K. Berberidis, and S. Theodoridis. Efficient least squares adaptive algorithms for fir transversal filtering. *IEEE Signal Processing Magazine*, 16(4):13–41, 1999.

[11] P. S. R. Diniz. *Adaptive Filtering: Algorithms and Practical Implementation*. Springer, New York, USA, 3rd edition, 2008.

EURODYN 2020
XI International Conference on Structural Dynamics
M. Papadrakakis, M. Fragiadakis, C. Papadimitriou (eds.)
Athens, Greece, 23–26 November 2020

ROBUST BAYESIAN OPTIMAL SENSOR PLACEMENT FOR MODEL PARAMETER ESTIMATION AND RESPONSE PREDICTIONS

Tulay Ercan[1], **Petros Koumoutsakos**[2] **and Costas Papadimitriou**[1]

[1] University of Thessaly, Department of Mechanical Engineering
Volos 38334, Greece
e-mail: {ercan, costasp}@uth.gr

[2] ETH Zurich, Computational Science and Engineering Laboratory
CH-8092, Switzerland
petros@ethz.ch

Keywords: Bayesian optimal experimental design, robust design, parameter inference, response predictions, structural dynamic

Abstract. *Optimal sensor placement (OSP) in complex systems implies a configuration that maximizes the information gain by the sensors. This configuration is identified by maximizing, with respect to the location of the sensors, an expected utility function on information-based measures. The resulting multi-dimensional integrals are estimated using asymptotic approximations and sampling techniques. Herein we extend such formulations to be robust to uncertainties in nuisance parameters associated with system and prediction error model conditions, and environmental variabilities. The nuisance parameters are not inferred from the collected data but they affect the learning or prediction processes. Robust designs are achieved by maximizing the expected amount of information in the data and minimizing its fluctuation due to uncertainties in the nuisance parameters. We demonstrate, through a number of examples in structural dynamics, the capabilities of the proposed OSP framework for model parameter estimation and model response predictions.*

1 INTRODUCTION

Optimal sensor placement (OSP) is an important component for numerous structural engineering applications. OSP aims to maximize the quality of the experimental or observational data in order to improve models and narrow the uncertainties in their parameters and their predictions for quantities of interest (QoI). Eventually such improved models are used to update the state of the structure, trace structural deterioration, update structural reliability and safety, prognose the remaining lifetime of structural components (e.g. fatigue lifetime) and design cost-effective maintenance actions. Bayesian OSP framework enables to select the design variables (type, number and location of sensors) to obtain most informative data to update posterior probability density function (PDFs) of model parameters for the purposes of parameter estimation, model selection and response prediction.

In this study, we outline a robust Bayesian OSP framework, based on information theory for parameter estimation and response reconstruction of linear systems. The information gain is quantified using the Kullback-Leibler divergence (KL-div) between the posterior and prior distribution of the model parameters or the response QoI. The Optimal Experimental Design (OED) framework is expanded to consider the uncertainties in the nuisance parameters arising from the variability in structural model parameters, environmental loads or prediction error model parameters. The nuisance parameters are not included in the parameters inferred by the Bayesian methodology. The utility function, chosen as the expected KL-div over all possible data, becomes a function of the design variables and the uncertain nuisance parameters. Thus robust design optimization techniques can be applied to find optimal sensor configurations that maximize the expected information gain and minimize the variability of the information gain over all possible values of the nuisance parameters. To demonstrate the efficiency of the proposed method, a simple spring mass chain system is selected.

2 BAYESIAN OPTIMAL EXPERIMENTAL DESIGN

2.1 Bayesian Parameter Estimation and Prediction of Output QoI

We consider a model of a structural system subjected to external loads. We define as $\underline{\theta} \in R^{N_\theta}$ the model parameters that will be estimated using a set of measured data $\underline{y} \equiv \underline{y}(\underline{\delta}) \in R^N$ of output quantities that depend on experimental design variables $\underline{\delta}$. The design variables $\underline{\delta}$ are related to the sensor configuration (number, type and location of sensors).We define as $\underline{\varphi}$ a set of nuisance parameters of the system model and/or the external loads that affect the output quantities of interest but they are not inferred from the available data. These parameters are related to factors that may be uncertain during the operation of the structure including environmental conditions and modeling assumptions. The values of the output QoI ($\underline{g}(\underline{\theta};\underline{\delta},\underline{\varphi}) \in R^N$) are predicted by the structural model at the measured locations, for specific values of the parameter set $\underline{\theta}$. These predictions depend on the model structure and the excitations, the sensor configuration $\underline{\delta}$ and the nuisance parameters $\underline{\varphi}$.

The discrepancy between the measurements and the model predictions is expressed as:

$$\underline{y} = \underline{g}(\underline{\theta};\underline{\delta},\underline{\varphi}) + \underline{e} \tag{1}$$

where $\underline{e}$ is due to the model and measurement error. The error $\underline{e}$ is modeled as a zero-mean Gaussian vector with covariance $\Sigma_e(\underline{\sigma}) \in R^{N\times N}$, where $\underline{\sigma}$ contains the parameters that define

the correlation structure of $\Sigma_e(\underline{\sigma})$. Herein the parameter set $\underline{\sigma}$ is included in the nuisance parameter set $\underline{\varphi}$. The Bayesian theorem is applied to estimate the posterior PDF $p(\underline{\theta} \mid \underline{y}, \underline{\delta}, \underline{\varphi})$ of the model parameters $\underline{\theta}$, with a prior $\pi(\underline{\theta})$, given the measured data $\underline{y}$ and the values of the nuisance parameters $\underline{\varphi}$.

We introduce an output vector QoI $\underline{z}$ given by

$$\underline{z} = \Psi(\underline{\delta}, \underline{\varphi})\underline{\theta} + \underline{\eta} \tag{2}$$

where $\Psi(\underline{\delta},\underline{\varphi}) \in R^{n \times N_\theta}$ has a known structure that depends on $\underline{\delta}$ and $\underline{\varphi}$, and $\underline{\eta}$ is the modeling error. Herein, for simplicity, a linear relation between the response QoI and the model parameters $\underline{\theta}$ is assumed. Also, the error is taken to be zero-mean Gaussian distribution with covariance matrix $\Sigma_\eta(\underline{s}) \in R^{n \times n}$. Using the posterior distribution of the model parameters, one can readily obtain the posterior distribution of the output QoI $\underline{z}$ as a function of $\Psi(\underline{\delta},\underline{\varphi})$ and $\Sigma_\eta(\underline{s})$.

2.2 Bayesian OSP for Parameter Estimation

One of the objectives of an experiment is to maximize the information contained in the data in order to estimate reliably the parameters of the model or for reliably predicting an output QoI. The information content of the data is quantified through the utility function chosen as the information gained by the experiment. The utility function is related to the relative entropy or the KL-divergence [1] between the prior and posterior PDF of the model parameters or the output QoI given an outcome $\underline{y}$ obtained from an experimental design $\underline{\delta}$. In the experimental design phase the data are not available and the expected utility function over all possible outcomes of the experimental data $\underline{y}$, is introduced to reflect the usefulness of the experiment in estimating the model parameters [1] or estimating an output QoI.

Using an asymptotic approximation for large numbers of data and assuming small prediction error, the expected utility function for model parameter estimation takes the form [2]:

$$U\left(\underline{\delta}, \underline{\varphi}\right) = -\int_{\Theta} H\left(\underline{\delta}; \underline{\theta}, \underline{\varphi}\right)\, \pi\left(\underline{\theta}\right) d\underline{\theta} + c_1 \tag{3}$$

where c_1 is constant,

$$H\left(\underline{\delta}; \underline{\theta}, \underline{\varphi}\right) = \frac{1}{2} N_\theta \ln\left(2\pi\right) - \frac{1}{2} \ln \det\left[Q\left(\underline{\delta}; \underline{\theta}, \underline{\varphi}\right) + \Sigma_\pi^{-1}\left(\underline{\theta}\right)\right] \tag{4}$$

is the posterior information entropy,

$$Q\left(\underline{\delta}; \underline{\theta}, \underline{\varphi}\right) = \nabla_{\underline{\theta}} g\left(\underline{\theta}; \underline{\delta}, \underline{\varphi}\right)^T \Sigma_e^{-1}\left(\underline{\theta}; \underline{\delta}, \underline{\varphi}\right) \nabla_{\underline{\theta}} g\left(\underline{\theta}; \underline{\delta}, \underline{\varphi}\right) \tag{5}$$

is the posterior covariance matrix approximated by the Fisher information matrix, and $\Sigma_\pi(\underline{\theta})$ is the covariance of the prior PDF of the model parameters $\underline{\theta}$, with $\nabla_{\underline{\theta}} = \left[\partial / \partial\theta_1, ..., \partial / \partial\theta_{N_\theta}\right]$. The prior PDF provides the necessary information to optimize the sensor configuration in the case where the Fisher information matrix is ill-conditioned due to insufficient information contained in the data.

2.3 Bayesian OSP for Response Prediction

The sensor configuration can be optimally designed to provide the highest information gain for predicting a set of output QoI. Using asymptotic approximation, assuming large number of data and small prediction error, the expected utility function for predicting output QoI is given in terms of the covariance matrix $P^z\left(\underline{\delta},\underline{\theta}\right)$ of the posterior uncertainty in the output QoI, in the form [3]:

$$U\left(\underline{\delta},\underline{\varphi}\right)=-\frac{1}{2}\int_{\Theta}\ln\det\left(P^z\left(\underline{\delta},\underline{\theta},\underline{\varphi}\right)\right)\pi\left(\underline{\theta}\right)d\underline{\theta}+c_2 \tag{6}$$

where c_2 is constant, $P^z(\underline{\delta},\underline{\theta},\underline{\varphi})$ depends on the sensor location $\underline{\delta}$, the model parameters $\underline{\theta}$ to be inferred from the data, and the values of the nuisance parameters $\underline{\varphi}$. The integral is over the uncertain parameter space associated with the model parameters $\underline{\theta}$. Using (2), the covariance matrix $P^z(\underline{\delta},\underline{\theta},\underline{\varphi})$ of the posterior PDF is expressed as

$$P^z\left(\underline{\delta},\underline{\theta},\underline{\varphi}\right)=\Psi(\underline{\delta},\underline{\varphi})\left[Q\left(\underline{\delta};\underline{\theta},\underline{\varphi}\right)+\Sigma_\pi^{-1}\left(\underline{\theta}\right)\right]^{-1}\Psi^T(\underline{\delta},\underline{\varphi})+\Sigma_\eta\left(\underline{\varphi}\right) \tag{7}$$

where $\Psi(\underline{\delta},\underline{\varphi})$ relate to the sensitivity of the output QoI with respect to the model parameters $\underline{\theta}$.

3 ROBUST OPTIMAL SENSOR PLACEMENT (ROSP)

The OSP should be designed to be robust to uncertainties arising from manufacturing variability, structural conditions not accounted into the modelling, environmental variabilities and modelling errors. To account for the uncertainties in the nuisance parameters, a robust design optimization technique is used to find the optimal values of the design variables. This optimal design is selected to maximize the expected amount of information in the data over all possible values of the nuisance parameters and also minimize the variability in this information due to the uncertainty in the values of the nuisance parameters.

The expected utility function $U(\underline{\delta},\underline{\varphi})$ depends on the uncertain nuisance parameters $\underline{\varphi}$. The respective minimization problem is expressed as

$$\underline{\delta}_{opt}=\arg\min_{\underline{\delta}}J(\underline{\delta})=\arg\min_{\underline{\delta}}[-\mu(\underline{\delta})+\alpha\sigma(\underline{\delta})] \tag{8}$$

where $\mu(\underline{\delta})$ is the expected utility

$$\mu(\underline{\delta})=E_{\underline{\varphi}}[U(\underline{\delta},\underline{\varphi})]=\int_{\Phi}U(\underline{\delta},\underline{\varphi})\ \pi(\underline{\varphi})\ d\underline{\varphi} \tag{9}$$

and $\sigma(\underline{\delta})$ is the standard deviation of the utility

$$\sigma^2(\underline{\delta})=E[(U(\underline{\delta},\underline{\varphi})-\mu(\underline{\delta}))^2]=\int_{\Phi}[U(\underline{\delta},\underline{\varphi})-\mu(\underline{\delta})]^2\ \pi(\underline{\varphi})\ d\underline{\varphi} \tag{10}$$

In this study the value of α in Equation (8) is equal to 1. Equation (8) is equivalent to minimizing the expected information entropy and its variability over all possible values considered for the nuisance parameters.

The multi-dimensional integrals in Equations (3) and (6) over the parameter space Θ and in Equations (9) and (10) over the uncertain parameter space Φ can be estimated using Monte Carlo or Sparse Grid [4] techniques. The optimization of (8) is performed using heuristic sequential sensor placement algorithms to overcome the large computational expense without sacrificing accuracy [5].

4 NUMERICAL EXAMPLES

We first demonstrate the effectiveness of the proposed ROSP methodology, on a 20 DOFs spring-mass chain system. The nominal mass and stiffness of each link in the chain are identical with $m = 0.085$ and $k = 600$ respectively. ROSP results are compared with the deterministic case.

In the first example, ROSP is performed to estimate the first three stiffness parameters of the system. Uniform prior PDF for the three stiffness parameters is assumed with lower and upper bounds taken to be 0.8 and 1.2 times the nominal stiffness values. The analysis is performed considering the uncertainty in the mass of the system. An uncertain nuisance parameter is assumed for the first mass of the system. The nuisance parameter follows a Gaussian distribution with mean equal the nominal mass value and standard deviation equal to 10% of the nominal mass value. Rayleigh damping is assumed with the mass and stiffness coefficients selected so that they correspond to 2% damping ratio for the first and the fifth mode of the system. The equations of motion are solved using the state space method for the system subjected to white noise input at the 20th DOF with 0.05 sec time step. It is assumed that the sensors measure acceleration time histories.

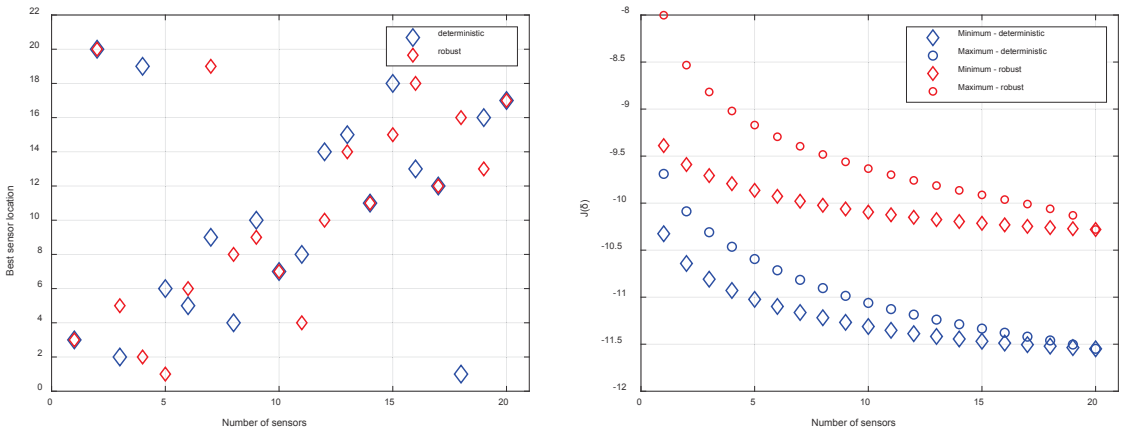

Figure 1: Comparison between the robust and deterministic OSP results (left) and the best and worst expected information entropy values (right) for parameter estimation.

In Figure 1, the optimal sensor locations and the corresponding best and worst (minimum and maximum) expected information entropy values for the robust and the deterministic cases are compared. Results are given as a function of the number of sensors. It can be seen that the expected utilities decrease as the number of sensors increases. The distance between maximum and minimum expected utility values quantify the information gain that can be achieved using the ROSP methodology. According to the comparison of deterministic and robust cases, the optimal sensor configurations and utility values are affected significantly when considering the uncertainty in the nuisance parameters. The difference in the optimal sensor configuration appears for configurations involving more than two sensors.

In the second example, OSP is performed for response prediction using a modal expansion technique [5]. Acceleration sensors at optimal locations are used to reconstruct the acceleration responses at all DOF of the system. Modal damping is used assuming that only four modes are contributing to the system dynamic. Robust analysis takes into consideration uncertain boundary conditions. Specifically, the fixity condition of the first link in the chain is assumed to be uncertain. The degree of fixity is simulated by replacing the base support by a spring. The stiffness of the added spring is assumed $k_0 = \varphi\, k$, where φ represents the uncertainty nuisance parameter taken as uniform distribution with lower bound 1 (simulating a flexible support) and upper bound 10 (simulating a fixed support).

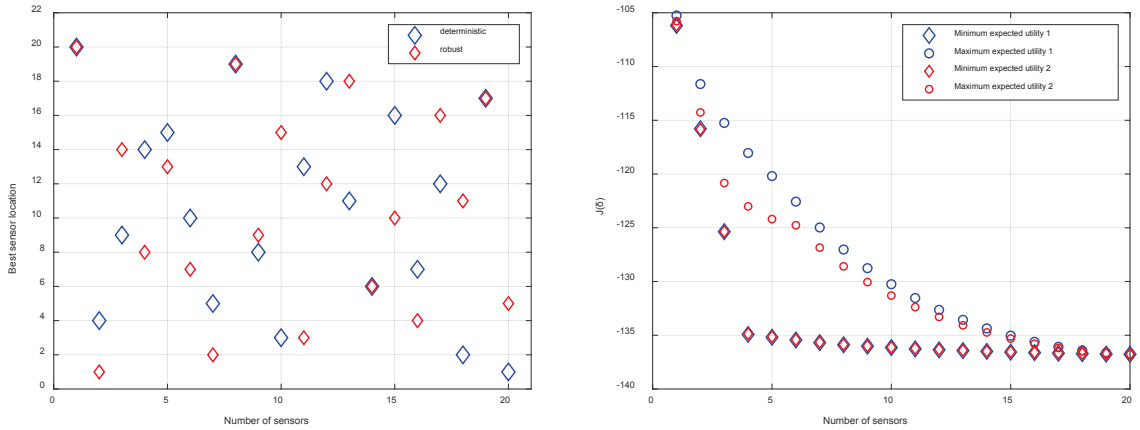

Figure 2: Comparison of the deterministic and robust OSP results throughout the best sensor locations (left) and the –utility values (right) for response prediction.

Figure 2 compares the deterministic and ROSP results for response prediction. Similar to the previous example, the information gain is a decreasing function of the number of sensors placed at their optimal position. The information gain for up to four sensors is significant for both deterministic and robust cases as the problem is ill-conditioned for less than four sensors. As observed by the small reduction in the information entropy values as a function of the number of sensors for more than four sensors, there is no significant information gained for accurate response prediction purposes from these additional sensors. This result holds for both robust and deterministic cases. It is also clear from the optimal sensor placement results that the optimal sensor configurations are affected significantly as a result of the uncertainty in the boundary condition.

5 CONCLUSIONS

We present a novel formulation for robust optimal sensor placement (ROSP) in structural dynamics by combining utility theory and information-based measures. The optimal sensor configuration maximizes the expected information gain computed by the KL divergence between prior and posterior distribution of the model parameters or the model predictions of an output QoI. Robust optimal configuration designs are proposed that take into account uncertainties in nuisance parameters that are not inferred from the data. Such parameters are associated with uncertain model conditions (e.g. boundary conditions), environmental variabilities, manufacturing variabilities as well as parameters of the prediction error models. The framework employs asymptotic approximations to simplify the computation of the integrals involved in the utility function. However, it is readily applicable to estimates of the expected utility functions that are based on full sampling techniques [7-9]. The multi-dimensional integrals involved

in the robust design optimization technique were estimated using Monte Carlo or sparse grid methods. The optimization is performed using heuristic sequential sensor placement algorithms to provide computationally efficient solutions. The effectiveness of the method was demonstrated for a multi-DOF linear spring-mass chain system. The proposed ROSP framework is general and can be extended to handle nonlinear structural dynamics models. It is also applicable to optimize the experimental design for a wide variety of systems encountered in engineering and applied sciences.

ACKNOWLEDGEMENT

This project has received funding from the European Union's Horizon 2020 research and innovation programme under the Marie Skłodowska-Curie grant agreement No 764547.

REFERENCES

[1] D. V. Lindley, "On a Measure of the Information Provided by an Experiment," *The Annals of Mathematical Statistics*, vol. 27, no. 4, pp. 986–1005, 1956.

[2] C. Argyris and C. Papadimitriou, "A Bayesian Framework for Optimal Experimental Design in Structural Dynamics," Model Validation and Uncertainty Quantification, *Volume 3 Conference Proceedings of the Society for Experimental Mechanics Series*, pp. 263–270, 2016.

[3] C. Papadimitriou, "Optimal Sensor Placement for Response Reconstruction in Structural Dynamics," *Model Validation and Uncertainty Quantification, Volume 3 Conference Proceedings of the Society for Experimental Mechanics Series*, pp. 205–210, 2019.

[4] T. Gerstner, M. Griebel, "Numerical integration using sparse grids," *Numerical algorithms*, vol. 18, no. 3-4, pp. 209, 1998.

[5] C. Papadimitriou, "Optimal sensor placement methodology for parametric identification of structural systems," *Journal of Sound and Vibration*, vol. 278, no. 4-5, pp. 923–947, 2004.

[6] C. Argyris, C. Papadimitriou, and P. Panetsos, "Bayesian Optimal Sensor Placement for Modal Identification of Civil Infrastructures," *Journal of Smart Cities*, vol. 2, no. 2, 2019.

[7] C. Argyris, S. Chowdhury, V. Zabel, and C. Papadimitriou, "Bayesian optimal sensor placement for crack identification in structures using strain measurements," *Structural Control and Health Monitoring*, vol. 25, no. 5, 2018.

[8] S. Verma, C. Papadimitriou, N. Lüthen, G. Arampatzis, and P. Koumoutsakos, "Optimal sensor placement for artificial swimmers," *Journal of Fluid Mechanics*, vol. 884, 2020.

[9] P. Weber, G. Arampatzis, G. Novati, S. Verma, C. Papadimitriou, and P. Koumoutsakos, "Optimal Flow Sensing for Schooling Swimmers," *Biomimetics*, vol. 5, no. 1, p. 10, 2020.

EURODYN 2020
XI International Conference on Structural Dynamics
M. Papadrakakis, M. Fragiadakis, C. Papadimitriou (eds.)
Athens, Greece, 23–26 November 2020

UNCERTAINTY QUANTIFICATION FRAMEWORK FOR STRUCTURAL MODEL OF WIND TURBINE BLADES

Paulo Gonzaga[1,2], Keith Worden[2], Nikolaos Dervilis[2], Nevena Stevanovic[1], Lars Oliver Bernhammer[1], Henrik Stensgaard Toft[1]

[1]Siemens Gamesa Renewable Energy
Borupvej 16, 7330 Brande, Denmark
{paulo.gonzaga} @siemensgamesa.com

[2] Dynamics Research Group - University of Sheffield
Mappin Street, Sheffield S1 3JD, United Kingdom
{k.worden, n.dervilis}@sheffield.ac.uk

Keywords: Wind Turbine Blade, Uncertainty quantification, Sensitivity Analysis, Gaussian Process.

Abstract. *Wind energy is in the forefront of the renewable energy sources and it is expected to show continuous expansion demanding more efficient design, simulation and production procedures. Nevertheless, with the rise of power ratings and the steep increase in size of the blades, there is a considerable need for the development of more reliable simulation predictions with quantified uncertainties and deeper understanding of the randomness that affects the system. The effect of structural uncertainties and imperfections on the properties of the composite material used for blades has long been confirmed. Many uncertainties in a wind turbine blade design relate directly to the uncertainties of material properties. Wind turbine blade models can rely on tens of thousands of parameters, including geometric, material and layup information. Some of these parameters can show diverse stochastic behaviours, which may impact prediction capacity, but are not easily included in an uncertainty study. Requirements for simulation accuracy and precision continue to intensify, together with the performance requirements. Uncertainty quantification is an important step towards an optimised structural design, i.e. it is important to analyse both data and model results to understand limitations of current modelling and data variability making informed decisions. This article shows the application of a non-intrusive uncertainty quantification framework to the structural model of a wind turbine blade, considering the main material property parameters as randomly-distributed inputs. The effects of these uncertainties and sensitivities of these parameters are investigated for stiffness distribution, mass and center of gravity (CG) of the blade and for their effect on the static deflection test. The numerical results are compared with experimental test data for validation.*

1 INTRODUCTION

The blades of a wind turbine are constructed by combining different composite materials - including glass and carbon fibre reinforced polymers with different fibre orientation - and a core material (typically wood or foam). The blades are required to withstand a diverse range of loads, while maintaining their aerodynamic profile and have a useful life of 20 years or more. These requirements mean that every aspect of their design, installation, operation and maintenance must be optimised.

Structural performance can be directly affected by uncertainties associated with models, making it harder to specify resistance and loadings. The conventional design approach has been to adopt characteristic values and safety factors to compensate for structural variations resulting from the production process. However, probabilistic analysis permits a more rigorous quantification of the various uncertainties, and ultimately will facilitate a more efficient design. Quantifying the confidence and predictive accuracy of model calculations is a necessary step toward model verification and validation (V&V); this is an enabling methodology for the development of computational models that can be used to make predictions with quantified confidence [1].

Uncertainty quantification (UQ) in wind applications (turbine models, wind forecasting, energy production) is still a young research theme, but the presence of uncertainties in wind turbine outputs, lifetimes, and failure probabilities leads to a conservative philosophy with high safety factors. Blades can be improved by using a probabilistic approach to design in which the effects of uncertainties are understood and quantified [2].

This paper describes the application of a UQ framework based on Monte Carlo simulation of a structural model of a wind turbine blade. The quantities of interest are the blade stiffness distribution, mass and centre of gravity (CG) location and static deflection under a specific loading. The material properties of the three main types of laminates used in the blade have been characterised as random inputs whose uncertainties are propagated to the QoIs (quantity of interest). A Gaussian process emulator is used to conduct sensitivity analysis on the parameters. Monte Carlo simulation with Latin Hypercube (MC-LHS) sampling is used for UQ. Results are validated against experimental data.

2 MODEL

2.1 Blade structural model

The cross-sectional model used in this study is based on the formulations of Krenk and Jeppesen [3]; utilising a line mesh in the calculation of the structural features, the torsion and shear properties of the cross-sections are formulated within a finite element method (FEM) with the warping function as unknown. The cross section is divided into straight elements with uniform trapezoidal thickness. Every component is simplified and lumped into a thin-walled shell structure with the help of so-called superelements. The Crs (cross-sectional) model also calculates the sectional mass by summing the contribution of each layer of the laminate. The calculation is repeated for each cross section throughout the blade (Fig.1) along the blade span. The blade's stiffness can be seen in Fig.2, normalised by the maximum value.

The QoIs for this study are the distributions of stiffness in flapwise (EI_Y), edgewise (EI_X) and torsional (GI_Z) directions, based on the blade reference frame shown in Fig. 1A. The model combines information from geometry, ply definition, layup and materials properties to calculate geometric and structural properties, mass and stiffness distributions. Elastic moduli are termed in accordance with a material coordinate system seen in Fig. 1B, where the 1-

direction corresponds to the 0° fibre direction.

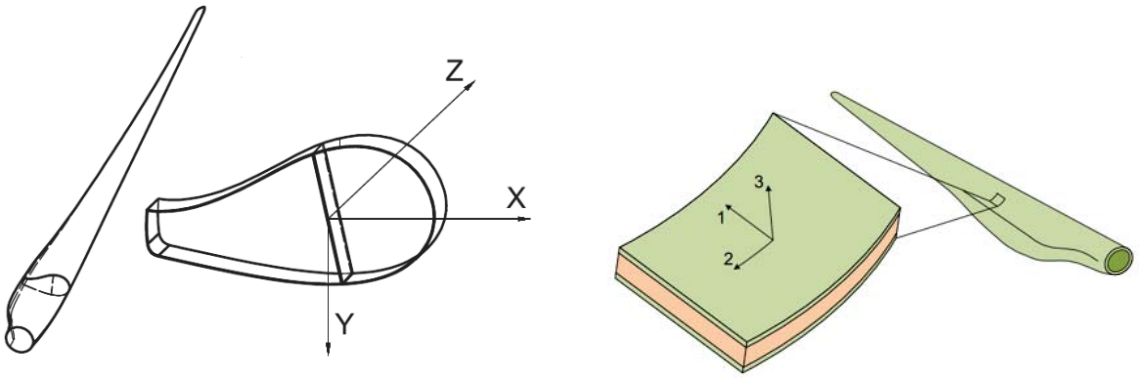

Figure 1: Reference system for wind turbine blade and material properties.

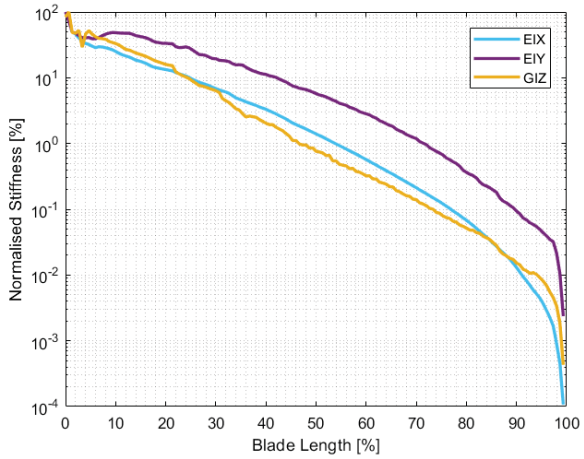

Figure 2: Wind Turbine Blade stiffness distribution - Deterministic results.

The blade layup is important information because, as can be seen in Fig.3 where it is plotted for normalised blade length X [%], there are substantial differences of composition along the blade. The blade studied in this paper has two main laminate types:

- UD: Unidirectional laminate
- BIAX: Bi-directional laminate

Results will show that the type and quantity of laminate used for specific regions of the blade have different impacts on the responses, meaning also that a few material properties have a much bigger influence in some model outputs than others.

2.2 Blade static deflection test

The blades are often considered the most critical structural component of the turbine. Therefore, safety standards require full-scale testing for every prototype and after major design changes. Overall, full-scale tests are seen as a final design verification with the following objectives:

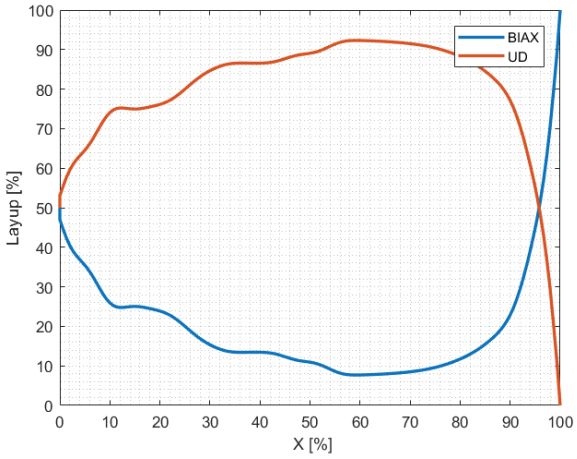

Figure 3: Wind turbine blade layup.

- validate assumptions;
- identify relevant failure modes;
- identify manufacturing details prone to damage initiation.

Requirements for blade testing are part of international standards (e.g. IEC-61400-23 and DNV GL-ST-0376) which manufacturers are required to comply with. The scope for certification static bending test (section 4.9 on [4]) involves (but is not limited to) testing in:

- positive flapwise direction (from pressure side to suction side);
- negative flapwise direction (from suction side to pressure side);
- positive edgewise direction (from trailing edge to leading edge);
- negative edgewise direction (from leading edge to trailing edge).

The blade static deflection test described in this section is not part of a certification campaign; it is a quality control test whose goal is to check whether the blade can withstand extreme load cases and gives evidence that the blade is neither too stiff nor too flexible. It is a way to evaluate blades per tolerance thresholds. The test setup consists of the blade supported at the root section and at midspan subjected to a negative flapwise load close to the tip. The blade is essentially kept in rigid-body statics due to its own weight pushing it on the supports.

The setup is illustrated by a 3D model in Fig. 4 together with the finite element model used to simulate the test. This model is based on the lengthwise stiffness distribution of the blade (which is characterised by the Crs model). Data from static deflection tests of 34 blades of the same type subjected to the same load will be compared in the UQ results.

3 RANDOM INPUT CHARACTERISATION

The characterisation of the uncertain inputs of an UQ problem is of utmost importance because poor input models will have a large effect on the interpretation of the uncertainty behaviour of the system. Bigoni [5] defines three main approaches to the *probability distribution estimation* of inputs:

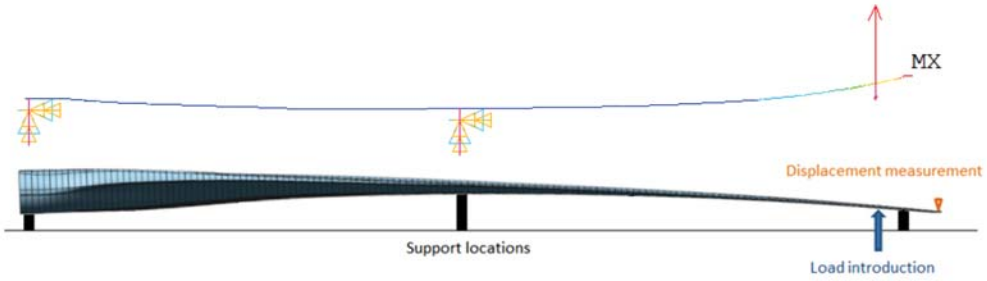

Figure 4: Wind Turbine Blade static test: Setup and finite element model.

- Assumption: probability distributions for the parameters are defined relying on experience and wisdom.
- Inference: the probability distributions are reconstructed using measurements of the quantity of interest.
- Measurement: measurements of the parameters are carried out, and probability distributions are fitted to these experiments.

The last approach is always preferred, but it is seldom available. The costs, effort and time necessary to characterise random parameters by experiments (that have to be repeated, generating enough samples to have a good fit) are usually too high.

The access to Siemens Gamesa Renewable Energy's material test database allowed this study to be conducted with experimental data for the estimation of material property probability distributions.

In this study the random variables are the material properties (Table 1) of the two main types of glass-fibre reinforcements (BIAX and UD) used in the blades. Fig. 3 shows the evolution of composition of the blade along its length.

Property	Description
E_{11}	Modulus of elasticity in direction 1 [Pa]
E_{22}	Modulus of elasticity in direction 2 [Pa]
E_{33}	Modulus of elasticity in direction 3 [Pa]
G_{12}	In-plane shear modulus of elasticity [Pa]
G_{13}	Out-of-plane shear modulus of elasticity [Pa]
G_{23}	Out-of-plane shear modulus of elasticity [Pa]
ρ	Laminate density [Kg m^3]
t	Laminate thickness [m]

Table 1: Laminate main material properties.

The material stiffness and strength for the glass-fibre laminates are determined from material testing of actual fibre-resin and core materials that are representative of the production blade laminates and sandwich configurations. Testing for each material property is carried out according to the relevant standard [6]. For each type of laminate, the main material properties were considered as random input parameters (Table 1). The nominal values and coefficient of variation were used to fit pdf to these inputs. The number of samples and coefficient of variation for each property, are presented at Table 2. The Gaussian distribution was used for all variables

so that the differential entropy is maximized for a given variance [7], which means this is the distribution with least assumptions and can be fitted only with information of variance and mean values.

BIAX					
Property	CoV %	# test	Property	CoV %	# test
E_{11}	4	15	G_{12}	3	30
E_{22}	4	15	G_{13}	3	5
E_{33}	4	15	G_{23}	3	5
ρ	0.6	27	t	2	27
UD					
Property	CoV %	# test	Property	CoV %	# test
E_{11}	3	15	G_{12}	3	15
E_{22}	5	15	G_{13}	3	15
E_{33}	5	15	G_{23}	3	15
ρ	0.6	9	t	3	9

Table 2: Materials properties experimental CoV.

Latin Hypercube Sampling (LHS) is widely used in Monte Carlo simulations as a way to improve accuracy and computational cost. LHS is a method to generate controlled random samples, the idea is to take the sampling point distribution close to the probability density function (pdf). It involves dividing the cumulative density function (cdf) into *n* equal partitions and then sampling a specified number of random data points in each partition. A MC-LHS (Monte Carlo with Latin Hypercube Sampling) was implemented for the materials properties previously defined by fitting pdfs to the coupon testing data and LHS from these pdfs. The fitted pdfs and the histogram of the LHS UD properties realisations can be seen in Fig. 5.

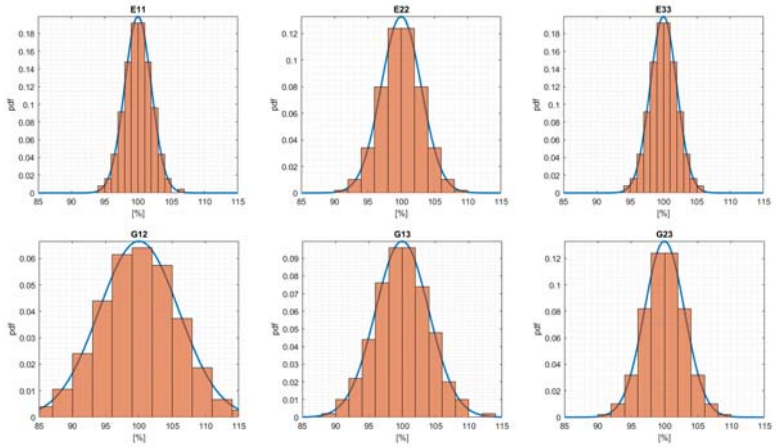

Figure 5: pdfs and histogram of UD random properties realisations from MC-LHS.

4 SENSITIVITY ANALYSIS

The software GEM-SA (Gaussian Emulator Machine - Sensitivity Analysis [8]), was used to calculate the main effects and total effects for each parameter. The emulator can be seen as a model of the model. The physics based model is treated as an unknown function, with the

possible ranges of the input parameters specified by probability distributions. Assuming this model is a smooth function of its inputs, then a response surface can be fitted to the training data using a least squares regression and the output can be estimated for any set of inputs, faster than using the physics based simulation. Details for this procedure are found in [9].

The emulator was trained using an LHS with 100 realisations of the deterministic code. This study relies on the following assumptions:

- No correlation between random variables (i.e. all properties were considered to be independent).
- No uncertainties in the geometry of the blade were considered.
- The CG and mass were assumed to be dependent exclusively on the density and thickness of the laminate.
- The static deflection was assumed to be dependent exclusively on the laminate's moduli.

Figs.6A and B show the contribution of the input parameters on the blade mass and CoG, respectively. As shown, the thickness of the UD is the most influential parameter both in the blade mass and in the blade CG.

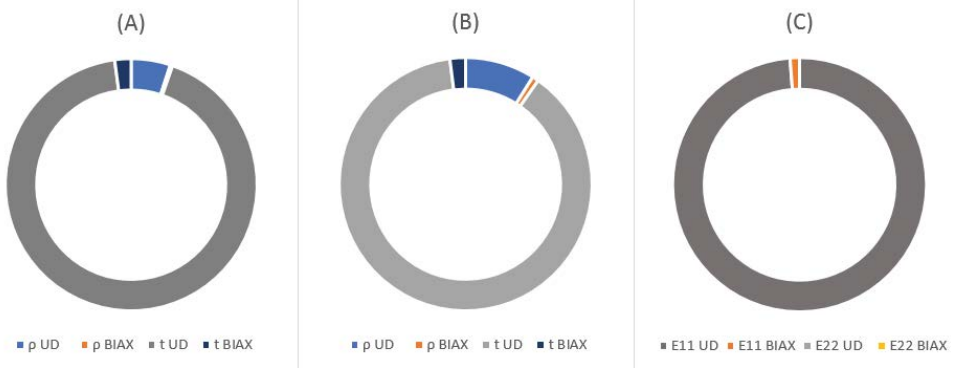

Figure 6: Blade mass, CG and static deflection sensitivity analysis - main effect.

Fig.6C shows the contribution of the material stiffness in the blade static deflection. The E_{11} of the UD dominates the variance of the static deflection test. This is coherent since the UD is the major laminate type in the spar cap, which is the substructure responsible for the flapwise blade stiffness. It is worth highlighting that the variation of the input parameters is limited (around 3 to 5%, shown in Table 2). In Table 3, the contributions can be seen for the main properties in each case: CG, mass and static deflection. The other parameters would need bigger variations to have a significant effect in the blade deflection.

5 UNCERTAINTY QUANTIFICATION

Monte Carlo (MC) simulation is the most applied methodology for uncertainty propagation, due to its straight forward implementation and non-intrusiveness to the deterministic model. It can be summarised in three steps:

1. construct probability density function (pdfs) for all random inputs independently
2. randomly sample from all the pdfs

Variance contribution (%)				
Property	CG	Mass	Property	Static Def
ρ UD	5.04	8.93	E11 UD	98.8
ρ BIAX	0.3	0.8	E11 BIAX	1.2
t UD	92.6	88.3	E22 UD	0.0
t BIAX	2.1	2.0	E22 BIAX	0.0

Table 3: Variance contribution - Sensitivity analysis.

3. evaluate the deterministic model

4. use the collection of realisations to compute relevant statistics of the quantity of interest

Even though the sensitivity analysis was dominated by few parameters, the MC simulation for CG, mass and static deflection were performed with the whole set of material properties of the laminates. The reason is because there could be cross-over effects between different parameters that could bring them to more relevance that might not be captured by the emulator.

MC results and fitted pdfs for experimental data can be seen in Figs. 7A, 7B and 8 for mass, CG, stiffness distribution and static deflection, respectively.

A total of 3000 realisations of the deterministic model were used on the MC simulation. The results are normalised by the experimental mean value. Table 4 shows the statistical moments for MC and experimental data.

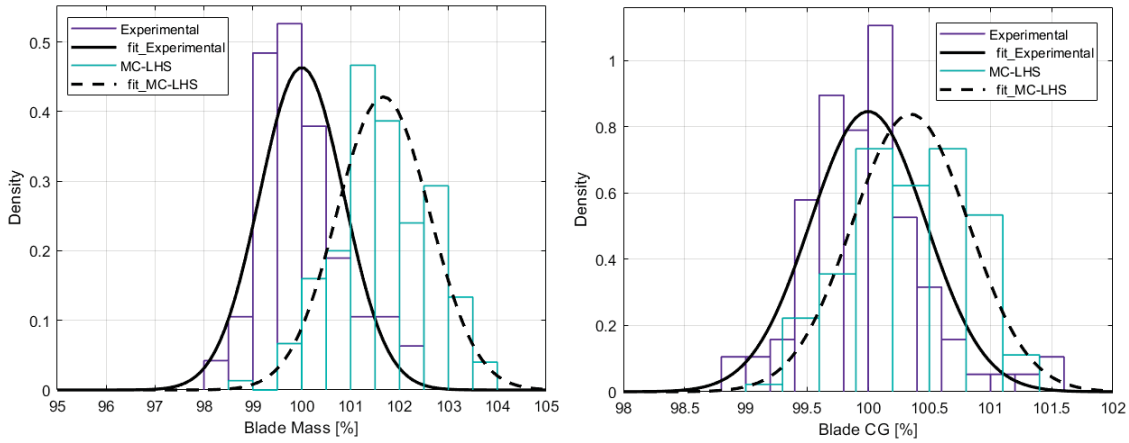

Figure 7: Blade mass and CG: Experimental and MC-LHS.

	Experimental		MC-LHS	
	μ (%)	σ (%)	μ (%)	σ (%)
Deflec.	100.0	2.2	99.9	3.0
Mass	100.0	0.9	101.7	0.9
CG	100.0	0.5	100.3	0.5

Table 4: Results summary: Mean values and standard deviation for experimental data and MC-LHS.

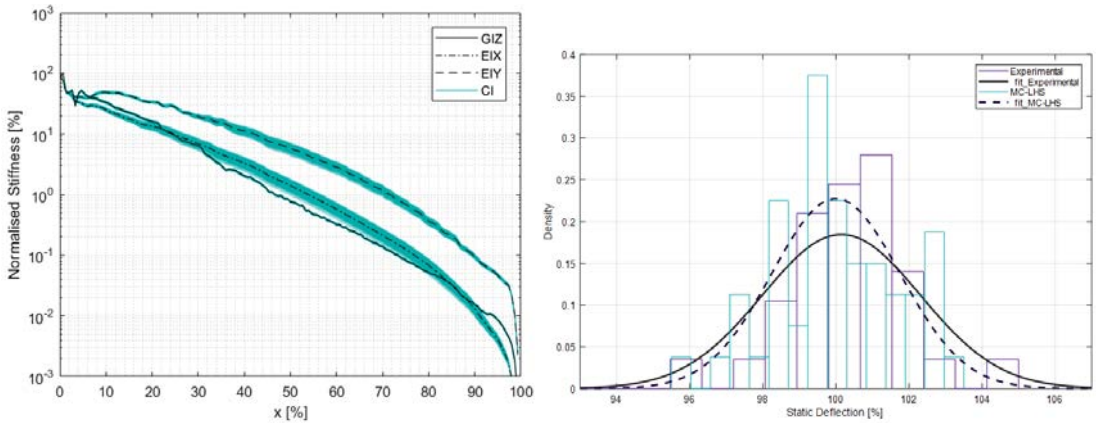

Figure 8: Blade stiffness distribution C.I. for normalised blade length and static deflection pdf .

6 DISCUSSION

The results for the UQ in the static deflection test can be given a high confidence as the deterministic model is accurate and the pdfs for both UQ and experimental data are in good agreement. Probabilistic simulations are heavily reliant of random input characterisation. Even though material properties are not highly uncertain (CoV of 3 - 5$\%$) there is still a considerable effect on the blade, which can be mostly seen in the flapwise stiffness (whilst the torsional stiffness is the least affected).

Comparison of the UQ results with experimental data test, showed the resulting variation of mass, CG location and static deflection can be reasonably explained by the uncertainties in the material properties of the 2 most used laminate types in the blade. The same order of variation is seen both in simulation and test data. The fact that the uncertainty in the E_{11} of the UD laminate (CoV 3 $\%$) is of the same order of the CoV in the static deflection test supports the Gaussian process sensitivity analysis results that it dominates the uncertainty (98.8$\%$ of variance contribution) and that the static deflection test can be accurately simulated by a beam model based on the blade stiffness distribution.

Mass and CG location present the same CoV for test data and MC simulations, although there is a small bias on the mean values. Under the current assumptions (section 4), this is a strong evidence that the uncertainty characterisation of the inputs (section 3) is representative of the blade production. Furthermore, this information is useful to update the model and have an even better numerical representation of the structure.

7 CONCLUSIONS

The present paper has investigated the effect of material properties uncertainties on the stiffness, mass and CG location as well as on static deflection of a wind turbine blade. The material properties were characterised by coupon testing statistical data. It is assumed that the uncertainty of these parameters can be modelled with a fitted normal distribution. In order to investigate combined effects on the stiffness and mass distribution, the parameters are simultaneously varied by means of LHS and the sensitivity described by means of a Gaussian emulator.

The material properties are not the only source of uncertainty in the characterisation of a wind turbine blade model. Still, the present study of propagating uncertainties in the materials properties of the blade is important because it shows that small uncertainties in these parameters have actually measurable effect on the characteristics of the blade.

It is also important to extend the uncertainties sources considered because blade stiffness, mass and CG can directly influence turbine loads and operation. Therefore, it is a natural step to extend the UQ framework to the turbine simulation, in order to have a best estimate of the impact uncertainties can have in the turbine in addition to other types of uncertainties (e.g. uncertainty in environmental parameters).

8 ACKNOWLEDGEMENTS

This project has received funding from the European Union's Horizon 2020 research and innovation programme under the Marie Skłodowska-Curie grant agreement No 764547.

REFERENCES

[1] Ben H Thacker, David S Riha, Daniel P Nicolella, Steve J Hudak, Luc J Huyse, Loren Francis, *Uncertainty quantification for structural dynamics and model validation problems: Reliability and optimization of structural systems, working conference*, 2003.

[2] Laurent Van den Bos, and Benjamin Sanderse, *Uncertainty quantification for wind energy applications - Literature review: Report SC-1701*, 2017.

[3] Steen Krenk, and Bo Jeppesen, *Finite elements for beam cross-sections of moderate wall thickness, computers and structures Volume 5*, 1989.

[4] Det Norske Veritas and Germanischer Lloy, *DNVGL-ST-0376: Rotor blades for wind turbines*, 2015.

[5] Daniele Bigoni, *Uncertainty quantification with applications to engineering problems, PhD Thesis: Technical University of Denmark* , 2015.

[6] International Organization for Standardization, *ISO 527-4 Tensile properties of isotropic and orthotropic fiber-reinforced plastic composites - Part 4: Test conditions for isotropic and orthotropic fibre-reinforced plastic composites*, 1997.

[7] Thomas M Cover, *Elements of information theory*, 1991.

[8] Tony O'Hagan, *The The Gaussian Emulation Machine for Sensitivity Analysis - Software* available in <http://www.tonyohagan.co.uk/academic/GEM/>, 2020.

[9] J. Oakley and A. O'Hagan, *Probabilistic sensitivity analysis of complex models: a Bayesian approach, Journal of the Royal Statistical Society, Series B, 66:751–769*, 2002.

EURODYN 2020
XI International Conference on Structural Dynamics
M. Papadrakakis, M. Fragiadakis, C. Papadimitriou (eds.)
Athens, Greece, 23–26 November 2020

SENSITIVITY ANALYSIS OF SAFETY PERFORMANCE OF BURIED PIPELINES UNDER SURCHARGE

Zhiqiang Wang[1,2] **and Zhenyu Lei**[1,2]

[1] Institute of Rail Transit, Tongji University
[2] Shanghai Key Laboratory of Rail Infrastructure Durability and System Safety, Tongji University
No. 4800, Cao'an Road, Jiading District, Shanghai 201804, P.R. China
e-mail: {1733359, leizhenyu}@tongji.edu.cn

Keywords: Surcharge, Safety performance, Pipeline, Monte-Carlo theory, Stochastic finite element method

Abstract. *In order to analyze the influence of surface soil loading on the safety performance of buried pipelines, based on the non-linear contact model, the pipe-soil interaction model under the action of surface soil loading is established by using the finite element software ANSYS. Then, based on the PDS module of ANSYS probability design, the sensitivity values of the four parameters of surcharge height H, soil density ρ, elastic modulus E and Poisson's ratio μ to the maximum Von Mises stress σ_{max} and horizontal maximum displacement x_{max} of the pipeline are analyzed. The results show that for σ_{max}, with the increase of ρ, σ_{max} increases significantly; with the increase of H, σ_{max} increases; with the increase of μ and E, σ_{max} decreases. For x_{max}, increasing ρ, x_{max} decreases significantly; increasing μ, x_{max} increases; increasing E and H, x_{max} decreases. It shows that the soil density has a great influence on the stress and displacement of the buried pipeline. The research results have certain engineering significance for the safety protection during the construction of buried pipelines.*

1 INTRODUCTION

Pipeline transportation is a safe and convenient way to transport resources. After the pipeline has been completed and put into operation, due to the influence of natural and human factors in the pipeline area, the external conditions will inevitably change, such as the surcharge phenomenon near the pipeline is very common. Surface surcharge causes pipeline deformation and stress change. When the stress and deformation exceed the pipeline's bearing range, the pipeline will fail and cause disastrous damage and accidents. Therefore, the study of the effect of surcharge on buried pipelines has an important guiding role and engineering value for ensuring the safe operation of pipeline engineering.

Because the model test is limited by the field conditions, more and more experts and scholars around the world use analytical method and finite element method to study the influence of surface surcharge on the mechanical properties of buried pipelines. Trichey [1] used finite element method to study the dynamic response of buried pipelines under the circular uniform load. Han et al [2] studied the effect of surface load on the mechanical properties of buried pipelines in hard rock area by establishing a three-dimensional numerical model of pipe-soil coupling. Li and Ding [3] established the calculation theory of pipe shear, bending moment and deformation, and obtained the quantitative evaluation method for the influence degree of the adjacent building load on underground pipelines. Li et al [4] established a three-dimensional pipe-soil interaction model to study the influence of the location and size of surface surcharge on the displacement, stress and ellipticity of pipelines. Shuai et al [5] analyzed the effect of loads on stress and strain of buried pipelines by establishing three-dimensional finite element model. Wang et al [6] comprehensively analyzed the mechanical parameters of buried pipelines through theoretical calculation and test, and studied the safety performance of buried natural gas pipelines under the heavy vehicle load.

For the analysis of the safety performance of buried pipelines under surcharge loading, previous studies have adopted deterministic analysis method, and a large number of trial calculations have been carried out to analyze the variation of displacement and stress of buried pipelines by changing the influencing factors several times. It is difficult for this method to consider the influence degree on the pipeline safety performance when a factor changes continuously, and when the influence factors increase, it cannot distinguish the contribution of each factor to the influence degree on the pipeline safety performance, so there is blindness in the analysis. In view of this, this paper chooses the surcharge height and characteristics (including the soil density, elasticity modulus and Poisson's ratio) as random variables, calculates the sensitivity of random parameters to pipeline safety performance by using ANSYS-PDS random analysis module, and obtains the correlation between parameters and the pipeline safety performance.

2 MECHANICAL MODEL AND CALCULATION PARAMETERS

The normal buried depth of the raw water steel pipe is about 2 meters, and the surface slag heaped load is about 2 meters high. The pipe is covered along the axis of the pipe, and its transverse width is about 12 meters, which is symmetrical to the center of the pipe. Steel tube diameter D=2.4m, wall thickness d=18mm, material elastic modulus E=2.1×10^{11}Pa, Poisson's ratio u=0.3, mass density ρ=7800kg/m^3.

3 FAILURE CRITERION OF BURIED PIPELINE

3.1 Strength checking standard

Because of the complex stress state of pipelines, Von Mises yield condition is often used to check the strength of pipelines. That is, when the maximum deformation ratio of pipelines reaches a certain value, the yield occurs [7]. The expression is as follows:

$$\sigma_{VonMises} = \sqrt{\frac{1}{2}\left[\left(\sigma_1 - \sigma_2\right)^2 + \left(\sigma_2 - \sigma_3\right)^2 + \left(\sigma_3 - \sigma_1\right)^2\right]} < \varphi\sigma_s \tag{1}$$

where σ_1, σ_2, σ_3 are the first, second and third principal stresses, φ is the design factor and σ_s is the yield stress of the pipe.

3.2 Stability check standard

The ratio of the maximum horizontal deformation Δx to the diameter D of the pipeline is defined as ellipticity Δ_θ. When the Δ_θ is greater than 3%, the section of the pipeline will lose stability [8].

$$\Delta_\theta = \frac{\Delta x}{D} \tag{2}$$

In this paper, the maximum Von Mises stress and horizontal maximum displacement of the pipeline are taken as the output variables to measure the safety performance of the buried pipeline.

4 ESTABLISHMENT AND SOLUTION OF FINITE ELEMENT MODEL

4.1 Constitutive model

The material nonlinearity should be considered in the analysis of the pipeline limit state. In this paper, the stress-strain relationship curve of three-fold line is chosen as the constitutive model of the pipeline. For soil constitutive model, Drucker-Prager material is used to simulate soil medium in ANSYS geotechnical finite element analysis.

4.2 Pipe-soil interaction model

In the modeling process of pipe, the commonly used models of pipe-soil interaction are elastic foundation beam model, soil spring model and non-linear contact model [9]. Compared with the non-linear contact model, the elastic foundation beam model and the soil spring model are simpler in calculation, but there are a lot of simplifications, which cannot better simulate the contact non-linear and non-linear friction between pipe and soil. Therefore, based on the non-linear contact model and the finite element software ANSYS, the pipe is regarded as a rigid body and the soil is regarded as a flexible body. A two-dimensional rigid-flexible surface contact is established to simulate the interaction between pipe and soil. The finite element model is shown in Figure 1.

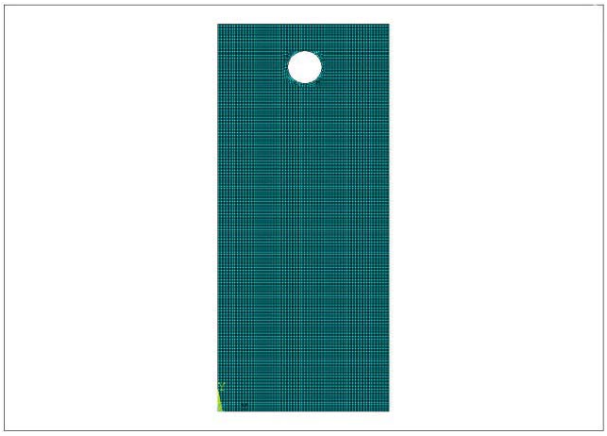

Figure 1: Schematic diagram of the finite element model.

4.3 Solution of finite element model

The displacement nephograms and equivalent stress nephograms of soil and pipeline can be obtained by solving the above finite element model, as shown in Figure 2.

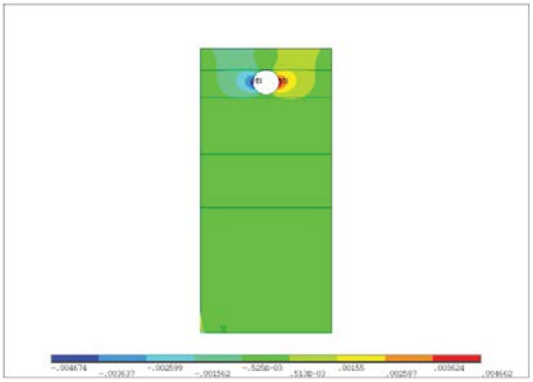

(a) X direction displacement of soil

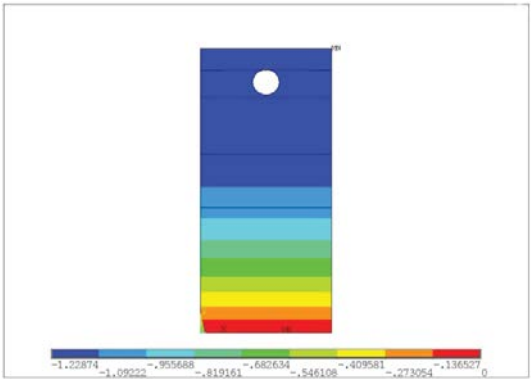

(b) Y direction displacement of soil

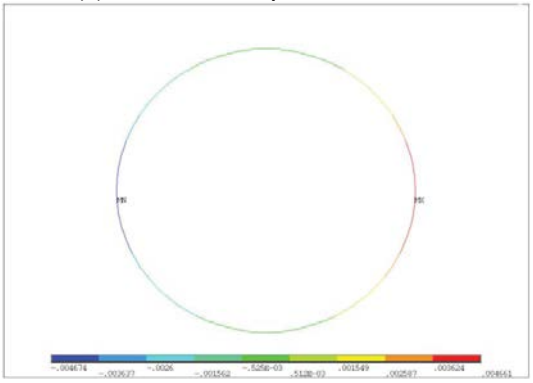

(c) X direction displacement of pipe

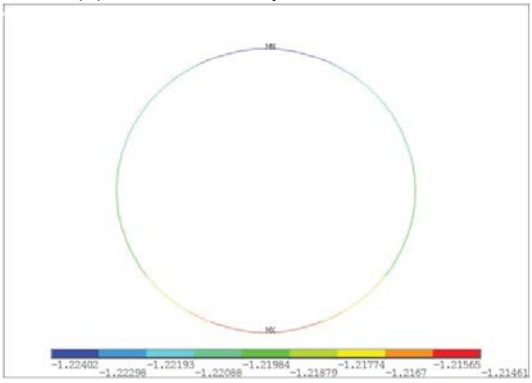

(d) Y direction displacement of pipe

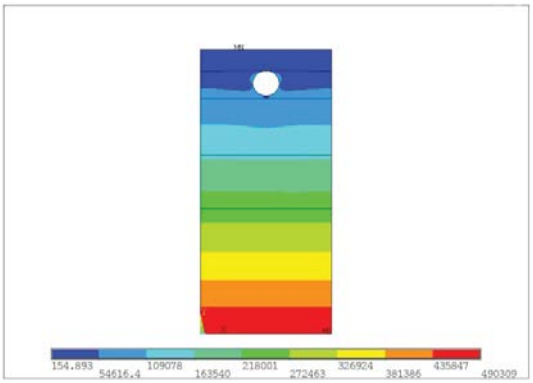

(e) Equivalent stress of soil

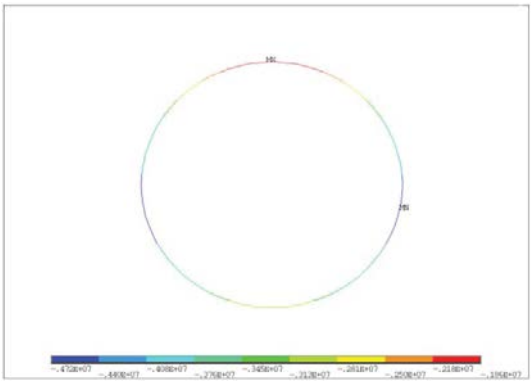

(f) Equivalent stress of pipe

Figure 2: Displacement and stress nephograms of soil and pipeline.

Based on the finite element model of pipe-soil interaction, the sensitivity analysis of the pipeline safety performance is carried out below.

5 SENSITIVITY ANALYSIS OF SAFETY PERFORMANCE

ANSYS PDS module [10] is designed based on the probability of finite element method, which can be used to study the influence of uncertain factors on the pipeline safety performance. In this module, Monte-Carlo method is used to simulate random parameters [11]. In the analysis, the random variables are parameterized, so that the random parameters can be randomly selected according to their probability distribution in a limited range. Finally, the response values of stress and displacement of pipelines can be obtained by calculation.

In this paper, four parameters of surcharge height H and characteristics of surcharge soil (including soil density ρ, elastic modulus E and Poisson's ratio μ) are taken as random input variables, without considering the correlation among variables, and all variables obey truncated normal distribution. The random distribution and eigenvalues are shown in Table 1.

Variable	Mean	Standard deviation	Minimum limit	Maximum limit
H/m	2	0.01	1.97	2.03
$\rho/10^3$ kg/m^3	1.80	0.09	1.53	2.07
E/ MPa	12.24	0.612	10.404	14.076
μ	0.3	0.015	0.255	0.345

Table 1: Statistical characteristics of random input variables.

5.1 Sensitivity analysis based on Spearman rank correlation coefficient

Sensitivity analysis is a method to evaluate the variation rate of structural response characteristics due to random parameter changing. It can be used to analyse the influence degree of random factors on structural response values [12-15]. Refer to literatures [16-18] for more cases related to this method.

The Spearman rank correlation coefficient is an important method for studying the correlation between test variables in nonparametric statistics and its sensitivity is expressed by the rank correlation coefficient. If the coefficient is close to -1 or 1, the input variable is considered to have a large influence on the output variable. If the calculated coefficient approaches 0, the effect is considered to be small. At the same time, if the coefficient is positive, it means that the output variable value increases with the increase of the input variable value; if the coefficient is negative, it means that the output variable value decreases with the increase of the input variable value.

5.2 Sensitivity calculation results

ANSYS-PDS module is used for sensitivity analysis. Monte-Carlo method and Latin hypercube method are adopted as probability analysis methods. The number n of cycles is set as 800, and the mean trend charts of σ_{max} and x_{max} are obtained as shown in Figure 3. With the increase of sampling times, the width of the confidence interval decreases, and the sampling mean approaches to the level, which indicate that 800 sampling times are enough.

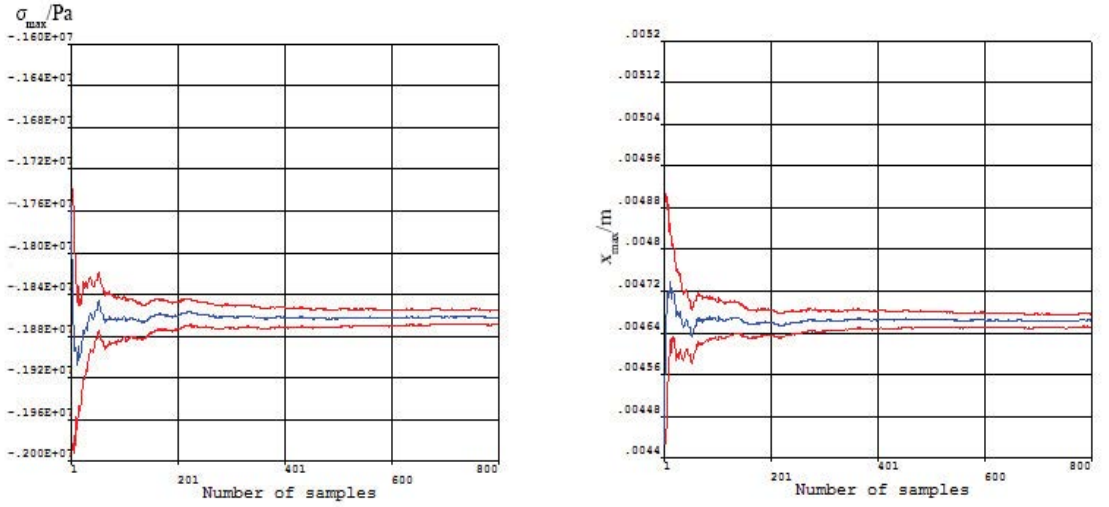

(a) The maximum Von Mises stress σ_{max} (b) The horizontal maximum displacement x_{max}

Figure 3: Average trend charts of σ_{max} and $x_{max.}$

The sensitivity values of σ_{max} and x_{max} to each random variable are shown in Table 2. According to the analysis data, the most significant influence on the maximum Von Mises stress σ_{max} of the pipeline is the density ρ of surcharge soil, which is 0.993, followed by the height H of surcharge soil, Poisson's ratio μ, and elastic modulus E of soil, which are 0.063, -0.021 and -0.017. The most significant influence on the maximum horizontal displacement x_{max} of the pipeline is the soil density ρ as well, which is -0.976, followed by elastic modulus E, height H and Poisson's ratio μ, which are -0.140, -0.073 and 0.025. Further analysis of the scatter plots shown in Figures 4 and 5 shows that with the increase of ρ, σ_{max} increases significantly; with the increase of H, σ_{max} increases; with the increase of μ and E, σ_{max} decreases; for the maximum horizontal displacement x_{max} of the pipeline, with the increase of ρ, x_{max} decreases significantly, with the increase of μ , x_{max} increases, with the increase of E and H, x_{max} decreases. It shows that the soil density has a great influence on the stress and displacement of the buried pipeline.

	H	ρ	E	μ
σ_{max}	0.063	0.993	-0.017	-0.021
x_{max}	-0.073	-0.976	-0.140	0.025

Table 2: Sensitivity values of σ_{max} and $x_{max.}$

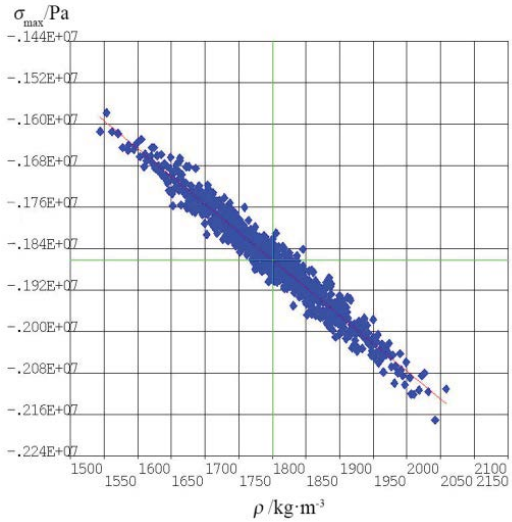

(a) Soil density ρ

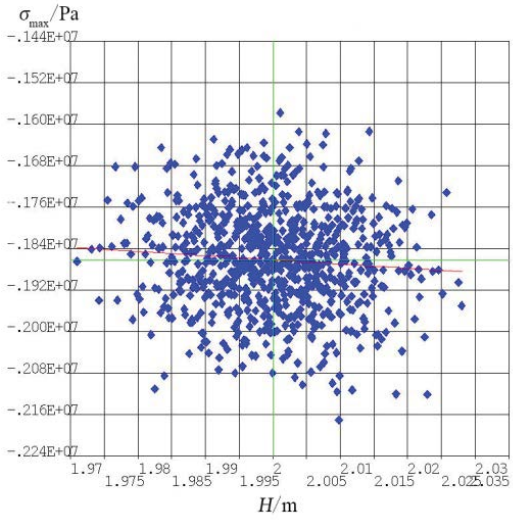

(b) Surcharge height H

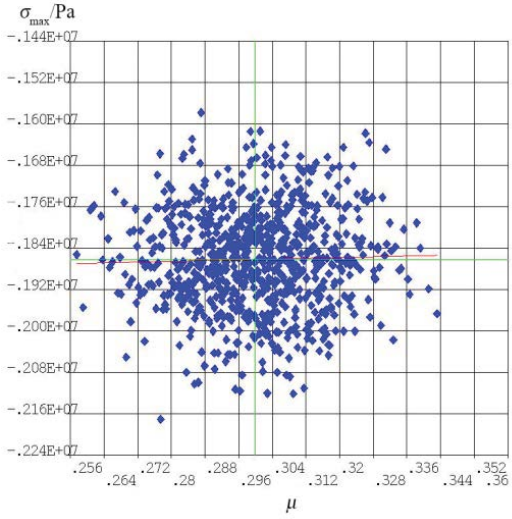

(c) Poisson's ratio μ

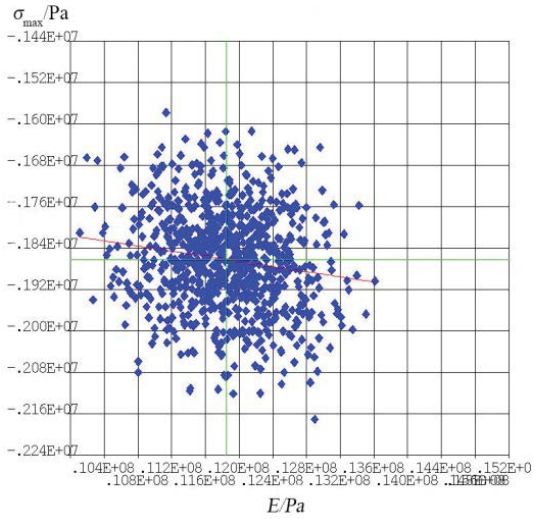

(d) Elastic modulus E

Figure 4: Scatter diagrams of input variables and $\sigma_{max.}$

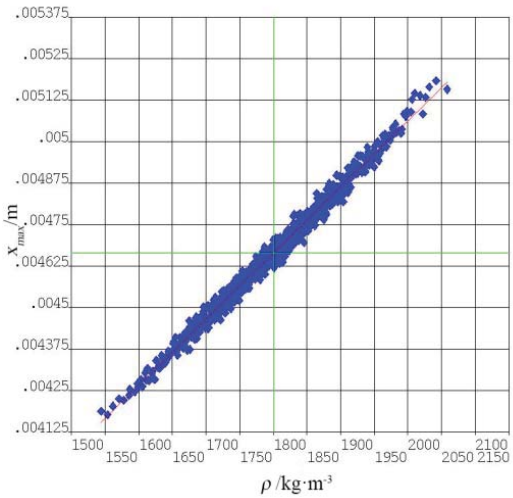

(a) Soil density ρ

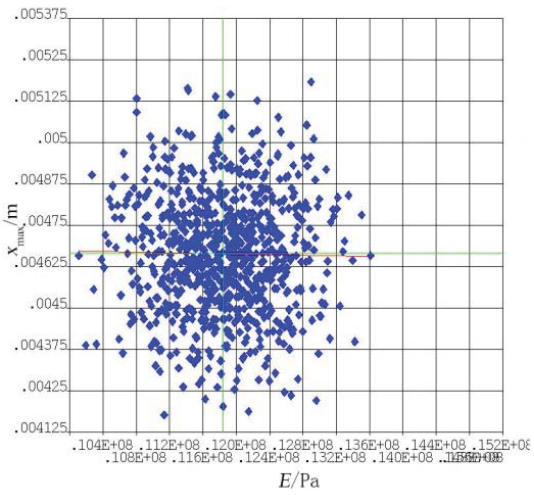

(b) Elastic modulus E

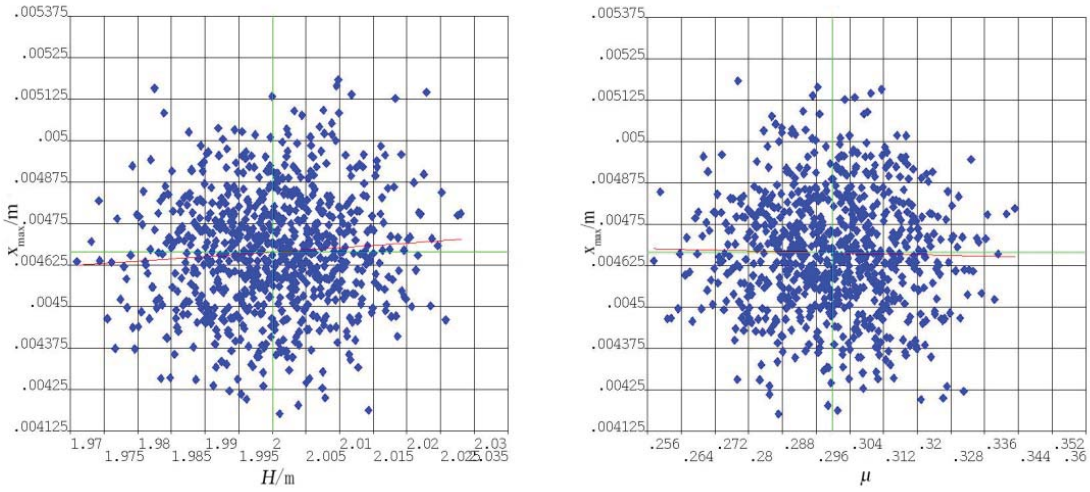

(c) Surcharge height H (d) Poisson's ratio μ

Figure 5: Scatter diagrams of input variables and $x_{max.}$

6 CONCLUSIONS

Based on the non-linear contact model, the pipe-soil interaction model of the buried pipeline under soil surcharge is established by using the finite element software ANSYS. Then, based on the ANSYS PDS module, the sensitivity values of the four parameters of surcharge height H and the characteristics of surcharge soil (including soil density ρ, elastic modulus E and Poisson's ratio μ) to the maximum Von Mises stress σ_{max} and the maximum horizontal displacement x_{max} of the pipeline are analyzed. The results show that the effect of soil surcharge on buried pipelines cannot be ignored.

(1) According to the sensitivity calculation results, for the maximum Von Mises stress σ_{max} of the pipeline, with the increase of ρ, σ_{max} increases significantly; with the increase of H, σ_{max} increases; with the increase of E and μ, σ_{max} decreases. The results show that the density of surcharge soil has the greatest influence on the stress of pipelines, while the elastic modulus of soil has the least influence on that.

(2) For the maximum horizontal displacement x_{max} of the pipeline, with the increase of ρ, x_{max} decreases significantly, with the increase of μ, x_{max} increases, with the increase of E and H, x_{max} decreases. It shows that the density of soil has the greatest influence on the horizontal displacement of the pipeline, while the Poisson's ratio of soil has less influence than other parameters.

(3) By the stochastic finite element analysis of the corresponding parameters of surcharge soil, it is easy to know which parameters are most sensitive to the pipeline stress and displacement, so that these parameters can be applied or prevented purposefully in engineering practice. The research results can provide some references for the construction and safety protection of buried pipelines.

CONFLICT OF INTEREST

The authors declare no conflict of interest.

ACKNOWLEDGMENT

The authors are greatly thankful for the financial support from the National Natural Science Foundation of China (11772230).

REFERENCES

[1] S. A. Trickey, I. D. Moore, Three-Dimensional Response of Buried Pipes under Circular Surface Loading, *Journal of Geotechnical and Geoenvironmental Engineering* 133, 219-223, 2017.

[2] C. J. Han, H. Zhang, J. Zhang, Q. Li, Effect of Surface Load on Stress and Strain of Buried Pipeline in Hard Rock Area, *Science and Technology of Safety Production in China* 11, 23-29, 2015.

[3] J. P. Li, S. J. Ding, Analysis of the Influence of Adjacent Building Loads on Underground Pipelines, *Journal of Tongji University (Natural Science Edition)* 32, 1553-1557, 2004.

[4] C. J. Li, S. F. Ma, C. L. Ji, L. Chen, Analysis of the Safety Impact of Surface Loading on Buried Pipeline, *Science and Technology of Safety Production in China* 11, 23-28, 2015.

[5] J. Shuai, X. L. Wang, Y. X. Ye, Stress Analysis of Pipeline Subject to Surface Load, *Journal of China University of Petroleum* 33, 99-103, 2009.

[6] Y. Q. Wang, X. G. Niu, Q. W. Tan, Safety Analysis for Buried Gas Pipeline under Heavy Vehicle Loads, *Journal of Safety Science and Technology* 7, 109-114, 2011.

[7] J. Shuai, Pipeline Mechanics, *Science Press*, Beijing, 2010.

[8] Design Regulations for Gas Pipeline Engineering, GB50251-2003.

[9] C. J. Han, H. Zhang, J. Zhang, X. Li, Mechanical Analysis on Buried Pipeline under Surface Tamping Load, *Science and Technology of Safety Production in China* 11, 61-67, 2015.

[10] S. Reh, J. Beley, S. Mukherjee, E. H. Khor, Probabilistic Finite Element Analysis Using ANSYS, *Structural Safety* 28, 17-43, 2005.

[11] J. Gao, Q. F. Luo, W. Che, Monte Carlo Theory and Its Implementation in ANSYS, *Journal of Qingdao Technological University* 29, 18-22, 2008.

[12] M. Baucells, E. Borgonovo, Invariant Probabilistic Sensitivity Analysis, *Management Science* 59, 2536-2549, 2013.

[13] P. Das, C. Shrubsole, B. Jones, I. Hamilton, Z. Chalabi, M. Davies, A. Mavrogianni, J. Taylor, Using probabilistic sampling-based sensitivity analyses for indoor air quality modelling, *Building and Environment* 78, 171-182, 2014.

[14] Y. Shu, Y. Shan, S. H. Zhou, X. W. Yang, Influence on vehicle-track-subgrade system dynamic response induced by track stiffness variation, *Journal of Tongji University (NATURAL SCIENCE)* 45, 721-731, 2017.

[15] X. Liu, L. Z. Jiang, P. Xiang, J. F. Mao, M. L. Wei, Analysis of train-bridge vertical random vibration based on a new point estimate method, *Journal of Vibration and Shock* 39, 15-21, 2020.

[16] Z. Y. Lei, Z. Q. Wang, Z. Jiang, Stress relaxation characteristics of rubber gasket under effect of random parameters, *Journal of Tongji University (NATURAL SCIENCE)* 47, 535-539, 2019.

[17] Z. Y. Lei, M. Liu, Waterproofness optimization for elastic rubber gaskets in shield tunnels with random parameters, *Applied Mathematics and Mechanics* 38, 899-910, 2017.

[18] Z. Y. Lei, M. Liu, Sensitivity analysis of waterproof performance of elastic rubber gasket in shield tunnel, *Journal of Tongji University (NATURAL SCIENCE)* 45, 336-341, 2017.

EURODYN 2020
XI International Conference on Structural Dynamics
M. Papadrakakis, M. Fragiadakis, C. Papadimitriou (eds.)
Athens, Greece, 23–26 November 2020

INCREMENTS AND DIFFERENTIALS IN THE STOCHASTIC ANALYSIS OF FRACTIONAL DIFFERENTIAL EQUATIONS

M. Di Paola[1], **A. Pirrotta**[1]

[1] Department of Engineering, University of Palermo
viale delle Scienze, 90128, Palermo, Italy
{mario.dipaola,antonina.pirrotta}@unipa.it

Keywords: Increments, Differentials, Itô Calculus, Fractional Differential Equations.

Abstract. *A clear definition of increments and differentials in the case of fractional differential equations enforced by white noise processes is of fundamental importance for the probabilistic characterization of the response process. In this paper it is shown that the increments for equations of the kind* $\left(D^{\alpha}X\right)(t)=W(t)$ *where* α *is the order of fractional derivative and* $W(t)$ *is a white noise process, strictly depend on the order of the fractional derivative at hand. It is shown that increments may be of order* $dt^{(\alpha-1/2)}$ *and thus range from* ∞ *up to* $dt^{1.5}$ *as* $\alpha=2$ *and so on.*

1 INTRODUCTION

In the stochastic dynamics of classical nonlinear systems, the Ito calculus is usually adopted [1-6]. In particular, dealing with the differential equation of systems enforced by normal white noise processes, the differential of the response in Ito form is $dX(t) = f(X,t)dt + dB(t)$, where $B(t)$ is the Brownian motion process whose formal derivative is the white noise. The r.h.s. of the previous equation is composed by two terms: the first one ($f(X,t)dt$) is an infinitesimal of order dt, while the second ($dB(t)$) is an infinitesimal of order $dt^{1/2}$ [7-16]. This vision opens the way to the Ito calculus and gives a whole scenario for the complete characterization of the response process $X(t)$ in probabilistic setting. Such a clear vision disappears for nonlinear fractional differential equations of the kind $\left(D^{\alpha}X\right)(t) = f(X,t) + W(t)$, where the symbol $\left(D^{\alpha}X\right)(t)$ is the fractional derivative of order α of the response process $X(t)$ and $W(t)$ is the white noise. For such an equation, the present state in the generic time *t* depends on the entire past history and thus the Ito form of the latter equation has not been defined in the past. This paper aims to give an insight on this fundamental matter. The question will be posed by making a distinction between increments and differentials in evaluating the response in presence of very irregular processes like white noise or, equivalently, Brownian motion processes.

2 PRELIMINARIES

In this section some concepts of Itô stochastic differential calculus [17] and of fractional differential equations [18] are reported for clarity's sake as well as for introducing the fundamental concepts to explain the difficulty involved in extending Itô calculus for fractional differential equations.

2.1 Itô calculus

Let the differential equation of a nonlinear system under normal white noise $W(t)$ be given as:

$$\dot{X}(t) + f(X,t) = W(t) \tag{1}$$

where $X(t)$ is the response process and $f(X,t)$ is a nonlinear function of $X(t)$. As $W(t)$ is a normal white noise, eq.(1) may be rewritten in Itô form as follows:

$$dX(t) + f(X,t) = dB(t) \tag{2}$$

where $B(t)$ is the so called Brownian motion process having independent increments and characterized in probabilistic settings by:

$$\begin{aligned} &E[dB(t)] = 0; \\ &E[dB(t_1)dB(t_2)] = 0; \quad \forall t_1 \neq t_2 \end{aligned} \tag{3}$$

$$\begin{aligned} &E[dB(t)^k] = qdt^{\frac{k}{2}} \\ &E[dB(t)^2] = qdt \end{aligned} \tag{4}$$

where $E[\bullet]$ means ensemble average.

The process $B(t)$ is nowhere differentiable, *q* is the strength of the white noise process. From eq. (4) it may be stated that $dB(t)$ is an infinitesimal of order $dt^{1/2}$. This produces in the clas-

sical rule of differentiation of a composite function $\Psi(X,t)$ twice differentiable on X and continuously differentiable on t, the following rule

$$d\Psi(X,t)=\frac{\partial\Psi(X,t)}{\partial t}dt+\frac{\partial\Psi(X,t)}{\partial x}dX+\frac{1}{2}\frac{\partial^2\Psi(X,t)}{\partial x^2}\left(dX\right)^2 \tag{5}$$

where the extra term involving the second order derivative of $\Psi(X,t)$ is present since $\left(dX\right)^2$ is of order *dt* and thus it may be not neglected. Eq. (5) is known as the Itô differential rule, and by properly selecting the trial function $\Psi(X,t)$ the various equations ruling the evolution of $X(t)$ in probabilistic setting may be readily found. An example of this is given by selecting that $\Psi(X,t)=X^k$, the equations in terms of statistical moments can be obtained; by selecting that $\Psi(X,t)=\exp\left(i\theta X\right)$ where θ is a real parameter, the equation of the characteristic function is readily found, the inverse Fourier transform of this equation returns the renowned Fokker-Plank (FPK) equation. Now the question is; if in eq. (1) the first order derivative is substituted by a fractional derivative of order $\alpha\in\mathbb{R}^+$ how can the stochastic analysis be performed? In the authors' opinion the main key to correctly answering this question is found by coming back to eq. (1), and by considering the various sample functions of $W(t)$ as an approximation by subdividing the time axis into small intervals of equal length Δt as shown in fig. (1a). The sample functions of $W(t)$ are considered as a step wise function, and in the k-th interval the amplitude is $N_k\sqrt{q/\Delta t}$ where N_k is a normal random variable with zero mean and unitary variance. The random variables N_k are independent of each another and thus $E[N_rN_s]=\delta_{rs}\,q/\Delta t$ where δ_{rs} is the Kronecker delta. In fig. (1.a) the j-th sample function is labeled as $W^{(j)}(t)$.

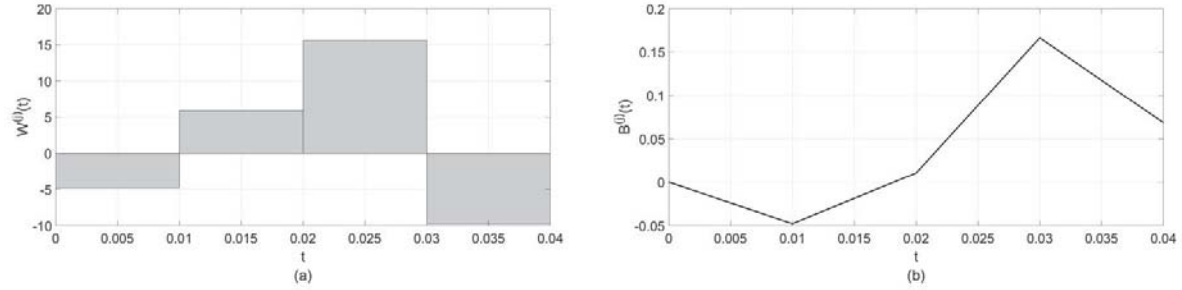

Figure 1 : j-th sample function of white noise (Fig.1a) and the correspondent Brownian motion (Fig.1b)

The correspondent sample function of the Brownian motion labeled as $B^{(j)}(t)$, is depicted in fig. (1b). As $t_k-t_{k-1}=\Delta t\to 0$ the approximations of $W^{(j)}(t)$ and $B^{(j)}(t)$ revert to the true j-th sample function of the white noise process and the correspondent j-th sample function of the Brownian motion process respectively.

3 FRACTIONAL DIFFERENTIAL EQUATION

Let us now suppose that the first order derivative is substituted by $\left(D^\alpha X\right)(t)$, that is:

$$\left(D^\alpha X\right)(t)=-f(X,t)+W(t) \tag{6}$$

where the symbol $\left(D^{\alpha}X\right)(t)$ stands for Riemann-Liouville fractional derivative defined as:

$$\left(D^{\alpha}X\right)(t)=\frac{1}{\Gamma(n-\alpha)}\left(\frac{d}{dt}\right)^{n}\int_{0}^{t}(t-\tau)^{n-\alpha-1}X(\tau)d\tau \tag{7}$$

where $n-1$ is the integer part of α. The inverse operator of the fractional derivative is the so called Riemann-Liouville fractional integral defined as:

$$\left(I^{\alpha}X\right)(t)=\frac{1}{\Gamma(\alpha)}\int_{0}^{t}(t-\tau)^{\alpha-1}X(\tau)d\tau;\quad \alpha\in\mathbb{R}^{+} \tag{8}$$

where $\Gamma(\bullet)$ is the Euler Gamma function ($\Gamma(\alpha)=\int_{0}^{\infty}e^{-t}t^{\alpha-1}dt$) that is the interpolating of the factorial.

In order to understand the problem at hand, namely, finding the characterization of $X(t)$ in a probabilistic setting we suppose that $f(X,t)=0$.

Eq. (6) is rewritten as:

$$\begin{cases}\left(D^{\alpha}X\right)(t)=W(t)\\ \quad X(0)=0\end{cases} \tag{9}$$

In particular, the above equation for $0\le\alpha\le 1$ rules the evolution of a quiescent viscoelastic bar under a white noise process. We start by assuming that the sample functions of $W(t)$ are approximated as in fig. (1a). In this figure an approximation of the white noise is depicted. The j-th sample function is represented as a stepwise function. As aforementioned, the amplitude of each step is $N_k^{(j)}\sqrt{q/\Delta t}$ where $N_k^{(j)}$ is the j-th realization of a normal standard variable (zero mean and unit variance). As $\Delta t\to 0$ the band limited white noise reverts into a true white noise. Then by assuming that the system is quiescent at $t=0$, the j-th sample function of $X(t)$ labelled as $X^{(j)}(t)$, correspondent to the j-th sample function of $W^{(j)}(t)$, is the Riemann-Liouville integral of the white noise is given as [19]

$$\underline{X}_m^{(j)}=\frac{\Delta t^{\alpha}}{\Gamma(1+\alpha)}\underline{V}_m(\alpha)\underline{W}_m^{(j)};\quad \alpha\in\mathbb{R}^{+} \tag{10}$$

where $\underline{X}_m^{(j)}$ is the vector collecting $X^{(j)}(t_k)=X_k^{(j)};\quad k=1,2,...,m$

$$\underline{X}_m^{(j)T}=[X_1^{(j)}\quad X_2^{(j)}\quad\dots\quad X_m^{(j)}]. \tag{11}$$

$\underline{W}_m^{(j)}$ is the m - vector of the amplitudes of the white noise represented in fig. (1a), namely:

$$\underline{W}_m^{(j)T}=\left(\frac{q}{\Delta t}\right)^{\frac{1}{2}}\left[N_1^{(j)}\quad N_2^{(j)}\quad\dots\quad N_m^{(j)}\right] \tag{12}$$

and $\underline{V}_m(\alpha)$ is a lower band triangular strip matrix defined [19]

$$\underline{V}_m(\alpha)=\begin{bmatrix}\omega_1(\alpha) & 0 & \cdots & 0\\ \omega_2(\alpha) & \ddots & \ddots & \vdots\\ \vdots & \ddots & \ddots & 0\\ \omega_m(\alpha) & \cdots & \omega_2(\alpha) & \omega_1(\alpha)\end{bmatrix} \tag{13}$$

where $\omega_k(\alpha)=k^\alpha-\left(k-1\right)^\alpha$. Eq. (10) gives the exact solution for the step wise representation of the white noise process.

It is worth noting at this point that a very similar representation of the Riemann-Liouville fractional integral is proposed by Grünwald-Letnikov [18], this representation implicitly assumes that the function at hand is continuous and differentiable up to the order $\left(n-1\right)$. Since this condition for $W(t)$ is violated owing to it's totally discontinuous the use of eq. (10) with $\underline{V}_m(\alpha)$ defined in eq. (13) and of $W(t)$ depicted in fig. (1a) is mandatory. Eq. (10) remains valid for $\alpha\in\mathbb{R}^+$, however the response $X_k^{(j)}$ to the step wise representation of the white noise depends upon the order of the fractional derivative. In fig. (2) a representative number of instants of the trajectories of the j-th sample function of $W(t)$ are plotted for different values of α.

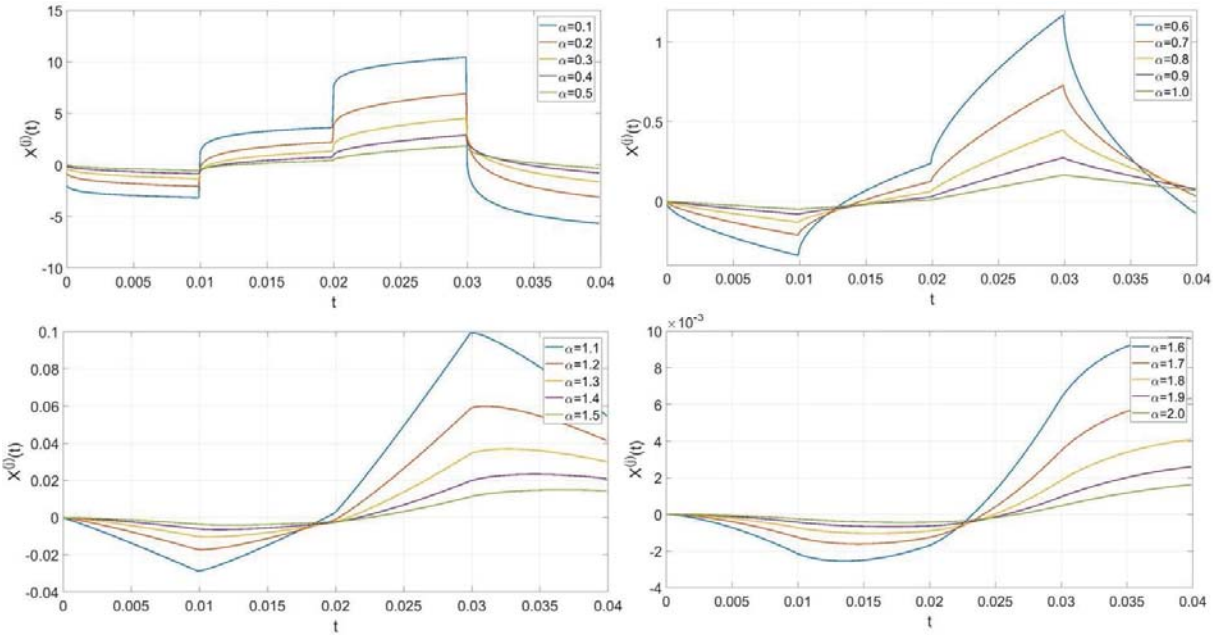

Figure 2: Few time instants of the response $X^{(j)}(t)$ for different values of α

As shown in fig.(2) we have very different scenarios for different values of α. In particular for $\alpha=0.5$ we have a continuous function with a vertical slope at the time t_k^+ (the apex + means immediately after t_k), and this behaviour does not change for $0<\alpha<1$; for $\alpha=1$ (Brownian motion) the response is a piece-wise function; for $\alpha=1.5$, $X^{(j)}(t)$ remains continuous with a discontinuity of first kind in t_k and this situation does not change for $1<\alpha<2$. For $\alpha>2$ the response is continuous with all the derivatives up to the integer part of α.

On the basis of these results we observe that an increment of $X^{(j)}(t)$ in passing from $X^{(j)}(t_{k-1})$ in $X^{(j)}(t_k)$, according to eq.(10) is given as:

$$X^{(j)}(t_k) - X^{(j)}(t_{k-1}) = \Delta X^{(j)}(t_k) = \frac{\sqrt{q}\Delta t^{\alpha-\frac{1}{2}}}{\Gamma(1+\alpha)} P_k^{(j)}(\alpha) \tag{14}$$

where $P_k^{(j)}(\alpha)$ is the j-th realization of a normal random variable (RV) $P_k(\alpha)$ defined as:

$$P_k^{(j)}(\alpha) = \left(\omega_k(\alpha) - \omega_{k-1}(\alpha)\right) N_1^{(j)} + \left(\omega_{k-1}(\alpha) - \omega_{k-2}(\alpha)\right) N_2^{(j)} + \ldots + \omega_1 N_k \tag{15}$$

and since it is a linear combination of independent normal random variables, the variance of $P_k(\alpha)$ is $\sum_{s=1}^{k}\left(\omega_s(\alpha) - \omega_{s-1}(\alpha)\right)^2 = \sigma_{P_k}^2$, and thus the variance is a finite quantity and the order of variance of $\Delta X(t_k)$ depends upon the order $\Delta t^{\alpha-1/2}$.

Now we turn out interest to the order of magnitude of the increments of the RV $\Delta X(t_k)$. As we have seen, the sample functions of $X^{(j)}(t)$ drastically depend upon the value of $\Delta X^{(j)}(t_k)$ therefore, we will consider the following different situations:

• $0 < \alpha < 1/2$. In this case $\Delta X^{(j)}(t_k)$ experiences a jump whose order of magnitude is $1/\Delta t^{1/2-\alpha}$ and thus as $\Delta t \to 0$ the RV $\Delta X(t_k)$ experiences an ∞ jump (like an instantaneous instability).

• $\alpha = 1/2$. In this case the RV experiences a jump of a finite quantity $\left(\sqrt{q}/\Gamma(1+\alpha)\right) P_k^{(j)}(\alpha)$ that is independent on the Δt selected.

• $1/2 < \alpha < 1$. In this case the RV $\Delta X(t_k)$ experiences an infinitesimal increment $\left(\sqrt{q}/\Gamma(1+\alpha)\right)\Delta t^{\alpha-1/2} P_k^{(j)}(\alpha)$ and thus the order of the RV is $\Delta t^{\alpha-1/2} > \Delta t$; to give an example, for $\alpha = 0.6$ the increment of $\Delta X(t_k)$ is $\frac{\sqrt{q}\Delta t^{0.1}}{0.894} P_k^{(j)}(\alpha)$.

• $\alpha = 1$. In this case $\Delta X(t_k) = B(t_k) - B(t_{k-1}) = \left(q\Delta t\right)^{1/2} P_k(1) = \left(q\Delta t\right)^{1/2} N_k$ and thus the increment is of order $\Delta t^{1/2} > \Delta t$ and $\Delta X(t_k)^2$ is of order Δt (increment of Brownian motion). It should be remarked that the increment only depends on the random variable N_k and not on the past history (the order of Markovianity is zero).

• $1 < \alpha < 1.5$. In this case the increment is $\left(\sqrt{q}/\Gamma(1+\alpha)\right)\Delta t^{\alpha-1/2} P_k^{(j)}(\alpha)$ with $0.5 < \alpha - 1/2 < 1$ and thus $\Delta X(t_k)$ is an infinitesimal quantity of order $\Delta t^{\alpha-1/2} > \Delta t$.

• $\alpha = 1.5$. In this case the increment coalesces with the differential order Δt and thus as $\Delta t \to 0$ the increment $\Delta X^{(j)}(t_k)$ is of order *dt*, and thus the increment and the differentials coalesce with each another.

• $1.5 < \alpha < 2$. In this case the increment is of order $1 < \alpha - 0.5 < 1.5$ and thus is a higher order infinitesimal than *dt*.

• $\alpha = 2$. This is a case of particular interest since $\omega_k(2) - \omega_{k-1}(2) = 2 \;\; \forall k \neq 1$ and $\omega_1(2) - \omega_0(2) = 1$ and the increment of RV $X(t_k)$ according to eq. (14) is given as:

$$\Delta X(t_k) = \frac{\sqrt{q}\Delta t^{1.5}}{2}\left(2\sum_{s=1}^{k-1} N_s + N_k\right) \tag{16}$$

and then $\left(2\sum_{s=1}^{k-1} N_s + N_k\right)$ is a normal zero mean RV, having variance $4(k-1)+1$ and thus $\Delta X(t_k)$ is a normal zero mean RV having a variance:

$$\sigma^2_{\Delta X}(t_k) = \frac{q\Delta t^3}{4}(4k+3) \tag{17}$$

From all of these observations, it is clear that in any case the order of the increments strictly depend on the value of α.

It must be stressed that the classical Brownian motion ($\alpha = 1$ in eq.9) is self-similar [20] that is the finite dimensional distribution for $a > 0$ $\{X(at); t \in T\} = \{a^H X(t); t \in T\}$, where H is the Hurst exponent. For $B(t)$ the Hurst exponent is 1/2, for the Lévy process, where the derivative is the stable white noise the Hurst exponent is the inverse of the instability index. These processes are called "fractional" but in the authors' opinion this is a misnomer introduced by Mandelbrot [21] but it may create confusion since one imagines that some fractional operator will appear, but this is not the case. In any case the fractional integral of the white noise is not in general self similar and hence, a deeper insight on this matter is necessary.

4 CONCLUSIONS

The extension of Itô calculus to the case in which some fractional operators appear is not currently available. In the authors opinion this is mainly due to the fact that the order of magnitude of the increments of the response process has to be defined in a correct way.

In this paper it is shown that for fractional differential equations of the kind $\left(D^\alpha X\right)(t) = W(t)$ the order of increments are $\Delta t^{\alpha-1/2}$ and thus, depending on the value of α it may experience jumps of order ∞ up to order dt^∞ for $\alpha = \infty$. This explains the difficulty for the extension of Itô calculus to fractional differential equations.

REFERENCES

[1] J. B. Roberts, P. D. Spanos, Random Vibration and Statistical Linearization, *Dover Publications*, ISBN: 9780486432403, 2003.

[2] R.A. Ibrahim, Parametric Random Vibration, *Research Studies Pr Ltd*, ISBN: 9780471908302, 1985.

[3] C.W. Gardiner, Handbook of Stochastic Methods: For Physics, Chemistry, and the Natural Sciences, *Springer Verlag*, ISBN: 9780387156071, 1986.

[4] Y.K. Lin, Probabilistic Theory of Structural Dynamics, *McGraw-Hill*, ISBN: 9781124016634, 1967.

[5] L. Arnold, Stochastic Differential Equations: Theory and Applications, *John Wiley & Sons Inc*, ISBN: 9780471033592, 1974.

[6] M. Grigoriu, Stochastic Calculus: Applications in Science and Engineering, *Birkhäuser*, ISBN: 978-0817642426, 2002.

[7] M. Di Paola, A. Pirrotta, Non-linear systems under impulsive parametric input, *International Journal of Non-Linear Mechanics* 34, 843–851, 1999.

[8] W. Feller, On the integro-differential equations of completely discontinuous Markov processes, *Transactions of the American Mathematical Society*. 48, 1948.

[9] M. Di Paola, G. Falsone, A. Pirrotta, Stochastic response analysis of non-linear systems under Gaussian inputs, *Probabilistic Engineering Mechanics* 7, 15–21, 1992.

[10] C. Proppe, The Wong-Zakai theorem for dynamical systems with parametric Poisson white noise excitation, *International Journal of Engineering Science* 40, 1165–1178, 2002.

[11] H.J. Pradlwarter, G.I. Schueller, On advanced Monte Carlo simulation procedures in stochastic structural dynamics, *International Journal of Non-Linear Mechanics* 32, 735–744, 1997.

[12] M. Di Paola, A. Pirrotta, Direct Derivation of Corrective Terms in SDE through Non-linear Transformation on Fokker-Planck Equation, *Nonlinear Dynamics* 36, 349-360, 2004.

[13] A. Pirrotta, Non-linear systems under parametric white noise input: digital simulation and response, *International Journal of Non-Linear Mechanics* 40, 1088-1101, 2005.

[14] A. Pirrotta, Multiplicative cases from additive cases: Extension of Kolmogorov-Feller equation to parametric Poisson white noise processes, *Probabilistic Engineering Mechanics* 22, 127-135, 2007.

[15] M. Di Paola, A. Pirrotta, M. Zingales, Itô Calculus extended to systems driven by alpha-stable Lévy white noises (a novel clip on the tails of Lévy motion), *International Journal of Non-Linear Mechanics* 42, 1046-1054, 2007.

[16] M. Di Paola, A. Pirrotta, M. Zingales, Stochastic analysis of external and parametric dynamical systems under sub-Gaussian Lèvy white-noise, *Structural Engineering and Mechanics* 28, 373-386, 2008.

[17] K. Ito, On a formula concerning stochastic differential, *Nagoya Mathematical Journal* 3, 55-65, 1951.

[18] I. Podlubny, Fractional differential equations: An introduction to fractional derivatives, fractional differential equations, to methods of their solution and some of their applications, *Academic Press*, ISBN: 9780125588409, 1998.

[19] N. Colinas-Armijo, M. Di Paola, Step-by-step integration for fractional operators, *Communications in Nonlinear Science and Numerical Simulation* 59, 292-305, 2018.

[20] G. Samorodnitsky, M.S. Taqqu, Stable non-Gaussian random processes: Stochastic Models with Infinite Variance, *Chapman and Hall/CRC*, ISBN: 978-0412051715, 1994.

[21] B. B. Mandelbrot, J. W. Van Ness, Fractional Brownian Motions, Fractional Noises and Applications, *SIAM Review* 10, 422-437, 1968.

EURODYN 2020
XI International Conference on Structural Dynamics
M. Papadrakakis, M. Fragiadakis, C. Papadimitriou (eds.)
Athens, Greece, 23–26 November 2020

A DEVELOPED ANALYTICAL NON-LINEAR MODEL OF ELASTOMERIC BEARINGS VERIFIED WITH NUMERICAL FINDINGS

Konstantinos N. Kalfas[1], **Davide Forcellini**[2]

[1] Southern Methodist University, Dept. of Civil and Environmental Engineering
Embrey Engineering Bldg, 3101 Dyer St, Dallas, TX 75205
e-mail: kkalfas@smu.edu

[2] University of Auckland, Dept. of Civil and Environmental Engineering
20 Symonds Street, Auckland CBD, Auckland 1010Auckland, New Zealand
e-mail: dfor295@aucklanduni.ac.nz

Keywords: Non-linearity, Analytical model, Elastomeric bearing, Numerical simulations

Abstract. *Multi-layer elastomeric bearings (EB) are used in civil engineering in many applications such as vibration control and base isolation in bridges and infrastructures. During strong seismic actions, EB can be subjected to both axial and shear loads. The recent theoretical model [1] considers the effects of both loads to study large deformation stability of EB. The present paper investigates the accuracy of this theory by comparing the proposed results with numerical findings, aiming to extend the current linear elastic model with a more accurate non-linear advanced formulation that can consider the behaviour of elastomeric bearings captured by numerical findings. In particular, such improvement is necessary in designing strategic structures, such as bridges or nuclear power plants. The developed model may be implemented in existing Finite Element Model (FEM) platforms and be widely used by the practitioners.*

1 INTRODUCTION

Base isolation and vibration control systems are the most common applications of EB towards the protection of structures and infrastructure assets from the effects of dynamic loads, such as earthquakes and vibrations. Isolation allows the decoupling of the structure from the ground by intentionally concentrating dynamic/seismic energy dissipation in a unique element with low horizontal stiffness between the substructure and the superstructure. In the past 20 years, extensive contributions developed models that can consider the complex mechanism of such systems. In particular, experimental tests that have been conducted [2-13] showed how the vertical and horizontal stiffness are related with the increase of the lateral displacement. Furthermore, numerical simulations were performed during the last decades [14-18], in order to model the non-linearity of EB and to predict the critical and post-critical mechanisms. More recently, Kumar et al. [19] investigated the effect of lateral displacement on vertical stiffness and the critical buckling load capacity of EB. In this background, Forcellini [20], Kalfas *et al.* [21-23], Kalfas and Mitoulis [24], and Rahnavard and Thomas [25] conducted numerical studies on EB with several platforms, such as Abaqus/ CAE and Opensees. In particular, Forcellini *et al.* [26] compared the numerical findings with the theoretical ones [1]. In this regard, numerical simulations apply isolators as finite elements inside structural models.

Other researchers studied simplified models that describe the behaviour of EB with the aim to be directly implemented in structural models. In particular, Forcellini and Kelly [1] described the stability of EB extending the original two-spring model of the bearing, developed by Kelly [27] and Kelly and Takhirov [28] to large deformations. The model is used to illustrate the influence of large deformations on the interaction between horizontal and vertical loads and assessing the post-buckling behaviour of EB.

The present paper investigates the accuracy of the theoretical model, particularly regarding the non-linear modelling of shear force – shear deflection and study its effects shown both by laboratory tests [29] and numerical studies [21-24]. The paper aims to extend the current linear elastic model with a more accurate non-linear advanced formulation. In this regard, the developed relationship can be implemented inside a finite element that reproduces the combined axial-shear behaviour. As shown by Forcellini *et al.* [26], Forcellini[30,31], and Canini and Forcellini [32,33] the role of non-linearity is fundamental in order to understand the cases where potentially EB becomes crucial for important structures such as bridges and nuclear power plants. In this regard, the paper first compares the numerical findings with the linear elastic theory. Subsequently, the procedure that was carried out in order to calibrate the most significant parameters is presented.

2 NUMERICAL SIMULATIONS IN SUPPORT OF THE ANALYTICAL MODEL

Abaqus/ CAE and Straus7 have been used here to perform numerical simulations (Fig. 1). The finite element (FE) models have been reproduced with layered systems that represent the alternating steel and rubber layers and the bolted connections. In particular, the models were performed in order to reproduce the experimental results by Ohsaki *et al.* [29].

The numerical models consist of two anchor plates at the upper and lower levels of the model (diameter: 1000 mm and thickness: 28 mm) and 30 rubber layers and 29 steel plates alternating each other. Each rubber layer had a thickness of 4 mm and the individual steel plate thickness was 3.1 mm, with a total thickness of 2x28 mm+30x4 mm+29x3.1 mm= 265.9 mm. The diameter of the intermediate layers was 700 mm and there was a hollow core, which run along the whole thickness of the bearing (internal diameter: 15 mm). The mesh consisted of 62,672 3D solid elements: 1,008 for each rubber layer and steel plate and 1,600 elements

for the anchor plates. Full integration elements were chosen in order to obtain more accurate results, especially in correspondence with the hourglass effect [34]. Boundary conditions are depicted in Fig. 1b (where X-, Y- and Z-axes can be seen). The bottom anchor plate was fixed (i.e. $UX=UY=UZ=URX=URY=URZ=0$). The axial load (along the *Z*-axis) and the horizontal displacement (along the *Y*-axis) were applied at the top anchor plate (where $UZ\neq0$ and $UY\neq0$). The remaining boundary conditions at the top anchor plate were: $UX=URY=URZ=0$, with $URX\neq0$. The elastic properties of the rubber layer and steel plates are shown in Table 1.

Two platforms were used to perform non-linear analyses with hyperelastic behaviour for the rubber layers. In Abaqus/ CAE, the Ogden material was used [35] and the hyperelastic properties were: $\mu_1= 0.41$ MPa, $\alpha_1= 1.6$, $\mu_2= 0.0012$ MPa and $\alpha_2= 6.2$ (as in [21]). These parameters led to a shear modulus of $G= 0.66344$ MPa and a Poisson's Ratio of $\nu= 0.49989$. Other parameters were: the stress scaling factor $S_{SF}= 1.6$, the creep parameter $A= 0.56$, the effective stress exponent $m= 4$ and the creep strain exponent $C= -1$. In Straus7, the rubber material was modelled with the Mooney and Rivlin model [36, 37] and the main parameters *C1* and *C2* (both equal to 0.16586 MPa) were calibrated with a parametric study. The compressibility modulus was set equal to 2,000 MPa.

	E [MPa]	ν
Rubber	1.99017	0.49989
Steel	205,000	0.3

Table 1: Elastic properties of the numerical models of rubber layers and steel plates.

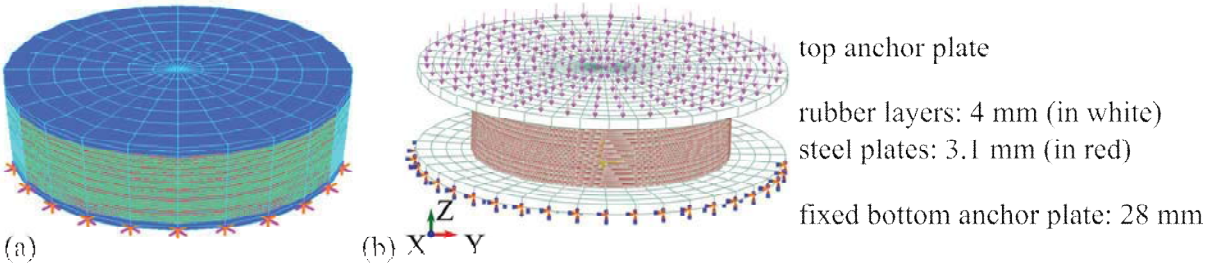

Figure 1. 3D numerical models: (a) Struss7, (b) Abaqus/ CAE

3 ANALYTICAL, LINEAR ELASTIC MODEL

The theory of stability of EB was firstly developed by Haringx [38] and later applied by Gent [39] that can be considered the basis for the theory of stability. In particular, EBs can be susceptible to a type of instability similar to that of an ordinary column but dominated by the low shear stiffness of a bearing, as described by the simplified two-spring linear elastic model that can be seen in Fig. 2 [27] and the developed theory [1].

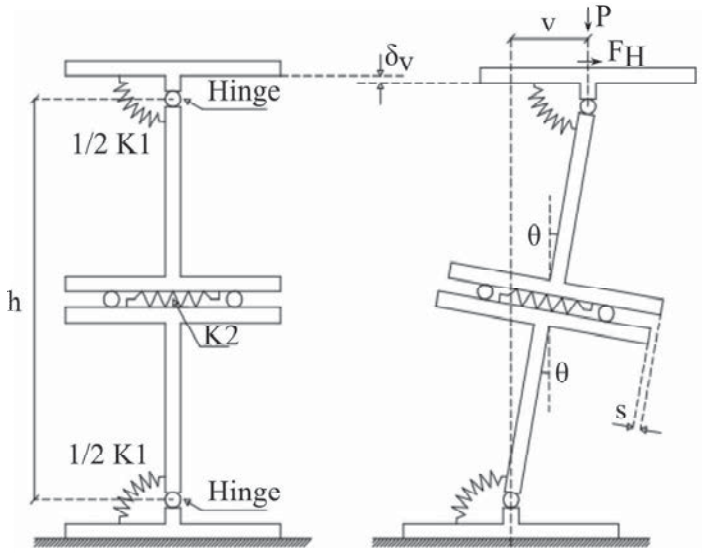

Figure 2. Linear elastic model

The formulation of the original model of the EB is based on three kinematic variables: the rotation θ, the vertical displacement δ_v and the horizontal displacement v. The equations can be condensed in the following:

$$[p \cdot \cos\theta + \lambda] \cdot [p \cdot \sin\theta + f \cdot \cos\theta] = \theta \tag{1}$$

where

$$p = \frac{P}{\sqrt{P_E P_S}} \tag{2}$$

$$f = \frac{F}{\sqrt{P_E P_S}} \tag{3}$$

$$\lambda^2 = \frac{P_S}{P_E} \tag{4}$$

$$P_E = \frac{\pi^2 \cdot E \cdot I_S}{h^2} \tag{5}$$

$$P_S = G \cdot A_s \tag{6}$$

EI_s is the bending stiffness, GA_s is the effective shear stiffness and λ^2 is the ratio between the Euler load (P_E) and the shear load (P_S), which generally tends to be a very small constant, usually of the order of 0.001 – 0.05 [1]. Since this model applies a linear isotropic material, the value of λ^2 does not depend on the shear modulus (G) and can be calculated as (by considering the Poisson's coefficient almost 0.5, for the rubber):

$$\lambda^2 = \frac{P_S}{P_E} = \frac{G \cdot A_S}{\frac{\pi^2 \cdot E \cdot I_S}{h^2}} = \frac{G \cdot A_S}{\frac{\pi^2 \cdot 2G \cdot (1+\nu) \cdot I_S}{h^2}} = \frac{A_S \cdot h^2}{\pi^2 \cdot 2(1+\nu) \cdot I_S} \cong 0.3377 \frac{A_S \cdot h^2}{I_S} \tag{5}$$

The above mathematical model is here compared with the results obtained from the numerical simulations where materials are set as linear elastic. Figure 3 compares the results for increasing vertical pressure p (i.e. 2 MPa, 5 MPa, 10 MPa and 14 MPa). It is possible to see that the linear elastic theoretical model is in close proximity to the results from the numerical simulations performed in Abaqus/ CAE and Straus7.

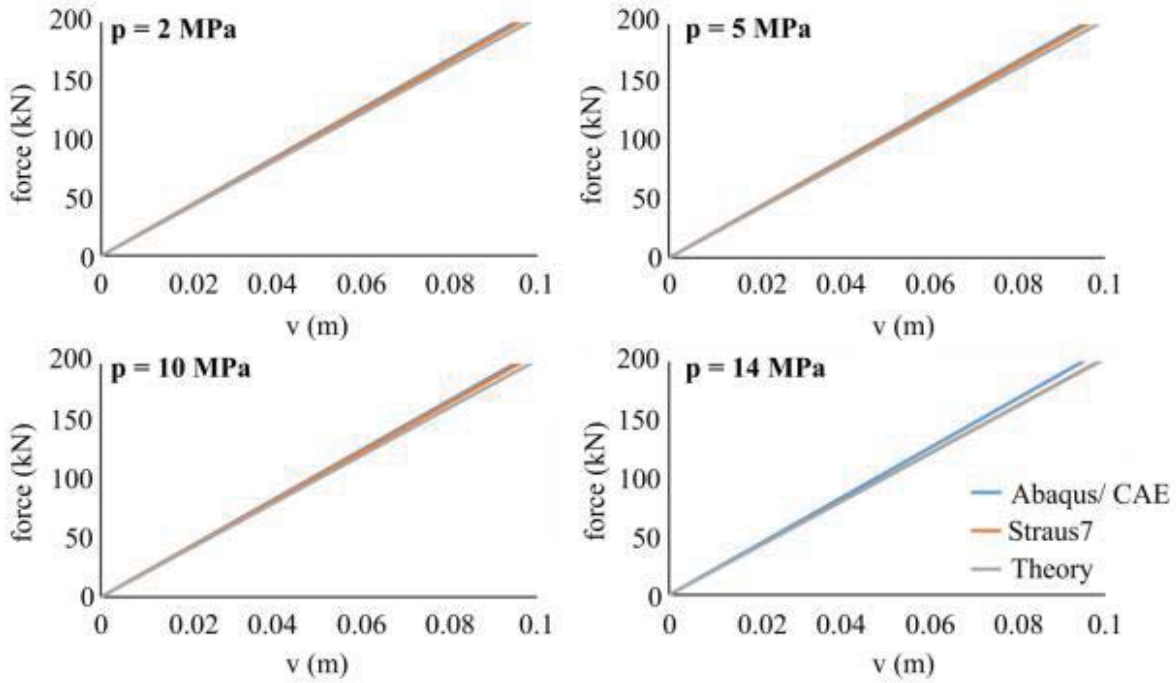

Figure 3. Comparison between linear assumptions (Abaqus/ CAE, Straus7 and Theory)

4 DEVELOPMENT OF THE NON-LINEAR ELASTOMERIC BEARING MODEL

In this section, the assumptions of the linear elastic material are neglected. Therefore, it is not possible to assume a linear relationship between G and E, as in Equation (7). In particular, λ^2 depends on the ratio between G and E and the assumption that it remains constant during the deformation needs to be removed. There are studies that describe the source of non-linearities of EB, such as the Mullin's effect [40, 41], which causes the reduction of the bulk modulus (volumetric elasticity). This paper aims to extend the linear theory by concentrating all the sources of non-linearity inside λ^2 and a new formulation of such parameter is proposed here. The formulation describes the behaviour of the EB by taking the horizontal displacement as the main kinematic variable. A non-linear relationship between such variable and λ^2 was built up with this form:

$$\lambda^2 = \lambda^2(v) = \alpha \cdot v^{\beta} \tag{8}$$

The power relationship was shown to be the best correlation between v and λ^2 and it was obtained adopting the least square regression technique. The correlation parameters α and β were calibrated considering R^2 value to be the measure of the correlation. Table 2 shows the parameters for the considered loading conditions.

	α	β	R^2
2 MPa	0.0014278	-0.0001	0.9991
5 MPa	0.00142	-0.026	0.9987
10 MPa	0.0106	-0.395	0.9976
14 MPa	0.0233	-0.576	0.9856

Table 2: Correlation parameters.

In order to implement formula (8) inside (1), an incremental solution was needed due to non-linearity. The Newton-Rapson algorithm was chosen as one of the most credited methods for solving non-linear problems. The new formulation was finally solved for the increasing vertical pressure p (2 MPa, 5 MPa, 10 MPa and 14 MPa) and compared with numerical simulations performed by Abaqus/ CAE and Strauss 7 (Fig. 4). It is worth noticing that for 2 MPa and 5 MPa the proposed formulation leads to a fairly linear relationship between the horizontal displacement and the horizontal force (λ^2 is fairly constant). For bigger values of p (10 MPa and 14 MPa), non-linearity behaviour becomes significant.

Figure 5 shows the proposed formulation (8) for the considered EB and it is possible to assess the relationship of λ^2 and the displacement. It is worth noticing that the variation is more significant for bigger values of vertical loads (10 MPa and 14 MPa), where non-linear behaviour needs to be considered.

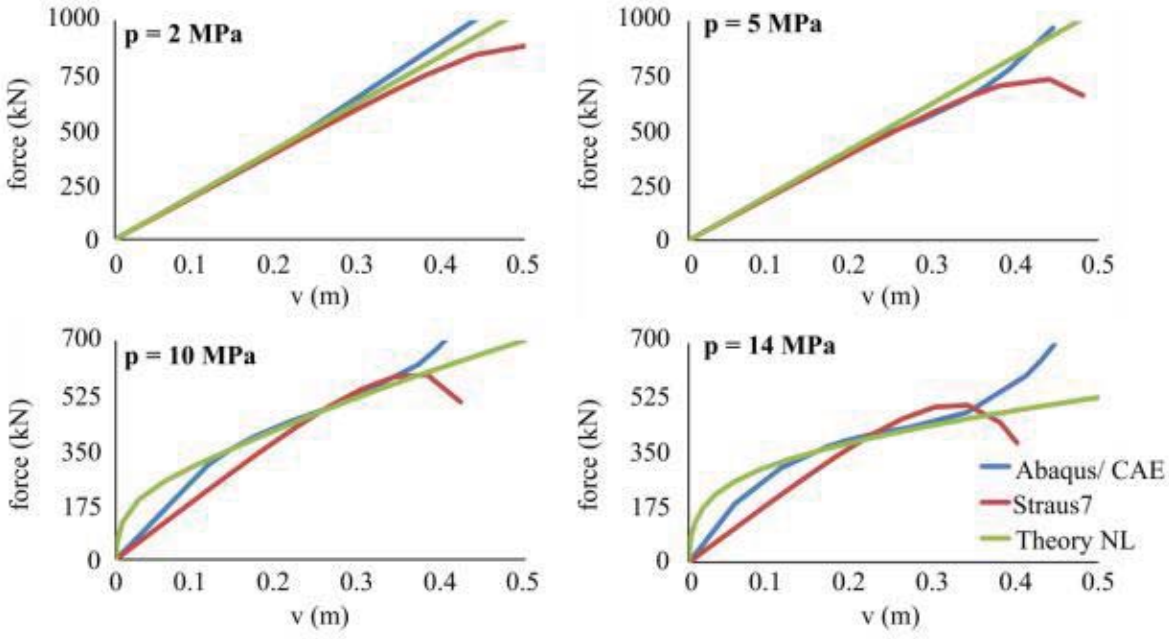

Figure 4. Comparison between non-linear results (Abaqus/ CAE, Straus 7 and the modified NL model)

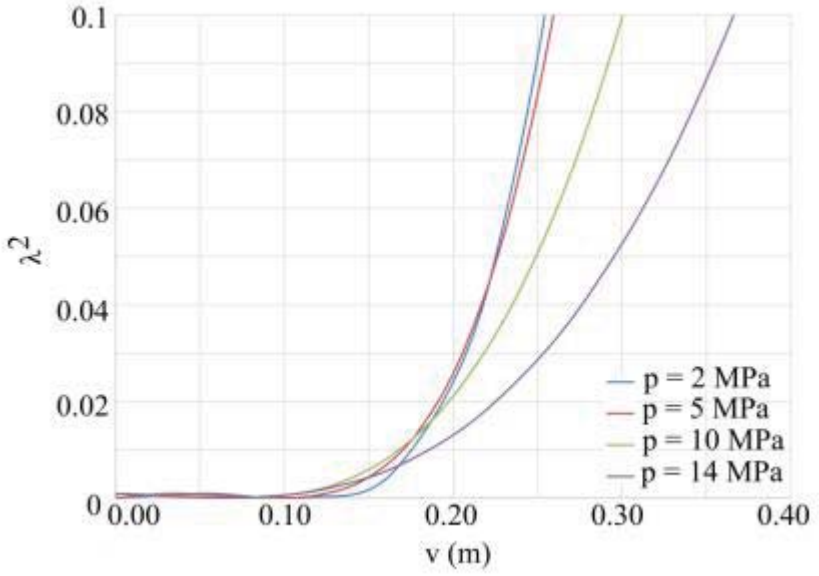

Figure 5. The proposed formulation (8)

5 CONCLUSIONS

The study conducted in this paper may be viewed as an original contribution to study the modelling of stability of EB with analytical models. In particular, the paper shows the credibility of the two-spring model by Forcellini and Kelly [1] in representing the linear behaviour of EB. The comparison between the theory and the numerical simulations performed with Abaqus/CAE and Straus7 showed good agreement under linear assumptions. The paper proposes the development of the original two-spring model by introducing a non-linear relationship between the λ^2 and the horizontal displacement. The proposed formulation can consider a more realistic non-linear behaviour of the EB and can be implemented in numerical codes. Overall, this study can be considered as a first step towards proposing a new easy-to-use approach that will assess the non-linear response of EB.

REFERENCES

[1] D. Forcellini, J. M. Kelly, Analysis of the large deformation stability of elastomeric bearings, *Journal of Engineering Mechanics*, 140.6:04014036, 2014.

[2] I. G. Buckle, H. Liu, Stability of elastomeric seismic isolation systems, *Proc., Seminar on Seismic Isolation, Passive Energy Dissipation and Control*, Applied Technology Council, Redwood City, CA, 293–305, 1993.

[3] I. G. Buckle, H. Liu, Critical loads of elastomeric isolators at high shear strain, *Proc., 3rd U.S.-Japan Workshop on Earthquake Protective Systems for Bridges*, National Center for Earthquake Engineering Research, Buffalo, NY, 1994.

[4] I. D. Aiken, J. M. Kelly, F. F. Tajirian, Mechanics of low shape factor elastomeric seismic isolation bearings, *Earthquake Engineering Research Center, Univ. of California, Berkeley, CA*, UCB/EERC-89/ 13, 1989.

[5] Civil Engineering Research Foundation (CERF), Evaluation findings for Scougal Rubber Corporation high damping rubber bearings, *Rep. No. HITEC 98-11 40373*, Washington, DC, 1998a.

[6] Civil Engineering Research Foundation (CERF), Evaluation findings for Skellerup base isolation elastomeric bearings, *Rep. No. HITEC 98-11 40376*, Washington, DC, 1998b.

[7] Civil Engineering Research Foundation (CERF), Evaluation findings for Tekton, Inc., steel rubber bearings, *Rep. No. HITEC 98-10 40365*, Washington, DC, 1998c.

[8] Civil Engineering Research Foundation (CERF), Summary of evaluation findings for the testing of seismic isolation and energy dissipating devices, *Rep. No. 40404*, Washington, DC, 1999.

[9] I. Buckle, S. Nagarajaiah, K. Ferrell, Stability of elastomeric isolation bearings: Experimental study, *J. Struct. Eng.*, 128:1, 3–11, 2002.

[10] G. Warn, A. Whittaker, M. Constantinou, Vertical stiffness of elastomeric and lead–rubber seismic isolation bearings, *J. Struct. Eng.*, 133.9, 1227– 1236, 2007.

[11] J. Sanchez, A. Masroor, G. Mosqueda, K. Ryan, Static and dynamic stability of elastomeric bearings for seismic protection of structures, *J. Struct. Eng.*, 139.7, 1149–1159, 2012.

[12] X. Han, C. A. Kelleher, G. Warn, T. Wagener, Identification of the controlling mechanism for predicting critical loads in elastomeric bearings, *J. Struct. Eng.*, 139.12: 04013016, 2013a.

[13] X. Han, G. Warn, A. Kasalanati, Dynamic stability testing of isolation systems composed of elastomeric bearings and implications for design, *Proc., Structures Congress, ASCE*, Reston, VA, 2140–2150, 2013b.

[14] S. Nagarajaiah, K. Ferrell, Stability of elastomeric seismic isolation bearings, *Journal of Structural Engineering*, 125.9, 946-954, 1999.

[15] G. P. Warn, A. S. Whittaker, Property modification factors for seismically isolated bridges, *J. Bridge Eng.*, 11.3, 371–377, 2006.

[16] G. Warn, A. Whittaker, M. Constantinou, Vertical stiffness of elastomeric and lead–rubber seismic isolation bearings, *J. Struct. Eng.*, 133.9, 1227-1236, 2007.

[17] G. Warn, J. Weisman, Parametric finite element investigation of the critical load capacity of elastomeric strip bearings, *Eng. Struct.*, 33.12, 3509–3515, 2011.

[18] J. Weisman, G. Warn, Stability of elastomeric and lead rubber seismic isolation bearings, *J. Struct. Eng.*, 138.2, 215–223, 2011.

[19] M. Kumar, A. S. Whittaker, M. C. Constantinou, An advanced numerical model of elastomeric seismic isolation bearings, *Earthquake Engineering and Structural Dynamics*, 43.13, 1955-1974, 2014.

[20] D. Forcellini, 3D Numerical simulations of elastomeric bearings for bridges, *Innovative Infrastructure Solution*, 1.1, 2016.

[21] K. N. Kalfas, S. A. Mitoulis, K. Katakalos, Numerical study on the response of steel-laminated elastomeric bearings subjected to variable axial loads and development of local tensile stresses, *Engineering Structures*, 134, 346-357, 2017a.

[22] K. N. Kalfas, S. A. Mitoulis, K. Katakalos, Numerical study on bridge elastomeric bearings subjected to large shear strain with emphasis on local tension, *16th World Conference on Earthquake Engineering*, 9-13 January 2017, Santiago, Chile, 2017b.

[23] K. N. Kalfas, S. A. Mitoulis, D. Konstantinidis, Influence of the steel reinforcement on the vulnerability of elastomeric bearings, *Journal of Structural Engineering*, 2020, DOI: 10.1061/(ASCE)ST.1943-541X.0002710.

[24] K. N. Kalfas, S. A. Mitoulis, Performance of steel-laminated rubber bearings subjected to combinations of axial loads and shear strains, *Procedia Engineering*, 99, 2979-2984, 2017c.

[25] R. Rahnavard, R. J. Thomas, Numerical evaluation of steel-rubber isolator with single and multiple rubber cores, *Engineering Structures*, 198, 109532, 2019.

[26] D. Forcellini, S. A. Mitoulis, K. N. Kalfas, Study of the response of elastomeric bearings with 3D numerical simulations and experimental validation, *Computational Methods in Structural Dynamics and Earthquake Engineering (COMPDYN) Conference*, Rhodes Island, Greece, 15-17 June 2017.

[27] J. M. Kelly, Earthquake-resistant design with rubber, *2nd Ed.*, Springer, London, 1997.

[28] J. M. Kelly, S. M. Takhirov, Tension buckling in multilayer elastomeric isolation bearings, *Journal of Mechanics of Materials and Structures*, 2, 1591–1605, 2007.

[29] M. Ohsaki, T. Miyamura, M. Kohiyama, T. Yamashita, M. Yamamoto, N. Nakamura, Finite-element analysis of laminated rubber bearing of building frame under seismic excitation, *Earthquake Engineering and Structural Dynamics*, 44.11, 1881-1898, 2015.

[30] D. Forcellini, Cost Assessment of isolation technique applied to a benchmark bridge with soil structure interaction, *Bulletin of Earthquake Engineering*, 15.1, 51-69, 2018a.

[31] D. Forcellini, Seismic assessment of a benchmark based isolated ordinary building with soil structure interaction, *Bulletin of Earthquake Engineering*, 16.5, 2021-2042, 2018b.

[32] A. Canini, Forcellini, D, 3D numerical simulations of a base-isolated residential building with soil structure interaction", *Computational Methods in Structural Dynamics and Earthquake Engineering (COMPDYN) Conference*, Rhodes Island, Greece, 15-17 June 2017.

[33] A. Canini, The role of non-linearity in the seismic assessment of a base isolated benchmark building with soil structure interaction effects, *International Conference on Structural Dynamics (EURODYN)*, Athens, Greece, 22-24 June 2020.

[34] Dassault Systèmes, ABAQUS/ CAE 6.13user's Manual, *Abaqus Ver. 6.13 Documentation*, Providence, RI, 2014.

[35] W. R. Ogden, Large Deformation Isotropic Elasticity–On the Correlation of Theory and Experiment for Incompressible Rubberlike Solids, *Proceedings of the Royal Society of London. Series A, Mathematical and Physical Sciences*, 326.1567, 565–584, 1972.

[36] M. Mooney, A theory of large elastic deformation, *J Appl Phys*, 11.9, 582–592, 1940.

[37] R. S. Rivlin, Large elastic deformations of isotropic materials IV. Further developments of the general theory, *Philosophical Transactions of the Royal Society of London. Series A, Mathematical and Physical Sciences*, 241.835, 379–397, 1948.

[38] J. A. Haringx, On highly compressible helical springs and rubber rods, and their application for vibration-free mountings, III, *Philips Res. Rep.*, 4, 206–220, 1948.

[39] A. N. Gent, Elastic stability of rubber compression springs, *J. Mech. Eng. Sci.*, 6.4, 318–326, 1964.

[40] L. Mullins, Softening of Rubber by deformation, *Rubber chemistry and technology*, 42, 339-362, 1969.

[41] J. Diani, B. Fayalle, P. Gilarmini, A review on the Mullins effect, *European Polymer Journal*, 45, 601-612, 2009. -

EURODYN 2020
XI International Conference on Structural Dynamics
M. Papadrakakis, M. Fragiadakis, C. Papadimitriou (eds.)
Athens, Greece, 23–26 November 2020

EXPERIMENTAL, THEORETICAL, AND NUMERICAL SIMULATION APPROACHES TO ASSESS THE COMPRESSIVE BEHAVIOR OF ELASTOMERIC BEARINGS

Manuel A. Guzmán Sánchez[1], Davide Forcellini[2], Ricardo Moreno Sánchez[1], and Diego H. Giraldo-Vásquez[1]

[1] Faculty of Engineering, University of Antioquia
Calle 67 No. 53-108, Medellín Colombia
e-mail: malberto.guzman@udea.edu.co, ricardo.moreno@udea.edu.co, dhernan.giraldo@udea.edu.co

[2] Civil and Environmental Engineering Department, University of Auckland
Symond Road, 20 Auckland, New Zealand
e-mail: dfor295@aucklanduni.ac.nz

Keywords: Elastomeric bearing, Compression, Stability, Experimental, Theoretical, Numerical simulations.

Abstract. *Elastomeric bearings may be applied as passive energy devices for seismic protection of structures and vibration control of systems and machinery. Their main loading state is compression combined with horizontal displacements and thus compressive behavior requires particular attention. In this study, three approaches (theoretical, experimental and numerical) are taken into account to study several scaled bearings with relative low shape factors. Compressive tests to scaled elastomeric bearings were performed and used to validate the large-displacement theory proposed by Forcellini and Kelly (2012). Relative large values of material variations, geometrical dimensions, and fabrication imperfections were taken into account in the validation of the theoretical model. Finite element modeling was performed using OpenSees, which is able to reproduce alternating rubber and steel layers subjected to vertical load conditions.*

1 INTRODUCTION

Elastomeric bearings have being used in applications such as bridges, buildings, and power generation plants due to their damping capacity, long life span, moderate cost since the 70s [1]. In addition, elastomeric bearings have been applied to control deformations in bridges and buildings due to vehicular traffic, wind, seismic activity, and thermal expansion, which generate cyclic loads in compression, shear, and torsion. Besides fulfilling the role of connectors between structural parts, they support relative large static loads in compression due to the weight of the structure [2, 3].

Bearings vertical behavior has been studied by experimental tests [4–8] using the results for design purposes. In [5], the authors studied the behavior of bearings used as seismic isolation systems under compression. Mechanical properties such as stiffness and damping ratio under axial loading were investigated [9–11]. Different rubber compounds were experimentally studied by [12] that evaluated physical and mechanical properties. Uniaxial compressive tests were performed by [13] on anisotropic laminated rubber bearings using v-shaped steel reinforcement shims with a predefined angle during the manufacturing process. Other authors [14] developed a failure model for rubber used in bearings by measuring local strains at failure using an image analysis approach. Recent studies [15, 16] obtained experimental results on high-damping rubber to validate constitutive models of elastomeric bearings.

Theoretical models have been proposed to consider the stability of bearings, which is controlled by the reduction of shear stiffness due to increasing axial load or increasing lateral displacements [8, 17–22]. There are contributions that propose mechanical models such as [23, 24]. Recently, [25] studied the stability of bearings subjected to large deformations, [26] presented a nonlinear analytical model based on [24] and capable of predicting the dynamic behavior at all displacement ranges. In addition, [27] developed an analytical model for the coupled horizontal-vertical behavior of bearings subjected to dynamic loads. Other theoretical models include [28–32].

Several finite element models (FEM) where proposed [33-37] and studies to predict critical loads, vertical and horizontal stiffness have been carried out [21, 38–40]. Recently, [41] studied and proposed several models by applying OpenSees, while [42] performed numerical simulations in LS-DYNA. Recently, [43] compared the large deformation response theory proposed in [25] with test results of [24] performing FEM using OpenSees. Other researchers [44] used different axial displacements to study the stress distribution within the rubber and steel reinforcing shims using ABAQUS, that was applied also by [45] that compared the three models proposed by [24, 28, 29]. Other studies focused on modeling civil structures to assess their dynamic response in order to design effective isolation systems [46–54].

Therefore, this paper aims at applying the experimental, theoretical, and FEM approaches to assess the behavior of elastomeric bearings under compressive loading states.

2 EXPERIMENTAL

Scaled bearings were manufactured using two natural rubber-based compounds typically used in elastomeric bearings with 15 and 45 phr (parts per hundred of rubber by mass) of carbon black as reinforcing filler, and nominal Shore A hardness of 55 and 70, respectively. Rubber compounds evaluated in this study have been analyzed previously in [55]. Shear properties of both rubber compounds we characterized for the FEM analysis using pure shear specimens following the recommendations of [56]. A displacement-controlled method was used at a deformation rate of 12 mm/min to approximately 40 % of shear strain. Three loading cycles were recorded, and from the stress-strain curves, shear modules were calculated from

the third loading cycle as the initial slope of the curves. Mean values of the shear modules of the 55 and 70 Shore A hardness compounds were 0.63 MPa and 1.13 MPa, respectively.

For the scaled bearings, different individual rubber thickness were chosen as shown in Table 1. The study analyzed two different shape factors, the geometrical parameter that characterizes a single rubber layer and defined as the ratio of the load area to the bulge area [57] (calculated using equation 1). Plan dimensions of all scaled bearings were fixed to 140x140 mm with a 5 mm edge cover, and 1 mm-thick steel reinforcement shims. Compression tests were performed using a SHIMADZU unidirectional testing machine with a load cell of 300 kN and a deformation rate of 5 mm/min.

$$S = \frac{(length)(width)}{2t(length + width)} \tag{1}$$

Name	Number of rubber layers (n)	Thickness of individual rubber layer (t, mm)	Shape factor (S)
B55-4	3	4	8.75
B55-6	3	6	5.83
B70-4	3	4	8.75
B70-6	3	6	5.83

Table 1: Characteristics of the bearings.

3 THEORETICAL MODEL

The large-displacement theory proposed by [25] uses the mechanical model shown in Figure 1 to assess the stability of elastomeric bearings due to vertical and horizontal loads (P and F_H respectively).

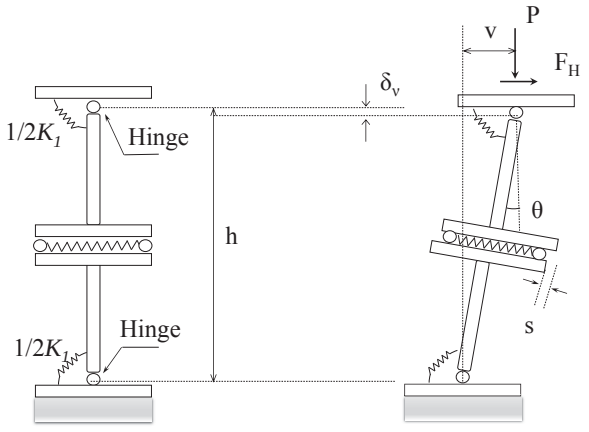

Figure 1: Two-spring model used by Forcellini and Kelly [25].

Where h is the total height of the bearing, δ_v and v the vertical and horizontal displacements respectively, s the shear displacement, and θ the relative rotation.

For compressive loads, $F_H = 0$ and P can be calculated as:

$$P = -\frac{P_S}{2\cos\theta} + \sqrt{\frac{P_S^2}{4\cos^2\theta} + \frac{P_E P_S(\theta - \theta_0)}{\sin\theta\cos\theta}} \tag{2}$$

Material variations, geometric, and fabrication imperfections are considered into the θ_0 angle expressed in radians [25]. P_E is the Euler load for a standard column defined as

$$P_E = \frac{\pi^2 EI_S}{h^2} \tag{3}$$

where EI_S the bending stiffness of the square section of the bearing calculated as

$$EI_S = E_c\left(\frac{1}{12}l^4\right) \tag{4}$$

where l is the length of a square section, and E_c the compressive modulus was calculated according to equation 5 taking into account the compression spring rate [56] and calculated as a function of the compressive force and compressive displacement from the force-displacement curve of the compressive test.

$$E_c = \frac{F_c tn}{Ad_c} \tag{5}$$

The compressive force F_c is obtained from the experimental test, A the loading area of the bearing, d_c the experimental vertical displacement, and h the total height of the bearing including steel shims. P_S from equation 2 is the shear stiffness of a unit element defined as

$$P_S = GA_S = GA\frac{h}{t_r} \tag{6}$$

where A is the plan area, and t_r the total rubber thickness. Finally, the vertical displacement δ_v can be calculated as

$$\delta_v = \frac{P}{P_S}h\sin^2\theta + (1-\cos\theta)h \tag{7}$$

4 NUMERICAL SIMULATIONS

Opensees (Open System for Earthquake Engineering Simulations), developed by the Pacific Earthquake Engineering Center (PEER), was applied to perform 3D FEM [58]. OpenSeesPL interface originally designed for soil analyzes was here applied by selecting shear-beam boundary conditions with side boundary nodes fixed vertically at gravity runs [59]. Figure 2 shows the mesh used for the 3D models, which contains 22464 elements and 24769 nodes. Furthermore, 10 mm-thick top and bottom steel plates are considered rigid ensuring that deformation concentrates only within the elastomer layers. Furthermore, a linear behavior in shear of the rubber compounds was assumed (shear modules of 0.63 MPa and 1.13 MPa for the 55 and 70 Shore A hardness compounds respectively). For the steel reinforcing shims, and both top and bottom steel plates, a shear modulus of 74.93 MPa and a density of 7850 kg/m^3 were considered.

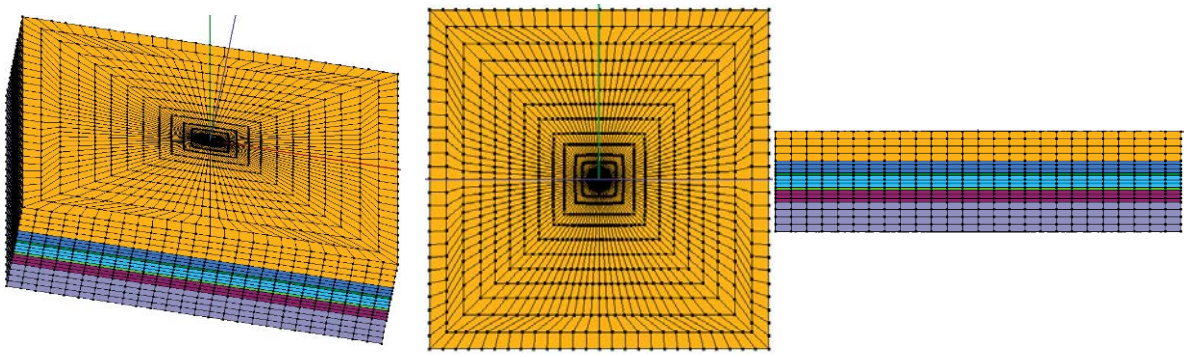

Isometric view Top view Front view

Figure 2: 3D model for the scaled elastomeric bearings.

A monotonic pushover analysis was carried out using the displacement-based method to simulate the conditions of a compressive load. Using this method, numerous displacements were applied to the 3D models with a total number of 10 steps. Several numerical simulations were performed for each bearing with increasing the vertical displacement. For each numerical simulation, the compressive force values were calculated from the maximum normal stress as the mean stress value at the center of each model.

5 DISCUSSION

Figure 3 shows the comparison of the experimental, theoretical, and numerical simulation approaches results for the different bearings. Regarding the comparison between the experimental and theoretical approaches, the large-displacement theory accounts for typical bearings with shape factors between 10 and 30 [25]. Since the shape factors considered in this study are smaller than those applied in the theory, relative large values of θ_0 (material variations and fabrication imperfections) were used, which are larger than those obtained in [25]. Among the bearings tested, higher values of θ_0 are observed for bearings with the lower shape factor, that is, bearings with 6 mm-thick individual rubber layers indicating that the number of rubber layers plays an important role besides the shape factor.

It is observed that the results of the numerical simulations showed an increased force-displacement response (Figure 3) because the model assumes an ideal bonding between rubber layers and steel reinforcing shims. In addition, the shape factor S seems not to affect significantly the comparison between the different approaches. And since the compressive stiffness of a rubber layer depends on the steel-rubber bond, a perfectly bonded surface yields in additional stiffness due to the kinematic constraint [60]. Furthermore, the numerical simulations assumed perfect bonding between the top and bottom outer rubber layers with the steel plates, while in the experimental tests surfaces in contact rely only on the friction between rubber and steel.

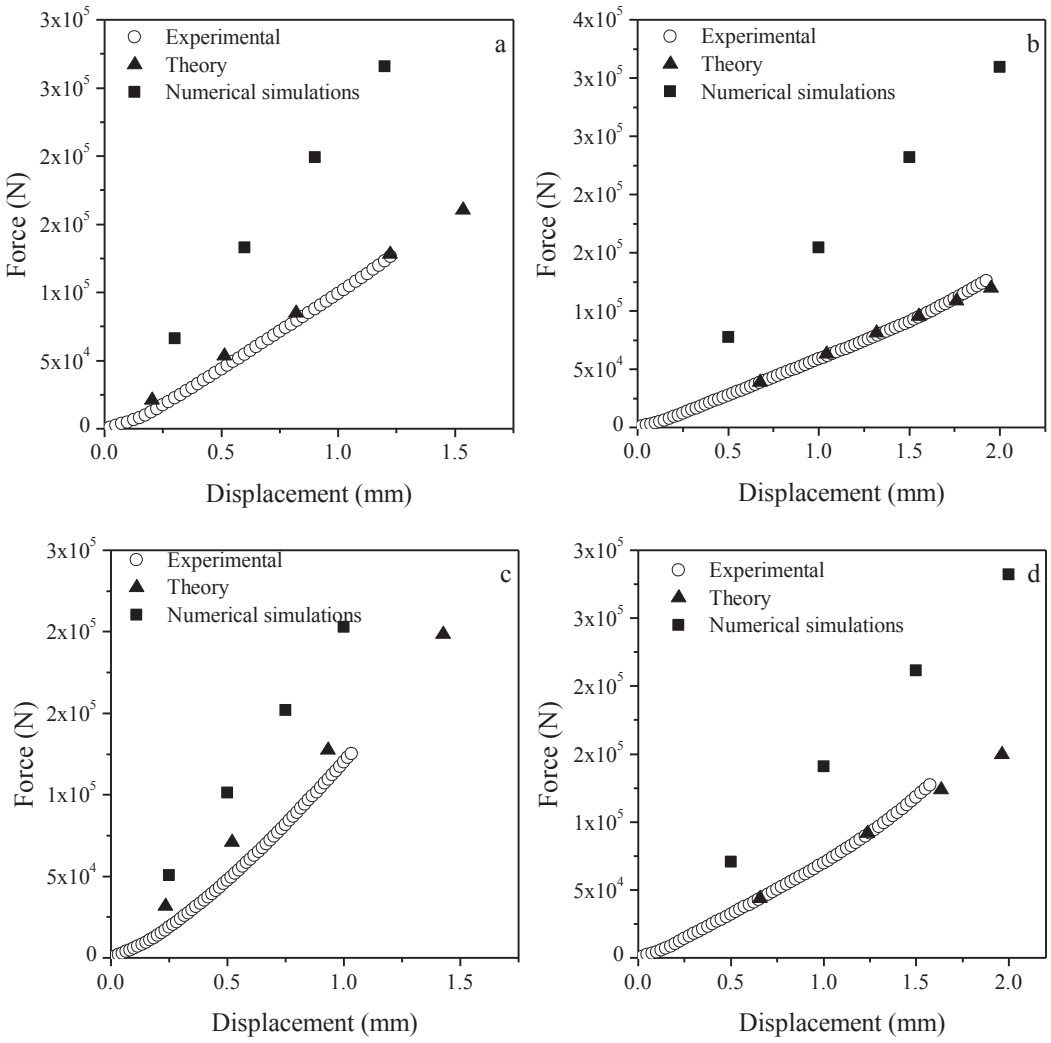

Figure 3: (a) B55-4, (b) B55-6, (c) B70-4, and (d) B70-6.

6 CONCLUSIONS

This study considered experimental, theoretical and numerical simulation approaches to assess the uniaxial compressive behavior of elastomeric bearings. The theoretical approach proposed by [25] was compared with experimental tests and numerical simulations using OpenSeesPL. Scaled bearings tested in this study had shape factors of 5.83 and 8.75, which are typical shape factors applied for viaducts but that are lower than the typical values used in the large-displacement theory. Calibration of θ_0 values was used to set the agreement between theoretical and experimental results. Although relative large values of θ_0 were taken into account due to material variations and manufacture imperfections, a good agreement between theoretical and experimental approaches was found for all the specimens. Relative errors (less than 6 %) were observed between experimental and theoretical results except for the bearings with the least total height (*i.e.*, bearings with $t = 4$ mm).Validation of the model using experimental data obtained in this study is considered of great importance and the model can be used in the design process of laminated elastomeric bearings. Linear properties of the materials were assumed for the numerical simulations in accordance with the characteristic shear curves of both compounds. Discrepancies can be addressed to linear assumptions and ideal bonding between internal steel shims and rubber layers and between the outer top and bottom

rubber covers and steel plates. Future studies will consider bearings with lower shape factors and an increased number of rubber layers.

REFERENCES

[1] F. Adebowale, Bridge bearings: Merits, Demerits, Practical Issues, Mainteinance and Extensive Surveys on Bridge Bearings, Royal Institute of Techonology, 2012.

[2] B. A. English, R. E. Klingner, and J. A. Yura, Elastomeric Bearings: Background information and field study, 1993.

[3] O. Hamzeh, J. L. Tassoulas, and E. B. Becker, Analysis of Elastomeric Bridge Bearings, 1995.

[4] C. W. Roeder and J. F. Stanton, Elastomeric bearings: state-of-the-art, *Journal of Structural Engineering* 109 (12), 2853–2871, 1984.

[5] A. Mori, A. J. Carr, N. Cooke, and P. J. Moss, Compression behaviour of bridge bearings used for seismic isolation, *Engineering Structures* 18 (5), 351–362, 1996.

[6] A. Mori, P. J. Moss, N. Cooke, and A. J. Carr, The behavior of bearings used for seismic isolation under rotation and axial load, *Earthquake Spectra* 15 (2), 225–244, 1999.

[7] A. Mori, P. J. Moss, N. Cooke, and A. J. Carr, The behavior of bearings used for seismic isolation under shear and axial load, *Earthquake Spectra* 15 (2), 199–224, 1999.

[8] I. Buckle, S. Nagarajaiah, and K. Ferrell, Stability of Elastomeric Isolation Bearings: Experimental Study, *Journal of Structural Engineering* 128 (1), 3–11, 2002.

[9] G. C. Manos, S. Mitoulis, V. Kourtidis, A. Sextos, and I. Tegos, Study of the behavior of Steel Laminated Rubber Bearings under prescribed loads, *10th World Conference on Seismic Isolation, Energy Dissipation and Active Vibrations Control of Structures*, 2007.

[10] H. Zhu, Z. Zhang, F. Zhou, H. Luo, and X. Deng, Horizontal mechanical behavior of elastomeric bearings under eccentric vertical loading: Full-scale tests and analytical modeling, *Construction and Building Materials* 125, 574–584, 2016.

[11] Y. Li, Z. Zong, X. Huang, J. Xia, and L. Liu, Experimental study on mechanical properties of high damping rubber bearing model, *Environmental Earth Sciences* 69, 1–6, 2017.

[12] S. Abedi Koupai, A. Bakhshi, and V. Valadoust Tabrizi, Experimental investigation on effects of elastomer components on dynamic and mechanical properties in seismic isolator compounds, *Construction and Building Materials* 135, 267–278, 2017.

[13] S. L. Burtscher and A. Dorfmann, Compression and shear tests of anisotropic high damping rubber bearings, *Engineering Structures* 26 (13), 1979–1991, 2004.

[14] C. S. Lewangamage, M. Abe, Y. Fujino, and J. Yoshida, Strain field measurements of rubber by image analysis and design criteria for laminated rubber bearings (LR), *Earthq*uake *Engineering and Structural Dynamics* 33 (4), 445–464, 2004.

[15] W. Wei, P. Tan, Y. Yuan, and H. Zhu, Experimental and analytical investigation of the influence of compressive load on rate-dependent high-damping rubber bearings, *Construction and Building Materials* 200, 26–35, 2019.

[16] W. Wei, Y. Yuan, A. Igarashi, P. Tan, H. Iemura, and H. Zhu, A generalized rate-dependent constitutive law for elastomeric bearings, *Construction and Building Materials* 106, 693–699, 2016.

[17] J. A. Haringx, On highly compressible helical springs and rubber rods and their application for vibration-free mountings, *Phillips Research Reports* 3, 401–449, 1949.

[18] A. N. Gent, Elastic stability of rubber compression springs, *Journal of Mechanical Engineering Science* 6 (4), 415–430, 1964.

[19] J. F. Stanton, A. W. Taylor, and C. W. Roeder, Stability of Laminated Elastomeric Bearings, *Journal of Engineering Mechanics* 116, 1351–1371, 1990.

[20] G. P. Warn, A. S. Whittaker, and M. C. Constantinou, Vertical Stiffness of Elastomeric and Lead – Rubber Seismic Isolation Bearings, *Journal of Structural Engineering* 133 (9), 1227–1236, 2007.

[21] G. P. Warn and J. Weisman, Parametric finite element investigation of the critical load capacity of elastomeric strip bearings, *Engineering Structures* 33 (12), 3509–3515, 2011.

[22] J. Sanchez, A. Masroor, G. Mosqueda, and K. Ryan, Static and Dynamic Stability of Elastomeric Bearings for Seismic Protection of Structures, *Journal of Structural Engineering* 139 (7), 1149–1159, 2013.

[23] C. G. Koh and J. M. Kelly, A simple mechanical model for elastomeric bearings used in base isolation, *International Journal of Mechanical Sciences* 30 (12), 933–943, 1988.

[24] S. Nagarajaiah and K. Ferrell, Stability of Elastomeric Seismic Isolation Bearings, *Journal of Structural Engineering* 125, 946–954, 1999.

[25] D. Forcellini and J. M. Kelly, Analysis of the large deformation stability of elastomeric bearings, *Journal of Engineering Mechanics* 140 (6), 1–10, 2014.

[26] S. M. V. Vemuru, S. Nagarajaiah, A. Masroor, and G. Mosqueda, Dynamic Lateral Stability of Elastomeric Seismic Isolation Bearings, *Journal of Structural Engineering,* 1–14, 2014.

[27] V. S. M. Vemuru, S. Nagarajaiah, and G. Mosqueda, Coupled horizontal–vertical stability of bearings under dynamic loading, *Earthquake Engineering & Structural Dynamics* 45, 913–934, 2015.

[28] X. Han and G. P. Warn, Mechanistic model for simulating critical behavior in elastomeric bearings, *Journal of Structural Engineering* 141 (5), 4014140, 2015.

[29] M. Iizuka, A macroscopic model for predicting large-deformation behaviors of laminated rubber bearings, *Engineering Structures* 22 (4), 323–334, 2000.

[30] X. Han, C. Kelleher, G. Warn, and T. Wagener, Identification of the Controlling Mechanism for Predicting Critical Loads in Elastomeric Bearings, *Journal of Structural Engineering* 4013016, 2013.

[31] M. Kikuchi, T. Nakamura, and I. D. Aiken, Three-dimensional analysis for square seismic isolation bearings under large shear deformations and high axial loads, *Earthquake Engineering & Structural Dynamics* 39, 1513–1531, 2010.

[32] S. Yamamoto, M. Kikuchi, M. Ueda, and I. D. Aiken, A mechanical model for elastomeric seismic isolation bearings including the influence of axial loading, *Earthquake Engineering & Structural Dynamics* 38, 157–180, 2009.

[33] P. B. Lindley, Plane-Stress Analysis of Rubber at High Strains Using Finite Element, *Journal of Strain Analysis* 6 (1), 45–52, 1971.

[34] P. B. Lindley, A Finite Element Programme for the Plane-Strain Analysis of Rubber, *Journal of Strain Analysis* 10 (1), 25–31, 1975.

[35] J. F. Stanton and C. W. Roeder, NCHRP Report 248 - Elastomeric bearings design, construction, and materials, 1982.

[36] C. W. Roeder, J. F. Stanton, and A. W. Taylor, NCHRP Report 298 - Performance of elastomeric bearings, 1987.

[37] O. Hamzeh, J. L. Tassoulas, and E. B. Becker, Behavior of Elastomeric Bridge Bearings: Computational Results, *Journal of Bridge Engineering* 3 (3), 140–146, 1998.

[38] D. Najjar, A. Kaadan, M. N. A. Eilouch, and A. Al Helwani, Multi-criteria decision making to improve the performance of base isolation rubber bearing, *Asian Journal of Civil Engineering* 18 (7), 1095–1112, 2017.

[39] D. Forcellini, S. Mitoulis, and K. N. Kalfas, Study on the response of elastomeric bearings with 3D numerical simulations and experimental validation, *6th ECCOMAS Thematic Conference on Computational Methods in Structural Dynamics and Earthquake Engineering*, 2017.

[40] W. Yang, X. Sun, M. Wang, and P. Liu, Vertical stiffness degradation of laminated rubber bearings under lateral deformation, *Construction and Building Materials* 152, 310–318, 2017.

[41] M. Kumar, A. S. Whittaker, and M. C. Constantinou, Mechanical Properties of Elastomeric Seismic Isolation Bearings for Analysis Under Extreme loading, *22nd Conference on Structural Mechanics in Reactor Technology*, 2013.

[42] R. Z. Wang, S. K. Chen, K. Y. Liu, C. Y. Wang, K. C. Chang, and S. H. Chen, Analytical Simulations of the Steel-Laminated Elastomeric Bridge Bearing, *Journal of Mechanics* 30 (4), 373–382, 2015.

[43] D. Forcellini, 3D Numerical simulations of elastomeric bearings for bridges, *Innovative Infrastructure Solutions* 1, 45, 2016.

[44] K. N. Kalfas and S. A. Mitoulis, Performance of steel-laminated rubber bearings subjected to combinations of axial loads and shear strains, *Procedia Eng*ineering, 199, 2979–2984, 2017.

[45] S. R. Moghadam and D. Konstantinidis, Simple mechanical models for the horizontal behavior of elastomeric bearings including the effect of support rotation, *Engineering Mechanics* 150, 996–1012, 2017.

[46] R. Kawatani, Y. Kobayashi, and H. Kawaki, Influence of elastomeric bearings on traffic-induced vibration of highway bridges, *Transportation Research Record* 1696, 76–82, 2000.

[47] M. Kawatani, C. Kim, and N. Kawada, Three-Dimensional Finite Element Analysis for Traffic-Induced Vibration of a Two-Girder Steel Bridge with Elastomeric Bearings, *Transportation Research Record,* 225–233, 2005.

[48] Y. Yang, K. Tsai, A. Elnashai, and T. Hsieh, An online optimization method for bridge dynamic hybrid simulations, *Simulation Modelling Practice and Theory* 28, 42–54, 2012.

[49] D. Su, Y. Fujino, T. Nagayama, J. Y. Hernandez, and M. Seki, Vibration of reinforced concrete viaducts under high-speed train passage: measurement and prediction including train–viaduct interaction, *Structure and Infrastructure Engineering* 6 (5), 621–633, 2010.

[50] A. Leopa, Theoretical Analysis of Dynamic Response of a Bridge Section Loading by the Impulsive Force, *Journal of Engineering Studies and Research* 18 (2), 50–56, 2012.

[51] D. Forcellini, Cost Assessment of isolation technique applied to a benchmark bridge with soil structure interaction, *Bulletin of Earthquake Engineering* 15, 51-69, 2017.

[52] A. Canini and D. Forcellini, 3D Numerical simulations of a base-isolated residential building with soil-structure interaction, *VI ECCOMAS Thematic Conference on Computational Methods in Structural Dynamics and Earthquake Engineering*, 2017.

[53] D. Forcellini, Seismic assessment of a benchmark based isolated building with soil structure interaction", *Bulletin of Earthquake Engineering* 16, 2021-2042, 2018.

[54] K. Kalfas and D. Forcellini, A developed analytical non-linear model of elastomeric bearings verified with numerical findings, *International Conference on Structural Dynamics*, 2020.

[55] M. Guzmán, D. Forcellini, R. Moreno, and D. Giraldo, Compressive Loading Assessment of Elastomeric Bearings through Experimental, Theoretical, and Numerical Simulation Approaches, *Journal of Applied Research and Techonology,* in-press.

[56] J. Sommer and O. Yeoh, Tests and specifications, in Engineering with rubber, 2ed, 2001.

[57] P. M. Sheridan, F. O. James, and T. S. Miller, Design of Components, in Engineering with Rubber - How to Design Rubber Components, 3ed, Carl Hanser Verlag GmbH & Co., 259–293, 2012.

[58] S. Mazzoni, F. McKenna, M. H. Scott, and G. L. Fenves, OpenSees, Open System for Earthquake Engineering Simulation. University of Berkley, 2011.

[59] J. Lu, A. Elgamal, and Z. Yang, OpenSeesPL - 3D Lateral Pile-Ground Interaction, 2012.

[60] M. S. Chalhoub and J. M. Kelly, Effect of bulk compressibility on the stiffness of cylindrical base isolation bearings, *International Journal of Solids and Structures* 26 (7), 743–760, 1990.

EURODYN 2020
XI International Conference on Structural Dynamics
M. Papadrakakis, M. Fragiadakis, C. Papadimitriou (eds.)
Athens, Greece, 23–26 November 2020

THE ROLE OF NON-LINEARITY IN THE SEISMIC ASSESSMENT OF A BASE ISOLATED BENCHMARK BUILDING WITH SOIL STRUCTURE INTERACTION EFFECTS

Andrea Canini[1]

[1] Head of Project Department in Slovakia and Poland at Dominion Steelcon A/S
Južná Trieda 82, 04017, Košice
andrea.canini@dominion-global.com

Keywords: Soil non-linearity, Non-linear isolation, Numerical Simulations, OpenSees, Soil Structure Interaction, Base Isolation, Ordinary buildings.

Abstract. *Advanced 3D numerical simulations of a soil-structure systems aim to assess non-linear behaviors of soil and structure and ultimately to describe realistic scenarios. The paper purpose is to simulate the effects of Soil Structure Interaction (SSI) on an ordinary base-isolated shear type building (BI), driving the assessment of the isolators by evaluating both their linear and non-linear behaviour. Non-linearity is also considered in the description of the soil which is modelled with hysteretic materials and advanced plasticity models that enable to reproduce soil hysteretic elasto-plastic shear response (including permanent deformations) and damping foundation impedances. Credited non-linear theories are applied in order to take into account appropriate flow rules as to reproduce the observed strong dilation tendency and resulting increase in cyclic shear stiffness and strength. The paper applies the open-source computational interface OpenSeesPL, implemented within the FE code OpenSees. The interface performs the 3D spatial soil domain, boundary conditions and input seismic excitation definition with convenient post-processing and graphical visualization of analysis results including deformed ground response time histories. Reproduce wave propagation adopting realistic boundaries is of crucial importance and significance in order to realistically reproduce SSI effects. The ultimate goal of the paper is the assessment of cases where BI becomes detrimental with particular attention to the structural performance by considering accelerations and displacements at various heights.*

1 INTRODUCTION

Base isolation (BI) is one of the most convincing solutions in order to protect structures from the destroying effects of earthquakes. This technique allows to decouple the structure from the ground by intentionally concentrating seismic energy dissipation in a unique element with low horizontal stiffness placed between the foundation and the structure. Many researchers have been carried on this issue, but few contributions have been focused on the effects of the soil structure interaction (SSI) on isolated buildings. Thanks to its benefits, BI has been spread all over the world in the last decades. For example, [1] showed that in Japan after the 1995 Kobe earthquake, the number of base-isolated buildings significantly increased from ten buildings to more than 150 buildings. In particular, [2] remarked that there was a significant increase in the application of base isolation to residential buildings after 1995. In Italy, the number of isolated buildings increased after L'Aquila earthquake to more than 400 [3], with many applications to residential buildings.

Extensive research has been conducted in the past 30 years regarding the effects of soil–structure interaction (SSI) on the seismic response of civil engineering structures. Even if many codes suggest to neglect SSI [4], [5], there are some researches where SSI is shown to be non-conservative for safety and cost reduction. In such cases, it is fundamental to take into account SSI in design procedures in order to predict its effects as detailed as possible [6], and [7].

The majority of publications study SSI simply by introducing springs, dashpots and artificial masses in the interface between the structure and the soil. This approach is generally accepted since modelling SSI is a challenging problem for numerical simulations. However, it could be insufficiently detailed in order to model the complexity of the problem. In particular, system response is directly connected with the mutual dynamic characteristics (natural frequencies) and thus with structural mass and stiffness, soil shear velocity and layer depth [8]. For this reason, the beneficial effects of BI can be strongly modified by soil deformability and energy dissipation in the ground [9], [10], [11] and [12].

This study aims at overcoming all previous simplifications considering a 3D numerical simulation of a soil-structure system applied to a shear type building isolated at the base. In particular, the soil has been performed with nonlinear hysteretic materials and advanced plasticity models. The proposed approach enables to drive the assessment of BI technique with evaluation of soil non-linear response into a unique twist. In this regard, the paper aims at assessing the cases where BI becomes detrimental. In particular, the study shows how considering the structure fixed at the base is non conservative and underestimates dynamic effects.

The study aims at considering the effects of SSI on a residential building, by taking into account the previous contributions such as [13], [14] and [15]. In particular, numerical simulations have been widely performed ([6],[16], [17], [18], [19], [20], [21], [22], [23], [24], [25], [26]), in order to study the dynamic interaction of a structure placed on a deformable soil. Taking into account these relevant contributions, the present study wants to consider a 3D soil-structure system that applies nonlinear hysteretic materials with plasticity models for the soil and a detail description of the structural system (building and foundation). The proposed model is able to reproduce soil hysteretic elasto-plastic shear response (including permanent deformations), damping foundation impedances and realistic boundary conditions at the base of soils and in correspondence with the interface between the soil and the structure.

The study allows to perform the behavior of a realistic base isolated building consisting of four stories shear type concrete structure. Its response at the base of the structure (foundation level) and along its height has been assessed. In this regard, with the development of the performance-based earthquake engineering methodology ([26], [27], [29] and [30]), there has

been an increasing attention to the floor acceleration, as one of the most useful engineering demand parameters to assess structural performance of buildings. In particular, many codes ([31] and [32]) are implementing new provisions based on floor performance [33]. In this regard, the paper aims to move in the direction of this new approach by calculating top floor accelerations and displacements and not just the peak values of such engineering demand parameters (EDP). The final goal is to provide valuable element-specific seismic assessment or design evaluations with a particular focus on the cases where BI technique can become detrimental due to SSI effects.

2 CASE STUDY

The paper must be written in English within a printing box of 16 cm x 24 cm, centered in the page. The paper goal is to perform a case study of a benchmark concrete structure (Figure 1) on different deformable soil conditions and adopting two typologies of isolators at the base.

The soil has been performed with nonlinear hysteretic materials and advanced plasticity models. This approach enables to assess SSI effects by reproducing soil hysteretic elasto-plastic shear response (including permanent deformations) and damping foundation impedances by applying the open-source computational interface OpenSeesPL [34] implemented within the FE code OpenSees [35].

It consists of a framework for saturated soil response as a two-phase material following the u-p (where u is displacement of the soil skeleton and p is pore pressure) formulation. This interface, implemented within the FE code OpenSees [35], has been originally calibrated for pile analysis. Here it has been modified in order to consider the presence of the system structure – foundation.

The study has been divided into several steps. The first step aims at calibrating the mesh and consist of eigenvalue analysis. In particular, the effects of the soil have been neglected by considering a hard soil (named soil A and with shear wave velocity equal to 1000 m/s) which reproduce rigid base conditions (see section 4.a). In the second step, soil is applied and the dynamic characteristics (in terms of natural periods) of the system (soil and structure) have been calculated. The third step consists of performing dynamic analysis.

Seven input motions (shown in Figure 3 and Table 1) were applied along the longitudinal direction (x-axis). These records were selected by following EC8 provisions [32], at section 4.3.3.4.3, Part 1 that allows to consider at least seven nonlinear time-history analyses, in accordance with 3.2.3.1, as described in [36]. Figure 3 shows the comparison between the mean response spectra of the selected ground motions (named MEAN in the figure) and the design spectra. They were chosen in order to significantly affect the dynamic behaviour of the structures in a wide range of periods: 0 - 2.5 s. The system performance has been assessed by considering accelerations and displacements as the main parameters. For all analysis, the Newmark transient integrator is used with $\gamma = 0.6$ and $\beta = 0.3$.

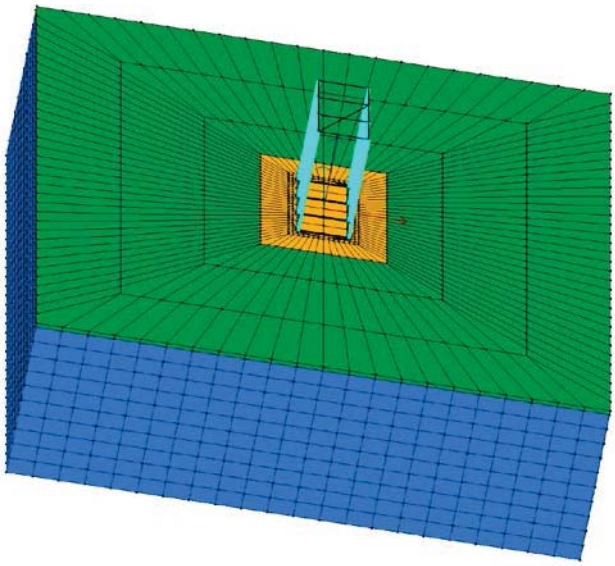

Figure 1: 3D Soil-structure OpenSees PL model [34].

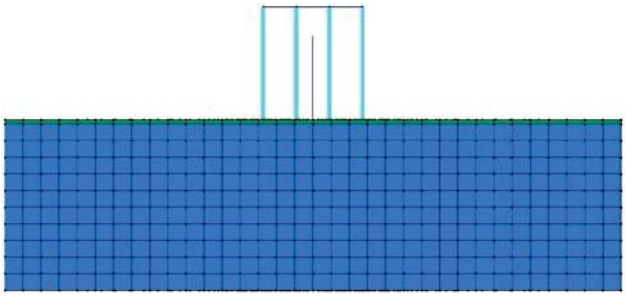

Figure 2: OpenSees PL [34] 3D system mesh – Vertical view.

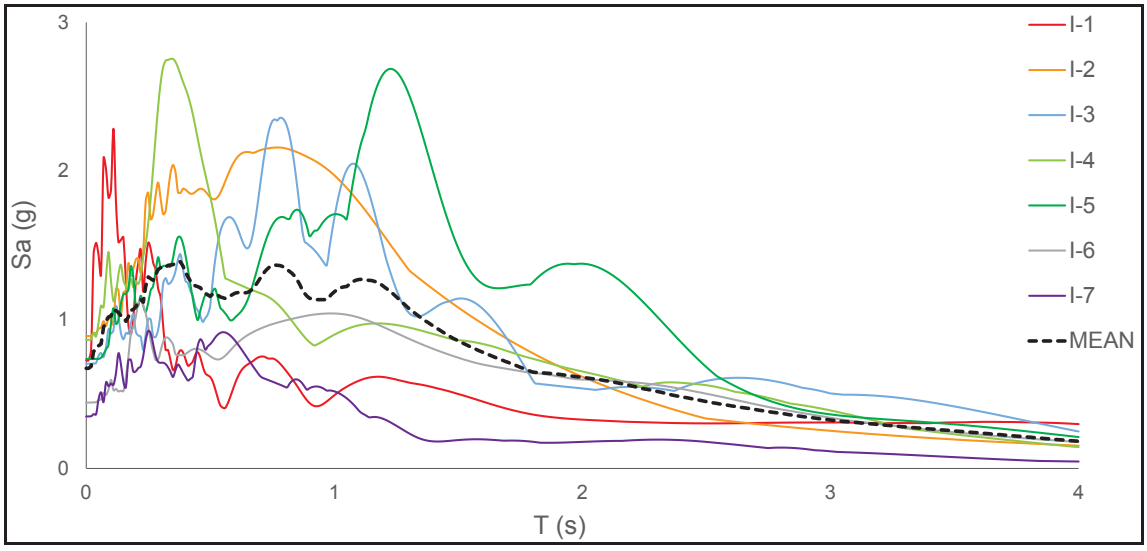

Figure 3: Input motions (response spectra).

Input motions	Station	PGA [g]	PGV [cm/s]	PGD [cm]	Duration [s]
n.1 Landers (1992)	Lucerne Valley	0.72	147.45	265.14	25.00
n.2 Northridge (1994)	Rinaldi Receiving	0.89	185.08	60.07	12.50
n.3 Northridge (1994)	Sylmar Converter	0.70	135.82	58.20	17.50
n.4 Northridge (1994)	Sylmar Hospital	0.87	139.54	50.37	15.00
n.5 Hyogo-Ken (1995)	Takatori	0.47	155.44	44.95	20.00
n.6 Erzincan (1992)	Erzincan	0.44	125.80	53.30	12.50
n.7 El Centro (1940)		0.35	38.47	82.44	17.50

Table 1 – Input motions (characteristics)

3 COMPUTATIONAL MODEL

The finite element model (FEM) has been built with OpenSees [35] that allows high level of advanced capabilities for modelling and analyzing non-linear responses of systems using a wide range of material models, elements and solution algorithms. In particular, numerical simulations follow the previous contributions [9], [14], [15], [16], [17], [37], [38], [39] [40], [41] and applies OpenSees PL [34] which consists of a framework for saturated soil response as a two-phase material following the u-p (where u is displacement of the soil skeleton and p is pore pressure) formulation and has been here modified in order to consider the presence of the system structure – foundation. Due to the high-level of non-linearity, some assumptions were important, for example, numerical damping was introduced in order to avoid the generation of high frequency noises that can cause instability of the computation process. Rayleigh numerical damping has been applied and equal to 2% and proportional to stiffness and mass (at 1 and 6 Hz) and it corresponds to mass-proportional and stiffness proportional coefficients respectively equal to 0.12542 and 0.00090946, as described in [39] and [40]. In additions, dynamic analyses were divided into four subsequent sub-steps in order to separate the various sources of numerical instabilities. In steps 1 and 2, linear properties (weight, Shear and Bulk modulus) were considered for the soil (without the structure) in order to reach the convergence. In step 3 the structure was added and all the properties have been changes from elastic to plastic by applying 25 load steps to reach convergence, then dynamic analysis were carried out in step 4 (for more details, see [39] and [40]. NewtonLineSearch algorithm [35] was used to speed of the solution.

The structure has been modelled with an equivalent 4-story concrete building (Figure 1 and Figure 2) and some approximations were assumed as a compromise between representativeness and computational time. A shear type behavior was considered for the building and a schematic geometry, based on 2 columns (15 m spaced) in the longitudinal direction and 4 in the transversal direction (10 m spaced), has been chosen as to maintain a plan and vertical regularity. The structure is assumed to be capacity designed and the presence of the isolation allows to remain in the elastic range and thus to model the columns with sixteen elasticBeamColumn elements, with a total height of 13.6 m (3.4 m for each floor). Seismic masses were assigned to each floor by calculating the structural self-weights of various elements (beams, columns, slabs, balconies, stairs). A rigid foundation has been assumed and modelled with a 28.4 m x 34.4 m 0.5-m thick concrete slab designed to maintain the stresses (induced by the seismic and vertical loads) inside the foundations in a range of acceptable values. In this regard, the foundation has been verified by calculating the eccentricity (the ratio between the overturning bending moment at the foundation level and the vertical forces) in the more detrimental condition of minimum vertical loads (gravity and seismic loads) and maximum

bending moments. For the fixed cases, the columns have been embedded inside the foundation material for 0.50 m, corresponding to the foundation thickness. The nodes at the base of the columns were linked together with equalDOF [35] in order to model rigid foundations. The interface between the columns and the foundations has been modelled with rigid beam-column links normal to the column longitudinal axis, as shown in [9], [13], [14], [15], [16], [17], [37], [38], [39], [40] and [41]. In particular, the elements of the foundation and the column elements are linked by connecting the outer nodes of these rigid links using the equalDOF (constraint in OpenSees for translations only) that connects two separate points (one belonging to the structure and the second to the soil) and imposes the displacements to be the same between the structure and the soil nodes [34] and [35]. Therefore, the system is able to capture the interaction between the columns and the foundation, including the potential settlement into the surrounding soil. Isolation devices at the base of the building have been modelled by applying the so called elastomericBearing element, [35] in order to overcome the previous publications where the structure was modelled with a single degree of freedom [14], [42] and [43]. (see Section 5). The slab is surrounded by a weak soil (named in the following with soil W), representing the infill layer of soil surrounding the foundation. Both the foundation and W soil have been modelled with the implemented material named Pressure Independent Multiyield [35].

Table 2 shows the values used for these two materials. The soil has been modelled with a 68.4m x 74.4m x 20.5m 3D mesh (Figure 1 and Figure 2), composed of 8228 brickUP linear isoparametric 8-nodes elements with 9660 nodes, [44] and with one-layer homogenous cohesive material (see also [14] and [45]) that was discretized in ten layers (0.5 m thickness for the first and 20 m for the others). Mesh dimensions have been determined following the suggestions indicated in [46] and [47] already applied in [9],[14], [15], [16], [17], [37], [38], [39], [40] and [41]. Discretization is built up with relatively small elements around the structure and gradually larger toward the outer mesh boundaries. The model applies hysteretic elasto-plastic materials in order to take into account realistic behavior of the soil, modified by the degradation of soil stiffness and energy dissipation [43]. Soil damping is directly computed by the implemented materials ([48] and [49]) that enable to consider many non-linear dynamic effects, such as permanent deformations, damping foundation impedances, hysteretic response and radiation damping). In particular, a Von Mises multi-surface ([44], [50]) kinematic plasticity model has been applied within the framework of multi-yield-surface plasticity [51] with an appropriate non-associative flow rule [52], [53], [54] and [55] that allows to control the magnitude of cycle-by-cycle permanent shear strain accumulation [48] and [56], with an associative flow rule deviatoric component, while non-associativity is restricted to the volumetric component. The adopted non-linear shear stress strain back-bone curves, represented by hyperbolic relation [57] and defined by two material constants (low-strain shear modulus and ultimate shear strength) are shown in Fig. 4 in correspondence with the considered soils (named Soil A, Soil B, Soil C and Soil D) which were modelled with four clay materials called Pressure Independent Multiyield [44], as shown in Table 3. Characteristic site periods have been calculated by assuming a uniform and damped soil and the linear formulation: $T = 4 H / Vs$, by [8]. H is the height of the soil layer and Vs the shear wave velocity of each layer. Base and lateral boundaries have been modelled to represent a small section of a presumably infinite (or at least very large) soil domain and allowing the seismic energy to be removed from the site itself ([9], [13], [14], [15], [16], [17], [37], [38], [39], [40] and [41]) and by modelling the real wave propagation with realistic boundaries at the base (at 20.5 m depth) and laterally located as far as possible from the structure as to decrease their effects on the response. In order to verify that they worked correctly, the response near the boundary where compared with the one resulted for free field conditions. In particular, at any special location,

symmetry conditions can be adopted and periodic boundaries [58] have been considered together with the penalty method to tie together the degrees of freedom of the left and right boundary nodes both longitudinally and vertically.

Paraments	Concrete	Soil W
Mass density (kN/ m3)	24	17
Reference Shear modul (kPa)	$1.25 \cdot 10^7$	$5.50 \cdot 10^4$
Reference Bulk modul (kPa)	$1.67 \cdot 10^7$	$1.50 \cdot 10^5$

Table 2 – Concrete and soil W parameters

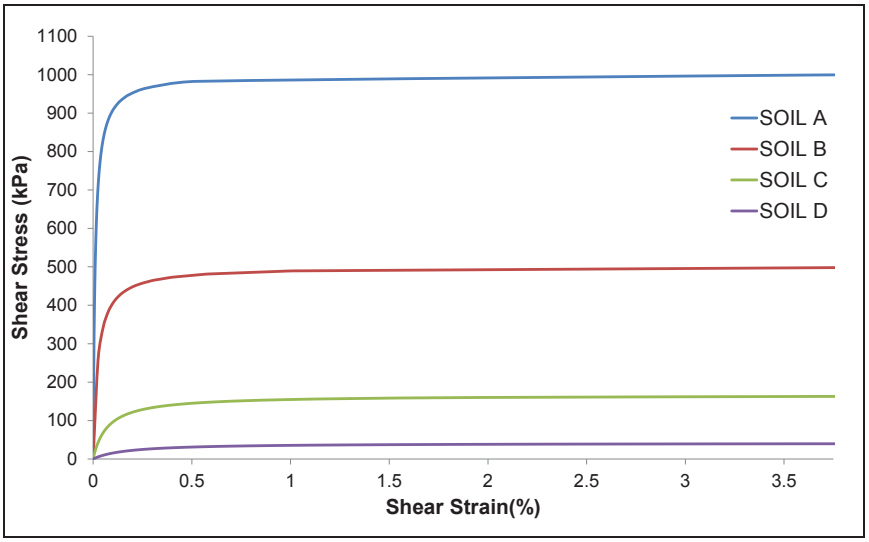

Figure 4 – Backbone curves

Parameters	Soil A	Soil B	Soil C	Soil D
Mass density (kN/m^3)	22.0	21.0	20.5	18.0
Reference Shear modul (kPa)	$5.60 \cdot 10^7$	$6.10 \cdot 10^6$	$1.72 \cdot 10^5$	$4.05 \cdot 10^4$
Reference Bulk modul (kPa)	$7.50 \cdot 10^7$	$1.30 \cdot 10^6$	$5.17 \cdot 10^5$	$1.89 \cdot 10^5$
Poisson Coefficient	0.20	0.30	0.35	0.40
Cohesion (kPa)	10000	500	160	10000
Shear wave velocity (m/s)	1600	540	290	1600
Characteristic site period (s)	0.05	0.148	0.276	0.533

Table 3 – Soil parameters

4 CALIBRATION

Calibration is the preliminary step in order to test OpenSees [35] potentialities in reproducing the non-linear problem. The soil non-linearity is tested, by considering the original configuration (without isolation) in two steps. The first step aims at assessing periods of the structure and a hard soil (shear velocity equal to 1600 m/s) has been calibrated in order to be stiffer than the structure to neglect SSI effects (simulating fixed based conditions), Figure 5, in the following named as FIX. In order to verify the consistency of the model accelerations time histories at the base of the mesh (the input motion) and at the top of the layer (and prop-

agating to the foundation) were considered were compared and found to be identical. Then the first four shape modes were compared with those obtained by SAP2000 [59] 3D numerical simulation and a simplified 1D scheme (Table 4).

The second step aims to consider the soil deformability, by calculating the period elongation of the soil-structure system due to the presence of the soil (Table 5) and it is worth to see that for example, the fundamental period of the structure (0.67 s) and the first period of the system increases with soil deformability (the ratio varies from 3.20% for soil B, to 7.08% for soil C and 19.7% for soil D). Then, transfer functions have been calculated as the ratio between the time histories of longitudinal accelerations at the base of the mesh (denoted as I in the figure) and the ones at the top of the soil layer (denoted as O) for the most severe input motion (input n. 2) in correspondence with the considered soils. Then, the characteristic soil periods of the layer have been calculated by assuming a linear layer of soil and following the linear formulation T = 4 H / Vs [8], where H is the height of the soil layer (20 m) and Vs the shear wave velocity of each layer. The transfer function peak values are shown to be close to the characteristic site periods (named with "linear" and represented with vertical lines in the figure).

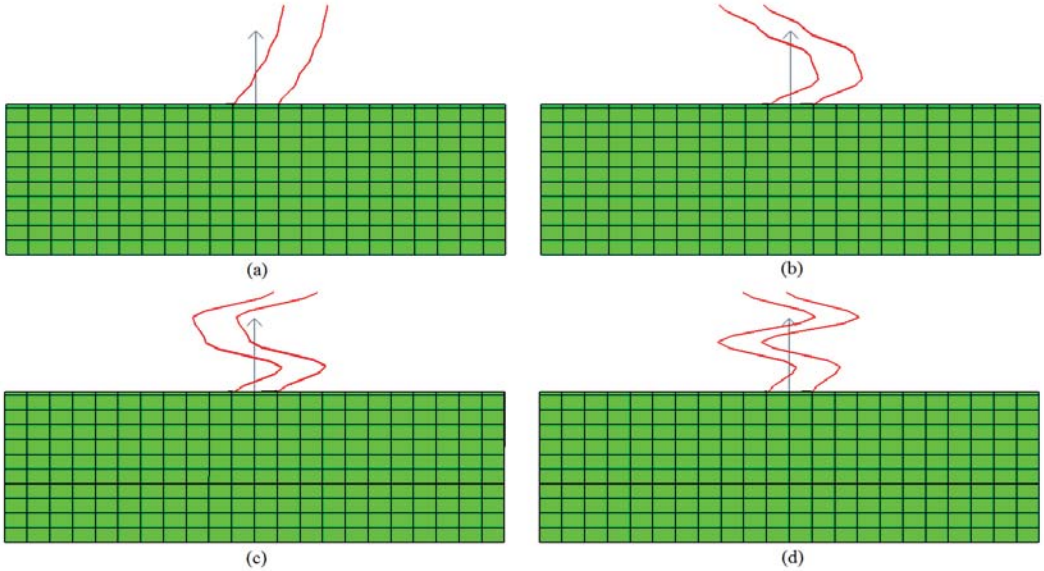

Figure 5 – Shape modes (Modes 1-4, Hard soil)

MODEL	T1 [s]	T2[s]	T3 [s]	T4[s]
3D (SAP 2000)	0.679	0.201	0.103	0.065
1D (Theory)	0.660	0.213	0.133	0.106
OpenSees	0.672	0.229	0.148	0.121

Table 4 –Natural Periods (longitudinal direction)

Soil Type	T1 [s]	T2[s]	T3 [s]	T4[s]
Soil A	0.678	0.236	0.150	0.121
Soil B	0.700	0.240	0.153	0.121
Soil C	0.726	0.282	0.238	0.151
Soil D	0.812	0.508	0.360	0.248

Table 5 – Period elongation due to soil deformability

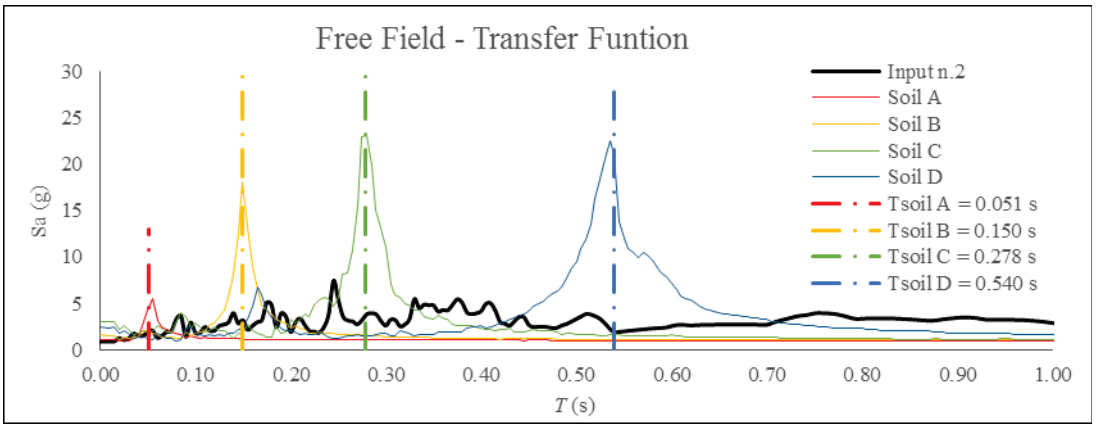

Figure 6 – Local effects assessment – transfer functions: comparison between the performed soils with the characteristic site periods [8]

5 BASE ISOLATION IMPLEMENTATION

The study performs the behavior of base isolation technique and it considers the effect of non-linearity by comparing two typologies of isolator models: a linear base isolation (BI-L) and a bilinear isolation (BI-NL), Figure 7. Isolators are consider in the longitudinal direction, by modelling significant high stiffness in the other directions (vertical and transversal) and applying the elastomericBearing element, (as shown in [9], [14], [15], [16], [17], [37], [38], [39], [40], [41] and [45]) which needs the calibration of 3 parameters: the initial elastic stiffness (named K), the yield strength (named Fy) and the post-yield stiffness ratio (alpha). Eigenvalue analysis were carried out in order to assess the effect of soil deformability and it was shown that the fundamental period increases for all the soil conditions to 3.35 s (Table 6), demonstrating that isolators perform their function to decouple the soil and the structure. It is worth to notice that comparing with the non-isolated cases (Table 5), the increases are more significant for soil A than in case of soil D, confirming that the efficiency of base isolation technique increases with rigid soils, as shown in [9].

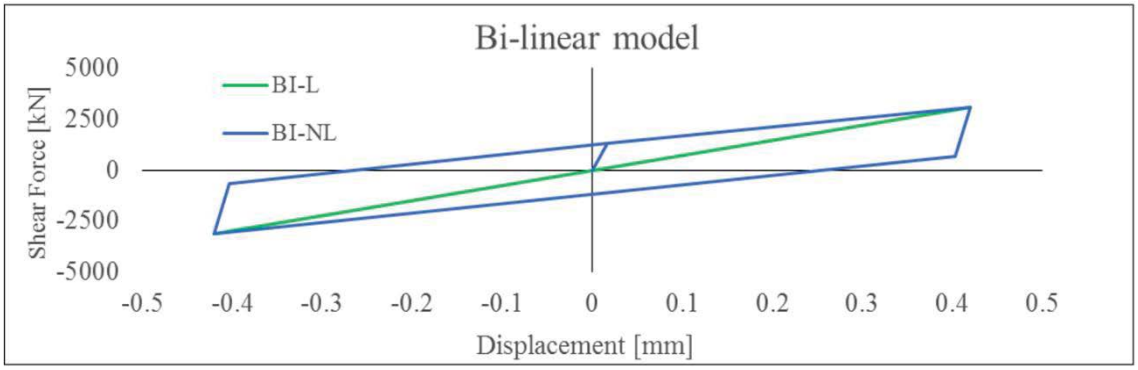

Figure 7 – Bi-linear model

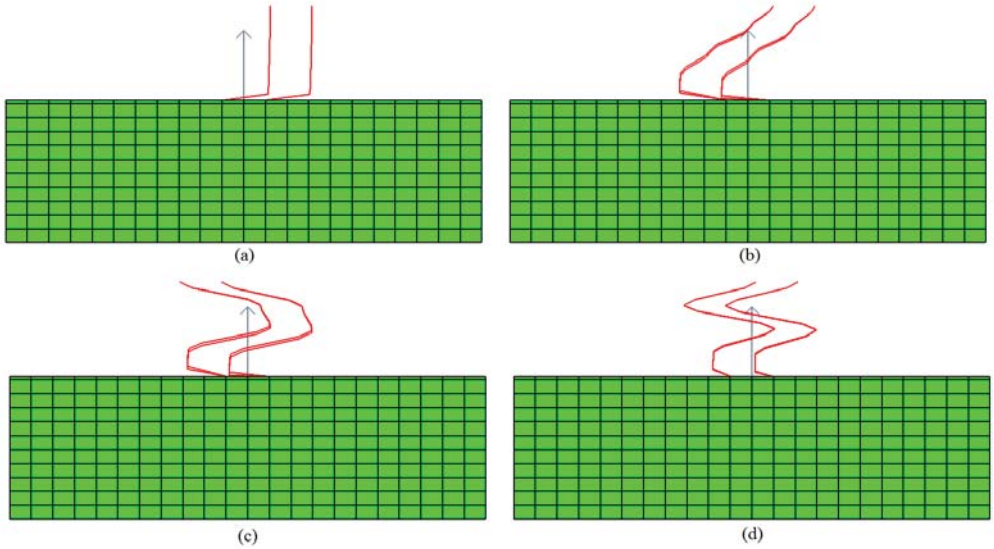

Figure 8 – Shape modes (BI model, Hard soil)

MODEL	$T_{1(iso)}$ [s]	$T_{2(iso)}$[s]	$T_{3(iso)}$ [s]	$T_{4(iso)}$[s]
Soil A	3.349	0.297	0.158	0.122
Soil B	3.352	0.297	0.158	0.122
Soil C	3.356	0.297	0.158	0.122
Soil D	3.370	0.297	0.167	0.158

Table 6 –Natural Periods of BI model in different soil conditions

6 DYNAMIC ANALYSES

This paragraph discusses the results of dynamic analyses, by considering the parameters that represent the performance of structures, following the new provisions included in many codes ([31] and [32]), as indicated [33] for multi freedom structures. The floor accelerations and displacements at each floor were chosen as engineering demand parameters (EDP), since in order to provide valuable element-specific seismic assessment or design evaluations. In particular, Figure 9 and Figure 10 show a comparison between time histories obtained with FIX and BI models, in terms of accelerations and displacements on top of the structure (z = 13.6 m) for input motion 2 (chosen because the most severe). In particular, the benefit of non-linear isolator is shown to significantly reduce the displacements after the first peak (at around 2.7 s) in correspondence with every considered soil. It is worth to notice that the largest displacements occur in correspondence of soil C, where the site fundamental period is relatively close to the second structural period (T2) both in FIX and BI configurations. In particular, for the FIX structure, T2 plays a significant role (modal participations mass ratio around 10%). When the isolation system is implemented (BI), T2 does not contribute to the seismic response of the structure (modal participations mass ratio almost 0%), since the mass of the structure is completely activated by T1 that has been shifted away from the period affected by the majority of ground motions.

Figure 11 shows that the most significant improvement of applying non-linear devices can be seen in by comparing the base shear time histories at the base of structure (z = 0.00 m) for the FIX case and at the top of the isolator for BI models. It is possible to assess how the isolation system performs its function by decoupling the structure from the soil. In addition, the results show also that in correspondence with soil D, the shear forces are bigger for the BI configurations that those calculated by the FIX case, demonstrating that high soil deformability can induce great damping in the system that reduces the forces more than what base isolation is able to do. This behaviour (already described by [9]) depends on the dissipation of seismic energy in the soil, that is shown to act as a natural base isolation.

As stated in [60] and [61], the first period of the isolated model become that of the isolation system and the second that of the structure. Table 7 shows the best reductions of the accelerations at the top of the structure occur with BI-L system. The average reductions are about 80%, 76% and 63% respectively for soil A, B and C. In correspondence of soil D have been observed reductions of about 53%, 15% and 60% for input n.2, n.4 and n.7, respectively. For input n.1, n.5 and n.6 small increments (of about 4%, 9% and 26%, respectively) and a significant increment for input n.3 (86%). For BI-NL case accelerations reductions are around 79%, 71% and 61% for soil A, B and C, while for soil D have been observed increments with all ground motions except for input n.1 and n.2 (where reductions are about 22% and 34%). The highest increment has been observed for BI-NL with input n.3 (107%).

Figure 9 shows the time histories of base shear forces in correspondence with input 3 that is shown to be the most severe. It is worth to see that soil deformability reduces base shear only for the case of FIX configurations. For BI models, it is confirmed that the response does not depend on soil deformability, since isolators decouple the structure from the soil. Non-linear models are shown to be more efficient than BI-L in reducing the peak values and in some cases modelling the isolator with linear assumptions can become more conservative and not realistic of the real behaviour of the structure. Table 9 shows the ratio between the results obtained in correspondence with BI-L and BI-NL respect the case of FIX configuration, respectively in column 4 and 5. The reduction operated between the BI-L and the FIX configuration is significantly high for soil A (between 60.4% and 87.3%), but when high soil deformability is considered (soil D), the linear bearings are not working properly and an increment of 151.1% occurs in correspondence with input 3. Similar trend can be seen for BI-NL cases and the reduction in correspondence with soil A are bigger that those resulted for BI-L (maximum: 91.1%). Their behaviour is shown to be more efficient even when soil deformability is applied and they perform properly in correspondence with soil D for all the input motions except for input 3, where there is an increment of 23.7% respect the FIX case. Last column of the table shows the ratio between BI-NL and BI-L results in terms of shear forces and it allows to assess the general benefit of NL over L models in correspondence with every soil condition. There is an exception for input motion, where linear isolations seem to perform better that what non-linear isolation does.

Overall, the results show that considering both soil and isolation non-linearity is significantly challenging because many parameters play important role and the assessment of the effects of non-linearity over linearity need to be related to the particular input motion considered.

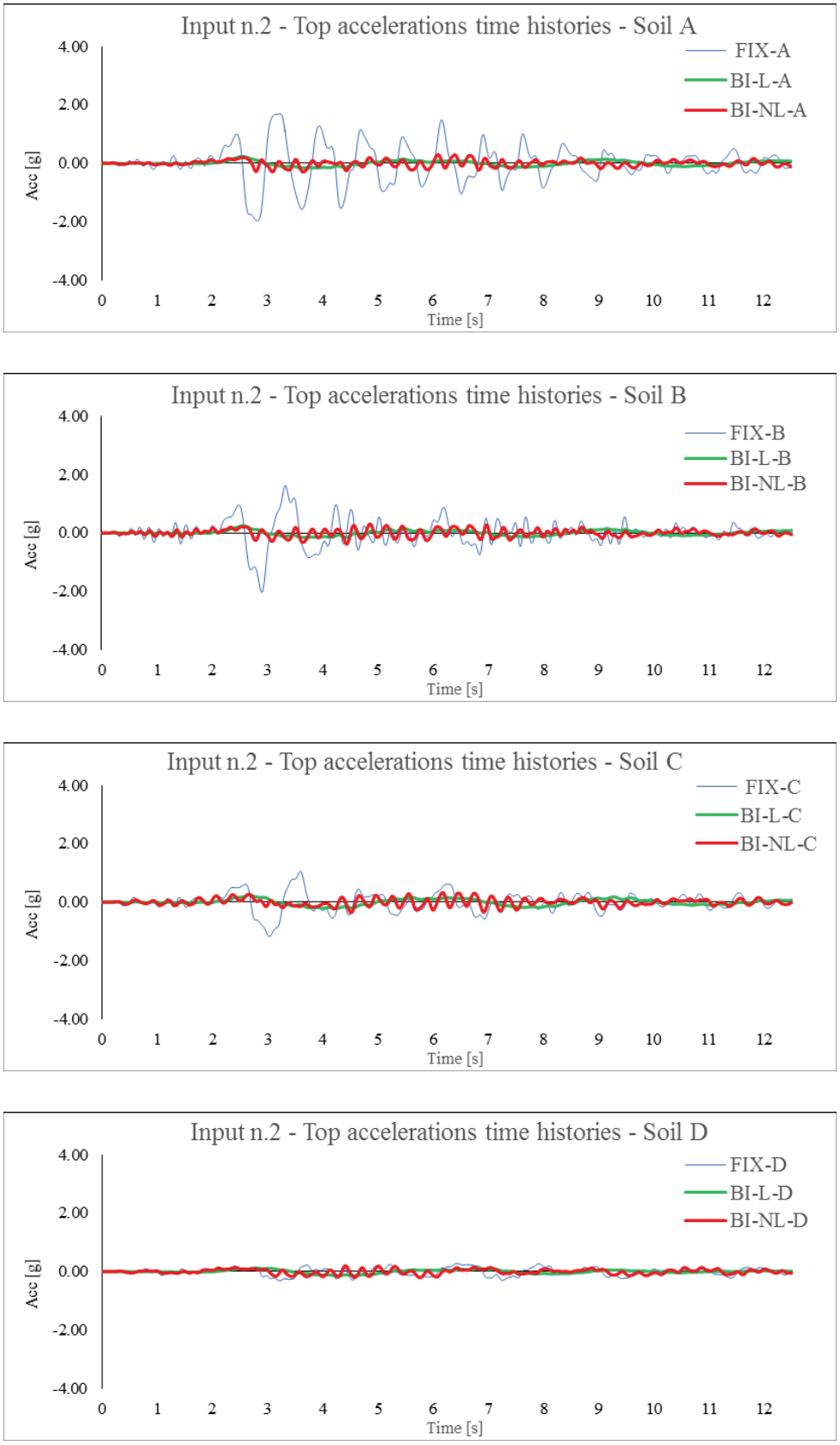

Figure 9 – Comparison accelerations Input-2 of FIX, BI-L and BI-NL (soil A, B, C and D)

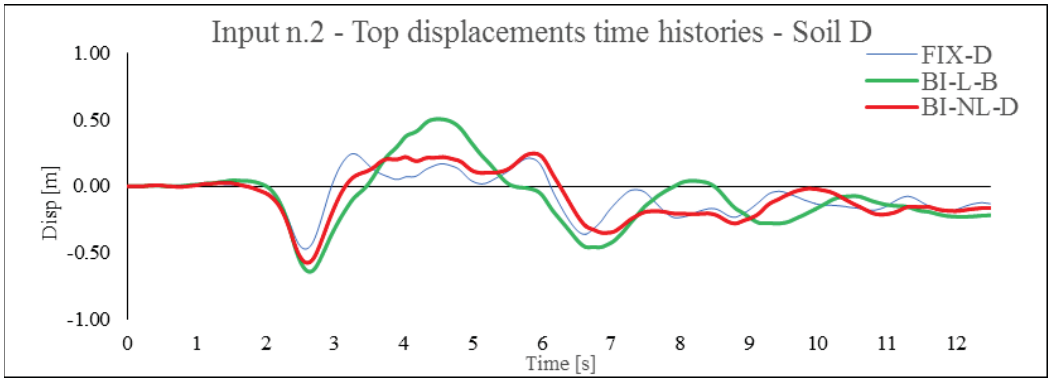

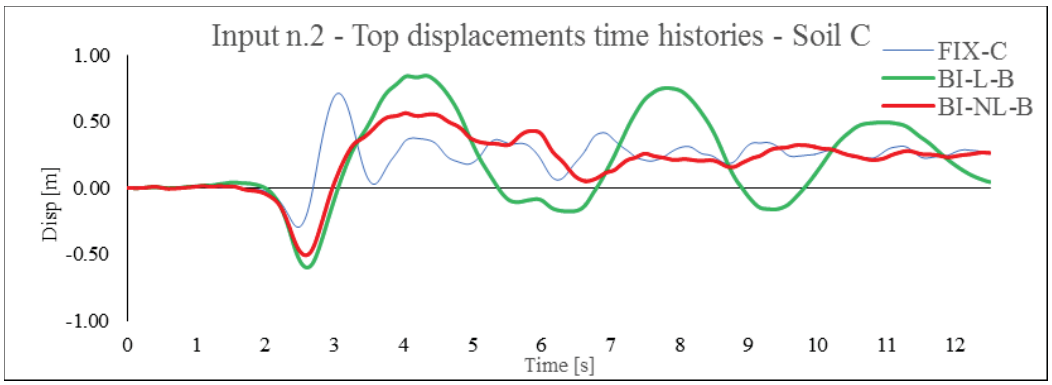

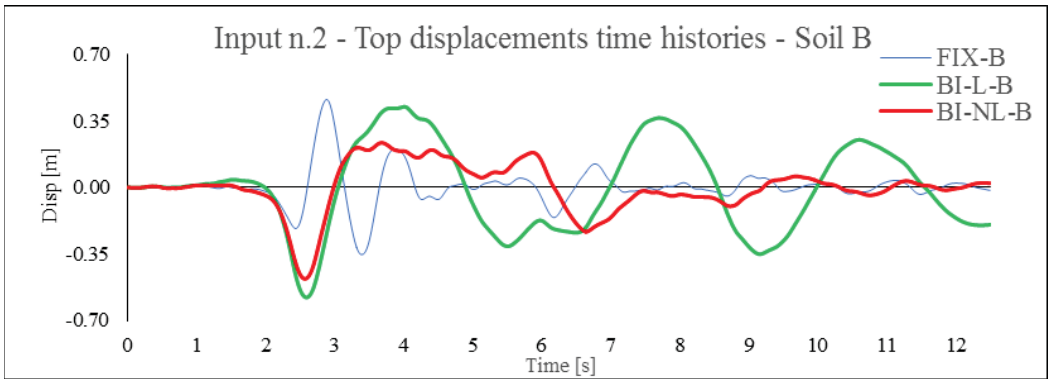

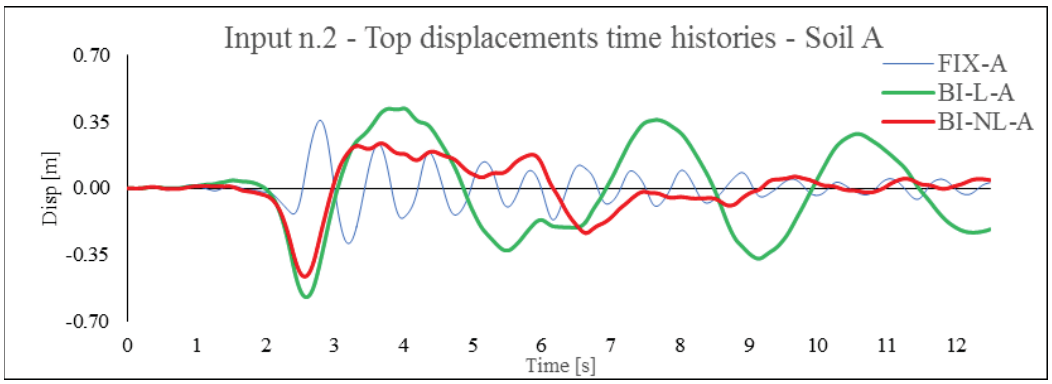

Figure 10 – Comparison displacements Input-2 of FIX, BI-L and BI-NL (soil A, B, C and D)

SOIL A	Top Acceleration [g]			BI-L-A	BI-NL-A	BI-NL-A
	FIX-A	BI-L-A	BI-NL-A	FIX-A	FIX-A	BI-L-A
Input n.1	1.15	0.31	0.24	-73.0%	-79.1%	-22.4%
Input n.2	1.70	0.24	0.30	-86.1%	-82.6%	24.8%
Input n.3	1.99	0.46	0.26	-77.1%	-86.7%	-42.1%
Input n.4	1.52	0.27	0.31	-82.3%	-79.7%	14.9%
Input n.5	1.09	0.27	0.29	-75.6%	-73.7%	7.8%
Input n.6	1.09	0.27	0.29	-75.6%	-73.7%	7.8%
Input n.7	0.93	0.09	0.24	-90.0%	-74.7%	153.9%

SOIL B	Top Acceleration [g]			BI-L-B	BI-NL-B	BI-NL-B
	FIX-B	BI-L-B	BI-NL-B	FIX-B	FIX-B	BI-L-B
Input n.1	0.90	0.32	0.29	-63.9%	-67.8%	-10.7%
Input n.2	1.62	0.24	0.31	-84.8%	-80.9%	25.9%
Input n.3	1.12	0.44	0.27	-60.5%	-76.2%	-39.8%
Input n.4	1.13	0.28	0.37	-75.3%	-67.6%	31.0%
Input n.5	1.50	0.32	0.49	-78.9%	-67.6%	53.9%
Input n.6	1.01	0.27	0.29	-73.6%	-71.8%	6.9%
Input n.7	0.66	0.10	0.24	-85.1%	-63.2%	147.0%

SOIL C	Top Acceleration [g]			BI-L-C	BI-NL-C	BI-NL-C
	FIX-C	BI-L-C	BI-NL-C	FIX-C	FIX-C	BI-L-C
Input n.1	0.59	0.33	0.26	-44.5%	-55.5%	-19.9%
Input n.2	1.05	0.24	0.33	-76.8%	-68.7%	34.8%
Input n.3	0.94	0.40	0.31	-56.9%	-66.7%	-22.8%
Input n.4	0.81	0.27	0.29	-67.1%	-64.8%	7.0%
Input n.5	1.06	0.29	0.49	-72.8%	-53.5%	71.3%
Input n.6	0.90	0.28	0.27	-68.9%	-70.4%	-4.8%
Input n.7	0.53	0.29	0.29	-44.6%	-44.6%	0.0%

SOIL D	Top Acceleration [g]			BI-L-D	BI-NL-D	BI-NL-D
	FIX-D	BI-L-D	BI-NL-D	FIX-D	FIX-D	BI-L-D
Input n.1	0.27	0.29	0.21	4.4%	-22.4%	-25.7%
Input n.2	0.28	0.11	0.20	-59.8%	-27.5%	80.5%
Input n.3	0.22	0.51	0.46	135.5%	113.6%	-9.3%
Input n.4	0.34	0.29	0.52	-15.2%	51.2%	78.2%
Input n.5	0.31	0.34	0.46	8.7%	49.2%	37.3%
Input n.6	0.28	0.35	0.35	25.7%	25.7%	0.0%
Input n.7	0.27	0.11	0.42	-60.2%	56.5%	293.3%

Table 7 – Top accelerations for FIX, BI-L and BI-NL for all input motions (soil A, B, C and D)

SOIL A	Top Displacements [mm]			BI-L-A	BI-NL-A	BI-NL-A
	FIX-A	BI-L-A	BI-NL-A	FIX-A	FIX-A	BI-L-A
Input n.1	130	839	594	547.4%	358.5%	-29.2%
Input n.2	357	421	236	17.7%	-33.8%	-43.8%
Input n.3	289	1014	425	250.9%	46.9%	-58.1%
Input n.4	191	698	484	265.1%	153.1%	-30.7%
Input n.5	274	866	615	216.1%	124.6%	-28.9%
Input n.6	163	737	531	352.2%	225.4%	-28.0%
Input n.7	103	237	125	130.8%	21.4%	-47.4%

SOIL B	Top Displacements [mm]			BI-L-B	BI-NL-B	BI-NL-B
	FIX-B	BI-L-B	BI-NL-B	FIX-B	FIX-B	BI-L-B
Input n.1	137	853	610	520.2%	343.4%	-28.5%
Input n.2	463	425	235	-8.2%	-49.2%	-44.7%
Input n.3	365	955	426	162.0%	16.7%	-55.4%
Input n.4	229	676	479	195.8%	109.6%	-29.2%
Input n.5	373	865	617	131.7%	65.2%	-28.7%
Input n.6	248	731	538	195.1%	117.4%	-26.3%
Input n.7	82	234	121	184.7%	47.1%	-48.3%

SOIL C	Top Displacements [mm]			BI-L-C	BI-NL-C	BI-NL-C
	FIX-C	BI-L-C	BI-NL-C	FIX-C	FIX-C	BI-L-C
Input n.1	210	895	663	326.6%	216.0%	-25.9%
Input n.2	712	844	563	18.6%	-20.9%	-33.3%
Input n.3	415	949	517	128.3%	24.5%	-45.5%
Input n.4	393	781	548	99.0%	39.6%	-29.8%
Input n.5	782	737	761	-5.8%	-2.8%	3.2%
Input n.6	398	804	627	101.8%	57.4%	-22.0%
Input n.7	100	140	140	39.8%	39.8%	0.0%

SOIL D	Top Displacements [mm]			BI-L-D	BI-NL-D	BI-NL-D
	FIX-D	BI-L-D	BI-NL-D	FIX-D	FIX-D	BI-L-D
Input n.1	602	1336	1074	121.8%	78.2%	-19.7%
Input n.2	245	506	246	106.0%	0.4%	-51.3%
Input n.3	602	964	551	60.0%	-8.5%	-42.8%
Input n.4	468	690	477	47.4%	1.9%	-30.9%
Input n.5	830	899	529	8.3%	-36.3%	-41.2%
Input n.6	457	748	573	63.6%	25.4%	-23.4%
Input n.7	131	230	160	75.7%	22.0%	-30.6%

Table 8 – Top displacements for FIX, BI-L and BI-NL for all input motions (soil A, B, C and D)

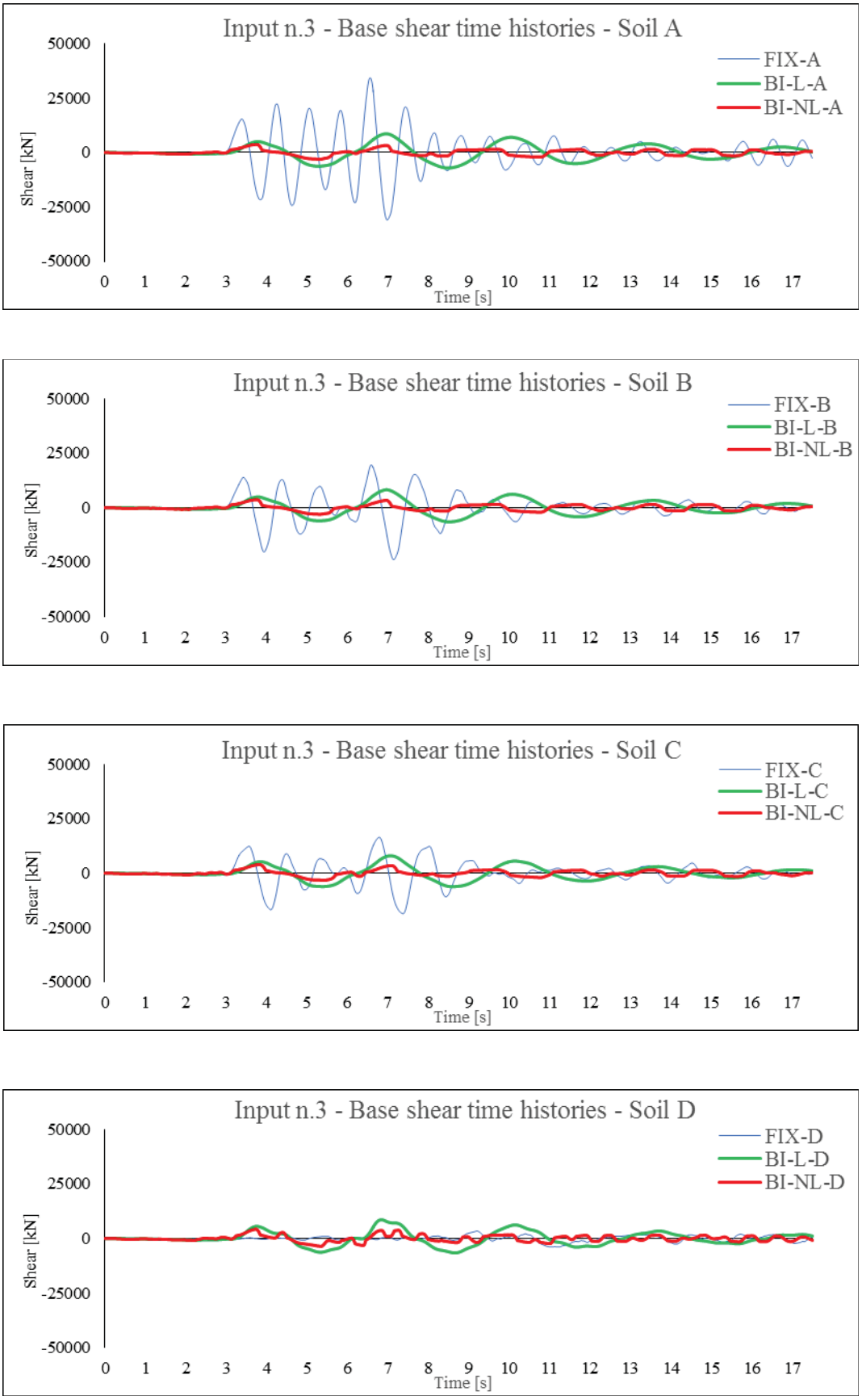

Figure 11 – Comparison base shear Input-3 of FIX, BI-L and BI-NL (soil A, B, C and D)

SOIL A	Base Shear [kN]			BI-L-A	BI-NL-A	BI-NL-A
	FIX-A	BI-L-A	BI-NL-A	FIX-A	FIX-A	BI-L-A
Input n.1	14848	5886	3752	-60.4%	-74.7%	-36.3%
Input n.2	31660	4029	2808	-87.3%	-91.1%	-30.3%
Input n.3	34370	8639	3720	-74.9%	-89.2%	-56.9%
Input n.4	19241	4895	3267	-74.6%	-83.0%	-33.3%
Input n.5	28457	6069	3797	-78.7%	-86.7%	-37.4%
Input n.6	18453	5165	3466	-72.0%	-81.2%	-32.9%
Input n.7	11788	1662	1718	-85.9%	-85.4%	3.4%

SOIL B	Base Shear [kN]			BI-L-B	BI-NL-B	BI-NL-B
	FIX-B	BI-L-B	BI-NL-B	FIX-B	FIX-B	BI-L-B
Input n.1	10268	5798	3762	-43.5%	-63.4%	-35.1%
Input n.2	24820	4044	3276	-83.7%	-86.8%	-19.0%
Input n.3	19583	8241	3701	-57.9%	-81.1%	-55.1%
Input n.4	13035	4657	3167	-64.3%	-75.7%	-32.0%
Input n.5	22529	5900	3753	-73.8%	-83.3%	-36.4%
Input n.6	16243	4976	3438	-69.4%	-78.8%	-30.9%
Input n.7	6504	1616	1691	-75.2%	-74.0%	4.7%

SOIL C	Base Shear [kN]			BI-L-C	BI-NL-C	BI-NL-C
	FIX-C	BI-L-C	BI-NL-C	FIX-C	FIX-C	BI-L-C
Input n.1	10134	5798	3870	-42.8%	-61.8%	-33.3%
Input n.2	15997	4539	3491	-71.6%	-78.2%	-23.1%
Input n.3	16560	8009	3916	-51.6%	-76.4%	-51.1%
Input n.4	12448	4725	3199	-62.0%	-74.3%	-32.3%
Input n.5	17201	5371	3786	-68.8%	-78.0%	-29.5%
Input n.6	15597	5151	3655	-67.0%	-76.6%	-29.0%
Input n.7	6581	1755	1755	-73.3%	-73.3%	0.0%

SOIL D	Base Shear [kN]			BI-L-D	BI-NL-D	BI-NL-D
	FIX-D	BI-L-D	BI-NL-D	FIX-D	FIX-D	BI-L-D
Input n.1	3813	5383	3568	41.2%	-6.4%	-33.7%
Input n.2	4291	2535	2094	-40.9%	-51.2%	-17.4%
Input n.3	3433	8620	4247	151.1%	23.7%	-50.7%
Input n.4	4527	5000	3667	10.5%	-19.0%	-26.7%
Input n.5	4833	6156	3730	27.4%	-22.8%	-39.4%
Input n.6	4270	5086	3752	19.1%	-12.1%	-26.2%
Input n.7	3935	1753	2140	-55.5%	-45.6%	22.1%

Table 9 – Base shear for FIX, BI-L and BI-NL for all input motions (soil A, B, C and D)

7 CONCLUSION

The study conducted in this paper may be viewed as an original contribution to seismic assessment of a residential benchmark BI building with SSI effects that considers the mutual effects of non-linearity both in the soil and in isolators. The FE computational model of the soil is based on an advanced constitutive formulation that enables to drive the assessment of structural behavior with the evaluation of soil non-linear response, by capturing the effects of accumulation of deformation in the ground. At the same time, the model of the structure allows to assess the structural performance by considering accelerations and displacements at various floors. Thanks to these potentialities, it was possible to demonstrate that isolation systems perform their functions consisting in decoupling the structure and the soil, by concentrating the deformations at the base of the buildings and by reducing the damage to the structure and thus to its contents. In particular, the paper shows that the effects of non-linear isolation are fundamental to be considered as well as soil deformability that can significantly modify the efficiency of base isolation technique. In this regard, the paper can be seen as a first attempt to propose new design considerations for engineers and consultants. Further analyses will be performed in order to consider advanced models of isolators and to extend the presented results.

8 END CREDITS

A special thanks goes to the company Dominion Global and especially Dominion Engineering and Construction division which sponsored the participation of the present paper to the EURODYN 2020 conference and least but not last my Employer Dominion Steelcon A/S that allowed me to attend the conference. Without this support this won't happened.

Another important contribution that allowed me publishing this job was given by the Dr. Davide Forcellini which supported me along the way.

REFERENCES

[1] Pan P, Zamfi rescu DAN, Nakashima M, Nakayasu N and Kashiwa H (2005), "Base-isolation Design Practice in Japan: Introduction to the Post-Kobe Approach," Journal of Earthquake Engineering, 9(1): 147–171.

[2] Fujita T. (1998) "Seismic isolation of civil buildings in Japan", Progress in Structural Engineering and Materials, I (3): 295-300.

[3] Clemente P. and Martelli A. (2019) "Seismically isolated buildings in Italy: State-of-the-art review and applications", Soil Dynamics and Earthquake Engineering 119 (2019) 471–487

[4] ATC-3-06. Amended tentative provisions for the development of seismic regulations for buildings. ATC Publication ATC 3-06, NBS Special Publication 510, NSF Publication 78-8, Applied Technology Council. US Government Printing Office: Washington, DC, 1978.

[5] Building seismic safety council, NEHRP. Recommended provisions for the development of seismic regulations for new buildings (and other structures). National earthquake hazards reduction programme: Washington, DC, 1985, 1988, 1991, 1994 (1997, 2000).

[6] Renzi S, Madiai C., Vannucchi G. (2013) "A simplified empirical method for assessing seismic soil-structure interaction effects on ordinary shear-type buildings." Soil Dynamics and Earthquake Engineering; 55: 100–107.

[7] J. E. Luco, Linear soil-structure interaction: a review. Earthquake Ground Motionand Its Effects on structures, 1982.

[8] Kramer S. L. (1996) "Geotechnical Earthquake Engineering", Prentice-Hall, International Series in Civil engineering and engineering Mechanics, William J. Hall Editor.

[9] Forcellini, D (2017). "Cost Assessment of isolation technique applied to a benchmark bridge with soil structure interaction." Bulletin of earthquake Engineering, DOI: 10.1007/s10518-016-9953-0.

[10] A. Vlassis, C. Spyrakos, Seismically isolated bridge piers on shallow soil stratum with soil-structure interaction. Computer and Structure 79: 2847-2861, 2001.

[11] N. Tongaonkar, R. Jandid, Seismic response of isolated bridges with soil-structure interaction. Soil dynamic and Earthquake Engineering 23(4):287-302, 2003.

[12] A. Ucak, P. Tsopeas, A.M. ASCE, Effect of soil-structure interaction on seismic isolated bridges. Journal of Structural Engineering, 2008.

[13] Elgamal, A., Lu, J., Forcellini, D. (2009). "Mitigation of Liquefaction-Induced lateral deformation in sloping stratum: Three-dimensional Numerical Simulation." Journal of Geotechnical and Geoenvironmental Engineering 135:11, 1672-1682.

[14] Forcellini, D., Gobbi, S., Mina, D. (2016) Numerical simulations of ordinary buildings with soil-structure interaction. VI International Conference on Structural Engineering, Mechanics and Computation (SEMC). Capetown, South Africa, 5-7 September 2016, ISBN 978-1-138-02927-9.

[15] Canini A., Forcellini, D. (2017) 3D Numerical simulations of a base-isolated residential building with soil-structure interaction. VI Eccomas Thematic Conference on Computational Methods in Structural Dynamics and Earthquake Engineering (COMPDYN 2017), Rhodes Island, Greece, 15–17 June 2017, DOI**:** 10.7712/120117.5482.16931.

[16] Forcellini D. (2020), "The Role of the Water Level in the Assessment of Seismic Vulnerability for the 23 November 1980 Irpinia–Basilicata Earthquake", Geosciences 2020, 10, 229

[17] Forcellini, D. (2020), "Soil–Structure Interaction Assessment of the 23 November 1980 Irpinia Basilicata Earthquake." Mina, D.; Geosciences 2020, 10, 152

[18] Figini, R., & Paolucci, R. (2016). Integrated foundation-structure seismic assessment through non-linear dynamic analyses. Earthquake Engineering & Structural Dynamics, (56), 1-6. http://doi.org/10.1002/eqe.2790.

[19] Iida M. (1998) "Three-dimensional non-linear soil building interaction analysis in the lakebed zone of Mexico City during the hypothetical Guerrero Earthquake." Earthquake Engineering and Structural Dynamics 1998; 27: 1483-1502.

[20] Mylonakis G, Gazetas G. (2000) "Seismic soil-structure interaction: beneficial or detrimental?" Journal of Earthquake Engineering; 4: 277–301.

[21] Pecker, A., Paolucci, R., Chatzigogos, C. T., Correia, A. a., & Figini, R. (2013). The role of non-linear dynamic soil-foundation interaction on the seismic response of struc-

tures. Bulletin of Earthquake Engineering, 12(3), 1157-1176. http://doi.org/10.1007/s10518-013-9457-0

[22] Pitilakis D, Dietz M, Wood DM, Clouteau D, Modaressi A. (2008) "Numerical simulation of dynamic soil-structure interaction in shaking table testing." Soil Dynamics and Earthquake Engineering 2008; 28(6): 453–467.

[23] Rayhani M.T, El Naggar M.H. (2012) "Physical and numerical modeling of seismic soil-structure interaction in layered soils. Geotechnical and Geological Engineering Journal; 30(2):331–342;

[24] Sáez, E., Lopez-Caballero, F., & Modaressi-Farahmand-Razavi, A. (2013). Inelastic dynamic soil-structure interaction effects on moment-resisting frame buildings. Engineering Structures, 51, 166-177. http://doi.org/10.1016/j.engstruct.2013.01.020

[25] Veletsos AS, Nair VV. (1975), "Seismic interaction of structures on hysteretic foundations". Journal of Structural Engineering, 101101; 109-129, 1975.

[26] Saouma V, Miura F, Lebon G, Yagome Y. (2011) "A simplifyed 3D model for soil-structure interaction with radiation damping and freefield input". Bulletin of Earthquake Engineering; 9(5):1387–1402.

[27] Priestley, M.J.N., Calvi, G.M. and Kowalsky, M.J. (2007), "Direct displacement-based seismic design", IUSS Press, Pavia, Italy, 720 pages.

[28] Garcia, R., Sullivan T.J. and Della Corte, G. (2010), "Development of a displacement-based design method for steel frame-RC wall buildings", J. Earthq. Eng., 14(2), 252-277.

[29] Maley, T.J., Sullivan, T.J. and Della Corte, G. (2010), "Development of a displacement-based design method for steel dual systems with buckling-restrained braces and moment resisting frames", J. Earthq. Eng., 14(1), 106-140.

[30] Sullivan, T.J., Calvi, P.M. and Nascimbene, R. (2013), "Towards improved floor spectra estimates for seismic design", Earthq. Struct., 4(1), 109-132.

[31] ASCE/SEI 7-10 (2010) ASCE Standard, Minimum design loads for buildings and other structures. American Society of Civil Engineers, Reston, VA

[32] CEN (2004) Eurocode 8 Design of structures for earthquake resistance. Part 1: General rules, seismic actions and rules for buildings. European standard EN 1998-1. European Committee for Standardization, Brussels, Belgium

[33] Calvi PM, Sullivan TJ (2014) Estimating floor spectra in multiple degree of freedom systems. Earthq Struct 7(1):17–38. doi:10.12989/eas.2014.7.1.017.

[34] Lu, J., Elgamal, A., and Yang, Z. (2011). "OpenSeesPL: 3D Lateral Pile-Ground Interaction, User Manual, Beta 1.0" (http://soilquake.net/openseespl/).

[35] Mazzoni, S., McKenna, F., Scott, M. H., Fenves, G. L. (2009). "Open System for Earthquake Engineering Simulation, User Command-Language Manual." (http://opensees.berkeley.edu/OpenSees/manuals/usermanual). Pacific Earthquake Engineering Research Center, University of California, Berkeley, OpenSees version 2.0.

[36] Pan P I, Maddaloni G and Cosenza E Eurocode 8 Compliant Record Sets for Seismic Analysis of Structures, Journal of Earthquake Engineering, 12:54–90, 2008 DOI: 10.1080/13632460701457173.

[37] D. Forcellini, S. A. Mitoulis, K. N. Kalfas, Study of the response of elastomeric bearings with 3D numerical simulations and experimental validation, *Computational Methods in Structural Dynamics and Earthquake Engineering (COMPDYN) Conference*, Rhodes Island, Greece, 15-17 June 2017.

[38] Forcellini, D (2018) "Seismic assessment of a benchmark based isolated building with soil structure interaction", Bulletin of Earthquake Engineering, DOI: 10.1007/s10518-017-0268-6.

[39] Forcellini D (2019) "Numerical simulations of liquefaction on an ordinary building during Italian (20 May 2012) earthquake" Bulletin of Earthquake Engineering https://doi.org/10.1007/s10518-019-00666-5.

[40] Forcellini, D (2020) "Soil-structure interaction analyses of shallow-founded structures on a potential-liquefiable soil deposit" Soil Dynamics and Earthquake Engineering; 133 (2020) 106108.

[41] K. N. Kalfas, D. Forcellini, A developed analytical non-linear model of elastomeric bearings verified with numerical findings, *International Conference on Structural Dynamics (EURODYN)*, Athens, Greece, 22-24 June 2020.

[42] Koutsourelakis, S., Prevost, J.H. Deodatis, G (2002) "Risk assessment of an interacting structure–soil system due to liquefaction" Earthquake Engineerig and Structural Dynamics; 31:851–879 (DOI: 10.1002/eqe.125).

[43] Caballero, F.L., Farahmand-Razavi, A. M. (2008) "Numerical simulation of liquefaction effects on seismic SSI" Soil Dynamics and Earthquake Engineering 28 (2008) 85–98

[44] Mroz, Z. (1967). "On the description of anisotropic work hardening." Journal of Mechanics and Physics of Solids, 15, 163-175.

[45] D. Forcellini, S. Gobbi (2015), Soil structure interaction assessment with advanced numerical simulations, Proceeding of Computational Method in Structural Dynamics and Earthquake Engineering conference (COMPDYN), Crete Island, 25 – 27 May 2015.

[46] Attewell, P. and Farmer, I.W. 1973. Attenuation of Ground vibrations from pile driving. Ground engineering, 6(4), 26-29.

[47] Jesmani M., Fallahi A.M., Kashani H.F. 2012. Effects of geometrical properties of rectangular trenches intended for passive isolation is sandy soils. Earth Sceince Research; 1 (2): 137-151.

[48] Yang Z., Elgamal A., Parra E. (2003). "A computational model for cyclic mobility and associated shear deformation." Journal of Geotechnical and Geoenvironmental engineering (ASCE), 129 (12): 1119-1127.

[49] Parra, E. (1996). "Numerical modeling of liquefaction and lateral ground deformation including cyclic mobility and dilation response in soil systems." Ph.D. thesis, Rensselaer Polytechnic Institute, Troy, N.Y.

[50] Iwan, W. D. (1967). "On a class of models for the yielding behavior of continuous and composite systems." Journal of Applied Mechanics, ASME 34, 612-617.

[51] Prevost, J.H. (1985). "A simple plasticity theory or frictional cohesionless soils." Soil Dynamics Earthquake Engineering, 4(1): 9-17.

[52] Dafalias, Y.F. 1986. Bounding surface plasticity I: mathematical formulation and hypo-plasticity. Journal of Engineering Mechanics, ASCE 112 (9), 966–987.

[53] Bousshine, L., Chaaba, A., De Saxce, G. 2001. Softening in stress-strain curve for Drucker-Prager nonassociated plasticity. International Journal of Plasticity 17 (1), 21–46.

[54] Nemat-Nasser, S., Zhang, J. (2002). "Constitutive relations for cohesionless frictional granular materials". International Journal Plasticity 18 (4), 531–547.

[55] Radi, E., Bigoni, D., Loret, B. (2002). "Steady crack growth in elastic-plastic fluid-saturated porous media". International Journal of Plasticity 18 (3), 345–358.

[56] Elgamal, A., Yang, Z., Parra, E. and Ragheb, A. (2003). "Modeling of cyclic mobility in saturated cohesionless soils." International Journal Plasticity 9:6, 883-905.

[57] Kondner, R. L. (1963). "Hyperbolic stress-strain response: Cohesive soils." Journal of the Soil Mechanics and Foundations Division, 89(SM1), 115-143.

[58] Law, H. K. Lam, I. P. (2001). "Application of periodic boundary for large pile group", Journal of Geotechnical Geoenvironmental. Engineering, 127-10, 889–892.

[59] Computer and Structures Inc. Structural and Eartquake Engineering software (https://www.csiamerica.com/products/sap2000)

[60] JM. Kelly, Earthquake-resistant design with rubber, London: Springer, 1993.

[61] F. Naeim, JM. Kelly, Design of seismic isolated structure – from theory to practice. New York, Jonh Wiley & Sons, Inc, 1999.

EURODYN 2020
XI International Conference on Structural Dynamics
M. Papadrakakis, M. Fragiadakis, C. Papadimitriou (eds.)
Athens, Greece, 23–26 November 2020

SENSITIVITY OF DEFORMATION DEMANDS IN BUILDINGS TO MODELING ASSUMPTIONS IN NONLINEAR SEISMIC ANALYSIS

Jørgen R. Roven[1], Emrah Erduran[2] and Amir M. Kaynia[3]

[1]Rambøll
Hoffsveien 4, 0275 Oslo, Norway
e-mail: jrroven@protonmail.com

[2] Dept. of Civil Engineering and Building Technology, Oslo Metropolitan University
Pilestredet 35, 0166 Oslo, Norway
e-mail: emrah.erduran@oslomet.no

[3] Norwegian Geotechnical Institute
Sognsveien 72, N-0855 Oslo, Norway
e-mail: amir.m.kaynia@ngi.no

Keywords: Performance based design, Nonlinear seismic analysis, Displacement demands, Damage assessment, Numerical Models

Abstract.

Performance-based design principles rely heavily on the estimation of engineering demand parameters through nonlinear static or dynamic analysis. The increased focus on nonlinear analysis in recent and upcoming building codes calls for a detailed investigation into the limitations of these procedures. This is especially true for nonlinear dynamic analysis, which is often referred to as "exact" or "benchmark" solution. This article examines the sensitivity of nonlinear analysis results to the assumptions made in the modeling of nonlinear element behavior. To this end, a four-story reinforced concrete building designed according to the recent European standards is modeled in OpenSEES computational environment. Nonlinear element behavior is modeled using several approaches from lumped plasticity models to force-based and displacement-based elements with fiber sections using complex stress-strain curves. The results of nonlinear static and dynamic analysis reveal that the modeling assumptions have a significant effect on both displacement demands at the story and global level. More specifically, the curvature demands at the bottom of the ground story columns are very significantly affected by the modeling assumptions, particularly for diplacement- and force-based elements.

1 INTRODUCTION

Current seismic design procedures rely on elastic analysis where earthquake ground motions are simulated using equivalent lateral forces. On the other hand, ordinary structures that are designed using elastic analysis procedures are expected to be forced well beyond their elastic limit. The safety of these structures is ensured by prescriptive measures without actually evaluating their real performance. Performance based design procedures aim to provide a more transparent approach by evaluating the performance of the structure under different hazard levels. These methods rely heavily on estimation of engineering demand parameters such as total or plastic deformations through nonlinear static and dynamic analysis. As performance based design procedures are used more and more in seismic design, the numerical models become more complex. The assumptions used in the numerical modeling phase such as inelastic material behaviour, cyclic degradation and geometric nonlineareties can have severe implications for the results of an analysis [1–4]. For example, plastic rotations and curvatures of structural elements such as columns and beams are widely used for the assessment of the structural state in seismic design [2] and have been shown to be sensitive to the numerical parameters used in the analysis [5]. Although some studies [3, 5] have commented on the sensitivity of the engineering demand parameters to the numerical modeling assumptions, a quantitative documentation of this sensitivity is vital as the performance based design methods begin to find their way into seismic design codes.

The objective of this study is to investigate the effects of numerical modeling assumptions on the engineering demand parameters (EDPs) obtained from nonlinear static and dynamic analyses. Section curvatures, roof drifts and interstory drift ratios are chosen as the EDPs as these parameters have been documented to be well-correlated with structural damage. This will be done by conducting nonlinear static analyses (SPO) and nonlinear response history analyses (NRHA) on a reinforced concrete moment resisting frame (MRF) designed according to EN-1998-1 [6]. The analyses are performed using the open system for earthquake engineering simulation (OpenSees), which is an advanced computational tool frequently used in research.

2 THE ANALYZED STRUCTURE AND NUMERICAL MODELS

The analyzed structure is a four-story reinforced-concrete frame. It is symmetric about both horizontal axes with five bays in both directions. Due to the regularity of the building in plan, only one of the inner frames was modeled and used in the analysis. Figure 1 shows the elevation view of the of this frame. The structure was designed according to EN-1998:2004 [6] assuming moderate ductility level (DCM). All structural elements were designed for exposure class XC3, M60. The concrete quality was chosen as C30/37 and the thickness of cover concrete is 35mm for all elements. The reinforcement is of quality B500C with a modulus of elasticity of 200 GPa. The cross sections of the structural elements are summarized in Table 1.

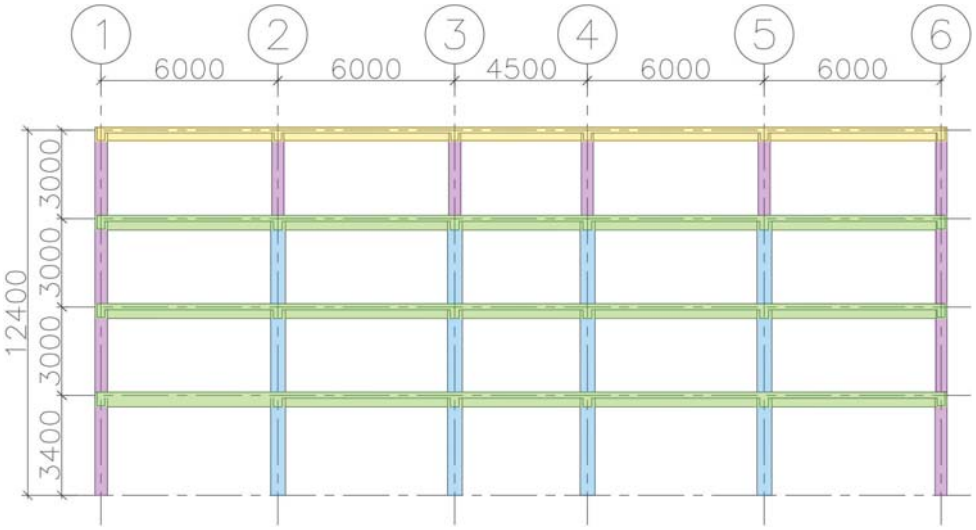

Figure 1: Elevation view of the analyzed frame (all measurements in mm)

Name	B [mm]	H [mm]	Color in Elevation View
Column 1	450	450	Pink
Column 2	500	500	Blue
Beam 1	300	500	Green
Beam 2	250	450	Yellow

Table 1: Cross sections of the structural elements of the frame shown in Figure 1.

The mass of the entire structure is 2 024 tons. The masses are lumped in their respective vertical level in nodes along axis 3. The natural periods for the first three modes were found to be 0.53, 0.17, and 0.10 seconds, respectively. Details of the structure can be found in [7]. For nonlinear response history analysis, damping of the system is modeled using 5% Rayleigh damping anchored at the $\omega_i = 0.707\omega_1$ (ω_1: the vibration frequency of the first mode) and $\omega_j = 31.4$ rad/s [8].

2.1 Structural Models

2.1.1 Element Models

All nonlinear analysis were carried out in the OpenSEES computational environment. Three types of structural element models were used in the analyses. The first element is a *force-based beam-column element* (FBE) that is based on the flexibility formulation and uses force interpolation functions for the variation of internal forces over the element length which represent the exact solution to the governing equations [9, 10]. The force-based approach relies on the equilibrium solution and, as such, even for nonlinear material response, FBE always satisfies the equilibrium conditions [11]. The inelastic properties are defined at integration points (IP) along the element, each contributing to the global inelasticity of the element [5]. The cross-sections of the elements have been modeled using fiber sections. Figure 2 illustrates a sample element with five integration points together with a sample fiber section where reinforcement, unconfined concrete and confined concrete fibers are depicted.

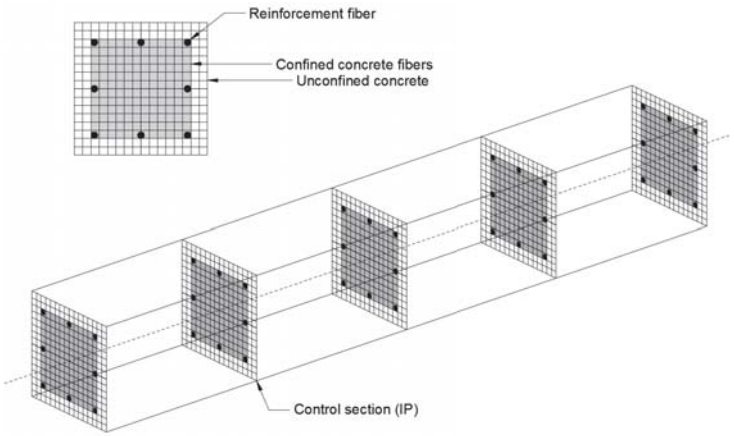

Figure 2: Illustration of the distributed plasticity model. One FE with five integration sections.

With regards to modeling softening behaviour, the stresses tend to localize in the most strained integration point (IP) of the most strained element [5]. As the number of integrations points are increased and the length of integration reduces, larger and larger rotations are required in the most strained IP for an element to produce same values of displacement, making the response nonobjective. Four to six IPs are necessary to accurately represent nonlinear material response and obtain an objective response [9].

The second element that was used in the analysis is the *displacement-based beam-column element* (DBE). This model is very similar to its force-based counterpart but uses the displacement formulation instead of the flexibility formulation. Despite their similarities, FBE and DBE cannot be modeled following the same approach. Most significantly, while the accuracy of the FBE can be improved by increasing either the number of integration points or the number of elements, the accuracy of the DBE can only be improved by increasing the number of elements.

The final element used in the present study is the *beam with hinges element* (BwH) which is also based on the flexibility formulation but the location and the weight of the integration points are predefined and based on the plastic-hinge formulation. This allows the users to specify plastic hinge lengths at the element ends. Two-point Gauss integration is used on the element interior while two-point Gauss-Radau integration is applied over lengths of $4Lp_I$ and $4Lp_J$ at the element ends [2, 12]. Figure 3 shows the underlying principles of the element together with the location of the integration points. The behaviour of the interior section can be modeled as linear elastic or inelastic; *e.g.* by using the fiber section shown in Figure 2. One of the most important parameters of BwH element is the plastic hinge length, l_p, which designates the part of the element where the nonlinear behavior is expected to occur, as the nonlinear behavior of the element depends, to a greater extent, to this parameter, especially if the interior of the element is modeled as linear elastic. There are different approaches to determine l_p, one of which is using empirical equations. One example can be found where Paulay and Priestly [13] provide an empirical formulation, and suggest that, for frame elements with normal proportions, this equation will lead to an approximate plastic hinge length of l_p = 0.5 h, where h is the depth of the cross section.

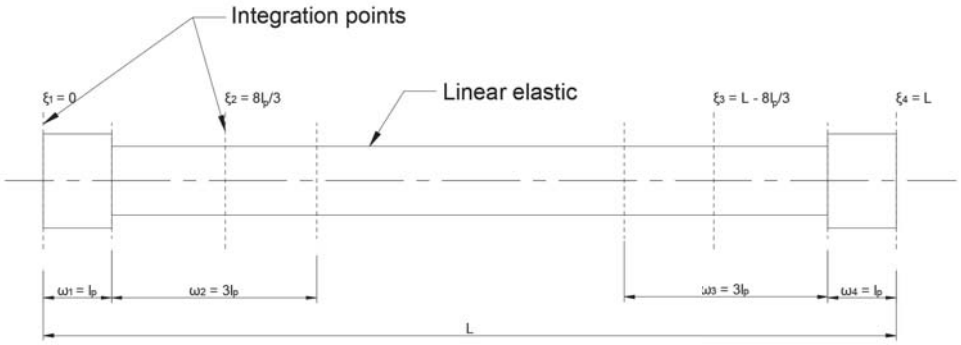

Figure 3: Beam with hinges element using the modified Gauss-Radeu integration rule.

2.1.2 Section and Material Models

All the cross-sections in the analysis were modeled using a fiber section as depicted in Figure 2. The material behavior at each fiber of the section is defined using a uniaxial stress-strain relationship. In order for a reliable nonlinear analysis, the concrete material model should be able to describe all material behaviours expected to occur before collapse during static and dynamic analyses. This includes, among other phenomena, strain softening and hardening, the effects of strain rates and confinement. To achieve this, the stress-straing model by Mander, Priestley and Park [14], which was based on Popovics model [15] and used extensively in literature (e.g. [2, 5, 16]), was used.

Two sets of parameters that were used for unconfined and confined concrete are presented in Table 2. The strain rate used in the calculations was 0.013 s^{-1}. The parameters shown in Table 2 were used as the input parameters for the CONCRETE04 material model in OpenSees. The reinforcement steel was modeled using the simplest model provided in OpenSees for steel, i.e STEEL01. The input parameters for this model were f_{yk} = 500 MPa, E_s = 200 GPa with a strain hardening ratio of b = 0.005.

Name	f_c	ϵ_c	ϵ_{cu}	E_c	ϵ_{ct}	ϵ_t
Unconfined concrete	-38.6	-0.00199	-0.0060	33.916	2.9	0.0855
Confined concrete nr.1	-47.9	-0.00420	-0.0142	-	-	-

Table 2: Concrete material parameters.

3 NUMERICAL ANALYSES

3.1 General

Nonlinear static analyses (NSA) and response history analyses (NRHA) were conducted using the elements described previously with different configurations. For the models using the DBE, each structural element was modeled using a different number of finite elements with two integration points. For the model using FBE such refinement is not necessary; instead the number of IPs per element has an effect and was thus varied. Similarly, only one finite element was used per structural element for the BwH elements. For the BwH element, the hinge length varied as well as the behavior of the interior section (elastic or inelastic). The different model configurations used in the analyses are summarized in Table 3. No NRHAs were performed using the DBE due to extremely long computational time and convergence issues.

Model	Configurations	Analyses
DBE	4, 8, 18 or 24 finite elements each using 2 IPs	NSA
FBE	One finite element using 2, 3, 4, 5, 6, 7 or 8 IPs	NSA and NRHA
BwH	$l_p = \{1.0\text{h} , 1.5\text{h} , 2.0\text{h}\}$ with elastic interior	NSA and NRHA
BwH	$l_p = \{1.0\text{h} , 1.5\text{h} , 2.0\text{h}\}$ with inelastic interior	NSA and NRHA

Table 3: Different model configurations

3.2 Nonlinear Static Analysis

NSA were performed to assess the behaviour of the structure and the different element formulations. The static pushover loads were applied at the nodes along axis 3 in a vertical pattern based on the eigenvectors of the first mode, making this a first-mode pushover analysis. P-δ effects were included in all analyses.

3.3 Nonlinear Response History Analysis

Nonlinear response history analyses were performed for a set of seven ground motion records for the different numerical models; in total 84 NRHAs. The ground motions records were selected for ground type C in EN 1998-1:2004 [6]. The ground motion records are listed in Table 4 with the corresponding parameters.

RSN	Name	Year	M_w	Rrap (km)	V_{s30} (m/sec)	PGA	SF
282	Trinidad	1980	7.2	76	312	0.22	2.32
720	Superstition Hills-02	1987	6.5	27	206	0.33	1.88
1003	Northridge-01	1994	6.7	27	309	0.64	0.76
1110	Kobe Japan	1995	6.9	25	256	0.25	1.67
4889	Chuetsu-Oki Japan	2007	6.8	33	315	0.37	1.29
5832	Iwate Japan	2010	6.9	31	248	0.40	1,121
6923	Darfield New Zealand	2010	7	31	255	0.47	0.99

Table 4: Ground motion records used for the analyses with the corresponding scale factors (SF).

The ground motions were scaled so that the spectral acceleration at the first natural period of the structure matches the elastic response spectrum defined in EN 1998 [6]. The scale factors used are also shown in Table 4. The scaled response spectra are plotted in Figure 4. The response of the structure is dominated by the first natural mode, hence scaling in this way is justified.

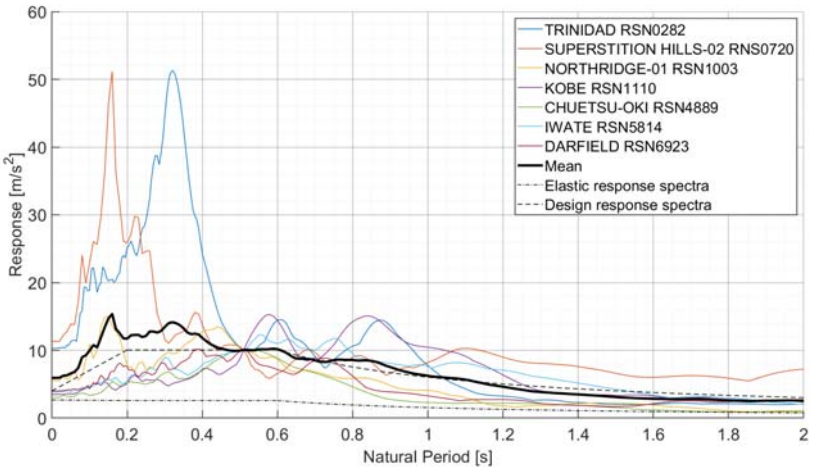

Figure 4: Response spectra scaled to match the elastic spectrum in EN-1998:2004 [6] at T_1.

4 RESULTS

4.1 Nonlinear Static Analysis

The capacity curves resulting from NSA for the different DBE models are shown in Figure 5. The results appear to converge to a stable solution as the number of FEs per member increases. As expected from the coarsely meshed models using DB elements, the base shear capacity of the structure is overestimated significantly for four- and eight-element models.

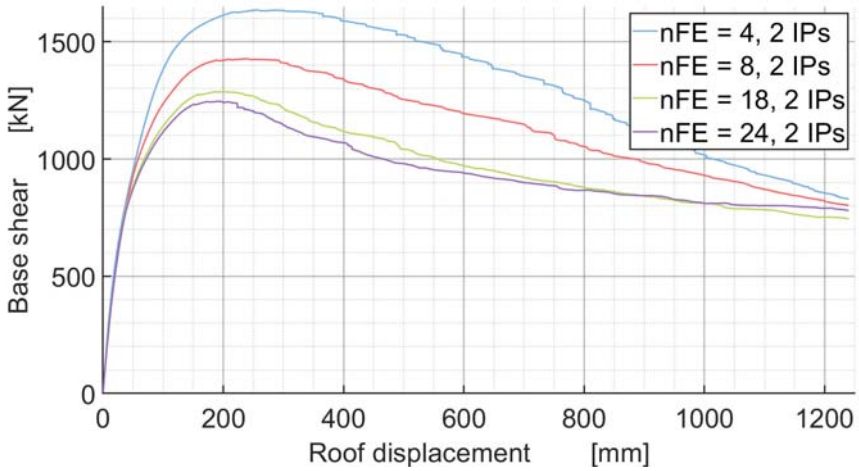

Figure 5: Base shear plotted against roof drift for different configurations of the DB model.

The response of the FBE model is nonobjective, i.e. as the number of IPs increases, the different curves do not converge towards a stable solution. Figure 6 presents capacity curves obtained from NSA using FBE. Figure 6 shows that increasing the number of IPs does not necessarily lead to a unique solution. Although the estimated maximum base shear load converges with increasing IP, the overall response, particularly, the immediate post-peak response shows discrepancies as the number of IPs increases. This can be attributed to the spread of nonlinearity over a larger part of the element as the number of integration points increases.

Comparing the computation time of NSA using DBE and FBE shows one of the significant disadvantages of DBE compared to the other elements, namely its poor efficiency. NSA using DBE with 18 FEs for each member provides a capacity curve quite similar to the one using FBE with 5 IPs per member. However, the computational time of the analysis with DBE is approximately five times that of the analysis with FBE.

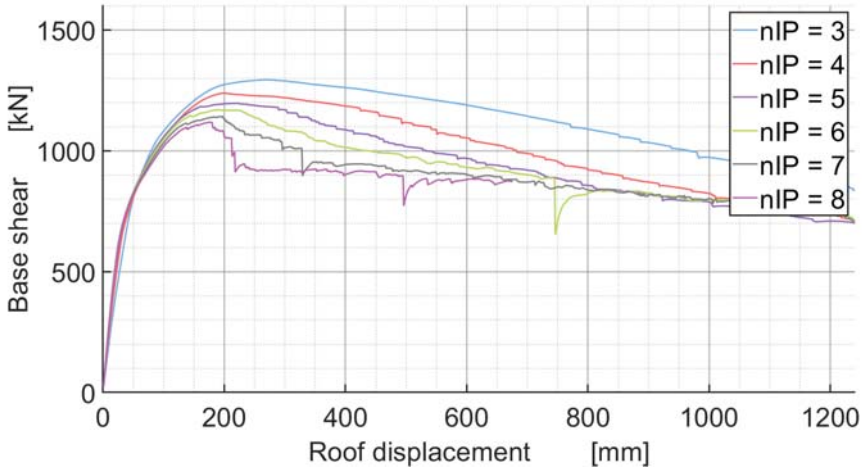

Figure 6: Base shear plotted against roof drift for different configurations of the FB model.

Using the BwH model, the models show similar responses for different plastic hinge lengths; see Figure 7. The stiffness of the structure immediately between first yielding (i.e. base shear around 500 kN) and the overall yielding is affected by the plastic hinge length if the element interior is modeled as elastic. When the element interior is inelastic, the capacity curves become virtually identical for different plastic hinge lengths. For the models where elements were defined with the inelastic fiber section in the interior, the response is generally softer. Note also that the model that used a hinge length of l_p = 2.0 h with an inelastic interior failed to converge at around 50 mm roof drift.

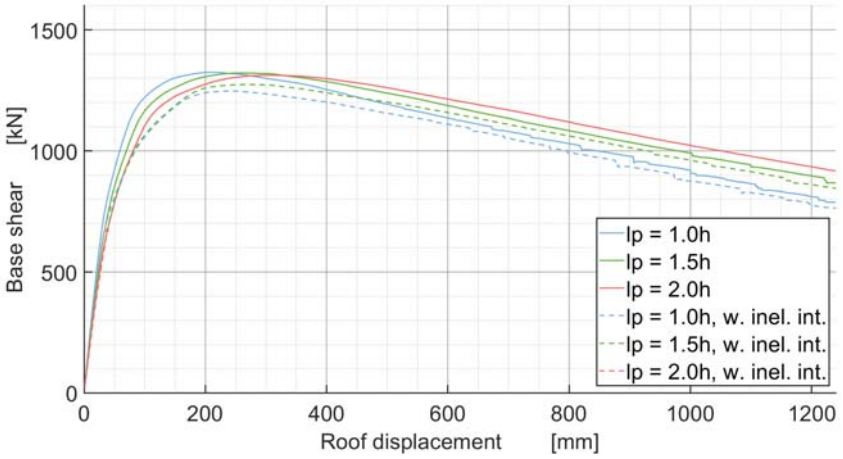

Figure 7: Base shear plotted against roof drift for different configurations of the BwH model.

One of the demand parameters that is strongly correlated with structural damage is the interstory drift ratio (IDR). Therefore, the effect of modeling assumptions on the IDR estimates

from NSA has been investigated. Figure 8 shows the IDRs for three different models at various roof drifts. From the IDR profiles at 2 and 4% roof drift, it can be seen that the three different models lead to very similar IDR estimates. As the roof drift increases, the DBE model starts displaying higher IDRs at the lower stories while the BwH leads to a higher estimate at the upper stories; Figure 8 (c).

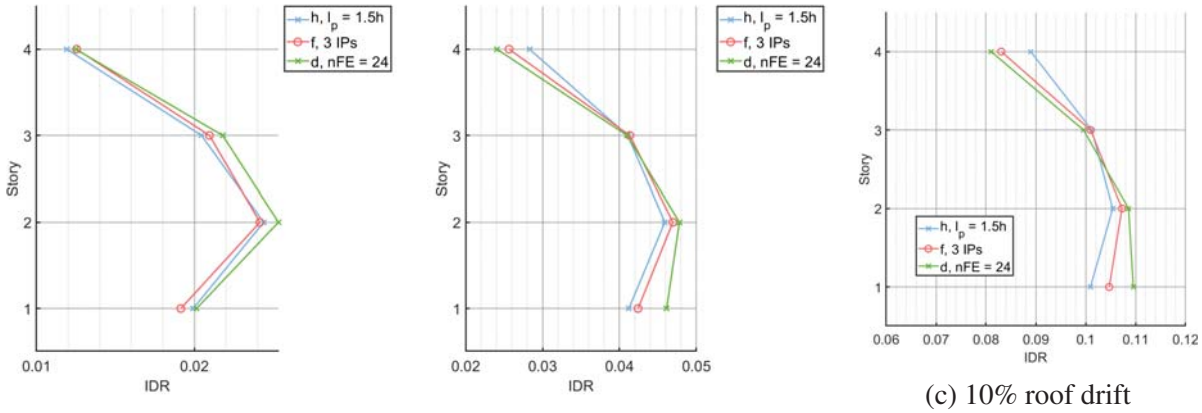

(a) 2% roof drift (b) 4% roof drift (c) 10% roof drift

Figure 8: IDRs for different element configurations at various roof drifts.

Curvature and curvature ductility at the element ends are often used as an indicator of damage at the element level. As such, variation of curvature estimates for different models can lead to a variation in the damage estimates. The curvature estimates at the bottom section of the ground story column in axis 3 from NSA is plotted against the roof drift in Figure 9. This plot illustrates how some of the model configurations give significantly different curvature estimates for a given roof drift even if the global demand estimates such as capacity curves and IDR estimates are rather similar. The most drastic variation is observed for FBE and DBE elements when the distance between the two integration points become rather short, either through increased number of IPs for FBE or through finer mesh for DBE.

Evaluating Figures 5 and 9 together presents a potential dilemma for use of displacement-based elements for nonlinear static analysis. More specifically, Figure 5 shows that in order to achieve a satisfactory capacity curve using DBEs, a fine mesh of 18 to 24 elements per member is necessary. However, using such a fine mesh leads to a potential problem that can have significant consequences as far as local behavior and damage estimates is concerned. As illustrated in Figure 9, using a very fine mesh, which is necessary to capture the global behavior satisfactorily, can lead to very high ductility demands for a given roof drift ratio compared to other models. These results are consistent with those found by Calabrese et al. [5] and others [17]; for softening behaviour, increasing the number of DB elements leads to nonobjective curvatures. The same issue can also be encountered for force-based elements when a high number of integration points is used as shown in Figure 9 and also reported by Calabrese et al. [5]. However, in case of FBE, the issue can be resolved by using less IPs, e.g. four or five, as these models produce very similar capacity curves compared to the model with 8 IPs.

With regards to the BwH model, Figure 9 shows results consistent with expectations. Since the characteristic length of the plastic hinge gets shorter, it must give higher values of curvature to produce the same displacements. As a result, the differences between the BwH model configurations are significant, although not as dramatic as FBE and DBEs with fine mesh.

The differences seen in curvature responses of these models can have direct implications for the estimated damage in the structural elements. It shows that when using a shorter hinge length or a finer mesh than the "correct" value, the level of damage may be greatly overestimated. Also, if a larger hinge length or a coarser mesh is used, the assessment may be unconservative.

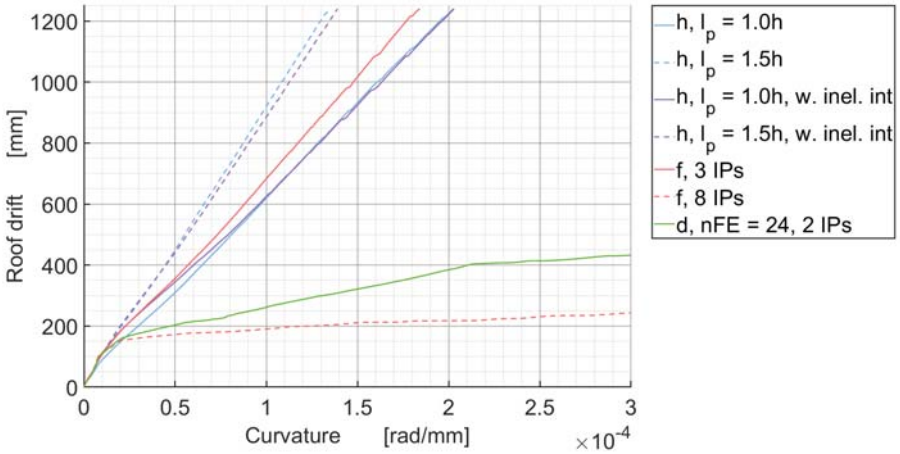

Figure 9: Roof drift plotted against the curvature in the monitored section.

4.2 Nonlinear Response History Analysis

The maximum interstory drift ratios obtained through NRHA for FBE, using different element configurations, are summarized in Figure 10. Here, it is seen that increasing the number of IPs beyond five appears to have little effect on the maximum IDR demands. Figures 11 and 12 shows the maximum IDRs for the BwH model, using elastic and inelastic interior, respectively. Both figures show that increasing the plastic hinge length for BwH elements lead to an increase in the maximum IDR demands for all ground motions.

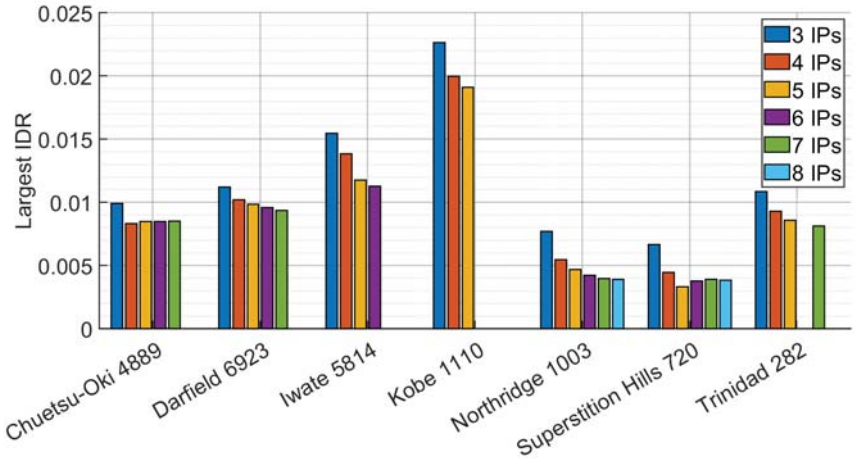

Figure 10: Maximum IDRs for the FB model.

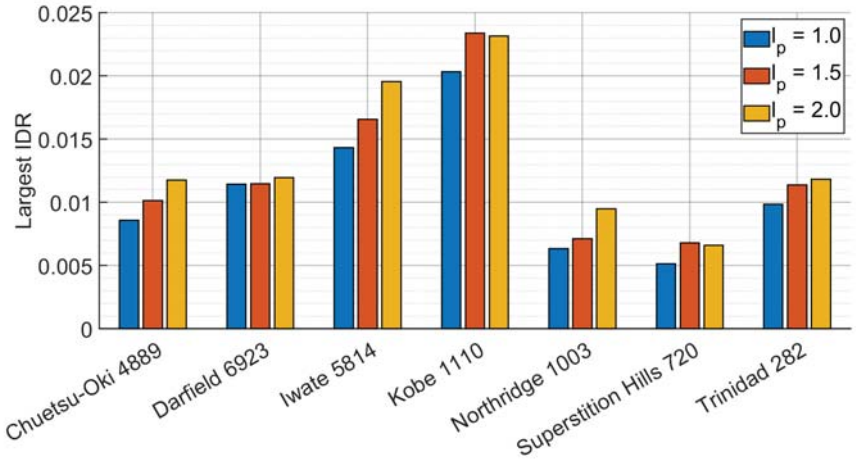

Figure 11: Maximum IDR for the BwH model using elastic interior.

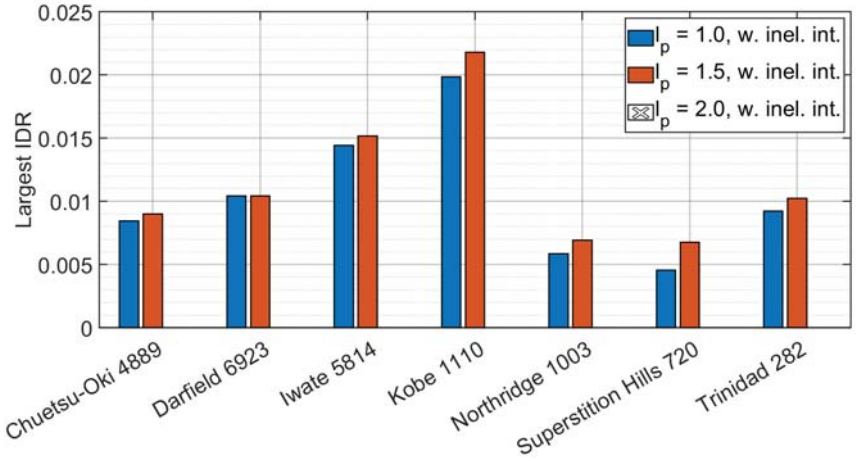

Figure 12: Maximum IDR for the BwH model using inelastic interior.

Figure 13 shows an overview of the mean value of the maximum roof drift ratios (RDR) and IDRs for the different model configurations. Across the various configurations, the trends shown for the RDRs and IDRs are very similar. For both parameters, it is evident that the peak responses decrease as the number of IPs increases for the FB model. For the BwH element, longer hinge lengths leads to larger peak values for both RDRs and IDRs. For elastic interiors, the peaks are somewhat larger when compared to the results from models using inelastic interiors.

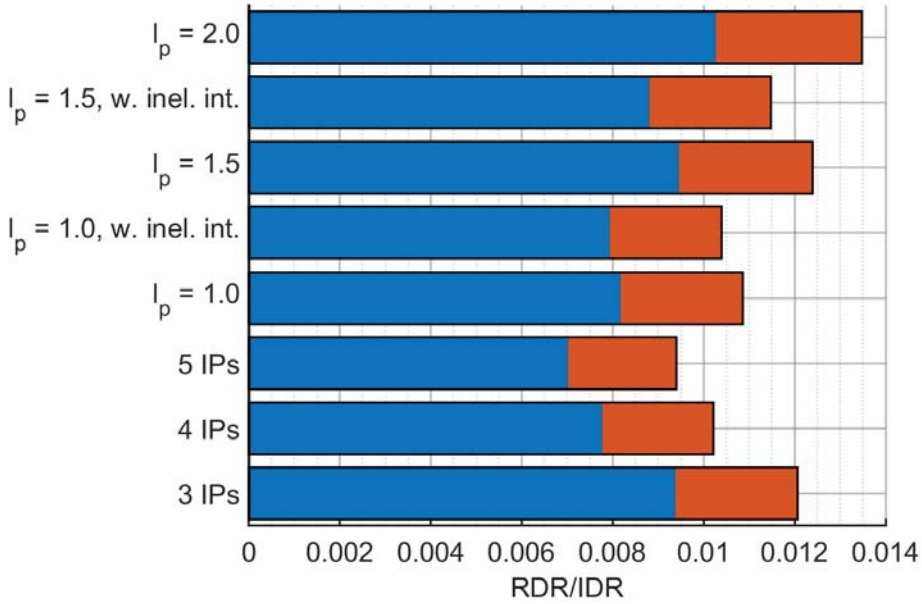

Figure 13: Mean values of RDRs and IDRs for the different numerical models. Blue bars represent RDRs while the values of the IDRs are represented by blue plus orange bars.

5 CONCLUSIONS

The objective of this study was to investigate the effect of modeling assumptions on deformation demand estimates of nonlinear static and dynamic analysis. This has been achieved through nonlinear static and dynamic analyses of a four-story reinforced concrete moment resisting frame using different model configurations. As a result of the analyses conducted, the following conclusions can be drawn:

- Use of displacement-based elements in nonlinear static analysis requires a fine mesh for a reliable capacity curve. Specifically, the base shear capacity of the structure can be significantly overestimated if less than 18 elements per member is used.
- Due to this requirement for a finer mesh, models created using displacement-based are computationally much more expensive compared to the models that use force-based elements.
- The modeling assumptions such as the number of integration points for forced-based element and the plastic hinge length for beam-with-hinges elements can have a significant effect on displacement demands such as interstory and roof drift ratios.
- The most significant impact of modeling assumptions have been observed for ductility estimates. For a given roof drift ratio, the ductility estimates can vary significantly from one model to another.
- The curvature estimates at the bottom of the ground story column from a displacement-based model with 24 elements per member are much higher compared to the other models. This is because, as the distance between the two element get smaller with finer mesh, very high curvatures at the exterior section can be required to achive the same roof displacement compared to other models with coarser mesh.

- Considering that a fine mesh is required in order to achieve a reliable capacity curve using displacement-based elements and the high curvature estimates for the same fine mesh, caution should be exercised when using this type of elements for nonlinear analysis.

- Force-based elements can also be susceptible to very high curvature estimates when a high number of integration points is chosen. To avoid this, the number of integration points has to be chosen carefully. The recommendation of using four to six IPs by Neuenhofer and Filippou [9] seems to provide satisfactory results at both global and local levels.

- The different types of elements available to an analyst, be it displacement-based, force-based or beam-with-hinges elements, have each their benefits as well as limitations and potential pitfalls. The different results show that an analyst must be able to assess what kind of phenomena are occurring in the numerical model in order to assess the objectivity of the results.

- More research that include a variety of structures and evaluate the sensitivity of more engineering demand parameters such as plastic rotations and hysteretic energy demands is necessary to enable the practitioners and researchers make informed decisions while developing nonlinear models.

References

[1] C. Zeris, D. Vamvatsikos, and P. Giannitsas. “Impact of Fe Modeling in the Seismic Performance Prediction of Existing Rc Buildings.” In: *ECCOMAS Thematic Conference on Computational Methods in Structural Dynamics and Earthquake Engineering*. Rethymno, 2007.

[2] M. H. Scott and G. L. Fenves. “Plastic Hinge Integration Methods for Force-Based Beam–Column Elements.” In: *Journal of Structural Engineering* 132.2 (2006), pp. 244–252.

[3] S. K. Kunnath and E. Erduran. *Pushover procedures for seismic assessment of buildings issues, limitations and future needs*. Tech. rep. Lisbon, Portugal, 2008, pp. 31–43.

[4] J. B. Mander. “Seismic Design of Bridge Piers.” Doctoral dissertation. University of Canterbury, 1983.

[5] A. Calabrese, J. P. Almeida, and R. Pinho. “Numerical Issues in Distributed Inelasticity Modeling of RC Frame Elements for Seismic Analysis.” In: *Journal of Earthquake Engineering* 14.sup1 (2010), pp. 38–68.

[6] Standard Norge. *NS-EN 1998-1 - Eurocode 8: Design of structures for earthquake resistance. Part 1: General rules, seismic actions and rules for buildings*. Lysaker, 2014.

[7] N. Øystad-Larsen, E. Erduran, and A. M. Kaynia. “Evaluation of effect of confinement on the collapse probability of reinforced concrete frames subjected to earthquakes.” In: *Procedia Engineering* 199 (2017), pp. 784–789.

[8] E. Erduran. “Evaluation of Rayleigh damping and its influence on engineering demand parameter estimates.” In: *Earthquake Engineering & Structural Dynamics* 41.14 (2012), pp. 1905–1919.

[9] A. Neuenhofer and F. C. Filippou. “Evaluation of Nonlinear Frame Finite-Element Models.” In: *Journal of Structural Engineering* 123.7 (1997), pp. 958–966.

[10] A. Neuenhofer and F. C. Filippou. “Geometrically Nonlinear Flexibility-Based Frame Finite Element.” In: *Journal of Structural Engineering* 124.6 (1998), pp. 704–711.

[11] E. Spacone, F. C. Filippou, and Fabio F. Taucer. “Fiber beam-column model for non-linear analysis of R/C frames: Part II. Applications.” In: *Earthquake Engineering and Structural Dynamics* 25.7 (1996), pp. 727–742.

[12] OpenSees wiki. *Beam With Hinges Element*. 2006. URL: http://opensees.berkeley.edu/wiki/index.php/Beam_With_Hinges_Element (Cited 03/13/2018).

[13] T. Paulay and M. Priestley. *Seismic Design of Reinforced Concrete and Masonry Buildings*. 1st ed. New York: John Wiley and Sons, 1992.

[14] J. B. Mander, M. J. N. Priestley, and R Park. “Theoretical Stress-Strain Model for Confined Concrete.” In: *Journal of Structural Engineering* 114.8 (1988), pp. 1804–1826.

[15] S. Popovics. “A numerical approach to the complete stress-strain curve of concrete.” In: *Cement and Concrete Research* 3.5 (1973), pp. 583–599.

[16] D.-C. Feng and X.-D. Ren. “Enriched Force-Based Frame Element with Evolutionary Plastic Hinge.” In: *Journal of Structural Engineering* 143.10 (2017).

[17] J. Coleman and E. Spacone. “Localization Issues in Force-Based Frame Elements.” In: *Journal of Structural Engineering* 127.11 (2001), pp. 1257–1265.

EURODYN 2020
XI International Conference on Structural Dynamics
M. Papadrakakis, M. Fragiadakis, C. Papadimitriou (eds.)
Athens, Greece, 23–26 November 2020

EFFECT OF THE JOINT STRENGTH ON THE PERFORMANCE OF ORDINARY MOMENT-RESISTING FRAMES UNDER A PROGRESSIVE COLLAPSE SITUATION

Mohammad Ali Mahdavipour[1], Dmitry Vysochinskiy[1]

[1] Department of Engineering Sciences, University of Agder
Jon Lilletuns vei 9, 4879 Grimstad, Norway
e-mail: {ali.mahdavipour, dmitry.vysochinskiy} @uia.no

Keywords: Progressive collapse, Panelzone, Column removal, Ductile fracture.

Abstract. *In standard design procedures of steel structures, buildings are usually designed for gravity and seismic load rather than a progressive collapse situation. When a structure is located in a low seismic zone, the codes have dictated fewer requirements regarding the beam-to-column strength ratio and the panelzone strength. In this study, a frame subassembly from an 8-story ordinary steel moment-resisting structure with different strength of exterior joints was investigated by numerical models under a column removal situation. The results revealed that although the beam-to-column strength ratio and the panelzone strength are generally less critical parameters in the seismic design of ordinary moment-resisting frames, they can have a notable effect on the fracture pattern and the capacity of the structure under a progressive collapse. Hence a special consideration about the joints strength is needed when a structure is aimed to be designed for a progressive collapse situation.*

1 INTRODUCTION

Progressive collapse is known as a rapid dynamic process that usually initiates from a local failure and propagates element-by-element to a global or partial collapse of the structure [1-4]. When a column is removed within a story of a steel structure, several sequential mechanisms act against the unbalanced vertical load. At very early stages, the beams and connections are under shear actions. In a subsequent stage as vertical displacement increases, the flexural moment at the beams becomes the dominant resisting mechanism in the frame. Finally, if the connections are ductile enough to undergo large deformations and adapt to a new configuration, the catenary action will be activated as the last resisting mechanism [1-3]. Since catenary action plays the main role in the frame resistance in progressive collapse, enough ductility of steel joints is required to develop catenary forces in the beams; otherwise, the premature global collapse of a multi-story steel structure might occur.

On the other hand, the standard design procedures of steel structures have been developed mostly for other dynamic loads like seismic load rather than a progressive collapse situation. Although the design methodology for seismic load and the progressive collapse is different, the seismic details in the steel structures would influence the performance of the connections and structures under a progressive collapse situation.

Two critical parameters of the seismic design of moment-resisting frames are the beam-to-column strength ratio and the panelzone strength. The codes [5, 6] have determined a maximum level of beam-to-column strength ratio to prevent plastic hinge formation in the columns and reduce the potential of the column-sway collapse. This limit is not obligatory for low-dissipative structures (ordinary moment frames) that are usually designed in a low-seismic zone [5, 6].

So far, the progressive collapse of steel structures has been investigated in many experimental and numerical studies [3, 7-16]; however, there are a few research studies to focus on the effect of the beam-to-column strength ratio and the panelzone strength, especially in ordinary moment frames that the strong-column-weak-beam criterion is usually neglected.

Kim and Kim [17] studied moment-resisting structures with both weak and strong panelzones by using macro-scale numerical models. The results of the nonlinear dynamic analyses showed that the influence of panelzone is dependent on the location of the removed column. The panelzone deformation could be notable if an exterior joint is engaged in the progressive collapse mechanism, while when all joints are interior, the effect of the panelzone deformation on the performance of the frame is not significant. For structures designed for high seismic load, it was also indicated that the panelzone consideration had little effect on the overall performance of the structure. In contrast, the performance of low-rise structures designed only for gravity loads could significantly be affected by the deformation of the panelzones, especially at the exterior bays. It was also reported that excessive panelzone distortion decreased the ductility demand of the beams in some cases.

In a similar study, Kordbagh and Mohammadi [18] investigated special moment-resisting frames under corner and middle column removal scenarios. The results revealed that considering panelzone in the structure with I-section columns notably increased the maximum and permanent vertical displacement of the frame, especially when the removed column was an exterior one. As a general conclusion, the panelzone effect must be considered for progressive collapse evaluation of moment-resisting structures if the panelzones were designed only for minimum requirements recommended by building codes.

Most of the previous studies used macro-level models to evaluate the effect of the beam-to-column strength ratio and the panelzone strength. Such models are not able to provide details about other level phenomena like the joints fracture mode and local plastic deformations.

2 OBJECTIVE AND SCOPE

In this paper, a frame subassembly from an exterior bay of an 8-story moment-resisting structure located in a low-seismic zone was studied under a column removal situation. In such structures, the beam-to-column strength ratio limit is usually ignored due to low seismic hazard. Therefore, two configurations of the selected subassembly with different beam-to-column strength ratios (and different panelzone strength) were investigated by nonlinear finite element simulations. A calibrated plasticity model in conjunction with a ductile damage initiation criterion was used to predict the performance of the subassemblies. These two subassemblies were compared in terms of the capacity and the pattern of ductile fracture.

3 DESCRIPTION OF THE FRAME SUBASSEMBLIES

An 8-story building with a steel moment-resisting system designed for a low-seismic area (e.g., Norway) with 0.1g design ground acceleration was selected as a case study. In terms of geometry, the structure was considered with four equal bays of 5 m (see Fig. 1(a)). Also, each story was assumed to be 3m in height. Besides seismic loads, the structure was designed for 30 kN/m and 12 kN/m uniformly distributed dead and live loads, respectively. The frame was designed according to EC8 [6] for a low ductility class with a behavior factor (q) equal to 2. In this ductility class controlling the strong-column-weak-beam criterion is not obligatory. It is worth mentioning that in the design process of this frame, strength criteria were dominant in the design of the sections, and the size of the beams was constant over the height of the building. All elements were selected from S355J2 structural steel with 355 MPa nominal yield strength. Welded Unreinforced Flange-Welded web (WUF-W) connections described in Fig. 1(c) were employed as the moment-resisting connections to resist lateral seismic loads. The weld access holes with the geometry adapted from AWS D1.8, 2016 [19] was implemented in the web of the beams to provide enough space for the flange Complete Joint Penetration welds (CJPs).

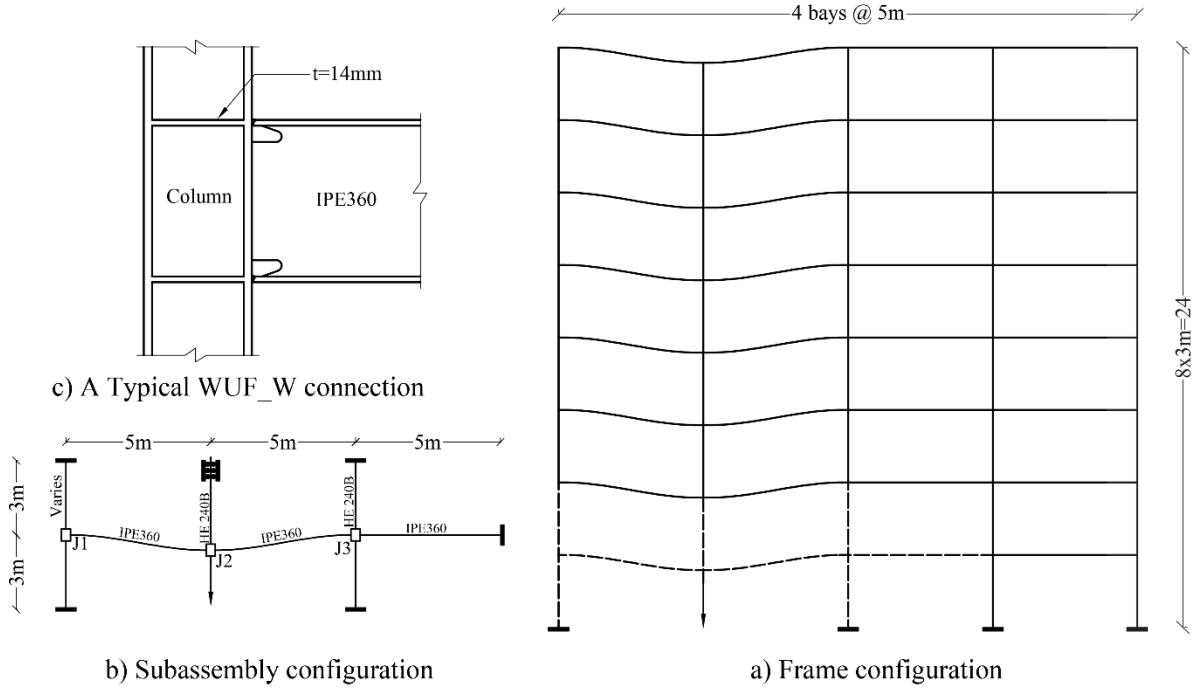

Figure 1: Configuration of a) the studied 8-story moment-resisting frame b) the subassembly c) Welded Unreinforced Flange-Welded web (WUF-W) connections.

Since analyzing the whole of the structure at the micro-level is challenging in terms of computational time and effort, a subassembly of the frame located at the first story as shown in Fig.1(b) was chosen for the finite element analyses. As it is apparent in this figure, this subassembly included three joints (J1, J2, and J3) connected by beams and columns with boundary conditions applied at the interface points between the subassembly and the rest of the frame. This subassembly was selected because the asymmetric strength of the joint J1 and J3 can also provide more detailed information regarding the effects of the beam-to-column joint strength. The previous studies also indicated that in this scenario, the panelzones have the most influence [17].

All design sections were the same in two subassemblies except the left column cross section that varies between HE180B and HE240B to study the effect of the beam-to-column strength ratio and the panelzone strength of the exterior joint. It should be noted that Subassembly-1 is from the original design of the frame that HE180B section was adequate as the left column for applied loads. On the other hand, in Subassembly-2, HE240B as the left column is a conservative design compared to the original frame.

4 NUMERICAL MODELS

4.1 Material model

Ductile fracture is known as a continuous process in which nucleation, growth, and coalescence of microvoids in ductile metals lead to form a new free surface in the material. Based on the prior studies [20-24], ductile fracture initiation is a function of equivalent plastic strain, stress triaxiality, strain rate, and Lode angle; however, the later one is less important when the structure is under tension load (positive triaxiality) [24, 25]. So far, several fracture models have been developed and utilized for predicting and evaluating the ductile fracture in steel structures. Some of these models are more complicated to be implemented (e.g., the Gurson-Tvergaard-Needleman model has over ten parameters for a single material [26]). Some other models (e.g., Johnson-Cook [20] and Bai-Wierzbicki [25]) are more appropriate for engineering applications where the uniaxial test is a standard test.

In this study, a phenomenological ductile damage model for predicting the onset of ductile fracture [27, 28] was used to investigate the fracture pattern of the studied subassemblies. In this model, it is assumed that the equivalent plastic strain at the onset of damage (ε_D^{pl}), is a function of stress triaxiality and strain rate [27]:

$$\varepsilon_D^{pl}(\eta, \dot{\varepsilon}^{pl}) \tag{1}$$

Where $\eta = {}^{\sigma_m}/_{\sigma_{eq}}$ is the stress triaxiality, σ_m is hydrostatic pressure and σ_{eq} is Mises equivalent stress. $\dot{\varepsilon}^{pl}$ also denotes the strain rate. Based on this definition, the damage variable can be defined as follows [7]:

$$D = \int \frac{d\varepsilon^{pl}}{\varepsilon_D^{pl}(\eta, \dot{\varepsilon}^{pl})} \tag{2}$$

This damage variable is an incremental state variable that increases monotonically with plastic deformations (ε^{pl}) to reach D=1 which indicates the fracture initiation. To use this model, a fracture strain curve in the space of ε^{pl}-η is needed. This curve was obtained by performing uniaxial tests under different triaxiality states for steel grade S355J2, as shown in Fig. 2. The described ductile fracture criterion was used in conjunction with the Mises plasticity and a linear isotropic hardening rule as the material model. To calibrate the stress-strain behavior of the

S355J2 material, five round smooth samples were tested under the uniaxial tensile test. Fig.3 shows the geometry of the samples.

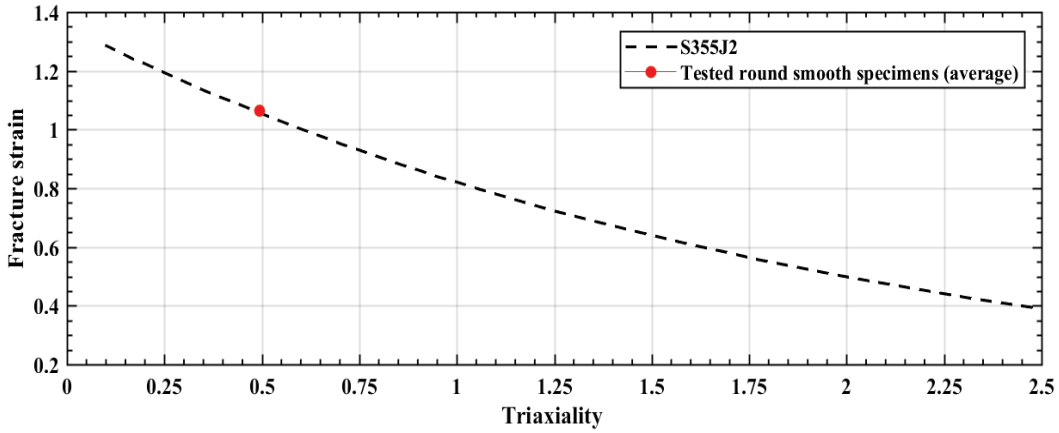

Figure 2: Fracture strain curve for S355J2 at different triaxiality.The curve adapted from [29].

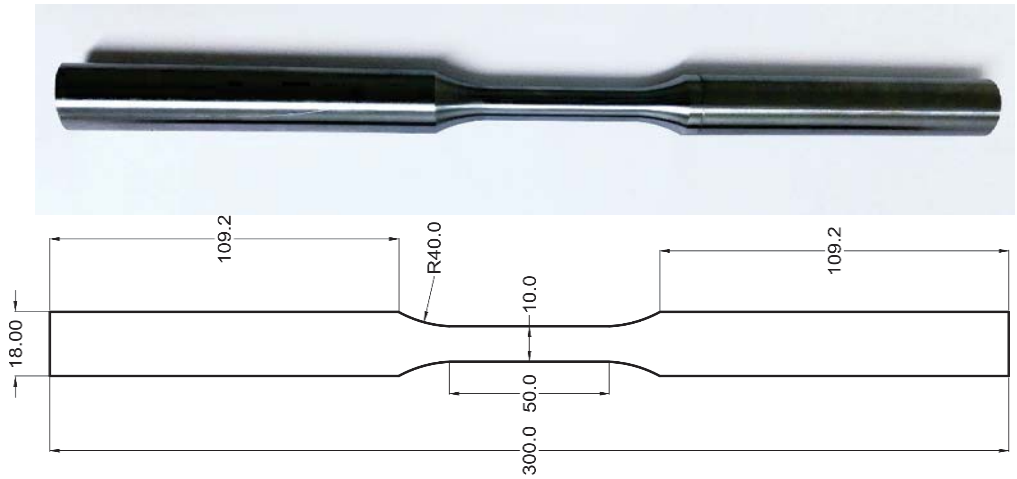

Figure 3: The geometry of round smooth tensile specimens.

All specimens were taken from a flat plate with 25mm thickness in the rolling direction. It should be noted that the effect of the strain rate was outside of the scope so that all tests were conducted at a strain rate of 0.002 mm/mm/s.

A 50mm axial extensometer and a digital image correlation system (DIC) were used to measure the elongation of the gage length. Using DIC can provide the fracture strain of each sample precisely. For example, as shown in Fig. 4, the fracture strain was 1.047 and 1.075 in sample MU1 and MU4, respectively. The engineering stress-strain curves for all tested samples are illustrated in Fig. 5.

To calibrate the ductile damage model an average fracture strain of all five samples ($\bar{\varepsilon}_f = 1.064$) was used. The point corresponding to the average fracture strain and triaxiality of the samples is plotted in Fig. 2 to validate the curve at least at one point. Since the stress triaxiality is varying after the necking of the samples, an average value was obtained ($\bar{\eta} = 0.49$) from the numerical simulation. Fig. 2 indicates a good agreement between the curve and experimental results for round smooth bar samples (plotted by a red circle).

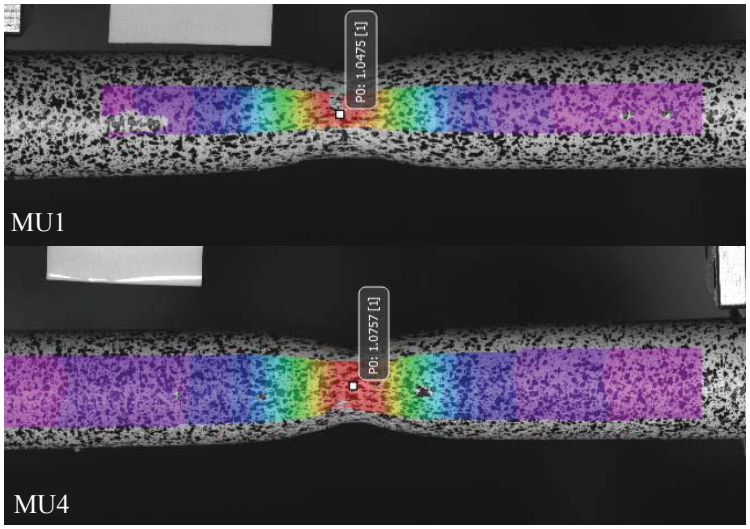

Figure 4: Fracture strain of samples MU1 and MU4 extracted from DIC.

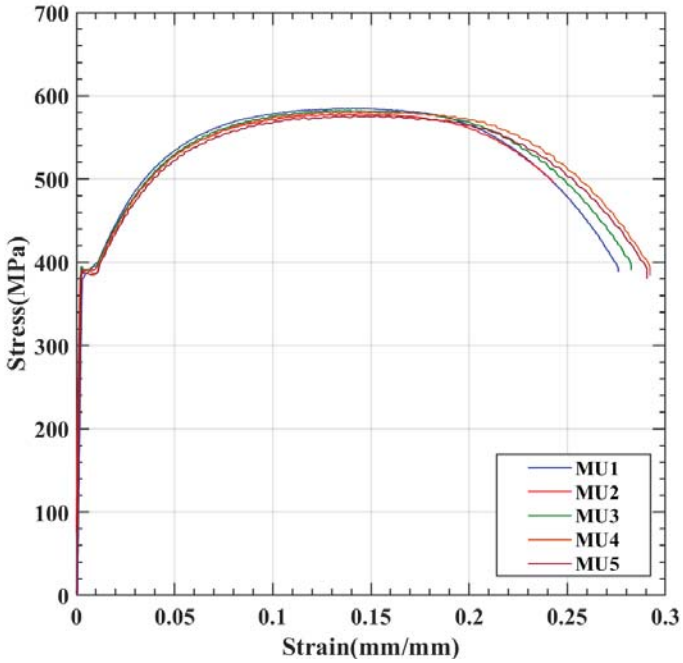

Figure 5: Engineering stress-strain curves for tested round smooth bar samples.

To use the test data in the material plasticity model, true stress-strain curves are required. Before the necking that the uniaxial state is governed, the true strain and stress can be obtained as follows:

$$\varepsilon_t = \ln(\varepsilon_e + 1)$$
$$\sigma_t = (1 + \varepsilon_e)\sigma_e \tag{3}$$

Where ε_t and σ_t are true strain and stress respectively, while ε_e and σ_e denote engineering values.

After necking, these relations are invalid due to stress triaxiality and strain localization. Therefore, a linear transition was assumed between the ultimate and the fracture point. The fracture strain could be obtained by DIC; however, the equivalent true fracture stress also

should be calculated to consider the triaxial stress state. Bridgman proposed an approximate conversion from a triaxial stress state into an equivalent stress σ_{eff} by using the geometry of the samples as follows [30]:

$$\sigma_{eff} = \frac{\sigma_t}{(1 + \frac{4R}{D}) \times ln(1 + \frac{D}{4R})} \tag{4}$$

Where D is the diameter of the sample, and R is the radius of curvature at the fracture point. These two parameters can be measured at the fracture point by image processing (e.g., See Fig. 6 for sample MU1).

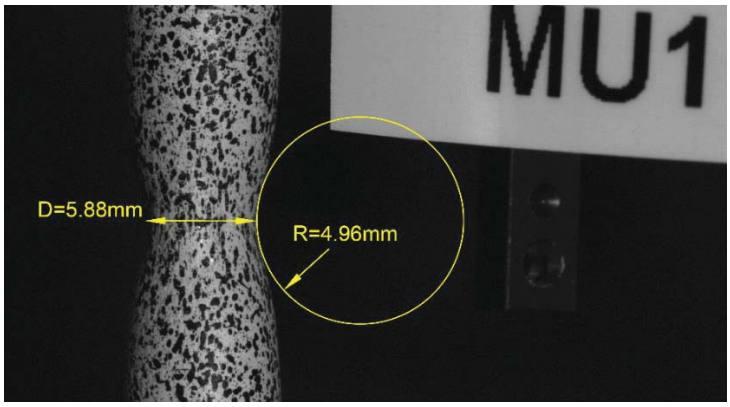

Figure 6: The diameter of the sample and the radius of curvature at the fracture point for sample MU1.

The calibrated material plasticity and damage model verified by numerical models. For instance, Fig. 7 compares the experimental and numerical force-displacement curves for the MU1 specimen. As this figure shows, there is a good agreement between numerical and experimental curves.

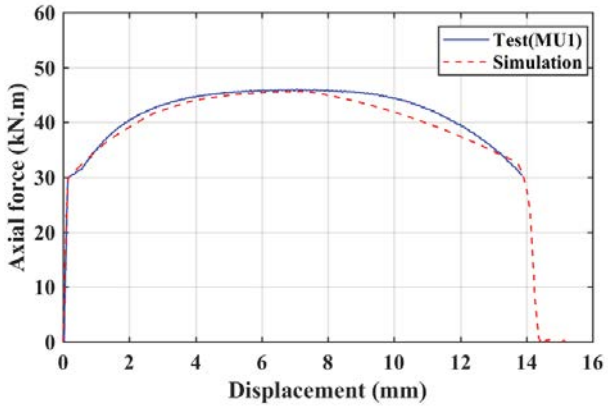

Figure 7: Ductile damage model verification for sample MU1.

4.2 Finite element models of the subassemblies

To predict the ductile fracture of two pre-described subassemblies, nonlinear finite element models were created in Abaqus/CAE. The explicit solver was employed due to its efficiency in conducting and converging extreme nonlinear behavior, particularly when a fracture and material separation are simulated. The simulations were implemented as a quasi-static to find the

capacity of the subassemblies and track the fracture behavior of the components under incremental displacement imposed at the point of the removed column.

For all nonlinear parts around the beam-to-column joints, the eight-node solid brick elements with reduced integration points (C3D8R) with a fine mesh were applied for the discretization of the models (see Fig. 8). These fine-meshed domains were assumed to have a length at least equal to the depth of beam or column that is known as the most probable place for plastic hinges formation. In these areas, the thickness of beams flanges and webs divided into at least four layers of element.

On the other hand, the middle parts of the beams and columns were modeled by a coarse mesh to reduce the time of analyses. To make an appropriate transition between the fine-meshed and the coarse-meshed areas a combination of C3D8R and six-node wedge element (C3D6) was used as shown in Fig. 8. It is worth mentioning that in numerical models, the properties of the welds were ignored.

An incremental displacement was applied to the removed column at joint J2, and the boundary conditions were defined as shown in Fig. 1(b). Also, it was supposed that beams flanges and columns at the joint level are laterally braced due to the slab system and secondary beams.

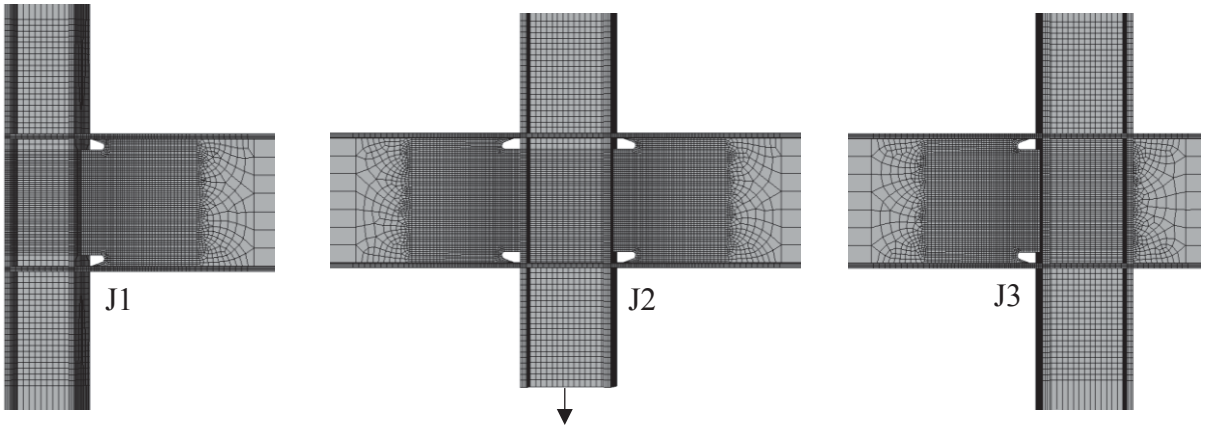

Figure 8: Finite element discretization of subassemblies with a fine mesh around the joints.

5 RESULTS

Fig. 9 compares the force-vertical displacement of two described subassemblies. Comparing of the subassemblies can be done in different aspects and parameters. In terms of yielding strength, both subassemblies provided approximately similar global yielding strength; however, due to the panelzone distortion in the Subassembly-1 with HE180B column, the panelzone in J1 was the first component that experienced plastic deformations, while the beam in this joint had a limited plastic strain even at the last step of the analysis. Moreover, this panelzone distortion imposed the maximum equivalent plastic strain (PEEQ) in the upper column of the joint J1. Forming plastic hinge and excessive lateral deformation of the column can increase the potential of post-yield buckling of the column under axial loads. In contrast, in the other subassembly (with HE240B column) the panelzone yielded after some plastification in the beam so that in the last step of the analysis, the maximum PEEQ occurred in the beam area while the upper column exhibited a low amount of plastic deformations.

Before any fracture initiation in the subassemblies, the Subassembly-2 with stronger joint J1 provided significantly more vertical strength. For example, in the vertical displacement of 877mm that is corresponding to the onset of fracture in the bottom flange of the joint J2 in the

Subassembly-2, the vertical strength of this subassembly was about 44% more than Subassembly-1.

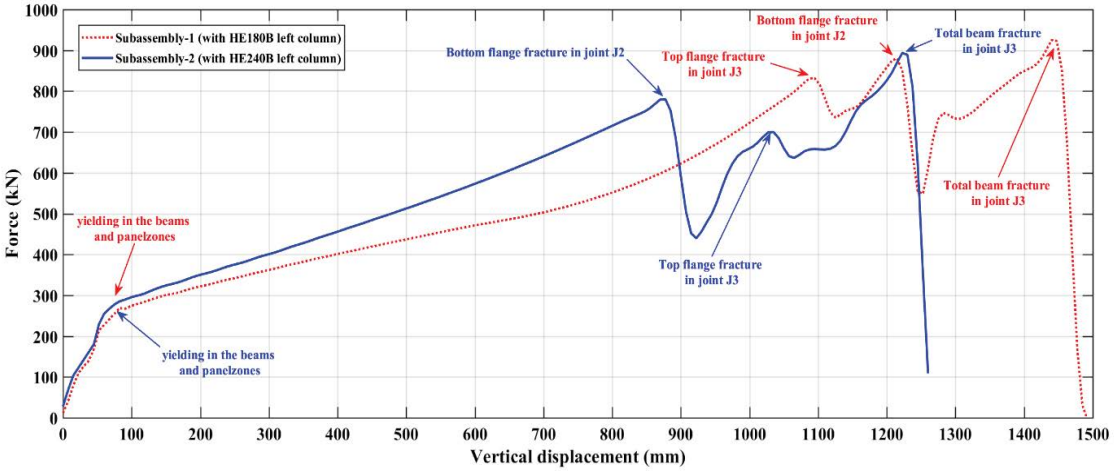

Figure 9: Vertical force-displacement curves for two studied frame subassemblies.

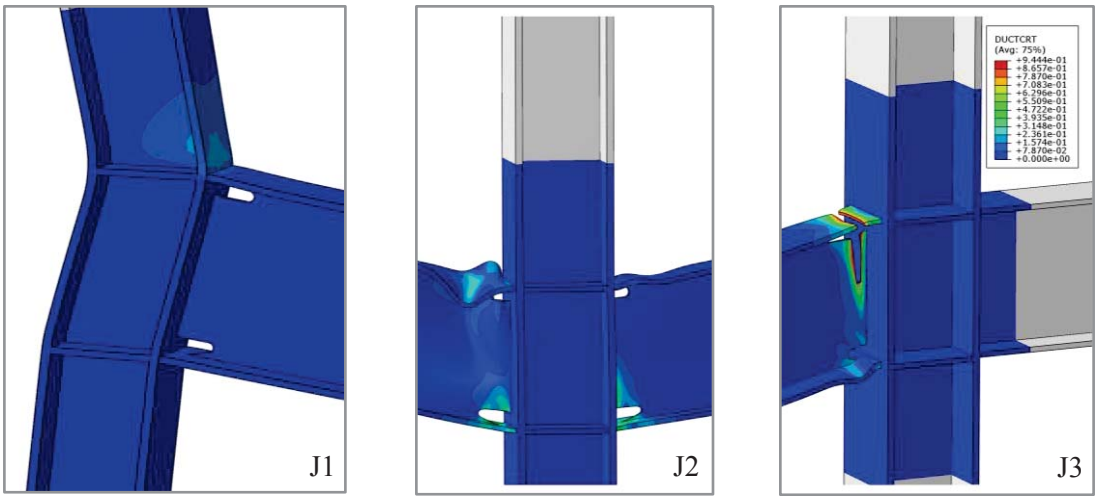

Figure 10: Distribution of ductile damage variable (D) at different joints in Subassembly-1 (ductile fracture initiated and developed firstly in J3)

In terms of ductile fracture initiation pattern, as shown in Fig.10 for the Subassembly-1, due to unbalanced stiffness and catenary action in the two sides beams, the fracture firstly initiated at the top flange of the beam in J3 joint and then developed to the web of the beam. When the right beam lost some amount of its stiffness, the fracture also initiated at the bottom flange in the other side beam in the joint J2.

On the other hand, the Subassembly-2 exhibited a vice-versa fracture initiation pattern. In other words, due to the stronger J1 joint, the stiffness and catenary action is more balanced than the Subassembly-1. As Fig.11 indicates the fracture initiated at the left beam of the joint J2. By developing the crack in the beam web and decreasing the beam stiffness, the J3 joint finally experienced the fracture at the top flange of the beam.

An interesting trend can be drawn from Fig.9 although the complete fracture of beams for both subassemblies happened in joint J3 and the cap vertical forces of both subassemblies are approximately similar, the Subassembly-1 exhibited larger vertical displacement than the Subassembly-2. This extra displacement caused by the excessive distortion of joint J1 (less stiffness) that delayed the activation of the catenary action in the beams. As a result, a weak panelzone

can significantly increase the vertical displacement demand of the frames and have to be considered in the frame analysis.

In addition, if the maximum vertical displacement demand obtained from the nonlinear dynamic analysis of the frame under similar column removal scenario was less than vertical displacement corresponding to ductile fracture initiation of subassemblies (in the capacity curves), using a simplified material model like a bilinear model can provide valid results in nonlinear dynamic analysis of the frame.

All these conclusions were made based on the assumption that welds material possesses higher toughness than base metal and the welds are without defects and significant stress and strain concentration.

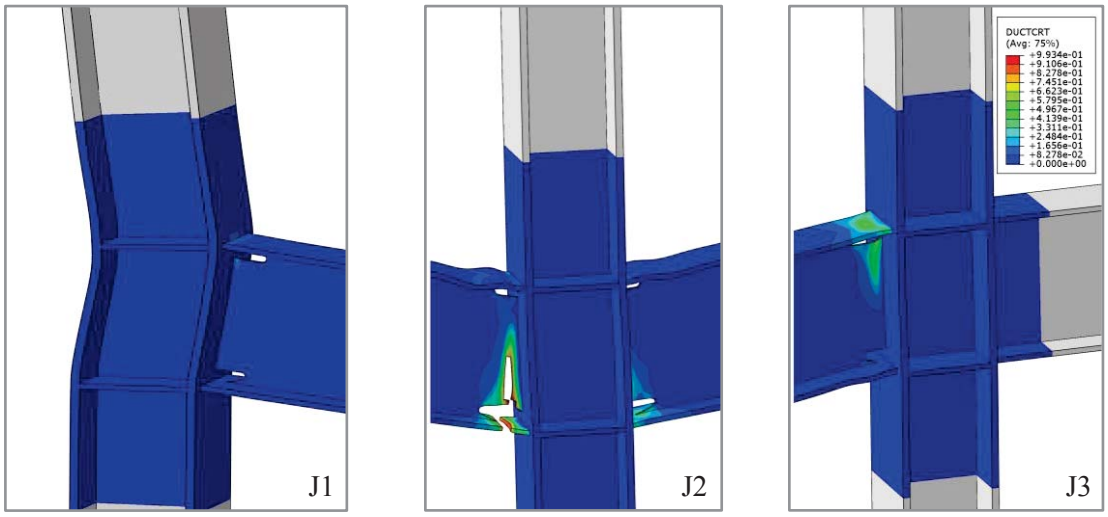

Figure 11: Distribution of ductile damage variable (D) at different joints in Subassembly-2 (ductile fracture initiated and developed firstly in J2)

6 CONCLUSIONS

A frame subassembly from an 8-story ordinary steel moment-resisting structure was studied for a column removal situation. The capacity and the fracture pattern of the subassembly obtained for different exterior joint strength. Based on the results from numerical models, the following conclusions can be drawn:

- The strength of the exterior joints in outer bays of such structures can significantly affect the fracture pattern and the capacity of the frame under a column removal situation.
- When an exterior weak joint was used, excessive plastic deformation of the panelzone led to an unbalanced state in catenary action so that the asymmetric force induced the fracture at the end of the right beam near to the interior joint. In contrast, when a stronger exterior joint was used, the rigidity of the panelzone led to make a balanced state in catenary action so that the fracture occurred at the left beam near to the middle joint that the column was removed.
- Before any fracture initiation, the vertical strength of the specimen with a stronger exterior joint showed about 44% more strength than the model with a weaker exterior joint; however, the maximum resisted vertical force for both models was approximately similar.

- In general, although the beam-to-column strength ratio and the panelzone strength usually are less critical in the standard procedure of design of moment-resisting structures in a low seismic zone, special consideration is needed when such structures are also designed for a progressive collapse situation.

REFERENCES

[1] Ellingwood BR, Smilowitz R, Dusenberry DO, Duthinh D, Lew HS, Carino NJ. Best practices for reducing the potential for progressive collapse in buildings. 2007.

[2] General Services Administration. Alternate path analysis & design guidelines for progressive collapse resistance. 2013.

[3] Sadek F, Main JA, Lew HS, Robert SD, Chiarito VP, El-Tawil S. An experimental and computational study of steel moment connections under a column removal scenario (NIST Technical Note 1669). National Institute of Standards and Technology; 2010.

[4] American Society of Civil Engineers. ASCE Standard ASCE/SEI 7-10: Minimum Design Loads and Associated Criteria for Buildings and Other Structures. Reston, Virginia2010.

[5] AISC. Seismic provisions for structural steel buildings (ANSI/AISC 341-10). Chicago(IL): American Institute of Steel Construction; 2010.

[6] European Committee for Standardization. Eurocode 8: Design of structures for earthquake resistance-part 1: general rules, seismic actions and rules for buildings (EN 1998-1). European Committee for Standardization,Brussels2004

[7] Botez M, Bredean L, Ioani A. Improving the accuracy of progressive collapse risk assessment: Efficiency and contribution of supplementary progressive collapse resisting mechanisms. Computers & Structures. 2016;174:54-65.

[8] Jiang B, Li G-Q, Usmani A. Progressive collapse mechanisms investigation of planar steel moment frames under localized fire. Journal of Constructional Steel Research. 2015;115:160-8.

[9] Jiang J, Li G-Q. Disproportionate collapse of 3D steel-framed structures exposed to various compartment fires. Journal of Constructional Steel Research. 2017;138:594-607.

[10] Khandelwal K, El-Tawil S. Collapse behavior of steel special moment resisting frame connections. Journal of Structural Engineering. 2007;133:646-55.

[11] Khandelwal K, El-Tawil S. Pushdown resistance as a measure of robustness in progressive collapse analysis. Engineering Structures. 2011;33:2653-61.

[12] Khandelwal K, El-Tawil S, Kunnath SK, Lew H. Macromodel-based simulation of progressive collapse: Steel frame structures. Journal of structural engineering. 2008;134:1070-8.

[13] Kim T, Kim J. Collapse analysis of steel moment frames with various seismic connections. Journal of Constructional Steel Research. 2009;65:1316-22.

[14] Rahnavard R, Fard FFZ, Hosseini A, Suleiman M. Nonlinear analysis on progressive collapse of tall steel composite buildings. Case studies in construction materials. 2018;8:359-79.

[15] Li L, Wang W, Teh LH, Chen Y. Effects of span-to-depth ratios on moment connection damage evolution under catenary action. Journal of Constructional Steel Research. 2017;139:18-29.

[16] Li L, Wang W, Chen Y, Lu Y. Experimental investigation of beam-to-tubular column moment connections under column removal scenario. Journal of Constructional Steel Research. 2013;88:244-55.

[17] Kim T, Kim J. Progressive collapse-resisting capacity of steel moment frames considering panel zone deformation. Advances in Structural Engineering. 2009;12:231-40.

[18] Kordbagh B, Mohammadi M. Influence of panel zone on progressive collapse resistance of steel structures. Journal of Performance of Constructed Facilities. 2018;32:04018014.

[19] American Welding Society (AWS) D1 Committee on Structural Welding. Structural welding code-seismic supplement (AWS D1.8/D1.8M:2016). MA: American Welding Society; 2016.

[20] Hancock J, Mackenzie A. On the mechanisms of ductile failure in high-strength steels subjected to multi-axial stress-states. Journal of the Mechanics and Physics of Solids. 1976;24:147-60.

[21] Johnson GR, Cook WH. Fracture characteristics of three metals subjected to various strains, strain rates, temperatures and pressures. Engineering fracture mechanics. 1985;21:31-48.

[22] McClintock FA. A criterion for ductile fracture by the growth of holes. Journal of applied mechanics. 1968;35:363-71.

[23] Rice JR, Tracey DM. On the ductile enlargement of voids in triaxial stress fields. Journal of the Mechanics and Physics of Solids. 1969;17:201-17.

[24] Bao Y, Wierzbicki T. On fracture locus in the equivalent strain and stress triaxiality space. International Journal of Mechanical Sciences. 2004;46:81-98.

[25] Bai Y, Wierzbicki T. A new model of metal plasticity and fracture with pressure and Lode dependence. International journal of plasticity. 2008;24:1071-96.

[26] Jia L-J, Ge H. Ultra-Low Cycle Fatigue Failure of Metal Structures Under Strong Earthquakes: Springer; 2018.

[27] Dassault Systèmes. Abaqus analysis user's manual. Simulia Corp. Providence, RI, USA2013.

[28] Hooputra H, Gese H, Dell H, Werner H. A comprehensive failure model for crashworthiness simulation of aluminium extrusions. International Journal of Crashworthiness. 2004;9:449-64.

[29] Hradil P, Talja A. Ductility limits of high strength steels. Research report VTT; 2016.

[30] Öchsner A. Continuum Damage and Fracture Mechanics: Springer; 2016.

EURODYN 2020
XI International Conference on Structural Dynamics
M. Papadrakakis, M. Fragiadakis, C. Papadimitriou (eds.)
Athens, Greece, 23–26 November 2020

NUMERICAL SIMULATIONS OF UNBURIED HP/HT SUBSEA PIPELINES SUBJECTED TO SEISMIC SCENARIOS

Daniele Mina[1], Davide Forcellini[2] and Hassan Karampour[3]

[1] Griffith University
Engineering building (G09), Engineering Drive, Southport QLD 4222, Australia
e-mail: minad@live.it

[2] University of Auckland
Engineering building 20 Symonds Street, Auckland 1010, New Zealand
e-mail: dfor295@aucklanduni.ac.nz

[3] Griffith University
Engineering building (G09), Engineering Drive, Southport QLD 4222, Australia
e-mail: h.karampour@griffith.edu.au

Keywords: numerical simulations, lateral buckling, seismic scenarios, HP/HT subsea pipelines

Abstract. *Vulnerability of subsea high pressure/high temperature (HP/HT) pipelines to seismic actions is studied numerically. This study focuses on the response of an unburied pipeline, laid on the seabed and resting on a sleeper. Two different scenarios are considered: (1) earthquake imposed on a laterally buckled pipeline and (2) earthquake imposed at temperatures lower than the lateral buckling temperature. The onset of yield and development of compressive local wrinkles in the wall thickness are calculated as the failure modes.*

1 INTRODUCTION

Resilience of pipelines during catastrophic events is a strategic issue that has a great impact on both society and the environment [1], being particularly vulnerable to high-intensity earthquakes as demonstrated during the 1989 Loma Prieta earthquake [2], the 1995 Kobe earthquake [3], and the Chi-Chi earthquake in 1999 [4]. Consequences of seismic events can potentially worsen in hazardous areas subjected to other risks, such as slope instability, landslide, soil liquefaction and fault movements [5]. International codes such as ALA [6] provide specifications for the seismic design of buried pipelines.

Previous studies investigated the seismic behaviour of offshore pipelines [7-9]. However, to the knowledge of the authors, the seismic studies of high pressure/high temperature (HP/HT) pipelines so far has been limited to buried and trenched pipelines [10]. A subsea HT/HP pipeline can undergo large bending stresses and strains due to lateral/upheaval buckling or free-spanning [11-14]. If the compressive strain in the pipe wall exceeds a certain limit, structural instability, in the form of local buckling/wrinkling may occur [15]. Periodic loading, such as flow-induced vibrations and earthquakes may cause fatigue cracks in this affected region [16]. In the current paper the seismic and thermal buckling responses of an unburied HP/HT subsea pipeline laid on an uneven seabed is investigated numerically. Structural responses of the pipeline under 17 recorded ground motions are considered in two scenarios:

(1) Scenario 1, where a controlled lateral buckle of the HP/HT pipeline is followed by the earthquake (EQ) input;
(2) Scenario 2, where the imposed EQ triggers the lateral buckle.

2 FINITE ELEMENT MODEL

Due to the lack of seafloor earthquake recordings, in the present study onshore ground motions are considered by neglecting the effects of the surrounding seawater layer on the pipeline response. Previous studies [17, 18] showed that the interaction between S-waves and P-waves, especially at resonant frequencies of propagating waves in the water, can mainly affect the vertical seafloor motion. Another contribution [19] considered a steel pipeline with outside diameter of OD = 350 mm, single span length of 16 meters and mechanical parameters (Table 1). By applying the commercial finite element analysis (FEA) package ABAQUS [20], in this section the same single span pipe (Figure 1) is considered and is placed on a soil domain characterized by two layers. The properties of the soil layers are shown in Table 2. The pipeline is modelled in ABAQUS using 2-node linear beam elements named PIPE31 [20]. The 16 m single span pipe is divided into 40 elements along its circumference and 100 elements in the longitudinal direction. The soil domain has surface dimensions of 48×48 m and a total depth of 40 meters. The adjacent spans are incorporated by simulating the boundary conditions with rotational springs (stiffness: 1.465×10^5 Nm/rad) and translational springs (stiffness: 1.1644×10^6 N/m) on either ends of the pipeline. The model presented in this paper was previously developed by [21] with the aim to apply a probability-based approach.

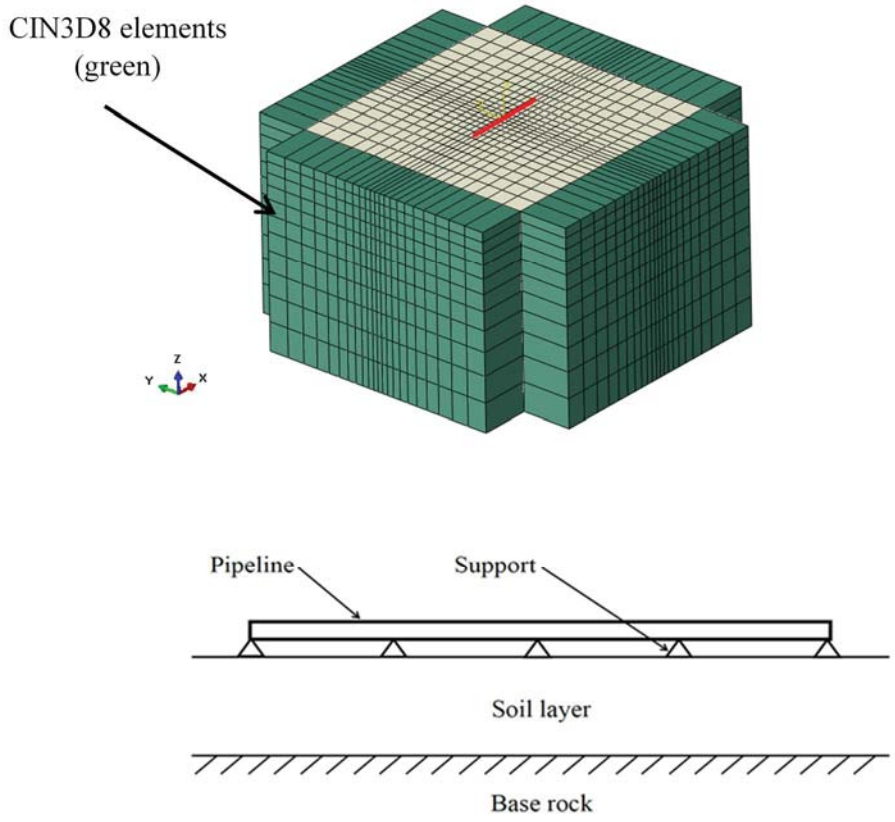

Figure 1: The FEA model, showing the pipeline and the soil and the numerical mesh used to validate the seismic analysis in comparison with the previous work [19].

Length, L (m)	16
Outer diameter, OD (mm)	350
Wall thickness, t (mm)	3
Mass density, ρ (kg/m^3)	7800
Young's modulus, E (MPa)	210000
Poisson's ratio, v	0.3
Damping ratio, ξ (%)	1.2

Table 1: Single span steel pipeline properties used in the seismic validation model.

Parameter	Soil layer	Base rock
Layer thickness, h (m)	30	10
Mass density, ρ (kg/m^3)	2000	3000
Shear modulus, G (MPa)	200	1800
Poisson's ratio, v	0.4	0.33
Damping ratio, ξ (%)	5	5

Table 2: Soil domain properties used in the seismic validation model.

Both the soil layer and the bedrock are discretised using three-dimensional C3D8R 8-node solid elements that allowed to model realistic seismic wave propagation at a depth far enough from the pipeline, so that the scaling effects can be neglected [22, 23]. Soil mesh size are chosen based on the Rayleigh wavelength parameters [24-27]. A variable mesh dimension is chosen, with soil elements becoming denser towards the centre and the surface of the soil domain (elements side length: 4 m on the lateral borders and 1 m at the centre of the model). The base boundary are constrained in order to simulate bedrock conditions (at 40 m depth from ground surface). CIN3D8 elements (Figure 1) constrain each node on one side of the lateral boundary of the soil domain in order to move the same as the analogous node on the opposite side (in both horizontal and vertical directions). Such conditions are used to simulate real wave propagation in a presumably infinite (or at least very large) soil domain, avoiding wave reflection disturbance and allowing the seismic energy to be removed from the site itself [28-32]. The damping ratios (Table 1 and Table 2) are added to the materials properties in the form of Rayleigh damping coefficients [33, 34]:

$$[C] = \alpha_d [M] + \beta_d [K] \tag{1}$$

where $[C]$ is the damping matrix, $[M]$ is the mass matrix and $[K]$ is the stiffness matrix, α_d and β_d are the mass-proportional and stiffness-proportional damping coefficients, respectively (Table 3).

Material	ξ (%)	α_d	β_d
Steel (pipeline)	1.2	0.14053	0.001018
Soil layer	5	0.58555	0.004240
Base rock	5	0.58555	0.004240

Table 3: Rayleigh damping parameters.

Based on an eigenvalue analysis, the pipe fundamental vibration frequency is found to be in the transverse direction and equal to 3.8992 Hz, which is close to the vibration frequency of 3.8556 Hz obtained by Bi and Hao [19]. The pipe-soil system frequencies, ω_1 and ω_3 are found to be equal to 1.7213 Hz and 2.0322 Hz, respectively. The mass-proportional and stiffness-proportional damping coefficients are calculated and represented in Table 3.

A seismic input motion, San Fernando earthquake with a PGA of 0.026*g*, is selected from the Pacific Earthquake Engineering Research Centre (PEER) [34] database and applied at the base of the bedrock along the transverse direction (*y*-direction shown in Figure 1). Time histories of maximum displacements obtained from the current and from Bi and Hao [19] models are shown in Figure 2. It should be noted that in Bi and Hao's work [19] the pipeline is modelled with 3D 20-node solid elements, whereas in the current work 2-node beam elements are used. Therefore, the negligible discrepancies in the amplitude observed between the two time histories in Figure 2 may be related to the different pipe element types. The results are in good agreement and show that the adopted beam model can predict the seismic wave propagation properly.

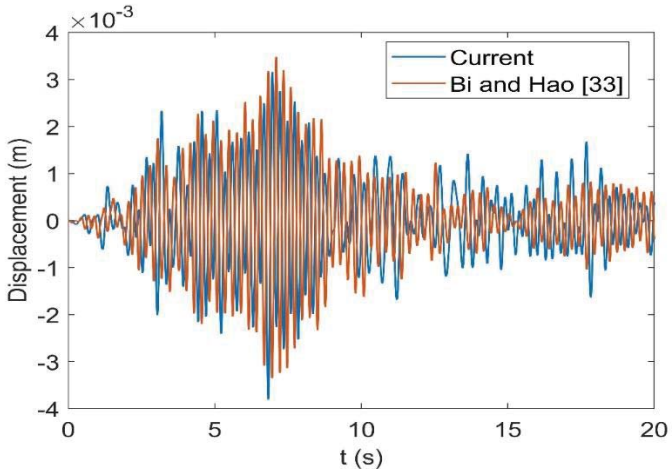

Figure 2: Seismic response of the pipeline in Figure 1, comparison between current results and Bi and Hao [19].

To study the interaction between thermal buckling and seismic disturbance, X65 steel pipeline with parameters represented in Table 4 is selected. The same pipeline is used in a thermal buckling study conducted by [36].

Length, L (m)	2000
Outer diameter, OD (mm)	254
Wall thickness, t (mm)	12.7
Thermal expansion coefficient, α (°C^{-1})	$1.01 \cdot 10^{-5}$
Young's modulus, E (MPa)	206000
Poisson's ratio, v	0.3
Lateral imperfection ratio, h_0/l_0	0.012
Submerged weight, q (N/m)	1500
Seabed friction coefficient, μ_1	0.5
Sleeper friction coefficient, μ_2	0.3
Sleeper height, h (m)	0.5

Table 4: Pipeline and seabed properties.

3 RESULTS

3.1 Thermal buckling

The pipeline with length of 2000 meters is laid on a rigid seabed (Figure 3 and Table 4), by using PIPE31 beam elements. A sleeper with height h = 500 mm (h/OD = 1.97), laid under the pipeline at its mid-length is used in order to control the lateral buckling [35] and is modelled with R3D4 shell elements (semicircular cross section). The seabed was meshed using R3D4 rigid shell elements [20]. Pipe element size is gradually decreased towards the midpoint area, where the length is set as half the diameter [15]. Both ends of the pipeline are pin-connected to the seabed using multiple point constraint (MPC) elements. The ends are far enough from the sleeper, to allow sufficient feed-in length into the buckle region. The sleeper is fixed to the seabed with a tie constraint. Mohr-Coulomb constitutive contact behaviour is used to model the interaction between the pipeline and the seabed and between the pipeline and the sleeper, with friction coefficients of μ_1 and μ_2, respectively (see Table 4). A large penalty stiffness coefficient is used to simulate hard contact definition between the pipeline and sleeper and soil [11]. To control the lateral buckling response, a sinusoidal initial imperfection was imposed on the pipeline at the point of contact with the sleeper with an amplitude to half wave-length ratio, h_0/l_0 = 0.012 and a schematic shape (Figure 3).

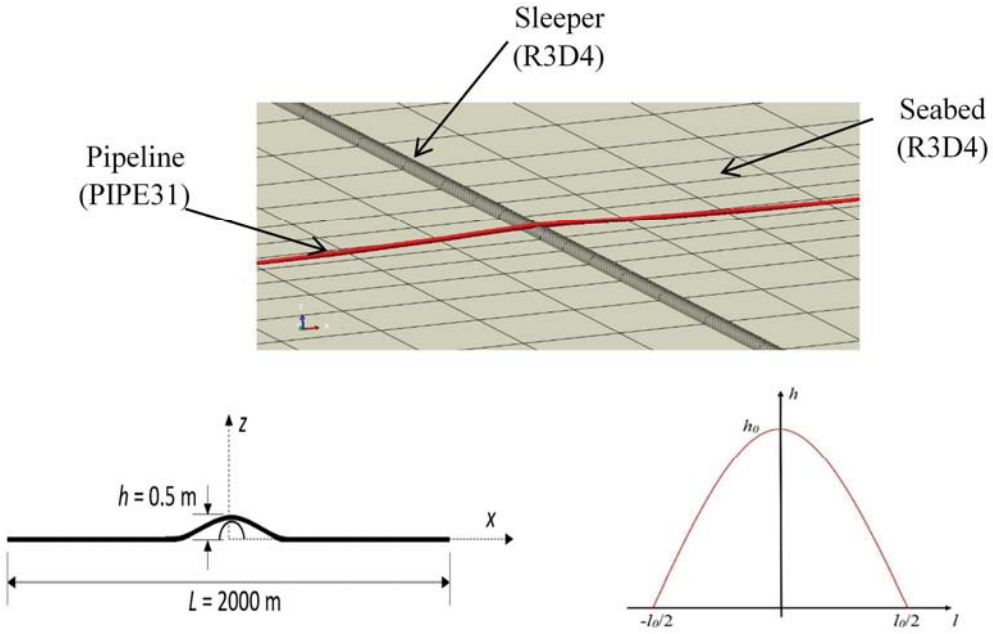

Figure 3: The pipeline and sleeper model used in the thermal buckling and seismic/thermal interaction models.

In order to obtain the thermal buckling response of the pipeline, the following load steps, in the mentioned sequence, are imposed to the pipeline, using a quasi-static dynamic analysis with geometric nonlinearity. (1) The self-weight is applied to the pipeline assuming a total buoyant weight of m = 153 kg/m (m included the submerged weight of the pipeline and its concrete coating). At the end of this load step, the pipeline deforms on the sleeper, with free-spans on either side of the sleeper and corresponding touchdown points [11, 36]. (2) An internal pressure of P_{int} = 12 MPa is applied to the pipeline, and (3) an increasing temperature change of ΔT is uniformly applied to the wall thickness. Due to the actions of the internal pressure and thermal

loading, the pipeline tends to expand. However, this expansion is balanced by the reaction of the soil, inducing axial forces in the wall thickness and causing a global lateral buckling in the pipeline [11, 15]. The maximum lateral buckle amplitude in the pipeline occurs at the contact point with the sleeper (Figure 4a). The temperature increased up to a critical value, after which the buckle amplitude monotonically upsurges with the corresponding increase in the temperature. The lateral buckle profiles at different temperatures are plotted in Figure 4b. The lateral buckle mode is shown to be similar to Hobb's mode 3 [37], as expected [11, 36]. In correspondence with the calculated (Figure 4a and 4b) critical temperature of the pipeline (T_{cr} = 26-30 °C), two scenarios are studied: scenario 1, post-buckle seismic input, and scenario 2 pre-buckle seismic input, by applying a total of 17 earthquake input motions from PEER database [35]. Input spectra of the selected 17 input motions are shown in Figures 5 and the characteristics of each input motion is outlined in Table 5.

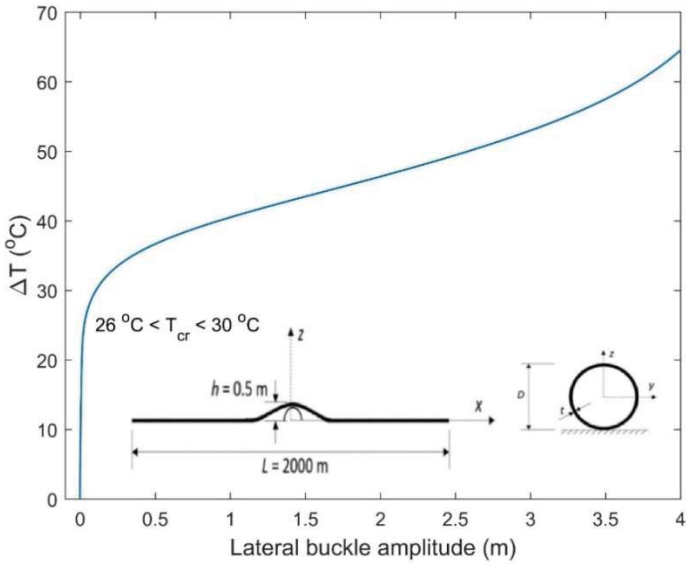

(a)

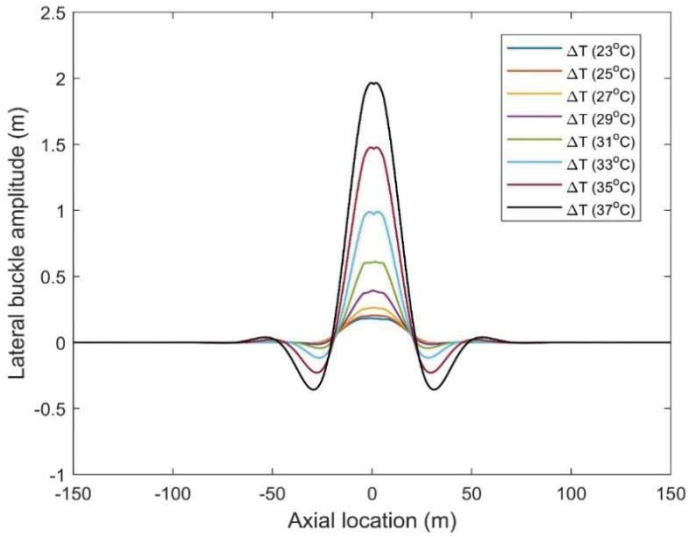

(b)

Figure 4: Lateral buckling response of the pipeline in Figure 3 with parameters in Table 4, showing, (a) temperature vs. the maximum buckle amplitude, (b) lateral buckle profile at different service temperatures.

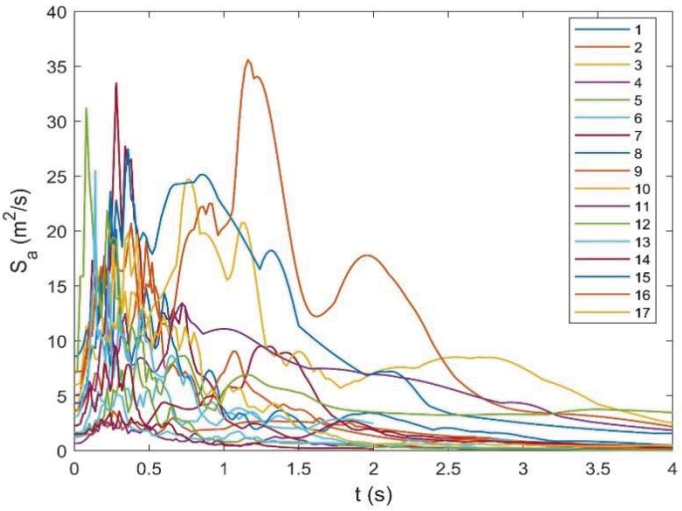

Figure 5: Seismic input spectra for the 17 EQ motions.

Site number - input motion (n.)	Site Code	PGA (m/s^2)	Duration (s)
1	A-ELC	1.24	40.0
2	A2E	1.66	40.0
3	CAP	5.01	40.0
4	CNP	3.53	25.0
5	H-PVB	3.68	40.0
6	SCS	6.00	40.0
7	B-ELC	0.66	40.0
8	H-C05	1.44	40.0
9	H-CAL	1.26	40.0
10	A-KOD	1.51	21.0
11	Northridge	8.57	15.0
12	Takatori	7.20	40.0
13	Llolleo	3.54	116.5
14	Erzincan	4.33	18.0
15	Lucerne Valley	7.12	48.2
16	Imperial Valley	3.09	22.0
17	Trinidad	2.28	21.4

Table 5: Characteristics of the selected seismic input motions.

3.2 Scenario 1: post-buckle seismic input

In addition to the self-weight (m = 153 kg/m) and internal pressure P_{int} = 12 MPa, the temperature in the pipeline is increased up to 31 °C (higher than the critical temperature). At this temperature, the pipeline has already buckled (see Figure 4b). Then, the seismic inputs are applied to the soil at a depth of 5 m below the seabed and in the y-direction (see Figure 3). The time histories of the lateral buckle amplitude at various stages of the loading are displayed in Figure 6. The lateral buckle profile and the crown stress distribution before and slightly after the application of the seismic input n.11 (Northridge) are shown in Figures 6b and 6c, respectively. It is worth noticing that the introduction of the seismic load significantly increases the buckle amplitude, and consequently the maximum stress at the crown of the buckled pipeline upsurges to a level slightly above the yield stress (448 MPa). The interaction buckle mode (solid line in Figure 6b) is similar to the thermal buckle mode (dashed line in Figure 6b).

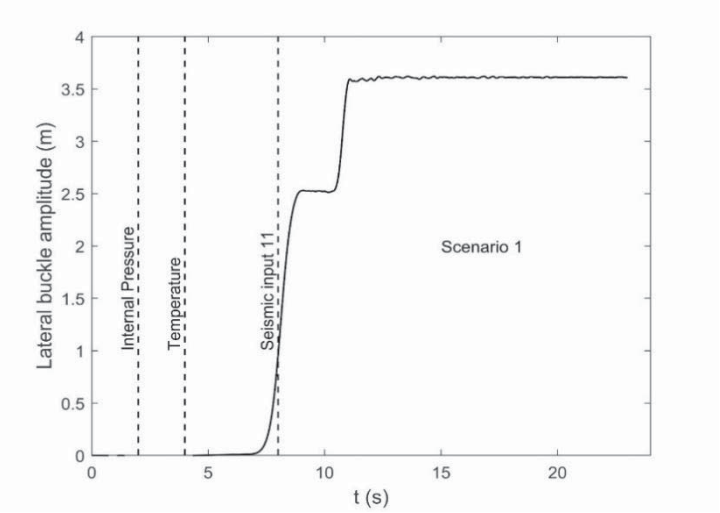

(a)

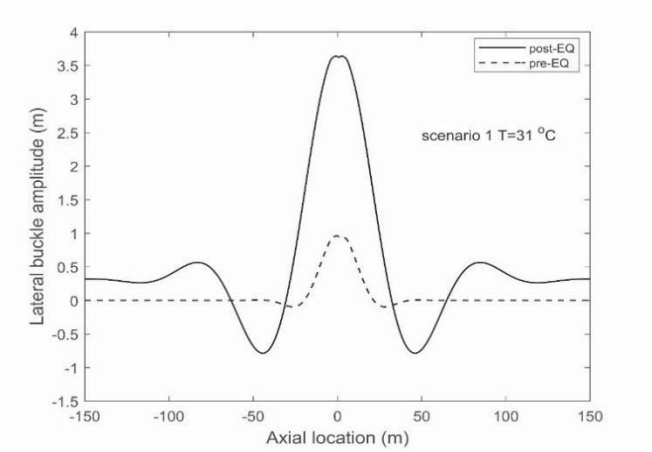

(b)

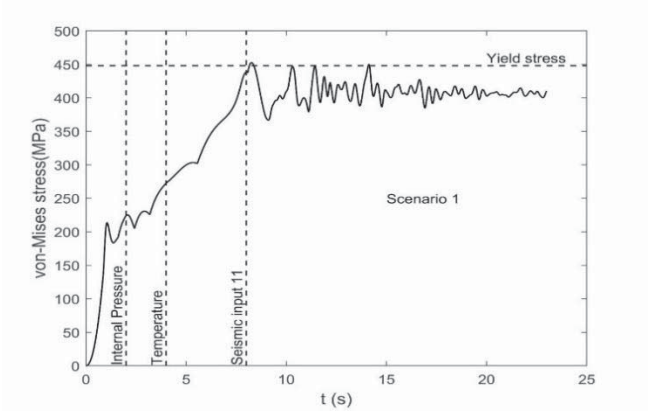

(c)

Figure 6: Scenario 1, (a) displacement time history, (b) the buckle profile, and (c) the von Mises stress time history in the buckle crown.

3.3 Scenario 2: pre-buckle seismic input

Following the application of the self-weight and the internal pressure, the temperature variation is kept at $\Delta T = 25$ °C (slightly below the critical temperature), and then the seismic input is applied. Results for the seismic input n.11 are shown in Figure 7, where $t = 0$ s corresponds to the onset of application of the seismic load. Due to the seismic action, the pipeline buckles with a maximum crown displacement of 3 m (Figure 7b). Several findings are considered. (1) Maximum displacement value is smaller than that calculated in scenario 1 (Figure 6b); (2) the buckle shape is symmetric and similar to the buckle shape under thermal loading only; (3) the maximum stress in the crown increased from 380 MPa to almost 440 MPa (Figure 7c), due to the combination of thermal and seismic actions. However, the maximum stress is still lower than the assumed yield stress (448 MPa).

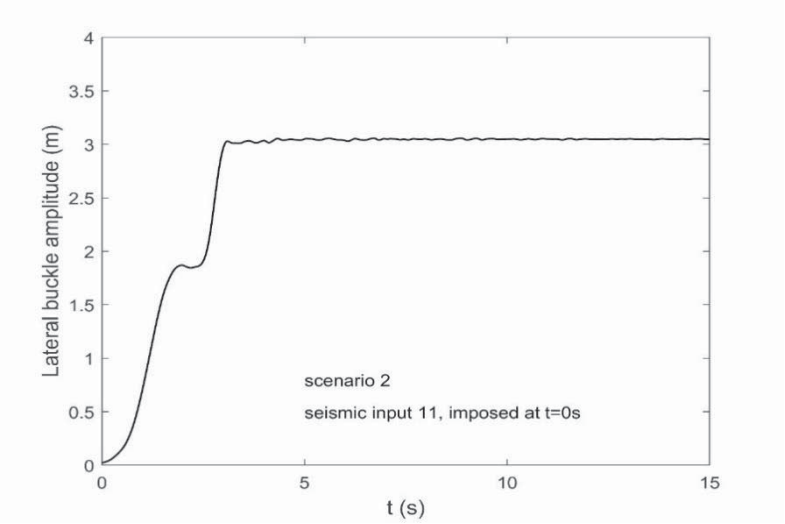

(a)

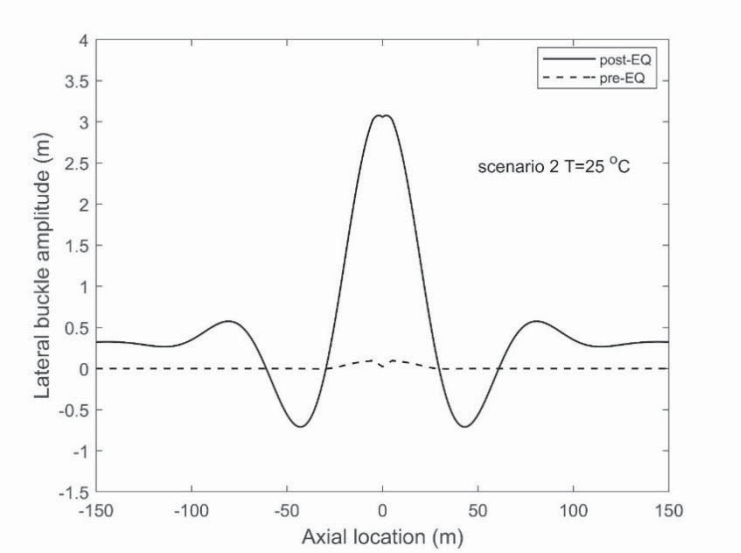

(b)

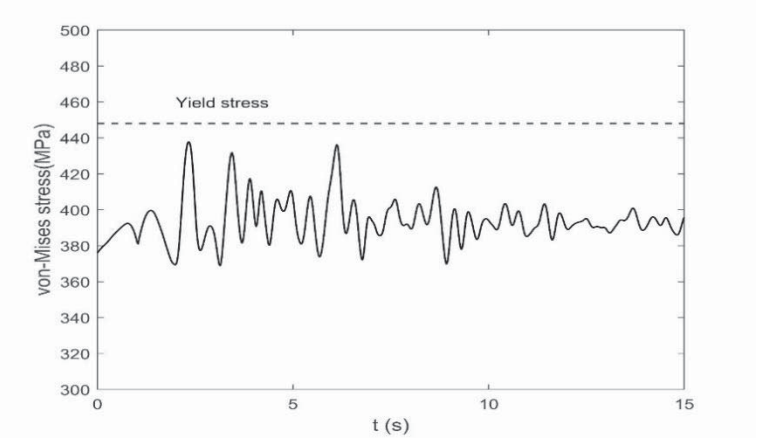

(c)

Figure 7: Scenario 2, (a) displacement time history, (b) the buckle profile, and (c) the von Mises stress time history in the buckle crown.

3.4 Bending response of the pipeline

It is worth noticing that even if the lateral buckling is not a failure mode by itself, yielding or rupture in the pipeline may occur when the bending stresses and local compressive strains exceed the ultimate values. In this regard, the bending response of the pipeline is assessed by modelling 1.27 m (5*D*) pipeline with 8-node linear brick elements (C3D8R) and by adopting isotropic bilinear material properties with yield stress of $\sigma_y = 448$ MPa and tangent modulus of $E_t = 0.01E$ (Table 4). Under symmetrical assumptions, half length of the pipe is modelled and a bending moment is applied at one end of the tube by applying a master/slave arrangement and by using MPC rigid elements (to restrain the ovalisation). The normalised moment-curvature response is shown in Figure 8, where moment is normalised to the plastic moment M_P, and curvature is normalised by the critical curvature k_c:

$$M_P = \sigma_y (D-t)^2 t \quad , \quad \kappa_c = \frac{t}{(D-t)^2} \tag{2}$$

At normalised moments $M/M_P > 0.9$, nonlinear material behaviour is observed, and is followed by a substantial increase in the curvature. The ultimate moment is reached at $1.08M_P$ (Figure 8a). Deformation and von Mises stress contours at selected stages of the curvature (I-IV) marked on the moment-curvature curve, are plotted in Figure 8b. At stage I, the von Mises stress in the pipe wall thickness reaches the yield stress. However, wrinkles in the compressive face (local buckle) start to appear at stage II. In stages III and IV, the compressive wrinkle progress substantially, and the cross section is significantly ovalised. The calculated critical strain in the pipe wall (ε_{cr}) at stage II (shown in Figure 8a) is $\varepsilon_{cr} = 1.576 \times 10^{-2}$ mm/mm, and it is about 1/4th of the well-known theoretical expression $\varepsilon_{cr} = 0.6\frac{2t}{D}$ as suggested in the previous experimental contribution [38] and recommendations of DNV [39].

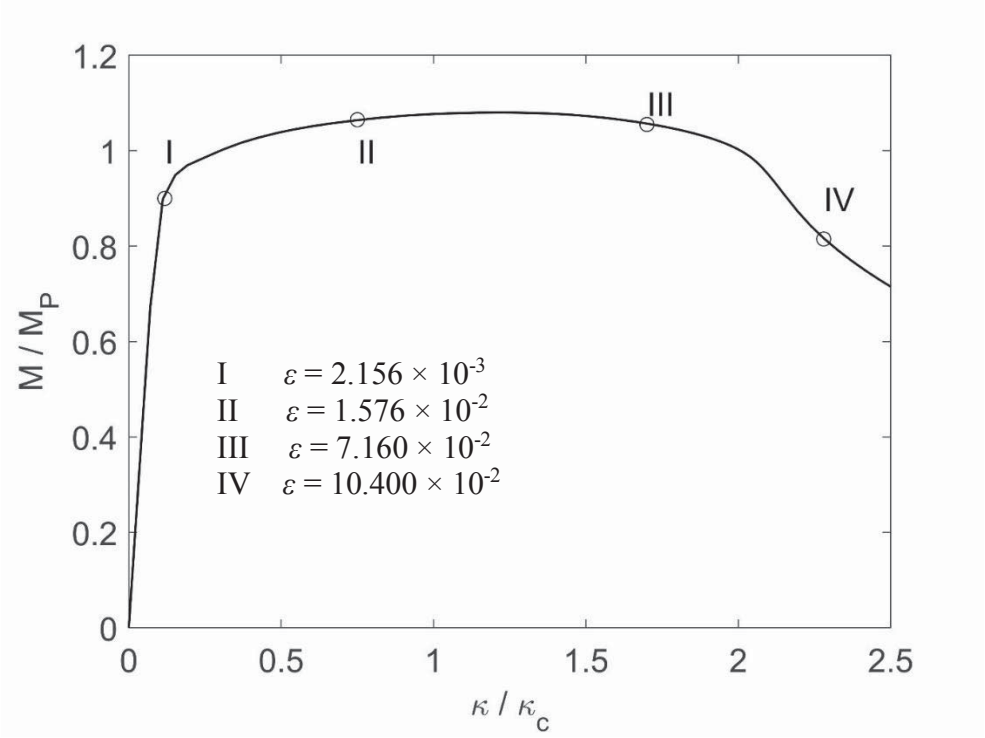

(a)

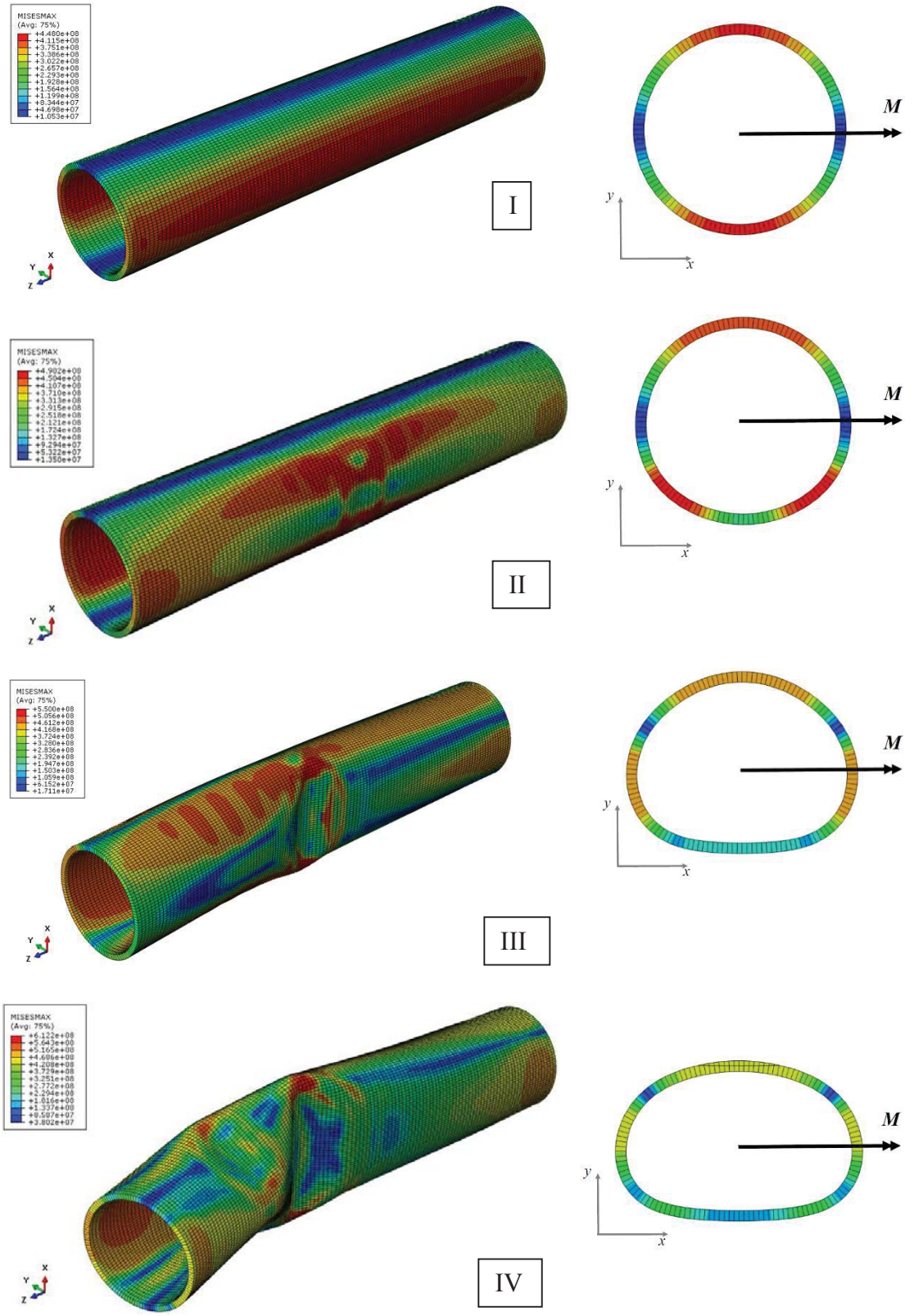

(b)

Figure 8: FEA pure bending response of the pipeline in Table 4, showing (a) the moment-curvature relationship and compressive strains, and (b) deformed shape and von Mises stress contours at selected stages of curvature.

4 CONCLUSIONS

A numerical model was proposed in order to study the interaction between earthquake and thermal buckling in a subsea pipeline. The thermal buckling response of the pipeline under action of buoyant self-weight, internal pressure and temperature variation from the inner fluid was analyzed. The interaction between seismic load and service loads (pressure and temperature) was studied using 17 earthquake inputs. The interaction study was conducted with two different scenarios: (1) the seismic input was imposed at a temperature of 31 °C (buckled pipeline) and (2) where the temperature was kept at 25 °C (unbuckled pipeline). Maximum stresses and compressive strains were compared. Future study will be conducted in order to assess analytical fragility curves.

REFERENCES

[1] Melissianos, V. E., Vamvatsikos, D., & Gantes, C. J. (2017). Performance-based assessment of protection measures for buried pipes at strike-slip fault crossings. Soil Dynamics and Earthquake Engineering, 101, 1-11.

[2] O'Rourke, T. D., Stewart, H. E., Gowdy, T. E., & Pease, J. W. (1991). Lifeline and geotechnical aspects of the 1989 Loma Prieta Earthquake.

[3] Lee, D. H., Kim, B. H., Lee, H., & Kong, J. S. (2009). Seismic behavior of a buried gas pipeline under earthquake excitations. Engineering structures, 31(5), 1011-1023.

[4] Hwang, H., Chiu, Y. H., Chen, W. Y., & Shih, B. J. (2004). Analysis of damage to steel gas pipelines caused by ground shaking effects during the Chi-Chi, Taiwan, earthquake. Earthquake spectra, 20(4), 1095-1110.

[5] Bai, Q., & Bai, Y. (2014). Subsea pipeline design, analysis, and installation. Gulf Professional Publishing.

[6] ALA (American Lifelines Alliance), (2001). Seismic Guidelines for Water Pipelines. Part 1- Guidelines. ASCE-FEMA, Washington, DC, USA.

[7] Bi, K., Hao, H., Li, C., & Li, H. (2017). Stochastic seismic response analysis of buried onshore and offshore pipelines. Soil Dynamics and Earthquake Engineering, 94, 60-65.

[8] Uckan, E., Akbas, B., Shen, J., Rou, W., Paolacci, F., & O'Rourke, M. (2015). A simplified analysis model for determining the seismic response of buried steel pipes at strike-slip fault crossings. Soil Dynamics and Earthquake Engineering, 75, 55-65.

[9] Vazouras, P., Dakoulas, P., & Karamanos, S. A. (2015). Pipe–soil interaction and pipeline performance under strike–slip fault movements. Soil Dynamics and Earthquake Engineering, 72, 48-65.

[10] Psyrras, N., Kwon, O., Gerasimidis, S., & Sextos, A. (2019). Can a buried gas pipeline experience local buckling during earthquake ground shaking?. Soil Dynamics and Earthquake Engineering, 116, 511-529.

[11] Karampour, H., Albermani, F., & Gross, J. (2013). On lateral and upheaval buckling of subsea pipelines. Engineering structures, 52, 317-330.

[12] White D, Cheuk C. Modelling the soil resistance on seabed pipelines during large cycles of lateral movement. Marine Structures. 2008;21:59-79.

[13] Zeinoddini, M., Parke, G. A. R., & Sadrossadat, S. M. (2011). Free-spanning submarine pipeline response to severe ground excitations: water-pipeline interactions. Journal of Pipeline Systems Engineering and Practice, 3(4), 135-149.

[14] Wang, Z., & van der Heijden, G. H. M. (2020). Snap behaviour in the upheaval buckling of subsea pipelines under topographic step imperfection. Marine Structures, 69, 102674.

[15] Karampour, H. (2018). Effect of proximity of imperfections on buckle interaction in deep subsea pipelines. Marine Structures, 59, 444-457.

[16] Xu, T., Lauridsen, B., & Bai, Y. (1999). Wave-induced fatigue of multi-span pipelines. Marine structures, 12(2), 83-106.

[17] Li, C., Hao, H., Li, H., & Bi, K. (2015). Theoretical modeling and numerical simulation of seismic motions at seafloor. Soil Dynamics and Earthquake Engineering, 77, 220-225.

[18] Boore, D. M., & Smith, C. E. (1999). Analysis of earthquake recordings obtained from the Seafloor Earthquake Measurement System (SEMS) instruments deployed off the coast of southern California. Bulletin of the Seismological Society of America, 89(1), 260-274.

[19] Bi, K., & Hao, H. (2016). Numerical simulation on the effectiveness of using viscoelastic materials to mitigate seismic induced vibrations of above-ground pipelines. Engineering Structures, 123, 1-14.

[20] ABAQUS, Simulia (2018), Analysis User Guide. Rhode Island, USA.

[21] Mina, D., Forcellini, D., & Karampour, H. (2020). Analytical fragility curves for assessment of the seismic vulnerability of HP/HT unburied subsea pipelines. Soil Dynamics and Earthquake Engineering, 137, 106308.

[22] Elgamal, A., Lu, J., & Forcellini, D. (2009). Mitigation of liquefaction-induced lateral deformation in a sloping stratum: Three-dimensional numerical simulation. Journal of geotechnical and geoenvironmental engineering, 135(11), 1672-1682.

[23] Forcellini, D., Gobbi, S., & Mina, D. (2016, September). Numerical simulations of ordinary buildings with soil-structure interaction. In VI international conference on structural engineering, mechanics and computation (SEMC). Capetown, South Africa (pp. 5-7).

[24] Forcellini D (2019) "Numerical simulations of liquefaction on an ordinary building during Italian (20 May 2012) earthquake" Bulletin of Earthquake Engineering https://doi.org/10.1007/s10518-019-00666-5.

[25] Forcellini, D (2020) "Soil- structure interaction analyses of shallow-founded structures on a potential-liquefiable soil deposit" Soil Dynamics and Earthquake Engineering 133 (2020) 106108.

[26] Forcellini D. (2020) "The role of the water level in the assessment of seismic vulnerability for the 23 November 1980 Irpinia-Basilicata earthquake", Geosciences 2020, 10, 229; doi:10.3390/geosciences10060229.

[27] Mina D., Forcellini D. (2020) Soil–Structure Interaction Assessment of the 23 November 1980 Irpinia Basilicata Earthquake Geosciences 2020, 10, 152; doi:10.3390/geosciences10040152.

[28] Forcellini D. (2020) "Probabilistic-Based Assessment of Liquefaction-Induced Damage with Analytical Fragility Curves", Geosciences 2020, 10, 2020, 315; doi:10.3390/geosciences10080315.

[29] Forcellini, D (2017) "Cost Assessment of isolation technique applied to a benchmark bridge with soil structure interaction." Bulletin of earthquake Engineering, DOI: 10.1007/s10518-016-9953-0.

[30] Forcellini, D (2018) "Seismic assessment of a benchmark based isolated building with soil structure interaction", Bulletin of Earthquake Engineering, DOI: 10.1007/s10518-017-0268-6.

[31] Law, H. K., & Lam, I. P. (2001). Application of periodic boundary for large pile group. Journal of Geotechnical and Geoenvironmental Engineering, 127(10), 889-892.

[32] Lu, J., Elgamal, A., & Yang, Z. (2011). OpenSeesPL: 3D lateral pile-ground interaction user manual (Beta 1.0). Department of Structural Engineering, University of California, San Diego.

[33] Kalliontzis, C. (1998). Numerical simulation of submarine pipelines in dynamic contact with a moving seabed. Earthquake engineering & structural dynamics, 27(5), 465-486.

[34] Hudson, M., Idriss, I. M., & Beikae, M. (1994). QUAD4M: a computer program to evaluate the seismic response of soil structures using finite element procedures and incorporating a compliant base. Center for Geotechnical Modeling, Department of Civil and Environmental Engineering, University of California, Davis.

[35] Ranf, R. T., Eberhard, M. O., & Berry, M. P. (2001). Pacific Earthquake Engineering Research Center. University of California, Berkeley.

[36] Wang, Z., Chen, Z., Liu, H., & Zhang, Z. (2017). Numerical study on lateral buckling of pipelines with imperfection and sleeper. Applied Ocean Research, 68, 103-113.

[37] Hobbs, R. E., & Liang, F. (1989). Thermal buckling of pipelines close to restraints.

[38] Stephens, D. R., Olson, R. J., & Rosenfeld, M. J. (1991). Pipeline monitoring: Limit state criteria (No. NG-18-188). Battelle, Columbus, OH (United States).

[39] Veritas, D. N. (2007). DNV-RP-F110. Global Buckling of Submarine Pipelines–Structural Design to High Temperature/High Pressure.

EURODYN 2020
XI International Conference on Structural Dynamics
M. Papadrakakis, M. Fragiadakis, C. Papadimitriou (eds.)
Athens, Greece, 23–26 November 2020

GRAVITY SYSTEM ENERGY DISSIPATION CONTRIBUTION IN SEISMIC PERFORMANCE OF SPECIAL STEEL MOMENT FRAMES

Francisco Flores[1,2*], Sebastian Pozo[2], Bryam X Astudillo[2] and Jose Vazquez[1]

[1] Universidad del Azuay
Avenida Veinte y Cuatro de Mayo
{fflores,jfvazquez}@uazuay.edu.ec

[2]Universidad de Cuenca
Avenida Doce de Abril
{francisco.flores, bryam.astudilloc, sebastian.pozo}@ucuenca.edu.ec

Keywords: Gravity System, Special Steel Moment Frames, Energy Dissipation

Abstract.

The effect of the gravity framing system on the seismic performance of steel frame buildings is an essential, but currently challenging, aspect of predicting building performance and evaluating community resilience in earthquakes. Analytical studies and field observations have indicated that the gravity framing system, can have a profound effect on the lateral behavior of steel-framed buildings. The main factors that affect the influence of the gravity framing are the gravity columns and the beam-column connections. The gravity columns improve the performances of steel structures providing what is known as continuous stiffness. On the other hand, gravity connections provide strength and another source of energy dissipation. Even though different studies have concluded that the gravity system improves considerably the collapse performance of special steel frame structures, it is still neglected at the design and analysis stage. One of the main reasons why the gravity system is not considered is the difficulty of modeling the beam-column connections. The cyclic hysteretic behavior of commonly used gravity connections presents strength degradation and pinching behavior.

Previous investigations have shown the importance of modeling accurately the cyclic behavior of the lateral resisting system, especially to capture dynamic instability. However, there are no studies regarding the effects of accuracy when modeling gravity connections. This paper investigates the effects of modeling the gravity connections on the seismic performance of special steel structures different approaches that vary in difficulty. The effectiveness of the approaches is illustrated through the analysis of an 8-Story building. Nonlinear dynamic response history analyses are conducted and the effect of the approaches used is evaluated in terms of deformations, energy dissipation and the collapse performance. The results obtained in this investigation show that modeling in detail the gravity connection´s hysteretic behavior is not relevant when the dissipation of energy is compared to the main lateral resisting system.

1 INTRODUCTION

Nonlinear performance assessment of structures is becoming in the present a common procedure to analyze and design structures under seismic loads. According to the current code (ASCE7-16), if the nonlinear analysis is required, it is necessary to establish the probability of collapse at a seismic hazard with a 2% probability of exceedance in 50 years. This kind of analysis require a detailed mathematical model that represent all the main sources of energy dissipation within the structure. The dissipation of energy, when a structure is subjected to earthquake loads, is expected to occur only at the lateral resisting system. In the case of Special Steel Moment Frames (SMFs), the dissipation of energy is expected to undergo at the ends of beams and at the base of the columns of the lateral resistant system. As a result, it is common practice to neglect the gravity system strength and energy dissipation contribution.

It has been proven through experience in real events and numerical investigations that the gravity system contribution could be important when SMFs are subjected to seismic loads. During the Northridge earthquake in 1994, multiple beam-to-column connections in SMFs presented brittle failures and did not dissipate energy as expected. However, structures did not collapse and the most likely reason behind this, is because the gravity system helped to resist the seismic loads [1]. As a consequence of this event, different numerical and laboratory test investigations were developed in order to evaluate the real capacity of gravity connections and their influence on the seismic performance of SMFs.

Liu and Astaneh [2] performed cyclic tests to different commonly used gravity system connections. It was found that shear tab connections moment capacity was approximately 20% the beam plastic moment strength (Mp) if the slab contribution was neglected and 35% Mp if not. Moreover, it was found that shear tab connections have a large inelastic rotation capacity. Gupta and Krawinkler [3] addressed the seismic performance of SMFs at various hazard levels including the gravity system. The gravity connections were modeled using a bilinear moment rotation constitutive law with a strength capacity of 40%Mp for positive bending and 20%Mp for negative bending. One of the main conclusions from this investigation was that the gravity system improves the seismic response of the structure when it is subjected to large drifts. However, it is stated by the authors that the contribution of the gravity column continuity appeared to be the most important having the gravity connections a much less important role. Flores et al. (2014) [4] studied the effect of the gravity system on the collapse performance of SMFs. The study focused on the influence of the gravity columns and the strength of the gravity connections. In the investigation, a simple hysteretic behavior with a backbone curve that presented strength degradation was used to represent the gravity connections behavior. The conclusions were that gravity connections had more influence in low rise buildings but the continuity of gravity columns is what improves the most the performance, especially in high rise buildings. Another investigation was performed by Elkady and Lignos 2014 [5] were the influence of the gravity system on the collapse performance of SMFs was also computed. In this investigation, a very detailed hysteretic behavior was used to model the gravity connections. The main conclusion from this paper regarding the influence of the gravity connections was that they improve the collapse performance of SMFs.

Despite the fact to be known that the gravity system improves the seismic performance of SMFs when subjected to large deformations, its contribution is still neglected in analysis and design. One of the main reasons why the gravity system is not incorporated is the complex hysteretic behavior that gravity connections have when subjected to cyclic loads. It has been established by studies like the one presented by Ibarra and Krawinkler [6], that certain hysteretic behavior characteristics are fundamental to capture the structural dynamic instability. For instance, in order to evaluate the collapse performance of SMFs it is necessary to incorporate

cyclic and strength degradation into the hysteretic behavior of beams and columns. These modelling recommendations apply to the main lateral resisting system and it has been assumed that they have the same effect on the gravity system. However, there is no investigation, to the author's knowledge, where the main lateral resisting system fulfills all the modelling requirements to perform complex analyses and the hysteretic behavior of the gravity connections is studied to evaluate their effectiveness.

In this investigation, an 8-Story Special Steel Moment Frame is analyzed including the gravity system. The structure is analyzed under different hazard levels using Far Field ground motions from the FEMA P-695 methodology [7]. The lateral resisting system of the structure incorporates detailed hysteretic models making it able to capture dynamic stability. On the other hand, the gravity system is included to evaluate the effect that gravity connection's hysteretic behavior has on the performance. Three different hysteretic behaviors are considered: a simple bilinear model, a hysteretic model that follows a backbone curve with strength degradation but with an arbitrary cyclic behavior and a more realistic complex model. The effects of the gravity connection's hysteretic behavior are evaluated by comparing nonlinear static capacity curves (pushover curves), first floor interstory drifts and maximum drifts along the building height. Additionally, the energy dissipated by the gravity system is compared among the models.

2 BUILDING OVERVIEW

The structure to be analyzed in this investigation is one of the buildings that have been extensively investigated since they formed part of the ATC 76-1 project [8]. In the former study, multiple Special Steel Moment Frames (SMFs) were analyzed using the FEMA P-695 to evaluate their collapse performance. The purpose of the project was to establish if the seismic performance factors provided by current codes are adequate. As mandated by the FEMA P-695 methodology the gravity system was not considered as part of the lateral resisting system.

The analyzed system is an 8-Story SMF designed using Response Spectrum Analysis (RSA) following the requirements given in AISC 341-05 [6] and ASCE/SEI 7-05 [9] with the exception that the deflection amplifier Cd was taken equal to the response modification factor, R, as specified in FEMA P-695. The seismic design category used for the design was Dmax as defined by the FEMA P695 (Site Class D, S_s=1.5g, S_1=0.6g). The SMF was designed considering fixed at the base of the columns and using Reduced Beam Sections (RBS) connections.

Figure 1 displays the plan view of the structure. The building has been designed using two lateral resisting systems in each direction. The figure also shows the gravity system in half the structure that is going to be evaluated. The gravity connections are considered to have flexural strength when the beam frames into the column´s strong axis. The height of the first story is 15ft and the rest is 13ft. The design loads are 90 psf as dead load (D) and as live load (L) 50 psf on all floors, except on the roof were 20 psf was used. The load combination considered to perform nonlinear static and dynamic analysis is 1.0 D + 0.25L.

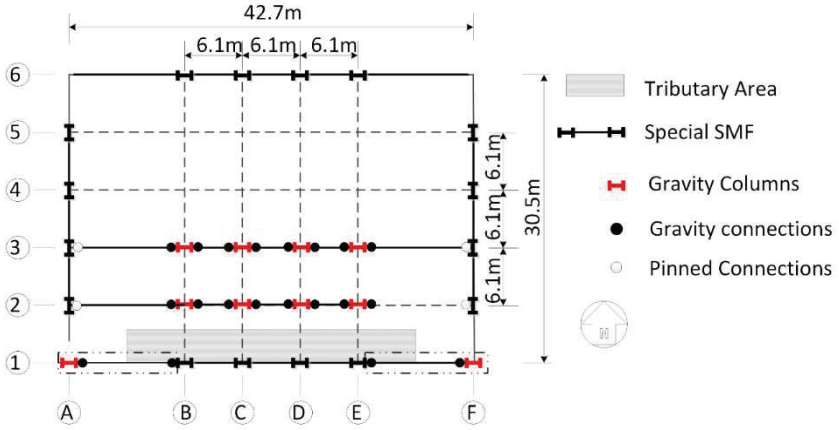

Figure 1 Plan View

The columns and beams of the gravity system were designed for the aforementioned loads using an A992 steel. The sections of the gravity system were designed following common practice, which is considering the gravity connections to have zero strength capacity. The column sections were considered the same along the height (W14x90), and the same beam sections were used on every floor (W24x55). It is important to point out that the gravity columns are considered continuous along their height in order to provide the benefits of continuous stiffness to the system Flores et al. [10]. This assumption implies that splices along the column's height provide full capacity.

3 SPECIAL STEEL MOMENT FRAME NONLINEAR MODEL

The purpose of this investigation is to evaluate the effect of modelling the gravity connections has on the performance of SMFs. However, the nonlinear mathematical model of the SMF, created in OpenSees [11], has to fulfill the minimum requirements to perform complex analyses such as evaluating the collapse performance. The material nonlinearities assumed in the 8-Story structure were represented using concentrated plasticity models at the panel zones and near the end of beams and columns. On the other hand, the geometric nonlinearities were incorporated using a leaning column when the gravity system was not explicitly modeled. The destabilizing load applied to this element corresponds to half of the building's gravity load minus the tributary load is taken by the SMF. Figure 2 displays a representation of the nonlinear mathematical model.

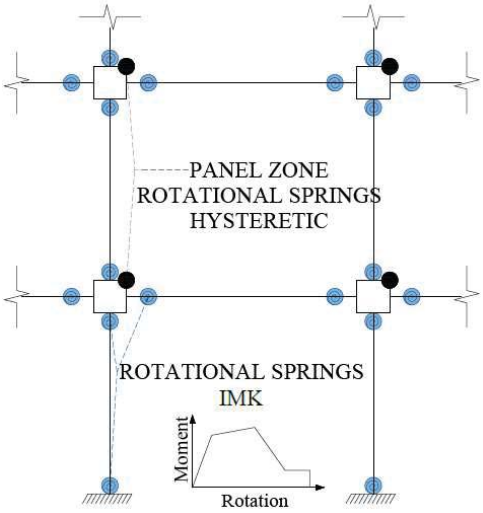

Figure 2 SMF Nonlinear Model

The hysteretic behavior assigned to beams and columns was proposed by Ibarra, Medina, and Krawinkler [12]. The backbone curve, as shown in Figure 3a, captures strength degradation. However, the cyclic behavior also incorporates strength and stiffness deterioration. All of these parameters are very important to capture residual deformations and dynamic instability [6]. The hysteretic behavior of beams and columns was calibrated using what is proposed by Lignos and Krawinkler [13]. One of the setbacks that column's hysteretic behavior currently have is that there is no phenomenological mathematical model that captures the Axial-Moment interaction. In order to overcome this, the flexural capacity of the column is reduced using a representative axial load which was taken equal to the gravity loads as proposed by Hartloper et al. [14]. Figure 3b and Figure 3c illustrates the hysteretic of one of the columns and one of the RBS connection respectively.

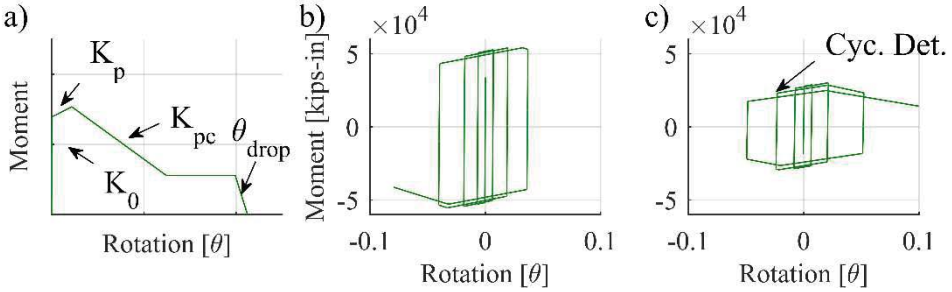

Figure 3 Beams and Columns Hysteretic Behavior a) Backbone curve b) Column c) RBS connection

The shear distortions that occur in the panel zone were modeled using a rectangular region composed of eight very stiff elastic beam-column elements and one nonlinear rotational spring (Figure 4a) proposed by Krawinkler [15]. The hysteretic backbone curve behavior is trilinear (Figure 4b) and represents shear yielding and column flange flexure yielding. The hysteretic behavior of these components is shown in Figure 4c.

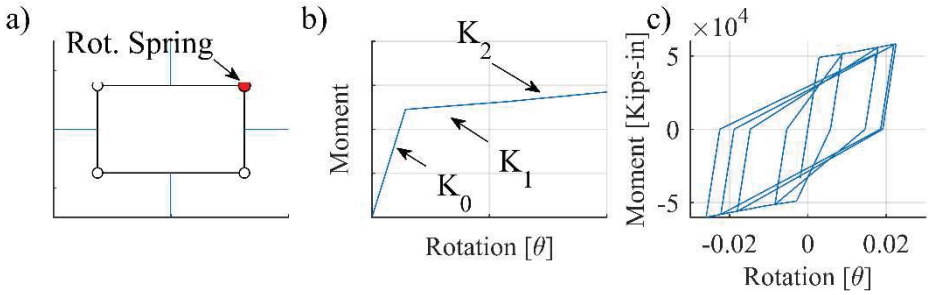

Figure 4 Panel Zone Model a) Geometry b) Backbone Curve c) Hysteretic behavior

4 GRAVITY SYSTEM NONLINEAR MODEL

In the case of the gravity system, columns, beams, and connections were explicitly modeled. The gravity columns were assumed to be continuous and pinned at the base in order to incorporate the continuous stiffness effect [10]. The gravity connections are the main point to be investigated in this study. The number of connections is generally much larger than the lateral resisting system connections, so the general trend is to assume that the influence is important. However, no investigation evaluates the importance of the detail required to model the gravity connections. Thus, in this investigation, three different hysteretic models are assigned to the connections, and the influence of the connection's flexural strength capacity is also evaluated. The flexural strength assigned to the connections was 0%, 15% and 35% the plastic capacity of the beams.

The importance of the gravity connection's hysteretic behavior is evaluated employing nonlinear static and dynamic analyses. In the first case, the back-bone curve will influence the structural force deformation response (pushover curve). In the second case, the gravity connection's cyclic behavior is going to influence the dynamic response. Each of the cyclic behavior assigned to the gravity connections is described in the following subsections.

4.1 Bilinear Model

This is the simplest of the nonlinear behaviors assigned to the gravity connections. In this case, an elastoplastic constitutive law is considered. The yielding rotation is equal to θ_y=0.008 and the maximum flexural capacity is a parameter to be investigated. Figure 5 illustrates the cyclic connection behavior.

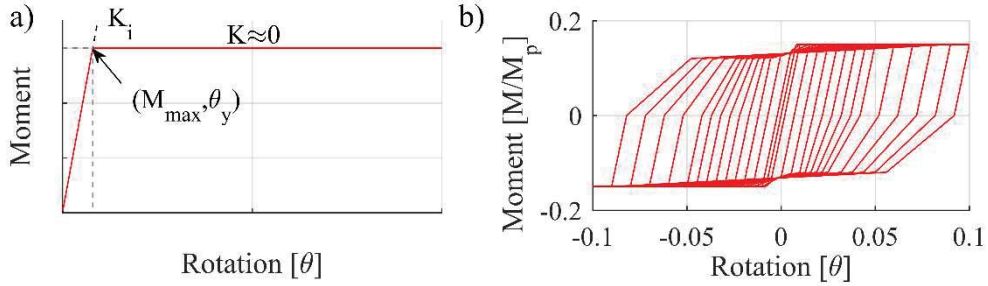

Figure 5 Gravity Connection Bilinear Hysteretic Behavior

4.2 ASCE41 Model

The hysteretic behavior assigned to the gravity connections in this model was based on what is recommended by ASCE41-17 [16] for Partially Restrained (PR) connections. Even though the former standard proposes the PR connections backbone curve model to be used in nonlinear static analyses, a cyclic behavior with pinching is considered in order to perform nonlinear

dynamic analysis. This model has strength degradation, but it does not include cyclic or stiffness deterioration. The yielding, and strength loss rotations are equal to θ_y=0.008 and θ_{drop}=0.08, respectively, as shown in Figure 6.

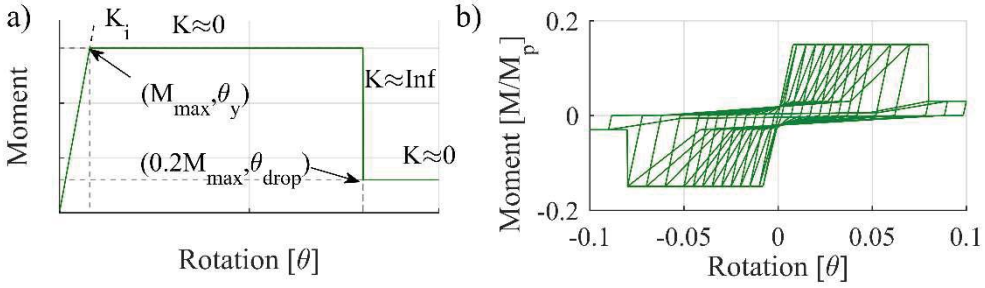

Figure 6 Gravity Connection Hysteretic Behavior

4.3 Deterioration Model

The final most detailed model has the purpose to investigate the importance of modeling accurately the gravity connections in the structural response. The cyclic behavior is based on real tests, and the mathematical model includes strength degradation, cyclic deterioration of strength and stiffness [5]. Unlike the two previously described cyclic simulations, this model presents a variation in stiffness, no reserved strength, and a more realistic pinching behavior. The backbone curve has a yielding (θ_y), maximum (θ_{max}) and dropping rotation (θ_{drop}) equal to 0.004, 0.03 and 0.08, respectively. Even though this model presents a maximum rotation different from the other two models, the initial stiffness is the same.

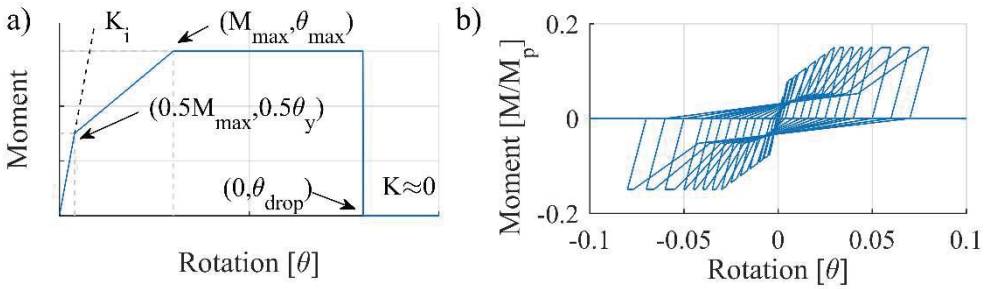

Figure 7 Gravity Connection Deterioration Hysteretic Behavior

5 NONLINEAR STATIC PUSHOVER CURVES

Static nonlinear pushover analyses are performed in order to evaluate the influence of the backbone curve on the capacity (overstrength) and the structure's ductility. The overstrength is the ratio between the maximum capacity and the design base shear. On the other hand, the ductility is computed following what is established by the FEMA P-695 methodology, the ratio between the displacement at which strength decreases 80% the maximum and the effective yielding displacement.

The models to be evaluated are the Special Steel Moment Frame (SMF) by itself, from now on called lateral system (LS), the SMF including the gravity columns (GC) and the three models incorporating the gravity connections (Bilinear, ASCE, and Deterioration). The flexural strength assigned to the gravity connections was 15% and 35% the beam plastic moment capacity.

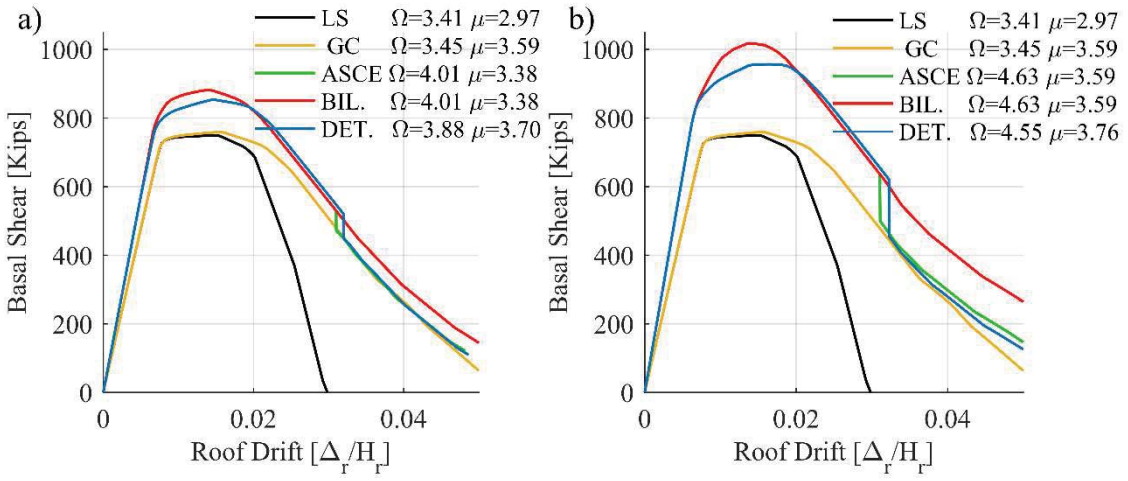

Figure 8 Pushover curves: a) Partial connections 15%Mp, b) Partial connections 35%Mp

Figure 8 a) and b) illustrate the force-roof drift capacity curves for the cases where the gravity connections have 15% and 35% flexural strength. Both figures include the capacity curve when the effect of the gravity column is considered, but the gravity connection's flexural strength is neglected (GC). The computed overstrength with the three different connection models are virtually the same with the exception of the Deterioration model that is around 4% smaller. These values are very similar, but the Deterioration model as expected, is more conservative. On the other hand, the ductility increases when compared to the LS model but among the models with different gravity connections, the ductility is very close. The difference between the bilinear and the other two models is seen on the post-yield stiffness where there is no strength loss. It has to be pointed out the maximum benefit from the gravity system on the post-yield stiffness is provided by the gravity columns. Therefore, in the static analysis the influence of the gravity system can be explained with an improvement of the overstrength due to partial connection capacity, and an improvement of the ductility and post-yield stiffness due to the gravity columns.

6 NONLINEAR DYNAMIC ANALYSES

Once the influence of the backbone curves was evaluated through nonlinear static analyses, nonlinear dynamic analyses are performed to measure the effects of the gravity connection's cyclic behavior. In this section, mathematical models are subjected to 44 ground Far-Field ground motions scaled to different intensity levels that represent different probability of recurrence. The seismic performance among all the models is compared using service, design, and maximum considered level earthquakes. In addition, the dissipated energy of the SMF and the gravity system is evaluated for all the mathematical models. Because the results obtained for the gravity connections with strength equal to 15% the beam plastic moment capacity were very similar to the 35%, only the latter are shown herein.

6.1 Service Level

The first comparison of the influence of the gravity connections is performed using the 44 Far Field ground motions scaled to represent a recurrence of 50% exceedance probability in 30 years (return period of 43 years). The comparison is done between the structure by itself (LS), the structure with gravity columns (GC) and the structure with the gravity system modeled with three different gravity connections. Figure 9 a) shows the first-floor inter-story drift for one of the ground motions that had somehow different results. Figure 9 b), on the other hand, displays

the maximum inter-story drift along the building's height. At this level of intensity, the difference in the results when different mathematical models on the gravity connections are used is negligible. As expected for small displacements, the gravity columns do not influence the structure's response.

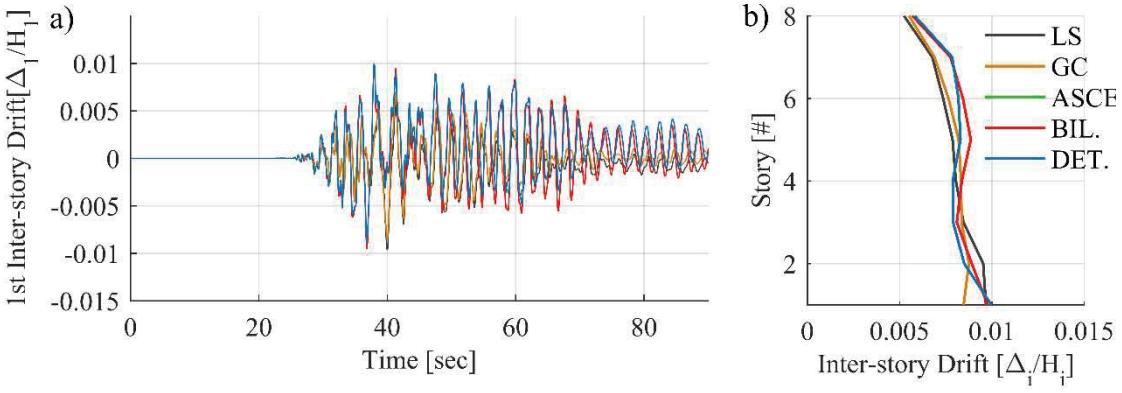

Figure 9 a) First Floor Inter-story Drift, b) Inter-story Drift Profile

Even though inter-story drift responses are widely used to evaluate structural seismic performance, energy balance is an alternative taken in this investigation in order to quantify the gravity system contribution. To the best of the author's knowledge, there are no investigations that evaluate the influence of the gravity connection's mathematical models by means of the dissipation of energy. Figure 10 a) displays the energy balance for all the models normalized by the input energy. The normalization is necessary in order to have comparable results because the input energy is larger for the structures that include the gravity system (stiffer). However, the purpose of this investigation is to quantify the amount of energy that the gravity system dissipates relatively to the main lateral resisting system.

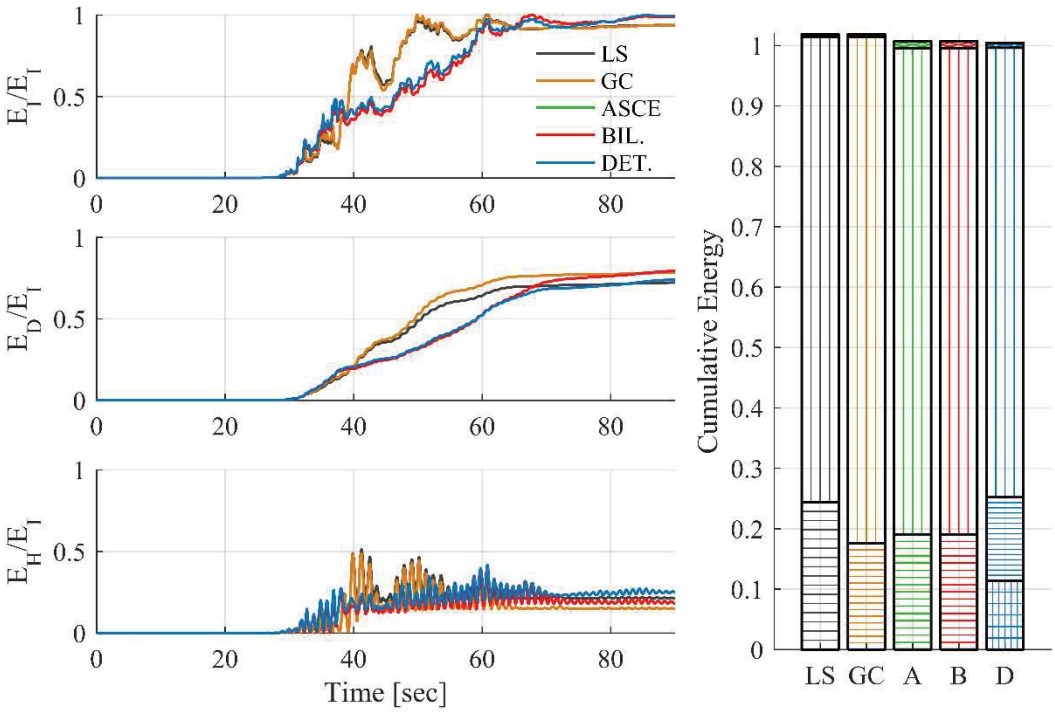

Figure 10 a) Normalized Input Energy b) Normalized Inherent Damping Energy c) Normalized Hysteretic Energy d) Energy Dissipation within the Structure

Figure 10 b) and c) illustrate the energy dissipated by the inherent and hysteretic damping for all models, respectively. It can be seen that, as expected at lower intensity levels, the inherent damping energy dissipation is larger than hysteretic energy because there is almost no damage. The ASCE and bilinear models give exactly the same results because these connections did not yield, while the deterioration model, for this specific earthquake, dissipated some energy. Figure 10 e) presents a bar graph with the percentages of the dissipated energy for each model. It can be seen that inherent damping energy is the one that dissipates the most for all models (around 75%). The Deterioration gravity connection model is the only one that presented energy dissipation within the gravity system. However, energy dissipated by the gravity system in comparison to the total energy (lateral plus inherent damping) is not considerable (around 10%).

6.2 Design Level

The second evaluation is performed using Design Level intensity earthquakes (return period of 475 years). At this intensity, it is expected that gravity and lateral system present damage. Thus, the mathematical models used to capture nonlinear behavior in the gravity connections could have an influence on the performance. Figure 11 displays results for one of the 44 analyzed ground motions. It is clear from Figure 11 a) and b), where the first-floor inter-story drift and maximum inter-story drift along the building are shown respectively, that the structure without the gravity system (LS) is subjected to very large displacements. As stated by different investigations [3, 4, 10], the gravity columns (GC) model improves the performance when SMFs are subjected to large deformations, and this is seen again in Figure 11. ASCE, Bilinear, and Deterioration models show slightly different results in terms of inter-story drifts and maximum drifts along the building's height. However, it is important to evaluate the importance of each mathematical model used for the gravity connections from an energy dissipation perspective.

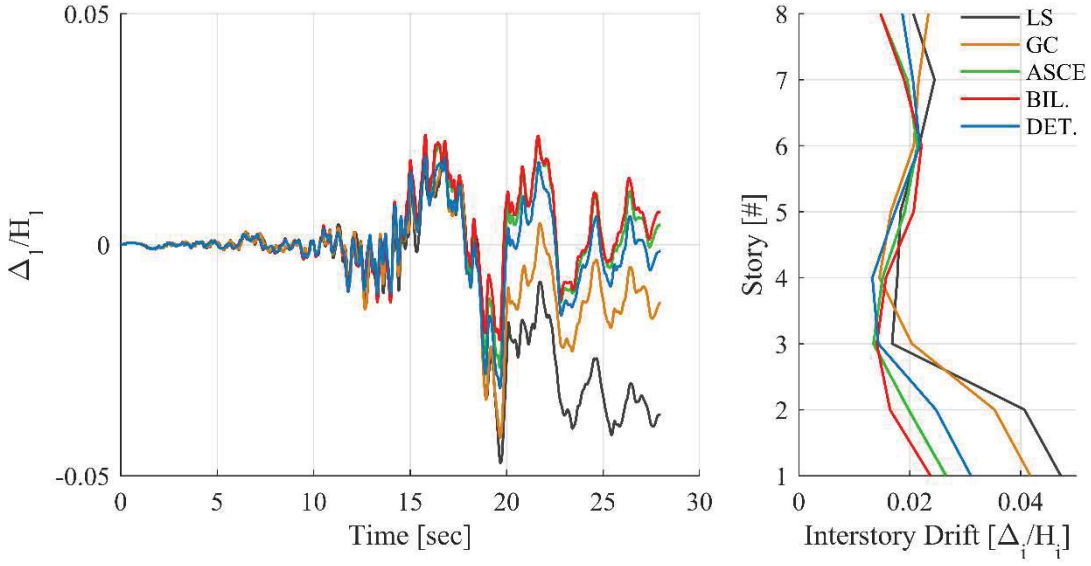

Figure 11 a) First Floor Interstory Drift b) Interstory Drift Profile

Figure 12 a) b) and c) display the normalized energy balance, the dissipated inherent damping energy, and the hysteretic damping energy, respectively. It can be seen from Figure 11b) and c) that the hysteretic energy is larger than inherent damping energy ,meaning that damage within the structures could be significant. The bar graph in Figure 12 d) illustrates the percentages of inherent damping, hysteretic lateral system, and hysteretic gravity system dissipated energy. At this level of intensity, it is clear that the lateral resisting system is the one that dissipates the vast majority of energy (around 70%). On the other hand, it is interesting to note that regardless of the mathematical model used for the gravity connections, the energy dissipated by the gravity system when compared to the main lateral resisting system is only a very small percentage. Even though the number of gravity connections is double the number of connections in the lateral resisting system, the amount of energy dissipated represents only 7% of the total dissipated energy. Therefore, modeling gravity connections in detail might not represent an important factor to consider when the seismic performance of SMFs is required.

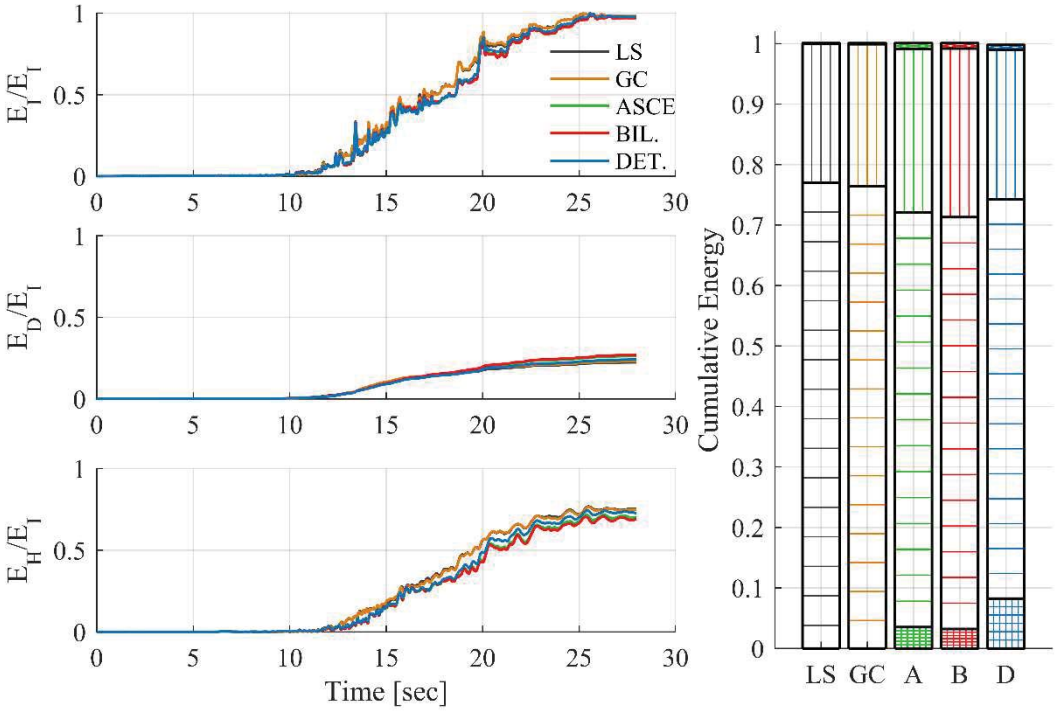

Figure 12 a) Normalized Input Energy b) Normalized Inherent Damping Energy c) Normalized Hysteretic Energy d) Energy Dissipation within the Structure

6.3 MCE Level

Analyses performed using ground motions scaled to the Maximum Considered Earthquake (MCE), which represent a 2% probability of exceedance in 50 years (return period of 2476 years) are in the present required in certain cases by codes like the ASCE7-16 [17]. In this section of the investigation, the influence of modeling the gravity connections is quantified performing nonlinear time history analyses using the 44 Far Field ground motions taken from the FEMA P-695 procedure. Figure 13 a) and b) illustrates the first inter-story drift and the maximum drift profile of one of the ground motions that caused large deformations within the structures. Figure 13 a) shows how the GC model improves drastically the performance of the LS model. On the other hand, the Bilinear ASCE and Deterioration models yielded similar results, but the bilinear model presented slightly larger deformations. Even though the results vary, the overall structural performance is quantified well by any of the mathematical models used to represent the gravity connections.

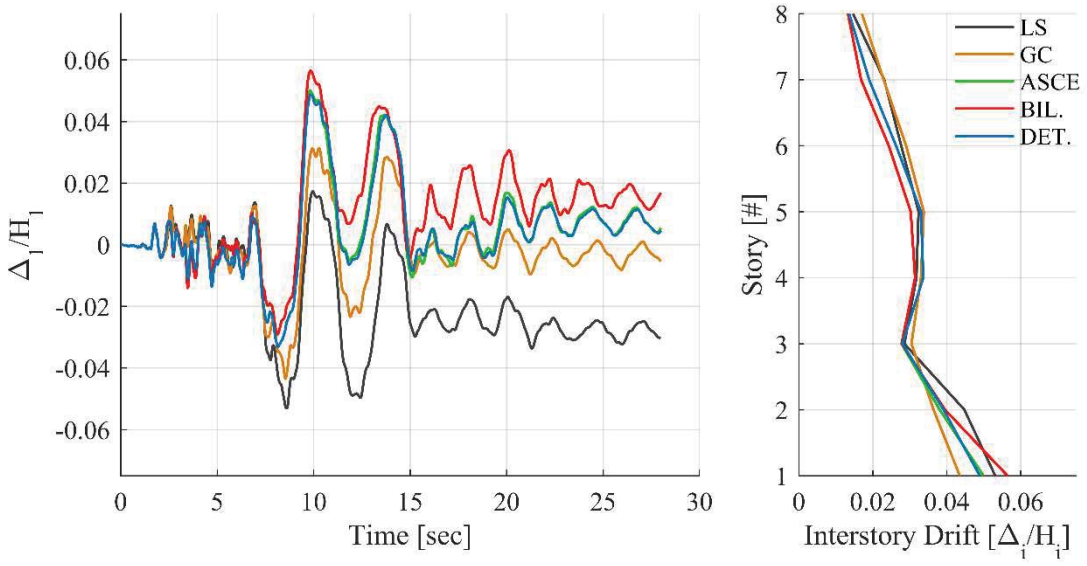

Figure 13 a) First Floor Interstory Drift b) Interstory Drift Profile

Figure 14 shows once again the influence of the gravity connections from a perspective of the dissipation of energy. Figure 14 a) b) and c) display the normalized energy balance, the dissipated inherent damping energy, and the hysteretic damping energy respectively. From Figure 14 b) it can be seen that the role of the inherent damping energy dissipation is almost negligible when compared to the hysteretic energy dissipated by the lateral and gravity system (Figure 14 c)). The bar graph in Figure 14 d) displays the amount of energy dissipated by inherent and hysteretic damping divided into the lateral and gravity system. Even though it is known that the gravity system has a positive effect on the performance of SMFs, it is interesting to see how much the influence is from an energy standpoint. According to Figure 14 d), the gravity system dissipates around 8% of the total energy regardless of the mathematical model used. The energy dissipated by the gravity system is even lower than dissipated energy by inherent damping. This is an important finding that could allow in the future and, with more research, incorporate the gravity connection´s nonlinear behavior in the analysis in a simple manner.

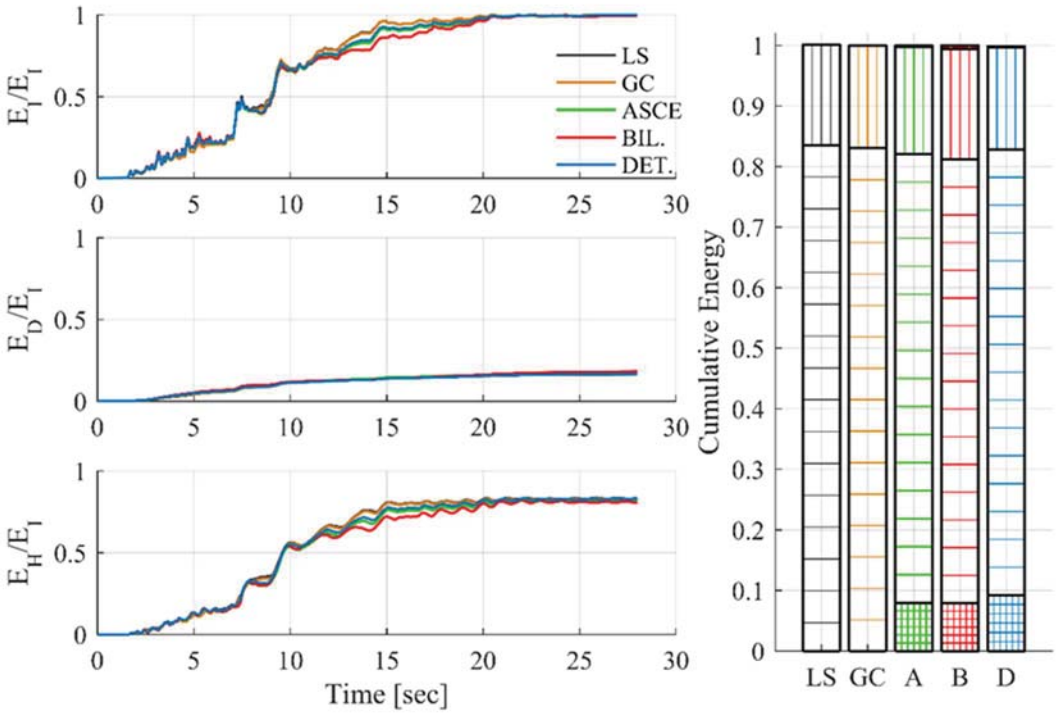

Figure 14 a) Normalized Input Energy b) Normalized Inherent Damping Energy c) Normalized Hysteretic Energy d) Energy Dissipation within the Structure

7 CONCLUSIONS

This investigation focused on the influence of modeling gravity connections on the performance of Special Steel Moment Frames (SMFs). An 8-Story SMF from the ATC76-1 investigation was taken as the structure to be evaluated under different conditions. Five different models were created within OpenSees in order to perform nonlinear static and dynamic analyses. The first model was the SMF by itself (LS), the second model includes the gravity columns only (GC), and the last three models include the whole gravity system modeling the gravity connections using different approaches. The gravity connections were modeled using a detailed approach (Deterioration model), an approach that includes strength degradation taken from the ASCE41-16 code (ASCE model) and a simple bilinear approach (Bilinear). Moreover, two gravity connection´s strengths were considered, 15% and 35% the plastic moment of the beams. After performing all the nonlinear static and dynamic analyses, the following conclusions were found:

- Gravity connection's strength improves the building overstrength regardless of the approach used for the mathematical model. However, the results in terms of energy dissipation the gravity system dissipated around 8% regardless of the mathematical model or connection strength.
- The difference between the Bilinear and the other two approaches that incorporate strength degradation is clearly seen in the pushover curve, where there is no sudden strength lost.
- At service level, the gravity connections have more influence than higher-level intensities. The Detailed mathematical model of the gravity connections was the only one that yielded and dissipated energy under service level ground motions.
- Even though the Deterioration model dissipated energy under different ground motions scaled at the service level, the amount was no considerable in comparison to

the energy dissipated by inherent damping and laterals system hysteretic energy together.

- The gravity columns did not have any influence at the service level.
- At the design level, the gravity system improves the building's seismic performance, especially the gravity columns. The time history responses have a slight variation depending on the approach used to model the gravity connections. However, the difference is not significant.
- The gravity connections dissipation of energy is virtually the same regardless of the approach used for the mathematical models. Moreover, the gravity system dissipation of energy is only 8% for the deterioration model and around 4% for the ASCE and Bilinear Model.
- At the MCE level, the gravity columns have a significant influence on the performance. The gravity connections did not influence the behavior drastically, and the energy dissipated was around 8 % for all models.

8 REFERENCES

[1] R.T. Leon, Composite connections, progress in Structural Engineering and Materials 1(2) (1998) 159-169.

[2] J. Liu, A. Astaneh-Asl, Cyclic testing of simple connections including effects of slab, Journal of Structural Engineering 126(1) (2000) 32-39.

[3] A. Gupta, H. Krawinkler, Behavior of ductile SMRFs at various seismic hazard levels, Journal of Structural Engineering 126(1) (2000) 98-107.

[4] F.X. Flores, F.A. Charney, D. Lopez-Garcia, Influence of the gravity framing system on the collapse performance of special steel moment frames, Journal of Constructional Steel Research 101 (2014) 351-362.

[5] A. Elkady, D.G. Lignos, Effect of gravity framing on the overstrength and collapse capacity of steel frame buildings with perimeter special moment frames, Earthquake Engineering & Structural Dynamics 44(8) (2015) 1289-1307.

[6] L.F. Ibarra, H. Krawinkler, Global collapse of frame structures under seismic excitations, Pacific Earthquake Engineering Research Center Berkeley, CA2005.

[7] P. FEMA, Quantification of building seismic performance factors, Washington, DC, 2009.

[8] G. NIST, GCR 10-917-8 (2010) Evaluation of the FEMA P-695 methodology for quantification of building seismic performance factors, National Institute of Standards and Technology, Gaithersburg (2011).

[9] A. ASCE, Minimum design loads for buildings and other structures, Reston, VA, 2010.

[10] F. Flores, F. Charney, D. Lopez-Garcia, The influence of gravity column continuity on the seismic performance of special steel moment frame structures, Journal of Constructional Steel Research 118 (2016) 217-230.

[11] F. McKenna, G.L. Fenves, M.H. Scott, Open system for earthquake engineering simulation, University of California, Berkeley, CA (2000).

[12] L.F. Ibarra, R.A. Medina, H. Krawinkler, Hysteretic models that incorporate strength and stiffness deterioration, Earthquake engineering & structural dynamics 34(12) (2005) 1489-1511.

[13] D.G. Lignos, H. Krawinkler, Deterioration modeling of steel components in support of collapse prediction of steel moment frames under earthquake loading, Journal of Structural Engineering 137(11) (2011) 1291-1302.

[14] A. Hartloper, D. Lignos, 11.29: Updates to the ASCE-41-13 provisions for the nonlinear modeling of steel wide-flange columns for performance-based earthquake engineering, ce/papers 1(2-3) (2017) 3072-3081.

[15] H. Krawinkler, S. Mohasseb, Effects of panel zone deformations on seismic response, Journal of Constructional Steel Research 8 (1987) 233-250.

[16] E. American Society of Civil, I. Structural Engineering, Seismic evaluation and retrofit of existing buildings, 2017.

[17] A. ASCE, Minimum design loads for buildings and other structures, Reston, VA, 2016.

EURODYN 2020
XI International Conference on Structural Dynamics
M. Papadrakakis, M. Fragiadakis, C. Papadimitriou (eds.)
Athens, Greece, 23–26 November 2020

SIMULATING THE CYCLIC BEHAVIOUR OF A SINGLE-BAY WIDE-FLANGED STEEL BRACED FRAME

Madhar A. Haddad[1*] **and Nigel G. Shrive**[2]

[1] AE Department, UAE University, Al Ain, UAE
e-mail: madhar@uaeu.ac.ae

[2] CE Department, University of Calgary, T2N 1N4, Calgary, Alberta, Canada
ngshrive@ucalgary.ca

Keywords: FE model, Large-size WF brace, Cyclic behaviour, Frame action.

Abstract. *Large size wide-flanged (WF) steel members are being used increasingly in steel braced frames to resist lateral cyclic actions. A finite element model is presented to simulate the cyclic behaviour of a large size WF bracing member in a single-bay diagonally braced frame. Shell elements are used to represent the components of the WF frame (beam columns, shear tabs, stiffener plates) and the brace components (WF specimen, gusset, net-section reinforcing and web plates). Multi-point constraints are used to connect the components. The effect of frame action on the hysteresis behaviour is investigated. Results indicate that the columns have a significant effect on the cyclic lateral hysteresis behaviour of WF braced frames. Recommendations for future cyclic WF simulations are presented.*

1 INTRODUCTION

Understanding the behaviour of concentrically braced frames (CBFs) subjected to cyclic lateral movements is necessary for the design of skeletal structures. In CBFs, the braces are expected to absorb the seismic energy through cyclic yielding and buckling, while the framing elements (beams and columns) remain elastic. Wide flange (WF) sections are being used as bracing members in building structures located in moderate and high seismic areas. WF members have the advantages of greater tensile resistance and longer fracture life when compared to tubular section braces (Popov and Black [1], Gugerli and Goel [2], Fell et al. [3], Tremblay et al. [4], Richard [5], Powell [6], Clark [7], Hsiao [8], Lai [9]).

Finite element models (FEMs) of braced frames need more attention than just modelling individual braces (Haddad et al. [10-18], Uriz et al. [19,20], Fell et al. [21], Myers et al. [22], Huang and Mahin [23,24], Lai [9]). FE modelling represents a complementary technique to develop understanding of the behaviour of braced frames under cyclic lateral movements in addition to experimental testing The FEMs presented in the current study were validated with the results of Haddad [16]. It is therefore reasonable to use these FEMs to simulate the response in CBFs. The shear tab-plate connection is adopted here as this connection detail is believed to be ductile and suitable for connecting the WF beams to the WF columns.

The objective of the current study is to build FEMs to capture the hysteresis response and assess the performance of single diagonal CBFs. The models are used to investigate the effects of brace inclination and frame action on the performance of the WF braced frames. The effect of restraining the vertical displacement of the centreline of the upper-flange of the beam on the hysteresis behaviour was investigated. The brace is connected to the frame, while the tab-plates are connected to the web of the beam by means of multi-point constraints (MPCs) representing the bolts for the latter.

2 BRACED FRAME AND DISPLACEMENT HISTORY

Brace W6 (10 × 77) of the tests reported by Tremblay et al. [4] was designed by the first author of the current study according to the AISC-05b [25] and AISC-05 (seismic) [26] provisions. This large-size WF-section brace and the framing elements (beam and columns) were manufactured from ASTM A992, Grade 50 steel [27] while the gusset, connection, doubler, and stiffener plates were made of ASTM A572 Grade 50 steel [28]. The end connections of the specimen represented the connections of a brace inside a frame in practice, with the minimum possible thickness for the gusset plates. The work-point was located at the intersection of the bottom-flange of the beam and the inner flange of the adjacent column to minimize the gusset plate dimensions (Sabelli [29]). The gusset was welded to the beam and column and detailed to accommodate inelastic rotation associated with out-of-plane buckling of the brace. Following the suggestion of Astaneh-Asl et al. [30], the free length of each gusset plate was thus defined to be twice the plate thickness. The free length of the gusset plates allows plastic hinges to develop in the end gussets which in turn reduces the demand on the mid-span plastic hinge. At connections, the net-sections were reinforced with cover plates, while the gusset plate and web were connected through a doubler plate. The design approach was weak-brace strong-gusset with all possible failure modes being considered. The effective length factor was taken as 0.9, as this accounts reasonably for the small capacity of the gusset plates to rotate out-of-plane compared to the WF member and is typically recommended for pin-pin compressive members.

Brace W6 met the stringent AISC-05 [26], AISC-10 [31], and the AISC-16 [32] seismic code limits with an effective slenderness ratio of 60 and a width-to-thickness ratio of 5.86. W6 was tested inside a 12 MN capacity frame in both compression and tension with 1.5 MN.m

capacity in bending. In practice, large-size section braces, similar to W6, are frequently selected and used in braced steel frame structures in locations of high seismic activity.

The lateral frame cyclic displacements in moderate and high seismic regions are implemented in the quasi-static cycles of the FEMs through the far-field symmetrical loading protocols of Izvernari et al. [33] and Fell et al. [3], respectively with an additional two cycles of a smaller amplitude between the previous loading protocols. These lateral frame cyclic displacements were developed in terms of frame drift ratio (Δ/hs). The lateral frame displacement (Δ) is equal to the corresponding frame drift ratio multiplied by the frame height (hs) as shown in Figure 1(a). For the individual brace models, these lateral frame cyclic displacements are transformed into axial brace cyclic displacements (δ) through the equation of Tremblay et al. [4].

$$\frac{\delta}{L_H} = 1.3\frac{\Delta}{h_s}\cos(\theta)\sin(\theta) \tag{1}$$

where θ is the angle of inclination of the brace with respect to the horizontal axis of the frame as shown in Figure 1(a). The 1.3 is the ratio of the length (L_H) between the far end hinges of the brace and the length (L_{cc}) between corresponding work-points along the axis of the brace that is typically used in the design of frames.

The cyclic axial displacements applied to the brace are divided by the distance between the plastic hinges at the ends of the brace to produce the normalized axial deformation shown in Figure 1(b). The angle of inclination of the brace with respect to the horizontal axis of the frame was 35 degrees.

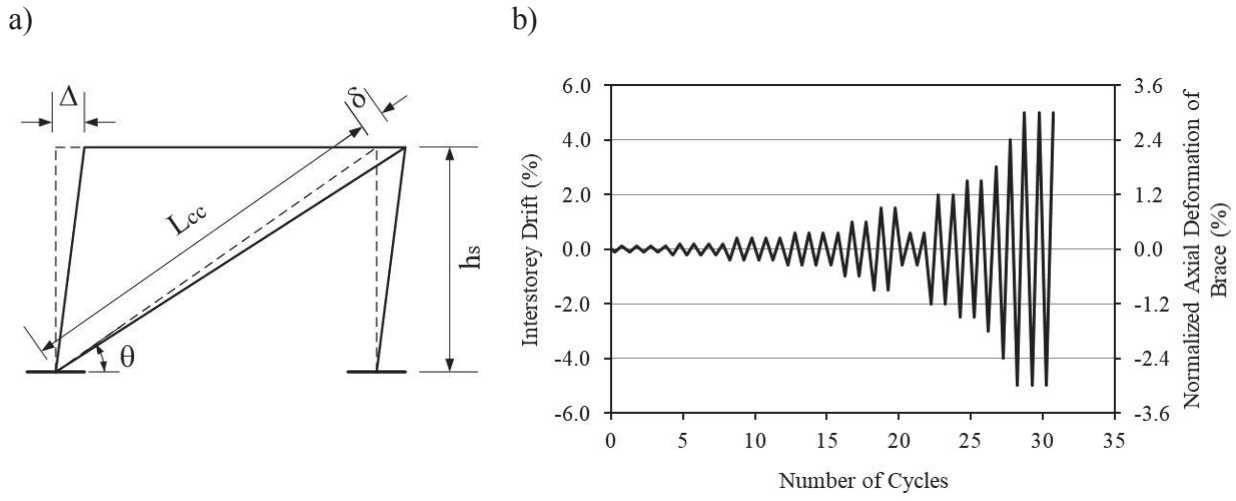

Figure 1(a): Concentrically braced frame and (b) Loading protocol.

3 DESCRIPTION OF THE FE MODEL

The nonlinear FE analyses were solved using Abaqus [34]. Four-node quadrilateral shell elements with nine integration points through the thickness of each element were used in meshing all components of the braced frames. Simpson's integration rule was used. The lateral cyclic displacements were applied at the centreline of the upper-flange of the beam. At this location, the out-of-plane translational degrees of freedom were restrained. In practice, this represents the connection of the centreline of the upper-flange of the beam to a concrete slab by means of double headed studs. The web of the beam at the beam mid-span was restrained against out-of-plane displacement to represent the presence or action of sub-beams. The columns were also

restrained against out-of-plane movement at the level of the upper-flange of the beam, simulating the presence of a concrete slab there. In addition, the vertical centreline of the web of the column is restrained against out-of-plane translation for a length equal to (d - 2k). This represents the presence of the beam intersecting the column in the out-of-plane direction of the frame. d is the depth of the intersecting beam and k is the k-distance as described in the WF steel sections of the AISC manual.

Stiffener plates are added to both sides of the beam in the vertical direction perpendicular to its web at the inner connection of the brace upper gusset plate to the beam bottom-flange. In the FE analysis, these beam stiffeners were perfectly connected to both the flanges and web of the beam. This in turn will guarantee that the axial cyclic force of the brace is transmitted to both flanges of the beam to prevent the possibility of the out-of-plane deformation of the web, especially when the braced frame is subjected to high lateral drift. In braced frames, stiffener plates are needed at these locations in practice for stability purposes that may result from the three-dimensional effect of the frames.

Fixed boundary conditions were applied at the base of each column and at the base of the left gusset of the brace. This represents the bottom braced frame connection to the base plates by means of welds. The far ends of the brace were connected to the frame by means of MPCs. Similarly, the doubler and connection plates were connected to the web and flanges of the WF specimen, respectively by means of MPCs. A tab-plate was used to connect the web of the beam at its far ends to the adjacent flange of each column by means of MPCs representing the bolts for the former (web of beam) and the weld for the latter (flange of column). Two types of MPC were used: the beam type for all except the MPC connecting the tab-plates to the web of the beam where the rotation about the Z-axis (axis of the bolts) is released.

In the FEM, the centrelines of the beam and column must align. Therefore, the shear tab-plates were offset a distance of one-half of the beam web thickness on one side or the other of the centreline of the column in the out-of-plane direction of the frame. The positive Z-direction was selected in the FEMs in the present modelling. In practice, the tab-plates are welded to the inner flanges of the columns with fillet welds on each side of the tab-plates. The weld was not modelled here: a beam type MPC was used instead to connect the tab-plates to the adjacent flanges of the columns. In addition, the beam has a 12.5 mm (½ in.) setback, or clearance, between the end of the beam and the face of the adjacent flange of the column in the plane of the frame in the current FEMs. Given the modelling approach adopted, residual stresses from welding were not included in the analyses.

The material in all elements was specified with the same initial Elastic modulus of 200 GPa and Poisson's ratio of 0.3, and a combined isotropic-kinematic hardening material model. This hardening model simulates the expansion, contraction and shift of the yield surface in stress space during compression-tension cyclic loading of the material.

The FE analyses of the WF braced frames were performed in two stages. First, the first modal shape of buckling was obtained from static linear analysis through the perturbation technique with ramp amplitude while multiplying the mid-span out-of-plane deformation of the brace by the geometric initial imperfection value of 0.2% of the total length of the brace according to Zeiman [35]. Second, the analysis of the WF braced frame model with the cyclic steps of applied lateral displacements was accomplished. Throughout the analysis, 1000 increments were used in each step with the full Newton-Raphson method being used to satisfy equilibrium at each increment.

The analytical average true stress-strain curve suggested by Haddad ad Shrive [36] was used here for the various components (brace, beam, and columns) of the WF braced frames. This analytical average true stress-strain curve was developed through trial and error utilizing a sim-

ple power-hardening law to obtain a hysteresis response that is a reasonable match to the experimental response for a single diagonal WF brace made from ASTM A992 grade 50 steel [27]. The yield surface is defined by:

$$F(\sigma_{ij}, k) = \sqrt{\frac{3}{2}(S_{ij} - \alpha_{ij}^{d})(S_{ij} - \alpha_{ij}^{d})} - \bar{\sigma}_y = 0 \tag{2}$$

In this equation, σ_{ij} is the stress tensor, α_{ij}^{d} is the deviatoric component of the backstress tensor S_{ij}, $\bar{\sigma}_y$ is a stress quantity related to the size of the yield surface and k is a hardening parameter that defines the size of the yield surface. With an initial yield stress of σ_{yo}, $\bar{\sigma}_y$ is defined as

$$\bar{\sigma}_y = \sigma_{yo} + k \tag{3}$$

Further, in Equation (2), the translation of the yield surface α_{ij}^{d} is subtracted from the corresponding stresses S_{ij}. The increment of the deviatoric part of the backstress tensor is defined according to Ziegler's [37] kinematic hardening rule as:

$$d\alpha_{ij}^{d} = \frac{H}{\bar{\sigma}_y}(S_{ij} - \alpha_{ij}^{d})\, d\epsilon_{eq}^{p} \tag{4}$$

where

$$H = \frac{d\sigma}{d\varepsilon^{p}} \tag{5}$$

4 SINGLE INCLINED BRACE

The axial displacement history (δ) is applied to the W6 brace producing a normalized axial hysteresis response that matches the hysteresis response of the experiment as shown in Figures 2(a) and (b), respectively. Further, the lateral displacements (Δ) are applied to the same W6 brace when inclined at 35 degrees to the horizontal axis. The normalized axial hysteresis loops for both the axial and inclined single brace W6 are shown in Figure 2(a). δ/L_H is the normalized axial displacement and $P_a/A_g F_y$ is the normalized axial response force. δ is the applied axial displacement; L_H is the distance between the plastic hinges at the ends of the brace and; P_a, A_g, and F_y are the load resistance, cross-sectional area, and yield strength of the WF brace member, respectively. The behaviour of the axial and inclined braces is identical. The normalized axial and lateral hysteresis responses of the inclined brace are shown in Figure 3.

Brace W6 first buckled in the compressive section of the ninth compressive-tensile loading cycle, both experimentally and in the FE analysis. Plastic hinges formed in the free lengths of the gusset plates at each end of the brace. In the tension portion of that cycle, the brace straightened and yielded. In the following cycles, the compressive capacity of the brace decreased markedly both experimentally and in the analysis as a result of the residual elongation. The bow shape of the buckled brace was enlarged in cycle ten, with the gusset plastic hinges becoming complete over the free-length cross-section. In the FEM, complete section plasticity was seen to occur in all subsequent cycles. The brace strength and stiffness reduced noticeably during the two smaller amplitude cycles of the loading sequence (cycles 21 and 22), followed by local

buckling during the compressive portion of cycle twenty-five. Fracture occurred during the tensile portion of cycle thirty-one.

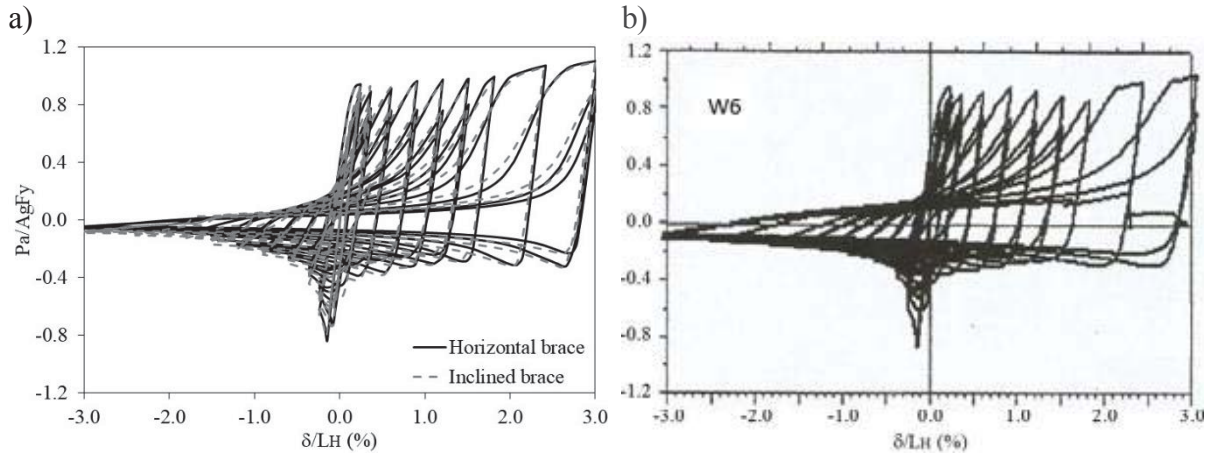

Figure 2: Normalized axial hysteresis response (a) Numerical and (b) Experimental.

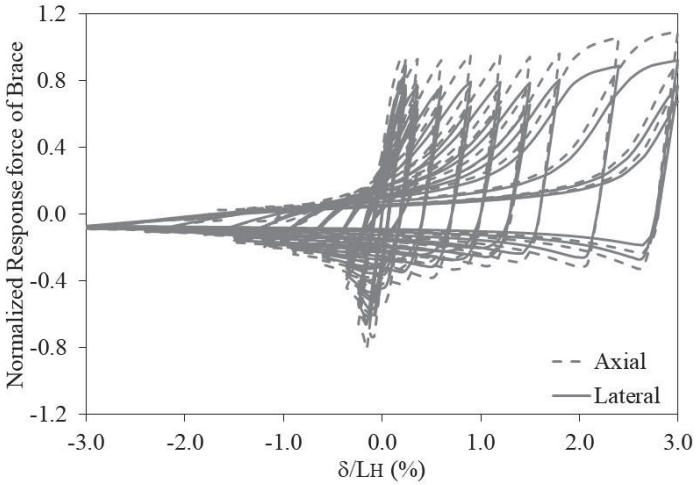

Figure 3: Normalized hysteresis response of the inclined brace.

5 FRAME ACTION

The W6 brace was modelled as a diagonal member inside a single frame with W10 × 77 or W14 × 370 columns and a W27 × 235 beam. The dimensions of the frame are height (hs) = 3.46 m (11.35 ft), width = 4.88 m (16.01 ft) centre-to-centre. All the sections selected met the stringent limits of compactness for seismic design according to the AISC 341-10 [29]. For the W10 × 77 columns and the W27 × 235 beam, local buckling occurred in the flange and web of the braced column, whereas the unbraced column has substantially less local buckling. The desired behaviour of the braced frame is seen when selecting a W27 × 235 beam with W14 × 370 columns: for instance, the local buckling failure mode did not occur in the columns. Active yielding at the base of the columns and at the tab-plates connection area in addition to the expected plastic hinges at the mid-span of the brace and the gussets are all shown in Figure 4.

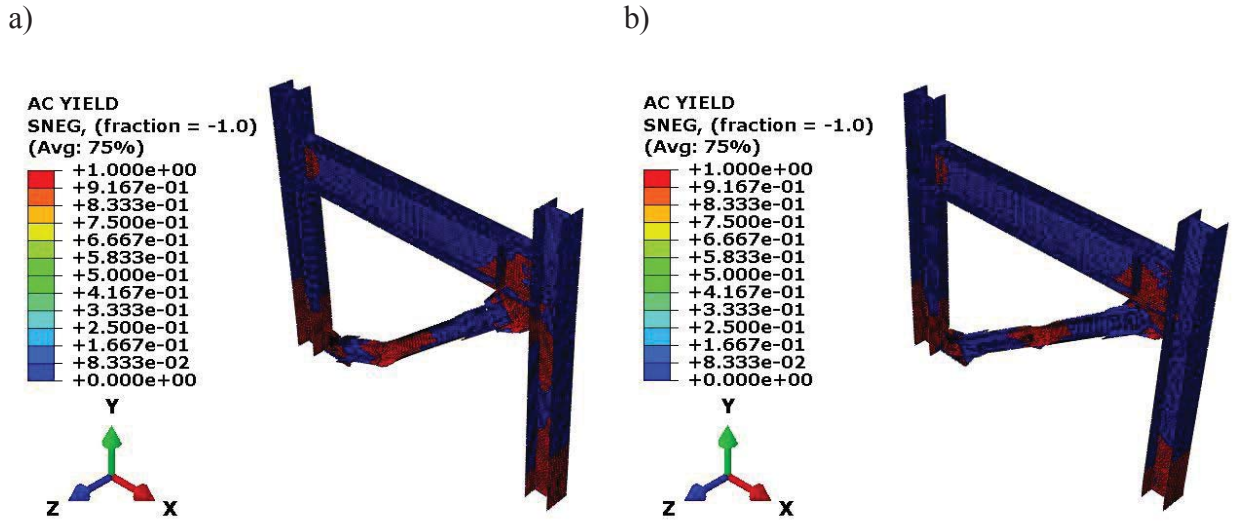

Figure 4: Active yield of the braced frame with the W27 × 235 beam and the W14 × 370 columns under lateral (a) compression and (b) tension deformation.

The applied lateral displacement of the frame (Δ) is transformed back to the axial displacements (δ) of the brace according to Equation (1) and normalized with respect the distance between the two end hinges of the brace (L_H). Having the same axial displacement for both the single brace and the braced frame facilitates comparison of the response. The lateral resistance (response) force (Pl) of the braced frame is normalized with respect to the axial yield force of the brace ($P_y = A_g F_y$). As such, the normalized lateral hysteresis behaviour of the braced frames with the W10 × 77 and W14 × 370 column sizes are shown in Figures 5(a) and (b), respectively.

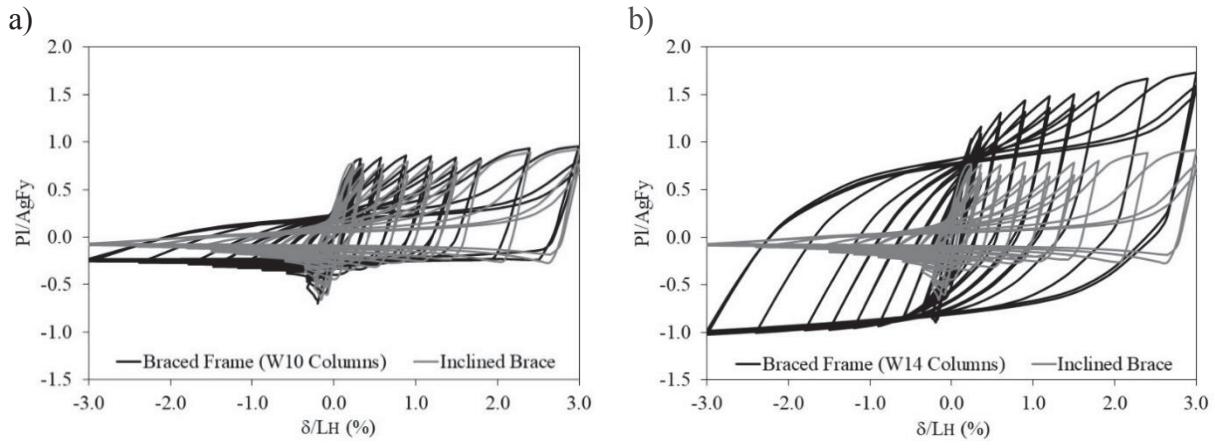

Figure 5: Normalized lateral hysteresis response of the (a) braced frame with the W10 columns and (b) braced frame with the W14 columns.

The maximum tensile and compressive normalized lateral response forces of the braced frame with the W10 × 77 columns are similar to those of the single inclined brace as seen in Figure 5(a), suggesting that the response of the braced frame is governed by the brace. On the other hand, the normalized lateral response forces of the braced frame with the W14 × 370 columns are greater than those for the single inclined brace as shown in Figure 5(b). Therefore, the columns contribute significantly to the seismic response of the concentrically braced frame.

Light roofs (metal decking with insulation or a sandwich panel) or heavy floors (composite metal decking or cast-in-place or precast concrete) are possible roof/floor system scenarios that can be used in residential or office buildings. The effect of releasing or restraining the vertical movement at the centreline of the upper flange of the beam simulates these scenarios, respectively. However, the deflection of the W27 × 235 beam was negligible for these scenarios, so the effect of restraining the vertical movement of the beam did not affect the hysteresis response of the braced frame.

6 CONCLUSIONS AND RECOMMENDATIONS

- The response of the individual brace and the same brace contained in a frame is different under the same loading protocol. This is mainly attributed to frame action.
- The columns contribute significantly to the seismic response of the concentrically braced frames.
- Yielding occurred in the columns regardless of the sizes examined here. Local buckling failure modes occurred in the W10 × 77 column when the frame was subjected to the high seismic load loading protocol. However, those modes did not occur when column size was increased to W14 × 370 or in the W27 × 235 beam.
- It is recommended to consider modelling the base plates with the anchorage rods. In addition, it recommended to model the bolts with holes and to consider the contact in between. It is also recommended to model the welds.

ACKNOWLEDGEMENT

The study was funded the Research Grants of the UAE University (SEED – G00001044 and UPAR – G00001916). In addition, thanks to the UAE University for providing the computational simulation facilities to conduct the current research.

REFERENCES

[1] E.P. Popov, R.G. Black, Steel struts under severe cyclic loadings, *Journal of Structural Engineering Division - ASCE* 107(ST9), 1857-1881, 1981.

[2] H. Gugerli, S.C. Goel, Inelastic Cyclic Behavior of Steel Bracing Members, *Report No. UMEE 82R1, Department of Civil Engineering*, University of Michigan, Ann Arbor, Michigan, 1982.

[3] B.V. Fell, A.M. Kanwinde, G.G. Deierlein, A.T. Myers, X. Fu, Buckling and Fracture of Concentric Braces under Inelastic Cyclic Loading, *Steel Tips, Structural Steel Education Council*, Moraga, CA., 2006.

[4] R. Tremblay, M. Haddad, G. Martinez, J. Richard, K. Moffatt, Inelastic Cyclic Testing of Large Size Steel Bracing Members, *Proceedings of the 14th World Conference on Earthquake Engineering*, Beijing, China, 2008 [Paper No. 05-05-0071].

[5] J. Richard, Étude Du Comportement Sismique de Bâtiments Industriels avec Systèmes de Contreventement en Acier de Faible Ductilité, *M.Sc. Thesis, Department of Civil, Geological and Mining Engineering, Montreal Polytechnic*, Montreal, QC, 2009.

[6] J. Powell, Evaluation of Special Concentrically Braced Frames for Improved Seismic Performance and Constructability, *A thesis submitted in partial fulfillment of the MSCE degree in Civil Engineering*, University of Washington, Seattle, 2009.

[7] K.A. Clark, Experimental Performance of Multi-Story X-Brace Systems, *A thesis submitted in partial fulfillment of the MSCE degree in Civil Engineering*, University of Washington, Seattle, 2009.

[8] P.C. Hsiao, Seismic Performance Evaluation of Concentrically Braced Frames, *A dissertation submitted in partial fulfillment of the PhD degree in Civil Engineering*, University of Washington, Seattle, 2010.

[9] J.W. Lai, Experimental and Analytical Studies on the Seismic Behavior of Conventional and Hybrid Braced Frames, *Ph.D. Thesis, Department of Civil Engineering*, University of California, Berkeley, CA., 2013.

[10] M. Haddad, T. Brown, N. Shrive, Finite Element Modeling of Concentrically Braced Steel Frames for Earthquakes, *Proceedings of the 13th World Conference on Earthquake Engineering*, Vancouver, BC., Canada. August 1-6, 2004 [Paper No. 2816].

[11] M. Haddad, R. Tremblay, Influence of Connection Design on the Inelastic Seismic Response of HSS Steel Bracing Members, *Proceedings of the 11th Inter Symposium and IIW Inter Conference on Tubular Structures*, Quebec City, Quebec, Canada, 2006 [pp. 639-646].

[12] M.A. Haddad, T.G. Brown, N.G. Shrive, Experimental cyclic loading of concentric HSS braces, *Canadian Journal of Civil Engineering* 38 (1), 110-123, 2011

[13] M.A. Haddad, T.G. Brown, N.G. Shrive, Finite element modeling of concentric HSS braces under cyclic loading, *Canadian Journal of Civil Engineering* 38(5), 493-505, 2011.

[14] M. Haddad, Concentric tubular steel braces subjected to seismic loading: Finite element modeling, *Journal of Constructional Steel Research* 104, 155-166, 2015.

[15] M. Haddad, R. Tremblay, L. Chen, L. Tirca, Cracking and Fracture of Concentric HSS Braces, *The 5th International Conference on Computational Methods in Structural Dynamics and Earthquake Engineering*, COMPDYN 2015. 25 - 27 May 2015 Crete Island, Greece [16p. paper].

[16] M. Haddad, Cyclic behavior and finite element modeling of wide flange steel bracing members, *Thin-walled Structures* 111, 65-79, 2017.

[17] M. Haddad, Intermediate HSS bracing members during seismic excitations: modeling, design, and behavior, *Frontiers of Structural and Civil Engineering* 12(1), 148-162, 2018. https://doi.org/10.1007/s11709-016-0375-5

[18] M. Haddad, R. Haddad, A. Al Qadi, H. Al-Mattarneh, Inelastic Cyclic Behavior and Fracture of Wide Flange Steel Brace Members, *Proceedings of the 16th European Conference on Earthquake Engineering*, Thessaloniki City, Greece, 2018.

[19] P. Uriz, Towards Earthquake Resistant Design of Concentrically Braced Steel Structures, *Ph.D. Thesis, Department of Civil Engineering*, University of California, Berkeley, CA., 2005.

[20] P. Uriz, F.C. Filippou, S.A. Mahin, Model for cyclic inelastic buckling of steel braces, *Journal of Structural Engineering - ASCE* 134(4), 619-628, 2008.

[21] B.V. Fell, A.M. Kanvinde, G.G. Deierlein, Large-Scale Testing and Simulation of Earthquake Induced Ultra Low Cycle Fatigue in Bracing Members Subjected to Cyclic Inelastic Buckling, *Report No. 172, Department of Civil and Environmental Engineering*, Stanford University, San Francisco, California, 2010.

[22] A.T. Myers, G.G. Deierlein, A.M. Kanvinde, Testing and Probabilistic Simulation of Ductile Fracture Initiation in Structural Steel Components and Weldments. *Report No. 170, Department of Civil and Environmental Engineering*, Stanford University, San Francisco, California, 2009.

[23] Y. Huang, S.A. Mahin, A cyclic Damage Plasticity Model: Implementation and Applications, *Proceedings of the 10th International LS-DYNA Users Conference*, Dearborn, Michigan USA. June 8-10, 2008 [14p. paper].

[24] Y. Huang, S.A. Mahin, Simulating the Inelastic Seismic Behavior of Steel Braced Frames Including the Effect of Low-Cycle Fatigue, *Report No. 2010/104, Pacific Earthquake Engineering Research Center*, University of California, Berkeley, CA., 2010.

[25] AISC, ANSI/AISC 360-05, Specification for Structural Steel Buildings, Chicago, IL: *American Institute of Steel Construction*, 2005.

[26] AISC 341-05, Seismic Provisions for Structural Steel Buildings, Chicago, *American Institute of Steel Construction*, 2005.

[27] ASTM A992 Standard Specification for Structural Steel Shapes.

[28] ASTM A572 Standard Specification for High-Strength Low-Alloy Columbium-Vanadium Steels of Structural Quality.

[29] R. Sabelli, Seismic Braced Frames — Design Concepts and Connections, An AISC short course, *North American Steel Construction Conference*, Montreal, QC, Canada, 2005.

[30] A. Astaneh-Asl, S.C. Goel, R.D. Hanson, Cyclic out-of-plane buckling of double-angle bracing, *Journal of Structural Engineering - ASCE* 111, 1135-1153, 1985.

[31] AISC 341-10, Seismic provisions for structural steel buildings. Chicago, *American Institute of Steel Construction*, 2010.

[32] AISC 341-16, Seismic Provisions for Structural Steel Buildings. Chicago, *American Institute of Steel Construction*, 2016.

[33] C. Izvernari, M. Lacerte, R. Tremblay, Seismic Performance of Multi-Storey Concentrically Braced Steel Frames Designed According to the 2005 Canadian Seismic Provisions, *Proceedings of the 9th Canadian Conference on Earth Engineering*, Ottawa, ON., 2007 [Paper No. 1419].

[34] Abaqus, User's Manual, Version, 11.6, *Hibbitt, Karlsson, and Sorensen, Inc.,* Providence, RI., 2011.

[35] R. Ziemian, Guide to Stability Design for Metal Structures, *John Wiley and Sons,* Hoboken, 2010.

[36] M. Haddad, N. Shrive, Investigating the inelastic cyclic behaviour of large-size steel wide-flange section braces, *Construction and Building Materials* 199(28), 92-105, 2019.

[37] H. Ziegler, A modification of Prager's hardening rule, *Quarterly of Applied Mathematics*, 17, 55-65, 1959.

EURODYN 2020
XI International Conference on Structural Dynamics
M. Papadrakakis, M. Fragiadakis, C. Papadimitriou (eds.)
Athens, Greece, 23–26 November 2020

NUMERICAL SIMULATIONS OF ELASTOMERIC BEARINGS BRACED WITH STEEL CABLES UNDER CYCLIC DISPLACEMENT

Hossain Talebi[1], Mohammad Reza Adibramezani[2], Nooshin Ghorbani Amirabad[3]

[1] Tehran south branch of the Islamic Azad University, Department of Civil Engineering, Tehran, Iran. E-mail: hosaintalebi70@gmail.com

[2] Tehran south branch of the Islamic Azad University, Department of Civil Engineering, Tehran, Iran. E-mail: mr_adib@azad.ac.ir

[3] Shahrood University of Technology, Department of Civil Engineering and Architecture, Shahrood, Iran. E-mail: n.ghorbani@shahroodut.ac.ir

Keywords: Cyclic Lateral Displacement, Multi-Layer Elastomeric Bearings, Multi-layer Elastomeric Bearings Braced with Steel Cable, Hysteresis Load-Displacement Behavior, Finite Element Analysis

Abstract. *One of the most important methods to improve the seismic performance of structures is the using of multi-layer elastomeric bearings (EB). The main purpose of applying this elastomeric device in the base level of structures is Separating of ground vibrations from body of structures. Recent researches have indicated although EB is capable to decrease damages of buildings, especially in irregular buildings despite of torsion cause of increasing roof displacement total collapse of buildings is likely so multi-layer elastomeric bearings braced with steel cable (EBBSC)to control displacement has been introduced. In this study, three different models of EBs have been studied. The first model is Simple multi-layer elastomeric bearings (SEB), the second model is multi-layer elastomeric bearing with vertical steel cable (EBBVSC), and the third model is multi-layer elastomeric bearing with diagonal steel cable (EBBDSC). By applying the cyclic lateral displacement to top level of specimens, their hysteresis load- displacement behavior was achieved under finite element analysis. The results have indicated increasing strength and stiffness for multi-layer elastomeric bearing braced with steel cable. In other hand, the strength and stiffness value in the EBDSC model in compare with the EBVSC model has been increased 28% and 32%, respectively.*

1. INTRODUCTION:

Reinforced elastomeric bearings have been used in the United States in non-seismic applications, such as bridge bearings and anti-vibration mounts, for over 30 years [Long, 1974; Stanton and Roeder, 1982]. The materials and fabrication techniques used in manufacturing seismic and non-seismic bearings are essentially the same. Seismic bearings decouple the motion of a structure from the motion of its foundation, increasing the fundamental period of the structure to a value beyond the range containing the principal earthquake energies. This can reduce the magnitude of the earthquake-induced forces by as much as a factor of 5 to 10 [Mayes, et al. 1988, Kelly, et al. 1989] and consequently reduce damage to the structure and its contents, and reduce danger to its occupants. [1], [2]. To decouple ground vibration from main body of structures, many devices such as types of dissipating steel fuses in buildings with rocking motion or the different models of Elastomeric Bearings have been suggested. [3], [4], [5]. In recent years many different approaches about EB have been performed. By J. S. Hwang et al. an analytical model for high damping elastomeric isolation bearings is presented. Both material tests and shaking table tests were performed to validate the proposed model, then Ten parameters have been identified from cyclic loading tests are included in the model. [6] To investigate the tension bulking behavior in multilayer elastomeric bearings it was presented the buckling solution to an ideal double-symmetric prismatic column clamped at both ends and free to sway and subjected to vertical loads at the ends only by James M. Kelly. [7], [8]. Furthermore, by G. P. Warn and et al. an experimental study to investigate the influence of lateral displacement on the vertical stiffness of elastomeric and lead–rubber seismic isolation bearings has been summarized. Two identically constructed low-damping rubber and lead–rubber seismic isolation bearings were subjected to a series of tests with varying levels of combined lateral displacement and axial compressive loading to study this relationship. The results of these tests showed the vertical stiffness decreases with increasing lateral displacement for each bearing tested. [9], [10], [11]. multilayer elastomeric isolator has enough stiffness to carry vertical load but it is soft in horizontal direction. It has been described the horizontal behavior of EB in spite of buckling in vertical load in large deformation by Forcellini, et al. with driving a simple two-spring model. [12], [13], [14]. In other case a series of experiments were conducted at University at Buffalo to characterize the behavior of elastomeric bearings in tension by Manish Kumar et al. Sixteen low damping rubber bearings from two manufacturers, with similar geometric properties but different shear moduli, were tested under various loading conditions to determine factors that affect cavitation in an elastomeric bearing. The effect of cavitation on the shear and axial properties of elastomeric bearings was investigated by performing post-cavitation tests. The test data were used to validate a phenomenological model of an elastomeric bearing in tension, which is implemented in OpenSees, ABAQUS and LS-DYNA. [15]. the other researches has performed analytical study to evaluated EB under axial and lateral loadings such as Vladimirs Gonca et al. [16] In 2017, by Forcellini et al. the response of the elastomeric bearings with 3D numerical simulation has been verified to experimental results. This paper aims to identify the accuracy of this theory using experimental results and de-tailed numerical simulations carried out on ABAQUS. The finite element (FE) model has been reproduced with a layered system able to represent the alternating steel and rubber layers and the bolted connections. The presented FE model can be used as a powerful tool for predicting the non-linear behaviors registered during the lab tests [17], [18], [19], [20]. Furthermore, in 2017, by Konstantinos N. Kalfas, a numerical study on the response of steel-laminated elastomeric bearings under cyclic shear and variable axial loads has been conducted to understand their behavior with emphasis placed on the tensile stresses within the elastomer, their stiffness and dissipation capacity. Extensive numerical re-

search was con-ducted with ABAQUS and the Ogden hyperplastic model was used for modelling the elastomeric material. The analyses showed that steel-laminated elastomeric bearings exhibit local tensile stresses, which alter significantly their stiffness and damping ratio. Most importantly, significant tensile stresses within the elastomer were observed locally, even when the bearings were subjected to a combination of shearing and compression. [21], [22], [23]. The cyclic loading experimental tests are an important part in the process of completing the design of the isolators, yet they are very expensive and time consuming. Using the accurate analytical modeling of hysteresis tests and knowing the limitations and the amount of error of the finite elements model and its effect on designing the isolated structure make it possible to reduce the financial and time expenses involved in designing seismic isolators along with experimental tests.[24] By Saedniya and et al., the cyclic loading of two different isolating systems, namely, the high damping rubber bearing (HDRB) and lead rubber bearing (LRB) have been modeled and analyzed in ABAQUS and the outcomes were compared with the experimental results attained by other researchers. After comparing the effective stiffness of the experimental sample with the analytical model of HDRB, the results have been shown that Yeoh function had the best performance in determining the effective stiffness of the isolating system with an error of less than 7%. [25]. Finally, in 2016, by Saman Rastgoo Moghadam, Dimitrios Konstantinidis, the effect of rotation on the horizontal behavior of elastomeric bearings using 3D Finite Element Analysis (FEA) has been investigated. It was observed that constitutive modeling assumptions can have a notable influence on the results, especially at low vertical pressure where the critical shear strain is large. Support rotation did not affect the critical displacement appreciably, but it significantly affects the critical shear force. It is observed that support rotation becomes important for bearings with low second shape factor, even if their first shape factor is large. [26]. In this study, three different models of multilayer elastomeric bearings have been evaluated by using of finite element analysis under cyclic lateral load and torsional displacement. To verify the results, as the first step, the laminated base isolation introduced by Rastgoo and et al. was analyzed in ABAQUS software. The results of this verification indicated appropriate coincidence for relative displacement- average stress curve in this study with results of Rastgoo and et al. research.

2. MODELING OF SPECIMENS:

Previous researches indicated although EBs can be prevented damaging of structural members cause of separating ground vibration from main body of structures during the earthquake, applying them in base level of structures have many significant points. One of the most important problem in this challenge is that using elastomeric layer as soft material can be caused buckling of EB under vertical load and it can be effected on stability of the EB in seismic loading. The second is that in the buildings equipped with EB cause of increasing period and roof displacement, in the strong ground motion, collapse prevention requirements seriously must be satisfied. Finally, in the irregular buildings in spite of torsion, initial torsion can be influenced on the behavior of EB under lateral load. so it seen that designing EBs with considering elements which they can be effective in stability would be useful. For this purpose, in this study, as it is shown in Fig. 1., three different models of EBs by performing finite element analysis in ABAQUS software by regarding two steps of loading have been evaluated.

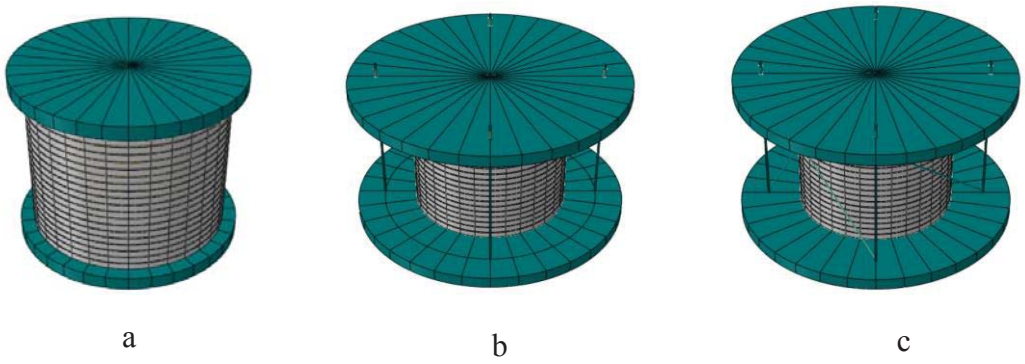

a b c

Figure 1. The different specimens of EBs: a. SEB, b. EBVSC, c. EBDSC

The main parts of these base isolation are including of anchor plate in top and bottom, rubber layers, and steel sheets. The geometrical dimensions for all of these parts have been gathered in Table 1. All of the interactions was considered as Tie. Furthermore, the mesh size for all of the parts was equal to 15mm. For the two specimens, EBVSC and EBDSC, the diameter of steel cable was regarded equal to 5mm. the material properties for steel in Table 2. and for rubber in Table 3. have been presented.

Table 1. Geometrical dimensions of studied EBs

Parts	Diameter(mm)	Thickness(mm)
Anchor Plate	250	21
Rubber Layer	140	10
Steel Sheet	140	2

Table 2. Material of properties for steel

Parts	Poisson Ratio	Ultimate Stress (N/mm^2)	Ultimate Strain	Yielding Stress (N/mm^2)	Elasticity Modulus ($N/mm^{2)}$)	Gravity (Kg/mm^3)
Steel Shims	0.3	370	0.15	280	205000	7.85E-6

Table 3. Hyperplastic properties of rubber

C_{10}	C_{01}
0.18	0.253
0.13	0.165
0.09	0.125
0.07	0.105
0.06	0.095
0.054	0.085
0.048	0.085
0.046	0.083
0.045	0.08
0.044	0.079

Two loading steps were introduced. in the first step a torsional displacement equal to 0.02 Rad as static/general, and in second step, a lateral cyclic displacement as static/general have been applied. The bottom anchor plate was fixed in through of the analysis. The specified boundary condition for specimens, and the cyclic displacement protocol has been shown in Fig. 2 and Fig. 3. respectively. To gain the results, it was made two set including of nodes in bottom anchor plate and nodes of top anchor plate as named “reaction force” and “displacement”. For reaction force set, RF1 and for displacement set, U1 as the history output was requested.

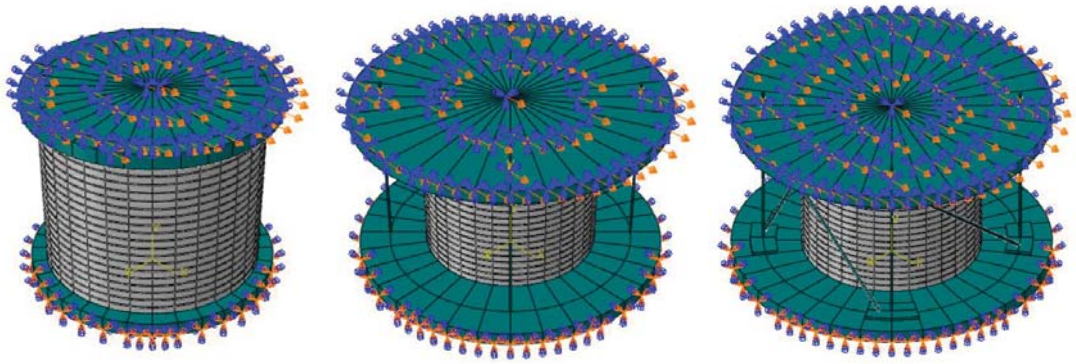

Figure 2. The boundary conditions and loadings in the specimens

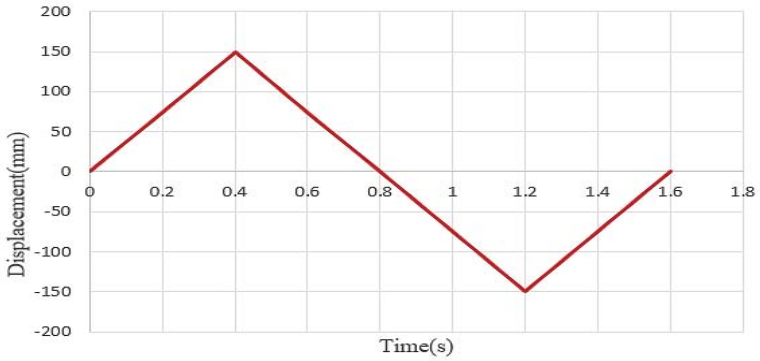

Figure 3. The cyclic displacement protocol

3. RESULTS OF FINITE ELEMENT ANALYSIS:

After analyzing all of the models, with getting summation of RF1 for all nodes belong to “reaction force” set and average of U1 for all nodes belong to “displacement” set, the hysteresis curve by combining U1 and RF1 have been plotted. As it has been shown in Fig. 4. Using of diagonal steel cable can be caused of increasing strength and stiffness in EB. Furthermore, increasing dissipation energy to this model comparing with EBVSC is visible.

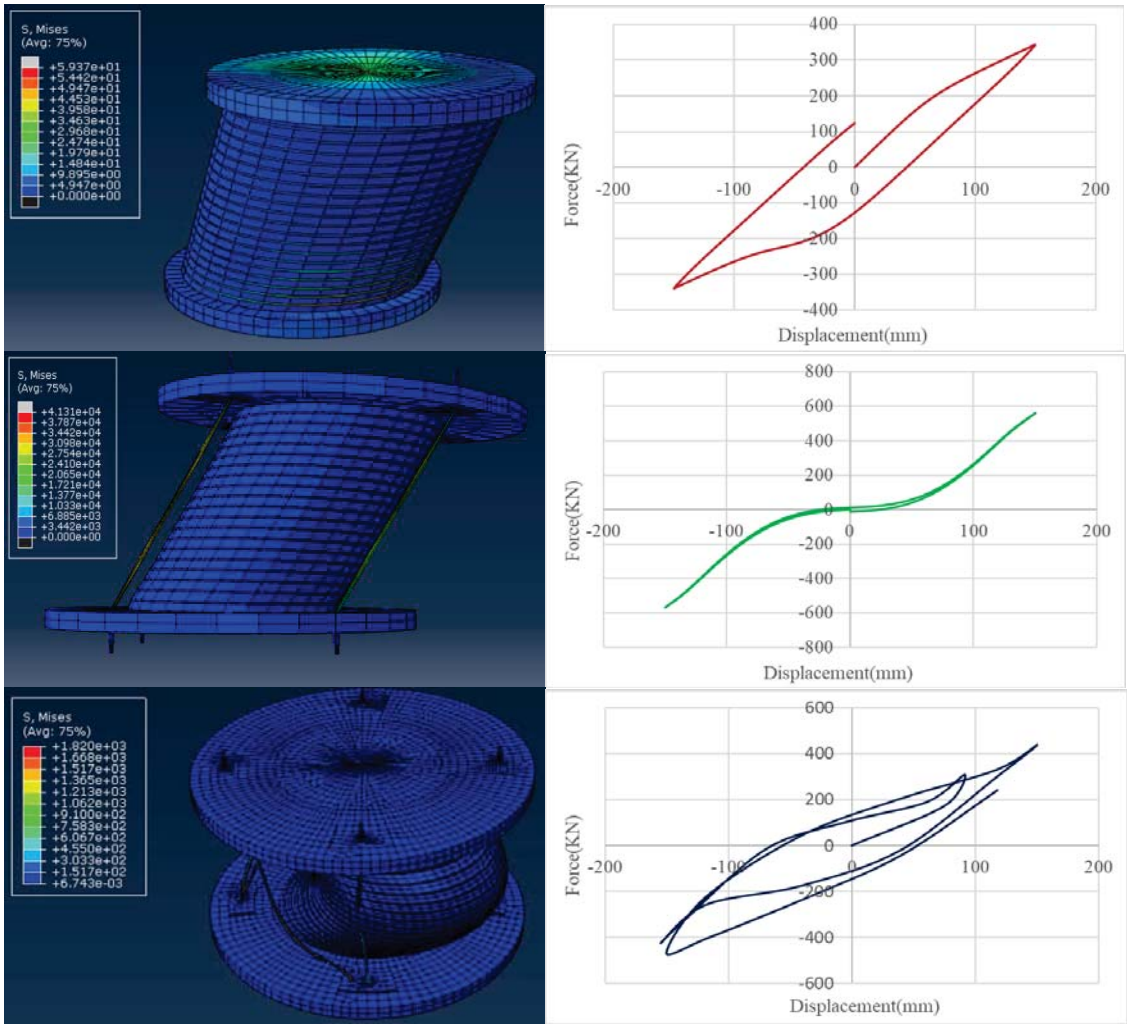

Figure 4. The cyclic displacement protocol

4. VERIFICATION:

In this study three different models of EB under finite element analysis by ABAQUS software was evaluated to verify the results due to finite element analysis, at first a kind of elastomeric bearing that has been studied by Saman Rastgoo Moghadam, and Dimitrios Konstantinidis, to investigate the effect of support rotation on the horizontal behavior of elastomeric bearings have been analyzed. For this purpose, according to Fig. 6. A multilayer elastomeric bearing with 20 rubber layers and 19 steel sheets between two anchor plates was investigated. The diameter of anchor plate which is located on upper and lower level, and its thickness were 320mm, and 21mm. Furthermore, the diameter of intermediate layered body, the thickness of steel sheets, and rubber layer were considered 280mm, 2mm, and 10mm, respectively. For whole models in this study all of the parts were considered as 3D, deformable, solid with 8-node elements.

a b

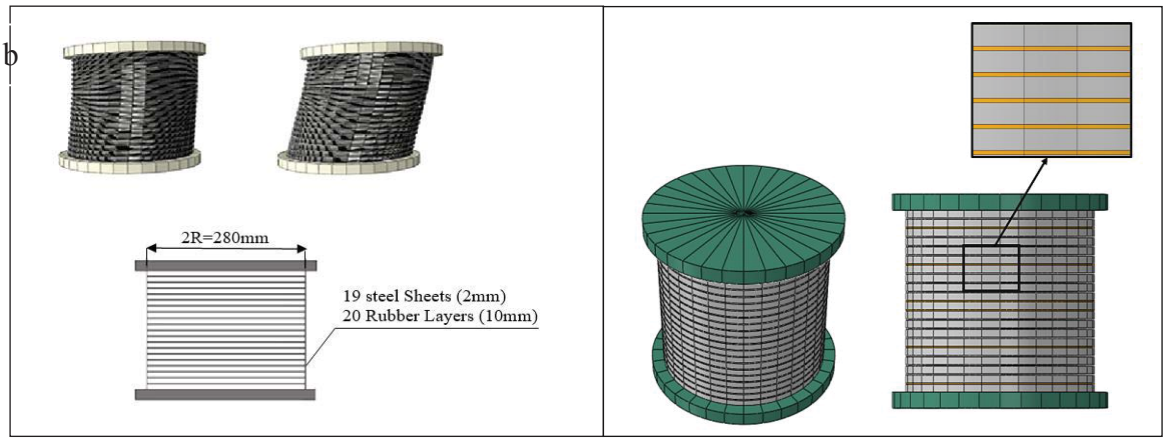

Figure5. a. the view of studied EB by Saman Rastgoo Moghadam and et al. b. EB Model in ABAQUS

in this study, the studied base isolation by Saman Rastgoo Moghadam and et al. other time analyzed to verify the future results. To make this model all of the geometrical dimensions and mechanical properties of material is completely similar to reference. For introducing of rubber's material properties has been used from Neo-Hookean model as it is presented to Table.4. All of the interactions to model this base isolation as surface to surface have been tied.

Table4. Neo-Hookean Model properties for the Rubber

Material Model	C10 (MPa)	D10 (MPa^{-1})
Neo-Hookean	0.45	0.001

Boundary conditions and loading for this model are illustrated in Fig. 7. Two loading steps were considered to apply load. In first step, a vertical load equal to 200KN (CFY=200E3 N), and a rotational displacement equal to 0.02Rad (UR3=0.02 Rad), and in the second step, a lateral load equal to 5 KN (CFX=5000 N), and propagating vertical load from previous step, have been introduced. The bottom anchor plate was fixes in all of during analysis. (UX=UY=UZ=URX=URY=URZ=0)

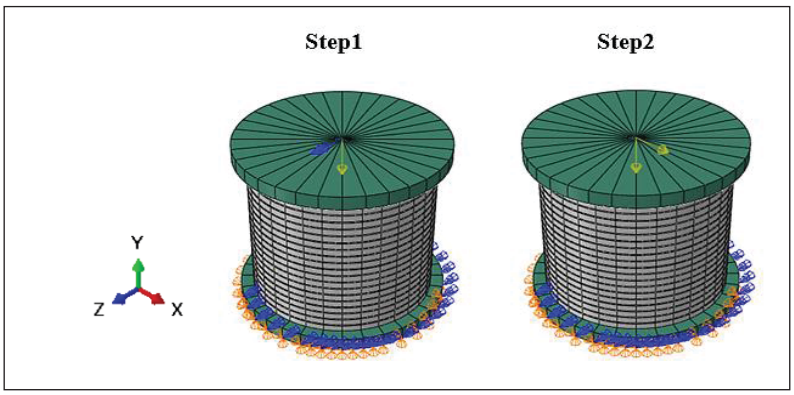

Figure6. Boundary Conditions and Loading.

After analyzing the history outputs including of reaction forces (RFX, RFY) for the bottom anchor plate, and displacements (U1, U2) for the top anchor plate were achieved. Furthermore, by introducing a set from all elements of the middle section of EB, average stress (P0) was reported, and then the relative displacement- stress behavior curve has been plotted. In this presented curve shown in Fig. 8., Uh, and Ur are lateral displacement, and the thickness of rubber, respectively.

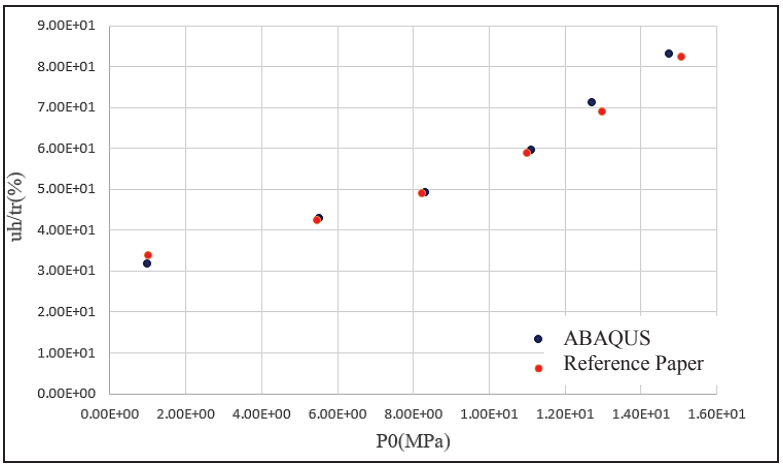

Figure 7. relative displacement-stress curve for studied EB by Saman Rastgoo Moghadam and et al.

5. CONCLUSIONS:

In this study, to control displacements in EBs, elastomeric bearings braced with steel cable has been investigated. By performing a finite element analysis for three different models of EBs under torsional displacement and cyclic lateral displacement, load-displacement hysteresis curves for all of them were achieved. Comparing the hysteresis behavior of specimens, increasing in strength and stiffness for the EBDSC was indicated. the strength and stiffness value in the EBDSC model in compare with the EBVSC model has been increased 28% and 32%, respectively.

6. REFERENCES:

[1] A. W. Taylor, A. N. Lin, and J. W. Martin, A Review of Seismic Isolation for Buildings, Historical Development and Research Needs, *Buildings,* 300-325; DOI:10.3390/buildings2030300, 2012.

[2] Andrew W. Taylor, Albert N. Lin, M. EERI, and Jonathan W. Martin, Performance of Elastomers in Isolation Bearings: A Literature Review, *Earthquake Spectra*, Vol. 8, No. 2, 1992.

[3] M. Hosseini, N. Ghorbani Abad, a structural fuse to create repairable buildings with see-saw motion in earthquake and it FE modeling, *The 11th Canadian Conference on Earthquake Engineering (11CCEE)*, July 21-24, 2015.

[4] M. Hosseini, N. Ghorbani Abad, introducing an innovative structural fuse for creation of repairable buildings with see-saw motion during earthquake and investigating it by nonlinear finite element modeling, *World Academy of Science, Engineering, and Technology Civil and Structural Engineering,* Vol:2, No:6, 2015.

[5] N. Ghorbani Abad, M.Hosseini, Yielding- curved- bars and hemisphere core energy dissipating device as the central support of repairable buildings with see-saw motion, *7th International Conference on Seismology and Earthquake Engineering*, May 12, 2015.

[6] J. S. Hwang, J. D. Wu, T.-C. Pan, and G. Yang, A mathematical hysteretic model for elastomeric isolation bearings, *Earthquake Enginerring structural dynamics*, DOI: 10.1002/eqe.120, 2002.

[7] J. M. Kelly, Tension Buckling in multilayer elastomeric bearings, *Journal of Mechanics of Materials and Structures*, 2,1591-1605,2007.

[8] J. M. Kelly, Earthquake Resistant Design with Rubber, 2nd Ed., Spriger, London, 1997.

[9] G. P. Warn, A. S. Whittaker, M. Constantinou, Vertical stiffness of elastomeric and lead–rubber seismic isolation bearings, *Journal of Structural Engineering,* 133.9,1227-1236,2007.

[10] G. P. Warn, A. S. Whittaker, Property modification factors for seismicslly isolated bridges, *J. Bridge Eng.,* 11.3,371-377,2006.

[11] G. P. Warn, J. Weisman, Parametric finite element investigation of the critical load capacity of elastomeric strip bearings, *Eng. Struc*., 33.12,3509-3515,2011.

[12] D. Forcellini, J. M. Kelly, Analysis of the large deformation stability of elastomeric bearings, *Journal of Engineering Mechanics*, 140.6:04014036, 2014.

[13] D. Forcellini, Seismic Assessment of isolation technique applied to benchmark bridge with soil structure interaction*, Bulletin of Earthquake Engineering*, 16.5,2021-2042,2018b.

[14] James M. Kelly, Maria Rosaria Marsico, Tension buckling in rubber bearings affected by cavitation, *Engineering Structures*, 56: 656–663, 2013.

[15] M. Kumar, A.S. Whittaker, M. C. Constantinou, Experimental investigation of cavitation in elastomeric seismic isolation bearings*, Engineering Structures*, 101 :290–305, 2015.

[16] V. Goncaa, S. Polukoshkob, Alexander Boykoc, Analytical and Experimental Research of Compressive Stiffness for Laminated Elastomeric Structures, 24th DAAAM International Symposium on Intelligent Manufacturing and Automation, 2013.

[17] D. Forcellini, S. Mitoulis, K. N. Kalfas, Study on the response of elastomeric bearings with 3D numerical simulations and experimental validation, *COMPDYN 2017 ,6th ECCOMAS Thematic Conference on Computational Methods in Structural Dynamics and Earthquake Engineering*, 2017.

[18] K.N. Kalfas, D. Forcellini. A developed analytical non-linear model of elastomeric bearings verified with numerical findings, *International Conference on Structural Dynamics (EURODYN)*, Athens, Greece, 22-24 June 2020.

[19] A. Canini, D. Forcellini, 3D Numerical simulations of a base-isolated residential building with soil-structure interaction. *VI Eccomas Thematic Conference on Computational Methods in Structural Dynamics and Earthquake Engineering (COMPDYN 2017)*, Rhodes Island, Greece, 15–17 June 2017, DOI: 10.7712/120117.5482.16931, 2017.

[20] D. Forcellini, "Seismic assessment of a benchmark based isolated building with soil structure interaction", *Bulletin of Earthquake Engineering*, DOI: 10.1007/s10518-017-0268-6, 2018.

[21] K.N. Kalfas, S. A. Mitoulis, K, Katakalos, Numerical study on the response of steel laminated elastomeric bearings subjected to variable axial loads and development of local tensile stresses, *Engineering Structures*, 134,346-357,2017a.

[22] K.N. Kalfas, S. A. Mitoulis, Performance of steel laminated rubber bearings subjected to combination of axial loads and shear strain, *Procedia Engineering*, 99, 2979-2984, 2017c.

[23] K.N. Kalfas, S. A. Mitoulis, D. Konstantinidis, Influence of the steel reinforcement on the vulnerability of elastomeric bearings, *Journal of Structural Engineering*, 2020.

[24] Juan C. Simo and James M. Kelly, Finite element analysis of the stability of multilayer elastomeric bearings, *Engineering Structure*, Volume 6. 1984.

[25] Majid Saedniya, Sayed Behzad Talaeitaba, Numerical modeling of elastomeric seismic isolators for determining force–displacement curve from cyclic loading, *International Journal of Advanced Structural Engineering*,11:361–376, 2019.

[26] Saman Rastgoo Moghadam, Dimitrios Konstantinidis, Finite element study of the effect of support rotation on the horizontal behavior of elastomeric bearings, *Composite Structures,* S0263-8223(16)31216-8, 2016.

EURODYN 2020
XI International Conference on Structural Dynamics
M. Papadrakakis, M. Fragiadakis, C. Papadimitriou (eds.)
Athens, Greece, 23–26 November 2020

CYCLIC BEHAVIOUR AND FRACTURE OF A SINGLE-BAY WIDE-FLANGED STEEL BRACED FRAME

Madhar A. Haddad[1*] **and Nigel G. Shrive**[2]

[1] AE Department, UAE University, Al Ain, UAE
e-mail: madhar@uaeu.ac.ae

[2] CE Department, University of Calgary, T2N 1N4, Calgary, Alberta, Canada
ngshrive@ucalgary.ca

Keywords: FE model, WF brace, Cyclic response, Fracture.

Abstract. *Concentrically braced frames (CBFs) are increasingly used in the construction of steel buildings located in moderate and high seismic regions. Wide flange (WF) sections represent a possible alternative to hollow structural steel sections as bracing members. The effects of plate thickness (tab or stiffener or gusset) and the number of bolts on the hysteresis response and fracture a single-bay WF steel braced frame subjected to reverse axial displacements has been assessed through a parametric study using finite element modelling. It is found that reducing the number of bolts while increasing their diameter and the thickness of tab-plates to satisfy the AISC standards for tab-plate connection design had negligible effect on the hysteresis response of the single-bay braced frame.*

1 INTRODUCTION

Optimizing the hysteresis response of CBFs is needed to increase their capacity in resisting lateral loads that result from ground motions. Under these motions, braces are expected to yield in tension and buckle in compression, reducing the impact of ground motions, and thereby preventing the catastrophic failure of buildings that could lead to human and economic losses. These braces are connected to the framing elements (beams and columns) by gusset plates. Beams are typically connected to columns by tab-plates. Vertical stiffener plates may also be needed in beams. The effects of these frame components on the hysteresis response of braced frames need to be analyzed and understood.

The finite element model (FEM) presented by Haddad and Shrive [1] was developed by extending previous models (Haddad et al. [2-7], Uriz et al. [8,9], Fell et al. [10], Myers et al. [11], Huang and Mahin [12,13], Lai [14]) and was used here to study the effects of various components of a single-bay frame on the hysteresis response and fracture life of the brace.

The longer fracture life of WF braces compared to hollow structural steel (HSS) section braces is advantageous (Popov and Black [15], Gugerli and Goel [16], Fell et al. [17], Tremblay et al. [18], Richard [19], Powell [20], Clark [21], Hsiao [22], Lai [14]). As there are a limited number of cyclic test data for individual WF braces, the possibility of presenting a reliable WF brace empirical fracture model based on the accumulated deformation, equivalent total ductility or tension-ductility is not feasible in the near future. Thus, both the significant cumulative plastic strain which is believed to be a reasonable damage index and a refined fracture model are used to assess the performance and predict the fracture life of the large-size WF braced frames simulated here. The FEMs presented here were validated by the results of Haddad [23]. It is therefore reasonable to use these FEMs to simulate the response and predict fracture in multi-storey braced frames and possibly even the whole structure.

Thus, the objective of the current study was to use the previously validated FE and fracture models to capture the hysteresis response and assess the behaviour of single-bay CBFs. The models were used to investigate the effects of the thickness of the tab-plates in relation to the number of bolts used to connect the tab-plates to the web of the beam on the behaviour and fracture of the WF braced frames. In addition, the effects of increasing thickness of gusset and stiffener plate were investigated.

2 FE AND FRACTURE MODELLING

Brace W6 (10 × 77) of the tests reported by Tremblay et al. [18] was modelled inside the single-bay braced frame of W14 × 370 columns and W27 × 235 beam sizes by Haddad and Shrive [1] using the FE analysis software (Abaqus [24]) as shown in Figure 1(a). Multi-point constraints (MPCs) were used to connect the frame components at corresponding nodes. The dimensions of the frame are height = 3.46 m (11.35 ft), width = 4.88 m (16.01 ft) centre-to-centre. The upper nodes at centreline of the beam upper flange were subjected to the loading protocol described in [1]. Lateral behaviour and out-of-plane deformation of the single-bay braced frame are shown in Figures 1(b) and (c), respectively with the corresponding von Mises stress distribution. The FE model was shown to be valid given the results. In addition to modelling of the braced frame presented in [1], the frame was modeled without the brace and beam-to-column connection with and without the brace in the current study.

The difference in response between the braced beam-column and the braced frame shown in Figure 2 basically results from the column and is not from the shear-tab beam-to-column connection or the beam. Therefore, the columns contribute significantly to the seismic response of the CBF. δ/L_H is the normalized axial displacement and P_a/A_gF_y is the normalized axial response force. δ is the applied axial displacement; L_H is the distance between the plastic hinges

at the ends of the brace and; P_a, A_g, and F_y are the load resistance, cross-sectional area, and yield strength of the WF brace member, respectively.

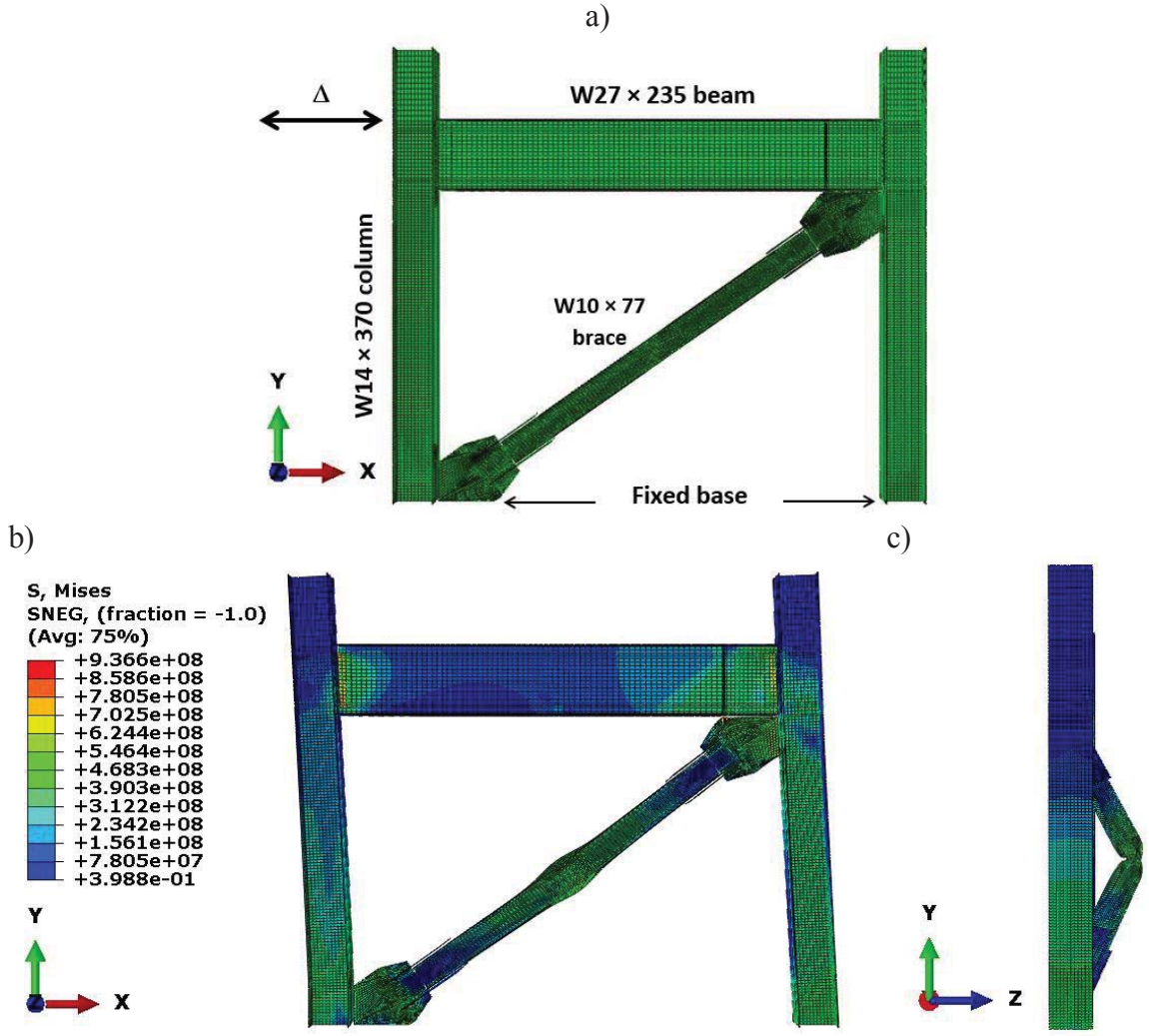

Figure 1(a): Single-bay concentrically braced frame, (b) lateral behaviour, and (c) out-of-plane deformation.

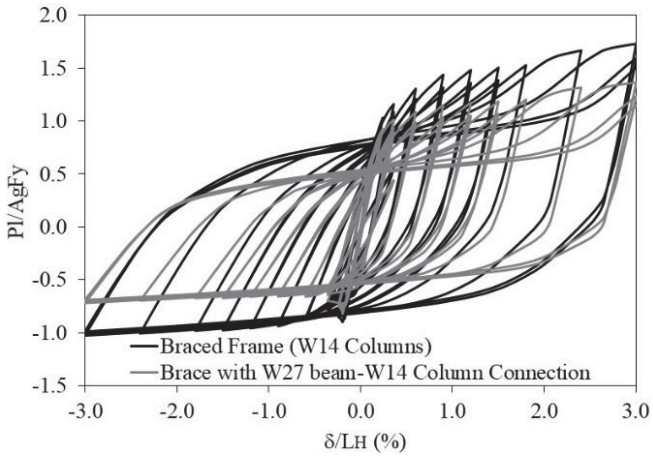

Figure 2: Normalized lateral hysteresis response of the braced frame with the W14 columns and the brace with the beam-to-column connection.

The effect of modelling the frame without the brace and the beam-column without the brace on the hysteresis behaviour is shown in Figure 3. The columns significantly affect the hysteresis response.

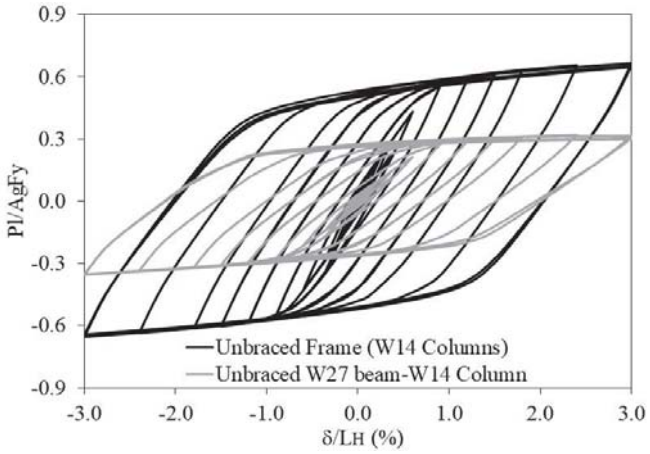

Figure 3: Normalized lateral hysteresis response of the unbraced frame and the unbraced beam-column.

A refined fracture model was implemented here to predict the fracture life of the brace. A strain-based approach to fracture prediction was defined, based on the accumulation of plastic strain. The increment in significant plastic strain in each portion of each cycle was summed as:

$$\varepsilon_{p\ significant} = \sum_{tensile} \int_{\varepsilon_1}^{\epsilon_2} exp^{|1.5T|}\, d\varepsilon_t - \sum_{compressive} \int_{\varepsilon_1}^{\epsilon_2} exp^{|1.5T|}\, d\varepsilon_c \quad (1)$$

In Equation (1), T is the triaxiality ratio (defined as the mean stress divided by the effective or von Mises stress) and the compressive strain is deducted from the tensile strain in each cycle. That is, the significant plastic strain is the sum of the magnitudes of the tensile and compressive strains (compressive strain being negative). When triaxiality is negative, strains are taken as compressive. In the fracture model, the monotonic tensile capacity is degraded during cyclic loading by the coefficient λ_{CVGM}. This coefficient is obtained from Equation 2:

$$\eta_{cyclic} = exp^{(\lambda_{CVGM}\varepsilon_p)} \left(\int_0^{\varepsilon_p} exp^{1.5T} d\varepsilon_p\right)_{monotonic} \quad (2)$$

where ε_p is the accumulated plastic strain and the values of the monotonic capacity (and thus λ_{CVGM}) were calibrated from the experimental results presented by Kanvinde and Deierlein [25] on monotonic and cyclic tests on notched bars manufactured from several types of steel.

3 THICKNESS OF PLATES (TAB OR STIFFENER OR GUSSET) AND NUMBER OF BOLTS

Shear tab-plate connections are economical to fabricate and simple to erect. This popular type of connection is the quickest connection to erect. It consists of a length of plate welded in the workshop to the column flange, onto which the supported beam web is bolted on site. The tab-plate welds are typically sized to the full length. These tab-plates are welded to the column flange at an offset distance of ½ the beam web thickness. A small clearance equal to 12.5 mm (½ in) the column width is typically left between the end of the supported beam and the supporting column flange. In the FE analysis, increasing the thickness of shear-tab plate connection

from 12.5 to 25 mm (½ to 1 in) has negligible effect on the hysteresis response of both the braced frame and braced beam-to-column connection as shown in Figures 4(a) and (b) for the braced frame and the braced beam-to-column connection, respectively. The effect of increasing the thickness of the tab-plates on the hysteresis response of the frame without the brace and the beam-to-column without the brace is minor as shown in Figures 5(a) and (b), respectively.

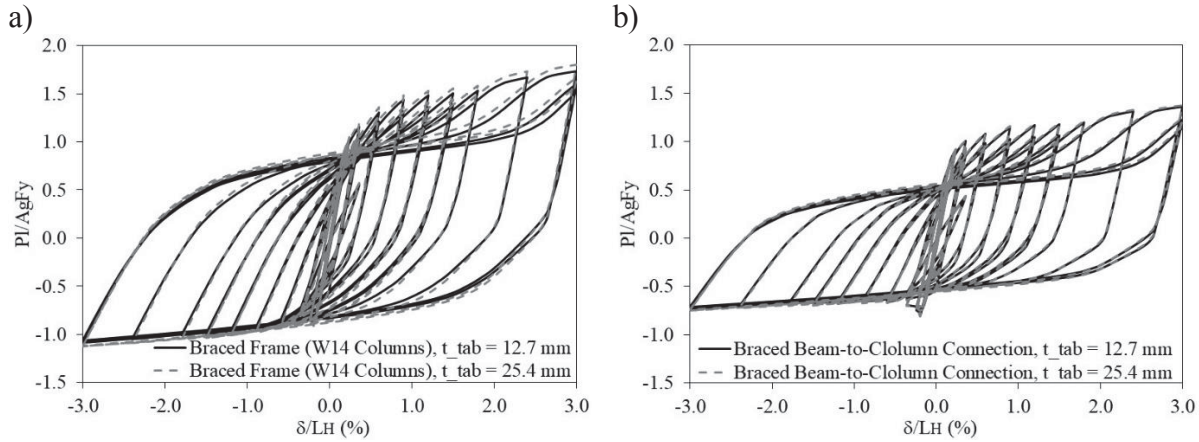

Figure 4: Effect of thickness of tab-plate on the lateral hysteresis response of the (a) braced frame and (b) braced beam-to-column connection.

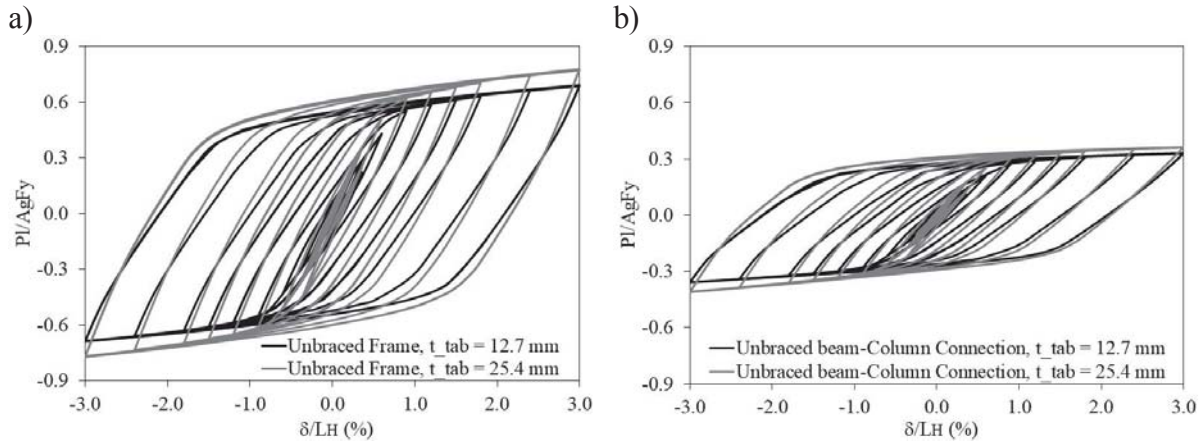

Figure 5: Effect of thickness of tab-plate on the cyclic hysteresis response of the (a) unbraced frame and (b) unbraced beam-to-column connection.

In the FEM, beam type MPCs were used to connect the tab-plate to the column flange at the same location used in practice. The rotation about the axis of the bolts was released in the MPCs connecting the tab-plate to the web of the beam. In addition, seven, five or three MPCs were used to represent the bolts connecting the tab-plates to the web of the WF beam. Reducing the number of the pin type MPCs representing the bolts results in a reduction of the yield demand on the shear-tab plate connection as shown in Figure 6(a) when the thickness of the tab-plate is 12.5 mm (½ in).

In practice, the holes through the plate are horizontal short-slotted rather than round holes. When calling for this type of connections, designers and fabricators commonly use horizontal slotted holes through either the beam or the tab-plate to give the field erection crews more leeway in making the connection on site. To study this effect a simple or pinned type MPC was used to connect the tab-plates to the far ends of the beam. The response is shown in Figure 6(b) when the thickness of tab-plates was 12.5 mm (½ in). Increasing the thickness of tab-plates to

25.4 mm (1 in) when using 3-bolts to comply with the increase in bolt diameter according to the AISC code results in an acceptable hysteresis response as shown in Figure 6(c).

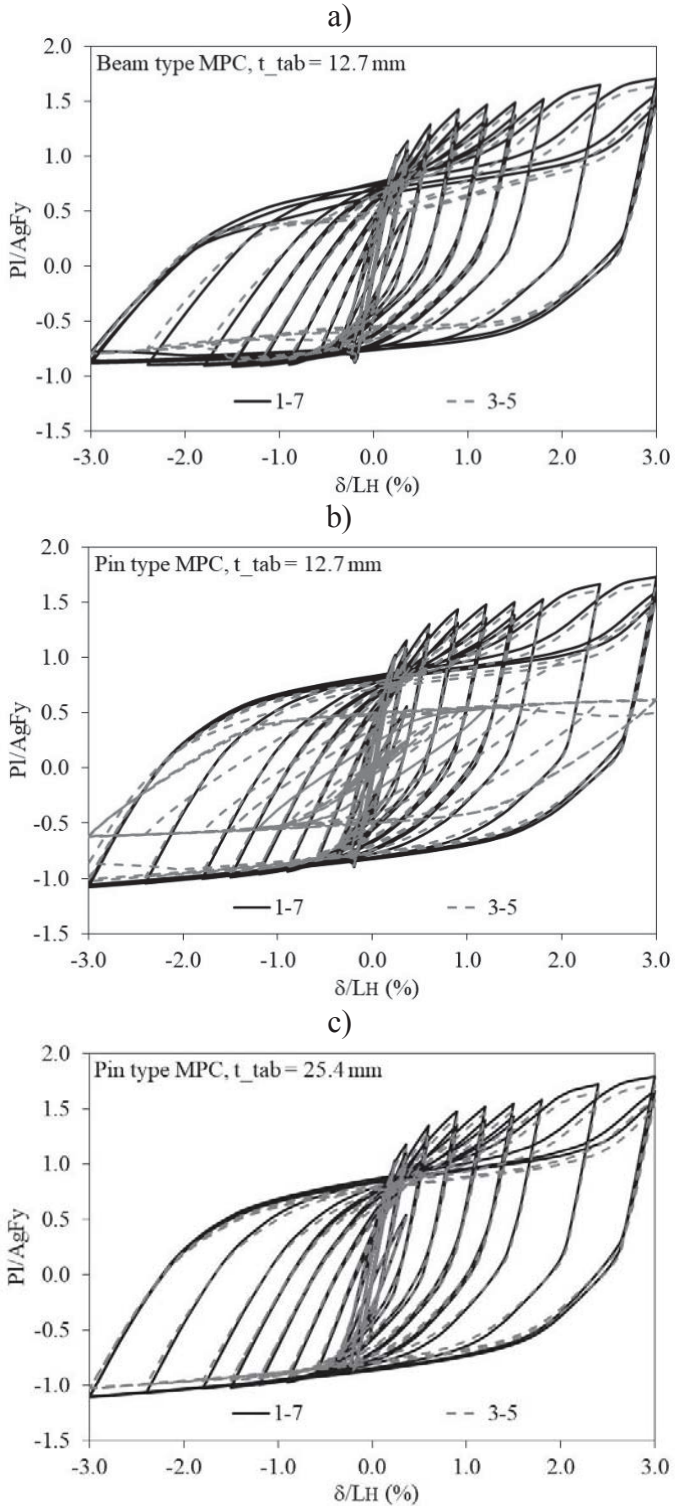

Figure 6: Effect of number of bolts and thickness of tab-plate on the cyclic hysteresis response for (a) beam type MPC with tab-plate thickness of 12.7 mm, (b) pin type MPC with tab-plate thickness of 12.7 mm, and (c) pin type MPC with tab-plate thickness of 25.4 mm. 1-7 means 7 MPCs, 3-5 means 3 MPCs.

The in-plane rotational capacity of the tab-plate connections comes from the distortion of the bolt holes in bearing, from the bolt deformation in shear and from the out-of-plane bending of the tab-plate. Tab-plates with long projections have the tendency of lateral torsional buckling (W27 compared to W18 or W21, for instance). For beams over 610 mm (24 in) nominal depth, the span to depth ratio of the beam should not exceed 20 and the vertical distance between extreme bolts should not exceed 530.86 mm (20.9 in) according to the standard fin-plates connection details of the British standards. The current W27 × 235 beam complies with the British standards. However, the effect of restraining the end beam away from the gusset connection on the hysteresis response is negligible. Therefore, increasing the thickness of tab-plates and reducing the number of bolts while increasing their sizes will reduce the possibility of lateral torsional buckling of the tab-plates.

The effect of increasing the thickness of the stiffener plates on the hysteresis response is negligible for the braced frame modelled in the current study.

Gusset plates must resist the full tensile and compressive capacities of the WF brace during significant cyclic loading [26-29] and permit large inelastic out-of-plane deformation when the brace buckles [30]. Increasing the thickness of gusset plates from 34.925 mm (1 3/8 in.) to 47.625 mm (1 7/8 in.) has a negligible effect on the hysteresis response as shown in Figure 7.

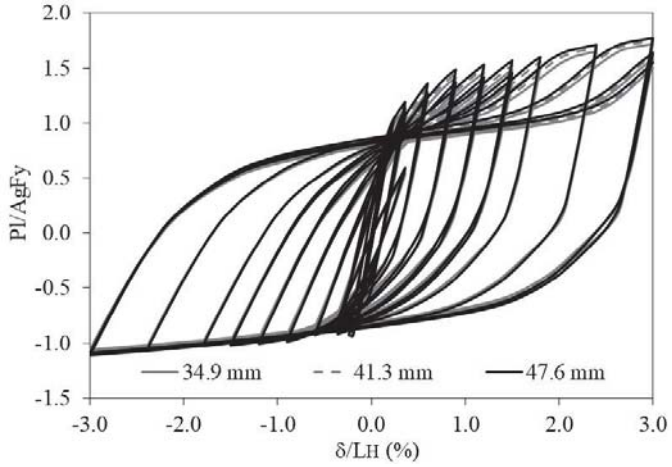

Figure 7: Effect of gusset thickness on the cyclic hysteresis response.

4 FRACTURE LIFE OF BRACE AND PERFORMANCE OF THE FRAME

The fracture life of the brace was not affected by the presence of the frame when using the calibrated cyclic void growth model (CVGM) for ultra-low cycle fatigue based on the significant cumulative plastic strains. A typical fracture life for the horizontal brace is shown in Figure 8. An average value of 2.90 was determined for the monotonic tensile capacity, which is similar to the value obtained by Kanvinde and Deierlein [25] for AW50 (ASTM A572 Grade 50) steel [31]. To predict the initiation of fracture of the WF brace the capacity was decreased with a degradation coefficient of 0.11, obtained by trial and error. The effect of reducing the number of bolts did not affect the fracture life of the brace.

The significant cumulative plastic strains were greater at both the corners of the gusset plate and at the tab-plates especially at the upper and lower locations of the MPCs connecting the tab-plates to the web of the beam compared to those at the mid-span plastic hinge of the WF brace member. This suggests that weld fracture may occur at these locations before the initiation of brace fracture at the mid-span plastic hinge.

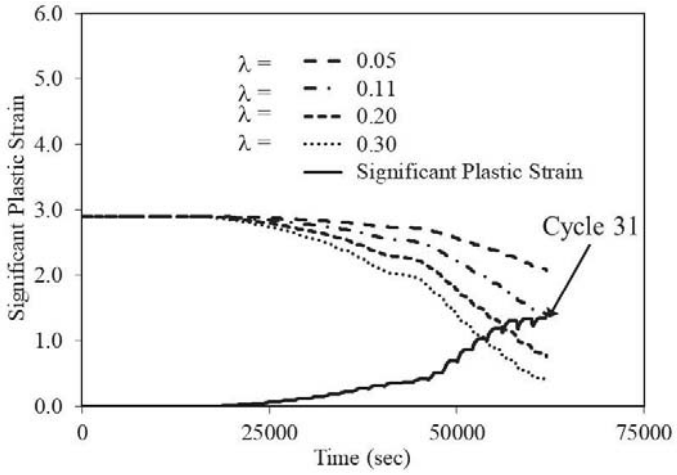

Figure 8: Fracture life of W6 brace.

5 CONCLUSIONS

- Increasing the thickness of the tab-plate will reduce the possibility of fracture of the weld connecting the tab-plate to the flange of the column. In addition, increasing the thickness of the tab-plate will force yielding in the web of the beam and prevent fracture of the tab-plates.
- Reducing the number of bolts while increasing both their diameter and the thickness of tab-plates to satisfy the AISC standards for tab-plate connection design had negligible effect on the hysteresis response of braced frames. Companies are producing bolts with larger diameters than what is available in the AISC tables.
- Reducing the number of bolts reduces the yielding demand on the connection and increases the rotational flexibility of the connection.

ACKNOWLEDGEMENT

The study was funded the Research Grants of the UAE University (SEED – G00001044 and UPAR – G00001916). In addition, thanks to the UAE University for providing the computational simulation facilities to conduct the current research.

REFERENCES

[1] M. Haddad, N. Shrive, Simulating the cyclic behaviour of a single-bay wide-flange steel braced frame, *Proceedings of the XI International Conference on Structural Dynamics*, EURODYN 2020, Athens, Greece, 23-25 November 2020.

[2] M. Haddad, T. Brown, N. Shrive, Finite Element Modeling of Concentrically Braced Steel Frames for Earthquakes, *Proceedings of the 13th World Conference on Earthquake Engineering*, Vancouver, BC., Canada. August 1-6, 2004 [Paper No. 2816].

[3] M.A. Haddad, T.G. Brown, N.G. Shrive, Finite element modeling of concentric HSS braces under cyclic loading, *Canadian Journal of Civil Engineering* 38(5), 493-505, 2011.

[4] M. Haddad, Concentric tubular steel braces subjected to seismic loading: Finite element modeling, *Journal of Constructional Steel Research* 104, 155-166, 2015.

[5] M. Haddad, R. Tremblay, L. Chen, L. Tirca, Cracking and Fracture of Concentric HSS Braces, *The 5th International Conference on Computational Methods in Structural Dynamics and Earthquake Engineering*, COMPDYN 2015. 25 - 27 May 2015 Crete Island, Greece [16p. paper].

[6] M. Haddad, Cyclic behavior and finite element modeling of wide flange steel bracing members, *Thin-walled Structures* 111, 65-79, 2017.

[7] M. Haddad, R. Haddad, A. Al Qadi, H. Al-Mattarneh, Inelastic Cyclic Behavior and Fracture of Wide Flange Steel Brace Members, *Proceedings of the 16th European Conference on Earthquake Engineering*, Thessaloniki City, Greece, 2018.

[8] P. Uriz, Towards Earthquake Resistant Design of Concentrically Braced Steel Structures, *Ph.D. Thesis, Department of Civil Engineering*, University of California, Berkeley, CA., 2005.

[9] P. Uriz, F.C. Filippou, S.A. Mahin, Model for cyclic inelastic buckling of steel braces, *Journal of Structural Engineering - ASCE* 134(4), 619-628, 2008.

[10] B.V. Fell, A.M. Kanvinde, G.G. Deierlein, Large-Scale Testing and Simulation of Earthquake Induced Ultra Low Cycle Fatigue in Bracing Members Subjected to Cyclic Inelastic Buckling, *Report No. 172, Department of Civil and Environmental Engineering*, Stanford University, San Francisco, California, 2010.

[11] A.T. Myers, G.G. Deierlein, A.M. Kanvinde, Testing and Probabilistic Simulation of Ductile Fracture Initiation in Structural Steel Components and Weldments. *Report No. 170, Department of Civil and Environmental Engineering*, Stanford University, San Francisco, California, 2009.

[12] Y. Huang, S.A. Mahin, A cyclic Damage Plasticity Model: Implementation and Applications, *Proceedings of the 10th International LS-DYNA Users Conference*, Dearborn, Michigan USA. June 8-10, 2008 [14p. paper].

[13] Y. Huang, S.A. Mahin, Simulating the Inelastic Seismic Behavior of Steel Braced Frames Including the Effect of Low-Cycle Fatigue, *Report No. 2010/104, Pacific Earthquake Engineering Research Center*, University of California, Berkeley, CA., 2010.

[14] J.W. Lai, Experimental and Analytical Studies on the Seismic Behavior of Conventional and Hybrid Braced Frames, *Ph.D. Thesis, Department of Civil Engineering*, University of California, Berkeley, CA., 2013.

[15] E.P. Popov, R.G. Black, Steel struts under severe cyclic loadings, *Journal of Structural Engineering Division - ASCE* 107(ST9), 1857-1881, 1981.

[16] H. Gugerli, S.C. Goel, Inelastic Cyclic Behavior of Steel Bracing Members, *Report No. UMEE 82R1, Department of Civil Engineering*, University of Michigan, Ann Arbor, Michigan, 1982.

[17] B.V. Fell, A.M. Kanwinde, G.G. Deierlein, A.T. Myers, X. Fu, Buckling and Fracture of Concentric Braces under Inelastic Cyclic Loading, *Steel Tips, Structural Steel Education Council*, Moraga, CA., 2006.

[18] R. Tremblay, M. Haddad, G. Martinez, J. Richard, K. Moffatt, Inelastic Cyclic Testing of Large Size Steel Bracing Members, *Proceedings of the 14th World Conference on Earthquake Engineering*, Beijing, China, 2008 [Paper No. 05-05-0071].

[19] J. Richard, Étude Du Comportement Sismique de Bâtiments Industriels avec Systèmes de Contreventement en Acier de Faible Ductilité, *M.Sc. Thesis, Department of Civil, Geological and Mining Engineering, Montreal Polytechnic*, Montreal, QC, 2009.

[20] J. Powell, Evaluation of Special Concentrically Braced Frames for Improved Seismic Performance and Constructability, *A thesis submitted in partial fulfillment of the MSCE degree in Civil Engineering*, University of Washington, Seattle, 2009.

[21] K.A. Clark, Experimental Performance of Multi-Story X-Brace Systems, *A thesis submitted in partial fulfillment of the MSCE degree in Civil Engineering*, University of Washington, Seattle, 2009.

[22] P.C. Hsiao, Seismic Performance Evaluation of Concentrically Braced Frames, *A dissertation submitted in partial fulfillment of the PhD degree in Civil Engineering*, University of Washington, Seattle, 2010.

[23] M. Haddad, N. Shrive, Investigating the inelastic cyclic behaviour of large-size steel wide-flange section braces, *Construction and Building Materials* 199(28), 92-105, 2019.

[24] Abaqus, User's Manual, Version, 11.6, *Hibbitt, Karlsson, and Sorensen, Inc.,* Providence, RI., 2011.

[25] A.M. Kanvinde, G.G. Deierlein, Micromechanical simulation of earthquake-induced fracture in steel structures, *Technical Report 145, John A. Blume Earthquake Engineering Center*, Stanford University, California, USA, 2004.

[26] M.A. Haddad, Design of concentrically braced steel frames for earthquakes, *A dissertation submitted in partial fulfillment of the PhD degree in Civil Engineering*, University of Calgary, Calgary AB, Canada, 2004. http://dx.doi.org/10.11575/PRISM/18398

[27] M. Haddad, R. Tremblay, Influence of Connection Design on the Inelastic Seismic Response of HSS Steel Bracing Members, *Proceedings of the 11th Inter Symposium and IIW Inter Conference on Tubular Structures*, Quebec City, Quebec, Canada, 2006 [pp. 639-646].

[28] M.A. Haddad, T.G. Brown, N.G. Shrive, Experimental cyclic loading of concentric HSS braces, *Canadian Journal of Civil Engineering* 38 (1), 110-123, 2011

[29] M. Haddad, Intermediate HSS bracing members during seismic excitations: modeling, design, and behavior, *Frontiers of Structural and Civil Engineering* 12(1), 148-162, 2018. https://doi.org/10.1007/s11709-016-0375-5

[30] A. Astaneh-Asl, S.C. Goel, R.D. Hanson, Cyclic out-of-plane buckling of double-angle bracing, *Journal of Structural Engineering - ASCE* 111, 1135-1153, 1985.

[31] ASTM A572 Standard Specification for High-Strength Low-Alloy Columbium-Vanadium Steels of Structural Quality.

EURODYN 2020
XI International Conference on Structural Dynamics
M. Papadrakakis, M. Fragiadakis, C. Papadimitriou (eds.)
Athens, Greece, 23–26 November 2020

EFFECT OF DIFFERENT CONFIGURATIONS OF A GEOFOAM-FILLED BARRIER IN VIBRATION SCATTERING AND ITS OPTIMIZATION BY GENETIC ALGORITHM

Mehran Naghizadehrokni[1], **Martin Ziegler**[2]

[1]RWTH Aachen University, PhD Applicant
Mies-van-der-Rohe-Str. 1, D-52074 Aachen
e-mail: Naghizadehrokni@geotechnik.rwth-aachen.de

[2] RWTH Aachen University, Professor
Mies-van-der-Rohe-Str. 1, D-52074 Aachen
e-mail: Ziegler@geotechnik.rwth-aachen.de

Keywords: Ground-born vibration isolation, Trench, Wave attenuation, optimization.

Abstract. *This paper deals with the effectiveness of various configurations of a geofoam-filled barrier including single, double and triangle wall trenches in isolating the ground vibrations induced by a harmonic load. A $3D$ finite element program (Plaxis) is used and the model is verified by the result of the analytical solution for the active scheme. Furthermore, a comprehensive parametric study is performed to evaluate the effect of geometrical factors including the depth, width and the length for all systems. The main assumption during the parametric study is treating each parameter as an independent variable and keeping other parameters constant. A genetic algorithm is a proper tool for optimizing all key parameters that can have mutual effects on the vibration attenuation since the vibration isolation is a non-linear problem. A genetic algorithm code is implemented with the help of Python Software and Finite Element Program (Plaxis) for all three systems and the optimized parameters for reaching 75% efficiency of the barrier are calculated. The result of the parametric study showed that the single wall system needs the lowest value of normalized depth for reaching the highest value of the efficiency. Also, the mutual study of all parameters proved that the results are very different from a single parametric study. The comparison of all systems demonstrated that a double wall barrier is the best system for different frequencies.*

1 INTRODUCTION

The number of people who are interested in living in the big towns are increasing. This growth in population results in constructing more buildings and transport networks in and around the city [1]. Therefore, residence will have more vibration problems from the vibration sources like the passing train, machine foundation, traffic and other constructional activities. The body and Rayleigh waves produced from these sources results in ground-born vibration. The vibration is transmitted through the ground surface to the foundation of the building and create distress to the buildings and their inhabitants [2]. Mitigation measures are used to solve this problem, which include control of the vibration at the source, along the propagation path and at the place of immission. This paper deals with mitigation measure in the transmission path through installing a geofoam-filled barrier for attenuating the incoming waves.

Different approaches including experimental and numerical methods have been carried out to solve the problem of vibration isolation by trench. Since the experimental test is too expensive and the parameters to be assessed are fixed, a numerical model is an effective alternative method for assessing governing parameters in vibration isolation.

Woods conducted a series of field tests for evaluating the efficiency of the open trench and suggested that 75% reduction in incoming waves is enough to have a successful system [3]. Multiple rows of geofoam-filled trenches were applied for screening train-induced ground vibration and the results showed that increasing the depth of the barrier up to $1\lambda_{\mathrm{r}}$ is enough to reach the highest value of efficiency and further increase in depth does not have an effect on isolation capability [4]. A full experimental study was investigated to assess the efficiency of open and geofoam-filled barrier and the normalized depth of 0.6 was selected as an optimum depth for both open and geofoam-filled trench [5]. Mahdavisefat et al. [6] performed a full-scale field experiment to study the effect of open and sand-rubber mixture-filled trench and the normalized depth of 1.5 is recommended by the authors for reaching $60-70\%$ of attenuation of the incoming waves.

Tulika et al. investigated the efficiency of open and in-filled barrier by developing a numerical model and concluded that low-density material performs better than high-density [7]. Beskos et al. developed a BEM to study the efficiency of open and concrete filled in homogeneous and layered soils [8]. A FEM was used to evaluate the governing parameters of water and geofoam-filled barrier by [9] and they concluded that depth of the trench is a key parameter for assessing the efficiency of the trench. Ahmad and Al-hussain compared the screening efficiency of the stiff and soft trenches and developed a simple model for predicting the efficiency of the trench in the active and passive schemes [10]. Naghizadehrokni et al. [11] did a full experimental and parametric study and they suggested that the depth and width of approximately $1\lambda_{\mathrm{r}}$ and $0.2\lambda_{\mathrm{r}}$, respectively are enough to reach the acceptable amount of efficiency for the active isolation.

Most studies have mainly focused on one system like rectangular single wall and few researchers compared the efficiency of different configurations of the trench and only a few parametric studies investigated the optimization of different parameters together. Therefore, a full parametric study for assessing the effect of various configurations of geofoam-filled trench is missing. For this purpose, three different systems including the single, double and triangle wall systems are analysed and the efficiency of the systems are compared. There is also a need for mutual optimization of governing factors in evaluating of trench efficiency. It is not possible to treat each parameter as an independent variable in vibration isolation problem.

2 NUMERICAL MODEL

A wave barrier creates a finite material discontinuity for the incoming waves by intercepting, scattering, diffraction and refraction of wave propagation in soil, which can decrease the vibration amplitude beyond the obstacle. A time domain numerical model using the finite element package, Plaxis (2019) is developed to assess the effectiveness of different isolation systems as the wave barriers for the active isolation due to harmonic load in vertical direction. A $3D$ view of the vibration isolation problem and the soil and geofoam properties are illustrated in Fig. 1. Here, the depth D, width W and the length L of the trench are dimensionless values, which are in relation to the Rayleigh wavelength. The geofoam-filled trench is installed at the normalized distance of 1.25 for all three systems. A normalized distance of 7 beyond the trench is selected for calculating the average amplitude reduction ratio.

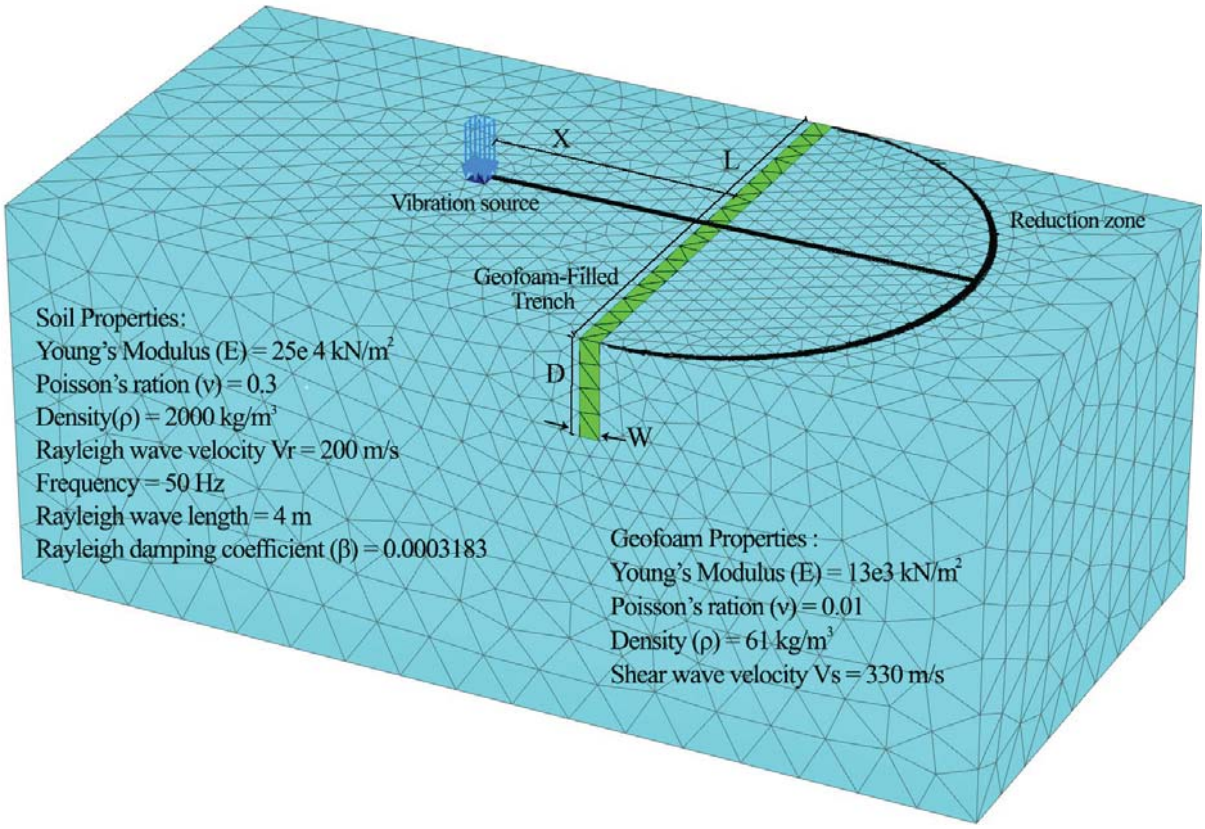

Figure 1: $3D$ model fir finite element analysis

3 ANALYTICAL VALIDATION OF FINITE ELEMENT METHOD

The developed model in Plaxis is verified by comparing the result of wave theory in terms of time of arriving to a specific point. There are two types of elastic waves in the elastic half-space theory including body and surface waves. Body waves are measured through equations 1 and 2.

$$V_p = \sqrt{\frac{E(1-\nu)}{\rho(1+\nu)(1-2\nu)}} \tag{1}$$

$$V_s = \sqrt{\frac{E}{2\rho(1+\nu)}} \tag{2}$$

The Rayleigh wave propagates along the surface of the half-space with a phase velocity, Vr, which is related to the shear wave velocity Vs and the poison's ratio. The Rayleigh wave velocity is calculated by:

$$K^6 - 8K^4 + (24 - 16\alpha^2)K^2 + 16(\alpha^2 - 1) = 1 \tag{3}$$

Where $K = Vr/Vs$ and $\alpha = Vs/Vp$.

Those equation are used just in an isotropic, homogeneous and elastic medium. For verifying the developed model for an open trench, a point at the location of $24\ m$ from the vibration source on the ground surface has been selected. The trench is located at the distance of $12\ m$ from the vibration source with the depth, width of and the length of 3, 0.25 and $10\ m$, respectively. Based on the equations of 1-3 the wave velocities are calculated as:

$$Vp = 406.6,\ Vs = 217.2,\ Vr = 200$$

Hence, the first time of arriving the waves to the selected point are measured as:

$$T_p = (24/406.3) = 0.059sec,\ T_s = (24/217.2) = 0.11sec,\ T_r = (24/200) = 0.12sec$$

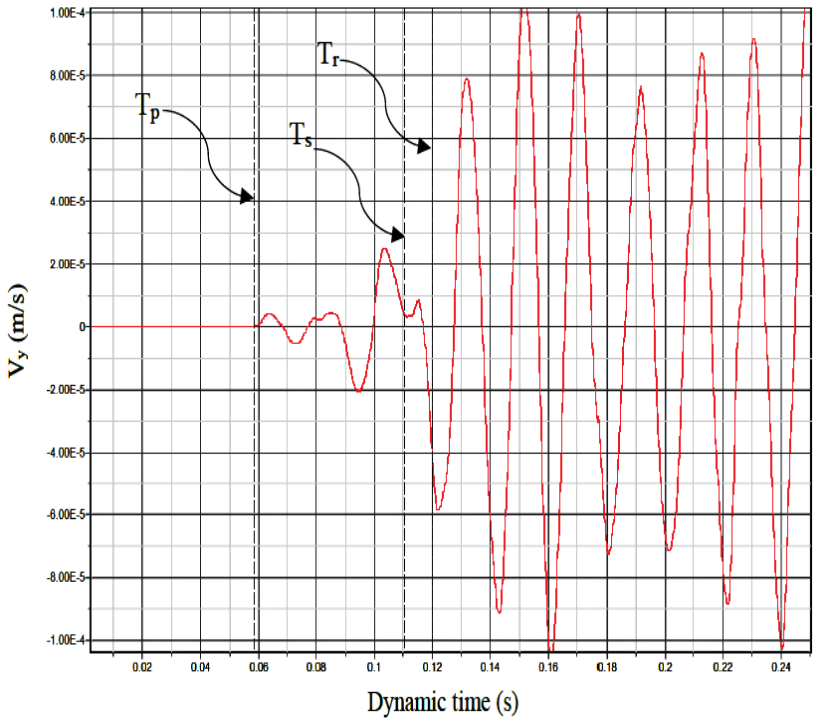

Figure 2: The motion of the selected point in homogeneous, isotropic and elastic soil media without damping

As it can be seen from Fig. 2 that the time of arriving of the body waves (P and S) to the selected point completely matches the analytical solution. The most important vibration will occur after arriving of the Rayleigh wave; that is 0.12 s and it is indicated as the third vertical dashed line. This confirms that the Rayleigh wave is the most important wave that should be considered in vibration isolation problem. Comparing the result of the developed numerical model and the analytical solution of the wave theory confirm the accuracy of Plaxis model.

4 SINGLE WALL SYSTEM

Fig. 3 shows the efficiency of an EPS Geofoam-filled obstacle as a function of normalized length. The average amplitude reduction ratio decreases dramatically with increasing the normalized length from 0.625 to approximately 2.5. It is apparent from the figure that the normalized length beyond around 2.5 does not create any further changes and $\overline{A}_r$ may be conservatively assumed to remind unchanged thereafter. Therefore, the normalized length of 2.5 is selected for the rest of the parametric study.

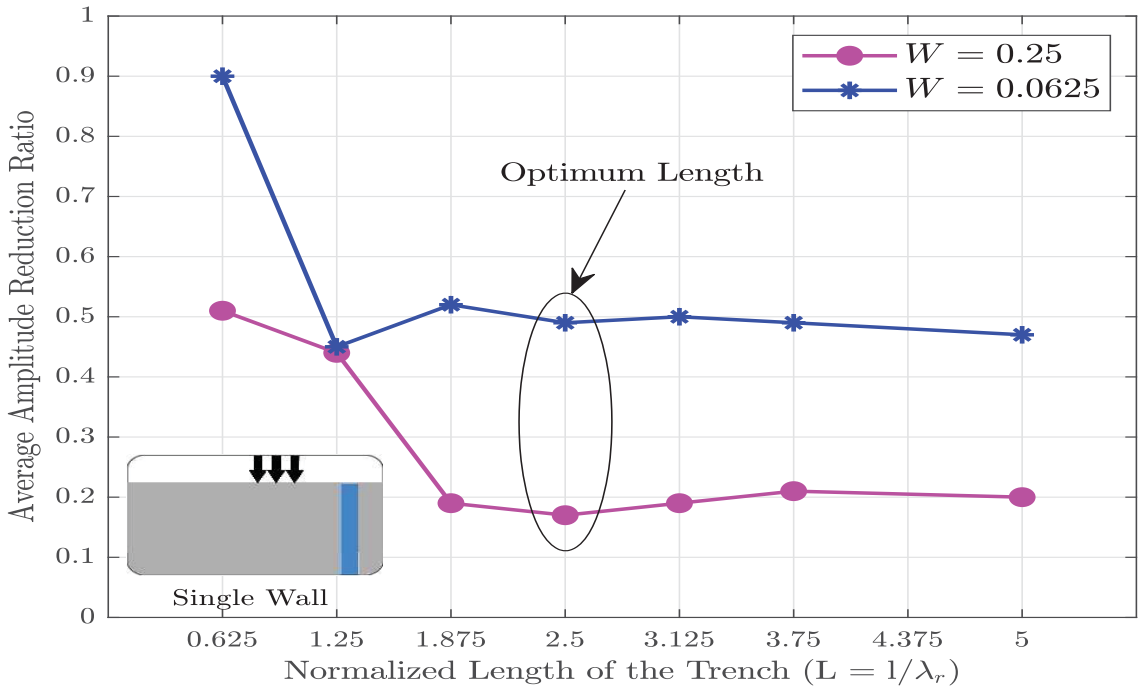

Figure 3: Influence of normalized length of the trench (normalized distance 1.25 from the vibration source, normalized depth of 1.25)

Fig. 4 illustrates the variation of $\overline{A}_r$ along the surface of soil domain for different trench depths. The effect of normalized trench depth is affected in a complex pattern with the effect of normalized trench widths. The efficiency of the trench reaches it's maximum value at D value around 1.25 for almost all widths. The optimum D has a close relationship with the width of the barrier and the efficiency of the trench increases gradually with increasing the normalized width for the same depth (optimum depth). Another important point in this figure is unexpected peaks and valleys in $\overline{A}_r$ value for various widths, which is caused by constructive and destructive interference of the barrier.

The importance of the normalized width on $\overline{A}_r$ is presented in Fig. 5. The width appears to play a significant role in screening efficiency of the trench. A reduction of approximately 50% is visible by increasing W from 0.0625 to 0.25 for almost all trench depths and it seems that $W = 0.25$ is an optimum width for achieving a reasonable amount of wave scattering. Increasing the normalized width means increasing the distance between two corners. The barrier bottom corners act as an additional geometric discontinuity and this issue results in mode conversation of incoming waves for converting part of the R-waves energy into the body waves

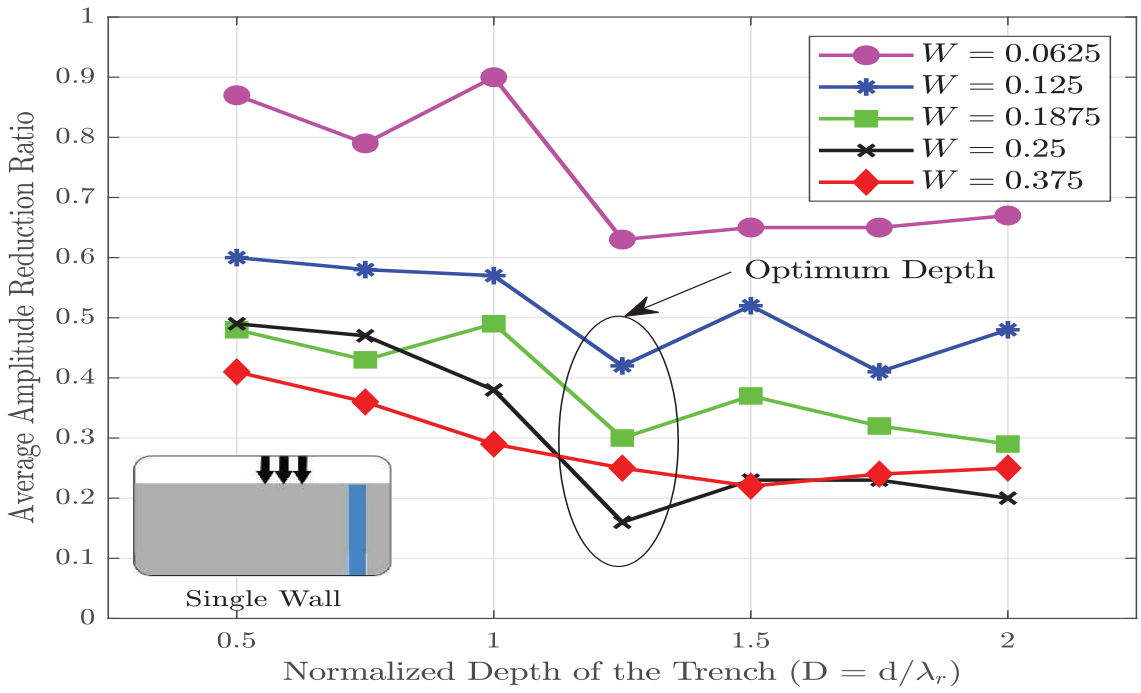

Figure 4: Influence of normalized depth of the trench

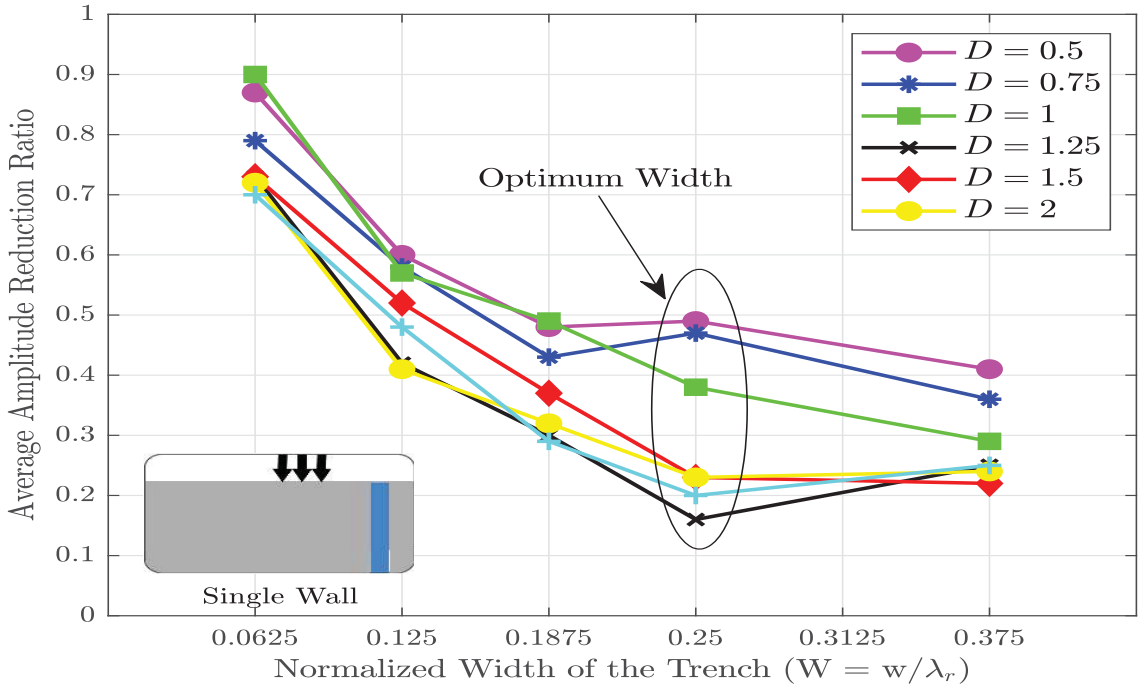

Figure 5: Influence of normalized width of the trench

5 DOUBLE WALL SYSTEM

The efficiency of the double wall system is compared with the single wall system with a thickness of $2W$, having the same width, depth and the length like the single wall obstacle. Hence, for this system the width of both barriers is considered as one width, which is W. This normalized width is the width for both trenches.

At the first step, a parametric study should be done for finding the optimum spacing between the barriers to achieve the best wave attenuation. The influence of spacing between trench walls is plotted in Fig. 6 with the constant normalized depth, width and length of 1, 0.25 and 2.5, respectively.

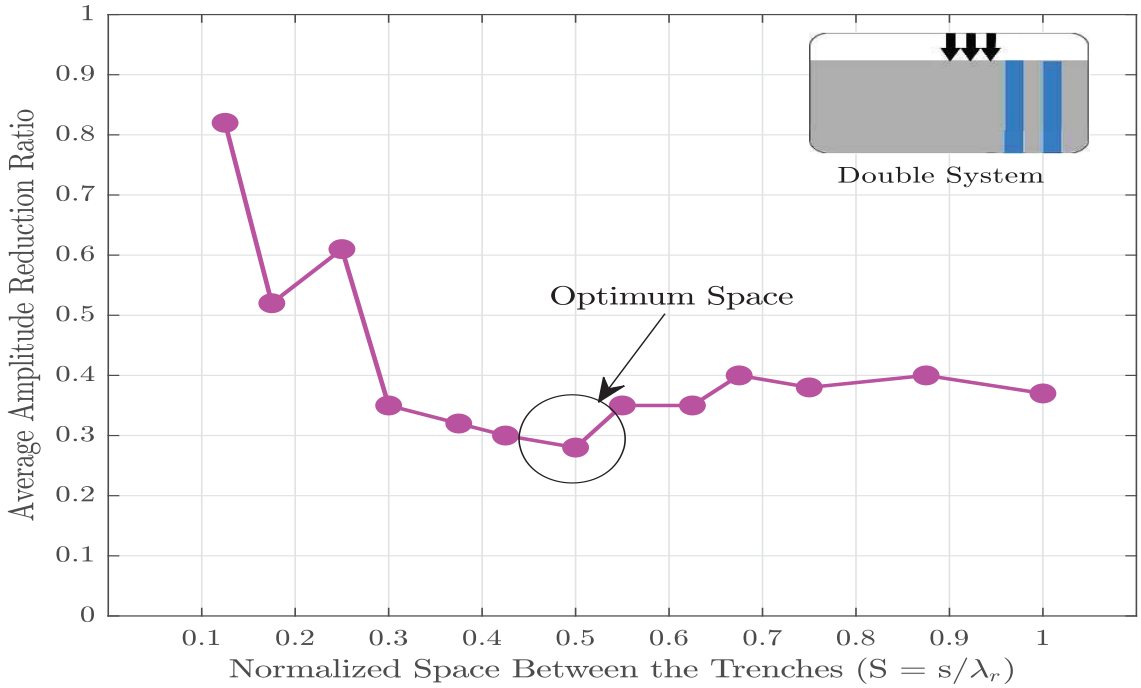

Figure 6: Influence of normalized space between the trenches

The normalized spacing (S) between the walls appears to govern the screening effectiveness of the trench. The efficiency of the double wall system is maximized at S value around 0.5. Therefore, the normalized optimum spacing between the wave barriers is considered as 0.5, which is compatible with the result of [5] for optimum spacing between trenches, for further parametric studies.

An investigation is done for finding the influence of the normalized length on wave attenuation like single wall system. The result of the parametric study doesn't show any specific change in comparison with the result of the single wall study. Therefore, to avoid the presentation of unchanged results, the normalized length of 2.5 is selected as the optimum length for this system.

Based on the information of Fig. 7, which is the calculated value of $\overline{A}_r$ as a function of the normalized depth, D for narrow trench ($W = 0.0625$) seems to govern the wave attenuation for the normalized depth between 0.5 and 1.5. For wider trenches, increasing the normalized depth of the barrier leads to blocking of more incident propagated waves until around $D = 1.25$, which is selected for the optimum depth of the trench for achieving approximately 80% of the barrier's efficiency for the wider trenches.

The effect of the width on $\overline{A}_r$ for an EPS Geofoam-filled barrier is presented in Fig. 8. It is obvious from the results that the value of average amplitude reduction ratio decreases dramatically with increasing the normalized width of the trench from 0.0625 to around 0.2 and thereafter, it remains at the constant value with increasing W to 0.375. An optimum width of almost 0.2 is enough for achieving the highest value of screening performance.

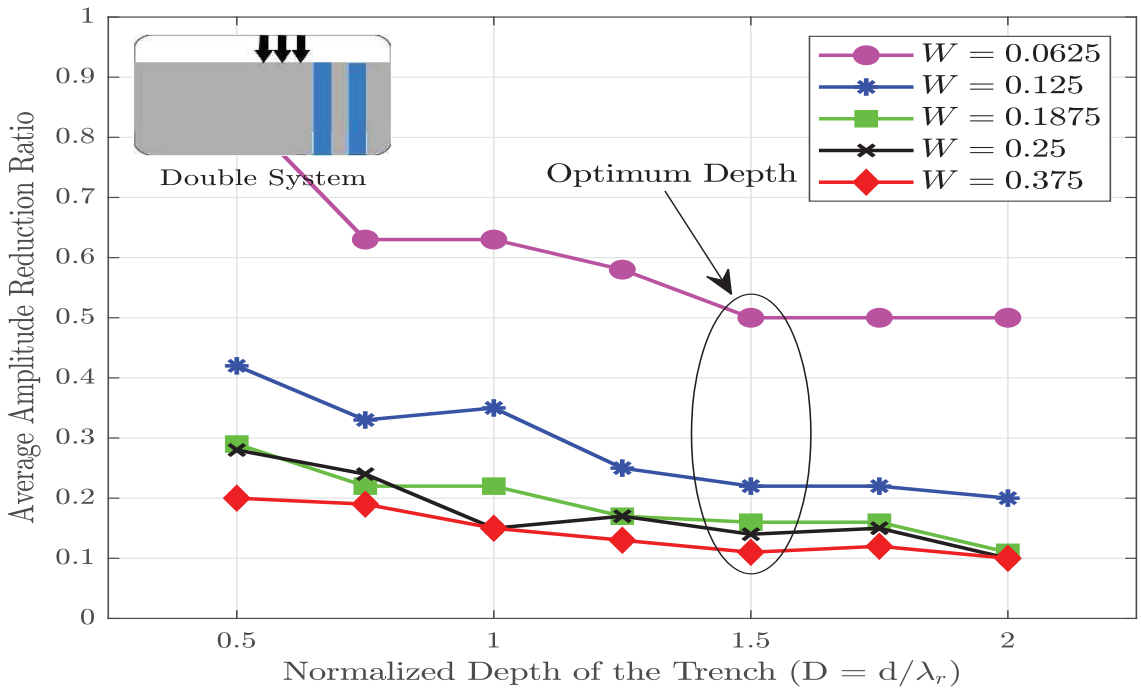

Figure 7: Influence of normalized depth of the trench

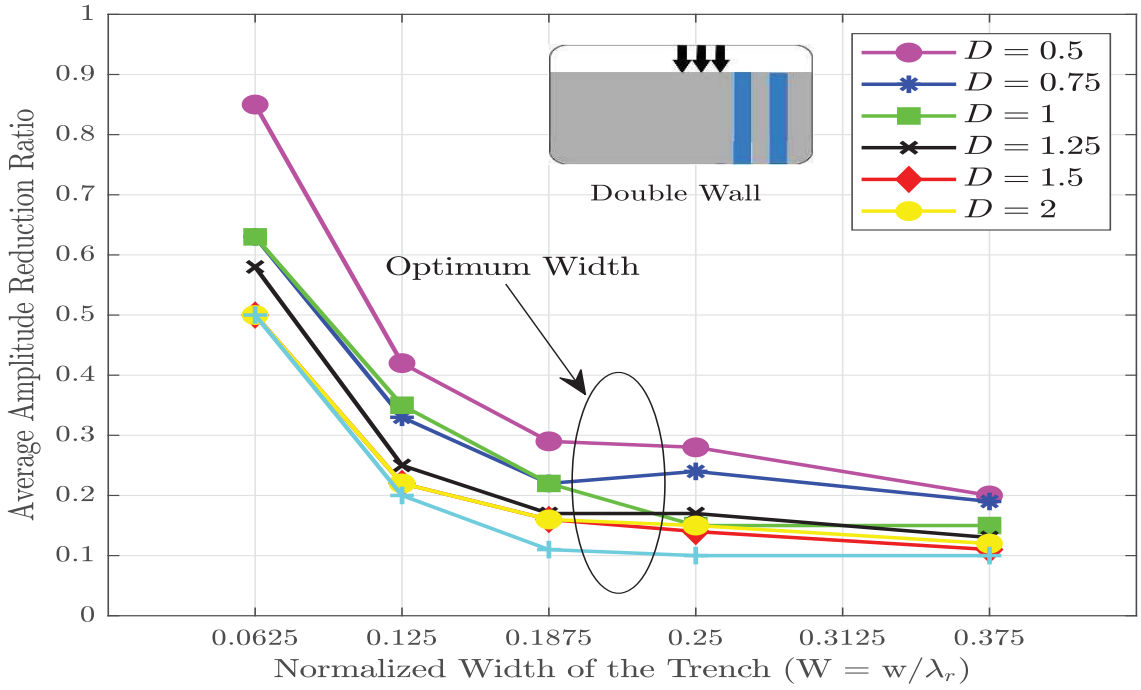

Figure 8: Influence of normalized width of the trench

6 TRIANGLE WALL SYSTEM AS WAVE BARRIER

For making a proper comparison with the single and double wall systems, triangle wall is considered with the same depth and the same area like single and double wall. However the width of the trench is different from those systems. Since increasing the width and the depth of the triangle trench leads to changing in the slope side wall of the trench, inclination

angle is proposed as an alternative parameter for measuring the efficiency of the barrier. As a consequence, the value of inclination angle is calculated with keeping the width of the trench at ground surface constant and calculating the inclination angle through increasing the depth.

A parametric study is done for finding the effect of the length on the efficiency of the trench and to see how far the results match with the results of the single and double wall systems. The results show that an optimum length of 2.5 is enough for the triangle wall system like for previous systems.

The effect of the normalized depth on the wave attenuation performance is presented in Fig. 9. The results reflect that in general a normalized depth of almost 1.5 appears to be the maximum depth for achieving at least 70% of system's effectiveness except for the narrow trench ($W = 0.125$). An approximately 50% reduction for almost all barrier with different normalized widths is seen by increasing D from 0.5 to 1.5

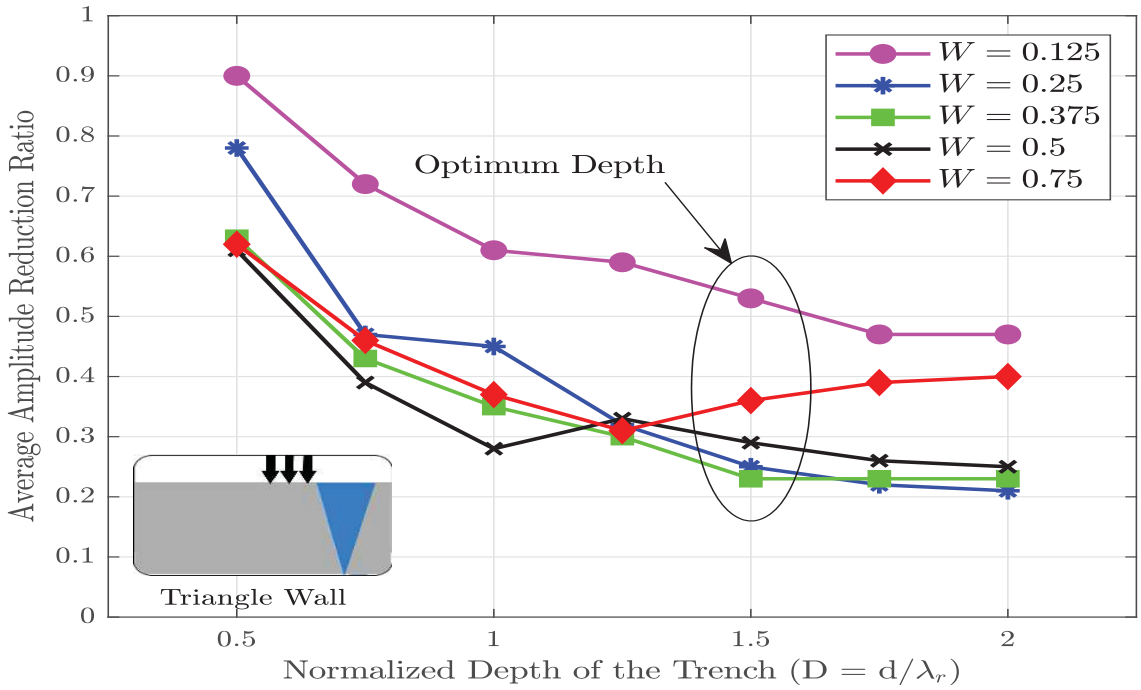

Figure 9: Influence of normalized barrier depth

The effect of varying the normalized width is studied by varying W from 0.125 to 0.75 which is the normalized width of the triangle wall system at the ground surface, while the normalized depth of the trench is varied from 0.5 to 4.

According to Fig. 10, vibration screening performance reaches the highest value when the normalized trench width is approximately 0.4 for shallow trenches ($D = 0.5$ to 1), which is considered as optimum W for shallow barriers. However, increasing the normalized depth ($D > 1$) leads to the highest value of wave attenuation when W is around 0.3. Therefore, a wider trench is needed (for $D < 1$) for reaching the highest value of screening performance, while by increasing the normalized depth of the trench ($D > 1$), a slender barrier is sufficient for reaching highest value of vibration isolation.

The performance of the trench inclination angle is investigated for $W = 0.125$ and three different normalized locations including 0.5, 1.25 and 2, respectively. Fig. 11 represent the effect of inclination on different situations.

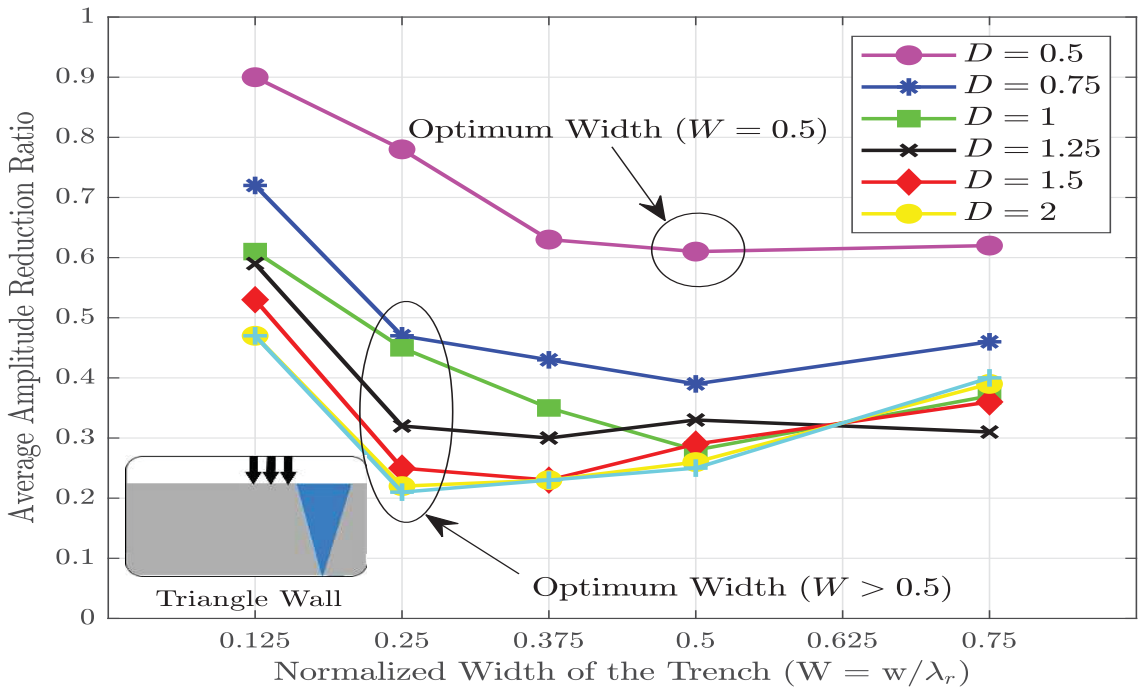

Figure 10: Influence of normalized width on the trench

It is observed that the average amplitude reduction ratio decreases dramatically with increasing the inclination angle from 35 to 60 degree. This angle is considered as the optimum angle for all locations.

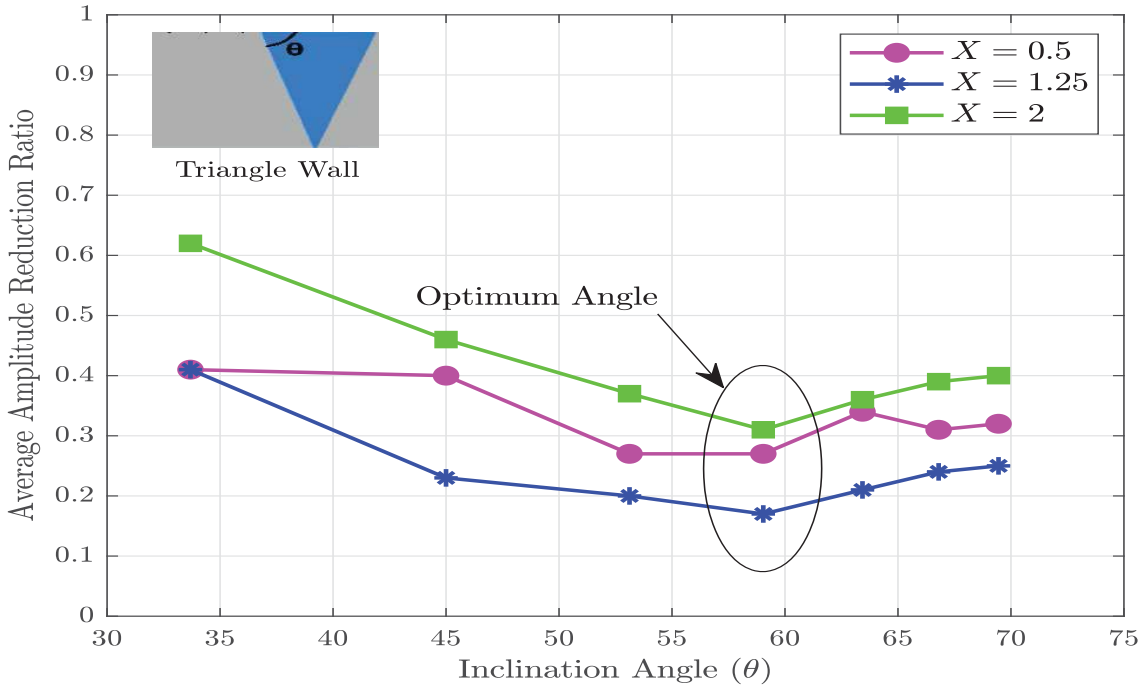

Figure 11: Influence of inclination angle of the trench with ground surface (normalized width 0.125)

7 COMPARISON OF DIFFERENT SYSTEMS

A comparison is performed between all proposed systems through calculating the screening performance as a function of D. The results are depicted in Fig. 12. The results show that the efficiency of the trench increases by increasing D for both widths ($W = 0.0625$ and 1). There is a considerable gap between the value of $\overline{A}_r$ for narrow and wide trenches that shows the significance of W.

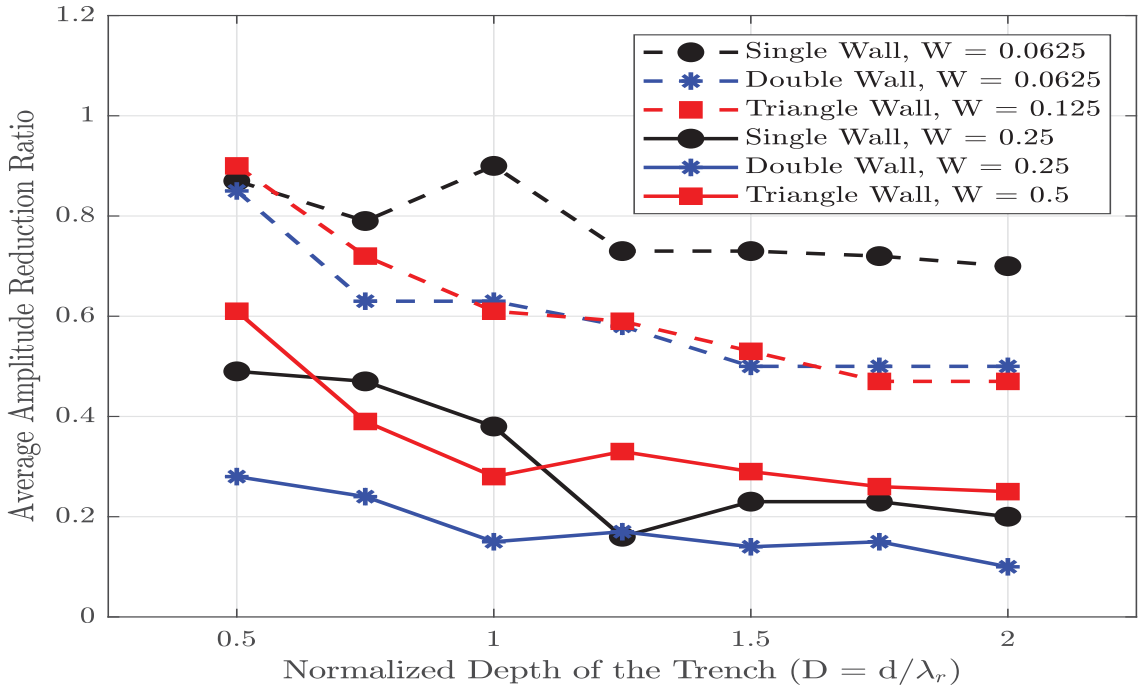

Figure 12: Comparison between different systems (normalized distance 2 from the vibration source)

Regarding the narrow trench, double wall systems has the highest value of screening efficiency for the normalized depth until 1. After this depth, double and triangle wall barriers have almost the same efficiency for all depths. However, the single wall system has the lowest value of efficiency in comparison with other systems.

As the width of the systems increases, the efficiency of all systems increases, too. However, the double wall system still performs better than the other systems in attenuating the incoming waves. There is a remarkable decrease in the amount of $\overline{A}_r$ for the single wall barrier which is the result of increasing the depth from 1 to 1.25. For making a comparison for the single and triangle wall system, it is divided into two different categories for shallower trenches ($D < 1$), in which triangle wall has better efficiency and deeper trenches ($D > 1$), in which single wall has more capability in blocking the incoming waves.

8 OPTIMIZATION PROCESS WITH GENETIC ALGORITHM

Until now, the problem of the vibration isolation has been solved for a specific parameter like depth, width, length or locations and keeping other factors constant. However, it is not reasonable to compute the wave barrier performance by allowing just one parameter to change since the parametric study proved that the dimensional and geometrical factors of a barrier are not independent and sometimes they may have an effect on each other. Therefore, it is imperative to study the mutual effect of all parameters including the dimensional and geometrical factors to

implement a successful wave barrier through optimal combination of parameters. This aim has been achieved through a genetic algorithm optimization technique for three different configurations of obstacles including the single, double and the triangle wall systems, respectively. It was tried to adjust the parameters to reach the same value of cross-sectional area for each system. The first step in the implementation of a genetic algorithm is to randomly create an initial population. Through reviewing empirical studies carried out and doing some trial and error for the initial population, population size equal 30 is found to be optimal for the problems in vibration isolation. Since the vibration isolation problem is an inherent complex and non-linear problem, the finite element program (Plaxis) and Python programming language are utilized as a fitness function to calculate the quality of a chromosome as a solution. A remote scripting interface is an option for building a model automatically in Plaxis and this ability creates a possibility to use Plaxis as a fitness function in genetic algorithm. The code is developed for vibration isolation study and all analyses steps are automatized. Another important feature of this code is the changeability of the soil and geofoam material, the geometrical dimensions and the shape of the barrier.

Woods suggested that a successful wave barrier should reach at least 75% mitigation in scattering of incoming waves. On the other hand, reaching to a deep trench like 5 or $6\ m$ is relatively tough and sometimes impossible in reality. All of these issues lead to create a restriction amount for $\overline{A}_r$ which is 0.75. In addition, we know that depth of the trench is one of the most important factors in achieving an acceptable efficiency for the wave mitigation. Therefore, defining a cost function for optimizing $\overline{A}_r$ value and simultaneously considering the depth of the barrier is a proper solution for increasing the importance of D in the optimization process. This is done by assigning two different constant coefficients including Alpha and Beta for $\overline{A}_r$ and the depth in a cost function, which are 0.995 and 0.005, respectively.

The next step is applying crossover, which is the genetic operator and uses to combine two chromosomes, or parents, to generate a crossover child for the next generation. Crossover is applied to the random selected parents with a crossover probability Pc of equal 0.8. The mutation operator is applied with a mutation probability Pm equal to 0.2. After completing the process of selection, recombination and mutation, the next population can be generated. This process of evaluation, selection, recombination and mutation is repeated until finishing the iteration number. A summary of implementation of the genetic algorithm for vibration isolation problem is presented in Fig. 13.

9 OPTIMIZATION OF DIFFERENT SYSTEMS

A genetic algorithm code with the above-mentioned properties is implemented in Python through writing a script for optimizing various parameters of the trench. It is mandatory to write a script that is readable by Plaxis for creating the model automatically including soil contour, borehole, soil model, structure, mesh, calculation phases, and calculating the efficiency of the trench.

A quantitative range for different parameters is defined for finding the optimal solutions of the problem. In order to make a proper comparison for all three configurations, the same depth and cross-sectional area is assumed for all three systems. For each system, different boundaries are defined as the maximum and minimum value for various variables, which are presented in Table 1.

A genetic algorithm is used for optimizing the important parameters of the barrier for the vibration isolation problem for reaching the efficiency of almost 75%. The variation of the parameters is assumed as the same value for having the equal cross-sectional area, while one of

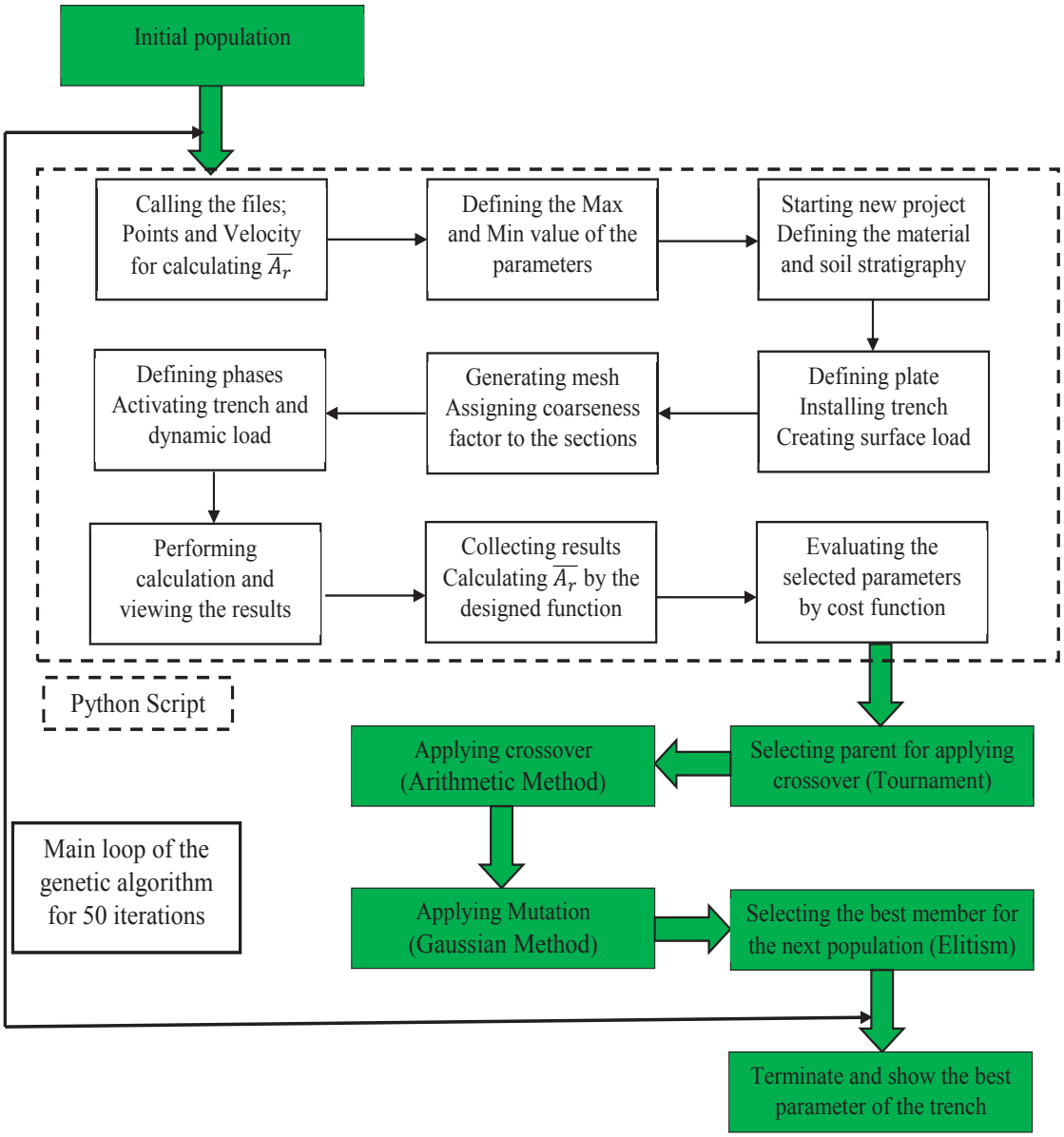

Figure 13: Implementation of the genetic algorithm for the vibration isolation problem

Type of system	Location (m)	Depth (m)	Width (m)	Length (m)	Distance (m)
Single	2-20	2-6	0.25-1	5-15	-
Double	2-20	2-6	0.25-1	5-15	2-4
Triangle	2-20	2-6	0.5-2	5-15	-

Table 1: Defined boundaries for different parameters in the genetic algorithm

the purposes of this study is evaluating the effect of the shape of the trench on mitigating of the incoming waves. The optimal parameters of geofoam-filled barrier for different systems in the case of active isolation and for the frequency of $50\ Hz$ is presented in Table 2.

The trench length for the single wall system is calculated with the same value of parametric study, so it is concluded that the length of $10\ m$ for the single wall system is suitable for reaching the desired efficiency. In addition, the space between the barriers for double wall system is in a

System	Location (m)	Depth (m)	Width (m)	Length (m)	Distance between trenches (m)	Efficiency (%)
Single Wall	5.38	2.96	0.95	10	-	78
Double Wall	4.06	2.6	1.2	6.05	2	78
Triangle Wall	2.18	2.98	1.92	8.15	-	74

Table 2: Optimized dimensions of the trench for different systems ($50Hz$)

good agreement with the result of parametric study.

An initial observation of the optimized parameters shows that the triangle wall system should be installed more near to the vibration source in comparison with other systems. In addition, the results show that the depth of the barrier is almost independent on the shape of the trench for the single and triangle wall systems, since the depth of the trench reminds almost has the same value for these systems. A pair of double wall barriers needs more width and lower depth in comparison with other configurations. Moreover, the length of the trench decreases in comparison with the other systems. Generally speaking, if reaching a depth of around $3m$ is difficult for a trench, double wall system is a good solution by having lower depth.

10 COMPARISON BETWEEN DIFFERENT SYSTEMS

Since the frequency of the applied load plays an important role in vibration isolation, a comparison has been done for different configurations with optimized parameters. By changing the frequency of the applied load, the average amplitude reduction ratio is calculated for the vertical response for the area beyond the trench and the results are illustrated in Fig. 14.

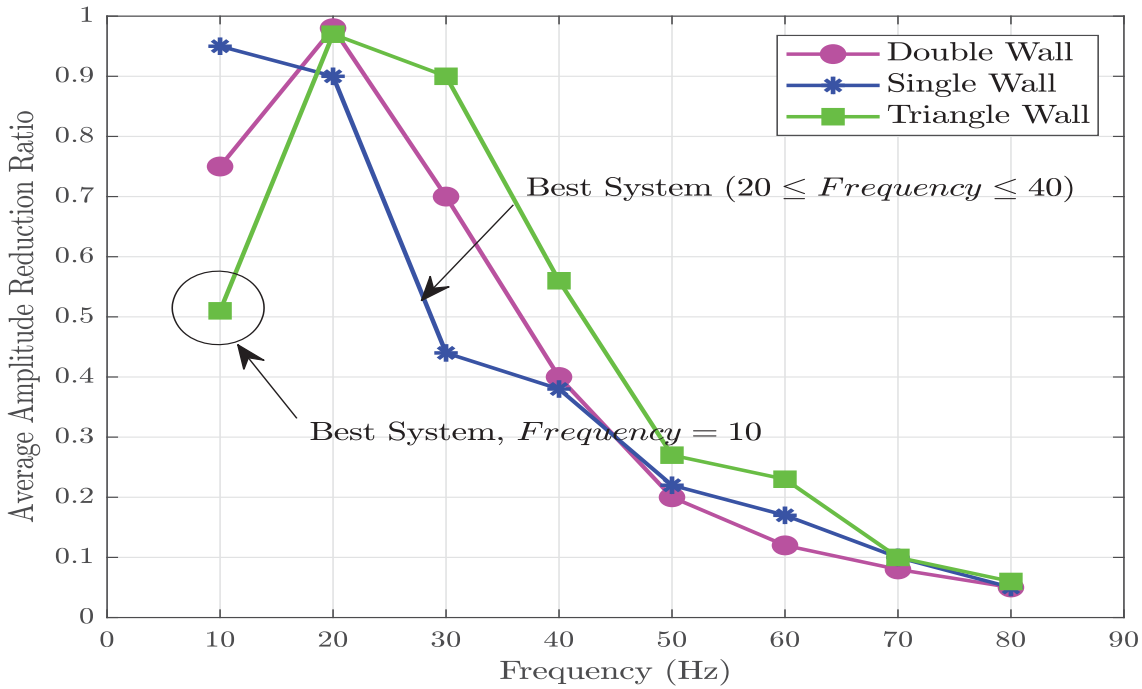

Figure 14: Influence of frequency of the applied load (Optimized parameters for all systems)

The results state that frequency of applied load plays a significant role in attenuating of incoming waves for various systems including the triangle, double and the single wall in orders.

Increasing the frequency of the load leads to a dramatic decrease in $\overline{A}_r$ value. For instance, increasing the frequency of the applied load from 20 to $70HZ$ results in reducing the average amplitude reduction ratios, which are approximately 85% for almost all systems.

11 Conclusion

The developed numerical model is verified by an analytical method. Then, a full parametric study is done for evaluating the effect of the governing factors including the depth, width and the length of the barrier in the active isolation and the results are compared. Three different systems including the single, double and the triangle wall are selected for assessing the effect of the shape of the trench on vibration isolation. Based on the results of parametric investigations:

- The normalized length of 2.5 is recommended for all three systems for having the highest amount of efficiency.
- The single wall system needs the lowest value of normalized depth for attenuating the incoming waves at an optimum depth, which is equal to 1.25. However, the optimum depth for double and triangle wall system is calculated to 1.5.
- The double wall system needs an optimum width of 0.2, which is the lowest width in comparison with other systems, whereas the optimum width of single wall system is calculated to 0.25. For triangle wall system, shallow trenches need more width ($W = 0.4$) to reach the highest value of efficiency in comparison with a deep trench, which is 0.3.
- The double wall is the best system for attenuating the highest amount of incoming waves in comparison with other systems.

Finally, the most significant finding of the research is the developed genetic algorithm code that can be used as a reference for geotechnical engineers for designing the barrier for achieving at least 75% mitigation in vibration amplitudes. In addition, the mutual study of all parameters demonstrated that the results are different to those of a single parametric study. The result of the comparison of all systems in the frequency domain revealed that the single and the double wall barriers are the best systems for the frequency in the range of $20-40\ Hz$ for the active isolation and the triangle wall system is highly recommended for the frequency of $10\ Hz$. However,

REFERENCES

[1] Kattis, S. E., D. Polyzos, and D. E. Beskos. “Modelling of pile wave barriers by effective trenches and their screening effectiveness.” *Soil Dynamics and Earthquake Engineering* 18.1 (1999): 1-10.

[2] Haupt, W. A. “Wave propagation in the ground and isolation measures.” (1995).

[3] Woods, Richard D. *Screening of suface waves in soils*. 1968.

[4] Pu, Xingbo, Zhifei Shi, and Hongjun Xiang. “Feasibility of ambient vibration screening by periodic geofoam-filled trenches.” *Soil Dynamics and Earthquake Engineering* 104 (2018): 228-235.

[5] Alzawi, Ashref, and M. Hesham El Naggar. “Full scale experimental study on vibration scattering using open and in-filled (GeoFoam) wave barriers.” *Soil Dynamics and Earthquake Engineering* 31.3 (2011): 306-317.

[6] Mahdavisefat, E., H. Salehzadeh, and A. A. Heshmati. “Full-scale experimental study on screening effectiveness of SRM-filled trench barriers.” *Géotechnique* 68.10 (2018): 869-882.

[7] Bose, Tulika, et al. “Efficiency of Open and Infill Trenches in Mitigating Ground-Borne Vibrations.” *Journal of Geotechnical and Geoenvironmental Engineering* 144.8 (2018): 04018048.

[8] Beskos, D. E., B. Dasgupta, and I. G. Vardoulakis. “Vibration isolation using open or filled trenches.” *Computational mechanics* 1.1 (1986): 43-63.

[9] Liyanapathirana, D. S., and Sanka D. Ekanayake. “Application of EPS geofoam in attenuating ground vibrations during vibratory pile driving.” *Geotextiles and Geomembranes* 44.1 (2016): 59-69.

[10] Ahmad, S., and T. M. Al-Hussaini. “Simplified design for vibration screening by open and in-filled trenches.” *Journal of geotechnical engineering* 117.1 (1991): 67-88.

[11] M. Naghizadehrokni and M. Ziegler and J. Sprengel. “A full experimental and numerical modelling of the practicability of thin foam barrier as vibration reduction measure.” *Soil Dynamics and Earthquake Engineering*, volume = 139, year = 2020, issn = 0267-7261, DOI: https://doi.org/10.1016/j.soildyn.2020.106416

EURODYN 2020
XI International Conference on Structural Dynamics
M. Papadrakakis, M. Fragiadakis, C. Papadimitriou (eds.)
Athens, Greece, 23–26 November 2020

EXPERIMENTAL INVESTIGATION OF 2D RAINBOW PHONONIC CRYSTALS FOR BROADBAND VIBRATION ATTENUATION

Han Meng[1], Dimitrios Chronopoulos[1], Nick Bailey[1], Zhuang Dong[2], and Jian Yang[2]

[1] University of Nottingham
Institute for Aerospace Technology & The Composites Group, Nottingham, NG8 1BB, UK
e-mail: han.meng@nottingham.ac.uk, dimitrios.chronopoulos@nottingham.ac.uk,
nick.bailey@nottingham.ac.uk

[2] University of Nottingham Ningbo China
Department of Mechanical, Materials and Manufacturing Engineering, Ningbo 315100, PR China
zhuang.dong@nottingham.edu.cn, jian.yang@nottingham.edu.cn

Keywords: 2D phononic crystal, Stopbands, Rainbow, Experimental, Additive manufacturing

Abstract. *Phononic crystals (PnCs) and metamaterials are nowadays widely investigated for vibration suppression owing to their stopbands that prohibit wave propagation. The application of PnCs and metamaterials is however limited by their narrow bandgaps especially for low frequencies. The recently introduced rainbow metamaterials composed of spatially varied oscillating unit cells are found to generate broader bandgaps than the periodic structures. 2D rainbow PnCs consisting of cubic blocks with internal voids connected by curved beam are proposed in the present paper. Masses of the cubic blocks differ due to different dimensions of internal voids. To prove the effects of rainbow design, two 2D block-beam lattice structures, with periodic and nonperiodic units respectively, were manufactured by additive manufacturing method. Frequency response functions of the manufactured PnCs were measured with a testing system containing a mechanical shaker, an impedance head and a laser Doppler vibrometer. Receptance functions of the PnCs in two directions were measured separately. The obtained experimental results show that the PnC with rainbow mass has extended bandgaps compared with the periodic one.*

1 INTRODUCTION

In recent years, a great deal of engineering materials and structures have been proposed for vibration and noise control [1-13]. Among all the promising structures, phononic crystals (PnCs) received much attention due to its outstanding wave control abilities. PnCs can be considered as engineered materials with designed macroscopic periodic structures that manifest outstanding properties such as bandgaps, i.e., frequency ranges within which acoustic/elastic waves cannot propagate and hence effectively attenuated. The existence of bandgaps enables a wide application of PnCs, such as wave filter, waveguide and wave trapping, vibration isolation, etc [7-13].

The bandgaps of PnCs are mainly generated by two phenomena, Bragg scattering and local resonances. The bandgaps by Bragg scattering occur when the wavelength of the propagating wave is comparable to the lattice dimension of the PnC [14-16]. This means it is hard to achieve Bragg scattering bandgaps in the low frequency ranges due to the limitation of lattice constant in application. In contrast, locally resonant bandgaps rely on the resonance of scattering units. The frequency of locally resonant bandgaps is much lower than that of Bragg scattering bandgaps [17-21].

Even though locally resonant PnCs can attenuation vibration greatly in the bandgaps at low frequencies, the bandwidth is still narrow for real-world applications. Broadening low frequency bandgaps remains a challenge for the design of PnCs. This consideration led to the design of nonperiodic structures. Zhu *et al*. [22] proposed rainbow wave trapping composed of grooves of different depth, Meng *et al*. [23-25] recently developed and manufactured beams with spatially varying resonators. These structures with rainbow profiles were found to possess enlarged locally resonant bandgaps compared with periodic structures. The concept of nonperiodicity opening new and innovative possibilities for design of PnCs and metamaterials.

Inspired by these results, we proposed a 2D rainbow PnCs consisting of spatially distributed cubic blocks connected by curved beams. The masses of blocks are adjusted by opening different internal voids. Two rainbow and periodic PnCs are manufactured with the employment of the additive manufacturing (AM) method, and tested with the frequency response functions (FRFs) measurement system. It is shown by the experimental results, broadband stopbands can be achieved in x and y directions as a result of the rainbow-based PnC design.

2 DESIGN OF 2D RAINBOW PHONONIC CRYSTALS

With the purpose of delivering the rainbow 2D PnCs, structures consisting of spatially distributed blocks connected by two curved struts are created as shown in Fig. 1. Each block contains a perforated hole in the middle. Masses of blocks differ due to the different diameters of internal voids. This maximum mass reduction is set as 70% in order to preserve the structural integrity of the blocks and to maintain the assumption that blocks act as rigid bodies. The masses of blocks are set as sinusoidally varied over the two directions of the rainbow structure with the aim of inducing a smooth near-periodicity and excluding rapid changes for consecutive masses. The two curved beams between blocks are inverted, which can both enhance stability and reduce transmission rigidity compared to straight ones. The cross-section and curvature of connection beams and consequently stiffness is fixed. The equivalent periodic structure is derived by setting the diameter of internal holes equal to the average hole diameter of the rainbow PnCs.

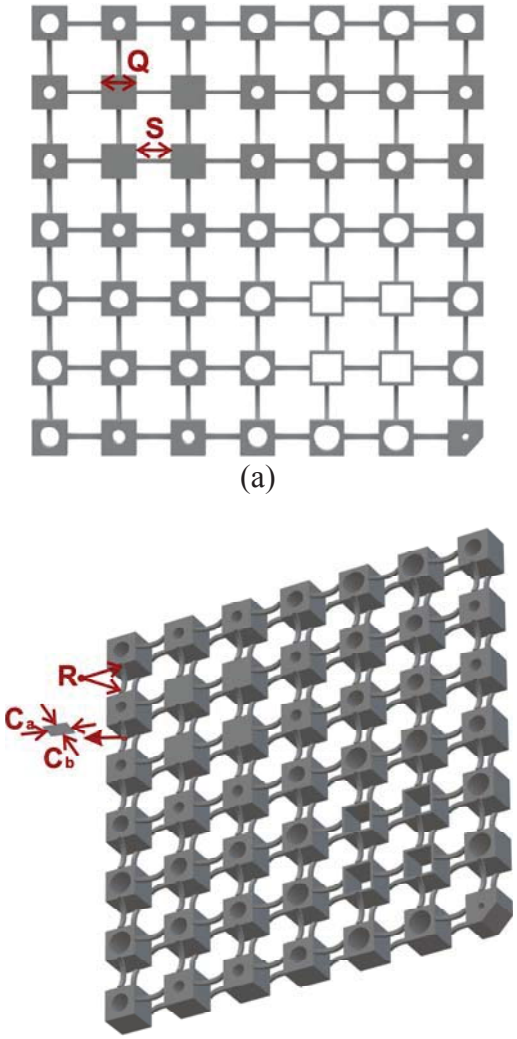

Figure 1: Schema of the 2D rainbow PnC, (a) top view, (b) global view. the labels show the geometric parameters block side length (Q), blocks distance (S), curvature radius of the curved beam (R), cross-section dimensions of the curved beams (C_a, C_b).

3 EXPERIMENTAL MEASUREMENT OF THE FRFS OF 2D PHONONIC CRYSTALS

3.1 Manufacturing of the PnCs

Influences of non-periodicity on the FRFs of the structure were explored experimentally with two rainbow and periodic PnCs. The two samples were manufactured by AM method. AM has become the most popular manufacturing method for PnCs and metamaterials owing to its distinct advantages over traditional subtractive manufacturing processes. AM technologies create structures by deposing materials layer-by-layer. A great number of AM technologies have emerged, including laser sintering, binder jetting and stereolithography, etc [26,27]. Given the geometrical dimension and structural physical parameter requirements as well as price factors, a Selective Laser Sintered (SLS) was selected for the fabrication of the 2D PnCs. A schematic illustration of the SLS process can be seen in Fig. 2.

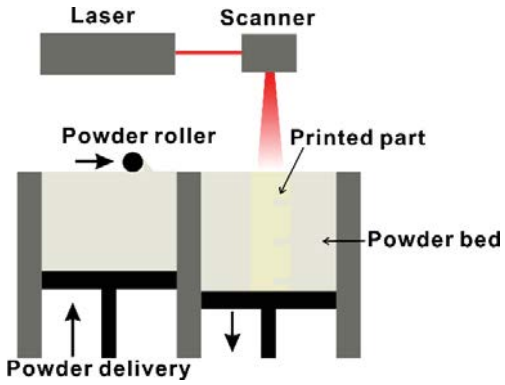

Figure 2: Schematic illustration of the SLS process [23].

The structural samples were fabricated using PA12 material. The printer employed a CO2 laser having a scan speed and hatch spacing of 0.35m/s and 0.3 mm, respectively. We note the nominal spot size of the laser was 0.46 mm and the layer thickness 0.12 mm. PA12 powder was used to fill the powder bed having dimensions 375 mm×375 mm×430 mm at a temperature of 170 °C. The theoretical size threshold below which the metamaterial manufacturing would present deviations from the designed CAD geometry was determined by the accuracy of the printer. The printer properties that affect manufacturing precision include the laser spot size, the layer thickness, the size of the powder and the laser scanning strategy. Features of sizes below 0.8 mm are expected to be fabricated with considerable mechanical properties [28].

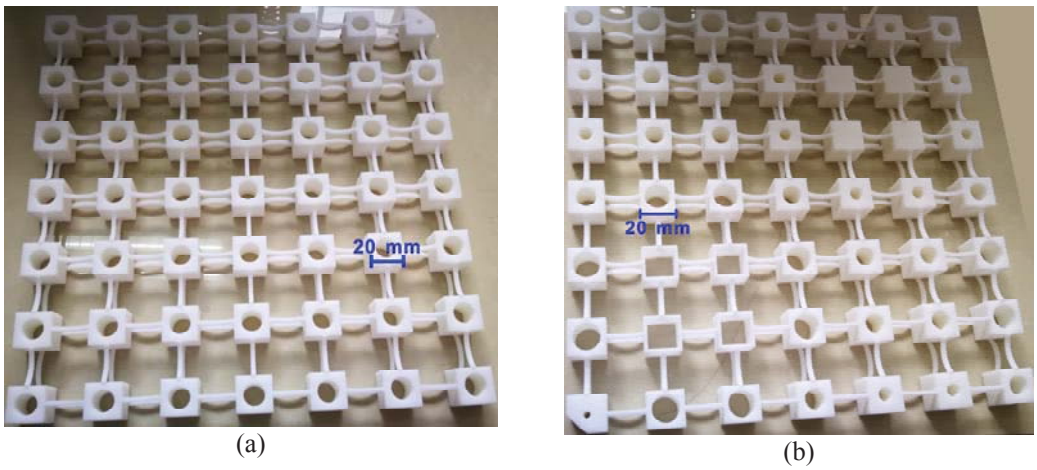

(a) (b)

Figure 3: Photographs of the manufactured (a) periodic PnC, and (b) rainbow PnC by laser sintering.

Photographs of the printed rainbow and periodic PnCs are shown in Figs. 3(a) and (b). The Young's modulus and material density of the printed structures were measured on small fabricated samples based on the ASTM standard and found to be 1.75GPa and 1000kg/m^3 respectively. The printed structures are composed of 7×7 cubic blocks. The side length of cubic blocks is $Q=20$ mm, the distance between blocks is $S=20$ mm, the curvature radius of the connection beam is $R=20$ mm, cross section dimensions of the curved beams are $C_a=C_b=2.5$ mm, the mass of the blocks are sinusoidally distributed in 2 directions as:

$$m_{ij}=\left(0.76+0.19\sin\left((i-1)\pi/3\right)+0.19\sin\left((j-1)\pi/3\right)\right)M \tag{1}$$

where M is the mass of original non-opening blocks, and $i, j = 1, 2, ..., 7$ represent the number of blocks in x and y directions. The block mass of corresponding periodic PnC is equal to the average block mass of the rainbow PnC, e.g. $m_{ij} = 0.76M$.

3.2 Experimental system

The samples were tested with the experimental setup presented in Fig. 4. Due to the large dimensions and masses of the structures, the PnCs were suspended on a metallic truss using rubber bands and plastic hooks to simulate free boundary conditions as shown in Fig. 5(a). The approach of suspending the tested structures has been proved effective by Elmadih *et al*. [29]. A mechanical shaker (Modal Shop 2060E) was employed to excite the PnCs with a chirp wave over the frequency range of 20~1000 Hz. The excitation signal was first generated by the computer and then sent to a junction box (Polytec VIB-E-400), afterwards it was amplified by the amplifier (Modal Shop 2050E09 amplifier) and sent to the shaker. The excitation forces on the PnCs were tested by an impedance head (PCB 288D01) which was bolted to the mechanical shaker on the opposite end. Displacements in two directions at the diagonal corner of the excitation point were measured with the laser Doppler vibrometer (Polytec PSV-400). The collected displacements and forces were sent back to the junction box and calculated by the software to solve out the FRFs. All measurements were taken with a frequency resolution of 1.25 Hz and are complexly averaged over 100 spectral sweeps. Schema of the complete experimental setup system can be seen in Fig. 5.

Figure 4: Photograph of experimental setup for FRFs test of 2D PnC

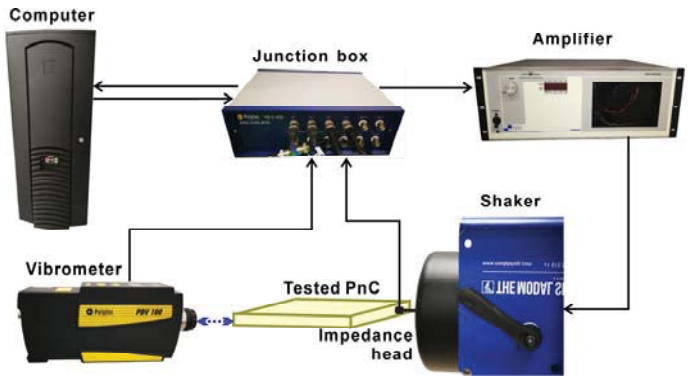

Figure 5: Schema of the experimental setup

3.3 Experimental results

The measured receptance values of the two PnCs are shown in Figs. 6(a)-(f). It can be seen that the rainbow PnC has broader bandgaps than that of the periodic structure of the same mass in x and y directions. The bandgaps of the rainbow PnC occur at the frequency range 470~550 Hz in two directions, within which the receptance values are significantly reduced by 20 dB. By contrast, the periodic PnC has bandgaps within the frequencies 420~470 Hz. Wavelengths at bandgaps are much larger than the lattice dimensions for both PnCs. The rainbow PnC has enhanced bandgaps by 60% than the periodic one. Meanwhile, it also can be seen that the reduction of receptance values within the bandgaps of the rainbow PnC is smaller than that of the periodic PnC. As discussed by Meng *et al*. [23], the enlarged bandwidth could cause smaller attenuation amplitude and thus smaller reduction of receptance values.

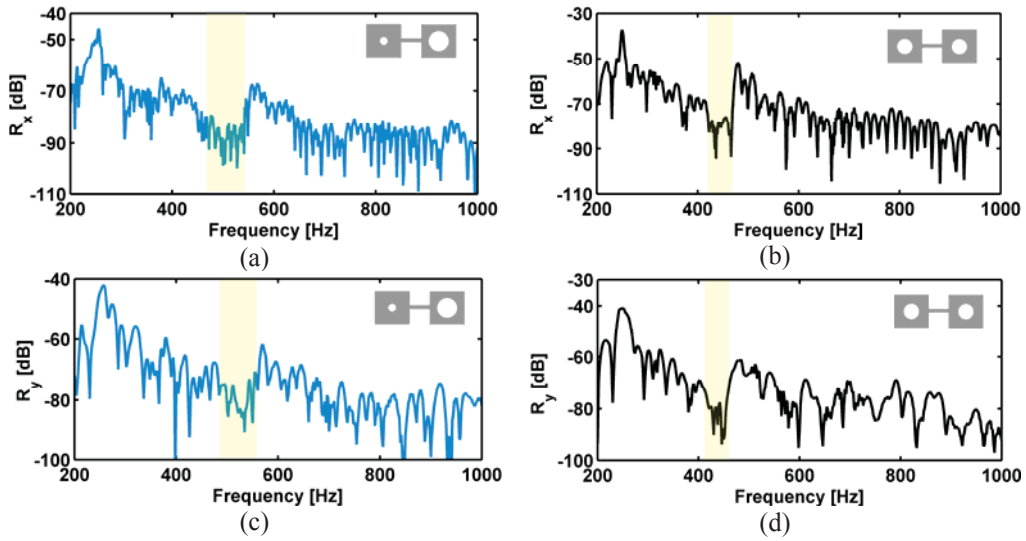

Figure 6: Experimental displacement FRFs of the rainbow PnC in x (a) and y (c) directions, and the periodic PnC in x (b) and y (d) directions

4 CONCLUSIONS

In this paper, the attenuation performance of 2D rainbow PnCs were investigated. Two PnCs with rainbow and periodic unit cells were manufactured by AM method. The PnCs were composed of spatially distributed blocks connected by curved beam. Internal voids were implemented to the blocks to adjust the local masses and generate nonperiodicity. The rainbow PnC contained blocks with masses sinusoidally varying in two directions. FRFs of the PnCs were measured experimentally. Results showed that the introduced rainbow PnC can have low frequency bandgaps much broader than periodic PnCs of equal mass. The method of introducing nonperiodicity displays a great potential for the designing of PnCs with enhanced attenuation performance.

REFERENCES

[1] J. Yang, Y. Xiong and J. Xing. Vibration power flow and force transmission behaviour of a nonlinear isolator mounted on a nonlinear base, *International Journal of Mechanical Sciences*, 115-116, 238-252, 2016.

[2] J. Yang, B. Shi and C. Rudd, On vibration transmission between interactive oscillators with nonlinear coupling interface, *International Journal of Mechanical Sciences*, 137, 238-251, 2018.

[3] B. Shi and J. Yang, Quantification of vibration force and power flow transmission between coupled nonlinear oscillators. *International Journal of Dynamics and Control*. 2-19. https://doi.org/10.1007/s40435-019-00560-7

[4] B. Shi, J. Yang and C. Rudd, On vibration transmission in oscillating systems incorporating bilinear stiffness and damping elements. International Journal of Mechanical Sciences, 150, 458-470, 2019.

[5] W. Dai, J. Yang and B. Shi, Vibration transmission and power flow in impact oscillators with linear and nonlinear constraints. *International Journal of Mechanical Sciences*, 168, 105234, 2020.

[6] J. Yang, J. Jiang and S. Neild (2019), Dynamic analysis and performance evaluation of nonlinear inerter-based vibration isolators. *Nonlinear Dynamics*. https://doi.org/10.1007/s11071-019-05391-x.

[7] M.I. Hussein, M.J. Leamy, M. Ruzzene, Dynamics of phononic materials and structures: Historical origins, recent progress, and future outlook, *Applied Mechanics Reviews*, 66, 040802, 2014.

[8] M. Kafesaki, M.M. Sigalas, N. García, Frequency Modulation in the Transmittivity of Wave Guides in Elastic-Wave Band-Gap Materials, *Physical Review Letters*, 85, 4044-4047, 2000.

[9] A. Khelif, A. Choujaa, S. Benchabane, B. Djafari-Rouhani, V. Laude, Guiding and bending of acoustic waves in highly confined phononic crystal waveguides, *Applied Physics Letters*, 84, 4400-4402, 2004.

[10] D. Richards, D.J. Pines, Passive reduction of gear mesh vibration using a periodic drive shaft, *Journal of Sound and Vibration*, 264, 317-342, 2003.

[11] V. Laude, L. Robert, W. Daniau, A. Khelif, S. Ballandras, Surface acoustic wave trapping in a periodic array of mechanical resonators, *Applied Physics Letters*, 89, 083515, 2006.

[12] Y. Pennec, B. Djafari-Rouhani, J. Vasseur, A. Khelif, P.A. Deymier, Tunable filtering and demultiplexing in phononic crystals with hollow cylinders, *Physical Review E*, 69, 046608, 2004.

[13] T.-T. Wu, W.-S. Wang, J.-H. Sun, J.-C. Hsu, Y.-Y. Chen, Utilization of phononic-crystal reflective gratings in a layered surface acoustic wave device, *Applied Physics Letters*, 94, 101913,2009.

[14] X. Li, Z. Liu, Coupling of cavity modes and guiding modes in two-dimensional phononic crystals, *Solid State Communications*, 133, 397-402, 2005.

[15] C.-Y. Lee, M.J. Leamy, J.H. Nadler, Frequency band structure and absorption predictions for multi-periodic acoustic composites, *Journal of sound and vibration*, 329, 1809-1822, 2010.

[16] T. Gorishnyy, C. Ullal, M. Maldovan, G. Fytas, E. Thomas, Hypersonic phononic crystals, *Physical review letters*, 94, 115501, 2005.

[17] Z. Liu, X. Zhang, Y. Mao, Y. Zhu, Z. Yang, C.T. Chan, P. Sheng, Locally resonant sonic materials, *Science*, 289, 1734-1736, 2000.

[18] S. Zuo, H. Huang, X. Wu, M. Zhang, T. Ni, Low-frequency band gap of locally resonant phononic crystals with a dual-base plate, *The Journal of the Acoustical Society of America*, 143, 1326-1332, 2018.

[19] S. Zhang, J. Hui Wu, Z. Hu, Low-frequency locally resonant band-gaps in phononic crystal plates with periodic spiral resonators, *Journal of Applied Physics*, 113, 163511, 2013.

[20] A. Mehaney, A.M. Ahmed, Locally Resonant phononic crystals at Low frequencies Based on porous Sic Multilayer, *Scientific reports*, 9, 1-12, 2019.

[21] O. McGee, H. Jiang, F. Qian, Z. Jia, L. Wang, H. Meng, D. Chronopoulos, Y. Chen, L. Zuo, 3D printed architected hollow sphere foams with low-frequency phononic band gaps, *Additive Manufacturing*, 30, 100842, 2019.

[22] J. Zhu, Y. Chen, X. Zhu, F.J. Garcia-Vidal, X. Yin, W. Zhang, X. Zhang, Acoustic rainbow trapping, *Scientific Reports*, 3, 1728, 2013.

[23] H. Meng, D. Chronopoulos, A.T. Fabro, W. Elmadih, I. Maskery, Rainbow metamaterials for broadband multi-frequency vibration attenuation: Numerical analysis and experimental validation, *Journal of Sound and Vibration*, 465, 115005, 2020.

[24] H. Meng, D. Chronopoulos, A.T. Fabro, I. Maskery, Y. Chen, Optimal design of rainbow elastic metamaterials, *International Journal of Mechanical Sciences*, 165, 105185, 2020.

[25] H. Meng, D. Chronopoulos, A.T. Fabro, Numerical simulation data for the dynamic properties of rainbow metamaterials, *Data in brief*, 28, 104772, 2020.

[26] N. Guo, M.C. Leu, Additive manufacturing: technology, applications and research needs, *Frontiers of Mechanical Engineering*, 8, 215-243, 2013.

[27] O. Abdulhameed, A. Al-Ahmari, W. Ameen, S.H. Mian, Additive manufacturing: Challenges, trends, and applications, *Advances in Mechanical Engineering*, 11, 1-27, 2019.

[28] D. Tasch, A. Mad, R. Stadlbauer, M. Schagerl, Thickness dependency of mechanical properties of laser-sintered polyamide lightweight structures, *Additive Manufacturing*, 23, 25-33, 2018.

[29] W. Elmadih, D. Chronopoulos, W. Syam, I. Maskery, H. Meng, R. Leach, Three-dimensional resonating metamaterials for low-frequency vibration attenuation, *Scientific Reports*, 9, 1-8, 2019.

EURODYN 2020
XI International Conference on Structural Dynamics
M. Papadrakakis, M. Fragiadakis, C. Papadimitriou (eds.)
Athens, Greece, 23–26 November 2020

ACOUSTIC PERFORMANCE EVALUATION OF A PANEL UTILIZING NEGATIVE STIFFNESS MOUNTING FOR LOW FREQUENCY NOISE CONTROL

Paradeisiotis Andreas[1], **Kalderon Moris** [1], **Antoniadis Ioannis**[1] **and Fouriki Lina**[1]

[1]National Technical University of Athens, Dynamics and Structures Laboratory, School of Mechanical Engineering,
Heroon Polytechniou 9, 15780 Zografou Athens, Greece
e-mail: aparadis@mail.ntua.gr

Keywords: noise control, acoustic panel, sound transmission loss, KDamper

Abstract. *In order to encounter the challenges of low frequency noise absorption below 100 Hz, primarily emitted from the engines in air and ground vehicles, a method of acoustic panel mounting is proposed based on the KDamper concept which utilizes the negative stiffness damping effect. The practical constraints in such applications relating to the thickness of the panel for adequate noise absorption, are compensated through the unique damping properties of the KDamper and the ability to attenuate low frequency excitation in a considerable range. Therefore, a preliminary implementation of an acoustic panel with appropriately designed elastic mounts incorporating negative stiffness elements, is evaluated in terms of acoustic performance. During the design stage of the mounting, the problem is approached as in the case of classic vibration isolation of a rigid mass, due to the nature of the low frequency excitation. However, the elasticity of the deformable thin plate is taken into account by modeling its dynamic behavior using generalized modal values. The investigation consists in establishing the theoretical framework of the problem for the examination of metrics such as the sound transmission loss (STL) and the optimization of the mounting in order to maximize the STL performance, accompanied by FEM simulations. Additionally, comparisons with conventionally mounted panels is provided for reference and to highlight the advantages of the proposed solution. Early results regarding the noise control capabilities of such a panel configuration, indicate the potential of this proposition in specific applications.*

1 INTRODUCTION

Researchers have reported several hazardous impacts of low-frequency noise on human health such as annoyance, headache, city-fatigue [5], etc. To attenuate low frequency sound, passive solutions such as foam layers, sound diffusing panels and blocks, sandwich panels and many others [14], constitute the most widespread means for acoustic treatment in a vast range of applications from room acoustics, to loudspeaker enclosures etc.. However, these means present certain limitations in the low frequency range, namely below 500 Hz approximately, which is very important regarding noise control in transportation media and inside buildings, among other applications. Traditional materials follow the mass density law for sound shielding. According to the mass-density law, sound transmission through a substance [19] is given by $T = \frac{1}{\rho t f}$, where ρ is density, t is thickness of the medium, and f is the sound wave frequency. Thus, for a particular frequency, doubling the thickness of the sound insulator would result in an increment of only 6 dB STL. Therefore, a thicker porous material is required for shielding of low frequency noise [11], but even a thick concrete wall fails to attenuate low levels of low frequency noise. To encounter these issues, other types of solutions have been proposed in the form of local dampers [13], perforated plates [4], meta- surfaces or meta-diffusers [8] and acoustic/elastic meta-materials [3] among others.

Lightweight single or double walls are very common solutions for partitioning in dwellings. They are typically composed of two leaves mounted on a wood or steel frame. The cavity between these leaves is filled by absorbing material to improve the acoustic performance in mid-to-high frequencies. The limited capability of the aforementioned conventional passive means at low frequencies, introduces a dilemma, provided that improvement of their performance is generally associated with an increase in weight and volume. Additionally, other solutions such as conventional passive vibration dampers have the ability to absorb at very specific frequencies, and they can also be very heavy.

Owing to the need of low frequency sound absorption, it is desired to develop a new generation of partitions capable of attenuating noise in low-to-high frequency range. To contribute to the solution the paper considers the application of the KDamping concept towards the design of highly dissipative low-frequency mounts. The KDamper is a novel passive vibration isolation and damping concept, based essentially on the optimal combination of appropriate stiffness elements, which include a negative stiffness element [1, 2]. In order to propose a solution to this problem, the STL of panels is initially examined, considering the sound propagation through a single, finite, rectangular thin plate. The acoustic behavior of a simply supported plate in this low frequency range, may be treated as a case of classic vibration control. The mounting of this plate is investigated and the way it participates in its STL performance. An equivalent analytical framework is presented describing the behaviour of a conventional panel supported by KDamper mounts incorporating the effect of the panel flexural stiffness. it is worth

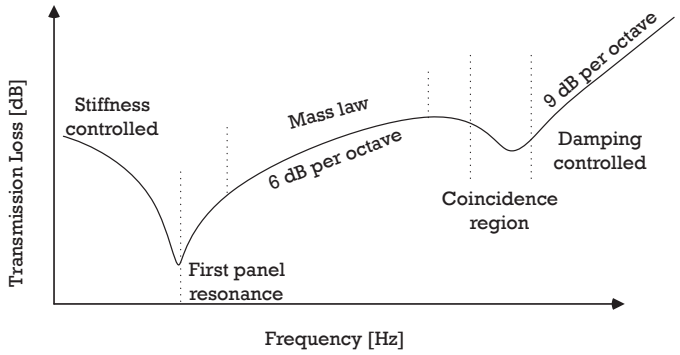

Figure 1: Typical STL profile of a panel.

noting that, the previous approaches considered the problem as in the case of classical vibration of a rigid mass ignoring any contribution of the plate's modes [17].

2 SOUND TRANSMISSION LOSS OF PANEL

In this section the theory of Sound Transmission Loss (STL) through a single panel is briefly presented. Various ways have been proposed regarding the modeling and simulation of the sound propagation through obstacles and the resulting STL [20, 15, 9]. In this work, the fundamental physics of the problem are investigated via an impedance based approach. According to this approach Transmission loss of sound occurs when there is an impedance mismatch between the propagation media of the traveling sound waves, thus sound is reflected and/or absorbed [9]. Direct sound transmission through thin panels depends on the mass, stiffness and damping of the system plate-support.

Figure 1 shows a typical form of the STL curve for sound propagation through a thin plate [7]. This curve presents five distinct regions in corresponding frequency ranges, depending on the properties of the system.

In a general case as in Fig. 2a, the STL is investigated via the assumption of a propagating plane wave between two different media. The impedance mismatch comes from the difference of impedance that the propagation medium of the incident waves Z_0, has from the propagation medium of the transmitted waves Z_1. In order to quantify the consequences of this mismatch, the transmission coefficient τ is introduced, defined as the ratio of the complex amplitude of the transmitted sound pressure to the complex amplitude of the incident sound pressure:

$$\frac{\tilde{p}_t}{\tilde{p}_i} = \tau = 2\frac{\tilde{Z}_1}{\tilde{Z}_1 + \tilde{Z}_0} \tag{1}$$

Figure 2 illustrates a wall, a rigid flat surface that consists only on mass, oscillating in an infinite rigid baffle with air on both sides, subjected to normal incident plane waves $\mathbf{p}_i = \tilde{p}e^{\jmath(\omega t - \kappa_0 z)}$. This particular case is refereed to as the "limp wall" assumption and the resulting frequency response of the STL is known as the "mass law".

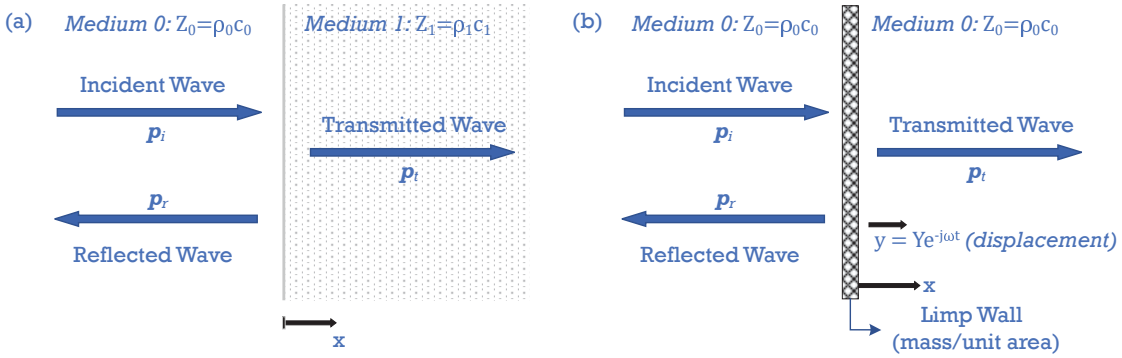

Figure 2: (a) Wave propagation in the presence of impedance mismatch (b) Limp wall assumption.

For frequencies higher than the natural frequency f_0, the STL is controlled by the mass per unit area of the panel. This corresponds to a 6 dB per octave increase of STL, while doubling the mass per unit area leads to a 6 dB per octave increase. Specifically, for a thin panel, neglecting stiffness and damping (limp wall):

$$STL = 10log\Big[\frac{\omega^2\overline{m}^2}{4(\rho_0 c_0)^2/cos^2\theta}\Big] \tag{2}$$

where θ is the angle of incidence of the propagated sound waves, c_0 is the speed of sound in air, ρ_0 the air density and $\overline{m}$ $[kg/m^2]$ is the mass per unit area of the panel. In the case of normal incident waves, $\theta = 0$.

Now, assuming that the same laws apply in case of a partition as illustrated in Fig. 3, by applying pressure and velocity continuity conditions at the interface of air and plate, the transmission coefficient comes as

$$\tau = \frac{2\tilde{Z}_0}{-\jmath(\omega m - k/\omega) + (2\tilde{Z}_0 + c)} \tag{3}$$

The imaginary part in the denominator of Eq. (3), indicates that the mass contribution ωm and the spring contribution $-k/\omega$ have a phase difference of 180° while the term $2\tilde{Z}_0$ indicates the radiation at both sides of the wall. The transmission coefficient can also be written as

$$\tau = \frac{\tilde{Z}_f}{\tilde{Z}_p + \tilde{Z}_f} \tag{4}$$

where $\tilde{Z}_p = -\jmath(\omega m + \jmath c - k/\omega)$ is the partition (mechanical) impedance and $\tilde{Z}_f = 2\tilde{Z}_0$ is the fluid loading impedance in both directions [9]. The

For the calculation of the Sound Transmission Loss (STL) in the case of a thin plate using the single DOF model as in Fig. 3, the expression of the mechanical impedance

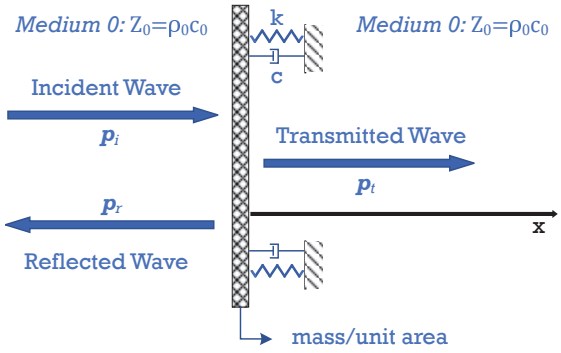

Figure 3: Wave propagation at a partition.

$\tilde{Z}_p$ can be rearranged to include the transfer function of the displacement as to the excitation, namely

$$\tilde{Z}_p = -\frac{1}{\jmath\omega}\frac{|\tilde{T}_{XF}|^{-1}}{A} \tag{5}$$

where A is the surface of the plate subjected to the excitation. Therefore, the STL is calculated as

$$STL = 10\log_{10}\frac{1}{|\tau|^2}\,[dB] \tag{6}$$

3 THE KDAMPER CONCEPT

The KDamper, which can be considered as an extension of the traditional Tuned Mass Damper (TMD), is a novel passive vibration isolation and damping concept, based essentially on the optimal combination of appropriate stiffness elements, including a negative stiffness element [1]. The KDamper supplements the inertial forces of the added TMD mass with the stiffness force of the negative stiffness element. This negative stiffness element can be realized by a number of ways such as pre-stressed disc (Belleville) springs, arranged in appropriate geometrical configurations [3]. Among others, this can provide significant comparative advantages, especially in the very low frequency range, such as better damping characteristics without the need of heavy additional masses.

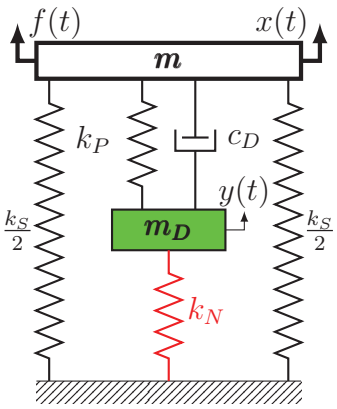

Figure 4: Schematic diagram of the KDamper oscillator.

The KDamper elements are calculated for a specific mass around a desired frequency f_0 or $\omega_0 = 2\pi f_0$ and the overall static stiffness comes as $k_0 = m\omega_0^2$, which also equals to

$$k_0 = \frac{k_P k_N}{k_P + k_N} + k_S \tag{7}$$

The overall static stiffness k_0 of the system is maintained.

Next, the basic parameters of the KDamper concept μ,κ and ρ, are defined as

$$\mu = m_D/m \tag{8}$$
$$\rho = \omega_D/\omega_0 \tag{9}$$
$$\kappa = -k_N/(k_P + k_N) \tag{10}$$

Finally, the non-dimensional parameters of the stiffness elements of the KDamper are defined as

$$\kappa_S = \frac{k_S}{k_0} = 1 + \kappa(1+\kappa)\mu\rho^2 \tag{11}$$
$$\kappa_P = \frac{k_P}{k_0} = (1+\kappa)\mu\rho^2 \tag{12}$$
$$\kappa_N = \frac{k_N}{k_0} = -\kappa\mu\rho^2 \tag{13}$$

leading to the calculation of the stiffness elements (k_S, k_P, k_N) of the oscillator. Furthermore k_D is defined as $k_D = k_P + k_N$, thus, for a specific damping ratio ζ_D, the damping constant is calculated as:

$$c_D = 2\zeta_D\sqrt{k_D m_D} \tag{14}$$

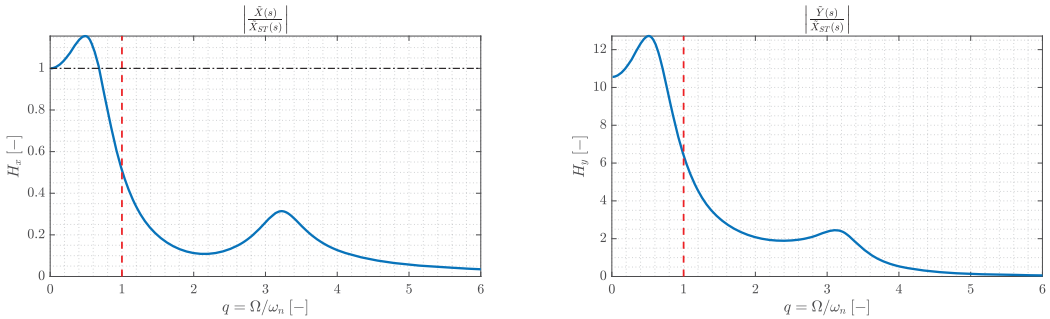

(a) Frequency response of $|\tilde{T}_{XK}|$.

(b) Frequency response of $|\tilde{T}_{YK}|$.

Figure 5: Frequency response of of the transfer functions of the KDamper.

Figures 5a and 5b, present the frequency response of the transfer functions of the dynamic magnification factor for both degrees of freedom (DOFs) x and y of the KDamper respectively, for an indicative set of parameters $\mu,\ \kappa$ and ρ. More information regarding the design of the KDamper can be found in [16].

4 SOUND TRANSMISSION LOSS OF DEFORMABLE THIN PLATE

The investigation in this paper is an extension of previous work [17, 16]. However, a slightly different approach is taken here, where the thin plate is now considered as elastic/deformable instead of rigid as before. The goal is to examine how this property of the plate, participates in the dynamics of the system and consequently, the acoustic performance.

In order to do that, the assumption that the bending stiffness of the deformable plate is in a way in series with the stiffness of the mounting, is formulated. This assumption is also investigated through modal analysis and frequency response with FEM. This is achieved by utilizing the generalized values of the structure, namely generalized mass and the corresponding generalized stiffness for the appropriate modes, calculated from modal analysis and FEM simulations, in order to construct a corresponding single degree of freedom (SDOF) model representing the dynamic behavior of the deformable thin plate.

4.1 THEORETICAL FORMULATION

In this section the KDamper theoretical framework is extended to include the case where the rigid mass is replaced by a deformable plate. Figure 6a, shows the equivalent dynamic SDOF model of a deformable plate and the approximate modification when the plate is mounted on elastic mounts.

Figure 6b, shows the equivalent model when the simple elastic mount is replaced with an elastic mount based on the design of the KDamper.

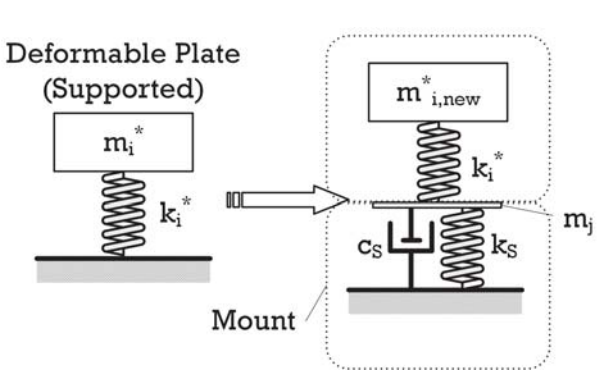

(a) Deformable plate on elastic mounts with stiffness k_S.

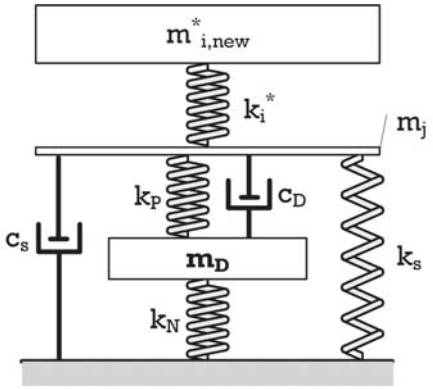

(b) Implementation of the mounting based on the KDamper.

Figure 6: Modelling of a mounted deformable plate.

The equation of motion of the equivalent SDOF model is

$$m_i^* \ddot{u} + c_i^* \dot{u} + k_i^* u = f(t) \tag{15}$$

while in the case of the simple elastic mount becomes

$$m_{i,new}^* \ddot{u}_1 + k_i^* (u_1 - u_2) = f(t) \tag{16}$$

$$m_j \ddot{u}_2 + c_S \dot{u}_2 + k_S u_2 + k_i^* (u_2 - u_1) = 0 \tag{17}$$

where m_j is the connecting mass which is assumed as neglible in order to act just as a connector, namely an additional DOF and k_S is the stiffness of the elastic mount which needs to be calculated.

In the case of the KDamper elastic mount, the equation of motion in matrix formulation comes as

$$\mathbf{M}\, \vec{\ddot{u}}(t) + \mathbf{C}\, \vec{\dot{u}}(t) + \mathbf{K}\, \vec{u}(t) = \vec{F}\, f(t) \tag{18}$$

where the mass ($\mathbf{M}$), damping ($\mathbf{C}$) and stiffness ($\mathbf{K}$) matrices, come as

$$\mathbf{M} = \begin{bmatrix} m_i^* & 0 & 0 \\ 0 & m_j & 0 \\ 0 & 0 & m_D \end{bmatrix}, \ \mathbf{C} = \begin{bmatrix} 0 & 0 & 0 \\ 0 & c_S + c_D & -c_D \\ 0 & -c_D & c_D \end{bmatrix}$$

$$\mathbf{K} = \begin{bmatrix} k_i^* & -k_i^* & 0 \\ -k_i^* & k_i^* + k_P' + k_S' & -k_P' \\ 0 & -k_P' & k_P' + k_N \end{bmatrix}, \ \mathbf{F} = \begin{bmatrix} 1 \\ 0 \\ 0 \end{bmatrix} \tag{19}$$

At this point, it should be highlighted that the Dashpots ($\mathbf{c_s}$,$\mathbf{c_D}$) shown in Figure 6a denote schematically the systems' hysteretic damping and they should not be confused

with the parallel dashpots that are usually employed when viscosity is considered. The loss factor η, can represent more accurately the dynamic response of nonlinear systems compared with the damping ratio which is defined on the grounds of the linear single degree of freedom (SDOF) viscous model [10, 6].

Therefore, the damping matrix is empty $\mathbf{C} = \begin{bmatrix} 0 \end{bmatrix}$ $(\mathbf{c_s} = \mathbf{c_D} = 0)$ and the hysteretic damping is introduced indirectly in the stiffness matrix $\mathbf{K} = \begin{bmatrix} \ \end{bmatrix}$,

where

$$k'_S = k_S \left(1 + \jmath n\right) \tag{20}$$

$$k'_P = k_P \left(1 + \jmath n\right) \tag{21}$$

The transfer matrix relative to the excitation, for each frequency ω, is calculated from the following expression:

$$\mathbf{TRF} = (-\omega^2 \mathbf{M} + \mathbf{K})^{-1} \mathbf{F} \tag{22}$$

where

$$\mathbf{TRF} = \left\{ \frac{\tilde{u}_1}{\tilde{F}} \quad \frac{\tilde{u}_2}{\tilde{F}} \quad \frac{\tilde{u}_3}{\tilde{F}} \right\}^T \tag{23}$$

Finally, the transfer function of the deformable plate mounted on KDamper mounts, is taken as $T_{XF_{KD}} = \frac{\tilde{u}_1}{\tilde{F}}$.

4.2 OPTIMIZATION OF THE KDAMPER PARAMETERS

The aim is the selection of the optimal values for the KDamper elements, in order to obtain the maximum possible STL performance, especially in the resonance region of the system in comparison to the initial case where the plate is simply supported on its edges.

4.2.1 OPTIMIZATION ALGORITHM

For the optimization, the "$fmincon$" function of the MATLAB software for local minimization of non-linear functions and constraints, is utilized. The optimization algorithm is formulated as follows:

$$\min_{\mathbf{x}} f(\mathbf{x}) \; s.t. \begin{Bmatrix} c(x) \leq 0 \\ c_{eq}(x) = 0 \\ \mathbf{A}\,\mathbf{x} \leq b \\ \mathbf{A_{eq}}\,\mathbf{x} = b_{eq} \\ lb \leq \mathbf{x} \leq ub \end{Bmatrix} \tag{24}$$

where $\mathbf{x}$ is the vector containing the optimization variables and $f(\mathbf{x})$ is the objective function to be minimized. In this case the vector $\mathbf{x}$ is

$$\mathbf{x} = \begin{Bmatrix} k_N & k_P & k_S \end{Bmatrix}^T \tag{25}$$

Regarding the objective function, the algorithm maximizes the minimum value of the STL of the model in Fig. 6b, namely

$$f(\mathbf{x}) = -\min(STL_{KD}) \tag{26}$$

Initially, the only constraint to which the optimization is subjected has to do with the static stability margin of the KDamper, which is defined as

$$\epsilon = \frac{k_{N_{lim}} - k_N}{k_N} \tag{27}$$

where

$$k_{N_{lim}} = \frac{k_P k_S}{k_P + k_S} \tag{28}$$

and is set to have a minimum value of 10%.
Therefore, the optimization problem becomes

$$\min_{\mathbf{x}} f(\mathbf{x}) \; s.t. \begin{Bmatrix} 0.1 - \epsilon \leq 0 \\ lb \leq \mathbf{x} \leq ub \end{Bmatrix} \tag{29}$$

with the optimization variables between the lower bounds

$$\mathbf{lb} = \begin{Bmatrix} -1 \times 10^6 & 0 & 0 \end{Bmatrix}^T \tag{30}$$

and the upper bounds

$$\mathbf{ub} = \begin{Bmatrix} 0 & 15 \times 10^5 & 1 \times 10^7 \end{Bmatrix}^T \tag{31}$$

The starting point $\mathbf{x}_0$ of the algorithm, is selected such that the stiffness element k_S is of the same order of magnitude as the stiffness element k_i^* of the deformable plate model.

4.2.2 CASE EXAMINATION: RECTANGULAR DRYWALL

A $0.625 \times 1.6\ m$ rectangular drywall is considered, according to real-life masonry applications. The width corresponds to the horizontal distance between the upright supporting beams providing the stable frame of the drywall. Typically, the height of such a drywall is around $3.2\ m$, meaning that it can be covered by two pieces with the

Table 1: Drywall properties.

$\overline{m}\ [kg/m^2]$	$W\ [m]$	$H\ [m]$	$t\ [m]$	$m\ [kg]$	$E\ [MPa]$	ν
8.35	0.625	1.6	12.5×10^{-3}	8.35	2900	0.31

dimensions consider here. The selected dimensions correspond also to a frontal surface of $1\ m^2$. The relevant properties of the drywall are summarized in Table 1.

Modal analysis via the finite element method (FEM), assuming simply supported boundary conditions as in Fig. 7a, gives the following generalized values for the fundamental mode of the plate, shown in Fig. 7b:

$$f_1^* = 31.39\ [Hz] \quad m_1^* = 2.82\ [kg] \tag{32}$$

In case of a simply supported rectangular thin plate this frequency may also be estimated accurately by the theoretical expression

$$\omega_{mn} = \sqrt{\frac{D}{\rho t}}\Big[\Big(\frac{m\pi}{l_x}\Big)^2 + \Big(\frac{n\pi}{l_y}\Big)^2\Big] \tag{33}$$

for $m = n = 1$ which corresponds to the 1^{st} mode and

$$D = \frac{Et^3}{12(1-\nu^2)} \tag{34}$$

where D is the plate flexural rigidity, t is the plate thickness, E the Young's modulus and ν is Poisson's ratio. The corresponding generalized mass and stiffness [18] are defined as

$$m_{11}^* = m/4 \tag{35}$$

$$k_{11}^* = \frac{1}{4} l_x l_y D \pi^4 \Big(\frac{1}{l_x^2} + \frac{1}{l_y^2}\Big)^2 \tag{36}$$

Based on these values an equivalent generalized stiffness is calculated for the formulation of the corresponding SDOF model. Based on expression (36), it can be easily shown that the generalized stiffness is minimized when $l_x = l_y$, i.e for a square plate. However, as it will be shown hereinafter, acoustic performance is optimized when stiffness is maximized; in that terms the square plate constitutes the less attractive configuration .

Next, it is assumed that the plate will be supported on fifteen (15) elastic mounts in a configuration that essentially divides the plate into two equal parts of $0.3125\ m \times 1.6\ m$, as presented in Fig. 8a. Initially, this configuration as a simply supported plate

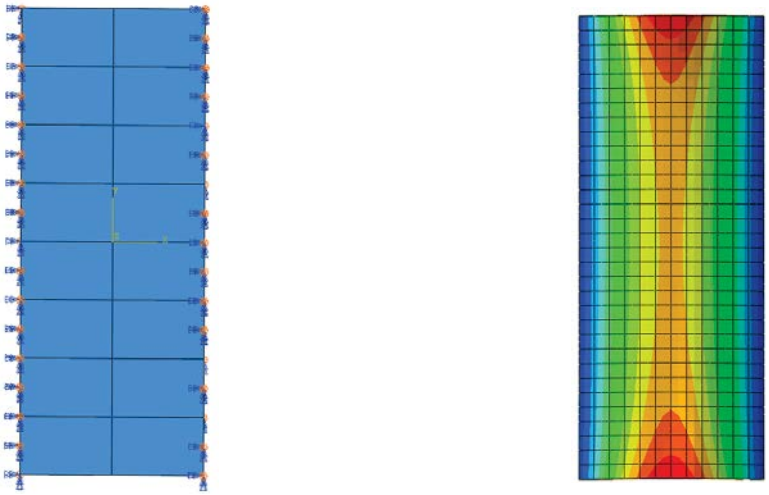

(a) Initial boundary conditions.

(b) Mode under consideration.

Figure 7: Simply supported drywall $0.625 \times 1.6\ m,\ A = 1\ m^2$.

is considered, in order to obtain a more indicative set of generalized values for the following case of the mounted plate, which come as:

$$f_1^* = 196.92\ [Hz] \quad m_1^* = 1.91\ [kg] \tag{37}$$

Using the objective function of Eq. (26), the algorithm searches for a solution in the frequency range $f_e = 1 : 1000\ Hz$. After the optimal set of parameters is calculated, the resulting stiffness k_S is divided into 15 springs and the FEM simulation is repeated in order to calculate the new generalized mass $m^*_{i,new}$. This procedure repeats a few times until there is a convergence of this value within a margin of error where any deviations become insignificant to the final results.

Then, for the generalized mass $m^*_{1,new}$ of the mounted plate, the corresponding element values of the KDamper come as in Table 2. The effect of the hysteretic behavior of KDamper is investigated parametrically for four (4) different loss factor η values and the results are illustrated in Fig. 9. The total loss factor η of a structure is the ratio of lost to reversible mechanical energy per radian cycle in a dynamic system. Nowadays, someone can easily find industrially produced rubber materials with specified loss factor values higher than $\eta = 0.4$ [12].

Figure 10, essentially compares the STL performance of the panel when utilizing elastic mounts - red-dashed line for simple elastic mounts and blue line for the optimized KDamper mounts - with the initial case as in Fig. 7, which is represented by the green line. Additionally, the mass law curve is represented for reference with the black-dashed line. When using elastic mounts the new generalized mass of the corresponding mode is higher, namely $m^*_{new} = 4.156\ kg$ compared to the initial $m^* = 2.819\ kg$. The same

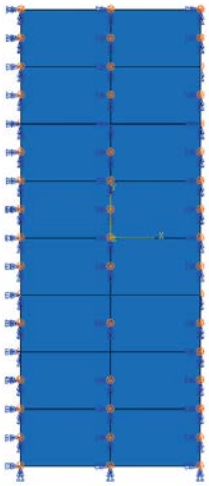

(a) Mounting points for the elastic mounts.

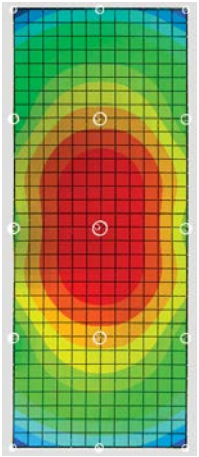

(b) Mode under consideration.

Figure 8: Drywall supported by 15 mounts.

η	μ	$f_i^*\ [Hz]$	$m_{i,new}^*\ [kg]$	κ	$k_S\ [N/m]$	$k_P\ [N/m]$	$k_N\ [N/m]$
0.05	0.01	42.73	4.159	5.247	5.280×10^5	4.348×10^4	-3.652×10^4
0.1	0.01	43.72	4.159	5.526	5.291×10^5	3.894×10^4	-3.297×10^4
0.2	0.01	26.76	4.154	1.478	5.225×10^5	2.739×10^5	-1.634×10^5
0.4	0.01	20.10	4.156	0.376	5.301×10^5	1.234×10^6	-3.371×10^5

Table 2: Values of KDamper parameters for assuming loss factor values $\eta = 0.05 : 0.4$.

mass m_{new}^* is also used for the mass law. Therefore, this fact alone is expected and it shows to improve the STL performance of the initial panel.

5 DISCUSSION

An increase in the loss factor, improves the acoustic performance of the panel at the design frequency and the uniformity of STL at the resonance frequency range. However, the design frequency shifts to lower values and at the same time, higher damping also translates to smaller oscillation amplitude for the added mass. Of course, arrangements with extraordinary high loss factors are not easily realized practically and that is something that has to be considered. For example, in this contribution the loss factor is selected η=0.2.

The resulting STL curves for the four cases are compared in Fig. 10. The STL curve of the ”mass law” (limp wall approximation) is presented as a reference for the performance in these cases. The obvious advantage of the proposed KDamper configuration is

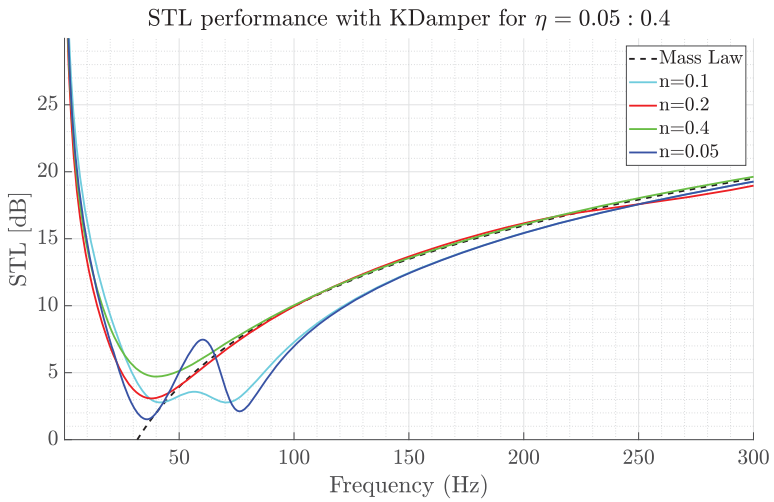

Figure 9: Resulting STL curves comparison with optimized $KDamper$ mount for different Loss factor η values.

the higher level of STL in the resonance region and the coincidence with the "mass law" curve for higher frequencies. On the other hand, the simple elastic mount configuration revealed little or no improvement in low frequencies compared with the simply supported panel, especially in the case of low damping but exhibited a similar behavior with the KDamper mounted panel for higher frequencies.

This impedance based approach for the calculation of the STL performance of a panel, demonstrates the viability and advantages of a KDamper based, mounted plate over conventional mounting mechanisms. The addition of the elastic mounts on a deformable plate, increases the generalized mass, therefore improves its acoustic performance. Compared to the simple elastic mounts, the KDamper provides an additional improvement in the resonance region. The main observation as shown in Fig. 6, is that the equivalent dynamic stiffness of the deformable plate and the stiffness of the mounting, operate approximately in series. Consequently, as it comes from the expression

$$k_{tot} = \frac{k_i^* k_S}{k_i^* + k_S} \tag{38}$$

the total stiffness of the model is restricted by the initial equivalent dynamic stiffness of the plate. An indicative graphical representation of Eq. (38), is shown in Fig. 11.

This implies that in order to utilize stiffer mounting -therefore increasing the eigenfrequency of the model where the total STL level is higher and the effect of the KDamper is more prevalent- requires a stiffer plate. To achieve that, either the mounting has to be more dense, namely dividing the plate into smaller "pieces" or the material of the

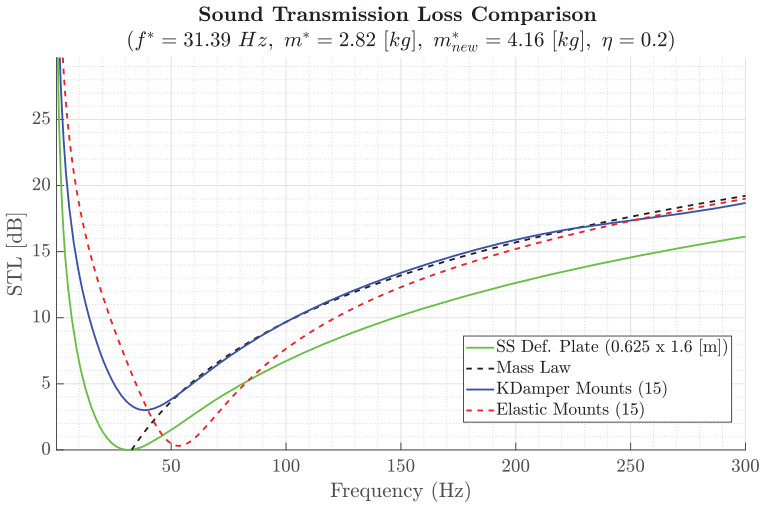

Figure 10: Comparison of the resulting STL curves with the optimized KDamper mount.

plate itself has to have higher Young's Modulus, thus higher bending stiffness D, or/and higher mass per unit surface.

6 CONCLUSIONS

A novel mount for acoustic panels was presented based on the KDamper concept, incorporating a negative stiffness element. The application of the mount in flexible panels was investigated based on analytical formulas and an equivalent "KDamper-Flexible panel model" was developed, to approximate more accurately the acoustic performance of the configuration compared to the "rigid mass" approach. The optimization algorithm of the system's parameters was described and an iterative procedure was followed to define the optimized set of parameters aiming to maximize the STL.

Then, a real-case scenario of a $0.625 \times 1.6\ m$ rectangular drywall was studied, comprising the reference arrangement for all the subsequent comparisons. The hysteretic behavior of the mount was examined for a range of loss factor (η) values, which control the design frequency, revealing the importance of a suitable rubber material to the system's performance. Finally, the superiority of the KDamper mounts was shown by comparison with the Simply-Supported panel and the simple elastic mounts. In case of the elastic supports an increase was observed at oscillating panel effective mass, resulting to an improved sound attenuation. The KDamper mounts proved advantageous compared with the simple elastic mounts improving at least four (4)dB the STL curve in the low frequency region. To the authors knowledge this improvement has not been observed in any other product being available on the market. Additionally, it was observed that the equivalent dynamic stiffness of the panel and the stiffness of the mounting, operate approximately in series. Hence, the total stiffness of the model is bounded by the

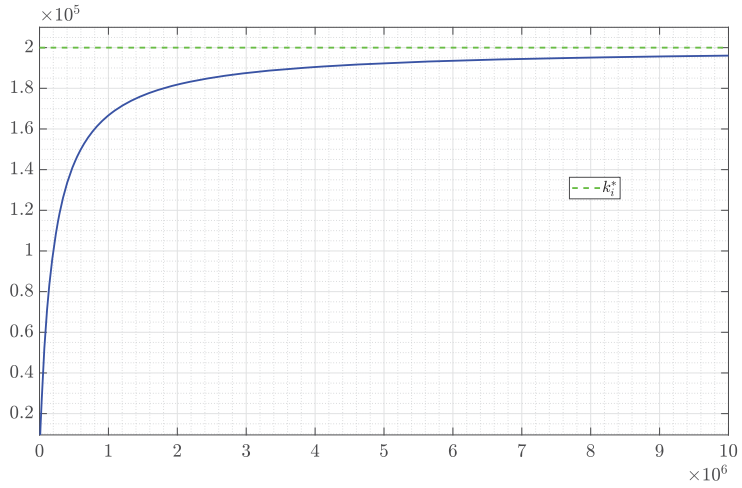

Figure 11: Springs in series configuration.

initial equivalent dynamic stiffness of the panel.

It should be noted that the approach followed in this paper, considers an equivalent mount-flexible panel model where the total system stiffness is calculated by applying a heuristic approach. Therefore, a topic for future work, is the calculation of the STL via a full numerical coupled structural-acoustic FE model and validate the performance experimentally.

7 ACKNOWLEDGMENTS

This research has been financed by the European Union's Horizon 2020 research and innovation programme under the Marie Sklodowska-Curie grant (grant agreement No INSPIRE-813424, "INSPIRE - Innovative Ground Interface Concepts for Structure Protection"). Dissemination of this work was also partially supported by COST (European Cooperation in Science and Technology) through the COST Action CA15125 – DENORMS: "Designs for Noise Reducing Materials and Structures".

References

[1] Antoniadis, I.A., Chronopoulos, D., Spitas, V., Koulocheris, D.: Hyper-damping properties of a stable linear oscillator with a negative stiffness element. Journal of Sound and Vibration **346**, 37–52 (2015)

[2] Antoniadis, I.A., Kanarachos, S.A., Gryllias, K., Sapountzakis, I.E.: Kdamping: A stiffness based vibration absorption concept. Journal of Vibration and Control **24**(3), 588–606 (2016)

[3] Antoniadis, I.A., Paradeisiotis, A.: Acoustic meta-materials incorporating the kdamper concept for low frequency acoustic isolation. Acta Acustica united with Acustica **104**(4), 636–646 (2018)

[4] Carbajo, J., Ramis, J., Godinho, L., Amado-Mendes, P.: Perforated panel absorbers with micro-perforated partitions. Applied Acoustics **149**, 108–113 (2019)

[5] Carfagni, M., Lenzi, E., Broner, M.P.N.: The effects of low frequency noise on people—a review. Journal of Sound and Vibration **58**(4), 483 – 500 (1978)

[6] Carfagni, M., Lenzi, E., Pierini, M.: The loss factor as a measure of mechanical damping. In: Proc. SPIE, Proceedings of the 16th International Modal Analysis Conference, vol. 3243, p. 580 (1998)

[7] Cowan, A.J.: Sound Transmission Loss of Composite Sandwich Panels. Ph.D. thesis, Department of Mechanical Engineering, University of Canterbury (2013)

[8] Jiménez, N., Cox, T.J., Romero-García, V., Groby, J.P.: Metadiffusers: Deep-subwavelength sound diffusers. Scientific reports **7**(1), 5389 (2017)

[9] Kim, Y.H.: Sound propagation: an impedance based approach. John Wiley & Sons (2010)

[10] Koblar, D., Boltežar, M.: Evaluation of the frequency-dependent young's modulus and damping factor of rubber from experiment and their implementation in a finite-element analysis. Experimental Techniques (nov 2013), ISSN 0732-8818

[11] Kumar, S., Lee, H.P.: The present and future role of acoustic metamaterials for architectural and urban noise mitigations. Acoustics **1**(3), 590–607 (2019), ISSN 2624-599X

[12] KURASHIKI: Product catalogue (Industrial Vibration Solutions) (2016)

[13] Liu, Z., Rumpler, R., Feng, L.: Broadband locally resonant metamaterial sandwich plate for improved noise insulation in the coincidence region. Composite Structures **200**, 165–172 (2018)

[14] Makris, S.E., Clive, L.D., MacGregor, J.S.: Transmission loss optimization in acoustic sandwich panels. The Journal of the Acoustical Society of America **79**(6), 1833–1843 (1986)

[15] Moore, J.A., Lyon, R.H.: Sound transmission loss characteristics of sandwich panel constructions. The Journal of the Acoustical Society of America **89**(2), 777–791 (1991)

[16] Paradeisiotis, A.: Applications of oscillators in energy conversion. Doctoral dissertation, School of Mechanical Engineering, National Technical University of Athens (2019)

[17] Paradeisiotis, A., Antoniadis, I.: Implementation of a low frequency acoustic isolation panel incorporating kdamper based mounts. In: Proceedings of ICOVP 2019, Crete, Greece (2019)

[18] Yang, Y., Lam, N.T.K., Zhang, L.: Estimation of response of plate structure subject to low veloctiy impact by a solid object. International Journal of Structural Stability and Dynamics **12**(06), 1250053 (dec 2012), ISSN 0219-4554

[19] Yang, Z., Dai, H.M., Chan, N.H., Ma, G.C., Sheng, P.: Acoustic metamaterial panels for sound attenuation in the 50–1000 hz regime. Applied Physics Letters **96**(4), 041906 (2010), doi:10.1063/1.3299007

[20] Zhang, S., Sheng, X.: Analysis of sound transmission loss of a rectangular plate with acoustic treatments. In: Proceedings of ISMA 2018 and USD 2018, pp. 2167–2181, Leuven, Belgium (2018)

EURODYN 2020
XI International Conference on Structural Dynamics
M. Papadrakakis, M. Fragiadakis, C. Papadimitriou (eds.)
Athens, Greece, 23–26 November 2020

A MACHINE MOUNT BASED ON THE KDAMPER FOR VIBRATION ABSORPTION AT LOW FREQUENCIES

Andreas Paradeisiotis[1], Konstantinos Tsioumanis[1], Ioannis Antoniadis[1], and Kalliopi Fouriki[1]

[1]National Technical University of Athens, Dynamics and Structures Laboratory, School of Mechanical Engineering
Heroon Polytechniou 9, 15780 Zografou Athens, Greece
e-mail: aparadis@mail.ntua.gr

Keywords: Vibration isolation, KDamper, Low frequency, Negative Stiffness.

Abstract. *The advantages of the negative stiffness damping effect for vibration absorption in very low frequencies (below 10 Hz) are utilized in this implementation in the form of a mounting mechanism based on the KDamper concept. Specifically, the mount is designed for the absorption of vertical vibrations for machines with mass in the order of 100 kg and rotational speeds in the area of 500 RPM. The design consists in the selection of the appropriate stiffness elements according to the KDamper concept, optimized for minimizing the displacement amplitude of the seismic mass. The included negative stiffness element is realized via a simple configuration of pre-stressed disc (Belleville) springs. Initial experimental measurements of an early prototype are used for comparison with the theoretical investigation and evaluation of the absorption capacity of the mounting mechanism. The results are compared with the predictions of the corresponding models. At the same time, the effects of the non-linear nature of the negative stiffness element are documented, among certain constraints and conditions required for the optimal operation of the system. This examination is demonstrated through the frequency response of the non-linear system using the theoretical models and experimental setup, its potential advantages compared to conventional elastic mounts.*

1 INTRODUCTION

Regarding vibration isolation with conventional elastic mounting, generally in the case of systems subjected to periodic excitation the resonant frequency has to be lowered by adjusting the stiffness of the mounting. Consequently, the frequency of the excitation falls in the isolation range. However, especially in cases where the excitation frequency is already very low, this could mean that the stiffness has to be decreased so much that it compromises the structural integrity of the system. Very low stiffness could also translate to prohibitive amplitude values of the response, especially since high damping ratios are not always easily achievable in a lot of cases.

For this reason, several different concepts have been proposed and implemented over the years, encountering the difficulties in low frequency vibration isolation. Some examples are the general concept of the Tuned Mass Damper (TMD), quasi-zero stiffness oscillators, the inerter and other concepts and variations of the aforementioned.

The design of a mounting mechanism for the absorption of vertical vibrations of rotating machines and all kinds of critical configurations, is examined in this paper. The seismic mass is considered to be 100 kg and the rotational speed around 500 RPM. This mount is based on the KDamper concept [1, 2], the schematic diagram of which is presented in Fig. 1.a.

The KDamper, which can be considered as an extension of the traditional Tuned Mass Damper (TMD), is a novel passive vibration isolation and damping concept, based essentially on the optimal combination of appropriate stiffness elements, including a negative stiffness element [1]. The KDamper supplements the inertial forces of the added TMD mass with the stiffness force of the negative stiffness element. This negative stiffness element can be realized by a number of ways such as pre-stressed disc (Belleville) springs, arranged in appropriate geometrical configurations [3]. Among others, this can provide significant comparative advantages, especially in the very low frequency range, such as better damping characteristics without the need of heavy additional masses and without sacrificing the static loading capacity of the structure by using very soft elastic mounting.

The KDamper elements are calculated for a specific mass around a desired frequency f_0 or $\omega_0 = 2\pi f_0$ and the overall static stiffness comes as $k_0 = m\omega_0^2$, which also equals to

$$k_0 = \frac{k_P k_N}{k_P + k_N} + k_S \tag{1}$$

The overall static stiffness k_0 of the system is maintained.

Next, the basic parameters of the KDamper concept μ,κ and ρ, are defined as

$$\mu = m_D/m \tag{2}$$
$$\rho = \omega_D/\omega_0$$
$$\kappa = -k_N/(k_P + k_N)$$

Finally, the non-dimensional parameters of the stiffness elements of the KDamper are defined as

$$\kappa_S = \frac{k_S}{k_0} = 1 + \kappa(1+\kappa)\mu\rho^2 \tag{3}$$
$$\kappa_P = \frac{k_P}{k_0} = (1+\kappa)\mu\rho^2$$
$$\kappa_N = \frac{k_N}{k_0} = -\kappa\mu\rho^2$$

leading to the calculation of the stiffness elements (k_S, k_P, k_N) of the oscillator. Furthermore k_D is defined as $k_D = k_P + k_N$, thus, for a specific damping ratio ζ_D, the damping constant is calculated as:

$$c_D = 2\zeta_D\sqrt{k_D m_D} \tag{4}$$

Figure 1 presents the schematic diagrams of the classic "m-c-k" and "TMD" oscillators along with the KDamper. For a direct comparison between the three concepts, it is appropriate to consider the same static stiffness k_0 for all. However for the TMD is taken that $f_{D,TMD} = f_{0,mck} = f_{0,KD}$. This modification makes the static stiffness of the TMD slightly higher and the reason for this is to exploit the anti-resonance nature of the oscillator. As for the stiffness elements, it is considered that $k_{S,TMD} = \omega_0^2 m_D$ and $k_{P,TMD} = \omega_D^2 m_D$.

The frequency response of the transfer functions for the three oscillators are compared in Fig.2. For a harmonic excitation, the KDamper minimizes the amplitude of the response $x(t)$ in a frequency band defined by the selection of its individual parameters, much more effectively than the TMD for a broader range of frequencies while utilizing much lighter added mass. The depth of the narrow band where the transfer functions of the TMD drop, is proportionate to its added mass and inversely proportionate to the damping element c_D, but of course c_D cannot be too low due to practical amplitude constraints of the internal mass.

2 EXPERIMENTAL IMPLEMENTATION OF KDAMPER

For this particular implementation, a conservative approach is taken, meaning that parameter κ is taken as just 45% of κ_{max} in order to ensure a static stability margin ϵ above 10%.

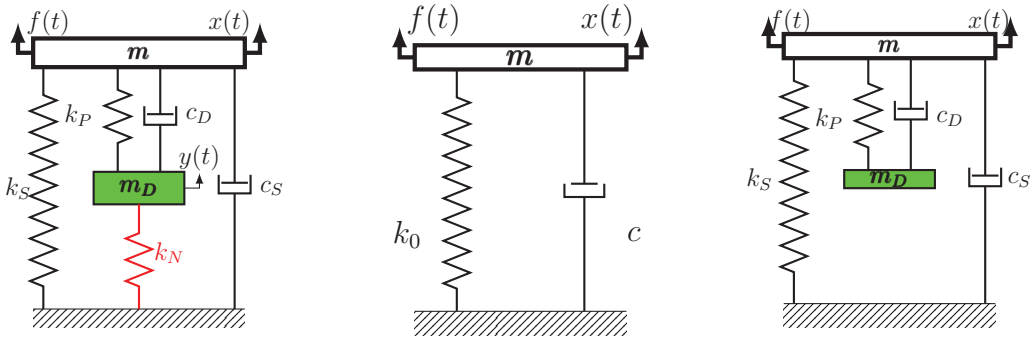

(a) "KDamper" (b) "m-c-k" (c) "TMD"

Figure 1: Schematic presentation of vibration isolation concepts.

μ	ζ_S	ζ_D	$f_0\,[Hz]$	$m\,[kg]$	$\kappa\,[\%\kappa_{max}]$
0.03	0.15	0.2	8.33	100	45
$k_0\,[N/m]$	$k_S\,[N/m]$	$k_P\,[N/m]$	$k_N\,[N/m]$	$c_S\,[Ns/m]$	$c_D\,[Ns/m]$
2.74×10^5	3.79×10^5	3.59×10^4	-2.68×10^4	1.57×10^3	66.36

Table 1: Values of KDamper parameters for 100 kg seismic mass.

Figure 3, presents the frequency response of the transfer functions of the dynamic magnification factor for both degrees of freedom (DOFs) x and y of the KDamper respectively, for an indicative set of parameters μ, κ and ρ. More information regarding the design of the KDamper can be found in [6].

2.1 NEGATIVE STIFFNESS ELEMENT REALIZATION

There are various structural configurations by which negative stiffness can be achieved, using either post-buckled beams or shells, pre-stressed spring configurations and many others [5]. In this implementation, the negative stiffness element of the oscillator is realized utilizing disc (Belleville) springs. The exerted force and the equivalent stiffness of this type of springs, are non-linear functions of the vertical displacement s of the inner diameter D_i. The height of the spring is denoted by l_0, D_e is the external diameter and $h_0 \approx l_0 - t$, where t is the thickness. The relevant notation is demonstrated in Fig. 4. More specific information about disc springs are provided by manufacturers [4]. Specifically, for the calculation of the exerted force of an individual spring as function

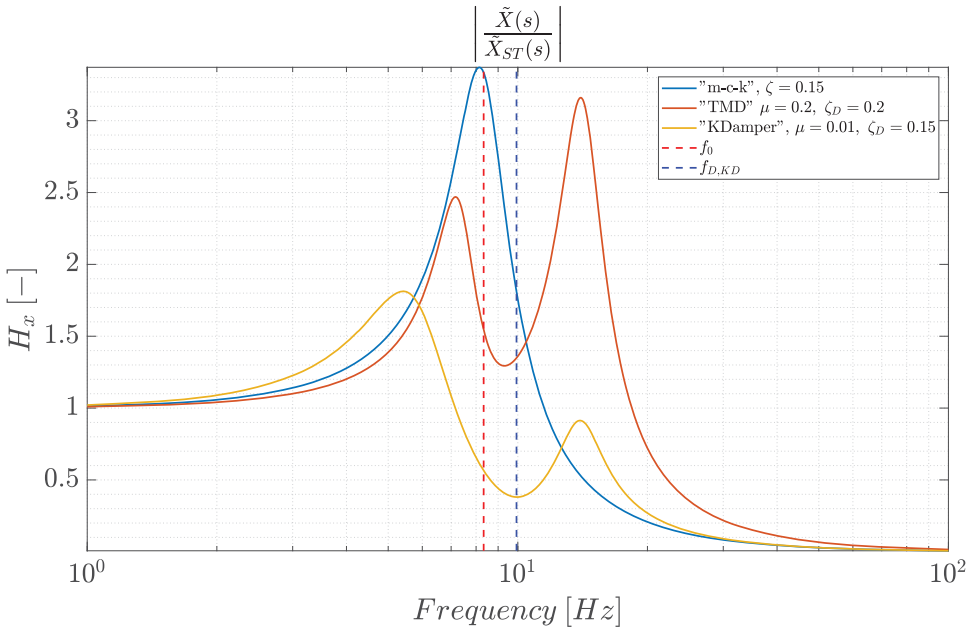

Figure 2: Magnification factor comparison of the three oscillators.

of the deformation s holds:

$$F(s) = F_c\Big[K_4^2\Big(\frac{h_0}{t} - \frac{s}{t}\Big)\Big(\frac{h_0}{t} - \frac{s}{2t}\Big) + 1\Big]s \tag{5}$$

where $F_c = F(s = h_0)$ is the exerted force when the disc is at its flattened position and is estimated as

$$F_c = \frac{4E}{1-\nu^2}\frac{t^3 h_0}{K_1 D_e^2}K_4^2 \tag{6}$$

By setting $\delta = D_e/D_i$ as the ratio of outer to inner diameter of the disc, parameters K_1 is defined as

$$K_1 = \frac{1}{\pi}\frac{\Big(\frac{\delta-1}{\delta}\Big)^2}{\frac{\delta+1}{\delta-1} - \frac{2}{ln(\delta)}} \tag{7}$$

while parameter K_4 depends on the type of the contact surfaces of the disc spring. In this particular case where $t < 1.25\ mm$, no contact surfaces (rounded edges) or reduced thickness are taken into account which corresponds to $K_4 = 1$.

Standard disc springs dimensioned in accordance with DIN 2093, have ratios of h_0/t up to 1.3. However, in order for such a disc to demonstrate negative stiffness behaviour, this ratio needs to be $h_0/t > \sqrt{2}$. Disc springs with a ratio above this value are categorized as non-standard. Furthermore, for $h_0/t > \sqrt{8}$ the disc becomes a bistable element, meaning that in a certain range of deformation s (snap-through region), the exerted force becomes negative, thus these type of discs may act as switch elements.

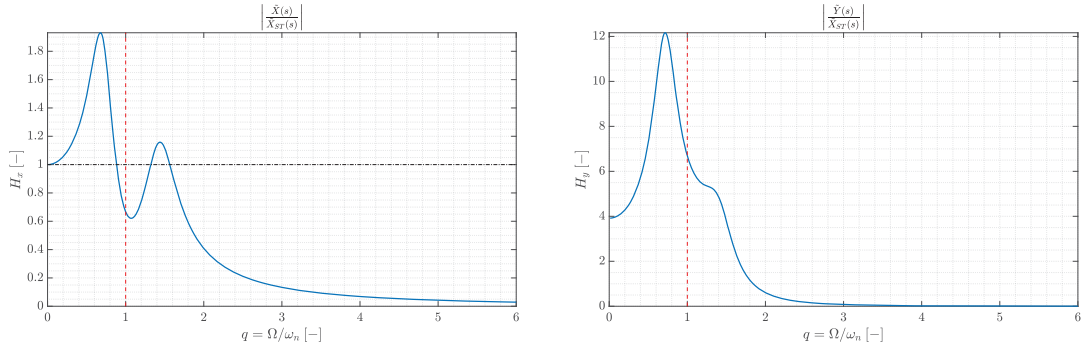

(a) Frequency response of $|\tilde{T}_{XK}|$. (b) Frequency response of $|\tilde{T}_{YK}|$.

Figure 3: Frequency response of the KDamper transfer functions.

On the other hand it has to be taken into account that as this ratio increases, considering all other parameters constant, the force F_c increases too and the developing stresses are getting higher. This fact would be problematic, especially for cyclic operation as in this case, due to low fatigue strength.

The range of the vertical displacement s where the disc exhibits the desired negative stiffness characteristics, is centred around the flat position of the disc where the exerted force is F_c and the negative stiffness value is at its maximum. This of course, translates to the application of a certain pre-stress condition on the spring, so that its stiffness falls in the negative stiffness region, at the equilibrium state of the oscillator.

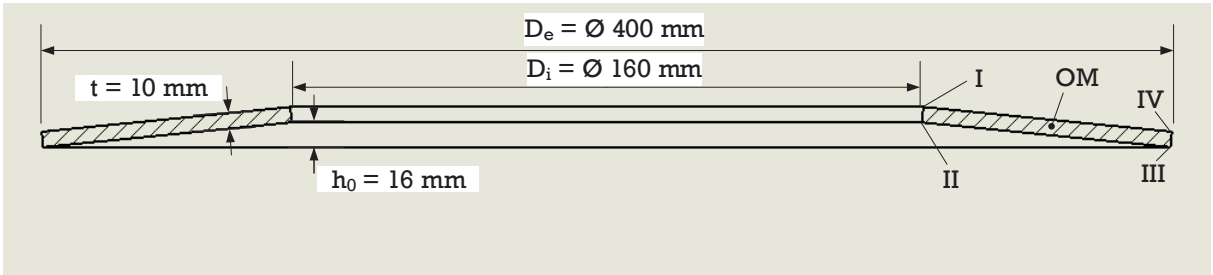

Figure 4: Notation and dimensions of disc springs.

δ	D_e/t	h_0/t	F_c $[N]$	$k_{N,max}$ $[N/m]$
2.5	40	1.6	1.2×10^3	-1.319×10^4

Table 2: Parameters of the disc spring.

$\rho\,[kg/m^3]$	$\sigma_{yield}\,[MPa]$	$E\,[MPa]$	ν
1060	44	2206	0.3

Table 3: Material properties of the disc spring.

Figure 5.a shows the resulting Force - Displacement curve for the selected disc spring, while Fig. 5.b demonstrates the equivalent stiffness of the spring as a function of the vertical displacement s. The dotted black line, indicates the zero value of k_N namely the threshold of negative stiffness. In order to achieve the required negative stiffness value, a total number of two such disc springs have to be configured in parallel. The resultingstiffness in this case is demonstrated in Fig. 5.b in comparison with the single spring curve.

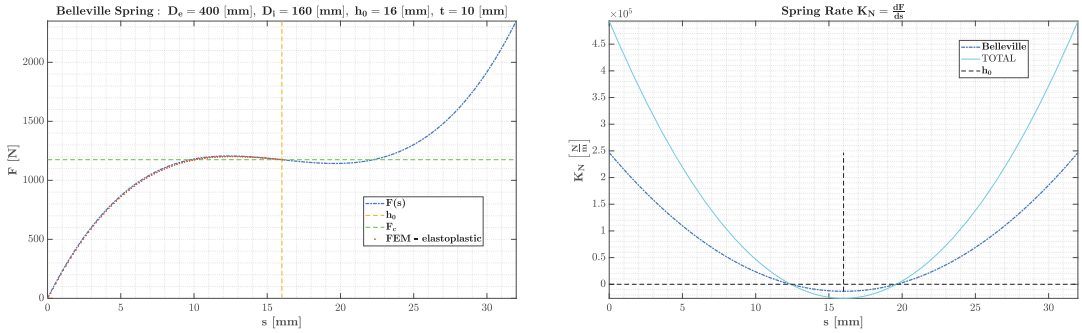

(a) Force-deformation curve of disc spring. Comparison with FEM simulation.

(b) Equivalent stiffness of the disc spring and of the parallel configuration.

Figure 5: Force-Displacement curves of "Belleville" disc springs.

Another aspect to be considered, concerns the generated stresses of the disc spring. Figure 6.a, shows the stresses as function of deformation s, at the five characteristic points of the spring. According to manufacturers, depending on the application, the value of the resulting stress σ_{OM} must be between certain limits to ensure smooth, as intended operation. Especially in dynamic applications this stress defines a nominal number of cycles of operation for the disc spring provided via endurance and fatigue strength diagrams.

Furthermore, due to the unstable nature of negative stiffness, once the pre-stressed flattened disc are attached inside the rest of the configuration, the exerted forces will produce deformation of the k_P stiffness element and consequently the k_S element leading to displacement of the internal and seismic mass up to a static equilibrium position.

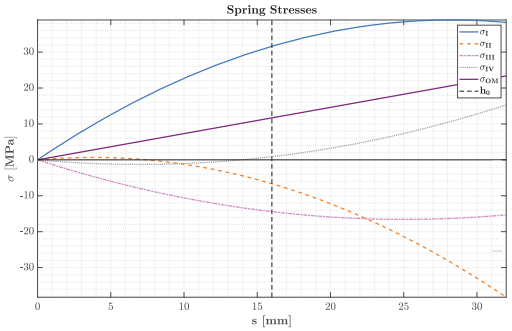

(a) Stresses during deformation of the disc spring.

(b) Disc springs in parallel configuration.

Figure 6: Stress development of the disc springs, and the configuration for the NSE.

2.2 ANALYTIC INVESTIGATION

In order to perform an initial evaluation of the performance of the system, two analytical models were formulated. The first, linear model, considers the value of the NSE k_N to be constant, as calculated by the initial dimensioning from the KDamper design. Utilizing this model, the transfer functions of the oscillator may be calculated along with indicative time response of the x and y DOFs and other important variables. This is important in order to have a frame of reference by which the non-linear response of the second model is evaluated and to calculate the expected order of magnitude of displacement, especially regarding the internal mass. The aforementioned second non-linear model considers the time-varying nature of the NSE, by incorporating the corresponding equations of the disc springs.

Considering a harmonic excitation of the form

$$F(t) = \tilde{F}e^{\jmath\Omega t} = \hat{F}e^{\jmath\Omega t} \tag{8}$$

where the amplitude of the force is taken as

$$\hat{F} = k_0 X_{ST} \tag{9}$$

which for $X_{ST} = 0.1\ mm$ results to $\hat{F} = 27.4\ N$.

As observed in Fig. 8.a, the response x of the initial mass and y of the internal mass of the non-linear model to a harmonic excitation of frequency $\Omega = \omega_0$, show negligible deviations from the linear response, both in phase and amplitude.

Figure 9.a shows the velocity response of both degrees of freedom x and y of the non-linear model, while Fig. 9.b shows the corresponding accelerations.

This velocity response can be used for direct comparison with the experimental measurements.

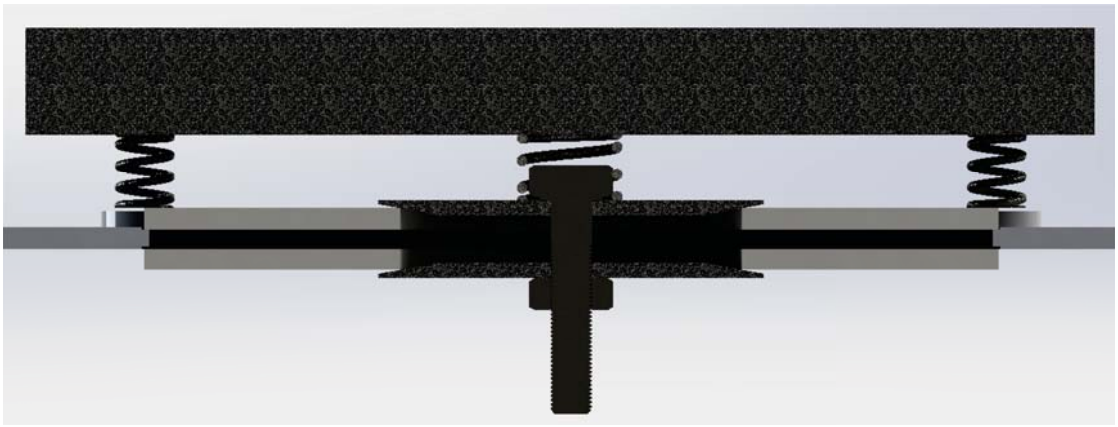

Figure 7: Design of the practical implementation of the mount. Cross section of front view.

3 EXPERIMENTAL TEST

A first prototype of the design presented thus far was structured and a preliminary run of experimental tests was performed in order to validate the analytical results and calculations. It should be noted that at that preliminary stage, no damping elements were added to the configuration, therefore the only dissipative mechanisms during these first tests were the structural damping of the various elements along with any frictional effects.

Figure 10.a presents the shape of the base acting as the ground where the disc springs of the NSE are positioned. This picture also shows the lower half of the NSE, namely the lower disc spring with its corresponding conical force-applying element and the screw via which the equivalent top part is later tied together. The surrounding helical springs implementing the k_S stiffness element of the KDamper can also be seen, positioned in the four corners around appropriate guides for the oscillating seismic mass in order to ensure proper vertical oscillation and avoid any slipping.

Figure 10.b shows the completed setup with the seismic mass on top, the NSE in its appropriate pre-stressed state where the disc springs are flat and the helical spring representing the k_P stiffness element of the KDamper, in between. The guide shown on the side, connects the exciter with the seismic mass in order to provide the necessary excitation for the tests.

Initially, the system is subjected to an impulse excitation, in an attempt to evaluate the eigenfrequency of the system along with its damping capacity. The measurements were undertaken by using appropriately positioned laser velocimeters. The response of the seismic mass, representing the x DOF of the KDamper, is presented in Fig. 11 along with the corresponding double-sided frequency spectrum $P_2(f)$.

The response of the internal mass, representing the y DOF of the KDamper, is pre-

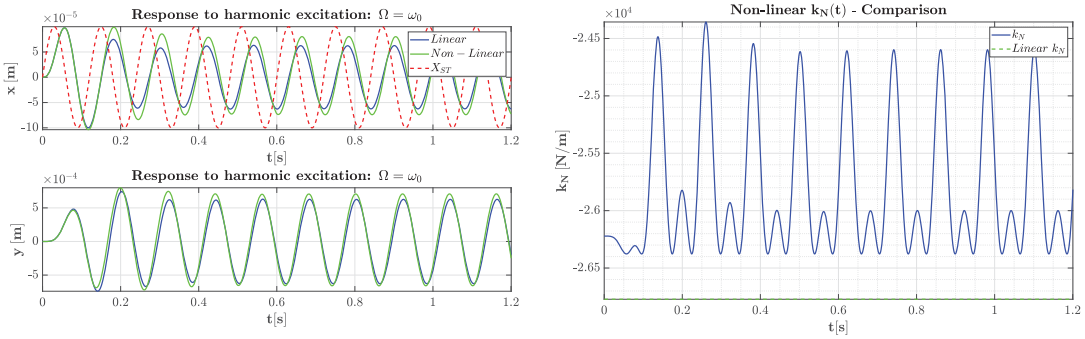

(a) Response of x and y to harmonic excitation with $\Omega = \omega_0$.

(b) Corresponding stiffness value response of the NSE.

Figure 8: Linear and non-linear models time response comparison to harmonic excitation.

sented in Fig. 12 along with the corresponding double-sided frequency spectrum $P_2(f)$. The spectra of these measurements show clearly a peak very close to the theoretical design frequency of $500RPM \approx 8.33\ [Hz]$. Specifically the response of the seismic mass shows the eigenfrequency of the system at $f = 8.582\ [Hz]$, while the response of the internal mass positions the eigenfrequency $f = 8.772\ [Hz]$, variations well within the margin of error.

Next, a frequency sweep was gradually applied, namely a harmonic excitation with varying frequency up to $50\ [Hz]$, in order to acquire a frequency response of the two DOFs for comparison with the theoretically estimated transfer functions.

The shape of the two spectra present some resemblance to the expected behavior, compared to Figs. 3.a and 3.b. The analytical model provides the two eigenfrequencies of the KDamper as $f_1 = 6.08\ [Hz]$ and $f_2 = 12.07\ [Hz]$ which appear to be comparable to the corresponding peaks of the measurements. Furthermore, the expected dip in amplitude is observable between these two frequencies. However, without exact knowledge of the excitation amplitude at each frequency, it is not possible to evaluate with any degree of certainty the level of isolation achieved by the system. For the same reason, it is difficult to extract definitive conclusions for the amplitude of the velocity response by comparing them to the theoretically calculated ones.

4 CONCLUSIONS

A machine mounting mechanism was designed based on the concept of the KDamper, for vertical vibration absorption of a 100 kg seismic mass at a frequency of interest approximately $8.33\ [Hz]$. Appropriate analytical models were formulated, simulating the expected performance of the mount and to be used for comparison with future experimental measurements. A first experimental setup has been constructed based on the

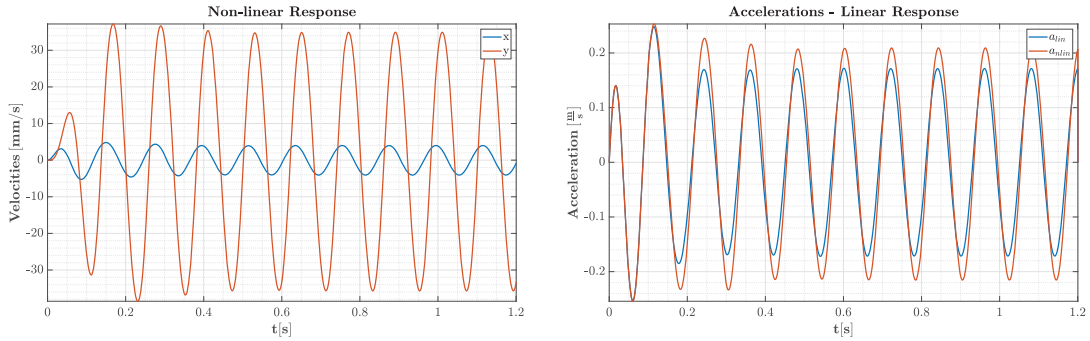

(a) Velocity response of non-linear model to harmonic excitation with $\Omega = \omega_0$.

(b) Acceleration response of non-linear model to harmonic excitation with $\Omega = \omega_0$.

Figure 9: Non-linear model time response comparison.

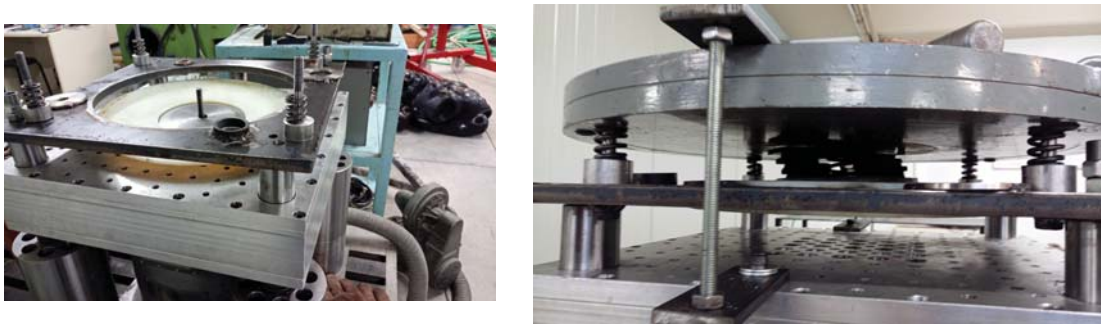

Figure 10: Experimental implementation of the KDamper design for 100 kg seismic mass.

above design and a preliminary set of measurements was undertaken in order to validate the projections of the theoretical analysis. However, various technical difficulties and the limited number of tests performed at this initial stage, cannot provide definitive conclusions as to the performance of the setup, although some values were verified, including some basic frequencies of the system.

The experimental setup is currently being updated and further tests will be performed in the near future to provide a clearer picture. Necessary future steps include the addition of either viscous or elastomeric damping elements in the appropriate positions of the system, along with more precise and targeted measurements.

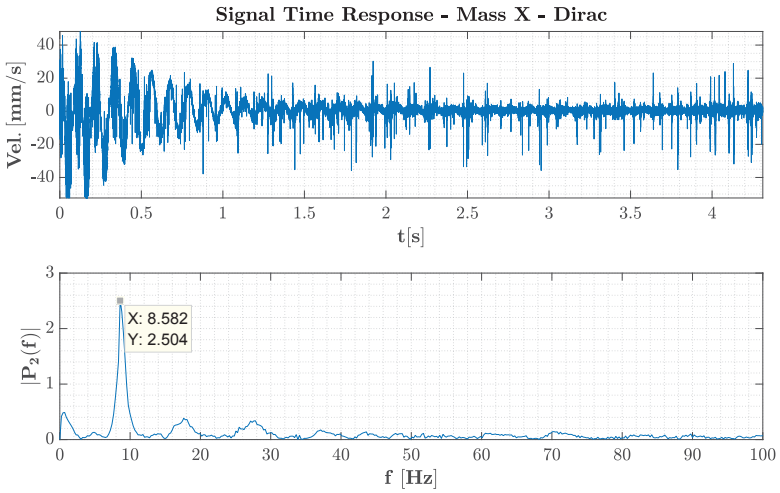

Figure 11: Velocity response of x DOF to impulse excitation along with the corresponding spectra.

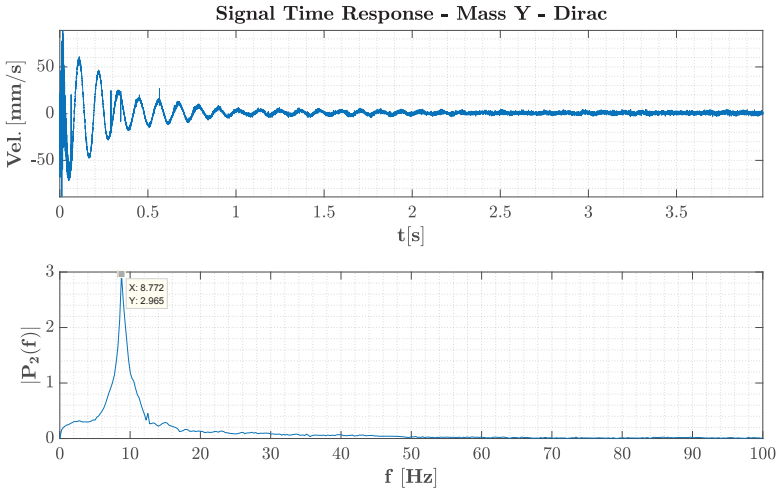

Figure 12: Velocity response of y DOF to impulse excitation along with the corresponding spectra.

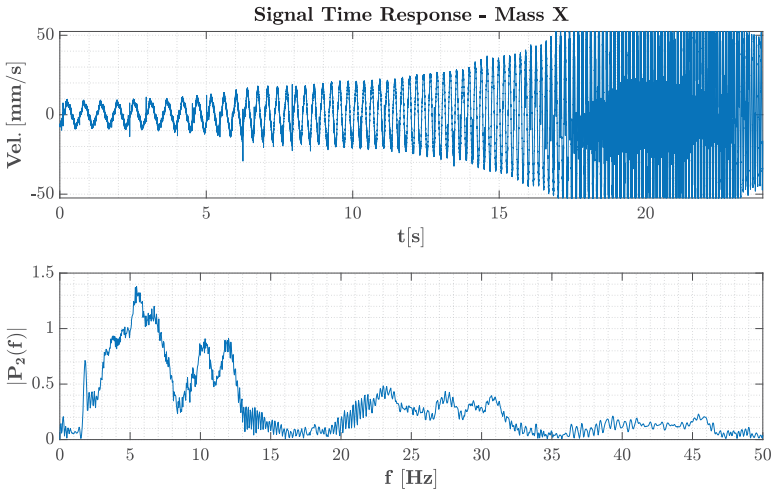

Figure 13: Velocity response of x DOF to frequency sweep along with the corresponding spectra.

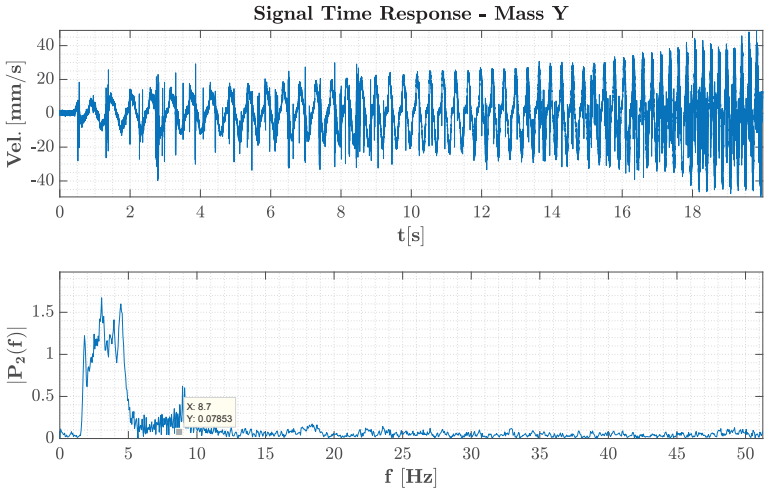

Figure 14: Velocity response of y DOF to frequency sweep along with the corresponding spectra.

5 ACKNOWLEDGMENTS

This research has been co-financed by the European Union and Greek national funds through the Operational Program Competitiveness, Entrepreneurship and Innovation, under the call RESEARCH – CREATE – INNOVATE(project code:T1EDK-02827, "Novel Seismic Protection Devices in All Spatial Directions - NOESIS").

References

[1] Antoniadis, I.A., Chronopoulos, D., Spitas, V., Koulocheris, D.: Hyper-damping properties of a stable linear oscillator with a negative stiffness element. Journal of Sound and Vibration **346**, 37–52 (2015)

[2] Antoniadis, I.A., Kanarachos, S.A., Gryllias, K., Sapountzakis, I.E.: Kdamping: A stiffness based vibration absorption concept. Journal of Vibration and Control **24**(3), 588–606 (2016)

[3] Antoniadis, I.A., Paradeisiotis, A.: Acoustic meta-materials incorporating the kdamper concept for low frequency acoustic isolation. Acta Acustica united with Acustica **104**(4), 636–646 (2018)

[4] Bauer, C.: Disc springs-theory and practice (2008), URL `https://www.christianbauer.com/en/img-cust/3_Theory_and_practice.pdf`

[5] Huang, H.H., Sun, C.T.: Wave attenuation mechanism in an acoustic metamaterial with negative effective mass density. New Journal of Physics **11**(1), 013003 (jan 2009), doi:10.1088/1367-2630/11/1/013003

[6] Paradeisiotis, A.: Applications of oscillators in energy conversion. Doctoral dissertation, School of Mechanical Engineering, National Technical University of Athens (2019)

EURODYN 2020
XI International Conference on Structural Dynamics
M. Papadrakakis, M. Fragiadakis, C. Papadimitriou (eds.)
Athens, Greece, 23–26 November 2020

DESIGN OF A BROADBAND ELASTIC METAMATERIAL VIA TOPOLOGICALLY OPTIMIZED INERTIAL AMPLIFICATION MECHANISMS

Osman Yuksel[1], **and Cetin Yilmaz**[2,*]

[1]Department of Mechanical Engineering, Kirklareli University
Kirklareli, Thrace, Turkey
e-mail: osmanyuksel@klu.edu.tr

[2] Department of Mechanical Engineering, Bogazici University
Bebek, Istanbul, Turkey
e-mail: cetin.yilmaz@boun.edu.tr
[*] Corresponding Author

Keywords: Phononic Band Gaps, Inertial Amplification, Topology Optimization, Elastic Metamaterials.

Abstract. *Elastic metamaterials enable to generate phononic band gaps below the Bragg limit. Most metamaterials in the literature are based on vibration absorption (local resonance) principle. In this study, a two dimensional elastic metamaterial is designed, which utilizes inertial amplification principle. This principle allows generating wide band gaps at low frequencies. Firstly, the theory of phononic gaps induced by inertial amplification in finite structures is discussed briefly utilizing a lumped parameter model. Afterwards, a compliant inertial amplification mechanism is introduced, which is the building block of the metamaterial designed in this paper. Topology optimization is performed on this mechanism to obtain a wide vibration stop band for a given mass constraint. Then, vibration transmissibilities of one dimensional finite periodic structures with various number of unit cells are presented. Subsequently, a two dimensional metamaterial is constructed by incorporating the topologically optimized compliant inertial amplification mechanisms. Finally, in-plane vibration isolation performance of this two dimensional system is demonstrated via vibration transmissibility plots.*

1 INTRODUCTION

Periodic structures are extensively studied for almost three decades since they can mitigate vibration transmission and can act as passive vibration isolation systems. Periodic structures which can inhibit wave propagation by generating phononic band gaps are generally known as phononic crystals. If band gaps can be generated below the Bragg limit then these structures are called elastic metamaterials. In the literature, there exist three methods to create band gaps (stop bands): Bragg scattering [1, 2], resonance scattering (local resonances) [3, 4], inertial amplification [5–7]. In Bragg scattering, stop band is created via employment of periodically varying mass and stiffness elements in the structure. However, in order to obtain band gaps at low frequency region, low stiffness and large mass elements are required. In resonance scattering (local resonances), periodic local resonators are added to the structure. Nevertheless, to have band gaps at low frequencies, one has to utilize large local resonators. In inertial amplification, displacement amplification mechanisms are employed to create inertial coupling induced vibration stop bands. In this method, effective dynamic inertia of the system is increased, thus low frequency band gaps can be attained without decreasing stiffness or increasing total mass of the structure.

Elastic metamaterials are formed by periodic inclusion of the smallest repeating constructive elements called unit cells. Unit cell design is quite important, since it determines the vibration stop band limits, i.e., vibration isolation frequency range. Hence, in order to obtain the widest possible stop band, structural optimization should be considered when designing a unit cell. To that end, topology optimization will be a proper choice since it determines optimum topology, shape and size of a structure simultaneously. On the other hand, vibration isolation level achieved with an elastic metamaterial depends on the number of unit cells used in the periodic structure. As the number of unit cells employed increases, vibration transmission through metamaterial decreases, hence vibration isolation performance increases.

In this paper, a two dimensional broadband elastic metamaterial is proposed to inhibit in-plane low frequency vibration transmission for a wide frequency range. The elastic metamaterial is constructed via incorporating topologically optimized compliant inertial amplification mechanisms (unit cell) in hexagonal form. Vibration transmissibility plots for several periodic designs are calculated and satisfactory levels of vibration isolation performances are demonstrated.

2 THEORY

2.1 Inertial Amplification

Inertial amplification [5, 6] is a phononic band gap generation method, in which broadband phononic band gaps can be attained at low frequency regions without decreasing stiffness or increasing mass of the structure. In order to show the effectiveness of the method, a lumped parameter inertial amplification mechanism model is provided in Fig. 1. In this model, the two masses denoted as m are connected with each other with an elastic spring which has stiffness k. On the other hand, the masses m and the mass m_a are connected with massless rigid rods. The mechanism has an isosceles triangle configuration, i.e., the angle between the rigid rods and the spring is θ. For this lumped parameter model, the input displacement is provided from the left side as y and the output is taken from the right side as x. Besides, the horizontal and the vertical displacements of the mass m_a are provided in terms of the input (y) and the output (x) displacements as $(x + y)/2$ and $(y - x)\cot(\theta)/2$, respectively.

The equation of motion of the lumped parameter inertial amplification mechanism shown in

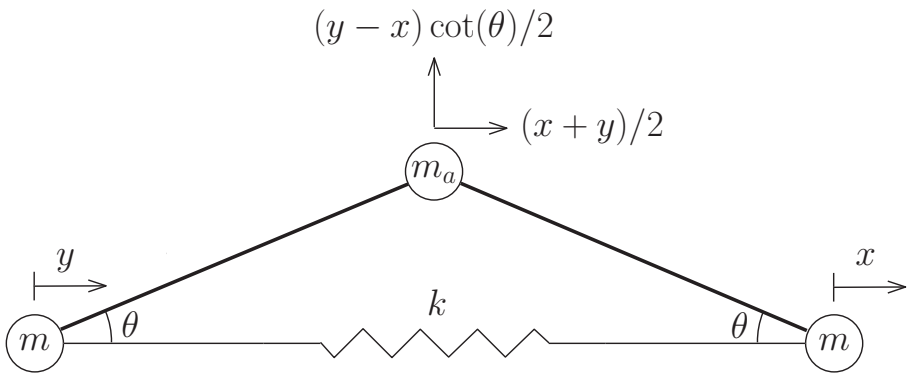

Figure 1: Lumped parameter inertial amplification mechanism.

Fig. 1 can be obtained by employing the Lagrange method as [8, 9]:

$$\left[m_a(\cot^2\theta+1)/4+m\right]\ddot{x}+kx=\left[m_a(\cot^2\theta-1)/4\right]\ddot{y}+ky \tag{1}$$

Equating the right hand side of Eq. 1 to zero and solving the resulting ordinary differential equation for the output x, one can find the resonance frequency as:

$$\omega_p=\sqrt{\frac{k}{m_a(\cot^2\theta+1)/4+m}} \tag{2}$$

Similarly, when one equates the left hand side of Eq. 1 to zero and solves for the input y, the antiresonace frequency can be found as:

$$\omega_z=\sqrt{\frac{k}{m_a(\cot^2\theta-1)/4}} \tag{3}$$

As can be seen from Fig. 1, the total mass of the structure (static mass) is:

$$m_s=2m+m_a \tag{4}$$

On the other hand, Eq. 2 can be rewritten as:

$$\omega_p=\sqrt{\frac{k}{m_d}} \tag{5}$$

Therefore, one can calculate the effective dynamic mass of the structure from Eq. 2 and Eq. 5 as:

$$m_d=\frac{4m+m_a(\cot\theta^2+1)}{4} \tag{6}$$

Similarly, antiresonance frequency can be redefined in terms of k, m_s and m_d as:

$$\omega_z=\sqrt{\frac{k}{m_d-m_s/2}} \tag{7}$$

The lumped parameter inertial amplification mechanism presented in Fig. 1 is a single degree of freedom low pass filter type vibration isolator. Hence, its displacement transmissibility for a given excitation frequency ω can be calculated as [8, 9]:

$$TR(\omega) = \frac{|x(\omega)|}{|y(\omega)|} = \frac{|1 - (\omega/\omega_z)^2|}{|1 - (\omega/\omega_p)^2|} \tag{8}$$

Vibration stop band is defined for the frequencies where transmissibility value obtained in Eq. 8 is less than 1 [8, 10]. Consequently, stop band starting frequency (ω_s) can be found by solving the expression below:

$$TR(\omega_s) = \frac{|x(\omega_s)|}{|y(\omega_s)|} = \frac{|1 - (\omega_s/\omega_z)^2|}{|1 - (\omega_s/\omega_p)^2|} = 1 \tag{9}$$

Solving Eq. 9 for ω_s, one can find the stop band starting frequency as:

$$\omega_s = \sqrt{\frac{2\omega_p^2\omega_z^2}{(\omega_p^2 + \omega_z^2)}} \tag{10}$$

Now, consider a situation in which angle θ is small. For small θ values, $\cot\theta^2$ term in the denominator of Eq. 6 becomes quite large. As a result, the effective dynamic mass of the lumped parameter inertial amplification mechanism becomes quite large. As the dynamic mass of the structure increases, the resonance and the antiresonance frequencies decrease to lower frequency region. Finally, following Eq. 10, the stop band starting frequency decrease, as well.

In order to give a clear view on the inertial amplification concept, a simple numerical example can be considered. Suppose that all masses are 1 kg, spring stiffness value is 1 N/m and consider a small θ value of 10° ($\pi/18$ rad). Then, static mass (m_s) of the model becomes 3 kg and effective dynamic mass (m_d) of the structure becomes 9.29 kg. Hence, the effective inertia of the system increases more than 3 fold. If the whole 3 kg mass was on the right side of the spring and there wasn't any amplification mechanism, the resonance frequency would be 0.577 rad/s and stop band would start at $\sqrt{2} \times 0.577 = 0.816$ rad/s. For the system with inertial amplification mechanism, the resonance and antiresonance frequencies are calculated as 0.328 rad/s and 0.358 rad/s, respectively. Hence, the stop band starts at 0.342 rad/s, which is less than half of 0.816 rad/s. As this simple example demonstrates, by employing inertial amplification method, one can obtain a vibration stop band at low frequency regions without sacrificing stiffness or increasing total mass of the structure.

2.2 Topology Optimization

Topology optimization [11] is a structural optimization method, in which optimum material layout is sought to obtain a structure that satisfies a certain mechanical performance in a given finite element design space. In the literature, there exist several topology optimization methods [12]. However, in this study, widely utilized modified solid isotropic material with penalization (modified-SIMP) [13] is employed. In this method, an individual finite element's stiffness value is defined as:

$$E_e(x_e) = E_{min} + x_e^p(E_0 - E_{min}) \qquad x_e \in [0, 1] \tag{11}$$

where x_e denotes the element's density which can take any value between 0 and 1, E_e denotes element's elastic modulus, E_{min} denotes a small elastic modulus value to prevent stiffness ma-

trix singularity, E_0 denotes the elastic modulus of the material, p denotes the penalization factor for stiffness.

Similarly, an individual element's physical density value can also be defined as [14]:

$$\rho_e(x_e) = \begin{cases} \rho_{min} + x_e(\rho_0 - \rho_{min}) & \text{if } x_e > 0.1 \\ \rho_{min} + x_e^d(\rho_0 - \rho_{min}) & \text{if } x_e \leq 0.1 \end{cases} \tag{12}$$

where x_e is the density of element e, ρ_e is the physical density of element e, ρ_{min} is a small density value to prevent mass matrix singularity, ρ_0 is the physical density of the material, d is the penalization factor for mass.

Using Eq. 11, global stiffness matrix $\boldsymbol{K}$ is defined as:

$$\boldsymbol{K} = \sum_{e=1}^{N} E_e(x_e)\boldsymbol{K_0} \tag{13}$$

where $\boldsymbol{K_0}$ is the stiffness matrix of an element that has unit elastic modulus and N is the total number of finite elements in the design domain. Here, the summation notation indicates the usual finite element notation to form global matrices from local matrices.

Similarly, using Eq. 12, global mass matrix $\boldsymbol{M}$ is defined as:

$$\boldsymbol{M} = \sum_{e=1}^{N} \rho_e(x_e)\boldsymbol{M_0} \tag{14}$$

where $\boldsymbol{M_0}$ is the mass matrix of an element that has unit density.

Moreover, the material volume is defined as:

$$V(\boldsymbol{x}) = \sum_{e=1}^{N} x_e \tag{15}$$

In this study, the objective of the topology optimization problem is maximization of the band gap width for a given mass constraint. For that purpose, $-\omega_2/\omega_1$ ratio is minimized, where ω_1 and ω_2 are the first two natural frequencies of the unit cell mechanism and the band gap resides between these frequencies. Hence, the topology optimization problem is given as [15]:

$$\begin{aligned} \text{min.}_{\ \boldsymbol{x}} \quad & f(\boldsymbol{x}) = -\frac{\omega_2(\boldsymbol{x})}{\omega_1(\boldsymbol{x})} \\ \text{s.t.} \quad & \boldsymbol{K u_1} = \omega_1^2 \boldsymbol{M u_1} \\ & \boldsymbol{K u_2} = \omega_2^2 \boldsymbol{M u_2} \\ & V(\boldsymbol{x}) = aV_0 \\ & 0 \leq x_e \leq 1 \qquad \text{for } e = 1, 2, ..., N \end{aligned} \tag{16}$$

where V_0 denotes the total design space area, a denotes the volume fraction defined as the ratio of solid area over total area, u_1 and u_2 are the eigenvectors for the 1st and the 2nd modes, respectively.

The topology optimization problem presented in Eq. 16 can be solved via optimality criteria (OC) [15, 16] method.

In a topology optimization problem, if an individual element's density value (i.e., x_e) is 0, then no material exists in that element. On the contrary, if an element's density value is 1, then it means that element is solid. At the end of the optimization process, the aim is to obtain a solid-void (1-0) type of design, which can be achieved via employing a sensitivity [17] and a post processing filter [18].

3 RESULTS

Topology optimization is conducted on the compliant inertial amplification mechanism shown in Fig. 2. The horizontal length of the mechanism is 120 mm, whereas the vertical length is 60 mm. The small square blocks that are found at the rightmost and leftmost ends have 4 mm by 4 mm dimensions. Four small flexure hinges that connect small square blocks and large triangular amplifier blocks have 4 mm horizontal and 1 mm vertical dimensions. Two long flexure hinges that reside at the center of the mechanism and connect large triangular amplifier blocks to each other have 8 mm horizontal and 1 mm vertical dimensions. Each of the large triangular amplifier blocks have 48 mm horizontal length and 29 mm vertical length. Two long flexure hinges at the center of the mechanism are connected at the middle to the large triangular blocks. Moreover, the slope of the hypotenuse of the triangular blocks is determined as 28° (0.489 rad), a value that prevents contact when a two dimensional periodic structure is constructed in hexagonal incorporation of compliant mechanisms with 60° ($\pi/3$ rad) angles. Finally, the isotropic material of construction is steel with elastic modulus $E_0 = 210$ GPa, density $\rho = 7800$ kg/m^3 and Poisson's ratio $\nu = 0.3$.

Topology optimization is performed on the compliant inertial amplification mechanism to obtain wide vibration stop bands for a given mass constraint. To that end, the topology optimization problem given in Eq. 16 is solved in the design space provided in Fig. 3 for roller-roller boundary conditions. Topology optimization is performed on the grey parts of the mechanism. Whereas, black solid parts of the mechanism are exempted of the optimization process, i.e., for the black solid parts element density value is fixed to 1 and can not be altered. In order to maintain the structural integrity [15] during the optimization process, a diagonal stair type solid framework, which is also exempted of the optimization routine, is utilized. According to the numerical studies performed, a volume fraction value of $a = 0.35$ is selected, since it is the optimum volume fraction value that provides the widest possible stop band. For the topology optimization finite element model, four node, quadrilateral, square, plane stress finite elements are employed. Finite element model discretization is 120 elements in horizontal by 60 elements in vertical, i.e., 7200 elements in total.

At the start of the optimization (i.e., for the mechanism in Fig. 3), first (non rigid mode) resonance frequency f_1 is found as 215.4 Hz, second (non rigid mode) resonance frequency is found as 1392 Hz, and f_2/f_1 ratio (an indicator of stop band width) is calculated as 6.46. As a result of topology optimization process, the design demonstrated in Fig. 4 is obtained. The topologically optimized design has its first resonance frequency f_1 at 200.2 Hz, second resonance frequency f_2 at 1594 Hz, thus, f_2/f_1 ratio is calculated as 7.96. As a result of topology optimization, f_2/f_1 ratio is increased by 23.2 %.

3.1 Unit Cell Mechanism

The unit cell mechanism of the two dimensional elastic metamaterial is obtained from the design provided in Fig. 4 by smoothing the sharp edges. To that end, the unit cell mechanism shown in Fig. 5 is obtained. For a fine mesh with 14050 four node, quadrilateral, plane stress

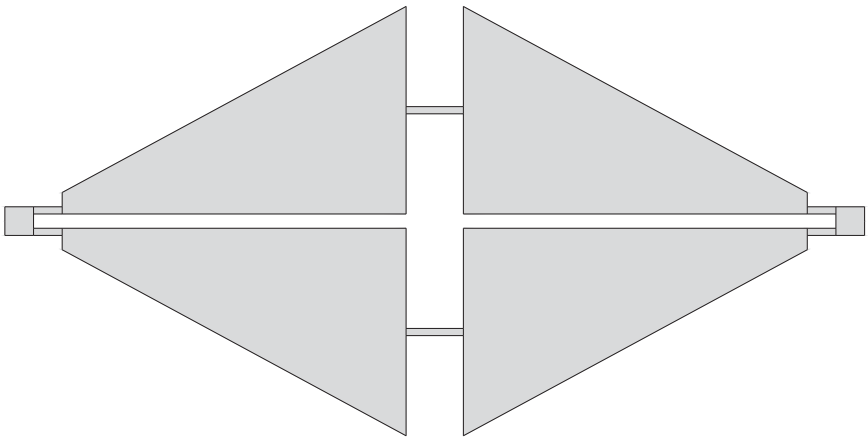

(a)

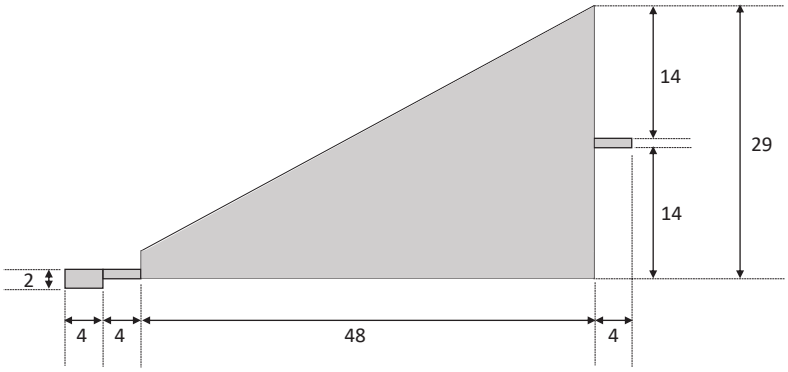

(b)

Figure 2: The compliant inertial amplification mechanism that is going to be topology optimized. (a) The whole mechanism, (b) the quarter mechanism showing the dimensions in mm.

finite elements, the first resonance frequency is observed at $f_1 = 172$ Hz and the second resonance frequency is observed at $f_2 = 1409$ Hz, whereas f_2/f_1 ratio is calculated as 8.19. Shift in resonance frequencies is an expected result, since the preliminary design in Fig. 4 has coarse mesh. However, the difference in f_2/f_1 ratios for both designs given in Fig. 4 and Fig. 5 is insignificant.

In order to see the vibration isolation performance of the compliant inertial amplification unit cell mechanism provided in Fig. 5, one has to perform frequency response function analysis. Consequently, vibration transmissibility of the unit cell structure given in Fig. 5 is calculated for roller-roller boundary conditions. In transmissibility analysis, a horizontal displacement input is provided from the left end of the structure, whereas horizontal output is taken from the right end. The vibration transmissibility plot for axial input and axial output case is shown in Fig. 6. As can be seen, between 171-1432 Hz, transmissibility value is below 1, hence this is the vibration isolation frequency range. The minimum vibration isolation amount achieved via one mechanism is calculated as 18 % within this frequency range (maximum vibration transmissibility of 82 %).

As the periodicity of the elastic metamaterial increases, vibration isolation level increases,

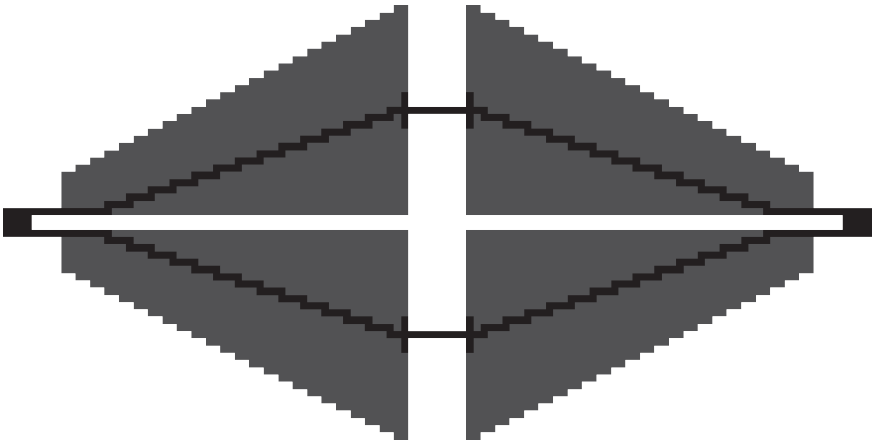

Figure 3: Topology optimization design space of the compliant inertial amplification mechanism. ($f_1 = 215.4$ Hz, $f_2 = 1392$ Hz, $f_2/f_1 = 6.46$).

as well [8, 10, 19, 20]. To that end, in order to observe how vibration isolation performance changes with the number of unit cell mechanisms employed in the elastic metamaterial, one dimensional periodic structures are formed utilizing various number of unit cell mechanisms. A one dimensional periodic structure constructed with four unit cells is given in Fig. 7 as an example. As in the case of the unit cell mechanism, for all of the one dimensional periodic structures, input displacement is provided from left end and output displacement is taken form right end. In Fig. 8, vibration transmissibility plots for one dimensional periodic structures that have 2, 4 and 6 unit cells are shown. As observed, vibration stop band occurs for the same frequency range (between 172-1418 Hz) for all of the periodic structures, a result which is encountered in the literature [8, 10, 19], as well. On the other hand, as the number of unit cells used in the periodic structure increases, vibration isolation level increases, as well. For the one dimensional periodic structure with two unit cell mechanisms utilized, minimum vibration isolation level achieved is calculated as 47 %. Vibration isolation level for the periodic structure with four unit cells is calculated as 84 %. Finally, vibration isolation level for the periodic structure with six unit cells is found as 96 %. In other words, for the periodic structure with six unit cells only 4 % of input vibration can reach to the output end.

3.2 Two Dimensional Broadband Elastic Metamaterial

A two dimensional elastic metamaterial can be constructed by incorporating the unit cell mechanisms in hexagonal formation as shown in Fig. 9. This two dimensional periodic structure has 483 mm horizontal length and 268 mm vertical length, and it is used to isolate in-plane excitations for a broad frequency range.

Vibration transmissibility plots for the two dimensional elastic metamaterial in Fig. 9 are provided in Figs. 10 and 11 for free boundary conditions. In Fig. 10, displacement transmissibility performance of the two dimensional periodic structure is demonstrated for an input provided from the left end and output displacement is taken from the right end (axial input vs axial output case). As can be seen, for a broad frequency range between 173-1420 Hz, less than 0.7 % of input vibration can reach to the output end. That is to say, by using the elastic metamaterial presented in Fig. 9 more than 99.3 % vibration isolation can be achieved between

Figure 4: Topologically optimized compliant inertial amplification mechanism. ($f_1 = 200.2$ Hz, $f_2 = 1594$ Hz, $f_2/f_1 = 7.96$).

173-1420 Hz for axial excitations. This result is also valid for transverse excitations, as well, considering the transmissibility data provided in Fig. 11. For the case shown in Fig. 11, an oblique in-plane displacement input that has both axial and transverse components is supplied to the two dimensional periodic structure from the left end whereas the axial and transverse output displacements are taken separately from the right end of the elastic metamaterial. As can be seen from Fig. 11, axial and transverse transmissibility plots show similar behavior with the axial input vs axial output case discussed in Fig. 10. As observed from Fig. 11, both of the axial and transverse excitations are mitigated more than 99 % within 173-1420 Hz frequency range. The transmissibility plots demonstrate that the two dimensional elastic metamaterial proposed in Fig. 9 is able to inhibit in-plane excitations for a broadband frequency region, and consequently can be used as a high performance passive vibration isolator.

4 CONCLUSIONS

In this study, a two dimensional elastic metamaterial which inhibits in-plane vibrations for a broad frequency range is proposed. The suggested two dimensional periodic structure is formed by incorporating topologically optimized compliant inertial amplification mechanisms in hexagonal formation. Vibration transmissibility plots indicate that, the proposed metamaterial can mitigate in-plane excitations for a broad frequency range that resides in the low frequency region. Vibration isolation levels achieved are quite satisfactory, hence, the suggested design can be utilized as a two dimensional passive vibration isolator for the specified broad frequency band.

ACKNOWLEDGEMENT

Cetin Yilmaz acknowledges the support from the Turkish Academy of Sciences Distinguished Young Scientist Award (TUBA-GEBIP).

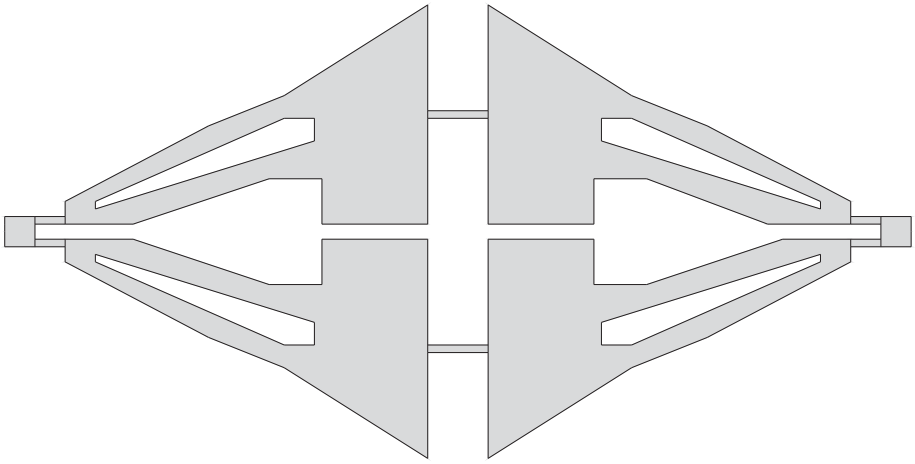

Figure 5: Topologically optimized unit cell mechanism of the periodic structure. ($f_1 = 172$ Hz, $f_2 = 1409$ Hz, $f_2/f_1 = 8.19$).

REFERENCES

[1] M. Sigalas, E. N. Economou, Elastic and acoustic wave band structure, *Journal of Sound and Vibration*, **158(2)**, 377–382, 1992.

[2] M. Sigalas, E. N. Economou, Band structure of elastic waves in two dimensional systems, *Solid State Communications*, **86(3)**, 141–143, 1993.

[3] Z. Liu, X. Zhang, Y. Mao, Y. Y. Zhu, Z. Yang, C. T. Chan, P. Sheng, Locally resonant sonic materials, *Science*, **289(5485)**, 1734–1736, 2000.

[4] C. Goffaux, J. Sanchez-Dehesa, Two dimensional phononic crystals studied using a variational method: Application to lattices of locally resonant materials, *Physical Review B*, **67(14)**, 144301, 2003.

[5] C. Yilmaz, G. M. Hulbert, N. Kikuchi, Phononic band gaps induced by inertial amplification in periodic media, *Physical Review B*, **76(5)**, 054309, 2007.

[6] C. Yilmaz, G. M. Hulbert, Theory of phononic gaps induced by inertial amplification in finite structures, *Physics Letters A*, **374(34)**, 3576–3584, 2010.

[7] C. Yilmaz, Identifying different phononic band gap generation methods, *5th International Conference on Phononic Crystals / Metamaterials, Phonon Transport and Topological Phononics, Tucson, Arizona, USA*, 23–24, 2019.

[8] O. Yuksel, C. Yilmaz, Shape optimization of phononic band gap structures incorporating inertial amplification mechanisms, *Journal of Sound and Vibration*, **355**, 232–245, 2015.

[9] O. Yuksel, Vibration isolator design with truss-like inertial amplification mechanisms, *Proceedings of the 5th International Congress on Advances in Mechanical Engineering, Istanbul, Turkey*, 447–455, December 16-19, 2019.

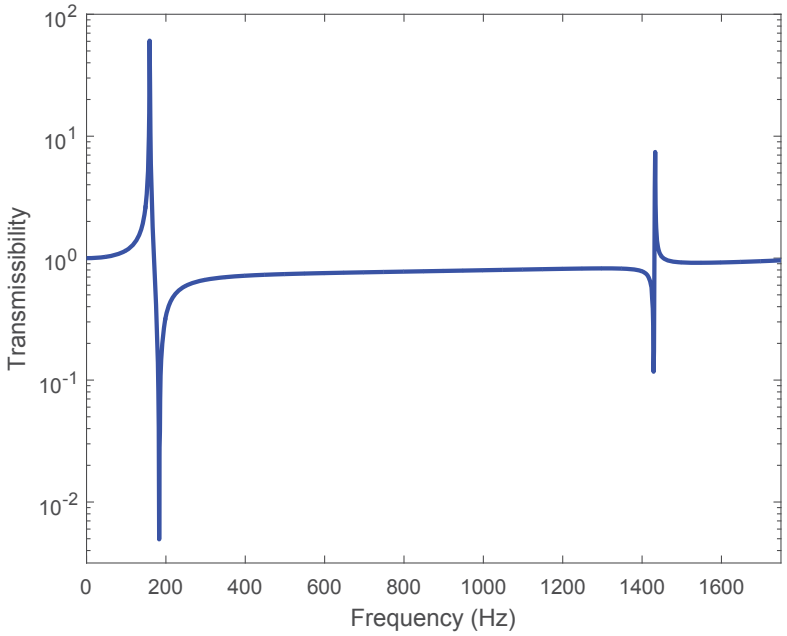

Figure 6: Vibration transmissibility plot of the topologically optimized inertial amplification mechanism provided in Fig. 5.

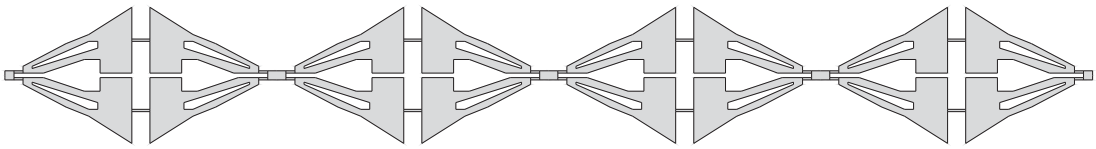

Figure 7: One dimensional periodic structure that has 4 unit cell mechanisms.

[10] G. Acar, C. Yilmaz, Experimental and numerical evidence for the existence of wide and deep phononic gaps induced by inertial amplification in two-dimensional solid structures, *Journal of Sound and Vibration*, **332(24)**, 6389–6404, 2013.

[11] M. P. Bendsoe, N. Kikuchi, Generating optimal topologies in structural design using a homogenization method, *Computer Methods in Applied Mechanics and Engineering*, **71(2)**, 197–224, 1988.

[12] O. Yuksel, An overview on topology optimization methods employed in structural engineering, *KLU Journal of Engineering and Science*, **5(2)**, 159–175, 2019.

[13] O. Sigmund, Morphology-based black and white filters for topology optimization, *Structural and Multidisciplinary Optimization*, **33(4)**, 401–424, 2007.

[14] J. Du, N. Olhoff, Topological design of freely vibrating continuum structures for maximum values of simple and multiple eigenfrequencies and frequency gaps, *Structural and Multidisciplinary Optimization*, **34(2)**, 91–110, 2007.

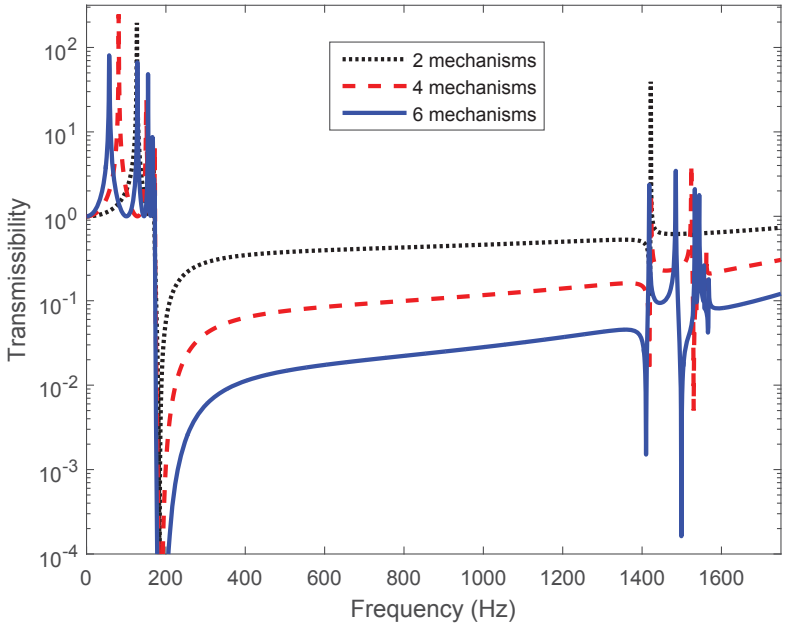

Figure 8: Vibration transmissibility plots of one dimensional periodic structures with various number of unit cell mechanisms.

[15] O. Yuksel, C. Yilmaz, Size and topology optimization of inertial amplification induced phononic band gap structures, *Proceedings of the ASME 2017 International Mechanical Engineering Congress and Exposition. Volume 13: Acoustics, Vibration and Phononics. Tampa, Florida, USA*, V013T01A007, 10 pages, November 3-9, 2017.

[16] E. Andreassen, A. Clausen, M. Schevenels, B. S. Lazarov, O. Sigmund, Efficient topology optimization in matlab using 88 lines of code, *Structural and Multidisciplinary Optimization*, **43(1)**, 1–16, 2011.

[17] O. Sigmund, On the design of compliant mechanisms using topology optimization, *Mechanics of Structures and Machines*, **25(4)**, 493–524, 1997.

[18] O. Sigmund, K. Maute, Topology optimization approaches, *Structural and Multidisciplinary Optimization*, **48(6)**, 1031–1055, 2013.

[19] S. Taniker, C. Yilmaz, Design, analysis and experimental investigation of three-dimensional structures with inertial amplification induced vibration stop bands, *International Journal of Solids and Structures*, **72**, 88–97, 2015.

[20] A. H. Orta, C. Yilmaz, Inertial amplification induced phononic band gaps generated by a compliant axial to rotary motion conversion mechanism, *Journal of Sound and Vibration*, **439**, 329–343, 2019.

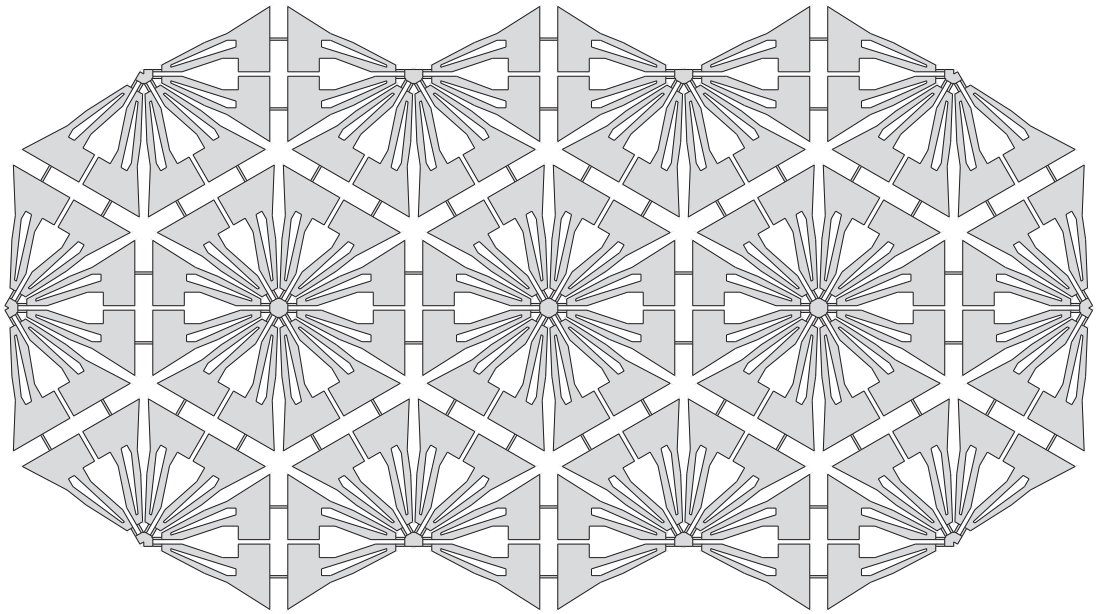

Figure 9: The two dimensional broadband elastic metamaterial.

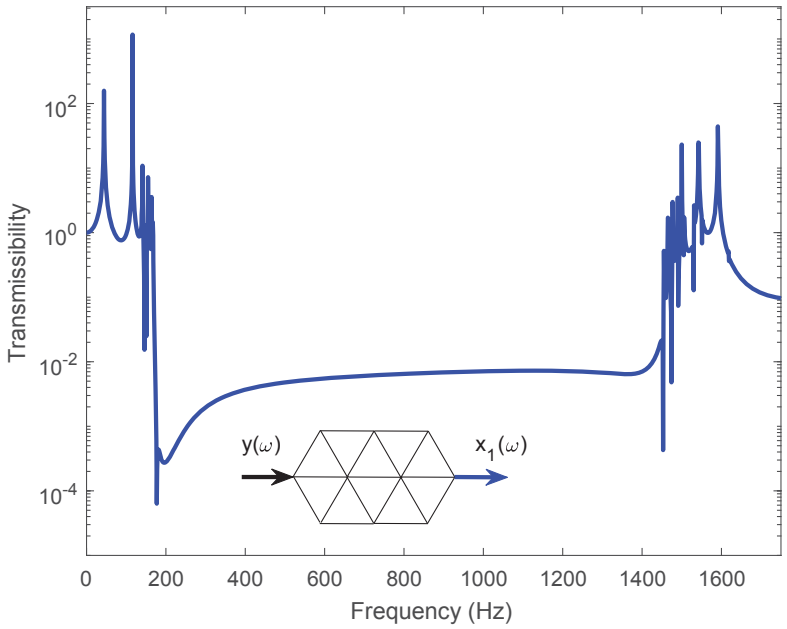

Figure 10: Axial displacement transmissibility plot of the broadband elastic metamaterial given in Fig. 9 for axial input.

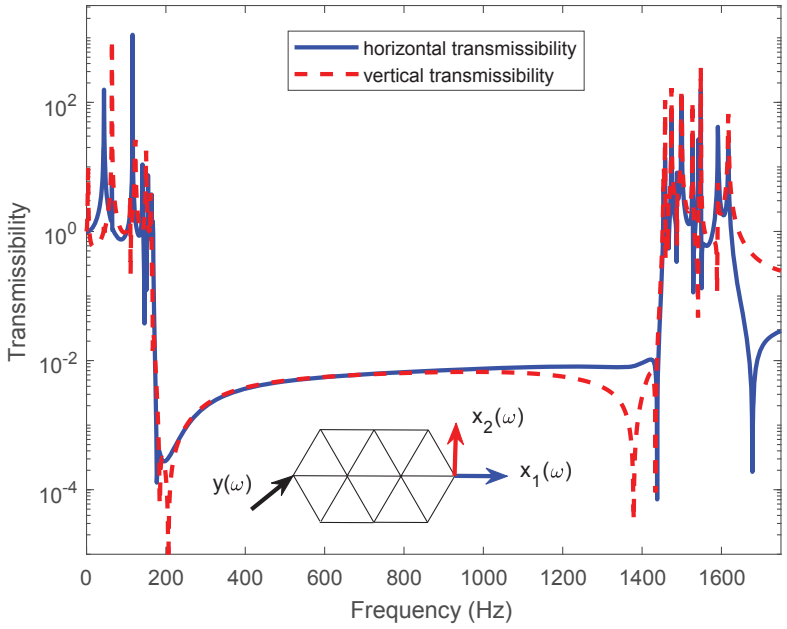

Figure 11: Axial (blue solid line) and transverse (red dashed line) displacement transmissibility plots of the broadband elastic metamaterial given in Fig. 9 for a 45 degree in-plane input.

EURODYN 2020
XI International Conference on Structural Dynamics
M. Papadrakakis, M. Fragiadakis, C. Papadimitriou (eds.)
Athens, Greece, 23–26 November 2020

VIBRATION ABSORPTION PERFORMANCE OF METAMATERIAL LATTICES CONSISTING OF IMPACT DAMPERS

Kyriakos Alexandros I. Chondrogiannis[1], Vasilis K. Dertimanis[1], Sami F. Masri[2] and Eleni N. Chatzi[1]

[1] Institute of Structural Engineering, ETH Zurich
Stefano-Franscini-Platz 5, 8093 Zurich, Switzerland
e-mail: {Chondrogiannis, v.derti, chatzi}@ibk.baug.ethz.ch

[2] Viterbi School of Engineering, University of Southern California
University Park, Los Angeles, CA 90089, USA
e-mail: masri@usc.edu

Keywords: Metamaterials, Impact-dampers, Nonlinear dynamics

Abstract. *In recent years, metamaterials are increasingly used in the field of vibration mitigation due to the unique potential these offer. Periodic placement of appropriately designed resonators, the so-called unit cells, has been shown to arrest the propagation of vibration within a specific frequency range, thus resulting in formation of a bandgap. In rendering metastructures efficient, the breadth of the bandgap should be maximized, while for application in structures, it is also necessary to shift the lower limit of the gap to lower frequencies. One potential solution to this direction is the use of nonlinearity at the unit cell scale. In this direction, the current study investigates finite lattice configurations, which consist of impact damper unit cells. The effectiveness of impact dampers in vibration attenuation has been successfully illustrated in limited degree of freedom systems, and is here extended for use in the metastructure sense, i.e., for multiple degree of freedom systems. For this purpose, a one dimensional lattice of a finite number of unit cells is considered. In order to study and better asses the behaviour of the configuration, variable parameters are taken into account, including the number of unit cells, stiffness and mass ratio, while a comparison to a conventional linear oscillator is further offered. For the evaluation of the system performance, several criteria are utilized, including the oscillation amplitude as well as the energy absorption from the primary system as a result of the individual impacts. The obtained results clearly indicate the ability of impact-based meta-structures to successfully contribute to vibration mitigation under appropriate design.*

1 INTRODUCTION

In recent years, attention has turned to resilience of large-scale civil structures under dynamic loading, and in particular under seismic excitation. In addressing this challenge, the research community has focused on the development of vibration mitigation systems, which are able to ensure structural safety, by minimizing the effects of the excitation onto the structure.

Mitigation of engineering vibration has been widely dealt using linear, passive or active methods. As for the first, several concepts have been developed, among which some take advantage of the favorable effects that increased damping can offer [1, 2, 4], while others influence the nature of the system's dynamic response by introducing secondary devices, which are attached to the main system. Some of the common practices of such methods include oil dampers [5], friction dissipaters [3], tuned mass dampers [8]-[11], as well as tuned liquid dampers [12]. A major disadvantage of such devices, however, lies in the narrow range of frequencies within which their contribution is beneficial. Indeed, there exist frequency regions where the existence of passive devices can even affect the dynamic response in a negative way, as for example in the case of tuned mass dampers. On the other hand, the active control schemes overcome the former difficulties by offering the ability to adapt to diverse loading situations [6, 7, 13, 14]. Nonetheless, considerable disadvantages to such an active approach pertain to the significantly higher costs and the continuous need for maintenance.

A novel idea, which has recently been exploited for civil engineering applications, is based on the concept of metamaterials [17]-[26]. These are configurations, characterized by extraordinary filtering properties, attained as a result of diversified mechanisms, such as their microscopic geometry, periodic arrangement, etc [27]. Appropriately designed resonators, the so-called unit cells, have been shown to arrest the propagation of vibration within a specific frequency range [15]-[16], this resulting in formation of a "bandgap". In rendering metastructures efficient, the breadth of the bandgap should be maximized, while for application in structures, it is also necessary to shift the lower limit of the gap to lower frequencies. One potential solution to this direction is the use of nonlinearity at the unit cell scale. In this direction, following the work of Dertimanis et al. [28], the current study investigates finite lattice configurations, which consist of impact damper unit cells. The effectiveness of impact dampers in vibration attenuation has been successfully illustrated in limited degree of freedom systems [29], and is here extended for use in the metastructure sense, i.e., for multiple degree of freedom systems. The general term used for nonlinear attachments to the primary system is nonlinear energy sinks (NES). Extended research has been carried out regarding several types of NES, including impact dampers [29, 34, 35]. The dynamics of impact phenomena has been investigated in multiple studies [36]-[38]. Significant contribution in the subject of impact dampers has been made in the work of Masri and colleagues on impact dampers, regarding their general motion [30], their stability analysis [31], as well as their dynamic response to random excitation [32]. There is also high relevance between impact dampers and particle dampers, the latter being investigated in the work of Lu et al. [33].

2 META-DAMPER

2.1 Unit cell

The idea of the meta-impactor is inspired by the beneficial effect that a single impact damper can have on a structure, under dynamic loading [29]. The unit cell consists of a rigid container of mass m, containing a laterally unconstrained mass μ, free to impact on the respective bounds (Figure 1).

The nonlinearity in the response results from the contact between the container and the inner mass at the time instances where the relative displacement of the two equals to the free clearance $D/2$. This leads to the outcome of impact realizations, which introduce a highly nonlinear behaviour. Furthermore, since the interaction between the two masses results in sudden changes in their velocity, the phenomenon of impact can be classified as non-smooth.

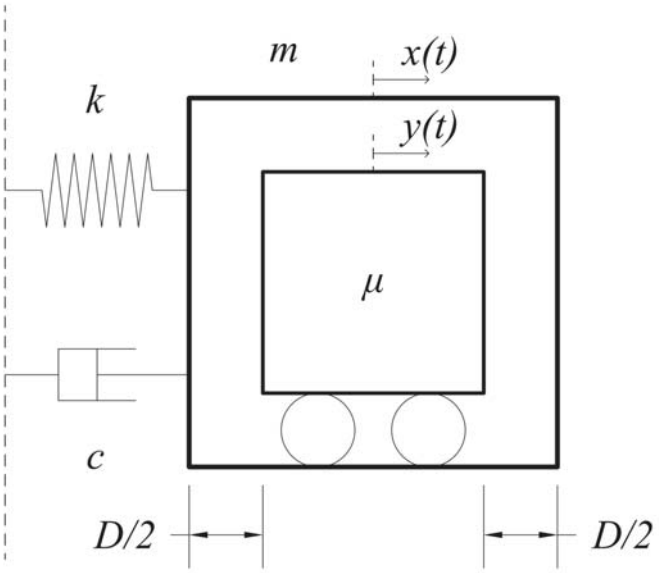

Figure 1: Impact damper unit cell.

2.2 Nonlinear lattice

The goals lies in shielding a target structure via coupling with the metamaterial configuration. The initial oscillator was a single degree of freedom system of mass M, stiffness K and damping C. The concept of the current work is based on the consecutive arrangement of impact damper unit cells. The resonators are connected elastically to each other with stiffness k, as well as to the protected mass on one end, and to a fixed support on the other, while damping c is also applied (Figure 2). In order to better assess the response of the system, excluding misleading effects from complicated input time histories, a harmonic excitation force $F(t)=A\sin(2\pi ft)$ was selected.

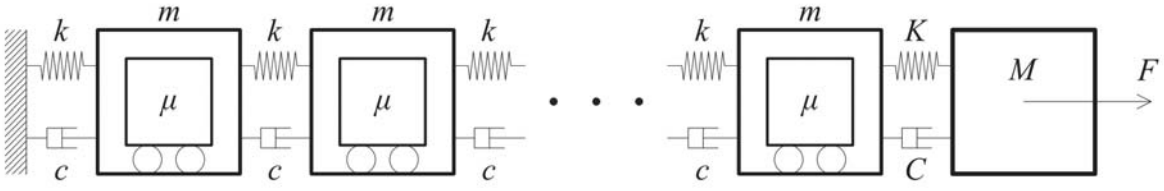

Figure 2: Nonlinear lattice.

2.3 Governing equations

The system is considered to comprise a linear behavior outside the impact events, so it can be described as a conventional, linear multiple degree of freedom system during those instances. It should be mentioned that there is no assumption regarding the number of impacts per cycle at the steady state.

The equations of motion for the first unit cell can be formulated as:

$$\begin{aligned} &m\ddot{x}_1(t)+c\dot{x}_1(t)+kx_1(t)+c[\dot{x}_1(t)-\dot{x}_2(t)]+k[x_1(t)-x_2(t)]=0 \\ &\mu\ddot{y}_1(t)=0,\ \ |x_1(t)-y_1(t)|<D/2 \end{aligned} \tag{1}$$

In the same pattern, the equations of motion for the *i*-th unit cell, $i=2,...,N-1$, are:

$$\begin{aligned} &m\ddot{x}_i(t)+c[\dot{x}_i(t)-\dot{x}_{i-1}(t)]+k[x_i(t)-x_{i-1}(t)]+c[\dot{x}_i(t)-\dot{x}_{i+1}(t)]+k[x_i(t)-x_{i+1}(t)]=0 \\ &\mu\ddot{y}_i(t)=0,\ \ |x_i(t)-y_i(t)|<D/2 \end{aligned} \tag{2}$$

For the last (*N*-th) unit cell the equations of motion are:

$$\begin{aligned} &m\ddot{x}_N(t)+c[\dot{x}_N(t)-\dot{x}_{N-1}(t)]+k[x_N(t)-x_{N-1}(t)]+C[\dot{x}_N(t)-\dot{X}(t)]+K[x_N(t)-X(t)]=0 \\ &\mu\ddot{y}_N(t)=0,\ \ |x_N(t)-y_N(t)|<D/2 \end{aligned} \tag{3}$$

whereas, for the primary structure they are formed as:

$$M\ddot{X}(t)+C[\dot{X}(t)-\dot{x}_N(t)]+K[X(t)-x_N(t)]=F(t) \tag{4}$$

Under the assumption of a sufficiently small duration of impact, it is further reasonable to consider that the post-impact displacement remains unaffected, opposite to the post impact velocities, which are altered discontinuously. In order to determine the latter, the coefficient of restitution *r*, related to the energy loss at every impact, is introduced [29]. Therefore, the additional equations describing the individual impacts can be defined as:

$$\begin{aligned} x_i^+ &= x_i^- \\ y_i^+ &= y_i^- \end{aligned} \tag{5}$$

$$r=-\frac{\dot{x}_i^+-\dot{y}_i^+}{\dot{x}_i^--\dot{y}_i^-} \tag{6}$$

where the coefficient of restitution ranges between $0<r<1$, zero representing purely plastic and unity perfectly elastic impacts [29]. Moreover, the conservation of momentum applies, which indicates:

$$m\dot{x}_i^+ + \mu\dot{y}_i^+ = m\dot{x}_i^- + \mu\dot{y}_i^- \tag{7}$$

Use of Eqs. 6, 7, results in the calculation of post impact velocities for the *i*-th unit cell.

$$\begin{bmatrix} m & \mu \\ 1 & -1 \end{bmatrix}\begin{bmatrix} \dot{x}_i^+ \\ \dot{y}_i^+ \end{bmatrix}=\begin{bmatrix} m\dot{x}_i^- + \mu\dot{y}_i^- \\ -r\dot{x}_i^- + r\dot{y}_i^- \end{bmatrix} \tag{8}$$

2.4 Simulation

In order to solve the system of differential equations, the system is brought into a nonlinear state space form as:

$$\begin{aligned} &\dot{z}(t)=g(z(t),F(t)),\ \text{where} \\ &z=\left[x_1,\dot{x}_1,y_1,\dot{y}_1\ |\ \ \ldots\ \ |x_N,\dot{x}_N,y_N,\dot{y}_N\ |\ X,\dot{X}\right]^T \end{aligned} \tag{9}$$

Subsequently, the derivatives of *z* for the first unit cell are calculated as:

$$\begin{aligned}
&\dot{z}_1(t) = z_2(t)\\
&\dot{z}_2(t) = -\frac{k}{m}z_1(t) - \frac{c}{m}z_2(t) - \frac{k}{m}[z_1(t) - z_5(t)] - \frac{c}{m}[z_2(t) - z_6(t)]\\
&\dot{z}_3(t) = z_4(t)\\
&\dot{z}_4(t) = 0, \quad |z_1 - z_3| < D/2
\end{aligned} \tag{10}$$

Similarly, for the the *i*-th unit cell, $i = 2,...,N-1$, these are:

$$\begin{aligned}
&\dot{z}_{4(i-1)+1}(t) = z_{4(i-1)+2}(t)\\
&\dot{z}_{4(i-1)+2}(t) = -\frac{k}{m}[z_{4(i-1)+1}(t) - z_{4(i-2)+1}(t)] - \frac{c}{m}[z_{4(i-1)+2}(t) - z_{4(i-2)+2}(t)]\\
&\qquad\qquad -\frac{k}{m}[z_{4(i-1)+1}(t) - z_{4i+1}(t)] - \frac{c}{m}[z_{4(i-1)+2}(t) - z_{4i+2}(t)]\\
&\dot{z}_{4(i-1)+3}(t) = z_{4(i-1)+4}(t)\\
&\dot{z}_{4(i-1)+4}(t) = 0, \quad |z_{4(i-1)+1} - z_{4(i-1)+3}| < D/2
\end{aligned} \tag{11}$$

and for the last (*N*-th) unit cell, these are respectively obtained as:

$$\begin{aligned}
&\dot{z}_{4N-3}(t) = z_{4N-2}(t)\\
&\dot{z}_{4N-2}(t) = -\frac{k}{m}[z_{4N-3}(t) - z_{4N-7}(t)] - \frac{c}{m}[z_{4N-2}(t) - z_{4N-6}(t)]\\
&\qquad\qquad -\frac{K}{m}[z_{4N-3}(t) - z_{4N+1}(t)] - \frac{C}{m}[z_{4N-2}(t) - z_{4N+2}(t)]\\
&\dot{z}_{4N-1}(t) = z_{4N}(t)\\
&\dot{z}_{4N}(t) = 0, \quad |z_{4N-3} - z_{4N-1}| < D/2
\end{aligned} \tag{12}$$

while for the linear oscillator are:

$$\begin{aligned}
&\dot{z}_{4N+1}(t) = z_{4N+2}(t)\\
&\dot{z}_{4N+2}(t) = \frac{K}{M}[z_{4N-3}(t) - z_{4N+1}(t)] + \frac{C}{M}[z_{4N-2}(t) - z_{4N+2}(t)] + \frac{1}{M}F(t)
\end{aligned} \tag{13}$$

The post impact velocities are computed as:

$$\begin{bmatrix} m & \mu \\ 1 & -1 \end{bmatrix} \begin{bmatrix} z^+_{4(i-1)+1} \\ z^+_{4(i-1)+2} \end{bmatrix} = \begin{bmatrix} mz^-_{4(i-1)+1} + \mu z^-_{4(i-1)+2} \\ -rz^-_{4(i-1)+1} + rz^-_{4(i-1)+2} \end{bmatrix} \tag{14}$$

3 ANALYSIS

The behaviour of the system was studied parametrically, calculating its response for each set of parameters. The analysis was performed using a MATLAB® environment, with integration carried out by means of the *ode45* function (AbsTol=eps, ReTol=eps$^{(2/3)}$, Refine=4 and MaxStep=0.001/sqrt(K/M), eps corresponding to the machine precision epsilon). Moreover, an event function is used, checking the condition $|x_i(t) - y_i(t)| = D/2$ for all unit cells. If at least one impact is detected, Eqns. 5, 8 are deployed for the calculation of post impact displacements and velocities.

The properties of the linear oscillator were chosen as M=1kg, f_n=1Hz and ζ_n=2%, while the harmonic excitation was chosen as $F(t)=\sin(2\pi t)$, with a unit amplitude and an excitation frequency matching the natural frequency of the linear oscillator. Furthermore, the coefficient of restitution is set constant at r=0.6, the clearance is set at D=0.1m and the damping between unit cells is set at c=0, throughout all parametric studies.

In order to better asses the effect of each parameter given to the system, parametric analyses were performed. Varying mass (m/M, μ/m) and stiffness (K/k) ratios were taken into consideration, in the range of $0.01 \leq m/M \leq 1.00$, $0.10 \leq \mu/m \leq 1.00$ and $10 \leq K/k \leq 100$ respectively.

The response of each system is calculated for the first 10 seconds. For the evaluation of the system's performance, several criteria are utilized, including the oscillation amplitude, maximum absolute acceleration, as well as the energy absorption from the primary system as a result of the individual impacts. The latter is calculated as the ratio between the total energy dissipation, resulting from all individual impacts, and the total energy inserted to the system by the external excitation [29].

$$E_{dis}(t)=\frac{\sum_{i=1}^{N-1}\int_0^t c[\dot{x}_i(\tau)-\dot{x}_{i+1}(\tau)]^2 d\tau+\sum_{p=1}^{P_t}\Delta p}{\int_0^t F(\tau)\dot{X}(\tau)dt} \tag{15}$$

where Δp is the amount of energy dissipation at the p-th impact, p=1,…, P_t and P_t is the number of impacts at any unit cell up to time t. Since in the current investigation c=0, the first part of the numerator is excluded.

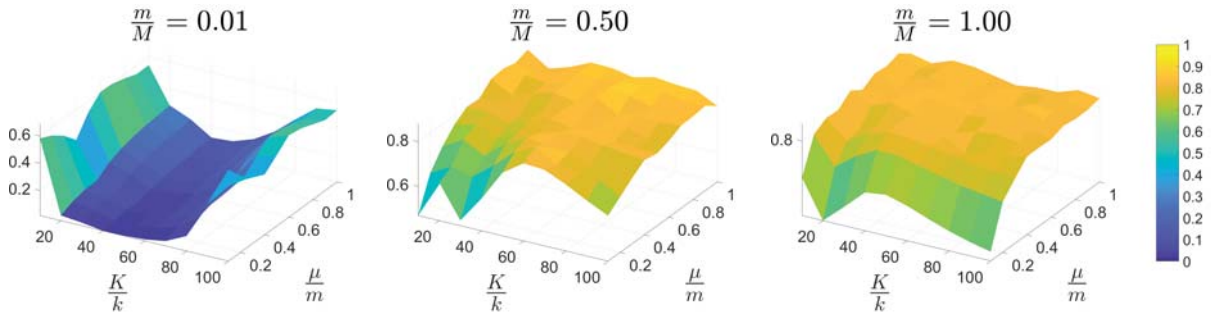

Figure 3: Energy absorption at 1 Hz for N=1 for varying mass and stiffness.

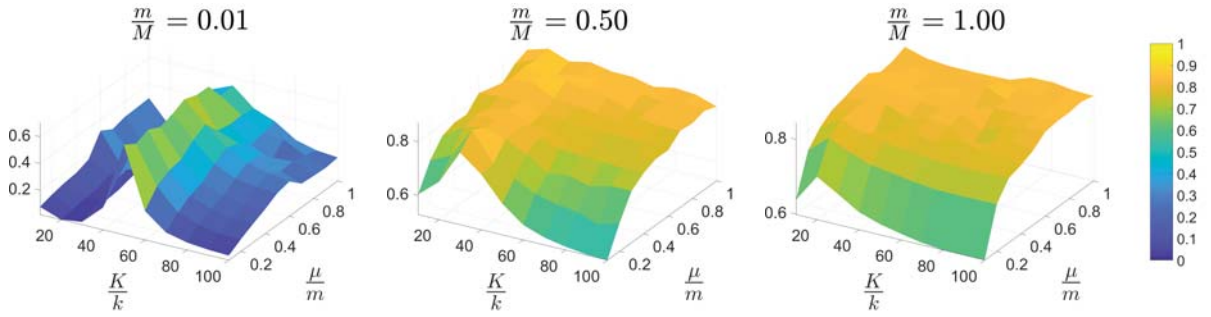

Figure 4: Energy absorption at 1 Hz for N=2 for varying mass and stiffness.

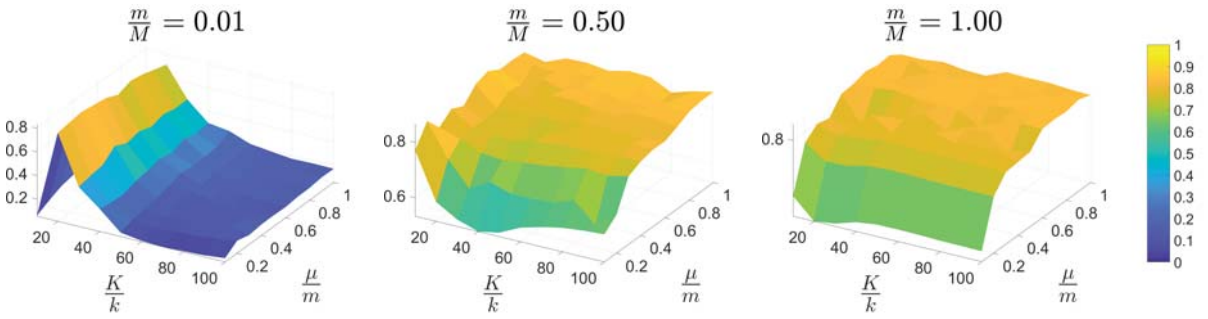

Figure 5: Energy absorption at 1 Hz for N=5 for varying mass and stiffness.

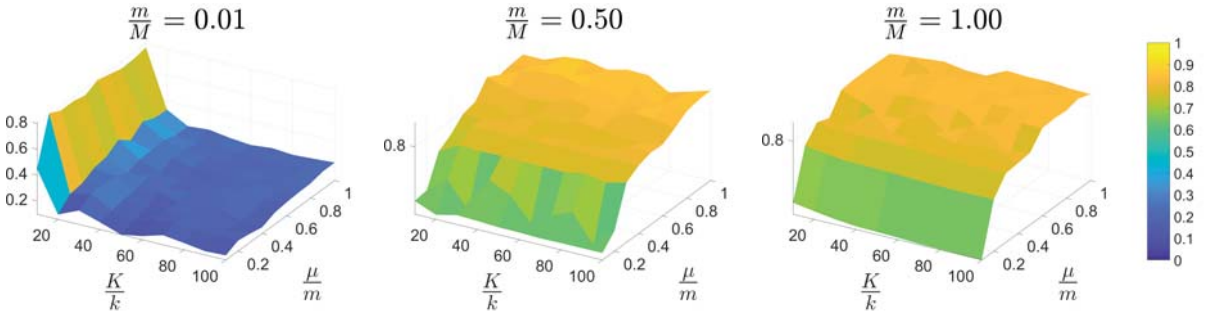

Figure 6: Energy absorption at 1 Hz for N=10 for varying mass and stiffness.

In Figs. 3-6 the results of energy absorption are presented. It is evident that for lower values of external mass ratio m/M the behavior of the system is dominated by the stiffness ratio. In those cases, the variation of the internal mass ratio μ/m does not significantly affect the energy absorption. As the external mass ratio increases, the importance is shifted towards the internal mass ratio as well, while for m/M=1, the internal mass ratio has the principal influence. As the number of unit cells increases, in combination with high values of external mass ratio, the amount of dissipated energy tends to become uniform and unaffected from the variation of the number of unit cells, as it can be inferred from Figs. 5, 6 for m/M=1.

Additional parametric analyses were carried out investigating the influence of the variation in the excitation frequency. For this purpose, the system's parameters were set to m/M=1, μ/m=0.1 and K/k=10. The simulation time is increased to 50s and the maximum absolute displacement and acceleration of the last 40s were recorded for the primary structure. Throughout these analyses, the excitation frequency varies between $0.1 \leq f / f_n \leq 4.0$.

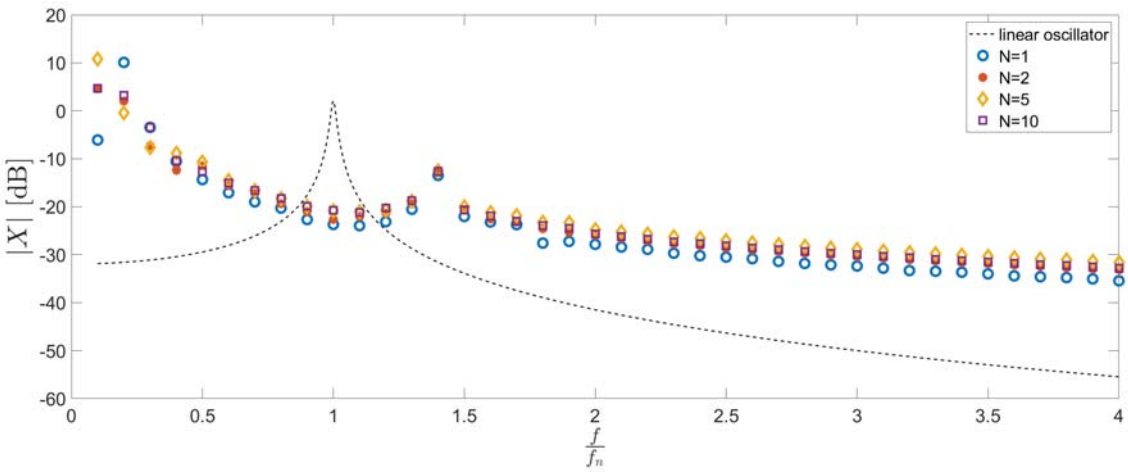

Figure 7: Maximum absolute displacement of the primary structure as a function of the applied frequency ratio.

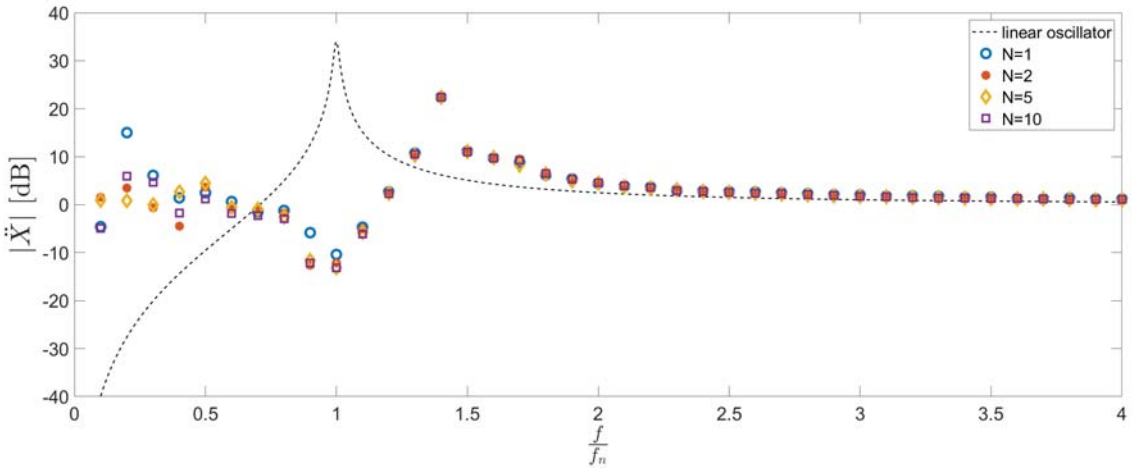

Figure 8: Maximum absolute acceleration of the primary structure as a function of the applied frequency ratio.

As inferred from Figs. 7, 8, a substantial mitigation of the dynamic load effect on the structure is observed for frequency ratios between 0.7 and 1.2. Considering that the damping between unit cells is set to zero, there is an amplification of the system's response in regions away from the resonance frequency. Moreover, it is observed that an increase in the number of unit cells does not have a notable effect on the attenuation properties of the configuration, especially in higher excitation frequencies. However, a distinctive peak at f / f_n=0.2 is indicated for N=1, which is not transferred to lattices with higher unit cell number.

4 CONCLUSIONS

The current study investigates the behavior of a highly nonlinear solution for attenuation of mechanical vibrations. The influence of critical parameters of the system was inspected, including mass and stiffness, number of unit cells, as well as excitation frequency. It is observed that high values of the external mass ratio m/M, as well as of the internal mass ratio μ/m, affect positively the system's vibration mitigation capabilities. Regarding the stiffness ratio, its influence is significant for lower values of the external mass ratio, while for higher values of the latter the amount of energy absorption is less affected by stiffness. The number of unit cells consisting the lattice does not seem to affect the behaviour of the system for high excitation frequencies, while for frequency ratio below unity there are some discrepancies in the behaviour of the system, the most notable being that of the single unit cell attachment. Further investigation is being performed by the authors in exploring this observation, which additionally requires consideration of the free clearance dimension. Moreover, the configuration is able to reduce the dynamic load effect within a frequency range centered around the resonance of the primary system, while some unfavourable effects were observed at adjacent frequencies. The results clearly indicate the effectiveness of the system under specific conditions, while it is also implied that proper adjustment of the metamaterial to specific structures can be challenging.

Acknowledgements

This work lies within the "INSPIRE" EU progamme. This project has received funding from the European Union's Horizon 2020 research and innovation programme under grant agreement No 813424.

REFERENCES

[1] Z. Liang, G.C. Lee, G.F. Dargush, and J. Song. Structural damping: Applications in Seismic Response Modification. *CRC Press*, Boca Raton, FL, USA, 2012.

[2] M.J.N. Priestley and D.N. Grant. Viscous damping in seismic design and analysis. *Journal of Earthquake Engineering*, 9(2):229–255, 2005.

[3] F. L´opez-Almansa, S.T. de la Cruz, and C. Taylor. Experimental study of friction dissipators for seismic protection of building structures. *Earthquake Engineering and Engineering Vibration*, 10(4):475–486, 2011.

[4] H.P. Zhu, D.D. Ge, and X. Huang. Optimum connecting dampers to reduce the seismic responses of parallel structures. *Journal of Sound and Vibration*, 330(9):1931–1949, 2011.

[5] Y.L. Xu and Z. Yu. Mitigation of three-dimensional vibration of inclined sag cable using discrete oil dampers - II. Application. *Journal of Sound and Vibration*, 214(4):675–693, 1998.

[6] L. Venanzi. A Review on Adaptive Methods for Structural Control. *The Open Civil Engineering Journal*, 10:653–667, 2016.

[7] W. Yu and S. Thenozhi. Active Structural Control with Stable Fuzzy PID Techniques. *Springer International Publishing*, Switzerland, 2016.

[8] R. Rana and T.T. Soong. Parametric study and simplified design of tuned mass dampers. *Engineering Structures*, 20(3):193–204, 1998.

[9] F. Sadek, B. Mohraz, A.W. Taylor, and R.M. Chung. A method of estimating the parameters of tuned mass dampers for seismic applications. *Earthquake Engineering and Structural Dynamics*, 26(6):617–635, 1997.

[10] J. Salvi and E. Rizzi. Optimum tuning of tuned mass dampers for frame structures under earthquake excitation. *Structural Control and Health Monitoring*, 22(4):707–725, 2015.

[11] S. Elias and V. Matsagar. Research developments in vibration control of structures using passive tuned mass dampers. *Annual Reviews in Control*, 44:129–156, 2017.

[12] R.O. Ruiz, D. Lopez-Garcia, and A.A. Taflanidis. Modeling and experimental validation of a new type of tuned liquid damper. *Acta Mechanica*, 227(11):3275–3294, 2016.

[13] M.S. Miah, E.N. Chatzi, V.K. Dertimanis, and F. Weber. Realtime experimental validation of a novel semiactive control scheme for vibration mitigation. *Structural Control and Health Monitoring*, 24(3):# e1878, 2017.

[14] M.S. Miah, E.N. Chatzi, V.K. Dertimanis, and F. Weber. Nonlinear modeling of a rotational MR damper via an enhanced BoucWen model. *Smart Materials and Structures*, 24(10):# 105020, 2015.

[15] M. Sigalas and E. Economou. Band structure of elastic waves in two dimensional systems. *Solid State Communications*, 86(3):141–143, 1993.

[16] M.S. Kushwaha, P. Halevi, G. Martinez, L. Dobrzynski, and B. Djafari-Rouhani. Theory of acoustic band structure of periodic elastic composites. *Physical Review B*, 49(4):2313–2322, 1994.

[17] V. La Salandra, M. Wenzel, O.S. Bursi, G. Carta and A.B. Movchan Conception of a 3D Metamaterial-Based Foundation for Static and Seismic Protection of Fuel Storage Tanks. *Frontiers in Materials*. 4:1-13, 2017.

[18] F. Basone, M. Wenze, O.S. Bursi, M. Fossetti. Finite locally resonant Metafoundations for the seismic protection of fuel storage tanks. *Earthquake Engng Struct Dyn*, 48: 232–252, 2019.

[19] I. Antoniadis, A. Paradeisiotis. Acoustic Meta-materials Incorporating the KDamper Concept for Low Frequency Acoustic Isolation. *Acta acustica united with acustica*, 104: 636-646, 2018.

[20] H. J. Xiang, Z. F. Shi, S. J. Wang, and Y. L. Mo. Periodic materials-based vibration attenuation in layered foundations: Experimental validation. *Smart Materials and Structures*, 21(11), 2012.

[21] Z. Shi, Z. Cheng, and H. Xiang. Seismic isolation foundations with effective attenuation zones. *Soil Dynamics and Earthquake Engineering*, 57(5-12):143–151, 2014.

[22] P. Roux, D. Bindi, T. Boxberger, A. Colombi, F. Cotton, I. Douste‐Bacque, S. Garambois, P. Gueguen, G. Hillers, D. Hollis, T. Lecocq, I. Pondaven. Toward Seismic Metamaterials: The METAFORET Project. *Seismological Research Letters*, 89 (2A): 582–593, 2018.

[23] P.-R. Wagner, V.K. Dertimanis, I.A. Antoniadis, and E.N. Chatzi. On the feasibility of structural metamaterials for seismic-induced vibration mitigation. *International Journal of Earthquake and Impact Engineering*, 1(1/2):20–56, 2016.

[24] V.K. Dertimanis, I.A. Antoniadis, and E.N. Chatzi. Feasibility Analysis on the Attenuation of Strong Ground Motions Using Finite Periodic Lattices of Mass in Mass Barriers. *Journal of Engineering Mechanics*, 142(9):# 04016060, 2016.

[25] A. Palermo, S. Krödel, K.H. Matlack, R. Zaccherini, V.K. Dertimanis, E.N. Chatzi, A. Marzani, and C. Daraio. Hybridization of Guided Surface Acoustic Modes in Unconsolidated Granular Media by a Resonant Metasurface. *Physical Review Applied*, 9(5):# 54026, 2018.

[26] R. Zaccherini, V.K. Dertimanis, A. Palermo, S. Krödel, A. Marzani, C. Daraio, and E.N. Chatzi. Resonant Metabarriers as Seismic Attenuators in Granular Media. *In Proceedings of the ISMA2018 conference on Noise and Vibration Engineering*, Leuven, Belgium, 2018.

[27] T. J. Cui, D.R. Smith, and R. Liu. Metamaterials, *Springer*, ISBN: 978-1-4419-0573-4, 2010.

[28] V.K. Dertimanis, S.F. Masri and E.N. Chatzi. On the vibration attenuation properties of finite periodic lattices of impact dampers. *IX ECCOMAS Thematic Conference on Smart Structures and Materials, SMART 2019*, Paris, France, 2019.

[29] A.F. Vakakis, O.V. Gendelman, L.A Bergman, D.M. McFarland, G. Kerschen and Y.S. Lee. Nonlinear Targeted Energy Transfer in Mechanical and Structural Systems, Vol. I & II, *Springer*, ISBN: 978-1-4020-9130-8, 2008.

[30] S.F. Masri. General Motion of Impact Dampers. *The Journal of the Acoustical Society of America*, 47:229–237, 1970.

[31] S.F. Masri and T.K. Caughey. On the Stability of the Impact Damper. *Journal of Applied Mechanics*, 33(3):586–592, 1967.

[32] S.F. Masri and A.M. Ibrahim. Response of the Impact Damper to Random Excitation. *The Journal of the Acoustical Society of America*, 53(1):200–211, 1973.

[33] Z. Lu, S.F. Masri and X. Lu. Studies of the performance of particle dampers attached to a two-degree-of-freedom system under random excitation. *Journal of Vibration and Control*. 17: 1454-1471, 2011.

[34] M.R. Duncan, C.R. Wassgren, and C.M. Krousgrill. The damping performance of a single particle impact damper. *Journal of Sound and Vibration*, 286(1–2):123–144, 2005.

[35] O.V. Gendelman. Analytic treatment of a system with a vibro-impact nonlinear energy sink. *Journal of Sound and Vibration*, 331:4599–4608, 2012.

[36] R.A. Ibrahim. Vibro-Impact dynamics: Modelling, Mapping and Applications, *Springer*, ISBN: 978-3-642-10156-4, 2009.

[37] M.F. Dimentberg and D.V. Iourtchenko. Random Vibrations With Impacts: A Review. *Nonlinear Dynamics*, 36(2–4):229–254, 1973.

[38] V.N. Philipchuk. Impact modes in discrete vibrating systems with rigid barriers. *International Journal of Non-Linear Mechanics*, 36(6):999–1012, 2001.

EURODYN 2020
XI International Conference on Structural Dynamics
M. Papadrakakis, M. Fragiadakis, C. Papadimitriou (eds.)
Athens, Greece, 23–26 November 2020

SEISMIC RESPONSE OF STRUCTURE EQUIPPED WITH A NON-INVASIVE EXTERNAL VISCOUS DAMPING SYSTEM.

Antonio Sabino[1], **Antonio Mannella**[1]

[1] Italian National Research Council
Construction Technologies Institute
Via Giosuè Carducci, 32 L'AQUILA
sabino@itc.cnr.it, mannella@itc.cnr.it

Keywords: existing building, retrofit, dissipation, viscous damper device; school building

Abstract. *The aim of this research is to evaluate the effectiveness of a seismic retrofit technique that involves the introduction of energy dissipation devices properly connected to an existing structure through a system of cables and leverisms, which are employed to amplify total or inter-story drift at device end. One of the main topics related to the introduction of energy dissipation devices, lies in the choice of their optimal setting within the structure to maximize the effectiveness without producing functionality limitations. The achievement of these objectives is therefore linked, regardless of the type adopted, to the amount of energy dissipated in each cycle, directly proportional to the displacements magnitude to which the device is subject. Many configurations proposed in the literature and currently adopted in professional practice provide additional dissipation systems variously connected to braces installed inside the structural frame and therefore able to exploit the inter-story drift produced by seismic input. The proposed system exploits top displacements of the structure with respect to the foundation level, transferred to the device through a system of cables properly configured and amplified with leverage. This paper represents the first step of the research, in which after a brief description of equation of motion for a simple SDOF system, it is take into account a existing RC school building in Italy to assess performances of the retrofitted structure equipped with the proposed system.*

1 INTRODUCTION

The introduction of seismic energy dissipation devices within existing structures represents an important seismic protection system widely adopted for framed structures. The deformability of these structures generally allows, in fact, to exploit inter-story drifts to activate the devices and achieve consistent levels of dissipation of input energy. Many configurations and geometrical arrangements [1,2] have been proposed in order to optimize the devices location, generally applied in series to a bracing placed inside the frame mesh and able to transfer to the device a fraction of the inter-story drift, depending on their geometric configuration. It is therefore clear that the deformability of the structure is an essential requirement for the effectiveness of dissipation systems. For situations where structures are not sufficiently flexible, interesting solutions have been developed by several authors, including a cable system solution (Damped cable system, DCS), initially proposed by the research team of the University of Buffalo [3,4], and further developed [5,6,7,8] also as part of a research project funded by the European Commission, named SPIDER (strand prestressing for internal damping of earthquake response). Likewise, dissipation systems designed to increase displacements at the dissipation system end have been proposed by various authors [9,10,11] and generally consist of levers or pulley systems able to amplify inter-story displacement. The system proposed in this paper, uses a system of steel cables capable to transmit a portion of the total roof displacement of the building to the foundation where, by means of a system of displacements amplification, transfer to the damper a resulting amplified displacement. Considering a simple shear frame, the proposed system is configured according to the following scheme in Figure 1: The cable used (6) is fixed with clamps (7) at the upper ends of the floor; the cable, therefore, is arranged in an X configuration along the diagonals of the frame and diverted at the base of the columns by pulleys (4). The cable then runs horizontally along the base of the frame; in this area it is connected to the end of a lever arm (1), to the opposite end of which the dissipation device is connected (2). The particular configuration of the cable, which runs along both diagonals of the building's elevation, continuing without interruption at foundation level, also allows the same to be always active in both directions of seismic loads. The portion of the cable placed on the diagonal in tension (blue wire), in fact, exerts a recall action on the cable portion placed along the compressed diagonal (red wire), not allowing deflection.

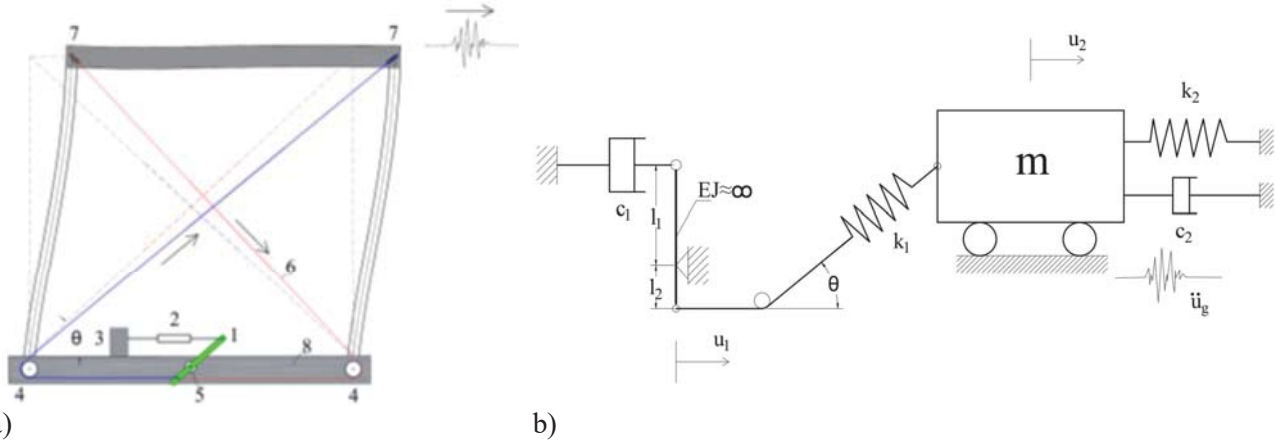

Figure 1 a) Conceptual model of simple 1-floor frame structure equipped with proposed system: 1 lever arm; 2 viscous damper (VD); 3 contrast; 4 pulleys; 5 pin; 6 wire; 7 clamp; 8 foundation; b) Mechanical model of a 2-DOF structure equipped with the proposed system.

The mechanical model of the SDOF system, equipped with the proposed system and reported in Figure 1, has been described in a previous paper by the authors [12], to which we refer you for details.

The model equipped with an additional damping system, with a linear viscous dissipation device, is described by the following general equation:

$$Fd = c_1 \dot{u}_d = \alpha_d \cdot c_2 \cdot \dot{u}_d \tag{1}$$

with $\dot{u}_d$ velocity at the device end and Fd device damping force.

The damping coefficient is then expressed as a function of the internal damping of the structure through the parameter α_d. With reference to the stiffness characteristics of the system, the structure stiffness k_2 and the stiffness of the elements constituting the additional dissipation system, i.e. the cable and the leverages, k_1, are defined; actually, as showed in the follow, the main stiffness component is represented by the cable extensional stiffness. As said, from the examination of the Figure 1 results that, in both directions of displacement, the part of the cable connecting the clamp placed in the direction of displacement with the lever arm is in tension (blue wire), while the remaining ones is not stressed (red wire) if friction in pulleys is neglected. In the evaluation of the extensional stiffness, therefore, it is necessary to refer to a length of the cable equal to half of the whole length. At this research stage the component related to the real viscous device elastic stiffness has been neglected, considering it rigid and neglecting friction in pulleys, pin etc... Added stiffness k_1 has been, then, expressed as a function of the stiffness of the bare structure through the coefficient α_k:

$$Fd = c_1 \dot{u}_d = \alpha_d \cdot c_2 \cdot \dot{u}_d \tag{2}$$

Finally, the amplification ratio produced by the leverage is defined through:

$$\alpha_M = \frac{l_1}{l_2} \tag{2a}$$

Description of the equations of the motion for a SDOF system are reported below:

$$\begin{cases} m\ddot{u}_2(t) + k_2 u_2(t) + \cos\theta\, \alpha_k k_2 \left(u_2(t)\cos\theta - u_1(t)\right) + c_2 \dot{u}_2(t) = -m\, \ddot{x}_g(t) \\ \alpha_M \alpha_d c_2 \cdot \dot{u}_1(t) - \alpha_k k_2 (u_2(t) \cdot \cos\theta - u_1(t)) = 0 \end{cases} \tag{3}$$

with symbols meaning reported in previous Figure 1.

The use of a displacement amplification system like that described, therefore, allows to overcome the usual limitations in the use of additional dissipation systems usually inserted inside the structural frames, as it is effective even for limited displacements, thanks to the introduction of leverage, displacements are transmitted amplified to the device, increasing the amount of dissipated energy. Another main objective in the development of the described system is to be able to carry out a seismic retrofit of a building, implementing interventions exclusively from the outside, without proceeding to demolition of non-structural elements, finishes and systems. The system of cables, in fact, will be applied primarily on all the building prospects, anchored through clamps to the external nodes of the roof or, if necessary, to intermediate stories. In this way, the clamps reaction is divided between the horizontal (beams) and vertical elements (columns) concurring into the node, stressing them with axial forces. The presence of rigid slabs in the structure also favors transferring seismic action to the frames equipped with the described system. Conversely, there is the possibility of interference between the path of the cables and architectural and functional projections present on the building prospect (balconies, etc. ...). Although variations to the cable path are possible, it is certainly easier to apply it on structures generally without such protrusions, but only windowed walls, such as schools or industrial buildings. In view of the importance that seismic vulnerability of existing school buildings assumes in many areas of the world and in

particular in Italy, where most of the existing school heritage is characterized by seismic performance below the standards required by current regulations, we proceed in the following to the evaluation of the specific characteristics of some of the most common structural types in the school heritage in order to assess in advance and in simplified form the applicability and effectiveness of the proposed system.

2 CASE STUDY BUILDING

The case study is related to the elementary school "Collina Castello" of Bisignano (Italy), built in 1983. The building has three floors plus a pitched roof and is characterized by a rectangular plan with dimensions of about 21.4 m × 15 m. The interstory heights range from about 3.2m to about 3.4m, for a total height of about 9.9m at the roof level. The rooftop has a maximum height of + 11.97 m. The reinforced concrete structure is characterized by a fairly regular frames, consisting of 4 main frames with 5 columns each arranged along the longitudinal direction, along transversal direction longitudinal frames are tied only by slabs and perimetral beams. The columns have dimensions of 50 cm × 40 cm and the longitudinal beams, at all levels, have section 40 cm × 60 cm. The main frames are connected by border beams with dimensions 50 cm × 40 cm arranged in transverse direction. The building was assumed as a benchmark structure for a Research Project financed by the Italian Department of Civil Protection and the authors of present paper take informations about geometrical and structural configuration from study belonging to it [13].

Figure 2 General views of the benchmark building

The modal analysis carried out by finite element model of the structure, generated by SAP2000 software [14] showed that the first vibration mode (0.79 s) is purely traslational along transversal direction, which is weakest direction because absence of beams. The second vibration mode is rotational with a period of 0.55 s and third vibration mode is purely translational along stiffer direction with a period of 0.51 s. Because of structural symmetry, the first three vibration modes excite about 85% of the mass in both the directions. The building presents windowed walls regularly arranged along the main facades and no prominent elements like balconies, bow-windows etc…

3 DESCRIPTION OF RETROFIT TECHNIQUE

The objective of the system is to carry out a seismic retrofit mainly intervening from outside, without the need of non-structural elements demolition or interruption to or limitation of the building's activity. Figure 3 shows a possible configuration of the cable system on the benchmark building main prospect. Each cable is connected to a different structure floor and

transfers the displacement of each floor to the lever (pinned at the foundation beam), to which the viscous damper is connected. To do so, may be required a foundation enlargement also with micropiles in order to absorb the forces related to the diversion of the cable, when it does not occur at a foundation beam-column joint, and to do not increase shear forces in the foundation beam. As can be seen, despite the non-uniform spans of the frame beams, the system configuration can be effectively adapted without restricting accessibility in the building. The passage of cables at the windowed walls, although they produce a visual obstacle, does not reduce the functionality of the windows (opening from the inside) nor the light entry in the building. Other building prospects and, if needed, internal frames, will be equipped with similar cables layout.

a)

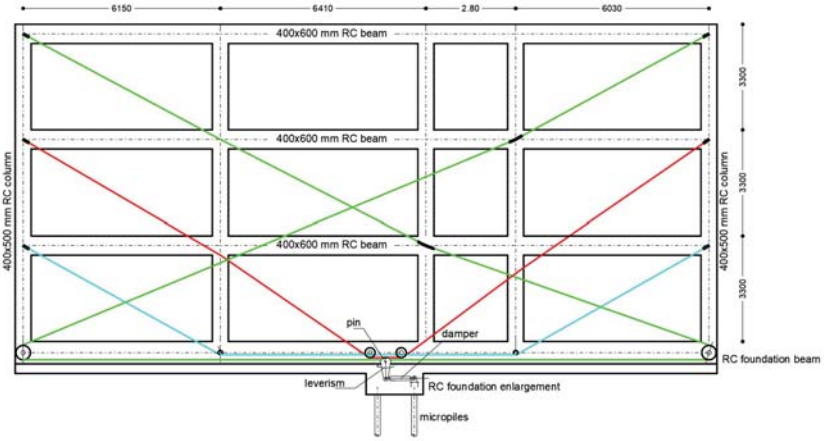

b)

Figure 3 (a) System layout on the main RC frame of the benchmark building: in green, red and cyan are represented, respectively, steel cables linking the 3th, 2th, and 1th floor to the foundation of the building; (b) Cable system layout depicted on the building prospect: steel cables (red lines), RC frame (dashed green lines);

In the present example only external façade frames are equipped with the system. Each cable is linked by means of a lever to the viscous damper device. Amplification factor α_M is set at 10 for all leverism devices. Characteristics of Linear viscous devices have been chosen so as to find equivalent commercial products; in particular damping coefficient is set at c = 160 kNsec/m and limit force F_L of 20 kN. The value choosen for limit force is related to the maximum cable tension compatible with the strenght of the beam-column joint where cable is clamped.

The leverage, in fact, also produces the amplification of the force generated by the damping device, inside the cable and at the cable clamped end, reaction are so limited to 200 kN ($\alpha_M \cdot F_L$). Higher limit force would require heavy beam-column joint reinforcement.

Each cable consist of a pair of Ø32 steel rods, connected at the deflection point, by a less stiff steel rope. Diversion point are arranged in corrispondence of beam-column joint to limit effects of reaction force on the existing frame elements and made to allow cable/rope sliding. In

the FEM model cable deflection was neglected. As a result of the insertion of the cable and device system, the dynamic properties of the structure undergo a modest variation, less than 2%, with a slight increase in the fundamental first vibration period (0.80 s). Higher modes are even less affected.

4 PERFORMANCE EVALUATION IN ORIGINAL AND RETROFITTED CONDITIONS

The seismic analyses were carried out with a non-linear dynamic approach using the finite element models of the building structure (Figure 4). As way of example of the results obtained, the responses computed before and after retrofit in terms of maximum interstory drift profiles and story displacements, for the main building in its principal direction x and y are compared in Figures 5. Seismic input used consist of a series of natural NTC spectum-compatible unscaled accelerograms [15], taken from a set of accelerograms extracted from the European Strong Motion Database (ESM), [16] through the REXEL software [17] for the Bisignano site, adopting a type B soil category, in the range of periods between 0.15 - 2 s.

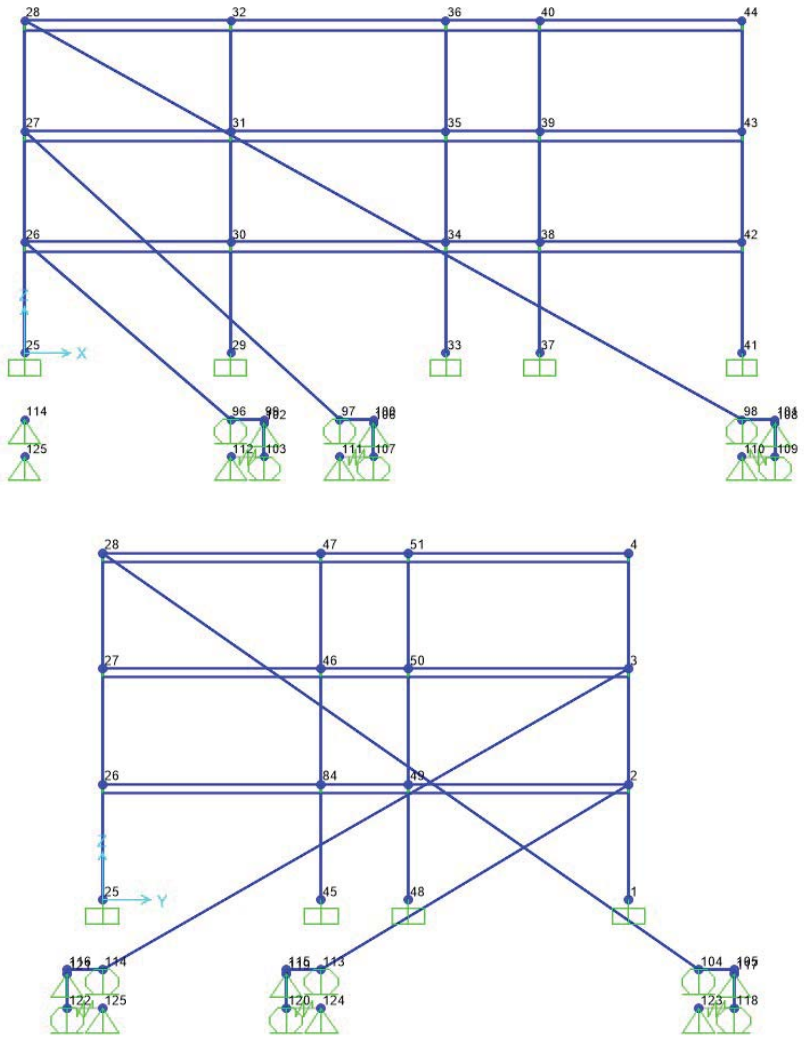

Figure 4 Equivalent SAP 2000 model view of the building longitudinal (X-dir) and trasversal (Y-dir) frames equipped with the damping system.

In the model used, for the sake of simplicity, the X-shaped cable is not modelled with real pattern on the building façade. Alternatively, only a angled strut with equivalent section and lenght of the cable and active in tension and compression was used, which links each edge floor beam-column joint with a leverism through proper node restrains/constrains.

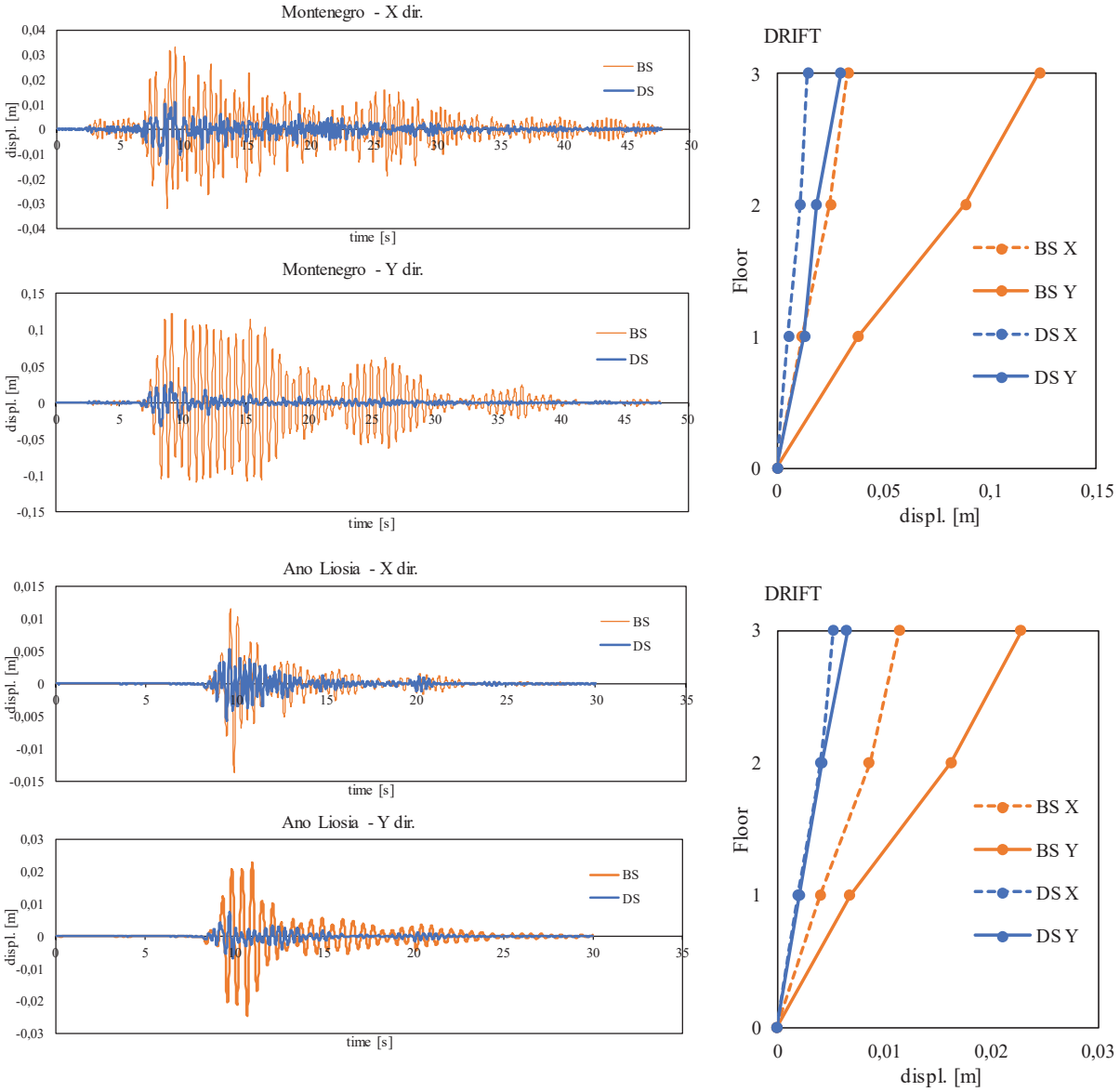

Figure 5 Top displacement and inter-story drift respectively for bare structure (BS – orange lines) and structure equipped with dissipative system (DS – blue lines) for Montenegro and Ano Liosia earthquakes.

Examination of the results shows a significant reduction in the displacements of the structure and story drifts. In particular, introduction of the damping system produces inter story drift reduction between 56% and 102%. It is clearly visible from results that efficiency of the system is higher in the weaker direction of the structure (Y-dir) than in the stiffer one, because cables with the same axial stiffness were used in both directions and therefore a different α_k ratio characterize two structure directions. This, as demonstrated in [12], is a very important feature in defining the response and efficiency of the damped system. Similar results are obtained for base shear as shown in the following Figure 6 for Montenegro earthquake.

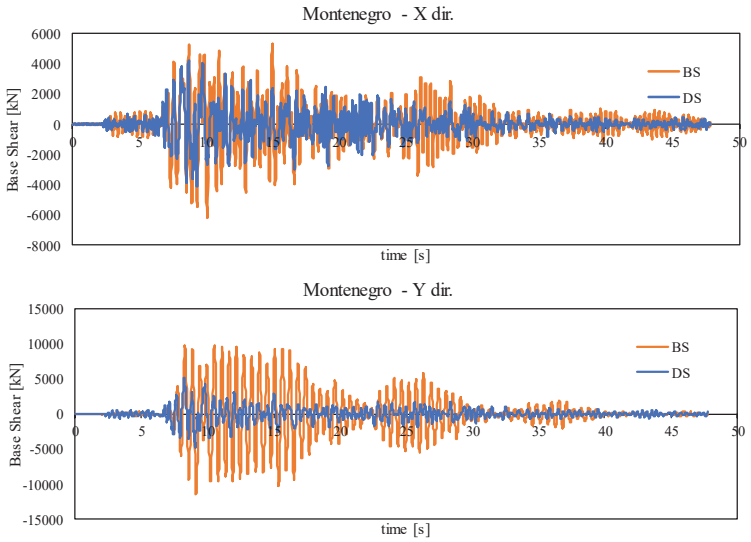

Figure 6 Base Shear respectively for bare structure (BS – orange lines) and structure equipped with dissipative system (DS – blue lines) for Montenegro earthquakes in X and Y direction.

In Figure 7 are presented Base Shear/ roof displacements and Viscous damping force/ device displacements histories. From the examination of the figure results a considerable amount of energy dissipated as result of the displacements amplification produced by the leverage, despite the low values of the force in the dissipation device, whose values it is convenient to keep low to avoid important interventions to strengthen the beam-column joints where cable are connected to the structure and relevant dimensions of the components of the described retrofit system.

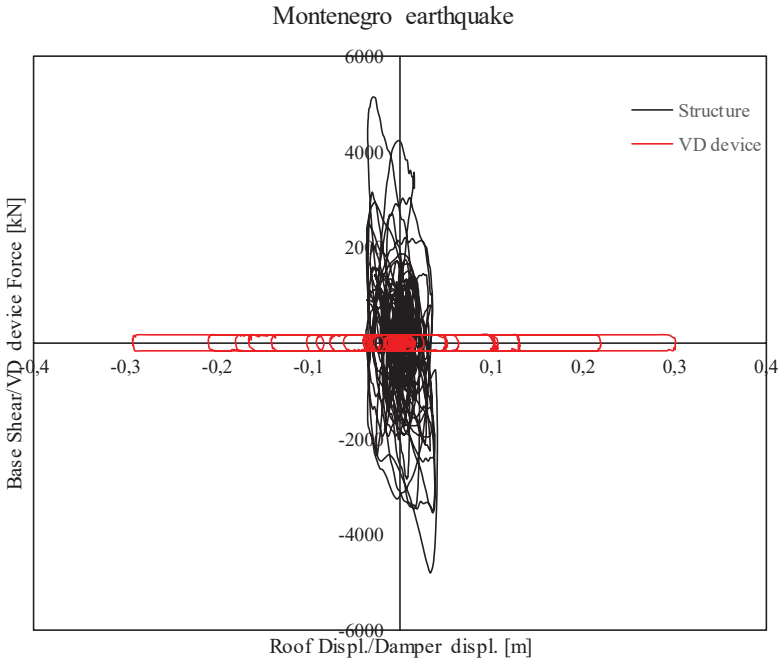

Figure 7 Base Shear/ roof displacements (black line) and Viscou damping (VD) force/ device displacements (red line) for Montenegro earthquake.

5 CONCLUSIONS

Present paper illustrates a seismic retrofit system for existing reinforced concrete structures by using additional viscous dampers connected to the structure by means of a system of cables and lever able to transmit the roof displacements to the base, where displacement amplification is carried out through a lever system and then transmitted to the dissipation device. The paper firstly provides motion equation system for a SDOF system and then describe results of application of the retrofit technique on a RC existing school building. Results show a high efficiency of the system in interstory drift and shear base reduction. The need for little or no demolition of non-structural elements and infills allows the structure to remain functional even during the execution of interventions and limit costs.

It is the aims of the authors to continue the research in order to investigate the effects on the system performances of the use of different dissipative devices (non-linear viscous and friction dampers, etc.) and application to more complex structures.

6 REFERENCES

[1] Constantinou, M.C., Tsopelas, P., Hammel, W., and Sigaher, A.N. Toggle-Brace-Damper Seismic Energy Dissipation System. *Journal of Structural Engineering* (ASCE) 2001, 127(2), 105-112;

[2] Sigaher, A.N.; Constantinou, M.C., Scissor-Jack-Damper Energy Dissipation System. *Earthquake Spectra* 2003, 19 (1), 133-158;

[3] Peckan G, Mander JB, Chen SS. Balancing lateral loads using tendon-based supplemental damping system. *Journal of Structural Engineering* (ASCE) 2000; 126: 896–905;

[4] Peckan G. Design of seismic energy dissipation systems for reinforced concrete and steel structures. PhD Dissertation, State University of New York at Buffalo, Buffalo, NY, 1998;

[5] Terenzi G. Dynamics of SDOF systems with nonlinear viscous damping. *Journal of Engineering Mechanics* (ASCE) 1999; 125: 956–963;

[6] Sorace S, Terenzi G. Non-linear dynamic modelling and design procedure of FV spring-dampers for base isolation. *Engineering Structures* 2001; 23: 1556–1567;

[7] Sorace, S.; Terenzi, G. (2011) The damped cable system for seismic protection of frame structures—Part II: Design and application. *Earthquake Engng Struct. Dyn.* 2012; 41:929–947;

[8] Naeem, A., Kim, J. Seismic performance evaluation of spring viscous damper cable system. *Engineering Structures* 176 (2018) 455-467;

[9] Saito, T.; Maegawa, T; Denno, S.; Sakai, S.; Uchikawa, M.; Kanagawa M.; Ryujin, H. New seismic response control system using block and tackle. *Proceedings of the 16th World Conference on Earthquake Engineering*, 16WCEE 2017. Santiago Chile 9-13 January 2017;

[10] Berton, S.; Bolander, E.B. Amplification system for supplemental damping devices in seismic applications. *Journal of Structural Engineering* 2005, 131(6), 979-983. Doi: 10.1061/(ASCE)0733-9445(2005) 131:6(979);

[11] Kang, J.; Tagawa, H.; Seismic response of steel structures with seesaw systems using viscoelastic dampers. *Earthquake Engng Struct. Dyn.* 2013; 42:779-794

[12] Sabino, A.; Mannella, A.; de Leo, A.M. Seismic Response of a Structure Equipped with an External Viscous Damping System. *Buildings* 2020, 10, 19.

[13] Sorace, S., Terenzi, G. Motion control-based seismic retrofit solutions for a R/C school building designed with earlier Technical Standards. *Bull Earthquake Eng* 2014; 12:2723–2744. DOI 10.1007/s10518-014-9616-y

[14] Computer and Structures, Inc. SAP2000 Ultimate Structural analysis programs—theoretical and users manual. Release no. 21.2.0, 2019, Berkeley;

[15] Nuove Norme Tecniche per le Costruzioni [New Italian Technical Standards for constructions]. DM 17 January 2018;

[16] Luzi L, Puglia R, Russo E & ORFEUS WG5. Engineering Strong Motion Database, version 1.0. Istituto Nazionale di Geofisica e Vulcanologia, Observatories & Research Facilities for European Seismology, 2016. DOI: 10.13127/ESM;

[17] Smerzini C., Galasso C., Iervolino I., Paolucci R. Ground motion record selection based on broadband spectral compatibility. *Earthquake Spectra* 2013. DOI 10.1193/052312EQS197M;

EURODYN 2020
XI International Conference on Structural Dynamics
M. Papadrakakis, M. Fragiadakis, C. Papadimitriou (eds.)
Athens, Greece, 23–26 November 2020

ADVANCED NEGATIVE STIFFNESS VIBRATION ABSORBER COUPLED WITH SOIL-STRUCTURE INTERACTION FOR SEISMIC PROTECTION OF BUILDINGS

Konstantinos A. Kapasakalis[1a], Antonios E. Alvertos[1b], Antonios G. Mantakas[1c], Ioannis A. Antoniadis[2], Evangelos J. Sapountzakis[1d]

[1] School of Civil Engineering, National Technical University of Athens, Greece
9, Iroon Polytechniou Str., 15780 Zografou
e-mail: kostiskapasakalis@hotmail.com, alvertos@otenet.gr, mantakasantonis@gmail.com, cvsapoun@central.ntua.gr

[2] Dynamics and Structures Laboratory, School of Mechanical Engineering,
National Technical University of Athens, Greece, 9 Iroon Polytechniou Str., 15780 Zografou
e-mail: antogian@central.ntua.gr

Keywords: KDamper, Negative Stiffness, Soil-Structure Interaction, Seismic Protection, Earthquake Engineering

Abstract. *Throughout the past decades, seismic isolation of structures has been studied rigorously as an approach to reduce seismic demand and mitigate structural damage. Research in this field has progressed significantly, starting from the use of simple elastomeric bearings for the decoupling of the superstructure from the base, to more complex devices that incorporate the use of an additional oscillating mass and negative stiffness elements. Characteristic examples of these devices are the Tuned Mass Damper (TMD) and the Quasi-Zero oscillators (QZSs). The KDamper is a novel passive vibration absorption concept, based essentially on the optimal combination of appropriate stiffness and mass elements, which include a negative stiffness element. The concept can be implemented using a system of prestressed elements in order to obtain the negative stiffness effects and might prove to achieve a significant advantage for seismic retrofitting.*

In this paper, the extended KDamper system is placed at the ground level and the soil-structure interaction (SSI) between the building foundations and superstructure is utilized as a means to effectively transfer the dynamic forces of the KDamper to the building and to distribute the required displacements between the structural elements and foundation, thus leading to absorption of the vibration energy. The configuration of the KDamper properties and tuning of its stiffness elements are studied herein. The effectiveness of the KDamper is subsequently investigated in view of the performance of a 4-storey building. A series of artificial accelerograms and real earthquake time histories are used as excitation. Results indicate the beneficial role of SSI on the reduction of the spectral acceleration and displacements, hence placing the concept as a compelling alternative to existing seismic protection technologies.

1 INTRODUCTION

During the latest years, seismic codes have significantly been altered with the intention to lead to resilient structures that perform better under seismic loads. To this end, seismic isolation has been one of the main approaches aiming to reduce structural seismic accelerations and, in this way, lead to earthquake-resistant design [1-6]. Therefore, a number of isolation devices from simple elastomeric bearings to more sophisticated roller bearings have been developed and advanced within the years. However, in order to isolate the building from its base, large displacements are required that are not always acceptable, hence rendering this system inadequate for retrofitting.

Seismic protection research focuses lately on devices which include: (a) negative stiffness elements (Negative Stiffness (NS) Devices and "Quazi-Zero Stiffness" (QZS) oscillators) and (b) Tuned Mass Dampers (TMDs). The concept of introducing additional oscillating masses (TMDs) has been employed in a variety of systems including skyscrapers and structure bases aiming to protect the structure from the dynamic effects of environmental loads (e.g. wind, wave and seismic) [7-11]. The main drawback of this method is the need of large additional masses, compared to the mass of the structure itself, as well as the detuning of the TMD parameters that affects the performance of the structure within the years.

A promising class of absorbers is based on increasing the damping by the appropriate introduction of negative stiffness elements. Proposed by Antoniadis et al. [12], the KDamper is a novel passive vibration absorption concept, based essentially on the optimal combination of appropriate stiffness and mass elements, which include a negative stiffness element. This vibration control system has been examined for the protection of bridges [13-17] wind turbines [18, 19] and structural systems [20,21]. In addition, the KDamper is implemented as an Absorption Base (KDAB) in the bases of structures [22-28]. In the recent work of Kapasakalis et al. [28], the KDAB is proven to be a possible supplement to BI, or can be alternatively implemented as a "stiff absorption base".

In this study, the EKD is implemented as a seismic protection measure within the base of a typical residential structure. The effects of the Soil-Structure interaction coupled with the KDamper damping properties are investigated and results indicate the significant benefits of the methodology at the seismic response of the structure.

2 OVERVIEW OF THE VIBRATION ABSORPTION METHODOLOGY

In this section, the extended KDamper concept (EKD) is presented and the fundamental principles of its function are provided in detail. A single degree of freedom (SDoF) oscillator is considered in which the KDamper is implemented between its rigid base and the oscillating mass. Throughout the paper, linear dynamic systems are considered to represent the stiffness elements of the KDamper while the effect of soil-structure interaction (SSI) is represented using non-linear springs.

2.1 The KDamper Vibration Absorber

Figure 1, illustrates the fundamental layout of various vibration isolation and damping concepts described in the literature and presented herein to facilitate the understanding of the KDamper concept. All strategies aim to minimize the response $x(t)$ of a low-damped (or undamped) SDoF comprising a mass m and static stiffness k due to the resulting motion of a base excitation $x_G(t)$. The Negative Stiffness Isolator (Fig. 1A) incorporates a negative stiffness element configured in parallel with the stiffness elements k of the system. To this end, the overall

stiffness of the configuration is reduced to $k_{QZS} = k + k_N \leq k$, hence leading to potential significant decrease of the overall static stiffness and consequently, instability of the system.

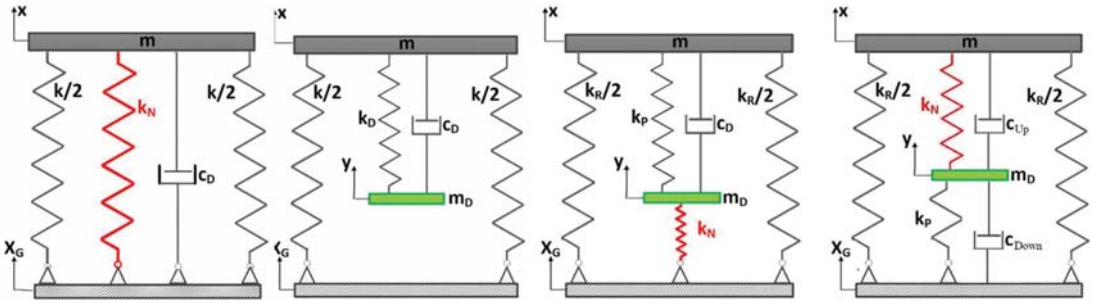

Figure 1. Schematic representation of the vibration absorption concepts considered: (A) Negative Stiffness (NS) isolator (or QZS), (B) Tuned Mass Damper (TMD), (C) KDamper concept and (D) Extended KDamper (EKD).

In a similar way to the Tuned Mass Damper (TMD, Fig. 1B), the KDamper (Fig. 1C) consists of an additional oscillating mass element (m_D) and two positive and negative stiffness elements k_P and k_N respectively. The negative stiffness element (k_N) serves as an indirect approach to increase the inertia of the oscillating mass (m_D) and consequently, increase the damping of the system. In addition, on the contrary to the NS isolator, the basic requirement of the KDamper is that the overall static stiffness of the system is maintained positive and, in this way, the risk of potential instability is eliminated. The total stiffness of the system with the KDamper can be expressed using the following formula:

$$k_R + \frac{k_P k_N}{k_P + k_N} = k_0 = (2\pi f_0)^2 m_{total} \tag{1}$$

Compared to the TMD, the KDamper uses an additional negative stiffness element k_N, which connects the additional mass to the base. Thus, the equation of motion of the KDamper becomes:

$$m\ddot{u}_S + k_R u_S + m_D \ddot{u}_D + k_N u_D = -(m + m_D)a_G \tag{2.a}$$
$$m_D \ddot{u}_D - C_D(\dot{u}_S - \dot{u}_D) - k_P(u_S - u_D) + k_N u_D = -m_D a_G \tag{2.b}$$

A closer examination at the equations above indicates that the additional negative stiffness element is an indirect way to increase the inertia of the KDamper mass m_D and to this end, increase the efficiency of the vibration absorption system without the need to incorporate large masses, contrary to the case of a conventional TMD.

2.2 Extended KDamper Concept (EKD)

The proposed vibration absorption concept is an extension of the KDamper referred to herein as the EKD system and is illustrated in Figure 1D. In a similar way to the KDamper, the EKD incorporates a system of masses, negative stiffness and positive stiffness elements as well as artificial dampers. The main variation would be the change of the system configuration where the positive stiffness spring (k_P) connects the damper mass (m_D) to the base of the system while the negative stiffness element (k_N), is attached between the damper mass (m_D) and the mass of the oscillator (m). Also, an additional artificial damper is adopted and placed in parallel with the negative stiffness element so that we end up having two dampers, namely C_{UP} and C_{DOWN}

Based on the original formulation of the KDamper expressions 2.a and 2.b, the following equations of motion for the EKD are derived:

$$m\ddot{u}_S + k_R u_S + m_D \ddot{u}_D + k_P u_D = -(m + m_D) a_G \tag{3.a}$$

$$m_D \ddot{u}_D - c_{UP}(\dot{u}_S - \dot{u}_D) - k_N (u_S - u_D) + c_{DOWN} \dot{u}_D + k_P u_D = -m_D a_G \tag{3.b}$$

As mentioned in the previous section, the stiffness parameters of the KDamper, and EKD respectively, are selected according to equation (1) in order to maintain the total stiffness of the system. However, an increase of the absolute value of k_N, or reduction of the absolute values of k_P or k_R, may endanger the static stability of the structure. In order to ensure that potential loss of the static stability is prevented, the possible variations of k_N, k_P and k_R should be taken into consideration in the design and optimization of the EKD parameters. The stiffness parameters of the system may present significant fluctuations due to numerous reasons, such as temperature variations, manufacturing tolerances, or non-linear behaviour of structural elements and the unpredictable behaviour of the foundation system (SSI). Consequently, an increase of the absolute value of k_N and/or a decrease of the values of k_P and k_R by a factor ε_N, ε_P and ε_R, respectively, may result in the system being unstable. This situation may happen in the following case:

$$(1 - \varepsilon_R) k_R + \frac{(1 - \varepsilon_P) k_P (1 + \varepsilon_N) k_N}{(1 - \varepsilon_P) k_P + (1 + \varepsilon_N) k_N} = 0 \tag{4}$$

Contrary to the KDamper concept, which foresees variation only in the negative stiffness element k_N, in the proposed extension of the KDamper concept (EKD), a variation in all stiffness elements is taken into consideration. Assuming either the negative stiffness ratio kn=k_N/k_0 or the absolute value of the negative stiffness element (k_N) is known, using the equations (1) and (4), the rest of the stiffness elements result as presented below:

$$kr = \frac{-b - \sqrt{b^2 - 4 * a * c}}{2a} \Rightarrow KR = kr * k_0 \tag{5.a}$$

$$kp = \frac{kn - kr * kn}{kr + kn - 1} \Rightarrow KP = kp * k_0 \tag{5.b}$$

Where parameters a, b and c are defined as:

$$(1 - \varepsilon_R) = R\,;\ (1 + \varepsilon_N) = N\,;\ (1 - \varepsilon_P) = P \tag{6.a, b, c}$$

$$a = R(P - N)\,;\ b = kn * N(P - R) + R(N - P)\,;\ c = -P * N * \mathrm{kn} \tag{6.d, e, f}$$

Finally, assuming that the following parameters are known:

1) the additional mass, m_D, and
2) the variations ε_N, ε_P and ε_R of the stiffness elements

The unknown parameters of the system are:

1) the nominal KDamper frequency f_0 (Eq. (1));
2) the negative stiffness ratio kn or the value of the negative stiffness element k_N and
3) the damping coefficients c_{DOWN} and c_{UP}.

3 EXTENSION OF THE EKD TO MULTI-STOREY STRUCTURES INCLUDING SOIL STRUCTURE INTERACTION (SSI) EFFECTS

In this section, the concept of the EKD is extended to multi-degree of freedom systems (MDoF) and applied to multi-storey buildings with aim to control their response to seismic excitations. For this purpose, an extension of the vibration control strategy from a simplified SDoF system (Fig. 1D) to MDoF systems is presented. In addition, Soil-Structure Interaction effects are considered in the analysis of the structural system using non-linear springs derived from numerical analysis of shallow foundation systems.

Based on the methodology presented herein, a numerical application is performed on a 4-storey typical concrete structure in order to assess its behaviour under seismic loading and demonstrate the beneficial role of SSI along with the application of EKD as a vibration absorption method.

3.1 The EKD as a Seismic Base Absorber

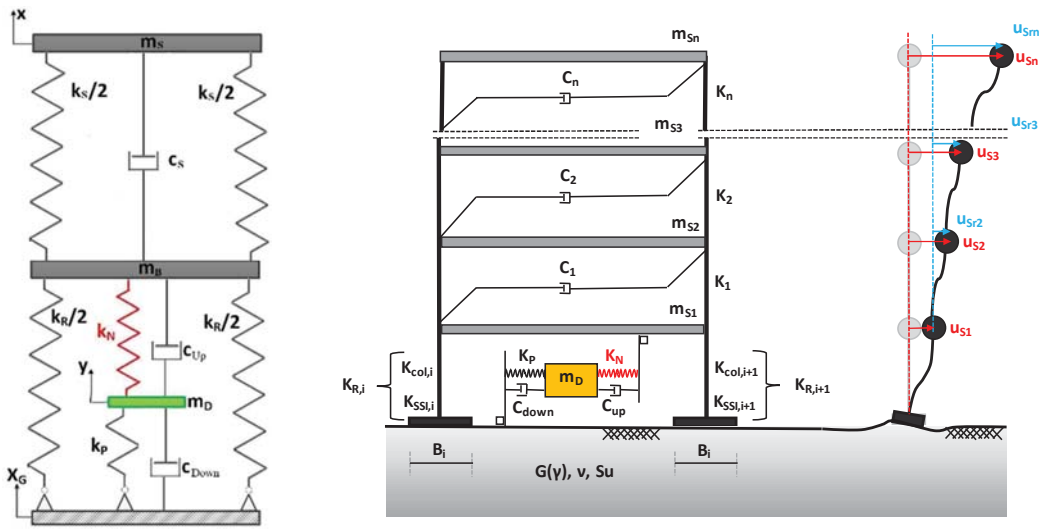

(A) (B)

Figure 2. (A) Implementation of the EKD as a seismic base absorber, (B) Multi-storey building with the proposed seismic vibration absorber system, EKD (sketch of the model) together with SSI effects.

The possible implementations of the KDamper and specifically of the Extended KDamper (EKD) might be numerous. In this study, the potential application of the EKD for seismic protection of structures is assessed and the EKD is implemented as a vibration base absorber. To this end, the EKD system is located between the base of the building and the superstructure. The corresponding configuration is illustrated in Fig. 2A and the equations of motion are derived as follows:

$$m_S(\ddot{u}_S+\ddot{u}_B)+c_S\dot{u}_S+k_Su_S=-m_Sa_G \tag{7.a}$$

$$m_B\ddot{u}_B+m_S(\ddot{u}_S+\ddot{u}_B)+c_{UP}(\dot{u}_B-\dot{u}_D)+k_N(u_B-u_D)+k_Ru_B=-(m_S+m_B)a_G \tag{7.b}$$

$$m_D\ddot{u}_D-c_{UP}(\dot{u}_B-\dot{u}_D)-k_N(u_B-u_D)+k_Pu_D+c_{DOWN}\dot{u}_D=-m_Da_G \tag{7.c}$$

where $u_S = x_S - x_B$, $u_B = x_B - x_G$, $u_D = x_D - x_G$. The natural frequencies of the subsystems and the rest of the parameters are defined as:

$$\omega_0 = 2\pi f_0 = \sqrt{k_0 / (m_S + m_B + m_D)}\ ;\ \omega_D = \sqrt{(k_P + k_N) / \mathrm{m}_D} \tag{8.a, b}$$

$$k_0 = k_R + \frac{k_P k_N}{k_P + k_N}\ ;\ m_D = \mu_D (m_S + m_B) \tag{8.c, d}$$

where ω_0 and ω_D refer to the natural frequencies of the total system and the EKD respectively, k_0 is the equivalent static stiffness of the EKD, m_B is the mass of the base, m_S the mass of the superstructure, m_D the mass of the EKD and μ_D the damper's mass ratio. In this study, the EKD parameters are selected according to Section 3.2 and Section 5 and refer to a typical 4-storey structure with total mass of *320 tn*. More details of the case study are presented in the following sections.

3.2 Extension of the EKD to Multi-Storey Structures

A planar *n*-storey building is considered and presented in the sketch of Fig. 2B, in which the proposed base absorber system, EKD is implemented for seismic protection between the base and the first floor of the structure. The following assumptions are made for the modelling of this system:

1. the total structure mass is concentrated at floor levels;
2. the slabs and girders on the floors are rigid when compared to the columns;
3. the columns are considered inextensible and weightless, providing the lateral stiffness of the structure;
4. the effect of soil-structure-interaction (SSI) is taken into consideration with the use of non-linear elastic springs coupled in series with the column stiffnesses of the first floor;
5. the superstructure is considered to remain within the elastic limit during the analysis.

As a result, the superstructure has *n* dynamic DoFs, represented by the relative to the ground displacements of the *n*-story masses m_{Sj} ($j=1, \ldots, n$), as presented in Fig. 2B, which are collected in the array $[u_{Sr}](t)=[u_{Sr1}(t), u_{Sr2}(t), \ldots, u_{Srn}(t)]^T$.

The parameter k_R refers to the coupling of the stiffness of the columns (k_{col}) connecting the foundation of the structure with the first floor together with the stiffness of the foundation system (k_{SSI}) that is derived due to the SSI effects. As a result, the total stiffness of the columns-foundations system is calculated as the k_R of the structure (Eq. 9). More details on the derivation of the k_R and incorporation of the SSI effects are provided in section 3.3 of this paper.

$$k_R = \frac{k_{SSI} k_{col}}{k_{SSI} + k_{col}} \tag{9}$$

The equations of motion Eq. (7) still apply, but now expressed in a matrix form, involving matrices with dimensions $r \times r$ with $r=n+1$:

$$[M][\ddot{u}(t)] + [C][\dot{u}(t)] + [K][u(t)] = -[\tau] a_G(t) \tag{10}$$

where the matrices and vectors entering Eq. (10) are defined as:

$$[K]_{(n+1)\times(n+1)} = \begin{bmatrix} [K_S]_{n\times n} & [0]_{n\times 1} \\ [0]_{1\times n} & [0]_{1\times 1} \end{bmatrix} + \begin{bmatrix} [0]_{(n-1)\times(n-1)} & [0]_{(n-1)\times 1} & [0]_{(n-1)\times 1} \\ [0]_{1\times(n-1)} & k_N + k_R - k_{col} & -k_N \\ [0]_{1\times(n-1)} & -k_N & k_P + k_N \end{bmatrix};$$

$$[C]_{(n+1)\times(n+1)} = \begin{bmatrix} [C_S]_{n\times n} & [0]_{n\times 1} \\ [0]_{1\times n} & [0]_{1\times 1} \end{bmatrix} + \begin{bmatrix} [0]_{(n-1)\times(n-1)} & [0]_{(n-1)\times 1} & [0]_{(n-1)\times 1} \\ [0]_{1\times(n-1)} & c_{UP} & -c_{UP} \\ [0]_{1\times(n-1)} & -c_{UP} & c_{UP} + c_{DOWN} \end{bmatrix}; \quad (11)$$

$$[u(t)]_{(n+1)\times 1} = \begin{bmatrix} [u_{st}]_{n\times 1}(t) \\ u_D(t) \end{bmatrix};$$

$$[M]_{(n+1)\times(n+1)} = \begin{bmatrix} [M_S]_{n\times n} & [0]_{n\times 1} \\ [0]_{1\times n} & m_D \end{bmatrix}; \; [\tau]_{(n+1)\times 1} = \begin{bmatrix} [M_S][\tau_S] \\ m_D \end{bmatrix}; \; m_{S,tot} = \sum_{i=1}^{n} m_i$$

where $[M_S]$, $[C_S]$ and $[K_S]$ are the n-dimensional matrices of mass, damping and stiffness of the original n-story building and $[\tau_S]$ is the $n\times 1$ influence vector of the superstructure associated with the ground motion $x_G(t)$. The parameter m_S now refers to the total multi-story structure mass and is $m_{S,tot}$ (Eq. (11)). This procedure can also be used in the case the n-story structure is mounted on a conventional or highly damped isolation base by appropriate modification of the matrices in Eq. (10).

3.3 Introduction of Soil-Structure Interaction (SSI) Effects

For the purposes of this study, the EKD is implemented as a vibration absorption technology positioned between the foundations and the first floor of the structure (Ground / 'Pilotis' level). As a consequence, the stiffness k_R (Fig. 2) is the resultant stiffness of both the columns and foundation system and can be expressed as in Eq. (9). The beneficial effect of the Soil-Structure Interaction (SSI) is taken into consideration with the use of non-linear spring stiffnesses (k_{SSI}) coupled in series with the stiffness of the ground floor columns (k_{col}). As a result, the benefits of a softer foundation response can be compared with the conventional approach of a fully fixed model.

The problem is analysed by employing the FE code ABAQUS and a typical foundation and column are modelled in 3D as depicted in Fig. 3A. The soil stratum is considered to be isotropic/homogeneous and modelled using non-linear 8-noded hexahedral continuum elements. The same is applied for the footing which is, however, considered to be elastic (Reinforced Concrete). The column is modelled using linear beam elements and is considered to be fixed on the top of the foundation. The interface between the foundation and the soil is considered to be 'fully bonded' with the foundation elements considered attached to the ground. The boundaries of the model have been strategically selected sufficiently far to avoid spurious boundary-effects on the system response. Static pushover analyses are subsequently undertaken in order to derive the non-linear soil-foundation stiffness relationships (k_{SSI}).

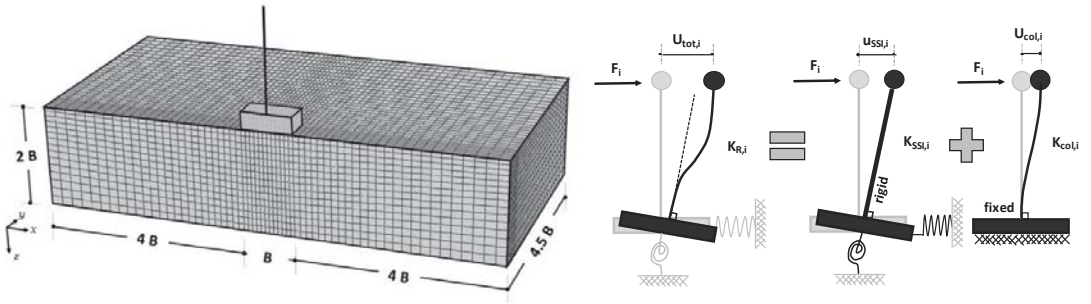

(A) (B)

Figure 3. (A) A view of the ABAQUS 3D FE model for a rigid footing with B=1.5m, (B) A simplified approach to account for the SSI effects (horizontal and rotational stiffness of the soil) for horizontal displacement at the top of each column.

Non-linear soil behaviour and stress-strain relationship is described by a simplified kinematic hardening model that follows a Von Mises failure criterion with associated flow rule. The formulation of this modified Von Mises model is adopted as a subroutine in ABAQUS code and has been parametrised by Gerolymos and Gazetas [29] and Anastasopoulos et al. [30] in order to appropriately simulate the response of clayey materials. Despite its simplicity, this constitutive model has been validated against physical model testing hence ensuring its ability to capture realistically the foundation behaviour and the non-linearity of the soil stiffness.

The foundation system is designed based on the properties and approximate loading of a typical residential 4-storey building as described in Chapter 5 of this paper. To this end, a series of parametric analyses have been conducted by adopting different foundation widths (B) and various material properties (S_u=70, 200 and 300 kPa) resulting in different FoS (Factor of Safety) against vertical loading. On the basis of empirical correlations, the initial, small strain, elastic modulus (E_0) of the soil was considered equal to $1800S_u$ and its non-linear behaviour is simulated realistically by the constitutive relations of the model.

As indicated in Fig. 3B, the equivalent soil-foundation stiffness (k_{SSI}) is calculated assuming a rigid column subjected to horizontal displacement at the top. The height of the column is equal to 3.5m, aligned with the height of the column considered in our case study (Section 5). As a consequence, the calculated stiffness (k_{SSI}), is a result of both the rotational and horizontal displacement of the soil footing and is expressed at the top of the rigid column.

The total stiffness (k_R) of the system can be then calculated as the resultant of the structural column stiffness (k_{col}) and the equivalent stiffness at the top of the beam due to the rotational and horizontal displacement of the footing (k_{SSI}). Results for a few foundation widths (B) and soil profiles that have been considered relevant for the study are presented in Fig. 4 below. The horizontal displacement at the top of the column is plotted against the reaction force (RF) and soil-foundation stiffness (k_{SSI}) respectively. All foundations considered below have a total FoS against vertical loading between 3.5 and 4 thus ensuring the stability of the structure under static loading. For the purposes of the study, the footing geometry selected represents a relatively soft foundation that allows deformation of the soil-foundation system during earthquake excitation as a means to reduce the forces transmitted to the structural members. This design is based on the idea of "rocking" foundations which has been investigated using numerical and physical models by several researchers [31-34].

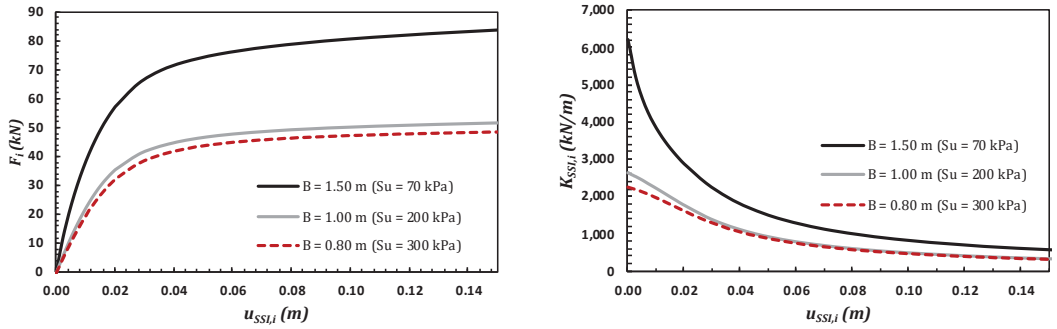

(A) (B)

Figure 4. (A) Reaction force (F) versus horizontal displacement at the top of the rigid column, (B) Soil-Foundation Stiffness (k_{SSI}) horizontal displacement at the top of the rigid column.

4 OPTIMIZATION OF THE EKD PARAMETERS

After the equations of motion of the EKD and structural system are derived, the aim is to determine efficient parameters for the proposed configuration in order to achieve an optimized vibration control strategy. As stated in the previous sections, the parameters f_0, k_N, c_{DOWN} and c_{UP} are the free design variables taken into consideration in the optimization problem, while parameters such as the additional damper mass m_D and the stability factors ε_N, ε_P, and ε_R are considered known. For the optimization process, a novel metaheuristic algorithm, harmony search algorithm (HS), is adopted. In this study, the optimization problem is formed according to the seismic design codes. The constraints and objective function are selected from the time-domain responses. The optimisation procedure is described in greater detail in the following sections.

4.1 Selection of Seismic Excitations Compatible to the Seismic Design Codes for the Analysis and Optimization of the EKD

The calculation of structural displacements, velocity and acceleration due to seismic excitation is usually undertaken according to seismic design codes (e.g. EC8) and the design response spectrum. As a consequence, the seismic intensity measures are within specified limits for a system with given properties (fundamental structural period and damping ratio). The parameters that mainly control these limits are the ground conditions, the expected seismic intensity, the damping ratio of the system as well as the fundamental period of the structure.

However, the application of such approach and the use of the code's Design Response Spectra for the selection of the extended KDamper parameters, is not considered adequate, since the application of the KDamper leads to MDoF systems with multiple eigenfrequencies. Therefore, analysis in the time-domain is required for the optimal design of the proposed base absorber. Strong earthquake records can be generated from various types of accelerograms such as synthetic records obtained from seismological models, real earthquake excitations and artificial accelerograms, compatible with a specific design response spectrum.

4.2 Generation of Artificial Accelerograms

In this section, a presentation of the details of the generation of artificial accelerograms based on the design response spectra is undertaken. This is a task that has been widely studied by researchers, overviews of which can be found among others in Giaralis and Spanos [35] and Cacciola and D'Amico [36]. For the purposes of this study, the approach followed is based on

generating a sample of artificial accelerograms with acceleration response spectra in accordance with the EC8 design response spectra. Artificial, spectrum-compatible accelerograms are generated using the SeismoArtif Software [37]. In this paper, the Artificial Accelerograms are designed to match the EC8 response spectra incorporating the following seismic properties: ground type C, spectral acceleration 0.36 g, spectrum type I and importance class II.

An artificial accelerogram is illustrated in Fig. 5A, along with its acceleration response spectrum (S_a) (Fig. 4B). A sample of 15 artificial accelerograms is generated and plotted in Fig. 5C along with the EC8 response spectrum for comparison with the design guidelines. An accurate match is observed with the EC8 acceleration response spectrum with characteristics: spectral acceleration 0.36 g, ground type C, spectrum type I and importance class II. More specifically, the percentage deviation is below *10%* in the range of periods from *0.2* to *2* sec, which are considered relevant for the structural performance.

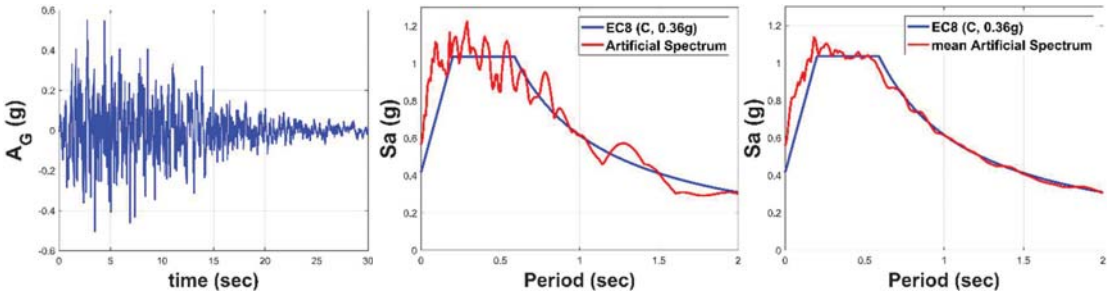

(A) (B) (C)

Figure 5. (A) Artificial Accelerogram, (B) Acceleration response spectrum of Artificial Accelerogram and (C) Mean Artificial acceleration response spectrum of the 15 generated Artificial Accelerograms compared to the EC8 acceleration response spectrum.

4.3 Evaluation of Optimization Constraints and Limitations

The design of the proposed control strategy must be efficient and realistic at the same time. For this reason, proper constraints that refer to the structural dynamic responses and therefore the EKD components must be applied. The structure's first floor drift is set as the objective function (mean of 15 maximum responses). The system is subjected to 15 Artificial Accelerograms generated according to section 4.1, with a mean PGA of *0.519g*.

Furthermore, the given parameters of the system with the EKD, i.e. the additional mass m_D and the stability factors ε_N, ε_P, and ε_R, as well as the limits of the free design variables sought in the optimization problem, f_0, k_N, c_{DOWN} and c_{UP}, must be within reasonable technological capabilities in order for design to be realistic. In particular:

i. In the previous work of KDamper, the stability factor ε_N that relates to the variation of the negative stiffness element k_N, is taken as *5%*. In this study, a variation in all stiffness elements is considered, making the design of the proposed vibration absorption concept rather conservative. The stability factors ε_P and ε_N are selected equal to *10%*, and the stability factor that relates to the stiffness element k_R is selected equal to 25%. The potential 25% stiffness reduction was selected based on an initial linear analysis with the EKD implemented in the structure assuming rigid footing. In this way, the anticipated displacement of the column top was calculated and the expected reduction of the k_{SSI} stiffness due to this deformation was estimated (approximately 25%, refer to Fig. 4B).

ii. The purpose of this design is to implement the proposed control strategy for seismic protection of building structures. Since KDamper can be implemented between the floors of structures, there are no strict limitations regarding the additional mass. According to the previous work of KDamper implemented as an Absorption Base (KDAB) of multi-story building structures with the same characteristics, [28], a *5%* additional mass is efficient and realistic.

iii. The negative stiffness element k_N, in the proposed configuration of EKD, is realized with pre-compressed springs. Based on previous indicative designs of KDamper with pre-compressed springs by Antoniadis et al. [12] and Kapasakalis et al. [27], for a total superstructure mass of *300 tn*, a realistic value of k_N is *-34171 kN/m*. In this work, the negative stiffness element absolute upper value is *|30000| kN/m*.

iv. The damping coefficients maximum value is set equal to *600 kNs/m* for the whole configuration (multiple KDamper devices can be implemented), therefore, common linear damping devices can be used.

v. The negative stiffness element stroke ($X_{S\text{-}D}$) is set as a constraint, with an upper limit value of *15 cm* which, based on previous work of Kapasakalis et al. [25], proves to be a realistic value for the design of the negative stiffness element with pre-compressed springs.

Finally, the limits of the free design variables are: 1) the nominal KDamper frequency f_0 (*Hz*) [*0.15 1.5*], 2) the negative stiffness element k_N (*kN/m*) [*-30000 -1*] and 3, 4) the damping coefficients c_{DOWN} and c_{UP} (*kNs/m*) [*1 600*].

5 NUMERICAL CASE STUDY ON A TYPICAL 4-STOREY STRUCTURE

A numerical case study has been conducted considering a 4-storey typical residential building. The structural system has 4 dynamic DoFs represented by the relative displacements of the 4 storeys with respect to the ground. The elastic modulus of reinforced concrete (assuming long-term cracked conditions) is equal to E=26 GPa. The mass of the building is considered to be concentrated at the floor levels, with m_i=80000 kg denoting the mass of the 4 storeys (i=1,…,4), while the columns are assumed to be weightless.
The superstructure's damping coefficients are mass and stiffness proportional (Rayleigh damping), with ζ_{Si}=0.02 (i=1,…,4).

The geometry of the model is presented in Fig. 6 below. A 15x15m floor in plan-view has been considered with 0.3x0.3m square columns. Analysis for different foundation widths (B) and soil material properties has been undertaken and results for a single case are presented herein. Therefore, the material under investigation has an undrained shear strength equal to S_u=70 kPa and a G_0=53 MPa. The footing width (B) is considered as 1.50m and a total FoS against vertical loading equal to 3.8 is calculated, hence ensuring the static stability of the system. For more details regarding the selection of the material properties refer to Section 3.3.

The soil-structure interaction is regarded in the excitation analysis as explicitly detailed in section 3 of this paper and the parameters of the EKD are optimized based on the methodology described in section 4. A Matlab-based code is incorporated to model the structure and extended KDamper system as a series of masses and springs; linear and non-linear representing the structural elements and soil-foundations respectively. A number of artificial and real seismic excitations are subsequently applied and the response of the structure is investigated. Results of the analysis are presented in Fig. 6 and Table 1 below.

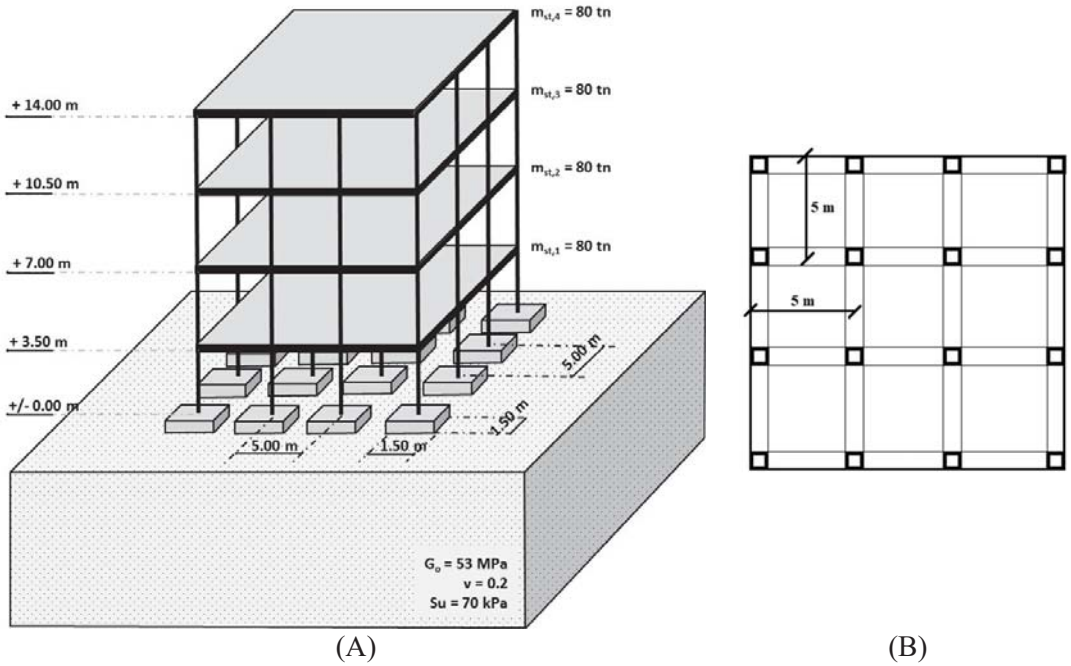

Figure 6 (A) Typical 4-storey residential building investigated as a case study, (B) Plan view of a typical floor of the building considered in this case study.

Structural System	Ensemble of 15 artificial accelerograms, PGA = 0.24 g					L'Aquila (2009), PGA = 0.40 g				
	$a_{s,4}$ (*g*)	$u_{s,1}$ (*cm*)	$u_{col,1}$ (*cm*)	$u_{SSI,1}$ (*cm*)	V_b (*kN*)	$a_{s,4}$ (*g*)	$u_{s,1}$ (*cm*)	$u_{col,1}$ (*cm*)	$u_{SSI,1}$ (*cm*)	V_b (*kN*)
Building with fixed footings	1.18	3.91	3.91	-	2,540	1.13	2.35	2.35	-	1,527
Building with SSI footings	1.08	6.67	2.02	4.65	1,310	0.89	5.72	1.85	3.88	1,204
Building with KDamper & fixed footings	0.35	3.32	3.32	-	640	0.29	3.60	3.60	-	745
Building with KDamper & SSI footings	0.29	3.29	1.36	1.93	518	0.29	4.50	1.61	2.90	400

Table 1: Dynamic response of the four examined residential building systems (with fixed footings, with SSI footings, with KDamper and fixed footings, with KDamper and SSI footings) for an ensemble of 15 artificial accelerograms (mean of 15 max values), and a real near fault earthquake record (L'Aquila, 2009, Mw = 6.3).

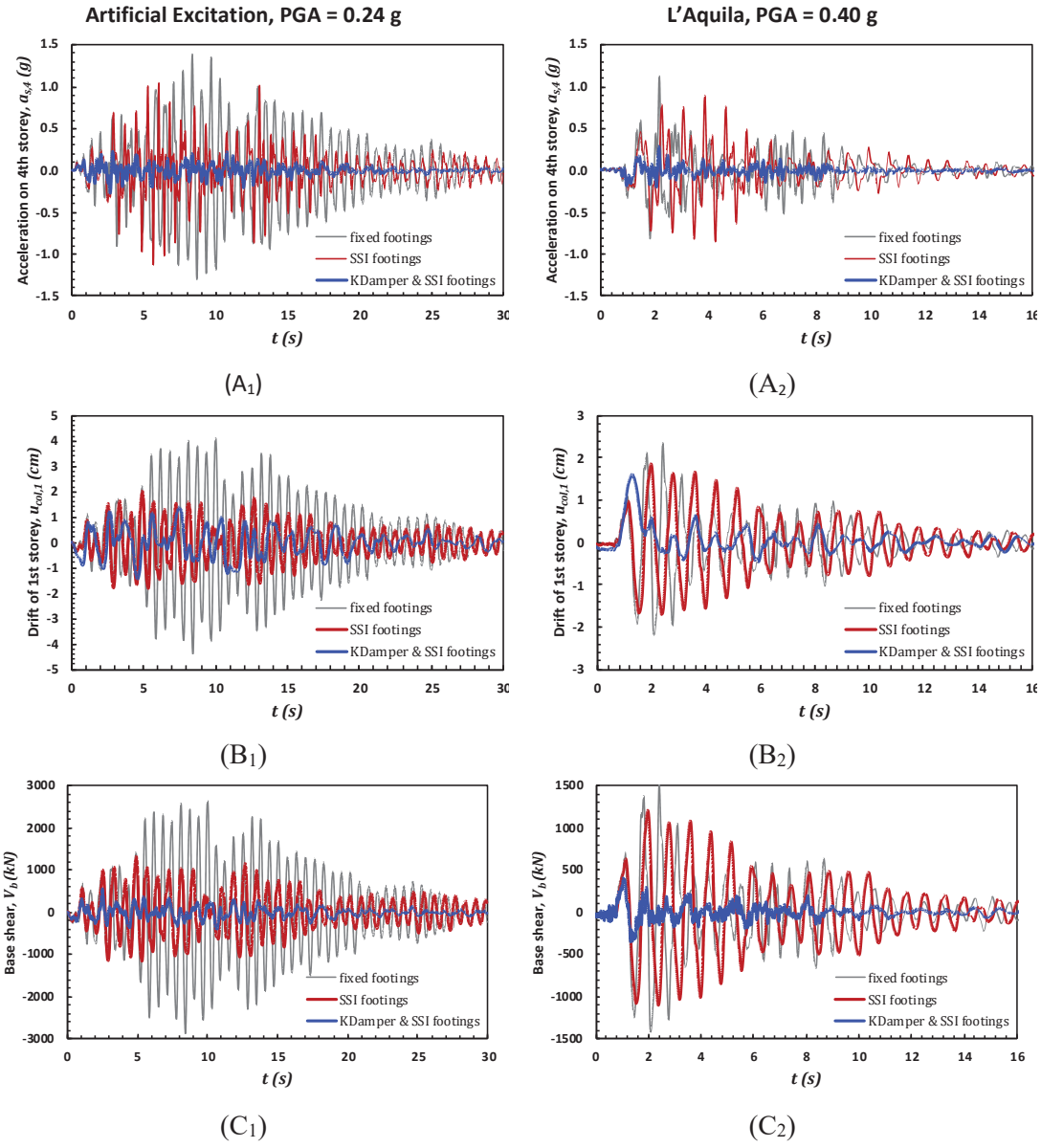

Figure 6. Comparative results in terms of (A) Absolute acceleration of the top storey of the structure (B) Horizontal displacement (drift) of the 1st floor and (C) Base shear-force of the structure for one artificial accelerogram (A_1, B_1, C_1) and the L'Aquila earthquake record (A_2, B_2, C_2) respectively.

A comparison between the response of the structural model considering a) fixed foundations, b) SSI effects by incorporating the non-linear stiffness of the soil and c) the extended KDamper coupled with SSI effects is undertaken for one of the artificial accelerograms (matching the EC8 design spectrum) and a real earthquake excitation. It can be observed that, the application of the extended KDamper along with the SSI effects lead to the main following results:

1. The EKD together with the SSI effects appear to improve the structural response under a dynamic seismic excitation, indicating that the non-linearity of the overall system stiffness parameters does not lead to detuning of the damper;
2. A 40-70% reduction of the absolute acceleration values of the building storeys is achieved, hence remaining within the structural limits;
3. The base shear values appear to be significantly reduced in accordance with the absolute acceleration values;
4. The total horizontal displacement of the first floor is slightly reduced compared to the fixed footings. However, as indicated in Fig. 7 below, due to the rotational and horizontal movement of the foundation the total displacement is distributed between the column and the footing (SSI) and consequently structural flexural displacements are reduced and remain within an acceptable region.

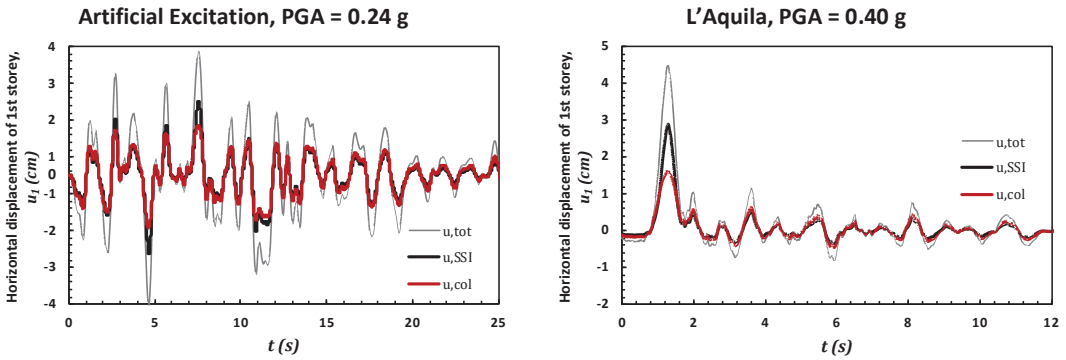

Figure 7. Distribution of the first storey total horizontal displacement due to the flexural deformation of the column (drift) and deformation due to SSI effects (horizontal and rotational movement of the footing), for the case of an artificial accelerogram (A), and the L'Aquila record (B)

As it can be observed in Fig. 7, although the displacement of the first storey for the case of an artificial accelerogram (u_{tot}) reached 3.36 cm, it was distributed both in the column, in the form of flexural deformation (u_{col}), and in the footing, in the form of predominantly rotational, and also translational displacement, due to the SSI effects (u_{SSI}). The maximum flexural deformation was a mere 1.37 cm, which is almost three times lower than the flexural deformation that was demanded in the case of the building with no seismic protection. The 1st-storey displacement is primarily undertaken by the SSI mechanism, meaning that during the shaking, the equivalent soil-foundation stiffness of a single footing 1.50 m x 1.50 m has dropped below the structural column stiffness of a single column, equal to 4,000 kN/m. In general, the distribution of the stiffness in the column-footing-soil system governs the distribution of the deformation in these components. It should be highlighted that for the case of either wider surface footings, or for footings whose rotational and horizontal displacement have been kinematically constrained, as in the case of footings connected with strap beams, the equivalent soil-foundation stiffness of the system increases dramatically, and hence the displacement is not distributed among the column and the foundation. Thus, the total displacement is undertaken by the columns leading to additional loading of the structural elements.

6 CONCLUSIONS

In this paper, the extended KDamper (EKD) is implemented as a seismic protection vibration control system located at the base of a typical building structure. The beneficial effects of soil-structure interaction (SSI) of a relatively soft foundation system along with the EKD as excitation absorber are investigated. An analytical approach for the selection of the EKD parameters aiming to optimize acceleration response, under base excitation, is considered and the initial structural system is introduced along with the vibration absorber concepts. A sample of Artificial Accelerograms with acceleration response spectra compatible to EC8 is generated, and a few real earthquake shaking records are considered. The concept is applied between the foundation system and the first floor of a 4-storey building that is examined as a case study herein. Results show significant reduction of the structural accelerations, drifts and base shear forces, hence placing the concept of a coupled EKD-SSI system as a compelling methodology for seismic protection of structures.

7 ACKNOWLEDGMENTS

This research has been financed by the European Union's Horizon 2020 research and innovation programme under the Marie Sklodowska-Curie grant (grant agreement No INSPIRE-813424, "INSPIRE - Innovative Ground Interface Concepts for Structure Protection").

8 REFERENCES

1. Warn GP, Ryan KL. A Review of Seismic Isolation for Buildings: Historical Development and Research Needs. *Buildings* 2012; **2**(3): 300–325. DOI: 10.3390/buildings2030300.
2. Reggio A, Angelis M De. Optimal energy-based seismic design of non-conventional Tuned Mass Damper (TMD) implemented via inter-story isolation. *Earthquake Engineering & Structural Dynamics* 2015; **44**(10): 1623–1642. DOI: 10.1002/eqe.2548.
3. Kunde MC, Jangid RS. *Seismic behavior of isolated bridges: A-state-of-the-art review*. vol. 3. 2003.
4. De Angelis M, Giannini R, Paolacci F. Experimental investigation on the seismic response of a steel liquid storage tank equipped with floating roof by shaking table tests. *Earthquake Engineering & Structural Dynamics* 2009: n/a-n/a. DOI: 10.1002/eqe.945.
5. Paolacci F, Giannini R, De Angelis M. Seismic response mitigation of chemical plant components by passive control techniques. *Journal of Loss Prevention in the Process Industries* 2013; **26**(5): 924–935. DOI: 10.1016/j.jlp.2013.03.003.
6. Whittaker AS, Kumar M, Kumar M. Seismic isolation of nuclear power plants. *Nuclear Engineering and Technology* 2014; **46**(5): 569–580. DOI: 10.5516/NET.09.2014.715.
7. Taniguchi T, Der Kiureghian A, Melkumyan M. Effect of tuned mass damper on displacement demand of base-isolated structures. *Engineering Structures* 2008; **30**(12): 3478–3488. DOI: 10.1016/j.engstruct.2008.05.027.
8. Tsai HC. The effect of tuned-mass dampers on the seismic response of base-isolated structures. *International Journal of Solids and Structures* 1995; **32**(8–9): 1195–1210. DOI: 10.1016/0020-7683(94)00150-U.
9. Palazzo B, Petti L, de Ligio M. Response of base isolated systems equipped with tuned mass dampers to random excitations. *Journal of Structural Control* 1997; **4**(1):

9–22. DOI: 10.1002/stc.4300040105.
10. Xiang P, Nishitani A. Optimum design for more effective tuned mass damper system and its application to base-isolated buildings. *Structural Control and Health Monitoring* 2014; **21**(1): 98–114. DOI: 10.1002/stc.1556.
11. Hashimoto T, Fujita K, Tsuji M, Takewaki I. Innovative base-isolated building with large mass-ratio TMD at basement for greater earthquake resilience. *Future Cities and Environment* 2015. DOI: 10.1186/s40984-015-0007-6.
12. Antoniadis I, Chronopoulos D, Spitas V, Koulocheris D. Hyper-damping properties of a stiff and stable linear oscillator with a negative stiffness element. *Journal of Sound and Vibration* 2015. DOI: 10.1016/j.jsv.2015.02.028.
13. Antoniadis I.A., Kapasakalis, K.A., Sapountzakis EJ. Isolation or Damping? A Soil-dependent approach based on the KDamper concept. *Proceedings of the 2nd International Conference on Natural Hazards & Infrastructure (ICONHIC 2019)*
14. Sapountzakis, E.J., Kapasakalis, K.A. AIA. Negative Stiffness Elements in Seismic Isolation of Bridges. *Proceedings of the 2nd International Conference on Natural Hazards & Infrastructure (ICONHIC 2019)*, 2019.
15. Kapasakalis KA, Alamir CHT, Antoniadis IA, Sapountzakis EJ. Frequency Base Design of the KDamper Concept for Seismic Isolation of Bridges. *Proceedings of the 14th International Conference on Vibration Problems (ICOVP 2019)*, 2019.
16. Bollano, P-O.N., Kapasakalis, K.A., Sapountzakis, E.J. AIA. Design and Optimization of the KDamper Concept for Seismic Protection of Bridges. *Proceedings of the 14th International Conference on Vibration Problems (ICOVP 2019)*, 2019.
17. Kapasakalis, K.A., Antoniadis I.A. SAE. Implementation of the KDamper Concept for Seismic Protection of Bridges. *Proceedings of the 14th International Conference on Vibration Problems (ICOVP 2019)*, 2019.
18. Kapasakalis, K.A., Sapountzakis, E.J., Antoniadis IA. Implementation of the KDamper Concept to Wind Turbine Towers. *Proceedings of the 6th International Conference on Computational Methods in Structural Dynamics and Earthquake Engineering (COMPDYN 2017)*, 2017.
19. Kapasakalis, K.A., Sapountzakis, E.J., Antoniadis IA. Optimal Design of the KDamper Concept for Structures on Compliant Supports. *Proceedings of the 16th European Conference on Earthquake Engineering (16ECEE 2018)*, 2018.
20. Kapasakalis, K.A., Sapountzakis, E.J., Antoniadis IA. KDamper Concept in Seismic Isolation of Multi Storey Building Structures. *Proceedings of the 9th GRACM International Congress on Computational Mechanics (9GRACM 2018)*, 2018.
21. Kapasakalis, K.A., Sapountzakis, E.J., Antoniadis IA. Kdamper concept in seismic isolation of building structures with soil structure interaction. *Proceedings of the 13th International Conference on Computational Structures Technology (CST2018)*, 2018.
22. Kapasakalis, K.A., Antoniadis, I.A., Sapountzakis EJ. Control of Multi Storey Building Structures with a New Passive Vibration Control System Com-bining Base Isolation with KDamper. *Proceedings of the 7th International Conference on Computational Methods in Structural Dynamics and Earthquake Engineering (COMPDYN 2019)*, 2019.
23. Kapasakalis, K.A., Antoniadis, I.A., Sapountzakis EJ. Implementation of the KDamper Concept for Base Isolation to a Typical Concrete Building Structure. *Proceedings of the 12th International Congress on Mechanics (12HSTAM2019)*.

24. Kapasakalis, K.A., Antoniadis, I.A. SEJ. KDamper Concept for Base Isolation and Damping of High-Rise Building Structures. *Proceedings of the 14th International Conference on Vibration Problems (ICOVP 2019)*, 2019.
25. Kapasakalis, K.A., Antoniadis, I.A. and Sapountzakis, E.J., "Implementation of the KDamper as a Stiff Seismic Absorption Base: A Preliminary Assessment", Vibration and Acoustics Research Journal, Vol. 1, No. 1, pp. 1-26, 2019.
26. Antoniadis, I.A., Kapasakalis, K.A., Sapountzakis EJ. Advanced Negative Stiffness Absorbers for the Seismic Protection of Structures. *Proceedings of the International Conference on Key Enabling Technologies 2019 (KEYTECH2019)*, 2019. DOI: https://doi.org/10.1063/1.5123704.
27. Kapasakalis, K.A., Antoniadis, I.A, Sapountzakis EJ. Novel Vibration Absorption Systems with Negative Stiffness Elements for the Seismic Protection of Structures. *4th National Conference on Earthquake Engineering and Engineering Seismology (Hellenic Association for Earthquake Engineering - HAEE / ETAM)*, 2019.
28. Kapasakalis, K.A., Antoniadis, I.A., Sapountzakis EJ. Performance Assessment of the KDamper as a Seismic Absorption Base. *Structural Control and Health Monitoring* 2019. DOI: 10.1002/stc.2482.
29. Gerolymos N., Gazetas G., 2005. Nonlinear Lateral Response of Caisson Foundations. Proceedings of the 1st Greece-Japan Workshop on Seismic Design, Observation, Retrofit of Foundations, Athens, Greece, pp. 125.
30. Anastasopoulos I., Gelagoti F., Kourkoulis R., Gazetas G., 2011. Simplified Constitutive Model for Simulation of Cyclic Response of Shallow Foundations: Validation against Laboratory Tests. Journal of Geotechnical & Geoenvironmental Engineering (ASCE),591 137(12).
31. Anastasopoulos I., Gazetas G., Loli M., Apostolou M., Gerolymos N. (2010) "Soil failure can be used for seismic protection of structures," Bulletin of Earthquake Engineering, 8(2), pp. 309-326.
32. Gajan S., Kutter B., Phalen J., Hutchinson T., Martin G. (2005) "Centrifuge modeling of load-deformation behavior of rocking shallow foundations," Soil Dynamics and Earthquake Engineering*, 25, pp. 773 - 783.*
33. Paolucci R., Shirato M., and Yilmaz M.T. (2008), "Seismic behaviour of shallow foundations: Shaking table experiments vs numerical modeling", Earthquake Engineering and Structural Dynamics, Vol. 37, pp. 577–595.
34. Loli M., Knappett J.A., Brown M.J., Anastasopoulos I., and Gazetas G. (2014), "Centrifuge Modeling of Rocking–isolated Inelastic RC Bridge Piers", Earthquake Engineering and Structural Dynamics*, 43, 15, pp. 2341-2359.*
35. Giaralis, A., and P. D. Spanos. "Wavelet-based response spectrum compatible synthesis of accelerograms—Eurocode application (EC8)." Soil Dynamics and Earthquake Engineering 29, no. 1 (2009): 219-235.
36. Cacciola P, D'Amico L. Response-Spectrum-Compatible Ground Motion Processes. Encycl. Earthq. Eng., 2015, p. 1–27. doi:10.1007/978-3-642-36197-5_325-1.
37. Seismosoft [2018]. SeismoArtif - A computer program for generating artificial earthquake accelerograms matched to a specific target response spectrum 2018. http://www.seismosoft.com.

EURODYN 2020
XI International Conference on Structural Dynamics
M. Papadrakakis, M. Fragiadakis, C. Papadimitriou (eds.)
Athens, Greece, 23–26 November 2020

OPTIMAL DESIGN OF ADVANCED NEGATIVE STIFFNESS ABSORBERS

Konstantinos A. Kapasakalis[1*], Ioannis A. Antoniadis[2], and Evangelos J. Sapountzakis[1]

[1] Institute of Structural Analysis and Antiseismic Research
School of Civil Engineering, National Technical University of Athens
Zografou Campus, GR-157 80 Athens, Greece
e-mail: kostiskapasakalis@hotmail.com, cvsapoun@central.ntua.gr

[2] Dynamics and Structures Laboratory
School of Mechanical Engineering, National Technical University of Athens
Zografou Campus, GR-157 80 Athens, Greece
e-mail: antogian@central.ntua.gr

Keywords: Negative Stiffness, Seismic Protection, Vibration Absorption, KDamper

Abstract. *Throughout the last decades, seismic isolation of structures has attracted the attention of civil engineers and scientists. Research around this field has progressed tremendously, starting from the use of simple elastomeric bearings for the decoupling of the superstructure from the foundation and moving towards the invention of more complex devices (characteristic examples being the Tuned Mass Dampers – TMDs or the Quasi-Zero Stiffness oscillators – QZSs) aiming to enhance structural dynamic behavior.*

In this paper, an extension of the KDamper (EKD) concept is proposed, for implementation as a seismic base absorber. The complexity of the EKD renders the conventional minmax (H∞) approach ineffective. For this reason, a constrained optimization problem is proposed for the selection of the optimal system parameters. The EKD is designed according to seismic design codes and the constraints and limitations of the EKD components are evaluated based on engineering criteria. A database of artificial accelerograms, compatible with the EC8 response spectra is generated. Sensitivity analysis is performed, and the effect of detuning is observed.

Based on a comparison with a conventional base isolated system, the EKD manages to retain the structure absolute acceleration at acceptable levels, while the structure relative displacement is drastically reduced, in the order of a few centimeters, rendering the implementation of the extended KDamper feasible using conventional structural elements, without the need for special types of bearing. Thus, EKD can be considered a possible retrofitting option for seismic protection.

1 INTRODUCTION

Seismic design codes for building structures, bridges and industrial facilities have changed with the intention of leading towards better seismic performance. Seismic isolation is perhaps the most popular approach to earthquake-resistant design. Contemporary seismic isolation systems provide horizontal isolation from the effects of earthquake shaking and an energy dissipation mechanism to reduce the large required base displacements, with the latter being the most important drawback of base isolation, as it prohibits retrofitting. Increasing the damping of the base isolation system, to reduce the large displacements, cannot be considered as a mainstream alternative due to the technological requirements and the increase of the inter-story drifts and floor accelerations. Numerous isolation devices have been developed, including elastomeric, frictional/sliding and roller bearings as well as fluid viscous and viscoelastic dampers. In the past few years, however, research focuses on the next generation of seismic protection devices that include: (a) the introduction of negative stiffness elements (Negative Stiffness Devices and "Quazi Zero Stiffness" oscillators) and (b) the implementation of additional masses (Tuned Mass Dampers).

The central concept of negative stiffness isolators is to significantly reduce the natural frequency of the system, lower than the predominant energy-containing frequencies of earthquake ground motions. Quazi Zero Stiffness (QZS) oscillators find numerous applications in seismic isolation [1–10]. The use of additional masses as a passive control strategy (TMDs) has been employed in a variety of systems, with skyscrapers [11–13] and implementations in the bases of structures [14–18], being the most interesting ones. TMDs are effective and reliable, but their usage presents significant drawbacks such as (a) detuning, which deteriorates the system performance, and (b) the need for large additional masses, that render the construction and placement of such configurations difficult.

In order to combine the advantages mentioned previously, without their respective drawbacks, a stiff and stable linear oscillator that incorporates a negative stiffness (NS) element, has been proposed in Antoniadis et al. [19]. The KDamper, first introduced in Antoniadis at al. [20], is essentially an extension of the conventional TMD concept, by the introduction of an appropriate NS element to the additional mass of the TMD. The KDamper is examined for the protection of bridge structure [21–25], Wind Turbines [26,27] and structural systems [28,29]. In addition, the KDamper is implemented as an Absorption Base (KDAB) in the bases of structures [30–36]. In the recent work of Kapasakalis et al. [35], the KDAB is proven to be a possible supplement to BI, or can be alternatively implemented as a "stiff absorption base".

This paper proposes an extension of the KDamper concept (EKD). The optimization problem is formed from which the optimal system parameters are selected. The constraints that refer to the dynamic responses and the limits of the free design variables, i.e. the EKD components, are evaluated base on engineering criteria. For the optimization process, the harmony search algorithm (HS) [37], a novel metaheuristic algorithm, is adopted. The EKD is designed according to seismic design codes. For this reason, artificial seismic excitations are generated, with compatible acceleration response spectra to EC8, using SeismoArtif [38] software. Finally, the system is compared to a conventional base isolated system, designed to have a natural frequency of *0.4 Hz*, in order to prove the efficiency of the EKD. The novel aspects of the innovative passive vibration control strategy developed here are summarized as follows:

i. Extended KDamper (EKD) presents similar/marginally superior results as compared to the previously optimal KDamper concept [35]. However, the proposed EKD foresees variation in all stiffness elements, while in the KDamper concept only the negative stiffness element is examined. Furthermore, the negative stiffness element stroke, which is critical for the whole configuration design, is dramatically reduced.

ii. The evaluation of the optimization constraints is based on engineering criteria. The realization of the additional mass, the damping coefficients and the stiffness elements are within reasonable technological capabilities and render the implementation of the EKD feasible.
iii. The EKD is designed according to seismic design codes. For this reason, the acceleration filter, used in the optimization procedure, is defined by a database of 30 Artificial Accelerograms, design to match the EC8 acceleration response spectra.
iv. The effects of detuning are observed via sensitivity analysis.

In conclusion, the essential features of the EKD design implemented in a SDoF system, as compared to a conventional base isolated system, are summarized as follows:

i. The EKD implemented in a SDoF system manages to retain the structure absolute acceleration in acceptable levels (base on the selected design Acceleration Filter) while at the same time the structure relative displacement is significantly low, as compared to conventional and highly damped base isolation systems.
ii. The small base displacement of the EKD with high Acceleration Filters, render its implementation feasible using conventional structural elements, without the need of special type of bearings. As a consequence, retrofitting is possible.

2 PROPOSED NEGATIVE STIFFNESS ABSORBER

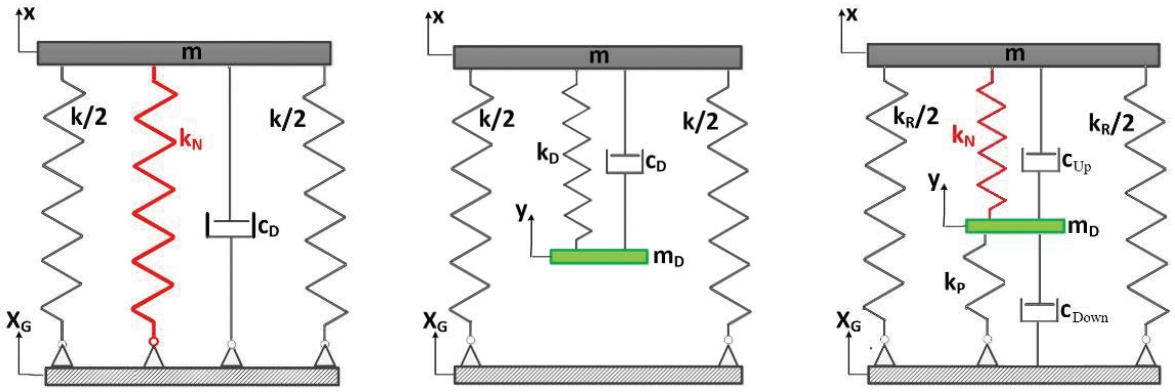

Figure 1: Schematic representation of the vibration absorption concepts considered: (A) Negative Stiffness (NS) isolator, (B) Tuned Mass Damper (TMD) and (C) Proposed Negative Stiffness Absorber (Extended KDamper).

The fundamental concept of the vibration control strategies presented in Figure 1 is to improve the dynamic behavior of an undamped (or low damped) SDoF system of mass m and static stiffness k to a base excitation of $x_G(t)$. The concept of the NS isolator is to add a negative stiffness element k_N in parallel to the original stiffness k of the system so that the overall stiffness of the system becomes $k_{QZS} = k + k_N \leq k$. However, this limits the static loading capacity of the structure. The proposed passive vibration absorption concept, presented in Figure 1.C is an extension of the KDamper (EKD) concept. Similarly to the KDamper, it incorporates a negative stiffness element. Contrary to the NS isolator, the first basic requirement of the EKD is that the overall static stiffness of the system is maintained:

$$k_R + \frac{k_P k_N}{k_P + k_N} = k = (2\pi f_0)^2 m_{total} \tag{1}$$

This way, the EKD overcomes the fundamental disadvantage of the NS isolator. Compared to the TMD (Figure 1.B), the EKD uses an additional negative stiffness element k_N, which

connects the additional mass to the structure, and a positive stiffness element which connect the additional mass to the base. Thus, the equation of motion of the EKD becomes:

$$\begin{gathered} m\ddot{u}_S + k_R u_S + m_D \ddot{u}_D + k_P u_D = -(m+m_D)a_G \\ m_D \ddot{u}_D - c_{UP}(\dot{u}_S - \dot{u}_D) - k_N(u_S - u_D) + c_{DOWN}\dot{u}_D + k_P u_D = -m_D a_G \end{gathered} \tag{2}$$

However, increasing the absolute value of k_N, or decreasing the absolute values of k_P or k_R, may endanger the static stability of the structure. Although theoretically the values of k_N, k_P, and k_R are selected according to Equation (1) to ensure the static stability, due to various reasons, such as temperature variations, manufacturing tolerances, or non-linear behavior, k_N, k_P and k_R may present significant variations in practice, since almost all negative stiffness designs result from unstable non-linear systems. Consequently, an increase of the absolute value of k_N and/or a decrease of the values of k_P *and* k_R by a factor ε_N, ε_P and ε_R, respectively, may result in the system being unstable:

$$(1-\varepsilon_R)k_R + \frac{(1-\varepsilon_P)k_P(1+\varepsilon_N)k_N}{(1-\varepsilon_P)k_P + (1+\varepsilon_N)k_N} = 0 \tag{3}$$

Contrary to the KDamper concept, which foresees variation only in the negative stiffness element k_N, in the proposed extension of the KDamper concept, a variation in all stiffness elements are taken into account. Assuming the negative stiffness ratio $kn=k_N/k_0$ or the absolute value of the negative stiffness element k_N is known, using Equations (1 and 3), the rest of the stiffness elements result:

$$kr = \frac{-b-\sqrt{b^2-4*a*c}}{2a} \Rightarrow KR = kr*k_0 \,;\; kp = \frac{kn-kr*kn}{kr+kn-1} \Rightarrow KP = kp*k_0 \tag{4}$$

Where parameters a, b and c are defined as:

$$\begin{gathered} (1-\varepsilon_R) = R \,;\; (1+\varepsilon_N) = N \,;\; (1-\varepsilon_P) = P \\ a = R(P-N) \,;\; b = kn*N(P-R) + R(N-P) \,;\; c = -P*N*\mathrm{kn} \end{gathered} \tag{5}$$

Finally, assuming that the following parameters are known: A) the additional mass, m_D, and B) the variations ε_N, ε_P and ε_R of the stiffness elements, the unknown parameters of the system are: i) the nominal EKD frequency f_0 (Equation (1)), ii) the negative stiffness ratio kn or the value of the negative stiffness element k_N and iii, iv) the damping coefficients c_{DOWN} and c_{UP}.

3 STATEMENT OF THE OPTIMIZATION PROBLEM

Once the equations of motion of the controlled system with the proposed configuration are stated, the goal now is to determine the "optimal" parameters such that the attained vibration control strategy turns out to be the best possible. As mentioned previously, the parameters f_0, k_N, c_{DOWN} and c_{UP} are the free design variables sought in the optimization problem, while other parameters such as the additional mass m_D and the stability factors ε_N, ε_P, and ε_R are supposed known. For the optimization process, the harmony search algorithm (HS), a novel metaheuristic algorithm, is adopted. In this paper, the optimization problem is formed according to the seismic design codes. The constraints and objective function are selected from the time-domain responses. The procedure from which the earthquake ground motions are selected for the optimization problem is described in section 3.1.

3.1 Selection of earthquake ground motion according to seismic design codes

Seismic design codes indicate that the structure's relative displacement and absolute acceleration, are within specified limits for a system with given characteristics (fundamental structure period and damping ratio). The parameters that mainly control these limits are the ground conditions, the expected seismic intensity, the damping ratio of the system as well as the fundamental period of the structure. A typical form of the so-called "Design Response Spectra" is depicted in Figure 2.

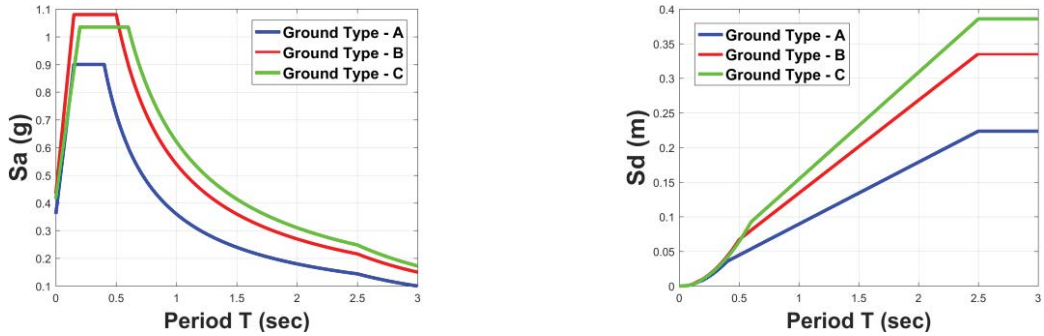

Figure 2. EC8 Design response spectra. (A) Spectral acceleration and (B) Spectral displacement.

However, the application of such approaches for the selection of the EKD parameters, isn't possible, since the application of the EKD leads to MDoF systems with multiple frequencies. Therefore, analysis in the time-domain is required for the optimal design of the proposed base absorber. Strong earthquake records can be generated from various types of accelerograms, the fundamental of which being: synthetic records, real earthquakes excitations, and artificial accelerograms, compatible with a specific design response spectrum, with the latter being the most suitable. For this reason, the approach followed in this paper is based on generating a database of artificial accelerograms, with response spectra closely compatible with the EC8 design response spectra using SeismoArtif Software [38]. In this paper, the Artificial Accelerograms are designed to match the EC8 response spectra with characteristics: ground type C, spectral acceleration 0.36 g and spectrum type I.

In Figure 3.A-B, an Artificial Accelerogram is presented, using the calculation method Artificial Accelerogram Generation and Adjustment, along with its acceleration response spectrum. In Figure 3.C, a comparison of the mean acceleration response spectrum of 30 Artificial Accelerograms with the EC8 design response spectrum is presented. An accurate match is observed. More specifically, the percentage deviation is under *10%* in the range of periods from *0.2* to *2* sec, which is of actual concern.

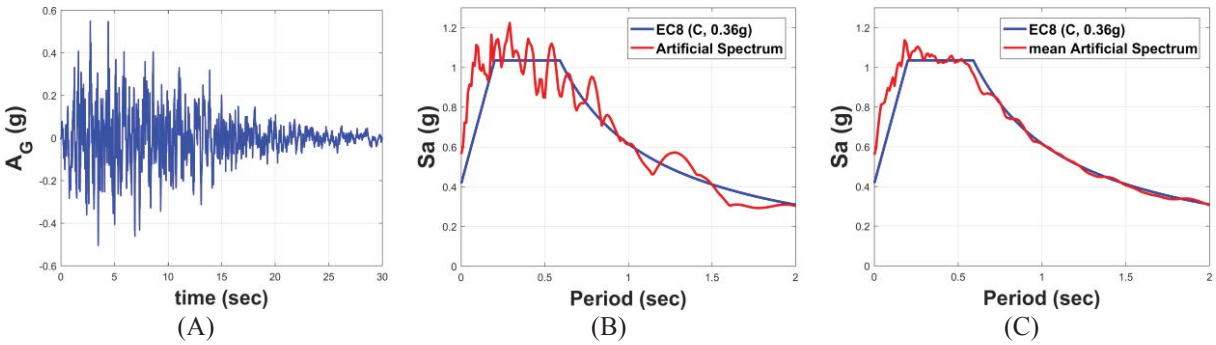

Figure 3. (A) Artificial Accelerogram, (B) response spectrum of Artificial Accelerogram and (C) mean Artificial acceleration response spectrum of 30 Artificial Accelerograms compared to the EC8 response spectrum.

3.2 Evaluation of optimization constraints and limitations

The design of the proposed control strategy must be efficient and realistic at the same time. For this reason, proper constraints that refer to the structural dynamic responses must be applied. More specifically, the system is subjected to 30 Artificial Accelerograms generated according to section 3.1. The relative structure displacement is set as the objective function (mean of 30 maximum responses). In order to better observe the efficiency of the proposed configuration, an acceleration filter is placed. Therefore, each set of optimized parameters of the extended KDamper refers to the maximum structure acceleration, expressed as a percentage of mean PGA. The mean PGA of the 30 Artificial Accelerograms of the database is *0.519g*. Furthermore, the given parameters of the system with the EKD, i.e. the additional mass m_D and the stability factors ε_N, ε_P, and ε_R, as well as the limits of the free design variables sought in the optimization problem, f_0, k_N, c_{DOWN} and c_{UP}, must be within reasonable technological capabilities in order for design to be realistic. In particular:

i. In the previous work of KDamper [17–22], the stability factor ε_N that relates to the variation of the negative stiffness element k_N, is taken as *5%*. In this paper, a variation in all stiffness elements is taken into account, making the design of the proposed vibration absorption concept pretty conservative, since all the stability factors ε_N, ε_P and ε_R are selected as *10%*.
ii. The purpose of this design is to implement the proposed control strategy for seismic protection of structures. Since KDamper can be implemented in the bases of structures, there are no strict limitations regarding the additional mass. According to the previous work of KDamper implemented as an Absorption Base (KDAB) in [30–33,35], a *5%* additional mass is efficient and realistic.
iii. The stiffness elements must be within reasonable technological capabilities. The negative stiffness element k_N, in the proposed configuration of EKD, is realized with pre-compressed springs. Based on previous indicative designs of KDamper with pre-compressed springs by Antoniadis et al. [20] and Kapasakalis et al. [34] (in Greek), for a total superstructure mass of *300 tn*, a realistic value of k_N is *-34171 kN/m*. In this paper, the negative stiffness element is set at least *50%* lower. The same reduction applies to the rest of the stiffness elements, k_R, and k_P.
iv. The damping coefficients maximum value is set *600 kNs/m* for the whole configuration, therefore common linear damping devices can be used.
v. The negative stiffness element stroke ($X_{S\text{-}D}$) is set as a constraint, with an upper limit that of *12 cm*, which based on previous work of Kapasakalis et al. [34] proves to be a realistic value for the design of the negative stiffness element with pre-compressed springs.

Finally, the limits of the free design variables are: 1) the nominal KDamper frequency f_0 (*Hz*) [*0.15 1.5*], 2) the negative stiffness element k_N (*kN/m*) [*-15000 0*] and 3, 4) the damping coefficients c_{DOWN} and c_{UP} (*kNs/m*) [*1 600*].

4 DYNAMIC PERFORMANCE

4.1 Optimization curves

Based on the previous, the set of optimized parameters, for a reference structure mass of *300 tn* is presented in Table 1. Each set of optimized parameters refers to the maximum structure acceleration. The extended KDamper (EKD) with Acceleration Filter as a percentage of PGA will be referred hereafter as EKD-*AF (%)*. The system dynamic responses (mean of 30 max values) of the proposed vibration absorption system (EKD) are presented in Figure 4.

Acceleration Filter, *AF*	f_0 (*Hz*)	k_N (*kN/m*)	k_P (*kN/m*)	k_R (*kN/m*)	C_{UP} (*kNs/m*)	C_{DOWN} (*kNs/m*)
30	0.3965	-5815.3	34587	8946	581.3	473.8
40	0.377	-4145.4	16601	7292	590.8	224.4
50	0.664	-9246.7	26575	19664	541.3	91.1
60	0.7287	-8909.3	21968	21591	571.9	262.6
70	0.9857	-14857	34747	38038	517.8	115.6
80	1.02	-12440	25887	36844	577.8	21.5

Table 1: Set of optimized parameters following the procedure described in section 3.2.

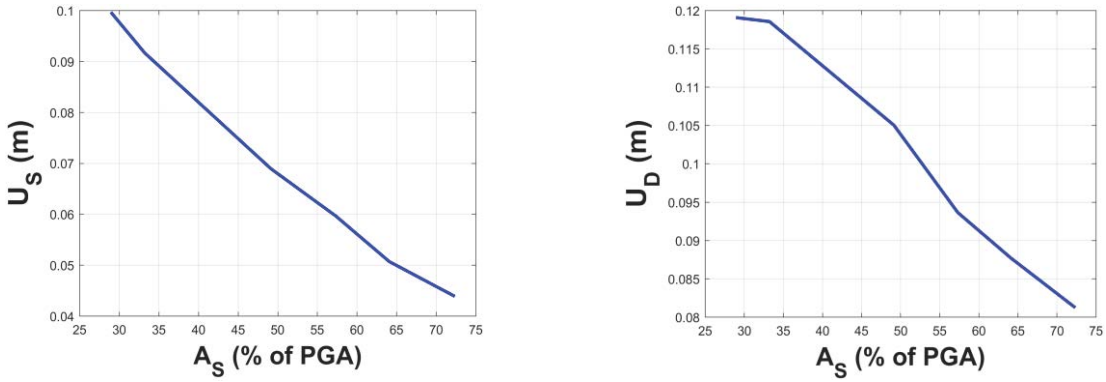

(A) (B)

Figure 4: (A) Structure relative displacement and (B) negative stiffness element stroke displacement maximum values over the structure absolute acceleration expressed as a percentage of the mean PGA (Acceleration Filter).

Furthermore, the EKD is compared with the previous optimal design of KDamper, as presented in Kapasakalis et al. [35]. For this reason, two sets of parameters of each concept, that present similar results, in terms of the structure's main dynamic responses, are selected and compared in Table 2.

Set #	System	A_S (*m/sec2*)	% (reduction)	U_S (*m*)	$U_{N.S.}$ (*m*) NS Stroke	ε_i (%)
Set #1	EKD	1.725	66.76	0.092	0.118	$\varepsilon_{N,P,R}=10$
	KDamper in [35]	2.085	59.83	0.093	0.363	$\varepsilon_N=5$
Set #2	EKD	3.755	27.65	0.0439	0.0812	$\varepsilon_{N,P,R}=10$
	KDamper in [35]	3.692	28.86	0.0379	0.163	$\varepsilon_N=5$

Table 2: Comparison of the SDOF system implemented with KDamper, designed in Kapasakalis et al. [35] and EKD proposed in this paper.

4.2 Time histories

In order to observe the efficiency of the EKD, it is compared with a conventional base isolated (BI) system with a damping ratio of *5%*. The BI system is designed to have a natural frequency of *0.4 Hz*. Comparative results between the conventional base isolated system (BI) and the EKD-*30* and EKD-*70*, are presented in Figure 5. The presented time histories relate to an Artificial seismic excitation.

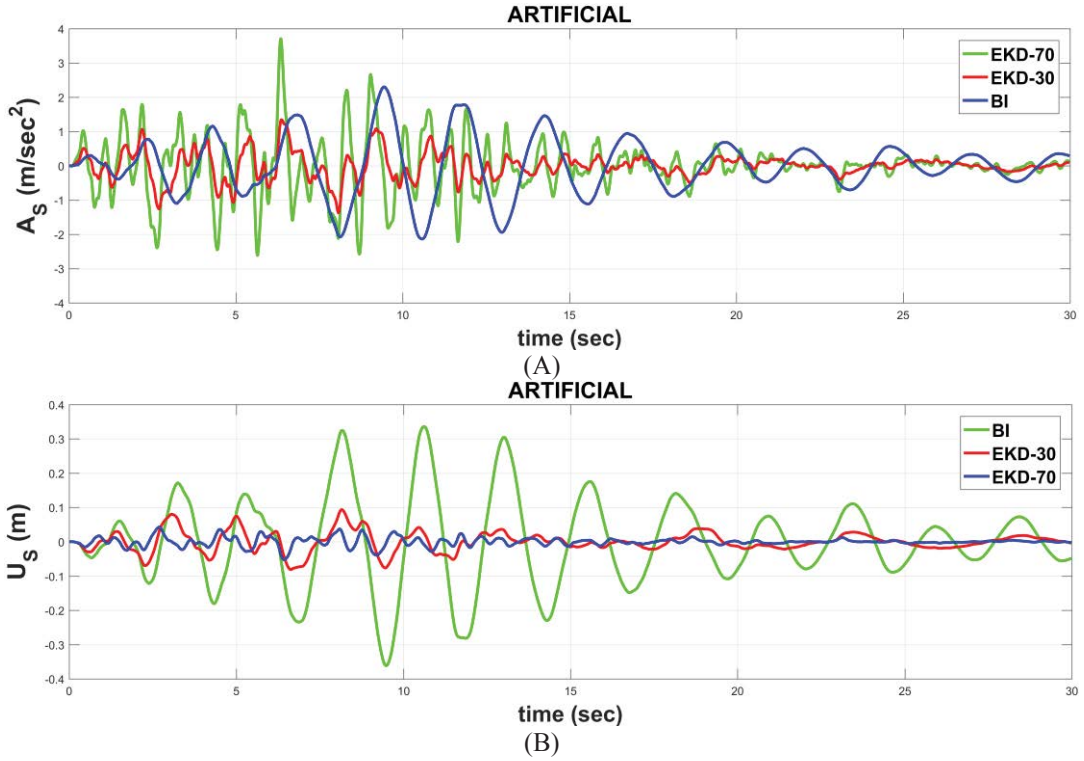

Figure 5: Comparative results, in terms of (A) structure's absolute acceleration (m/sec^2) and (B) structure relative displacement, between the BI, EKD-30, and EKD-70 systems, for an Artificial Accelerogram.

5 EFFECT OF DETUNING

It is important to analyze how the main system responses vary by shifting the optimal EKD parameters from their respective values (effect of detuning). We expect that as the system parameters depart from their optimal values (Table 1), the effectiveness of the proposed passive vibration control strategy decreases. In Figure 6, we observe the effect of detuning of the EKD-*50* set of optimized parameters. The stiffness elements of the EKD are designed to have a *10%* variation as described in section 3 of the paper. In Figures 6.A-C, the system main responses are depicted in a range of *20%* variation of the optimal stiffness elements. Sensitivity analysis reveals that the variation of the stiffness elements k_N and k_R have a greater influence on the system responses, up to *30%*, compared to k_D (up to *10%*). In Figures 6.D-E, we observe that the variation of the damping coefficient that is parallel to the negative stiffness element, k_N, presents an increased influence as compared with the camping coefficient parallel with k_D. Finally, the effect of the variation of the additional mass has no significant influence on the system responses.

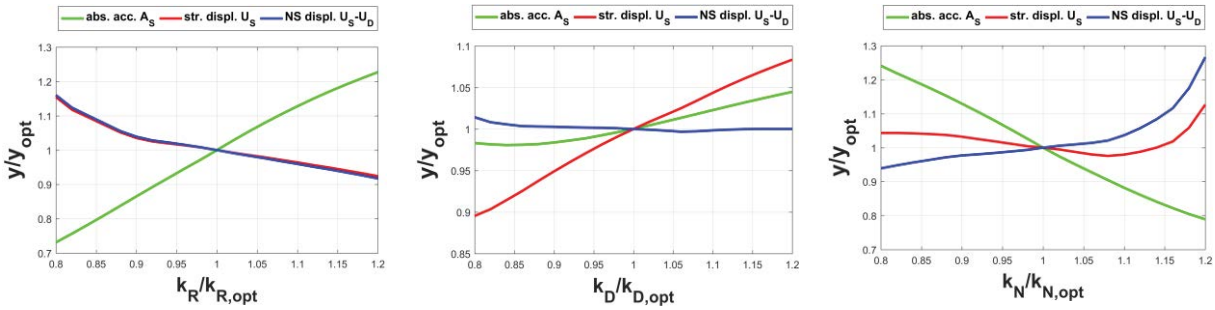

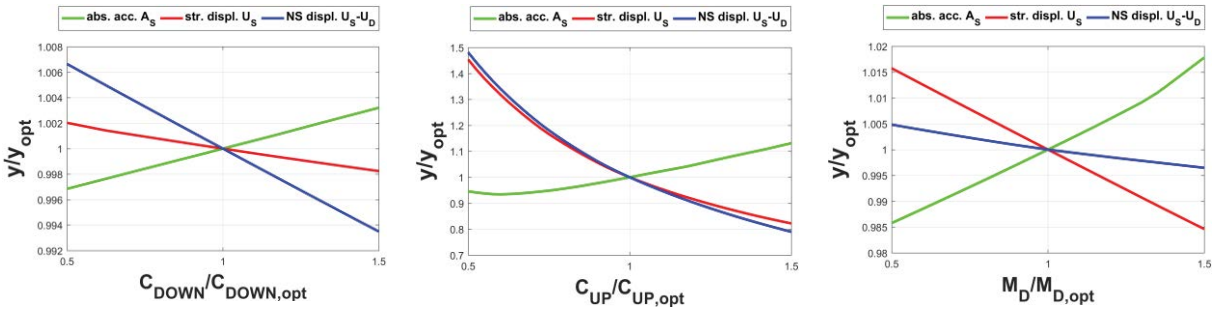

(D) (E) (F)

Figure 6: Sensitivity analysis. Main system responses (mean of 30 max values) by varying the system parameters. (A-C) 20% variation of the stiffness elements and (D-F) 50% variation of the damping coefficients and additional mass.

6 ACKNOWLEDGMENTS

This research has been co-financed by the European Union and Greek national funds through the Operational Program Competitiveness, Entrepreneurship and Innovation, under the call RESEARCH – CREATE – INNOVATE (project code: T1EDK-02827).

European Union
European Structural and Investment Fund
EPAnEK 2014-2020
OPERATIONAL PROGRAMME
COMPETITIVENESS
ENTREPRENEURSHIP
INNOVATION
ΕΣΠΑ 2014-2020
Partnership Agreement 2014 - 2020
Co-financed by Greece and the European Union

7 CONCLUSIONS

In this paper, an extension of the KDamper (EKD) concept is proposed, for implementation as a seismic base absorber. The optimization problem is stated, from which the optimal system parameters are selected. The evaluation of the optimization constraints is based on engineering criteria, from previous indicative designs of the KDamper implemented as an absorption base. In order to better observe the efficiency of the proposed configuration, an acceleration filter is placed as a constraint. Therefore, each set of optimized parameters of the EKD refers to the maximum structure acceleration, expresses as a percentage of PGA. The EKD is designed according to seismic design codes, therefore a database of artificial accelerograms, compatible with the EC8 response spectra is generated, to define the acceleration filter (AF). Sensitivity analysis is performed, and the effect of detuning is discussed accordingly. A comparison with a conventional base isolated system is then made in order to prove the efficiency of the proposed seismic base absorber (EKD). Finally, the following conclusive comments can be made:

- EKD presents similar/marginally superior results as compared to the previously optimal KDamper concept [35], while it foresees variation in all stiffness elements (ε_N, ε_P, ε_R=*10%*), while in the KDamper concept only the negative stiffness element (ε_N=*5%*) is examined. Furthermore, the negative stiffness element stroke is reduced by *50-67%*, which is critical for the whole configuration design.
- The evaluation of the optimization constraints is based on engineering criteria and render the implementation of the EKD feasible. As compared with previous indicative designs of KDamper, all the stiffness elements are at least *50%* lower. Thus, the realization of the additional mass, the damping coefficients, and the stiffness elements are within reasonable technological capabilities.

- Based on the performed sensitivity analysis, the EKD is not vulnerable to detuning.
- The EKD implemented in a SDoF system manages to retain the structure absolute acceleration at acceptable levels (base on the selected design Acceleration Filter) while at the same time the structure relative displacement is significantly low, as compared to conventional and highly damped base isolation systems (*50%-80%* lower).

REFERENCES

1. Carrella A, Brennan MJ, Waters TP. Static analysis of a passive vibration isolator with quasi-zero-stiffness characteristic. *Journal of Sound and Vibration* 2007; **301**(3–5): 678–689. DOI: 10.1016/j.jsv.2006.10.011.
2. Nagarajaiah S, Pasala DTR, Reinhorn A, Constantinou M, Sirilis AA, Taylor D. Adaptive Negative Stiffness: A New Structural Modification Approach for Seismic Protection. *Advanced Materials Research* 2013; **639–640**: 54–66. DOI: 10.4028/www.scientific.net/amr.639-640.54.
3. DeSalvo R. Passive, Nonlinear, Mechanical Structures for Seismic Attenuation. *Journal of Computational and Nonlinear Dynamics* 2007; **2**(4): 290. DOI: 10.1115/1.2754305.
4. Iemura H, Pradono MH. Advances in the development of pseudo-negative-stiffness dampers for seismic response control. *Structural Control and Health Monitoring* 2009; **16**(7–8): 784–799. DOI: 10.1002/stc.345.
5. Sarlis AA, Pasala DTR, Constantinou MC, Reinhorn AM, Nagarajaiah S, Taylor DP. Negative Stiffness Device for Seismic Protection of Structures. *Journal of Structural Engineering* 2012; **139**(7): 1124–1133. DOI: 10.1061/(asce)st.1943-541x.0000616.
6. Pasala DTR, Sarlis AA, Nagarajaiah S, Reinhorn AM, Constantinou MC, Taylor D. Adaptive Negative Stiffness: New Structural Modification Approach for Seismic Protection. *Journal of Structural Engineering* 2013; **139**(7): 1112–1123. DOI: 10.1061/(ASCE)ST.1943-541X.0000615.
7. Sarlis AA, Pasala DTR, Constantinou MC, Reinhorn AM, Nagarajaiah S, Taylor DP. Negative Stiffness Device for Seismic Protection of Structures: Shake Table Testing of a Seismically Isolated Structure. *Journal of Structural Engineering* 2016. DOI: 10.1061/(asce)st.1943-541x.0001455.
8. Sun T, Lai Z, Nagarajaiah S, Li HN. Negative stiffness device for seismic protection of smart base isolated benchmark building. *Structural Control and Health Monitoring* 2017. DOI: 10.1002/stc.1968.
9. Wang M, Sun F fei, Jin H jian. Performance evaluation of existing isolated buildings with supplemental passive pseudo-negative stiffness devices. *Engineering Structures* 2018. DOI: 10.1016/j.engstruct.2018.09.049.
10. Shen Y, Peng H, Li X, Yang S. Analytically optimal parameters of dynamic vibration absorber with negative stiffness. *Mechanical Systems and Signal Processing* 2017. DOI: 10.1016/j.ymssp.2016.08.018.
11. Qin L, Yan W, Li Y. Design of frictional pendulum TMD and its wind control effectiveness. *Journal of Earthquake Engineering and Engineering Vibration* 2009; **29**(5): 153–157.

12. McNamara RJ. Tuned Mass Dampers for Buildings. *Journal of the Structural Division* 1977; **103**(9): 1785–1798.

13. Luft RW. Optimal Tuned Mass Dampers for Buildings. *Journal of the Structural Division* 1979; **105**(12): 2766–2772.

14. Taniguchi T, Der Kiureghian A, Melkumyan M. Effect of tuned mass damper on displacement demand of base-isolated structures. *Engineering Structures* 2008; **30**(12): 3478–3488. DOI: 10.1016/j.engstruct.2008.05.027.

15. Tsai HC. The effect of tuned-mass dampers on the seismic response of base-isolated structures. *International Journal of Solids and Structures* 1995; **32**(8–9): 1195–1210. DOI: 10.1016/0020-7683(94)00150-U.

16. Palazzo B, Petti L, de Ligio M. Response of base isolated systems equipped with tuned mass dampers to random excitations. *Journal of Structural Control* 1997; **4**(1): 9–22. DOI: 10.1002/stc.4300040105.

17. Xiang P, Nishitani A. Optimum design for more effective tuned mass damper system and its application to base-isolated buildings. *Structural Control and Health Monitoring* 2014; **21**(1): 98–114. DOI: 10.1002/stc.1556.

18. Hashimoto T, Fujita K, Tsuji M, Takewaki I. Innovative base-isolated building with large mass-ratio TMD at basement for greater earthquake resilience. *Future Cities and Environment* 2015. DOI: 10.1186/s40984-015-0007-6.

19. Antoniadis I, Chronopoulos D, Spitas V, Koulocheris D. Hyper-damping properties of a stiff and stable linear oscillator with a negative stiffness element. *Journal of Sound and Vibration* 2015. DOI: 10.1016/j.jsv.2015.02.028.

20. Antoniadis IA, Kanarachos SA, Gryllias K, Sapountzakis IE. KDamping: A stiffness based vibration absorption concept. *JVC/Journal of Vibration and Control* 2018; **24**(3): 588–606. DOI: 10.1177/1077546316646514.

21. Antoniadis I.A., Kapasakalis, K.A., Sapountzakis EJ. Isolation or Damping? A Soil-dependent approach based on the KDamper concept. *Proceedings of the 2nd International Conference on Natural Hazards & Infrastructure (ICONHIC 2019)*, 2019.

22. Sapountzakis, E.J., Kapasakalis, K.A. AIA. Negative Stiffness Elements in Seismic Isolation of Bridges. *Proceedings of the 2nd International Conference on Natural Hazards & Infrastructure (ICONHIC 2019)*, 2019.

23. Kapasakalis KA, Alamir CHT, Antoniadis IA, Sapountzakis EJ. Frequency Base Design of the KDamper Concept for Seismic Isolation of Bridges. *Proceedings of the 14th International Conference on Vibration Problems (ICOVP 2019)*, 2019.

24. Bollano, P-O.N., Kapasakalis, K.A., Sapountzakis, E.J. AIA. Design and Optimization of the KDamper Concept for Seismic Protection of Bridges. *Proceedings of the 14th International Conference on Vibration Problems (ICOVP 2019)*, 2019.

25. Kapasakalis, K.A., Antoniadis I.A. SAE. Implementation of the KDamper Concept for Seismic Protection of Bridges. *Proceedings of the 14th International Conference on Vibration Problems (ICOVP 2019)*, 2019.

26. Kapasakalis, K.A., Sapountzakis, E.J., Antoniadis IA. Implementation of the KDamper Concept to Wind Turbine Towers. *Proceedings of the 6th International Conference on Computational Methods in Structural Dynamics and Earthquake Engineering*

(COMPDYN 2017), 2017.

27. Kapasakalis, K.A., Sapountzakis, E.J., Antoniadis IA. Optimal Design of the KDamper Concept for Structures on Compliant Supports. *Proceedings of the 16th European Conference on Earthquake Engineering (16ECEE 2018)*, 2018.
28. Kapasakalis, K.A., Sapountzakis, E.J., Antoniadis IA. KDamper Concept in Seismic Isolation of Multi Storey Building Structures. *Proceedings of the 9th GRACM International Congress on Computational Mechanics (9GRACM 2018)*, 2018.
29. Kapasakalis, K.A., Sapountzakis, E.J., Antoniadis IA. Kdamper concept in seismic isolation of building structures with soil structure interaction. *Proceedings of the 13th International Conference on Computational Structures Technology (CST2018)*, 2018.
30. Kapasakalis, K.A., Antoniadis, I.A., Sapountzakis EJ. Control of Multi Storey Building Structures with a New Passive Vibration Control System Com-bining Base Isolation with KDamper. *Proceedings of the 7th International Conference on Computational Methods in Structural Dynamics and Earthquake Engineering (COMPDYN 2019)*, 2019.
31. Kapasakalis, K.A., Antoniadis, I.A., Sapountzakis EJ. Implementation of the KDamper Concept for Base Isolation to a Typical Concrete Building Structure. *Proceedings of the 12th International Congress on Mechanics (12HSTAM2019)*, 2019.
32. Kapasakalis, K.A., Antoniadis, I.A. SEJ. KDamper Concept for Base Isolation and Damping of High-Rise Building Structures. *Proceedings of the 14th International Conference on Vibration Problems (ICOVP 2019)*, 2019.
33. Antoniadis, I.A., Kapasakalis, K.A., Sapountzakis EJ. Advanced Negative Stiffness Absorbers for the Seismic Protection of Structures. *Proceedings of the International Conference on Key Enabling Technologies 2019 (KEYTECH2019)*, 2019. DOI: https://doi.org/10.1063/1.5123704.
34. Kapasakalis, K.A., Antoniadis, I.A, Sapountzakis EJ. Novel Vibration Absorption Systems with Negative Stiffness Elements for the Seismic Protection of Structures. *4th National Conference on Earthquake Engineering and Engineering Seismology (Hellenic Association for Earthquake Engineering - HAEE / ETAM)*, 2019.
35. Kapasakalis, K.A., Antoniadis, I.A., Sapountzakis EJ. Performance Assessment of the KDamper as a Seismic Absorption Base. *Structural Control and Health Monitoring* 2019. DOI: 10.1002/stc.2482.
36. Kapasakalis KA, Antoniadis IA, Sapountzakis EJ. Implementation of the KDamper as a Stiff Seismic Absorption Base: A Preliminary Assessment. *Vibration and Acoustics Research Journal* 2019; **1**(1).
37. Zong Woo Geem, Joong Hoon Kim, Loganathan GV. A New Heuristic Optimization Algorithm: Harmony Search. *SIMULATION* 2001; **76**(2): 60–68. DOI: 10.1177/003754970107600201.
38. Seismosoft [2018]. SeismoArtif - A computer program for generating artificial earthquake accelerograms matched to a specific target response spectrum 2018. http://www.seismosoft.com.

EURODYN 2020
XI International Conference on Structural Dynamics
M. Papadrakakis, M. Fragiadakis, C. Papadimitriou (eds.)
Athens, Greece, 23–26 November 2020

DYNAMIC ANALYSIS OF AN ACTIVE ISOLATION MOUNT USING FEEDFORWARD AND FEEDBACK CONTROL SCHEMES

Grigorios M. Chatziathanasiou[1], **Nikolaos A. Chrysochoidis**[2], **and Dimitris A.Saravanos**[3]

[1,2,3]Department of Mechanical Engineering and Aeronautics, University of Patras, Rion-Patras, Greece
e-mail: grigoris.chatziathanasiou@gmail.com, nchr@mech.upatras.gr, saravanos@mech.upatras.gr

Keywords: Piezoelectric Active mount, Isolation System, Transmissibility

Abstract. *This paper presents the simulation of dynamic analysis and performance of a 2-Degree-of-Freedom active vibration isolation system. Vibration isolation is studied on both feedforward and feedback schemes, exploiting their transmissibility reduction capabilities and different effects to the system dynamics. The 2-DoF system is mounted on the isolated structure of interest, while the disturbance is induced through the secondary structure. The two structures are connected with an active mount, where a passive spring-damper element and a piezoelectric actuator are parallelly placed. In feedforward approach, the optimal controller input is calculated a-priori and offline, while in the feedback scheme, LQR and Proportional-Derivative control algorithms are tested and compared. The results demonstrate great vibration suppression capabilities to the structure of interest, as both force transmissibility and displacement are considerably degraded.*

1 INTRODUCTION

Engine induced vibration in means of transportation influences not only the lifetime and reliability of the structure, but also the user comfort and satisfaction. In order to suppress the unwanted vibrations transmitted from the engine to the cabin structure through the connecting mounts, various methods have been developed, which increase the mount isolating capabilities. Conventional passive mounts have been widely used in the past, however their frequency compensation limitations and considerable addition of mass [1] has led to the development of active mounts. Active mounts introduce new requirements to the existing isolation system, such as sensors and external energy in order to induce the appropriate actuating input, however their ability to suppress vibration transmissions at all frequencies have made them very appealing. Among the various types of actuators used in antivibration mounts, such as electromagnetic [2] and hydraulic actuators [3], piezoelectric actuators have gathered most of the scientific interest due to their high force generation, reliability, quick response and minimum energy consumption [4].

For the active vibration isolation to be efficient, the vibration control researcher must choose between various control techniques, including adaptive feedforward control[5], such as LMS, RLS and FxLMS [6], feedback control, such as the Delayed Resonator [7], PID control [8], [9], and LQR [10], and their combinations [11]. Although both feedforward and feedback control schemes have been widely investigated and tested, little literature has been dedicated to exploiting their different interference with the systems dynamics. Moreover, the theoretical approach of vibration transmissibility of 2-DoF vibrating systems has been covered by [12], however no control scheme was taken under consideration. For these reasons, this paper deals with the simple 2-DoF isolation system and explores how the different control approaches affect the system dynamics and transmissibility. For the feedforward scheme, the optimal controller input is calculated a priori and offline, while for the demonstration of feedback control, LQR and Proportional-Derivative control algorithms are taken under consideration. The 2-DoF model is presented in Section 2, while in Section 3, the feedforward and feedback control designs are presented. The different effects of the control algorithms to the system dynamics and disturbance rejection capabilities are illustrated and discussed in Section 4. Section 5 summarizes the main concluding remarks of this work.

2 DYNAMIC 2-DOF MODEL

The 2-DoF model is illustrated in Figure 1a and is simulating a fuselage-engine system, where the isolation system is mounted between the main mass m_1 (fuselage/structure of interest) and the secondary mass m_2 (engine), while the disturbance is induced through the secondary mass m_2 (engine). The active mount connecting the two masses is a system that consists of a passive component of a spring-damper capable to operate solely, and the active part using a linear piezoelectric actuator. The active part operates synergistically with the passive one and is installed parallel to the passive components. The actuator is assumed to have zero damping and contributes only to the stiffness of the mount, introducing an actuating force to the system through the converse piezoelectric effect: $F_{act} = \bar{e}\Delta\varphi$, where $\bar{e}$ is the piezoelectric stress coefficient of the actuator and $\Delta\varphi$ the electric potential applied to the actuator [13], as shown in Figure 1b.

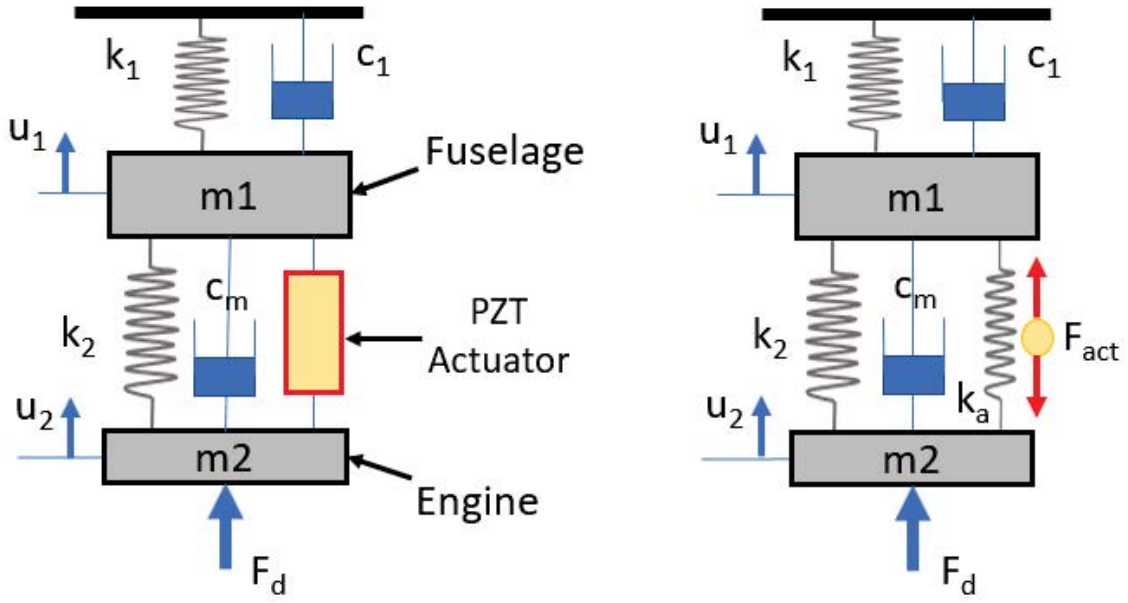

Figure 1: 2-DoF isolation model

Applying equations of motion to each degree of freedom, the dynamic equation that describes the 2-DoF system is presented as follows:

$$\begin{bmatrix} m_1 & 0 \\ 0 & m_2 \end{bmatrix}\begin{Bmatrix} \ddot{u}_1 \\ \ddot{u}_2 \end{Bmatrix}+\begin{bmatrix} c_1+c_m & -c_m \\ -c_m & c_m \end{bmatrix}\begin{Bmatrix} \dot{u}_1 \\ \dot{u}_2 \end{Bmatrix}+\begin{bmatrix} k_1+k_m & -k_m \\ -k_m & k_m \end{bmatrix}\begin{Bmatrix} u_1 \\ u_2 \end{Bmatrix}=\begin{Bmatrix} \bar{e}\Delta\varphi \\ F_d-\bar{e}\Delta\varphi \end{Bmatrix} \quad (1)$$

where m_1, m_2 are the main and secondary mass, respectively, $u_1, u_2, \dot{u}_1 \dot{u}_2 \ddot{u}_1 \ddot{u}_2$ are the displacements, velocities, and accelerations of m_1, m_2 respectively, k_1, c_1 are the stiffness and viscous damping of m_1, $k_m = k_2 + k_a$ is the equivalent mount stiffness with k_2 representing the stiffness of the passive mount and k_a the stiffness of the actuator, c_m is the passive mount viscous damping and F_d is the disturbance force. In our case the disturbance is introduced from the engine operation.

Transforming (1) to the frequency domain, we derive:

$$\begin{bmatrix} k_1+k_m+(c_1+c_m)j\omega-m_1\omega^2 & -k_m-c_m j\omega \\ -k_m-c_m j\omega & k_m+c_m j\omega-m_2\omega^2 \end{bmatrix}\begin{Bmatrix} U_1 \\ U_2 \end{Bmatrix}=\begin{Bmatrix} \bar{e}\Delta\varphi \\ F_d-\bar{e}\Delta\varphi \end{Bmatrix} \quad (2)$$

where ω is the angular frequency, U_1, U_2 are the amplitudes of the m_1, m_2 displacements at the corresponding ω and $j = \sqrt{-1}$ is the imaginary number.

The force transmissibility is defined as:

$$T_F(\omega)=\frac{F_1(\omega)}{F_d(\omega)} \quad (3)$$

where $F_1(\omega)$ is the transmitted force to the isolated mass of interest for the frequency ω and is equal to:

$$F_1(\omega)=k_m[u_2(\omega)-u_1(\omega)]+c_m[\dot{u}_2(\omega)-\dot{u}_1(\omega)]-k_1u_1(\omega)-c_1\dot{u}_1(\omega) \quad (4)$$

when no control is applied and

$$F_1(\omega) = k_m[u_{2,contr}(\omega) - u_{1,contr}(\omega)] + c_m[\dot{u}_{2,contr}(\omega) - \dot{u}_{1,contr}(\omega)] \\ -k_1 u_{1,contr}(\omega) - c_1 \dot{u}_{1,contr}(\omega) + F_{act}(\omega) \quad (5)$$

when control is applied. All the X_{contr} terms refer to the controlled values which differ from the baseline results for each angular frequency, due to the existence of $F_{act}(\omega)$.

The model parameters used, are presented in Table 1:

Parameter	Term	Value
Mass [kg]	m_1	30
	m_2	7
Damping [N*s/m]	c_1	143
	c_2	18
Stiffness [n/m]	k_1	$150*10^4$
	k_2	$5.2*10^4$
	k_a	$8.2*10^4$
Disturbance [N]	F_d	5
Piezoelectric Stress Coefficient [N/V]	$\bar{e}$	1

Table 1: System Parameters

3 DESIGN OF CONTROLLER

The control is implemented in State Space. The State Space representation of the isolating system (Plant) is:

$$\dot{x} = Ax + Bu \\ y = Cx \quad (6)$$

where $x = [u_1 \ u_2 \ \dot{u}_1 \ \dot{u}_2]'$: the state vector,
$\dot{x}$: time derivative of x,
u: system input F_{act},
y: system output

$$A = \begin{bmatrix} 0 & 0 & 1 & 0 \\ 0 & 0 & 0 & 1 \\ -\frac{k_1 + k_m}{m_1} & \frac{k_m}{m_1} & -\frac{c_1 + c_m}{m_1} & \frac{c_m}{m_1} \\ \frac{k_m}{m_2} & -\frac{k_m}{m_2} & \frac{c_m}{m_2} & -\frac{c_m}{m_2} \end{bmatrix}$$: the state matrix, $$B = \begin{bmatrix} 0 \\ 0 \\ \frac{1}{m_1} \\ -\frac{1}{m_2} \end{bmatrix}$$: the input matrix

C : the output matrix that depends on the control scheme.

3.1 Feedforward Control

The Feedforward Control scheme is presented in Figure 2, where $G_d = {}^1/_{m_2}$.

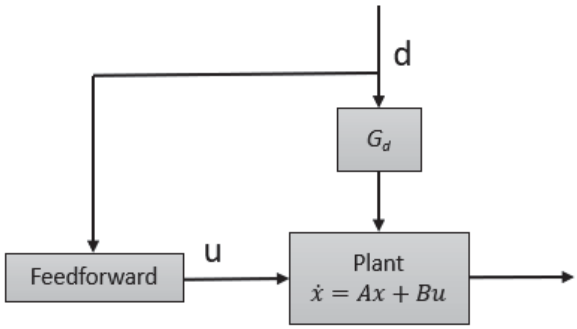

Figure 2: Feedforward Control

In case of a known disturbance d and considering that the control system operates in steady state conditions (i.e. an aircraft or yacht traveling with cruise speed), it is reasonable to compute, offline, a feedforward isolating signal in advance and apply it at an appropriate time [14]. Assuming that, due to the operation of the active force, the remaining disturbance on the main mass is negligible ($U_1 = 0$), the optimal $F_{act} = \bar{e}\Delta\varphi$ and corresponding U_2 can be found for each given combination of ω and F_d by (7).

$$\begin{bmatrix} k_m + c_m j\omega & 1 \\ k_m + c_m j\omega - m_2\omega^2 & 1 \end{bmatrix} \begin{Bmatrix} U_2 \\ \bar{e}\Delta\varphi \end{Bmatrix} = \begin{Bmatrix} 0 \\ F_d \end{Bmatrix} \tag{7}$$

We are performing a forced response of the system (Figure 1), solving the system of Equation (7) for each frequency step in the range of 15-50Hz for a periodic disturbance $F_d = 5sin\omega t$. It can be easily understood that the terms of mass, stiffness and viscous damping corresponding to the main structure do not affect the controller input. Variation of the required actuation Force F_{act} as a function of disturbance frequency is presented in Figure 3, where $f_{n1} = 20.6Hz$ and $f_{n2} = 37.9Hz$ are the 2-DoF system eigenfrequencies. The main observation is that the required actuation force is not related to the system modal characteristics.

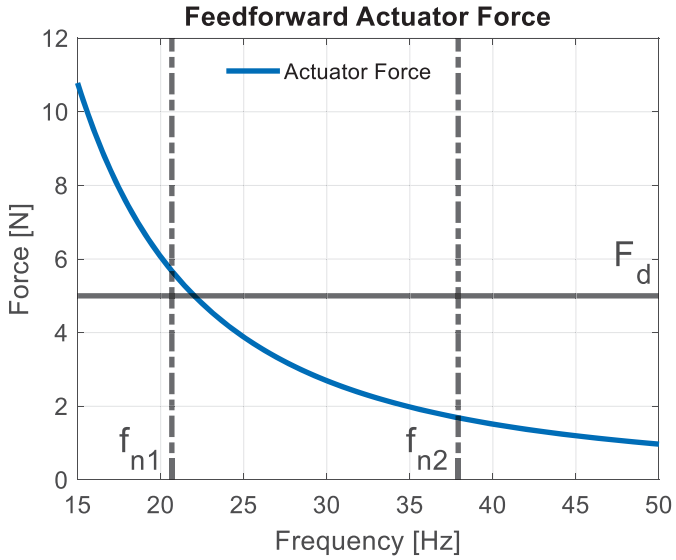

Figure 3: Optimal feedforward input

3.2 Feedback Control

3.2.1 LQR Controller

The Linear Quadratic Regulator Control scheme is presented in Figure 4:

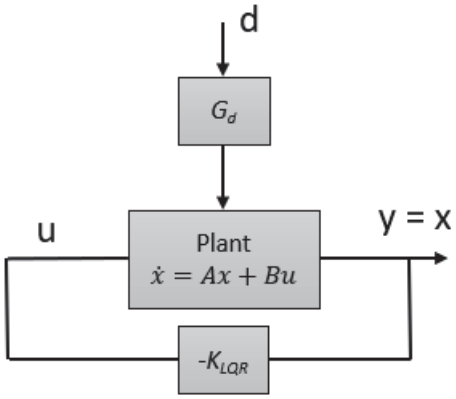

Figure 4: LQR Control

The presented isolation system is controllable: *rank(Ć)=4*, where $\acute{C}$ is the controllability matrix, so if all State Space variables are measured: $C = [1\ 1\ 1\ 1]$, an optimal controller K_{LQR} can be found, utilizing the LQR theory. The term "optimal" here, refers to the minimization of the cost function:

$$J = \int_{t_0}^{t_1} (x^T Q x + u^T R u) dt \tag{8}$$

where *Q* and *R* are positive-definite matrices which represent the weight that penalizes the state vector *x* and the energy cost for input *u*, respectively. The optimal controller K_{LQR} is given by:

$$K_{LQR} = R^{-1} B^T P \tag{9}$$

where the matrix P is found by solving Riccati's equation:

$$A^T P + PA - PBR^{-1} B^T P + Q = 0 \tag{10}$$

The control law that minimizes the cost function *J* is: $u = -K_{LQR} x$, so the State Space expression of the system with the external disturbance will be:

$$\dot{x} = Ax + Bu + G_d d = A(x - BK_{LQR})x + G_d d \tag{11}$$

Moreover, it is assumed that the energy cost of the electric potential is subordinate, so 2 Cases with small weights were taken under consideration: *Case 1: R = 0.001, Case 2: R = 0.0001*.

The vibration reduction of the main mass is more important from the one of the secondary mass, so the state variable weights for *Cases 1 and 2* are chosen as:

$$Q = \begin{bmatrix} 10 & 0 & 0 & 0 \\ 0 & 10 & 0 & 0 \\ 0 & 0 & 1 & 0 \\ 0 & 0 & 0 & 1 \end{bmatrix}$$

3.2.2 PD Controller

Proportional-Derivative control is implemented as shown in Figure 5:

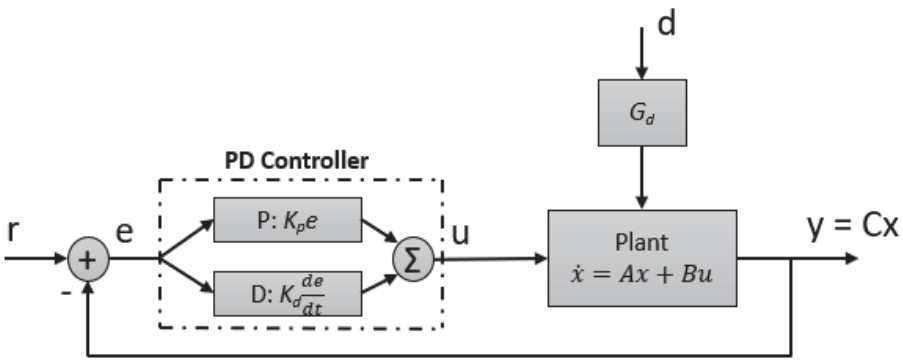

Figure 5: PD Controller

The measured variable here is the displacement of m_1: $u_1 = x_1$, so the output matrix is $C = [1\ 0\ 0\ 0]$. The Integral term from the Proportional-Integral-Derivative PID scheme is neglected, because this term would affect the integral of u_1, which is a parameter with no physical meaning.

The measured output is compared to the reference value r (here $r = 0$) and the error e is calculated and used as input to the PD controller. The output of the controller serves as the isolating input force and is defined as:

$$\begin{aligned} u &= K_p e + K_d \frac{d(e)}{dt} = K_p (r - y) + K_d \frac{d(r - y)}{dt} \\ &= -K_p y - K_d \frac{d(y)}{dt} = -K_p Cx - K_d C\dot{x} \end{aligned} \tag{12}$$

where K_p and K_D denote the proportional and derivative gain, respectively, so the State Space expression of the system with the external disturbance will become:

$$\begin{aligned} \dot{x} &= Ax + Bu + G_d d \\ \dot{x} &= Ax - BK_p Cx - BK_d \dot{x} + G_d d \\ \dot{x}(I + BK_d C) &= (A - BK_p C)x + G_d d \\ \dot{x} &= A'x + B'd \end{aligned} \tag{13}$$

where:

$$\begin{aligned} A' &= (I + BK_d C)^{-1}(A - BK_p C) \\ B' &= (I + BK_d C)^{-1} G_d \end{aligned} \tag{14}$$

are the new state and input matrices, respectively. The selected gains are: $K_p = 2 * 10^6$ and $K_d = -100$.

4 ACTIVE ISOLATION SIMULATION AND RESULTS

The simulation was carried out in the frequency domain. The results reveal the vibration reduction capabilities if the applied disturbance is a harmonic excitation at a specific frequency. In order to compare the change in the system dynamics and vibration reduction capabilities of each control mechanism, the displacements of the two masses and the transmissibility

to the main mass are presented with and without control (baseline). Moreover, in order to extract meaningful deductions both near and away from resonance, the analysis focused on 2 frequencies: (1) near resonance: $f_1 = 21Hz$ and (2) away from resonance: $f_2 = 30Hz$.

4.1 Feedforward Results

The vibration isolation is evident for both targeted frequencies, as shown in Figure 6. Drastic reductions are calculated locally at the frequencies of interest. Near resonance (Figure 6a), both main and secondary mass displacements are heavily reduced, resulting to extreme reduction of transmissibility, as well. The targeted frequency away from resonance (Figure 6b) also demonstrates great vibration isolation capabilities, as both main mass displacement and transmissibility show great reductions. Moreover, the displacement of the secondary mass inducing the vibration, is also degraded. Another important remark is the fact that, each calculated actuation force reduces the transmitted vibration not only exactly on the targeted frequency, but in a bandwidth of at least 10Hz. This is a useful result in case of multi-DoF problems, where the system uncertainty is higher, and the system parameters are not fully known. It is easily understood that the feedforward control, as discussed in Section 3.1, heavily interferes with existing system dynamics, dramatically changing the displacement amplitude, as well as the force transmissibility. The dB reductions of transmissibility for each targeted frequency are shown in table Table 2.

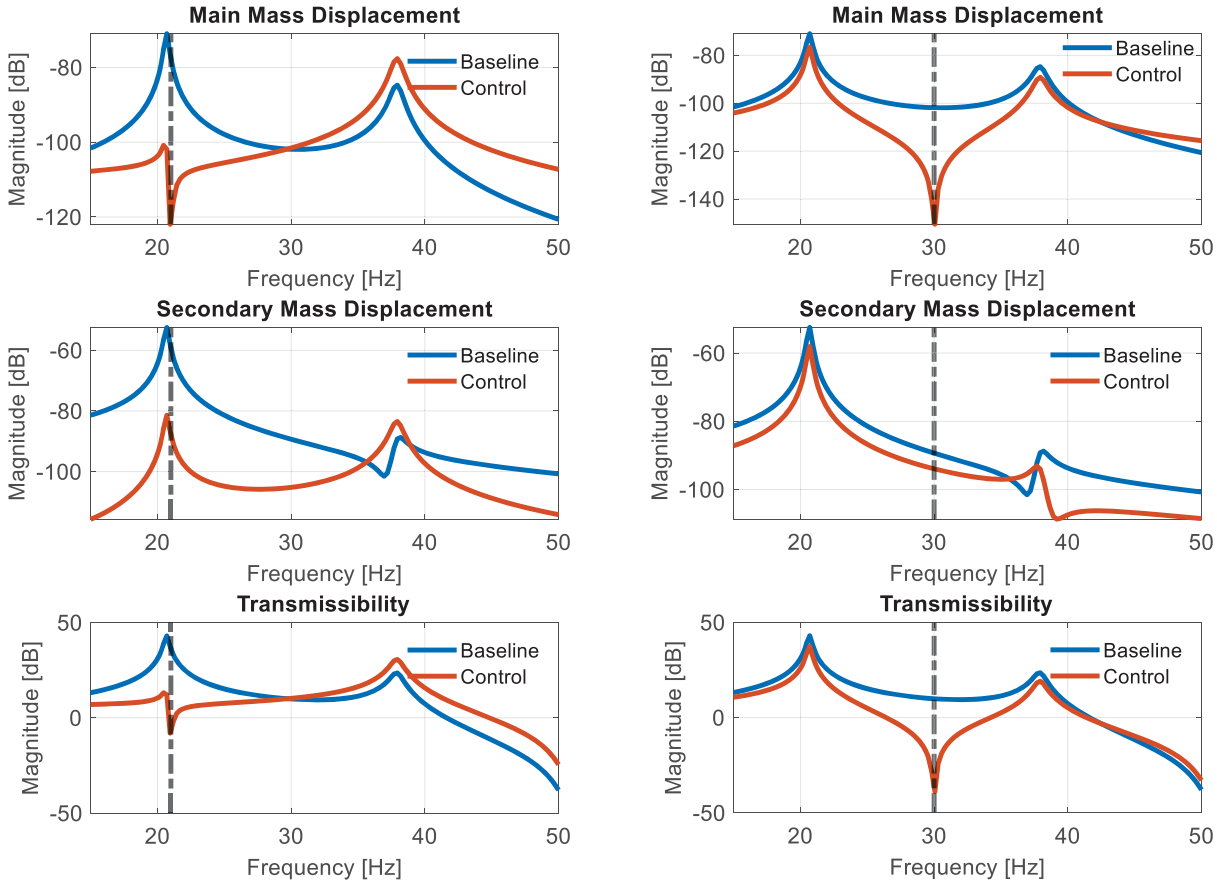

a. Focus on 21Hz

b. Focus on 30Hz

Figure 6: Feedforward Control Results

4.2 Feedback Results

The selected parameters of LQR and PD control influence the existing isolation system dynamics in the way that is illustrated in Figure 7. As shown in Figure 7, both LQR Cases do not seem to satisfactory isolate the structure of interest in the whole frequency bandwidth, except for the resonance. This implies that LQR control slightly changes the system dynamics, mainly adding damping to the resonance, so it may not be appropriate for dynamic isolation applications. Furthermore, to implement LQR control, all state variables must be measured, which is not realistic and might be an impossible task for multi-DOF systems.

From the results of Figure 7, it can also be seen that by choosing appropriate controller gains K_p and K_D, the isolation capabilities of PD control can be satisfactory, especially near resonance. K_p and K_D terms change the stiffness and damping system matrices, respectively, shifting the resonance away from its baseline values. As a result, the displacements of both targeted frequencies are reduced in both masses, using the same gains. The transmissibility is affected analogously, meaning that it appears decreased compared to the baseline. However, reduced performance is recorded compared to the feedforward control. Achieved reductions are summarized in Table 2. The bandwidth of the vibration reduction using the existing values of K_p and K_D is over 25Hz.

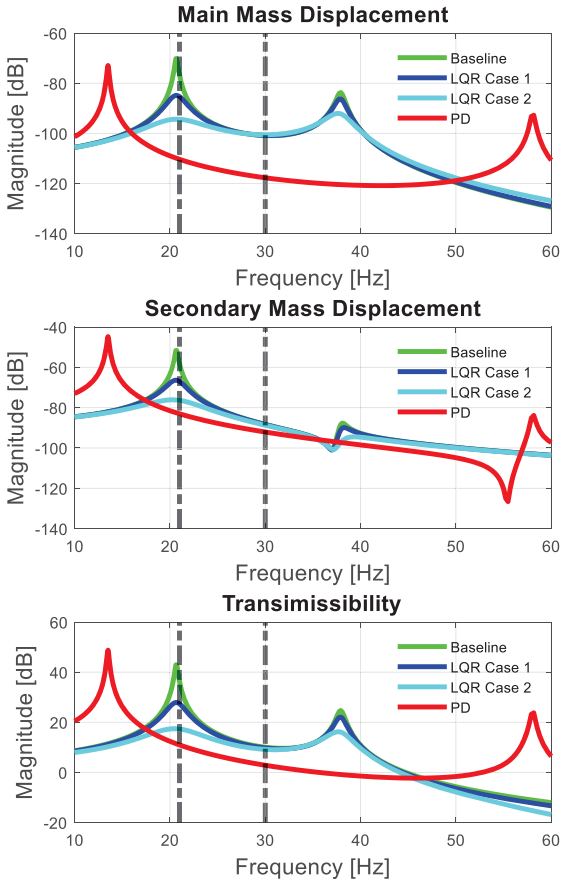

Figure 7: Feedback Control Results

	Control scheme			
	Feedforward		PD Feedback	
Frequency [Hz]	21	30	21	30
dB Reduction	**45**	**47**	**28**	**7**

Table 2: Transmissibility dB Reduction

5 CONCLUDING REMARKS

Current paper investigates with a simple paradigm of a 2-DoF system the concept of eliminating the force transmitted from an operating engine to the fuselage. The proposed antivibration system is based on the development of an active engine mount using piezoelectric device to reduce/ eliminate the transmitted force from the engine to the fuselage. This simple system was selected in order to investigate the dynamic interference and isolating capabilities of two different control algorithms, the feedforward and feedback control. The main contribution of this paper is the demonstration that the proposed feedforward control achieves significant reduction to the transmitted forces at specific frequencies of interest having minimum interference to the studied system modal characteristics. On the other hand, the feedback control interferes with the dynamic characteristics of the system, such as the stiffness and damping matrices, by shifting or damping the existing resonance. The results of displacement and force transmissibility reduction demonstrated better results for the proposed feedforward control. However, this is applicable only in the case that the exact characteristics of the disturbance are a priori known. Going a step forward, combining the two methodologies so that feedforward control simultaneous with feedback input, online calculates the potential change in frequency or amplitude of the disturbance, could lead to a more robust concept of engine vibration isolation.

REFERENCES

[1] E. I. Rivin, “Passive engine mounts-some directions for further development,” *SAE Tech. Pap.*, 1985, doi: 10.4271/850481.

[2] X. Huang, S. J. Elliott, and M. J. Brennan, “Active isolation of a flexible structure from base vibration,” *J. Sound Vib.*, vol. 263, no. 2, pp. 357–376, 2003, doi: 10.1016/S0022-460X(02)01057-X.

[3] A. J. Hillis, A. J. L. Harrison, and D. P. Stoten, “A comparison of two adaptive algorithms for the control of active engine mounts,” *J. Sound Vib.*, vol. 286, no. 1–2, pp. 37–54, 2005, doi: 10.1016/j.jsv.2004.09.023.

[4] I. Chopra, “Review of state of art of smart structures and integrated systems,” *AIAA J.*, vol. 40, pp. 2145–2187, Jan. 2002, doi: 10.2514/3.15309.

[5] M. A. Beijen, M. F. Heertjes, H. Butler, and M. Steinbuch, “Disturbance feedforward control for active vibration isolation systems with internal isolator dynamics,” *J. Sound Vib.*, vol. 436, pp. 220–235, 2018, doi: 10.1016/j.jsv.2018.09.010.

[6] F. Ranglin, Z. Weicun, and F. Dongshuai, “Comparative study of active engine mount control methods,” *Proc. 2017 9th Int. Conf. Model. Identif. Control. ICMIC 2017*, vol. 2018-March, no. Icmic, pp. 600–605, 2018, doi: 10.1109/ICMIC.2017.8321526.

[7] N. Olgac and B. T. Holm-Hansen, “A Novel active vibration absorption technique:

Delayed resonator," *Journal of Sound and Vibration*, vol. 176, no. 1. pp. 93–104, 1994, doi: 10.1006/jsvi.1994.1360.

[8] Y. Li, X. Wang, R. Huang, and Z. Qiu, "Active vibration and noise control of vibro-acoustic system by using PID controller," *J. Sound Vib.*, vol. 348, pp. 57–70, 2015, doi: 10.1016/j.jsv.2015.03.017.

[9] S. Zhang, R. Schmidt, and X. Qin, "Active vibration control of piezoelectric bonded smart structures using PID algorithm," *Chinese J. Aeronaut.*, vol. 28, no. 1, pp. 305–313, 2015, doi: 10.1016/j.cja.2014.12.005.

[10] A. M. Mahil, M. A. Shah, and W. F. Faris, "Active engine mounting controller design using linear quadratic regulator and proportional integral derivative," *Int. J. Autom. Control*, vol. 5, no. 3, pp. 284–297, 2011, doi: 10.1504/IJAAC.2011.042858.

[11] T. Kai, Y. Nakamura, and S. Wakui, "Implementation of floor vibration feedforward using an absolute displacement sensor combined with acceleration PI feedback," *2012 IEEE Int. Conf. Ind. Technol. ICIT 2012, Proc.*, pp. 1104–1109, 2012, doi: 10.1109/ICIT.2012.6210087.

[12] Z. Li, "Vibration transmissibility of two-DOF vibrating systems," *INTER-NOISE 2019 MADRID - 48th Int. Congr. Exhib. Noise Control Eng.*, no. 1, 2019.

[13] H. S. Tzou and C. I. Tseng, "Distributed piezoelectric sensor/actuator design for dynamic measurement/control of distributed parameter systems: A piezoelectric finite element approach," *J. Sound Vib.*, vol. 138, no. 1, pp. 17–34, 1990, doi: 10.1016/0022-460X(90)90701-Z.

[14] M. Yasuda, T. Osaka, and M. Ikeda, "Feedforward control of a vibration isolation system for disturbance suppression," *Proc. IEEE Conf. Decis. Control*, vol. 2, no. December, pp. 1229–1233, 1996, doi: 10.1109/cdc.1996.572662.

EURODYN 2020
XI International Conference on Structural Dynamics
M. Papadrakakis, M. Fragiadakis, C. Papadimitriou (eds.)
Athens, Greece, 23–26 November 2020

AN INNOVATIVE VOXEL-BASED APPROACH FOR THE OUT-OF-PLANE HOMOGENIZED LIMIT ANALYSIS OF NON-PERIODIC MULTI-LEAF MASONRY WALLS

Gabriele Milani[1] **and Simone Tiberti**[2]

[1] Department ABC, Technical University of Milan
Piazza Leonardo da Vinci 32, 20133 Milan, Italy
e-mail: gabriele.milani@polimi.it

[2] Department ABC, Technical University of Milan
Piazza Leonardo da Vinci 32, 20133 Milan, Italy
e-mail: simone.tiberti@polimi.it

Keywords: masonry multi-leaf walls, voxel based mesh, limit analysis, homogenization

Abstract. *A recurring construction technique in many European countries (Italy included) is based on the erection of multi-leaf walls. Their seismic vulnerability is usually high, due to the fact that the wythes are poorly or by no means connected one each other. Hence, masonry buildings with multi-leaf walls regularly display an insufficient strength against out-of-plane actions (such as those caused by earthquakes and those causing the highest vulnerability), which leads to partial or total collapse. This paper proposes a novel approach devoted to the out-of-plane analysis of masonry multi-leaf walls at collapse, with special attention given to the case of non-periodic masonry – in which the units display different geometries and are randomly arranged in the walls. This approach is based on the so-called "voxel strategy", in which the 3D finite element mesh of a multi-leaf wall is created directly from the rasterized images of its external wythes. Every pixel of the rasterized images is transformed into its 3D counterpart (the "voxel", indeed), which is then converted into a solid finite element. The "voxel strategy" for generating the finite element mesh is translated into a MATLAB function, which is itself part of a broader limit analysis approach based on the upper bound theorem, that aims at deriving homogenized out-of-plane failure surfaces. These represent macroscopic out-of-plane strength criteria for the selected non-periodic multi-leaf masonry walls; they are expressed in terms of flexural and torsional moments around the horizontal and vertical axes of the considered wall. The approach also enables the extraction of the deformed shapes at collapse for single out-of-plane load conditions. The homogenized out-of-plane failure surfaces are the results of an upper bound limit analysis problem coupled with homogenization, aptly formulated as a standard-form linear programming problem. The solid finite elements of the created mesh are rigid, and the velocity jumps at the interfaces between adjacent finite elements obey a Mohr-Coulomb failure criterion with separate tension and compression cut-offs and associated flow rule. A case study is investigated to benchmark the procedure, namely a rubble masonry three-leaf wall with absente interconnection between leaves.*

1 INTRODUCTION

Multi-leaf walls are quite common in the architectural heritage of several European countries. They are usually structured as follows: two external wythes (called also layers) of masonry are erected, leaving a thinner in-between void that is later filled with loose material (e.g. stone chips) or low-quality mortar. Multi-leaf walls are often characterized by a rate of transversal interconnection among the wythes that is either very poor or wholly absent most of the times. This entails an insufficient resistance against out-of-plane actions: the outer wythe is often ejected, weakening the construction up to the point where its partial or even total collapse is a very likely occurrence. Unfortunately, in historical masonry buildings the presence of multi-leaf walls is only revealed after the local or global failure of the structure. On the left, it is possible to observe the ejection of the external wythe caused by the seismic action, although in this case the building is still standing. On the right, it is possible to observe that the inner wythe of the multi-leaf wall is basically absent, suggesting a total lack of transversal interconnection between the outer wythes. At present, very few papers are available with the study of multi-leaf masonry walls (they are equally subdivided between experimental [1]-[4] and numerical approaches [5]-[8]), due to the complexity that is typical of this kind of walls, therefore it is very difficult to employ micro- or macro-modelling approaches. In general, these walls are characterized by peculiar geometries and units' arrangements that make each of them a unique instance; an extremely refined analytical model at the microscale is then required, which would make any numerical analysis very cumbersome and computationally unfeasible. On the other hand, it is also very difficult to properly investigate the mechanical properties of the masonry constituents in these walls, not to mention the impossibility to run extensive and effective experimental tests, thus ruling out any possibility of defining a reliable macroscale model for such kind of masonry. Eventually, assessing the actual rate of transversal interconnection between adjacent layers represents another delicate issue to be addressed for these walls.

The pairing of homogenization and limit analysis seems to offer once more an acceptable solution to all the aforementioned issues; this is especially true when considering the fact that in many cases it is paramount to only assess the out-of-plane behavior at collapse of these walls in a swift and straightforward way, and limit analysis with a homogenized approach is potentially a very powerful tool in this sense.

Therefore, this paper presents a homogenized limit analysis model aiming at investigating the out-of-plane collapse behavior of non-periodic multi-leaf masonry walls, which is a novelty due to the substantial lack of dedicated models in this regard. Specifically, the out-of-plane collapse behavior is addressed by extracting out-of-plane homogenized failure surfaces for the multi-leaf walls, which actually represent out-of-plane macroscopic strength criteria for the considered wall. The out-of-plane kinematics of the multi-leaf wall is governed by a Kirchhoff-Love plate model; each wythe of the wall is provided with its own average strain rate tensor components, whereas a single average curvature rate tensor is introduced for the wall. The out-of-plane homogenized failure surfaces are derived from the solution of a mixed limit analysis-homogenization problem, written into a MATLAB script as a standard-form linear programming problem; a custom-built post-processing phase enables also the extraction of the deformed configurations at collapse ("failure modes") for the considered multi-leaf wall.

The representative element of volume, irregular both in plane and along the thickness, is meshed by means of a very refined voxel-based discretization where dissipation is allowed at the interfaces between voxels. Interfaces, where all plastic dissipations occur, behave following a cohesive-frictional failure criterion with limited tensile strength and cap in compression. Such homogenization approach has been first applied to random one-leaf masonry in [9][10] with a

2D pixel discretization, then extended with simple on-thickness integration to multi-leaf masonries in [11]-[12], finally changed in a more complex voxel procedure applied first to periodic masonry in- and out-of-plane loaded in [13] and to rubble masonry in [14]-[17]. In these last attempts, it is stressed how the representative element of volume was discretized by means of voxels. Conversely, here it is worth mentioning that the novelty of the numerical procedure here discussed stands in the generalization of the voxel approach to three-leaf masonry with external leafs constituted by the irregular assemblage of stones/blocks. The possibility of a partial interlocking among leafs is in principle accounted for and any configuration of the blocks both externally and along the thickness can be easily taken into account by means of the discretization into small voxels.
This paper is structured as follows: Section 2 offers a short presentation of the upper bound limit analysis problem with homogenization as formulated for the present application, including a short overview of the kinematic model here used as well as the several constraints required in the linear programming problem. Section 3 presents a preliminary numerical application of this model, consisting of a three-leaf rubble masonry wall. The effects on the out-of-plane collapse behavior coming from the possible presence of separate but similar masonry bonds in the outer wythes is finally investigated.

2 HOMOGENIZATION PROBLEM FORMULATION IN CASE OF MULTI-LEAF WALLS

This section presents very concisely the bases of the mathematical formulation of the homogenized limit analysis problem, used to derive out-of-plane homogenized failure surfaces for multi-leaf masonry walls Such formulation requires the definition of a kinematic model that accounts for the presence of different layers.

Analogous to the single leaf-case [10][13][14], a representative element of volume REV large enough to account for the irregular disposition of the stones in the leaf is a-priori selected, in the same way done for irregular textures made by only one leaf. Then, each leaf is meshed into rigid-infinitely resistant voxel finite elements with dissipation at the interfaces between contiguous voxels, behaving as Mohr-Coulomb interfaces. One of the main advantages is to deal exclusively with interfaces parallel to the material axes frame of reference. A standard linear programming problem is then written and solved to estimate homogenized failure surfaces. Full details of the numerical implementation for single leaf irregular textures –not reported here for the sake of conciseness- can be found in [10][13][14], where the reader is referred for further details.

The main difference with respect to the single-leaf formulation lies in the definition of separate average strain rate tensors for each wythe; conversely, the average curvature rate tensor is still unique for all the wythes. This modification is enforced to reproduce separate in-plane behaviors for each wythe, as is usually the case in multi-leaf walls where the wythes are not so well connected; the use of a single average curvature rate tensor for all the wythes instead represents a simplification of the out-of-plane behavior, for which the multiple wythes cannot bend differently with respect to each other, therefore removing the possibility of disconnection between the wythes along the out-of-plane direction (in this case, axis Z). Even though multi-leaf walls in general do not behave as sandwich structures, it is also well known that their inner core usually consists of either loose materials such as stone chips or materials that display poor mechanical properties. Therefore, it is totally reasonable to suppose that there is no actual contact between the outer wythes and the inner core, which justifies the simplifications adopted in the present formulation.

The difference between the single- and multi-leaf formulation is displayed in Figure 1, where the macroscopic quantities involved in each case are highlighted.

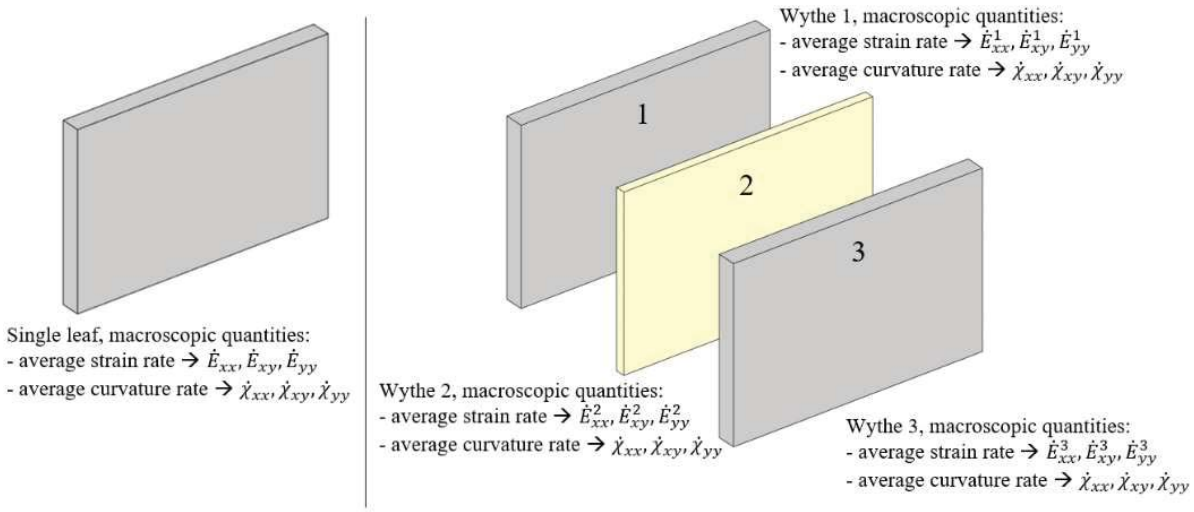

Figure 1: Difference in terms of macroscopic quantities between the single-leaf (left) and multi-leaf case (right).

Since each voxel of the multi-leaf wall is rigid and bereft of rotation rate, its kinematics is fully determined by the displacement rate field of its centroid $\{\dot{u}_x, \dot{u}_y, \dot{u}_z\}$, where axis Z represents the transversal direction. The use of a Kirchhoff-Love plate model leads to the following expressions for the three components of the displacement rate field, written for each wythe in the general case of a three-leaf masonry wall:

$$\dot{u}_x = \dot{u}_{x,per} + \dot{E}^1_{xx} x_G + \dot{E}^1_{xy} y_G + \dot{\chi}_{xx} z_G x_G + 0.5 \dot{\chi}_{xy} z_G y_G \tag{1}$$

$$\dot{u}_y = \dot{u}_{y,per} + \dot{E}^1_{xy} x_G + \dot{E}^1_{yy} y_G + \dot{\chi}_{yy} z_G y_G + 0.5 \dot{\chi}_{xy} z_G x_G \tag{2}$$

$$\dot{u}_z = \dot{u}_{z,per} - 0.5 \dot{\chi}_{xx} {x_G}^2 - 0.5 \dot{\chi}_{yy} {y_G}^2 - 0.5 \dot{\chi}_{xy} x_G y_G \tag{3}$$

$$\dot{u}_x = \dot{u}_{x,per} + \dot{E}^2_{xx} x_G + \dot{E}^2_{xy} y_G + \dot{\chi}_{xx} z_G x_G + 0.5 \dot{\chi}_{xy} z_G y_G \tag{4}$$

$$\dot{u}_y = \dot{u}_{y,per} + \dot{E}^2_{xy} x_G + \dot{E}^2_{yy} y_G + \dot{\chi}_{yy} z_G y_G + 0.5 \dot{\chi}_{xy} z_G x_G \tag{5}$$

$$\dot{u}_z = \dot{u}_{z,per} - 0.5 \dot{\chi}_{xx} {x_G}^2 - 0.5 \dot{\chi}_{yy} {y_G}^2 - 0.5 \dot{\chi}_{xy} x_G y_G \tag{6}$$

$$\dot{u}_x = \dot{u}_{x,per} + \dot{E}^3_{xx} x_G + \dot{E}^3_{xy} y_G + \dot{\chi}_{xx} z_G x_G + 0.5 \dot{\chi}_{xy} z_G y_G \tag{7}$$

$$\dot{u}_y = \dot{u}_{y,per} + \dot{E}^3_{xy} x_G + \dot{E}^3_{yy} y_G + \dot{\chi}_{yy} z_G y_G + 0.5 \dot{\chi}_{xy} z_G x_G \tag{8}$$

$$\dot{u}_z = \dot{u}_{z,per} - 0.5 \dot{\chi}_{xx} {x_G}^2 - 0.5 \dot{\chi}_{yy} {y_G}^2 - 0.5 \dot{\chi}_{xy} x_G y_G \tag{9}$$

Where (1)-(3) refers to wythe 1, (4)-(6) to wythe 2, (7)-(9) to wythe 3, $\{\dot{u}_{x,per}, \dot{u}_{y,per}, \dot{u}_{z,per}\}$ is the periodic velocities of the element, $\{\dot{E}^t_{xx}, \dot{E}^t_{xy}, \dot{E}^t_{yy}\}$ are the components of the average in-plane strain rate tensor of each t-th wythe of the multi-leaf wall and $\{\dot{\chi}_{xx}, \dot{\chi}_{xy}, \dot{\chi}_{yy}\}$ are the components of the average curvature rate tensor (with $\dot{\chi}_{yx}$ equal to $\dot{\chi}_{xy}$ for symmetry). In com-

pliance with the hypothesis of a Kirchhoff-Love plate model, such kinematics satisfies the requirements of $\dot{\chi}_{xx} = -\frac{\partial^2 \dot{u}_z}{\partial x^2}$, $\dot{\chi}_{yy} = -\frac{\partial^2 \dot{u}_z}{\partial y^2}$, and $\dot{\chi}_{xy} = -2\frac{\partial^2 \dot{u}_z}{\partial x \partial y}$.. When compared with a classic homogenization problem, the novelty is that a different in-plane average strain rate tensor is enforced in the different leaves (3 in this case), so the total number of macroscopic unknowns is here equal to 12, namely 9 in-plane macroscopic strain rates $\{\dot{E}^1_{xx}, \dot{E}^1_{xy}, \dot{E}^1_{yy}, \dot{E}^2_{xx}, \dot{E}^2_{xy}, \dot{E}^2_{yy}, \dot{E}^3_{xx}, \dot{E}^3_{xy}, \dot{E}^3_{yy}\}$ and 3 curvature rates $\{\dot{\chi}_{xx}, \dot{\chi}_{xy}, \dot{\chi}_{yy}\}$, instead of the classic 6 components originally included in the single-leaf formulation.

A master-slave formulation is also adopted to reduce the computational effort, which consists in considering the stones/blocks infinitely resistant, i.e. assuming only 6 kinematic unknowns for all the voxels belonging to the same stone. The relations that link the kinematic field of a single finite element and that of the masonry unit to which it belongs, are the following:

$$\dot{u}^S_x = \dot{u}^M_x + \dot{\theta}^M_{yy}(z^S_G - z^M_G) \tag{10}$$

$$\dot{u}^S_y = \dot{u}^M_y - \dot{\theta}^M_{xx}(z^S_G - z^M_G) \tag{11}$$

$$\dot{u}^S_z = \dot{u}^M_z + \dot{\theta}^M_{xx}(y^S_G - y^M_G) - \dot{\theta}^M_{yy}(x^S_G - x^M_G) \tag{12}$$

Where $\dot{u}^M_x$, $\dot{u}^M_y$, and $\dot{u}^M_z$ are the components of the displacement rate field of a generic masonry unit (the "master element", superscript M) expressed according to Eqs. (1)-(9), x^M_G, y^M_G, and z^M_G are the coordinates of the centroid of the stone/block, $\dot{u}^S_x$, $\dot{u}^S_y$, and $\dot{u}^S_z$ are the components of the displacement rate field of a generic finite element belonging to the considered masonry unit (the "slave element", superscript S), expressed according to Eqs. (1)-(9) as well. $\dot{\theta}^M_{xx}$ and $\dot{\theta}^M_{yy}$ are the rotations of the master element about the X and Y axes, respectively; in fact, the kinematics of any master element is here enriched to enable the occurrence of macroscopic rotations, which are displayed in the deformed shape of the multi-leaf wall associated to an out-of-plane load condition.

No modifications with respect to the single leaf case are needed by the constraints related to the periodicity of the velocity field at the boundaries. Conversely, the equation that expresses the normalization of the dissipated external power - needs to be modified as follows:

$$\begin{aligned} P^{ext} &= \Sigma_{xx}\dot{E}^1_{xx} + \Sigma_{yy}\dot{E}^1_{yy} + \Sigma_{xy}\dot{E}^1_{xy} + (\dots) + \Sigma_{xx}\dot{E}^n_{xx} + \Sigma_{yy}\dot{E}^n_{yy} + \Sigma_{xy}\dot{E}^n_{xy} + \\ &\quad + M_{xx}\dot{\chi}_{xx} + M_{yy}\dot{\chi}_{yy} + M_{xy}\dot{\chi}_{xy} = 1 \\ P^{ext} &= \Sigma_{xx}\sum_{t=1}^{n}\dot{E}^t_{xx} + \Sigma_{yy}\sum_{t=1}^{n}\dot{E}^t_{yy} + \Sigma_{xy}\sum_{t=1}^{n}\dot{E}^t_{xy} + \\ &\quad + M_{xx}\dot{\chi}_{xx} + M_{yy}\dot{\chi}_{yy} + M_{xy}\dot{\chi}_{xy} = 1 \end{aligned} \tag{13}$$

Eventually, the homogenized limit analysis problem is once more formulated as a linear programming problem. The objective function that ought to be minimized is still the dissipated

internal power, and the equality constraints are still given by periodicity conditions and constraints for plastic flow in continuum, provided that they include the modifications introduced in the previous equations. In the usual standard form, the components of the average strain tensors are split with a decomposition assuring that optimization variables are all non-negative:

$$\dot{E}_{ij}^{t} = \dot{E}_{ij}^{t,+} - \dot{E}_{ij}^{t,-} \qquad i,j = x,y \tag{14}$$

The standard form for this linear programming problem can therefore be written as follows:

$$\text{Minimize} \quad \boldsymbol{C^T X} \tag{15}$$

$$\text{Subject to} \quad \boldsymbol{AX = B} \tag{16}$$

$$\boldsymbol{X \geq 0} \tag{17}$$

Where $\boldsymbol{C^T X}$ is the dissipated internal power, $\boldsymbol{X}$ collects all non-negative optimization variables, according to Eq. (14), which include macroscopic strain and curvature rates, master elements velocities, periodic velocities and plastic multipliers and $\boldsymbol{AX=B}$ collects all the equality constraints, which include among the others Eqs. (10)-(13).

An efficient linear programming solver as CPLEX is utilized to deal with several variables and the need to recursively solve Eqs. (15)-(17) to find an approximation of the homogenized strength domain, also changing the REV considered (an operation needed when the external leaves are constituted by irregular stones disposed randomly and the identification of a suitable test window is required [10]).

3 CASE STUDY

A multi-leaf case study is investigated in terms of out-of-plane homogenized failure surfaces. The case study deals with a three-leaf wall whose outer wythes consist of rubble masonry. Two separate sets of mechanical parameters (cohesion, friction angle, tensile strength, and compressive strength) are employed: one set is dedicated to simulate the properties of the outer wythes, the other set is dedicated to simulate the properties of the inner wythe, which is supposed to consist of low quality mortar. Both sets are listed in Table 1.

Type of interface	Cohesion [MPa]	Friction angle [°]	Tensile strength [MPa]	Compressive strength [MPa]
Outer wythes	0.15	30	0.1	1.5
Mortar inner wythe	0.05	35	0.02	0.5

Table 1: Mechanical properties for the material employed.

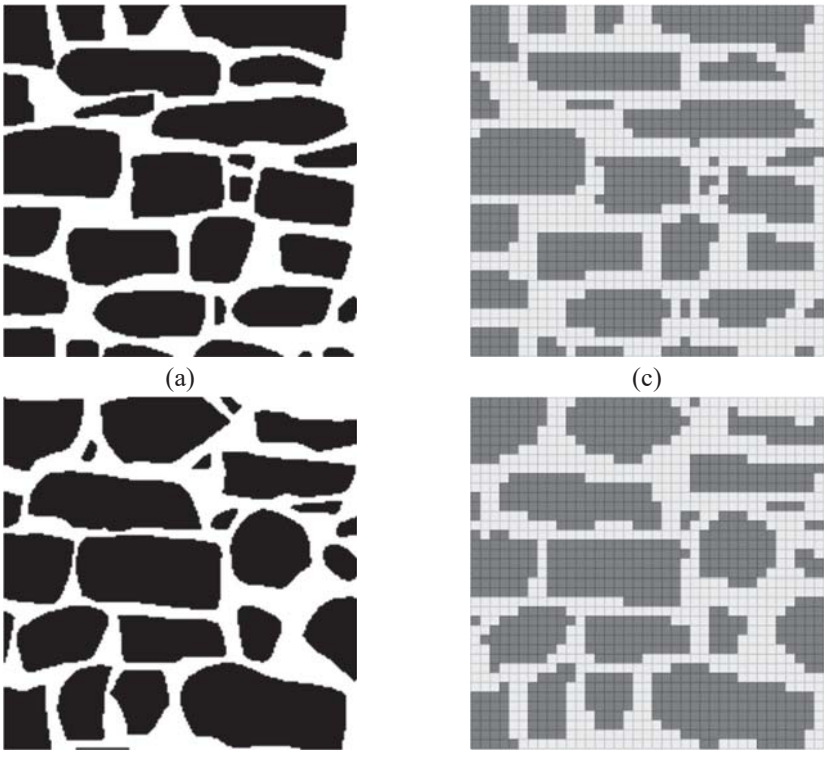

Figure 2: (a) Test-window C of case study 1; (b) test-window B of case study 1; (c) in-plane configuration of both the outer wythes for Instance 1, and of one wythe of Instance 2; (d) in-plane configuration of the other outer wythe of Instance 2.

3.1 Three-Leaf Rubble Masonry Wall

The case study under consideration consists of a three-leaf wall whose outer wythes are rubble masonry walls. Two instances of such wall are created aiming at investigating how the possible presence of different rubble masonry bonds influences the out-of-plane response of a three-leaf wall: specifically, one is named “Instance 1” and considers test-window C of case study 1 illustrated in [10][18], as the masonry bond for both outer wythes (Figure 2a), whereas the other is named “Instance 2” and employs the previous masonry bond for a single wythe, considering instead test-window B of the same case study as the masonry bond for the opposite wythe (Figure 2b). In both instances, a 5×5 coarsing strategy is employed to reduce the number of finite elements in the analytical models (Figure 2c and Figure 2d), see also [10][18] for a better insight into the coarsing strategy adopted to speed up computations; the outer wythes are supposed to be 40 cm thick and the mortar inner one 15 cm thick. The 3D finite element meshes of the two instances are shown in Figure 3 along with their exploded view: the outer wythes employ 16 finite elements over the thickness, while the mortar inner one employs 6 finite elements over the thickness.

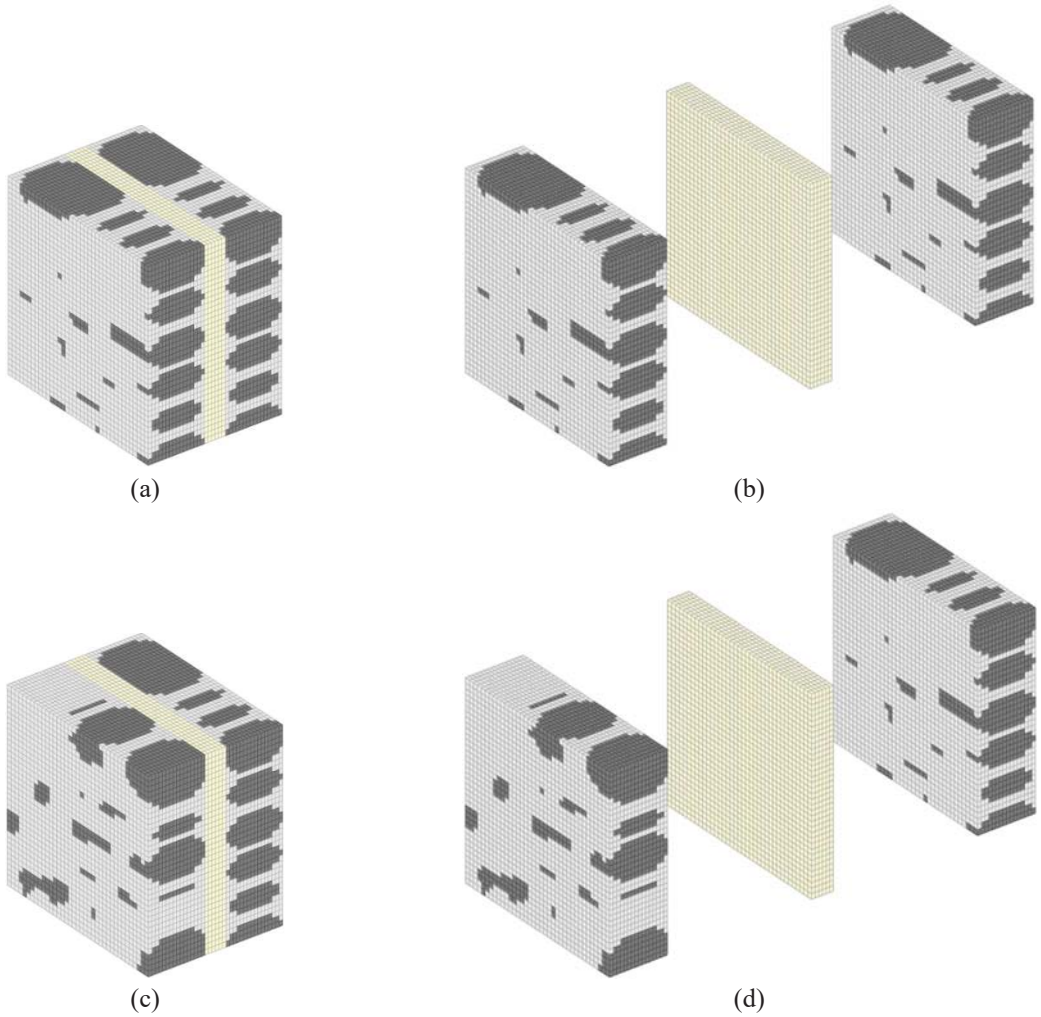

Figure 3: Case study considered to benchmark the procedure: (a) 3D finite element mesh for Instance 1; (b) exploded view of the 3D finite element mesh for Instance 1; (c) 3D finite element mesh for Instance 2; (d) exploded view of the 3D finite element mesh for Instance 2.

Figure 4 shows the comparison between the two instances in terms of flexural and torsional out-of-plane homogenized failure surfaces. It is possible to observe that Instance 2 (the one with different rubble masonry bonds in the outer wythes) displays larger failure surfaces in both the flexural and torsional cases: this means that, when it comes to rubble masonry three-leaf walls, the presence of different bonds in the outer wythes somehow increases the out-of-plane resistance of the wall, probably due to the combined effect of the two different types of irregularity at the extremities.

The deformed shapes at collapse ("failure modes") of the two instances of this case study are shown in Figure 5, which come from the single application of M_{xx}, M_{yy}, and M_{xy}. The outcomes of both the out-of-plane homogenized failure surfaces are corroborated: in fact, it is possible to observe how Instance 2 shows less widespread crack patterns for all the applied moments, suggesting a more compact (and, in the end, stiffer) out-of-plane response with respect to Instance 1.

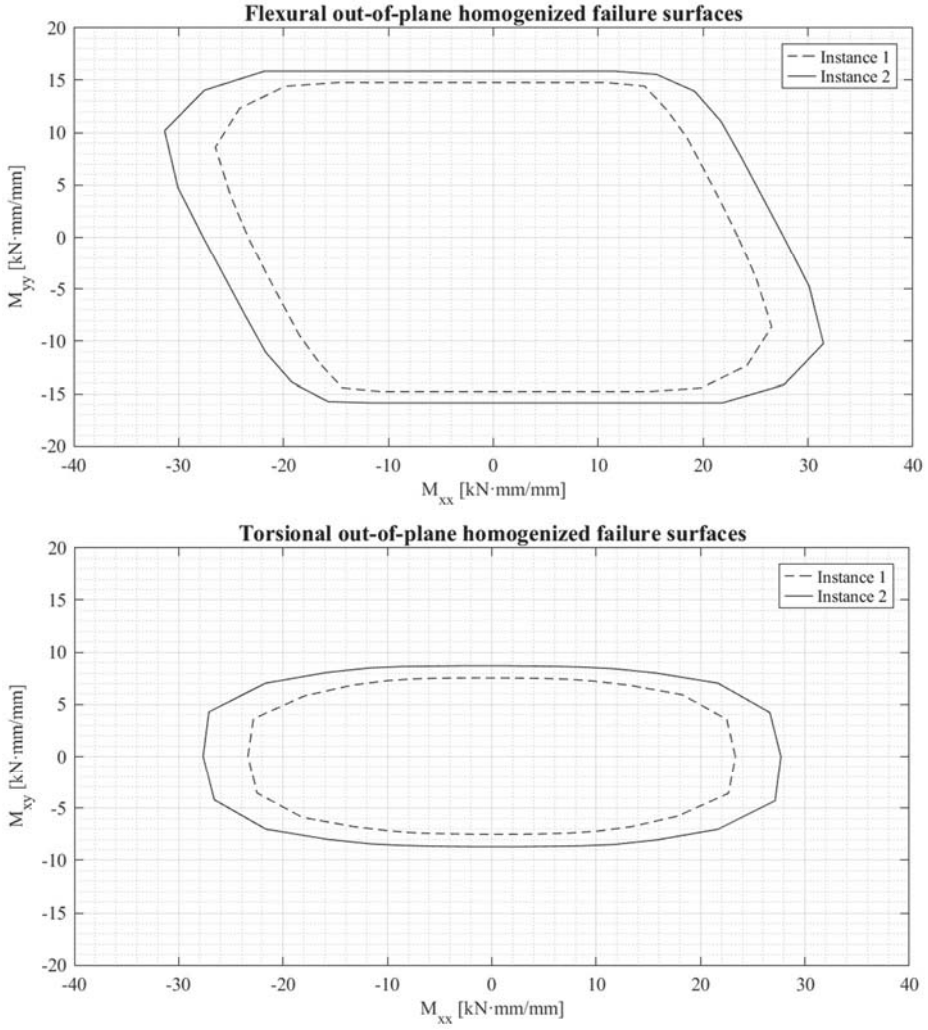

Figure 4: Flexural and torsional out-of-plane homogenized failure surfaces for the two instances of the first case study.

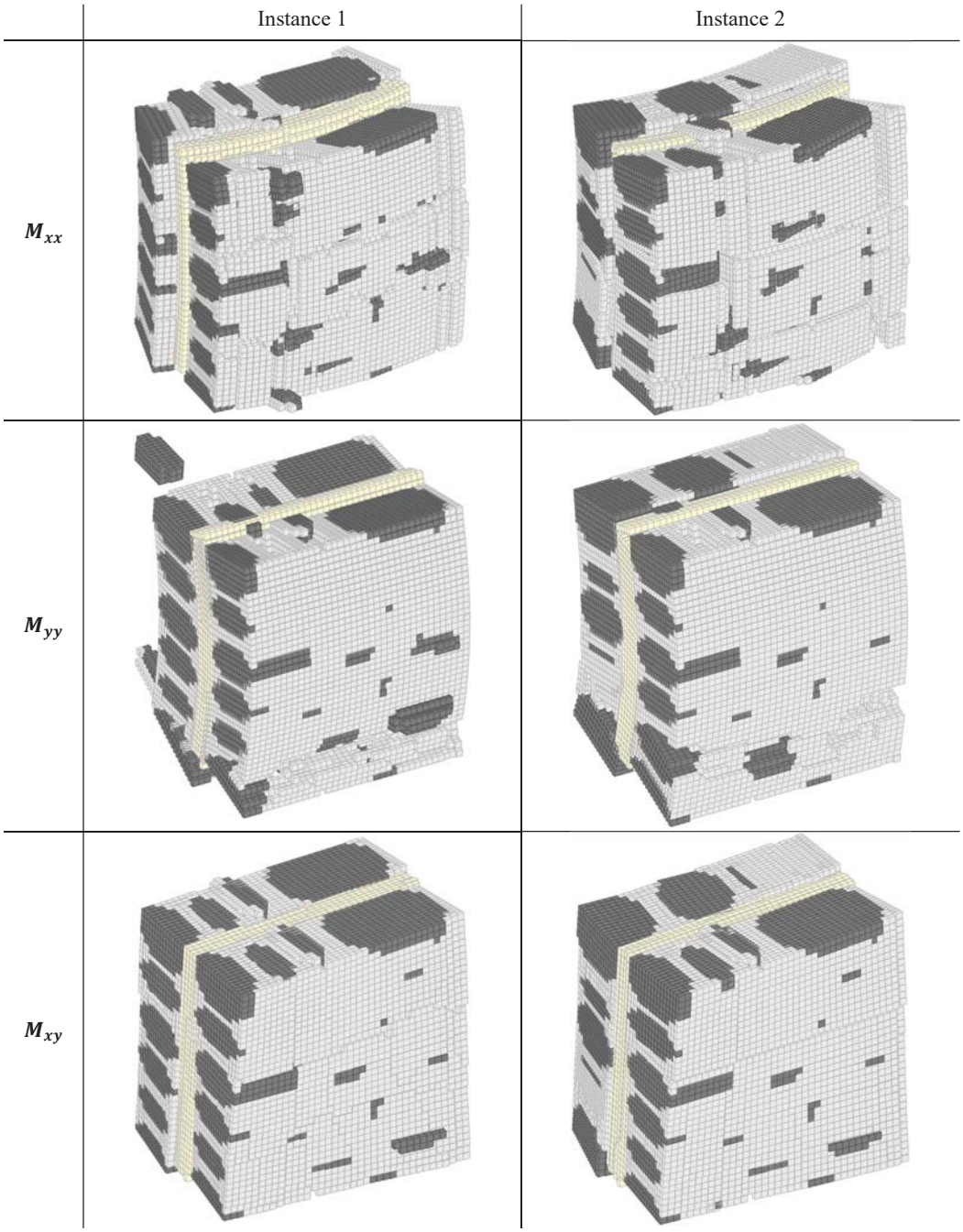

Figure 5: Failure modes under M_{xx}, M_{yy}, and M_{xy} for the two instances of the first case study.

4 CONCLUSIONS

The paper presented the first results obtained with a simple homogenized limit analysis model able to predict the ultimate out-of-plane behavior of non-periodic multi-leaf walls. The approach proposed enabled the derivation of out-of-plane homogenized failure surfaces for the multi-leaf wall, which can be useful for a quick assessment of the out-of-plane ultimate behavior of entire façades. The out-of-plane homogenized failure surfaces were obtained from the iterated solution of a standard linear programming problem with coupled kinematic limit analysis and homogenization hypotheses. The multi-leaf wall was discretized into infinitely resistant small voxels and the homogenization problem was solved in the rigid-plastic case

following a Kirchhoff-Love plate formulation. A preliminary numerical application was discussed, relying into a three-leaf non-periodic masonry wall, where external leaves consisted of rubble masonry. The effect due to the possible presence of separate but similar masonry bonds in the outer wythes were also investigated, showing that the presence of two different wythes increases the out-of-plane response of the wall both under flexural and torsional actions. The effects induced by (i) the presence of quasi periodic masonry for the external leaves and (ii) a good transversal interconnection between the outer wythes are two future issues to be investigated. A final implementation of the homogenization procedure at a structural level for the determination of the seismic vulnerability of entire multi-leaf masonry façades will be the last step of the research.

5 ACKNOWLEDGMENTS

The analyses were partially developed within the activities of ReLUIS (Rete dei Laboratori Universitari di Ingegneria Sismica – Network of the Italian University Laboratories of Seismic Engineering), for the research program funded by the Department of Civil Protection, Executive Project 2019, gratefully acknowledged by the authors.

REFERENCES

[1] L. Binda, J. Pina-Henriques, A. Anzani, A. Fontana, P.B. Lourenço, A contribution for the understanding of load-transfer mechanisms in multi-leaf masonry walls: Testing and modelling, *Engineering Structures*, 28 (8), 1132-1148, 2006.

[2] H. Derakhshan, M.C. Griffith, J.M. Ingham, Airbag testing of multi-leaf unreinforced masonry walls subjected to one-way bending, *Engineering Structures*, 57, 512-522, 2013.

[3] B. Silva, M. Dalla Benetta, F. Da Porto, C. Modena, Experimental assessment of in-plane behaviour of three-leaf stone masonry walls, *Construction and Building Materials*, 53, 149-161, 2014.

[4] B. Silva, A.E. Pigouni, M.R. Valluzzi, C. Modena, Calibration of analytical formulations predicting compressive strength in consolidated three-leaf masonry walls, *Construction and Building Materials*, 64, 28-38, 2014.

[5] M.A. Ramalho, A. Taliercio, A. Anzani, L. Binda, E. Papa, A numerical model for the description of the nonlinear behaviour of multi-leaf masonry walls, *Advances in Engineering Software*, 39(4), 249-257, 2008.

[6] G. Milani, 3D upper bound limit analysis of multi-leaf masonry walls, I*nternational Journal of Mechanical Sciences*, 50(4), 817-836, 2008.

[7] G. Milani, 3D FE limit analysis model for multi-layer masonry structures reinforced with FRP strips, *International Journal of Mechanical Sciences*, 52, 784–803, 2010.

[8] S. Casolo, G. Milani, Simplified out-of-plane modelling of three-leaf masonry walls accounting for the material texture, *Construction and Building Materials*, 40, 330-351, 2013.

[9] S. Tiberti, G. Milani, L. Macorini, A novel pixel limit analysis homogenization model for random masonry, *AIP Conference Proceedings*, 1978, art. no. 450008, 2018.

[10] S. Tiberti, G. Milani, 2D pixel homogenized limit analysis of non-periodic masonry walls, *Computers and Structures*, 219, 16-57, 2019.

[11] S. Tiberti, G. Milani, Simple Homogenized Numerical Model for the Analysis of Multi-leaf Masonry Walls, *RILEM Bookseries*, 18, 992-999, 2019.

[12] S. Tiberti, G. Milani, In- and out-of-plane analysis of multi-leaf masonry walls via an elementary homogenized numerical procedure, *Proceedings of the International Masonry Society Conferences*, 222279, 57-63, 2018.

[13] S. Tiberti, G. Milani, Fast brick-based homogenized limit analysis for in- and out-of-plane loaded periodic masonry panels, *Computers and Structures*, 231, art. no. 106206, 2020.

[14] S. Tiberti, G. Milani, Seismic vulnerability of masonry walls through an innovative voxel limit analysis homogenization approach, *COMPDYN Proceedings*, 1, 1202-1208, 2019.

[15] S. Tiberti, G. Milani, Voxel approach for 3D in-plane homogenized failure surfaces of non-periodic masonry, *AIP Conference Proceedings*, 2186, art. no. 100008, 2019.

[16] S. Tiberti, G. Milani, 3D limit analysis voxel approach for the homogenization of masonry with irregular bond, *AIP Conference Proceedings*, 2116, art. no. 420004, 2019.

[17] S. Tiberti, G. Milani, 3D voxel homogenized limit analysis of single-leaf non-periodic masonry, *Computers and Structures*, 229, art. no. 106186, 2020.

[18] S. Tiberti, G. Milani, 3D homogenized limit analysis of non-periodic multi-leaf masonry walls, *Computers and Structures*, under review, 2020.

EURODYN 2020
XI International Conference on Structural Dynamics
M. Papadrakakis, M. Fragiadakis, C. Papadimitriou (eds.)
Athens, Greece, 23–26 November 2020

EXPERIMENTAL AND NUMERICAL STUDY OF HISTORIC MASONRY WITH BED JOINT REINFORCED REPOINTING

Anastasios Drougkas, Lucia Licciardello, Jan G. Rots and Rita Esposito

Delft University of Technology
Stevinweg 1, 2628 CN Delft, The Netherlands
e-mail: {A.Drougkas, L.Licciardello, J.G.Rots, R.Esposito}@tudelft.nl

Keywords: seismic assessment & strengthening, historic masonry structures, full-scale testing, numerical analysis

Abstract. *Induced seismicity due to gas extraction in the province of Groningen in the Netherlands has a noticeable impact on building structures. Historic masonry structures in the area, which are non-engineered and lacking empirical design features often present in traditionally seismic regions, are especially vulnerable to dynamic loading. Compounding the problem, gas extraction additionally generates soil settlement, which can induce damage to masonry buildings and thus reduce their capacity to bear seismic loads.*

The objective of this paper is the evaluation of the performance of a widely used structural intervention method applied in masonry structures in the Groningen region of the Netherlands. This method, initially developed against soil subsidence damage, consists in the embedment of stainless steel helical bars in repointed bed joints. Additionally, diagonal anchors are placed in drilled holes across existing cracks in the masonry. The increase in induced seismicity in Groningen raises the question whether this intervention technique can additionally enhance the behaviour of masonry structures during seismic loading.

A masonry wall was experimentally tested in two configurations: a) a pre-damaged state, with simulated damage typical of imposed soil settlement, and b) a post-damaged and post-intervention state, this being the wall from the previous configuration after being tested to its maximum base shear and subsequently strengthened. Differences between the two configurations in terms of stiffness, peak force and prevalent damage patterns are discussed.

Accompanying the experimental campaign, results of finite element simulations of the strengthened wall are presented. The strengthened wall is simulated using non-linear macro-modelling techniques. The model accounts for the experimentally simulated damage as well as for the damage arising after the testing in the first configuration. The analysis results clarify and quantify the experimental observations on the strengthened wall, particularly as regards stress development and bond-slip in the reinforcement bars.

Based on the experimental and numerical results, the effectiveness of the intervention in restoring the strength of the wall and in preventing the re-emergence of major diagonal cracking is confirmed.

1 INTRODUCTION

1.1 State of the art and motivation

Induced seismicity is the term used for describing low-magnitude ground shaking caused by human activity. It is characterised by high frequency of incidence, potentially exceeding hundreds of events every year in a single location. Among the main human activities linked to the generation of induced seismicity events is gas extraction [1]. While these low-magnitude earthquakes typically do not pose a threat to the structural safety of buildings and infrastructure, they can gradually reduce the durability and aesthetic integrity of structures through the formation and accumulation of light damage.

Soil-subsidence and uplift are responsible for the formation of damage in structures. The difference in stiffness between the superstructure/foundation and the soil causes the induction of bending and shear strain in buildings, an effect known as soil-structure interaction [2]. Gas extraction, in addition to inducing seismicity, leads to soil subsidence over wide geographic areas. Masonry structures are particularly vulnerable to soil-structure interaction effects due to their high stiffness and low tensile strength.

Due to the presence of soft clay, sand and peat top-soils, the Dutch region of Groningen has continuously experienced soil subsidence. Over the preceding decades, repair measures have been employed against the effects of soil movement in historic and traditional masonry buildings. One such widely employed measure consists in the placement of stainless steel helical bars in bed joints repointed using a high strength mortar. Additional bars are placed across cracks formed in masonry through drilled pilot holes. In more recent times, gas extraction operations in the region have not only exacerbated soil subsidence, but have been the cause of induced seismicity. This combined action poses substantial risk to the durability of the masonry building stock in the region, including both vernacular and monumental structures [3]. The role of the embedded reinforcement bars in enhancing the seismic capacity of masonry buildings, a role for which it was not originally intended, has not been sufficiently studied.

The role of embedded steel or CFRP reinforcement in masonry has received some attention in the literature, in both experimental and numerical studies [4, 5, 6]. However, the role of bed joint reinforced repointing as the main means of strengthening has not been sufficiently investigated, particularly in full-scale structures.

1.2 Objectives

The main objective of the paper is the evaluation of the overall role of bed joint reinforced repointing for masonry walls on structural behaviour under in-plane earthquake loading. The conditions in Groningen require that the walls be tested in a combination of subsidence- and earthquake-induced loads. Further, the nature of induced seismicity requires that structural behaviour be evaluated for both low- and high-magnitude loading.

The strengthening technique is evaluated in terms of contribution to capacity and ductility. Additionally, the shift in failure mode during low- and high-magnitude loading is an important parameter to consider.

1.3 Methodology

The effectiveness of the strengthening was evaluated through preliminary experimental testing of masonry walls with dimensions and layout commonly encountered in Groningen. Two walls with a window opening and simulated damage were tested up to light damage. Subse-

quently, one of the walls was strengthened and re-subjected to the light damage loading protocol. Finally, both the unstrengthened and strengthened walls were tested up to failure.

Following the experimental testing, a numerical campaign was executed. The primary objective of the campaign was the simulation of the strengthened wall test. Different modelling techniques were employed in order to establish the influence of the modelling approach on the results.

This paper focuses on the numerical simulation of the in-plane testing of the strengthened wall. The experimental results of both the unstrengthened and strengthened walls are detailed in a separate work [7]

2 EXPERIMENTAL CAMPAIGN

2.1 Testing of constituent materials

The units were solid clay bricks measuring $210 \times 50 \times 100\ mm^3$ in length $\times$ height $\times$ width. The width of the walls is equal to the width of the units. These units are very typical in traditional clay-brick masonry construction in the Netherlands, including in Groningen, and feature a high compressive strength [8].

The construction mortar was an O-type lime cement mortar, with an expected compressive strength of $2.4\ N/mm^2$ at 28 days. While this mortar type is not typically recommended for load-bearing members in new construction, it offers a reasonable approximation of traditional mortars while simultaneously not requiring excessive curing time before developing a compressive strength sufficient for low-rise construction. The thickness of all mortar joints was $10\ mm$.

The properties of the units and mortar as determined experimentally are shown in Table 1.

Parameter	Symbol	Units	Average	Coefficient of variation
Unit compressive strength	$f_{c,u}$	N/mm^2	28.31	0.10
Mortar compressive strength	$f_{c,m}$	N/mm^2	3.59	0.09

Table 1: Results of masonry constituent material tests.

2.2 Testing of masonry composite

Masonry wallets were subjected to different mechanical tests for the determination of the properties of the masonry composite. Further, the mechanical properties of the unit-mortar interface were determined experimentally.

Compressive tests on the masonry composite were executed according to EN 1052-1 [9], both normal and perpendicular to the bed joints (vertical and horizontal directions).

The shear strength of the unit-mortar interface was characterised through triplet testing according to EN 1052-3 [10]. The tensile strength of the interface was determined through manually-operated bond-wrench testing according to EN 1052-5 [11].

The results of the masonry composite tests are summarised in Table 2.

2.3 Layout of masonry walls

The masonry wall samples measured $3070 \times 2690 \times 100\ mm^3$ in length $\times$ height $\times$ width, with an eccentric window opening measuring $780 \times 1510\ mm^2$ in length $\times$ height. The masonry was constructed in single-wythe running bond, with a concrete lintel constructed over the open-

Parameter	Symbol	Units	Average	Coeff. of variation
Horizontal compressive strength	$f_{c,x}$	N/mm^2	13.11	0.18
Vertical compressive strength	$f_{c,y}$	N/mm^2	12.93	0.07
Horizontal compressive fracture energy	$G_{c,x}$	N/mm	35.06	0.19
Vertical compressive fracture energy	$G_{c,y}$	N/mm	28.63	0.11
Horizontal Young's modulus	E_x	N/mm^2	3207	0.18
Vertical Young's modulus	E_y	N/mm^2	3190	0.24
Initial shear strength	f_{v0}	N/mm^2	0.13	-
Friction coefficient	μ	-	0.82	-
Shear fracture energy	G_v	N/mm	0.30	-
Flexural bond strength	f_w	N/mm^2	0.08	0.32
Flexural bond fracture energy	G_w	N/mm	0.0069	-
Density	ρ	kg/m^3	1708	0.07

Table 2: Material properties of masonry composite.

ing. The walls were constructed in a single day by an experienced mason. The samples were were constructed directly atop a steel HEB 300 beam and capped with a HEB 600 beam.

For the simulation of damage caused by soil settlement, thin plastic sheets were introduced at targeted locations between the units and the mortar, thus preventing the formation of the unit-mortar interface bond, but allowing the mortar to develop its compressive strength. This damage is designated as 'pre-damage' in this paper. It consists in diagonal cracks near the edges of the window, as would be formed from a sagging deformation towards the right of the wall.

The layout of the walls, along with the disposition of the pre- and post-damage, can be seen in Figure 1a.

2.4 Strengthening method and intervention materials

The strengthening method consists in two interventions: a) the embedment of horizontal helical bars in repointed bed joints and b) the insertion of diagonal helical bars in pilot holes across formed cracks, without grout or other anchoring measures.

The repair mortar used in this application is a strong cementitious intervention material that can be injected in mortar joints. Its expected compressive strength at 28 days is 45 N/mm^2. For the repointing of the bed joints, a 40 *mm* portion of the joint was removed from one face of the wall. Subsequently, helical bars were placed in the groove singly or in pairs and the groove was completely filled with the repair mortar. This intervention method introduces some eccentricity to the wall, since the bars are not placed centrally along the thickness of the wall and since the repair mortar, applied on a single face, is much stiffer than the construction mortar.

The helical bars are stainless steel grade ASTM 304, with a diameter of 6 *mm*. The steel has a yield strength of 215 N/mm^2 and a tensile strength of 505 N/mm^2. The bond-slip behaviour of the bars was investigated in two setups: a) in bars embedded in repair mortar for testing the behaviour of the bed joint reinforcement and b) in bars inserted vertically in masonry prisms for testing the behaviour of the diagonal reinforcement [12]. The test results were fitted to the piecewise Model Code 2010 bond-slip model [13]:

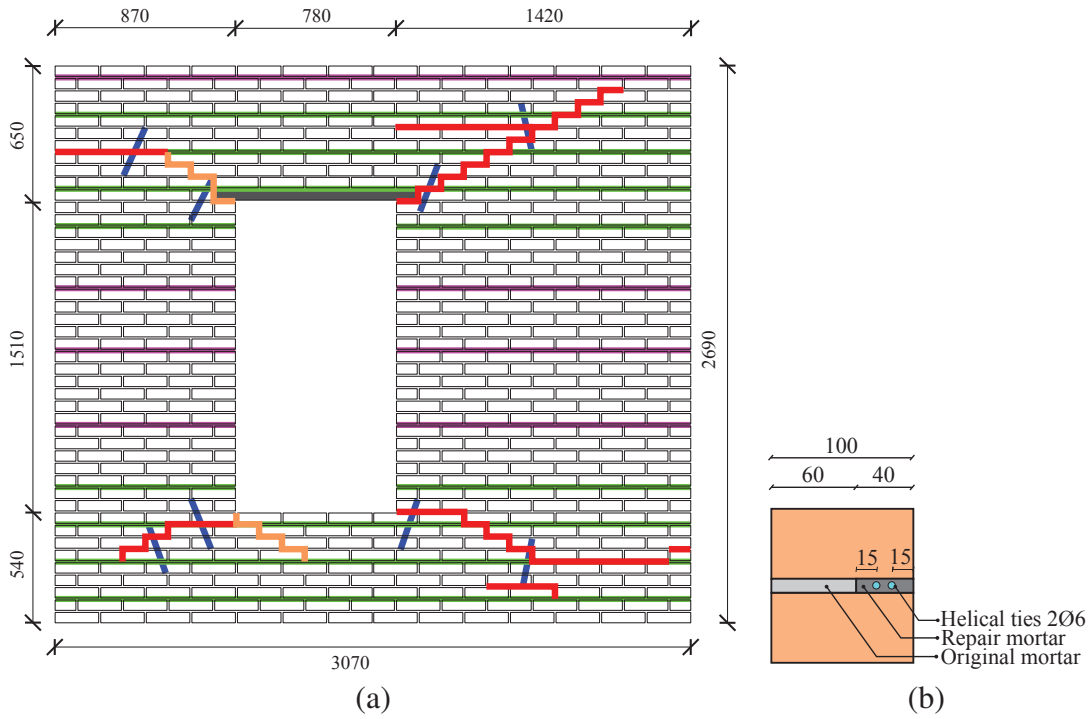

Figure 1: a) Layout of strengthened masonry wall. Pre-damage in orange, post-damage in red. Single bed joint bars in purple, double bed joint bars in green, diagonal anchors in blue. b) Cross-section of repointed joint. All dimensions in *mm*.

$$\tau_0(s) = \begin{cases} \tau_{max}\,(s/s_1)^a & \text{for} \quad 0 \le s \le s_1 \\ \tau_{max} & \text{for} \quad s_1 \le s \le s_2 \\ \tau_{max} - \left(\tau_{max} - \tau_f\right)(s - s_2)\,/\,(s_3 - s_2) & \text{for} \quad s_2 \le s \le s_3 \\ \tau_f & \text{for} \quad s_3 \le s \end{cases} \tag{1}$$

where a is a numerical parameter controlling the shape of the initial branch, τ_{max} is the peak bond stress, τ_f is the residual bond stress and s_1, s_2 and s_3 are slip values determining the inflection points of the bond-slip curve. The value of s_1 is here considered as the elastic limit for the bond-slip. The experimentally determined bond-slip properties according to Eq. 1 are summarised in Table 3.

	s_1	s_2	s_3	τ_{max}	τ_f	a
	mm	mm	mm	N/mm^2	N/mm^2	-
Bed joint	5.0	110.0	120.0	2.0	0.05	0.7
Diagonal	20.0	45.0	50.0	1.3	0.05	0.7

Table 3: Numerical parameters for Model Code 2010 bond-slip model.

The properties of the repair materials are summarised in Table 4. The repair mortar was tested at 28 days and the properties of the bars are determined according to the properties of ASTM 304 stainless steel.

Material	Parameter	Symbol	Units	Average	Coeff. of variation
Repair mortar	Compressive strength	$f_{c,M}$	N/mm^2	46.42	0.09
	Flexural strength	$f_{b,M}$	N/mm^2	7.68	0.24
Helical bar	Young's modulus	E_s	N/mm^2	193000	-
	Yield strength	$f_{y,s}$	N/mm^2	215	-
	Tensile strength	$f_{t,s}$	N/mm^2	505	-

Table 4: Mechanical properties of repair materials.

2.5 Testing procedure for masonry walls

A vertical compressive load of $0.12\,N/mm^2$ was applied on the top beam. The testing setup allowed rotation of the top (cantilever configuration). The horizontal in-plane load was applied in displacement control through a horizontal actuator to the top steel beam. Digital image correlation and an arrangement of sensors were employed for monitoring the deformation and crack pattern of the walls.

Both walls were initially tested in their un-strengthened, pre-damaged state up to light damage. The damage due to this test, similar in pattern for both walls, was documented and designated as 'post-damage' and was concentrated at the mortar joints. These cracks propagate from the corners of the window, both as extensions of the pre-damage and in new locations, and propagated primarily in a diagonal direction. One wall was subsequently strengthened using the repair mortar and helical bars and diagonal ties. Finally, both walls were tested up to failure. The geometric layout of the bars is illustrated in Figure 1a, while a cross-section of a repointed bed joint can be seen in Figure 1b.

The loading protocol for in-plane shear-compression was designed in order to simulate the loading that may arise in regions were both soil settlement and induced seismicity are encountered [7]. Thus, the loading protocol for both tests was composed of three phases. In phase 1, low-magnitude repeated in-plane displacement was applied. In phase 2, low magnitude cyclic loading was applied. In phase 3 the target displacement per cycle was increased in magnitude up to failure of the wall. The loading protocol is detailed in Table 5. The net displacement refers to the displacement of the top beam with respect to an external reference point, excluding rotations of the setup and horizontal displacement of the bottom beam with respect to the external reference.

2.6 Experimental results

The results of the in-plane tests are illustrated in terms of force displacement graphs obtained in phase 3 in Figure 2. The eccentric placement of the window results in noticeable difference in the capacity and stiffness of the unstrengthened wall in the negative and positive direction. The unstrengthened wall presents substantial residual drift accumulation for negative displacement, whereas the residual drift is reduced in magnitude and oscillates according to the loading direction in the strengthened case.

Despite the wall having sustained substantial damage in the initial test, the strengthening technique not only restores the strength and stiffness of the wall, but modestly enhances these parameters. Similarly enhanced is the ductility of the wall, with limited reduction in the shear force after attaining its peak value. Further, the strengthening reduces the difference between the response in the negative and positive directions.

The crack patterns registered through digital image correlation for both the unstrengthened

Phase	Cycle	Runs	Net horizontal displacement	
				mm
1	C1	30	0.73	-
	C2	30	0.92	-
	C3	30	1.09	-
	C4	30	1.28	-
	C5	30	1.50	-
2	C6	30	0.73	-0.75
	C7	30	0.92	-0.96
	C8	30	1.13	-1.15
	C9	30	1.33	-1.37
	C10	30	1.53	-1.58
	C11	30	1.72	-1.77
	C12	30	1.93	-1.98
3	C13	4	2.48	-2.52
	C14	4	7.87	-7.91
	C15	2	13.28	-13.29
	C16	2	26.76	-26.79
	C17	2	40.25	-40.30
	C18	2	53.77	-53.80
	C19	2	67.26	-67.28
	C20	2	80.76	-63.31

Table 5: Loading protocol for the in-plane shear-compression test.

and strengthened walls are illustrated in Figure 2. In the unstrengthened wall the diagonal cracking around the window is prevalent. The presence of the bars in the strengthened wall produces a shift in the arrangement of the crack pattern. The bed joint reinforcement prevents for the most part the diagonal cracks from propagating, resulting in the formation of more pronounced horizontal cracks. These cracks are well-defined at the top of the two piers, but are more distributed at the base of the piers. Damage in the spandrel is significantly limited compared to the unstrengthened case. Both piers in both tests are generally undamaged due to the predominance of rocking in their response. Toe crushing was not extensive due to the low vertical load.

3 NUMERICAL SIMULATION OF STRENGTHENED WALL

3.1 Modelling approach

The modelling campaign presented here focuses on the strengthened wall. Analyses of the unstrengthened wall, with the absence of pre-damage, have been presented in a previous work [14].

For the simulation of the in-plane experiment, a finite element macro-modelling approach is adopted in this paper. In this approach, the masonry composite is modelled as a plane stress orthotropic continuum, with no distinction between units and mortar in the analysis domain. The mean edge length of the finite element mesh was 30 *mm*. Each cycle of the loading protocol was executed once. A regular Newton-Raphson scheme was employed for the iterations and an energy norm of 0.1% was used as a convergence criterion at each load step.

The finite element model was constructed and analysed using the DIANA finite element

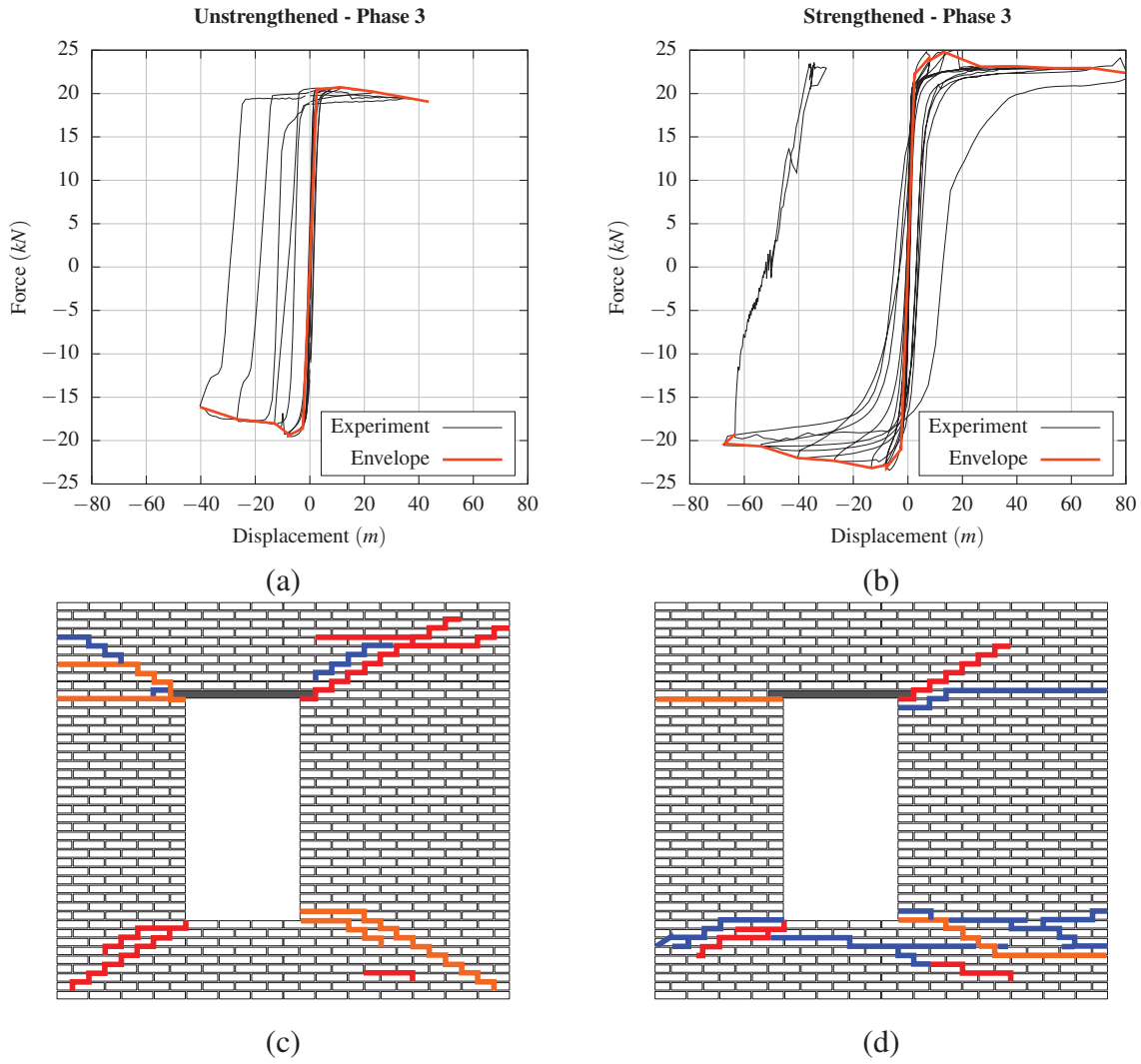

Figure 2: Force-displacement graphs for phase 3: a) unstrengthened wall and b) strengthened wall. Experimentally obtained damage patterns for: c) unstrengthened wall and d) strengthened wall. Damage arising in phase 1 (orange), in phase 2 (red) and in phase 3 (blue).

program. Material non-linearity was modelled using the Engineering Masonry Model, jointly developed by TU Delft and DIANA FEA [15]. Within an anisotropic total strain context, the model accounts for the compressive, shear and tensile failure of the masonry composite.

The tensile strength of the masonry composite in two orthogonal in-plane directions is calculated as a function of the masonry bond, unit-mortar bond strength, friction angle and shear strength.

In the direction normal to the continuous bed joints (vertical), the tensile strength of masonry is determined at the load of first cracking during the bond strength test, empirically equal to:

$$f_{t,y} = \frac{2}{3} f_w \tag{2}$$

In the direction parallel to the bed joints (horizontal), the tensile strength of masonry is equal to:

$$f_{t,x} = \tau_{max} / \tan(\alpha) \tag{3}$$

where α is the angle between the staircase crack and the bed joint (here equal to 0.50 rad) and τ_{max} is equal to:

$$\tau_{max} = \max\left[0, f_{v0} - \sigma_y \mu\right] \tag{4}$$

where σ_y is the vertical stress, compression being negative. Diagonal staircase cracking, defined as the opening of a crack at an angle of α from the horizontal, is evaluated against the diagonal tensile strength, calculated as:

$$f_{t,a} = \frac{f_{t,x} f_{t,y}}{f_{t,x}^2 \sin^2\left(\frac{\pi}{2} - \alpha\right) + f_{t,y}^2 \cos^2\left(\frac{\pi}{2} - \alpha\right)} \tag{5}$$

The reinforcement bars were modelled as truss elements embedded in the plane stress elements. Their bond-slip behaviour is modelled by considering a uniaxial constitutive relation between slip and bond stress according to Eq. 1. Yielding of the bars is also considered with a uniaxial constitutive relation between axial strain and stress according to the properties of ASTM 304 stainless steel. The material properties as summarised in Table 2 and Table 3 were used as input for the model without further calibration.

To model the pre- and post-damage, reduced strength and stiffness were assigned to the damaged areas of the masonry. The compressive strength was left unchanged due to the damage having been caused by opening of the unit-mortar interface. The tensile and shear strength, as well as the tensile and shear fracture energy, were reduced to zero in order to account for the artificial absence of bond in the pre-damage and the loss of interface cohesion in the post-damage due to crack opening. The Young's modulus was reduced by 50% in all damaged locations.

The top steel beam was modelled as an elastic beam element in perfect bond with the masonry wall. The model was clamped at the base and unrestrained at the top. Out-of-plane effects that may arise due to the eccentricity of the reinforcement were not considered in the model.

4 NUMERICAL ANALYSIS RESULTS

The numerical force-displacement curve for phases 1 and 2, in comparison with the experimentally derived curve, is presented in Figure 3. The stiffness of the structure is approximated well. The peak force is overestimated by 20% in the positive direction, but predicted with good accuracy in the negative direction. The hysteresis loops are also better approximated in the negative direction.

The numerically obtained crack patterns are shown in Figure 4 at the instances of peak negative and positive applied displacement. The cracking pattern matches the experimentally obtained damage to a significant extent, with the exception of the re-opening of the diagonal crack at the upper left corner of the window for positive displacement instead of the formation of a new horizontal crack propagating towards the edge of the wall. The difference in the crack pattern for positive displacement is possibly linked to the overestimation of the peak force in that loading direction. It is interesting to note that this horizontal crack was formed in the unstrengthened wall during phase 1 but was not formed in the wall that was eventually strengthened.

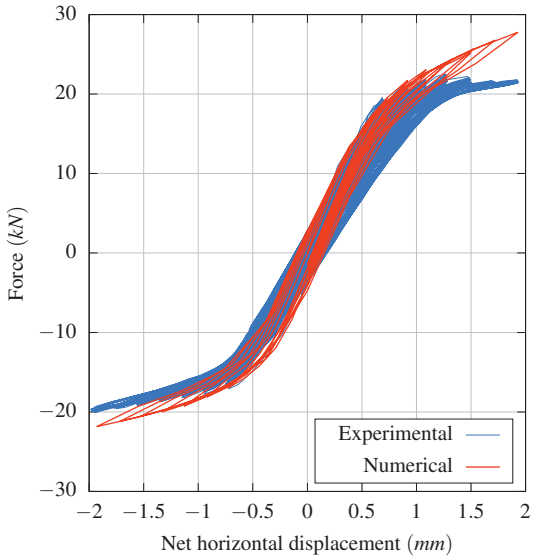

Figure 3: Comparison of experimental with numerically-derived force-displacement curve for phase 2.

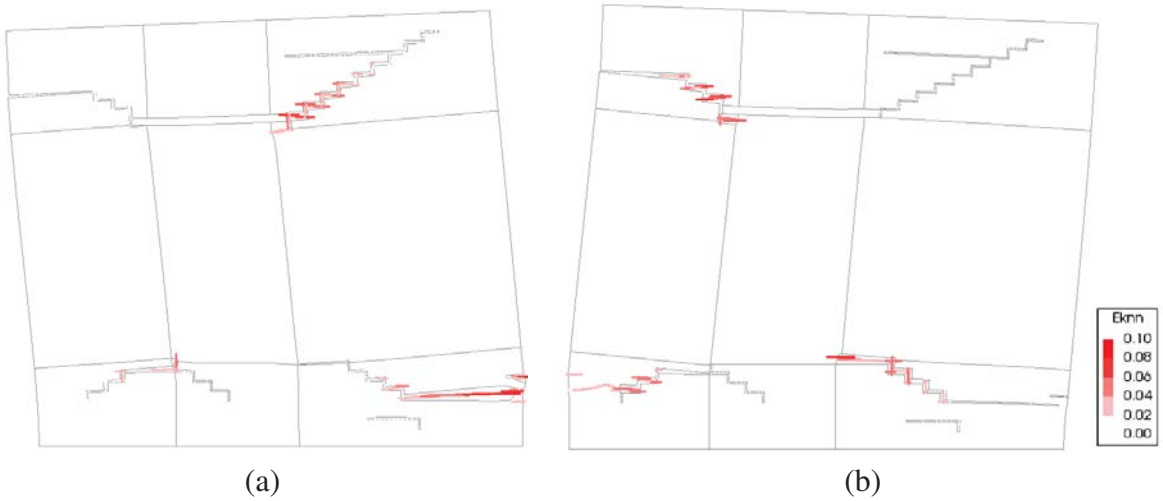

Figure 4: Numerically obtained crack patterns, as crack strain vectors parallel to the crack in red, for phase 2 at: a) peak negative displacement ($-1.98\ mm$) and b) peak positive displacement ($1.93\ mm$).

The bed joint reinforcement, being oriented in parallel with the main direction of cracking, did not register any substantial slipping. The maximum axial stress borne by the bed joint bars was $53.2\ N/mm^2$ well below the yield strength ($215\ N/mm^2$). The maximum slip of the diagonal anchors was roughly $0.26\ mm$, while the maximum axial stress was limited to $1.5\ N/mm^2$.

The numerical force-displacement curve for phase 3, in comparison with the experimentally derived curve, is presented in Figure 5. The stiffness of the structure is well approximated, as is the capacity in the negative direction. As in the simulation of the previous phase, an overestimation of the capacity in the positive direction was obtained, but this overestimation is much reduced in this phase. The hysteresis cycles are well approximated up to a displacement of $20\ mm$ and $40\ mm$ in the positive and negative directions respectively. The residual resistance of the wall in the positive direction is very well approximated and is slightly overestimated in

the negative direction.

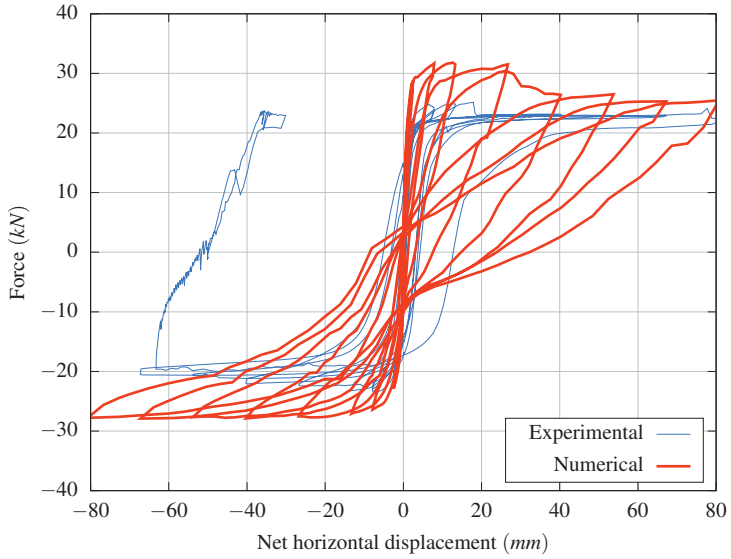

Figure 5: Comparison of experimental with numerically-derived force-displacement curves for phase 3.

The cracking pattern obtained numerically for phase 3 is shown in Figure 6. In the negative loading direction the network of mostly horizontal cracks formed at the lower right portion of the base of the wall is reproduced numerically. The cracks at the lower left of the window are partially reproduced, while the horizontal crack starting at the upper right edge of the window is partially reproduced in the simulation. For applied positive displacement, the horizontal crack at the upper left edge of the window propagates to a greater degree and is in better agreement with the experimental results. The length of the crushed toe is negligible due to the low ratio of applied vertical stress over the compressive strength.

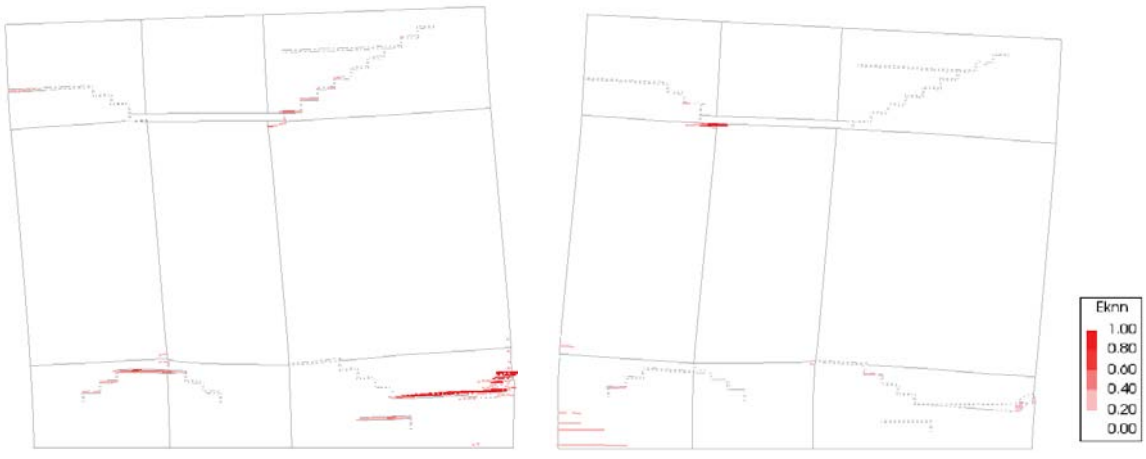

(a) (b)

Figure 6: Numerically obtained crack patterns, as crack strain vectors parallel to the crack in red, for phase 3 at: a) peak negative displacement and b) peak positive displacement.

Similarly to the results obtained in phase 1 and 2, slipping in the horizontal bars is negligible.

However, the peak axial stress registered at the lower right of the opening for maximum applied horizontal displacement was 239.1 N/mm^2, which is slightly higher than the yield strength. The maximum slip of the diagonal anchors was 8.2 *mm* and the maximum axial stress 21.9 N/mm^2.

The behaviour of the reinforcement at key locations on the structure is detailed in Figure 7. The axial stress of the bed joint reinforcement follows a generally linear correlation with the applied net displacement, up to an applied displacement of 40 *mm*. For higher applied displacement the peak axial stress hovers at a plateau of roughly 230 N/mm^2, which is higher than the yield stress of 215 N/mm^2. The bond-slip at the diagonal bars above the window opening remain below than 1 *mm* for an applied displacement lower than 7.91 *mm*. For higher levels of applied displacement, the bond-slip obtained at the peak of the load cycle increases linearly with the net horizontal displacement.

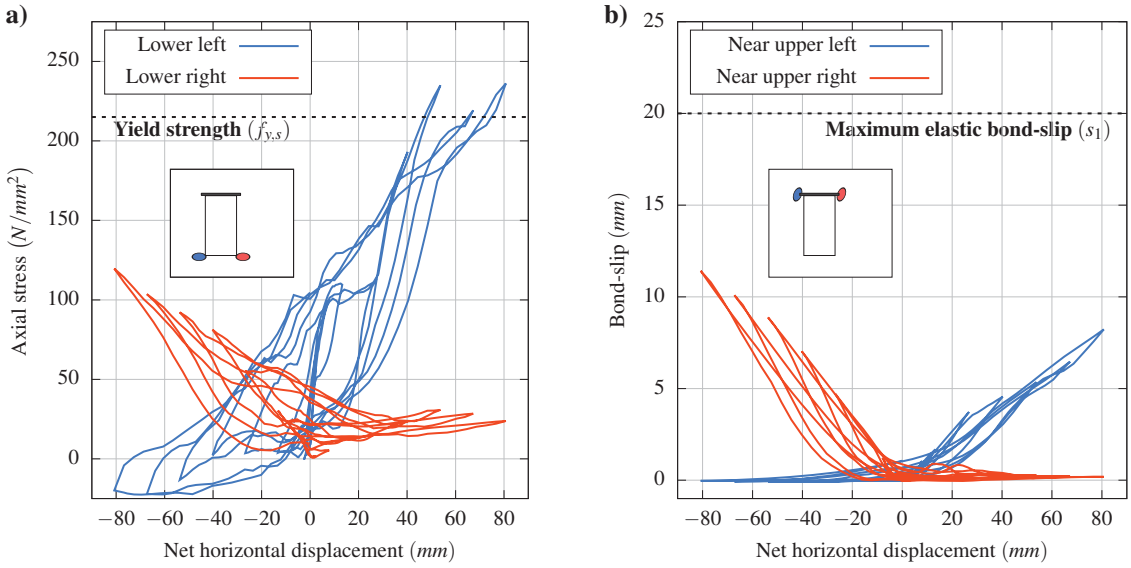

Figure 7: Numerically calculated behaviour of reinforcement during phase 3: a) axial stresses at bed joint reinforcement bars below the window opening and b) bond-slip of diagonal anchors above window opening. Locations of measurement indicated in colour-coded wall drawing insets.

It is generally concluded that the diagonal anchors, due to the low stiffness of their bond with the masonry, develop very low axial stresses and exhibit substantial bond-slip. Increasing the bond with the masonry through an enhancement of the mechanical anchoring of these bars could potentially increase their contribution to the behaviour of the strengthened wall. Conversely, the bed joint bars, which feature a stronger bond with the repair mortar, contribute more substantially to the response of the wall through the restraint of diagonal crack propagation. Bond-slip is negligible but yielding occurs below the window opening for high applied net displacement. Due to their orientation, these bars do not contribute to the rocking mode capacity of the piers, but are nevertheless effective in reducing crack propagation, particularly in the spandrel.

Overall, without resorting to any undue calibration of material parameters, the numerical effort is able to reproduce the main characteristics of the response registered in the experiments. This renders the numerical results a valuable tool in the assessment of the performance of the reinforcement, direct measurements of which were not possible to be acquired during the experiments. Finally, the capture of the main characteristics of the response through the model paves the way for application in larger and more complex cases.

5 CONCLUSIONS

The performance of bed joint reinforced repointing as employed for masonry structures in the Groningen region of the Netherlands was investigated. A masonry structure subjected to settlement-induced damage, followed by in-plane seismic loading was experimentally tested. The structure was strengthened using a technique widely employed in practice but lacking in rigorous experimental validation.

The reinforcement was experimentally shown to provide a modest increase to the in-plane stiffness and force capacity of masonry walls, in addition to a substantial increase in displacement capacity. This is accomplished despite the presence of damage induced by settlement and prior seismic loading. The strengthening is shown to prevent new diagonal cracks from forming in the spandrels, reduces the obtained crack width and reduces the crack propagation length.

The experimental tests were simulated numerically for assisting in the interpretation of the experimental results and for the investigation of the performance of the bed joint reinforcement and anchors. The numerical reproduction of the tests highlights crucial aspects in the performance of the reinforcement. Minimal bond-slip occurs and high axial stresses are developed in the bed joint bars. Conversely, the diagonal anchors exhibit substantial slipping and low axial stresses. It is therefore concluded that the contribution of the bed joint reinforcement is more substantial than that of the anchors.

ACKNOWLEDGEMENTS

This research was funded by the Rijksdienst voor het Cultureel Erfgoed (RCE), part of the Ministerie van Onderwijs, Cultuur en Wetenschap (OCW), subsidy No. MS-2018-189, which is gratefully acknowledged.

REFERENCES

[1] G. Foulger, MP. Wilson, JG. Gluyas, BR. Julian, RJ. Davies. Global review of human-induced earthquakes. *Earth-Science Reviews*, **178**, 438–514, 2018.

[2] M. Son, EJ. Cording. Evaluation of Building Stiffness for Building Response Analysis to Excavation-Induced Ground Movements. *Journal of Geotechnical and Geoenvironmental Engineering*, **133**, 995–1002, 2007.

[3] P. Van Staalduinen, K. T, JG. Rots. Onderzoek naar de oorzaken van bouwkundige schade in Groningen Methodologie en case studies ter duiding van de oorzaken. Report no. CM-2018-01, Delft University of Technology, 2018.

[4] VG. Haach, G. Vasconcelos, P. Lourenço. Parametrical study of masonry walls subjected to in-plane loading through numerical modeling. *Engineering Structures*, **33**, 1377–1389, 2011.

[5] N. Ismail, RB. Petersen, MJ. Masia, JM. Ingham. Diagonal shear behaviour of unreinforced masonry wallettes strengthened using twisted steel bars. *Construction and Building Materials*, **25**, 4386–4393, 2011.

[6] RB. Petersen, MJ. Masia, R. Seracino. In-Plane Shear Behavior of Masonry Panels Strengthened with NSM CFRP Strips. I: Experimental Investigation. *Journal of Composites for Construction*, **14**, 754–763, 2010.

[7] L. Licciardello, JG. Rots, R. Esposito. Performance of unreinforced masonry strengthened with bed joint reinforced repointing. In *12th International Conference on Structural Analysis of Historical Constructions, Barcelona, Spain*, 2020.

[8] S. Jafari, JG. Rots, R. Esposito, F. Messali. Characterizing the Material Properties of Dutch Unreinforced Masonry. *Procedia Engineering*, **193**, 250–257, 2017.

[9] CEN. *EN 1052-1 - Methods of test for masonry - Part 1: Determination of compressive strength*. 1999.

[10] CEN. *EN 1052-3 - Methods of test for masonry - Part 3: Determination of initial shear strength*. 2002.

[11] CEN. *EN 1052-5 - Methods of test for masonry - Determination of bond strength by the bond wrench method*. 2005.

[12] L. Licciardelo, R. Esposito. Experimental study on unreinforced masonry strengthened with bed joint reinforcement. Report no. CM1B07-2, Delft University of Technology, 2019.

[13] Federátion Internationale du Béton. *The fib Model Code for Concrete Structures 2010*. Wiley and Sons, 2013.

[14] PA. Korswagen, M. Longo, E. Meulman, JG. Rots. Crack initiation and propagation in unreinforced masonry specimens subjected to repeated in-plane loading during light damage. *Bulletin of Earthquake Engineering*, **17**, 4651–4687, 2019.

[15] JG. Rots, F. Messali, R. Esposito, S. Jafari, V. Mariani. Computational modelling of masonry with a view to Groningen induced seismicity. In *Structural Analysis of Historical Constructions: Anamnesis, diagnosis, therapy, controls - Proceedings of the 10th International Conference on Structural Analysis of Historical Constructions, SAHC 2016*, 227–238, 2016.

EURODYN 2020
XI International Conference on Structural Dynamics
M. Papadrakakis, M. Fragiadakis, C. Papadimitriou (eds.)
Athens, Greece, 23–26 November 2020

SEISMIC VULNERABILITY EVALUATION OF LONGHU PAGODA, SICHUAN, PRC

Peixuan Wang[1], Jacopo Scacco[1], Gabriele Milani[1], and Shengcai Li[2]

[1] Politecnico di Milano, Department of Architecture Built Environment and Construction Engineering
Piazza Leonardo da Vinci, 32, 20133, Milan, Italy
peixuan.wang@polimi.it, jacopo.scacco@polimi.it, gabriele.milani@polimi.it

[2] Yangzhou University, College of Civil Science and Engineering
Huayang Avenue, No. 198, Yangzhou, Jiangsu, China
lisc@yzu.edu.cn

Keywords: Masonry pagoda, FE simulation, Damage characteristics, Dynamic analysis, Earthquake

Abstract. *As an important historical relic of human being, masonry pagoda is the great significance in the eastern and western architectural cultures. These pagodas usually have large self-weight, low material strength, complex structure, which have been seriously affected by nature and man made because of their ages. Most of the existing masonry pagodas in China which have been seriously damaged urgently need detailed structural safety assessment, repair and reinforcement. In this paper, a simplified 3D model was used to evaluate the seismic vulnerability of masonry pagodas reliably. According to the previous numerical research in the field and post-earthquake surveys experience, assume for masonry a Concrete Damage Plasticity CDP material model, pushover analyses and non-linear dynamic analyses are carried out by Abaqus software. The aim is to predict the state, characteristics and distribution of damage of the structure in an accurate way. The approach is applied to Longhu pagoda (built in 1342 A.D.) which is the only yuan dynasty masonry pagoda in Sichuan province of China. Longhu pagoda is a brick pagoda with dense eaves, with a square plane and a height of about 33 meters. Affected by the Wenchuan earthquake in 2008, a north-south crack appeared from the bottom to the top of the pagoda's body. Despite the artificial repair of the cracks, the pagoda still faces the risk of structural damage. Through numerical simulation, the seismic performance of the pagoda can be evaluated, which can not only predict the hidden danger and weak link in its structure, but also provide useful reference for the reinforcement and repair of the pagoda.*

1 INTRODUCTION

China is an ancient country with a history of 5,000 years, and has countless architectural wonders with exquisite structures and beautiful shapes [1]. The ancient masonry pagoda which is one of Chinese significant art treasures draws on the basic mechanical principles of the barrel structure, and integrates into the history and culture of the China. It is a reflection of the skills of high-rise buildings in ancient, is an important milestone in the development of Buddhism, and is also a distinctive sign on human masonry architectures [2-7].

The ancient Chinese pagoda was introduced with Buddhism and first appeared in Han Dynasty They were large-scale constructed in Sui Dynasty and reached its peak in Tang and Song Dynasties. The early plane of pagoda was square, evolved into octagon with time, and the height of pagoda became higher and higher. The construction method of them is using stacked bricks in traditional Chinese techniques, which is similar to other masonry buildings. Although their shape is ever-changing, and the use and functions are also different, almost all pagodas contain three parts (Figure 1): pagoda pedestal, pagoda body, pagoda spire, and some of them built underground palaces with scriptures reserved in it [8-15].

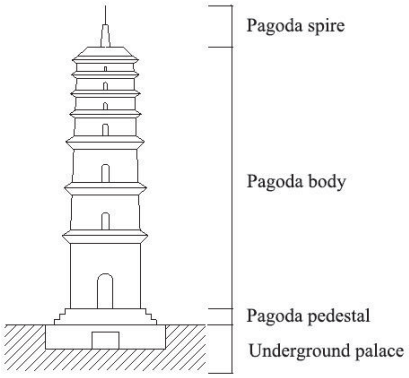

Figure 1: Schematic diagram of ancient pagoda structure

As far as pagodas' structures and material properties are concerned, they have the advantages of high compressive strength, weather resistance, fire resistance, corrosion resistance, low cost and so on. However, because Chinese masonry materials are mostly a mixture of glutinous rice juice, lime and sand, the pagodas' ability to resist tensile, shear and bending is poor. After hundreds of years influence from weather, war and other artificial destruction, these Chinese pagodas have suffered sorts of damages. Meanwhile, relevant research depicts that most structural damage and collapse of pagodas were caused by earthquakes [16]. China is located in the intersection of the Pacific Rim earthquake belt and the Eurasian earthquake belt. According to the collection of statistics, there were three major earthquakes with seismic wave magnitudes greater than or equal to 8.5 in the 20th century, and two of them occurred in China. Therefore, It is one of the countries most severely affected by earthquake disasters in the world. The seismic activity in this area has characteristics of wide distribution, high intensity, high frequency [17-19].

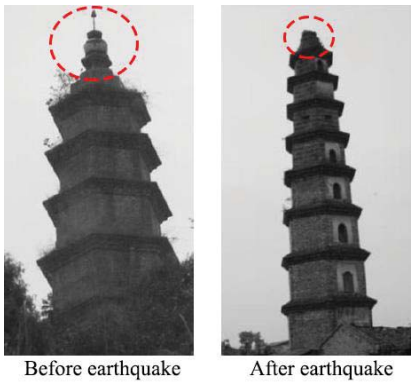

(a) Damage characteristics 1)

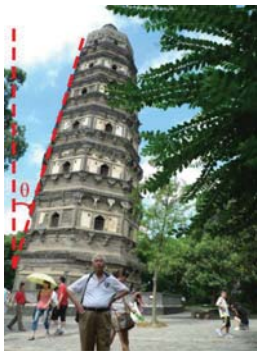

(b) Damage characteristics 2)

(c) Damage characteristics 3)

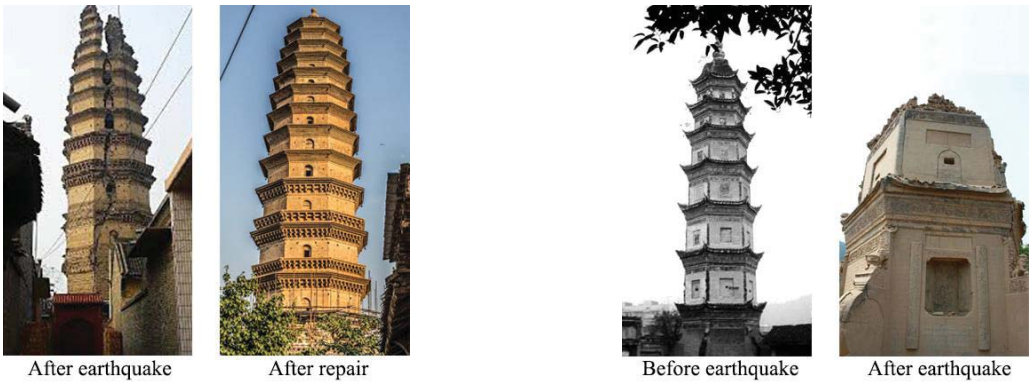

(d) Damage characteristics 4) (e) Damage characteristics 5)

Figure 2: Damage characteristics of pagodas [19]

After subjected to earthquakes, the accumulation of damage will lead to collapse of pagoda that is major threat of structural safety. The main damage characteristics of pagodas which were made by earthquake are following (Figure 2): 1) the tilt and collapse of pagoda spire, 2) the tilt and bend of pagoda body, 3) the break in the middle part of the pagoda, 4) the split of pagoda body along the central axis, 5) overall collapse [19].

In recent years, scholars have made outstanding contributions to the research on the dynamic performance, seismic resistance and structural damage of masonry pagoda structure. Y.G. Shen et al. discussed the seismic mechanism and dynamic performance of ancient masonry pagodas in China based on site surveys, subsequent reinforcement data, and the structural characteristics of Xi'an Xiaoyan pagodas [20-21]. J.L. Yuan et al. used a classical theoretical method to calculate the model, combined with the actual pulsation method test results, established a more accurate numerical analysis model of Wenfeng Pagoda which is located in Yangzhou, and guide the seismic identification and reinforcement [22-25]. J.L. Lu, F. Zhu et al. also carried out dynamic characteristic tests and numerical calculations on various Chinese ancient pagodas. The weak links and damage mechanisms of the model structure under the action of earthquakes were also be observed which can provide a reference basis for further pagodas' damage identification, seismic response, maintenance and repair [26-31]. Subsequently, more and more scholars began to use FE software to build 3D models of pagodas to analyse the elastic and plastic properties of structures and materials, then obtained their seismic performance [32-40].

On the other hand, western scholars have also studied the seismic performance of pagoda structures such as churches, bell towers, castles, and tobacco countries. Anzani et al. took the Italian Civic Tower and the Noto Church as research objects, and analysed the effects of vertical cracks on masonry buildings. They concluded that these cracks were the main cause of the collapse of the tower [41]. G. Milani et al. also applied nonlinear static and dynamic analysis methods to assess the seismic performance of bell towers, churches, pagoda, and promoted the advancement of numerical simulation technology for masonry buildings [42,43]. Marco Valente et al. researched eight masonry towers in northeastern Italy, and conducted nonlinear static and dynamic analysis. The conclusion is drawn that the results obtained by the nonlinear static analysis method are slightly conservative [44].

In general, the current FE simulation technology has been widely used in the research of seismic vulnerability of ancient pagodas, and most of them has focused on the dynamic characteristics testing, seismic response analysis, seismic performance, reinforcement and structural damage. However, because of the complex and divers destruction factors, it is easy

to find that the current research selection of pagodas' structure features are not diversified and typical, the results which have been concluded is still limited.

Therefore, the theory and technology of the vulnerability analysis of masonry structures of pagodas in China still need to be improved. With the help of FE simulation, analysing the response of typical pagodas influenced by earthquakes, deducing the possible damage patterns, especially after the earthquake, finding the damage parts in time, predicting the development of damage, evaluating the extent of damage effectively, and proposing reasonable protection and reinforcement measures are still topics which are worthy to be focus on and need more in-depth research.

This paper selects Longhu pagoda which is a typical masonry pagoda as a case study. The pagoda has been damaged (now partially repaired) by Wenchuan earthquake which was the largest earthquake since the founding of China, and its main damage is cracks. Through Abaqus simulation, this research studied the seismic reaction and damage characteristics of Longhu pagoda during the Wenchuan earthquake, and provided the vulnerability analysis and seismic reinforcement repair of masonry pagoda, and all of the research results have important practical significance.

2 HISTORICAL CONTEXT AND LOCATION

Longhu pagoda (Figure 3) which was built in 1342 A.D. is located in Xiaoquan, Deyang, Sichuan province (East longitude 104°17′, North latitude 31°15′) and is the only preserved masonry pagoda made in Yuan dynasty (Figure 4). Because of its tall and straight appearance (around 12 m), it is the commanding point and visual center of Xiaoquan town. The early architectural features of Longhu pagoda are obvious, which is an significant evolution illustration of Chinese masonry pagoda. Meanwhile, it occupies an special position in the urban space with an important historical value [8, 9].

Figure 3: Longhu pagoda

Figure 4: Location of Longhu pagoda

Longhu pagoda has a square plan with 13 layers of eaves outside it, and is roughly 33 meters tall which contains 2 meters of stylobate and 31 meters of body. The main entrance of the pagoda is in the south, and the size of its eaves shrink from bottom to top especially above 8th layer, depicting a parabolic shape facade. The pagoda's body has windows on four sides, some of them are real, while others are decoration (Figure 5). From second to ninth layer, there are three windows on each side, but the number decreased to one on the upper layers [8].

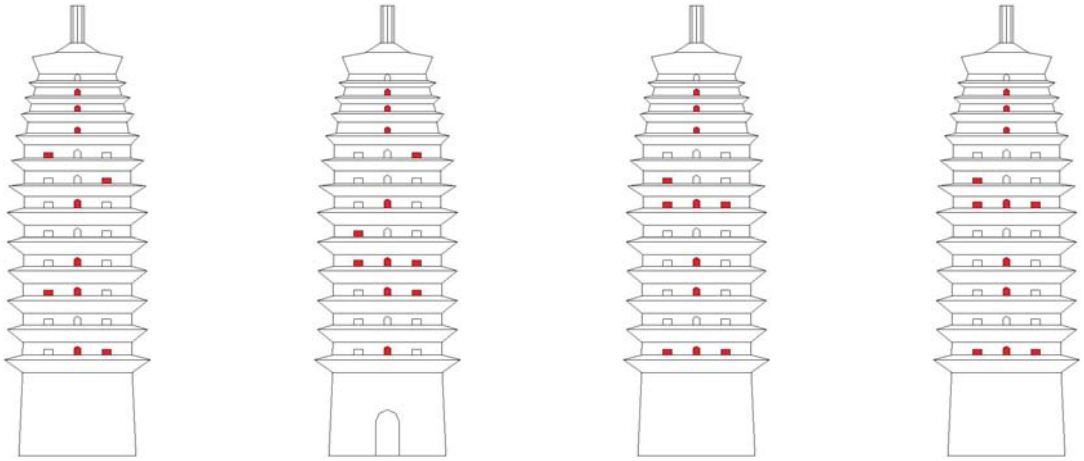

(a) East facade (b) South facade (c) West facade (d) North facade

Figure 5: Real windows of Longhu pagoda

Actually, there are only five real floors (Buddhas can be found in each of them) and a heavenly palace (a dome that penetrates the eleventh to thirteenth eaves) inside the pagoda (Figure 6). In each floor, there is a central room, with caissons and Dougongs on the roofs of the first to fourth floors, while the caisson of the fifth floor is empty that through to heavenly palace. Between the exterior and the central room, stairs spiral up clockwise connecting each center room (Figure 7).

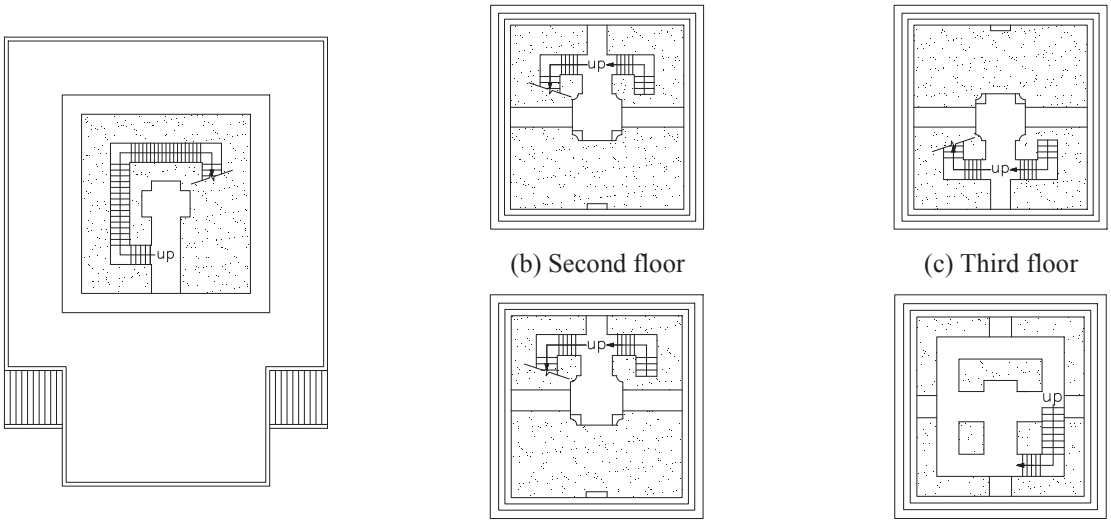

(a) First floor (b) Second floor (c) Third floor

(d) Fourth floor (e) Fifth floor

Figure 6: Plans of each floor in Longhu pagoda (Source: Adapted from document available in [8])

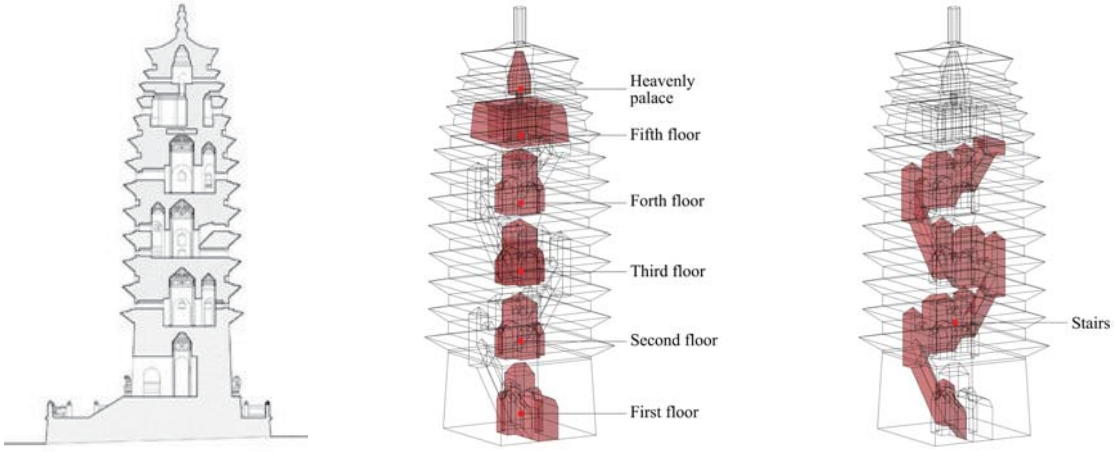

(b) Section (c) Central room of each floor (d) Stairs

Figure 7: Internal structure of Longhu pagoda (Source: Adapted from document available in [45])

3 EARTHQUAKE HISTORY

Sichuan province which is known as Chinese earthquake-prone area sits in the hinterland of southwest China (between east longitude 97°21′-108°33′ and north latitude 26°03′-34°19′). The province which shows various geomorphology from east area to west area is composed of mountains, hills, plain basins and plateaus. Its terrain is complex and diverse, and has a large height difference (Figure 8).

On May 12, 2008, a 8.0 magnitude Richter earthquake occurred in Wenchuan, Sichuan province, China, and the epicenter was in a small town whose name is Yingxiu. It was caused by the sudden release of long-term accumulated tectonic stress energy in the Longmen Mountain fault zone between the Qinghai-Tibet Plateau and the Sichuan Basin. The hypocenter depth that close to the surface is 10 km to 20 km, and whole earthquake lasted a long time (182 s - 194 s). Wenchuan earthquake is destructive and has a strong impact, its maximum acceleration peak value which appeared after the start of the crustal movement (65 s - 82 s) is nearly 424 cm/s^2. According to incomplete statistics, the earthquake killed around 69227 people, injured 376443 people, and 17923 people were missing. Large numbers of architectures were collapsed and cultural relics were severely damaged, which resulted immeasurable losses [45].

The position of Longhu pagoda is not very far away from the epicenter (about 100 km), and it was influenced by the east-west seismic wave. Because of the seismic intensity distribution map of Wenchuan earthquake, issued by the China Seismological Bureau (Figure 9), the earthquake damages to Longhu pagoda's structure should be analysed according to 8 degrees.

After Wenchuan earthquake, the aftershocks, which continued in Deyang area, also caused further damages of the pagoda. On July and August in 2008, Longhu pagoda suffered by many aftershocks which brought a long-term swing, and further increased the width, depth and length of the pagoda's cracks. Fortunately, with the earthquake rescue project, the pagoda received timely and effective protection that help it to defend against risks made by aftershocks.

Figure 8: Chinese Earthquake Belt

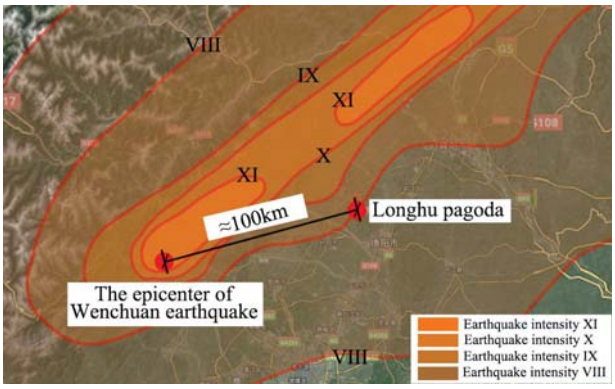

Figure 9: Earthquake intensity distribution of Wenchuan earthquake (2008) (Source: Adapted from document available in [45])

4 GEOMETRICAL AND DAMAGE SURVEY

The Longhu pagoda, which has been subjected to a huge earthquake load, suffered great damage during the Wenchuan earthquake, but it did not collapse. All of the damage can be concluded in the following [45]:

1) Through on-site observation, no significant tilt of the pagoda body was found, the status of its foundation was good, and only the lower part collapsed.

2) From the bottom to the top of the pagoda, a north-south crack appeared. The crack developed along the height, and the higher the position, the wider the crack width (Figure 10).

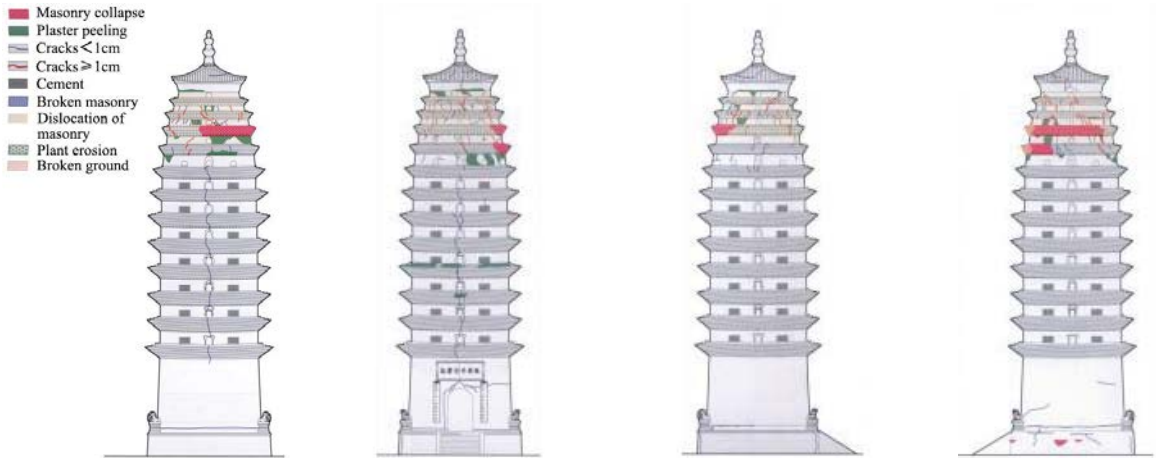

(a) North facade (b) South facade (c) West facade (d) East facade

Figure 10: Cracks on the Longhu pagoda (Source: Adapted from document available in [45])

3) The damage of Longhu pagoda from the outer 9 layers (the inner 5 floors) to the top was severe. The diagonal cracks at the four corners were wide and the maximum crack width was 10cm, which caused the pagoda instability.

4) Corresponding to the mentioned cracks, some cracks could also been found on the roofs or the walls around the doors which connect it central rooms and stairs.

5) There are dense and severe oblique cracks around the walls of the central rooms, these walls are facing collapse and the surrounding eaves (from outer 9 to 11 floor) already collapsed in many places.

6) Cracks also appeared in the central rooms of each floor. Their width increased along the height, and the tops of the five floor partially collapsed.

7) The windows on both the south and north sides of each floor were severely damaged, and some of them which located above outer 8 floors (inner 5 floors) were severely collapsed.

8) The pagoda spire is basically intact, and only a few cracks can be found.

5 NUMERICAL SIMULATIONS

With the aim to analyse the seismic vulnerability of the pagoda and to study how the damage spread within the structure, several non-linear numerical simulations are performed by means of FE-based software Abaqus.

A numerical model based on a macro-modeling approach is here proposed. The discretization of the pagoda is made by means of around 87000 solid linear elements (Figure 12 (a)). Such an amount is a reasonable compromise between reliability and computational speedy. Concerning the boundary conditions for the purpose of the study, as the condition of foundations results to be in good condition, fixed supports are considered at the base of the pagoda. The non-linearities of the material are introduced taking advantage of the already implemented constitutive model Concrete Damage Plasticity. CDP is a isotropic plastic-damage based model which allows a differential behavior under compression and tension. Its yield surface follows the Drucker-Prager function, which shape is opportunely modified in order to approximate a Mohr-Coulomb surface. Other parameters are input with the scope to smooth the yield surface and tackle computational issues. However, a lower value of the viscosity parameter is always preferable in order to not lead to an overestimation of the capacity of the structure. The behavior under compression is described by a parabolic softening (Figure 11), whereas the tensile behavior follows a linear or exponential softening. In this work as the tensile non-linear properties are input through a fracture energy approach (Table 1) a linear softening is accounted. The degradation of the elastic stiffness is determined by two variables of damage dt and dc, functions of the plastic strains. Such variables vary between a value of 0 for the undamaged material and 1 for the material that has completely lost any stiffness In the following tables a list of material properties is provided along with the parameters related to the definition of yield surface of CDP (Table 2).

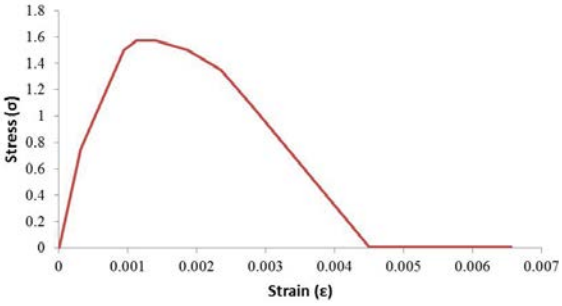

Figure 11: Stress-strain curve for the masonry material

Young's Modulus	1600 MPa
Specific Weight	18 kN/m^3
Compression Strength	1.5 MPa
Tensile Strength	0.05 MPa
Tensile Fracture Energy	0.007 N/mm

Table 1: Mechanical properties

Dilatancy Angle	Eccentricity	fb0/fc0	Viscosity Parameter
10°	0.1	1.16	0.0001

Table 2: Input parameters in the CDP

Firstly, an eigenvalues analysis is carried out with the scope to validate the efficacy of the model and to obtain the different vibration modes (Figure 12). As expected from a structure like-tower the first two vibration modes are translational modes respectively along the Z^- direction and X^- direction. The frequencies related to the first and second mode are very close

(1.61 Hz and 1.67 Hz) giving a clear indication of an almost equal stiffness of the structure in the two directions. The third mode is the rotational one corresponding to a frequency of around 5.17 Hz.

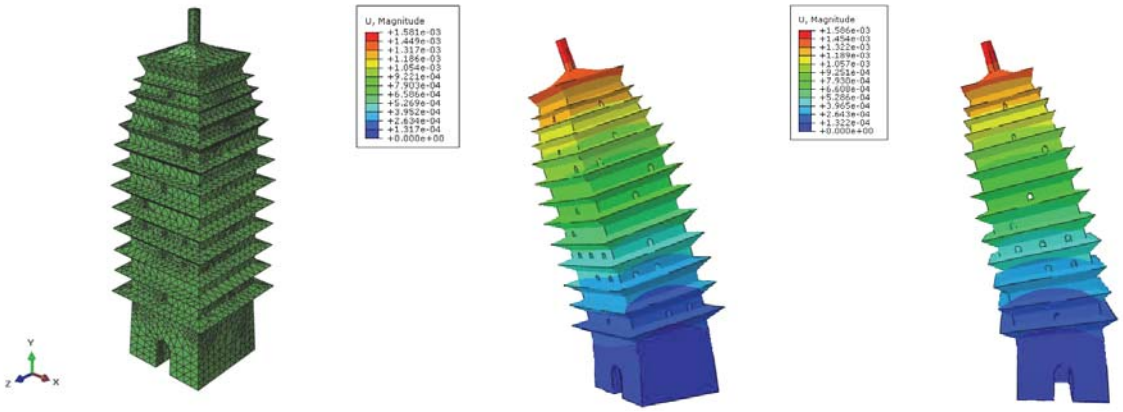

(a) Geometric configuration and discretization of the pagoda in Abaqus

(b) 1st mode: 1.61 Hz

(c) 2nd mode: 1.67 Hz

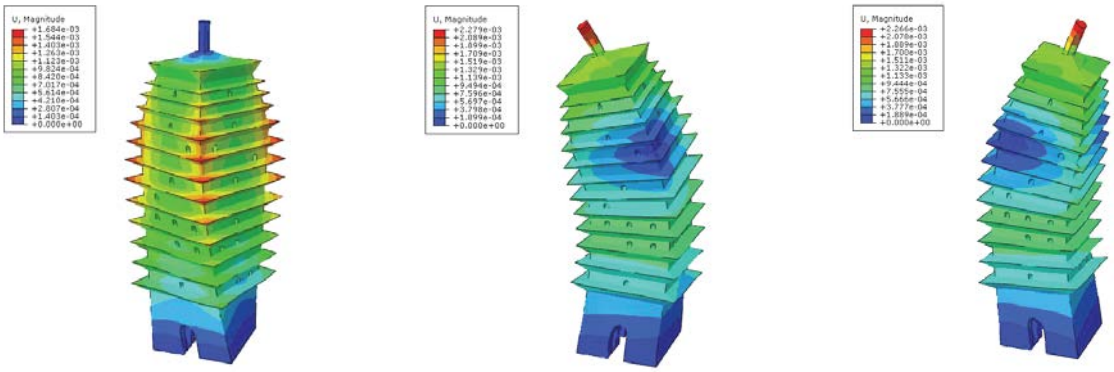

(d) 3rd mode: 5.17 Hz

(e) 4th mode: 6.97 Hz

(f) 5th mode: 6.99 Hz

Figure 12: Different vibration modes in numerical simulations

6 PUSHOVER ANALYSIS

Four different pushover analyses are performed (one for each direction) by applying a uniform distribution along the height. Despite of the symmetry of the structure, some differences in the damage among the four analyses deserve to be deeply discussed. For each analysis it is provided the progressive crack configuration along with the capacity curve Load Factor-Displacement.

6.1 Pushover X^- direction

The first analysis is carried out by "pushing" the structure along the direction E-W. The damage starts to spread at the bottom of the structure and just above the main entrance. This latter then develops in a vertical crack which involves almost 2/3 of the total height on the south facade. On the north facade it is provided the damage configuration at the last step where a diagonal crack occurs. The global behavior of the structure is described by the capacity curve. From this latter it is possible to identify that around a load factor of 0.15 g the pagoda stopped working under elastic regime (in correspondence of almost 0.03 m).

Afterwards, the non-linear response is described by a plateau in correspondence of a load factor nearby 0.16 g and a final displacement of about 0.13 m (Figure 13).

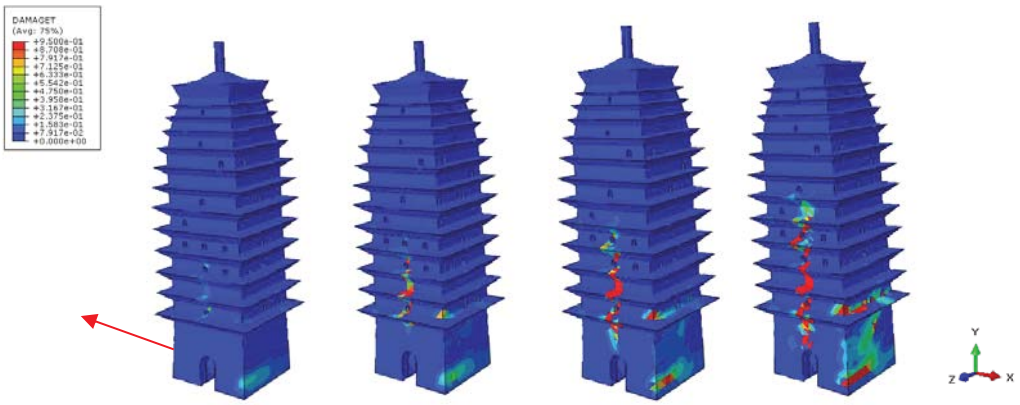

(a) Damage on the east facade and south facade

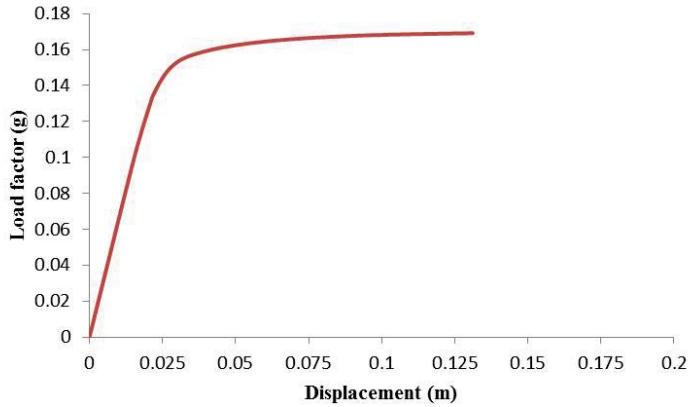

(b) Load factor-displacement curves

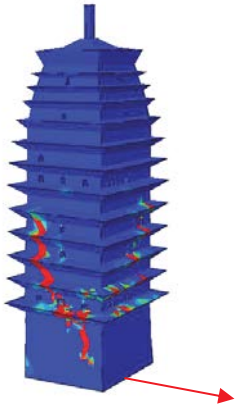

(c) Damage on the west facade and north facade

Figure 13: Results of pushover analysis in X^- direction

6.2 Pushover X^+ direction

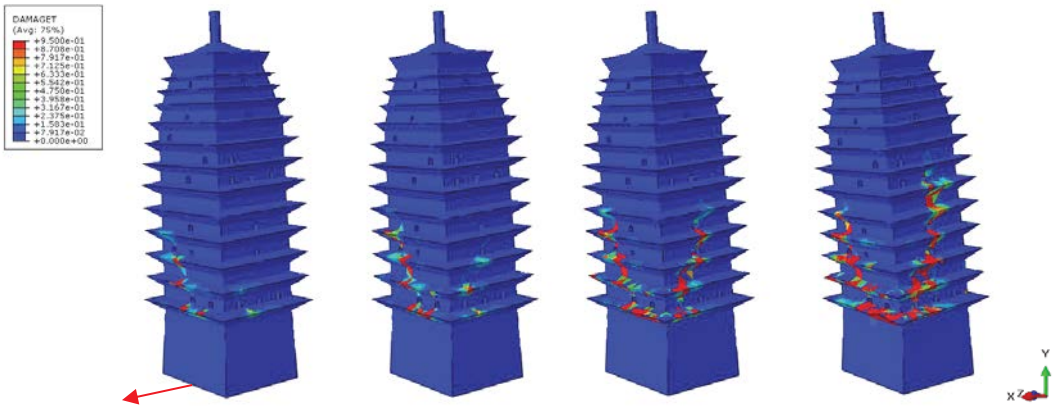

(a) Damage on the east facade and north facade

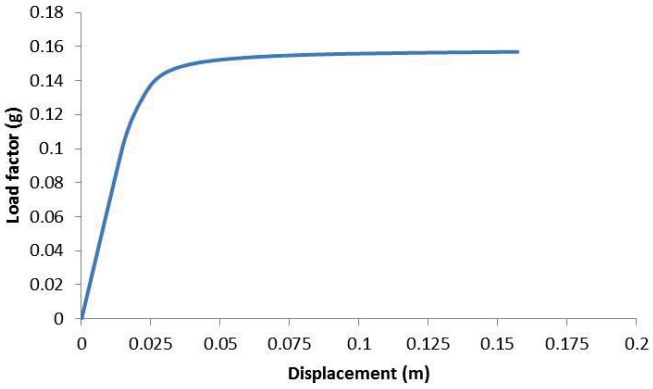

(b) Load factor-displacement curves

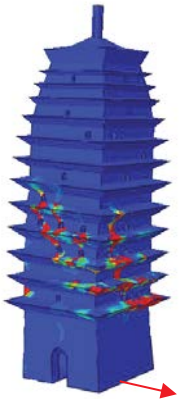

(c) Damage on the east facade and south facade

Figure 14: Results of pushover analysis in X^+ direction

From the pushover along the W-E direction a similar capacity curve is obtained. However, a different spread of the damage can be noticed. Indeed, the first crack occurs on the East facade where the presence of the stairs represent a weakness of the structure (Figure 14). On the North facade the crack is pretty similar with the one obtained in the previous analysis but involving more the upper part of the structure. Even on the South facade it is noticeable a difference. In place of a vertical crack, a more diffused damage characterizes the center of the structure.

6.3 Pushover Z^- direction

The pushover analysis along S-N direction is characterized by the lowest value of load factor (0.12 g) and displacement (0.13 m). Again, the presence of the stairs probably induces on the East facade a concentration of damage, leading to a overturning mechanism just above the first floor (Figure 15).

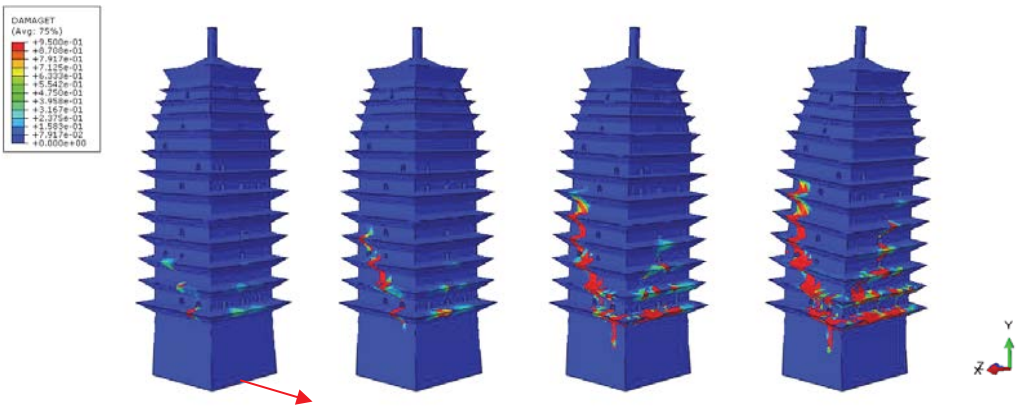

(a) Damage on the east facade and north facade

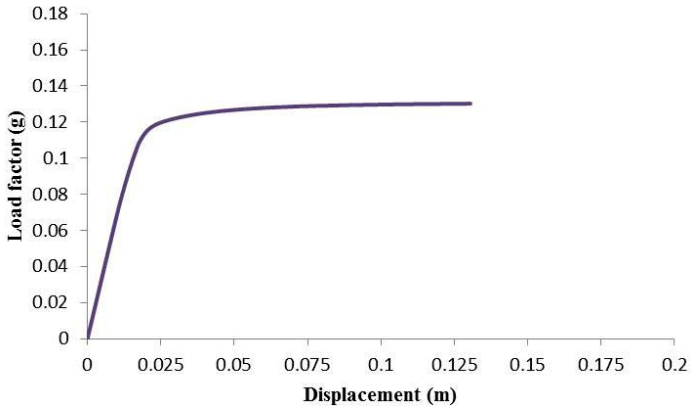

(b) Load factor-displacement curves

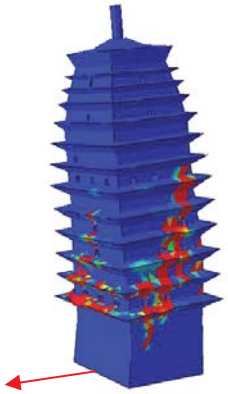

(c) Damage on the west facade and north facade

Figure 15: Results of pushover analysis in Z^- direction

6.4 Pushover Z^+ direction

The analysis along the N-S direction leads to a damage configuration almost purely vertical on both facades. The capacity load factor results close to 0.16 g with a final displacement slightly above the previous analyses: 0.18 m (Figure 16).

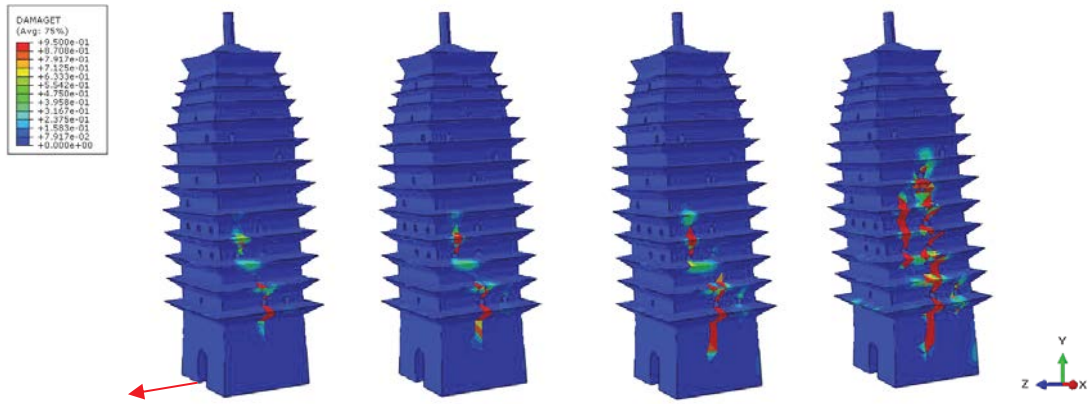

(a) Damage on the east facade and south facade

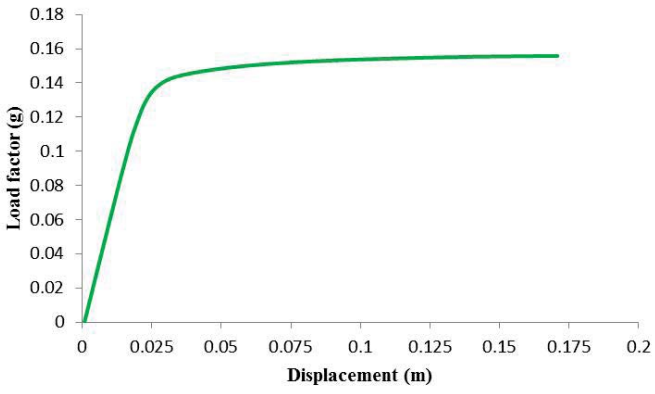

(b) Load factor-displacement curves

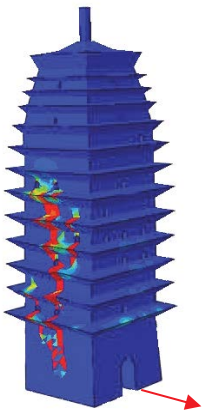

(c) Damage on the south facade and west facade

Figure 16: Results of pushover analysis in Z^+ direction

6.5 Dynamic Analysis

Along with the above discussed non-linear static analyses, a dynamic non-linear analysis is presented in this section. A real accelerogram recorded on 12 May 2008 has been filtered and corrected and applied to the pagoda along the E-W direction in order to provide a numerical comparison with pushover analyses and even with the real damage configuration observed after the Wenchuan earthquake. The PGA is almost equal to 0.2 g in correspondence of 2.76 sec. As it is noticeable from the crack evolution, by means of dynamic analysis it is possible to track the damage of the pinnacle, impossible to obtain with pushover analysis. The rest of the damage is pretty similar with the one resulting from the Pushover X^- (Figure 17). A vertical crack occurred on the North facade along with a diagonal crack on the East facade, involving even the upper part of the structure in correspondence of the openings.

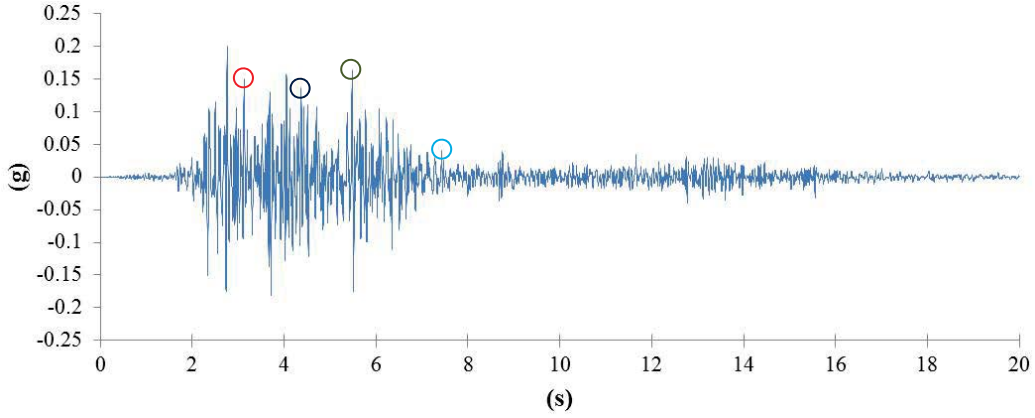

(a) Accelerogram of Wenchuan earthquake which has been filtered and corrected

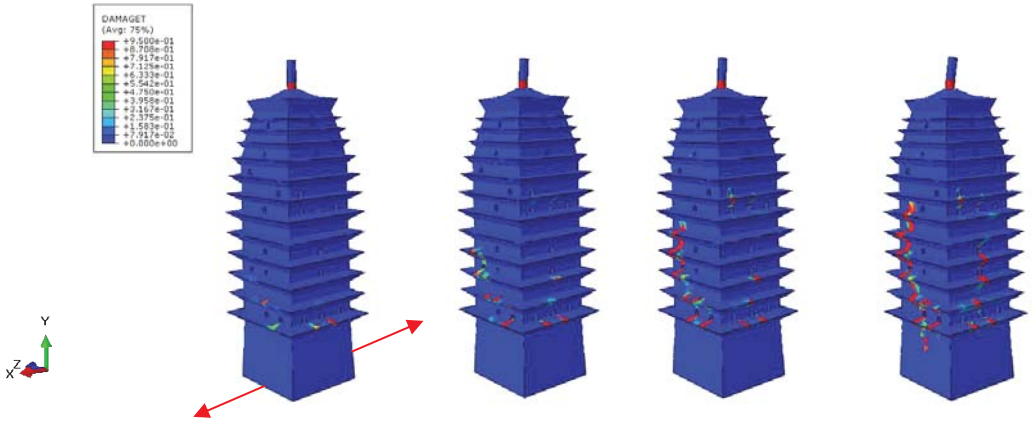

Figure 16: Results of dynamic analysis

7 CONCLUSIONS

In this paper, the Longhu pagoda which is located in the high-intensity area of the Wenchuan earthquake was taken as the case study.Combined with relevant survey data, a solid model was created by CAD, and Abaqus was used for seismic dynamic response analysis. In the numerical simulation, the load factors and displacement were used as the analysis objects. The damage process of the pagoda was evolved, and its weak parts were found out. By comparing with the relevant data, the damage characteristics of the Longhu

pagoda in the earthquake were attempted to be summarized. The main conclusions are as follows:

1) The Abaqus software is used for mode analysis and dynamic analysis. The mode analysis can reflect the dynamic characteristics of the structural model, and illustrates the reliability of the FE simulation. In the numerical simulation, the stress concentration in the windows is more obvious, and the cracks show X shape along them. At the same time, the location of the internal staircase is also the main weak link of the structure, and the cracks develop diagonally on the building surface along the direction of the stair construction.

2) Without considering the dynamic interaction between soil and structure, the cracks of Longhu pagoda first appeared at the door and window openings of the first floor, and gradually developed along the weak links of each floor. The final simulation results indicate that the structure of first floor is in an elastic state, and the structures of second, third, and fourth floors are in a state of slight damage. More than five floors, its structure may reach a serious damage state, which is close to the ultimate damage.

3) Several non-linear static and dynamic analyses have been presented on the particular case of the Longhu pagoda, severely affected by Wenchuan earthquake. The most remarkable outcome to highlight is the great efficacy of pushover analyses in reproducing the damage observed after the earthquake, specifically the vertical crack on the South and North facades. On the one hand the non-linear dynamic analysis allows to put in evidence the accuracy provided by the pushover analyses but moreover gave useful information about the crack propagation of the upper part and nearby the pinnacle. On the other hand, pushover analysis seem to underestimate the capacity load that in average settles down around 0.16 g.

ACKNOWLEDGEMENTS

Mrs Peixuan Wang would like to acknowledge the financial support received by Chinese Scholarship Council, Popular Republic of China PRC (CSC Scholarship) for performing her Ph.D. program at the Technical University of Milan, Italy.

The analyses were partially developed within the activities of ReLUIS (Rete dei Laboratori Universitari di Ingegneria Sismica – Network of the Italian University Laboratories of Seismic Engineering), for the research program funded by the Department of Civil Protection, Executive Project 2019, gratefully acknowledged by the authors.

REFERENCES

[1] H.L. Xu, Chinese Ancient Pagoda Shape, *China Forestry Publishing*, 2006.

[2] J.H. Si, K. Li, J.L. Lu, et al., Numerical Analysis of Seismic Damage of Masonry Pagoda structure in Chongshou Temple, *Journal of Xi'an University of Technology*, 34(02): 153-158, 2018.

[3] C. Ge, M.Z. Tian, Research on the Safety Evaluation of Ancient Stone Pagodas in the Earthquake: a Case Study of Qingjing Pagoda, *Chinese Cultural Relics Research*, (02):46-50, 2013.

[4] L. Yao, Research and Application of Dynamic Characteristics Modeling Technology of Ancient Masonry Pagoda, *Yangzhou University*, 2003.

[5] M.Q. Zhang, Architectural Features of Ancient Pagoda in Sichuan Province, *Chongqing University*, 2009.

[6] H.D. Li, C. Ge, Killing with Kindness： Seismic Wisdom of Ancient Chinese Buildings, *National Geographic*, (06): 74-79, 2009.

[7] Z.W. Luo, Chinese Ancient Pagoda, *Beijing: China Youth Publishing House*, 1985.

[8] Y. Liu, Study on the Damage Characteristics of the Longhu Pagoda in the Wenchuan Earthquake, *Yangzhou University*, 2012.

[9] D.Y. Ren, Experimental Study on the Impact of Earthquake Damage on the Dynamic Characteristics of Masonry Pagoda, *Yangzhou University*, 2016.

[10] Z.X. Zhou, J.S. Ma, H. Z, Nonlinear FE Analysis of Seismic Performance of Bolin Pagoda, *Industrial Architecture*, 40(02): 74-76+63, 2010.

[11] D.H. Li, L. Wei, Historical Damage and Seismic Mechanism of Ancient Masonry Pagodas, *Architecture Science*, 6(01): 13-18, 1990.

[12] Y.Z. Tao, Reinforcement of Chinese Leaning Pagoda: Huqiu Pagoda in Suzhou Province, *Journal of Architectural Structures*, 8(12): 177-180, 1987.

[13] J.L. Wang, Analysis of the Research Status of Ancient Masonry Structures, *Earthquake resistance and Reinforcement of Engineering*, 33(04): 116-119, 2011.

[14] Z.L. Zhan, Ancient Pagoda Tilting and Strengthening Technology, *China Railway Press*, 2011.

[15] Q.F. Yao, J.L. Lu, Y. Zhang, Discussion on Anti-seismic Reinforcement Measures of Masonry Ancient Pagoda, *Industrial Architecture*, 37(09): 115- 118, 2007.

[16] Y. Pan, C. Wang, C.L. Ji, et al., Investigation and Analysis of Earthquake Damage to Ancient Masonry Pagodas during the Wenchuan Earthquake, *Sichuan Building Science Research*, 38(06): 156-159, 2012.

[17] Q. Zhou, W.M. Yan, X.S. Yang, et al., Damage to Ancient Buildings Caused by the Wenchuan Earthquake, *Heritage and Archeology*, 22(01): 37-45, 2010.

[18] Y. Zheng, Y.T Zhang, Investigation and Reflection on the Damage of the Main Buildings in the Wenchuan Earthquake, *Journal of Huazhong University of Science and Technology (Urban Science Edition)*, 26(02): 95-98+102, 2009.

[19] Q.F. Xie, J.Y. Xue, H.T. Zhao, Investigation and Enlightenment of Ancient Buildings in Wenchuan Earthquake, *Journal of Architectural Structures*, 31(S2):18-23, 2010.

[20] Y.G. Shen, Analysis of Seismic Performance and Foundation Structure of Xiaoyan Pagoda, *Xi'an University of Architecture and Technology*, 2010.

[21] P. Chen, D. Zhao, Q.F. Yao, Discussion on Seismic Capacity of Xi'an Xiaoyan Pagoda, J*ournal of Xi'an University of Architecture and Technology*, 31(02): 149-151, 1999.

[22] J.L. Yuan, S.C. Li, Q.Y. Lu et al., Research on Modeling Method of Dynamic Characteristics of Ancient Masonry Pagoda, *Engineering Earthquake Resistance*, 21(01): 22-25, 1998.

[23] J.L. Yuan, S.C. Li, D.Q. Liu et al., Research and Application of Seismic Identification Method for Ancient Masonry Pagoda, *Journal of Yangzhou University (Natural Science Edition)*, 2(03):30-31, 1999.

[24] J.L. Yuan, Simplified Calculation Method of Basic Period of Ancient Masonry Pagoda, *Earthquake Engineering and Engineering Vibration*, 35(02): 151-156, 2015.

[25] J.L. Yuan, H. Fan, H.B. Chen et al., Experimental Study on Dynamic Characteristics of Huqiu Pagoda, *Engineering Mechanics*, 22(05): 158-164, 2005.

[26] J.L. Lu, J.Z. Li, K. Li, Test and Analysis of Dynamic Characteristics of Pagoda in Cideng Temple, *Journal of Xi'an University of Technology*, 33(01): 7-12, 2017.

[27] J.L. Lu, Dynamic Characteristics and Structural Damage Analysis of Masonry Pagoda, *Mechanics and Practice*, 38(05):506-566, 2016.

[28] J.L. Lu, J.H. Si, P.G. Tian, Test and Analysis of the Dynamic Characteristics of the Pagoda of Xingjiao Temple, *Architecture Structure*, 47(21): 105-108, 2017.

[29] T.C. Chen, H. Deng, X.H. Luo, Study on Dynamic Test and Characteristics of Jinbiezhou Pagoda, *Vibration and Shock*, 29(04): 193-196, 2010.

[30] F. Zhu, Experimental Study on Seismic Performance of Chinese Dinosaur Pagoda, *Harbin Institute of Technology*, 2011.

[31] Y.X. Hu, Research on Modal Parameter Identification of Ancient Masonry Pagoda Based on Environmental Dynamic Test, *Yangzhou University*, 2012.

[32] J.Y. Wei, Study on Seismic Protection of Ancient Pagodas: Analysis of Linear Elastic Seismic Response of Ancient Pagodas, *Xi'an University*, 2005.

[33] J.Y. Yue, Y.T. Wang, Research on the Dynamic Characteristics of Kaifeng Pagoda, *Architecture science*, 24(03): 15-24, 2008.

[34] J.Y. Yue, Y.W. Peng, Study on Dynamic Characteristics of Huiming Pagoda in Tang Dynasty, J*ournal of Huazhong University of Science and Technology (Urban Science Edition)*, 25(04): 107-110, 2008.

[35] J. Gao, D.F. Su, Structural Characteristics and Seismic Performance of Fawang Pagoda in Xianyou Temple, *Earthquake Resistance and Reinforcement of Engineering*, 30(05): 107-110, 2008.

[36] T.T. Zheng, Analysis of Seismic Performance of Ancient Masonry Pagodas and Discussion of Reinforcement Schemes, *Xi'an University of Architecture and Technology*, 2008.

[37] J.F. Hou, S.J. Su, S.L. Wang, Test and Research on the Dynamic Characteristics of a Masonry Pagoda, *Sichuan Building Science Research*, 36(01): 141-144, 2010.

[38] J.Y. Wei, D.P. Zhang, Study on Dynamic Characteristics of Ancient Masonry Pagoda, *Earthquake Resistance and Reinforcement of Engineering*, 30(05): 103-106, 2008.

[39] X.L. Li, J.L. Lu, Analysis of Xuanzang Pagoda in Xuanjiao Temple Frequency Domain Seismic Response, *Journal of Xi'an University of Technology*, 31(04): 422-427, 2015.

[40] Y. Pan, Z.C. Wang, F. Shang et al., Study on the Isolation and Reinforcement Scheme of an Ancient Masonry Pagoda in Sichuan Province, *Journal of Southwest Jiaotong University*, 53(03): 540-547, 2018.

[41] Anzani, L. Binda, G. Mirabella Roberti, The Effect of Heavy Persistent Actions into the Behavior of Ancient Masonry, *Material and Structures*, 33(04): 251-261, 2000.

[42] G. Milani, M. Simoni, A. Tralli, Advanced Numerical Models for the Analysis of Masonry Cross Vaults: A Case Study in Italy, *Engineering Structures*, 76: 339 – 358, 2014.

[43] M. Valente, G. Milani, Advanced Numerical Insights into Failure Analysis and Strengthening of Monumental Masonry Churches under Seismic Actions, *Engineering Failure Analysis*, 103: 410-430, 2019.

[44] M. Valente, G. Milani, Non-linear Dynamic and Static Analyses on Eight Historical Masonry Towers in the North-East of Italy, *Engineering Structures*, 11(04): 241-270, 2016.

[45] Investigation Report on the Status Longhu Pagoda in Deyang, Sichuan Province, China, *Chinese Cultural Heritage Research Institute*, 2011.

EURODYN 2020
XI International Conference on Structural Dynamics
M. Papadrakakis, M. Fragiadakis, C. Papadimitriou (eds.)
Athens, Greece, 23–26 November 2020

ADAPTIVE LIMIT ANALYSIS OF HISTORICAL MASONRY STRUCTURES MODELED AS NURBS SOLIDS

Nicola Grillanda[1], Andrea Chiozzi[2], Gabriele Milani[1] and Antonio Tralli[2]

[1] Department of Architecture, Built Environment and Construction Engineering (ABC), Politecnico di Milano, Piazza Leonardo da Vinci 32, 20133, Milan, Italy. nicola.grillanda@polimi.it, gabriele.milani@polimi.it

[2] Department of Engineering, University of Ferrara, Via Saragat 1, 44100 Ferrara, Italy. andrea.chiozzi@unife.it, tra@unife.it

Keywords: Historical masonry structures, NURBS, adaptive limit analysis, genetic algorithm.

Abstract. *In this work, we propose an adaptive upper bound limit analysis based on the representation of geometry through NURBS-solids. A NURBS-solid is a closed volume identified by boundary NURBS surfaces (Non-Uniform Rational Bezier Spline). Differently from using NURBS surfaces representing masonry shell-elements, NURBS-solids allow an accurate representation of masonry three-dimensional macro-blocks, such as vaults or walls with variable thickness. The initial model is subdivided into very few macro-elements, each one is still a NURBS solid and is considered as a rigid block. Since dissipation occurs only along interfaces, NURBS boundary surfaces represent possible fracture zones. An upper bound limit analysis is applied. The minimum kinematic multiplier is found by modifying the initial subdivision of solids until the real collapse mechanism is reproduced. This automatic research is performed through a Genetic Algorithm. A simple numerical example is finally reported.*

1 INTRODUCTION

The field of historical masonry structures includes a wide range of different masonry construction typologies, such as vaulted structures, churches, towers, castles, monumental buildings, and aggregates.

The interest in the study of these structures through new advanced computational strategies became higher after recent seismic events, which underlined the strong vulnerabilities of historical masonry constructions to horizontal loads [1–3]. In the analysis of masonry structures, the peculiar characteristics of historical masonry structures have to be taken into account: the nonlinearities of masonry material (i.e. negligible tensile stress compared with good compressive behavior), typical presence of curved geometries, uncertainties on interlockings, coexistence of different and irregular masonry textures and presence of damage. Above all methods adopted [4], one of the most suited numerical tools is limit analysis. The limit analysis of masonry structures has been introduced for the first time by Heyman [5], who suggested to treat masonry as a no-tension material. In this theory, the structure is simplified as an assembly of rigid bodies with null tensile resistance and both crushing and sliding failures avoided. This allowed to analyze of the statics of curved masonry structures through simple procedures based on the static theorem of limit analysis [6,7], such as the construction of the thrust surface for the analysis of masonry arches. Among the methods proposed in last years, it is worth mentioning the so-called Thrust Network Method [8], which consists of a lower bound limit analysis of masonry vaults through the construction of the thrust surface, which is the three-dimensional extension of the thrust line.

As regards methods based on the kinematic theorem of limit analysis, procedures based on the finite element method have been proposed [9]. Here, rigid elements with nonlinear interfaces are often adopted. Nonlinearities are represented by assigning a three-dimensional failure domain which allows a refined representation of mechanical parameters of masonry. Moreover, recently some homogenization procedures have been presented for a reliable determination of the three-dimensional failure surface, opening the access to a wide field of applications [10–12].

However, analyses based on the kinematic theorem of limit analysis can lead to inaccurate results if the geometrical representation and the mechanical models are not able to reproduce the real collapse mechanism. In order to overcome such limitations, a new adaptive upper bound limit analysis has been proposed by the authors [13]. In this method, the geometry of a masonry vault is modeled through NURBS surfaces (Non-Uniform Rational Bezier Spline, [14]). The use of NURBS is particularly suited for curved masonry structures, because it allows an accurate representation of complex geometries [15]. The masonry vault is discretized through very few shell elements, each one is still a NURBS surface. An upper bound limit analysis is applied. Elements are idealized as curved rigid blocks and jump of velocities are allowed only along interfaces according to an associated flow rule. A properly defined homogenized failure domain is required. Therefore, interfaces assume the meaning of possible fracture lines. In order to find the real collapse mechanism, i.e. the real position of fracture lines, a mesh adaptation procedure is applied. By maintaining a low total number of elements, the mesh is adaptively modified until the minimum kinematic multiplier is reached. This optimization procedure is conducted through a Genetic Algorithm (GA) [16], even if other metaheuristic approaches can be followed [17]. Different typologies of masonry structures have been studied through this GA-NURBS limit analysis [18–26].

Despite the great versatility of the method, it is still limited to constructions which can be described through plate or shell elements. However, there are many masonry structures which do not behave as assemblies of surfaces, such as arches and vaults with variable thickness,

monumental triumphal arches, and complex buildings. Therefore, a new adaptive upper bound limit analysis based on the use of NURBS solids is presented. A NURBS solid is a closed region of space delimited by NURBS boundary surfaces.
The use of solids, which can be characterized by curved boundaries, allows the representation of curved objects without geometrical limitations. In this new method, a masonry structure is modeled in Rhinoceros by using NURBS solid-entities and then imported into MATLAB, in which an adaptive upper bound limit analysis is applied. A simple example on a masonry arch with variable thickness is presented to prove the effectiveness of the method.

2 NURBS SOLIDS: GEOMETRIC DESCRIPTION

In the geometrical description of three-dimensional objects, NURBS functions (Non-Uniform Rational Bezier Spline, [14]) are commonly adopted in the modern modeling software, such as Rhinoceros or SolidWorks. NURBS basis functions are built on B-splines basis functions, which are piecewise polynomial functions defined by a non-uniform knots vector (i.e. non-equidistant points in a parametric domain) $\Xi = \left\{\xi_1, \xi_2, ...\xi_{n+p+1}\right\}$, where p and n denote respectively the polynomial order and the total number of basis functions. Given a set of weights w_i and the i-th B-spline basis function $N_{i,p}$, then the NURBS basis function $R_{i,p}$ can be written as follows:

$$R_{i,p}(\xi) = \frac{N_{i,p}(\xi)}{\sum_{j=1}^{n} N_{j,p}(\xi)\, \mathrm{w}_j} \tag{1}$$

Starting by NURBS basis function, a NURBS surface $\mathbf{S}(u,v)$ of degree p in the u-direction and q in the v-direction is a parametric surface in the three-dimensional Euclidean space defined as follows:

$$\mathbf{S}(u,v) = \sum_{i=0}^{n}\sum_{j=0}^{m} R_{i,\mathrm{j}}(u,v)\mathbf{B}_{i,j} \tag{2}$$

where $\mathbf{B}_{i,j}$ are the control points.

Consider now a limited region of space $D \subset \mathbb{R}^3$ whose frontier ∂D is a piecewise regular and oriented surface. A NURBS solid is defined as a closed region of space D in which the boundary ∂D is an assembly of NURBS surfaces and no information is provided for the space internal to the boundary. In other words, a NURBS solid is exhaustively described by its frontier ∂D as follows:

$$D = \partial D = \bigcup_{k=1}^{M} \mathbf{S}_k\left(u,v\right) \tag{3}$$

where M is the total number of boundary NURBS surfaces, and each boundary surface is identified by the classical NURBS description (see Equation 2).
Geometrical models composed of NURBS surfaces can be easily imported in MATLAB from Rhinoceros through the IGES standard file [27] and the available functions within the IGES toolbox [28]. However, this is not the case of NURBS solids, which are not supported by the IGES standard file. Therefore, a new IGES format, called "IGESsolid" and a new function "iges2matlab" [29] has been written specifically to import solids in the MATLAB environment. An example of NURBS solid in Rhinoceros and in MATLAB, representing a portion of a masonry arch with variable thickness, is reported in Figure 1.

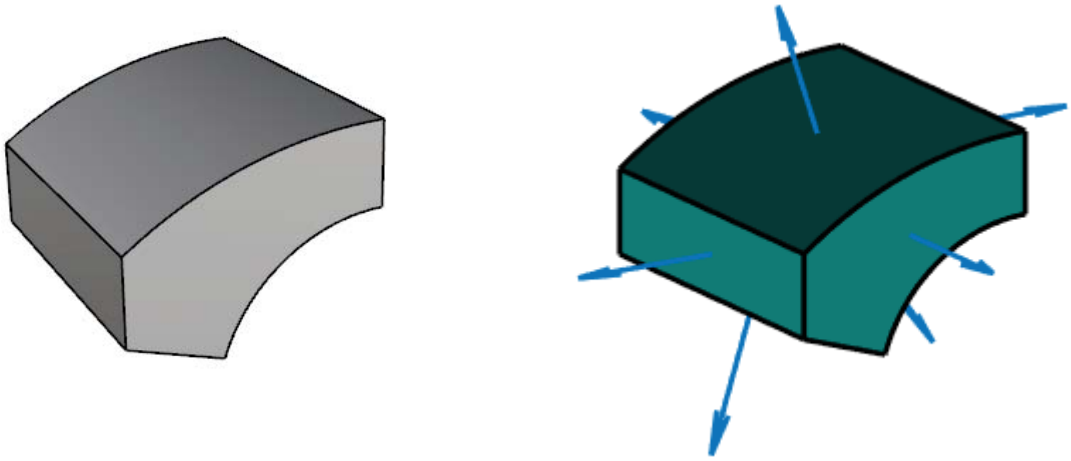

(a) (b)

Figure 1. NURBS solid in (a) Rhinoceros and (b) MATLAB.

A NURBS solid can be subdivided into one or more solids directly within MATLAB. The subdivision of solids is a fundamental step for the adaptive limit analysis procedure which will be described in the next Section. This operation is conducted through a new algorithm written by the authors specifically for the subdivision of solids in MATLAB. Without going in detail about this algorithm, the subdivision is performed by defining an additional NURBS surface, which represents the "splitting object". For each boundary surface, a surface-surface intersection problem (SSI) is solved. Once the common curve between the boundary surface and the splitting surface is determined, the boundary comes split into two (or more) boundaries, in which each one is a partition of the original boundary. After a procedure of re-assembling of the new sub-boundaries, two new NURBS solids are obtained (see Figure 2).
Therefore, the core of this subdivision procedure is the SSI algorithm. The SSI problem has been widely investigated in the scientific literature [30], the procedure here implemented has been developed by improving the formulation presented in [31].

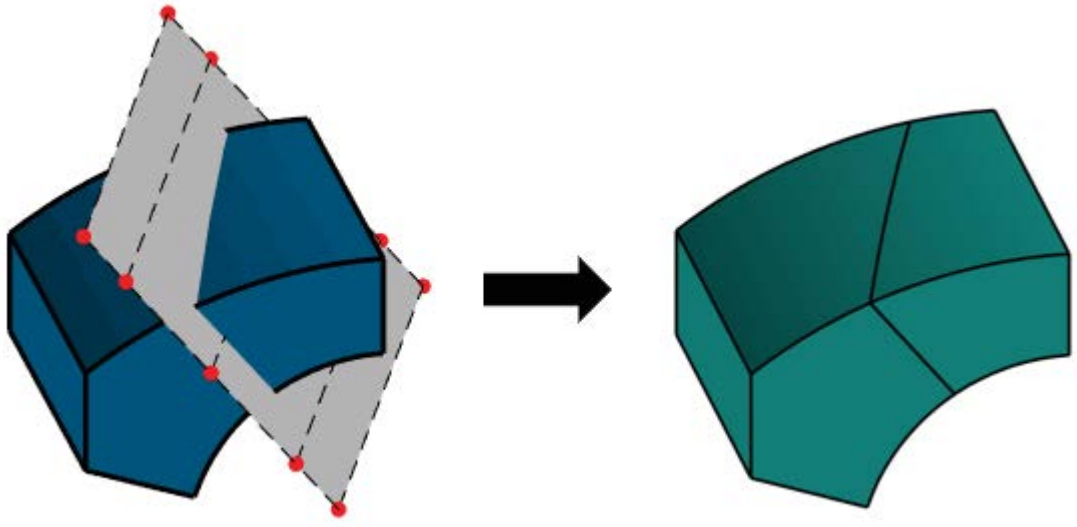

Figure 2. NURBS solid subdivided through a planar NURBS surface.

Once the subdivision of solids is completed, the volume V and the centroid $\mathbf{G}$ of each solid can be evaluated. As it is well known, these properties are determined as follows:

$$V = \iiint_D dxdydz \tag{4}$$

$$\mathbf{G} = \frac{\iiint_D \nabla \cdot \mathbf{F}(x,y,z)\, dxdydz}{V}, \text{ such that } \nabla \cdot \mathbf{F}(x,y,z) = x\mathbf{i} + y\mathbf{j} + z\mathbf{k} \tag{5}$$

These volume integrals can be easily converted in surface integrals by applying the divergence theorem (also known as the Gauss's theorem), for which:

$$\iiint_D \nabla \cdot \mathbf{F}(x,y,z)\, dxdydz = \iint_{\partial D} \mathbf{F}(x,y,z) \cdot \mathbf{n}_e dS \tag{6}$$

where $\mathbf{n}_e$ is the normal external unit vector for ∂D. For NURBS surfaces, the normal unit vector is so defined:

$$\mathbf{n}_e = \frac{\mathbf{S}_u(u,v) \times \mathbf{S}_v(u,v)}{\left\| \mathbf{S}_u(u,v) \times \mathbf{S}_v(u,v) \right\|} \tag{7}$$

where $\mathbf{S}_u(u,v)$ and $\mathbf{S}_v(u,v)$ denote respectively the two partial derivative vectors. Provided that in a NURBS solid the frontier ∂D is a composition of NURBS surfaces (Equation 1), Equation 6 can be re-written as follows:

$$\iiint_D \nabla \cdot \mathbf{F}(x,y,z) dxdydz = \sum_{k=1}^{M} \iint_{Q_k} \mathbf{F}\left(x(u,v), y(u,v), z(u,v)\right) \cdot \left(\mathbf{S}_{k,u}(u,v) \times \mathbf{S}_{k,v}(u,v)\right) dudv \tag{8}$$

in which Q_k is the standard parametric domain associated to the *k*-th surface. This integral can be solved in MATLAB through the Gauss integration. Equation 8 is applied to solve all volume integrals on NURBS solids. Therefore, it is adopted in the evaluation of volumes, weights, centroids, and in the application of volume forces.

3 ADAPTIVE KINEMATIC LIMIT ANALYSIS

A masonry structure is here represented as an assembly of few rigid blocks, in which each block is a NURBS solid. A procedure of kinematic limit analysis is defined. The kinematic of each block is defined through the six degrees of freedom $\left\{u_x^i, u_y^i, u_z^i, \Phi_x^i, \Phi_y^i, \Phi_z^i\right\}$ of its centroid in the three-dimensional space *Oxyz*. Interfaces between elements, which are the NURBS surfaces of the common boundaries, are the only zones where jumps of velocities are supposed to occur. Therefore, dissipation is allowed only at interface according to a rigid-plastic behavior. A three-dimensional failure surface, which consists of a Mohr-Coulomb failure surface with tension cut-off and linear cap in compression [32], is assigned to the masonry material. In this way, crushing and sliding failures are automatically included in the computation. It is clear that, by using high values of ultimate compression strength and friction angle, the typical Heyman condition [5] can be reproduced. The internal plastic dissipation at the generic interface is evaluated according to the associated flow rule:

$$\Delta\tilde{\mathbf{u}} = \left(\dot{\boldsymbol{\lambda}}^T \frac{\partial f}{\partial \boldsymbol{\sigma}} \right)^T \tag{9}$$

where $\Delta\tilde{\mathbf{u}}$ is the jump of velocity in the local reference system, $\dot{\boldsymbol{\lambda}}$ is the vector containing the non-negative plastic multiplier, f is the three-dimensional failure domain, and $\boldsymbol{\sigma}$ is the stress vector. The associated flow rule is applied by discretizing the interface into a series of points. Since the use of NURBS allows the presence of curved interfaces, the discretization is conducted by defining a triangularization of the NURBS surface (the procedure described in [33] is used). In Figure 3(a) and example of discretization with local reference systems is showed, whereas Figure 3(b) reproduces a linearization of the adopted three-dimensional failure surface.

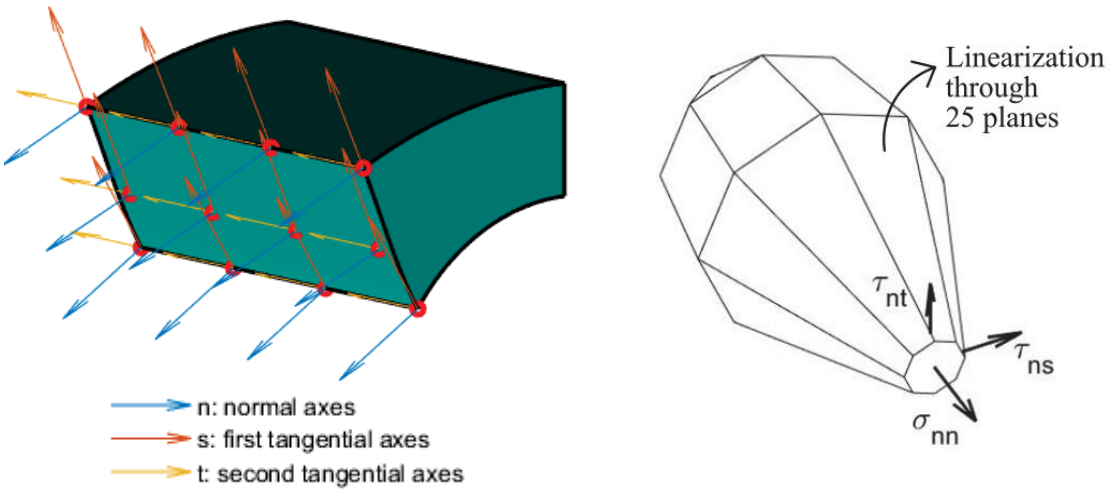

(a) (b)

Figure 3. (a) Discretization of the curved interface into points and local reference systems, (b) linearized three-dimensional failure surface.

The total internal dissipation is thus determined as follows:

$$P_{\text{int}} = \sum_i \int_{S_i} \left(\boldsymbol{\sigma} \cdot \Delta\tilde{\mathbf{u}}\right) dS = \sum_i \int_{S_i} \dot{\boldsymbol{\lambda}}^T \cdot \left(\boldsymbol{\sigma}^T \frac{\partial f}{\partial \boldsymbol{\sigma}} \right)^T dS \tag{10}$$

A configuration of loads, distinguished in dead loads (permanent) $\mathbf{F}_0$ and live loads (depending on a multiplier λ) $\lambda \cdot \boldsymbol{\Gamma}_0$, is defined. If the vector of velocities is indicated as $\mathbf{U}$, the power dissipated by the external loads is defined as:

$$P_{ext} = \left(\mathbf{F}_0 + \lambda \cdot \boldsymbol{\Gamma}_0\right)^T \mathbf{U} \tag{11}$$

The solution of the kinematic problem is obtained by applying the Principle of Virtual Powers. By normalizing the power dissipated by live loads, i.e.:

$$\boldsymbol{\Gamma}_0^T \mathbf{U} = 1 \tag{12}$$

the problem can be written with the following linear programming formulation:

$$\min\left\{\lambda = P_{\text{int}} - \mathbf{F}_0^T \mathbf{U}\right\} \text{ such that } \begin{cases} \mathbf{A}\mathbf{x} = \mathbf{b} \\ \dot{\boldsymbol{\lambda}} \geq 0 \end{cases} \tag{13}$$

where $\mathbf{x} = \left[\mathbf{U}, \dot{\boldsymbol{\lambda}}\right]$ is the vector of unknowns, $\mathbf{A}$ and $\mathbf{b}$ are respectively the overall equality constraints matrix (which include geometric constraints, compatibility constraints and normality condition) and the corresponding right hand side vector.

The presented upper bound formulation provides the configuration of velocities of each block at failure, i.e. a kinematic mechanism, and an associated load multiplier, which is an upper bound of the collapse multiplier. In order to optimize the kinematic multiplier, the real collapse mechanism has to be found.

The mechanism depends on how solids have been initially subdivided. Therefore, changing the position and/or the shape of the NURBS surfaces adopted as splitting objects, different mechanisms can be found. A genetic algorithm (GA) [16] is applied to move these NURBS surfaces and find the subdivision associated to the minimum kinematic multiplier. Given the lower number of parameters involved in the meta-heuristic optimization, the optimized mechanism is usually found after very few iterations.

4 NUMERICAL EXAMPLE

The first result obtained through the novel NURBS solids-based formulation is here presented. A masonry arch characterized by variable thickness is here analyzed under a simple pointed load. Geometry and load condition are depicted in Figure 4(a). This type of arch has been originally presented by Lamé and Clapeyron [34] and successively studied in [35]. These arches are constructed with a layer of radial voussoirs disposed at the intrados and additional horizontal layers of masonry above. Therefore, the shape of the arch is different between intrados and extrados, resulting in a variable thickness. In presence of simple vertical load, Lamé and Clapeyron observed that this kind of arches fails by developing fracture lines that start radially at the intrados (i.e. following the radial joints given by voussoirs), and then propagate upward becoming almost vertical. A representative scheme of this crack pattern is shown in Figure 4(b). This observation has been confirmed in [35].

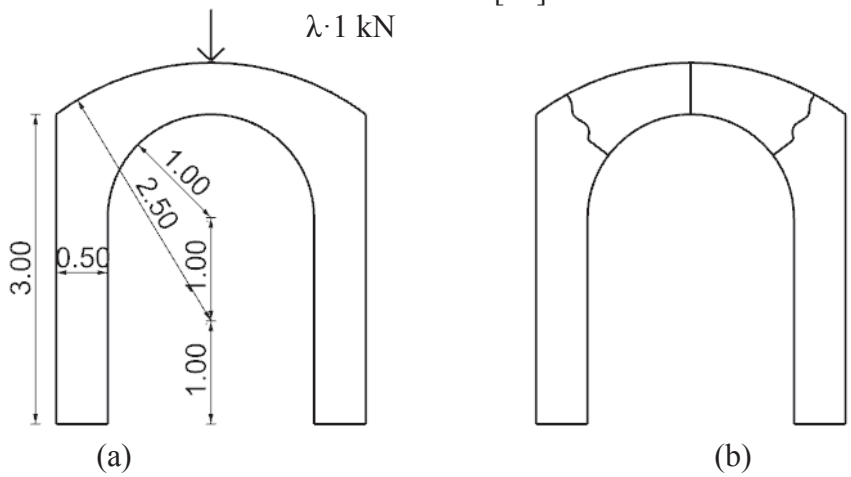

Figure 4. Arch with radial voussoirs at the intrados and a horizontal layer of masonry above: (a) geometry and load condition analyzed, and (b) typical crack pattern under vertical loads [34,35].

As a preliminary evaluation, the masonry arch has been analyzed as 2D problem (width has been assumed unitary) through a heterogeneous kinematic limit analysis. Two different subdivisions into rigid blocks have been adopted. In the first one, the arch is subdivided through radial joints starting from the intrados, whereas horizontal joints have been adopted for piers, see Figure 5(a). In the second one, two different mesh have been adopted for the intrados and the extrados, in order to better take into account the two different layers of voussoirs. Whereas radial joints have been maintained at the intrados, triangular blocks have been assigned to the masonry material located above the radial voussoirs, see Figure 5(b). A value of 18 kN/m3 has been adopted as specific weight. A null tensile strength has been assigned, cohesion and friction angle are respectively equal to 0.02 MPa and 30°, and finally the compression strength has been assumed equal to 2.6 MPa. Results obtained for both the mesh are shown in Figure 5(c,d). It can be noted that a lower load multiplier has been found for the second mesh, in which the crack pattern observed in [34,35] can be better reproduced.

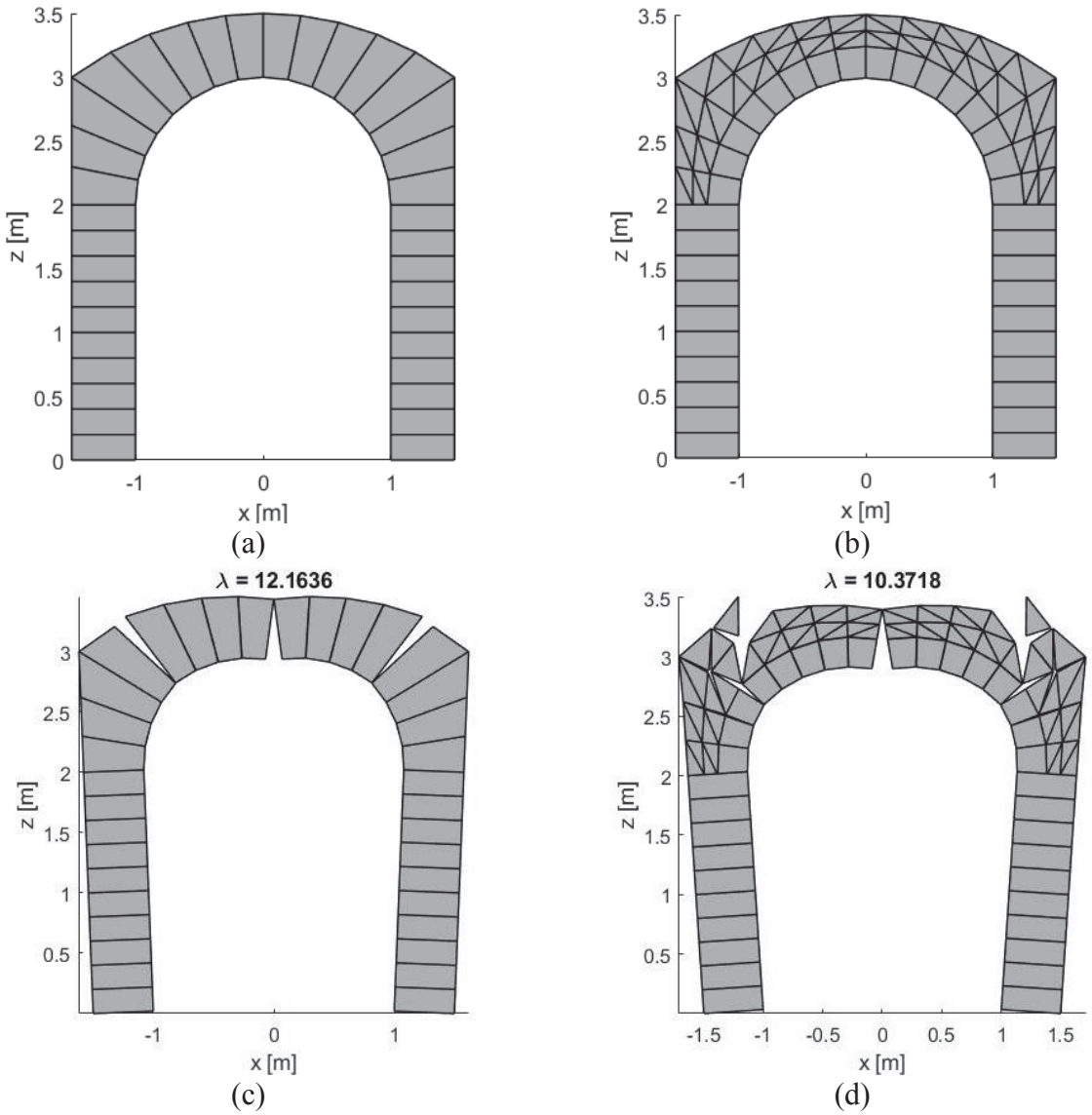

Figure 5. Limit analysis of the masonry arch with heterogeneous approach: (a,b) two different initial mesh, and (c,d) corresponding collapse mechanism and load multiplier.

The study through adaptive limit analysis through NURBS solids is now presented. A representation through two NURBS solids is reported in Figure 6(a). A width equal to 2 m has been assigned. In order to correctly compare this example to the previous ones, the live load condition here used consists of a linear load equals to 1 kN/m distributed along the extrados line belonging to the symmetry plane of the arch. According to the symmetry of the problem, the subdivision of the masonry arch is governed by two planar NURBS surfaces that move symmetrically. The shape of these surfaces is governed by three parameters, summarized by the vector **a** and depicted in Figure 6(b). It can be observed that, if the second or the third parameter are not null, the surface is not more planar and the resulting fracture surface on the solid is curved. The same material parameters have been adopted for this model.

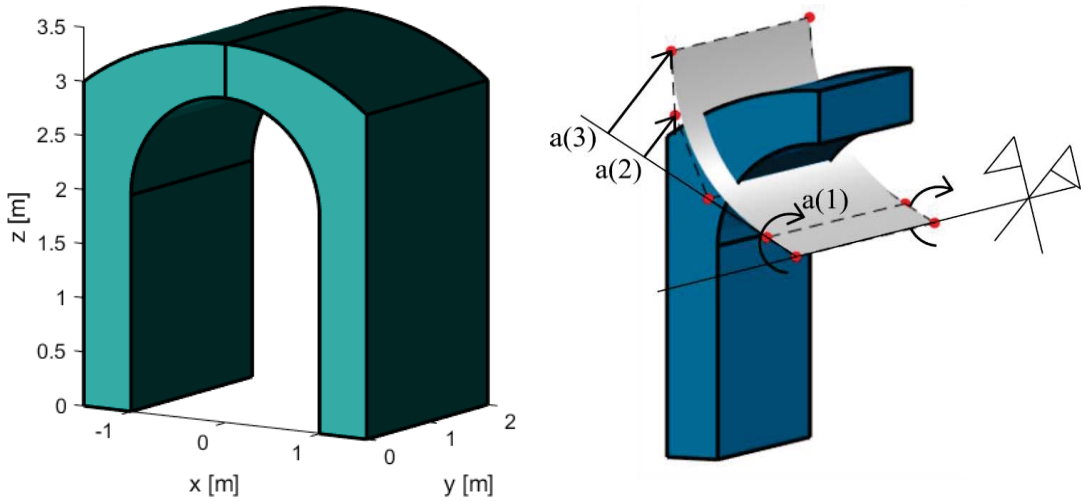

Figure 6. (a) NURBS model of the arch, and (b) NURBS surfaces adopted for the subdivision.

Results are shown in Figure 7. Figure 7(a, b) depicts the collapse mechanism found and the corresponding live load multiplier, whereas in Figure 7(c) the convergence diagram deriving from the application of the GA is reported. As it was expected, the arch collapses for the formation of curved cracks that are almost vertical near the extrados. The load multiplier resulted lower than values obtained through the heterogeneous approaches (9.37 compared with 10.37 and 12.16), denoting a higher precision in the definition of the collapse mechanism for the adaptive approach.

This method is computationally cheap because it allows to study complex geometries by using a very reduced number of elements, still maintaining the exact geometry of the case study.

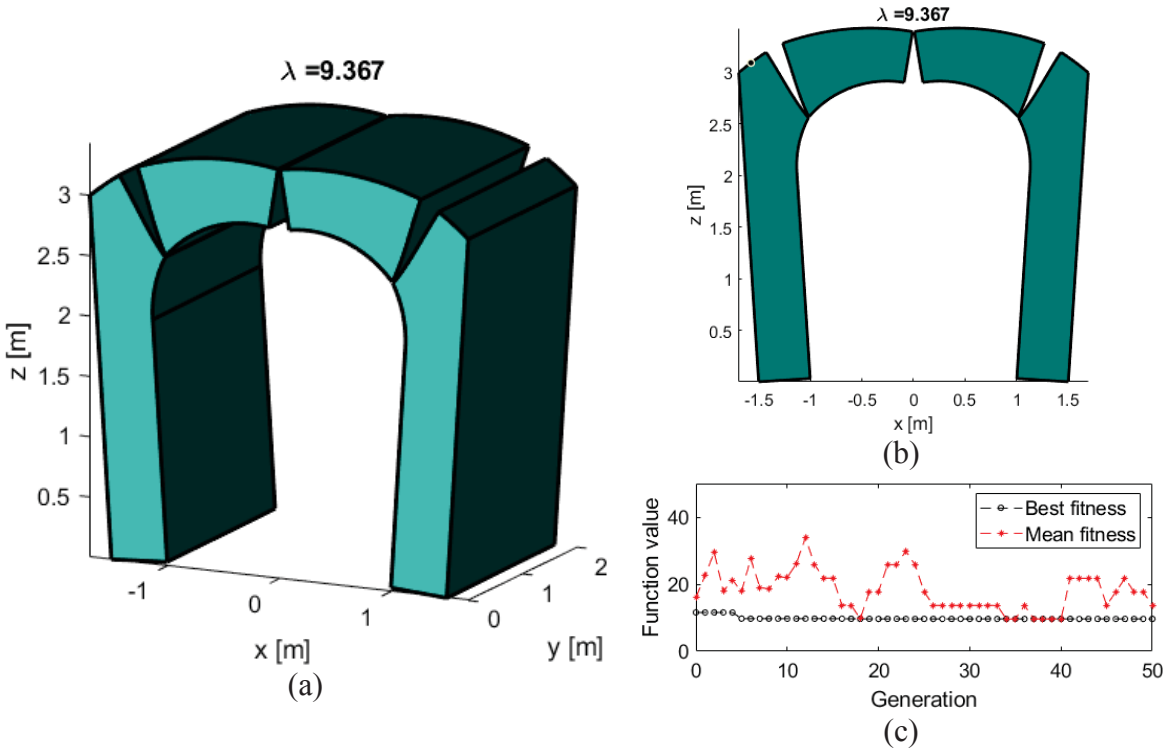

Figure 7. Results obtained through adaptive limit analysis: load multiplier and collapse mechanism in (a) axonometric and (b) frontal view, and (c) convergence diagram.

5 CONCLUSIONS

A new adaptive upper bound limit analysis based on the use of NURBS solids has been presented. A given masonry structure is modeled through NURBS solids and then imported into MATLAB. The model is then subdivided through NURBS surface and analyzed through an adaptive upper bound limit analysis is applied. By using a Genetic Algorithm, the initial subdivision is then modified to reproduce the real collapse mechanism and identify the collapse multiplier.

The presented method has been applied on a masonry arch with variable thickness and results have been compared with classical heterogeneous limit analysis procedures. A good agreement has been observed between results obtained. The use of NURBS solids allowed the exact representation of curved geometries of structures that cannot be represented with standard shell elements. The collapse mechanism is identified with good precision thanks to the automatic mesh adaptation. Moreover, the subdivision of solids through NURBS surfaces allows the identification of curved fracture zones within the macroblocks in easy way.

Future research will be focused on the use of the presented method for the analysis of monumental masonry constructions subjected to horizontal actions.

REFERENCES

[1] M. Valente, G. Milani, E. Grande, A. Formisano, Historical masonry building aggregates: advanced numerical insight for an effective seismic assessment on two row housing compounds, *Engineering Structures*, 190, 360–379, 2019. doi:10.1016/j.engstruct.2019.04.025.

[2] M. Valente, G. Milani, Earthquake-induced damage assessment and partial failure mechanisms of an Italian Medieval castle, *Engineering Failure Analysis*, 99, 292–309, 2019. doi:10.1016/j.engfailanal.2019.02.008.

[3] M. Pavlovic, E. Reccia, A. Cecchi, A Procedure to Investigate the Collapse Behavior of Masonry Domes: Some Meaningful Cases, *International Journal of Architectural Heritage*, 10, 67–83, 2016. doi:10.1080/15583058.2014.951797.

[4] P. Roca, M. Cervera, G. Gariup, L. Pelà, Structural analysis of masonry historical constructions. Classical and advanced approaches, *Archives of Computational Methods in Engineering*, 17, 299–325, 2010. doi:10.1007/s11831-010-9046-1.

[5] J. Heyman, The stone skeleton, *International Journal of Solids and Structures*, 2, 249–256, 1966.

[6] P. Block, M. DeJong, J. Ochsendorf, As hangs the flexible line: Equilibrium of masonry arches, *Nexus Network Journal*, 8, 13–24, 2006. doi:10.1007/s00004-006-0015-9.

[7] M. Como, *Statics of historic masonry constructions*, Berlin Heidelberg, 2013.

[8] P. Block, J. Ochsendorf, Thrust network analysis: A new methodology for three-dimensional equilibrium., *Journal of the International Association for Shell and Spatial Structures*, 48, 1–7, 2007.

[9] E. Milani, G. Milani, A. Tralli, Limit analysis of masonry vaults by means of curved shell finite elements and homogenization, *International Journal of Solids and Structures* 45, 5258–5288, 2008. doi:10.1016/j.ijsolstr.2008.05.019.

[10] G. Milani, P.B. Lourenço, A. Tralli, Homogenised limit analysis of masonry walls, Part I: Failure surface, *Computers & Structures*, 84, 166–180, 2006. doi:10.1016/j.compstruc.2005.09.004.

[11] G. Milani, P.B. Lourenço, A. Tralli, Homogenised limit analysis of masonry walls, Part II: Structural examples, *Computers & Structures*, 84, 181–195, 2006. doi:10.1016/j.compstruc.2005.09.004.

[12] G. Milani, P.B. Lourenço, A. Tralli, 3D homogenized limit analysis of masonry buildings under horizontal loads, *Engineering Structures*, 29, 3134–3148, 2007. doi:10.1016/j.engstruct.2007.03.003.

[13] A. Chiozzi, G. Milani, A. Tralli, A Genetic Algorithm NURBS-based new approach for fast kinematic limit analysis of masonry vaults, *Computers & Structures*, 182, 187–204, 2017. doi:10.1016/j.compstruc.2016.11.003.

[14] L. Piegl, W. Tiller, *The NURBS Book*, Springer, Berlin, 1995. doi:10.1007/978-3-642-59223-2.

[15] A. Cazzani, M. Malag , E. Turco, Isogeometric analysis: a powerful numerical tool for the elastic analysis of historical masonry arches, *Continuum Mechanics and Thermodynamics*, 28, 139–156, 2016. doi:10.1007/s00161-014-0409-y.

[16] R.L. Haupt, S.E. Haupt, *Practical Genetic Algorithms*, John Wiley & Sons, New York, 1998.

[17] N. Grillanda, A. Chiozzi, G. Milani, A. Tralli, Efficient meta-heuristic mesh adaptation strategies for NURBS–based upper–bound limit analysis of general curved three-dimensional masonry structures, *Computers & Structures*, 236, 106271, 2020. doi:10.1016/j.compstruc.2020.106271.

[18] A. Chiozzi, G. Milani, A. Tralli, Fast kinematic limit analysis of FRP reinforced masonry vaults through a new genetic algorithm nurbs-based approach, Proceedings of the 7th European Congress on Computational Methods in Applied Sciences and Engineering, 3, 5326–5339, 2016.

[19] A. Chiozzi, G. Milani, N. Grillanda, A. Tralli, Fast and reliable limit analysis approach for the structural assessment of FRP-reinforced masonry arches, *Key Engineering Materials*, 747, 196–203, 2017. doi:10.4028/www.scientific.net/KEM.747.196.

[20] A. Chiozzi, G. Milani, N. Grillanda, A. Tralli, A fast and general upper-bound limit analysis approach for out-of-plane loaded masonry walls, *Meccanica*, 53, 1875–1898, 2018. doi:10.1007/s11012-017-0637-x.

[21] A. Chiozzi, N. Grillanda, G. Milani, A. Tralli, UB-ALMANAC: An adaptive limit analysis NURBS-based program for the automatic assessment of partial failure mechanisms in masonry churches, *Engineering Failure Analysis*, 85, 201–220, 2018. doi:10.1016/j.engfailanal.2017.11.013.

[22] N. Grillanda, A. Chiozzi, F. Bondi, A. Tralli, F. Manconi, F. Stochino, A. Cazzani, Numerical insights on the structural assessment of historical masonry stellar vaults: the case of Santa Maria del Monte in Cagliari, *Continuum Mechanics and Thermodynamics*, 1–24, 2019. doi:10.1007/s00161-019-00752-8.

[23] N. Grillanda, A. Chiozzi, G. Milani, A. Tralli, Collapse behavior of masonry domes under seismic loads: an adaptive NURBS kinematic limit analysis approach,

Engineering Structures, 200, 2019. doi:10.1016/j.engstruct.2019.109517.

[24] N. Grillanda, M. Valente, G. Milani, A. Chiozzi, A. Tralli, Advanced numerical strategies for seismic assessment of historical masonry aggregates, *Engineering Structures*, 212, 2020. doi:10.1016/j.engstruct.2020.110441.

[25] N. Grillanda, M. Valente, G. Milani, ANUB-Aggregates: a fully automatic NURBS-based software for advanced local failure analyses of historical masonry aggregates, *Bulletin of Eartquake Engineering*, 1–27, 2020. doi:10.1007/s10518-020-00848-6.

[26] A. Chiozzi, N. Grillanda, G. Milani, A. Tralli, NURBS-based kinematic limit analysis of FRP-reinforced masonry walls with out-of-plane loading, *Frattura Ed Integrità Strutturale*, 51, 9–23, 2020. doi:10.3221/IGF-ESIS.51.02.

[27] P.R. Kennicott, *Initial Graphics Exchange Specification, IGES 5.3*, U.S. Product Data Association, 1966. https://books.google.com/books?id=FHPhGwAACAAJ&pgis=1.

[28] P. Berstrong, "IGES Toolbox," MATLAB Central File Exchange User Community. (2006). https://it.mathworks.com/matlabcentral/fileexchange/13253-iges-toolbox.

[29] N. Grillanda, "iges2matlab," MATLAB Central File Exchange User Community. (2019). https://it.mathworks.com/matlabcentral/fileexchange/70461-iges2matlab.

[30] V. Skytt, Challenges in Surface-Surface Intersections, in: *Computational Methods for Algebraic Spline Surfaces*, Springer, Berlin, Heidelberg, 2005: pp. 11–26. doi:10.1007/3-540-27157-0_2.

[31] G. Casciola, S. Morigi, The SSI problem in solid modelling with NURBS surfaces (in Italian), 1995.

[32] G. Milani, A. Taliercio, Limit analysis of transversally loaded masonry walls using an innovative macroscopic strength criterion, *International Journal of Solids and Structures*, 81, 274–293, 2016. doi:10.1016/j.ijsolstr.2015.12.004.

[33] L. Piegl, M. Richard, Tessellating trimmed NURBS surfaces, *Computer-Aided Design*, 27, 16–26, 1995.

[34] M.G. Lamé, E. Clapeyron, Mémoire sur la stabilité des vo tes, *Annales Des Mines*, 8, 789–836, 1823.

[35] H. Alexakis, N. Makris, Limit equilibrium analysis of masonry arches, *Archive of Applied Mechanics*, 85, 1363–1381, 2015. doi:10.1007/s00419-014-0963-6.

EURODYN 2020
XI International Conference on Structural Dynamics
M. Papadrakakis, M. Fragiadakis, C. Papadimitriou (eds.)
Athens, Greece, 23–26 November 2020

AN AUTOMATIC AND FAST PROCEDURE FOR THE NUMERICAL ANALYSIS OF CURVED MASONRY STRUCTURES

J. Scacco[1], G. Milani[1], and P. B. Lourenço[2]

[1] Department of Architecture, Built Environment and Construction Engineering ABC
Politecnico di Milano, Piazza Leonardo Da Vinci 32, 20133 Milan, Italy
E-mail addresses : jacopo.scacco@polimi.it; gabriele.milani@polimi.it

[2] Department of Civil Engineering, ISISE
University of Minho, Azurém, 4800-058 Guimarães, Portugal
Email address: pbl@civil.uminho.pt

Keywords: discrete model, auto-mesh, homogenization, masonry vault.

Abstract. *A fast and innovative discrete model approach coupled with homogenization procedure is here presented. The method is able to comply with the main features required for an accurate simulation of masonry curved elements, such as the orthotropy and the typical in-and-out-of-plane coupled behavior exhibited by masonry vaults. Furthermore, homogenization techniques directly implemented in the method allows reducing consistently the number of variables, leading to a fair combination of accuracy and reasonable computational time. The discrete model is an assembly of elastic units joint by non-linear interfaces. These latter are modeled with 3D linear brick elements and Concrete Damage Plasticity (CDP) is used for modeling the non-linear mechanical properties coming from the homogenization step. In order to overcome potential difficulties during the preparation of the model, the discretized mesh is obtained automatically by means of an ad-hoc script implemented by the Authors. The proposed approach is validated taking advantage of numerical data already available on a cloister vault. The numerical comparison shows the reliability of the method and its efficacy in the simulation of both global behavior and crack pattern, requiring a low computational effort.*

1 INTRODUCTION

The vulnerability of historical masonry structures when subjected to seismic loads is well known and preservation is a fundamental task in order to preserve the structures that assumed the role of a cultural landmark. In such historical buildings, the most fascinating and peculiar elements are represented by arches, vaults and domes. However, at the same time, these elements represent often the most vulnerable part of the whole structure. The methodologies according to which curved masonry elements were designed in the past result highly effective for static loads [1]. On the other hand, strong knowledge about the behavior of such elements when subjected to dynamic loads is still missing. From the numerical point of view, the issues are related to the difficulty of balancing reliable results with a reasonable computing time. Several approaches have been developed in literature ranging from methodologies enable to effectively combine ancient and current methods as kinematic limit analyses [2] to approaches that allow a full non-linear analysis. This latter can be faced with both macro-modeling [3] and micro-modeling [4]. The first case leads to an easy numerical implementation simulating the material as a continuum, but the choice of a suitable constitutive model may result cumbersome. On the contrary, a micro-modeling procedure can allow a distinction of all the different constituents but my lead to a huge number of variables and to not practical computing time. These numerical issues can be overtaken by applying homogenization procedures, that ensure a detailed evaluation of the non-linear behavior of masonry at meso-scale [5,6] Such information is then transferred at the structural level in a second step.

In this paper, an innovative and automatic procedure for the non-linear analysis of curved masonry structures is presented.

At the macro-scale level, the structure is described as a repetition of elastic cells joint by interfaces. Such a discrete approach allows reproducing properly the orthotropic behavior of masonry. The non-linear properties coming from homogenization are lumped exclusively at the interfaces, that are modeled as flat brick elements along with a Concrete Damage Plasticity model already available in Abaqus. The main advantage of the method is the direct implementation of the homogenized parameter at the structural level, where even the mesh of the discrete model is created automatically employing a MATLAB script.

The efficacy of the method has been already described for the case of brick walls loaded out-of-plane, in the unreinforced and TRM-reinforced configuration in [7]. The extension of the method even to curved structures is suitable as the modeling of interfaces with flat 3D elements leads to a full coupling of in-and-out-of-plane actions. In such a way the influence of the normal stress related to the gravity loads on the non-linear behavior in flexion is automatically taken into account. The number of variables involved in the numerical simulations is very low when compared to micro approaches, opening the way to further application of the method on reinforced structures.

With the aim to validate the proposed approach, some non-linear simulations have been carried out on a cloister vault, of which experimental and numerical data are available in the literature [8].

2 METHODOLOGY

In this section, a general overview of the method is provided. The validation and its implementation are deeply discussed in [7] and the interested readers are directed to this research for a point of reference.

The first main step is the implementation of a discrete mesh of the curved structure. In the case of the wall, such a step resulted straightforward and without complexity due to the simplicity of the geometrical model. On the contrary, the realization of a discrete mesh for vaults

and domes may lead to a tedious procedure. In fact, the flat 8-noded brick elements employed as interfaces have a thickness that, even though negligible, implies the presence of gaps in the intersections. In order to overcome such limitations, a MATLAB script was implemented by the Authors, enable to provide an automatic discretized mesh. Moreover, the non-linear homogenized properties are assigned automatically to the interfaces according to their orientation. The non-linearity is introduced by taking advantage of the constitutive model Concrete Damage Plasticity (CDP), already available in Abaqus. Its applicability for modeling masonry structures has been widely proved in [9,10] where several non-linear analyses were performed. With such a model, a differential behavior in tension and compression is introduced, following a softening exponential law in the first case and a parabolic softening law in the second one.

Even if CDP is a continuum isotropic constitutive model, its use in a discrete approach allows preserving the orthotropy peculiar to masonry, opening the way to the implementation even in FEM-based software that does not provide an orthotropic constitutive model.

In this paper, a cloister vault, already numerically reproduced in literature, is selected in order to show the capability of the model. The automatic mesh procedure starts with the definition of a rough but structured mesh of the inner surface of the curved structure.

Each 4-noded shell element of the coarse mesh generates correspondent elastic units of the final discrete mesh. In order to create the space for interfaces, each element is scaled by acting on the 3D coordinates of four vertices. Then, the elements are automatically joined with the surrounding ones, generating additional 4-noded narrow elements. These latter will be converted to the non-linear 3D interfaces in the final model. After this stage, each 4-noded element is partitioned, creating a new mesh for the subsequent discrete model.

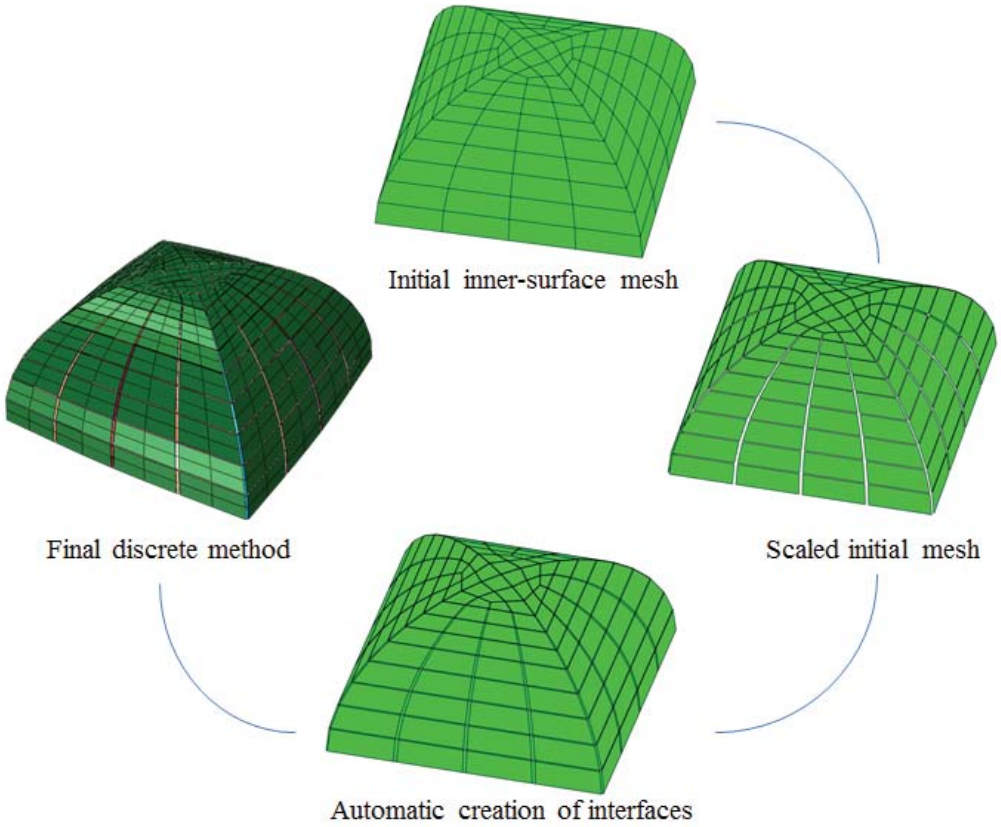

Figure 1: Steps for the automatic implementation of the discrete mesh.

The final model is then obtained by extrusion of the discrete shell mesh. A different quantity can be applied to each node, making possible the modeling of vaults with variable thickness.

In this work, the cloister vault has been modeled with 160 elastic units having a rough mesh of 4 elements on the plane r-s.

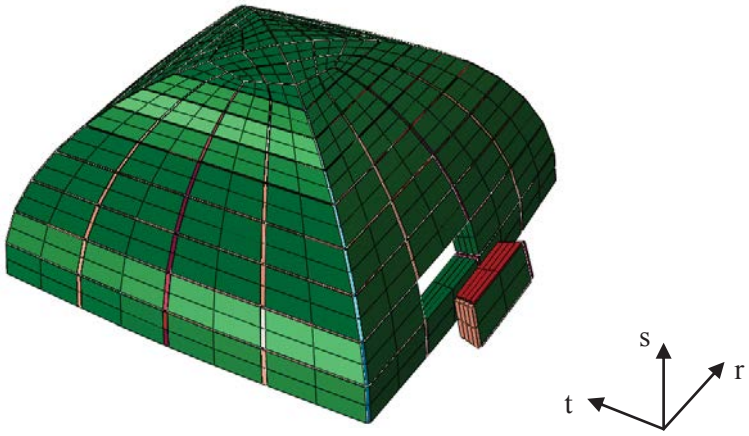

Figure 2: Mesh configuration in detail of the homogenized cloister vault.

According to the experience of the Authors, for reproducing properly the flexural behavior of curved masonry structures, 4 elements along the depth of the dome is a sufficient number.

The possibility to assign automatically the homogenized mechanical properties according to the orientation of the interfaces is a promising starting point for the upcoming research by the Authors. Indeed, semy-analytical approaches [6] might be directly implemented inside the script, leading to a full comprehensive homogenization procedure for curved structures.

Numerical analyses on the cloister vault are available in [8,12]. For the sake of consistency, the same homogenized mechanical properties defined in [8] for both directions, are input in the Concrete Damage Plasticity.

Figure 3: Detail of non-linear interfaces

3 RESULTS

The cloister vault, with a square base of 2.2 m*2.2 m, used for the validation of the method was tested by Foraboschi in 2006 and described in [11]. The test consisted in inducing the collapse of the vault by the application of a concentrated force applied at the top. Several non-linear FE simulations are already available by means of heterogeneous and macroscopic ap-

proaches. From these latter, a comparison in terms of load-displacement curves is here provided with the proposed method.

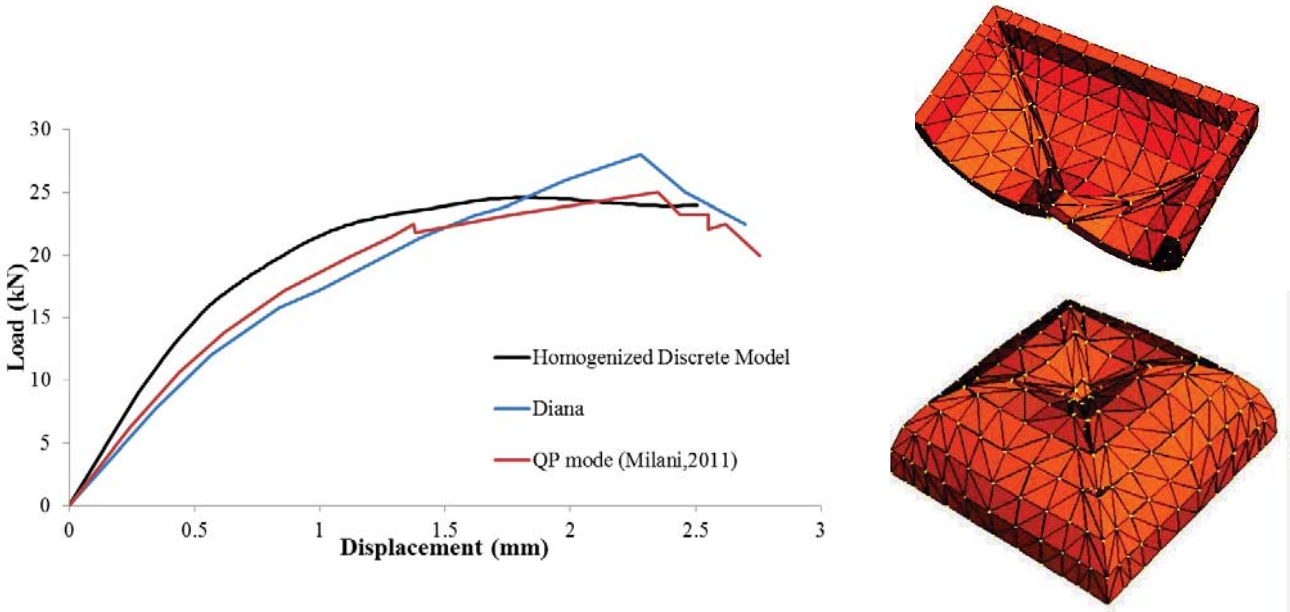

Figure 4: Comparison in terms of load-displacement curves of the proposed method with previous numerical analyses (Left); Collapse mechanism obtained by means of QP non-linear analysis by Milani, 2011 (Right).

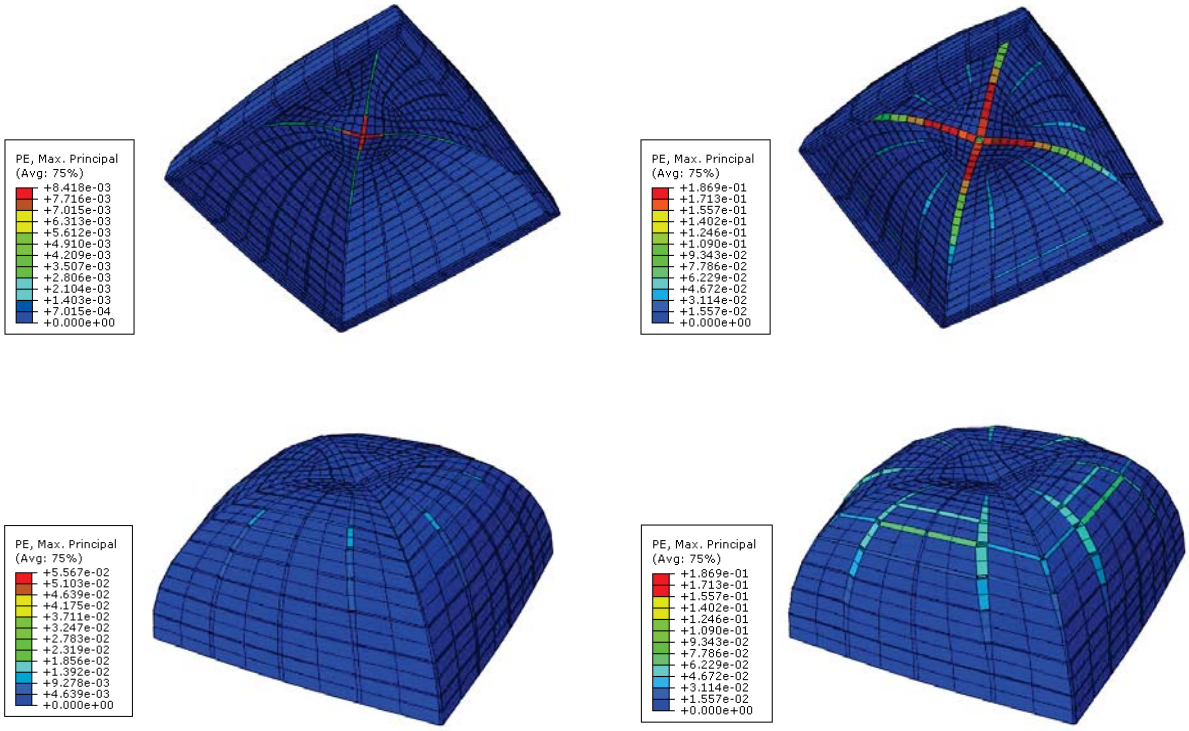

Figure 5: Evolution of crack pattern at the intrados (Top), at the extrados (Bottom).

The global behavior described by DIANA analyses and by other numerical approaches implemented in [8,12] presents a final displacement around 2.7 mm and a peak load within the range of 25-28 kN. The discrete homogenized approach provides a global behavior that fits

satisfactorily the numerical references, with a maximum load nearby 25 kN and maximum capacity in displacement around 2.5 mm. The slight difference in the first branch may be attributed to the discrete nature of the method, which does not allow the non-elastic behavior in all the structures but only at the interfaces.

The crack pattern is provided in terms of plastic strains (PE in Abaqus). The cracks start to spread symmetrically along the diagonal at the intrados. Afterward, a circular flexural hinge is determined by the openings at the extrados of the parallels at approximately 2/3 of the height, causing the impossibility to carry further loads.

4 CONCLUSIONS

In the present work, a validation of an innovative discrete homogenized method applied on a masonry cloister vault has been provided. First of all, a short overview of already existing methods is discussed to highlight the required features for a new approach and the necessity of implementing it. A discrete method, when complemented with previous homogenization procedures, is presented as the right approach for meeting the following requirements: non-linear simulation, low-number of variables involved, preservation of orthotropy of material like-masonry, necessity of keeping coupled the in-out-of-plane effects.

The method, already validated on UR and RE out-of-plane-loaded walls, is extended to the case of a cloister vault, experimentally tested in 2006 and numerically simulated several times by different approaches.

The numerical model of the vault is conceived as a repetition of elastic units jointed by non-linear interfaces. These latter are input as flat 8-noded bricks and the non-linearities are introduced by means of the constitutive model Concrete Damage Plasticity, available in the Abaqus library. The discretized mesh is obtained automatically through a MATLAB script implemented by the Authors and the homogenized mechanical properties are, as well, assigned by an automatic procedure to each interface according to their orientation, preserving the orthotropic behavior.

Finally, the homogenized outcome, in terms of load-displacement curves, revealed an excellent capacity to reproduce numerical results coming from more advanced and consuming approaches. Even the evolution of the crack pattern is fully consistent with the information available in the literature.

Moreover, given the low computational burden, it is the opinion of the Authors that interesting extension to reinforced curved elements may be proposed in future works, by applying in a second moment the reinforcement.

REFERENCES

[1] Huerta S. Mechanics of masonry vaults: the equilibrium approach. *Proc. 1st Int. Congr. Struct. Anal. Hist. Constr. Guimaraes*, 47–70, 2001.

[2] Grillanda N, Chiozzi A, Milani G, Tralli A. On Collapse Behavior of Reinforced Masonry Domes under Seismic Loads, *Key Engineering Materials*, 275–82, 2019.

[3] Bianchini N, Mendes N, Lourenco PB. Seismic assessment of masonry cross vaults through numerical seismic assessment of masonry cross vaults through numerical nonlinear static and dynamic analysis, *COMPDYN 2019 7th International Conference on Computational Methods in Structural Dynamics and Earthquake Engineering,* 2019.

[4] Bove M, Castellano A, Fraddosio A, Scacco J, Milani G, Piccioni MD. Experimental and Numerical Analysis of FRCM Strengthened Parabolic Tuff Barrel Vault, *Key Engineering Materials*, 213–20, 2019.

[5] Silva LC, Lourenço PB, Milani G. Derivation of the out-of-plane behaviour of masonry through homogenization strategies: Micro-scale level. *Comput. Struct.*, **209**, 30–43, 2018.

[6] Milani G, Bertolesi E. Quasi-analytical homogenization approach for the non-linear analysis of in-plane loaded masonry panels. *Constr. Build. Mater.*, 146, 723–43, 2017.

[7] Scacco J, Ghiassi B, Milani G, Lourenço PB. A fast modeling approach for numerical analysis of unreinforced and FRCM reinforced masonry walls under out-of-plane loading. *Compos. Part B Eng.*, 180, 107553, 2020.

[8] Milani G, Tralli A. A simple meso-macro model based on SQP for the non-linear analysis of masonry double curvature structures. *Int. J. Solids Struct.*, 49, 808–34, 2012.

[9] Valente M, Milani G. Effects of Geometrical Features on the Seismic Response of Historical Masonry Towers E ff ects of Geometrical Features on the Seismic Response of Historical Masonry Towers. *J. Earthq. Eng.*, 1–33, 2017.

[10] Tiberti S, Milani G. Historic City Centers After Destructive Seismic Events , The Case of Finale Emilia During the 2012 Emilia-Romagna Earthquake : Advanced Numerical Modelling on Four Case Studies Abstract : 1059–78, 2017.

[11] P. Foraboschi, Masonry structures externally reinforced with FRP strips: tests at the collapse [in Italian], *Proceedings of I Convegno Nazionale''Sperimentazioni su Materiali e Strutture''*, 2006.

[12] G. Milani, E. Milani, A. Tralli, Upper bound limit analysis model for FRPreinforced masonry curved structures. Part II: Structural analyses, *Comput. Struct*. 87 (23–24), 1534–1558, 2009b.

EURODYN 2020
XI International Conference on Structural Dynamics
M. Papadrakakis, M. Fragiadakis, C. Papadimitriou (eds.)
Athens, Greece, 23–26 November 2020

THE MODELLING OF MULTIPLE LEAF MASONRY WALLS OF THE ARQUATA DEL TRONTO FORTRESS AS A NON-SMOOTH DYNAMICAL SYSTEM

Angela Ferrante[1*], Ersilia Giordano[1], Francesco Clementi[1], Vasilis Sarhosis[2], Gabriele Milani[3], Stefano Lenci[1]

[1] Department of Civil and Building Engineering, and Architecture, Polytechnic University of Marche, via Brecce Bianche, 60131, Ancona, Italy
e-mail: a.ferrante@pm.univpm.it, e.giordano@pm.univpm.it, francesco.clementi@univpm.it, s.lenci@univpm.it

[2] School of Civil Engineering, University of Leeds
LS2 9JT Leeds, UK
e-mail: V.Sarhosis@leeds.ac.uk

[3] Department of Architecture, Built Environment and Construction Engineering ABC, Polytechnic of Milano, Piazza Leonardo da Vinci 32, 20133, Milan, Italy
e-mail: gabriele.milani@polimi.it

Keywords: Cultural Heritage, Masonry, Multiple Leaf Walls, Damage Assessment, Discrete Element Method, Non-Smooth Contact Dynamics method.

Abstract. *In the present paper has been reported the Non-Smooth Contact Dynamics method (NSCD) used for the damage evaluation of the multiple leaf masonry walls of the medieval fortress of Arquata del Tronto, strongly affected by the last Centre Italy earthquakes of August and October 2016. Pursuing this approach, a system of rigid blocks has been used for the assembly of the masonry structure. By means of contacts between blocks, which are governed by the Signorini's impenetrability condition and by dry-friction Coulomb's law, the building exhibits discontinuous dynamics. Finally, the NSCD method has proved to be an effective instrument for investigating the dynamical behaviour of the masonry structures under the ground seismic accelerations. Indeed, several possible failure mechanisms have been confirmed through the numerical results, which have given a deep insight into the seismic vulnerability of this damaged medieval fortress.*

1 INTRODUCTION

In the structural mechanics became relevant the attention for the damage assessment of historical masonry buildings, which are commonly complex, with irregular geometries, heterogeneity and absence of a box behaviour due to defective connections between different structural parts, in particular walls and floors, that often play a fundamental role. However, the knowledge of the dynamical behaviour is crucial for a reliable seismic vulnerability assessment, which became more and more important due to recent catastrophic earthquakes that stroked Italy in the last few decades (Umbria-Marche 1997–1998, Abruzzo 2009, Emilia-Romagna 2012, Marche-Lazio-Umbria-Abruzzo 2016) [1]–[3].

In October 2016, two major earthquakes occurred in the Marche region in the Centre of Italy, causing widespread damage especially on the historical structures. The epicentre of the second one stroked Norcia, Visso, Arquata del Tronto, Accumoli and Amatrice, and a lot of damages to cultural heritage were also done in the cities of Tolentino, San Severino, Camerino, and Matelica.

To investigate the mechanical behaviour of masonry structures, commonly Finite Element Methods is utilized, often including very sophisticated constitutive laws taking into account post-elastic behaviours and damage [4]–[8]. This method, while being very appealing, do not focus on the possible non-smooth nature of the dynamic response, which can come sliding and impacting between different blocks, and situation that is common just before and during the collapse [9]–[13].

Moreover, the ancient masonry structures can be considered as discontinuous structural systems, which is composed of units (e.g. bricks, stones, blocks, etc.), bonded together with or without mortar. Thus, defining the constitutive model and the material properties for a numerical model is meaningful to adequately represent the dynamical behaviour of a real structure, to take into account the variation of masonry properties and the range of stress state types that exist in masonry structures [14]–[16].

Hence, the progressive damage of the Arquata del Tronto medieval fortress, in the province of Ascoli Piceno (AP), is examined throughout the paper and it is based on an advanced numerical point of view. The measured damage evaluation is relative to the long sequence of strong earthquakes that struck Central Italy in 2016, plunging the area into chaos for several months (see Figure 1) [17].

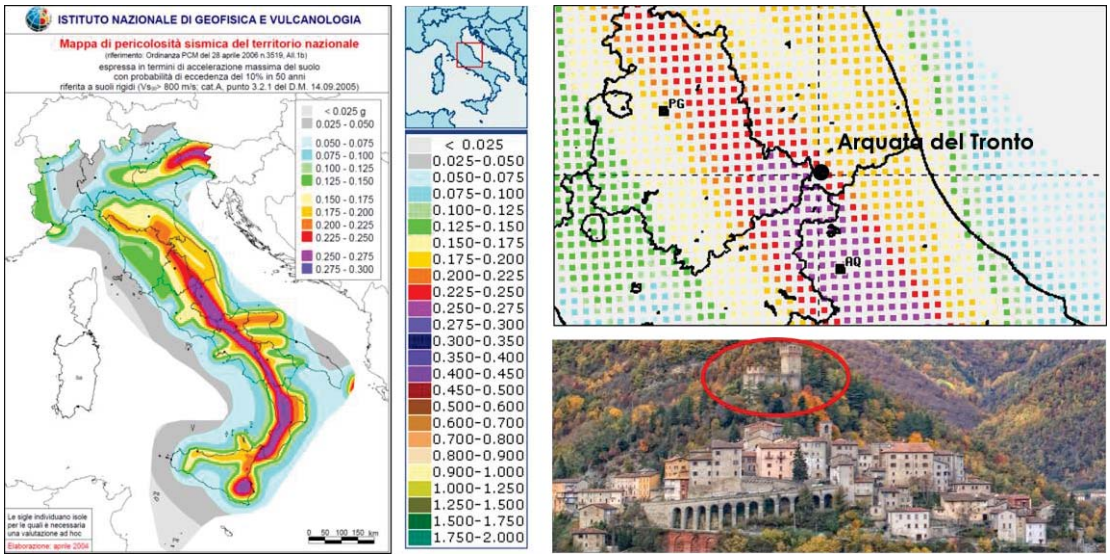

Figure 1: Macroseismic intensity map of the Central Italy area (https://emidius.mi.ingv.it/) and localization of the Arquata del Tronto (AP) medieval fortress

An advanced numerical model is here utilized to have an insight into the modalities of progressive damage and the behaviour of the structure under strong nonlinear dynamic excitations, namely a Non-Smooth Contact Dynamic method (NSCD) adopting a full 3D detailed discretization [18], [19].

In accordance with the NSCD method, the fortress is structured as a system of rigid bodies, assuming frictional sliding and perfect plastic impacts between the blocks. The structure exhibited a complex dynamic behaviour, because of the geometrical nonlinearity and the non-smooth nature of the contact laws [13], [20], with a focus on the possible non-smooth nature of the dynamic response, which can come commonly just before and during the collapse.

The main aim of the survey is to confirm the weakness zones, the efficacy of past interventions and to evaluate the acceleration of the activation of different mechanisms, by means of the discontinuous approaches, to address comparison between the numerical and the real damages, and, at the same time, to confirm the powerful of the model.

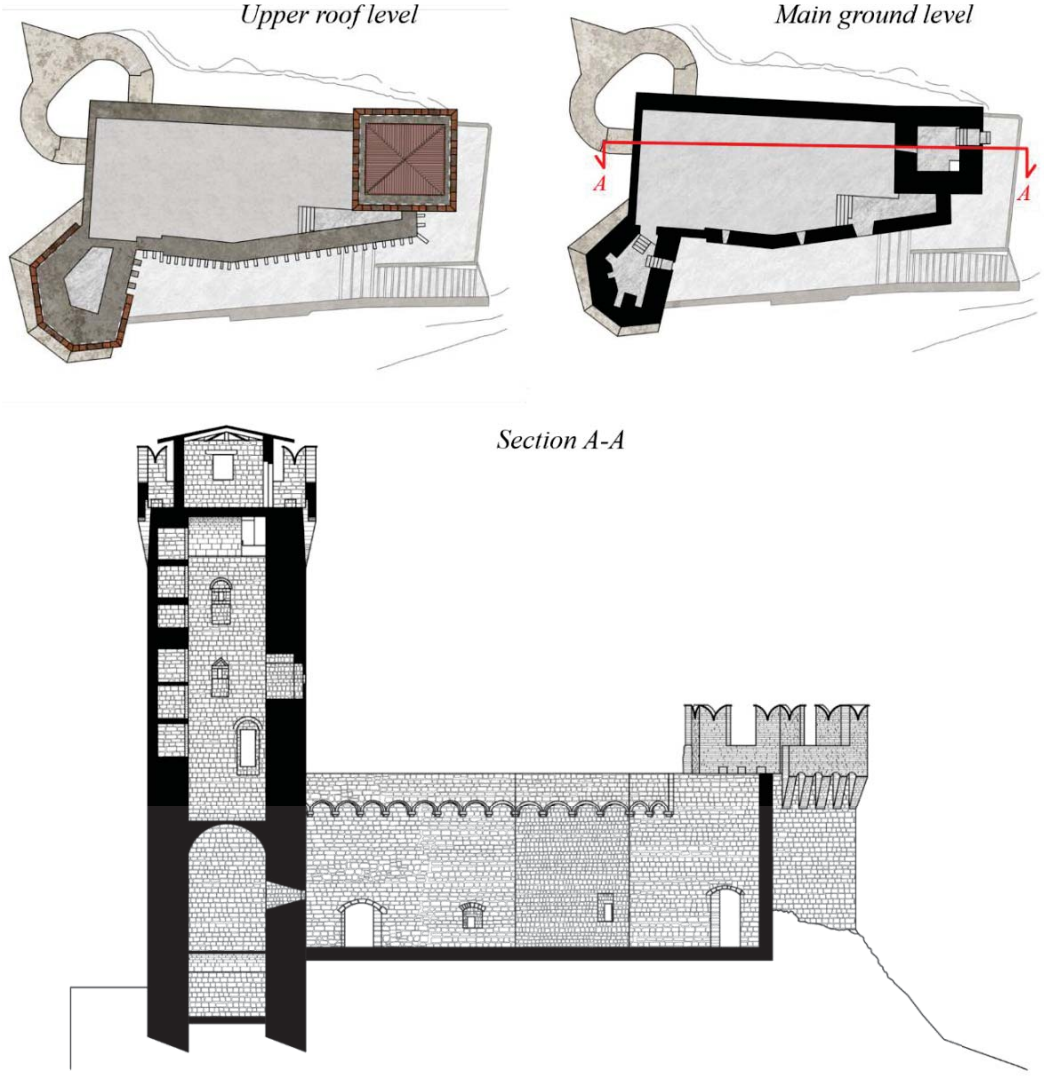

Figure 2: Geometric configuration of the Arquata del Tronto (AP) medieval fortress

2 HISTORICAL DEVELOPMENTS OF THE MEDIEVAL FORTRESS

The fortress of Arquata del Tronto, in Figure 2 and Figure 3, which is a typical example of Umbria-Marche Apennines fortified architecture of the XIII century, is mainly made by cal-

careous stone masonry walls made of multiple leaf, which can be prone to disintegration under strong dynamic actions. The fortress is in a strategical position, located on the border between the Ascoli and Norcia's administrations, and was damaged but left standing by the magnitude 6.2 earthquake event occurred in August 2016 that flattened the town centre. The medieval fortress lost *chemin de ronde* and was one of the few buildings in the town to remain still standing after the main shock. It was then severely damaged by further quakes that rattled the region in October 2016, demonstrating a not proper transverse bond for most of the masonry walls.

Moreover, the first built element of the fortress is the tower with the hexagonal plant and height of 12 m, located in the South-East edge, which encloses an irregular pentagonal environment. At the base, it is visible the gate of the ancient walled now escape tunnels. Between the XIV and XV centuries was built the North tower, with a square base and height of 24 m, which was destined sighting and extreme defence. On its top, there is a quadrangular room that was built in the early years of the XX century. The last built part is a circular tower with a diameter of 10 m and a height of 12 m, located at the South-West corner.

Following earthquakes occurred in 1703, the fortress of Arquata del Tronto suffered serious damages. Therefore, various retrofitting interventions were carried out in subsequent years. The last restoration work, before the seismic sequence of 2016, was made in the last decade of XX century.

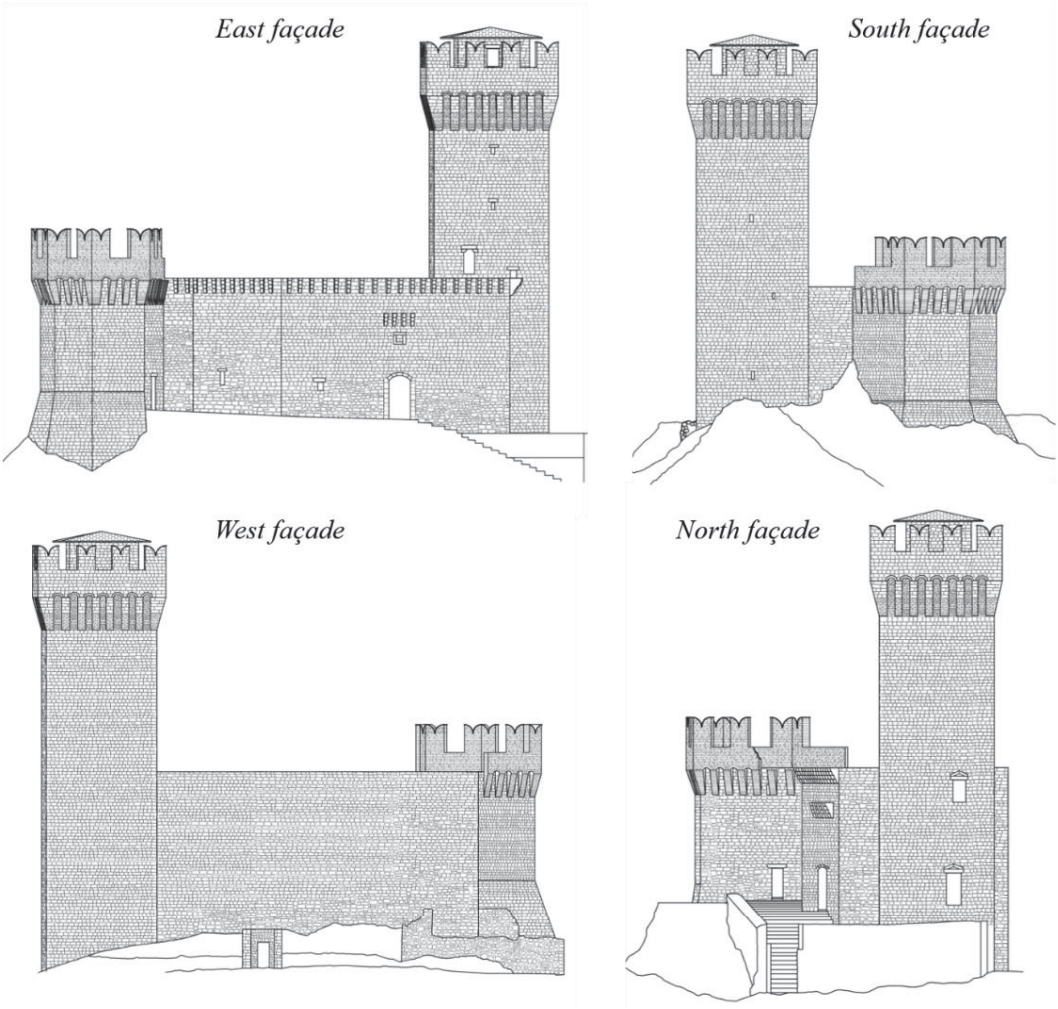

Figure 3: Geometric configuration of the Arquata del Tronto (AP) medieval fortress

2.1 Damage of the Arquata del Tronto fortress after the Central Italy earthquakes of 2016

Globally, the Arquata del Tronto medieval fortress has suffered extended damages after the shocks of the Central Italy seismic sequence of 2016.

The major cracks appeared on the upper part of the masonry towers, with the complete overturning of the merlons and the collapse of the protruding turret, visible in Figure 4a-b. Moreover, there are widespread crumbling of the multiple leaf masonry walls, partially showed in Figure 4c.

Figure 4: Views of the global (a, b) and of the multiple leaf masonry walls (c) damages of the Arquata del Tronto (AP) medieval fortress after the seismic sequence of 2016

3 THE NON-SMOOTH CONTACT DYNAMICS METHOD

The NSCD method belongs to the family of Discrete Element methods, distinguishing from the classical Distinct Element method for three differences: (i) it integrates the non-smooth contact laws directly, (ii) it uses an implicit integration scheme, and (iii) it does not account for any structural damping. It is important to stress the fact that the NSCD method is based on some modelling simplifications. The main assumption is that bodies are rigid, and their dynamics is governed by the equation of motion and by the frictional contact conditions. To describe the frictional contact laws, we must introduce some basic definitions. In the following, the notation adopted in [21] is used (scalars, vectors, and tensors are explicitly declared, and italic letters are used for all of them). Given two arbitrary bodies B_i and B_j, let P_i and P_j (Figure 5a) be the points of possible contact on the boundaries of B_i and B_j, respectively, and let n be the outer unit vector, orthogonal to the boundary of B_i in P_i. We define $g = (P_j - P_i)\cdot n$ the gap between P_i and P_j (a dot means scalar product), $(\dot{u}_n, \dot{u}_t)$ the normal and tangential velocities of P_j with respect to P_i, and (r_n, r_t) the normal and tangential reactive forces of B_i on B_j.

The contact conditions are:

1) The Signorini's law of impenetrability (Figure 5b)

$$g \geq 0, r_n \geq 0, g r_n = 0, \tag{1}$$

which, in the case of contact $g = 0$, is equivalent to the following Kuhn–Tucker conditions [18]

$$\dot{u}_n \geq 0, r_n \geq 0, \dot{u}_n r_n = 0, \tag{2}$$

written in term of relative normal velocity.

2) The dry-friction Coulomb's law (Figure 5c) that governs the behaviour in the tangential direction

$$|r_n| \leq \mu r_n; \begin{cases} r_t < \mu r_n \rightarrow \dot{u}_t = 0 \\ |r_t| = \mu r_n \rightarrow \dot{u}_t = -\lambda \frac{r_t}{|r_t|}, \end{cases} \tag{3}$$

with the friction coefficient and λ an arbitrary positive real number.

If q is the vector of the system configuration parameters (unknown translations and rotations of each body), and p is the global vector of reaction forces, the equation of motion can be written as follows

$$M\ddot{q} = f(q, \dot{q}, t) + p, \tag{4}$$

where M is the mass matrix, and f is the vector of external forces.

The local pairs $(\dot{u}_n, \dot{u}_t)$ and (r_n, r_t), characteristic of each contact, are related to the global vectors $\dot{q}$ and p, respectively, through linear maps which depend on q. Since the contact laws (1) - (3) are non-smooth, velocities $\dot{q}$ and reactions p are discontinuous functions of time. They belong to the set of bounded variation functions, i.e. functions which, at each time, have finite left and right limits. Since the accelerations are not defined when the velocities are discontinuous, Eq. (4) is reformulated in the integral form [18], [21], and it is solved numerically using a time-stepping approach, where t time is discretized into time intervals, and, within each time interval $[t_i, t_{i+1}]$, the equation of motion is integrated as follows

$$M(\dot{q}_{i+1} - \dot{q}_i) = \int_{t_i}^{t_{i+1}} f(q, \dot{q}, t)dt + \bar{p}_{i+1}, \tag{5a}$$

$$q_{i+1} = q_i + \int_{t_i}^{t_{i+1}} \dot{q}(t)dt. \tag{5b}$$

Where $\bar{p}_{i+1}$ is the impulse in $[t_i; t_{i+1}]$. The primary variables of the problem are the velocity vector $\dot{q}_{i+1}$ and the impulse vector $\bar{p}_{i+1}$ at the instant t_{i+1}. In the NSCD method, the integrals in (5a, 5b) are evaluated by means of an implicit time integrator. The overall set of global Eq. (5a, 5b) and local contact relations (1) and (2), where the reactions are approximated by the average impulses in $[t_i; t_{i+1}]$, is condensed at the contact local level, and then they are solved by means of a non-linear Gauss–Seidel by block method.

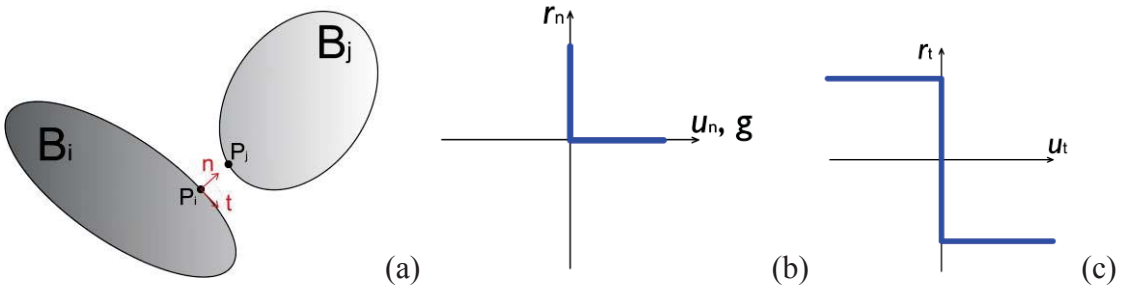

Figure 5: The interaction between two bodies (a) Signorini's law (b) Coulomb's law (c)

The relations (1) imply a perfectly plastic impact, i.e., the Newton law with restitution coefficient equal to zero. A perfect plastic impact law makes impossible to describe bouncing phenomena, and, furthermore, overestimates the energy dissipated during impacts. However, in case of systems of bricks or stones, the restitution coefficient has low values, and bouncing phenomena can be neglected. Since we are interested in the dynamical interactions between different parts of the fortress, we neglect blocks deformability. It follows that the numerical results obtained depict an overall picture of the fortress dynamics and describe the failure mechanisms of the whole structure, due to blocks rocking and sliding, but they do not describe the stresses and strain distributions within each block.

The values of friction coefficient range from 0.3 to 1.2, according to different combinations of units and mortars [22]. As a first attempt, we assume the value = 0.5 for the interface block/block of the external and internal leaf, = 0.3 for the infill and the interface between it and the leaf, and = 0.9 for the interface block/foundation to observe, mainly, the dynamics of the fortress without the structure-foundation interaction. Finally, we note that damping is not considered here and only friction and perfect plastic impacts dissipate energy.

The LMGC90© code is used, due to its ability to compute the interaction of a large number of bodies, based on the NSCD method, also assessing the seismic vulnerability of the structures [23]. As visible in Figure 6, very detailed models have been created to understand better the influence of local and global mechanisms within the analysed medieval fortress and, where possible, the presence of some past retrofitting interventions is also considered.

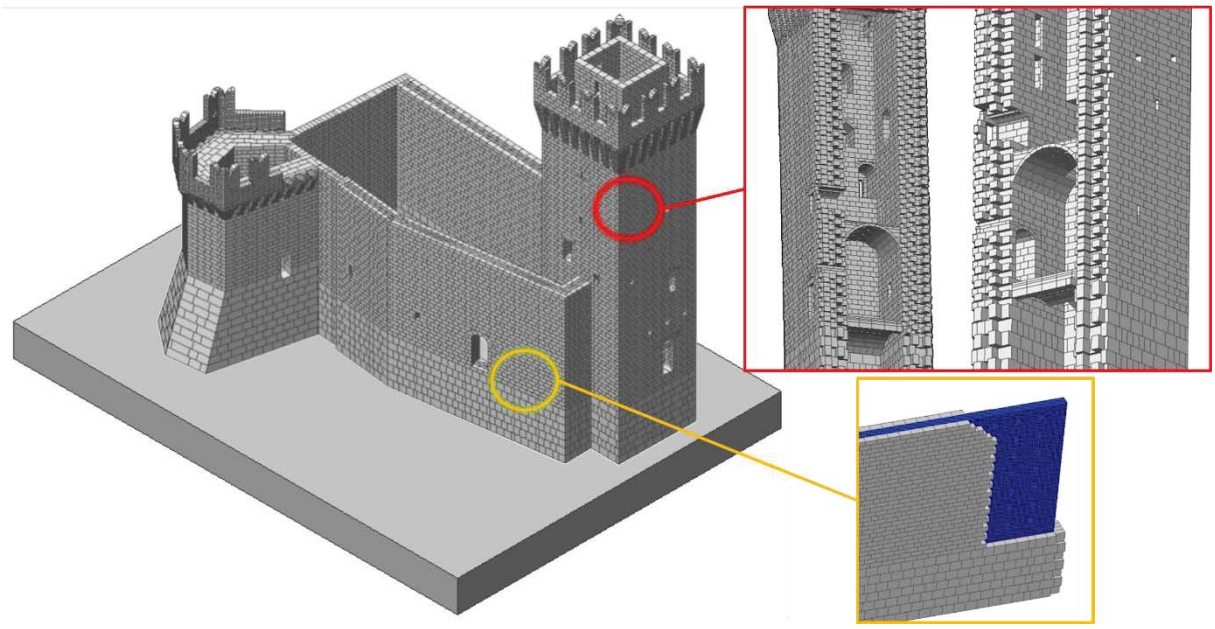

Figure 6: 3D discrete element model of the Arquata del Tronto (AP) medieval fortress

4 NUMERICAL RESULTS

The main results of the nonlinear dynamic analyses are reported in Figure 7. For this purpose, it has been applied to the main shock of the seismic sequence of 2016 in the Centre of Italy. The dynamic action used in the nonlinear analyses is recorded near Arquata del Tronto (AP) in 24th August 2016 Amatrice (AMT station in Italian Accelerometric Archive (ITACA)) with M_w=6.0.

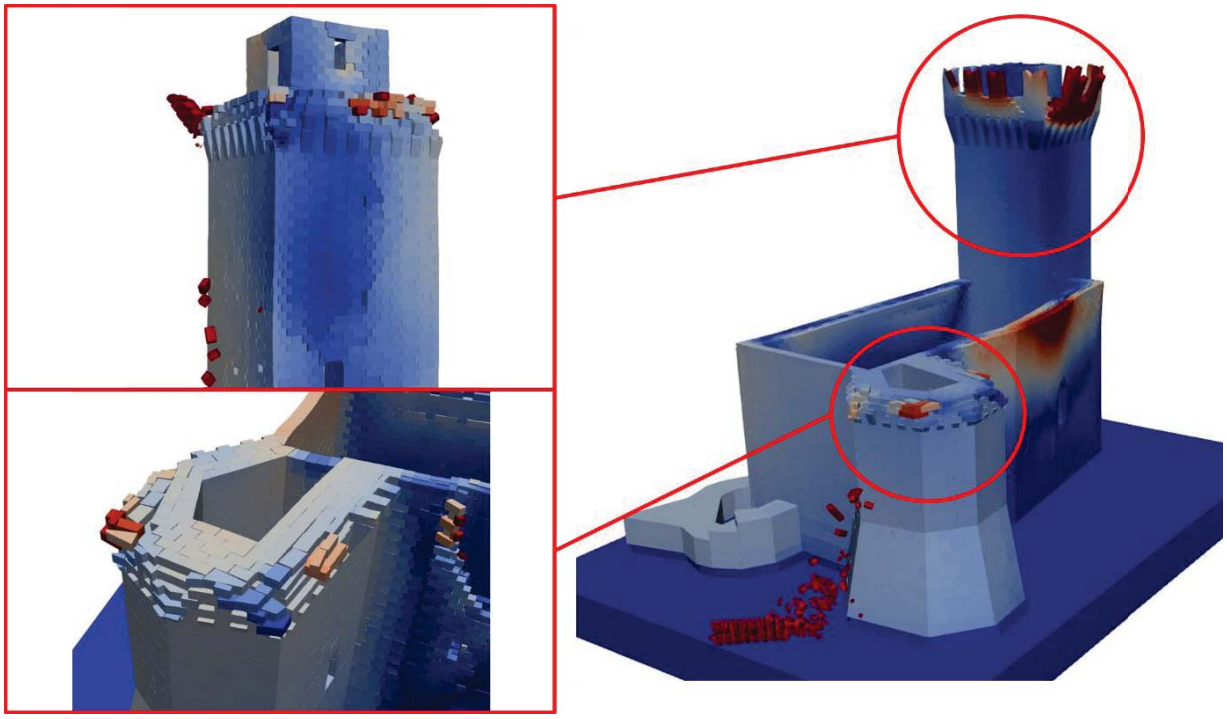

Figure 7: Failure mechanism of the Arquata del Tronto (AP) medieval fortress

Thus, from the numerical results, both the role played by the actual geometry and the insufficient resistance of the constituent materials are envisaged, showing a good match with actual crack patterns and collapses observed after the seismic sequence. Finally, the numerical analyses provide a valuable picture of the actual behaviour of the fortress, thus giving useful hints for the reconstruction and future effective strengthening interventions.

5 CONCLUSIONS

The results obtained for the Arquata del Tronto medieval fortress stroked by the Central Italy seismic sequence are here briefly reported and summarized, underline the high vulnerability of this type of multiple leaf masonry walls, and especially of the upper where merlons are placed.

A discontinuous approach and the NSCD method, implemented in the LMGC90© is used in order to assess numerically the real damage. The NSCD method combines modelling simplicity and great predictive capabilities.

Its simplicity comes from the following fundamental simplifying assumptions: (i) block rigidity; (ii) simple contact laws between blocks; (iii) absence of any damping. As a result, the mechanical behaviour of the masonry structures is influenced by only the friction coefficient. This is a significant consequence for modelling ancient buildings since the determination of the mechanical properties of these masonries is always uncertain and variable. Despite its simplicity, the model can predict a large variety of dynamical behaviours of the historical structures and their seismic vulnerability.

The numerical investigation pointed out that no collapse mechanism passes the safety check. This outcome suggests that the reconstruction of the collapsed parts on the top of the towers if pursued, should be complemented by specific strengthening devices.

REFERENCES

[1] L. Krstevska *et al.*, "In-situ experimental testing of four historical buildings damaged during the 2009 L'Aquila earthquake," *COST ACTION C26 Urban Habitat Constr. under Catastrophic Events - Proc. Final Conf.*, p. 652880, 2010.

[2] G. Milani, "Lesson learned after the Emilia-Romagna, Italy, 20–29 May 2012 earthquakes: A limit analysis insight on three masonry churches," *Eng. Fail. Anal.*, vol. 34, pp. 761–778, Dec. 2013.

[3] N. Cavalagli, G. Comanducci, and F. Ubertini, "Earthquake-induced damage detection in a monumental masonry bell-tower using long-term dynamic monitoring data," *J. Earthq. Eng.*, p. 13632469.2017.1323048, Aug. 2017.

[4] A. Formisano, G. Vaiano, F. Fabbrocino, and G. Milani, "Seismic vulnerability of Italian masonry churches: The case of the Nativity of Blessed Virgin Mary in Stellata of Bondeno," *J. Build. Eng.*, vol. 20, pp. 179–200, Nov. 2018.

[5] G. Milani and M. Valente, "Failure analysis of seven masonry churches severely damaged during the 2012 Emilia-Romagna (Italy) earthquake: Non-linear dynamic analyses vs conventional static approaches," *Eng. Fail. Anal.*, vol. 54, pp. 13–56, Aug. 2015.

[6] E. Giordano, F. Clementi, A. Nespeca, and S. Lenci, "Damage Assessment by Numerical Modeling of Sant'Agostino's Sanctuary in Offida During the Central Italy 2016–2017 Seismic Sequence," *Front. Built Environ.*, vol. 4, Jan. 2019.

[7] G. Brandonisio, G. Lucibello, E. Mele, and A. De Luca, "Damage and performance evaluation of masonry churches in the 2009 L'Aquila earthquake," *Eng. Fail. Anal.*, vol. 34, pp. 693–714, Dec. 2013.

[8] E. Giordano, A. Ferrante, E. Ribilotta, F. Clementi, and S. Lenci, "Damage Assessment of San Francesco Church in Amandola Hit by Central Italy 2016-2017 Seismic Event," *Key Eng. Mater.*, vol. 817, pp. 627–633, Aug. 2019.

[9] A. Ferrante, F. Clementi, and G. Milani, "Advanced numerical analyses by the Non-Smooth Contact Dynamics method of an ancient masonry bell tower," *Math. Methods Appl. Sci.*, p. mma.6113, Feb. 2020.

[10] F. Clementi, G. Milani, A. Ferrante, M. Valente, and S. Lenci, "Crumbling of Amatrice clock tower during 2016 Central Italy seismic sequence: Advanced numerical insights," *Frat. ed Integrità Strutt.*, vol. 14, no. 51, pp. 313–335, Dec. 2019.

[11] A. Ferrante, F. Clementi, and G. Milani, "Dynamic Behavior of an Inclined Existing Masonry Tower in Italy," *Front. Built Environ.*, vol. 5, Mar. 2019.

[12] A. Ferrante, E. Ribilotta, E. Giordano, F. Clementi, and S. Lenci, "Advanced Seismic Analyses of 'Apennine Churches' Stroked by the Central Italy Earthquakes of 2016 by the Non-Smooth Contact Dynamics Method," *Key Eng. Mater.*, vol. 817, pp. 309–316, Aug. 2019.

[13] F. Clementi, A. Ferrante, E. Giordano, F. Dubois, and S. Lenci, "Damage assessment of ancient masonry churches stroked by the Central Italy earthquakes of 2016 by the non-smooth contact dynamics method," *Bull. Earthq. Eng.*, Apr. 2019.

[14] E. Ribilotta, E. Giordano, A. Ferrante, F. Clementi, and S. Lenci, "Tracking Modal Parameter Evolution of Different Cultural Heritage Structure Damaged by Central Italy

Earthquake of 2016," *Key Eng. Mater.*, vol. 817, pp. 334–341, Aug. 2019.

[15] G. Standoli, E. Giordano, G. Milani, and F. Clementi, "Model Updating of Historical Belfries Based on Oma Identification Techniques," *Int. J. Archit. Herit.*, pp. 1–25, Feb. 2020.

[16] R. Maio, R. Vicente, A. Formisano, and H. Varum, "Seismic vulnerability of building aggregates through hybrid and indirect assessment techniques," *Bull. Earthq. Eng.*, vol. 13, no. 10, pp. 2995–3014, Oct. 2015.

[17] A. M. D'Altri, G. Castellazzi, and S. de Miranda, "Collapse investigation of the Arquata del Tronto medieval fortress after the 2016 Central Italy seismic sequence," *J. Build. Eng.*, vol. 18, pp. 245–251, Jul. 2018.

[18] J. J. Moreau, "Unilateral Contact and Dry Friction in Finite Freedom Dynamics," in *Nonsmooth Mechanics and Applications*, Vienna: Springer Vienna, 1988, pp. 1–82.

[19] B. Chetouane, F. Dubois, M. Vinches, and C. Bohatier, "NSCD discrete element method for modelling masonry structures," *Int. J. Numer. Methods Eng.*, vol. 64, no. 1, pp. 65–94, Sep. 2005.

[20] J. V. Lemos, "Discrete Element Modeling of Masonry Structures," *Int. J. Archit. Herit.*, vol. 1, no. 2, pp. 190–213, May 2007.

[21] M. Jean, "The non-smooth contact dynamics method," *Comput. Methods Appl. Mech. Eng.*, vol. 177, no. 3–4, pp. 235–257, Jul. 1999.

[22] G. Vasconcelos and P. B. Lourenço, "Experimental characterization of stone masonry in shear and compression," *Constr. Build. Mater.*, vol. 23, no. 11, pp. 3337–3345, Nov. 2009.

[23] F. Dubois, V. Acary, and M. Jean, "The Contact Dynamics method: A nonsmooth story," *Comptes Rendus Mécanique*, vol. 346, no. 3, pp. 247–262, Mar. 2018.

EURODYN 2020
XI International Conference on Structural Dynamics
M. Papadrakakis, M. Fragiadakis, C. Papadimitriou (eds.)
Athens, Greece, 23–26 November 2020

DAMAGE ASSESSMENT OF CHURCHES IN THE CITY OF CAMERINO AFTER THE 2016 CENTRAL ITALY SEISMIC SEQUENCE

E. Giordano[1], A. Ferrante[1], F. Clementi[1] and S. Lenci[1]

[1] Dept. of Civil and Building Engineering, and Architecture, Polytechnic University of Marche, Ancona, Italy
e-mail: {e.giordano,a.ferrante}@pm.univpm.it, {francesco.clementi,lenci}@univpm.it

Keywords: Central Italy Earthquakes, Masonry churches, Finite Element Model, Linear Dynamic Analysis, Total Strain Crack Model, Non-Linear Static Analysis

Abstract. *In the present work, the importance of considering the exact nonlinear and three-dimensional behavior of masonry structures is shown, in order to highlight all the structural deficiencies of different churches damaged by the last Centre Italy earthquake in the city of Camerino. For this purpose, the exact geometries of the structures are reconstructed, while information regarding the mechanical properties of masonry material are derived from previous investigations and literature references. Based on this information, different numerical models are used to reconstruct the damages.*
Different three-dimensional FE models, endowed with an elastic plastic (softening) damage constitutive law, are adopted to determine the seismic vulnerability of the building by means of nonlinear static analyses using the smeared fracture energy approach. With this method it is possible to establish, with a right degree of approximation, the areas where the most important cracks are expected and, in general, the location of the potential damage caused by horizontal forces.

1 INTRODUCTION

Italy in the last years was hit by several earthquakes, the last one was that of 2016/2017 Central Italy, characterized by four principal shooks: 24th August 2016 Mw=6.0, 26th October 2016 Mw=5.9, 30th October 2016 Mw=6.5 and 18th January 2017 Mw=5.5. This swarm interested a large area between Marche, Abruzzo, Lazio and Umbria regions. These areas are characterized by spread little villages with many religious buildings, having been territories belonging to Papal State up to 1870. The churches showed, again, their high vulnerability to the horizontal forces [1–12], due to their complex geometry and state of conservation. Whit the aim to find an appropriate method to evaluate the actual vulnerability and to predict the possible seismic damages of these structures, three different churches were analyzed. The case studies are in Camerino, a village in Marche Region hinterland. Camerino has been often hit by strong quakes (Figure 1), noteworthy is the 1799 swarm with a maximum intensity of 6.1 that provoked 60 dead in the village and heavy damages at the structures.

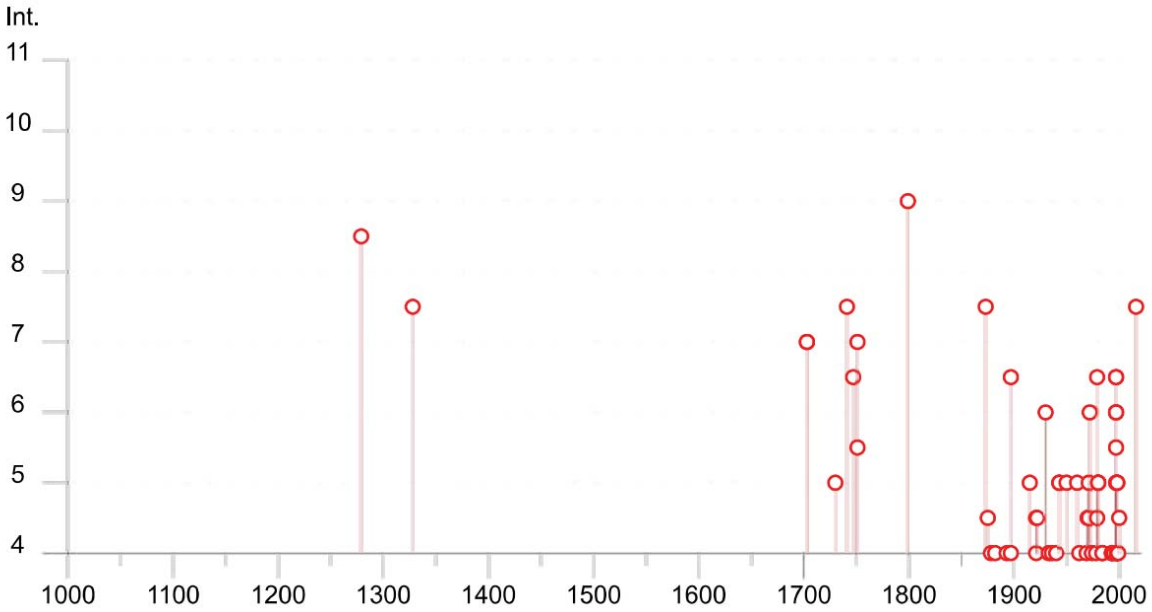

Figure 1 Earthquakes felt in Camerino during the years, from 1000 to 2017 (https://emidius.mi.ingv.it/ [13])

The analyzed churches are shown in Figure 2, they are:

- Santa Maria in Via Church
- San Venanzio Church
- Santa Maria Annunziata Church

Two of them are in the red zone, Santa Maria in Via and Santa Maria Annunziata, whereas San Venanzio is in Nord-Est neighborhood. The churches were studied using 3D Finite Element Models, on with whom linear and non-linear analyses were carried out in order to stress, once again, the capacity of this modeling type to predict the seismic vulnerability, since it would be a useful resource to design interventions to prevent cracks and failures occurrence [14,15].

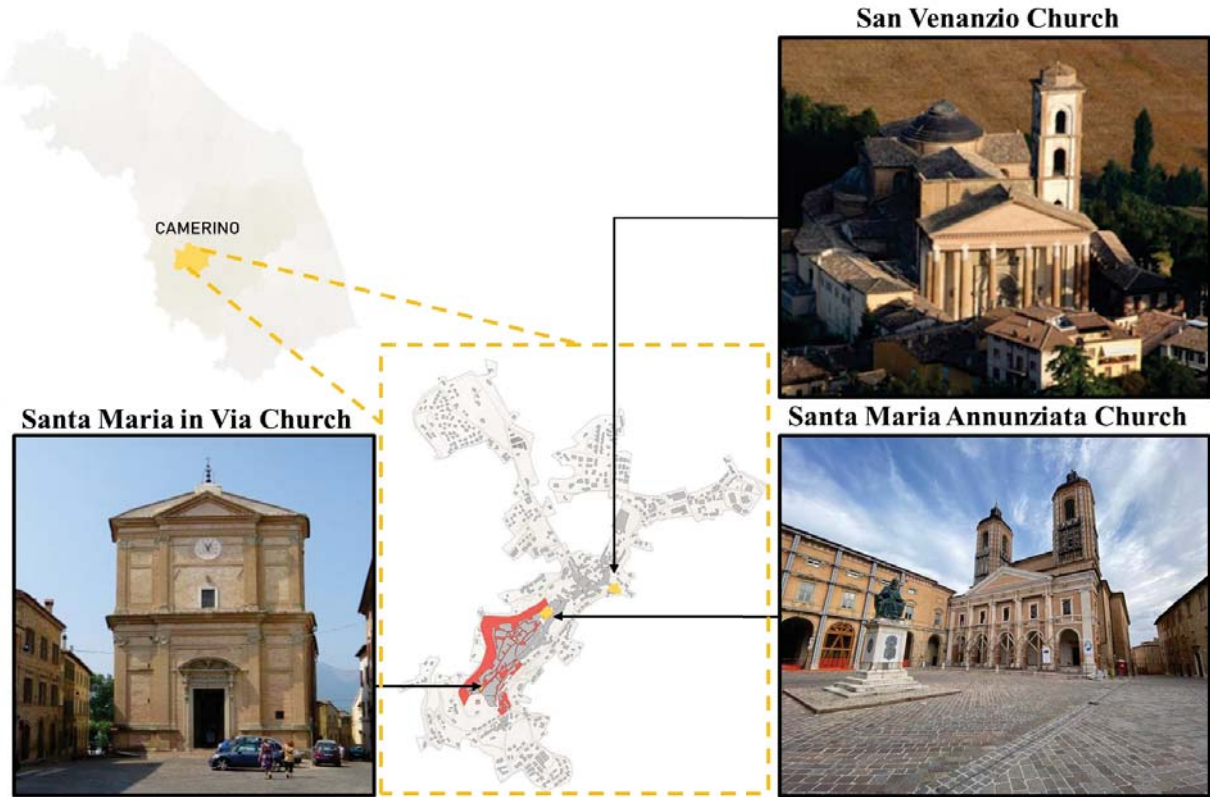

Figure 2 Geographical localization of the churches analyzed

2 CASE STUDIES

2.1 Historical development

Santa Maria in Via Church (S_M_V)

The firsts proofs of a church presence date back to 1299, it was probably a little church that was converted later to guard the Madonna enthroned with the child, painting brought by Crusaders from Smirne. The church reformation started in 1639 by the Angelo Giori Cardinal will and ended in 1642. The church was hit by different earthquakes during the centuries, the strong 1799 quake caused the collapse of the masonry vault that covered the principal room, that was replaced by a camorcanna vault (light vault). During the 1997 Earthquake, there were static damages and in the connections of the light vault with the trusses od roof. The work of restoration was completed only in 2006.

San Venanzio Church (S_V)

San Venanzio Church dates back to the XII century, it was built on the ruins of a little church erected on the place of Saint's martyrium. In the XIII century, the church acquired importance and became Collegiata. The church was subject to different works during the years, subsequently the 1799 earthquake was necessary a radical reconstruction for the heavy damage suffered. The works were carried out by the architect Luigi Poletti, they started in 1836 and ended in 1875 on the 9 of May. In 1979 the transept foundations were consolidated with micro piles and the principal walls were reinforced by concrete injections. In the “90s also the crypt columns' foundations were consolidated. During the “97 earthquakes, the failure of sac-

risty and apse foundations occurred. After this event also these foundations were reinforced with R.C. piles and the roofs and masonry walls were repaired.

Santa Maria Annunziata Church (S_M_A)
The first the structure edification seems to date back to the V century, while the first proof of a Romanesque church, consecrated to San Giuseppe, date to the XIII century. The first important interventions go back to 1259 when the Svevi's devastation and the population increment pushed on a complete renovation. In 1279 the church was hit by a strong earthquake, it provoked the bell-tower collapse, that was rebuilt subsequently. In 1748/49 the façade was transformed by a two hundred style at Barocco style. The 28th June of 1799 a new earthquake hit the church, followed by a heavy makeover carried out by Andrea Vinci architect, a Vanitelli's student. The new church had a portico in front as an extension of the Palazzo Vescovile. The works ended the 8th of September of 1932, when the church was devoted to Santissima Maria Annunziata. After the "97 earthquake the church was reinforced by steel connections on the roof base to provide the box-behavior.

2.2 Geometric survey

Santa Maria in Via Church (S_M_V)
The nave of the church has an elliptic shape with a larger diameter of about 28m and smaller of 13m, on both sides there are four chapels (Figure 3-a). On the two sides of the entry, there are two symmetric rooms that are a baptizer and a chapel. The sacristy and the oratory are on the sides of the presbytery. On the south side, there is the bell-tower high 15m. The bearing structure is made of solid bricks with an inner core of poor materials. The hall is covered by a camorcanna vault and the roof is made by wood trusses

San Venanzio
The basilica has a Latin-cross (39mx68m) layout with the principal nave of double-length respect the lateral ones Figure 3-b. The principal nave is divided by the others whit fourteen Corinthian columns built with blocks stone and solid bricks. Under the presbytery, there is the crypt covered by cross vaults supported by Porfido columns. The crypt is accessed through two symmetrical stairs in the transept. The bell-tower is on the north-west side with a height of 45 m, three different orders are visible on it. On the principle nave there is a light barrel vault covered by a wood roof. The bearing structure is made of solid bricks

Santa Maria Annunziata Church (S_M_A)
The church has a Latin-cross layout (29mx70m), the naves are divided by columns and pillars on which rest round arches Figure 3-c. Under the church, there is a large crypt cover by cross and barrel vaults. On the two sides of the facade, arrears of six meters, there are two identical bell-towers of 40 m high covered by domes. The naves are covered by camorcanna vaults and the roof is made of wood trusses. The bearing structure is made of solid bricks and stone blocks

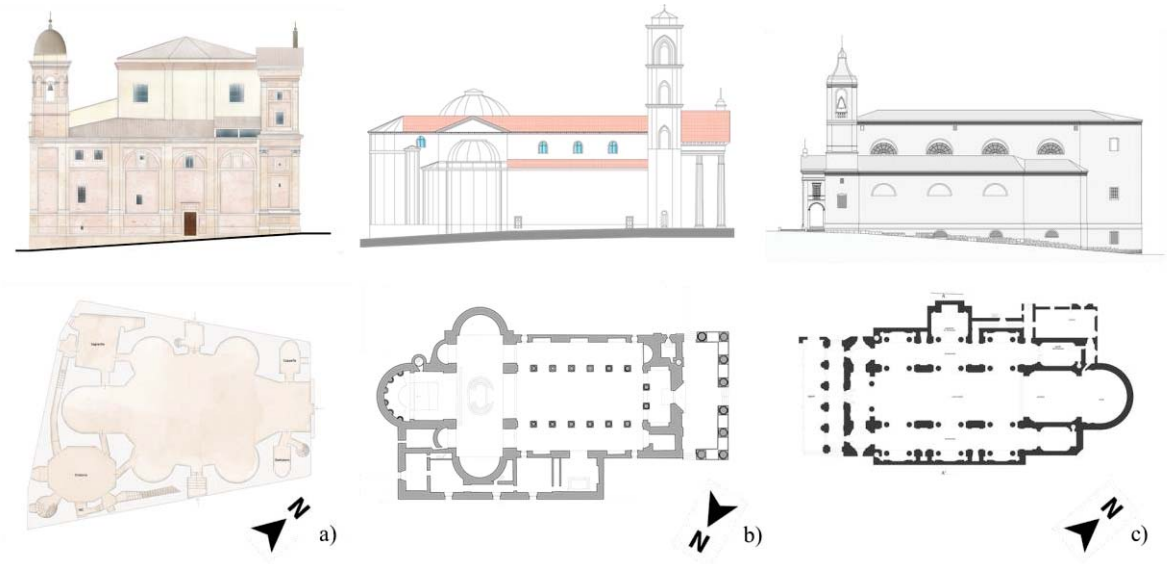

Figure 3 Geometric configuration; a) Santa Maria in Via; b) San Venanzio; c) Santa Maria Annunziata

2.3 Damage suffered during the Central Italy Earthquake

The 2016 earthquakes caused damages to all these churches. Indeed, comparing the accelerations recorded to Camerino during the 30th October quake with the maximum acceleration expected to preserve the human life, according to the Italian code [16], they have been, in North direction, twice respect to expected values Figure 4.

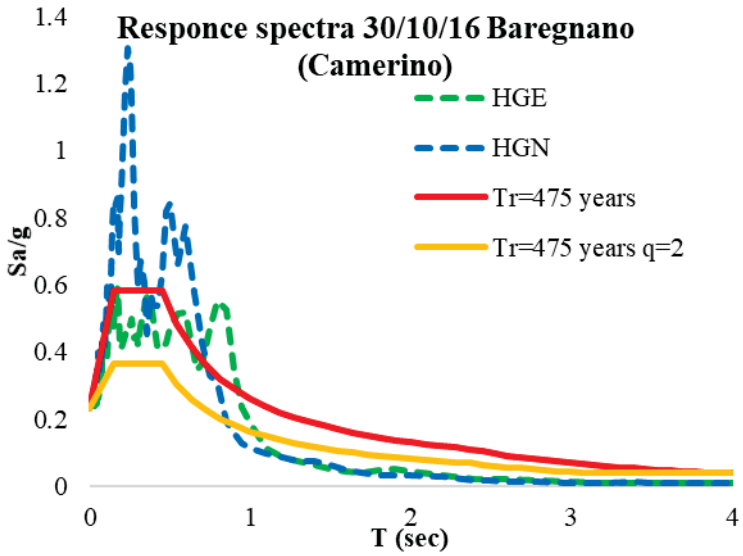

Figure 4 Comparison between the maximum acceleration expected for the SLV and accelerations recorded

The most damage church is Santa Maria in Via. After the 26th October earthquake, the bell-tower collapsed and a lot of spread cracks appeared, during the 30th October quake the cracks made worst, and partial collapses occurred on the two sides of the façade Figure 5-a. The roof collapse happened after the 18th January 2017 earthquake, provoking the tambour and light vault failure.

The second more damaged church is Santa Maria Annunziata Figure 5-c, it showed significative cracks in both the bell-towers in correspondence of the spiral stairs and near the façade connections. The narthex had cracks on the connection to the façade, probably provoke by a hammering mechanism. On the opposite sides of the presbytery, two symmetric cracks show the activation of its out-of-plane mechanism. The church internally had shear cracks on the pillars and between the change of materials.
San Venanzio, instead, had deep cracks on the light vaults, on the arches and walls Figure 5-b. All of them were declared unsafe after the earthquakes, today the only reopened is the less damage, or rather, San Venanzio.

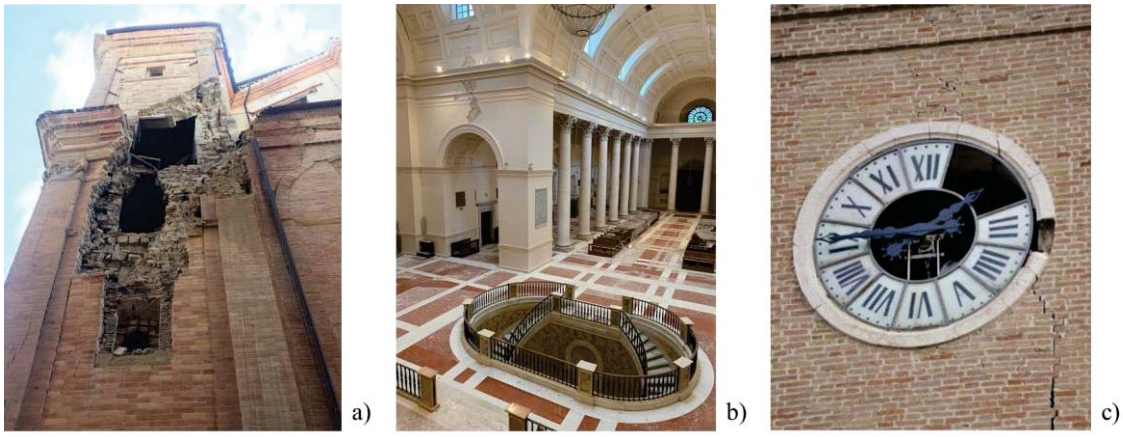

Figure 5 Some cracks after the Central Italy Earthquake, a) Partial collapse of one façade side of Santa Maria in Via; b) Cracks spread on the walls and the vault of San Venanazio; c) Crack in correspondence of the Clock of one Santissima Annunziata bell-tower

3 NUMERICAL MODEL

The churches were studied using Finite Element Models (FEMs), by means of MidasFEA© software [17], as it is impossible to simplify this type of buildings with the common softwares. The masonry was considered as homogeneous and isotropic material, whose post elastic behavior was considered using the Total Strain Crack Model, assign a parabolic law in compression, a Hordjik law in tension and a linear law for the shear [18–20].

The geometries were reproduced carefully and subsequently discretized with 4-nodes tetrahedral brick elements Figure 6. In the Table 1 are reported the number of elements, nodes and degree of freedom used for each case study.

Church	Element	Nodes	d.o.f.
S_M_V	483 885	109 694	345 414
S_V	230 046	61 422	175 723
S_M_A	601 019	163 030	489 090

Table 1 Finite Element Models characteristics

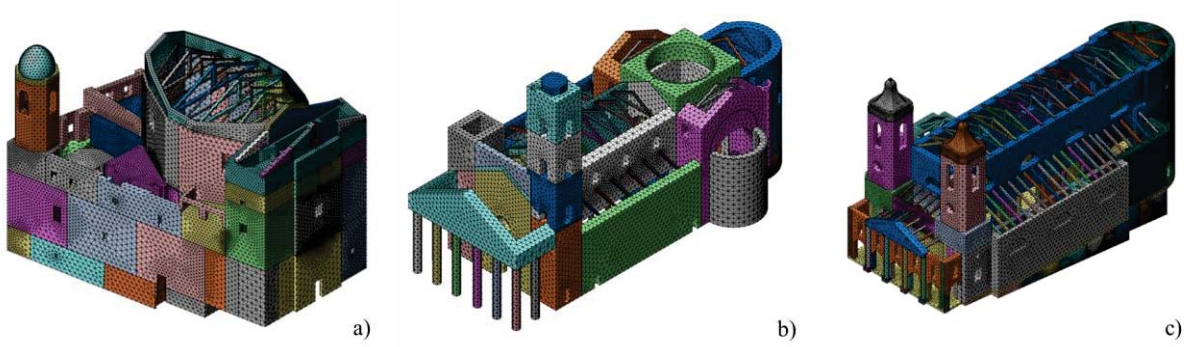

Figure 6 Numerical Models of a) Santa Maria in Via; b) San Venanzio; b) Santa Maria Annunziata

3.1 Dynamic analysis

Firstly, the numerical models were submitted to dynamic linear analyses using Lancoz method. A lot of modal shapes were necessary to move the 85% of the total mass in both the direction, the number of modes are respectively 414 for Santa Maria in via, 230 for the San Venanzio and 474 for the Santa Maria Annunziata

The principal modal shapes periods, for each church, are compared with the spectrums recorded during the strongest quake of the 2016 seismic swarm, the Figure 7 shows that their periods are near the maximum accelerations recorded periods.

In all the models the bell-towers are moved from one of the principal modes, indeed, in all the cases, they showed cracks after the earthquakes. The two long churches, San Venanzio and Santa Maria Annuziata, have as other vulnerable elements the longitudinal walls, instead, the façade is a vulnerable element for the Santa Maria in via church, in effect it has two long cracks on both sides.

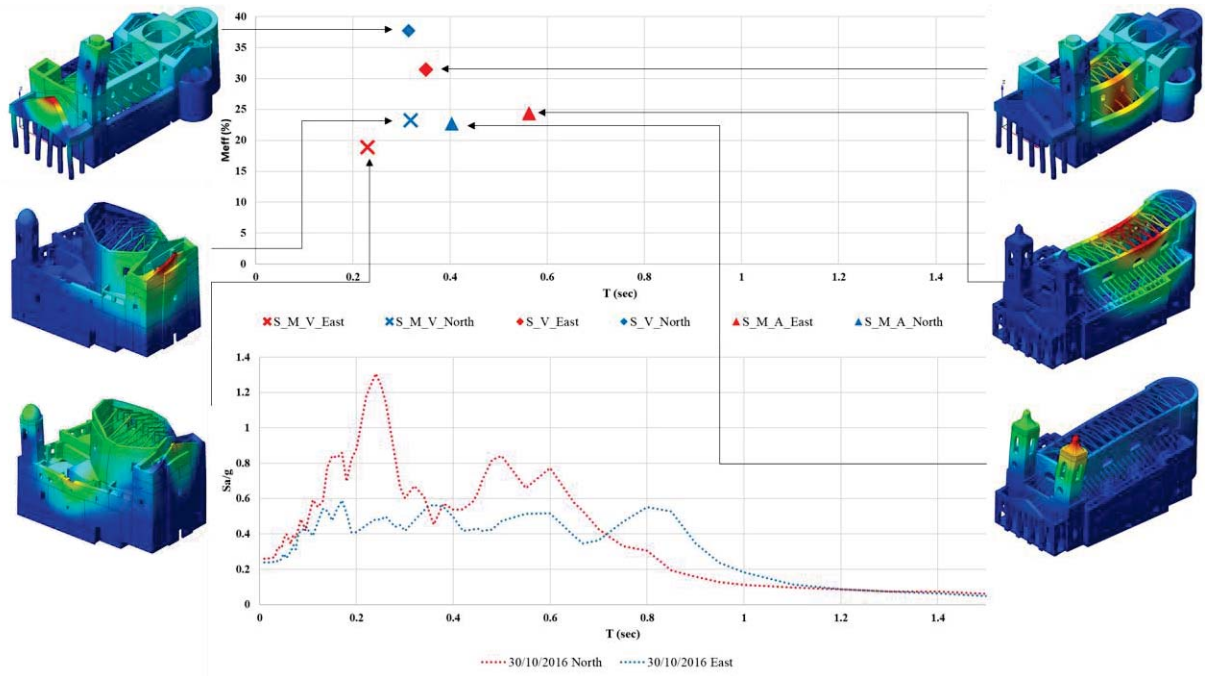

Figure 7 Distribution of principal modal shapes in the North and East directions and comparison with the pseudo-acceleration response spectra of the main shock of Central Italy 2016-2017 seismic sequence.

3.2 Nonlinear static analysis

Subsequently, the models were used to carry out the non-linear static analyses, following the guidelines of the Italian Code [16,21] two different force distributions were used, one proportional to the modal shapes (PushMode) and the other masses proportional (PushMass).

To perform the PushMode the models were subjected to response spectrum analysis using as input the Limit State of Significant Damage (SLSD or SLV in Italian) spectrums considering "Class II" and ordinary structures. The nodal forces were obtained combining with the CQC algorithm the responses in each direction, considering the number of modes necessary to move the 85% of the total mass.

The analyses were performed using the arch-length iteration, using 0.1 as initial load, 1000 as maximum number of iteration and a 10^{-3} as convergence limit.

From these analyses, the capacity curves of each church were obtained for different control nodes. The curves show different behaviors and resistances for both in the directions and control nodes chosen, due to the geometry complexity. In Figure 8 are reported the capacity curves of one control node for each church obtain by PushMass analysis in +X-Direction and +Y-Direction.

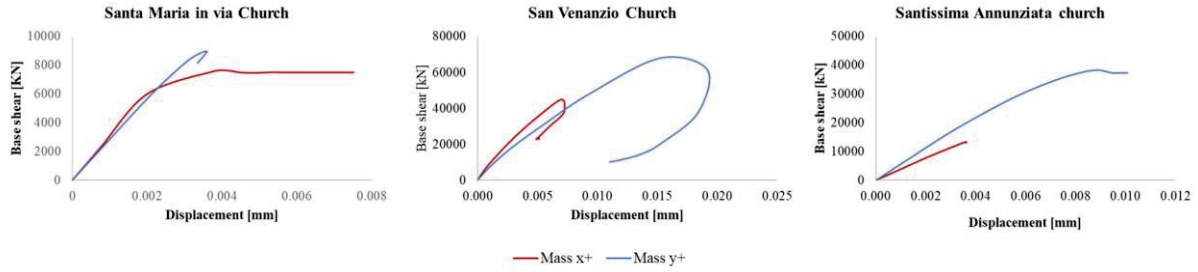

Figure 8 Examples of PushMass curves in +X-Direction and +Y-Direction of a control node for each church

Comparing the numerical cracks with the real damages it is possible to confirm the readability of the numerical models **Figure 9**.

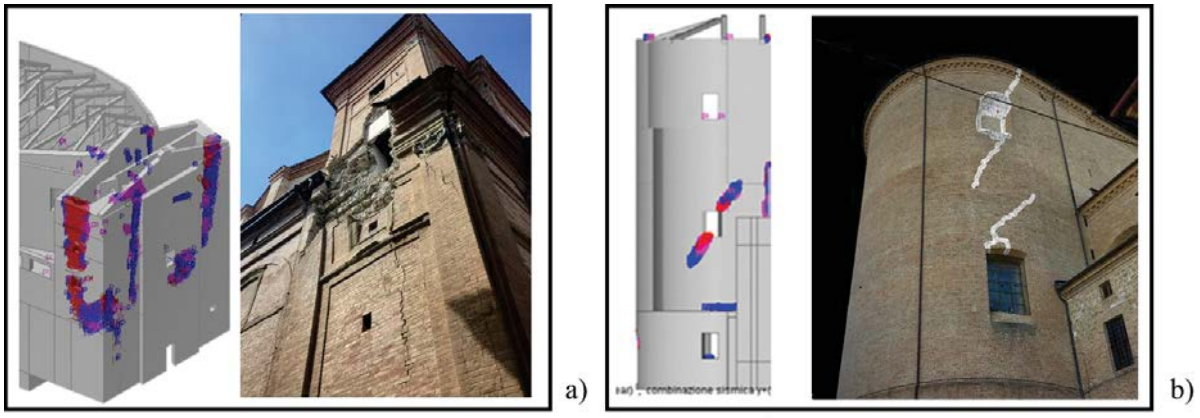

Figure 9 Correspondence between numerical and real cracks for a) Santa Maria in Via; b) Santa Maria Annunziata

4 CONCLUSIONS

The paper presents an accurate study of three churches, Santa Maria in Via, San Venanzio and Santissima Annunziata, located in the crater area of 2016 Central Italy Earthquake, precisely in Camerino, a village in the hinterland of Marche Region. The churches, seriously damaged, were studied with FEM using linear and nonlinear analysis. The nonlinear static analyses show as this type of analysis is able, with a good approximation, to reproduce the real cracks occurred, even if it overestimates the seismic capacity, since it doesn't include the change of frequencies produced by the damage evolution.

REFERENCES

[1] F. Clementi, A. Ferrante, E. Giordano, F. Dubois, S. Lenci, Damage assessment of ancient masonry churches stroked by the Central Italy earthquakes of 2016 by the non-smooth contact dynamics method, Bull. Earthq. Eng. (2019). doi:10.1007/s10518-019-00613-4.

[2] E. Giordano, F. Clementi, A. Nespeca, S. Lenci, Damage Assessment by Numerical Modeling of Sant'Agostino's Sanctuary in Offida During the Central Italy 2016–2017 Seismic Sequence, Front. Built Environ. 4 (2019). doi:10.3389/fbuil.2018.00087.

[3] A. Ferrante, F. Clementi, G. Milani, Advanced numerical analyses by the Non-Smooth Contact Dynamics method of an ancient masonry bell tower, Math. Methods Appl. Sci. (2020) mma.6113. doi:10.1002/mma.6113.

[4] F. Clementi, G. Milani, A. Ferrante, M. Valente, S. Lenci, Crumbling of Amatrice clock tower during 2016 Central Italy seismic sequence: Advanced numerical insights, Frat. Ed Integrità Strutt. 14 (2019) 313–335. doi:10.3221/IGF-ESIS.51.24.

[5] G. De Matteis, M. Zizi, Preliminary Analysis on the Effects of 2016 Central Italy Earthquake on One-Nave Churches, in: 2019: pp. 1268–1279. doi:10.1007/978-3-319-99441-3_136.

[6] G. Milani, M. Valente, Failure analysis of seven masonry churches severely damaged during the 2012 Emilia-Romagna (Italy) earthquake: Non-linear dynamic analyses vs conventional static approaches, Eng. Fail. Anal. 54 (2015) 13–56. doi:10.1016/j.engfailanal.2015.03.016.

[7] A. Ferrante, F. Clementi, G. Milani, Dynamic Behavior of an Inclined Existing Masonry Tower in Italy, Front. Built Environ. 5 (2019). doi:10.3389/fbuil.2019.00033.

[8] A. Formisano, G. Vaiano, F. Fabbrocino, G. Milani, Seismic vulnerability of Italian masonry churches: The case of the Nativity of Blessed Virgin Mary in Stellata of Bondeno, J. Build. Eng. 20 (2018) 179–200. doi:10.1016/j.jobe.2018.07.017.

[9] E. Giordano, F. Clementi, A. Barontini, M. Giovanna, E. Chatzi, F. Luís, Damage detection and optimal sensor placement in health monitoring of " Collegiata di Santa Maria " in Visso (Central Italy) Damage detection and optimal sensor placement in health monitoring of " Collegiata di Santa Maria " in Visso (Central Italy), (2019) 44–53.

[10] E. Giordano, A. Ferrante, E. Ribilotta, F. Clementi, S. Lenci, Damage Assessment of San Francesco Church in Amandola Hit by Central Italy 2016-2017 Seismic Event,

Key Eng. Mater. 817 (2019) 627–633. doi:10.4028/www.scientific.net/KEM.817.627.

[11] A. Ferrante, E. Ribilotta, E. Giordano, F. Clementi, S. Lenci, Advanced Seismic Analyses of "Apennine Churches" Stroked by the Central Italy Earthquakes of 2016 by the Non-Smooth Contact Dynamics Method, Key Eng. Mater. 817 (2019) 309–316. doi:10.4028/www.scientific.net/KEM.817.309.

[12] E. Ribilotta, E. Giordano, A. Ferrante, F. Clementi, S. Lenci, Tracking Modal Parameter Evolution of Different Cultural Heritage Structure Damaged by Central Italy Earthquake of 2016, Key Eng. Mater. 817 (2019) 334–341. doi:10.4028/www.scientific.net/KEM.817.334.

[13] INGV, Istituto Nazionale di Geofisica e Vulcanologia, (2020). https://emidius.mi.ingv.it/.

[14] B. Faggiano, A. Marzo, A. Formisano, F.M. Mazzolani, Innovative steel connections for the retrofit of timber floors in ancient buildings: A numerical investigation, Comput. Struct. 87 (2009) 1–13. doi:10.1016/j.compstruc.2008.07.005.

[15] A. Formisano, C. Castaldo, G. Chiumiento, Optimal seismic upgrading of a reinforced concrete school building with metal-based devices using an efficient multi-criteria decision-making method, Struct. Infrastruct. Eng. 13 (2017) 1373–1389. doi:10.1080/15732479.2016.1268174.

[16] Ministero delle Infrastrutture e dei Trasporti, DM 17/01/2018 - Aggiornamento delle "Norme Tecniche per le Costruzioni" (in italian), (2018) 1–198.

[17] Midas FEA, Analysis and Algorithm Manual, (2016).

[18] J.G. Rots, Smeared and discrete representations of localized fracture, Int. J. Fract. 51 (1991) 45–59. doi:10.1007/BF00020852.

[19] P.B. Lourenço, Recent advances in masonry modelling: micromodelling and homogenisation, in: Multiscale Model. Solid Mech. Comput. Approaches, 2009: pp. 251–294. doi:10.1142/9781848163089_0006.

[20] J.G. Rots, R. de Borst, Analysis of Mixed-Mode Fracture in Concrete, J. Eng. Mech. 113 (1987) 1739–1758. doi:10.1061/(ASCE)0733-9399(1987)113:11(1739).

[21] Ministero delle infrastrutture e dei trasporti, Circolare 21 gennaio 2019 n. 7 C.S.LL.PP. Istruzioni per l'applicazione dell'aggiornamento delle "Norme Tecniche per le Costruzioni" di cui al D.M. 17/01/2018 (in Italian), Suppl. Ord. Alla G.U. n. 35 Del 11/2/19. (2019).

EURODYN 2020
XI International Conference on Structural Dynamics
M. Papadrakakis, M. Fragiadakis, C. Papadimitriou (eds.)
Athens, Greece, 23–26 November 2020

AUTOMATIC ASSESSMENT OF PARTIAL FAILURE MECHANISMS IN RETROFITTED HISTORICAL MASONRY AGGREGATES THROUGH ADAPTIVE NURBS LIMIT ANALYSIS

Nicola Grillanda[1], **Marco Valente**[1] **and Gabriele Milani**[1]

[1]Department of Architecture, Built Environment and Construction Engineering (ABC), Politecnico di Milano, Piazza Leonardo da Vinci 32, 20133, Milan, Italy. nicola.grillanda@polimi.it, marco.valente@polimi.it, gabriele.milani@polimi.it

Keywords: Historical masonry aggregates, local mechanisms, NURBS, adaptive limit analysis.

Abstract. *The aim of this work is to propose a new automatic procedure for the seismic assessment of partial failure mechanisms in historical masonry aggregates. Starting from the geometrical survey, a three-dimensional model of the whole aggregate is derived. The model is discretized through few NURBS surfaces (Non-Uniform Rational Bezier Spline) and imported into the MATLAB environment. A procedure of kinematic limit analysis is applied to a pre-selected part of the construction. The walls selected are subdivided into few elements, each one is a portion of the initial NURBS surface and is assumed as a rigid body. Rigid-plastic interfaces are defined on the boundary of each element. As a result, the kinematic limit analysis provides a local mechanism involving the selected walls and an associated kinematic multiplier. An optimization procedure, here conducted by using a Genetic Algorithm, is applied with the aim of finding the collapse multiplier. The procedure can take into account the most spread reinforcement techniques adopted in historical constructions, such as tie-rods and FRP strips, which maintain a local response to horizontal loads. An application to a historical masonry aggregate, located in the center of Arsita (Teramo, Italy), is finally presented.*

1 INTRODUCTION

Historical centers are often the final result of a high number of masonry construction built adjacent to each other. The seismic response of masonry constructions aggregates is affected by several factors, such as geometrical irregularities, uncertainties on connections between walls, difficulties on the identification of masonry mechanical parameters, lack of design details, and pre-existent damage, resulting quite difficult to predict. Seismic events occurred during last years (L'Aquila 2009, Emilia Romagna 2012, Central Italy 2016) damaged severely a huge number of masonry historical constructions [1–4], including residential building aggregates. Therefore, the implementation of an efficient numerical method for the correct prediction of the seismic response of historical masonry aggregates before and after the application of the most typical retrofitting interventions is a very actual problem.

Several numerical methods are available. Focusing the attention on masonry building aggregates, the typical approaches include index-based methods [5,6], local failures analyses through limit analysis techniques [7], Equivalent Frame-based methods [8–10], and Finite Element-based static and dynamic nonlinear analyses [11–14]. However, considering the typical lack of global behavior of this structural typology (see also the huge number of local collapses observed during the last earthquakes [15]), local analyses cannot be neglected in the evaluation of the seismic vulnerability [16–18]. Moreover, the application of a thorough number of local analyses is also recommended by the Italian code [19] for masonry buildings in general.

The typical retrofitting strategies on masonry aggregates are aimed at achieving the global response of the structure under horizontal loads. However, it has to be pointed out that this result usually requires too invasive interventions that are not allowed for historical constructions, for which the original construction cannot be subjected to strong modifications for reasons of cultural heritage preservation. As regards historical constructions, local interventions are usually preferred, such as the application of steel or timber ties [20,21], FRP strips, TRM or FRCM [22,23]. These interventions are aimed at avoiding the most critical out-of-plane mechanisms. As a result, the structural response is still local, but the collapse takes place through a different local mechanism to which a higher horizontal load multiplier is associated. Therefore, the seismic vulnerability evaluation still requires local analyses, allowing studies through limit analysis techniques.

The theory of limit analysis for historical masonry constructions was originally developed by Heyman [24], who proposed to treat masonry as a no-tension material. However, more accurate modelling strategies can be followed to take into account crushing and shear failures. Some recent homogenized limit analysis techniques have been presented [25–27]. In order to decrease the required computational effort, deriving from the reproduction of the correct collapse mechanisms by using refined mesh, a novel limit analysis approach has been presented by some of the Authors [28]. In this procedure, an upper bound formulation is applied on a masonry structure discretized through a reduced number of NURBS surfaces (Non-Uniform Rational B-Spline, [29]). NURBS objects are parametric functions commonly adopted in the CAD modelling that allow representing curved geometries with few surfaces. NURBS surfaces are adopted to represent walls and vaults and are idealized as rigid elements with internal dissipation allowed only along edges. Since the method is based on a reduced number of rigid elements, a mesh adaptation procedure is applied to minimize the kinematic load multiplier and determine the real collapse mechanism. A Genetic Algorithm (GA) [30] is usually applied, even if different meta-heuristic algorithms can be adopted [31]. The method has been adopted to study several typologies of historical masonry structures [32–35], sometimes considering the presence of reinforcement [36–39]. In this work, the adaptive NURBS limit analysis is adopted to study a complex case of historical masonry aggregate located in the center of Arsi-

ta (Abruzzo region) [40,41]. A disposition of tie-rods has been hypothesized on the constructions, and the local mechanisms are compared with those found in the unreinforced case.

2 ADAPTIVE NURBS-BASED LIMIT ANALYSIS

This novel limit analysis approach for historical masonry aggregates is based on a discretization of the whole construction through NURBS (Non-Uniform Rational B-Spline [29]) surfaces. The geometrical representation via NURBS allows representing each wall by using a single surface (even in presence of openings), resulting in a very reduced number of overall elements. Moreover, curved structural elements, such as arches and vaults, can be reproduced through very few surfaces. For sake of simplicity, we refer to [29] for a complete theoretical dissertation on the NURBS geometrical entities and the main algorithms involved.
The NURBS model is imported into the MATLAB environment, where each surface is converted into a 3D macro-element once thickness and offset properties are assigned. Each surface can be subdivided into few elements, each one deriving by a trimmed NURBS surface which is a partition of the initial one.
The assumption of infinitely rigid elements is here followed. Non-linearities are included in the computation by defining rigid-plastic interfaces at the contacts between rigid elements. A simple kinematic limit analysis can be defined in this model. The kinematic of each rigid element is defined through the six degrees of freedom of its gravity center. Relative velocities can occur at interfaces only. In order to properly evaluate the amount of plastic dissipation related to velocity jumps at interfaces, each one is discretized through points in which a local reference system ($\mathbf{n}$, $\mathbf{s}$, $\mathbf{t}$) (Figure 1(a)) is defined, and a three-dimensional failure surfaces (typically a Mohr-Coulomb domain with tension cut-off and linear cap in compression, Figure 1(b)) is assigned. A classic associative plastic flow rule is adopted.

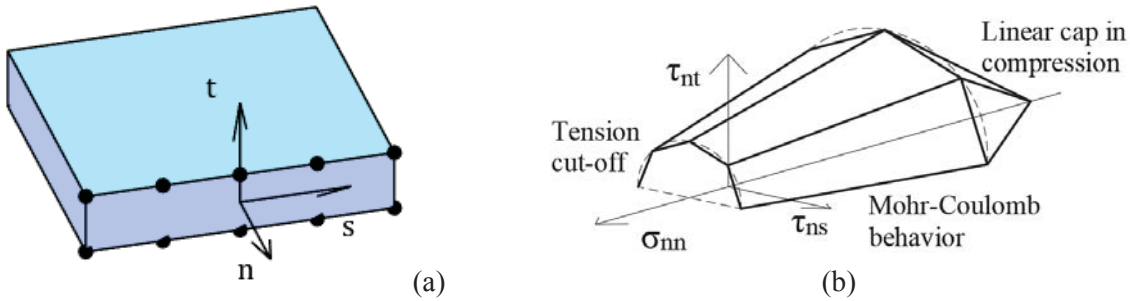

Figure 1. (a) Discretization of interfaces and local reference system, (b) three-dimensional failure surface.

Therefore, interfaces assume the meaning of possible fracture lines. A configuration of dead- and live-load (respectively $\mathbf{F}_0$ and $\boldsymbol{\Gamma}$) is defined. The live-load multiplier Γ is found by applying the Principle of Virtual Powers. The procedure can be summarized in form of standard linear programming problem:

$$\min\left\{\Gamma = \sum_i P_{\text{int}}^i - P_{\mathbf{F}_0}\right\} \text{ such that } \begin{cases}\mathbf{A}_{eq}\mathbf{x} = \mathbf{b}_{eq} \\ \dot{\boldsymbol{\lambda}} \geq 0\end{cases} \tag{1}$$

where:

$\sum_i P_{\text{int}}^i$ is the total amount of internal dissipated power;

$P_{\mathbf{F}_0} + P_{\boldsymbol{\Gamma}}$ is the power dissipated by the external loads;

$\mathbf{x}$ is the vector of unknowns, which include the velocity components of each element and the non-negative plastic multipliers $\dot{\boldsymbol{\lambda}}$;

$\mathbf{A}_{eq}$, $\mathbf{b}_{eq}$ are respectively the overall equality constraints matrix (containing geometric constraints, plastic compatibility, and normalization condition of live loads power) and the corresponding right-hand side vector.

The solution of the presented linear programming problem allows defining a horizontal load multiplier α_0 and a mechanism. The mechanism will depend on the assumed position of fracture lines and, in agreement with the kinematic theorem of limit analysis, the associated horizontal load multiplier will be an upper bound of the collapse multiplier. Therefore, the initial mesh must be adjusted to find the real position of fracture lines. A Genetic Algorithm (GA) is here applied for the mesh adaptation procedure [30]. In this way, a good estimation of the horizontal load multiplier and the correct collapse mechanism is automatically provided.

3 APPLICATION TO HISTORICAL MASONRY AGGREGATES

When local mechanisms in historical masonry aggregates are investigated, dead loads represent self-weights and masses applied on each wall, whereas live loads are constituted by a distribution of horizontal loads proportional to masses (as recommended by the Italian code [19]). In other words, the vector of the power dissipated by the dead loads can be written as follows:

$$P_{\mathbf{F}_0} = \sum_{i=1}^{N_E} \left(W_i \cdot \dot{u}_z^i + F_i^P \cdot \dot{u}_z^P \right) = \mathbf{F}_0^T \cdot \mathbf{x} \tag{2}$$

where:

N_E is the number of elements adopted;

W_i is the weight if the i-th element;

F_i^P is the vertical load given by the non-structural mass applied to the point P;

$\dot{u}_z^i$, $\dot{u}_z^P$ are the vertical components of the velocity vectors respectively of the gravity center and the point P.

The power dissipated by live loads can be derived directly from $P_{\mathbf{F}_0}$:

$$P_\Gamma = \sum_{i=1}^{N_E} \left(\Gamma W_i \cdot \dot{u}_h^i + \Gamma F_i^P \cdot \dot{u}_h^P \right) = \mathbf{\Gamma}^T \cdot \mathbf{x} \tag{3}$$

where:

$\dot{u}_h^i$, $\dot{u}_h^P$ are the horizontal components of the velocity vectors;

Γ is the horizontal load multiplier (which is named α_0 in the Italian code [19]).

This procedure can be applied to evaluate the horizontal load multiplier of complex local mechanisms in historical masonry aggregates. It has to be pointed out that masonry aggregates can present very complex structures, with coexistence of different levels of interlockings that make their structural response quite difficult to predict. Therefore, the proposed code allows performing local analyses on a pre-selected number of walls belonging to the same structural unit. The pre-selected walls are those supposed to be involved in the local failure. Different levels of interlockings can be taken into account by assigning different values of resistance parameters to interfaces located at the corners. In addition to this, the procedure can take into account the most spread retrofitting interventions for these constructions. It is worth noting that the common use of FRP strips or tie-rods maintains still local the structural response under horizontal load, since the aim of these interventions is mainly to avoid the most critical local mechanisms. This allows to easily take into account the contribution of these retrofitting techniques by using local analyses. In the adaptive NURBS limit analysis, the presence of tie-rods can be included by using simple kinematic conditions. Considering the i-th tie-rods applied between the points P and Q (located on different walls), an additional equa-

tion is assigned as a geometrical constraint. The constraint given by the presence of tie-rods is described as follows:

$$\dot{u}_k^P - \dot{u}_k^Q = 0 \tag{4}$$

where:

k is the direction defined by the tie-rod;

$\dot{u}_k^P, \dot{u}_k^Q$ are the velocities along the direction k respectively of the points P and Q.

4 CASE STUDY

A masonry aggregate located in the historical center of Arsita has been adopted for the analyses. Arsita is a small village in the center of Italy that was hit by the 2009 earthquake. As a consequence of this event, 17 masonry aggregates have been inspected by a scientific team set up by ENEA (Italian National Agency for New Technologies, Energy and Sustainable Economic Development), resulting in the publication of the Post-Earthquake Reconstruction Plan for the Arsita Municipality [40,41]. The masonry aggregate here presented is the first one among those studied by ENEA (see Figure 2). This construction is composed of three structural units, here named A, B and C. A and B are residential buildings, whereas C constitutes the Church of Santa Vittoria. The whole construction is approximately 47 m long and 15 m wide. The maximum height is about 15 m in correspondence to the bell tower. The construction is characterized by thick walls. An average value of 70 cm has been observed in units A and B. The church is characterized by thicker walls, with an average value of 90 cm and a maximum of 200 cm in the façade. Several vaulted elements (mainly semicircular barrel vaults) can be found within the central nave of the church and on the first floor of unit B. According to [40,41], the masonry is composed of irregular stones and bad quality mortar.

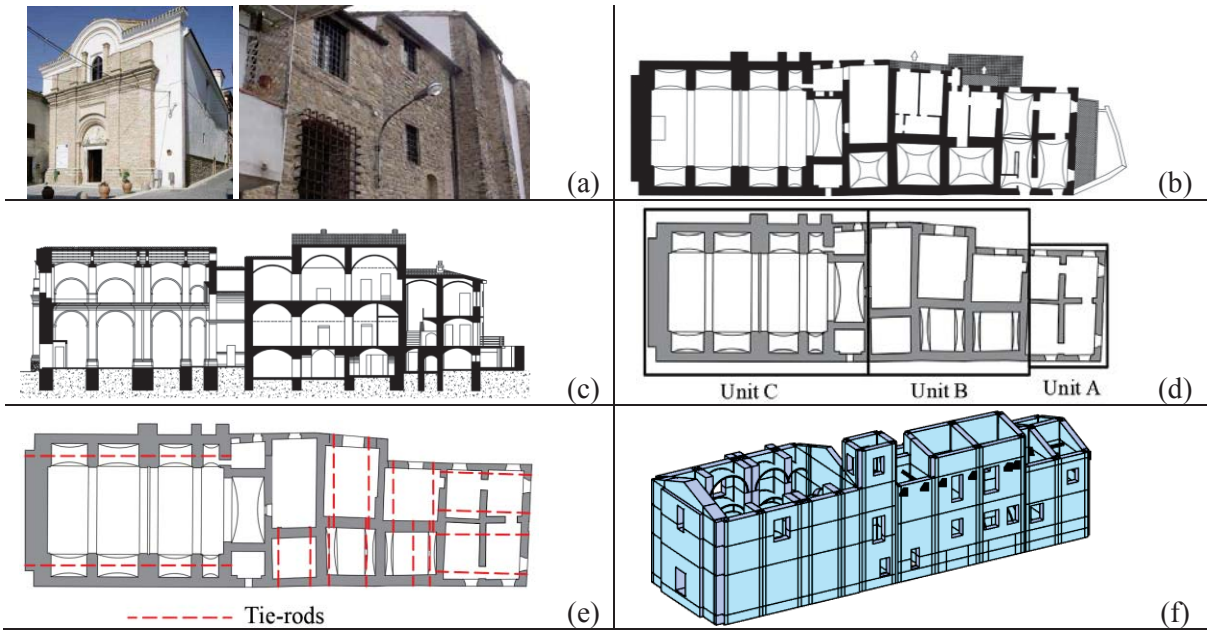

Figure 2. Aggregate "Il Corso": (a) some photos of the aggregate (pictures taken from [40]), (b) plan view, (c) section along the longitudinal direction, (d) identification of the structural units, (e) hypothesized position of tie-rods and (f) 3D NURBS model.

Since this masonry aggregate does not have tie-rods or concrete edgings, the first study has been performed on the unreinforced case [35]. After that, a disposition of tie-rods has been hypothesized to increase the horizontal load multiplier associated with the obtained collapse

mechanisms. The disposition of the tie-rods here assumed is reported in Figure 2(e). Therefore, the adaptive NURBS-based limit analysis has been re-applied to this case study to show how local failures are affected by the application of such retrofitting interventions. As in the unreinforced case [35], good interlocking has been assumed between walls belonging to the same structural unit, whereas the different structural units have been hypothesized as disconnected from each other. Considering the presence of not regular masonry texture, an isotropic Mohr-Coulomb behavior has been assigned [42]. The tensile stress is assumed equal to 0.05 MPa for walls and 0.1 MPa for vaulted elements. As shown in [43], a not null tensile stress is usually needed for slender barrel vaults in churches, since these elements are often too slender to sustain their self-weight in comparison with what is recommended in the classical Heyman's theory [44]. The ultimate compression strength has been assumed equal to 2 MPa, whereas cohesion and friction angle are supposed 0.035 MPa and 22°, respectively.

The new results in terms of local failures, horizontal load multipliers, and spectral accelerations (a_0*), are depicted in Figure 3, together with failure mechanisms of the unreinforced case. In general, the presence of tie-rods allows a notable increase in the values of horizontal load multipliers. Values higher than 1 are mainly related to the presence of thick walls. In two cases, the initial overturning mechanisms convert into vertical flexure mechanisms with participation of the transversal walls (see Figure 3(b) and Figure 3(f)). Then, the other walls belonging to structural unit B (Figure 3(c)) collapse through the partial overturning of the top part in the reinforced case (Figure 3(d)). Finally, the horizontal response of the vaults within the central nave is still the most critical failure mechanism, even if its horizontal load multiplier increases from 0.106 to 0.225. This is mainly due to the high slenderness of the barrel vaults, which cannot counteract the rotation of the supporting walls. As it can be observed in Figure 3(g, h), the collapse occurs initially through the overturning of walls that supports the vaults, whereas a partial overturning takes place once tie-rods have been applied at the quote of the barrel vaults first row. It is clear that higher values of horizontal load multiplier could be found by applying some tie-rods at different quotes, in order to avoid the partial overturning failures of the walls located within the central nave.

It is worth noting that the use of NURBS has been particularly useful in the study of this construction, where there is a high number of curved structural elements that affect its horizontal structural capacity. Finally, this code allows to reproduce several structural conditions, in terms of loads applied and representation of interlocking conditions. However, it is clear that a thorough knowledge of the real structural details is needed in order to correctly estimate the structural behavior under horizontal loads.

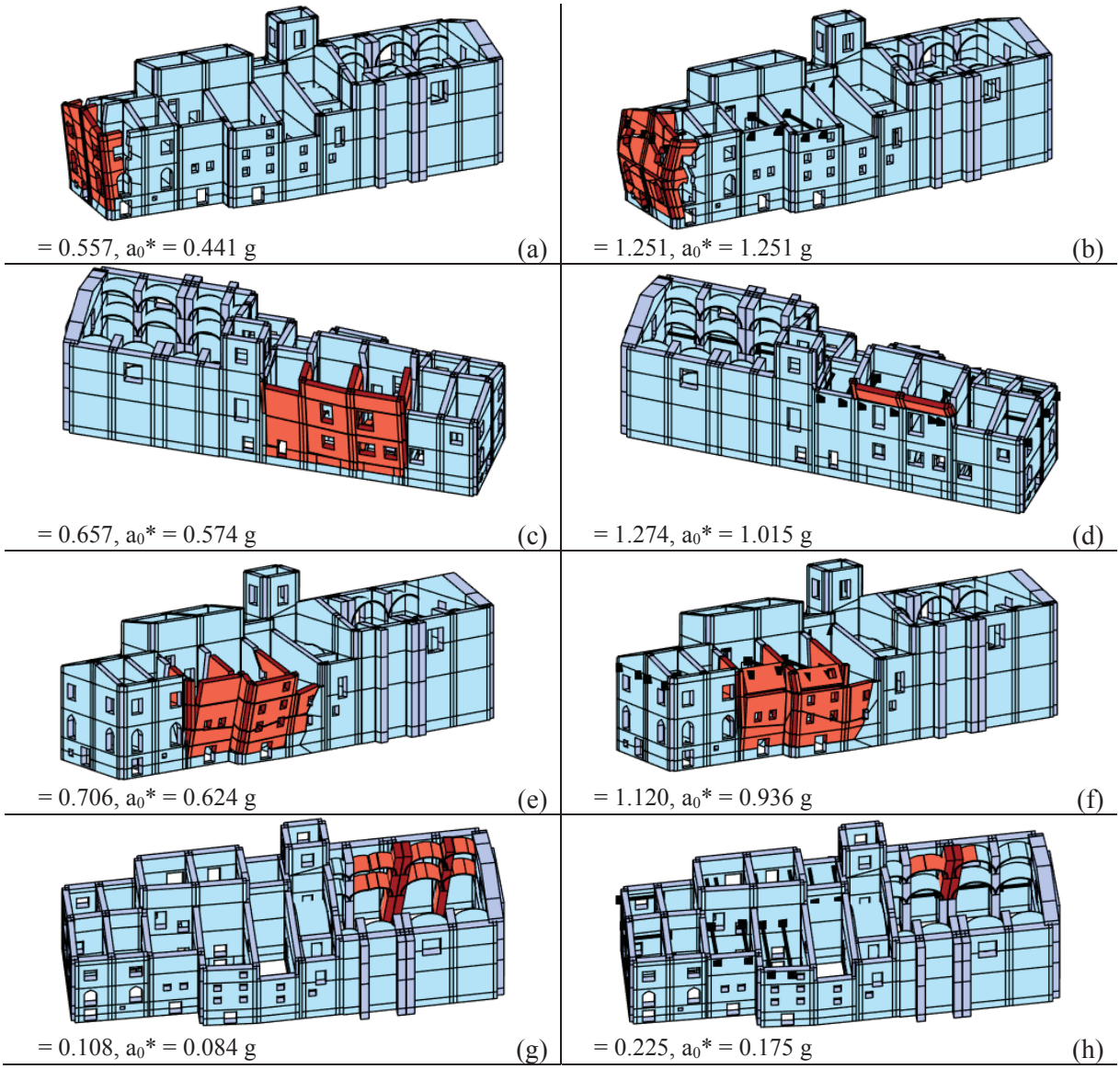

Figure 3. Local failures in the unreinforced (on the left column) and the reinforced case (on the right column): (a, b) unit A, (c-f) unit B, (g, h) unit C.

5 CONCLUSIONS

A novel computational procedure for the assessment of partial failure mechanisms in historical masonry aggregates has been presented. The procedure uses a NURBS discretization of the geometry of the whole structure, allowing to easily represent curved elements and, more in general, the complex geometries typical of historical constructions. A kinematic limit analysis with mesh adaptation governed by Genetic Algorithm is applied. In this way, both standard and non-standard local mechanisms in masonry aggregates, i.e. deriving from the interaction between different structural elements, can be predicted with good precision and the associated horizontal load multiplier is correctly estimated. The procedure allowed to take into account, in an easy way, the effects of the most common retrofitting strategies, such as the application of tie-rods, which maintains a local structural response but affects the shape of the local mechanisms, avoiding the occurrence of the most critical ones. Finally, the use of few NURBS rigid elements maintains a low computational effort. The reliability of this method

has been demonstrated through the application on a complex historical masonry aggregate in both unreinforced and reinforced cases.

REFERENCES

[1] C.F. Carocci, Small centres damaged by 2009 L'Aquila earthquake: on site analyses of historical masonry aggregates, *Bulletin of Earthquake Engineering*, 10, 45–71, 2012. doi:10.1007/s10518-011-9284-0.

[2] M. Valente, G. Milani, Seismic response and damage patterns of masonry churches: seven case studies in Ferrara, Italy, *Engineering Structures*, 177, 809–835, 2018. doi:10.1016/j.engstruct.2018.08.071.

[3] L. Sorrentino, S. Cattari, Seismic behaviour of ordinary masonry buildings during the 2016 central Italy earthquakes, *Bulletin of Earthquake Engineering*, 2018. doi:10.1007/s10518-018-0370-4.

[4] G. Fiorentino, A. Forte, E. Pagano, F. Sabetta, C. Baggio, D. Lavorato, C. Nuti, Damage patterns in the town of Amatrice after August 24th 2016 Central Italy earthquakes, *Bulletin of Earthquake Engineering*, 16, 1399–1423, 2018. doi:10.1007/s10518-017-0254-z.

[5] P.B. Lourenço, J.A. Roque, Simplified indexes for the seismic vulnerability of ancient masonry buildings, *Construction and Building Materials*, 20, 200–208, 2006. doi:10.1016/j.conbuildmat.2005.08.027.

[6] A. Formisano, N. Chieffo, M. Mosoarca, Seismic vulnerability and damage speedy estimation of an urban sector within the municipality of San Potito Sannitico (Caserta, Italy), *Open Civil Engineering Journal*, 11, 1106–1121, 2017. doi:10.2174/1874149501711011106.

[7] L. Milano, A. Mannella, C. Morisi, A. Martinelli, Illustration and kinematic analysis of local collapse mechanisms in existing masonry buildings, 2010. (in Italian)

[8] P. Roca, C. Molins, A.R. Marí, Strength capacity of masonry wall structures by the equivalent frame method, *Journal of Structural Engineering*, 131, 1601–1610, 2005. doi:10.1061/(ASCE)0733-9445(2005)131:10(1601).

[9] S. Lagomarsino, A. Penna, A. Galasco, S. Cattari, TREMURI program: An equivalent frame model for the nonlinear seismic analysis of masonry buildings, *Engineering Structures*, 56, 1787–1799, 2013. doi:10.1016/j.engstruct.2013.08.002.

[10] A. Formisano, A. Massimilla, A Novel Procedure for Simplified Nonlinear Numerical Modeling of Structural Units in Masonry Aggregates, *International Journal of Architectural Heritage*, 12, 1162–1170, 2018. doi:10.1080/15583058.2018.1503365.

[11] M. Valente, G. Milani, E. Grande, A. Formisano, Historical masonry building aggregates: advanced numerical insight for an effective seismic assessment on two row housing compounds, *Engineering Structures*, 190, 360–379, 2019. doi:10.1016/j.engstruct.2019.04.025.

[12] A.B. Habieb, M. Valente, G. Milani, Base seismic isolation of a historical masonry church using fiber reinforced elastomeric isolators, *Soil Dynamic and Earthquake Engineering*, 120, 127–145, 2019. doi:10.1016/j.soildyn.2019.01.022.

[13] A.B. Habieb, M. Valente, G. Milani, Effectiveness of different base isolation systems for seismic protection: numerical insights into an existing masonry bell tower, *Soil Dynamic and Earthquake Engineering*, 125, 2019. doi:10.1016/j.soildyn.2019.105752.

[14] J. Scacco, G. Salazar, N. Bianchini, N. Mendes, C. Cullimore, L. Jain, Seismic assessment of the church of Carmo convent, in: Congress on Numerical Methods in Engineering, 2019.

[15] G. Milani, Lesson learned after the Emilia-Romagna, Italy, 20–29 May 2012 earthquakes: A limit analysis insight on three masonry churches, *Engineering Failure Analysis*, 34, 761–778, 2013. doi:10.1016/J.ENGFAILANAL.2013.01.001.

[16] M. Valente, G. Milani, Advanced numerical insights into failure analysis and strengthening of monumental masonry churches under seismic actions, *Engineering Failure Analysis*, 103, 410–430, 2019. doi:10.1016/j.engfailanal.2019.05.009.

[17] M. Valente, G. Milani, Earthquake-induced damage assessment and partial failure mechanisms of an Italian Medieval castle, *Engineering Failure Analysis*, 99, 292–309, 2019. doi:10.1016/j.engfailanal.2019.02.008.

[18] N. Grillanda, M. Valente, G. Milani, A. Chiozzi, A. Tralli, Advanced numerical strategies for seismic assessment of historical masonry aggregates, *Engineering Structures*, 212, 110441, 2020. doi:10.1016/j.engstruct.2020.110441.

[19] CIRCOLARE 21 gennaio 2019, n. 7 C.S.LL.PP. Istruzioni per l'applicazione dell' Aggiornamento delle "Norme tecniche per le costruzioni" di cui al decreto ministeriale 17 gennaio 2018.

[20] A. Murano, J. Ortega, G. Vasconcelos, H. Rodrigues, Influence of traditional earthquake-resistant techniques on the out-of-plane behaviour of stone masonry walls: Experimental and numerical assessment, *Engineering Structures*, 201, 109815, 2019. doi:10.1016/j.engstruct.2019.109815.

[21] N. Bianchini, N. Mendes, P. Lourenço, Seismic evaluation of Bagan heritage site (Myanmar): The Loka-Hteik-Pan temple, *Structures*, 24, 905–921, 2020. doi:10.1016/j.istruc.2020.01.020.

[22] J. Scacco, G. Milani, M. Bove, A. Castellano, A. Fraddosio, M.D. Piccioni, Experimental and numerical analysis of the effectiveness of FRCM strengthening on a parabolic tuff barrel vault, *AIP Conference Proceedings*, 2186, 100005, 2019. doi:10.1063/1.5138011.

[23] J. Scacco, B. Ghiassi, G. Milani, P.B. Lourenço, A fast modeling approach for numerical analysis of unreinforced and FRCM reinforced masonry walls under out-of-plane loading, *Composites Part B Engineering*, 180, 107553, 2020. doi:10.1016/j.compositesb.2019.107553.

[24] J. Heyman, The stone skeleton, *International Journal of Solids and Structures*, 2, 249–256, 1966.

[25] G. Milani, P.B. Lourenço, A. Tralli, Homogenised limit analysis of masonry walls, Part I: Failure surface, *Computers & Structures*, 84, 166–180, 2006. doi:10.1016/j.compstruc.2005.09.004.

[26] E. Milani, G. Milani, A. Tralli, Limit analysis of masonry vaults by means of curved shell finite elements and homogenization, *International Journal of Solids and Structures*, 45, 5258–5288, 2008. doi:10.1016/j.ijsolstr.2008.05.019.

[27] G. Milani, Homogenized limit analysis of FRP-reinforced masonry walls out-of-plane loaded, *Computional Mechanics*, 43, 617–639, 2009. doi:10.1007/s00466-008-0334-7.

[28] A. Chiozzi, G. Milani, A. Tralli, A Genetic Algorithm NURBS-based new approach for fast kinematic limit analysis of masonry vaults, *Computers & Structures*, 182, 187–204, 2017. doi:10.1016/j.compstruc.2016.11.003.

[29] L. Piegl, W. Tiller, *The NURBS Book*, Springer, Berlin, 1995. doi:10.1007/978-3-642-59223-2.

[30] R.L. Haupt, S.E. Haupt, *Practical Genetic Algorithms*, John Wiley & Sons, New York, 1998.

[31] N. Grillanda, A. Chiozzi, G. Milani, A. Tralli, Efficient meta-heuristic mesh adaptation strategies for NURBS–based upper–bound limit analysis of general curved three-

dimensional masonry structures, *Computers & Structures*, 236, 106271, 2020. doi:10.1016/j.compstruc.2020.106271.

[32] A. Chiozzi, G. Milani, N. Grillanda, A. Tralli, Fast kinematic limit analysis of masonry walls with out-of-plane loading, in *Proceedings of the 6th International Conference on Computational Methods in Structural Dynamics and Earthquake Engineering* (COMPDYN 2017). doi:10.7712/120117.5576.17224.

[33] N. Grillanda, A. Chiozzi, F. Bondi, A. Tralli, F. Manconi, F. Stochino, A. Cazzani, Numerical insights on the structural assessment of historical masonry stellar vaults: the case of Santa Maria del Monte in Cagliari, *Continuum Mechanics and Thermodynamics*, 1–24, 2019. doi:10.1007/s00161-019-00752-8.

[34] N. Grillanda, A. Chiozzi, G. Milani, A. Tralli, Collapse behavior of masonry domes under seismic loads: an adaptive NURBS kinematic limit analysis approach, *Engineering Structures*, 200, 109517, 2019. doi:10.1016/j.engstruct.2019.109517.

[35] N. Grillanda, M. Valente, G. Milani, ANUB-Aggregates: a fully automatic NURBS-based software for advanced local failure analyses of historical masonry aggregates, *Bulletin of Earthquake Engineering*, 1–27, 2020. doi:10.1007/s10518-020-00848-6.

[36] A. Chiozzi, G. Milani, A. Tralli, Fast kinematic limit analysis of FRP reinforced masonry vaults through a new genetic algorithm nurbs-based approach, *Proceedings of the 7th European Congress on Computational Methods in Applied Sciences and Engineering* (ECCOMAS 2016), 3, 5326–5339, 2016.

[37] A. Chiozzi, G. Milani, N. Grillanda, A. Tralli, Fast and reliable limit analysis approach for the structural assessment of FRP-reinforced masonry arches, *Key Engineering Materials*, 747, 196–203, 2017. doi:10.4028/www.scientific.net/KEM.747.196.

[38] N. Grillanda, A. Chiozzi, G. Milani, A. Tralli, On Collapse Behavior of Reinforced Masonry Domes under Seismic Loads, *Key Engineering Materials*, 817, 275–282, 2019. doi:10.4028/www.scientific.net/KEM.817.275.

[39] A. Chiozzi, N. Grillanda, G. Milani, A. Tralli, NURBS-based kinematic limit analysis of FRP-reinforced masonry walls with out-of-plane loading, *Frattura Ed Integrità Strutturale*, 51, 9–23, 2020. doi:10.3221/IGF-ESIS.51.02.

[40] R. Chiarini, M. Indirli, Piano di ricostruzione del comune di Arsita (Te) a seguito dell'evento sismico del 6/04/2009, 2013.

[41] M. Indirli, S. Bruni, F. Geremei, G. Marghella, A. Marzo, L. Moretti, A. Formisano, C. Castaldo, L. Esposito, G. Florio, R. Fonti, E. Spacone, S. Biondi, E. Miccadei, I. Vanzi, A. Tralli, C. Vaccaro, T. Gambatesa, The reconstruction plan of the town of Arsita after the 2009 Abruzzo (Italy) seismic event, in: *Proceedings of the 9th International Conference on Structural Analysis of Historical Constructions* (SAHC 2014), 14–17.

[42] S. Tiberti, G. Milani, 2D pixel homogenized limit analysis of non-periodic masonry walls, *Computers & Structures*, 219, 16–57, 2019. doi:10.1016/j.compstruc.2019.04.002.

[43] G. Ramaglia, G.P. Lignola, A. Prota, Collapse analysis of slender masonry barrel vaults, *Engineering Structures*, 117, 86–100, 2016.

[44] J. Heyman, The safety of masonry arches, *International Journal of Mechanical Sciences*, 11, 363–385, 1969.

EURODYN 2020
XI International Conference on Structural Dynamics
M. Papadrakakis, M. Fragiadakis, C. Papadimitriou (eds.)
Athens, Greece, 23–26 November 2020

MITIGATION OF AMPLIFIED RESPONSE OF RESTRAINED ROCKING WALLS THROUGH HORIZONTAL DAMPERS

Fabio Solarino[1,2], Linda Giresini[1], and Daniel V. Oliveira[2]

[1]Department of Energy, Systems and Territory Engineering (DESTEC)
University of Pisa - Largo Lucio Lazzarino, 1, 56126, Pisa (PI), Italy
solarino.fabio@gmail.com, linda.giresini@unipi.it

[2] ISISE, Institute of Science and Innovation for Bio-Sustainability (IB-S), Department of Civil Engineering
University of Minho - Azurém, P-4800-058, Guimarães, Portugal
danvco@civil.uminho.pt

Keywords: Damping, Rocking, Restrained rocking, Non-linear dynamic analysis.

Abstract. *Failure mechanisms in masonry walls are commonly due to the low tensile strength of masonry that could cause overturning or pounding due to the interaction with transverse walls. In this paper, the influence of dissipative devices easing the dynamic stability of rocking blocks is studied considering the main parameters affecting the response. Normalized rotation time-histories are obtained for six geometrical configurations under several acceleration records in order to analyse possible resonant effects and beneficial reductions due to the presence of a damper, accounted for in the equation of motion of the one-sided restrained rocking block. Rocking response spectra obtained for undamped systems show that possible beat phenomena may arise for certain geometrical configurations and restraint stiffness values. A design equation for the damping coefficient is proposed for the anti-seismic device and its influence on restrained façade walls under real strong motions is analysed.*

1 INTRODUCTION

Recent seismic events demonstrated that out-of-plane mechanisms are commonly developed in historical constructions causing relevant cracks and sometimes leading to catastrophic collapses. This can be due to not proper wall-to-diaphragm connections [1] or to slender walls as those of church façades [2, 3, 4, 5]. Portions of the building can tilt as rigid blocks around plastic hinges developed during earthquakes, even of low entity, involving complex phenomena of friction, impact, sliding and possible overturning [6, 7]. The most significant way to treat these problems, due to the many uncertainties that affect them, is a probabilistic approach considering univariate and bivariate fragility curves [8].

Kinematic approach is considered one of the most valid tools for the assessment of local modes, based on the assumption of the "most probable" mechanisms that can be developed during a seismic event. This method is widely used worldwide and the Italian national code [9] suggests this approach as a valid preliminary verification for successive global assessment. Besides more complex models can account for horizontal restraints or frictions, the method is based on the pseudo-static application of virtual work principle and collapse mechanisms have to be assumed, thus setting the limit of the approach.

Recent developments were done on rocking analysis, capable of assessing the dynamic stability of rigid restrained blocks and suitable to understand the behavior of tilting objects during seismic motion [2, 10, 11]. Newly published national Italian standards [9, 12] allows the assessment of local mechanisms through the use of nonlinear dynamic analysis of rigid bodies. During the oscillation of rocking structures, the seismic energy is dissipated through the impacts and this can be accounted for in the equation of motion through a cofficient of restitution, whose experimental estimation is of crucial relevance [13]. The rocking block can be free-standing, namely without restraints [14] or with vertical [15] or horizontal [16] elastic restraints. If a further source of energy dissipation is desired, to control the stability of the rocking wall, the restraint could be characterized by a viscous damper.

In this contribution, a damper device is intended to be designed in order to control possible damages occurring on out-of-plane masonry walls. This paper aims at understanding the influence of damping and stiffness of anti-seismic devices through rocking analysis.

2 EQUATION OF MOTION AND RESONANCE CONDITION

The full equation of motion of a damped restrained rocking block in one-sided vibrations under seismic force reads:

$$I_0\ddot{\theta} + sign(\theta)mgR\sin A_\theta + T_K + T_{K'} + T_D = m\ddot{u}_g R\cos A_\theta, \tag{1}$$

where I_0 is the polar moment of inertia of the block with mass m oscillating about the pivot points O and O' of an angle θ (Figure 1), R is the semi diagonal of the block and $A_\theta = \alpha - sign(\theta)\theta$, in which α is the angle between the direction of R and the vertical, being also the inverse of the slenderness of the block ($\alpha = \tan^{-1}(s/h) \simeq s/h = 1/\lambda$). The term T_K relates to the contribution of a horizontal spring, referring to the elastic stiffness of the damper or to separate restraints (steel ties). For the scope of this work the pre-tensioning and yielding are not considered, being the spring indefinitely linear elastic characterized by particular axial stiffness, K, whose term reads

$$T_K = sign(\theta)KR_t^2 cos(A_t)(sin\alpha_r - sinA_t), \tag{2}$$

where $A_t = \alpha_t - sign(\theta)\theta$ and geometrical parameters, R_t and α_t define the position of the spring. $T_{K'}$ is the term given by horizontal bed springs, simulating eventual lateral transversal

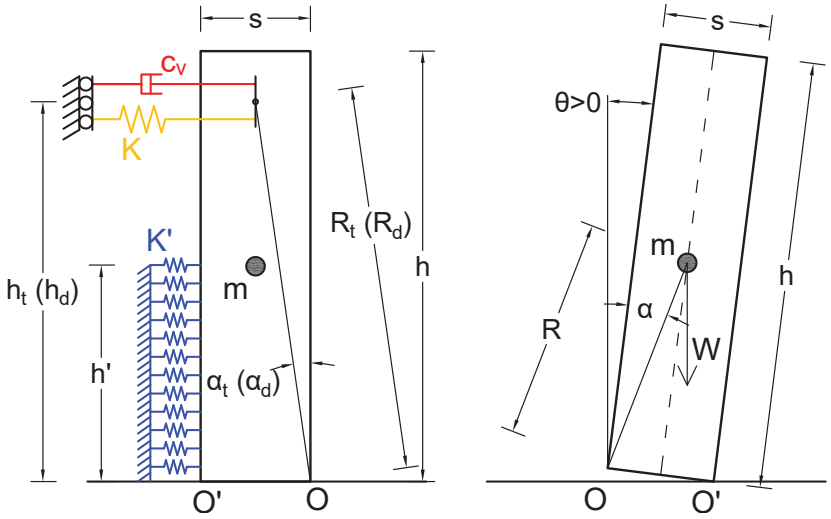

Figure 1: Rocking block model restrained by damper in one-sided motion: geometry and definition of positive rotation.

walls of stiffness (per unit length), K'. Assuming,

$$A = sign(\theta)s^2\, sin\theta\, cos\theta(1 - cos\theta) \tag{3}$$

$$B = sin^2\theta\, cos\theta - cos^3\theta + cos^2\theta \tag{4}$$

$$C = sign(\theta)\, sin\theta\, cos^2\theta \tag{5}$$

the spring bed term can be defined as follows:

$$T_{K'} = sign(\theta)K'h'\left(A + \frac{Bh'}{2} + \frac{Ch'^2}{3}\right) \tag{6}$$

where, h' is the effective height of the spring bed (Figure 1). The term T_d depends upon the damping, c, and the relative velocity between the damper ends, $\dot{u}_d$, function of $\dot{\theta}$, in this specific case, and reads

$$T_d = cR_d^2 cos^2 A_d\dot{\theta}, \tag{7}$$

where $A_d = \alpha_d - sign(\theta)\theta$ and, at the same way of horizontal spring term, R_d and α_d define the position of the damper (Figure 1). For the specific case of damper and elastic spring at the same position, $\alpha_d = \alpha_t$, and $R_d = R_t$. It can be noted that the sign of damping term is directly given by the sign of rotational velocity, $\dot{\theta}$, thus no $sign$ function is necessary in this case.

Previous studies demonstrated that amplified response can be achieved in certain circumstances associated with resonance conditions [16]. Depending on the direction of motion, two rocking systems can be defined, one referring to clockwise rotation (single spring in tension) and the other to anticlockwise direction (spring bed in compression). Thus, calling the frequency ratio $p = \sqrt{mgR/I_0}$, resonance frequencies can be computed for both systems,

$$\omega_r^+ = p\sqrt{\left(\frac{KR_t^2}{mgR} - 1\right)} \tag{8}$$

and

$$\omega_r^- = p\sqrt{\left(\frac{8K'R^2}{3mg} - 1\right)} \tag{9}$$

Even if circular frequency of the rocking system varies during the oscillation, it was seen that the horizontal elastic restraint behaves like a "filter" for the output signal. This aspect is confirmed in Figure 2 showing the comparison between the fast fourier transform (FFT) of the displacement response in restrained and in free-standing configuration, under free vibration. The restrained configuration is defined, here, by the presence of a bidirectional indefinitely linear elastic tie with stiffness equal to $K = 1.0e6$ N/m. The restrained rocking block response

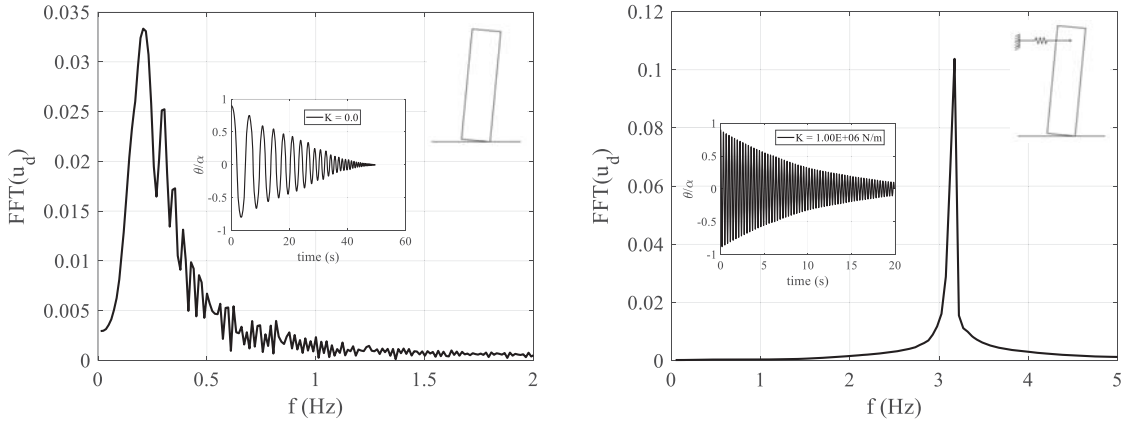

(a) (b)

Figure 2: Fast fourier transform of horizontal displacement read at the level of restraint; (a) free-standing block; (b) restrained block.

is characterized by a reduced frequency content if compared to the free-standing configuration. Ideally, if such a restrained system is forced by excitations with similar frequencies, dangerous amplified responses may arise and should be controlled. Artificial inputs with similar frequency content have been adopted in recent studies in order to cause resonant response [17]. In this paper, possible resonance circumstances are investigated under real ground motion, which are characterized by a complex frequency content but representative of realistic situations.

3 GEOMETRIES AND HYPOTHESIS

Geometries of unit length were selected in order to study two different slenderness ratios ($\lambda = 10, 13$) and three different wall thickness values ($s = 0.3; 0.6$ and 0.9 m), resulting in a total of six geometrical layouts representative of common masonry wall façades. The masonry weight density was assumed equal to 21 kN/m^3 for all blocks. The analysis of damped restrained rocking blocks requires the definition of horizontal restraint elastic stiffness, representing a possible steel tie rod placed at a certain height of the wall. Moreover, for the definition of the elastic impact with transverse walls, a value of stiffness (per unit length) needs to be set. A realistic value of K' can be based on transversal walls thickness, t, and effective with, L_{eff}, with equivalent lateral elastic modulus, E_x,

$$K' = E_x t / L_{eff}. \tag{10}$$

label	λ [-]	s [m]	h [m]	m [kg]	R [m]	I_0 [kg m^2]
block1	10	0.3	3.0	1926	1.51	5837
block2	10	0.6	6.0	7706	3.01	93401
block3	10	0.9	9.0	17339	4.52	472847
block4	13	0.3	3.9	2505	1.96	12773
block5	13	0.6	7.8	10018	3.91	204374
block6	13	0.9	11.7	22541	5.87	1034645

Table 1: Geometrical parameters of selected blocks.

However, if the system global stiffness in the positive direction equates the one in negative direction [16], the spring bed stiffness becomes a function of horizontal restraint stiffness:

$$K_{sys} = K'_{sys} \rightarrow K' = K\frac{3}{8}\frac{R_t^2}{R^3 cos\alpha}. \tag{11}$$

A reference value of tie stiffness, K_d, can be calculated starting from a design value of steel tie rod diameter, ϕ_d, based on simple equilibrium criterium (Equation 12) assuming the seismic action as a horizontal equivalent static force acting at the center of gravity of the block. The length of the tie rod is assumed $10\,$m.

$$T_d h_t + Ws/2 = \mu W h/2, \tag{12}$$

where $T_d = \sigma_d \frac{\pi \phi_d^2}{4}$ is the force given by the tie, applied at height h_t, computed considering a *S275* steel, a design stress value, $\sigma_d = \frac{0.7 f_{u,k}}{1.05}$. W is the self weight of the block and $\mu = 0.2$ is the collapse multiplier.

Even if it is hard to define a critical damping for rocking blocks (appropriate for single-degree-of-freedom oscillators), mainly because of the non-constant value of eigenfrequency [18], a reference value of damping can be defined starting from the capacity curve of the free-standing block. The damping becomes function of the solely geometry of the block and a characteristic event time, δ_t [17],

$$c_d = \frac{F_0}{v} = \frac{\mu W}{\delta_u/\delta_t} = 2mg\delta_t/h \tag{13}$$

The viscous-elastic damper, which is ruled by a stiffness, K and a coefficient of damping c, is located at the top of the wall. Furthermore, dampers are ideally bilinear.

It is worth noting that the yielding of the steel tie rod was not considered, as outer the scope of the study.

4 ANALYSIS AND RESULTS

The influence of the wall geometries and of the viscous-elastic damper on the dynamic stability of the rocking walls are studied under free and forced vibration in one-sided motion. For the latter analyses, a selection of several (> 40) real accelerograms was done in order to consider a wide range of frequency content and intensity levels. Strong motion accelerations are selected among recent seismic events that stroke Central Italy during 2016-2017 and past events characterized by high level of magnitude (i.e. $M_w > 5.0$) (Table 2). Two limit states are defined for the scope of these analyses as reference values of moderate ($\theta/\alpha = 0.4$) and limited ($\theta/\alpha = 0.1$) rocking.

Event name	Event date-(UTC)time [yyyy/mm/dd-hh:mm]	Municipality	M_w
Central Italy	2017/01/18-13:33	Cagnano Amiterno	5.0
Central Italy	2017/01/18-10:25	Montereale	5.4
Central Italy	2017/01/18-10:14	Capitignano	5.5
Central Italy	2016/10/30-06:40	Norcia	6.5
Central Italy	2016/10/26-19:18	Ussita	5.9
Central Italy	2016/10/26-17:10	Castelsantangelo sul Nera	5.4
Central Italy	2016/08/24-02:33	Norcia	5.3
Central Italy	2016/08/24-01:36	Accumoli	6.0
Emilia 2^{nd} shock	2012/05/29-07:00	Medolla	6.0
Emilia 1^{st} shock	2012/05/20-02:03	Finale Emilia	5.8
L'Aquila	2009/04/06-01:32	L'Aquila	6.1
Bam	2003/12/26-01:56	Bam	6.6
Bingöl	2003/05/01-00:27	Turkey	6.3
Duzce	1999/11/12-16:57	Pınarlar Köyü	7.3
Umbria-Marche 2^{nd} shock	1997/09/26-09:40	Foligno	6.0
Turkey	1995/10/01-15:57	Dinar	6.2
Greece	1995/06/15-00:15	Fokida	6.5
Western Iran	1990/06/20-21:00	Rudbar-Tarom	7.4
Irpinia	1980/11/23-18:34	Laviano	6.9
Northwestern Uzbekistan	1976/05/17-02:58	Gazli, Bukhara	6.7

Table 2: List of selected seismic events.

4.1 Undamped rocking response spectra

The construction of design response spectra is common in civil engineering with the aim of defining the seismic input of a given structure [14]. This method is valid for structures that may be related to classical single degree of freedom systems for which an equivalent period can be defined. Commonly 5% of damping ratio is considered to take into account the capability of the building on dissipating energy.

Even if rocking systems are characterized by an amplitude-dependent eigenfrequency, a rocking spectrum can be defined for a given geometry evaluating the maximum response in terms of normalized rotations under a certain seismic event, for different values of horizontal restraint stiffness. Figures 3 and 4 show the rocking spectra obtained for the undamped restrained rocking block2 in one-sided motion (K' and K calculated according to Equation 11 and 12, respectively, Section 3) under 1995/10/01 - 6.2 M_w and 2016/10/30 - 6.5 M_w - Norcia earthquakes (Table 2). 50 values of K were chosen within the range $0 \leq K \leq K_d$. A limit state of moderate rocking was considered corresponding to $\theta/\alpha = 0.4$ [3]. Amplifications are clearly visible for different values of K where beats and resonant effects develop (Figure 3). This not monotonic trend observed when the stiffness monotonically increases or decreases suggests near-resonant conditions. Response time-histories are shown upon the corresponding spectrum peaks (Figure 5). Although values of K different from zero should correspond to a more stable response (since the block is ideally "more stable"), the peaks on the rocking spectrum demonstrate the opposite. Indeed, as shown in Figure 5(a), even low values of stiffness result in an amplification response up to three times. For the spectrum built for Norcia

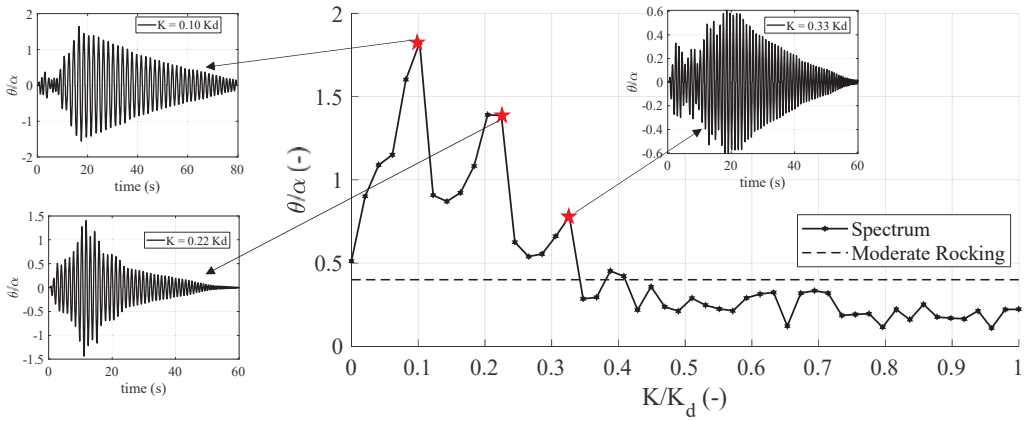

Figure 3: Rocking spectrum obtained for restrained block2 in one-sided motion under 1995/10/01 - 6.2 M_w - Dinar (Turkey) earthquake; resonant-like responses shown for $K/K_d = 0.10$, 0.22 and 0.33.

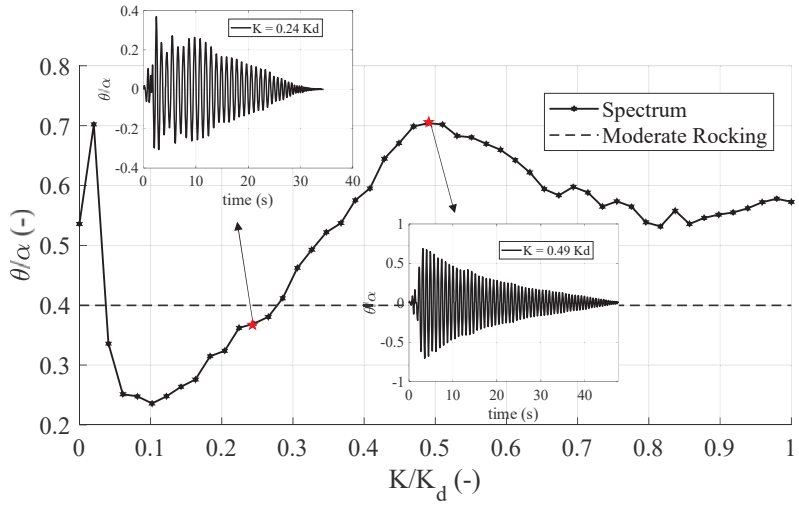

Figure 4: Rocking spectrum obtained for restrained block2 in one-sided motion under 2016/10/30 - 6.5 M_w - Norcia earthquake; resonant-like responses shown for $K/K_d = 0.24$ and 0.49 .

earthquake (Figure 4), maximum rotations are beyond the moderate limit state only for stiffness values ranging between $0.02 < K/K_d < 0.3$, while amplified responses, sometimes overcoming the free-standing peak, are obtained elsewhere (e.g. $K = 0.49\,K_d$, Figure 5(b)).

Among all selected geometries, block2 and block5 ($s = 0.6$ m, see Table 1) are more sensitive to resonant-like effect under strong-motions, while other geometries respond in a stabler manner. Given a certain slenderness, the moment of inertia plays a crucial role in the frequency content of the block (blocks with thickness $s = 0.3$ and 0.9 m show a reduced amplification response).

4.2 Damped free vibration

To better study the influence of damping in the rocking stability of rigid blocks, preliminary analyses are performed on block1 under free vibrations. For this purpose, an initial normalized rotation, $(\theta/\alpha)_0$ is set equal to 0.9, corresponding to the 90% of the ultimate kinematic displacement capacity ($u_G = s/2$), read at the center of gravity. Moreover, in order to isolate

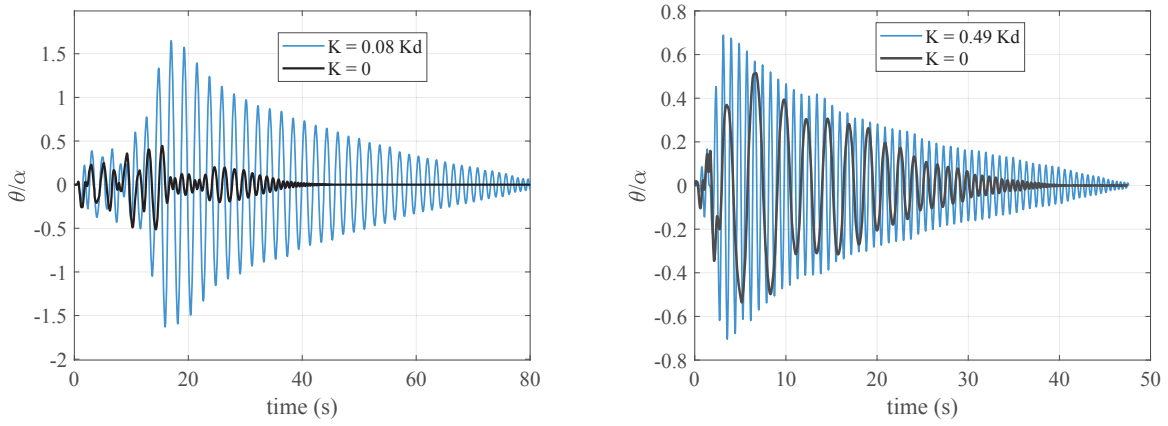

(a) (b)

Figure 5: Comparison between free and restrained rocking block responses; (a) block2 - 1995/10/01 - 6.2 M_w - Dinar earthquake; (b) block2 - 2016/10/30 - 6.5 M_w - Norcia earthquake.

the influence of viscous damping, a unit value of restitution coefficient is set ($e = 1.0$), corresponding to perfectly elastic impacts. Firstly, responses under two-sided motion are computed. Secondly a realistic value of K' is set in order to simulate the presence of transversal walls under both free and restrained configuration ($K = 0.0$, and $K = K_d$, respectively) [16].

Assuming the clockwise direction as the positive rotation (Figure 1), the damping contribution takes the sign of rotational velocity, $\dot{\theta}$, coherent with the self weight term, among the others. The validation of sign and shape of T_d term is shown in Figure 6 for free vibration of block1 in two-sided motion for the particular case of $c = 0.1\%\, c_d$.

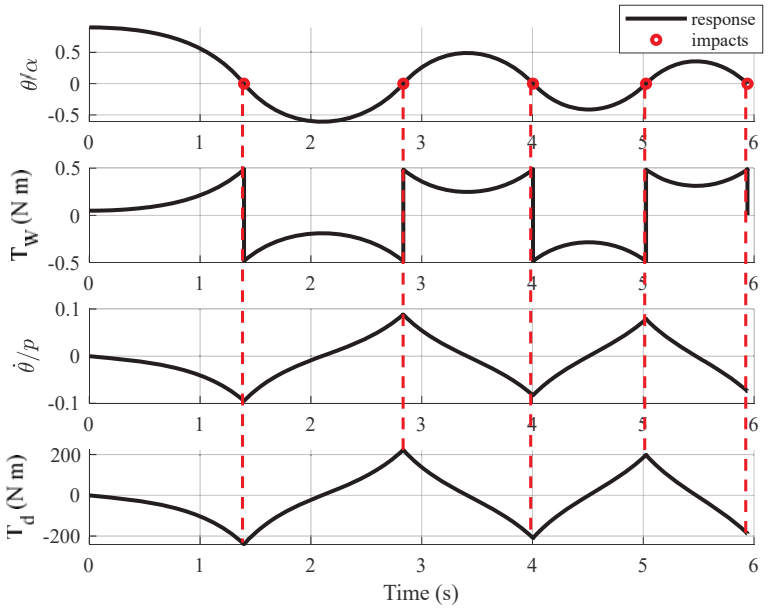

Figure 6: Validation of damping term sign for a simple free vibration time-history analysis of free-standing block1 in two-sided motion ($K = K' = 0.0$); from top to bottom: (i) normalized rotation; (ii) self weight term; (iii) normalized rotational velocity.

Figures 7 shows the influence of four different values of damping ($c = 0.0; 0.1; 1.0;$ and $5.0\%\, c_d$) on the damped free-standing block1 under two- and one-sided motion (i.e. without and with the presence of transversal walls with equivalent spring bed stiffness $K' = 4.5e8$ N/m/m, [16]). The beneficial effect of increased damping coefficient is clearly visible from the Figures. The damping device decreases the successive peaks and delays the first impact time, as evidently demonstrated passing from $c = 1.0\%$ to $c = 5\%\, c_d$.

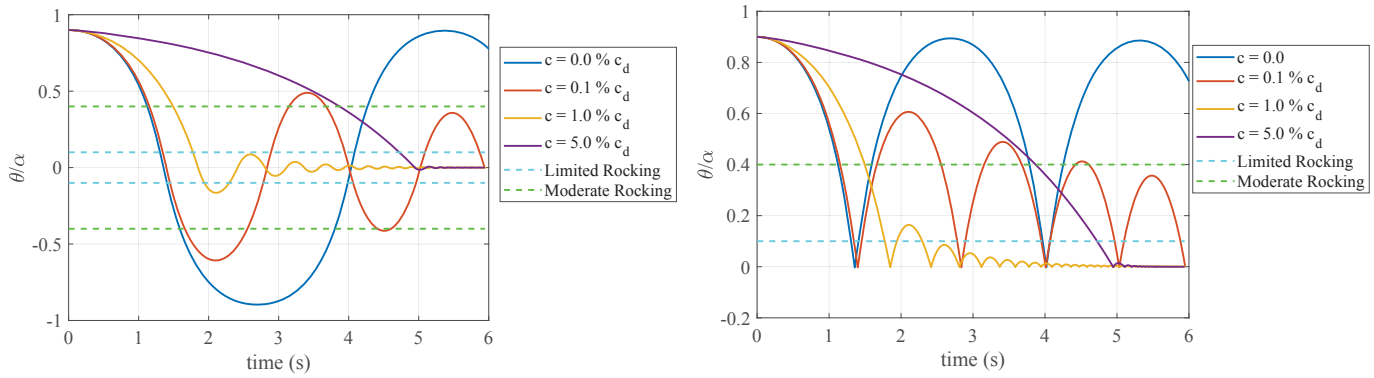

Figure 7: Influence of damping on free-standing rocking block1 under free vibrations; (a) two-sided motion; (b) one-sided motion.

The effect of dampers is also studied for the restrained configuration (that is with K different from zero) in one-sided motion, setting $K = K_d$ as defined in Section 3. The first impact time is strongly reduced by the presence of the tie re-centering the block in its "zero" position (Figure 8). It is visible an increased rotational frequency due to the restrained condition. This aspect could be problematic in terms of repeated cyclic stresses on the transverse walls, where masonry could crush for the attainment of compressive strength. It is interesting to note that, for the same value of damping coefficient, despite the more "regular" response if compared to the free-standing configuration, higher normalized rotations are obtained for the restrained block. Indeed, as confirmed in Figure 9, setting $c = 1.0\%\, c_d$, the peak reduction is gradual for the restrained block, only corresponding to 27% reduction after the first impact, while a reduction of 82% of normalized rotation is obtained for the free-standing block.

4.3 Damped forced vibration

Nonlinear analyses of the restrained ($K = K_d$) blocks with the same geometries are performed under real inputs in order to study the influence of dampers on façade-like walls. The lateral stiffness per unit length is computed according to Equation 11. For the purpose of this work, a value of $E_x = 1.5e9$ N/m/m can be used according to [12]. Moreover, 30 cm thickness and 1.0 m length can be assumed. The analytical value of the coefficient of restitution, $e_H = 1 - \frac{3}{2} sin^2\alpha$, based on [18] is set.

The beneficial effect of damping is clear in Figure 10 where a significant reduction of maximum normalized rotation is obtained for higher values of damping. Amplified response is obtained for the undamped cases characterized by high and longer oscillations probably caused by the bouncing and near resonant effects given by the tie. For higher values of damping, the rotation time-histories shape is similar during the first impacts only, as successive frequency

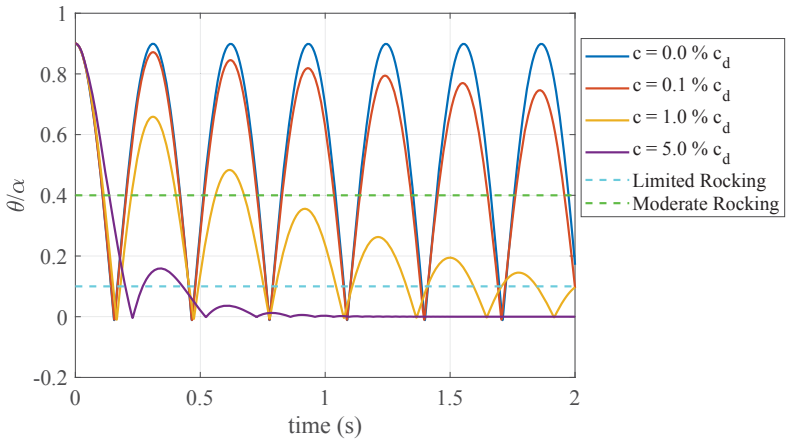

Figure 8: Influence of damping on restrained rocking block1 under free vibration in one-sided motion.

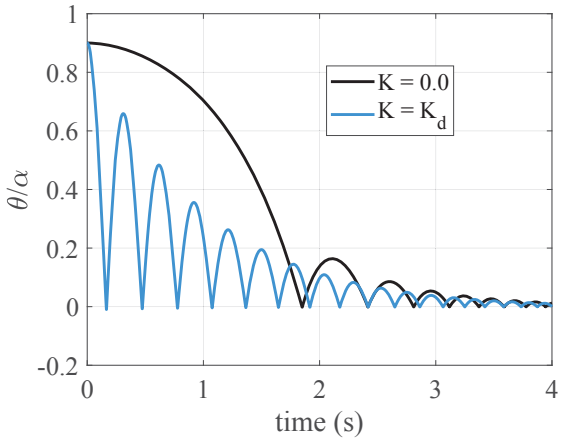

Figure 9: Comparison between free and restrained configuration under free damped vibration in one-sided motion; block1, $c = 1.0\%\, c_d$.

and peaks values are affected by damping force. Besides the response is strongly dependent on the geometry of the block and the type of input, damping values of $c > 10.0\%\, c_d$ should fulfil the limited rocking limit state.

5 CONCLUSIONS

This paper analysed the dynamic response of out-of-plane rocking walls with a viscous-elastic damper at the top under recorded acceleration time histories. Six different geometries were tested to investigate the role of size and slenderness of the rigid block in the dynamic response. From the non-linear analyses outcomes, a not monotonic trend in rocking spectra was observed when the stiffness was monotonically increased or decreased. The rocking spectra are therefore recommended in the design of whatsoever horizontal restraint for rocking walls to avoid such undesired amplifications due to near-resonance conditions. Moreover, the influence of damping was investigated in free and forced vibrations. As for the response in free vibrations, the beneficial effect of a greater damping coefficient was clearly visible, since it caused a reduction of consecutive peaks and delayed the first impact time. The effect of dampers was also

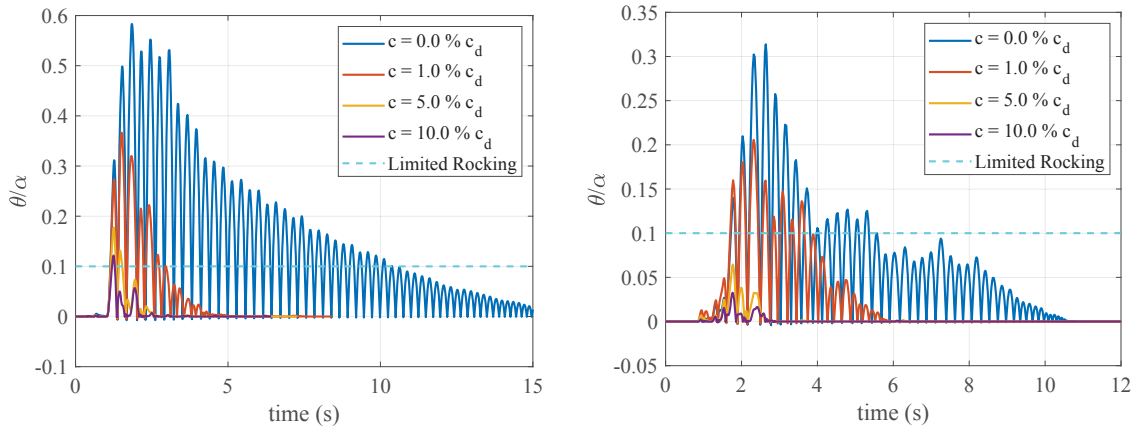

Figure 10: Influence of damping on restrained block1 under real seismic input; (a) 2016/10/26 - 5.4 M_w Castelsantangelo sul Nera earthquake; (b) 2016/08/24 - 6.0 M_w Accumoli earthquake.

studied for the restrained configuration in one-sided motion. The first impact time was strongly reduced by the presence of the tie that re-centered the block in its "zero" position. Moreover, the resulting increased rotational frequency due to the restrained condition could be problematic in terms of repeated cyclic stresses on the transverse walls, where masonry could crush for the attainment of compressive strength. Forced vibrations responses also results in advantageous use of damper devices for the control of rocking motion of walls, considered in a realistic one-sided configuration sensitive to possible resonant behaviors. Not only maximum normalized rotations are strongly reduced by higher values of damping, but responses time-histories present relevant changes in terms of frequency and shape after the first impacts. A value of $c > 10\% \, c_d$ can be evaluated as the corresponding design value for the limited rocking limit state, but further analyses are necessary and intended in order to account for pretensioning and plasticity of the steel and for the possible development of multi-degree-of-freedom mechanisms.

REFERENCES

[1] F. Solarino, D. Oliveira, and L. Giresini, "Wall-to-horizontal diaphragm connections in historical buildings: A state-of-the-art review," *Engineering Structures*, vol. 199, 2019.

[2] L. U. Argiento, A. Maione, and L. Giresini, "The corner failure in a masonry building damaged by the 2016-2017 central Italy earthquake sequence," in *COMPDYN 2019 7th ECCOMAS Thematic Conference on Computational Methods in Structural Dynamics and Earthquake Engineering*, (Crete; Greece; 24th-26th June 2019), pp. 633–650, 2019.

[3] C. Casapulla, L. Giresini, L. U. Argiento, and A. Maione, "Nonlinear Static and Dynamic Analysis of Rocking Masonry Corners Using Rigid Macro-Block Modeling," *International Journal of Structural Stability and Dynamics*, vol. 19, no. 11, p. 1950137, 2019.

[4] C. Casapulla, L. U. Argiento, and A. Maione, "Seismic safety assessment of a masonry building according to Italian Guidelines on Cultural Heritage: simplified mechanical-based approach and pushover analysis," *Bulletin of Earthquake Engineering*, vol. 16, no. 7, pp. 2809–2837, 2018.

[5] C. Casapulla, P. Jossa, and A. Maione, "Rocking motion of a masonry rigid block under seismic actions: A new strategy based on the progressive correction of the resonance response," *Ingegneria Sismica*, vol. 27, no. 4, pp. 35–48, 2010.

[6] C. Casapulla, "Dry rigid block masonry: Safe solutions in presence of Coulomb friction," *WIT Transactions on the Built Environment*, vol. 55, pp. 251–261, 2001.

[7] Y. Ishiyama, "Motions of rigid bodies and criteria for overturning by earthquake excitations," *Earthquake Engineering and Structural Dynamics*, vol. 10, pp. 635–650, 1982.

[8] L. Giresini, F. Taddei, C. Casapulla, and G. Mueller, "Stochastic assessment of rocking masonry façades under real seismic records," in *COMPDYN 2019 7th ECCOMAS Thematic Conference on Computational Methods in Structural Dynamics and Earthquake Engineering*, (Crete; Greece; 24th-26th June 2019), pp. 673–689, 2019.

[9] D. M. 17/01/2018, "Aggiornamento delle "norme tecniche per le costruzioni" (in italian)," 2018.

[10] C. Casapulla, A. Maione, and L. U. Argiento, "Performance-based seismic analysis of rocking masonry façades using non-linear kinematics with frictional resistances: a case study," *International Journal of Architectural Heritage*, 2019.

[11] L. Giresini, F. Solarino, O. Paganelli, D. V. Oliveira, and M. Froli, "One-sided rocking analysis of corner mechanisms in masonry structures: influence of geometry, energy dissipation, boundary conditions," *Soil Dynamics and Earthquake Engineering*, vol. 123, pp. 357–370, 2019.

[12] C.S.LL.PP. Ministero delle infrastrutture e dei trasporti, "Circolare applicativa 21 gennaio 2019, n. 7 (in italian)," 2019.

[13] L. Giresini, M. Sassu, and L. Sorrentino, "In situ free-vibration tests on unrestrained and restrained rocking masonry walls," *Earthquake Engineering & Structural Dynamics*, vol. 47, no. 15, pp. 3006–3025, 2018.

[14] N. Makris and D. Konstantinidis, "The rocking spectrum and the limitations of practical design methodologies," *Earthquake Engineering and Structural Dynamics*, vol. 32, no. 2, pp. 265–289, 2003.

[15] N. Makris and M. F. Vassiliou, "Dynamics of the Rocking Frame with Vertical Restrainers," *Journal of Structural Engineering*, vol. 141, no. 10, 2015.

[16] L. Giresini, "Design strategy for the rocking stability of horizontally restrained masonry walls," in *COMPDYN 2017 6th ECCOMAS Thematic Conference on Computational Methods in Structural Dynamics and Earthquake Engineering* (M. F. M. Papadrakakis, ed.), (Rhodes Island), 2017.

[17] L. Giresini, F. Solarino, F. Taddei, and G. Mueller, "Near resonance conditions and effects of damping in rocking restrained masonry walls," *submitted in Earthquake Eng. Struct. Dyn.*, 2020.

[18] G. Housner, "The behavior of inverted pendulum structures during earthquakes," *Bulletin of the Seismological Society of America*, vol. 53, no. 2, pp. 403–417, 1963.

EURODYN 2020
XI International Conference on Structural Dynamics
M. Papadrakakis, M. Fragiadakis, C. Papadimitriou (eds.)
Athens, Greece, 23–26 November 2020

THE SPECTRAL ACCELERATION IN THE SEISMIC VULNERABILITY ASSESSMENT OF A HISTORIC MASONRY BUILDING. A COMPARISON BY USING SEVERAL APPROACHES ON A CASE STUDY

Renato Sante Olivito[1], **Saverio Porzio**[1*], **and Carmelo Scuro**[2]

[1] Department of Civil Engineering, University of Calabria, Via P. Bucci, Cubo 39B, 87036 Rende CS, Italy
e-mail: {renato.olivito, saverio.porzio}@unical.it

[2] Department of Physics, University of Calabria, Via P. Bucci, Cubo 31B, 87036 Rende CS, Italy
carmelo.scuro@unical.it

Keywords: Historic masonry structures, seismic vulnerability, collapse mechanisms, spectral acceleration, multi-control points.

Abstract. *This paper concerns the seismic vulnerability assessment of a historic masonry building by means of the spectral acceleration values detected with several approaches. This comparison is related to the particular geometrical-configuration of the case study, which makes the structure particularly prone to collapse mechanisms. These accelerations are evaluated in the static and dynamic nonlinear framework through the most common Finite Element Method (FEM) strategies employed by the scientific community. In particular, the nonlinear static analysis is performed by using a multi-control point pushover methodology allowing the detection of the most damaged areas in the building in which the nodes are located. The nonlinear dynamic analysis is performed by using an artificial accelerogram, and the damage cracks patterns are compared with the ones provided by the static approach. Afterward, a comparison between the spectral accelerations obtained with the FEM approaches and the limit analysis, according to the kinematic theorem, is proposed. This simplified analysis is used to investigate two of the most relevant out-of-plane failure mechanisms, previously highlighted by the global nonlinear investigations. The results show interesting aspects of the seismic resilience of the building, the San Fili Castle of Stignano, in the province of Reggio Calabria (southern Italy), which is strongly influenced by the absence of the box-like behavior.*

1 INTRODUCTION

The mitigation of seismic vulnerability is an excellent interest task for researchers, especially in seismic prone areas such as southern Italy [1, 2]. Structures that characterize old cities have several uncertainties affecting the geometrical and mechanical features. They are the result of many modifications that happened throughout the centuries. In order to take into account these complexities, different devices, and numerical methodologies have been successfully utilized as a support for the seismic investigation. For these reasons, this study concerns the seismic assessment of a historic masonry building by using both nonlinear static and dynamic analyses.

The case study is the San Fili Castle of Stignano (province of Reggio Calabria, south of Italy, Figure 1), a fortified residential building built in the XVIII century all in rubble masonry [3]. This artifact was taking into account owing to its particular geometrical configuration. A Finite Element (FE) model was developed with ABAQUS software by meshing the 3D geometric model provided by the Digital Photogrammetry [4]. Moreover, the Concrete Damage Plasticity (CDP) model, available in the computer program, was adopted to describe the nonlinear behavior of masonry [5]. Preliminary sensitivity analyses were carried out to calibrate the dimensions of the mesh and test the effect of some simplifications on the geometry [4, 6-8].

The spectral acceleration values obtained with FE Method (FEM) approaches were compared with the ones provided by the limit analysis according to the kinematic method. In particular, this simplified analysis was used to investigate two of the most relevant out-of-plane failure mechanisms, highlighted by the global nonlinear analyses. The results of the nonlinear static analysis were presented in terms of pushover curves related to different control points at the top level, as the center of mass of this level and three vertexes of the prismatic volume of the building, which has a triangular plan. For these points, displacement time-histories derived from the dynamic analysis were also presented together with the time history of the base shear in order to compare these results with those provided by the pushover analysis.

(a) (b)

Figure 1: (a) Localization of the town of Stignano; (b) San Fili Castle.

2 NON-LINEAR STATIC AND DYNAMIC ANALYSES

The first step for the seismic assessment is obtaining a proper model of the investigated structure. However, these buildings are complex geometry, which requires simplifications in

order to obtain FE model able to reproduce the structural behavior realistically, as it is studied in the papers by Tiberti *et al.* [9, 10]. In order to reduce the computational burden and obtain a convergent behavior of the solution in all ABAQUS simulations, a sensitivity analysis to set the correct mesh seed is also performed. In the latter, the mesh size is related to the natural frequencies and the participating mass for the three main modes.

Moving on, the nonlinear Pushover Analysis (PA), according to the N2 method adopted by Structural Codes [11, 12], is carried out. Through this method, the seismic vulnerability is evaluated by the conversion of the multi-degree of freedom system (MDOF) into the equivalent system with a single degree of freedom (SDOF) by using the modal participation factor. The PA consists in applying the vertical action including gravity loads and then in considering the seismic forces, acting separately along the positive and negative geometric directions (X and Y) of the analyzed structure [13].

In the simulations, a mass-proportional force distribution pattern is assumed, corresponding to a uniform horizontal acceleration pattern. As a matter of fact, the triangular shape of the building suggests to considerer three Boundary Control Points (BCPs) [14] onto the three vertexes. Their selection plays a very important role in the evaluation of the seismic vulnerability because the three nodes, namely C1, C2, and C3, show different displacement values at the collapse time. In Figure 2, the results of +Y PA are reported.

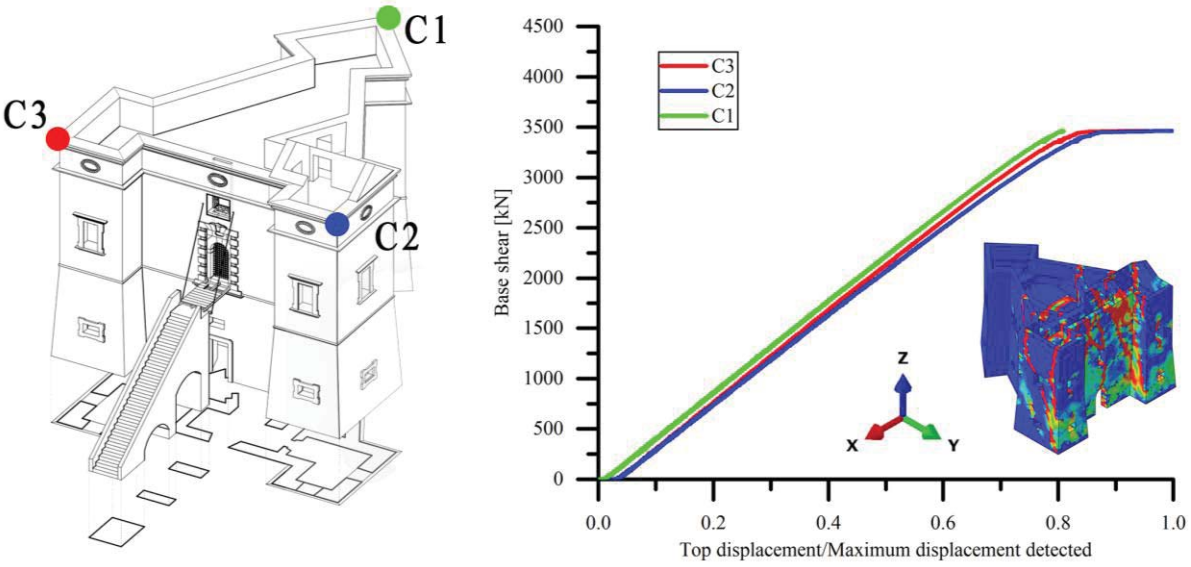

(a) (b)

Figure 2: (a) Localization of the three BCPs onto the San Fili Castle; (b) Results of PA for +Y direction.

In Table 1, the results of PAs are reported in terms of:

- safety factors F_S, which is the ratio between displacement capacity d^*_C and seismic demand d^*_D of the SDOF system,
- behavior factor q^*, which is the ratio between the elastic forces and the yield ones of the SDOF system, which represents the ductility of the structure,
- and spectral acceleration, which is the ratio between shear force F^* and participating mass m^*,

for the three BCPs.

Subsequently, the validation of PA results has been performed by using the Response History Analysis (RHA) based on the application of an artificial accelerogram along the X or Y directions [15-17]. In these analyses, the same model used in PAs is now subject to gravity loads, in the first phase, and, in the second phase, to an accelerogram applied to the base separately for each direction. With the aid of RHAs, the time histories of base shear, damage variables, and displacements of the control points might be assessed [18]. Figure 3 shows the results of RHA in Y direction.

Load direction	BCP	$F_S=d^*_C/d^*_D$	q^*	$a^*=F^*/m^*$
+X	C1	0.23	2.69	2.56
	C2	0.27	2.32	2.97
	C3	0.38	2.20	3.14
-X	C1	0.31	2.17	3.18
	C2	0.38	2.15	3.20
	C3	0.35	2.38	2.89
+Y	C1	0.19	2.86	2.40
	C2	0.23	2.66	2.59
	C3	0.22	2.68	2.57
-Y	C1	0.34	2.03	3.39
	C2	0.28	2.02	3.41
	C3	0.26	2.17	3.17

Table 1: Summary results of PAs in terms of safety and behavior factors.

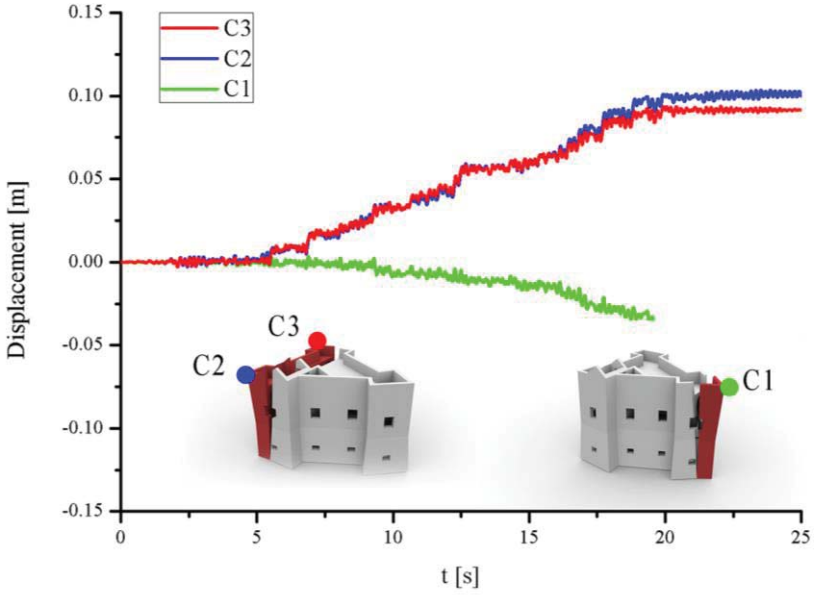

Figure 3: Results of RHA for Y direction in terms of top displacements of BCPs.

3 LIMIT ANALYSIS WITH KINEMATIC APPROACH

The previous seismic analyses highlighted the onset of out-of-plane mechanisms, which occur on the perimeter walls denoting the lack of box-like-behavior. In order to compare the

spectral acceleration provided by the different approaches (PAs, RHAs, and KAs), two out-of-plane mechanisms were analyzed: Simple Overturning (SO) and Vertical Overturning with 2 side wings (VO) (Figure 4). These mechanisms refer to the rocking west tower of the north front which collapses firstly in the +Y PA and reaches higher displacements than all other simulations. The BCP C2 is placed above this structural element, and the detrimental effect of the static thrust of a masonry vault was considered. At the first stage, two linear kinematic analyses were carried out in order to evaluate the corresponding multiplier at collapse α_0 by using the Virtual Work Theorem (VWT) [2, 19]. In the calculation, masonry walls are considered as an assemblage of macro-elements made of a no-tension material with an infinite compressive strength. In the next stage, according to NTC 2018, the nonlinear kinematic analysis was used in order to calculate the spectral acceleration values a^* of the SDOF system.

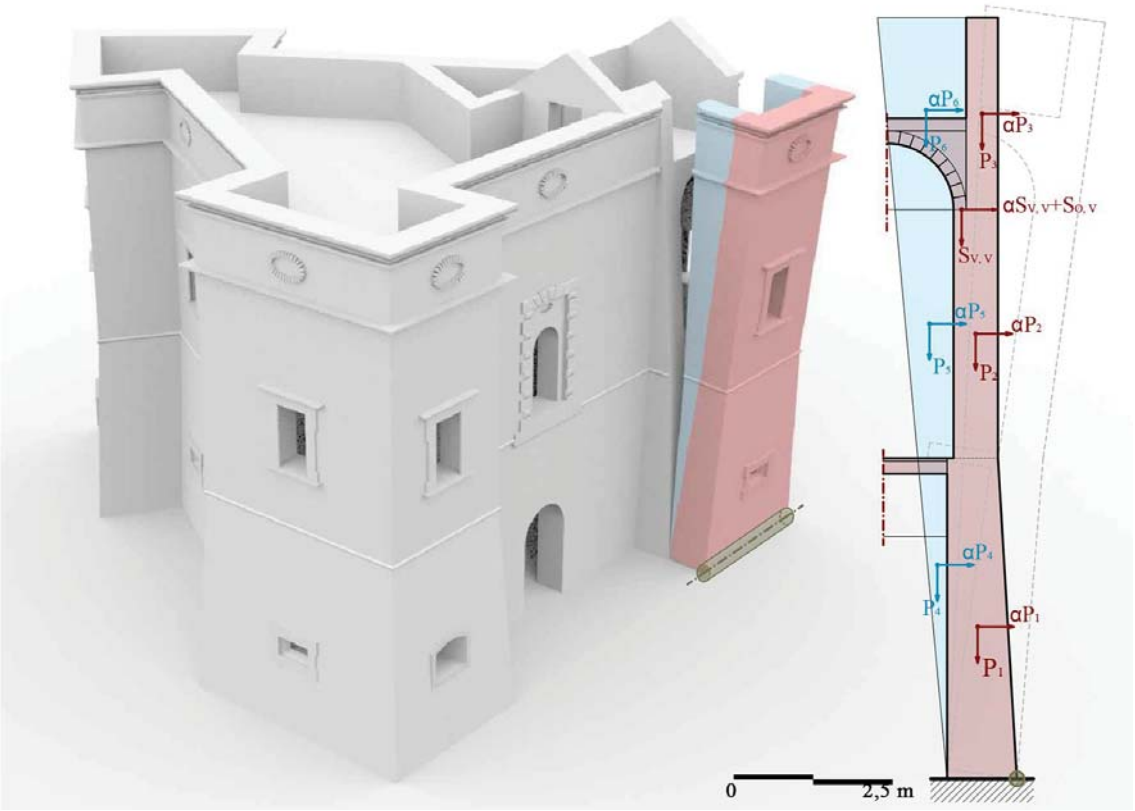

Figure 4: KAs calculation scheme.

4 COMPARISON OF SPECTRAL ACCELERATION VALUES

With regard to the spectral acceleration, a comparison among all types of analyses is reported in Table 2. In numerical analyses, the values concerning node C2 are taken into account along the +Y load direction in PAs as well as the Y direction in RHAs. In the case of KAs, the spectral accelerations are calculated on the ultimate displacement configuration of the SDOF equivalent system. As evidenced by the reported results, the seismic response obtained through the different numerical approaches is comparable. The RHA provides higher spectral accelerations than the PA, but the values are quite comparable in terms of magnitude. This confirms the difficulty in the numerical modeling of very complex structures, especially in the case of nonlinear dynamic analysis which represent the best investigation tool. Regarding the analytical approach, there is a discrepancy with the results of the numerical insight. The lowest values obtained for the KA are mainly due to the non-refinement of the simplified method, which is more conservative since the accelerations obtained are calculated on a single

failure mechanism. On the contrary, the numerical calculation involving the entire structure and a* values are assessed as the ratio of Base-shear to participating mass. However, KA is a quick tool for the seismic analysis of masonry walls. Even today, the design of localized interventions, such as the insertion of tie-rods for achievement of the box-like behavior, takes place through simplified approaches [20].

Pushover Analysis +**Y**: a_{PA}^* [m/s^2]	Response History Analysis **Y**: a_{RHA}^* [m/s^2]		Kinematic Analysis: a_{KA}^* [m/s^2]	
BCP: C2	Positive values	Negative values	SO	VO
2.59	2.90	2.75	0.89	1.10

Table 2: Spectral acceleration values obtained with the different approaches.

5 CONCLUSIONS

The nonlinear static analysis is performed with the purpose of highlighting the seismic vulnerability of the case study. Owing to the triangular plan of the building, a multi-control point approach is used. The dynamic simulations allowed the seismic capacity of the San Fili Castle to be drawn clearly. The results, in terms of both damage and seismic resilience, are quite in agreement with those provided by pushover analysis. Also, it is noteworthy that the kinematic approaches lead to lower spectral acceleration values. However, these simplified investigations might be useful to improve the connection conditions between macro-elements by using traditional techniques such as steel tie-roads. In addition, this first study of the problem in question could be applied to the implementation of the Internet of Things paradigm to a structural health monitoring system of the building in order to conduct real-time analyses with data acquired using accelerometers [21, 22].

REFERENCES

[1] R. S. Olivito, S. Porzio, C. Scuro, and R. Codispoti, "Evaluations on the seismic vulnerability of masonry churches: A case study in Amantea (Cosenza - Italy)," 2018.

[2] R. S. Olivito, S. Porzio, and A. Tedesco, "An Interdisciplinary Approach for the Seismic Vulnerability Assessment of Historic Masonry Buildings: The Case Study of the Ex Jesuits College in Amantea (Italy)," in *RILEM Bookseries* vol. 18, ed: Springer Netherlands, 2019, pp. 1247-1256.

[3] R. S. Olivito and S. Porzio, "A new multi-control-point pushover methodology for the seismic assessment of historic masonry buildings," *Journal of Building Engineering,* vol. 26, 2019.

[4] R. S. Olivito, S. Porzio, M. F. Funari, C. Scuro, and F. Demarco, "A numerical-geometrical methodology to represent out-of-plane mechanisms of unreinforced masonry structures by using pushover analysis," presented at the COMPDYN 2019, Crete, Greece, 2019.

[5] C. Scuro, S. Tiberti, S. Porzio, R. Olivito, and G. Milani, "Study of the interface behaviour between fictile tubules bricks and mortar: numerical and experimental analysis," in *IOP Conference Series: Materials Science and Engineering*, 2019, p. 012027.

[6] C. Scuro, F. Lamonaca, R. Codispoti, D. L. Carn , and R. S. Olivito, "Experimental and numerical analysis on masonry arch built with fictile tubules bricks," *Measurement,* vol. 130, pp. 246-254, 2018.
[7] C. Scuro, S. Tiberti, R. Codispoti, G. Milani, and R. S. Olivito, "Fictile tubules: A traditional Mediterranean construction technique for masonry vaulted systems," *Construction and Building Materials,* vol. 193, pp. 84-96, 2018.
[8] R. S. Olivito, C. Scuro, S. Porzio, R. Codispoti, and F. Demarco, "Seismic vulnerability of ancient masonry buildings: The case study of low-rise towers," in *AIP Conference Proceedings*, 2019, p. 420007.
[9] S. Tiberti, C. Scuro, R. Codispoti, R. S. Olivito, and G. Milani, "Experimental and numerical analysis of historical aseismic construction system," in *Structural Analysis of Historical Constructions*, ed: Springer, 2019, pp. 910-918.
[10] S. Tiberti, C. Scuro, S. Porzio, R. S. Olivito, and G. Milani, "Experimental and numerical analysis on an ancient anti-seismic technique," in *AIP Conference Proceedings*, 2019, p. 100009.
[11] Circolare, "Circolare 2 febbraio 2009, n. 617 Istruzioni per l'applicazione delle Nuove norme tecniche per le costruzioni ," 2009.
[12] NTC, "Aggiornamento delle Norme tecniche per le costruzioni," decreto 17 - 1 - 2018, Gazzetta Ufficiale 42, 20 - 02 - 2018, Ordinary Suppl2018.
[13] F. Clementi, V. Gazzani, M. Poiani, and S. Lenci, "Assessment of seismic behaviour of heritage masonry buildings using numerical modelling," *Journal of Building Engineering,* vol. 8, pp. 29-47, 2016.
[14] M. Valente and G. Milani, "Damage assessment and collapse investigation of three historical masonry palaces under seismic actions," *Engineering Failure Analysis,* 2019/01/17/ 2019.
[15] R. S. Olivito, R. Codispoti, and C. Scuro, "A seismic analysis for masonry constructions: The different schematization methods of masonry walls," in *AIP Conference Proceedings*, 2017, p. 090007.
[16] M. Valente and G. Milani, "Non-linear dynamic and static analyses on eight historical masonry towers in the North-East of Italy," *Engineering Structures,* vol. 114, pp. 241-270, 2016/05/01/ 2016.
[17] R. S. Olivito, C. Scuro, R. Codispoti, and S. Porzio, "A seismic analysis for ancient Trentacapilli Palace with different schematization methods of masonry walls," in *Proceedings of the International Masonry Society Conferences*, 2018, pp. 2555-2562.
[18] G. Fortunato, M. F. Funari, and P. Lonetti, "Survey and seismic vulnerability assessment of the Baptistery of San Giovanni in Tumba (Italy)," *Journal of Cultural Heritage,* vol. 26, pp. 64-78, 2017.
[19] M. Betti and L. Galano, "Seismic analysis of historic masonry buildings: the vicarious palace in Pescia (Italy)," *Buildings,* vol. 2, pp. 63-82, 2012.
[20] A. Formisano and G. Milani, "Seismic vulnerability analysis and retrofitting of the SS. Rosario church bell tower in finale emilia (Modena, Italy)," *Frontiers in Built Environment,* vol. 5, 2019.
[21] F. Lamonaca, P. Sciammarella, C. Scuro, D. Carni, and R. Olivito, "Internet of things for structural health monitoring," in *2018 Workshop on Metrology for Industry 4.0 and IoT*, 2018, pp. 95-100.
[22] C. Scuro, P. F. Sciammarella, F. Lamonaca, R. S. Olivito, and D. L. Carni, "IoT for structural health monitoring," *IEEE Instrumentation and Measurement Magazine,* vol. 21, pp. 4-9 and 14, 2018.

EURODYN 2020
XI International Conference on Structural Dynamics
M. Papadrakakis, M. Fragiadakis, C. Papadimitriou (eds.)
Athens, Greece, 23–26 November 2020

FRAGILITY ASSESSMENT OF UNREINFORCED MASONRY WALLS UNDERGOING EARTHQUAKE-INDUCED LOCAL FAILURE MECHANISMS

Marco Nale[1], Andrea Chiozzi[1], Riccardo Lambroghini[1], Fabio Minghini[1], Marco Rigolin[1] and Antonio Tralli[1]

[1] Department of Engineering, University of Ferrara
Via Saragat 1, Ferrara, Italy
e-mail: {marco.nale, andrea.chiozzi, fabio.minghini, antoniomichele.tralli}@unife.it
{riccard.lamborghini, marco.rigolin}@student.unife.it

Keywords: Fragility functions, Masonry, Local failure mechanisms, Seismic vulnerability.

Abstract. *Damage observations from strong earthquakes show that unreinforced masonry buildings have exhibited recurrent local failure mechanisms and constitute a serious life-safety hazard. This contribution is aimed at evaluating the fragility functions for unreinforced masonry walls in the presence of local failure mechanisms induced by out-of-plane loading. The out-of-plane response consists of the overturning of the entire or a part of the wall insufficiently connected to the rest of the structure. The wall can be idealized as a number of rigid bodies undergoing rocking motion. They are assumed to undergo one-sided rocking or vertical spanning strip wall displacing as an assembly of a coupled rigid body. In this study, we use a set of 44 ground motions from earthquake events that occurred in Italy from 1972 to 2017. For any given wall undergoing a specific collapse mechanism, the probability of collapse is evaluated through a Multiple Stripe Analysis (MSA). Then, a fragility curve is fitted to the MSA data points. The procedure outlined may be extended to obtain typological fragility functions as a combination of the fragility curves corresponding to the various mechanisms analyzed. A preliminary application of the procedure to the historical centre of Ferrara, Italy, is described.*

1 INTRODUCTION

The out-of-plane behavior of UnReinforced Masonry (in the following, URM) structures subjected to ground motion excitations has been widely investigated. Recent seismic events have shown that overturning of entire or parts of walls represents one of the most serious life hazards [1]. Ancient buildings not conceived with specific design criteria against earthquake actions are generally more vulnerable than new buildings, because of the inadequacy of connections of walls to transverse stabilizing walls and floor structures.

In Italy, the seismic analysis of masonry structures based on the study of local collapse mechanisms starts with Giuffrè [2] and a design method based on kinematic analysis is currently reported by the Italian building code [3]. Another approach, often more accurate, makes use of the motion equations of rocking rigid blocks subjected to a given acceleration time history. In this context, the study of rocking oscillators starts with the seminal paper by Housner [4], which derives the out-of-plane response of a parapet wall considered as a single degree of freedom (SDOF) system. Following Housner, the research focuses on the dynamic response of rigid blocks subjected to pulse or earthquakes excitations [5]. In particular, it is shown that this response is characterized by strong nonlinearity and dynamic instability.

Later, other models are developed to approximate the rocking response of complex multi-block systems with an equivalent SDOF system [6]. In particular, a useful SDOF idealization for the displacement-based analysis of the out-of-plane bending of URM walls is proposed in [7].

The increasing interest in a probabilistic approach that allows taking account of uncertainties, vulnerabilities and risk in earthquake engineering provides a description of the structural response by means of dynamic analyses. In PEER-PBEE framework [8], the fragility curve represents one of the main key tools. Several studies provide fragility curves for rocking blocks as a function of various intensity measures [9, 10].

The aim of the present study is to propose a dynamic approach using rigid block modeling to derive fragility curves for two types of very frequent local failure mechanisms. In particular, we analyze one-sided rocking and one-way vertical spanning strip walls (VSSW) displacing as an assembly of two rigid bodies. Section 2 reviews the mechanical models used to reproduce the out-of-plane behavior. Section 3 presents the procedure for evaluating the fragility curves and reports some results. As a case study, a preliminary application to the historical centre of Ferrara (Figure 1), Italy, is presented.

a) b)

Figure 1: Typical URM buildings in the historical centre of Ferrara

2 MECHANICAL MODELS REVIEWS

This section presents the equations of motion for the one-sided rocking and two-block rocking mechanisms. The dynamic response of the rigid blocks to prescribed acceleration time histories is obtained from a specifically suited MATLAB code that numerically solves the nonlinear equations with a 4^{th}-5^{th} order Runge-Kutta integration technique.

2.1 One-sided rocking

A rectangular block resting on a horizontal plane and presenting a vertical one-sided restraint is considered (Figure 2). The friction coefficient is assumed large enough to avoid sliding between the block and the plane.

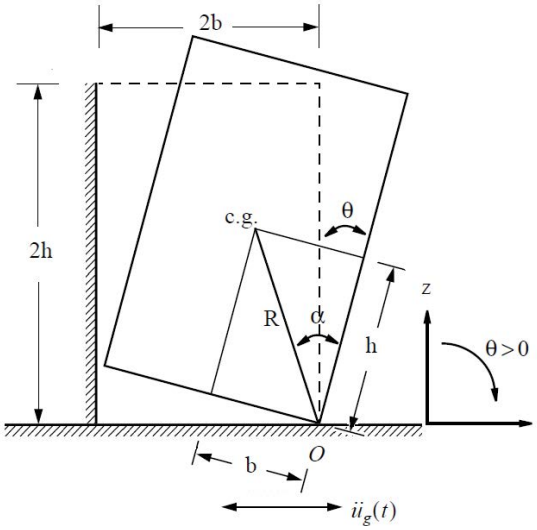

Figure 2: One-sided rocking under ground motion.

The equation of motion that governs the one-sided rocking response can be written as follows:

$$I_0\ddot{\theta} + gM_bR\sin(\alpha-\theta) = -M_bR\ddot{u}_g\cos(\alpha-\theta) \tag{1}$$

with R being the distance between block centroid and rotation centre O, θ the angular rotation, I_0 the polar second moment of area, α the angle between R and the vertical edge of the block, M_b the block mass of the block and g the gravity. The presence of a vertical restraint makes rotation θ remain positive.

In this paper, a coefficient of restitution is accounted for to estimate the energy dissipation. This coefficient, defined as the ratio between angular velocities after ($\dot{\theta}^+$) and before ($\dot{\theta}^-$) the generic impact, takes the following form [11]:

$$\eta_{1s} = \left(1-\frac{3}{2}\sin^2\alpha\right)^2\left(1-\frac{3}{2}\cos^2\alpha\right) \tag{2}$$

2.2 Two-block mechanism

A wall with a deformed shape corresponding to the formation of pivot interfaces at the top, the bottom, and an intermediate height is now considered (Figure 3). The main parameters that describe the mechanism are angles α_1 and α_2, defining the slenderness of the two blocks; M_{b1} and M_{b2} represent the masses of the blocks and I_{01} and I_{02} their polar second moments of area.

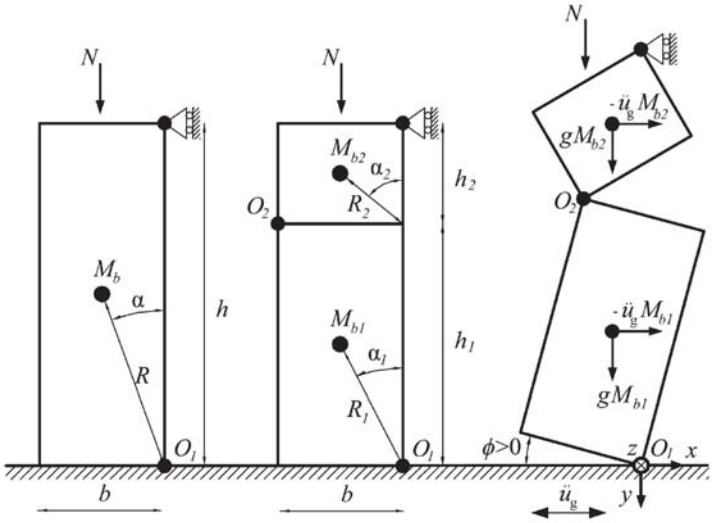

Figure 3: two block mechanism under ground motion

The equation of motion can now be written in the following form (the interested reader is referred to [12] for more details):

$$\left(I_{01}+B_1 I_{02}+B_2 M_{b2} R_2^2\right)\ddot{\phi}+\left(C_1 I_{02}+C_2 M_{b2} R_2^2\right)\dot{\phi}^2+gAR_2\left[M_{b1}+M_{b2}\left(1+\frac{B_2}{4A^2}\right)\right]= \\ -A\left(M_{b1}+M_{b2}\right)R_2\cot\left(\alpha_1-\phi\right)\ddot{u}_g+Q \tag{3}$$

The coefficient of restitution for this mechanism, depending of the block slendernesses, is defined as [12]:

$$\eta_{tb}=\frac{M_{b1}R_1^2+I_{01}\dfrac{\tan\alpha_2}{\tan\alpha_1}-2M_{b1}R_1^2\sin^2\alpha_1+M_{b2}R_1^2\left[2+\dfrac{\sin\alpha_1\cos\alpha_1}{\tan\alpha_2}-\sin^2\alpha_1\left(4+\dfrac{\tan\alpha_2}{\tan\alpha_1}\right)\right]}{M_{b1}R_1^2+I_{01}-I_{02}\dfrac{\tan\alpha_2}{\tan\alpha_1}+M_{b2}R_1^2\left[2+\sin\alpha_1\cos\alpha_{11}\left(\dfrac{1}{\tan\alpha_2}+\tan\alpha_2\right)\right]} \tag{4}$$

This coefficient decreases with wall slenderness and elevation of the intermediate hinge. The experimental evidence shows that the coefficient of restitution ranges between 0.84 and 0.90 of the predicted value [13].

3 FRAGILITY ANALYSIS

The fragility curve is defined as a conditional probability of failure.

$$P\left(C\middle|IM=x\right)=\Phi\left(\frac{\ln\left(x/\theta\right)}{\beta}\right) \tag{5}$$

where x is the median value of the selected Engineering Demand Parameter (EDP), while θ is the capacity related with the collapse damage state. Coefficient β is the logarithmic standard deviation of the demand conditioned on the Intensity Measure (*IM*). Fragility parameters may be estimated from an Incremental Dynamic Analysis (IDA) or a Multiple Stripe Analysis (MSA). In this contribution, the second approach is chosen.

3.1 Ground motion selection

A set of 44 natural ground motions from the ITACA [14] is used. The ground motion set collects the horizontal components of acceleration time histories recorded in Italy during 23 earthquake events occurred from 1972 to 2016. The ground motions are selected with a large range of peak ground acceleration (PGA) and peak ground velocity (PGV). The intensity measure used for the fragility curves is the PGA, which is the key strong motion parameter for seismic design in Italy [3].

3.2 Engineering Demand Parameter

An appropriate choice of the EDPs is necessary for the fragility analysis. The EDP for an overturning block may be chosen as the ratio between block rotation θ and slenderness angle α (see Figure 1):

$$EDP = \theta/\alpha \tag{6}$$

Values of the EDP larger than zero imply that the structure starts to rock. When the EDP exceeds 1, the overturning occurs. This definition of the overturning condition is a simplification on the safe side. In fact, a rocking block might exhibit a higher EDP without overturning [15].

3.3 Multiple Stripe Analysis (MSA)

This type of analysis consists of a series of time history analyses for a specified set of *IM* levels [16]. Compared with the IDA, the MSA offers the advantage of a reduced computational effort. The maximum likelihood criterion is then used to fit the computed fragilities with suitable analytical functions (Figure 4).

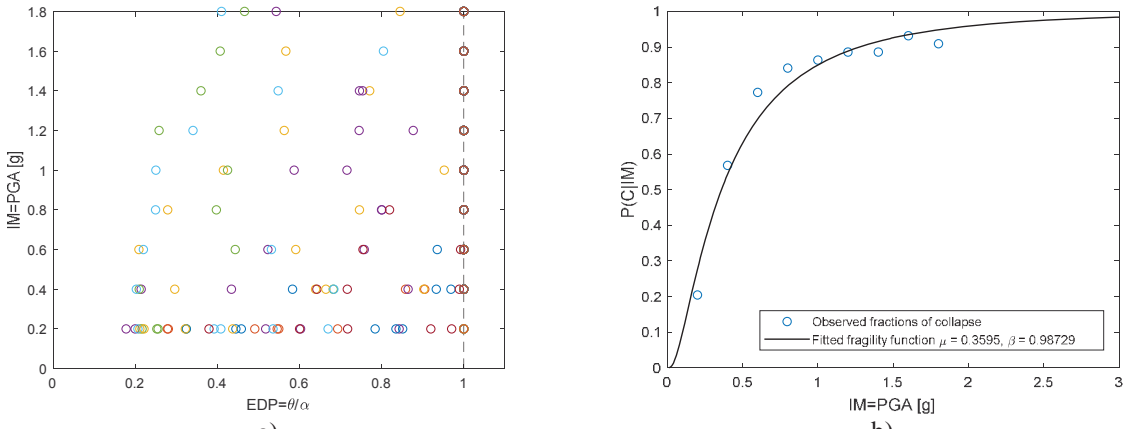

a) b)

Figure 4: a) example of MSA results. b) collapse probability as a function of IM and estimated fragility curve.

3.4 Fragility curves

A survey of an aggregate of buildings in the historic centre of Ferrara, Italy, has been preliminary carried out to form a "population" of masonry walls. The probability of occurrence of the one-sided rocking and two-block mechanism is estimated based on peculiar characteristics of the the surveyed buildings. The corresponding fragility curves are evaluated (Figure 5). These curves describe the vulnerability of the aggregate according with the analyzed mechanisms. It is worth noting that the rocking mechanism is more vulnerable than the two-block mechanism. This greater vulnerability relies upon the nature of the rocking mechanism, which has a trigger acceleration lower than that of the two-blocks mechanism.

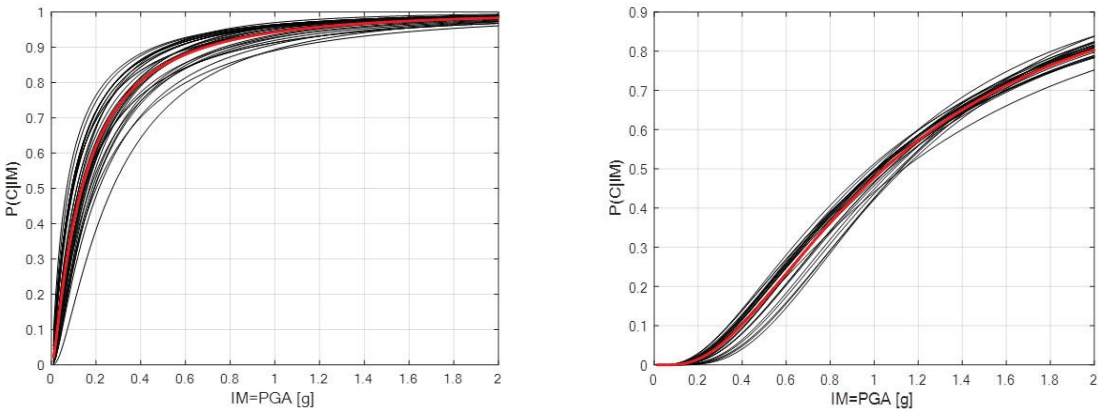

a) b)

Figure 5: a) one-sided rocking fragility curves; b) two block mechanism fragility curves. (the red line represents the average curve)

4 CONCLUSIONS

The paper presents a procedure for evaluating the analytical fragility curves of out-of-plane loaded URM walls with a non-linear dynamic approach.

In a future research, a suitable combination of the obtained fragility curves taking account of the probability of occurrence of the various collapse mechanisms could allow to define typological fragility curves for classes of URM buildings.

5 ACKNOWLEDGEMENTS

The present research was carried out within the activities of the (Italian) University Network of Seismic Engineering Laboratories–ReLUIS in the research program funded by the (Italian) National Civil Protection – Progetto Esecutivo 2019/21 – WP2.

REFERENCES

[1] L. Sorrentino, S. Cattari, F. da Porto, G. Magenes, and A. Penna, "Seismic behaviour of ordinary masonry buildings during the 2016 central Italy earthquakes," *Bull. Earthq. Eng.*, vol. 17, no. 10, pp. 5583–5607, Oct. 2019.

[2] A. Giuffré, "A Mechanical Model for Statics and Dynamics of Historical Masonry Buildings," in *Protection of the Architectural Heritage Against Earthquakes*, Vienna: Springer Vienna, 1996, pp. 71–152.

[3] Ministero delle Infrastrutture e dei Trasporti, "D.M. 17.01.18 Aggiornamento delle 'Norme Tecniche per le costruzioni,'" Ministero delle Infrastrutture e dei Trasporti, Italy, 2018.

[4] G. W. Housner, "The behavior of inverted pendulum structures during earthquakes," *Bull. Seismol. Soc. Am.*, vol. 53, no. 2, pp. 403–417, 1963.

[5] C.-S. Yim, A. K. Chopra, and J. Penzien, "Rocking response of rigid blocks to earthquakes," *Earthq. Eng. Struct. Dyn.*, vol. 8, no. 6, pp. 565–587, 1980.

[6] M. J. DeJong and E. G. Dimitrakopoulos, "Dynamically equivalent rocking structures," *Earthq. Eng. Struct. Dyn.*, vol. 43, no. 10, pp. 1543–1563, Aug. 2014.

[7] K. Doherty, M. C. Griffith, N. Lam, and J. Wilson, "Displacement-based seismic analysis for out-of-plane bending of unreinforced masonry walls," *Earthq. Eng. Struct. Dyn.*, 2002.

[8] G. G. Deierlein, H. Krawinkler, and C. A. Cornell, "A framework for performance-based earthquake engineering," *Pacific Conf. Earthq. Eng.*, 2003.

[9] E. G. Dimitrakopoulos and T. S. Paraskeva, "Dimensionless fragility curves for rocking response to near-fault excitations," *Earthq. Eng. Struct. Dyn.*, vol. 44, no. 12, pp. 2015–2033, 2015.

[10] A. Chiozzi, M. Nale, and A. Tralli, "Fragility assessment of non-structural components undergoing earthquake induced rocking motion," in *XVII Convegno ANIDIS-L'ingegneria Sismica in Italia*, 2017, pp. 449–458.

[11] L. Sorrentino, O. AlShawa, and L. D. Decanini, "The relevance of energy damping in unreinforced masonry rocking mechanisms. Experimental and analytic investigations," *Bull. Earthq. Eng.*, vol. 9, no. 5, pp. 1617–1642, Oct. 2011.

[12] L. Sorrentino, R. Masiani, and M. C. Griffith, "The vertical spanning strip wall as a coupled rocking rigid body assembly," *Struct. Eng. Mech.*, vol. 29, no. 4, pp. 433–453, Jul. 2008.

[13] F. Graziotti, U. Tomassetti, A. Penna, and G. Magenes, "Out-of-plane shaking table tests on URM single leaf and cavity walls," *Eng. Struct.*, vol. 125, pp. 455–470, Oct. 2016.

[14] F. Pacor *et al.*, "Overview of the Italian strong motion database ITACA 1.0," *Bull. Earthq. Eng.*, vol. 9, no. 6, pp. 1723–1739, Dec. 2011.

[15] E. G. Dimitrakopoulos and M. J. DeJong, "Overturning of Retrofitted Rocking Structures under Pulse-Type Excitations," *J. Eng. Mech.*, vol. 138, no. 8, pp. 963–972, 2012.

[16] J. W. Baker, "Efficient Analytical Fragility Function Fitting Using Dynamic Structural Analysis," *Earthq. Spectra*, vol. 31, no. 1, pp. 579–599, Feb. 2015.

EURODYN 2020
XI International Conference on Structural Dynamics
M. Papadrakakis, M. Fragiadakis, C. Papadimitriou (eds.)
Athens, Greece, 23–26 November 2020

SEISMIC VULNERABILITY COMPARATIVE ASSESMENT OF SOME SAMPLES OF CURCHES AFFECTED BY LAST ITALIAN EARTHQUAKES

Generoso Vaiano[1], Michele D'Amato[2], and Antonio Formisano[1]

[1] Department of Structures for Engineering and Architecture, University of Naples "Federico II"
Piazzale Tecchio, 80 – 80125 Naples (Italy)
e-mail: generoso.vaiano@inwind.it; antoform@unina.it

[2] Department of European and Mediterranean Cultures: Architecture, Environment and Cultural Heritage (DICEM), University of Basilicata
Via Lanera, 20 – 75100 Matera (Italy)
michele.damato@unibas.it

Keywords: Cultural Heritage, Masonry churches, Seismic vulnerability, Damage index, Risk analysis

Abstract. *In this paper, seismic vulnerability and risk assessment of two churches samples, located in Teramo and Ischia island in the Naples gulf, both affected by the most recent earthquakes occurred in Italy, are presented. An overview of some simplified methods particularly suitable for seismic evaluations at a territorial scale of ancient churches is presented. In particular, the damage index provided by the post-earthquake usability form adopted by the Italian Civil Protection Department, the vulnerability and risk analysis method implemented in a recent work and defined LV0, and the LV1 method contemplated in the Italian Guidelines for Cultural Heritage have been calculated for the examined samples of churches. These methods have an increasing precision level and they may be applied as well in sequence at a different scale for screening and identifying the present priorities and, consequently, for designing the required interventions. The obtained results have been compared to each other in order to evaluate, starting from the most precise Italian Guidelines method, if the other simplified analysis techniques are more or less effective in predicting the large scale seismic behaviour of churches. Finally, the comparison among the achieved indexes allows for the evaluation of the health state of inspected churches, so to both plan additional in-depth evaluations and program a priority scale in performing future retrofitting interventions.*

1 INTRODUCTION

Seismic vulnerability represents the building attitude to suffer damages related to an assigned earthquake. In order to assess vulnerability of buildings, it is sufficient to detect the damages caused from seismic events, associating them with the shock intensity. A building can show structural damages to load-bearing elements and/or non-structural ones. Damage typologies depend on structure geometry, age, materials, construction site, proximity to other buildings and placement of non-structural elements, as well as on the earthquake duration and intensity. In order to reduce structural damages and the loss of life, buildings need to be secured. Current Italian standards and guidelines [1-3] require that structures should have certain seismic criteria in order to exhibit a ductile response during a seismic event.
Seismic vulnerability assessment of historic buildings represents an enormous applicative relevance problem and constitutes an important preliminary step in masonry heritage safeguarding. A common monumental building typology exposed at seismic risk is represented by masonry churches. In fact, in many cases churches, due to their singular geometry, have shown a vulnerability greater than that of other historical masonry building types. In particular, the presence of large halls without intermediate walls, usual poor masonry mechanical properties, large walls having high slenderness, pushing roof elements, colonnades, decorative elements not effectively constrained to the walls and lack of intermediate floors give an extremely variable seismic response of churches [4-9].
The systematic observation of the typical damage scenarios reported by churches following earthquakes has also highlighted how the seismic response is attributable to local collapse mechanisms connected to the loss of balance and the consequent transformation into a kinematic motion of one or more portions of the construction, which detach from it due to crack occurrence [10-19]. These observations led to the classification of 28 collapse mechanisms developed by the Italian Department of Civil Protection [8, 20]. The possible kinematic mechanisms assessment is not an easy solution problem: detailed structural analyses carried out using software or finite element methods [21-24], have high computational costs, so to make very difficult their application for a territorial scale analysis, and, therefore, simplified methodologies can be preferred [25-31].
For this reason, in this paper three simplified methodologies are investigated in order to assess seismic vulnerability of churches placed in two zones affected by last Italian earthquakes. In particular, the damage indexes detected after seismic events have been evaluated and compared to those deriving from application of both Italian Guidelines on Cultural Heritage and a method developed by a research group of the University of Basilicata (UniBas) defined as *LV0*, with the final goal to evaluate the more or less reliability of these latter two methodologies to predict the large scale seismic behaviour of examined churches.

2 LARGE SCALE ASSESSMENT METHODOLOGIES

2.1 The church form (A-DC model – Italian Civil Protection Department)

The proposed methodology, developed by the Italian Civil Protection Department [20], is based on the evaluation of a damage index (i_d) calculated through the observation of 28 potential local collapse mechanisms that could be activated during a seismic event.
Local mechanisms are (Figure 1):

1. Façade overturning
2. Top overturning
3. In-plane damages

4. Narthex
5. Transverse response of the hall
6. Shear mechanism into lateral walls
7. Longitudinal response of the colonnade
8. Hall or central aisle vaults
9. Lateral aisles vaults
10. Transept wall overturning
11. Shear mechanism into transept walls
12. Transept vault
13. Triumphal arches
14. Dome
15. Lantern
16. Apse overturning
17. Apse shear mechanism
18. Presbytery or apse vaults
19. Roof elements: hall
20. Roof elements: transept
21. Roof elements: apse
22. Chapel overturning
23. Shear mechanism into chapel walls
24. Chapel vaults
25. Interaction due to irregularities
26. Projections
27. Bell tower
28. Belfry

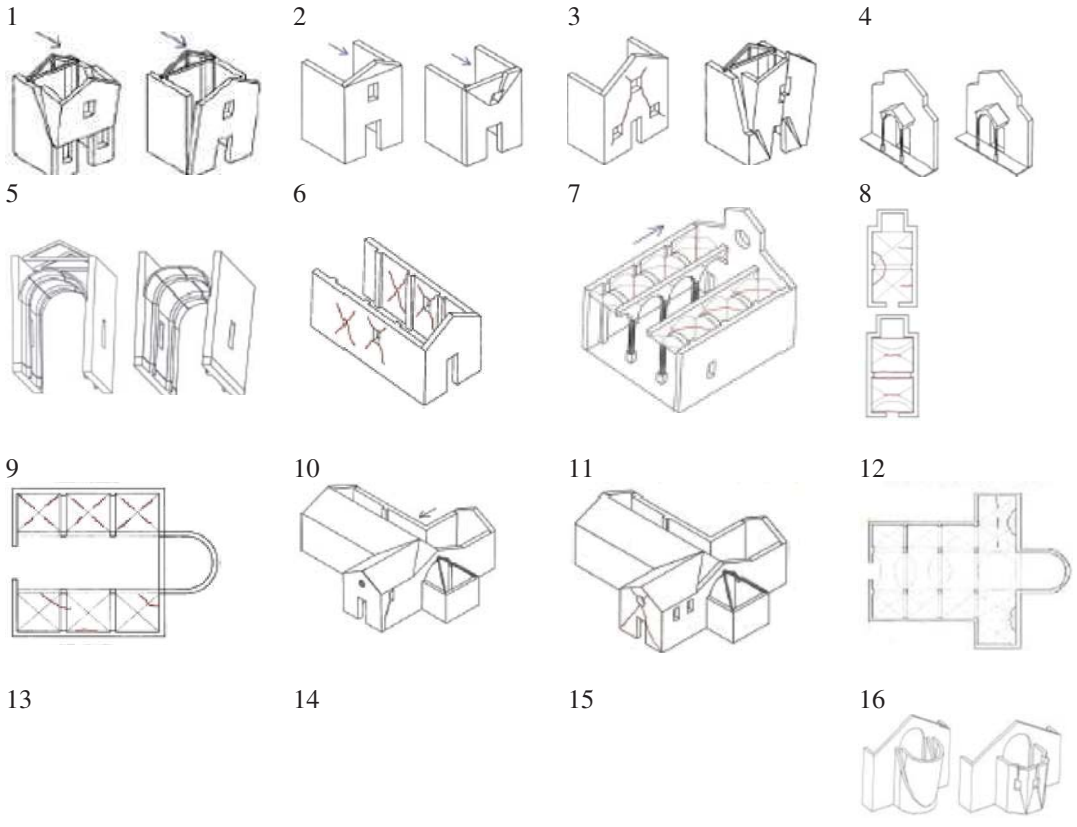

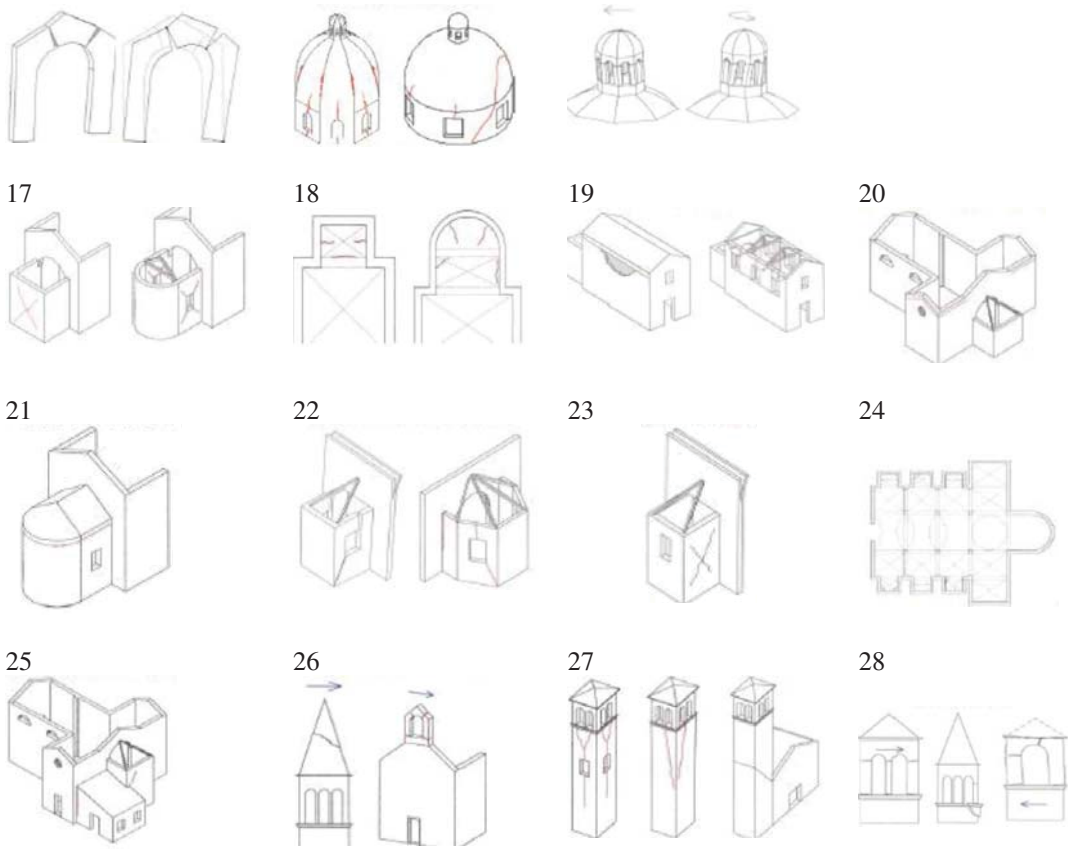

Figure 1: Local mechanisms of churches

For each possible mechanism, a damage value d_k between 0 (no damage) and 5 (collapse) may been assigned, and the resulting global damage index i_d is calculated as the ratio of the sum of the detected damage values d_k to the potential mechanisms number n (<=28) multiplied by 5 according to the following relationship:

$$i_d = \Sigma d_k / 5n \quad (1)$$

The application of the above formula provides damage index values i_d ranging from 0 (no damage) to 1 (total collapse of the church examined).

2.2 Vulnerability and risk analysis method (UniBas)

In this methodology, developed by a research group of University of Basilicata (UniBas), the resulting seismic risk of churches at a territorial scale is based on the evaluation of the following three tools, which an independent score is assigned to [25, 30, 32]:

- *Tool 1*: attention priority on actions related to the buildings according to their exposure value (*E*);
- *Tool 2*: description, classification and mapping of seismic hazard (*H*);
- *Tool 3*: evaluation and quantification of the seismic vulnerability level (*V*).

The seismic risk score is assessed through a correlation among exposure (*E*), threats (*H*) and seismic vulnerability (V) according to the following relationship [33, 34]:

$$R = E \times H \times V \quad (2)$$

In particular, *Tool 1* considers socio-cultural values, i.e. antiquity, historical, symbolic and

aesthetic factors, and economic values, i.e. use, financial and scientific factors.
Tool 2 provides the *H* score through the analysis of threats, which are classified into sporadic events and continuous processes (depending on their occurrence probability), as shown in Table 1. Every threats have a score according to the damage severity, namely absent, medium and catastrophic. The seismic hazard index (*H*) is obtained by summing these scores and assumes values between 0 and 2,15.

	Parameters	Damage gravity		
		Absence	**Average**	**Catastrophic**
Sporadic Events	earthquake and tsunami threat	0	0,20	0,40
	landslides	0	0,15	0,25
	volcanic threat	0	0,20	0,40
	hydro-methodological threat	0	0,15	0,25
	chemical-technological threat	0	0,15	0,25
	forest fires	0	0,15	0,25
Continuous Events	erosion threat	0	0,05	0,10
	physical stress of threat	0	0,05	0,10
	air pollution	0	0,01	0,05
	socio-organizational threat	0	0,01	0,05
	demographic decline	0	0,01	0,05

Table 1: Scenarios description and classification of threats according to the damage severity.

Finally, the *Tool 3* provides the *V* score, that is the seismic vulnerability. This tool is based on the assessment of 13 parameters (see Table 2), of which 10 are derived from the Italian 2nd level GNDT vulnerability datasheet [35]. Each parameter is characterised by 4 classes having an assigned score and the vulnerability index is defined through the following relation:

$$IV=\sum^{n}_{i=1} v_i \cdot p_i \quad (2)$$

where:
v_i is the parameter class score, depending from building properties;
p_i is weight correlated to the parameter importance.
Depending on the vulnerability index obtained, it is possible to define three different vulnerability levels as follows:

- *low*: $0 < IV \leq 10.81$;
- *medium*: $10.81 < IV \leq 55.52$;
- *high*: $55.52 < IV \leq 100$.

Total seismic risk (R) is obtained by applying the following relation [32]:

$$R=IV\times(H+1) \quad (3)$$

	Parameters	Classes				Weight
		A	B	C	D	
1	Position of the building and foundations	0	1,35	6,73	12,12	0,75
2	In-plane configuration	0	1,35	6,73	12,12	0,50
3	In-elevation configuration	0	1,35	6,73	12,12	1,00
4	Distance among walls	0	1,35	6,73	12,12	0,25
5	Non-structural elements	0	0	6,73	12,12	0,25
6	Resistant system type and organization	0	1,35	6,73	12,12	1,50
7	Resistant system quality	0	1,35	6,73	12,12	0,25
8	Floors	0	1,35	6,73	12,12	1,00
9	Roofs	0	1,35	6,73	12,12	1,00
10	Conservation state	0	1,35	6,73	12,12	1,00
11	Environmental alterations	0	1,35	6,73	12,12	0,25
12	Construction system negative alterations	0	1,35	6,73	12,12	0,25
13	Fire vulnerability	0	1,35	6,73	12,12	0,25

Table 2: The UniBas form for seismic vulnerability evaluation of churches.

2.3 The LV1 Method (Italian Guidelines on Cultural Heritage)

The Italian LV1 method provides a statistical-based method to assess the vulnerability of masonry churches [8]. This methodology is based on 28 mechanisms defined in Section 2.1 and the vulnerability index i_v, framed in the range [0÷1], is assessed through vulnerability indicators and seismic upgrading devices according to the following formula:

$$i_v = \frac{1}{6}\frac{\sum_{k=1}^{28}\rho_k\left(v_{ki}-v_{kp}\right)}{\sum_{k=1}^{28}\rho_k}+\frac{1}{2} \tag{4}$$

where:

i_v is the vulnerability index;
k represents the 28 collapse mechanisms potentially activated;
ρ_k is the mechanism weight;
v_{ki} is the vulnerability score related to the k-*th* mechanism;
v_{kp} is the score connected to the upgrading device related to the k-*th* mechanism.

The inactive collapse mechanisms have ρ_k=0; instead the activated mechanisms n. 4 and 15 have ρ_k = 0.5, those with numbers 10, 11, 12, 18, 20, 22, 23, 24, 25 and 26 have a value between 0.5 and 1 in relation to their importance and the remaining activated ones have ρ_k=1.
For each mechanism, the possible seismic protection devices and vulnerability indicators are suggested in [8] and a score depending from effectiveness or severity degree variable between 1 and 3 must be defined. Table 3 shows the vulnerability issues and seismic upgrading devices for the most commonly detected local collapse mechanism, namely the façade overturning.

Through Table 4 it is possible to calculate the indicators v_{ki} and v_{kp} related to vulnerability parameters and anti-seismic devices, respectively.

01 – Façade overturning			
Possibility of activation of collapse mechanism: YES [ ] NO[ ]			
YES	NO	Seismic protection devices	Importance
[ ]	[ ]	Presence of metal tie road	[ ] [ ] [ ]
[ ]	[ ]	Presence of constraining elements	[ ] [ ] [ ]
[ ]	[ ]	Connection systems at angles of walls	[ ] [ ] [ ]
YES	NO	Vulnerability issues	Importance
[ ]	[ ]	Presence of pushing elements (arches, vaults, beams)	[ ] [ ] [ ]
[ ]	[ ]	Presence of big windows	[ ] [ ] [ ]

Table 3: Seismic protection devices and vulnerability issues suggested in [8] for façade overturning mechanism.

Number of vulnerability parameters or seismic protection devices	Importance	Score (v_k)
at least 1	3	3
at least 2	2	
1	2	2
at least 2	1	
1	1	1
None	0	0

Table 4: v_k scores assigned to vulnerability factors and seismic protection devices.

Starting from vulnerability index i_v (eq. 4), it is possible to define an ultimate limit state (ULS) seismic acceleration:

$$a^*_{g(SLU)} = 0.025 \cdot 1.8^{5.1-3.44 \cdot i_v} \tag{5}$$

For safety check, it is required to evaluate the return period corresponding to the ULS as follows:

$$T_{ULS} = T_{R1} \cdot 10^{\log(\frac{T_{R2}}{T_{R1}}) \cdot \log(\frac{a_{ULS} S}{F_C a_1 S_1}) / \log(\frac{a_2 S_2}{a_1 S_1})} \tag{6}$$

where T_{R1} and T_{R2} are the return periods of the seismic hazard and represent the limits of the interval where T_{ULS} is located, a_1S_1 and a_2S_2 are the corresponding peak acceleration values on rigid ground taking into account the topographical conditions and FC is the confidence factor.

The safety index referred to the ULS is the ratio between the capacity return period at the ultimate limit state T_{ULS} and the corresponding reference (demand) return period $T_{R,ULS}$:

$$I_{S,ULS} = T_{ULS}/T_{R,ULS} \tag{7}$$

$I_{S,ULS}$ value greater than or equal to one means that the building is in safe conditions, while values lower than the unit show that the building needs seismic upgrading interventions.

3 THE CASE STUDIES

3.1 Teramo's churches

Teramo is the provincial capital of the homonymous province, located in the Italian Abruzzo region. The 12 investigated churches in the current study, depicted in Figure 2 [22], are:

1. Saint John church. Hall: 16.50x14.30m, average height 10.00m. There are no apse and bell tower.
2. Saint Anastasio church. Hall: 14.70x7.20m, average height 6.70m. Apse: 7.50x3.50m, average height 7.15m. There is a bell tower.
3. Holy Mary of Carmine church. Hall: 11.30x6.20m, average height 7.20m. Apse: 6.45x5.00m, average height 7.00m. There is a bell tower.
4. Saint Nicola church. Hall: 11.00x4,60m, average height 3.50m. There are no apse and bell tower.
5. Saint Catherine of Alexandria church. Hall: 13.40x6.50m, average height 7.50m. There are no apse and bell tower.
6. Saint Luca church. Hall: 8.00x4.00m, average height 6.00m. There are no apse and bell tower.
7. Saint Mary de Praediis church. Hall: 14.50x9.00m, average height 5.00m. Apse: 3.00x1.50m, average height 5.00m. There is not a bell tower.
8. Saint Michael Archangel church. Hall: 16.50x14.30m, average height 10.00m. There are no apse and bell tower.
9. Saint Francis of Assisi church. Hall: 11.40x7.00m, average height 7.80m. Apse: 5.85x5.80m, average height 6.00m. There is a bell tower.
10. Saint John in Pergulis church. Hall: 14.90x9.30m, average height 8.00m. There are no apse and bell tower.
11. Holy Salvatore church. Hall: 10.70x7.20m, average height 8.00m. There are no apse and bell tower.
12. Saint Stephen church. Hall: 14.40x5.25m, average height 5.85m. Apse: 5.25x3.40m, average height 3.50m. There is a bell tower.

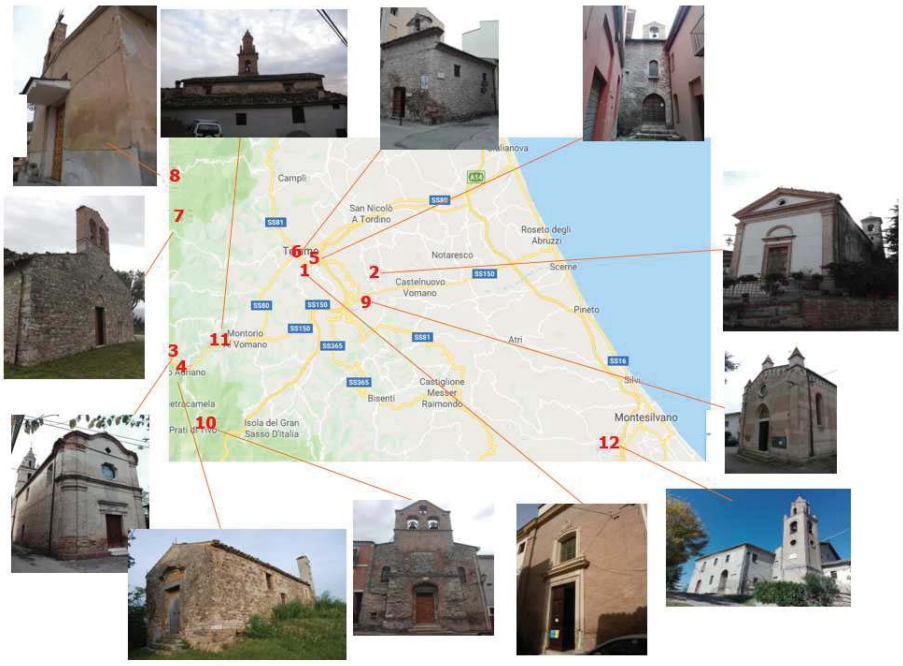

Figure 2: Location of the 12 churches investigated in the city of Teramo.

3.2 Ischia's churches

Ischia is an Italian island belonging to the Phlegrean islands archipelago located in the northern area of the Gulf of Naples. The 10 investigated churches showed in Figure 3 [22] are:

1. Saint Francis of Paola church. Hall: 19.50x3.30m, average height 7.00m. Apse: 3.40x3.30m, average height 8.50m. There is a bell tower.
2. Saint Vito church. Hall: 22.00x4.80m, average height 7.10m. Apse: 4.80x2.80m, average height 10.00m. There is a bell tower.
3. Most Holy Annunciation church. Hall: 6.50x3.90m, average height 6.55m. Apse: 4.80x4.00m, average height 6.55m. There is not a bell tower.
4. Saint Sebastiano church. Hall: 17.30x6.30m, average height 12.30m. Apse: 6.30x4.60m, average height 8.00m. There is a bell tower.
5. Saint Michael Archangel church. Hall: 8.60x5.20m, average height 8.00m. Apse: 5.20x4.70m, average height 8.00m. There is not a bell tower.
6. Saint Mary of Loreto church. Hall: 30.00x5.80m, average height 11.00m. Apse: 8.15x5.80m, average height 10.00m. There is a bell tower.
7. Saint Francis of Assisi church. Hall: 21.00x8.40m, average height 10.00m. Apse: 9.00x6.80m, average height 12.00m. There is not a bell tower.
8. Most Holy Annunciation coven. Hall: 11.00x5.60m, average height 7.00m. Apse: 6.00x5.50m, average height 7.40m. There is a bell tower.
9. Saint Mary of Soccorso church. Hall: 14.80x6.80m, average height 7.50m. Apse: 4.60x4.10m, average height 8.50m. There is a bell tower.
10. Saint Gaetano church. Hall: 17.00x5.80m, average height 13.70m. Apse: 4.70x1.70m, average height 7.15m. There is not a bell tower.

Figure 3: Location of the 10 churches investigated in the Ischia island

4 APPLICATION OF THE METHODOLOGIES

4.1 Teramo's churches

Collapse mechanisms and damage indices of churches calculated according to the form delivered by the Italian Civil Protection Department are reported in the Tables from 5 to 16.

For each mechanism, a different colour for each damage value between 0 (no damage) and 5 (collapse) is assigned, as shown in Figure 4.

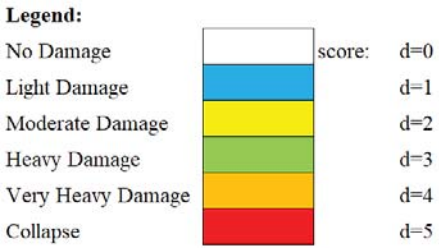

Figure 4: Colours assigned to damage scores

Activated mechanisms	Seismic Damage
Facade overturning	
In-plane damages	
Transverse response of the hall	
Shear mechanism into lateral walls	
Longitudinal response of the colonnade	
Hall or central aisle vaults	
Lateral aisles vaults	
Roof elements: hall	

Table 5: St. John Church's activated mechanisms.

Activated mechanisms	Seismic Damage
Facade overturning	
Top overturning	
In-plane damages	
Transverse response of the hall	
Shear mechanism into lateral walls	
Hall or central aisle vaults	
Triumphal arches	
Apse overturning	
Apse shear mechanism	
Presbytery or apse vaults	
Roof elements: hall	
Roof elements: apse	
Interaction due to irregularities	
Bell tower	
Belfry	

Table 6: St. Anastasio Church's activated mechanisms.

Activated mechanisms	Seismic Damage
Facade overturning	
Top overturning	
In-plane damages	
Transverse response of the hall	
Shear mechanism into lateral walls	
Hall or central aisle vaults	
Triumphal arches	
Apse overturning	
Apse shear mechanism	

Activated mechanisms	Seismic Damage
Facade overturning	
Top overturning	
In-plane damages	
Transverse response of the hall	
Shear mechanisms into lateral walls	
Roof elements: hall	
Projections (sailing, spiers, pinnacles, statues)	

Presbytery or apse vaults	
Roof elements: hall	
Roof elements: apse	
Interaction due to irregularities	
Bell tower	
Belfry	

Table 7: Most Holy Annunciation Church's activated mechanisms.

Facade overturning	
Top overturning	
In-plane damages	
Transverse response of the hall	
Roof elements: hall	
Interaction due to irregularities	
Projections (sailing, spiers, pinnacles, statues)	

Table 8: St. Nicola Church's activated mechanisms.

Activated mechanisms	Seismic Damage
In-plane damages	
Shear mechanisms into lateral walls	
Roof elements: hall	
Projections (sailing, spiers, pinnacles, statues)	

Table 9: St. Catherine of Alessandria Church's activated mechanisms.

Activated mechanisms	Seismic Damage
Facade overturning	
Top overturning	
In-plane damages	
Transverse response of the hall	
Shear mechanism into lateral walls	
Roof elements: hall	
Projections (sailing, spiers, pinnacles, statues)	

Table 10: St. Luca Church's activated mechanisms.

Activated mechanisms	Seismic Damage
Facade overturning	
Top overturning	
In-plane damages	
Transverse response of the hall	
Shear mechanism into lateral walls	
Longitudinal response of the colonnade	
Apse overturning	
Apse shear mechanism	
Presbytery or apse vaults	
Roof elements: hall	
Roof elements: apse	
Projections (sailing, spiers, pinnacles, statues)	

Table 11: St. Mary de Praediis Church's activated mechanisms.

Activated mechanisms	Seismic Damage
Facade overturning	
Top overturning	
In-plane damages	
Transverse response of the hall	
Shear mechanism into lateral walls	
Roof elements: hall	
Projections (sailing, spiers, pinnacles, statues)	

Table 12: St. Michael Archangel Church's activated mechanisms.

Activated mechanisms	Seismic Damage
Facade overturning	
Top overturning	
In-plane damages	
Transverse response of the hall	

Activated mechanisms	Seismic Damage
Facade overturning	
Top overturning	
In-plane damages	
Transverse response of the hall	

Shear mechanism into lateral walls	
Triumphal arches	
Apse overturning	
Apse shear mechanism	
Presbytery or apse vaults	
Roof elements: hall	
Roof elements: apse	
Projections (sailing, spiers, pinnacles, statues)	
Bell tower	
Belfry	

Table 13: St. Francis of Assisi Church's activated mechanisms.

Roof elements: hall	
Roof elements: apse	
Projections (sailing, spiers, pinnacles, statues)	

Table 14: St. John in Pergulis Church's activated mechanisms.

Activated mechanisms	Seismic Damage
Facade overturning	
In-plane damages	
Transverse response of the hall	
Shear mechanism into lateral walls	
Hall or central aisle vaults	
Transept wall overturning	
Transept shear mechanisms	
Transept vaults	
Roof elements: hall	
Roof elements: transept	
Interaction due to irregularities	
Bell tower	
Belfry	

Table 15: Most Holy Salvatore Church's activated mechanisms.

Activated mechanisms	Seismic Damage
Facade overturning	
Top overturning	
In-plane damages	
Transverse response of the hall	
Shear mechanism into lateral walls	
Hall or central aisle vaults	
Roof elements: hall	
Roof elements: transept	
Bell tower	
Belfry	

Table 16: St. Stephan Church's activated mechanisms.

The filling of the previous forms for all of the investigated churches has lead towards the evaluation of the following damage index i_d:

- St. John Church (Table 5): i_d =(1/40)= 0,02
- St. Anastasio Church (Table 6): i_d = (19/75) = 0.25
- Most Holy Annunciation Church (Table 7): i_d = (11/75)= 0,15
- Saint Nicola Church (Table 8): i_d= (3/35)= 0,08.
- Saint Catherine of Alessandria Church (Table 9): i_d= (5/20)= 0,25
- Saint Luca Church (Table 10): i_d= (10/35)= 0,29
- Saint Mary de Praediis Church (Table 11): i_d= (16/60)= 0,27
- Saint Michael Archangel Church (Table 12): i_d= (8/35)= 0,23
- Saint Francis of Assisi Church (Table 13): i_d= (4/70) = 0,06
- Saint John in Pergulis Church (Table 14): i_d= (4/35)= 0,11
- Most Holy Salvatore Church (Table 15): i_d= (5/65)= 0,08

- Saint Stephan Church (Table 16): i_d= (13/50)= 0,26

The results obtained from applying the *LV0* method to the churches inspected in Teramo are shown in Table 17.

Churches	Vulnerability Index
St. John	21,22
St. Anastasio	51,52
Holy Mary of Carmine	31,32
St. Nicola	53,18
St. Catherine of Alexandria	66,32
St. Luca	22,23
St. Mary de Praediis	39,06
St. Michael Archangel	37,37
St. Francis of Assisi	22,23
St. John in Pergulis	28,96
Most Holy Salvatore	45,44
St. Stephen	30,64

Table 17: Vulnerability indexes of Teramo's churches using vulnerabily method implemented by the University of Basilicata (UniBas).

Table 18 shows vulnerability indexes and results of the ULS safety checks achieved from the *LV1* method developed in the Italian Guidelines for Cultural Heritage described in Section 2.3.

Churches	Vulnerability Index	Safety Index
St. John	0,23	1,41
St. Anastasio	0,39	0,57
Holy Mary of Carmine	0,32	0,81
St. Nicola	0,31	0,85
St. Catherine of Alexandria	0,32	0,66
St. Luca	0,43	0,44
St. Mary de Praediis	0,57	0,57
St. Michael Archangel	0,41	0,49
St. Francis of Assisi	0,24	1,29
St. John in Pergulis	0,31	0,88
Most Holy Salvatore	0,25	1,21
St. Stephen	0,38	0,57

Table 18: Vulnerability indexes and ULS safety checks for Teramo's churches using LV1 method.

4.2 Ischia's churches

The damage indexes of Ischia's churches deriving from the "*A-DC model*" form developed by the Italian Civil Protection Department have been evaluated started from filling Tables from 19 to 28.

Activated mechanisms	Seismic Damage
Facade overturning	
Top overturning	
In-plane damages	
Transverse response of the hall	
Shear mechanism into lateral walls	
Longitudinal response of the colonnade	
Hall or central aisle vaults	
Lateral aisles vaults	
Triumphal arches	
Dome	
Apse overturning	
Apse shear mechanism	
Roof elements: hall	
Roof elements: apse	
Bell tower	
Belfry	

Table 19: St. Francis of Paola Church's activated mechanisms.

Activated mechanisms	Seismic Damage
Facade overturning	
Top overturning	
In-plane damages	
Transverse response of the hall	
Shear mechanism into lateral walls	
Longitudinal response of the colonnade	
Hall or central aisle vaults	
Lateral aisles vaults	
Triumphal arches	
Dome	
Apse overturning	
Apse shear mechanism	
Roof elements: hall	
Roof elements: apse	
Bell tower	
Belfry	

Table 20: St. Vito Church's activated mechanisms.

Activated mechanisms	Seismic Damage
Facade overturning	
Top overturning	
In-plane damages	
Transverse response of the hall	
Shear mechanism into lateral walls	
Transept wall overturning	
Shear mechanism into transept walls	
Transept vaults	
Triumphal arches	
Apse overturning	
Apse shear mechanism	
Presbytery or apse vaults	
Roof elements: transept	
Roof elements: apse	

Activated mechanisms	Seismic Damage
Facade overturning	
Top overturning	
In-plane damages	
Shear mechanism into lateral walls	
Lateral aisles vaults	
Dome	
Apse overturning	
Apse shear mechanism	
Presbytery or apse vaults	
Roof elements: hall	
Roof elements: apse	
Chapel overturning	
Shear mechanism into chapel walls	
Chapel vaults	

Projections (sailing, spiers, pinnacles, statues)	
Facade overturning	

Table 21: Most Holy Annunciation Church's activated mechanisms.

Interaction due to irregularities	
Bell tower	
Belfry	

Table 22: St. Sebastiano Church's activated mechanisms.

Activated mechanisms	Seismic Damage
Facade overturning	
In-plane damages	
Transverse response of the hall	
Shear mechanism into lateral walls	
Hall or central aisle vaults	
Dome	
Apse overturning	
Apse shear mechanism	
Roof elements: hall	
Roof elements: apse	
Chapel overturning	
Shear mechanism into chapel walls	
Chapel vaults	
Projections (sailing, spiers, pinnacles, statues)	

Table 23: St. Michael Archangel Church's activated mechanisms.

Activated mechanisms	Seismic Damage
Facade overturning	
Top overturning	
In-plane damages	
Transverse response of the hall	
Shear mechanism into lateral walls	
Longitudinal response of the colonnade	
Lateral aisles vaults	
Triumphal arches	
Dome	
Apse overturning	
Apse shear mechanism	
Presbytery or apse vaults	
Roof elements: hall	
Roof elements: apse	
Interaction due to irregularities	
Bell tower	
Belfry	

Table 24: St. Mary of Loreto Church's activated mechanisms.

Activated mechanisms	Seismic Damage
Facade overturning	
In-plane damages	
Transverse response of the hall	
Shear mechanism into lateral walls	
Hall or central aisle vaults	
Lateral aisles vaults	
Triumphal arches	
Apse overturning	
Apse shear mechanism	
Presbytery or apse vaults	
Roof elements: hall	
Roof elements: apse	
Shear mechanism into chapel walls	

Activated mechanisms	Seismic Damage
Facade overturning	
In-plane damages	
Transverse response of the hall	
Shear mechanism into lateral walls	
Hall or central aisle vaults	
Apse overturning	
Apse shear mechanism	
Presbytery or apse vaults	
Roof elements: hall	
Roof elements: apse	
Interaction due to irregularities	
Projections (sailing, spiers, pinnacles, statues)	
Bell tower	

Chapel vaults	
Interaction due to irregularities	

Table 25: St. Francis of Assisi Church's activated mechanisms.

Belfry	

Table 26: Most Holy Annunciation Coven's activated mechanisms.

Activated mechanisms	Seismic Damage
Facade overturning	
Top overturning	
In-plane damages	
Transverse response of the hall	
Shear mechanism into lateral walls	
Hall or central aisle vaults	
Lateral aisles vaults	
Triumphal arches	
Dome	
Apse overturning	
Apse shear mechanism	
Roof elements: hall	
Roof elements: apse	
Chapel overturning	
Shear mechanism into chapel walls	
Chapel vaults	
Projections (sailing, spiers, pinnacles, statues)	
Bell tower	
Belfry	

Table 27: St. Mary of Soccorso Church's activated mechanisms.

Activated mechanisms	Seismic Damage
Facade overturning	
In-plane damages	
Shear mechanism into lateral walls	
Hall or central aisle vaults	
Triumphal arches	
Dome	
Apse overturning	
Apse shear mechanism	
Presbytery or apse vaults	
Roof elements: hall	
Roof elements: apse	
Chapel overturning	
Shear mechanism into chapel walls	
Chapel overturning	
Shear mechanism into chapel walls	
Chapel vaults	
Projections (sailing, spiers, pinnacles, statues)	

Table 28: St. Gaetano Church's activated mechanisms.

The damage indexes of the inspected churches have been calculated on the basis of the previous tables, leading to the following results:

- St. Francis of Paola church (Table 19): i_d =(7/80)= 0,09
- Saint Vito church (Table 20): i_d= (6/80)= 0,08
- Most Holy Annunciation church (Table 21): i_d= (12/65)= 0,16
- Saint Sebastiano church (Table 22): i_d= (17/80)= 0,19
- Saint Michael Archangel church (Table 23): i_d= (23/70)= 0,33
- Saint Mary of Loreto church (Table 24): i_d= (16/85)= 0,18
- Saint Francis of Assisi church (Table 25): i_d= (8/80)= 0,10
- Most Holy Annunciation Coven church (Table 26): i_d= (4/70)= 0,06
- Saint Mary of Soccorso church (Table 27): i_d= (8/80)= 0,10
- Saint Gaetano church (Table 28): i_d= (4/75)= 0,05

The application of the *LV0* method (developed by a reserach group pf the University of Basilicata) has led to the results depicted in Table 29. Finally, Table 30 shows vulnerability index

values and ULS safety checks obtained through *LV1* method developed by the Italian Guidelines for Cultural Heritage as described in Section2.3.

Churches	Vulnerability Index
St. Francis of Paola	25,93
St. Vito	25,93
Most Holy Annunciation	38,64
St. Sebastiano	34,33
St. Michael Archangel	46,46
St. Mary of Loreto	32,66
St. Francis of Assisi	24,25
Most Holy Annunciation coven	21,56
St. Mary of Soccorso	23,24
St. Gaetano	32,33

Table 29: Vulnerability indexes of Ischia's churches using the LV0 method.

Churches	Vulnerability Index	Safety Index
St. Francis of Paola	0,36	1,16
St. Vito	0,36	1,18
Most Holy Annunciation	0,42	0,85
St. Sebastiano	0,43	0,78
St. Michael Archangel	0,48	0,66
St. Mary of Loreto	0,43	0,78
St. Francis of Assisi	0,40	0,93
Most Holy Annunciation coven	0,40	0,93
St. Mary of Soccorso	0,34	1,30
St. Gaetano	0,36	1,21

Table 30: Vulnerability indexes and ULS safety checks for Ischia's churches using LV1 method.

4.3 Comparison of results

All results from examined methodologies are grouped in Tables 31 and 32, respectively, for Teramo's churches and Ischia's ones. In the first column of Tables 31 and 32 the ranking is reported in descending order (from the worst church to the best one) in terms of vulnerability indexes (I_v) defined according to the *LV1* method developed in the Italian Guidelines for Cultural Heritage. In the subsequent columns of the above mentioned tables, the safety indexes (I_s) of the *LV1* method, the vulnerability indexes calculated on the basis of the *LV0* method, indicating the method proposed by a UniBas research group and expressed in percentage terms and the damage indexes i_d resulting from filling the "A-DC model" form, developed by

the Italian Civil Protection Department, after the post-earthquake emergency phase have been reported too.

Church	I_v (LV1 method)	I_s (LV1 method)	I_v (LV0 method)	i_d (A-DC form)
St. Luca	0,435	0,44	0,22	0,30
St. Michael Archangel	0,414	0,495	0,37	0,27
St. Mary of Praediis	0,388	0,57	0,39	0,27
St. Anastasio	0,388	0,57	0,52	0,25
St. Stephan	0,38	0,573	0,31	0,26
St. Catherine of Alessandria	0,322	0,664	0,66	0,20
St. Mary of Carmine	0,322	0,813	0,32	0,15
St. Nicola	0,315	0,848	0,53	0,08
St. John in Pergulis	0,309	0,88	0,29	0,11
St. Salvatore	0,255	1,21	0,45	0,08
St. Francis of Assisi	0,244	1,29	0,22	0,05
St. John	0,229	1,41	0,21	0,02

Table 31: Comparison between al examined methodologies for Teramo's churches

Church	i_v (LV1 method)	I_s (LV1 method)	I_v (LV0 method)	i_d (A-DC form)
St. Michael Archangel	0,48	0,659	0,46	0,33
St. Sebastiano	0,43	0,779	0,34	0,19
St. Mary of Loreto	0,43	0,782	0,33	0,18
Most Holy Annunciation	0,42	0,85	0,24	0,10
St. Francis of Assisi	0,40	0,93	0,39	0,16
Most holy Annunciation Coven	0,36	1,05	0,26	0,08
St. Francis of Paola	0,36	1,165	0,26	0,09
St. Vito	0,36	1,18	0,22	0,06
St. Gaetano	0,36	1,21	0,32	0,05
St. Mary of Soccorso	0,34	1,3	0,23	0,07

Table 32: Comparison between al examined methodologies for Ischia's churches

For comparison purpose, it is believed that damage indexes provided by the Italian Civil Protection Department form represent the reference values, since they have been proposed starting from damages occurred after last Italian earthquakes. From comparison in term of vulnerability index, it has been detected that the *LV0* method provides very frequently lower

values (82% of the cases examined). In particular, this always occurs for the Ischia's churches, while for the Teramo's ones the *LV0* indexes are greater than damage indexes only in four cases. These results allow to say that the *LV0* method, even if it provides a ranking similar to that of the A-DC form, is not on the safe side in predicting the vulnerability of examined churches. On the other hand, it seems that the *LV1* method is good in predicting the vulnerability ranking and indexes of churches under investigation.
Finally, from A-DC form values, it has been revealed that churches usable only after prompt interventions are those characterised by indexes in the range between 0,2 and 0,3, while the worst conditions that carry out the church unusable are obtained for a damage index higher than 0,3. This limit value could be reached for vulnerability indexes greater than 0,32 and 0,40, respectively, in the areas of Teramo and Ischia. This is due to the fact that Teramo belongs to a territory with seismicity greater than that of Ischia.

5 CONCLUSIONS

In the context of the cultural heritage conservation and protection it is essential to have an adequate knowledge of the existing constructions, which allows to well identify the structural element for a reliable seismic safety assessment and the choice of the intervention strategies for improving their structural performance. To this purpose, it is preferable to perform analyses with sophisticated finite element programs. However, the use of such programs for vulnerability assessment at a territorial scale is not suitable, since it would take too long time. For these reasons expeditious methodologies are preferred. In this paper three different quick vulnerability analysis methods, namely the *LV1* Italian Guidelines method, the "Church form –A-DC model" developed by the Italian Civil Protection and the *LV0* methodology developed by a research group of the University of Basilicata, have been proposed and applied to two samples of churches located in Teramo and in the Ischia island, both affected by the last Italian earthquakes. The churches of these two areas have in common many features, but there are also some structural differences which have modified the values of their vulnerability index. A comparative seismic risk and vulnerability analysis considering the above three methods has been conducted at a territorial level for both areas considered.
From the analyses carried out, it can be revealed that the damage indexes provided by the Italian Civil Protection Department A-DC form represent the reference values, since they have been calculated on the basis of the damages really occurred after last earthquakes. In particular, churches usable only after prompt interventions are those characterised by indexes in the range between 0,2 and 0,3, while unusable church have damage index higher than 0,3. This limit value could be reached for vulnerability indexes greater than 0,32 and 0,40, respectively, in the areas of Teramo and Ischia. This occurred since Teramo belongs to a territory with seismicity greater than that of Ischia. Starting from this evidence, it has been detected that the LV1 method provides, in the cases analysed, more conservative results with respect to LV0 method, even if providing, similarly to the A-DC form, a macro-element approach is followed in evaluating the vulnerability index.

REFERENCES

[1] Ministry of Infrastructures and Transports (2018). Ministerial Decree 17 January 2018, *Updating of Technical Codes for Constructions* (in Italian). Official Gazette n. 42 of 20/02/18, Ordinary Supplement n. 8, 2018.

[2] DPCM, *Guidelines for the cultural heritage seismic risk assessment and reduction with reference to the construction technical standards referred the M.I.T. decree of 2008 (in Italian)*, Italy, 2011.

[3] R. Cecchi, M. Calvi, *Guidelines for Evaluation and Mitigation of Seismic Risk to Cultural Heritage with Reference to Technical Standard for Construction* (In Italian), Ministry for Cultural Heritage and Activities, Department of Civil Protection Agency, Gangemi, Rome, Italy, 2010.

[4] J. Leite, P. B. Lourenco, and J. M. Ingham, Statistical Assessment of Damage to Churches Affected by the 2010 – 2011 Canterbury (New Zealand) Earthquake Sequence, *Journal of Earthquake Engineering* 17, 73–97, 2017.

[5] M. Valente, G. Barbieri, and L. Biolzi, Damage assessment of three medieval churches after the 2012 Emilia earthquake*, Bulletin of Earthquake Engineering*, doi:10.1007/s10518-016-0073-7, 2016.

[6] R. Fonti, A. Borri, R. Barthel, M. Candela, and A. Formisano, Rubble masonry response under cyclic actions: experimental tests and theoretical models, *International Journal of Masonry Research and Innovation*, 2, no. 1, 2017.

[7] M. Como, *Statics of Historic Masonry Constructions*, Springer Berlin Heidelberg, 2013.

[8] A. Anthoine, *In-plane behaviour of masonry: A literature review*. Report EUR 13840 EN, Comission of the European Communities, JRC - Institute for Safety Technology, Ispra, Italy, 1992.

[9] F. Parisi, N. Augenti, Evolutionary strength domains of unreinforced masonry spandrel panels including strain softening, *In: Proceedings of the 9th Pacific conference on earthquake engineering, April 14–16,* Auckland, New Zealand, 2011.

[10] A. Formisano, P. Di Feo, M.R. Grippa, G. Florio, L'Aquila earthquake: A survey in the historical centre of Castelvecchio Subequo. *COST ACTION C26: Urban Habitat Constructions under Catastrophic Events - Proceedings of the Final Conference*, pp. 371-376, 2010.

[11] V. Gattulli, E. Antonacci, F. Vestroni, Field observations and failure analysis of the Basilica S. Maria di Collemaggio after the 2009 L'Aquila earthquake, *Engineering Failure Analysis* 34, 715–734, 2014.

[12] J. Leite, P.B. Lourenco, J.M. Ingham, Statistical Assessment of Damage to Churches Affected by the 2010 – 2011 Canterbury (New Zealand) Earthquake Sequence, *Journal of Earthquake Engineering* 17, 73–97, 2017

[13] G. Milani, M. Valente, Comparative pushover and limit analyses on seven masonry churches damaged by the 2012 Emilia-Romagna (Italy) seismic events: Possibilities of non-linear finite elements compared with pre-assigned failure mechanisms, *Engineering Failure Analysis*, 129–161, 2015.

[14] M. Valente, G. Barbieri, L. Biolzi, L., Damage assessment of three medieval churches after the 2012 Emilia earthquake, *Bulletin of Earthquake Engineering*,10.1007/s10518-016-0073-7, 2016.

[15] S. Lagomarsino, S. Podestà, Seismic vulnerability of ancient churches: II. Statistical analysis of surveyed data and methods for risk analysis, *Earthquake Spectra* 20, 395–412, 2004.

[16] E. Ramirez, P.B. Lourenco, M. D'Amato, M., Seismic assessment of the Matera Cathedral. *RILEM Bookseries, 18, 11th International Conference on Structural Analysis of Historical Constructions*, Cusco, Perù, 11-13 September 2018, 1346-1354, 2019.

[17] M. D'Amato, R. Gigliotti, R. Laguardia, Comparative seismic assessment of ancient masonry churches. *Frontiers in Built Environment, 5:56*. doi: 10.3389/fbuil.2019.00056, 2019

[18] D. Díaz Fuentes, P. A., Baquedano Julià, M., D'Amato, M. Laterza. Preliminary Seismic Damage Assessment of Mexican Churches after September 2017 Earthquakes. International Journal of Architectural Heritage. https://doi.org/10.1080/15583058.2019.1628323, 2019

[19] S. Lopez, M. D'Amato, L. Ramos, M. Laterza, P. B. Lourenço, Simplified formulation for estimating the main frequencies of ancient masonry churches. *Frontiers in Built Environment, 5:18*. doi: 10.3389/fbuil.2019.00018, 2019

[20] Presidency of Ministers Council, Department of the Civil Protection, *Manual for compilation of the form for survey of the damage to cultural heritage, Churches, MODEL A-DC* (in Italian), (S. Papa, G. Di Pasquale editors), 2013.

[21] M. Betti, M. Vignoli, Numerical assessment of the static and seismic behaviour of the basilica of Santa Maria all'Impruneta (Italy), *Construction and Building Materials* 25 4308–4324, 2011.

[22] F. Clementi, V. GAzzani, M. Poiani, P.A. Mezzapelle, S.Lenci, Seismic assessment of a monumental building through nonlinear analyses of a 3D solid model. Journal of Earthquake Engineering, 2017a.

[23] F. Clementi, A. Pierdicca, A. Formisano, F. Catinari, S. Lenci, Numerical model upgrading of a historical masonry building damaged during the 2016 Italian earthquakes: the case study of the Podestà palace in Montelupone (Italy), *Journal of Civil Structural Health Monitoring* 7 (5), pp. 703-717, 2017b.

[24] A. Formisano, G. Vaiano, F. Fabbrocino, G. Milani, Seismic vulnerability of Italian masonry churches: The case of the Nativity of Blessed Virgin Mary in Stellata of Bondeno, *Journal of Building Engineering* 20, pp. 179-200. DOI: 10.1016/j.jobe.2018.07.017, 2018.

[25] F. Fabbrocino, G. Vaiano, A. Formisano, M. D'Amato, Large scale seismic vulnerability and risk of masonry churches in seismic prone areas: two case study, *Frontiers in Built Environment* 5:102, doi: 10.3389/fbuil.2019.00102, 2019.

[26] M. D'Amato, M. Laterza, D. Diaz Fuentes, Simplified Seismic Analyses of Ancient Churches in Matera's Landscape. *International Journal of Architectural Heritage* 14(1), 119-138, https://doi.org/10.1080/15583058.2018.1511000, 2020.

[27] A. Formisano, Local- and global-scale seismic analyses of historical masonry compounds in San Pio delle Camere (L'Aquila, Italy) *Natural Hazards* 86, 465-487. DOI: 10.1007/s11069-016-2694-1, 2017.

[28] A. Formisano, A. Marzo, A. Simplified and refined methods for seismic vulnerability assessment and retrofitting of an Italian cultural heritage masonry building, *Computers and Structures* 180, 13-26, doi: 10.1016/j.compstruc.2016.07.005, 2017.

[29] A. Formisano, G. Ciccone, A. Mele, Large scale seismic vulnerability and risk evaluation of a masonry churches sample in the historical centre of Naples, *AIP Conference Proceedings*, 1906, art. no. 090003, doi: 10.1063/1.5012360, 2017.

[30] D. D. Fuentes, M. Laterza, M. D'Amato, Seismic Vulnerability and Risk Assessment of Historic Constructions: The Case of Masonry and Adobe Churches in Italy and Chile, *RILEM Bookseries, 18, 11th International Conference on Structural Analysis of Historical Constructions*, Cusco, Perù, 11-13 September 2018, 1127–1137, 2019.

[31] M. Valente, G. Milani, Seismic assessment of historical masonry towers by means of simplified approaches and standard FEM, *Construction and Building Materials*, 74-104, 2016.

[32] D. Diaz Fuentes, *Diseño de herramientas de evaluación del riesgo para la conservación del patrimonio cultural inmueble: Aplicación en dos casos de estudio del norte andino chileno,* Publicaciones Digitales ENCRYM – INAH, Mexico, 2016.

[33] UNDRO, *Natural disasters vulnerability Analysis.* United Nations Disaster Relief Organisation, 1979.

[34] FEMA, *Primer for Design Professionals (FEMA 389),* Department of Homeland Security Emergency Preparedness and Response Directorate, Washington, D.C., 2004.

[35] GNDT (National Group for Earthquakes Defense), *First and second level form for exposure, vulnerability and damage survey (masonry and reinforced concrete)* (in Italian), Rome, 1994.

EURODYN 2020
XI International Conference on Structural Dynamics
M. Papadrakakis, M. Fragiadakis, C. Papadimitriou (eds.)
Athens, Greece, 23–26 November 2020

A MULTIDISCIPLINARY APPROACH FOR THE ASSESSMENT OF THE DYNAMIC AND SEISMIC BEHAVIOUR OF ARCHAEOLOGICAL STRUCTURES IN HIERAPOLIS OF PHRYGIA, TURKEY

F. Lorenzoni[1], M. Salvalaggio[2], M.R. Valluzzi[2*], J. Boaga[1], R. Deiana[2]

[1] University of Padova – Department of Geoscience
Via Gradenigo, 6 35131 Padova, Italy
{filippo.lorenzoni; jacopo.boaga}@unipd.it

[2] University of Padova – Department of Cultural Heritage
Piazza Capitaniato 7, 35139 Padova, Italy
*mariarosa.valluzzi@unipd.it (corresponding author){matteo.salvalaggio; rita.deiana}@unipd.it

Keywords: Non-destructive tests, modal analysis, geophysical prospections, dynamic behavior, seismic assessment, archaeological structures, discrete element method

Abstract. *The knowledge path applied to the conservation of archaeological sites represents a crucial phase with the aim of qualifying materials and structural features, as well as identifying vulnerabilities for the selection of possible interventions. The use of non-destructive testing (NDT) techniques can significantly contribute to understand the overall structural behavior and correctly simulate the response through suitably calibrated numerical models. Archeological ruins often show several vulnerabilities due to the presence of incomplete structures, discontinuities, deterioration, and cumulated damages. In this framework, the paper describes a multidisciplinary approach for the structural assessment and conservation of some incomplete structures in the archeological site of Hierapolis of Phrygia (TR). The region is still nowadays characterized by high seismicity. This study is part of a bigger project consisting of the development of an archaeo-seismic park in Hierapolis. On this site, preserved and visible seismic effects on structures and soils making an educational function for valorization, prevention, and conservation purposes. The applied methodology consists of the execution of structural and geophysical inspections on selected structures (e.g,. Roman Bath complex, Nymphaeum) to experimentally define their dynamic response and characterize soil properties for an accurate simulation of the seismic behavior. Dynamic identification test on structures (with the support of other NDTs), ground penetrating radar (GPR), electrical resistivity tomography (ERT) and seismic prospection methods on soils were applied. The outcomes are used to calibrate and validate numerical models, mainly based on the discrete element method (DEM), able to simulate the dynamic behavior of structures composed by large stone blocks with thin mortar layers or massive multi-leaves freestanding walls, which represent the main structural types in Hierapolis. The study has been used to define an appropriate methodology to choose practical and reliable solutions for inspections and the correct selection of numerical tools for structural analyses and simulations.*

1 INTRODUCTION

Archaeological sites reveal important signs of our culture and history. Nowadays, the structure of ancient buildings appears often incomplete, e.g., lacking of bearing walls and piers, of horizontal components (floor and roofs, vaults and domes), and of mutual connections. Moreover, some monuments with peculiar functions in the past (e.g., amphitheater, nymphaea, temples) were built as relevant massive constructions, whose stability is also jeopardized by local failures, despite their thick sections. All those structures require particular care for their conservation in the current environmental conditions, and present high vulnerability to dynamic actions [1].

In such a context, the archaeological site of Hierapolis of Phrygia (Turkey) is paradigmatic, because: a) it includes a large variability of remains belonging to constructions that had various functions from its foundation as Greco-Roman city (around 3rd century B.C.) up to its abandonment (about the 14th century); b) it extends on a wide area (over 40 hectares) having high seismicity (expected peak ground acceleration PGA=0.4g) [2]. The site has been studied for over seven decades from the Italian Archaeological Mission in Hierapolis (MAIER) [3], that contributed to the excavations and restoration works for its valorization and use. The final aim is to complete the recovering of the whole site to make an archaeo-seismic park, i.e., a site where visitors can appreciate the ruins also in terms of their important seismic history.

In this paper, the results of an integrated multi-disciplinary approach aimed at analyzing the current structural conditions of typical remains in the area are discussed. The research involved the geophysical investigation of soil to identify the current seismic parameters, which integrated a series of structural investigations. They were based on dynamic tests used for the calibration of numerical models able to evaluate the seismic vulnerability and simulate the mechanical behavior under the expected earthquake.

Two categories of constructions were analyzed: (i) massive large travertine block remains (as for the Roman Baths and Latrines); (ii) multi-layer thick masonry structures (as for the Nymphaeum of Apollo and the Martyrion of St. Philip) [4][5][5].

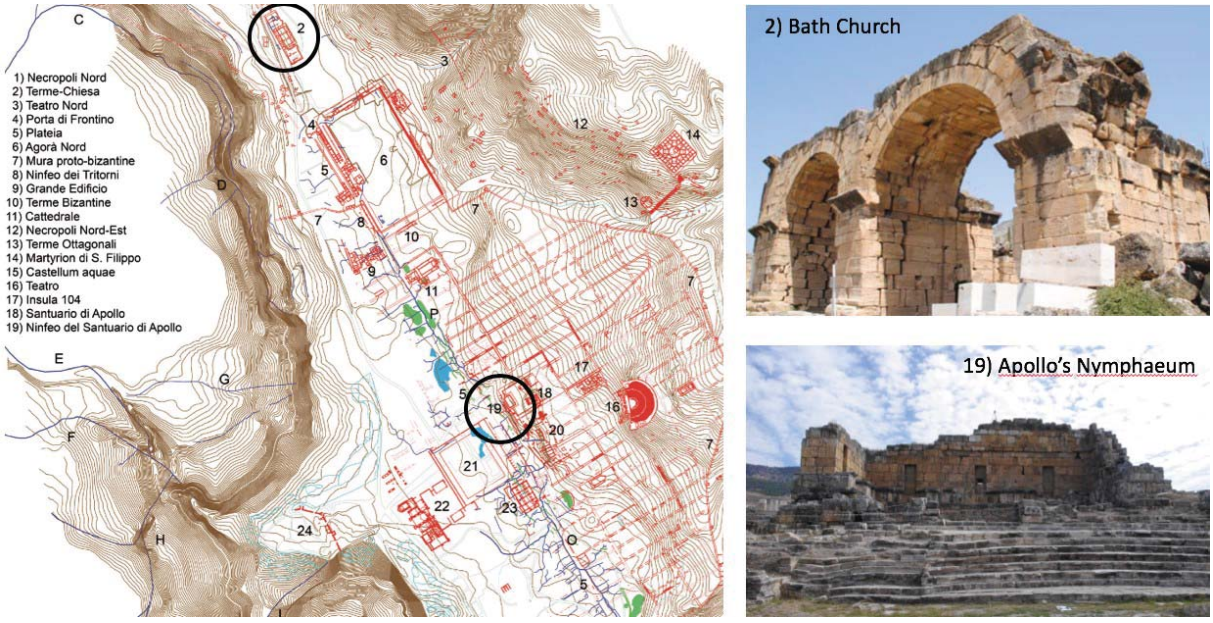

Figure 1: Archaeological chart of Hierapolis (after [7]) with location of two investigated monuments.

2 MATERIALS AND METHODS

Two extensive on-site investigation campaigns were performed by the authors in 2015 and 2018. Structural inspections and geophysical prospections were combined and integrated to assess the quality of building materials and their conservation condition, and to characterize the soil properties of some emblematic monuments in the archaeological site. Onsite testing on structures included visual inspections, critical and structural surveys, dynamic identification tests, sonic pulse velocity test, ground penetrating radar (GPR) applications, and video-endoscopy. Prospections on ground were performed through MASW (multichannel analysis of surface waves) and HVSR (horizontal to vertical spectral ratio) methods, to characterize the seismic properties of soils and identify the possible local amplification of the response during earthquakes. ERT (electrical resistivity tomography) measurements were also performed to support the seismic characterization of soil in its laterally and in-depth variation.

2.1 Geophysical prospections

The use of geophysical measurements in the characterization of soils and in the structure analysis supports since decades geological and engineering studies [8][9][10][11]. In the framework of this multidisciplinary project controlled source seismic refraction, surface wave, passive seismic measurements, as well as ERT and GPR data were collected across the Roman Bath and the Nymphaeum area in front of the Apollo temple, to characterize the shallow soil system. Seismic acquisitions were performed using vertical geophones (4.5 Hz natural frequency) and a Geode system digital seismograph, covering a maximum total array length of 94 m. Table 1 shows the acquisition parameters for the seismic controlled source measurements.

Controlled source seismic prospection	
Instrument	N. 2 Geode digital seismographs
Source	5 kg Sledgehammer on steel plate
Trigger system	Electric circuit
Receivers	24-48 vertical geophones
Receiver spacing	1 - 2 m
Survey length	47 - 94 m
Record length	2 s
Sampling	0.25 ms
Electrical resistivity tomography (ERT)	
Instrument	Iris Syscal Pro 72
Power source	External battery
Electrodes	48
Electrode spacing	1 - 2 m
Survey lenght	47 - 94 m
Stacks	3-6
Time	250 ms
Ground penetrating radar (GPR)	
Instrument	PulseEkko Pro (500 MHz antenna) IDS Ris Hi-Mod Dual frequency (200-600 MHz)

Table 1: Details of controlled-source seismic measurements at Hierapolis.

2.2 Structural investigations

The combination of modal analysis using ambient vibrations on the upper structures and seismometers on the ground demonstrated to be very useful to define the fundamental frequencies and assess possible resonance, local amplification phenomena and soil-structure interactions.

The outcomes of onsite inspections were used to create and calibrate engineering models, i.e. numerical (Finite Element, FE [12][13]) and Discrete Element, DE [14][15]) methods and kinematic limit analyses [16][17], able to assess the global and local seismic vulnerability of the structures.

Ambient vibrations tests (AVT) and output-only identification techniques were performed to identify modal parameters (natural frequencies, damping ratios and mode shapes) of Roman Bath and Apollo's Nymphaeum monuments. A network of accelerometers connected to an acquisition unit was installed in specific points of the two buildings. A preliminary FE model was constructed to analyze mode shapes and select the optimum sensor locations. Tests consisted in acquiring data implementing several setups, over a predetermined period, at a specific sampling rate. Time series acquired at a sampling frequency of 100 Hz were composed by 131'072 points with an overall signal recording duration of 21'51''.

3 RESULTS

The results of geophysical prospections were combined and integrated with ones of the structural investigations. Moreover, the outcomes of inspections on structures were used to calibrate and validate analytical and numerical models, able to simulate the dynamic response and assess the seismic vulnerability of the site monuments. A selection of the analysis carried out for the archaeological remains of Hierapolis are reported hereinafter.

3.1 Soil characterization

Controlled-source seismic surveys were used for both refraction seismic method [18] and surface wave method. The refraction method was used to estimate the 2D structure of the subsoil beneath the monuments and evaluate the velocity of compressional seismic velocities (Vp). The surface method was indeed used to estimate the shear velocities (Vs) characteristic of the first subsoil and the Vs_{30} seismic soil classification for a seismic design (according to Eurocode 8 [19]). The shear seismic wave velocity (Vs) is the most critical parameter for the seismic response analysis [20][19] and it was estimated onsite by the MASW technique [21]. 2D seismic surveys enhanced the lateral variation complexity of the studied subsoil, while Vs surveys showed a progressive improvement of mechanical behaviour of the subsoil in deep, thus highlighting the presence of a shallow thin layer of loose sediment overlying a deep fractured rock. In term of seismic soil characterization, being Vs_{30} = 760 m/s, the site is classifiable as soil B, according to ('Deposits of very dense sand, gravel or very stiff clay, at least several tens of m in thickness, characterized by a gradual increase of mechanical properties with depth') [19]. The passive seismic method allowed evaluating the possible soil resonance frequency behaviour: the results of HVSR [22] analysis were consistent with the previous surveys, indicating a resonance frequency peak of 16 Hz, to be related to a main seismic impedance contrast at 6 m depth. Moreover, the combination of ERT and seismic methods outside the eastern part of the Roman Bath with the GPR measurements provided new information about the fractured system of the soil.

All geophysical methods confirmed the presence of multistep normal faults in the shallow layers around the Roman Bath and the Nymphaeum of Apollo. These information supported the structural analysis with seismic soil classification and geometrical description of the faults system, which is responsible for the structural damage of the buildings still standing in the site.

3.2 Dynamic and structural characterization

Ambient vibration data collected through dynamic identification tests were pre-processed applying a high-pass filter with cut-off frequency of 1 Hz and a decimation of 2 (Nyquist frequency of 25 Hz), with segment length of 1024 points and 66.67% window overlap. System identification was performed using a modal analysis software, implementing a non-parametric frequency domain techniques, i.e., Enhanced Frequency Domain Decomposition (EFDD) [23]. Peaks in the frequency domain related to structural frequencies were selected and the corresponding mode shapes and damping ratios identified.

In the case of the Roman Bath complex, it was rather difficult to excite the structure through ambient vibrations; therefore, an additional external input was necessary. Modal analysis results demonstrated that the structure, despite the high level of damage, is able to show a unitary dynamic response with clear mode shapes (Figure 2). On the contrary, in the case of Apollo's Nymphaeum, it was very difficult to identify a global dynamic response, due to the stiff and rigid walls that composed the building. In this case, the predominant effect of out-of-plane failure of blocks was detected.

All the performed inspections (both visual and instrumental) were used to construct and validate structural models, later used for the seismic assessment.

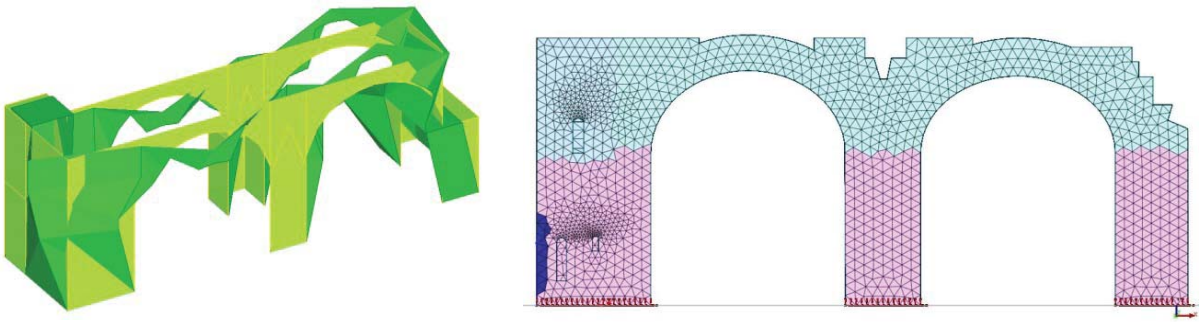

a) b)

Figure 2: Characterization of dynamic response through modal analysis (a) and creation of FEM model (b) of Roman Bath complex.

3.3 Structural and seismic assessment

The structural and seismic assessment of the investigated structures was performed through a combination of local and global analyses, able to simulate their seismic response. Outcomes of in-situ surveys were implemented to validate the adopted behavioral models.

The assessment procedure was performed according to the Italian [24] and European [19] codes. Target spectrum was calculated according to FEMA-368 guidelines, with PGA of 0.33g, average return period Tr=475 years, damping 5%, magnitude Mmin=6.0 and Mmax=7.0, and minimum and maximum distance from the epicenter of 0 and 25 km respectively.

DEM has proven to be an effective tool to simulate the response of structures composed by large blocks of stone connected through thin mortar layers. Blocks can be considered rigid

and displacements lumped at joint interfaces, while seismic behavior is ruled by rocking phenomena rather than structural resistance. The Nymphaeum of Apollo is an extraordinary example of this type of archaeologic remain, made of huge travertine blocks and average 4 m thick wings. Structural survey was limited to external accessible leaves, but allowed to validate previous data and detect some thickness values of top travertine blocks. On this basis, a statistical analysis on unit dimensions was performed [25].

The DE model was generated in 3DEC environment [26] (Figure 3.a). The structure was discretized by means of rigid block through the automatic generation of joints tool, on the basis of the statistical distribution, assuming that inner infill has a composition similar to external leaves. Linear and nonlinear properties were lumped at the interfaces, characterized according to [27], on the basis of calibration results of a preliminary FE model [28].

Nonlinear dynamic time-histories analyses were performed. Artificial time-histories of 25 s length were generated from the elastic spectrum, according to [19], and final deformed configurations were observed at progressive levels of PGA. Results showed that up to about 0.5g no significant damage occur (Figure 3.b). At about 0.75g, some blocks shift from the original positions, leaving small gaps in the interfaces (Figure 3.c); this is best observable in the intersection of North and East walls. The simulation at extremely high PGA levels (e.g., from 1g to 1.25g) show the partial collapse of the outward portion of North wing and of the end of West one (Figure 3.d, e). This provided a qualitative approximation of possible failure modes. Major response is due to out-of-plane mechanism, as detected by experimental mode shapes.

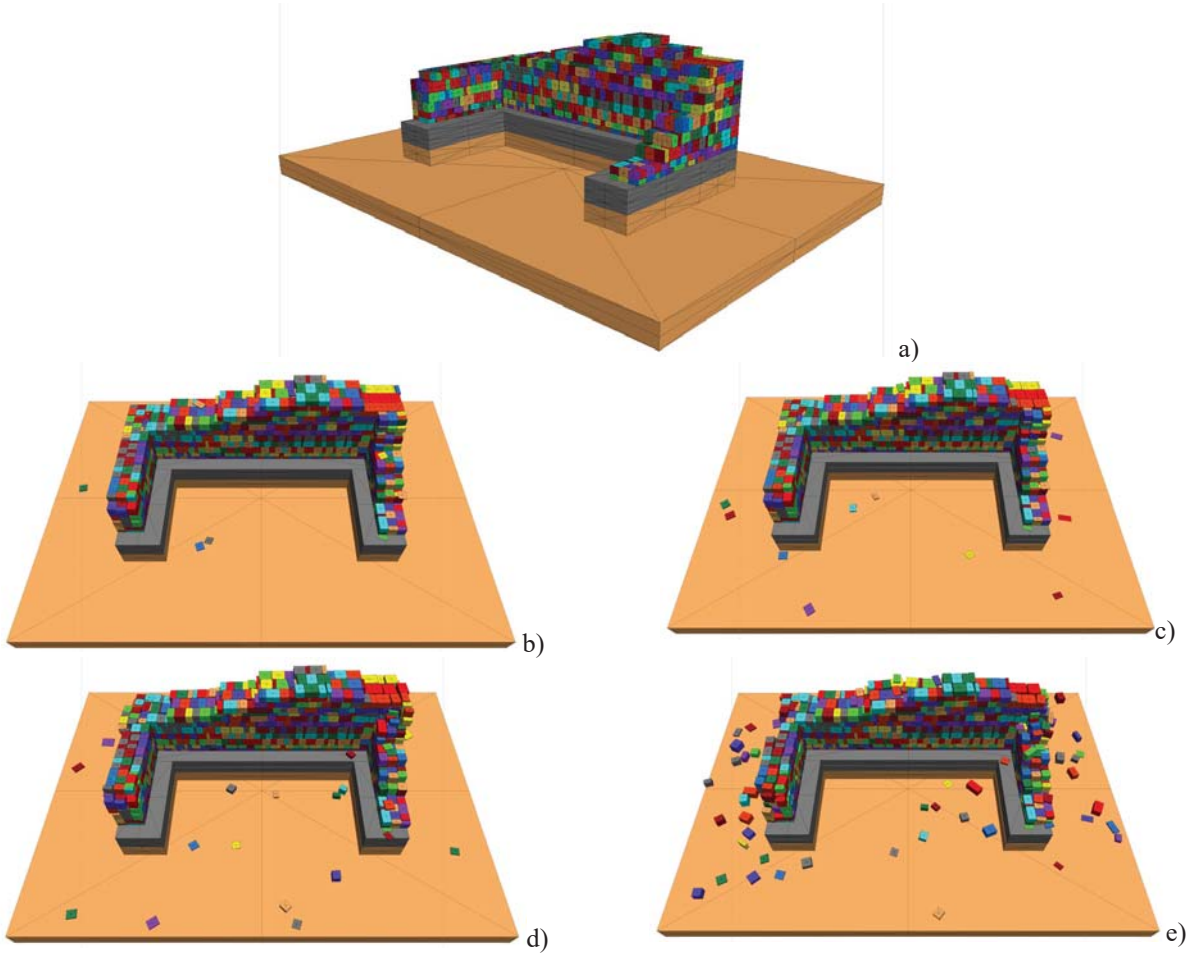

Figure 3: DE model of Nymphaeum of Apollo (a) and final configuration of time-histories analyses for increasing PGAs: 0.50g (b), 0.75g (c), 1.00g (d), 1.25g (e).

4 CONCLUSIONS

The paper presented an integrated methodology for the assessment of archaeological structures in Hierapolis of Phrygia (Tukey). Structural inspections and geophysical prospections on selected structures were used to experimentally define the dynamic response and characterize the soil properties for a reliable simulation of their seismic behavior. On one hand, dynamic tests were able to identify modal parameters and assess the response (thus determining whether or not the buildings show a unitary behavior, despite the high level of damage). On the other hand, indirect information on soil properties and foundations supported the structural analysis with seismic soil classification and geometrical description of the shallow faults system.

Test results were implemented to calibrate and validate numerical models, i.e., a combined modeling approach involving FE and DE methods. DEM was particularly suitable to perform dynamic simulations, as the typical monumental structures in the site are made of large stone blocks with thin mortar layers or massive multi-leaves freestanding walls.

This study could represent a basis to define appropriate procedures to choose practical and reliable solutions for inspections and the correct selection of numerical tools for structural analyses and simulations of incomplete structures in archaeological sites.

ACKNOWLEDGMENTS

This work was supported by the Italian Ministry of University and Research (MIUR) programme PRIN 2015 “Archeology of urban landscapes in Asia Minor between late Hellenism and Byzantine age. Multidisciplinary approaches to the study of Hierapolis in Phrygia” (PI G. Semeraro, University of Salento; local coordinator M.R. Valluzzi, University of Padova).

REFERENCES

[1] N.N. Ambraseys, Earthquakes and Archaeology, *Journal of Archaeological Science* 33, 1008-1016, 2006.

[2] P. L. Hancock, E. Altunel, Faulted Archaeological Relics at Hierapolis (Pamukkale), Turkey, *Journal of Geodynamics*, 24, 21–36, 1997.

[3] F. D’Andria, Hierapolis of Phrygia: its Evolution in Hellenistic and Roman Times, in: D. Parrish (ed.), *JRA supp. 45*, 96–115, 2001.

[4] P. Mighetto, F. Galvagno, Le Terme-Chiesa e la Sfida della Conservazione dei Segni dell’attività Sismica: i Primi Interventi di Messa in Sicurezza e di Consolidamento del Complesso Monumentale, in: F. D’Andria, M. P. Caggia, T. Ismaelli (eds.), *Hierapolis di Frigia V - Le attività delle campagne di scavo e restauro 2004-2006*, Istanbul, 2012. (In Italian).

[5] L. Campagna, N. Sulfaro, C. Terranova, Nuove Ricerche al Ninfeo del Santuaro di Apollo, in: F. D’Andria, M. P. Caggia, T. Ismaelli (eds.), *Hierapolis di Frigia VIII - Le attività delle campagne di scavo e restauro 2007-2011*, Istanbul, 2016 (In Italian).

[6] M.R. Valluzzi, C. Marson, S. Taffarel, M. Salvalaggio, R. Deiana, J. Boaga, Structural Investigations and Modelling of Seismic Behaviour on Ruins in the Monumental Area

of Hierapolis of Phrygia, in: Aguilar R., Torrealva D., Moreira S., Pando M.A., Ramos L.F. (eds), *Structural Analysis of Historical Constructions. An Interdisciplinary Approach*. RILEM Bookseries, 18, 1849–1857, 2019.

[7] G. Scardozzi (ed.), *Nuovo Atlante di Hierapolis di Frigia. Cartografia Archeologica della Città e delle Necropoli*, Istanbul, 2015 (In Italian).

[8] P.M. Soupios, P. Georgakopoulos, N. Papadopoulos, V. Saltas, A. Andreadakis, F. Vallianatos, A. Sarris, J.P. Makris, Use of Engineering Geophysics to Investigate a Site for a Building Foundation, *Journal of Geophysics and Engineering*, 4, 94–103, 2007.

[9] M.H. Loke, Electrical Imaging Surveys for Environmental and Engineering Studies: A practical guide to 2-D and 3-D surveys, Malaysia, 1999.

[10] E. Cardarelli, G. De Donno, I. Oliveti, C. Scatigno, Three-dimensional Reconstruction of a Masonry Building Through Electrical and Seismic Tomography Validated by Biological Analyses, *Near Surface Geophysics*, 16, 2018.

[11] M.R. Valluzzi, F. Lorenzoni, R. Deiana, S. Taffarel, C. Modena, Non-destructive Investigations for Structural Qualification of the Sarno Baths, Pompeii. *Journal of Cultural Heritage*, 201940, 280-287, 2019.

[12] P.B. Lourenço, Computations of Historical Masonry Constructions, *Prog. Struct. Eng. Mater.*, 4, 301-319, 2002.

[13] A. Elyamani, P. Roca, O. Caselles, J. Clapes, Seismic Safety Assessment of Historical Structures using Updated Numerical Models: The case of Mallorca cathedral in Spain, *Engineering Failure Analysis*, 74, 54-79, 2017.

[14] J.V. Lemos, Discrete Element Modeling of Masonry Structures. *International Journal of Architectural Heritage*, 1, 190–213, 2007.

[15] A. Mordanova, G. de Felice, Seismic Assessment of Archaeological Heritage Using Discrete Element Method, *International Journal of Architectural Heritage*, 2018.

[16] R. Aguilar, R. Marques, K. Sovero, C. Martel, F. Trujillano, R. Boroschek, Investigations on the Structural Behaviour of Archaeological Heritage in Peru: from Survey to Seismic Assessment, *Engineering Structures*, 95, 94-111, 2015.

[17] E. Di Miceli, G. Monti, V. Bianco, M.G. Filetici, Assessment and Improvement of the Seismic Safety of the "Bastione Farnesiano" in the Central Archeological Area of Rome: a Calculation Method between need to Preserve and Uncertainties, *International Journal of Architectural Heritage*, 11, 198-218, 2017.

[18] D. Palmer, Refraction Seismics. The Lateral Resolution of Structure and Seismic Velocity, *Geophysical Press*, 1986.

[19] CEN, Eurocode 8 – Design of Structures for Earthquake Resistance. Part 1: General Rules, Seismic Actions and Rules for Buildings, 2004.

[20] J. Boaga, An Efficient Tool for Cultural Heritage Seismic Soil Classification: FTAN Method in Venice Historical Centre and its Lagoon (Italia), *Geosciences Journal*, 17, 2013.

[21] C.B. Park, R.D. Miller, J. Xia, Multichannel Analysis of Surface Waves, *Geophysics*, 64, 800–808, 1999.

[22] M. Nogoshi, T. Igarashi, On the Amplitude Characteristics of Microtremor (Part 2), *Jour. Seism. Soc. Japan*, 24, 26-40, 1971 (in Japanese with English abstract).

[23] R. Brincker, C. Ventura, P. Andersen, Damping Estimation by Frequency Domain Decomposition*, Proc. of the IMAC 19, International Modal Analysis Conference*, USA, 2001.

[24] Cons. Sup. LL. PP., Circolare 2 febbraio 2009, n. 617, Istruzioni per l'Applicazione delle « Norme Tecniche per le Costruzioni » di cui al D.M. 14/01/2008 G.U. del 26/02/2009 n. 47, supplemento ordinario n. 27/2009 (In Italian).

[25] J. Kim, Assessment of the Dynamic Behaviour of Masonry Structures with Advanced 3D Discrete Element Code. SAHC Master Thesis, University of Padova, Italy, 2018.

[26] Itasca, 3DEC - Three-dimensional Distinct Element Code. Version 5. Minneapolis, MN: Itasca Consulting Group, 2012.

[27] M.J. DeJong, Seismic Assessment Strategies for Masonry Structures, PhD Thesis, MIT, 2009.

[28] TNO, DIANA FEA 10.2, Delft, 2017.

EURODYN 2020
XI International Conference on Structural Dynamics
M. Papadrakakis, M. Fragiadakis, C. Papadimitriou (eds.)
Athens, Greece, 23–26 November 2020

VALIDATION OF A STRUCTURAL MODEL OF A LARGE TIMBER TRUSS WITH SLOTTED-IN STEEL PLATES AND DOWELS

Pierre Landel[1,2] **and Andreas Linderholt**[2]

[1]Research Institutes of Sweden
e-mail: pierre.landel@ri.se

[2]Linnaeus University Sweden
e-mail: {pierre.landel, andreas.linderholt}@lnu.se

Keywords: Glued-Laminated-Timber (Glulam) truss, slotted-in steel plates and dowels connection, experimental and numerical modal analysis, stiffness, damping, induced vibrations in timber structure.

Abstract. *The dynamic response to time varying loads, e.g. wind loads or earthquakes, is in many cases decisive when designing a tall timber building. The structural parameters governing the dynamic behaviour are the mass, the damping and the stiffness. The last two parameters are not well-known at serviceability levels for timber structures in general and for timber connections specifically. Results from forced vibration tests on single components and on a full-scale truss for an eight-storey residential building have been analyzed. In parallel, a detailed Finite Element (FE) model of a large Glulam truss with slotted-in steel plates and dowels connections has been developed and simulations have been made. The damping caused by the structural components, the embedment of fasteners and friction of mating surfaces of components in the selected connection types is quantified experimentally. The materials' stiffness values in the model were evaluated. The results from this study bring knowledge on the structural dynamic properties of large timber structures with mechanical connections and will facilitate the performance prediction of new tall timber buildings for better comfort at higher levels in environmentally friendly expansions of our cities.*

1 INTRODUCTION

Tall timber buildings are becoming more common due to their environmental benefits and low weights. Large engineered wood products such as Glulam members or Cross-Laminated-Timber plates are often used. For instance, the largest column of the 18-storey Mjøstårnet in Norway, is made of glued spruce lumbers and has a cross sectional area equal to 625 x 1485 mm^2. To assemble the structural elements, slotted-in steel plates and dowels are used [1]. This connection technique has traditionally been used in long-span bridges and roof structures. Moreover, the density and the modulus of elasticity of the wood material are well known; they are lower than the corresponding values for steel and concrete. When the height of timber buildings rises in cities around the world, new types of challenges appear for structural designers. One of them is wind-induced vibrations which appears to be annoying for the occupants at lower heights for buildings made of timber than for traditional high-rise buildings [2]. Mass, stiffness and damping matrices (denoted M, K and C) need to be fairly well known to accurately predict responses of structures subjected to time varying excitations. For tall timber buildings, it is relevant to analyze the accuracy of the mass and stiffness matrices used by structural designers in FE-analysis for serviceability load levels. Unfortunately, some dynamical properties of large timber structures are not well known [2]. The damping is the least known dynamical property and recently started research projects aim to close the knowledge gap through ambient vibration tests [3, 4, 5] and forced vibration tests of tall timber buildings [6].

The load distribution in timber structures depends on the stiffness of the structural elements and the stiffness of the connections. Glulam structures are usually modeled as beam elements with well-known stiffness but the load distribution in connections with multiple fasteners is uncertain. The joints are often modelled either with constrains in displacement and rotation, i.e. clamped, or only with constrains in displacement, i.e. pinned [1]. Most connections in Glulam structures consist of many steel dowels and several slotted-in steel plates in parallel. However, most of the experimental and numerical studies have been performed on single dowel connections. Building design codes for timber structures propose simple parameters to evaluate the slip of single connections, e.g. [7] and [8] but better slip models for connections with multiple fasteners and several shear planes are needed [9]. Wood is a complex material to model: high orthotropy, inhomogeneities at different scales and large variability, and this must be considered when predicting the embedment between timber and steel [10]. Phenomenological models for embedment have recently been developed based on the beam on foundation approach [11], with elastic and plastic foundation modulus [12]. Such material models are suitable for beam element models to predict deformations and load capacity. Constitutive models with non-linear material stiffness and embedment stiffness with criteria for yielding and softening [13, 14, 15] have also been developed recently and they are applicable to solid FE-models mainly to predict load capacity but not focusing on the deformations at serviceability levels.

Damping in timber structures has mainly been studied experimentally through cyclic tests, representing seismic load histories, on single components or large structures [16], but not much through vibrational tests to assess the damping at serviceability levels [17]. Standard values of the critical viscous damping ratio are set to 1 % and 1.5 % for timber bridges without respectively with mechanical connections when designed for pedestrian induced vibrations [18].

2 FORCED VIBRATION TESTS ON A LARGE TIMBER TRUSS

2.1 The Glulam truss

A truss made of Glulam members assembled with slotted-in steel plates and dowels connections has been vibrational tested in the factory where it was manufactured, in Töreboda, Sweden. It has 14 Glulam members of quality GL30c according to [19], an overall height of 18.5 m and a width of 4.3 m. It is now part of the lateral stabilizing timber structure of a six-storey residential building and it stands up on a concrete foundation to prevent the building from collapse in case of strong winds. The short elements, diagonals and beams have a rectangular cross-section of 215 x 360 mm. The first column has a rectangular cross-section of 215 x 540 mm. The second column is composed of a similar cross-section glued with 90 x 215 members on each side to form a T-shaped cross-section. Holes, cutting and details for the Glulam members were made with a CNC-machine. The steel plates and the dowels are made of S355JO steel quality. The plates are 8 mm thick and weight between 8 and 37 kg. The dowels are 12 mm in diameter and have a length of 210 mm. Each connection has two steel plates and 8 to 45 dowels hammered in each timber member. In total there are 650 dowels and 28 steel plates in the truss. Heavy steel feet with welded 8 mm plates, weighting 88 and 106 kg, are mounted with dowels at the end of both columns. The overall weight of the Glulam truss including the steel elements is 4280 kg and the densities of the timber members have been measured and the mean density was evaluated to 426.8 kg/m^3.

2.2 The vibration test

When the truss was assembled, forced vibrations tests (FVT) were made at the factory. With overhead cranes, the truss was lifted from the ground with lift straps placed close to the center of gravity of the truss, see figure 1. Excitations were made in different directions on and close to the steel foot of the lower column (bottom end) with a short-sledge impulse hammer. During the tests, fourteen tri-axial piezo electrical accelerometers at the center of each truss connection and twelve single axial accelerometers on the middle of the short Glulam elements were used. The accelerometers, with a sensitivity of 100 mV/g ($\pm$ 10 %), were glued on one side of the Glulam members. The data were recorded with an LMS data acquisition system with 56 input channels that measured 50 accelerations in the X- Y- or Z-directions, see figure 1, and the excitation force from the impulse hammer.

Further information on the Glulam truss properties and details of the vibration test performed are available in paper [20].

3 A NUMERICAL MODEL OF THE LARGE TIMBER TRUSS

3.1 The 3D FE-model with solid elements

The Glulam truss has been modeled, as an FE-model, to numerically evaluate the structural dynamic properties and compare them with the experimental results. The model was developed using the pre- and post-processor MSC Simxpert and analyzed with the FE-solver MSC Nastran. The model consists of 1 726 778 eight-noded solid elements (CHEXA) and 523 961 six-noded solid elements (CPENTA) with a total of 2 715 641 nodes. Different element sizes have been used with densified meshes around details such as the holes for the dowels in the timber members and the steel parts and coarser meshes in areas without complexity, see figure 2. To ensure continuity between solid elements from the same part but with non-congruent meshes, contact constraints paired and permanently glued slaves contact bodies to masters contact bod-

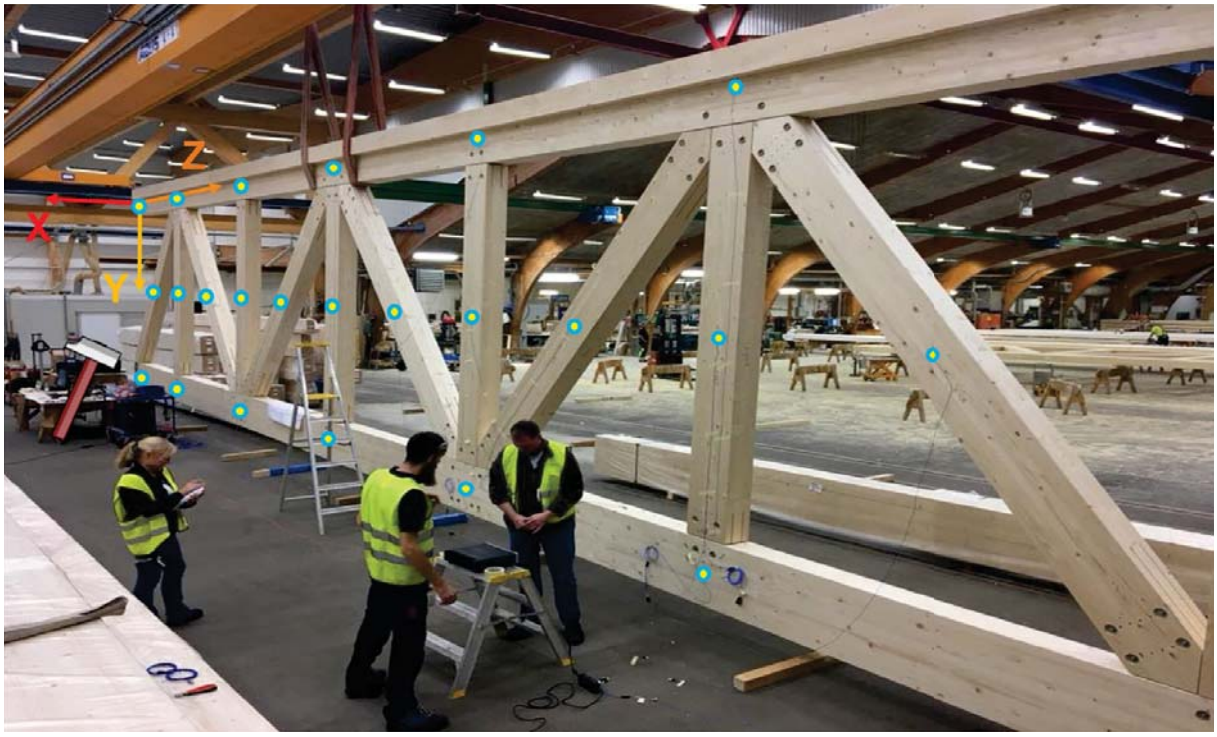

Figure 1: The Glulam truss during a forced vibration test.

Modulus of elasticity parallel to the fiber direction	Modulus of elasticity perpendicular to the fiber	Shear modulus in the 0,90-plane	Shear modulus in the 90,90-plane	Poisson's ratios
$E_0 \in [10.5, 11.8]$ in GPa	E_{90} = 300 MPa	$G_{0,90}$ = 650 MPa	$G_{90,90}$ = 65 MPa	$\nu_{0,90}$ = 0.5
				$\nu_{90,90}$ = 0.2
acc. to [20]	acc. to [19]	acc. to [19]	acc. to [19]	acc. to [21]

Table 1: The material properties used in the FE-models of the Glulam members.

ies with non-congruent meshes. Permanent glue contacts constrained parts of different material together, i.e. timber member to dowel and dowel to steel plates. The MSC Nastran node-to-segment contact method has been used and it created multi-point constraint equations among the nodes from a slave body which met the surface of a master body. Then, the augmented Lagrange multiplier method was used to embed constraints into the modal analysis.

Steel parts were modeled using an isotropic material model with a Young's modulus of 210 GPa, a Poisson's ratio of 0.3 and a density of 7850 kg/m^3. The Glulam members were modeled using an orthotropic material model with the six stiffness parameters presented in Table 1.

Two spring elements representing the hoisting loops were attached to the ground and to several points of the upper timber column with an interpolation constraint element (RBE3). The RBE3 elements defined the motion at a reference grid point as the weighted average of the motions at a set of other grid points. The axial stiffness of the springs was calibrated to match the natural frequency of the global bouncing mode in the Y-direction from the experimental results.

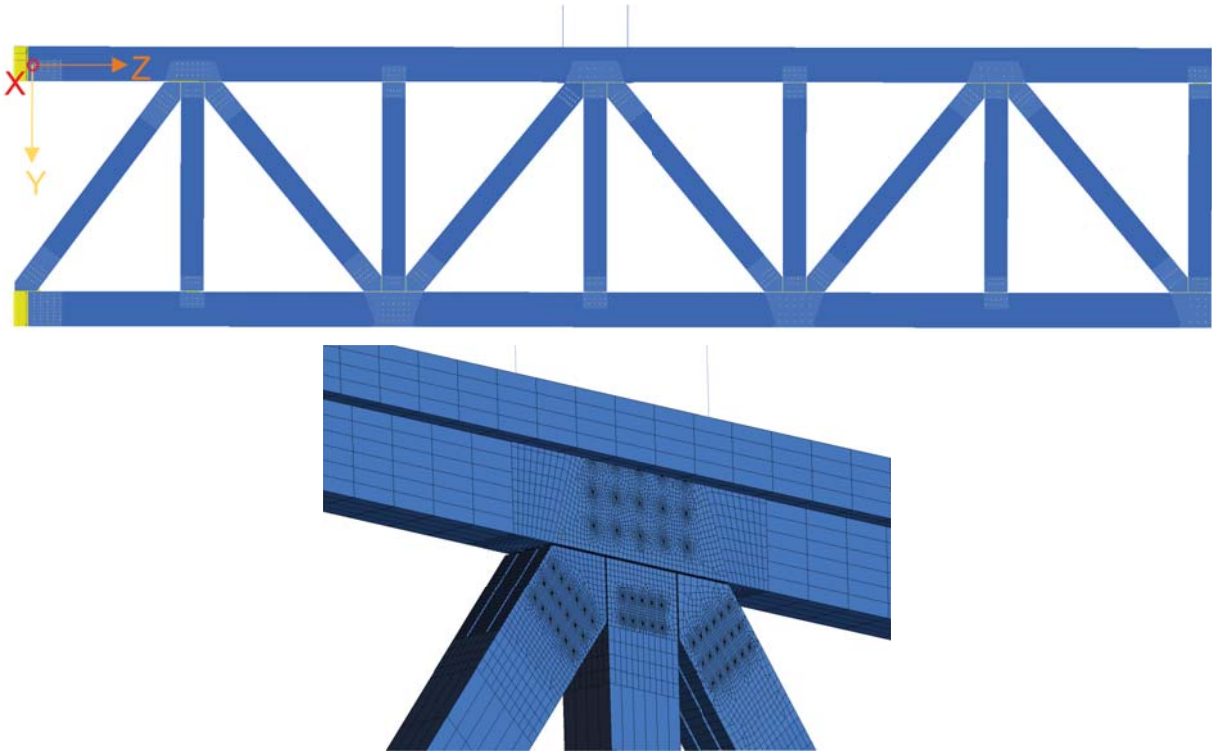

Figure 2: a) the FE-model representing the truss and b) the meshing details of the top-middle connection.

3.2 The numerical analysis

In a structural dynamic system without damping, the vectors of displacement, u, and acceleration, $\ddot{u}$, are related to the mass matrix $[M]$, the stiffness matrix $[K]$ and the excitation force vector, p, according to the equation of motion:

$$[M]\ddot{u} + [K]u = p \tag{1}$$

The eigenfrequencies and eigenmode shapes of the model were extracted using the normal mode analysis in MSC Nastran implementing the block shifted Lanczos eigenvalue extraction method. The numerical mode shapes with very low displacement out of the plane of the truss, which is the structurally operational plane, and with eigenfrequencies between 5 and 130 Hz were investigated.

4 COMPARISON AND DISCUSSION

During the FVT, five eigenmodes corresponding to motion in the plane of the truss and with eigenfrequencies between 5 Hz and 100 Hz were identified and their corresponding mode shapes and damping values were extracted. From the numerical analysis, 23 in-plane eigenmodes were calculated. Modal Assurance Criterion (MAC) values comparing the experimental modes shapes Φ_r^X, stemming from modal testing, to the analytical mode shapes Φ_s^A, stemming from the FE-analysis, are calculated according to equation 2 and are presented in the matrix in figure 3.

$$MAC_{r,s} = \frac{(\Phi_r^{X^T} \Phi_s^A)^2}{\Phi_r^{X^T} \Phi_r^X \Phi_s^{A^T} \Phi_s^A} \tag{2}$$

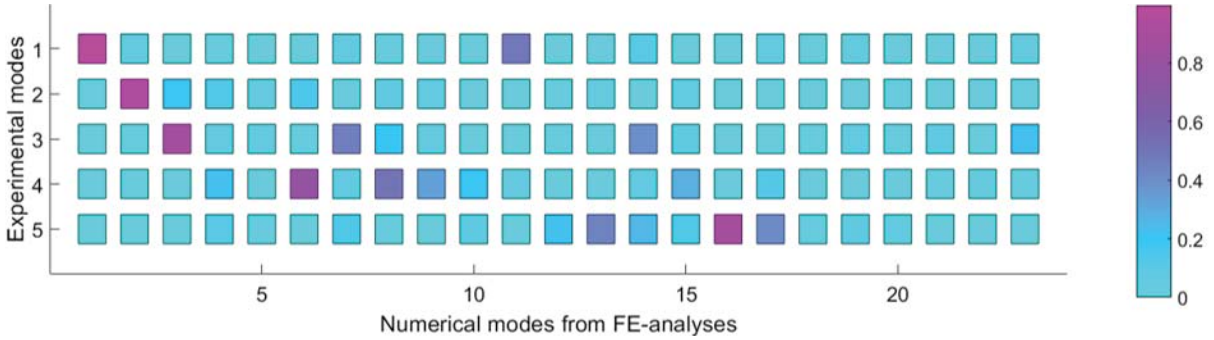

Figure 3: A representation of the MAC matrix comparing experimental mode shapes to numerical mode shapes.

According to the MAC values, five numerical modes (mode 1, 2, 3, 6 and 16) have high consistency with the five experimental modes ; their MAC values are between 0.88 and 0.99. Table 2 presents graphical representations of the mode shapes, the eigenfrequencies, the experimental damping and the MAC values of the paired eigenmodes. The numerical eigenmode 2 corresponds to a local motion of the end of the pillar and matches in both eigenfrequency and shape the paired experimental eigenmode 2. The numerical eigenmodes 3, 6 and 16 are stiffer and have eigenfrequencies 10 % higher than their experimental counterparts. These modes are global bending vibration modes and are of interest when investigating structural timber trusses aimed for stabilization against lateral forces e.g. wind loads. The total mass of the glulam and the stiffness of the single elements are correct at a global scale. At a smaller scale, slightly lower than the diameter of the dowels, timber presents large variability in the density and in the orthotropic stiffnesses [22]. At this lower scale, the embedment stiffness between timber and dowels is sensitive to the local variations of the modulus of elasticity and the shear modulus. Higher frequencies in the numerical models can signify that this embedment stiffness in the FE-model is overestimated. Linear material model for timber with standard elastic modulus stemming from clear wood testing might not be suitable. Bi-linear material models with a yield criterion for timber friction and gaps between timber and dowels should be considered in FE-models made of solid element to predict the dynamic properties of timber structures. The damping ratios (relative to the critical viscous damping) from the test data of the experimental modes 2, 3, 4 and 5 vary between 0.6 % and 1.0 %. They are lower than the damping ratios of timber floors tested in lab [17] and the standard values for timber bridges [18].

Experimental results	Numerical results
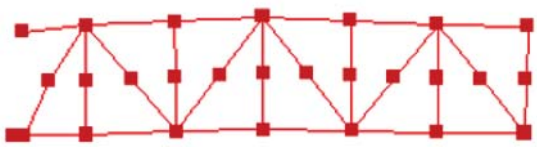	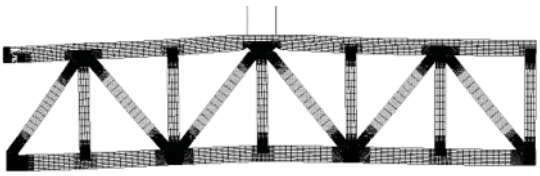
Exp. 1: 8.97 Hz and ζ_1 = 1.7 %	Num. 1: 8.97 Hz (0%) and $\mathrm{MAC}_{1,1} = 0.99$
	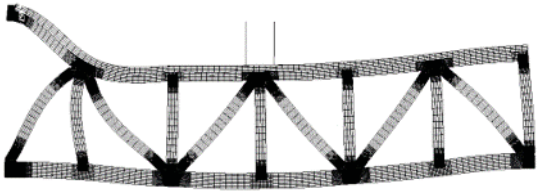
Exp. 2: 25.25 Hz and ζ_2 = 0.9 %	Num. 2: 26.9 Hz (+6%) and $\mathrm{MAC}_{2,2} = 0.99$

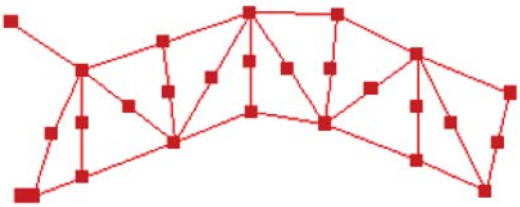	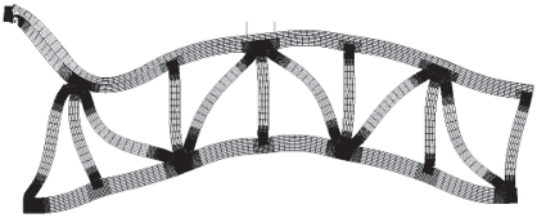
Exp. 3: 42.65 Hz and ζ_3 = 1.0 %	Num. 3: 47.5 Hz (+11%) and $\text{MAC}_{3,3} = 0.97$
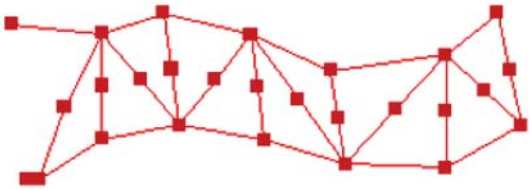	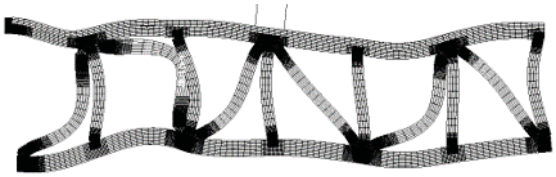
Exp. 4: 61.57 Hz and ζ_4 = 0.6 %	Num. 6: 67.7 Hz (+10%) and $\text{MAC}_{4,6} = 0.88$
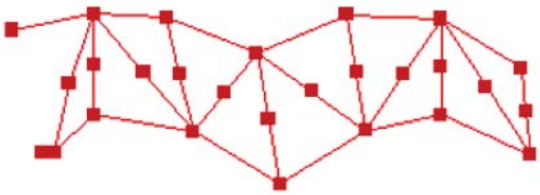	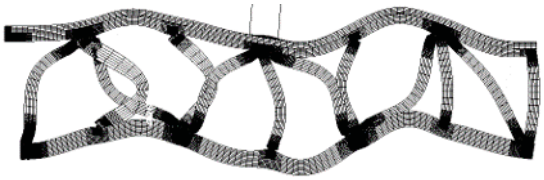
Exp. 5: 92.78 Hz and ζ_5 = 0.7 %	Num. 16: 103 Hz (+11%) and $\text{MAC}_{5,16} = 0.9$

Table 2: Experimental and numerical eigenmodes and their MAC values.

5 CONCLUSIONS

There is still limited knowledge on the stiffness and damping of real timber connections for dynamic loads. This study, comparing modal data measured on a real large structure and modal data from a detailed 3D FE-model, shows the suitability of modal analysis methods. Non-linear embedment stiffness between timber and the dowels is likely to be important and further studies on damping properties in timber structures must be performed to better evaluate the dissipation of energy. The FE-model presented in this article will be further developed and reduced in coming investigations.

6 ACKNOWLEDGEMENT

We would like to express our thanks to Moelven Töreboda AB for the opportunity and the help to measure in their factory while manufacturing had to run with a tight schedule for the building project. The authors gratefully acknowledge the funding for the project “Tall Timber Buildings – concept studies” from Formas the Swedish Research Council for Environment, Agricultural Science and Spatial Planning [Dnr: 942-2015-115].

REFERENCES

[1] Kjell Arne Malo, Rune B Abrahamsen, and Magnus A Bjertnaes. Some structural design issues of the 14-storey timber framed building “Treet” in Norway. *European Journal of Wood and Wood Products*, 74(3):407–424, 2016.

[2] Marie Johansson, Andreas Linderholt, Kirsi Jarnerö, and Pierre Landel. Tall timber buildings - a preliminary study of wind-induced vibrations of a 22-storey building. In *WCTE World Conference on Timber Engineering*, 2016.

[3] Thomas Reynolds, Daniele Casagrande, and Roberto Tomasi. Comparison of multi-storey cross-laminated timber and timber frame buildings by in situ modal analysis. *Construction and Building Materials*, 102:1009–1017, 2016.

[4] Angela Feldmann, Huang Haoyu, Wen-Shao Chang, Richard Harris, Philipp Dietsch, Martin Gräfe, and Carsten Hein. Dynamic properties of tall timber structures under wind-induced vibration. In *WCTE 2016, World Conference on Timber Engineering*, 2016.

[5] Samuel Cuerrier Auclair, Lin Hu, Sylvain Gagnon, and Mohammad Mohammad. Effect of type of lateral load resisting system on the natural frequencies of mid- to high-rise wood buildings. In *WCTE 2018, World Conference on Timber Engineering*, 2018.

[6] Rune Abrahamsen et al. Dynamic response of tall timber buildings under service load - the DYNATTB research program. In *EURODYN 2020, XI International Conference on Structural Dynamics*, 2020.

[7] CEN. Eurocode 5: Design of timber structures – part 1-1: General – common rules and rules for buildings. European Standard EN 1995-1-1, Comité Européen de Normalisation, 2004.

[8] SIA. Timber structures. Swiss Standard SIA 265, Swiss Society of Engineers and Architects, 2012.

[9] Robert Jockwer and André Jorissen. Load-deformation behaviour and stiffness of lateral connections with multiple dowel type fasteners. In *INTER 2018, International Network on Timber Engineering Research*, 2018.

[10] Patrick Racher and Jean-François Bocquet. Non-linear analysis of dowelled timber connections: a new approach for embedding modelling. *Electronic Journal of Structural Engineering*, 5, 2005.

[11] Romain Lemaître, Jean-François Bocquet, Michael Schweigler, and Thomas Bader. Beam-on-foundation modelling as an alternative design method for timber joints with dowel-type fasteners–part 2: Modelling techniques for multiple fastener connections. In *INTER 2019, International Network on Timber Engineering Research*, 2019.

[12] Michael Schweigler, Thomas Bader, Jean-François Bocquet, Romain Lemaître, and Carmen Sandhaas. Embedment test analysis and data in the context of phenomenological modeling for dowelled timber joint design. In *INTER 2019, International Network on Timber Engineering Research*, 2019.

[13] Bo-Han Xu, Mustapha Taazount, Abdelhamid Bouchaïr, and Patrick Racher. Numerical 3d finite element modelling and experimental tests for dowel-type timber joints. *Construction and Building Materials*, 23:3043–3052, 2009.

[14] Luis F. Sirumbal-Zapata, Christian Málaga-Chuquitaype, and Ahmed Y. Elghazouli. A three-dimensional plasticity-damage constitutive model for timber under cyclic loads. *Computers Structures*, 195:47–63, 2018.

[15] Carmen Sandhaas, Ani Khaloian Sarnaghi, and Jan-Willem van de Kuilen. Numerical modelling of timber and timber joints: computational aspects. *Wood Science and Technology*, 54:31–61, 2020.

[16] Mislav Stepinac, Iztok Šušteršič, Igor Gavrić, and Vlatka Rajčić. Seismic design of timber buildings: Highlighted challenges and future trends. *Applied Sciences 10*, 4:1380, 2020.

[17] Nathalie Labonnote, Anders Rønnquist, and Kjell Arne Malo. Prediction of material damping in timber floors, and subsequent evaluation of structural damping. *Materials and Structures 48*, 6:1965–1975, 2015.

[18] CEN. Eurocode 5: Design of timber structures – part 2: Bridges. European Standard EN 1995-2, Comité Européen de Normalisation, 2004.

[19] CEN. Timber structures – glued laminated timber and glued solid timber – requirements. European Standard EN 14080, Comité Européen de Normalisation, 2013.

[20] Pierre Landel, Andreas Linderholt, and Johansson. Marie. Dynamical properties of a large glulam truss for a tall timber building. In *WCTE 2018, World Conference on Timber Engineering*, 2018.

[21] Hans Joachim Blaß and Ireneusz Bejtka. Numerische Berechnung der Tragfähigkeit und der Steifigkeit von querzugverstärkten Verbindungen mit stiftförmigen Verbindungsmitteln (in german). Technical report, Karlsruher Institut für Technologie (KIT), 2008.

[22] Sven Thelandersson and Hans J. Larsen. *Timber engineering*. John Wiley Sons, 2003.

EURODYN 2020
XI International Conference on Structural Dynamics
M. Papadrakakis, M. Fragiadakis, C. Papadimitriou (eds.)
Athens, Greece, 23–26 November 2020

SHEAR STRENGTHENING OF MASONRY PANELS USING A GFRP-REINFORCED MORTAR COATING

G. Castori[1], E. Speranzini[1], M. Corradi[1,2], S. Agnetti[3] and G. Bisciotti[3]

[1] University of Perugia, Dept. of Engineering
Via Duranti 92, 05100, Perugia Italy
e-mail: giulio.castori@unipg.it emanuela.speranzini@unipg.it

[2] Northumbria University, Dept. of Mechanical & Construction Engineering
Wynne-Jones Building, NE1 8ST Newcastle Upon Tyne, United Kingdom
e-mail: marco.corradi@northumbria.ac.uk

[3] Kimia ltd., Ponte Felcino, 06134 Perugia, Italy
e-mail: stefano.agnetti@kimia.it giordano@kimia.it

Keywords: Conservation engineering, Shear walls, Retrofit, Composite materials

Abstract. *The use of new composite materials for reinforcement of heritage masonry structures, especially in seismic prone areas, is of interest structural engineers and conservators. However, the need to increase the structural performance of masonry structures is often in contrast with the principles of conservation in terms of reversibility, limited visual impact, compatibility of new materials with masonry. With the aim at striking a balance between structural safety and heritage protection, this paper investigates strengthening stone and brickwork masonry walls using glass-fiber reinforced polymer (GFRP) meshes embedded into a coating of lime or cement mortar. An experimental research program was undertaken in the laboratory on large-scale wall panels. Both clay brick and stone work specimens were tested, with and without strengthening. Single-sided and double-sided strengthenings were considered, as it is often not practicable to apply the reinforcement to both sides of a wall. Static tests were carried out on twelve masonry panels, under in-plane diagonal shear loading. The mechanisms by which load was carried were observed, varying from the initial, uncracked state, to the final, fully cracked state. The results demonstrate that a significant increase of the in-plane shear capacity of masonry can be achieved by using the proposed retrofitting technique. The experimental data were used to assess the effectiveness of the strengthening, and a finite element (FE) numerical model is discussed and calibrated against experimental results. The FE model was used to investigate further aspects of the reinforced masonry under shear-loading.*

1 INTRODUCTION

The performance of historic and heritage masonry buildings during previous earthquakes in Italy and other parts of Europe has demonstrated that many structural failures could be attributed to inadequate shear capacity of their wall panels [1, 2, 3]. This was particularly serious not only for very old ashlar stone masonry buildings, but also for those buildings, often more recently built, made of brickwork masonry [4]. The use of very weak lime mortar in construction and inadequate construction methods, not fulfilling the so-called "rules of the art" as defined in historic manuals and recent studies constitute the primary reasons for poor performance.

While it is not socially and economically acceptable to demolish these unsafe buildings, it is possible to retrofit them. A large portion of its programmed economic stimulus in Italy is associated with upgrading the building stock through, for instance schemes for improvement of structural safety of old masonry buildings against the seismic loading (Fig. 1). The anticipated cost benefit of lightweight composite reinforcements that can be easily transported and applied without interfering with the use of the buildings, against the conventional steel/concrete, are presented in Table 1. This table also reports the grade of reversibility and compatibility for different traditional and innovative retrofitting methods for shear walls [5, 6].

Reinforcement method	Brickwork masonry	Stone work masonry	Grade of structural efficiency	Reversibility of intervention	Compatibility with masonry
Lime grout injections	Unsuitable	Suitable/ Unsuitable*	High	Low	Good
Deep repointing of mortar joints with lime new mortar	Suitable/ Unsuitable*	Suitable/ Unsuitable*	Low to Medium	High	Very Good
Epoxy-bonded FRP jacketing	Suitable	Suitable	High	Low	Very Low
Reinforced Concrete Jacketing	Suitable	Suitable	Very High	Low	Very Low
FRCM Jacketing	Suitable	Suitable	Medium to High	High	Good

* highly depends on the masonry type, dimensions the mortar joints, if there are internal voids in the shear walls

Table 1: Reinforcement of shear walls: commercially available methods.

During the past two decades applications of Fiber Reinforced Polymer (FRP) products have increased significantly, most notably for seismic retrofitting. Among many beneficial characteristics of FRP materials are light weight, ease of installation, high tensile strength, and immunity to corrosion [7, 8, 9].

With regard to shear walls, it is well known that FRP jackets can provide additional shear capacity, confinement and clamping force within wall leaves, enhancing wall performance especially when stressed by the action of an earthquake. However, serious limitations remain for the use of epoxy adhesives. These resins are typically employed to fix the composite reinforcements to masonry. Their long term behavior, as well their "compatibility" with masonry materials and the limited "reversibility" of these interventions are object of debate in the scientific community [10]. Conservation bodies often do not authorize the use of epoxy-bonded

FRPs on listed masonry buildings and different retrofitting solutions have been recently proposed.

Figure 1: Examples of different methods to retrofit shear walls: a. Epoxy-bonded Carbon FRP, b. Steel mesh reinforced concrete jacketing, c. Grout Injection in the internal core of multi-leaf stone walls.

The most important Italian Conservation Body (*Soprintendenza Archeologia, Belle Arti e Paesaggio*) supervises around 9.66 M heritage items (archeological sites, heritage buildings and museum assets) with a density of about 33.3 items/100 km^2. In Italy, the density of this enormous quantity of assets is much higher in seismic prone areas (Tuscany, Campania, Marche and Umbria have a density of 40, 41, 49 and 53 items/100 km^2, respectively). In this situation, to overcome the limitations of the use of epoxy-bonded reinforcement, the use of inorganic, i.e. lime or cement based, coatings reinforced with composites meshes has been proposed. The final result is a Fiber Reinforced Cementitious Mortar (FRCM) [11, 12, 13]: this can be easily used to create a jacket, to apply to one or both surfaces of the shear walls. Low fire resistance of FRPs is an issue that can be resolved by using FRCMs: composite materials are embedded in the mortar jacketing and this can also protect the reinforcement.

To verify the effectiveness of FRCM reinforcement with respect to real-scale laterally loaded wall panels, to study the structural behaviour of FRCM reinforced members and to investigate some specific aspects of the modelling of shear walls, shear tests on large-scale panels reinforced with FRCM have been performed. The variables considered in this test program included masonry type, single-side and double-side reinforcement, and method of application of the reinforcement (preventive method, i.e. reinforcement applied to un-cracked walls, or repair method, i.e. reinforcement used to repair damaged or cracked shear walls). Combined experimental and analytical research is underway at the Structures Laboratory of the University of Perugia to investigate the effectiveness of FRCM jackets on the seismic performance of shear walls. Some preliminary results on shear walls tested under simulated seismic loading are presented in the paper. Analytical research, leading to a seismic design approach is also presented. Design performance levels are compared with experimentally obtained drift capacities, verifying the applicability of the design procedure.

2 EXPERIMENTAL VALIDATION

2.1 Wall geometry and test method

The specimens in this study are twelve full-scale shear walls, made of solid bricks or ashlar stone blocks. The walls are 1200 x 1200 mm. The nominal thickness of the brick and stone walls was 240 mm. Thus, all the test specimens had been constructed at once by an expert mason at the Structures Laboratory (Lastru) of the University of Perugia, located in Terni, Italy.

a. b.

Figure 2:Realization of full-scale shear walls: a. Solid bricks test specimens, b. shear test setup.

Figure 2 shows the test setup: the shear wall panel is subjected to a diagonal, compressive, in-plane loading and fails by a diagonal shear crack, typically originating from the panel's centroid where the stresses are maximum. A highly strained region is assumed to form in the panel's centre at the crack location.

Hence for a linear elastic membrane under in-plane loading, the plane-stress components σ_{xx}, σ_{xy} and σ_{yy} at the panel's centroid are given by:

$$\sigma_{xx} = \sigma_{yy} = -0.56\frac{F}{A_n}$$
$$\sigma_{xy} = \sigma_{yx} = 1.05\frac{F}{A_n}$$

where F is the diagonal force and A_n is the wall horizontal cross section.

The principal stresses σ_I and σ_{II} are:

$$\sigma_I = 0.50\frac{F}{A_n}$$
$$\sigma_{II} = -1.62\frac{F}{A_n} \quad (2)$$

According to the interpretation provided by the RILEM guidelines (Fig. 3), at failure ($F=F_{max}$), σ_I is equal to the masonry tensile strength f_t:

$$f_t = \sigma_I = 0.50 \frac{F_{max}}{A_n} \tag{3}$$

The masonry shear strength, τ_0, at failure, is then given by:

$$\tau_0 = \frac{f_t}{1.5} \tag{4}$$

The two sides of each wall panel have been labelled with letters A and B. Contact instrumentation (LVDT: Linear Variable Differential Transformers) was used to measure the deformation of the panels along the unloaded (in tension) and loaded (in compression) wall's diagonals. The change in length of the wall's diagonal in compression (Δl_{CSA} and Δl_{CSB} for side A and B of the wall panel, respectively) and in tension (Δl_{TSA} and Δl_{TSB}), are giving the compressive and tension strains as:

$$\begin{aligned} \varepsilon_{CSA} &= \frac{\Delta l_{CSA}}{l_{CSA}} \qquad & \varepsilon_{TSA} &= \frac{\Delta l_{TSA}}{l_{TSA}} \\ \varepsilon_{CSB} &= \frac{\Delta l_{CSB}}{l_{CSB}} \qquad & \varepsilon_{TSA} &= \frac{\Delta l_{TSA}}{l_{TSA}} \end{aligned} \tag{5}$$

where l_{CSA} and l_{CSB} are the gage lengths of the LVDTs applied along the compressed diagonals on side A and B, respectively. Similarly, l_{TSA} and l_{TSB} are the gage lengths for the stretched wall diagonals. Hence, the compressive and tensile axial strains, ε_c and ε_t, and the shear strain, γ, are given by

$$\varepsilon_C = \frac{\varepsilon_{CSA} + \varepsilon_{CSB}}{2} \tag{6}$$

$$\varepsilon_T = \frac{\varepsilon_{TSA} + \varepsilon_{TSB}}{2}$$

$$\gamma = \left|\varepsilon_C\right| + \varepsilon_T \tag{7}$$

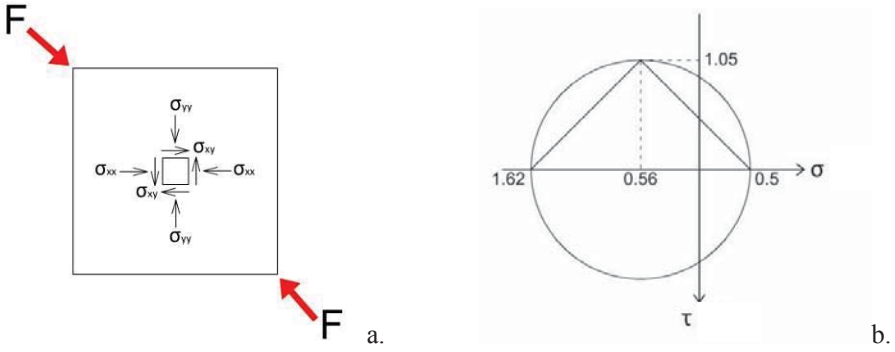

Figure 3: : a. Components of plane stress at panel centroid,
b. Graphical interpretation: Mohr's circle (tangential stress (τ), normal stress (σ)) (units in MPa).

A value of the shear stiffness modulus (G), representative of the cracked condition of the masonry, was calculated starting from the tangential stress (τ) versus angular strain (γ) curve. This was obtained by taking into account the envelope curve of the loading and unloading cycles and by constructing a bilinear curve, with a subtended equivalent-area to the tangential

stress (τ) versus angular strain (γ) curve. The equivalent bilinear curve is made of a horizontal and an inclined lines. The bilinear was calculated using the following procedure:
- The horizontal line of the bilinear was determined starting from the ultimate tension (τ_u) of the load test and ends at the ultimate angular strain (γ_u)
- By imposing energy equality, i.e. the equality between the area (A) underlying the diagram of the envelope curve and that of the bilinear equivalent, the value of the average angular deformation of the panel at the end of the inclined section of the bilinear (γ_y)

$$\gamma_y = 2\left(\gamma_u - \frac{A}{\tau_u}\right) \tag{8}$$

- The slope of the inclined line was thus obtained represents the value of the modulus of shear stiffness G (Fig. 4)

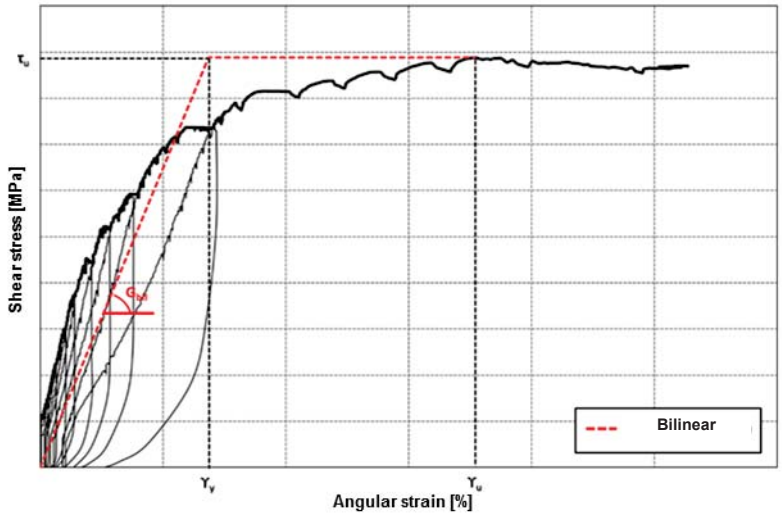

Figure 4: Determination of the shear modulus (G).

	Type of Masonry	Single- or Double side Reinforcement	Mesh Type	Coating Material
MAT-01-U	Brickwork Masonry	-	-	-
MAT-02-D		Double	1	Basic M15
MAT-03-S		Single	1	Basic M15
MAT-04-D		Double	2	Basic M15
MAT-05-S		Single	2	Basic M15
MAT-06-S		Single	1	Betonfix RCA
MAT-07-S		Single	2	Betonfix RCA
PIE-01-U	Stone Masonry	-	-	-
PIE-02-D		Double	1	Basic M15
PIE-03-S		Single	1	Basic M15
PIE-04-D		Double	2	Basic M15
PIE-05-S		Single	2	Basic M15

Table 2: Reinforcement of shear walls: test matrix.

Table 2 shows the test matrix: it can be noted that a total of twelve full-scale wall panels were tested: seven walls were made of solid bricks (MAT-series), while the remaining five (PIE-series) was constituted by ashlar (rubble) calcareous stones. The letter designations U, D and S were used to identify unreinforced, double-sided and single-sided strengthenings, respectively.

2.2 Materials and retrofitting method

A composite grid, made of fiberglass (GFRP), was applied, using an inorganic mortar, to the prepared surface of the wall panels. To connect the two coatings on the wall surfaces, composite connectors were also inserted into holes cut horizontally and transversally into the walls. The composite grids were fully embedded in the mortar coating and were secured in place by fixing them to the composite connectors. The same structural mortar used in the grid application was also employed to fill the holes.

Reinforcement application is not difficult and it can be carried on both uncracked and damaged shear walls. Furthermore, it is worth noting that the proposed retrofitting method can be used as a rapidly deployable emergency repair technique or a long-term and permanent strengthening procedure suitable for seismic protection of heritage buildings. Different methods of applying FRCM composite strengthening systems to the walls were investigated.

		Type 1	Type 2
Mesh	Material	Fiberglass, AR	Fiberglass, AR
	Weight density (dry fiber) (g/m^2)	235	465
	Weight density (pre-preg) (g/m^2)	335	581
	Mesh size (mm)	50 x 50	35 x 30
	Mesh unit uensile strength (kN/m)	63	110
Single Cord	Young's modulus (GPa)	72	72
	Elongation at Failure (%)	3.5	1.5
	Tensile strength (MPa)	1200	1200

AR = Alkali Resistant

Table 3: Two types of fiberglass mesh used for reinforcement: physical and mechanical properties.

Two types of composite grids have been used for shear reinforcement. The main mechanical properties of the GFRP meshes are listed in Table 3. These values are given in the produced data sheet (Kimia ltd., Perugia, Italy). The superficial weight density, and mesh size of Type 1 are 335 g/m^2 (for impregnated, pre-preg, fibres) and 50 x 50 mm, respectively, while higher values characterized the Type 2. A detail of the GFRP meshes are shown in Figures 5 and 6.

Two types of mortars (*Basic M15* and *Betonfix RCA*) were used for the coating (Tab. 2): Both are ready-to-use mortars, having a special fibre-reinforced composition. *Basic M15* is a lime (hydraulic) mortar and the producer (Kimia ltd.) reports in the data sheet a compressive strength > 15 MPa. On opposite *Betonfix RCA* is a cement mortar with a compressive strength > 25 MPa.

Figure 7 and Table 4 show the masonry units (brick and typical stone) and the main mechanical properties.

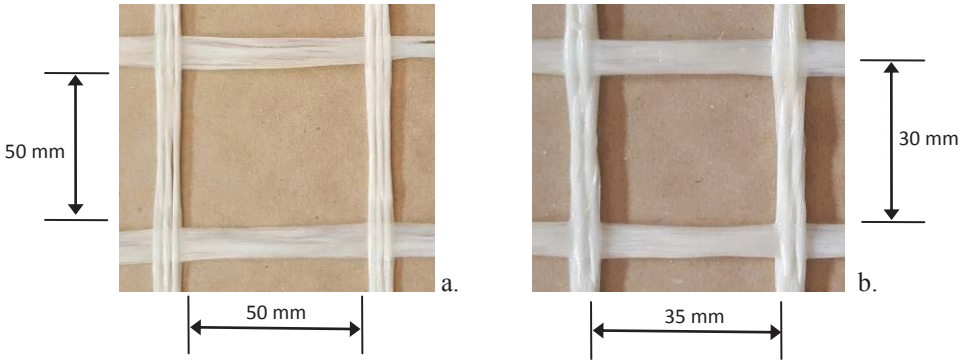

Figure 5: The two types of fiberglass mesh used for reinforcement: a. Type 1, b. Type 2

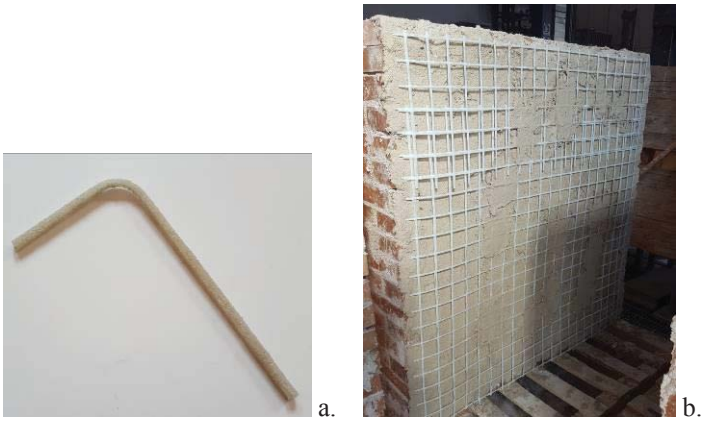

Figure 6: Reinforcement materials and application: a. Fiberglass L-shaped connectors, b. Detail of the mesh reinforcement before the application of the second layer of mortar coating.

Figure 7: a. Used materials for wall construction: Solid bricks (240 x 120 x 55 mm); b. Bonding pattern, c. Ashlar calcareous stone.

Brick	Dimensions (mm)	240 x 120 x 55
	Compressive strength (MPa)	39.00
	Bending strength (MPa)	3.61
Bedding mortar	Compressive strength (MPa)	2.69
	Bending strength (MPa)	0.76

Table 4: Bricks and mortar properties.

2.3 Test results and analysis

Table 5 shows the results in terms of the maximum load F_{max}, masonry tensile strength f_t and shear modulus. A multi-letter designation MAT has been used for brickwork panels, while this was PIE for stone work specimens. A further letter (U = unreinforced, S = single-sided reinforcement, D = double-sided reinforcement) has been adopted to specify the type of reinforcement. All GFRP-reinforcements have been applied to undamaged, sound, wall panels. Ten wall panels were reinforced (6 single-sided reinforcements, and 4 double-sided) with the GFRP grid, applied using a low-cement mortar. Panel 1 in both brickwork (MAT) and stone (PIE) series was the control panel and unreinforced.

	Wall Thickness (mm)	Single- or Double-side Reinforce-ment	F_{max} (kN)	f_t (MPa)	G (MPa)
MAT-01-U	240	-	67.03	0.077	1080
MAT-02-D	291	Double	205.0	0.236	1490
MAT-03-S	260	Single	100.3	0.117	1052
MAT-04-D	297	Double	199.8	0.233	2512
MAT-05-S	270	Single	113.4	0.133	2703
MAT-06-S	267	Single	120.9	0.141	1624
MAT-07-S	265	Single	120.9	0.138	1834
PIE-01-U	245	-	73.80	0.084	2092
PIE-02-D	303	Double	182.3	0.206	2034
PIE-03-S	285	Single	136.1	0.155	954
PIE-04-D	307	Double	209.6	0.242	876
PIE-05-S	293	Single	138.2	0.160	1902

Table 5: Results of shear tests.

For the brickwork panels, the test results show that the increase in the shear load capacity (F_{max}) is nearly three times, for double-sided reinforcement, that of the load capacity without the GFRP composite. However, for single-sided reinforcement, this increment reduced to about 70%, ranging from 49.5 % (MAT-02-D) to 80.5 % (MAT-06-S). The brickwork specimens showed the largest increase in shear capacity. The shear modulus variations were smaller in percentage and more scattered: for single-sided reinforcement, the stiffness of the wall panels increased in a range between -3.6 % and 150%.

Results from the shear tests on stone work panels are also shown in Table 5; they indicate that the average shear capacity of both single- and double-sided reinforced panels was 84 % and 164% stronger than the unreinforced wall panel.

For both brickwork and stone unreinforced panels, the shear load – angular strain curves show a quasi-elastic behaviour with a weak yield plateau: this was mainly caused by the development of a diagonal cracks along the compressed diagonal. The two unreinforced panels (denoted MAT-01-U and PIE-01-U) presented a brittle, zig-zag shaped failure along the compressed diagonal. Cracking appeared suddenly in the mortar joints and, more rarely, in the bricks, producing the instant failure of the masonry walls.

For the reinforced wall panels, shear load – angular strain curves underline two stages of the global behaviour: a first elastic and a second plastic (Figs. 8 and 9). The elastic phase of

the curves of the reinforced panels are characterized by the steeper slope as those of the unreinforced, regardless to the type of the composite reinforcement (Type 1 or Type 2). The load corresponding to the elastic limit and the ultimate load are much higher than that of unreinforced control panels. The gain in strength is quite significant. Thus, a first consequence of the reinforcement is the increase of the shear capacity of the walls. Moreover, it can be also noted an important increase of the post-elastic deformation capability of the reinforced walls, emphasized by the presence of a relevant post-elastic plateau. Because tests were conducted in load stroke-control (and not displacement-control) this is a pseudo-ductility and reader should be alerted about the limitations of the post-peak test data. Figure 10 shows the typical failure modes on both unreinforced and reinforced wall panels.

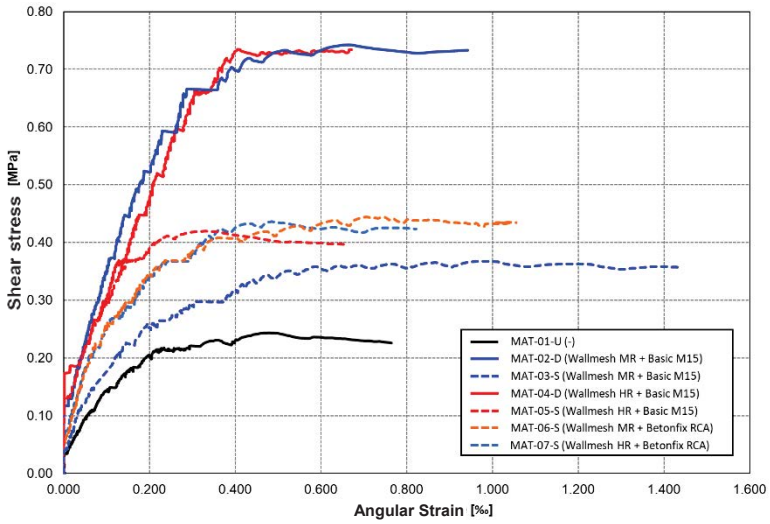

Figure 8: Envelope of the shear stress (τ) versus angular strain (γ) curves for the brickwork panels.

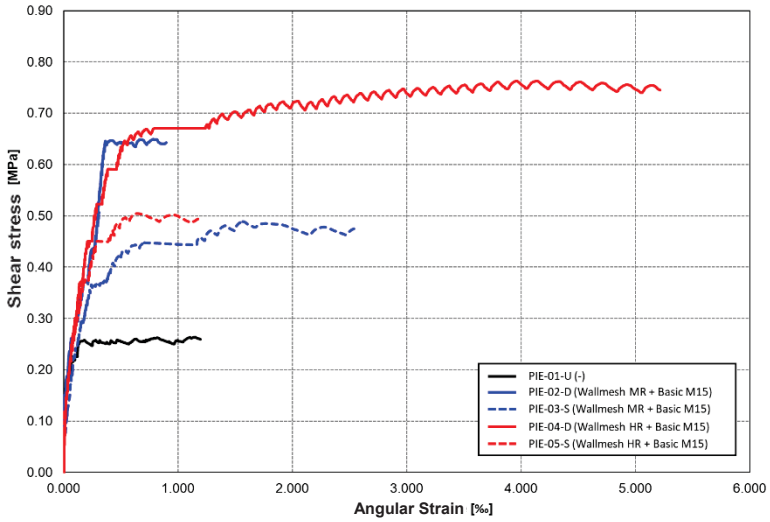

Figure 9: Envelope of the shear stress (τ) versus angular strain (γ) curves for the stone panels.

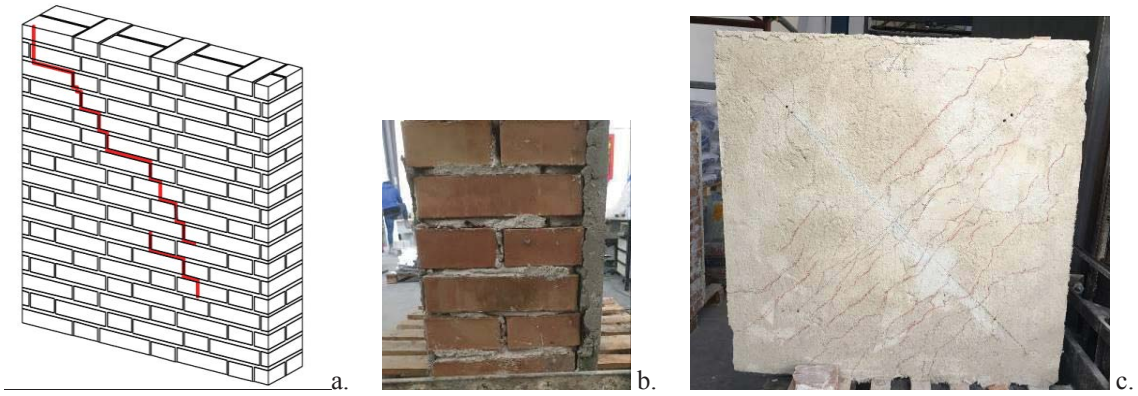

a. b. c.

Figure 10: Failure modes: a. Unreinforced brickwork panel, b. Single-sided reinforced brickwork specimens, c. Shear cracks on the double-sided reinforced wall.

3 NUMERICAL SIMULATION

3.1 FE model

The experimental data were implemented numerically, via non-linear constitutive laws, in a commercial FE modelling code. Accounting for the brickwork masonry nonlinear behavior [14, 15, 16], 3D finite element (FE) models were thus adopted. To this end, after defining their geometry with CAD drawings, the panels were discretized by means of iso-parametric solid elements (Solid 65), having 8 nodes with 3 Degrees of Freedom (DOF) at each node. To facilitate the analysis, the periodically repeating patterns of the brick masonry typology was modelled by dividing each periodic unit cell into ten cuboid subcells (ten brick units, three head and one bed joints) characterized by different material properties (Figure 11).

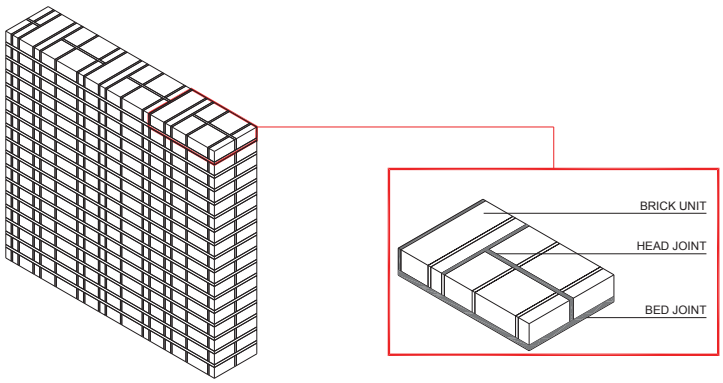

Figure 11: Derivation of periodic unit cell.

Since all units were identically oriented and the masonry layout did not change through the thickness, for convergence checking, each periodic unit cell was then modelled with a sufficient number of elements through the height of each sub-cell. After performing a sensitivity analysis varying the mesh size, the mesh of all FE models was thus refined so as to have three elements (18.33 × 20 × 20 mm) across each brick unit, two elements (18.33 × 20 × 3.33 mm) across each bed joint and a single element (7 × 20 × 20 mm) across each head joint (it is important to remark that in this two latter cases the size of the mesh was dictated by the thickness of the mortar joints).

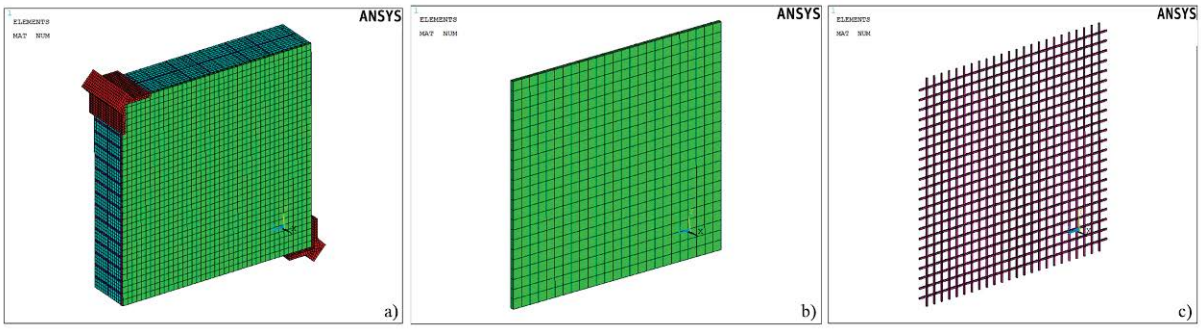

Figure 12: FE model with mesh discretization: a. Reinforced model; b. Mortar coating; c. GFRP mesh.

As for reinforcement, a shared node approach was instead used for simulating the GFRP meshes embedded into the mortar coating. Accordingly, the connection between the mortar matrix and the reinforcement was achieved treating the glass meshes (modelled by means of 2-noded uniaxial tension-compression Link 180 elements) as a slave material, which is merged to the surrounding master material.

This allows to capture the more critical details avoiding distorted meshes as well as shear lock effects. Figure 12 shows the full FE model, which is characterized by 85,642 elements and 90,356 nodes, with 271,068 DOF.

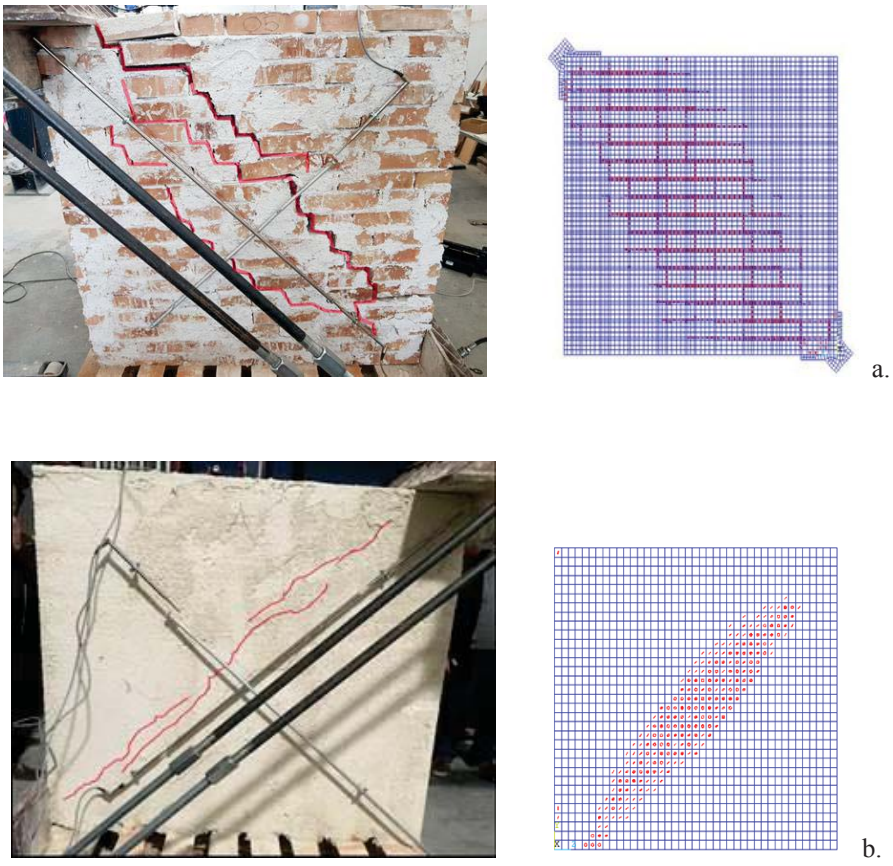

Figure 13. Experimental vs FE model crack pattern: a. Unreinforced face; b. Reinforced face.

To model the behavior of brickwork masonry, a 3d nonlinear analysis was implemented through the use of a damage mechanic approach. Based on this, a tensile cut-off failure criterion was adopted for each masonry component (brick units, bead and head joints). The aforementioned elastic-plastic model, generally used for brittle materials such as concrete, can account for either crushing or cracking failure modes using a smeared model. More specifically, the cracking pattern observed during the damaging process of both bricks and mortar joints was simulated by means of only 2 material parameters (assigned according to the material properties obtained through the experimental tests): compressive (f_c) and tensile (f_t) strength. Moreover, to increase the reliability of the proposed analysis, the simulation of the contacts between the panel and loading plates was performed using unilateral contact interfaces. Accordingly, surface-to-surface contact elements were adopted, determining the contacting properties for the tangent and normal behavior through the use of a trial-and-error procedure. In detail, a Coulomb friction law was used assuming that at each interface sliding may (or may not) occur by introducing a coefficient of friction ($\mu = 0.3$).

3.2 FEA results

According to the aim of simulating the in-plane response of the specimens and therefore providing an interpretation of the detected damage pattern, FE analyses were developed, in which each model was firstly subjected to self-weight, followed by a ramped 9000 N shear load. Figure 13 reports the cracking pattern observed during the FE analysis on the panels. In agreement with the damage observed at the end of the experimental tests, cracking is not present on the whole panel, but mainly on its bed and head joints. More specifically, following predominant horizontal cracking initiated at the specimen mid-height, when the interface bond strength was attained, stepped diagonal cracks spread (through horizontal and vertical joints) along the compressed diagonal.

As shown in Table 6, in order to evaluate the efficiency and accuracy of the proposed FEM, the estimates of the ultimate shear capacity were then compared with laboratory outcomes. Even in this case, it can be emphasized how FE models satisfactorily reproduce the observed ultimate capacities, since in all cases the maximum deviations between predicted and measured response (i.e., error of the model) were found to be no more than 14%.

	Predicted in-plane capacity (kN)	Experimental in-plane capacity (kN)	Error of the model (-)
MAT-01-U	67.5	67.03	1.01
MAT-02-D	176.25	205.0	0.86
MAT-03-S	112.5	100.3	1.12
MAT-04-D	172.5	199.8	0.86
MAT-05-S	112.5	113.4	0.99
MAT-06-S	135	120.9	1.12
MAT-07-S	135	120.9	1.12

Table 6. Experimental vs predicted shear load capacities.

4 CONCLUSIONS

This research has investigated the shear behavior of stone and brickwork masonry walls, strengthened using GFRP meshes embedded into a mortar coating. Full-scale shear tests and numerical simulations were performed to determine the strength capacity of wall panels reinforced with the proposed retrofitting method.

The following conclusions can be drawn:

- brickwork panels, test results show that the increase in the shear load capacity, for double-sided reinforcement, is nearly three times higher than the shear capacity of unreinforced wall panels. For single-sided reinforcement, this increment reduced to about 70 %, ranging from 49.5 % to 80.5 %. The brickwork specimens showed the largest increase in shear capacity. The shear modulus variations were smaller in percentage and more scattered: for single-sided reinforcement, the stiffness of the wall panels increased in a range between -3.6 % and 150 %.

- Stone work panels, they indicate that the average shear capacity of both single- and double-sided reinforced panels was 84 % and 164 % stronger than the unreinforced wall panel.

- For both brickwork and stone unreinforced panels, the shear load – angular strain curves showed a quasi-elastic behaviour with a weak yield plateau: this was mainly caused by the development of a diagonal shear crack along the compressed diagonal. For the reinforced panels, shear load – angular strain curves underline two stages of the global behaviour: a first elastic and a second plastic.

- Although the number of tested panels was limited and not exhaustive, we can remark that the reinforcement caused a significant increase of the ultimate strength of the panels; the typical failure mode was due to masonry crushing.

- Furthermore, this initial attempt to model the GFRP-reinforced wall panels, while not complete, demonstrates that structural modeling is possible given accurate information on material property evolution and structural response of both unreinforced and reinforced panels. In addition, we require a better understanding of boundary conditions at interface coating-to-masonry. As we continue this part of the program we wish to develop further examples and isolate those details that are critical to making accurate predictions. The experimental data were implemented numerically using a non-linear constitutive law and adopting a 3D finite element model. The results of the numerical analysis are in agreement with the observations of the experimental tests: unit (stone or bricks) cracking was not noted, but failure mainly occurred at the bed and head joints. Moreover, the numerical ultimate shear capacity was then compared with laboratory results in order to evaluate the efficiency and accuracy of the proposed FEM. Considering that the maximum error of the numerical simulation was 14 %, it can be highlighted that FE model satisfactorily reproduced the observed experimental ultimate capacities.

REFERENCES

[1] S. Boschi, L. Galano, V. Vignoli, Mechanical characterisation of Tuscany masonry typologies by in situ tests, *Bulletin of Earthquake Engineering*, 17(1), 413-38, 2019.

[2] M. Corradi. A. Borri, A database of the structural behavior of masonry in shear, *ulletin of Earthquake Engineering*, 9, 3905-30, 2018.

[3] G. Castori, A. Borri, A. De Maria, M. Corradi, R. Sisti, Seismic vulnerability assessment of a monumental masonry building, *Engineering Structures*, 136, 454-465, 2017.

[4] Y. Boffill, H. Blanco, I. Lombillo, L. Villegas, Assessment of historic brickwork under compression and comparison with available equations. *Construction and Building Materials*, 207, 258-272, 2019.

[5] M. Corradi, A. Borri, G. Castori, R. Sisti, The Reticulatus method for shear strengthening of fair-faced masonry, *Bulletin of Earthquake Engineering*, 14(12). 3547-3571, 2016.

[6] A. Borri, M. Corradi, A. Vignoli, Seismic upgrading of masonry structures with FRP. Proceeding of 7th International Conference on inspection appraisal repairs and maintenance of buildings and structures, Nottingham, UK, 2001

[7] R. Capozucca, Experimental analysis of historic masonry walls reinforced by CFRP under in-plane cyclic loading. *Composite Structures*, 94 (1), 277-289, 2011.

[8] T. Stratford, G. Pascale, O. Manfroni, B. Bonfiglioli, Shear strengthening masonry panels with sheet glass-fiber reinforced polymer. *Journal of Composites for Construction*, 8(5), 434-443, 2004.

[9] T.C. Triantafillou, Strengthening of masonry structures using epoxy-bonded FRP laminates. *Journal of Composites for Construction*, 2, 96-104, 1998.

[10] ICOMOS Charter, Principles for the analysis, conservation and structural restoration of architectural heritage. ICOMOS 14th General Assembly and Scientific Symposium, Victoria Falls, 2003, Zimbabwe.

[11] T.C. Triantafillou, C.G. Papanicolaou, Shear strengthening of reinforced concrete members with textile reinforced mortar (TRM) jackets. *Materials and structures*, 39(1), 93-103, 2006.

[12] F.G. Carozzi, G. Milani, C. Poggi, Mechanical properties and numerical modeling of Fabric Reinforced Cementitious Matrix (FRCM) systems for strengthening of masonry structures. *Composite structures*, 107, 711-725, 2014.

[13] S. Casacci, C. Gentilini, A. Di Tommaso, D.V. Oliveira, Shear strengthening of masonry wallettes resorting to structural repointing and FRCM composites. *Construction and Building Materials*, 206, 19-34, 2019.

[14] P.B. Lourenço, J.T. Rots, J. Blaauwendraad, Two approaches for the analysis of masonry structures: micro and macro-modeling, *Heron*, 40(4), 313-340, 1995.

[15] D. Addessi, S. Marfia, E. Sacco, J. Toti, Modeling approaches for masonry structures, *Open Civil Engineering Journal,* 8, 288-300, 2014.

[16] V. Sarhosis, J.V. Lemos, A detailed micro-modelling approach for the structural analysis of masonry assemblages, *Computers and Structures*, 206, 66-81, 2018.

[17] M. Betti, L. Galano, A. Vignoli, Finite element modelling for seismic assessment of historic masonry buildings, Earthquakes and their impact on society. Earthquakes and Their Impact on Society. Springer, Berlin, 2016.

EURODYN 2020
XI International Conference on Structural Dynamics
M. Papadrakakis, M. Fragiadakis, C. Papadimitriou (eds.)
Athens, Greece, 23–26 November 2020

EFFECTS OF IMPULSIVE ACTIONS DUE TO SEISMIC JERK AND LOCAL FAILURES IN MASONRY STRUCTURES

Massimo Mariani[1] **and Francesco Pugi**[2]

[1] Studio Ricerche Applicate
06123 Perugia, Italy
ricercheapplicate@libero.it

[2] Aedes Software: Ricerca e Sviluppo
56028 San Miniato, Pisa, Italy
info@aedes.it

Keywords: masonry structures, seismic motion, jerk, impulsive forces

Abstract. *Recent studies [1-9] highlighted aspects of the seismic motion and the structural response which are usually ignored or not properly considered: the chaotic and spatial nature of the seismic motion, the importance of the vertical seismic component and its effect on the vulnerability of the structures. Considering seismic acceleration as a vector in space, the path outlined by the vector at each instant is the 3D representation of the accelerograms. The study of spatial accelerograms reveals interesting new aspects related to the variation of acceleration and the impulsive nature of the seismic motion. The seismic jerk (first derivative of acceleration and third derivative of displacement) is the fundamental component of the impulsive actions associated to high frequency content of the seismic motion. During the seismic event, the continuous variation of acceleration, in terms of modulus and direction, causes impulses (hammering, shaking, disconnection, etc.). In masonry structures they lead to local failures of the connections, disaggregation and damage accumulation with loss of ductility. Monitoring the seismic jerk in three directions may provide more significant information on the damage rather than monitoring the interstory drift. A design process is finally outlined: the study of the seismic motion impulsive content leads to solutions for structural retrofit aimed at strengthening masonry elements and improvement of connections.*

1 SEISMIC MOTION: ACCELERATION

The classic representation of a seismic event is a set of acceleration time series (also known as accelerograms) where ground acceleration is sampled in three mutually orthogonal directions.

By combining the three components of ground acceleration, one may plot a 3D path where each point is defined by the three components of the acceleration vector applied in the origin of the system. In this chart acceleration is not plotted against time but time is involved in indirect manner since each point corresponds to a different instant.

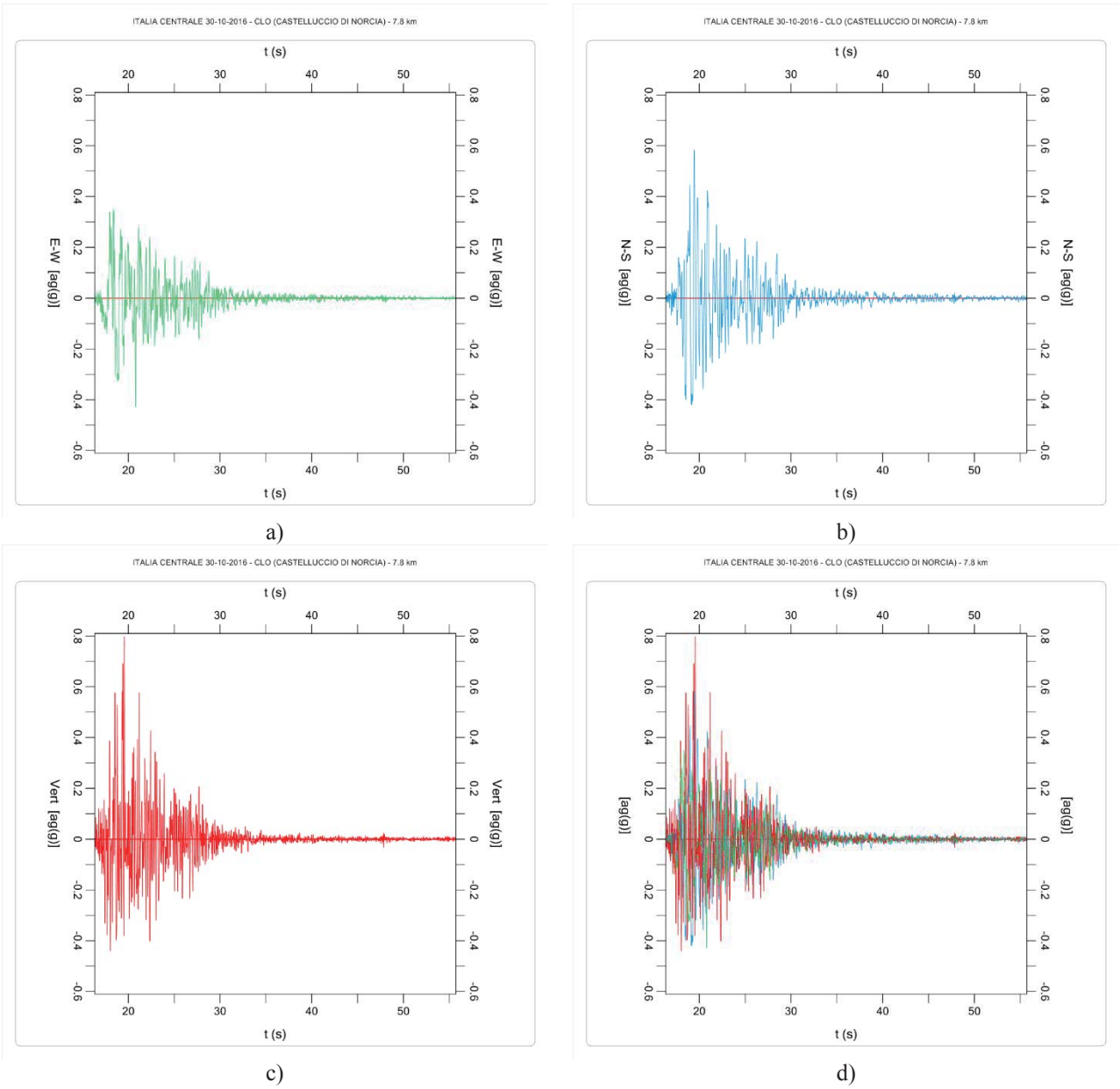

Figure 1. Traditional representation of accelerogram as time series: each component of ground acceleration is plotted against time. (a) EW component; (b) NS component; (c) Vertical component and (d) the three components overlaid in the same chart.

The 3D chart represents the seismic ground motion in a unified way: it highlights the simultaneity of the three components of ground acceleration and allows for direct comparison between them.

The graphic elaboration was carried out by means of the original software Seismic3D [10] specially developed for the purpose. Starting from the seismic event records, the software performs several elaborations aimed at studying the seismic ground motion.

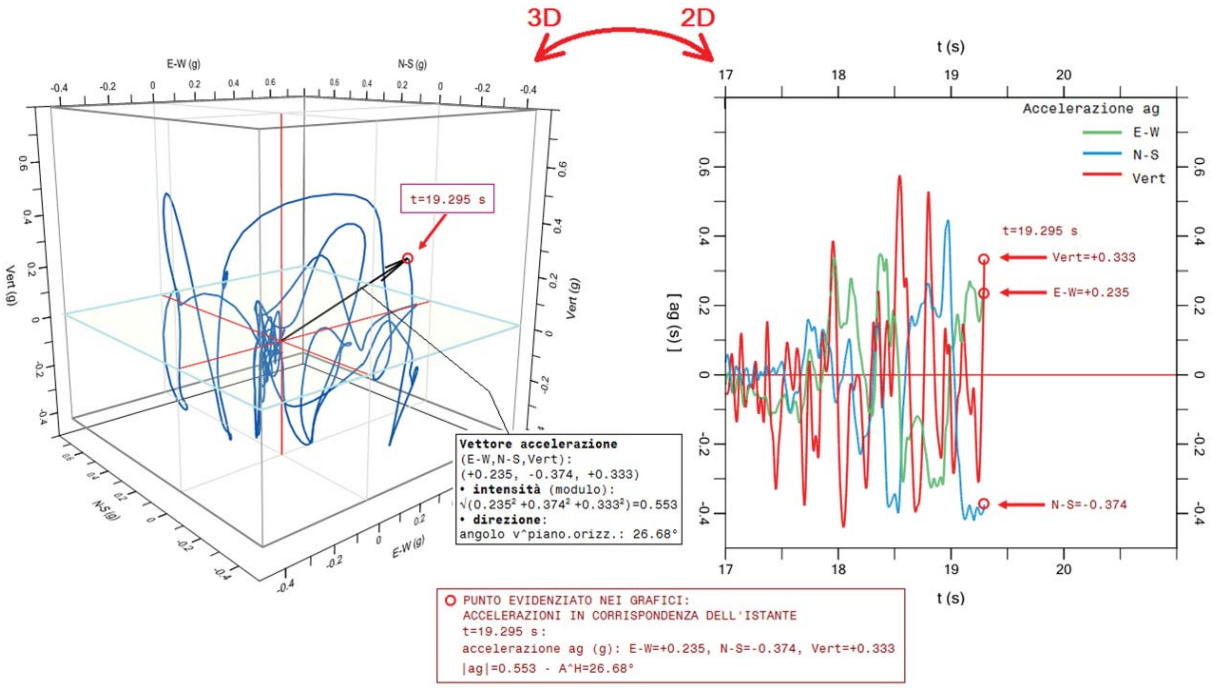

a)

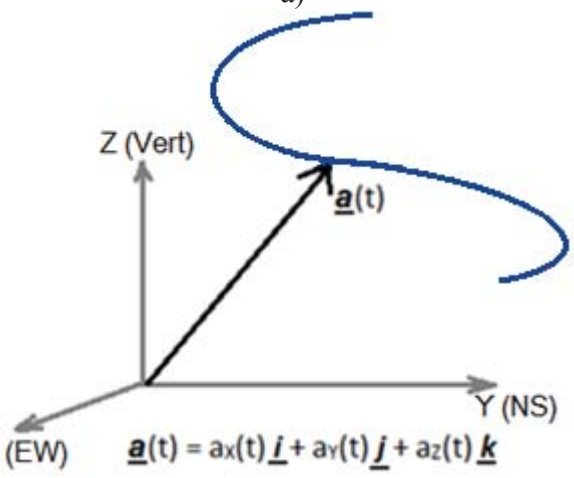

b)

Figure 2. (a) Evolution of the accelerogram from time series to 3D path (from plane to space) (b) Acceleration path outlined at any time by the acceleration vector

The 3D curve has the shape of a tangle: the more similar are the three components of acceleration the more compact and spherical is the tangle. In the following, the term “tangle” refers to the acceleration path when 2 or 3 components are considered.

Figures 1-2 show the evolution of the accelerogram from three separated time series in the plane (t, ag) to one 3D path in the space (a_gEW, a_gNS, a_gVert). The elaboration is based on

ground acceleration records at station CLO (Castelluccio di Norcia) from 30 October 2016 Norcia earthquake in Central Italy (mainshock).

The accelerograms in Figure 1 represent acceleration in a bracket duration: time span between the first and last peak exceeding 0.010 g.

At each instant, the acceleration vector is characterized by magnitude and direction. Magnitude (or modulus) is given by the square root of the sum of the squares of the three components. By ignoring one of the components, the 3D path is reduced to its projection on the plane of the other two components. For instance, by ignoring the vertical component we get a 2D path in the horizontal plane (a_gEW, a_gNS). Comparison between the 3D path and its projection on the horizontal plane highlights the contribution of the vertical component to total ground acceleration (Figure 3).

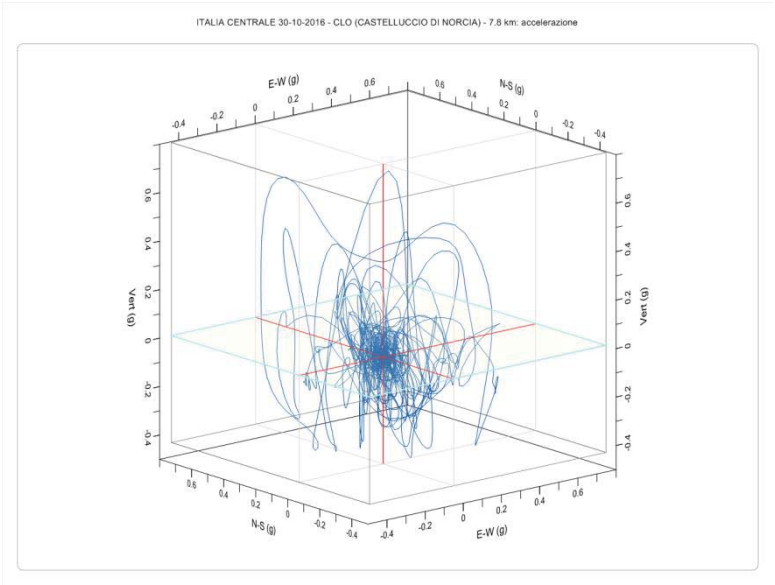

a)

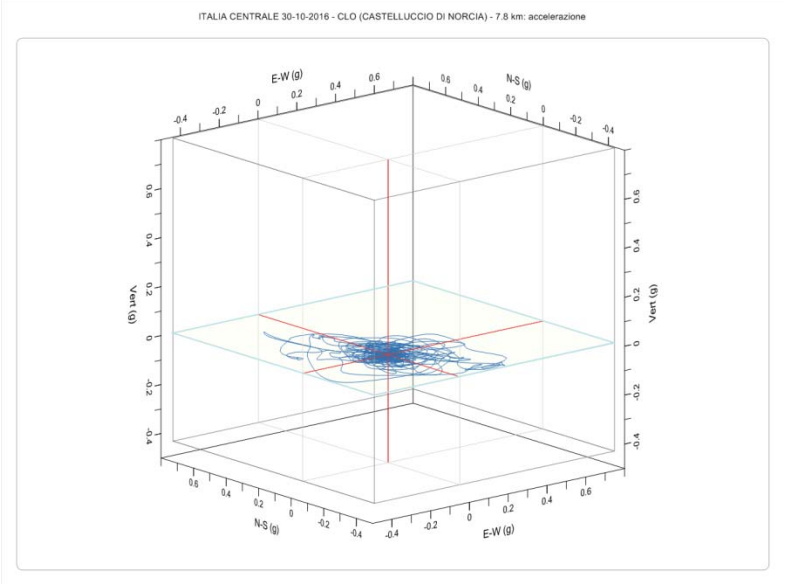

b)

Figure 3. Acceleration paths (or tangles).
(a) 3D path considering the three components; (b) 2D path ignoring vertical component

Figure 4 shows the projection of the 3D acceleration path (tangle) on the horizontal plane (a_gEW, a_gNS) and on the vertical planes (a_gEW, a_gVert) and (a_gNS, a_gVert). By comparing the 2D tangles one may observe that in this particular record the maximum values of the three acceleration components are very similar to each other.

The charts show the chaotic nature of the acceleration paths and the sharp variation in magnitude and direction of the acceleration vector. The plane accelerogram as time series shows the variation of one acceleration component at a time. Even when the time series of the three components are overlaid in the same chart, they cannot explicitly represent the real nature of the seismic motion. The ground acceleration records conceal a more complex reality which is finally revealed by their combination into the plot of the acceleration paths.

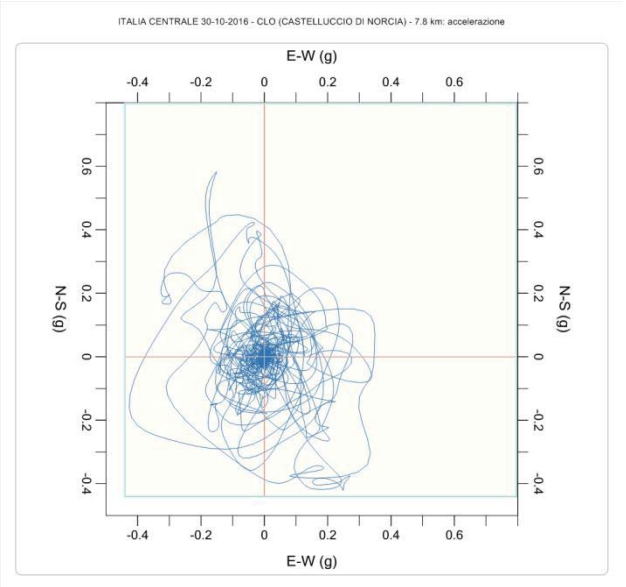

a)

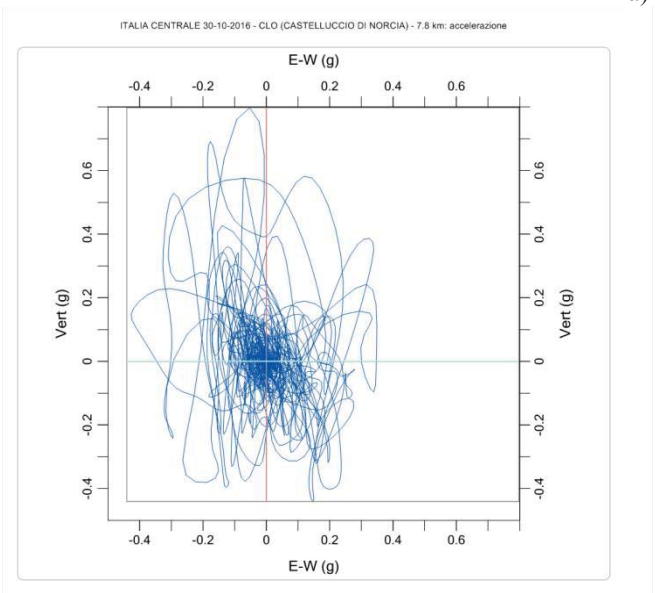

b)

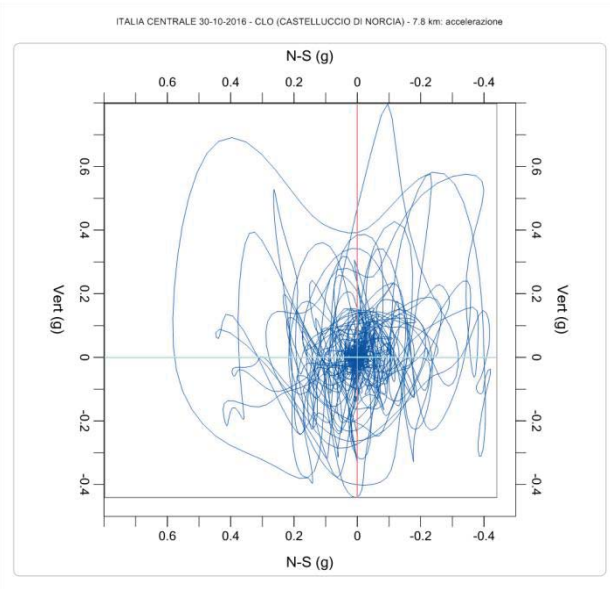

c)

Figure 4. Projections of the acceleration path on:
(a) horizontal plane (agEW,agNS); (b) vertical plane (agEW, agVert); (c) vertical plane (agNS, agVert)

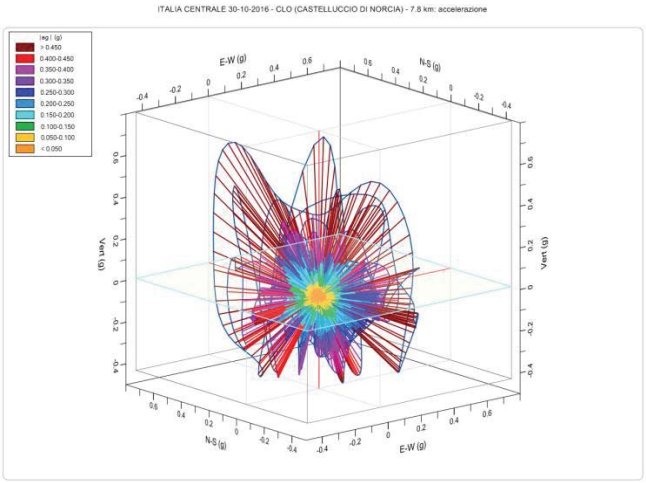

Figure 5. 3D Accelerogram: freezing motion of acceleration vector with color scale based on its magnitude

An interesting re-elaboration of the 3D chart can be obtained by "freezing" the motion of the acceleration vector at given time intervals, visualized with a color scale based on its magnitude (Figure 5).

As can be seen in Figure 5, the highest accelerations correspond to the "borders" of the path (characterized by dark red vectors) but the central core associated to lower accelerations (yellow or orange vectors) appears very dense showing countless variations in magnitude and directions which characterize a significant part of the seismic event.

To better understand the level of complexity one could zoom in the central core. Figure 6 shows the core in different levels of magnification. In order to reach this level of details, the acceleration record has been considered in a wide bracket duration, the time span between the first and last peak exceeding 0.005 g (15.385 s - 57.360 s, duration 41.985 s). In Figure 7 the same sequence is presented in the vertical plane (a_gNS, a_gVert).

These figures recall the fractals: whatever the scale, the curve always presents the same characteristics.

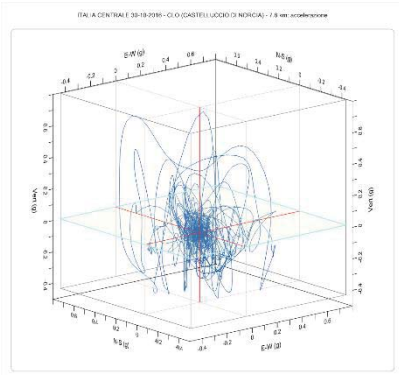

a) full box

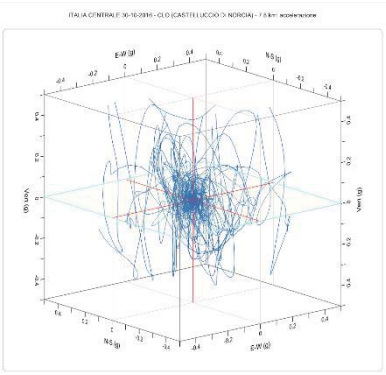

b) limit box: 0.500 g

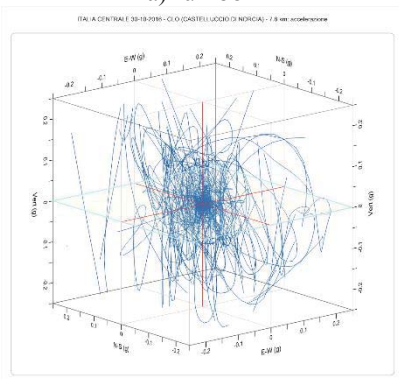

c) limit box: 0.250 g

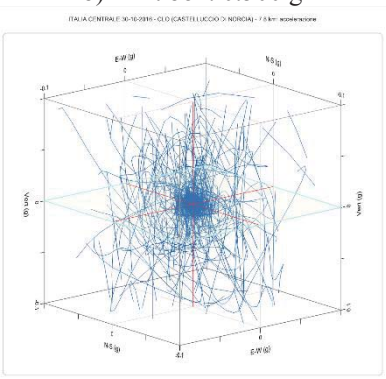

d) limit box: 0.100 g

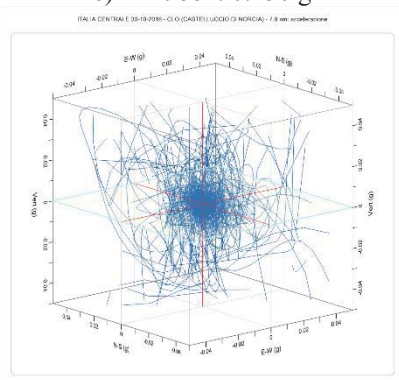

e) limit box: 0.050 g

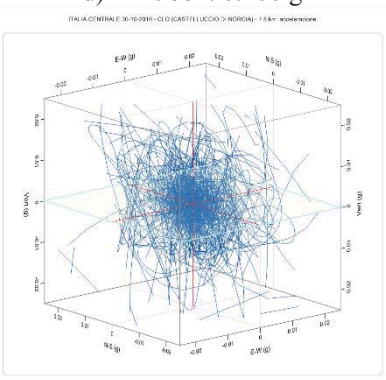

f) limit box: 0.025 g

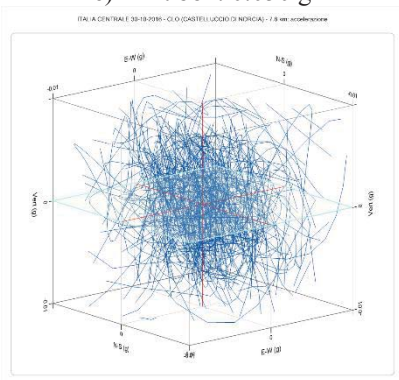

g) limit box: 0.010 g

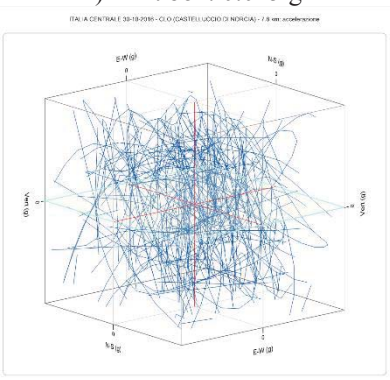

h) limit box: 0.005 g

Figure 6. Different levels of magnification of the acceleration path: 3D view

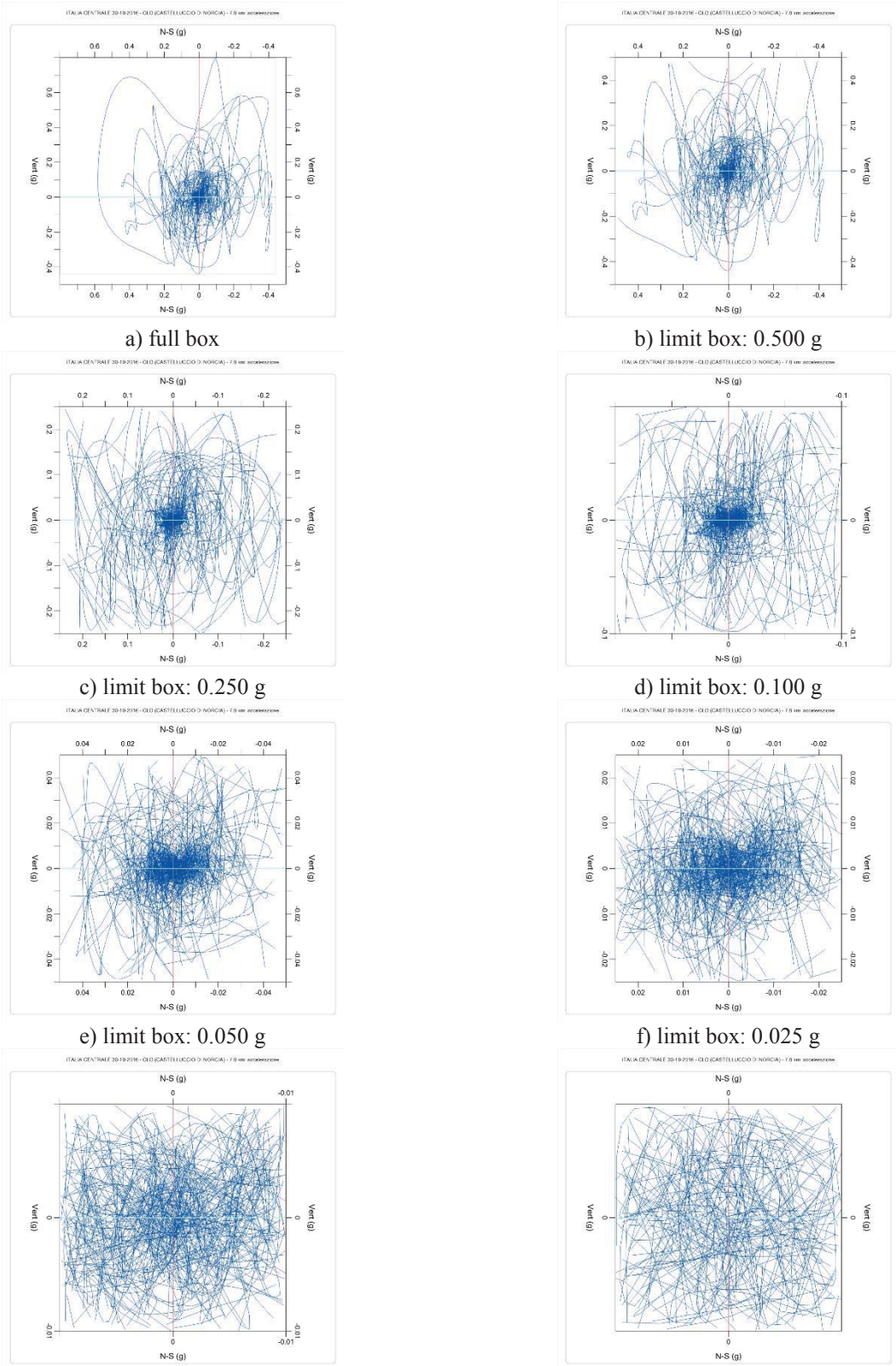

a) full box

b) limit box: 0.500 g

c) limit box: 0.250 g

d) limit box: 0.100 g

e) limit box: 0.050 g

f) limit box: 0.025 g

g) limit box: 0.010 g

h) limit box: 0.005 g

Figure 7. Different levels of magnification of the acceleration path: projection on vertical plane NS-Vert

The charts show what happened in Castelluccio di Norcia on 30 October 2016 in about 40 seconds. Considering the bracket time span between the first and last acceleration peak exceeding 0.250 g, we obtain the chart shown in Figure 8 for a time span of 6.48 s (17.435 s to 23.915 s). The red labels in the chart point out the acceleration reached at each second. In this way "time" re-appears in the chart highlighting the progression of the path.

In 6 seconds, the ground motion was characterized by violent accelerations especially in the vertical direction. The ground accelerations generated inertial and impulsive forces which caused collapses and severe damages to the buildings. A destruction happened in a very short time interval caused by a chaotic event, extremely different in its nature from the static actions that stress the buildings under operating conditions.

The 3D accelerograms, that are the paths outlined by the acceleration vector, indicate a new perspective: studying the shape of the curves and their evolution throughout the duration of the seismic event. The continuous changes of the acceleration vector in terms of magnitude and direction suggest to further investigate on the variation of acceleration. In fact, the safety verification applied in terms of resistance and deformation under inertial forces, may not be enough to fully describe the structural response. Assessment of the structural capacity cannot ignore verifications on the impulsive effects, that are the forces related to the short time intervals in which accelerations change, increase, decrease or change sign.

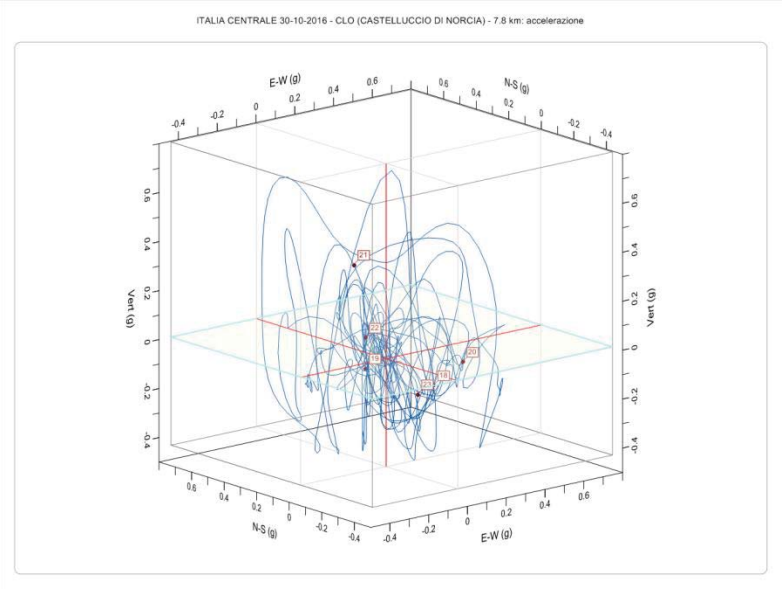

Figure 8. 3D Accelerogram at station CLO during 2016 Norcia mainshock: about 6 seconds while acceleration is above 0.25 g

2 JERK: FIRST DERIVATIVE OF ACCELERATION

The time derivative of acceleration (TDoA), that is the velocity of acceleration or the third derivative of displacement, is referred to as jerk and associated to the symbol j:

$$\boldsymbol{j} = \frac{d\boldsymbol{a}}{dt} \tag{1}$$

Since force acting on a body is equal to mass times acceleration, the jerk is related to the variation of the force acting on the body:

$$\boldsymbol{F} = m\boldsymbol{a} \Rightarrow \boldsymbol{j} = \frac{\left(\frac{d\boldsymbol{F}}{dt}\right)}{m} \tag{2}$$

In absence of jerk, a mass in constant acceleration is subject to static loading (constant force) and in this condition vibrations cannot occur. Therefore, when a body in motion undergoes vibration, jerk is always there.

Tong et al. (2005) [11] investigated on seismic jerk stating from the need of obtaining quantitative understanding about its amplitude, duration and frequency content. The study is based on records from the 1999 Chi-Chi Earthquake in Taiwan (M_W 7.6, 17:47, 20 September 1999) and one of its aftershocks (M_W 6.2, 00:14, 22 September 1999). At that time, jerk sensors were not widely available; therefore, jerk time series were obtained from ground acceleration records via numerical methods. This methodology, which can be applied to other seismic events where jerk records are not available, was implemented in the software Seismic 3D [10]

Seismic acceleration is a discrete signal, therefore seismic jerk can be calculated by the following mi-point differentiation formula:

$$j(t_i) = \frac{a(t_{i+1}) - a(t_{i-1})}{2\Delta t} \quad (i = 2, \dots, N-1) \tag{3}$$

where: $a(t_i)$ is the acceleration at instant t_i, N is the number of samples, Δt is the sampling period.

The formula is applied separately for each of the three components of the jerk vector **j.**

The accuracy of the jerk elaboration relies on the accuracy of the acceleration records and the sampling rate. Ground acceleration records of the main seismic events on the Italian territory are provided by ITACA [12] with a sampling period of 5 ms (200 Hz). The records are also corrected to reduce errors in high and low frequency; therefore, quality of the records is excellent for the purposes of this work.

At this point it comes naturally to represent the variation of jerk both as time series of its three components and as 3D path outlined by the jerk vector in space. In this way one can get graphs like the ones seen for acceleration.

In the 3D graph of the acceleration path it is worth noticing that the **j** vector is tangent to the path at each point.

Figure 9 shows the time series of the three jerk components at station CLO (Castelluccio di Norcia) from the 30 October 2016 Norcia earthquake. Table 1 summarize the maximum amplitude of acceleration (PGA) and jerk (PGJ) for each of the three components, and the instant in the record when they occur.

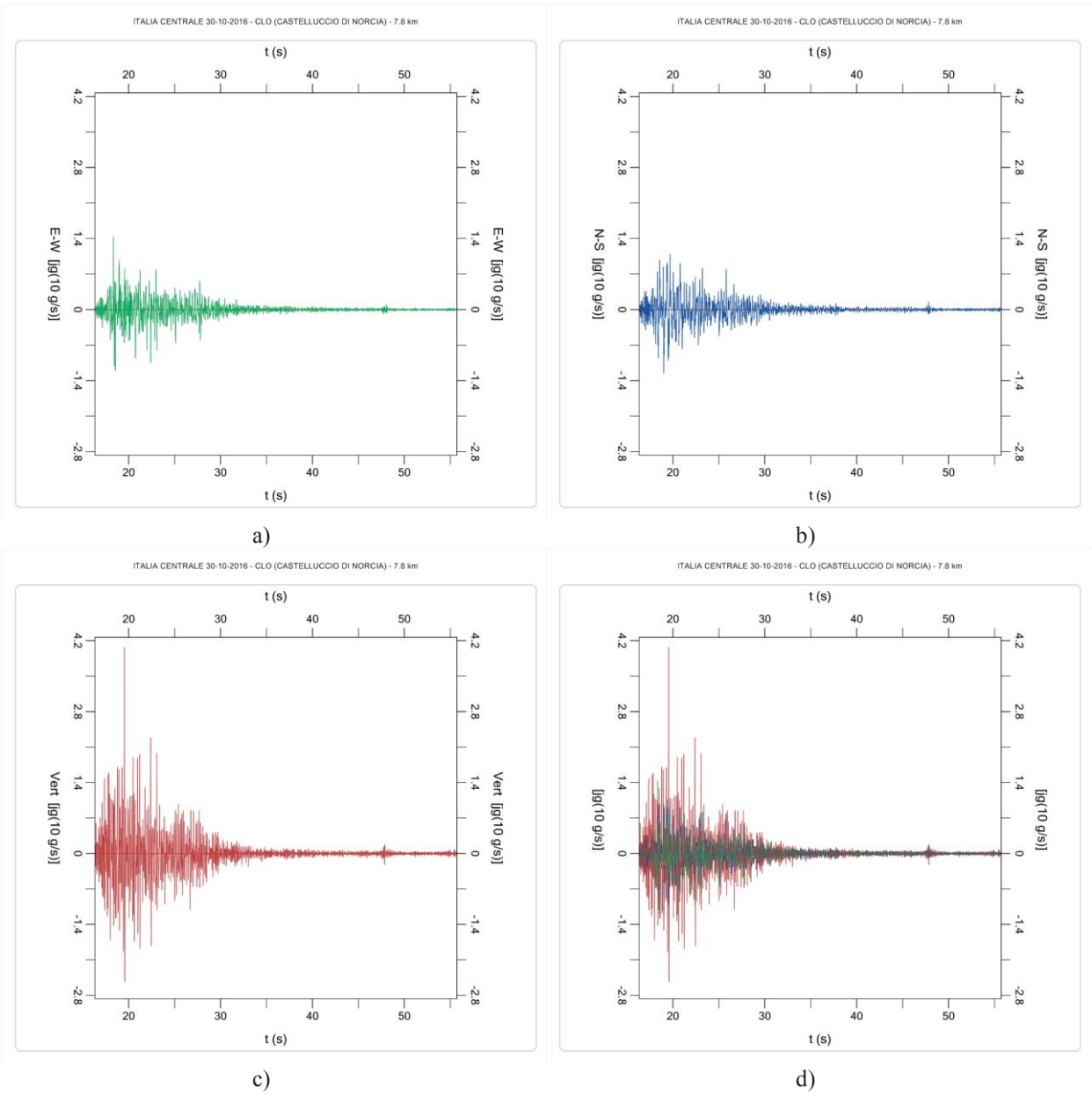

Figure 9. Jerk time series: each component of ground jerk plotted against time. (a) EW component; (b) NS component; (c) Vertical component and (d) the three components overlaid in the same chart.

	EW	t (s)	NS	t (s)	Vert.	t (s)
PGA (g)	0.427	20.775	0.583	19.445	0.797	19.560
PGJ (g/s)	14.36	18.335	12.50	18.995	40.70	19.540

Table 1. Station CLO (Castelluccio di Norcia), 30 October 2016 Norcia earthquake. Maximum acceleration (PGA) and maximum jerk (PGJ) for each of the three components and corresponding time instant

The maximum values of jerk (PGJ) occur at different instants of time than the ones of acceleration (PGA). They occur in a time interval between 18 s and 21 s and there is not a clear relationship with the occurrence of PGA values in the three directions.

In this event both vertical acceleration and jerk are rather strong with respect to the horizontal component. Vertical acceleration almost reached 0.8 g (Figure 1) and the vertical PGJ of about 40 g/s (Figure 9) is almost double than the horizontal ones.

In order to understand the relationship between acceleration and jerk, let us consider the time series of their vertical component focusing on a small time interval between 19.3 s and 19.8 s (0.5 s) in which both PGA and PGJ occur.

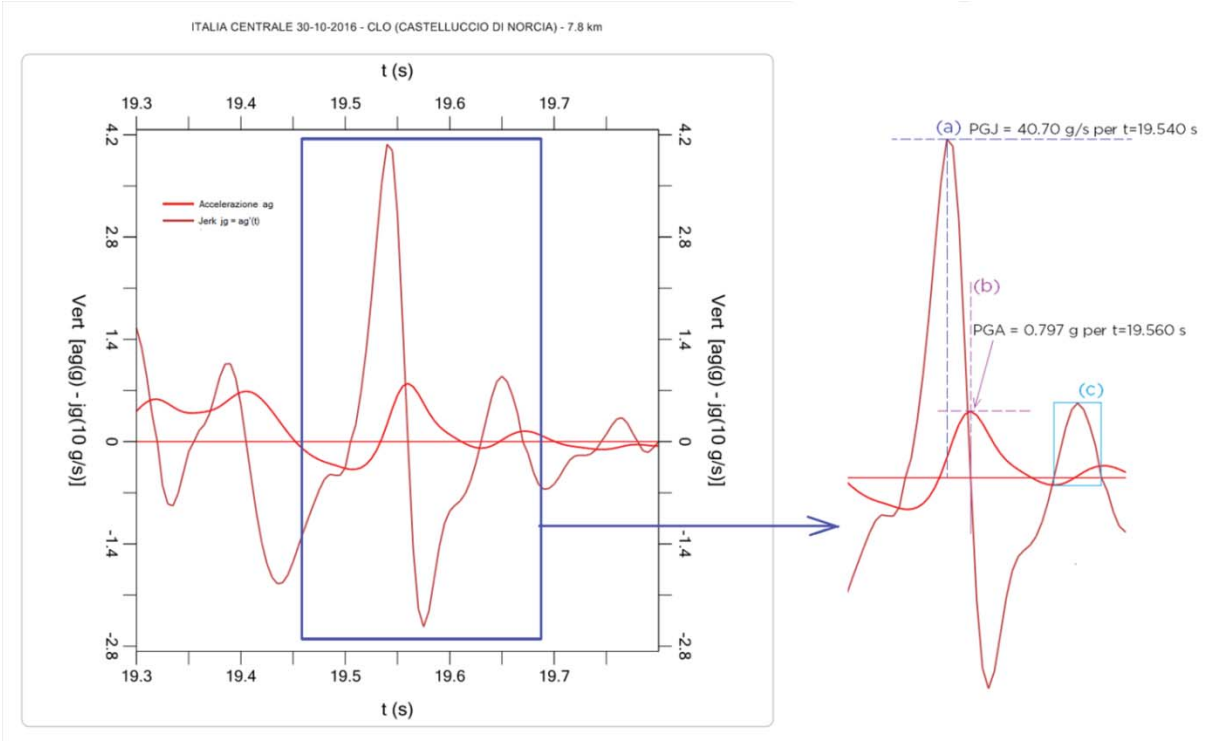

Figure 10. Comparison between acceleration and jerk time series. The detail on the right shows how the points where jerk is zero correspond to local maximum or minimum of acceleration.

Since jerk is the first derivative of acceleration it is equal to zero when acceleration shows a local maximum or minimum.

The detail in Figure 10 highlights (a) the absolute maximum of jerk (PGJ); (b) the absolute maximum of acceleration correspondent (like other local maximum) to zero in jerk; (c) the sector between two consecutive zeros of jerk correspondent to local minimum and maximum of acceleration.

Figure 11 shows the time series of acceleration and jerk for the three components in the time span between 18.0 s and 21.0 s. Jerk time series feature a higher number of fluctuations between positive and negative values: this is even more evident from the detail in Figure 12. Throughout the seismic event, the secondary fluctuation of acceleration corresponds to significant jerk peaks of alternate sign. The operation of derivation generates a “jerky” function characterized by denser peaks, that is in strict terms, by higher frequencies.

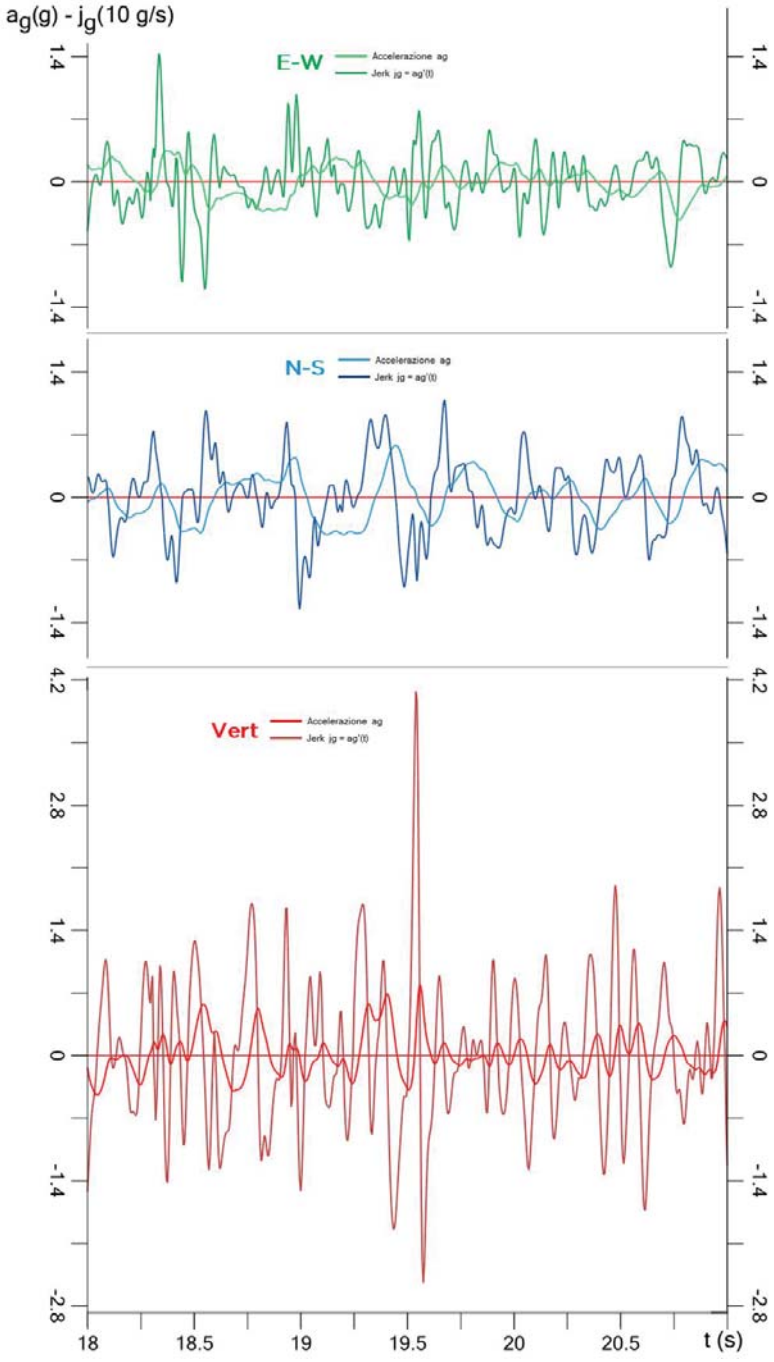

Figure 11. Acceleration and jerk time series for the three components (EW, NS, Vert)

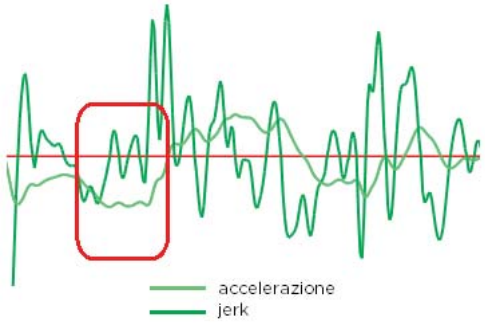

Figure 12. Secondary fluctuation of acceleration correspondent to jerk peaks

The graphs of jerk variation in space as the 3D path outlined by the **j** vector are similar to the ones already seen for acceleration. Comparison between acceleration and jerk paths is given in Figure 13 (3D view), Figure 14 (EW-NS plane), Figure 15 (EW-Vert plane) and Figure 16 (NS-Vert plane).

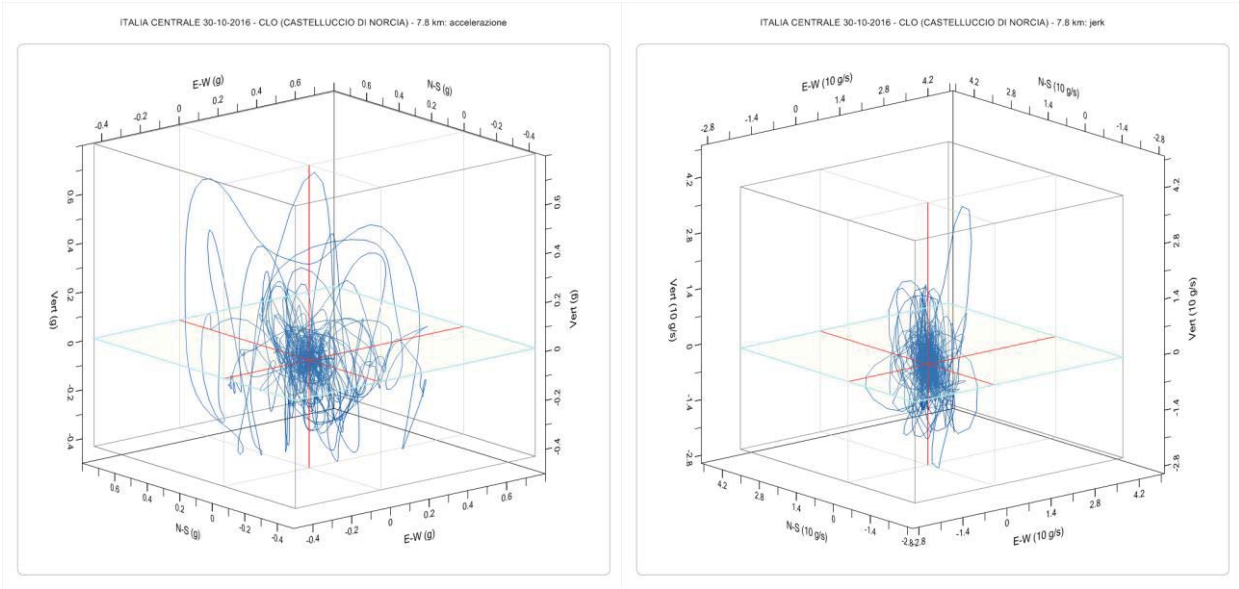

a) b)

Figure 13. Comparison between (a) acceleration and (b) jerk paths: 3D view

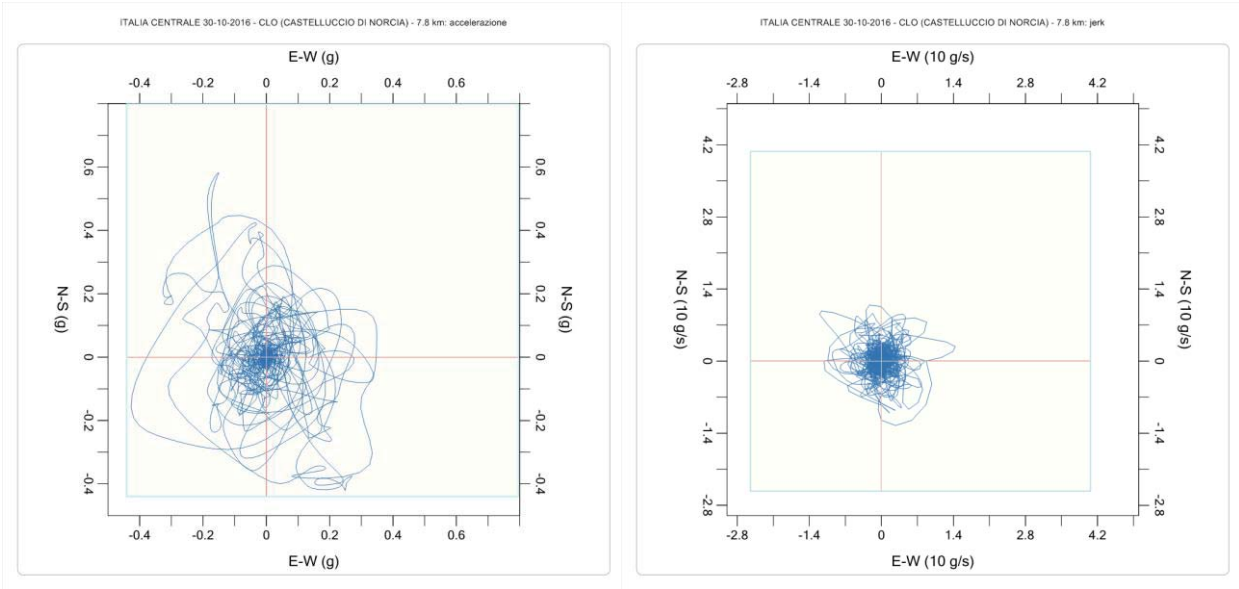

a) b)

Figure 14. Comparison between (a) acceleration and (b) jerk paths: projection on horizontal plane EW-NS

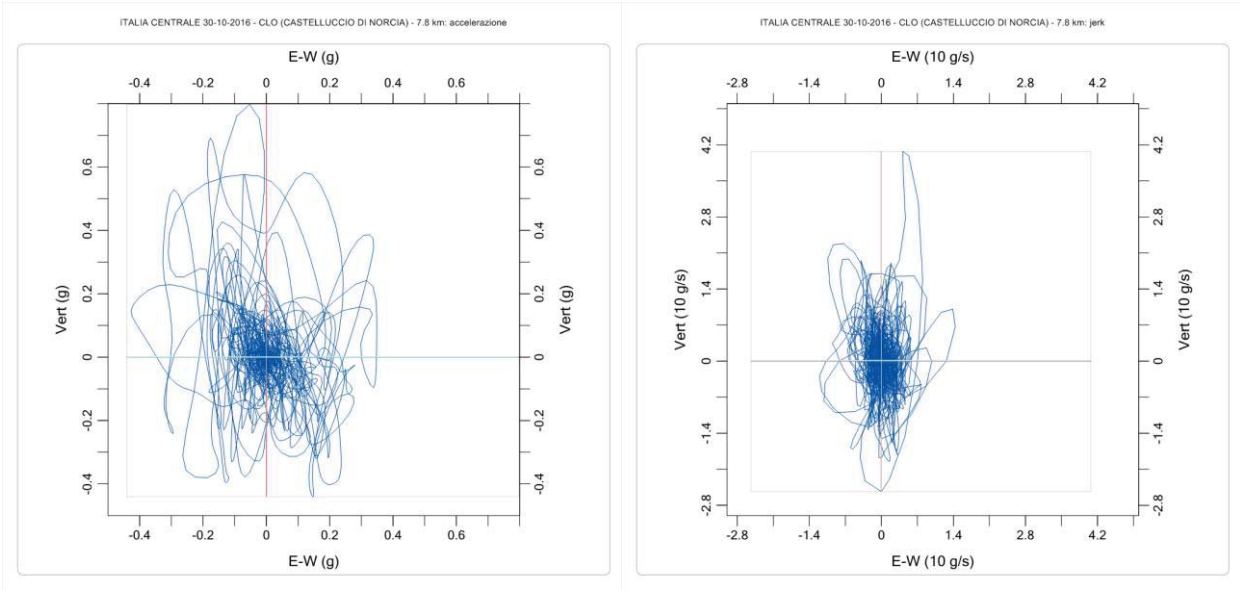

a) b)

Figure 15. Comparison between (a) acceleration and (b) jerk paths: projection on vertical plane EW-Vert

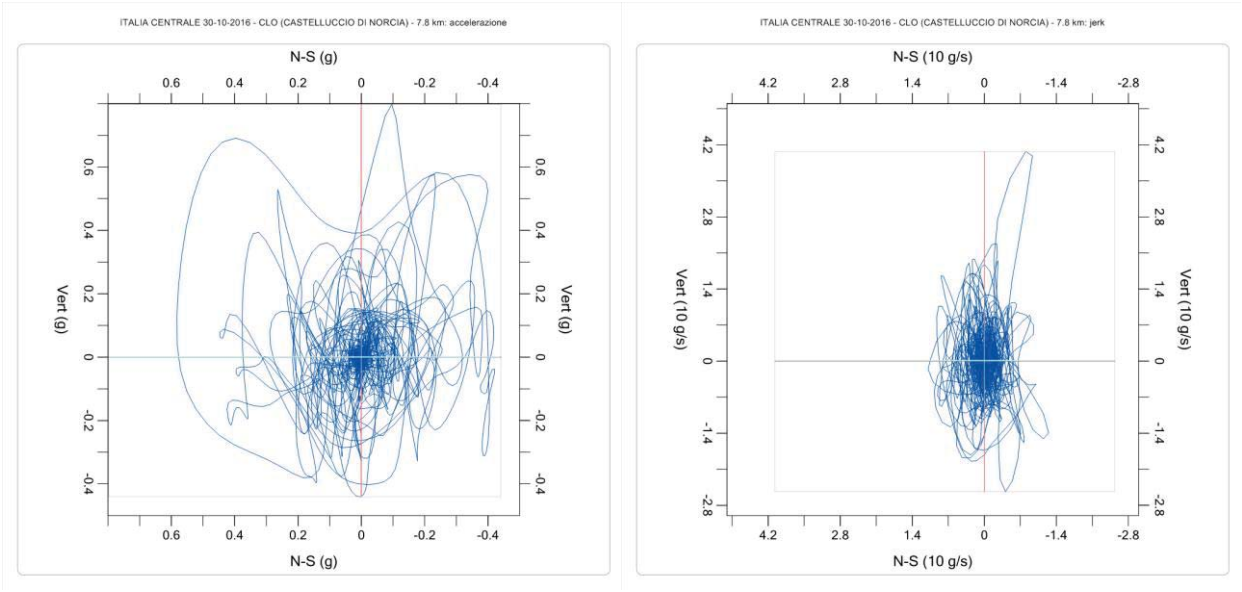

a) b)

Figure 16. Comparison between (a) acceleration and (b) jerk paths: projection on vertical plane NS-Vert

All the views highlight that the jerk tangle is denser than the acceleration one: this is in agreement with what previously noted in the comparison between acceleration and jerk time series. The projection of the jerk tangle on the vertical planes appears stretched in the vertical direction and this points out the importance of the vertical seismic component.

It is worth noticing that even the jerk paths feature a fractal type shape. Figure 17 shows different levels of magnification of the jerk path, from the box which envelopes the curve to the 0.5 g/s box.

This proves the chaotic nature of the represented phenomenon: the zoom in the core of the paths clearly highlights that, although the amplitude is lower, the number of fluctuations is

very high: this leads to the hypothesis that the phenomenon may disrupt the intimate constitutive bonds of the materials.

Since jerk is the first derivative of acceleration, a good way to understand its evolution is to represent the $\boldsymbol{j}$ vector on the acceleration path. Applying differential geometry of curves in $\mathbb{R}^3$, it can be proved that at the i-th instant t_i the vector $\boldsymbol{j}(t_i)$ is tangent to the curve in the point $\boldsymbol{a}(t_i)$. The modulus of vector $\boldsymbol{j}$ is given by the square root of the sum of the squares of its three components, each one being the time derivative of the correspondent acceleration component evaluated at instant t_i:

$$|\boldsymbol{j}(t_i)| = j_{3D}(t_i) = \sqrt{j_{EW}^2(t_i) + j_{NS}^2(t_i) + j_{Vert}^2(t_i)} \quad (i = 2, \dots, N-1)$$
$$where: \qquad (4)$$
$$j_{EW}(t_i) = \left.\frac{da_{EW}(t)}{dt}\right|_{t=t_i}, \quad j_{NS}(t_i) = \left.\frac{da_{NS}(t)}{dt}\right|_{t=t_i}, \quad j_{Vert}(t_i) = \left.\frac{da_{Vert}(t)}{dt}\right|_{t=t_i}$$

Jerk $\boldsymbol{j}$ is the rate of change of acceleration, that is, velocity of acceleration: there is complete analogy with velocity $\boldsymbol{v}$ as rate of change of displacement. Figure 18 shows the jerk vector on the 3D accelerogram (acceleration path). The bracket duration is defined as the time span between the first and last acceleration peak exceeding 0.250 g (17.435 – 23.915 s). The j vector is represented at instant t = 19.375 s by a red arrow, which of course is tangent to the curve from any point of view.

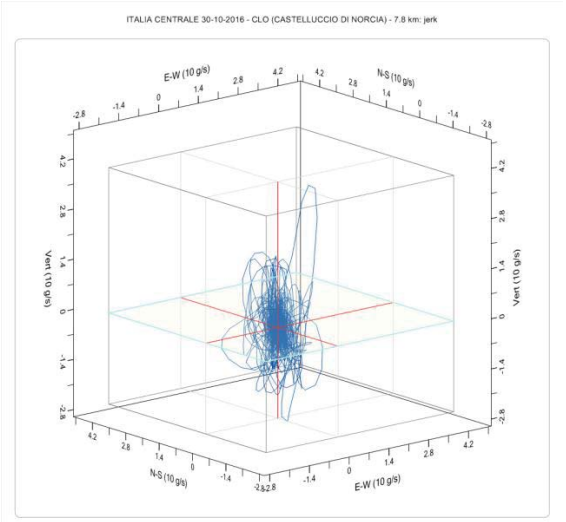

a) full box

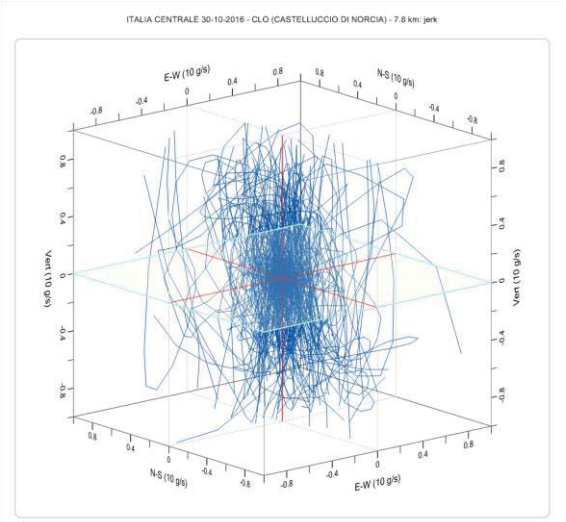

b) limit box: 10 g/s

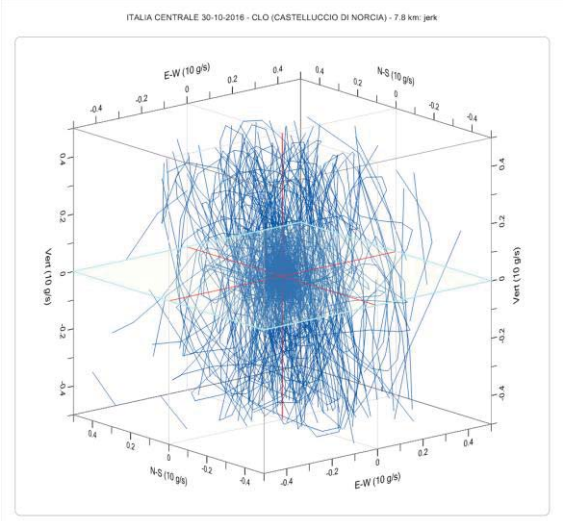

c) limit box: 5 g/s

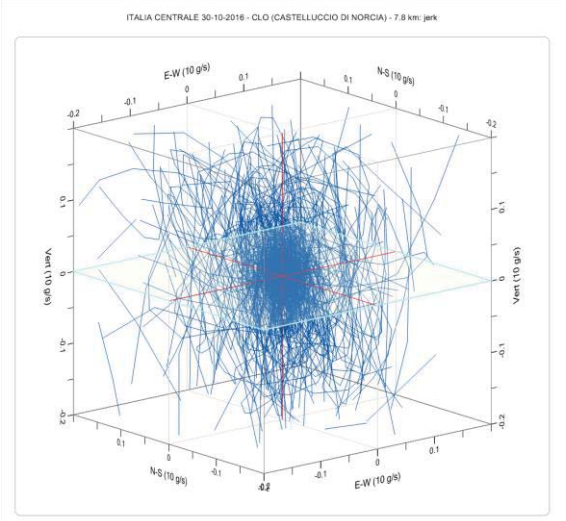

d) limit box: 2.5 g/s

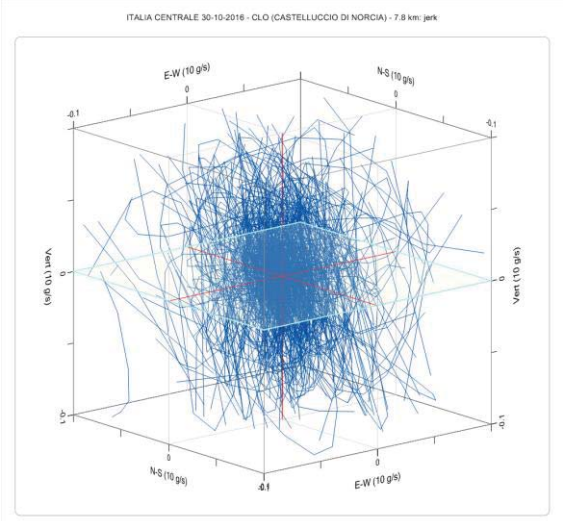

e) limit box: 1 g/s

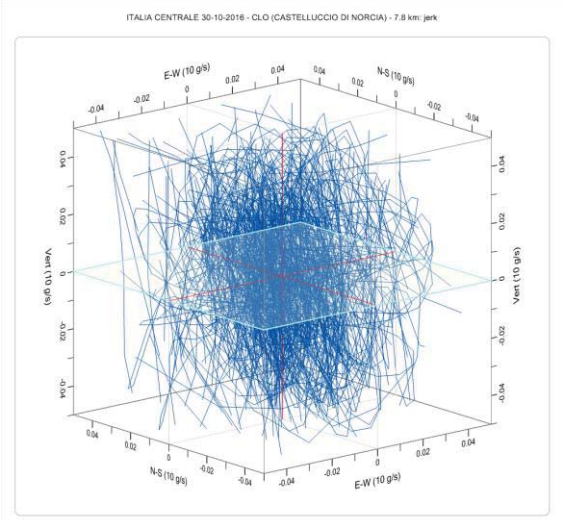

f) limit box: 0.5 g/s

Figure 17. Different levels of magnification of the 3D jerk path

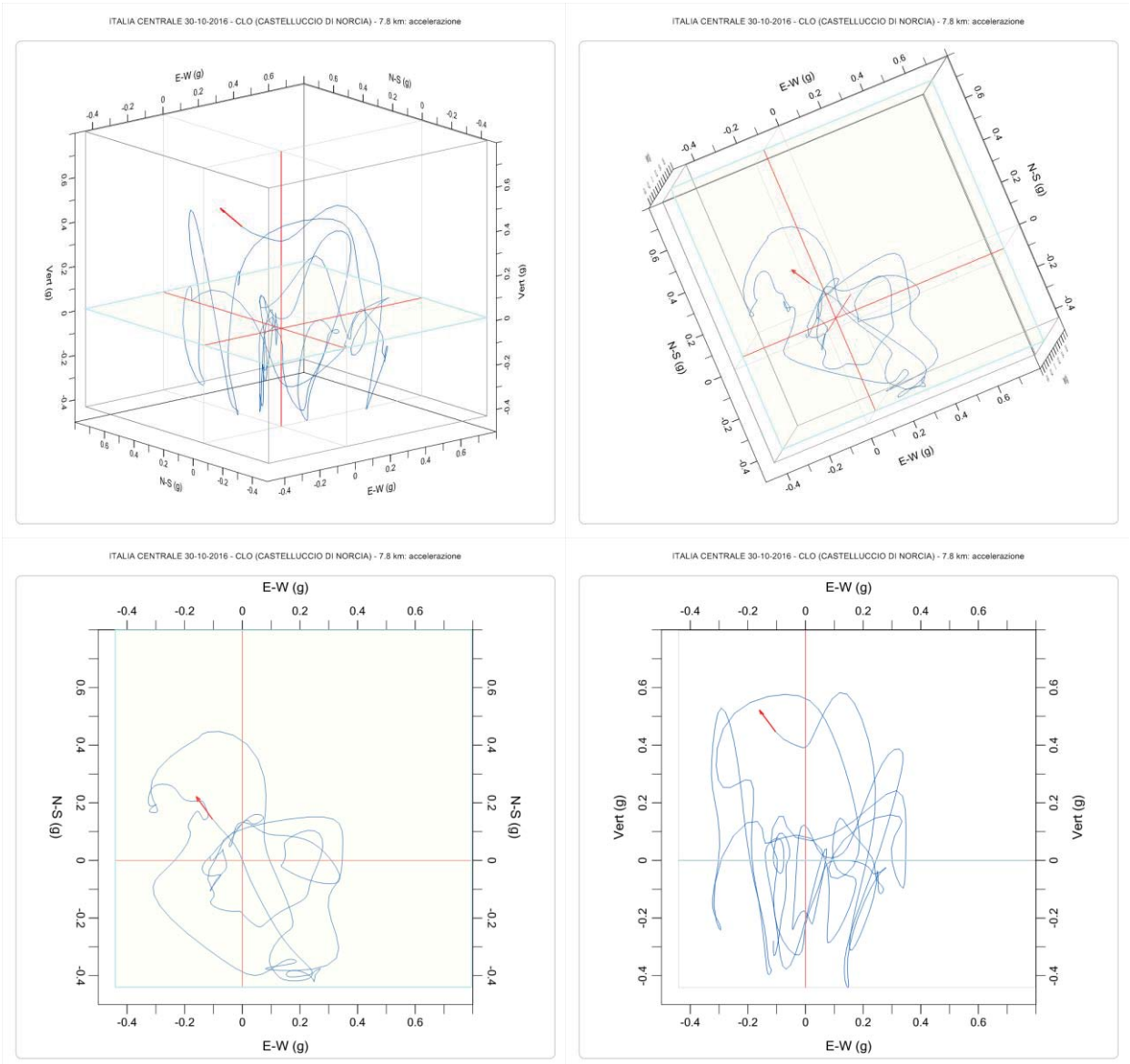

Figure 18. The jerk vector on the 3D accelerogram (acceleration path) from different points of view

Considering acceleration and jerk as vectors in space, PGA and PGJ may not only be expressed for the three separated components but also with respect to the magnitude (modulus) of the vectors. Therefore, Table 2 updates Table 1 with the inclusion of global PGA and PGJ and the instant when they occurred.

	EW	t (s)	NS	t (s)	Vert.	t (s)	3D	t (s)
PGA (g)	0.427	20.775	0.583	19.445	0.797	19.560	0.829	19.410
PGJ (g/s)	14.36	18.335	12.50	18.995	40.70	19.540	41.69	19.540

Table 2. Station CLO, 30 October 2016 Norcia mainshock. Peak ground acceleration (PGA) and peak ground jerk (PGJ). Three separated components and magnitude of the 3D vectors

Peaks of vectors magnitude are of course higher than the peaks of the singular components and they generally occur at different time instants. The maximum effects of seismic ground motion, both in terms of acceleration and jerk, did not occur along one of the three axes of the reference system (X,Y, Z) but along a random direction in space.

Figure 19 shows the time series of acceleration and jerk magnitude (3D) for two different bracket duration. The maximum values of these time series are given in Table 2 as 3D values.

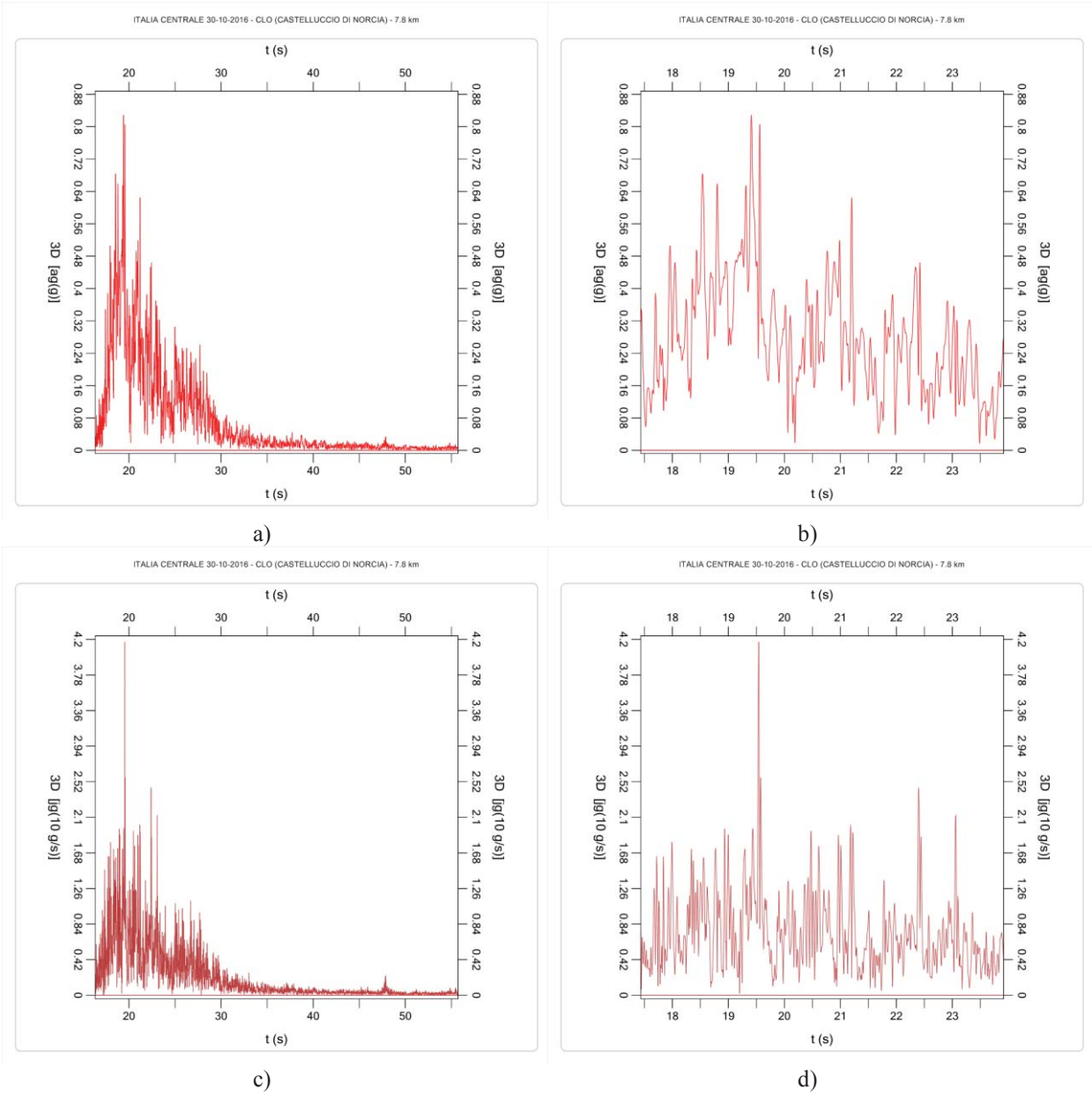

Figure 19. Station CLO, 2016 Norcia mainshock: acceleration and jerk 3D magnitude time series.
(a, b) acceleration time series; (c, d) jerk time series;
(a, c) time series cut-of at the acceleration threshold of 0.010 g (16.330 - 55.715 s);
(b, d) time series cut-of at the acceleration threshold of 0.025 g (17.435 - 23.915 s).

3 IMPULSIVE FORCES DUE TO JERK

During a seismic event, ground acceleration varies quickly, and the correspondent inertial forces also fluctuate in short time intervals of the order of few milliseconds. This sharp variation causes "jolts", that is, impulsive forces that act very briefly. Therefore, jerk could become a useful parameter for structural analysis and design if it is considered with the corresponding impulsive forces. A new approach is introduced below.

The study is based on ground acceleration records at station CLO (Castelluccio di Norcia) from 30 October 2016 Norcia mainshock: the same records considered in previous paragraphs.

Impulsive forces due to seismic jerk are distinct from inertial forces due to acceleration. The former are generated by the variation of acceleration and may be much higher than the latter. Their influence on a structure depends on the frequency content of the jerk and the dynamic properties of the structure itself.

The integral of jerk is, by its own definition, an acceleration. Since acceleration, according to Newton's Second Law, is force per unit mass, the definite integral of jerk in the interval between two consecutive zeros may be referred to as "impulsive force per unit mass" (F_{imp}/m). Two consecutive zeros of jerk correspond to a maximum and a minimum of acceleration, or vice-versa. The signed area bounded by the jerk function in that interval corresponds to the impulse of acceleration or deceleration. Therefore, considering the interval between instants t_1 and t_2, the impulsive force per unit mass is given by:

$$\frac{F_{imp}}{m} = \int_{t_1}^{t_2} j(t)\, dt \tag{5}$$

This expression can be applied to any of the three jerk components, each one characterized by its own sequence of zeros.

Figure 20 illustrates the definition of impulsive force per unit mass as the area bounded by the jerk function $j(t)$ between two consecutive zeros. Yellow color indicates the positive impulsive force corresponding to an interval where acceleration increases: $a(t)$ goes from a minimum to a maximum. Instead, green color indicates the previous negative impulsive force corresponding to the interval where acceleration decreases going from a maximum to a minimum.

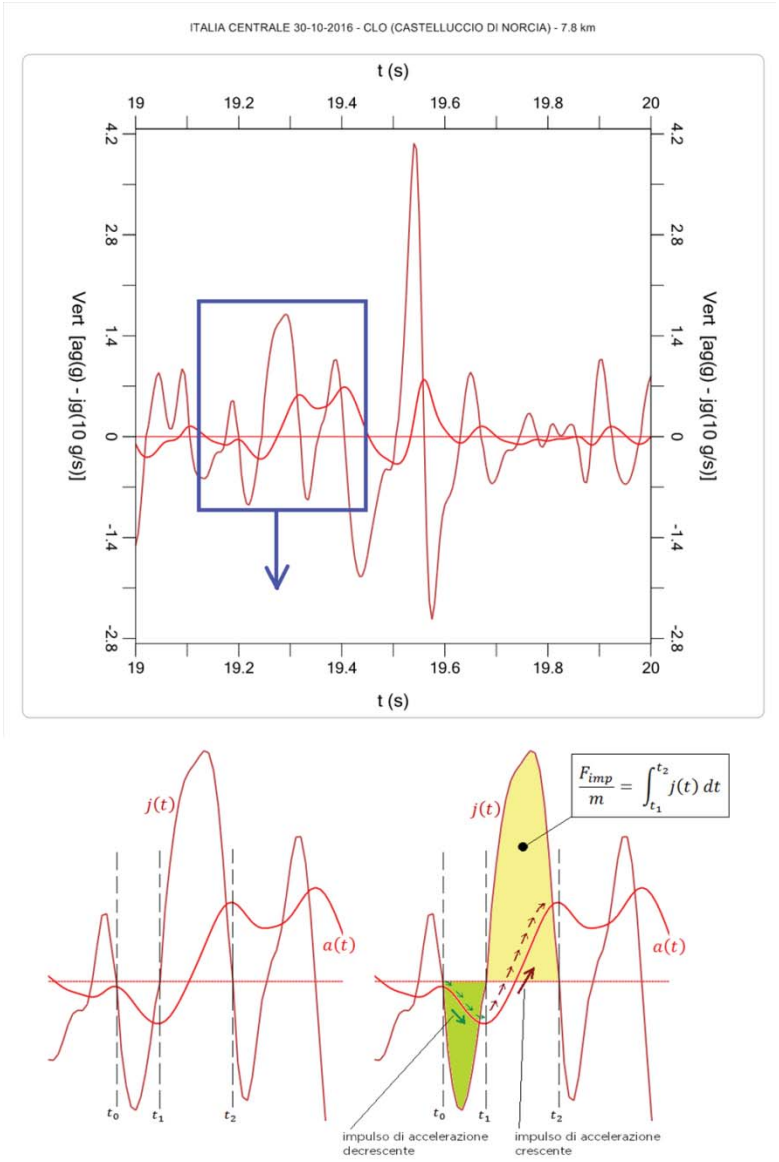

Figure 20. Impulsive force per unit mass, defined as the integral of jerk between two consecutive zeros

Figure 20 refers to the vertical component of the ground motion recorded at station CLO (Castelluccio di Norcia) from 30 October 2016 Norcia mainshock in the time interval (19.000 – 20.000 s).

It is worth noticing the very short duration of the impulsive forces. The considered jerk zeros correspond to the following instants in the record: t_0 = 19.200 s, t_1 = 19.245 s, t_2 = 19.320 s. The negative impulsive force corresponding to decreasing acceleration lasts 45 ms while the following positive impulsive force lasts 75 ms.

Thus, impulsive force may be calculated throughout the record for each time interval between two consecutive jerk zeros. The result is a step function that represents the time series of impulsive force per unit mass.

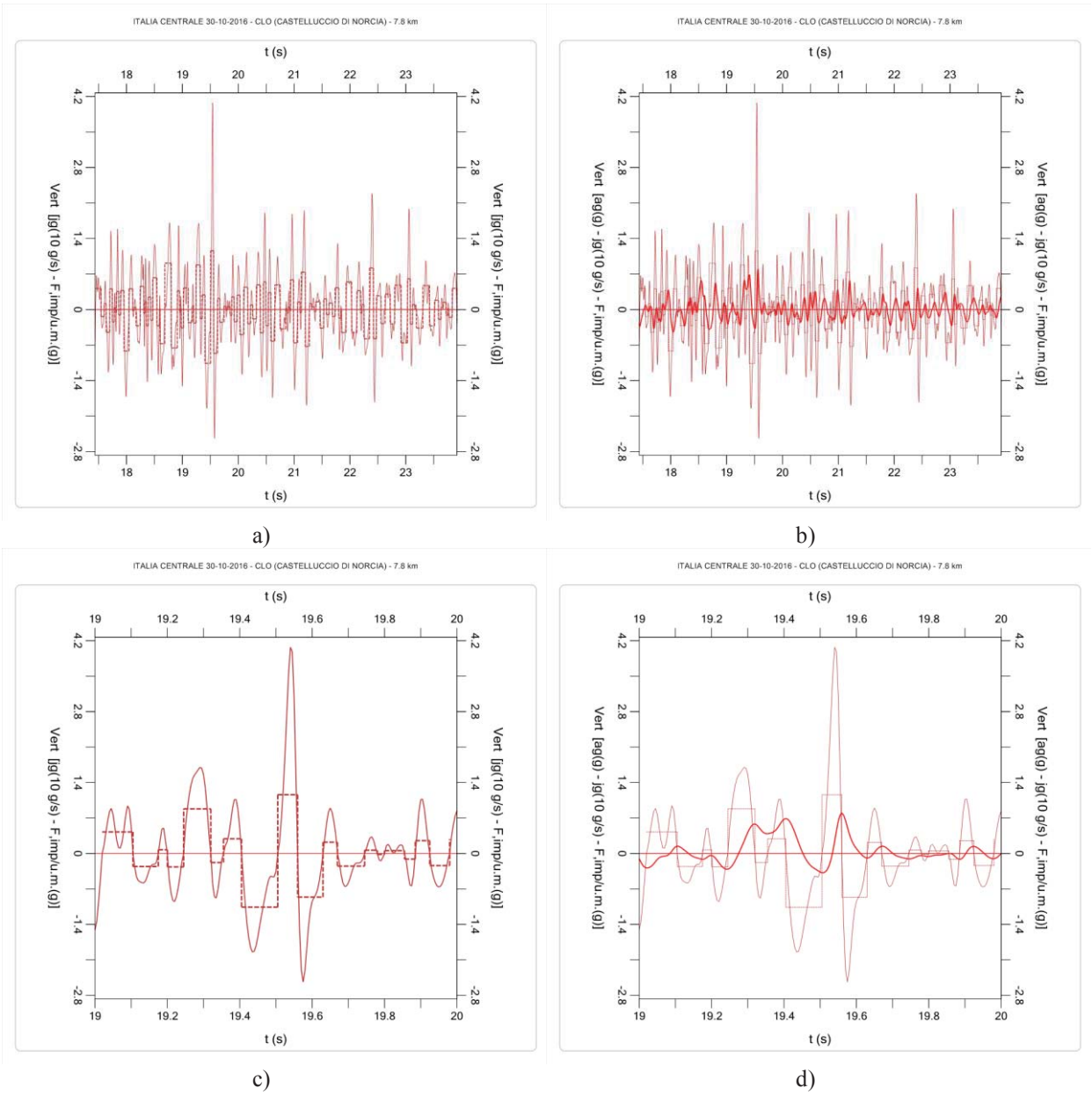

Figure 21. Jerk and impulsive forces per unit mass for the vertical seismic component. CLO - 30 October 2016 Norcia mainshock

Figure 21 shows jerk time series and step function of impulsive forces per unit mass (dashed line) for the vertical component of the reference seismic motion. The graphs on the right (b, d) also display the correspondent acceleration time series. The graphs at the top (a, b) refer to the time span between first and last acceleration peak exceeding 0.250 g, while the graphs at the bottom (c, d) refer to a shorter time interval (19.000 – 20.000 s).

The detail shown in Figure 22 highlights an important aspect: the value of the impulsive force cannot be directly correlated to the jerk level because it depends also on the time interval between two zeros. Therefore, lower jerk peaks with longer duration may yield higher impulsive forces than higher jerk peaks with shorter duration (cfr. Impulsive forces A and B in Figure 22).

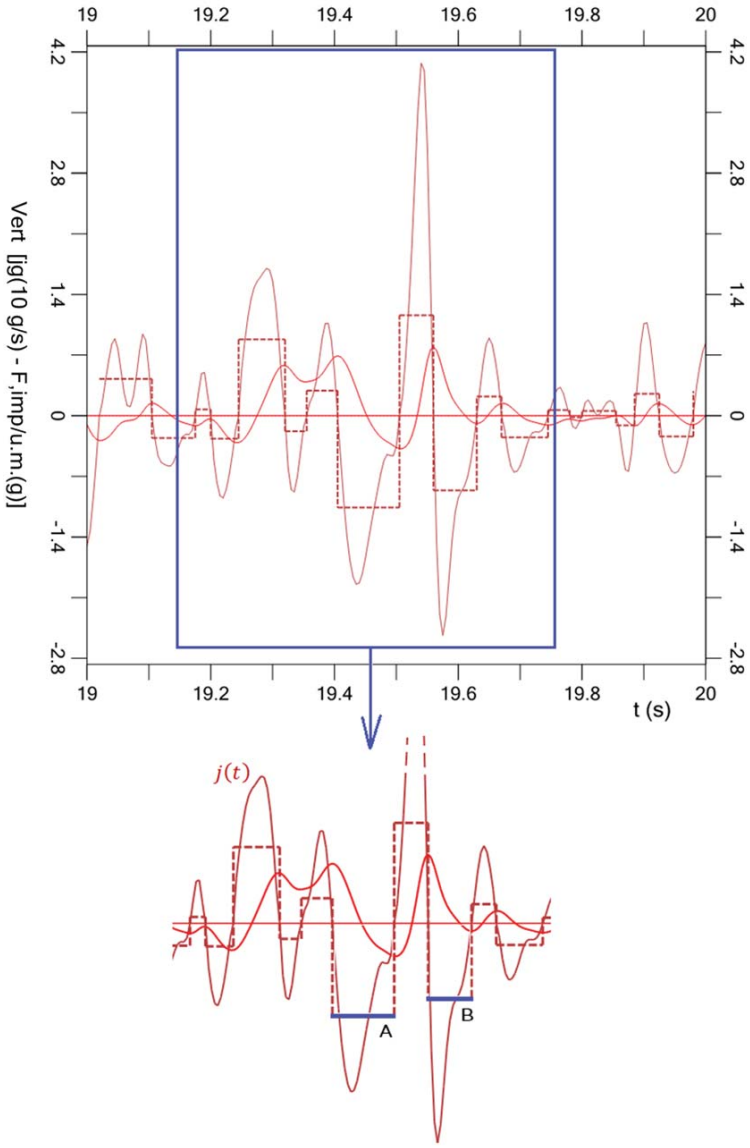

Figure 22. Peaks of jerk and correspondent impulsive forces

This behavior has general validity, it applies to all the components of seismic motion and different seismic events: the maximum values of jerk and impulsive force do not occur at the same time. The same happens between peaks of acceleration and peaks of jerk. Therefore, we get to the following property: PGA, PGJ and $F_{imp,max}$ are not simultaneous and there is not a direct relationship between them. This applies for any seismic event, any station, any of the three components of seismic motion.

Figures 23-25 show, for the reference seismic motion, the time series of impulsive force for each of the three components cut-off at the acceleration threshold of 0.250 g. The graphs on the left also include overlaid jerk time series (scale is uniform among the graphs on the left and among the graphs on the right).

Figure 26 shows the time series of the three components of impulsive forces overlaid in the same graph.

Thus, the dynamic nature of the seismic action is expressed, through jerk, by a series of consecutive impulses which determine vibrations; these are concept well known in Mechani-

cal Engineering, where forces induced by jerk are kept under control e.g. in order to optimize production processes [13].

Table 3 extends the information given in Table 2 with the maximum impulsive forces so to compare them with PGA and PGJ. Given their instantaneous nature and the independence between the three components, the impulsive forces are not combined in a unified 3D value. However, given the chaotic nature of the seismic motion, high values of impulsive force may occur simultaneously in different directions.

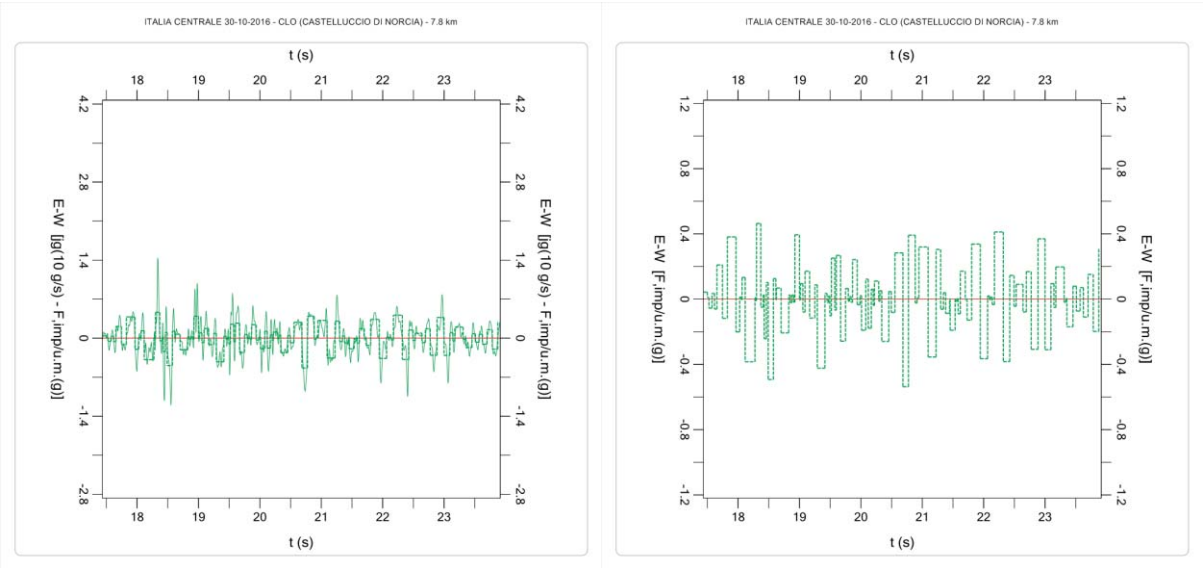

Figure 23. Jerk and impulsive force per unit mass: EW component

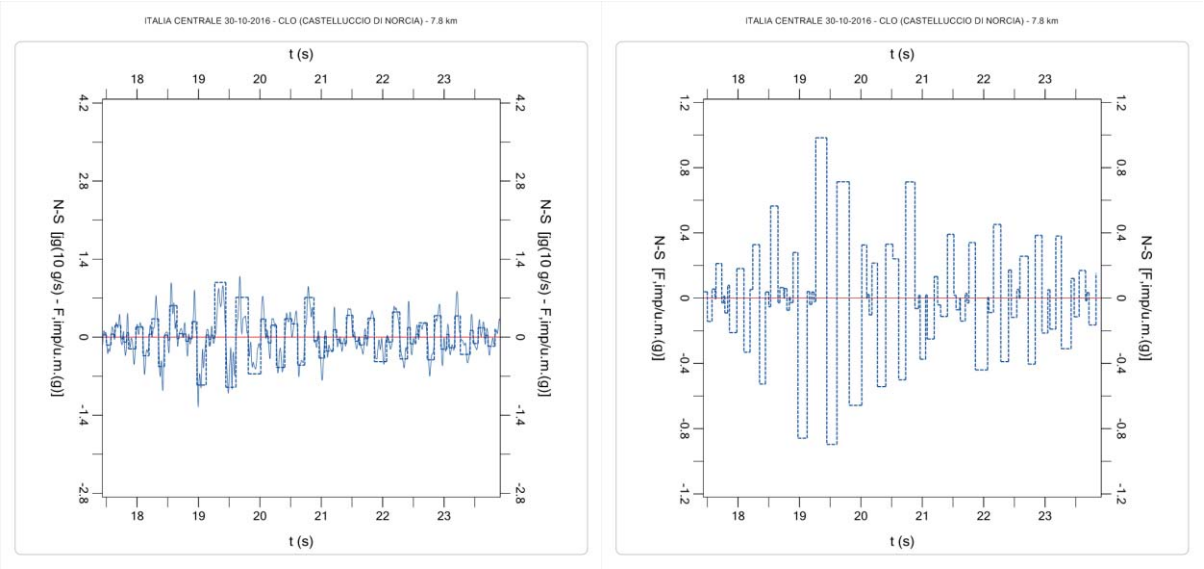

Figure 24. Jerk and impulsive force per unit mass: NS component

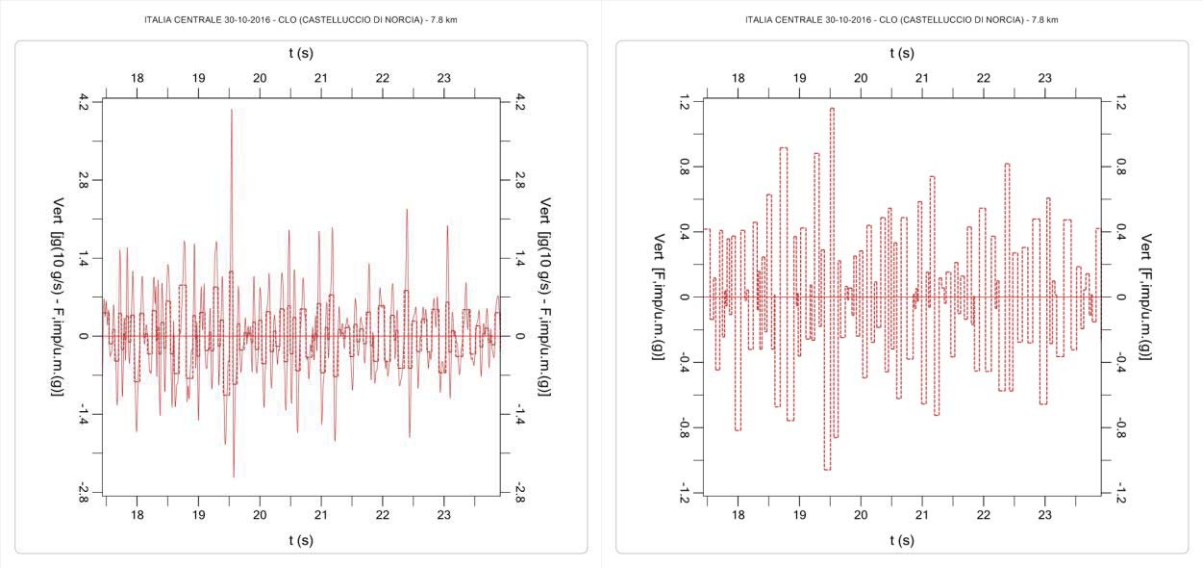

Figure 25. Jerk and impulsive force per unit mass: vertical component

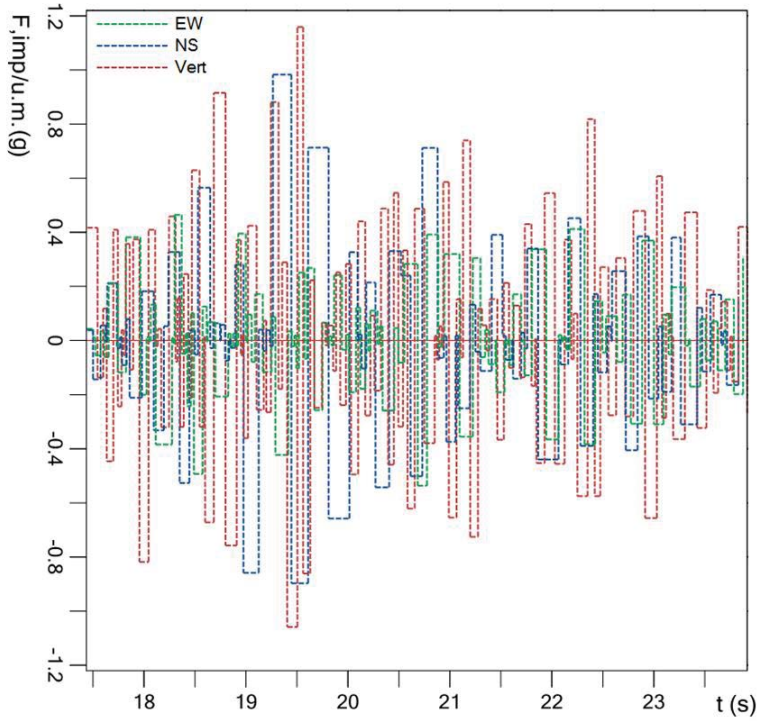

Figure 26. Time series of impulsive force per unit mass. All three components overlaid

Table 3 made clear how high the values of impulsive forces may be: for the reference seismic event (CLO, 30 October 2016 Norcia mainshock) the vertical impulsive force per unit mass exceeds gravity and reaches 1.159 g.

This means that during the seismic event there was a short time interval (55 ms, 19.505 s – 19.560 s) where the vertical "jolt" induced a force which exceeded weight (force of gravity) by more than 15%. Structures were subject to very demanding dynamic stress causing damages and collapses which cannot be fully understood if the analysis considers only the inertial forces due to ground acceleration.

Jerk thresholds significant for building damages need to be identified. Tong et Al. (2005) [11] highlighted that jerk larger than 2 g/s causes discomfort in people inside buildings. It is a threshold much higher (about 10 times higher) than criteria used by the transportation industry to ensure passenger comfort (about 0.2 g/s). The threshold of 10 g/s is the one within which structural damages may become severe.

Furthermore, the effects of jerk must be related to its frequency content: these aspects may be addressed through Fourier analysis.

	EW	t (s)	NS	t (s)	Vert.	t (s)	3D	t (s)
PGA (g)	0.427	20.775	0.583	19.445	0.797	19.560	0.829	19.410
PGJ (g/s)	14.36	18.335	12.50	18.995	40.70	19.540	41.69	19.540
$\frac{F_{imp,max}}{m}$ (g)	0.537	20.685 20.775 (**90** ms)	0.984	19.265 19.445 (**180** ms)	1.159	19.505 19.560 (**55** ms)		

Table 3. Peaks of acceleration, jerk and impulsive force per unit mass. Station CLO, 2016 Norcia mainshock

4 FREQUENCY ANALYSIS

The frequency content of a time series is expressed by the Fourier amplitude spectrum. Identification of the dominant frequency of the seismic motion is crucial for the comparison with the fundamental frequency of the structures.

Tong et al. (2005) [11], in their study on the 1999 Chi-Chi earthquake in Taiwan, provided Fourier amplitude spectra both for acceleration and jerk. The dominant frequency contents of the acceleration and jerk time series are between 1 and 10 Hz; however, jerk distributes in a much wider frequency band and its higher frequency contents are prominent.

This characteristic, observed for the first time in this seismic event in Taiwan, is confirmed for all seismic events in the Italian territory elaborated in this work. The jerk Fourier spectrum features a window of dominant frequency wider than the acceleration one. The jerk higher frequency content appears more important.

A parameter that characterized the frequency content is the mean period T_m, defined as the average of periods in the Fourier spectrum, each weighted by the square of its Fourier amplitude (Rathje et al. [14])

While the mean period of acceleration is generally quite large with values even higher than 1 s, the mean period of jerk is much lower with values comparable to typical fundamental periods of buildings.

Fourier analysis has been performed on the seismic records from station CLO (Castelluccio di Norcia) for 30 October 2016 Norcia earthquake. Figures 27-29 show the Fourier amplitude spectra of acceleration and jerk with the indication of the mean period for the three components of the seismic motion (EW, NS, Vert.).

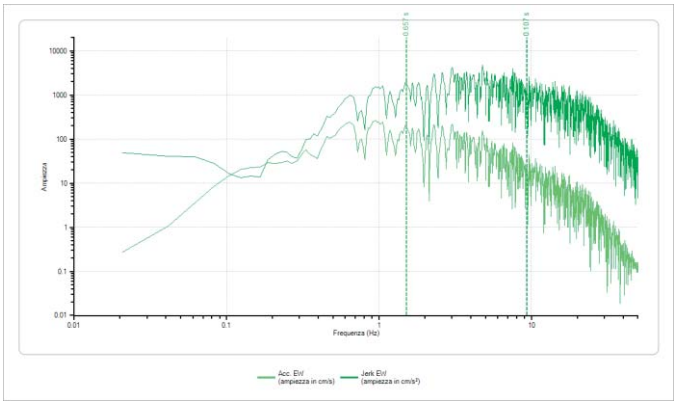

Figure 27. CLO, 2016 Norcia earthquake:
acceleration and jerk Fourier amplitude spectra for EW component

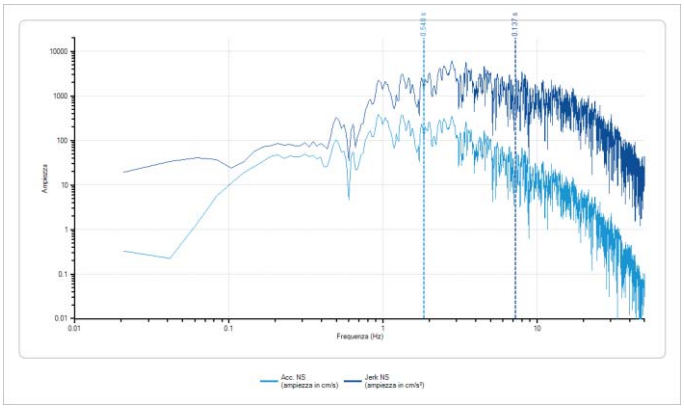

Figure 28. CLO, 2016 Norcia earthquake:
acceleration and jerk Fourier amplitude spectra for NS component

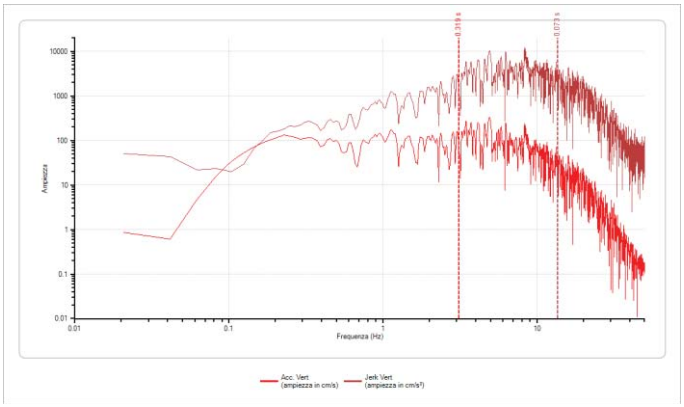

Figure 29. CLO, 2016 Norcia earthquake:
acceleration and jerk Fourier amplitude spectra for vertical component

T_m(s)	EW	NS	Vert.
Acceleration	0.657	0.540	0.319
Jerk	0.107	0.137	0.073

Table 4. Mean period of acceleration and jerk. CLO, 2016 Norcia earthquake

Table 4 highlights an important aspect: the main frequencies of the vertical component are significantly higher than the horizontal ones. This is also evident by the overlaid three-components Fourier spectra shown in Figures 30-31 for acceleration and jerk respectively. The jerk mean periods appear very close to fundamental periods of rigid structures like masonry buildings. This points out the prospect of critical issues caused by impulsive action on structural elements.

Records from CLO station for 30 October 2016 Norcia earthquake have been taken as reference for the elaborations presented so far, but the highlighted observation can be generalized and deepened through the analysis of a larger number of records.

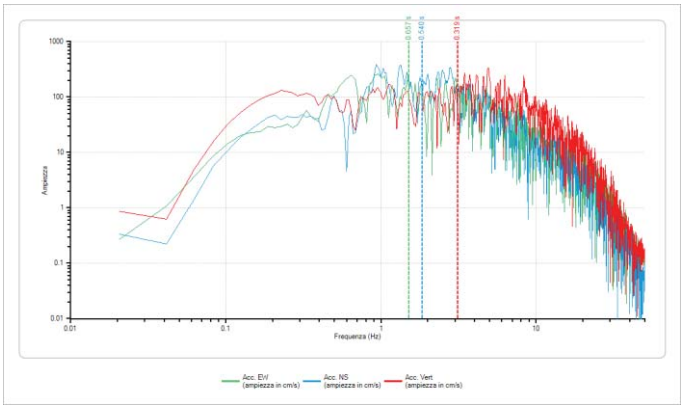

Figure 30. CLO, 2016 Norcia earthquake:
overlaid Fourier spectra for the three components of acceleration

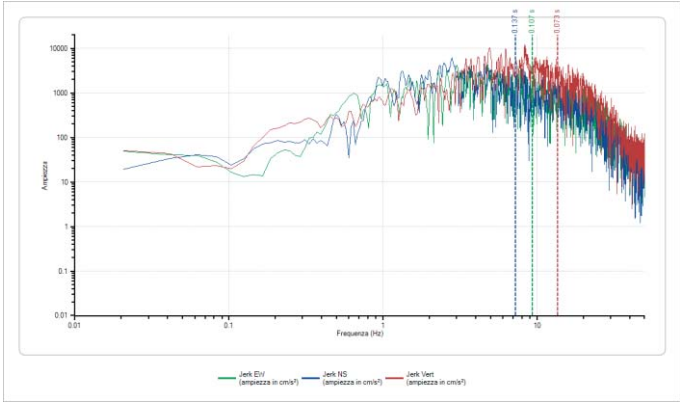

Figure 31. CLO, 2016 Norcia earthquake:
overlaid Fourier spectra for the three components of jerk

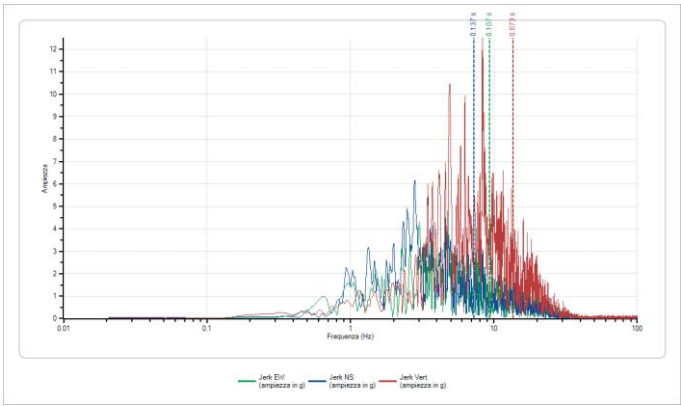

Figure 32. CLO, 2016 Norcia earthquake:
overlaid Fourier spectra for the three components of jerk
(logarithmic scale for frequency, natural scale for amplitude)

5 SEISMIC EVENTS ON ITALIAN TERRITORY: ELABORATIONS AND ANALYSES

The following study is based on ground motion records provided by ITACA project [12] for 8 reference seismic events: 30 October 2016 Norcia; 24 August 2016 Accumuli; 29 May 2012 Emilia; 6 April 2009 L'Aquila; 26 September 1997 Umbria-Marche; 23 November 1980 Irpinia; 19 September 1979 Valnerina; 6 May 1976 Friuli.

ITACA database provides records of these events taken from numerous stations. The signals are already corrected, thus, can be directly elaborated for the purposes of this work.

The performed elaborations highlighted some common aspects:

- the farer is the station from the epicenter, the shorter is jerk duration and the lower is its peak value.
- the farer is the epicenter the lower are the impulsive forces per unit mass; however, they remain higher than peak ground acceleration.
- the mean period of the vertical jerk component is always significantly lower than the horizontal components. Jerk represents the impulsive content of the seismic motion which is enhanced in the vertical component.
- stations farer form epicenter show attenuation of impulsive content through jerk drop. Vertical jerk component attenuates with respect to other horizontal components.

As an example, Table 5 reports the results for three stations recording 30 October 2016 Norcia mainshock.

Through statistical elaboration of the records, trend lines correlating PGA, PGJ and Impulsive Forces may be outlined.

This constitutes the first step for considering impulsive forces in structural design. If ground jerk and correspondent impulsive forces are not known, an estimation is required in order to evaluate their effects on structures.

30 October 2016 Norcia earthquake. Station and epicentral distance ➔	1_1 - CLO Castelluccio di Norcia, 7.8 km	1_2 - ACC Accumuli 18.6 km	1_3 - FBR Fabriano 59.1 km
Acceleration, Jerk and Impulsive Force per unit mass			
$\Delta t(j_g \geq 2.0$ g/s)	31.440 (16.410 - 47.850)	13.750 (7.395 - 21.145)	7.905 (17.465 - 25.370)
EW: PGA	0.427	0.434	0.079
PGJ	14.36	18.25	5.39
F_{imp} max	0.537	0.744	0.155
NS: PGA	0.583	0.392	0.066
PGJ	12.50	12.15	3.46
F_{imp} max	0.984	0.660	0.121
Vert.: PGA	0.797	0.558	0.049
PGJ	40.70	35.88	2.21
F_{imp} max	1.159	0.887	0.095
Mean period from Fourier amplitude spectra (T_m)			
EW: Acc.	0.657	0.397	0.234
Jerk	0.107	0.081	0.054
NS: Acc.	0.540	0.456	0.247
Jerk	0.137	0.083	0.060
Vert.: Acc.	0.319	0.179	0.232
Jerk	0.073	0.044	0.060

Seismic parameters and unit of measure:

$\Delta t(j_g \geq 2.0$ g/s)	(s)	Time span between first and last jerk peak exceeding 2.0 g/s
PGA	(g)	Peak ground acceleration
PGJ	(g/s)	Peak ground jerk
F_{imp} max	(g)	Maximum impulsive force per unit mass (based on jerk)
T_m	(s)	Mean period from Fourier amplitude spectra

Table 5. Acceleration and jerk and impulsive forces for 30 October 2016 Norcia earthquake

Among all the ground station records available for the 8 events considered, the ones taken into account in the statistical analysis were those with bracket duration of ground acceleration record longer than 100 ms when the threshold of 0.005 g is applied. In total 447 station records were considered. For each of them and for each of the three components (EW, NS, Vert.) the following parameters were elaborated by means of the software Seismic 3D:

1. peak ground acceleration (PGA)
2. peak ground jerk (PGJ)
3. maximum value of impulsive force per unit mass (F_{imp})
4. mean period (T_m) of acceleration and jerk from Fourier spectra

The statistical elaboration was performed separately for horizontal and vertical components. In the pursuit of useful correlation between the considered parameters, distinction between the two horizontal components (coming from different stations) appears inappropriate.

The correlations obtained between PGA, PGJ and F_{imp} are illustrated in Figures 33, 34, 35.

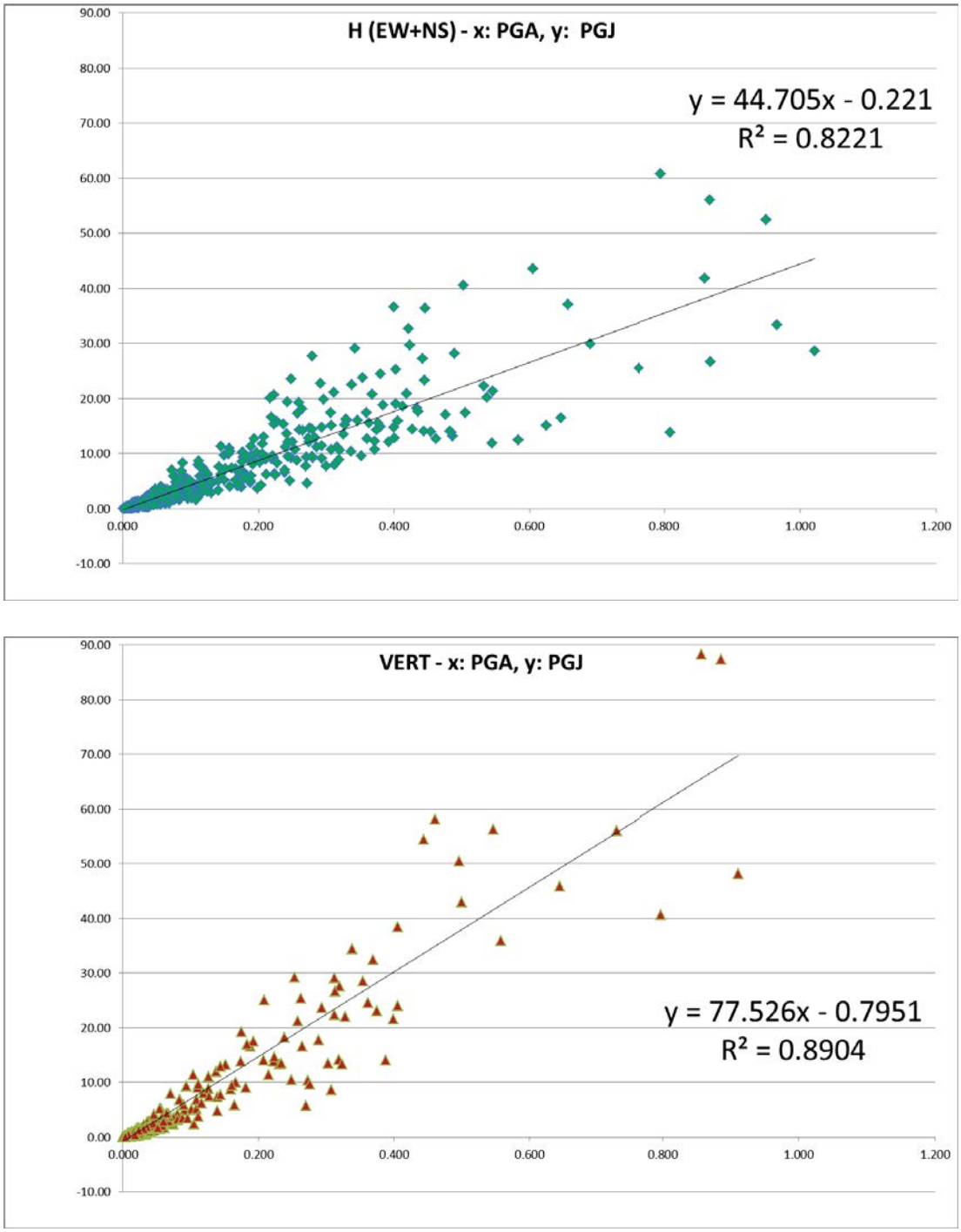

Figure 33. Correlation PGA-PGJ for horizontal and vertical components

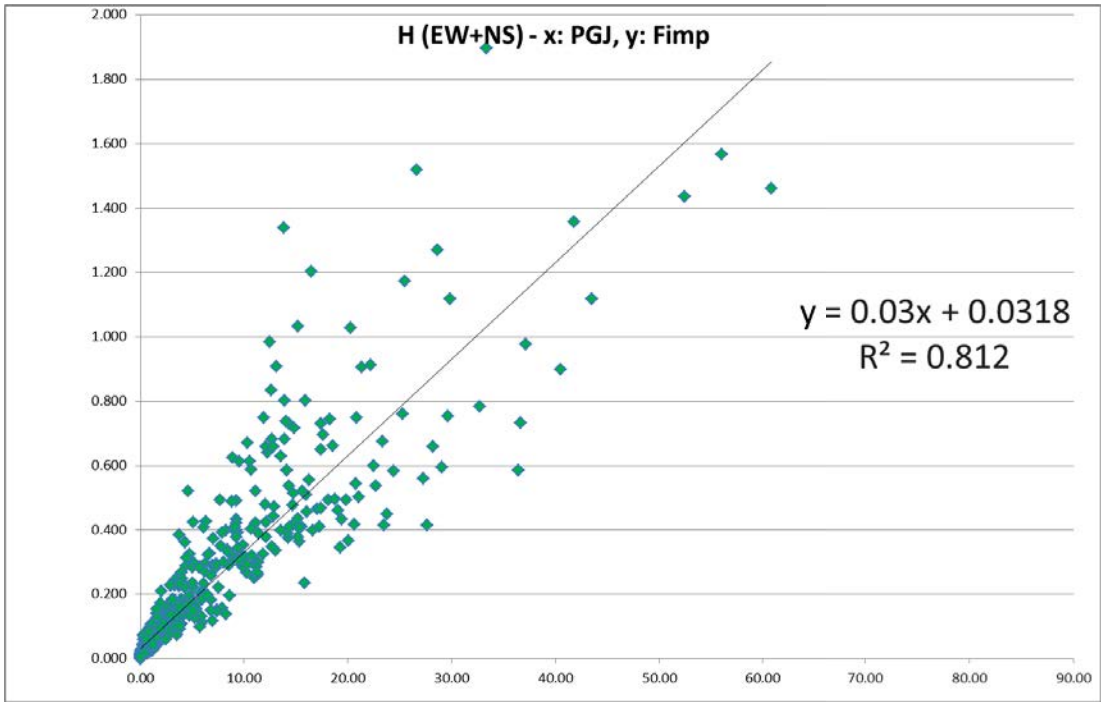

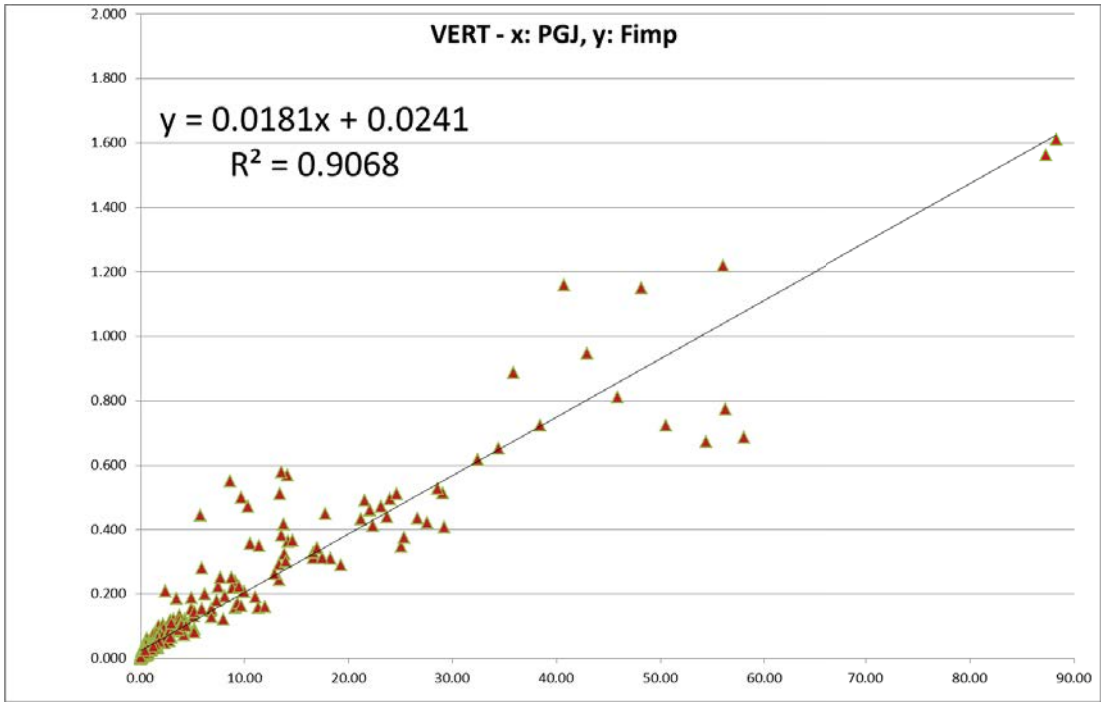

Figure 34. Correlation PGJ-Fimp determined through (5), for horizontal and vertical components

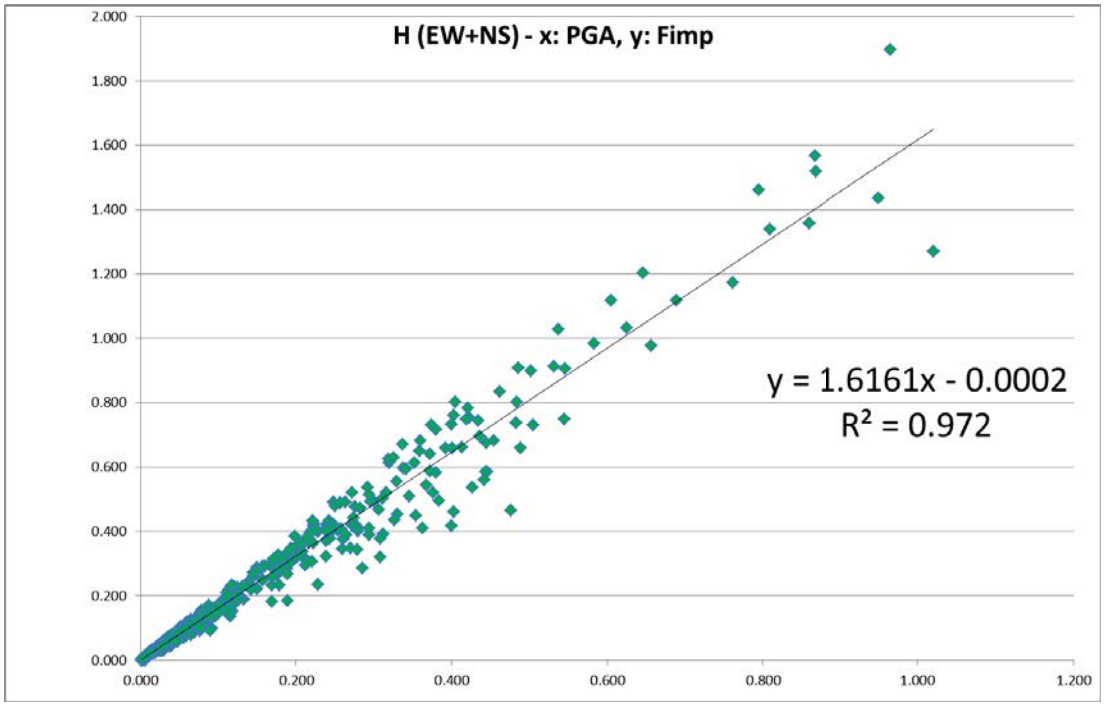

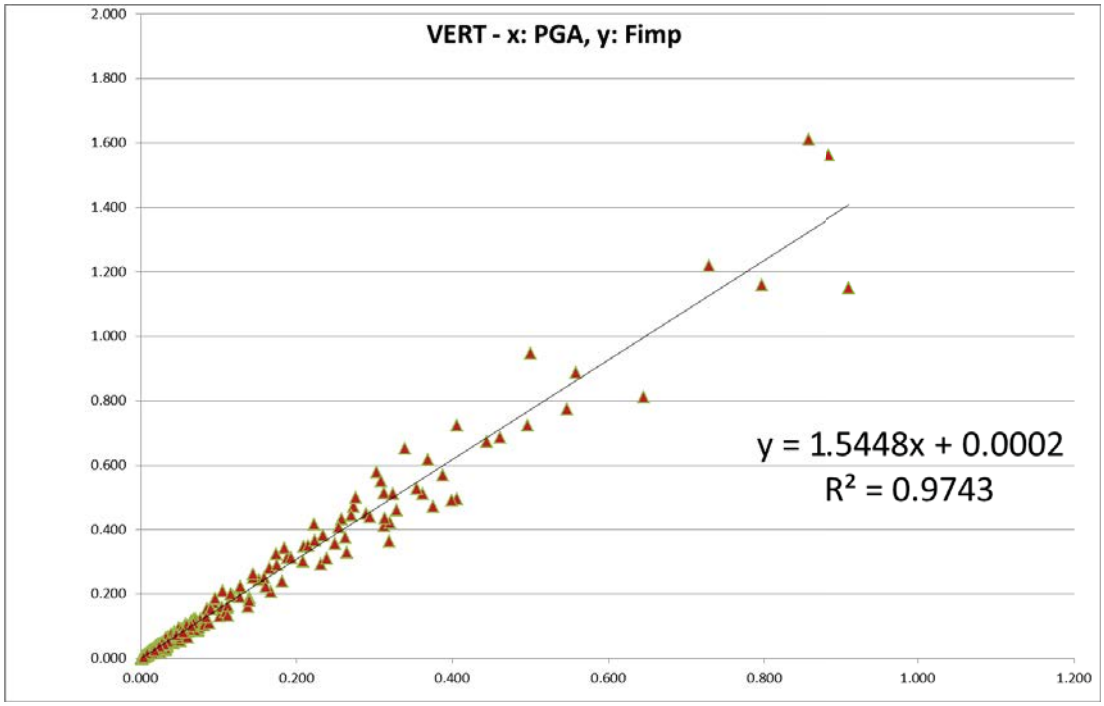

Figure 35. Correlation PGA-F_{imp} for horizontal and vertical components

The PGA-F_{imp} graphs show an excellent correlation: the relationship between peak ground acceleration and peak impulsive force is well described by the trend line.

Acceleration, jerk and impulsive force are generated by a chaotic phenomenon: the analytical operations carried out for determining jerk (through derivation of acceleration) or for calculating the impulsive forces are processes which do not correspond to a predefined analytical function.

The correlation between PGA and impulsive forces, obtained through elaboration of the main seismic events in Italy, is an intrinsic property of the events themselves. The fact that the cor-

relation has a coefficient of determination very close to 1 represents an excellent support for estimating the impulsive actions based on ground acceleration data.

The correlation obtained through statistical analysis between PGA (s) and PGJ (g/s) and between PGA (g) and maximum impulsive force per unit mass (g) are summed up in the following expressions (H stand for horizontal component, V stands for vertical component):

$$PGJ_H = 44.705\, PGA_H - 0.221 \quad (6)$$

$$PGJ_V = 77.526\, PGA_V - 0.795 \quad (7)$$

$$F_{imp,max,H} = 1.616\, PGA_H \quad (8)$$

$$F_{imp,max,V} = 1.545\, PGA_V \quad (9)$$

In order to validate the relationships determined through statistical analysis on Italian seismic events, we operate a comparison between the jerk values elaborated by Tong et al. [11] for the 1999 Chi-Chi earthquake in Taiwan and those calculated from PGA with expressions (6-7).

Station	Component	PGA (g)	PGJ (g/s) (Tong et Al.)	PGJ (g/s) (Mariani, Pugi)	PGJ delta vs Tong et Al.	F_{imp} (g)
CHY028	EW	0.630	21.50	27.94	30%	1.018
	NS	0.764	26.30	33.93	29%	1.235
	VERT	0.342	23.20	25.72	11%	0.529
TCU095	EW	0.378	13.80	16.68	21%	0.611
	NS	0.712	31.80	31.61	-1%	1.150
	VERT	0.255	19.80	18.97	-4%	0.394

Table 6. Comparison between the elaborations of Tong et Al. (2005) [11] and Mariani and Pugi (2020)

CHY028 station yields a difference of about 30% for the horizontal component. The difference is rather high, but it drops to 11% for the vertical component. Given the fact that the seismic event in Taiwan has no relation whatsoever with the Italian events and that the analytical procedure for calculating jerk (based on numerical differentiation) has been carried out independently, the result is satisfactory. Considering that the impulsive phenomenon is particularly associated to the vertical component, the value of 25.72 g/s estimated through (7) is in good agreement with the 23.20 g/s in Tong et Al. Moreover, these jerk values are rather high, definitely higher than the 10 g/s threshold considered the cause of important damages on buildings: the values of 25.72 and 23.20 g/s would result in similar effects induced on the structures.

A surprisingly high agreement is obtained for TCU095 station where the peak ground jerk for the NS component is practically coincident with the value calculated through (7): 31.61 vs. 31.80 (g/s). Also, the vertical jerk component is very close: 18.97 vs 19.80 g/s.

The statistical investigation carried out on jerk should be completed with the analysis of the frequency content. In fact, the effects of seismic motion depend on the way they are filtered by the structures: a reliable model for the evaluation of jerk impulsive action effects on structures requires a frequency analysis which could be carried out through the study of the mean period from Fourier amplitude spectra.

The definition of a statistical value of the mean period T_m would provide a realistic estimation of the main frequencies of acceleration and jerk.

The mean period T_m calculated from Fourier spectra has no relations with peak ground acceleration, peak ground jerk or maximum impulsive forces. Therefore, the investigation on the mean periods is carried out comparing directly the T_m values of the 447 station records considered. Some stations yielded T_m values significantly far from average due to local site effects. Since the scope of the analysis is the pursuit of a T_m value which could be representative of acceleration and jerk for generic events, it is preferable to associate it to the median value rather than the mean. The median value is less influenced by extremely large or small values and gives a better idea of which is the "typical" value.

Figures 36-41 report for the three components of acceleration and jerk the following information:

- the mean period T_m for each station considered. The graphs also show the mean value (black line) and the median value (red line) which in all the cases is lower than the mean.
- the frequency distribution with discretization of the periods in intervals of 0.1 s for acceleration and 0.025 s for jerk

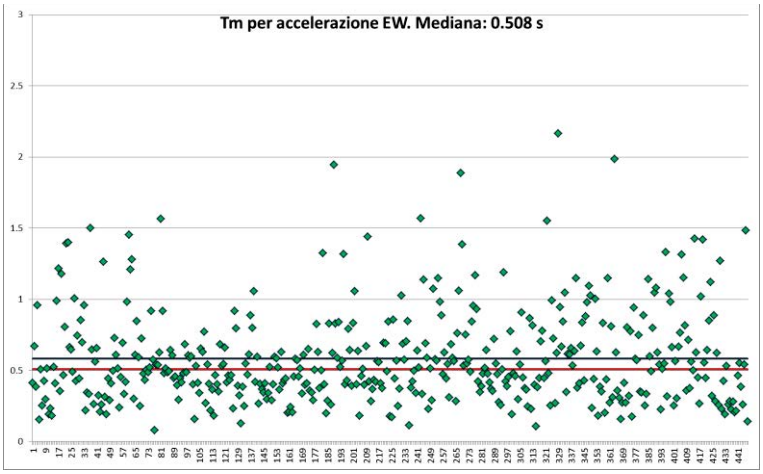

Classe	Frequenza	
0.1	0.22%	1
0.2	4.25%	19
0.3	12.75%	57
0.4	13.20%	59
0.5	18.79%	84
0.6	14.54%	65
0.7	11.41%	51
0.8	4.47%	20
0.9	5.82%	26
1	3.58%	16
1.1	3.13%	14
1.2	2.24%	10
1.3	1.12%	5
1.4	1.57%	7
1.5	1.34%	6
Altro	1.57%	7

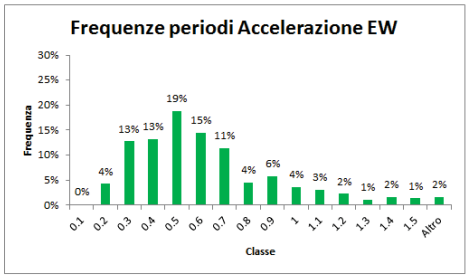

Figure 36. Statistical elaboration on the mean period T_m of acceleration EW component

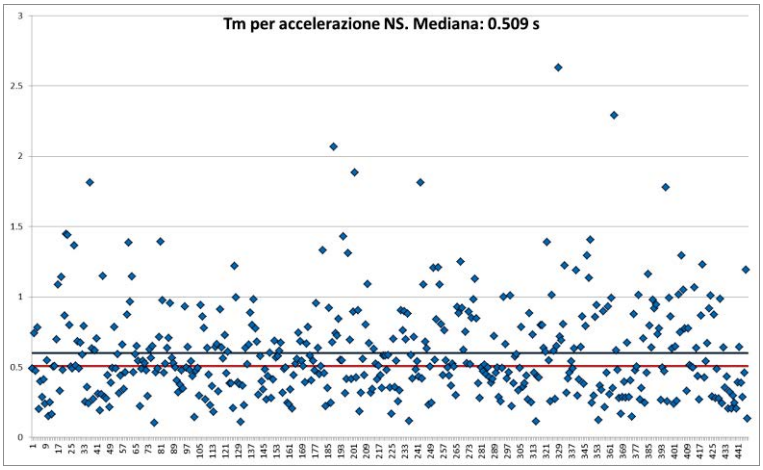

Classe	Frequenza	
0.1	0.00%	0
0.2	3.36%	15
0.3	13.65%	61
0.4	11.86%	53
0.5	18.79%	84
0.6	12.30%	55
0.7	11.63%	52
0.8	7.38%	33
0.9	5.59%	25
1	5.59%	25
1.1	2.46%	11
1.2	1.79%	8
1.3	1.79%	8
1.4	1.34%	6
1.5	0.89%	4
Altro	1.57%	7

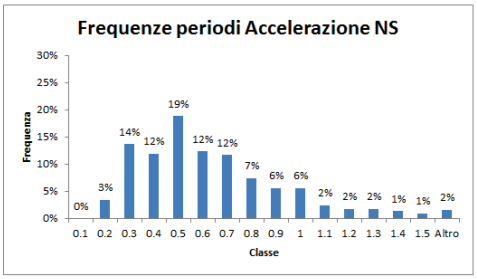

Figure 37. Statistical elaboration on the mean period T_m of acceleration NS component

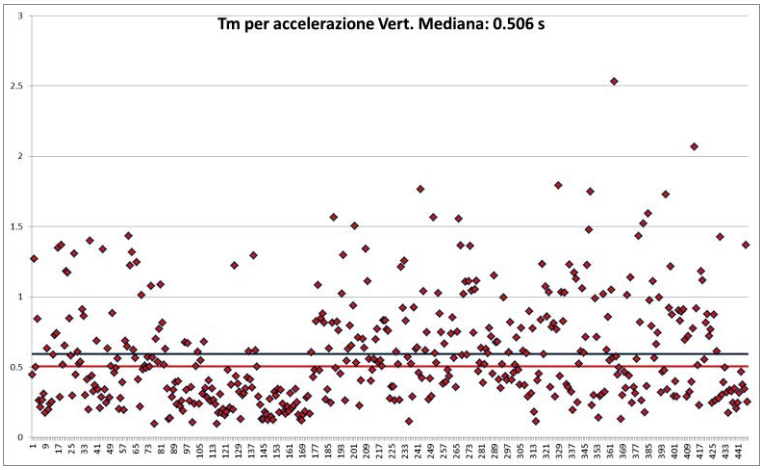

Classe	Frequenza	
0.1	0.45%	2
0.2	8.95%	40
0.3	15.21%	68
0.4	14.32%	64
0.5	10.29%	46
0.6	10.51%	47
0.7	8.95%	40
0.8	6.49%	29
0.9	6.71%	30
1	2.68%	12
1.1	4.03%	18
1.2	2.91%	13
1.3	2.68%	12
1.4	2.24%	10
1.5	0.89%	4
Altro	2.68%	12

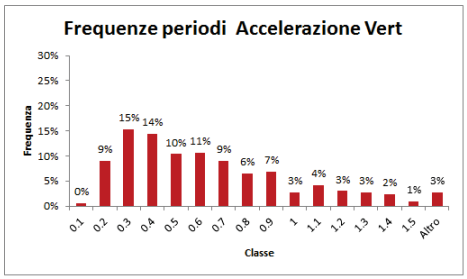

Figure 38. Statistical elaboration on the mean period T_m of acceleration vertical component

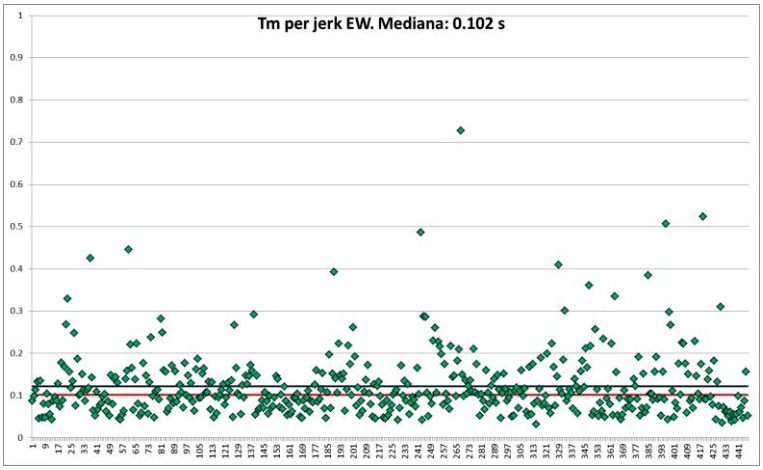

Classe	Frequenza	
0.025	0.00%	0
0.05	6.71%	30
0.075	19.46%	87
0.1	22.60%	101
0.125	16.78%	75
0.15	10.96%	49
0.175	9.17%	41
0.2	4.03%	18
0.225	2.91%	13
0.25	1.79%	8
0.275	1.34%	6
0.3	1.12%	5
Altro	3.13%	14

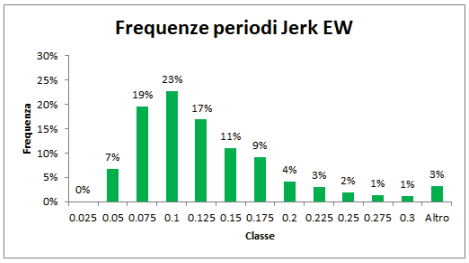

Figure 39. Statistical elaboration on the mean period T_m of jerk EW component

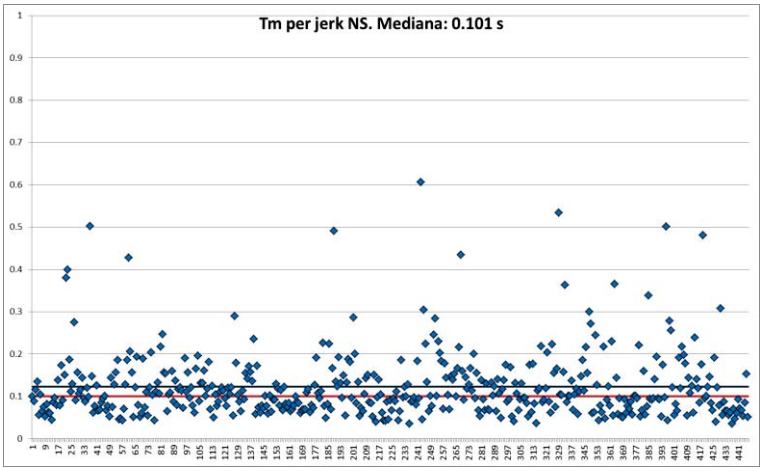

Classe	Frequenza	
0.025	0.00%	0
0.05	5.37%	24
0.075	21.25%	95
0.1	22.15%	99
0.125	17.45%	78
0.15	10.29%	46
0.175	7.38%	33
0.2	5.59%	25
0.225	3.58%	16
0.25	1.79%	8
0.275	0.45%	2
0.3	1.34%	6
Altro	3.36%	15

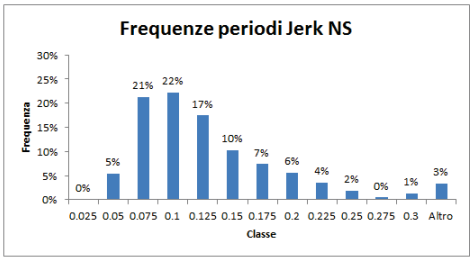

Figure 40. Statistical elaboration on the mean period T_m of jerk NS component

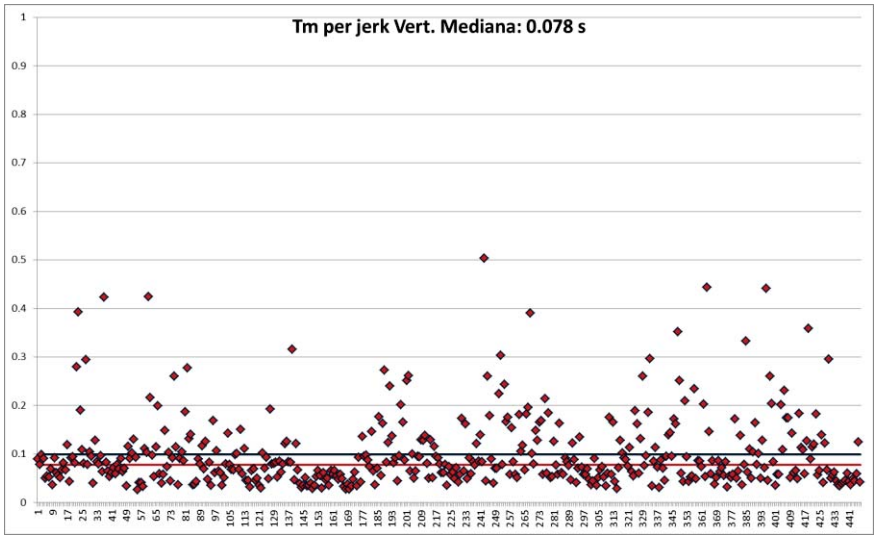

Classe	Frequenza	
0.025	0.00%	0
0.05	21.48%	96
0.075	27.52%	123
0.1	19.69%	88
0.125	8.50%	38
0.15	6.71%	30
0.175	4.25%	19
0.2	3.58%	16
0.225	1.79%	8
0.25	0.89%	4
0.275	1.79%	8
0.3	1.12%	5
Altro	2.68%	12

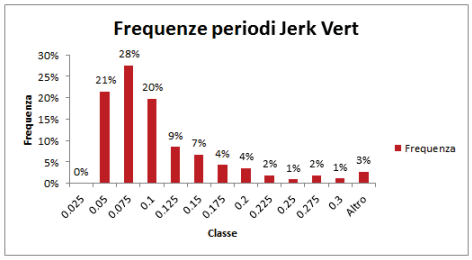

Figure 41. Statistical elaboration on the mean period T_m of jerk vertical component

Table 7 sums up the representative values of the mean periods and the main contribution to the distribution.

	T_m (s) and main contribution to the distribution	
Component	Acceleration	Jerk
EW	0.508 (19% for 0.500)	0.102 (23% for 0.100)
NS	0.509 (19% for 0.500)	0.101 (22% for 0.100)
Vert.	0.506 (15% for 0.300)	0.078 (28% for 0.075)

Table 7. Representative T_m for acceleration and jerk

From the analysis of the Fourier spectra it is evident that the main jerk frequencies are much higher than the acceleration ones. This aspect was already clear by the comparison of the Fourier spectra elaborated for Castelluccio di Norcia records of 2016 Norcia earthquake (Figures 27-29). This highlights the very nature of jerk which can be associated to the impulsive content of acceleration.

Moreover, while for acceleration there are not significant differences among the horizontal and vertical components, all characterized by $T_m \cong 0.500$ s, for jerk the difference is substantial ($T_m \cong 0.100$ s for horizontal components and $T_m \cong 0.075$ s for the vertical).

Therefore, jerk consists of higher frequency than acceleration and the vertical component accentuate this characteristic with respect to the horizontal components.

Jerk vertical component is particularly important since it represents the most impulsive content of seismic motion.

The conception that buildings, being designed to resist vertical loading, can undergo impulsive seismic action without damages while they suffer only the horizontal seismic action effects, is definitely overcome.

Moreover, in lights of the study on jerk, the negative effects of the vertical seismic component involve failures triggered by the rapid alternation of compression and decompression induced by vertical vibrations.

The seismic motion is a dynamic phenomenon; thus, the structural response is totally different from that under static loading.

Where the main frequencies of the seismic motion are close to the fundamental frequencies of buildings, seismic effects undergo maximum amplification and structural elements are subject to the most demanding actions.

Studying the different building typologies one can identify the cases where jerk effects may be critical and potentially cause damages: e.g., the fact that jerk mean periods are close to fundamental periods of masonry buildings suggests to investigate the link between impulsive forces and local damages such as masonry disaggregation and connection failures.

6 EFFECTS OF IMPULSIVE ACTIONS ON BUILDINGS

During this research, the few available studies on the variation of seismic acceleration were collected. Based on the various considerations of the authors and the results of this work, the following 7 aspects may be highlighted:

1) Inertial force induced by acceleration and impulsive action due to variation of acceleration are two complementary aspects: both should be considered when assessing the structural behavior (Tong et Al. [11]);
2) During 1999 Chi-Chi earthquake acceleration records obtained from sensor placed at different levels of seven-story RC building showed that jerk amplification is substantially similar to that of acceleration (Tong et Al. [11]);
3) The attenuation of the Jerk design response spectrum with respect to the elastic spectrum is lower than what occur for acceleration. For low periods (rigid structures) the impact reduction factor R_J is practically equal to 1, so the jerk design response spectrum is almost coincident with the elastic one (Haoxiang He et Al. [15]).
4) In general, improving ductility jerk effect will reduce, that is, the impact reduction factor R_J increases, in a manner similar to the behavior factor q for acceleration spectra (Haoxiang He et Al. [15]). For the horizontal components of the seismic motion, useful information for design purposes are given by the jerk response spectra illustrated in Figures 42-43 (Haoxiang He et Al. [15]).
5) The propagation of jerk vibrational waves is directly related to stress concentration and local damages, which in homogeneous material are initiated by molecular bond separation (Y. Xueshan et Al. [16]). In the case of masonry, it comes naturally to extend this concept to the macroscopic level of stones separation for mortar disaggregation.
6) In existing masonry buildings, strengthening interventions aimed at confining the structural elements prevent local concentration of stresses and improve the response with respect to jerk (Sofronie [17-18]). Considering the short duration of the impulsive action and the rigid-brittle behavior of masonry, such interventions may be verified in terms of resistance. In general, in existing masonry buildings, it is crucial to ensure resistance with respect to local damages such as masonry disaggregation and failure of connections between different structural elements.

7) The effects of jerk are particularly important in vertical direction. In fact, the vertical components are more impulsive than the horizontal ones, as described by the lower mean period in Fourier spectra (Table 7).

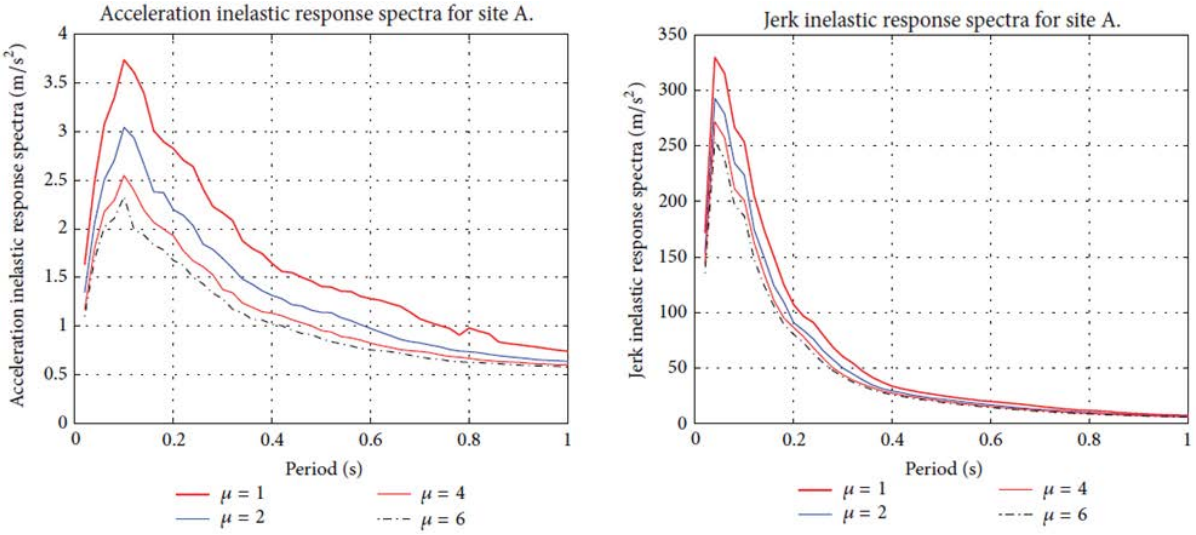

Figure 42. Acceleration and jerk inelastic response spectra for site A.
Statistical elaboration by Haoxiang He et Al. [15]

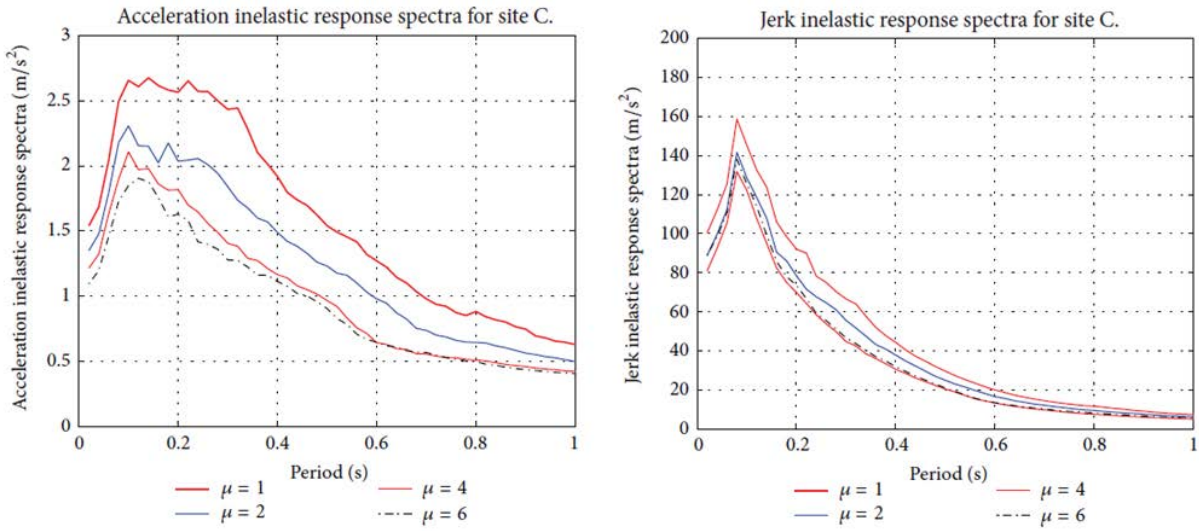

Figure 43. Acceleration and jerk inelastic response spectra for site C.
Statistical elaboration by Haoxiang He et Al. *[15]*

In light of the correlation between seismic jerk and physical damage of materials and structural elements during a seismic event, some considerations on seismic monitoring activity should be made.

At the moment, drift ratio, that is the relative displacement between two floors divided by the vertical distance between them, is the main parametric indicator of damage condition in a monitored building [19].

This parameter is monitored through software processing real-time measurements of displacements acquired through double integration of accelerometer time-series data. Other mon-

itored parameter are the periods of vibration, the peak ground acceleration (PGA) and peak structure acceleration (PSA), but only in the two horizontal direction X and Y.

Drift ratio is truly representative of damage condition in framed steel or RC structures; but in masonry structures, very rigid and strongly characterized by brittle types of failures, this parameter appears less consistent with respect to jerk monitoring.

The difference between the two parameters is also the possibility to represent through jerk the spatial effects of seismic motion, including the vertical component: drift ratio completely disregards this aspect.

Furthermore, jerk monitoring may provide important information on the assessment of local failures in other structural typologies: e.g. joint failures in steel frames [20, 21].

Given the relation between high values of impulsive forces and damage in areas with high stress concentration, the maximum values of jerk (PGJ and PSJ) play a significant role in the assessment of the negative effects induced by the seismic motion.

Placement of triaxial jerk sensor, available for some years now [16], or the real-time analytical calculation of jerk time series, may further enhance the quality of the monitored information with clear benefits on the quick definition of the damage scenarios, one of the main objectives of seismic monitoring.

The negative effects of the vertical jerk component are highlighted by the impulsive nature of the phenomenon and the high vertical stiffness of the structure. Therefore, amplification effects due to high similarity between fundamental period of the structures and jerk mean period should be investigated.

Jerk is characterized by high frequencies. The statistical analysis on the main recent seismic events in Italy found that the representative mean period of the vertical jerk component is about 0.075 s, which is very close to the fundamental period of vertical vibration of many rigid structures, such as masonry buildings.

To be more specific about the amplification of the structural response in terms of displacements and internal actions, considering that seismic input is a combination of many harmonic excitations, we can refer to the theory of driven harmonic oscillators with viscous damping.

Study of the simple oscillator leads to an amplification factor C_{ampl} given in expression (10):

$$C_{ampl} = \frac{1}{\sqrt{\left(1 - \frac{T_1^2}{T^2}\right) + 4\,\xi_{eq}^2\,\frac{T_1^2}{T^2}}} \tag{10}$$

where: T_1 is the fundamental period of the structure; T is the period of the applied force (in this case coincident with the mean period of vertical jerk component); ξ_{eq} is the equivalent viscous damping coefficient.

By applying (10) we get that with a period of the applied force T = 0.075 s, the vertical impulsive effect is amplified for fundamental periods T_1 in the range [0 - 0.105 s] with maximum amplifications for T_1 in the range [0.050 s – 0.090 s].

With T = 0.050 s, the amplification is obtained for T_1 in the range [0 - 0.070 s] with maximum amplifications for T_1 in the range [0.040 s – 0.060 s].

With T = 0.050 s, the amplification is obtained for T_1 in the range [0 - 0.140 s] with maximum amplifications for T_1 in the range [0.075 s – 0.120 s].

In all the examined cases, amplification occurs for ranges of vertical fundamental periods T_1 which include those of a wide class of masonry buildings. This aspect is crucial for determining the vertical impulsive actions along the building elevation and their effects on the structural elements.

Moreover, the structural effects of the impulsive actions are also affected by jerk variation, that is, the time derivative of jerk referred to as snap [21-22]. We can imagine that the variation of acceleration generates a "jolt" which in turn contains a series of smaller "jolts" related to higher-order derivatives. Snap can be represented in space as a vector with one component tangent to the acceleration path (thus parallel to jerk) and one orthogonal component associated to the change of direction. When the changes of direction are particularly important, strengthening elements able to resist "jolts" along different and suddenly variable directions should be designed. Therefore, the strengthening intervention should provide resistance distributed as much as possible.

7 CONSTRUCTION DETAILS FOR MASONRY ELEMENTS STRENGTHENING

In light of the findings of this research about the effects of impulsive actions on existing masonry buildings, two construction details of particular strengthening interventions are presented.

The interventions aim at enhancing the resistance of structural discontinuity regions, load application points, stress concentration areas, joints, etc., in agreement with current Technical Standards (Italian guidelines: CNR DT 214/2018 - Istruzioni per la valutazione della robustezza delle costruzioni, §6.1.1).

This work highlighted the importance of masonry confinement and improvement of connections between distinct structural elements, both in vertical and horizontal planes. The interventions aim at enhancing structure robustness through three-dimensional ties.

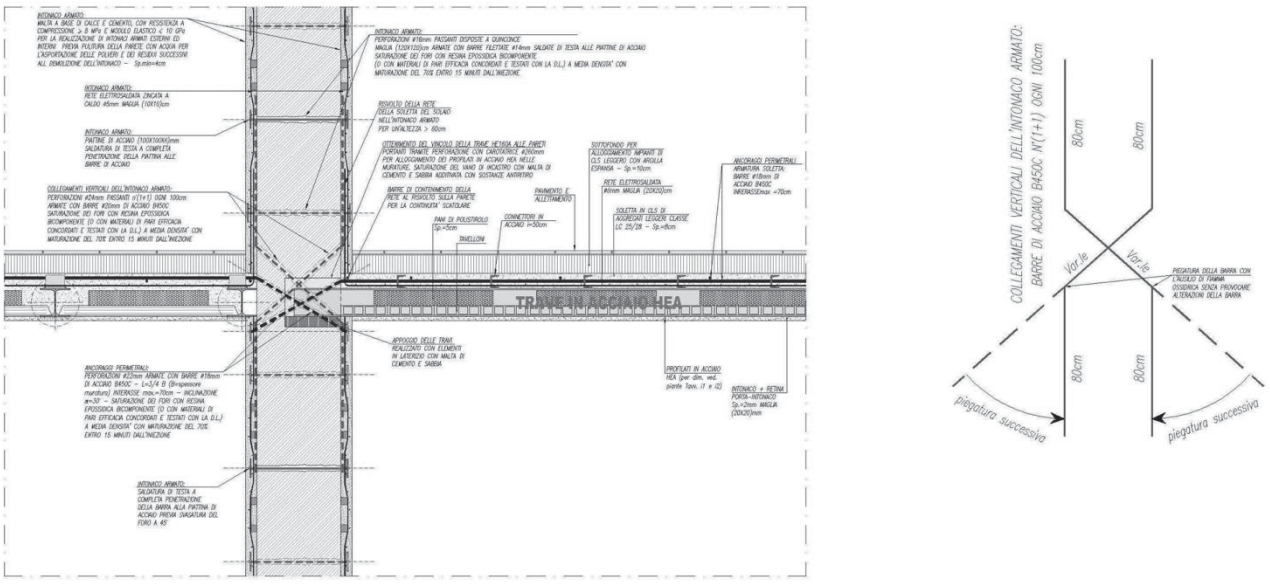

Figure 44. Vertical connection between reinforced mortar and internal masonry pier in correspondence of a steel slab (original drawings by Massimo Mariani)

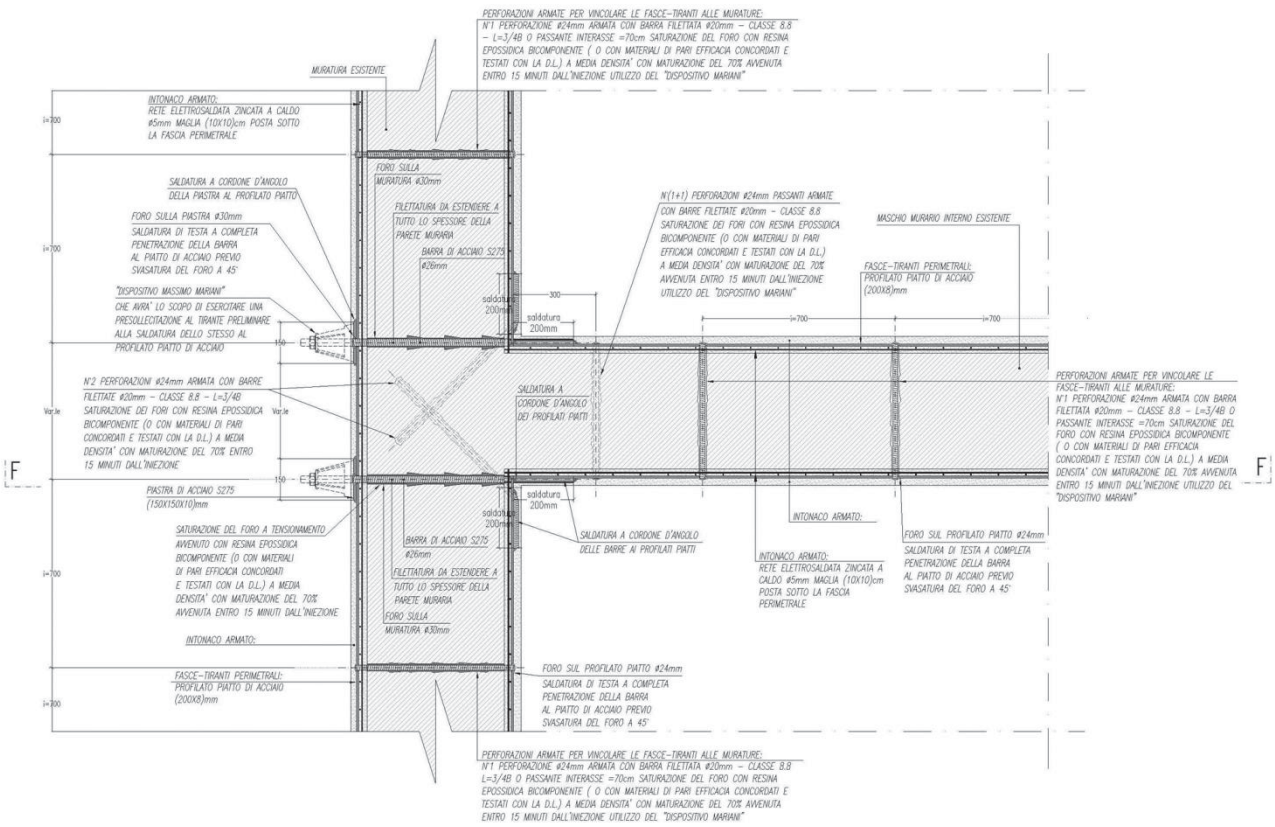

Figure 45. Horizontal connection between orthogonal masonry piers in presence of reinforced mortar on both faces and internal wrapping with steel plates connected to masonry through the "Dispositivo Massimo Mariani", a device allowing to manually prestress the connection jacks in order to enhance the collaboration between steel plate and masonry structure. Prestress is exerted through torque wrench; ties and steel plate are fully covered by the mortar (original drawings by Massimo Mariani)

8 CONCLUSIONS

This work outlined that the variation of acceleration covers an important role in the design of strengthening interventions on existing structures, in particular for masonry buildings. The variation of acceleration is responsible of local failures such as masonry disaggregation and loss of connection between structural elements.

In this context, particularly important is the vertical component of the seismic motion. In that direction the structures feature a non-dissipative behavior and the seismic input may undergo amplification related to resonance phenomena.

As indicated by current technical standards, the seismic evaluation of a structure cannot prescind form an accurate assessment of the local capacities. The latter should always precede analyses that count on the structural dignity of the elements and assess the behavior of the structure as a whole.

This research will be continued by the Authors with the objective of dimensioning the strengthening elements applied in the proposed construction details and providing design solution and analysis methods that take into account the effects of the three-dimensional impulsive actions.

ACKNOWLEDGEMENTS

The authors appreciate the support of colleagues and collaborators that contributed to this research. They would like to thank Luca Ranocchia, Alessia Travanti and Nicola Pero Nullo for the composition and drawing of the construction details; Fulvio Massimo Mariani for the selection of records on ITACA database; Alessio Francioso for the elaborations of Fourier spectra. They also wish to thank Aedes Software for the software Seismic3D developed by Francesco Pugi as part of applied research activities.

REFERENCES

[1] Mariani M.: Terremoto e caos: un nuovo percorso di analisi del comportamento dei sismi, Ingenio, 23.12.2017

[2] Mariani M., Pugi F.: Effetti negativi del sisma verticale sul comportamento delle pareti esistenti in muratura, Ingenio, 25.07.2018

[3] Mariani M., Pugi F., Francioso A.: Sisma verticale: amplificazione della vulnerabilità degli edifici esistenti in muratura, Ingenio, 01.10.2018

[4] Mariani M., Pugi F., Francioso A.: Sisma verticale: modellazione e analisi in ambito professionale sugli edifici esistenti in muratura, Ingenio, 20.12.2018

[5] Mariani M., Pugi F.: Circolare NTC2018: finalmente si dovrà progettare considerando il sisma verticale, Ingenio, 18.02.2019

[6] Mariani M., Pugi F.: Circolare NTC2018: "sisma verticale" da considerare in entrambe le analisi non lineari statica e dinamica, Ingenio, 12.03.2019

[7] Mariani M., Pugi F.: "Sisma verticale" nelle NTC 2018: edifici esistenti e comportamento strutturale "atteso", Ingenio, 03.04.2019

[8] Mariani M., Pugi F., Francioso A.: Vertical component of the seismic action: amplified vulnerability of existing masonry buildings, CompDyn 2019, Crete, Greece, 24–26 June 2019

[9] Mariani M., Pugi F.: La componente sismica verticale è sempre da considerare perché rilevante vicino e lontano dalla sorgente, Ingenio, 07.11.2019

[10] Seismic3D, software, 2020. Sviluppo: F. Pugi, Test: F. Pugi, M. Mariani.

[11] M. Tong, G.-Q. Wang, G.C. Lee: Time derivative of earthquake acceleration, Earthquake Engineering and Engineering Vibration, Vol. 4, No. 1, pp.1-16, June, 2005.

[12] ITACA: ITalian ACcelerometric Archive, http://itaca.mi.ingv.it/ItacaNet_30/#/home

[13] Weihan Weng, Jeffrey Kuo: Jerk decision for free-form surface effects in multi-axis synchronization manufacturing, International Journal of Advanced Manufacturing Technology, 105, pp.799-812, November, 2019.

[14] E.M. Rathje, N.A. Abrahamson, J.D. Bray: Simplified frequency content estimates of earthquake ground motions, J. Geotech. Geoenviron. Eng., 124(2), pp. 150-159, 1998.

[15] Haoxiang He, Ruifeng Li, Kui Chen: Characteristics of Jerk Response Spectra for Elastic and Inelastic Systems, Shock and Vibration, Vol. 2015, Article ID 782748.

[16] Y. Xueshan, Q. Xiaozhai, G.C. Lee, M. Tong, C. Jinming: Jerk and Jerk Sensor, 14th World Conference on Earthquake Engineering, October 12-17, 2008. Beijing, China.

[17] R. Sofronie: Seismic strengthening of masonry in buildings and cultural heritage, SÍSMICA 2004, 6° Congresso Nacional de Sismologia e Engenharia Sísmica, pp.81-100.

[18] R. Sofronie: On the seismic jerk, Journal of Geological Resource and Engineering, Vol. 4, pp.147-152, 2017.

[19] Çelebi, M.: Health monitoring of Buildings Using Threshold Drift Ratios - Now an Established Method, International Conference on Structural Health Monitoring, Vancouver, B.C., Canada, October 2007.

[20] M. Wakui, J. Iyama, T. Koyama: Estimate of plastic deformation of vibrational systems using the high- order time derivative of absolute acceleration, in: Proceedings of the 16th World Conference on Earthquake Engineering, Santiago, 2017.

[21] M. Wakui, J. Iyama: Threshold value and applicable range of nonlinear behavior detection method using second derivative of acceleration, Japan Architectural Review, Vol. 2, No. 2, pp.153-165, April, 2019.

[22] D. Eager, A.M. Pendrill, N. Reistad: Beyond velocity and acceleration: jerk, snap and higher derivatives, European Journal of Physics, 37 (2016) 065008 (11pp).

Historical references about the spatial representation of seismic motion:

[23] B.J. Morrill: *Evidence of record vertical accelerations at Kagel Canyon during the earthquake*, in: The San Fernando, California, earthquake of February 9, 1971, United States Government Printing Office, Washington, 1971.

[24] W.K. Cloud, D.E. Hudson: *A simplified instrument for recording strong-motion earthquakes*, Bulletin of the Seismological Society of America, Vol. 51, No. 2, pp.159-174, April, 1961.

[25] Ronald F. Scott: *The calculation of horizontal accelerations from seismoscope records*, Bulletin of the Seismological Society of America, Vol. 63, No. 5, pp.1637-1661, October, 1973.

[26] C. Arnold, R.Reitherman: *Building configuration and seismic design: the architecture of earthquake resistance*, NSF-CEE 81064, National Science Foundation, Washington, 1981.

EURODYN 2020
XI International Conference on Structural Dynamics
M. Papadrakakis, M. Fragiadakis, C. Papadimitriou (eds.)
Athens, Greece, 23–26 November 2020

ANALYSIS OF RC CONTAINMENTS OF NUCLEAR PLANTS UNDER AEROPLANE IMPACT LOADS

Mohamed Ihab S. Elmasry [1], Nabil H. Alashkar [2], and Mostafa M. Hassan [3]

[1] Professor of Structural Engineering at the Construction and Building Engineering Department,
Dean of the School of Engineering and Technology, Port Said Branch
Arab Academy for Science, Technology and Maritime Transport, Alexandria
e-mail: elmasryi@aast.edu

[2] Professor of Structural Engineering at the Construction and Building Engineering Department
Arab Academy for Science, Technology and Maritime Transport, Alexandria
e-mail: nelashkar@aast.edu

[3] Research assistant at construction and building engineering department
Arab Academy for Science, Technology and Maritime Transport, Alexandria
e-mail: hassan92mostafa@yahoo.com

Keywords: Stability, Riera, RC Containment, Impact, Aeroplanes.

Abstract. *Nuclear power plants are considered vital structures for generating electricity worldwide. In general, a nuclear power plant structure includes two containments, external and internal ones. The internal containment surrounds the main reactor as a primary shield. The external containment is considered as a final shield between the internal of the reactor and the environment. This paper studies the integrity of external containment after being hit by different aeroplanes. Analytical model is constructed using ANSYS® software in order to simulate the RC containment including the circular shell and dome subjected to impact of different aeroplanes. An existing design of the typical external containment is used in modeling. According to ASCE 58, the circular wall and the dome are considered lined with inner steel liner plates in order to reduce the radiation emission to the environment in case of accidents. The studied external RC containment is subjected to the impact of different aeroplanes, Boeing 747-200c and Boeing 707-320. Riera Method is used to simulate the impact load with respect to time at the outer surface of the external shell, at a vertical level of 30m above the upper foundation level. The impact load is concentrated at 16 nodes at the outer surface of containment. Heavy weight concrete is used for the RC containment with a compressive strength of 60MPa. The analysis of RC containment after the impact of the different aeroplanes showed the displacement, velocity, acceleration and the shape of the cracks. It was found that the containment is stable after the impact of an aeroplane, but clear damage affected the elements within the impact region. From the impact of different aeroplanes on RC containment, Boeing 747-220c is the most damaging according to results concerning the displacement, velocity and acceleration on the RC containment.*

1 INTRODUCTION

Nuclear Power Plants include several structures such as the internal, external containment structures and others. The external RC containment structure is the physical building that separates the reactor from the outer atmosphere, and houses the internal containment structure that surrounds the nuclear reactors and the associated chain reactions [1]. Most typical current external containment structures ranges from 150 to 200 feet tall with a diameter of approximately 150 feet. The RC containment structure should be airtight to prevent the release of radioactive particles into the atmosphere. The secondary containment is necessary when radiation levels at the site boundary exceed the allowable limits [1], [2].

Concrete containments for Boiling Water Reactor Mark II and parts of Mark III are mainly reinforced deformed bar concrete, whereas for the Pressurized Water Reactors both deformed bar and pre-stressed concrete containments are common. The design loads consist mainly of internal pressure, temperature, tornado, and earthquake, all of which result in different states of stresses in the concrete elements such as tension, compression, radial and tangential shears. These loads are categorized as axisymmetric loads, such as the internal pressure and temperature, and non-axisymmetric loads, such as tornadoes and earthquakes [1]. In addition, most current external containment structures have been designed as RC structures. Concrete containment structures lined with steel are even more economical than steel containment structures for dry containment design [1]. This is attributed to the fact that a steel containment structure would require a concrete shield structure, thus concrete is required in either case, and the more economical choice is typically used.

The response of the containment structure due to impact of an aeroplane can be determined by equating the work done by the impact load to the strain energy produced in the structure through applying the three basic principles of mechanics: conservation of energy, conservation of linear momentum, and virtual work principle. In addition, in the evaluation of the aeroplane crash on the outer containment structure, the following steps are considered [3]:

- Global structural response including excessive structural deformations or displacements.
- Localized structural damage due to the effects of missile impact, including penetration, perforation, scabbing, that may lead to the failure of structural elements as a result of the effects of an aeroplane impact.

In the carried out analysis, the normal impact was chosen, according to Riera formulation, since it corresponds to the worst condition for the containment structure accident scenario. It was also assumed that the concrete may undergo gradual failure modes representing the progressive cracking and crushing of concrete itself caused by the abrupt stiffness changes [3]. Moreover in the impact analysis, the damping effect was considered to be negligible as it does not affect the maximum response to impulse loading. Moreover, concrete as a construction material is commonly used for biological shielding in nuclear power plants and atomic research and testing facilities [4].

1.1 Problem Definition

The damage caused by missile impact might lead to the leakage of nuclear radiation. Earlier research showed that RC containments with thicknesses greater than 1.4 m, permanent damage is negligible, whereas for thicknesses lower than 1.0 m considerable plastic strains occurred on opposite surfaces of the containment shell [5]. This is the case where the impact load of an aeroplane on the outer RC containment results from the effects of a finite amount of kinetic energy that depends upon the inertial and stiffness properties of the missile and

target structure [3]. This paper studies and evaluates the effects of impact caused by impact of an aeroplane Boeing 747-200c upon typical external RC containment of the nuclear power plants. Nonlinear response of such impact is studied then analyzed to identify the propagating damage in the containment structure. Two different aeroplanes were hitting the external RC containment, were made as parametric study to show the most damage aeroplane on the RC containment and its effect on displacement, velocity and acceleration of the RC containment.

1.2 Case Study

The studied RC outer containment consists of 3 major components, the cylindrical wall, the hemispherical dome, and the cylindrical base mat foundation as shown in Figure(1) at which the external RC containment wall is fixed to the foundation. In addition, based on an existing design, the cylindrical wall is assumed to be 1.2m thickness whereas the thickness of the RC hemispherical dome is assumed to be 1.05m [1]. The effective concrete cover is 150mm at both faces till the reinforcement. The height of the cylindrical wall from the top of foundation till the spring line is 36.45 m. The total height of containment from the top of foundation till the apex of the dome is 60m. The cylindrical wall and dome of the RC containment is axisymmetric, inner diameter of the containment is 45 m as shown in Figure (1).

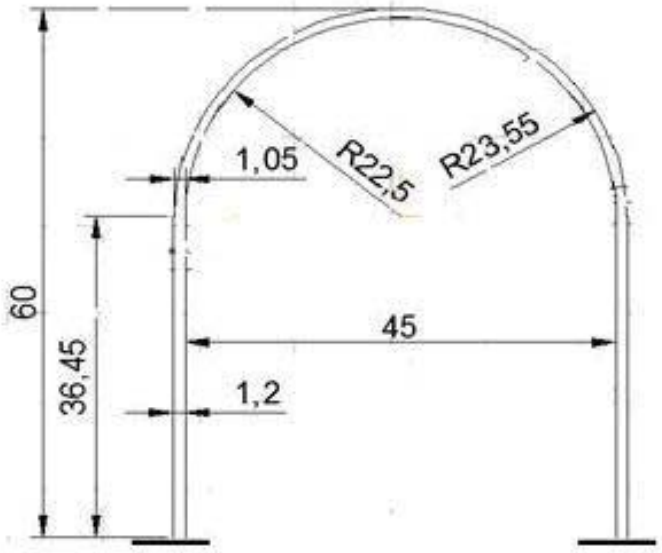

Figure 1: Section elevation of the RC containment wall and dome

The massive concrete containment structure was described as follows as per [2]. The RC dome is typically three and a half feet thick with two layers of reinforcement for the typical containment structure; #18 bars at 12 inches [6]. The cylindrical walls are even larger in order to carry the entire dead load including the shell to the base slab. The walls are at least four feet thick with #18 vertical bars at 12 inches for each face and #18 horizontal bars on both sides of the vertical reinforcing as shown in Figure (2).

Moreover, since the containment structure must be airtight to prevent any fission emissions from bypassing, and knowing that concrete as a material is porous, then the studied containment is assumed to have a steel liner on the entire internal surface. This lining thus acts as a part of the system for the concrete wall. Based on [2], [1] the required minimum thickness for the steel liner plates is a quarter of an inch; however, the studied existing design considered the steel liner plate of thickness three-eighths of an inch as shown in Figure (2).

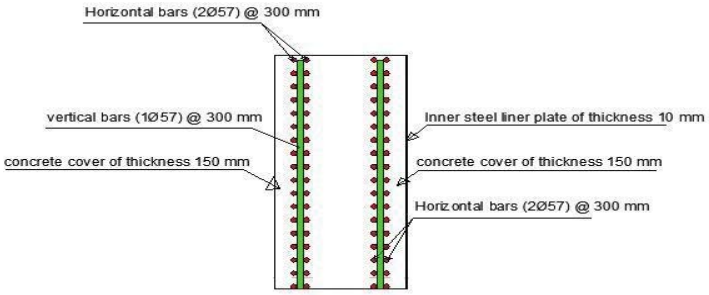

Figure 2: Cross section elevation details of shell wall reinforcement

2. MODELING

In the finite element model applied in ANSYS® software, the connection between the foundation and the cylindrical wall is assumed to be fixed. In addition, the local details in the RC containment structure, including penetrations, temporary openings, and embedded parts, were not considered in modeling. The meshing of the containment volume is as shown in Figure (3).

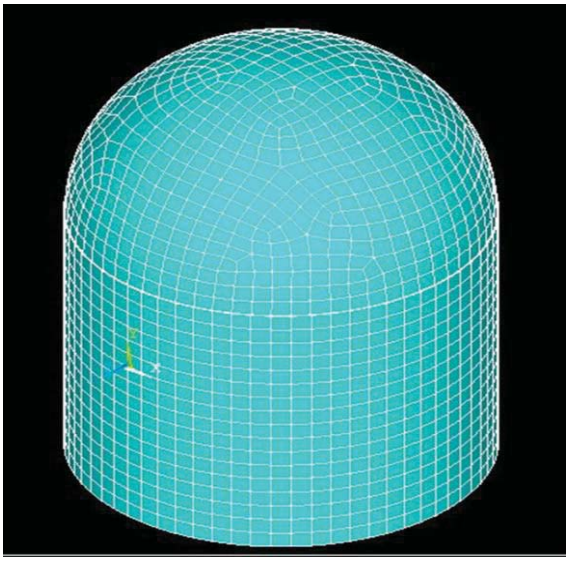

Figure 3: Meshing of the external RC containment building

2.1. Jet Impact Modeling on RC Containment

Impact loads due to the effects of a finite amount of kinetic energy that depends on the inertial and stiffness properties of missile and target structure, differs from the “impulse” load that is generally a force independent of the inertial and stiffness properties of missile and target. As a result of a jet impact, kinetic energy is transferred from the aeroplane to the building walls and thereby absorbed by the building components in the form of strain energy.

From literature review, it was observed that the Riera method is an efficient in evaluating damage of RC structures from severe impact loads. The riera method is an approximate method for constructing a force-time history for an aeroplane striking a rigid wall based on a known distribution of mass and crushing characteristics of the aeroplane along the length [7], [8]. This is the case where the riera approach assumes that the aeroplane can be represented like a soft missile. Moreover, it is assumed that as the aeroplane strikes the target, a part of it close to the target gets crushed and the remaining portion of projectile undergoes elastic deformation.

The basic assumptions of the Riera method [7] can be summarized in:

- The target is rigid
- The aeroplane axis is perpendicular to the target; angle of incidence is 90 degree.
- The aeroplane is separated into two parts, one being uncrushed and moving with velocity (v) and the other crushed with zero velocity.
- All crushing takes place within a local region adjacent to the rigid target.
- The crushing or material behavior of the missile is rigid-perfectly plastic.
- The crushed mass of the aeroplane moves with the target structure.

Consequently, some parameters clearly affect the impact scenario. Such parameters include the velocity and impact angles of the aeroplane, the mass and stiffness of the aeroplane as a function of the aeroplane length as shown in Table (1) [3].

Air plane type	**Boeing 747-200c**	**Boeing 707-320**
Mass at take-off (Kg)	350000	150000
Engine mass (Kg)	4 x 21300	4 x8100
Impact speed (m/s)	269	272

Table 1: Parameters of different aeroplanes

Furthermore, it is assumed that the load versus time curve affect a constant equivalent area to the average of total cross-sectional area of fuselage and wings. Thus, the impact contact area of the Boeing 747-200c in the analysis model is assumed to be 37 m^2 [3]. Moreover, in this analysis, the load is assumed to act on 16 nodes as concentrated point loads on the outer external RC wall of the containment. Figure (4) shows a schematic of the distribution of the loads on the loaded nodes.

Figure 4: Impact load distribution on nodes in the impact region

The impact force, F(t), acting on the rigid fixed containment is calculated with the riera method as shown in Figure (5) [3].

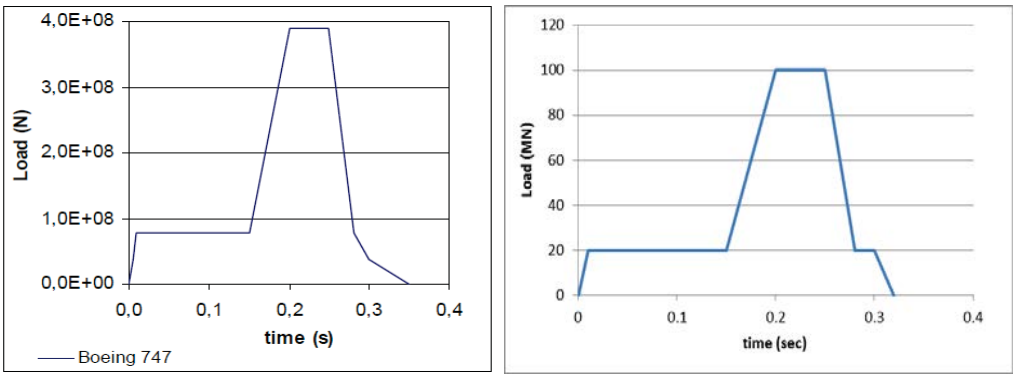

(a)- Boeing 747-200c (b)-Boeing 707-320

Figure 5: Load-time history curve of different aeroplanes

The key formula in the computation of the force applied to the rigid target, F(t), or the impact force time history is given by equation (1) [8].

$$F(t)=Pc(x)+\mu(x)(dx/dt)^2 \quad (1)$$

where x (t) is the crushed length of the missile, the distance from the nose of the missile when uncrushed to the point at which crushing has progressed at time t, Pc(x) is the static force required to axially crush a cross-section of the missile at location x, and μ(x) is the mass per unit length at location x.

2.2. Containment Materials Modelling

2.2.1. Concrete modelling

The concrete material is assumed to be homogenous and isotropic. The compressive multi-linear stress-strain relationship for concrete [9], as defined by ANSYS®, is shown in Figure (6), and calculated by the following equations:

$$f_c = E_c \varepsilon \quad \text{for } 0 < \varepsilon < \varepsilon_1 \quad (2)$$

$$f_c = f_c' \quad \text{for } \varepsilon_o < \varepsilon < \varepsilon_{cu} \quad (3)$$

$$f_c = E_c \varepsilon / (1 + (\varepsilon/\varepsilon_o)^2) \quad \text{for } \varepsilon 1 < \varepsilon < \varepsilon o \quad (4)$$

$$\varepsilon_1 = (0.3 \times f_c)/ E_c \quad (5)$$

$$\varepsilon_o = (2 f_c)/ E_c \quad (6)$$

Where ε_1 is the strain corresponding to 0.3 f_c, ε_o is the strain at peak point, and ε_{cu} is the ultimate compressive strain [9].

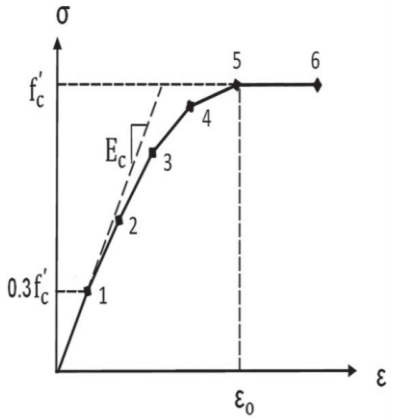

Figure 6: Uniaxial compressive stress-strain curve for concrete

Furthermore, the Poisson ratio for concrete is taken 0.2, and the modulus of elasticity, E_c, is calculated from Equation (7), whereas the modulus of rupture for concrete, f_r, is calculated from Equation (8) according to [10] specifications [9].

$$E_c = 4700\sqrt{f'c} \quad (7)$$

$$f_r = 0.62\sqrt{f'c} \quad (8)$$

In the analysis, the uniaxial compressive strength of concrete is assumed to be 60 MPa, whereas the uniaxial rupture stress f_r is assumed to be 4.8 MPa. Moreover, the shear transfer coefficients ranges from 0.0 to 1.0, with 0.0 representing a smooth crack (complete loss of shear transfer) and 1.0 representing a rough crack (no loss of shear transfer). This specification may be made for both the closed and open crack as shown in Table (2) [11], [12].

Input strength parameter	Values
Open shear transfer coefficient	0.3
Closed shear transfer coefficient	0.9
E (Modulus of Elasticity of concrete)(MPA)	36406.043

Table 2: Concrete strength input data

2.2.2. Reinforcing Rebar Modeling

The reinforcement rebar used in the containment structure is according to ASTM A-615 Grade 60 steel [13]. The stress-strain curve of the reinforcing bar is assumed to be elastic perfectly plastic as shown in Figure (7). Figure (7) also shows the bilinear material model defining the linear isotropic hardening of the reinforcement in which the yield stress is assumed to be 400 MPA, the elastic modulus, E_s is assumed 2×10^5 N/mm^2, and the Poisson ratio assumed 0.3 [13].

In addition, within ANSYS® software, rebar reinforcement is treated as an equivalent uniaxial material, the reinforcement layers were thus defined using the smeared reinforcement option of the SOLID65 element. The reinforcement is assumed to be uniformly spread throughout the defined layer and has uniaxial stiffness only in each direction. The amount of reinforcement was defined by material number and the orientation angles of the reinforcing bars. The shell wall reinforcements for horizontal and vertical are modeled as continuous layers inside the wall section, and the same applies for the dome reinforcements. The thicknesses of the reinforcement layers were calculated from Equation (9) [12].

$$h=A/s \tag{9}$$

Where h is the equivalent reinforcement layer in each direction, A is the cross section area of the reinforcement rebar, and S is the spacing between the reinforcement rebar in each direction.

2.2.3. Steel Liner Modeling

The (0.9375 cm) thick steel liner plate has a bilinear isotropic hardening plasticity model in which its yield stress is 165 Mpa as shown in Figure (8), and the elastic modulus, E_S, and the Poisson's ratio are assumed to be 2×10^5 N/mm^2 and 0.3 respectively [13].

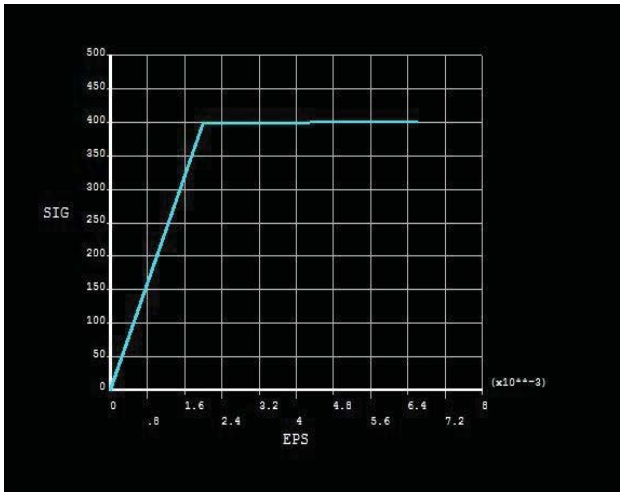

Figure 7: Stress strain curve for steel reinforcing rebar

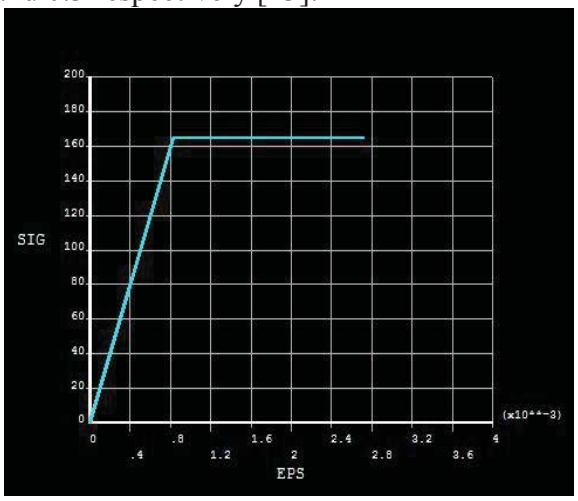

Figure 8: Stress strain curve for the inner steel liner plate

2.3. Used Model Elements from ANSYS® Library

2.3.1SOLID65 element

The SOLID65 element is used for the 3D modelling of the RC wall and dome. The solid element is capable of cracking in tension and crushing in compression. The element is defined by eight nodes having three degrees of freedom at each node: translations in the nodal X, Y, and Z directions and the isotropic material properties. The element has one solid material and up to three rebar materials. The orientation of any rebar layer is defined by two angles in degrees from the element coordinate system [12]. The assumptions for the SOLID65 element include that the concrete material is homogenous and isotropic where cracking is permitted in three orthogonal directions at each integration point.

2.3.2. SOLID45 element

The SOLID45 element is used for the 3D modeling for the inner steel liner plate. The

element is defined by eight nodes having three degrees of freedom at each node: translations in the nodal x, y, and z directions [12].

2.4. Failure criteria of concrete

The concrete material model predicts the failure of brittle materials. Both cracking and crushing failure modes are accounted for. The criterion for failure of concrete due to a multi axial stress state can be expressed in the form [14], [12]:

$$\frac{F}{fc} - S \geq 0 \tag{10}$$

Where:

F = a function of the principal stress state (σ_{xp}, σ_{yp}, σ_{zp}).

S = failure surface expressed in terms of principal stresses and five input parameters f_t, f_c, f_{cb}, f_1 and f_2 .

f_c = uniaxial crushing strength .

σ_{xp}, σ_{yp}, σ_{zp} = principal stresses in principal directions.

If Equation (10) is satisfied, the material will crack or crush.

However, the failure surface can be specified with a minimum of two constants, f_t and f_c. The other three constants default to [14]:

$$f_{cb} = 1.2\ fc \tag{11}$$

$$f_1 = 1.45\ fc \tag{12}$$

$$f_2 = 1.725\ fc \tag{13}$$

These default values are valid only for stress states where the condition is satisfied.

$$|\sigma h| \leq \sqrt{3}\ f_c \tag{14}$$

$$\sigma_h = \text{hydrostatic stress state} = \frac{1}{3}(\sigma_{xp} + \sigma_{yp} + \sigma_{zp}) \tag{15}$$

Both the function F and the failure surface S are expressed in terms of principal stresses denoted as σ_1, σ_2, and σ_3 where:

σ_1 =max (σ_{xp}, σ_{yp}, σ_{zp})

σ_3 =min (σ_{xp}, σ_{yp}, σ_{zp})

and $\sigma 1 \geq \sigma_2 \geq \sigma_3$. The failure of concrete is categorized into four domains:

1. $0 \geq \sigma_1 \geq \sigma_2 \geq \sigma_3$ (compression - compression - compression)
2. $\sigma_1 \geq 0 \geq \sigma_2 \geq \sigma_3$ (tensile - compression - compression)
3. $\sigma_1 \geq \sigma_2 \geq 0 \geq \sigma_3$ (tensile - tensile - compression)
4. $\sigma_1 \geq \sigma_2 \geq \sigma_3 \geq 0$ (tensile - tensile - tensile)

3. ANALYSIS OF RESULTS

A full transient dynamic analysis was applied with considering a small displacement transient response. The impact analysis is considered seven load steps in impact load-time curve as shown in Figure (5-a). The transient dynamic analysis requires two sets of initial conditions since the dynamic equations are of second order. The initial displacement, u_o, and

initial velocity ($\mathring{u}_o$) are assumed to be zero. In addition, the initial accelerations ($\ddot{u}_o$) are also assumed to be zero [5]. Furthermore, Damping was also included in the analysis through identifying the mass damping and stiffness damping. Thus, Rayleigh damping with coefficient β=0 was applied to the model. The coefficient α was reflected with a magnitude of 3.0 for the RC and 0.1 for the structural steel such that the damping matrix, C, was identified from equation (16) [5].

$$C=\alpha m+\beta K \tag{16}$$

The outer RC containment response under the impact load of an aeroplane Boeing 747-200c was studied at different time instances. Figure (9) shows the deformation shape of the impact region at time 0.2sec. It was observed that the elements within the impact region deformed in the direction of loading, which generated significant large tensile stresses at the inner surface of steel liner plates, and compressive stresses at the outer surface of concrete. The maximum displacement was found to be 46.658mm in the region of impact at time 0.2 sec. Meanwhile, other regions near the impact showed maximum displacements of 1.958 mm outside the containment as shown in Figure (10).

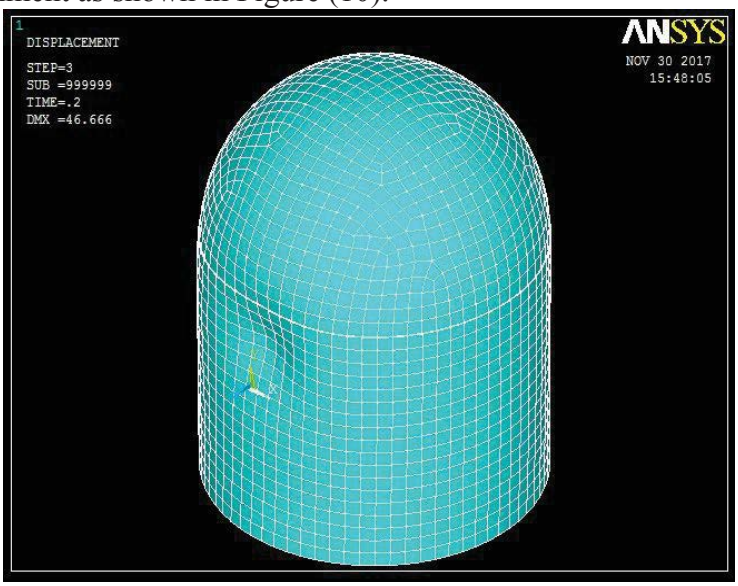

Figure 9: Deformation shape of the containment at time 0.2 sec

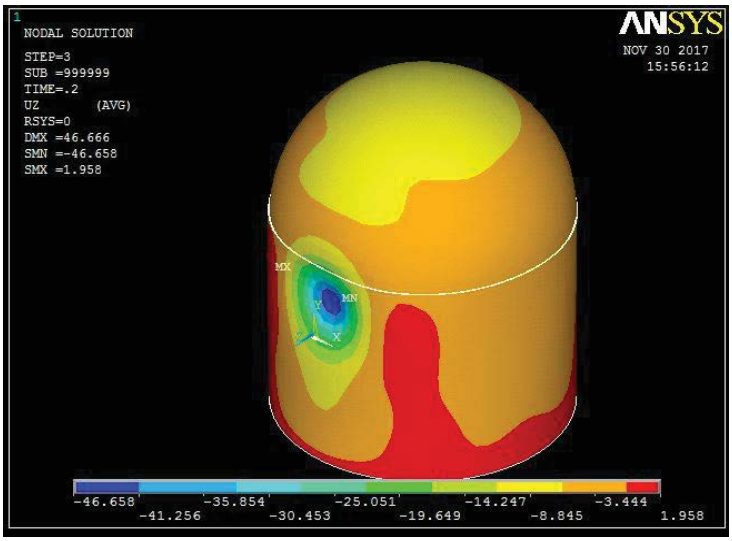

Figure 10: Displacement distribution of the containment at time 0.2 sec

The impact effect on the displacement of the RC containment

The maximum displacement of the RC containment is at the impact region which reached a value of 46.658 mm. The displacement vanished at a distance of 16 m from the impact region along the circumference direction from right and left hand sides as shown in Figure (11).

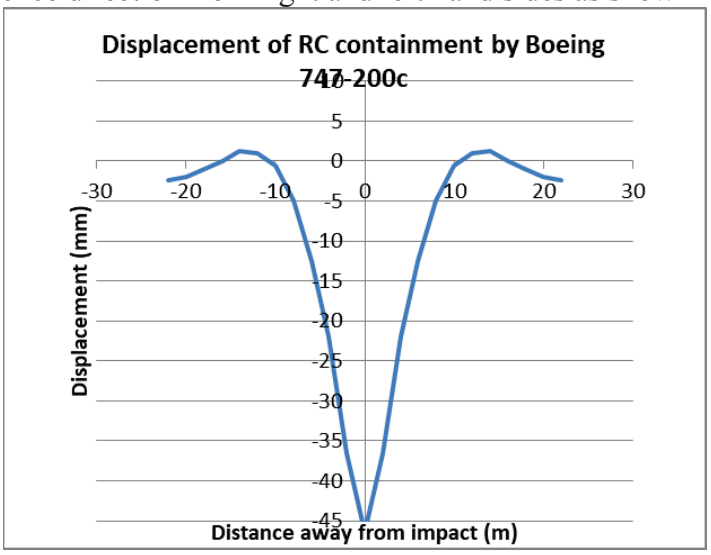

Figure 11: Containment displacement with respect to distance from the impact region at time 0.2 second

The impact effect on the velocity of the RC containment

The velocity of the RC containment reached a value of 2.145 m/sec at the impact region. The velocity vanished at a distance of 16m from the impact region along the circumference direction from left and right hand sides as shown in Figure (12).

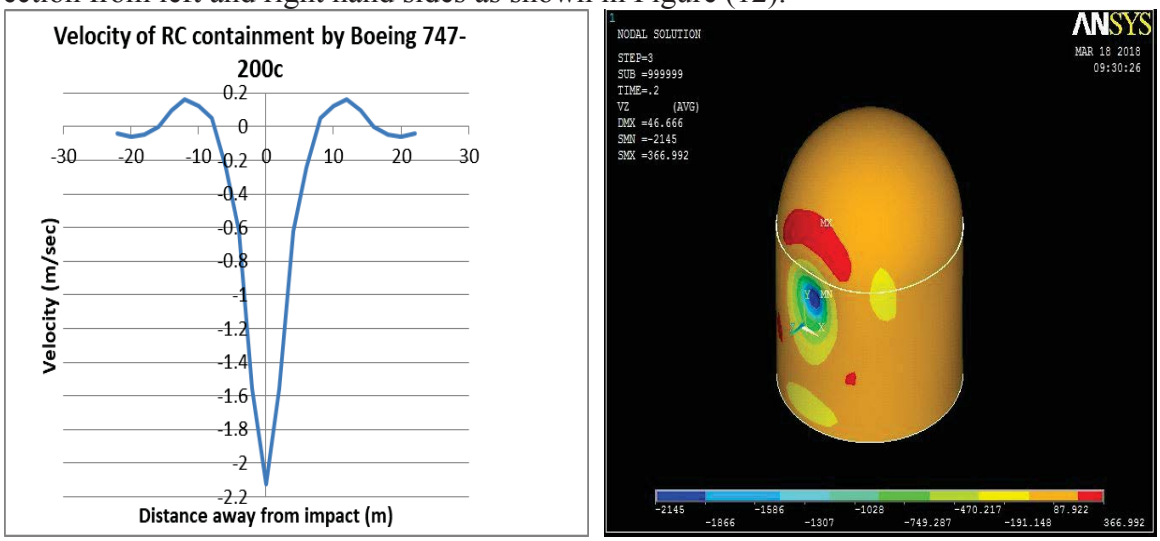

(a)- Velocity of the RC containment along the circumference (b) - Velocity distribution of the RC containment

Figure 12: Velocity of the RC containment due to impact of an aeroplane Boeing 747-200c at time 0.2 second

The impact effect on the acceleration of the RC containment

The acceleration of the RC containment reached a value of 147.151 m/sec^2 at the impact region in direction of loading. The acceleration vanished at a distance of 18m from the impact region along the circumference direction as shown in Figure (13).

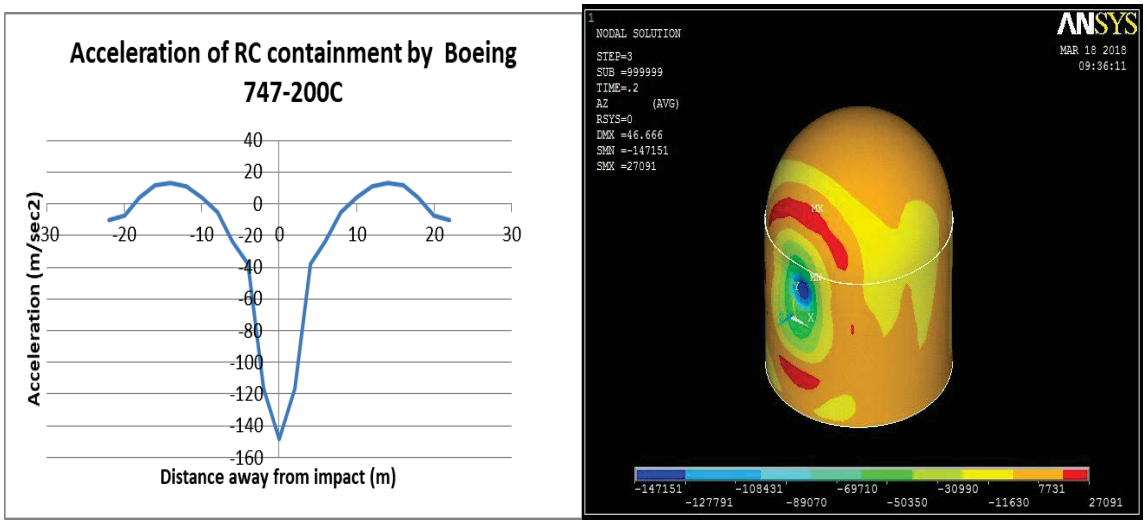

(a)- Acceleration of the RC containment along the circumference (b)- Acceleration distribution of the RC containment

Figure 13: Acceleration of containment with respect to distance away from impact region at time 0.2 second

The impact effect on the cracks of the RC containment

From the previous mentioned results, thus, the elements within the impact region were clearly crushed. In addition some tension cracks (flexure cracks) appeared at the bottom of the fixation of containment. In addition, shear cracks appeared far from the impact region as shown in Figure (14). The failure criterion for the concrete built in Ansys12 due to a multi-axial stress state was used to identify cracks. This is the case where in a concrete element, cracking occurs when the principal tensile stress in any direction lies outside the failure surface. After cracking, the elastic modulus of the concrete element is set to zero in the direction parallel to the principal tensile stress direction. In addition, crushing would occur when all principal stresses are compressive and lies outside the failure surface. Consequently, the elastic modulus is set to zero in all directions, and the element effectively disappears [15], [12]. It was observed that the RC containment remained fully intact after the impact of an aeroplane, and the damage region extended 34m from the impact region of aeroplane at both sides of the impact. The severe damage was clear in the impact region of the studied aeroplane.

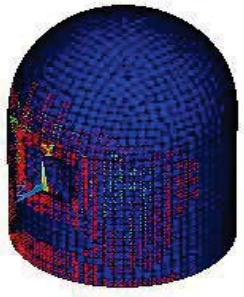

Figure 14: Crack propagation within the RC containment

The effect of different aeroplanes impact on RC containment

The parameter used in this model is modeling the studied RC containment to be hit with

different aeroplanes such as Boeing (747-200c) at speed of 269 m/sec, Boeing (707-320) at speed 103 m/sec. This is in order to see the effects on the displacement of RC containment as shown in Figure (15 (a),(b),(c),(d)). The two aeroplanes impact varies according to velocity, mass and the size of the effective impact area. This effective impact area is calculated as the area of a circular with a diameter equal to the maximum fuselage diameter (maximum body diameter) of each aeroplane.

The maximum displacement of RC containment reached a maximum value of 46.658mm on being hit with Boeing 747-200c in contrast to Boeing 707-320 where the displacement reached 38.299 mm as shown in Figure (15). It was observed that the displacement of the RC containment due to the impact of Boeing 747-200c was greater than the impact of Boeing 707-320 by 17.91%.

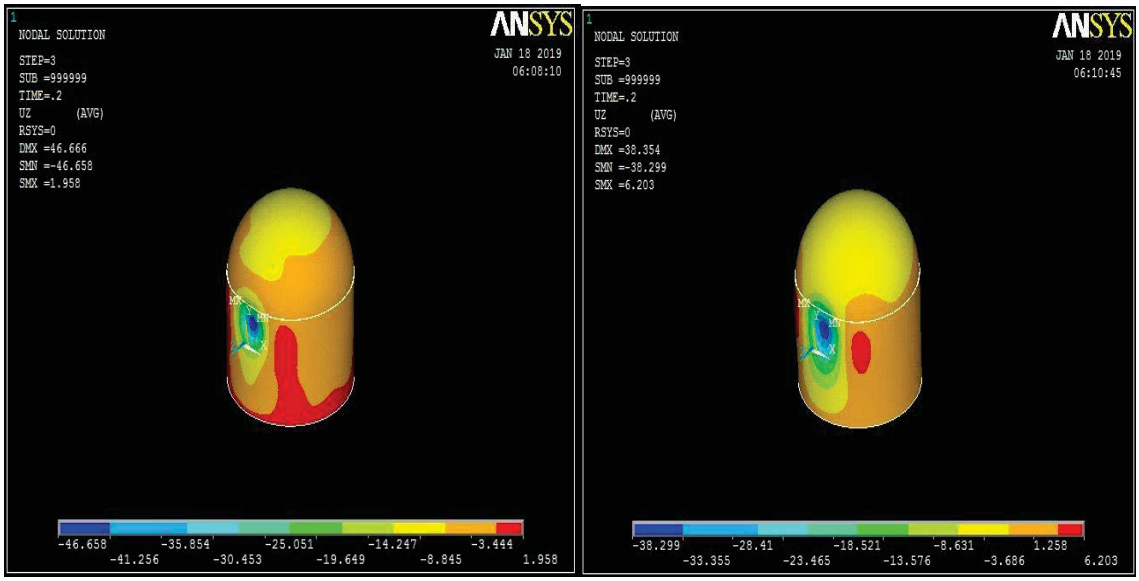

(a) Impact of Boeing 747-200c (b) Impact of Boeing 707-320

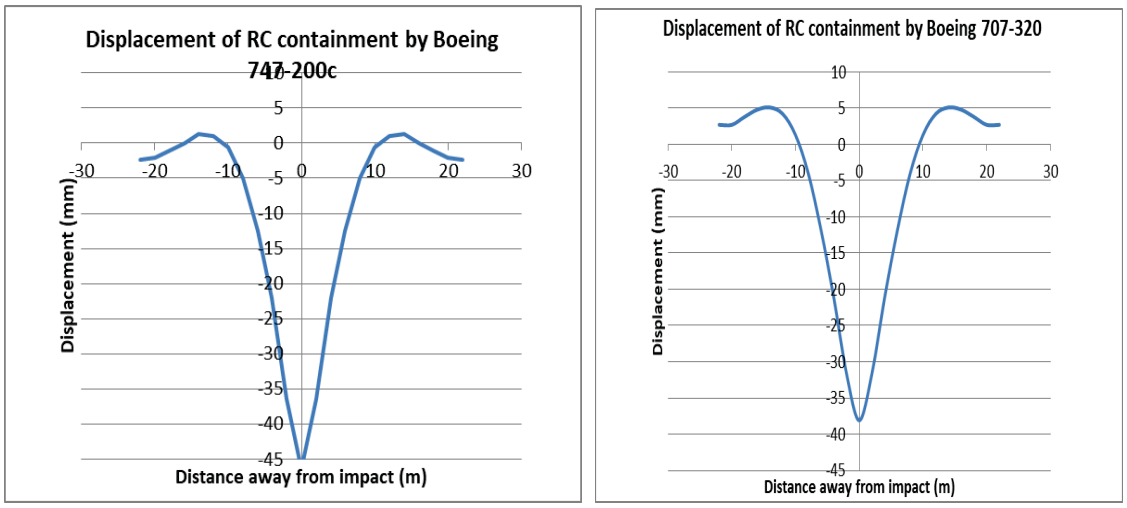

(c) Impact of Boeing 747-200c (d) Impact of Boeing 707-320

Figure 15: Displacement of RC containment due to impact of different aeroplanes at time of 0.2 second

The velocity of the RC containment reached a value of 2.145 m/sec due to impact of Boeing 747-200c at 0.2 second as shown in Figure (16 (a)). The velocity of the RC containment reached a value of 1.049 m/sec due to impact of Boeing 707-320 at 0.2 second as shown in Figure (16 (b)). It was observed that the velocity of the RC containment due to the impact of Boeing 747-200c was greater than the impact of Boeing 707-320 by 51.095%.

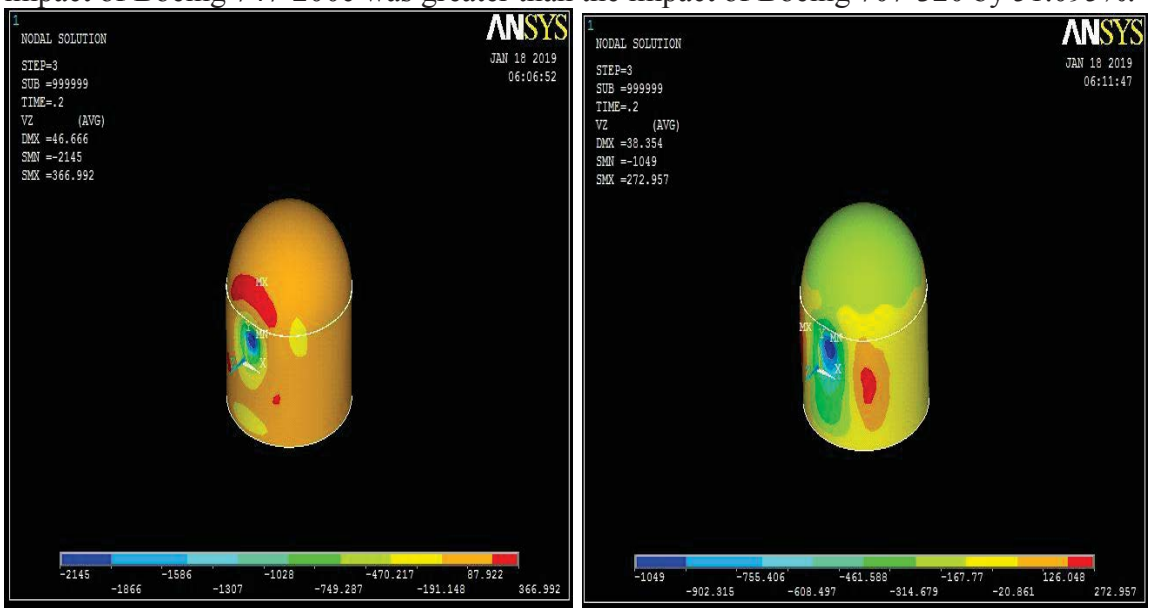

(a) Impact of Boeing 747-200c (b) Impact of Boeing 707-320

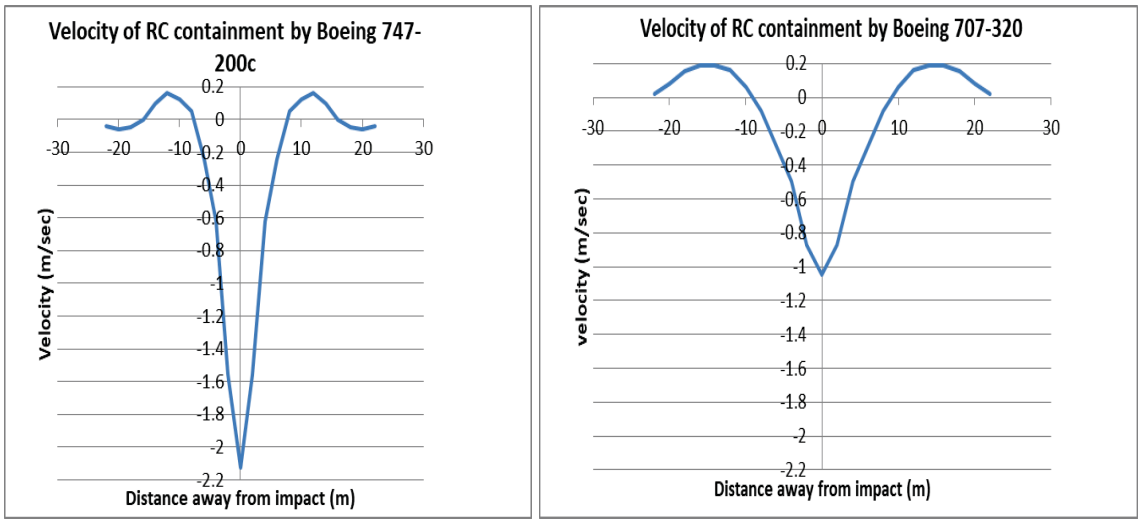

(c) Impact of Boeing 747-200c (d) Impact of Boeing 707-320

Figure 16: Velocity of RC containment due to impact of different aeroplanes at time of 0.2 second

Furthermore, the acceleration of the RC containment reached a value of 147.151 m/s^2 due to the impact of Boeing 747-200c at 0.2 second as shown in Figure (17 (a)). In contrast, the acceleration of the RC containment reached a value of 32.471 m/s^2 due to impact of Boeing 707-320 at 0.2 second as shown in Figure (17 (b)). It was observed that the acceleration of the RC containment due to the impact of Boeing 747-200c was greater than the impact of Boeing 707-320 by 77.93%.

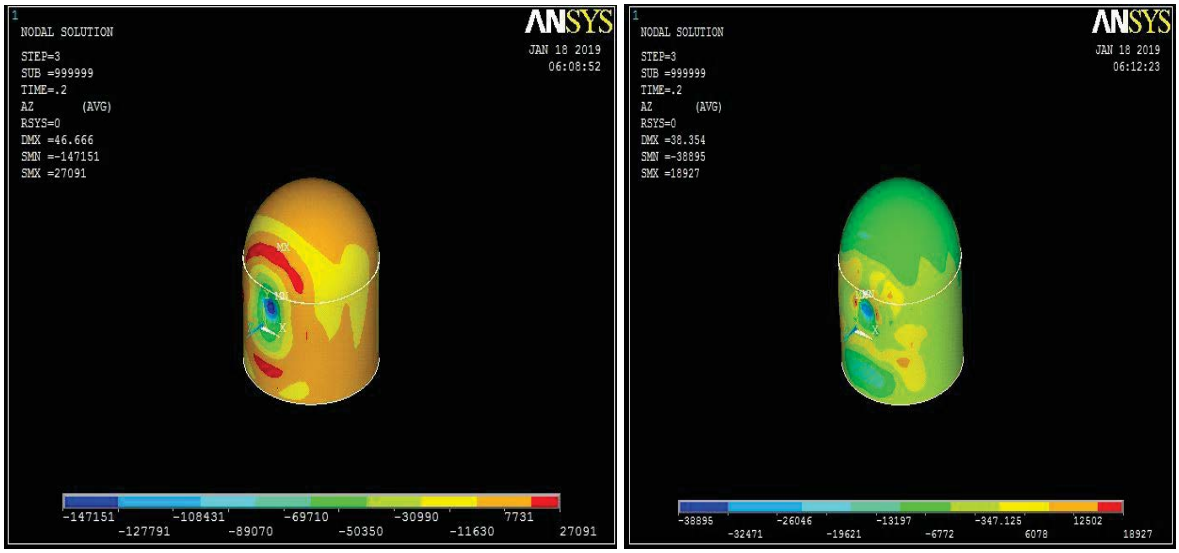

(a) Impact of Boeing 747-200c (b) Impact of Boeing 707-320

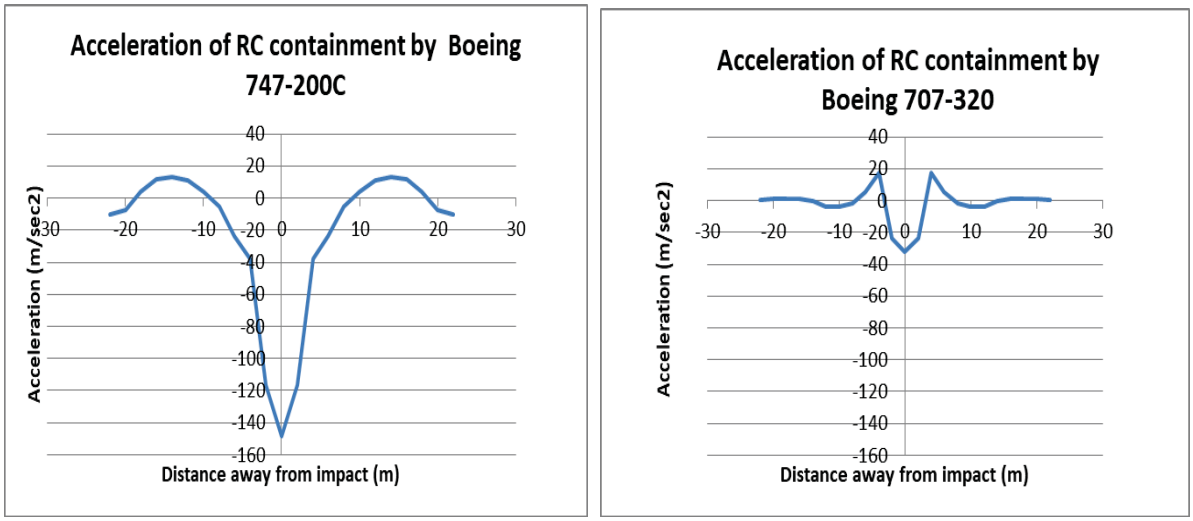

(c) Impact of Boeing 747-200c (d) Impact of Boeing 707-320

Figure 17: Acceleration of RC containment due to impact of different aeroplanes at time of 0.2 second

4. CONCLUSIONS AND RECOMMENDATIONS

The external RC containment is used as the case study designed according to ASCE 58. The external RC containment structure is subjected to normal impact load of a Boeing 747-200c aeroplane using the Riera method load time curve in order to see the response of the containment and to analyze the resulting deformations, displacements and shapes of cracks that would occur due to the impact of an aeroplane. The elements within the impact region showed locally damage indicated from displacement, velocity and acceleration. The maximum displacement, velocity and acceleration in direction of loading were 46.658 mm, 2.145 m/sec and147.151 m/sec^2 respectively reached a maximum value within impact region due to the impact load of an aeroplane Boeing 747-200c. From all the above results it was observed that locally damage has been occurred to the elements within the impact region only due to impact of an aeroplane Boeing 747-200C. It was observed that the displacement, velocity and acceleration of the RC containment due to the impact of Boeing 747-200c were greater than the impact of Boeing 707-320 by 17.91%, 51.095%, and 77.93% respectively. It

was observed that Boeing 747-200c aeroplane is more damaging than Boeing 707-320 aeroplane.

5. REFERENCES

[1] S.Czerniewski, The Feasibility of Modern Technologies for Reinforced Concrete Containment Structures of Nuclear Power Plants, Report of master science, KANSAS State University, 2009.

[2] ASCE standard 58, Structural Analysis and Design of Nuclear Plant Facilities,1980.

[3] G .Forasassi, R.Lofrano, Preliminary analysis of an aircraft impact, Report of RICERCA DI SISTEMA ELETTRICO,2010 .

[4] KP.Mehta, P.J.Monteiro, Concrete Microstructure, Properties, and Materials, Electronic Book page 529-531, 2006.

[5] I.Němec , Š.Sychrová, I.Ševčík, J.Kabeláč, L.Weis, Study of a Nuclear Power Plant Containment Damage Caused by Impact of a Plane, International Refereed Journal of Engineering and Science (IRJES),Vol (1), PP 48-53, 2012.

[6] ACI standard 359, Code for Concrete Reactor Vessels and Containments, 2007.

[7] J.D Riera, on the stress analysis of structures subjected to aircraft impact forces, Nuclear Engineering Design, Vol (8), PP 415–426, 1968.

[8] R.J.James, J.Y.R.Rashid, Severe Impact Dynamics of Reinforced Concrete Structures, Sixth European Conference on Structural Dynamics, EURODYN, 2005.

[9] W.D.Salman, Nonlinear Behavior of Reinforced Concrete Continuous Deep Beam, International Journal of Engineering Research & Technology (IJERT),Vol (4), ISSN: 2278-0181,2015.

[10] ACI standard 318, Building Code Requirements for Structural Concrete, 2008.

[11] Y.Ding, S.Jaffer, Development of finite element models for the study of ageing effects in CANDU 6 concrete containment buildings, Canadian Nuclear Laboratories Chalk River, ON K0J 1J0, Canada, 2015.

[12] ANSYS 12.1, Theory Reference Manual ,2012.

[13] H .Teh Hu, J.I.Liang, Ultimate analysis of BWR Mark III RC containment subjected to internal pressure, Article in Nuclear Engineering and Design 195(1):1-11, DOI: 10.1016/S0029-5493(99)00163-6,2015.

[14] K.J.William , E.P.Warnke , Constitutive model for the tri-axial behavior of concrete. IABSE reports of the working commissions, BERGAMO, ITALY, 1974.

[15] L. Dahmani, A.Khennane, Crack identification in reinforced concrete beams using ANSYS software. Article in Strength of Materials, DOI: 10.1007/s11223-010-9212-6, 2010.

EURODYN 2020
XI International Conference on Structural Dynamics
M. Papadrakakis, M. Fragiadakis, C. Papadimitriou (eds.)
Athens, Greece, 23–26 November 2020

DESIGN AND ANALYSIS OF AN X-STRUCTURED VIBRATION ISOLATION MOUNT (X-MOUNT) WITH WIDER QUASI-ZERO-STIFFNESS RANG

Jing Bian, Xingjian Jing *

Department of Mechanical Engineering, The Hong Kong Polytechnic University
Hong Kong, China
jing.bian@connect.polyu.hk; xingjian.jing@polyu.edu.hk

Keywords: Passive vibration isolation; Nonlinear stiffness; Negative stiffness; Quasi-zero-stiffness; X-shaped structure

Abstract. *Increasing demands for high performance of vibration control drives the development of nonlinear vibration control devices to overcome the limitations of traditional linear vibration control methods. A novel and compact X-structured mount (X-mount) with an oblique spring is designed and investigated in this paper which demonstrates beneficial nonlinear stiffness and damping, tunable payload and resonant frequency property, and a special enlarged quasi-zero-stiffness region, which thus lead to excellent vibration isolation performance without instability or other strong nonlinear response such as jump phenomenon. The X-mount is designed, based on a bio-inspired X-shaped structure, and a special oblique spring is introduced which can effectively widen the working quasi-zero-stiffness range by employing negative stiffness due to a special contact stiffness. The oblique spring can also help to reduce the dynamic stiffness achieving an ultra-low natural frequency and broadband effective vibration isolation range. The mathematical modeling, theoretical analysis and experiment results show the high performance of this X-mount, potentially providing a promising solution for vibration control in many engineering practices.*

INTRODUCTION

Vibration generated by machines or other environmental sources are often troublesome and unavoidable. However, their influences on dynamical systems or structures can be suppressed through properly designed vibration isolators. To achieve an effective vibration suppression effect, the natural frequency of an isolation platform must be smaller compared with the excitation frequency. For the low-frequency vibration environment, this requirement can be achieved by using a soft spring/stiffness component, but this might sacrifice the static loading capacity of the isolation platform. To conquer this intractable problem, some quasi-zero-stiffness (QZS) vibration isolators are developed to achieve a low dynamic frequency and maintain the static loading capacity simultaneously [1-11]. A traditional QZS isolator consists of three springs, where the negative stiffness provided by the horizontal springs is designed to offset the positive stiffness from the vertical spring, thus quasi-zero-stiffness is achieved. While, QZS isolators could lead to unstable problems, e.g., jump phenomenon, multi-stable [8, 11, 12]. Moreover, QZS isolators are limited in large vibration motion and very sensitive to the loading. Therefore, proper nonlinearity should be considered to avoid the strong nonlinear problems and the disadvantages mentioned above. For instance, the benefits of the applications of the geometric nonlinearity was summarized in Gatti et al [13] which may provide solutions for the problems above. The applications of the QZS in shock isolation can be found in [9, 14, 15]. The methods of realizing negative stiffness and QZS inlcude horizontal spring [7, 10, 11, 16], buckled beams [14] or magnetic components [1, 17] and structures [2]. Another important component for an isolation system is its damping. The limitation of the linear damping is that increasing the linear damping can suppress the resonant peak but will deteriorate the performance in higher frequencies. Therefore, nonlinear damping attracts attentions recently for the advantages. Among the nonlinear damping, the displacement-dependent damping shows advantages in both of the resonance and the high frequencies [18, 19].

Recently, a bio-inspired structure called X-shaped or limb-like structure (LLS) attracted many attentions due to the beneficially nonlinear stiffness and damping properties, and could be conveniently designed for many engineering applications [6, 12, 20-26], which presents an alternative and totally new approach for creating QZS or negative stiffness with only simple bio-inspired structure design. Based on this X-shaped structure, an innovative X-mount is thus proposed in this paper. This X-mount is optimally designed with a special oblique spring which can reduce the equivalent stiffness before contact and achieve a wider QZS range when the contact happens. This contact stiffness can contribute to remove/offset the negative stiffness after the zero-stiffness point, and the combination effect enhances the system isolation performance with an obviously enlarged QZS range. In addition, the obliqueness of this spring can be used for reducing the system stiffness further to achieve an ultra-low natural frequency and broadband effective isolation range. Experimental validation is conducted, together with theoretical analysis to verify the effectiveness of the proposed method.

1 MATHEMATICAL MODELLING

1.1 Static force

The X-mount is presented in Fig. 1 with specification of the structural parameters. The structural parameters are defined as: L is the length of the rod, θ is the initial assembly angle, n is the number of the layer, M is the isolated mass and K is the stiffness of the spring. z-axis is the vertical direction and x-axis is the horizontal direction, φ is the rotational angle of the rod, Δx is the relative displacement in the horizontal direction, z_1 is the total relative displacement in vertical direction. By changing H, the initial angle θ_1 between the oblique spring

and the horizontal plane can be adjusted correspondingly. Introducing β to describe the oblique level of the spring. l_0 is the original length of the spring and l_1 is the tension length of the spring. $\Delta l = l_1 - l_0$ is the deformation length.

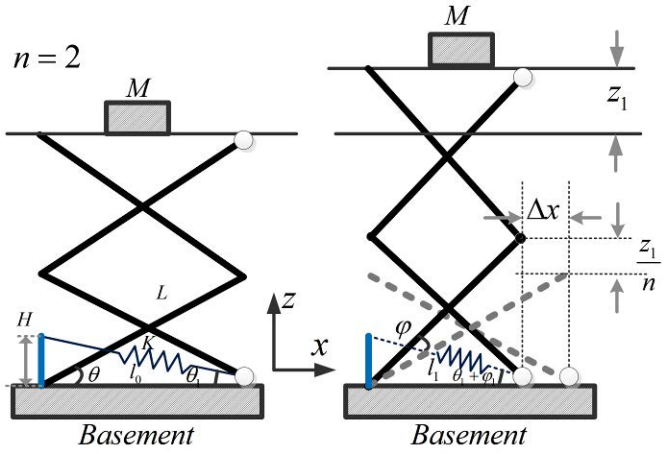

Figure 1: X-mount with an oblique spring

The variable φ, Δx and Δl can be obtained as

$$\Delta x = L(cos(\theta) - cos(\theta + \varphi)) = L\,cos(\theta) - \sqrt{L^2 - (L\,sin(\theta) + \frac{z_1}{n})^2} \tag{1}$$

$$\varphi = arctan\left(\frac{L\,sin(\theta) + \frac{z_1}{n}}{L\,cos(\theta) - \Delta x}\right) - \theta \tag{2}$$

$$\Delta l = \sqrt{H^2 + (Lcos(\theta) - \Delta x)^2} - \sqrt{H^2 + (Lcos(\theta))^2} \tag{3}$$

And other parameters are defined as

$$\varphi_1 = arctan(\frac{H}{Lcos(\theta) - \Delta x}) - arctan(\frac{H}{Lcos(\theta)}) \tag{4}$$

$$\alpha = (\theta + \varphi) - (\theta_1 + \varphi_1) \tag{5}$$

As shown in Fig. 2(a), the static force before the contact can be obtained as

$$F_1 = \frac{1}{2}(K\Delta l_1 \sin(\theta_1 + \varphi_1) + \cos(\theta_1 + \varphi_1)\tan(\theta + \varphi) + \frac{\sin(\alpha)}{\cos(\theta + \varphi)}) \tag{6}$$

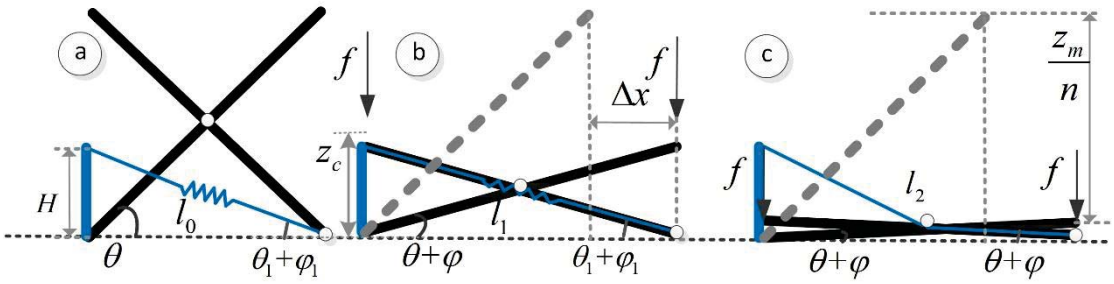

Figure 2: The loading process

And the parameters after contact are defined as follows:

$$l_2 = \frac{1}{2}L + \sqrt{(\frac{1}{2}Lcos(\theta+\varphi))^2 + (H - \frac{1}{2}Lsin(\theta+\varphi))^2} \tag{7}$$

$$\Delta l_2 = l_2 - l_0 \tag{8}$$

Where the relative spring forces and geometric angles are defined as

$$f_{s2} = K\Delta l_2,\ f_o = 2f_{s2}cos\ (\theta'),\ f_{ov} = f_o cos\ (\theta'') \tag{9}$$

$$\theta' = \frac{\theta_2 + \pi/2 + \theta + \varphi}{2},\ \theta'' = \theta' - \theta_2 \tag{10}$$

The static force after the contact can be obtained as

$$F_2 = f_{s2}(sin(\theta+\varphi) - f_{s2}tan(\theta+\varphi)cos\ (\theta')sin(\theta'') + \frac{1}{2}f_{ov} \tag{11}$$

The whole loading process can be combined and written as a piecewise function:

$$F = \begin{cases} F_1, if\ z_1 < z_c \\ F_2, if\ z_1 \geq z_c \end{cases} \tag{12}$$

1.2 Dynamic model

By utilizing the Lagrange equation, the dimensionless dynamic equation of the X-mount can be written as follows

$$z_1'' + Kf_{eq}(z_1) + 2\xi_x z_1' = \Omega^2 A_0\ cos\ \Omega\tau \tag{13}$$

Where ξ_x in the nonlinear damping ratio which can be found in [20] and the piecewise stiffness can be written as

$$f_{eq}(z_1) = \begin{cases} f_b(z_1), if\ z_1 \geq -z_c \\ f_a(z_1), if\ z_1 < z_c \end{cases} \tag{14}$$

And the stiffness before contact and after contact can be obtained as

$$f_b(z_1) = \Delta l \frac{\partial(\Delta l)}{\partial z_1},\ f_a(z_1) = \Delta l_2 \frac{\partial(\Delta l_2)}{\partial z_1}\frac{\partial z_1}{\partial z} \tag{15}$$

2 ANALYSIS RESULTS

2.1 Optimal working position

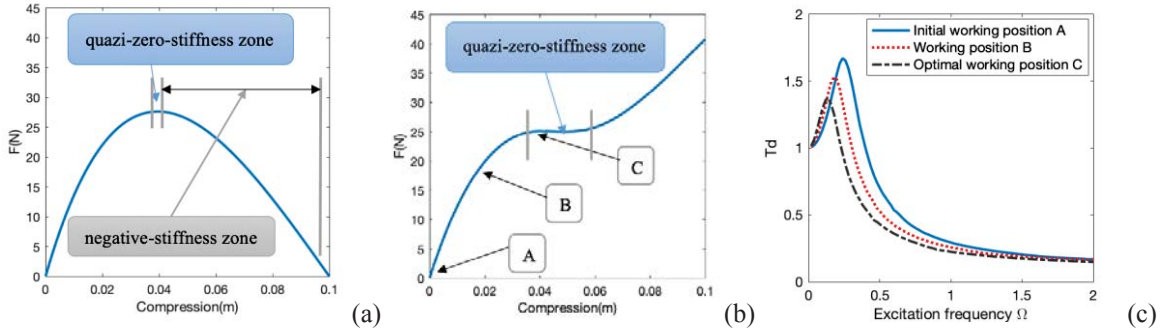

Figure 4: Optimal working position analysis: (a) static force curve with horizontal spring, (b) static force

curve with oblique spring and the contact stiffness, (c) the relative isolation performance

In Fig 4, the parameters are set as K=10000, M=10, A=0.005, L=0.1, $\theta = \pi/6$, n=2, $\beta = 0.6$, $c_r = 0.15$, $c_h = 1$. Fig. 4(a) shows the static force of the X-mount with a horizontal spring which has a very limited QZS zone. While, with the oblique spring and the contact stiffness in Fig. 4(b), the negative stiffness can be offset effectively by the vertical positive stiffness due to the contact, and the X-mount can maintain the QZS in a considerable wide range. In the Fig. 4(c), the displacement transmissibility curves are obtained with three working positions: A, B and C. The result shows the X-mount in the optimal working position C (working angle is 0.314) has the best vibration isolation performance: wider isolation frequency range and smaller transmissibility value in the resonance. Both are desirable properties for vibration isolation.

2.1 Comparison with benchmark QZS isolator

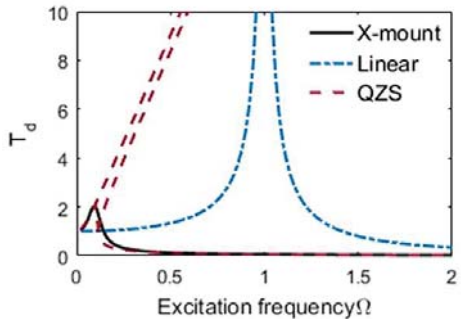

Figure 5: Comparison result of the X-mount, linear isolator and benchmark QZS isolator

The comparison results are shown in Fig. 5. Three models are evaluated and compared: the linear isolator with the linear stiffness and damping, the benchmark QZS isolator and the X-mount. The advantages of the X-shaped systems are obvious. Firstly, compared with the linear isolator and the QZS, the X-mount shows great suppression effect on the resonant peak and the widest isolation frequency range. The QZS isolator can only be effective when the excitation frequency is larger than unstable frequencies. Most importantly, the X-mount has superior stability compared with the QZS isolator. In the ultra-low frequencies, the QZS isolator appears the multi-steady states and the jump phenomenon which are very dangerous for the application. This unstable state demonstrates the QZS has strong nonlinear property which is sensitive to the initial conditions and the perturbation and leads to the system unsafe in these jump frequency range. While, the X-mount shows a very week nonlinear property which is more stable.

3. EXPERIMENTAL VALIDATION

The experimental setup is shown in Fig. 6(a), the whole X-mount has two layers (n=2) with rod length L=0.075m. An oblique spring with stiffness coefficient K=2300 N m^{-1} is installed in the bottom of the X-mount.

In Fig. 6(b), position A is the initial working angle, position B is the situation when the loading increased to 3N, position C (without contact) is the optimal working position with loading of 5.5N. When the loading continues increasing to 5.6 N, the system reaches to position D (with contact) which is also in the QZS range. In Fig. 7(c), it is clear the resonant frequency shifts to the lower frequency range as the working position is tuned from the initial

position A to the optimal positions (C and D). With the working position C and D, the X-mount has an ultra-low resonant frequency around 1Hz and the transmissibility peak decreases as well. In both positions C and D, the X-mount has ultra-low resonant frequencies and excellent isolation transmissibility performances which effectively confirmed the effectiveness of the enlarged QZS range. Without the special designed oblique spring and the contact stiffness, the QZS range is very narrow and position D will not exist.

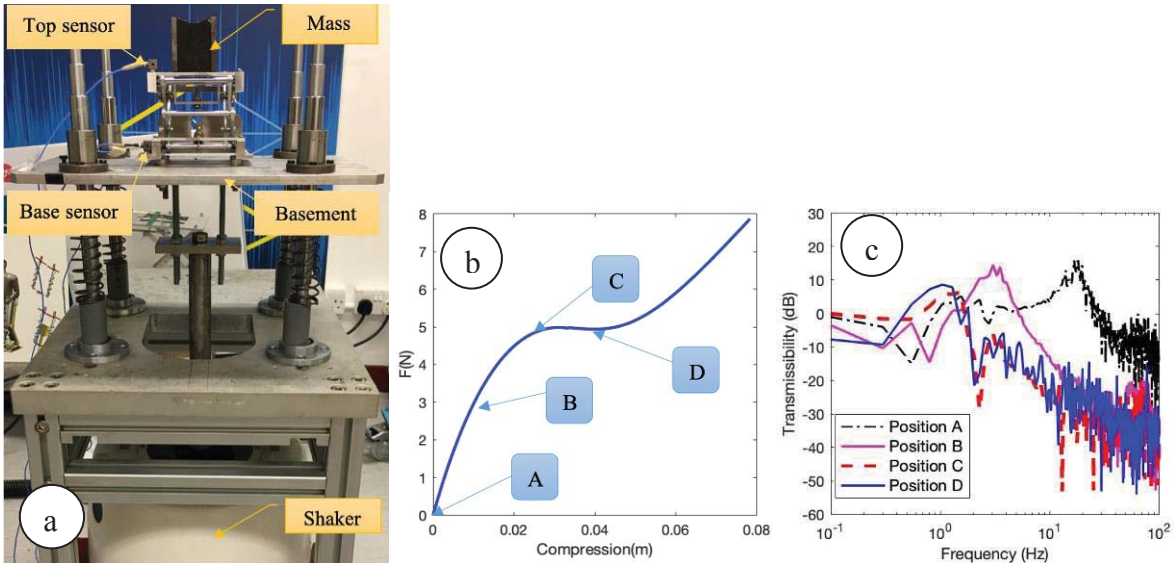

Figure 6. Working position influence: (a)experimental setup, (b) static force curves, (c) transmissibility.

4. CONCLUSIONS

A novel and compact X-mount are designed and investigated in this paper. This X-mount demonstrates beneficial nonlinearities (stiffness and damping), tunable payload and resonant frequency property, and excellent isolation performance with enhanced QZS effect. More specially, the QZS range of this X-mount can be effectively enlarged with a special designed oblique spring via the combination effect of the negative stiffness and the contact stiffness. The X-mount has desirably weak nonlinearities which can achieve superior isolation performance (lower resonant amplitude and wider isolation frequency range) and maintain the stability without the dangerous nonlinear problems, e.g., instability, bifurcation, jump phenomenon and chaos. Therefore, this novel X-mount provides a promising solution for the vibration control and could be conveniently applied in a wide range of engineering practice.

ACKNOWLEDGEMENT

The work is supported by a general research fund (GRF) of HK RGC (Ref. 15206717) and an innovation and technology fund (ITF) project of HK ITC (ITP/020/19AP)

REFERENCES

[1] Y. S. Zheng, X. N. Zhang, Y. J. Luo, Y. H. Zhang, S. L. Xie, Analytical study of a quasi-zero stiffness coupling using a torsion magnetic spring with negative stiffness, *Mechanical Systems and Signal Processing* 100, 135-151, 2018.

[2] J. X. Zhou, Q. Y. Xiao, D. L. Xu, H. J. Ouyang, Y. L. Li, A novel quasi-zero-stiffness strut and its applications in six-degree-of-freedom vibration isolation platform, *Journal of Sound and Vibration* 394, 59-74, 2017.

[3] A. Carrella, M. J. Brennan, I. Kovacic, T. P. Waters, On the force transmissibility of a vibration isolator with quasi-zero-stiffness, *Journal of Sound and Vibration* 322, 4-5, 707-717, 2009.
[4] A. D. Shaw, S. A. Neild, D. J. Wagg, Dynamic analysis of high static low dynamic stiffness vibration isolation mounts, *Journal of Sound and Vibration* 332, 6, 1437-1455, 2013.
[5] X. T. Sun, X. J. Jing, Multi-direction vibration isolation with quasi-zero stiffness by employing geometrical nonlinearity, *Mechanical Systems and Signal Processing* 62-63, 149-163, 2015.
[6] X. T. Sun,X. J. Jing, A nonlinear vibration isolator achieving high-static-low-dynamic stiffness and tunable anti-resonance frequency band, *Mechanical Systems and Signal Processing* 80, 166-188, 2016.
[7] C. Liu and K. P. Yu, A high-static–low-dynamic-stiffness vibration isolator with the auxiliary system, *Nonlinear Dynamics* 94, no. 3, 1549-1567, 2018.
[8] A. Carrella, M. J. Brennan, T. P. Waters, V. Lopes, Force and displacement transmissibility of a nonlinear isolator with high-static-low-dynamic-stiffness, *International Journal of Mechanical Sciences* 55, no. 1, 22-29, 2012.
[9] B. Tang,M. J. Brennan, On the shock performance of a nonlinear vibration isolator with high-static-low-dynamic-stiffness, *International Journal of Mechanical Sciences* 81, 207-214, 2014.
[10] T. D. Le, K. K. Ahn, Experimental investigation of a vibration isolation system using negative stiffness structure, *International Journal of Mechanical Sciences* 99-112, 2013.
[11] C. C. Lan, S. A. Yang, Y. S. Wu, Design and experiment of a compact quasi-zero-stiffness isolator capable of a wide range of loads, *Journal of Sound and Vibration* 333, no. 20, 4843-4858, 2014.
[12] Z. Wu, X. Jing, J. Bian, F. Li, R. Allen, Vibration isolation by exploring bio-inspired structural nonlinearity, *Bioinspir Biomim* 10, no. 5, p. 056015, Oct 8 2015.
[13] G. Gatti, M. J. Brennan, and B. Tang, Some diverse examples of exploiting the beneficial effects of geometric stiffness nonlinearity, *Mechanical Systems and Signal Processing* 125, 4-20, 2019.
[14] X. C. Huang, Y. Chen, H. X. Hua, X. T. Liu, Z. Y. Zhang, Shock isolation performance of a nonlinear isolator using Euler buckled beam as negative stiffness corrector: Theoretical and experimental study, *Journal of Sound and Vibration* 345, 178-196, 2015.
[15] L. X. Yan, S. H. Xuan, X. L. Gong, Shock isolation performance of a geometric anti-spring isolator, *Journal of Sound and Vibration* 413, 120-143, 2018.
[16] I. Kovacic, M. J. Brennan, T. P. Waters, A study of a nonlinear vibration isolator with a quasi-zero stiffness characteristic, *Journal of Sound and Vibration* 315, no. 3, 700-711, 2008.
[17] D. L. Xu, Q. P. Yu, J. X. Zhou, S. R. Bishop, Theoretical and experimental analyses of a nonlinear magnetic vibration isolator with quasi-zero-stiffness characteristic, *Journal of Sound and Vibration* 332, no. 14, 3377-3389, 2013.
[18] J. Y. Sun, X. C. Huang, X. T. Liu, F. Xiao, H. X Hua, Study on the force transmissibility of vibration isolators with geometric nonlinear damping, *Nonlinear Dynamics* 74, no. 4, 1103-1112, 2013.
[19] B. Tang, M. J. Brennan, A comparison of two nonlinear damping mechanisms in a vibration isolator, *Journal of Sound and Vibration* 332, no. 3, 510-520, 2013.
[20] J. Bian, X. J Jing, Superior nonlinear passive damping characteristics of the bio-inspired limb-like or X-shaped structure, *Mechanical Systems and Signal Processing,* 2018.
[21] X. T. Sun, X. J Jing, Analysis and design of a nonlinear stiffness and damping system with a scissor-like structure, *Mechanical Systems and Signal Processing* 66-67, 723-742, 2016.
[22] X. J Jing, L. L Zhang, X. Feng, B. Sun, Q. K. Li, A novel bio-inspired anti-vibration structure for operating hand-held jackhammers, *Mechanical Systems and Signal Processing* 118, 317-339, 2019.
[23] X. Feng,X. J. Jing, Human body inspired vibration isolation: Beneficial nonlinear stiffness, nonlinear damping & nonlinear inertia, *Mechanical Systems and Signal Processing* 117, 786-812, 2019.
[24] H. H. Dai, X. J. Jing, C. Sun, Y. Wang, X. K. Yue, Accurate modeling and analysis of a bio-inspired isolation system: with application to on-orbit capture, *Mechanical Systems and Signal Processing* 109, 111-133, 2018.
[25] C. C. Liu, X. J. Jing, F. M. Li, Vibration isolation using a hybrid lever-type isolation system with an X-shape supporting structure, *International Journal of Mechanical Sciences* 98, 169-177, 2015.
[26] B. Sun,X. J. Jing, A tracked robot with novel bio-inspired passive "legs", *Robot. Biomim.* 4 ,1-14, 2017.

EURODYN 2020
XI International Conference on Structural Dynamics
M. Papadrakakis, M. Fragiadakis, C. Papadimitriou (eds.)
Athens, Greece, 23–26 November 2020

CALCULATION DISPERSIONS AND ERRORS OF SHIP HULL AND SUPERSTRUCTURE VIBRATIONS

Lech Murawski[1], **Do Van Doan**[1]

[1] Gdynia Maritime University, Faculty of Marine Engineering
Morska Street 83 – 87, 81-225 Gdynia, Poland
e-mail: l.murawski@wm.am.gdynia.pl, dodoan.vimaru@gmail.com

Keywords: Finite element method, Ship hull vibrations, Propeller's excitation, Main engine's excitation

Abstract. *The ship hull vibration has a great impact on the performance, safety of the devices, structures and the sailor's comfort when working on the ship. With increases in ship sizes and speeds, shipboard vibration becomes a significant concern in the design and construction of ships. Therefore, designing a ship without any excessive vibration is an important issue and should be studied through analysis right in the design phase. To ensure minimum vibration in a proposed new design; avoid damage to structures, machinery or equipment (mechanically suitable); meeting the requirements of the crew's living environment and working conditions. The ship's natural and forced vibrations are determined to right from the design stage, which will help ship designers and structures avoid dangerous resonance areas. In the study, a finite element model representing the entire ship hull, including the deckhouse and machinery propulsion system, has been developed using commercial software for vibration analyses of the container ships. The basic elements of a hull vibration system include basic mass, elastic properties as well as damping and exciting forces. In order to control or limit the vibration response, it is necessary to modify the mass and/or elastic properties; by increasing damping; reducing excitation forces or changing the excitation frequency. Increasing damping may be useful in solutions to local structural vibration problems and in some machine and equipment problems but not as a practical solution to reduce hull vibration. The influence of different modeling methods on the obtained calculation results was investigated. The impact of various operating parameters on the vibration level was also analyzed. In particular, the impact of modelling methods, added water mass, loading conditions and sources of excitations, was taken into account. The results are compared with some empirical formulas. As a result, the calculation confidence level was estimated. The calculation results have been verified by comparison with measurement tests carried out on the real ship.*

1 INTRODUCTION

Seagoing ships, particularly those equipped with slow-speed diesel engines, are exposed to excessive vibration of the ship's superstructure and hull [1, 2]. Ship's hull vibrations have a major impact on navigation safety. They have an impact on the marine structures and equipment reliability and on the comfort of maritime crews, which is also connected with navigation safety. In most cases, two main systems of the ship are distinguished: the ship's hull (with superstructure and main engine body) and the power transmission system (crankshaft, main engine shafting, propeller), as shown in figure 1. The ship's adverse dynamic characteristics are very difficult to change once it is built. Therefore, it is very important to correctly determine the expected vibration levels when designing units. All global classification societies require reliable computational analyses (often verified by measurement tests) of dynamic characteristics of the ship's propulsion system and of the propulsion system influence on the seagoing ship's hull and superstructure vibration levels.

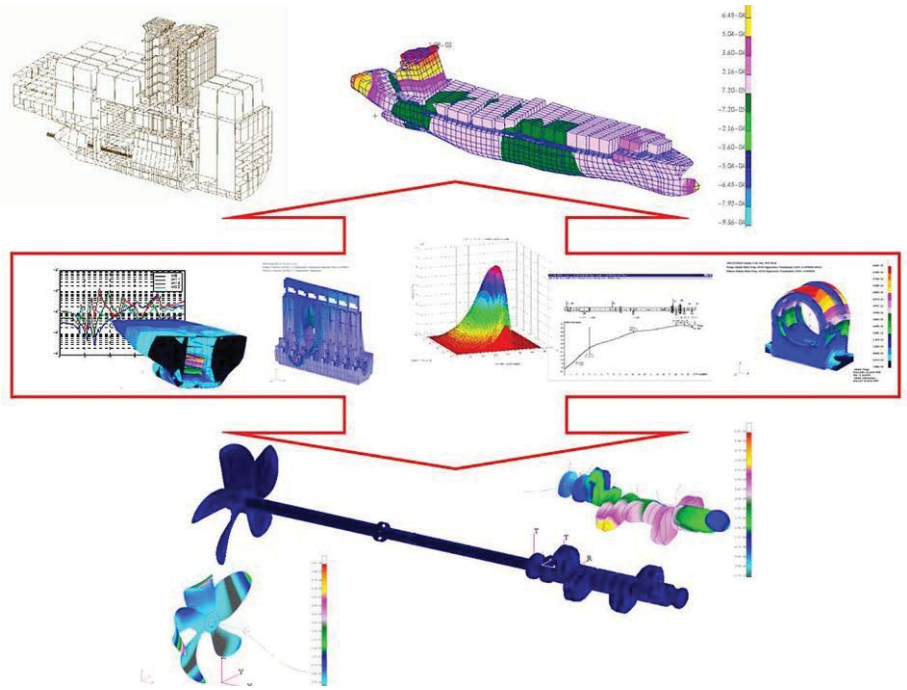

Figure 1: Interactions between the ship's hull and propulsion system through boundary conditions.

Mainly, the power transmission system [3, 4, 5] induces the forces that excite significant vibrations. Environmental impact functions are less important because they do not generate continuous vibration. The purpose of the presented analyses is to identify the main forces, which excite the ship's superstructure and hull vibrations, to test their effects on vibration levels, and to verify the assumptions of the computational methodology. The numerical calculations results have been verified by comparison with the measurement tests.

2 BASIC ASSUMPTIONS

As already mentioned, only propeller excitations and engine excitations will be considered. The rotating propeller is generating six variable components, generalized hydrodynamic forces and a variable field of pressures induced over the propeller on the ship's deck transom. The variable total pressure head causes uncoupled longitudinal vibrations of the power transmission system (main engine shafting + crankshaft), which generate dynamic reactions of the thrust bearing. Transverse hydrodynamic forces generate flexural vibrations of the main en-

gine shafting that result in variable reactions of the radial bearings: the stern bearing and the intermediate bearings. On the other hand, the main engine, and in particular the variable, radial mass and gas forces (from piston-crank system), are the source of unbalanced forces and moments of the main engine. In general, these are also six components: three forces and three force moments. Forces and moments are partially compensated by the correct ignition order choice in the engine cylinders. However, usually not all of them: for selected harmonic components, generalized forcing forces may be non-zero. On the other hand, variable forces cause torsional vibration of the power transmission system. Torsional vibration causes deformation of the crankshaft inside crank, which leads to coupled longitudinal vibrations. Such vibrations are another source of variable thrust bearing reactions.

A list of basic forces exciting vibrations of the hull and superstructure [4, 6, 7] of a ship equipped with a low-speed engine directly driving the propeller is given in figure 2. Drive dynamics analysis is necessary to determine hull vibration correctly; nevertheless, the power transmission system vibration analysis requires knowledge of the boundary conditions, i.e. the hull's stiffness dynamic characteristics. The couplings between the hull and the drive shall be taken into account in any detailed analysis of ship's vibrations.

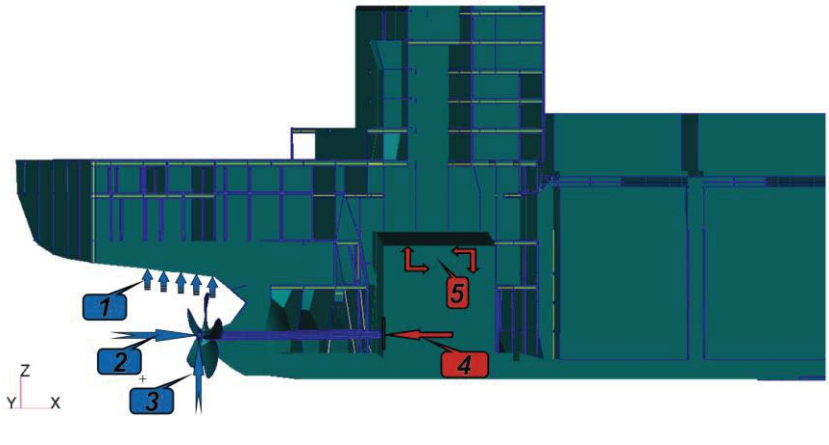

Figure 2: Forces exciting the ship's hull and superstructure vibration.

The dynamic forces indicated schematically in figure 4.25 have the following meanings:

1. pressure pulses induced on the ship's deck transom by the propeller;
2. longitudinal hydrodynamic forces exciting uncoupled longitudinal vibrations of the power transmission system and, consequently, variable reactions of the thrust bearing;
3. transversal hydrodynamic forces and moments causing flexural vibrations of the main engine shafting and, consequently, variable reactions of the transversal radial bearings (stern bearings and intermediate bearings);
4. dynamic reactions of the thrust bearing from coupled longitudinal vibrations of the power transmission system;
5. unbalanced moments (and, possibly, forces) of the main engine coming from the radial gas and mass forces of the piston-crank system.

In the present paper, only the steady-state vibrations, i.e. the ship's vibrations, will be analysed; when all machinery and equipment are operating under the steady operating conditions (constant power and rotational speed). It is assumed that any operation disturbance is small compared to the fixed size. In this case, the mathematical model can be brought into a series of linear differential equations with fixed parameters. The constant and set parameters are both mass and mass moment of inertia, as well as rotational speed, power (moment), forcing

frequency, etc. In addition, in typical marine structures, the vibration damping has a negligible effect on the natural vibrations frequency. In such a case, the finite element method (FEM) that the author uses, applies relatively simple methods of solutions. Therefore, the number of elements (of differential equations) can be very large; the analysed models can be detailed.

The container ship were analysed in the work: a medium-sized, with a capacity of approximately 2700 TEU (standard containers). The ship's length is equal to 207 m, main engine (MAN B&W 8S70MC-C) power: about 25 thousand kW, nominal rotational speed: 91 rpm, and the five-blades propeller. The FEM model for the ship are shown in figure 3.

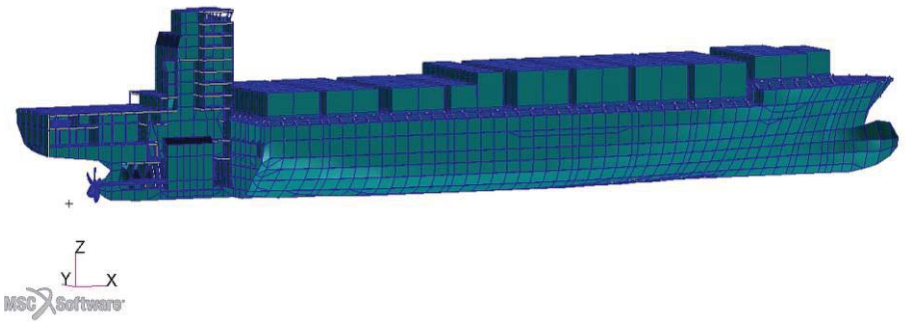

Figure 3: FEM model of a 2700 TEU container ship.

3 NATURAL VIBRATIONS

Free vibrations allow a qualitative assessment of the ship's excessive vibration risk [8]. For example, the position of the ship's hull beam vibration nodes (relative to the position of the main engine) makes it possible to decide on the purchase of the main engine balancing devices (stern and/or bow balancer). The comparison of the forcing frequency with the free vibration frequency of the ship's superstructure allows, yet at the stage of the initial design, to make major structural changes in order to avoid excessive vibrations. For example, low-frequency vibrations of the main engine body may prove its foundation poor or the double bottom too susceptible in the engine room area. When analysing the ship's natural vibration, we can distinguish:

- global vibrations (vertical, horizontal, torsional) of the hull beam,
- main engine body vibrations,
- ship's superstructure vibrations,
- local vibration of decks and other structural elements of the hull.

All of the above types of vibration can be coupled. Figure 4 shows examples of global hull beam vibrations. These are vertical and torsional vibration forms with frequencies from 1.6 to 4.6 Hz. Most often, the "beam-type" forms of the ship's hull free vibrations are benign due to their very low frequencies. They are usually outside the range of the forcing frequency generated by the drive. At a rated speed of 91 rpm, the basic forcing frequency of the 8-cylinder engine is of 12.1 Hz and the basic excitations frequency of 5-blade propeller is of 7.6 Hz. The ship's hull is an example of typical superresonant vibrations with a big offset. Of course, the forcing frequency may be similar to the higher forms of the ship's hull beam free vibrations. For this reason, at least the first dozen free vibration forms should be taken into account when analysing global vibration of ships.

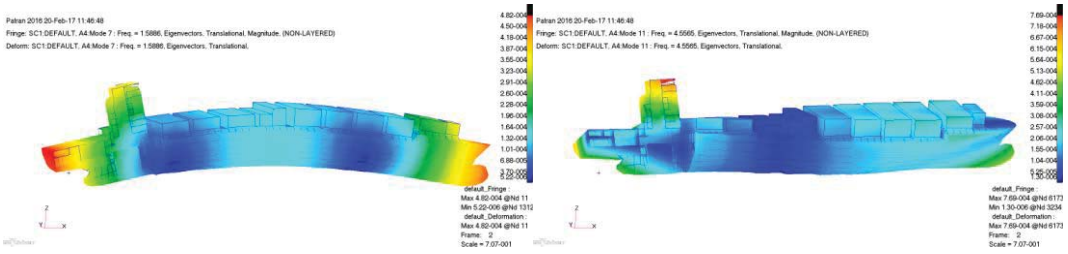

Figure 4: Global natural vibrations of 2700 TEU container ship.

Ship's superstructure vibrations are the most important. They are often coupled with the vibrations of the ship's hull and main engine. Figure 5a shows the forms of the discussed ships' superstructure free vibrations. The main engine body vibrations are also important for two reasons. When excessive, they can be dangerous to the engine reliability, but they can also be a source of forcing other marine structures and equipment. Figure 5b shows the transversal form of the 2700 TEU container ship main engine body natural vibrations.

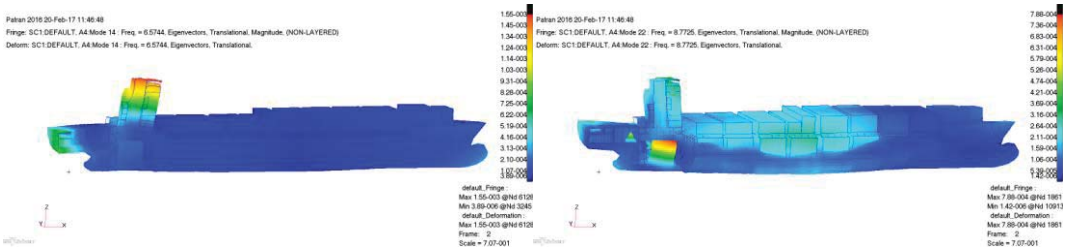

Figure 5: Superstructure and main engine body vibrations of the container ship.

Good consistency between vibration measurements and calculation results is particularly difficult to obtain in marine conditions [4, 9]. Many important design decisions depend on the results of the computational analyses. The reliability and the distribution of the vibration calculation results are a fundamental question in numerical analyses of complex structures. Free vibrations depend only on the stiffness and mass distribution (the damping effect is negligible). Therefore, the confidence level of the free vibration calculation is relatively high. However, the actual level of the forced amplitude may significantly differ from that resulting from the computational analyses. This is due, among others, to poor knowledge of the size of the structural damping in marine conditions. There are no good methods for calculating the damping.

The mass matrix is affected by the ship's performance characteristics. The effect of the ship's loading state on its frequencies and the free vibration forms was examined. The importance of taking into account the masses of associated water that accompanies the hull vibrations was also assessed. If the associated water phenomenon is taken into account, the free vibration frequencies are reduced. The natural vibration frequency decreases by approximately 25%, when the hull wetness is taken into account. This applies mainly to vertical forms with a small number of vibration nodes. The more vibration nodes, the less impact of the associated water. For example, the frequency drop for the 6-node vibration form is of 16%. The hull wetting effect on horizontal vibration is also slightly less, not more than 20%. The addition of the associated water mass also changes the order of the free vibration form occurrence. The effect of the added water on the vibrations of the superstructure and main engine is much lower, it does not exceed 6%. This is because neither the superstructure nor the engine body is directly wetted. This impact is so small that it is acceptable not to include the associated water in analyses focused on these ship's elements.

The effects of cargo condition changes on the free vibration frequencies of both ships are also analysed. As we would expect, the ship's cargo (ballast state -> design cargo state) reduces the hull free vibration frequency. The measured vibration amplitude levels, which are normally checked once a ship is built, during marine tests (ballast condition), may significantly differ from the operational ones (cargo condition). It may be possible to eliminate the excessive vibrations in the superstructure by adding a large effective mass, e.g. by filling a space located high up in the superstructure with sand.

Before calculating forced vibrations, it is necessary to decide on the calculation method. There are two main methods: direct integration and modal superposition. The most common method is the modal superposition of free vibration. In this method, the free vibration forms are added together in an appropriate manner. In this case, we should verify the assumption of the number of free vibration forms included in the summation to forced vibrations. The impact of the quantities of free vibration forms taken into account was verified by analysing the results of the 2700 TEU container ship analyses. Given the nominal speed of the power transfer system (91 rpm) and the fact that the fifth and the eighth harmonic components are the basic forcing force components (number of propeller blades and number of engine cylinders), a maximum frequency of the main forcing forces can be determined at 8 and 12 Hz. The focus was on propeller excitations. For this reason, the key range of excitations is from 0 to 7.6 Hz. A number of variants of forced vibration calculations were carried out, taking into account the different number of free vibration forms. Calculation variants with the following number of free vibration forms included were adopted, from 10 modes (up to 7 Hz - all basic forms of hull and superstructure free vibration forms) to 150 modes (up to 20 Hz - forms with frequencies up to 2.5 times the frequency of the propeller excitations). Figure 6 shows the longitudinal amplitudes of the vibration velocity of the main engine body (MEF—heads on the bow side), the hull in the deck transom area (DTR), and the top of the superstructure (STL—bridge wing), depending on the number of free vibration forms taken into account.

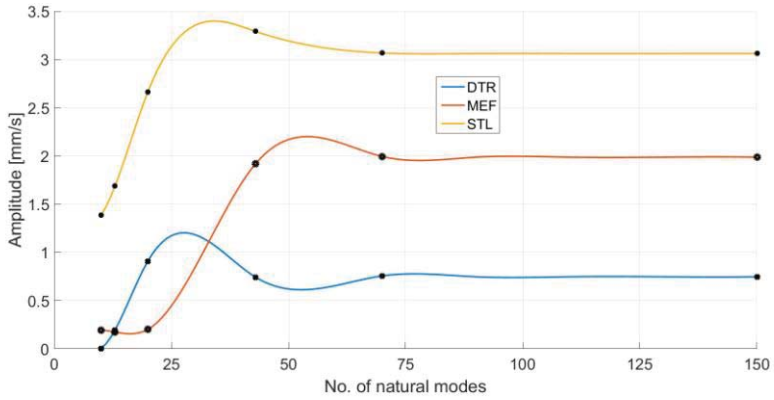

Figure 6: Amplitude of the longitudinal forced vibration velocity depending on the number of natural vibration modes considered.

We should note that if there are not enough free vibration forms to be taken into account, even forced vibration forms might be wrong. For example, the amplitude of the main engine heads longitudinal vibrations, which are more than twice the amplitude of the deck transom. If the free vibration frequency range is from 0 to 9 Hz (20 forms), the calculation results indicate that the heads vibration amplitude is four times less (!) than the deck transom amplitude. Also, the shape of the resonance curves can be changed at an insufficient number of free vibration forms considered. When using the modal superposition method, the band of the free vibration frequencies to be determined should be at least twice as wide as the forcing frequency band so

that the results of the vibration amplitude (velocity) calculations are correct. Forced vibration phases are less sensitive to the number of determined forms of natural vibration. In specific cases, for drives with high-frequency excitations (medium-velocity engines), it is admissible to extend the frequency range of forced vibrations 1.5 times when determining the essential of free vibration forms. In the considered case, taking into account the first 70 free vibration forms (up to 16 Hz) is sufficient.

4 FORCED VIBRATIONS

When calculating the analysed model forced vibrations, the damping matrix must be specified. Damping depends on a large number of factors. The damping is greatly affected by the structure wetting with seawater. It is very difficult to precisely define the damping; practically, it is possible only using experiments. Its values can be found in numerous publications [3, 9]. For steel welded structures, the author believes that vibration increase factor of 20–25 is a good approximation. However, it is very important to verify the calculation analyses using correctly performed measurement tests.

When analysing the hull and superstructure dynamics, two main sources of forcing are to be taken into account: from the propeller and from the main engine [3, 5]. The vibration amplitudes (forcing forces) summation must take into account the time history phase angles between propeller' blades and engine's cranks. In the case of excitations induced by the propeller, the dominant force is the harmonic component associated with the number of propeller blades (for the concerned ship, the 5th component). Engine excitations are represented by a whole spectrum of harmonic components, the most dangerous of which is related to the number of engine cylinders. Power systems with the same number of propeller blades and engine cylinders should not be used in shipbuilding because of the high risk of excessive vibration due to the summation of identical harmonic components. However, even for different numbers of cylinders and propeller blades, harmonic components summation may be unfavourable, as marine low-velocity engines have high collateral harmonic components. For the analysed 8-cylinder engine, the 5th harmonic component is significant. As it has already been stressed, the vibration phases caused by the propeller depend on its blades position, while the vibration phases caused by the main engine depend on the crankshaft crank position. For these reasons, the angular mutual alignment of the propeller and crankshaft may significantly affect the superstructure vibrations level [5].

When minimising vibrations, the selected point vibration amplitude and phase must be determined first, for both sources of excitations. For the main engine excitations, the vibrations caused by the coupled longitudinal vibrations and the vibrations caused by the main engine unbalanced moments are to be added together. Propeller excitations consist of water pressure pulses on the deck transom and of forces induced by drive uncoupled longitudinal vibrations and of the main engine shafting flexural vibrations. Only the 5th harmonic component will be considered in this analysis, as the principal propeller excitations are of the fifth order, and only the same order vibrations can be vectorially added. Figure 7 summarise the longitudinal vibrations levels of the superstructure bridge wing, produced by the propeller and main engine. Summary results by excitations type are presented.

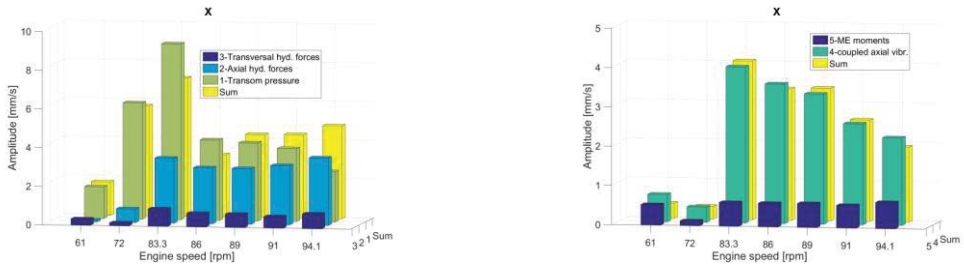

Figure 7: Vibration velocity amplitudes for the container ship in the longitudinal direction on the bridge wing, excited by the propeller and main engine.

Since the total vibrations from the propeller and main engine have similar amplitude levels, it is possible to minimise the vibration by changing the propeller and crankshaft crank angular position. Each vibration direction and each drive rotational speed can be minimised. The admitted optimum angle (the propeller blade optimal translation angle in relation to the first crankshaft crank) is α=-20.3°, it gives a minimum level of superstructure longitudinal vibrations at the nominal engine rotational speed. In reality, the propeller and the crankshaft relative angular position are very often random. Therefore, the distribution of calculation results compared to the measurement tests can be significant. Figure 8 shows the size of distribution, i.e. errors which may result from the accidental propeller and crankshaft phasing for the 5th harmonic component. The reference level is the average of the expected vibration amplitudes.

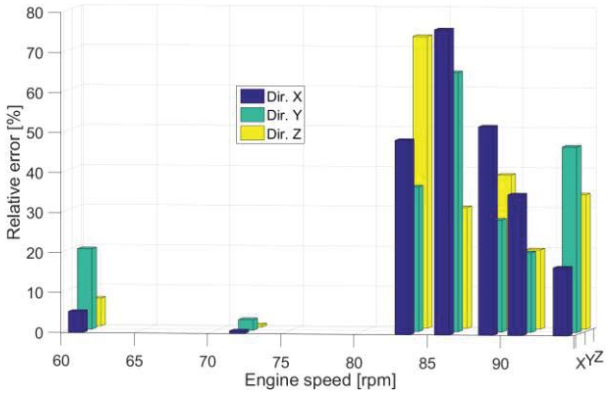

Figure 8: Expected vibration amplitude result distribution of the 5th harmonic component, for the 2700 TEU container ship's variable propeller and engine phasing.

During measurements, total vibrations from all harmonic components are measured and standardised. At rated rotations, the expected 5th harmonic component results distribution is about ±60%. However, the total vibration amplitudes distribution will be smaller. The difference in the 5th harmonic results is to be multiplied by its percentage in the total vibration. It was assumed that the propeller has one dominant harmonic component, i.e. the first blade (5th harmonic).

The measurement tests of the 2700 TEU container has been performed. A comparison of the results of calculations with the results of measuring tests is shown in figure 9. As the measurements results normally give the values of vibration velocity effective amplitude, the calculation analyses results have been recalculated accordingly. The comparison was presented for the most important hull reference points: the superstructure bridge wing.

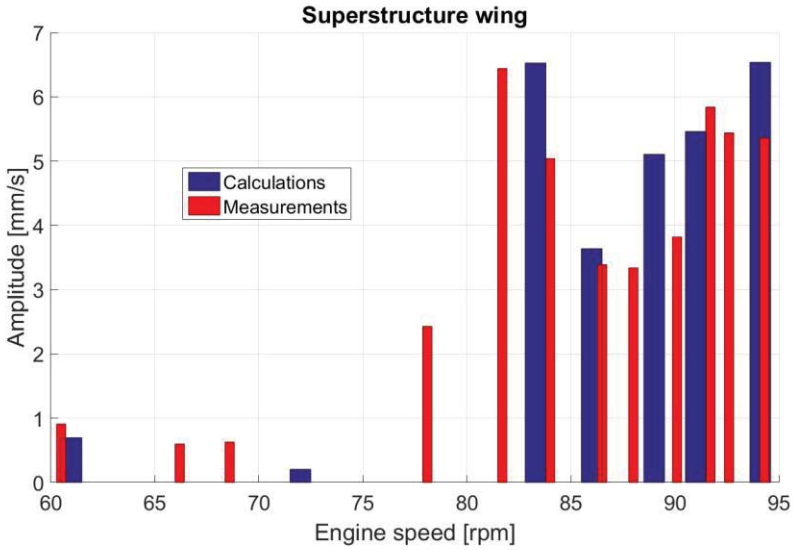

Figure 9: Measurement and calculation verification of the superstructure bridge wing vibrations, for the 2700 TEU container ship, in ballast condition

The presented measurement and calculation verification fully confirmed the validity of the assumptions made and of the used calculation methods. The consistency between the measurement tests and the numerical calculations is highly satisfactory, in the light of the analyses carried out for the expected dispersions and errors in the numerical modelling of a physical object, the hull.

5 CONCLUSIONS

The main engine meaning (in comparison to propeller) varies with its rotational speed, with ship cargo state and the direction of the vibrations to be considered. Therefore, it is impossible to eliminate ships vibrations to levels not noticeable by the crew and passengers. Due to the complexity of the ship structures vibration phenomenon, it is also difficult to reduce them effectively, especially after the ship has been built. For this reason, in-depth calculation analyses of the ship dynamics are extremely important at the design stage. However, it is important to be aware of the inevitable calculation results dispersion (and of measurement tests, also).

Based on the performed analyses, it can be concluded that resonant frequencies should be provided for in calculations with good accuracy. However, even correctly performed calculations of vibration amplitudes may significantly differ from the amplitudes obtained by measurement tests. It should be stressed that measurements, especially those carried out in marine conditions, are also subject to a number of significant errors and dispersions.

REFERENCES

[1] J.F. Wilson, Dynamic of offshore structures, *John Wiley & Sons,* New Jersey 2003.

[2] I. Senjanović, N. Vladimir, M. Tomić, N. Hadžić, Š. Malenica, Some aspects of structural modelling and restoring stiffness in hydroelastic analysis of large container ships, *Ships and Offshore Structures* 9 (2), 199-217, 2014.

[3] *ABS GUIDANCE NOTES ON SHIP VIBRATION* 2006

[4] F. Besnier, S. Du, A. Ergin, O.A. Hermundstad, S.Y. Hong, R. Iaccarino, M.L. Kaminski, J.H. Liu, H. Mumm, L. Murawski, H. Shuri, Dynamic Response, *16th International Ship and Offshore Structures Congress (ISSC)*, 2006.

[5] L. Murawski, Static and Dynamic Analyses of Marine Propulsion Systems, *Oficyna Wydawnicza Politechniki Warszawskiej*, Warszawa 2003.

[6] L. Murawski, Forces exciting vibrations of ship's hull and superstructure, *Polish Maritime Research* 4(46), 15-21, 2005.

[7] L. Murawski, Ship structure dynamic analysis – effects of made assumptions on computation results, *Polish Maritime Research* 2(48), 3-7, 2006.

[8] Y. Yumei, C. Hongyu, Z. Deyou, H. Ming, Predicting method of natural frequency for ship's overall vertical vibration, *Shipbuilding* 65 (3), 2014

[9] I. Asmussen, W. Menzel, H. Mumm, Ship Vibration, *Germanischer Lloyd*, 5/2001.

EURODYN 2020
XI International Conference on Structural Dynamics
M. Papadrakakis, M. Fragiadakis, C. Papadimitriou (eds.)
Athens, Greece, 23–26 November 2020

EVALUATION OF A PUSHOVER PROCEDURE FOR ASYMMETRIC R/C BUILDINGS WITH VARIOUS TORSIONAL PROPERTIES

Grigorios E. Manoukas[1], **and Asimina M. Athanatopoulou**[1]

[1] Department of Civil Engineering, Aristotle University
University Campus, 54124, Thessaloniki, Greece
e-mail: {grman,minak}@civil.auth.gr

Keywords: Pushover analysis, asymmetric buildings, torsionally stiff/flexible buildings, biaxial seismic excitation, nonlinear dynamic analysis, seismic response.

Abstract. *In the present paper a recently developed multimode pushover procedure is evaluated for asymmetric systems with various torsional properties. The procedure is applicable to asymmetric in plan buildings under concurrent action of two horizontal seismic components and its main advantage is that it does not require independent analysis in two orthogonal directions. Thus, the use of simplified directional combination formulae, which is not valid in the nonlinear range, is avoided. The preliminary evaluation of the proposed methodology led to quite satisfactory results. However, the studies conducted up to date are limited to 'torsionally stiff' buildings. Hence, in the present study the procedure is applied to 'torsionally similarly stiff' and 'torsionally flexible' systems too. In particular, a set of nine reinforced concrete buildings are analyzed for 20 earthquake excitations. The values of selected response quantities are compared to those resulting from a conventional pushover analysis variant as well as from nonlinear dynamic analysis. The whole evaluation study leads to the derivation of useful conclusions.*

1 INTRODUCTION

The vast majority of buildings belong to the category of asymmetric in plan structures, i.e. they do not possess any axis of symmetry. The earthquake analysis and design of such buildings should be based on spatial models and should take into account the so-called multi-directional seismic effects, namely the concurrent action of at least the two horizontal seismic components. When linear or nonlinear time history analysis is applied these effects are taken into account directly, by concurrent application of accelerograms along two orthogonal directions. On the other hand, when modal response spectrum or linear static method of analysis are applied a fundamental assumption is adopted. In particular, it is considered that the same design spectrum represents both horizontal seismic components and the analysis is carried out independently for each direction. Then the directional combination is conducted using SRSS (Square Root of the Sum of the Squares) formula or the percentage combination rule. The latter approach is adopted by seismic codes (eg., [1], [2], [3]) even for the implementation of nonlinear static method.

In recent years many researchers investigated the issue of application of pushover analysis to asymmetric buildings under biaxial seismic excitation and presented several relevant methodologies. The majority of them is based also on simplified directional combination formulae. For example, Reyes and Chopra [4], [5] extended the well-known Modal Pushover Analysis [6] in order to include asymmetric buildings under bi-axial seismic excitation. They proposed independent implementation of the procedure along two orthogonal directions and directional combination of the results using SRSS formula. The same approach is also adopted for the extension of N2 method for asymmetric in plan buildings [7], [8], for the Improved Modal Pushover Analysis [9], for the Improved Consecutive Modal Pushover Analysis [10] and for the pushover procedure proposed by Shakeri and Ghorbani [11].

However, the simplified directional combination rules are based on the superposition principle which is not valid in the nonlinear range of behaviour. Thus, the use of such rules is a major shortcoming of the aforementioned methodologies found in literature as well as of those prescribed by seismic codes. In order to overcome this shortcoming Manoukas et al. [12], [13], [14] developed a multimode pushover procedure for asymmetric in plan buildings which does not require independent analysis for each direction, hence directional combination is avoided. The main idea of the procedure is that the seismic response of a multi-degree-of-freedom (MDOF) system under biaxial seismic excitation can be expressed as superposition of the responses of a series of equivalent single-degree-of-freedom (E-SDOF) systems under uniaxial excitation. The properties of the E-SDOF systems (mass, stiffness, damping factor) are calculated using proper formulae which are derived from the equations of motion and take directly into account the concurrent action of the two horizontal seismic components.

The evaluation studies published in the past [12], [13], [14] demonstrated that the proposed procedure provides quite satisfactory results. However, the studies conducted up to date are limited to the so called 'torsionally stiff' buildings. Hence, the scope of the current study is the validation of the procedure for asymmetric in plan systems including 'torsionally similarly stiff' and 'torsionally flexible' buildings [15]. After a brief outline of the procedure, a series of applications to reinforced concrete buildings is presented. In particular, nine multi-storey buildings are analyzed for 20 biaxial seismic excitations. The values of selected response quantities are compared to those resulting from a conventional pushover analysis variant as well as from nonlinear dynamic analysis. The whole study leads to the derivation of useful conclusions.

2 SUMMARY OF THE PROCEDURE

The theoretical background of the proposed procedure has already been presented by Manoukas et al. in previous papers [12], [13], [14]. Hence, in the present study only some key points are briefly outlined. Apart from the well-known assumptions on which all pushover variants are based, an additional one is introduced. In particular, it is considered that the two horizontal seismic components $\ddot{u}_{g(t)X}$ and $\ddot{u}_{g(t)Y}$ are proportional to each other, i.e.:

$$\ddot{u}_{g(t)Y} = \kappa \ddot{u}_{g(t)X} = \kappa \ddot{u}_{g(t)} \tag{1}$$

where κ is a constant factor. Although this is not the case for earthquake excitations, this assumption should be considered as reasonable, since it is in fact equivalent to the common assumption of seismic codes which specify that the same design spectrum represents both horizontal seismic components and the directional combination can be conducted using the percentage combination rule where a factor equal to 0.3 (similar to κ) is applied.

Thanks to the aforementioned assumptions, it has been demonstrated [12], [13], [14] that the motion of an N-DOF system subjected to the seismic excitation given in Eq. (1) is governed by N uncoupled equations, each one corresponding to a 'modal' E-SDOF system:

$$M^*_{XYi}\,\ddot{D}_i + 2\,M^*_{XYi}\,\omega_i\zeta_i\,\dot{D}_i + V_{XYi} = -M^*_{XYi}\,\ddot{u}_g \tag{2}$$

where $D_i = q_i / v_{XYi}$, $\dot{D}_i$, $\ddot{D}_i$ are the displacement, velocity and acceleration of the i^{th} (i = 1…N) E-SDOF system, ω_i, ζ_i and q_i are the natural frequency, the damping ratio and the 'modal' co-ordinate of the elastic vibration mode i and:

$$V_{XYi} = V_{Xi} + \kappa V_{Yi} \tag{3}$$

$$M^*_{XYi} = M^*_{Xi} + \kappa(v_{Xi}\,L_{Yi} + v_{Yi}\,L_{Xi}) + \kappa^2 M^*_{Yi} \tag{4}$$

$$L_{Xi} = \boldsymbol{\delta}_{,X}^T \boldsymbol{M} \boldsymbol{\varphi_i} \tag{5}$$

$$L_{Yi} = \boldsymbol{\delta}_{,Y}^T \boldsymbol{M} \boldsymbol{\varphi_i} \tag{6}$$

$$v_{XYi} = v_{Xi} + \kappa v_{Yi} \tag{7}$$

where $\boldsymbol{M}$ is the NxN mass matrix, $\boldsymbol{\varphi_i}$ is the 'modal' vector of mode i, V_{Xi}, V_{Yi} are the 'modal' base shears parallel to X and Y axes respectively, M^*_{Xi}, M^*_{Yi} and v_{Xi}, v_{Yi} are the effective modal masses and the modal participation factors of mode i due to independent uniaxial excitations, while $\boldsymbol{\delta}_{,X}$, $\boldsymbol{\delta}_{,Y}$ are the influence vectors for independent uniaxial excitations.

Eq. (2) demonstrates that the nonlinear response of an N-degree of freedom system subjected to the seismic excitation given in Eq. (1), can be expressed as the sum of the responses of N SDOF systems under uniaxial excitation, each one corresponding to a vibration 'mode' and having the properties given in Eqs. (3) to (7) and in Table 1. The properties that each E-SDOF would have in case of uniaxial excitation (parallel to X axis) are also tabulated in the second column of Table 1. Notice that the displacements of E-SDOF systems is correlated to the roof displacement u_{Ni}.

The implementation of the proposed methodology should be conducted for the following possible combinations of the horizontal seismic components:

$$\ddot{u}_{gX} + \kappa \ddot{u}_{gY} \tag{8}$$

$$\ddot{u}_{gX} - \kappa \ddot{u}_{gY} \tag{9}$$

$$\ddot{u}_{gY} + \kappa \ddot{u}_{gX} \tag{10}$$

$$\ddot{u}_{gY} - \kappa \ddot{u}_{gX} \tag{11}$$

The properties of the E-SDOF systems should be modified properly for each combination. Consideration of the four combinations with opposite sign (e.g., $-\ddot{u}_{gX} - \kappa\ddot{u}_{gY}$ instead of $\ddot{u}_{gX} + \kappa\ddot{u}_{gY}$) is not necessary because it leads to identical properties for the E-SDOF systems and as a consequence to identical results.

The sequence of steps needed for the implementation of the proposed methodology are shown in the flowchart of Fig.1.

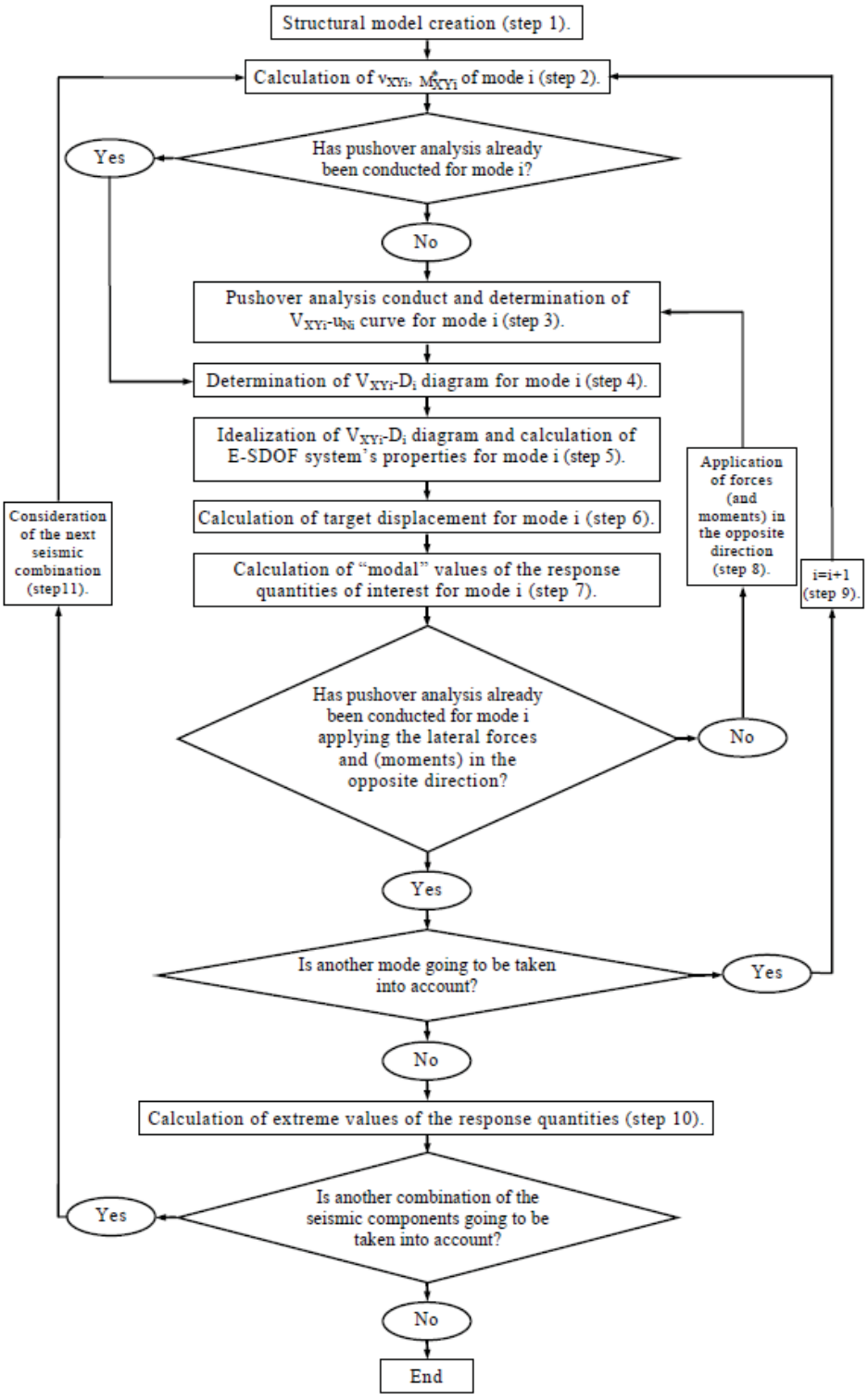

Figure 1: Flowchart of the proposed methodology.

Property	Uniaxial excitation $\ddot{u}_{gX}$	Biaxial excitation $\ddot{u}_{gX} + \kappa\ddot{u}_{gY}$
Mass	M^*_{Xi}	$M^*_{XYi} = M^*_{Xi} + \kappa(v_{Xi} L_{Yi} + v_{Yi} L_{Xi}) + \kappa^2 M^*_{Yi}$
Resisting force	V_{Xi}	$V_{XYi} = V_{Xi} + \kappa V_{Yi}$
Displacement	$D_i = u_{Ni} / v_{Xi} \varphi_{Ni}$ (roof displacement u_{Ni})	$D_i = u_{Ni} / v_{XYi} \varphi_{Ni} = u_{Ni} / (v_{Xi} + \kappa v_{Yi}) \varphi_{Ni}$ (roof displacement u_{Ni})
Damping factor	$2 M^*_{Xi} \omega_i \zeta_i$	$2 M^*_{XYi} \omega_i \zeta_i$

Table 1: Properties of the i^{th} E-SDOF system.

3 EVALUATION STUDY

3.1 Structural modeling and design

It has been demonstrated in previous studies [12], [13], [14] that the proposed methodology produces quite satisfactory results for buildings characterized as 'torsionally stiff' according to the definition given by Chopra and Goel [15] and other researchers. In the framework of the current paper, the procedure is applied to 'torsionally similarly stiff' and 'torsionally flexible' asymmetric in plan buildings too.

In particular, nine multi-storey asymmetric in plan (but regular in elevation) reinforced concrete buildings with various torsional properties are analyzed for 20 seismic excitations. The buildings are characterized by a string symbol comprising 2 or 3 letters and a number indicating the number of storeys (4, 8 or 12). The meaning of the letters is as follows:

- 'ts' ('torsionally stiff'): Asymmetric buildings with plan given in Fig. 2. 'ts' models are characterized as 'torsionally stiff' [15], given that in the first two vibration modes the motion is dominated by lateral displacements.
- 'tss' ('torsionally similarly stiff'): Asymmetric buildings identical to 'ts' models except that the mass moment of inertia of each diaphragm is multiplied by 2. 'tss' models are characterized as 'torsionally similarly stiff' [15], given that in the first two vibration modes lateral and torsional motions are strongly coupled.
- 'tf' ('torsionally flexible'): Buildings identical to 'ts' models except that the mass moment of inertia of each diaphragm is multiplied by 4. 'tf' models are characterized as 'torsionally flexible' [15], given that in the first mode the motion is dominated by torsion.

For example, the symbol tf8 corresponds to a 'torsionally flexible' building with 8 storeys.

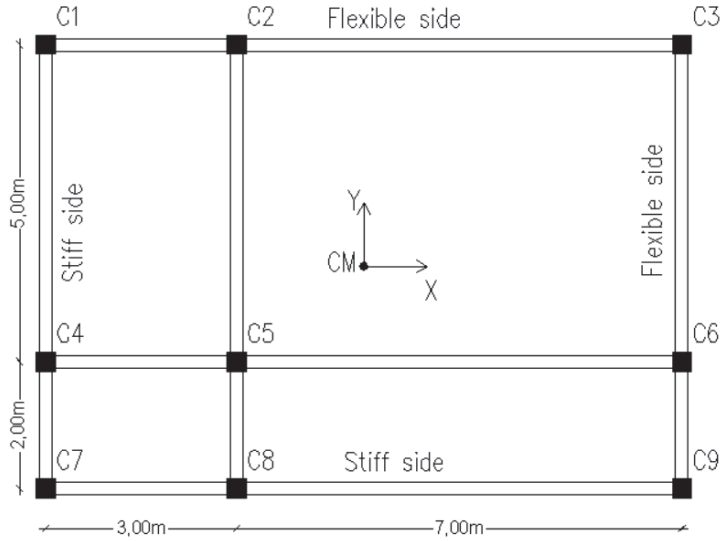

Figure 2: Floor plans of the analyzed buildings.

All buildings are designed using the modal response spectrum method of analysis [3], [16] for Peak Ground Acceleration (PGA) equal to 0.16g. The design is conducted with the aid of the software package NEXT v.2004 which is developed by 'Computec Software' and widely used by engineering professionals in Greece. The mass and the mass moment of inertia of each storey (Table 2) are concentrated to the mass center of the diaphragms. The first six natural periods of the examined models are tabulated in Table 3, while the modal participating mass ratios are shown in Table 4.

The inelastic analyses of the buildings are conducted using the program SAP 2000. The inelastic behavior is represented through plastic hinges possessing elastic-perfectly plastic moments-rotations relations.

Buildings	Mass (t)	Mass moment of inertia (tm^2)
ts4	68	844.33
ts8	86.5	1074.04
ts12	107	1328.58
tss4	68	1688.66
tss8	86.5	2148.08
tss12	107	2657.16
tf4	68	3377.32
tf8	86.5	4296.16
tf12	107	5314.32

Table 2: Storey masses and mass moments of inertia.

Buildings	T_1	T_2	T_3	T_4	T_5	T_6
ts4	0.381	0.368	0.244	0.120	0.116	0.077
ts8	0.667	0.642	0.416	0.200	0.191	0.126
ts12	1.061	1.027	0.649	0.311	0.297	0.193
tss4	0.393	0.371	0.331	0.124	0.117	0.105
tss8	0.683	0.648	0.569	0.205	0.193	0.171
tss12	1.081	1.034	0.893	0.318	0.301	0.264
tf4	0.506	0.375	0.360	0.160	0.118	0.114
tf8	0.863	0.658	0.628	0.261	0.197	0.186
tf12	1.344	1.047	1.004	0.400	0.307	0.290

Table 3: Natural periods T_i (sec).

Buildings	m_{1x}^*	m_{1y}^*	m_{2x}^*	m_{2y}^*	m_{3x}^*	m_{3y}^*	m_{4x}^*	m_{4y}^*	m_{5x}^*	m_{5y}^*	m_{6x}^*	m_{6y}^*
ts4	74.94	7.28	8.13	74.59	0.84	1.93	9.73	1.27	1.35	10.09	0.11	0.28
ts8	71.43	4.56	5.15	70.44	0.65	1.49	11.32	0.52	0.55	12.19	0.10	0.28
ts12	68.00	5.56	6.11	67.07	0.55	1.17	1.70	0.51	0.54	12.65	0.09	0.26
tss4	38.10	20.77	39.68	40.23	6.13	22.79	4.63	3.10	5.68	5.29	0.88	3.25
tss8	43,88	16.11	28.76	43.54	4.59	16.84	7.11	2.23	4.20	7.25	0.67	3.52
tss12	44.32	17.12	26.39	44.83	3.96	11.85	7.93	2.18	3.76	8.19	0.64	3.05
tf4	2.01	3.02	79.95	2.73	1.94	78.04	0.26	0.41	10.62	0.43	0.31	10.79
tf8	2.12	3.03	73.52	2.35	1.58	71.11	0.32	0.48	11.51	0.26	0.15	12.26
tf12	2.31	3.36	69.93	3.45	2.42	67.00	0.36	0.53	11.80	0.31	0.17	12.58

Table 4: Modal participating mass ratios m_{ix}^*, m_{iy}^* (%).

3.2 Ground motions

The buildings are analyzed for 20 accelerograms obtained from the PEER database [17] and tabulated in table C-3 of FEMA 440 [18]. The accelerograms are scaled to PGA equal to 0.40g in order to ensure that the analyzed buildings undergo extensive nonlinear deformation. The scaled acceleration response spectra of the 20 seismic excitations along with the mean response spectrum are shown in Fig. 3. Each accelerogram is applied simultaneously along two orthogonal directions with the same intensity.

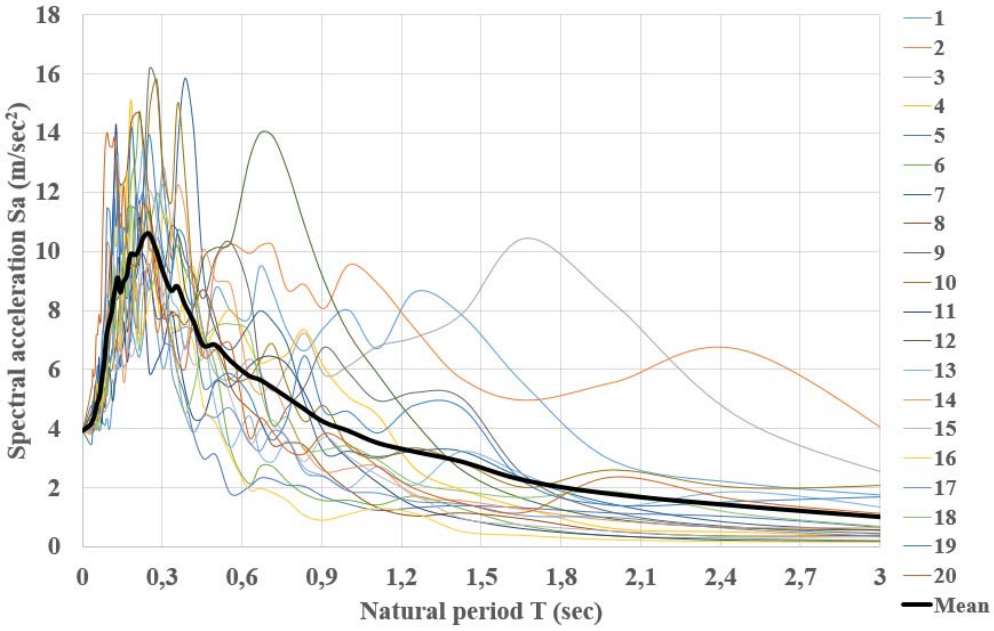

Figure 3: Acceleration response spectra of the 20 seismic excitations.

3.3 Analysis process

Two alternative pushover procedures are implemented:

- The proposed methodology (PM). Due to the simultaneous action of the same earthquake excitation along two horizontal axes, the factor κ (Eq. (1)) is equal to 1. Thus, the combinations of the seismic components (Eqs. (8) to (11)) are limited to two: $\ddot{u}_{gX} + \ddot{u}_{gY}$ (PM+) and $\ddot{u}_{gX} - \ddot{u}_{gY}$ (PM-).
- A conventional procedure (CP) which differs from PM in the following three points: i) CP is applied for independent uniaxial excitations along X and Y axes and the percentage combination rule is used for the calculation of the extreme values of the response parameters (step 10 in Fig. 1), ii) in steps 2 to 4 v_{Xi}, M^*_{Xi}, V_{Xi} or v_{Yi}, M^*_{Yi}, V_{Yi} are used instead of v_{XYi}, M^*_{XYi}, V_{XYi} and iii) step 11 is omitted.

For both procedures the first six vibration modes are taken into account, while the Complete Quadratic Combination (CQC) rule is used for the 'modal' superposition. The target roof displacement for each mode is estimated multiplying by the quantity $v_{XYi}\varphi_{Ni}$ (PM) and $v_{Xi}\varphi_{Ni}$ or $v_{Yi}\varphi_{Ni}$ (CP) the response of the corresponding E-SDOF system. The latter is determined with the aid of nonlinear dynamic analysis. For each building, the floor displacements and the storey drifts at the center of mass (CM), at the flexible side (C3) and at the stiff side (C7) of the plan are calculated.

The values of the response quantities resulting from the two alternative pushover procedures are compared to those obtained by Nonlinear Dynamic Analysis (NDA), which is con-

sidered as 'exact' solution. For each response parameter $R_{j,s}$ calculated by means of pushover analysis for an excitation j, the error with regard to the NDA E_j is determined as follows:

$$E_j\,(\%) = 100\frac{R_{j,s} - R_{j,d}}{R_{j,d}} \tag{12}$$

where $R_{j,d}$ is the value of the relevant parameter resulting from NDA. Furthermore, the mean error *ME* for the 20 excitations is determined using Eq. (13):

$$ME\,(\%) = \frac{1}{20}\sum_{j=1}^{20} E_j = 100\,\frac{1}{20}\sum_{j=1}^{20}\left(\frac{R_{j,s} - R_{j,d}}{R_{j,d}}\right) \tag{13}$$

3.4 Results

In Figs. 4 to 15 the mean errors of the calculated response parameters are shown. The two combinations of PM (PM+ and PM-) provide an upper bound and a lower bound value for each response parameter. The 'exact' value (NDA) for 304 of 432 displacements and for 289 of 432 drifts lies in this range. For the vast majority of response quantities (408 of 432 displacements and 405 of 432 drifts) PM is conservative. This means that the number of modes taken into account is adequate. Non-conservative values are observed mainly for the stiff side of 'torsionally similarly stiff" buildings. The *ME* of the more conservative combination (PM+ or PM-) for displacements range between -13% and 155%, while for drifts between -14% and 211%. In comparison with CP, the absolute values of *ME* resulting from PM are smaller for 384 of 432 displacements and for 357 of 432 drifts. The *ME* of CP range between 0% and 240% for displacements and between 0% and 241% for drifts. Concerning the influence of the torsional properties of the buildings, no remarkable differences in the accuracy of response quantities of the center of mass is identified. However, the proposed procedure tends to highly overestimate both displacements and drifts of the flexible side of 'torsionally similarly stiff" buildings. On the other hand, the mean errors of the response quantities of the stiff side are generally smaller in comparison with 'torsionally stiff' and 'torsionally flexible' buildings. Obviously, this phenomenon may be attributed to the action of torsion. Finally, it is worth noticing that no correlation between the ductility required for each excitation and the corresponding error has been observed.

4 CONCLUSIONS

In the present paper a recently developed multimode pushover procedure is evaluated for asymmetric systems with various torsional properties. The procedure is applicable to asymmetric in plan buildings under concurrent action of two horizontal seismic components and its main advantage is that it does not require independent analysis in two orthogonal directions. Thus, the use of simplified directional combination formulae, which is not valid in the nonlinear range, is avoided. The evaluation study conducted in the present paper leads to the verification of some already derived conclusions [12], [13], [14]:

- The proposed methodology provides for each response parameter an upper limit and a lower limit which in the majority of cases envelope the 'exact' value.
- In general, the mean errors with regard to the nonlinear dynamic analysis results are smaller than those resulting from a conventional procedure based on simplified directional superposition rules.

Furthermore, it seems that the proposed methodology provides more reasonable estimation of the seismic response of 'torsionally stiff' and 'torsionally flexible' in comparison with 'torsionally similarly stiff' buildings.

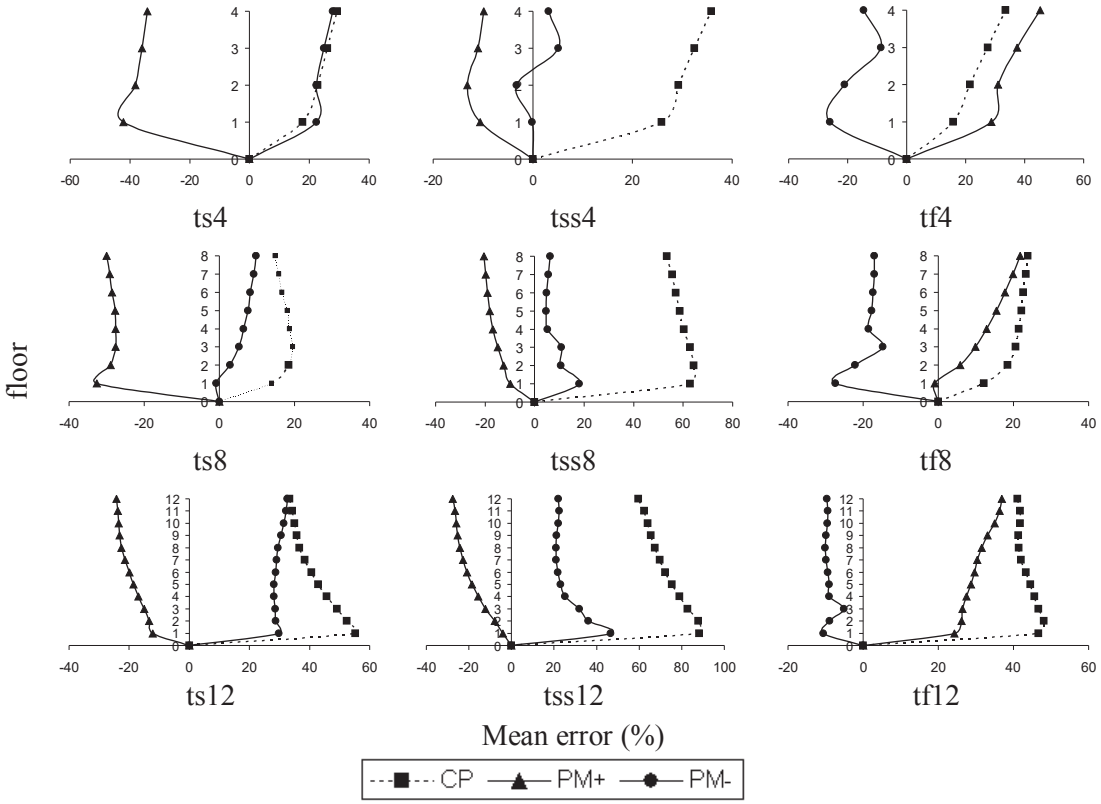

Figure 4: *ME* (%) of floor displacements along *X* axis at CM.

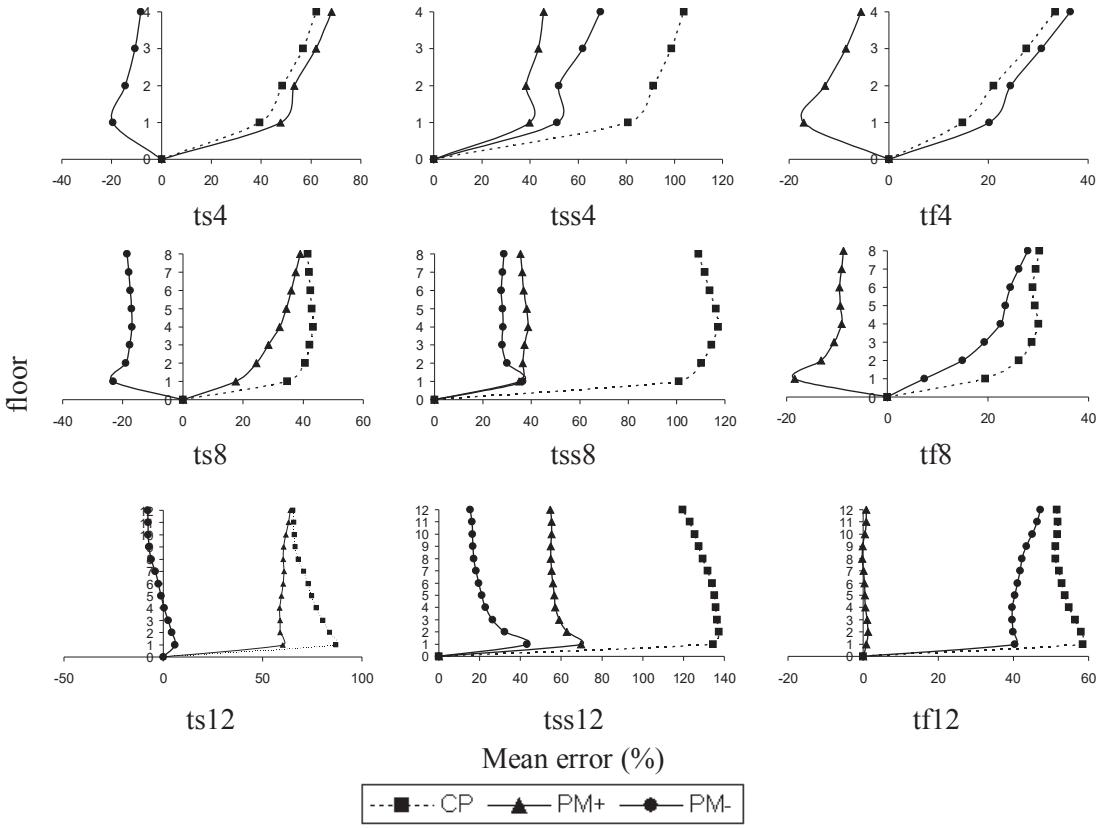

Figure 5: *ME* (%) of floor displacements along *Y* axis at CM.

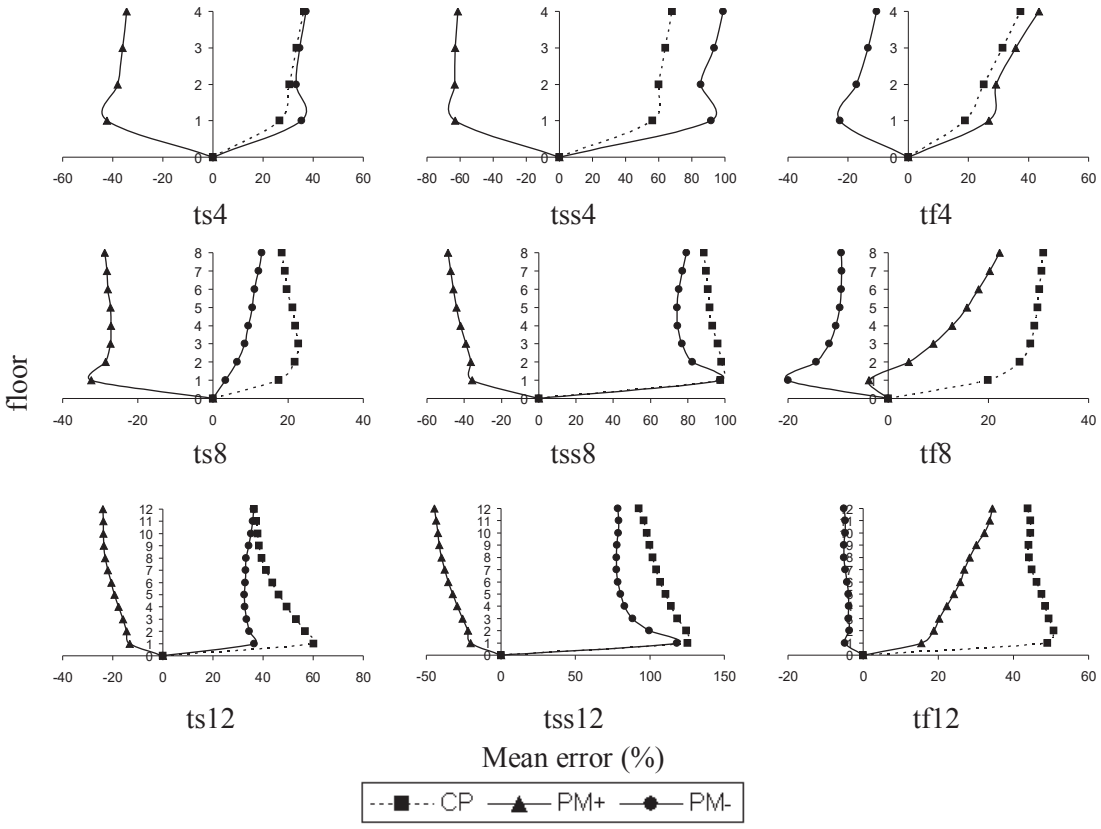

Figure 6: *ME* (%) of floor displacements along *X* axis at C3.

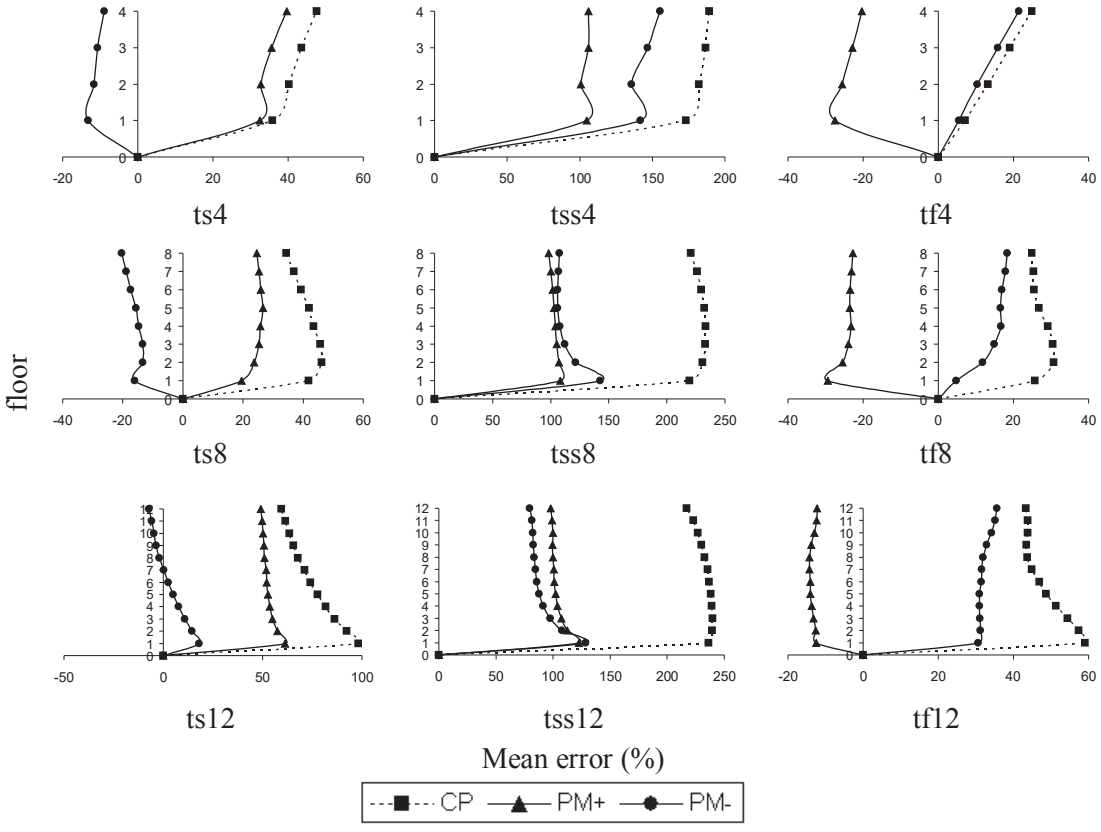

Figure 7: *ME* (%) of floor displacements along *Y* axis at C3.

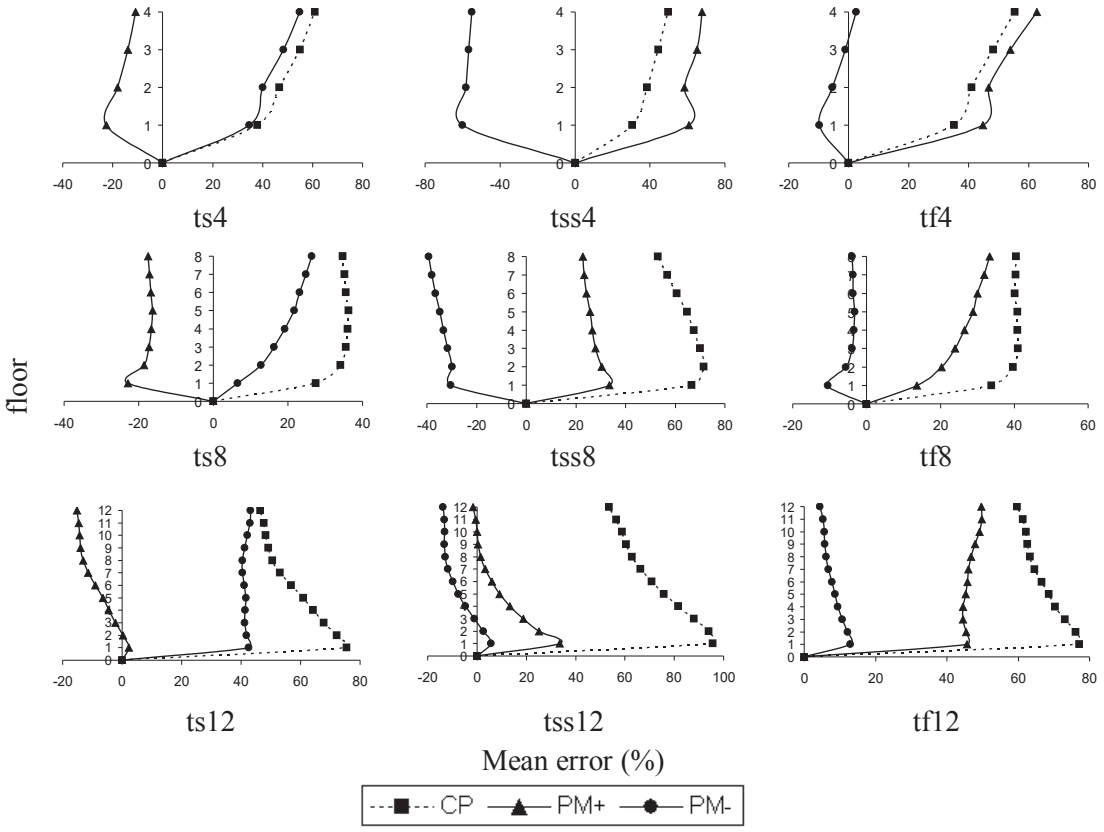

Figure 8: *ME* (%) of floor displacements along *X* axis at C7.

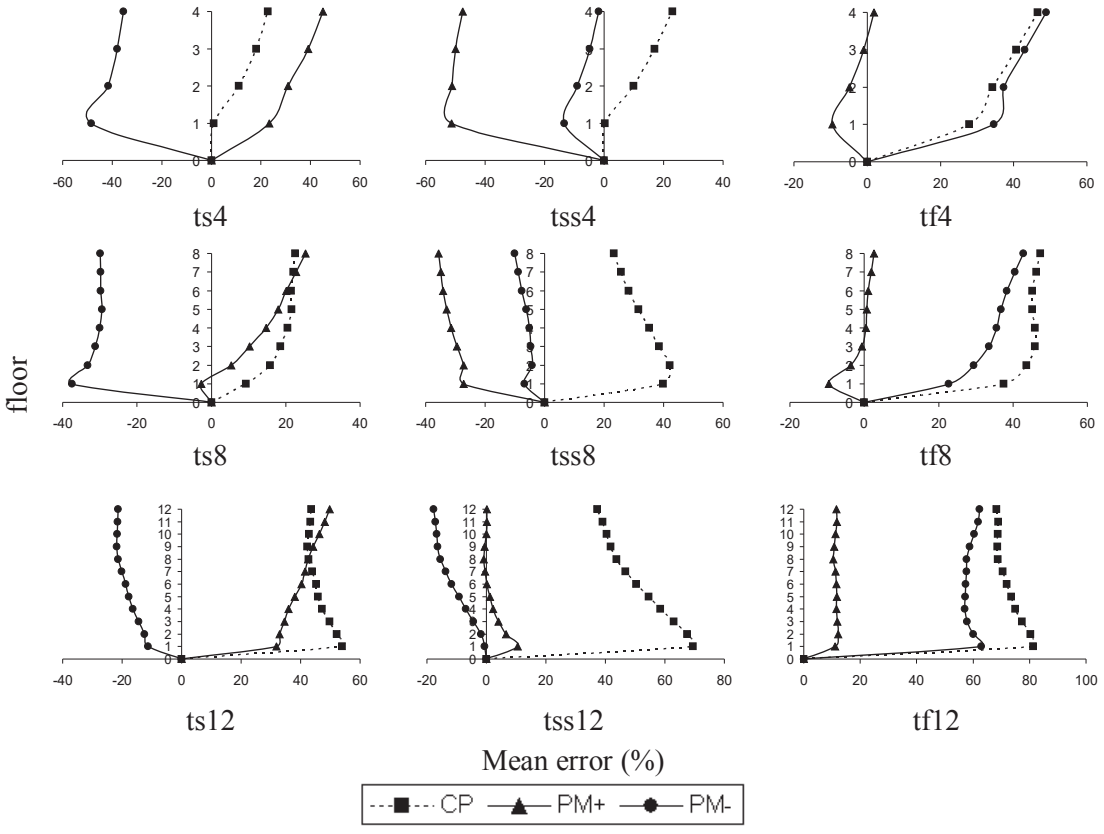

Figure 9: *ME* (%) of floor displacements along *Y* axis at C7.

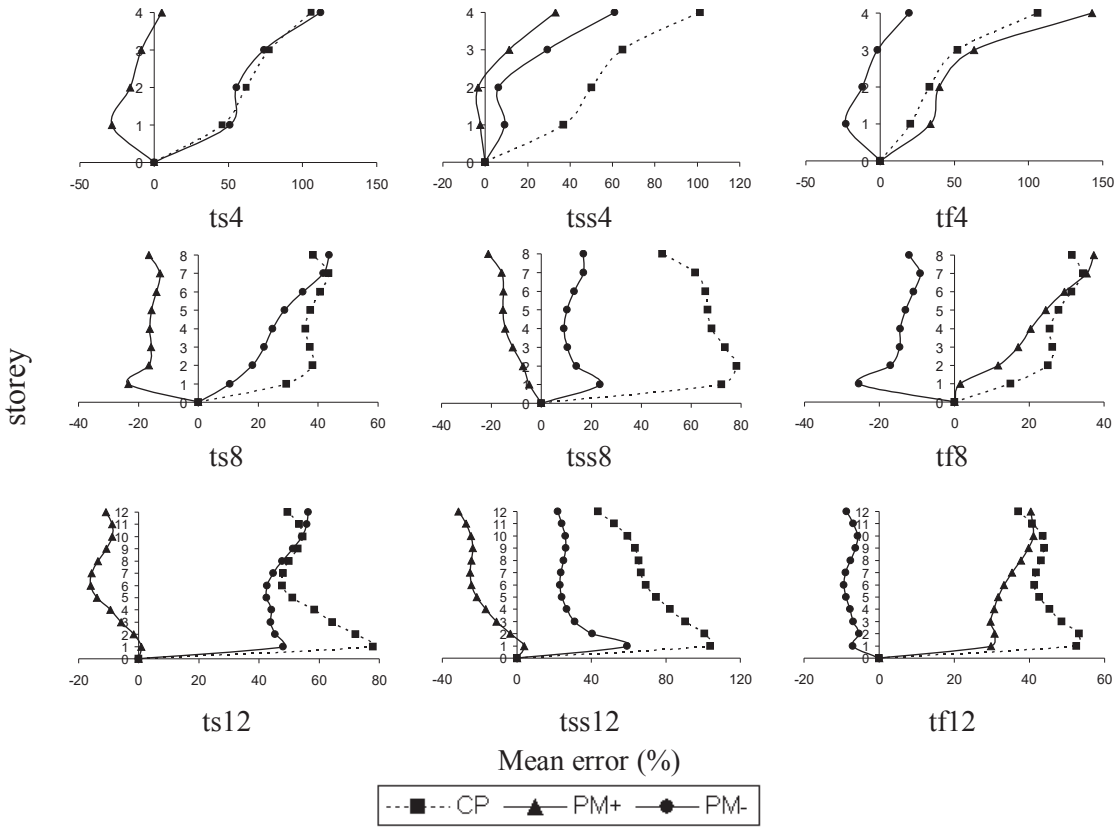

Figure 10: *ME* (%) of storey drifts along *X* axis at CM.

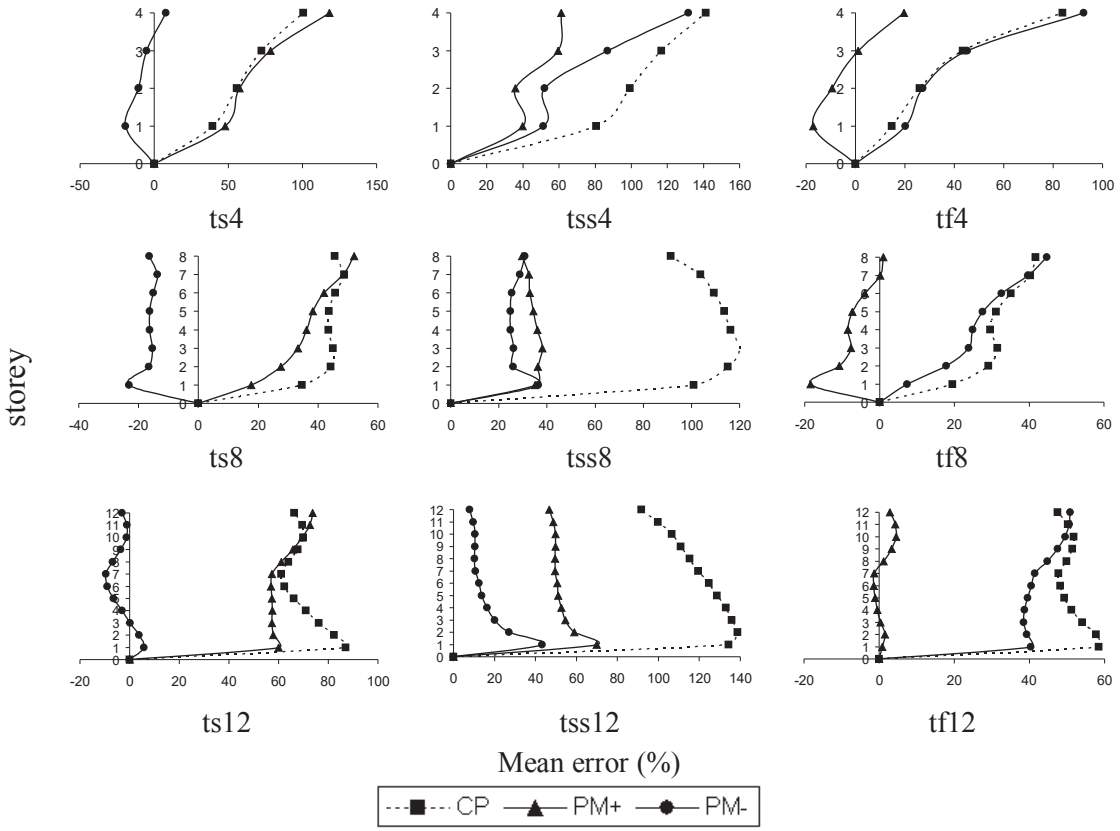

Figure 11: *ME* (%) of storey drifts along *Y* axis at CM.

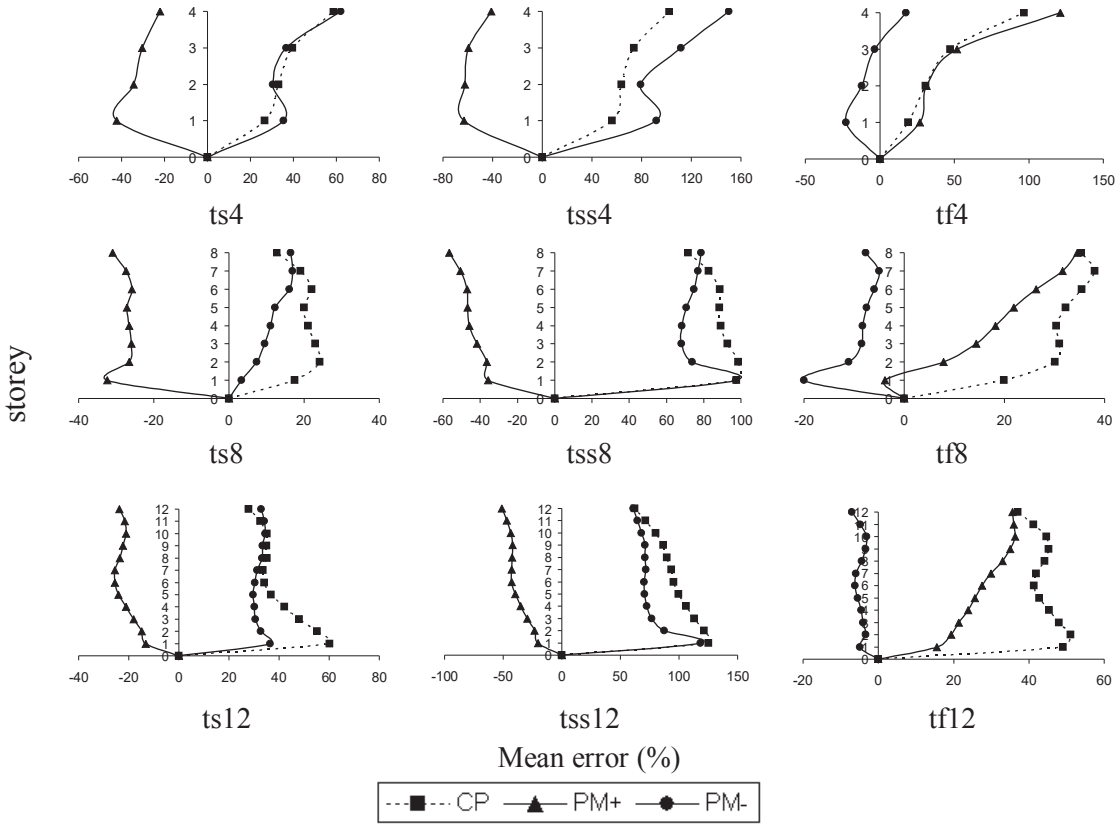

Figure 12: *ME* (%) of storey drifts along *X* axis at C3.

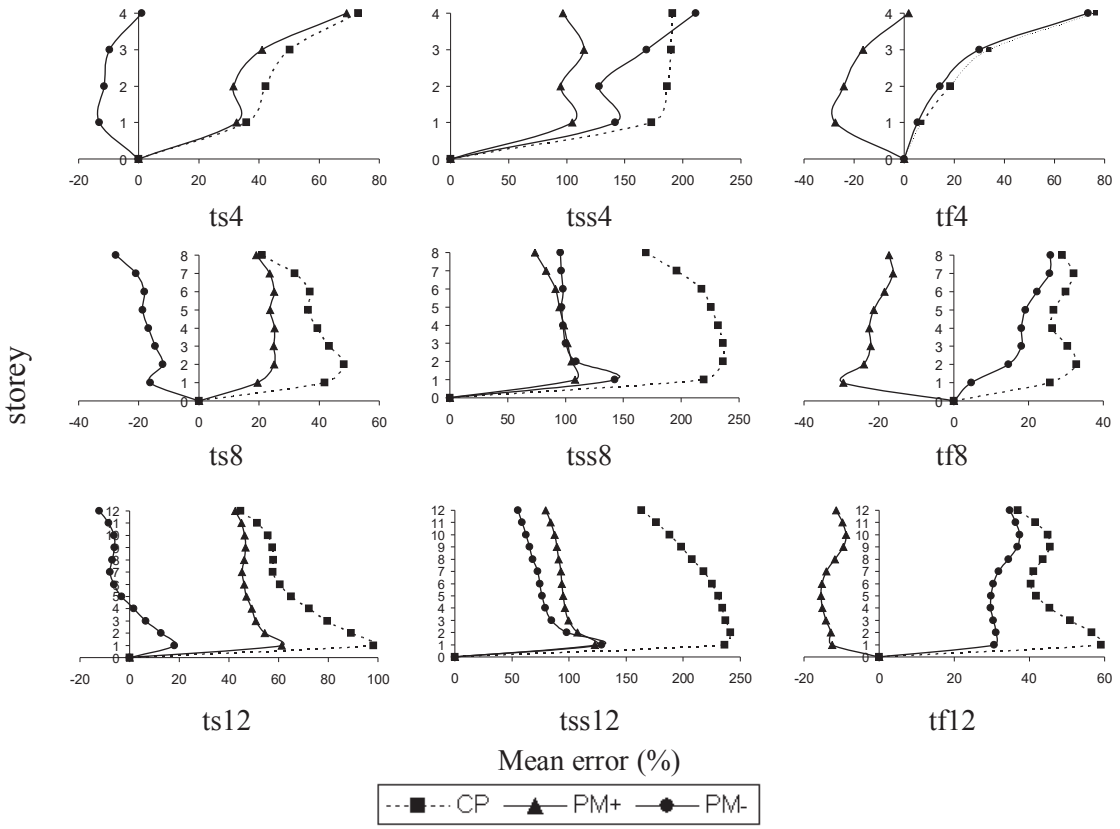

Figure 13: *ME* (%) of storey drifts along *Y* axis at C3.

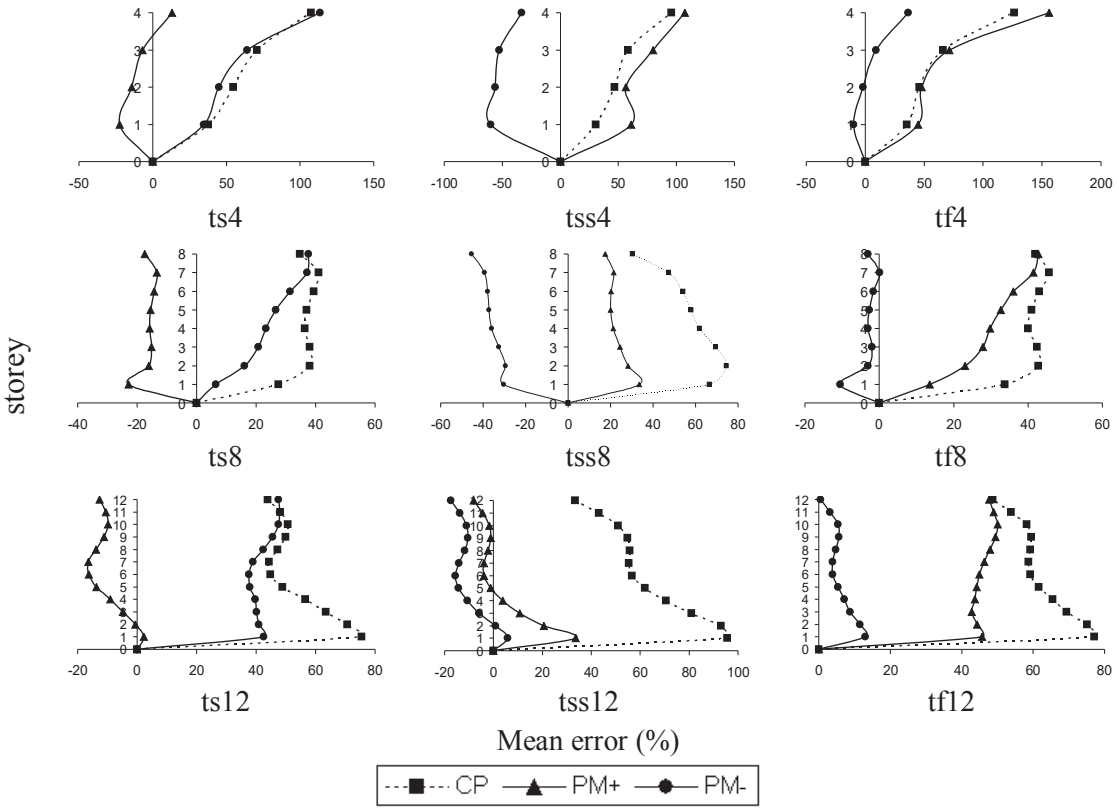

Figure 14: *ME* (%) of storey drifts along *X* axis at C7.

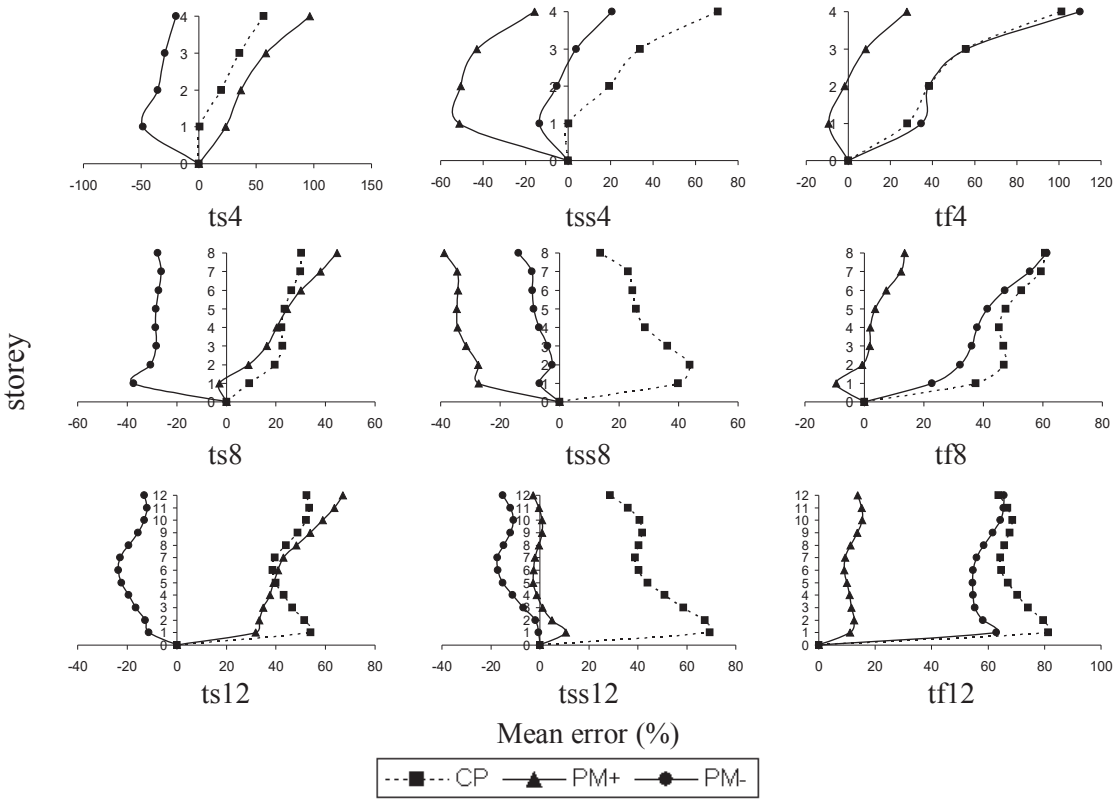

Figure 15: *ME* (%) of storey drifts along *Y* axis at C7.

REFERENCES

[1] ASCE (American Society of Civil Engineers), Seismic rehabilitation of existing buildings, ASCE/SEI 41-06 Standard, 2008.

[2] ATC (Applied Technology Council), Seismic evaluation and retrofit of concrete buildings, Vol. 1. Report No. ATC-40, Redwood City, 1996.

[3] CEN (European Committee for Standardization), Design of structures for earthquake resistance, Eurocode 8, Brussels, 2004.

[4] J.C. Reyes, A.K. Chopra, Three dimensional modal pushover analysis of buildings subjected to two components of ground motion, including its evaluation for tall buildings, *Earthquake Engineering and Structural Dynamics* 40(7), 789-806, 2011a, DOI: 10.1002/eqe.1060.

[5] J.C. Reyes, A.K. Chopra, Evaluation of three-dimensional modal pushover analysis for unsymmetric-plan buildings subjected to two components of ground motion, *Earthquake Engineering and Structural Dynamics* 40(13), 1475-1494, 2011b, DOI: 10.1002/eqe.1100.

[6] A.K. Chopra, R.K. Goel, A Modal Pushover Analysis procedure to estimating seismic demands of buildings: theory and preliminary evaluation, PEER Report 2001/03, *Pacific Earthquake Engineering Research Centre, University of California*, Berkeley, 2001.

[7] P. Fajfar, D. Marusic, I. Perus, The extension of the N2 method to asymmetric buildings, *Proceedings of the 4th European Workshop on the Seismic Behavior of Irregular and Complex Structures, 4EWICS*, Paper No. 41, Thessaloniki, Greece, August 26-27, 2005.

[8] G. Magliulo, G, Maddaloni, E. Cosenza, Extension of N2 method to plan irregular buildings considering accidental eccentricity. *Soil Dynamics and Earthquake Engineering* 43, 69-84, 2012, DOI: 10.1016/j.soildyn.2012.07.032.

[9] A.F. Belejo, R. Bento, Improved Modal Pushover Analysis in seismic assessment of asymmetric plan buildings under the influence of one and two horizontal components of ground motions, *Soil Dynamics and Earthquake Engineering* 87, 1-15, 2016, DOI: 10.1016/j.soildyn.2016.04.011.

[10] J.Z. Zhang, X. Jiang, G.Q. Li, An improved consecutive modal pushover procedure for estimating seismic demands of multi-storey framed buildings, *The Structural Design of Tall and Special Buildings* 26(4), Article number e1336, 2017, DOI: 10.1002/tal.1336.

[11] K. Shakeri, S. Ghorbani, A pushover procedure for seismic assessment of buildings with bi-axial eccentricity under bi-directional seismic excitation, *Soil Dynamics and Earthquake Engineering* 69, 1-15, 2015, DOI: 10.1016/j.soildyn.2014.10.018.

[12] G.E. Manoukas, A.M. Athanatopoulou, I.E. Avramidis, Multimode pushover analysis for asymmetric buildings under biaxial seismic excitation based on a new concept of the equivalent single degree of freedom system, *Soil Dynamics and Earthquake Engineering* 38, 88-96, 2012, DOI: 10.1016/j.soildyn.2012.01.018.

[13] G.E. Manoukas, I.E. Avramidis, Evaluation of a multimode pushover procedure for asymmetric in plan buildings under biaxial seismic excitation, *Bulletin of Earthquake Engineering* 12(6), 2607-2632, 2014, DOI: 10.1007/s10518-014-9600-6.

[14] G.E. Manoukas, I.E. Avramidis, Improved multimode pushover procedure for asymmetric in plan buildings under biaxial seismic excitation – Application to tall buildings, *The*

Structural Design of Tall and Special Buildings 24(6), 397-420, 2015, DOI: 10.1002/tal.1171.

[15] A.K. Chopra, R.K. Goel, Evaluation of the modal pushover analysis procedure for unsymmetric-plan buildings, *Proceedings of the First European Conference of Earthquake Engineering and Seismology*, Geneva, Switzerland, September 3-8, 2006.

[16] CEN (European Committee for Standardization), Design of concrete structures, Eurocode 2, Brussels, 2002.

[17] PEER (Pacific Earthquake Engineering Research Centre), Strong motion database, http://peer.berkeley.edu/smcat/, 2003, Accessed July 1 2017.

[18] FEMA (Federal Emergency Management Agency) - ATC (Applied Technology Council), Improvement of nonlinear static seismic analysis procedures, Report No. ATC-55 (FEMA 440), 2004.

EURODYN 2020
XI International Conference on Structural Dynamics
M. Papadrakakis, M. Fragiadakis, C. Papadimitriou (eds.)
Athens, Greece, 23–26 November 2020

OPTIMUM STRUCTURAL DESIGN OF A CUBESAT SUBJECTED TO LAUNCHER MECHANICAL ENVIRONMENT

Adham Salem[1], **Amir Tawfik**[1], **Eslam Saleh** [1]**and Hesham Ibrahim**[2]

[1]Research Assistant Mechatronics Department, German University in Cairo Egypt.
adham.adel@student.guc.edu.eg, amir.tawfik@student.guc.edu.eg, eslam.saleh@student.guc.edu.eg

[2] Associate Professor,Mechatronics Department, German University in Cairo, Egypt.
hesham.hamed-ahmed@guc.edu.eg

Keywords: CubeSat, Random Vibration, Optimization, Fatigue Analysis

Abstract. *This paper presents structural analyses and optimization of a student's CubeSat project to be launched in a lower thermosphere orbit. The static and dynamic responses of the primary and secondary structures are simulated, using ANSYS Finite Element Software, being subjected to the mechanical environments of two candidate launchers. The mass of the primary structure is optimized subject to quasi-static loading, during launching phase, given certain constraints on the strength and stiffness imposed by the P-POD provider and the candidate launchers. In addition, random base excitation response, and hence fatigue life estimation, are performed in order to ensure that the primary and secondary structures will safely survive the launching phase. Finally, the structural response of some selected subsystems, modeled in detail and simulated individually, are compared with their lumped mass approximations, which are simulated as part of the whole CubeSat, in order to investigate the outcome of such approximations.*

1 INTRODUCTION

The CubeSat is a modular pico-class-satellites which are early-developed by the Space Systems Design Laboratory at Stanford University. The simplest standardized solution is the 1-Unit CubeSat, a cube-shaped satellite with 100x100x100 mm dimensions and a weight of up to 1,33 kg. This category of satellites, though encapsulated in an Orbital Deployer (P-POD), developed by California Polytechnic State University, is launched as a secondary payload. CubeSat missions are among the most enticing and advanced categories in the space industry, because a cluster of such pico-satellites may easily replace a large cluster. When testing new components and applications, CubeSat missions have proved useful for space-qualified use in future. In addition, these uniform pico-satellites made the university's space technology readily available as a subject in undergraduate and postgraduate programs, where they were originally started. Ampatzoglou et al. [1] designed and tested a 2U nanosatellite, to be launched and working in the lower thermosphere. They developed a hybrid subsystem based on both aluminum and composite materials, fulfilling all design and test requirements and successfully launched into orbit, proving the feasibility of the new design. Barsoum et al. [2] presented hands on experience of the configuration process and strength analyses of a student's CubeSat project. They preformed static and random vibration analysis, and fatigue life analysis in order to the primary structure will safely mechanical environment design will survive the mechanical environments launched safely. Eiswy et al. [3] presented the overall design process of the structure subsystem of 1-U CubeSat mission. they implemented the static and modal analysis using finite element method. Raviprasad et al. [4] they provided the modal, harmonic and random vibration analysis of the nano-satellite mission and findings were compared with the standard mechanical specifications of the CubeSat and launch vehicle providers. Oh et al. [5] introduced a CubeSat mission structure concept, based on the 1U Model, developed by the Chosun University Space Technology Synthesis Laboratory. Furthermore, the validity of their proposed design was investigated through quasi-static and modal analysis. Swartwout [6] Submitted a comprehensive review of the first one hundred CubeSat missions, together with an on-orbit performance assessment while classifying missions by size, origin and mission life. It was found that many design and deployment defects, while correctable, still haunt the CubeSat missions at the university. Furthermore, for this type of missions the P-POD launch container, not the CubeSat model, has proven to be the true supporting technology. Alminde et al. [7] Addressed the educational value of the CubeSat university projects by explaining the overall architecture of the AAU-CubeSat university project launched in space on 30 June 2003. Results from the operation phase were presented, suggesting further work on pico-satellite designs. Noca et al. [8] presented the project organization, mission and satellite description of their first pico-satellite project, Swiss-Cube, developed at the Federal Institute of Technology Space Center in Lausanne. Technical and programmatic lessons were discussed, since the main objective of this project was to provide practical experience of the entire cycle of satellite production. Cote et al. [9] outlined the power, propulsion, and structure subsystems of Worcester Polytechnic Institute's initial endeavor to experiment a CubeSat. Each of the three subsystems teams managed to design and specify a baseline set of components for their subsystem and to perform rudimentary testing. Castello [10] built a MATLAB toolbox to help CubeSat developers understand the limitations of CubeSat, automate their systems, and decrease design development time while meeting initial requirements. Cghan [11] the design analysis of the structure and mechanisms subsystem of their second CubeSat project at the Technical University of Istanbul. Two separate designs were proposed, and the final selection was based on certain target performance parameters. Bürger

et al. [12] Presented static and modal analysis of the structure subsystem of a CubeSat project developed at the Brazilian Aeronautics Technology Institute. Arroyave et al. [13] proposed a design protocol that would help in meeting the unique structural specifications of CubeSat missions. In addition, they evaluated the static and dynamic behaviour of some case studies by performing static, modal, harmonic, and random vibration analyses, subject to special mechanical load conditions. The current work presents structural analyses and optimization of a student's CubeSat project to be launched in a lower thermosphere orbit. The static and dynamic responses of the primary and secondary structures are simulated, using ANSYS Finite Element Software, being subjected to the mechanical environments of two candidate launchers. The mass of the primary structure is optimized subject to static and natural frequency constraints,In addition, random base vibration response, and hence fatigue life are performed in order to ensure that the primary and secondary structures will safely survive the launching phase. Finally, the structural response of some selected subsystems, modeled in detail and simulated individually, and compared with their lumped mass approximations, which are simulated as part of the whole CubeSat, in order to investigate the outcome of such approximations.

2 MODEL OVERVIEW

The current pico-satellite project is a 1-U CubeSat, made for earth observation purposes and is based on commercial of the shelf (COTS) components[18][19]. The primary structure is assembled by four corner rails connected, by stainless steel screws, to four side panels made of Aluminum 6061-T6. Inside the enclosure, four spacer rods, made of brass, where installed to support the Printed Circuit Boards (PCBs) of the different satellite subsystems. Inside the structure, the following components are placed from top to bottom. An optical earth observation camera is installed at the top with its lens penetrating from the top cover. A Communication (COMM) system board responsible for the communication between the CubeSat and the ground station. An On-Board Computer (OBC) board that controls the CubSat based on the commands incoming from the ground station. An Attitude and Directional Control (ADC) unit responsible for the positioning and orientation of the Cubesat. Lastly, an Electrical Power Supply (EPS) unit that powers the CubeSat circuitry. The initial proposed mass budget of the CubeSat, before the optimization, is 1.076 Kg namely: the structure mass 360 g, camera mass 210 g, COMM mass 75 g, OBC mass 75 g, ADC mass 156 g and EPS including its batteries 200 g. Two CubeSat models were investigated throughout the current work; the first one is based on a detailed configuration of the interior and the second one is based on lumped mass representation of the PCBs. Figure 1 shows the proposed detailed layout of the CubeSat with and without the side panels.

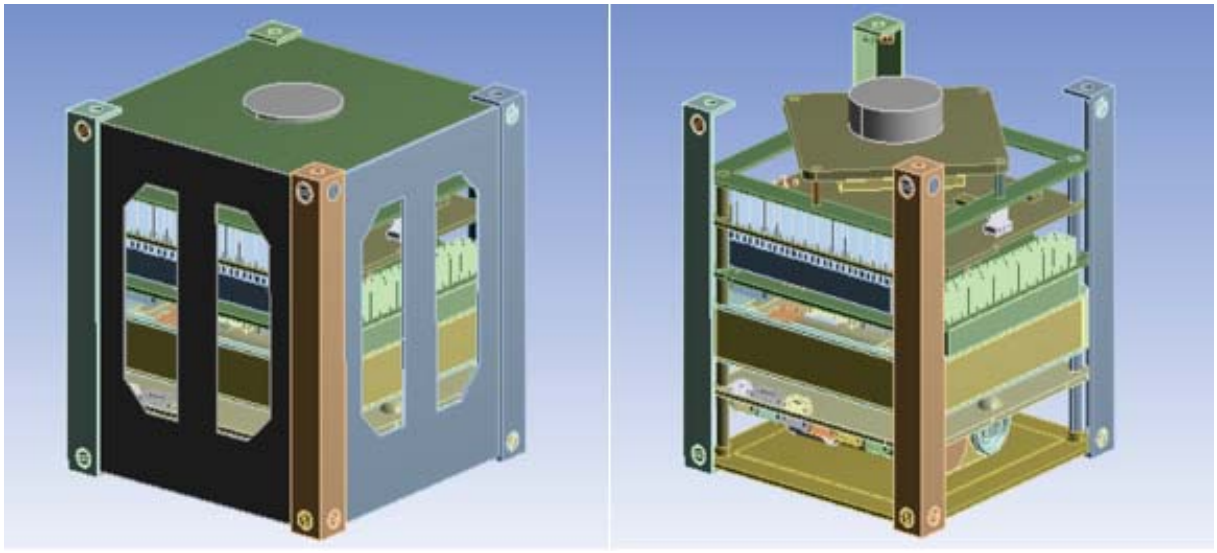

Figure 1: Layout of the proposed primary structure with(left) and without(right) side panels

3 RESULT AND DISCUSSION

3.1 Static analysis of the Assembly

All the analyses presented, hereinafter, are intended to check the static and dynamic behaviour, of the current proposed CubeSat primary structure and its PCBS, in response to the mechanical environment of Soyuz and Dnepr as two candidate launchers. The static response of the satellite structures is simulated while being exposed to a quasi-static acceleration of 13g in the X, Y and Z directions simultaneously. The primary structure is assumed to be clamped through the whole length of the rails [1]. Figures 2 and 3 show the distributions of the equivalent stress and total deformations, respectively, of the lumped mass model. It is shown that the structure experiences maximum stress of 18.786 MPa which is fairly safe in terms of yield stress when compared to the 276 MPa which is the yield stress of the aluminum 6061-T6 and it is seen in Figure 3 that the structure responds with a maximum value of total deflection equals 0.1501 mm which is found very acceptable in terms of the static deflection interference of the different components of the satellite as per the interior static envelop of the proposed configuration. However, for the detailed model shown Figure 4, the equivalent stress increased to 43.127 MPa and the total deformation 0.021066 mm as shown in Figure 5. Taking a closer look at the detailed model, the maximum stress value appeared to be at the pins of the COMM board where these pins are absent in the lumped mass model.

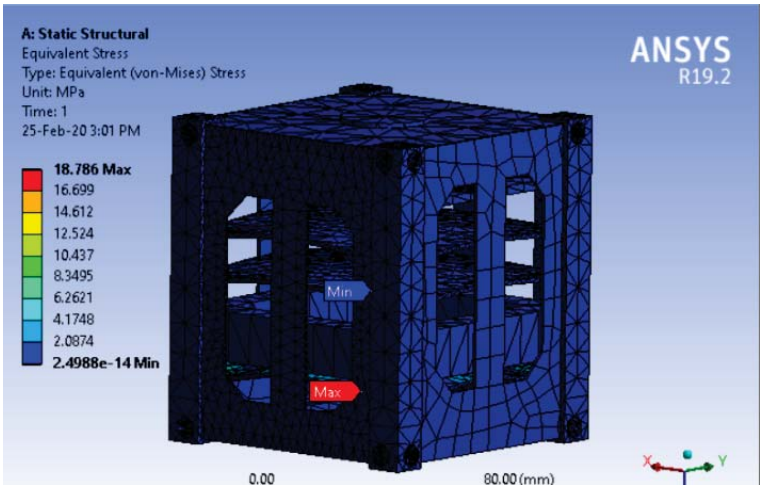

Figure 2: Equivalent Von-Mises stress lumped mass model

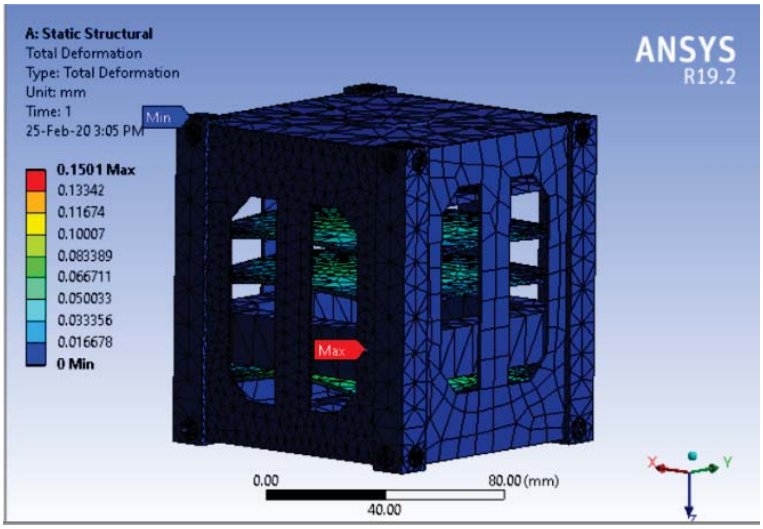

Figure 3: Total Deformation in lumped mass model

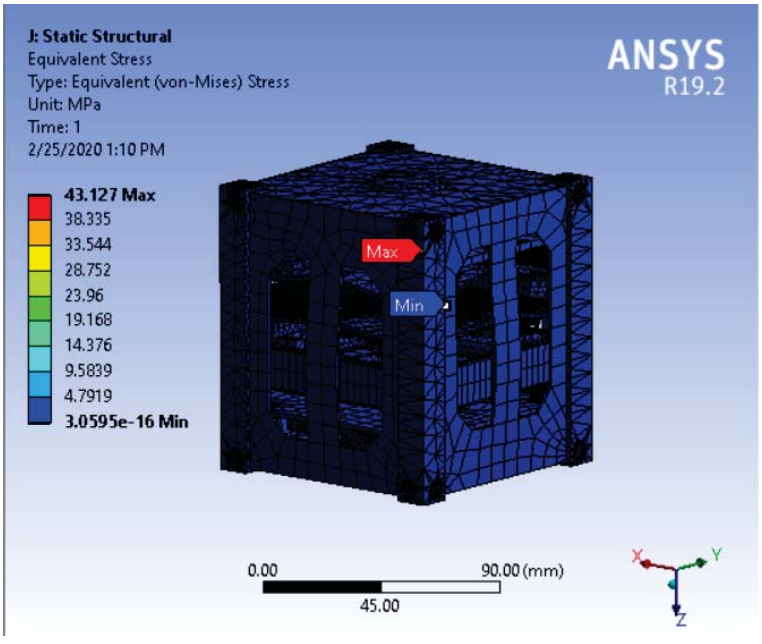

Figure 4: Equivalent Von-Mises stress in fully detailed model

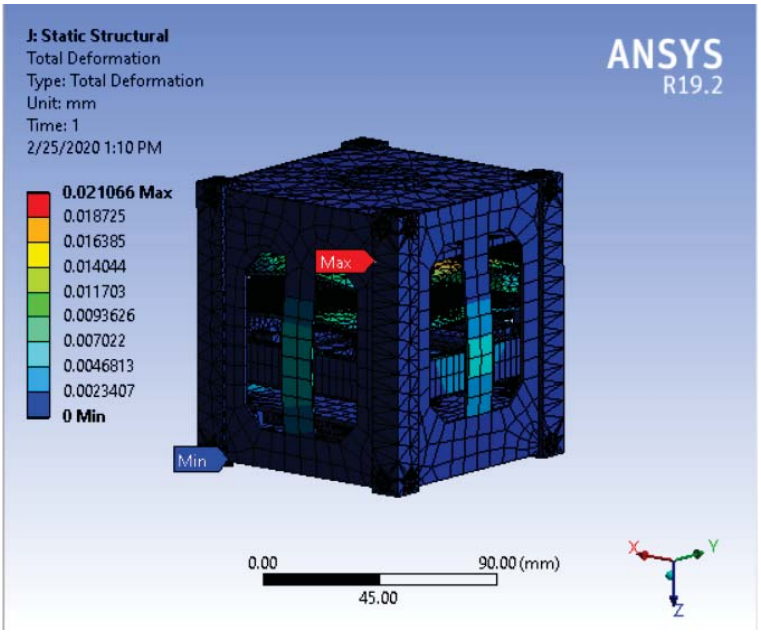

Figure 5. Total Deformation in fully detailed model

3.2 Modal Analysis

Modal analysis was conducted on both, lumped mass and detailed models, for the first six mode shapes as shown in Table 1. It is shown in the results that the first natural frequency of the lumped mass model is 199.81 Hz while in the detailed model the value jumped high to be 562.52 Hz which can be attributed to the more even distribution of the masses on each printed circuit board compared to the lumped mass modeling. The fundamental frequency of both models were found above the lower threshold value of 100 Hz specified by launcher providers.

Mode	Natural Frequencies [Hz]	
	Detailed	Lumped mass
1	562.52	199.81
2	609.68	292.36
3	702.01	304.37
4	785.64	537.79
5	843.19	683.27
6	859.68	686.14

Table 1: Natural frequencies for detailed and lumped mass models

3.3 Static Structural and Modal analyses of PCBs

This section presents the quasi-static response and natural frequencies of each subsystem PCB analyzed separately. There are four commonly used in most CubeSat missions namely: COMM, OBC, ADC and EPS. All of the PCBs are simulated assuming that they are supported from their corner holes. Table 2 shows the static analysis on the COMM board yielding the highest stress value when compared to other PCBs with a value of 50.5 MPa, which is almost similar to the maximum of 43.127 MPa displayed in the analysis of the detailed model and a total deformation of 0.02 mm. Figure 6 shows the maximum stress at the pins of the COMM board same as at the detailed model. In addition, the first mode shape in the detailed model appeared at the COMM board at 562.52 Hz which is approximately the same as the first mode shape of the COMM board which was analyzed separately.

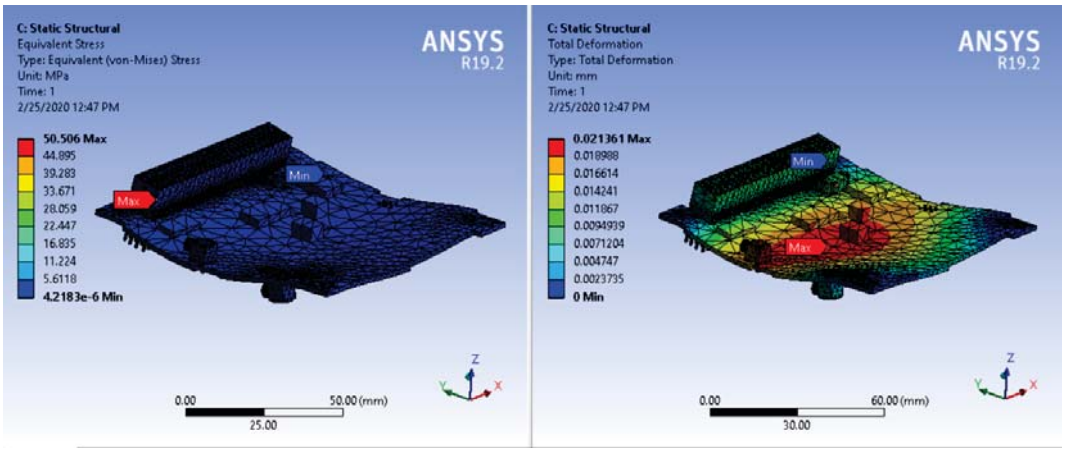

Figure 6: Quasi-static response of COMM PCB: Stress and deformation

Analysis	Value
Von-Mises Stress	50.506 [MPa]
Total Deformation	0.021361 [mm]
Safety Factor	5.5

Table 2: Quasi-static response of COMM PCB

3.4 Optimization

The Objective of the optimization was to minimize the mass of the CubeSat, while keeping it safe under launch loads by limiting the factor of safety of the structure to 2 or more. The mass of the initial proposed design of the CubeSat was 1.076 Kg and the mass of primary structure itself is 0.36012 Kg. After conducting the optimization process, Using surface response optimization method, the CubeSat total mass is dropped to 0.899 Kg which is 16% less than the initial total mass of the CubeSat. To ensure the safety of the structure, static analysis is implemented on the optimized model with the same loading conditions and it yielded nearly same results compared to those prior to the optimization as shown in Figure 7 and 8.

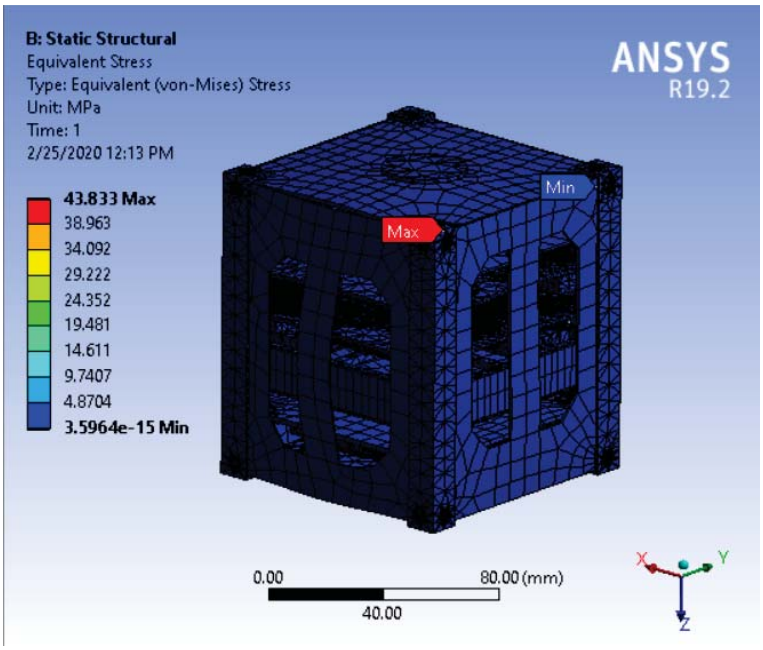

Figure 7: Equivalent Von-Mises for the detailed optimized model

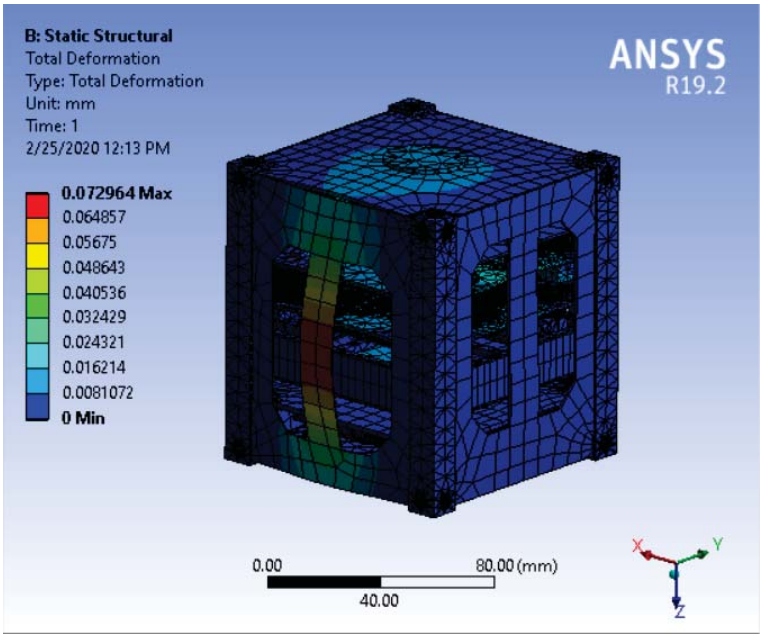

Figure 8: Total Deformation for the detailed optimized model

3.5 Fatigue analysis

This section presents the fatigue analysis of the optimized Cubesat primary structure subjected to random vibration induced by two candidate launchers, namely: Soyuz and Dnepr. The main purpose of preforming this analysis is to identify the stress peak of each launching phase, corresponding to the resonance frequencies of the primary structure to be used later in assessing the effect of cumulative fatigue. Tables 3 and 4 show the PSD (Power Spectral Density) random vibration loading of Soyuz and Dnepr respectively, specifying the expected duration of each launching stage[16][17].

Event	Frequency Band (Hz)						Time (s)
	20-50	50-100	100-200	200-500	500-1000	1000-2000	
	PSD, Power Spectral Density $10^{-3}g^2/HZ$						
1st Stage	5.0	5.0 10.0	10.0 25.0	25.0	25.0 10.0	10.0 5.0	120
2nd & 3rd Stage	2.5	2.5 5.0	5.0 10.0	10.0	10.0 5.0	5.0 2.5	480
Fregat Stage	2.0	2.0	2.0	2.0	2.0-1.0	1.0	1100

Table 3: The limit flight levels of random vibrations of Soyuz launcher [16]

Event	Frequency Band (Hz)							Time (s)
	20-40	40-80	80-160	160-320	320-640	640-1280	1280-2000	
	PSD, Power Spectral Density $10^{-3}g^2/HZ$							
Lift Off,	7.0	7.0	7.0	22.0	35.0	35.0	17.0	35
LV Flight			22.0	35.0		17.0	5.0	
1st Stage Burn	7.0	7.0	7.0	7.0	9.0	9.0	4.5	831
				9.0		4.5		

Table 4: The limit flight levels of random vibrations of Dnepr launcher [17]

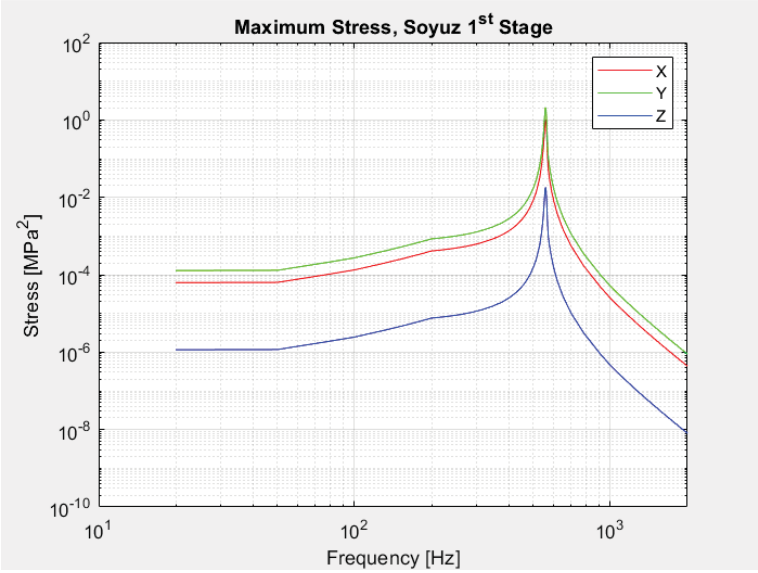

Figure 9: Random vibration response of Soyuz 1^{st} Stage in X, Y and Z (Hz – MPa^2)

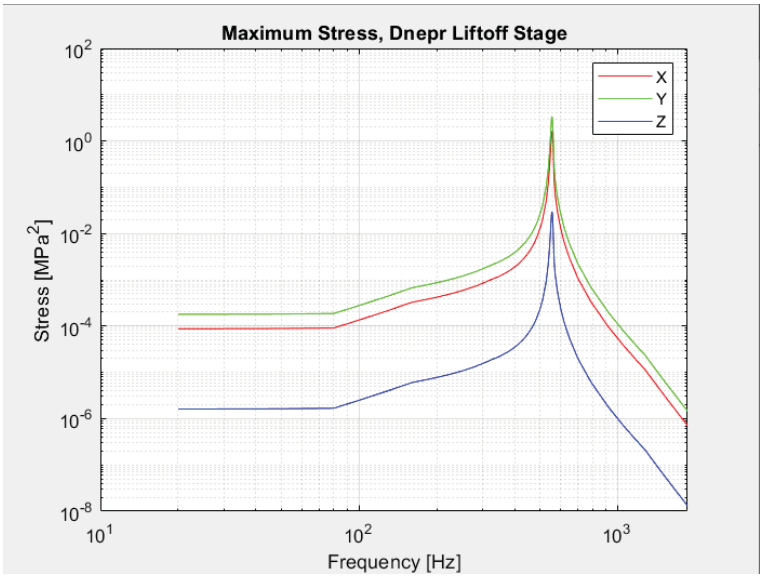

Figure 10: Random vibration response of Dnepr Lift Off, LV Flight in X, Y and Z (Hz – MPa^2)

PSD stress calculated on 24 different points namely, 4 points at the connections between the 4 PCBs and the spacer rods, 4 points at the center of the side panels and 4 points at the middle nodes of the PCBs. From the results of Dnepr simulations, it was found that the liftoff stage yielded the highest stress level, as shown in Figure 10 , which occurred at the point of connection between the spacer rod and the COMM board. It is seen in the Figure 9 that x direction the peak value was 1.02 MPa^2/Hz, y direction was 2.09 MPa^2/Hz and z direction was 1.83E-02 MPa^2/Hz at 557.84 Hz, as in Figure 10 it is seen that x direction the peak value was 1.65 MPa^2/Hz, y direction was 3.39E MPa^2/Hz and z direction was 2.96E-02 MPa^2/Hz at 557.93Hz. As mentioned before the number of stress cycles *ni*, at one frequency found to be most influential, will be calculated while assuming that this frequency will happen to last for the total duration of the given launching stage. Therefore, the frequency peak was found to have the highest (*ni*/*Ni*) value, for the given launching stage, will be considered in calculating the total cumulative effect of all stages.

Referring to the S-N curve of the selected aluminum alloy, it was found that all of the stress levels reported in the previous section fall in the category of high cycle fatigue. Therefore, it would be conservative to use 1E+8 as the number of cycles to fail for all the simulated values of the stress. Miner's law for cumulative fatigue has been implemented for both launcher cases. as shown in table 5 and table 6 number of cycles (*ni*) at stress peak and number of cycles to fail (*Ni*) at each loading phase and then sum the all values to get total cumulative effect of all stages as shown. The total cumulative in launcher Soyuz value is 0.02845 while in launcher Dnepr value is 0.0157.

Loading phase		No. of cycles at 1st stress peak ni	No. of cycles to fail at 1st stress peak Ni	ni/Ni
1st Stage	X	66940.8	1×10^8	0.00067
	Y	66951.6	1×10^8	0.000669516
	Z	66940.8	1×10^8	0.000669408
2nd Stage & 3rd Stage	X	267806.4	1×10^8	0.002678
	Y	267806.4	1×10^8	0.002678
	Z	267806.4	1×10^8	0.002678
Fregat Stage	X	613723	1×10^8	0.006137
	Y	613723	1×10^8	0.006137
	Z	613723	1×10^8	0.0061372
Total cumulative effect of all stages				0.028454214

Table 5: Cumulative fatigue damage analysis subject to Soyuz random load

Loading phase		No. of cycles at 1st stress peak ni	No. of cycles to fail at 1st stress peak Ni	ni/Ni
Lift Off, LV Flight	X	19527.6	1×10^8	0.0002
	Y	19527.55	1×10^8	0.000195276
	Z	19527.55	1×10^8	0.000195276
1st Stage Burn	X	463639.8	1×10^8	0.004636
	Y	267739.2	1×10^8	0.002677
	Z	267806.4	1×10^8	0.002678
Total cumulative effect of all stages				0.010577681

Table 6: Cumulative fatigue damage analysis subject to Dnepr random load

The Modified Goodman-line method was implemented to determine the fatigue factor of safety based on highest stressed location, out of those previously checked using Miner's cumulative fatigue life assessment. The number of stress cycles, of the aforementioned stress location, was calculated using the fundamental frequency and the whole time duration of all launching stages which represent quite conservative assumption. Table (7) shows the stress results of the highest stressed location, which happened to be the maximum out all launching stages, of the two candidate launchers. The fatigue limit of Aluminum 6061-T6 was assumed to be 96.5 MPa as per Yahr [20] for a full reversed cycle, while the maximum stress amplitude was assumed to be 4.5 times the root mean square value (RMS), by converting the random vibration response of the critical launching stage from frequency domain to time domain [21]. It was found that both candidate launchers are fatigue safe with a minimum factor of safety of 2.46, depicted by Dnepr, despite the very conservative assumptions implemented while applying Goodman method compared to those previously used in Miner's cumulative fatigue assessment which proved over safe as well.

Stage	Direction	RMS [MPa]	Stress [MPa]	σ_a	Factor of Safety n
Soyuz 1st Stage	X	3.9211	17.64495	17.64495	5.468986877
	Y	5.6137	25.26165	25.26165	3.820019674
	Z	0.52708	2.37186	2.37186	40.68536929
	Resultant		30.904	30.904	3.122
Dnepr Liftoff	X	4.9712	22.3704	22.3704	4.313736008
	Y	7.1171	32.02695	32.02695	3.013087415
	Z	0.66825	3.007125	3.007125	32.09045184
	Resultant		39.183	39.183	2.46

Table 7 Fatigue life Assessment using Modified Goodman-line factor of safety

4 CONCLUSIONS

This work presented structural analyses and optimization of a student's CubeSat project subject to the mechanical environments of two candidate launchers. The structural response of some selected subsystems, modeled in detail and simulated individually and as part of the whole CubeSat, are simulated and compared with their lumped mass approximations. In terms of the quasi static response due to launcher g-loads, it was found the primary structures of the detailed and lumped mass models displayed similar stress values, in magnitudes and locations. while the some fine details of the subsystems PCBs, which were absent in the lumped mass model, showed stress levels more than two time those of the lumped mass one. Modal analysis results of both models showed that the fundamental frequency of the detailed model higher than the lumped mass one by 281.5% which can be attributed to the much even distribution of component masses of the detailed PCBs model. Therefore, such significant difference in the simulated frequencies could affect the accuracy of the modal assurance coefficient provided to launcher providers. Furthermore, optimization of the primary structure has implemented and the results showed a mass reduction of 16%, which made it 0.899 Kg instead of an initial value of 1.076 Kg.Finally, fatigue life assessments were implemented to the CubeSat primary structure and its PCBs, using Miner's law and Goodman – line method, subject to random vibrations induced by both candidate launders. It was found that both candidate launchers are fatigue safe with a minimum factor of safety of 2.46, depicted by Dnepr, despite the very conservative assumptions implemented while applying Goodman method compared to those previously used in Miner's cumulative fatigue assessment which proved over safe as well.

REFERENCES

[1] A. Ampatzoglou, and V Kostopoulos, “Design, Analysis, Optimization, Manufacturing, and Testing of a 2U Cubesat”, International Journal of Aerospace Engineering Volume 2018, Article ID 9724263.

[2] George I. Barsoum, A., Hesham H. Ibrahim, Mina A. Fawzy, “Static and Random Vibration Analyses of a University CubeSat Project”, Journal of Physics: Conference Series, Volume 1264, 2019.

[3] Eisawy, M., Hussain, A., Merza, Z., Hesham H. Ibrahim, Nada, T., ” Emirates Aviation College CubeSat Project: Tuning of Natural Modes, Static and Dynamic Analyses of the Strength Model,” 5th International Conference on Recent Advances in Space Technologies, Istanbul, Turkey, June 2011.

[4] Raviprasad S. and Nayak N. S., Dynamic analysis and verification of structurally optimized nano-satellite systems, Journal of Aerospace Science and Technology, Vol. 1, pp. 78 - 90, doi: 10.17265/2332-8258/2015.02.005, (2015).

[5] Oh H. U., Jeon S. H., and Kwon S. C., Structural design and analysis of 1U standardized STEP Cube Lab for on-orbit verification of fundamental space technologies, International Journal of Materials, Mechanics and Manufacturing, Vol. 2, No. 3, August (2014).

[6] Swartwout, M., The first one hundred CubeSats: A statistical look, Journal of Small Satellites, Vol. 2, No. 2, pp. 213-233, (2013).

[7] Alminde L., Bisgaard M., Vinther D., Viscor T., and Stergard K., Educational value and lessons learned from the AAU-CubeSat project, Proceedings of 3rd International Conference on Recent Advances in Space Technologies (RAST), Istanbul, Turkey, 20-22 Nov., 10.1109/RAST.2003.1303391, (2003).

[8] Noca M., Jordan F., Steiner N., Choueiri T., George F., Roethlisberger G., Scheidegger N., PeterContesse H., Borgeaud M., Krpoun R., and Shea H., Lessons learned from the first Swiss picosatellite: SwissCube, 23rd Annual/USU Conference on Small Satellites, Utah-USA, August 10-13, (2009).

[9] Cote K., Gabriel J., Patel B., Ridley N., Taillefer Z., and Tetreault S., Mechanical, power, and propulsion subsystem design for a CubeSat, BSc. Qualifying Project, Aerospace Engineering, Worcester Polytechnic Institute, UK, March (2011).

[10] Castello B. R., CubeSat mission planning toolbox, MSc. Thesis, Aerospace Engineering, California Polytechnic State University, USA, June (2012).

[11] Cġhan M, A new conceptual structure design for nanosatellites, MSc. Thesis, Aeronautics and Astronautics Engineering, Institute Of Science And Technology, Ġstanbul Technical University, June (2011).

[12] Bürger E. E., Loureiro G., Costa L. L., Hoffmann C. T., Zambrano D. H., and Jaenisch G. P., Development and analysis of a Brazilian CubeSat structure, 22nd International Congress of Mechanical Engineering (COBEM 2013) November 3-7, Ribeirão Preto, SP, Brazil, (2013).

[13] Arroyave J. E. H., Pérez J. A. F., Colín A. and Reyes B. B., CubeSat system structural design, 67th International Astronautical Congress (IAC), Guadalajara, Mexico, 26-30 September (2016).

[14] Poly Picosatellite Orbital Deployer MK III ICD, the CubeSat Program, California Polytechnic State University-SanLuis, CA 93407.

[15] Abdelal, G. F., Abuelfoutouh, N., and Gad, A. H. Finite element analysis for satellite structures: applications to their design, manufacture and testing. Springer Science and Business Media, 2012.

[16] Soyuz User's Manual March 2012.

[17] Dnepr User Guide November 2001.

[18] PCB: COMM from ISISspace. https://www.isispace.nl/

[19] PCBs :OBC, ADC and EPS from GOMSpace. https://gomspace.com/home.aspx

[20] Yahr, G. T. Fatigue Design Curves for 6061-T6 Aluminum. United States. doi:10.1115/1.2842286.

[21] http://www.caefatigue.com/wp-content/uploads/CAEF-34-RMS-Stress-Levels1.pdf.

EURODYN 2020
XI International Conference on Structural Dynamics
M. Papadrakakis, M. Fragiadakis, C. Papadimitriou (eds.)
Athens, Greece, 23–26 November 2020

WIND EFFECTS ON LOW-RISE BUILDINGS WITH NEIGHBOURING STRUCTURE AS OBSTACLES

Rodríguez-Alcántara, J. U.[1], **Pozos-Estrada, A.**[2] **and Gómez-Martínez, R.**[3]

[1] PhD Student in Institute of Engineering of National Autonomous University of Mexico, Mexico City.
JRodriguezA@iingen.unam.mx

[2] Researcher in Institute of Engineering of National Autonomous University of Mexico, Mexico City.
{APozosE, RGomezM}@ iingen.unam.mx

Keywords: Low-Rise Buildings, Pressure Coefficient, Wind Tunnel, Neighboring structure.

Abstract. *Experimental studies of the wind effects on a low-rise building considering two different turbulent wind speeds and one type of terrain category were carried out at the boundary layer Wind Tunnel operated by the Institute of Engineering of UNAM (IIUNAM). The model considered was a cube made of acrylic, instrumented with 125 taps. Two experimental setups were considered, the first one considered the evaluation of the wind effects on the isolated model (with no obstacles surrounding it), while the second one evaluated the effects of placing a body of identical shape next to the studied model. The second setup considered six different separations between the models. For both experimental setups, wind direction was varied from 0 ° to 180 ° with increments of 10 °, and including the angles of 45 ° and 135 °. Mean, maximum and minimum pressure coefficients were obtained for each arrangement in order to make a comparison between the values obtained in each tap. The results show that the consideration of a neighboring structure has an important impact on the pressure coefficients due mainly to Venturi effects and vortex shedding. It was also observed that the separation between the instrumented model and the obstacle serves as an important parameter to evaluate the increase or decrease of the wind pressures with respect to the isolated model.*

1 INTRODUCTION

In recent years, research on construction and the environment has taken a different direction than the traditional one, trying to minimize the impact on the environment and provide better comfort for the inhabitants. The presence of tall buildings on areas with a high density of low-rise buildings, results in the presence of turbulent wind flows that disturb people's activities. Narrow corridors within an industrial or residential area accelerate flows giving the perception of a greater impact of the wind effect, affecting the activities in these areas.

In some countries, the effects of wind are studied in suburban and urban areas with different building configurations, and their impact on the comfort of people or activities are carried out in predefined spaces [1, 2]. These studies are often developed with Computational Fluid Dynamics (CFD) and later validated with a few wind tunnel tests. These studies are carried out to confirm that the speeds, within spaces confined by neighboring buildings, do not exceed the recommended values for the pleasant stay of the inhabitants. In the event of finding speeds greater than permissible, it is proposed to build barriers that reduce the wind impact and generate greater comfort areas.

In Mexico, the use of any comfort criteria is an unusual practice during the structural design stage, which may lead to serious problems during unfavorable environmental conditions. In this work, experimental studies of the wind effects on a low-rise building by considering two different turbulent wind speeds and one type of terrain category were carried out at the boundary layer Wind Tunnel operated by the Institute of Engineering of UNAM (IIUNAM). The model considered was a cube made of acrylic, instrumented with 125 taps. Two experimental setups were considered, the first one considered the evaluation of the wind effects on the isolated model (with no obstacles surrounding it), while the second one evaluated the effects of placing a body of identical shape next to the studied model. The second setup considered six different separations between the models. For both experimental setups, wind direction was varied from 0 ° to 180 ° with increments of 10 °, including the angles of 45 ° and 135 °. The results show that the consideration of neighboring structures has an important impact on the pressure coefficients due mainly to Venturi effects and vortex shedding.

2 BACKGROUND

The first wind tunnel of UNAM was inaugurated in 1966, in which important projects such as the wind load analysis of the Palace of Sports was studied; however, due to its dimensions, this tool is considered to have significant limitations when addressing current problems of modern wind engineering [3]. Therefore, in 2006, researchers from the Institute of Engineering (IIUNAM) joined efforts to develop a design for a new wind tunnel that was revised and modified by AIOLOS. The new facility was built by a Mexican company and was finally inaugurated in 2015. The boundary layer Wind Tunnel, operated by IIUNAM, is a tool for experimental study of the effects of wind on civil structures through dimensional and similarity analysis in a long-length test section (Figure 1). One of the main dimensional parameters is the geometric scale, which involves not only the scaling of the model, but also the terrain and consequently the scaling of atmospheric conditions.

For practical purposes in civil engineering, within the troposphere there are three main sublayers, the Planetary Boundary Layer (PBL), whose height is associated with a geostrophic height the Atmospheric Boundary Layer (ABL) whose thickness is associated with a gradient height, and the Atmospheric Surface Layer (ASL) which is the closest layer to the ground and usually represents the bottom 10% of the PBL (usually 100 m), its height is mainly defined by vegetation [4]. In the laboratory, ABL is often considered, and ASL is implicitly represented.

The correct simulation of one or the other must adequately replicate the mean velocity and turbulence intensity profiles associated with certain category of terrain based on the logarithmic law or the power law. In order to achieve proper representation in an artificial way, there are several methods, the most commonly used is the Counihan method [5], which uses a barrier, an elliptical needle set and a series of roughness elements distributed throughout the test section, which represent the idealized topography of some terrain. When defining the terrain and model simulation scale, an iterative "test and error" process is required. Based on works by Balendra [6] and Endo [7], in this study the ASL of an urban terrain was adequately represented. The mean wind velocity and turbulence intensity profiles measured were associated with an open country terrain for real velocity values of 13.23 m/s and 21.45 m/s. The geometric scale used was 1:50, while the calculated speed scale was 1:5.

The Silsoe Cube is one of the models that has been tested by various researchers, both on real and reduced laboratory scales. This model has been used for calibration of rigid models and tests of low-rise buildings [8]. It is important to note that this model is usually used for terrain category 2 (open country terrain). Based on the geometric scale mentioned above, the Silsoe Cube was scaled producing a 0.20 m cubic model which was constructed with $4x10^{-3}$m thickness acrylic plates to ensure model rigidity. When the model is oriented to ±45° on the turntable, and when the projected length is greater than 0.20 m, the effective blockade is less than 1% of the cross-sectional area of the tunnel test section 2 (Figure 1). Each face of the model was instrumented with 25 sensors (taps) providing a total number of 125 (Figure 3). The recording of pressure fluctuations and sensor distribution was proposed based on distributions suggested in the literature, as well as on the distribution of pressures obtained by CFD simulations [9, 10]. The sampling rate for the pressure records was 256 Hz and the sampling time was 45 seconds (real-scale observation time is 10 min), obtaining a total of 11,520 samples for each wind direction.

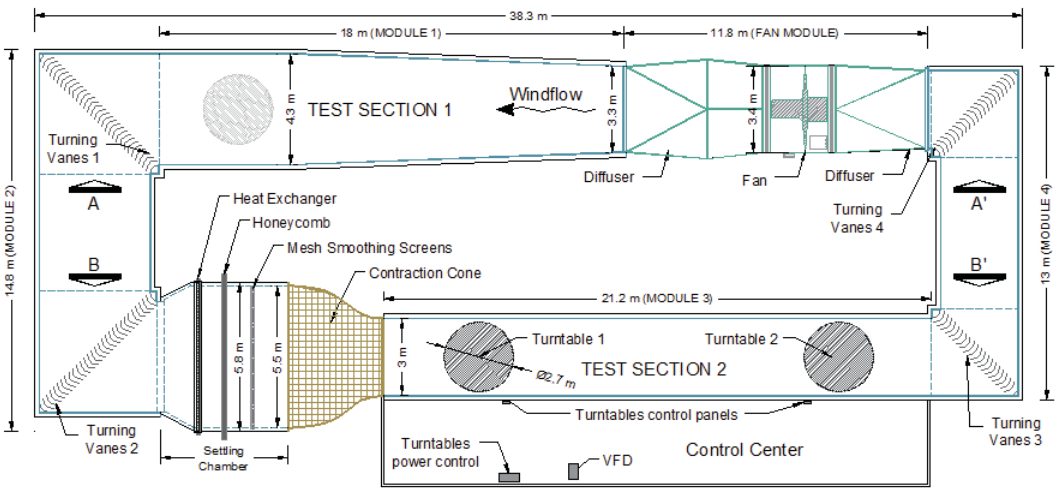

Figure 1. Diagram of the UNAM boundary layer wind tunnel [8]

3 WIND TUNNEL TESTS

Two scaled wind speeds were considered in the tests, the first one was 3.53 m/s and the second one was 5.72 m/s. The previous velocities correspond to mean wind speeds at 10 m height of 13.23 m/s and 21.45 m/s in real scale, respectively. One of the tests consisted in the evaluation of the pressure distribution over the isolated acrylic cube, this test was called Arrangement 0 (Figure 3a). This pressure distribution was used as reference to evaluate the im-

pact of having a structure, with the same geometry as the cube, next to the reference structure. The proposed arrangements for the reference structure with one identical next to it were chosen based on two relevant criteria. Firstly, to get the most common arrangement in the construction of industrial and housing complexes by using satellite images. Figure 2 shows two of these arrangements. The side and aspect ratios (d/b and H/b) of the structures are very similar, where d, b and H represent the length, width, and height of the structure, respectively. Figure 2a shows a minimum separation distance between them, whereas Figure 2b shows that the separation distances are increased. It is noted that variations in the height of bluff bodies in the proximity of the studied model are out of the scope of the present study. This aspect of variations in height requires further investigation.

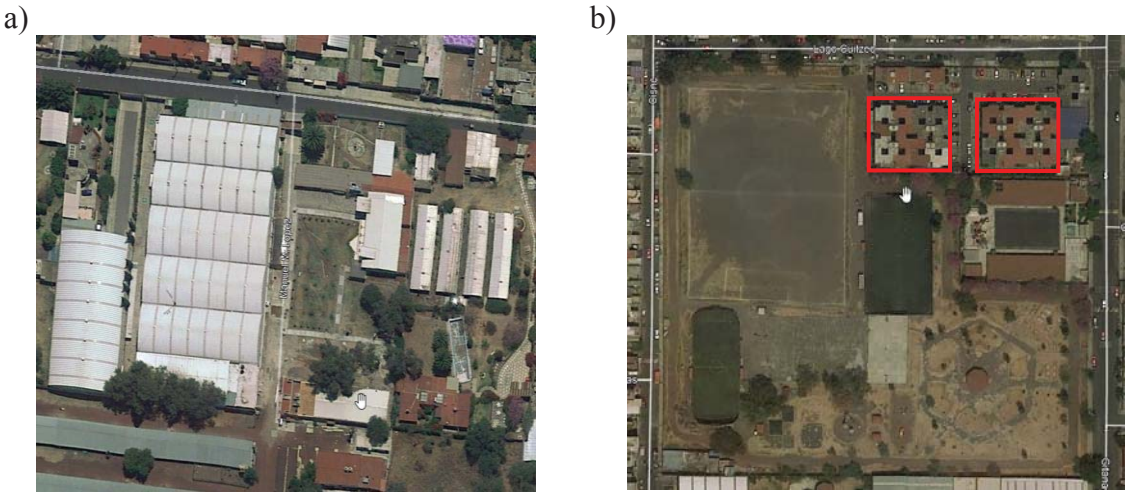

Figure 2. (A) Industrial buildings confined with less separation between them; (b) Two identical buildings in an open terrain with narrow corridors between

Secondly, three of the most important phenomena that can be identify due to the interference of an object in the flow of the wind are:

- Venturi effect. Neighboring buildings, due to their dimensions, shape and orientation, can cause a "bottleneck" effect, accelerating airflow and consequently pressure alterations.
- Wind deviation in vertical direction. When there is a higher body in the leeward zone, the wind flow that affects its windward face is diverted downward increasing the velocities and pressures in areas close to this face. Buildings under this face may have higher pressure coefficients.
- Effects of vortex shedding. One building located at the leeward of another can be significantly affected by the turbulence wake caused by the blockage of the wind flow in windward, which can cause considerable dynamic effects and changes in pressures.

Figure 3b shows Arrangement 1 that consisted in the instrumented acrylic model (Silsoe Cube, [11, 12]), and next to it a wood obstacle placed at a gap that was varied from 0.5H to 3.5H, with 0.5H increments, where H is the total height of the cube (H = 0.20 m). This arrangement was located on turntable 2 (Figure 1), which allows the model to be rotated to simulate different wind directions (θ). The wind directions considered were 0°, 30°, 45°, 60°, 90°, 120°, 135°, 150° and 180°; angles at which it is expected to obtain the most critical external pressures/suctions on the reference model. As mentioned previously, two scaled wind speeds were considered. The wind tunnel tests carried out with these velocities were employed to evaluate if the wind speed affected the values of the External Pressure Coefficients (*EPC*), or

if they could be considered independent of the wind speed when there were obstacles with edges (bluff bodies) in the proximity of the studied model.

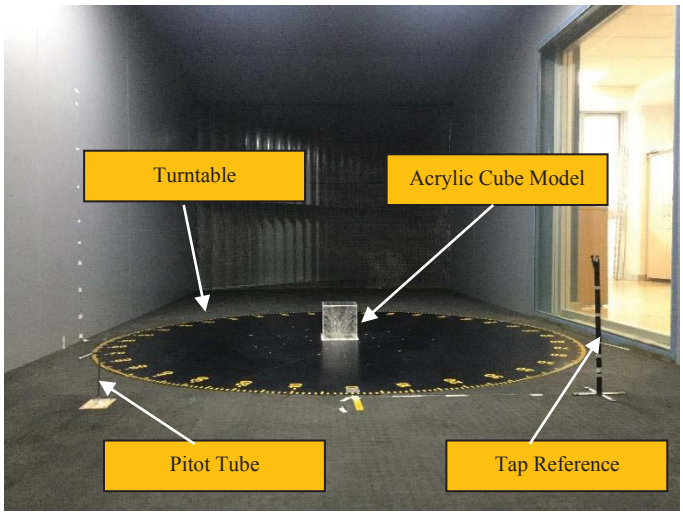

Figure 3a. Arrangement 0. Isolated model

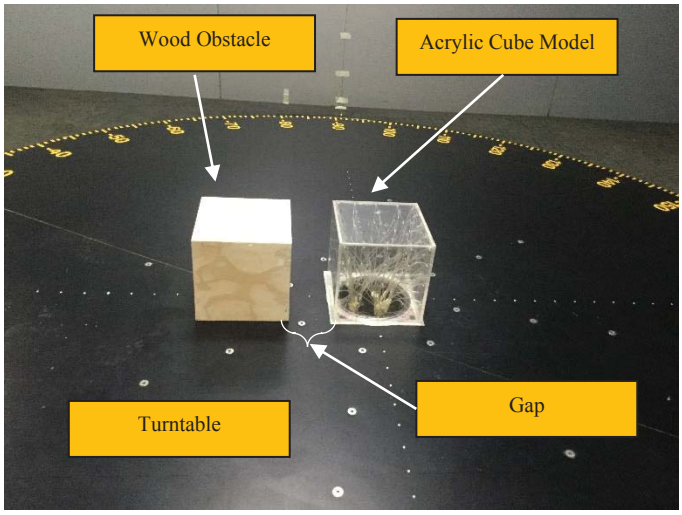

Figure 3b. Arrangement 1. Model with obstacle next to it

4 COMPARISON AND VALIDATION OF RESULTS

Once the pressure records on the different faces of the reference model were acquired, *EPC* were obtained for each tap, this coefficient is defined as the relationship between the pressure difference (ΔP) on a given surface and the dynamic pressure of the undisturbed flow (Pq), see ec. (1):

$$EPC = \frac{\Delta P}{P_q} \tag{1}$$

where:

$$\Delta P = P - p_s \tag{2}$$

$$P_q = P_T - p_s \tag{3}$$

P is the pressure measured on the taps.
p_s is the static pressure of the undisturbed wind flow, measured with a Pitot Tube in the center of the turntable, prior to the tests of the arrangements.
P_T is the total pressure of the undisturbed wind flow, measured with a Pitot tube in the center of the turntable, prior to the tests of the arrangements.

Table 1 shows the average *EPC* values for each face of the cube and each of the arrangements studied for a gap G = 2.0H. Table 1 shows that EPC values increase or decrease on the different surfaces of the model for each of the arrangements, with respect to the isolated model.

Face	***Wind Incident angle (θ)***								
Isolate Cube	***0 °***	***30 °***	***45 °***	***60°***	***90°***	***120°***	***135°***	***150°***	***180°***
Left side wall	*-0.5984*	*-0.5636*	*-0.5250*	*-0.4178*	*-0.3175*	*-0.3620*	*-0.3755*	*-0.4472*	*-0.6608*
Windward	*-0.4824*	*0.4223*	*0.2030*	*-0.0985*	*-0.6995*	*-0.5503*	*-0.4483*	*-0.3310*	*-0.2922*
Right side wall	*-0.6608*	*0.0332*	*0.3305*	*0.4887*	*0.5285*	*0.3250*	*0.2432*	*-0.0576*	*-0.5984*
Leeward	*-0.2923*	*-0.3626*	*-0.4126*	*-0.4637*	*-0.6539*	*-0.2202*	*0.4274*	*0.5851*	*0.4824*
Roof	*-0.5944*	*-0.6685*	*-0.6633*	*-0.6526*	*-0.6156*	*-0.6664*	*-0.6296*	*-0.6091*	*-0.5944*
Arrangement 1 (Model with obstacle next to it, V =3.53 m/s, G = 2.0H)									
Left side wall	*-0.7414*	*-1.0122*	*-1.0318*	*-0.7998*	*-0.8596*	*-0.7650*	*-0.9124*	*-0.9815*	*-1.1485*
Windward	*-0.3836*	*0.0773*	*-0.2035*	*-0.5191*	*-1.5691*	*-0.9588*	*-1.1092*	*-0.8789*	*-0.6477*
Right side wall	*-0.6094*	*-0.0940*	*0.0952*	*0.1861*	*0.1946*	*0.2097*	*0.0499*	*-0.2922*	*-1.1799*
Leeward	*-0.3802*	*-0.7341*	*-0.7935*	*-0.7925*	*-1.4219*	*-0.2726*	*0.1288*	*0.2944*	*0.3368*
Roof	*-0.6635*	*-1.1006*	*-1.1772*	*-1.1194*	*-1.4339*	*-1.1682*	*-1.2474*	*-1.3709*	*-1.3000*
Arrangement 1 (Model with obstacle next to it, V = 5.72 m/s, G = 2.0H)									
Left side wall	*-0.7041*	*-0.8453*	*-0.8269*	*-0.8029*	*-0.6270*	*-0.6368*	*-0.6302*	*-0.7230*	*-0.8929*
Windward	*-0.3103*	*0.1077*	*-0.0203*	*-0.2187*	*-0.9296*	*-0.9299*	*-0.9459*	*-0.8359*	*-0.5106*
Right side wall	*-0.8139*	*-0.3086*	*0.0730*	*0.1170*	*0.1924*	*0.2040*	*0.1223*	*-0.0280*	*-0.8156*
Leeward	*-0.3567*	*-0.5401*	*-0.6177*	*-0.6576*	*-1.0084*	*-0.5915*	*0.0118*	*0.1380*	*0.2786*
Roof	*-0.6045*	*-0.8740*	*-0.9671*	*-1.0110*	*-1.1307*	*-1.0721*	*-1.0291*	*-1.0034*	*-0.9964*

Table 1. Mean EPC values

The ratio of the EPC of each arrangement and the isolated model is known as the Interference Factor (F_I), which represents the reduction or increase in pressures and suctions that are acting on the faces of the reference model as a result of the obstacle. This is:

$$F_I = \frac{EPC_{AO}}{EPC_I} \tag{4}$$

where:

EPC_{AO} = External pressure coefficient in isolated model with obstacle.
EPC_I = External pressure coefficient in model.

Ec. (4) was used to determine F_I values for each of the arrays, Table 2 shows the results obtained.

Face	*Wind Incident angle (θ)*								
	0 °	*30 °*	*45 °*	*60°*	*90°*	*120°*	*135°*	*150°*	*180°*
	Arrangement 1a (Model with obstacle next to it, V =3.53 m/s, G = 2.0H)								
Left side wall	*1.2389*	*1.7959*	*1.9654*	*1.9144*	*2.7074*	*2.1133*	*2.4298*	*2.1948*	*1.7380*
Windward	*0.7952*	*0.1831*	*-1.0026*	*3.2392*	*2.2432*	*1.7423*	*2.4743*	*2.6553*	*2.2165*
Right side wall	*0.9221*	*-2.8313*	*0.2879*	*0.3808*	*0.3683*	*0.6452*	*0.2050*	*0.5073*	*1.9717*
Leeward	*1.3006*	*2.0245*	*1.9233*	*1.7091*	*2.1745*	*1.2380*	*0.3014*	*0.5032*	*0.6981*
Roof	*1.1162*	*1.6464*	*1.7748*	*1.7153*	*2.3293*	*1.7531*	*1.9813*	*2.2507*	*2.1871*
	Arrangement 1b (Model with obstacle next to it, V = 5.72 m/s, G = 2.0H)								
Left side wall	*1.1767*	*1.4999*	*1.5751*	*1.9218*	*1.9749*	*1.7590*	*1.6782*	*1.6167*	*1.3512*
Windward	*0.6433*	*0.2551*	*-0.9992*	*2.2208*	*1.3290*	*1.6898*	*2.1100*	*2.5254*	*1.7475*
Right side wall	*1.2317*	*-2.4356*	*0.2209*	*0.2393*	*0.3641*	*0.6277*	*0.5031*	*0.4855*	*1.3629*
Leeward	*1.2203*	*1.4896*	*1.4970*	*1.4182*	*1.5421*	*2.6863*	*0.2752*	*0.2359*	*0.5775*
Roof	*1.0170*	*1.3075*	*1.4581*	*1.5492*	*1.8367*	*1.6088*	*1.6345*	*1.6474*	*1.6762*

Table 2. Interference Factor

Figure 5 and 6 show the F_I values for arrangement *1* with a gap of *2.0H* between the acrylic model and the wooden obstacle.

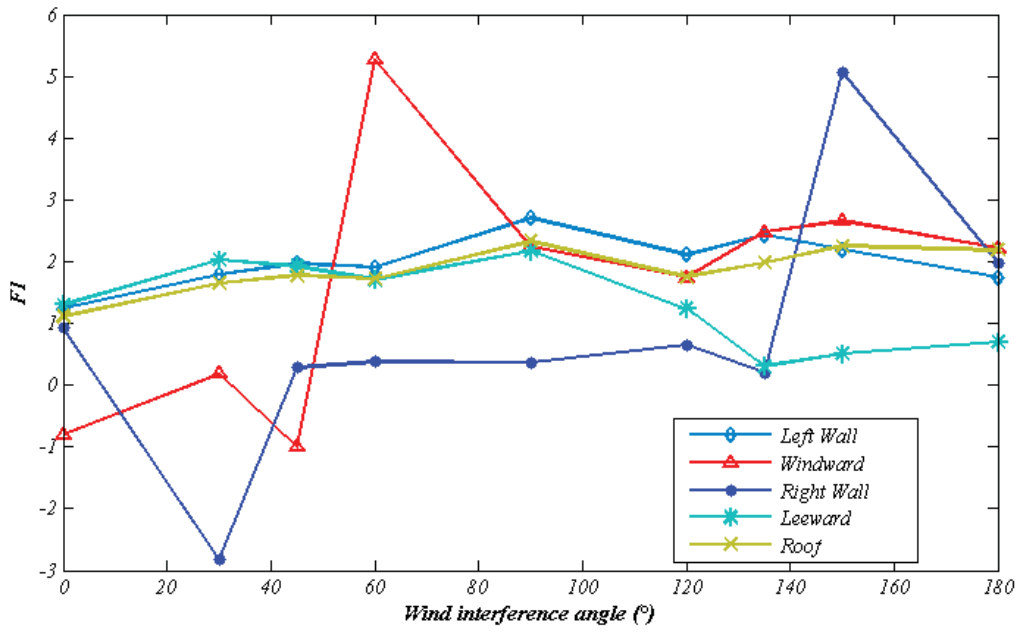

Figure 4. Variation of FI with wind direction for different faces of the reference model. Arrangement 1, V = 3.53 m/s and G = 2.0H

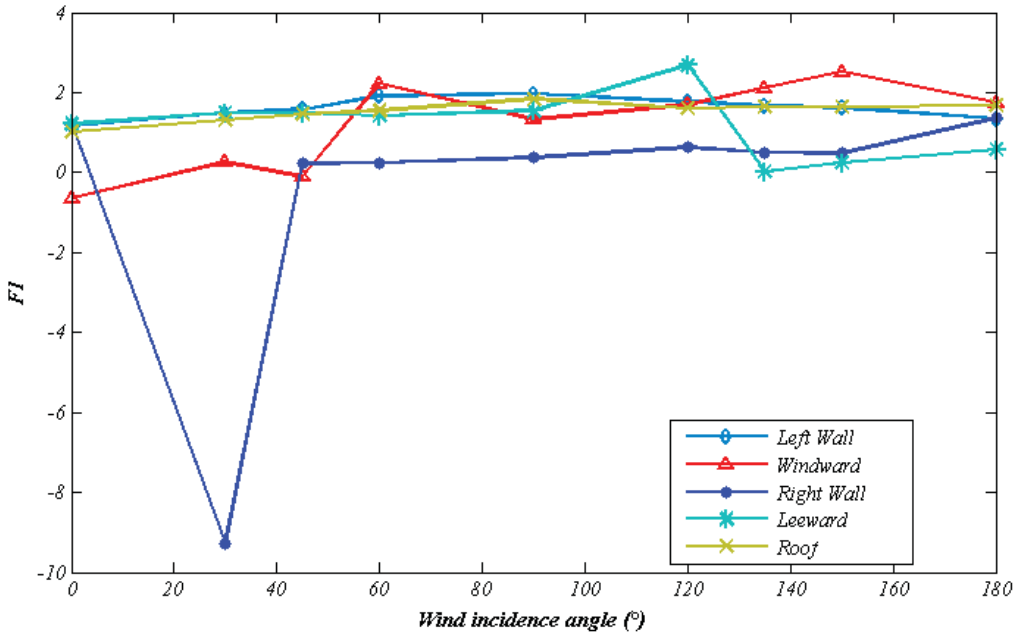

Figure 5. Variation of FI with wind direction on different faces of the reference model. Arrangement 1, V = 5.72 m/s and G = 2.0H

It can be observed from Figures 5 and 6 that F_I varies about 1. If the F_I value is above 1, the pressures or suctions observed in the isolated model are increased, in some cases by more than 100%, in the presence of the obstacles of each arrangement. On the other hand, if the F_I value is below 0, the pressures on the reference model have changed sign and became suctions, or vice versa.

For F_I values between the range of 0 and 1, the pressures or suctions decrease, since the zones are protected by the presence of the obstacle, this is known as the "Shielding Effect".

Figures 7 to 10 present the variation of F_I for other values of wind speed and separation.

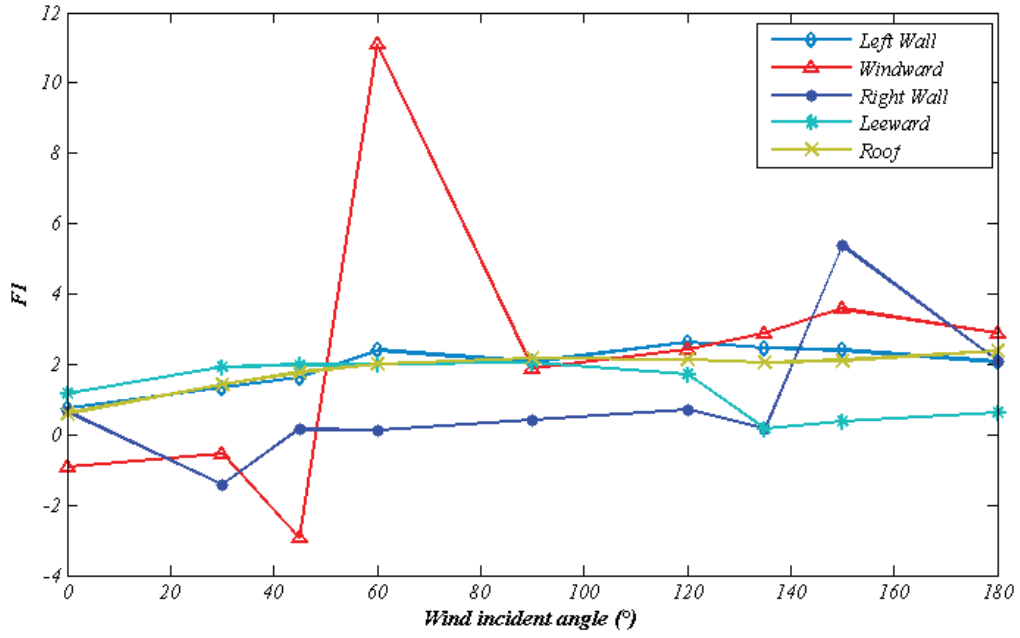

Figure 6. Variation of F_I with wind direction on different faces of the reference model. Arrangement 1, V = 3.53 m/s and G = 0.5H

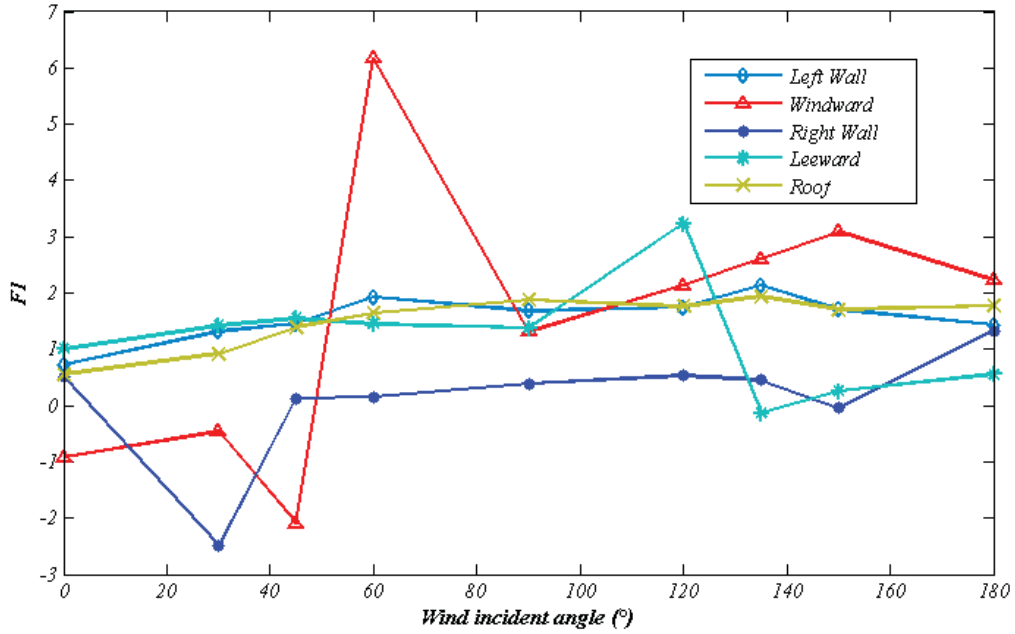

Figure 7. Variation of FI with wind direction on different faces of the reference model. Arrangement 1, V = 5.72 m/s and G = 0.5H

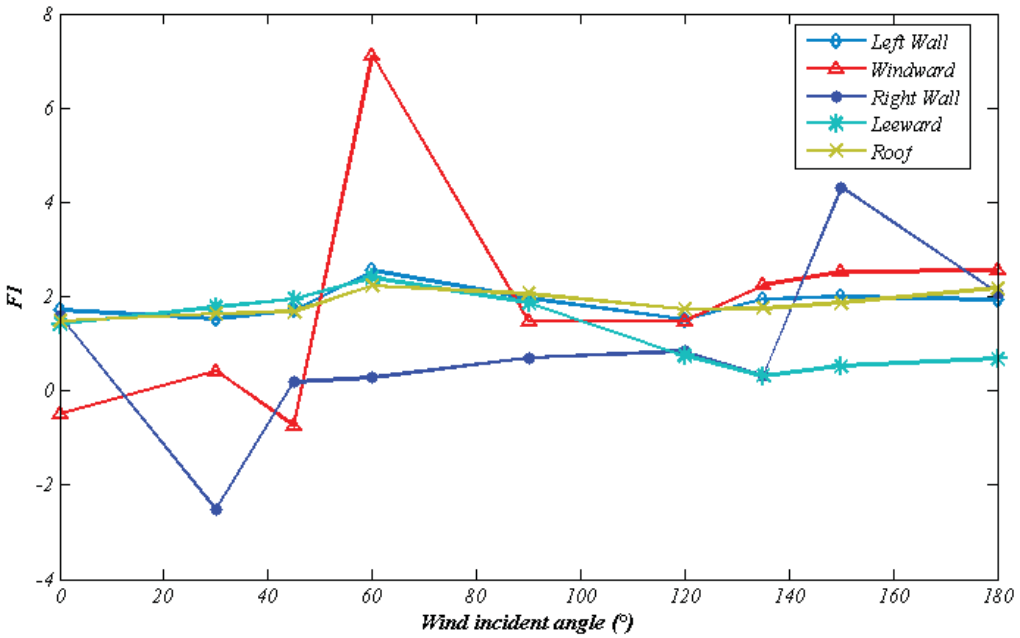

Figure 8. Variation of F_I with wind direction on different faces of the reference model. Arrangement 1, V = 3.53 m/s and G = 3.5H

In all cases, the Left wall and Roof face showed F_I values from 0 to 2. The same applies to the leeward face between the angles of 0° to 110°, then there is a transition at 120°, because at this angle, this face is the one that receives the flow of the wind in a direct way. When V = 3.53 m/s, the F_I at this angle decrease and then is equal almost to zero, while at the speed of V = 5.72 m/s, there is an increase of F_I to 2.5 on average and then descend to values almost to zero.

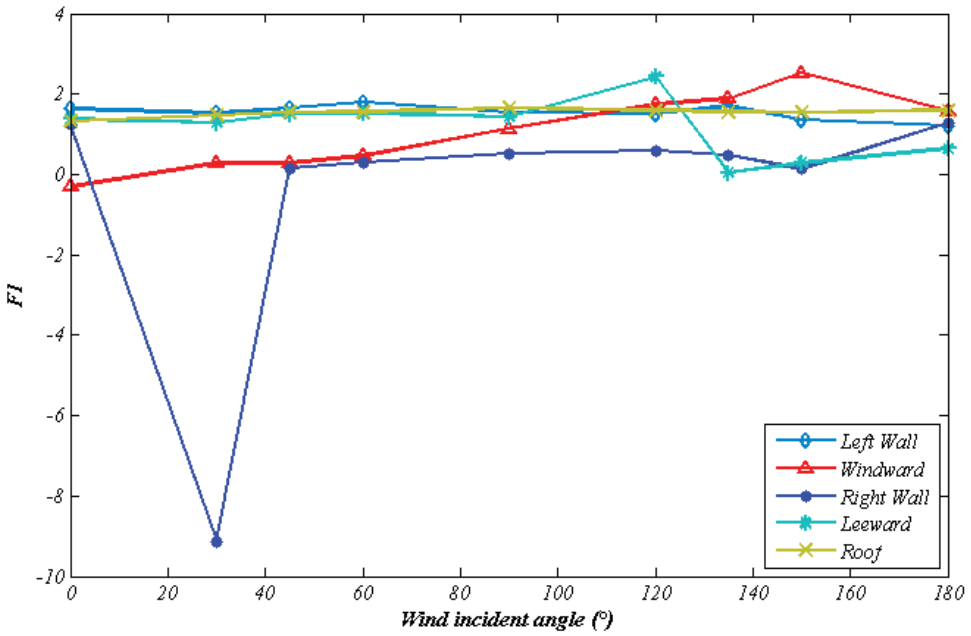

Figure 9. Variation of F_I with wind direction on different faces of the reference model Arrangement 1, V = 5.72 m/s and G = 3.5H

In the case of windward, no great variation between the values of Arrangement 1 for separations of 2.0H and 3.5H are observed (Figures 5 and 9), but by decreasing the gap to 0.5H there is a double F_I increase for the wind direction of 60° (Figure 7). This is probably cause by the combination of Venturi effect and vortex shedding due to the near edge of the obstacle.

Finally, for the right wall there is a considerable increase in the negative values of F_I at the wind incidence of 30° for separations of 2.0H and 3.5H (Figures 6 and 10) for wind speed equal to 5.72 m/s, while for a wind speed of 3.53 m/s the F_I values are almost identical to the other arrangements. Further, for low speeds, the F_I value is increased at 150°wind incidence (Figures 5, 7 and 9).

The shielding effect can be observed on the right wall from 45° to 135° and in the leeward wall about 135° to 180°. This is due to the deviation of the wind flow on the leeward face and the right wall face, reducing the effects of wind pressures.

5 CONCLUSIONS

- The presence of obstacles next to studied structure is an important consideration for wind design.
- The experimental results show that the wind effects caused by obstacles on the neighborhood modify the *EPC*.
- The main mechanisms that cause this variation are the vortex shedding, the reduction of the wind flow area (Venturi effect) and the vertical flow caused by obstacles located in the leeward area.
- The variation of the wind speed affects the interference factors.
- The gap between the reference model and the adjacent obstacle is an important parameter for generating the phenomena described in this work; variation of this measure will be considered for future testing.

ACKNOWLEDGEMENTS

We thank the Instituto de Ingeniería de la UNAM and the Consejo Nacional de Ciencia y Tecnología (CONACyT) for the financial support. This work was partly supported by UNAM-PAPIIT IN101318.

REFERENCES

[1] Zhang, X., Tse, K., Weerasuriya, A. U., Li, S. W., Kwok, K. C. S., Mak, C. M., Niu, J. y Lin, Z. Evaluation of pedestrian wind comfort near 'lift-up' buildings with different aspect ratios and central core modifications. *Building and Environment,* Vol 124, pp. 245-257. 2017.

[2] Kang, G., Kim, J. J., Kim, D. J., Choi, W., y Park S.J. Development of a computational fluid dynamics model with tree drag parameterizations: Application to pedestrian wind comfort in an urban area. *Building and Environment*, Vol 124, pp. 209-218. 2017.

[3] Gomez-Martínez, R., Pozos-Estrada, A., Sánchez-García, R. y Escobar, J.A. Contemporary wind engineering in Mexico, *Proceedings of INTED2011 Conference*, 7-9 march, Valencia, Spain. 2011.

[4] ASCE. Wind Tunnel Studies of Buildings and Structures, *ASCE Manuals and Reports on Engineering Practice No. 67*, USA. 1999.

[5] Counihan, J. Adiabatic Atmospheric Boundary Layer: A review and analysis of data from the period 1880-1972. *Atmospheric Enviroment,* Vol 9, pp. 871-905. 1975.

[6] Balendra, T., Shah, D.A., Tey, K.L., y Kong, S.K. Evaluation of flow characteristics in the NUS-HDB Wind Tunnel, *Journal of Wind Engineering and Industrial Aerodynaics*, vol. 90, pp. 675–688, Singapore. 2002.

[7] Endo, M., Bienkiewicz, B., y Ham, H.J. Wind-tunnel investigation of point pressure on TTU test building, *Journal of Wind Engineering and Industrial Aerodynamics*, Vol. 94, pp. 553-578. 2006.

[8] Amaya-Gallardo, E., Pozos-Estrada, A., y Gomez, R. Comparison of pressure coefficients of two cubic low-rise buildings tested in a boundary layer wind tunnel, *6th Structural Engineers World Congress*, 14-17 November, Cancun, Mexico. 2017.

[9] Amaya-Gallardo, E., Pozos-Estrada, A., y Gómez, R. Estudio del comportamiento del viento en naves industriales con mecánica de fluidos computacional, *XIX Congreso Nacional de Ingeniería Estructural*, 12-15 noviembre, Puerto Vallarta, Jalisco, México. 2014.

[10] Amaya-Gallardo, E., Pozos-Estrada, A., y Gómez, R. Simulación experimental y numérica para la obtención de coeficientes de presión sobre un cubo: estudio comparativo, *XX Congreso Nacional de Ingeniería Estructural*, 16-19 noviembre, Mérida, Yucatán, México. 2016.

[11] Richards, P. J., Hoxey, R. P., y Short, L.J. Wind pressures on a 6m cube, *Journal of Wind Engineering and Industrial Aerodynamics*, vol. 89, pp. 1553–1564, New Zealand. 2001.

[12] Richards, P. J., Hoxey, R. P., Connell, B. D., y Lander, D. P. Wind-tunnel modelling of the Silsoe Cube. *Journal of Wind Engineering and Industrial Aerodynamics*, vol 95(9-11), pp. 1384-1399. 2007.

EURODYN 2020
XI International Conference on Structural Dynamics
M. Papadrakakis, M. Fragiadakis, C. Papadimitriou (eds.)
Athens, Greece, 23–26 November 2020

FLEXURAL PERFORMANCE OF DOUBLE HOOKED END STEEL FIBRE REINFORCED CONCRETE BEAMS UNDER CYCLIC LOADING

Demewoz W. Menna[1], **Aikaterini S. Genikomsou**[1], **and Mark F. Green**[1]

[1]Department of Civil Engineering, Queen's University
58 University Avenue, Kingston, Ontario, K7L 3N6, CANADA
e-mail: 18dwm@queensu.ca, aikaterini.genikomsou@queensu.ca, greenm@queensu.ca

Keywords: Steel Fibre Reinforced Concrete, Cyclic loading, Energy dissipation

Abstract. *Steel fibre reinforced concrete (SFRC) is examined experimentally under cyclic loading. The effect of volumetric ratio and type of fibres on the mechanical properties and flexural strength of the SFRC beams are accessed. Multiple prismatic concrete specimens with two different types of steel fibres are fabricated and tested, under four-point bending according to ASTM C1609. Compressive and tensile strength characteristics using cylindrical specimens are determined. The two fibres have similar length to diameter ratio but different size. Two volumetric ratios (0.5% and 1%) are analyzed for each type of fibre. By increasing the volumetric ratio of the fibres, significantly are increased both the tensile and the compressive strengths. Higher post crack peak load and greater cumulative energy dissipation under cyclic loading are attained by increasing the steel fibre content. By adding 1% the volume of concrete, up to 93% the ultimate flexural strength under cyclic loading is enhanced. Although the two fibres have similar aspect ratios, steel fibre type B (larger size) shows higher flexural strength and energy dissipation than steel fibre type A (smaller size).*

1 INTRODUCTION

It is desirable that all existing and new reinforced concrete constructions remain safe and in service or be easily returned to service after a catastrophic event, so as to minimize the socio-economic impact on society. To minimize and/or avoid structural failures a promising approach is to use concrete with better mechanical properties. Among the various mechanical performance improvement techniques for concrete, the steel fibre reinforced concrete developed in the last 20 years, distinguished by its exclusive mechanical properties and durability performance. Steel fibres improve the tensile strength, energy absorption capacity, flexural strength, ductility and flexural toughness of concrete [1]. The fibres either resist the internal stress or transfer to a stable matrix in concrete and limit growth and propagation of cracks. The mechanical properties of steel fibre reinforced concrete (SFRC) are affected by fibre volume fraction, geometry, distribution and the bond strength between fibre and matrix [2, 3].

The volumetric ratio of steel fibres is a key parameter that affects the post-crack flexural performance of SFRC. Previous research [3] investigated the effect of single hooked-end steel fibres content and strain rate in both regular and high strength concretes. The research outcomes indicated that for both regular and high strength concrete, the flexural strength and corresponding deflection increased with the volume fraction of fibres (V_f). Steel fibres with V_f equal to 1.0% and 2.0% in regular concrete increased the ultimate flexural resistance by 13% and 63%, respectively. Likewise, the deflection at the ultimate flexural load significantly improved by the increase in the volume of fibres leading to more ductile failure. However, the 28^{th} day compressive strength and modulus of elasticity of regular concrete are slightly affected by the addition of fibres. The average increase in compressive strength due to the addition of fibres up to 1.5% by volumetric ratio is found to be less than 10% [4].

Previous studies have proved that the aspect ratio (length to diameter ratio, l/d) of fibres has a significant impact on the mechanical properties of SFRC. The common aspect ratios of steel fibres vary between 50 to 100 [5]. The flexural and split tensile strengths of steel fibre reinforced concrete increase with an increase in aspect ratio. This increase in mechanical properties attributes to the improvement of heterogeneous distribution and flocculation of fibres with the increase in aspect ratio [5]. However, fibres could have similar aspect ratio with different length and diameter. The effect of variation in length and diameter without changing the aspect ratio of the fibres on the property of SFRC needs further investigation.

The interfacial bond between fibre and matrix plays a significant role in the capacity of fibres to transfer applied stresses in cracked concrete. Mechanical anchorage is one of the main methods used to improve the bond between matrix and steel fibres. Among the different types of steel fibres, end hook fibres are commonly used due to their advantage to gradually straighten prior to significant slippage [6]. Abdallah and Fan [7] studied the anchorage mechanics of single and double end hooked fibres by conducting pullout tests. The double hooked end fibres showed 50% and 25% higher maximum pullout load and total pullout work, respectively compared to the corresponding single hooked end fibres within normal strength concrete. As a result, these recently developed end hooked fibres are recommended for improved mechanical properties for regular and high strength concrete.

Although the flexural performance of SFRC under monotonic loading has been studied by various researchers, very limited data are found under cyclic loading. Recent developments on high-performance steel fibres also require the evaluation of flexural strength under cyclic loading. This paper presents experimental results on the flexural behaviour of double end hooked steel fibre reinforced concrete under cyclic loading. The effects of volumetric ratio of two double hooked end fibres with similar aspect ratios on the compressive strength, tensile strength and cyclic flexural resistance are investigated. The findings of this study provide a

better understanding of the energy dissipation characteristics under repeated loading and a wider application of the double end hooked fibres, which have been recently provided to the market.

2 EXPERMENTAL PROGRAM

Five different concrete batches are prepared: one control mix without steel fibres and four SFRC with different fibre type and volumetric ratio. The concrete mix design was prepared based on Kosmatka et al. [8] and the mixture composition is presented in Table 1. General use Portland-Limestone (GUL) type cement that meets the standards of the Canadian Standards Association (CSA) A3001 and ASTM C595 and water to cement ratio equal to 0.5 were used. Natural coarse aggregates with a maximum size of 9.5 mm and natural sand fine aggregate were used.

Mixture	Steel fibre		Batch weight (kg/m^3)					SP	Slump
	Type	V_f(%)	Cement	Water	Gravel	Sand	Fibre	(ml)	(mm)
CS	-	-	456	228	768	891.3	-	-	120
FRCA0.5	A	0.50	456	228	764	882.1	39.0	23	130
FRCA1	A	1.00	456	228	760	873.0	78.0	28	125
FRCB0.5	B	0.50	456	228	764	882.1	39.0	23	130
FRCB1	B	1.00	456	228	760	873.0	78.0	28	125

Table 1: Concrete mixture proportion and slump test results.

Figure 1 presents the type and dimensions of the steel fibres. Two types of double hooked end steel fibres with lengths of 35 mm (type A) and 60 mm (type B) were used. Tensile strengths of 1850 MPa and 1600 MPa were reported by the manufacturing company for fibre type A and type B, respectively. Both types of fibres have similar aspect ratio equal to 65. Fiber volume fractions (V_f) of 0% (control specimen), 0.5% and 1.0 % by volume of concrete were investigated. The equivalent amount of fibre were 0, 39.0, and 78.0 kg/m^3 of concrete, respectively. Super plasticizer (SP) was added to improve the workability of the fibre reinforced concrete.

Type A Type B

Figure 1: Types of Steel fibres (type A and type B).

Three prisms with dimensions of 76 x 76 x 292 mm for the flexural test and nine 100 mm x 200 mm cylindrical specimens for both tensile and compressive strength tests were casted for each mixture group. Thus, in total 15 prisms were tested in flexure, 15 cylinders were tested in compression (28 days), 15 cylinders were tested in compression (90 days) and 15 cylinders were tested in tension (28 days). The prisms were tested at the age of 90 days.

2.1 Cyclic flexural test setup

The SFRC prisms were tested under four-point bending according to ASTM C1609 [9] and the test setup is shown in Figure 2(a). A 250 kN testing frame (INSTRON 8802) was used for the flexural tests. Displacement controlled loading with a constant rate of 0.6 mm/min for both loading and unloading was used. The loading protocol contains nine cycles starting at 0.25 mm with an incremental increase of 0.5 mm in each cycle up to 4.25 mm, as shown in Figure 2(b). After completing all 9 cycles, the loading continued until the net deflection hits 6 mm, to determine the residual strength. The prisms were supported by two roller bearings one free to move and the other pinned. An aluminum frame connected to the prism was used to support the bar holding the linear potentiometer (LP) and the net deflection of the prisms was measured relative to the midspan of the specimen.

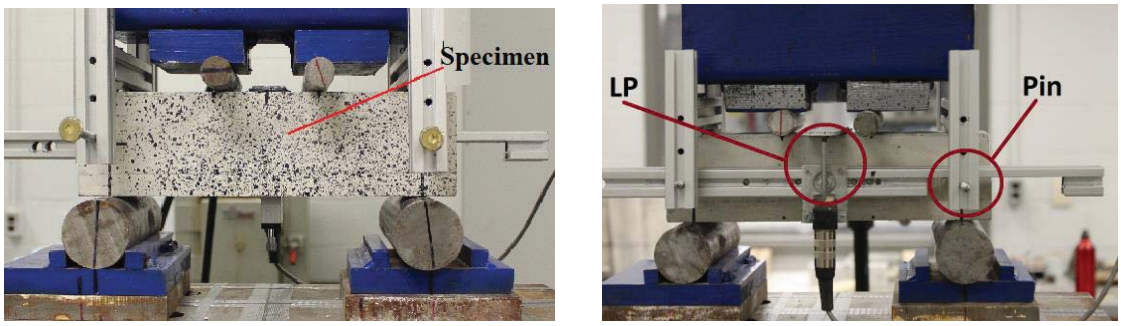

(a)

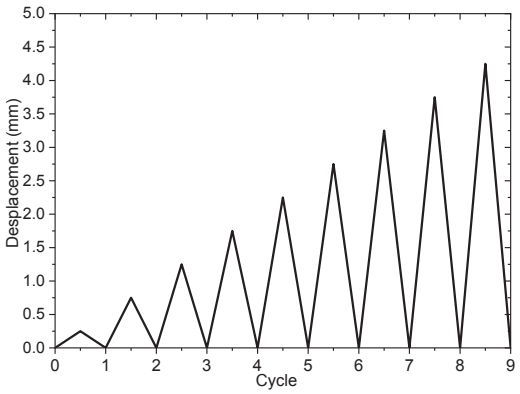

(b)

Figure 2: Cyclic flexural test: (a) setup and (b) loading protocol.

3 RESULTS AND DISSCUSSION

3.1 Compressive and tensile strengths of SFRC

Table 2 summarizes the compressive and tensile strength results (mean values), where SD represents the standard deviation of the strengths between the specimens of similar mixture composition. Due to the addition of superplasticizer (SP), the SFRC specimens gained strength slower than the corresponding control specimens without SP. Superplasticizers will retard the hydration process when the adsorption of the superplasticizer is greater than hydrated cement [10]. Cement pastes containing superplasticizers are reported to have a slower rate in decreasing porosity over time due to lower hydration rate [11]. As a result, at the 28th day age, most of the fibre reinforced concrete cylinders had slightly lower compressive strength compared to the corresponding control specimens (without fibres). These results coincide

with the experimental findings [12]. However, at the 90th day age, the SFRC had up to 19% higher compressive strength than the control specimen. This increase in compressive strength attributes to the improvement of anchorage between the matrix and fibre as the matrix strength increases with the hydration process.

Mixture	28th day compression		90th day compression		28th day tension	
	$f_c(MPa)$	SD (MPa)	$f_c(MPa)$	SD (MPa)	$f_t(MPa)$	SD (MPa)
CS	38.93	0.43	39.50	0.54	4.32	0.43
FRCA0.5	34.36	1.67	46.14	1.80	5.86	0.06
FRCA1	32.74	3.41	47.14	3.43	6.70	0.09
FRCB0.5	35.65	3.71	47.70	1.99	5.54	0.06
FRCB1	43.03	1.76	44.46	3.15	8.07	0.45

Table 2: Compressive and tensile strength test results.

Figure 3 presents typical compressive stress-strain plots. The steel fibres increase the strain corresponding to the peak compressive stress and this strain increased with the percentage ratio of steel fibre; similar trends have been reported by other researchers [13, 14]. After the peak stress, the SFRC underwent a more ductile failure with extended softening behaviour. The ductility was directly proportional to the fibre content. Regarding the failure mode, multiple cracks were observed on the cylinders with a higher volume of fibres. This was mainly due to the contribution of fibres to produce more ductile failure by bridging cracks. The tensile strength of the SFRC increased as the fibre content increased. As presented in Table 2, by increasing the fibre content from 0.5% to 1.0% by volume of concrete resulted in 35.6% to 55% increase in tensile strength for steel fibre type A and 28.5% to 86.8% for steel fibre type B. The highest tensile strength is recorded for SFRC with 1.0% fibre type B (FRCB1) with a value equal to 8.07 MPa.

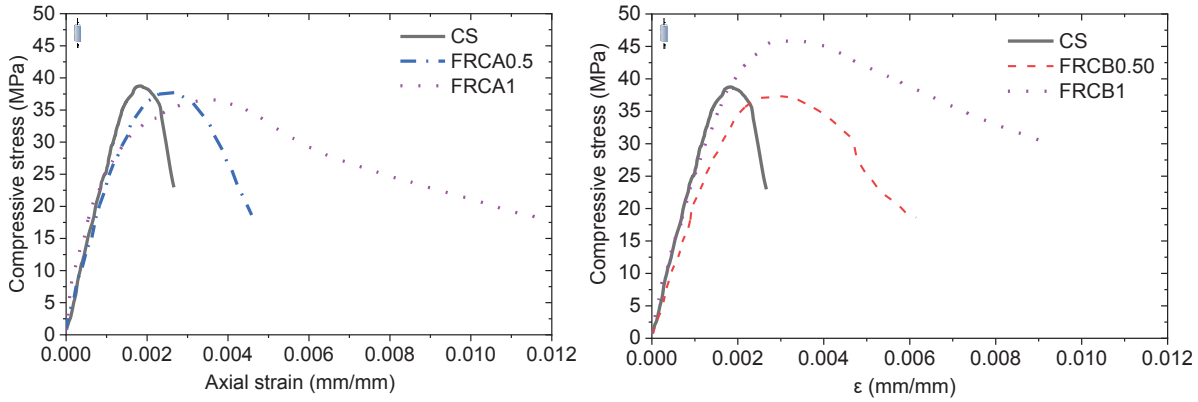

Figure 3: Typical stress-strain response of SFRC cylinders under compression at 28 days age.

3.2 Flexural response under cyclic loading

Typical hysteresis response of the tested specimens under cyclic loading is shown in Figure 4. The fibres became effective following the crack formation and enabled the SFRC to be ductile (Figure 4(a) and Figure 4(b)), while the plain control specimen suddenly failed at a very small deflection (0.123 mm) (Figure 4(c)). At the initial cycles, the SFRC prisms were in the elastic range and the area under the hysteresis was smaller. During the subsequent cycles,

the specimens entered to an elastic-plastic region and the area under the hysteresis increased with the formation of multiple cracks. Then, the material damage started to be progressed and the residual deformation during the unloading appeared. The slope of loading and unloading path decreased with the increased number of cycles, due to the stiffness degradation caused from the material damage [12]. The ultimate flexural strength (f_u, MPa) can be determined using equation 1. In equation 1, P_u denotes the peak load (in N) and L, b, and d denote clear span, width, and depth of the prism in mm.

$$f_u = \frac{P_u L}{bd^2} \tag{1}$$

For both type A and type B fibres, the ultimate flexural strength of SFRC increased with the increase in fibre volumetric ratio. The average ultimate flexural strength versus fibre percentage is shown in Figure 4(d). For the fibre volumetric ratio 0.5% by volume of concrete, the two different fibres show similar response, the ultimate flexural strength is around 11% higher than the control specimen (plain concrete). Although the two fibres have similar aspect ratio, at the 1.0% fibre percentage, the steel fibre type B (longer and thicker fibre) showed superior ultimate flexural strength than the steel fibre type A (shorter and thinner fibre). The recorded ultimate flexural strength at 1.0% fibre volumetric ratio for fibre type A and type B are 41% and 93% higher than the control specimen, respectively.

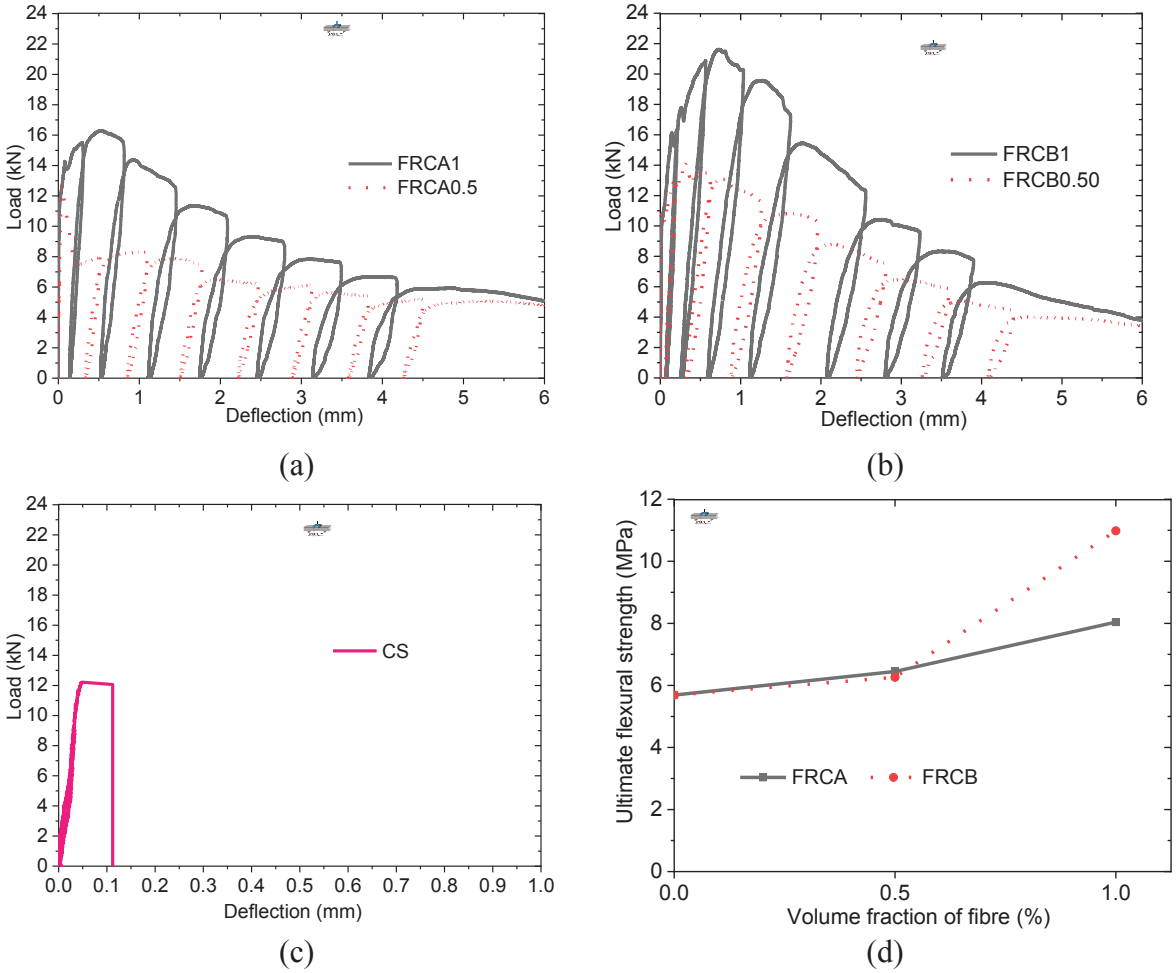

Figure 4: Cyclic flexural test results: (a,b,c) strength versus deflection curves, (d) ultimate flexural strength versus fibre volume fraction.

3.2.1 Energy dissipation

The area under the hysteresis of the load-deflection curve represents the energy dissipated during the loading and unloading cycle [12]. Energy dissipation capacity is essential for structural performance under cyclic loading (e.g., during earthquakes). Structures can survive seismic loads only if they can dissipate the energy exerted by the earthquake [15]. The cumulative energy dissipation versus displacement is plotted in Figure 5. The cumulative energy dissipated by the specimens is calculated by summing up the area under the load-deflection curve before reaching the specified displacement. For both steel fibre types, the cumulative dissipated energy considerably increased with the increase in fibre content. The total energy dissipation at 4.0 mm is 28.66 kNmm and 47.01 kNmm for FRCA0.5 and FRCA1, respectively. Fibre type B showed significantly higher energy dissipation characteristics than fibre type A. The energy dissipation at 1% steel fibre type B (FRCB1) at 4 mm displacement is 34% higher than the fibre type A (FRCA1). This higher energy dissipation characteristic of fibre type B might be due to its better distribution and higher mechanical anchorage from its longer end hook.

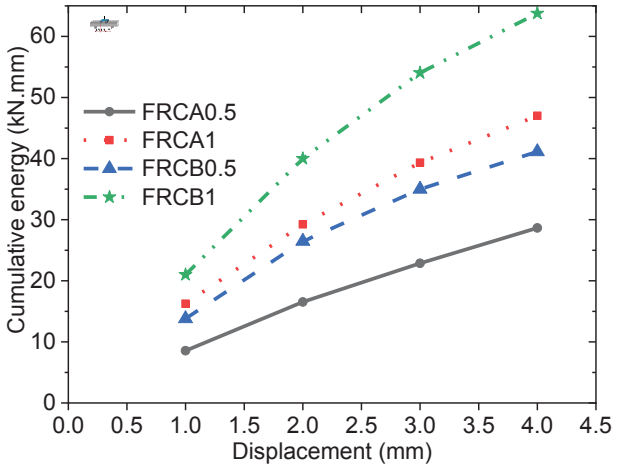

Figure 5: Cumulative energy dissipation of specimens.

4 CONCLUSIONS

The flexural performance of double hooked end steel fibre reinforced concrete prisms tested under cyclic loading was experimentally studied. The following conclusions can be made:

- The steel fibre reinforced concrete (SFRC) specimens showed increased tensile strength, ductility and compressive strength at the 90th day age while slightly reduced compressive strength at the 28th day, when compared to the plain concrete specimens.
- The double hooked end steel fibres enhanced the ductility and ultimate flexural strength of the specimens. The improvement in the flexural strength increased with the increase in the volume fraction of steel fibres. The ultimate flexural strengths of FRCA1 and FRCB1 are 41% and 93% higher than the control plain concrete specimens.
- The cumulative energy dissipation under cyclic loading significantly increased with the increase in fibre content for both steel types.
- Although the two fibres had similar aspect ratios to each other, steel fibre type B (longer and thicker) showed superior flexural strength and energy dissipation characteristics than steel fibre type A (shorter and thinner) showed.

REFERENCES

[1] Y. Mohammadi, S. Singh, S. Kaushik, Properties of steel fibrous concrete containing mixed fibres in fresh and hardened state, *Construction and Building Materials*, 22, no. 5, 956-965, 2008.

[2] T. J. M. Uygunoğlu, Investigation of microstructure and flexural behaviour of steel-fiber reinforced concrete, *Materials and Structures*, 41, 8, 1441-1449, 2008.

[3] D.-Y. Yoo, Y.-S. Yoon, N. J. C. Banthia, Flexural response of steel-fiber-reinforced concrete beams: Effects of strength, fiber content, and strain-rate, *Cement and Concrete Composites*, 64, 84-92, 2015.

[4] J. Thomas and A. Ramaswamy, Mechanical properties of steel fiber-reinforced concrete, Journal of materials in civil engineering, 19, no. 5, pp. 385-392, 2007.

[5] Ş. Yazıcı, G. İnan, and V. Tabak, Effect of aspect ratio and volume fraction of steel fiber on the mechanical properties of SFRC, *Construction and Building Materials*, 21, no. 6, 1250-1253, 2007.

[6] T. S. Ng, S. J. Foster, M. L. Htet, T. N. S. Htut, Mixed mode fracture behaviour of steel fibre reinforced concrete, *Materials and structures*, 47, no. 1-2, 67-76, 2014.

[7] S. Abdallah and M. Fan, Anchorage mechanisms of novel geometrical hooked-end steel fibres, *Materials and Structures*, 50, no. 2, 139, 2017.

[8] S. Kosmatka, B. Kerkhoff, R. McGrath, and R. Hooton, "Design and Control of Concrete Mixtures, eighth Canadian Edition," *Cement Association of Canada, Ottawa, ON, Canada,* 2011.

[9] Standard, Standard test method for flexural performance of fiber-reinforced concrete (using beam with third-point loading), ASTM C1609/C1609M − 19, 2019.

[10] N. Singh, R. Sarvahi, N. Singh, Effect of superplasticizers on the hydration of cement, *Cement and Concrete Research*, 22, no. 5, 725-735, 1992.

[11] P. Gu, P. Xie, J. J. Beaudoin, C. Jolicoeur, Investigation of the retarding effect of superplasticizers on cement hydration by impedance spectroscopy and other methods, *Cement and concrete research*, 24, no. 3, 433-442, 1994.

[12] B. Boulekbache, M. Hamrat, M. Chemrouk, S. Amziane, Flexural behaviour of steel fibre-reinforced concrete under cyclic loading, *Construction and Building Materials*, 126, 253-262, 2016.

[13] F. Bencardino, L. Rizzuti, G. Spadea, R. N. Swamy, Stress-strain behaviour of steel fiber-reinforced concrete in compression, *Journal of Materials in Civil Engineering*, 20, no. 3, 255-263, 2008.

[14] M. Nataraja, N. Dhang, A. Gupta, Stress–strain curves for steel-fiber reinforced concrete under compression, *Cement and concrete composites*, 21, no. 5-6, 383-390, 1999.

[15] N. Ganesan, P. Indira, M. Sabeena, Behaviour of hybrid fibre reinforced concrete beam–column joints under reverse cyclic loads, *Materials & Design*, 54, 686-693, 2014.

EURODYN 2020
XI International Conference on Structural Dynamics
M. Papadrakakis, M. Fragiadakis, C. Papadimitriou (eds.)
Athens, Greece, 23–26 November 2020

DISCUSSION ON THE CAPACITY DESIGN OF COLUMNS IN LOW-RISE BARE AND INFILLED RC MOMENT FRAMES

Alexios Papasotiriou[1] **and Asimina Athanatopoulou**[2]

[1] Ph.D. candidate, Aristotle University of Thessaloniki
AUTH University Campus 54124 - Greece
e-mail: apapasso@civil.auth.gr

[2] Professor, Aristotle University of Thessaloniki
AUTH University Campus 54124 - Greece
minak@civil.auth.gr

Keywords: Reinforced concrete, Capacity design, Masonry infills.

Abstract. *Column capacity design rule is of crucial importance in modern seismic resistant design of moment-frame structures. However, the implementation of this rule in modern codes is still based on an empirical method of design, which lacks the capacity to account for the actual dynamic response of the structure. The lack of column capacity design to completely protect the columns from yielding has been discussed many times in the literature since the '70s. The current study examines the seismic behavior of a large number of moment-frames, using the non-linear dynamic analyses. In total, 20 basic R/C frame configurations (moment frames with 2, 4, 6 and 8 stories, consisting of columns with various strength) are investigated, along with four different masonry infill setups, each one with 12 different infill types (in total 980 different models), against 60 recorded ground motions, scaled to 10 different seismic intensity levels. The results revealed that 2, 4 and 6 story frames designed according to EC-8 failed regularly to fulfill the objectives of the column capacity design. The deformation demand on the columns was found to be systematically higher for frames with fewer stories, and in some cases, even columns overdesigned by a factor of 2 exhibited a deformation demand beyond the yielding point. Subsequently, statistical analysis was used to identify causal relationships between various structural and dynamic properties of the frames and the magnitude of the ductility demand on the columns. Many of these relationships were quantified, and the relevant investigation allowed deriving semi-empirical formulae, that can effectively predict the ductility demand on the columns according to specific characteristics of the structure. On the basis of these findings a brief discussion on the shortcomings of the current method for column capacity design is made, as well as general suggestions for the improovment of its efficiency and effectiveness.*

1 INTRODUCTION

In earthquake resistant design of Reinforced Concret (RC) moment frames capacity design of columns is applied to transfer the demand for inelastic deformation to the beams and to mitigate the risk of story mechanisms. Simple provisions for the so-called “strong column - weak beam” design rule were already incorporated in ACI 318-71 [1]. However, these provisions did not account for the uncertainties involved in the beam and column response, and no overstrength factor was used. Park and Paulay [2] were the first to introduce a rigorous procedure for the column capacity design. They investigated comprehensively the “column sidesway” and “beam sidesway” mechanisms and demonstrated the need for the introduction of a column overstrength factor as high as 2.0 in order to completely protect the columns from yielding. Subsequent work of Paulay (eg. [3,4,5]) laid the basis for the column capacity design rule which, despite the several alternative proposals made by other researchers in the ensuing decades, still remains in use in the modern seismic design codes (e.g. [6,7,8]) with only minor modifications.

Paulay [4] used the non-liner dynamic analysis on 6, 12 and 18-storey frames to evaluate the proposed capacity design method, and found that they exhibited a quite satisfactory seismic performance. Nonetheless, he noticed that the six-story frame suffered greater damage and some column yielding, and ascribed this to the lower overall overstrength factor ($\omega \cdot \Phi_0$) and the lower fundamental period of the six-story frame. Other researchers, however, also found that the capacity design of the columns does not prevent completely the formation of plastic hinges at the columns. For instance, A. Kappos [9] performed a large number of parametric, non-linear dynamic analyses on 10-storey RC frames, in an attempt to evaluate the many already existing criteria for the capacity design of the columns, as well as to verify the efficiency of a new design method, based on non-linear methods of analysis. He found that in order to completely preclude the yielding of columns at the upper storeys an overstrength factor greater than 2 was required, while values greater than 1,5 were required to preclude the formation of column sidesway mechanisms. In another study, Panagiotakos and Fardis [10] used non-linear dynamic analysis to assess the effect of the EC-8 [6] capacity design rules on the seismic performance of 12 RC frame structures of 3, 4 and 12 storeys. The authors found that capacity design does not preclude the yielding of the columns. More interestingly however, the analysis results demonstrate that the average damage of columns increases for the frames with fewer storeys.

In the present study, investigation on the results from a large number of Non-Linear (N/L) dynamic analyses demonstrated clearly that the demand for inelastic deformation on the columns gets grater for frames with fewer storeys. More specifically, 20 basic R/C frame configurations (moment frames of 2, 4, 6 and 8 storeys) were studied, both bare and infilled with 12 different types of UnReinforce Masonry (URM) infills, against 60 recorded ground motions, scaled to 10 different seismic intensity levels. Many of the examined frame types, including the frames designed according to EC-8, exhibited a deformation demand on the columns of the upper stories beyond the yielding point. Statistical analysis on the results allowed the connection between the demand for inelastic response of the columns and certain characteristics of the frames. As a result, semi-empirical formulae were derived, which predict the demand for inelastic deformation on the basis of particular structural characteristics and the intensity of the seismic action.

2 PROBLEM STATEMENT

The basic idea behind the column capacity design rule is most commonly described on the basis of an idealized model of the beam-column joint, which illustrates the desired over-strength of the columns though the moment equilibrium of the joint (Fig. 1a). In this model, it is implied that both columns can contribute with their full bending capacity in order to overcome the sum of the yielding moments of the beams. However, this model is incomplete, as it does not account for the equilibrium of the forces acting on the joint. After taking into account these forces (Fig. 1b), it becomes apparent that it is impossible for the two columns to provide simultaneously their full moment capacity. This problem was already known to Park and Paulay [2], and the "dynamic amplification factor" (ω) was introduced in the New Zealand code (e.g. NZS-3101 - Appendix D [8]) as a remedy to it. Many modern codes overlook the exact nature of the capacity design of the columns, however, it is thought (e.g. [9]) that an accurate description of the problem is the basis for identifying the numerous sources of uncertainties associated with the capacity design of columns.

In principle, the equilibrium of the beam-column node is completely described by the differential equation of dynamics, however, the non-linear nature of the problem does not allow for an analytical solution. Hence, all the methods currently proposed, involve either the use of an amplification factor (such as the aforementioned dynamic amplification factor), whose value is determined empirically or the use of non-linear methods of analysis for the design of the structures. Nevertheless, the ductility demand on the columns, despite being not predictable analytically, is still determined by the underlying laws of dynamics. So, if a large data set of suitable non-linear dynamic analyses were available, distinctive response patterns should emerge, unveiling the deterministic nature of the problem. The present study exploits this idea, and uses statistical analysis on such a data set, in order to establish a quantitative relationship between the ductility demand on the columns and certain dynamic properties of the structure. Such properties are the equivalent seismic forces of each storey and the corresponding base shear, the capacity of each story to withstand lateral loads, and the "Sway-Potential Index" (SPI) initially introduced by Priestley and Calvi [11].

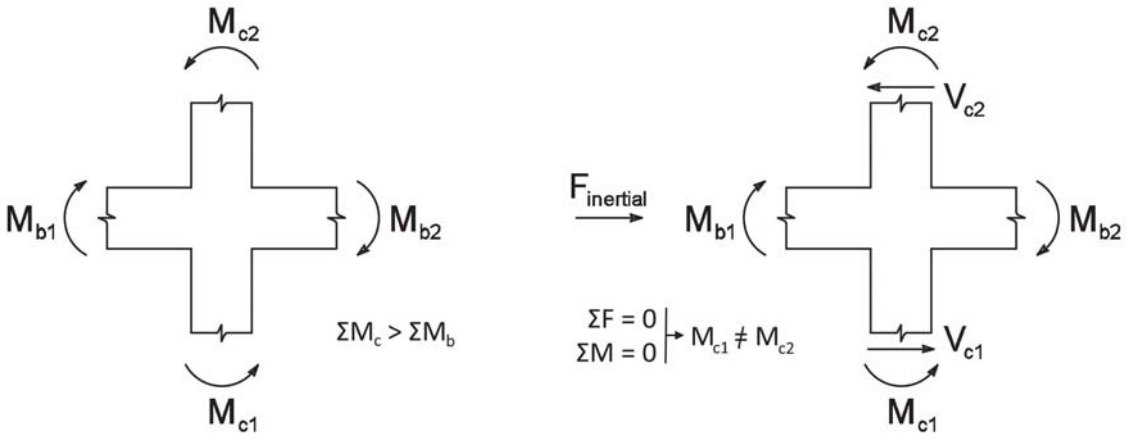

Figure 1: Simplistic (a) and complete (b) model with regard to the column capacity design.

3 INVESTIGATED R/C FRAMES AND N/L ANALYSIS MODELING PARAMETERS

Four groups of frames with a height of two, four, six and eight storeys are investigated. Each group consists of five moment frames with columns of different section size, as follows:

frame type 1: Moment frames designed for a low seismic load, according to the old Greek seismic code.
frame type 2: Moment frames designed according to EC-8[6], without the capacity design of the columns.
frame type 3: Moment frames fully complying with EC-8, with the smallest possible column sections.
frame type 4: Moment frames with overdesigned columns, fully complying with EC-8. The columns in this category have a section depth 50% larger than that of the corresponding columns in category 3.
frame type 5: Moment frames with overdesigned columns, fully complying with EC-8. The column sections in this category have double the depth of the corresponding column sections in category 3.

The seismic load used for designing the frames complies with EC-8[6] and has been calculated in accordance with the greek annex, for soil type "C" and seismic zone II. In all cases, the reinforcing details -and therefore the hysteretic behavior of beams and columns- fulfill the requirements of EC2[12] and EC8. Furthermore, special care was taken not to overdesign the frames of each of the five categories. The design procedure for the frames was based on the linear method of analysis (modal analysis), which was carried out using SAP2000 v19 [13] software. Following the standard practice for tall buildings, the column section size is reduced on the upper floors. However, in these cases, additional models with columns of a constant section across all stories were also investigated, in order to capture the potential effect of the varying column sections to the global response of the structure.

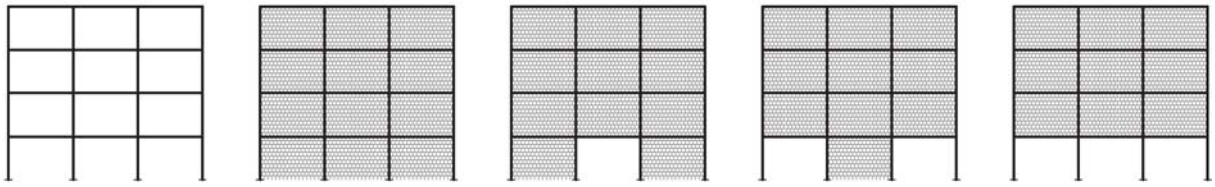

a: Bare frame b: uniform infill c: partial infill d: partial infill e: soft ground storey

Figure 2. Different types of infill arrangement under investigation (eg. four-story frames).

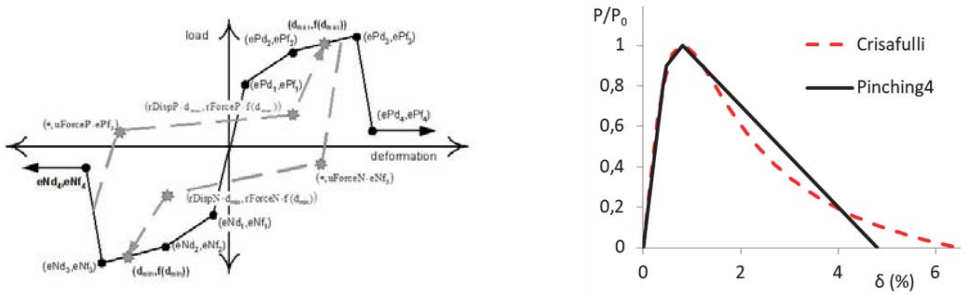

(a) (b)

Figure 3. Idelized masonry backbone curve (a) and loading/unloading curves for material "pinching4" (b)

To simulate the seismic response of both the bare and the infilled frames, non-linear dynamic analysis is employed using Opensees [14]. For each frame, four cases of different infill arrangements are considered, ranging from the uniform infill distribution to the fully open ground story, as depicted in Fig. 2. For each type of infill arrangement, four different levels of masonry panel strength and three levels of infill ductility were considered (Table 1) in order to cover the most common types of URM infills, including infill walls with openings. The mechanical characteristics of the infill panels are specified in terms of interstorey drift and masonry shear force, and they take the predetermined values of Table 1 for all the frame types, regardless of the frame layout. Additionally, the frame members were carefully modeled in order to preclude secondary characteristics -not included in the investigation- from influencing the analysis results.

Infill Type	Strength category	Plasticity category	Characteristic values for the infill panel			
			V_0 (kN)	V_u (kN)	δ_0 (‰)	δ_u (‰)
1	1	1	33.3	0	4.0	12
2	1	2	33.3	0	6.0	27
3	1	3	33.3	0	8.0	48
4	2	1	84.8	0	4.0	12
5	2	2	84.8	0	6.0	27
6	2	3	84.8	0	8.0	48
7	3	1	147	0	4.0	12
8	3	2	147	0	6.0	27
9	3	3	147	0	8.0	48
10	4	1	216	0	4.0	12
11	4	2	216	0	6.0	27
12	4	3	216	0	8.0	48

Table 1: Overview of the characteristics of the 12 infill types.

The frames are modeled using nonlinear force-based beam-column elements with distributed plasticity [15] and fiber sections, to accurately simulate the post-elastic behavior of the structural elements, as well as the interaction between axial force and bending behaviour. In modeling the floor diaphragmatic action special care was taken to not affect the behavior of the beams by constraining their axial deformation (because of the axial-moment interaction). Uniaxial materials “comcrete01” and “steel4” were adopted for modeling the hysteretic behavior of concrete and reinforcing steel respectively. The infill walls were modeled using the equivalent strut method. Each infill panel was modeled as a pair of diagonal compression-only struts, the mechanical characteristics of which are listed in table 1. The “pinching4” hysteretic law (Fig. 3) was used to define the nonlinear behavior of the struts, as it has been shown to be the most accurate model available in Opensees for implementing the equivalent strut method [16].

The non-linear dynamic analyses were performed using a sample of 60 normalized ground motion records obtained from the PEER strong motion database. The records have been appropriately selected to conform to the elastic spectrum for soil type C according to EC8 (so as to correspond to the design spectrum used in frame design, figure 4). To this end, the geometric mean square error (MSE) between the spectral acceleration of each record and the target spectrum in the range 0.15sec ~ 5.0sec was used as the main selection criterion, while various seismic parameters were utilized to additionally confine the selected set. More specifically the following limiting values were adopted: magnitude M5.5 ~ M8.5, epicentric distance Rjb = 10

km ~ 50 km, mean shear wave velocity at the upper 30 m Vs,30 = 240 m/sec ~ 400 m/sec and significant duration d5-95 = 10 sec ~ 30 sec. The values above were chosen to exclude unlikely events, and also as a means for better matching to the target spectrum. The record suite comprises of both far-fault and near-fault events and covers uniformly a rather wide range of earthquake characteristics with regard to the frequency content and to the most common seismic intensity measures. The scaling of the records was based on the minimization of MSE[17]. Finally, each bare or infilled frame was analyzed for ten different earthquake intensity levels covering a range of 5% to 225% of the intensity corresponding to the seismic design load of the frames. These 10 records comprise a coarse Incremental Dynamic Analysis (IDA) [18], which is used for assessing the change in the seismic response of the frames as the seismic intensity increases.

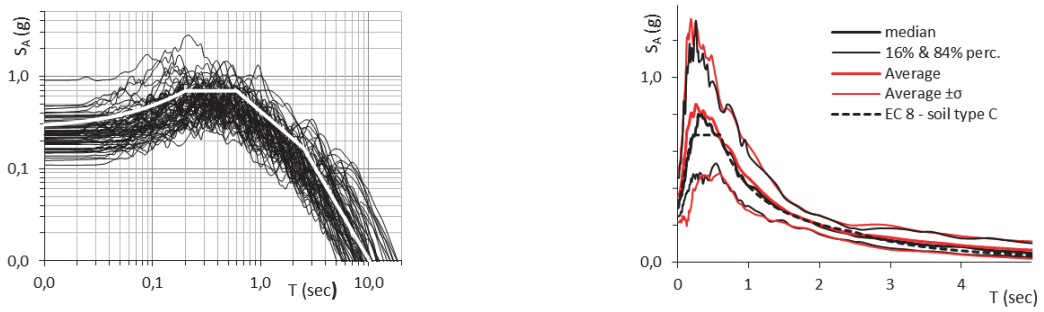

(a) (b)

Figure 4. a: Response spectra (5%) of the un-scalled earthquake records. EC-8 elastic spectrum is superimposed as a white line. b: 16, 50 and 84 percentile spectra of the scaled records.

4 ASSESSMENT OF THE DUCTILITY DEMAND ON THE COLUMNS

The ductility demand on the columns is assessed at the story level, as the average normalized curvature at the top ($\Phi_{av.t}$) and the bottom ($\Phi_{av.b}$) of the storey columns, as follows:

$$\Phi_{av.b} = \sum_{i=1}^{4}\left(\frac{\Phi_{i,b}}{\Phi_{i,y}}\right) \quad , \qquad \Phi_{av.t} = \sum_{i=1}^{4}\left(\frac{\Phi_{i,t}}{\Phi_{i,y}}\right) \tag{1, 2}$$

$\Phi_{i,t}$ and $\Phi_{i,b}$ are the median curvature demand for the 60 time-histories on the top and the bottom section of column i, and $\Phi_{i,y}$ is the yield curvature of the column. The total ductility demand (Φ_{av}) at the story level is subsequently calculated as the average of $\Phi_{av.t}$ and $\Phi_{av.b}$. Φ_i values less than 1 indicate that the bending demand at the respective column section did not surpass the yielding moment of this section in the respective time-history. Accordingly, $\Phi_{av.t}$ and $\Phi_{av.b}$ values less than 1 indicate that on average the maximum bending demand was lower than the bending capacity of the columns' sections (top and bottom section, respectively). $\Phi_{av.t}$ and $\Phi_{av.b}$ are not necessarily concurrent, however statistical analysis on the results of the present study revealed that almost always a story mechanism occurs when both $\Phi_{av.t}$ and $\Phi_{av.b}$ take values larger than 1. Since $\Phi_{av.t}$ is usually lower than $\Phi_{av.b}$, Φ_{av} values slightly larger than 1 do not necessarily imply that both $\Phi_{av.t}$ and $\Phi_{av.b}$ values are larger than 1. However, the difference between $\Phi_{av.t}$ and $\Phi_{av.b}$ is small and of no particular importance, with the only exception of the ground-storey columns.

5 RESULTS AND DISCUSSION

5.1 Bare frames

A large number of structural and dynamic characteristics of the frames were considered as possible factors that determine the ductility demand on the columns. These include the bending capacity of the structural members, the total number of storeys in the frame, the natural period, the seismic intensity etc. In order to estimate the relationship between the ductility demand and these parameters, linear regression analysis was initially employed, without, however, any success. Regression analysis is a powerful statistical method for examining the possible relationship between a set of independent variables and a dependent one, however, it requires to be able to formulate the problem in hand in a polynomial form, and this was found to be impossible in the case of the seismic demand on the columns. Subsequently, an exhaustive examination of the covariance between each independent variable and the ductility demand was performed, and the combination of the most significant of them into formulae that correlate with the response measures was accomplished via trial and error. The following expression is an example of such a formula ($\Phi_{av.i}$ is the Φ_{av} value at storey i, "$\propto$" is the proportionality symbol):

$$\Phi_{av,i} \quad \propto \quad \frac{V_0}{\Sigma M_{c1}} \cdot \left(\frac{F_i}{1.5 \cdot \Sigma M_{ci}} \right)^{2/3} \cdot \frac{\Sigma M_{bi}}{\Sigma M_{ci} + \Sigma M_{ci+1}} \tag{3}$$

The first term ($V_0/\Sigma M_{c1}$) in this expression is a measure of the seismic intensity to the base-shear capacity of the structure ratio. V_0 is the design base shear force calculated as:

$$V_0 = Sa_{(T1)} \cdot m \tag{4}$$

where $Sa_{(T1)}$ is the spectral acceleration according to the design spectrum at T_1, and m is the total mass of all the storeys (T_1 is the fundamental period from the modal analysis). $\Sigma M_{c,1}$ is the sum of the design moment resistance of the ground storey columns, and it is a measure of the actual capacity of the structure to withstand lateral loads. The physical meaning of the first term is that the ductility demand on the columns is proportional to $Sa_{(T1)}$ and inversely proportional to the capacity of the structure to withstand lateral loads.

The second term is a measure of the ratio of the inertial forces acting on storey i (the story for which the ductility demand is calculated) to the capacity of this very storey to withstand lateral loads. F_i (the inertial force) is calculated assuming a triangular distribution of the equivalent lateral load, as follows:

$$F_i = \frac{2 \cdot i}{N \cdot (N+1)} \cdot V_0 \tag{5}$$

where N is the total number of storeys in the frame, i the particular storey counting from the ground, and V_0 the base shear. $\Sigma M_{c,i}$ is the sum of the design moment resistance of the columns of storey i. So, the second term of Equation 3 is a measure of the inertial forces to the lateral force capacity ratio at storey i. Factor 1.5 stands for the shear span of the columns, which is approximately half the height of the storey. The use of the accurate shear span value (according to the modal analysis) was found to result in slightly more reliable results. However, the difference is insignificant, and the approximate value used herein has the advantage of being readily available without the need of any structural analysis of the frame. The physical meaning of the second term is that higher story-level inertial forces -and consequently higher

ductility demand- appears on structures with fewer storeys, as well as on the upper storeys of each structure. This relation however, is not linear, as the exponent ⅔ suggests. Extensive investigation via trial and error lead to the conclusion that the lack of linearity is not a consequence of an incorrect estimation of the distribution of the inertial forces.

The third term is the SPI, initially introduced by Priestley and Calvi [11]. It is the ratio between the sum of the bending resistance of the beams to the sum of the bending resistance of the columns on the respective storey and the storey above it, and serves as a measure of the structure's ability to redistribute the demand for inelastic deformation across multiple stories. SPI, however, was found to be irrelevant to the ductility demand on the columns of the ground story, and so for the ground storey SPI is disregarded.

Equation 3 contains the minimum number of parameters that are absolutely necessary for establishing proportionality to $\Phi_{av.i}$. However, in order to produce a formula that actually fits the data generated by the time-history analyses, a proportionality factor and a constant factor have to be introduced. These factors were defined using regression analysis, resulting in the following equation that best fits the data of the present study:

$$\Phi_{av,i} = 65.8 \cdot \frac{V_0}{\Sigma M_{c1}} \cdot \left(\frac{F_i}{1.5 \cdot \Sigma M_{ci}} \right)^{2/3} \cdot \frac{\Sigma M_{bi}}{\Sigma M_{ci} + \Sigma M_{ci+1}} + 0.495 \quad (6)$$

Finally, this equation can be expanded in order to predict the ductility demand for seismic intensity levels other than the seismic intensity of the design earthquake, by multiplying with the ratio of the ground acceleration of the supposed seismic action to the design ground acceleration (α_g/α_{gd}), with an exponent of 1.5:

$$\Phi_{av,i} = \left(\frac{\alpha_g}{\alpha_{gd}} \right)^{3/2} \cdot \left[35.85 \cdot \frac{V_0}{\Sigma M_{c1}} \cdot \left(\frac{F_i}{1.5 \cdot \Sigma M_{ci}} \right)^{2/3} \cdot \frac{\Sigma M_{bi}}{\Sigma M_{ci} + \Sigma M_{ci+1}} + 0.495 \right] \quad (7)$$

Equation 7 fits the data with a considerably high coefficient of determination (R^2). In Fig. 5a the results for seismic intensity level 5 are ploted, while Fig. 5b displays aggregated results for seismic intensity levels 4~7 (75% ~ 150% of the design earthquake). It should be noted that $\Phi_{av.t}$ also correlates well with Equation 7 (R^2=0.907 for seismic intensity level 5), while $\Phi_{av.b}$ correlates more loosely (R^2=0.780 for seismic intensity level 5). In all three cases, however, the coefficient of determination can get significantly higher if outliers are omitted (for example, frame types 1 and 5). The reliability of Equation 7 can also be improved by using more accurate data (for example T_1 and column shear span). However, the purpose of Equation 7 is not to serve as an accurate predictor of the ductility demand of the columns, but rather to demonstrate that the ductility demand is unambiguously determined by certain properties of the structure. Equation 7 may not fit well other data sets (for example results from frames with a different aspect ratio or mass distribution), while Equation 3 -which is not quantified- underlines a potentially more universal principle about the proportionality of the ductility demand to specific characteristics of the structure. Obviously, however, more research is needed in order to confirm that Equation 3 is indeed generally valid.

The unexpected discovery during the above investigation was that the ductility demand on the columns depends on the number of storeys of the frame, as well as on the actual storey under examination, as indicated by the term $F_i/(1.5 \cdot \Sigma M_{ci})$. This means that low-rise structures are more vulnerable to the formation of a storey mechanism, regardless of the regulatory framework they comply with. Besides, higher storeys in bare frames are also more vulnerable (though in the common practice the presence of infill walls may eliminate the additional risk). Another issue being highlighted by Equation 3 is that a small increase in the column strength

can have a significant effect on the protection against the formation of a story mechanism, since the bending resistance of the columns contributes to the denominator of all the three terms of Equation 3. However, this also implies that the resistance of modern buildings to the formation of story mechanism may arise from other factors leading to over-strengthened columns (for example the minimum reinforcement requirement), which also affect the first two terms of Equation 3, and not necessarily from the column capacity design (which in principle affects only the 3rd term).

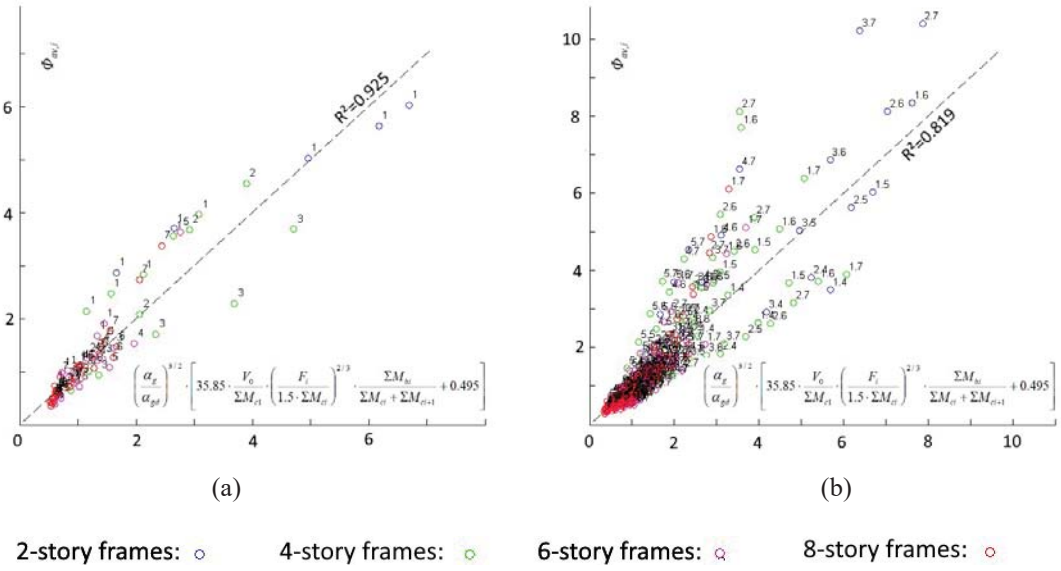

Figure 5: Prediction of the ductility demand on the columns on the basis of Equation 7. a: for seismic intensity level 5 (the numbers indicate the storey number). b: for seismic intensity levels 4~7 (the numbers indicate the frame type and the intensity level).

5.2 Infilled frames

Adding strong infill walls to the frames leads in concentration of the demand for inelastic deformation to fewer storeys, which effectively protects the rest storeys from large post-elastic deformation. The change in the distribution of the ductility demand along the height of the frames (from that of the bare frame to the one of the frames with strong infill walls) happens progressively as the infill strength increases, in a complicated, difficult to quantify manner. Nevertheless, as the infill strength increases, the maximum ductility demand on the columns tends to appear on the storey sustaining the maximum damage (usually one of the lower storeys), while the columns of the other storeys remain near -or within- the elastic response domain. As a result of this behavour, the term $(F_i/1.5\cdot M_{ci})^{2/3}$ which describes the distribution of the ductility demand along the frames' height in the case of the bare frames, does not apply to the infilled frames.

The behavior of the infilled frames is further complicated because the infill walls dissipate seismic energy and provide resistance to lateral loads, an effect that has a different impact on frames with a different number of storeys and different layout. So, Equation 3 is completely inadequate for describing the ductility demand on the columns of the infilled frames. Moreover, due to the many more parameters simultaneously affecting the seismic response of the infilled frames, it proved impossible to derive a universal formula for predicting the ductility demand. Nevertheless, the influence of each parameter on the seismic response is still recognizable, and some of them can be still jointed in formulae that partially describe the seismic response of the structure.

As an example, Equation 8 utilizes the strength of the structural elements and the infill walls of the first and the second storey, to predict $\Phi_{av.t}$ at the ground storey:

$$\Phi_{av,t} = \left(\frac{1600-\Sigma V_{inf2}}{80}\right)\cdot\frac{V_0-(0.8-d)\cdot 0.65\cdot\Sigma V_{inf1}}{\Sigma M_{c1}}\cdot\frac{\Sigma M_{bi}}{\Sigma M_{c1}+\Sigma M_{c2}+0.2\cdot\Sigma V_{inf1}}\cdot\frac{\Sigma M_{c2}+\Sigma V_{inf2}}{\Sigma M_{c1}+0.5\cdot\Sigma V_{inf1}} \quad (8)$$

The first term $[(1600\text{-}\Sigma V_{inf1})/80]$ is a general factor for the detrimental infill effect (gets higher as the infill strength increases). ΣV_{inf2} is the sum of the shear strength of the infill walls on the second storey.

The second term accounts for the contribution of the infill in withstanding seismic loads and dissipating seismic energy. This contribution was found to depend on the stiffness of the frame, which is roughly represented by the depth (d) of the column sections. ΣV_{inf1} is the sum of the shear strength of the infill walls on the ground storey. V_0 is the design base shear force calculated on the basis of the design spectrum, as already described.

The third term is a version of the SPI, modified due to the presence of infill walls. Finally, the fourth factor accounts for the irregularities induced by the infill. This factor reflects the unfavorable effect of even the uniformly distributed infill, due to the damage concentration.

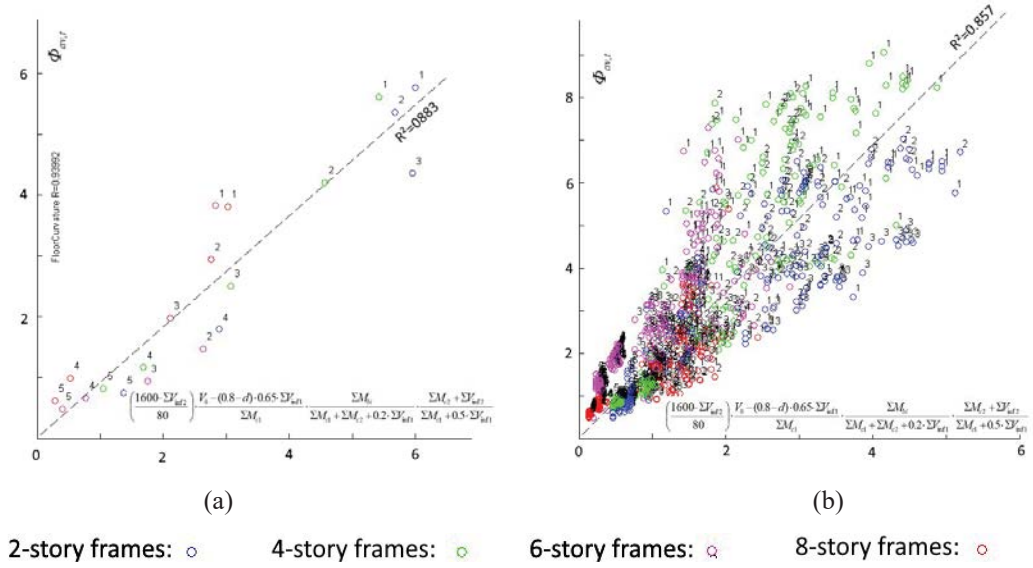

Figure 6: Prediction of the ductility demand on the columns on the basis of Equation 8, for seismic intensity level 5 (the numbers indicate the frame type). a: for the bare frames. b: for all the infilled frames (48 different infill types of uniform and non-uniform arraignment).

The many empirical constant factors utilized in equation 8 were defined either by trial and error or by partial regression analyses, in order to best fit the empirical data. Figure 6 depicts the relation between the values predicted by Equation 8 and the actual $\Phi_{av.t}$ values for seismic intensity level 5 (the design earthquake). As already mentioned, it has been impossible so far to derive a formula accounting for all the parameters that affect the ductility demand on the columns of the infilled frames. Moreover, partial formulae like the one in Equation 8 are purely empirical and, due to the large number of the arbitrary factors involved, they lack the robustness of Equation 3. Moreover, Equation 8 has a lower correlation with the actual empirical data than Equation 3. Nevertheless, Equation 8 still provides an insight into the mechanisms being activated by the addition of infill walls, and this insight is particularly useful in the context of the capacity design of the columns. Further research may allow drawing

more reliable and definitive conclusions about the infill effect on the ductility demand on the columns.

6 CONCLUSIONS

Historically, the view that the column capacity design is not necessary to completely preclude yielding of the columns has prevailed in the relevant research. However, to this day different seismic design codes call for different protection levels against the formation of story mechanisms, by utilizing different column overstrength factors. Moreover, the predominant method for the column capacity design is still based on the simplistic model of Fig. 1a. and utilizes a single general overstrength factor. While this method has been in use for decades now successfully, the present study demonstrates that it cannot ensure a uniform level of protection against the formation of a story mechanism for all the different structures or even for all the columns within the same structure. Based on the current results, the following conclusions may be drawn:

- Most seismic design codes formulate the column capacity design methodology on the base of the simplified beam-column joint model. However, this model is fundamentally incomplete. It misleads the designer about the nature of the column capacity design and has been many times criticized in the literature. The adoption of an accurate model, fully accounting for the equilibrium of the lateral forces acting on the beam-column joint, is of paramount importance for implementing an effective and efficient method for the column capacity design.
- In order to provide a uniform level of protection for all the columns within the structure, as well as for every different structure, the column capacity design should account for the number of stories of the building, the specific story being checked, and the presence of infill walls. More specifically, the results of the present study demonstrated that low- to mid-rise buildings are more vulnerable to the column sidesway mechanism. Higher storeys of bare frames were also found to be more vulnerable; however, the presence of infill was found to effectively mitigate the additional risk at the upper storeys of the investigated frames.
- Since infill walls are not considered load resisting members in R/C structures, the introduction of an additional general level of protection accounting for a minimum nominal level of adverse infill effect seems to be a reasonable choice.
- A more effective and efficient method for column capacity design can be established on the basis of formulae like Equation 3 or even Equation 8. Such a method could ensure a uniform level of protection both for all the columns in a structure, and all the different structures. A method like this can still be based on a general criterion, which however, will have the form of an ultimate acceptable ductility demand, rather than that of an arbitrary overstrength factor.

7 AKNOWLEGMENTS

Results presented in this work have been produced using the AUTH Compute Infrastructure and Resources. The earthquake records were obtained from the Pacific Earthquake Engineering Research Center (PEER) database. Time-history analyses were performed using OPENSEES software developed at Berkley University.

REFERENCES

[1] ACI Committee 318, Bulding code requirements for reinforced concrete (ACI 318-71), *American Concrete Institute*, Detroit, 1971

[2] R. Park, T. Paulay, Reinforced concrete structures, *John Wiley & Sons*, 1975.

[3] T. Paulay, An application of capacity design philosophy to gravity load dominated ductile reinforced concrete frames, *Bulletin of the New Zealand National Society for Earthquake Engineering,* 11.1, 50-61, 1978

[4] T. Paulay, Developments in the design of ductile reinforced concrete frames, *Bulletin of the New Zealand National Society for Earthquake Engineering*, 12.1, 35-43, 1979

[5] T. Paulay, A Critique of the Special Provisions for Sesmic Design of the Building Code Requirements for Reinforced Concrete (ACI 318-83), *Journal of the ACI,* 83.2, 274-83, 1986

[6] Eurocode 8 (EN 1998-1:2005), Design provisions for earthquake resistance of structures, *European Committee for Standardization*, 2005

[7] ACI Committee 318, Building Code Requirements for Structural Concrete (ACI 318-08), *American Concrete Institute*, USA, 2008

[8] NZS 3101:2006, Concrete Structures Standard, *New Zealand Standards*, Wellington, 2006

[9] Kappos A. J, Influence of capacity design method on the seismic response of R/C columns, *Journal of Earthquake Engineering* 1.02, 341-399, 1997

[10] Panagiotakos T. B, Fardis M. N, Effect of column capacity design on earthquake response of reinforced concrete buildings, *Journal of Earthquake Engineering*, 2.01, 113-145, 1998

[11] M.N. Priestley, G.M. Calvi, Towards a capacity-design assessment procedure for reinforced concrete frames, *Earthquake Spectra* 7.3, 413-437, 1991

[12] Eurocode 2 (EN 1992-1-1), Design of concrete structures - General rules and rules for buildings, *European Committee for Standardization*, 2005

[13] CSI, SAP2000 Integrated Software for Structural Analysis and Design. *Computers and Structures Inc.*, Berkeley, California

[14] F. McKenna, G.L. Fenves, M.H. Scott, Open System for Earthquake Engineering Simulation, *University of California*, Berkeley, California, 2000

[15] M. H. Scott, Numerical integration options for the force-based beam-column element in OpenSees, *OpenSEES Wiki, http://opensees.berkeley.edu*, 2011

[16] N. Mohammad N, L. Liberatore, F. Mollaioli, S. Tesfamariam, Modeling of Masonry Infilled RC Frames Subjected to Cyclic Loads: State of the Art Review and Modelling with OpenSees, *Engineering Structures,* 150, 599-621, 2017

[17] D. Michaud, P. Léger, Ground motions selection and scaling for nonlinear dynamic analysis of structures located in Eastern North America, *Canadian Journal of civil engineering*, 41(3), 232-244, 2014

[18] D. Vamvatsikos, C. A. Cornell, Incremental dynamic analysis. *Earthq Eng Struct Dyn,* 31, 491-514, 2002

EURODYN 2020
XI International Conference on Structural Dynamics
M. Papadrakakis, M. Fragiadakis, C. Papadimitriou (eds.)
Athens, Greece, 23–26 November 2020

ELASTIC AXIS OF BUILDINGS UNDER EARTHQUAKE EXCITATION

Terzi Vasiliki[1] **and Athanatopoulou Asimina**[2]

[1] Laboratory Teaching Staff, Department of Civil Engineering, Aristotle University of Thessaloniki
[2] Professor, Department of Civil Engineering, Aristotle University of Thessaloniki
Aristotle University Campus, 54124, Thessaloniki, Greece
[1]e-mail: terziv@civil.auth.gr, [2]e-mail: minak@civil.auth.gr

Abstract. *The elastic axis of multistory buildings is defined as the intersection of two vertical principal bending planes which are perpendicular. The elastic axis intersects each story at a point which has the property of the rigidity center. Single-story and special classes of multi-story buildings, such as isotropic ones possess an elastic axis. Taking into account the dynamic nature of earthquake excitation the following question arises: under the action of a torsional earthquake component, is it possible to locate a stable vertical axis around which the structural system will be rotated under any torsional ground motion? For this purpose, monosymmetric single-story and isotropic monosymmetric multi-story buildings are studied analytically. The equation of motion is expressed in the time domain and transferred by Fast Fourier Transform in the frequency domain. Mathematical expressions of the coordinates of the torsional axis at each story level are produced, taking into account that each floor behaves as a rigid in-plane diaphragm. The derived equations indicate that the dynamic torsional axis depends not only on the geometrical and mechanical characteristics of the system but also on mass, damping and excitation frequency. Numerical examples are included for enhancing the comprehension of the derived equations. The divergence of the coordinates of the static and dynamic definition of elastic axis is discussed.*

Keywords: elastic axis, earthquake torsional effects, isotropic buildings, monosymmetric buildings

1 INTRODUCTION

The damage state of the structural facilities following an earthquake excitation usually discloses: (i) the torsional nature of buildings behavior; and (ii) the significance of torsional ground motion [1-4]. The main causes of torsion are the following: (i) stiffness eccentricity, which is attributed to the asymmetric distribution of load bearing elements; (ii) inertial eccentricity, which is attributed to the asymmetric distribution of masses and live loads [5]; (iii) torsional earthquake component, which is attributed to the wave passage effect [6-7] or the incoherency of ground motion [8]; various parameters that are not considered in the design phase, such as non-structural elements, yield strength of bearing elements, differences between actual values of mechanical parameters and computed ones. Thus, multi-story buildings presenting asymmetries in plan are submitted in a coupled lateral-torsional motion during earthquake excitation. The most vulnerable in terms of risk of collapse elements are those that are located in the perimeter of a structure due to significant swaying caused by twisting [9].

According to the aforementioned, the necessity to take into account torsional effects during the design phase arises. Therefore, the notion of eccentricity is introduced by various codes [10] and two types of it are defined: (i) structural eccentricity which is the distance between the center of mass (CM) and the center of rigidity (CR), is attributed to the lack of symmetry in plan and is responsible for the natural or inherent torsional moment; (ii) accidental eccentricity, which is attributed to uncertainty in determination of center of mass, uncertainty in location of center of rigidity and the possible influence of torsional ground motion input. It is expressed with the aid of the structure's dimensions in plan [5, 11].

The center of rigidity (CR) can be easily determined in single-story buildings [10], is usually denoted as CR, called elastic center and is accompanied by two axes denoted I,II, called principal directions [12]. The properties of the elastic center (CR, I, II) are the following: (i) the static response of a single-story building can be defined by two pure bending states along I, II axes and one pure torsional state about CR; (ii) Only translational motion is produced when arbitrary horizontal forces are applied along principal directions. In this case, CR corresponds to the bending center (BC) and axes I, II correspond to the translational planes; (iii) Only rotation is produced when arbitrary torsional moment is applied at the story level. In this case, CR corresponds to the center of twist or torsion (TC); (iv) If arbitrary horizontal force is applied at the story level, the resultant of internal shear forces passes through CR, only under the condition that the rotation of the story is restrained. In this case, CR corresponds to the shear center (SC). The aforementioned properties are independent of the applied loads and depend only on the structural geometry and mechanical characteristics [13].

The definition and existence of the elastic axis in multi-story buildings presents some difficulties [11] and has been investigated by various researchers [13-18]. However, there is a certain multi-story buildings category that the elastic axis and the principal bending planes can be defined. In this case, the elastic axis is a unique vertical axis that the rigidity center of each story belongs and is independent of the load distribution along the vertical direction as well [10]. The aforementioned category corresponds to buildings that consist of homotropic vertical elements [13]. Homotropicity is expressed by the same elastic deformation law for all vertical elements under horizontal loading, and therefore the horizontal stiffness matrices of the aforementioned elements are proportional [19-22]. Homotropic buildings can be divided in the following categories: (i) isotropic, all elements follow the same homotropicity rule and their horizontal stiffness matrices receive the following form: $\mathbf{K}_n = k_n \cdot \mathbf{K}_o$, where k_n is the proportionality constant and $\mathbf{K}_o$ is the characteristic stiffness matrix; (ii) orthotropic, elements along X, and Y directions follow different homotropicity rules and their horizontal stiffness matrices

receive the following forms: $\mathbf{K}_{\mathrm{xn}} = \mathrm{k}_{\mathrm{xn}} \cdot \mathbf{K_{ox}}$, $\mathbf{K}_{\mathrm{yn}} = \mathrm{k}_{\mathrm{yn}} \cdot \mathbf{K_{oy}}$, where $\mathrm{k}_{\mathrm{xn}}, \mathrm{k}_{\mathrm{yn}}$ are the proportionality constants and $\mathbf{K_{ox}}$, $\mathbf{K_{oy}}$ are the characteristic stiffness matrices; (iii) complex isotropic-coaxial, the vertical elements can be divided into two or more subsystems that belong to type (i) or (ii) [13].

All the aforementioned studies refer to the definition of elastic axis under the application of static horizontal forces or moments. Since the torsional effects are attributed to a purely dynamic phenomenon the two-fold question that arises is the following: (i) Is it possible to define a dynamic elastic axis under the application of transient horizontal forces or moments?; (ii) Will this axis be different than the elastic axis defined by the static loading? The present paper utilizes the notion of twist center which coincides with the center of rigidity in order to define the dynamic elastic axis. In particular, monosymmetric single-story and monosymmetric isotropic multistory buildings are excited by a torsional ground motion and the center of twist of each story is determined. Once the centers of twist line up in a vertical axis, the dynamic elastic axis is possible to be defined. The position of the dynamic axis is compared with the position of the known elastic axis.

2 MATHEMATICAL FORMULATION

The equation of motion of any structural system is the following:

$$\boldsymbol{M} \cdot \ddot{\boldsymbol{U}}(t) + \boldsymbol{C} \cdot \dot{\boldsymbol{U}}(t) + \boldsymbol{K} \cdot \boldsymbol{U}(t) = \boldsymbol{F}(t) \tag{1}$$

where $\mathrm{M}, \mathrm{C}, \mathrm{K}$ are the mass, damping and stiffness matrices respectively. $\mathrm{U(t)}$ and $\mathrm{F(t)}$ are the displacement and force vectors respectively. The damping matrix, $\boldsymbol{C}$ is represented by Rayleing damping by the following expression [23]:

$$\boldsymbol{C} = a \cdot \boldsymbol{M} + b \cdot \boldsymbol{K} \tag{2}$$

where the constants a, b are related to the modal damping ratio, ζ by the following expressions:

$$a = \frac{2 \cdot \zeta \cdot \omega_i \cdot \omega_j}{\omega_i + \omega_j} \qquad b = \frac{2 \cdot \zeta}{\omega_i + \omega_j} \tag{3}$$

where ω_i, ω_j are the eigenfrequencies of the ith and jth eigenmode respectively.

The equation of motion (1) in the time domain is coupled due to the participation of accelerations, $\ddot{U}(t)$; velocities, $\dot{U}(t)$; and displacements, $U(t)$. Therefore, the Fast Fourier Transform is applied to both parts of equation (1).

$$(\boldsymbol{K} - \Omega^2 \cdot \boldsymbol{M} + i \cdot \Omega \cdot \boldsymbol{C}) \cdot \boldsymbol{U}(\Omega) = FFT(\boldsymbol{F}(t)) \tag{4}$$

It is assumed that each story plate behaves as an in-plane rigid diaphragm. Therefore, each story has three degrees of freedom: (i) translation at X axis, u_x; (ii) translation at Y axis, u_y; (iii) rotation around Z axis, θ_z. The constraint equations between two points $i(x_i, y_i)$ and $j(x_j, y_j)$ that belong to the diaphragm are the following [24].

$$\begin{aligned} u_{xj} &= u_{xi} - \Delta y_{ij} \cdot \theta_z, \ \Delta y_{ji} = y_i - y_j \\ u_{yj} &= u_{yi} + \Delta x_{ij} \cdot \theta_z, \ \Delta x_{ji} = x_i - x_j \end{aligned} \tag{5}$$

Furthermore, it is assumed that the masses of the individual vertical resisting elements are negligible and the mass distribution is uniform at the floor levels. Therefore, the center of mass, CM coincides with the geometric center of the diaphragm. The center of mass of a system is

the point on the diaphragm through which the resultant of the inertial forces of the diaphragm is passing through.

2.1 Single-story symmetric buildings

A single-story building which is symmetric at the X axis is depicted in Fig. 1. The structure has three degrees of freedom: (i) translation at X axis, u_x; (ii) translation at Y axis, u_y; (iii) rotation around Z axis, θ_z. Furthermore, the inertial characteristics of the single-story are: the translational mass, m; and the mass moment of inertia, J_m.

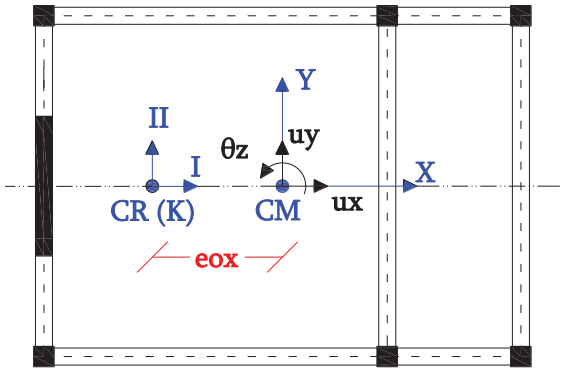

Figure 1: Single-story building symmetric at X axis.

The mass, stiffness and damping matrices of the system under study are represented by the following equations.

$$\boldsymbol{M} = \begin{bmatrix} m & 0 & 0 \\ 0 & m & 0 \\ 0 & 0 & J_m \end{bmatrix}$$

$$\boldsymbol{K} = \begin{bmatrix} k_{xx} & 0 & 0 \\ 0 & k_{yy} & k_{yz} \\ 0 & k_{yz} & k_{zz} \end{bmatrix} \qquad \boldsymbol{C} = \begin{bmatrix} c_{xx} & 0 & 0 \\ 0 & c_{yy} & c_{yz} \\ 0 & c_{yz} & c_{zz} \end{bmatrix} \tag{6}$$

The displacement and force vector are expressed by the following relationships in time domain.

$$\boldsymbol{U}(t)^T = [u_x(t) \quad u_y(t) \quad \theta_z(t)] \qquad \boldsymbol{F}(t)^T = [0 \quad 0 \quad -J_m \cdot \ddot{\theta}_g(t)] \tag{7}$$

where $\ddot{\theta}_g(t)$ is the rotational base excitation. The aforementioned vectors receive the following expressions in the frequency domain.

$$\boldsymbol{U}(\Omega)^T = [u_x(\Omega) \quad u_y(\Omega) \quad \theta_z(\Omega)] \qquad \boldsymbol{F}(\Omega)^T = [0 \quad 0 \quad FFZ] \tag{8}$$

where FFZ is the Fast Fourier Transform of the rotational moment, $-J_m \cdot \ddot{\theta}_g(t)$.

Finally, the equation of motion for the single-story building, which is symmetric with respect to X axis is expressed as follows:

$$\begin{bmatrix} k_{xx} - \Omega^2 \cdot m + i \cdot \Omega \cdot c_{xx} & 0 & 0 \\ 0 & k_{yy} - \Omega^2 \cdot m + i \cdot \Omega \cdot c_{yy} & k_{yz} + i \cdot \Omega \cdot c_{yz} \\ 0 & k_{yz} + i \cdot \Omega \cdot c_{yz} & k_{zz} - \Omega^2 \cdot J_m + i \cdot \Omega \cdot c_{zz} \end{bmatrix} \cdot \begin{bmatrix} u_x(\Omega) \\ u_y(\Omega) \\ \theta_z(\Omega) \end{bmatrix} = \begin{bmatrix} 0 \\ 0 \\ FFZ \end{bmatrix} \tag{9}$$

The dynamic elastic center can be defined as the point which belongs to the diaphragm, and that under a rotational base excitation is only rotated without being translated at all. Therefore,

using the diaphragm's constraint equations (5), the coordinates of the dynamic elastic center can be defined as follows:

$$x_K = -\frac{u_y(\Omega)}{\theta_z(\Omega)} \qquad y_K = \frac{u_x(\Omega)}{\theta_z(\Omega)} \tag{10}$$

By solving equation (9) and replacing the expressions of the displacements at CM in equation (10), the coordinates of the dynamic elastic center receive the following form.

$$x_K = \frac{k_{yz} + i \cdot \Omega \cdot c_{yz}}{k_{yy} - \Omega^2 \cdot m + i \cdot \Omega \cdot c_{yy}} \qquad y_K = 0 \tag{11}$$

From Equation 11 the following observations can be made.

- The coordinates depend on: (i) stiffness terms (k_{yy}, k_{yz}) related to the translational degree of freedom, Y which is perpendicular to the axis of symmetry, X; (ii) translational mass, m ; (iii) damping terms (c_{yy}, c_{yz}); and (iv) frequency of excitation, Ω.
- The coordinates do not depend on the rotational earthquake component ($\ddot{\theta}_g(t)$).
- The coordinates do not depend on the mass moment of inertia, J_m.
- The coordinates as expressed in the frequency domain, are complex numbers. Their imaginary part is attributed to the damping terms exclusively.
- In case that the dynamic terms, such as mass and damping, are ignored or the excitation frequency is very small ($\Omega \approx 0$) the coordinates of the dynamic elastic center coincide with the coordinates of the elastic center as defined by the application of a static moment ($x_K = k_{yz}/k_{yy}$).
- The deviation of the static values of the coordinates is expected at the high frequency range. This is important taking into account that the rotational earthquake accelerations are dominated by frequencies higher than the corresponding translational accelerations [8].

2.2 Two-story isotropic monosymmetric buildings

Fig. 2 depicts the plan view of an isotropic monosymmetric building. The main assumption regarding the inertial characteristics is that they remain the same at each story level. Furthermore, the centers of mass of all stories belong on the same vertical axis. Each story level has a translational mass, m and a mass moment of inertia, J_m. The vector of displacements for all six degrees of freedom and the mass matrix of the two-story isotropic building are given by following Equation 12.

$$\boldsymbol{u} = \begin{bmatrix} u_{x1} \\ u_{x2} \\ u_{y1} \\ u_{y2} \\ \theta_1 \\ \theta_2 \end{bmatrix}, \qquad \boldsymbol{M} = \begin{bmatrix} m & 0 & 0 & 0 & 0 & 0 \\ 0 & m & 0 & 0 & 0 & 0 \\ 0 & 0 & m & 0 & 0 & 0 \\ 0 & 0 & 0 & m & 0 & 0 \\ 0 & 0 & 0 & 0 & J_m & 0 \\ 0 & 0 & 0 & 0 & 0 & J_m \end{bmatrix} \tag{12}$$

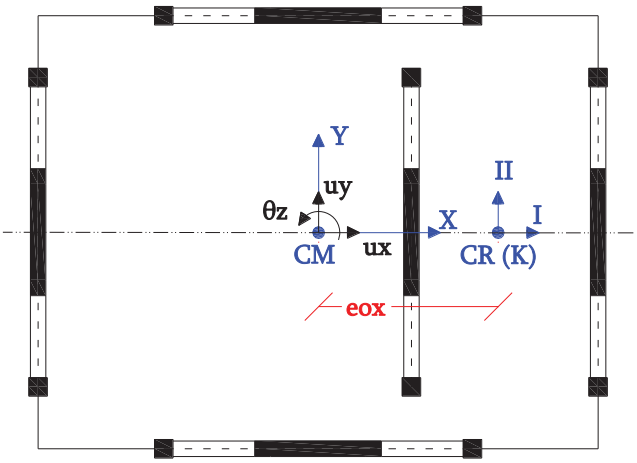

Figure 2: Plan view of isotropic building.

Furthermore, the main characteristic of the isotropic buildings behavior is that all the planar frames participating in the structural system, have proportional stiffness matrices. The frames may consist of mixed-type resisting elements, such as for example moment frames coupled with shear walls. Therefore, the following equation is valid [25].

$$\boldsymbol{K}_i = k_i \cdot \boldsymbol{K}_o \tag{13}$$

where $\boldsymbol{K}_i$ is the stiffness matrix of each frame participating in the structural system, K_o is the characteristic stiffness matrix and k_i is the proportionality constant. The stiffness matrix of the two-story structure is expressed by the following relationships [20].

$$\boldsymbol{K} = \begin{bmatrix} k_{xx} \cdot \boldsymbol{K_o} & 0 & 0 \\ 0 & k_{yy} \cdot \boldsymbol{K_o} & k_{yz} \cdot \boldsymbol{K_o} \\ 0 & k_{yz} \cdot \boldsymbol{K_o} & k_{zz} \cdot \boldsymbol{K_o} \end{bmatrix} \qquad \boldsymbol{K_o} = \begin{bmatrix} K_{o1} & K_{o2} \\ K_{o2} & K_{o3} \end{bmatrix} \tag{14}$$

The damping matrix is expressed by Rayleigh damping and it is given by equation (2).

The displacement and force vector are given by the following relationships, expressed in the frequency domain.

$$\boldsymbol{U}(\Omega)^T = [u_{x1}(\Omega) \quad u_{x2}(\Omega) \quad u_{y1}(\Omega) \quad u_{y2}(\Omega) \quad \theta_{z1}(\Omega) \quad \theta_{z2}(\Omega)]$$
$$FFT(\boldsymbol{F}(t))^T = [0 \quad 0 \quad 0 \quad 0 \quad FFZ_1 \quad FFZ_2] \tag{15}$$

where the indices 1,2 denote the first and second floor respectively and FFZ is the Fast Fourier Transform of the moment $-J_m \cdot \ddot{\theta}_g(t)$.

After performing some mathematical calculations (see Appendix), the complex matrix which is multiplied by the displacement vector receives the following form.

$$\boldsymbol{K_{comp}} = \begin{bmatrix} k_{xx} \cdot \boldsymbol{K_{ox}} & 0 & 0 \\ & k_{yy} \cdot \boldsymbol{K_{oy}} & k_{yz} \cdot \boldsymbol{K_{o,imag}} \\ symm. & & k_{zz} \cdot \boldsymbol{K_{oz}} \end{bmatrix} \tag{16}$$

where the 2x2 submatrices receive the following expressions (see A8, A10, A14):

$$\boldsymbol{K_{0x}} = \begin{bmatrix} (K_{o1} - \Omega^2 \cdot m/k_{xx} + i \cdot \Omega \cdot \alpha \cdot K_{o1} + i \cdot \Omega \cdot b \cdot m/k_{xx}) & K_{o2} \cdot (1 + i \cdot \Omega \cdot a) \\ K_{o2} \cdot (1 + i \cdot \Omega \cdot a) & (K_{o3} - \Omega^2 \cdot m/k_{xx} + i \cdot \Omega \cdot \alpha \cdot K_{o3} + i \cdot \Omega \cdot b \cdot m/k_{xx}) \end{bmatrix} \tag{17}$$

$$\boldsymbol{K_{0y}} = \begin{bmatrix} \left(K_{o1} - \Omega^2 \cdot m/k_{yy} + i \cdot \Omega \cdot \alpha \cdot K_{o1} + i \cdot \Omega \cdot b \cdot m/k_{yy}\right) & K_{o2} \cdot (1 + i \cdot \Omega \cdot a) \\ K_{o2} \cdot (1 + i \cdot \Omega \cdot a) & \left(K_{o3} - \Omega^2 \cdot m/k_{yy} + i \cdot \Omega \cdot \alpha \cdot K_{o3} + i \cdot \Omega \cdot b \cdot m/k_{yy}\right) \end{bmatrix}$$

$$\boldsymbol{K_{0z}} = \begin{bmatrix} (K_{o1} - \Omega^2 \cdot J_m/k_{zz} + i \cdot \Omega \cdot \alpha \cdot K_{o1} + i \cdot \Omega \cdot b \cdot J_m/k_{zz}) & K_{o2} \cdot (1 + i \cdot \Omega \cdot a) \\ K_{o2} \cdot (1 + i \cdot \Omega \cdot a) & (K_{o3} - \Omega^2 \cdot J_m/k_{zz} + i \cdot \Omega \cdot \alpha \cdot K_{o3} + i \cdot \Omega \cdot b \cdot J_m/k_{zz}) \end{bmatrix}$$

$$\boldsymbol{K_{0,imag}} = (1 + i \cdot \Omega \cdot a) \cdot \boldsymbol{K_0}$$

Finally, the equation of motion of the two-story isotropic building can be written as follows.

$$\boldsymbol{K_{comp}} \cdot \begin{bmatrix} \boldsymbol{u_x}(\Omega) \\ \boldsymbol{u_y}(\Omega) \\ \boldsymbol{\theta_z}(\Omega) \end{bmatrix} = \begin{bmatrix} \mathbf{0} \\ \mathbf{0} \\ \boldsymbol{FFZ}(\Omega) \end{bmatrix} \tag{18}$$

where $\boldsymbol{u_x}(\Omega), \boldsymbol{u_y}(\Omega), \boldsymbol{\theta_z}(\Omega)$ are 2-dimensional vectors of translations $u_{x1}(\Omega), u_{x2}(\Omega), u_{y1}(\Omega), u_{y2}(\Omega)$ and rotations $\theta_{z1}(\Omega), \theta_{z2}(\Omega)$ at each story level; $\mathbf{0}$ is a 2-dimensional zero force vector; and $\boldsymbol{FFZ}(\Omega)$ is a 2-dimensional moment vector of FFZ_1, FFZ_2.

The coordinates of the dynamic elastic axis are determined using equations (5) and receive the following forms.

$$\begin{gathered} \boldsymbol{X_{Ko}} = \left(\boldsymbol{K_{oy}} \cdot k_{yy}\right)^{-1} \cdot \left(\boldsymbol{K_{o,imag}} \cdot k_{yz}\right) \\ \boldsymbol{Y_{Ko}} = \mathbf{0} \end{gathered} \tag{19}$$

where $\boldsymbol{X}_{Ko}, \boldsymbol{Y}_{Ko}$ are square matrices. In this particular case of symmetry, the matrix $\boldsymbol{Y}_{Ko}$ contains zero terms. Therefore, the elastic axis is located on X axis, the axis of symmetry. The diagonal terms of matrix $\boldsymbol{X}_{Ko}$ denote the coordinates of the elastic center at each story-level. The off-diagonal terms must be zero. In case that the off-diagonal terms are not zero then the elastic axis does not exist.

2.3 n-story monosymmetric isotropic buildings

A typical plan view of N-story isotropic building which is symmetric with respect to X axis is depicted in Fig. 2. The plate of each story behaves as a rigid in-plane diaphragm. Therefore, each story has three degrees of freedom: two translations at the X, Y axes and one rotation around Z axis.

The displacement and force vector are given by the following relationships, expressed in the frequency domain.

$$\begin{gathered} \boldsymbol{U}(\Omega)^T = [u_{x1}(\Omega) \quad u_{x2}(\Omega) \quad \ldots \quad u_{y1}(\Omega) \quad u_{y2}(\Omega) \quad \ldots \quad \theta_{z(n-1)}(\Omega) \quad \theta_{zn}(\Omega)] \\ FFT(\boldsymbol{F}(t))^T = [0 \quad 0 \quad \ldots \quad 0 \quad 0 \quad \ldots \quad FFZ_{(n-1)} \quad FFZ_n] \end{gathered} \tag{20}$$

where the indices 1,2,…,n denote the first, second and nth floor respectively and FFZ is the Fast Fourier Transform of the moment $-J_m \cdot \ddot{\theta}_g(t)$.

The inertial characteristics are the same for each story. In particular, each story has a translational mass, m and a mass moment of inertia, J_m. Therefore, the mass matrix of the n-story isotropic building is a 3n-dimensional matrix and it can be written as follows.

$$\boldsymbol{M} = \begin{bmatrix} m & 0 & 0 & 0 & . & . & 0 & 0 \\ 0 & m & 0 & 0 & . & . & 0 & 0 \\ 0 & 0 & m & 0 & . & . & 0 & 0 \\ 0 & 0 & 0 & m & . & . & 0 & 0 \\ .. & . & . & . & . & . & . & . \\ . & . & . & . & . & . & . & . \\ 0 & 0 & 0 & 0 & . & . & J_m & 0 \\ 0 & 0 & 0 & 0 & . & . & 0 & J_m \end{bmatrix} \tag{21}$$

Taking into account the proportionality of the stiffness matrices of the planar frames and the symmetry with respect to X axis, the stiffness matrix, $\boldsymbol{K}$ of the n-story building is a 3n-dimensional matrix and can be expressed by equation (14). However, the characteristic stiffness matrix, $\boldsymbol{K_o}$ is an n-dimensional matrix and receives the following form:

$$\boldsymbol{K_0} = \begin{bmatrix} K_{o11} & K_{o12} & K_{o13} & K_{o14} & \dots & \dots & K_{o1(n-1)} & K_{o1n} \\ & K_{o22} & K_{o23} & K_{o24} & \dots & \dots & K_{o2(n-1)} & K_{o2n} \\ & & K_{o33} & K_{o34} & \dots & \dots & K_{o3(n-1)} & K_{o3n} \\ & & & K_{o44} & \dots & \dots & K_{o4(n-1)} & K_{o4n} \\ & & & & \ddots & \dots & \vdots & \vdots \\ & & symm. & & & \ddots & \vdots & \vdots \\ & & & & & & K_{o(n-1)(n-1)} & K_{o(n-1)n} \\ & & & & & & & K_{onn} \end{bmatrix} \tag{22}$$

The damping matrix is expressed by Rayleigh damping, it is expressed by equation (2).

Following the same notion as in the case of the two-story building, the complex matrix which is multiplied by the displacement vector can be expressed by equation (16). However, the diagonal terms of each submatrix, $\boldsymbol{K_{ox}}, \boldsymbol{K_{oy}}, \boldsymbol{K_{oz}}$ receive the following forms.

$$\begin{aligned} \boldsymbol{K_{0x(ij)}} &= K_{oij} - \Omega^2 \cdot m/k_{xx} + i \cdot \Omega \cdot \alpha \cdot K_{oij} + i \cdot \Omega \cdot b \cdot m/k_{xx} \\ \boldsymbol{K_{0y(ij)}} &= K_{oij} - \Omega^2 \cdot m/k_{yy} + i \cdot \Omega \cdot \alpha \cdot K_{oij} + i \cdot \Omega \cdot b \cdot m/k_{yy} \\ \boldsymbol{K_{0z(ij)}} &= K_{oij} - \Omega^2 \cdot J_m/k_{zz} + i \cdot \Omega \cdot \alpha \cdot K_{oij} + i \cdot \Omega \cdot b \cdot J_m/k_z \end{aligned} \tag{23}$$

where $i = j = 1{:}\,1{:}\,n$

The off-diagonal terms of each submatrix, $\boldsymbol{K_{ox}}, \boldsymbol{K_{oy}}, \boldsymbol{K_{oz}}$ are the same and receive the following forms.

$$\boldsymbol{K_{0(ij)}} = K_{oij} \cdot (1 + i \cdot \Omega \cdot a) \tag{24}$$

where $i \neq j$.

The imaginary matrix, $\boldsymbol{K_{0,imag}}$ is represented by equation (17).

The equation of motion in the frequency domain is represented by equation (18). However, $\boldsymbol{u_x}(\Omega), \boldsymbol{u_y}(\Omega), \boldsymbol{\theta_z}(\Omega)$ are n-dimensional vectors of translations rotations at each story level; $\mathbf{0}$ is a n-dimensional zero force vector; and $\boldsymbol{FFZ}(\Omega)$ is a n-dimensional moment vector of FFZ_i.

Finally, the coordinates of the dynamic elastic axis can be calculated by equations (19) where $\boldsymbol{X_{Ko}}, \boldsymbol{Y_{Ko}}$ are n-dimensional matrices. The diagonal terms of each matrix denote the coordinates of the elastic center at each story-level. The off-diagonal terms must be zero. In case that the off-diagonal terms are not zero then the elastic axis does not exist.

3 NUMERICAL APPLICATIONS

In the present section a characteristic numerical example for each structural formulation is presented. A MATLAB code has been written in order to apply the final equations for the estimation of the coordinates of the elastic center or axis [26]. The code also performs a modal analysis, in order to estimate the eigenfrequencies and calculate further the Rayleigh damping components, a, b. The Rayleigh damping matrix takes into account all the eigenfrequencies in the case of single-story buildings. In the case of multi-story building the MATLAB code has the capability to take into account more than three eigenfrequencies. The stiffness matrix is calculated by the application of the Finite Element Method while the mass matrix is calculated according to the inertial data.

3.1 Single-story symmetric building

Fig. 3 depicts a single-story building which is symmetric with regard to X axis.

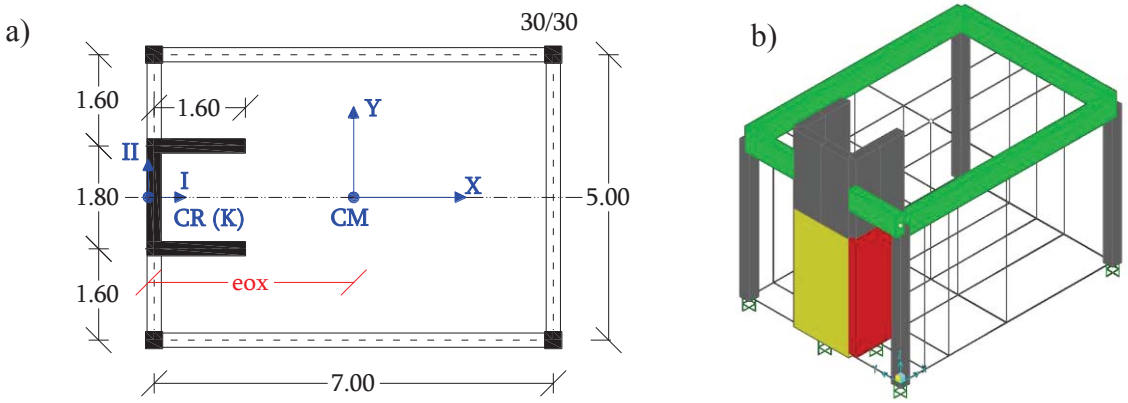

Figure 3: Single-story symmetric building: a) plan view; b) finite element model.

The vertical supporting elements consist of four columns (30/30) and a C shaped shear wall. The horizontal supporting elements consist of a rectangular plate which behaves as a rigid in plane diaphragm and five beams (20/60), which are located at the perimeter of the plate. The height of the building equals 4.5m. The material characteristics are: E=2.8e7kN/m^2; v=0.2. The uniform vertical load of the plate equals to 12kN/m^2 and the modal damping ratio equals 5%. Fig.3 also depicts the structure's finite element model. The simulation of the C shaped shear wall follows the notion of the equivalent frame model.

Taking into account the geometry of the plate and the vertical uniform load, the mass matrix can be calculated under the assumption of diaphragmatic function. In the following equations the stiffness matrix, mass and damping characteristics are given.

$$K = \begin{bmatrix} 238720.458 & 0 & 0 \\ 0 & 214041.096 & -770547.945 \\ 0 & -770547.945 & 3329528.158 \end{bmatrix} \quad m = 42.813\text{tn} \quad a = 2.0894$$

$$J_m = 264.016\text{tnm}^2 \quad b = 6.442 \cdot 10^{-4}$$

Fig.4 depicts the real and imaginary parts of the coordinates of the elastic center, which are calculated according to equation (11). The following two cases are studied: (i) $\zeta = 5\%$; (ii) $\zeta = 0\%$. The real parts of the coordinates coincide with the static values $(x_k = -3.6m, y_k = 0)$ while the imaginary parts are zero, except for very small values of periods or for very large values of frequencies.

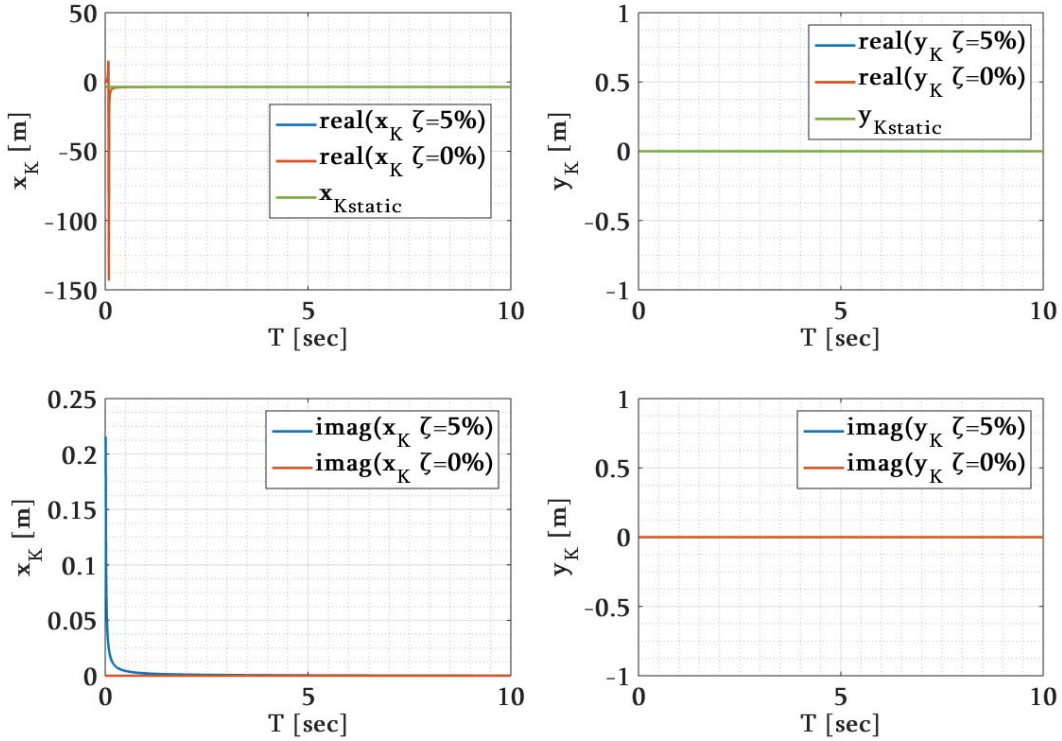

Figure 4: Coordinates of elastic center for a single-story building symmetric with regard to X axis.

3.2 Two-story isotropic symmetric building

Fig.5 depicts a two-story isotropic building. The vertical supporting elements are three walls of 200/25 dimensions and two walls of 160/25 dimensions. The horizontal supporting element is a plate of 3m x 6m which behaves as a rigid in plane diaphragm. The height of each story equals 3.5m. The material characteristics are: E=2.9e7kN/m^2; v=0.2. The inertial characteristics at each story are: translational mass equal to 18tn and polar moment of inertia equal to 67.5tnm^2. The modal damping ratio equals 5%. Fig.5 also depicts the structure's finite element model.

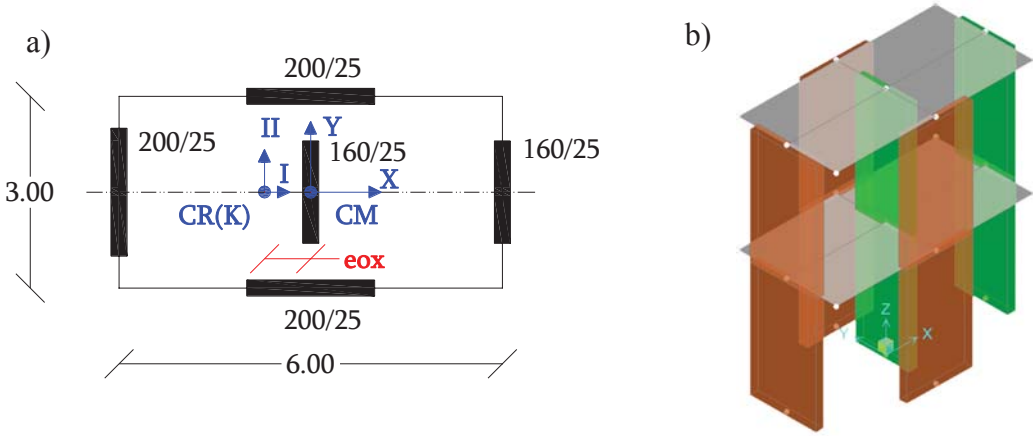

Figure 5: Two-story isotropic building: a) plan view; b) finite element model.

The terms participating in the stiffness matrices according to equations (16, 17) and the coefficients of Rayleigh damping matrix taking into account the first three eigenfrequencies are given in the following.

$$k_{xx} = 361993.161\,,\ k_{yy} = 465153.413$$
$$k_{yz} = -336159.689,\ k_{zz} = 3529724.779$$
$$\boldsymbol{K_o} = \begin{bmatrix} 8 & -2.5 \\ -2.5 & 1 \end{bmatrix} \qquad a = 3.947 \qquad b = 5.944 \cdot 10^{-4}$$

Using well known equations the coordinates of the static elastic axis are determined [25]: $XX_{static} = -0.7227\text{m}$; $YY_{static} = 0\text{m}$. Fig.6 depicts the values of the matrix of the dynamic elastic axis. The coordinate values in X axis deviate from the stable values for the case of zero damping, which is unrealistic and in the small period or high frequency range. This is attributed solely to the presence of inertia according to equation (17). The off-diagonal terms receive zero values for the case that the damping ratio of the structure equals 5%. Furthermore, the coordinate values in Y axis receive zero values. Therefore, the real dynamic elastic axis exists and coincides with the static elastic axis.

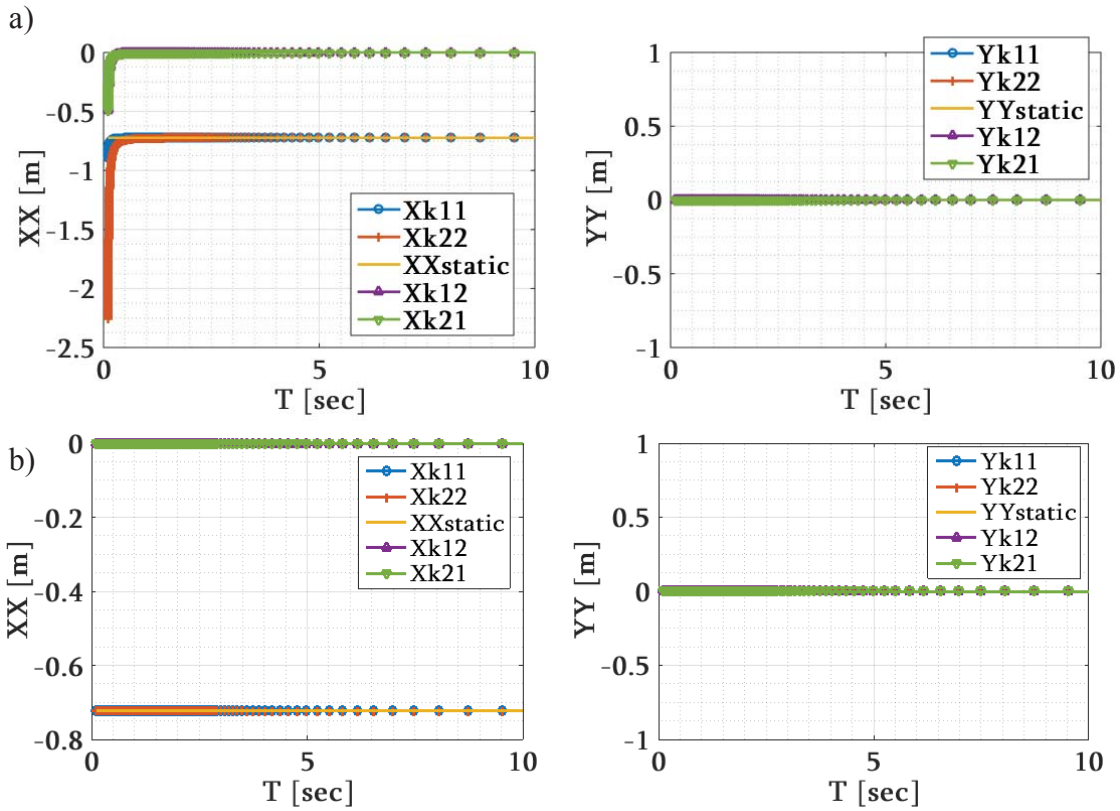

Figure 6: Coordinates of elastic axis for a two-story isotropic building: a) ζ =0%; b) ζ =5%.

3.3 Five-story isotropic building

Fig.7 depicts the plan view of a five-story isotropic building which is symmetric with respect to X axis.

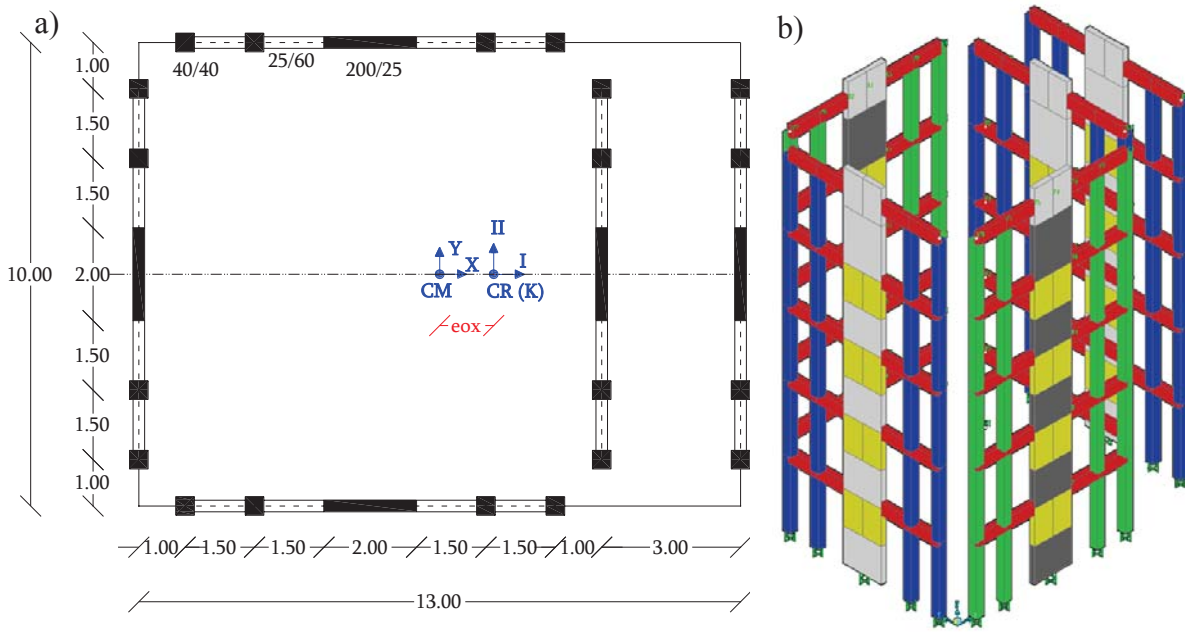

Figure 7: Five-story isotropic building: a) plan view; b) finite element model.

The vertical supporting elements consist of 20 columns (40/40) and five walls (200/25). The horizontal supporting elements consist of a square plate (13mx10m) which behaves as a rigid diaphragm and twenty beams (25/60). The height of each story equals to 3.5m. The material characteristics are: E=2.9e7kN/m^2; v=0.2. The inertial characteristics of each story are: translational mass equal to 200tn and mass moment of inertia equal to 4483.33tnm^2. The modal damping ratio equals 5%. Fig.7 also depicts the structure's finite element model.

The terms participating in the stiffness matrices according to equation (18) are:

$$k_{xx} = 2, k_{yy} = 3$$

$$k_{yz} = 3.5,$$

$$k_{zz} = 146.75$$

$$\boldsymbol{K}_o = \begin{bmatrix} 135.686 & -76.379 & 16.963 & -1.457 & 0.112 \\ & 118.982 & -74.930 & 16.747 & -1.253 \\ & & 118.767 & -73.955 & 14.608 \\ & symm. & & 107.895 & -49.359 \\ & & & & 35.903 \end{bmatrix} \cdot 1e4$$

The coefficients of Rayleigh damping matrix taking into account the first three eigenfrequencies (damping case 1) and the first six eigenfrequencies (damping case 2) are given in the following.

$$a_{3eigen} = 0.9153 \qquad a_{6eigen} = 1.2104$$

$$b_{3eigen} = 0.0025 \qquad b_{6eigen} = 0.001$$

Fig.8 a) and c) depicts the diagonal terms for the two damping cases. A deviation from the static values of the elastic axis is observed at short period range. However, the deviation refers to the third decimal place, and therefore it can be ignored. The increase of the number of eigenfrequencies that participate in the Rayleigh damping matrix, reduces the aforementioned deviation but in small percentage. Fig.8 b) and d) depicts the off-diagonal terms for the two damping cases as well. The values of the terms are considered to be negligible and equal to zero. Therefore, the dynamic elastic axis as defined by the rotational excitation of the structure coincides with the static elastic axis.

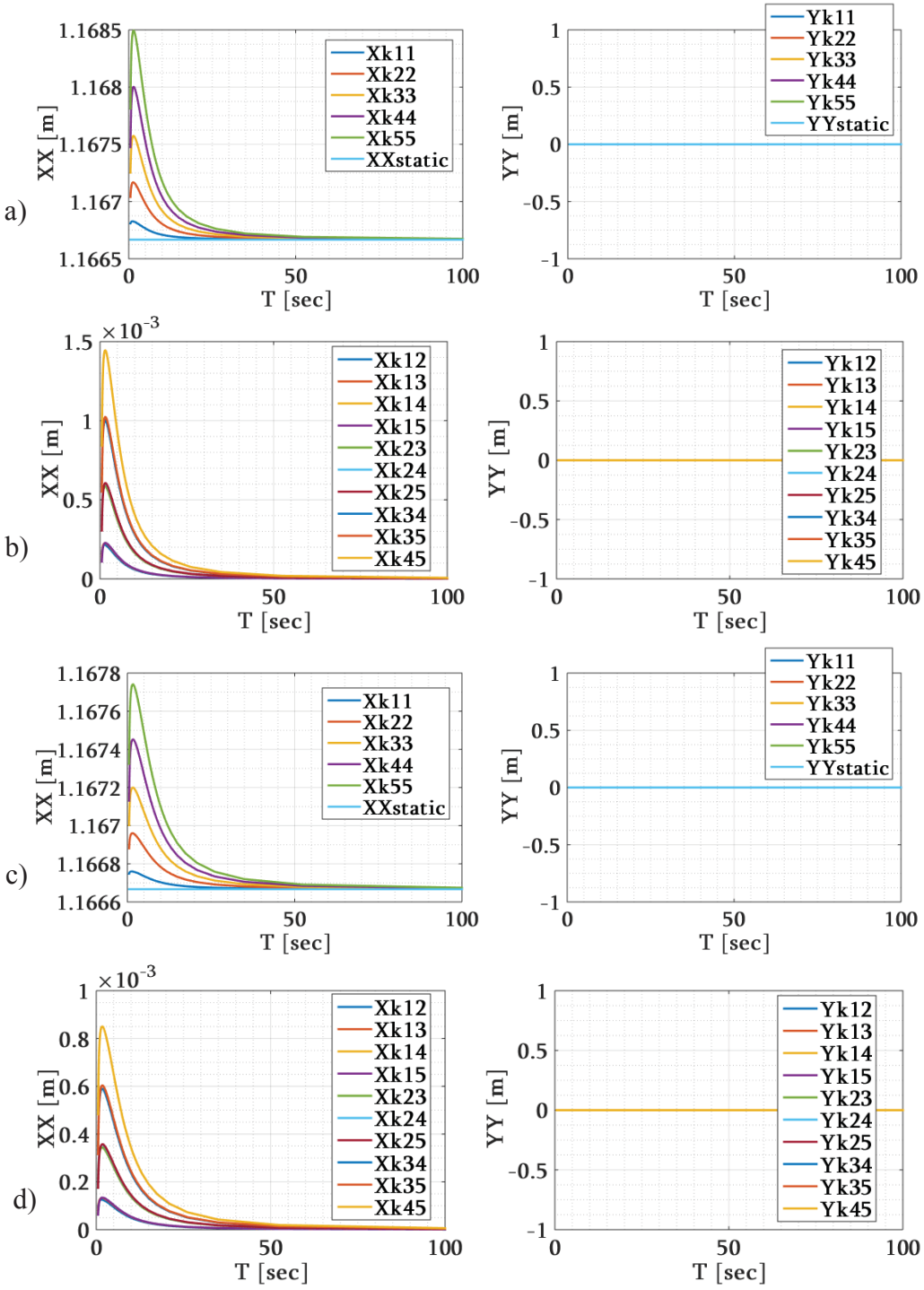

Figure 8: Coordinates of elastic axis for a five-story isotropic building: a) diagonal terms, damping case 1; b) off-diagonal terms, damping case 1; c) diagonal terms, damping case 2; d) off- diagonal terms, damping case 2.

4 CONCLUSIONS

The investigation of the existence of a torsion axis under the action of torsional seismic load has led to the development of analytical formulae for the determination of the torsional axis

under torsional excitation in single story monosymmetric and in multistory isotropic monosymmetric buildings. The determination of the torsional axis has led to the following conclusions:

- A torsional axis can be defined under dynamic excitation in single story monosymmetric and isotropic monosymmetric buildings.
- The location of the torsional axis under dynamic loading depends not only on the geometrical and mechanical characteristics of the structural systems, as the static elastic axis but also on the translational mass and damping characteristics.
- The location of the dynamic torsional axis is independent of the torsional earthquake component and the mass moment of inertia of each story-level.
- The deviation of the coordinates between the static and the dynamic definition of the elastic axis is observed in the high frequency range.
- Characteristic numerical examples are presented for each case under study. Especially for the case of multistory isotropic buildings, the deviation of the elastic axis coordinates from the static values is reduced if more eigenfrequencies are taken into account during the calculation of damping matrix.

The investigation is continued in other types of buildings: asymmetric isotropic buildings and mixed type R/C buildings.

REFERENCES

[1] GC. Hart, RM. DiJulio, M. Lew, Torsional response of high rise buildings, *Journal of Structural Division (J Struct Div) ASCE* 101, 397-414, 1975.

[2] H. Sezen, AS. Whittaker, KJ. Elwood, KM. Mosalam KM, Performance of reinforced concrete buildings during the August 17, 1999 Kocaeli, Turkey earthquake, and seismic design and construction practice in Turkey, *Engineering Structures* 25, 103-14, 2003.

[3] WY. Kam, S. Pampanin, K. Elwood, Seismic performance of reinforced concrete buildings in the 22 February Christchurch (Lyttelton) earthquake, *Bull. N. Z. Soc. Earthq. Eng.* 44 (4), 2011.

[4] SC. Alih, M. Vafaei, Performance of reinforced concrete buildings and wooden structures during the 2015 MW 6.0 Sabah earthquake in Malaysia. *Engineering Failure Analysis* 102, 351-368, 2019.

[5] SA. Anagnostopoulos, MT. Kyrkos, KG. Stathopoulos KG, Earthquake induced torsion in buildings: Critical review and state of the art, *Earthquakes and Structures* 8 (2), 305-377, 2015.

[6] NM. Newmark, Torsion in symmetrical buildings, *Proceedings of the 4th World Conference on Earthquake Engineering*, Santiago, Chile, Vol. 2, 19-32, 1969.

[7] JE. Luco, DA. Sotiropoulos, Local characterization of free-field ground motion and effects of wave passage, *Bulletin of Seismological Society of America* 70(6), 2229-2244, 1980.

[8] JC. De La Llera, AK. Chopra, Accidental torsion on buildings due to base rotational excitation, *Earthquake Engineering and Structural Dynamics* 23; 1003-1021, 1994.

[9] IN. Doudoumis, NI. Doudoumis, Centres of rigidity in multi-story asymmetric diaphragm systems for general lateral static loading, *Engineering Structures* 150; 39-51, 2017.

[10] EM. Marino, PP. Rossi, Exact evaluation of the location of the optimum torsion axis, *The Structural Design of Tall and Special Buildings* 13, 277-290, 2004.

[11] D. Basu, S. Giri, Accidental eccentricity in multistory buildings due to torsional ground motion, *Bull Earthquake Eng* 13, 3779-38080, 2015.
[12] A. Roussopoulos, Distribution of horizontal forces by a rigid plate in spatial structures. Case of seismic forces, their distribution and regime, *Technika Chronika Technical Chamber of Greece*, No. 17, September 132, pp. 871-884 (in Greek), 1932.
[13] T. Makarios, K. Anastassiadis, Real and fictitious elastic axes of multi-story buildings: Theory, *The Structural Design of Tall Buildings (Struct Design Tall Build)* 7, 33-55, 1998.
[14] CL. Kan, AK. Chopa, Elastic earthquake analysis of torsionally coupled multistory buildings, *Earhquake Eng Struct Dynam* 5(4), 395-412, 1977.
[15] IN. Doudoumis, AM. Athanatopoulou, Invariant torsion properties of multistory asymmetric buildings, *Struct Des Tall Special Build* 1, 79-97, 2008.
[16] AM. Athanatopoulou, IN. Doudoumis, Principal directions under lateral loading in multistory asymmetric buildings, *Struct Des Tall Special Build* 17(4): 773-94, 2008.
[17] GK. Georgoussis, Modal rigidity centre: it's use for assessing elastic torsion in asymmetric buildings, *Earthquakes Struct* 2010 1(2), 163-75, 2010.
[18] M. Bosco, EM. Marino, PP. Rossi, An analytical method for the evaluation of the in-plan irregularity of the non-regularly asymmetric buildings, *Bull Earthq Eng* 11, 1423-45, 2013.
[19] T. Shiga, Torsional vibrations of multi-story buildings, *Proceedings of the Third World Conference on Earthquake Engineering*, Vol. 2, New Zealand, 569-584, 1965.
[20] K. Anastassiadis, Caracteristiques elastiques spatiales des batiments a etages, *Annales* de I' I.T.B.T.P., No. 435, June, 1985.
[21] K. Anastassiadis, Axes propres de vibration spatial des batiments a etages, *Annales* No 442: 15-28, 1986.
[22] CL. Kan, AK. Chopra, Elastic earthquake analysis of a class of torsionally coupled buildings, *Journal of the Structural Division ASCE* April: 821-838, 1989.
[23] AK. Chopra, Dynamics of Structures: Theory and Applications to Earthquake Engineering, *Prentice-Hall Inc.,* 1995.
[24] I. Avramidis, A. Athanatopoulou, K. Morfidis, The Finite Element Method: Simulation and Analysis of Structures, *Sofia*, 2016.
[25] Athanatopoulou A.M., Makarios T., and Anastassiadis K., Earthquake Analysis of Isotropic Asymmetric Multistory Buildings, *Journal of Structural Design of Tall and Special Buildings* 15, 417-443, 2006.
[26] MATLAB R2019b. *The Mathworks Inc*.

APPENDIX

Two-story isotropic symmetric building

The equation of motion in the frequency domain receives the following form.

$$(\boldsymbol{K} - \Omega^2 \cdot \boldsymbol{M} + i \cdot \Omega \cdot \boldsymbol{C}) \cdot U(\Omega) = FFT(\boldsymbol{F}(t)) \tag{A1}$$

The displacement and force vector in frequency domain, receive the following forms.

$$\boldsymbol{U}(\Omega)^T = [u_{x1}(\Omega) \quad u_{x2}(\Omega) \quad u_{y1}(\Omega) \quad u_{y2}(\Omega) \quad \theta_{z1}(\Omega) \quad \theta_{z2}(\Omega)]$$
$$FFT(\boldsymbol{F}(t))^T = [0 \quad 0 \quad 0 \quad 0 \quad FFZ_1 \quad FFZ_2] \tag{A2}$$

The stiffness matrix of the two-story isotropic building is expressed by the following form

$$\boldsymbol{K}=\begin{bmatrix} k_{xx}\cdot\boldsymbol{K_o} & 0 & 0 \\ 0 & k_{yy}\cdot\boldsymbol{K_o} & k_{yz}\cdot\boldsymbol{K_o} \\ 0 & k_{yz}\cdot\boldsymbol{K_o} & k_{zz}\cdot\boldsymbol{K_o} \end{bmatrix} \qquad \boldsymbol{K_o}=\begin{bmatrix} K_{o1} & K_{o2} \\ K_{o2} & K_{o3} \end{bmatrix}$$

$$\boldsymbol{K}=\begin{bmatrix} k_{xx}\cdot K_{o1} & k_{xx}\cdot K_{o2} & 0 & 0 & 0 & 0 \\ k_{xx}\cdot K_{o2} & k_{xx}\cdot K_{o3} & 0 & 0 & 0 & 0 \\ 0 & 0 & k_{yy}\cdot K_{o1} & k_{yy}\cdot K_{o2} & k_{yz}\cdot K_{o1} & k_{yz}\cdot K_{o2} \\ 0 & 0 & k_{yy}\cdot K_{o2} & k_{yy}\cdot K_{o3} & k_{yz}\cdot K_{o2} & k_{yz}\cdot K_{o3} \\ 0 & 0 & k_{yz}\cdot K_{o1} & k_{yz}\cdot K_{o2} & k_{zz}\cdot K_{o1} & k_{zz}\cdot K_{o2} \\ 0 & 0 & k_{yz}\cdot K_{o2} & k_{yz}\cdot K_{o3} & k_{zz}\cdot K_{o2} & k_{zz}\cdot K_{o3} \end{bmatrix} \tag{A3}$$

The mass matrix is expressed by the following equation

$$\boldsymbol{M}=\begin{bmatrix} m & 0 & 0 & 0 & 0 & 0 \\ 0 & m & 0 & 0 & 0 & 0 \\ 0 & 0 & m & 0 & 0 & 0 \\ 0 & 0 & 0 & m & 0 & 0 \\ 0 & 0 & 0 & 0 & J_m & 0 \\ 0 & 0 & 0 & 0 & 0 & J_m \end{bmatrix} \tag{A4}$$

The damping matrix following the notion of Rayleigh damping.

$$\boldsymbol{C}=a\cdot\boldsymbol{K}+b\cdot\boldsymbol{M}$$

$$\boldsymbol{C}=\begin{bmatrix} a\cdot k_{xx}\cdot K_{o1}+b\cdot m & a\cdot k_{xx}\cdot K_{o2} & 0 & 0 & 0 & 0 \\ a\cdot k_{xx}\cdot K_{o2} & a\cdot k_{xx}\cdot K_{o3}+b\cdot m & 0 & 0 & 0 & 0 \\ 0 & 0 & a\cdot k_{yy}\cdot K_{o1}+b\cdot m & a\cdot k_{yy}\cdot K_{o2} & a\cdot k_{yz}\cdot K_{o1} & a\cdot k_{yz}\cdot K_{o2} \\ 0 & 0 & a\cdot k_{yy}\cdot K_{o2} & a\cdot k_{yy}\cdot K_{o3}+b\cdot m & a\cdot k_{yz}\cdot K_{o2} & a\cdot k_{yz}\cdot K_{o3} \\ 0 & 0 & a\cdot k_{yz}\cdot K_{o1} & a\cdot k_{yz}\cdot K_{o2} & a\cdot k_{zz}\cdot K_{o1}+b\cdot J_m & a\cdot k_{zz}\cdot K_{o2} \\ 0 & 0 & a\cdot k_{yz}\cdot K_{o2} & a\cdot k_{yz}\cdot K_{o3} & a\cdot k_{zz}\cdot K_{o2} & a\cdot k_{zz}\cdot K_{o3}+b\cdot J_m \end{bmatrix} \tag{A5}$$

The complex matrix, which is multiplied by the displacement vector is calculated by the following expression.

$$\boldsymbol{K_{comp}}=(\boldsymbol{K}-\Omega^2\cdot\boldsymbol{M}+i\cdot\Omega\cdot a\cdot\boldsymbol{K}+i\cdot\Omega\cdot b\cdot\boldsymbol{M})$$

$$\boldsymbol{K_{comp}}=\left[\begin{array}{cc:cc:cc} K_{comp}(1,1) & K_{comp}(1,2) & 0 & 0 & 0 & 0 \\ & K_{comp}(2,2) & 0 & 0 & 0 & 0 \\ \hdashline & & K_{comp}(3,3) & K_{comp}(3,4) & K_{comp}(3,5) & K_{comp}(3,6) \\ & & & K_{comp}(4,4) & K_{comp}(4,5) & K_{comp}(4,6) \\ \hdashline & symm. & & & K_{comp}(5,5) & K_{comp}(5,6) \\ & & & & & K_{comp}(6,6) \end{array}\right] \tag{A6}$$

$$\boldsymbol{K_{comp}}=\begin{bmatrix} \boldsymbol{K_{comp,1}} & \boldsymbol{0} & \boldsymbol{0} \\ & \boldsymbol{K_{comp,2}} & \boldsymbol{K_{comp,3}} \\ symm. & & \boldsymbol{K_{comp,4}} \end{bmatrix}$$

The complex matrix can be divided at six 2-dimensional symmetric matrices. The terms of the first submatrix are calculated in the following.

$$\begin{aligned} &K_{comp}(1,1)=k_{xx}\cdot K_{o1}-\Omega^2\cdot m+i\cdot\Omega\cdot a\cdot k_{xx}\cdot K_{o1}+i\cdot\Omega\cdot b\cdot m\Rightarrow \\ &K_{comp}(1,1)=k_{xx}\cdot(K_{o1}-\Omega^2\cdot m/k_{xx}+i\cdot\Omega\cdot\alpha\cdot K_{o1}+i\cdot\Omega\cdot b\cdot m/k_{xx}) \\ &K_{comp}(1,2)=k_{xx}\cdot K_{o2}+i\cdot\Omega\cdot a\cdot k_{xx}\cdot K_{o2}=k_{xx}\cdot K_{o2}\cdot(1+i\cdot\Omega\cdot a)=K_{comp}(2,1) \\ &K_{comp}(2,2)=k_{xx}\cdot K_{o3}-\Omega^2\cdot m+i\cdot\Omega\cdot a\cdot k_{xx}\cdot K_{o3}+i\cdot\Omega\cdot b\cdot m\Rightarrow \\ &K_{comp}(2,2)=k_{xx}\cdot(K_{o3}-\Omega^2\cdot m/k_{xx}+i\cdot\Omega\cdot\alpha\cdot K_{o3}+i\cdot\Omega\cdot b\cdot m/k_{xx}) \end{aligned} \tag{A7}$$

Therefore, the first submatrix can be written as:

$$\boldsymbol{K_{comp,1}}=\begin{bmatrix} k_{xx}\cdot(K_{o1}-\Omega^2\cdot m/k_{xx}+i\cdot\Omega\cdot\alpha\cdot K_{o1}+i\cdot\Omega\cdot b\cdot m/k_{xx}) & k_{xx}\cdot K_{o2}\cdot(1+i\cdot\Omega\cdot a) \\ k_{xx}\cdot K_{o2}\cdot(1+i\cdot\Omega\cdot a) & k_{xx}\cdot(K_{o3}-\Omega^2\cdot m/k_{xx}+i\cdot\Omega\cdot\alpha\cdot K_{o3}+i\cdot\Omega\cdot b\cdot m/k_{xx}) \end{bmatrix}$$

$$\boldsymbol{K_{comp,1}}=k_{xx}\cdot\boldsymbol{K_{0x}} \tag{A8}$$

$$\boldsymbol{K_{0x}}=\begin{bmatrix} (K_{o1}-\Omega^2\cdot m/k_{xx}+i\cdot\Omega\cdot\alpha\cdot K_{o1}+i\cdot\Omega\cdot b\cdot m/k_{xx}) & K_{o2}\cdot(1+i\cdot\Omega\cdot a) \\ K_{o2}\cdot(1+i\cdot\Omega\cdot a) & (K_{o3}-\Omega^2\cdot m/k_{xx}+i\cdot\Omega\cdot\alpha\cdot K_{o3}+i\cdot\Omega\cdot b\cdot m/k_{xx}) \end{bmatrix}$$

The terms of the second submatrix are calculated in the following.

$$K_{comp}(3,3)=k_{yy}\cdot\left(K_{o1}-\Omega^2\cdot m/k_{yy}+i\cdot\Omega\cdot\alpha\cdot K_{o1}+i\cdot\Omega\cdot b\cdot m/k_{yy}\right)$$

$$
\begin{aligned}
K_{comp}(3,4) &= k_{yy} \cdot K_{o2} \cdot (1 + i \cdot \Omega \cdot a) \\
K_{comp}(4,3) &= K_{comp}(3,4) \\
K_{comp}(4,4) &= k_{yy} \cdot \left(K_{o3} - \Omega^2 \cdot m/k_{yy} + i \cdot \Omega \cdot \alpha \cdot K_{o3} + i \cdot \Omega \cdot b \cdot m/k_{yy}\right)
\end{aligned} \tag{A9}
$$

Therefore, the second submatrix can be written as:

$$
\boldsymbol{K_{comp,2}} = \begin{bmatrix} k_{yy} \cdot \left(K_{o1} - \Omega^2 \cdot m/k_{yy} + i \cdot \Omega \cdot \alpha \cdot K_{o1} + i \cdot \Omega \cdot b \cdot m/k_{yy}\right) & k_{yy} \cdot K_{o2} \cdot (1 + i \cdot \Omega \cdot a) \\ k_{yy} \cdot K_{o2} \cdot (1 + i \cdot \Omega \cdot a) & k_{yy} \cdot \left(K_{o3} - \Omega^2 \cdot m/k_{yy} + i \cdot \Omega \cdot \alpha \cdot K_{o3} + i \cdot \Omega \cdot b \cdot m/k_{yy}\right) \end{bmatrix}
$$

$$
\boldsymbol{K_{comp,2}} = k_{yy} \cdot \boldsymbol{K_{0y}} \tag{A10}
$$

$$
\boldsymbol{K_{0y}} = \begin{bmatrix} \left(K_{o1} - \Omega^2 \cdot m/k_{yy} + i \cdot \Omega \cdot \alpha \cdot K_{o1} + i \cdot \Omega \cdot b \cdot m/k_{yy}\right) & K_{o2} \cdot (1 + i \cdot \Omega \cdot a) \\ K_{o2} \cdot (1 + i \cdot \Omega \cdot a) & \left(K_{o3} - \Omega^2 \cdot m/k_{yy} + i \cdot \Omega \cdot \alpha \cdot K_{o3} + i \cdot \Omega \cdot b \cdot m/k_{yy}\right) \end{bmatrix}
$$

The terms of the third submatrix are calculated in the following.

$$
\begin{aligned}
K_{comp}(3,5) &= k_{yz} \cdot K_{o1} \cdot (1 + i \cdot \Omega \cdot a) \\
K_{comp}(3,6) &= k_{yz} \cdot K_{o2} \cdot (1 + i \cdot \Omega \cdot a) \\
K_{comp}(4,5) &= K_{comp}(3,6) \\
K_{comp}(4,6) &= k_{yz} \cdot K_{o3} \cdot (1 + i \cdot \Omega \cdot a)
\end{aligned} \tag{A11}
$$

Therefore, the third submatrix can be written as:

$$
\boldsymbol{K_{comp,3}} = \begin{bmatrix} k_{yz} \cdot K_{o1} \cdot (1 + i \cdot \Omega \cdot a) & k_{yz} \cdot K_{o2} \cdot (1 + i \cdot \Omega \cdot a) \\ k_{yz} \cdot K_{o2} \cdot (1 + i \cdot \Omega \cdot a) & k_{yz} \cdot K_{o3} \cdot (1 + i \cdot \Omega \cdot a) \end{bmatrix}
$$

$$
\boldsymbol{K_{comp,3}} = k_{yz} \cdot \boldsymbol{K_{0,imag}} \tag{A12}
$$

The terms of the fourth submatrix are calculated in the following.

$$
\begin{aligned}
K_{comp}(5,5) &= k_{zz} \cdot (K_{o1} - \Omega^2 \cdot J_m/k_{zz} + i \cdot \Omega \cdot \alpha \cdot K_{o1} + i \cdot \Omega \cdot b \cdot J_m/k_{zz}) \\
K_{comp}(5,6) &= k_{zz} \cdot K_{o2} \cdot (1 + i \cdot \Omega \cdot a) \\
K_{comp}(6,5) &= K_{comp}(5,6) \\
K_{comp}(6,6) &= k_{zz} \cdot (K_{o3} - \Omega^2 \cdot J_m/k_{zz} + i \cdot \Omega \cdot \alpha \cdot K_{o3} + i \cdot \Omega \cdot b \cdot J_m/k_{zz})
\end{aligned} \tag{A13}
$$

Therefore, the fourth submatrix can be written as:

$$
\boldsymbol{K_{comp,4}} = \begin{bmatrix} k_{zz} \cdot (K_{o1} - \Omega^2 \cdot J_m/k_{zz} + i \cdot \Omega \cdot \alpha \cdot K_{o1} + i \cdot \Omega \cdot b \cdot J_m/k_{zz}) & k_{zz} \cdot K_{o2} \cdot (1 + i \cdot \Omega \cdot a) \\ k_{zz} \cdot K_{o2} \cdot (1 + i \cdot \Omega \cdot a) & k_{zz} \cdot (K_{o3} - \Omega^2 \cdot J_m/k_{zz} + i \cdot \Omega \cdot \alpha \cdot K_{o3} + i \cdot \Omega \cdot b \cdot J_m/k_{zz}) \end{bmatrix}
$$

$$
\boldsymbol{K_{comp,4}} = k_{zz} \cdot \boldsymbol{K_{0z}} \tag{A14}
$$

$$
\boldsymbol{K_{0z}} = \begin{bmatrix} (K_{o1} - \Omega^2 \cdot J_m/k_{zz} + i \cdot \Omega \cdot \alpha \cdot K_{o1} + i \cdot \Omega \cdot b \cdot J_m/k_{zz}) & K_{o2} \cdot (1 + i \cdot \Omega \cdot a) \\ K_{o2} \cdot (1 + i \cdot \Omega \cdot a) & (K_{o3} - \Omega^2 \cdot J_m/k_{zz} + i \cdot \Omega \cdot \alpha \cdot K_{o3} + i \cdot \Omega \cdot b \cdot J_m/k_{zz}) \end{bmatrix}
$$

Finally, the 6-dimensional complex matrix can be written in the following form.

$$
\boldsymbol{K_{comp}} = \begin{bmatrix} k_{xx} \cdot \boldsymbol{K_{ox}} & 0 & 0 \\ & k_{yy} \cdot \boldsymbol{K_{oy}} & k_{yz} \cdot \boldsymbol{K_{o,imag}} \\ symm. & & k_{zz} \cdot \boldsymbol{K_{oz}} \end{bmatrix} \tag{A15}
$$

EURODYN 2020
XI International Conference on Structural Dynamics
M. Papadrakakis, M. Fragiadakis, C. Papadimitriou (eds.)
Athens, Greece, 23–26 November 2020

EVALUATION OF VIBRATION CHARACTERISTICS OF RC AND PPC BEAM MEMBERS UNDER CYCLIC TRAIN LOADING

M. TOKUNAGA[1]

[1] Railway Technical Research Institute
2-8-38, Hikari-cho, Kokubunji-shi, Tokyo, Japan
e-mail: tokunaga.munemasa.68@rtri.or.jp

Keywords: Railway viaduct, resonance, fatigue test, RC member, PPC member

Abstract. *Resonance phenomenon during train passing has been observed because of the increased in train operation speed in high-speed railway, the spread of low stiffness girder such as PPC and SRC girder, and the advances in measurement technology. An example has been reported in which significant resonance is generated, which is caused by a decrease in stiffness due to the progress of cracks in concrete members. The stiffness of members must be evaluated in consideration of the action hysteresis during the design life time, i.e. the magnitude and the cyclic number of the load. The aim of this paper is to evaluate the vibration characteristics of RC and PPC beam members in operating condition and the variation of stiffness and damping of the beam after repeated loads of about 2 million times was evaluated based on fatigue tests of 4 specimens. Static loading tests made it clear that the effective stiffness of RC members decreases with respect to increasing load magnitude and it is consistent with the previous evaluation formula. On the other hand, the effective stiffness of the PPC member is overestimated in the case of the previous evaluation formula, and is consistent with Branson's cubic law. From the fatigue tests, the effective stiffness decreases by about 6 to 16% for RC members and 10 to 33% for PPC members after 2 million cyclic loading. The equivalent damping is from 4.0% for RC members, according to the load magnitude and decreases to about 0.5%, and 1.5% to 0.5% for PPC members after 2 million cyclic loading. This means that the repeated loading accompanying the train pass contributes to increasing the dynamic response, especially with a large degree of influence on the PPC members. Finally, dynamic analyses implementing the experimental results implied that excessive response can occur after millions of train passage, especially in the case of PPC members, even if it were not observed in the initial stage of operations.*

1 INTRODUCTION

The phenomenon of vibrational resonance during train passing has been confirmed following the enhanced operational speeds of high-speed railways, the spread of low-stiffness girder such as the PPC and SRC girders, and the advances in measurement technology [1]. For example, there was a study reporting that significant resonance was generated from a decrease in stiffness of concrete members owing to crack progression. As such, further refinement of the impact coefficient is required in the dynamic response evaluation of such members, largely depending on their natural frequencies or their rigidities [2]. In view of this, the stiffness of concrete members must be evaluated in consideration of their experience during the design lifetime, i.e. the magnitude and cyclic number of the repeated loads. Thus, the stiffness of RC members was evaluated herein, under the assumption of an operational condition [3]. Moreover, the hysteresis characteristics of PPC members were evaluated under the same use condition, whereas in the past such characteristics were partially studied in the architectural field, under the occurrence of earthquakes [4, 5, 6].

This paper aims to evaluate the vibration characteristics of RC and PPC beam members under a specific operational condition in beam stiffness and damping variations after a fatigue test of approximately two million times of repeated loading.

2 EXPERIMENT

2.1 Specimen

Figure 1 shows the design details of the specimens, which consists of both RC and PPC members, of which the latter has become widely popular in railway structures in recent years. Herein, the ratio of tensile rebars and the amount of introduced pre-stress were assumed by reference to specifications of general railway bridges. The tensile reinforcement ratio of RC and PPC member are 1% and 0.6%, respectively. The prestressing coefficient of PPC member λ is 0.71.

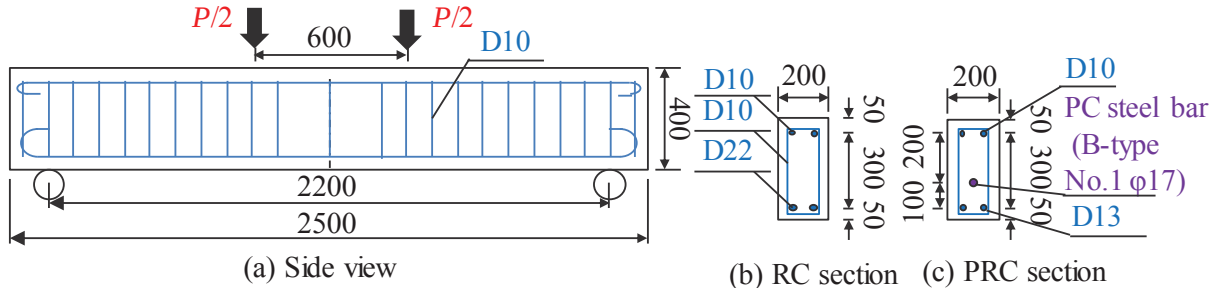

Figure 1: Design details of specimens

2.2 Loading pattern

Figure 2 illustrates the static cyclic loading test for evaluating the basic hysteresis characteristics of the members, with increments of 20kN in the load control through the tensile rebar's yield point and 2 mm as displacement control after yield. At each increasing load level, the number of repetitions was three times. Moreover, a 5-kN load was maintained during unloading.

In the dynamic loading test, the upper limit load was increased to 70, 120 and 170kN, with assumed 50-kN reinforcement stress (of approximately 100 MPa) of dead load based on a 5-Hz excitation frequency. In this test, the number of repetitions at each load level was two million.

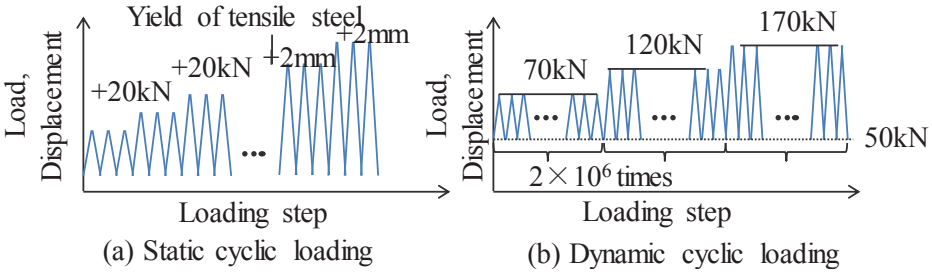

Figure 2: Loading pattern

2.3 Static load-displacement relationship

Figure 3 shows the load–displacement relationship obtained from the static and dynamic loading test. Apparently, the stiffness (effective stiffness K_{eq}) at unloading and reloading decreased in the region where cracks occurred, whereas it decreased on the skeleton curve (after δ_c in the figure). Moreover, the residual displacement at unloading in the RC members increased with respect to increasing load as compared to the PPC members. The hysteresis characteristics of PPC members exhibited a stronger tendency to point towards the origin during unloading when compared with those of the RC members; as the residual displacement decreased, the effective stiffness showed decreasing tendency. That is, the prestress introduced for the purpose of reducing the crack width was found to influence reduction in the stiffness of the entire beam system.

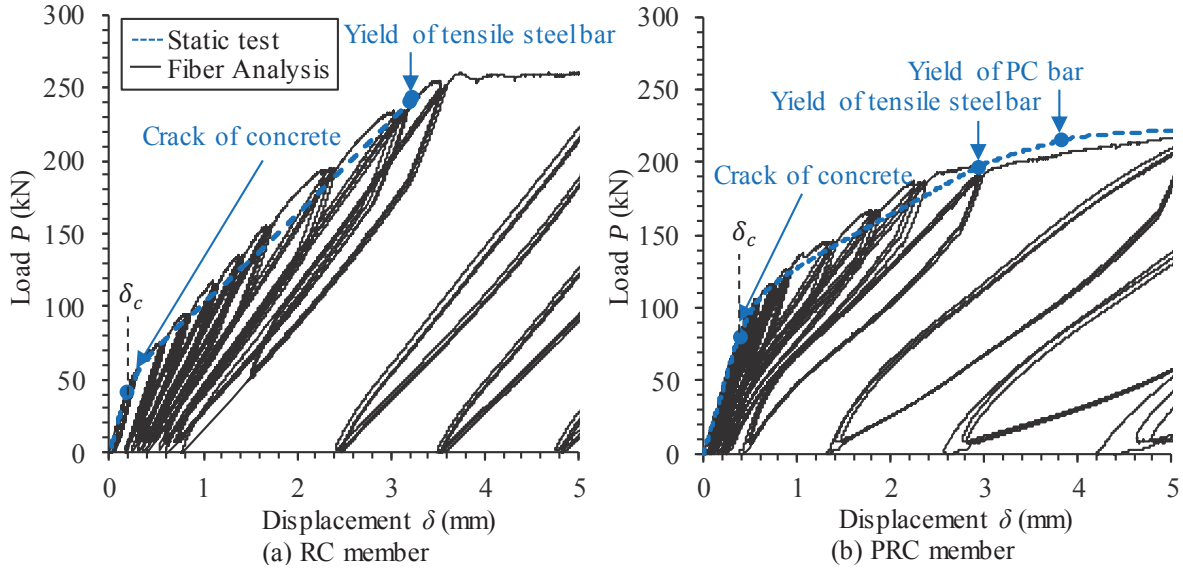

Figure 3: Load-displacement relationship obtained from static and dynamic loadings

2.4 Dynamic characteristics variation due to cyclic loading

Figures 4 shows the effective stiffness and equivalent damping of RC members obtained from the static and dynamic loading tests. Displacement of the horizontal axis was the maximum displacement experienced in the past at each loading step. On one hand, effective stiffness was the active stiffness connecting the maximum and minimum load points of the loop on the load–displacement relationship under cyclic loading. On the other hand, equivalent damping ratio was the equivalent viscous damping of the hysteresis damping calculated from the area of the same loop.

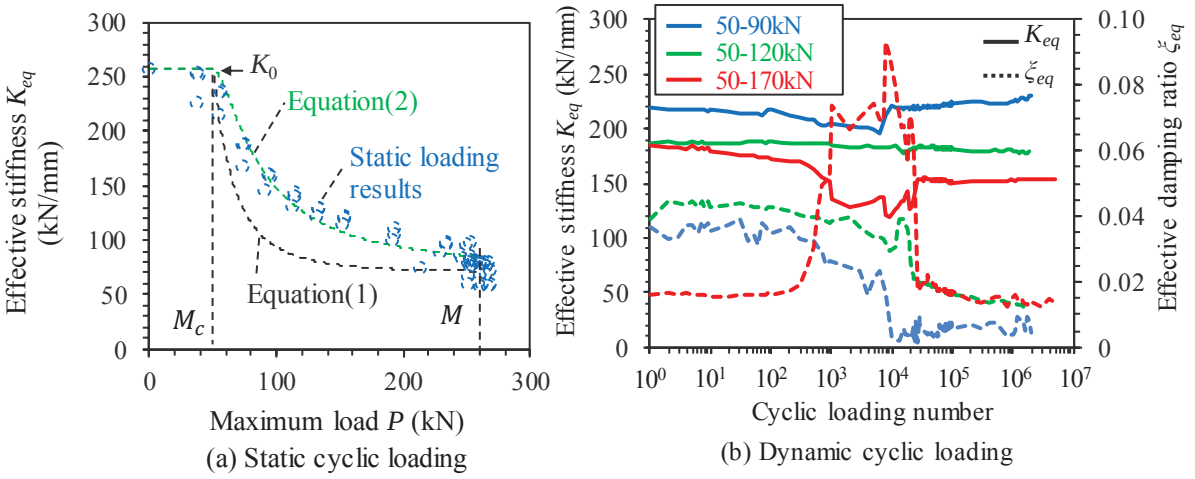

Figure 4: Effective stiffness and equivalent damping of RC members

The ACI 318-08 [7] technique is based on the method proposed by Branson [8, 9], which uses the effective stiffness K_e,

$$K_e = \left(\frac{M_{cr}}{M_{max}}\right)^3 K_0 + \left\{1 - \left(\frac{M_{cr}}{M_{max}}\right)^3\right\} K_{cr} \tag{1}$$

where K_0 is the gross sectional stiffness (uncracked concrete section); K_{cr} the sectional stiffness of the fully cracked section; M_{max} the applied maximum bending moment; M_{cr} the cracking moment. In practical designs, the secant stiffness is calculated by Eq. (1) (Railway Technical Research Institute 2004).

Wakui et al. (1996) proposed a method to predict the flexural stiffness at reloading by using the following equation.

$$K_{s,RC} = \left(\frac{M_{cr}}{M_{max}}\right)^{1.6} K_0 + \left\{1 - \left(\frac{M_{cr}}{M_{max}}\right)^{1.6}\right\} K_e \tag{2}$$

Hereafter, test results are compared with above two equations for the sake of conforming the applicability especially for PPC members under cyclic loading condition.

For the RC member, the static loading test results confirmed that the effective stiffness decreases with an increase of loading amplitude after δ_c. The obtained effective stiffness K_{eq} of the RC member was consistent with stiffness $K_{s,RC}$ during reloading by the static cyclic loading test.

Results of the fatigue test by dynamic loading indicated that the RC members achieved K_{eq} of approximately 220kN/mm to about 11% at 50–90kN and approximately 189kN/mm to nearly 6% at 50-120kN in 50–90kN. At 170-kN load, K_{eq} decreased from 184kN/mm to approximately 16%. Moreover, ξ_{eq} showed the tendency to increase with increasing load and to decrease with increasing number of repeated loads. Specifically, it decreased from 4.0% to 0.5% at 50–90kN and from 167kN/mm to within 4.5%–1.2% at 50–120kN. The change was small at nearly 1.5% at 50-170kN. K_{eq} exhibited a sharp decline of roughly 25% while ξ_{eq} increased rapidly from approximately 1.5% to 9% at repetitions of almost 500 to 20,000 times at 50–170kN. Crack width and residual displacement in this region increased simultaneously, indicating that there is a possibility of deterioration of aggregate mesh in the concrete at the cracked area. Nonetheless, the mesh was improved by repeated loading thereafter, where K_{eq}, ξ_{eq} must have settled to the value prior to 500 times of repeated loadings.

For the PPC member, the effective stiffness decreases with respect to increasing loading amplitude after δ_c. These results were consistent with the stiffness K_e obtained by using Branson's law, with overestimated $K_{s,RC}$.

Figures 5 shows the effective stiffness and equivalent damping of PPC members obtained from the static and dynamic loading tests. For the PPC members, results for the dynamic loading test indicated that K_{eq} decreased almost 10% from the initial stiffness 275kN/mm when the cyclic loading amplitude is 50-90kN loading. It decreased almost 33% from 240kN/mm when the loading amplitude is 50-120kN and almost 20% from 167kN /mm when the loading amplitude is 50-170kN. These results show the stiffness of PPC member significantly decreases when compared to RC members due to cyclic loading. ξ_{eq} exhibited a tendency to increase with respect to increasing loading amplitude and to decrease with increasing frequency of repeated loads. Particularly, it ranged within 0.5% and 1.5% when the cyclic loading amplitude is 50-90kN. It decreased from 1.5% to 0.5% when the amplitude is between 50 and 120kN and from 2.3% to 1.2% when the amplitude is between 50 and 120kN. Both RC and PPC members showed a tendency of stiffness reduction and damping reduction by the repeated loading, towards a greater or a lesser extent. Especially for PPC members, the dynamic response is expected to shift to the direction of increase due to repeated loading accompanying the train passing.

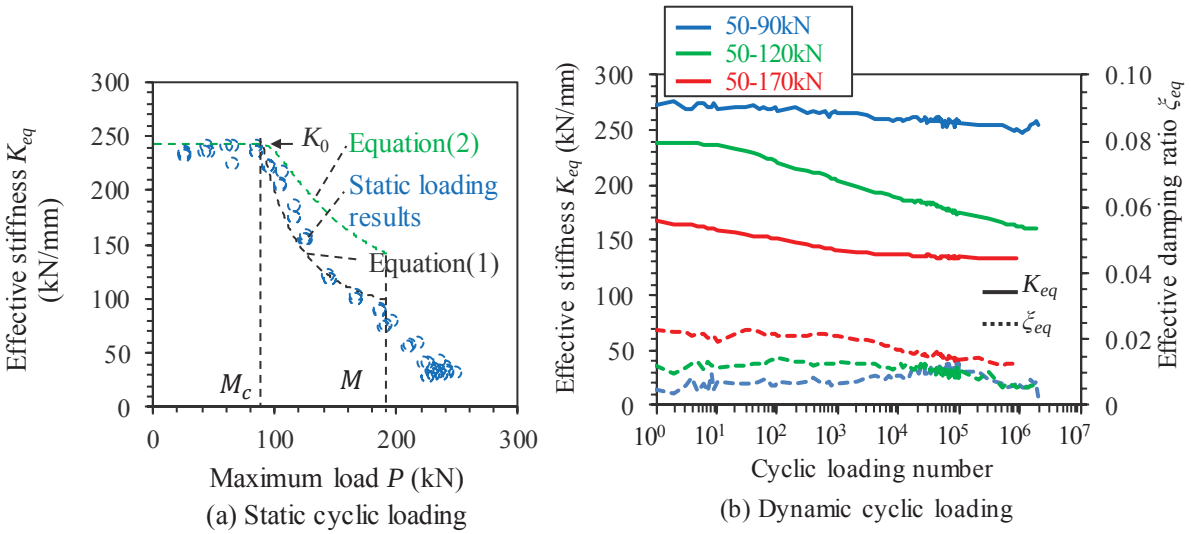

Figure 5: Effective stiffness and equivalent damping of PPC members

3 ANALYSIS

Previously mentioned experimental results were implemented into dynamic analysis expecting a number of train passage.

In the analyses, girders were modeled by elastic beam elements of which initial natural frequency was set to be $f = 50\sim80L_b^{-0.8}$. As shown in figure 6, the coefficient 50 implies that the girder frequency is approximately minimum stiffness defined in Eurocode. The initial damping ratio ξ was set to be 0.02. As shown in figure 7, the stiffness and modal damping ratio decrease with the number of the repeated loading cycle. Considering the test results, the stiffness was supposed to decreases 20% for RC members and 35% for PPC members at 1 million times cyclic loading. The damping ratio decreases from 2% to 1% at 1 million times cyclic loading for both members. The unit weight per length was set to be 200kN/m. Train load was modeled by moving concentrated load which suppose 12 cars and 300pph of running speed and 120kN of axial loads.

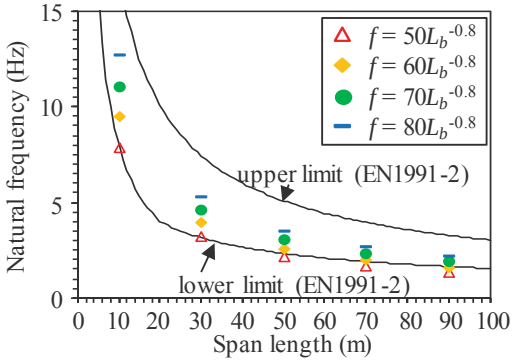

Figure 6: Initial natural frequency

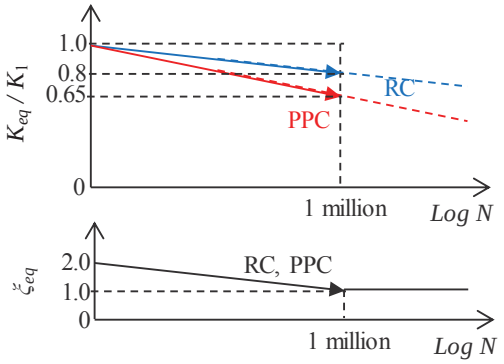

Figure 7: Dynamic characteristics deterioration

Figure 8 shows the displacement increase obtained by dynamic analyses. In the case of RC girder of which span is 10m, the displacement response grows with the cyclic number and exceeds the serviceability limit after 1 million cyclic loadings only when initial frequency is $50L_b^{-0.8}$. In the case of RC girder of which span is 30m, it doesn't exceed the serviceability limit even after 1 million cyclic loadings. In the case of PPC girders, the displacement increases more in the case of RC girders, and it tends to exceed the serviceability limit after 1 million cyclic loadings when initial frequency is $50L_b^{-0.8}$ and $60L_b^{-0.8}$. These results imply that excessive response can occur after millions of cyclic loading, especially in the case of PPC members, even if it were not observed in the initial stage of operations.

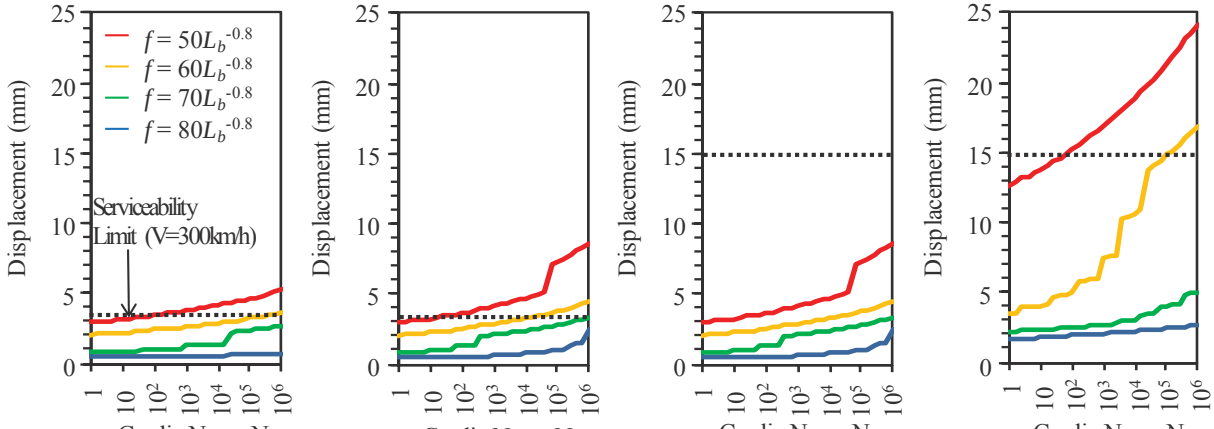

Figure 8. Displacement increase obtained by dynamic analyses

4 CONCLUSIONS

This study has evaluated the vibration characteristics of RC and PPC beam members under operational condition, based on fatigue tests. From these results, the following conclusions may be drawn:

- From static loading tests, it is found that the effective stiffness of RC members decreas-es with respect to increasing load, which is consistent with a previous evaluation formula. Nevertheless, the effective stiffness of the PPC members is overestimated relative to the same previous evaluation formula, which is consistent with Branson's cubic law.

- As a result of repeated dynamic loading, the effective stiffness decreases by approximately 6% to 16% for the RC members and 10% to 33% for the PPC members. Equivalent damping for the RC members is from 4.0% (relative to load size) and decreases to

around 0.5%, whereas for the PPC members it decreases from 1.5% to 0.5%. This means that repeated loading accompanying the train passing contributes to the shift to-wards increasing dynamic response, especially directing a large degree of influence on the PPC members.

- Dynamic analyses implementing the experimental results implied that excessive response can occur after millions of train passage, especially in the case of PPC members, even if it were not observed in the initial stage of operations.

REFERENCES

[1] Ito, Y., Y. Oono, K. Yoshida, S. Nishiyama & A. Tanabe (2017), Proposal of simple health index for double reinforced RC slab girder railway bridges, Journal of Structural Engineering 63A, pp. 876-887 (in Japanese).

[2] Sogaba, M., N. Matsumoto, M. Kanamori, M. Sato & H. Wakui (2005), Impact factors of concrete girders coping with train speed-up, Quarterly Report of RTRI, 46(1), pp. 46-52.

[3] Wakui, H., N. Matsumoto & T. Watanabe (1991), An evaluation method of flexural rigidity of reinforced concrete girders for computing deflection, RTRI report, 5(11), pp. 55-62.

[4] Hayashi, M., S. Okamoto, S. Otani, H. Kato & J. Fu (1995), Hysteresis model for prestressed concrete members and its effect on earthquake response, Journal, Prestressed Concrete Japan Prestressed Concrete Engineering Association, 37(4), pp. 57-67 (in Japanese).

[5] Sugano, S. (1970), Experimental Study on Restoring Force Characteristic of Reinforced Concrete Members, Ph.D. Thesis, University of Tokyo (in Japanese).

[6] Takeda, T. M. A. Sozen & N. N. Nielsen (1970), Reinforced concrete response to simulated earthquakes, Journal of the Structural Division, 96(2), pp. 2557-2573.

[7] ACI Committee 318 (2008), Building code requirements for structural concrete. ACI 318-08 and Commentary. ACI, Farmington Hills, Michigan.

[8] Branson, D.E. (1963), Instantaneous and time-dependent deflections of simple and continuous reinforced concrete beams, HPR Report 7, pp. 1-78.

[9] Branson, D.E. (1977), Deformation of Concrete Structures. McGraw-Hill, New York.

[10] Railway Technical Research Institute (2004), Design Standards for Railway Structures and Commentary (Concrete Structures). Maruzen Co., Ltd. Tokyo (in Japanese).

EURODYN 2020
XI International Conference on Structural Dynamics
M. Papadrakakis, M. Fragiadakis, C. Papadimitriou (eds.)
Athens, Greece, 23–26 November 2020

EXPERIMENTAL STUDY ON THE FRACTURE BEHAVIOR OF AN RC PILE GROUP FOUNDATION USING A CENTRIFUGE MODEL

Y. Miyachi[1], K. Hayashi[1], S. Takahashi[1], T. Saito[1]

[1] Department of Arch. and Civil Eng., Toyohashi University of Technology
1-1 Hibarigaoka, Tempaku-cho, Toyohashi, Aichi, Japan
e-mail: y173540@edu.tut.ac.jp, hayashi@ace.tut.ac.jp, s183515@edu.tut.ac.jp, tsaito@ace.tut.ac.jp

Keywords: *Centrifuge experiment, Dynamic response, Dry Sand, Bending fracture, Maximum inertial force*

Abstract. *It is reported the pile foundations of many buildings were damaged by the 2016 Kumamoto Earthquake. The main shock of the massive earthquake measured magnitude 7.3. The city hall, built using an RC pile foundation was damaged, and inclined. Little is known about the fracture behavior of the soil-pile-superstructure interaction under a strong earthquake. This study investigated the fracture mode of RC pile foundations and the relationship between the pile fracture and the dynamic response of a superstructure and attempted to evaluate the ultimate lateral strength of a RC pile foundation.*

A shaking table test under a 50G centrifuge field was conducted to investigate the bending fracture behavior of RC pile members. A miniature RC pile model was proposed for the centrifuge experiment. The diameter of the pile model was 25 mm (prototype scale: 1.25 m) and consisted of mortar (17.1 MPa in compressive strength), 4 main reinforcements (1.2 mm in diameter), and a spiral hoop reinforcement (0.8 mm in diameter at intervals of 5 mm). The pile model demonstrated elasto-plastic behavior according to the element test without surrounding soil. It showed sufficient bending deformation capacity and the maximum strength exceeded the full plastic moment. The specimen for the centrifuge experiment was composed of dry soil, RC pile models, footing, and a superstructure. The footing was supported by four vertical pile models. The relative density of the dry soil (Toyoura dry sand) was 60%. The mass of the superstructure was 7.45kg (931ton in prototype scale), and the mass of the footing was 1.77kg (221ton in prototype scale). The natural period of the superstructure was 0.63 sec. This value corresponds to a 10-floor RC building. During the shaking table test, a total of 11 Rinkai waves, with different amplitudes, were input. A Rinkai wave is an artificial wave expected to form off the coast of Japan. The maximum acceleration of each shaking ranged between 0.41 m/s^2 to 7.06 m/s^2.

In the test result, bending fracture occurred at the pile head when the maximum input acceleration was 2.97 m/s^2. When the input acceleration was further increased, the inertial force acting on the superstructure also increased and exceeded the evaluated strength. Finally, at maximum inertial force of superstructure, the displacement of the footing further increased.

1 INTRODUCTION

In the 2016 Kumamoto Earthquake (the main shock of the earthquake was measured at magnitude 7.3), it was reported that several pile foundations of buildings were damaged [1]. Mashiki city hall, which had an RC pile foundation structure was damaged and inclined after the earthquake. Through damage investigation after the earthquake, it was found that some piles were severe damaged, and the city hall had to be rebuilt. The relationship between damage to the piles and the dynamic response of a superstructure under dry soil-RC pile-superstructure interaction is, the most part, unclear.

Few studies have investigated the facture behavior of RC pile foundations under soil-RC pile-superstructure interaction. Previous studies were conducted using a large shaking table test [2, 3], and a centrifuge model [4, 5]. Tamura et al., conducted shaking table tests using a large scale laminar shear box [2]. They revealed the dynamic behavior and failure mechanisms of small diameter RC pile models (diameter: 150mm) during soil liquefaction. Shibata et al., conducted a shaking table test of small diameter RC pile using E-Defense, which is largest shaking table in the world. The diameter of the RC pile model was 150mm, which was 1/10 of the full scale RC pile. It investigated the bending-induced damage mechanism and revealed the influence of axial load variation on the pile damage [3]. Even with the shaking table test under 1G field it is hard to reproduce the ultimate behavior of a large diameter RC pile. On the other hand, the centrifuge model test is available to reproduce the ultimate behavior of a large diameter RC pile. Kimura et al., conducted pushover loading and cyclic loading tests using small diameter RC pile models on dry sand under a centrifuge field [4]. According to the test result of the load-deformation relationship and observation of test specimen, the bending fractures had occurred at the RC pile models. Nevertheless, an evaluation method for ultimate strength hasn't been discussed. Higuchi et al., examined soil-large diameter RC pile interaction behavior until the main bar of the pile models yielded, using a dynamic centrifuge test [5]. However, there has not been any research on the strongly nonlinear behavior of soil-large diameter RC pile-superstructure interaction. Further, an evaluation of the ultimate lateral strength of RC pile foundation has not been undertake.

This study investigated the fracture mode of RC pile foundations and the relationship between the pile fracture and the dynamic response of a superstructure and attempted to evaluate the ultimate lateral strength of a RC pile foundation.

2 PILE MODEL FOR CENTRIFUGE TEST

2.1 RC pile model

The experiment was conducted under a 50G field using the centrifuge test system of the Disaster Prevention Research Institute at Kyoto University. An RC pile model (hereinafter called 'the pile model') that could reproduce elasto-plastic behavior was used to conduct the experiment. Figure 1 shows the details of the pile model. The pile model was designed to reproduce the elasto-plastic behaviour of concrete piles. It consisted of mortar, 4-main reinforcement bars (diameter: 1.2mm, yield strength: 374N/mm^2), and a spiral hoop reinforcement bar at intervals of 5mm (diameter: 0.8mm, yield strength: 432N/mm^2). The diameter of the pile model was 25mm (full scale: 1.25m). Table 1 shows a comparison of pile cross sections: the main reinforcement ratio and the hoop reinforcement ratio of the pile model almost correspond to the example cross section suggested by examples from foundation structures in Japan [6]

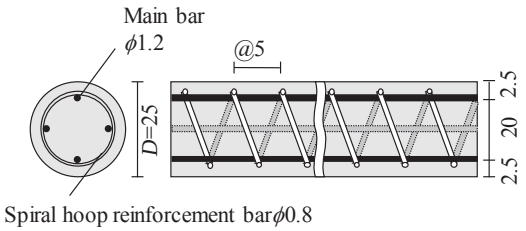

Figure. 1: Cross section of RC pile model (mm)

Table 1: Comparison of pile cross section

		Pile Model (Model scale)	Example cross-section (Real scale)
Diameter		25mm	1800mm
Main reinforcement bar	Rebar	4-ϕ1.2	45-D29
	Ratio	0.92%	1.13%
Hoop reinforcement bar	Rebar	ϕ0.8@5	D13@150
	Ratio	0.27%	0.26%

2.2 Static loading test

The static loading test was conducted to evaluate the performance of the pile model. Figure 2 shows the loading system of the test. The bottom of the pile model was rigidly jointed to a reaction force jig, and the top connected to a horizontal loading device by a pin jig and a vertical roller jig. The horizontal deformation was measured by a laser displacement transducer. The horizontal cyclic loading was input to 37.5mm (shear span ratio=1.5*D*, full scale: 1.875m) above the critical section, and the loading device was controlled according to rotation angles of 0.005, 0.01, 0.02, 0.04, 0.06, 0.08, 0.1, and 0.15 rad. The rotation angle of the pile model was calculated using the distance between the laser displacement transducer and the critical section (37.5mm). The compressive strength of the mortar of the pile model was 17.1 Mpa. The axial force for the pile model was 1,126N (full scale: 2.8MN). It was same value as the axial force for each pile model of the shaking table test, which is described later. The ultimate strength (loading capacity) of the pile model in this test is calculated as equation (1)

$$Q_u = \frac{M_u}{L} \tag{1}$$

where M_u is the full plastic moment of the pile model, and L is the shear span (37.5mm).

Figure 3 shows the relationship between load and rotation angle in full scale. The red line indicates the calculated ultimate strength (loading capacity, full scale: Q_u= 1.56MN). The RC pile model used in this study performed degradation behavior after reached ultimate strength. This behavior reproduced to a real RC member.

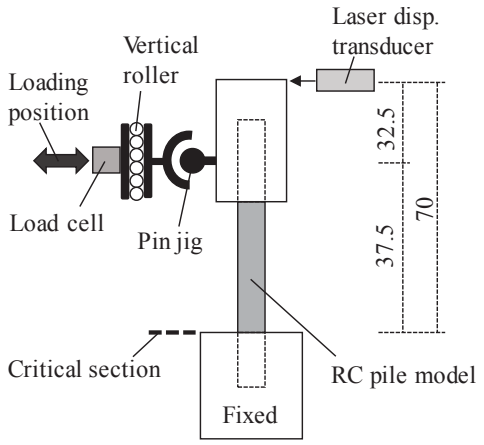

Figure 2: System of the test (mm)

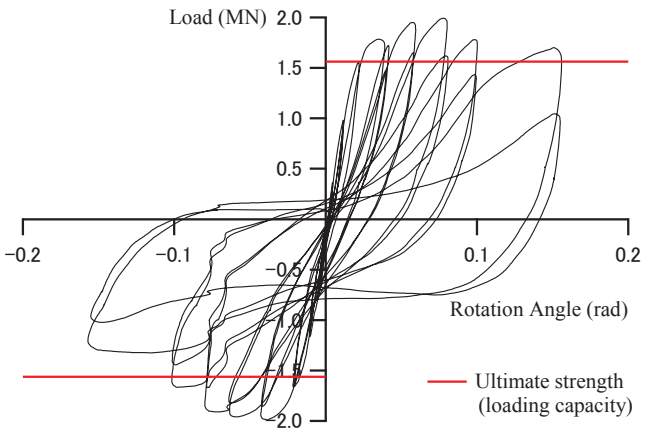

Figure 3: Test result

3 DYNAMIC CENTRIFUGAL MODEL TEST

3.1 Specimen

The shaking table test was conducted under a 50G field, the same as the static loading test in the previous section, using a centrifugal loading device at the Disaster Prevention Research Institute, Kyoto University. Figure 4 shows the specimen of the test and Table 2 shows its properties. The specimen was composed of dry soil, RC pile models, footing, and superstructure. The footing was supported by four 200 mm long piles with rigid connections at the pile head and bottom. The distance of the pile models was 150mm (full scale: 6*D*, 7.5m) in *X* direction, and 62.5mm (full scale: 2.5*D*, 3.13m) in *Y* direction. The mass of the footing was 1.77 kg while the mass of the superstructure was 7.42 kg. Therefore, the total mass was 4,503N (full scale: 11.3MN) and the axial force for each pile model was 1,126N (full scale: 2.8MN). This was roughly equivalent to the static loading test in the previous section. The primary natural period of the superstructure was 0.013 seconds (0.63 seconds in full scale). The primary natural period of the superstructure and the acting axial force of the pile were equivalent to a 10 story RC building (roughly a 35 m high building, with 5 to 6 m column spans). The soil consisted of Toyoura dry sand with a relative density of 60%

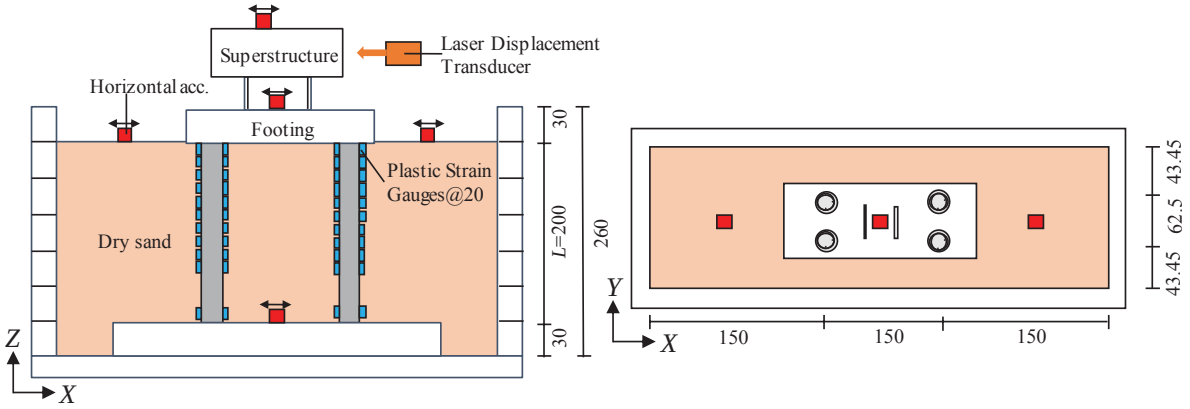

Figure 4 : Specimen of the shaking table test

Table 2: Properties of the spacimen

			Scaling Law	Unit	Full Scale	Model Scale
Piles	Length		1/λ	m	10	0.2
	Diameter		1/λ	mm	1250	25
	moment of inertia of area		$1/\lambda^4$	cm^4	1.29×10^7	2.08
	Yield stress of mortar		1	N/mm^2	17.1	17.1
	Main bar	Diameter	1/λ	mm	60	1.2
		Yield stress	1	N/mm^2	374	374
	Shear reinforcement bar	Diameter	1/λ	mm	40	0.8
		Pitch	1/λ	mm	250	5
		Yield stress	1	N/mm^2	432	432
Footing	Mass		$1/\lambda^3$	kg	221250	1.77
Superstructure	Mass		$1/\lambda^3$	kg	927500	7.42
Soil	Density		1	%	60	60

3.2 Shaking and measurement plan

The shaking was programmed to impose gradually progressive damage to the pile model using gradually increasing amplitudes of horizontal unidirectional input waves. A total of 11 Rinkai waves (JBDPA 1992) of different amplitudes were input. A Rinkai wave is an artificial wave expected to form off the coast of Japan. The maximum acceleration of each shaking ranged between 0.41 m/s^2 to 7.06 m/s^2 (from shaking 1 to 11). As showed in Figure 4, the accelerometers to measure the horizontal acceleration of the superstructure, footing, ground surface and bottom of the soil tank (input) were installed. Also, the horizontal displacement of the footing section was measured by laser displacement transducers. Plastic strain gauges were attached to the surface of the pile models to measure axial strain.

3.3 Test result

Figure 5-7 shows the main time history (0 to 50s) of the horizontal acceleration of the superstructure, footing, ground surface and input (bottom of the soil tank), vertical displacement and inclination angle of the superstructure, and horizontal displacement of the footing for shaking 2(elastic state), 4(plastic hinge occurred) and 11(final shaking) respectively. They are shown at full scale below. Figure 8 shows the damage to the pile model after the test.

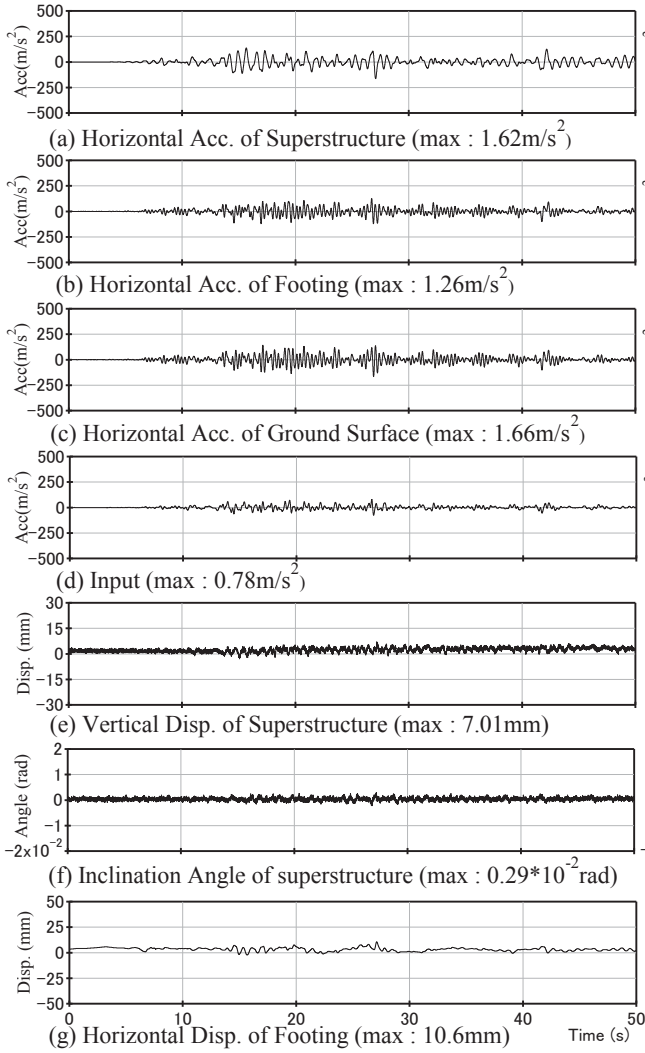

(a) Horizontal Acc. of Superstructure (max : 1.62m/s^2)
(b) Horizontal Acc. of Footing (max : 1.26m/s^2)
(c) Horizontal Acc. of Ground Surface (max : 1.66m/s^2)
(d) Input (max : 0.78m/s^2)
(e) Vertical Disp. of Superstructure (max : 7.01mm)
(f) Inclination Angle of superstructure (max : 0.29*10^{-2}rad)
(g) Horizontal Disp. of Footing (max : 10.6mm)

Figure 5: The main time history of shaking 2

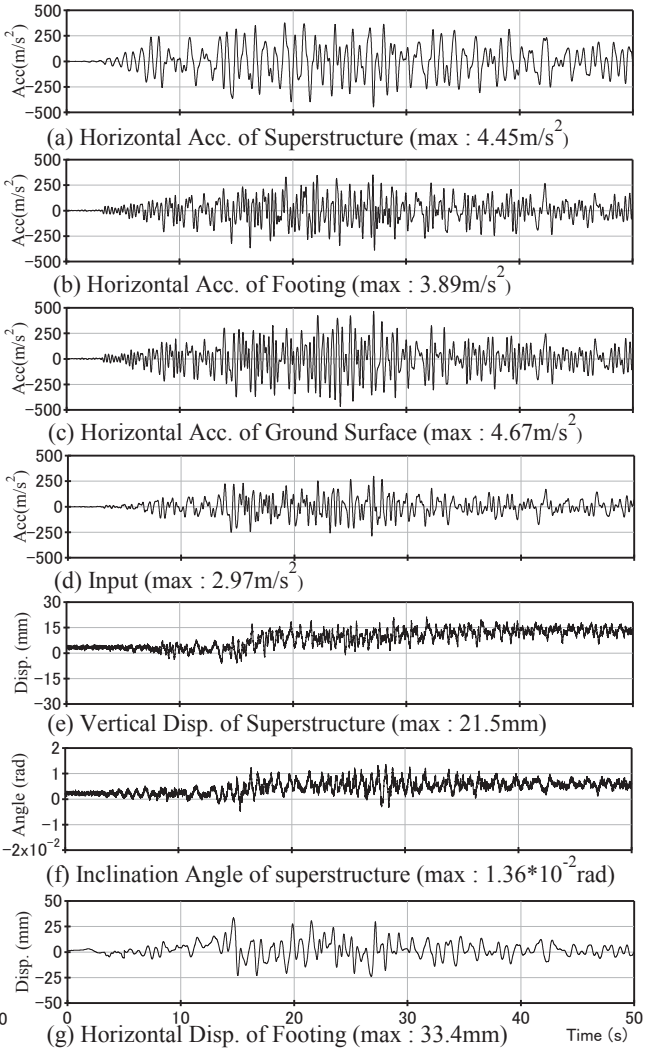

(a) Horizontal Acc. of Superstructure (max : 4.45m/s^2)
(b) Horizontal Acc. of Footing (max : 3.89m/s^2)
(c) Horizontal Acc. of Ground Surface (max : 4.67m/s^2)
(d) Input (max : 2.97m/s^2)
(e) Vertical Disp. of Superstructure (max : 21.5mm)
(f) Inclination Angle of superstructure (max : 1.36*10^{-2}rad)
(g) Horizontal Disp. of Footing (max : 33.4mm)

Figure 6: The main time history of shaking 4

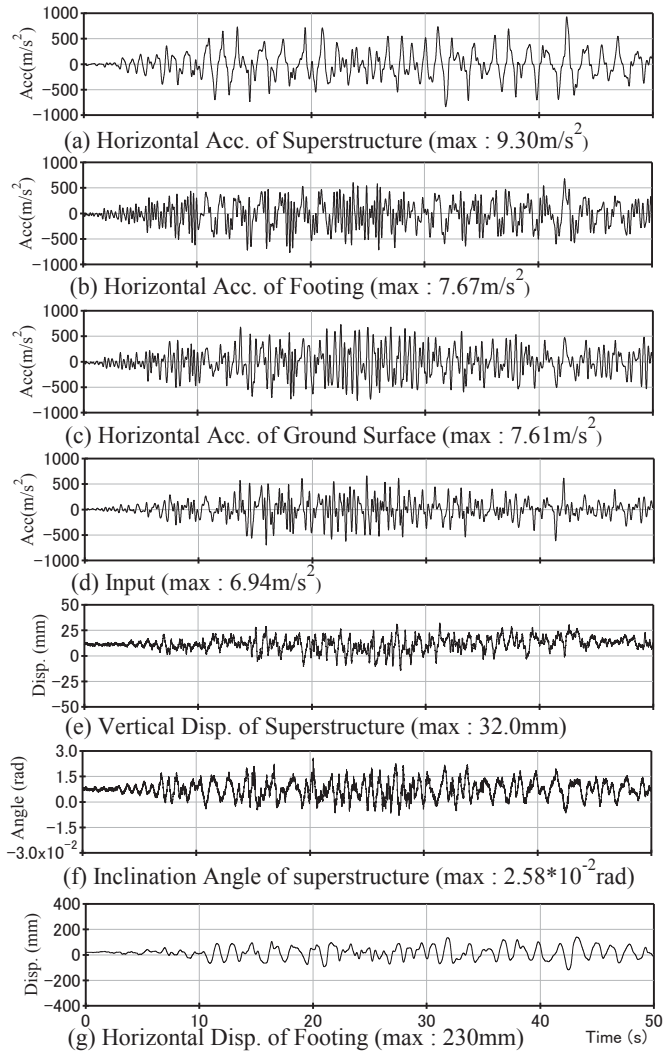

Figure 7: The main time history of shaking 11

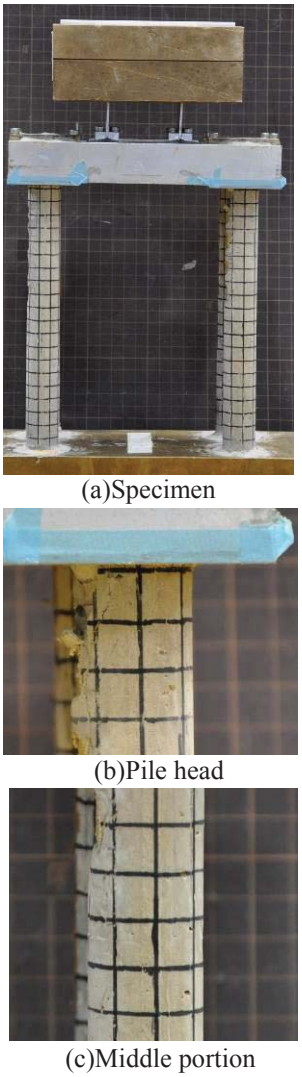

Figure 8: The damage of the pile model

In the test results, bending fracture occurred at the pile head. During shaking 2, the maximum response acceleration of the superstructure was 2.08 times larger than the input, and the maximum response acceleration of the footing was 1.62 times larger than the input. In contrast, during shaking 4, the maximum response acceleration of the superstructure was 1.50 times larger than the input, and the maximum response acceleration of the footing was 1.31 times larger than the input. This reduction of the response acceleration indicates that the bending fracture occurred at the pile head and formed a plastic hinge. During the final shaking (shaking 11), the damage of the pile model further progressed and the inclined angle of the superstructure also increased.

3.4 Relationship between relative displacement of the footing and inertial force

Figure 9 shows the relationship between the relative displacement of the footing to the bottom of the soil tank and the inertial force of superstructure and footing during shaking 2, 4, and 11. During shaking 2, the pile model kept a still elastic state according to the strain gauges. The blue dotted line indicates the initial stiffness based on the behavior during shaking 2. However, during shaking 4, the pile model performed elasto-plastic behavior because the plastic hinge occurred at the pile head and reached plastic state according. During shaking 11, maximum inertial force was 9.41MN. The relationship showed obvious nonlinear behavior. It indicates the pile model had reached ultimate condition.

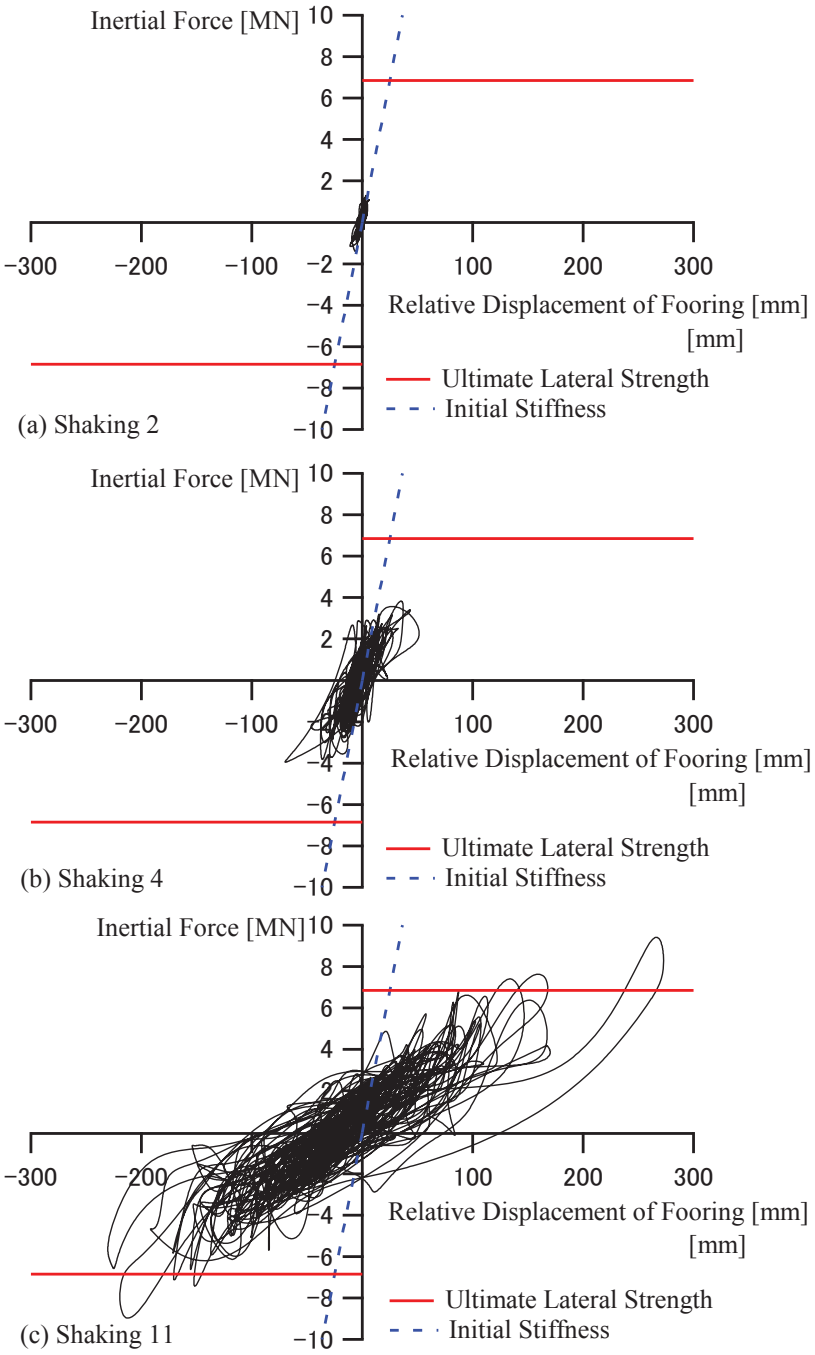

Figure 9: Relationship between the relative displacement of the footing and inertial force

4 ULTIMATE LATERAL STRENGTH OF AN RC PILE FOUNDATION IN THE CASE OF BENDING FRACTURE MODE

4.1 Evaluation method of an RC pile foundation

Broms proposed an equation to evaluate the ultimate lateral strength of a single pile [7]. The equation assumes that lateral reactions of soil are distributed in a triangle shape. The evaluation value of ultimate lateral strength Q is calculated as equation (2)

$$Q = 2.38\left(\frac{M_u}{K_p\gamma B^4}\right)^{\frac{2}{3}} K_p\gamma B^3 \tag{2}$$

where M_u is the full plastic moment of the pile, K_p is the coefficient of passive earth pressure, γ is the unit weight of soil, and B is the diameter of the pile.

4.2 Pile group effect

It is known that the strength of piles at the rear of a building is smaller than piles at the front if the pile foundation is affected by the pile group effect. In case of dry soil ground, the horizontal plastic ground reaction coefficient (pile group effect) κ is defined as less than 3. For a single pile, κ is determined as 3. Pile group effect κ is determined from equation (3) [8]

$$\kappa = \left\{ a\left(\frac{R}{B} - 1.0\right) + 0.4 \right\} \leq 3 \tag{3}$$

$$a = 0.55 - 0.007\phi$$

where R is the distance between front and rear piles.

Internal friction angle ϕ is calculated by equation (4) [9]

$$\phi = 32.5 - 20.6\frac{D_r - 40}{100} \tag{4}$$

where D_r is the relative density of the soil.

4.3 Comparison between the test result and evaluation value

In figure 9, the red line indicates the evaluated ultimate lateral strength. The strength of the front pile was calculated by equation (2). The strength of back side pile was determined by equation (2) and multiplied by pile group effect κ. The strength of the back pile was calculated by equation (5). The evaluated value was 6.85MN and maximum inertial force in the test result was 9.41MN. Therefore, the value was 72.8% of the test result. The value was estimated on the safe side.

$$Q_{back} = 2.38\left(\frac{M_u}{K_p\gamma B^4}\right)^{\frac{2}{3}} K_p\gamma B^3 \times \frac{\kappa}{3} \tag{5}$$

5 CONCLUSIONS

This paper conducted a dynamic centrifuge model test of the dry soil-RC pile-superstructure interaction. In addition, the author tried to evaluate the ultimate lateral strength of an RC pile foundation with surrounding ground. The following results were obtained.

1) An RC pile model was proposed for this study. According to the result of the static loading test, the pile model strength reached full plastic moment and then performed degradation behavior. This behavior reproduced to a real RC pile member.
2) A dynamic centrifuge model test of dry soil- RC pile-superstructure interaction was conducted. Bending failure (plastic hinge) occurred at the head of the pile models. This plastic hinge caused the reduction of response acceleration.
3) The ultimate lateral strength of an RC pile foundation was evaluated. The estimated value was smaller than the test result, and evaluated on the safe side.

6 ACKNOWLEDGEMENTS

This work is partially supported by a Kurata Grant awarded by the Hitachi Global Foundation. The authors are grateful to Associate Professor Shuji Tamura of Tokyo Institute of Technology for their valuable assistance throughout the centrifugal tests.

REFERENCES

[1] Architectural Institute of Japan, Report on the Damage Investigation of the 2016 Kumamoto Earthquakes, 2018.6 (In Japanese)

[2] Tamura, S., Suzuki Y., Tsuchiya T., Fujii S. and Kagawa T. “Dynamic Response and Failure Mechanisms of a Pile Foundation During Soil Liquefaction by Shaking Table Test with a Large-Scale Laminar Shear Box”, Proc., of 12th World Conf. on Earthq. Engrg. 2000.1, Reference No. 903

[3] K. Shibata, H. Funahara, T. Nagano, Y. Kawamata, S. Tamura. “Damage mechanism of reinforced concrete piles with axial load variation based on E-Defense shaking table tests” Proc. the 7th International Conf. on Earthquake Geotechnical Eng., pp4978-4985, 2019.6

[4] M. Kimura, T. Adachi, T. Yamanaka & Y. Fukubayashi, “Failure mechanism of axially-loaded concrete piles under cyclic lateral loading” Centrifuge 98, Kimura, Kusakabe & Takemura (eds), 1998 Balkema, Rotterdam

[5] S. Higuchi, T. Tsutsumiuchi, R. Otsuka, K. Ito, J. Ejiri, “Centrifugal Vibration Test of RC Pile Foundation”, Japan Society of Civil Engineers, Vol68, Issue 4, pp642-651, 2012

[6] Architectural Institute of Japan, Design problems in foundation engineering, 2004.2 (in Japanese)

[7] B. B. Broms, “Lateral Resistance of Piles in Cohesion Less Soils”, Journal of Soil Mechanics and Foundation Division, ASCE, Vol90, Issue 3, pp123-156, 1964

[8] Architectural Institute of Japan, Recommendations for Design of Building Foundations, AIJ, 2001.10 (in Japanese)

[9] Public works research institute: TECHNICAL NOTE of PWRI, No.4283, 2014.3 (in Japanese)

EURODYN 2020
XI International Conference on Structural Dynamics
M. Papadrakakis, M. Fragiadakis, C. Papadimitriou (eds.)
Athens, Greece, 23–26 November 2020

SSI EFFECTS ON R/C ONE-STOREY BUILDINGS UNDER SEISMIC LOADINGS

Paraskevi K. Askouni [1], Dimitris L. Karabalis [2] and Dimitri E. Beskos [4,3]

[1, 2,3] Department of Civil Engineering, University of Patras, 26504 Rio, Greece
askounie@gmail.com [1]
karabali@upatras.gr [2]
d.e.beskos@upatras.gr [3]

[4] Department of Disaster Mitigation for Structures, College of Civil Engineering, Tongji University, Shanghai, China
d.e.beskos@upatras.gr [4]

Keywords: Seismic analysis, Reinforced Concrete structures, Asymmetrical structures, Soil-Structure Interaction, Damage index, Elastoplastic analysis.

Abstract. *In this work, a series of seismic analyses of one-storey, one-span reinforced concrete (R/C) asymmetrical building frames under 2-D and 3-D conditions is performed and the effect of deformable soil on the seismic response of the structure is determined and discussed. A comparison is performed between the elastic behavior of R/C sections according to the building codes' provisions to possible inelastic behavior resulting in the analyses. The time history analyses aim at clarifying the role of SSI in the seismic behavior of simple R/C structures while investigating the possible elastic or elastoplastic behavior of critical sections with the aid of a realistic damage index. The conclusions drawn from these linear and nonlinear time history analyses provide helpful guidelines for the safer seismic design of structures.*

1 INTRODUCTION

According to current design codes [1], consideration of dynamic Soil-Structure Interaction (SSI) is usually required only for the design of special structures, structures supported on very soft soils, and structures on special foundations. Seismic codes usually neglect SSI for the design of common building structures since it is assumed that SSI results in decreased internal forces of the structural elements. However, recent research has shown that the deformability of the supporting soil may have a strong impact on the seismic response of common, low-rise reinforced concrete (R/C) buildings [2-3] as well as of special structures [4]. The present paper aims at presenting preliminary results of an ongoing investigation on the role of SSI on the seismic response of ordinary, low-rise symmetric and asymmetric one-storey R/C building frames. Both two dimensional (2-D) and three dimensional (3-D) buildings are considered.

2 DESCRIPTION OF CASE STUDIES AND ANALYSIS

In this work, simple 2-D and 3-D, one-span and one-storey R/C building frames are examined, as shown in Fig.1. The 2-D R/C one-storey frames have one span of 6.0 m and height 3.0 m, consisting of two vertical elements connected with a horizontal beam (Fig. 1.a). The cross-section of one column is constant at $0.40*0.40m^2$, while the cross-section of the other column increases in successive steps from $0.40x0.40m^2$ to $0.30x2.00m^2$, where the greater dimension of the later lies in the plane of the frame and is referred herein as "wall". In this way, a simple geometrical asymmetry of the frame is introduced. The horizontal R/C beam has a constant cross-section of $0.25x0.50m^2$.

Similarly, the 3-D one-storey R/C building frames consist of one slab 5.0m x 4.0m, supported by perimetric beams and 4 columns at the corners (Fig. 1.b). The height of the frame is 4.0m. The cross-section of the three columns, i.e. C1, C3 and C4 (Fig. 1.b) remains constant at $0.40x0.40m^2$, while the cross-section of one column, i.e. C2, increases in successive steps from $0.40x0.40m^2$ to $0.30x2.00m^2$ and is referred herein as wall. The cross-section of the horizontal beams remains constant at $0.25x0.60m^2$. The slab is 0.15m thick and considered to act as a rigid diaphragm.

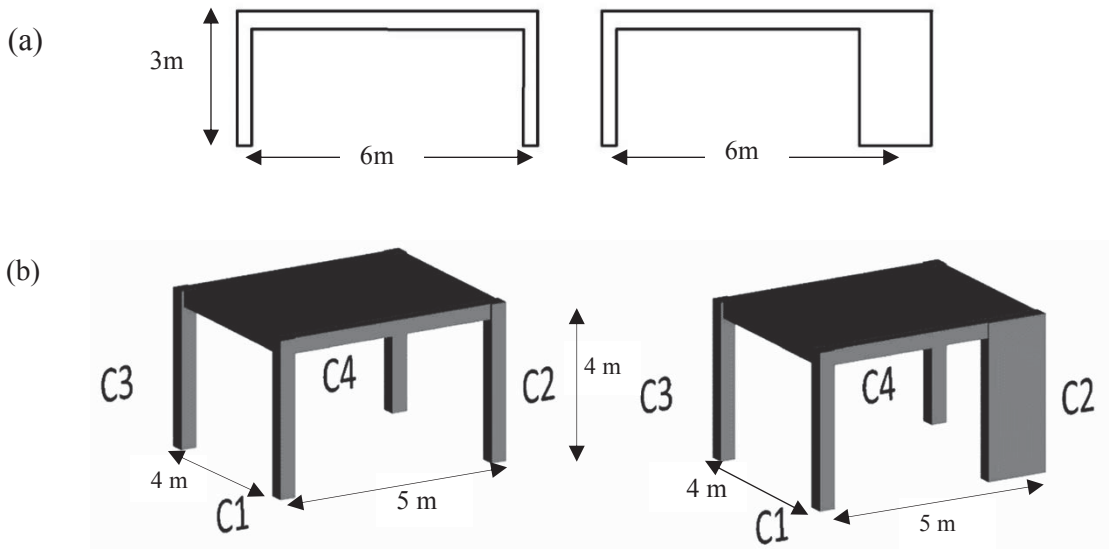

Figure 1: 2-D and 3-D symmetrical and asymmetrical frames under study.

In all 2-D and 3-D frames, the material is concrete C20/25 with steel reinforcement B500c. On the 2-D building frames, a uniformly distributed load of 34 kN/m is applied on the horizontal beam, approximately incorporating the entire dead and live load for typical structures with domestic/residential and office use [5]. For the 3-D building frames, a dead load of 12.24 kN/m acts directly on the beams, simulating the weight of a perimeter wall, while the load on the floor consists of 2.0 kN/m^2 dead load and 0.6 kN/m^2 live load [5].

The 2-D and 3-D building frames are dimensioned according to the current codes [1, 6] for medium ductility class using the typical fixed base assumption (Fig. 2.a,c). The dimensioning assumptions are zone ground acceleration a_g=0.36g, spectrum type I, importance factor γ_I=1.00, viscous damping ratio ξ=5%, and soil type C [1]. For all 2-D frames, the behavior factor is considered as q=3.30, while for the 3-D frames the behavior factor is considered according to the current codes [1]. Capacity design of R/C 2-D and 3-D frames is performed.

The foundation of the 2-D and 3-D frames consists of footings connected to each other with R/C beams (Fig. 2.a-d), all dimensioned according to the current codes [1, 6]. In addition to the above, for the 3-D frames only, a mat foundation is considered (Fig. 2.e), dimensioned according to the current codes [1, 6].

The effect of SSI is considered through discrete elements of a simple spring-dashpot-mass system, as shown in Fig. 2.b,d. The values of the parameters of the spring-dashpot-mass system are calculated according to Gazetas [7]. For the purposes of this study, the soil properties are Poisson ratio ν_s=0.4, soil density ρ_s=1750 kgr/m^3, modulus of elasticity E_s=150MPa, and shear velocity V_s= 175 m/sec, corresponding to a medium clay.

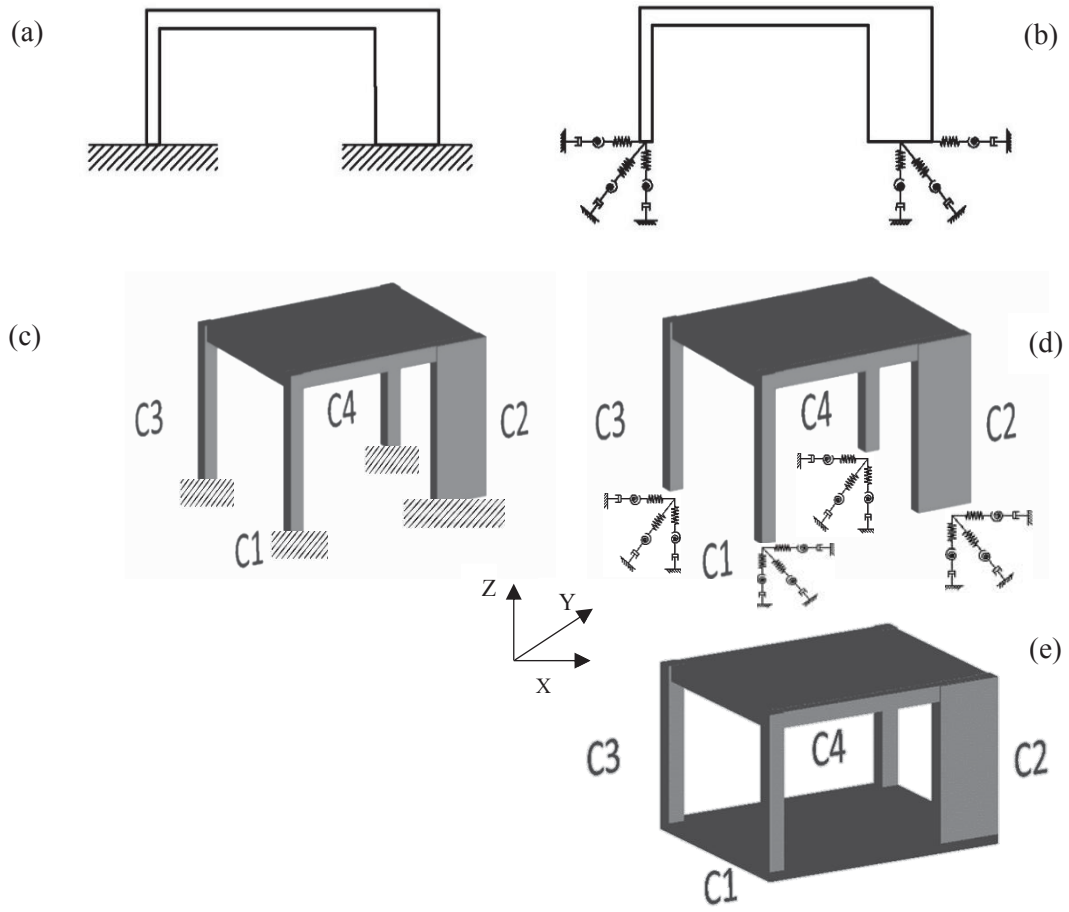

Figure 2: 2-D (a, b) and 3-D (c, d, e) frames on rigid soil (a, c) and deformable soil (b, d, e).

The 2-D building frames are analyzed by the ETABS software [8] using an artificial accelerogram compatible to the design spectrum of Eurocode 8 [1] based on the earthquake of Argostoli (Kefalonia, Greece) of 2014 [9] and constructed by ETABS [8]. A stiffness reduction of R/C elements is performed according to the current codes [1,6] while they are considered to maintain elastic behavior. Elastoplastic analyses are performed in the time domain using the fiber model of Sfakianakis and Fardis [10] and Sfakianakis [11]. According to this elastoplastic model of R/C sections, point hinges at both ends of all R/C elements are applied including all material and section properties of interest, i.e. dimensions, reinforcement, reduced stiffness, elastoplastic mechanical properties, deformation, curvature limits, etc. Possible shear failure of R/C elements is checked according to the Greek Interventions Regulation "KANEPE" [12]. The elastic and elastoplastic time-history analyses are performed by ETABS [8], first assuming a rigid base and then SSI.

Similarly, the 3-D building frames are studied using elastic and elastoplastic analyses and the earthquake of Vasiliki (Lefkada, Greece) of 2015 [9]. The numerical investigation of the structural response is affected by the incidence angle of the horizontal seismic input [2,13]. The effect of the incidence angle of the seismic motion is investigated here by analyzing the 3-D buildings for incidence angles $\varphi=0°$ and $\varphi=90°$, which are along the two primary geometrical axes, and $\varphi=45°$, which is close to the direction of the diagonal axis.

For the elastoplastic behavior of R/C elements the following response parameters/procedures are used:

1. The maximum interstorey drift ratio (IDR) is calculated for each dynamic analysis and compared with the limits of the performance levels for R/C framed structures according to FEMA 356 [14]. At the performance level IO - Immediate Occupancy, corresponding to the performance level DL - Damage Limitation of EC8 [1], the limit of IDR is 1%. At the performance level LS - Life Safety, corresponding to the performance level SD – Severe Damage [1], the limit of IDR is 2%. At the performance level CP - Collapse Prevention, corresponding to the performance level NC-Near Collapse [1], the limit of IDR is 4%.
2. A simple damage index is employed to evaluate the elastoplastic behavior of R/C elements and frames. For each elastoplastic analysis, the final deformations/curvatures and the maximum internal forces/moments of each point hinge are checked, and each vertical member is classified according to the limits of performance levels [1]. In the Greek Interventions Regulation "KANEPE" [12] values of damage indices r_R for damaged R/C elements without repair or retrofit are provided. A correspondence between the performance levels of [1] and r_R of [12] is noticed as shown in Table 1. The values of the index r_R vary in the range of 0~1, where 0 indicates collapse and 1 refers to elastic behavior [12]. If different states of performance levels are indicated at the ends of an R/C element, the element is ranked using the lower of the two indices.

Performance level [1]	Description of Performance Level	Damage index, r_R [12]
A≤DL	Elastic behavior – Operational	1.00
A≤DL	Damage Limitation - light damages	0.90
DL≤SD	Severe Damage - significant structural damages, retaining full vertical load-bearing capacity	0.80
SD≤NC	Near Collapse – heavy damages at the verge of collapse	0.50
>NC	Collapse- total element loss	0

Table 1: Correlation of Damage Index [12] and Performance Levels [1].

The damage index estimation is extended for the whole one-storey frame, as quantified by the overall structural damage index r_g, expressed as [15]

$$r_g = \frac{\sum_{i=1}^{n}(V_{Rd,c,i} \cdot r_{R,i})}{\sum_{i=1}^{n} V_{Rd,c,i}} \quad (1)$$

where n is the number of vertical structural elements, r_R is the element damage index (Table 1), and $V_{Rd,c}$ is the design shear resistance of the R/C member without shear reinforcement [6].

The estimation of the loading capacity of the frame, considering structural asymmetry, can be expressed by the general modified damage index r_f as [15]

$$r_f = \frac{r_g \cdot K_R}{\gamma_I} \quad (2)$$

where K_R is a factor expressing the geometric symmetry/normality of the structure with values ranging from 1.0, for normal/symmetric structures to 0.8 for asymmetric ones, and γ_I is the importance factor [1, 15]. The range of values of r_f is 0~1, where 0 indicates "collapse" and 1 elastic behavior. This damage index procedure presents the advantages of simplicity, calculation speed, and the ability to roughly characterize a whole R/C frame.

3 RESULTS OF SEISMIC RESPONSE

3.1. 2-D building frames

In this section, the numerical results of the 2-D frame analyses are shown and discussed. The following parameters are examined and presented in the plots.

- *I(wall)/I(col)* is the ratio of the moment of inertia of the wall to the column. The ratio *A(wall)/A(col),* which involves the cross-sections, is defined similarly.
- *M(s)/M* is the ratio of the maximum absolute value of the internal bending moment of a vertical element when SSI is considered to the corresponding value, at the same location, considering rigid soil. This ratio is considered at the lower end ("bot") and the upper end ("up") of the vertical element. The ratio of the internal shear forces *V(s)/V* is defined similarly.
- Interstorey drift ratio (IDR) with the notation "r.s." for rigid soil, or "ssi" for SSI consideration.
- r_R is the damage index of each vertical element and r_f is the frame damage index.

The internal axial forces of R/C elements are not examined here because of their high compressive strength. The internal force diagrams refer only to internal forces of vertical elements, which are considered as the main structural elements undertaking the seismic action.

As shown in Figs. 3-4, the elastic M(s)/M, at the top and base section of C1, as well as the elastic V(s)/V of C1, increases along with the increase of the wall section. The elastic M(s)/M at the top and base and the elastic V(s)/V of the wall, C2, decrease along with the increase of its cross-section (Figs. 3-4). The column is burdened due to SSI, while the wall benefits from SSI.

As shown in Fig. 5, the elastoplastic M(s)/M of C1 increases at its base up to 1.18 for I(wall)/I(col)=22.89 and decreases for greater wall sections to 0.99, while at its top section increases up to 1.95 for I(wall)/I(col)≈52 and decreases for greater wall sections to 1.05. The elastoplastic M(s)/M of the wall base increases up to 1.14 for I(wall)/I(col)=22.89 and decreases almost linearly to 0.29 for I(wall)/I(col)=93.75 (Fig. 5). The elastoplastic M(s)/M of the wall top section increases rapidly up to 2.24 for I(wall)/I(col)=11.72 and for greater wall sections decreases to 0.53 for I(wall)/I(col)=93.75 (Fig. 5).

As shown in Fig. 6, the elastoplastic V(s)/V of C1 increases up to 1.39 for A(wall)/A(col)=2.81 and decreases to 1.02 for A(wall)/A(col)=3.75. The elastoplastic V(s)/V of C2 is almost stable around the value 1.07~1.09 for A(wall)/A(col)≤2.81 and decreases for larger wall sections to 0.33 for A(wall)/A(col)=3.75 (Fig. 6).

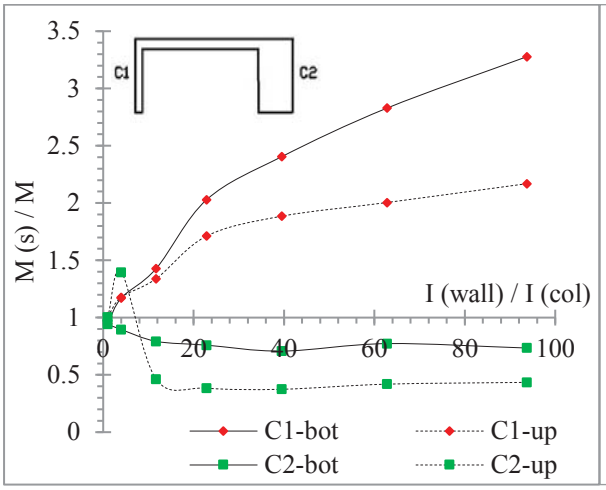

Figure 3: Elastic M(s)/M versus I(wall)/I(col).

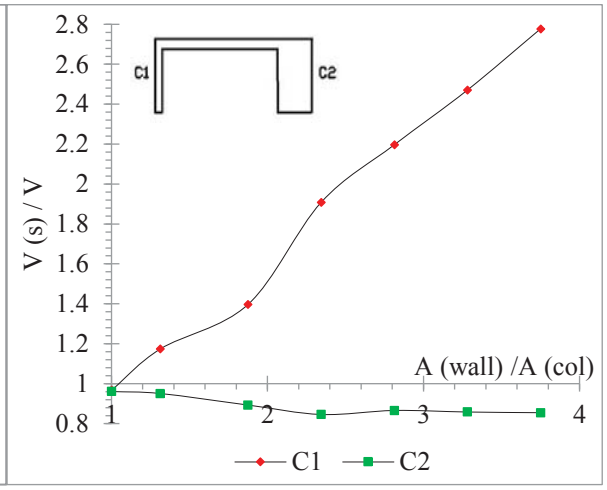

Figure 4: Elastic V(s)/V versus A(wall)/A(col).

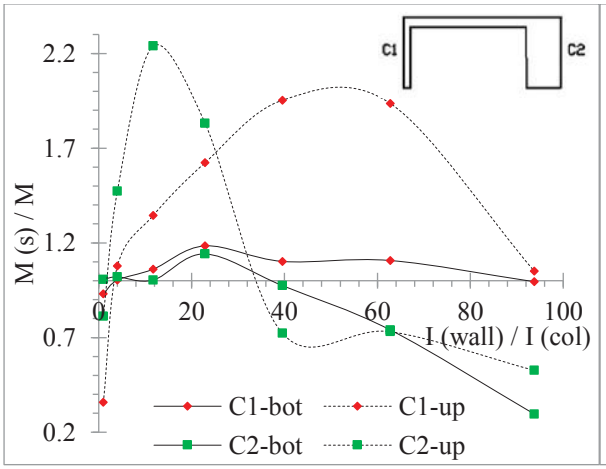

Figure 5: Elastoplastic M(s)/M versus I(wall)/I(col).

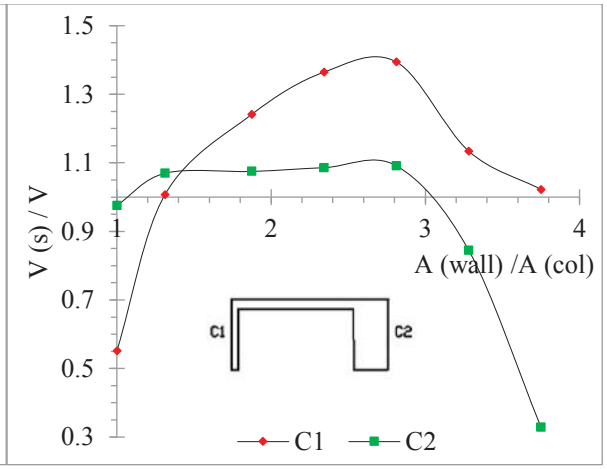

Figure 6: Elastoplastic V(s)/V versus A(wall)/A(col).

As shown in Fig. 7, the elastic IDR for both rigid soil and SSI decreases along with the increase of the wall section. Both remain below the limit of 1% [14], while the elastic IDR with SSI is greater than the respective for rigid soil. As shown in Fig. 8, the elastoplastic IDR for SSI is greater than the IDR for rigid soil for almost all wall sections. The elastoplastic IDR for rigid soil remains within the limit of 2% [14] (Fig. 8). The elastoplastic IDR for SSI remains almost below the limit of 2% [14] for all sections except for A(wall)/A(col)=2.81, where it exceeds slightly 2% while staying constantly within 4% [14] (Fig. 8).

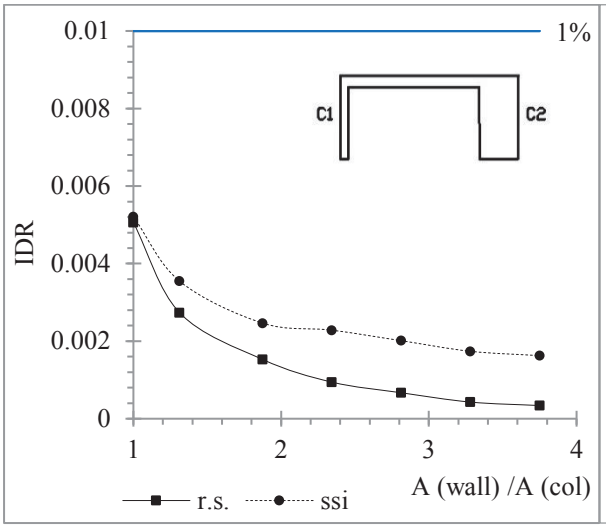

Figure 7: Elastic IDR versus A(wall)/A(col).

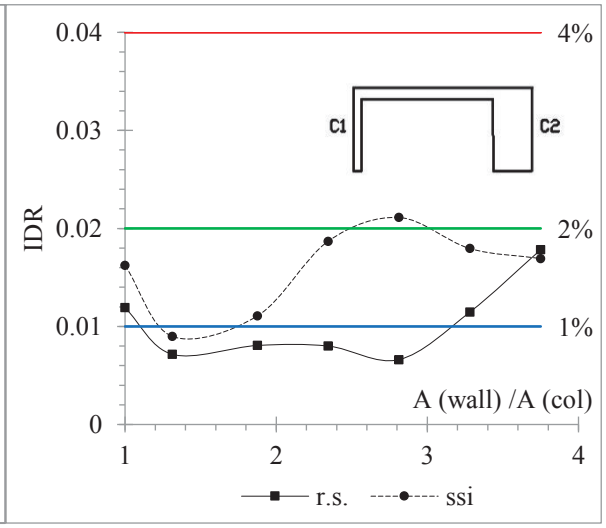

Figure 8: Elastoplastic IDR versus A(wall)/A(col).

As shown in Fig. 9, the r_R of C1 and C2 fluctuates for SSI and for rigid soil in the range of overlapping values 0~1 for both boundary conditions. As shown in Fig. 10, the frame damage index has smaller values for SSI than for rigid soil for A(wall)/A(col):1.31~2.81, indicating more damage is expected for SSI at this range of wall sections.

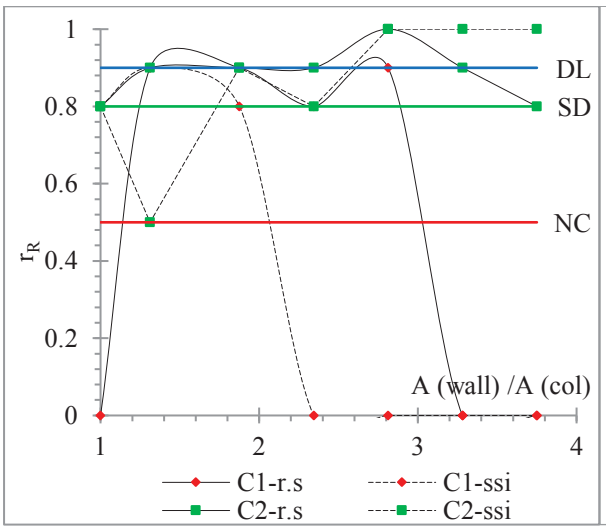

Figure 9: r_R versus A(wall)/A(col).

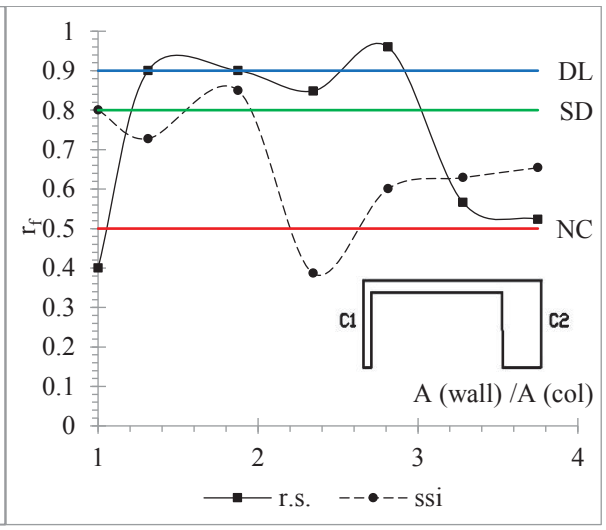

Figure 10: r_f versus A(wall)/A(col).

3.2. 3-D building frames – numerical results and discussion

Similarly to the analysis of plane frames, the following parameters are examined and presented in the plots regarding 3-D, 1-storey R/C building frames.

- *M(s)/M* is the ratio of the maximum absolute value of the internal bending moment of when SSI via footings with connecting beams is considered, at the lower end ("bot") and the upper end ("up") of the vertical element. *M(m)/M* is a similar ratio when SSI via foundation mat is considered. These ratios are examined at both internal transverse axes of R/C vertical elements. Here, due to lack of space, only the plots regarding the major internal moment ratio (*M3*) defined for the transverse axis of R/C vertical elements, coinciding here to the Y-axis, are shown.

- *V(s)/V* is the ratio of the shear forces defined similarly when SSI via footings with connecting beams is considered. *V(m)/V* is the respective ratio when SSI via foundation mat is considered. There are presented here only the plots of major shear force ratio (*V2*) defined for the transverse axis of R/C vertical elements, coinciding here to the X-axis.
- *IDR* with the notations "r.s." for rigid soil, or "s" for SSI via footings with beams, or "m" for SSI via foundation mat, on both horizontal global axes, X and Y.
- r_R is the damage index of each vertical R/C element and r_f is the frame/storey damage index.

As shown in Fig. 11, considering footings for the incidence angle φ=90°, the elastic M3(s)/M3 of the top and base section of C1 increases along with the increase of the wall section, up to 2.73~3.01 for I(wall)/I(col)=93.75, while remains close to 1 for the top and base sections of C3 and C4 and decreases to 0.86 for the base section of the wall and 0.39 for the top section of the wall for I(wall)/I(col)=93.75. Considering foundation mat for φ=0° (Fig. 12), a similar form of the plot is obvious with greater values on average, such as that the elastic M3(m)/M increases close to 2.09 for C3 and C4, at their top and base sections, close to 1 for the base section of the wall, up to 12.51 for the top section of the wall and up to 8.53 for the top section of C1 and 15.36 for the base section of C1 for I(wall)/I(col)=93.75.

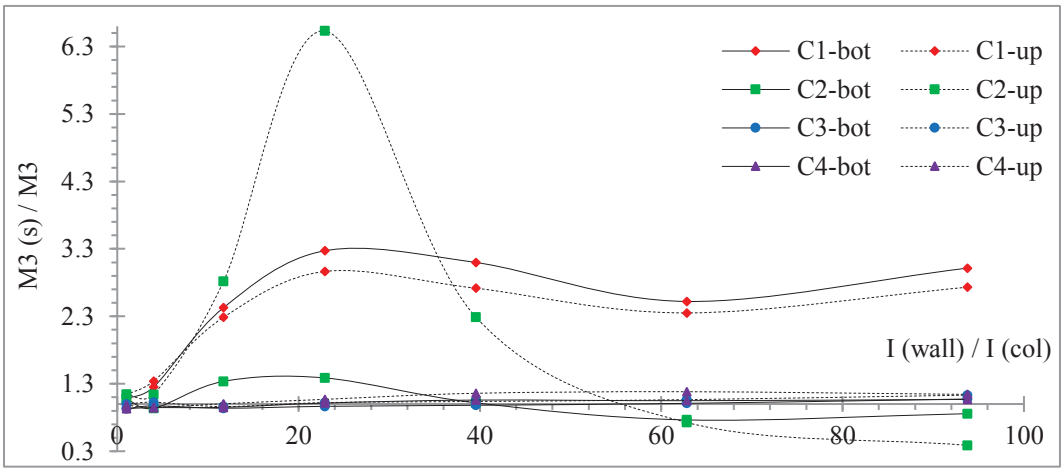

Figure 11: Elastic M3(s)/M3 versus I(wall)/I(col) for footings and φ=90°.

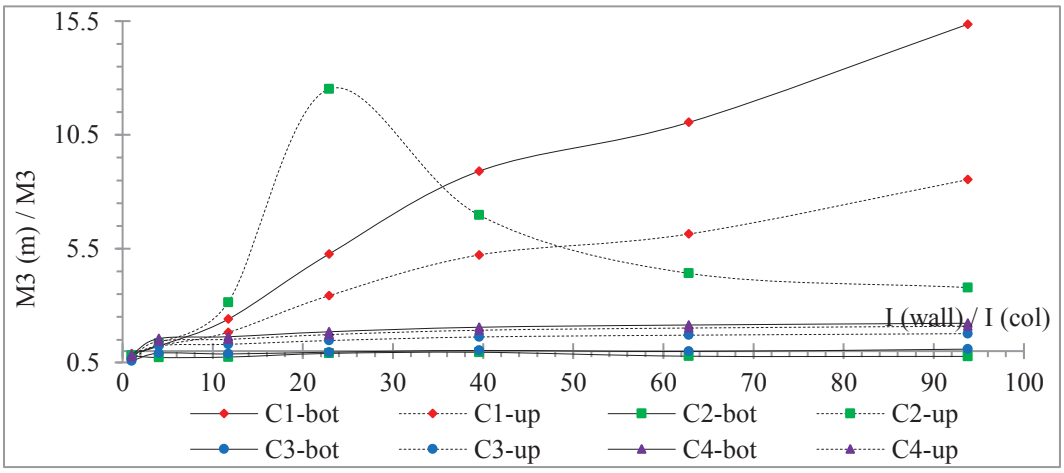

Figure 12: Elastic M3(m)/M3 versus I(wall)/I(col) for foundation mat and φ=0°.

As shown in Fig. 13, comparing foundation mat to rigid soil for φ=45º, the elastoplastic M3(m)/M of C3 and C4, at their top and bottom sections, increases slightly along with the increase of the wall section up to 1.13~1.27 for I(wall)/I(col)=93.75, while for the top and bottom sections of C1 increases intensely up to 2.12~2.20. The elastoplastic M3(m)/M3 of the top section of C2 increases intensely along with the increase of the wall section up to 3.44 for I(wall)/I(col)=93.75, while for the relevant bottom section has almost steady decreased values around 0.63~0.71 (Fig. 13).

As shown in Fig. 14, comparing footings to rigid soil for φ=90°, a similar form of the plot of elastoplastic M3(s)/M3 is observed to the previous paragraph (Fig. 13) with smaller general values. The elastoplastic M3(s)/M3 of C1, C3, and C4, at their top and base sections, varies with overlapping values tending to decrease along with the increase of the wall section in the range of 0.9~1.29 (Fig. 14). The elastoplastic M3(s)/M3 of the top section of the wall varies tending to increase up to 1.33 for I(wall)/I(col)=39.55 and decreases for greater wall sections close to 1 for I(wall)/I(col)=93.75 (Fig. 14). Respectively, the elastoplastic M3(s)/M3 of the base sections of C2 and C3 varies tending to decrease to 0.77 for I(wall)/I(col)=62.81 and increases to 1 for I(wall)/I(col)=93.75 (Fig. 14). The top sections of all vertical elements tend to show greater values of the elastoplastic M3(s)/M3 than the respective bottom sections (Figs. 13-14).

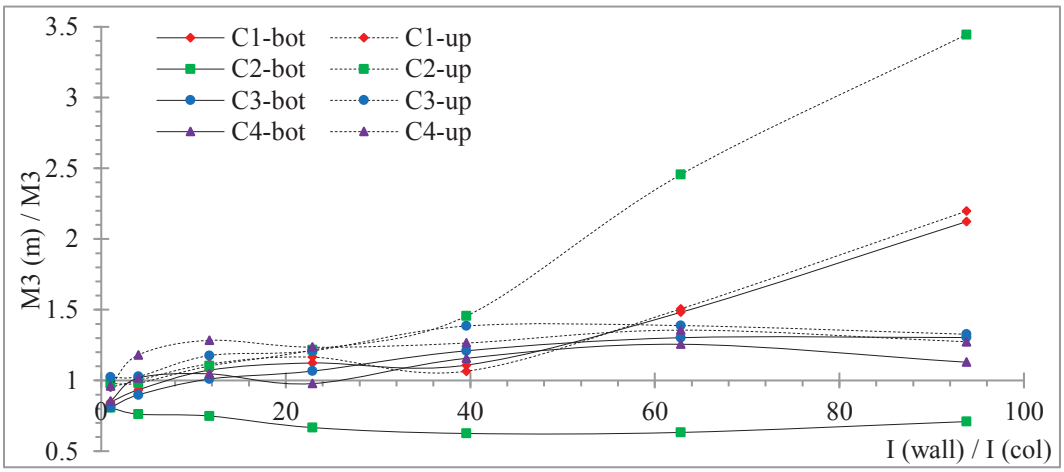

Figure 13: Elastoplastic M3(m)/M3 versus I(wall)/I(col) for foundation mat and φ=45°.

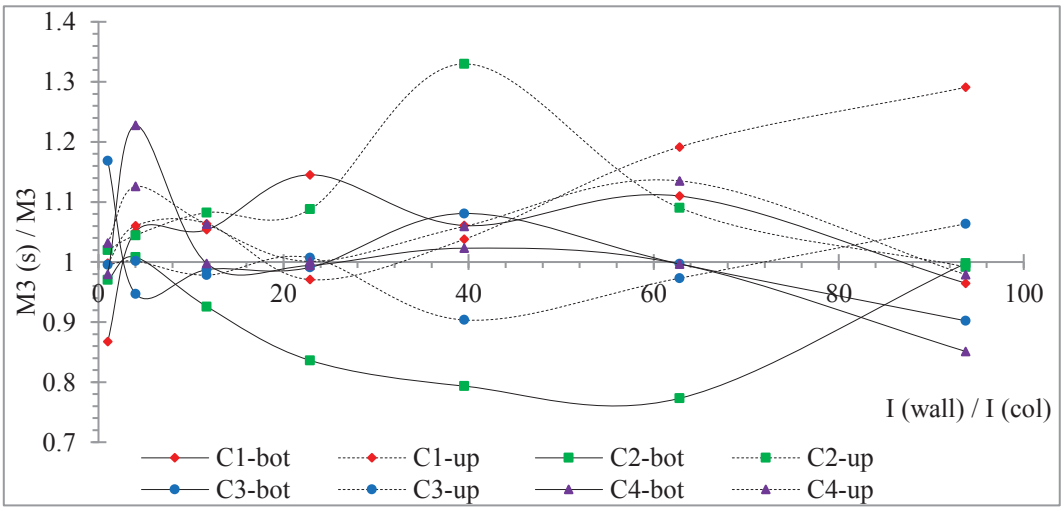

Figure 14: Elastoplastic M3(s)/M3 versus I(wall)/I(col) for footings and φ=90°.

As shown in Fig. 15, comparing foundation mat to rigid soil for φ=0°, the elastic V2(m)/V2 of C1 increases along with the increase of the wall section up to 12.33 for A(wall)/A(col)=3.75. The elastic V2(m)/V2 of C4 increases up to 2.17 for A(wall)/A(col)=3.75, while the elastic V2(m)/V2 for C2 and C3 remains close to 1 for all wall sections (Fig. 15).

For footings and φ=90°, as in Fig. 16, the elastic V2(s)/V2 of C1 increases up to 3.14 for A(wall)/A(col)=2.34 and varies to 2.89 for A(wall)/A(col)=3.75. The elastic V2(s)/V2 of C3 and C4 increases along with the increase of A(wall)/A(col) up to 1.10 for A(wall)/A(col)=3.75 (Fig. 16). The elastic V2(s)/V2 of the wall increases up to 1.66 for A(wall)/A(col)=2.34 and decreases variably for greater wall sections, e.g. to 1 for A(wall)/A(col)=3.75 (Fig. 16).

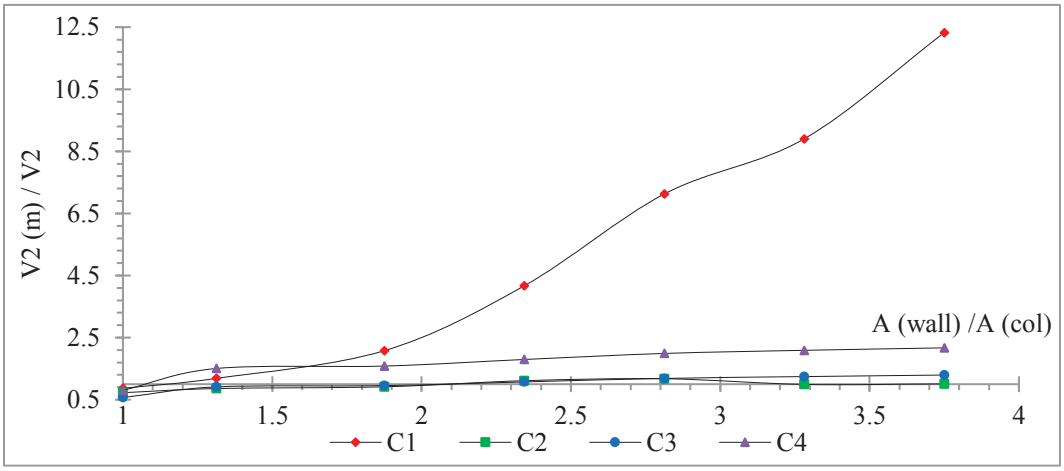

Figure 15: Elastic V2(s)/V2 versus A(wall)/A(col) for foundation mat and φ=0°.

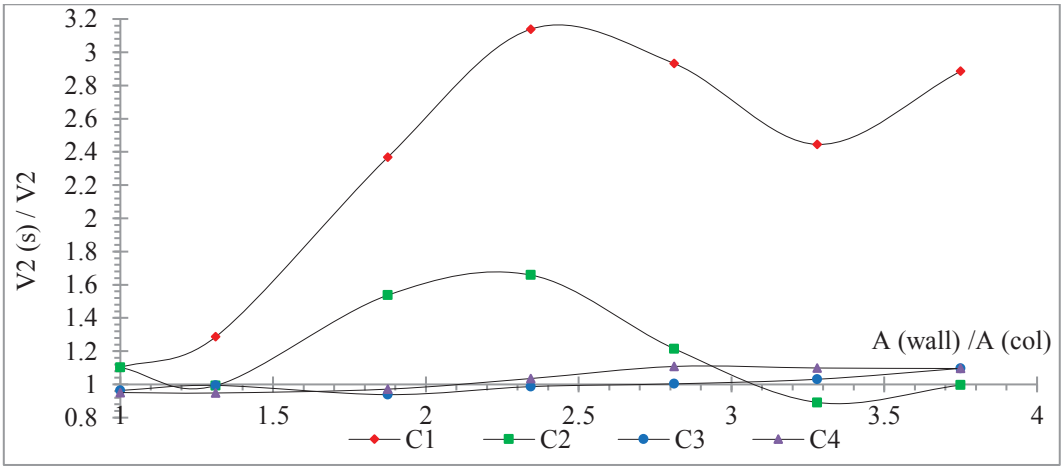

Figure 16: Elastic V2(s)/V2 versus A(wall)/A(col) for footings and φ=90°.

Considering the foundation mat to rigid soil for φ=45°, as in Fig. 17, the elastoplastic V2(m)/V2 increases for the columns along with the increase of the wall section up to 2.24 for C1, to 1.34 for C3, and 1.16 for C4, all values for A(wall)/A(col)=3.75. Respectively, the elastoplastic V2(m)/V2 of the wall decreases to 0.79 for A(wall)/A(col)=3.75 (Fig. 17).

Similarly, as shown in Fig. 18, for foundation mat and φ=0°, the elastoplastic V2(m)/V2 increases for the columns along with the increase of the wall section up to 1.67 for C1, to 1.38 for C3 and 1.56 for C4, all for A(wall)/A(col)=3.75. Respectively, the elastoplastic V2(m)/V2 of the wall decreases to 0.50 for A(wall)/A(col)=3.75 (Fig. 18).

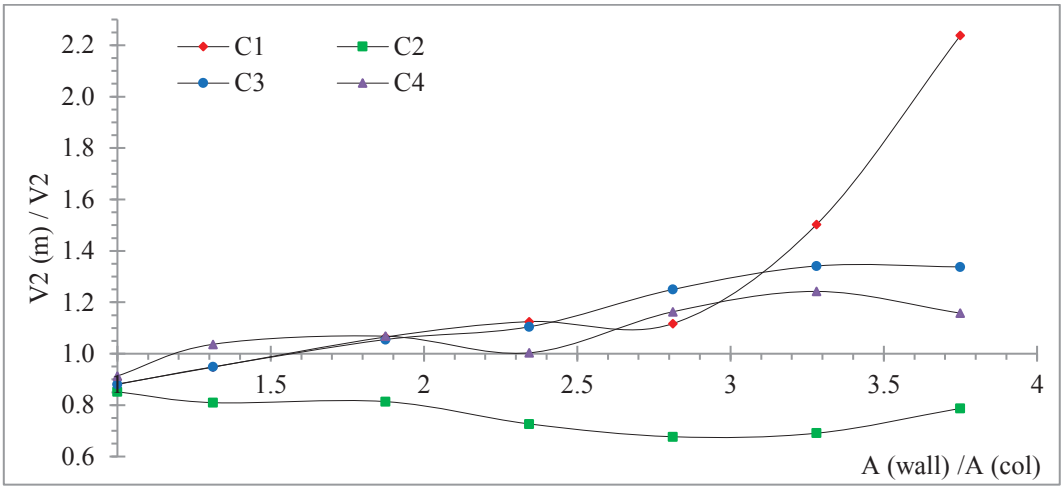

Figure 17: Elastoplastic V2(m)/V2 versus A(wall)/A(col) for foundation mat and φ=45°.

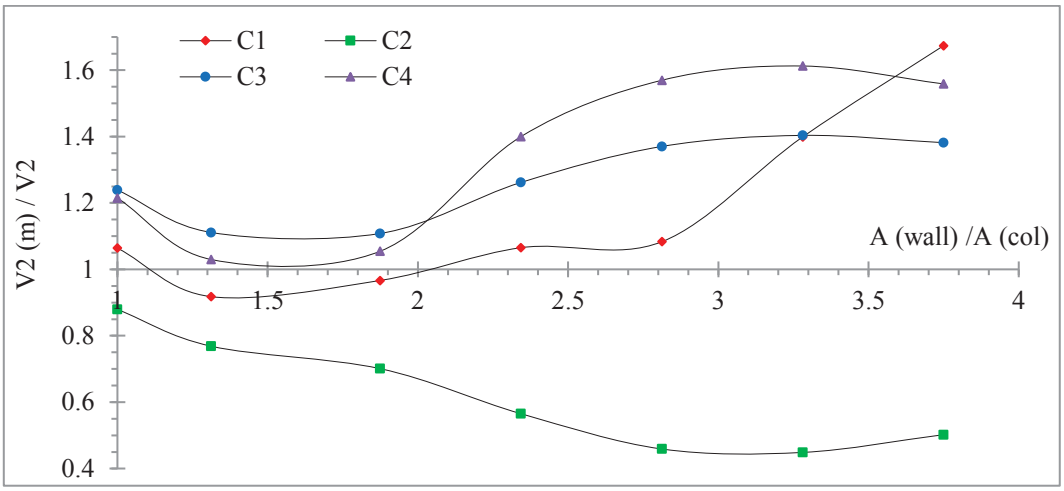

Figure 18: Elastoplastic V2(m)/V2 versus A(wall)/A(col) for foundation mat and φ=0°.

As shown in Fig. 19, for φ=0°, the elastic IDR on the X-axis for rigid soil decreases along with the increase of the wall section to 0.0044 for A(wall)/A(col)=3.75, for footings to 0.0058, while for foundation mat increases to 0.01, all values for A(wall)/A(col)=3.75. For φ=0°, as in Fig. 20, the elastic IDR on Y-axis for rigid soil decreases to 0.004 for A(wall)/A(col)=3.75, for footings to 0.0055, while for foundation mat remains in the range of 0.0145~0.0135, e.g. over the limit of 1% [14]. For all incidence angles on both axes, the elastic IDR is greater for the foundation mat, less for the rigid soil, while for footings has intermediate values closer to the rigid soil.

As shown in Fig. 21, for φ=45º, the elastoplastic IDR for all boundary conditions on X-axis decreases along with the increase of the wall section in the range of 1-2% [14], where the IDR for foundation mat has greater values close to 2%, the IDR for rigid soil has fewer values and the IDR for footings has intermediate values closer to ones for the rigid soil. For φ=90º, the elastoplastic IDR on Y-axis for all boundary conditions increases along with A(wall)/A(col) in the range of 1-2% [14], where the IDR for foundation mat has greater values, while the IDRs for rigid soil and footings have fewer overlapping values to each other (Fig. 22).

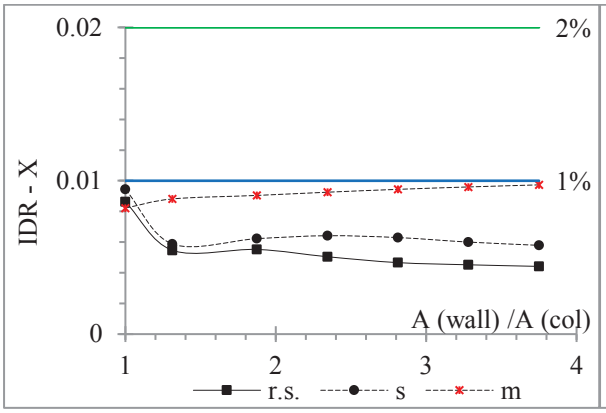

Figure 19: Elastic IDR on X-axis versus A(wall)/A(col) for φ=0°.

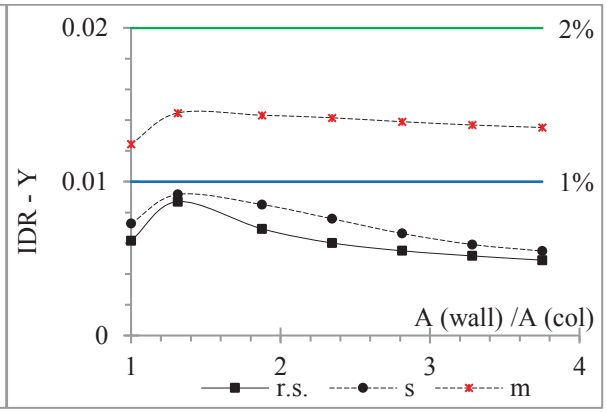

Figure 20: Elastic IDR on Y-axis versus A(wall)/A(col) for φ=0°.

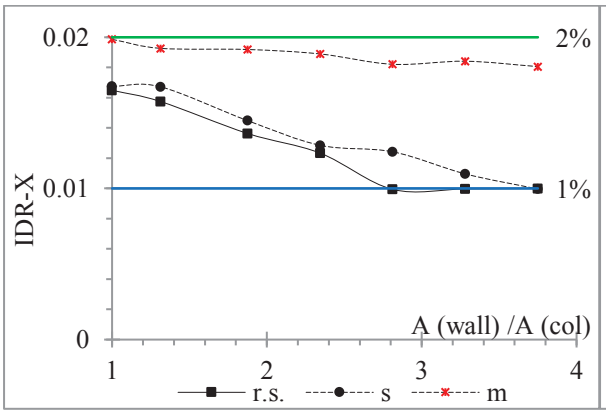

Figure 21: Elastoplastic IDR on X-axis versus A(wall)/A(col) for φ=45°.

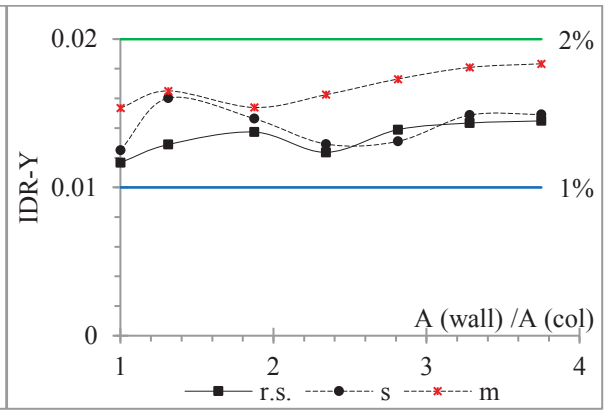

Figure 22: Elastoplastic IDR on Y-axis versus A(wall)/A(col) for φ=90°.

As shown in Fig. 23, for φ=0º, the damage index for all elements varies in the range of 0~0.9, e.g. approaching to collapse while less than DL performance level. For φ=0º, as in Fig. 24, the r_f for rigid soil decreases variably along with the increase of A(wall)/A(col) with greater values than for the other boundary conditions for A(wall)/A(col)=1.31~1.88 and smaller for A(wall)/A(col)≥2.81. Respectively, the r_f for foundation mat increases with smaller values for A(wall)/A(col)=1.31~1.88 and greater for A(wall)/A(col)≥2.34 and the r_f for footings tend to variably decrease with intermediate values to the other ones (Fig. 24).

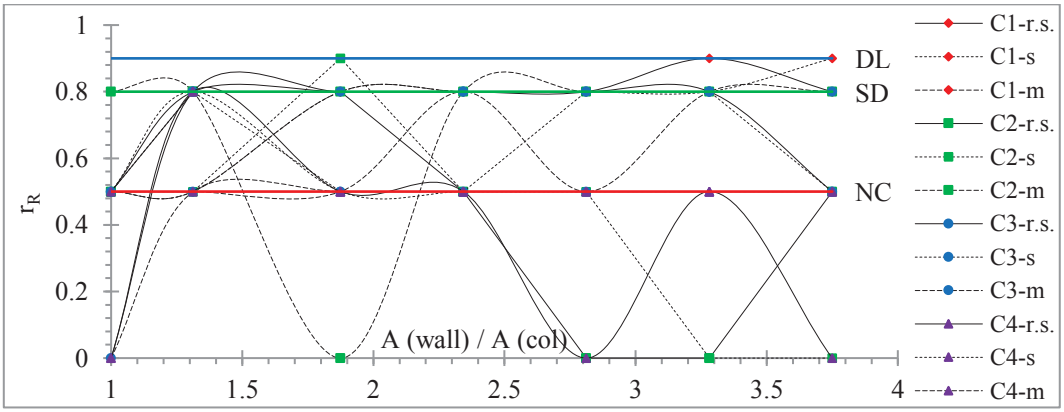

Figure 23: r_R versus A(wall)/A(col) for φ=0°.

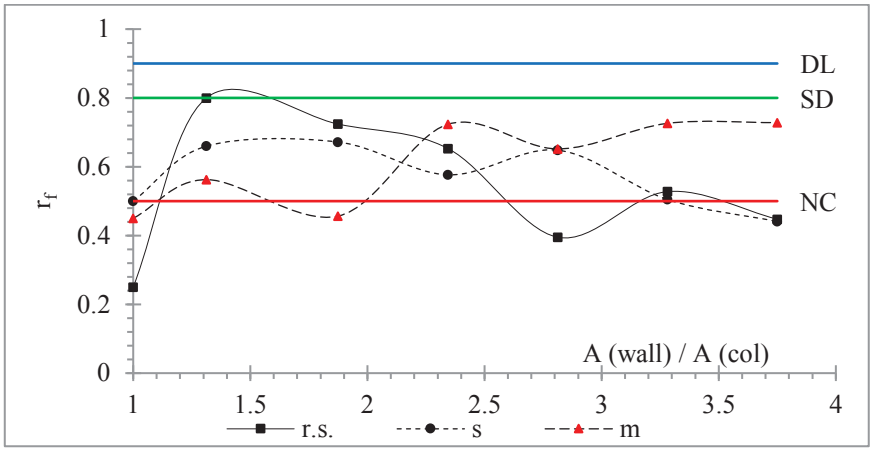

Figure 24: r_f versus A(wall)/A(col) for φ=0°.

Comparing the effect of the incidence angle of the earthquake on the analyses, the plot of the elastic M3(s)/M3 has a greater range of values for φ=90°, while the plot of the elastoplastic M3(m)/M2 has a greater range of values for φ=45° (Figs. 11-14). The plot of the elastic V2(m)/V2 has a greater range of values for φ=0°, while the plot of the elastoplastic V2(m)/V2 has a greater range of values for φ=45° (Figs. 15-18). The plots of the elastic IDR on X and Y axes have a greater range of values for φ=0°, while the plot of the elastoplastic IDR on X-axis has a greater range of values for φ=45° and the plot of the elastoplastic IDR on Y-axis has a greater range of values for φ=90° (Figs. 19-22). The plot of the damage index r_f tends to a smaller range of values, indicating more damages, for φ=0° (Fig. 24).

4 CONCLUSIONS

SSI affects strongly the structural seismic response and proves to be necessary for the design of low-rise usual R/C buildings. From the current analyses of the selected 2-D and 3-D building frames, the following conclusions can be stated.

1. The elastic M(s)/M and V(s)/V of the columns increase along with the increase of the wall section, while the respective ratios of the wall decrease. Indicatively, for example, the elastic M(s)/M of the column is greater by 349% at its base and 389.6% at its top for the greatest wall section, while the elastic V(s)/V of the column is greater by 227%, compared to the respective ones of the wall. Respectively, for comparison purposes, the elastoplastic M(s)/M of the column tends to be greater by 233% at its base and 9% at its top for the greatest wall section, while the elastoplastic V(s)/V of the column is greater by 209%, compared to the respective ones of the wall.

   The elastoplastic M(s)/M and V(s)/V of all vertical elements have a fluctuating behavior because their elastoplastic hinges act as "movable" limits of the internal moment depending on deformation and loading conditions at the end of each element for every time step. If in an elastoplastic hinge a limit is reached, then this acts as a barrier and influences rapidly all other elements by rapidly transmitting an extra load to them. In general, the columns carry more load considering SSI compared to the rigid soil, where their top sections tend to be burdened more than their respective base sections, in terms of the elastoplastic M(s)/M ratio, e.g. greater than 75% for I(wall)/I(col)=39.55~62.81. The wall tends to generally benefit from SSI compared to the rigid soil. Thus, its top section occasionally tends to larger values of the elastoplastic M(s)/M ratio, e.g. up to 124% greater than its respective base, for I(wall)/I(col)=11.72.

Also, in 3-D building frames, the column C1, connected to the wall through a beam along the X-axis, tends to be burdened more than the other columns from SSI, e.g. having greater elastic M(s)/M ratio at its base by 668% and at its top by 382% and elastoplastic M(s)/M at its base by 93% and at its top by 73%, as well as greater elastic V(s)/V by 613% and elastoplastic V(s)/V by 163%, all values calculated for the greatest wall section.

2. The elastic IDRs for SSI and rigid soil decrease along with the increase of the wall section under the limit of 1%, which refers to the Immediate Occupancy performance level, while the elastic IDR for SSI is greater than the one for rigid soil. The latter is observed in 2-D frames, for SSI via footings as compared to rigid soil, and in 3-D, 1-storey buildings, for SSI via footings with tie beams, as well as via foundation mat, compared to rigid soil. However, in both 2-D and 3-D frames, the elastoplastic IDRs vary in a greater range of values, e.g. 1~2%, than the elastic IDRs, e.g. less than 1.5%.
   In general, smaller values of r_f, such as less than 0.73, are observed along with greater values of elastoplastic IDR, such as closer to 2%, indicating heavier damages, corresponding to the Severe Damage performance level.
3. The incidence angle of the seismic motion affects each response parameter differently. This means that for each response parameter the greater range of values of the respective plots is observed for different incidence angles, which are not always the same for all response parameters. Therefore, a general conclusion, defining the "most detrimental angle of incidence", is not obvious.
4. The foundation mat tends to increase the average range of values of the internal moment and shear ratio compared to separate footings connected with beams. The plots of the elastoplastic internal moment and shear ratio have a more fluctuating form for footings than for foundation mat. In general, at the examined 3-D R/C building frames, the foundation mat tends to affect their seismic response more negatively, though more stably, than the footings.

REFERENCES

[1] Eurocode 8 (EC8). Design of structures for earthquake resistance - Part 1: General rules, seismic actions and rules for buildings; Part 3: Strengthening and repair of buildings; and Part 5: Foundations, retaining structures and geotechnical aspects. Brussels: European Committee for Standardization (CEN); 2004.

[2] Mantzaras G, Karabalis DL. The role of SSI in the redistribution of internal forces in concrete buildings due to seismic excitation. COMPDYN 2015, Crete, Greece, (Paper C1611).

[3] Lampropoulou A. "Investigation of the Distribution of Base Shear of Plane Frame Structures with Soil-Structure Interaction", Master of Science Dissertation, Department of Civil Engineering, University of Patras 2009 (in Greek).

[4] Mylonakis G, Syngros C, Gazetas G, Tazoh T. The role of soil in the collapse of 18 piers of Hanshin Expressway in the Kobe earthquake. Earthquake Engineering and Structural Dynamics. 2006; 35.5: 547-575.

[5] Eurocode 1 (EC1). Actions on structures - Part 1-1: General actions, Densities, self-weight, imposed loads for buildings. Brussels: European Committee for Standardization (CEN); 2001.

[6] Eurocode 2 (EC2). Design of concrete structures - Part 1-1: General rules and rules for buildings. Brussels: European Committee for Standardization (CEN); 2004.

[7] Gazetas G. Analysis of machine foundation vibrations: State of the art. International Journal of Soil Dynamics and Earthquake Engineering; 1983:2.1:2-42.
[8] ETABS. Integrated Building Design Software. Computers and Structures Inc. CSI. Berkeley, USA. 2015.
[9] Institute of Engineering Seismology and Earthquake Engineering (ITSAK). Institute of Engineering Seismology and Earthquake Engineering. Database of earthquake records available at http://www.itsak.gr/db/data; 2017 [accessed 1 December 2017].
[10] Sfakianakis MG, Fardis MN. Bounding surface model for cyclic biaxial bending of R/C sections. Journal of Engineering Mechanics. 1991;117.12:2748-68.
[11] Sfakianakis MG. Biaxial bending with axial force of reinforced, composite and repaired concrete sections of arbitrary shape by fiber model and computer graphics. Advances in Engineering Software. 2002; 33.4:227-242.
[12] Greek Interventions Regulation (KANEPE). Greek Organization for Earthquake Planning and Protection (EPPO). Greek Ministry for Environmental Planning and Public Works. Athens (In Greek); 2017.
[13] Hatzivassiliou M, Hatzigeorgiou G. Seismic sequence effects on three-dimensional reinforced concrete buildings. Soil Dynamics and Earthquake Engineering, 2015, 72: 77-88.
[14] FEMA-356. Prestandard and Commentary for the Seismic Rehabilitation of Buildings. Washington, D.C.: Federal Emergency Management Agency; 2000.
[15] Eurocode 8-Draft prENV. Design provisions for earthquake resistance of structures - Part 1-4: Strengthening and repair of buildings. Brussels: European Committee for Standardization (CEN); 1998.

EURODYN 2020
XI International Conference on Structural Dynamics
M. Papadrakakis, M. Fragiadakis, C. Papadimitriou (eds.)
Athens, Greece, 23–26 November 2020

THE RESPONSE OF DIFFERENT BUILDINGS TO FREE-FIELD EXCITATION – A STUDY USING DETAILED FINITE ELEMENT MODELS

Lutz Auersch[1], **Susanne Ziemens**[1]

[1] Federal Institute of Material Research and Testing,
Berlin 12200 Germany
e-mail: lutz.auersch-saworski@bam.de

Keywords: building vibration, office building, residential building, soil-building resonance, floor resonance, column/wall resonance.

Abstract. *A study on building vibrations has been performed by finite element calculations. Family houses, multi-storey residential buildings, office buildings and office towers have been modelled in detail. The frequency-dependent response due to a free-field excitation has been evaluated for walls, columns and floors. The ratio of building amplitudes to free-field amplitudes starts with $u_B/u_0 = 1$ at zero frequency and is usually lower than 1 at 50 Hz, the end of the frequency range considered here. In between, amplifications occur due to several reasons. There are „soil resonances“ where the whole building is vibrating on the compliant soil, “column resonances” where the upper storeys are vibrating on the compliant columns, and the “floor resonances” where the floors are vibrating excited by their supports. Results are presented for all building types, but a special focus is set on office buildings. A parameter study shows the influence of the stiffness of the soil, the number of storeys, and the width of the building. It has been found that the “soil resonance” is strongly modified by the low-frequency floor resonances for the normal office building. The main resonance of a twenty-storey office tower is determined equally by the “soil mode” and the “column mode”. It is an important observation for these office buildings that the resonances can differ for different parts of the building such as the centre, the edge, the corner, and the core of the building. This leads to non-uniform vibration modes across the building, which look like another type of “floor resonance” and which have been observed in several real building projects. Experimental results will be shown which can confirm the calculated phenomena.*

1 INTRODUCTION

The response of buildings to ground vibration had been studied by experiments and some rules have been derived. The transfer from free-field to foundation amplitudes and to floor amplitudes had been established for small residential buildings [1,2]. These rules, however, cannot be applied to larger and more complex buildings, namely to office buildings with their column-type rather than wall-type structure. Therefore, a finite-element analysis of different building types has been performed where the parametric study of office buildings was of high interest [3].

2 DIFFERENT BUILDINGS

The basic office building consists of four storeys, three lines of thirteen columns, and 5 x 2 x 12 floors (Fig. 1). The columns and floors are of concrete with the material parameters

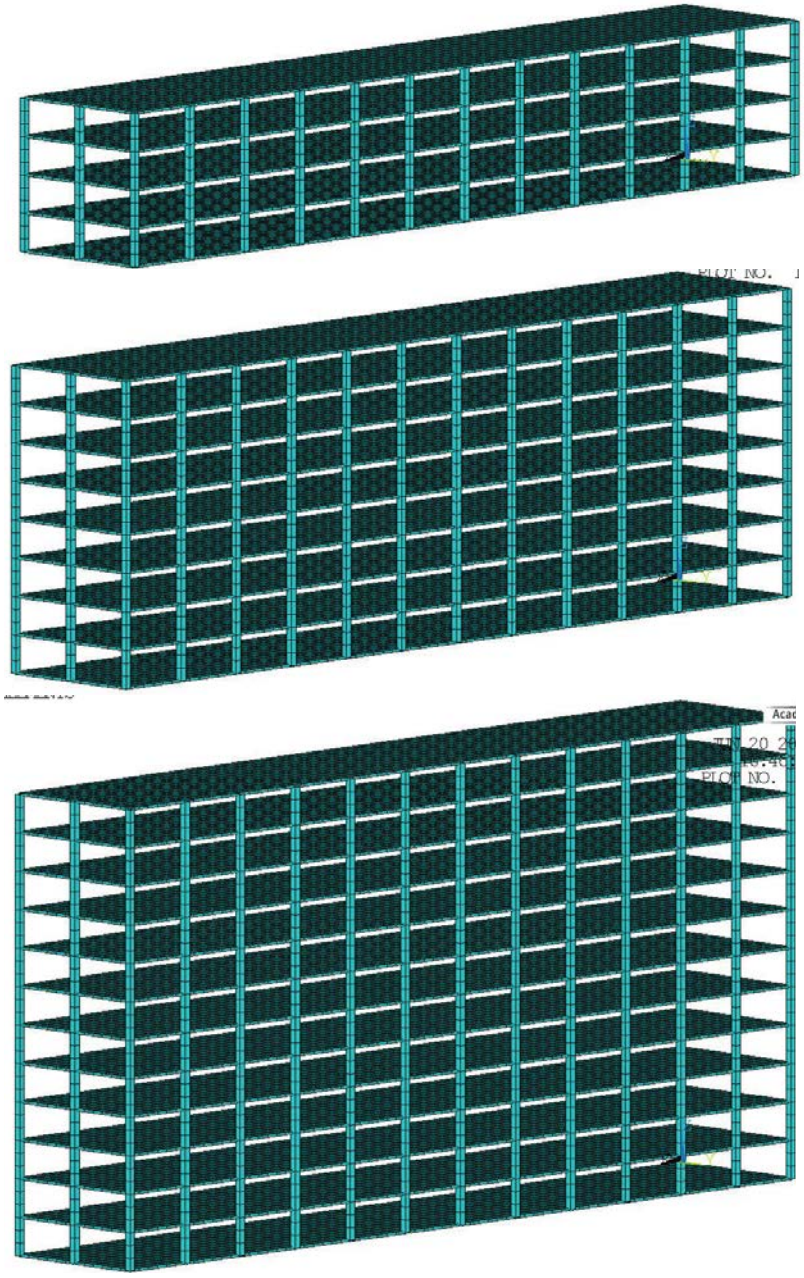

a)

b)

c)

Figure 1: Office buildings with 2 x 12 floor bays and a) 4, b) 8, and c) 12 storeys.

$E_C = 3\ 10^{10}$ N/m^2 the elasticity modulus, $\rho_C = 2.5\ 10^3$ kg/m^3 the mass density, and the geometrical parameters 3 m x 0.6 m x 0.6 m for the columns and 6 m x 6 m x 0.2 m for the floors. There is a 2 m x 2 m shallow foundation under each column of which the stiffness is calculated as $k = 4\ G/(1-\nu)\ \sqrt{A/\pi}$ and the damping as $c = 3.4\ A/\pi(1-\nu)\ \sqrt{G\rho}$. The soil parameters $G = 8\ 10^7$ N/m^2 the shear modulus, $\nu = 0.33$ the Poisson ratio, $\rho = 2\ 10^3$ kg/m^3 the mass density are used together with the foundation area $A = 2$ m x 2 m.

The number of storeys has been varied between 4, 8, and 12, see Figure 1. The number of rows of floors has been varied between two (the standard) and three. The stiffness of the soil has been varied between $G = 4.5$, 8 and 18 10^7 N/m^2.

High-rise office buildings of 20 storeys have been analysed with a different ground plan (Fig. 2). There are 4 x 3 floor bays of 6 m x 6 m which are completely supported by columns as before (Fig. 2a) or supported by an additional inner core of walls with $d_W = 0.2$ m (Fig. 2b).

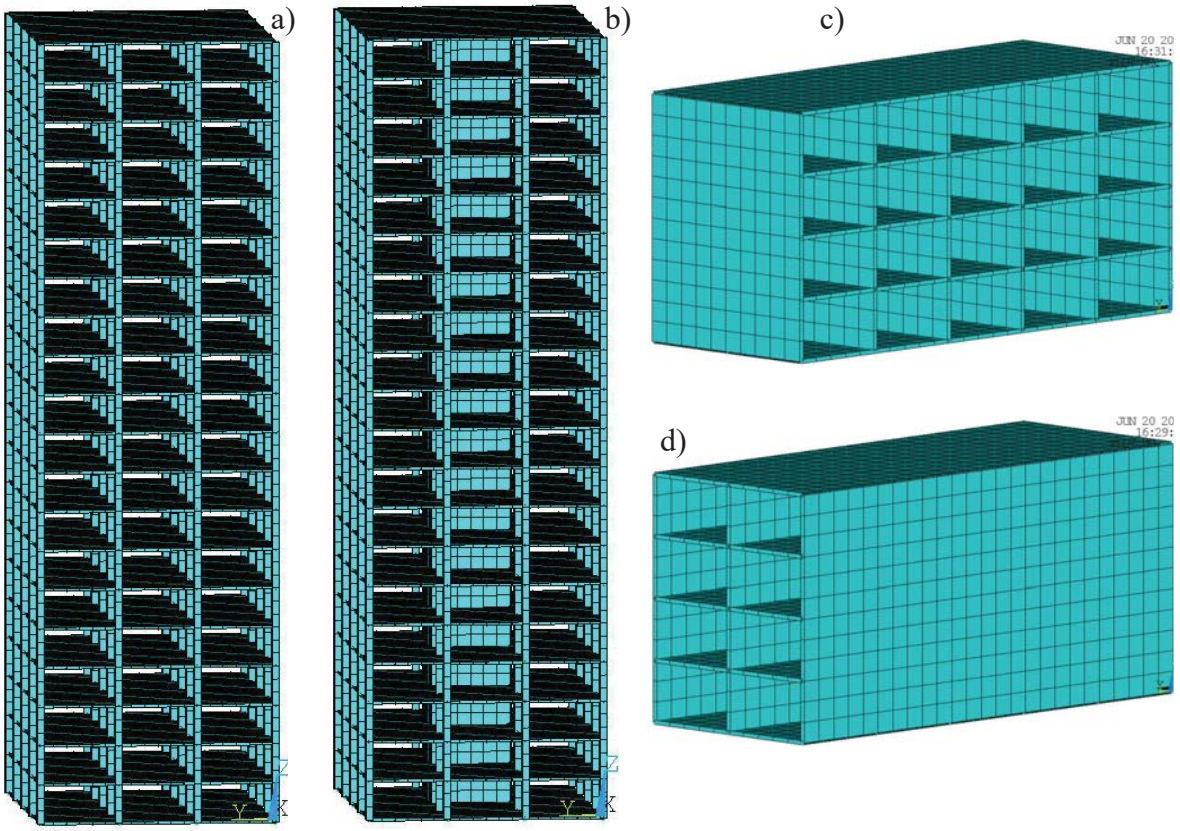

Figure 2: Office towers of 3 x 4 floor bays and 20 storeys, a) without core walls, and b) with core walls, 4-storey residential buildings with 2 x 5 floor bays and c) walls across and d) walls along the building.

Two 4-storey wall-type residential buildings have been analysed (Fig. 2c,d). Both buildings have 2 x 5 floor bays of 5 m x 5 m width, and one building has its walls across the building and the other has its walls along the building. Whereas the floors are of concrete, the walls are made of masonry with the material parameters $E_M = 5\ 10^9$ N/m^2 the elasticity modulus, $\rho_M = 2.5\ 10^3$ kg/m^3 the mass density, and a thickness of $d_W = 0.25$ m.

A small 2-storey residential building with varying floor dimensions (Fig. 3) is analysed once with equal floors in the storeys and once with a different floor of 7 m x 6 m in the ground floor.

All buildings are excited by a constant harmonic free-field of frequencies between 1 and 50 Hz. The response of the building is plotted as the ratio to the free-field amplitude giving the frequency-dependent transfer functions of the different building points.

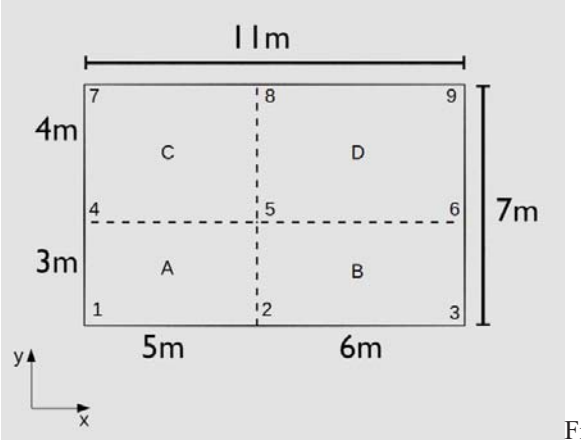

Figure 3: 2-storey residential building, floor plan.

3 A PARAMETER STUDY FOR OFFICE BUILDINGS

3.1 Transfer functions and vibration modes

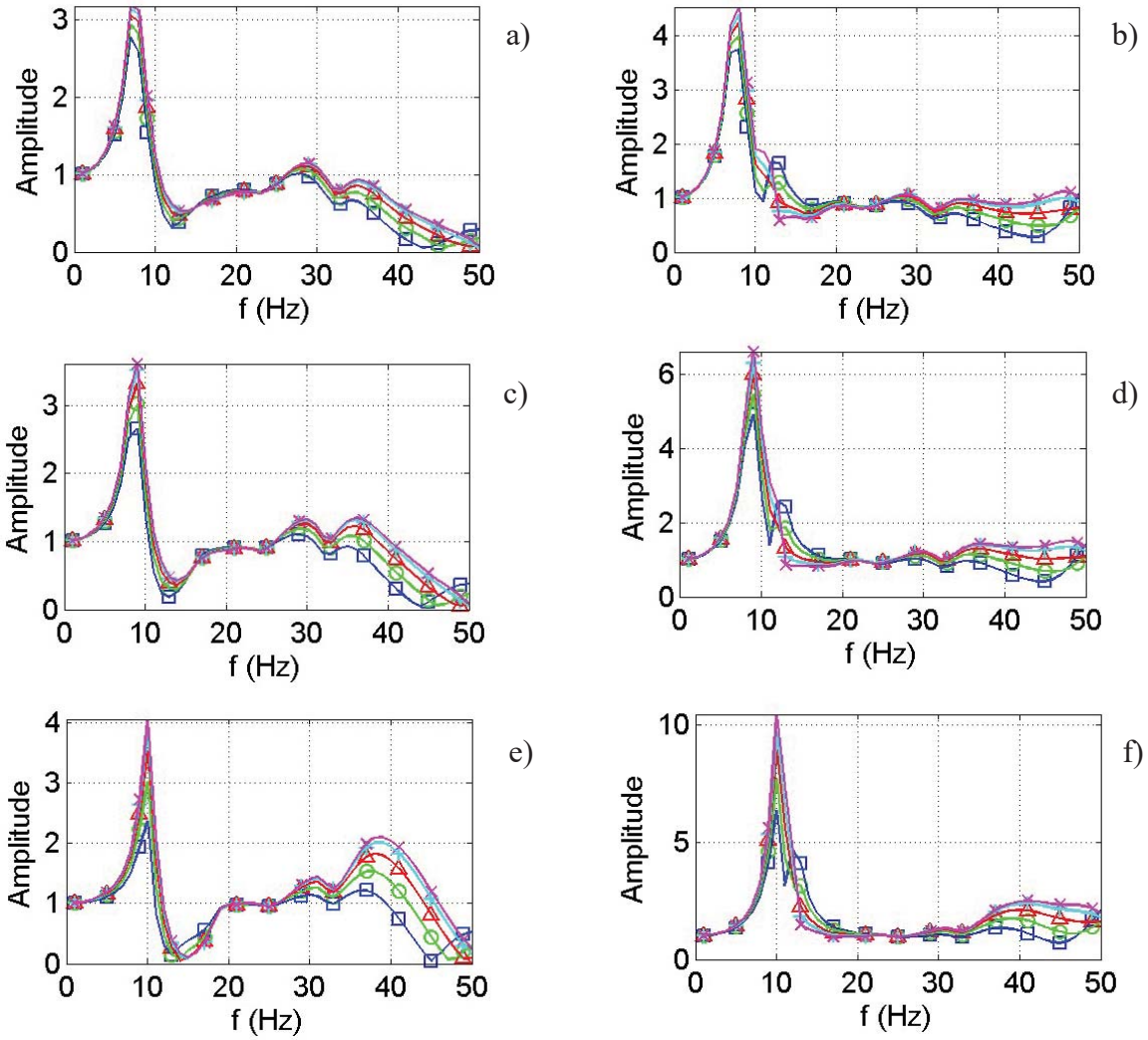

Figure 4: Transfer functions of the 4-storey office buildings, a,c,e,g) mid columns, b,d,f,h) floors, ☐ ground, ○ 1st, △ 2nd, + 3rd storey, × roof, a,b) soft soil, c,d) medium soil, e,f) stiff soil, g,h) average of all storeys, ☐ soft, ○ medium, and △ stiff soil.

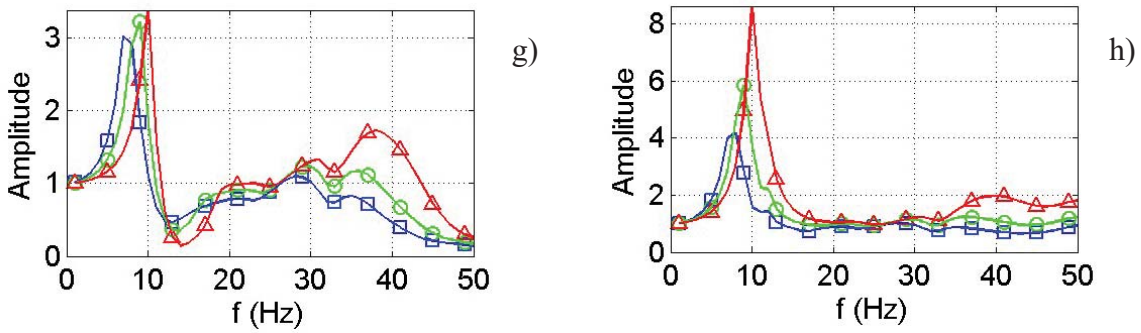

Figure 4: continued.

The freefield-building transfer functions are shown in Figure 4c,d for the five storeys of the standard office building. Figure 4c shows the transfer functions for a central column, and Figure 4d for the midpoint of a central floor. These transfer functions show some general characteristics. All freefield-building transfer functions start with $V = 1$ at zero frequency and usually end below $V < 1$ at 50 Hz. That means that the free field is not modified by the building at low frequencies whereas the free field is reduced by the building at high frequencies. In between, amplifications of the free field can occur due to several reasons. The standard office building shows an amplification at 9 Hz for the column as well as for the floor points where the floor amplitudes are higher at $V \approx 6$ compared to the column points at $V \approx 3$. The points higher in the building (the upper storeys) have a little higher amplitudes. This is also true for a weak amplification at 29 and 37 Hz. Another weak amplification can be found at 13 Hz for the floor points. To be complete, there is also a relative maximum of almost $V \approx 1$ at 15 Hz for the outer columns.

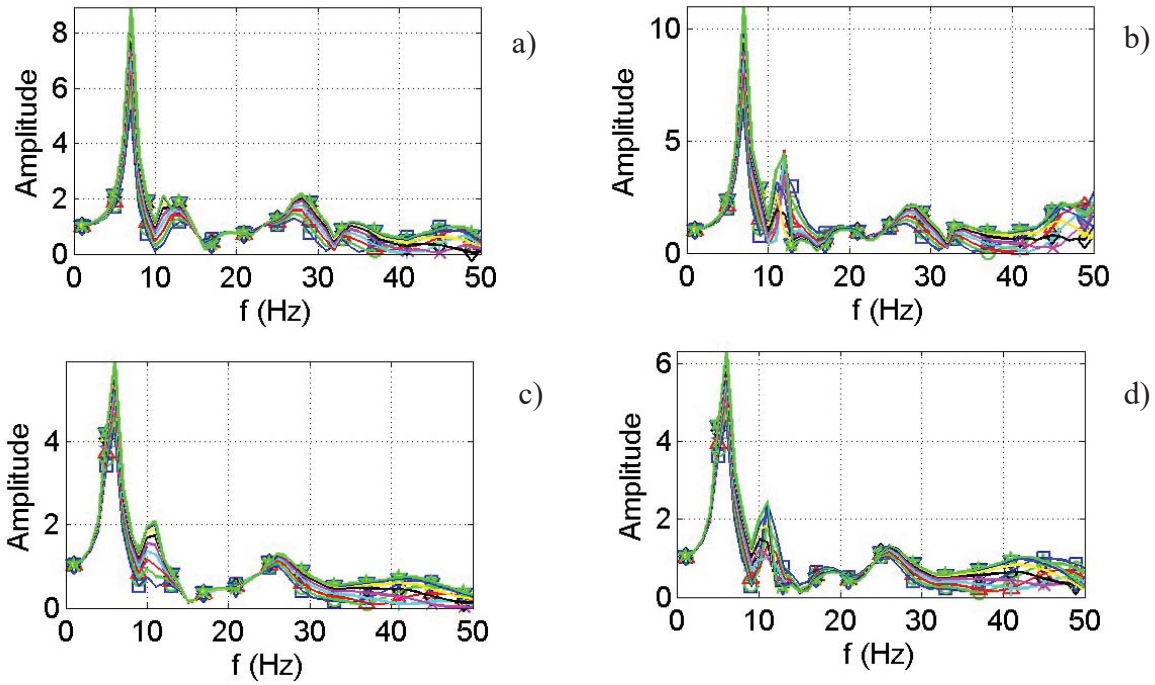

Figure 5: Transfer functions of the 8- (a,b) and 12-storey buildings (c,d), a,c,e,g) mid columns, b,d,f,h) floors, □ ground, ○ 1st, △ 2nd, + 3rd storey, × 4th, ◇ 5th, 6th, 7th, roof, e,f) average of all storeys, □ 4-storey, ○ 8-storey, and △ 12-storey building.

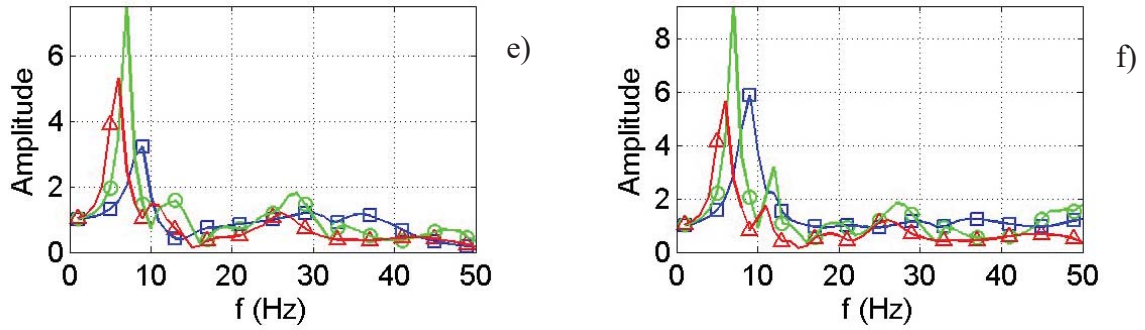

Figure 5: continued.

The results for the variation of the soil can be found in Figures 4a,b,e,f. If the stiffness of the soil is modified once to the soft (Fig. 4a,b) and once to the stiff side (Fig. 4e,f), the fundamental resonance frequency is shifted to 7 Hz and to 10 Hz. At the same time, the amplitudes are increased from 3 to 4 for the columns and from 4 to 10 for the floors from the soft to the stiff soil. The stiff soil yields also a more pronounced second maximum at 13 Hz. Corresponding to that, a common minimum can be observed at 13 Hz for the columns which is also strongest for the stiffest soil.

The variation of the number n of storeys of the office building is shown in Figure 5. The transfer functions of higher office buildings show a lower resonance frequency, 7 Hz for the 8-storey building and 6 Hz for the 12-storey building. The second maximum is now a little stronger ($V \approx 4$) at 11 or 12 Hz.

Finally in Figure 6, it is demonstrated that the fundamental resonance does not change if the total width of the storey floor is increased from 2 x 6 m to 3 x 6 m.

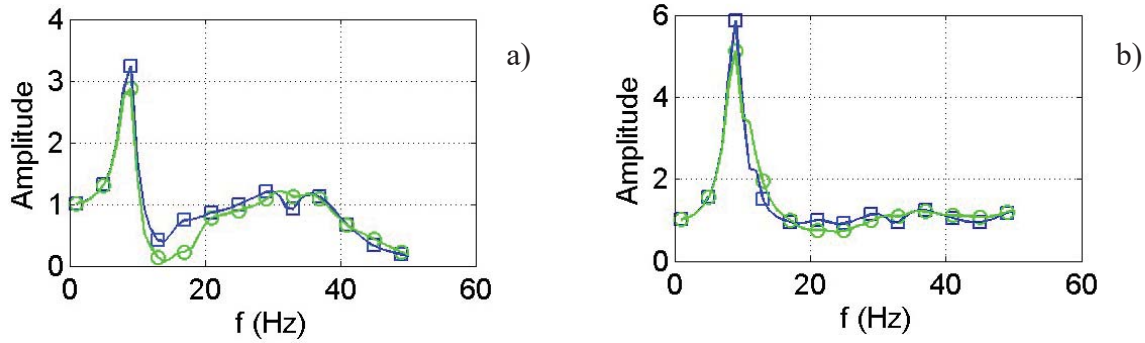

Figure 6: Transfer functions of the office buildings with □ 2 x 12, and, ○ 3 x 12 floor bays, a) mid columns, b) floors, average of all storeys.

Some mode shapes of the different buildings are shown in Figure 7. The 4-storey office building shows clear equal deformations of each storey for the first resonance frequency at 9 Hz (Fig. 7a). The maximum displacement occurs in the middle of the building along the central columns. It looks like a resonance of the entire floor of the storey, but it is the resonance of the central building on the soil, see more examples in [4,5]. Figure 7b shows the local floor resonances at 12 Hz which are in anti-phase for the top and the bottom floors. The 12-storey building (Fig. 7c) has clearly increasing amplitudes from bottom to top at the first resonance frequency of 6 Hz, that means a vertical deformation of the whole building which is called the "column mode".

The resonance amplitudes vary with the stiffness of the soil and the height of the building. The highest amplitudes are for the 8-storey building with $V = 8$ for the columns and $V = 10$

for the floors. This can be explained by the coupling of different modes, see the next section. For the 8-storey building, the “soil mode”, the “floor mode”, and the “column mode” coincide. The 12-storey building with the lowest resonance frequency has a combination of the “soil mode” and the “column mode”. The 4-storey building has a coincidence of the soil and the floor mode. Therefore, the 4-storey building and the 12-storey building have only medium strong resonances of $V = 6$ at the floors. The amplitudes increase with the stiffer soils as the theoretical soil-building resonance frequency comes closer to the floor resonance frequency and reaches $V = 10$ for the stiff soil of $G = 18\ 10^7$ N/m^2.

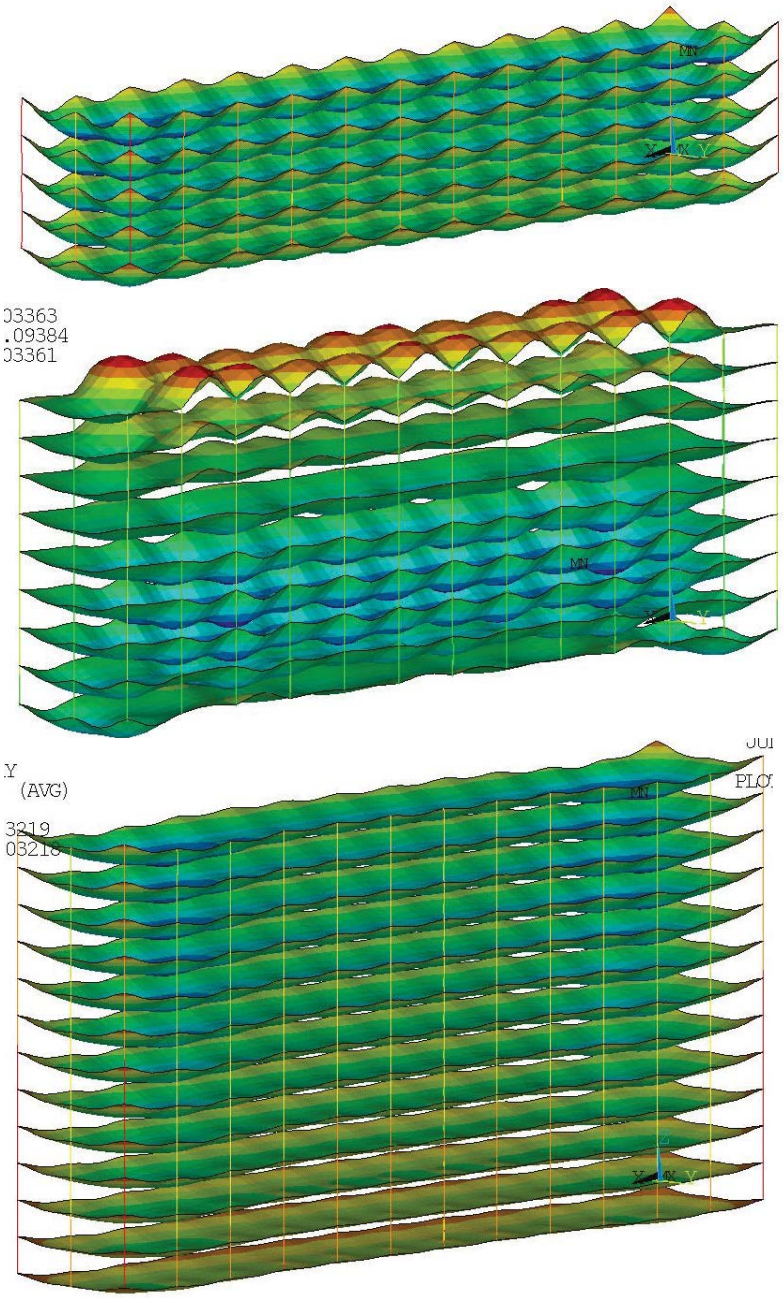

Figure 7: Vibration modes of the column-type office buildings with a) 4, b) 8, c)12 storeys, at 9 Hz (a), 12 Hz (b), and 6 Hz (c).

3.2 Analysis of resonance frequencies and the coupling of modes

All these resonance frequencies are analysed in more detail by Figure 8. The fundamental

resonance frequencies from the finite element calculations are compared with the theoretical soil-building resonance frequencies. The theoretical soil-building frequency $f_S = \sqrt{k/m}$ compares the stiffness k of the foundation and the mass m of the building. Therefore, the theoretical soil-building resonance frequency varies with $f_S \sim v_S = \sqrt{G/\rho}$ and with $f_S \sim n^{-0.5}$. There are differences between the soil-building resonance frequency for the whole building, for the outer building (with a lower mass and a higher resonance frequency), and for the central building (with a higher mass and a lower resonance frequency). The fundamental resonance frequencies from the finite-element calculation are even lower than the theoretical ones. The difference is 11.7 Hz to 9 Hz for the standard soil of $G = 8\ 10^7$ N/m^2 ($v_S = 200$ m/s), from 8.7 Hz to 7.5 Hz for the soft soil of $v_S = 150$ m/s, and greatest for the stiff soil $v_S = 300$ m/s from 17.5 Hz to 10 Hz. Moreover, the power laws from the finite-element calculations are clearly weaker than the theoretical laws. All these observations indicate another influence on the fundamental resonance.

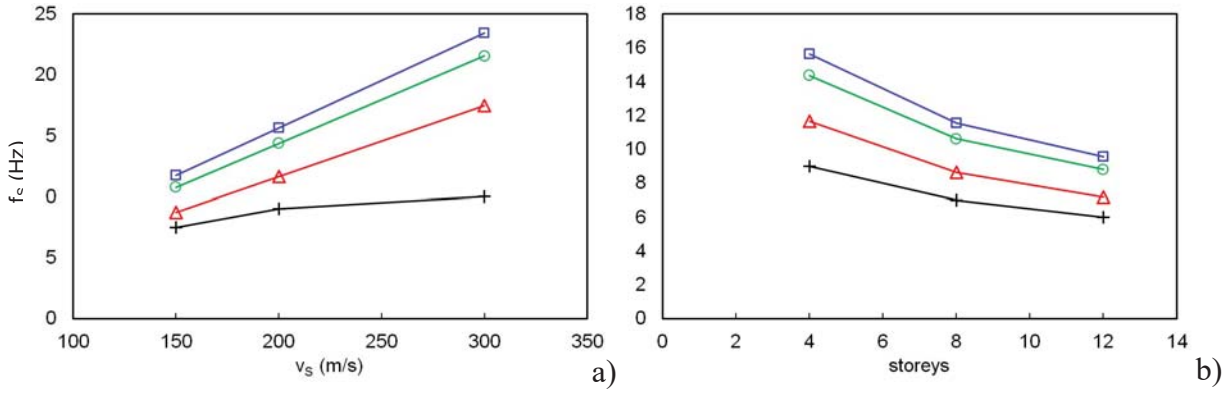

Figure 8: Theoretical soil building resonance frequencies for ○ the whole building, △ the inner building and □ the outer building, + the fundamental resonance frequency from the finite-element calculation, a) variation of the soil, b) variation of the number of the storeys.

This influence is identified as the influence of the floor resonance. Approximately, the floors are clamped at each column and the rotation along the sides is prevented due to the interaction with the neighbouring floors. The theoretical floor resonance frequency is therefore 13.7 Hz, see [4]. This floor resonance frequency is not far from the soil-building resonance frequency so that both resonances work together and yield a lower fundamental resonance frequency.

The higher office buildings have lower soil-building resonance frequencies which are further away from the floor resonance frequency. Therefore, the floors have a weaker influence on the soil-building resonance frequency. There is another influence in case of higher buildings. The upper storeys are amplified compared to the lower storeys. This "column mode" means a stronger mass effect than for a rigid building, and this yields also a reduction of the soil-building resonance frequency.

4 OFFICE TOWERS

The two 20-storey office towers considered here can be seen in Figure 9 with their typical vibration modes. Figures 9a,b,d show the column mode of the tower without and with core walls where the amplitudes are increasing from the bottom to the top of the building. Figure 9c shows a second "column mode" at 9 Hz where top and bottom of the building are in anti-phase.

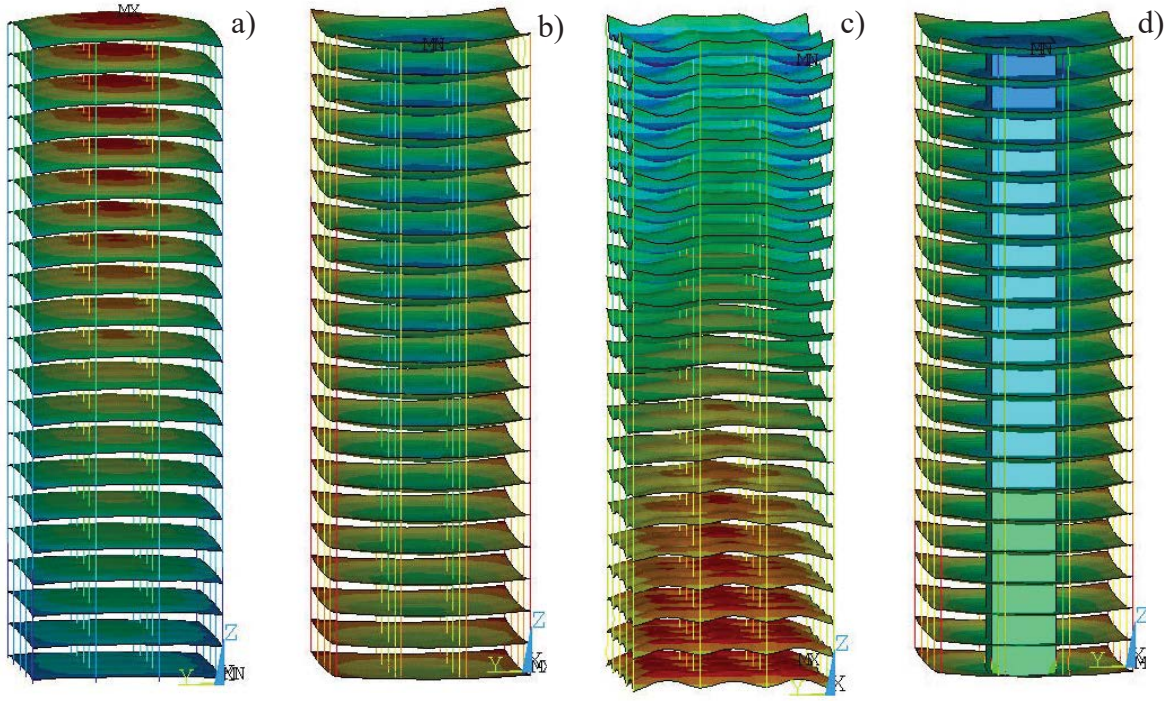

Figure 9: Vibration modes of the 20-storey office towers without (a,b,c) and with (d) core walls, a) 4 Hz, b) 4 Hz (imaginary part), c) 9 Hz, d) 4 Hz.

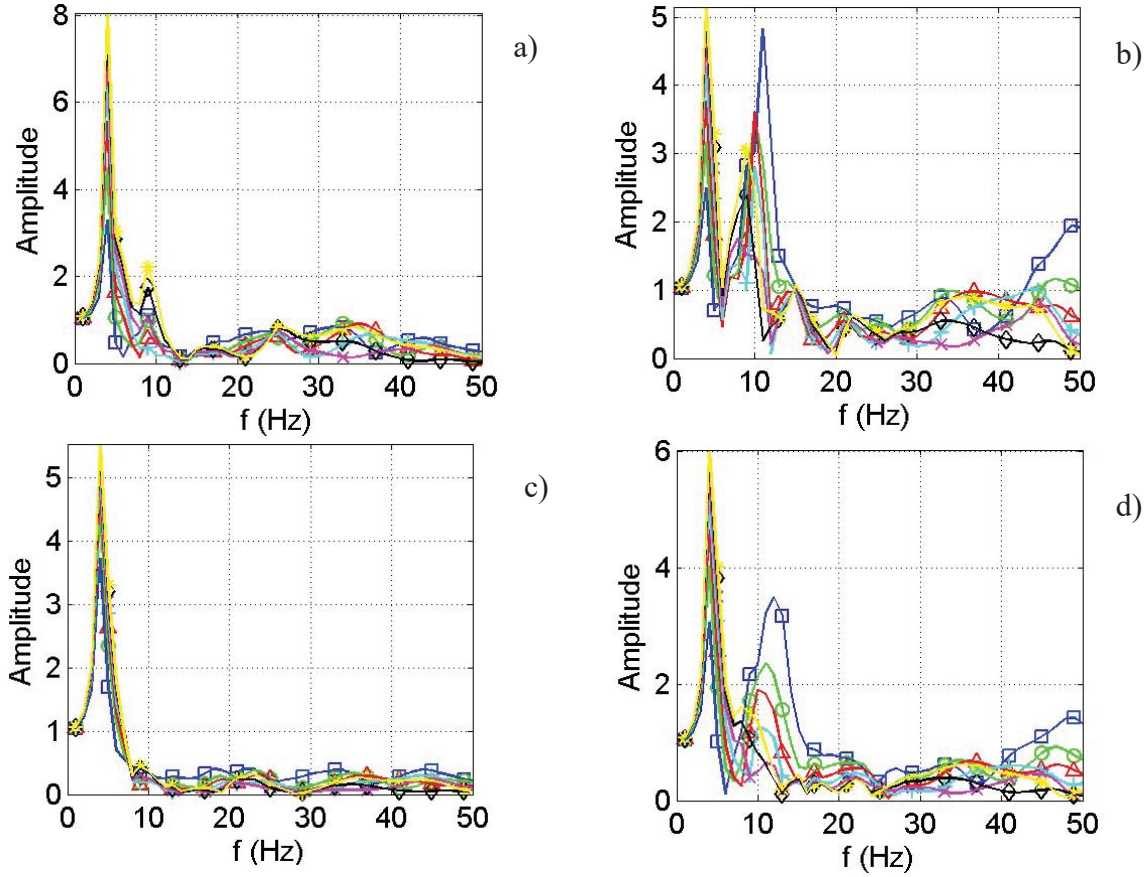

Figure 10: Transfer functions of the 20-storey buildings (a,b) without and (c,d) with core walls, a,c) mid columns, b,d) floors, □ ground, ○ 4th, △ 7th, + 10th, × 13th, ◇ 16th, ∗ 19th storey.

The transfer functions of the two tower buildings have some similarities (Fig. 10a,c). The main resonance is at 4 Hz and a considerable amplification from bottom to top can be observed. The tower without core reaches amplitudes of $V = 8$ and some influence of the floors at 9 Hz can be found. The tower with core has lower amplitudes with a maximum of $V = 5$. Some floor resonances can be seen at 11 to 13 Hz for the floor points (Fig. 10b,d).

The main resonance of the twenty-storey office towers is determined similarly by the "soil mode" and the "column mode". The theoretical soil-building resonance frequency is 6 Hz and the theoretical column resonance is also $f_C = v_L/4H \approx 6$ Hz, see [6] for details. Both together yield a fundamental resonance frequency of 4 Hz.

The floor resonance frequencies depend on the position of the floor. It is lowest with $f_0 = 11$ Hz at the corner, with $f_0 = 12$ Hz at the edge of the storey, it is higher with $f_0 = 15$ Hz near the core, and highest with $f_0 = 24$ Hz inside the core.

5 RESIDENTIAL BUILDINGS

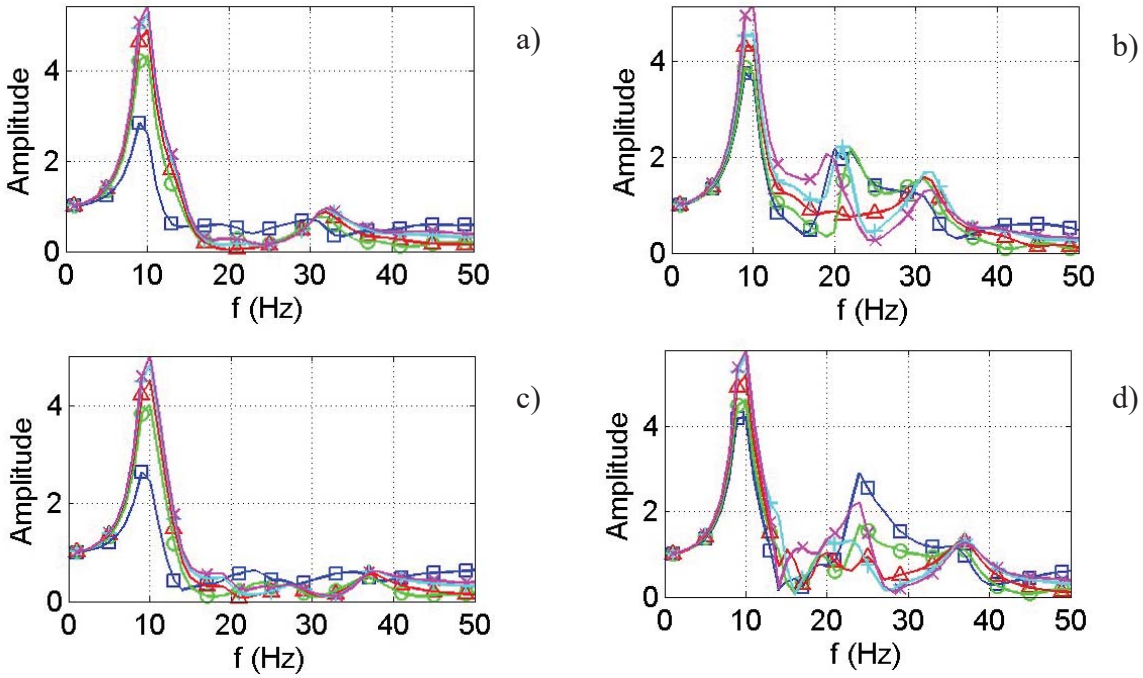

Figure 11: Transfer functions of the 4-storey residential buildings (a,b) with walls across and (c,d) walls along the building, a,c) mid wall, b,d) floors, □ ground, ○ 1st, △ 2nd, + 3rd storey, × roof.

The two types of 4-storey residential buildings have a different orientation of the walls and there is only a small difference of the building mass. Therefore, they have almost the same theoretical soil-building resonance frequency at 12 Hz. The resonance frequency of a rigid building is reduced to 10 Hz for the flexible building (Fig. 11) which is due to a small effect of the floor mode and the wall mode. The floor resonances are at 20 Hz in case of the longitudinal walls and at 24 Hz in case of the transverse walls. The resonance frequency in case of the longitudinal walls is defined by a clamped boundary at the central wall and a hinged boundary at the outer wall. This yields the eigen frequency $f_0 = 20$ Hz for the floor span of 5 m. In case of the transverse walls, the boundary condition is clamped-clamped which yields the higher floor resonance frequency. The 20 Hz floor resonance can be found in Figure 11b, but the amplitudes are not higher than $V = 2$. The floor resonance amplitudes are

reduced by the compliance of the soil. Around 20 Hz, the foundation and wall amplitudes are very low so that the floor resonance amplitudes are limited (absorber effect).

Figure 12 shows two floor resonances of the residential building, the first at 23 Hz, the second at 37 Hz. Both floor modes comprise anti-phase motions. At 24 Hz, the top and bottom floors are in anti-phase (Fig. 12a), at 37 Hz, all floors are in anti-phase to the walls (Fig. 12b).

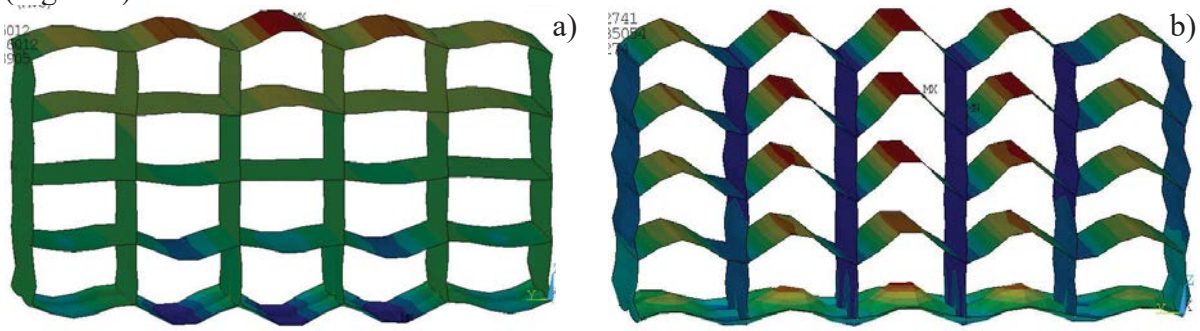

Figure 12: Vibration modes of the residential building with walls across the building, at a) 24 Hz, and b) 37 Hz.

Finally, the small 2-storey residential building is analysed in Figure 13. The highest soil-building resonance of 15 Hz can be found. All four rooms have different dimensions, but no floor resonance can be seen in Figure 13b, not even for the largest room. Only if the ground and the first storey have different walls, the floor resonance at 17 Hz can be found with a high amplitude of $V = 8$ (Fig. 13d). The resonance frequency agrees with the resonance frequency of a 6 m x 7 m large plate which is hinged at all boundaries.

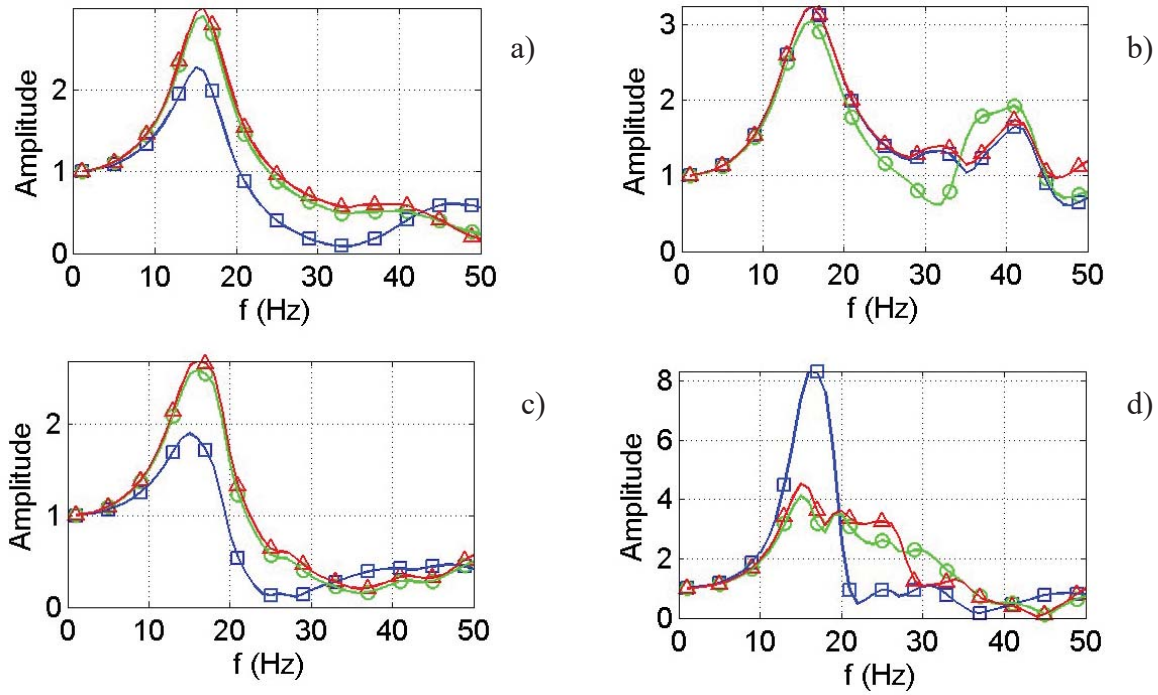

Figure 13: Transfer functions of the 2-storey residential buildings, a,b) with regular floors and c,d) with a separated large floor a,c) mid wall, b,d) floors, □ ground, ○ 1st floor, △ roof.

6 COMPARISON OF THE DIFFERENT BUILDING TYPES

All buildings have a clear fundamental resonance which is mainly a soil-building resonance in most cases. The floor resonance can be observed for all buildings, but not so

clearly. The column resonances as an effect of the flexibility of the columns can be found for the high office buildings. Moreover, many anti-phase modes have been found in many buildings, floor against columns/walls, inner against outer building, and top against bottom. A column-type office building is obviously not a rigid structure.

The highest resonance amplitudes have been found for the stiffest soil, the highest building, and for the separated floor in the small residential building with amplitudes of $V = 8$ to 10. The amplitudes are reduced with increasing frequencies, strongest for the office towers which have amplitudes below $V < 1$ above 7 Hz, even lower for the tower with core walls. The residential buildings start with amplitudes below $V < 1$ at 15 Hz, the small residential building starts at 20 Hz. The office buildings have the highest amplitudes at higher frequencies, usually at $V \approx 1$, even higher for the stiff soil, whereas the soft soil yields amplitudes below $V < 1$ starting from 30 Hz. In general, the column-type office buildings have been identified as the most sensible buildings.

7 EXPERIMENTAL RESULTS

The soil-building resonance which is dominant in the theoretical results has also been found in measurements of small residential buildings (Fig. 14 from [2]). The soil-building resonance frequencies have been measured in the range of 5 to 10 Hz. These lower frequencies have been attributed to an inhomogeneous soil with a soft material on top of the soil.

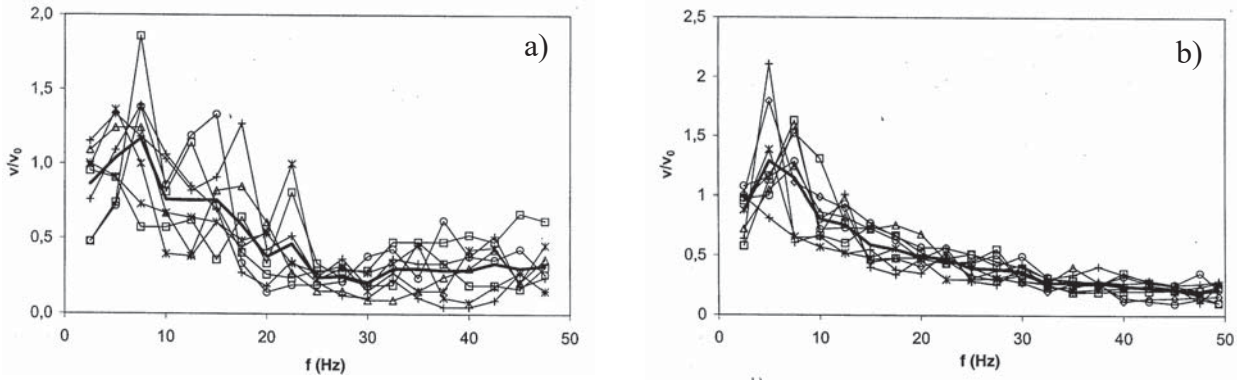

Figure 14: Transfer functions of several small residential buildings measured during pile driving (a) and train passages (b), eight buildings and the average (thick line).

Many measured floor resonances have been evaluated in [6,7]. The resonance amplitudes (compared to the free field) are in the range of $V = 1$ to 10. The low floor resonance amplitudes of the present numerical study are probably due to the very regular modelling of the building. All reducing effects are stronger if all the same floors act together, for example reducing the foundation amplitudes [6]. Also, the regular interaction of the inner and outer columns leads to an anti-phase floor excitation and smaller resonance amplifications.

The wall or column resonance has been observed in some measurements of 6- to 8-storey buildings [1]. The strongest wall and column effect can be found in the office towers. Such a tower building has been measured and also modelled in detail. The resulting soil-building transfer functions have been compared (Fig. 15). The wall/column mode resonance with increasing amplitudes at higher storeys can be clearly seen below 10 Hz in theory and measurements. The floor resonances follow between 10 and 17 Hz.

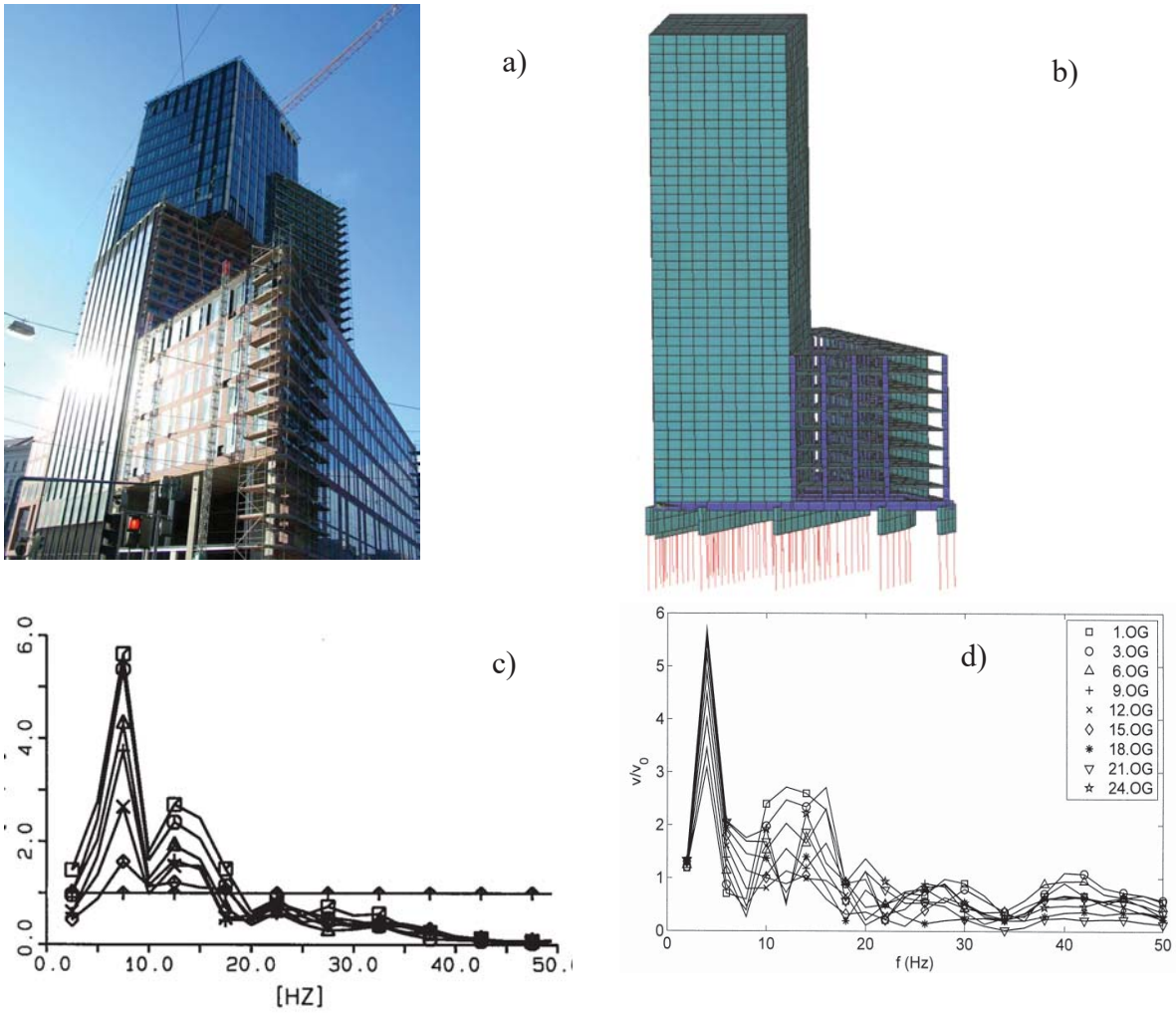

Figure 15: Office tower (a), finite element model (b), measured transfer functions (c, □ 24th, ○ 21st, △ 18th, + 15th, × 12th, ◇ 6th, ♦ ground storey), and calculated transfer functions (d).

8 REAL BUILDING PROJECTS

Finally, some real building projects are presented. The real building projects are not as regular as the buildings of the preceding parameter study. The foundation consists of end-bearing piles which are necessary for the soft sandy soil under building 1 (Fig. 16a). Buildings 2 and 3 (Fig. 16b, e) are above from traffic lines (motorway or metro) so that pile foundations are used close to the traffic lines while plate foundations are used for the rest of the building. The building plan is also irregular, for example triangular for building 1 (Fig. 16c). The building structure is usually mixed with core walls and columns.

Some building-soil transfer functions are given in Figure 17a-d for building 1. The transfer functions of the core wall display the soil-building resonance at 10 Hz and a quit regular behaviour at higher frequencies. The column near the core wall (Fig. 17b) shows some more column deformations but still the basic resonance at 10 Hz. The column in the column section has a lower resonance at 7.5 Hz with a strong amplification from bottom to top (Fig. 17c). The floor resonances are between 15 and 20 Hz (Fig. 17d).

Building 2 has a 10-storey and a 20-storey part where the 10-storey part is situated above the metro line. The side parts include the walls whereas the middle parts are built with columns. The soil-building transfer functions of the wall part (Fig. 17 e, f) show only the floor

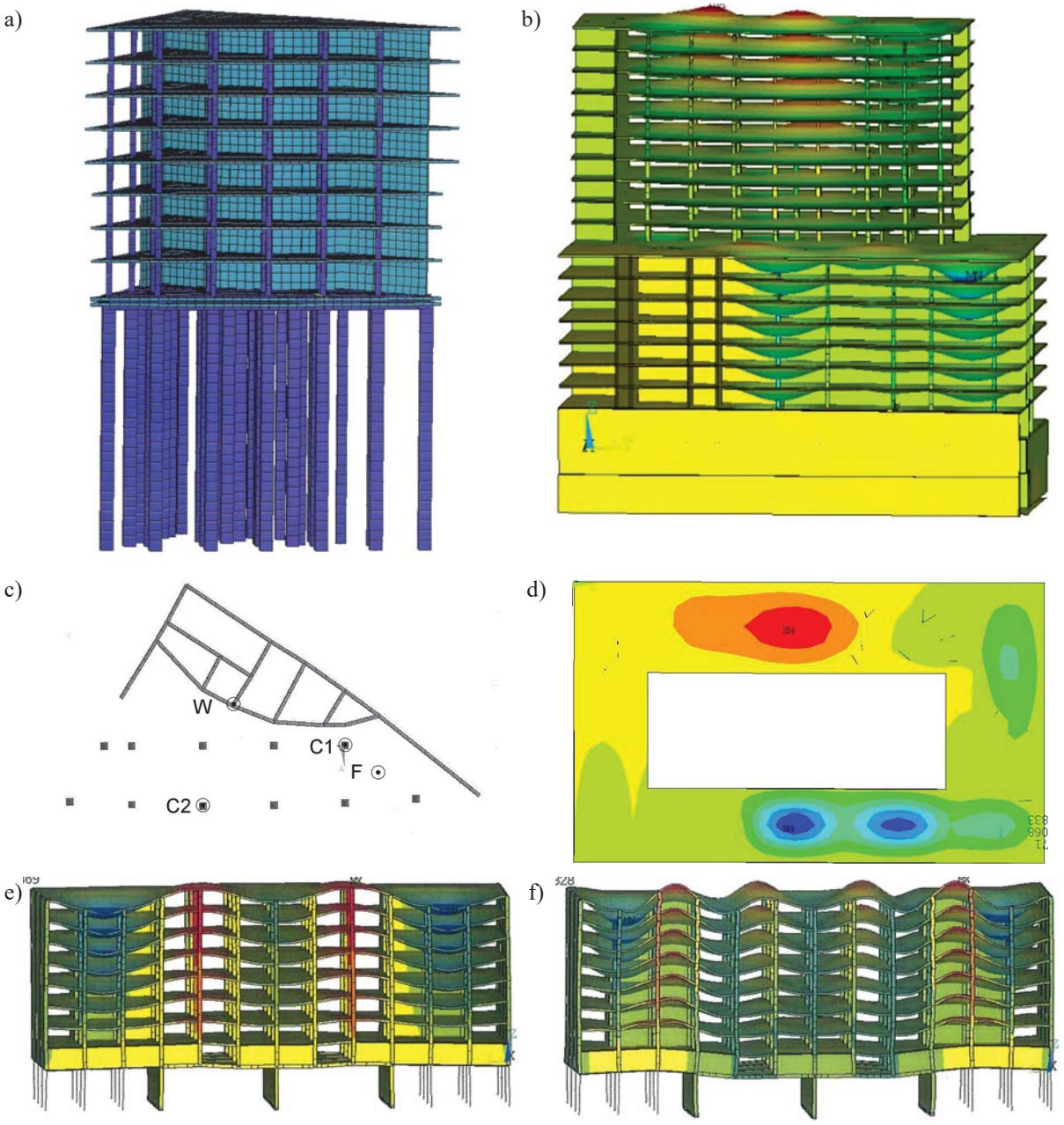

Figure 16: (a, c) Building 1 on piles with core walls and columns, (b, d) building 2 above metro line vibration modes at 12 and 8 Hz, (e, f) Building 3 above motorway, modes at 9 and 14 Hz.

resonances at 20 Hz. The column part (Fig. 17 g, h) show a strong column resonance at 10 Hz and some floor resonances around 25 Hz.

Building 3 has eight storeys and lies above a motorway. The floors are built on rather small columns (0.35 m x 0.35 m). Walls at the two ends and at two staircases at the back side provide the stiffness. The building-soil transfer of a column near the staircase (Fig. 17i) has a higher column resonance at 8 Hz than a column in the column section with 5 Hz (Fig. 17j).

The vibration modes in Figure 16 show the basic building resonance always at the softest part of the building, in the front (the column section) of building 3 (Fig. 16e), and at the central columns of building 2 (Fig. 16d). This result from irregular realistic buildings underlines the observation of the preceding parameter study with regular buildings.

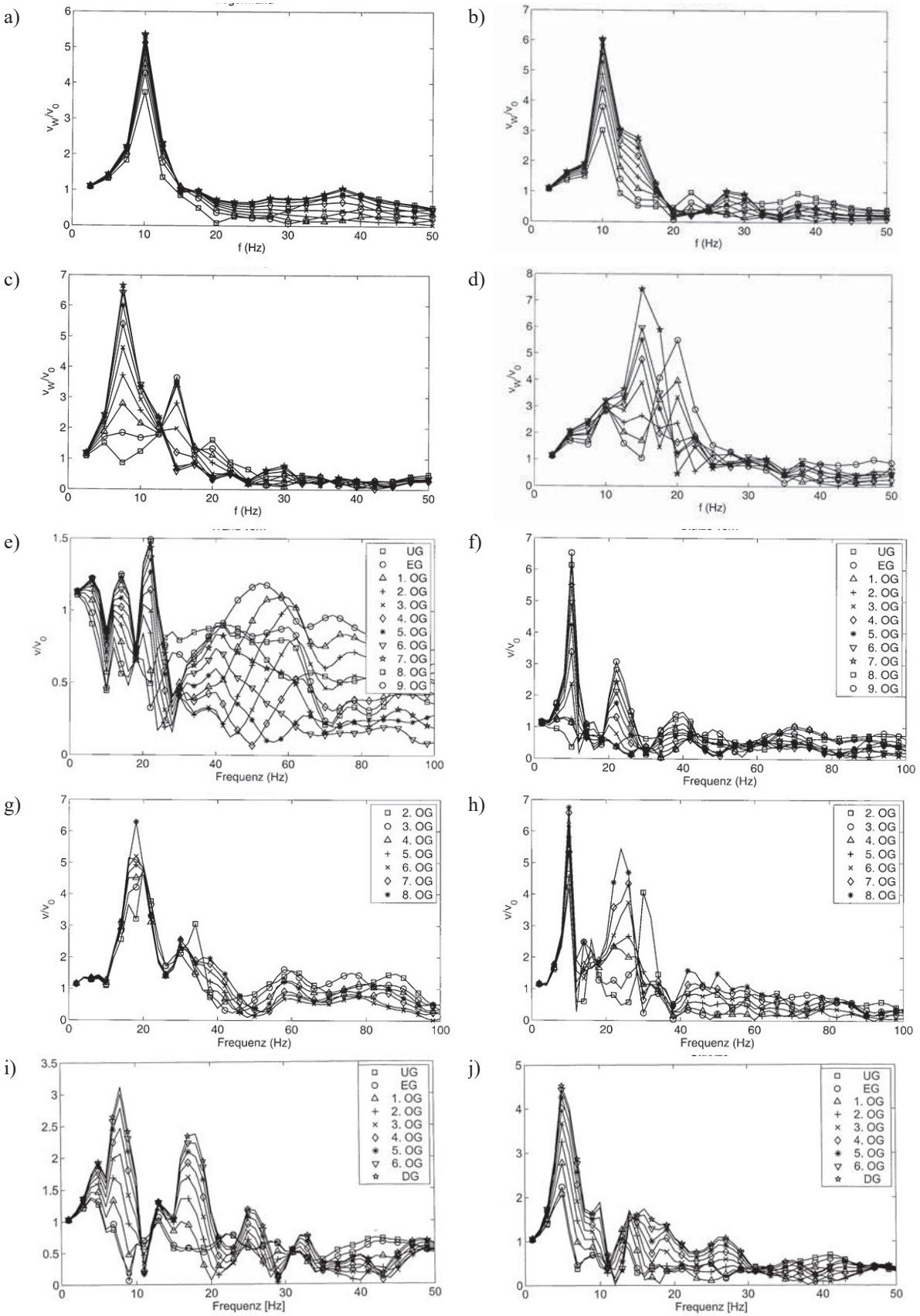

Figure 15: Transfer functions of building 1 (a-d), 2 (e-h), and 3 (i, j), walls (a, e), near-wall columns (b, e, i), columns (c, f, j), near-wall floors (g) near-column floors (d, h).

9 CONCLUSIONS

Different types of buildings have been modelled by the finite element method and calculated in frequency domain to obtain the transfer functions of the floor, wall and column points compared to the free-field excitation. Soil-building, floor and wall/column resonances have been observed. Strong coupling effects between these modes have been found for the office buildings. The fundamental resonance is a combination of the soil and floor mode in case of the lower office buildings or a combination of the soil and column mode in case of high office buildings. The combined resonance frequencies are usually smaller than the theoretical soil-building resonance frequencies. The characteristics of the office buildings compared to the residential buildings are the higher flexibility of the columns compared to the walls and the lower floor resonance frequencies because of the less constrained support conditions. The low floor resonance frequencies are close to the soil-building resonance frequency and induce strong coupling effects. The compliance of the soil under the foundations leads to a reduction of the resonance amplitude of the floors. A clear floor resonance has only been found for the irregular 2-storey residential building. Measurements show higher resonance amplitudes of the floors as real buildings have more irregular variations than the building models here. Measured examples of the soil-building and the column resonance show a good agreement between theory and experiment. The results of this study should help to find simplified models for a fast prediction of ground-induced building vibrations [8-10].

REFERENCES

[1] L. Auersch, S. Said, W. Schmid, W. Rücker, Erschütterungen im Bauwesen: Messergebnisse an verschiedenen Gebäuden und eine einfache Berechnung von Fundament-, Wand- und Deckenschwingungen, *Bauingenieur* 79, 185-192 and 291-299, 2004.

[2] L. Auersch, Dynamic stiffness of foundations on inhomogeneous soils for a realistic prediction of the vertical building resonance. *Journal of Geotechnical & Geoenvironmental Engineering* 134, 328-340, 2008.

[3] S. Ziemens, Numerische Untersuchung der Erschütterungsausbreitung in Gebäuden und deren Wechselwirkung mit dem Baugrund, Bachelor Thesis. TU Berlin (F. Rackwitz), 2019.

[4] L. Auersch, Amplification and reduction phenomena of soil-building interaction by finite-element boundary-element calculations and simplified methods, *Proc. of ninth European Conference on Structural Dynamics (EURODYN 2014)*, Porto, 2014, 591-597.

[5] L. Auersch, A. Romero, P. Galvín, Respuesta dinámica de edificaciones producida por campos de ondas incidentes considerando la interacción suelo-estructura, *Revista Internacional de Métodos Numéricos para Cálculo y Diseño en Ingeniería* 30, 256-263, 2014.

[6] L. Auersch, Building response due to ground vibration – simple prediction model based on experience with detailed models and measurements, *International Journal of Acoustics and Vibrations* 15, 101-112, 2010

[7] L. Auersch, S. Said, Methods and phenomena of single and coupled floor vibrations – measurements in apartment and office buildings, *Building Acoustics* 22, 81-108, 2015.

[8] N. Breitsamter, Ersatzmodelle zur Bestimmung der Schwingungsantwort von Gebäuden bei Anregung durch Bodenerschütterungen, PhD Thesis, TU München, 1996.

[9] C. Meinhardt, Einflussgrößen für das Schwingungsverhalten von Gebäuden zur Prognose von Erschütterungsimmissionen, PhD Thesis, TU Berlin, 2008.

[10] W. Rücker, L. Auersch: A user-friendly prediction tool for railway induced ground vibrations: Emission – Transmission – Immission. In: B. Schulte-Werning et al. (Eds): Noise and Vibration Mitigation for Rail Transportation Systems, Notes on Numerical Fluid Mechanics and Multidisciplinary Design, Volume 99, Springer Berlin / Heidelberg, 2008, 129-135.

EURODYN 2020
XI International Conference on Structural Dynamics
M. Papadrakakis, M. Fragiadakis, C. Papadimitriou (eds.)
Athens, Greece, 23–26 November 2020

INVESTIGATION OF AN ACTIVELY CONTROLLED ROBOT ARM FOR VIBRATION SUPPRESSION IN MILLING

Muhammet Ozsoy[1], Neil D. Sims[1], and Erdem Ozturk[2]

[1]Department of Mechanical Engineering, The University of Sheffield
Mappin Street Sheffield S1 3JD, UK
e-mail: mozsoy1@sheffield.ac.uk, n.sims@sheffield.ac.uk

[2] Advanced Manufacturing Research Center with Boeing, The University of Sheffield
Wallis Way, Rotherham, Sheffield S60 5TZ, UK
e-mail: e.ozturk@sheffield.ac.uk

Keywords: Robotic-assisted milling, Proof-mass actuator, Active chatter suppression, Stability, Flexible structures.

Abstract. *In recent years, the use of robotic systems to enhance the productivity of machining operations has received significant attention from the research and manufacturing communities. Robots have the potential to further improve productivity, for example by providing automated workpiece fixturing, or by providing a flexible and reconfigurable platform from which a variety of subtractive or additive manufacturing operations could be performed. One possible approach is the use of a robotic arm to provide additional fixturing or support of the workpiece during the machining operation. This can increase the stiffness of the workpiece system during machining, which can improve productivity by limiting the onset of undesirable vibrations such as chatter. Chatter is a form of self-excited vibration which leads to low surface quality of the workpiece, shortens the cutting tool life and increases the cutting forces. In this paper, an actively controlled robot arm is simulated in order to suppress the chatter, in an effort to further improve the chatter stability. During the milling operation, preload can be applied through the robot to support the flexible structure, however, the robot cannot suppress high-frequency forces. Since the stiffness and damping ratio of the large flexible structure vary during the operation due to material removal, active vibration control is performed. A proof-mass actuator is proposed that can provide 45 N force up to 2000 Hz with 2 mm stroke. The dynamic properties of the device are identified experimentally as part of a model of a robot fixture prototype. The robotic arm is modelled as a three degree of freedom system; this is combined with a simplified representation of the workpiece dynamics, and the proof-mass actuator, within a Matlab environment. The effect of active control on the chatter stability is evaluated, focussing initially on the use of direct velocity feedback as a control strategy. Estimated chatter stability predictions, along with time, frequency domain simulation results, show that the application of active control method in robotic-assisted machining can suppress the chatter vibrations during machining and hence increase productivity.*

1 INTRODUCTION

Thin-walled structures such as jet engine parts and aerospace fuselage components are common in the aeronautical industry. However, large flexibility of these components leads to excessive vibrations which are called chatter vibration during machining. Chatter is a form of self-excited vibration which leads to low surface quality of the workpiece, shortens the cutting tool life and increases the cutting forces. Milling stability theory [1] can be used to improve the chatter stability by selection of the process parameters which are cutting speed, feed rate and depth of cut. Also, in order to increase the productivity of the process, dynamic stiffness and damping ratio of the workpiece can be improved. There are many techniques with fixed supports [2] and mobile supports [3] to avoid chatter but an interesting current approach is to use robotic systems as part of the machining system. Robots can be used to directly machine components, yet they tend to exhibit very low stiffness which exacerbates excessive vibration. Recently, considerable literature has grown up around the theme of robotic assisted machining. Robots can be used to improve the fixturing or support of the workpiece during machining. The method is called robotic assisted milling when a robot supports a workpiece from the opposite surface to the milling process.

For instance, Ozturk et. al. [4] presented a new concept called robotic assisted milling of thin-walled structures. The authors used two types of end effectors to support the workpiece from the back surface. Experimental results showed that the surface roughness decreased considerably by using moving support. During the milling, robot and the cutting tool moved synchronously. As it is mentioned in the paper, the process was monitored not controlled. The authors did not take account of stiffness change during machining. As the workpiece's stiffness changes due to the material removal, the supporting force needs to be adjusted to achieve better dynamic response improvement.

Fei et al. [5] presented a moving damper to increase the stability of the process. Stability of the process increased substantially. Nonetheless, since the moving damper is fixed to the machine itself, it can be used for only a particular workpiece unless the moving damper design is changed. The authors also investigated the deformation model for moving fixture [6]. Surface quality and machining errors are improved. Esfandi and Tsao [7] suggested using an industrial robotic manipulator to avoid machining vibrations for turning process of the thin walled cylindrical structures. The results encouraged the use of manipulator which provides higher cutting stiffness. Nevertheless, the robot sometimes influences negatively the stability of the machining process given that the robotic arm itself is not rigid.

Some researchers have also studied the effect of the supporting preload force. Bo et al. [8] investigated the influence of supporting force of moving support on machining stability during mirror milling operation of the thin-walled structure. Supporting force influences not only machining stability but also the dynamic behaviour of the workpiece.

In this paper, an actively controlled robot arm which is modelled as a three degree of freedom system, is simulated for milling process in time and frequency domain. The aims are to improve chatter stability, select the most effective actuator assembly point, and compare the effect of the contact type between robot and workpiece. In section 2, contact parameter identification using the receptance coupling formula is presented. In section 3, an inertial actuator which can provide active control for robotic assisted milling is introduced. The effect of the active control on the chatter stability improvement is simulated and evaluated, focussing on the direct velocity feedback (DVF) as a control strategy. In the last section, the stability lobe diagram is estimated for the process.

2 IDENTIFICATION OF CONTACT PARAMETERS

The proposed robot and machine tool configuration is shown schematically in Figure 2.1. Here, a flexible robot is pushed against a flexible workpiece via a soft contact interface whose dynamics must be identified. The machining stability can be improved by using an active vibration control device on the end effector. During the milling operation, preload will be applied through the STAUBLI TX90 robot to stiffen the flexible workpiece. It should be noted that for the purposes of this proof-of-concept experiment, a nominal 'thin walled workpiece', is replaced by a solid workpiece block that is mounted on a flexure. The contact parameters which are stiffness and damping ratio, between the end-effector that is hard rubber, and the flexure are identified by receptance coupling formula [9]. Parameters are identified when 240 N support force is applied to the flexure.

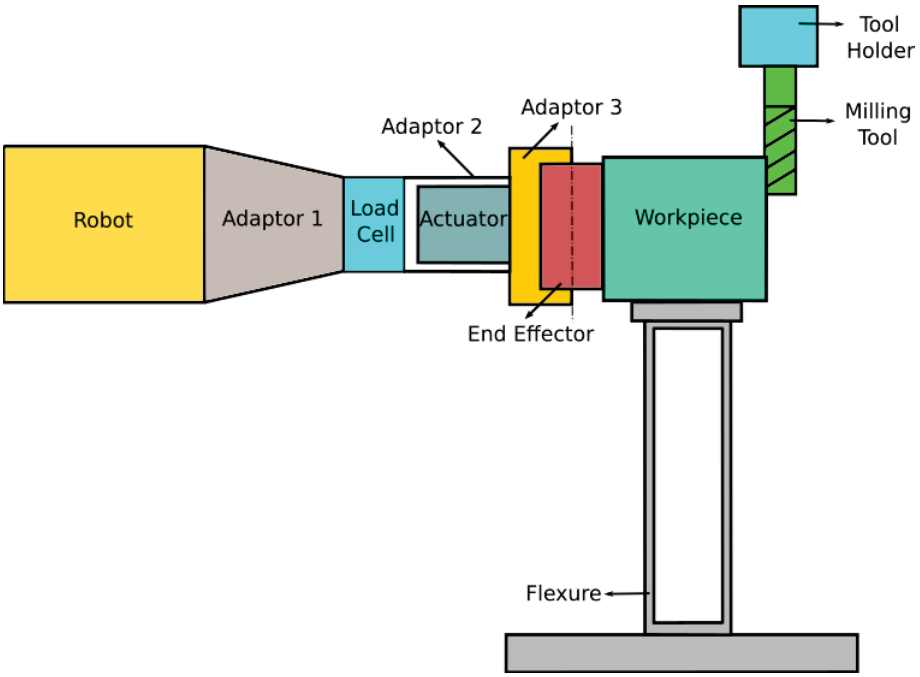

Figure 2.1: Actively Controlled Robot Arm for Milling

The workpiece and robot are modelled as single and three degree of freedom system, respectively. The combined system's frequency response function (FRF) is calculated as;

$$FRF_{combined} = FRF_{part} - FRF_{part}(FRF_{part} + FRF_{robot} + \frac{1}{K'})FRF_{part} \tag{1}$$

$$K' = k + iwc \tag{2}$$

where $FRF_{combined}$, FRF_{part}, FRF_{robot}, k, c and w are the combined FRF, workpiece FRF, robot FRF, contact stiffness, damping and the frequency, respectively.

As a first step, flexure and robot were tested using a modal hammer and accelerometer. The flexure FRF was measured at its midpoint. Since the robot's stiffness varies due to the configuration, the robot was tested on the end-effector while the robot was not touching the flexure but very close to the measurement point. Then, the experiments were repeated with

hard rubber supporting the workpiece at the middle point of the flexure. The flexure flexibility is improved 61% by utilizing preload through the robot as seen in Figure 2.2. Seeing that the experimental contact is flexible, the coupled system's natural frequency is changed from 380 Hz to 399 Hz. The contact stiffness and damping are identified for flexible contact as 4.5e5 N/m and 35.5 Ns/m, respectively.

Also, the combined FRF is estimated for rigid contact. If the contact was assumed as rigid contact, which can be provided with a metal castor end-effector presented by Barrios et. al. [10] by using a different robot, natural frequencies would have been shifted close to robot's natural frequencies which are 32, 76 and 136 Hz.

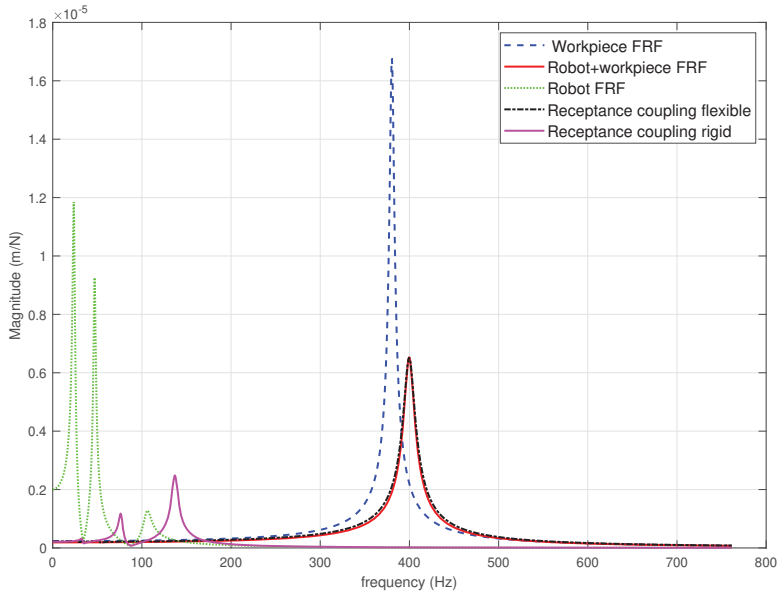

Figure 2.2: Frequency Response Functions and Receptance Coupling Model

3 ACTIVE CONTROL AND SIMULATION RESULTS

Active control is simulated for robotic assisted milling by using an actuator as shown in Figure 2.1. The direct velocity feedback (DVF) control system is selected as it is a model free control method and easy to apply. Once it is implemented, only the gain needs to be adjusted. An inertial actuator is chosen as this approach is easily deployed on the robot's end effector.

3.1 Inertial Actuator

The inertial actuator seen in Figure 3.1 can be represented by a vibrating mass m_p with a damper c_p and spring k_p. The mass is excited by a electromagnetic force f_a according to the voltage input V_{in}. The transfer function between the mass displacement x and the voltage input V_{in} can be written as,

$$\frac{x(s)}{V_{in}(s)} = \frac{G_1 G_2}{ms^2 + cs + k} \tag{3}$$

where G_1 is the electromagnetic gain and G_2 is the power amplifier gain [11].

The transfer function between the reaction force f_a and the voltage input V_{in} can be written as,

$$\frac{f_a(s)}{V_{in}(s)} = \frac{-G_1 G_2 m s^2}{ms^2 + cs + k} = g_a \frac{s^2}{s^2 + 2\zeta\omega_p s + \omega_p^2} \tag{4}$$

where ω_p is the natural frequency, ζ is the damping ratio of the actuator and g_a is the actuator gain [11].

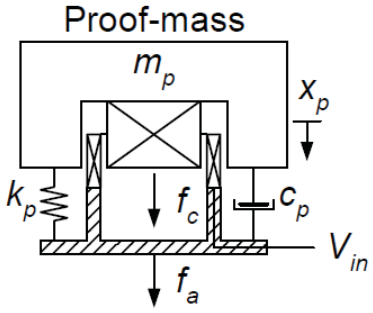

Figure 3.1: Proof-Mass Actuator [12]

An inertial actuator which is a model of Micromega Dynamics, is used to perform the simulations. This actuator has a mode at 8.4 Hz and is capable of applying up to 45 N supporting force up to 2000 Hz. Its transfer function [13] can be written as:

$$\frac{f_a(s)}{V_{in}(s)} = 5\frac{s^2}{s^2 + 15.834s + 2785.6} \tag{5}$$

3.2 Case Studies

In this section, 4 cases which show the effect of the actuator, actuator assembly point, and effect of the contact parameters, are presented. Time domain solutions are solved by ODE 45 function within a Matlab environment. This function implements a Runge-Kutta method with a variable time step for the time domain solution. Robot and workpiece are modelled as a three and single degree of freedom, respectively. Model parameters and cases can be seen in Table 3.1 and Table 3.2.

Table 3.1: Model Parameters

Parameters	Value (kg)	Parameters	Value (N/m)	Parameters	Value (Ns/m)
M_1	32.8	K_1	7.3e5	C_1	573
M_2	21.6	K_2	1.88e6	C_2	368
M_3	21.4	K_3	9.47e6	C_3	1210
M_4	0.748	K_4	4.5e5	C_4	35.5
M_a	1	K_5	4.27e6	C_5	25
		K_a	2785.6	C_a	15.83

Table 3.2: Cases

Case Number	Explanation
Case 1	Preloaded case, without actuator
Case 2	Actuator on the end-effector, flexible contact
Case 3	Actuator on the end-effector, rigid contact
Case 4	Actuator on the workpiece, flexible contact

The first case is uncontrolled and has a flexible contact. Three degree of freedom robot supports the workpiece. Vibration on the workpiece is suppressed by applying preload through the robot. Its spring-mass model can be seen in Figure 3.2.

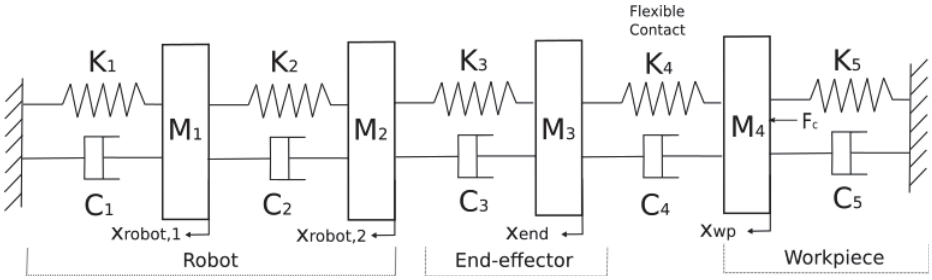

Figure 3.2: Flexible Contact Without Actuator

The natural frequency of the workpiece is shifted from 380 Hz to 399 Hz in this configuration. The model natural frequency is calculated by Cramer's rule [14]. The amplitude of the workpiece is reduced by around 61%. This scenario matches the results already presented in Figure 2.2.

Case 2 is with the actuator mounted on the end-effector seen in Figure 3.3. So as to carry out the direct velocity feedback (DVF) control method, vibration of the end-effector is differentiated to velocity and the velocity is multiplied with feedback gain to drive the actuator.

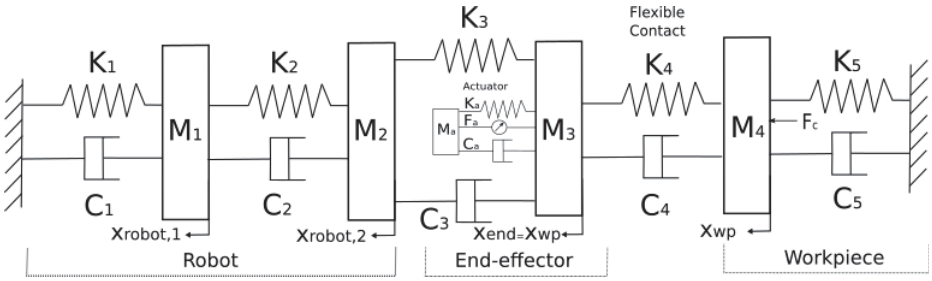

Figure 3.3: Actuator on the End-effector with Flexible Contact

The simulated FRF for this case is shown in Figure 3.4. The input force is implemented on the end-effector and workpiece while output is measured on workpiece for both simulations. Direct FRF (red dashed line) for the workpiece has only one mode at 399 Hz yet the cross FRF (blue solid line) has two modes at 19 Hz and 54 Hz. In practice when the optimum gain limit is exceeded, the system becomes unstable due to actuator nonlinearities such as force and stroke

saturation. So, the optimum actuator gains were determined via simulations and the best case scenario is presented in Figure 3.5. In the simulations, a sinusoidal excitation force of 100 N at 399 Hz, was applied to the workpiece to approximately represent the forces due to the milling operation. Figure 3.5 shows the simulated workpiece response under these conditions. It can be seen that the actuator cannot provide enough force to suppress the vibration on the workpiece since the vibration on the end-effector is too small due to the flexible contact. Consequently, the actuator is ineffective and the workpiece vibrations are not suppressed.

Nevertheless, if the system is excited with 100 N at 19 Hz, vibration on the workpiece is suppressed by 23% shown in Figure 3.5b. Vibration on the workpiece is decreased up to feedback gain g=800. Gain greater than 800 makes the system unstable due to the actuator nonlinearity.

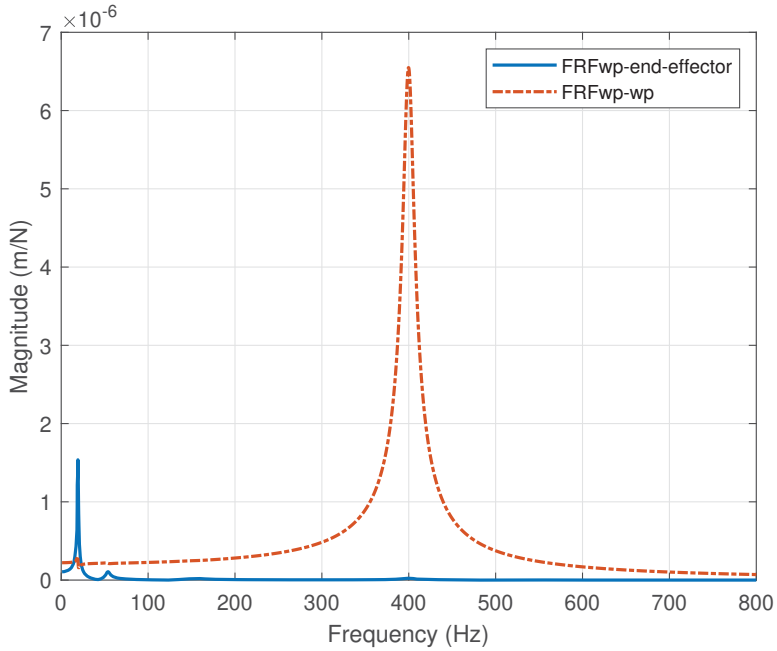

Figure 3.4: Frequency Domain Model for Case 2

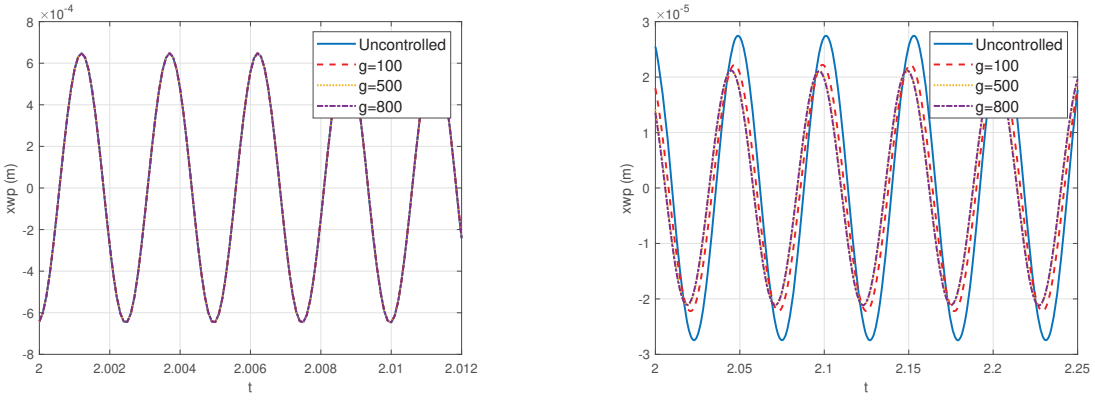

(a) Excitation Force at 399 Hz

(b) Excitation Force at 19 Hz

Figure 3.5: Workpiece Vibration for Case 2

Case 3 is with the actuator on the end-effector with rigid contact (metal castor) as shown in Figure 3.6. Since the vibration on the end-effector is equal to workpiece's vibration, the actuator can provide the vibration suppression on the workpiece. Rigid contact decreases the natural frequencies to 34, 65, 160 Hz. All three modes are damped by active control.

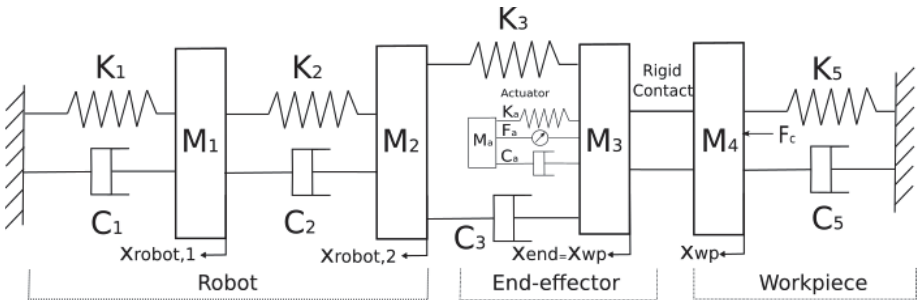

Figure 3.6: Actuator on the End-effector with Rigid Contact

To excite the system a sinusoidal force which is 50 N at 65 Hz is applied. 65 Hz is the most flexible frequency for the workpiece. Actuator force varies from 13 N to 45 N for the gains: 100 (dashed red line), 500 (dotted yellow line), 1000 (dash-dot purple line), 2500 (solid green line) and blue solid line is for the uncontrolled system shown in Figure 3.7. Workpiece vibration is suppressed around 90% for the case 3. Since the maximum produced force by the actuator is 45 N, gain can be increased up to 2500 for this excitation force value. If the gain is selected greater than 2500, the system will be unstable owing to the force saturation.

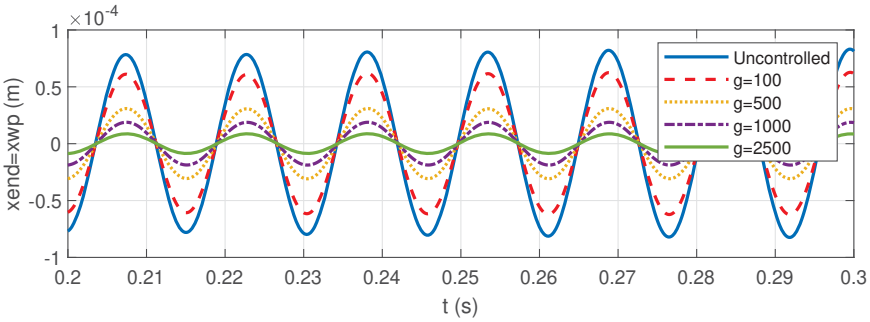

Figure 3.7: Time Domain Model with Rigid Contact

Case 4 with actuator on the workpiece can be seen in Figure 3.8. The contact between the end-effector and the workpiece is flexible. In this case, the support is fixed support since the actuator is assembled directly to the workpiece. 50 N at 399 Hz sinusoidal excitation force is implemented. Optimum gain is determined as 5000, yet the gain only can be increased to 150 owing to the actuator force limitation. Time domain result is shown in Figure 3.9. Actuator force varies from 20 N to 45 N for the gains 10 (dashed red line), 50 (dotted yellow line), 100 (dash-dot purple line), 150 (solid green line). Vibration on the workpiece is suppressed around 90%. If the gain was increased up to 5000 without actuator force limitation, vibration on the workpiece could have been suppressed around 99%.

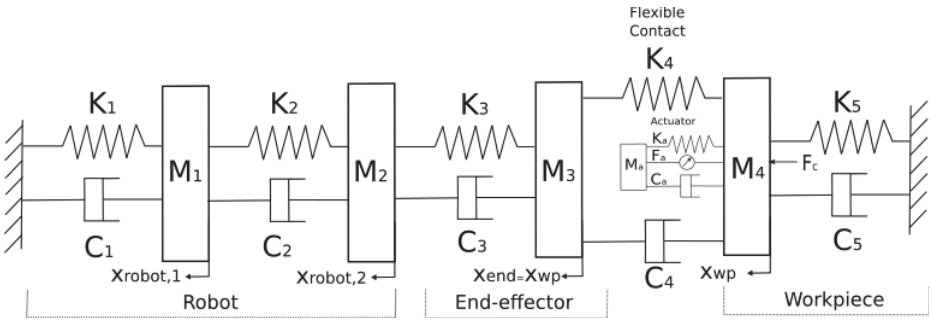

Figure 3.8: Actuator on the Workpiece

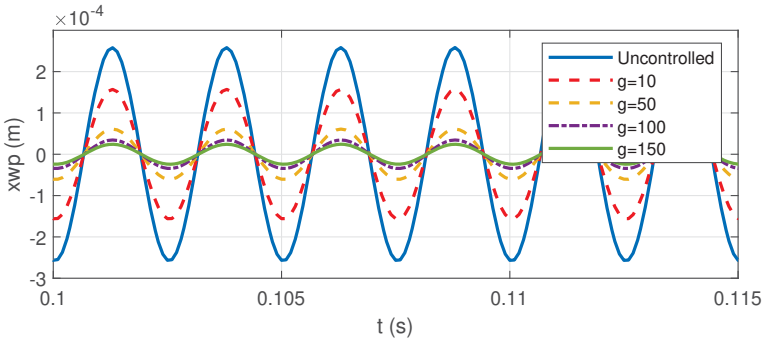

Figure 3.9: Time Domain With Actuator on the Workpiece

All the cases are compared in regards of workpiece vibration whilst the robot applies the preload to the midpoint of the flexure. The effect of preload point can affect the results slightly, which is given in the next section.

3.3 The Effect of Robot Position

The robot applied the preload to the midpoint of the flexure in the previous section. The flexibility of the flexure is improved 61%. However, if the robot applies the preload to the edge point of the flexure, the flexibility is improved 51%. Case 4 results are compared for both robot's preload position and it is presented in the Figure 3.10. The DVF control method is applied with the same gains (10, 50, 100, 150) to the case 4 for both robot's position. In terms of controlled vibration results, there is no significant difference.

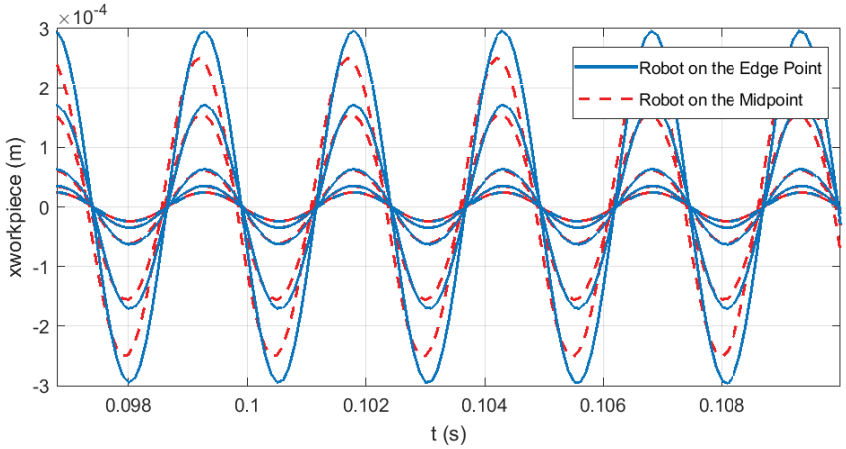

Figure 3.10: Comparison of Robot's Position Effect on Vibration Result

All cases are evaluated regarding vibration of the workpiece. By using active control through the robot, the dynamic response of the structure can be improved significantly. Contact parameters and the actuator assembly point are very critical in order to get a well damped and stable system. Selection of the end-effector and the actuator assembly point must be taken into consideration for further applications. From a machining context the implications of this vibration suppression can be considered from the perspective of the chatter stability. This is considered in the next section.

4 STABILITY LOBE DIAGRAM

Selection of proper axial depth of cut and spindle speed is important to avoid chatter vibrations [1]. Stability lobe diagram is often used to select optimal parameters so as to improve productivity. The stability lobe diagram is estimated for the robot configurations described in Section 3 in order to demonstrate the performance improvement that can be obtained from a manufacturing context.

The stability lobe diagrams were obtained using Budak and Altintas's method [15]. Details of this approach are outside the context of the current contribution, but the theory and method is widely reported elsewhere [1, 15]. Down milling was a assumed, with a 20 mm diameter 4 tooth tool and a radial immersion of 3 mm. The workpiece was assumed to have a cutting stiffness of Ks=796e6 N/m2, Kt=768e6 N/m2, corresponding to Al-7075-T6 material. With reference to Figure 4.1, five scenarios are shown:

- Flexible workpiece without active control and preload (blue solid line)
- Case 1: With preload which is implemented through the robot arm (red dashed line)
- Case 3: With the actively controlled robot arm by the inertial actuator on the end-effector, rigid contact (for g=150 dotted green line, for g=2500 purple dash-dot line)
- Case 4: With the actively controlled robot arm by the inertial actuator on the workpiece, flexible contact (for g=150 black solid line)

SLD is not developed for case 2 since the FRF was no improved in this scenario.

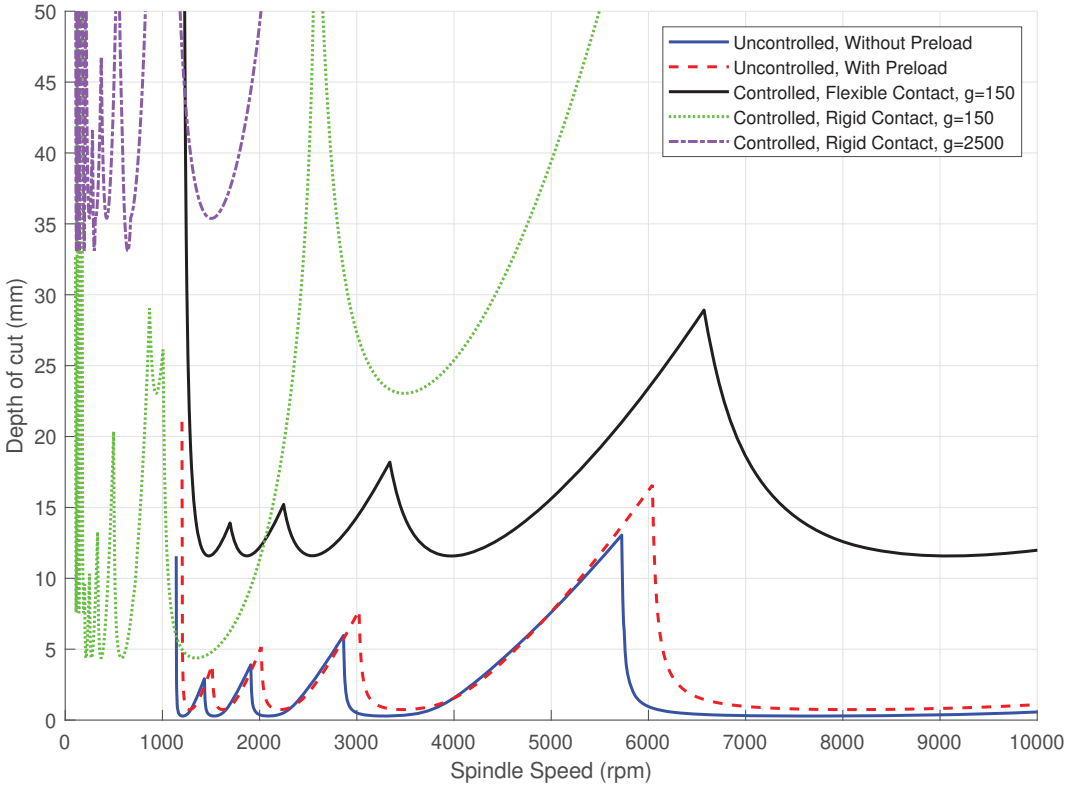

Figure 4.1: Stability Lobe Diagram

Comparison of the limiting (min) depth of cut for each cases can be seen in Table 4.1.

Table 4.1: Comparison of the Limiting Depth of Cut b_{lim}

Cases	blim (mm)
Uncontrolled, Without Preload	0.29
Case 1, Uncontrolled, With Preload (240 N)	0.74
Case 3, Controlled, Actuator on the End-Effector, Rigid Contact, g=150	4.38
Case 3, Controlled, Actuator on the End-Effector, Rigid Contact, g=2500	33.09
Case 4, Controlled, Actuator on the Workpiece, g=150	11.58

As seen in Figure 4.1 and Table 4.1, the depth of cut is increased around 2.5 times with preload through the robot arm. To achieve greater depth of cut, active vibration control is applied. The greatest depth of cut is achieved when the actuator is assembled on the end-effector with rigid contact, gain=2500. However, when the actuator is mounted directly onto the workpiece, the depth of cut is improved more than when the actuator is mounted on the end-effector.

5 CONCLUSIONS

The purpose of the current study is to determine the dynamic response improvement in milling operation by using an actively controlled robot arm. The concept is evaluated in terms

of the contact type between the robot, workpiece, and actuator. Direct velocity feedback (DVF) control method is performed in order to improve the dynamic response. It is concluded that the actively controlled robot arm can improve the productivity of the milling process by decreasing the vibration on the workpiece.

In the conducted simulations, workpiece vibration is damped around 61% by applying preload through the robot to the midpoint of the flexure. An inertial actuator is mounted on the end-effector and the workpiece for different cases to compare the effect of the actuator assembly point on the dynamic response. An actuator on the end-effector with flexible contact cannot improve the dynamic response of the workpiece except at low frequencies. However, when the actuator is assembled on the end-effector with rigid contact, the vibration on the workpiece is significantly decreased to around 90%. If the actuator is mounted directly onto the workpiece, rather than via the robot, then the workpiece vibration decreases by around 90%. Similar performance improvements can be observed in the so-called stability lobe diagram for a machining scenario. To summarise, the work has proved the concept of using a robotically assisted active vibration control system, for the machining of flexible workpieces. It has been shown via simulations that improved machining stability can be achieved even when accounting for the flexibility of the robot and the workpiece to robot contact.

As future work, all the simulations will be validated by experimental study. Direct velocity feedback control method will be compared with more sophisticated control methods such as PID, LQG, LQR and H_∞. Finally, different end-effectors can be designed to compare the contact parameter effect on the chatter stability.

REFERENCES

[1] Y. Altintas, *Manufacturing automation: metal cutting mechanics, machine tool vibrations, and CNC design*. Cambridge university press, 2012.

[2] K. Kolluru, D. Axinte, and A. Becker, "A solution for minimising vibrations in milling of thin walled casings by applying dampers to workpiece surface," *CIRP Annals-Manufacturing Technology*, vol. 62, no. 1, pp. 415–418, 2013.

[3] C. Sun, P. L. Kengne, A. Barrios, S. Mata, and E. Ozturk, "Form error prediction in robotic assisted milling," in *Procedia CIRP*, vol. 82. Elsevier, 2019, pp. 491–496.

[4] E. Ozturk, A. Barrios, C. Sun, S. Rajabi, and J. Munoa, "Robotic assisted milling for increased productivity," *CIRP Annals*, 2018.

[5] J. Fei, B. Lin, S. Yan, M. Ding, J. Xiao, J. Zhang, X. Zhang, C. Ji, and T. Sui, "Chatter mitigation using moving damper," *Journal of Sound and Vibration*, vol. 410, pp. 49–63, 2017.

[6] J. Fei, B. Lin, J. Xiao, M. Ding, S. Yan, X. Zhang, and J. Zhang, "Investigation of moving fixture on deformation suppression during milling process of thin-walled structures," *Journal of Manufacturing Processes*, vol. 32, pp. 403–411, 2018.

[7] N. Esfandi and T.-C. Tsao, "Robot assisted machining of thin-walled structures," *IFAC-PapersOnLine*, vol. 50, no. 1, pp. 14 594–14 599, 2017.

[8] Q. Bo, H. Liu, M. Lian, Y. Wang, and K. Liu, "The influence of supporting force on machining stability during mirror milling of thin-walled parts," *The International Journal of Advanced Manufacturing Technology*, pp. 1–13, 2018.

[9] T. L. Schmitz and K. S. Smith, *Machining dynamics*. Springer, 2014.

[10] A. Barrios, S. Mata, A. Fernandez, J. Munoa, C. Sun, and E. Ozturk, "Frequency response prediction for robot assisted machining," *MM Science Journal*, vol. 2019, no. 04, pp. 3099–3106, 2019.

[11] A. Preumont, *Vibration control of active structures*. Springer, 1997, vol. 2.

[12] S. Huyanan and N. D. Sims, "Vibration control strategies for proof-mass actuators," *Journal of Vibration and Control*, vol. 13, no. 12, pp. 1785–1806, 2007.

[13] Operational and M. Manual, *Micromega Dynamics*. Belgium, 2019.

[14] S. S. Rao, "Mechanical vibrations fifth edition in si units," 2012.

[15] Y. Altintaş and E. Budak, "Analytical prediction of stability lobes in milling," *CIRP Annals-Manufacturing Technology*, vol. 44, no. 1, pp. 357–362, 1995.

EURODYN 2020
XI International Conference on Structural Dynamics
M. Papadrakakis, M. Fragiadakis, C. Papadimitriou (eds.)
Athens, Greece, 23–26 November 2020

AN EVALUATION OF THE CURRENT APPROACHES AND RECOMMENDATIONS FOR MORE RATIONAL APPROACHES FOR ASSESSING THE SEISMIC TORSIONAL STABILITY OF BUILDINGS

Bryam Astudillo[1*], Francisco Flores[1, 2], Sebastian Pozo[1] and Finley Charney[3]

[1] Department of Civil Engineering, Universidad de Cuenca
Av. 12 de Abril s/n, Cuenca, Ecuador
{bryam.astudilloc; francisco.flores; sebastian.pozo}@ucuenca.edu.ec

[2] Department of Civil Engineering, Universidad del Azuay
Av. 24 de Mayo 7-77, Cuenca, Ecuador
fflores@uazuay.edu.ec

[3] Department. of Civil Engineering, Virginia Tech,
Blacksburg, VA 24060
fcharney@vt.edu

Keywords: Accidental torsion, response spectrum analysis, response history analysis

Abstract. *Building codes for seismic resistant design of building structures generally include requirements for imposing an "accidental" torsion response. Methods for incorporating such effects into the analysis are ad-hoc at best and have not changed significantly over the past 50 years. This is despite the tremendous advanced in analytical and computational capabilities over the same period. The current building code methodology for including accidental torsion depends on the analytical method. For linear static approaches, lateral forces are applied at an eccentricity that depends on the sensitivity of the system to torsional effects. Where modal response spectrum analysis (MRSA) is used, the torsion may be included by imposing a mass offset or adding the accidental torsion as in linear static analysis. Where linear or nonlinear time history analysis is utilized, the mass offset approach has been used almost exclusively.*

In a recent report published by FEMA (FEMA P-2012), it was found that the dynamic mass offset procedure could produce grossly unsafe designs relative to the static load approach for torsionally sensitive systems. For this reason, it was recommended that the mass-offset approach not be used in MRSA or in linear time history analysis (LTHA) for systems with extreme torsional irregularities. A recent supplement to ASCE 7-16 included the restriction on MRSA but not on time history analysis. In this paper, the mass-offset approach for including accidental torsion in the dynamic analysis is evaluated in detail and compared with the static analysis for different building configurations. It was found that for the analyzed buildings, MRSA predicts well the demands obtained using LTHA, and hence, the prohibition of the mass offset approach for accommodation accidental torsion should be extended to response history analysis.

1 INTRODUCTION

Current codes and standards such as the ASCE 7-16 [1] provide three approaches that can be used to perform a seismic structural design considering accidental torsion in buildings using linear analyses. The first approach implemented uses the equivalent lateral force (ELF) procedure, the second one uses modal response spectrum analysis (MRSA), and the third uses linear time history analysis (LTHA).

The ELF procedure uses a linear static analysis to represent the seismic force distributed along the building´s height. This procedure concentrates the seismic loads at the center of mass of each floor. In addition, if the building is torsionally irregular, accidental torsion is included in two steps: 1) moving the applied load to an eccentricity of 0.05 times the building width perpendicular to the direction of loading, 2) amplifying the effect if the torsion is considerable. The amplification factor A_x is calculated using equation (1), The factor is computed using the maximum (δ_{max}) and average displacements (δ_{avg}). The amplification factor need not be taken as less than 1.0, and has an upper limit of 3.0.

$$A_x = (\delta_{max}/1.2\delta_{avg})^2 \qquad (1)$$

The modal response spectrum analysis uses the modal shapes of the structure to calculate its dynamic response. When this procedure is used, two methodologies are proposed to incorporate accidental torsion if the structure is torsionally irregular. The first one consists in adding accidental torsion to the modal response as a static load. For this purpose, the modal analysis is carried without a mass eccentricity. The second method, which is commonly used, is to explicitly incorporate the eccentricity in the dynamic properties of the model by applying a mass eccentricity to the building so the effect of accidental torsion is inherent.

The linear response history analysis approach uses ground motions scaled to the design spectrum to calculate the building's response. Accidental torsion is explicitly included by moving the center of mass. This approach demands more computational resources than the previous ones but has certain advantages, such a retaining the signs of the computer response quantities.

In a recent report, FEMA P-2012 [2], it was found that the dynamic mass offset procedure could result in unsafe building designs relative to the static load approach for torsionally sensitive systems. Similar findings were reported in De la Llera and Chopra (1994) [3]. FEMA P-2012 recommends that the mass-offset approach not to be used in linear dynamic analysis. However, a 2019 update to ASCE 7 included the prohibition for modal response spectrum analysis but not for linear response history analysis. Thus, the main focus of this paper is to establish differences in responses when the mass-offset approach is used in ELF, MRSA and LTHA. First, displacement and rotation demands are computed using the ELF and MRSA approaches in a series of one-story buildings with different configurations. Then, the paper studies the pertinence of MRSA to capture the same demands produced in the LTHA and, therefore, note a contradiction in that recommendation regarding the prohibition of MRSA for torsional sensitive buildings in ASCE 7.

2 METHODOLOGY

The FEMA P-2012 recommendations state that the difference between the ELF and the MRSA is critical under torsionally sensitive buildings. Therefore, to compare both design methodologies three-dimensional models with different plan ratios (PR) and lateral system distributions were used. The models are based on a previous torsional research building stud-

ied by Flores et al (2018) [4], which consists of a 9-story building with buckling restrained braces (BRBs) as a lateral resisting system. However, in this research, only the top floor was taken as a one-story building, varying the lateral system positions as seen in Figure 1a to investigate different torsional irregularities. The element sections are shown in Figure 1b. Also, the archetype present leaning columns uniform distributed on the building area to capture geometric second-order effects.

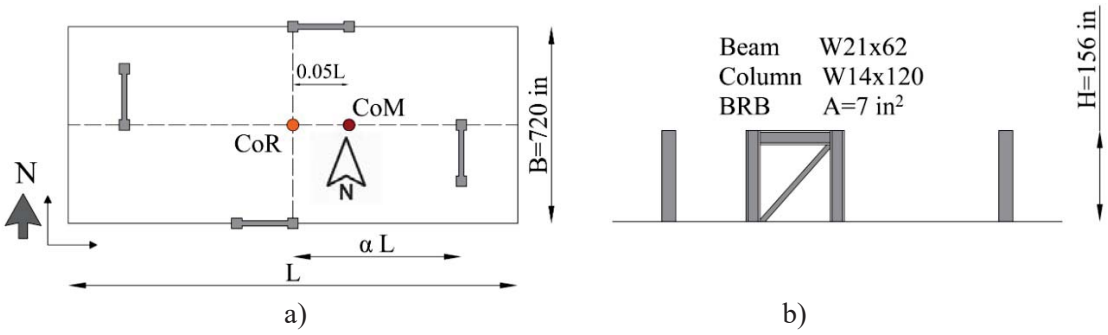

Figure 1 a) Plan View and b) elevation view

The mass of the building was assigned with lumped masses distributed according to Figure 2, and each node on the grid had a lateral mass only acting in each direction (i.e. North-South and East-West). The rotational mass moment of inertia was generated automatically by linking all nodes with a rigid diaphragm. In order to consider accidental torsion, a portion of the mass was shifted from the left to the right side, so each side sum (1-*x*)*M*/2 and (*x*)*M*/2, respectively. The value for *x* was chosen as 0.50 and 0.60, giving rise to eccentricities of 0% and 5% respectively. The total mass assigned to the structure was calculated to obtain a fundamental period of 1 second approximately on each lateral direction for merely academic purposes.

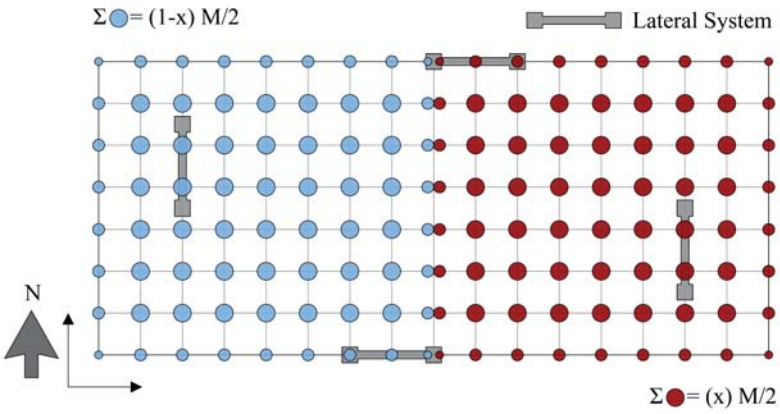

Figure 2 mass shifting eccentricity

With the base archetype configuration, several models were developed varying the plan ratio (PR) and the position of the North-South lateral system (NS-LS) respect of the building's length (L). Meanwhile, the East-West (EW) plan dimension and the lateral resistant system remains invariant for all the models. Three PR ratios were used: 2 to 1, 3 to 1, and 4 to 1. In

addition, several positions of the NS-LS were considered which are defined by the parameter α, where α represents the distance of the NS-LS from the geometric center. It is necessary to clarify that the positions of the NS lateral system are always symmetric respect to the geometric center. It means that when α is equal to 50%, the NS lateral system will be located at the perimeter, while for α equal to 0%, the NS will be located at the geometric center.

The three-dimensional elastic models were implemented using the software OpenSees [5]. Also, the models consider a 5% Rayleigh damping ratio applied on the 1st and the 3rd modes of the structure. The damping ratio was selected to be consistent with the design spectrum that uses a 5% target damping.

2.1 Equivalent Lateral Force vs. Modal Response Spectrum Analysis.

The previously defined models were used to determine the differences in design parameters and demands between the equivalent lateral force (ELF) and the modal response spectrum analysis (MRSA) design approaches. The equivalent lateral force (ELF) procedure was performed with a concentrated load corresponding to the weight of the structure (W) times the spectral acceleration ($Sa(T_1)$) consistent with the NS translational mode (i.e. 1sec.). Initially, the load was applied to an eccentricity of 5%, then at an eccentricity of A_x times 5%. Meanwhile, modal response spectrum analysis (MRSA) was performed using all the modes of the building (three), with a CQC modal combination. The design response spectrum corresponds to a D_{max} seismic risk as defined in FEMA P-695 [6] with a maximum spectral acceleration (S_d) of 1.0, and a one-second acceleration (S_1) of 0.6.

One of the initial considerations of building design is to determine if the building has torsion irregularities. The ASCE 7-16 uses the maximum story drift at a building's edge and the average story drift given a static force applied at 5% eccentricity to evaluate torsional irregularities. FEMA P-2012 defines this ratio as the Torsional Irregular Ratio (TIR). ASCE 7-16 also allows calculating the TIR with the MRSA as established in the commentary (i.e. performing a combination of the maximum and average drift for each mode). Therefore, the TIR is calculated with both methods to assess the differences under a variety of building configurations.

After computed and compared the TIR, the demands of the ELF analysis were adjusted with the amplification factor A_x to increase the torsional effects, calculated with the equation (1). The ELF final demands and the demands obtained with the MRSA were compared in terms of the maximum displacement reached in the NS direction and the maximum rotation of the rigid diaphragm. This evaluation was carried to study the initial statement of the FEMA P-2012 that MRSA leads to unconservative design for torsional sensitive buildings, and extend the study to rotational demands as a new indicator of torsional effects.

2.2 Modal Response Spectrum Analysis vs. Linear Time History Analysis.

Once the difference between the ELF and the MRSA was assessed, a comparison between the latter one and the linear time history analysis (LTHA) was performed. The demands were assessed in terms of the NS displacements and the rotation of the rigid diaphragm as well to make comments on the FEMA P-2012 recommendation about limiting the use of linear dynamic analysis.

The LTHA was conducted using 11 ground motions obtained from the Far-Field dataset provided by the FEMA P-695 document that represents a D_{max} seismic risk corresponding with the design spectrum used in the previous analyses. The 11 ground motions were matched to the spectrum using a spectral matching process [7] to reduce the variances between the ground motion response spectrum used for the LTHA and the design response spectrum used

for the MRSA. In the comparisons, the LTHA demands were considered as the average response of the 11 ground motions following the ASCE 7 code methodology.

3 RESULTS AND DISCUSSIONS

3.1 Response comparison RSA vs Static

First, the Torsional Irregular Ratio was calculated using the static method and the dynamic MRSA. The results for plan ratios 2, 3 and 4-to-1 for different locations of the NS-LS are shown in Figure 3a. It can be seen that TIR calculated with the static method increases when the NS-LS is moved towards the CoR. This is consistent with the figure shown in commentary C12.8.4.3 of ASCE 7-16, which shows the torsional amplification factor. However, when calculating the TIR with the MRSA, this value does not necessarily increase when the NS-LS is moved toward the center. This happened due to the dynamic properties when the mass is shifted to one side as will be explained in the following subsections.

Additionally, Figure 3b shows the torsional amplification factor A_x that was used to increase accidental torsion for the static method in the models. It has to be mentioned that the dynamic methods do not need to increase the demands with their corresponding A_x as is mentioned in the newest code version (ASCE7-16).

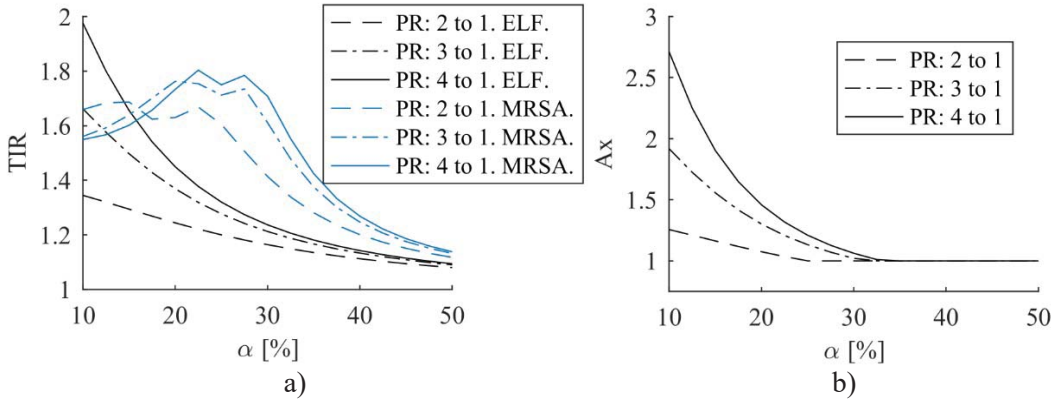

Figure 3 a) TIR calculated using ELF and MRSA and b) Torsional Amplification Factor for ELF

Figure 4 shows the drift's demands measured at the North-East and North-West corners (NE and NW, respectively) of each building configuration. Additionally, it shows the maximum drift envelope for MRSA. It should be noted the sensitivity of the demands to the location of the NS-LS and the plan-ratio. For the static method, the drift demands increase when the NS-LS is moved towards the center, and that increment rate is greater when the plan-ratio is larger. On the other hand, for MRSA, the drift demands start to increase when the NS-LS is moved towards the center but it reaches a point where the demands tend to stabilize or even decrease as happened with the TIR. Additionally, it should be noted that the increment rate remains almost the same for all building plans which drastically differs from the ELF.

Thus, it can be said that models with NS-LS at the perimeter have similar maximum responses for both methods despite their plan ratio. In contrast, when the NS-LS was moved towards the center, the calculated demands start to differ, especially for longer plan ratios (e.g. 4 to 1 plan ratio). Therefore, it can be inferred that a design based on the ELF will end up with more robust elements. This is congruent with [3] and helps to explain the findings stated in

[2], [8], where buildings designed with ELF had a better collapse performance than buildings designed with MRSA.

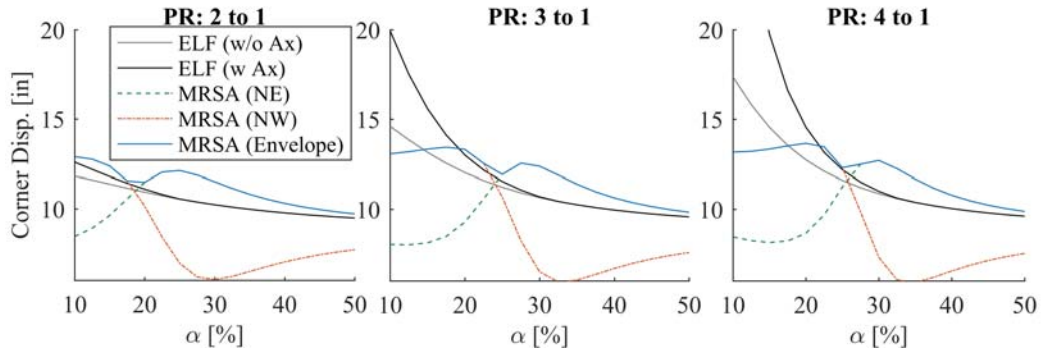

Figure 4 ELF and MRSA maximum corner displacements

Since the MRSA gives only positive results, using displacements can bias the evaluation of torsional effects. However, the diaphragm rotations can help to evaluate the torsional effects on buildings modeled with a rigid diaphragm. Rotation demands for ELF and MRSA are shown in Figure 5.

Once again, the ELF produces demands that increase with greater plan-ratios and NS-LS located towards the center. In the case of MRSA, the rotation demands increase until a given configuration and then start to decrease, similar to drift demands. It is also seen that the rotations produced by MRSA decrease with greater plan ratios, contrary to the behavior of ELF.

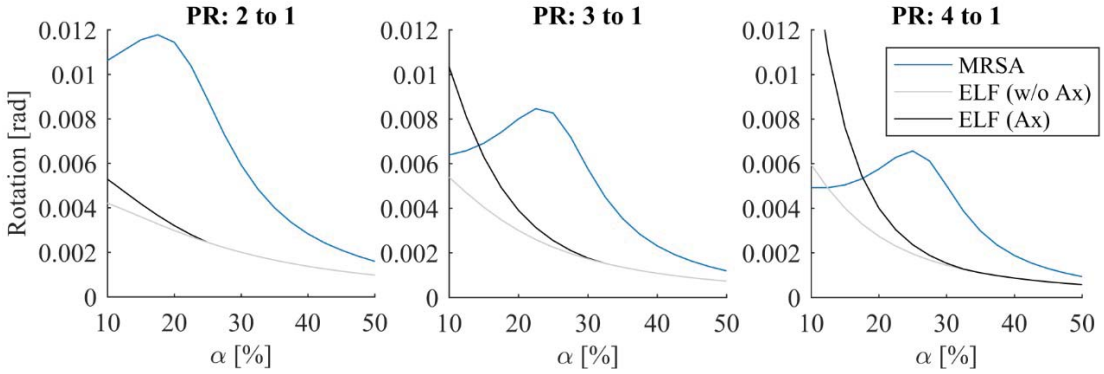

Figure 5 ELF and MRSA maximum diaphragm rotations

3.2 Response comparison LTH vs RSA

As seen before, for models sensitive to torsional effects (low alphas and larger plan ratios), the MRSA produced lower demands than the static method. This could be the reason why ELF designed buildings have a better collapse performance when compared to buildings designed with MRSA. However, it does not mean that the MRSA underestimates the elastic demands produced in those models in relation to LTH as it will be shown in this section. Figure 6 shows the maximum drift for the NE and NW corners resulting from MRSA and LTH with mass shifted 5%L to the east side. It is seen that both methods give similar absolute maximum

results. It could have been expected that when the mass is shifted into the east direction, the NE corner will have larger forces and therefore larger displacements as happens on the ELF. In agreement, the NW corner will have fewer demands and displacements. However, it can be seen that once a certain location of the NS-LS is reached, a different behavior occurred and it can be explained with the interaction of the modes and their participation factors. That mode interaction causes that for torsional sensitive configurations (i.e. with the NS-LS located toward the center) the opposite corner is subjected to higher demands. This involves that, for a given location (i.e. α=20-25% for the analyzed building) the maximum demands for both corners are the same. In the case of MRSA, the sign and the time when maximum demands occurred are lost. This can cause a misinterpretation that there are not torsional effects, and if the TIR is calculated based on the average of those values rather than the average at each mode as explained in the ASCE commentary, there would be a TIR of 1.

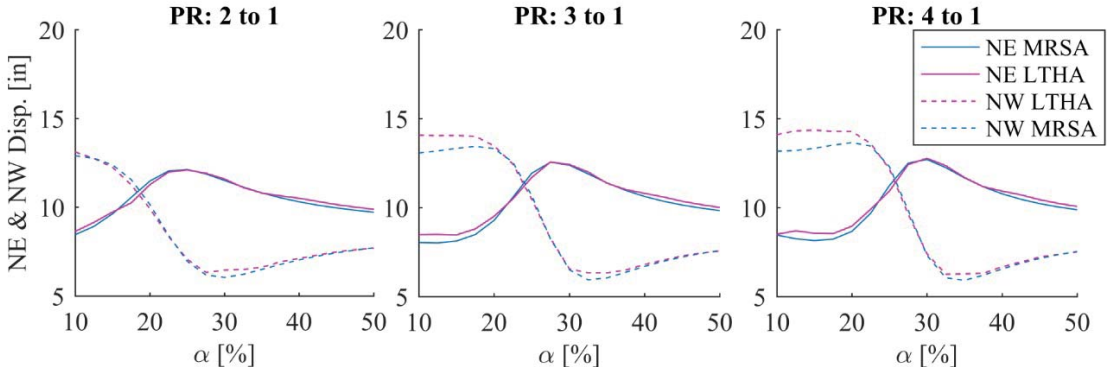

Figure 6 LTH and RSA maximum corner displacements

It must be noted that those maximum drifts don't happen at the same time as can be assessed in LTHA. Thus, when the maximum drift is reached at one of the corners, the other corner is subjected to fewer drifts than what is predicted in MRSA due to the loss of sign and time of events. This is illustrated in Figure 7 where the maximum displacements for both methods are equal but the demands of the opposite edge differ when time and sign are accounted in LTHA. When the MRSA predicts the same maximum displacement for both corners (i.e. α=20-25%), LTHA shows the bigger differences between them, even reaching displacements with different signs.

This phenomenon was studied by tracking the rotations to evaluate whether there were torsional effects or not, and in fact, it was found that the point where both corners have the same maximum displacement, the diaphragm rotation reaches its maximum value as shown in Figure 8. So, it must be noted that the maximum displacements were reported, however, they do not occur at the same time. Under this circumstance, the RSA could not be effective if torsional effects are predicted by only having the displacements as a reference but the diaphragm rotation can work as a new parameter to account for torsional effects. Once again, it is seen that both methods give almost the same results (of course, RSA requires less computational effort).

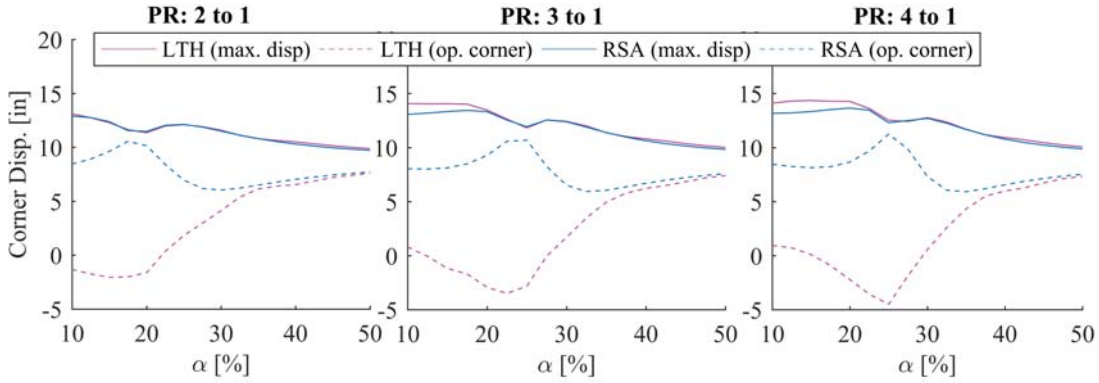

Figure 7 LTHA and RSA maximum corner displacements and displacement of the opposite corner

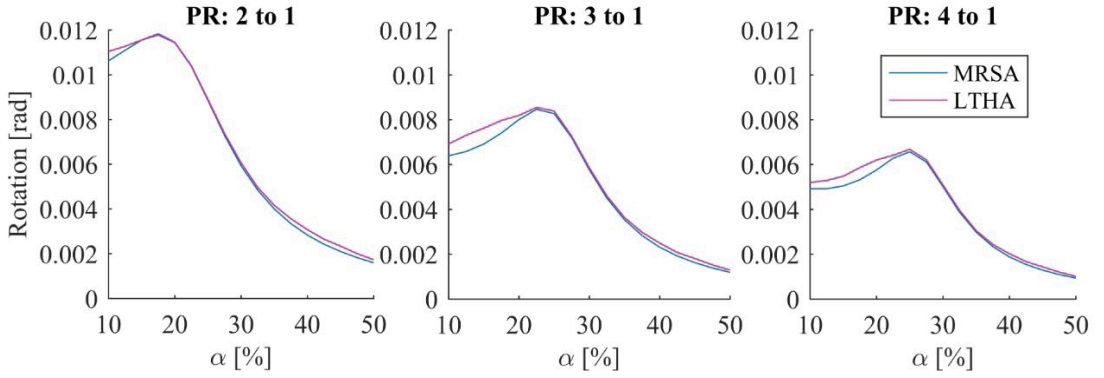

Figure 8 LTH and RSA diaphragm comparison

Now, going a step further to explain why the NW corner increased its maximum displacements, the modal shapes and participation factors for some models are shown in Figure 9. It is clear that when there is no eccentricity, each mode is purely translational or rotational (i.e. the participation factors are 100% in NS, EW or rotation). Then, when a 5% mass offset is added, there cannot be identified a purely torsional and translation mode, instead, the 1st and 3rd mode are a mix of them and it is reflected in the participation factors. For configurations where the NS-LS is located towards the perimeter (e.g. α equal to 0.5), the 1st mode takes over the NS translation while the 3rd mode takes over the torsional component. The opposite happens when the NS-LS is moved towards the center; the 1st mode starts to control the torsional response while the 3rd mode controls the NS translation. However, this implies that for some configurations, the 1st and 3rd mode shares almost the same participation over translation and torsion as happens when α is set between 0.25 and 0.30 for plan ratio 4 to 1. In this last case, the 1st mode generates a larger translation in the east corners while the 3rd mode generated larger translation in the west corners and since its period and participation are almost the same, the displacements are also similar. That is why it could be misinterpreted that since both displacements are similar, there would not be rotation when actually that is when the maximum rotation is reached due to the combined effects of modes. In the case of the 2nd mode, it always remains as translational in the EW direction.

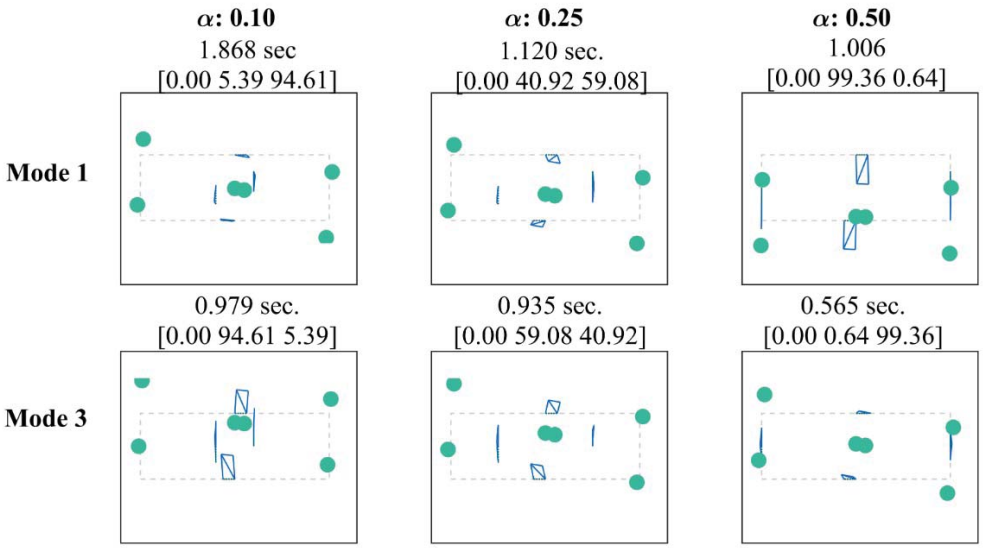

Figure 9 Modal response analysis for Plan Ratio 4 to 1 with different alpha values

4 CONCLUSIONS

The linear dynamic behavior of a structure differs from the static behavior; thus drifts and rotation demands are dependent on the method that was used.

- Starting with TIR, the static method shows an increment of the TIR when the NS LS is moved towards the center. However, MRSA causes the TIR to saturate once a given configuration is achieved, making the TIR decrease despite the NS LS is moved to-wards the center.
- Additionally, TIR calculated with static method increases for greater plan ratios for all values of alpha. MRSA produces the same behavior of the TIR but only for large values of alpha (greater than 25) before they saturate. For low alpha values, the TIR in MRSA can even decrease for greatest plan ratios but there is not much difference within the plan ratios.
- For larger values of alpha (greater than 25), the TIR calculated with MRSA is greater than the TIR calculated with the static method. It was also noted that after the saturation point, values of TIR calculated with the static method can be great than those computed with MRSA, especially for larger plan ratios.
- For large values of alpha, drifts calculated with MRSA are greater than those produced by the static procedure. However, for low alphas, the static procedure caused greater drifts demands even without the torsional amplification factor (Ax). Once again, the differences are more notorious for larger plan ratios.
- In terms of diaphragm rotations, both methods cause different behaviors. For the static procedure, rotations increased when alpha values decreased while for MRSA rotations increase up to the saturation point following what it was seen for the TIR. Additionally, it can be seen that the static method causes larger rotations for larger plan ratios. However, the MRSA behaves like the opposite; fewer rotations are expected for larger plan ratios.

This would lead to misinterpretations of the indirect forces that the orthogonal lateral system will receive due to torsion.

Linear time history analysis demands can be predicted with MRSA for all the configurations under analysis.

- The major differences between MRSA and LTH drifts and rotation demands were seen in torsional sensitive configurations (lower alphas). However, MRSA allows predicting well the demands obtained in the LTHA analysis for the prototype under study. This implies that further comments or recommendations about the mass-offset technique must apply to MRSA and LTHA in the same manner.
- Maximum rotations are reached in configurations where the modal participation factors for a 5% mass offset, in each degree of freedom, are not concentrated in one mode only. This also happens to be the configuration where both opposite edges reach the same maximum displacements.
- For configurations with large values of alpha (e.g. less torsional sensitive configurations), the displacement demands produced in the edge closer to the shifted center of mass are larger. However, due to dynamic characteristics, for low alpha values, after the saturation point, the edge in the opposite direction to the mass offset has larger displacement demands. This contra intuitive result that occurs due to inertial forces present in dynamic analyses.
- The torsional behavior of a structure can be evaluated using RSA despite it gives positive results only. For the purpose, not only drift demands must be evaluated but diaphragm rotations. It can also help to avoid results misinterpretations due to the loss of sign and time occurrence associated with MRSA. Regarding this topic, more work should be done to use the diaphragm rotations and edge lengths to be an indicator of the torsional effects.

REFERENCES

[1] ASCE 7, *Minimum Design Loads and Associated Criteria for Buildings and Other Structures*. American Society of Civil Engineers, Reston, VA., 2016.

[2] FEMA P-2012, *Assessing Seismic Performance of Buildings with Configuration Irregularities*. Federal Emergency Management Agency, 2018.

[3] J. C. de la Llera and A. K. Chopra, "Accidental torsion in buildings due to stiffness uncertainty," *Earthq. Eng. Struct. Dyn.*, vol. 23, no. 2, pp. 117–136, Feb. 1994, doi: 10.1002/eqe.4290230202.

[4] F. Flores, F. A. Charney, and D. Lopez-Garcia, "The Influence of Accidental Torsion on the Inelastic Dynamic Response of Buildings during Earthquakes," *Earthq. Spectra*, vol. 34, no. 1, pp. 21–53, Feb. 2018, doi: 10.1193/100516EQS169M.

[5] S. Mazzoni, F. McKenna, M. H. Scott, and G. L. Fenves, "OpenSees command language manual," *Pac. Earthq. Eng. Res. PEER Cent.*, vol. 264, 2006.

[6] FEMA P-695, *QUANTIFICATION OF BUILDING SEISMIC PERFORMANCE FACTORS.* Federal Emergency Management Agency, 2009.

[7] J. R. Jayamon and F. A. Charney, "Multiple Ground Motion Response Spectrum Match Tool for Use in Response History Analysis," in *Structures Congress 2015*, Portland, Oregon, 2015, pp. 2497–2509, doi: 10.1061/9780784479117.216.

[8] D. J. DeBock, A. B. Liel, C. B. Haselton, J. D. Hooper, and R. A. Henige, "Importance of seismic design accidental torsion requirements for building collapse capacity:

IMPORTANCE OF DESIGN ACCIDENTAL TORSION REQUIREMENTS FOR BUILDINGS," *Earthq. Eng. Struct. Dyn.*, vol. 43, no. 6, pp. 831–850, May 2014, doi: 10.1002/eqe.2375.

EURODYN 2020
XI International Conference on Structural Dynamics
M. Papadrakakis, M. Fragiadakis, C. Papadimitriou (eds.)
Athens, Greece, 23–26 November 2020

VIBRATION CONTROL BY STRUCTURAL COUPLING IN ADJACENT STRUCTURES USING STOCHASTIC ANALYSIS

Augusto de Souza Pippi[1], José Luis Vital de Brito[1], Suzana Moreira Avila[2] and Graciela Doz[1]

[1] Universidade de Brasília – Campus Universitário Darcy Ribeiro, Brasília – 70910-900, Brasil
augustopippi@hotmail.com; jlbrito@unb.br; graciela@unb.br

[2] Universidade de Brasília – Campus do Gama, Brasília – 72444-240, Gama (Brasília), Brasil
avilas@unb.br

Keywords: Structural Control, Coupled Buildings, Stochastic analysis, Passive Control

Abstract. *The structural coupling technique originated in the USA in the 70's, when Klein et al. [1] connected two adjacent structures through wire ropes to prevent pounding between them. This technique has been shown to be efficient not only to prevent the pounding phenomenon, but also to control the amplitude of vibration of coupled structures and to avoid possible severe structural damage caused by earthquakes or strong winds. The study of random vibrations arose from the need to assess the reliability structures that operate in a random environment. Stochastic dynamic analysis aims to evaluate the response of dynamic systems subject to stochastic inputs. One of the main premises of this analysis is to consider that the structure is known and deterministic, that is, its properties are not subject to random variations. The structure excitation is managed through probabilistic properties, generating the problem response as a function of variances. Thus, this paper aims to evaluate the difference between the deterministic and stochastic response in two adjacent structures, when using the structural coupling technique for vibration control. In addition, a parametric analysis is performed in order to verify the importance of the soil and filter parameters applied in the state matrix, in the stochastic analysis. Adjacent building models are used considering the shear frame structure behavior. The dampers that connect the structures are passive and their positions, quantities and mechanical properties are optimized by the particle swarm algorithm, in which the excitation in deterministic analysis is provided by the acceleration record of the 1940 El Centro earthquake. For stochastic excitation, a Gaussian stationary random process is used, in which it is applied through a filter, applied directly on the coupled system state matrix. The deterministic results of the uncoupled structures indicated the importance of choosing the base acceleration used as excitation in dynamic models. Reductions in vibration amplitude of up to 60% were observed. In the stochastic analysis, the reductions in floor vibration amplitude remained in the 50% range both structures. It has been seen that there are considerable differences when using deterministic analysis and stochastic analysis. However, the use of coupling structural control technique increases the system reliability.*

1 INTRODUCTION

The first researches on the structural coupling technique were carried out in the United States, in the 70s, when Klein *et al.* [1] connected two adjacent structures using steel cables, in order to avoid pounding between them. Later, Klein and Healy [2] developed an algorithm for semi-active control and found that to ensure that the system is controllable, the natural frequencies of adjacent buildings should be different. From these works, several researches were developed using the coupling technique, evaluating several control devices in the connection between the buildings [3-9].

The studies of random vibrations arose from the need to evaluate the reliability of structures that operate in a random environment. As examples, we can mention: winds in tall buildings and bridges, waves of the sea, earthquakes in civil structures, acceleration in satellites, among others [10]. A stochastic process, or a random process, is a mathematical model of a dynamic process in which dependence on the parameter time (t) is governed by probabilistic laws [11].

Stochastic dynamic analysis aims to evaluate the response of dynamic systems subject to stochastic inputs. One of the main premises of this analysis is to consider that the parameters of the structure are known and deterministic, that is, its properties are not subject to random variations. The excitation of the structure is managed through probabilistic properties, generating the response of the problem as a function of variances. Thus, it is possible to assess the reliability of the analysis and work, for example, with the probability of failure of a given system.

The objective of this work is to optimize the parameters of viscofluid dampers that connect two adjacent buildings through the deterministic dynamic response and the stochastic response, in order to verify the difference in the optimization results. Afterwards, a study is carried out on the importance of the parameters of the soil and filter, applied in the stochastic analysis, in the damping constant of the viscofluid dampers.

2 METHOLOGY

The models of adjacent buildings are considered to have shear frame behavior. The connection devices are of the passive type, and their positions, quantity and mechanical properties, are optimized through the particle swarm algorithm. In the deterministic analysis, an excitation provided by the acceleration record of the 1940 El Centro earthquake is used. In the stochastic analysis, a random Gaussian stationary process is considered and applied through a filter, used directly on the state matrix of the coupled system. This improved matrix contains soil and filter parameters.

3 MATHEMATICAL FORMULATION

The mathematical formulation for adjacent coupled buildings with deterministic base excitation is based on studies [7, 8, 12-13]. For stochastic excitation with white noise as an input, the formulation is based on studies [14-18].

3.1 Adjacent Coupled buildings

The adjacent buildings are considered as shear frame structures in this work, that is, the entire mass on the floor is considered concentrated in the beam, in which it is infinitely rigid in relation to the columns. In this way, rotations in the nodes are prevented and the stiffness of the structure is provided by the columns. The distance between the buildings is enough to install a connection device, however, it is not considered in the calculations. The type of control

used is a linear viscoelastic damper, that is, a device classified as passive. Finally, the movement of the ground is uniform in both structures.

Let the coupled models shown in Fig.1 in that the structure 1 contains $n+m$ floors and the structure 2, n floors. The mass, stiffness and damping properties of buildings have, respectively, the values of m_i^j, k_i^j, c_i^j, in which, i indicates the floor number and j the building $(j = 1, 2)$. The springs and dampers of the control system have the mechanical properties k_n^3 and c_n^3, being n the floor on which the elements are situated. Both structures are excited by acceleration in the ground $\ddot{X}_g$. Lastly, $x_{n+m}^1(t)$ and $x_n^2(t)$ are the displacements of models in the time domain. Thus the velocities and accelerations are, respectively, $\dot{x}_{n+m}^1(t)$, $\dot{x}_n^2(t)$, $\ddot{x}_{n+m}^1(t)$ and $\ddot{x}_n^2(t)$. The free-body diagram is shown in Fig. 2.

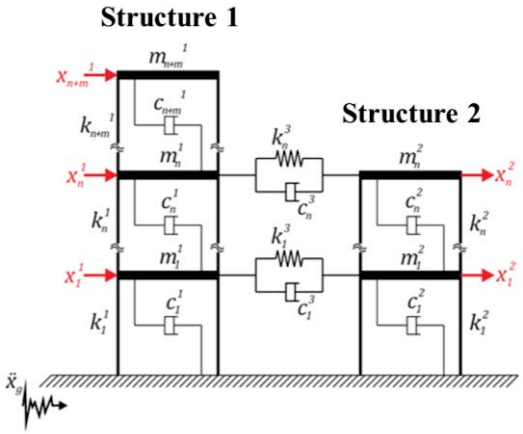

Figure 1: Model for adjacent coupled buildings.

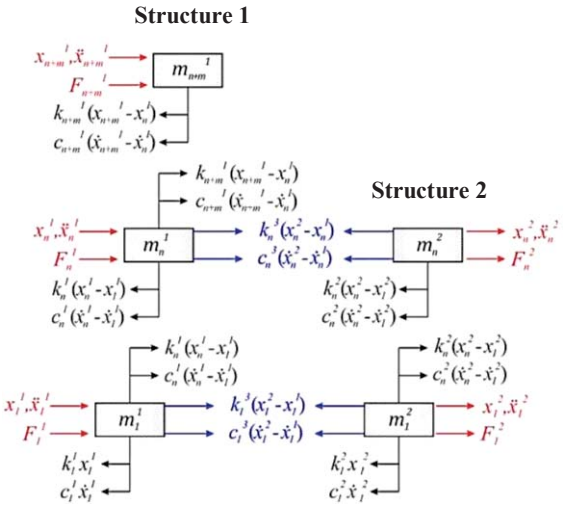

Figure 2: Free-body diagram.

Applying Newton's second law, the equation of motion for the coupled system is as follows:

$$\mathbf{M}_{ee}\,\ddot{\mathbf{x}}_{ee}(t) + \mathbf{C}_{ee}\,\dot{\mathbf{x}}_{ee}(t) + \mathbf{K}_{ee}\,\mathbf{x}_{ee}(t) = \mathbf{f}(t) \tag{1}$$

In which: $\mathbf{M}_{ee}$, $\mathbf{C}_{ee}$ and $\mathbf{K}_{ee}$ are the mass, damping and stiffness matrices of the coupled system, respectively; the vectors $\ddot{\mathbf{x}}_{ee}(t)$, $\dot{\mathbf{x}}_{ee}(t)$ and $\mathbf{x}_{ee}(t)$ are the ones that contain the values of

accelerations, velocities and displacements, respectively, in the two structures; $\mathbf{f}(t)$ is the external force vector, which in this case is the acceleration in the base.

One way to represent the above equation is by state-space. In this way, the second order differential equation (Eq. 1) is transformed into a set of first order equations. For a structural system, the state variables are displacements and velocities. If a system contains n degrees of freedom, then it is separated into $2n$ first order equations. The state vector $\boldsymbol{z(t)}$ is then given by:

$$\boldsymbol{z(t)} = \begin{bmatrix} x_{ee}(t) \\ \dot{x}_{ee}(t) \end{bmatrix} \tag{2}$$

And the first order equation is given by:

$$\dot{\boldsymbol{z}}(\boldsymbol{t}) = \boldsymbol{A}\boldsymbol{z}(\boldsymbol{t}) + \boldsymbol{B}\ddot{X}_g \tag{3}$$

In which:

$$\boldsymbol{A} = \begin{bmatrix} \boldsymbol{0} & \boldsymbol{I} \\ -\boldsymbol{M}_{ee}^{-1}\boldsymbol{K}_{ee} & -\boldsymbol{M}_{ee}^{-1}\boldsymbol{C}_{ee} \end{bmatrix}$$

$$I = identity\ matrix \tag{4}$$

$$\boldsymbol{B} = \begin{Bmatrix} 0 \\ -1 \end{Bmatrix}$$

Matrix $\boldsymbol{A}$ is the system state matrix, the vector $\boldsymbol{B}$ represents the disturbance vector. Being $\boldsymbol{C_y}$ the system output matrix, the structure response can be obtained as:

$$\boldsymbol{y(t)} = \boldsymbol{C_y z(t)} \tag{5}$$

$$\boldsymbol{C_y} = \begin{bmatrix} \boldsymbol{I} & \boldsymbol{0} \\ \boldsymbol{0} & \boldsymbol{I} \\ -\boldsymbol{M}_{ee}^{-1}\boldsymbol{K}_{ee} & -\boldsymbol{M}_{ee}^{-1}\boldsymbol{C}_{ee} \end{bmatrix} e\ \boldsymbol{y(t)} = \begin{Bmatrix} x_{ee}(t) \\ \dot{x}_{ee}(t) \\ \ddot{x}_{ee}(t) \end{Bmatrix}$$

3.2 Stochastic response in State-Space

In this formulation, it is considered that the system disturbance is given by a random process of white noise of average zero with power spectral density function (PSDF) of constant intensity S_0. The covariance matrix $\boldsymbol{S}$ of $\boldsymbol{y(t)}$ is given by:

$$\boldsymbol{S_{ij}} = \boldsymbol{E}[\boldsymbol{y_i y_j}] \tag{6}$$

where $E[.]$ is the expectation operator and y_i is the $i-nth$ element of the vector $\boldsymbol{y(t)}$.

As the process is random and it is considered white noise with zero mean, then $\boldsymbol{S}$ satisfies the following differential equation:

$$\dot{\boldsymbol{S}} = \boldsymbol{A}\boldsymbol{S}^{\boldsymbol{T}} + \boldsymbol{S}\boldsymbol{A}^{\boldsymbol{T}} + \boldsymbol{D} \tag{7}$$

Where $\boldsymbol{D}$ is the covariance matrix between the state and the excitation vectors and $D_{ij} = 0$ except $D_{2n,2n} = 2\,\pi S_0$.

Still, considering that the excitation is stationary, $\boldsymbol{D}$ is independent of time, so the stationary solution of Eq. (7) can be obtained by solving the Lyapunov matrix equation:

$$\boldsymbol{AS^T + SA^T + D = 0} \tag{8}$$

When using the PSDF to represent a stationary Gaussian random process $x_g(t)$, can be used a white noise filter $x_0(t)$ through two linear filters:

$$\begin{gathered}\ddot{x}_g(t) + 2\xi_g\omega_g\dot{x}_g(t) + \omega_g^2 x_g(t) = -\left(x_f(t) + x_0(t)\right) \\ \ddot{x}_f(t) + 2\xi_f\omega_f\dot{x}_f(t) + \omega_f^2 x_f(t) = -\ddot{x}_0(t)\end{gathered} \tag{9}$$

In which ω_g, ω_f, ξ_g and ξ_f are soil parameters (sub index g) and filter parameters (sub index f). Equation (9) lead to the following PSDF described by Clough and Penzien [15]:

$$G_{cp}(\omega) = S_0\left(\frac{1+4\xi_g^2\left(\frac{\omega}{\omega_g}\right)^2}{\left[1-\left(\frac{\omega}{\omega_g}\right)^2\right]^2+4\xi_g^2\left(\frac{\omega}{\omega_g}\right)^2}\right)\left(\frac{\left(\frac{\omega}{\omega_f}\right)^4}{\left[1-\left(\frac{\omega}{\omega_f}\right)^2\right]^2+4\xi_f^2\left(\frac{\omega}{\omega_f}\right)^2}\right) \tag{10}$$

Being S_0 the intensity of the process. The stochastic response of the structure is obtained through Eq. (8), in which the state vector $\boldsymbol{y(t)}$, the improved state matrix $\boldsymbol{A}$ (with the addition of the filter), are:

$$\boldsymbol{y} = \left\{\boldsymbol{x^T} \quad \boldsymbol{\dot{x}^T} \quad \boldsymbol{x_f} \quad \boldsymbol{\dot{x}_f} \quad \boldsymbol{x_g} \quad \boldsymbol{\dot{x}_g}\right\}^T \tag{11}$$

$$\boldsymbol{A} = \begin{bmatrix} [0] & [I] & \{0\}^T & \{0\}^T & \{0\}^T & \{0\}^T \\ -\boldsymbol{M}_{ee}^{-1}\boldsymbol{K}_{ee} & -\boldsymbol{M}_{ee}^{-1}\boldsymbol{C}_{ee} & -\{1\}^T\omega_f^2 & -\{1\}^T 2\xi_f\omega_f & \{1\}^T\omega_g^2 & \{1\}^T 2\xi_g\omega_g \\ \{0\} & \{0\} & 0 & 1 & 0 & 0 \\ \{0\} & \{0\} & -\omega_f^2 & -2\xi_f\omega_f & \omega_g^2 & 2\xi_g\omega_g \\ \{0\} & \{0\} & 0 & 0 & 0 & 1 \\ \{0\} & \{0\} & 0 & 0 & -\omega_g^2 & -2\xi_g\omega_g \end{bmatrix} \tag{12}$$

The elements of the covariance matrix $\boldsymbol{D}$ with dimensions $(2n+4)\,x\,(2n+4)$ are $D_{ij} = 0$ except $D_{2n+4,2n+4} = 2\pi S_0$.

With the covariance matrix $\boldsymbol{S}$ it is possible to obtain the standard deviation of root mean square (RMS) values of displacements σ_d through:

$$\sigma_d = \sqrt{diag(\boldsymbol{TST^T})} \tag{13}$$

where $\boldsymbol{T}$ is a transformation matrix, which for this case, has the form:

$$T_{2n+4,2n+4} = \begin{bmatrix} I_{n,n} & [0] \\ [0] & [0] \end{bmatrix} \tag{14}$$

For a given stochastic excitation, the maximum displacement can be obtained through the peak factor (p_f). Studies by Der Kiureghian [14], indicate that the maximum displacement (μ_{dmax}) is obtained as follows:

$$\sigma_{dmax} = \max(\sigma_d)$$
$$p_f = \sqrt{2\ln(\nu_e \tau)} + \frac{0.5775}{\sqrt{2\ln(\nu_e \tau)}} \tag{15}$$

Where σ_{dmax} is the maximum standard deviation of the displacements obtained in the stochastic analysis. In the second equation, it is the modified mean zero crossing rate and the duration of the excitation. For a degree of freedom (SDOF) system subject to white noise as excitation at the base ν_e is given by:

$$\nu_e = \begin{cases} (1.90\xi^{0.15} - 0.73)\nu & (\xi < 0.54) \\ \nu & (\xi \geq 0.54) \end{cases},$$
$$\nu = \frac{\omega}{\pi} \tag{16}$$

In the above equation ν is zero-crossing rate of the response, ω and ξ are the natural frequency and damping ratio of the SDOF structure, respectively. For multiple degrees of freedom, the natural frequency and damping rate of the dominant vibration mode should be used.

Thus, the maximum displacement is given by:

$$\mu_{dmax} = p_f \sigma_{dmax} \tag{17}$$

3.3 Particle swarm optimization (PSO)

The PSO was used to obtain the positions, quantity and optimum properties of the dampers in the analysis. The PSO algorithm was developed by Kennedy and Eberhart [19] and is based on a population of individuals that adapt and stochastically return to previously well-defined regions.

The objective function used is formed by two parts. The first consists of minimizing the square of the RMS of the maximum interstory drift of the two adjacent buildings (Eq. 17). The second is intended to decrease the value of the sum of squares of these RMS (Eq. 18).

$$f_{obj1} = \max\{\max(\{\Delta\}^1)^2 \quad \max(\{\Delta\}^2)^2\} \tag{18}$$

$$f_{obj2} = \sum_{i=1}^{n+m}\left(\{\Delta\}_i^1\right)^2 + \sum_{i=1}^{n+m}\left(\{\Delta\}_i^2\right)^2 \tag{19}$$

$$f_{objtotal} = f_{obj1} + f_{obj2} \tag{20}$$

$$\begin{cases} \{\Delta\}_i^j = x_i^j \\ \{\Delta\}_i^j = x_i^j - x_{i-1}^j \qquad 1 < i \leq n_{floor} \end{cases} \tag{21}$$

where $\{\Delta\}^j$ is the vector that contains the RMS of the interstory drift of each building ($1 \leq j \leq 2$) and x_i^j is the RMS of the absolute displacement calculated on each floor.

4 NUMERIC STUDY

One model of adjacent structures was chosen, containing the largest, 8 floors and the smallest, 4 floors, as shown in Fig. 3.

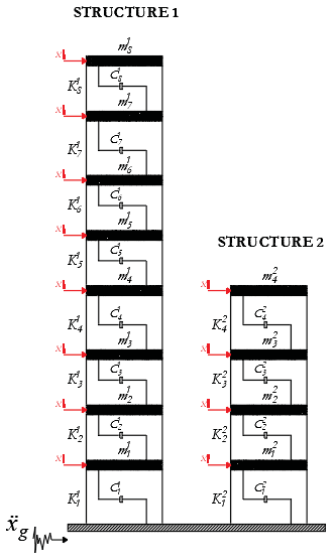

Figure 3: Models of adjacent buildings.

The floor mass considered is m_i^j = 30 t, floor-to-floor height H_i^j = 3.0 m and stiffness per floor k_i^j = 12.58 MN/m. The damping matrices were calculated using the Rayleigh method, considering a 3% damping ratio for all modes. In the deterministic analysis, accelerations on the ground of the 1940 El Centro earthquake were used, whose record of accelerations is shown in Fig. 4.

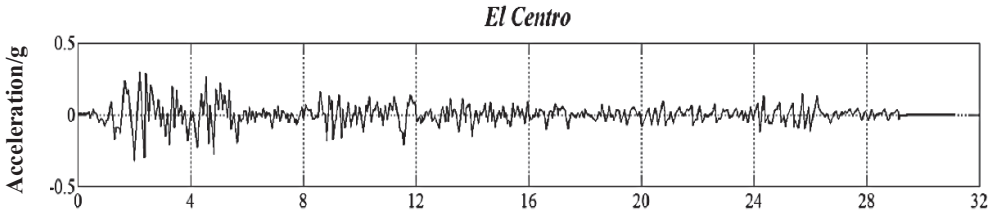

Figure 4: Record of 1940 El Centro earthquake accelerations.

The stiffness and damping values of the connection device between adjacent buildings vary from zero to 10.10^6 Ns/m. These devices are based on passive dampers available on the market (Taylor Device, Inc).

On first stochastic analysis, for comparison with the deterministic analysis, Clough and Penzien's PSDF was used, as described in Eq. (10). The soil parameters are based on the work of [20-22] and are described in Table 1.

ω_g (rad/s)	ξ_g	ω_f (rad/s)	ξ_f
5π	0.6	0.5π	0.6

Table 1: Parameters of PSDF.

For the process intensity S_0, a value suggested by Clough and Penzien [15] representing the NS component of the 1940 El Centro earthquake was used, and has the value of

$S_0 = 0.0047937\ m^2/s^3$. Fig. 5 shows the spectrum using the parameter values described above.

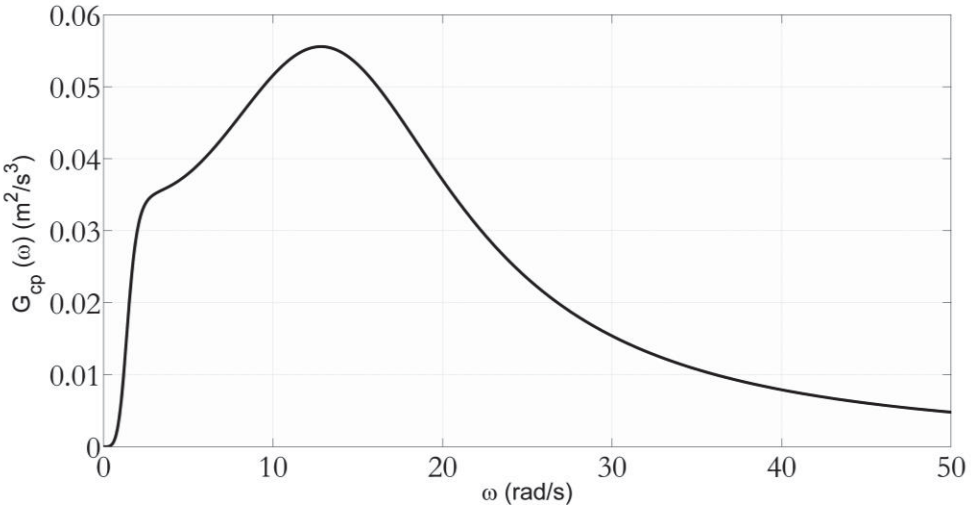

Figure 5: Clough and Penzien PSDF.

5 RESULTS AND DISCUSSIONS

The results are separated into two parts. The first part presents the results of the comparative analysis of the performance of the control technique by structural coupling using deterministic and stochastic analysis. The second part presents the results of the parametric analysis of the influence of soil and filter parameters on the structural coupling technique performance using stochastic analysis.

5.1 Comparative study

The first two natural frequencies (ω) in both structures are shown in Table 2. In parentheses are the frequencies f in Hertz, where $f = \omega/2\pi$.

Structure	First frequency (rad/s)	Second frequency (rad/s)
1	3.78 (0.60)	11.21 (1.78)
2	7.11 (1.13)	20.48 (3.26)

Table 2: Natural frequencies of adjacent structures.

In this stage, three analyses are performed. The first analysis (RMS-D) consists of optimizing the parameters of the viscofluid damper, which connects the two structures, through a deterministic analysis using the objective function of Eq. (20). In the second analysis (RMS-S), optimization is performed through stochastic responses with the same objective function as the first analysis. In the third analysis (MD-D), optimization is performed, in a deterministic analysis, with the objective function (Eq. 20) modified. The values of Δ (Eq. 18 and Eq. 19) are now the absolute values of interstory drift and no longer the RMS of those displacements.

The Eq. (20) with absolute values of interstory drift is used by [7, 9, 12]. The results of optimization are shown in Table 3. Table 4 shows the results of the interstory drift RMS. The results of the maximum interstory drift are shown in Table 5 and the maximum displacement values are shown in Table 6. The values in parentheses are those of the coupled system.

Analysis	Objective Function	Damping Constant (Ns/m)	Position (floor)
RMS-D	0.00052986	1,816,143.80	3
RMS-S	0.00038953	305,282.23	1 and 4
MD-D	0.004551	505,569.80	1 and 4

Table 3: Optimization results.

Analysis	Structure	RMS Interstory Drift (mm)	Reduction
RMS-D	1	13.38 (6.95)	48%
	2	16.40 (6.25)	62%
RMS-S	1	17.70 (8.39)	53%
	2	25.50 (7.10)	72%
MD-D	1	13.38 (6.95)	48%
	2	16.40 (5.87)	64%

Table 4: RMS of Interstory drift results.

Analysis	Structure	Maximum Interstory Drift (mm)	Reduction
RMS-D	1	37.65 (21.91)	42%
	2	60.57 (24.22)	60%
RMS-S	1	48.06 (22.81)	52%
	2	37.20 (19.28)	48%
MD-D	1	37.65 (22.25)	41%
	2	60.57 (23.83)	61%

Table 5: Maximum Interstory drift results.

Analysis	Structure	Maximum Displacement (m)	Reduction
RMS-D	1	0.180 (0.134)	26%
	2	0.176 (0.077)	56%
RMS-S	1	0.255 (0.133)	48%
	2	0.106 (0.059)	44%
MD-D	1	0.180 (0.132)	27%
	2	0.176 (0.078)	56%

Table 6: Maximum displacement results.

For the uncoupled system, in the deterministic analysis, the structure 2 has a greater amplitude of interstory drift than the larger structure (structure 1) and also, both have similar max-

imum amplitudes. This is due to the energy content in the frequency range of the 1940 El Centro earthquake, as shown in Fig. 6.

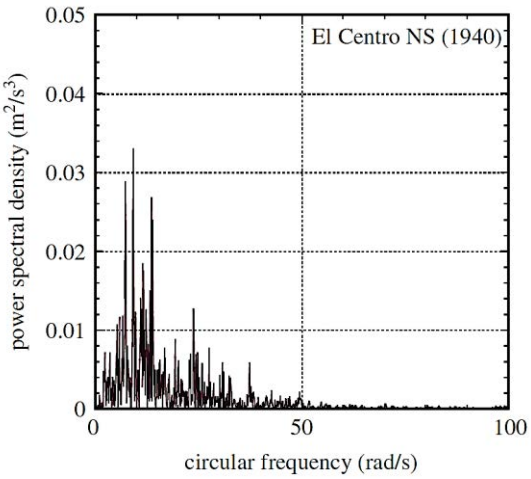

Figure 6: Power density function of the 1940 El Centro earthquake [23].

Stochastic analysis resulted in more economical dampers when compared to deterministic analysis. Also, the maximum displacements are higher (29%) for structure 1 and smaller (66%) for structure 2, in comparison with the deterministic analysis. Even so, the efficiency of the coupling technique was better in the stochastic analysis, in which the randomness of earthquakes is considered.

5.2 Parametric study

This study aims to verify the influence of the soil and filter parameters, applied in the state matrix $\boldsymbol{A}$ (Eq. 12), on the damping coefficient (C^3) of the dampers. The parameters are ω_g, ω_f, ξ_g e ξ_f. Each parameter was varied one by one, keeping the other three constants with values described in Table 1.

The results for natural soil frequency ω_g are shown in Fig. 7. The parameter was varied from 0.1π to 10π.

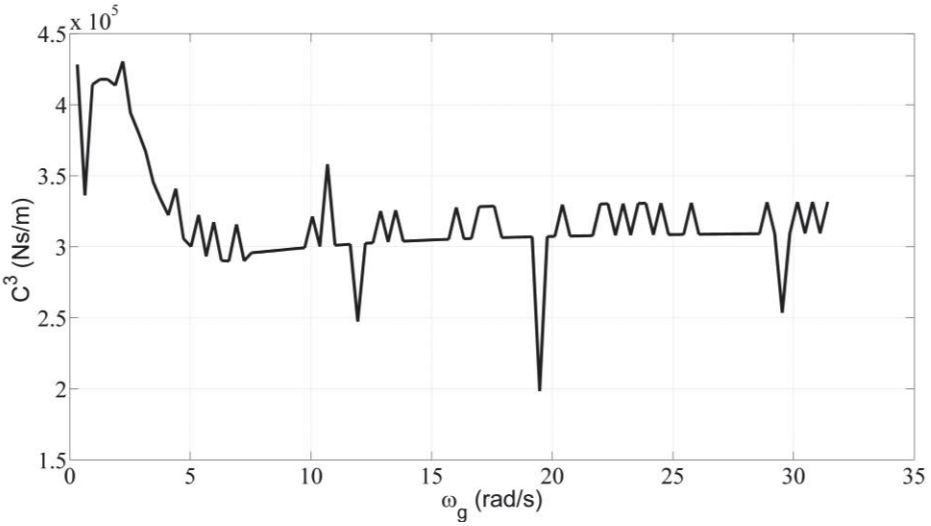

Figure 7: Influence of the ω_g on the damping coefficient.

There is an influence of the soil natural frequency in the optimization of the damper. The C^3 value changes around 300,000 Ns/m, close to the answer of the previous comparative study. This means that this parameter generates a little variation in the optimization, that is, its values are not significant in the analysis. The number of dampers varied between 1 and 2. For the filter frequency ω_f, the results are shown in Fig. 8. The frequency was varied from 0.1π to 10π.

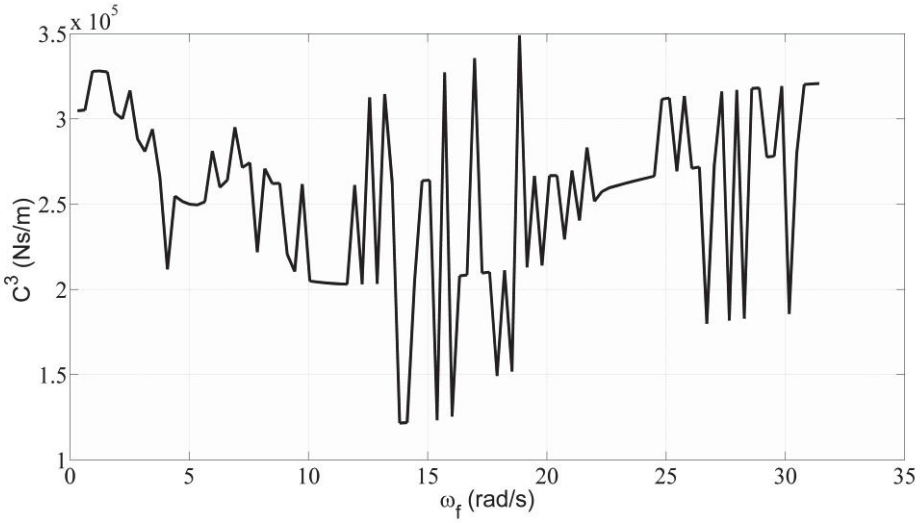

Figure 8: Influence of the ω_f on the damping coefficient.

The filter frequency generated a more intense variation on the damping coefficient. Thus, it is important that the frequency is carefully chosen, since this parameter strongly influences the dampers that connect the two structures.

The responses for the soil ξ_g and filter ξ_f damping ratio are shown in Fig. 9 and Fig. 10. The damping ratios varied from 0.01 to 1.

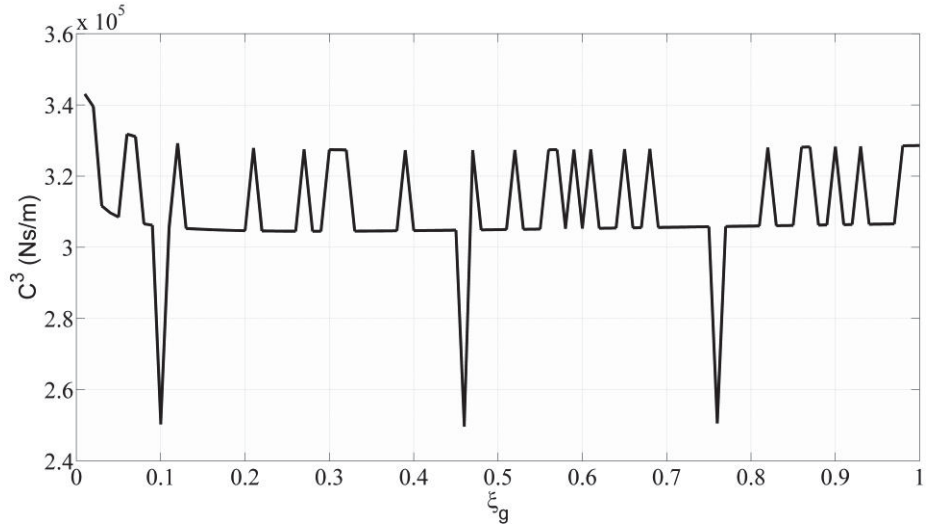

Figure 9: Influence of the ξ_g on the damping coefficient.

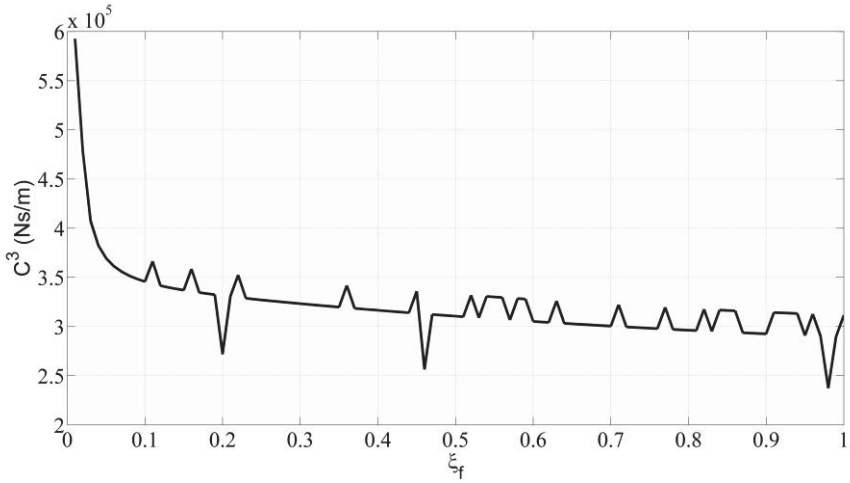

Figure 10: Influence of the ξ_f on the damping coefficient.

The soil damping ratio has a greater influence in the damping constant of the control system that connects the two structures. Even so the values are close to the average, showing a low standard deviation, thus, it has a low influence in the optimization.

6 CONCLUSIONS

This work aimed to study the vibration control technique through structural coupling using different perspectives in the optimization. In addition, a parametric study was carried out to verify the influence of soil and filter parameters on the damping constant of the control device that connects the two adjacent structures.

The deterministic results of the uncoupled structures indicated the importance of choosing the base acceleration used as excitation in dynamic models. In this analysis, for example, the more rigid structure (structure 2) obtained amplitudes of vibrations similar to the more flexible structure (structure 1).

The efficiency of the control technique by structural coupling was observed in both deterministic and stochastic analysis. In the deterministic analysis, there were reductions of up to 60% in the vibration amplitudes in the structure 1. For the structure 2, a 42% reduction on the maximum interstory drift was observed. In the stochastic analysis, the reductions on the vibration amplitudes of the floors, remained in the range of 50% in the structures. In the more flexible structure, the reduction on the vibration amplitudes was more efficient than in the rigid structure, different from that observed in deterministic analysis.

Comparing the results between the two analysis, the maximum displacements in the structure 2 were greater in the stochastic analysis. For structure 1, the displacements were smaller. It was observed that the maximum interstory drift are higher in the structure 2 in the deterministic analysis. In the stochastic analysis, these displacements demonstrate the opposite behavior, with the interstory drift being smaller in the structure 2. However, the interstory drift RMS maintained the same behavior in the three analysis. The use of the structural coupling technique approximated the maximum response between the three analysis.

The difficulty in predicting the real characteristics of earthquakes, makes the stochastic analysis important in the evaluation of the maximum response in dynamic problems. It has been shown that there are considerable differences when using deterministic and stochastic analysis. However, the use of the coupling structural control technique increases the reliability of the system, since it approximates the responses of the analysis performed.

In the parametric analysis, the influence of the soil and filter constants on the mechanical characteristics of the damper that connects the two structures was verified. The parameter that generated the greatest variation in the damping coefficient was the filter frequency. As the optimum properties of the dampers depend on the response of the structures, it makes the choice of these variables a crucial point in the analysis. Since the characteristics of the earthquake and the real behavior of the structure during the earthquake are not known, this analysis demonstrated that the value of the optimal damping constant has a low standard deviation for the soil parameters, however, this deviation is considerable for filter parameters. Thus, for this analysis, changes in soil characteristics can be discarded.

ACKNOWLEDGEMENTS

The authors would like to thank the Research Support Foundation of the Federal District (FAP-DF) and the Coordination for the Improvement of Higher Education Personnel (CAPES) for financial support for this paper.

REFERENCES

[1] R.E. Klein, C. Cusano, J. Stukel, Investigation of a method to stabilize wind induced oscillations in large structures, *ASME Winter Annual Meeting*, Paper No. 72, 1972.

[2] R.E. Klein, M.D. Healy, Semi-Active Control of Wind Induced Oscillations in Structures, *Proc. 2nd International Conference on Structural Control*, 354-369, 1987.

[3] B.D. Westermo, The Dynamics of Interstructural Connection to Prevent Pounding, *Earthquake Engineering and Structural Dynamics* 18, 687-699, 1989.

[4] J.E. Luco, C.P. Barros, Optimal Damping Between Two Adjacent Elastic Structures, *Earthquake Engineering and Structural Dynamics* 27, 649-659, 1998.

[5] Y.L. Xu, Q. He, J.M. Ko, Dynamic response of damper-connected adjacent buildings under earthquake excitation, *Engineering Structures* 21, 135-148, 1999.

[6] L.A. Pérez, S. Avila, G. Doz, Seismic Response Control of Adjacent Buildings Connected by Viscous and Hybrid Dampers, *Dynamics of Civil Structures* 4, 433-440. 2014.

[7] L.A. Pérez Peña, Resposta Dinâmica de Edificações Adjacentes Acopladas: Considerações sobre a Interação Solo–Estrutura, *Tese de Doutorado*, Universidade de Brasília, 2017.

[8] K. Bigdeli, W. Hare, J. Nutini, S. Tesfamariam, Optimizing damper connectors for adjacent buildings, *Optimization and Engineering* 17, 47-75, 2016.

[9] A. Pippi, P. Bernardes JR., S. Avila, M. De Morais, G. Doz, Dynamic Response to Different Models of Adjacent Coupled Buildings, *Journal of Vibration Engineering & technologies* 8, 247-256, 2019.

[10] A. Preumont, Random Vibration and Spectral Analysis, *Spring Science*, ISBN: 9789048144495, 1994.

[11] T.T. Soong, M.A. Grigoriu, Random Vibration Mechanical and Structural Systems, *Prentice-Hall Inc.*, ISBN: 0137523610, 1993.

[12] K. Bigdeli, Optimal Placement and Design of Passive Damper Connectors for Adjacent Structures, *Master thesis of applied science*, University of British Columbia, 2012.

[13] M.E. Uz, M.N.S. Hadi, Earthquake Resistant Design of Buildings, *Taylor & Francis Group*, ISBN: 9780815391722, 2018.

[14] A. Der Kiureghian, On Response of Structures to Stationary Excitation, A report on research sponsored by the National Science Foundation, *report nº UCB/EERC-79/32*, 1979.

[15] R.W. Clough, J. Penzien, Dynamics of Structures, *McGraw-Hill Education*, ISBN: 9780071132411, 1993.

[16] E. De La Fuente, An efficient procedure to obtain exact solutions in random vibration analysis of linear structures, *Engineering Structures* 30, 2981-2990, 2008.

[17] C. Martínez, O. Curadelli, M.E. Compagnoni, Optimal design of passive viscous damping systems for buildings under seismic excitation, *Journal of Constructional Steel Research* 90, 253-264, 2013.

[18] O. Curadelli, M. Amani, Integrated structure-passive control design of linear structures under seismic excitations, *Engineering Structures* 81, 256-264, 2014.

[19] J. Kennedy, R. Eberhart, Particle swarm optimization, *Proceedings of IEEE International Conference on Neural Networks* 5, 1942–1948, 1995.

[20] G. Deodatis, Non-stationary stochastic vector processes: seismic ground motion applications, *Probabilistic Engineering Mechanics* 11, 149-168, 1996.

[21] Z. Liu, W. Liu, Y. Peng, Random function based spectral representation of stationary and non-stationary stochastic processes, *Probabilistic Engineering Mechanics* 45, 115-126, 2016.

[22] J. Chen, F. Kong, Y. Peng, A stochastic harmonic function representation for non-stationary stochastic processes, *Mechanical System and Signal Processing* 96, 31-44, 2017.

[23] I. Takewaki, Critical Excitation Methods in Earthquake Engineering, *Elsevier*, ISBN: 9780080994369, 2013.

EURODYN 2020
XI International Conference on Structural Dynamics
M. Papadrakakis, M. Fragiadakis, C. Papadimitriou (eds.)
Athens, Greece, 23–26 November 2020

STUDY OF A HYBRID INVERTED PENDULUM TUNED MASS DAMPER BEHAVIOR USING A PID CONTROL

Jonas P. Falcão[1], Ledymar F. Moreno[2], José L. V. de Brito[1], Marcus V. G. de Morais[2], and Suzana M. Avila[2]

[1]Graduate Program in Structures and Civil Construction, University of Brasilia, Darcy Ribeiro Campus, Asa Norte, Brasília, DF 70910-900, Brazil.
email:jonaspfalcao@hotmail.com, jlbrito@unb.br

[2]Graduate Program in Engineering Materials Integrity, University of Brasilia, Campus of Gama, 72444-240, Gama, DF, Brazil.
e-mail:ingfoncault@gmail.com, mvmorais@unb.br, avilas@unb.br

Keywords: Tuned mass damper, Vibration, Inverted pendulum, Hybrid control, PID controller.

Abstract. *Tuned mass dampers are devices well known in the literature. It is an auxiliary mass system that correctly tuned when connected to the structure vibrates out of phase with it, having the energy transferred to itself and thus reducing the vibration level of the main system. Among the geometries of this type of damper stands out the pendular one. However, recent studies show that inverted pendulum configuration would be more appropriate and efficient. The inverted pendulum problem itself is widely discussed in the literature, but its application as a structural control device acting as a tuned mass damper has not been sufficiently studied. The originally passive control device can be designed to operate in a hybrid manner with the addition of an active controller to the system. This configuration has the advantage of being more robust than passive, which only works well in the design frequency range, and requires lower control forces than purely active control. In this work a hybrid inverted pendulum mass damper (TMD-HIP) is proposed, where in addition to tuning it from the pendulum length and mass, an active control device is added. The active force used is designed as a PID controller with optimized gains. Numerical simulations are performed using the MATLAB computational package and its SIMULINK control toolbox. Several forms of external excitation are considered in the analysis. From the results it appears that the TMD-HIP is a good alternative for reducing excessive vibration. Although it is a preliminary model, it is a basis for studies in this area to evolve to more sophisticated model and full-scale applications.*

1 INTRODUCTION

The design and construction of slender and flexible structures, such as wind turbines, observation towers and high buildings, have increased in recent years. These structures are subjected to dynamic actions such as: wind, earthquakes, waves, heavy traffic, human occupation and rotating machines. These vibrations are undesirable both from the point of view of safety and environmental comfort, since they can reach the ultimate limit state, that is, collapse of the structure, or the service limit state, caused by excessive vibrations causing discomfort to the occupants [1].

One of the solutions to reduce undesirable levels of vibration in structures is the so-called structural control. It is a technology that promotes changes in the structure stiffness and damping properties, both by adding external devices and by applying external forces [2, 3]. It can be classified as passive, active, hybrid and semi-active [2].

Passive control already has several applications implemented in practice in structures around the world [4]. One of the most used devices is the so-called Tuned Mass Damper (TMD), it is an auxiliary mass attached to the structure, which properly tuned, vibrates out of phase, thus reducing the dynamic response of the main system [2, 5-12].

Among the possible geometric configurations used for TMD we have the simple pendulum [12-20]. Alternatively, Ahn *et al.* [21] proposed a TMD type as inverted pendulum (TMD-IP). The authors showed that equivalent performance of a simple pendulum can be achieved, but with shorter inverted pendulum lengths.

Despite being a problem widely studied in the control literature [22], the inverted pendulum system functioning as a TMD has not been adequately explored in the literature yet [4, 7, 23-28].

Resende *et al.* [26] presented an experimental-numerical study of an inverted pendulum system to control a reduced model of one degree of freedom. The study concluded that, based on experimental results, the TMD-IP showed satisfactory reductions of more than 50% in the response amplitudes of the main system, indicating good potential for the development of future practical applications.

Passive control, however, has deficiencies, as it does not function properly outside the design frequency range. The active control, which is a more robust control in relation to the passive, requires external energy supply, high magnitudes actuator forces and eventual stability problems. In this way, hybrid control, which combines passive and active control, presents itself as a more robust alternative and requires lower magnitude force than those of purely active control [1]. In the literature proposals for hybrid mass dampers can be found [29-34]. It is the combination of a passive TMD with an active control actuator, having already been implemented in practice [35].

In this work, the originally passive TMD-IP can be designed to operate in a hybrid manner with the addition of an active controller to the system. A hybrid inverted pendulum mass damper (TMD-HIP) is proposed, where in addition to tuning it from the pendulum length and mass, an active control device is added. The active controller used is a PID controller with optimized gains. From the analysis of the results it appears that the TMD-HIP is a good alternative for reducing excessive vibrations. Although being a preliminary model, it could be a basis for future studies in this area, to evolve to more sophisticated modelling and full-scale applications.

2 MATHEMATICAL MODEL

The system of two degrees of freedom (2DoF) studied in this work is shown in Figure 1. It represents the main system with a translational degree of freedom with an inverted coupled pendulum having a rotational degree of freedom. Considering small displacements, where $\mathbf{sin}\,\boldsymbol{\theta} \cong \boldsymbol{\theta}$, the hypothesis is of a linear system and the equations of motion are given by:

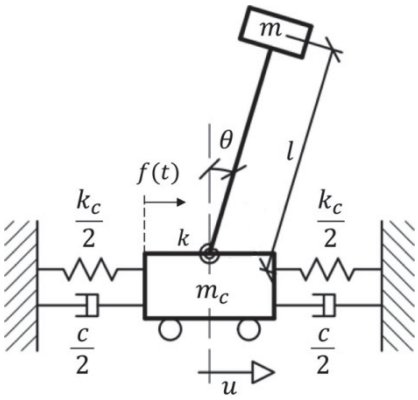

Figure 1: Mass-spring-damper model with inverted pendulum [26].

$$\begin{aligned}&(m_c + m + \rho l)\ddot{u} + \left(ml + \frac{\rho l^2}{2}\right)\ddot{\theta} + c\dot{u} + k_c u = f(t)\\&\left(ml + \frac{\rho l^2}{2}\right)\ddot{u} + \left(ml^2 + \frac{\rho l^3}{3}\right)\ddot{\theta} + \left(k - mgl - \frac{\rho g l^2}{2}\right)\theta = 0\end{aligned} \tag{1}$$

where:

m_c *is* the mass of the main system;
k_c is the stiffness of the main system;
c is the damping of the main system;
ρ is the linear specific mass of the pendulum;
l is the length of the pendulum;
m is the pendulum top mass;
k is the pendulum rotational stiffness;
g is the gravity acceleration;
$f(t)$ is the external dynamic force.

Applying the Laplace transform to each equation and solving the system with two algebraic equations, the transfer functions for the translational and rotational displacement are obtained and given, respectively, by:

$$\begin{aligned}G_u(s) &= \frac{(4\rho l^3 + 12ml^2)s^2 + (12k - 6\rho g l^2 - 12mgl)}{As^4 + Bs^3 + Cs^2 + Ds + E}\\G_\theta(s) &= \frac{-(6\rho l^2 + 12ml)s^2}{As^4 + Bs^3 + Cs^2 + Ds + E}\end{aligned} \tag{2}$$

where:

$$
\begin{aligned}
A &= \rho^2 l^4 + 4\rho\, l^3 (m_c + m) + 12 m_c m l^2 \\
B &= 4cl^2 (3m + \rho l) \\
C &= 4k_c l^2 (3m + \rho l) + 12k(\rho l + m_c + m) - 6\rho g l^2 (\rho l + m_c + 3m) - 12mgl(m_c + m) \\
D &= 12kc - 6cgl(\rho l + 2m) \\
E &= 12kk_c - 6k_c gl(\rho l + 2m)
\end{aligned}
\tag{3}
$$

3 PID CONTROLLER

The PID controller is a combination between the proportional derivative control (PD) and the proportional integral control (PI). The combination of these two types of control combines the increased damping provided by the PD control with the improvement of the system stability and the steady state error generated by the PI control [36]. Therefore, from the PID control it is possible to obtain a significant improvement in the behaviour of the system for both the transient and steady state behaviour.

The block diagram of the system with hybrid PID control consists of adding a sensor, a PID controller and a reference input as shown in Figure 2. The sensor captures the output signal and converts it to the same unit as the reference signal in order to compare these values. However, as the system response and the reference signal already have the same unit, then the transfer function of the sensor is unitary. As the aim is to reduce the displacements, the reference is taken equal to zero. The actuator force is applied at the translational main system.

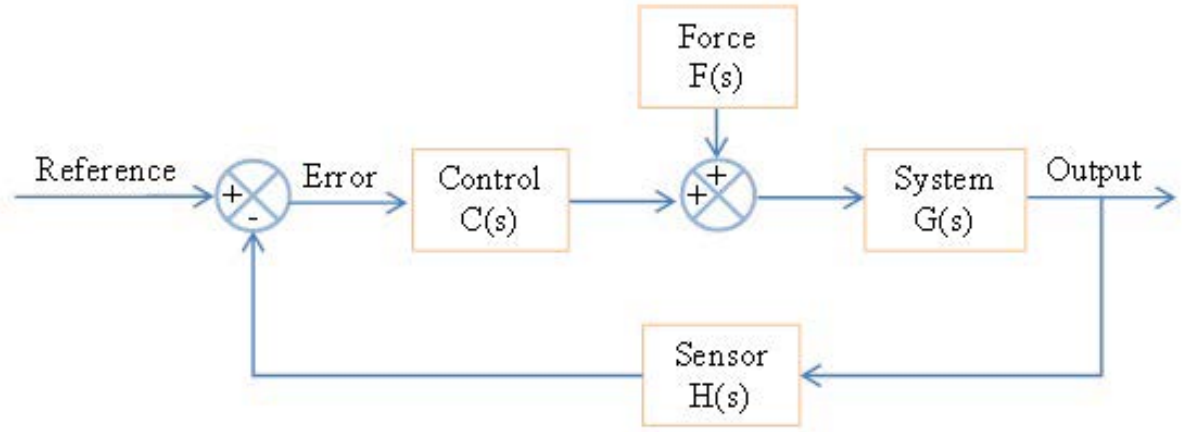

Figure 2: Block diagram of closed-loop system.

The controller transfer function is obtained from the optimization of P, I, D and N values, where N is a filter coefficient. The controller transfer function is given by:

$$
C(s) = P + I\frac{1}{s} + D\frac{N}{1 + N\frac{1}{s}} \tag{4}
$$

In order to verify the performance of the PID controller, a preliminary result of the vibration control is obtained through an inverted pendulum system analysis as shown in Figure 3.

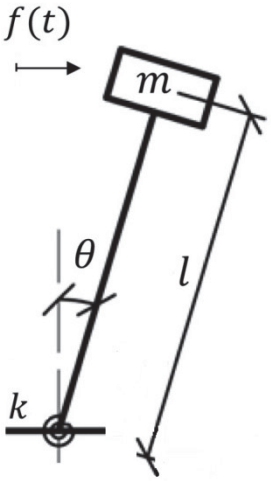

Figure 3: Inverted pendulum system.

The motion equation for this system is given by:

$$\left(ml^2+\frac{\rho l^3}{3}\right)\ddot{\theta}+\left(k-mgl-\frac{\rho g l^2}{2}\right)\theta=f(t)l \tag{5}$$

Applying the Laplace transform, the following system transfer function is obtained:

$$G_\theta(s)=\frac{1}{\left(ml+\frac{\rho l^2}{3}\right)s^2+\left(\frac{k}{l}-mg-\frac{\rho g l}{2}\right)} \tag{6}$$

The physical parameters adopted for the model are: ρ=0.24 kg/m, l=0.24 m, m=0.097 kg, k=2.23 N.m/rad and g=9.781 m/s^2.

The loading is a harmonic force with amplitude equal to 0.10 N and frequency of 15.7 rad/s. The evolution of angular displacement over time for the system without control and with PID control is shown in Figure 4.

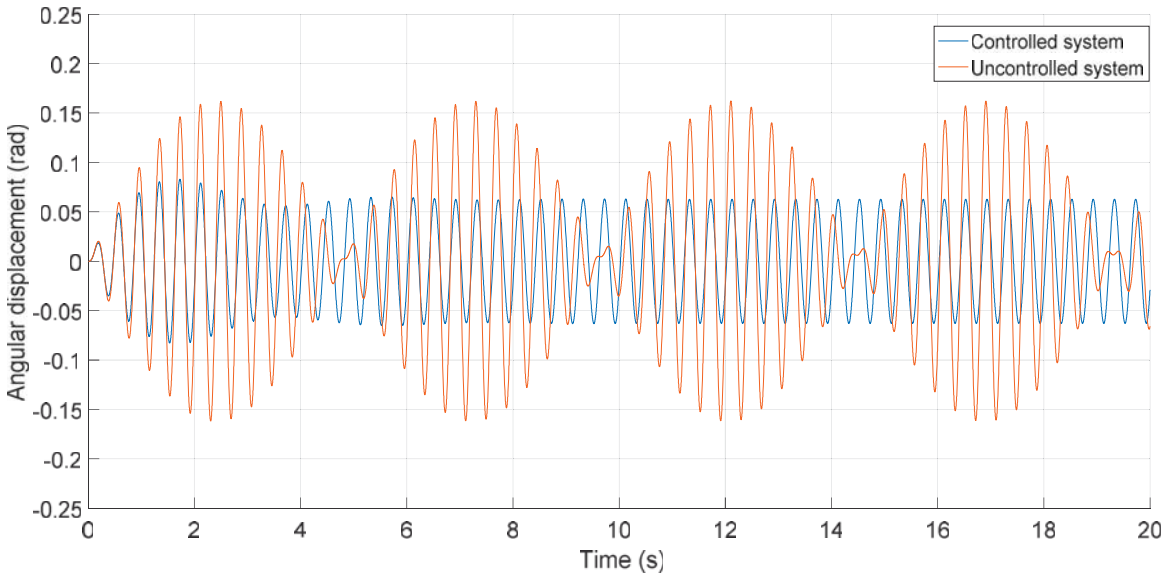

Figure 4: Angular displacement time history of an inverted pendulum subjected to harmonic loading.

It is verified that the maximum displacement of the system without control is 0.162 rad, while for the system with active control the maximum displacement is 0.083 rad, that is, there is a reduction of 48.76% in the value of the angular displacement of the inverted pendulum. In addition, the displacements are below 0.174 rad (10°), so the hypothesis that the system has a linear behaviour is met.

Then, a step excitation with amplitude equal to 0.10 N and duration of 5 s is applied. The response of the structure in the time domain in this case is shown in Figure 5 both for the system without control and for the system with PID control.

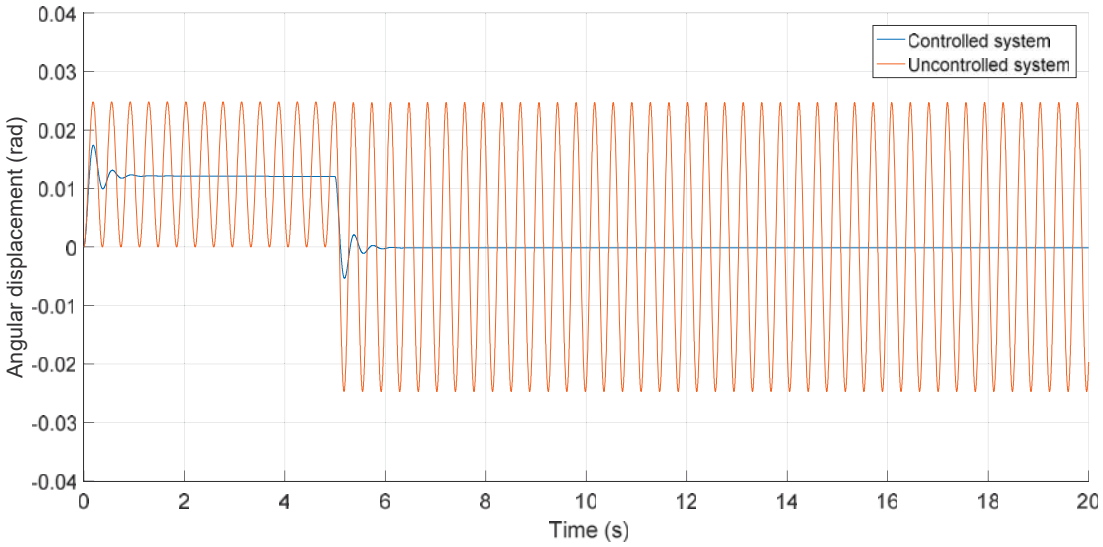

Figure 5: Angular displacement time history of an inverted pendulum subjected to step loading.

The maximum displacement of the system without control is 0.025 rad, while the system with active control shows a maximum displacement of 0.017 rad, that is, there is a reduction of 32%. As the displacements are below 0.174 rad (10°), the hypothesis that the system has a linear behaviour is met.

Therefore, it is verified that the control by means of PID presents satisfactory performance in reducing the dynamic response of the inverted pendulum presented.

4 RESULTS AND DISCUSSIONS

The parameters considered for the 2DoF model are: m_c=1.13317 kg, c=0.546 N.s/m, k_c=328.34 N/m, ρ=0.24 kg/m, l=0.24 m, m=0.097 kg, k=2.23 N.m/rad and g=9.781 m/s^2. Two loading cases were analyzed: harmonic loading $f(t)=f_o\sin(\omega t)$ where f_o =0.32 N and ω=15.7 rad/s and step loading with amplitude equal to 0.32 N and duration of 5 s. It is worth noticing that all the parameters above are the ones of the experimental model presented by Resende *et al.* [26].

4.1 Modal analysis and frequency analysis

It was developed a modal analysis of the following cases: system without control, applying passive control, active control and hybrid control.

The natural frequency of system without control is 17.02 rad/s. The addition of an inverted pendulum introduces one extra degree of freedom at the system and influences the modal parameters of the structure, leading to new values of natural frequencies, which are 14.27 rad/s and 20.12 rad/s. The mode shapes for passive control model are given by the following eigen-

vectors: [10.75 1.00] for the first mode of vibration and [-15.78 1.00] for the second mode of vibration, where the first column represents the angular displacement and the second column represents the translational displacement.

As the addition of a PID controller acts applying a control force at the system in order to reduce vibrations and it does not change the physical properties of the system, the mass and stiffness matrixes remain the same and consequently the modal proprieties too. Thus, natural frequencies and mode shapes of the without control model are the same of active control model, as well as these modal proprieties of the passive control model are the same of those of the hybrid control model. Therefore, PID controller does not produce any change in the modal parameters of the system.

Besides that, it is developed a frequency analysis of the same study of modal analysis: without control, passive control, active control and hybrid control. Figure 6 shows the frequency response function for an amplitude force of 0.32 N.

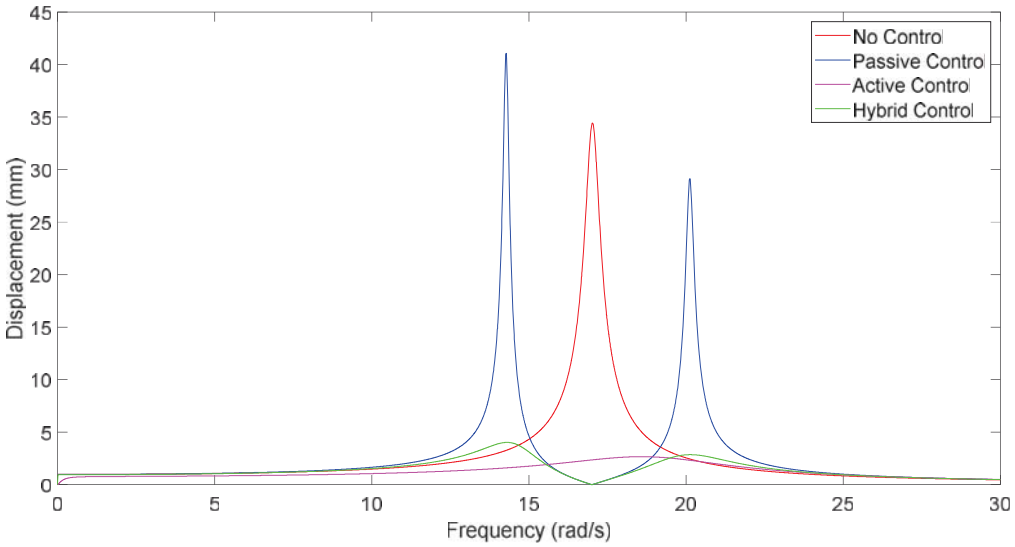

Figure 6: Displacement response in frequency domain (without control, TMD-IP, AC, TMD-HIP).

Table 1 summarizes the values of natural and resonant frequencies and peak response for all the case studied.

	No control	Active control	Passive control	Hybrid control
Natural Frequency (rad/s)	17.02	17.02	14.27 and 20.12	14.27 and 20.12
Resonant Frequency (rad/s)	17.02	18.58	14.27 and 20.12	14.31 and 20.15
Peak Response (mm)	34.43	2.67	41.07 and 29.13	4.02 and 2.86

Table 1: Natural and resonant frequencies and peak response.

The resonant frequency of the system without control is 17.02 rad/s. The addition of an inverted pendulum as passive control changes resonant frequencies. In this model, the resonant frequencies are the same of natural frequencies: 14.27 rad/s and 20.12 rad/s. Besides that, it is verified that for frequencies between 15.02 rad/s and 19.18 rad/s, the permanent response of the passive control model is less than the without control model. Therefore the passive control works well only in a range of frequency pre-established in the design.

The addition of PID controller changes slightly the resonant frequency which for the active control model is 18.58 rad/s and for hybrid control model are 14.31 rad/s and 20.15 rad/s. It can be seen a little difference for resonant frequencies between without control model and active control model, and between passive control model and hybrid control model. This little difference happens because although PID controller acts applying a control force to the system, it works improving damping which changes the bandwidth frequency and consequently resonant frequencies.

Besides that, it is verified that active control model presents the minimum peak response when compared with the other models. On the other hand, the amplitude response of the hybrid control model is lower than active control model in a frequency range between 15.62 rad/s and 18.92 rad/s. Therefore, depending on the frequency range of external exciting force, it can be better to design using active or hybrid control in order to minimize peak permanent response.

4.2 Response due to harmonic loading

Figure 7 shows the time domain response for harmonic loading using passive control and PID hybrid control. The optimization of the values of P, I, D and N is performed using the Simulink/MATLAB toolbox and limiting the control forces to 50% of the magnitude of the dynamic excitation forces. The values of the parameters found are P = 7.5, I = 0.9, D = 5.0 and N = 1720. The hybrid control shows a rise time equal to 851 s and a settlement time equal to 1430 s.

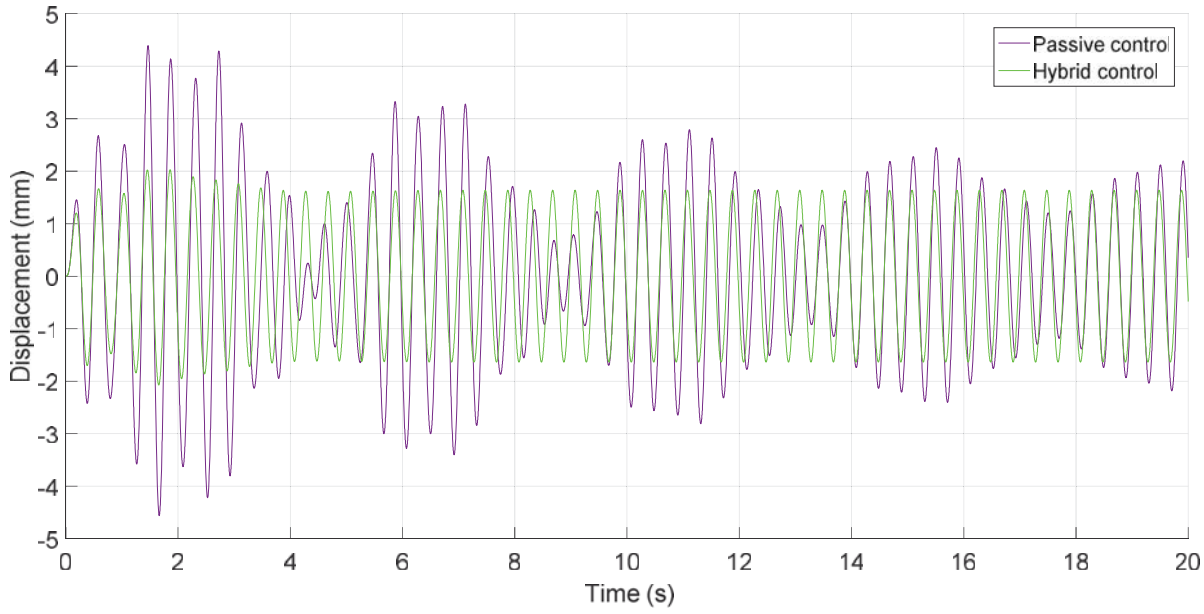

Figure 7: Displacement time history of the main system for harmonic loading (TMD-IP and TMD-HIP).

Figure 8 shows the time domain response for harmonic loading using PID active control and PID hybrid control. The optimization of the values of P, I, D and N for active control is performed using the Simulink/MATLAB toolbox and equalling the maximum displacements from the two PID controllers. The values of the parameters found for PID active control are P = 81.3, I = 97.3, D = 6.1 and N = 2337. The active control shows a rise time equal to 8.74 s and a settlement time equal to 15.5 s.

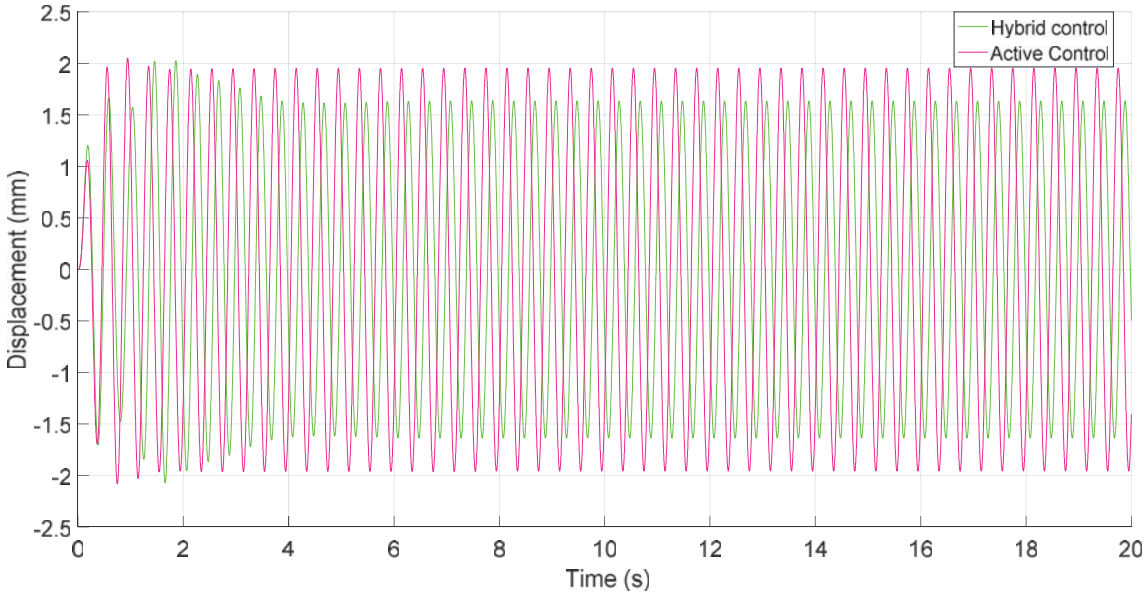

Figure 8: Displacement time history of the main system for harmonic loading (AC and TMD-HIP).

Figure 9 shows the comparison of displacement time history between the uncontrolled system and the system with TMD-HIP because this was the one that shows the smallest displacements compared to passive control and PID active control.

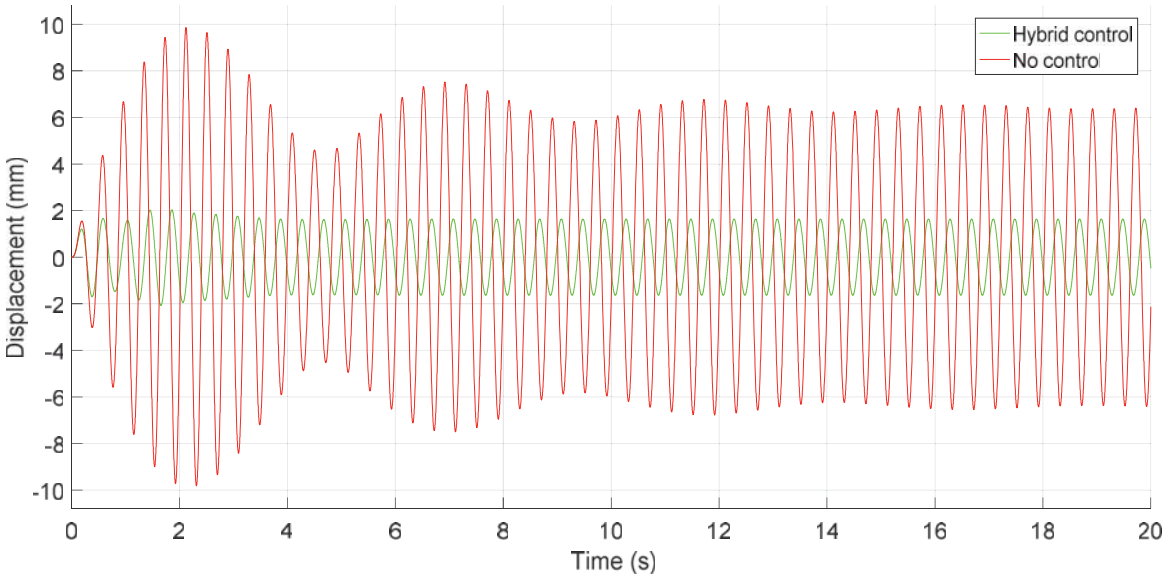

Figure 9: Displacement time history of the main system for harmonic loading (without control and TMD-HIP).

Table 2 shows the maximum and RMS displacement values of the main system for the harmonic loading case.

	No control	Passive control	Active control	Hybrid control
U_{max} (mm)	9.76	4.36	2.08	2.07
RMS(mm)	5.60	2.45	1.38	1.26

Table 2: Displacements due to harmonic loading.

The system with passive control shows a reduction of 55.3% in the maximum displacement of the structure in relation to the system without control. The system with hybrid control shows a reduction of 78.8% and 52.5%, respectively, in relation to the system without control and the system with passive control. It is verified that there are time ranges where the response with passive control is lower than the one with hybrid control.

Although the maximum displacement results comparing the active hybrid control are approximately the same, there is a reduction of 8.7% of the response regarding the hybrid control in relation to the active control during the steady state phase.

Regarding the RMS response, the system with passive control shows a reduction of 56.2 % compared to the system without control, while the system with hybrid control presents a reduction of 77.5% and 48.57%, respectively, in relation to the system without control and the system with passive control. Regarding the RMS of the systems with PID controller, the system with hybrid control shows a reduction of 8.7% in relation to the system with active control.

The control force is limited to 50% of amplitude value of the external action, and therefore the hybrid control shows to be feasible in practice. In the case of active control, it is found that to maintain the same maximum displacement obtained through the hybrid control during the transient response, a control force of 0.26 N is required, which corresponds to 81.2% of the amplitude of the external excitation. Therefore, it is verified that the capability of the actuator when using active control is 62.5% higher than when using hybrid control.

The maximum angular displacement of the system with passive control is equal to 0.081 rad, which allows using the small displacement hypothesis, as this value is less than 0.174 rad (10^o).

4.3 Response due to step loading

Figure 10 shows the time history response of the structure for a step load considering the system with passive control and with hybrid control. The values of P, I, D and N found were P = 47.0, I = 12.6, D = 3.6 and N = 1716. The hybrid control shows rise time equal to 64.6 s and settlement time equal to 113 s.

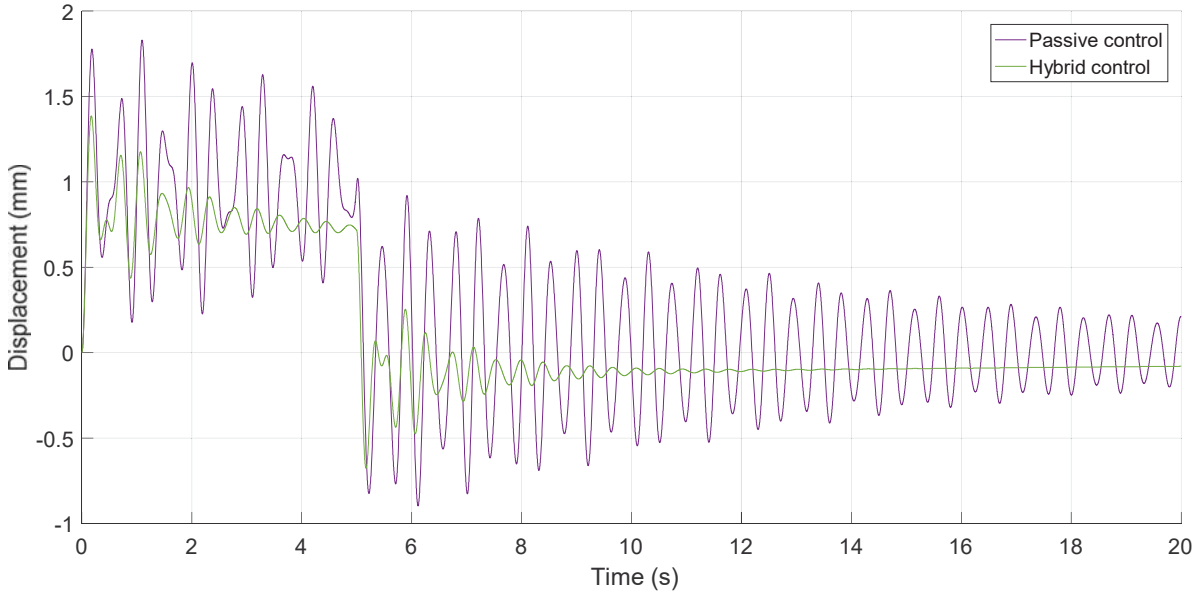

Figure 10: Displacement time history of the main system for step loading (TMD-IP and TMD-HIP).

Figure 11 shows the time history response using PID active control and PID hybrid control. The optimization of P, I, D and N values for active control is performed using the Simulink/MATLAB toolbox in order to approach the maximum response obtained using the two PID controllers. The values of the parameters found for PID active control are P = 49.8, I = 24.7, D = 3.5 and N = 2177. The active control shows a rise time equal to 33.1 s and a settlement time equal to 57.7 s.

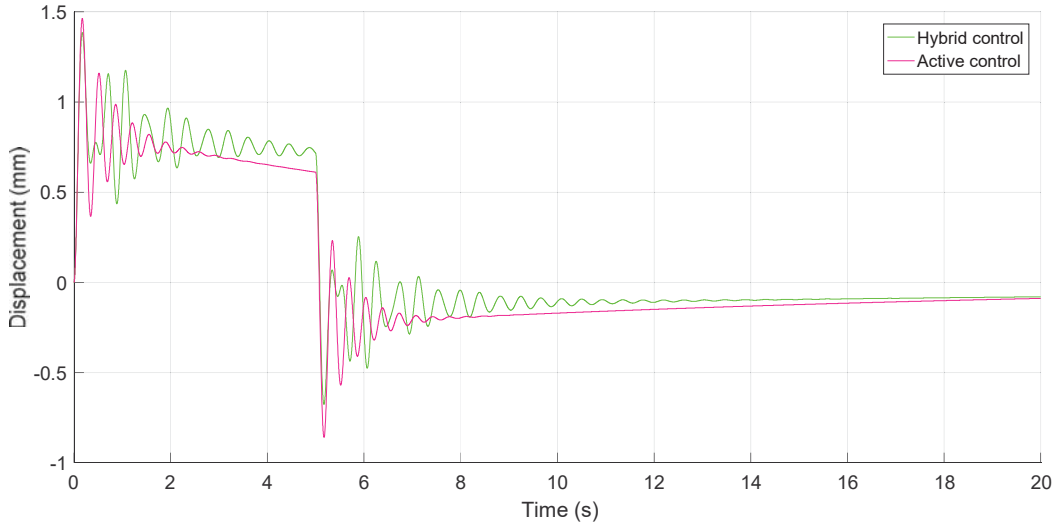

Figure 11: Displacement time history of the main system for step loading (AC and TMD-IP).

As the hybrid control shows better results than the passive control and PID active control, the response in the time domain is compared considering the system without control and with hybrid control as shown in Figure 12.

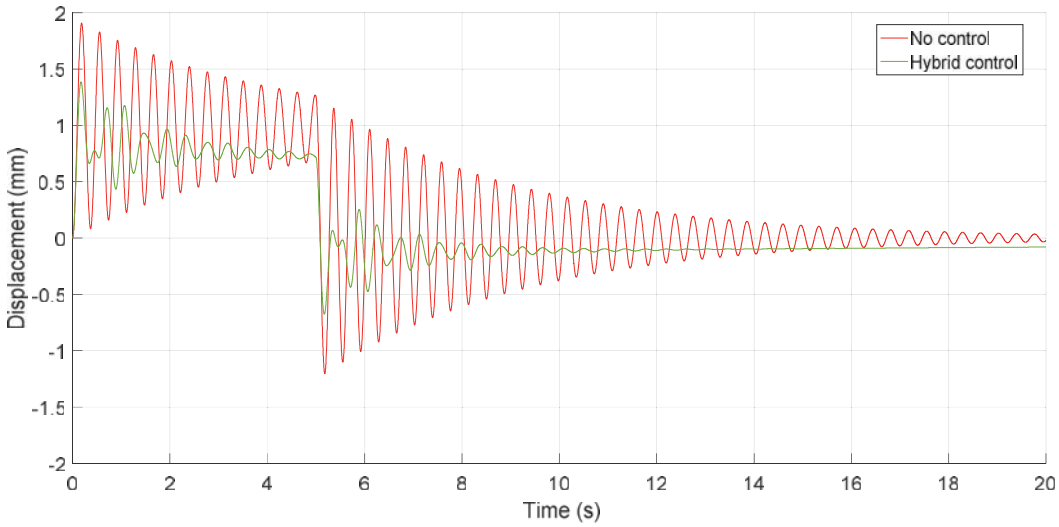

Figure12: Displacement time history of the main system for step loading (without control and TMD-IP).

Table 3 shows the maximum and RMS displacement values of the main system for the step loading case.

	No control	Passive control	Active control	Hybrid control
U_{max}(mm)	1.95	1.83	1.46	1.39
RMS(mm)	1.34	1.27	1.05	1.01

Table 3: Displacements due to step loading.

The system with passive control shows a reduction of 6.1% in the maximum displacement of the structure in relation to the system without control. The system with hybrid control presents a reduction of 28.7% and 24.0% in the displacement, respectively, compared to the system without control and the system with passive control. It is verified that there are ranges of time that the response of the system with passive control is lower than that of the hybrid control.

As for the PID controllers, although the maximum displacement between the active control and the hybrid control diverges by 3.96% during the transient phase, the hybrid control goes to zero faster than active control for longer times.

Despite the reduction in the amplitude response due to the step loading, when using the hybrid control, it is less than of the one due to the harmonic loading, the hybrid control is still an efficient alternative to attenuate vibrations due to step loadings.

Regarding to the RMS response, the system with passive control shows a reduction of 5.2% in relation to the system without control, while the system with hybrid control shows a reduction of 24.6% and 20.4%, respectively, in relation to the system without control and to the system with passive control.

The maximum control force obtained for the hybrid control is 0.09 N which represents only 27.5% of magnitude of external excitation. Therefore, the use of external energy is lower and because of this, the hybrid control system to minimize vibrations is a viable alternative in structures subjected to step loads. In the case of active control, it is found that to maintain the maximum displacement approximately equal to the one obtained with the hybrid control during the transient response, a control force of 0.12 N is required, which corresponds to 37.5% of the amplitude of the external excitation. Therefore, it is verified capability of the actuator needed when using active control is 33.3% higher than when using hybrid control.

The maximum angular displacement of the system with passive control is equal to 0.012 rad, being therefore less than 0.174 rad and allowing the use of the linear regime hypothesis for angular displacement.

5 CONCLUSIONS

In this work, the use of a TMD-HIP is studied, in order to verify the potential of this device. The analyses are performed using the parameters of the passive experimental model presented by Resende *et al.* [26]. Two loading cases are considered and the active control force is obtained through a PID controller.

Installing an inverted pendulum influences the modal proprieties of the system, while the addition of a PID controller does not change them. On the other hand, PID controller changes slightly resonant frequencies.

Passive control model reduces permanent response only in a frequency range when compared to the without control model. Although active control model presents the minimum peak permanent response, there is a specific frequency range where permanent amplitude response of the hybrid control is lower than that corresponding to the active control model.

Verifying the response in terms of maximum displacement, the use of hybrid control is shown as an efficient alternative, since it manages to reduce the maximum response by almost 85% when compared to the system without control.

In regard to RMS response, the hybrid control manages to reduce the response by almost 80% when compared to the system without control.

The required control forces vary from just 25% to 50% of amplitude of external actions, which can be considered satisfactory and feasible in practice.

The hybrid control shows better results to reduce the response of structures subjected to harmonic loading than to impulse loading, since in the case of step loads the structure needs an additional time to accommodate the response due to this type of excitation.

It is found that the TMD-HIP performs satisfactorily in reducing the translational response of the main system, with more significant reductions than the passive TMD-HIP presented by Resende *et al.* [26].

Compared to purely active control, the TMD-HIP leads to greater response reductions requiring small actuator force amplitudes.

For future work it is intended to implement this hybrid control in the experimental model. It is also worth mentioning that this device shows potential, based on more in-depth future studies for use on a real scale.

6 ACKNOWLEDGMENTS

The authors of this research are grateful for the financial support of the Foundation of Support to the Research of Federal District (FAPDF), the Post-Graduate Decanate of the University of Brasília (DPG-UnB), the Program of Alliances for Education and Training, the Organization of American States, the Coimbra Group of Brazilian Universities (PAEC-OEA/ GCUB) and the Coordination for the Improvement of Higher Education Personnel (CAPES).

REFERENCES

[1] S.M. Avila, Controle Híbrido para Atenuação de Vibrações em Edifícios, PhD Thesis*, Pontifical Catholic University of Rio de Janeiro, Brazil,* 2002. (In Portuguese).

[2] M.C. Constantinou, T.T. Soong, G.F. Dargush, Passive Energy Dissipation Systems in Structural Engineering, *John Wiley & Sons, Chichester*, 1998.

[3] J.J. Connor, Introduction to Structural Motion Control, *Prentice Hall*, 2002.

[4] D.V. Resende, Estudo Numérico-Experimental de Controle Utilizando um Pêndulo Invertido, *Master Thesis, University of Brasilia, Brazil*, 2018.

[5] J.E.C. Carmona, S. M. Avila, G. Doz, Proposal of a Tuned Mass Damper With Friction Damping to Control Excessive Floor Vibrations, *Engineering Structures,* 148, 81-100, 2017.

[6] S. Bagheri, V. Rahmani-Dabbagh, Seismic Response Control with Inelastic Tuned Mass Dampers, *Engineering Structures,* 172, 712-722, 2018.

[7] P.L. Bernardes, M.V.G. Morais, S.M. Avila, Experimental Study of an Inverted Tuned Mass Damper, *25th ABCM International Congress of Mechanical Engineering, Uberlandia, Brazil*, 2019.

[8] C.C. Kennedy, C.D.P. Pancu, Use of Vectors in Vibration Measurement and Analysis. *Journal of the Aeronautical Sciences*, 14, 11, 603-630, 1947.

[9] S.Y. Kim, C.H. Lee, Optimum Design of Linear Multiple Tuned Mass Dampers Subjected to White-Noise Base Acceleration Considering Practical Configurations. *Engineering Structures*, 171, 516-528, 2018.

[10] K. Majchern, Z. Wojcicki, Kinematically Excited Parametric Vibration of a Tall Building Model with a TMD—Part 1: Numerical Analyses. *Archives of Civil and Mechanical Engineering,* 14(1), 204-217, 2014.

[11] L.A. Martins, F.A. Lara-Molina, E.H. Koroishi, Optimal Design of a Dynamic Vibration Absorber with Uncertainties. *Journal of Vibration Engineering &Technologies*, 8, 133-140, 2019.

[12] Z. Shu, S. Li, X. Sun, M. He, Performance-Based Seismic Design of a Pendulum Tuned Mass Damper System, *Journal Earthquake Engineering*, 23, 334-355, 2019.

[13] G.B. Colherinhas, M.V.G. Morais, M.A.M. Shzu, S.M. Avila, Genetic Optimization of Tower Vibrations with Pendulum TMD. *COMPDYN 2015-5th ECCOMAS Thematic Conference on Computational Methods in Structural Dynamics and Earthquake Engineering, Crete Island, Greece*, 2015.

[14] G.B. Colherinhas, M.A.M. Shzu, S.M. Avila, M.V.G. Morais, Wind Tower Vibration Controlled by a Pendulum TMD using Genetic *Optimization: Beam Modelling, Procedia Engineering,* 199, 1623-1628, 2017.

[15] G.B. Colherinhas, M.V.G. Morais, M.A.M. Shzu, S.M. Avila, Optimal Pendulum Tuned Mass Damper Design Applied to High Towers Using Genetic Algorithms: Two-DOF Modeling, *International Journal of Structural Stability and Dynamics*, 19, 10, 1950125 (17 pages), 2019, doi.org/10.1142/S0219455419501256.

[16] A. Deraemaeker, P. Soltani, A Short Note on Equal Peak Design for the Pendulum Tuned Mass Dampers, *Proceedings of the Institution of Mechanical Engineers, Part K: Journal of Multi-Body Dynamics*, 2017.

[17] R.R. Gerges, B.J. Vickery, Optimum Design of Pendulum-Type Tuned Mass Dampers, *The Structural Design of Tall and Special Buildings*, 14, 353-368, 2005.

[18] R. Lourenco, Design Construction and Testing of an Adaptive Pendulum Tuned Mass Damper, *Master Thesis, Waterloo Ontario, Canada*, 2011.

[19] T. Nagase, T. Hisatoku, Tuned-Pendulum Mass Damper Installed in Crystal Tower. *The Structural Design of Tall Buildings*, 1, 35-56, 1992.

[20] F.S. Oliveira, A.L. Zuluaga, S.M. Avila, J.L.V. Brito, Design Criteria for a Pendulum Absorber to Control High Building Vibrations. *Journal of Innovations in Materials Science and Engineering*, 1, 82-89, 2014.

[21] N.D. Ahn, H. Matsuhisa, L.D. Viet, M. Yasuda, Vibration Control of an Inverted Pendulum Type Structure by Passive Mass-Spring-Pendulum Dynamic Vibration Absorber, *Journal of Sound and Vibration*, 307, 187-201, 2007.

[22] K. Ogata, Modern Control Engineering, *Prentice-Hall, New Jersey*, 2009.

[23] P.L. Bernardes, S.M. Avila, G.B. Colherinhas, M.V.G. Morais, Optimization of Inverted Pendulum Damper Parameters for Vibration Control in Tall Buildings, *XXXVIII Iberian-Latin American Congress on Computational Methods in Engineering, Florianópolis, Brazil, CILAMCE-0234*, 2017.

[24] P.V.B. Guimarães, M.VG. Morais, S.M. Avila, Tuned Mass Damper Inverted Pendulum to Reduce Offshore Wind Turbine Vibrations, *Vibration Engineering and Technology of Machinery, Mechanisms and Machine Science, Springer, Switzerland*, 23, 379–388, 2014.

[25] D.V. Resende, M.V.G. De Morais, S.M. Avila, Experimental Study of a Passive Inverted Pendulum Control System, *VETOMAC XIV MATEC Web of Conferences 211*, 02005, (6 pages), 2018, doi.org/10.1051/matecconf/201821102005.

[26] D.V. Resende, M. V. G. De Morais, S. M. Avila, Experimental Analysis of One-Degree-of-Freedom (1DoF) Dynamic System Controlled by Optimized Inverted Pendulum, *Journal of Vibration Engineering & Technologies*, 8, 2020, doi.org/10.1007/s42417-020-00198-2.

[27] P.V.B. Guimarães, Controle Semiativo de Modelo de Pendulo Invertido para Aergeradores Off-shore, *Master Thesis University of Brasilia, Brazil*, 2016. (In Portuguese).

[28] P.L.Bernardes Jr, Amortecedor Tipo Pendulo Invertido para Controle de Vibrações em Edifícios Altos, *Master Thesis, University of Brasilia, Brazil*, 2018. (In Portuguese).

[29] A. Di Matteo, C. Masnata, A. Pirrotta, Hybrid Passive Control Strategies for Reducing the Displacements at the Base of Seismic Isolated Structures, *Frontiers Built Environment*, 5:132, 2019, doi.org/10.3389/fbuil.2019.00132.

[30] S. Chesné, G. Inquieté, P. Cranga, F. Legrand, B. Petitjean, Innovative Hybrid Mass Damper for Dual-Loop Controller, *Mechanical Systems and Signal Processing*, 115*,* 514-523, 2019.

[31] C. Collete, S. Chesné, Robust Hybrid Mass Damper, *Journal of Sound and Vibration,* 375, 19-27, 2016.

[32] J. Salvi, E. Rizzi, E. Rustighi, N.S. Ferguson, On The Optimization of a Hybrid Tuned Mass Damper for Impulse Loading, *Smart Materials and Structures* 24 (8), 085010 (15 pages), 2015, doi.org/10.1088/0964-1726/24/8/085010

[33] A. Preumont, D. Alaluf, R. Bastaits, Hybrid Mass Damper: A Tutorial Example, Active and Passive Vibration Control of Structures. *CISM International Centre for Mechanical Sciences, Springer, Vienna*, 558, 179-211, 2014.

[34] T. Engle, H. Mahmoud, A. Chulahwat, Hybrid Tuned Mass Damper and Isolation Floor Slab System Optimized for Vibration Control, *Journal of Earthquake Engineering* 19, 1197-1221, 2015.

[35] B.F. Spencer, M.K. Sain, Controlling Buildings: A New Frontier in Feedback, *IEEE Control Systems Magazine on Emerging Technology*, 17, 6, 19-35, 1997.

[36] B.C. Kuo, Automatic Control System, *Prentice-Hall*, *New Jersey*, 2010.

EURODYN 2020
XI International Conference on Structural Dynamics
M. Papadrakakis, M. Fragiadakis, C. Papadimitriou (eds.)
Athens, Greece, 23–26 November 2020

A COMPARISON OF GAIN DESIGN CRITERIA FOR CLOSED-LOOP MODEL UPDATING

Lars Lynge Hansen[1], **Thomas Akselsen**[1], **Ünal Korkmaz**[1], **Martin Dalgaard Ulriksen**[2]

[1]M.Sc. Student, Aalborg University
Niels Bohrs Vej 8, 6700 Esbjerg, Denmark
e-mail: llha14@student.aau.dk, taksel15@student.aau.dk, akorkm15@student.aau.dk

[2] Department of Energy Technology, Aalborg University
Niels Bohrs Vej 8, 6700 Esbjerg, Denmark
e-mail: mdu@et.aau.dk

Keywords: Closed-loop model updating, output feedback, gain design

Abstract. *A conventional procedure for structural model updating is to solve an inverse problem with the aim of minimizing the discrepancy between an experimental target feature vector and a model-predicted one. The inverse problem to be solved is often ill-posed as the number of model parameters to be updated typically exceeds the number of target features. One way to confront this issue is to expand the target feature vector through closed-loop model updating, where gains are used to form multiple closed-loop eigenstructures from which target features are obtained. Besides confronting the ill-posedness of the inverse problem, the closed-loop model updating procedure also allows one to tailor the sensitivities of the target features by adequate design of the feedback gains. The present paper offers a comparative study in which the merit of different gain design criteria is examined for closed-loop sensitivity-based model updating. More specifically, the gains will be designed through eigenstructure assignment in an optimization setting where different cost functions, including the nuclear norm and the condition number of the sensitivity matrix, will be tested. Updating results will be shown for a numerical model of a shear building.*

1 INTRODUCTION

Within the fields of civil and mechanical engineering, numerical models are used extensively for structural design, analysis, health monitoring, and so forth [1]. In order to ensure adequate models, a selected subset of their parameters are updated to minimize the discrepancy between target features from the physical structure—for example, system poles, which are used in this paper—and the corresponding features predicted by the model. In this setting, the updating procedure involves solving an inverse problem, and an issue in this regard is that the number of updating parameters typically exceeds the number of identified poles, hence resulting in an under-determined system of equations. Furthermore, the sensitivities of the poles to the updating parameters are often relatively low [2, 3].

A suggested procedure to expand the target space, and hereby obtain a determined or over-determined system of equations, is to test the structure under known perturbations [4]. However, this approach suffers from its often limited practicality. In order to avoid testing under known perturbations, the use of output feedback to form multiple closed-loop systems has been proposed [5, 6, 7]. Different studies have examined the use of randomly generated gains to over-determine the system of equations [8, 9, 10], while another approach enables one to tailor the sensitivities through gain design in an eigenstructure assignment setting [11, 12]. The present paper addresses the latter by exploring the merit of different gain design criteria for sensitivity-based closed-loop updating of structural models. Specifically, four different criteria are examined; namely, maximization of three different norms of the sensitivity matrix and minimization of the condition number of the sensitivity matrix. The incentive for using each of the four criteria is outlined from a theoretical outset, and the performance is evaluated in the context of a comparative study with a numerical shear building model.

The paper is organized as follows: Section 2 presents the background theory of output feedback and eigenstructure assignment. The model updating procedure is outlined in section 3, section 4 describes the four gain design criteria, and section 5 contains a numerical examination of the merit of using the different criteria in closed-loop model updating. Finally, section 6 closes the paper with a conclusion.

2 OUTPUT FEEDBACK

A discrete-time, linear, and time-invariant state-space representation of a structural system is given by

$$x_{k+1} = A_d x_k + B_d u_k, \tag{1a}$$

$$y_k = C x_k, \tag{1b}$$

where $x_k \in \mathbb{R}^n$ is the state, $u_k \in \mathbb{R}^r$ the input, and $y_k \in \mathbb{R}^m$ the output, while $A_d \in \mathbb{R}^{n\times n}$, $B_d \in \mathbb{R}^{n\times r}$, and $C \in \mathbb{R}^{m\times n}$ are the system matrices. It should be noted that (1b) is only valid when measurements are displacements, velocities, non-collocated accelerations, or collocated accelerations if the direct transmission term is subtracted. Throughout this paper, it is assumed that one of the stated conditions is met.

When system (1) operates under static output feedback, the input is given by

$$u_k = -G y_k + v_k, \tag{2}$$

where $G \in \mathbb{R}^{r\times m}$ is the gain matrix and $v_k \in \mathbb{R}^r$ is some unmeasured excitation. Plugging (2) into (1) yields the closed-loop system

$$x_{k+1} = (A_d - B_d G C) x_k + B_d v_k, \tag{3}$$

with the non-defective closed-loop state matrix defined as $\bar{A} = A_d - B_d G C$.

2.1 Eigenstructure assignment

Let $\begin{Bmatrix} \lambda_1 & ... & \lambda_p \end{Bmatrix}$ denote a subset of $p \leq n$ closed-loop poles that are to be placed and $\Psi = \begin{bmatrix} \psi_1 & ... & \psi_p \end{bmatrix} \in \mathbb{C}^{n \times p}$ the corresponding eigenvectors. The eigenvalue problem of the closed-loop system (3) is given by

$$(A_d - B_d G C)\psi_j = \psi_j \lambda_j, \tag{4}$$

which can be rewritten into

$$\begin{bmatrix} A_d - I\lambda_j & -B_d \end{bmatrix} \begin{Bmatrix} \psi_j \\ GC\psi_j \end{Bmatrix} = 0. \tag{5}$$

By defining $Z = C \begin{bmatrix} \psi_1 & ... & \psi_p \end{bmatrix} \in \mathbb{C}^{m \times p}$ and $\Gamma = GC \begin{bmatrix} \psi_1 & ... & \psi_p \end{bmatrix} \in \mathbb{C}^{r \times p}$, it follows that

$$GZ = \Gamma, \tag{6}$$

so when the number of placed poles is equal to the number of outputs, the gain follows as

$$G = \Gamma Z^{-1}. \tag{7}$$

In the case of homogeneous sensing, Z is poorly conditioned, which will typically result in a subset of the unplaced poles being unstable [7]. To resolve the instability issue, (6) is over-determined by setting $p = n$ and then

$$GZW^{1/2} = \Gamma W^{1/2}, \tag{8}$$

where $W \in \mathbb{R}^{n \times n}$ is a diagonal weighting matrix with $\alpha_i > 1$ assigned to the subset of poles used in the updating and ones assigned to the rest. The weighted least-squares solution is then given by

$$G = \Gamma W^{1/2}(ZW^{1/2})^{\dagger} = \Gamma W Z^H (ZWZ^H)^{-1}, \tag{9}$$

where superscripts † and H denote the pseudo-inverse and Hermitian transpose, respectively.

3 MODEL UPDATING FORMULATION

Let $\Lambda_{\mathcal{S}}, \Lambda_{\mathcal{M}} \in \mathbb{C}^{qp}$ denote physically estimated and model-predicted poles for q different closed-loop systems, then the unknown parameters $\theta \in \mathbb{R}^s$ are estimated through the following constrained optimization problem:

$$\begin{aligned} &\arg\min_{\theta \in \mathbb{R}^s} ||\Lambda_{\mathcal{S}} - \Lambda_{\mathcal{M}}(\theta)||_2^2 \\ &\text{subject to} \quad \forall i \in [1, s] : \tau_i \leq \theta_i \leq \eta_i, \end{aligned} \tag{10}$$

where τ and η are lower and upper bounds on θ. The procedure is to form enough closed-loop systems to ensure that $qp \geq s$, such that the optimization problem is well-posed. Worth of explicit note is that the number of poles selected for each of the q gain can differ, but a fixed number, p, is assumed here to promote simplicity.

4 GAIN DESIGN

In order to obtain a determined or over-determined system of equations, q gains are designed and gathered in the compound gain matrix

$$\mathcal{G} = \begin{bmatrix} G_1 & G_2 & ... & G_q \end{bmatrix} \in \mathbb{R}^{r \times qm} \tag{11}$$

from which we place the poles

$$\Lambda = \begin{Bmatrix} \Lambda_{G_1} & ... & \Lambda_{G_q} \end{Bmatrix} \in \mathbb{C}^{qp}. \tag{12}$$

The design of $\mathcal{G}$ can be carried out on the basis of different criteria; of which the four outlined in subsection 4.2 are examined in the present paper. Regardless of what criterion one opts for, the general aim is to maximize the Fisher information that the target features carry on the model parameters to be updated.

4.1 Fisher information on updating parameters

For an observable variable, λ, that carries information on θ, the Fisher information matrix is defined as [13]

$$\mathcal{F} = -E\left(\frac{\partial^2 \ln(p(\lambda_i;\theta))}{\partial\theta_i \partial\theta_j}\right), \tag{13}$$

in which $E(\bullet)$ denotes the expected value of $\bullet$. Assuming that λ_i is Gaussian and that the covariance, Σ, does not depend on θ, the Fisher information matrix can be expressed as

$$\mathcal{F} = J_{\mathcal{G}}^H \Sigma^{-1} J_{\mathcal{G}}, \tag{14}$$

where $J_{\mathcal{G}} \in \mathbb{C}^{qp \times s}$ is the non-defective sensitivity matrix

$$J_{\mathcal{G}} = \begin{bmatrix} J_{G_1} \\ \vdots \\ J_{G_q} \end{bmatrix} = \begin{bmatrix} \frac{\partial \Lambda_{G_1}}{\partial \theta} \\ \vdots \\ \frac{\partial \Lambda_{G_q}}{\partial \theta} \end{bmatrix}. \tag{15}$$

4.2 Gain design criteria

The present subsection outlines four gain design criteria that aim to maximize the model parameter estimation accuracy by increasing the inherent Fisher information. The merits of the criteria are explored and compared in a numerical example in section 5.

4.2.1 Nuclear norm

If $\Sigma = \gamma I$, which is often assumed with $\gamma \in \mathbb{R}^+$, then $\mathcal{F} \propto J_{\mathcal{G}}^H J_{\mathcal{G}}$. This suggests to design the gains such that

$$\tilde{\mathcal{G}} = \arg\max_{\mathcal{G}} \|J_{\mathcal{G}}\|_*, \tag{16}$$

where $\tilde{\mathcal{G}}$ is the optimal gain based on the cost function and $\|J_{\mathcal{G}}\|_*$ is the nuclear norm,

$$\|J_{\mathcal{G}}\|_* = \text{trace}\left(\sqrt{J_{\mathcal{G}}^H J_{\mathcal{G}}}\right) = \left\| \begin{matrix} \sigma_1 \\ \vdots \\ \sigma_{qp} \end{matrix} \right\|_1 \tag{17}$$

with σ_i being the i'th singular value of $J_{\mathcal{G}}$. It is worth mentioning that this norm promotes sparsity.

4.2.2 Frobenius norm

The Frobenius norm, which is given by

$$\|J_{\mathcal{G}}\|_F = \sqrt{\text{trace}(J_{\mathcal{G}}^H J_{\mathcal{G}})} = \left\| \begin{matrix} \sigma_1 \\ \vdots \\ \sigma_{qp} \end{matrix} \right\|_2, \tag{18}$$

also contains the dot product of the sensitivity matrix, thus a cost function is formulated as

$$\tilde{\mathcal{G}} = \arg\max_{\mathcal{G}} \|J_{\mathcal{G}}\|_F. \tag{19}$$

Note that, unlike the nuclear norm, the Frobenius norm does not promote sparsity.

4.2.3 Individual gain evaluation

The cost functions based on the nuclear and Frobenius norms aim to increase the sensitivity by maximizing the ℓ_1- and ℓ_2-norms of the singular values of the sensitivity matrix. Another approach is to design gains individually, where each gain increases sensitivity to a specific parameter by maximizing the ℓ_2-norm of the associated column in the sensitivity matrix. Hence,

$$\tilde{G}_i = \arg\max_{G_i} \|J_{G_{i_{\bullet i}}}\|_2, \tag{20}$$

such

$$\tilde{\mathcal{G}} = [\tilde{G}_1 \dots \tilde{G}_q]. \tag{21}$$

4.2.4 Condition number

The model updating formulation (10) is solved iteratively on the basis of the linearized Taylor approximation

$$J_{\mathcal{G}}(\theta^{(i+1)} - \theta^{(i)}) = \Lambda_{\mathcal{S}} - \Lambda_{\mathcal{M}}^{(i)}. \tag{22}$$

Evidently, the parameter estimation involves (pseudo-)inversion of $J_{\mathcal{G}}$, thus a cost function is defined as

$$\tilde{\mathcal{G}} = \arg\min_{\mathcal{G}} \kappa(J_{\mathcal{G}}), \tag{23}$$

where $\kappa(J_{\mathcal{G}})$ is the condition number of the sensitivity matrix.

5 NUMERICAL EXAMPLE

The merit of the four cost functions for gain design is tested numerically by comparing model updating results for the 10-level shear building shown in figure 1. We refer to a *target model* and *nominal model*, with the latter being the one to be updated. Mass, damping, and stiffness values for the nominal model are shown in figure 1. The target model, which in this example replaces a physical system, is identical to the nominal model except for inter-story stiffness reductions of 10 % and 5 % at the first and second floor, respectively. Two sine sweep inputs, which only excite the first open-loop mode, are applied at floor one and two, while outputs are taken as displacements at floor two, four, six, and eight with a sampling frequency of 100 Hz. The outputs are imposed with 2 % Gaussian white noise, and the system identification is performed

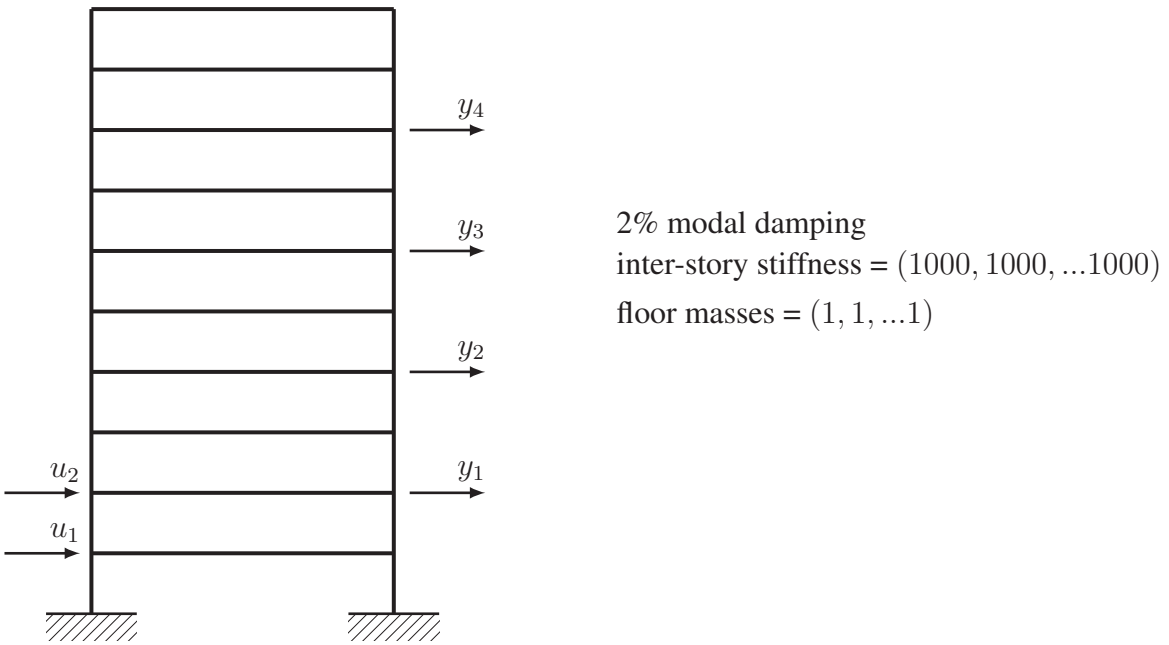

Figure 1: Nominal model of the structure for the numerical example.

using a subspace identification algorithm [14]. The model updating analysis is performed in a Monte Carlo setting with 1000 simulations, where the first closed-loop pole is extracted as target feature. The inter-story stiffnesses between floor one, two, and three are chosen as the updating parameters, thus three gains are designed in order to obtain a determined system of equations for the model updating. The gains are designed with the cost functions defined in section 4.2, and the optimization is carried out using a genetic algorithm (GA). For more information on GAs, the reader is referred to [15].

The closed-loop poles are placed using (9), where the constraints listed below are applied. The first constraint ensures stability, the second ensures that the poles can be estimated, the third limits the damping, and the fourth provides the lower and upper bounds on θ. For the selected τ and η, it has been numerically verified that the nominal and target models both comply with the other constraints.

- $\mathbb{R}(\lambda_{\mathcal{S}}) < 0$
- $|\mathbb{I}(\lambda_{\mathcal{S}})| > 1$
- $\frac{-\mathbb{R}(\lambda_{\mathcal{S}})}{|\lambda_{\mathcal{S}}|} < 0.1$
- $\tau = 0.80$ and $\eta = 1.20$.

The model updating is carried out by minimization of (10) using the "fmincon"-algorithm in MATLAB®. Converged parameter estimation results are shown in figure 2 and listed in tables 1-2 for the under-determined open-loop formulation and the determined closed-loop formulations using each of the four gain design criteria. Evidently, the model parameters do not converge to the exact values for the open-loop formulation or the closed-loop ones based on the nuclear and Frobenius norms as gain design criteria. The parameter estimation fails when using either the nuclear or Frobenius norm to design $\mathcal{G}$, because a subset of the closed-loop poles are approximately equal, which results in an ill-conditioned sensitivity matrix. For the

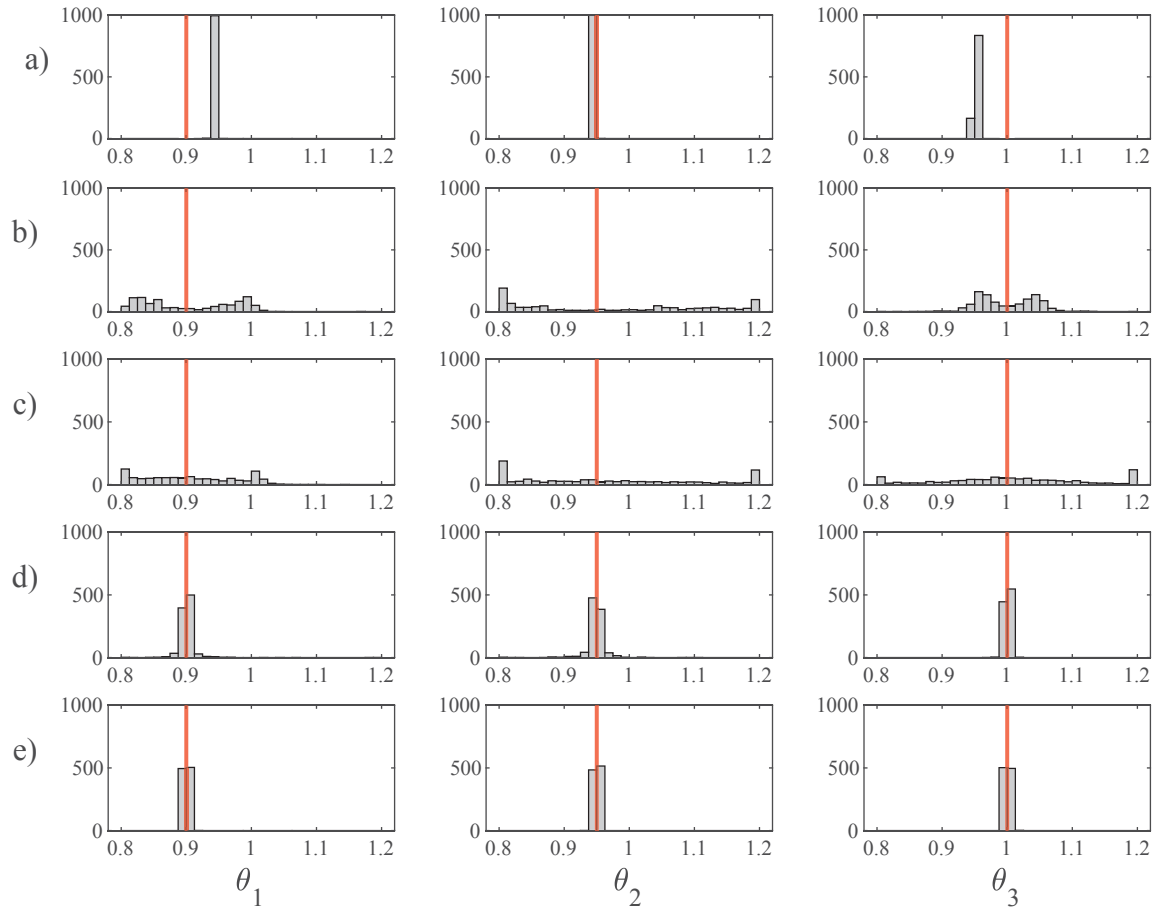

Figure 2: Estimation results for θ_i in a) open loop and in closed loop using gains designed based on b) nuclear norm, c) Frobenius norm, d) individual, and e) condition number. The exact θ_i-values are indicated with a red vertical line.

cost function that minimizes the condition number of the sensitivity matrix, the mean values are converged to the exact θ_i-values and with standard deviations comparable to those obtained in open loop. Evidently, the condition number-based cost function allows for the most accurate parameter estimation.

	E(θ_i)				
	Open-loop	Nuclear	Frobenius	Individual	Condition number
θ_1	0.943	0.904	0.907	0.902	0.900
θ_2	0.945	0.976	0.969	0.949	0.950
θ_3	0.950	0.999	1.010	1.000	1.000

Table 1: Mean values for the updated θ_i-values. The exact values are $\theta_1 = 0.9$, $\theta_2 = 0.95$, and $\theta_3 = 1$.

	std.(θ_i)				
	Open-loop	Nuclear	Frobenius	Individual	Condition number
θ_1	0.001	0.071	0.073	0.019	0.001
θ_2	0.001	0.146	0.137	0.018	0.002
θ_3	0.001	0.045	0.112	0.002	0.002

Table 2: Standard deviations for updated θ_i-values.

6 CONCLUSION

The paper offers a comparative study in which the merit of different gain design criteria is examined for closed-loop model updating. Gains are designed through eigenstructure assignment in an optimization setting where different cost functions are tested numerically in the context of a 10-level shear building. The gains are designed in order to maximize the parameter estimation accuracy, and the numerical example shows that, out of the four gain design criteria explored in this study, minimizing the condition number of the sensitivity matrix yields the most accurate parameter estimates.

REFERENCES

[1] M.I. Friswell, J.E. Mottershead, ”Finite element model updating in structural dynamics”, Kluwer Academic Publishers, 1995.

[2] B.H. Koh, L.R. Ray, ”Feedback controller design for sensitivity-based damage localization”, *Journal of Sound and Vibration*, 273(1), 317-335, 2004.

[3] M.D. Ulriksen, D. Tcherniak, P.H. Kirkegaard, L. Damkilde, ”Operational modal analysis and wavelet transformation for damage identification in wind turbine blades”, *Structural Health Monitoring*, 15(4), 381–388, 2016.

[4] N.G. Nalitolela, J.E.T. Penny, M.I. Friswell, ”A mass or stiffness addition technique for structural parameter updating”, *The International Journal of Analytical and Experimental Modal Analysis*, 7(3), 157-168, 1992.

[5] L.R. Ray, L. Tian, ”Damage detection in smart structures through sensitvity enhancing feedback control”, *Journal of Sound and Vibration*, 227(5), 987-1002, 1999.

[6] L.J. Jiang, J.J. Tang, K.W. Wang, ”An Optimal Sensitivity-Enhancing Feedback Control Approach via Eigenstructure Assignment for Structural Damage Identification”, *Journal of Vibration and Acoustics*, 129(6), 771-783, 2007.

[7] M.D. Ulriksen, D. Bernal, ”Output feedback in the design of eigenstructures for enhanced sensitivity”, *Mechanical Systems and Signal Processing*, 112, 22-30, 2018.

[8] M.D. Ulriksen, D. Bernal, ”On the use of complex gains in virtual feedback for model updating”, Proceedings of the International Conference on Structural Engineering Dynamics (ICEDyn) 2019, Viana do Castelo, Portugal.

[9] M.S. Jensen, T.N. Hansen, M.D. Ulriksen, D. Bernal, ”Physical and Virtual Implementation of Closed-loop Designs for Model Updating”, In book: Proceedings of the 13th International Conference on Damage Assessment of Structures, Springer, 363-371, 2020.

[10] T.N. Hansen, M.S. Jensen, M.D. Ulriksen, D. Bernal, ”On the model order in parameter estimation using virtual compensators”, In book: Proceedings of the 13th International Conference on Damage Assessment of Structures, Springer, 498-506, 2020.

[11] D. Bernal, M.D. Ulriksen, ”Virtual Closed Loop Parameter Estimation: A Review”. Proceedings of the International Conference on Structural Engineering Dynamics (ICEDyn) 2019, Viana do Castelo, Portugal.

[12] M.D. Ulriksen, D. Bernal, ”On Gain Design in Virtual Output Feedback for Model Updating”, In book: Proceedings of the 13th International Conference on Damage Assessment of Structures, Springer, 372-379, 2020.

[13] S.M. Kay, ”Fundamentals of statistical signal processing: Estimation theory”, Prentice Hall, 1993.

[14] P.V. Overschee, B.D. Moor, ”Subspace identification for linear systems”, Kluwer Academic Publishers, 1996.

[15] M. Mitchell, ”An introduction to genetic algorithms”, The MIT Press, 1996.

EURODYN 2020
XI International Conference on Structural Dynamics
M. Papadrakakis, M. Fragiadakis, C. Papadimitriou (eds.)
Athens, Greece, 23–26 November 2020

ADEQUACY OF ACCIDENTAL ECCENTRICITY IN ACCOUNTING FOR THE EFFECTS OF THE TORSIONAL COMPONENT OF EARTHQUAKES ON THE SEISMIC DAMAGE

Konstantinos E. Morfidis[1], Konstantinos G. Kostinakis[2], and Nikolaos G. Pneymatikos[3]

[1] Assistant Researcher, EPPO-ITSAK
55535 Pylaia, Thessaloniki, Greece
kmorfidis@itsak.gr

[2]Assistant Professor, Aristotle University of Thessaloniki
54124 Thessaloniki, Greece
kkostina@civil.auth.gr

[3]Associate Professor, University of West Attica
12243 Athens, Greece
pnevma@uniwa.gr

Keywords: seismic rotational components, seismic torsional component, seismic rocking components, r/c structures, seismic damage, eccentricity effects

Abstract. *The influence of the torsional component of earthquake excitations on the response of reinforced concrete (R/C) structures is the aim of this work. The structure that is going to be examined is asymmetric in plan and regular in elevation 5-storey R/C building. In most studies, seismic input is modeled only using the translational components of the ground acceleration, while the torsional one is ignored. This is due to the observation that the torsional component has minimal effect on low-rise buildings. Hence, the accelerometers used would not measure it, leading to a lack of records. Nowadays, technology provides such instruments and relative records have been made available. Indicative of this is that design response spectra for rotational components are introduced in the design codes. In this paper, nonlinear dynamic time history analyses of the selected R/C building are performed (a) considering the torsional component of the excitation and (b) without it. From the numerical results it is shown that the impact of torsional component in structural response must be taken into account. Moreover, the extracted results indicate that the provided by Eurocodes values for the accidental eccentricity can effectively capture the effects of the torsional component on the seismic damage.*

1 INTRODUCTION

Generally, the seismic analysis and design of new buildings, as well as the assessment of the seismic performance of existing ones, are only conducted by applying the translational components of earthquakes, thus ignoring the effects of the rotational components on the structural response. The main reason for the above assumption is the fact that earthquake records that include rotational components were not available since the last years, because these components are difficult to be recorded by accelerographs in the free field. Thus, some researchers attempted to derive rotational components by combining mathematical equations with the properties of surface and body waves and geological parameters of soil. Nevertheless, during the last years it has been made feasible to record real ground motion with rotational components too. The rotational components of an earthquake record consist of the torsional component, which is the rotation about vertical axis, and the other two rocking components, which are the rotations about the two horizontal axes. The effects of these components of earthquakes on structures have been studied by a number of investigators and it was found that their contribution may significantly affect the seismic response and the damage of structures.

A lot of seismology scientists focus on rotational records over the last years. Droste and Teisseyre [1] using the signals taken from an array of seismographs calculated the rotational excitations. Takeo [2] using a gyro-sensor with combination of inertial angular displacement sensor measure the rotation motion during an earthquake happened in April 1998 in Japan. Advances in rotational seismology about instrumentation, theory and observations are presented in the work of Igel et al. [3]. More cheaper sensors based on electrochemical magnetohydrodynamic technology used from Liu et al. [4] and Wassermann et al. [5]. There are a lot of procedures that calculate rotational time series from translational recordings. A Single Station Procedure (SSP), is one of them. A number of researchers such as Lee and Trifunac [6], Castellani and Boffi [7], Li et al. [8] and Basu et al. [9], presented their work based on SSP. Site soil conditions are connected with rotations earthquake excitations. This link is proposed in the work of Sbaa et al. [10]. Perron et al. [11] show that the interaction of translation and rotation records seems to be useful, for engineering seismology applications and for investigation of the composition of the wavefield and this has a result to avoid a deployment of dense arrays.

Considering the torsional component, current seismic code provisions allow to ignore it when conducting the seismic analysis (with the exception of special structures e.g. towers, masts and chimneys, see [12]), but they recommend the shifting of mass center in order to account for the effects of this component on the seismic response. The shifting of mass center is achieved with the aid of the accidental eccentricity. Bozev et al. [13], performed analysis accounting the rotational components of seismic action on towers, masts and chimneys according to EN1998-6. Zembaty [14], work on rotational seismic code definition in EN1998-6, for slender tower-shaped structures. Zembaty and Boffi [15], apply response spectrum analysis using horizontal and rotational spectra described in Eurocode, and show the effect of rotational excitation to moments diagram along the height of a tall tower.

A lot of works investigated the effect of rotational components of ground motion on structural response. The influence of rotational components on a base-isolated nuclear power plant was investigated by Wolf et al. [16]. Furthermore, rotational components of near-fault earthquakes effects on triple concave friction pendulum base-isolated asymmetric structures is investigated by Tajammolian et al. [17]. Another application of rotational excitation in a base-isolated building and the rocking mode identification was done by Politopoulos [18]. A simplified relation for the application of rotational components to seismic design codes and calculation of response of multiple-support structures subjected to horizontal and rocking components are presented in references [19], [20]. Basu et al. [21], [22], suggests an equivalent accidental eccentricity to account for the effects of torsional ground motion on structures.

Torsion in building due to base rotational excitation was investigated by De-La-Llera and Chopra, [23]. Yin et al. performed earthquake time history analysis using recorded rotation ground excitation at a structure [24]. A parametric study on the effect of rotational ground motions on building structural responses is also examined by Vicencio and Alexander [25].

In the present paper the adequacy of the accidental eccentricity as a parameter to capture the effects of the torsional component on the seismic damage is further investigated. For this purpose, one 3D asymmetric 5-storey R/C building with structural system consisting of frames and walls is examined. The building is analyzed with the aid of nonlinear time-history analysis using an adequate number of real ground motions with translational and torsional components. Two different categories of structural models for the building and the seismic excitation are investigated: a) a model taking into account the translational and the torsional components of the seismic motion applied to the mass center of the building and b) models taking into account only the translational components of the seismic motion, but using different values of the accidental eccentricity. Then, a comparison between the above models is carried out in order to examine the effectiveness of the accidental eccentricity in capturing the effects of torsional component of seismic motion. Useful results are derived concerning the effectiveness of the specific Eurocode provisions as regards the proposed values for accidental eccentricities.

2 THE EXAMINED BUILDING: DESCRIPTION - MODELING - DESIGN

The data of the building which was used in the present investigation are outlined in Fig. 1. This building is asymmetric in plan but regular in elevation according to the EN1998-1 [26].

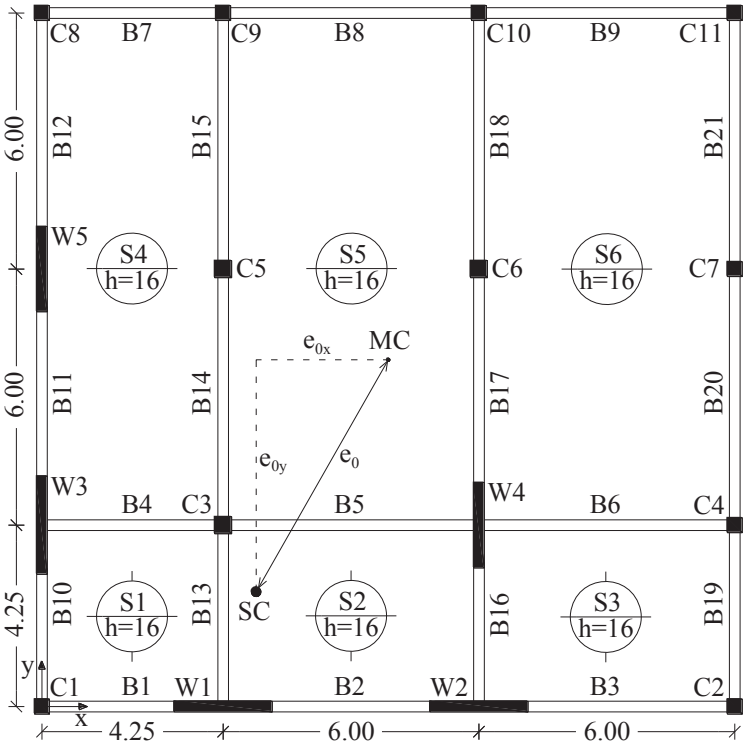

Dimensions of the cross-sections of R/C members (b/h):

Storey	Height	Beams (in cm)
1^{st}-2^{nd}	3.2m	25/55
3^{rd}-4^{th}	3.2m	25/50
5^{th}	3.2m	20/45

Storey	Columns	Walls
1^{st}-3^{rd}	35/35 (C3,C5, C6: 40/40)	W1,W2, W3: 230/25
4^{th}-5^{th}	30/30	W4,W5: 200/25

Behavior factor: q=3.0

Structural eccentricities e_{0x}, e_{0y}, torsional radii r_x, r_y, and Radius of gyration l_s:

e_{0x}(m)	e_{0y}(m)	r_x(m)	r_y(m)	l_s(m)
3.1	5.44	7.87	9.44	6.7

MC: Mass Center
SC: Stiffness Center

Structural type / Ductility class	Ductile Wall System / Medium (DCM)
Concrete / Steel	C20/25 / S500B
Slab loads	Dead G=1.0kN/m^2, Live Q=2.0kN/m^2
Masonry loads	Perimetric beams 3.6kN/m^2, Internal beams 2.1kN/m^2
Design spectrum for elastic analysis (§2.2.2.5 of EN1998-1)	Reference PGA a_{gR}=0.24g; Importance class: II $\rightarrow \gamma_I$=1 $\rightarrow a_g$=0.24g (Ground type: C)

Figure 1: Data of the examined 5-storey R/C building

In the framework of design the examined building was analyzed for static loads (1.35G+1.50Q) and for seismic loads (G+0.3Q±E, taking into consideration the accidental torsion effects) using the elastic modal response spectrum analysis, as defined in EN1998-1 [26]. The R/C members were designed following the provisions of EN1992-1-1 [27] and EN1998-1 [26]. As regards the modeling of building the following assumptions (compatible to the provisions of EN1988-1) were made:

- The floor slabs were assumed to act as rigid diaphragms,
- The beam-wall joints were modeled as perfectly rigid,
- The building was considered to be fully fixed to the ground,
- The infill walls were considered only as vertical loads and not as seismic resistant structural elements,
- The flexural and shear stiffness properties of the R/C members' cross-sections were considered to be equal to one-half of the corresponding stiffness of the uncracked ones.

As regards the modeling in the framework of the nonlinear time history analyses, for the R/C structural elements' nonlinear behavior force-based beam-column elements were implemented in OpenSees software [28], using a 5-point Gauss – Lobato integration scheme. Fiber sections, describing exactly the reinforcement detailing were assigned to the beam, column and wall elements. In addition, appropriate material constitutive laws (according to EN1992-1-1 and EN1998-1) were utilized for the steel rebar, the unconfined and confined concrete regions respectively.

3 THE SEISMIC RECORDS

The building models were subjected to the 6.4 moment magnitude, M_w, earthquake excitation (mainshock) which happened at 2015/11/17 in Kefalonia Island, Greece, as well as to six of the aftershocks of the seismic sequence (in total 7 earthquake records according to provisions of EN1998-1). The mainshock's epicenter latitude and longitude were 38.16^o and 20.50^o degrees respectively. The event depth was 10.7 km. The record history of translational and torsional component was provided by by Argonet project, a 3D accelerometric array implemented on the island of Kefalonia in Greece, [10], [[11] and is ostensive shown in Fig. 2.

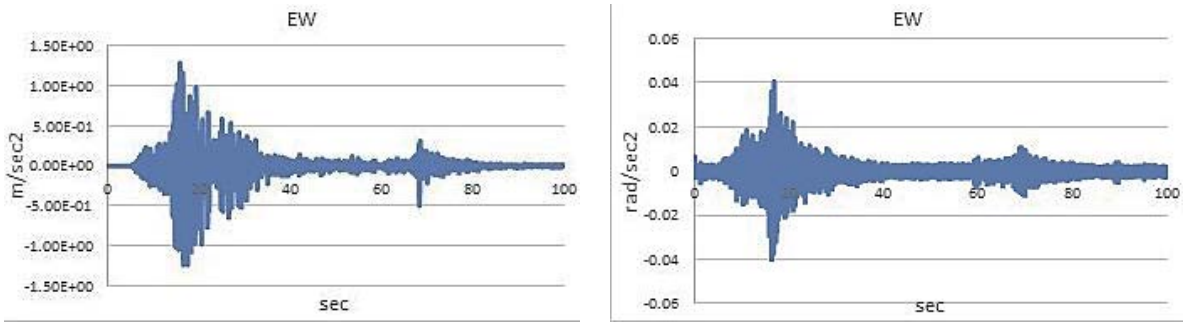

Figure 2: Two components of the mainshock: translational and torsional ones.

4 DESCRIPTION OF THE PARAMETRIC INVESTIGATION

The procedure followed in order to accomplish the aim of the present study comprises of a series of analyses of the selected building, according to the following characteristics:

- Nonlinear time history analyses using the 7 selected seismic records with 2 (only translational) or 3 (2 translational and 1 rotational) components.
- Application of the (2 or 3) seismic components of each record to the Mass Center of the building (MC), as well as to positions at distances from the MC equal to the following

values of accidental eccentricity: e_a=±0.025L, e_a=±0.05L, e_a=±0.1L και e_a=±0.2L. The aforementioned distances are measured along the line that connects the MC with the Stiffness Center (SC) of the building, whereas L denotes the building's dimension along the diagonal of its plan view. The description of the abovementioned distances is given in Fig. 3.

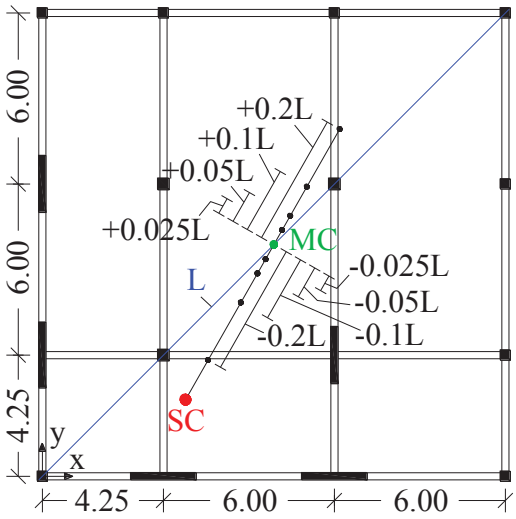

Figure 3: Positions of application of the 2 (or 3) components of the seismic records

- In order to account for two different seismic intensities corresponding to certain performance levels suggested by EN1998-3 (§2.1) [29], the accelerograms were scaled to two different values of Peak Ground Acceleration (PGA). More specifically, the scaling factors adopted in the present study correspond to the following performance levels:

a) Performance level of Significant Damage (SD). According to EN1998-3 (§2.1(3)P) this performance level corresponds to a reference return period of 475 years, which, in turn, corresponds to PGA=a_g·S=0.276g, where a_g=0.24g and S=1.15 are the design ground acceleration and the soil factor respectively used for the elastic analysis of the buildings (EN1998-1 (§3.2.1(3) and §2.1(4)) and the Greek National Annex). So, in this case the 7 selected records were scaled to PGA=0.276g.

b) Performance level of Near Collapse (NC). According to EN1998-3 (§2.1(3)P) this performance level corresponds to a reference return period of 2475 years, which, in turn, corresponds to PGA=1.72·a_g·S=0.475g (EN1998-1 (§3.2.1(3) and §2.1(4)) and the Greek National Annex). So, in this case the selected 7 records were scaled to PGA=0.475g.

For each one of the 7 seismic records the following analyses were conducted (Table 1):

A/A	Accidental Eccentricity e_a	Number/Type of excitations
1,2	±0.025L	3 / (2 translational + 1 torsional)
3,4	±0.05L	3 / (2 translational + 1 torsional)
5,6	±0.10L	3 / (2 translational + 1 torsional)
7,8	±0.20L	3 / (2 translational + 1 torsional)
9,10	±0.025L	2 / (2 translational)
11,12	±0.05L	2 / (2 translational)
13,14	±0.10L	2 / (2 translational)
15,16	±0.20L	2 / (2 translational)
17	0	2 / (2 translational)
18	0	3 / (2 translational + 1 torsional)

Table 1: Parameters of analyses for each one of 7 selected records and performance levels (NC and SD)

Consequently, in total 252(=7·18·2) nonlinear time history analyses were conducted.

With regard to the damage measures that were used, the following parameters were chosen, the use of which has been well documented in the relative literature:

- Maximum interstorey drift ratios along building's axes X, Y (Fig. 1).
- Maximum roof rotations about the vertical axis of the building (axis Z).
- Maximum roof accelerations along building's axes X, Y (Fig. 1).

5 RESULTS

In the current section the main results extracted from the parametric investigation (section 4) are presented and discussed. The Figures 4, 5 and 6 illustrate the ratios of maximum values of the examined seismic Response Parameters (RP), (i.e. the values of interstorey drifts along the axes X (DrX) and Y (DrY), the rotations of floors considered as rigid diaphragms about the vertical axis Z (Rz) and the accelerations of floors along the axes X (AccX) and Y (AccY)) extracted from analyses performed considering 3 components of seismic excitation (the two translational and the torsional) applied to MC(e_a=0) and the corresponding values exported from analyses performed considering the 2 translational components of seismic excitation and several values for the accidental eccentricity (e_a≠0, see Fig. 3). More specifically, the values of the ratios of the examined RP in Figs. 4, 5, 6 are calculated by means of Eq. (1).

$$\frac{RP(e_a=0)}{RP(e_a\neq 0)}=\frac{(1/7)\cdot\sum_{i=1}^{7}\left\{\max\left[RP_{storey1,\dots},RP_{storey5}\right]_{i,e_a=0}\right\}}{(1/7)\cdot\sum_{i=1}^{7}\left\{\max\left[RP_{storey1,\dots},RP_{storey5}\right]_{i,e_a\neq 0}\right\}} \quad \left[\begin{array}{l}RP=DrX,\ DrY,\ Rz,\ AccX,\ AccY,\\ \max(Drx,DrY),\max(Accx,AccY)\end{array}\right] \tag{1}$$

Where: i is the seismic record (i=1÷7), e_a=0 indicates the analyses of the building considering 3components of excitation (the two translational and the torsional) applied to MC, and e_a≠0 indicates the analyses of the building considering 2 components of excitation (only the translational components) and several values for the accidental eccentricity (i.e. e_a=±0.025L, ±0.05L, ±0.10L and ±0.20L).

It is obvious that when the values of these ratios tend to 1.00 then the analyses in which the 2 translational seismic components and accidental eccentricities are considered (e_a≠0) export almost equal values of RPs with the corresponding analyses in which 3 seismic components are considered in MC (e_a=0).

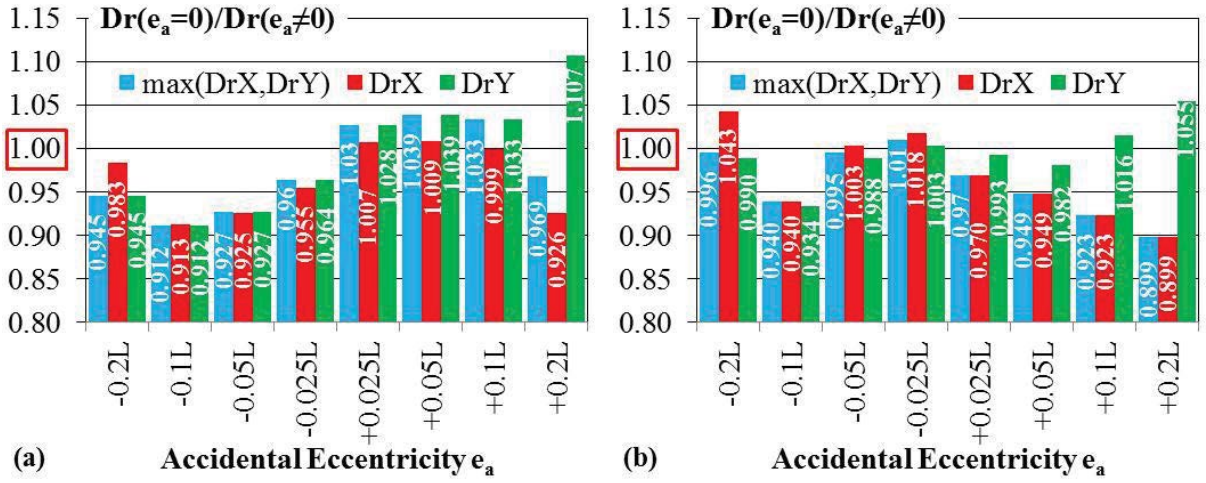

Figure 4: Ratios of the maximum interstorey drifts along the direction of X (DrX), Y (DrY) axes and max(DrX, DrY) extracted by analyses performed considering 3 seismic components applied to MC (e_a=0) and those extracted by analyses performed considering 2 seismic components in several distances from MC (e_a≠0): (a) Performance level SD, (b) Performance level NC

Fig. 4 illustrates the ratios of interstorey drifts DrX, DrY and the maximum values between them max(DrX,DrY). More specifically, the Fig. 4(a) presents the ratios which correspond to analyses conducted considering the performance level SD, whereas the Fig. 4(b) presents the ratios extracted considering the performance level NC. The study of this figure leads to the following main conclusions:

- The values of accidental eccentricity e_a for which the analyses conducted considering the two translational seismic components lead to ratios $Dr(e_a=0)/Dr(e_a\neq0)$ close to 1 fluctuate between +0.025L and +0.1L in case of performance level SD. The corresponding range of values of e_a in case of analyses for performance level NC is between -0.05L and -0.025L.
- Generally, the higher values of $e_a(=\pm0.2L)$ fail to lead to values of ratios $Dr(e_a=0)/Dr(e_a\neq0)$ close to 1. Exception to this conclusion is the value -0.2L in case of performance level NC.

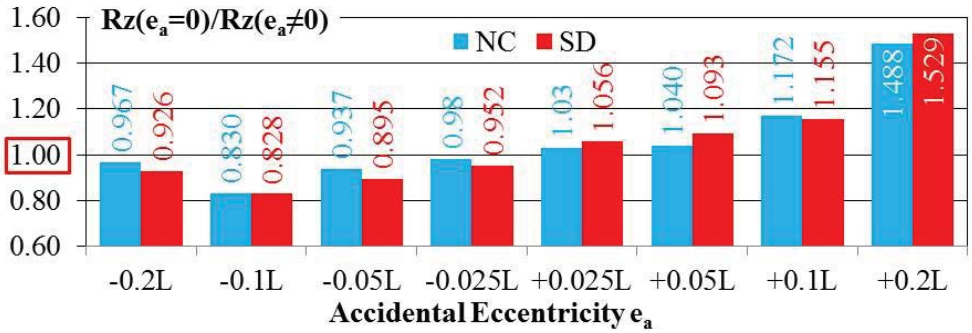

Figure 5: Ratios of the maximum floor rotations about the vertical axis Z (Rz) extracted by analyses performed considering 3 seismic components applied to MC ($e_a=0$) and those extracted by analyses performed considering 2 seismic components in several distances from MC ($e_a\neq0$).

Fig. 5 illustrates the ratios of the floor rotations about the vertical axis Z ($Rz(e_a=0)/Rz(e_a\neq0)$) extracted from analyses for performance levels NC and SD. The main conclusions that can be drawn from this figure are the following:

- The values of accidental eccentricities e_a which lead to values of ratios $Rz(e_a=0)/Rz(e_a\neq0)$ closer to 1 are located between -0.025L and +0.05L. Thus, as in case of ratios $Dr(e_a=0)/Dr(e_a\neq0)$ the smaller values of e_a are more effective than the larger ones.
- No significant diversification is observed between the results of analyses for performance levels NC and SD as regards the relation e_a–$Rz(e_a=0)/Rz(e_a\neq0)$.

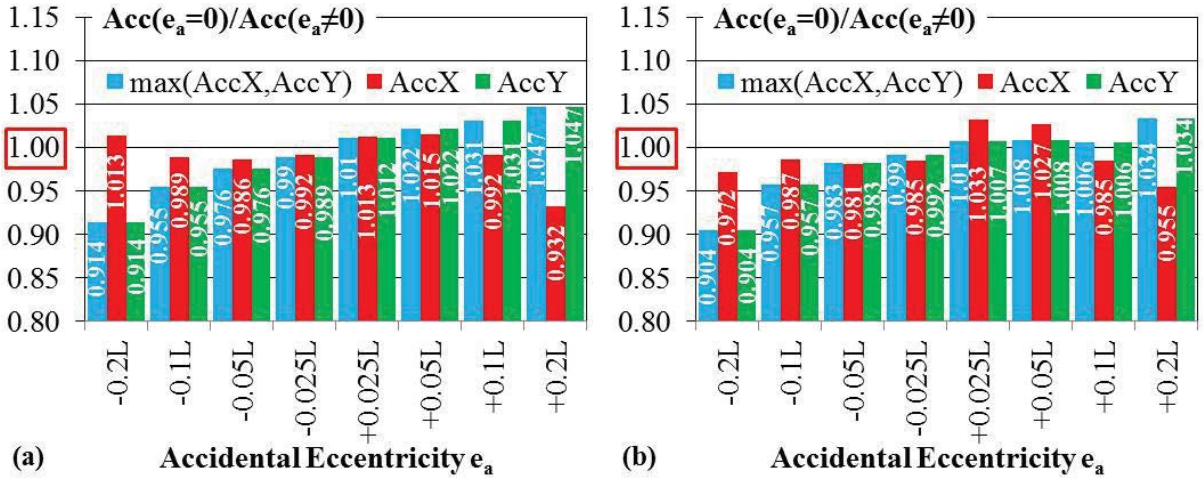

Figure 6: Ratios of the maximum floor acceleration along the direction of X (AccX), Y (AccY) axes and max(AccX, AccY) extracted by analyses performed considering 3 seismic components applied to MC ($e_a=0$) and those extracted by analyses performed considering 2 seismic components in several distances from MC ($e_a\neq0$): (a) Performance level SD, (b) Performance level NC

Fig. 6 illustrates the ratios of floor accelerations AccX, AccY and the maximum values between them max(AccX, AccY). The Fig. 6(a) presents the ratios which correspond to analyses conducted considering as performance level the level SD, whereas the Fig. 6(b) presents the ratios extracted considering the performance level NC. The study of Fig. 6 leads to the conclusion that while the convergence of $Acc(e_a=0)/Acc(e_a\neq0)$ ratio values to 1 is achieved using mainly low values of e_a as in the case of $Dr(e_a=0)/Dr(e_a\neq0)$ ratios the range of these values is greater in the current case. More specifically, in both examined cases of performance level (i.e. NC and SD) the values of e_a which lead to $Acc(e_a=0)/Acc(e_a\neq0)$ ratio values closer to 1 fluctuate between -0.05Land +0.05L.

The Figures 7 and 8 illustrate the variation along the height of the values of interstorey drifts along axes X (DrX) and Y (DrY) extracted from analyses considering performance levels SD and NC. These are the mean (according to EN1998-1) values of DrX and DrY all over the used seismic records (Eq. 2).

$$\text{meanDrX}_j(\%)=\frac{1}{7}\cdot\sum_{i=1}^{7}\left\{\text{DrX}_{j,i}(\%)\right\}\ ,\ \text{meanDrY}_j(\%)=\frac{1}{7}\cdot\sum_{i=1}^{7}\left\{\text{DrY}_{j,i}(\%)\right\}\quad (j=1\div5) \tag{2}$$

Where: i is the seismic record (i=1÷7) and j (j=1÷5) is the storey.

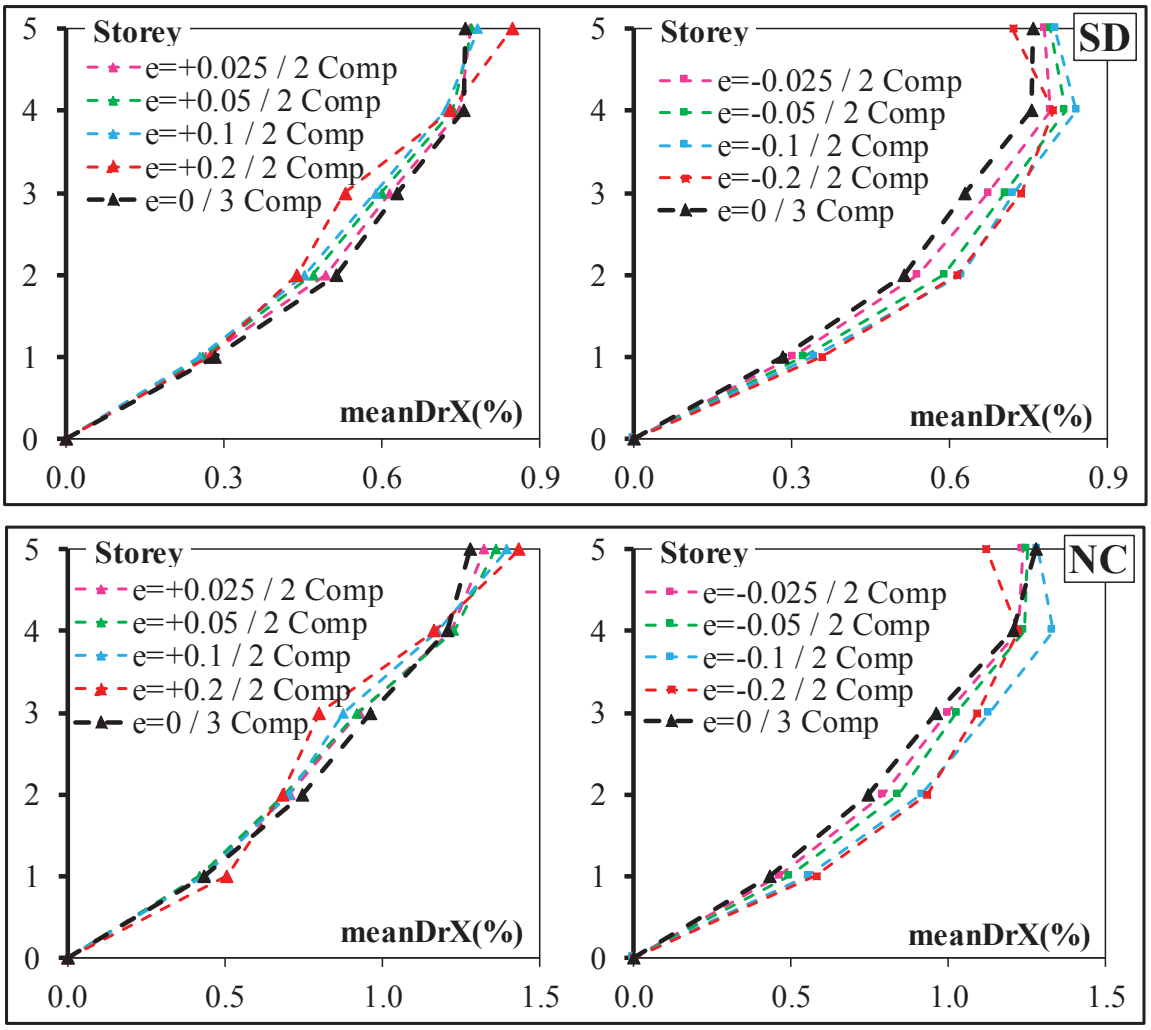

Figure 7: Variation along the height of the interstorey drift mean values along axis X all over the used seismic records

The presentation of diagrams of Figs. 7 and 8 aims to illustrate in more details the comparison between the results extracted from analyses conducted using 3 seismic components applied to MC and the corresponding results extracted from analyses conducted using 2 seismic components and several values for accidental eccentricity (Fig. 3).

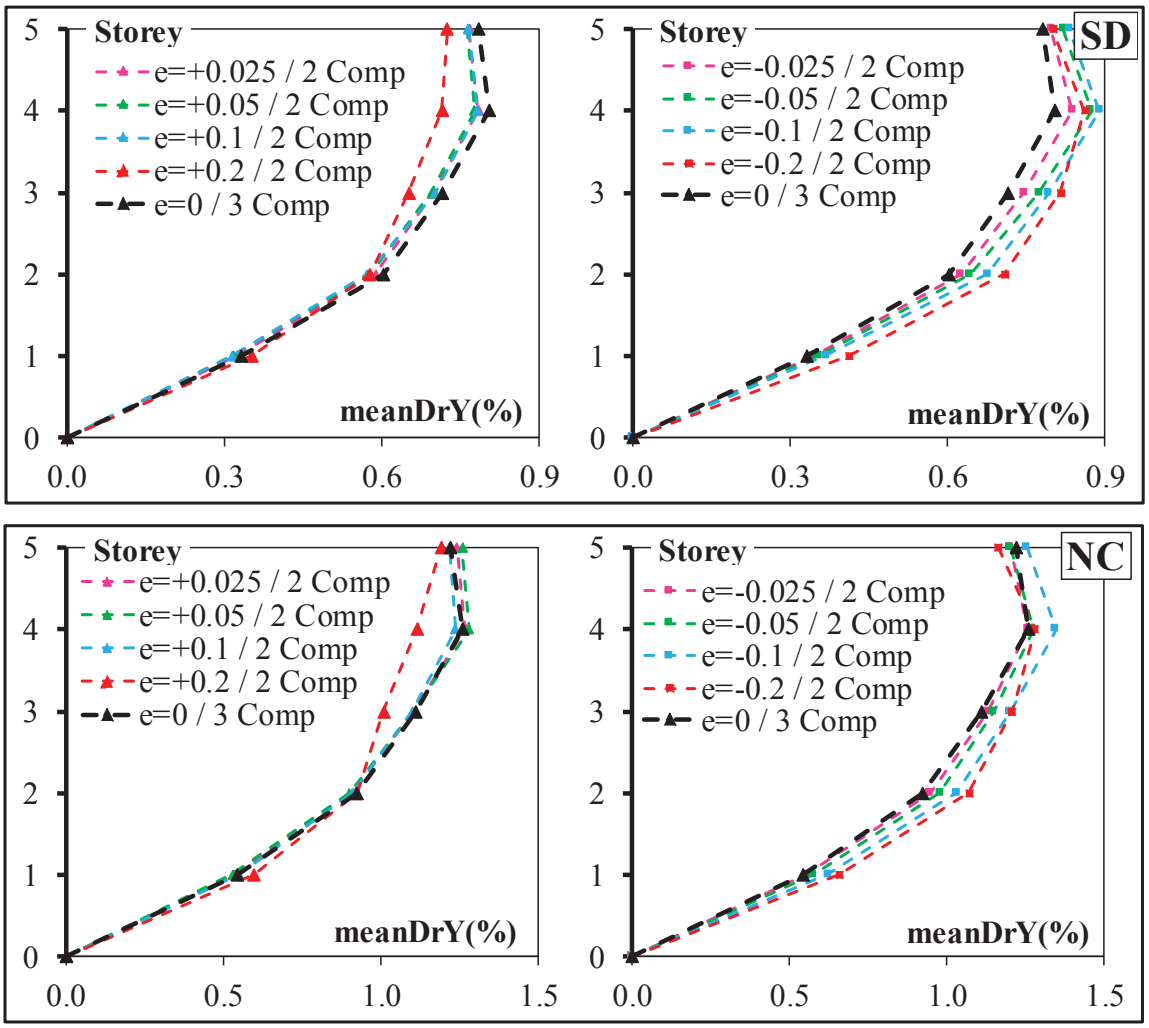

Figure 8: Variation along the height of the interstorey drift mean values along axis Y all over the used seismic records

The study of Figs. 7 and 8 confirms the main conclusion which was extracted from the study of Fig. 4. Thus, it is confirmed that the mean DrX (and DrY) values extracted from analyses conducted considering 2 (translational) seismic components and low values for accidental eccentricity e_a are closer to the corresponding values extracted from analyses conducted considering 3 seismic components applied to the MC.

6 CONCLUSIONS

The current paper deals with the investigation of the adequacy of the accidental eccentricity as a parameter to capture the effects of the torsional seismic component on the seismic damage. To this end, an 3D asymmetric 5-storey R/C building with structural system consisting of frames and walls is analysed using nonlinear time-history analysis and seven real ground motions with translational and torsional components. These ground motions were scaled to PGA values which correspond to performance levels indicated by Eurocodes. In order to achieve the goals of investigation two different categories of models for the building

and the seismic excitation were used: a) a model in which the translational and the torsional components of the seismic motion are applied to the mass center of the building and b) models in which only the translational components of the seismic motion are considered in different distances of building's mass center (i.e. consideration of several values for the accidental eccentricity). For the comparison of the above models three different seismic response parameters were used. These parameters are the interstorey drifts and the accelerations of floors along the two building's principal axes as well as the rotations of floors considered as rigid diaphragms about the its vertical axis, which are well-known damage indices.

The main conclusion which was extracted from the aforementioned investigation is that the results of the two categories of models converge generally for values of accidental eccentricity equal or lower of the 5% of building's floor length. This is an indication that the accidental eccentricity which is provided by the Eurocodes is capable to capture adequately the effects of the torsional seismic component on the seismic damage. However, the above conclusion is based on only one building and for this reason is essentially an initial conclusion which requires extended investigation.

REFERENCES

[1] Droste Z, Teisseyre R. Rotational and displacement components of ground motion as deduced from data of the azimuth system of seismographs. *Publ Inst Geophys Pol Acad Sci***,** 97, 157–167, 1976.

[2] Takeo M. Rotational motions observed during an earthquake swarm in April 1998 offshore to, Japan. *Bull Seismol Soc Am*, 99, 1457–1467, 2009. doi:10.1785/0120080173.

[3] Igel H, Brokesova J, Evans J, Zembaty Z. Advances in rotational seismology: instrumentation, theory, observations, and engineering. *J Seismol***,** 16, 571–572, 2012. doi:10.1007/s10950-012-9307-6.

[4] Liu CC, Huang BS, Lee WHK, Lin C-J. Observing rotational and translational ground motions at the HGSD station in Taiwan from 2007 to 2008. *Bull Seismol Soc Am*,99,1228–1236, 2009. doi:10.1785/0120080156.

[5] Wassermann J, Lehndorfer S, Igel H, Schreiber U. Performance test of a commercial rotational motions' sensor. *Bull Seismol Soc Am***,** 99, 1449–1456, 2009. doi:10.1785/0120080157

[6] Lee VW, Trifunac MD. Rocking strong earthquake accelerations. *Soil Dynamics and Earthquake Engineering*, 6, 75–89,1987.

[7] Castellani A, Boffi G. On the rotational components of seismic motion. *Earthquake Engineering Structural Dynamic*, 18, 785–797, 1989.

[8] Li H-N, Sun L-Y, Wang S-Y. Improved approach for obtaining rotational components of seismic motion. *NuclEng Des.*, 232, 131–137, 2004.

[9] Basu D, Whittaker AS, Constantinou MC. On estimating rotational components on ground motion using data recorded at a single station. *Journal Engineering Mechanics ASCE*,138(9),1141–1156, 2012.

[10] Sarah Sbaa, Fabrice Hollender, Vincent Perron, Afifa Imtiaz, Pierre-Yves Bard, Armand Mariscal, Alain Cochard and Alain Dujardin, Analysis of rotation sensor data from the SINAPS@ Kefalonia (Greece) post-seismic experiment - link to surface geology and wavefield characteristics, *Earth, Planets and Space*, 69, 124, 2017.

[11] Vincent Perron, Fabrice Hollender, Armand Mariscal, Nikolaos Theodoulidis, Chrisostomos Andreou, Pierre-Yves Bard, Cécile Cornou, Régis Cottereau, Edward Marc Cushing, Alberto Frau, Sébastien Hok, Agisilaos Konidaris, Philippe Lan-glaude, Aurore Laurendeau, Alexandros Savvaidis, and Angkeara Svay Accelerometer, Velocimeter Dense-Array, and Rotation Sensor Datasets from the Sinaps@ Postseismic Survey (Cephalonia 2014–2015 Aftershock Sequence), *Seismological Research Letters*, 89(2A),2018.doi:10.1785/0220170125.

[12] EN 1998-6, Eurocode 8: Design of structures for earthquake resistance – Part 6: Towers, masts and chimneys. European Committee for Standardization, 2005.

[13] Bonev, Z., Blagov, D., Vaseva, E. and Mladenov, K. Accounting the rotational component of Seismic action on towers, masts and chimneys according to BDS EN 1998-6. *International conference UACG-2009: Science and Practice. Fascicule VIII, Vol. XLIV* 185-195, 2009.

[14] Zembaty Z. Rotational seismic code definition in Eurocode 8, Part 6, for slender tower-shaped structures. *Bull Seismol Soc Am*.,99(2B), 1483–1485, 2009.

[15] Zembatyy Z, Boffi G. Effect of rotational seismic ground motion on dynamic response of slender towers. *European Earthquake Engineering*,8, 3-11, 1994.

[16] Wolf JP, Obernhueber P, Weber B. Response of a nuclear plant on aseismic bearings to horizontally propagating waves. *Earthquake Engineering Structural Dynamic***,** 11, 483–499, 1983.

[17] H. Tajammolian, F. Khoshnoudian, V. Loghman, Rotational components of near-fault earthquakes effects on triple concave friction pendulum base-isolated asymmetric structures, Engineering structures 142, 110-127, 2017.

[18] Politopoulos I. Response of seismically isolated structures to rocking-type actions. *Earthquake Engineering Structural Dynamic*, 39, 325–342, 2010.

[19] Falamarz-Sheikhabadi, M. R., and Ghafory-Ashtiany, M. Rotational components in structural loading. *Soil Dynamics and Earthquake Engineering***,** 75, 220–233, 2015.

[20] Falamarz-Sheikhabadi, M. R., Zerva, A., and Ghafory-Ashtiany, M. Mean absolute input energy for in-plane vibrations of multiple-support structures subjected to horizontal and rocking components. *J. Probab. Eng. Mech.*, 45, 87, 2016.

[21] Basu D, Constantinou MC, Whittaker AS. An equivalent accidental eccentricity to account for the effects of torsional ground motion on structures. *Engineering Structures*, 69, 1–11, 2014.

[22] Basu D, Whittaker AS, Constantinou MC. Characterizing the rotational components of earthquake ground motion. Technical repost MCEER 12-0005, 2012.

[23] De-La-Llera JC, Chopra AK. Accidental torsion in buildings due to base rotational excitation. *Earthquake Engineering Structural Dynamic*,23,1003–1021, 1994.

[24] Yin J, Nigbor RL, Chen Q, Steidl J. Engineering analysis of measured rotational ground motions at GVDA. *Soil Dyn Earthq Eng*, 87, 125–137, 2016. doi:10.1016/j.soildyn.2016.05.007.

[25] Felipe Vicencio and Nicholas Alexander A parametric study on the effect of rotational ground motions on building structural responses Soil Dynamics and Earthquake Engineering, 118, 191–206, 2019.

[26] EN 1998-1, Eurocode 8: Design of structures for earthquake resistance – Part 1: General rules, seismic actions and rules for buildings. European Committee for Standardization, 2005.

[27] EN 1992-1-1, Eurocode 2: Design of concrete structures – Part 1-1: General rules and rules for buildings. European Committee for Standardization, 2005.

[28] McKenna F and Fenves G (2004) Open System for Earthquake Engineering Simulation. Pacific Earthquake Engineering. Research Center, Berkeley, California. (Available from: http://opensees.berkeley.edu). Accessed on June 20, 2016.

[29] EN 1998-3, Eurocode 8: Design of structures for earthquake resistance – Part 3: Assessment and retrofitting of buildings. European Committee for Standardization, 2005.

EURODYN 2020
XI International Conference on Structural Dynamics
M. Papadrakakis, M. Fragiadakis, C. Papadimitriou (eds.)
Athens, Greece, 23–26 November 2020

SUB-STRUCTURING APPROACH OF THE PREDICTION OF BUILDING VIBRATIONS INDUCED BY RAILWAY TRAFFIC

CHAO HE[1], SHUNHUA ZHOU[2], PEIJUN GUO[3], and HONGGUI DI[4]

[1] Shanghai Key Laboratory of Rail Infrastructure Durability and System Safety, Tongji University, Shanghai, 201804, China; and Key Laboratory of Road and Traffic Engineering of the Ministry of Education, Tongji University, Shanghai, 201804, China
e-mail: chaohe1990@gmail.com

[2]Shanghai Key Laboratory of Rail Infrastructure Durability and System Safety, Tongji University, Shanghai, 201804, China; and Key Laboratory of Road and Traffic Engineering of the Ministry of Education, Tongji University, Shanghai, 201804, China

[3]Department of Civil Engineering, McMaster University, Hamilton, ON L8S 4L7, Canada

[4]Shanghai Key Laboratory of Rail Infrastructure Durability and System Safety, Tongji University, Shanghai, 201804, China; and Key Laboratory of Road and Traffic Engineering of the Ministry of Education, Tongji University, Shanghai, 201804, China

Keywords: Building vibrations; Railway traffic; Sub-structuring approach; dynamic stiffness method.

Abstract. *This paper presents a sub-structuring approach to predict the building vibrations generated by railway traffic. The three-dimensional building is simulated by rectangular plates supported by a distribution of columns and is modelled by the dynamic stiffness method. The building model is coupled with the layered half-space by using the continuity condition. The building vibrations generated by surface railways and underground railways are examined by two case studies. In the two cases, the analytical models are applied to calculate the incident wave field generated by railway traffic. The proposed method shows sufficient efficiency, making it suitable for performing many types of parametric studies and large-scale vibration predictions. It is found that the building vibration levels decrease as the distance from the building to the railway line increases, which is induced by the attenuation of the waves due to geometrical spreading in the soil. The floating slab can significantly reduce the building vibration levels starting from its cut-off frequency.*

1 INTRODUCTION

Ground-borne vibrations induced by railway traffic can make annoyance to the dwellers and interrupt the usage of sensitive equipment in the nearby building [1–3]. Therefore, a correct prediction method for those vibrations is important, which decides whether or not a vibration mitigation countermeasure should be used. In the past decades, the prediction of building vibrations generated by railway traffic has been paid much attention. A series of approaches, either numerical or (semi) analytical, have been proposed.

The numerical approach has the advantage in simulating the complex geometry of the building and ground. Since it requires a large amount of computational efforts and storage, various kinds of methods were proposed to improve the efficiency. In terms of the building vibrations generated by the surface railway traffic, Jean and Villot [4] proposed a two-dimensional (2D) finite element–boundary element (FE-BE) model, while Fiala et al. [5] developed a three-dimensional (3D) FE-BE model. Villot et al. [6] proposed a two-and-a-half dimensional (2.5D) methodology to predict the building vibrations induced by surface trains. There were also some studies focusing on the building vibrations induced by underground railway traffic by using numerical approaches. Lopes et al. [7–8] proposed a sub-structuring approaches, in which a 2.5D finite element-Perfectly Matched Layers (FE–PML) method was used to simulate the track–tunnel–ground system, while a 3D FE method was applied to model the building. Coulier et al. [9] developed a 2.5-D FE-BE model for the coupled tunnel-soil-building system. Recently, a two-step time-frequency numerical method was develop by Yang et al. [10] to calculate the vibrations of a large-scale building induced by underground railway traffic. A train-track coupled dynamic model proposed by Zhai [11–12] was applied to calculate the rail supporting forces in the first step, while a 3D FE model was developed to predict the building vibrations in the second step.

Despite the rapid advances in computing technology, the numerical approach is still not a feasible solution for the prediction of large-scale vibrations. On the contract, the (semi) analytical method is quite efficient and suitable for predicting large-scale vibrations and performing certain parametric studies. Although a number of analytical models were proposed to predict the ground vibrations induced by surface railway traffic [13–16] and underground railway traffic [17–21]. However, less attention was paid to analytical modelling of the building vibrations induced by railway traffic. Recently, an efficient method was proposed by Hussein et al. [22] to compute the building vibrations from underground tunnels, in which the PiP model was used to calculate the incident waves generated by underground railway traffic, and a 2D framed structure composed of horizontal and vertical beams was applied to simulate the building response. Clot et al. [23] proposed a 3D analytical method to predict the vertical building vibrations generated by a harmonic load acting on the ground surface.

This paper proposes an efficient method to calculate the vertical vibrations of buildings induced by railway traffic by using sub-structuring approach. A multi-story building constructed on a multi-layered half-space is considered. The 3D building is simplified as rectangular plates supported by columns and simulated by the dynamic stiffness method. By using the continuity condition between the building foundations and ground, the building is coupled with the stratified soil. Two case studies on building vibrations generated by surface railways and underground railways are presented to demonstrate the high efficiency of the proposed approach.

2 MODELLING METHOD

In this section, the modelling method for the vertical building vibrations generated by incident waves is proposed. A building with N story is located on a multi-layered half-space (Fig-

ure 1). The building floors are simplified as rectangular floors, while the supported columns are simulated as rods, as shown in Figure 2. The columns on each floor are distributed in an $N_x \times N_y$ grid pattern. The shallow foundations are considered in this study to support the building.

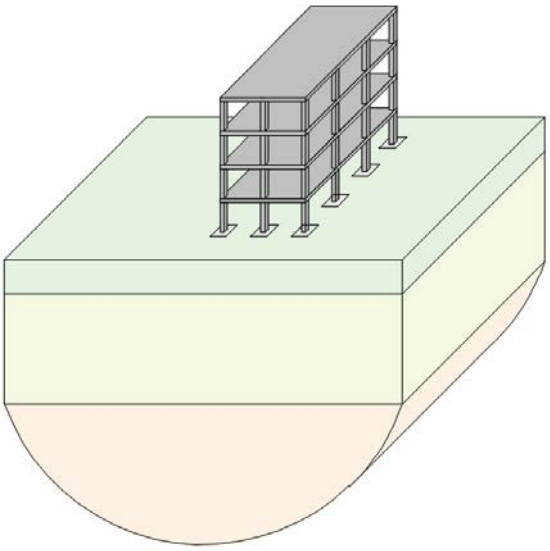

Figure 1: A building constructed in a milti-layered half-space.

2.1 DYNAMIC STIFFNESS MATRIXES FOR COLUMNS AND FLOORS

For a rod with a length L_c and cross-sectional area A_c, the relationship between the forces and displacements at the two edges can be obtained in the frequency domain as:

$$\hat{F}_{jk}^{2n} = c_{11}^{n}\hat{u}_{jk}^{2n} + c_{12}^{n}\hat{u}_{jk}^{2n+1},\ \hat{F}_{jk}^{2n+1} = c_{12}^{n}\hat{u}_{jk}^{2n} + c_{11}^{n}\hat{u}_{jk}^{2n+1}, \tag{1}$$

with

$$c_{11}^{n} = \mathrm{i}\xi E_c A_c \frac{1+\mathrm{e}^{-\mathrm{i}2\zeta L_c}}{1-\mathrm{e}^{-\mathrm{i}2\zeta L_c}},\ c_{12}^{n} = -2\mathrm{i}\xi E_c A_c \frac{\mathrm{e}^{-\mathrm{i}\zeta L_c}}{1-\mathrm{e}^{-\mathrm{i}2\zeta L_c}}, \tag{2}$$

where $\xi = \omega(\rho_c/E_c)^{1/2}$ is the axial wavenumber, with E_c and ρ_c being Young's modulus and density of the column.

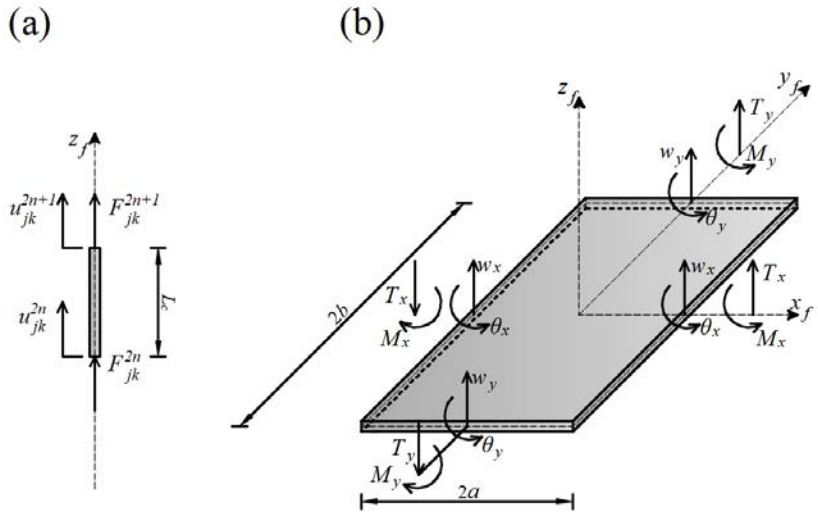

Figure 2: (a) Supported column (j, k) and sub-plate j for the story n.

The dynamic stiffness method is applied to calculate the vertical vibration of a rectangular plate. According to the superposition method [24], the plate displacement consists of four parts: symmetric-symmetric (SS), antisymmetric-antisymmetric (AA), symmetric-antisymmetric (SA), and antisymmetric-symmetric (AS):

$$\hat{w}(x_f, y_f) = \hat{w}_{SS}(x_f, y_f) + \hat{w}_{AA}(x_f, y_f) + \hat{w}_{SA}(x_f, y_f) + \hat{w}_{AS}(x_f, y_f) \tag{3}$$

A triangular series expansion is subsequently applied to those displacement and force components. Taking the symmetric-symmetric part as an example, the corresponding displacement components $\hat{\mathbf{u}}_{SS}$ and force components $\hat{\mathbf{t}}_{SS}$ are expressed as:

$$\begin{aligned} \hat{\mathbf{u}}_{SS} &= \left[\hat{w}_{xSS},\quad \hat{\theta}_{xSS},\quad \hat{w}_{ySS},\quad \hat{\theta}_{ySS}\right]^{\mathrm{T}} = 2\hat{\mathbf{U}}_{SS0}\mathbf{H}_{SS0} + \sum_{m=1}^{M}\hat{\mathbf{U}}_{SSm}\mathbf{H}_{SSm}, \\ \hat{\mathbf{t}}_{SS} &= \left[\hat{T}_{xSS},\quad \hat{M}_{xSS},\quad \hat{T}_{ySS},\quad \hat{M}_{ySS}\right]^{\mathrm{T}} = 2\hat{\mathbf{Q}}_{SS0}\mathbf{H}_{SS0} + \sum_{m=1}^{M}\hat{\mathbf{Q}}_{SSm}\mathbf{H}_{SSm}, \end{aligned} \tag{4}$$

where the rotations θ_x, θ_y, shear forces T_x, T_y, and moments M_x, M_y are shown in Figure 2, whose expressions were given in Ref. [25]. $\hat{\mathbf{U}}_{SS} = [\hat{\mathbf{U}}_{SS0}, \hat{\mathbf{U}}_{SS1}, ..., \hat{\mathbf{U}}_{SSM}]^{\mathrm{T}}$ and $\hat{\mathbf{Q}}_{SS} = [\hat{\mathbf{Q}}_{SS0}, \hat{\mathbf{Q}}_{SS1}, ..., \hat{\mathbf{Q}}_{SSM}]^{\mathrm{T}}$ are the projections of the displacement $\hat{\mathbf{u}}_{SS}$ and force $\hat{\mathbf{t}}_{SS}$, with

$$\mathbf{H}_{SS0} = 0.5\mathbf{I}_4, \quad \mathbf{H}_{SSm} = \begin{bmatrix} \cos\dfrac{m\pi y_f}{b_f} & 0 & 0 & 0 \\ 0 & \cos\dfrac{m\pi y_f}{b_f} & 0 & 0 \\ 0 & 0 & \cos\dfrac{m\pi x_f}{a_f} & 0 \\ 0 & 0 & 0 & \cos\dfrac{m\pi x_f}{a_f} \end{bmatrix}, \tag{5}$$

Following the procedure proposed by Nefovska-Danilovic [24], the dynamic stiffness matrix for a rectangular plate can be subsequently obtained, which is given by:

$$\mathbf{K}_f = \frac{1}{2}\mathbf{T}_1 \begin{bmatrix} \mathbf{K}_{SS} & 0 & 0 & 0 \\ 0 & \mathbf{K}_{AA} & 0 & 0 \\ 0 & 0 & \mathbf{K}_{SA} & 0 \\ 0 & 0 & 0 & \mathbf{K}_{AS} \end{bmatrix} \mathbf{T} \tag{6}$$

where $\mathbf{K}_{SS}$, $\mathbf{K}_{AA}$, $\mathbf{K}_{SA}$, and $\mathbf{K}_{AS}$ represent the dynamic stiffness matrixes for each symmetric part, while $\mathbf{T}$ and $\mathbf{T}_1$ are the transformation matrixes. The expressions of those matrixes were given by Nefovska-Danilovic [24].

The external force can only be applied to the edges of the plate in the dynamic stiffness method. Therefore, each floor may consist of multiply plates. Considering each plate as an element with four nodes that corresponds to the four edges, an assembly procedure that is used in the FE method can obtain the system equation for each building floor n:

$$\begin{bmatrix} \hat{\mathbf{Q}}_I^n \\ \hat{\mathbf{Q}}_R^n \end{bmatrix} = \begin{bmatrix} \mathbf{K}_{II}^n & \mathbf{K}_{IR}^n \\ \mathbf{K}_{RI}^n & \mathbf{K}_{RR}^n \end{bmatrix} \begin{bmatrix} \hat{\mathbf{U}}_I^n \\ \hat{\mathbf{U}}_R^n \end{bmatrix}, \tag{7}$$

where $\hat{\mathbf{U}}_I^n$ and $\hat{\mathbf{Q}}_I^n$ are the projections of the displacements and forces at the edges supporting by columns, while $\hat{\mathbf{U}}_R^n$ and $\hat{\mathbf{Q}}_R^n$ are those at other edges.

2.2 COUPLING OF THE FLOOR AND COLUMN

To couple the building floor with the supported column, the continuity condition at the connect positions is applied, which gives

$$\begin{cases} \hat{\mathbf{T}}_j^n = \dfrac{-1}{b}\mathbf{E}\mathbf{H}_j^n(\hat{\mathbf{F}}_j^{2n-1} + \hat{\mathbf{F}}_j^{2n}), \quad \hat{\mathbf{u}}_j^{2n-1} = \hat{\mathbf{u}}_j^{2n} = \left[\mathbf{H}_j^n\right]^{\mathrm{T}}(\hat{\mathbf{w}}_j^n), \quad n = 1, \ \ldots, N-1 \\ \hat{\mathbf{T}}_j^N = \dfrac{1}{b}\mathbf{E}\mathbf{H}_j^N(\hat{\mathbf{F}}_j^{2N-1}), \quad \hat{\mathbf{u}}_j^{2N-1} = \left[\mathbf{H}_j^N\right]^{\mathrm{T}}(\hat{\mathbf{w}}_j^N), \qquad n = N \end{cases} \tag{8}$$

where $\hat{\mathbf{u}}_j^l = \left[\hat{u}_{j1}^l, \ \hat{u}_{j2}^l, \ \ldots, \ \hat{u}_{jN_y}^l\right]^{\mathrm{T}}$ and $\hat{\mathbf{F}}_j^l = \left[\hat{F}_{j1}^l, \ \hat{F}_{j2}^l, \ \ldots, \ \hat{F}_{jN_y}^l\right]^{\mathrm{T}}$ (l = 1, 2, …, 2N − 1) represent the displacement and force components of the supported columns, respectively. $\mathbf{E}$ is a (2M + 1) × (2M + 1) diagonal matrix with E(1, 1) = 0.5 and E(m, m) = 1 ($m \geq 2$). $\mathbf{H}_j^n$ has the following expression:

$$\mathbf{H}_j^n = \begin{bmatrix} 1 & 1 & \cdots & 1 \\ \cos\dfrac{\pi y_1}{b_j^n} & \cos\dfrac{\pi y_2}{b_j^n} & \cdots & \cos\dfrac{\pi y_2}{b_j^n} \\ \sin\dfrac{\pi y_1}{2b_j^n} & \sin\dfrac{\pi y_2}{2b_j^n} & \cdots & \sin\dfrac{\pi y_{N_y}}{2b_j^n} \\ \vdots & \vdots & \ddots & \vdots \\ \cos\dfrac{M\pi y_1}{b_j^n} & \cos\dfrac{M\pi y_2}{b_j^n} & \cdots & \cos\dfrac{M\pi y_{N_y}}{b_j^n} \\ \sin\dfrac{(2M-1)\pi y_1}{2b_j^n} & \sin\dfrac{(2M-1)\pi y_2}{2b_j^n} & \cdots & \sin\dfrac{(2M-1)\pi y_{N_y}}{2b_j^n} \end{bmatrix}, \tag{9}$$

Substituting Eq. (1) into Eq. (8) gives the following relationship:

$$\begin{cases} \hat{\mathbf{Q}}_I^1 = \mathbf{K}_c^{11}\hat{\mathbf{U}}_I^1 + \mathbf{K}_c^{12}\hat{\mathbf{U}}_I^2 + \mathbf{G}^0\hat{\mathbf{F}}^0 + \mathbf{D}^0\hat{\mathbf{u}}^0, \qquad n = 1 \\ \hat{\mathbf{Q}}_I^n = \mathbf{K}_c^{n,n-1}\hat{\mathbf{U}}_I^{n-1} + \mathbf{K}_c^{n,n}\hat{\mathbf{U}}_I^n + \mathbf{K}_c^{n,n+1}\hat{\mathbf{U}}_I^{n+1}, \quad n = 2, \ \ldots, N-1 \\ \hat{\mathbf{Q}}_I^N = \mathbf{K}_c^{N,N-1}\hat{\mathbf{U}}_I^{N-1} + \mathbf{K}_c^{N,N}\hat{\mathbf{U}}_I^N, \qquad n = N \end{cases} \tag{10}$$

where $\hat{\mathbf{u}}^0$ and $\hat{\mathbf{F}}^0$ are the vertical displacements and forces between the columns and the foundations, respectively. Since the buildings are assumed to be directly fixed the foundation, the continuity condition between the columns and foundations gives:

$$\hat{\mathbf{u}}^0 = \hat{\mathbf{u}}^{fs}, \ \hat{\mathbf{F}}^0 = \hat{\mathbf{F}}^{fs}, \tag{11}$$

The Combination of Eqs. (7), (10) and (11) gives the system equation for the whole building:

$$\begin{bmatrix} \hat{\mathbf{F}}^{fs} \\ \mathbf{0} \end{bmatrix} = \begin{bmatrix} \mathbf{K}^{ss} & \mathbf{K}^{sb} \\ \mathbf{K}^{bs} & \mathbf{K}^{bb} \end{bmatrix} \begin{bmatrix} \hat{\mathbf{u}}^{fs} \\ \hat{\mathbf{U}}^b \end{bmatrix} \tag{12}$$

2.3 BUILDING VIBRATIONS INDUCED BY INCIDENT WAVES

When an incident wave acts on the shallow foundations, the induced vibrations can be determined by:

$$\hat{\mathbf{u}}^{fs} = \hat{\mathbf{u}}^s = -\hat{H}^s\mathbf{I}\hat{\mathbf{F}}^{fs} + \hat{\mathbf{u}}^{s,iw} \tag{13}$$

where $\hat{\mathbf{u}}^s$ denotes the vertical displacements of soils at the geometric center of each foundation; $\hat{\mathbf{u}}^{s,iw}$ is the corresponding incident displacement field. $\hat{H}^s$ is the soil compliance that represents the vertical displacement at the driving point induced by a rectangular distribute load. The transfer matrix method [14] is used to calculate the soil compliance in this study.

Substituting Eq. (13) into Eq. (12) gives the system equation for the calculation of the building vibrations induced by the incident waves:

$$\begin{bmatrix} 1/\hat{H}^s \mathbf{I}\hat{\mathbf{u}}^{s,iw} \\ \mathbf{0} \end{bmatrix} = \begin{bmatrix} \mathbf{K}^{ss} + \mathbf{K}^s & \mathbf{K}^{sb} \\ \mathbf{K}^{bs} & \mathbf{K}^{bb} \end{bmatrix} \begin{bmatrix} \hat{\mathbf{u}}^0 \\ \hat{\mathbf{U}}^b \end{bmatrix} \tag{14}$$

3 APPLICATION

3.1 BUILDING VIBRATIONS FROM SURFACE RAILWAY

In the first numerical case, the proposed method is used to calculate the vertical building vibrations generated by surface railways. As shown in Figure 3, the track system consists of the rails, pads, sleepers and ballast. The rails in this model are simulated as Euler-Bernoulli beams, while the rail pads are modelled as continuous spring. The sleepers are simplified as a continuous mass and the ballast is modelled as a continuous distributed vertical spring and mass. A harmonic load acting on the rails is considered as the excitation. An analytical model proposed by Sheng et al. [14] is used to calculate the incident displacement field $\hat{\mathbf{u}}^{s,iw}$ generated by a harmonic load acting on a railway track.

In this case, the UIC60 rail with a bending stiffness $E_rI_r = 6.3 \times 10^6$ N/m^2 and a mass per unit length $m_r = 60.34$ kg/m is considered. The equivalent stiffness of the rail pads per unit length k_{rp} is 3.5×10^8 N/m^2, and its loss factor $\eta_{rp} = 0.15$. The Mass of sleepers per unit length m_s is 490 kg/m, while the mass of ballast per unit length m_b is 1200 kg/m. the ballast has a smeared stiffness $k_b = 3.15 \times 10^8$ N/m^2 and a loss factor $\eta_b = 1$. The contact width of railway and ground is 2.7 m.

The soil consists of a layer with a depth of 2 m on top of a homogeneous half-space. The first layer has a shear wave velocity $C_s = 150$ m/s, a compression wave velocity $C_p = 306$ m/s, and density $\rho_s = 1900$ kg/m^2. The bottom half-space has a shear wave velocity $C_s = 230$ m/s, a compression wave velocity $C_p = 443$ m/s and a density $\rho_s = 2023$ kg/m^2. The material damping ratio β_s for the two layers are 0.05 and 0.04, respectively.

A four-story building with two spin is located in the vicinity of the railway line. The distance between the centerline of the track to the nearest column alignment of the building d = 10 m, 20 m, and 30 m is considered. The geometry of the building is shown in Figure 4. The building floors with a length of 8 m, a width of 4 m, and a thickness of 0.3 m are supported by square columns with a side length of 0.3 m and a height of 3 m. the material of the building floors and columns are concrete with Young's modulus of 35 GPa, a density of 2500 kg/m^3, and a Poisson's ratio of 0.2.

Four observation points are considered, as shown in Figure 4. The observation points A and C are located at the center of each spin of the first floor, while the observation points B and D are at the center of each spin of the fourth floor.

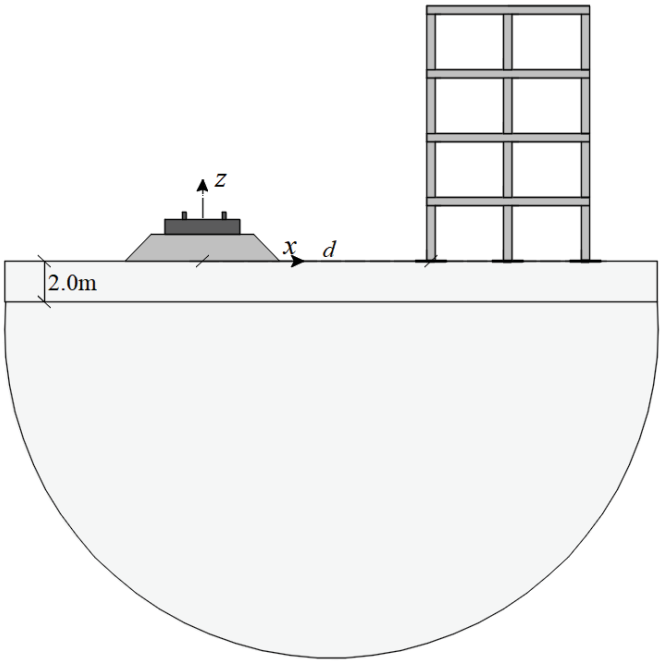

Figure 3: Geometry of the surface railway-soil-building system.

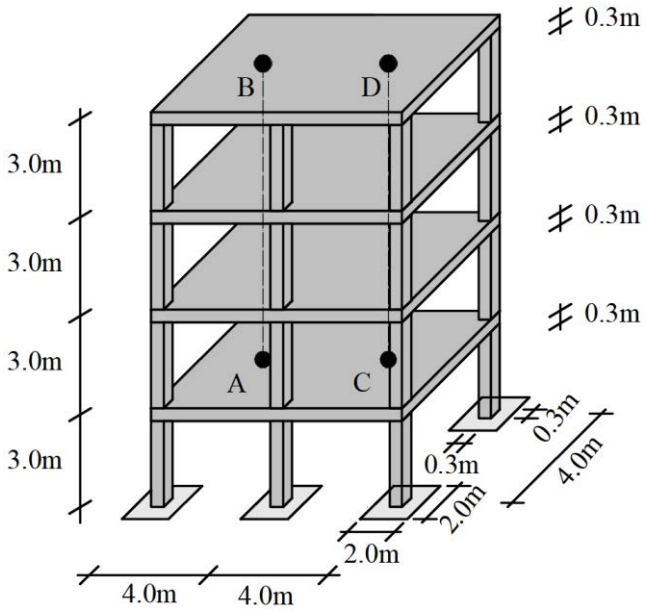

Figure 4: Geometry of the building.

Figure 5 shows the vertical displacements of the building at the four observation points induced by a harmonic load acting on the rails of the surface railway. As expected, the displacement amplitude decreases as the distance from the building to the railway line increases. Since the attenuation of the waves due to geometrical spreading in the soil is slow in the low-frequency range, the magnitude of the displacement decreases slightly as distance from the building to the railway line increases. When the distance *d* increases from 10m to 20 m and 30m, the vibration levels decrease approximately 5 dB and 8dB, respectively. However, as the frequency increases, the attenuation due to geometrical spreading accelerates. The vibration level of the building decreases significantly as the distance increases.

A personal computer with 8 GB RAM and 2.6 GHz processor is used to calculate the results in this case. The average calculation times for each frequency (f) is 2.5 minutes, which shows its advantage of high computational efficiency.

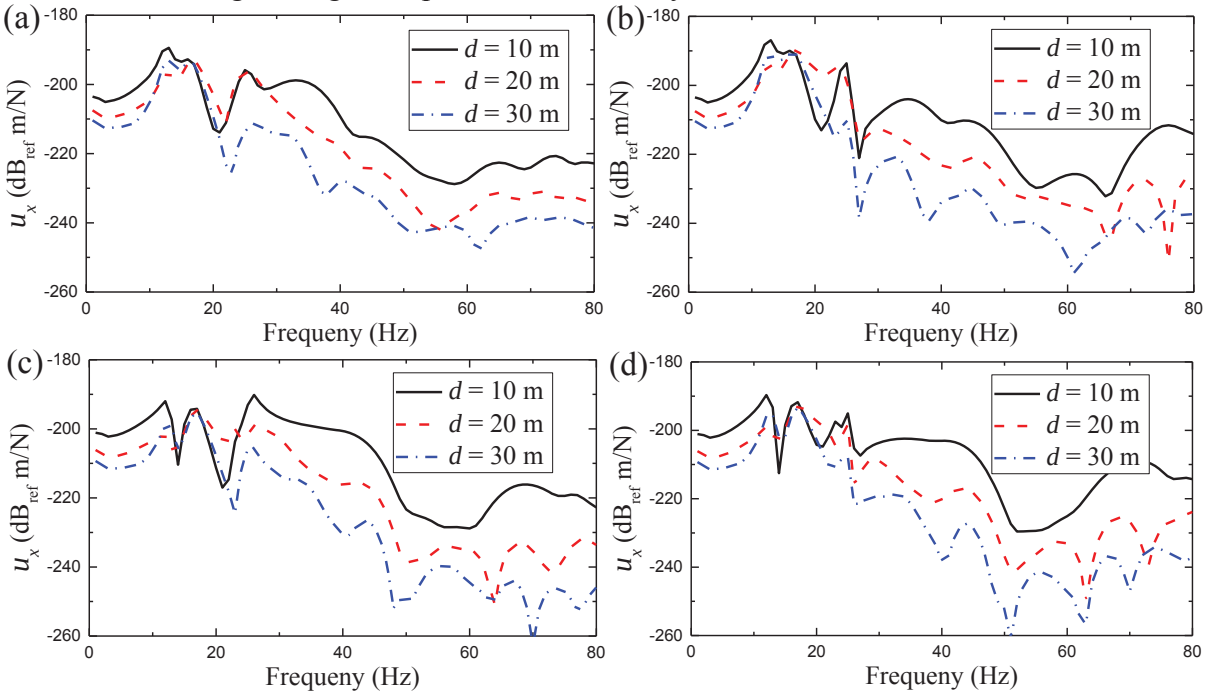

Fig. 5. Vertical displacements of the building at the observation point (a) A, (b) B, (c) C, and (d) D induced by a harmonic load acting on the rails of the surface railway.

3.2 BUILDING VIBRATIONS FROM UNDERGROUND RAILWAY

This section investigates the building vibrations induced by underground railways. As shown in Figure 6, a circular tunnel embedded in a two layered half-space is considered. A fully-coupled analytical method [19] is used to calculate the incident displacement field $\hat{\mathbf{u}}^{s,iw}$. The tunnel is simulated as a cylindrical thin shell. The soil is considered as a layered elastic half-space and simulated by the transfer matrix method [26–28]. A model of a double-beam is used to model the track slab and rails. A harmonic load acting on the rails is considered as the excitation. The derivation of this method was proposed in detail by He et al. [19].

In this study, the tunnel with an out radius of 3.0 m and a thickness of 0.25 m is made of concrete with Young's modulus E_t = 50 GPa, a density ρ_t = 2500 kg/m^3, and a Poisson's ratio ν_t = 0.2. The depth of the tunnel is 10 m below the ground surface. The UIC 60 rails is considered in this case. The rail pads in this case have a smeared stiffness k_{rp} = 116 MN/m^2. Two kinds of slabs are considered. The first one is a directly-fixed slab, and the second one is a floating slab with the isolation frequency f_n = 10 Hz and 20 Hz being considered. Two kinds of slabs have a mass per unit length of 3500 kg/m and a bend stiffness of 1430 MNm^2. The properties of the soil and building are the same as those in Section 3.1.

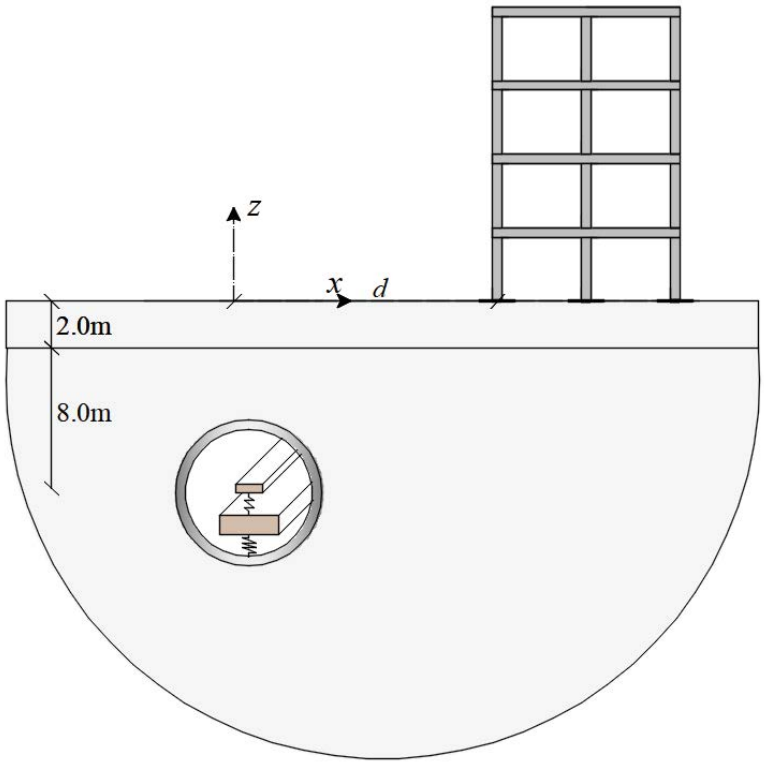

Figure 6: Geometry of the underground tunnel-soil-building system.

Figure 7 presents the vertical displacements of the building at the four observation points induced by a harmonic load acting on the rails of the underground railway. The insert gain (IG) that represents the difference of the building vibration levels between the two kinds of slabs is calculated and presented. By comparing the building responses for the directly-fixed slab with those for the floating slab, we can find that the floating slab has a good isolation effectiveness after the cut-off frequency $\sqrt{2}f_n$. However, the floating slab also can increase the vibration levels for the frequency that is less than the cut-off frequency. Especially at the isolation frequency of the floating slab track, a major peak can be observed at the IG curves.

The calculation times for each frequency (f) is 9 minutes in this numerical case, indicating that the proposed method has a high computational efficiency when calculating the building vibrations generated by underground railway traffic.

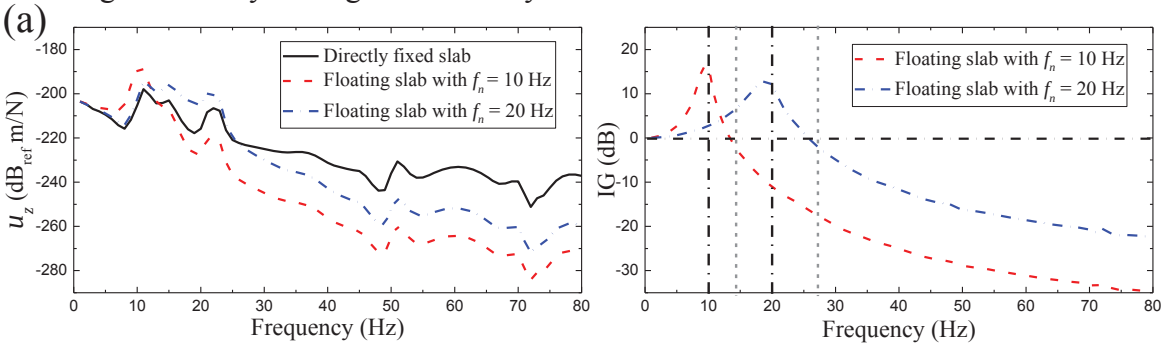

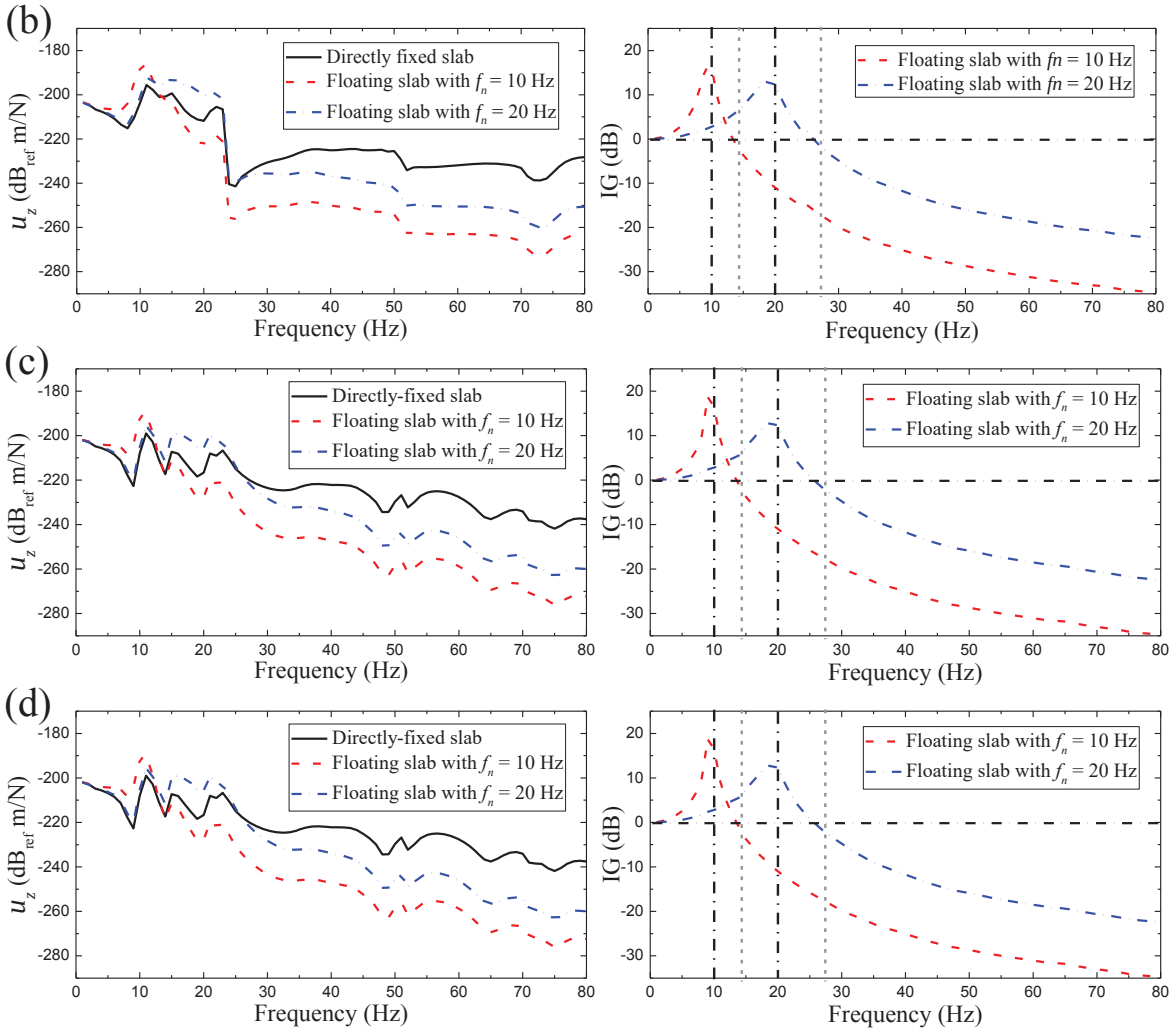

Figure 7: Vertical displacements of the building at the observation point (a) A, (b) B, (c) C, and (d) D induced by a harmonic load acting on the rails of the underground railway.

4 CONCLUSIONS

A sub-structuring method was proposed to calculate the vertical building vibrations induced by railway traffic. The 3D building is simulated by rectangular plate supported by a distribution of columns. The dynamic stiffness method was used to obtain the solution for rectangular plates and columns. The 3D building model was subsequently obtained by coupling the plate model with the column model. The building model was coupled with the layered half-space by satisfying equilibrium and compatibility condition at the building foundations.

Two case studies on building vibrations generated by surface railways and underground railways are proposed. In this first case, an analytical model was used to calculate the incident wave filed generated by surface railway traffic. In the second case, the tunnel-soil system was simulated by a fully-coupled analytical model. The numerical results demonstrated that the building vibration levels decreases as the distance from the building to the railway line increases, which is induced by the attenuation of the waves due to geometrical spreading in the soil. The floating slab can significant reduces the building vibration levels starting from its cut-off frequency.

REFERENCES

[1] D.J. Thompson, G. Kouroussis, E. Ntotsios, Modelling, simulation and evaluation of ground vibration caused by rail vehicles, Vehicle Syst. Dyn. 57(7), 936-983, 2019.

[2] S. Zhou, C. He, P. Guo, F. Yu, Dynamic response of a segmented tunnel in saturated soil using a 2.5-D FE-BE methodology, Soil Dyn. Earthquake Eng. 120, 386-397, 2019.

[3] X. Sheng, A review on modelling ground vibrations generated by underground trains, Int. J. Rail Transp. 7(4), 241-261, 2019.

[4] P. Jean, M. Villot, Study of the vibrational power injected to a wall excited by a ground surface wave, J. Sound Vib. 231(3), 721–726, 2000.

[5] P. Fiala, G. Degrande, F. Augusztinovicz, Numerical modelling of ground-borne noise and vibration in buildings due to surface rail traffic, J. Sound Vib. 301(3), 718–738, 2007.

[6] M. Villot, P. Ropars, P. Jean, E. Bongini, F. Poisson, Modeling the influence of structural modifications on the response of a building to railway vibration, Noise Control Eng. J., 59(6), 641, 2011.

[7] P. Lopes, P. Alves Costa, M. Ferraz, R. Calçada, A. Silva Cardoso, Numerical modeling of vibrations induced by railway traffic in tunnels: From the source to the nearby buildings, Soil Dyn. Earthquake Eng. 61-62, 269–285, 2014.

[8] P. Lopes, P. Alves Costa, R. Calçada, A. Silva Cardoso, Influence of soil stiffness on building vibrations due to railway traffic in tunnels: Numerical study, Comput. Geotech. 61, 277–291, 2014.

[9] P. Coulier, G. Lombaert, G. Degrande, The influence of source–receiver interaction on the numerical prediction of railway induced vibrations, J. Sound Vib. 333, 2520–2538, 2014.

[10] J. Yang, S. Zhu, W. Zhai, G. Kouroussis, Y. Wang, K.Y. Wang, et al., Prediction and mitigation of train-induced vibrations of large-scale building constructed on subway tunnel, Sci. Total Environ. 668, 485-499, 2019.

[11] W. Zhai, Two simple fast integration methods for large-scale dynamic problems in engineering, Int. J. Numer. Methods Eng. 39, 4199–4214, 1996.

[12] W. Zhai, K. Wang, C. Cai, Fundamentals of vehicle-track coupled dynamics, Vehicle Syst. Dyn. 47, 1349–1376, 2009.

[13] V.V. Krylov, Ground vibration boom from high speed train: prediction and reality, The Acoustic Bulletin July/August, 15-22, 1998.

[14] X. Sheng, C.J.C. Jones, M. Petyt, Ground vibration generated by a load moving along a railway track. J. Sound Vib. 228, 129-156, 1999.

[15] A.V. Metrikine, S.N. Verichev, J. Blaauwendraad, Stability of a two-mass oscillator moving on a beam supported by a visco-elastic half-space. I J Solids Struct. 42(3–4), 1187-1207, 2005.

[16] Y.C. Li, S.J. Feng, H.X. Chen, Z.L. Chen, D.M. Zhang, Random vibration of train-track-ground system with a poroelastic interlayer in the subsoil, Soil Dyn. Earthquake Eng. 120, 1-11, 2019.

[17] J.A. Forrest, H.E.M. Hunt, A three-dimensional tunnel model for calculation of train-induced ground vibration, J. Sound Vib. 294 (4e5), 678–705, 2006.

[18] M.F.M. Hussein, S. François, M. Schevenels, H.E.M. Hunt, J.P. Talbot, G. Degrande, The fictitious force method for efficient calculation of vibration from a tunnel embedded in a multi-layered half-space, J. Sound Vib. 333, 6996–7018, 2014.

[19] C. He, S.H. Zhou, H.G. Di, P.J. Guo, J.H. Xiao, Analytical method for calculation of ground vibration from a tunnel embedded in a multi-layered halfspace, Comput. Geotech. 99, 149–164, 2018.

[20] C. He, S.H. Zhou, P.J. Guo, H.G. Di, X.H. Zhang, F. Yu, Theoretical modelling of the dynamic interaction between twin tunnels in a multi-layered half-space, J. Sound Vib. 456, 65–85, 2019.

[21] C. He, S.H. Zhou, P.J. Guo, H.G. Di, X.H. Zhang, A theoretical model on the influence of ring joint stiffness on dynamic responses from underground tunnels, Constr. Build. Mater. 223, 69–80, 2019.

[22] M. Hussein, H. Hunt, K. Kuo, P. Alves Costa, J. Barbosa, The use of sub-modelling technique to calculate vibration in buildings from underground railways, P. I. Mech. Eng. F-J. Rai. 229(3), 303–314, 2015.

[23] A. Clot, R. Arcos, J. Romeu, Efficient Three-Dimensional Building-Soil Model for the Prediction of Ground-Borne Vibrations in Buildings, J. Struct. Eng. 143(9), 04017098, 2017.

[24] M. Nefovska-Danilovic, Dynamic Analysis of Soil-structure System Using Spectral Element Method, Ph.D. thesis, Belgrade, 2012.

[25] A.W. Leissa, Vibration of plates. NASA, SP-160; 1969.

[26] W.T. Thomson, Transmission of elastic waves through a stratified solid medium, J. Appl. Phys. 21, 89–93, 1950.

[27] X. Sheng, C.J.C. Jones, D.J. Thompson, Ground vibration generated by a harmonic load acting on a railway track, J. Sound Vib. 225(1), 3–28, 1999.

[28] C. He, S.H. Zhou, P. Guo, H.G. Di, J.H. Xiao, Dynamic 2.5-D Green's function for a point load or a point fluid source in a layered poroelastic half-space, Eng. Anal. Bound. Elem. 77, 123–137, 2017.

EURODYN 2020
XI International Conference on Structural Dynamics
M. Papadrakakis, M. Fragiadakis, C. Papadimitriou (eds.)
Athens, Greece, 23–26 November 2020

A TUNED MASS DAMPER INERTER CONTROL DEVICE FOR BASE ISOLATED STRUCTURES

Salah Djerouni[1], Mouncef Eddine Charrouf[1], Abdelhafid Ounis[1], Mahdi Abdeddaim[2] and Nassim Djedoui[2]

[1] LARGHYDE Laboratory, Department of civil engineering and hydraulics, faculty of science and technology, Biskra University Algeria
P.O.B 145 RP, Biskra, Algeria 07000
e-mail: (s.djerouni, Mouncef-charrouf, abdelhafid.ounis)@univ-biskra.dz

[2] Faculty of science and technology, Biskra University Algeria
P.O.B 145 RP, Biskra, Algeria 07000
(m.abdeddaim,n.djedoui)@univ-biskra.dz

Keywords: inerter, base-isolated, optimal, tuned mass damper inerter

Abstract. *The recent earthquakes history shows that the conception of resistant, safe, and economical structures is daily challenges for structural engineers. Among the newest vibration control devices figures the inerter which is a device capable of developing a large fictive mass using rotational inertia. In this research work, a conventional passive tuned mass damper (TMD) is compared with an inerter based mass damper (TMDI) which consists of tuned mass damper attached to an inerter. The two devices are used to control the vibration of a base-isolator structure (BI) submitted to earthquake excitations. For this purpose, an eight (8) storey structure is equipped with a (TMDI) at the base floor compared with case TMDI in zeros inertance case TMD, the inerter is fixed to the (TMD) on one side and grounded on the second side. A set of dynamic parameters are optimized by exploring predefined bounds, the optimal parameters* ***(frequency tuning, damping tuning, inertance ratio, mass ratio)*** *are then used to confirm and perform a time history analysis is under different earthquake records. The obtained results demonstrated good performance and effectiveness of the structure equipped with a (TMDI) in terms of bearing displacement as well as top floor acceleration.*

1 INTRODUCTION

In recent years, seismic vibration control constituted a field of interest for a large number of researchers. The motivation behind such interest is the protection of lives and structures against earthquakes; this can be achieved by introducing passive, active, or semi-active control devices [1, 2].

In the same context, many researchers presented and investigated numerous devices which lead to acceptable results in terms of response reduction (e.g., base-isolated (BI), tuned liquid damper (TLD), magneto-rheological damper (MR), tuned viscous mass damper (TVMD), viscous mass damper (VMD), tuned inerter damper (TID), tuned mass damper (TMD)) [3, 4]. One of the widespread devices is the (TMD), a passive control device used to absorb and limit the vibration in a structure or a building [5]. It's attached to the main structure with mechanical elements small mass, viscous spring, and linear elastic dashpot to mitigate and decrease maximum displacement of main structure induced by numerous natural hazards [6]. As it is well known the (TMD) efficiency is mainly related to its mass. However, a large mass constitutes a constant challenge for the structural and architectural design of any building, hence a larger (TMD) mass involves bigger vertical loads and base shear but also a large space occupancy [2, 7].

In order to overcome these weaknesses or in other words disadvantages, a new mechanical device is known as "Inerter" has attracted the interest of researchers in several areas, this latter can be associated with (TMD) to obtain a larger mass [8, 9]. Furthermore, this tool has the possibility of developing a large fictive virtual mass proportional to the relative acceleration between its nodes [10]. The association of a (TMD) and an inerter is denoted tuned mass damper inerter (TMDI) [9]. The concept of mechanical inerter was introduced by Engineer Smith in 2002 at Cambridge University, it was firstly used in Formula One cars under the "J damper" name. Today, an inerter mechanism is capable to produce an equal and opposite inertia force at two ends, the force is proportional to the relative acceleration which can be analogous to a very large physical mass [8]. The factor of proportionality is known as inertance, the "mass amplification effect" can reach a magnitude from 1 to 350 times or higher the mass of a conventional (TMD) [11].

Undoubtedly, inertance plays a majority part of the apparent mass of (TMD) [12]. The inerter mechanism purposes divers' possibilities to be used in several domains (e.g., motors bike, turbine tower, train, mechanical vibration, vehicle cars, skyscraper, and automobile suspensions). Hence, several inerter types can be found (e.g., ball screw type, rack pinion gear flywheel type, hydraulic motor, fluid inerter type, electro-magnetic inerter) [13].

Along with (TMDs) base-isolation technology is widely used in order to secure buildings and prevent them from irreversible damages or collapse due to earthquake actions [14]. Nowadays, the extensive used of vertical building lead to the appearance of a large number of high rise buildings with multiple usages. As it is well known (BI) technique that contributes significantly to the reduction of both acceleration and inter-story drift response by shifting the frequency of the structure to the small acceleration branch in the response spectrum [15].

On the other hand, base-isolation involves large deformations and displacements due to smaller stiffness at the base of the structure [16].In order to overcome the large deformations issue is base-isolated buildings multiple solutions were proposed, a hybrid control strategy that combines (BI) technology and additional control systems are one of the recommended solutions. Yang [17] was one of the first researchers to propose such a solution, by combining base-isolation with (TMD) at the top of the building or above the base-isolated level. In this regard, researchers found that (TMD) can reduce maximum response if the input period is up-

per than the fundamental period of the base-isolated building [6, 7, 18]. However, most of the (TMD) has a frequency mistuning problem; if a mistuning occurs it can either reduce the performance or at times amplify the response of the main building, with this in the background, the author or the researcher De-Domenico focused on the possibility of enhancing the effects of (TMD) by transforming it into a (TMDI) via the inerter [12]. Therefore, the objective of his work is centered to evaluate the ground motion response of a base-isolated building equipped with tuned mass damper inerter (TMDI) which consists of a (TMD) mounted in series with viscous damper and elastic stiffness elements connected with an inerter. The latter is attached between the secondary mass of (TMD) and the ground, it worth noticing that a (TMD) is a particular condition of a (TMDI) when the inertance is set to be null [12]. The results obtained show a response reduction of the base-isolated system, especially the bearing displacement. Newly, a hybrid control strategy presented by De Domenico and Ricciardi demonstrated the efficiency of combining a BI and a (TMDI), it also shows that the (BI-TMDI) combination is more effective compared to a (BI-TMD) [12, 19-21].

In this work, a base-isolated building is equipped with a (TMDI). The second end of the inerter is grounded (fixed to the ground) or in other words, inerter with a single terminal exists. The system is submitted to a set of earthquake records with the aim of finding optimal parameters of (TMDI) and (TMD) such as frequency, damping, and inertance. Although the idea of using passive (TMDI) to control displacements in BI structures is not novel, this work aims to present optimal parameters without using optimization algorithms.

2 MATHEMATICAL MODEL

Figure 1(a) shows the model of an *n*-story base-isolated structure equipped with a TMD-Inerter on the ground floor. The masses of the building are concentrated at floor levels. Figure 1(b) illustrations the models of ideal inerter made by (rack, pinion, gear, and a flywheel) this is the inerter concept used in this paper. The location of TMD-Inerter is connected between ground and base-isolation. The hypothesis is made in such a way to disregard the impact of the rotational degrees of freedoms (*n*-DOF) in the models. The other key assumptions made for the structural system are the following: First, the inerter device must function sufficiently in any spatial direction and motion. Second, considering the only horizontal direction of earthquake applied. Third, the effects of soil-structure interaction is neglige. Finally, over the earthquake excitation, the building behavior remains linear elastic.

According to d'Alembert's principle, the general equation of motion model for the present hybrid system can be written as follows:

$$[M]\{\ddot{x}(t)\}+[C]\{\dot{x}(t)\}+[K]\{x(t)\}=-[M_{\partial}]\{\Im\}\{\ddot{x}_g\} \tag{1}$$

In equation (1); *[M]; [K]; [C];* are *[(n+1)×(n+1)];* mass the corresponding stiffness; and damping coefficient matrices of the system respectively. Further, $\ddot{x}(t),\dot{x}(t),x(t)$ are (n) dimensional acceleration; velocity; displacement vectors respectively, and the dots signifying the derivative with respect to time. $[M_{\partial}]$, $\{\Im\}$, $\{\ddot{x}_g\}$ are respectively the real mass matrix where $(\beta=0)$, the distribution unit vector with size *(n+1)*, earthquake ground acceleration motion vector.

The (TMDI) and (BI) components are denoted m_d; c_d; k_d; m_b; c_b; k_b, respectively. Clearly b denotes the apparent mass of inerter with two terminals, the latter integrated or mounted to (TMD) with a second terminal fixed to the grounded (inerter with only one terminal exist).

Equation (1); can be rearranged in transfer function (TF) method, more specifically "*State Space"* form, it will result in the following writing:

$$\begin{cases} \dot{\theta} = A.\theta + B.\psi \\ y = E.\theta + D.\psi \end{cases} \tag{2}$$

Where $[A],[B]$ are unknown or defines state or system matrix of order *(2n×2n)*, the input matrix is of the order *(2n×q)*; respectively, expressed as:

$$[A] = \begin{bmatrix} \Theta & \Psi \\ -M^{-1}.K & -M^{-1}.C \end{bmatrix} \; ; \; [B] = \begin{bmatrix} \Theta \\ -M^{-1}.M_{\partial} \end{bmatrix} \tag{3}$$

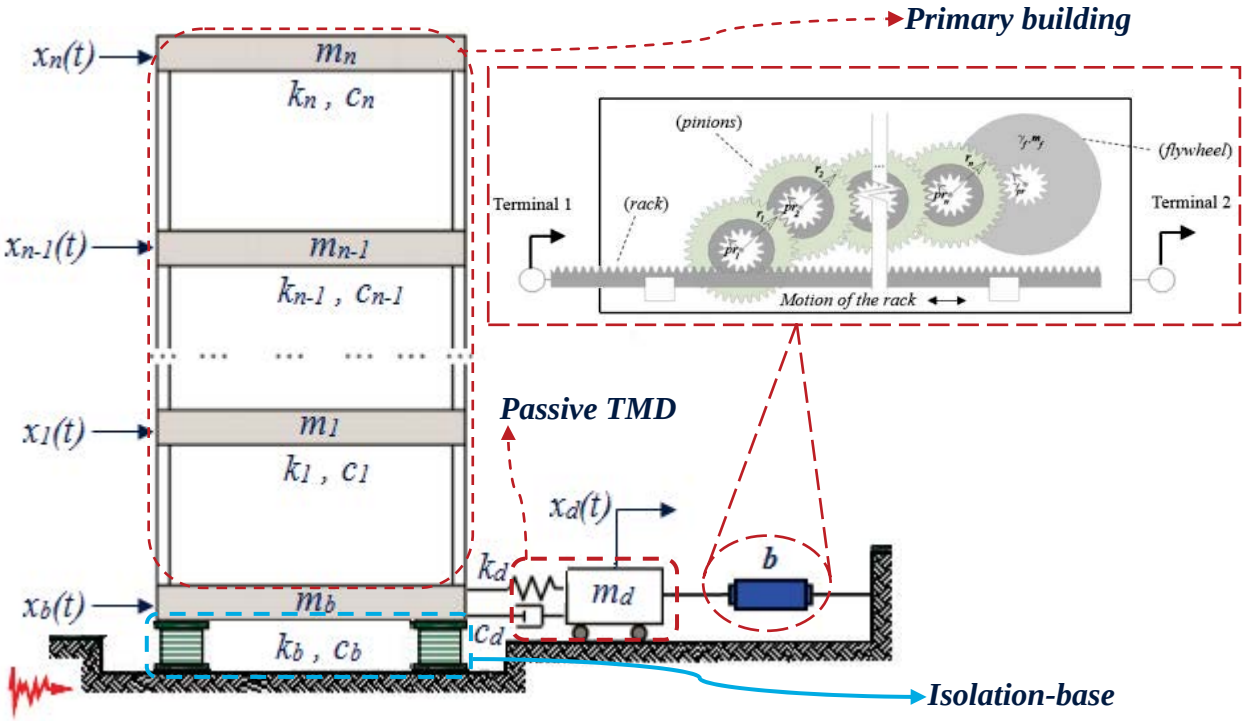

Figure 1. Simplified model of benchmark building integrating with (BI) and (TMDI) connected between (BI) and ground (i);(ii) Schematic representation of the two-terminal inerter device [12, 22].

For the building controlled with (TMDI), the structural matrices (mass, rigidity, and damping) of the system can be written as:

$$[M] = \begin{bmatrix} m_d + b & 0 & \cdots & & 0 \\ 0 & m_b & \cdots & & \vdots \\ \vdots & \vdots & m_1 & \cdots & \\ & & \vdots & \ddots & \\ \vdots & & & m_{n-1} & \vdots \\ 0 & \cdots & \cdots & 0 & m_n \end{bmatrix} \begin{Bmatrix} \ddot{x}_d(t) \\ \ddot{x}_b(t) \\ \ddot{x}_1(t) \\ \ddots \\ \ddots \\ \ddot{x}_{n-1}(t) \\ \ddot{x}_n(t) \end{Bmatrix} \tag{4}$$

$$[K]=\begin{bmatrix} K_d & -K_d & 0 & \cdots & 0 \\ -K_d & K_b+K_d+K_1 & -K_1 & 0 & \vdots \\ 0 & -K_1 & \ddots & \cdots & \\ 0 & 0 & & \vdots & \vdots \\ \vdots & \vdots & \vdots & K_{n-1}+K_n & -K_n \\ 0 & \cdots & 0 & -K_n & K_n \end{bmatrix} \begin{Bmatrix} x_d(t) \\ x_b(t) \\ x_1(t) \\ \ddots \\ \ddots \\ x_{n-1}(t) \\ x_n(t) \end{Bmatrix} \tag{5}$$

$$[C]=\begin{bmatrix} C_d & -C_d & 0 & \cdots & 0 \\ -C_d & C_b+C_d+C_1 & -C_1 & 0 & \vdots \\ 0 & -C_1 & \ddots & \cdots & \\ 0 & 0 & & \vdots & \vdots \\ \vdots & \vdots & \vdots & C_{n-1}+C_n & -C_n \\ 0 & \cdots & 0 & -C_n & C_n \end{bmatrix} \begin{Bmatrix} \dot{x}_d(t) \\ \dot{x}_b(t) \\ \dot{x}_1(t) \\ \ddots \\ \ddots \\ \dot{x}_{n-1}(t) \\ \dot{x}_n(t) \end{Bmatrix} \tag{6}$$

Therefore, the natural frequencies of the (BI) and (TMDI) respectively can be obtained using the following equation:

$$\omega_b=\sqrt{\frac{K_b}{m_b}} \;\; ; \;\; \omega_d=\sqrt{\frac{K_d}{\left(m_d+b\right)}} \tag{7}$$

And their damping ratio factors are evaluated by the following formulas:

$$\xi_b=\frac{C_b}{2.\mathrm{m}_b.\omega_b} \;\; ; \;\; \xi_d=\frac{C_d}{2.(\mathrm{m}_d+\mathrm{b}).\omega_d} \tag{8}$$

Moreover, the modal mass and the inertance ratio, which is expressed as:

$$\mu=\frac{m_d}{\sum_{j=1}^{j=n} m_j} \;\; ; \;\; \beta=\frac{b}{\sum_{j=1}^{j=n} m_j} \;\; ; \;\; and \;\; j=\left(1,2,..,n\right) \tag{9}$$

The mechanical layout of an ideal linear inerter device is a mechanism with two terminals, and both terminals of the inerter device should be connected, on one side to the moving attached mass (TMD) and on the other side to the structure, ideally the floor slab or to the ground.

The force of both ends is positively correlated with the relative acceleration and can be expressed by the following formula [3, 10]:

$$F_{Left}=F_{Right}=b\times\left(\ddot{u}_{Left}-\ddot{u}_{Right}\right) \tag{10}$$

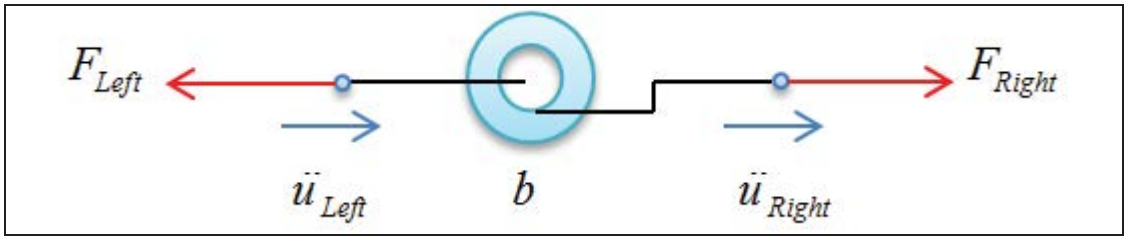

Figure 2. Schematic of ideal linear inerter device

As it can be seen in Figure 2, the constant of inertance (apparent mass) marked *b* can be expressed by the following relationship or formula below:

$$b = I_b \times \left(\frac{2 \times \pi}{L_b} \right)^2 \tag{11}$$

Where the moment of inertia of the flywheel is marked I_b; and the lead of the ball screw is marked L_b.

3 NUMERICAL STUDY

In order to develop and assess the performance of the hybrid strategy, an eight-story benchmark base-isolated building is chosen and equipped with TMD-Inerter, the building is submitted to several earthquakes ground motion, the responses are compared with a building equipped with a (TMDI)(β=0) , it means case (TMD). The mass, stiffness, damping, and frequency of the benchmark building are listed in Table 1 and Table 2 for BI parameters:

Storey	m_j *ton*	c_j *kN.s / m*	k_j *kN / m*	ω_j *rad / sec*	T_j sec	f_j *Hz*
1	345.6	490	3.4×10^5	5.24	1.19	0.83
2	345.6	467	3.26×10^5	14.0	0.45	2.23
3	345.6	410	2.85×10^5	22.55	0.28	3.58
4	345.6	386	2.69×10^5	30.22	0.21	4.81
5	345.6	348	2.43×10^5	36.89	0.17	5.87
6	345.6	298	2.07×10^5	43.06	0.14	6.85
7	345.6	243	1.69×10^5	49.54	0.13	7.89
8	345.6	196	1.37×10^5	55.96	0.11	8.91

Table 1. Benchmark building parameters [23].

	m_b *ton*	c_b *kN.s / m*	k_b *kN / m*
Base-isolator (BI)	450	26.17	18.050

Table 2. Base-isolator parameters [23].

3.1 Optimization and results

In order to find and investigate the performance of the optimal parameters, an optimization procedure is carried out on TMD-Inerter, in which the inerter's 2nd extremity is grounded. The optimization is achieved by the variance of four different parameters simultaneously. The range of the frequency ratio υ is bounded as [0.85, 1.12] and the damping ratio ξ range is set as [0.01, 0.2] while the inertance β is bounded as [0 , 1] where the mass ratio $\mu_{TMDI} = \beta - \mu_{TMD}$ is calculated in function of the continuously changing inertance factor. Figures 3-6, show the result in form of surf plots, in which it can be seen that the optimal tuning parameters lead to the minimization of the bearing displacement and top floor acceleration response under different earthquakes (El Centro, Northridge, Kocaeli, Imperial valley) respectively. The response reduction is clearly visible. This validates the fact that increasing the mass M_{tmdi} + b, could improve the base-isolation performance. Moreover, for a null inertence factor, where the system is equivalent to a conventional (TMD), the results are represented in Figure 5-6, it can be seen that the improvement of the response is directly related to the increase in the mass ratio. These findings show that the optimal parameters of the system allow increasing the linear stiffness of base-isolation. Hence, resulting in more effective reduction effect in terms of bearing displacement and top floor acceleration due to the increased of base-isolation restoring force. Therefore, the influence of the damping ratio and mass ratio and frequency ratio on the design parameters is significant and should be manipulated with an exceptional attention.

The results related to the optimization are listed in Table 3.

Remark: The bound use for the optimization parameters using later by [12].

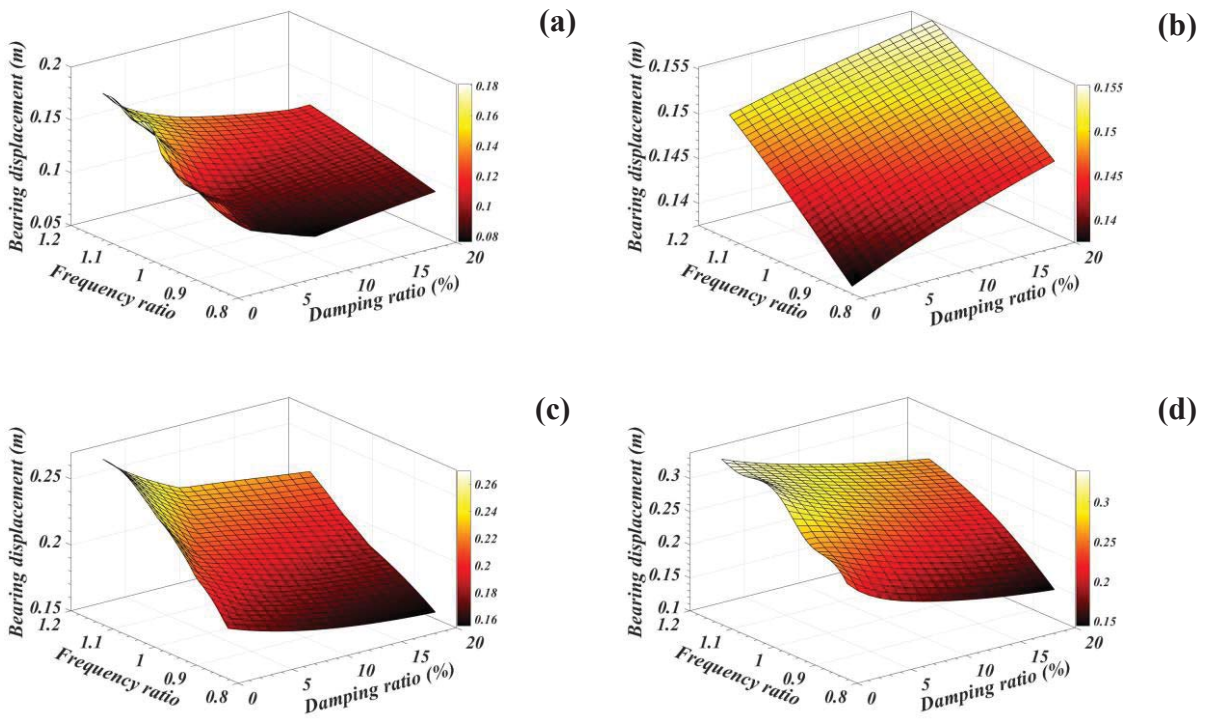

Figure 3. Bearing displacement of (BI-TMDI).(a) El Centro,(b) Northridge,(c) Kocaeli,(d) Imperial valley

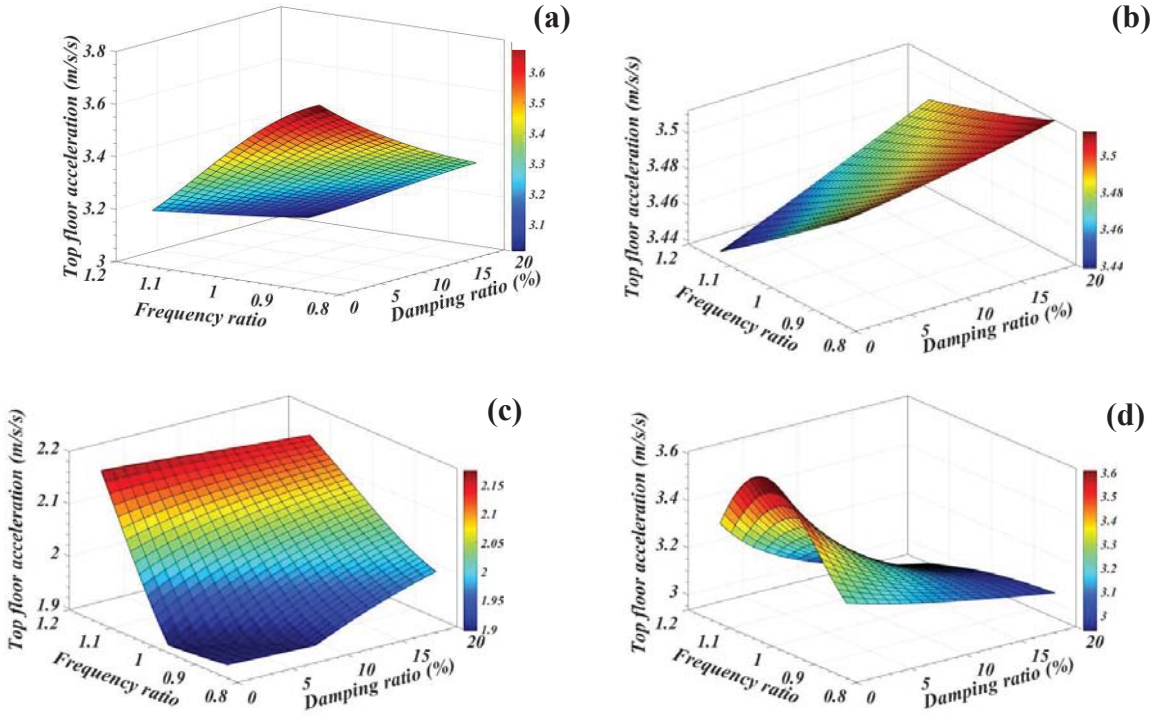

Figure 4. top floor acceleration of (BI-TMDI) .(a) El Centro,(b) Northridge,(c) Kocaeli,(d) Imperial valley

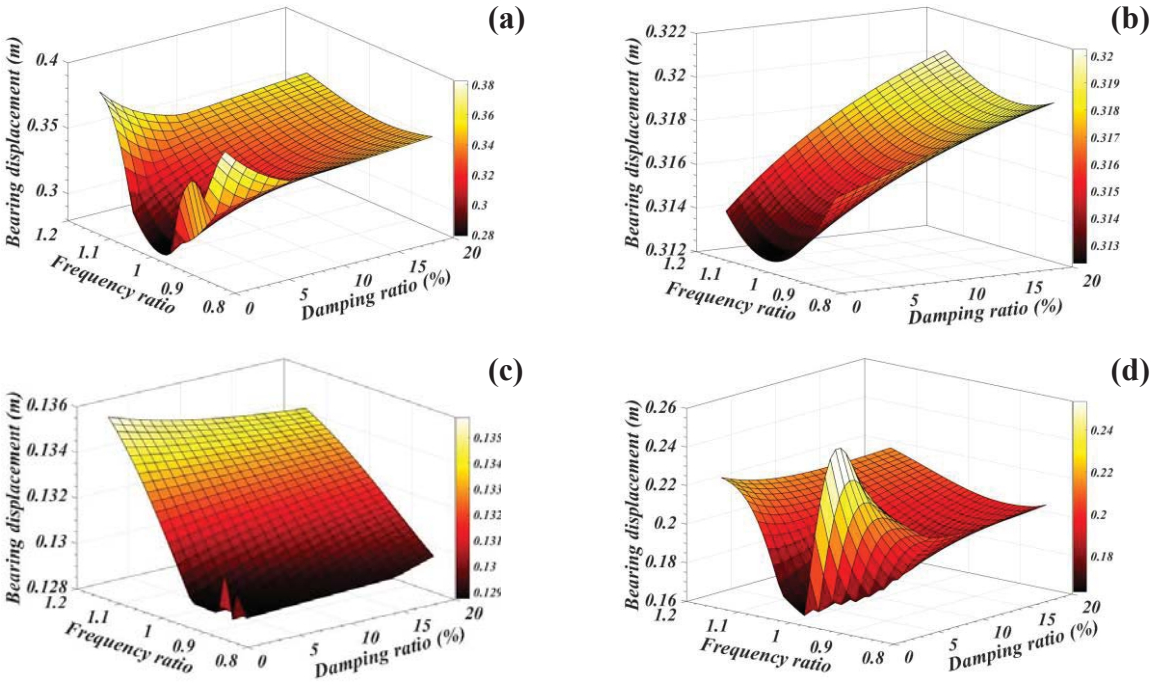

Figure 5. Bearing displacement of (BI-TMD) $(\beta=0)$.(a) El Centro,(b) Northridge,(c) Kocaeli,(d) Imperial valley

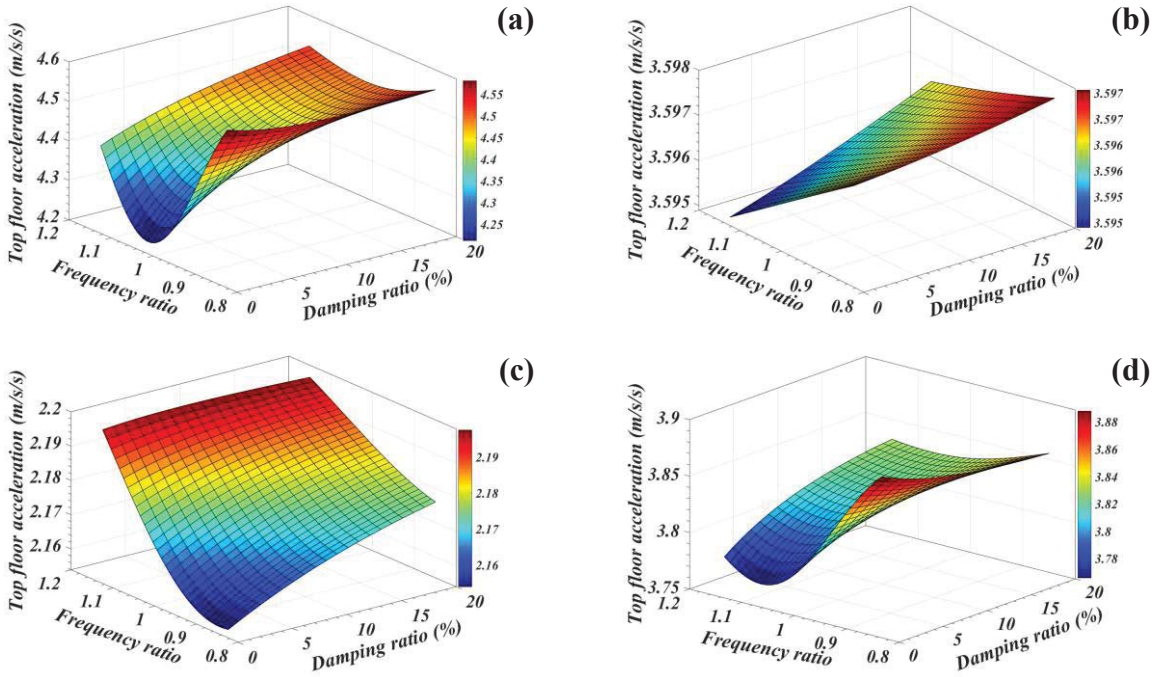

Figure 6. top floor acceleration of (BI-TMD) $(\beta=0)$.(a) El Centro,(b) Northridge,(c) Kocaeli,(d) Imperial valley

In order to compare the control systems strategy performance, the mean values of the optimal parameters obtained after optimization are given in Table 3. It must be noted that the value of β , υ , ξ for a TMDI system larger than those of a TMD system.

	β	υ	ξ
TMD	0	0.97	0.01
TMDI	0.55	1.1375	0.115

Table 3. Optimal values of each Hybrid systems (BI-TMD), (BI-TMDI)

3.2 Time history analysis of *n*-DOF

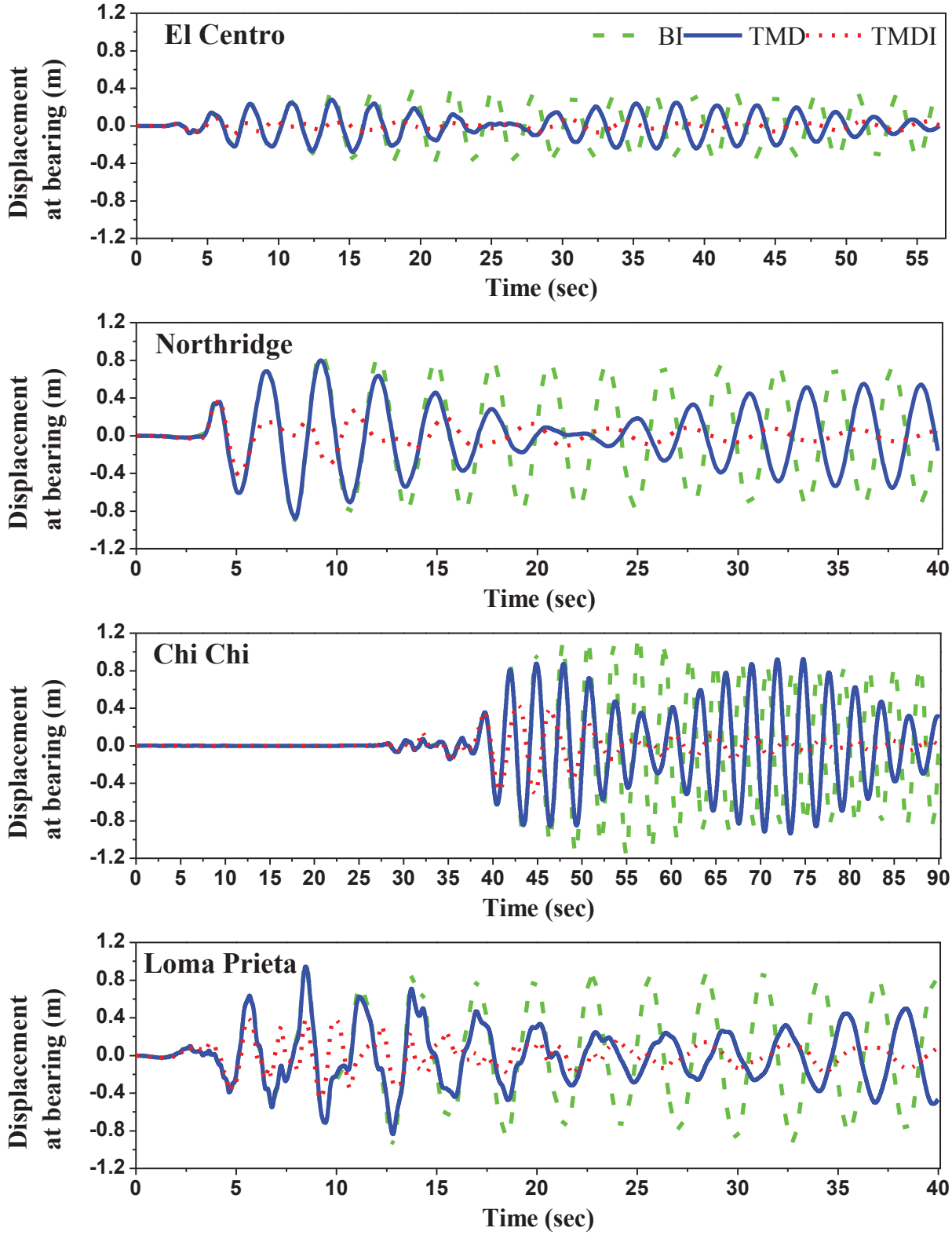

Figure 7. Time history of bearing displacement using a tuned mass damper inerter (TMDI) and a tuned mass damper (TMD).

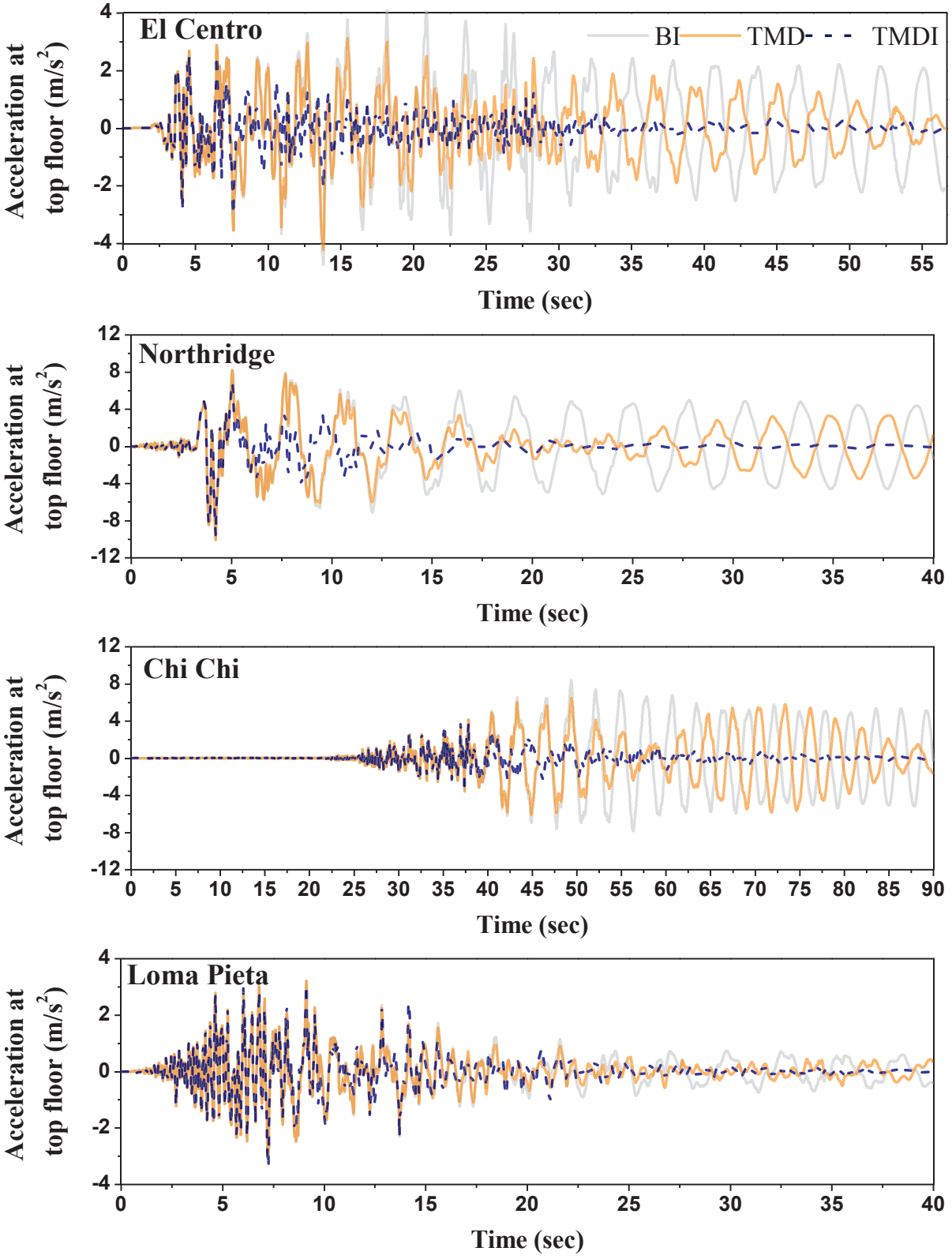

Figure 8. Time history of the top floor acceleration of the (eight-storey) base-isolated building, isolated with leading rubber bearing (LRB) and equipped with the single tuned mass damper inerter (TMDI), tuned mass damper (TMD).

Earthquake Name	Station Name	Years	PGA *(g)*	M_w	Distance. Epic *(km)*
El Centro	El Centro	1940	0.30	6.9	16.90
Northridge	San Marino	1994	0.84	6.69	40.32
Chi-Chi	HWA025	1999	0.33	7.62	90.78
Loma Prieta	Sunol-Forest fire station	1989	0.29	6.93	61.90
Kocaeli	Fatih	1999	0.16	7.51	93.86
Imperial valley	Brawley Airport	1979	0.25	5.01	25.84

Table 4.List of records earthquakes considered in this paper.

Time history analysis is conducted on the system using optimal parameters for further verification. The comparison is made under the input of the recorded accelerograms selected from the pacific earthquake engineering research center (peer ground motion database). Six natural seismic signals are investigated: El Centro, Northridge, Chi-Chi, Loma Prieta, Kocaeli, and Imperial Valley. Specifications of these earthquakes are listed in Table 4. Moreover, Table 3, contains the optimal parameters, such as inertance ratio β , frequency tuning f , and damping tuning ξ , for each TMDI and TMD device combined to a *BI* system. The corresponding response time histories of the BI reference building without and with control devices (both the total base displacement and roof acceleration response) are displayed in Figures 7 and 8, respectively. The figures are elaborated for different earthquakes. For comparison purposes, in each graph, the response of base-isolated building equipped with (TMDI) has been plotted along with the response of the BI structure equipped with a conventional (TMD) and the uncontrolled response of the base-isolated building (without any control device) which serves as a reference.

Figures 7 and 8, show that for the El Centro record, 31% and 78% response reduction in terms of bearing displacement is obtained using TMD and TMDI respectively, 11% and 37% response reduction in terms of top floor acceleration using TMD and TMDI respectively. For Northridge record, 5% reduction is obtained using TMD, and 55% reduction is obtained with TMDI in terms of bearing displacement, 1%, and 4% reduction in terms of top floor acceleration is obtained using TMD and TMDI, respectively. Chi-Chi record 19% and 56% response reduction in terms of bearing displacement, 22%, and 54% response reduction in terms of top floor acceleration under both TMD and TMDI, respectively. Loma Prieta record 4% and 52% response reduction in terms of bearing displacement using TMD and TMDI, respectively, a very small reduction in terms of top floor acceleration is obtained using both devices.

Moreover, the Chi-Chi earthquake made the utmost important amplification of the response in the median part of the ground motion, contrary to El Centro, Loma Prieta and Northridge earthquakes which produced the utmost important amplification of the response in the initial part of the ground motion. It is worth noticing that the displacement response of the additional mass such as TMD or TMDI should not surpass the displacement response of the uncontrolled base-isolated building.

4 CONCLUSIONS

The present paper studied the possibility of enhancing a base-isolated building dynamical performance. The building was equipped with tuned mass damper inerter (TMDI), optimal parameters of the (TMDI) were investigated and explored through a set of predefined bounds. The performance of the proposed system where compared to a conventional tuned mass damper (TMD), the main target of the hybrid strategy proposed in this work is to reduce the bearing displacement without increasing significantly the acceleration. With this in the background, the following main concluding remarks can be drawn:

- Numerical simulation shows that a recently control device known as tuned mass damper inerter TMDI is effective in controlling the lateral displacement (with a significant reduction of the average bearing displacement value of almost 60% compared to a TMD only which achieved a 15% reduction in average. In terms of top floor acceleration, a reduction average of 23% was obtained using TMDI while a 10% reduction average was obtained using a TMD.
- The results demonstrated that adding a grounded inerter leads to significant response reduction in terms of top floor acceleration and bearing displacement simultaneously.
- It has been demonstrated that the use of the inerter in along with a TMD to form a TMDI is a very practical control strategy.
- The use of the inerter integrated to a TMD results in a lightweight system, with superior capability and reliability compared to conventional TMD.
- A TMDI device designed with an optimal approach can effectively reduce the bearing displacement of a base-isolated building and as well as other response quantities such as top floor acceleration, compared to a conventional (TMD).
- The determination of a suitable apparent or physical mass $(M_{TMD}+b)$ should consider control performance, physical feasibility, and economic price.

REFERENCES

1. Djedoui, N., A. Ounis, and M. Abdeddaim. *Active Vibration Control for Base-Isolated Structures Using a PID Controller against Earthquakes*. in *International Journal of Engineering Research in Africa*. 2016. Trans Tech Publ.
2. Stanikzai, M.H., et al., *Seismic response control of base-isolated buildings using tuned mass damper.* Australian Journal of Structural Engineering, 2019: p. 1-12.
3. Abdeddaim, M., A.A. Kasar, and N. Djedoui. *Seismic vibration control using a novel inerto-elastic damper*. in *MATEC Web of Conferences*. 2018. EDP Sciences.
4. Stanikzai, M.H., et al., *Seismic response control of base‐isolated buildings using multiple tuned mass dampers.* The Structural Design of Tall and Special Buildings, 2019. **28**(3): p. e1576.
5. Guenidi, Z., et al., *Control of adjacent buildings using shared tuned mass damper.* Procedia engineering, 2017. **199**: p. 1568-1573.
6. Charrouf, M.E., et al., *COMBINED CONTROL STRATEGY FOR EARTHQUAKE INDUCED VIBRATIONS IN STRUCTURES*, in *4th Eurasian Conference on Civil and Environmental Engineering (ECOCEE)* 2019: lSTANBUL. p. 13.
7. Salah, D., et al., *Optimization of the seismic response of buildings with hybrid control using Tuned Mass Damper (TMD) and base isolation*, in *The First International Conference on Materials, Environment, Mechanical and Industrial Systems ICMEMIS'19* 2019: Djelfa p. 6.
8. Chen, M.Z. and Y. Hu, *Inerter and Its Application in Vibration Control Systems*. 2019: Springer.
9. Marian, L. and A. Giaralis, *The tuned mass-damper-inerter for harmonic vibrations suppression, attached mass reduction, and energy harvesting.* Smart structures and systems, 2017. **19**(6): p. 665-678.
10. Mahdi Abdeddaim, A.K., Djedoui Nassim,Abdelhafid Ounis, *A Novel inerto-viscous damper for seismic vibration control*, in *ANCRiSST2019-The 14th International Workshop on Advanced Smart Materials and Smart Structures Technology*. July 2019: Italy-Rome. p. 5.
11. Tai, W.-C., *Optimum Design of a New Tuned Inerter-Torsional-Mass-Damper Passive Vibration Control for Stochastically Motion-Excited Structures.* Journal of Vibration and Acoustics, 2020. **142**(1).
12. De Domenico, D. and G. Ricciardi, *An enhanced base isolation system equipped with optimal tuned mass damper inerter (TMDI).* Earthquake Engineering & Structural Dynamics, 2018. **47**(5): p. 1169-1192.
13. Xu, K., et al., *Using tuned mass damper inerter to mitigate vortex-induced vibration of long-span bridges: Analytical study.* Engineering Structures, 2019. **182**: p. 101-111.
14. Djedoui, N., et al., *Semi-Active Fuzzy Control of Tuned Mass Damper to Reduce Base-Isolated Building Response under Harmonic Excitation.* Jordan Journal of Civil Engineering, 2018. **12**(3).
15. DJEDOUI, N. and A. OUNIS, *TUNED MASS DAMPER FOR BASE ISOLATED STRUCTURES.* Sciences & Technologie. B, Sciences de l'ingénieur, 2014(40): p. 29-34.
16. Djedoui, N., et al., *Hybrid control systems for rigid buildings structures under strong earthquakes.* Asian Journal of Civil Engineering (BHRC), 2017. **18**(6): p. 893-909.
17. Yang, J., A. Danielians, and S. Liu, *Aseismic hybrid control systems for building structures.* Journal of Engineering Mechanics, 1991. **117**(4): p. 836-853.

18. P., X. and N. A., *Optimum design for more effective tuned mass damper system and its application to base‐isolated buildings.* Structural Control and Health Monitoring, 2014. **21**(1): p. 98-114.
19. Pietrosanti, D., M. De Angelis, and M. Basili, *Optimal design and performance evaluation of systems with Tuned Mass Damper Inerter (TMDI).* Earthquake Engineering & Structural Dynamics, 2017. **46**(8): p. 1367-1388.
20. Ye, K., et al., *Analytical solution of seismic response of base‐isolated structure with supplemental inerter.* Earthquake Engineering & Structural Dynamics, 2019. **48**(9): p. 1083-1090.
21. Li, L. and Q. Liang, *Effect of inerter for seismic mitigation comparing with base isolation.* Structural Control and Health Monitoring, 2019. **26**(10): p. e2409.
22. Petrini, F., A. Giaralis, and Z. Wang, *Optimal tuned mass-damper-inerter (TMDI) design in wind-excited tall buildings for occupants' comfort serviceability performance and energy harvesting.* Engineering Structures, 2020. **204**: p. 109904.
23. Yang, J.N., Z. Li, and S. Liu, *Stable controllers for instantaneous optimal control.* Journal of engineering mechanics, 1992. **118**(8): p. 1612-1630.

EURODYN 2020
XI International Conference on Structural Dynamics
M. Papadrakakis, M. Fragiadakis, C. Papadimitriou (eds.)
Athens, Greece, 23–26 November 2020

FUNDAMENTAL PERIOD RELATIONSHIP OF RC-BUILDINGS IN ALICANTE PROVINCE (SPAIN). A FIRST STEP TO SOIL-STRUCTURE RESONANCE MAPS

N. Agea-Medina [1], A. Kharazian [1], S. Molina [1,2], J. Galiana-Merino [3,4] and J.L. Soler-Llorens [2]

[1] Multidisciplinary Institute for Environmental Studies "Ramón Margalef" (IMEM), University of Alicante. {noelia.agea, alireza.kharazian}@ua.es

[2] Dept. Earth Sciences and Environment - Faculty of Sciences - University of Alicante.
{sergio.molina, jl.soler}@ua.es

[3] University Institute of Physics Applied to Sciences and Technologies, University of Alicante, Spain
juanjo@dfists.ua.es

[4] Dept. Physics, Systems Engineering and Signal Theory, Polytechnic School, University of Alicante, Spain

Keywords: noise measurements, fundamental period, resonance, vulnerability

Abstract. *South and South-East of Spain are the regions with a higher seismic hazard in Spain Consequently, all the municipalities in Alicante province has to develop seismic emergency planning. Besides, the south of Alicante province and, in particular, the cities of Elche and Alicante are located in a sedimentary deposit, which can reach hundreds of meters, so site effects can be important. Additionally, most of the building stock belongs to periods without seismic normative, increasing, therefore, their vulnerability. Furthermore, following the damage caused by earthquakes in Spain, it has been observed that there are significant differences in the spatial distribution of damage from site to site in buildings with similar seismic behavior, located in a similar site. Hence, many authors have stated that the main factor responsible for the different damage distribution could be the building height. The seismic response of a building depends on its dynamic characteristics (fundamental period, T, damping ratio, ξ, and modal shape) and on the input ground motion. Among the existing methods to determine the T and ξ parameters, the best ones probably are to record weak earthquakes (or near explosions) or induced vibrations inside the building. However, both techniques need a very expensive and time-consuming effort when it is applied to a large number of buildings. A possible alternative is the measurement of ambient vibrations. In this work, ambient vibration measurements were performed at the geometrical center of the plan on the top floor of buildings with different height and year of construction in the municipality of Alicante and Elche (both in the Alicante province), assuming that this point coincides with the mass center of the floor. The preliminary results follow a linear relationship between the number of stories and the fundamental period. Finally, the results have been used to estimate the probability of resonance in several districts of both municipalities.*

1 INTRODUCTION

Spain has a moderate seismic hazard, compared with other European countries like Italy or Greece. However, South and South-East regions had been affected by damaging earthquakes and according to the updated seismic hazard map developed by [1], the expected peak ground acceleration (PGA) for an exceedance probability of 10% in 50 years is 0.24g (Granada province) and 0.23g (Alicante province). In this work, we have chosen two of the most important cities of Alicante province, in terms of population and number of buildings, that is, Elche and Alicante cities. Both cities are located above a sedimentary deposit with hundreds of meters deep, making it possible to feel the effects of small to moderate shallow earthquakes (5 to 10 km), which are very common in this area. According to the update of the seismic hazard maps [1], the PGA for exceedance probability of 10% in 50 years is 0.18g for Alicante and 0.20g for Elche.

The last damaging earthquake in Spain was the Lorca earthquake (May 11, 2011 with a moment magnitude of Mw = 5.2 and a focal depth of 4.6 km). Although the magnitude was not severe, the observed damage was very high. More than 300 buildings were demolished and many others repaired. Concretely in this city, [2] analyzed the dynamic behavior of the buildings before and after the Lorca earthquake. They concluded that the fundamental period of the buildings shows a permanent increase following a process of damage such as an earthquake. The fundamental period (T) is a parameter widely used to evaluate the seismic response of the buildings.

In contrast, the damping factor is not usually used as an indicator of damage in structures. The damping assessment is a complex problem due to all the variables involved. That fact is due to depending on many factors such as structure and soil characteristics [3].

Several studies have used the recorded ambient vibrations to obtain the seismic response of the building, e.g., [2, 4, 5, 6, 7, 8, 9, 10, 3, 11 and 12]. In essence, their results do not differ from other methods such as earthquake registration or forced vibration techniques.

Therefore, the main objective in the present work is to develop an empirical relationship between the fundamental period and the number of floors using the recorded ambient vibration on the top floor of the buildings in Alicante and Elche cities. Both cities represent the construction model of the Mediterranean coastal area. The obtained relationship will be used not only to establish the fundamental period of the current building stock but also to compare its evolution if damaging earthquakes would happen in the area.

2 DATA ACQUISITION AND ANALYSIS

Alicante and Elche have approximately 24,162 and 34,395 buildings respectively. The height of the buildings can be classified as low-rise (1 to 3 stories) with a 49 % for Alicante and 67 % for Elche; mid-rise (4 to 6 stories) with a 30 % for Alicante and 21 % for Elche and high-rise (>6 stories) with a 21 % for Alicante and 11 % for Elche. For this study, we have carried out a random selection of reinforced concrete buildings in both cities. Table 1 shows the selected buildings with information about the height, year of construction, and location.

The fundamental period of the buildings was estimated through ambient vibration measurements using a three-component digital seismometer Güralp 6TD. This is a broadband instrument with an on-board 24-bit digitizer and configurable output. The duration of the records was 10 minutes and the equipment was located on the top floor of the buildings (Figure 1). If some disturbance occurred during the recording time, the duration of the measurement was increased by 5 more minutes. [13] was used to compute the Fourier amplitude spectra and the fundamental period for each longitudinal direction. Finally, the building period was assigned as the average of both horizontal components.

Building number	Cadastral reference	Number of storeys	Year of construction
no 1	1474122YH0317C	2	2007
no 2	4377901YH0347G	2	2004
no 3	4204101YH2540C	2	> 2007
no 4	7463801YH1476C	3	> 2007
no 5	0175726YH2407E	3	2007
no 6	1671701YH0317B	4	1986
no 7	1278012YH0317G	4	1960
no 8	0791301YH0309B	4	1960
no 9	1083323YH0318C	5	1959
no 10	0891608YH0309B	5	1960
no 11	1274701YH0317C	5	1968
no 12	2787301YH0328F	5	1979
no 13	0889504YH0308H	6	1976
no 14	0878314YH0307H	6	1971
no 15	1183715YH0318C	6	1989
no 16	4677303YH0347H	7	2005
no 17	7663901YH1476D	7	1983
no 18	7662807YH1476B	7	1985
no 19	1479009YH0317G	8	1977
no 20	2789710YH0328H	8	1975
no 21	7662802YH1476B	8	1984
no 22	9788403XH9398H	9	2006
no 23	0487603YH0308E	9	1975
no 24	7666501YH1476F	9	1983

Table 1: Information of the selected buildings in Alicante and Elche.

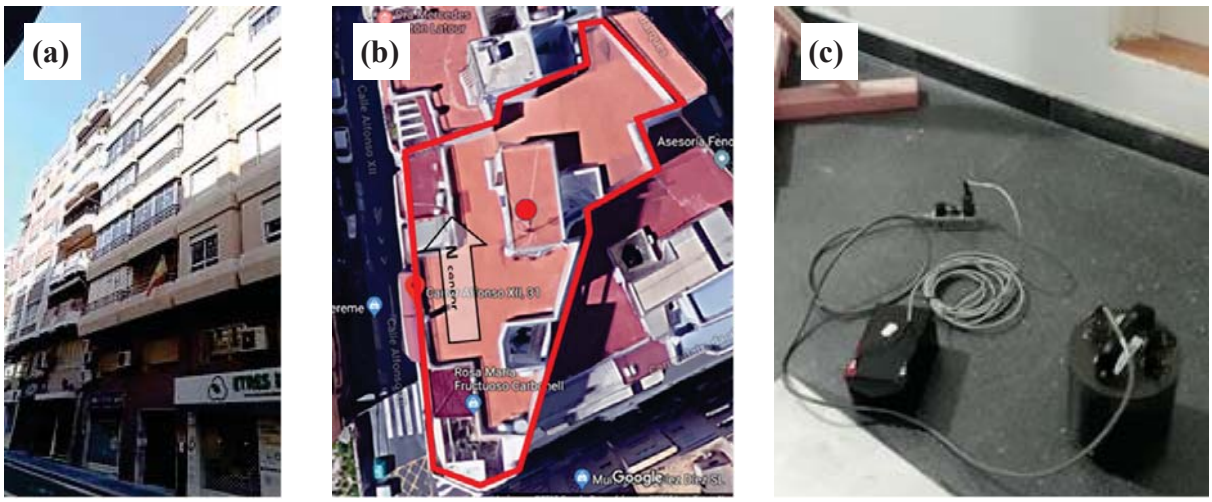

Figure 1: a) Main front of one of the studied buildings (no 19). b) Aerial view of the building with the location of the sensor and its orientation. c) Equipment arrangement during measurement inside the building.

Additionally, microzonification campaigns in urban areas of both cities were carried out using a 1 Hz Mark L-4C-3D seismographs connected to a Reftek digitizer. Regarding the number of H/V measurements, a total number of 123 and 90 measures were taken for Alicante and Elche, respectively. In both cases, the measurements were carried out leaving a separation of about 500 meters between them. In this case, attending to the expected resonant frequencies and the recommendations proposed in [14] the duration of the records was set up to 30 minutes.

3 FUNDAMENTAL PERIOD

To determine the fundamental period of the selected buildings of Alicante and Elche, the sensor was located in the available highest part of these buildings. In this way, the sensor records all the vibrations that pass through the building, assuming that the sensor is in the mass center of the floor [2].

The recorder noise can be produced by environmental factors (e.g. wind) or coming from different artificial sources such as traffic noise, elevators, presence of people, etc. The method is based on the fact that these sources of noise, excluding strong harmonic sources close to the instrument, contain energy with a broad spectrum and the building acts as a filter enhancing its dynamic properties [2].

Once the data were collected, the power spectral density of both horizontal components was determined for each building. An example is shown in Figure 2. As it can be observed, the steeper peak indicates the fundamental frequency of the building in that direction. However, erroneous peaks may appear as a result of the interaction with adjacent buildings or due to the building's own geometry, so the analysis has to be performed carefully.

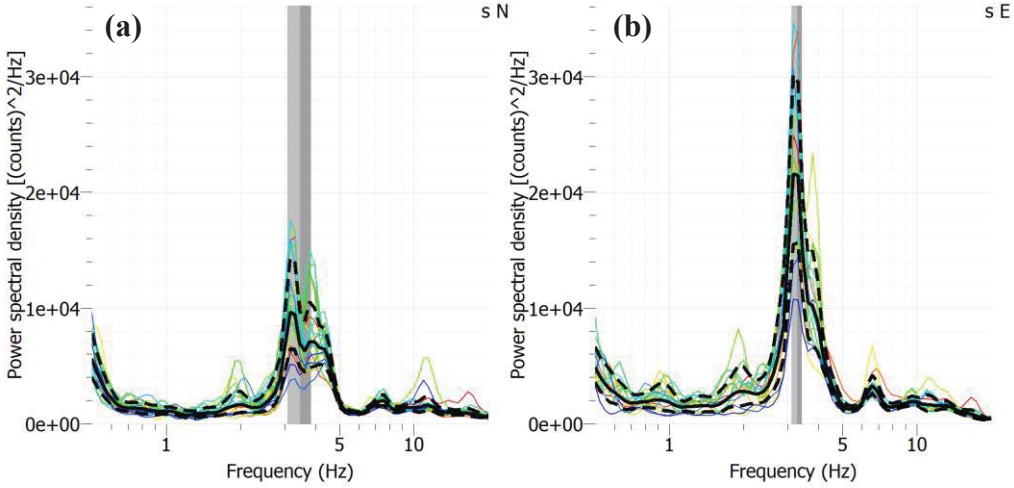

Figure 2: Power spectral density for North and East components of the building no 19.

The obtained results for the buildings of both cities show that the natural vibration period increases with the number of storeys (Table 2). In Table 2 it can be seen that the lowest value of the average fundamental period is 0.13 ± 0.06 sec for buildings with two floors and the highest value is 0.40 ± 0.14 sec for buildings with nine floors.

N (storeys)	T (sec)
2	0.13 ± 0.06
3	0.15 ± 0.02
4	0.16 ± 0.03
5	0.20 ± 0.03
6	0.23 ± 0.05
7	0.37 ± 0.01
8	0.36 ± 0.04
9	0.40 ± 0.14

Table 2: Average value of the fundamental periods obtained for buildings with different number of storeys.

Linear regression has been made using the commonly applied expression, T = a N, where T is the period and N is the number of storeys. The obtained relationship is as follow:

$$T = 0.045\ N \text{ with } \sigma = 0.035 \tag{3.1}$$

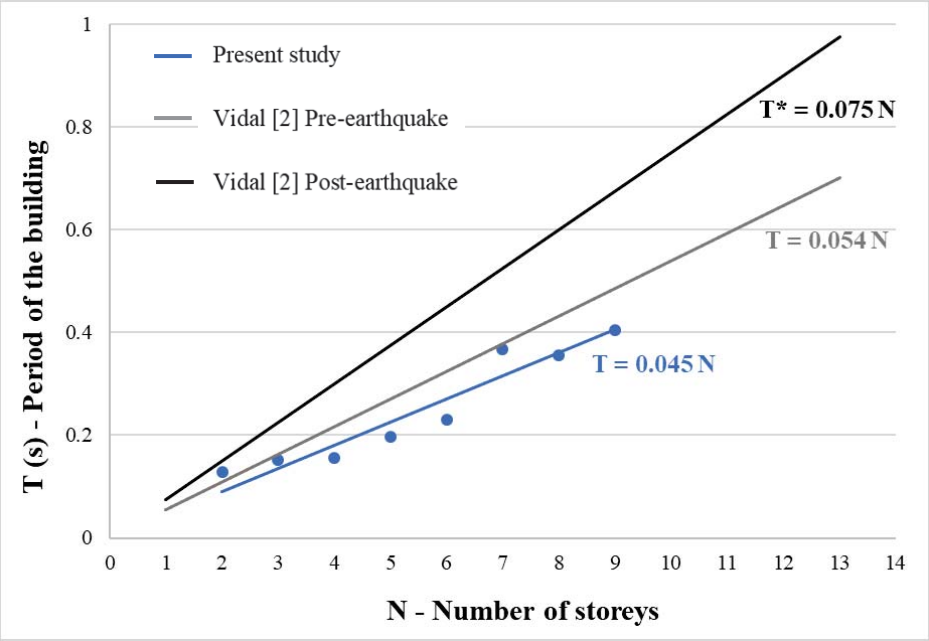

Figure 3: Relationship between the period of the building (T) and the number of storeys (N). Blue line represented the one obtained in this study while black a grey line represents the one obtained by [2] before (T) and after earthquake (T*).

Equation (3.1) has a correlation coefficient of $R^2 = 0.912$ and an average standard deviation of $\sigma = 0.035$. In Figure 3, the obtained relation is compared with the ones obtained by [2] in the Lorca city before and after the 2011 earthquake. The comparison shows that the obtained linear adjustment presents the lowest slope, providing a period of 0.39 sec for a 9 storeys building while [2] will assign 0.49 sec. As [2] used buildings with height up to 13 storeys, the difference can be due to a lack of data in our results so future studies will include buildings with higher height. If we assume that the slope increases for damaged buildings, our lower slope will also be indicative of a lower vulnerability of the reinforced-concrete buildings analyzed. The obtained results are also quite similar to other previous studies carried out in Europe using ambient vibrations, e.g., [4, 5 and 12].

4 RESONANCE PROBABILITY

The phenomenon of resonance occurs when the fundamental period of the buildings coincides with the predominant period of the soil. Resonance phenomenon results in an amplification of the movement of the structure, increasing the damage in the building. If the fundamental period of the building and the predominant period of the soil are different enough, the phenomenon of resonance will not exist.

In the present study, the predominant period of the soil was obtained using the H/V technique [15]. In Figure 4, an example is shown.

The probability of resonance (IR) of each of the buildings has been assigned using the ratio (in percentage) between the fundamental period of the building and the natural period of the soil. Thus, we have assumed the following classification: no resonance for IR <60%; slight resonance for IR between 60% and 75%; moderate for IR between 75% and 90% and full resonance for IR higher than 90%.

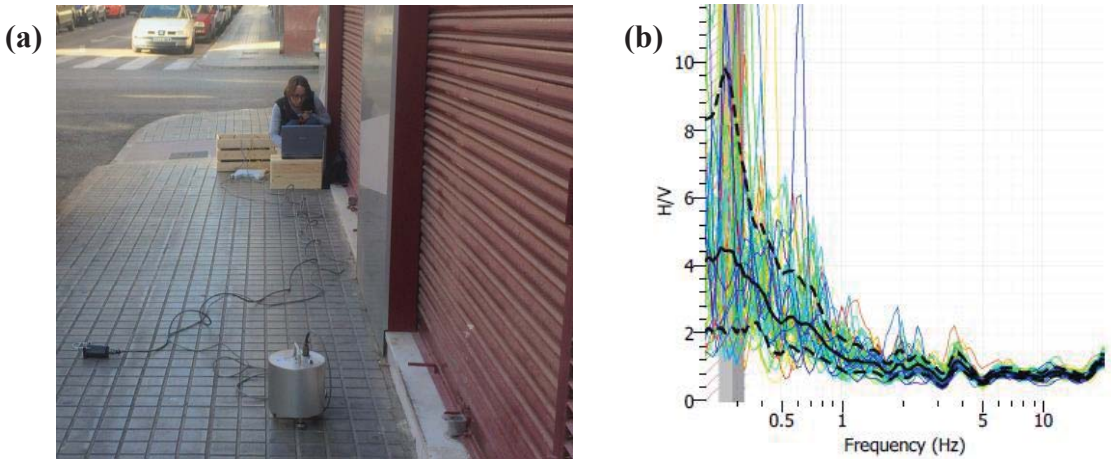

Figure 4: Example of the ambient noise measurements carried out in the vicinity of the building shown in Figure 1 (no 19). a) Field measurement and b) obtained H/V curve.

Table 3 shows the obtained fundamental period for the buildings and the predominant period of the soil as close as possible to the position of the building. In the right column is indicated the probability of resonance. Table 3 shows that, only one of the studied buildings is classified like moderate. The rest of the buildings do not show probability of resonance.

Building number	Storeys	T(s) Building	T(s) Soil	Resonance probability
no 1	2	0.088	3.690	no resonance
no 2	2	0.102	3.440	no resonance
no 3	2	0.196	3.850	no resonance
no 4	3	0.163	3.330	no resonance
no 5	3	0.141	0.270	no resonance
no 6	4	0.185	3.330	no resonance
no 7	4	0.132	3.500	no resonance
no 8	4	0.153	3.100	no resonance
no 9	5	0.196	3.270	no resonance
no 10	5	0.156	3.100	no resonance

no 11	5	0.214	3.690	no resonance
no 12	5	0.221	0.260	**moderate**
no 13	6	0.218	2.940	no resonance
no 14	6	0.290	3.070	no resonance
no 15	6	0.185	0.070	no resonance
no 16	7	0.372	3.030	no resonance
no 17	7	0.359	3.330	no resonance
no 18	7	0.373	3.230	no resonance
no 19	8	0.307	3.500	no resonance
no 20	8	0.372	0.260	no resonance
no 21	8	0.389	3.230	no resonance
no 22	9	0.492	2.670	no resonance
no 23	9	0.241	3.470	no resonance
no 24	9	0.481	3.330	no resonance

Table 3: Fundamental periods measured in Alicante and Elche and the probability of resonance.

5 CONCLUSIONS

Ambient vibration measurements have been carried out in reinforced concrete buildings within the urban areas of Alicante and Elche in order to obtain the fundamental period and a relationship with the height of the building. From the obtained results, it can be concluded:

a) The obtained period-height relationship shows a similar behavior than the obtained by [2] in Lorca, but our slope is lower. This can be due to the lack of data in the regression or it may indicate a lower vulnerability of the reinforced-concrete buildings chosen for Alicante and Elche when compared with Lorca city.
b) Our period-height relationship has been used to propose a probability of soil-structure resonance and only one of the studied buildings has been assigned moderate resonance probability.

The next step in this research will be to continue the data acquisition to a higher number of buildings (also with higher heights), what will improve the estimated linear regression. Additionally, this will allow us to compute resonance probability maps for the whole cities using not only the fundamental period of the soil but also, considering the secondary peaks observed in the HV curves of some areas. These secondary peaks may appear due to the presence of more superficial contrasts and might have additional effects on certain buildings.

6 ACKNOWLEDGMENTS

The study has received funding from the European Union's Horizon 2020 research and innovation programme under grant agreement No 821046, the Ministerio de Economía, Industria y Competitividad through research project CGL2016-77688-R, the Generalitat Valenciana through the research project AICO/2016/098 with the collaboration and funding provided by Elche and Alicante municipalities.

REFERENCES

[1] IGN-UPM Working Group (2012). Actualización de Mapas de Peligrosidad Sísmica de España 2012. Editorial Centro Nacional de Información Geográfica, Madrid.

[2] Vidal, F., Navarro, M., Aranda, C. And Enomoto, T. (2014). Changes in dynamic characteristics of Lorca RC buildings from pre- and post- earthquake vibration data. Bull Earthquake Eng 12: 2095-2110. https://doi.org/10.1007/s10518-013-9489-5

[3] Satake N, Suda K, Arakawa T, Sasaki A, Tamura Y (2003) Damping evaluation using full-scale data of buildings in Japan. J Struct Eng ASCE 129(4):470–477HS. Atamturktur, B. Moaveni, C. Papadimitriou, Model Validation and Uncertainty Quantification, *Volume 3: Proceedings of the 32nd IMAC, A Conference and Exposition on Structural Dynamics*, 2014.

[4] Oliveira CS, Navarro M (2010) Fundamental periods of vibration of RC buildings in Portugal from in-situ experimental and numerical techniques. Bull Earthq Eng 8:609–642

[5] Gallipoli MR, Mucciarelli M, Vona M (2009) Empirical estimate of fundamental frequencies and damping for Italian buildings. Earthq Eng Struct Dyn 38:973–988

[6] Gallipoli MR, Mucciarelli M, Šket-Motnikar B, Zupan´ci´c P, Gosar A, Prevolnik S, Herak M, Stipˇcevi´c J, Herak D, Milutinovi´c Z, Olum´ceva T (2010) Empirical estimates of dynamic parameters on a large set of European buildings. Bull Earthq Eng 8:593–607

[7] Navarro M, Sánchez FJ, Feriche M, Vidal F, Enomoto T, Iwatate T, Matsuda I, Maeda T (2002) Statistical estimation for dynamic characteristics of existing buildings in Granada, Spain, using microtremors. Structural Dynamics, Eurodyn 2002, 1, 807–812, Balkema

[8] Navarro M, Vidal F, Enomoto T, Alcalá FJ, Sánchez FJ, Abeki N (2007) Analysis of site effects weightiness on RC building seismic response. The Adra (SE Spain) example. Earthq Eng Struct Dyn 36:1363–1383

[9] Navarro M, Oliveira CS (2005) Dynamic properties of existing RC buildings using measurements of ambient vibrations. Structural Dynamics, Eurodyn 2005, 3, 1847–1852, Millpress

[10] Navarro M, Oliveira CS (2006) Experimental techniques for assessment of dynamic behaviour of buildings. In: Oliveira CS, Roca A, Goula X. Assessing and managing earthquake risk. Volume 2, part II, chapter 8, Springer, pp 159–183

[11] Kobayashi H, idorikawa S, Tanzawa H, Matsubara M (1987) Development of portable measurement system for ambient vibration test of building. J Struct Constr Eng (Transactions of Architectural Institute of Japan) 378:48–56

[12] Kobayashi H, Vidal F, Feriche M, Samano T, Alguacil G (1996) Evaluation of dynamic behaviour of building structures with microtremors for seismic microzonation mapping. In: The 11th world conference on earthquake engineering, Acapulco, México, 23–28 June 1996

[13] Geopsy® (available at www.geopsy.org)

[14] SESAME (2004) Guidelines for the implementation of the H/V spectral ratio technique on ambient vibrations. Measurements, processing and interpretation. SESAME Europe-

an research project WP12-deliverable D23.12. http://sesame-fp5.obs.ujf-grenoble.fr/Delivrables/Del-D23-HV_User_Guidelines.pdf

[15] Nakamura Y (1989) A method for dynamic characteristics estimation of subsurfaceusing microtremor on the ground surface, Q. Rep. Railw. Tech. Res. Inst. 30, 25–33

EURODYN 2020
XI International Conference on Structural Dynamics
M. Papadrakakis, M. Fragiadakis, C. Papadimitriou (eds.)
Athens, Greece, 23–26 November 2020

MEASURING THE DYNAMIC DISPLACEMENTS OF BRIDGES USING GEOPHONE DATA: APPLICATION AND VALIDATION ON A LIVELY FOOTBRIDGE

Paolo Borlenghi[1], **George Piniotis**[2], **Harris Perakis**[2], **Vassilis Gikas**[2], **Carmelo Gentile**[1]

[1] Department of Architecture, Built environment and Construction engineering; Politecnico di Milano;
Piazza Leonardo da Vinci, 32 - 20133 Milan, Italy
e-mail: {paolo.borlenghi, carmelo.gentile}@polimi.it

[2] School of Rural and Surveying Engineering; National Technical University of Athens;
15780, Athens, Greece
e-mail: {vgikas, hperakis}@central.ntua.gr, piniotis@survey.ntua.gr

Keywords: Structural dynamic displacement, Cable-stayed bridge, Field test, Geophone, Signal integration

Abstract. *Dynamic displacement is a highly valuable information for the evaluation of bridge safety and performance, providing data on the dynamic behaviour of the structure under service loads. However, its measure is often challenging and costly: traditional techniques require a fixed support and a direct connection (or a clear line-of-sight) with the target point that is rarely present in large-scale infrastructures, making their deployment in long-term monitoring often not feasible. In this study, an indirect measuring approach deploying an electro-dynamic velocity sensor (geophone) and digital filtering is adopted to measure human-induced dynamic displacements on a lively footbridge. These sensors have an excellent cost to performance ratio, do not require any powering and, overall, are easy to install and deploy for a long time. Furthermore, geophones measure velocities and consequently only "one integration step" is needed to obtain displacements. The field test was performed with the bridge partially open to pedestrian passages, the geophone was placed in different positions directly on the deck, and a reference measure of the vertical displacement was obtained from a laser-based system placed nearby. Appropriate digital filtering is then applied on the geophone data before the integration. The calibration of digital filters and the validation of the results was carried out comparing the reconstructed vertical displacements from geophone data and the directly measured vertical displacements from the state-of-art measuring device. Under the assumption of pure dynamic loading, some promising results were obtained, reaching a tenth of a millimetre accuracy for the integrated signals.*

1 INTRODUCTION

Structural dynamic displacement is a highly valuable information for the evaluation of structural safety and performance, providing data on the dynamic behaviour of the structure under service loads. Furthermore, contemporary pedestrian bridges are often slender structures, prone to human-induced vibrations [1], making the control of displacement of great interest.

However, measuring dynamic displacement is often challenging and costly: traditional techniques require reference fixed points that are rarely found in large-scale structures, making the deployment in long-term monitoring often not feasible. Particularly, traditional displacement transducers, e.g. LVDT, requires direct contact both with the target measurement point and with external fixed support. Laser-based or radar-based systems, such as Laser Doppler vibrometer or Ground-based Microwave Interferometer [2], respectively, can provide noncontact measures of dynamic displacements but they still require a line-of-sight to the target point.

In recent years, some promising applications of low-cost satellite-based systems for structural displacement measures, such as GPS [3] or GNSS [4], were carried out but the lack of accuracy often remains an issue.

Another interesting approach is based on indirect measurements with accelerometers or velocimeters. These sensors are small, relatively low-cost, and easy to install and deploy for long time. The main drawback of these technologies is the need for signal processing when performing double or single integration for displacement reconstruction. Indeed, if direct integration is performed, the presence of noise in the recorded data and the inaccurate measures in the low-frequency range brings to erroneous estimation of displacements [5]. For this purpose, various digital filters can be applied: Butterworth filter [6], Baseline Correction [7], finite impulse response filter (FIR filter) [8], or Spectral Subtraction [9] are some examples.

Among the technologies that record accelerations and velocities, geophones are of interest for their cost to performance ratio and the null power demand. Geophones are a well-established technology in the field of seismology, mainly used for measuring ground motion-induced velocities, showing remarkable results in estimating the dynamic displacements [5]. In addition, geophones are well-suited sensors for Operation Modal Analysis of civil engineering structures (see e.g. [10]), making their deployment in a monitoring system of twofold interest: (a) identifying the modal characteristics of the structure; (b) monitoring the maximum displacements induced by operational loads.

More recently, geophones were widely deployed to evaluate the deformations that occur to railway track foundations, during the passage of trains [11-12]. Bowness et al. [6] describe a technique to filter and integrate geophone signals in the context of railway track monitoring. Firstly, the signals are deconvoluted to consider the frequency-dependent sensitivity and the phase lag of the sensor. Indeed, these instruments have a limited linear frequency range, above its natural frequency, typically between 4 and 12 Hz, and when dealing with excitations that have a dominant frequency close to the natural frequency of the sensor, deconvolution is always needed. Secondly, a band-pass filter with a range of 0.3–15 Hz is applied: the high-pass removes the low-frequency drift while the low-pass removes noise at high frequencies. However, defining the cut-off frequency can be challenging, considering that the filter becomes unstable when approaching 0 Hz. Bowness et al. [6] define the lowest cut-off frequency equal to 0.2 Hz.

Notwithstanding, the promising applications of geophones in the monitoring of railway track deformations or recording of strong motion-induced displacements, very few studies are

present in the literature for the application of geophones to record structural dynamic displacements of bridges.

The present paper investigates the application of geophones in the measurement of dynamic displacement of pedestrian bridges. The procedure was exemplified on a cable-stayed pedestrian bridge: the human-induced vibrations are recorded in the same point with a geophone and a state-of-art technology for measuring dynamic displacement (i.e. a Laser Tracker). Therefore, to estimate the dynamic displacement from the geophone data, digital filtering was applied before signal integration. The validation of the results and the calibration of the digital filter was performed through the comparison between reconstructed (from geophone data) and directly measured (from the Laser Tracker) displacements. Particularly, the following steps were involved:

(i) performing a field test on the selected cable-stayed bridge, measuring the human-induced vibrations with multiple setups (subsequent measures in different points) deploying a geophone and a state-of-art measuring device;
(ii) performing the deconvolution of the geophone data with SEISMOWIN [13] software;
(iii) selecting and calibrating a digital filtering method (i.e. pass-band filter [6]) to minimise the difference between the measured and reconstructed dynamic displacements; and
(iv) consequently, developing a MATLAB-based algorithm to perform the filtering and the integration of geophone data for long-term monitoring purposes.

2 ADOPTED MEASURING DEVICES

Geophones are electro-dynamic velocity transducers that produce an output signal in voltage proportional to the recorded speed. The signal is generated by the relative movements of a coil suspended around a core magnet. Therefore, geophones are passive sensors and do not require any power supply. The main drawbacks of this technology are the limited frequency range and the limited excursion of the coil. In the low frequency range – below the resonant frequency of the sensors – the signal is attenuated, and a proper signal deconvolution must be performed. The limited excursion is given by the limited length of the suspended system.

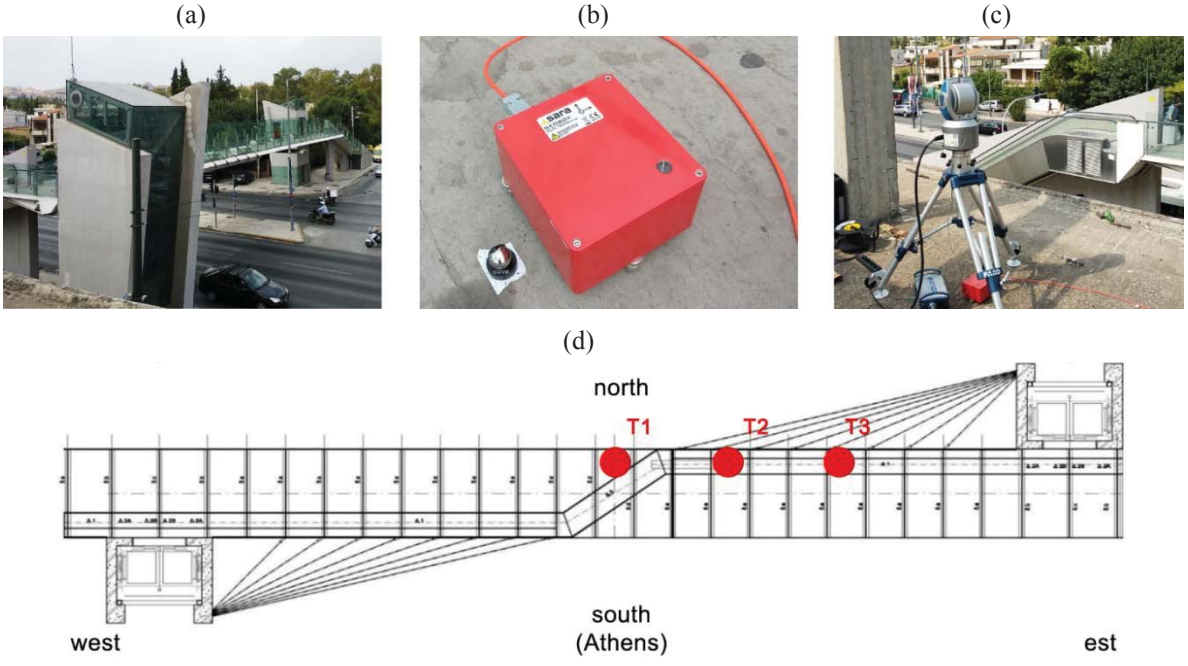

Figure 1: (a) Tested bridge; (b) Laser Tracker target and Geophone; (c) Laser Tracker; (d) Experimental setup.

The indirect measures of displacement were conducted with a high-sensitive seismometer (Fig. 1b), namely a SARA GEOBOX SS45 (nominal sensitivity 78 V/ms^{-1}; natural frequency 4.5 Hz). These specific geophones are of interest for the very good performance in the low-frequency range with a usable dynamic band – before an appropriate signal deconvolution – defined by the manufacturer of 0.2-400 Hz.

The direct measurements of displacements were conducted with a laser tracker, namely the FARO Vantage (Fig. 1c). The Vantage is a portable, three dimensional coordinate measuring instrument that determines the position of a special Spherically Mounted Retroreflector (SMR), through the extremely accurate measurement of a zenith angle, an azimuth angle and a radial distance from the instrument. It uses a phase shift Absolute Distance Meter (ADM), providing a Maximum Permissible Error (MPE) accuracy of ±16μm+0.8μm/m for the radial distance measurements, while its angular Maximum Permissible Error (MPE) accuracy is ±20μm+5μm/m. According to FARO, the typical performance of the sensor is half the MPE values. Vantage has a working range of 0m to 80m and it is capable of making static and dynamic measurements as well, since its maximum sampling frequency is 1 kHz.

3 BRIDGE DESCRIPTION AND TEST PROGRAMME

The test bridge (Fig. 1a), named "Bridge of dreams", is a cable stayed, composite bridge located in the North of Athens, Greece, crossing over the main road that leads to the Olympic Stadium Complex [14]. The bridge is suspended from two composite pylons using 16 fully-locked galvanized cables, anti-symmetrically distributed on each side of the structure. It has an overall length of 76.0 m, a free span of 31.5 m and is 4.0 m wide.

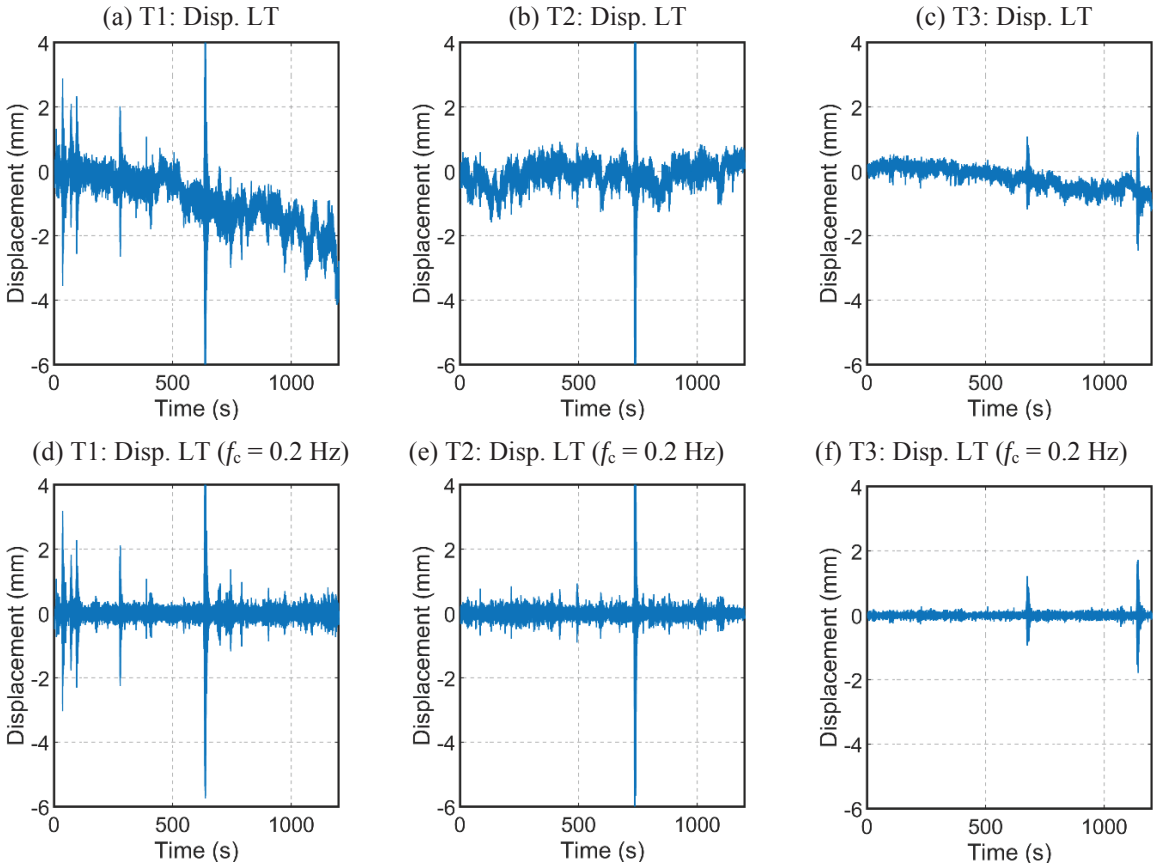

Figure 2: Laser tracker time-series of the 3 measured points: comparison between the non-filtered data (a-c) and the filtered data with a Bandpass Butterworth Filter with a lower cut-off frequency (f_c) of 0.2 Hz (d-f).

The field test was performed with the bridge partially open to pedestrian passages; the geophone was placed in different positions directly on the deck (Fig. 1d), and a reference measure of the vertical displacement was obtained from the laser tracker placed on the roof of a nearby building (Fig. 1c). Particularly the test involved the following steps: (i) positioning of the state-of-art measuring device on the top of a nearby building to obtain a clear line-of-sight to the target point (the small sphere in Fig. 1b); (ii) positioning of the geophone (the red box in Fig. 1b) and the target point in the selected position (Fig. 1d); (iii) recording of human-induced vibration with both devices for 1200 seconds with a sampling rate of 200 Hz.

4 SIGNAL PROCESSING AND DATA ANALYSIS

The calibration of digital filters and the validation of the results was carried out comparing the reconstructed vertical displacements from geophone data and the directly measured vertical displacements from the laser tracker (LT).

The recorded time-series of displacement from the LT are shown in Fig. 2. Figs. 2a-c illustrates the raw displacement data obtained just subtracting the initial recorded value. As mentioned earlier, the test was performed with the bridge partially open to pedestrian passages. During the test the number of people that were walking or staying (several benches are present on the bridge deck) changed continuously, creating an overall increase of quasi-static loads; this effect is particularly visible in the first recording (T1, Fig. 2a). To obtain a pure dynamic displacement, the effects of the quasi-static loads and the noise in the high frequency range were removed with a pass-band filter with cut-off frequencies of 0.2 Hz and 15 Hz (Figs. 2d-f).

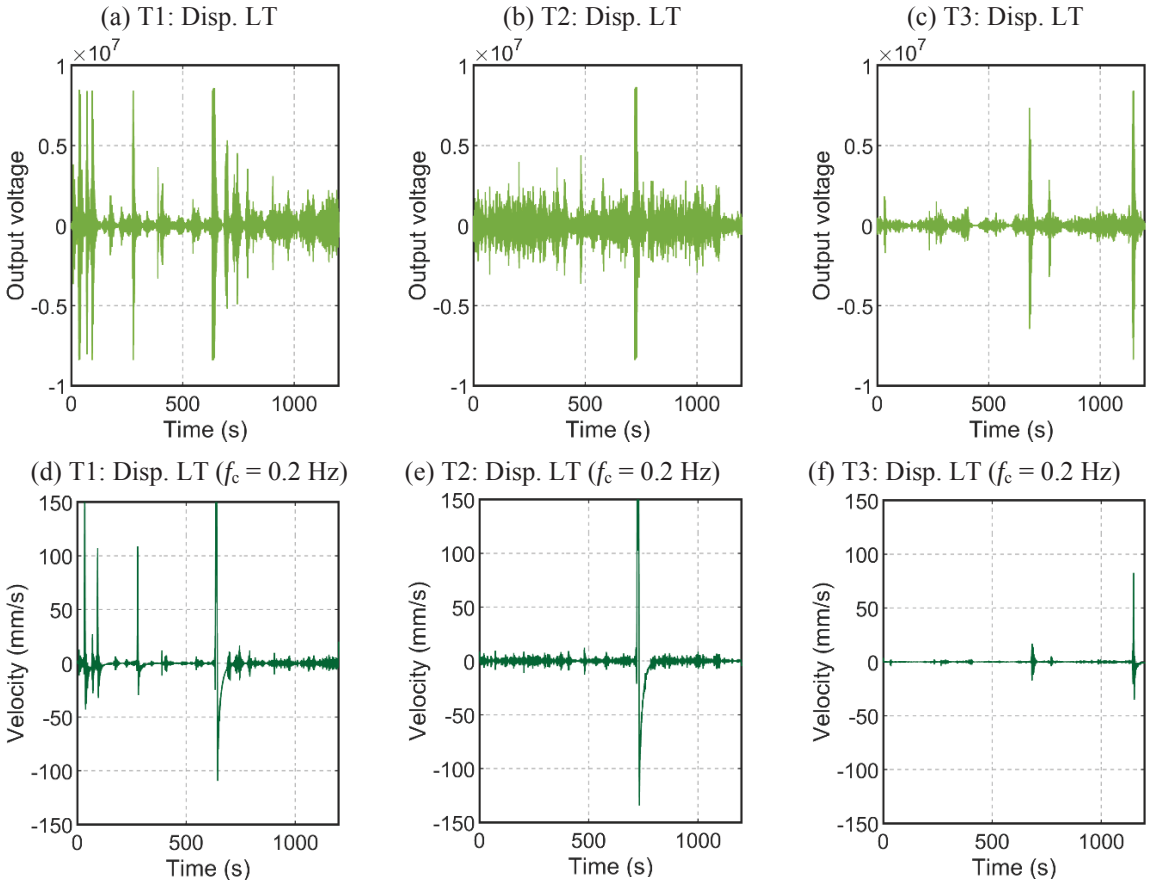

Figure 3: Geophone time-series from of the 3 measured points: comparison between the raw data (a-c) and the deconvoluted velocity data (d-f).

The recorded signals from the geophone are shown in Fig 3. Figs. 3a-c illustrates the raw output voltages: the sharp peaks, particularly visible in the first recording, are caused by high dynamic loads given by people running on the deck. In these instances, the signal reached the threshold given by limited excursion of the coil, resulting in a clipping of the recorded data. This is particularly visible in the deconvoluted velocity data (Figs. 3d-f): the clipped signals results in abnormal speed increases that must be removed or ignored.

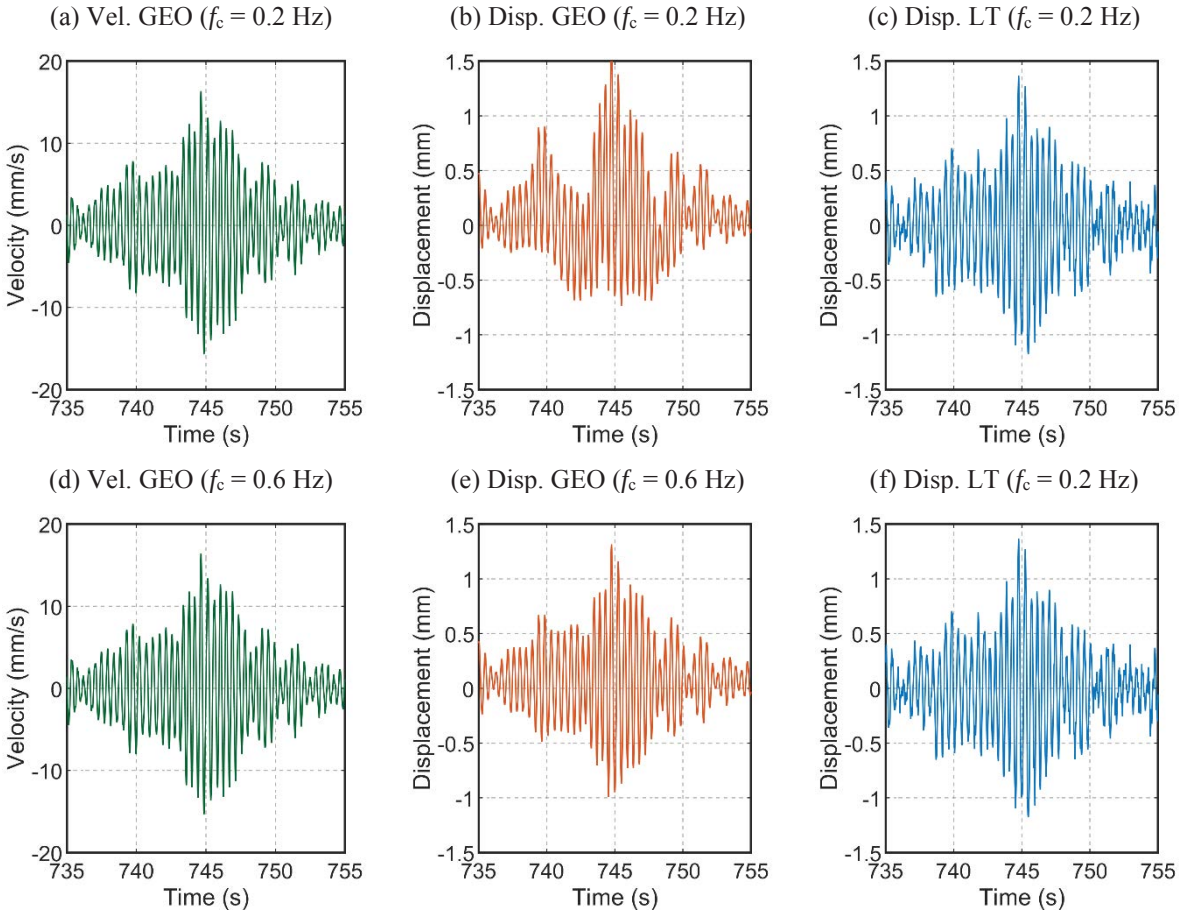

Figure 4: Time-series of 20 sec from T1: geophone velocities (a, d) and reconstructed displacements (b, e) with different cut-off frequency (f_c) and reference laser tracker displacements (c, f).

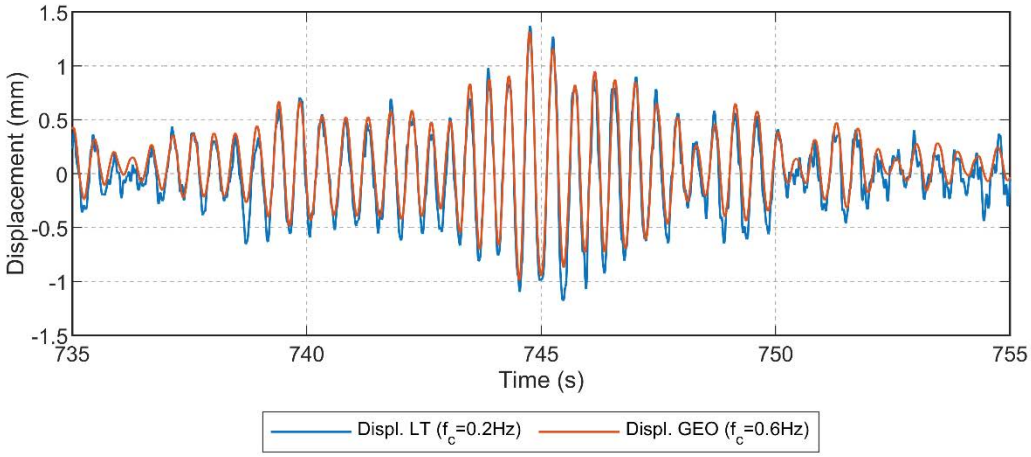

Figure 5: Time-series of 20 sec from T1: comparison between the reconstructed displacements from the geophone (f_c = 0.6 Hz) and the reference laser tracker displacements (f_c = 0.2 Hz).

Subsequently, a pass-band Butterworth filter was applied on the velocity data before the integration. The difference between the references and the reconstructed displacements were minimised with a manual tuning of the cut-off frequencies of the filter. To exemplify the calibration procedure, in Fig. 4 and Fig. 6 are shown few seconds of the time-series recorded at T1 and T3. Firstly, a lower cut-off frequency (f_c) of 0.2 Hz was adopted showing some distortion in the reconstructed displacements (Figs. 4b, 6b). The best match was obtained with f_c =0.6 Hz.

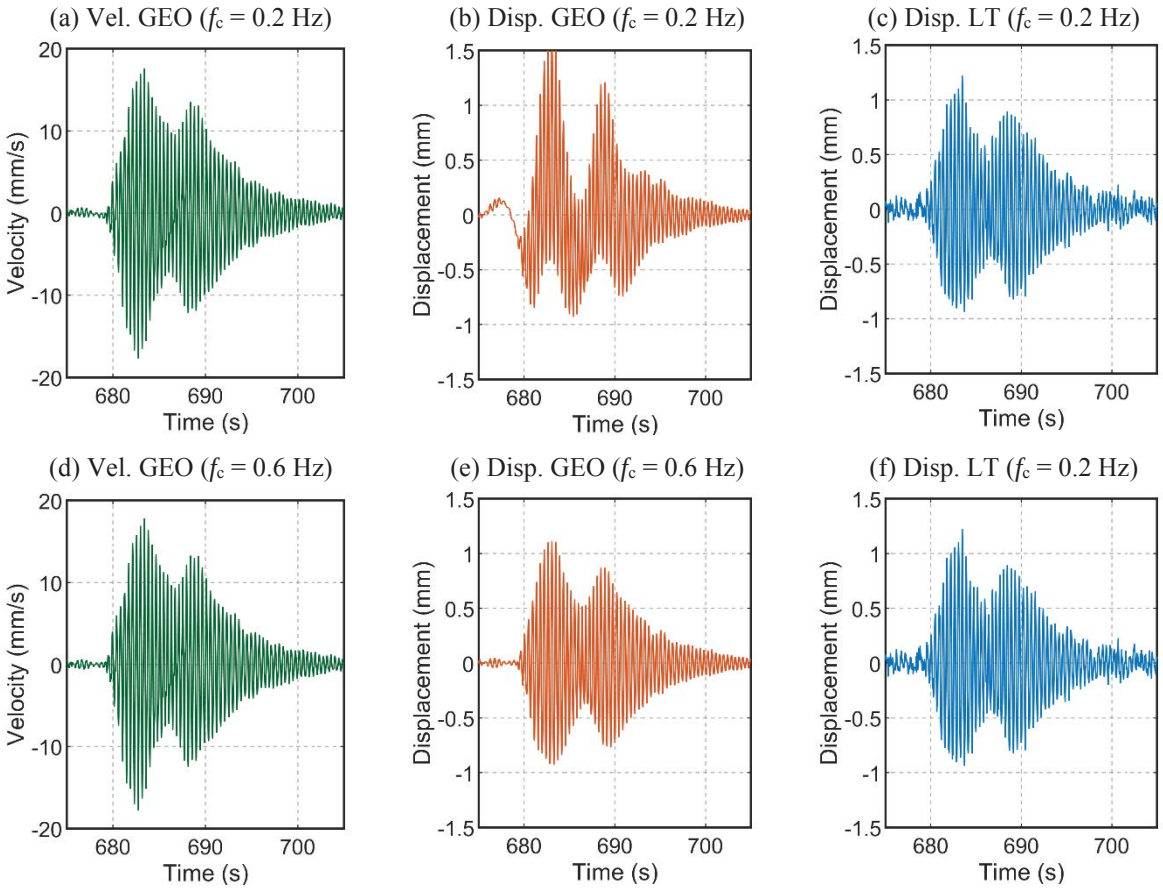

Figure 6: Time-series of 30 sec from T3: geophone velocities (a, d) and reconstructed displacements (b, e) with different cut-off frequency (f_c) and reference laser tracker displacements (c, f).

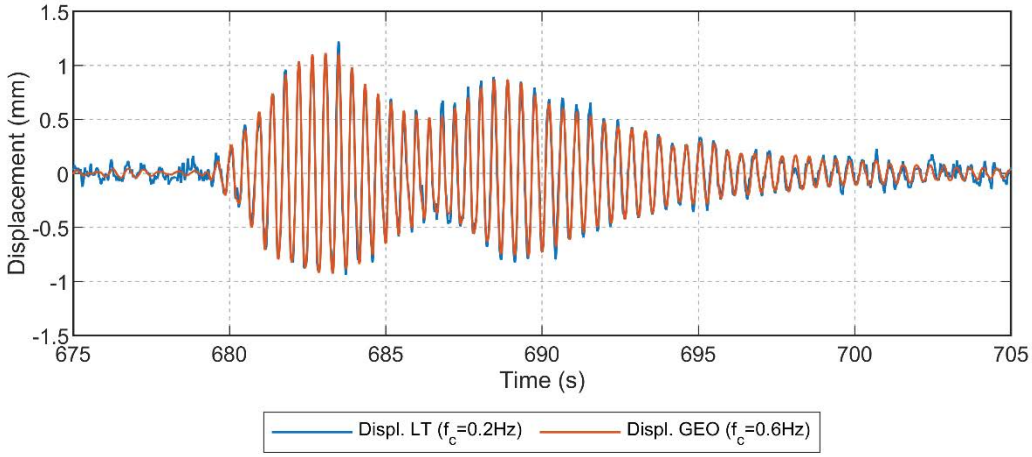

Figure 7: Time-series of 30 sec from T3: comparison between the reconstructed displacements from the geophone (f_c = 0.6 Hz) and the reference laser tracker displacement (f_c = 0.2 Hz).

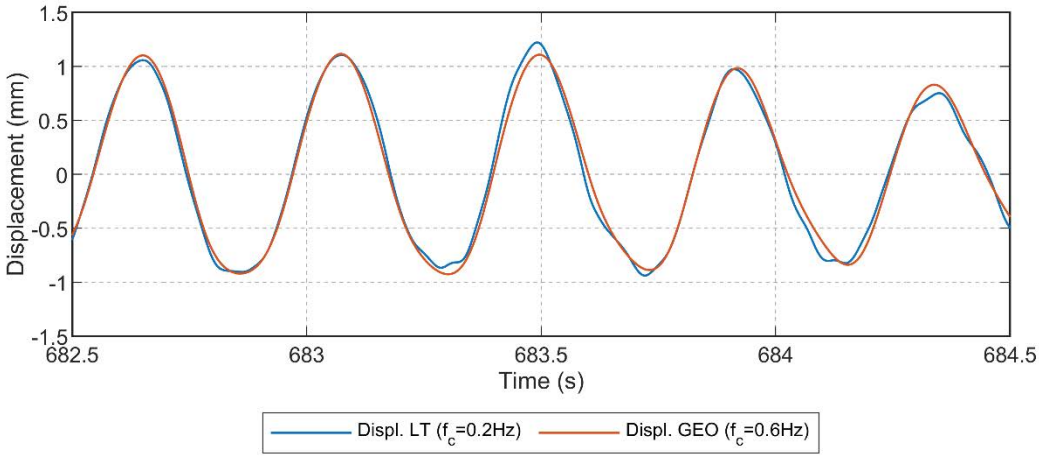

Figure 8: Focus on a time-series of 2 sec from T3: comparison between the reconstructed displacements from the geophone (f_c = 0.6 Hz) and the reference laser tracker displacement (f_c = 0.2 Hz).

Figs. 5 and 7 demonstrates the very good agreement between the reconstructed and the reference displacements.

5 CONCLUSIONS

Previous studies have demonstrated the successful application of digital signal processing on the velocity data recorded with geophones to reconstruct the displacements of railway track foundations and strong-motion induced displacements. In this study, an application of digital filtering for the reconstruction of human-induced displacements on a pedestrian cable stayed bridge is illustrated. The results from the investigated structure suggest the following conclusions:

1) Under the assumption of pure dynamic loading, it is possible to reconstruct the induced displacements from the geophone data by simply applying a Butterworth filter before the integration;
2) Approximately, a tenth of a millimetre accuracy was obtained for the integrated signals (Fig. 8);
3) The cut-off frequencies of the filter are connected to the dynamic characteristics of the investigated structure and to its operational loads;
4) Consequently, from a Structural Health Monitoring perspective, the filter calibration must be performed each time a long-term monitoring is installed;
5) Despite the generally very good accuracy in terms of reconstructed displacement, the sensor reached its measurement threshold several times, making impossible to reconstruct the maximum displacements experienced during the test. Further investigations are needed to reconstruct the clipped signals.

The promising results suggest the future application of the proposed signal processing strategy for the continuous monitoring of the dynamic displacement of bridges. In addition, more tests on structures with higher and lower stiffness have already been planned.

REFERENCES

[1] E. Caetano, Á. Cunha, F. Magalhães, C. Moutinho, Studies for controlling human-induced vibration of the Pedro e Inês footbridge, Portugal. Part 1: Assessment of dynamic behaviour, *Engineering Structures* 32(4), 1069-1081, 2010.

[2] C. Gentile, G. Bernardini, An interferometric radar for non-contact measurement of deflections on civil engineering structures: Laboratory and full-scale tests, *Structure and Infrastructure Engineering* 6(5), 521-534, 2010.

[3] F. Moschas, S. Stiros, Measurement of the dynamic displacements and of the modal frequencies of a short-span pedestrian bridge using GPS and an accelerometer, *Engineering Structures* 33(1), 10-17, 2011.

[4] J. Yu, X. Meng, X. Shao, B. Yan, L. Yang, Identification of dynamic displacements and modal frequencies of a medium-span suspension bridge using multimode GNSS processing, *Engineering Structures* 81, 432-443, 2014.

[5] D.M. Boore, J.J. Bommer, Processing of strong-motion accelerograms: needs, options and consequences, *Soil Dynamics and Earthquake Engineering* 25, 93-115, 2005.

[6] D. Bowness, A. C. Lock, W. Powrie, J. A. Priest, D. J. Richards, Monitoring the dynamic displacements of railway track, *in: Proceedings of the Institution of Mechanical Engineers, Part F: Journal of Rail and Rapid Transit* 221(1), 13-22, 2007.

[7] D. M. Boore, Effect of baseline corrections on displacements and response spectra for several recordings of the 1999 Chi-Chi, Taiwan, earthquake, *Bulletin of the Seismological Society of America* 91(5), 1199-1211, 2001.

[8] H. S. Lee, Y. H. Hong, H. W. Park, Design of an FIR filter for the displacement reconstruction using measured acceleration in low-frequency dominant structures, *International Journal for Numerical Methods in Engineering* 82(4), 403-434, 2010.

[9] B. Coelho, P. Hölscher, F. Barends, Enhancement of double integration procedure through spectral subtraction, *Soil Dynamics and Earthquake Engineering* 31(4), 716-722, 2011.

[10] C. Gentile, A. Ruccolo, F. Canali, Continuous monitoring of the Milan Cathedral: dynamic characteristics and vibration-based SHM, *Journal of Civil Structural Health Monitoring* 9(5), 671-688, 2019.

[11] J. A. Priest, W. Powrie, L. Yang, P. J. Grabe, C. R. I. Clayton, Measurements of transient ground movements below a ballasted railway line, *Geotechnique* 60(9), 667-677, 2010.

[12] B. Coelho, P. Hölscher, J. Priest, W. Powrie, F. Barends, An assessment of transition zone performance, *in: Proceedings of the Institution of Mechanical Engineers, Part F: Journal of Rail and Rapid Transit* 225(2), 129-139, 2011.

[13] SARA electronic instruments, SEISMOWIN front-end 1.4.0, Perugia, Italy.

[14] V. Gikas, P. Karydakis, T. Mpimis, G. Piniotis, H. Perakis, Structural integrity verification of cable stayed footbridge based on FEM analyses and geodetic surveying techniques, *Survey Review* 48(346), 1-10, 2016.

EURODYN 2020
XI International Conference on Structural Dynamics
M. Papadrakakis, M. Fragiadakis, C. Papadimitriou (eds.)
Athens, Greece, 23–26 November 2020

SEISMIC RESPONSE OF ADJACENT BUILDING STRUCTURE CONNECTED WITH SUPERELASTIC DAMPER: COMPARISON WITH YIELD DAMPER

Sourav Gur[1], Pranay Singh[2], and Koushik Roy[3]

[1] Assistant Professor, Department of Civil and Environmental Engineering, Indian Institute of Technology (IIT) Patna, Bihta, Bihar 801103, India
e-mail: sgur@iitp.ac.in

[2] Master of Technology Student, Department of Civil and Environmental Engineering, Indian Institute of Technology (IIT) Patna, Bihta, Bihar 801103, India
e-mail: pranay_1911ce13@iitp.ac.in

[3] Assistant Professor, Department of Civil and Environmental Engineering, Indian Institute of Technology (IIT) Patna, Bihta, Bihar 801103, India
e-mail: koushik@iitp.ac.in

Keywords: Adjacent buildings, Earthquake, Vibration Control, SMA damper, Yield damper

Abstract. *Use of the supplemental damping systems (i.e. viscous or yield dampers), to mitigate the seismic hazard of adjacent building structures (two connected buildings), is proven to be a practical and very efficient approach. In the context of energy dissipation capacity and developing damper/ energy absorber, shape memory alloy (SMA) is well known for its high energy dissipation capacity (super-elasticity). In the present study, the superior seismic response control efficiency of SMA damper is explored over the yield damper. Response of two adjacent structures (steel building frames) connected with SMA damper and yield damper is evaluated through nonlinear dynamic time-history analysis, under a set of recorded near-fault ground motions. The robustness of the improved performances is studied under varying characteristics of damper strength, the building structure time period, as well as different scenarios of seismic loading. Finally, it is demonstrated that, the use of SMA damper significantly improves the floor displacement control efficiency over the yield damper and also provides considerable reduction in the peak absolute floor acceleration.*

1 INTRODUCTION

Construction of sustainable and resilient building structures is an important issue in structural engineering field. Specifically, modern cities are coming up with high rise buildings with very little clearance between them, putting them at risk of mutual pounding in case of an intense earthquake. Various researches are going on to prevent these poundings by connecting these buildings using active, passive or semi-active control devices [1–4]. The concept of vibration control using passive dampers is widely accepted and has frequently been implemented in the civil engineering structures due to its low maintenance costs, reliable performance in real time and low energy requirement. These passive devices respond to the relative responses of the connected buildings. These can be easily installed between the gaps of the buildings without the need for any additional space for its installation or working. These devices serve the dual benefits: (a) prevent the mutual pounding of the buildings and (b) dissipate a part of the seismic energy coming to the buildings.

Some of the popular passive control devices include linear and non-linear viscous dampers, MR damper, viscoelastic or Maxwell dampers, yield dampers, and friction dampers [5–10]. Application of viscous damper and/or viscoelastic damper in buildings does not reduce floor displacement significantly, whereas increases the floor acceleration. MR damper shows high control efficiency in case of semi-active devices. Use of hysteretic dampers such as metallic yield dampers and friction dampers provides good control efficiency but provides high level of residual displacement after a seismic event, therefore hindering immediate occupancy. Thus, researchers are actively involved to find some suitable passive energy dissipation devices for reducing building structural vibration. In this regard, use of advance and smart material gain attention from researcher community [11–13]. In recent years Shape Memory Alloy (SMA) is gaining significant popularity as damper material for passive vibration control device [14–18]. Two important characteristics of the flag-shaped hysteresis of SMA are (a) the hysteresis loop is fat enough to dissipate the input seismic energy and (b) the loop leaves no residual displacement on unloading. To reduce the response of building structure SMA spring is already used in mass damper [19,20] or as a supplement of conventional damper [15,18,21]. It has been shown in several previous studies [19,20] that, compare to the conventional viscous damping (as present in inverse pendulum dampers or mass dampers), hysteretic damping (as present in case of SMA or yield damper) provides much higher control efficiency, due to its higher energy dissipation capacity. Further, the primary application of mass damper or inverse pendulum dampers are mainly for reduction of displacement in single flexible structure, not in case of two connected building structurers. Thus in present study, SMA damper and yield dampers are considered to demonstrate the seismic response reduction control efficiency of adjacent and connected building structures.

In this paper, the focus is laid to demonstrate the superior control efficiency of SMA damper over yield damper in case of connected building structure system. Therefore, presently the performance of super-elastic shape memory alloy damper is assessed to reduce vibration of multistoried building frame under seismic excitation and compare with conventional metallic yield damper. Non-linear time-history analyses are performed to determine the control efficiency of the SMA damper and yield damper. An extensive parametric study is performed considering a wide range of damper parameters and building parameters, as well as under various scenarios of ground motions.

2 MODELLING OF DAMPERS

This section will provide a brief idea about the force-deformation hysteresis behaviour of the yield damper and super-elastic SMA damper.

2.1 Force deformation hysteresis of yield damper

Under cyclic loading, all types of metallic material dissipate energy through yielding and show stable bi-linear force deformation behaviour. Thus, the force deformation hysteresis loop of yield damper is modeled through the parametric Bouc-Wen model [17,22,23], as shown in Fig.1. According to this model, the nonlinear force deformation in a steel member is expressed as

$$F_s(x,Z) = \alpha_s k_s x + (1-\alpha_s) F_{ys} Z$$
$$\dot{Z} = \left(\frac{\delta}{q_s}\right)\dot{x} - \left[\left\{\left(\frac{\gamma}{q_s}\right)|\dot{x}||Z||Z|^{(\eta-1)}\right\} + \left\{\left(\frac{\beta}{q_s}\right)\dot{x}|Z|^{\eta}\right\}\right] \quad (1)$$

where, k_s is the initial elastic stiffness of the yield damper, α_s is the ratio of post to pre yield stiffness (i.e. rigidity ratio) of the yield damper, F_{ys} and q_s are the yield strength and yield displacement of the yield damper, x and $\dot{x}$ are the relative displacement and velocity of the yield damper, variable Z is a non-dimensional quantity, which represents the hysteretic behaviour of metallic material in the yield damper. Here, parameters δ, γ, β and η in Eq. (1) controls the shape and transition of the hysteresis loop.

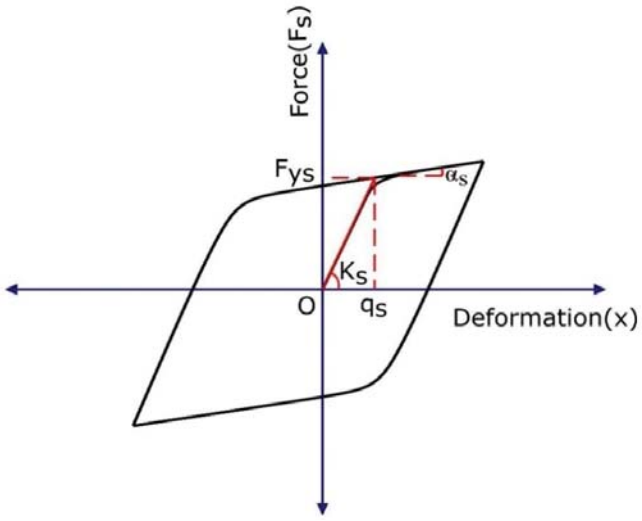

Figure-1: Bi-linear force-deformation hysteresis of yield damper

2.2 Force deformation hysteresis of SMA damper

Super-elasticity and the energy dissipation capability of SMA are primarily exploited in the vibration control applications. Fig. 2 shows that the force-deformation hysteresis of super-elastic SMA damper. The hysteresis behaviour of SMA has been characterized by different types of thermos-mechanical phenomenological models [16,23]. Out of several alternatives, the Graesser-Cozzarelli model [24] has been widely employed for studying the dynamic characteristic of SMA based system. The model is based on the parametric Bouc-Wen model [22]

with an added term incorporating the effect of super-elasticity. The one-dimensional form of this model is given as

$$\dot{F}_{sma}\left(\dot{x},F_B\right)=k_{sma}\left[\dot{x}-\left|\dot{x}\right|\left|\frac{F_{sma}-F_B}{F_{ysma}}\right|^{(\eta-1)}\left(\frac{F_{sma}-F_B}{F_{ysma}}\right)\right]$$
$$F_B=\alpha_{sma}k_{sma}\left[x-\left(\frac{F_{sma}}{k_{sma}}\right)+f_T\left|x\right|^{c'}erf\left(a'x\right)\right] \tag{2}$$

Here, F_{sma} is the restoring force, x and $\dot{x}$ are the relative displacement and velocity of the SMA damper, k_{sma} is the initial stiffness of SMA in austenite phase, F_{ysma} is the force triggering the forward-transformation from the austenite to martensite phase, α_{sma} is a constant determining the ratio of pre to post transformation stiffness, a' is a constant controlling the amount of recovery, the parameter η controls the sharpness of the loop, c' decides the slope of unloading path, F_B is one-dimensional back stress given by the Eq. (2), f_T is a constant to control the type and size of hysteresis

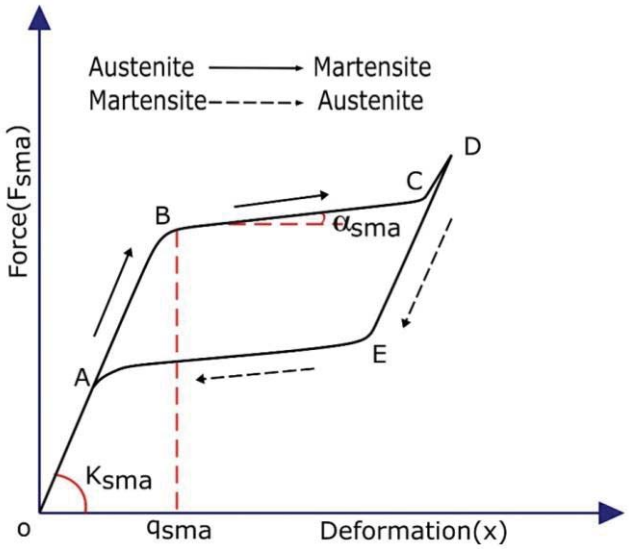

Figure-2: Force-deformation hysteresis of super-elastic shape memory alloy damper

3 SIMULATION DETAILS

This section provides the important details of the simulation process in terms of the equation of motion and ground motion information, as discuss below.

3.1 Nonlinear dynamic analysis

A two dimensional flexible and stiff building frame structure idealized as shear type building and connected by SMA damper or yield damper system has been considered here, as shown in Fig. 3 (a). The mechanical model of the SMA or yield damper system is shown in Fig. 3 (b), consist of super-elastic SMA spring or steel spring, respectively. Since, yield damper or SMA damper dissipate significant amount of input seismic energy via hysteresis loop, thus they will behave non-linearly, and both the building will behave linearly. With linear superstructure behaviour, the equation of motion can be written as

$$\begin{aligned}[M_1]\{\ddot{u}_1\}+[C_1]\{\dot{u}_1\}+[K_1]\{u_1\}+\{F_h\}&=-[M_1]\{r_1\}\ddot{u}_g\\ [M_2]\{\ddot{u}_2\}+[C_2]\{\dot{u}_2\}+[K_2]\{u_2\}-\{F_h\}&=-[M_2]\{r_2\}\ddot{u}_g\end{aligned} \tag{3}$$

Here, $[M_1]$, $[C_1]$ and $[K_1]$ are the mass, damping, and elastic stiffness matrices of flexible building of order $(n_1 \times n_1)$; $[M_2]$, $[C_2]$ and $[K_2]$ are the mass, damping, and elastic stiffness matrices of stiff building of order $(n_2 \times n_2)$, respectively. $\{u_i\} = \{u_{1i} \quad u_{2i} \quad u_{3i} \quad \cdots \quad u_{n_i i}\}^T$ is the lateral displacement vector (of order n_1 for flexible building and n_2 for stiff building) relative to the ground, where $i = 1$ for flexible building and $i = 2$ for stiff building. $\{r_i\}$ is the influence coefficient vector containing pseudo-elastic deformation of the stories under unit deformation of the ground, $\ddot{u}_g$ is the ground acceleration from the earthquake and $\{F_h\}$ is the hysteresis force of the yield or SMA damper.

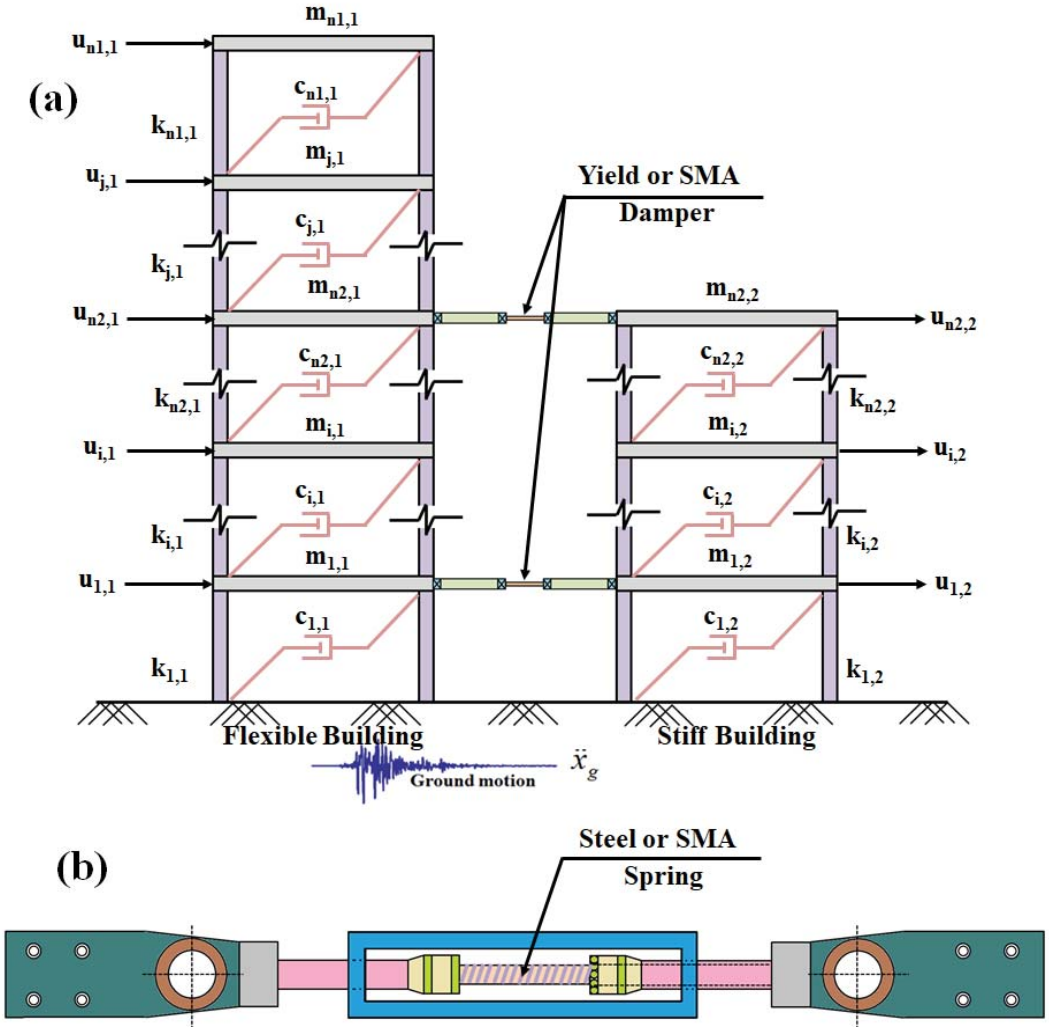

Figure-3: (a) Idealized model of the flexible and stiff building frame structures connected by the yield damper and super-elastic SMA damper. (b) Idealization mechanical model of yield damper and super-elastic SMA damper.

Hysteresis force $\{F_h\}$ is estimated using Eq. (1) for yield damper and Eq. (2) for SMA damper. In case of yield damper, yield strength is define as $F_{ys} = F_{0ys} W$ (here F_{0ys} is the normal-

ized yield strength) and for the super-elastic SMA damper, transformation strength is define as $F_{ysma} = F_{0sma} W$ (here F_{0sma} is the normalized transformation strength). Here, $W = (m_{i1} + m_{i2}) g/2$ is the average floor weight of flexible and stiff building. Numerical values of the different parameters of the build structure, yield damper and super-elastic SMA damper are provided in Table-1, based on the previous studies [17,23].

Table -1: Values of parameters adopted for buildings, yield damper, and SMA damper

Building Structure	*Yield damper*	*SMA damper*
Flexible building time period = 1.00 s Stiff building time period = 0.50 s Damping ratio = 2.00 %	Normalized yield strength $F_{0ys} = 0.100$ Hysteresis of yield damper $\alpha_s = 0.05,\ q_s = 0.025$ m $\delta = 1.0,\ \gamma = 0.5,\ \beta = 0.5$ $\eta = 0.5$	Normalized transition strength $F_{0sma} = 0.125$ Hysteresis of SMA damper $\alpha_{sma} = 0.10,\ q_{sma} = 0.035$ m $a' = 2500,\ c' = 0.001$ $f_T = 0.07,\ \eta = 3.0$

3.2 Ground motion selection

Response output of dynamic analysis of any structure strongly depends on the characteristic of the input excitation and thus ground motion selection is very important for assessment of the structural performance. A set of real earthquakes i.e. fault normal component of the ground motion with near fault characteristics (pulse type features) are adopted for the numerical study. Fig. 4 shows the spectral acceleration of the selected ground motions [25].

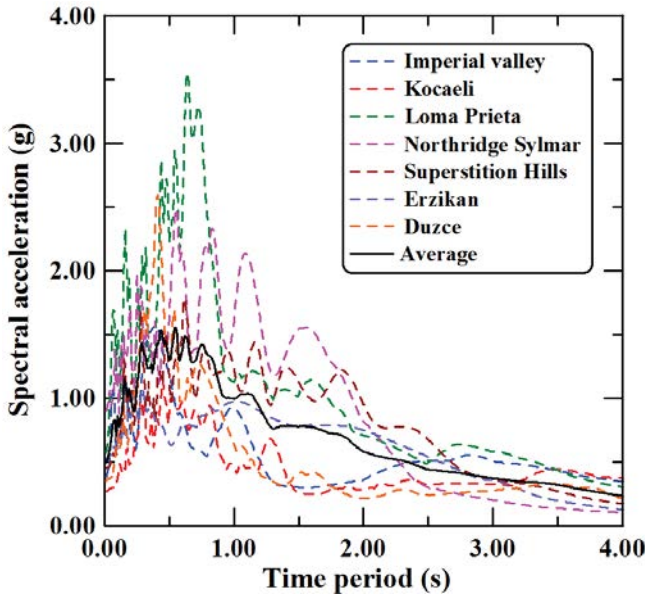

Figure-4: Spectral acceleration plot of selected ground motion

During the selection process of ground motion, consideration has been put to capture the wide range variations in PGAs and dominant frequency contents of the near fault type ground motion. Also, these ground motions are scaled accordingly, whenever needed for parametric study. Table-2 provides some salient characteristics of the adopted ground motions for the

present study. More detailed information about those ground motions are provided in a recent study by Gur et al [23,25,26].

Table-2: Set of ground motion time histories for response evolution

GM Number	Earthquake	Station	PGA (in g)	Dominant Period (sec)
GM-1	Imperial Valley (10/15/1979)	ElCentro array #5, 230	0.379	0.39
GM-2	Kocaeli (08/17/1999)	Yarimca 060 (Koeri)	0.268	0.45, 0.60
GM-3	Loma Prieta (10/18/1989)	LGPC, 000	0.563	0.47, 0.64
GM-4	Northridge Sylmar (01/17/1994)	Sylmar-Converter	0.897	0.59, 0.84
GM-5	Superstition Hills (11/24/1987)	PTS, 225	0.455	0.28, 0.64
GM-6	Erzikan (03/13/1992)	Erzikan NS comp.	0.515	0.29
GM-7	Duzce (11/12/1999)	Duzce, 180 (ERD)	0.348	0.41

4 RESULTS AND DISCUSSION

Performance of the controlled building structure is studied through the numerical simulation under a set of real, recorded near fault type ground motions as mentioned in the above section. Control efficiency of different types of control system i.e. yield damper, super-elastic SMA damper has been demonstrated through comparing the top floor acceleration and displacement of the flexible and stiff building structure.

4.1 Response analysis

To obtain the response of the isolated building under the earthquake excitation, step-by-step Newmark-beta (average acceleration technique) numerical integration method [27] is used with the time step $\Delta t = 0.0001$ seconds. Here, it is assumed that the damper system will dissipate input seismic excitation energy through its non-linear force deformation hysteresis loop and both the flexible and stiff buildings will remain in their linear-elastic regime. Thus, to obtain the correct solution at each time step, equation of motion of the building structures (both flexible building as well as stiff building) with the connected yield or SMA damper need to be solved iteratively. This iteration process continues until the error in any measured response quantities at the current time step becomes less than or equal to a tolerance limit δ_{tol}, and in the present study it has been considered as 10^{-5}. Different parameters for the numerical solution are adopted from Table-1.

A nonlinear time history analysis is first carried out to examine the responses of the linear steel building with and without passive yield and SMA dampers. In this case, the flexible and stiff building frames, yield damper, and SMA damper are simulated using Table-1 parameter. In this case of response analysis, a seven-story flexible building and a five-story stiff building

is considered. The Yarimca 060 (Koeri) record of the 1999 Kocaeli earthquake is selected as the input ground motion [23,25,26]. Time history responses are presented in Fig. 5. Figs. 5 (a) and 5(b) shows the variation of top floor acceleration of flexible and stiff buildings with respect to time, while Figs. 5(c) and 5(d) shows the variation of top displacement of flexible and stiff buildings with respect to time. It can be observed that, for both flexible and stiff building, yield damper increases top floor acceleration than the uncontrolled building structure. In terms of the floor displacement control efficiency, yield damper shows high level of reduction in the top floor displacement; however, SMA damper significantly improves this displacement control efficiency than yield damper. Such a noticeable improvement in the control efficiency of SMA damper can be explained from its energy dissipation capacity. It can be observed from Fig. 5 (e) that the hysteresis loop size (damper's strength) of SMA damper is more than yield damper, which causes more dissipation of seismic energy and thereby reduces the top floor displacement of the buildings.

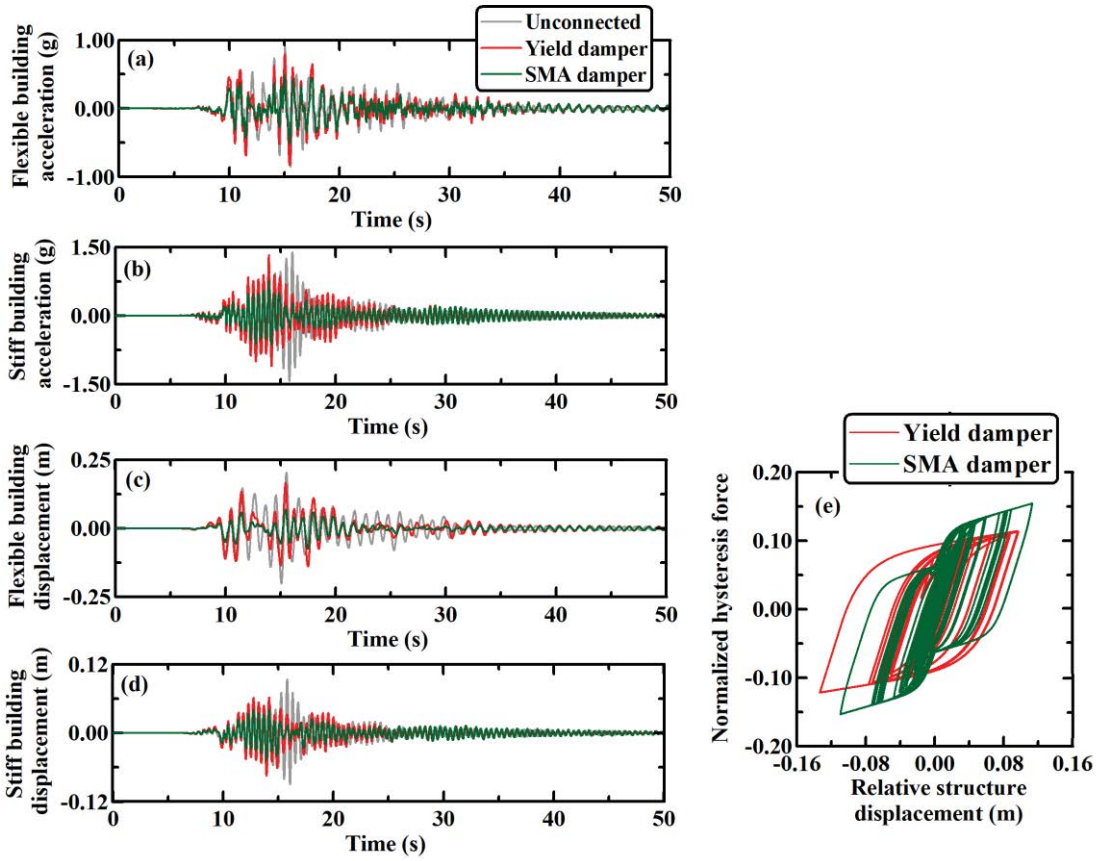

Figure-5: Time-history response of the top floor acceleration of (a) flexible building structure and (b) stiff building structure; top floor displacement of the (c) flexible building structure and (d) stiff building structure under Kocaeli (1999) earthquake. (e) Normalized force-deformation hysteresis loop of the yield damper and SMA damper.

As it can be observed in Fig. 5 (a) and (b) in contrast, super-elastic SMA damper shows reduction in top floor acceleration than unconnected buildings and as well as yield damper. This can be explained from the FFT plots of top floor acceleration of the flexible and stiff buildings, as shown in Fig. 6 (a) and (b), respectively. Fig. 6 (a) and (b) shows that, near to the fundamental frequency of the flexible and stiff buildings (i.e. 1.0 Hz and 0.5 Hz), FFT amplitude of top floor acceleration is much lower in case of SMA damper connected building structure than yield damper connected building structure or unconnected building structure.

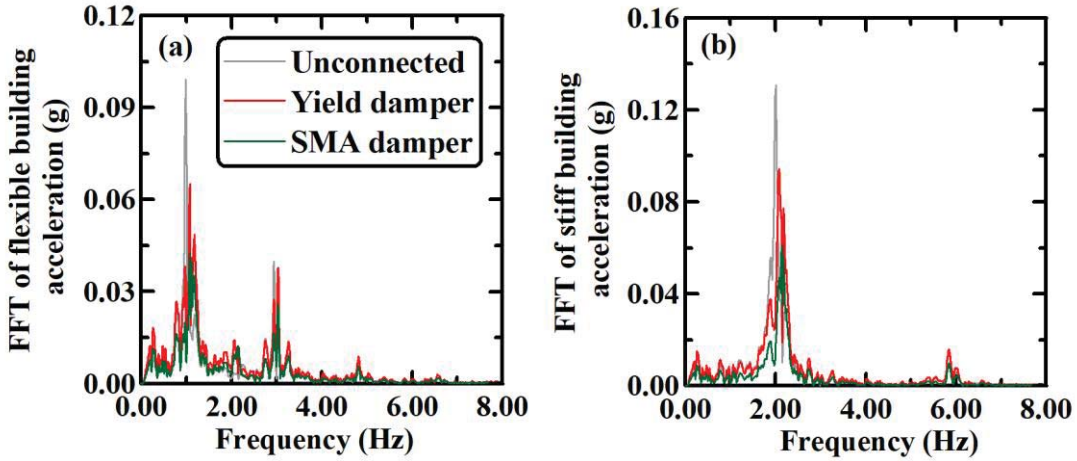

Figure-6: FFT of top floor acceleration (a) flexible building and (b) stiff building structures.

Table-3 provides the top floor absolute acceleration and top floor displacement, respectively, for flexible and stiff buildings without any dampers (only building), and buildings connected with yield or SMA dampers, under all the ground motion mentioned above in Table-2. Observing the values in Table-3 it is clear that, both the dampers reduces acceleration and displacement responses, however SMA dampers provides superior control efficiency than yield damper.

Table-3: Top floor responses of buildings under different earthquakes

GM Number	Flexible Building			Stiff Building		
	Only Building	Yield Damper	SMA Damper	Only Building	Yield Damper	SMA Damper
Top floor maximum absolute acceleration (in g)						
GM-1	2.030	1.684	0.996	1.553	1.767	1.129
GM-2	0.982	0.962	0.651	1.464	1.428	0.705
GM-3	2.353	2.081	1.436	2.677	3.637	2.123
GM-4	1.645	1.805	1.076	2.780	2.231	1.371
GM-5	2.286	2.177	1.574	2.286	2.165	1.229
GM-6	1.174	1.189	0.772	1.937	1.274	0.874
GM-7	1.721	1.662	1.091	2.725	1.830	1.035
Top floor maximum displacement (in m)						
GM-1	0.428	0.333	0.161	0.099	0.102	0.064
GM-2	0.232	0.186	0.079	0.104	0.075	0.054
GM-3	0.525	0.452	0.214	0.228	0.241	0.158
GM-4	0.276	0.281	0.147	0.188	0.133	0.080
GM-5	0.537	0.516	0.255	0.109	0.139	0.091
GM-6	0.370	0.285	0.138	0.082	0.079	0.046
GM-7	0.298	0.280	0.139	0.165	0.116	0.073

4.2 Parametrical study

In this section, parametrical study is performed to demonstrate the superior control efficiency of SMA damper over yield damper. Here, peak acceleration and peak displacement of top floor are measured under all seven ground motions and the average response is reported herein.

As reported in previous studies [16, 17], normalized strength of yield or SMA damper is an important design parameter, and the optimal choice of this parameter will maximize the control efficiency. Fig 7 depicts the effect of normalized yield strength (for steel) or transformation strength (for SMA) of the dampers on the response parameters (i.e. peak top floor acceleration, peak top floor displacement for flexible and stiff building).

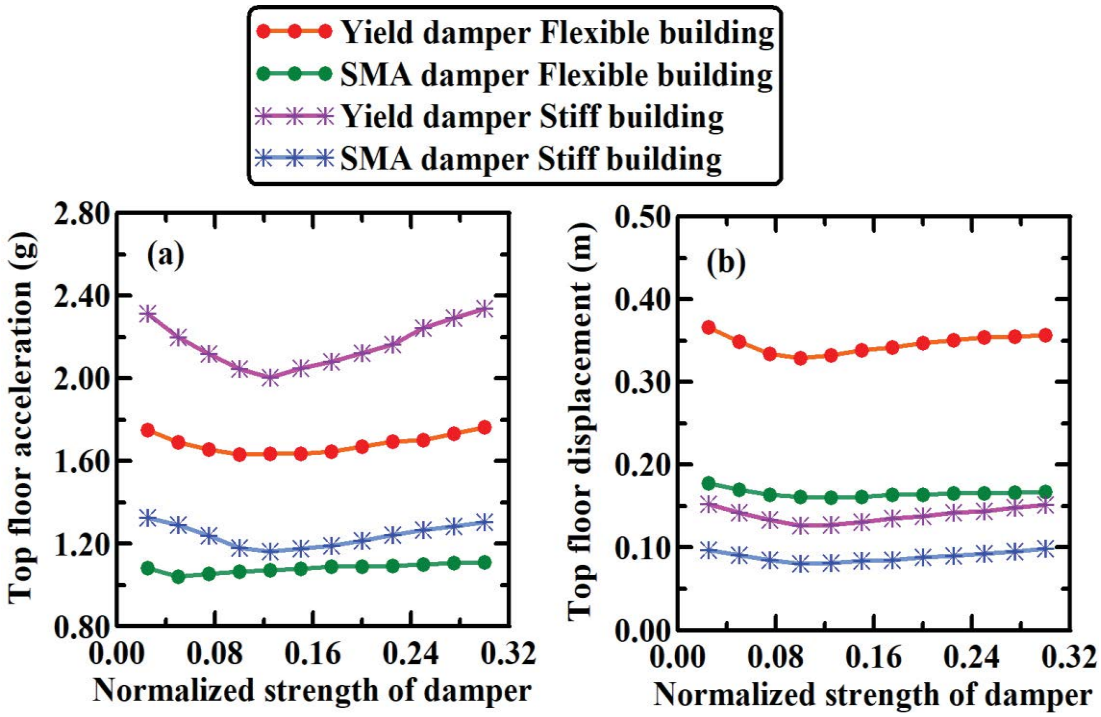

Figure-7: Variation of (a) peak top floor acceleration and (b) peak top floor displacement with respect to the normalized strength of yield damper and SMA damper, for flexible and stiff building.

Fig. 7 (a) and (b) shows variation of peak top floor acceleration and peak top floor displacement of the buildings connected by yield damper and SMA damper, where top floor acceleration and displacements were lesser in case SMA dampers connected building than yield damper. For all the values of normalized strength of damper, stiff building connected with yield damper system shows maximum top floor acceleration; whereas flexible building in SMA damper connected system shows the least (see Fig. 7 (a)). For top floor displacement, flexible building connected with yield damper system shows maximum top floor displacement for all the values of normalized strength of damper, whereas stiff building in SMA damper connected system shows the least (see Fig. 7 (b)). In case of flexible building structure, SMA damper reduces maximum 33.53 % top floor acceleration and 54.71 % top floor displacement. Similarly, for stiff building structure, SMA damper reduces 48.53 % top floor acceleration and 35.03 % top floor displacement.

Next, the effect of time period of flexible building structure on the response parameters are studied, and shown in Fig. 8. Variation of the top floor peak acceleration and peak displacement with respect to the time period of the flexible building are shown in Figs. 8 (a) and 8(b). As expected, for both the dampers (yield and SMA), with the increasing flexibility (i.e. time period) of the flexible structure, top floor peak absolute acceleration reduces. Fig. 8(a) shows that in comparison to the yield damper, SMA damper reduces top floor peak acceleration more in case of stiff building than the flexible building. Compare to the yield damper, SMA damper reduces top floor peak acceleration by 35.07 % for the flexible building structure, and 53.76 % for the stiff building structures. Opposite to the top floor peak acceleration, for both flexible and stiff buildings connected with yield damper and/or super-elastic SMA dampers, top floor peak displacement increases with the increasing time period of flexible structure (Fig. 8 (b)). Here, for the flexible building, SMA damper control efficiency is more than yield damper. In case of stiff building, displacement control efficiency for both SMA and yield damper are comparable. In terms of displacement control efficiency, SMA damper reduces top floor peak displacement up to 55.01 % for the flexible building, and 21.62 % for stiff building, when compare to the yield damper.

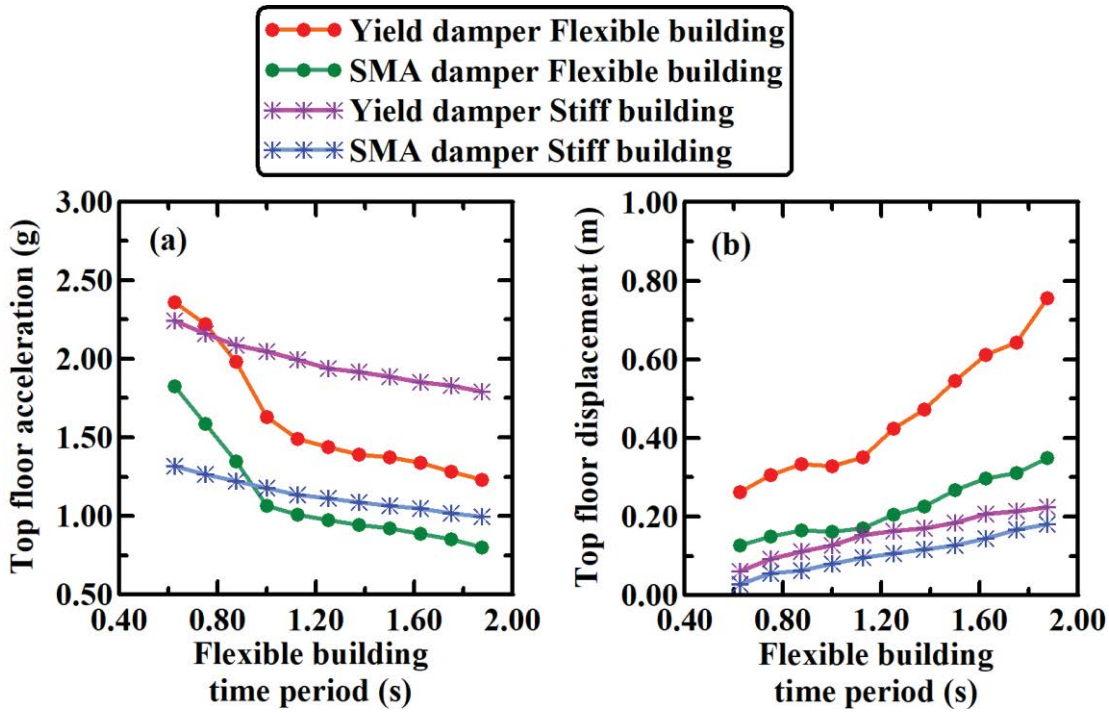

Figure-8: Variation of (a) peak top floor acceleration and (b) peak top floor displacement with respect to the flexible building time period, for flexible building and stiff building, connected with SMA damper and yield damper

Finally, the control efficiency of different type of damper has been studied under the varying peak ground acceleration (PGA); keeping frequency contents of the ground motions unaltered. This is achieved just by up-scaling individual ground motions by suitable factors i.e. multiplying the ordinates of the ground motion by some suitable factors. Variation of the different response quantities (i.e. top floor peak acceleration and displacement) under the varying PGAs are shown in Fig. 9. As expected, for both types of damper, the responses increase monotonically with increasing PGA. In any type of building structures (flexible or stiff), responses of SMA dampers connected building system are consistently lesser than the responses of yield dampers connected building system. At lower values of PGA, control efficiency of

SMA damper is almost comparable with yield damper. Whereas for higher values of PGA, SMA damper shows significant improvement in control efficiency than yield damper. Such aspect strengthens the fact that, the control efficiency of SMA damper over yield damper increases while subjected to a larger intensity of earthquakes. In terms of the floor acceleration control efficiency, SMA damper reduces top floor peak acceleration by 14.07 % for flexible building and 21.83 % for stiff building, when compare to the yield damper. Similarly, for floor displacement, SMA damper reduces top floor peak displacement by 35.67 % for flexible building and 19.45 % for stiff building, relative to the yield damper.

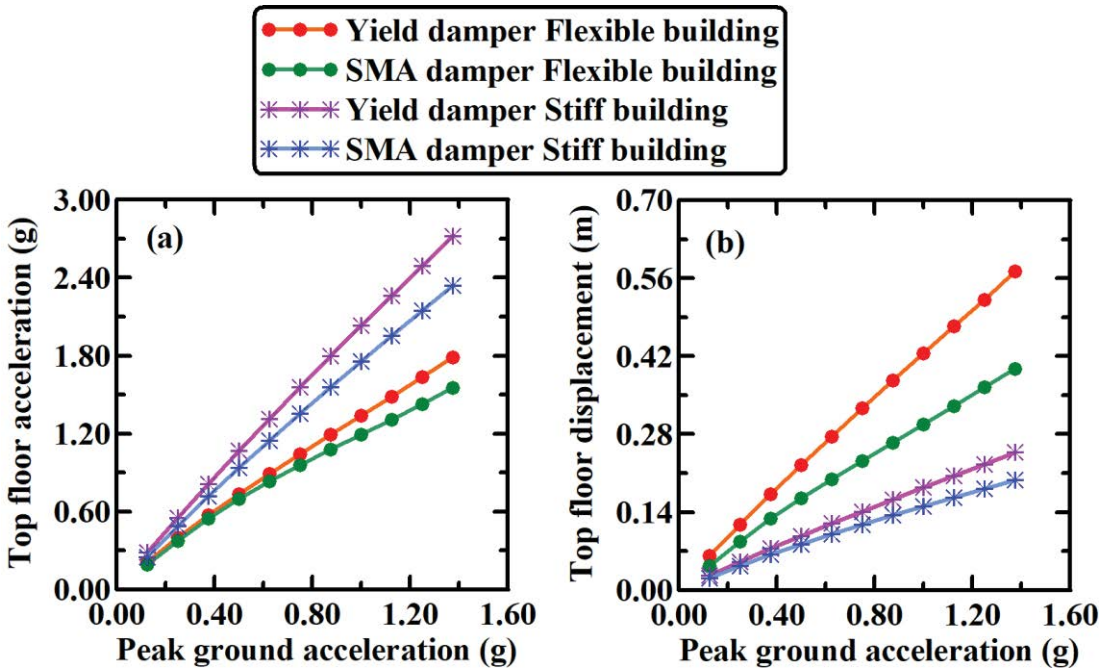

Figure-9: Variation of (a) peak top floor acceleration and (b) peak top floor displacement with respect to the peak ground acceleration for flexible building to stiff building, connected with SMA damper and yield damper

5 CONCLUSIONS

Performance of yield damper and SMA damper as passive control device in connected buildings are compared using non-linear dynamic response analysis under seven ground motions obtained from past earthquakes. Analyses results show that both the dampers help to reduce floor responses (peak acceleration and displacement) for connected buildings than unconnected buildings. Here, performance of both the dampers are evaluated under varying parameters like normalized strength of dampers, time period of buildings, peak ground acceleration. Response analysis shows that, SMA dampers significantly reduce the top floor responses (peak acceleration and displacement) when compare with the yield dampers. Finally, all the parametrical studies confirmed the superior control efficiency of SMA Damper over yield damper for connected buildings under the seismic excitation. Parametrical study results show that, compare to the yield damper, SMA damper reduces top floor peak absolute acceleration as high up to 35 % for flexible building and 55 % for stiff building. When displacement control efficiency is considered (in terms of the top floor peak displacement), compare to the yield damper, SMA damper provides 55 % more reduction for the flexible building, and 35 % more reduction for the stiff building.

REFERENCES

[1] Y.Q. Ni, J.M. Ko, Z.G. Ying, Random seismic response analysis of adjacent buildings coupled with non-linear hysteretic dampers, *Journal of Sound and Vibration* 246, 403–417, 2001.

[2] Z.G. Ying, Y.Q. Ni, J.M. Ko, Stochastic optimal coupling-control of adjacent building structures, *Computers and Structures* 81, 2775–2787, 2003.

[3] I. Takewaki, Earthquake input energy to two buildings connected by viscous dampers, *Journal of Structural Engineering (ASCE)* 133, 620–628, 2007.

[4] D.D. Ge, H.P. Zhu, D.S. Wang, M.S. Huang, Seismic response analysis of damper-connected adjacent structures with stochastic parameters, *Journal of Zhejiang University: Science A* 11, 402–414, 2010.

[5] V.A. Matsagar, R.S. Jangid, Viscoelastic damper connected to adjacent structures involving seismic isolation, *Journal of Civil Engineering and Management* 11, 309–322, 2005.

[6] A. V. Bhaskararao, R.S. Jangid, Seismic response of adjacent buildings connected with friction dampers, *Bulletin of Earthquake Engineering* 4, 43–64, 2006.

[7] A. V. Bhaskararao, R.S. Jangid, Harmonic response of adjacent structures connected with a friction damper, *Journal of Sound and Vibration* 292, 710–725, 2006.

[8] C.C. Patel, R.S. Jangid, Seismic response of adjacent structures connected with maxwell dampers, *Asian Journal of Civil Engineering*, 11, 585–603, 2010.

[9] S.D. Bharti, S.M. Dumne, M.K. Shrimali, Seismic response analysis of adjacent buildings connected with MR dampers, *Engineering Structures* 32, 2122–2133, 2010.

[10] C.C. Patel, R.S. Jangid, Optimum parameter of viscous damper for damped adjacent coupled system, *Journal of Civil Engineering and Science*, 1, 22–30, 2012.

[11] Y.L. Han, Q.S. Li, A.Q. Li, A.Y.T. Leung, P.-H. Lin, Structural vibration control by shape memory alloy damper, *Earthquake Engineering & Structural Dynamics* 32, 483–494, 2003.

[12] Y. Zhang, S. Zhu, A shape memory alloy-based reusable hysteretic damper for seismic hazard mitigation, *Smart Materials and Structures* 16, 1603–1613, 2007.

[13] Y. Jia, L. Li, C. Wang, Z. Lu, R. Zhang, A novel shape memory alloy damping inerter for vibration mitigation, *Smart Materials and Structures* 28, 115002, 2019.

[14] J. McCormick, R. DesRoches, D. Fugazza, F. Auricchio, Seismic vibration control using superelastic shape memory alloys, *Journal of Engineering Materials and Technology, Transactions of the ASME* 128, 294–301, 2006.

[15] O.E. Ozbulut, S. Hurlebaus, Re-centering variable friction device for vibration control of structures subjected to near-field earthquakes, *Mechanical Systems and Signal Processing* 25, 2849–2862, 2011.

[16] S. Gur, S.K. Mishra, G.N. Frantziskonis, Thermo-mechanical strain rate-dependent behavior of shape memory alloys as vibration dampers and comparison to conventional dampers, *Journal of Intelligent Material Systems and Structures* 27, 1250–1264, 2016.

[17] S. Gur, S.K. Mishra, K. Roy, Stochastic seismic response of building with super-elastic damper, *Mechanical Systems and Signal Processing* 72–73, 642–659, 2016.

[18] H. Qian, H. Li, G. Song, Experimental investigations of building structure with a superelastic shape memory alloy friction damper subject to seismic loads, *Smart Materials and Structures* 25, 125026, 2016.

[19] S.K. Mishra, S. Gur, S. Chakraborty, An improved tuned mass damper (SMA-TMD) assisted by a shape memory alloy spring, *Smart Materials and Structures* 22, 095016, 2013.

[20] S. Gur, S.K. Mishra, S. Bhowmick, S. Chakraborty, Compliant liquid column damper modified by shape memory alloy device for seismic vibration control, *Smart Materials and Structures* 23, 105009, 2014.

[21] B. Silwal, R.J. Michael, O.E. Ozbulut, A superelastic viscous damper for enhanced seismic performance of steel moment frames, *Engineering Structures* 105, 152–164, 2015.

[22] Y.K. Wen, Equivalent linearization for hysteretic systems under random excitation, *Journal of Applied Mechanics, Transactions ASME* 47, 150–154, 1980.

[23] S. Gur, Y. Xie, R. DesRoches, Seismic fragility analyses of steel building frames installed with superelastic shape memory alloy dampers: Comparison with yielding dampers, *Journal of Intelligent Material Systems and Structures* 30, 2670–2687, 2019.

[24] E.J. Graesser, F.A. Cozzarelli, Shape-memory alloys as new materials for aseismic isolation, *Journal of Engineering Mechanics* 117, 2590–2608, 1991.

[25] S. Gur, S.K. Mishra, S. Chakraborty, Performance assessment of buildings isolated by shape-memory-alloy rubber bearing: Comparison with elastomeric bearing under near-fault earthquakes, *Structural Control and Health Monitoring* 21, 449–465, 2014.

[26] S. Gur, G.N. Frantziskonis, S.K. Mishra, Thermally modulated shape memory alloy friction pendulum (tmSMA-FP) for substantial near-fault earthquake structure protection, *Structural Control and Health Monitoring* 24, 1–15, 2017.

[27] R. Villaverde, Fundamental Concepts of Earthquake Engineering, CRC Press, ISBN 9781420064957 (1st Edition)

EURODYN 2020
XI International Conference on Structural Dynamics
M. Papadrakakis, M. Fragiadakis, C. Papadimitriou (eds.)
Athens, Greece, 23–26 November 2020

SURFACE WAVE PROPAGATION FROM DROP-PROJECTILE TESTS: PHYSICAL AND NUMERICAL MODELLING

Vipul Kumar[1,2], **S.P.G. Madabhushi**[1]

[1] Schofield Center, Department of Engineering
University of Cambridge
e-mail: {vk337, mspg1}@cam.ac.uk

[2] Geotechnical Engineer
Mott MacDonald, UK
e-mail: vipul.kumar@mottmac.com

Keywords: Rayleigh Waves, Ground-borne vibrations, Centrifuge Modelling, Numerical Analysis, High-Speed Trains

Abstract. *Surface wave propagation can be investigated with the help of centrifuge and numerical modelling. An electromagnetic drop-projectile apparatus was used to generate surface waves in soil upon the impact of a spherical metal ball with a shallow foundation. A 3D LS-DYNA FE model was developed and first calibrated against the analytical solutions for the soil displacement at the ground surface due to the arrival of Rayleigh waves. The 3D model was then validated with the results of vertical acceleration obtained from geotechnical centrifuge test for homogeneous soil layer profile. The numerical results show that LS-DYNA can reliably be used as a numerical tool to simulate surface wave propagation. Following the validation, a parametric numerical study was performed to assess the impact of stiffness contrast in soil layers on surface wave propagation. In this parametric study, soil layer with relatively lower stiffness (shear wave velocity) was modelled below a stiffer upper layer. The attenuation of vertical acceleration of the surface waves at an increasing distance away from the source were investigated and compared between the results of geotechnical centrifuge test and numerical models. The results of parametric analysis tend to suggest that the presence of soft soil at shallow depth can amplify the amplitude of vertical accelerations within the stiffer upper layer. This effect however is likely to be localised near the source of vibration.*

1 INTRODUCTION

Inter-city high speed rail is one of the most efficient means of transportation systems and an attractive and viable alternative for promoting travel and commerce as compared to air or car-based land transport. Today, Spain and China have one of the largest high-speed rail networks in the world. After the success of High Speed 1 (HS1), Britain is now planning and moving ahead with the early stages of construction of its new high-speed railway line – High Speed 2 (HS2). The projected operational speed of trains on HS2 network will be 100 m/s with the proposed track alignment passing through cuttings and embankments with sub-surface conditions varying from soft alluvium and/or deep peat layers to stiff glacial till.

The increased operational speed of high-speed trains has also led to some notable case histories [1,2,3] of excessive ground-borne vibrations. Ground-borne vibrations are generated due to the wheel-axle pressure acting on the rails as shown in Figure 1. The vibrations due to geo-dynamic track-soil interaction tends to amplify as the train speed approaches critical velocity (Rayleigh wave velocity) of the subgrade supporting the tracks [4,5]. It is possible for modern-day high-speed trains to exceed this critical velocity if the soil below tracks consists of soft silty clays, peats and/or organics which typically have shear wave velocity in the range of 40-60 m/sec.

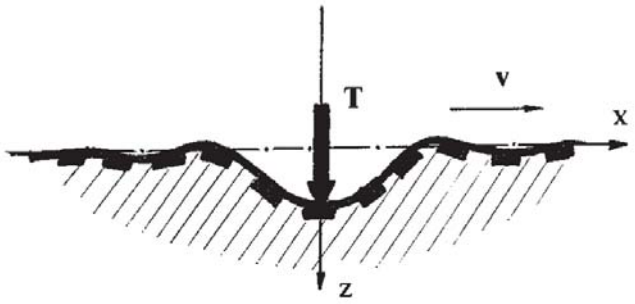

Figure 1: Wheel-axle pressure acting on rails [6]

Although the relevance of understanding propagation of surface waves (in the form of Rayleigh waves) is important to the high-speed rail industry, the phenomenon has not been that well understood experimentally. One of the earliest endeavors in studying surface wave propagation was with the means of full-scale tests [7] to understand efficacy of active and passive isolation systems as mitigation measures against excessive vibration. Since it is not always feasible to perform full-scale tests, some researchers have investigated the feasibility of centrifuge modelling to generate and measure surface vibrations in scaled-down models. A novel drop-ball apparatus [8] was developed to generate surface waves from a falling spherical metal ball under the effect of centrifugal acceleration. Piezoelectric accelerometers buried in the centrifuge package provided an estimate of geometric and material damping coefficients for surface waves. An enhancement was developed [9] to drop multiple balls to simulate a moving surface load and study the effect of geometry and material of wave barrier in attenuating the surface wave motion.

When the observations from full-scale or model-scale centrifuge tests are not available, numerical analysis in the form of BEM (Boundary Element Method), FEM (Finite Element Method), FDM (Finite Difference Model) and coupled FEM-BEM (2.5D) methods have been used for the propagation of surface waves generated due to high-speed trains. 2D and 2.5D BEMs were used [10,11] to assess the effect of geometry of structures such as wave barrier and stiffness contrast ratio between a structure (for example, wave barrier or embankment)

and in-situ soil on the propagation and attenuation of surface waves. Although, FEM/FDM are computationally expensive than BEM, several researchers [12-15] have used these methods for the flexibility of modelling 3D track-structure geometry, moving train loads and the ability to predict the effects of surface wave propagation along the length of track and in far-field (away from the track), which are generally obtained with some approximation in 2D (FEM/FDM/BEM) and 2.5D BEM-FEM coupled models.

In this paper, we discuss the development of drop-ball centrifuge test to generate surface waves in a medium of homogeneous, dry sand. A 3D FE numerical model is proposed which is calibrated with analytical solution of particle displacement at soil surface due to arrival of Rayleigh waves and afterwards, calibrated with the results from centrifuge test. A parametric study is performed with the FE model to demonstrate the possible effect of soil stiffness contrast in a layered soil profile on surface wave propagation.

2 PHYSICAL MODELLING OF GROUND-BORNE VIBRATIONS

In centrifuge modelling, the stress state of soil at a certain depth in the prototype can be replicated under the centrifugal acceleration of N*g. Scaling laws used to correlate stress, strain and other behaviour in a prototype and scaled-down centrifuge model are presented in Table 1 [14].

Parameter	Dimensions	Model/Prototype
Length	L	1/N
Velocity	LT^{-1}	1
Acceleration	LT^{-2}	N
Mass	M	$1/N^3$
Time (dynamic)	T	1/N
Frequency	T^{-1}	N

Table 1: Scaling laws for centrifuge modelling

Centrifuge tests were performed on the 10 m beam centrifuge at the Schofield Center (UK). The results from centrifuge experiment reported in this paper correspond to centrifugal acceleration 40 (N) times the gravitational acceleration. Only a brief discussion of the centrifuge model is presented below; the details of drop-ball system and preliminary centrifuge test results are discussed in another paper [17].

2.1 Centrifuge model for calibration of numerical model

The centrifuge model was prepared by pouring Hostun HN31 silica sand from an automatic sand pourer in an 850 mm (internal) diameter model container, to a height of approximately 232 mm. The material parameters of Hostun HN31 silica sand are presented in Table 2. An average relative density of about 50% was achieved for the homogeneous sand bed.

Parameter	Value
Density of solid particle (kg/m^3)	2650
Minimum Void Ratio	0.555
Maximum Void Ratio	1.01
d_{50} (mm)	0.334

Table 2: Material parameters of Hostun HN31 silica sand [16]

Time-lag in the arrival of shear waves generated by Air Hammer [15] placed near the bottom of model container and recorded by piezoelectric accelerometers at different elevations in the sand bed were used to derive in-situ shear wave velocity profile. Surface waves were generated by dropping spherical metal ball onto a circular metal foundation placed at the top of soil surface [17] as shown in Figure 2.Vertical accelerations in the soil were recorded by MEMS-type accelerometers buried at shallow depth and at an increasing radial distance away from the metal foundation.

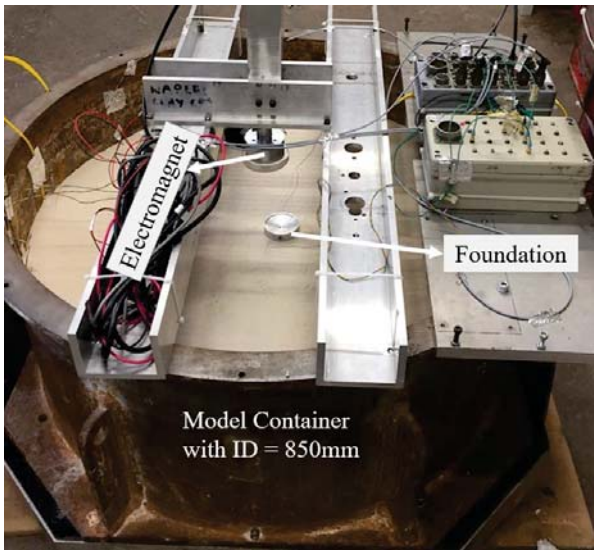

Figure 2: Centrifuge Model with Drop-Ball Apparatus (homogeneous soil layer)

3 NUMERICAL MODELLING OF GROUND-BORNE VIBRATIONS

Numerical analysis for surface wave propagation is performed with LS-DYNA (http://www.lstc.com/) using Explicit Solver. The explicit solution technique is based on integration of constant accelerations over a time increment. It is important that an FE model is appropriately discretised in space and time domains to avoid numerical dispersion and errors due to mesh size and analysis time step.

An FE mesh with coarse element size acts like a low-pass filter which can filter high-frequency waveforms unable to propagate over large element size. Spatial discretisation (mesh element size) of FE mesh is based on the highest frequency of propagating surface wave (f_{max}) and Rayleigh wave velocity (V_R) of the medium. The minimum mesh element size (d_{min}) can be chosen as one-tenth of the minimum wavelength propagating through the medium [18]. The minimum time-step for integration of accelerations in the explicit solution scheme is then derived as the ratio of minimum mesh element size (d_{min}) and Rayleigh wave velocity (V_R) [19].

3.1 Validation with analytical solution

A 3D LS-DYNA FE model (Figure 3) was developed to simulate Lamb's problem [20] where the surface waves are generated by a point impulse load acting on a semi-infinite elastic medium. This step serves as a benchmark exercise before the application of LS-DYNA FE for simulating surface wave propagation observed in centrifuge test. The time-dependent impulse load has the form[21]:

$$F(t) = F_b \frac{t}{(t^2 + \tau_p^2)} \quad (1)$$

The peak amplitude of the pulse and pulse width it modulated with parameters F_b and τ_P with their respective amplitudes taken as 2.0×10^{-6} and 6.0×10^{-4}. Taking advantage of the symmetry of the problem, only a quarter-geometry is modelled in FE analysis with an edge length of 1m along each cartesian axes. The soil parameters adopted for this analysis correspond to shear wave velocity (V_s) of 60 m/sec [19] modelled with *MAT_ELASTIC in LS-DYNA. Since only finite dimensions of soil domain are modelled, special boundary elements were placed around the bounded domain to absorb outgoing waves and minimise their reflection back into the model domain. Absorbing boundaries along the outer planes of geometry were modelled with perfectly matched layers (PML) using *MAT_PML_ELASTIC in LS-DYNA [22]. The perfectly matched layers were modelled with the same elastic properties as that of the soil domain with 8 elements through the depth. For geometry planes along the axis of symmetry, the nodes were constrained against translation in the normal direction and the nodes of PML elements were fully fixed against translation using *BOUNDARY_SPC.

Using the guidelines presented above, a 3D mesh with uniform element size of 10 mm was adopted for analysis resulting in approximately 1.26 million solid elements. The time-step used for analysis was taken as 1.36×10^{-5} sec. The solid elements were modelled with *SECTION_SOLID with fully integrated selectively reduced formulation (Elform = 2). To dampen any spurious oscillations in the elastic medium, a nominal damping of 0.1% was defined using *DAMPING_FREQUENCY between a frequency range of 20 Hz to 0.5 kHz. The impulse load (Equation 1) was defined using *DEFINE_CURVE and applied to a node along the axis of symmetry using *LOAD_NODE in the vertical direction. The total analysis run time was adopted as 0.03 sec and was analysed with double-precision LS-DYNA R11 explicit solver.

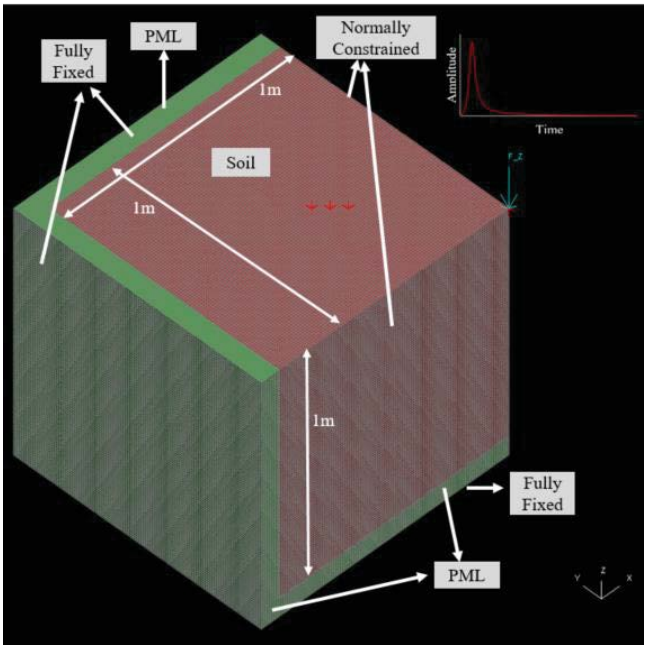

Figure 3: 3D LS-DYNA model for validation with Lamb's problem

Vertical displacement time histories of nodes at pre-defined locations on surface were obtained from the numerical analysis and compared with the analytical solution [21]. As shown in Figure 4, the numerical solution captures the arrival of P-waves and S-waves before the arrival of Rayleigh waves which causes peak particle displacement [7,22]. The Rayleigh wave velocity (V_R) calculated from the numerical solution as the time-lag (dt = 0.001031 sec) be-

tween the arrival of peak particle displacement at two node locations (distance = 0.49 m; distance = 0.55 m) is 54.9 m/sec, which matches reasonably with the theoretical value of 56.7 m/sec [19]. This step shows a good agreement between theoretical solutions and numerical analysis with LS-DYNA for Rayleigh wave propagation.

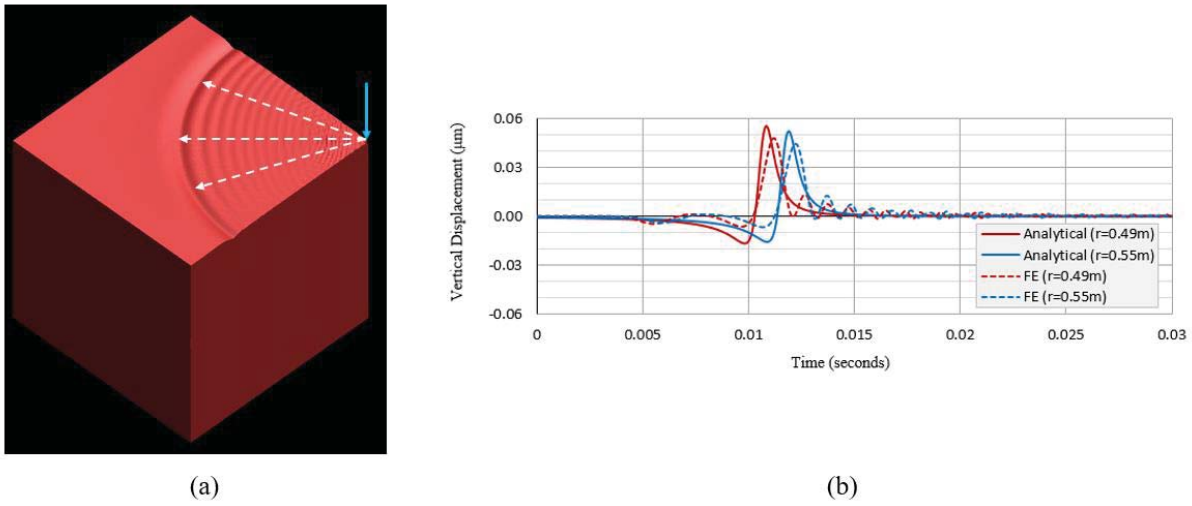

(a) (b)

Figure 4: (a) Deformed Shape of FE mesh (magnified by 5.0×10^5) showing wave propagation at $t = 0.16$ *sec*, (b) Comparison of vertical displacement time-histories between theoretical and LS-DYNA analysis

3.2 Validation with centrifuge test

After validating LS-DYNA with analytical solutions for Rayleigh wave propagation, the FE model was modified to represent the physical dimensions of centrifuge test in Section 2.1. The modified 3D quarter-model has lateral dimensions equal to the internal radius of the model container (425 mm) and a model height of 232 mm (Figure 5).

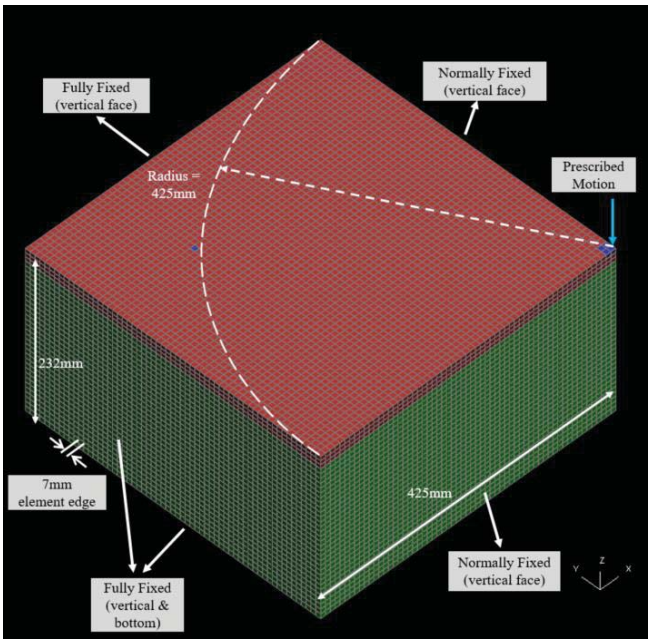

Figure 5: 3D LS-DYNA model for validation with centrifuge test

The model container in centrifuge test was cylindrical, the 3D FE model was modelled with a parallelepiped mesh domain to maintain a uniform and regular shape of 3D solid element with straight edges. Although, this approximation resulted in model domain with its diagonal length greater than radius of centrifuge model container (425 mm), it was unlikely to influence the acceleration calculated in soil close to the source of vibration in the FE model.

The soil was modelled as a linear elastic material with a uniform shear wave velocity of 120 m/sec [17] taken at the depth of MEMS-accelerometers in soil. The model boundaries (*BOUNDARY_SPC) were also updated to represent the fixed condition at the interface of soil-model container, thereby allowing for reflection of outgoing waves back into the model domain. The vertical acceleration measured at the circular foundation (source) in centrifuge test was directly applied in the FE model with *BOUDNARY_PRESCRIBED_MOTION. All the results presented hereafter refer at model scale unless stated otherwise.

The vertical acceleration measured at the metal foundation from the centrifuge test for a drop height of 100 mm and its corresponding FFT is presented in Figure 6. Based on the maximum cutoff frequency at the source of about 1500 Hz, a minimum mesh size of 8 mm was obtained. This cutoff frequency is significantly higher than what can typically propagate through soil (typically in the range of 10-25 Hz at 1g). Nevertheless, the mesh element size was further reduced to 7 mm purely from the perspective of placing FE nodes at the locations of MEMS-accelerometers placed in soil in the centrifuge test.

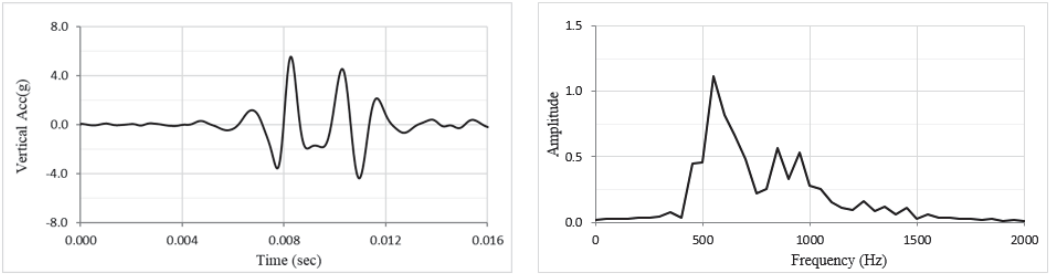

Figure 6: (a) Vertical acceleration measured at foundation disk (source), (b) FFT spectrum

The vertical accelerations (model-scale) at a depth of 18 mm from surface and at 60 mm and 90 mm lateral distance with from the source were compared (Figure 7) between the results obtained from centrifuge tests and from the 3D FE model. The preliminary results suggest that the arrival of the first peak in the acceleration pulse match reasonably well with the experimental measurements.

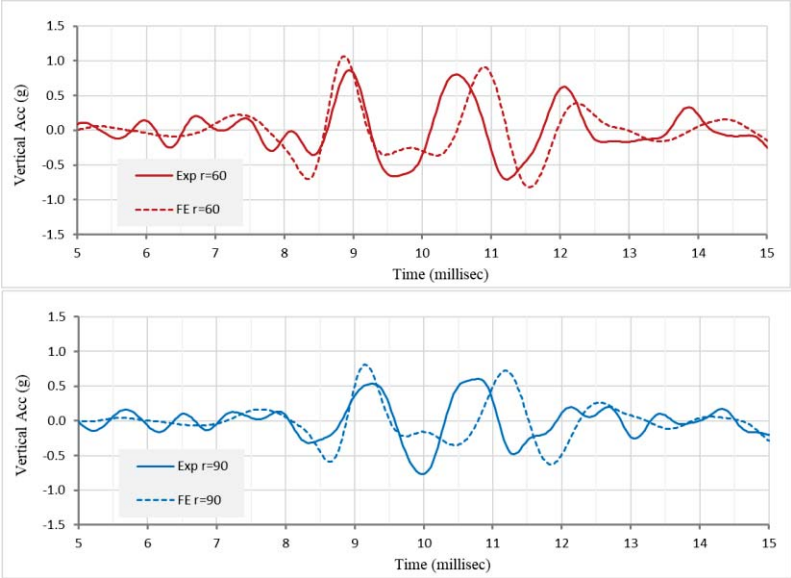

Figure 7: Comparison of vertical acceleration between centrifuge test and numerical model

3.2.1. Parametric study – soil stiffness

Amplification of the surface wave vibrations have generally been reported for sites where soft soil conditions were present below the stiff track-structure. Remediation measures such as piled embankments with piles ending in a competent stratum or ground improvement with dry deep mixing method to a certain depth below the track-structure [1, 3] were applied to reduce the amplification of vibrations. The 3D FE model previously calibrated with the results of centrifuge test was updated for non-uniform soil stiffness as shown in Figure 8. It was assumed that the stiff upper layer has a prototype thickness of 0.72 m (or, 18 mm at model scale). A uniform shear wave velocity of 60 m/sec was assumed for the soft soil layer which is similar to the values reported in literature [1, 17, 24].

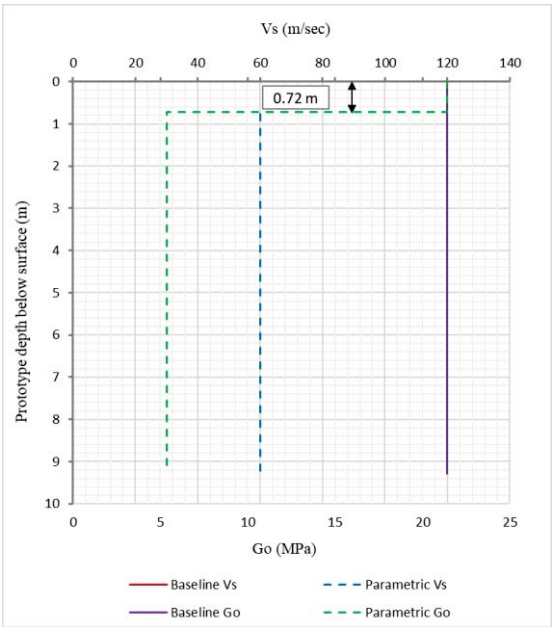

Figure 8: Comparison of shear wave velocity (and equivalent small-strain stiffness (G_o)) profile assumed for baseline and parametric FE analyses

In order to numerically assess the effect of having soft soil conditions at a shallow depth, the FE model was re-run with vertical acceleration at source (Figure 6) and with 'stiff soil over soft soil' shear wave velocity profile (Figure 8). Vertical acceleration time histories (Figure 9) at 60 mm and 90 mm (lateral distance) from the source were compared with the ones obtained with uniform shear wave velocity profile. In Figure 10, the peak amplitude of first arrival of vertical accelerations (prototype level) were plotted at an increasing distance (resultant of lateral distance from source and depth below soil surface) from the source for centrifuge test and numerical analysis with uniform and layered soil (stiffness) profiles. The preliminary results tend to suggest that a presence of soft soil layer at a shallow depth from the source of vibration can potentially amplify the vibration.

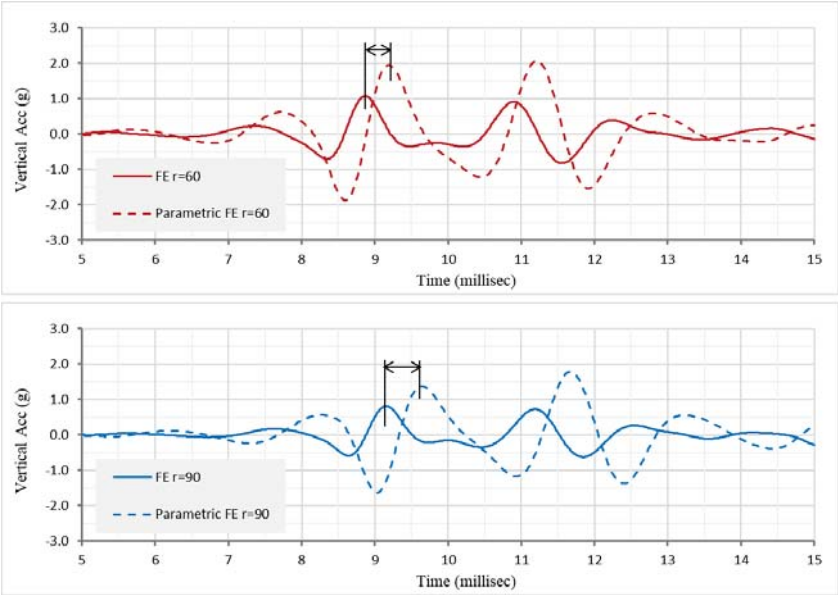

Figure 9: Comparison of vertical acceleration from numerical model for Uniform and Layered soil profile (Stiff soil over soft soil)

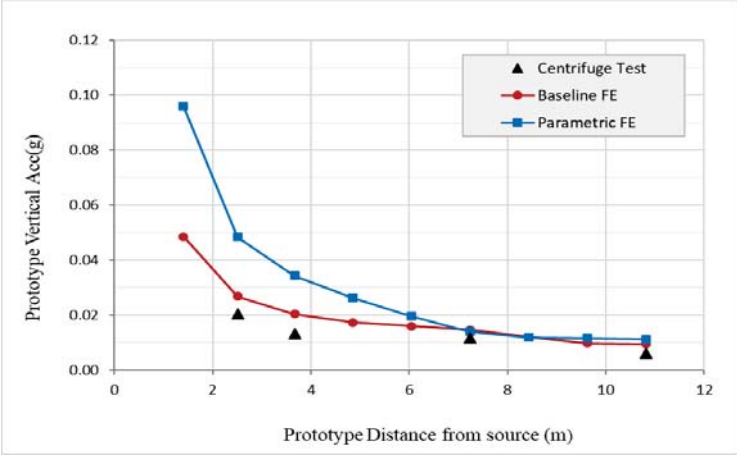

Figure 10: Attenuation of vertical acceleration from source

4 CONCLUSIONS

This paper forms part of an ongoing research into the generation and propagation of surface waves with the help of a series of centrifuge tests. In this paper, finite element analysis was used as tool to simulate ground-borne vibrations generated by a stationary point impulse load. Following conclusions are drawn from the preliminary results presented in this paper:

- Reliability of LS-DYNA as a numerical tool for modelling surface wave propagation was presented by validating the numerical response with analytical solutions. Infinite domain was represented in a finite domain model by modelling solid elements along outer boundaries with Perfectly Matched Layers (PML).
- Another 3D FE model was developed without the absorbing boundaries to simulate the physical conditions of the centrifuge model container. This model was validated with the results from centrifuge test.
- Parametric FE study was performed to investigate the potential effect of soft soil at a shallow depth from the source of vibration.
- The results from numerical analysis tend to suggest that the presence of soft soil at shallow depth can amplify the amplitude of vibrations in the stiff upper layer as compared to a homogenous soil layer with uniform soil stiffness.
- The attenuation of vertical accelerations at an increasing distance from source suggest that the effect of soft soil on the surface wave propagation tend to decay rapidly and could be a localised phenomenon. At sufficiently far away distance from the source, the attenuated accelerations levels are similar regardless of soil stiffness profile.
- It is likely that closer to the point of impact, plastic strains develop in soil which would lead to faster attenuation and lower amplitude of vertical acceleration in the centrifuge test results as compared to the numerical predictions obtained with an assumption of soil behaving as a linear elastic material. At a far away distance from the source, this behaviour would diminish and soil behaviour could be assumed as linear elastic.

5 ACKNOWLEDGEMNTS

The authors would like to thank colleagues and technical staff at the Schofield Center for their insightful opinions, time and support.

The first author would also like to acknowledge the Mott MacDonald Research Fund in supporting research at Cambridge University and Dr. Barnali Ghosh, Tony O'Brien and Imran Farooq for their guidance.

REFERENCES

[1] K. Adolfsson, B. Andreasson, P. E. Bengtsson, and P. Zackrisson, 'High speed train X2000 on soft organic clay - measurements in Sweden', in *Geotechnical engineering for transportation infrastructure. Proceedings of the 12th European conference on soil mechanics and geotechincal engineering, Amsterdam, June 1999. Vol. 3.*, 1999.

[2] C. MADSHUS and A. M. KAYNIA, 'High-Speed Railway Lines on Soft Ground: Dynamic Behaviour At Critical Train Speed', *J. Sound Vib.*, vol. 231, no. 3, pp. 689–701, 2000.

[3] R. F. Woldringh and B. M. New, 'Embankment design for high speed trains on soft soils', in *Geotechnical engineering for transportation infrastructure. Proceedings of the 12th European conference on soil mechanics and geotechincal engineering, Amsterdam, June 1999. Vol. 3.*, 1999.

[4] R. G. Payton, 'Transient motion of an elastic half-space due to a moving surface line load', *Int. J. Eng. Sci.*, vol. 5, no. 1, pp. 49–79, 1967.

[5] L. Fryba, 'Vibration of Solids and Structures under Moving Loads', in *Vibration of Solids and Structures under Moving Loads*, 1972, pp. 83–93.

[6] V. V. Krylov, 'Vibrational impact of high-speed trains. I. Effect of track dynamics', *J. Acoust. Soc. Am.*, 1996.

[7] R. D. Woods, 'Screening of Surface Waves in Soils', *J. Soil Mech. Found. Div.*, vol. 94, no. 4, pp. 951–980, 1968.

[8] J. F. Semblat and M. P. Luong, 'Wave propagation through soils in centrifuge testing', *J. Earthq. Eng.*, vol. 2, no. 1, pp. 147–171, 1998.

[9] K. Itoh, M. Koda, K. I. Lee, O. Murata, and O. Kusakabe, 'Centrifugal simulation of wave propagation using a multiple ball dropping system', *Int. J. Phys. Model. Geotech.*, vol. 2, no. 2, pp. 33–51, 2002.

[10] S. François, M. Schevenels, B. Thyssen, J. Borgions, and G. Degrande, 'Design and efficiency of a composite vibration isolating screen in soil', *Soil Dyn. Earthq. Eng.*, 2012.

[11] G. Kouroussis, D. P. Connolly, B. Olivier, O. Laghrouche, and P. A. Costa, 'Railway cuttings and embankments: Experimental and numerical studies of ground vibration', *Sci. Total Environ.*, 2016.

[12] M. Banimahd, P. K. Woodward, J. Kennedy, and G. M. Medero, 'Behaviour of train–track interaction in stiffness transitions', *Proc. Inst. Civ. Eng. - Transp.*, vol. 165, no. 3, pp. 205–214, 2012.

[13] H. Holm, B. Andréasson, P. Bengtsson, A. Bodare, and H. Eriksson, 'Mitigation of Track and Ground Vibrations by High Speed Trains at Ledsgard, Sweden', *Swedish Deep Stab. Res. Cent.*, vol. Report 10, pp. 7–60, 2002.

[14] G. Madabhushi, *Centrifuge modelling for civil engineers*. 2017.

[15] B. Ghosh and S. P. G. Madabhushi, 'An efficient tool for measuring shear wave velocity in the centrifuge', in *International Conference on Physical Modelling in Geotechnics*, 2002, pp. 119–124.

[16] G. Tsinidis, K. Pitilakis, and G. Madabhushi, 'On the dynamic response of square tunnels in sand', *Eng. Struct.*, 2016.

[17] V. Kumar and S. P. G. Madabhushi, 'Surface wave propagation in centrifuge testing using Electromagnetic Drop-Projectile system "in-press"', in *Proceedings of the 4th European Conference on Physical Modelling in Geotechnics*.

[18] J. F. Semblat, J. J. Brioist, and M. P. Luong, 'Mean-stress dependent damping of seismic waves in sand', in *Earthquake geotechnical engineering. Proceedings of the 2nd international conference on earthquake geotechnical engineering, Lisbon, June 1999. (3 vols.).*, 1999.

[19] A. Zerwer, G. Cascante, and J. Hutchinson, 'Parameter estimation in finite element simulations of Rayleigh waves', *J. Geotech. Geoenvironmental Eng.*, 2002.

[20] H. Lamb, 'On the Propagation of Tremors over the Surface of an Elastic Solid', *Philos. Trans. R. Soc. A Math. Phys. Eng. Sci.*, 1904.

[21] M. Bath, A. J. Berhout, and R. T. Beyer, 'Mathematical Aspects of Seismology (Vol. 17 of Handbook ofGeophysical Exploration), 2nd Enlarged Ed. by Markus Bath and A. J. Berhout ', *J. Acoust. Soc. Am.*, 1986.

[22] L. S. T. Corporation, 'LS-DYNA Keyword User's Manual Volume II R11 r:10572'. 2018.

[23] G. F. Miller and H. Pursey, 'On the Partition of Energy between Elastic Waves in a Semi-Infinite Solid', *Proc. R. Soc. A Math. Phys. Eng. Sci.*, vol. 233, no. 1192, pp. 55–69, 1955.

[24] A. M. Kaynia, C. Madshus, and P. Zackrisson, 'Ground vibration from high-speed trains: Prediction and countermeasure', *J. Geotech. Geoenvironmental Eng.*, 2000.

EURODYN 2020
XI International Conference on Structural Dynamics
M. Papadrakakis, M. Fragiadakis, C. Papadimitriou (eds.)
Athens, Greece, 23–26 November 2020

GAP MONITORING IN REFURBISHMENT TASKS IN A FERRONICKEL FURNACE AT CERRO MATOSO SA

Diego A. Tibaduiza[1], Jersson Leon[2], Luis Bonilla[3], Bernardo Rueda[3], Oscar Zurita[3], Juan Carlos Forero[3], Jaime Vitola[4], Dario Segura[4], Edwin Forero[4], Maribel Anaya[4]

[1]Departamento de Ingeniería Eléctrica y Electrónica. Universidad Nacional de Colombia, Bogotá, Colombia.
Cra 45 No. 26-85, Bogotá, Colombia
e-mail: dtibaduizab@unal.edu.co

[2] Departamento de Ingeniería Mecanica y Mecatrónica. Universidad Nacional de Colombia, Bogotá, Colombia.
Cra 45 No. 26-85, Bogotá, Colombia
e-mail: jxleonm@unal.edu.co

[3] Cerro Matoso S.A, Montelíbano, Colombia. email: bernardo.s.rueda@south32.net.

[4] MEM (Modelling-Electronics and Monitoring Research Group), Faculty of Electronics Engineering, Universidad Santo Tomás, Bogotá 110231, Colombia; maribelanaya@usantotomas.edu.co

Keywords: Gap monitoring, ultrasonics, ferronickel, furnace.

Abstract. *Cerro Matoso SA (CMSA) is one of the world's major producers of ferronickel. As one of the companies leaders of this sector, CMSA is continuously changing and improving all its processes to ensure the business sustainability, one of these improvements is the refurbishment of one of its electric furnaces. This procedure will replace the current furnace sidewalls of one of its electric furnaces in order to process material of new compositions by applying new refractory brick lining. This procedure will require the shut down of the furnace which will generate a contraction of the bricks mainly in the hearth of the furnace. During the furnace startup, the behavior of the hearth will tend to recover its position in such a way that it will expand, for this reason it is planned to left a gap between the skew the hearth lining. Such gap is allowed for bricks to expand properly, however,it is important to highlight that this gap must be closed since the molten material can be filtered through such spaces causing catastrophic damage. Therefore, the need arises to establish a process for monitoring the growth of the hearth of the furnace. In this work, the ultrasound method was used for gap monitoring by detecting pressure exerted by the expansion of the bricks on the metallic shell. Measurements were made without pressure, with 300 and 600 psi to demonstrate the problem of closing the expansion gap. Results show that the developed methodology can detect when the gap is closed by using ultrasonic inspection and the use of two gap monitoring indicators.*

1 INTRODUCTION

To implement new technologies that allow Cerro Matoso SA (CMSA) to enhance its operational efficiency, a series of activities have been proposed that seek to optimize fundamental aspects in the production chain of ferronickel. As a smelting industry, CMSA is interested in monitoring the state of the refractory walls of its furnaces in search of more informed decision making in order to increase the furnace efficiency and prolonged campaign life. Due to the continuous operation, the refractory walls of the furnace show deterioration through its use, this is caused mainly by mechanical, thermal stress cracks and chemical attack resulting in loss of heat transfer capability, shrinkage and change of thermal conductivity of the refractories [6]. Due to the nature of smelting furnaces, it is nearly impossible to drill into the lining while the furnace is in operation and directly evaluate the refractory thickness and condition [5].Because of this limitation the industry demand non-destructive testing (NDT) methods for furnace refractory walls during operation. Some of the NDT techniques commercially available that have been used to measure the refractory wall thickness in furnaces are: Radioactive Tracers, Infrared (IR) Thermography, Electromagnetic (EM) / Microwave Techniques, Ultrasonic, Acousto Ultrasonic-Echo (AU-E), among others [6]. In the industry, there exists Furnace Integrity Monitoring System (FIMS) which are based on the utilization of Acoustic Emission (AE) signal detection, however, these systems are not available for refractory gap monitoring. Three case studies of FIMS using ultrasound sensors to monitor furnaces are described in the work of Sadri et al., in 2018 [7] . In all three cases, the Acousto Ultrasonic-Echo (AU-E) measurements in combination with other data such as thermocouple readings and surveying information, resulted in the extension of furnace campaign life by improving the accuracy and reliability of thermal furnace models. An acoustic emission-based furnace integrity monitoring system was developed by Gebsky and Sadri in 2012 [2], in this system, the capability of detecting emissions related to the fracture development in the furnace wall, movement of the refractory and electrode arcing is satisfactory accomplished. An Integrated Furnace Control system for shielded arc smelting of the 75 MW Cerro Matoso Line 2 Furnace is described in [4], it is aimed to detect the gap between the bricks of the furnace hearth when it shrinks and then expands. As a contribution to the need for a gap monitoring system, this work presents a furnace refractory gap monitoring methodology that uses data from the ultrasonic pulse echo technique and the current indicators for the detection of the presence of a gap in the refractory bricks. The remainder of this paper is organized as follows. The second section presents a theoretical background that briefly describes the most relevant concepts of the measurement technique used in the proposed methodology. Section 3 is devoted to present the gap measurement methodology and section 4 describes the data acquisition process. Then, section 5 shows the experimental results and their corresponding discussion. Finally, the last section outlines the main conclusions.

2 THEORETICAL BACKGROUND

In this section, some concepts about the methods used in the gap monitoring methodology are summarized, we recommend reviewing the bibliography for deepen understanding of the methods.

2.1 Ultrasonic inspection

Ultrasound is a non-destructive inspection technique that is used to measure different characteristics in materials. These include, for example, the measurement of thickness as an element of quality in manufacturing processes or as an element of continuous monitoring in processes

where changes in the structure can be a critical element to consider.

2.2 Signal to noise ratio SNR or S/N

Signal to noise ratio is a measure that allows comparing the level of the desired signal to the level of the background noise [3]. In general terms, it allows to know how well is the signal captured in relation to the noise in the acquisition.

2.3 Fast Fourier Transform (FFT)

Fourier Analysis is a kind of analysis very common in the analysis of signals, it allows to convert a signal from its original domain to another domain, for example to change from the time or space to the frequency domain. FFT is a kind of algorithm to apply Fourier Analysis and allows to compute the discrete Fourier transform of a sequence by decomposing a sequence into components of different frequencies.

3 GAP MONITORING METHODOLOGY

Gap Monitoring methodology considers the following elements, first, data acquisition, second, data pre-processing, third, index calculation and evaluation. For gap monitoring indicators, two measurements are considered as illustrated in figure 1 and figure 2 which results in two possible methodologies. The first approach considers the use of the signal to noise ratio (SNR) and the second approach calculates the FFT to extract the dc component.

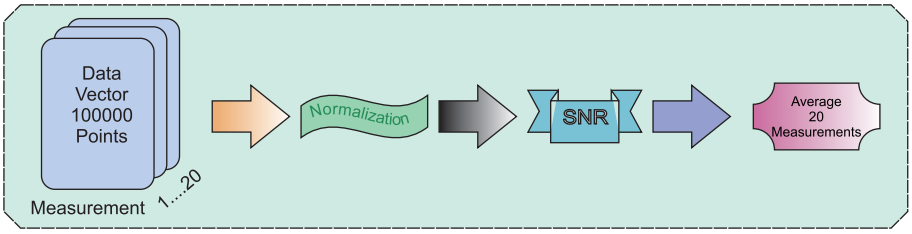

Figure 1: Methodology I - Signal to noise ratio

In both methodologies, pre-processing and normalization are considered in order to avoid data acquisition biases such as noise, coupling of the sensors, and others [1]. Measures from the experiment are averaged to facilitate comparisons and avoid biases before the application of the indicators and the final gap detection [8].

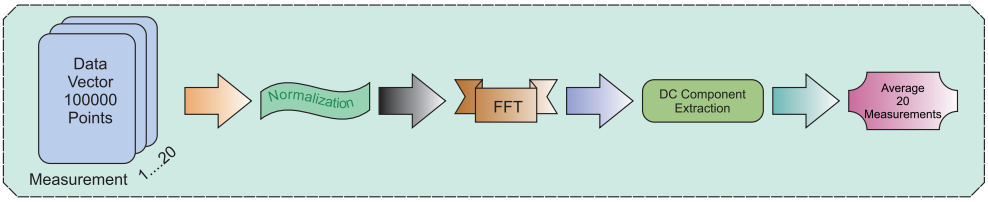

Figure 2: Methodology II - DC component extraction

4 EXPERIMENTAL SETUP

Since it is impossible to create a gap when the furnace is in operation, CMSA built a model to evaluate the methodology as in Figure 3. This model is in scale 1:1 and represents a small

section of the skew. As it is possible to observe there is an expansion paper between bricks and shell.
The experiment was designed so that samples were taken at different points of the external wall (iron shell), these samples were taken when the refractory bricks in the internal part had a gap (without pressure), then with 300 psi and finally, 600 psi. This pressure was applied to the skew by a hydraulic jack to emulate the pressure applied by the bricks to the shield once the gap is closed. For this experiment, three indicators of the acquired signal were proposed to observe measurement magnitude changes with respect to the applied pressure, the first magnitude is the signal to noise ratio, the second is to the power spectrum, and finally, the third is extracting the DC level of the acquired signal. The results indicated that there are two evaluations that could be taken into account to detect the pressure in the inner wall and these are, the calculation of signal to noise ratio and the extraction of the DC component. Both cases can differentiate when pressure is applied to the shield by the inner wall and hence determine the existence of a gap.

Figure 3: Experimental setup for gap evaluation

5 EXPERIMENTAL RESULTS

Excitation of the structure was performed by the use of pulses at a frequency of 55-kilohertz and 1000 volts of amplitude as it is shown in figure 4. The signal in the figure includes an attenuation 1:100. This excitation signal was applied by a commercial source with reference Humboldt C369NH/AH/0009. The receiving signal from the structure is captured by the ultrasonic sensor and it is digitized by using a tiepie HS04 oscilloscope. In each acquisition, clock and excitation signal are considered to determine the echo from the structure.

In this work, signals from six positions in the external shield are considered to evaluate the methodology, these positions are labeled as A3, A4, A5, A6, A7 and A8. The sensor location was defined at the same height as the first bricks that are in contact with the gap. For each position, 200 measurements were obtained, averaged, and compared with the others results to avoid the influence of noise.

5.1 Signal to noise ratio

Figure 5 shows the average results for each load condition (0, 300 and 600 psi) when the methodology applied was the signal to noise ratio.

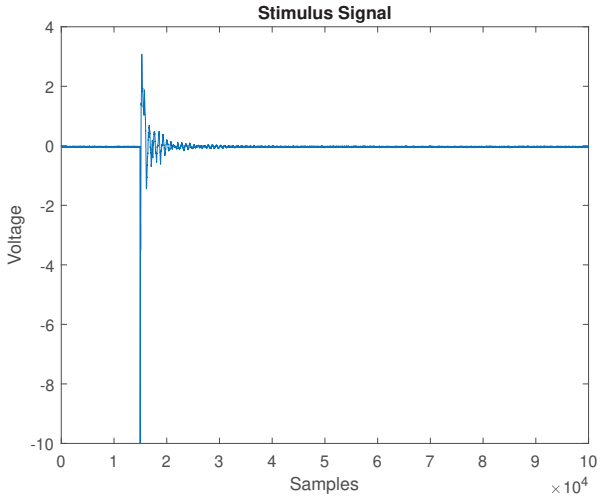

Figure 4: Stimulus Signal

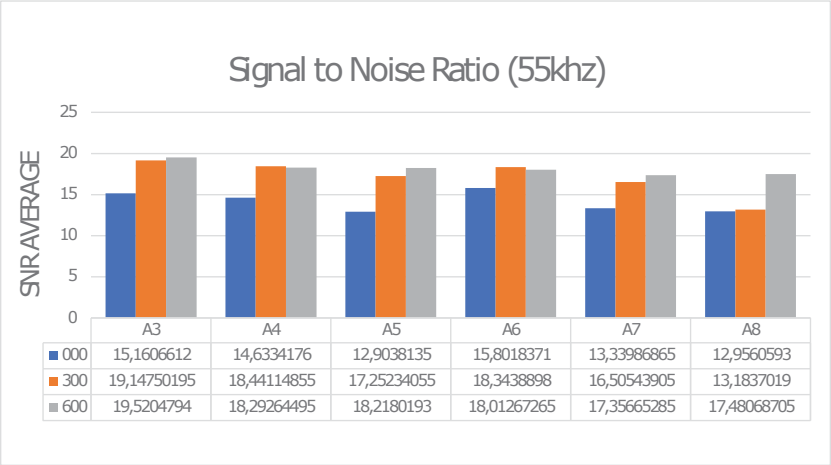

Figure 5: SNR Levels

In all cases, it is possible to evidence the influence of an existence of a gap in the signal to noise ratio, Figure 5 also shows that there are changes in the SNR in each pressure condition that were evaluated.

5.2 DC Levels

In the second analysis, spectral decomposition is used. The methodology includes the use of the FFT and the extraction of the first value to determine the presence of a gap in the configuration. Results of this process were averaged using 20 DC components, figures 6 and 7 shows the frequency decomposition for two points at the three different pressures.

As can it be seen in figure 8, the DC level of the measured signal decreases when pressure is applied by the intern wall. In the same way, as in the methodology with SNR, there are different values for each pressure condition.

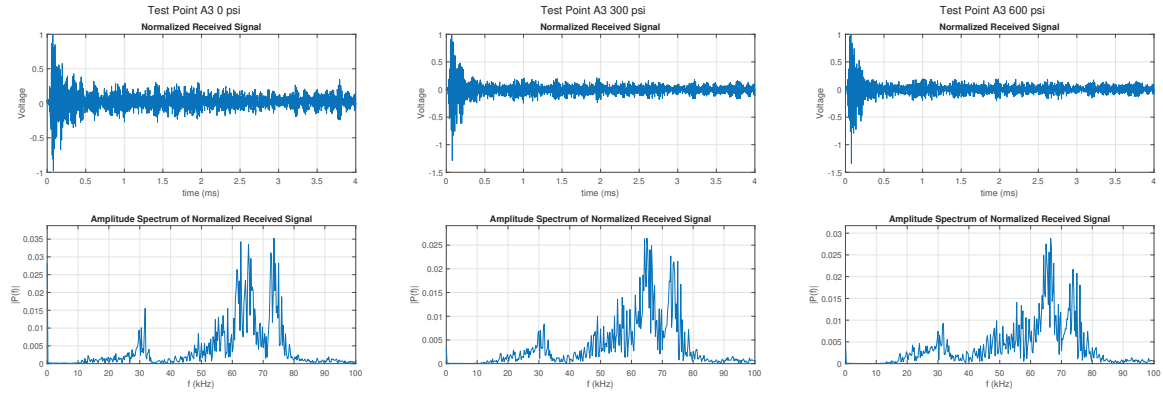

(a) Position A3 - 0 psi (b) Position A3 - 300 psi (c) Position A3 - 600 psi

Figure 6: FFT Signals - position A3

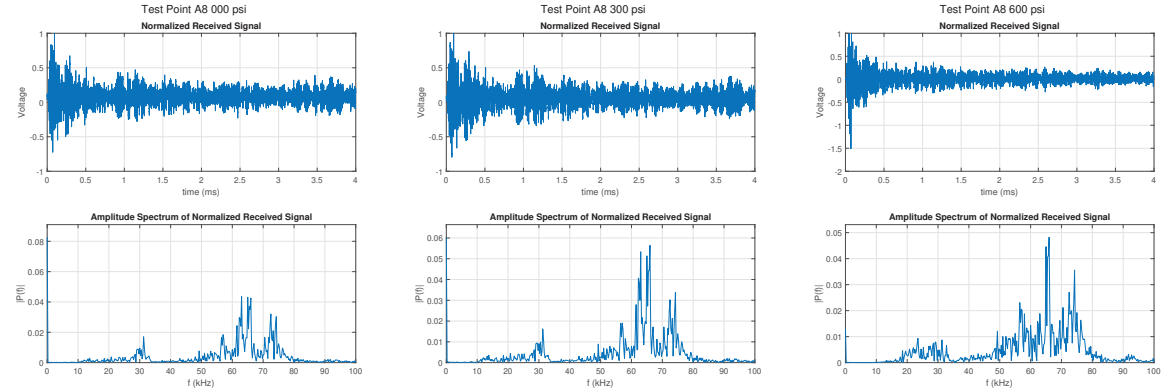

(a) Position A8 - 0 psi (b) Position A8 - 300 psi (c) Position A8 - 600 psi

Figure 7: FFT Signals - position A8

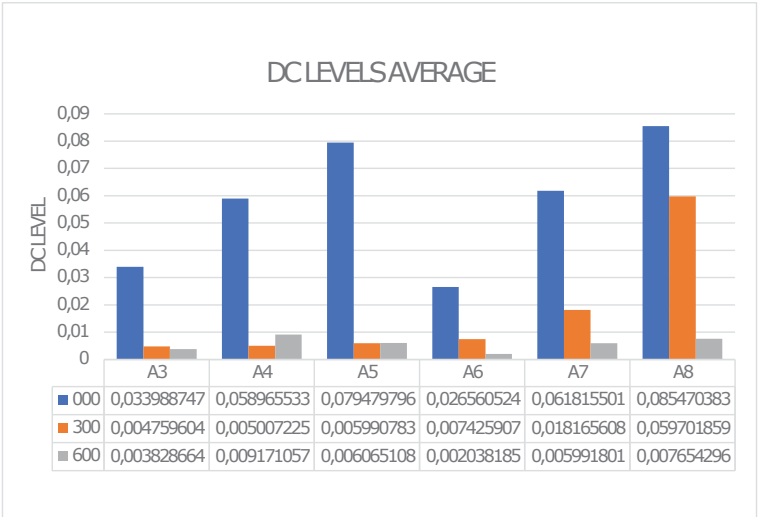

Figure 8: DC Levels

6 CONCLUSIONS

Results showed that two indicators could be taken into account for gap monitoring in a furnace with refractory bricks, these are, signal to noise ratio and the extraction of the DC components. These indicators present a difference when a gap exists and allow also to determine differences when there is a pressure from the skew to the external shield. This is an important result because by simple visual inspection it is not possible to determine variations in the wall because most of the signal is attenuated by the external shield which results in the presence of noise in the signal. For the results, the normalization of the measurements is an essential task since it prevents different factors in the signal acquisition (like sensor pressure, actuator pressure, coupling gel, surface imperfections, and others) to affect the data used by these methodologies.

The experiments were performed on a test-bed that does not consider the temperature. However, a task in the future is verifying the methodology's immunity to the temperature changes. It is expected that temperature can affect the measurements, however from previous experiences with this kind of signals, these changes are evidenced as an offset to all the measurements which can be removed by compensation techniques.

Although each methodology provide interesting results, one option that could be studied is to fuse both indicators in a single methodology to increase the reliability of the procedure for online monitoring applications.

7 ACKNOWLEDGMENT

This work has been funded by the Colombian Ministry of Science through the grant number 839, *"Convocatoria para el registro de proyectos que aspiran a obtener beneficios tributarios por inversión en CTeI a partir del 2019"*.

REFERENCES

[1] Maribel Anaya. *Design and validation of structural health monitoring system based on bio-inspired algorithms*. PhD thesis, Universitat Politècnica de Catalunya, 7 2016.

[2] Pawel Gebski and Afshin Sadri. Structural integrity monitoring of smelting furnaces based on acoustic emission data acquisition and analysis. In *18th World Conference on Non-destructive Testing*, pages 16–20, 2012.

[3] Will Gragido, Johnl Pirc, Nick Selby, and Daniel Molina. Chapter 4 - signal-to-noise ratio. In Will Gragido, Johnl Pirc, Nick Selby, and Daniel Molina, editors, *Blackhatonomics*, pages 45 – 55. Syngress, Boston, 2013.

[4] J Janzen, T Gerritsen, N Voermann, ER Veloza, and RC Delgado. Integrated furnace controls: Implementation on a covered-arc (shielded arc) furnace at cerro matoso. In *Proceedings of the 10th International Ferroalloys Congress*, pages 659–669, 2004.

[5] A Sadri, WL Ying, and D Chataway. Non-destructive testing (ndt) and monitoring of refractory lining in operating furnaces. In *UNITECR 2017, September 26 – 29, 2017, CentroParque Convention - Conference Center, Santiago, Chile*, 2017.

[6] A Sadri, WL Ying, P Gebski, P Szyplinski, T Goff, and B van Beek. A comprehensive review of acousto ultrasonic-echo (au-e) technique for furnace refractory lining assessment. In *54th annual conference of metallurgists, COM*, 2015.

[7] Afshin Sadri, Mitchell Henstock, Peter Szyplinski, and Wai Lai Ying. Progressing towards furnace modernization by utilizing comparative analysis of acousto ultrasonic-echo (au-e) monitoring: Case studies. In *Extraction 2018*, pages 547–557. Springer, 2018.

[8] Jaime Vitola, Francesc Pozo, Diego Tibaduiza, and Maribel Anaya. A sensor data fusion system based on k-nearest neighbor pattern classification for structural health monitoring applications. *Sensors*, 17(2):417, 2017.

EURODYN 2020
XI International Conference on Structural Dynamics
M. Papadrakakis, M. Fragiadakis, C. Papadimitriou (eds.)
Athens, Greece, 23–26 November 2020

ON THE ESTIMATION OF VON MISES EQUIVALENT STRESS IN RANDOM VIBRATION ANALYSIS

Federico Perotti, Francesco Foti and Luca Martinelli

Department of Civil and Environmental Engineering, Politecnico di Milano
Piazza Leonardo da Vinci, 32 20133 Milan Italy
{federico.perotti, francesco.foti, luca.martinelli}@polimi.it

Keywords: structural dynamics, random vibration, seismic analysis, stress assessment

Abstract. *Linear random vibration analysis aims to the probabilistic characterization of response functions; classical procedures are targeted to the time histories of output kinematic variables, such as displacement, velocity and acceleration, and to parameters which are linearly related to them, such as internal forces, deformations, stress components ecc. Much less attention has been devoted, by researcher and developers, to the case of response variables which are non-linearly dependent of the lagrangian coordinates or their derivatives; the most typical among these is the Von Mises equivalent stress, whose square value is quadratic in the components of the stress tensor, and thus in the lagrangian coordinates. The topic is of relevance especially for the structural safety of industrial equipment and systems, which is usually based on local stress integrity assessment.*

In the paper an innovative analytical procedure to deal with the probabilistic characterization of the VM stress is proposed as an extension of the classical approach adopted for linear output parameters. To this aim the matrix of the quadratic form delivering is decomposed into the sum of suitable factors; each of them deserves the same treatment as for linear parameters.

The various features related to the numerical implementation of the procedure for stationary or non-stationary (evolutionary) random excitation are discussed, with reference to both the application via direct frequency domain treatment and to the modal superposition approach; an example is finally shown and commented.

1 INTRODUCTION

Linear random vibration analysis is a powerful tool for the probabilistic characterization of the response of linearized systems to dynamic perturbative forces, both for the case of environmental interactions and for excitations of anthropic nature.

Aim of the analysis is usually the assessment of both the functionality under serviceability loads and the structural integrity under exceptional loads. The first is naturally checked in the linear range, in which no damage occurs. For the second, which should imply inelastic behavior and/or large deformations, elastic methods are nevertheless accepted in many situations. A typical example is represented by the integrity assessment of equipment components in industrial plants, which can be performed (see ASME B31.30) by means of elastic methods against complex damage phenomena, such as ratcheting, ….

Linear random vibration analysis aims to the probabilistic characterization of response functions; classical procedures are targeted to the time histories of output kinematic variables, such as displacement, velocity and acceleration, and to parameters which are linearly related to them, such as internal forces, deformations, stress components ecc. Much less attention has been devoted to the case of response variables which are non-linearly dependent of the lagrangian coordinates or their derivatives; the most typical among these is the Von Mises equivalent stress, whose square value is quadratic in the components of the stress tensor, and thus in the lagrangian coordinates. The topic is crucial for the structural safety of industrial equipment and systems, which is usually based on local stress integrity assessment.

The extreme-value distribution of the Von Mises (VM in the following) stress is addressed in [1] by estimating, through the Rice formula, the outcrossing rate of an ellipsoid by the stress component vector process; the derivation is performed for stationary gaussian random processes. In the same context, in [2] the estimation of the RMS value of the VM stress is pursued; classical approaches are here exploited such as modal analysis and frequency domain integration.

In this paper the approach proposed in [2] is cast into the more general framework of non-stationary (evolutionary) random processes. For the stationary case an innovative analytical procedure to deal with the probabilistic characterization of the VM stress is proposed as an extension of the classical approach adopted for linear output parameters. To this aim the matrix of the quadratic form delivering the equivalent stress is decomposed into the sum of suitable factors; each of them deserves the same treatment as for linear parameters. The various features related to the numerical implementation of the procedure for stationary or non-stationary (evolutionary) random excitation are discussed, with reference to both the application via direct frequency domain treatment and to the modal superposition approach; an example is finally shown and commented.

2 STRESS RESPONSE TO RANDOM DYNAMIC EXCITATION

The response of a linear *n* dof system is considered, governed by the following equations of motion

$$\mathbf{m}\ddot{\mathbf{q}}(t) + \mathbf{c}\dot{\mathbf{q}}(t) + \mathbf{k}\mathbf{q}(t) = \mathbf{F}\mathbf{g}(t) \tag{1}$$

where **m**, **c** and **k** are respectively the mass, damping and stiffness matrices, **F** is a matrix of load amplitude coefficients and **g***(t)* is the vector listing the functions that define the time variation of the loads.

Assuming non-stationary (evolutionary) random excitation, the time histories of the loads can be expressed (see Priestley [3]) according to the Fourier-Stieljes integral formulation

$$\mathbf{g}(t) = \int_{-\infty}^{\infty} \mathbf{\Psi}(t, f) \exp(i2\pi ft) d\mathbf{G}(f) \tag{2}$$

where $\mathbf{\Psi}(t, f)$ is a diagonal matrix listing deterministic, slowly varying envelope functions. $d\mathbf{G}(f)$ is an orthogonal process related to a zero-mean stationary process, having a Spectral Power Density (SPD) $\mathbf{S}_g(f)$, through the relation

$$E\left[d\mathbf{G}(f_1) d\mathbf{G}^*(f_2) \right] = \delta(f_1 - f_2) \mathbf{S}_g(f_1) \tag{3}$$

In such setting, the response of the system can be expressed, by integrating in the frequency domain, through the following expression

$$\mathbf{q}(t) = \int_{-\infty}^{\infty} \mathbf{\Gamma}(t, f) \exp(i2\pi ft) d\mathbf{G}(f) \tag{4}$$

The $\mathbf{\Gamma}(t, f)$ function appearing in (4) is in turn obtained via the time convolution

$$\mathbf{\Gamma}(t, f) = \int_{-\infty}^{\infty} \mathbf{h}(u) \mathbf{F} \mathbf{\Psi}(t-u, f) \exp(-2\pi fu) du \tag{5}$$

where $\mathbf{h}(u)$ is the matrix of the unit impulse response functions of the system.

If we now express a generic stress component as a linear combination of the configuration vector components we can write:

$$\sigma_{jk}(t) = \mathbf{z}^T \mathbf{q}(t) = \mathbf{z}^T \int_{-\infty}^{\infty} \mathbf{\Gamma}(t, f) \exp(i2\pi ft) d\mathbf{G}(f) \tag{6}$$

so that

$$\sigma_{jk}^2(t) = \mathbf{q}^T(t) \mathbf{z} \mathbf{z}^T \mathbf{q}(t) = \mathbf{z}^T \mathbf{q}(t) \mathbf{q}^T(t) \mathbf{z} \tag{7}$$

Note that, if modal analysis is performed, by expressing the configuration vector as a linear combination $\mathbf{q}(t) = \mathbf{\Phi} \mathbf{y}(t)$ of the system eigenvectors, we get the following

$$\sigma_{jk}^2(t) = \mathbf{q}^T(t) \mathbf{z} \mathbf{z}^T \mathbf{q}(t) = \mathbf{y}^T(t) \mathbf{u} \mathbf{u}^T \mathbf{y}(t) \tag{8}$$

where $\mathbf{u} = \mathbf{\Phi} \mathbf{z}$ and $\mathbf{y}(t)$ is the vector of modal coordinates.

If direct analysis is performed, i.e. without modal expansion, the mean square value of the stress component can thus be expressed, from (7), as

$$E\left[\sigma_{jk}^2(t) \right] = \mathbf{z}^T E\left[\mathbf{q}(t) \mathbf{q}^T(t) \right] \mathbf{z} = \mathbf{z}^T \mathbf{\mu}_q \mathbf{z} \tag{9}$$

i.e. as a function of the covariance matrix $\mathbf{\mu}_q$; taking expressions (3) to (5) into account the latter can be in turn obtained from the following derivation

$$\begin{aligned}
\mathbf{\mu}_q &= E\left[\mathbf{q}(f_1) \mathbf{q}^T(f_2) \right] = \\
&= \left[\int_{-\infty}^{\infty} \int_{-\infty}^{\infty} \mathbf{\Gamma}(t, f_1) E\left[d\mathbf{G}(f_1) d\mathbf{G}^*(f_2) \right] \mathbf{\Gamma}^*(t, f_2) \exp\left(i2\pi \left(f_1 - f_2 \right) t \right) \right] = \\
&= \left[\int_{-\infty}^{\infty} \int_{-\infty}^{\infty} \mathbf{\Gamma}(t, f_1) \mathbf{S}_g(f_1) \mathbf{\Gamma}^*(t, f_2) \delta(f_1 - f_2) \exp\left(i2\pi \left(f_1 - f_2 \right) t \right) df_1 df_2 \right] = \\
&= \int_{-\infty}^{\infty} \mathbf{\Gamma}(t, f) \mathbf{S}_g(f) \mathbf{\Gamma}^*(t, f) df
\end{aligned} \tag{10}$$

A time-varying (evolutionary) SPD is consistently defined as:

$$S_{\sigma_{jk}}(f,t) = \mathbf{z}^T \boldsymbol{\Gamma}(t,f)\mathbf{S}_g(f)\boldsymbol{\Gamma}^*(t,f)\mathbf{z} = \mathbf{z}^T \mathbf{S}_q(f,t)\mathbf{z} \tag{11}$$

For a stationary excitation we get the following:

$$\boldsymbol{\Psi}(f,t) = \mathbf{I} \quad ; \quad \boldsymbol{\Gamma}(f,t) = \mathbf{H}(f)\mathbf{F} \quad ; \quad S_{\sigma_{jk}}(f) = \mathbf{z}^T \mathbf{H}(f)\mathbf{F}\mathbf{S}_g(f)\mathbf{F}^T\mathbf{H}^*(f)\mathbf{z} \tag{12}$$

in which $\mathbf{H}(f)$ is the usual matrix of Frequency Response Functions, i.e. the inverse of the Mechanical Impedance matrix $\mathbf{E}(f)$, so that

$$\mathbf{H}(f) = \mathbf{E}^{-1}(f) = \left[-(2\pi f)^2 \mathbf{m} + (i2\pi f)\mathbf{c} + \mathbf{k} \right]^{-1} \tag{13}$$

3 THE ESTIMATION OF THE VON MISES EQUIVALENT STRESS

Starting from the stress tensor components the equivalent Von Mises stress can be expressed by the following quadratic form

$$\sigma_{VM}^2(t) = \boldsymbol{\sigma}^T(t)\mathbf{A}\boldsymbol{\sigma}(t) \tag{14}$$

where **A** is a 6*x*6 symmetric positive definite matrix, whose entries are given in the Appendix. By expressing the stress components as linear functions of the configuration we get

$$\sigma_{VM}^2(t) = \boldsymbol{\sigma}^T(t)\mathbf{A}\boldsymbol{\sigma}(t) = \mathbf{q}^T(t)\mathbf{Z}\mathbf{A}\mathbf{Z}^T\mathbf{q}(t) = \mathbf{q}^T(t)\mathbf{B}\mathbf{q}(t) \tag{15}$$

in which ***Z*** is a matrix of dimension $6xn_c$, being n_c the number of lagrangian coordinates affecting the computation of the stress tensor $\boldsymbol{\sigma}$.

Expressions (15), (4) and (5) formally solve the problem of the Von Mises stress evaluation. When the evaluation of the expected value of the squared VM stress is addressed, however, it can be easily verified that an approach similar to equations (8)-(10) is problematic. To overcome these problems, the matrix **B**, symmetric and positive definite, can be decomposed in terms of its eigenvectors, i.e.

$$\mathbf{B}\bar{\mathbf{R}} = \bar{\mathbf{R}}\boldsymbol{\Lambda} \quad \rightarrow \quad \mathbf{B} = \bar{\mathbf{R}}\boldsymbol{\Lambda}^{1/2}\boldsymbol{\Lambda}^{1/2}\bar{\mathbf{R}}^T = \mathbf{R}\mathbf{R}^T \tag{16}$$

$$\sigma_{VM}^2(t) = \mathbf{q}^T(t)\mathbf{R}\mathbf{R}^T\mathbf{y}(t) = \mathbf{q}^T(t)\left(\sum_{i=1}^{M} \mathbf{r}_i\mathbf{r}_i^T \right)\mathbf{q}(t) = \sum_{i=1}^{M} \mathbf{r}_i^T\mathbf{q}(t)\mathbf{q}^T(t)\mathbf{r}_i \tag{17}$$

It is worth noting that, having applied the eigenvector transformation, we have obtained in (17) an expression which is simply the sum of *M* terms having exactly the same form as obtained in (8) for the linear response parameter (generic stress component); one the expectation operator is applied, it can be now interchanged with the summation, leading to an expression which is the sum of terms sharing the same form as in (9), i.e.

$$E\left[\sigma_{VM}^2(t)\right] = E\left[\sum_{i=1}^{M} \mathbf{r}_i^T\mathbf{q}(t)\mathbf{q}^T(t)\mathbf{r}_i \right] = \sum_{i=1}^{m} \mathbf{r}_i^T E\left[\mathbf{q}(t)\mathbf{q}^T\right]\mathbf{r}_i = \sum_{i=1}^{m} \mathbf{r}_i^T\boldsymbol{\mu}_q\mathbf{r}_i \tag{18}$$

The efficiency of the proposed procedure deserves further comments when applied within the context of the modal superposition approach. In such setting, by expressing the configuration vector as a linear combination $\mathbf{q}(t) = \boldsymbol{\Phi}\mathbf{y}(t)$ of the system eigenvectors, we get the following alternative formulation

$$\begin{aligned} \sigma_{VM}^2(t) &= \boldsymbol{\sigma}^T(t)\mathbf{A}\boldsymbol{\sigma}(t) = \mathbf{q}^T(t)\mathbf{Z}\mathbf{A}\mathbf{Z}^T\mathbf{q}(t) = \mathbf{y}^T(t)\boldsymbol{\Phi}^T\mathbf{Z}\mathbf{A}\mathbf{Z}^T\boldsymbol{\Phi}\mathbf{y}(t) \\ &= \mathbf{y}^T(t)\boldsymbol{\beta}^T\mathbf{A}\boldsymbol{\beta}\mathbf{y}(t) = \mathbf{y}^T(t)\mathbf{D}\mathbf{y}(t) \end{aligned} \tag{19}$$

It can be observed, on practical grounds, that each row of the (*n*,6) $\mathbf{\Phi}^T\mathbf{Z}$ matrix lists the components of the stress tensor occurring when the corresponding modal shape is imposed to the system; these are often available through commercial software, so that the final matrix **D** can be assumed as available also for large and complex structural models.

Again, the eigenvalue decomposition of the matrix **D**, which is symmetric and positive definite, can be considered, leading to the following factorization:

$$\mathbf{D}\overline{\mathbf{S}} = \overline{\mathbf{S}}\mathbf{\Lambda} \quad \rightarrow \quad \mathbf{D} = \overline{\mathbf{S}}\mathbf{\Lambda}^{1/2}\mathbf{\Lambda}^{1/2}\overline{\mathbf{S}}^T = \mathbf{S}\mathbf{S}^T \tag{20}$$

Since **D**, from its definition (19), has maximum rank equal to six, the squared VM stress can be now expressed as a quadratic form in the normal coordinates given as the combination of six terms having the same form as in equation (8), i.e.

$$\begin{aligned}\sigma_{VM}^2(t) = \mathbf{y}^T(t)\mathbf{S}\mathbf{S}^T\mathbf{y}(t) = \mathbf{y}^T(t)\left(\sum_{i=1}^{M}\mathbf{s}_i\mathbf{s}_i^T\right)\mathbf{y}(t) = \sum_{i=1}^{M}\mathbf{y}^T(t)\mathbf{s}_i\mathbf{s}_i^T\mathbf{y}(t) = \\ = \sum_{i=1}^{M}\mathbf{s}_i^T\mathbf{y}(t)\mathbf{y}^T(t)\mathbf{s}_i\end{aligned} \tag{21}$$

The computation of (19) requires availability of the (*p*,*M*) matrix **S** (with $M \le 6$), which can be clearly much less expensive than the direct storage of **D,** the latter being implicit in the method proposed in [2].

The variance of the VM stress can thus be expressed in terms of the covariances $\sigma_{y_j y_k}$ among normal-mode response functions, i.e.

$$E\left[\sigma_{VM}^2(t)\right] = \sum_{i=1}^{M}\mathbf{s}_i^T E\left[\mathbf{y}(t)\mathbf{y}^T(t)\right]\mathbf{s}_i = \sum_{i=1}^{M}\sum_{j=1}^{p}\sum_{k=1}^{p} s_{i,j}\sigma_{y_j y_k} s_{i,k} \tag{22}$$

In the stationary case $\sigma_{y_j y_k}$ can be, in turn, expressed via the following frequency integral

$$\sigma_{y_j y_k} = \int_{-\infty}^{+\infty} S_{y_j y_k}(f)\,df = \mathbf{\varphi}_j^T\mathbf{F}\int_{-\infty}^{+\infty}\bar{H}_j(f)\bar{H}_k(f)\mathbf{S}_g(f)df\;\mathbf{F}^T\mathbf{\varphi}_k \tag{23}$$

In the integral (21) the modal Frequency Response Functions (FRFs) appear, defined as:

$$\bar{H}_j(f) = \frac{1}{\left(2\pi f_j\right)^2 M_j}\frac{1}{1-\dfrac{f^2}{f_j^2}+i2\xi_j\dfrac{f}{f_j}} = \frac{1}{\left(2\pi f_j\right)^2 M_j}\tilde{H}_j(f) \tag{24}$$

In (22) f_j, M_j and ξ_j are respectively the modal frequency, mass and damping ratio.

In the case of perfect correlation of input forces, typical of one-component seismic excitation, the input spectral matrix becomes a scalar SPD; in addition, in can be noted that:

$$\mathbf{\varphi}_j^T\mathbf{F} = -\mathbf{\varphi}_j^T\mathbf{m}\mathbf{r} = -\Gamma_j M_j \tag{25}$$

where **r** is a vector having non zero (unit) components along coordinates expressing displacement components parallel to the seismic input and Γ_j is the usual modal participation factor. Upon substitution of (24,25) into (23) we obtain the following:

$$\sigma_{y_j y_k} = \int_{-\infty}^{+\infty} S_{y_j y_k}(f)\,df = \frac{\Gamma_j\Gamma_k}{16\pi^4 f_j^2 f_k^2}\int_{-\infty}^{+\infty}\tilde{H}_j(f)\tilde{H}_k(f)S_{\ddot{u}}(f)df \tag{26}$$

in which the SPD of the free-field ground acceleration is now introduced in the integral.

It is worth noting that all the quantities appearing in equation (26) can be easily computed (the integral) or obtained by standard structural analysis software, as the participation factors and modal frequencies. Given that the matrix **D** can be obtained as well from the standard code, and its eigenvalues easily computed, the evaluation of the mean square VM stress is easily at hand.

Finally, the most general case in which 3D seismic excitation is applied in addition to static loading can be addressed upon simple superposition of effects, by stating:

$$\sigma_{VM}^2(t) = \left\{\boldsymbol{\sigma}^{(x)T}(t) + \boldsymbol{\sigma}^{(y)T}(t) + \boldsymbol{\sigma}^{(z)T}(t) + \boldsymbol{\sigma}^{(st)T}\right\} \mathbf{A} \left\{\boldsymbol{\sigma}^{(x)}(t) + \boldsymbol{\sigma}^{(y)}(t) + \boldsymbol{\sigma}^{(z)}(t) + \boldsymbol{\sigma}^{(st)}\right\} \tag{27}$$

By expressing the stress vector in terms of the normal response, applying again the eigenvalue decomposition to the matrix **D**, considering that the normal coordinates are zero-mean processes and taking the average of (27) it can be derived that the SRSS rule can be adopted for combining the static effect and the effect of the three components of excitation, provided that the latter are uncorrelated.

3 CASE STUDY

The preceding criteria have been applied, as a first test, to a problem obtained upon drastic simplification of a real life case; this was an equipment component located in a seismically isolated industrial building. Isolation was acting only in the horizontal plane; accordingly, the vertical excitation applied to the component is by far the most significant.

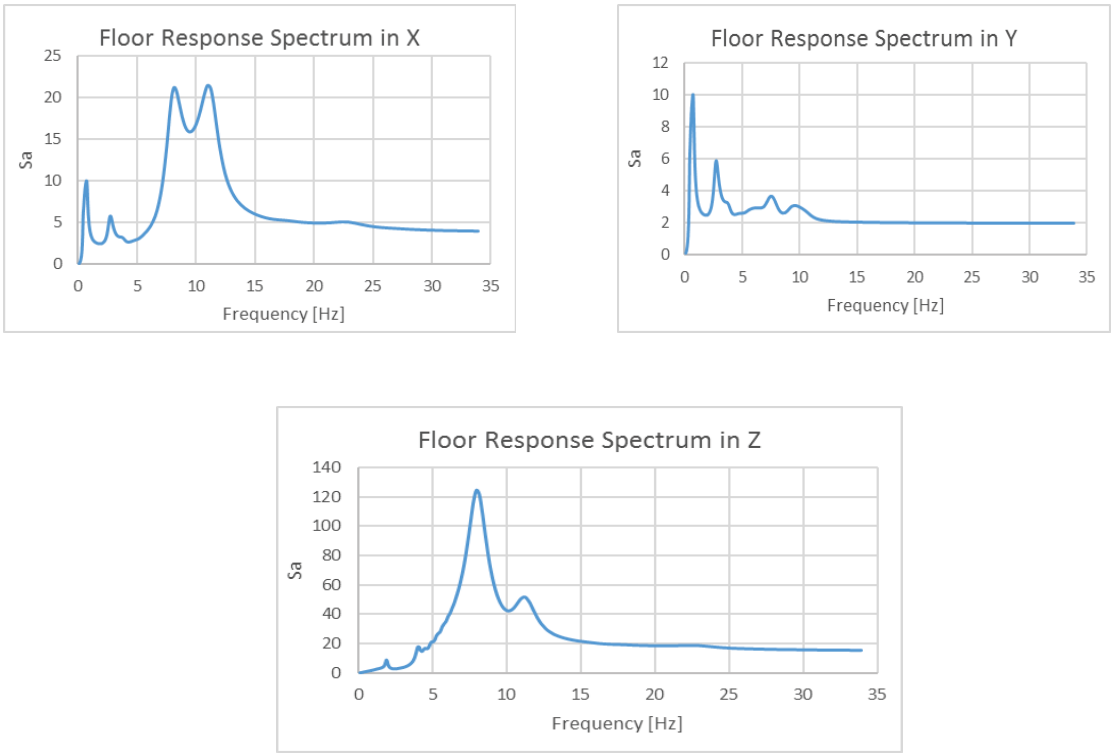

Figure1. Floor response spectrum in X, Y (horizontal) and Z (vertical) direction.

Figures 1 and 2 show the floor response spectra (FRS) applied to the system and a triplet of spectrum-compatible accelerograms obtained from the FRS; seven triplets were generated for the subsequent comparisons. In Table 1 the natural frequencies of the first ten normal modes of the model are given, spanning a range which is quite typical for a broad class of equipment components.

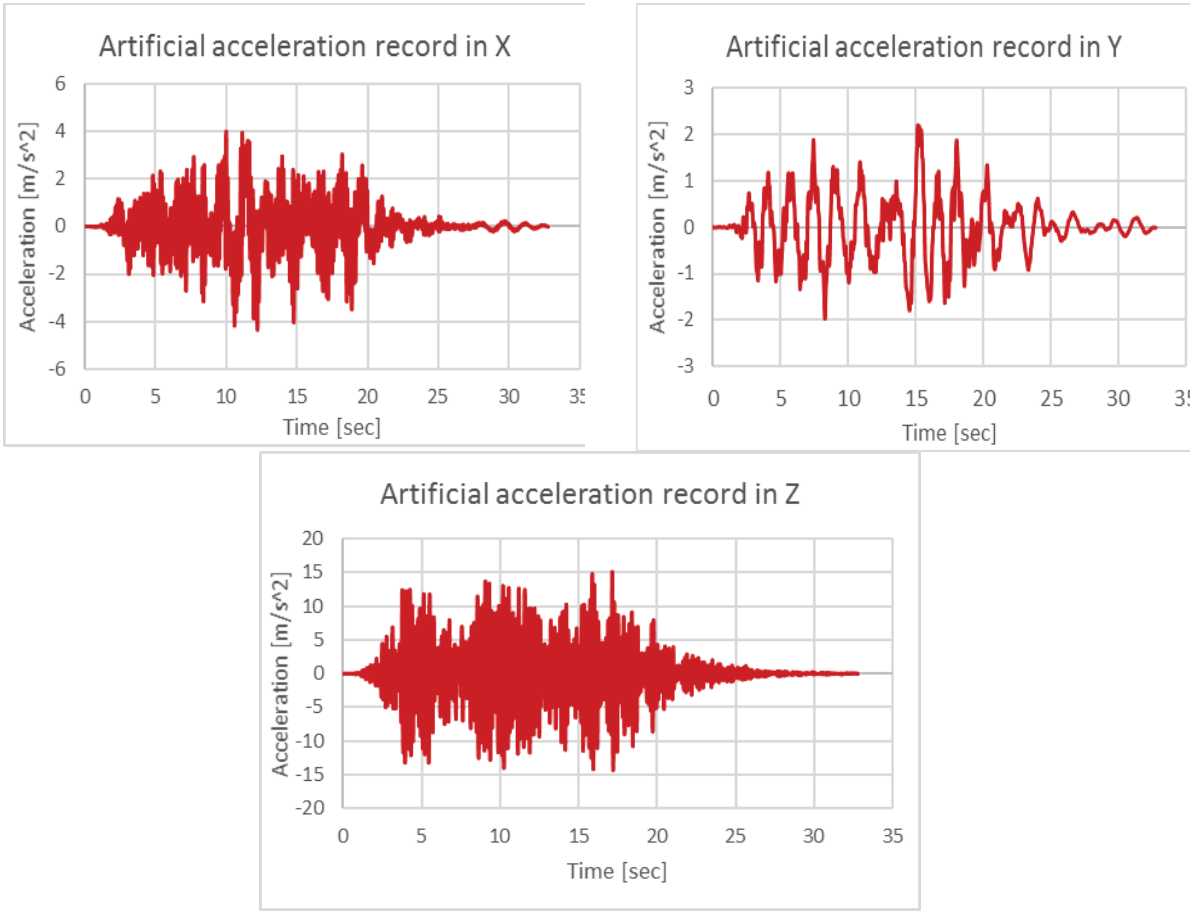

Figure 2. Artificial acceleration records in X, Y (horizontal) and Z (vertical) direction.

11.728	11.755	40.698	61.899	85.527
127.03	171.51	202.23	207.04	284.71

Table 1: Natural frequencies [Hz] of the example model.

The subsequent figure 3 shows the Finite Element mesh and the point where the stress assessment was performed. In these points the mean square Von Mises stress has been evaluated according to the following procedures:

- application of formulas (22) and (23),
- step-by-step time domain analysis, performed for the seven FRS compatible triplets of accelerograms; the mean square VM stress is obtained by simply averaging the values obtained in the seven cases,
- application of the ANSYS procedure based on [2].

In the following tables the result of the comparison is shown, suggesting the following general comments;

- the proposed method outcomes are generally in excellent agreement with the ones of the ANSYS procedure,
- both random vibration based procedures deliver slightly larger results when compared to step-by-step analysis, this being justified by the stationarity assumption.

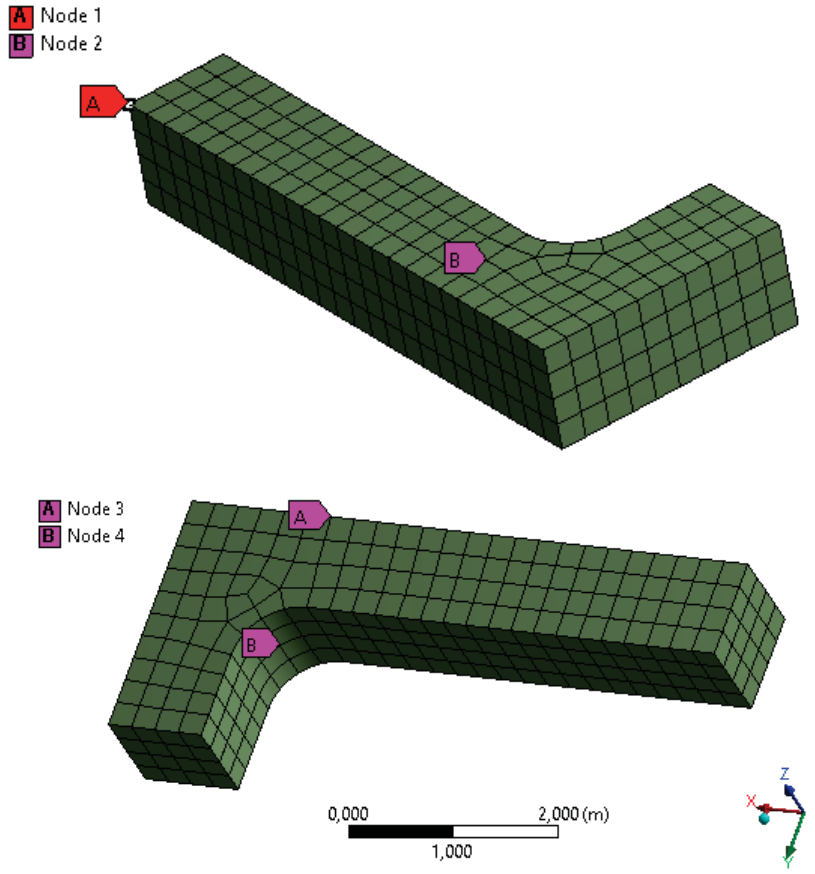

Figure 3. FE mesh and points for stress evaluation.

Direction	T History	RV Ansys	RV (22-23)	Error TH vs. Ansys	Error TH vs. RV
	[MPa]	[MPa]	[MPa]	[%]	[%]
X	1,20	1,29	1,29	7,65	8,13
Y	1,82	2,18	2,08	19,75	14,50
Z	27,82	30,06	30,22	8,05	8,63

Table 2: stress evaluation at point 1

4 CONCLUSIONS

A numerical procedure has been proposed in the paper for estimating the RMS value of the Von Mises equivalent stress within a random vibration analysis. The procedure is based on a transformation allowing the VM stress, which is a quadratic form in the coordinates, to be represented as the sum of linear output quantities; on this basis standard procedures targeted to the latter parameters can be exploited.

Some tests performed on a simple FE system are shown, in which the results obtained by means of the procedure are satisfactorily compared to the ones obtained by the method available in the software ANSYS and to the ones computed by a time-domain step-by-step procedure. The results here shown open the way to applications performed via more common design approaches, such as the response spectrum method.

Direction	T History	RV Ansys	RV (22-23)	Error TH vs. Ansys	Error TH vs. RV
	[Mpa]	[Mpa]	[Mpa]	[%]	[%]
X	0,12	0,13	0,13	8,02	8,38
Y	0,12	0,20	0,13	72,42	14,26
Z	4,34	4,90	4,92	12,99	13,53

Table 3: stress evaluation at point 2

Direction	T History	RV Ansys	RV (22-23)	Error TH vs. Ansys	Error TH vs. RV
	[Mpa]	[Mpa]	[Mpa]	[%]	[%]
X	0.25	0.27	0.27	7.64	8,53
Y	0,17	0,21	0,20	17.81	13.93
Z	2.77	3.14	3.16	13.2	13,76

Table 4: stress evaluation at point 3

Direction	T History	RV Ansys	RV (22-23)	Error TH vs. Ansys	Error TH vs. RV
	[Mpa]	[Mpa]	[Mpa]	[%]	[%]
X	0,23	0,26	0,26	9.65	9.32
Y	0,03	0,26	0,03	-	11.71
.3Z	2.85	3.07	3.09	7.78	8.30

Table 5: stress evaluation at point 4**.**

ACKNOWLEDGMENT

Facundo Ignacio Garzon performed the computations here shown in Chapter 3 as a part of his MS thesis. The technical discussions with Prof. Antonietta Lo Conte (Department of Mechanical Engineering – Politecnico di Milano) are also gratefully acknowledged.

REFERENCES

[1] H. Madsen, Extreme-value statistics for nonlinear stress combination, *Journal of Engineering Mechanics* **111**, 1121-1129, 1985.

[2] D.J. Segalman, G.W.G. Fulcher, G.M. Reese, R.V. Field Jr, An efficient method for calculating R.M.S. Von Mises stress in a random vibration environment, *Journal of Sound and Vibration* **230**(2), 393-410, 2000.

[3] M.B. Priestley, Spectral analysis of non-stationary random processes, *Journal of Sound and Vibration* **6**, 86-97, 1967.

APPENDIX

$$A_{11} = A_{22} = A_{33} = 1 \quad ; \quad A_{44} = A_{55} = A_{66} = 3 \quad ; \quad A_{12} = A_{13} = A_{23} - \frac{1}{2}$$

(other coefficients are zero)

EURODYN 2020
XI International Conference on Structural Dynamics
M. Papadrakakis, M. Fragiadakis, C. Papadimitriou (eds.)
Athens, Greece, 23–25 November 2020

INTERRELATION BETWEEN NEW HILBERT-HUANG TRANSFORM-BASED SEISMIC INTENSITY PARAMETERS AND STRUCTURAL DAMAGE

Magdalini Tyrtaiou[1], **Anaxagoras Elenas**[2]

[1] Department of Civil Engineering, Institute of Structural Statics and Dynamics,
Democritus University of Thrace, 67100 Xanthi, Greece
e-mail: mtyrtaio@civil.duth.gr

[2] Department of Civil Engineering, Institute of Structural Statics and Dynamics,
Democritus University of Thrace, 67100 Xanthi, Greece
e-mail: elenas@civil.duth.gr

Keywords: Seismic intensity parameters, Hilbert-Huang Transform (HHT), Hilbert Spectrum (HS), Park and Ang damage index, Multivariate statistics.

Abstract. *In this study, new proposed seismic intensity parameters based on Hilbert-Huang Transform (HHT) analysis are presented and associated with the seismic damage potential. The HHT is a procedure utilized to gain a better insight into complex seismic signals. Its use to the process of a seismic excitation leads to the evaluation of Hilbert Spectrum (HS). From the investigation of Hilbert Spectrum, derived from velocity-time histories, new frequency-related parameters are evaluated. A first application of the suggested new parameters reveals the interrelation between them and the structural damage of two reinforced concrete frame structures. The results are compared with the corresponding ones obtained from conventional seismic parameters with well-known seismic structural damage interrelation. Park-Ang global structural damage index ($DI_{PA,global}$) is used to describe the postseismic structural damage. Thus, a set of recorded seismic accelerograms from all over the word is applied on a seven-story reinforced concrete frame structure, and the values of $DI_{PA,global}$ index are evaluated through nonlinear dynamic analyses and considered subsequently as numerical reference values. Two statistical methods, namely correlation analysis, and multiple linear regression analysis, are applied to the set of conventional parameters and the set of new parameters separately to confirm their interrelation with the caused structural damage. The numerical results validate the significant ability of the proposed HHT-based new seismic intensity parameters to approximate the postseismic structural damage, which presented to be equal to this attained from the established parameters.*

1 INTRODUCTION

In earthquake engineering, a quick and accurate estimation of seismic hazard in both existing and planned structures remains a significant task for study. Knowing the level of the seismic hazard is indispensable for the determination of the planning process before, during, and after a severe seismic excitation. In general, the seismic intensity is a metric of the effect or the power of seismic damage potential. Thus, in the earthquake engineering and engineering seismology scientific literature, several seismic intensity parameters are presented and interrelated with the structural damage [1-9].

These parameters are evaluated by signal processing techniques meaningful mainly for stationary data and interrelated with the structural damage quantified by different damage indices. However, the seismic signals as the most signals in nature are nonlinear and non-stationary. In the last years a new, signal processing method, namely Hilbert-Huang Transform (HHT) analysis, has been developed [10-14] for that kind of signals. The HHT analysis is based on the local characteristic time scale of the data and, thus, considered as the most appropriate method for the processing of non-stationary and nonlinear signals like seismic accelerograms. In this research, the Hilbert Spectra derived from several worldwide natural earthquake records are investigated, and new seismic intensity parameters based on their features are proposed.

Subsequently, one first application of the proposed HHT-based seismic intensity parameters is presented and their interrelationship with the seismic structural damage, expressed by Park and Ang overall structural damage index [15, 16], is emerged. For the verification of this interdependence, two statistical methods, the correlation analysis, and the multiple linear regression analysis are utilized. The results are compared with the corresponding ones that occurred by several seismic parameters, already established in the scientific literature by their interrelation with the structural damage. The first statistical procedure reveals the interrelation between the new proposed seismic parameters and the structural damage. Whereas the second one proves that these parameters are able to accomplish the development of a rapid technique for the investigation of the seismic vulnerability of existing buildings.

2 HILBERT-HUANG TRANSFORM (HHT)

The HHT is a time-frequency analysis technique that offers higher frequency resolution and more accurate timing of transient and non-stationary signal events than other more common techniques for the analysis of nonlinear signals (e.g., Fourier transform, wavelet analysis) which assume that signals are stationary within the time window of observation. In contrary to the last analysis techniques, HHT is associated with adaptive bases that describe the most signals in nature [17-19].

The HHT presented first by Huang et al. [10] and can be separated into two parts: the empirical mode decomposition (EMD) and the Hilbert spectral analysis (HSA).

2.1 Empirical Mode Decomposition (EMD)

The EMD decomposes any complex signal data into non-sinusoidal oscillatory modes, and each of them represents an intrinsic mode function (IMF). The following conditions define the IMF:

1. In the whole signal, the number of extrema and zero-crossings must be either equal or differ at most by one, and

2. at any point, the mean value of the envelope defined by the local maxima and the envelope defined by the local minima must be zero.

The following procedure is performed, taking into account the above definition. For the seismic signal $X(t)$ in the study, all the local maxima are identified and connected by a cubic spline

to create the upper envelope $u_{max}(t)$ of the signal. An identical procedure is performed for the local minima and the lower envelope $u_{min}(t)$ of the signal is created. The two envelopes must enclose the whole signal between them. The mean value of the two envelopes assigned as m_1 is provided in Eq. (1).

$$m_1(t) = \frac{(u_{max}(t) - u_{min}(t))}{2} \tag{1}$$

Moreover, the difference between the seismic signal and the $m_1(t)$ is the first component

$$h_1(t) = X(t) - m_1(t) \tag{2}$$

By going on the procession, the signal is considered to be the first component $h_1(t)$ and then

$$h_{11}(t) = h_1(t) - m_{11}(t) \tag{3}$$

where $m_{11}(t)$ is the new mean of the two envelopes of $h_1(t)$. This process is repeated for k times and $h_{1k}(t)$ is provided by

$$h_{1k}(t) = h_{1(k-1)}(t) - m_{1k}(t) \tag{4}$$

The $h_{1k}(t) = c_1(t)$ consists of the first IMF of the signal in the study, and it should contain the shortest period of it. After that, the residue $r_1(t)$ is derived by subtracting the first IMF from the initial signal

$$r_1(t) = X(t) - c_1(t) \tag{5}$$

The residue $r_1(t)$ contains components of longer periods and then is considered as new signal. The new data are submitted to the same iteration mentioned above process until all the functions $r_j(t)$ are obtained

$$r_j(t) = r_{(j-1)}(t) - c_j(t),\ j = 2, 3, \dots, n \tag{6}$$

The sifting procedure stops when one of the two following criteria comes true:

1. The value of the component $c_n(t)$, or the value of the residue r_n(t), is less than a predetermined one.

2. The residue r_n(t) is a monotonic function with only one extreme or a constant, and therefore, no further IMFs can be extracted from it.

Finally, the initial seismic signal $X(t)$ is resulting from the summation of all IMFs and the residue r_n(t) as presented in Eq. (7).

$$X(t) = \sum_{J=1}^{n} c_j\,(t) + r_n\,(t) \tag{7}$$

2.2 Hilbert Spectral Analysis (HSA)

During HSA the Hilbert transform is applied to each intrinsic mode function (IMF), $c_j(t)$,

$$y_j(t) = \frac{1}{\pi}\ P \int_{-\infty}^{\infty} \frac{c_j(\tau)}{t-\tau}\ d\tau \tag{8}$$

where P denotes the Cauchy principal value of the integral. The IMF $c_j(t)$ and the Hilbert transform $y_j(t)$ form an analytical signal $z_j(t)$

$$z_j(t) = c_j(t) + iy_j(t) = a_j(t)e^{i\theta j(t)} \tag{9}$$

where $a_j(t)$ is the radius of the rotation of the analytical signal and $\theta_j(t)$ is the instantaneous phase function and are defined as

$$a_j(t) = \sqrt{c_j^2(t) + y_j^2(t)} \tag{10}$$

$$\theta_j(t) = arctan[\frac{y_{j(t)}}{c_j(t)}] \tag{11}$$

The instantaneous angular velocity of the rotation ω_j(t) is computed from the derivative of the phase function, and ω_j(t), the instantaneous frequency can be calculated as presented in Eq. (12).

$$\omega_j(t) = \frac{d\theta_j(t)}{dt} = 2\pi \cdot f_j(t) \rightarrow f_j(t) = \frac{\omega_j(t)}{2\pi} = \frac{d\theta_j(t)}{dt} \tag{12}$$

By using the above equations, the IMF components are designated as

$$c_j(t) = Re(a_j(t)e^{i\theta j(t)}) = a_j(t)cos\theta_j(t) \tag{13}$$

where Re() is the real part of the analytical signal $z_j(t)$. Therefore, the initial signal can be written as:

$$X(t) = Re\left[\sum_{j=1}^{n} a_j(t)cos(\int 2\pi \cdot f_j(t)dt\right] \tag{14}$$

The residue term r_n(t) of the initial signal X(t) in Eq. (7), has been left out in Eq. (14) because it is either a monotonic or a constant function. From the Eq. (14) is revealed that the amplitude and frequency are functions of time and can be presented in a three-dimensional plot forming the time-frequency distribution of the amplitude. This time-frequency representation of the amplitude is called the Hilbert Amplitude Spectrum, or simply Hilbert Spectrum (HS) (see Figure 1). Subsequently, the quantities of instantaneous amplitude and frequency refer to the three-dimensional Hilbert Spectrum and not to j-th intrinsic mode function (IMF) separately.

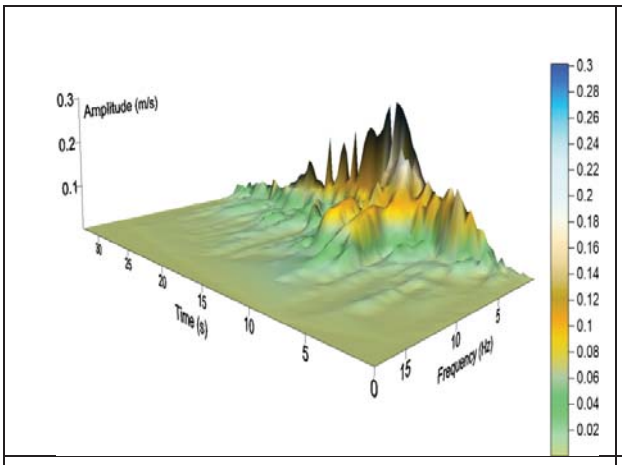

Figure 1. Hilbert Spectrum of seismic excitation.

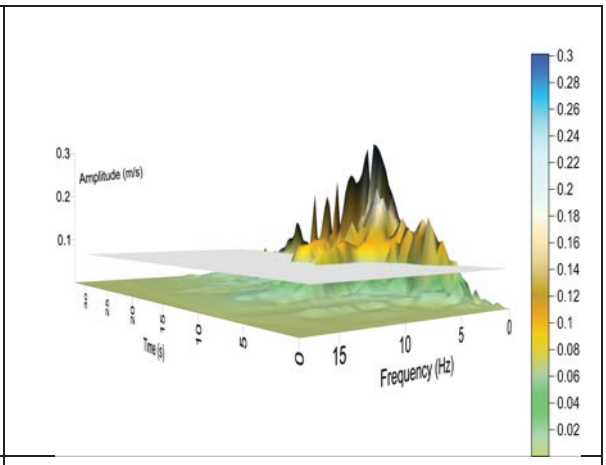

Figure 2. A layer crosses the amplitude-axis of Hilbert Spectrum vertically at $A_{(mean,HHT)}$.

3 NEW PROPOSED HHT-BASED SEISMIC INTENSITY PARAMETERS

In this study, HHA is applied to several seismic excitations, and the Hilbert Spectrum of the velocity-time history of every excitation is obtained. From the analysis and the processing of these Hilbert Spectra, new proposed seismic intensity parameters are resulting.

In particular, as aforementioned, every Hilbert spectrum, which presents the distribution of time-frequency-amplitude, leads to a time-frequency-energy (square of the amplitude) description of a signal. From the illustrated Hilbert spectrum plot, the volume of the confined space is

evaluated. The numerical value of the volume, limited from every produced Hilbert spectrum of seismic velocity, consists of an essential seismic feature because it reveals the amount of the released energy during the seismic excitation of the considered record. For this research, the specific volume is considered as a new seismic parameter, which is denoted as $V_{(HHT)}$ and is defined in Eq. (15),

$$V_{(HHT)} = \int_0^{f_{max}} \int_0^{t_{max}} a(f,t) \cdot df \cdot dt \tag{15}$$

where f_{max} is the maximum instantaneous frequency, t_{max} the total duration of the seismic signal, and $\alpha(f,t)$ denotes the instantaneous amplitude.

The area of the general surface $S_{(HHT)}$ provided by the Hilbert Spectrum, which is a function of two variables, HS(f,t) is defined in Eq. (16).

$$S_{(HHT)} = \int_0^{f_{max}} \int_0^{t_{max}} \sqrt{1 + \left(\frac{da(f,t)}{df}\right)^2 + \left(\frac{da(f,t)}{dt}\right)^2} \cdot df \cdot dt \tag{16}$$

The maximum, the mean value, and their difference of instantaneous amplitude $\alpha(f,t)$ that are obtained from the analytical signal are presented in Eq (17)-(19).

$$A_{(max,HHT)} = max(\alpha(f,t)) \tag{17}$$

$$A_{(mean,HHT)} = mean\big(\alpha(f,t)\big) \tag{18}$$

$$A_{(dif,HHT)} = A_{(max,HHT)} - A_{(mean,HHT)} \tag{19}$$

Moreover, the corresponding values of volume and area above the parallel to the time-frequency layer that intersects the amplitude-axis of Hilbert Spectrum at the value of $A_{(mean,HHT)}$ (see Figure 2), denoted as $V_{(Pos,HHT)}$ and $S_{(Pos,HHT)}$, are presented respectively in Eq. (20) and Eq. (21).

$$V_{(Pos,HHT)} = \int_0^{f_{max}} \int_0^{t_{max}} a(f,t) \cdot df \cdot dt \;\; , a \geq a_{mean} \tag{20}$$

$$S_{(Pos,HHT)} = \int_0^{f_{max}} \int_0^{t_{max}} \sqrt{1 + \left(\frac{da(f,t)}{df}\right)^2 + \left(\frac{da(f,t)}{dt}\right)^2} \cdot df \cdot dt \;\; , a \geq a_{mean} \tag{21}$$

In the end, the following quantities that come of the combination of the above parameters are evaluated, as described in Eq. (22)-(25).

$$VA_{(max,HHT)} = V_{(HHT)} \cdot A_{(max,HHT)} \tag{22}$$

$$VA_{(mean,HHT)} = V_{(HHT)} \cdot A_{(mean,HHT)} \tag{23}$$

$$VA_{(dif,HHT)} = V_{(HHT)} \cdot \big(A_{(max,HHT)} - A_{(mean,HHT)}\big) \tag{24}$$

$$A_{(Pos,HHT)} = \frac{V_{(Pos,HHT)}}{S_{(Pos,HHT)}} \tag{25}$$

The volume $V_{(HHT)}$ obtained from the Hilbert spectrum is increased while it is multiplied by the maximum and mean amplitude and their difference. The quantities, $VA_{(max,HHT)}$, $VA_{(mean,HHT)}$, $VA_{(dif,HHT)}$, are three new quantities that are representative of every seismic record since every one of them includes two or three characteristic features of each record. In the case where the difference between the mean and maximum amplitude is minimal, the quantity $VA_{(dif,HHT)}$ is statistically equivalent to one of the other two quantities.

Finally, the volume $V_{(Pos,HHT)}$ is divided by the $S_{(Pos,HHT)}$, and new parameter $A_{Pos,HHT}$ is obtained, which can be considered as the mean amplitude of the positive volume (volume above the $A_{(mean,HHT)}$-layer) of the Hilbert spectrum.

4 CONVENTIONAL SEISMIC INTENSITY PARAMETERS

Besides the HHT-based seismic parameters, several well-known and extensively surveyed parameters are also used in this study to validate the significance of the results referring to the estimated structural vulnerability by the new parameters. These already established seismic parameters are presented in Table 1.

Description	Symbol	Reference
Peak Ground Acceleration	PGA	(Meskouris, 2000) [20]
Peak Ground Velocity	PGV	(Meskouris, 2000) [20]
Peak Ground Displacement	PGD	(Meskouris, 2000) [20]
Ratio PGA/PGV	PGA/PGV	(Meskouris et al., 1993) [21]
Central Period	CP	(Vanmarcke and Lai, 1980) [22]
Arias Intensity	I_{Arias}	(Arias, 1970) [23]
Strong Motion Duration of Trifunac-Brady	SMD_{TB}	(Trifunac and Brady, 1975) [24]
Seismic Power	$P_{0.90}$	(Jennings, 1982) [25]
Root Mean Square Acceleration	RMS_a	(Meskouris, 2000) [20]
Seismic Intensity of Fajfar-Vidic-Fischinger	I_{FVF}	(Fajfar et al., 1990) [26]
Housner's Spectrum Intensity	SI_H	(Housner, 1952) [27]
Cumulative Absolute Velocity	CAV	(Cabãnas et al., 1997) [1]
Destructiveness Potential of Araya-Saragoni	DP_{AS}	(Araya and Saragoni, 1984) [28]
Spectral Displacement	SD	(Chopra, 1995) [29]
Spectral Velocity	SV	(Chopra, 1995) [29]
Spectral Acceleration	SA	(Chopra, 1995) [29]
Seismic Absolute Input Energy	E_{inp}	(Uang and Bertero, 1990) [30]
Kappos Spectrum Intensity	SI_K	(Kappos, 1990) [31]
Spectrum Intensity of Martinez-Rueda	SI_{MR}	(Martinez and Rueda, 1998) [32]
Effective Peak Acceleration	EPA	(ATC 3-06, 1978) [33]
Maximum effective peak acceleration	EPA_{max}	(ATC 3-06, 1978) [33]

Table 1: Established seismic parameters.

5 SEISMIC DAMAGE INDICES

Damage indices (DIs) are quantities that perform the damage status of a structure with a single numerical value that can be efficiently utilized in calculations for the vulnerability assessment of a structure and their correlation with the single-value of a seismic intensity parameter. In this study, the overall structural damage index of Park and Ang ($DI_{global,PA}$) is employed [15, 16].

Park and Ang damage index is an index defined as the ratio between the initial and the reduced resistance capacity of a structure during a seismic excitation evaluated by nonlinear dynamic analysis. The classification of the structural damage status, according to $DI_{PA,global}$ values are presented in the table below.

Structural damage index	Structural damage level			
	Low	Medium	Great	Total
$DI_{PA,global}$	≤ 0.3	$0.3 < DI_{PA,global} \leq 0.6$	$0.6 < DI_{PA,global} \leq 0.8$	$DI_{PA,global} > 0.80$

Table 2. Structural damage level (DL) classification according to $DI_{PA,global}$.

The structural damage located in the "Great" (G) level is non-repairable, and damage level characterized as "Total" (T) signifies the partial or complete collapse of the structure. Thus, it is essential to be known if the caused damage of an earthquake is located in the "Low" (L) or "Medium" (M) level which means that the structure is repairable or if the damage is characterized as "Great" or "Total" which means that the structure is not repairable.

6 SEISMIC EXCITATIONS

A total number of 80 natural seismic excitations derived from ground strong motions all over the world (Table 3) are employed, and the association of their destructive power with the caused damage on the constructions is achieved using the aforementioned seismic index [2-4]. The utilized earthquakes generate for statistical reasons, a broad spectrum of damage (Low, Medium, Great, and Total) as presented in Table 2. Table 4 and Table 5 provide the categorization per PGA range and Richter magnitude scale for the used excitations, respectively. Subsequently, all the seismic parameters described above are evaluated for every utilized seismic excitation, and the results are correlated with the structural damage.

Country	Number of seismic excitations
Albania	1
Armenia	1
California	14
Canada	2
France	2
Iceland	2
Iran	9
Italy	11
Japan	6
Mexico	2
New Zealand	7
San Salvador	1
Turkey	19
Uzbekistan	3

Table 3: Number of excitations employed per country.

PGA Range [g]	Number of seismic excitations
0.01-0.1	7
0.1-0.2	17
0.2-0.3	10
0.3-0.4	9
0.4-0.5	5
0.5-0.6	4
0.6-0.7	5
0.7-0.8	5
0.8-0.9	7
> 0.9	11

Table 4: Number of excitations employed per PGA range.

Magnitude [Richter]	Number of seismic excitations
4-5	1
5-6	10
6-7	42
7-8	27

Table 5: Number of excitations employed per magnitude.

7 REINFORCED CONCRETE FRAME STRUCTURES

All the utilized accelerograms are applied to a seven-story reinforced concrete frame structure with a total height of 22 m. The examined structure is designed in agreement with the rules of the recent Eurocodes for structural concrete and aseismic structures, EC2 (2000) [34] and EC8 (2004) [35], and shown in Figure 3, where the dimensions are provided in meter and centimeter, respectively. The cross-section of the beams are T-shapes with 30 cm width, 20 cm plate thickness, 60 cm total beam height. The effective plate width is 1.15 m at the end-bays and 1.80 m at the middle-bay. The distance between frames in the three-dimensional structure has been chosen to be 6 m. The building has been considered as an "importance class II", "ductility class Medium," and "subsoil of type B".

Additionally, to the dead weight and the seismic loading, snow, wind, and live loads have been taken into account. The fundamental period of the frame is 0.95 s. After the design procedure of the reinforced concrete frame structure, a nonlinear dynamic analysis has been occurred using the software computer program IDARC2D [36] for the evaluation of the structural seismic response for every seismic excitation utilized in the present study. The hysteretic behavior of beams and columns has been specified at both ends of each one using a three-parameter Park model.

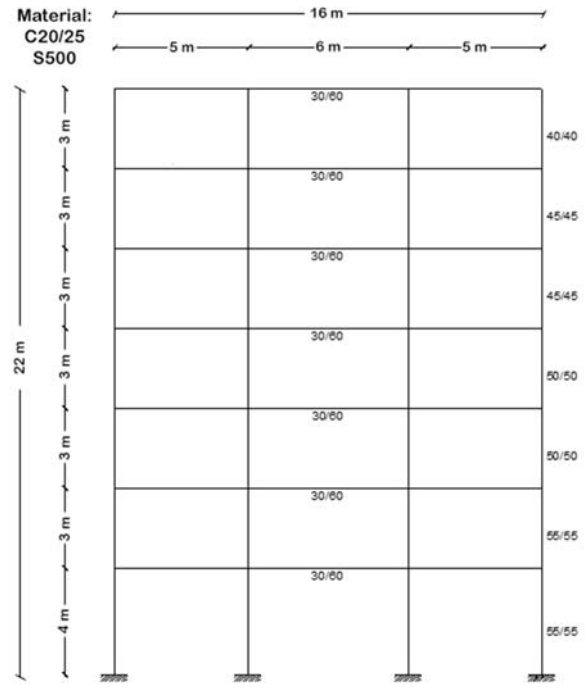

Figure 3a: Seven-story reinforced concrete frame.

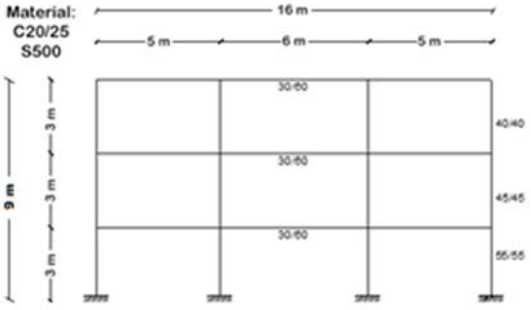

Figure 3b: Three-story reinforced concrete frame.

This model incorporates stiffness degradation, strength deterioration, non-symmetric response, slip-lock, and a trilinear monotonic envelope. The parameter values, which specify the above degrading parameters, have been chosen from experimental results of cyclic force-deformation characteristics of typical components of studied structure [16, 37]. Thus, the nominal parameters for stiffness degradation and strength deterioration have been chosen. In contrast, no pinching has been taken into account. From the derived response parameters of the nonlinear dynamic analysis, this study is concentrated on the overall structural damage index of Park and Ang ($DI_{PA,global}$). Figures 4a and 4b present the $DI_{PA,global}$ index per number of employed excitations, for each examined reinforced concrete frame.

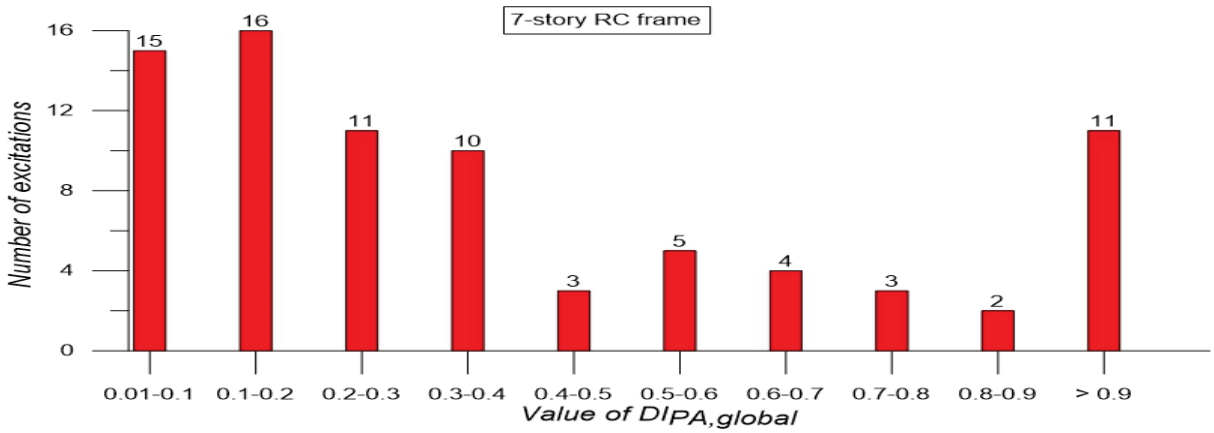

Figure 4a: Number of employed excitations per $DI_{PA,global}$ range for the seven-story frame.

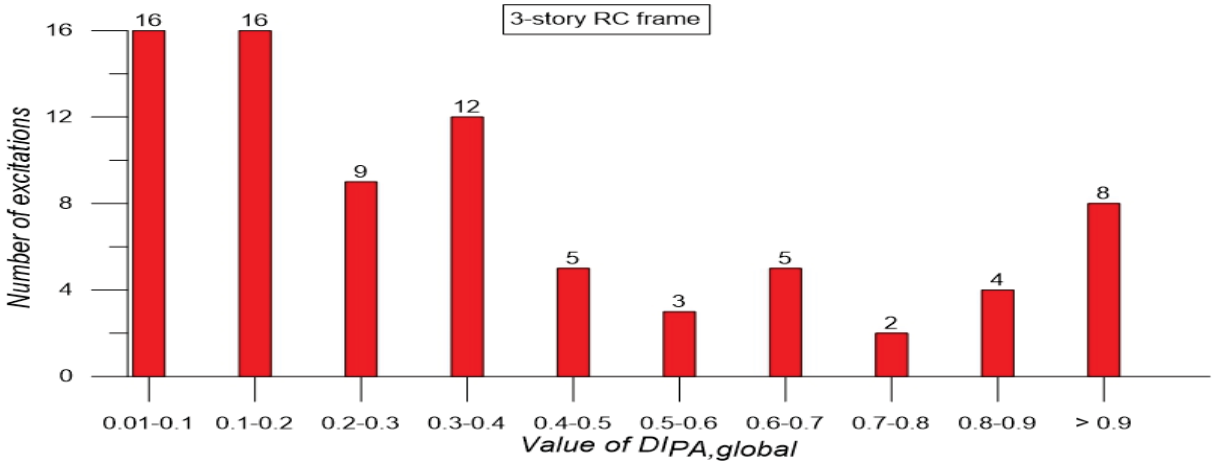

Figure 4b: Number of employed excitations per $DI_{PA,global}$ range for the three-story frame.

Also, the second concrete frame construction with three stories is used to strengthen the reliability of the results that occurred by the new proposed seismic parameters. The three-story reinforced concrete frame structure has a total height of 9 m and presents a similar layout of columns and beams to these of the seven-story RC frame, as shown in Figure 3b. After the application of the same set of seismic excitations to the second concrete frame, a nonlinear dynamic analysis using the software computer program IDARC2D [36] has been also occurred, and the new values of $DI_{PA,global}$ have been evaluated.

8 NUMERICAL RESULTS OF SEISMIC PARAMETERS EVALUATION

Applying the HHT technique to the seismic velocity time-histories of all the examined earthquakes, the instantaneous frequencies and amplitudes as functions of time are calculated using a code of the program MATLAB [38]. From the instantaneous values, time-frequency distributions of amplitude are formed, and thus, the Hilbert Spectrum for every seismic velocity signal is plotted. From the derived Hilbert Spectra, the new parameters for every seismic record are evaluated, and their statistical values are presented in Table 6. In addition, all the conventional seismic intensity parameters are evaluated, and their statistical values are presented in Table 7.

Parameter	Min Value	Max Value	Average	Standard Deviation
$V_{(HHT)}$ (m/s)	0.205	69.376	6.422	10.286
$S_{(HHT)}$ (-)	153.591	4062.689	1185.912	871.246
$A_{(max,HHT)}$ (m/s)	0.011	7.475	0.515	1.245
$A_{(mean,HHT)}$ (m/s)	0.001	0.469	0.046	0.106
$A_{(dif,HHT)}$ (m/s)	0.010	7.022	0.470	1.143
$V_{(Pos,HHT)}$ (m/s)	0.060	7.393	1.303	1.306
$S_{(Pos,HHT)}$ (-)	0.387	313.910	71.763	67.229
$VA_{(max)}$ (m^2/s^2)	0.005	322.619	13.789	51.616
$VA_{(mean)}$ (m^2/s^2)	0.0002	29.670	1.245	4.756
$VA_{(dif,HHT)}$ (m^2/s^2)	0.005	292.948	12.544	46.912
$A_{(Pos,HHT)}$ (m^2/s^2)	0.002	0.388	0.038	0.067

Table 6: Statistical values of the HHT-based parameters.

Parameter	Min Value	Max Value	Average	Standard Deviation
PGA (m/s^2)	0.304	13.615	4.541	3.446
PGV (m/s)	0.030	1.152	0.352	0.251
PGD (m)	0.003	4.341	0.290	0.713
PGA/PGV (g·s/m)	0.314	3.248	1.420	0.687
CP (s)	0.052	0.802	0.223	0.125
I_{ARIAS} (m/s)	0.015	17.041	2.823	3.551
SMD_{TB} (s)	2.080	39.100	15.203	16.150
$P_{0.90}$ (m^2/s^4)	0.005	7.442	1.740	2.037
RMS_a (m/s^2)	0.038	1.636	0.533	0.393
I_{FVF} ($m \cdot s^{3/4}$)	0.041	2.095	0.633	0.462
SI_H (m)	0.096	5.082	1.432	1.153
CAV (g·s)	0.058	4.652	1.214	1.009
DP_{AS} (m·s)	0.000	0.226	0.032	0.045
SD (m)	0.006	0.369	0.083	0.073
SV (m/s)	0.051	2.408	0.599	0.487
SA (m/s^2)	0.058	1.975	0.653	0.469
E_{inp}(m^2/s^2)	0.001	6.175	0.690	1.173
SI_K (m)	0.016	1.024	0.259	0.218
SI_{MR} (m/s)	0.042	1.391	0.466	0.350
EPA (g)	0.018	1.001	0.360	0.252
EPA_{max} (g)	0.030	1.035	0.387	0.269

Table 7: Statistical values of the conventional seismic intensity parameters.

9 INTERDEPENDENCE BETWEEN SEISMIC PARAMETERS AND $DI_{PA,global}$

The dependence of every seismic parameter with the employed damage index (DI) is examined by occurring correlation analysis between them. Correlation analysis reveals if a systematic change in one variable implies a systematic change in the other. Thus, the dependence between the two variables is established, and the occurrence of the one affects the probability of occurrence of the other. For identifying the correlation between every seismic parameter and damage index separately, Pearson r and Spearman ρ correlation coefficients are used. A value of ± 1 for a correlation coefficient indicates a perfect degree of association between the two variables of every examined pair (seismic parameter, damage index), while this relationship becomes weaker when the correlation coefficient value approximates zero. A correlation coefficient above the value 0.5 indicates a low correlation; a coefficient in the range [0.5-0.8] indicates a medium correlation, while a coefficient, higher than 0.8, indicates a strong correlation. The correlation coefficients are calculated by the program STATGRAPHICS Centurion [39].

The Pearson r correlation coefficient measures the degree of linearity between two related variables and is described by the following equation

$$r = \frac{N\sum xy - \sum(x)(y)}{\sqrt{[N\sum x^2 - \sum(x^2)][N\sum y^2 - \sum(y^2)]}} \tag{26}$$

where N is the number of observations, $\sum xy$ is the sum of the products of paired scores, $\sum x$ is the sum of x scores, $\sum y$ is the sum of y scores, $\sum x^2$ presents the sum of squared x scores, and $\sum y^2$ presents the sum of squared y scores.

The Spearman ρ rank correlation coefficient measures the degree of monotone ranking between two related variables and is defined from the following equation.

$$\rho = 1 - \frac{6\sum d_i^2}{n(n^2-1)} \tag{27}$$

Where ρ is Spearman rank correlation, d_i is the difference between the ranks of corresponding variables, and n is the number of observations. The correlation coefficients are presented in Tables 8 and 9.

Parameter	$DI_{PA,global}$	
	Pearson coefficient	Spearman coefficient
PGA (m/s^2)	0.557	0.684
PGV (m/s)	0.592	0.906
PGD (m)	0.445	0.765
PGA/PGV (g·s/m)	-0.445	-0.483
CP (s)	0.088	0.299
I_{ARIAS} (m/s)	0.462	0.779
SMD_{TB} (s)	0.088	0.108
$P_{0.90}$ (m^2/s^4)	0.590	0.720
RMS_a (m/s^2)	0.646	0.794
I_{FVF} ($m \cdot s^{3/4}$)	0.561	0.927
SI_H (m)	0.589	0.906
CAV (g·s)	0.534	0.720
DP_{AS} (m·s)	0.461	0.781
SD (m)	0.688	0.933
SV (m/s)	0.650	0.911

SA (m/s^2)	0.640	0.786
E_{inp}(m^2/s^2)	0.436	0.904
SI_K (m)	0.685	0.920
SI_{MR} (m/s)	0.599	0.703
EPA (g)	0.693	0.723
EPA_{max} (g)	0.682	0.733

Table 8: Pearson and Rank correlation coefficients of conventional seismic parameters with $DI_{PA,global}$.

Parameter	$DI_{PA,global}$	
	Pearson coefficient	Spearman coefficient
$V_{(HHT)}$ (m/s)	-0.233	-0.238
$S_{(HHT)}$ (-)	0.530	0.766
$A_{(max,HHT)}$ (m/s)	0.265	0.457
$A_{(mean,HHT)}$ (m/s)	-0.381	-0.538
$A_{(dif,HHT)}$ (m/s)	0.560	0.898
$V_{(Pos,HHT)}$ (m/s)	0.605	0.879
$S_{(Pos,HHT)}$ (-)	0.554	0.885
$VA_{(max)}$ (m^2/s^2)	0.443	0.875
$VA_{(mean)}$ (m^2/s^2)	0.637	0.935
$VA_{(dif,HHT)}$ (m^2/s^2)	0.447	0.891
$A_{(Pos,HHT)}$ (m^2/s^2)	0.444	0.876

Table 9: Pearson and Rank correlation coefficients of HHT-based seismic parameters with $DI_{PA,global}$.

10 MULTIVARIATE REGRESSION ANALYSIS (MRA)

Multiple Regression Analysis (MRA) allows the assessment of the relationship between one dependent variable (DV) and several independent variables (IVs). Regression techniques can be applied to a data set in which the IVs are correlated with one another and with the DV to varying degrees [39].

The IVs are combined to predict a value of DV for each subject according to the following equation form, and the result of the regression represents the best prediction of a DV from several continuous (or dichotomous) IVs.

$$Y' = A + B_1X_1 + B_2X_2 + \ldots + B_kX_k \tag{28}$$

Y' is the predicted value on the DV, A is the Y-intercept (the value of Y when all the X values are zero), the X_i represents the various IVs (of which there are k), and the B_i (i=1, …, k) are the coefficients assigned to each of the IVs during regression. Although the same intercept and coefficients are used to predict the values on the DV for all cases in the sample, a different Y'value is predicted for each subject as a result of inserting the subject's X values into the equation. The goal of regression is to arrive at the set of B values, called "regression coefficients", for the IVs that bring the Y' values predicted from the equation as close as possible to the Y values obtained by measurement.

In this research, the damage index $DI_{PA,global}$ is used as a dependent variable (DV), and two sets of parameters are used as independent variables (IVs). The first set contains the conventional seismic parameters and the second the HHT-based parameters. A general goal of regression is to identify the fewest IVs necessary to predict the DV, where each IV predicts a substantial and independent segment of variability in the DV. The reduction of the explanatory variables from the initial regression model (with all the conventional or HHT-based parameters as IVs) is accomplished in the present study by a stepwise elimination procedure combined with

an appropriate elimination criterion. Thus, a successive elimination of the IVs is realized with a p-value greater than or equal to 0.05 as long as the Mean Absolute Error (MAE) is getting reduced. The p-value for each term tests the null hypothesis that the coefficient of the variable in the model is equal to zero (no effect). A low p-value (< 0.05) indicates that the null hypothesis is rejected. When a predictor has a low p-value, it constitutes a significant addition to our model because changes in the predictor's value are related to changes in the dependent variable. The elimination method leads to the selection of IVs, which may not present the highest correlation with the DV, but they present the highest power effect (F-ratio) and low collinearity with the other selected IVs, providing so, a more significant model. In the end, the best model considered is the one with the fewest significant IVs, the smallest SEE and MAE, the highest R^2 and adjusted R^2 and with the highest power (F-ratio). The F-ratio indicates how well the model fits the data and tests the null hypothesis when it is compared with F critical values obtained from given F-Tables [39].

The R^2 is a value percent, which indicates that the model as fitted explains the percentage equal to this value of the variability in the DV equation. Adjusted R^2 will always be less than or equal to R^2, and it balances the R^2 value by the number of data points and independent variables in the model. The adjusted R^2 statistic is more suitable for comparing models with different numbers of independent variables. The adjusted R^2 and the adjusted R^2 are getting decreased, adding a useless independent variable in the model.

For the construction of the best regression models, the multiple regression analysis is applied to a subset of seventy seismic excitations, while the other ten excitations are used to test the effectiveness of the constructed models. All the above calculations are also realized by the software program STATGRAPHICS Centurion XVII [39]. The best-attained regression models for the damage index in the study as DV and for each set of IVs separately are presented below.

Models 1 and 2 are the best fitted statistical models, with and without constant term, respectively, to the set of the conventional parameters as IVs and $DI_{PA,global}$ of the seven-story concrete frame as DV. The constructed models are presented in Eqs. (29)-(30).

$$DI_{PA,global} = 0.192123 - 0.170151 \cdot PGA/PGV - 0.0127411 \cdot I_{Arias} - 0.552931 \cdot SV + 1.70315 \cdot SI_K + 0.92999 \cdot EPA \quad (29)$$

$$DI_{PA,global} = -0.0862897 \cdot PGA/PGV - .0146593 \cdot I_{Arias} - 0.582707 \cdot SV + 1.96585 \cdot SI_K + 0.946831 \cdot EPA \quad (30)$$

Investigating the HHT-based parameters was observed that $A_{(max,HHT)}$ and $A_{(dif,HHT)}$ parameters as well $VA_{(max,HHT)}$ and $VA_{(dif,HHT)}$ presented perfect correlation (equal to 1.0) for the excitations in study because of the very small values of $A_{(mean,HHT)}$ parameter. Thus, the parameters $A_{(dif,HHT)}$ and $VA_{(max,HHT)}$ decided to be removed, and the first investigated models were Models (3)-(4) (Eqs 31-32), which consisted of nine HHT-based parameters with and without constant respectively. From Tables (12)-(13) it is obvious that in Models (3)-(4) there are parameters with P-value > 0.05 and for this reason, a reduction of them has occurred until Models (5)-(6) (Eqs 33-34) with five parameters were obtained.

In the end, the best results were attained by removing the parameter $S_{(HHT0)}$, which P-value was 0.0458 close to 0.05. Hence, Models (7)-(8) are the best models with and without constant term obtained from the regression analyses for the set of HHT-based parameters as IVs and the examined damage index for the seven-story structure as DV, using the training sample of the seventy seismic excitations. These models are presented in Eqs (35)-(36).

$$DI_{PA,global} = 0.0181109 + 0.0000436157 \cdot S_{(HHT)} + 0.102817 \cdot V_{(HHT)} - 0.0923962 \cdot V_{(Pos,HHT)} - 0.00181203 \cdot S_{(Pos,HHT)} + 0.637458 \cdot A_{(max,HHT)} - 6.94883 \cdot A_{(mean,HHT)} + 6.79734 \cdot A_{(Pos,HHT)} + 0.163871 \cdot VA_{(mean,HHT)} - 0.0434509 \cdot VA_{(dif,HHT)} \quad (31)$$

$$DI_{PA,global} = 0.0000484984 \cdot S_{(HHT)} + 0.105145 \cdot V_{(HHT)} - 0.0938841 \cdot V_{(Pos,HHT)} - 0.00179545 \cdot S_{(Pos,HHT)} + 0.628084 \cdot A_{(max,HHT)} - 6.83837 \cdot A_{(mean,HHT)} + 6.90182 \cdot A_{(Pos,HHT)} + 0.156813 \cdot VA_{(mean,HHT)} - 0.0433545 \cdot VA_{(dif,HHT)} \quad (32)$$

$$DI_{PA,global} = 0.0179463 + 0.0000631707 \cdot S_{(HHT)} + 0.0678431 \cdot V_{(HHT)} - 0.00196269 \cdot S_{(Pos,HHT)} + 6.79454 \cdot A_{(Pos,HHT)} - 0.0190404 \cdot VA_{(dif,HHT)} \quad (33)$$

$$DI_{PA,global} = 0.000068291 \cdot S_{(HHT)} + 0.0694873 \cdot V_{(HHT)} - 0.00195125 \cdot S_{(Pos,HHT)} + 6.91811 \cdot A_{(Pos,HHT)} - 0.0195237 \cdot VA_{(dif,HHT)} \quad (34)$$

$$DI_{PA,global} = 0.0629837 + 0.064319 \cdot V_{(HHT)} - 0.00129891 \cdot S_{(Pos,HHT)} - 0.0176613 \cdot VA_{(dif,HHT)} + 6.51428 \cdot A_{(Pos,HHT)} \quad (35)$$

$$DI_{PA,global} = 0.0703044 \cdot V_{(HHT)} - 0.00101145 \cdot S_{(Pos,HHT)} - 0.0192978 \cdot VA_{(dif,HHT)} + 6.9586 \cdot A_{(Pos,HHT)} \quad (36)$$

The results of the mentioned models that describe the relationship between the damage index and the conventional parameters are presented in Tables (10)-(11), while the corresponding results that refer to the new proposed parameters are presented in Tables (12)-(17). Tables (18)-(19) present the results of the corresponding variance analyses.

Parameter	Estimate	Standard Error	Lower Limit	Upper Limit	P-Value
CONSTANT	0.1921	0.0579	0.0765	0.3077	0.0015
PGA/PGV	-0.1702	0.0337	-0.2376	-0.1027	0.0000
I_{Arias}	-0.0127	0.0019	-0.0166	-0.0089	0.0000
SV	-0.5529	0.1492	-0.8510	-0.2549	0.0004
SI_K	1.7032	0.3172	1.0694	2.3369	0.0000
EPA	0.9300	0.1280	0.6742	1.1858	0.0000

Table 10: Results for Model 1.

Parameter	Estimate	Standard Error	Lower Limit	Upper Limit	P-Value
PGA/PGV	-0.0863	0.0241	-0.1343	-0.0383	0.0006
I_{Arias}	-0.0147	0.0020	-0.0186	-0.0107	0.0000
SV	-0.5827	0.1600	-0.9022	-0.2632	0.0005
SI_K	1.9659	0.3301	1.3067	2.6250	0.0000
EPA	0.9468	0.1375	0.6723	1.2214	0.0000

Table 11: Results for Model 2.

Parameter	Estimate	Standard Error	Lower Limit	Upper Limit	P-Value
CONSTANT	0.0181	0.0495	-0.0809	0.1171	0.7156
$S_{(HHT)}$	0.0000	0.0000	0.0000	0.0001	0.1959
$V_{(HHT)}$	0.1028	0.0189	0.0650	0.1406	0.0000
$V_{(Pos,HHT)}$	-0.0924	0.0619	-0.2163	0.0315	0.1410
$S_{(Pos,HHT)}$	-0.0018	0.0006	-0.0030	-0.0006	0.0039
$A_{(max,HHT)}$	0.6375	0.2396	0.1582	1.1167	0.0100
$A_{(mean,HHT)}$	-6.9488	3.0281	-13.0059	-0.8917	0.0253
$A_{(Pos,HHT)}$	6.7973	1.3948	4.0074	9.5873	0.0000
$VA_{(mean,HHT)}$	0.1639	0.0915	-0.0192	0.3470	0.0784
$VA_{(dif,HHT)}$	-0.0435	0.0115	-0.0664	-0.0205	0.0003

Table 12: Results for Model 3.

Parameter	Estimate	Standard Error	Lower Limit	Upper Limit	P-Value
$S_{(HHT)}$	0.0000	0.0000	0.0000	0.0001	0.1151
$V_{(HHT)}$	0.1051	0.0177	0.0698	0.1404	0.0000
$V_{(Pos,HHT)}$	-0.0939	0.0614	-0.2166	0.0288	0.1312
$S_{(Pos,HHT)}$	-0.0018	0.0006	-0.0030	-0.0006	0.0038
$A_{(max,HHT)}$	0.6281	0.2365	0.1552	1.1010	0.0101
$A_{(mean,HHT)}$	-6.8384	2.9916	-12.8204	-0.8564	0.0257
$A_{(Pos,HHT)}$	6.9018	1.3555	4.1913	9.6124	0.0000
$VA_{(mean,HHT)}$	0.1568	0.0888	-0.0208	0.3345	0.0825
$VA_{(dif,HHT)}$	-0.0434	0.0114	-0.0661	-0.0206	0.0003

Table 13: Results for Model 4.

Parameter	Estimate	Standard Error	Lower Limit	Upper Limit	P-Value
CONSTANT	0.0179	0.0490	-0.0800	0.1159	0.7155
$S_{(HHT)}$	0.0001	0.0000	0.0000	0.0001	0.0458
$V_{(HHT)}$	0.0678	0.0075	0.0528	0.0829	0.0000
$S_{(Pos,HHT)}$	-0.0020	0.0005	-0.0029	-0.0010	0.0001
$A_{(Pos,HHT)}$	6.7945	0.5856	5.6246	7.9645	0.0000
$VA_{(dif,HHT)}$	-0.0190	0.0020	-0.0230	-0.0151	0.0000

Table 14: Results for Model 5.

Parameter	Estimate	Standard Error	Lower Limit	Upper Limit	P-Value
$S_{(HHT)}$	0.0001	0.0000	0.0000	0.0001	0.016
$V_{(HHT)}$	0.0695	0.0060	0.0575	0.0815	0.000
$S_{(Pos,HHT)}$	-0.0020	0.0005	-0.0029	-0.0010	0.000
$A_{(Pos,HHT)}$	6.9181	0.4754	5.9687	7.8675	0.000
$VA_{(dif,HHT)}$	-0.0195	0.0015	-0.0225	-0.0166	0.000

Table 15: Results for Model 6.

Parameter	Estimate	Standard Error	Lower Limit	Upper Limit	P-Value
CONSTANT	0.0630	0.0448	-0.0265	0.1524	0.1645
$V_{(HHT)}$	0.0643	0.0075	0.0493	0.0793	0.0000
$S_{(Pos,HHT)}$	-0.0013	0.0004	-0.0020	-0.0006	0.0007
$VA_{(dif,HHT)}$	-0.0177	0.0019	-0.0215	-0.0138	0.0000
$A_{(Pos,HHT)}$	6.5143	0.5829	5.3502	7.6783	0.0000

Table 16: Results for Model 7.

Parameter	Estimate	Standard Error	Lower Limit	Upper Limit	P-Value
$V_{(HHT)}$	0.0703	0.0062	0.0579	0.0828	0.0000
$S_{(Pos,HHT)}$	-0.0010	0.0003	-0.0016	-0.0004	0.0014
$VA_{(dif,HHT)}$	-0.0193	0.0015	-0.0224	-0.0162	0.0000
$A_{(Pos,HHT)}$	6.9586	0.4934	5.9736	7.9437	0.0000

Table 17: Results for Model 8.

	Model 1	Model 2	Model 7	Model 8
Total Df	69	70	69	70
Model Df	5	5	4	4
Residual Df	64	65	65	66
R^2 (%)	81.9681	89.7659	82.1602	91.1003
R^2-Adjusted (%)	80.5594	89.1361	81.0623	90.6957
F-Ratio	58.19	114.03	74.84	168.9
SEE	0.1702	0.1829	0.168008	0.169247
MAE	0.1217	0.1263	0.11411	0.116569

Table 18: Analysis of variance for the best-constructed models.

	Model 3	Model 4	Model 5	Model 6
Total Df	69	70	69	70
Model Df	9	9	5	5
Residual Df	60	61	64	65
R^2 (%)	85.6463	93.0352	83.2466	91.8720
R^2-Adjusted (%)	83.4932	92.1218	81.9378	91.3718
F-Ratio	39.78	90.54	63.60	146.94
SEE	0.1569	0.1557	0.1641	0.1630
MAE	0.1046	0.1052	0.1115	0.1122

Table 19: Analysis of variance for other investigated models.

In Tables (10)-(13), the results present the 95% confidence intervals for the coefficients in the multilinear models and the estimated standard errors. Each variable coefficient in a model is interpreted as the mean change in the dependent variable based on a one-unit change in the corresponding independent variable keeping all other variables fixed.

Finally, the best models, Models (1)-(2) for the conventional seismic parameters and Models (7)-(8) for the HHT-based parameters were selected and compared. According to these, the detected critical F-value is ranging from 3.76 to 4.14. Thus, observing the calculated F-values in Table 14 (the smallest calculated value is F=58.19) and comparing them with the critical ones, the null hypothesis is rejected, and the increased power of every model is resulting. In Table 14 observing the standard deviation of the residuals (SEE) and the average value of the residuals (MAE) are presented to be smaller in models 3 and 4 which refer to the set of new proposed parameters while the corresponding values of R^2 (or Adjusted R^2) presented to be higher for the last models. Thus, according to the statistical indices models, 3 and 4 accomplish a more extensive and accurate explanation of the $DI_{PA,global}$ than models 1 and 2. These results also become apparent in the figures below.

The scatterplots in Figures (5)-(6) illustrate the results of evaluated $DI_{PA,global}$ using the non-linear dynamic analysis against the estimated values of $DI_{PA,global}$ using the MRA while figures 7-8 present the Standard Errors of Estimation for every $DI_{PA,global}$ estimated by MRA for the two sets of seismic intensity parameters,

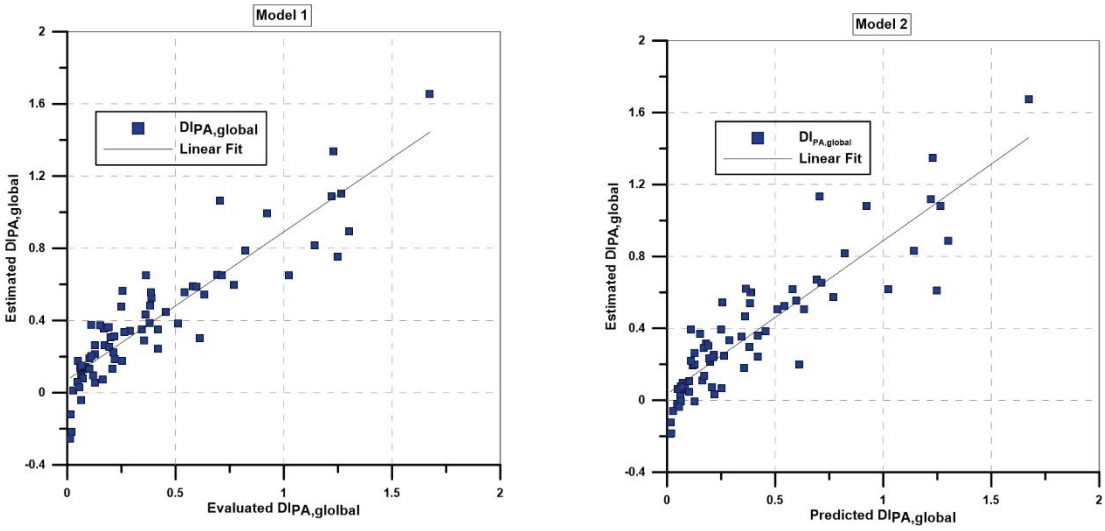

Figure 5: Evaluated vs. predicted $DI_{PA,global}$ resulting from conventional parameters.

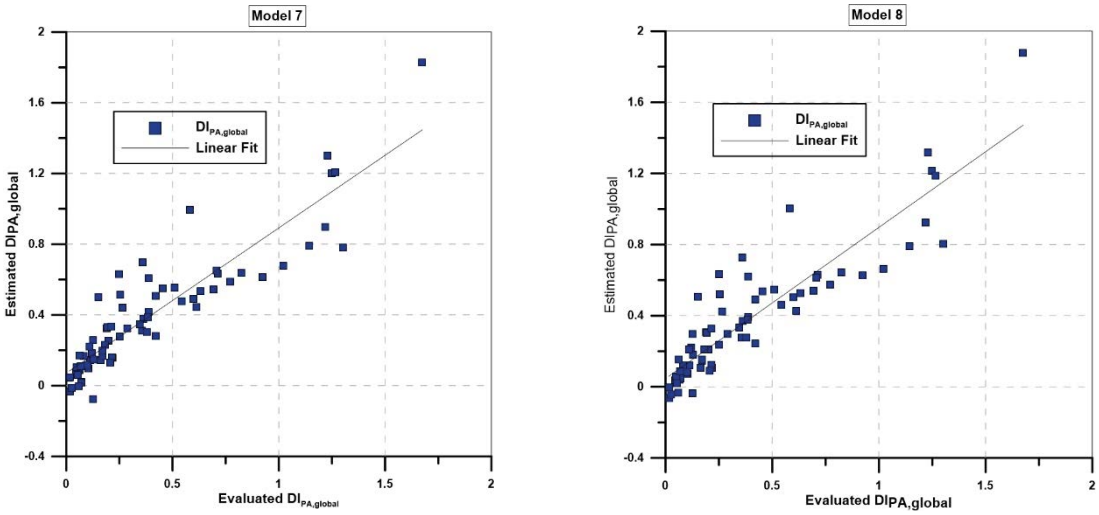

Figure 6: Evaluated vs. predicted $DI_{PA,global}$ resulting from HHT-based parameters.

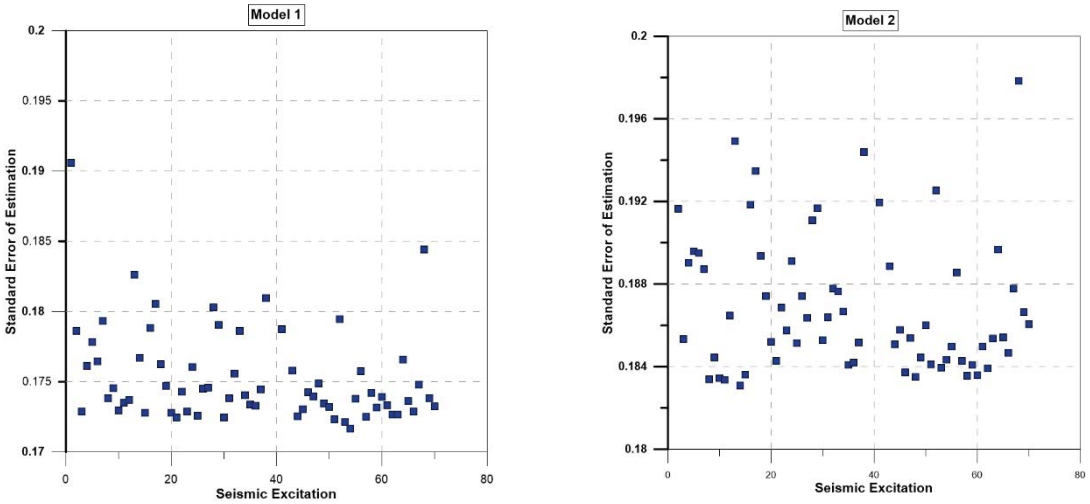

Figure 7: Standard Errors of Estimations for models using conventional parameters.

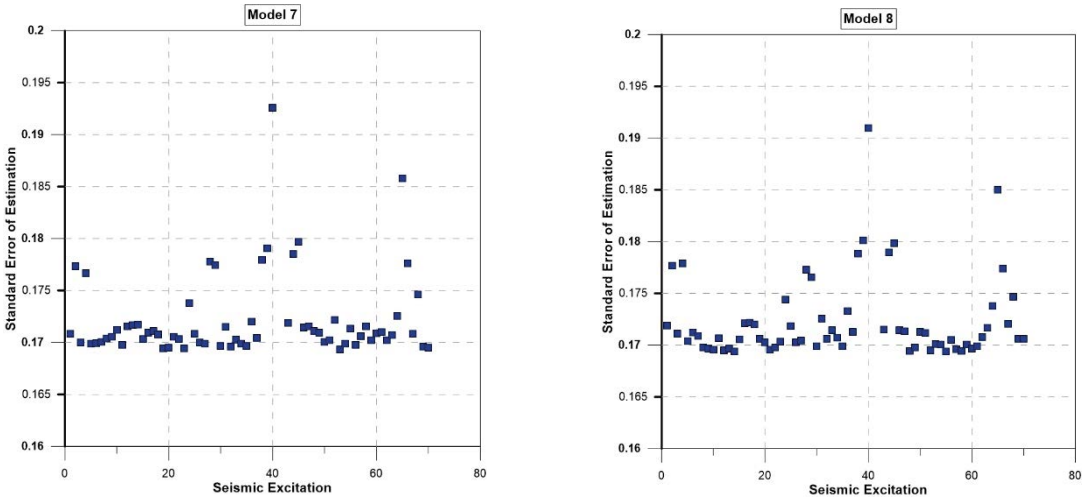

Figure 8: Standard Errors of Estimations for models using HHT-based parameters.

After the comparison between the new HHT-based parameters and twenty well-established parameters for the determination of their effectiveness to the estimation of postseismic damage of a seven-story structure, a new comparison has occurred. Two more regression models, Model 9 and 10, have been constructed using the new HHT-based parameters as IVs and $DI_{PA,global}$ obtained from the second frame as DV, after the application of the same set of seismic excitations. Hence, Models 9 and 10 are the best fitted statistical models, with and without constant term, respectively, to the set of the HHT-based parameters as IVs and $DI_{PA,global}$ of the three-story concrete frame as DV.

$$DI_{PA,global} = -0.0130677 + 1.4473 \cdot A_{(max,HHT)} - 10.0006 \cdot A_{(mean,HHT)} + 1.83459 \cdot VA_{(mean)} + 4.89072 \cdot A_{(Pos,HHT)} \quad (37)$$

$$DI_{PA,global} = 1.4233 \cdot A_{(max,HHT)} - 10.2049 \cdot A_{(mean,HHT)} + 1.85385 \cdot VA_{(mean,HHT)} + 4.88059 \cdot A_{(Pos,HHT)} \quad (38)$$

	Model 9	Model 10
Total Df	69	70
Model Df	4	4
Residual Df	65	66
R^2 (%)	82.1478	90.3628
R^2-Adjusted (%)	81.0492	89.9247
F-Ratio	74.78	154.71
SEE	0.1843	0.1831
MAE	0.1208	0.1189

Table 20: Analysis of variance for Models 9-10.

From Table 20 becomes obvious that the results of the second frame are similar to these obtained from the first one (Models 7-8). Thus, it can be concluded that the utilization of HHT-based parameters for the estimation of seismic damage of the three-story frame is so efficient as for damage estimation of the seven-story frame. Consequently, the presented HHT-based parameters used for the determination of seismic vulnerability to be equally effective to tall and short buildings.

11 PREDICTION OF $DI_{PA,global}$ USING THE CONSTRUCTED MODELS

As aforementioned, a set of ten seismic excitations is utilized to test the effectivity of the constructed statistical models. Thus, every one of the best-derived models for the seven-story concrete frame is applied to the set of ten earthquake excitations independent of the set of seventy earthquakes used for the regression analysis. From the new seismic excitations, the two sets of parameters are evaluated, and after their application to the equations of the best models, the values of $DI_{PA,global}$ are predicted using STATGRAPHICS Centurion XVII program. The results of the predicted values and their classification, according to the damage levels (DL) described in Table 2, are presented below. Specifically, in Table 21, the evaluated by nonlinear dynamic analysis damage index and its classification for these seismic excitations are displayed as opposed to the predicted ones from the constructed regression models.

Seismic Excitations	Evaluated Values	DL	Model 1		Model 2		Model 3		Model 4	
			Fitted Values	DL	Fitted Values	DL	Fitted Values	DL	Fitted Values	DL
Friuli	0.541	M	0.452	M	0.363	M	0.470	M	0.453	M
Central Italy	0.056	L	0.117	L	0.056	L	0.066	L	0.025	L
Ardal	0.367	M	0.455	M	0.445	M	0.371	M	0.342	M
Amberley New Zealand	0.394	M	0.505	M	0.458	M	0.430	M	0.440	M
Amberley New Zealand	1.289	T	0.833	T	0.904	T	0.969	T	1.047	T
Amberley New Zealand	0.221	L	0.043	L	0.061	L	0.220	L	0.299	L
Amberley New Zealand	0.193	L	0.156	L	0.139	L	0.261	L	0.273	L
Amberley New Zealand	0.617	G	0.750	G	0.732	G	0.626	G	0.688	G
Amberley New Zealand	0.895	T	0.597	M	0.617	G	0.707	G	0.787	G
Amberley New Zealand	1.424	T	1.252	T	1.315	T	0.907	T	0.954	T

Table 21: Predicted values of $DI_{PA,global}$ oppose to evaluated ones.

The observation of the results reveals that a very significant approximation of the damage level is achieved. From the predicted values of $DI_{PA,global}$ the damages are not correctly classified for only one earthquake for both sets of parameters.

12 CONCLUSIONS

Hilbert Huang Transform is a time-frequency analysis technique that offers more detailed and accurate frequency resolution as a function of time considered to be an improved procedure for non-stationary and nonlinear signal events as the seismic excitations. Several numbers of natural seismic signals are analyzed utilizing HHT analysis, and their Hilbert Spectra are derived. Physical and geometric features from these spectra are connected with seismic features, and new HHT-based seismic intensity parameters are conducted.

The new proposed seismic parameters are evaluated for all the velocity-time histories of the seismic excitations in the study, and an application of them is presented, revealing a strong interrelation with the structural damage caused by an earthquake excitation. Park and Ang overall structural damage index $DI_{PA,global}$, evaluated by nonlinear dynamic analysis, is used to express the earthquake damage of a seven-story and a three-story reinforced concrete structure in the study. The powerful interdependence between the new seismic parameters and the utilized damage index is validated by two statistical procedures the correlation analysis and the multiple linear regression analysis. The correlation analysis interrelates the evaluated $DI_{PA,global}$ with the investigated parameters, while the multilinear regression analysis is utilized to prove that these parameters can attain a significant estimation of the postseismic structural damage. This ability is also tested by the application of a set of new seismic signals to the best statistical models obtained from the multiple regression analysis in order to be predicted the caused damage level of the structure.

The obtained results from the statistical procedures for the set of the new proposed parameters are compared with the corresponding ones extracted from a set of established parameters, and their effectiveness presented to be of the same significance with the last ones.

Finally, according to all the above results, the ability of the new HHT-based seismic parameters to assess the seismic vulnerability of a structure with high approximation accuracy is certified. Consequently, the proposed set of the seismic intensity parameters based on Hilbert-Huang Transform can be considered one more powerful tool for the scientific community in order to early postseismic damage in structures to be accomplished and crucial decisions before and after an earthquake to be made.

REFERENCES

[1] L. Cabãnas, B. Benito, M. Herráiz, An approach to the measurement of the potential structural damage of earthquake ground motions, *Earthquake Engineering and Structural Dynamics* 26, 79-92, 1997.

[2] A. Elenas, Interdependency between seismic acceleration parameters and the behavior of structures, *Soil Dynamic Earthquake Engineering* 16, 317-322, 1997.

[3] A. Elenas, Correlation between seismic acceleration parameters and overall structural damage indices of buildings, *Soil Dynamic Earthquake Engineering* 20, 93-100, 2000.

[4] A. Elenas, K. Meskouris, Correlation study between seismic acceleration parameters and damage indices of structures, *Engineering Structures* 23, 698-704, 2001.

[5] A. Elenas, Seismic-Parameter-Based Statistical Procedure for the Approximate Assessment of Structural Damage, *Mathematical Problems in Engineering*, Article ID 916820, 2014.

[6] A. Elenas, Seismic-Parameter-Based Statistical Procedure for the Approximate Assessment of Structural Damage, *Mathematical Problems in Engineering*, Article ID 916820, 2014.

[7] N. Nanos, A. Elenas, P. Ponterosso, Correlation of different strong motion duration parameters and damage indicators of reinforced concrete structures, *Proceedings of the 14th World Conference on Earthquake Engineering. Beijing*, 2008.

[8] V.C. Vui, R.R. Hamid, Correlation between seismic parameters of far-fault motions and damage indices of low-rise reinforced concrete frames, *Soil Dynamics and Earthquake Engineering* 66,102-112, 2014.

[9] K. Kostinakis, A. Athanatopoulou, K. Morfidis, Correlation between ground motion intensity measures and seismic damage of 3D R/C buildings, *Engineering Structures* 82, 151-167, 2015.

[10] N. Huang, Z. Shen, S.R. Long, M.C. Wu, H.H. Shih, Q. Zheng, et al., The empirical mode decomposition and the Hilbert spectrum for nonlinear and non-stationary time series analysis, *Proceedings of the Royal Society of London A: Mathematical, Physical and Engineering Science* 454, 903-995, 1998.

[11] N. Huang, Z. Shen, S.R. Long, A new view of nonlinear water waves: The Hilbert spectrum, *Annual Review of Fluid Mechanics* 31, 417-457, 1999.

[12] N. Huang, M.L. Wu, W. Qu, S. Long, S. Shen, Applications of Hilbert–Huang transform to non-stationary financial time series analysis applied stochastic models in business and industry, *Applied Stochastic Models in Business and Industry* 19, 245–268, 2003.

[13] R.R. Zhang, S. Ma, E. Safak, S. Hartzell, Hilbert–Huang transform analysis of dynamic and earthquake motion recordings, *ASCE, Journal Engineering Mechanics* 129, 861–875, 2003.

[14] R.Q. Yan, R.X. Gao, A tour of the Hilbert–Huang transform: An empirical tool for signal analysis, *IEEE Instrumentation and Measurement Magazine* 10, 40–45, 2007.

[15] Y.J. Park, A.H-S. Ang, Mechanistic seismic damage model for reinforced concrete, *Journal of Structural Engineering* 111, 722–739, 1985.

[16] Y.J. Park, A.H-S. Ang, Y.K. Wen, Damage-limiting aseismic design of buildings, Earthquake Spectra 3,1–26, 1987.

[17] P.F. Alvanitopoulos, I. Andreadis, A. Elenas, Interdependence between damage indices and ground motion parameters based on Hilbert–Huang transform, *Measurement Science and Technology* 21, 1-14, 2010.

[18] E. Vrochidou, P.F. Alvanitopoulos, I. Andreadis, A. Elenas, Structural damage estimation in mid-rise reinforced concrete structure based on time-frequency analysis of seismic accelerograms, *IET Science, Measurement and Technology* 10, 900-909, 2016.

[19] M. Tyrtaiou, A. Elenas, Novel Hilbert spectrum-based seismic intensity parameters interrelated with structural damage, *Earthquakes and Structures* 16, 197-208, 2019.

[20] K. Meskouris, Structural Dynamics: Models, Methods, Examples, *Ernst & Sohn, Berlin*, 2000.

[21] K. Meskouris, W.B. Krätzig, U. Hanskötter, Nonlinear computer simulations of seismically excited wall-stiffened reinforced concrete buildings, *Proceedings of the 2nd International Conference on Structural Dynamics (EURODYN '93), Balkema, Lisse, The Netherlands*, 49-54, 1993.

[22] E.H. Vanmarcke, S.S.P. Lai, Strong-motion duration and RMS amplitude of earthquake records, *Bulletin of the Seismological Society of America* 1980 70, 1293–1307, 1980.

[23] A. Arias, A measure of earthquake intensity, *In Hansen RJ, editors, Seismic Design for Nuclear Power Plants. MIT Press. Cambridge, MA, USA*, 438-483, 1970.

[24] M.D. Trifunac, A.G. Brady, A study on the duration of strong earthquake ground motion, *Bulletin of the Seismological Society of America* 65, 581–626, 1975.

[25] P.C. Jennings, Engineering seismology, *In H. Kanamori, E. Boschi, editors, Earthquakes: Observation, Theory and Interpretation. Italian Physical Society, Varenna, Italy*, 138-173, 1982.

[26] P. Fajfar, T. Vidic, M. Fischinger, A measure of earthquake motion capacity to damage medium-period structures, *Soil Dynamics and Earthquake Engineering* 9, 236–242, 1990.

[27] G.W. Housner, Spectrum intensities of strong-motion earthquakes, *Proceedings of the Symposium on Earthquake and Blast Effects on Structures, EERI, Oakland, CA, USA*, 20-36, 1952.

[28] R. Araya, G.R. Saragoni, Earthquake accelerogram destructiveness potential factor, *Proceedings of the 8thWorld Conference on Earthquake Engineering, EERI, El Cerrito, CA, USA*, 835-842, 1984.

[29] A.K. Chopra, Dynamics of Structures, *Prentice-Hall. Englewood Cliffs, NJ, USA*, 1995.

[30] C.M. Uang, V.V. Bertero, Evaluation of seismic energy in structures, *Earthquake Engineering & Structural Dynamics* 19, 77–90, 1990.

[31] A.J. Kappos, Sensitivity of calculated inelastic seismic response to input motion characteristics, *Proceedings of the 4th U.S. National Conference on Earthquake Engineering, EERI, Oakland, CA, USA*, 25-34, 1990.

[32] J.E. Martinez-Rueda, Scaling procedure for natural accelerograms based on a system of spectrum intensity scales, *Earthquake Spectra* 14, 135–152, 1998.

[33] ATC 3-06 Publication, Tentative Provisions for the Development of Seismic Regulations for Buildings, *US Government Printing Office, Washington, DC, USA*, 1978.

[34] Eurocode 2: Design of Concrete Structures—Part 1: General Rules and Rules for Buildings, *European Committee for Standardization, Brussels, Belgium*, 2000.

[35] Eurocode 8: Design of Structures for Earthquake Resistance—Part 1: General Rules, Seismic Actions, and Rules for Buildings, *European Committee for Standardization, Brussels, Belgium*, 2004.

[36] A.M. Reinhorn, H. Roh, M. Sivaselvan, et al., IDARC2D version 7.0: a program for the inelastic damage analysis of structures, *Tech. Rep. MCEER-09-0006, MCEER, State University of New York at Buffalo, New York, NY, USA*, 2009.

[37] G.A. Gholamreza, R. Elham, Maximum damage prediction for regular reinforced concrete frames under consecutive earthquakes, *Soil Dynamics and Earthquake Engineering* 14, 129-142, 2018.

[38] The Math Works Inc. MATLAB and Statistics Toolbox Release 2016b, *Natick, Massachusetts, USA*, 2016.

[39] B.G. Tabachnick, L.S. Fidell, Using multivariate statistics, 6th edition, *Pearson Education Inc., Upper Saddle River, NJ, USA*, 2013.

[40] K.C.G. Ong, Z. Wang, M. Maalej. Adaptive magnitude spectrum algorithm for Hilbert–Huang transform based frequency identification, *Engineering Structures* 30, 33-41, 2008.

[41] Statpoint Technologies Inc. STATGRAPHICS Centurion XVII User Manual, *StatPoint, Herndon, VA, USA*, 2016.

EURODYN 2020
XI International Conference on Structural Dynamics
M. Papadrakakis, M. Fragiadakis, C. Papadimitriou (eds.)
Athens, Greece, 23–26 November 2020

TYPHOON FRAGILITY ANALYSIS AND CLIMATE CHANGE IMPACT ASSESSMENT OF FILIPINO CULTURAL HERITAGE ASSET ROOFS

G. Sevieri[1] **and C. Galasso**[2,3]

[1] Dept. of Civil, Environmental and Geomatic Engineering, University College London
Gower Street, London, WC1E 6BT, United Kingdom
g.sevieri@ucl.ac.uk

[2] Dept. of Civil, Environmental and Geomatic Engineering, University College London
Gower Street, London, WC1E 6BT, United Kingdom
c.galasso@ucl.ac.uk

[3] Scuola Universitaria Superiore (IUSS) Pavia
Piazza della Vittoria 15, Pavia, 27100, Italy
carmine.galasso@iusspavia.it

Keywords: typhoon risk assessment; typhoon risk prioritization; Cultural Heritage; climate change.

Abstract. *Cultural Heritage (CH) assets are especially vulnerable to natural hazards (e.g., earthquake-induced ground shaking, typhoon-induced strong wind, and flooding) due to the lack of hazard-resistant features and to aging-induced extensive structural degradation. These considerations, together with their high historical/cultural value, justify the prioritization/implementation of disaster risk reduction (DRR) and resilience-enhancing strategies for the preservation of such assets.*

This paper proposes a probabilistic, simulation-based framework for the derivation of wind fragility relationships for CH roofs. Roof-panel pullout and pullover failure modes are used to model the progressive failure of the roof system, thus enabling the integration of fastener corrosion effects and load redistribution into the proposed fragility model. Monte-Carlo sampling is used to propagate the uncertainties related to wind-induced demands and roof component (i.e., fasteners and panels) capacities. Climate projections are used to assess the impact of climate change on wind hazard variations, and ultimately on the asset wind risk profile over time.

An illustrative application of the proposed procedure is presented with reference to 25 heritage buildings in Iloilo City, Philippines.

1 INTRODUCTION

The 2019 Pacific typhoon season was the costliest ever recorded. It was an above-average year with a total of 17 typhoons recorded in the Philippine Area of Responsibility (PAR, the northwestern Pacific area where the Philippines' national meteorological agency, PAGASA, monitors weather occurrences). The costliest event was the typhoon Kammuri (locally known as Tisoy), which caused PHP 5.9 billion (USD 116 million) of damage to crops and agriculture [1]. In addition, more than 68,000 houses, schools, and other structures were reported destroyed and at least 463,000 were also damaged, including several cultural heritage (CH) assets. Various studies available in the scientific literature discuss how climate change is going to affect the frequency and intensity of future tropical cyclones in the Philippines [2, 3], with a shift towards stronger storms with an estimated intensity increases of 2-11% by 2100, as well as changes in their paths [4, 5]. This, in turn, will lead to an increase in typhoon-induced economic losses [6].

Typhoon-related economic losses in the Philippines are not just due to the adverse environmental conditions. Rapid population growth along the coast together with highly-vulnerable structures/infrastructure contribute to intensify the typhoon-risk of Filipino buildings [7]. Particularly vulnerable in this sense are CH asset roofs (i.e., wood frame and light-weight metal sheet, LWMS) because of the general lack of any hazard-resistant design considerations, presence of non-engineered structures/detailing, and material/structural degradation due to aging. In particular, non-engineered CH roofs have been recognized as the most vulnerable component in the building envelope due to typhoon-induced wind uplift. In addition, CH assets have a fundamental role for local communities. They contribute to creating citizens' sense of place, which is key to form a community's identity, and to promoting local, sustainable jobs related to cultural tourism – a priority sector in several developing countries.

The Filipino government, as well as other stakeholders, are promoting disaster risk reduction (DRR) strategies to improve the resilience of the country and its built environment. This requires a deep understanding of the risk associated to the built environment as well as its variation over time due to degradation/aging and potential effect of climate change. Several methods for typhoon risk assessment/prioritization at building specific and portfolio level, respectively, are available in the scientific literature (e.g., [8, 9]). Those adopted for building-specific risk assessment usually rely on refined numerical models and require specific data (e.g., roof geometry, number/location of purlins/fasteners, material properties) to be performed/collected. They allow an analyst to model material degradation as well as uncertainties in the definition of both structural capacity and wind-induced demands but with a high computational cost [10]. However, the required information is hardly available when CH assets located in developing countries are analysed. High population density, the adaptive reuse of CH assets for private/commercial activities, and diffused material degradation/lack of any maintenance plan all act as disruptive factors during data collection. On the other hand, scoring-based risk prioritization methods are commonly adopted at portfolio level (i.e., for the assessment of a large number of structures in a given region of interest) [11, 12]. These approaches require only few data about the assets under investigation, but they do not properly consider the variation of the risk during the time due to climate change and material degradation.

A simplified probabilistic, simulation-based framework for the calculation of typhoon risk for CH asset roofs in the Philippines is herein proposed to address the above-mentioned gaps. The proposed approach can be used both for risk prioritization at portfolio level and for preliminary risk assessment at building specific level. In fact, by considering a simplified geometry of the roof, the proposed method allows corrosion of fasteners and LWMS as well as fastener

failure progression to be explicitly modelled with relatively low computational cost and requiring only few basic data about the structure.

The proposed procedure is tested in this study on 25 CH assets in Iloilo city, Philippines, which is an important heritage hub for tourism in the Philippines. It is one of the most highly urbanized cities of the south-eastern tip of Panay island in the Philippines [13] and also capital city of the province. Fine examples of historic luxury buildings constructed in the first half of the 20th century during the American colonization can be found in the historic street Calle Real [14].

2 FILIPINO CULTURAL HERITAGE ASSETS

The procedure proposed in this study has been developed within the *Cultural Heritage Resilience & Sustainability to multiple Hazards* (CHeRiSH) project [7], funded by the UK Newton Fund. This project aims to develop a multi-level risk and resilience assessment framework for CH assets in the Philippines exposed to multiple natural hazards.

The definition of CH assets is usually based on both tangible (e.g., architectural/ historical value) and intangible (e.g., socio-cultural factors) criteria [15]. However, the Filipino law considers only the building year of construction as the main criterion for the eligibility of a structure as CH asset [16]. Structures which are at least fifty years old can be declared to be a "Heritage House", so that fairly recent reinforced concrete (RC) frame-type structures and unreinforced masonry (URM) buildings are often part of the Filipino CH portfolio.

The twenty-five CH assets analysed in this study (Figure 1) have been surveyed during a field trip in Iloilo City, Philippines, in July 2019 by a research group composed of members from the University College London (UCL, United Kingdom), the De La Salle University (DLSU, Philippines) and Central Philippines University (CPU, Philippines) [7].

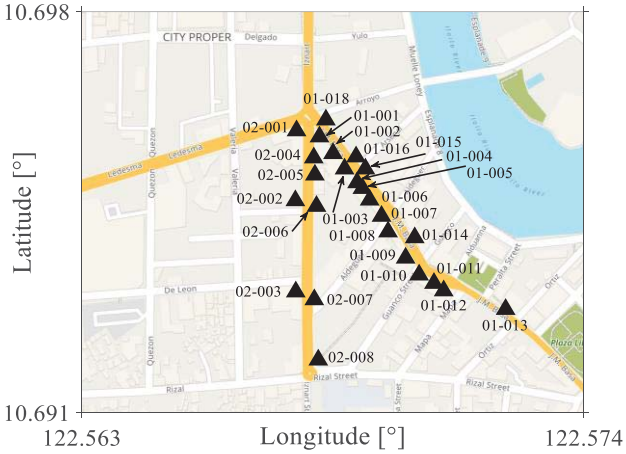

Figure 1: Surveyed CH buildings in Iloilo city, Philippines.

The surveyed CH portfolio is composed of 24 RC structures and one URM building date back to the first half of the 20th century. Most of them are two-story, plan-regular buildings and part of construction blocks with different shapes (e.g., triangular, rectangular) and compositions (i.e., a block can be the result of building aggregation during the time, or not).

Nineteen CH roofs out of twenty-five are made of timber frames with LWMS and metal fasteners (i.e., screws or nails). This represents the most common and vulnerable Filipino CH roof typology, and then it is the focus of the present study. Post-event surveys in the Philippines highlight that most economic losses in high-wind hazard areas are due to the breach of the building envelope [17]. This includes roof panel uplift, roof-to-wall connection failure and roof system damage, among others. Once the roof is damaged or even collapsed, walls lose lateral

supports and the global stability of the construction is heavily compromised. The local capacity of fasteners and LWMS clearly play a fundamental role in the determination of the global capacity of the roof. Corrosion phenomena, which can affect the strength of both fasteners and LWMS, must then be considered in the typhoon-risk quantification both at building specific and portfolio level. As shown in Figure 2, most of the surveyed CH roofs were characterised by diffused and heterogeneous corrosion levels [7].

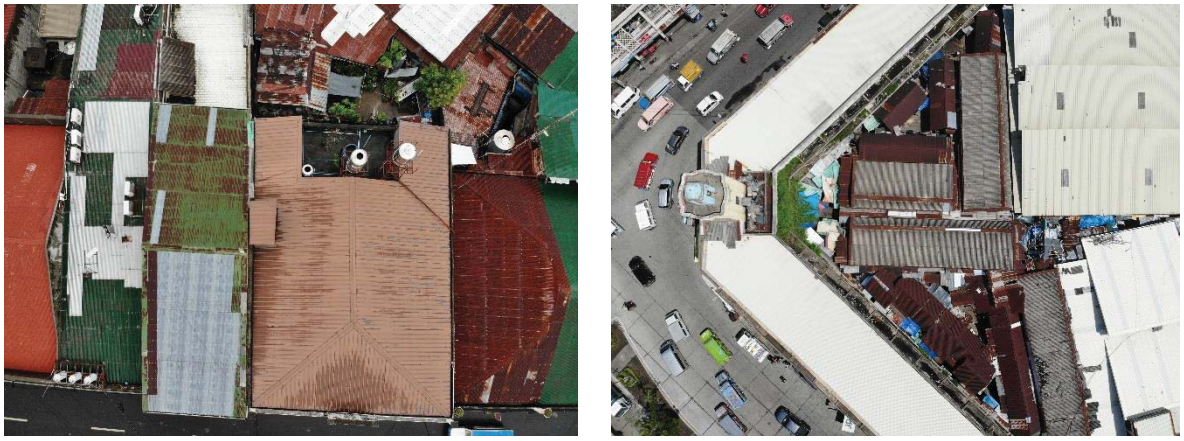

Figure 2: Two samples of Filipino CH roofs.

3 TYPHOON RISK ASSESSMENT FOR FILIPINO CULTURAL HERITAGE ASSET ROOFS AND CLIMATE CHANGE IMPACT

3.1 Typhoon risk assessment framework

In this study, Performance-Based Wind Engineering (PBWE) [18] is used as the conceptual framework to define the typhoon risk of CH asset roofs. In the context of PBWE, the performance of a structure/structural component is assessed through the probabilistic description of a set of decision variables, DVs [19]. Each DV is a quantitative proxy for the specific structural performance/damage in terms of metrics of interest for various stakeholders and/or the society in general, e.g., repair cost, downtime, and people affected (casualties/injuries). Once an intensity measure, IM (stochastically describing the hazard intensity at a site of interest), a relevant engineering demand parameter, EDP (synthetically expressing the structural response to wind loads), and a damage-measure parameter, DM (quantifying the structural damage due to wind load in relation to the considered performances and EDP) are defined, risk can be computed as the mean annual frequency (MAF) (or annual probability) of exceeding a specified value in terms of a relevant DV,

$$\lambda[DV] = \int\int\int G[DV|DM]\, dG[DM|EDP]\, dG[EDP|IM]\, |d\lambda[IM]| \,. \qquad (1)$$

In the previous equation $\lambda[\cdot]$ is the mean annual rate of exceedance, while $G[\cdot]$ indicates the complementary cumulative probability distribution function (CCDF) [19].

In this study, the 3-sec gust speed (v) at 10 m height in open terrain [20] is used as IM while the ratio between damaged LWMS and their total number R_{damage} is used as DM. In this way, the term $dG[DM|IM]$ in Equation 1 can be directly derived (as discussed in the following), rather than using $dG[DM|EDP]\, dG[EDP|IM]$.

Damage-to-loss (or consequence) models [21], which describe the relationship between DM and DV, are then needed to derive $G[DV|DM]$. Since no damage-to-loss models are specifically available for Filipino buildings, those developed by the Federal Emergency Management

Agency (FEMA, 2014) [22] in terms of direct repair cost for residential buildings in the USA are used in this study. This assumption is somehow justified by the fact that the prescriptions included in the Filipino building codes [19] are fully consistent with the recommendations of US building codes [7], across the years. Moreover, the damage-to-loss curves reported in Figure 3 are defined in terms of percentage of building replacement value rather than in absolute terms. Hence, even if this specific aspect will require more investigation in future studies, it still allows one to illustrate/test the validity of the proposed procedure and to obtain loss results for relative comparisons/risk prioritization exercises for the selected case-study portfolio.

The damage-to-loss curves adopted in this study consider direct repair costs associated to roof covering, roof framing and content. It is worth noting that the damage-to-loss curves presented in this section represents the expected loss L given R_{damage}, that is $\mathbb{E}[L|R_{\text{damage}}]$.

Details of the proposed fragility analysis framework and the approach to model climate change impact on wind hazard are presented in the next two sections.

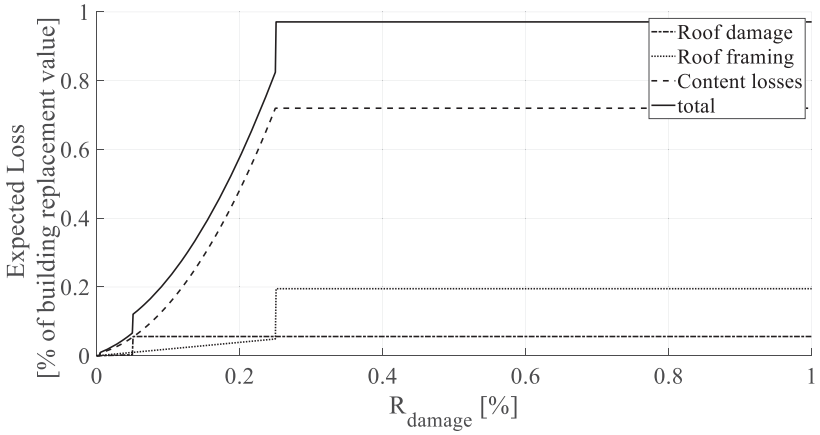

Figure 3: Damage-to-loss curves adopted in this study.

3.2 Impact of climate change on wind hazard

One of the specific objectives of this study is to investigate climate change impact on the typhoon risk assessment outputs for Filipino CH roofs. Climate change is leading to a rise in the temperature of the world's oceans. As their surface temperature increases, oceans provide more energy to convert into tropical cyclones [23]. This is the thermodynamic phenomenon due to climate change that will cause the globally averaged intensity of tropical cyclones to shift towards stronger storms, from being a category 3 (severe tropical storm) to a category 4 (typhoon) by the end of the 21st century. Not only the intensity of tropical storm is going to be affected by climate change, but also their frequencies, paths and velocities [5].

These variations of the environmental conditions may affect the wind hazard of the country and ultimately the wind risk profile of building roofs. The Type I (Gumbel) distribution is typically adopted in the scientific literature (e.g., Garciano et al., 2005 [24]), and in structural codes (e.g., the National Structural Code of the Philippines, NSCP, 2015 [20]) to model probabilistically the 3-sec gust speed (v) at 10 m height in open terrain. Climate change effects can be incorporated in the hazard model by modifying the cumulative distribution function (CDF) of the 3-sec gust speed, $\mathrm{F}_v(v,t)$, through a function $\gamma_{\text{mean}}(t)$ expressing the time-dependent percentage change in the considered gust wind speed [10],

$$\mathrm{F}_v(v,t) = \exp\left(-\exp\left(-\left(\frac{\frac{v}{1+\frac{\gamma_{\mathrm{mean}}(t)}{100}}-v_g}{\sigma_g}\right)\right)\right). \quad (2)$$

In the previous equation, v_g and σ_g are the location and scale parameters of the CDF, respectively. In Iloilo City, where the case-study buildings considered in this paper are located, these parameters can be assumed as $v_g = 25.21$ m/s and $\sigma_g = 5.75$ m/s [24]. Recent studies assume a time-dependent linear change in wind speed $(\gamma_{\mathrm{mean}}(t))$ and discuss how the use of different functions does not really affect the the wind risk profile [10, 23]. The projected changes in wind speed over the next 50 years is assumed equal to 4%; this climate scenario is in agreement to the studies available in the scientific literature for similar geographical locations [25].

4 PROPOSED FRAGILITY MODEL

4.1 Overview

The fragility model proposed in this study is based on a simplified geometry of the roof, which is divided into N_{ms} LWMS, each of which is supported by a constant number of purlins (N_p) and connected through a constant number of fasteners (N_f). LWMS are also assumed not interacting with each other, thus allowing the parallelization of the procedure and a further reduction of the computational burden. Only a few information about the roof are thus needed to perform the fragility analysis, namely: number of LWMS, number of purlins, number of fasteners, distance between purlins (d_p), fastener typology/geometry, LWMS typology/geometry and dead load (D). Once the roof geometry is defined, the limit state function for a given damage state, $g(R,Q)$ (i.e., R is the component capacity, while Q is the wind-induced demand), is derived at fastener level in order to facilitate the integration of failure progression and degradation into the fragility model.

Specifically, when the number of fasteners failing under a given load condition reaches a specific threshold, treated as random variable as well, the LWMS is assumed to fail. Only refined numerical models can properly consider all the factors affecting such a threshold value, such as wind direction, location of the failed fasteners and wind pressure distribution. However, in this study a triangular probability distribution bounded by 10% and 80% (the average is 33.3%) is adopted for the definition of the threshold, as proposed in [27]. Once the safety of each LWMS is checked, R_{damage} is calculated as ratio of failed LWMS over N_{ms}. This procedure is repeated varying the wind speed v needed for the definition of Q.

Monte Carlo sampling is used to propagate the considered uncertainties. Once a wind-speed value v is selected, the uplift loads W are randomly generated for each fastener of each LWMS. For the same elements, pullout and pullover capacities are randomly generated as well (as discussed in the following). A corrosion model is implemented to reduce the resisting sections of fasteners and LWMS over time, thus reducing the capacity R. The starting degradation level is treated as random variable to consider the heterogeneity of the 'health' state of different metal sheets as observed during the field trip.

4.2 Wind load

Assuming that LWMS, purlins and fasteners can be considered as components and claddings (C&C), the uplift wind load W (N/m^2) is defined according to the American Society of Civil Engineers (ASCE 7-10, 2010) [28] and NSCP (2015) [19], that is

$$W = q_h\left(GC_p - GC_{pi}\right). \tag{3}$$

In the previous equation, q_h (N/m^2) is the velocity pressure evaluated at the mean roof height of h; G is the gust factor; C_p (NSCP 2015 Figures 207E.4-2A to 207E.4-7) is the external pressure coefficient; and C_{pi} (NSCP 2015 Table 207A.11-1) is the internal pressure coefficient. In both codes, q_h is evaluated as:

$$q_h = 0.613\, K_h\, K_{zt}\, K_d\, v^2, \tag{4}$$

where K_h (NSCP 2015 Table 207E.3-1) is an exposure factor accounting for the terrain exposure condition; K_{zt} is a topography factor; and K_d (NSCP 2015 Table 207A.6-1) is a wind directionality factor accounting for the reduced probability of unfavourable building orientation and wind direction.

In this study, the parameter needed for the definition of the wind load W are treated as random variables in order to properly account for the uncertainties (Tables 1 and 2).

Table 1: Statistical model of the wind load parameters.

Parameters	Category	Mean	Coefficient of Variations (CoV)	Statistical model	Reference
GC_p		see Table 2		Normal	
GC_{pi}	Partially enclosed	0.46	0.33	Normal	Ellingwood and Tekie, 1999 [29]
K_h	Exposure B (0 – 9.1 m)	0.71	0.19	Normal	
K_d		0.89	0.16	Normal	
K_{zt}		Deterministic (= 1)			

Table 2: Statistics of the gust pressure coefficient GC_p.

Metal sheet panel position		Mean	Coefficient of Variations (CoV)	Reference
(Wind from all directions) 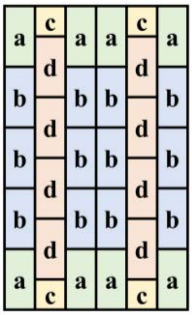	a	−1.768	0.12	Lee and Rosowsky, 2005 [30]
	b	−1.455	0.12	
	c	−1.425	0.12	
	d	−0.855	0.12	

4.3 Dead and total loads

The value of the dead load D needed for the calculation of the demand Q depends on the weights of roof panel material and the roof system. This load counteracts the effect of wind uplift, thus contributing to stabilize the roof and increase its resistance. In this study, the dead load is modelled as a deterministic value equal to 0.2 kN/m^2 and assumed to remain constant in time (added weight due to re-roofing, if any, is not considered here).

4.4 Uplift resistance

The uplift failure of the system fastener-LWMS is governed by two main mechanisms: pullout and pullover failure modes. The resistance R mainly depends on the fastener typology (i.e., screws or nails), material strengths as well as the geometry of the structural system (e.g., distance between fasteners, distance between purlins). If the forces due to the wind uplift act parallel to the length of the fasteners and perpendicular to the holding members, the nominal pullover resistance per screw and nail ($P_{n,\text{over}}$ in N) is computed as

$$P_{n,\text{over}} = 1.5\, t\, d_w\, F_{u1}, \tag{5}$$

Where, in the case of screws, t (mm) is the thickness of the member in contact with the screw head, d_w (mm) is the larger of the diameter of the washer and the screw head and F_{u1} (MPa) is the ultimate tensile strength of the member in contact with screw head or washer. Whereas, in the case of nails, d_w is the diameter of the nail head.

The definition of the pullout resistance for screws ($P_{n,\text{out,screw}}$ in N) is based on the design criteria provided by the NSCP (2015),

$$P_{n,\text{out,screw}} = 0.85\, t_c\, d\, F_{u2}, \tag{6}$$

where t_c (mm) is the lesser of the depth of penetration and thickness of the element not in contact with the screw head, d (mm) is the nominal screw diameter, and F_{u2} (MPa) is the ultimate tensile strength of the member not in contact with the screw head or washer.

In the case the roof structure consists of wood purlins, nails are generally used as fasteners. In this case, according to the National Design Specification (NDS) for Wood Construction (AWC, 2017) [31], the pullout capacity for single smooth shank nail used as wood-to-wood and metal-to-wood connections ($P_{\text{out,nail}}$ in N) can be expressed as

$$P_{\text{out,nail}} = K_w\, G_{\text{out}}^{5/2}\, d_s\, P, \tag{7}$$

where, G_{out} is the specific gravity of the wood based on oven-dry weight, d_s (mm) is the shank diameter of the nail, P (mm) is the penetration of the nail in the member holding the nail point, and K_w is a constant having a value of 9.515, which is converted from the original value of 1380 (in empirical unit) for SI unit consistency.

The parameters needed for the definition of the roof panel capacity are treated as random variables to properly account for the epistemic uncertainties involved in the fragility calculation and to 'balance' the simplified geometry of the proposed model. In particular, the geometric parameters of the resisting elements (i.e., d_w, t_c, d, d_s, P) are considered normally distributed with mean values equal to the nominal values assumed during the analysis or measured during field surveys. More specifically, 4d and 8d fasteners (i.e., nominal diameters equal to 2.9 and 3.3 mm, respectively) are usually found for such a roof typology [25, 32]. Therefore, if observed data are not available, fastener typology and size can be randomly generated. Whereas, the coefficients of variations are derived from studies related to Filipino roofs available in the scientific literature [8, 33]. Table 3 summarises the statistical model for the pullout/pullover capacity adopted in this study.

Table 3: Statistical model of the capacity parameters.

Parameters	Mean	Coefficient of Variations (COV)	Statistical model
t	0.79 mm	0.1	Normal
d_w	Nominal or assumed value	0.05	Normal
d	Nominal or assumed value	0.05	Normal
d_s	20% of d	0.025	Normal
P	Nominal or assumed value	0.25	Normal
F_{u1}	147 MPa	0.35	Log Normal

F_{u2}	215 MPa	0.1	Log Normal
t_c	Nominal or assumed value	0.025	Normal
G_{out}	Nominal or assumed value	0.25	Normal

4.5 Load redistribution and corrosion effects

Load redistribution among fasteners and corrosion effects are key issue to derive system-level capacity. When a fastener fails, its load is redistributed among the closest resisting elements until the equilibrium is achieved. 90% of the load of the failed fastener is redistributed between those located on parallel purlins, while the remaining 10% goes to fasteners which are on the same purlin. In the proposed procedure, the load is redistributed until the equilibrium is achieved each time that a fastener fails and if the metal sheet is still safe [10]. Once the load is redistributed to other fasteners, these can fail and a rapid damage progression can occur.

Corrosion affects the effective section of fasteners and LWMS, thus reducing the uplift resistance of the roof panels over time. The corrosion model adopted in this study is the one proposed by Nguyen et al. (2013) [34], which considers two types of corrosions: embedded and atmospheric. The former is generated by corrosive agents that are within the surrounding wood, such as wood acidity and timber moisture content. Only parts inside the wood, such as the shank of nails are affected. Whereas, the atmospheric corrosion is due to corrosive agents within the surrounding air, such as airborne salinity and airborne pollution agents. The parts of the cladding exposed to the air, such as the heads of nails and screws as well as the LWMS surfaces, are affected by this type of corrosion. The parameters needed for the definition of the corrosion model are derived from the environmental data provided by PAGASA [35].

5 RESULTS

5.1 Fragility analysis

The fragility analysis has been carried out for all the 19 CH assets previously introduced by varying the gust wind speed v from 0 to 100 m/s with 2 m/s steps and by increasing the corrosion depths by considering 10-year steps from 0 to 50 years (i.e., observation year, y). Moreover, ten-thousand steps are considered within the Monte Carlo sampling, while the log-normal CDF is used to fit the analysis results by applying the maximum likelihood estimation (MLE) method [36]. For the sake of clarity, only the fragility curves for building with ID ‘01-001’ and ‘02-003’ (Figure 4) are discussed in this section. The building ‘01-001’ has 2.6-mm shank diameter screws with a 500-mm spacing, while the building ‘02-003’ has 2-mm shank diameter nails with 250-mm spacing. When the fragility curves are derived for year 0, so without increasing the initial corrosion depths, the two CH asset roofs show similar fragility relationships. When time passes, the corrosion affects more the roof ‘02-003’ (Figure 4b) than the roof ‘01-001’ (Figure 4a); in fact, the distance among fragility curves is larger in Figure 4b. This is mainly due to the fact that nails are affected by both embedded and atmospheric corrosion, because of the use of wood purlins. Whereas, screws are generally subjected to only atmospheric corrosion, which usually achieves value smaller than the embedded one [34]. In general, the fragility curves derived in this study show that CH roofs with nails as fasteners are more sensitive to corrosion than the screw ones.

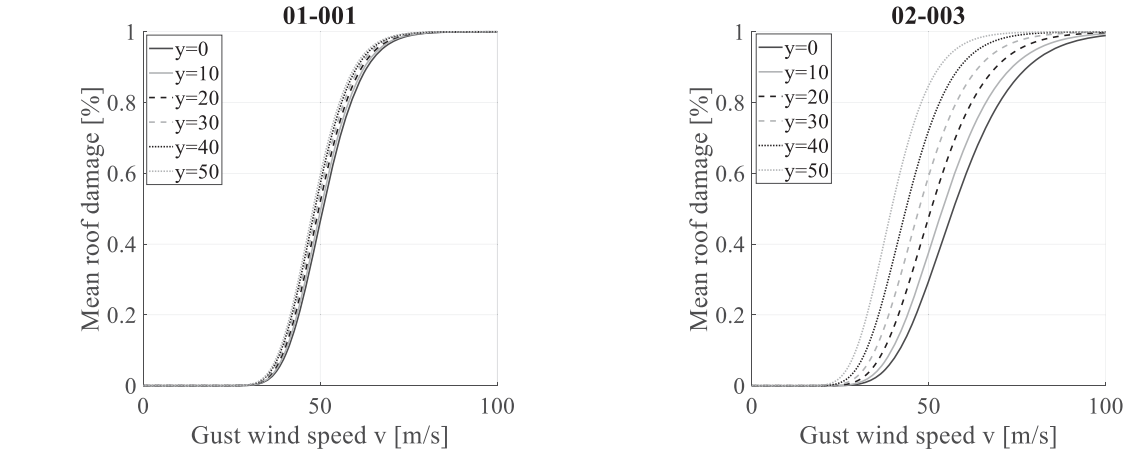

Figure 4: Fragility curves derived for different observation years (y): a) building 01-001 (screws), b) building 02-003 (nails).

5.2 Risk assessment

The results of the fragility analysis are then used to calculate the expected loss in terms of percentage of building replacement value as a function of the mean annual frequency (MAF) of the 3-sec gust speed v (i.e., simplified loss curves are derived, Figure 5). The calculation is repeated by varying the reference year from 0 to 50 years to account for both corrosion effects and climate change impact.

Loss curves calculated considering the reference year equal to 0 are very close, thus reflecting the result obtained for the fragility curves. The variation of the reference year affects more the roof '02-003' (nails) than the '01-001' one (screws). This is mainly due to the corrosion effect rather than the climate change, as explained before.

It is worth noting that the loss curves presented in this section are derived considering the expected values of damage-to-loss curves $\mathbb{E}[L|R_{\text{damage}}]$ (section 3.1). A comprehensive discussion of this problem would require considering the uncertainty related to the damage-to-loss curves, that means to consider $p[L|R_{\text{damage}}]$.

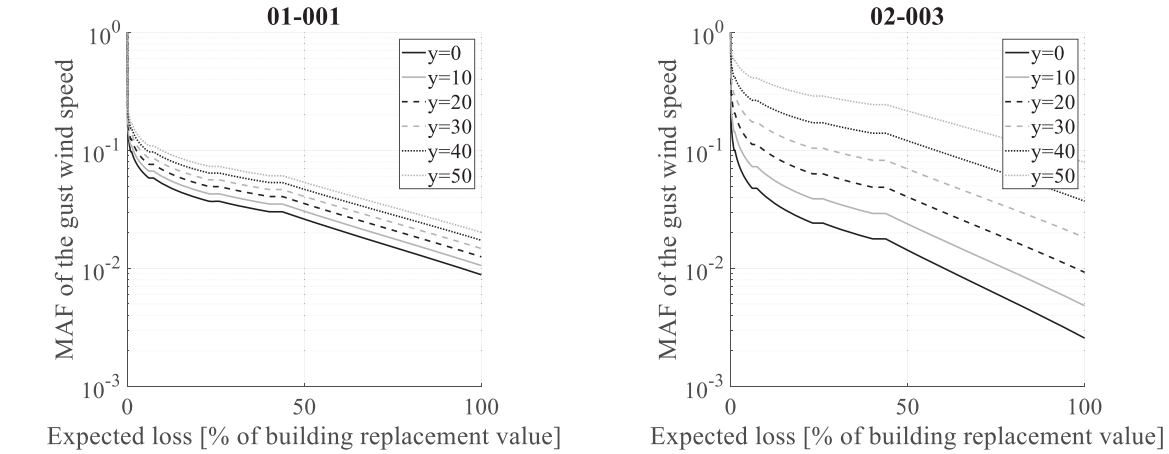

Figure 5: Loss curves: a) building 01-001 (screws), b) building 02-003 (nails).

5.3 Risk prioritization

The previous results are finally used to calculate the expected annual loss (EAL) [37] for each CH asset by varying the reference year. The resulting EAL are then used to prioritize the building portfolio by proposing a typhoon risk prioritization index I_{TR}. The index related to the k-th CH assets considering the i-th reference year is defined as,

$$I_{TR,i,k} = \frac{(100-1)}{(\mathrm{EAL}_{\max,i} - \mathrm{EAL}_{\min,i})} \left(\mathrm{EAL}_{i,k} - \mathrm{EAL}_{\min,i}\right) + 1, \quad (8)$$

where, $\mathrm{EAL}_{\max,i}$ and $\mathrm{EAL}_{\min,i}$ are the maximum and minimum EAL within the analysed portfolio. The resulting indices are arbitrarily categorized in three groups, respectively "green, yellow and red tags" by defining two thresholds. As a proof of concept, in this study the thresholds are selected to be equal to 33% and 66% for the calculated typhoon risk index. The results reported in Figure 6 show that the variation of the reference year of analysis leads to a small variation of the prioritization index. This fact indicates that even if corrosion and climate change affect the risk analysis at building-specific scale (previous section), the initial conditions of the analysed CH assets are more important for the definition of the typhoon risk prioritization scheme.

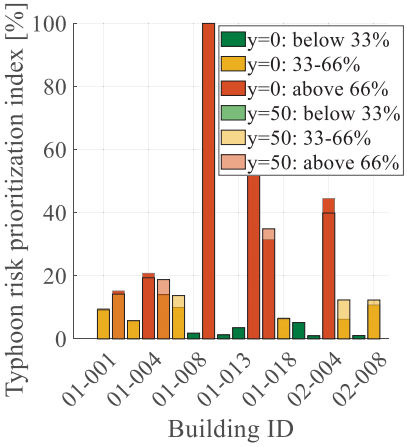

Figure 6: Typhoon risk prioritization index.

6 CONCLUSIONS

The Philippines is particularly prone to natural hazards, such as typhoons and earthquakes. Last catastrophic events have emphasized that the Filipino built environment is highly vulnerable to typhoons. This is likely to be worsened in the future because of the impact of climate change on typhoon intensities, frequencies and paths. Among the most vulnerable buildings, CH assets deserve special attention because of their intangible value for local communities, and their fundamental role in sustaining cultural tourism. Hence, typhoon risk assessment methods at building specific level and typhoon risk prioritization schemes at portfolio level, suitably defined for CH assets, are fundamental to prioritize disaster risk reduction and resilience-enhancing strategies.

This paper has presented a simulation-based approach for CH roof fragility derivation in which roof panel pullout and pullover failure mechanisms, corrosion effects and load redistribution (after fastener failure) have been explicitly modelled. Filipino CH asset roofs are made of timber frames and light-weight metal sheet (LWMS) with steel screws and nails used as fasteners; this structural typology has been the main focus of the study. A simplified model for the roof geometry, at the base of the proposed approach, has enabled 1) to reduce the required computational burden for fragility assessment; and 2) to probabilistically model

capacities/demands. The proper balance between refinement level and uncertainty consideration/propagation makes the proposed approach especially suitable for both risk prioritization and preliminary risk assessment at building specific level.

The analysis of 25 CH assets in Iloilo City, Philippines, has shown the feasibility of the proposed approach and has enabled the evaluation of the impact of the climate change on the risk assessment at building specific level and on the prioritization scheme. The results of the analysis have revealed that corrosion may strongly affect the fragility results for the considered CH roofs. Therefore, given the lack of maintenance activities in several developed countries corrosion around the world, corrosion effect must be considered in the typhoon fragility/risk assessment. Results of the analysis have also shown that climate change affects more the risk assessment estimates at building specific level than the prioritization scheme.

7 ACKNOWLEDGMENTS

This study was performed in the framework of the "CHeRiSH: Cultural Heritage Resilience & Sustainability to multiple Hazards" project funded by the UK British Council. The University of the Philippines Visayas (UPV), the Central Philippine University (CPU), and the De La Salle University (DLSU), Manila, are acknowledged for the technical support during the fieldwork.

REFERENCES

[1] Republic of the Philippines - National Disaster Risk Reduction and Management Council, Situational Report No.19 Regarding Response Actions and Effects of Typhoon "TISOY" (I.N. KAMMURI). Camp Aguinaldo, Quezon City, Philippines, 2019.

[2] T.R. Knutson, J.L. McBride, J. Chan, K. Emanuel, G. Holland, C. Landsea, I. Held, J.P. Kossin, A.K. Srivastava, M. Sugi. Tropical cyclones and climate change. *Nat. Geosci*. 3, 157-163, 2010.

[3] K. Emanuel, Global warming effects on U.S. hurricane damage. *Weather. Clim. Soc*. 3, 261-268, 2011.

[4] W.N. Holden, S.J. Marshall, Climate change and typhoons in the Philippines: Extreme weather events in the anthropocene, *Integrating Disaster Science and Management: Global Case Studies in Mitigation and Recovery*, Elsevier Inc., pp. 407- 421, 2018.

[5] W. Mei, S.P. Xie, F. Primeau, J.C. Mc Williams, C. Pasquero, Northwestern Pacific typhoon intensity controlled by changes in ocean temperatures. *Sci. Adv.*, 4, 1- 8, 2015.

[6] E. Strobl, The impact of typhoons on economic activity in the Philippines: evidence from nightlight intensity (No. 589), *ADB economics working paper series*, 2019.

[7] G. Sevieri, C. Galasso, D. D'Ayala, R. De Jesus, A. Oreta, M.E.D.A. Grio, R. Ibabao, A multi-hazard risk prioritization framework for cultural heritage assets. *Nat. Hazards Earth Syst. Sci.*, in review, 2020.

[8] B. Song, C. Galasso, L. Garciano, WARP^2: Wind Assessment of Roofs to Pullout & Pullover for Priority Cultural Heritage Structures in the Philippines. *Proceedings of the 13th International Conference on Applications of Statistics and Probability in Civil Engineering (ICASP13)*. Seoul, South Korea, 2019.

[9] H. Masoomi, M. R. Ameri, J.W. Van De Lindt, Wind Performance Enhancement Strategies for Residential Wood-Frame Buildings. *J. Perform. Constr. Facil*. 32, 2018.

[10] M. G. Stewart, Climate change impact assessment of metal-clad buildings subject to extreme wind loading in non-cyclonic regions, *Sustain. Resilient Infrastruct*, 1, 32- 45, 2016.

[11] R. Gentile, C. Galasso, Y. Idris, I. Rusydy, E. Meilianda, From rapid visual survey to multi-hazard risk prioritisation and numerical fragility of school buildings in Banda Aceh, Indonesia. *Natural Hazards and Earth System Sciences Discussions*, 19, 1365-1386, 2019.

[12] G. Pita, J. P. Pinelli, K. Gurley, J. Mitrani-Reiser. State of the art of hurricane vulnerability estimation methods: A review, *Nat Hazards Rev*., 16, 2, 2015.

[13] Philippine Statistics Autorithy, Census of Population 2015: "Region VI (Western Visayas)". Total Population by Province, City, Municipality and Barangay. *Report 2016-070*, 2016.

[14] Iloilo City Cultural Heritage Conservation Council (ICCHCC), Implementing Rules and Regulations for the Downtown Central Business District (CBD) Heritage Zone. Iloilo City, Philippines, 2010.

[15] United Nations Educational, Scientific and Cultural Organization (UNESCO), Operational Guidelines for the Implementation of the World Heritage Convention, *Report WHC.17/01*, 2017.

[16] Republic Act No. 10066, National Cultural Heritage Act of 2009, 2009.

[17] Q. Yang, R. Gao, F. Bai, T. Li, Y. Tamura, Damage to buildings and structures due to recent devastating wind hazards in East Asia. *Nat Hazards*., 92, 1321-1353, 2018.

[18] M. Ciampoli, F. Petrini, G. Augusti, Performance-Based Wind Engineering: Towards a general procedure, *Struct Saf*., 33, 367-378, 2011.

[19] J. Moehle, G. G. Deierlein, A framework methodology for performance-based earthquake engineering. *Proceedings of 13th World Conference on Earthquake Engineering*, Vancouver, BC, Canada, 3812–4, 2004.

[20] Association of structural engineers of the Philippines, National Structural Code of the Philippines, Manila, 2015.

[21] A. J. Kappos, G. Panagopoulos, C. Panagiotopoulos, G. Penelis, A hybrid method for the vulnerability assessment of R/Cand URM buildings. *Bull Earthq Eng*., 4, 391–413, 2006.

[22] Federal emergency management agency (FEMA) - Mitigation division, Multi-hazard loss estimation methodology – hurricane model, *Hazus–MH 2.1 Technical manual*, Washington, D.C., 2014.

[23] J. B. Elsner, J. P. Kossin, T. H. Jagger, The increasing intensity of the strongest tropical cyclones, *Nature*, 455, 7209, 92-95, 2008.

[24] L. Garciano, M. Hoshiya, O. Maruyama, Development of a regional map of extreme wind speeds in the Philippines, *Struct Eng Eng*., 22, 1, 15-26, 2005.

[25] M. G. Stewart, J. D. Ginger, D. J. Henderson, P. C. Ryan, Fragility and climate impact assessment of contemporary housing roof sheeting failure due to extreme wind, *Eng Struct*., 171, 464-475, 2018.

[26] A. Silang, S. N. Uy, J. M. Dado, F. A. Cruz, G. Narisma, N. Libatique, G. Tangonan, Wind Energy Projection for the Philippines Based on Climate Change Modeling, *Energy Procedia*., 52, 26-37, 2014.

[27] K. M. C. Konthesingha, M. G. Stewart, P. Ryan, J. Ginger, D. Henderson, Reliability based vulnerability modelling of metal-clad industrial buildings to extreme wind loading for cyclonic regions. *J Wind Eng Ind Aerodyn*., 147, 176–85, 2015.

[28] American Society of Civil Engineers (ASCE), ASCE 7-10. Minimum Design Loads for Buildings and Other Structures (ASCE/SEI 7-10), *American Society of Civil Engineers*, Reston, VA, 2010.

[29] B. R. Ellingwood, P. B. Tekie, Wind load statistics for probability-based structural design, *J Struct Eng*., 125, 4, 453-463, 1999.

[30] K. H. Lee, D. V.Rosowsky, Fragility assessment for roof sheathing failure in high wind regions, *Eng Struct*., 27, 857-868, 2005.

[31] American Wood Council (AWC), National Design Specification for Wood Construction. Leesburg, VA, 2017.

[32] Y. Dong, Y. Li, Reliability of Roof Panels in Coastal Areas Considering Effects of Climate Change and Embedded Corrosion of Metal Fasteners. *ASCE-ASME J Risk Uncertain Eng Syst Part A Civ Eng*., 2, 1, 2016.

[33] I. P. R. Alvarez, J. A. M. Colobong, C. Q. Decal, A. B. S. Tan, Pull-Out and Pull-Over Failure Probability of Residential House Roofs due to Extreme Wind Speeds: a Case Study in Malate, Metro Manila, *BSc thesis, De La Salle University*, 2013.

[34] M. N. Nguyen, R. H. Leicester, C. H. Wang, G. C. Foliente, Corrosion effects in the structural design of metal fasteners for timber construction, *Struct Infrastruct Eng*., 9, 3, 275-284, 2013.

[35] Philippine Atmospheric Geophysical and Astronomical Services Administration. PAGASA website. http://bagong.pagasa.dost.gov.ph/. Published 2020.

[36] J. W. Baker. Efficient analytical fragility function fitting using dynamic structural analysis. *Earthq Spectra*, 31, 1, 579-599, 2015.

[37] K. M. Solberg, R. P. Dhakal, J. B. Mander, B. A. Bradley, Computational and rapid expected annual loss estimation methodologies for structures, *Earthq Eng Struct Dyn*., 37, 1, 81-101, 2007.

EURODYN 2020
XI International Conference on Structural Dynamics
M. Papadrakakis, M. Fragiadakis, C. Papadimitriou (eds.)
Athens, Greece, 23–26 November 2020

MODAL PROPERTIES OF A FLOOR WITH SINGLE-LEAF PLYWOOD ON TIMBER JOISTS: EXPERIMENTAL AND NUMERICAL MODELLING

Lars V. Andersen[1], **Nina Jørgensen**[1], **Gitte S. Iversen**[1] **and Jannick B. Hansen**[2]

[1] Department of Engineering, Aarhus University
Inge Lehmanns Gade 10, DK-8000 Aarhus C, Denmark
e-mail: lva@eng.au.dk

[2] Aarhus School of Engineering, Aarhus University
Inge Lehmanns Gade 10, DK-8000 Aarhus C, Denmark
e-mail: jbah@ase.au.dk

Keywords: Wood, Timber, Floor, Vibration, Modal Analysis, Model Calibration.

Abstract. *The paper addresses the modal properties of a wooden floor consisting of a plywood board fastened by screws to timber joists. The overall aim of the study has been to examine how well finite-element models can be calibrated to match the dynamic properties of a mock-up, studied in the laboratory in a scale of 1:2. The paper proposes the use of output-only modal analysis, also known as operational modal analysis (OMA), using brushes of various stiffnesses to excite the floor. In order to avoid uncertainties related to the supports, free–free boundary conditions are considered. This has been modelled experimentally by suspending the test specimens in rubber bands. Modes up to about 500 Hz were extracted, using an array of accelerometers, and the experimental results were then used as a basis for model calibration and model validation. Two overall approaches to finite-element modelling of the wooden floor are studied in the paper. The first approach employs a solid model with all parts of the structure (plywood and joists) modelled as orthotropic, linear elastic materials. The second approach considers a structural model with the plywood leaf modelled as a laminate shell using Mindlin thick-plate theory and the joists modelled using Timoshenko beam theory. Firstly, the finite-element models of each individual component of the floor, i.e. each beam or plate, are updated with the use of the measured modal properties. Secondly, in order to validate the finite-element models of the assembled floor, their modal properties are compared with the results obtained experimentally. In the validation step, no further updating is performed, but various configurations of the connections between the wooden beams and the plywood board are included in the study. An artificial elastic layer and modelling of the individual lines of screws are introduced within the solid model to allow more realistic modelling of the connection. In this context, the kinematic constraints enforced within the shell–beam model are discussed.*

1 INTRODUCTION

Vibrations in a floor can be caused by walking on the floor as well as other sources inside or outside a building. At low frequencies from 1–80 Hz, this can be felt as whole-body vibrations or heard, for example, as rattling noise. In the frequency range 20–250 Hz, the structure-borne vibrations lead to reradiated noise. The noise and vibration may cause annoyance to the inhabitants of a building and, in severe cases, health problems [1–3].

The vibrations of a floor and the related reradiated structure-borne noise are greatly influenced by the modal properties of the floor. These properties are subject to large uncertainties due to natural variations in the material [4,5] and the usage of the floor [6–9] as well as the support conditions and internal joints [10,11]. This entails detailed information about the individual floor if a reliable computational model of the floor is to be constructed. Without such knowledge, the error in the estimate of the natural frequency of a floor may exceed 20 %.

Before a computational model based on, for example, the finite-element (FE) method can be calibrated to match the modal properties identified from measured accelerations, the model must first be able to represent the dynamic response in the frequency range of interest. This paper concerns the frequency ranges relevant to whole-body vibration and reradiated structure-borne noise. For low vibration levels at these frequencies, reinforced concrete floors may be modelled as shells with isotropic, linear elastic material behaviour of the concrete, accounting for the steel reinforcement as layers with additional stiffness in the direction of the rebar. However, a similarly simple approach cannot be used for wooden floors. Timber is an orthotropic material, and the position and orientation of each joist or layer in a plywood laminate must be accounted for explicitly. Furthermore, the uncertainties of the material properties as well as the internal joints between the beams and the plates must be addressed.

The purpose of the paper is to analyse whether FE models based on different overall concepts can be used to model the dynamic behaviour of a wooden floor consisting of a single-leaf plywood board attached to four timber beams by screws in different configurations. Free–free conditions and an empty floor have been considered to avoid additional uncertainties related to the supports and usage of the floor. An experimental campaign has been conducted with the aim of extracting the modal parameters of a mock-up built in scale 1:2. The modal properties of the individual components, i.e. the timber beams and the plywood board, have also been determined experimentally to allow a stepwise model updating. Usually, the modal properties would be obtained by experimental modal analysis (EMA) [12–15], but this paper proposes the use of output-only modal analysis—or operational modal analysis (OMA)—as an alternative to this [16,17], applying diffuse white-noise excitation with soft and medium-stiff brushes.

Two FE modelling concepts are considered: a) a solid FE model and b) a structural FE model. The models are compared regarding their ability to represent the modal properties of the individual components before validating the FE models of the assembled floor with various configurations of the connections.

The overall geometry, connectivity and material properties of the studied wooden floor are presented in Section 2. Section 3 provides an overview of the experimental campaign. Firstly, the experimental setup and testing procedure for each of the tests are described, and then the results are presented. Next, Section 4 introduces the FE models. The geometry, material modelling, discretization, and assembly strategy are all described with focus on the solid FE models. The calibration and validation of the FE models then follow in Section 5. A sensitivity study is first performed to quantify the importance of each material property in the orthotropic material models. A model updating of each beam and the plate is conducted, before the models of the assembled floors with different configurations of screws are validated. Finally, a short summary, the main conclusions, and suggestions for future work are presented in Section 6.

2 DEFINITION OF THE FLOOR MODEL

Ideally, to examine how well an FE model may replicate the modal properties of a wooden floor structure, the FE model should be compared to and validated by a physical floor model in full scale. However, a full-scale model of a floor requires a considerable amount of space and time to build in a laboratory. Further, as the experimental campaign was conducted in the Dynamics Laboratory of Aarhus University School of Engineering, the mock-up of the floor panel should fit into the available test stand. Hence, it was chosen to construct the mock-up in smaller scale, approximately 1:2 compared to a full-size floor. While this allowed easier handling of the timber beams and the plywood plates constituting the floor panel, it still provided an experimental model representative of the kinematic and dynamic behaviour that can be expected for a full-size floor. The geometry and dimensions of the down-scaled model are shown in Figure 1. All beams (*Södra reglar*) came from the same badge in order to get insight into the variation in material properties that can be expected even in that case. Also, two plywood boards (*Keflico Selex Radiata Pine Krydsfiner*) from the same badge were tested to examine the variation in material properties before the modelling of the assembled floor panel.

Prior to conducting the tests and setting up the FE models, it was necessary to have an initial idea of the material properties as well as their upper and lower bounds to be used in the model updating and calibration process. With the initial values, FE analysis and simple hand calculations could be carried out for the beams as well as the boards in order to get insight into the eigenfrequencies and the related eigenmodes, such that the sampling frequency, recording time, and the position of accelerometers used for measurements could be chosen on an informed basis. The upper and lower bounds could be used in the FE model updating (calibration) procedure.

Tables 1–2 show the material properties of the timber beams, based on two different overall assumptions. Thus, for the beams, two sets of parameters are given assuming that the wood is either isotropic (Table 1) or orthotropic (Table 2). In any case, the material is assumed to

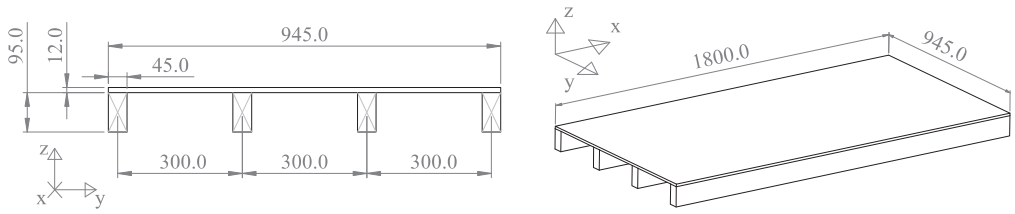

Figure 1: Down-scaled panel section (measures in mm).

	Young's modulus [MPa] E	Poisson's ratio [-] ν
Lower limit	5 600	0.10
Upper limit	17 000	0.49
Initial value	12 440	0.334

Table 1: Isotropic material properties for the beams. Mass density: $\rho = 450$ kg/m^3.

	Young's modulus [MPa]			Shear modulus [MPa]			Poisson's ratio [-]		
	E_1	E_2	E_3	G_{12}	G_{13}	G_{23}	ν_{12}	ν_{13}	ν_{23}
Lower limit	5 600	230	230	440	440	21	0.34	0.34	0.20
Upper limit	17 000	1 200	1 200	1 600	1 600	125	0.72	0.72	0.60
Initial value	12 440	812	812	1 136	1 136	83.4	0.568	0.568	0.44

Table 2: Orthotropic material properties for the beams. Mass density: $\rho = 450$ kg/m^3.

	Young's modulus [MPa]			Shear modulus [MPa]			Poisson's ratio [–]		
	E_1	E_2	E_3	G_{12}	G_{13}	G_{23}	v_{12}	v_{13}	v_{23}
Lower limit	5 860	3 220	1 005	290	61.5	20.5	-0.108	0.156	0.116
Upper limit	12 460	9 820	1 505	940	211.5	170.5	0.142	0.656	0.616
Initial value	9 820	7 180	1 305	680	151.5	110.5	0.042	0.456	0.416

Table 3: Orthotropic material properties for the plywood *single-layer plate*. Mass density: ρ = 500 kg/m^3.

	Young's modulus [MPa]			Shear modulus [MPa]			Poisson's ratio [–]		
	E_1	E_2	E_3	G_{12}	G_{13}	G_{23}	v_{12}	v_{13}	v_{23}
Lower limit	8 200	270	560	350	590	33	0.21	0.12	0.01
Upper limit	21 700	770	1 460	900	1 540	88	0.71	0.62	0.51
Initial value	16 300	570	1 100	680	1 160	66	0.51	0.42	0.31

Table 4: Orthotropic material properties for the plywood *lamina*. Mass density: ρ = 500 kg/m^3.

undergo linear elastic deformation given the very low excitation levels associated with the experiment. It should be noted here that wood is behaving as an orthotropic material. Modelling the wood as isotropic will overestimate the shear moduli as well as the Young's moduli in the directions orthogonal to the grain. The intervals for the values are chosen based on the previous study by Flodén et al. [14], and the initial values are a qualified guess based on the mass density that has been provided by the supplier.

Next, Tables 3–4 show the material properties for the plywood boards in terms of lower and upper bounds as well as the assumed initial values. Here, it was judged that an isotropic material behaviour would be inappropriate, even for the first few eigenmodes. Instead, two alternatives based on orthotropic behaviour were considered: a "smeared-out model" with a single-layer plate (Table 3) and a model with five plies, or laminae, with identical properties by having different orientation of the grain (Table 4). Here, the material properties were inspired by the work on Scots Pine carried out by Gerrand [18]. It is noted that, for the individual lamina, E_1 is the Young's modulus in the grain direction while E_2 is the Young's modulus in the transverse direction parallel to the annual rings. In the single-layer plate model, E_1 is the Young's modulus in direction 1 in which most of the laminae have the grain direction, and E_2 is then the in-plane direction orthogonal to direction 1. The difference between E_1 and E_2 is assumed to be small, since three laminae are present in direction 1, whereas two laminae are present in direction 2.

In addition to the material properties, the assembly between the individual parts of the floor must also be modelled correctly in an FE model. In the present analyses, the plywood board was attached to the beams by screws of the brand Carl Ras (Panel Twistec Ruspert with Fibercut Point no. 4848-0653). The screws had the length 40 mm, and the head had a diameter of 4.0 mm. A total of six configurations were considered for the assembly:

- Panel A: One line of screws per beam, c–c distance of screws: 191 mm
- Panel B: One line of screws per beam, c–c distance of screws: 95.5 mm
- Panel C: One line of screws per beam, c–c distance of screws: 47.8 mm
- Panel D: Three lines of screws per beam, c–c distance of screws: 191 mm
- Panel E: Three lines of screws per beam, c–c distance of screws: 95.5 mm
- Panel F: Three lines of screws per beam, c–c distance of screws: 47.8 mm.

At the ends of the beams, the screws were placed 40 mm from the edges.

Figure 2 shows the overall placement of the screws in Panel A. Further, in the lower–right corner of the figure, an encircled area can be found, indicated by the letter A. This refers to

Figure 3 which provides an overview of the screw positions in all six cases, i.e. Panels A–F. As described below, a part of the research has focused on testing whether a single screw present in the width direction of each beam (Panels A–C) provide a line coupling. Also, it has been examined whether three screws present across the beams (Panels D–F) provide a rigid coupling such that the beams can be considered fully merged with the board.

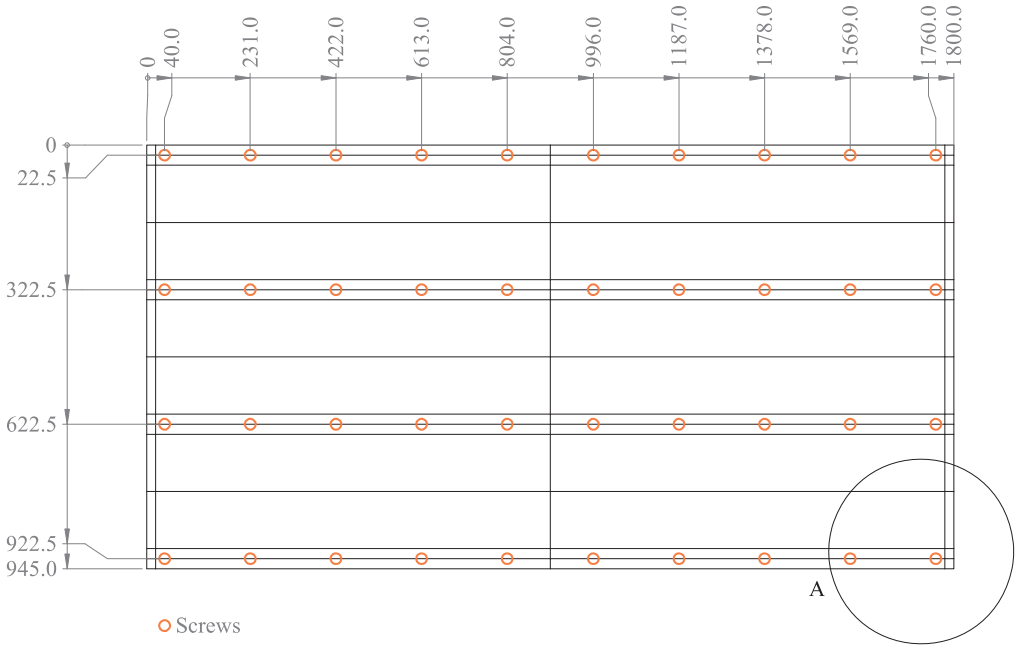

Figure 2: Top view of the floor model with placement of the screws in Panel A.

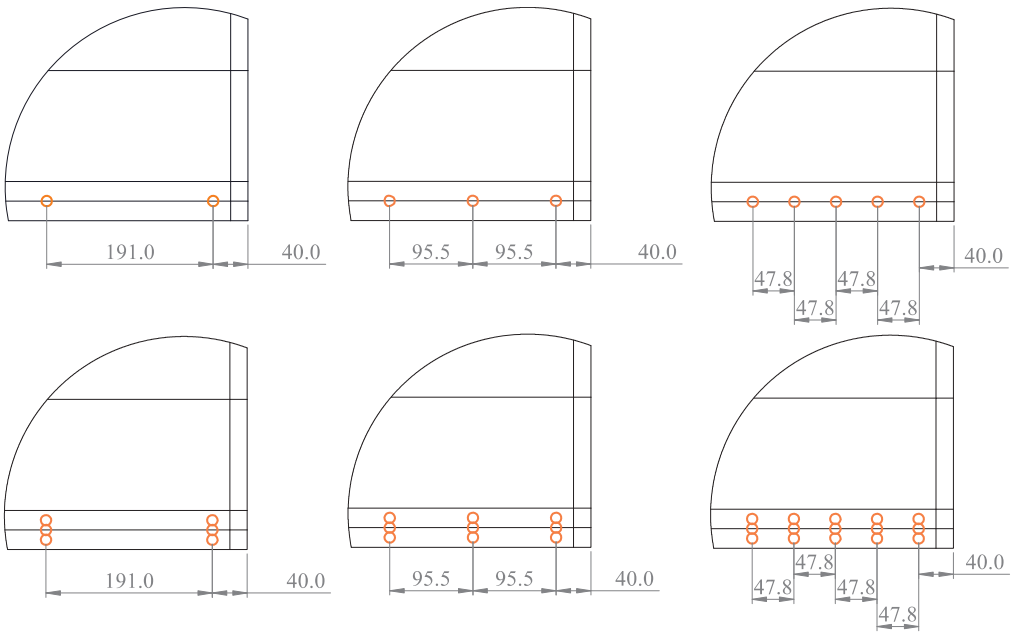

Figure 3: Position of the screws within the encircled area indicated in Figure 2. Top row, left to right: Panel A, Panel B, and Panel C; bottom row, left to right: Panel D, Panel E, and Panel F.

3 EXPERIMENTAL SETUP AND TESTING

The overall purpose of the experimental campaign was to collect reliable data that could be used for the validation and calibration of the FE models. For real floors, constituting a part of a building, uncertainties are associated not only with the material properties but also the support conditions and the usage of the floor, as discussed, for example, by Andersen and co-workers [7–10]. In order to minimize the possible influence of such uncertainties, an empty floor was considered, and so-called free–free conditions (i.e. an unsupported floor) were assumed. In practice, this was established by suspending the test specimens in rubber bands tied at one end to the test rig. Following the procedure suggested by Dickow [19], the other end of the rubber bands was tied by a knot to the eyebolts installed in the test specimens (see Figures 6, 8 and 10). This provides well-defined connections with no sliding or uncertain mechanisms involved.

The experiments were carried out as Output Only Modal Analysis (OMA) [16], using brushes to excite the test specimens. To allow a stepwise calibration of the FE model, updating the material properties of the beams and the boards before analysing the assembled floor, the experimental campaign was conducted in three main steps:

- OMA of the four timber beams, one at a time, conducting four tests for each beam (see Subsection 3.1)
- OMA of the two plywood boards, one at a time, conducting four tests for each board (see Subsection 3.2)
- OMA of the assembled floor, using Board no. 2 and Beams no. 1–4, conducting three to four tests for each of the six panel configurations (see Subsection 3.3).

The specimens were not dismounted between the different tests. For the OMA of the individual beams and boards, a soft brush was utilized for excitation, and for the assembled floor, the same brush as well as a medium soft brush were applied to excite a wider range of frequencies.

The data collection was performed with sensors from Brüel & Kjær (B&K) and a data acquisition system National Instruments (NI):

- 20 pcs. B&K Type 4508-B-002, Piezoelectric CCLD Accelerometer, 1000 mV/ms^{-2}
- 1 pc. B&K Type 4508-B, Piezoelectric CCLD Accelerometer, 100 mV/ms^{-2}
- B&K Type UA-1407, Plastic Mounting Clips
- B&K Type 4294, Accelerometer Calibrator, hand-held
- NI Type cDAQ-9178, CompactDAQ Chassis
- 5 pcs. NI Type 9234, C Series Sound and Vibration Input Module
- Stanley 0-77-030 Moisture Meter
- TinyTag Type TGP-4500, Temperature and Relative Humidity Logger.

Furthermore, a level was used to make sure that the various specimens were mounted in a horizontal position, and a scale was used to determine the weights.

The experimental data were recorded using NI SignalExpress [20] with DAQ Assistant [21] installed. Analyses were carried out using ARTeMIS Modal Pro [22], and a quick pre-analysis of the recorded data was performed in MATLAB [23] using the OMA Toolbox [16] to see whether reasonable eigenfrequencies modes were obtained. In the instrumentation of the specimens, care was made to place accelerometers such that global as well as local modes of vibration would be registered. For the assembled floor, accelerometers should therefore not be placed only on top of the beams, but also on the boards in the mid-spans between the beams. Examples of global bending and local vibration modes for the assembled floor can be seen in Figure 4.

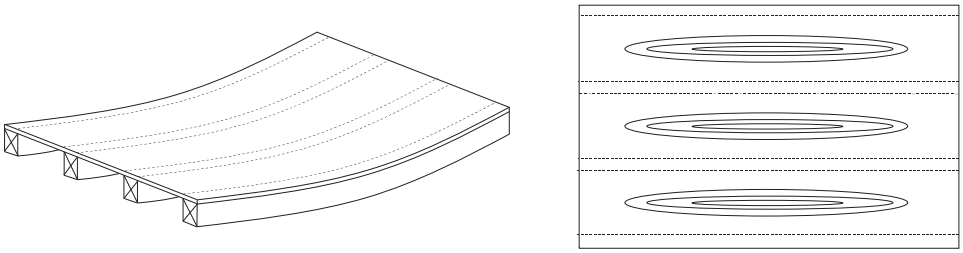

Figure 4: Example eigenmodes of panel: Global bending (left); local plate deflection between joists (right).

3.1 Output-only modal analysis of the individual beams

Figure 5 shows the position of the accelerometers mounted on each single beam in the first step of the experimental campaign. Further, Figure 6 shows the experimental setup with one of the beams mounted in the test rig. Nine accelerometers were placed on the top flange of the beam and another nine accelerometers were placed on one side. No accelerometers were placed on the bottom flange or on the other side, since no modes with significant deformation of the cross-section were expected within the considered frequency range. All wires were carefully attached to a wooden rod placed above the beam to avoid any collisions with the beam during the experiment. Each test lasted 30 s, and the data was acquired at a sampling frequency of 2 049.2 Hz. The soft brush was applied for excitation.

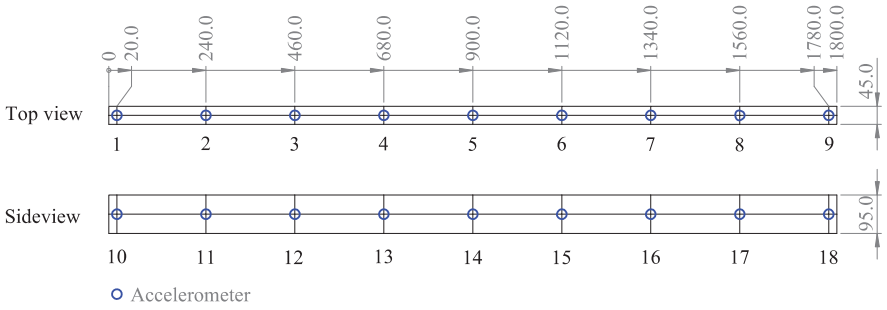

Figure 5: Position of the accelerometers mounted on each single beam.

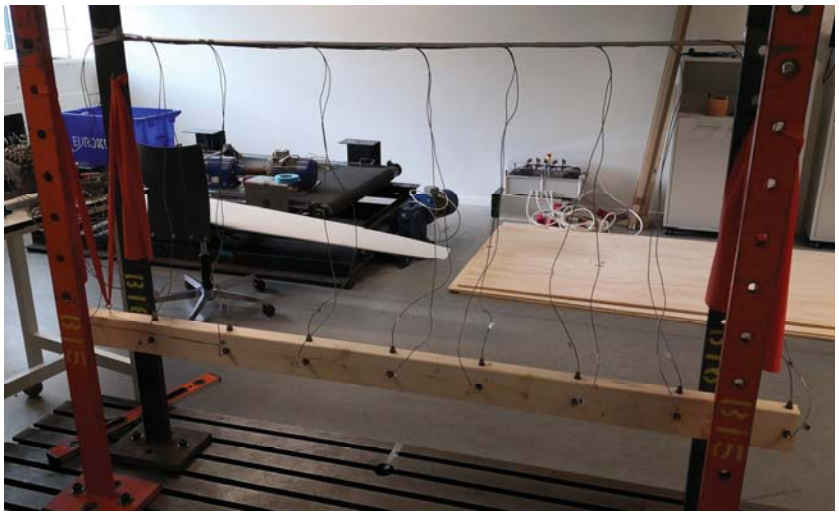

Figure 6: One of the wooden beams placed in the test stand.

3.2 Output-only modal analysis of the board

Figure 7 shows the positions of the eyebolts and the accelerometers mounted on each single plywood board. Figure 8 illustrates the experimental setup with one of the boards mounted in the test rig. It should be noted that Figure 7 indicates the positions at which the beams were later placed (the sides as well as the centre lines of the beams). The accelerometer positions were carefully chosen to capture as many modes as possible within the considered frequency range. Also, the eyebolts were placed at the positions where preliminary analyses based on the initial material properties in Table 4 indicated a small deflection in the first eight eigenmodes. Each test lasted 120 s, and the sampling frequency was set to 1 652.9 Hz. The soft brush was applied for excitation.

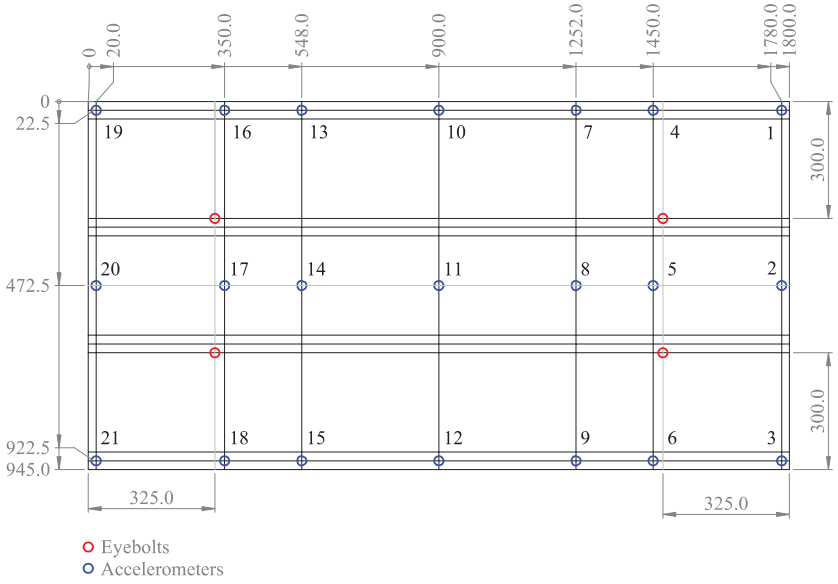

Figure 7: Position of the accelerometers on each of the plywood boards (top view).

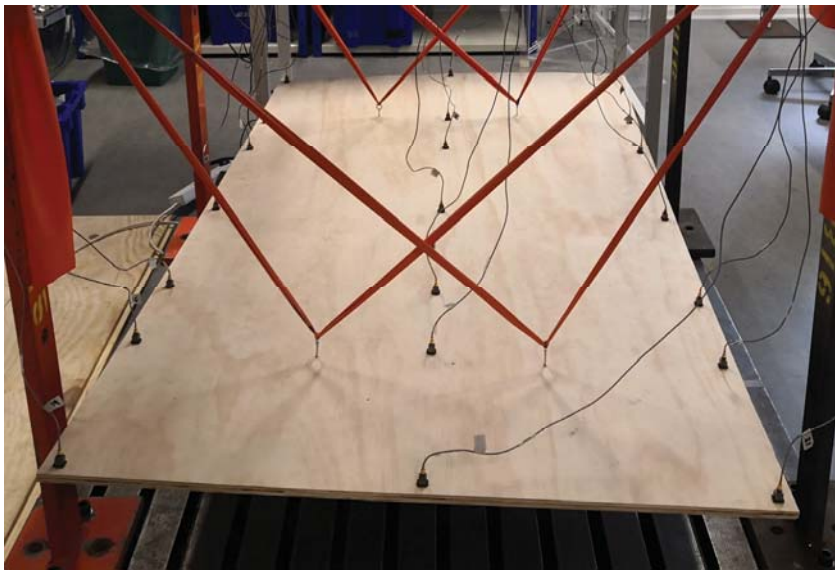

Figure 8: One of the plywood boards placed in the test stand.

3.3 Output-only modal analysis of the complete floor panel

The positions of the accelerometers and the eyebolts mounted on the assembled floor panel are shown in Figure 9. Again, the positions have carefully been selected based on a preliminary FE analysis using the initial material properties for the timber beams (Table 2) and the plywood

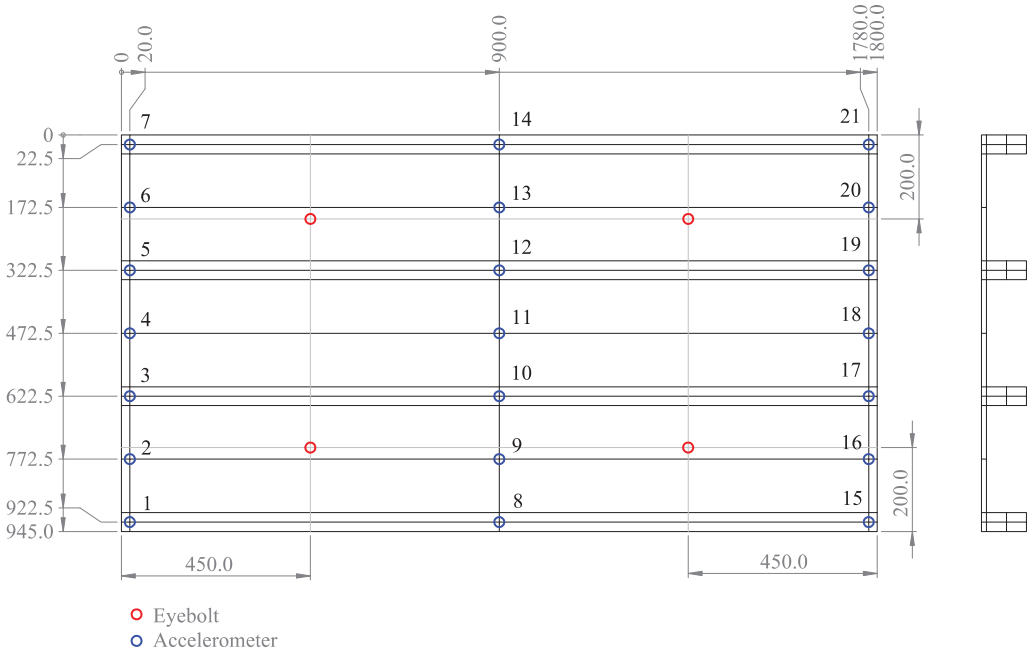

Figure 9: Position of the accelerometers on the assembled floor (top view).

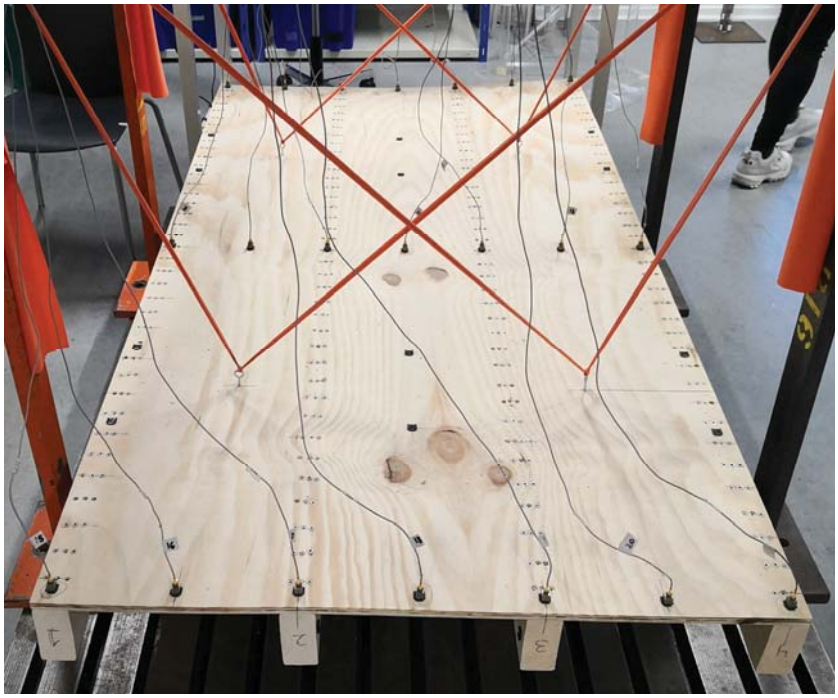

Figure 10: The mock-up of the floor (Panel F) mounted in the test rig.

board (Table 4). Figure 10 shows the setup with the assembled floor panel installed in the test rig. The photograph illustrates Panel F, i.e. the configuration with three screws over the width of each beam and with 47.8 mm between the screws in the longitudinal direction. Among the considered panel configurations, this is the most rigid connection between the beams and the board. Each test lasted 45 s, and the sampling frequency was set to 1 652.9 Hz. The soft and medium soft brushes were applied for excitation.

3.4 Results of the experimental campaign

The mass densities of the individual beams were found to be 415.32, 539.19, 444.31, and 442.85 kg/m^3, for Beams 1, 2, 3, and 4, respectively. Thus, Beam 2 had a relatively high mass density compared to the other beams, even though all beams came from the same badge. The mass densities of the boards were 490.09 and 483.25 kg/m^3, for Plates 1 and 2, respectively.

A full report of the experimental results is beyond the scope of the paper. However, information about the mean values of the eigenfrequencies extracted for each of the components as well as for the assembled floor are given in Tables 5–7. The first eigenfrequency of the beams is related to bending in the horizontal plane, i.e. with respect to the weak axis of the cross section, and it lies close to 70 Hz. Mode 2 relates to bending in the vertical plane, i.e. with respect to the strong axis. As expected, the corresponding eigenfrequency is approximately twice as high as the eigenfrequency related to Mode 1. It is furthermore interesting to note that Modes 4 and 7 are the first and second torsional modes according to the finite-element models. Given the instrumentation of the beams, these modes were not captured in the OMA. This explains that these modes are missing in Table 5.

The plates (plywood boards) were much more flexible than the beams. Here, the first ten eigenmodes had frequencies in the interval from around 10 Hz to approximately 80 Hz. With the chosen position of the accelerometers, all the first ten modes could be captured by OMA. It is noted that the first mode at around 10–12 Hz relates to torsion, whereas the second mode relates to bending of the plates. Except for Modes 4 and 5, Plate 1 had a stiffer response than Plate 2, i.e. the extracted eigenfrequencies for Plate 1 are higher than those for Plate 2.

Finally, Table 7 shows that the eigenfrequencies related to the first ten modes of the assembled floor panels lie in the range 15 Hz to 200 Hz. By comparison with FE models of the six panels, it was identified that Mode 2 of Panel B was not captured by the OMA. The same problem occurred for Modes 1 and 2 of Panel D. Interestingly, the eigenfrequencies related to some of the modes, e.g. Modes 1, 4, 5 and 10, are close to being identical for the various configurations of the screws. For Mode 10, only Panel A with the smallest amount of screws has a significantly lower eigenfrequency than the other configurations. However, for some of the modes, e.g. Modes 7 and 9, there is a marked difference between the panels with few or many screws. The number of screws in the longitudinal direction and the number of screws across each beam are equally important. It should in this context be mentioned that the first eight eigenmodes of the full panel do not involve bending of the beams which are relatively stiff.

Further, the relative variations in the extracted eigenfrequencies of all specimens are shown in Figure 11. For a given eigenmode of the beams it can be observed that the associated eigenfrequencies of the individual beams differed up to about 5 percent from the mean value based on all four beams. As also seen in Table 5, Beam 2 provided consistently higher eigenfrequencies than the other beams for the first four modes. The higher mass density of Beam 2 is therefore associated with an even higher stiffness. For the plates, some variation also occurs, and it can be observed that none of the boards provides frequencies that are consistently higher than the other board. This indicates that the eigenfrequencies are very sensitive to variations of the material properties in the different laminae and in different directions or planes.

	Beam 1	Beam 2	Beam 3	Beam 4
Mode 1	69.04	73.67	68.91	68.54
Mode 2	144.75	147.34	142.83	145.08
Mode 3	187.77	195.86	180.73	191.28
Mode 4 (5)	351.54	376.22	367.59	358.37
Mode 5 (6)	372.88	360.58	354.83	382.39
Mode 6 (8)	573.50	590.22	558.82	570.83
Mode 7 (9)	650.37	660.26	682.02	673.72
Mode 8 (10)	831.65	836.11	795.96	805.30

Table 5: Average eigenfrequencies (Hz) for the beams based on four OMA tests on each beam. The mode numbers given in parenthesis refer to the mode numbers obtained by the finite-element models.

	Plate 1	Plate 2
Mode 1	12.26	10.49
Mode 2	15.06	14.63
Mode 3	27.41	25.73
Mode 4	32.27	33.23
Mode 5	35.79	36.59
Mode 6	42.84	41.16
Mode 7	52.74	49.97
Mode 8	54.07	53.30
Mode 9	77.83	75.19
Mode 10	80.59	78.42

Table 6: Average eigenfrequencies (Hz) for the plates based on four OMA tests on each plate.

	Panel A	Panel B	Panel C	Panel D	Panel E	Panel F
Mode 1	15.64	15.69	15.54		15.50	15.57
Mode 2	13.94		16.01		16.51	16.75
Mode 3	32.08	34.26	35.55	34.84	36.05	36.35
Mode 4	41.93	42.19	42.24	42.14	42.24	42.37
Mode 5	56.26	58.11	59.19	58.65	59.62	59.99
Mode 6	81.48	85.73	87.30	86.49	88.48	89.35
Mode 7	105.12	115.50	119.72	116.93	122.20	124.36
Mode 8	139.69	142.67	143.02	142.01	142.79	143.12
Mode 9	161.82	168.45	172.41	170.73	174.93	175.91
Mode 10	191.32	198.41	200.79	197.23	200.29	200.42

Table 7: Average eigenfrequencies (Hz) for the panels based on three to four OMA tests on each panel.

Figure 11 shows that some of the panel configurations provide eigenfrequencies that are significantly lower than other configurations. Especially, in eigenmode 2, Panel A (which has the smallest amount of screws) provides an eigenfrequency that is about 20 percent lower than that of Panel F (which has the largest amount of screws). This clearly demonstrates that the connectivity between the beams and the plate has a large impact on the modal properties of the floor, even for the first eigenmodes. It should again be noted that Mode 2 of Panel B and Modes 1 and 2 of Panel D were not captured during the experiments.

Finally, Figure 11 shows that there was a small scatter in the repeated recordings for the individual structural members as well as the floor panels. Part of this variation can be attributed to the changing environmental conditions caused, primarily, by an irregularity in the operation

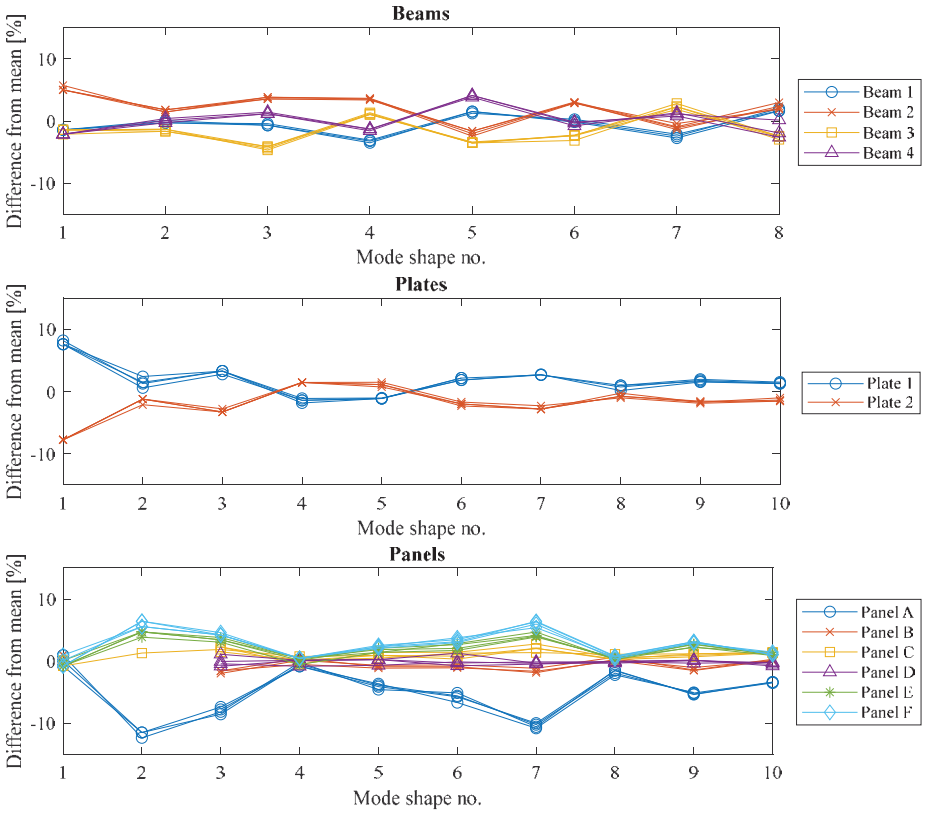

Figure 11: Relative variations in the experimentally measured eigenfrequencies.

of the ventilation system in the laboratory. During the experimental campaign, the temperature varied between 20.2 °C and 22.6 °C, and the relative humidity varied between 28.6 % and 50.3 %. It was observed that one of the plywood boards, Plate 1, warped because of a change in moisture content, and for this reason, only Plate 2 was used for the floor assembly.

4 FINITE-ELEMENT ANALYSIS OF THE WOODEN FLOOR PANEL

The finite-element modelling process followed the same steps as the experimental campaign in order to allow a direct comparison, validation and calibration of the FE models. Thus, as a first step, the individual beams and plates were modelled. Two overall concepts were applied: a three-dimensional (3D) solid FE model of each part developed in Abaqus, and a 3D structural FE model developed of each individual part developed in MATLAB.

The MATLAB model of the beam was based on two-node Timoshenko beam elements using the standard cubic Hermite interpolation functions. Linear interpolation was used for the axial and torsional deformations, assuming Saint-Venant torsion. Since the beam theory assumes that cross sections remain undeformed, only E_1, G_{12} and G_{13} influence the stiffness when utilizing an orthotropic material model. It is noted that the torsional stiffness depends on a combination of G_{12} and G_{13}, whereas transverse shear depends on either G_{12} or G_{13}, depending on direction.

For the plywood boards, the MATLAB model employed Mindlin thick-plate theory. Nine-node elements with quadratic Lagrange interpolation of the displacements and rotations were utilized. Selective integration was applied for the in-plane directions of the element to avoid locking, and a three-point Gauss quadrature rule was applied over the thickness of each ply. The model allows the introduction of a laminate composite with orthotropic behaviour of each

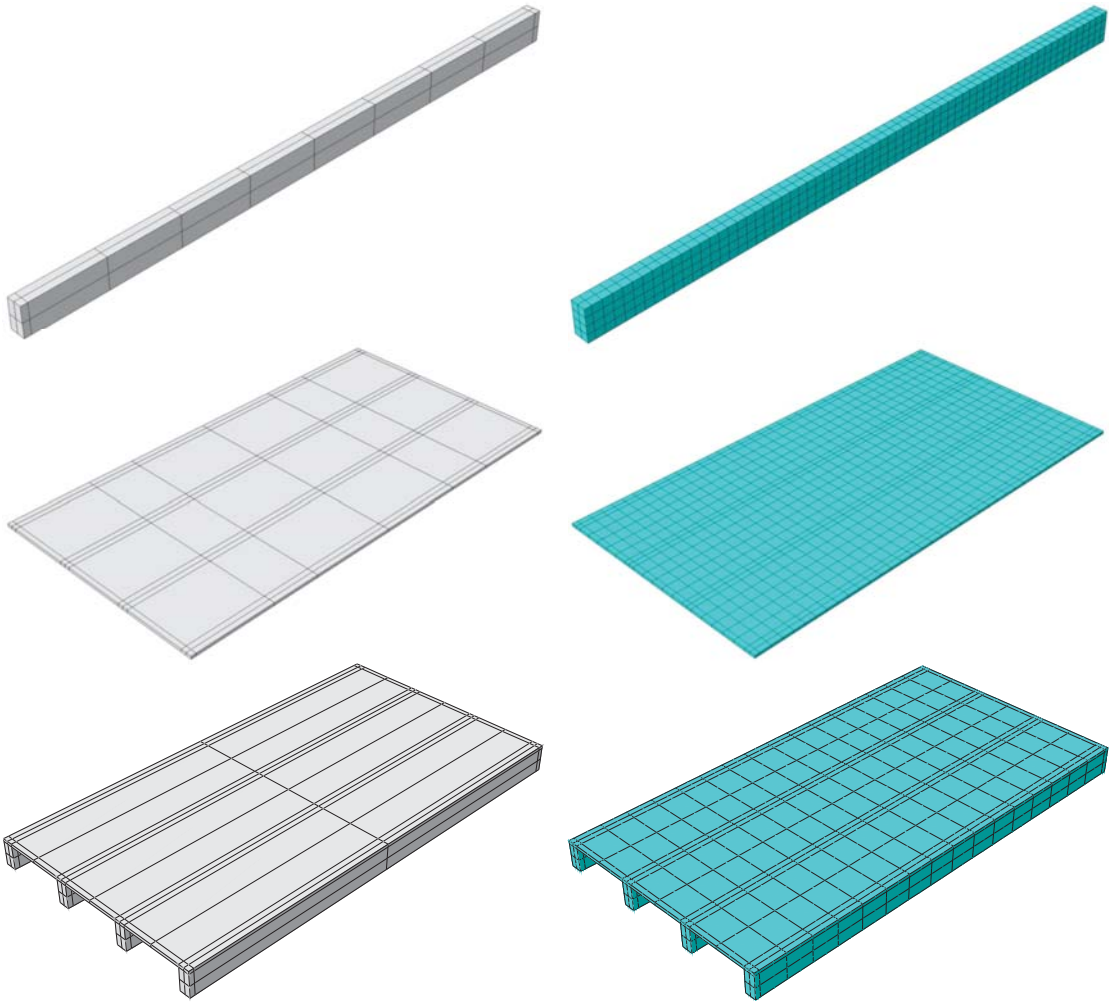

Figure 12: Solid finite-element models of a single beam (top), a plate (middle), and a floor panel (bottom). Left: Division of the geometry. Right: Structured mesh with solid cubes.

layer, or ply. A layup with a 0°–90°–0°–90°–0° configuration was implemented, assuming that the thickness of each ply was the same, corresponding to one-fifth of the plate thickness.

The Abaqus solid FE models of a beam and a plate are illustrated in Figure 12 which also shows a model of an assembled floor panel in which the beams are simple merged with the plate. Generally, the divisions of the models were introduced to allow the evaluation of the displacements at the positions where the accelerometers were placed in the experimental tests. The same strategy was used for the beams and plates in MATLAB. It is noted that the accelerometers were not modelled in any of the models. This implies a modelling uncertainty, but the errors related to the modal properties are assumed to be small.

The 3D solid models are based on 20-node iso-parametric brick elements with quadratic Lagrange interpolation of the displacements and full integration. The Abaqus models were implemented via Python scripting to allow easy modification of material properties and geometry. Further, the input files for Abaqus/Standard are directly transferable to FEMtools [24]. As explained in Section 5, this was later used for automatic model updating aimed at identification of the material properties. However, it should be noted that orthotropic material behaviour must be treated with care, because Abaqus and FEMtools order the material properties differently.

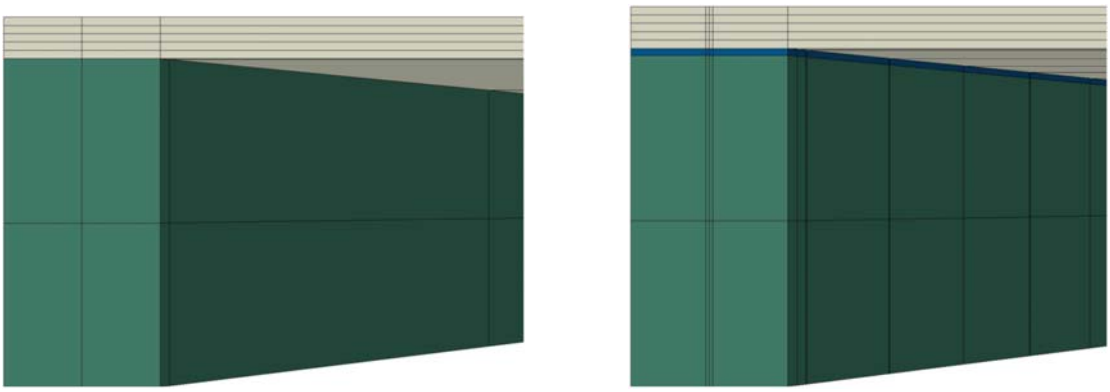

Figure 13: Configurations of the coupling between the beams and the plate in the 3D solid finite-element model. Left: Merged model with direct coupling of the beams to the plate. Right: Coupling via an artificial layer.

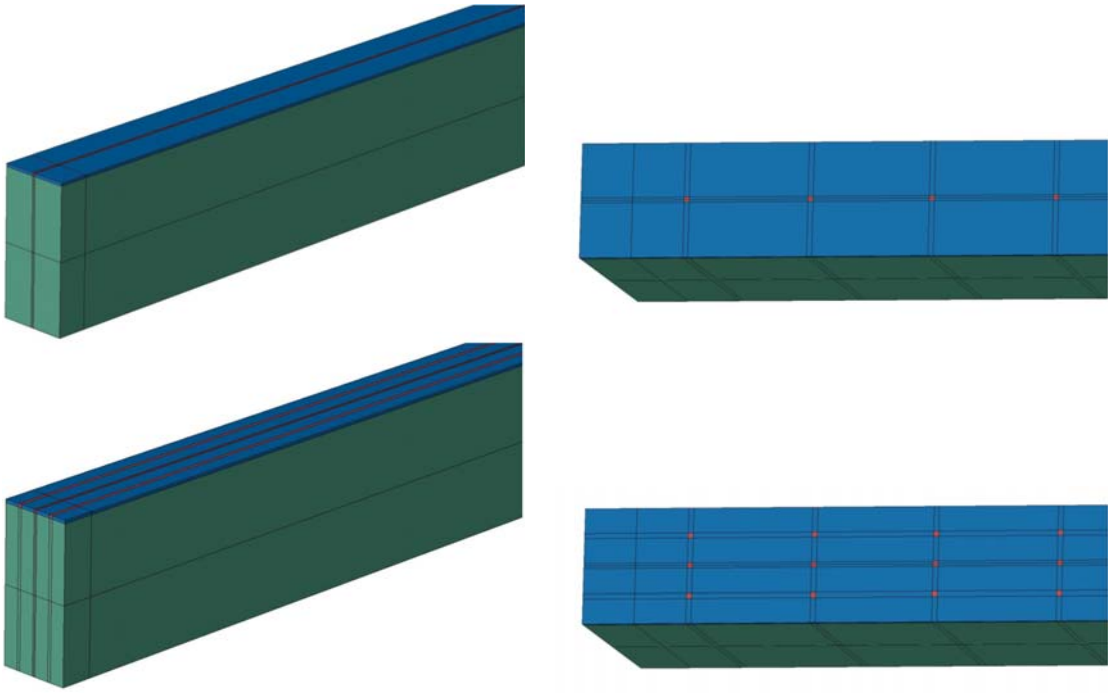

Figure 14: Modelling approaches for the screwed connections between the beams and the plate. "Line" couplings (left) and "point" couplings (right) for a single line of screws (top) or three lines of screws (bottom).

Different approaches to coupling of the beams and the plate were tested in the solid FE model. The simplest configuration merely introduced a full coupling by merging the beams with the plate. To allow a more realistic modelling of the coupling, a 2 mm thick artificial elastic layer was introduced in the remaining models, as illustrated in Figure 13. Based on a previous study by Dickow et al. [25], the layer was assumed to have a mass density of 450 kg/m^3, a Young's modulus of 4 MPa, and a Poisson's ratio of 0.05.

As shown in Figure 14, two strategies were used to model the screws: "line" couplings with 4 mm wide zones resembling the single lines of screws in Panels A–C or the three lines of screws in Panels D–F; "point" couplings with 4 mm × 4 mm zones at the positions of the individual screws. The material in the zones representing the screws was assumes to be steel with the mass density 7 850 kg/m^3, the Young's modulus 210 000 MPa, and the Poisson's ratio 0.30.

5 MODEL CALIBRATION AND UNCERTAINTIES

Based on the experimental tests, reported in Section 3, the FE models of Section 4 were calibrated by updating the material properties. The strategy was to first calibrate the models of the beams and plates separately and then to couple the various parts as suggested in Section 4 without additional modification of the properties. A comparison can then be made of the results obtained using the initial properties (see Tables 1–4) and the optimized values. The properties of the artificial coupling layer were not modified in this process, and as such the comparisons serve as a validation of the material properties and modelling approach for this layer.

Before the model calibration, a preliminary sensitivity study was performed to quantify the importance of each material property. The solid model of each part was employed for this analysis. In the following model calibration, only the material properties with significant influence on the eigenfrequencies were included as variables. This ensured a robust optimization at a relatively low computational cost while still exploiting close to the entire potential for fitting the models to the results of the experimental tests. In any case, the material in each beam, and in each ply of the boards, was assumed to be homogeneous.

For the beam with isotropic material behaviour, the Young's modulus is equally important for all modes, whereas Poisson's ratio only influences modes dominated by shear – since in this case $G = E/(2 + 2\nu)$. However, the isotropic beam models were found to provide a poor match to the test results with no possibility to fit more than the first four to five modes within a reasonable accuracy. Hence, only the orthotropic model was used for further analysis. Here, Figure 15 (left) shows the results of the sensitivity analysis. Clearly, the Young's modulus E_1 in the grain direction has a strong influence on four of the first five modes. Mode 4 is dominated by the shear moduli G_{12} and, especially, G_{13}. It is noted that this is the first torsional mode, which explains the weak dependence on E_1. In any case, none of the remaining six material properties have any significant impact, i.e. only E_1, G_{12} and G_{13} are important for the orthotropic beams.

For the plywood board, Figure 15 (right) shows the results of the sensitivity study. Interestingly, G_{12} is very important for Mode 1, and it also has a strong influence on Modes 3 and 5. Mode 1 is the first torsional mode of the board which lies at a frequency slightly below that of the first bending mode (Mode 2). For Modes 2–5, E_1 has the larger impact on the eigenfrequencies. A weak influence can be seen from E_2, G_{23} and ν_{12}, while the remaining properties have no or extremely little influence. However, it may be expected that G_{12} and G_{13} are important for the eigenfrequencies related to higher modes where shear in bending becomes pronounced.

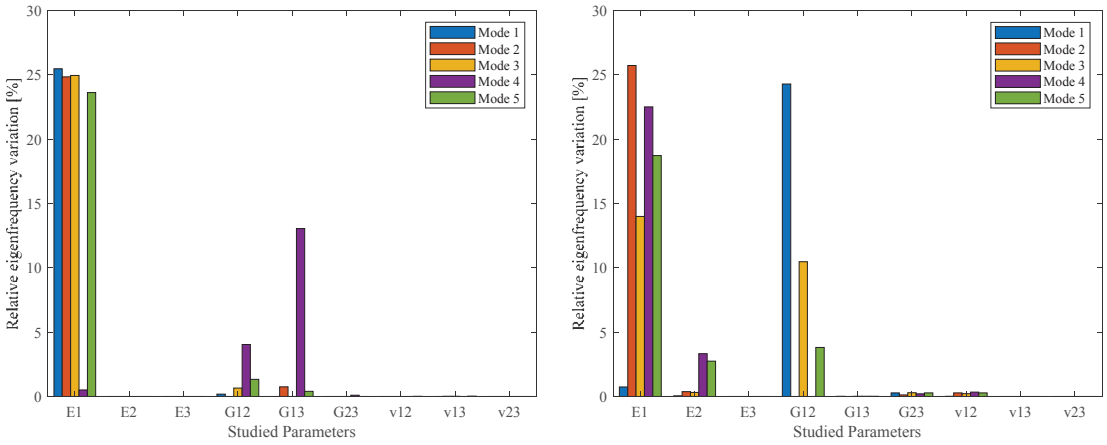

Figure 15: Change in the first five eigenfrequencies due to a variation of each material property by about ±25 % relatively to the initial values suggested for the beams in Table 2 (left) and for the plates in Table 4 (right).

The model updating was performed in FEMtools using, as input, the experimental results from ARTeMIS and the FE models from Abaqus. The initial values as well as the upper and lower bounds for the material properties given in Tables 2 and 4 were used. However, the mass densities found for each specimen using the scales were employed (see Subsection 3.4). As already mentioned, the isotropic beam models will not be analysed further. Likewise, the plate model with a single layer of orthotropic material will not be further regarded in the present analysis, although model updating showed that fair results could be achieved with this type of model for the first few modes of the individual plywood boards.

The model updating was performed based on a comparison of the eigenfrequencies f_i as well as the mode shapes $\{\boldsymbol{\Phi}_i\}$, using the Modal Assurance Criterion (MAC) [26]:

$$\mathrm{MAC}_{ij} = \frac{\left|\left\{\boldsymbol{\Phi}_i^{\mathrm{FE}}\right\}^H \left\{\boldsymbol{\Phi}_j^{\mathrm{EX}}\right\}\right|^2}{\left\{\boldsymbol{\Phi}_i^{\mathrm{FE}}\right\}^H \left\{\boldsymbol{\Phi}_i^{\mathrm{FE}}\right\} \left\{\boldsymbol{\Phi}_j^{\mathrm{EX}}\right\}^H \left\{\boldsymbol{\Phi}_j^{\mathrm{EX}}\right\}}. \tag{1}$$

Here *H* denotes the Hermitian of the vector, the superscripts FE and EX refer to "Finite-Element model" and "Experimental test", respectively, and the indices *i* and *j* refer to Modes *i* and *j*. A MAC value of (nearly) 1 implies that there is (almost) correspondence between the modal vectors for Mode *i* of the FE model and mode *j* of the experiment. This does not guarantee that the modes are (nearly) identical. For example, the related eigenfrequencies may be different, and the response at points that are not included as nodes in the vectors may deviate. On the other hand, if the MAC value is (close to) zero, it can be expected that the modes are inconsistent.

For each structural component, i.e. Beams 1–4 and Plates 1 and 2, the following updating procedure was applied:

- The nodes of the FE model (FE nodes) corresponding to the positions of the accelerometers (experimental nodes) were identified.
- The FE nodes and the experimental nodes were paired in FEMtools.
- The eigenmodes of the FE model and experiment were compared and the modes with MAC values of at least 60 % were included as basis for the model updating.
- A maximum of five iterations were performed to optimize the selected material properties.
- In each iteration, a normalized sensitivity matrix, $[\mathbf{S}]$, was determined, defining the dependence of each observed eigenfrequency on each of the material properties, e.g.,

$$S_{12} = \frac{\partial f_2}{\partial E_1}\frac{E_1}{f_2}. \tag{2}$$

  Here f_2 is the second eigenfrequency of the FE model and E_1 is the value of the Young's modulus in the grain direction of the considered beam or ply based on the previous iteration. See, for example, [17, 18] for further details.
- The change in the material properties was found as $\{\Delta\mathbf{P}\}_{k+1} = [\mathbf{S}]_k^{-1}\left(\left\{\mathbf{f}_k^{\mathrm{EX}}\right\} - \left\{\mathbf{f}_k^{\mathrm{FE}}\right\}\right)$.
- The material properties were updated as $\{\mathbf{P}\}_{k+1} = \{\mathbf{P}\}_k + \{\Delta\mathbf{P}\}_{k+1}$.
- If the difference between the eigenfrequencies of the experiment and the FE model was overall below a given threshold, or if the improvement from one iteration to the next was below a given tolerance, the iteration was terminated even if five iterations had not been reached. The standard values EPS1 = 0.01 and EPS2 = 0.001 were used in FEMtools.

It is noted that the process corresponded to a gradient-based optimization procedure, using a least-squares approach, since there were more eigenfrequencies than material properties.

Table 8 and Figure 16 show the results of the model calibration for the beams. Here, only E_1, G_{12} and G_{13} have been used as variables in the optimization. Compared to the initial values, Young's in the grain direction, E_1, was reduced for Beams 1, 3 and 4, whereas an increase was necessary for Beam 2 in order to provide an optimal fit to the experiment. For all beams, the shear moduli G_{12} and G_{13} were reduced significantly. With reference to Figure 16, the solid FE models developed in Abaqus and the Timoshenko beam FE model implemented in MATLAB provided very similar results for the first seven modes when using the initial values of the material properties. However, the eigenfrequencies deviated about 10 % from the measured values. For Mode 8, there is a large discrepancy between the results of the two FE models. It is noted that this mode occurred at around 800 Hz (see Table 5), i.e. at a very high frequency. After the model updating with the use of FEMtools, a much better fit was obtained. It was thus possible to fit the first eight eigenfrequencies within a relative error of 0–5 %, compared to the experiments for the respective beams. It should be mentioned that an optimization of the MATLAB model was achieved by the introduction of a torsional shear modulus, $G_T = \alpha(G_{12} + G_{13})$. With a proper tuning of the parameter α, a good match of the MATLAB model with the Abaqus model could be obtained, regarding the torsional modes that were not captured experimentally.

Table 9 and Figure 17 show the results of the model updating for the two plywood boards. Poor results were achieved with the initial values of the material properties, but after the model updating with FEMtools, a fair fit was obtained for the first ten modes. It can be observed that the five-layer solid model developed in Abaqus and the Mindlin-shell-element model developed in MATLAB provide similar results both before and after the updating process. Slightly better results were obtained for Plate 2, compared to Plate 1, and as mentioned above, Plate 1 could

Property		Initial value	Beam 1	Beam 2	Beam 3	Beam 4	Average
E_1	(MPa)	12 440	9900	14 256	10 360	10 810	11 332
G_{12}	(MPa)	1 136	635	679	582	531	607
G_{13}	(MPa)	1 136	631	592	815	809	711

Table 8: Model updating of beams with orthotropic material behaviour.

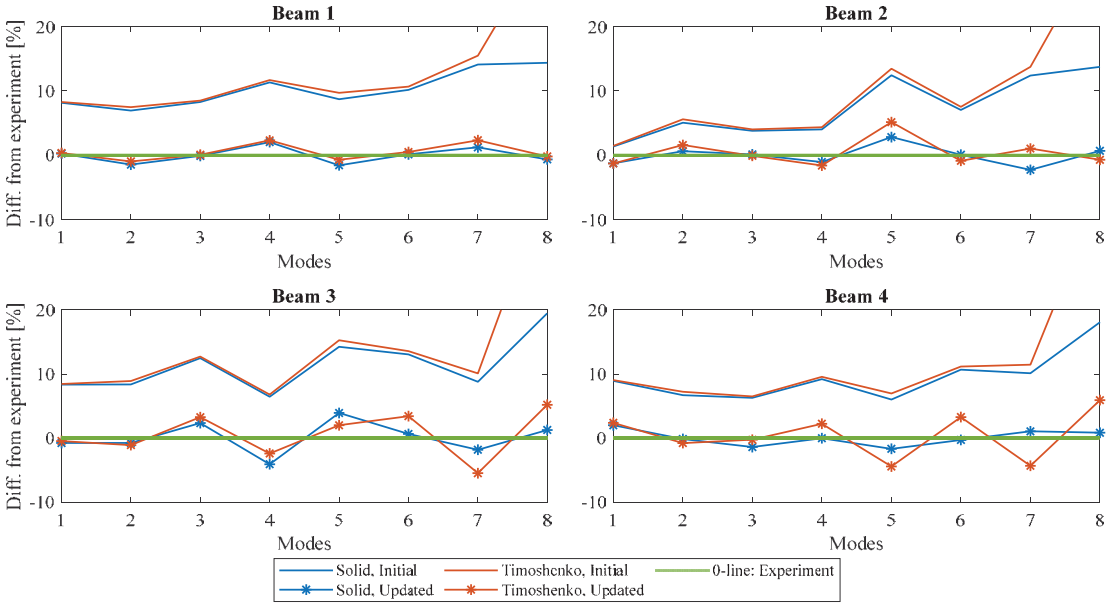

Figure 16: Eigenfrequencies for Modes 1–8 of the beams – deviation from the test results.

		Initial value	Plate 1	Plate 2	Average
E_1	(MPa)	16 300	9 396	8 487	8 942
E_2	(MPa)	570	511	1 031	771
G_{12}	(MPa)	680	1 178	932	1 055

Table 9: Model updating of plywood boards with five-layers of orthotropic material.

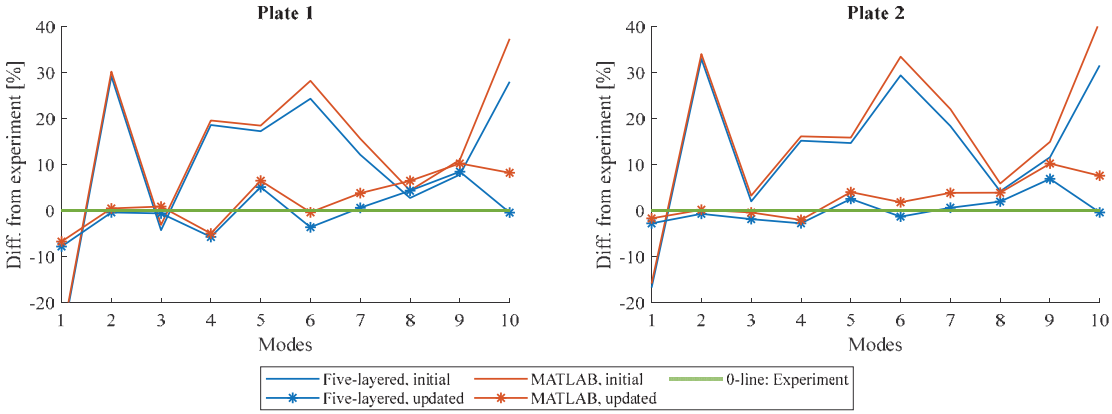

Figure 17: Eigenfrequencies for Modes 1–10 of the plywood boards – deviation from the test results.

not be used in the subsequent assembly of the floor panels, since it was twisted due to uncontrolled variations of the environmental conditions (temperature and humidity) in the laboratory.

Finally, the FE models of the assembled floor panels were compared with the experimental results. Figure 18 shows the results for Panels A–F, based on three different sets of material properties:

- The initial values based on a qualified guess and literature study (see Tables 2 and 4)
- The average updated values of the material properties (see Tables 8 and 9, the last columns)
- The exact updated values of the material properties for each of the structural components (see Tables 8 and 9, the columns for Beams 1–4 and Plate 1).

The deviations from the test results are quantified in terms of the Normalized Relative Frequency Difference (NRFD) [12]:

$$\mathrm{NRFD}_i = \frac{\left| f_i^{\mathrm{FE}} - f_i^{\mathrm{EX}} \right|}{f_i^{\mathrm{EX}}} \cdot 100\ \%\,, \tag{3}$$

where f_i^{FE} and f_i^{EX} are the eigenfrequencies of Mode i obtained by FE modelling and experimental testing, respectively.

The general trend in Figure 18 is that the NRFD is about 30 % for the models employing the initial values of the material properties. For Panel A, the merged FE model provides a very poor result. This was to be expected, given that Panel A has the weakest coupling of the beams and the plate with only a single line of screws for each beam and with almost 200 mm distance between the screws. However, even when modelling the connection between the beams and the plate more realistically, the initial values of the properties lead to erroneous results.

A significant improvement in the accuracy of the FE models was achieved by using the average material properties obtained by model updating. Except for three modes of Panel A, the first ten eigenfrequencies of all the considered panel configurations have an NRFD below 15 % when the beams are merged to the plate within the FE models. When the connections were modelled appropriately, NRFD values below 5 % were obtained with the average values

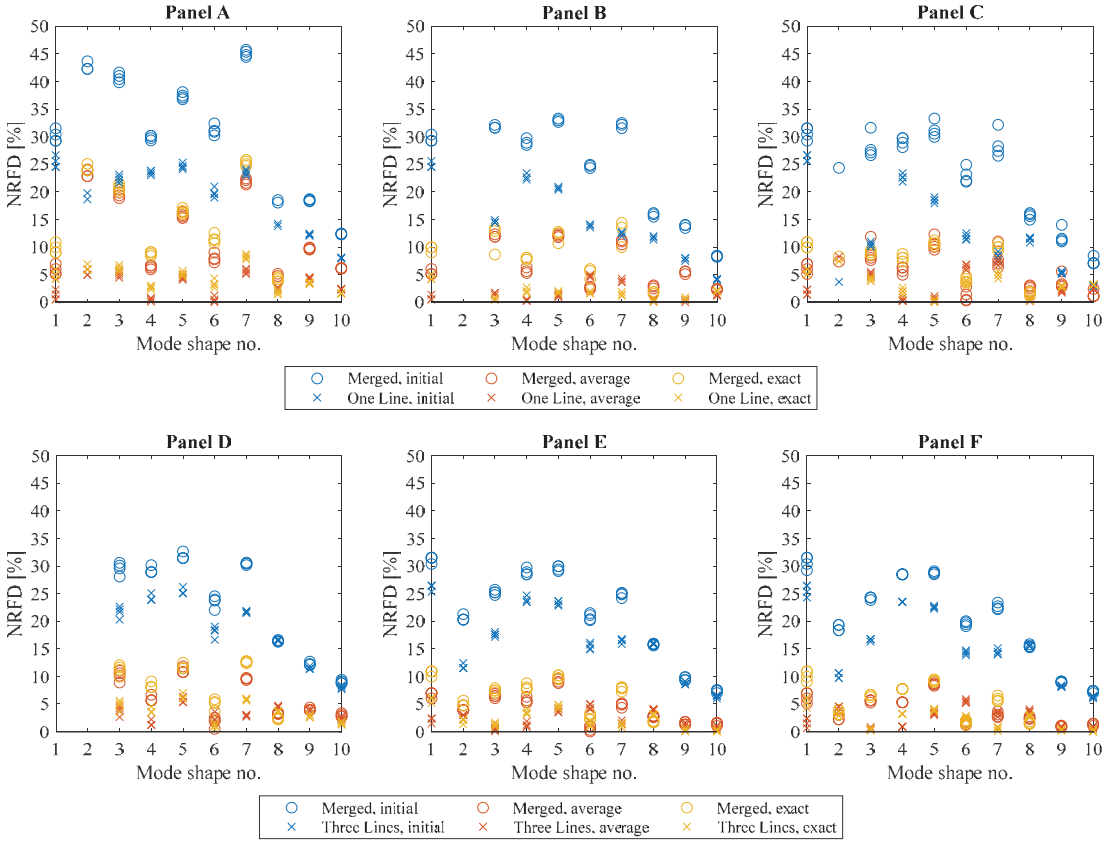

Figure 18: Normalized Relative Frequency Difference (NRFD) plots for the solid FE models of Panels A–F.

of the material properties. Interestingly, no significant improvement could be achieved by using the exact updated values for the individual structural components. For some of the modes, in some of the panels, the average material properties provided the better match, and for the other combinations of modes and panels, the exact updated values resulted in a more accurate fit.

As an alternative to the solid models of the floor panels, a structural FE model based on Timoshenko beam and Mindlin shell elements was implemented in MATLAB. The coupling of the beam and shell elements was introduced in terms of Lagrange multipliers, assuming a rigid link between the nodes of the beams and the nodes of the shell to which they were tied. Kinematically, this introduces a severe constraint, since the beams cannot rotate relative to the shell. Hence, the structural FE model was only able to produce useful results for Panels D–F. For Panels A–C (especially Panels A–B) with the single line of screws coupling each beam to the board, some modes of vibration could not be represented by the MATLAB model.

6 CONCLUSIONS AND SUGGESTIONS FOR FURTHER RESEARCH

A mock-up of a single-leaf floor panel consisting of four timber beams and a plywood board was analysed. An output-only modal analysis (OMA) was conducted for the individual structural components, and it was found that a significant variation in the eigenfrequencies can exist for similar beams coming from the same badge. One of the tested beams was about 25 % heavier than the other beams, and the difference in stiffness was even higher. Hence, some of the eigenfrequencies of the beam with the larger density were higher than the corresponding eigenfrequencies of the other beams.

Three-dimensional finite-element (FE) models were developed in Abaqus and MATLAB, in both cases assuming orthotropic material properties of the wood and modelling the plywood with five layers of the same material. In Abaqus, a solid model was used for the plywood boards and the beams, whereas the MATLAB models were based on structural finite elements employing Timoshenko beam theory and Mindlin plate theory. It was found that only three material properties, E_1, G_{12} and G_{13}, have significant influence on the modal properties of the beams, and only E_1, E_2 and G_{12} are important for the plywood boards.

The results of the experiments and the finite-element models developed in Abaqus were used as input for a model update utilizing the software FEMtools. It was possible to obtain a good match of the first eight eigenfrequencies of the individual beams and the first ten eigenfrequencies of the individual plywood boards within five iterations of the gradient-based updating procedure. Post analysis showed that the MATLAB models provided almost equally accurate results for the individual components when using the updated material properties.

Six configurations of the assembled floor were considered. In all cases, the plywood board was fastened to the beams by screws. Three different distances between the screws in the longitudinal direction were considered, and either one single or three lines of screws were used per beam. The panels were all analysed by OMA, and the panel with single lines of screws and the largest distance between the screws was found to have significantly lower eigenfrequencies than the panel with shorter distance between the screws and three lines of screws per beam.

The experimental results for the floor panels were used to validate the FE models of the panels. It was found that the FE models performed poorly when the plywood board was simply merged with the beams within the models. When introducing an artificial soft elastic layer and a model of the screws into the FE models, higher accuracy could be obtained. A further improvement was achieved by using the updated material properties. However, no conclusion could be made whether the exact values extracted for each individual component should be used, or if average values based on all beams or plates should be employed. In any case, the relative error between the eigenfrequencies of the mock-ups and the FE models of the floor panels were about 0–5 %.

It was found that an FE model based on structural finite elements, i.e. beam and shell elements, could not represent the response of the panels with only single lines of screws and the longer distances between the screws. With a direct coupling between the nodes of the beams and those of the plate, the link is too rigid. One idea for future research is to develop a model with a flexible link between the beams and the plate, using the existing OMA results to calibrate the translational and rotational springs of this coupling.

Further, the present analyses all assumed that the material in each beam is homogeneous, and that the material in all layers of the plywood boards is identical and homogeneous within each layer. Obviously, wood is a heterogeneous material with significant variations of the properties from one position to another. This was demonstrated, for example, by the variation in material density between the four beams in this study. Future research on the heterogeneity of timber and plywood, and its impact on the modal properties of floor panels, is proposed. Identification based on the mode shapes, not only the eigenfrequencies, should be performed.

ACKNOWLEDGMENTS

The authors would like to thank Peter Olsen and Jørgen Holm, Aarhus School of Engineering, Aarhus University, as well as Thomas Kabel, Department of Engineering, Aarhus University, for their involvement in various parts of the research project that was funded by the university.

REFERENCES

[1] M.G. Smith, I. Croy, O. Hammar, M. Ögren, K.P. Waye, Nocturnal vibration and noise from freight trains impacts sleep, Proc. Meet. Acoust. 19 (2013). https://doi.org/10.1121/1.4800407.

[2] T. Münzel, F.P. Schmidt, S. Steven, J. Herzog, A. Daiber, M. Sørensen, Environmental Noise and the Cardiovascular System, J. Am. Coll. Cardiol. 71 (2018) 688–697. https://doi.org/10.1016/j.jacc.2017.12.015.

[3] E. Pedersen, City dweller responses to multiple stressors intruding into their homes: Noise, light, odour, and vibration, Int. J. Environ. Res. Public Health. (2015). https://doi.org/10.3390/ijerph120303246.

[4] P. Persson, C. Frier, L. Pedersen, L.V. Andersen, L. Manuel, Influence of uncertain parameters on modal properties of wood floors, in: A. Zingoni (Ed.), Adv. Eng. Mater. Struct. Syst. Innov. Mech. Appl., CRC Press, Taylor & Francis Group, London, London, 2019.

[5] H.U. Lim, L. Manuel, P. Persson, L.V. Andersen, A surrogate model to describe uncertainties in wood floor modal frequencies, in: A. Zingoni (Ed.), Adv. Eng. Mater. Struct. Syst. Innov. Mech. Appl., CRC Press, Taylor & Francis Group, London, London, 2019.

[6] L. Pedersen, C. Frier, L. Andersen, Flooring-systems and their interaction with usage of the floor, in: Conf. Proc. Soc. Exp. Mech. Ser., 2017. https://doi.org/10.1007/978-3-319-54777-0_25.

[7] C. Frier, L. Pedersen, L.V. Andersen, Non-structural Masses and Their Influence on Floor Natural Frequencies, in: S. Pakzad (Ed.), Dyn. Civ. Struct. Vol. 2. Conf. Proc. Soc. Exp. Mech. Ser., Springer, Cham, 2019: pp. 59–65. https://doi.org/10.1007/978-3-319-74421-6_9.

[8] C. Frier, L. Pedersen, L.V. Andersen, Floor Vibrations and Elevated Non-structural Masses, in: 2020: pp. 103–110. https://doi.org/10.1007/978-3-030-12115-0_13.

[9] L.V. Andersen, C. Frier, L. Pedersen, P. Persson, Influence of Furniture on the Modal Properties of Wooden Floors, in: 2020: pp. 197–204. https://doi.org/10.1007/978-3-030-12075-7_22.

[10] L.V. Andersen, C. Frier, L. Pedersen, Probabilistic Analysis of Modal Properties for Floor Systems with Uncertain Support Conditions, in: S. Pakzad (Ed.), Dyn. Civ. Struct. Vol. 2. Conf. Proc. Soc. Exp. Mech. Ser., Springer, Cham, 2019: pp. 67–75. https://doi.org/10.1007/978-3-319-74421-6_10.

[11] L.V. Andersen, P.H. Kirkegaard, Vibrations in a multi-storey lightweight building structure: Influence of connections and nonstructural mass, in: Res. Appl. Struct. Eng. Mech. Comput. – Proc. 5th Int. Conf. Struct. Eng. Mech. Comput. SEMC 2013, 2013.

[12] J. Negreira, A. Sjöström, D. Bard, Low frequency vibroacoustic investigation of wooden T-junctions, Appl. Acoust. 105 (2016) 1–12. https://doi.org/10.1016/j.apacoust.2015.11.016.

[13] G. Kouroussis, L. Ben Fekih, T. Descamps, Assessment of timber element mechanical properties using experimental modal analysis, Constr. Build. Mater. (2017). https://doi.org/10.1016/j.conbuildmat.2016.12.081.

[14] O. Flodén, K. Persson, G. Sandberg, A multi-level model correlation approach for low-frequency vibration transmission in wood structures, Eng. Struct. 157 (2018) 27–41. https://doi.org/10.1016/J.ENGSTRUCT.2017.11.062.

[15] P. Persson, O. Flodén, Towards uncertainty quantification of vibrations in wood floors, in: Proc. 25th Int. Congr. Sound Vib., Hiroshima, Japan, 2018: pp. 1–8.

[16] R. Brincker, C.E. Ventura, Introduction to Operational Modal Analysis, 2015. https://doi.org/10.1002/9781118535141.

[17] E. Orlowitz, A. Brandt, Comparison of experimental and operational modal analysis on a laboratory test plate, Meas. J. Int. Meas. Confed. (2017). https://doi.org/10.1016/j.measurement.2017.02.001.

[18] C. Gerrand, The equivalent orthotropic elastic properties of plywood, Wood Sci. Technol. 21 (1987) 335–348. https://doi.org/10.1007/BF00380201.

[19] K.A. Dickow, Prediction of Noise Transmission in Lightweight Building Structures, Department of Civil Engineering, Aalborg University, 2014.

[20] SignalExpress 2015 version 15.0.0, National Instruments, Austin, Texas, USA, 2015.

[21] DAQ Assistant version 7.0.0, National Instruments, Austin, Texas, USA, 2019.

[22] ARTeMIS Modal Pro version 6.0.2.2, Structural Vibraton Solutions, Aalborg, Denmark, 2019.

[23] MATLAB version 9.6.0.1072779 (R2019a), Mathworks, Natick, Massachusetts, USA, 2019.

[24] FEMtools version 4.1.0, Dynamic Design Solutions, Leuven, Belgium, 2019.

[25] K.A. Dickow, P.H. Kirkegaard, L.V. Andersen, An evaluation of test and physical uncertainty of measuring vibration in wooden junctions, in: Int. Conf. Noise Vib. Eng. 2012, ISMA 2012, Incl. USD 2012 Int. Conf. Uncertain. Struct. Dyn., 2012.

[26] R.J. Allemang, The modal assurance criterion - Twenty years of use and abuse, Sound Vib. 37 (2003) 14–23.

[27] T. Lauwagie, E. Dascotte, Layered Material Identification using Multi-Model Updating, in: Proc. 3rd Int. Conf. Struct. Dyn. Model. – Test, Anal. Correl. Valid. – Madeira Island, Port., 2002.

[28] T. Lauwagie, Vibration-based methods for the identification of the elastic properties of layered materials, KU Leuven, 2005.

EURODYN 2020
XI International Conference on Structural Dynamics
M. Papadrakakis, M. Fragiadakis, C. Papadimitriou (eds.)
Athens, Greece, 23–26 November 2020

COMPARATIVE EVALUATION OF THE METHODS PROPOSED BY THE GREEK CODE FOR STRUCTURAL INTERVENTION (KAN.EPE.) FOR THE ESTIMATION OF CURVATURE DUCTILITY

Konstantinos E. Morfidis[1], Christos Z. Karakostas[2] and Sotiria P. Stefanidou[3]

[1]Assistant Researcher ITSAK-EPPO
Dassyliou Street, Eleones, 55535 Pylaia, Thessaloniki, Greece
kmorfidis@itsak.gr

[2]Research Director ITSAK-EPPO
Dassyliou Street, Eleones, 55535 Pylaia, Thessaloniki, Greece
christos@itsak.gr

[3]Postdoctoral Researcher ITSAK-EPPO
Dassyliou Street, Eleones, 55535 Pylaia, Thessaloniki, Greece
sotiria.stefanidou@gmail.com

Keywords: R/C structures, Ductility of R/C members, Structural Intervention, KAN.EPE.

Abstract. *The ductility factor in terms of R/C cross-sections' curvatures ($\mu_{1/r}$ or μ_{ϕ}) possesses a significant role in the framework of the Greek code for structural intervention (KAN.EPE.). This factor is used for the classification of the verification methods in either those which are expressed in terms of forces or deformations, for the calculation of the required mechanical volumetric ratio of the confining reinforcement in case of interventions aiming to increase the local ductility of R/C members and for the estimation of the ductility in terms of chord rotations μ_{θ}. The factor μ_{θ} is, according to KAN.EPE., the parameter which better describes the inelastic deformations at the ends of R/C members where the flexural deformations coexist with shear deformations and rotations of end-sections due to anchorage slip of the reinforcement bars. Due to the fact that $\mu_{1/r}$ and μ_{θ} factors are crucial for the evaluation of R/C members' seismic performance, KAN.EPE. provides different methodologies for their estimation. In the present paper a primary comparative evaluation of them is attempted, with emphasis on the investigation of the equation that is proposed by KAN.EPE. for the relation between μ_{θ} and $\mu_{1/r}$. For this investigation, a R/C column with rectangular cross-section and different concrete grades, and levels of longitudinal and transverse reinforcement is examined. The results of the analyses performed herein can be characterized only as indicative for the range of the values of $\mu_{1/r}$ and μ_{θ} factors which can be extracted by the methods proposed by KAN.EPE. Thus, the results of the present paper provide a motivation for further investigations about more proper alternative relations between the $\mu_{1/r}$ and μ_{θ} factors.*

1 INTRODUCTION

In the provisions of the code for structural interventions (KAN.EPE.) [1] which is applied in Greece for the evaluation of seismic capacity and the interventions of Reinforced Concrete (R/C) buildings, the seismic performance of the linear R/C structural members which are characterized as "quasi-ductile" is verified in terms of deformations, in case of inelastic analysis procedures. Additionally, one of the potential types of interventions for the critical regions of linear R/C members (when the target is the improvement of their capacity against flexure with axial force) is the increase of their local ductility. In both aforementioned cases, the chord rotations in the critical regions of the linear R/C members at flexural yield (θ_y) and failure (θ_u) must be estimated. To this end, KAN.EPE. recommends equations (derived through regression analyses of validated experimental results) which lead to the required estimation of the values of θ_y and θ_u and subsequently the estimation of the ductility in terms of chord rotations (μ_θ). Based on the available local ductility μ_θ KAN.EPE. classifies the failure mechanisms as "quasi-ductile" or "brittle" ones.

Another significant parameter which is used in KAN.EPE. for the assessment and redesign of linear "quasi-ductile" R/C structural members is the curvature ductility $\mu_{1/r}$ (the symbol μ_φ is also used for the same parameter). More specifically, $\mu_{1/r}$ is used for the classification of failure mechanisms as "quasi-ductile" or "brittle" ones, for the determination of the required mechanical volumetric ratio of confining hoops in the critical regions of the linear R/C members (where the increase of the local ductility is required), and for the verification of the selected values for the local R/C members' ductility "m". Thus, KAN.EPE. provides alternative methods for the calculation of $\mu_{1/r}$.

It must also be stressed that according to KAN.EPE. the relation between μ_θ and $\mu_{1/r}$ is used for the estimation of the available plastic chord rotation in critical regions of R/C structural members after the interventions, as well as the for the determination of the appropriate mechanical volumetric ratio of confining hoops when the chord rotations are utilized to define the targeted performance level.

The scope of the present investigation is a primary comparative evaluation of the different methodologies which KAN.EPE. proposes for the estimation of $\mu_{1/r}$, with emphasis on the equation that is proposed for the relation between μ_θ and $\mu_{1/r}$. To this end, a R/C column with rectangular cross-section and different concrete grades, and levels (mechanical volumetric ratios) of longitudinal and transverse reinforcement was used.

2. BRIEF PRESENTATION OF THE PROVISIONS OF KAN.EPE. ABOUT THE ESTIMATION OF THE DUCTULITY OF R/C MEMBERS

It is well-known that in the framework of earthquake resistance design of new R/C structures, as well as for the seismic evaluation of existing ones, the estimation of the ductility of R/C members (i.e. their ability to deform plastically without significant loss of strength) is a process of paramount importance. Generally, the ductility is defined in terms of displacements ($\mu_\delta=\delta_u/\delta_y$), rotations of members' ends ($\mu_\theta=\theta_u/\theta_y$) and curvatures of cross-sections ($\mu_{1/r}=\varphi_u/\varphi_y$), (e.g. [2], [3]). Recognizing this fact, KAN.EPE. provides (see comments of §7.1.2.1) that for the critical failure mechanism in crucial regions of structural members due to bending moments (with or without axial force) the parameters which are appropriate for the simulation of their mechanical behavior are the bending moments (M) as stress measure and the curvatures 1/r as deformation measure. However, theoretical and experimental studies indicate that especially in case of R/C members' crucial regions when the inelastic behavior is controlled by flexure (i.e. bending moments with or without axial force) the parameter which better describes their deformation is the chord rotation "θ" at the ends (see KAN.EPE. §7.1.2.1 com-

ments). This is based on the fact that in R/C elements the flexural deformations coexist with shear deformations and rotations of end-sections due to anchorage slip of the reinforcement bars in the region of their ends (e.g. [4], [5]). The definition of the chord rotation θ_{ch} of a R/C member is illustrated in Fig. 1. Therefore, in Chapter 7 KAN.EPE. provides equations for the estimation of the chord rotation at flexural yield (θ_y), as well as at flexural failure (θ_u). Using these equations one can estimate the ductility of R/C members in terms of chord rotation ($\mu_\theta=\theta_u/\theta_y$).

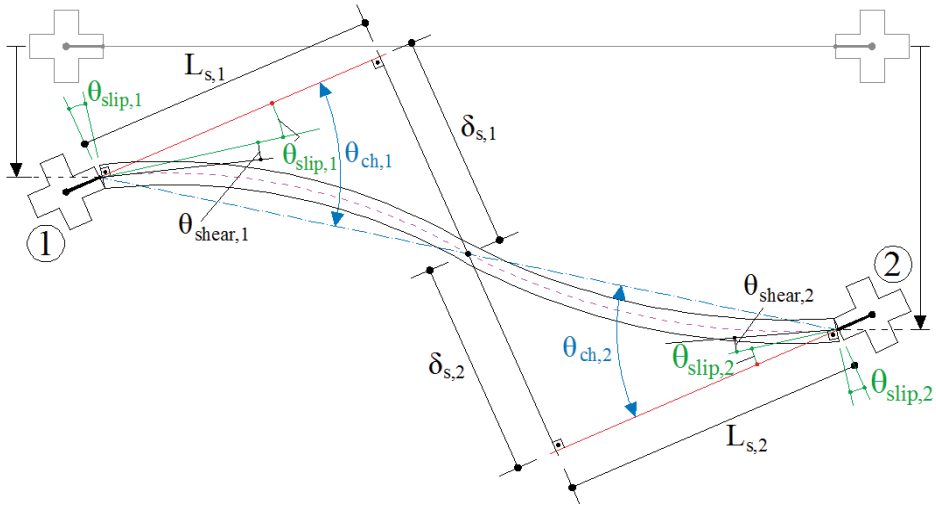

Figure 1: Definition of the chord rotation θ_{ch} at the ends of a R/C member

However, despite the fact that the utilization of the chord rotations at the ends of R/C members is considered as more efficient for the evaluation of their inelastic flexural behavior, KAN.EPE. in §8.2.3 (where provisions about the interventions with the objective to increase the local ductility are given) states that the required mechanical volumetric ratio of the confining reinforcement must be estimated through a selected target value of the curvature ductility $\mu_{1/r,req}$ (§8.2.3c) for all the critical cross-sections of primary members. Besides, in §8.2.3d it is stated that when the redesign objective is expressed in terms of required maximum permitted values of chord rotations θ_d, then the corresponding curvature ductility $\mu_{1/r}$ (which is used for the calculation of the confining reinforcement) can be estimated using reliable relations between μ_θ and $\mu_{1/r}$. To this end, it is permitted in the comments of §8.2.3d the utilization of the Eq. (1):

$$\mu_{1/r} = 3\cdot\mu_\theta - 2 \tag{1}$$

According to the comments of §8.2.3d, the values of μ_θ ($=\theta_u/\theta_y$) in Eq. (1) are calculated on the basis of the skeleton behavior diagram of Appendix 4.4 (Fig. 2).

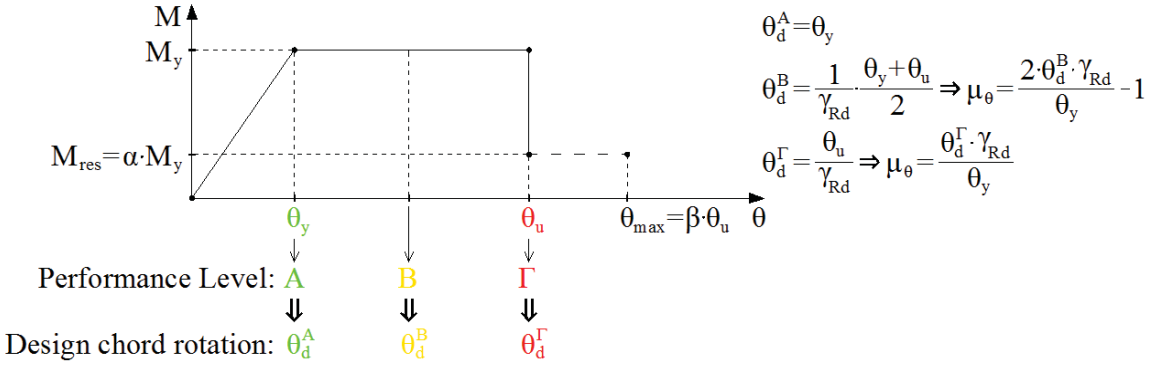

Figure 2: Calculation of the design values of θ for the three performance levels proposed by KAN.EPE.

Eq. (1) is also proposed (solved for μ_θ) in the comments of §6.5 for the approximative estimation of the available plastic chord rotation in the critical regions of R/C members after the required interventions (according to the comments of §6.5, μ_θ is approximately equal to ductility in terms of displacements μ_δ, i.e. $\mu_\theta \cong \mu_\delta$).

The available curvature ductility $\mu_{1/r}$ is also used for the choice of the proper verification method. The verification methods are classified in methods which are expressed in terms of forces or deformations. This classification is based on the anticipated type of members' failure (ductile or brittle). More specifically, in §4.1.4iii KAN.EPE. states that if the available ductility $\mu_{1/r}$ is greater than 3.0, then the members' behavior is characterized as "quasi-ductile", and the proper verification method in this case is expressed in terms of deformations.

Obviously, the estimation of the curvature ductility $\mu_{1/r}$ is of great interest within the framework of KAN.EPE. Therefore, the following methods are proposed for its calculation:

- Using the cross-sections' moment-curvature (M-1/r) diagrams (§6.4, see Fig. 3). The sequence of the steps which should be performed is described in §6.4b (a modified sequence for the case in which the member's ductility is achieved through external confinement using steel components or FRP is presented in §6.4c). However, the calculation of the (M-1/r) diagrams requires the utilization of cross-sections' analysis dedicated software.

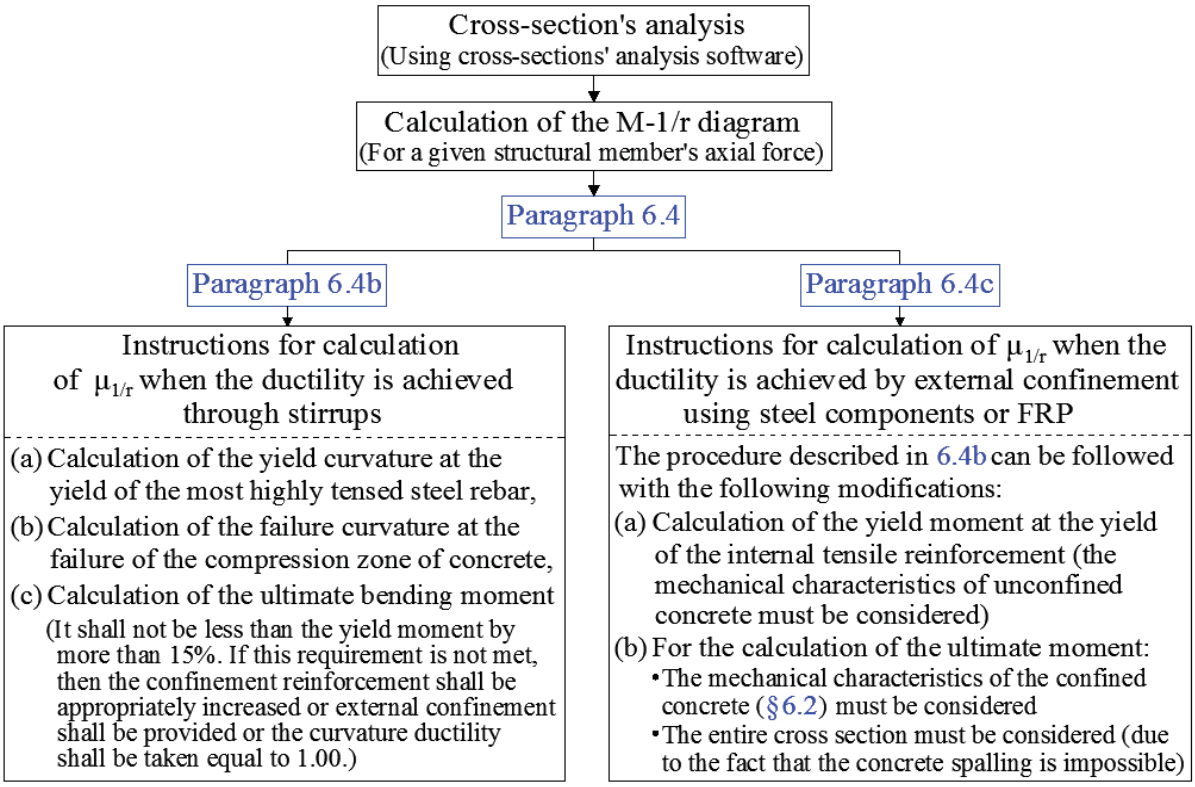

Figure 3: The provisions given by KAN.EPE. for the estimation of $\mu_{1/r}$ using the M-1/r diagrams

- Utilizing the φ_u and φ_y values which can be calculated using the provisions of §7.2.4 and §7.2.2 respectively (see comments of §6.4b). In these paragraphs it is stated that the calculation of φ_y and φ_u can be optionally accomplished using the methods that are given in Appendices 7A and 7E. These methods are based on specific assumptions and for this reason are not always applicable. It must be noted that regarding the calculation of φ_y, approximate semi-empirical expressions are also given in Appendix 7A.
- Using approximative (but reliable) closed-form expressions from the literature (comments of §6.4). As an example, KAN.EPE. recommends the expression:

$$\mu_{1/r} = \frac{f_{cc}}{f_c} \cdot \frac{\lfloor \varepsilon_{cu,c} - (\varepsilon_{cc}/3) \rfloor}{1.75 \cdot \nu \cdot \varepsilon_{sy}} \text{ with } (\varepsilon_{cu,c} \geq 0.004) \quad (2)$$

Where: f_{cc} and f_c are the strength of the confined and the unconfined concrete respectively, $\varepsilon_{cu,c}$ is the compressive failure strain of the confined concrete in the cross-section's core, ε_{cc} is the compressive strain of concrete which corresponds to the strength of the confined concrete f_{cc}, ε_{sy} is the yield strain of the longitudinal rebars' steel, and ν is the normalized axial force.

Eq. (2) is applied to the spalled cross-section in case of confinement through stirrups or continuous steel laminates and to the entire cross-section in case of confinement through steel cage, jacket of FRP. In the latter case Eq. (2) takes the following form:

$$\mu_{1/r} = \frac{f_{cc}}{f_c} \cdot \frac{\varepsilon_{cu,c}}{2.6 \cdot \nu \cdot \varepsilon_{sy}} \quad (3)$$

Figure 4 illustrates the methods for the estimation and the applications which are provided by KAN.EPE. for the curvature ductility $\mu_{1/r}$.

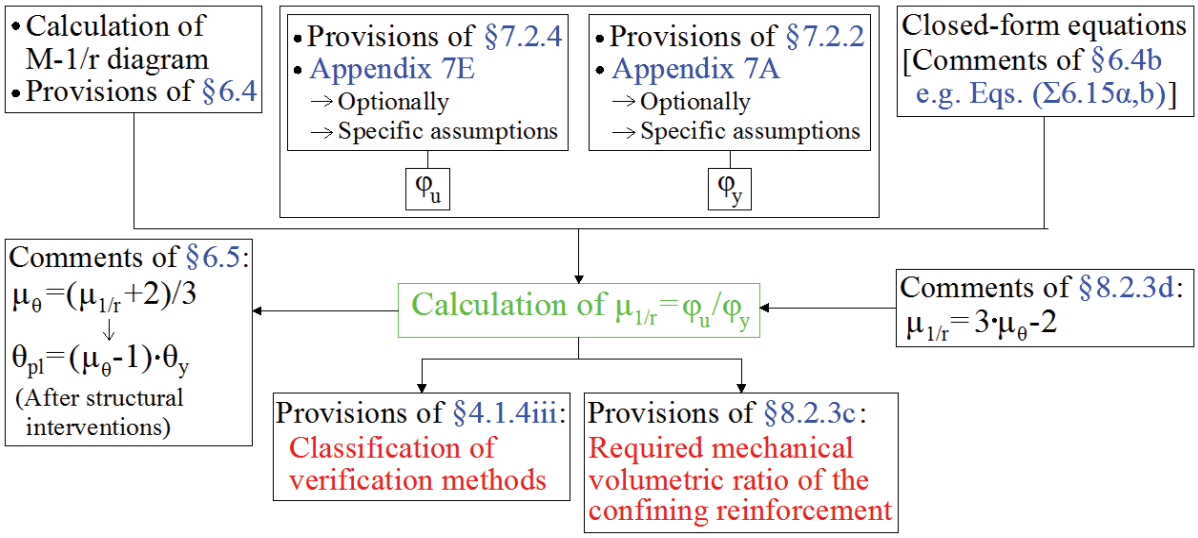

Figure 4: Ductility $\mu_{1/r}$ – methods for estimation and the corresponding applications proposed by KAN.EPE.

3. PARAMETRIC INVESTIGATIONS

3.1 Data, details and description of the parametric investigations

In order to evaluate the different procedures which are proposed by KAN.EPE. for the estimation of the curvature ductility $\mu_{1/r}$, a R/C column with rectangular cross-section and different characteristics regarding the concrete grade as well as the longitudinal and transverse reinforcement was used. Figure 5 illustrates the data of the examined column. The clear length of the column was taken equal to 3m, whereas as construction year 1990 was considered.

It must be noted that the assumed stress-strain diagram for the confined concrete was based on the model which KAN.EPE. provides in §6.2.1. The corresponding diagram for the unconfined concrete was based on the model presented in EN1992-1-1 [6]. As regards the assumed stress-strain diagram for the steel of rebars and stirrups, the model which is proposed in Appendix 7E was considered. The combination of the different assumptions for the concrete grades, the longitudinal reinforcement and the transverse reinforcement led to 64 different

analysis cases. For each case the curvature ductility $\mu_{1/r}$ and the chord rotation ductility μ_θ were calculated for 18 values of column's normalized axial force between ν=0.0 and ν=0.85.

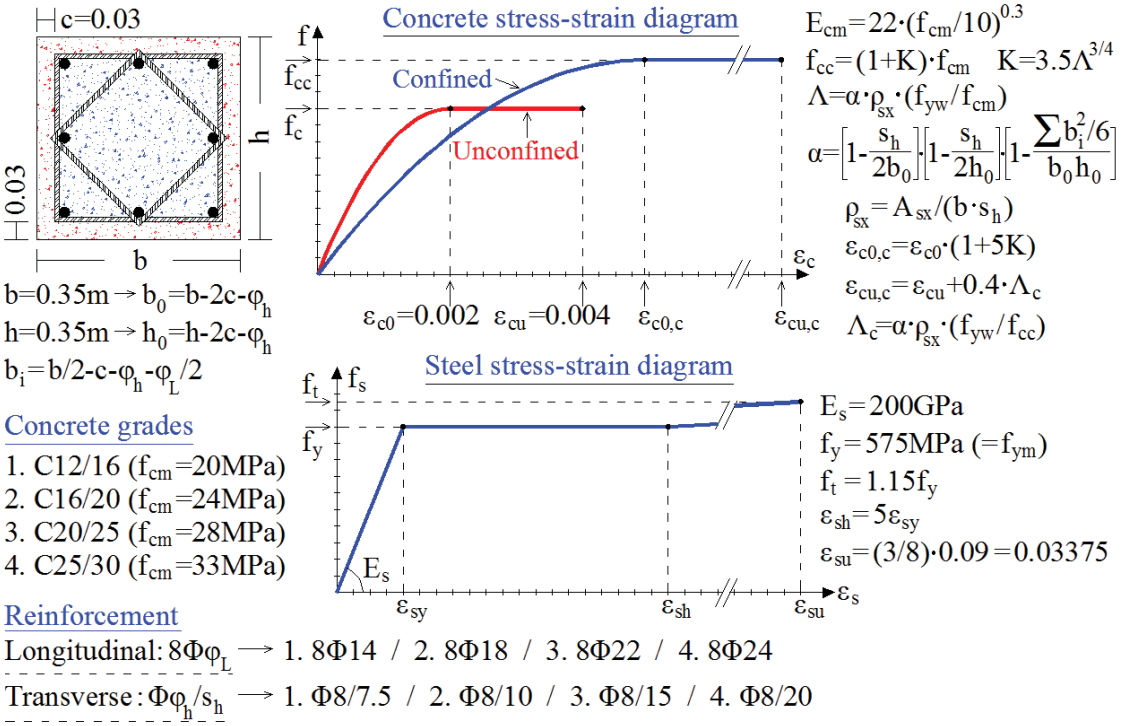

Figure 5: The different cases and the corresponding parameters which are considered in the investigation

Regarding the M-1/r diagrams, two different approaches were followed (Fig. 6):

- Consideration of a bi-linearized equivalent elasto-plastic diagram which results from the analytically evaluated (through cross-section analysis) curve assuming a horizontal branch after the effective yield curvature $\varphi_{y,eff}$ (Fig. 6a). In this case the ultimate moment M_u is taken as equal to the effective yield moment $M_{y,eff}$. It also must be noted that in this case M_u and $\varphi_{y,eff}$ are calculated using the "equal areas" rule.
- Consideration of a bi-linearized equivalent elasto-plastic diagram which results from the analytically evaluated (through cross-section analysis) curve assuming a sloping branch after the effective yield curvature $\varphi_{y,eff}$ (Fig. 6b). The ultimate moment M_u is taken as equal to the ultimate moment evaluated by the cross-section analysis. In this case, the yield curvature $\varphi_{y,eff}$ and the slope (αK_{el}) of the branch after the effective yield are calculated using the "equal areas" rule.

In both cases the assumption that the initial stiffness (K_{el}) is determined as the secant stiffness that corresponds to a moment equal to the 60% of $M_{y,eff}$ was made.

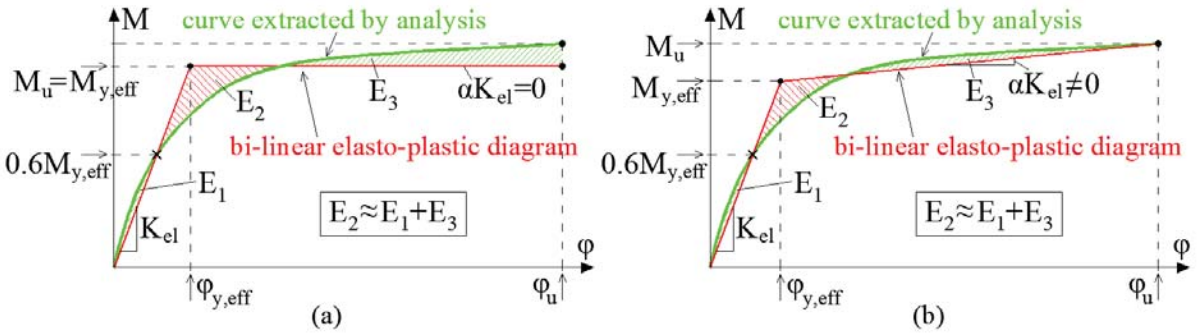

Figure 6: The two utilized approaches for the bilinearization of the M-1/r diagrams

For the cross-sections' analyses the XTRACT software [7] was utilized, whereas for all other required calculations (for example the implementation of flow charts of Appendices 7A and 7E) appropriate computer programs using the Fortran programming language were developed.

3.2 Results of the parametric investigations

In this section the results of $\mu_{1/r}$ and μ_θ calculations for the cross-sections which are illustrated in Fig. 5 on the basis of KAN.EPE. provisions are presented in three stages:

- At the first stage (Subsection 3.2.1) the results pertaining to the calculation of the curvature ductility $\mu_{1/r}$ are presented and briefly discussed.
- At the second stage (Subsection 3.2.2) the results pertaining to the calculation of the curvature in terms of the members' ends chord rotation μ_θ are presented and briefly discussed.
- Finally, at the third stage (Subsection 3.2.3) the proposed relation between $\mu_{1/r}$ and μ_θ (Eq. 1) is implemented and compared with the relations provided directly from the various $\mu_{1/r}$ and μ_θ calculation methods that are used in stages one and two.

3.2.1 Comparison between the methods provided by KAN.EPE. for the $\mu_{1/r}$ calculation

As it was mentioned in section 2, the three methods for the estimation of $\mu_{1/r}$ (Fig. 4) which are provided by KAN.EPE. are compared using the data of Fig. 5. It must be noted that regarding the method which is based on the calculation of the M-1/r diagram, both approaches illustrated in Fig. 6 for its bilinearization were implemented. Thus, the following four different values of curvature ductility $\mu_{1/r}$ for each one of the 64 different examined cases were calculated (the symbol μ_φ instead of $\mu_{1/r}$ will be used from now on in the present paper, i.e. $\mu_\varphi=\mu_{1/r}$):

(a) μ_φ^{SBH}: the value of the curvature ductility $\mu_{1/r}$ which is based on the bilinearization of the M-1/r diagram considering a horizontal branch after the effective yield curvature (Fig. 6a).
(b) μ_φ^{SBI}: the value of the curvature ductility $\mu_{1/r}$ which is based on the bilinearization of the M-1/r diagram considering an inclined branch after the effective yield curvature (Fig. 6b).
(c) μ_φ^{KAP}: the value of the curvature ductility $\mu_{1/r}$ which is based on the procedures which are proposed by KAN.EPE. in Appendices 7A and 7E for the estimation of φ_y and φ_u respectively.
(d) μ_φ^{KAE}: the value of the curvature ductility $\mu_{1/r}$ which is based on the closed-form expression proposed by KAN.EPE. (Eq. 2).

The diagrams of Figs. 7, 8, 9 illustrate the variation of the calculated μ_φ values in relation to the normalized axial force $\nu(=N/bhf_c)$. It must be noted that after the initial evaluation of the μ_φ-ν curves it was observed that the results which correspond to cross-sections with confinement reinforcement Φ8/7.5 and Φ8/10 were qualitatively almost the same. Thus, only the results that correspond to confinement reinforcement Φ8/7.5 along with the results extracted considering confinement reinforcement Φ8/15 and Φ8/20 will be illustrated. Moreover, for the same reason the results which correspond to the longitudinal reinforcement 8Φ24 are omitted because are qualitatively almost the same with the results for longitudinal reinforcement 8Φ22. Finally, almost the same conclusion is valid regarding the concrete grades C20/25 and C25/30. Thus, the presentation of the results concerning the concrete grade C25/30 is also omitted. The three above initial observations constitute conclusions that can be mentioned in the framework of the present investigation, namely the behavior of the μ_φ-ν curves extracted from the methods proposed by KAN.EPE. presents no significant qualitatively chances in the case of high-level confinement, in the case of high ratios of longitudinal reinforcement and in the case of high concrete grades.

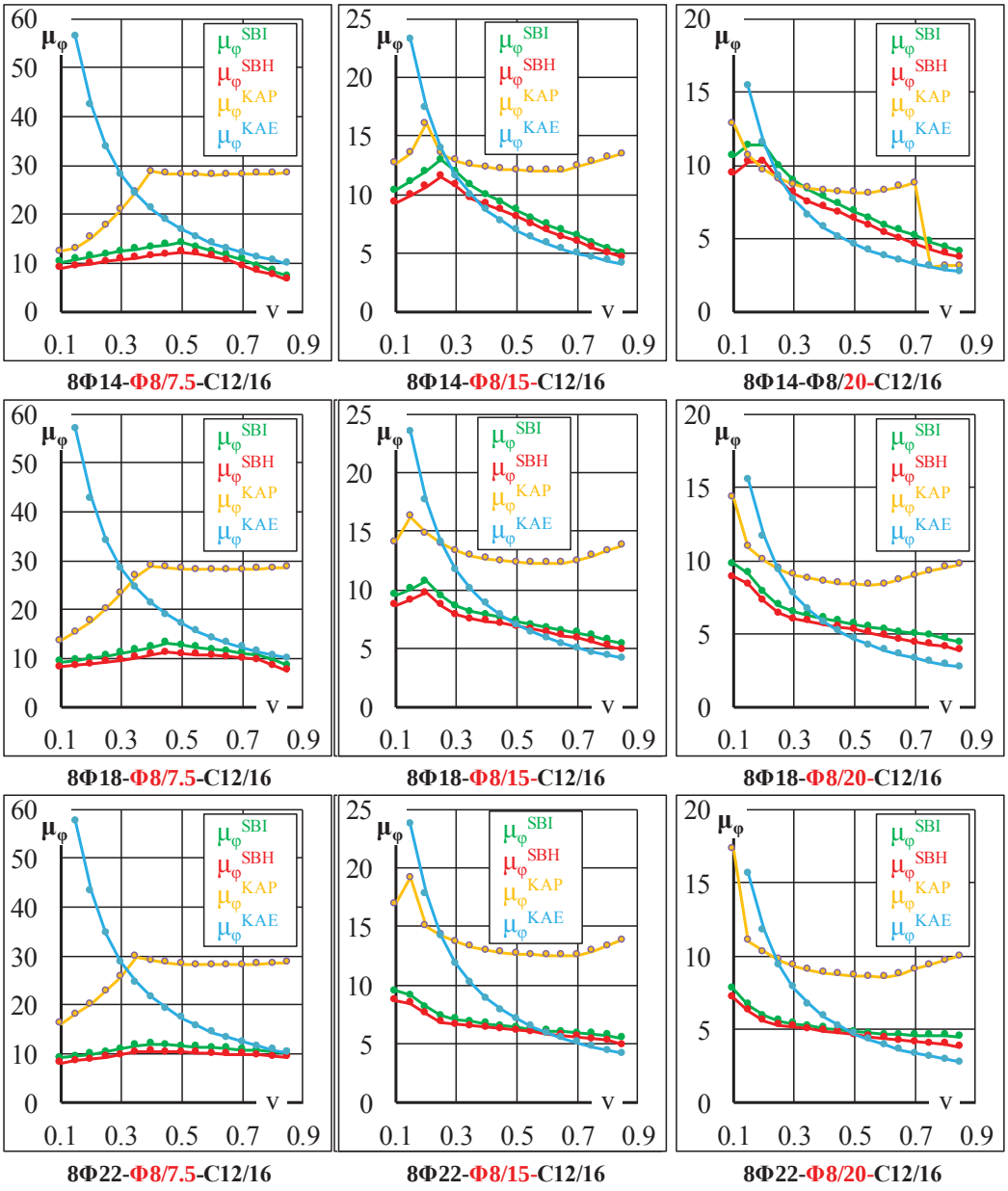

Figure 7: Variation of the μ_φ values calculated through the examined methods in relation to ν – Concrete C12/16

From the study of Fig. 7 the following main conclusions can be extracted:

- The differences between μ_φ^{SBH} and μ_φ^{SBI} values are very small, as it was expected because the only difference between the two methods of bilinearization is the calculation of the effective yield curvature $\varphi_{y,eff}$ (in both cases the values of φ_u are equal). These differences (of $\varphi_{y,eff}$ and consequently of μ_φ) fluctuate between 8% and 17% for the 64 studied cases.
- The μ_φ^{SBH} (or μ_φ^{SBI}) and μ_φ^{KAE} values have small differences for ν>0.5. This means that the approximative closed-form Eq. 2 is capable to provide results which are close to the results based on the reliable method of the calculation of M-1/r diagram in the range ν=0.5-0.85. On the contrary, use of Eq.2 leads to extremely large (and nonrealistic) values for μ_φ in the range ν=0.1-0.3. The above described behavior of the μ_φ values which are extracted from Eq. 2 (rapid decrease of μ_φ for small ν values and small decrease for large values of ν) is due to the fact that this equation consists of a quotient that contains the normalized axial force ν in the denominator.

- The methods which are based on the bilinearization of M-1/r diagrams (values μ_φ^{SBH} and μ_φ^{SBI}) extract relatively constant values (almost horizontal μ_φ-ν curves mainly in cases of longitudinal reinforcement 8Φ18, 8Φ22) in comparison with the other two studied methods.
- The curve μ_φ^{KAP}-ν consists of two distinguishable branches especially in case of high confinement level (Φ8/7.5). In the first branch (ν≈0-0.37) the values of μ_φ are increasing, whereas for ν>0.4 the corresponding values remain almost constant. For medium confinement level the curve μ_φ^{KAP}-ν has also two braches but the first one is stopped for ν≈0.15. Finally, for low level confinement level (Φ8/20) the curves μ_φ^{KAP}-ν have intense downward trend for (ν≈0-0.15), whereas for ν>01.5 remain almost constant. The only exception regards the case of low ratio of longitudinal reinforcement (8Φ14) in which after the value ν=0.7 the curve μ_φ^{KAP}-ν shows an abrupt decrease.
- Finally, regarding the differences between the μ_φ^{SBH} (or μ_φ^{SBI}) and μ_φ^{KAP} values, it must be noted that are in general much higher from all other comparison cases for ν>0.3.

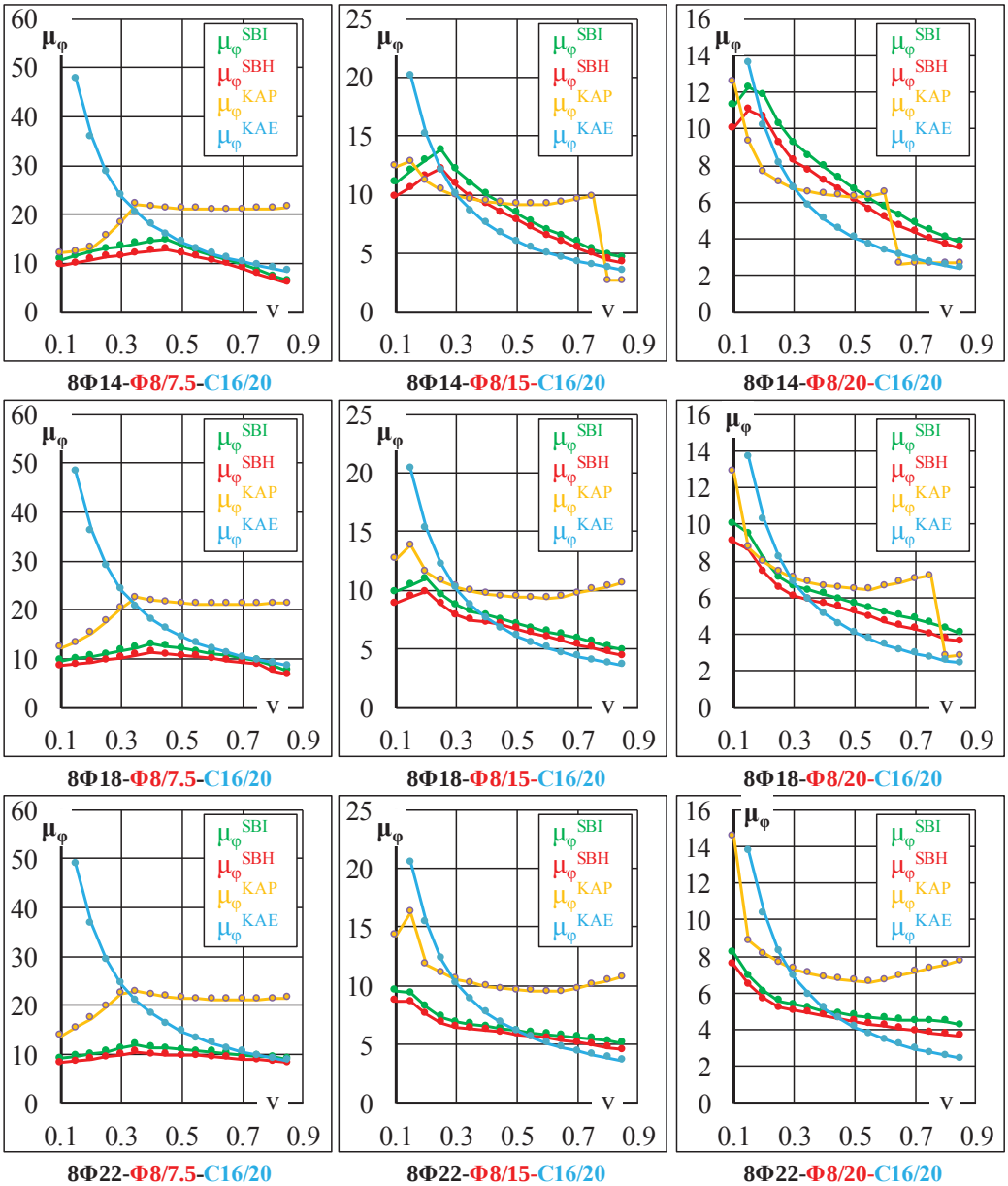

Figure 8: Variation of the μ_φ values calculated through the examined methods in relation to ν – Concrete C16/20

From the combined study of Figs. 7 and 8 the following significant differences regarding the conclusions which were already presented above can be referred:

- In cases of transverse reinforcement Φ8/7.5 and Φ8/10 the only significant diversification is the reduction of the differences between the values μ_φ^{SBH} (or μ_φ^{SBI}) and μ_φ^{KAP}.
- In case of transverse reinforcement Φ8/20 the μ_φ^{KAP} values significantly converge to μ_φ^{SBH}, μ_φ^{SBI} and μ_φ^{KAE}, especially for low and medium longitudinal reinforcement ratio in the entire range of ν values.
- With the exception of the case of transverse reinforcement Φ8/7.5, the closed-form expression (Eq. 2) provides values closer to the values that are extracted from the other more detailed methods proposed by KAN.EPE. especially for ν>0.2.
- The abrupt drop of μ_φ^{KAP} values appears mainly in cases which correspond to low ratios of transverse reinforcement and low and medium ratios of longitudinal reinforcement.

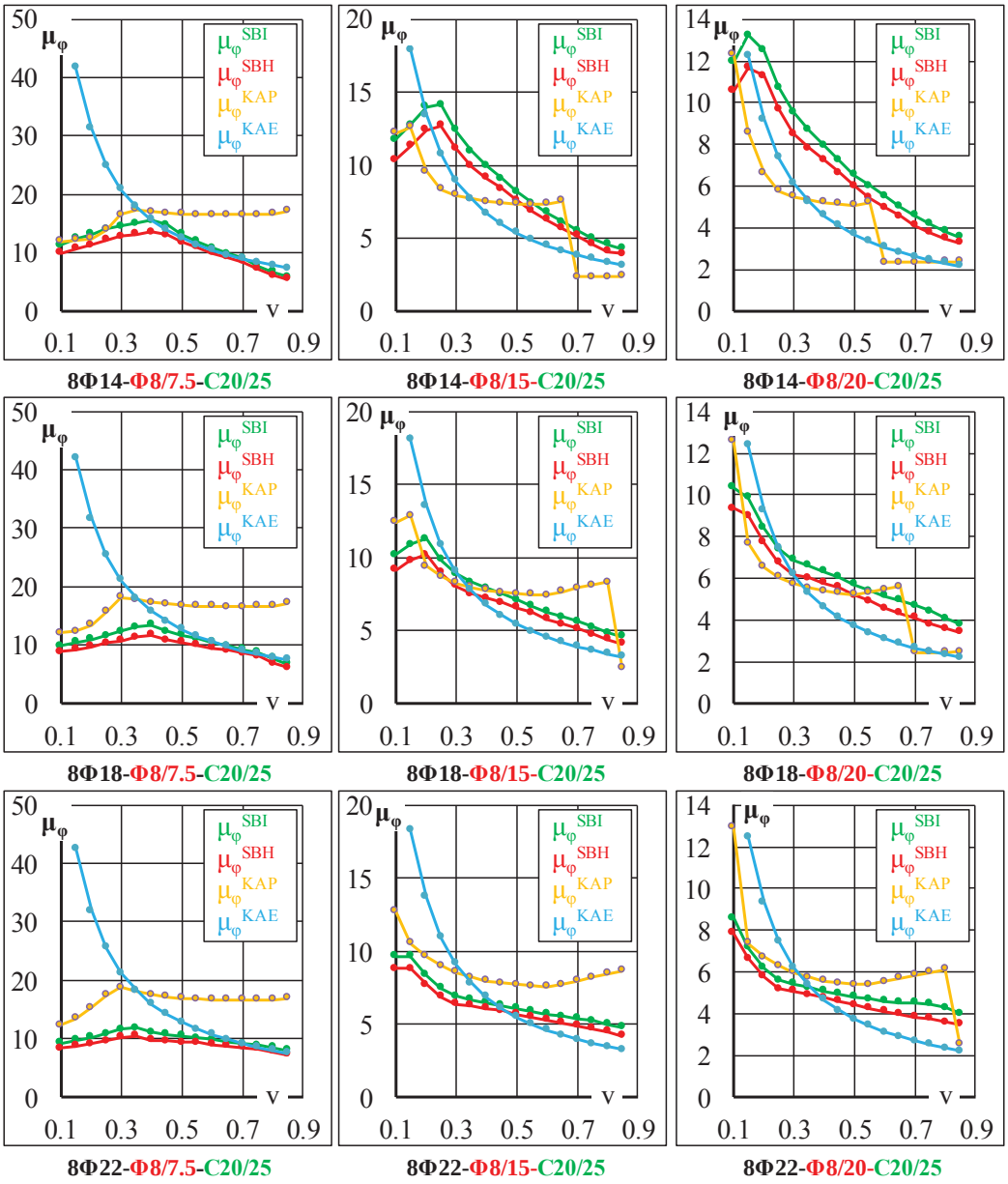

Figure 9: Variation of the μ_φ values calculated through the examined methods in relation to ν – Concrete C20/25

Finally, from the combining study of Figs. 8 and 9 the following significant differences are observed:

- The differences between the μ_φ^{SBH} (or μ_φ^{SBI}) and μ_φ^{KAP} values are even smaller in case of the higher concrete grade C20/25.
- The occasionally observed abrupt drops of the μ_φ^{KAP} values appear more often and for lower values of ν in case of the higher concrete grade C20/25.

3.2.2 Comparison between the methods provided by KAN.EPE. for the μ_θ calculation

As it was mentioned in section 2 of the present paper, KAN.EPE. provides closed-form expressions for the estimation of the chord rotation at flexural yield (θ_y, equation Σ.2a for beams and columns), as well as at flexural failure (θ_u, equation Σ.11a). Moreover, as it was also mentioned in section 2, KAN.EPE. in §6.5 provides the implementation of the ductility in terms of chord rotation ($\mu_\theta=\theta_u/\theta_y$) for the relation between μ_θ and μ_φ through Eq. 1. The examination of equation Σ.2a (comments of §7.2.2d of KANE.EPE) leads to the conclusion that the estimation of θ_y requires the calculation of the yield curvature φ_y (or $(1/r)_y$), whereas the estimation of θ_u on the basis of equation Σ.11a (comments of §7.2.4b of KANE.EPE) is independent from φ_u. Thus, the different approaches regarding the estimation of μ_θ are focused on the method that is used for the calculation of φ_y. In other words, in the framework of the present investigation the equation proposed by KAN.EPE. for the estimation of θ_y is considered as a function of φ_y (i.e. $\theta_y=\theta_y(\varphi_y)$). Consequently, the ductility in terms of chord rotation μ_θ is also considered (only for the scope of the present investigation) as a function of φ_y (i.e. $\mu_\theta=\mu_\theta(\varphi_y)$). For this reason, three different approaches for the estimation of μ_θ (on the basis of equations Σ.2a and Σ.11a) were examined for the 64 cases of Fig. 5:

- $\mu_\theta^{SBH}=\mu_\theta(\varphi_y^{SBH})$: the value of μ_θ estimated using the value of $\varphi_{y,eff}$ extracted from the bilinearization of M-1/r diagram considering a horizontal branch after the effective yield curvature (Fig. 6a).
- $\mu_\theta^{SBI}=\mu_\theta(\varphi_y^{SBI})$: the value of μ_θ estimated using the value of $\varphi_{y,eff}$ extracted from the bilinearization of M-1/r diagram considering an inclined branch after the effective yield curvature (Fig. 6b).
- $\mu_\theta^{KAP}=\mu_\theta(\varphi_y^{KAP})$: the value of μ_θ estimated using the value of φ_y extracted from the procedure proposed by KAN.EPE. in Appendix 7A.

The initial evaluation of the diagrams μ_θ^{SBH}-ν, μ_θ^{SBI}-ν and μ_θ^{KAP}-ν, indicates that the greater differences between the three investigated approaches for the calculation of μ_θ are those between μ_θ^{SBH} (or μ_θ^{SBI}) and μ_θ^{KAP}. This conclusion was expected since the differences between $\theta_y(\varphi_y^{SBH})$ and $\theta_y(\varphi_y^{SBI})$ are significantly smaller than the corresponding differences between $\theta_y(\varphi_y^{SBH})$ (or $\theta_y(\varphi_y^{SBI})$) and $\theta_y(\varphi_y^{KAP})$.

Another significant observation is that the greater differences between μ_θ^{SBH} (or μ_θ^{SBI}) and μ_θ^{KAP} correspond generally to the case of transverse reinforcement Φ8/7.5. Thus, only the diagrams μ_θ-ν extracted from the cross-sections with Φ8/7.5 are illustrated in Fig. 10.

The main conclusions which arise from the study of Fig. 10 are the following:

- The curves μ_θ^{SBH}-ν and μ_θ^{SBI}-ν are in any case descending, which means that the ductility in terms of chord rotations is reduced as the normalized axial force ν increases.
- The curves μ_θ^{KAP}-ν are also in the majority of the studied cases descending, but the corresponding decrease of μ_θ^{KAP} values is generally lower than the decrease of the μ_θ^{SBH} and μ_θ^{SBI} values. However, mainly in case of the lower ratio of longitudinal reinforcement 8Φ14 (and secondarily in case of 8Φ18) the curves μ_θ^{KAP}-ν do not have the same behavior in the entire range of the ν values. More specifically, for ν<0.2-0.3 the μ_θ^{KAP}-ν curves drop significantly, but for greater ν values remain almost constant.

- In the vast majority of the examined cases the μ_θ^{KAP} values are greater than the μ_θ^{SBH} and μ_θ^{SBI} values, with the exception the cases of concrete grades C16/20, C20/25 and C25/30 and for ν values lower than 0.2-0.3.
- Generally, the differences between the μ_θ^{KAP} values and the μ_θ^{SBH} and μ_θ^{SBI} values decrease as the concrete grade increases.

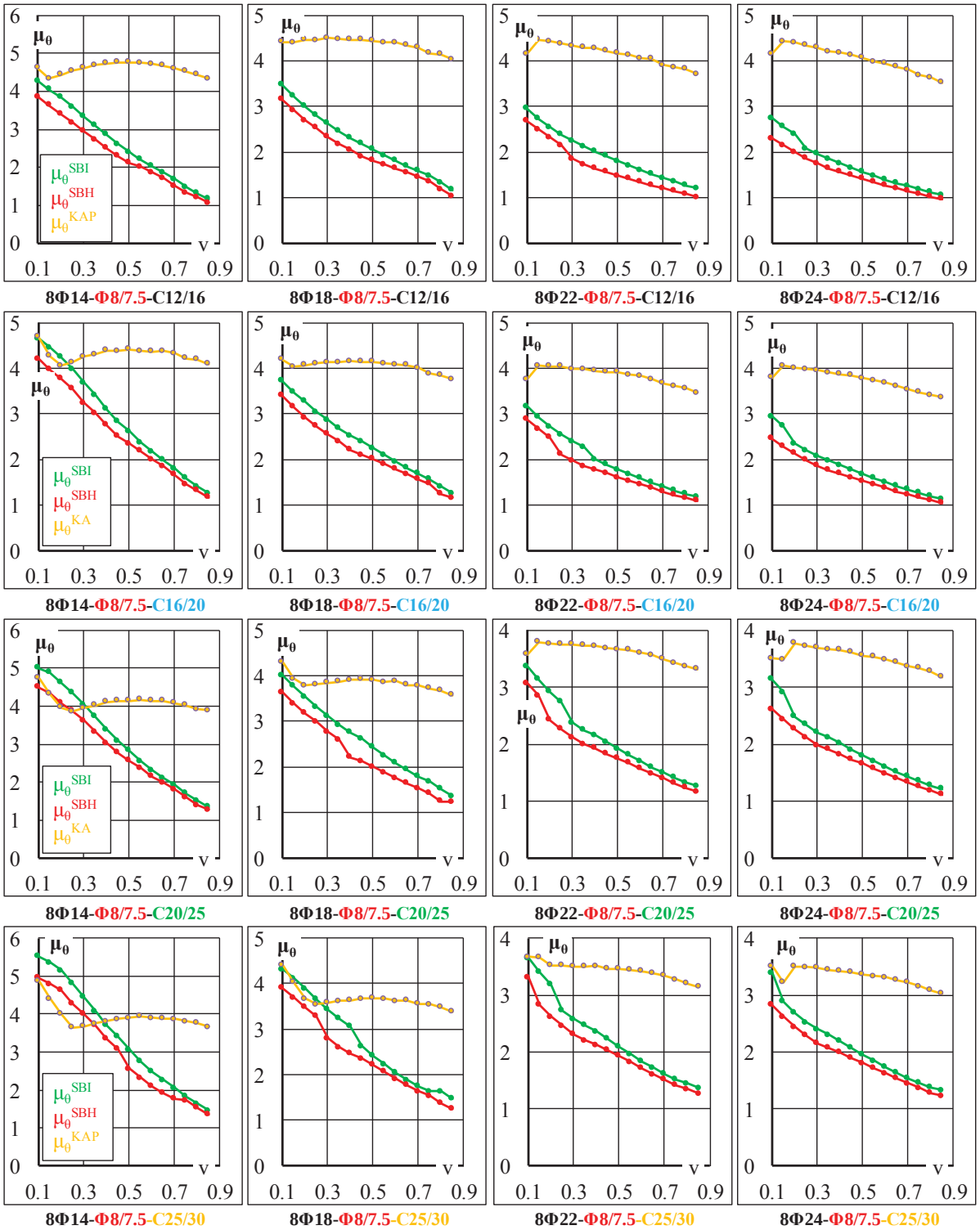

Figure 10: Variation of the μ_θ values calculated through the examined methods in relation to ν

3.2.3 Investigation of the relation between $\mu_\varphi(=\mu_{1/r})$ and μ_θ proposed by KAN.EPE.

In section 2 it was stressed that according to KAN.EPE. one of the applications of the ductility factor μ_φ is the estimation of ductility factor μ_θ using Eq. 1. Besides, one of the main targets of the present paper is the examination of this relation. Thus, in this subsection the results of this examination are presented.

Four different approaches for the estimation of μ_θ were examined and compared. Two of them are based on equations Σ.2a (comments of §7.2.2d of KANE.EPE) and Σ.11a (comments of §7.2.4b of KANE.EPE). The first one [$\mu_\theta(\varphi_y^{SBH})=\theta_y(\varphi_y^{SBH})/\theta_u$] is based on the estimation of φ_y from the bilinearization of M-1/r diagram considering a horizontal branch after the effective yield curvature (Fig. 6a), whereas the second one [$\mu_\theta(\varphi_y^{KAP})=\theta_y(\varphi_y^{KAP})/\theta_u$] is based on the estimation of φ_y from the procedure which are proposed by KAN.EPE. in Appendix 7A. These approaches were already used for the comparison between them in the previous subsection 3.2.2. The other two approaches for the estimation of the ductility factor μ_θ are based on the utilization of the relation between μ_θ and μ_φ proposed by KAN.EPE. (Eq. 1). More specifically, Eq. 1 was implemented twice using the values of μ_φ^{SBH} and μ_φ^{KAP} (see subsection 3.2.1) as follows:

$$\mu_\theta\left(\mu_\varphi^{SBH}\right)=\frac{1}{3}\cdot\left(\mu_\varphi^{SBH}+2\right) \tag{4a}$$

$$\mu_\theta\left(\mu_\varphi^{KAP}\right)=\frac{1}{3}\cdot\left(\mu_\varphi^{KAP}+2\right) \tag{4b}$$

The aforementioned four approaches for the estimation of ductility factor μ_θ were compared in two pairs. Each one of these pairs consists of one μ_θ value calculated on the basis of equations Σ.2a and Σ.11a and one μ_θ value calculated using the Eqs. (4a), (4b). More specifically the following two pairs of μ_θ values were compared:

- The values $\mu_\theta(\varphi_y^{SBH})$ and $\mu_\theta(\mu_\varphi^{SBH})$
- The values $\mu_\theta(\varphi_y^{KAP})$ and $\mu_\theta(\mu_\varphi^{KAP})$

The comparisons were performed for the 64 cases of Fig. 5 and for 18 values of column's normalized axial force between ν=0.0 and ν=0.85. Thus, the relation between the μ_θ values calculated through the theoretical definition $\mu_\theta=\theta_y/\theta_u$ (considered as reference values) and the corresponding values calculated approximately though Eqs. (4a), (4b) was investigated for a great range of ν values. In substance, the ability of the proposed by KAN.EPE. Eqs. (4a), (4b) to approach effectively the reference values of μ_θ calculated by the theoretical definition for various levels of normalized axial force was investigated. Due to the fact that the presentation of all μ_θ-ν curves leads to very complex diagrams which are very difficult for studying, only the curves which correspond to maximum and minimum differences between $\mu_\theta(\varphi_y^{SBH})$ and $\mu_\theta(\mu_\varphi^{SBH})$ values (as well as between $\mu_\theta(\varphi_y^{KAP})$ and $\mu_\theta(\mu_\varphi^{KAP})$ values) are presented in Figs. 11, 12.

From the study of the diagrams of Fig. 11, the following conclusions can be mentioned:

- Generally, the approximative Eq. (4a) provides greater values for μ_θ ($\mu_\theta(\mu_\varphi^{SBH})$) than the application of its theoretical definition ($\mu_\theta(\varphi_y^{SBH})$). However, there are few cases in which the opposite occurs. These cases correspond to ν<0.1-0.2 in combination with high level of transverse reinforcement (i.e. Φ8/7.5 or Φ8/10) or to the lower level of transverse reinforcement (i.e. Φ8/20) in combination with high grades of concrete (i.e. C20/25 or C25/30).
- The method which is based on the theoretical definition of μ_θ ($\mu_\theta(\varphi_y^{SBH})$) provides declining μ_θ-ν curves for the entire range of ν values. On the contrary, the approximative Eq. (4a) provides μ_θ-ν curves which are ascending for ν values between 0.1 and 0.3-0.5, and declin-

ing for greater ν values mainly in case of high level of transverse reinforcement (Φ8/7.5 or 10).

- In all examined cases the maximum differences between $\mu_\theta(\varphi_y^{SBH})$ and $\mu_\theta(\mu_\varphi^{SBH})$ values correspond to the maximum level of transverse reinforcement (Φ8/7.5). On the contrary, with very few exceptions, the minimum differences correspond to the minimum level of transverse reinforcement (Φ8/20).

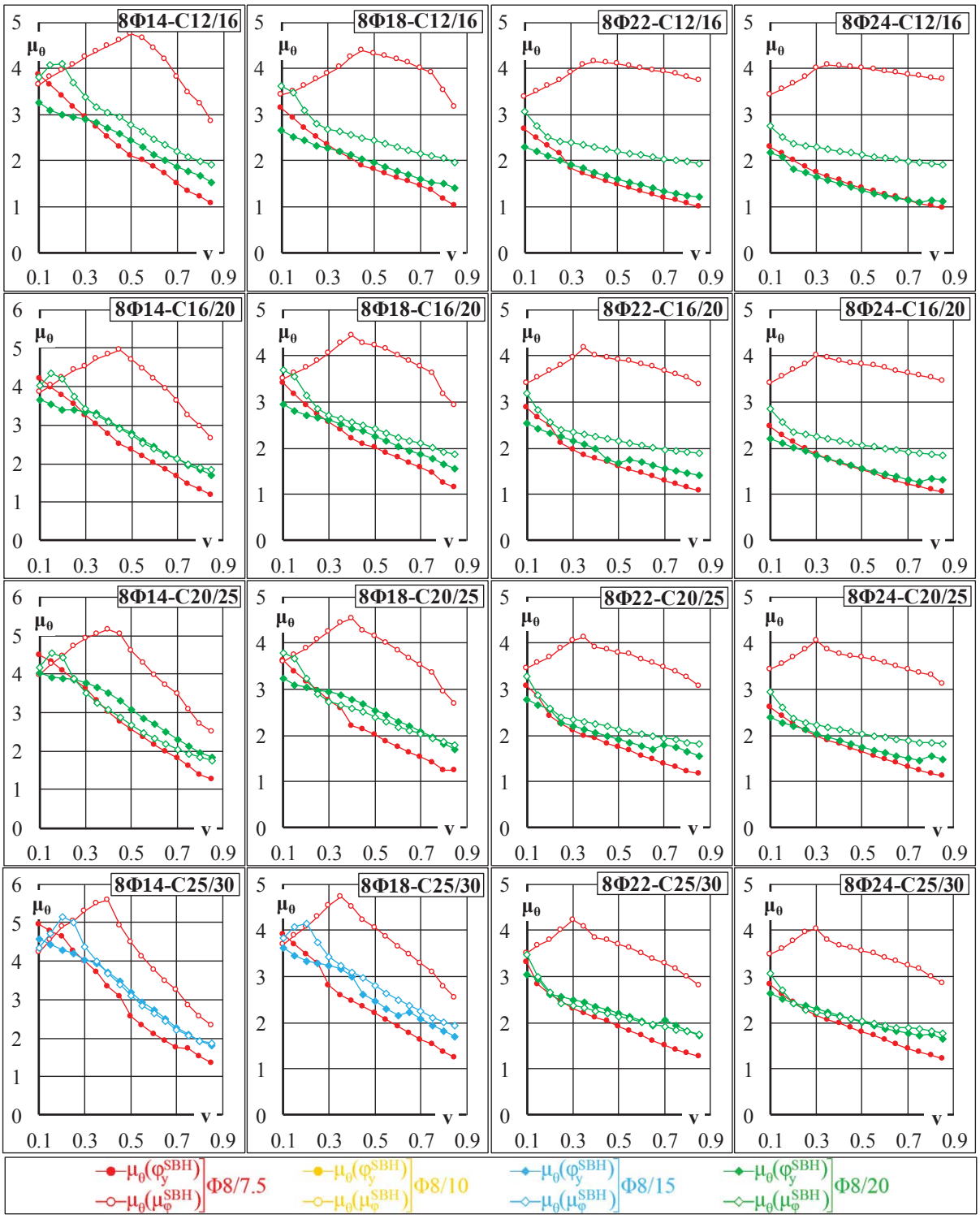

Figure 11: Max and min differences between the μ_θ values extracted by the equation proposed by KAN.EPE. for the relation μ_θ-μ_φ and the μ_θ values extracted by its theoretical definition and the bilinearization of M-μ_φ diagram

- In the vast majority of the studied cases the rate of variation between $\mu_\theta(\varphi_y^{SBH})$ and $\mu_\theta(\mu_\varphi^{SBH})$ values is greater for ν values less than 0.3-0.4.

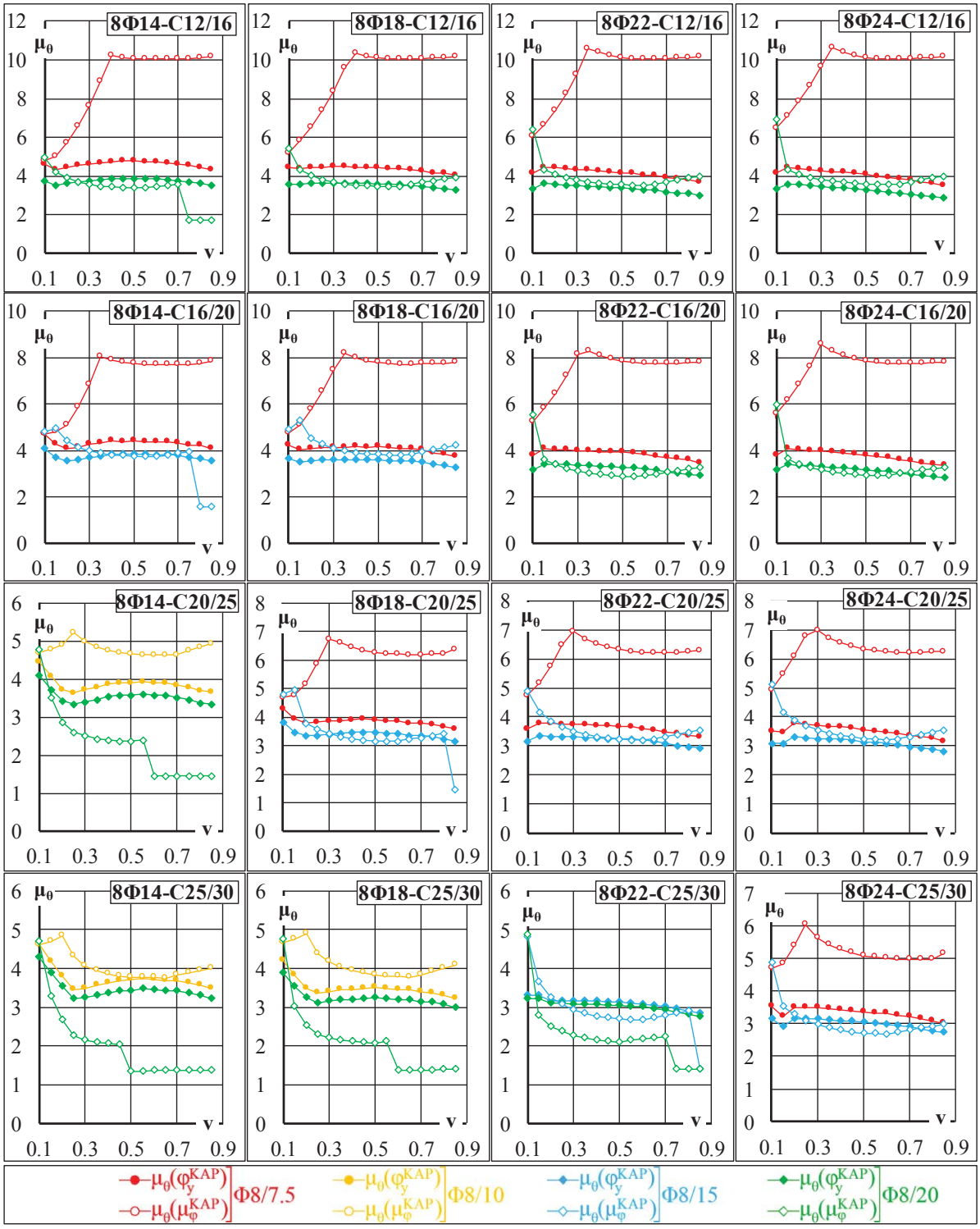

Figure 12: Max and min differences between the μ_θ values extracted by the equation proposed by KAN.EPE. for the relation μ_θ-μ_φ and the μ_θ values extracted by its theoretical definition and the procedure of Appendix 7A

The main conclusions which arise from the study of Fig. 12 are the following:

- The maximum differences between $\mu_\theta(\varphi_y^{KAP})$ and $\mu_\theta(\mu_\varphi^{KAP})$ values correspond to the maximum level of the transverse reinforcement (Φ8/7.5) mainly in cases of concrete grades

C12/16 and C16/20. In the cases of other two assumed concrete grades (mainly in case of C25/30) the maximum differences correspond to the minimum level of the transverse reinforcement (Φ8/20). The minimum differences generally correspond to low levels of transverse reinforcement (Φ8/15 or Φ8/20). Some exceptions are observed for concrete grades C20/25 and C25/30.

- The method which is based on the theoretical definition of μ_θ ($\mu_\theta(\varphi_y^{KAP})$) provides almost horizontal (slightly declining) μ_θ-ν curves for the entire range of ν values. As regards the $\mu_\theta(\mu_\varphi^{KAP})$-ν curves no general conclusion is extracted, since for the cases Φ8/7.5 and Φ8/10 the curves are ascending for low ν values whereas for the cases Φ8/15 and Φ8/20 the curves are mainly declining.
- In the vast majority of the studied cases the rate of variation between $\mu_\theta(\varphi_y^{KAP})$ and $\mu_\theta(\mu_\varphi^{KAP})$ values is greater for ν values less than 0.1-0.2.
- The approximative Eq. (4b) provides greater values for μ_θ ($\mu_\theta(\mu_\varphi^{KAP})$) than the application of its theoretical definition ($\mu_\theta(\varphi_y^{KAP})$) in the vast majority of cases where transverse reinforcements Φ8/7.5, Φ8/10 and Φ8/15 are applied. The opposite occurs in the vast majority of cases where transverse reinforcement Φ8/20 is applied.

Generally, from the combined study of the conclusions extracted from Figs. 11 and 12 the following basic remarks can be stressed:

(a) The Eq. (1) proposed by KAN.EPE. for the relation between μ_θ and μ_φ fails in many of the examined cases to approach effectively the μ_θ values which are calculated using the theoretical definition of $\mu_\theta(=\theta_y/\theta_u)$ in combination with the procedures proposed by KAN.EPE. for the estimation of θ_y and θ_u.

(b) The results provided by Eq. (1) approach more effectively the μ_θ values which are calculated using the theoretical definition of μ_θ only in cases where low levels of transverse reinforcement (Φ8/15 or Φ8/20) are applied.

4. CONCLUSIONS

In the present paper the methods which are proposed by the Greek code for structural intervention (KAN.EPE.) for the estimation of the ductility factors in terms of curvatures (μ_φ) and in terms of chord rotations at the ends of R/C members (μ_θ), as well as the relation between them were comparatively evaluated. The ductility factors μ_φ and μ_θ possess significant roles within the framework of KAN.EPE. Thus, several methods for their estimation as well as an equation for their relation are proposed. In order to achieve the goals of the present investigation, a R/C column with rectangular cross-section and different data regarding the concrete grade as well as the longitudinal and transverse reinforcement mechanical volumetric ratios was analytically investigated. The main conclusions extracted from the present study can be summarized to the following points:

- The methods proposed by KAN.EPE. for the estimation of the ductility in terms of curvatures ($\mu_{1/r}$ or μ_φ) provide in many of the examined cases values with significant differences between them. However, these differences generally decrease as the concrete grade increases.
- The methods which are based on the bilinearization of M-1/r diagrams for the estimation of the ductility in terms of chord rotations μ_θ, provide significantly different μ_θ values in comparison with the method based on the estimation of φ_y through the procedure of Appendix 7A of KAN.EPE. Generally, the latter provides higher μ_θ values. However, these differences decrease as the concrete grade increases.
- Equation (1) proposed by KAN.EPE. for the relation between μ_θ and μ_φ, approaches more effectively the μ_θ values which are calculated using the theoretical definition of μ_θ only in

cases where low levels of transverse reinforcement (Φ8/15 or Φ8/20) are applied. On the contrary, in cases of high level of transverse reinforcement (Φ8/7.5 or Φ8/10) the corresponding approach is not sufficient.

Finally, it must be stressed that the above-mentioned conclusions can only be considered as indicative for the range of the results which are provided by the various methods proposed by KAN.EPE. for the estimation of μ_φ and μ_θ. In any case, all these methods are well-documented and the differences between them can be simply considered as a result of the different assumptions on which are based. However, especially for the provision of KAN.EPE. pertaining to the relation between μ_φ and μ_θ the results of the present paper provide a motivation for further investigations (e.g. on the basis of their theoretic definition and/or extensive parametric analyses) for more efficient alternative approaches.

REFERENCES

[1] KAN.EPE (2017). Code of structural interventions. Earthquake Planning and Protection Organization of Greece (EPPO).

[2] GG. Penelis and AJ. Kappos, Earthquake-Resistant Concrete Structures, Taylor and Francis, ISBN 0 419 18720 0, 1997.

[3] MN. Fardis, Seismic Design, Assessment and Retrofitting of Concrete Buildings (based on EN-Eurocode 8), Springer, ISBN 978-1-4020-9841-3, 2009.

[4] TB. Panagiotakos and MN. Fardis, Deformations of Reinforced Concrete Members at Yielding and Ultimate, *ACI Structural Journal* V.98(No. 2), 135-148, 2001.

[5] D. Biskinis and MN. Fardis, Deformations of concrete members at yielding and ultimate under monotonic or cyclic loading (including repaired and retrofitted members, *Report Series in Structural and Earthquake Engineering*, University of Patras, Department of Civil Engineering, Report No. SEE 2009-01, 2009.

[6] EN1992 (Eurocode 2), Design of Concrete Structures, Part 1-1: General rules and rules for buildings, European Committee for Standardization, 2005.

[7] Imbsen Software Systems, XTRACT: Version 3.0.5. Cross-sectional structural analysis of components, Sacramento, CA, 2006.

EURODYN 2020
XI International Conference on Structural Dynamics
M. Papadrakakis, M. Fragiadakis, C. Papadimitriou (eds.)
Athens, Greece, 23–26 November 2020

SEISMIC PERFORMANCE OF EXISTING BUILDINGS CONCRETE SHEAR WALL

S. A. Hossain[1], A. Bagchi[2]
[1]Ph.D. student (Structural and Earthquake Engineering),
Department of Building, Civil and Environmental Engineering
Concordia University, Montreal, Canada
Lecturer, Department of Civil & Environmental Engineering and Construction Management
College of Engineering, University of Texas, Tyler, USA
shossain@uttyler.edu
[2]Professor and Chair, Department of Building, Civil and Environmental Engineering
Concordia University, Montreal, Canada
Ashutosh.Bagchi@concordia.ca

Abstract - This article presents a study on the seismic performance of reinforced concrete shear wall buildings with focus on shear strength of walls that are designed using the seismic design provisions of the National Building Code of Canada. A set of buildings, four, six and eight storeys with a simple configuration and different heights have been considered here. While the static and linear dynamic analyses indicate the robustness in the design but dynamic time history analysis indicates deficiency in the shear capacity in the plastic hinge region. It is observed that a dynamic amplification factor for shear on flexural walls governs the shear demand. Here, a simple method has been proposed to estimate the amplified shear demand and to enhance shear resistance of a structural wall economically to avoid unintended shear failure.

Keywords: Reinforced concrete, Shear wall, seismic demand, dynamic analysis.

1. Introduction

Failure of structural walls in shear has been identified as one of the reasons that can diminish the expected level of performance and lead to the big financial loss. For instance, the amount of America's financial losses in the 1990s' is estimated to be twenty times bigger than that of three earlier decades all together [1]. This is despite the fact that all the structural walls are designed according to the building code requirements, but these structural walls have still been a challenge and are failing with different reason including inadequate shear capacity. They should have adequate displacement capacity to ensure the satisfactory level of performance of the wall [2-3]. Building codes in various jurisdictions including Canada have moved towards performance-based design approaches. The National Building Code of Canada (NBCC 2005; has been provided in an objective based code format which provides under the "Alternative Solution"; category that a structure can be designed not only to have adequate strength, but also for the performance attributes, such as deformability. Although, the current seismic design approach of ductile RC shear wall provided by the NBCC 2005 and CSA A23.3-04 is more rational than the earlier editions; yet, despite all improvements made to them they do not specially address the higher mode effects on the base shear demand in the shear walls [4]. It also should be noted that even such improvements provided under "alternative solutions" that gives way for PBSD can still result in a major brittle shear failure. For instance, an increase in participation of higher modes of vibration can result in decrease of building drifts, and in a sense, a more desirable level of performance. But, on the other hand, such increase can also cause considerable increase in shear force demand at the base of the shear walls, particularly after formation of plastic hinge. If not taken into account, such magnification can result in a brittle shear failure, and turn the seeming desired level of

performance into a major loss. Hence, it is very inevitable that still it requires a lot of study and research on this field to mitigate these problems.

2. Literature review

Higher modes of vibration play an important role for enhanced shear demand. Blakeley et al. [5], were the first pioneer the idea that higher modes of vibration not only magnifies the elastic shear demand at the base of shear walls, but also increases the demand more appreciably after the structure enters inelastic phase and plastic hinge forms.

The recent work of Boivin and Paultre [6], shows that for the regular multi-storey ductile RC cantilever or coupled walls, the capacity design shear envelope determined from (CSA A23.3-04) to prevent shear failure can largely underestimate the shear force demand under design level ground motions, even when the wall response is slightly inelastic. This kind of underestimation results from a deficiency of the present codes to account for dynamic amplification effects, in the elastic and inelastic regimes, due to higher lateral modes. Boivin and Paultre [6], identified two sources of underestimation: (i) the 2005 NBCC spectral accelerations underestimate the elastic responses of higher lateral modes of the walls because their traditional 5% damping overestimate actual damping (about 2% on average) and that makes reducing the higher mode responses; and (ii) as per CSA standard A23.3-04, the capacity design method for shear strength design do not account for the dynamic amplification of shear forces due to inelastic effects of higher modes.

Boivin and Paultre [4], also noted that the capacity design method prescribed by CSA standard A23.3-04 to prevent unintended plastic hinges above the base plastic hinging region is not free from such a problem because it is formulated based on amplified elastic forces which is tributary of the analysis method, static or dynamic, used to derive these forces.

For New Zealand code and standard of the time, they recommended the shear force relative to the moment capacity (allowing for different sources of strength such as actual yield strength of steel greater than minimum specified) be calculated and then to be magnified based on their number of stories and class of importance. Their work then became the basis for modifying structural wall's base shear in many standards of the time.

Among many other countries, the earlier edition of Canadian Standard, CSA A23.3-94 (CSA 2001) also adapted New Zealand's approach (NZS 1995) in which was recommended as:

[1] $1 \leq J/1.25 * (0.9+N/10)$ $N \leq 6$

[2] $1 \leq J/1.25 * (1.3+N/30) \leq 1.8$ $N > 6$

In that J/1.25 is to adopt the original formulas into Canadian Standard; J is a reduction coefficient in NBCC that accounts for higher modes of vibration in the Equivalent static load method, and 1/1.25 is to account for the difference between probable and nominal values used in Canadian and New Zealand standard respectively. However, the New Zealand approach is not recommended in the current standard of practice A23.3-04 anymore.

Another approach that is compared with the results of this study are proposed by Filiatrault et al. [7], suggested that the shear demand to be calculated using the ESL method formula, $V = U * V_e / R$ (NBCC 1995), in which V is the design base shear, V_e is the equivalent lateral force at the base, U is a calibration factor equal to 0.6, and R is the force modification factor. But they suggested that the R to be replaced by a factor R_v equal to 1.0 in seismic zones $Z_a \geq Z_v$ and 1.5 when $Z_a < Z_v$. On the other hand, Ghosh and Markevicius [8], suggested that the base shear to be calculated using $0.25W \times a + M_y / (0.67h_n)$ equation in which W is the seismic weight, a is the design peak ground acceleration, and M_y is the yield moment of the wall, and hn is the building total height.

Currently, no method of analysis is capable of capturing the effect of higher modes of vibration but dynamic analysis. Yet, an elastic dynamic analysis is not sufficient if plastic hinge forms in the shear wall. That is because vibrating in the elastic range constitutes only a small portion of the effect of higher modes and the major portion of base shear magnification takes place after formation of plastic hinge that an elastic analysis is not capable of

capturing it. However, because of its complication, inelastic dynamic analysis of RC structures is not an approach of common practice. On the other hand, the initial approach for seismic design of RC shear walls used in most building codes is the equivalent lateral load method. Beside the fact that the Canadian code and standard do not implicitly address deficiency of such effects, the existing recommendations suggested for inclusion of the effects of higher modes of vibration still either underestimate or well overestimate the base shear demand in walls, or seems not to cover a large range of building heights.

3. Objectives

The objective of this research is to do a comparative study of different analyses methods like equivalent lateral force method, response spectrum analysis and dynamic time history analysis of reinforced concrete shear walls using Canadian National building Code and to check the design adequacy of reinforced concrete shear walls as per CSA A23.3-04, with seismic demand analyses from these Static, linear dynamic and dynamic time history analyses. And to propose any suitable solution, if any discrepancy arises between seismic demand and shear wall capacity as per Canadian design standards considering linear and non-linear dynamic analysis, which is usually not considered in standard practice.

4. Methodology

A set of buildings with a simple configurations and different heights have been modeled in ETABS. The seismic design parameters are considered for Vancouver locations. It has been utilized the real seismic database from PEER (Pacific Earthquake Research Institute). Fifteen ground motion records have used for this study. These 15 records have ratios of peak acceleration (A) to peak velocity (V) close to 1 which represents the seismicity of Vancouver, [9]. A comparative study has been performed between, ELF method, Response Spectrum analysis and Dynamic Time History analysis.

Three reinforced concrete RC office buildings with shear wall of 4, 8, and 16 storey heights and 3 bays by 3 bays in plan were modeled and performed analysis and design in ETABS. The buildings fall into the category of regular symmetric buildings according to NBCC 2015. The floors are designed as floor plates. The buildings are of heights equal to 15.8, 30.4, and 59.6 m, respectively covering limits of the applicability of the ESL methods as permitted by NBCC 2015. The range of heights considered here also cover both flexural and shear behaviour of walls. In low rise buildings the shear behaviour is dominant and in the high building the flexural behaviour is dominant.

The periods obtained from modal analysis are found to be more than the corresponding values of T_a by empirical formula in all the buildings. Therefore, the fundamental periods of the buildings are revised to maximum $2T_a$ as recommended in NBCC 2015.The design live load is equal to 2.4 kN/m^2 for all floors except for the first storey which is 4.8 kN/m^2. The snow load is calculated to be 2.3 kN/m^2. The dead load is 0.85 kPa for exterior walls, 1.0 kPa for partitions on floors, 0.5 kPa for ceiling and mechanical services for all floors and 0.5 kPa for roofing. It has been considered ductile shear walls, with R_d=3.5 and R_o=1.6 for the lateral force resisting system as stated in the code, where R_o and R_d are overstrength and ductility factors, respectively.

Located in Vancouver, location of high seismic activity region in Canada, the buildings are assumed to be founded on class “C” soil. The initial stiffness of the members is estimated based on the CSA-A23.3-04 provisions for seismic resisting buildings and is kept unchanged over every few floors. For instance, the eight storey walls are modelled with a flexural rigidity of $0.68EI_g$ for storey one to flour, and $0.64EI_g$ for stories five to eight.

The following two methods are used for scaling the 15 historical earthquake records (PEER database) to fit them into the response spectrum provided in the code. It has been used Seismosignal software to analyse these ground motion data. The scaling methods considered here are: (i) Partial Area Method (PAM) and (ii) Ordinate Methods (OM). For the ordinate method (OM), the accelerograms were scaled by a ratio of “design spectral

ordinate'', and "spectral ordinate of the accelerograms" both at the fundamental period T1; In the Partial Area Method (PAM), the accelerograms were scaled by a ratio of the area under the design spectrum of an accelerogram, both within the same period interval "T1' to "1.2T1"; The typical spectra from the 15 accelerograms and ETABS models are shown in below figures 4(a) and 4(b):

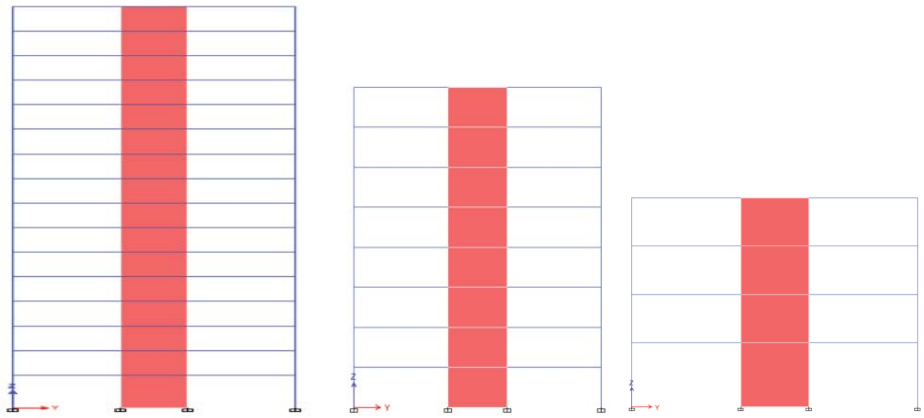

Fig.4(a) – ETABS Models (16, 8 and 4 Storey Building)

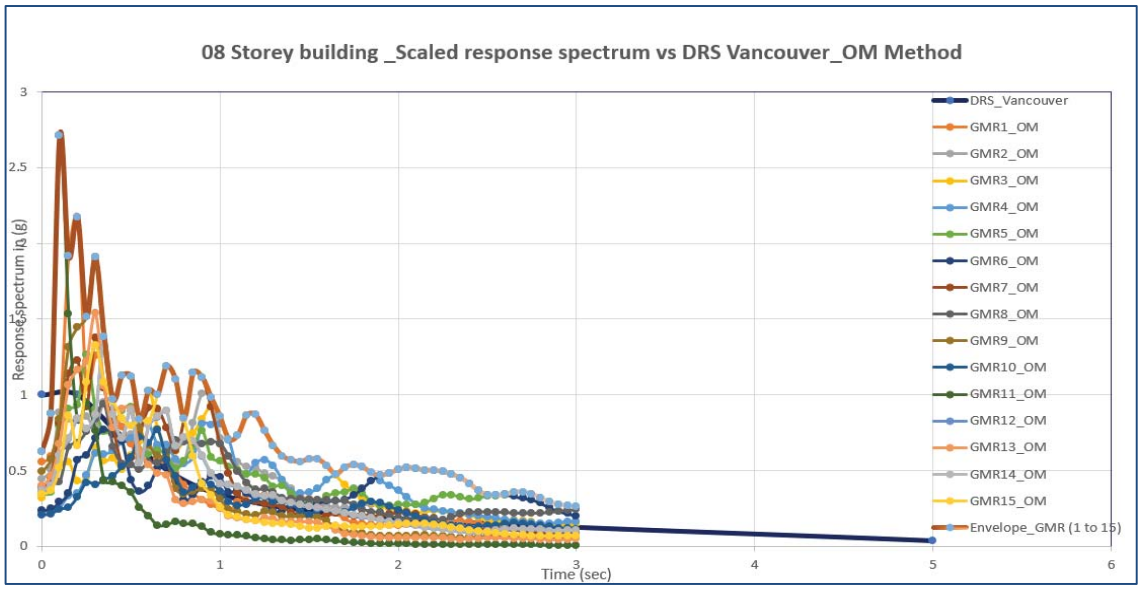

Fig. 4(b): Envelope scaled response spectrum vs design response spectrum, Vancouver, 8 Storey building

5. Assessments of Results

For comparison, the base shear demand and its distribution along the height of the critical wall for each building for different analysis methods are shown in below figures 5(a), 5(b) and 5(c); It has been observed that the base shear demand increases with the storey height with the same floor area. But this increase is not directly proportional to seismic weight of the buildings. Effect of time period and higher mode affect come into play in this scenario. In Fig 5(d), it has been plotted the factored base shear demand to factored shear capacity in static analysis. And the D/C ratio is less than one. And in Fig 5(e) it has been plotted the ratio of factored base shear demand to base shear capacity from detail time history analysis. And the D/C ratio is greater than one shows inadequacy in shear wall design that is usually not considered in standard practice.

Moreover, it can be observed the increase of higher mode effect with building height from this diagram, 5(d) and 5(e); It can be seen also that the ratio of factored base shear demand to factored shear capacity increases with the increase of building height but that increment is not proportional to the story height. This is because, with the increase of height the inelastic rotation requirement become the more dominant parameter in shear wall design. Therefore, it will be seen later in this paper that it seems more reasonable to dynamically amplify the shear capacity of the wall rather than using the common approach which is amplifying the factored or probable shear demand resulting from elastic analyses.

It has been observed from Fig 5(e) that difference of shear demand capacity ratio in 04 storey and 08 storey is not significant, but the ratio increases from 1.49 to 1.68 from 08 storey to 16 storey respectively. It needs to be noted that in below Figures, EMP-T, Revised-T, and DRS denote the base shear due to time period based on code empirical equation, code limit and ETABS calculation considering design response spectrum respectively.

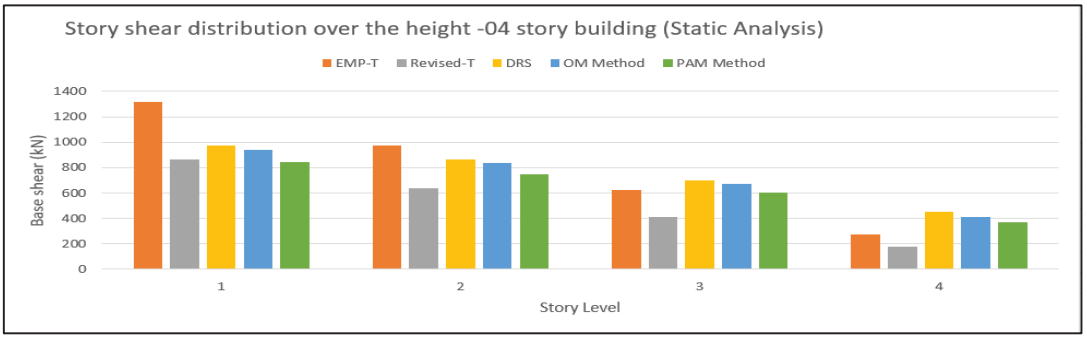

Fig. 5(a): Storey shear distribution over the height, 04 storey building (Static analysis)

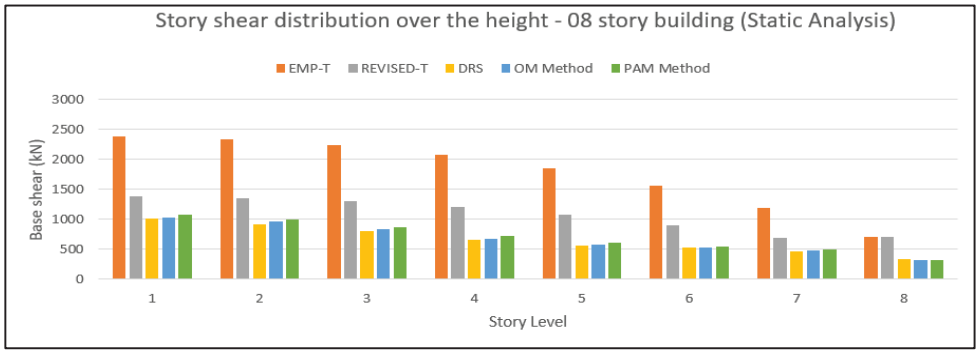

Fig. 5(b): Storey shear distribution over the height, 08 storey building (Static analysis)

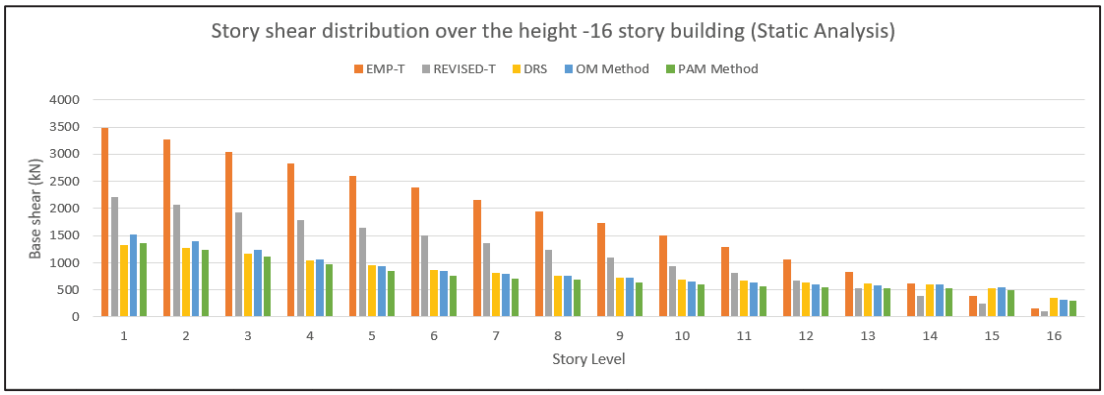

Fig.5©: Storey shear distribution over the height, 16 storey building (Static analysis)

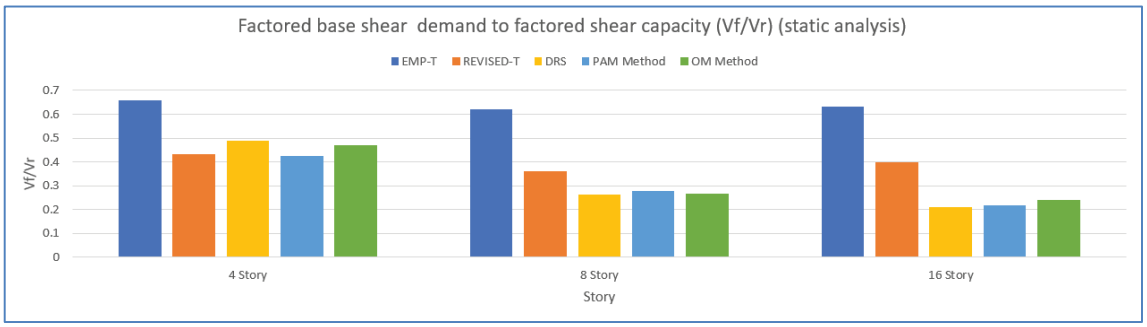

Fig. 5(d): Ratio of probable base shear demand vs factored shear capacity (static analysis)

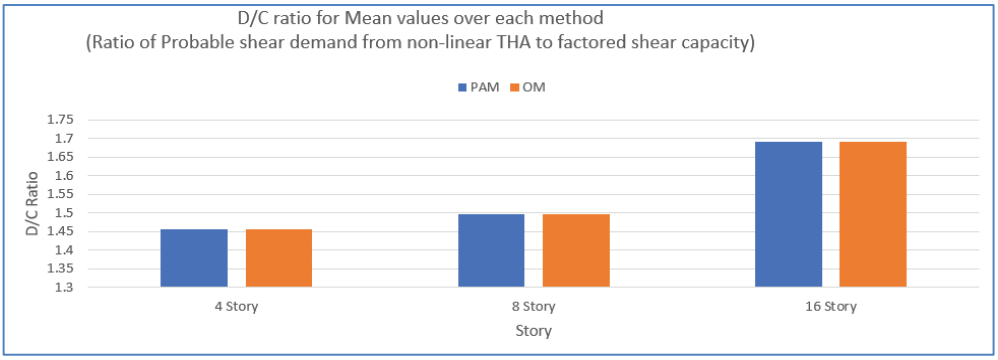

Fig. 5(e): Ratio of probable shear demand vs factored shear capacity (Dynamic time History analysis

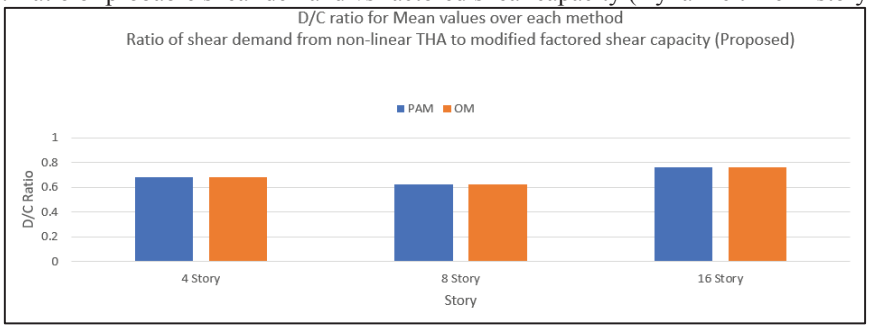

Fig.5(f): Ratio of probable shear demand vs modified factored shear capacity (Dynamic time History analysis)-Proposed

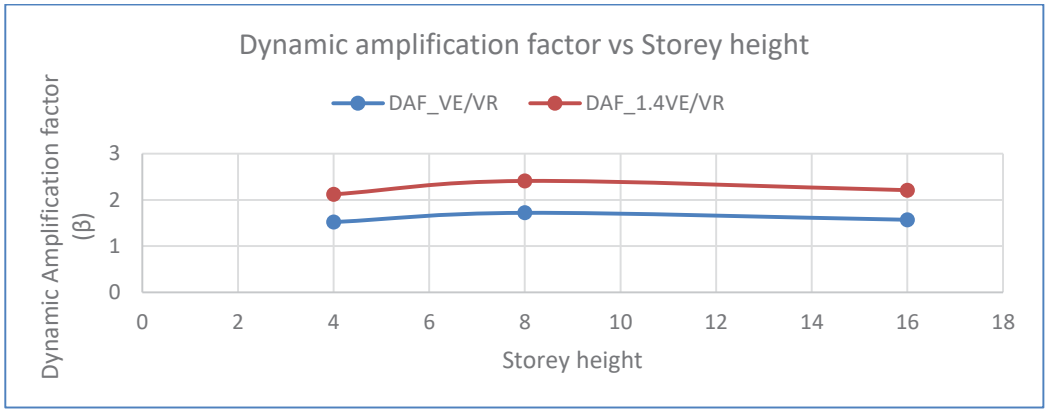

Fig.5(g) Variation of Dynamic amplification factor with Storey height

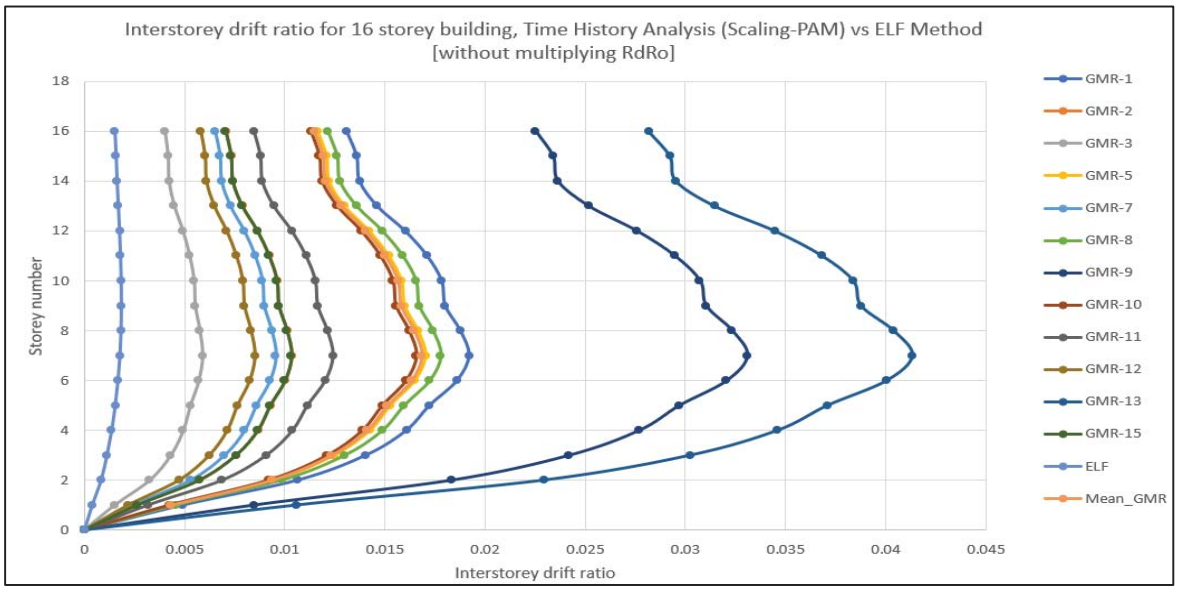

Fig. 5(h): Interstorey drift ratio for 16 storey building Time History Analysis (scaling PAM) vs ELF method

It has been plotted the variation of dynamic amplification factors in different proposed method vs storey height in Fig 5(g). The fundamental periods are increasing with increasing of storey height. In these calculations it has been considered minimum wall thickness as per Canadian standards. It has been observed that the interstorey drift ratio of 16 storey building Fig 5(h) as per 1.0DL+0.5LL+1.0Ex load combination is within the limit. ($0.002*R_d*R_o$)/IE=0.011<0.025), but as per load combination from time history analysis the interstorey drift is not within the code limit ($0.017*R_d*R_o$)/IE=0.095; This is because of higher base shear demand. It has been shown detailed discussions and conclusions in section 8.0;

6. Summary of cost to increase shear strength at critical regions: [RS Mean data-2009]

It has been designed the shear walls for all buildings in this study (4, 8 and 16 storey) as per Canadian standards and calculated additional reinforcement cost to provide additional shear capacity using the proposed approach mentioned in this study and summarized in below table. It has not been shown the detail design calculation in this paper due to page limitations.

It has been found that a very negligible effect on cost increase in this study, max (0.3%);

Table 6.1 – Modification factors for shear strength vs additional cost

Building height and cost	Modification Factors for Shear Strength in the critical Region [Proposed]		Additional reinforcements for increasing the critical Region Shear Strength (ton)	Additional Cost for increasing the critical Region's Shear Strength (CDN $)	Additional Cost Relative to the Total Cost (%)
16 Storey ($14 m)	VE/VR	1.58	5.0	16000	0.25
	1.4VE/VR	2.21	11.0	31000	0.3
08 Storey ($5.5m)	VE/VR	1.72	3.52	11000	0.20
	1.4VE/VR	2.42	5.72	18000	0.33
04 Storey ($2.5m)	VE/VR	1.52	1.1	3676	0.15
	1.4VE/VR	2.21	1.5	5000	0.2

Table 6.2 - D/C ratio due to Dynamic Time History Analysis

Storey	Partial Area Method (PAM)/Ordinate Method (OM)
04	1.46
08	1.49
16	1.69

7. Comparison of results

It has been compared the result of this study (proposed VE/VR or 1.4 VE/VR as a multiplication factor) with previous New Zealand code and study of Filiatrault et. Al. [7], and summarized in below table (Table-7.1). It has been observed that, the original New Zealand approach (NZS 1995) and that of adapted CSA A23.3-94 (the original New Zealand approach multiplied by J/1.25) results in shear values those are also comparable with the values from inelastic analysis of this study. From below table, it can be observed that both of the New Zealand and that of adapted to standard CSA A23.3-94 give close estimation of shear demand, they are at the lower bound that can be viewed as an underestimation of shear demand.

However, using VE/VR or 1.4VE/VR ratio as an amplifying multiplier gives a better estimate of shear demand that are comparable to results from the New Zealand approach. Moreover, the proposed approach gives even a better result compared to those of New Zealand approach even in case of using probable shear demand V_p as the multiplicand. Here V_p, V_r and V_n denote probable base shear demand, factored shear capacity and nominal shear capacity of wall respectively.

Table 7.1– Variation of shear demand (Proposed) from Dynamic Time History Analysis (%)

		Proposed						New Zealand						Filiatraul
		VE/VR			1.4VE/VR			βv			J/1.25 βv			
		Vr	Vn	Vp	Vr	Vn	Vp	Vr	Vn	Vp	Vr	Vn	Vp	
16 Storey	Mean	-6.5	3.8	14.1	30.7	45.3	59.8	8.2	20.2	32.27	-22.05	-13.3	-4.7	-93.5
08 Storey	Mean	15.3	28.12	12.37	61.9	79.36	57.32	4.31	15.9	1.66	-24.8	-16.5	-26	-92.8
04 Storey	Mean	35.27	50.3	14.5	89.3	110.4	60.3	15.6	28.4	-2.1	-16.7	-7.4	-29.5	-89.9

8. Discussions and Conclusion

The present study focuses on the evaluation of buildings based on National Building Code of Canada. Equivalent static load method, response spectrum analysis and dynamic time history analysis have been carried out in the design and evaluation process. The different findings from this study are summarized as follows:

The static and response spectrum analyses indicate the robustness in the design that the shear demands on the shear walls are below the shear capacities (D/C<1), while the dynamic time history analysis indicates deficiency in the shear capacity in the plastic hinge region. Based on the nonlinear dynamic analysis, it has been found that the shear demand in the walls is well above the capacity (D/C>1); It has been proposed dynamic amplification factors for modification of such deficiency. The ratio of probable base shear demand to factored shear capacity are found 1.46, 1.49 and 1.68 for 04, 08, and 16 storey buildings respectively. For calculation of probable base shear calculation, it has been considered flexural overstrength as per CSA A23.4-04.

It is determined that the shear capacity of a wall in the hinge region where the shear critical section is located, needs to be increased by a factor of VE/VR or1.4VE/VR in order to keep the shear demand lower than the capacity.

Here, VE represents the base shear due to time period from empirical equation and VR represents base shear due to revised time period as per Canadian code. The dynamic amplification factors for 4, 8, 16 storeys are determined 1.52, 1.72, 1.57 respectively for multiplication factor VE/VR and 2.12, 2.41, 2.21 respectively for multiplication factor 1.4VE/VR.

The dynamic amplification factor with respect to different storey are plotted in Fig. 5(g). It is not a straight-line variation. Since dynamic amplification factor depends on frequency ratio (β) and damping ratio. And the frequency depends on the stiffness and mass of the building. Here, β represents VE/VR or 1.4VE/VR.

It has been found a good agreement ratio of the engineering design parameters, moment, shear and deflection with respect to empirical time period and revised time periods (not shown in this paper) with this proposed multiplication factors, VE/VR and 1.4VE/VR. It has been observed also that the D/C ratio shown in Table-6.2 (D/C>1), which is failing due to considering detail time history analysis base shear has a good agreement with this multiplication factors (VE/VR or 1.4VE/VR) as well as the dynamic amplification factors.

The proposed factor has been proposed to apply to the shear capacity of the wall rather than shear demand from elastic analysis. And after applying these factors with shear capacity, it has been plotted D/C ratio in Fig 5(f), which is less than one.

It is shown in Table 7.1, the variation of proposed shear demand from dynamic time history analysis in percentage and VE/VR and 1.4VE/VR shows all positive values.

From Table 7.1, it has been observed also that using these factors (VE/VR or 1.4VE/VR as an amplifying multiplier factor gives a better estimate of shear demand that are comparable to results from the New-Zealand approach and Filiatraul et.al. [7].

It also can be observed from detail shear reinforcement calculation of these buildings as per CSA A23.4, that the proposed approach results in a better estimate of shear demand on wall in any case, whether magnifying the probable shear demand $[(M_p/M_f) * V_f]$ obtained from elastic analysis or magnifying shear capacity of the wall from capacity design approach. It needs to mention that to increase the shear capacity, it has been used CSA A23.4, ductility approach to apply those proposed multiplication factors. The probable base shear demand has been calculated from CSA A23.4 capacity design approach, that plotted in Fig. 5 (e) and can be commented that the Canadian capacity design for shear wall design is adequate for linear static and response spectrum analysis but it is inadequate for the shear demand from dynamic time history analysis. For probable shear demand calculation, it has been used γ_w equal to 3.49; It can be noted that the value of γ_w equal to 4 approximates the theoretical overstrength limit before shear strength design of ductile walls is controlled by elastic shear force, [4].

It has been studied also the effect of wall thickness on base shear demand and interstorey drift ratio. It has been observed that by increasing wall thickness from 450 mm to 500mm on 08 storey building, there is not significant base shear changed. Whereas, the interstorey drift can be reduced by 22 percent (not shown in this paper). It has been done detail cost analysis also due to increase of reinforcement for increasing section shear capacity considering ductile design and found that the shear strength of the walls can be modified at a relatively small expense; as compared with the whole buildings. It is estimated at 0.2, 0.33 and 0.3 percent of the building total cost for 4, 8 and 16 storeys building respectively; the shear capacity in walls can be increased such that D/C ratio is lower than one. The results are tabulated in Table 6.1; Hence, it can be commented that using the proposed scheme for shear capacity modification of shear walls, a well-defined level of performance for buildings can be achieved and it can be related to the design shear forces estimated using the equivalent static load method provided in the building code.

In this study for analysis process 5% damping is considered for all buildings, the effect of other damping is not considered. It has been considered Newmark method for time-history analysis base shear calculation in ETABS modelling. Since the configuration of the buildings studied here is simple and symmetric, the effect of accidental torsion is found to be negligible.

9. References

[1] FEMA 2000 a. Action plan for performance based seismic (FEMA-349), Federal Emergency Management Agency, Washington, D.C.

[2] Paulay, T. and Priestley, M.J.N. 1992. Seismic Design of Reinforced Concrete and Masonry Buildings, John Wiley and Sons, Inc., New York.

[3] Adebar P., Mautrie., and DeVall R., 2005. Ductility of concrete walls: the Canadian seismic design provisions 1984 to 2004, Canadian Journal of Civil Engineering, 32: 1124-1137;

[4] Boivin, Y., and Paultre, P. 2010. Seismic performance of a 12-storey ductile concrete shear wall system designed according to the 2005 National building code of Canada and the 2004 Canadian Standard Association standard A23.3. Canadian Journal of Civil Engineering, 37(1): 1-16.

[5] Blakeley, R.W.G., Cooney, R.C., and Megget, L.M. 1975. Seismic shear loading at flexural capacity in cantilever wall structures. Bulletin of the New Zealand National Society for Earthquake Engineering, 8(4): 278-290.

[6] Boivin and Paultre, 2012. Seismic force demand on ductile reinforced concrete shear walls subjected to western North American ground motions: Part 1 – parametric study. Can. J. Civ. Eng. Vol. 39, 2012

[7] Filiatrault, A., D'Aronco, D., and Tinawi, R. 1994. Seismic shear demand of ductile cantilever walls: a Canadian code perspective. Canadian Journal of Civil Engineering, 21(3): 363-376.

[8] Ghosh, S.K., and Markevicius, V.P. 1990. Design of Earthquake resistant shear walls to prevent shear failure. In Proceedings of Fourth U.S. National Conference of Earthquake Engineering, Palm Springs, Calif., 20-24 May 1990.

[9] Naumoski, N., Tso, W.K. and Heidebrecht A.C., 1998. A selection of representative strong motion earthquake records having different A/V ratios, Earthquake Engineering Research group, McMaster University, Hamilton, Canada.

EURODYN 2020
XI International Conference on Structural Dynamics
M. Papadrakakis, M. Fragiadakis, C. Papadimitriou (eds.)
Athens, Greece, 23–26 November 2020

EFFECTS OF ALTERNATING AXIAL FORCES ON THE RECYCLING RESPONSE OF REINFORCED CONCRETE BRIDGE FRAMES STRENGTHENED BY TENSION-TIES

Angelos A. Liolios [1*], George D. Hatzigeorgiou [2], Panagiotis K. Panetsos [1], and Dimitrios K. Konstantinidis [3]

[1] Egnatia Odos S.A., Bridge Maintenance and Structural Health Monitoring Department, Thermi-Thessaloniki, Greece,
e-mail: aliolios@egnatia.gr, angelosliolios@gmail.com, ppane@egnatia.gr

[2] Hellenic Open University, School of Science and Technology, Patras, Greece,
e-mail: hatzigeorgiou@eap.gr

[3] International Hellenic University, Alexander Technological Educational Institute, Department of Environmental Engineering, Thessaloníki, Greece
e-mail: dkon@cie.teithe.gr

Keywords: Seismic Strengthening of RC Structures, Tension-Ties, Alternating Axial Forces, Multiple Earthquakes Simulation

Abstract. *The influence of varying and alternating axial forces, compressive or tensional ones, on the behavior of Reinforced Concrete (RC) framed structures, seismically strengthened by tension-tie elements, is investigated experimentally and computationally. The experimental investigation concerns the flexure-shear behavior of the structural elements (beam, columns) in a specimen of a two-columns one-story RC frame subjected to a recycling loading simulating seismic excitation. This frame has dimensions and reinforcement configurations that have been used commonly in older substandard RC structures, without anti-seismic design and with typical shear problems. Additional permanent vertical compressive axial loads on the two columns and gravity loads on the beam have not been applied, in order to investigate the influence of varying axial forces and vertical earthquake components. The specimen-frame is examined first as bare, and then as strengthened by X-ties. Next, the computational simulations of these two experiments are performed by a pseudo-dynamic relaxation approach simulating multiple earthquakes. Particular emphasis is given to the operation of tension-tie elements, which have a unilateral behavior. It is proved that ties-strengthening improves the structural seismic behavior and can prevent the flexure-shear failure. A very satisfactory coincidence of the computational with the experimental results has been found. Finally, the investigation shows that the effects of alternating axial forces can be very important for the seismic behavior of RC framed structures. This holds also for two-columns framed piers in bridges subjected to transverse horizontal or vertical seismic components, as is the case of near-field seismic excitations.*

1 INTRODUCTION

As well-known, see e.g. [1-10], variations in axial force can influence strength, stiffness, bending and shear behavior, and deformation capacity of reinforced concrete (RC) columns. In multi-floor RC buildings, the axial loads of the columns are continuously changing during a seismic excitation. This change is particularly significant in perimeter columns, affecting the seismic behavior of the entire structure [5].

Relevant experimental research work on seismic flexural behavior of columns under variable axial loads has already been successfully carried out, see e.g. [3-5]. In these investigations, the seismic behavior of column-specimens with constant axial load was compared with the seismic behavior of specimens similar to the first ones, but under variable axial load. However, the changing axial load was and remained in compressive values range. The same is holding for experiments concerning RC frames having additional vertical loads, see e.g. [5,13,18,20].

On the other hand, in low-rise RC buildings, that do not have additional vertical loads, the changing axial forces do not always remain as compressive ones during a seismic excitation. So, axial forces can be alternated from compressive to tensile ones, meaning that their sign switches from negative to positive ones. The same may hold for highway overcrossings under transverse horizontal seismic excitations, and especially for two-column framed-piers (two-column bents) of RC bridges, when the vertical earthquake component is important for near-field seismic excitations [7-11]. In the above mentioned research it is concluded that excessive tension or tensile strain of the column may lead to shear strength degradation, and therefore vertical excitation can be one of the causes of shear failure. Moreover, tension in the columns has the potential to degradate the shear capacity, which is mainly due to the degradation of the concrete contribution to this capacity.

The above shear capacity degradation and other degradation reasons (seismic, environmental, anti-seismic design according to old codes, etc.) can result to the necessity of seismic strengthening and rehabilitation of RC structures. As well-known, various traditional methods for such seismic strengthening are available [1,6,12,13-14, 47]. Among them, steel bracing systems can be used, and especially buckling resistant braces (BRB), [15-18]. So, the above appearance of alternating axial forces may also be the case for RC frames seismically strengthened with tie-tension (cable) elements [19-21]. Particularly for these cable elements, which are tension-only elements [52-53], their unilateral behavior must be strictly taken into account [22]. This leads to the problem formulation as an Inequality Problem of Structural Engineering, for which a numerical solution requires the use of optimization methods [23-25].

In the present work, the effects of alternating axial forces, compressive or tensile ones, on the recycling behavior of a single-span single-story RC specimen-frame, seismically strengthened with two diagonal tie-tension steel rods (X-bracing), is experimentally and computationally investigated. The investigation focuses on the effect of alternating axial force on the shear strength and on the active stiffness (rigidity) of the structural elements (beam, columns) of the frame. This specimen-frame has dimensions and reinforcement configurations that refer to older RC substandard structures, which have been constructed in Greece and in other seismically active regions without anti-seismic design provided by current Seismic Codes. So, this RC specimen-frame appears typical shear failure problems, such as insufficient concrete confinement and low shear ratio in the columns and beam.

Concerning the seismic strengthening with diagonal tie-tension rods, emphasis is given to the operation of tie-tension elements, which have unilateral behavior, i.e. they can undergo tensile stresses but do not get compressive ones. In both experimental and computational investigation, the frame response is examined first as bare, and then as strengthened by tension-

ties. The frames do not have additional vertical loads, so the changing axial force does not always remain compressive, but changes sign. This concerns the cases where the vertical component is important in near-field seismic excitations or spatial variability of ground motion has to be taken into account [26-27].

2 SUMMARY OF THE EXPERIMENTAL INVESTIGATION

The realized experimental investigation is extensively analyzed in the publications [28, 29]. The research concerns the shear-critical RC frame-specimen shown in Fig. 1., which has no additional vertical loads other than the dead weight. This frame-specimen was first tested without strengthening (bare test-specimen).

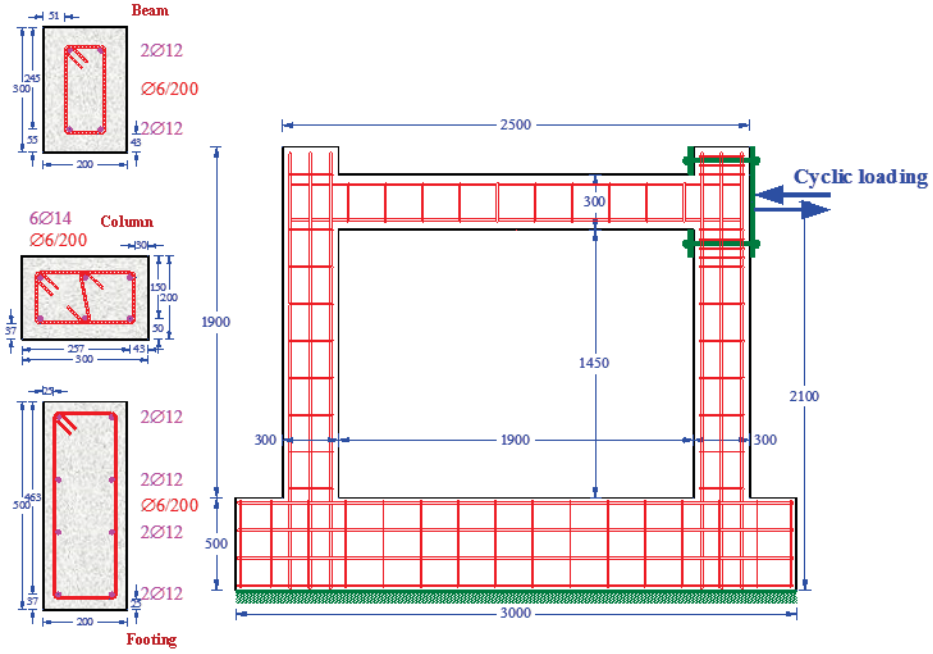

Figure 1: Dimensions and reinforcement configurations of the bare test-specimen [28, 29].

Subsequently, the same frame was tested after being strengthened with two diagonally mounted (X-bracing system) steel tie-tension rods of diameter 16 mm in cross-section, as shown in details in Fig. 2. The displacement-controlled loading history applied to both frames consists of five different and continuously increasing charging steps at ± 1.0, ± 3.6, ± 12.0, ± 22.5 and ± 45.5 mm and two equal charging cycles at each step, (as is further shown in Fig. 7 (d)).

The mode of failure of the control specimen (bare frame) of Fig. 1 is shown in Fig. 3. This is a flexure-shear mode of failure, not symmetric and much more pronounced at the left column, and it has been occurred for the imposed displacement of + 44.5 mm. As concerns the strengthened frame subjected to the same imposed displacement history, the cracking pattern at the end of the test is presented in Figure 4. There it is shown that critical flexure-shear failure of the left column has been prevented. Two distinctive flexural plastic hinges have been only formed in the beam extremities while both beam-column joints of the frame remained undamaged and practically elastic. Finally, the Figure 5 shows the comparative experimental load-displacement diagram for the bare and the strengthened frame. The load abrupt reductions (strength decay) are due to alternating axial forces.

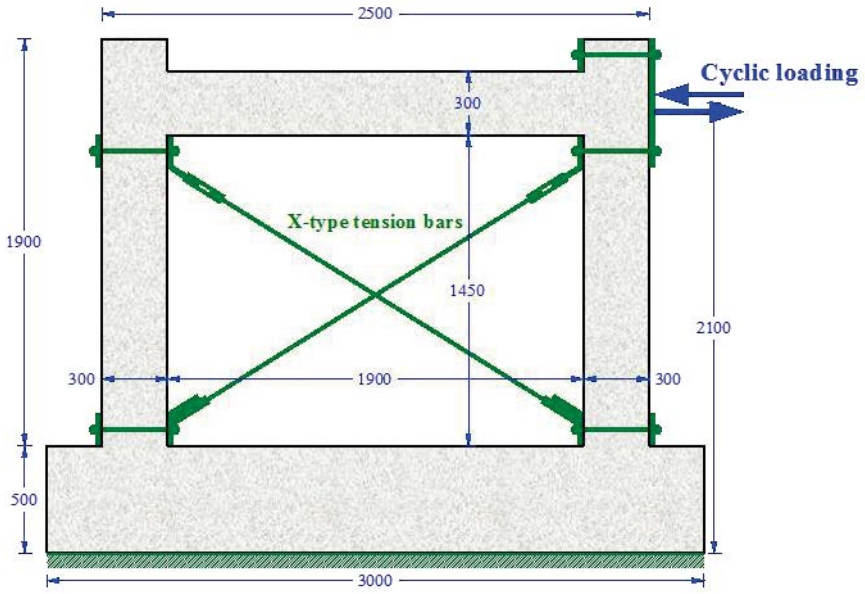

Figure 2: Dimensions and X-bracing of the strengthened test-specimen [28, 29].

Figure 3. Flexure-shear failure occurred at the left column of the bare test-frame [28, 29].

Figure 4. Cracking pattern of the steel X-braced RC frame at the end of the test [28, 29].

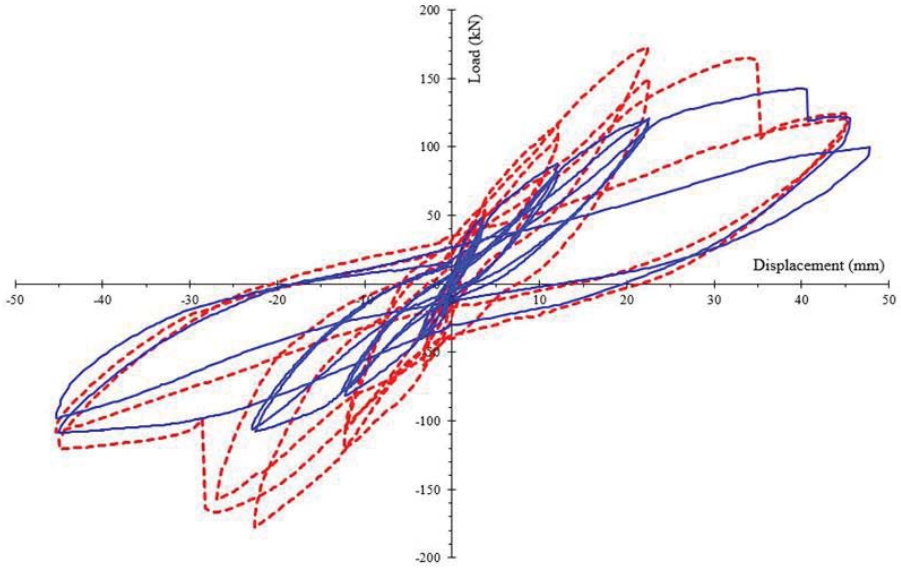

Figure 5: Experimental hysteresis load-displacement diagramme of the ties-strengthened frame (dashed red lines) in comparison to the diagramme of the bare frame without ties (continuous blue lines).

In general, the comparisons of the cyclic performance between the original bare and the X-bracing strengthened specimens indicate a significantly enhanced behavior: The load capacity in the bare frame is 120.82kN and in the strengthened frame is 178.18kN. So, an increase of 47.48% in the load capacity is recorded.

3 COMPUTATIONAL SIMULATION OF THE EXPERIMENTS TAKING INTO ACCOUNT ALTERNATING AXIAL FORCES

3.1 The computational method of analysis in general

The computational simulations of the above experiments concerns in general the dymamic response of RC framed-structures strengthened by tension-tie elements. In references [28, 30, 31] a developed methodology is presented, which concerns the dynamic analysis of RC structures strengthened by ties under multiple earthquakes. This methodology focuses on studying the seismic response of multistory RC frame structures in a practical and economic way according to suggestions of [1,6,32,33]. So, RC finite elements belonging to macroscopic models are used instead of microscopic fiber ones. For this purpose, the Ruaumoko computational code [34] is used for inelastic analysis in an appropriate way.

In order to simulate the imposed displacement-controlled loading, a pseudo - dynamic relaxation procedure [35] is applied simulating multiple earthquakes procedures [22,30,36,37]. Thus, the imposed displacements are considered as pseudo-events of a seismic sequence. These are adjusted to have a time-duration much bigger than the fundamental eigen-period of the investigated frame. Special attention and treatment is given herewith to the effects of alternating axial force on the behavior of the shear critical structural elements, in particular with

respect to the bending moment-curvature diagrams in sections, the active flexural stiffness and the cyclic shear strength, as discussed below.

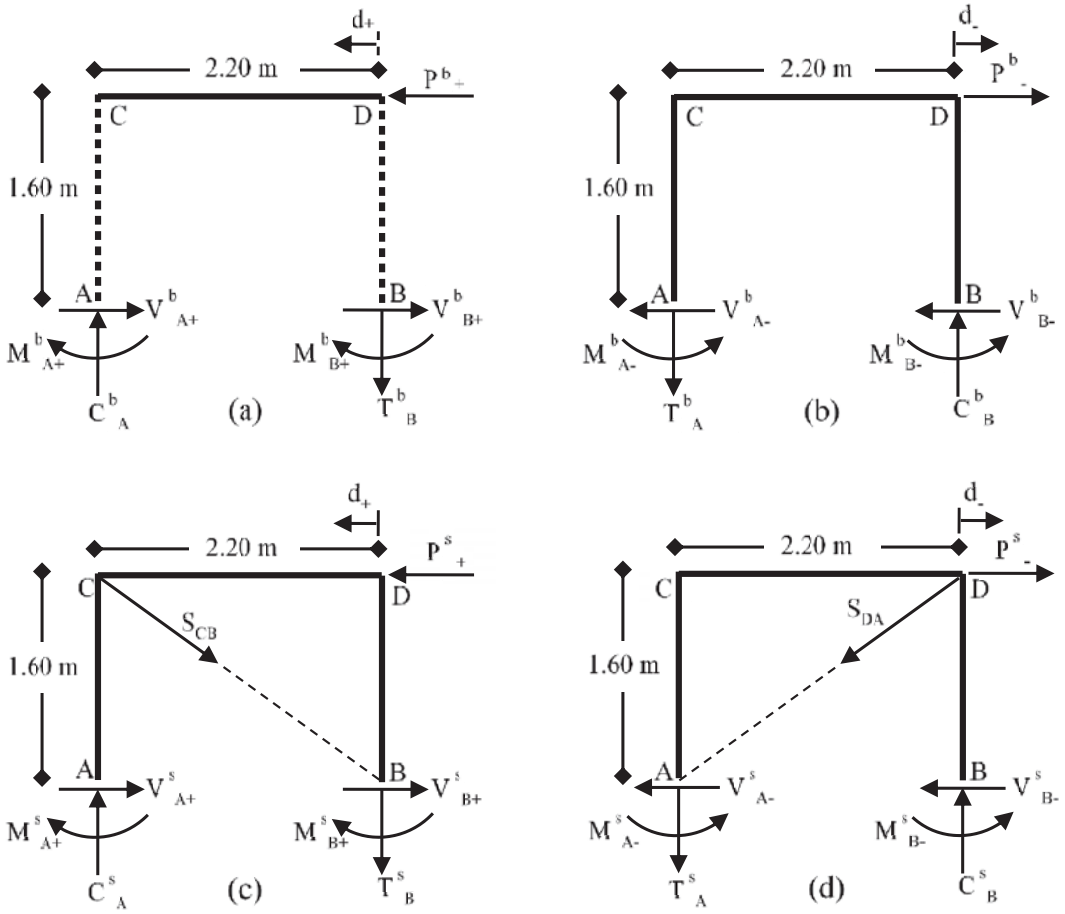

Figure 6. The alternating behaviour of the specimen-frames for the cyclic imposed displacements: (a), (b) bare frame, (c), (d) strengthened frame.

In Figure 6 the alternating behaviour of the specimen-frames of Fig. 1 and Fig. 2 due to the cyclic imposed displacements is shown. As has been reported in sections 2, the load was imposed to the right top corner joint (see Fig. 1 and Fig. 2) denoted as node D in Fig. 6. Taking into account the real axial deformation of the beam CD, this loading on node D has as result a non-symmetric behavior. This means e.g. that the shear-reactions V_A and V_B have no-equal value, but in any case, must satisfy the equilibrium condition $V_A + V_B = P$. So, equality for the shear-reactions V_A and V_B holds only under the theoretical linear-elastic assumption. Figure 6 shows the alternating frame behavior concerning the alternating axial forces, tensional or compressive ones, which are developed in the structural elements at each semi-cycle of imposed displacement, (d_{+}) ή (d_{-}), for the bare and the strengthened frame. As concerns the strengthened frame, for positive imposed displacement d_+ only the descending tie CB is activated- see Fig. 6 (c). Similarly, for the reversal negative imposed displacement d_-, only the ascending tie AD is activated- see Fig. 6(d).

Obviously, for positive (from right to left) imposed displacement d_+ on node D -see Fig. 6, (a)-the right column BD is under tension axial load T_B, whereas the left column AC and the

beam CD are under compression axial loads. On the contrary, for the reversal negative imposed displacement d- on node D, the left column AC and the beam CD appear tension, whereas the right column BD appears compression - see Fig. 7. (b). Thus, in every semi-cycle of the imposed displacements, an appropriate adaptive estimate for the effective flexural stiffness EI_{eff} of the structural members has to be realized, taking into account whether they are in compressive or in tensional state. This is in agreement with the already mentioned-see also [3,4,7,45-51]- well-known fact, that variable axial force affects, due to by it induced cracking, on the one hand the effective flexural stiffness EI_{eff}. and on the other hand the available cyclic shear strength V_R.

So, based on experimental research, they are known-see e.g. [3]- semi-empeirical relations of the form $EI_{eff} = (a_1 + a_2 P).EI_g$ for compressive axial force P, and $EI_{eff} = (a_3 - a_4 P).EI_g$ for tensional axial force P. Similarly, they are known semi-empeirical relations of the form $V_c = a(1+bP)^n$ for compressive axial force P, and $V_c = c(1-dP)^m$ for tensional axial force P, where V_c is the concrete shear strength and a,b,c,d,m,n are experimental parameters. Especially for the available cyclic shear strength V_R, the Eurocode EC8 [39] provides the formula

$$V_R = \frac{1}{\gamma_{el}} \cdot \left[\frac{(h-x)\lambda_1}{2L_s} + (1 - 0.05\lambda_2) \cdot \left[0.16\lambda_3 (1 - 0.16\lambda_4) A_c \sqrt{f_{cm}/\mathrm{CF}} + V_w \right] \right] \quad (1)$$

For the meaning of the various symbols, see [39,40]. Especially for the parameter λ_1, it depends on the variable axial force $N(t)$, i.e. $\lambda_1 = \lambda_1(N)$, and must be emphasized that $N(t)$ is positive when it is compressive, but it is taken zero when it is tensional.

Finally, concerning the shear critical structural behavior, and especially the question, whether the flexural failure precedes the shear one or not, use of Moment versus Chord Rotation (M - θ) final elastic-plastic diagrams for the critical sections are constructed and used according to Makarios [40].

3.2 Some representative computational results

Next, some representative results by applying the above numerical simulation for the experimental process are reported. So, the alternating axial forces developed in the columns AC and BD and in the beam CD of the bare frame are shown in Fig. 7(a), 7(b) and 7(c), respectively, in dependence of the imposed displacement history on node D shown in Fig. 7(d).

As is already reported in section 2.1, the shear capacity and the stiffness of RC members is affected by the level of axial force. Compressive axial force increases and tensile axial force decreases the shear capacity and the stiffness of the columns. When the failure of the bare frame had occurred at imposed displacement of 44.5 mm, the left column AC was in compression, while the right column BD was in tension. The left column AB has appeared bigger compressive axion force than the right column BD-see Fig. 4. Note that although compressive axial force increases the shear capacity, it also increases the demand owing to the increase in the stiffness of the column. So, the left column AC "attracted" bigger portion of the horizontal load P than the right column BD, i.e. $V_A > V_B$, and when its shear resistance had been overcome by V_A, a shear failure had occurred in the left column AC.

Based on the above considerations, the mode of failure of the control specimen (bare frame) of Fig. 1 can be predicted numerically and explained. As the imposed displacement history is applied on the node D, the flexure-shear mode of failure is not symmetric and as shown in Fig. 3 it is much more pronounced at the left column.

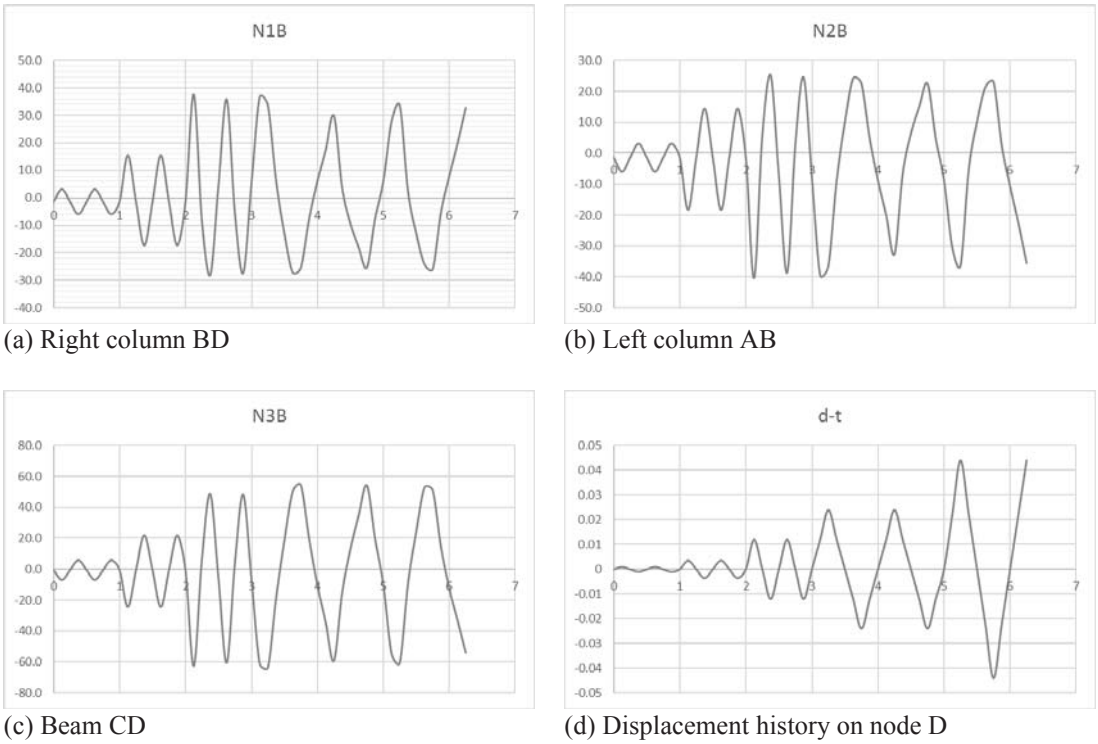

(a) Right column BD (b) Left column AB

(c) Beam CD (d) Displacement history on node D

Figure 7. Alternating axial forces for the bare frame-specimen: (a) Right column BD, (b) Left column AB, (c) Beam CD, and (d): The history of the imposed displacement on node D.

The range-values of the alternating axial forces for the bare frame, as well as for the strengthened frame, are shown in the Table 1. These axial forces are due to both loading: on the one hand due to dead weight loading and on the other hand due to imposed displacement loading. The first ones, i.e. the compressive (negative, -) axial forces due to static dead weight loading, are: -2.89 kN for the columns AC and BD, and -0.46 kN for the beam CD.

As the total values in Table 1 show, the tensional (positive, +) axial forces in the strengthened frame are slightly reduced in comparison to the corresponding values of the bare frame. On the contrary, the compressive (negative, -) axial forces in the strengthened frame are significantly increased in comparison to the corresponding values of the bare frame. So, the shear capacity for the members of the strengthened frame is increased.

Structural Member	Bare Frame		Strengthened frame	
	max	min	max	min
Right column BD	+50.91	-35.97	+45.26	-91.17
Left column AC	+33.12	-48.11	+33.10	-109.08
Beam CD	+59.38	-68.47	+53.21	-147.48

Table 1: Extreme values [in kN] of the alternating axial forces in the structural members.

Next, for the strengthened with ties frame-specimen it is shown in Figure 8 the computational hysteresis load-displacement diagramme (continuous blue lines) in comparison to the corresponding experimental diagramme (dashed red lines). This comparison proves a good agreement between the computational results and the corresponding experimental ones. Moreover, the load abrupt reductions (strength decay) due to alternating axial forces are covered (captured) very satisfactorily.

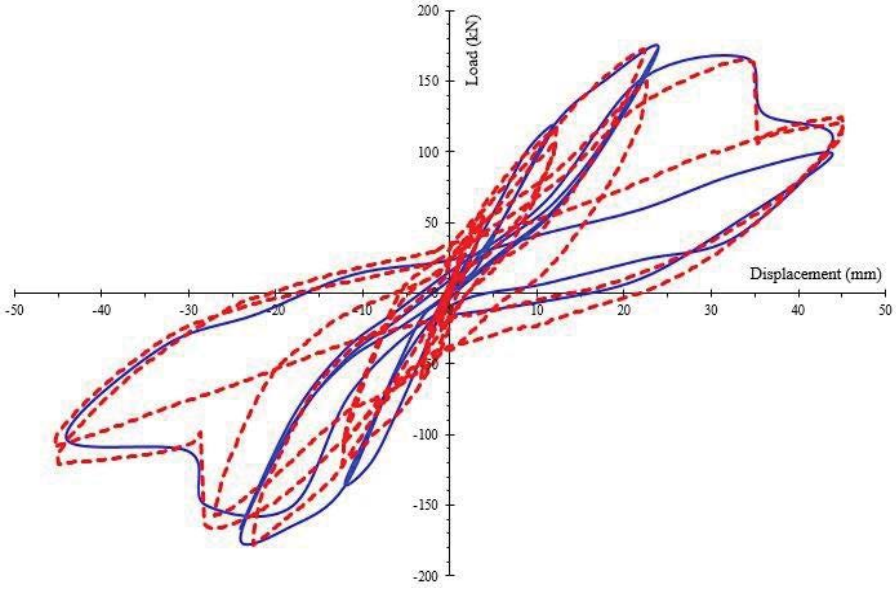

Figure 8: Strengthened with ties frame: Comparison of the computational hysteresis load-displacement diagramme (continuous blue lines) with the corresponding experimental diagramme (dashed red lines).

Finally, in Table 2 they are given indicative results, which prove the effectiveness of the strengthening by ties. The table values in columns (2) and (3) concern, respectively, the Total Damage Index DI_G and the Local Damage Index DI_L for the flexural bending moment in the base of the left column AC. These damage indices are computed according to Park & Ang formula [41,42]. In columns (4) they are given the maximum horizontal load P_{top}, which can be undertaken for both, the bare and the ties-strengthened test-frame of the experimental investigation.

FRAME	DI_G	DI_L	P_{top} [kN]
(1)	(2)	(3)	(4)
Bare	0.694	0.973	122.8 kN
Strengthened	0.001	0.001	181.9 kN

Table 2: Damage indices and maximum horizontal load P_{top}.

4 APPLICATION CONSIDERATIONS FOR FRAMED BENTS OF BRIDGES

The numerical approach presented in the previous section 3 and calibrated on the basis of the experimental results of section 2, can be effectively applied in various practical cases, which concern strengthening by tension-ties under alternating axial forces. Such cases are, e.g: (a) horizontal seismic excitation in low-rise RC framed buildings, that do not have additional

dead weight vertical loads, in coupled shear-walls systems [3], etc, (b) vertical seismic excitation due to near-field seismic excitations, especially for RC bridge systems, [7-10], (c) horizontal seismic excitation transverse to longitudinal axis of bridges having RC framed two-column bridge-bents, (d) horizontal seismic excitation of bridges with restrainer-cable systems [38]. Especially for the (c) case, where alternating axial forces have significant effects on the seismic behavior of framed bridge-bents, some typical examples are next considered.

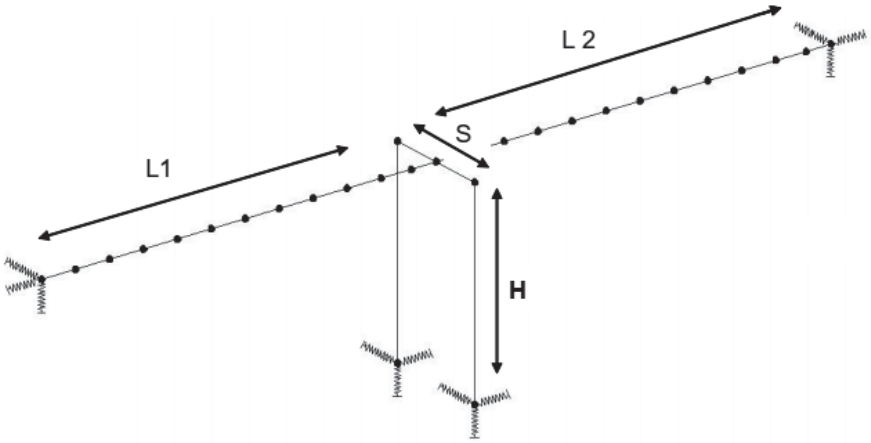

Figure 9: Simulation model of the typical two-span highway overcrossing bridge considered in [8].

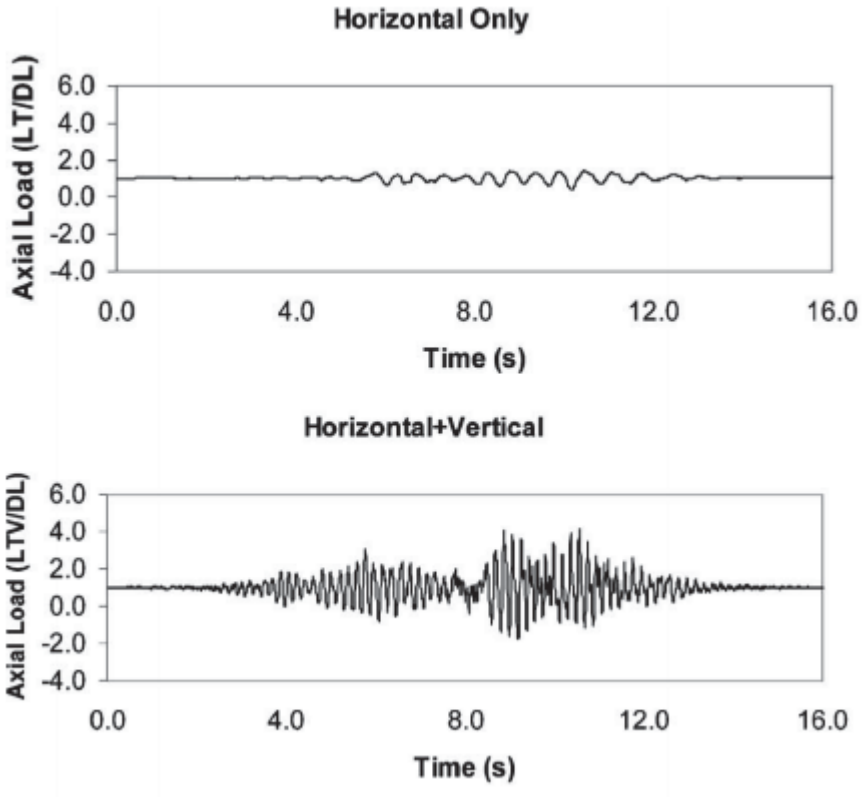

Figure 10. Time history response of axial force demand in the columns of the bridge considered in [8].

In above Fig. 9 it is shown a typical case for highway overcrossings [8] with one framed-pier. Figure 10 shows a typical response of the above bridge columns under horizontal longitudinal and vertical seismic actions. The computed axial force is considered as positive when it is compressive and is normalized by the dead axial load, which means that values below 0.0 indicate a state of axial tension in the column.

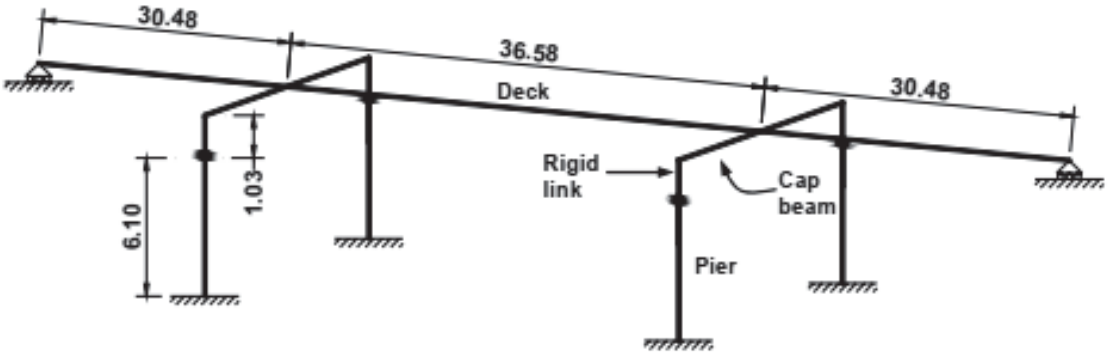

Figure 11: The FHWA Bridge #4 considered in [9] with two-colums framed piers.

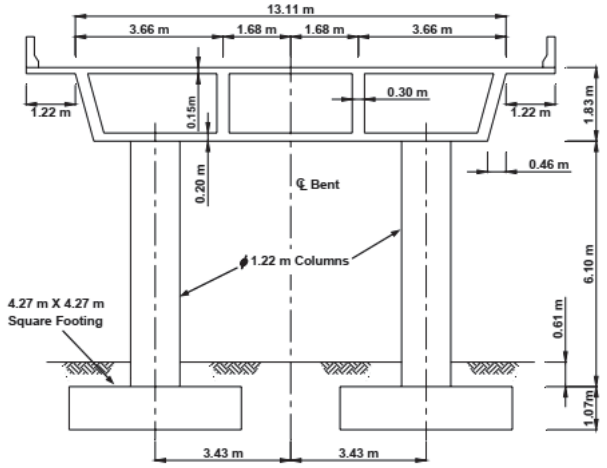

Figure 12: The cross section of the two-colums framed piers in FHWA Bridge #4 of [9].

Figures 11 and 12 show the case of a FHWA bridge considered in [9] with two framed-bent piers. Obviously, the above bents, i.e. two-column framed-piers, under transverse (to bridge axis) horizontal (along the bent) seismic excitations, may appear alternating axial forces on their columns. The same holds for the cases shown in Figure 13 and which are considered in [43,44]. The last case-(b) in Fig. 13- concerns the middle tall-pier of the high Evripos cable-stayed bridge in Chalkis, Evoia, Greece.

Concerning the seismic strengthening of above considered two-columns framed piers by bracing systems, the indicative case of using BRB (buckling resistant braces) diagonal "structural fuses" proposed in [17] is shown in Fig. 14.

In general, for strengthening by ties-bracing systems in bridges, the numerical treatment can be realized by using the herein proposed methodology.

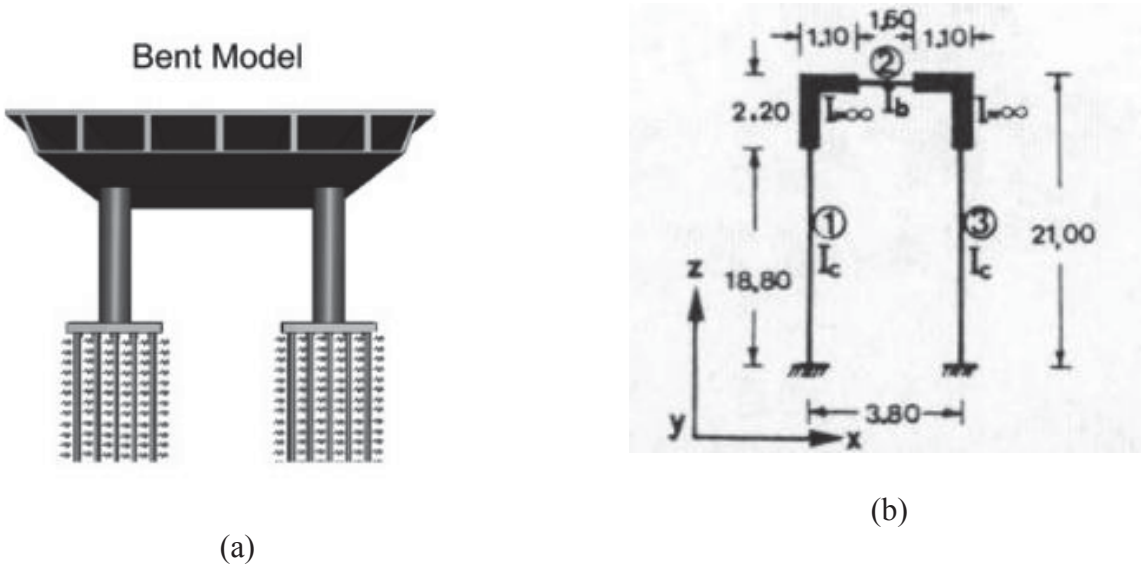

Figure 13: Two-columns framed bridge piers considered: (a) in [43], (b) in [44], Evripos bridge.

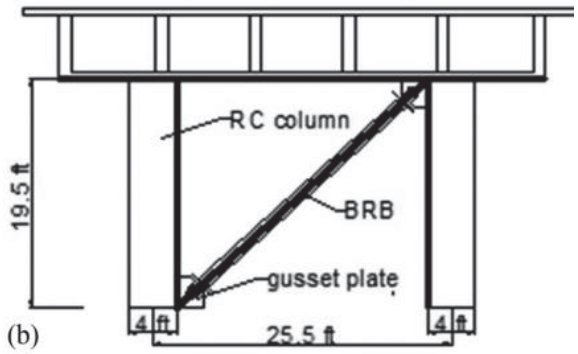

Figure 14: A two-columns framed pier strengthened by an BRB diagonal "structural fuse" proposed in [17].

5 CONCLUDING REMARKS

Based on available experimental results for shear-critical RC frame-specimens, a numerical approach has been presented and calibrated for the seismic strengthening by tension-ties under alternating axial forces. This approach can be used for the numerical treatment of the general problem concerning the tension-ties strengthening of framed-bents in existing bridges. Moreover, this approach can be used for the construction of fragility curves for the seismic vulnerability of bridges strengthened by ties. As well-known, see e.g. [54], fragility curves are very important for practical reasons concerning the evaluation of seismic risk in existing bridges. Thus, fragility curves for ties-strengthened bridges is an interesting research field. In

general must be taking into account that the numerical treatment of strengthening by bracing systems in existing bridges requires the estimation of various uncertain parameters. For this purpose, relevant results of significant recent research are now available and can be used [55-58].

REFERENCES

[1] Penelis, G., Penelis, Gr. *Concrete Buildings in Seismic Regions*. CRC Press, Taylor and Francis Group Ltd, London, 2nd edition, 2018.

[2] Penelis, G., Kappos, A. *Earthquake Resistant Concrete Structures*. CRC Press, London, 2010.

[3] Paulay, T. Priestley, M.J.N. *Seismic design of reinforced concrete and masonry buildings.* Wiley, New York, 1992.

[4] Abrams, D.P. *Influence of axial force variations on flexural behavior of reinforced concrete columns,* ACI Struct. J., 84(3), 246-254, 1987.

[5] Tsonos, A.G., I.A. Tegos, and G.Gr. Penelis. *Influence of Axial Force Variations on Seismic Behaviour of R/C Columns*, (in Greek). Tech. Chron.-A, Greece, Vol. 12, No 2, pp. 82-100, 1992.

[6] Fardis, M.N. *Seismic design, assessment and retrofitting of concrete buildings: based on EN-Eurocode 8*. Springer, Berlin, 2009.

[7] Saadeghvaziri, M.A., Foutch, D.A. *Dynamic behaviour of R/C highway bridges under the combined effect of vertical and horizontal earthquake motions*. Earthquake Engineering and Structural Dynamics, Vol. 20(6), pp. 535-549, 1991

[8] Kunnath, S. K., Erduran, E., Chai, Y. H., & Yashinsky, M. *Effect of near-fault vertical ground motions on seismic response of highway overcrossings.* Journal of Bridge Engineering, 13(3), 282-290, 2008.

[9] Kim, S. J., Holub, C. J., & Elnashai, A. S. *Experimental investigation of the behavior of RC bridge piers subjected to horizontal and vertical earthquake motion*. Engineering Structures, 33(7), 2221-2235, 2011.

[10] Makris, N., & Zhang, J. *Seismic response analysis of a highway overcrossing equipped with elastomeric bearings and fluid dampers*. Journal of Structural Engineering, 130(6), 830-845, 2004.

[11] Carydis, P., Castiglioni, C., Lekkas, E., Kostaki, I., Lebesis, N., & Drei, A. *The Emilia Romagna, May 2012 earthquake sequence: The influence of the vertical earthquake component and related geoscientific and engineering aspects.* Ingegneria Sismica, 29(2-3), 31-58, (2012.

[12] Dritsos, S.E.. *Repair and Strengthening of Reinforced Concrete Structures*, (in Greek), University of Patras, Greece, 2017.

[13] Kakaletsis, D.J. David, K.N. and Karayannis, C.G. *Effectiveness of Some Conventional Seismic Retrofitting Techniques for Bare and Infilled R/C Frames*. Structural Engineering and Mechanics, 39 (4), 499-520, 2011.

[14] Rousakis, T. C., Karabinis, A. I., Kiousis, P. D., & Tepfers, R. *Analytical modelling of plastic behaviour of uniformly FRP confined concrete members.* Composites Part B: Engineering, 39(7-8), 1104-1113, 2008.

[15] Antonopoulos, T.A. and Anagnostopoulos, S.A. *Seismic evaluation and upgrading of RC buildings with weak open ground stories*. Earthquakes and Structures, 3(3-4), pp. 611-628, 2012.

[16] El-Bahey S, Bruneau M. *Buckling restrained braces as structural fuses for the seismic retrofit of reinforced concrete bridge bents*. Engineering Structures; 33:1052–1061, 2011.

[17] Wei, X., & Bruneau, M. *Case study on applications of structural fuses in bridge bents*. Journal of Bridge Engineering, 21(7), 2016.

[18] Karalis, A.A., Georgiadi-Stefanidi, K.A., Salonikios, T.N., Stylianidis, K.C., Mistakidis, E.S. *Experimental and numerical study of the behaviour of high dissipation metallic devices for the strengthening of existing structures*. In: M. Papadrakakis et al., (eds.), Proceedings of COMPDYN 2011, ECCOMAS, 2011.

[19] Markogiannaki, O. and Tegos, I. *Strengthening of a Multistory R/C Building under Lateral Loading by Utilizing Ties*. Applied Mechanics and Materials, 82, 559-564, 2011.

[20] Massumi, A. and Absalan, M. *Interaction Between Bracing System and Moment Resisting Frame in Braced RC Frames*. Archives of Civil and Mechanical Engineering, 13(2), 260-268, 2013.

[21] D. S. Sophianopoulos, K.S. Papachristou, T. Papatheocharis, P. Tsopelas, P. Perdikaris, *Theoretical – Experimental Investigation and Optimization of the Seismic Strengthening of Existing RC Buildings with Pilotis via Steel Concentric X-Braces: I. Parametric Study, II. Experiments*. Proceedings of the 8th Hellenic National Conference of Steel Structures, Tripoli, Greece, October 2-4, 2014.

[22] Liolios, A.A. *A computational investigation for the seismic response of RC structures strengthened by cable elements*. In: Papadrakakis M. et al (eds), Proceedings of COMPDYN 2015, pp. 3997-4010, 2015.

[23] Panagiotopoulos, P. *Hemivariational Inequalities. Applications in Mechanics and Engineering*, Springer Verlag, Berlin, 1993.

[24] Mistakidis, E.S., Stavroulakis, G.E. *Nonconvex optimization in mechanics. Smooth and nonsmooth algorithmes, heuristic and engineering applications*. Kluwer, London, 1998.

[25] Rousis, M.G., Koumousis, V.K. *Elastoplastic frame analysis with softening in the form of mixed complementarity problem.* In: Proceedings of the 7 th GRACM Congress, Athens, 2010.

[26] Maniatakis, C.A., Psycharis, I.N., Spyrakos, C.C. *Effect of higher modes on the seismic response and design of moment-resisting RC frame structures*. Engineering Structures, Vol. 56, pp. 417-430, 2013.

[27] Sextos, A.G., Pitilakis, K.D., Kappos, A.J. *Inelastic dynamic analysis of RC bridges accounting for spatial variability of ground motion, site effects and soil–structure interaction phenomena. Part 1: Methodology and analytical tools*. Earthquake Engineering and Structural Dynamics, 2003, Vol. 32(4), pp. 607-627.

[28] Liolios, A.A. *A study on the strengthening of reinforced concrete structures with emphasis on the use of tension-ties: Computational and experimental investigation*. PhD Dissertation Thesis, (in Greek), Democritus University of Thrace, Dept. of Civil Engineering, Xanthi, Greece, 2019.

[29] Liolios, A.A., Efthymiopoulos, P., Mergoupis, T., Rizavas, V. and Chalioris, C. *Reinforced concrete frames strengthened by tension-tie elements under cyclic loading: Experimental investigation*, In: Papadrakakis, M. et al.(eds.), Proceedings of COMPDYN 2017: Computational Methods in Structural Dynamics and Earthquake Engineering, paper C18197, 2017.

[30] Liolios, A., Liolios, A.A., and Hatzigeorgiou, G. *A Numerical Approach for Estimating the Effects of Multiple Earthquakes to Seismic Response of Structures Strengthened by Cable-Elements*. Journal of Theoretical and Applied Mechanics, Vol.43, No. 3, pp. 21-32, 2013.

[31] Liolios, A.A., Chalioris, C. *Reinforced concrete frames strengthened by tention-tie elements under cyclic loading: A computational approach*. In: Papadrakakis, M., et al. (eds.) Proceedings of

COMPDYN 2017: Computational Methods in Structural Dynamics and Earthquake Engineering, paper C18195.

[32] Fardis, M. N., Carvalho, E. C., Fajfar, P., and Pecker, *A. Seismic Design of Concrete Buildings to Eurocode 8.* CRC Press, Taylor and Francis Group, New York, 2015.

[33] Fardis M.N. *Modelling of concrete buildings for practical nonlinear seismic response analysis.* Architecture, Civil Engineering, Environment Journal, Silesian University of Technology, 3(1), 31-46, 2010.

[34] Carr, A.J. *RUAUMOKO - Inelastic Dynamic Analysis Program*. Department of Civil Engineering, University of Canterbury, Christchurch, New Zealand, 2008.

[35] Papadrakakis, M. *A method for the automatic evaluation of the dynamic relaxation parameters.* Computer Methods in Applied Mechanics and Engineering, Vol. 25(1), pp. 35-48, 1981.

[36] Hatzigeorgiou, G. & Liolios, A. *Nonlinear behaviour of RC frames under repeated strong ground motions*. Soil Dynamics and Earthquake Engineering, 30(10), 1010-1025, 2010.

[37] Liolios, A.A., Hatzigeorgiou, G., and Liolios, A. *Effects of multiple earthquakes to the seismic response of structures.* Building Materials and Structures – Journal for Research in the Field of Materials and Structures, Vol.55, No. 4, pp. 3-14, 2012.

[38] Priestley, M.J.N., Seible, F.C., Calvi, G.M. *Seismic Design and Retrofit of Bridges*. Wiley, 1996.

[39] EC8, Eurocode 8 (CEN 2004). *Design of Structures for Earthquake Resistance, Part 3: Assessment and Retrofitting of Buildings*, (EC8-part3), EN 1998-3, Brussels.

[40] Makarios, T. *Modelling of characteristics of inelastic member of reinforced concrete structures in seismic nonlinear analysis*. Ch. 1, pp. 1-41, In: Gualtiero Padovani and Manuel Occhino (Editors): *Focus on Nonlinear Analysis Research*, Nova Publishers, New York, 2013.

[41] Park, Y. J. & Ang, A. H. S. (1985). *Mechanistic seismic damage model for reinforced concrete.* Journal of Structural Engineering, ASCE, 111(4), 722-739.

[42] Mitropoulou, C. C., Lagaros, N. D., & Papadrakakis, M. *Numerical calibration of damage indices.* Advances in Engineering Software, 70, 36-50, 2014.

[43] Kotsoglou, A., & Pantazopoulou, S. *Response simulation and seismic assessment of highway overcrossings*. Earthquake Engineering & Structural Dynamics, 39(9), 991-1013, 2010.

[44] Kalevras, V. & Stathopoulos, S. *Optimization of the design for middle bent-pier of the tall Evripos bridge.* In: Proceedings of 8th Hellenic Concrete Conference, TEE, Xanthi-Kavala, Greece, 1987.

[45] Achillopoulou, D.V., Karabinis, A.I.. *Investigation of shear transfer mechanisms in repaired damaged concrete columns strengthened with RC jackets*. Structural Engineering and Mechanics, Vol. 47(4), pp. 575-598, 2013.

[46] Konstantinidis, D., Kappos, A. J. and Izzuddin, B. A. *Analytical modelling of unconfined and confined high strength concrete under reverse cyclic loading*. In: Proceedings of the 13th World Conference on Earthquake Engineering, Vancouver, Canada, paper no. 2064, 2004.

[47] Papanikolaou, V. K., Thermou, G. E., & Kappos, A. J. *Moment-curvature analysis of R/C jacketed rectangular sections including interface slip under cyclic loading*. In: Proceedings of 15th World Conference on Earthquake Engineering, Lisbon, Portugal, 2012.

[48] Rousakis, T., Nistico, N., Karabinis, A. *Upgraded experimental database of uniformly FRP confined concrete columns for assessment of existing recommendations*. In: The 6th International Conference on FRP Composites in Civil Engineering–CICE, pp. 13-15, 2012.

[49] Megalooikonomou, K. G., Tastani, S. P., & Pantazopoulou, S. J. *Effect of yield penetration on column plastic hinge length*. Engineering Structures, vol. 156, 161-174, 2018.

[50] Kim, T. H., Kim, Y. J., & Shin, H. M. *Seismic performance assessment of reinforced concrete bridge columns under variable axial load.* Magazine of Concrete Research, 59(2), 87-96, 2007.

[51] Mariani, V., Tanganelli, M., Viti, S., & De Stefano, M. *The effects of the axial load variation on the seismic performance of existing RC buildings*. In: M. Papadrakakis, V. Papadopoulos, V. Plevris (eds.), *Proceedings of COMPDYN 2015,* Crete, Greece.

[52] Filiatrault A, Tremblay R. *Design of tension-only concentrically braced steel frames for seismic induced impact loading*. Eng Struct; 20(12):1087–96, 1998.

[53] Papagiannopoulos GA. *On the seismic behaviour of tension-only concentrically braced steel structures.* Soil Dyn Earthq Eng; 115: 27–35, 2018.

[54] Liolios, A. A., Panetsos, P., Liolios, A., Hatzigeorgiou, G., Radev, S. *A Numerical Approach for Obtaining Fragility Curves in Seismic Structural Mechanics: A bridge Case of Egnatia Motorway in Northern Greece.* Lecture Notes in Computer Sciences, Vol. 6046, pp. 477-485, Springer, 2010.

[55] Tsompanakis, Y., Lagaros, N. D., & Papadrakakis, M. (Eds.). *Structural Design Optimization Considering Uncertainties.* Taylor & Francis, CRC Press, London, 2008.

[56] Papadrakakis, M., Stefanou, G., & Papadopoulos, V. (Eds.). *Computational methods in stochastic dynamics*. Berlin: Springer, 2011.

[57] Papadrakakis, M., Fragiadakis, M., & Lagaros, N. D. (Eds.). *Computational methods in earthquake engineering*. Berlin, Germany: Springer, 2011.

[58] Papadrakakis, M., & Stefanou, G. (Eds.). *Multiscale modeling and uncertainty quantification of materials and structures*. Springer, Berlin, 2014.

EURODYN 2020
XI International Conference on Structural Dynamics
M. Papadrakakis, M. Fragiadakis, C. Papadimitriou (eds.)
Athens, Greece, 23–26 November 2020

CORRECTION OF LASER DOPPLER VIBROMETER MEASUREMENTS AFFECTED BY SENSOR HEAD VIBRATION USING TIME DOMAIN TECHNIQUES

Abdel Darwish[1], Ben Halkon[1], Sebastian Oberst[1], Robert Fitch[1] and Steve Rothberg[2]

[1]School of Mechanical and Mechatronic Engineering, Faculty of Engineering& IT,
University of Technology Sydney, 15 Broadway, Ultimo, NSW 2007, Australia
e-mail: {Abdel.Darwish, Benjamin.Halkon, Sebastian.Oberst, Robert.Fitch}@uts.edu.au

[2]Wolfson School of Mechanical, Electrical and Manufacturing Engineering,
Loughborough University, Ashby Road, Loughborough, Leicestershire, LE11 3TU, U.K.
e-mail: S.J.Rothberg@lboro.ac.uk

Keywords: Vibration measurement; laser Doppler vibrometer; instrument vibration correction; time domain signal processing.

Abstract. *Despite widespread use in a variety of areas, in-field applications of laser Doppler vibrometers (LDVs) are still somewhat limited due to their inherent sensitivity to vibration of the instrument sensor head itself. Earlier work, briefly reviewed herein, has shown it to be possible to subtract the instrument vibration via a number of means, however, it has been difficult up to now to truly compare the performance of these. This is compounded by the constraint that a frequency domain based approach only holds for stationary vibration signals while, particularly for in-field applications, an approach that is also applicable to transient signals is necessary. This paper therefore describes the development of a novel time domain post-processing based approach for vibrating LDV measurement correction and compares it with the frequency domain counterpart. Results show that, while both techniques offer significant improvements in the corrected LDV signal when compared to a reference accelerometer measurement, the time domain based correction outperforms the frequency domain based method by a factor of eight.*

1 INTRODUCTION

Laser Doppler vibrometers (LDVs) have become indispensable tools both within industrial and research domains, especially where non-contact operation is advantageous [1]. Despite the considerable amount of published research, in-field applications of LDVs - which might include their incorporation into unmanned aerial vehicles for example - remains arguably limited, at least partly due to their sensitivity to vibration of the instrument itself. However, if this limitation was eliminated, it could enable remote vibration measurement campaigns in hazardous environments, for example facilitating the more accurate and rapid detection of remnant mines or structural health monitoring of remote infrastructure.

LDVs are based on an interferometric optical arrangement, meaning they measure target surface vibration *relative* to the instrument; conversely, more traditional contacting vibration transducers measure *absolute* surface vibration. In other words, instrument vibration, usually caused by the surrounding environment, is indistinguishable from that of the target in the resulting measurement. A common solution to this problem is to isolate the LDV using passive [2] or active anti-vibration mounting arrangements [3]. However, such solutions can be too heavy, ineffective or costly. The contemporary solution [4–6] is to independently measure the instrument vibration and use this information to correct the LDV measurement, thereby recovering the intended target vibration measurement.

Correction by measuring the instrument vibration has previously been carried out conveniently and effectively in the frequency domain [4–6], however, this is only appropriate for the statistically stationary signals that are typically encountered. Oftentimes, however, and in particular in field based measurement campaigns, vibration profiles may be transient in nature and an alternative, time domain based approach may, therefore, be more appropriate. Correction based in the time domain has previously been carried out using either an internal damper, which the reference beam is incident upon or an external accelerometer [7–9]. However, until now, no comparison has been been made of the two types of approach due to alternative experimental setups or effectiveness metrics. The development of a novel, post-processing, time domain based approach and its comparison with the frequency domain based alternative is, therefore, the focus of this article.

2 FREQUENCY DOMAIN BASED PROCESSING

It has been rigorously shown, both mathematically and experimentally, that correction of erroneous LDV measurements requires the subtraction of an independent simultaneous measurement of the instrument/optical element vibration [4, 5]. In the case of a single beam LDV, this measurement is conveniently achieved in practice using a single, ‘correction accelerometer’ mounted somewhere along the laser beam axis, generally on the back of the housing. To experimentally confirm the validity of the correction, a second ‘reference accelerometer’ is typically mounted to the target at the measurement location to offer a ‘true’ target vibration measurement. For statistically stationary velocity signals, frequency domain processing is a convenient means by which subtraction of the correction accelerometer signal can be realised while simultaneously performing the required integration and temporal alignment. The framework for this frequency domain based processing approach for the correction of erroneous LDV measurement is already well-established and the description is therefore intentionally kept brief in what follows.

2.1 Sensitivity adjustment and time delay correction

Accelerometer sensitivities are adjusted, with reference to the LDV, using a broadband frequency domain based relative calibration procedure. By necessity, this includes integration, readily achieved in the frequency domain, of the accelerometer signals. Ratios of the vibration levels over the frequency range of interest are used to revise the accelerometer sensitivities. Furthermore, due to inevitable differences between accelerometer and LDV signal conditioning electronics, finite time delays, independent of the sensitivity adjustment, exist between the digitised signals. Again, taking the LDV as the reference, these can be similarly readily estimated in the frequency domain from the signal phase differences [4, 5].

2.2 Instrument vibration correction

Among other typical practical measurement factors, including the accuracy of the positioning of the correction transducer to accurately determine the instrument vibration in the laser beam direction, the mean error reduction achieved depends upon the relative levels of instrument and target vibration. For vibration levels and frequency ranges of relevance to 'real-world' measurement campaigns, that is an RMS of 1 $\mathrm{mm\,s^{-1}}$ to 10 $\mathrm{mm\,s^{-1}}$ over the frequency range 2.5 Hz to 100 Hz, comparison of the LDV signal to the reference accelerometer typically yields a significant mean error reduction between 15 and 30 dB [4–6]. As previously derived [6], the mean error reduction, R, is calculated using:

$$R = -10 \log_{10} \left(\frac{\mathrm{MSE_{corr}}}{\mathrm{MSE_{m}}} \right) \ \mathrm{dB} \tag{1}$$

where $\mathrm{MSE_m}$ and $\mathrm{MSE_{corr}}$ are the mean square error of the LDV signal before and after correction, respectively, when taking the reference accelerometer signal as the 'true' vibration signal. For N spectral lines, the general formulation is:

$$\mathrm{MSE_{signal}} = \frac{1}{2} \sum_{n=1}^{N} (A_{\mathrm{signal}}(n) - A_{\mathrm{true}}(n))^2 + (B_{\mathrm{signal}}(n) - B_{\mathrm{true}}(n))^2 \tag{2}$$

where $A_{\mathrm{signal}}(n)$ and $B_{\mathrm{signal}}(n)$ are the real and imaginary parts, respectively, of either the measured or corrected LDV signal at the nth spectral line. Similarly, $A_{\mathrm{true}}(n)$ and $B_{\mathrm{true}}(n)$ are the equivalents for the reference accelerometer signal.

3 TIME DOMAIN BASED PROCESSING

While there are some earlier studies in which erroneous measurements from LDVs subject to instrument vibration are resolved in real time or using time domain based techniques [7–9], they are few in number and diverse in approach with each employing a different metric to gauge the efficacy of the correction. This makes it somewhat difficult to contextualise the relative performances as well as to compare each with the established frequency domain based approach previously described. An early approach used a purely mechanical means to perform the compensation, incorporating an internal damper into the optical arrangement, upon which the reference beam was incident [7]. However, this system performance is unlikely to be consistent over a sufficiently wide frequency range as a result of damper resonances. Other known solutions employ a correction accelerometer, with the compensation being performed either in real-time [8] or in post-processing [9]. In the former, it is unclear where the accelerometer was mounted geometrically, only that it was mounted to the probe laser beam optics. Recent work

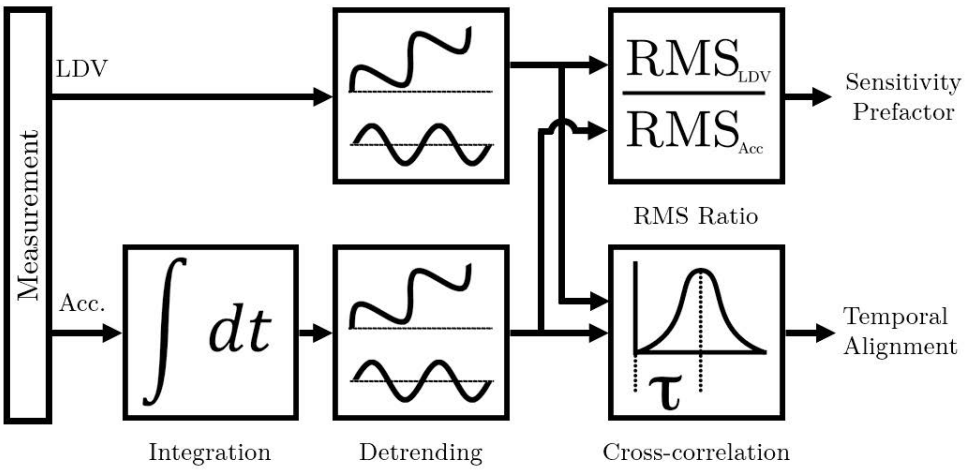

Figure 1: The time domain based accelerometer calibration procedure with "Acc." representing either the correction or the reference accelerometer signal.

has shown that the accelerometer must be on the laser beam axis for complete correction in the presence of arbitrary six degree-of-freedom instrument vibration [5]. In the latter, some useful enhancements to the preceding frequency domain based approach are introduced, in particular the means to undertake signal time delay compensation using time series data.

Offering complementarity to the earlier approaches, the method proposed herein is entirely based in the time domain and, for the moment, is performed in post-processing on recorded signals. In this respect, it does not differ to the frequency domain based approach, previously summarised, and, as such, the required experimental arrangement is common. While the motivation for the novel approach is to extend current capability to processing of *non-stationary* signals, in order to directly compare with the frequency domain equivalent, using the same previously defined metric, R, *stationary* vibration signals only are considered herein.

3.1 Sensitivity adjustment and time delay correction

As for the corresponding stage in the frequency domain based processing approach, accelerometer sensitivities and signal finite time delays are determined with the LDV taken as the reference. Figure 1 schematically depicts the time domain based processing calibration procedure for a single accelerometer; this can be replicated for as many accelerometers as are required. Again, the accelerometer signals must first be integrated and this is straightforwardly achieved here using the cumulative trapezoidal method. However, the integration of accelerometer signals commonly leads to the introduction of errors such as a DC offset and drift. Detrending is intended to remedy this and is achieved by subtracting a least squares fit of a first order polynomial from the integrated signal. Since this might remove genuine as well as spurious signal content, the LDV signal is subjected to the same for consistency.

With the accelerometer and LDV signals both represented as velocities, an RMS ratio can then be used to revise the accelerometer sensitivities; all subsequent measurements acquire signals accordingly adjusted. Meanwhile, the finite time delays between the LDV and accelerometer signals which occur as a result of differences between the signal processing electronics in the measurement chain, are estimated using a cross-correlation function as follows [9]:

$$r_{xy}(\tau) = \frac{1}{T}\int_0^\infty x(t)y(t+\tau)dt \tag{3}$$

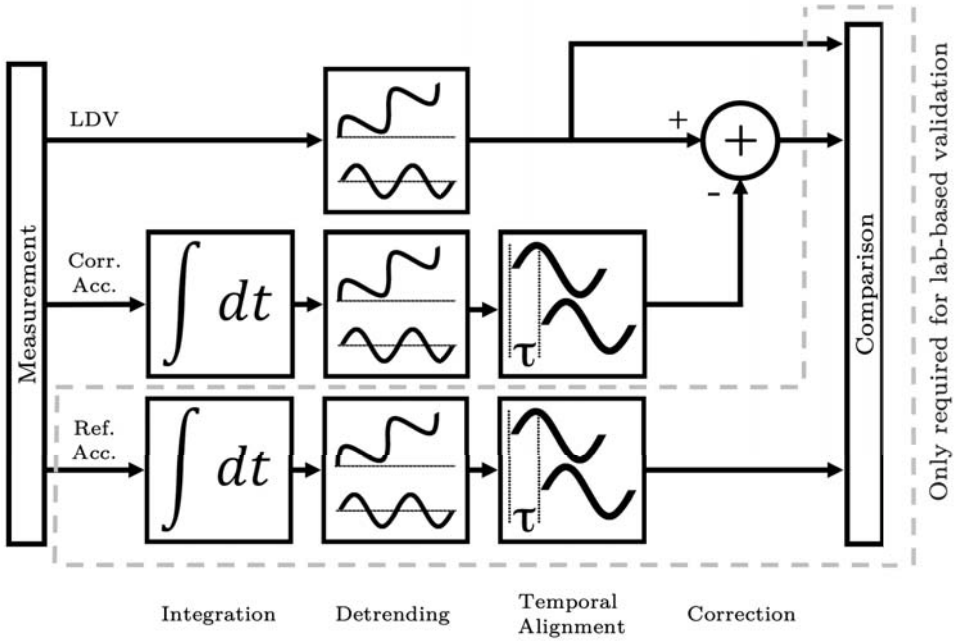

Figure 2: The time domain processing correction procedure with "Corr. Acc." and "Ref. Acc." representing the correction and reference accelerometer signals, respectively.

where τ is the time delay between the signals, x and y are the two signals, t is time and $r_{xy}(\tau)$ the cross-correlation function in which the peak will occur at the time delay between the signals.

3.2 Instrument vibration correction

Figure 2 schematically depicts the time domain based processing correction procedure. The first, "Integration", and second, "Detrending", steps are consistent with those previously described. The third, "Temporal alignment", step incorporates the finite time delay in the accelerometer signals. This is achieved by time-shifting each accelerometer signal relative to the LDV signal by the amount previously determined, τ. Since this is only possible in integer units of the time step, a high sample frequency is required to maximise the accuracy of the temporal alignment between the signals. This time-shifting results in regions at the start and at the end of the measurement duration where samples for all three signals are not present and these regions are therefore truncated. The total original measurement duration may therefore need to be slightly longer than that which is ultimately required.

The final signal processing step in Figure 2, "Correction", refers to the LDV signal correction and is given mathematically by [4]:

$$U_{\text{corr}}(t) = U_{\text{m}}(t) - U_0(t) \tag{4}$$

where $U_{\text{m}}(t)$ is the measured LDV signal, $U_0(t)$ is the integrated correction accelerometer signal and $U_{\text{corr}}(t)$ is the fully corrected LDV signal.

Ultimately, and only possible in the lab-based experimental validation approach described herein, the "Comparison" step in Figure 2 determines the efficacy of the correction procedure. This is achieved by comparing the corrected LDV signal with the final reference accelerometer signal. The performance metric used here is the previously described mean error reduction, R, given by (1). To calculate this in the time domain, an appropriate formulation of the MSE

should be used, given by [6]:

$$\mathrm{MSE}_{\mathrm{signal}} = \overline{\big(U_{\mathrm{signal}}(t) - U_{\mathrm{true}}(t)\big)^2} \tag{5}$$

where $U_{\mathrm{true}}(t)$ is the reference accelerometer, $U_{\mathrm{signal}}(t)$ is either the measured or corrected LDV signal and $\overline{(\cdot)}$ signifies the time average. Direct comparison can now be made between processing techniques in both the time and frequency domains.

4 EXPERIMENTAL VALIDATION

4.1 Setup

An experimental setup, common with that implemented in earlier work [4–6], depicted in Figure 3 was arranged, whereby independent control of the target vibration and of the LDV vibration was possible. The target vibration is the measurement of interest while the base vibration simulates the effect of a vibrating platform on the LDV measurement. Both target and base vibrations were created using electrodynamic shakers independently powered and driven using uncorrelated broadband white noise signals up to 200 Hz, generated by a Siemens PLM Simcenter SCADAS Mobile data acquisition system.

Mounted to the base vibration shaker, using a custom-made aluminium mounting bracket such that the LDV sensitive direction was aligned with the shaker vibration direction, was a Polytec Compact Laser Vibrometer NLV-2500-5. The bracket also contained an Endevco 770-10-U-120 (200 $\mathrm{mV/g}$ nominal) DC-response accelerometer, rigidly mounted with synthetic beeswax. This correction accelerometer was aligned with the probe laser beam axis to be optimally effective [4]. The target shaker was suspended from above using an overhead crane, providing isolation from the large base motion shaker. Mounted to the shaker spigot was a second similar Endevco accelerometer providing the 'true' vibration measurement.

4.2 Data collection and processing

The Siemens acquisition system was used to record the various time data throughput vibration signals at the maximum sampling frequency of 204.8 kHz for a duration of 8 s. This extremely high oversampling factor assists in the accurate temporal alignment of the three signals in the time domain, as previously mentioned. The acquired data were processed as five separate 1.6 s segments for both processing methods. In the frequency domain, these acquisition parameters lead to a spectral resolution of 0.625 Hz and a bandwidth of 102.4 kHz. The DC component was excluded from the calculation of R in frequency domain processing. The mean error reduction for both the time and frequency domain based approaches was averaged over the five segments with the standard error of the mean taken as the uncertainty in each result.

4.3 Results comparison

Frequency domain based accelerometer calibration for the model and conditioning used yielded a time delay of -138.5 ± 13.2 µs with the corresponding time domain based method value of -125.0 ± 1.1 µs in agreement. Since the estimation using the time domain based method yielded a lower uncertainty, a time delay of -125.0 µs was subsequently used for both correction procedures. It should be noted that, due to the necessary signal truncation following time domain based temporal alignment, comparisons between time and frequency domain approaches are not of *exactly* identical signal content. In this case, however, the difference is only 26 out of over 300,000 samples and it is therefore unlikely this will significantly affect the

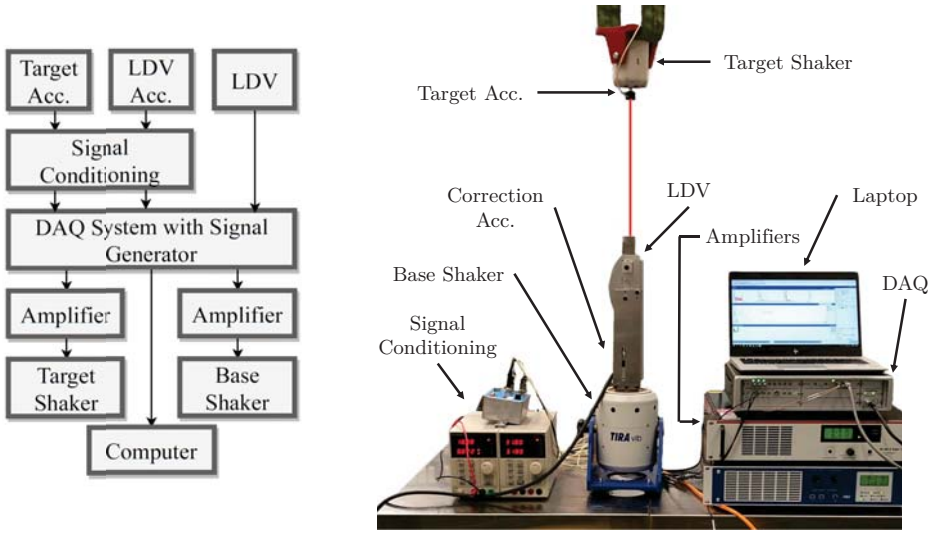

(a) (b)

Figure 3: Experimental setup used to simulate a LDV target vibration measurement during base motion vibration: (a) block diagram representation and (b) physical setup.

results.

As can be seen qualitatively by comparing Figure 4 (a) and Figure 4 (b), this frequency domain based processing method yields significant improvements in the corrected versus the uncorrected LDV signal over the range 25 Hz to 200 Hz. However, the performance below 25 Hz is relatively poor, likely due to the lower signal level in this range owed to the shaker-amplifier dynamic characteristics.

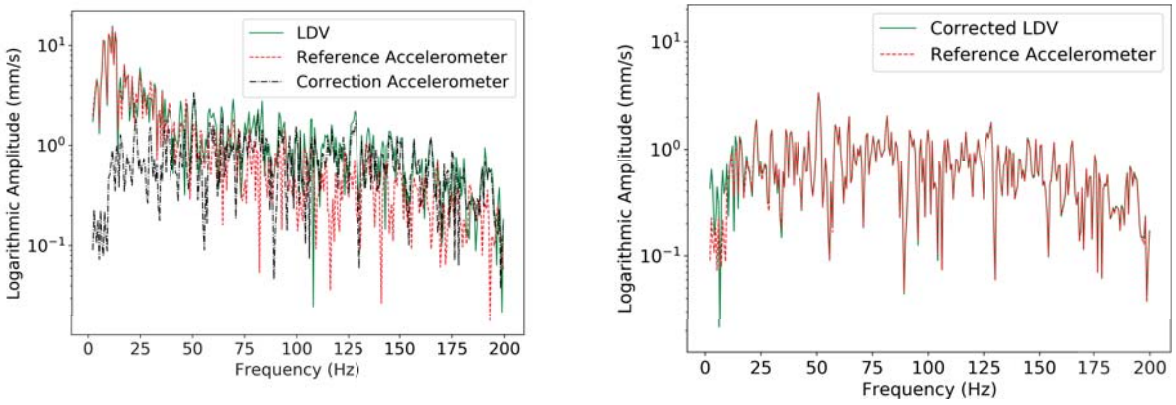

(a) (b)

Figure 4: Frequency domain processing spectra for a 1.6 s segment in the range 0.625 Hz - 200 Hz: (a) all signals before correction and (b) corrected LDV and reference accelerometer signals.

As can be seen in Figure 5 for a 100 ms segment of data, the time domain based processing method proposed here also offers significant improvement in the corrected versus the uncorrected LDV signal. However, in the time domain, the effect of speckle noise [1] is apparent, manifested as instantaneous spikes not present in the reference accelerometer signal.

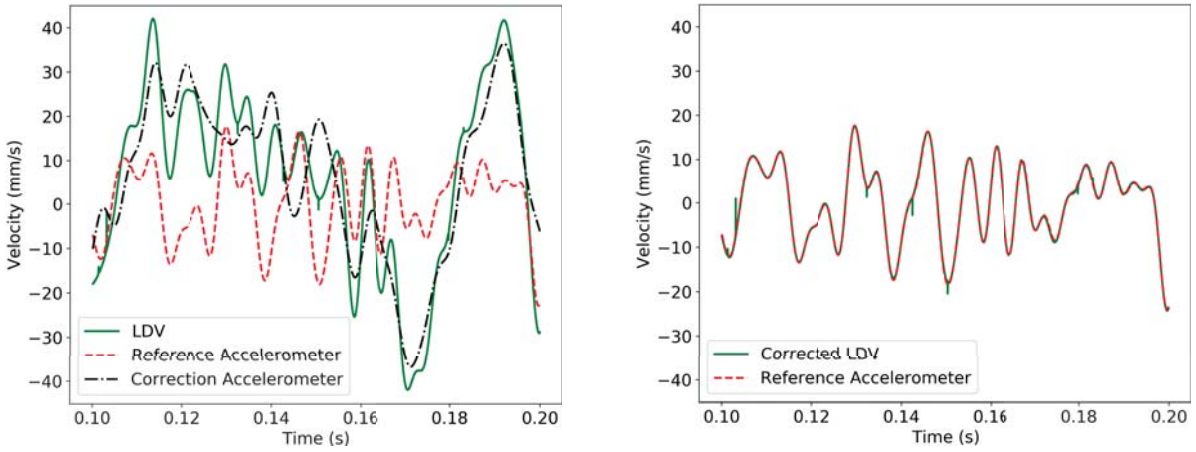

(a) (b)

Figure 5: A 100 ms segment of data from time domain processing: (a) all signals before correction and (b) corrected LDV and reference accelerometer signals.

The quality of the correction for the two alternative methods can be compared quantitatively using the mean error reduction, R, which can be seen in Table 1. Here it is shown that the time domain processing method outperforms the established frequency domain based processing method by a factor of eight.

Table 1: The mean error reduction for the five 1.6 s segments along with their logarithmic uncertainties calculated as the standard error of the mean.

	R	
Frequency Domain	$25.3^{+1.8}_{-1.3}$	dB
Time Domain	$34.5^{+2.1}_{-1.4}$	dB

5 CONCLUSIONS

While correction of LDV measurements in the presence of instrument vibration has typically been carried out in the frequency domain and for *stationary* vibration signals only, extension to vibration signals that are *transient* in nature requires an alternative, time domain based approach. Furthermore, the direct comparison of existing time domain based approaches with the established, frequency domain approach is challenging. In this paper, therefore, the totally general theoretical basis for complete measurement correction was extended to include a completely time domain based approach.

Validation using a conventional experimental arrangement consisting of a vibrating LDV instrumented with a correction accelerometer and a vibrating target similarly instrumented to provide a true vibration reference measurement, has been shown. Throughput time data for statistically stationary vibration signals have been acquired and processed in both frequency and time domain processing. It has been shown that, while both approaches lead to significant improvements in the quality of the corrected LDV measurement, the time domain based approach described here yields a mean error reduction value, R, eight times higher than the previously described frequency domain based approach.

This improvement is a significant finding and offers a viable alternative to the established frequency domain equivalent for *stationary* vibration signals, provided time data signals can be acquired with a high oversampling factor. Moreover, it now extends the capability to perform complete correction of LDV measurements in the presence of *transient* instrument vibration, such vibrations being more likely to occur in real-world in-field applications for example in measurement campaigns from unmanned aerial vehicles.

Future investigations will explore the sensitivity of the time domain based approach to reduced sample frequency signals and identify the sources of the performance gap. Improved frequency domain approach performance, including the estimate of accelerometer signal time delays, will be realised. Ultimately, however, deployment of the time domain based approach for transient signal processing will be the most significant follow-up to the work presented here.

REFERENCES

[1] S.J. Rothberg, M.S. Allen, P. Castellini, D. Di Maio, J.J.J. Dirckx, D.J. Ewins, B.J. Halkon, P. Muyshondt, N. Paone, T. Ryan, H. Steger, E.P. Tomasini, S. Vanlanduit and J.F. Vignola, An international review of laser Doppler vibrometry: Making light work of vibration measurement, *Optics and Lasers in Engineering*, **99**, 11–22, 2017.

[2] A. Dräbenstedt, X. Cao, U. Polom, F. Pätzold, T. Zeller, P. Hecker, V. Seyfried, and C. Rembe, Mobile seismic exploration, *AIP Conference Proceedings*, **1740**, 030001, 2016.

[3] S. Oberst, E. Nava-Baro, J.C.S. Lai and T.A. Evans, An Innovative Signal Processing Method to Extract Ants' Walking Signals, *Acoustics Australia*, **43**, 87-96, 2015.

[4] B.J. Halkon and S.J. Rothberg, Taking laser Doppler vibrometry off the tripod: correction of measurements affected by instrument vibration, *Optics and Lasers in Engineering*, **91**, 16–23, 2017.

[5] B.J. Halkon and S.J. Rothberg, Towards laser Doppler vibrometry from unmanned aerial vehicles, *Journal of Physics: Conference Series*, **1149**, 012022, 2018.

[6] B.J. Halkon and S.J. Rothberg, Establishing correction solutions for Scanning Laser Doppler Vibrometer measurements affected by sensor head vibration, *Mechanical Systems and Signal Processing* (under review), arXiv:2006.10918 [physics.ins-det], 2020.

[7] H. Kim, Y. Lee, C. Kim, T. Chang and M. Kang, Laser Doppler vibrometer with body vibration compensation, *Optical Engineering*, **42**, 2291-2295, 2003.

[8] L.A. Jiang, M.A. Albota, R.W. Haupt, J.G. Chen and R.M. Marino, Laser vibrometry from a moving ground vehicle, *Applied Optics*, **50**, 2263-2273, 2011.

[9] M. Klun, D. Zupan, J. Lopatič and A. Kryžanowski, On the application of laser vibrometry to perform structural health monitoring in non-stationary conditions of a hydropower dam, *Sensors (Switzerland)*, **19**, 3811, 2019.

EURODYN 2020
XI International Conference on Structural Dynamics
M. Papadrakakis, M. Fragiadakis, C. Papadimitriou (eds.)
Athens, Greece, 23–26 November 2020

THE DISSIPATIVE CHARACTERISTICS OF OBLATE PARTICLES IN GRANULAR DAMPERS

Furkan Terzioglu[1], **Jem A. Rongong**[1], **and Charles E. Lord**[1]

[1] The University of Sheffield, Department of Mechanical Engineering
Mappin Building, Mappin Street, Sheffield, S1 3JD, United Kingdom
fterzioglu1@sheffield.ac.uk, j.a.rongong@sheffield.ac.uk, c.lord@sheffield.ac.uk

Keywords: granular damping, friction, impact, irregular particle, sphericity, circularity, discrete element method.

Abstract. *In numerical models for granular dampers, particles are generally considered to be perfect spheres. However, in practical engineering applications these particles can slightly deviate from being true spheres. It has been observed experimentally that sphericity, which defines the proximity degree of a shape to a sphere, plays an important role in the amplitude dependent behaviour of granular dampers. This paper mainly examines the significance of the sphericity level for slightly oblate particles in a granular damper that are subjected to sinusoidal vibrations in the same direction as standard gravity. This investigation is carried out by evaluating the dissipated power from the granular medium by utilizing three-dimensional discrete element method simulations. Apart from the effect of amplitude of vibrations in the dissipated power, the relative contributions of frictional and inelastic collisional damping mechanisms in the overall power dissipation, are also investigated for varying sphericity levels of the oblate particles.*

1 INTRODUCTION

Granular (or particle) damping is an effective passive damping approach that involves many small spherical particles (typically 0.05 mm – 5 mm in diameter) located inside an enclosure that is fixed to a vibrating structure. The kinetic energy from vibration is transmitted to the particles by collisional momentum exchanges between the particles and the boundaries of the enclosure. Granular dampers dissipate the transmitted kinetic energy through inter-particle and particle-enclosure boundary interactions. This is unlike common viscoelastic dampers which generally dissipate the stored elastic energy.

Interest in granular damping is rapidly increasing in engineering fields because such dampers are robust, cost-effective, easy to retro-fit and relatively insensitive to the environment and excitation frequency. [1–4]. As a result, granular dampers have been successfully applied in numerous mechanical systems to solve noise and vibration problems, such as a desk-top banknote processing machine [5], the exterior panel of a launch vehicle [6], a gear transmission system [7], and an automotive oil pan [8].

Despite their conceptual simplicity, granular dampers have quite complex and distinctive behaviour. Since the particles are generally hard, made from materials such as metal and ceramic, surface friction plays an important role in energy dissipation, which leads to significant non-linearity in the form of amplitude dependent behaviour [9,10]. Granular damping has been studied extensively and this non-linearity is the likely reason for the existence of many contradictory findings in the literature. To improve understanding, studies have been undertaken to investigate the sensitivity of granular damping against damper parameters, such as coefficient of restitution between impacting bodies, coefficient of friction in contacting surfaces, particle number and individual stiffness of particles and enclosure walls [11–13]. More recently, it has also been shown that an approximated granular damper model in Discrete Element Method (DEM) simulations can adequately represent the essential properties of a real granular damper without matching parameters exactly provided the total mass is represented accurately [14]. This presumably arises from the compensation feature of multiple particles against the small variations of parameters from exact ones. It should be noted that this 'universal response' approach is only valid when using relatively large numbers of particles.

Previous studies have reported that granular dampers exhibit the characteristic properties of both friction dampers and single impact dampers since the main damping mechanisms of granular dampers are surface friction and inelastic collision within the granular media [15]. Furthermore, it has been also emphasized before that understanding of the damping mechanisms would provide an efficient way to increase the performance of such dampers [1]. Accordingly, a few attempts have been made to identify relative contributions of damping mechanisms in granular damping [15–18]. However, much uncertainty still exists and the literature on this topic is very scarce.

Although the hard particles used in granular dampers typically have a high level of durability, over time their shape may deviate from a true sphere due to harsh working conditions or intense collisional events. Moreover, non-spherically shaped particles may be deliberately used either for cost reasons or to avoid practical design issues such as the packing problem in small voids or because of manufacturing tolerances. Therefore, the investigation of irregular particles has grown in importance [19–21]. However, there is no notable study that focuses upon slightly oblate particles in granular dampers.

The aim of this study is to provide a numerical investigation on slightly oblate hard particles in a granular damper undergoing harmonic vibrations in the same direction as gravity. Several three dimensional DEM simulations are carried out to find the effects of particle sphericity levels on the dissipative behaviour. Steady-state cumulative power loss calculations are

utilized to characterize the amplitude dependent granular damper in every simulation. The contributions of frictional and collisional energy dissipation mechanisms on the total dissipation are computed.

2 DEM MODEL FOR OBLATE PARTICLES

DEM is a numerical scheme for analyzing granular matter, in which the motion of every particle is tracked in time. The full time history of interest is broken into a series of very short time steps over which the equations of motion for each particle are solved. Where particles interact with one another, or with the physical boundaries of the system being studied, appropriate force-displacement and force-velocity relations for the contact are employed. The fundamental theory of DEM was originally presented by Cundall and Strack [22] and was first applied to granular dampers more than 20 years ago [23]. The use of DEM is attractive in the study of granular damping because it provides a way to control and observe the contact parameters and their effect on overall damping achieved.

2.1 Oblate particle generation

Although several algorithms have been developed recently that allow irregular particles to be defined and used directly within the DEM field, the most common method is the multi-sphere approach. In this approach, two or more overlapping spherical particles are rigidly joined together. Relatively complex shapes can be produced as the spheres are allowed to intersect each other. The use of the sphere as the building block provides computational benefits including the existence of advanced contact detection algorithms and contact models. Thus, the oblate particles used in this study are formed by employing the multi-sphere approach in the EDEM 2020 software [24].

Shape is an important indicator which defines a particle in numeric computational fields – especially for rock-like irregular particles [25]. If a large number of spheres is used in the multi-sphere approach, non-spherical shapes can be represented more precisely. However, it also causes significant increases in computational times. Hence, irregular shapes should be modeled conducting a balance between computational efficiency and closeness of representation. In this study, oblate particles are generated considering these criteria and are shown in Figure 1.

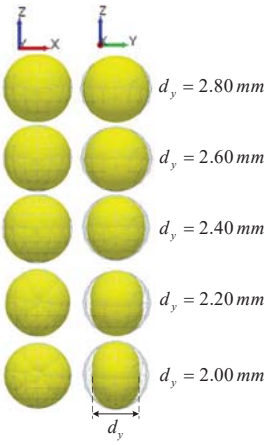

Figure 1: Created particle types for simulations with respect to a $3\,mm$ diameter perfect sphere mesh template.

It should be noted that the reference perfect sphere diameter used in this study is 3 mm and particle resizing occurs along the local y-axis (i.e. d_y changes) as can be seen in Figure 1,

whilst the other lengths (d_x , d_z) are kept constant. In this investigation, the lower limit for d_y was set at 2 mm, which represents a moderate change in particle shape.

The relative similarity of oblate particles to the reference sphere can be described using the sphericity index [25] which can be written as,

$$\psi = \sqrt[3]{\frac{c^2}{ab}} \tag{1}$$

Here, a , b and c are the corresponding lengths (largest to smallest, respectively) along the three local axes. In this paper, only the smallest length of the oblate particles is adjusted and therefore, $c = d_y$, $a = b = d_x = d_z = 3\,\text{mm}$.

Since oblate particles are created by deforming a sphere along one axis, a two dimensional parameter called the circularity index can also be used to define the shape. Circularity is defined in the local YZ axis as shown below [20].

$$C = \sqrt{\frac{4\pi A_{YZ}}{P_{YZ}{}^2}} \tag{2}$$

where A_{YZ} and P_{YZ} are respectively the projection area of a particle on the YZ axis and the perimeter of the particle. Sphericity and circularity values for the oblate particles used in this work, are presented in Table 1.

Particle minor axis length, d_y [mm]	Sphericity, ψ [-]	Circularity, C [-]
2.00	0.763	0.970
2.20	0.813	0.980
2.40	0.862	0.989
2.60	0.909	0.995
2.80	0.955	0.999
3.00	1.000	1.000

Table 1: Shape parameters of oblate particles.

2.2 Contact force model

In DEM, although particles are created as completely rigid bodies, contacts between them are deformable. Contacts are traditionally modeled using spring and dashpot elements as shown in Figure 2a, which allow relatively rapid calculations to be performed. For perfect spheres, force-displacement relationships have already been defined and tested for suitability [26–28]. As the multi-sphere is employed, these validated models can be applied to address the load-deformation behaviour of oblate particles. The contact model used in EDEM 2020 for this study is briefly summarized below considering the spheres shown in Figure 2a.

Normal elastic force between the spheres is determined using the well-known non-linear Hertzian contact model.

$$\boldsymbol{F}_{N_e} = -\underbrace{\frac{4}{3} E^{eq} \sqrt{R^{eq}}}_{k_N} \delta_N{}^{3/2} \boldsymbol{e}_N \tag{3}$$

Here, $\boldsymbol{e}_N$ is the unit vector from the centre point of sphere under consideration to the contact point and δ_N is the normal overlap of sphere. In this expression, the equivalent elastic modulus (E^{eq}) and the equivalent radius (R^{eq}) can be found by $1/E^{eq} = \left(1-\nu_1^2\right)/E_1 + \left(1-\nu_2^2\right)/E_2$ and $1/R^{eq} = 1/\mathrm{R}_1 + 1/\mathrm{R}_2$, where E, R and ν are elastic modulus, radius and Poisson's ratio of relevant spheres, respectively. In order to define inelastic (i.e. dissipative) part of normal force between the spheres, a coefficient of restitution (e) based approach is employed [29]:

$$\boldsymbol{F}_{N_d} = -\underbrace{2\sqrt{\frac{5}{6}}\frac{\ln(e)}{\sqrt{\ln^2(e)+\pi^2}}\left(2m^{eq}E^{eq}\sqrt{R^{eq}\delta_N}\right)^{1/2}}_{c_N}\frac{d\boldsymbol{r}_{\boldsymbol{rel}_N}(t)}{dt} \tag{4}$$

where equivalent mass (m^{eq}) is defined using the individual masses of spheres $1/m^{eq} = 1/m_1 + 1/m_2$ and $d\boldsymbol{r}_{\boldsymbol{rel}_N}(t)/dt$ denotes the normal relative velocity between the spheres in contact.

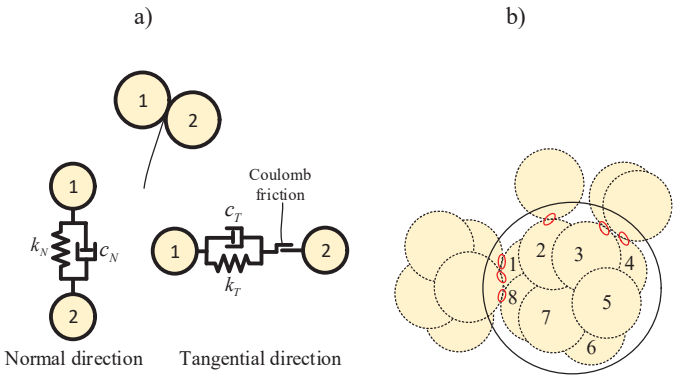

Figure 2: a) Modelling at the contact point of two contacting spheres, b) contacts of an irregular particle constructed with many spheres.

On the other hand, tangential elastic force is determined according to normal overlap defined as Mindlin and Deresiewicz method [16]. Unlike the original method in which many incremental elastic-plastic loading and unloading steps exist [30], a simplified version of this method is used to define tangential elastic force-displacement relation as given below.

$$\boldsymbol{F}_{T_e} = -(1-\vartheta)\underbrace{8G^{eq}\sqrt{R^{eq}\delta_N}}_{k_T}\delta_T\boldsymbol{e}_{\boldsymbol{T}} \tag{5}$$

While equivalent shear modulus (G^{eq}) is defined by $1/G^{eq} = \left(1-\nu_1^2\right)/G_1 + \left(1-\nu_2^2\right)/G_2$ with shear modulus of spheres (G), δ_T and $\boldsymbol{e}_{\boldsymbol{T}}$ stands for the tangential overlap and the unit vector along tangential overlap, respectively. Additionally, tangential inelastic force can be also formed using the similar approach as for normal direction. However, shear friction should be also taken into consideration in tangential direction. Thus, the widely used Coulomb friction model is added to tangential contact model:

$$\boldsymbol{F}_{T_d} = -(1-\vartheta)\underbrace{2\sqrt{\frac{5}{6}}\frac{\ln(e)}{\sqrt{\ln^2(e)+\pi^2}}\left(8m^{eq}G^{eq}\sqrt{R^{eq}\delta_N}\right)^{1/2}}_{c_N}\frac{d\boldsymbol{r}_{\boldsymbol{rel}_T}(t)}{dt} - \vartheta\gamma_f\left|\boldsymbol{F}_N\right|\boldsymbol{e}_{\boldsymbol{T}} \tag{6}$$

where $d\boldsymbol{r}_{rel_T}(t)/dt$ is the tangential relative velocity between the spheres and γ_f is coefficient of friction. ϑ is for indicating whether slipping occurs or not as seen in Equation 7.

$$\vartheta = \begin{cases} 1 & |\boldsymbol{F}_T| > \gamma_f |\boldsymbol{F}_N| \\ 0 & otherwise \end{cases} \tag{7}$$

It should be also noted that although the contact model is presented considering sphere – sphere contacts, it would be also valid for sphere – cylindrical enclosure contacts if one assumes $R_{enclosure} \to \infty$ and $m_{enclosure} \to \infty$ in above expressions.

For an irregularly shaped particle modelled using multi-sphere approach, contact force calculation procedure should be performed accounting all existing contacts of all individual spheres which constitute the particle. For example; as can be seen in Figure 2b, 8 perfect spheres which form the irregular particle have different number of contacts with other particles (e.g. number 1 has 2 contacts while number 8 has 1 contact) and the effects of the total 6 contacts can be only obtained by looking all 8 spheres. Thus, the resultant force acting on the particle can be computed as follows for a particle:

$$\boldsymbol{R}_F = \sum_i \left\{ \sum_{j(i)} \left(\boldsymbol{F}_{N_e} + \boldsymbol{F}_{N_d} + \boldsymbol{F}_{T_e} + \boldsymbol{F}_{T_d} + \boldsymbol{F}_g \right) \right\} \tag{8}$$

where i and $j(i)$ are the indices which count the total spheres forming the particle and the total contacts involved by sphere i, respectively. $\boldsymbol{F}_g$ is the gravitational force acting on the corresponding sphere. The resultant moment acting on the particle can be also determined by vectorial product of the resultant force and the position vector of particle mass center ($\boldsymbol{r}_c$).

$$\boldsymbol{R}_M = \boldsymbol{r}_c \times \boldsymbol{R}_F \tag{9}$$

2.3 DEM simulation procedures

In three dimensional DEM simulations, detected contacts of particle – particle and particle – enclosure pairs are considered to perform the given contact force computation procedure at a solution time step. After the calculation of resultant forces and moments, Euler-Newton equations of motions are numerically solved to find updated translational and rotational kinematics (i.e. positions, velocities and accelerations) of every particle by utilizing central-difference formulae.

The time step needs to be set small enough to capture particle overlaps, avoid propagating disturbances of a particle far from away and decrease numerical inaccuracies in simulations. Although several other approaches have been available to estimate a time step for realistic simulations in DEM, the Rayleigh time step criterion is used in the present study [31]. The time interval used in the simulations is chosen to be approximately %50 – %35 of the Rayleigh time step according to the particle type to ensure the reliability of simulations.

Even though there have been studies which investigate the characteristics of granular damping considering the dynamics of host structure [12,32], it is useful to carry out investigations on the damper alone to determine energy dissipation behaviour independently from the host structure [33,34], so that the damper can be adopted to any structure. This study involves a cylindrical enclosure filled with oblate particles subjected to vertical sinusoidal vibrations.

Particles are given the properties of stainless steel while the material of enclosure is chosen as polymethylmethacrylate (PMMA). The properties of these materials and the dimensions of

the enclosure are given in Table 2. The contact properties used in the simulations (i.e. friction and restitution coefficients) are determined as presented in this table. These parameters are selected according to a comprehensive study in which stainless steel – stainless steel and PMMA – stainless steel interactions were experimentally examined to extract the contact properties between those for DEM simulations [35].

Enclosure parameters		**Particle parameters**	
Material	PMMA	Material	Steel
Elastic modulus	3.3 GPa	Elastic modulus	206 GPa
Poisson's ratio	0.37	Poisson's ratio	0.30
Diameter	0.02 m	Density	7800 kg/m^3
Height	0.04 m	Nominal total mass	0.04 kg
Other simulation parameters			
Particle-enclosure friction coefficient	0.4		
Particle-particle friction coefficient	0.4		
Particle-enclosure restitution coefficient	0.92		
Particle-particle restitution coefficient	0.92		
Time step	~5x10^{-7} s		

Table 2: Parameters and properties of numerical simulations.

To allow a comparative study to be undertaken, it was considered desirable that the total mass of particles remained the same for different particle types. In order to achieve a suitable clearance level (75% – 80% filling ratio or 20% – 25% clearance ratio) for practical damping in every simulation configuration [11], the total particle mass was set to 0.04 kg. However, because particles are discrete but had different sizes, the total mass varied by up to the mass of half a particle, as shown in Figure 3a. Figure 3a also shows that a greater deviation in shape from a perfect sphere results in an increase in the number of particles required to achieve the target mass. Before any vibrational loading was applied, all particles were allowed to settle in the enclosure by the gravitational effect (see Figure 4).

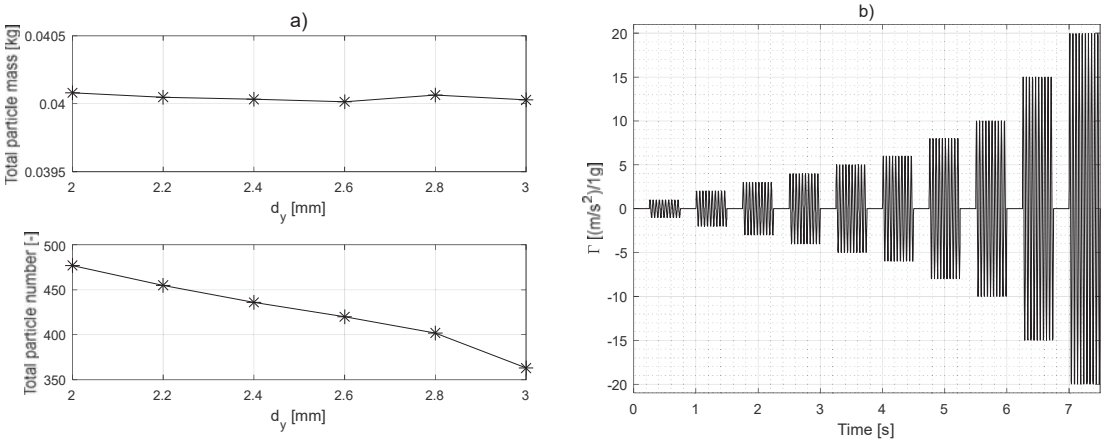

Figure 3: a) Changes in total particle mass and total particle number in terms of particle type, b) given vibration signal.

Behaviour of the granular medium under steady-state vibration was studied by prescribing sinusoidal motion for the enclosure at a frequency of 20 Hz. The effect of vibration intensity

was investigated by increasing the amplitude in steps, with the response being calculated for ten cycles at each level, as shown in Figure 3b. These vibrational levels are represented by commonly used non-dimensional acceleration (Γ).

$$\Gamma = \frac{A\omega^2}{g} \tag{10}$$

where A and ω are displacement magnitude and angular frequency of vibrations, respectively. In the vibration signal, time gaps are provided between each vibrational level to let the particles become stationary before the next excitation.

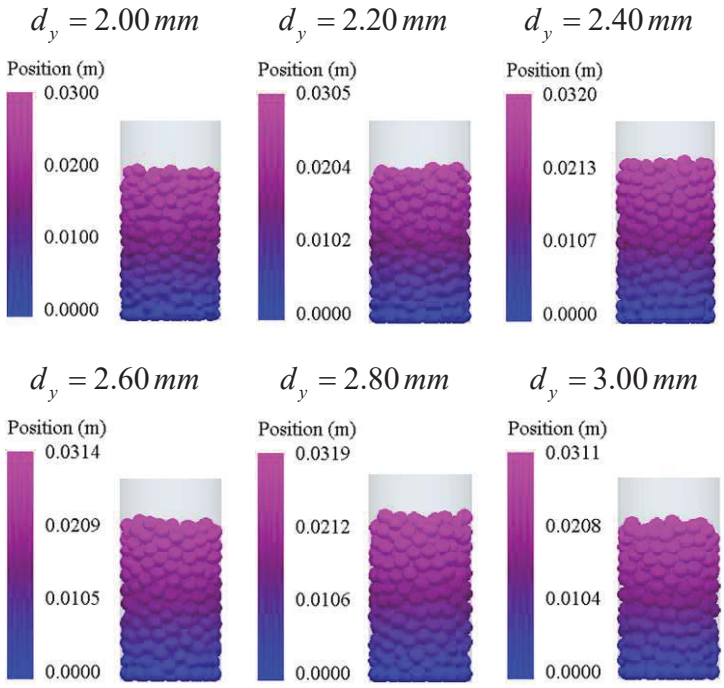

Figure 4: Views of granular oblate particles in the enclosure after settling process (i.e. stationary positions).

3 DISSIPATED ENERGY CALCULATION

Total cumulative dissipated energy in the simulations can be obtained by utilizing an incremental numeric computation scheme. For a single contact, total dissipated energy increments (ΔE_C) are computed integrating the scalar product of dissipative forces (i.e. in normal direction, $\boldsymbol{F}_{N_d}$ and in tangential direction, $\boldsymbol{F}_{T_d}$) and corresponding relative velocities between the contacting bodies through the contact time, T_c. In order to account all N number of contacts in the current computation step, this calculation is repeated for every contact, and then the effects of every contact is summed accordingly as following.

$$\Delta E_C = \sum_{k=1}^{N} \int_{T_c^{(k)}} \left\{ \left| \boldsymbol{F}_{N_d}^{(k)}(t) \cdot \frac{d\boldsymbol{r}_{rel_N}^{(k)}(t)}{dt} \right| + \left| \boldsymbol{F}_{T_d}^{(k)}(t) \cdot \frac{d\boldsymbol{r}_{rel_T}^{(k)}(t)}{dt} \right| \right\} dt \tag{11}$$

where $\boldsymbol{r}_{rel_N}$ and $\boldsymbol{r}_{rel_T}$ represent the relative positions of contacting bodies with respect to each other in normal and tangential directions, respectively, while t stands for time. In addition, the computation time step of the energy dissipation calculation scheme should be sufficiently larger than the contact durations to account all contacts within a single step.

The tangential dissipation can arise from either friction between the bodies in contact or restitution of the bodies unlike the normal dissipation where whole dissipation is caused by only collisional restitution. Frictional dissipation is solely employed if slipping, in which the tangential force is higher than the maximum static friction force between the contacting bodies, is occurred. The frictional cumulative dissipation steps can be separately determined as given in below.

$$\Delta E_C^f = \gamma_f \sum_{k=1}^{N} \int_{T_c^{(k)}} \left| \boldsymbol{F}_N^{(k)}(t) \cdot \frac{d\boldsymbol{r}_{rel_T}^{(k)}(t)}{dt} \right| dt \tag{12}$$

Collisional dissipation can then be obtained by subtracting the frictional loss from the total dissipation energy.

$$\Delta E_C^c = \Delta E_C - \Delta E_C^f \tag{13}$$

4 RESULTS

4.1 Overall dissipative behaviour of oblate particles

To assess the general damping behaviours of oblate particles against different vibrational amplitudes and the relationship between the dissipation and the granular motional behaviour, cumulative total dissipated energies were extracted separately for every vibrational case in all simulations. Figure 5 presents some of those dissipated energy results. In these results, the last five vibration periods at each vibration level are considered. Simulations were repeated to determine the effects of packing on the results. The results verified that packing effects stay very small except at the amplitude $\Gamma = 1$.

The first set of analyses belongs to very small oscillations (i.e. $\Gamma = 1.0$). Under such small vibrations, the particles inside the enclosure have almost no relative motions with respect to each other, they only follow the enclosure motion (i.e. solid-like behaviour) since the particles do not overcome the gravitational and the static frictional forces within the granular media. Thus, the dissipated energies are extremely small, and they do not exhibit obvious steady-state behaviors since a few individual particle movements that induce energy dissipation can be instantly observed due to wave propagation through the granular media from the bottom boundary of the enclosure. These instantaneous dissipation increases can be more likely seen for perfect spheres owing to their smooth circular surfaces. In addition, numerical errors in computational operations and initial packing may also considerably affect these small outcomes.

It is apparent from Figure 5 that huge differences surprisingly emerge between the particle types at several vibration amplitudes. Further investigation into granular media indicates that this is mainly connected with the dissimilarities of granular motional states which the particles are in. For instance; in Figure 5d, there are two groups of result: one is high dissipation group, and the other is low dissipation. At this vibration level, the high energy dissipation group is at the onset of two-sided bouncing bed behaviour in which the granular particle cluster impacts the bottom and the top boundaries of enclosure during a period of vibration (i.e. 2 collective impacts with the enclosure in a period), thereby transferring the momentum effectively to the granular media. On the other hand, the granular media in low dissipation group generally collides with only the bottom boundary in a vibration period (one-sided bouncing bed), while it slightly touches to the top boundary in this period (mild collision).

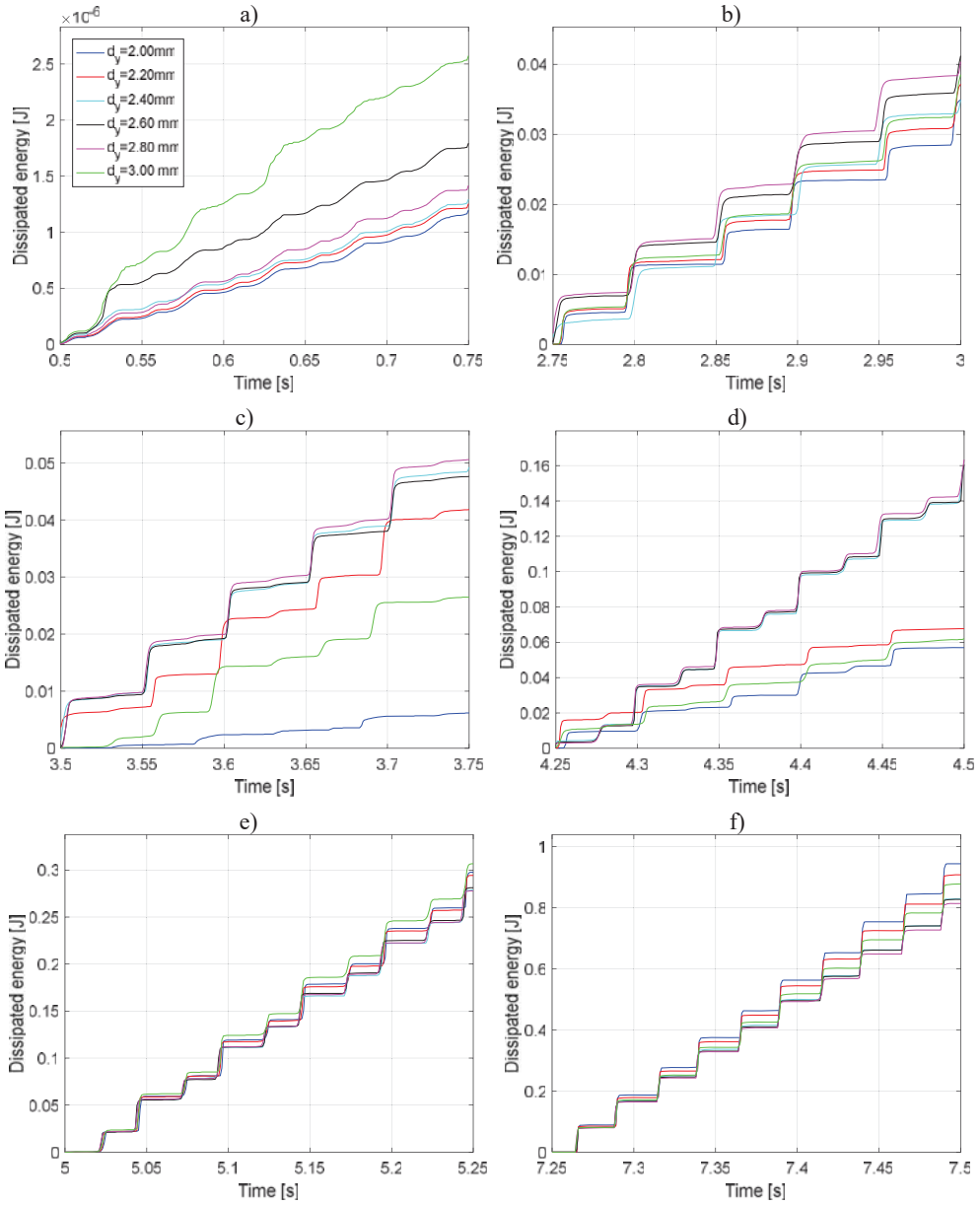

Figure 5: Total cumulative dissipated energy characteristics for 5 vibrational periods of a) $\Gamma = 1$, b) $\Gamma = 4$, c) $\Gamma = 5$, d) $\Gamma = 6$, e) $\Gamma = 8$, f) $\Gamma = 10$.

The defined dissipation groups in Figure 5d are also valid at $\Gamma = 5$ as can be seen in Figure 5c. At this vibration level, the high dissipation group members exhibit similar behaviour to that seen previously except that the granular cluster impacts the top boundary once in every two periods. Although the members of low dissipation group have similar motion, the most squashed particle type somehow executes impacts with quite less intensive than the other members as can be clearly seen in Figure 5c.

Figure 6 shows the total potential energy in the particles throughout the simulation. Observed motional behaviours of granular media at various vibrational sequences are marked with different colors. Purple represents solid-like behaviour, while magenta and cyan stand for one-sided bouncing bed with fluidization of a few of the particles on the top layer and one-sided bouncing bed with fluidization of the uppermost layers of particles, respectively. As one can see in this figure, red marked potential energy regions are clearly more uneven and scat-

tered than other vibrational cases. This result may be explained by the fact that the granular media shows relatively higher level of fluidization in which a reasonable amount of particle indistinctly floats in these loading ranges. Another possible reason for this is that the collective motion of granular media is not symmetric at every vibrational period in these cases as it is in other vibration scenarios. The motions within these red marked ranges are described as following: dotted red is one-sided complete bouncing bed with few individual top particles-top wall impacts in every period, dot-dashed red is one-sided complete bouncing bed with few individual top particles-top wall impacts once in every two periods, dashed red is one-sided complete bouncing bed and mild collective collision with the top wall once in every two periods and flat red is one-sided complete bouncing bed and mild collective collision with the top wall in every period. The last phenomena observed in the simulations is two-sided complete bouncing bed that is marked with blue in total potential energy plots.

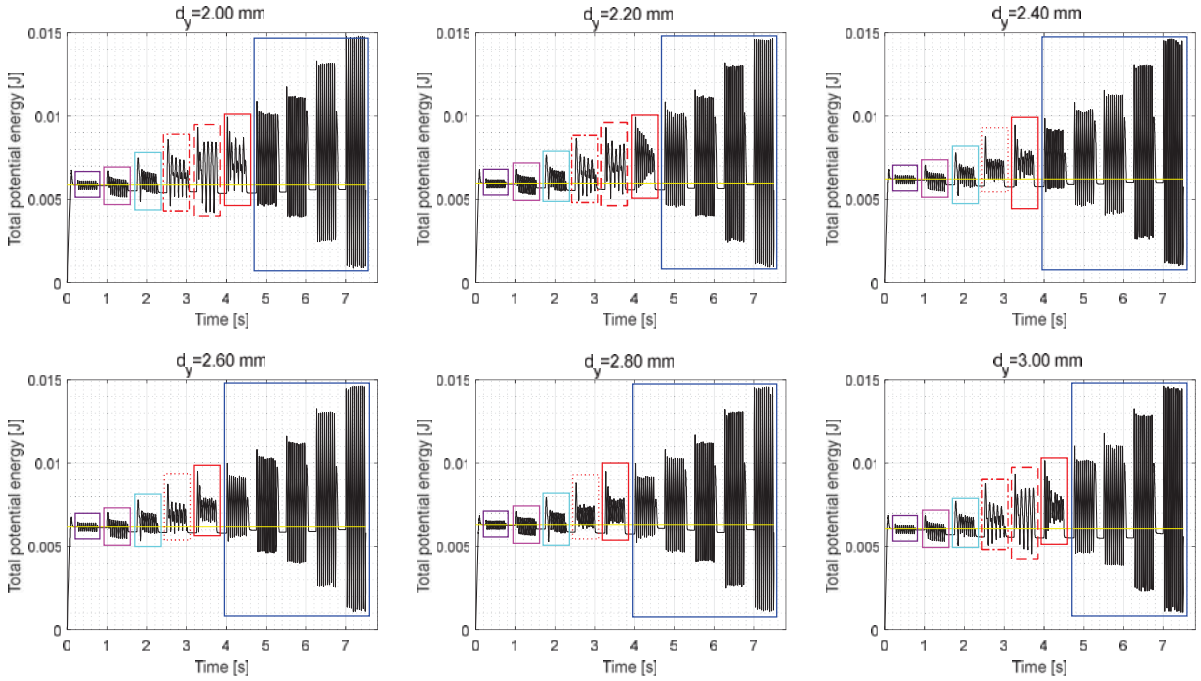

Figure 6: Total potential energy changes of simulated particles in time, yellow flat line indicates the total potential energy at the stationary positon of particles.

4.2 Damping characterization of oblate particles

In order to compare the damping behaviour of oblate particle types, the energy dissipation rates in a steady-state vibration period (i.e. power loss) were determined by integrating the cumulative dissipated energies through this period.

$$Power\,loss = \frac{1}{T}\int_{T} E_C(t)\,dt \tag{14}$$

The power losses are illustrated with respect to either sphericity or circularity for every simulated vibrational level in Figure 7 and Figure 8, respectively. The perfect sphere results are also included in these figures as a reference of default particle type used in most typical granular damper applications. In these graphs, the contribution of damping mechanisms of granular damping (i.e. friction and impact) on overall power loss are also shown to illustrate the macroscale damping behaviour of oblate particles. In addition to this, particle-particle and

particle-enclosure frictional losses are separately depicted in these plots to show dominance of interaction type.

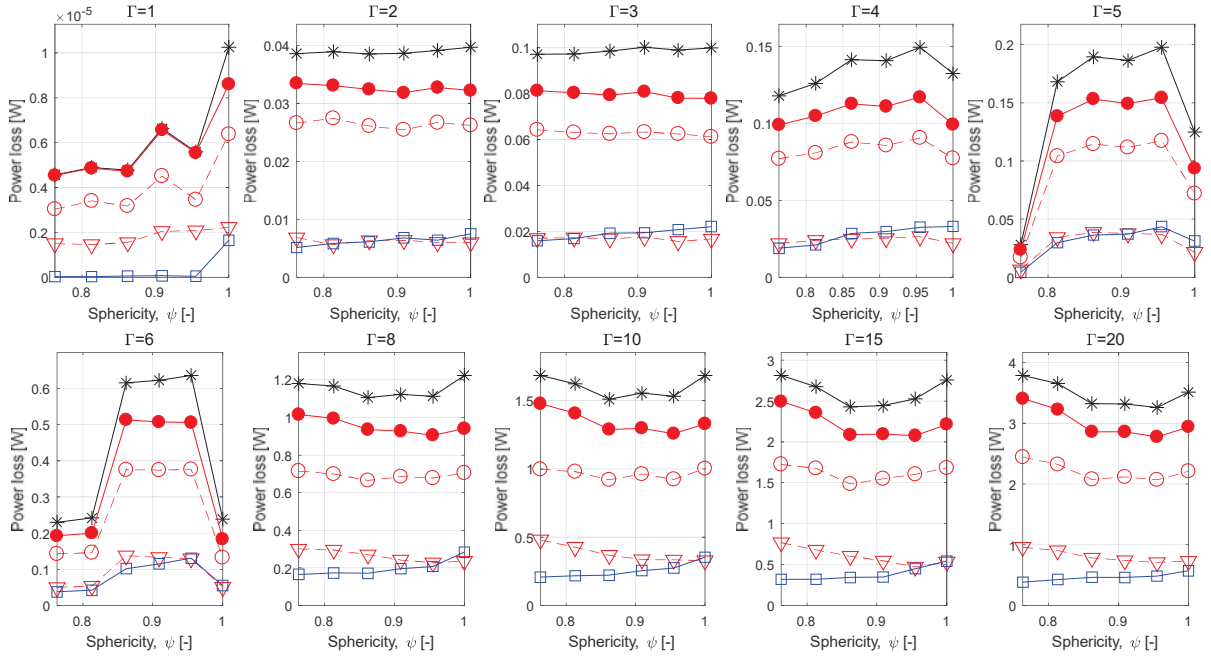

Figure 7: Power loss changes in terms of sphericity at different vibration levels: total loss (—✳—), frictional loss (—●—), inter-particle frictional loss (—⊖—), particle-enclosure frictional loss (—▽—), collisional loss (—□—).

If one looks into the total power loss results omitting the reference particle (i.e. the perfect sphere: $\psi = 1$ and $C = 1$) in both charts, it can be found that there are three damping regimes according to the vibrational intensity in which the total loss is affected by particle shape. The first one is 'inclining' regime where the total power loss generally increases with increasing sphericity or circularity level before $\Gamma \approx 5$. This increasing behaviour becomes moderate at higher amplitudes, whilst it is very slight for small vibrations. Afterwards, there is 'transition' regime up to $\Gamma \approx 8$. Although increasing tendency in total power loss continues in this regime, a dramatic jump is also observed because of impacts with the upper surface of the cavity, as discussed in the previous section. The last damping regime is 'declining' in which the power loss is decreasing with increasing sphericity or circularity unlike the other regimes and this falling behaviour is more apparent at higher vibration amplitudes. Together, these findings suggest that damping is optimised at different amplitudes, depending on particle shape. The results also indicate that there is an oblate particle type which provides more damping than the perfect sphere for almost all vibrational levels. Thus, it can be preferable in granular applications to use very slight oblate particle if the vibrations ensure working before two-sided complete bouncing bed. Otherwise, in two-sided complete bouncing bed state, it is more appropriate to employ highly flattened particles. However, it should be noticed that these results need to be supported by quantitative data from experimental works.

For a given non-dimensional acceleration level, it can be highlighted from the power loss plots that the most dominant damping mechanism is friction for every particle type. Besides, particle-particle frictional interactions are responsible for most of frictional dissipation. In fact, it is reported that particle-particle contacts contribute most of overall dissipation (i.e. particle-enclosure boundary interactions have minor effects on dissipation) as similarly mentioned before [18]. The dominancy of frictional loss leads that the overall damping behaviour stated in the previous paragraph completely reflects the frictional energy dissipation.

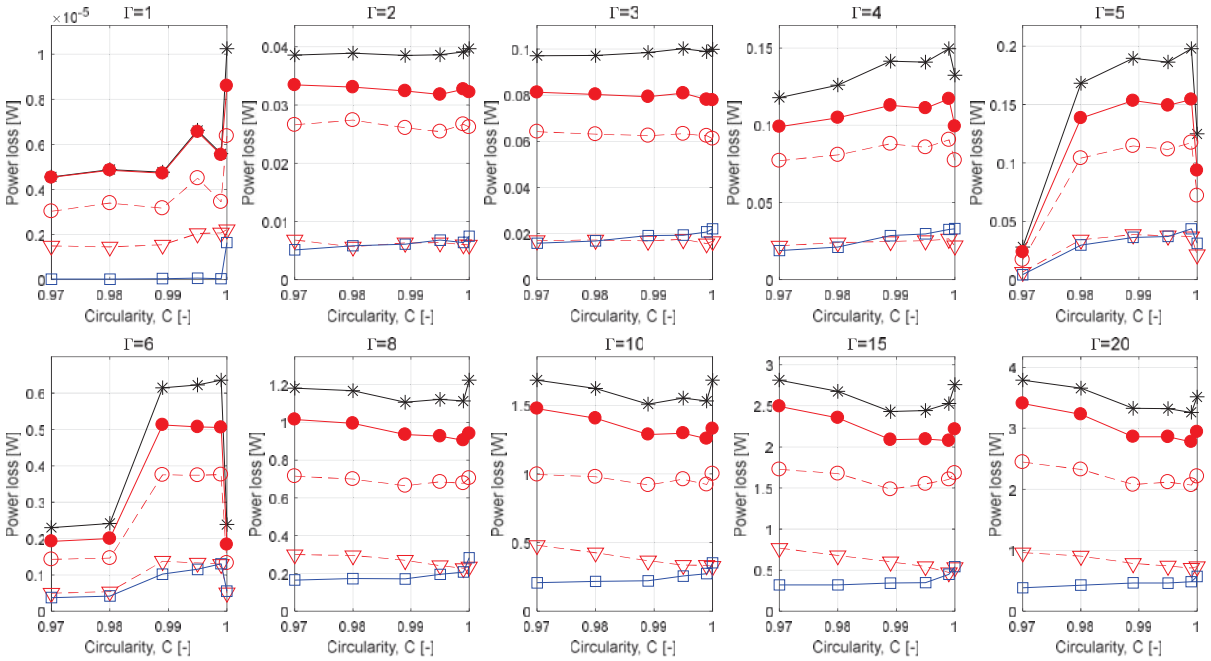

Figure 8: Power loss changes in terms of circularity at different vibration levels: total loss (—✳—), frictional loss (—●—), inter-particle frictional loss (–⊖–), particle-enclosure frictional loss (–▽–), collisional loss (—□—).

One unanticipated result is that collisional loss always increases with sphericity or circularity whatever the damping regime. It is believed that this occurs because flatter (i.e. low sphericity or low circularity) particles have fewer intense collisions (i.e. high overlap, high impact velocity). Additionally, an interesting correlation is found between collisional and particle-enclosure frictional loss characteristics along sphericity or circularity. As can be seen in Figure 7 and Figure 8, they generally have the same tendency before two-sided bouncing bed behaviour (i.e. $\Gamma < 8$) while the power loss trends of those seem opposite after this threshold vibration intensity.

5 CONCLUSIONS

This study set out to assess the effect of oblate particle usage in granular dampers undergoing vertical harmonic excitations by conducting numerical studies. The investigation has shown that the damping performance and the motional behaviour is sensitive to the sphericity level of the particles as well as the vibration amplitude. The power loss results in this study indicate that three damping regimes exist, each depends on vibration level and sphericity of the particles. Additionally, there is generally an oblate particle type which can be chosen rather than the typical perfect sphere to provide higher damping to main structures according to the motional state. Also, it has been shown that the general damping characteristics of particles follow the frictional dissipation behaviour which is the dominant mechanism in granular damping. This research extends the existing literature on damping from irregular particles. However, experimental investigations should be also conducted to confirm these numerical outcomes.

REFERENCES

[1] H. V Panossian, Non-obstructive particle damping: New experiences and capabilities, in: 49th AIAA/ASME/ASCE/AHS/ASC Struct. Struct. Dyn. Mater. Conf., Schaumburg, Illinois, 2008. doi:10.2514/6.2008-2102.

[2] H. V Panossian, Structural damping enhancement via non-obstructive particle damping technique, J. Vib. Acoust. 114 (1992) 101–105. doi:10.1115/1.2930221.

[3] S.S. Simonian, Particle beam damper, in: Proc. SPIE 2445, Smart Struct. Mater. 1995 Passiv. Damping, San Diego, California, 1995: pp. 149–160. doi:10.1117/12.208884.

[4] B.M. Shah, D. Pillet, X.M. Bai, L.M. Keer, Q. Jane Wang, R.Q. Snurr, Construction and characterization of a particle-based thrust damping system, J. Sound Vib. 326 (2009) 489–502. doi:10.1016/j.jsv.2009.06.007.

[5] Z. Xu, M. Yu Wang, T. Chen, A particle damper for vibration and noise reduction, J. Sound Vib. 270 (2004) 1033–1040. doi:10.1016/S0022-460X(03)00503-0.

[6] B. Knight, D. Parsons, A. Smith, Evaluating attenuation of vibration response using particle impact damping for a range of equipment assemblies, in: AIAA Aerosp. Des. Struct. Event, Boston, Massachusetts, 2013: pp. 1–9.

[7] Y.C. Chung, Y.R. Wu, Dynamic modeling of a gear transmission system containing damping particles using coupled multi-body dynamics and discrete element method, Nonlinear Dyn. 98 (2019) 129–149. doi:10.1007/s11071-019-05177-1.

[8] F. Duvigneau, S. Koch, E. Woschke, U. Gabbert, An effective vibration reduction concept for automotive applications based on granular-filled cavities, JVC/Journal Vib. Control. 24 (2018) 73–82. doi:10.1177/1077546316632932.

[9] J.A. Rongong, G.R. Tomlinson, Amplitude dependent behaviour in the application of particle dampers to vibrating structures, in: 46th AIAA/ASME/ASCE/AHS/ASC Struct. Struct. Dyn. Mater. Conf., Austin, Texas, 2005: pp. 6433–6441. doi:10.2514/6.2005-2327.

[10] W. Liu, G.R. Tomlinson, J.A. Rongong, The dynamic characterisation of disk geometry particle dampers, J. Sound Vib. 280 (2005) 849–861. doi:10.1016/j.jsv.2003.12.047.

[11] J.J. Hollkamp, R.W. Gordon, Experiments with particle damping, in: Proc. SPIE 3327, Smart Struct. Mater. 1998 Passiv. Damping Isol., San Diego, California, 1998: pp. 2–12. doi:10.1117/12.310675.

[12] Z. Lu, S.F. Masri, X. Lu, Parametric studies of the performance of particle dampers under harmonic excitation, Struct. Control Heal. Monit. 18 (2011) 79–98. doi:10.1002/stc.359.

[13] A. Papalou, S.F. Masri, Performance of particle dampers under random excitation, J. Vib. Acoust. 118 (1996) 614–621. doi:10.1115/1.2888343.

[14] M. Sánchez, G. Rosenthal, L.A. Pugnaloni, Universal response of optimal granular damping devices, J. Sound Vib. 331 (2012) 4389–4394. doi:10.1016/j.jsv.2012.05.001.

[15] K. Mao, M.Y. Wang, Z.Z. Xu, T. Chen, Simulation and characterization of particle

damping in transient vibrations, J. Vib. Acoust. 126 (2004) 202–211. doi:10.1115/1.1687401.

[16] C.X. Wong, M.C. Daniel, J.A. Rongong, Energy dissipation prediction of particle dampers, J. Sound Vib. 319 (2009) 91–118. doi:10.1016/j.jsv.2008.06.027.

[17] K. Mao, M.Y. Wang, Z. Xu, T. Chen, DEM simulation of particle damping, Powder Technol. 142 (2004) 154–165. doi:10.1016/j.powtec.2004.04.031.

[18] Y. Wang, B. Liu, A. Tian, W. Tang, Experimental and numerical investigations on the performance of particle dampers attached to a primary structure undergoing free vibration in the horizontal and vertical directions, J. Sound Vib. 371 (2016) 35–55. doi:10.1016/j.jsv.2016.01.056.

[19] M. Sánchez, C.M. Carlevaro, L.A. Pugnaloni, Effect of particle shape and fragmentation on the response of particle dampers, J. Vib. Control. 20 (2014) 1846–1854. doi:10.1177/1077546313480544.

[20] H. Pourtavakoli, E.J.R. Parteli, T. Pöschel, Granular dampers: Does particle shape matter?, New J. Phys. 18 (2016). doi:10.1088/1367-2630/18/7/073049.

[21] J.M. Bajkowski, B. Dyniewicz, M. Gębik-Wrona, J. Bajkowski, C.I. Bajer, Reduction of the vibration amplitudes of a harmonically excited sandwich beam with controllable core, Mech. Syst. Signal Process. 129 (2019) 54–69. doi:10.1016/j.ymssp.2019.04.024.

[22] P.A. Cundall, O.D.L. Strack, A discrete numerical model for granular assemblies, Geotechnique. 29 (1979) 47–65. doi:10.1680/geot.1979.29.1.47.

[23] B.L. Fowler, E.M. Flint, S.E. Olson, Effectiveness and predictability of particle damping, in: Proc. SPIE 3989, Smart Struct. Mater. 2000 Damping Isol., Newport Beach, California, 2000: pp. 356–367. doi:10.1117/12.384576.

[24] D. Markauskas, R. Kačianauskas, A. Džiugys, R. Navakas, Investigation of adequacy of multi-sphere approximation of elliptical particles for DEM simulations, Granul. Matter. 12 (2010) 107–123. doi:10.1007/s10035-009-0158-y.

[25] I. Cruz-Matías, D. Ayala, D. Hiller, S. Gutsch, M. Zacharias, S. Estradé, F. Peiró, Sphericity and roundness computation for particles using the extreme vertices model, J. Comput. Sci. 30 (2019) 28–40. doi:10.1016/j.jocs.2018.11.005.

[26] Y. Tatemoto, Y. Mawatari, T. Yasukawa, K. Noda, Numerical simulation of particle motion in vibrated fluidized bed, Chem. Eng. Sci. 59 (2004) 437–447. doi:10.1016/j.ces.2003.10.005.

[27] L. Vu-Quoc, X. Zhang, L. Lesburg, Normal and tangential force-displacement relations for frictional elasto-plastic contact of spheres, Int. J. Solids Struct. 38 (2001) 6455–6489. doi:10.1016/S0020-7683(01)00065-8.

[28] T. Iwasaki, M. Satoh, T. Koga, Analysis of collision energy of bead media in a high-speed elliptical-rotor-type powder mixer using the discrete element method, Powder Technol. 121 (2001) 239–248. doi:10.1016/S0032-5910(01)00384-9.

[29] Y. Tsuji, T. Tanaka, T. Ishida, Lagrangian numerical simulation of plug flow of cohesionless particles in a horizontal pipe, Powder Technol. 71 (1992) 239–250. doi:10.1016/0032-5910(92)88030-L.

[30] L. Vu-Quoc, X. Zhang, Accurate and efficient tangential force-displacement model for

elastic frictional contact in particle-flow simulations, Mech. Mater. 31 (1999) 235–269. doi:10.1016/S0167-6636(98)00064-7.

[31] EDEM, EDEM software user manual, (2020).

[32] R.D. Friend, V.K. Kinra, Particle impact damping, J. Sound Vib. 233 (2000) 93–118. doi:10.1006/jsvi.1999.2795.

[33] M. Ben Romdhane, N. Bouhaddi, M. Trigui, E. Foltête, M. Haddar, The loss factor experimental characterisation of the non-obstructive particles damping approach, Mech. Syst. Signal Process. 38 (2013) 585–600. doi:10.1016/j.ymssp.2013.02.006.

[34] B. Darabi, J.A. Rongong, Polymeric particle dampers under steady-state vertical vibrations, J. Sound Vib. 331 (2012) 3304–3316. doi:10.1016/j.jsv.2012.03.005.

[35] C.X. Wong, M.C. Daniel, J.A. Rongong, Prediction of the amplitude dependent behaviour of particle dampers, in: AIAA/ASME/ASCE/AHS/ASC Struct. Struct. Dyn. Mater. Conf., Honolulu, Hawaiii, 2007: pp. 4167–4182. doi:10.2514/6.2007-2043.

EURODYN 2020
XI International Conference on Structural Dynamics
M. Papadrakakis, M. Fragiadakis, C. Papadimitriou (eds.)
Athens, Greece, 23–26 November 2020

PREDICTION OF BEAM DYNAMICS IN CABLE-BEAM SYSTEMS THROUGH EXPERIMENTAL-NUMERICAL DECOUPLING

Mohammad Hadi Jalali[1], **Geoff Rideout**[2],

[1] Memorial University
St. John's, NL, Canada
e-mail: mjalalinodou@mun.ca

[2] Memorial University
St. John's, NL, Canada
e-mail: gdrideout@mun.ca

Keywords: Cable-Beam System, FRF-based Decoupling, Finite Element Model Updating.

Abstract.

Interactions between cable and structure affect the modal properties of cabled structures such as overhead electricity transmission and distribution line systems. Modal properties of an in-service pole, without the effects of conductors, are potentially useful for condition monitoring, but are difficult to determine. This paper presents a frequency-based decoupling method to extract modal properties of a beam with the effects of cable filtered out. A scalable experimental lab-scale pole-line for a cable-beam system consisting of a cantilever beam and stranded cable is used to validate the method. A finite element model for the stranded cable is developed and optimized using FRF-based nonlinear optimization based on experimentally obtained FRF and the FRFs of the assembled system are measured. The (unknown) FRF of the cantilever beam is predicted by substructural decoupling of the numerical cable dynamic model (known FRF matrix) from the measured assembled cable-beam dynamic model (known FRF matrix). Comparison of the estimated and directly-measured beam FRF's show good agreement, demonstrating that the method can be used to filter out the effects of cable on the modal properties of the structure in cabled structures.

1 INTRODUCTION

Dynamic interaction between cables and the main structure in cabled structures such as cable-stayed bridges, guyed towers, cable-stayed wind turbines, and power transmission lines has been a topic of interest of researchers for many years. The focus of this study is power transmission lines and dynamic interaction between the conductor (cable) and the pole. The authors are developing a global NDE (Non-destructive Evaluation) method to detect damage at any location, based on vibration response from modal impact testing at a single arbitrary location [1]–[5]. Since power lines (conductors) are attached to the poles, vibrations of the conductors affect the modal properties of the pole. Removing the effect of the conductors to reveal pole properties requires a structural dynamic method to decouple the cable dynamic model from the assembled cable-pole dynamic model.

There are many studies in the literature about the interaction between cables and structures as a coupled system. Gattulli et. al. [6] investigated linear coupled vibration of two masonry walls connected by a cable. The system was modeled as two cantilever beams connected by a cable and the effect of different parameters on coupled vibration behavior was investigated. Potenza et. al. [7] and Gattulli et. al. [8] studied the same system using nonlinear analysis. Jalali et. al. [3] developed an analytical model to study the effect of cable sag and bending stiffness on coupled vibration behavior of a cable-beam system. Cable bending stiffness and sag had significant effects. The analytical results were verified by experiments on a lab-scale cable-beam system. Li et. al. [9] presented a simplified computational model for a high-voltage transmission tower-line system to study the coupling behavior of adjacent tower spans and cables due to seismic excitations. Reviewing the literature in cable-beam system dynamic analysis reveals that all the published papers studied the dynamic interaction of cable and beam in linear or nonlinear analysis and there is no research dealing with extraction of dynamic properties of the beam as an independent substructure.

Dynamic substructuring methods and the reverse problem (inverse dynamic substructuring) are well established [10]–[14]. Inverse dynamic substructuring or decoupling is a relevant issue for subsystems that cannot be measured separately, since they are coupled to their neighboring substructure(s) in operational conditions [15]. In this paper, a frequency-based or FRF-based decoupling technique is used to extract beam dynamics in a cable-beam system with the effects of connected cable filtered out. An experimental reduced-scale cable-beam set up of a cantilever beam connected to a stranded cable was built to measure the assembled system FRFs and a finite element model for the cable was developed and optimized using FRF-based optimization. The cable numerical model was then decoupled from the assembled (measured) system through experimental-numerical FRF-based decoupling.

The paper is outlined as follows. A summary of theory behind FRF-based decoupling is presented in Section 2 and FRF-based finite element model updating is described briefly in Section 3. Section 4 describes the cable-beam system and finite element model updating of the cable. Decoupling results and discussion are presented in Section 5 and conclusion and future work are presented in Section 6.

2 SUBSTRUCTURE DECOUPLING

In a cable-beam system (Figure 1), the cable and the beam are "substructures" of the assembled system and the purpose of substructure decoupling is to find the dynamics of beam subsystem (*B*) as a "standalone" component that is completely decoupled from subsystem cable (*C*).

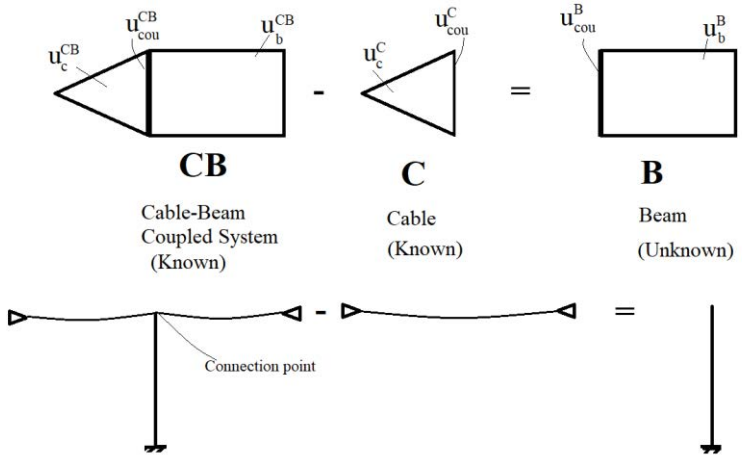

Figure 1. Substructure decoupling schematic

Assuming the dynamics of system *CB* and *C* are known, a dynamic stiffness representation of the assembled system *CB* in compact form is [15]:

$$\boldsymbol{Z}^{CB}\boldsymbol{u}^{CB} = \boldsymbol{f}^{CB} + \boldsymbol{g}^{CB}$$

$$\begin{bmatrix} \boldsymbol{Z}_{cc}^{CB} & \boldsymbol{Z}_{ccou}^{CB} & \boldsymbol{0} \\ \boldsymbol{Z}_{couc}^{CB} & \boldsymbol{Z}_{coucou}^{CB} & \boldsymbol{Z}_{coub}^{CB} \\ \boldsymbol{0} & \boldsymbol{Z}_{bcou}^{CB} & \boldsymbol{Z}_{bb}^{CB} \end{bmatrix} \begin{bmatrix} \boldsymbol{u}_c \\ \boldsymbol{u}_{cou} \\ \boldsymbol{u}_b \end{bmatrix} = \begin{bmatrix} \boldsymbol{f}_c \\ \boldsymbol{f}_{cou} \\ \boldsymbol{f}_b \end{bmatrix} + \begin{bmatrix} \boldsymbol{0} \\ \boldsymbol{g}_{cou} \\ \boldsymbol{0} \end{bmatrix} \tag{1}$$

And subsystem *C*:

$$\boldsymbol{Z}^{C}\boldsymbol{u}^{C} = \boldsymbol{f}^{C} - \boldsymbol{g}^{C}$$

$$\begin{bmatrix} \boldsymbol{Z}_{cc}^{C} & \boldsymbol{Z}_{ccou}^{C} \\ \boldsymbol{Z}_{couc}^{C} & \boldsymbol{Z}_{coucou}^{C} \end{bmatrix} \begin{bmatrix} \boldsymbol{u}_c^{C} \\ \boldsymbol{u}_{cou}^{C} \end{bmatrix} = \begin{bmatrix} \boldsymbol{f}_c \\ \boldsymbol{f}_{cou} \end{bmatrix} - \begin{bmatrix} \boldsymbol{0} \\ \boldsymbol{g}_{cou}^{C} \end{bmatrix} \tag{2}$$

where $\boldsymbol{u}^{CB} = \begin{bmatrix} \boldsymbol{u}_c \\ \boldsymbol{u}_{cou} \\ \boldsymbol{u}_b \end{bmatrix}$ is the vector of DOF of system *CB* (**Error! Reference source not found.**) (the superscripts are omitted for brevity), $\boldsymbol{u}^{C} = \begin{bmatrix} \boldsymbol{u}_c^{C} \\ \boldsymbol{u}_{cou}^{C} \end{bmatrix}$ is the vector of DOF of substructure *C*, $\boldsymbol{Z}^{CB}$ and $\boldsymbol{Z}^{C}$ are the stiffness matrices of system *CB* and *C*, respectively (stiffness matrix is the inverse of FRF matrix ($\boldsymbol{Z} = \boldsymbol{H}^{-1}$)). Vectors $\boldsymbol{f}^{*}$ are the external force vectors and vectors $\boldsymbol{g}^{*}$ represent the additional disconnection forces (with non-zero entries only at the interface DOF) felt from the decoupling of the neighboring components [15]. When two substructures are in contact and (de)coupling is carried out, compatibility and equilibrium conditions at the connected interface DOFs must always be satisfied. The compatibility condition ($\boldsymbol{u}_{cou}^{C} = \boldsymbol{u}_{cou}$) states that the displacements of connected interface DOF must be compatible and the equilibrium condition ($\boldsymbol{g}_{cou} + \boldsymbol{g}_{cou}^{C} = \boldsymbol{0}$) states that the connection forces between the substructures should be in equilibrium. A more systematic description of the problem can be written by introducing the Boolean matrices $\boldsymbol{B}$ and $\boldsymbol{L}$ and writing the compatibility and equilibrium in a compact from: [15]

$$\boldsymbol{B}\boldsymbol{u} = \begin{bmatrix} \boldsymbol{B}^{CB} & \boldsymbol{B}^{C} \end{bmatrix} \begin{bmatrix} \boldsymbol{u}^{CB} \\ \boldsymbol{u}^{C} \end{bmatrix} = \boldsymbol{u}_{cou}^{C} - \boldsymbol{u}_{cou} = \boldsymbol{0} \tag{3}$$

$$\boldsymbol{L^T g} = [\boldsymbol{L}^{CB^T} \quad \boldsymbol{L}^{C^T}] \begin{bmatrix} \boldsymbol{g}^{CB} \\ \boldsymbol{g}^{C} \end{bmatrix} = \begin{bmatrix} \mathbf{0} \\ \mathbf{0} \\ \mathbf{0} \\ \boldsymbol{g}_{cou} + \boldsymbol{g}_{cou}^{C} \end{bmatrix} = \mathbf{0} \tag{4}$$

Eq. (3) presents the compatibility equation and Eq. (4) presents the equilibrium equation. Therefore, the decoupling problem can be described in the following equations:

$$\begin{bmatrix} \boldsymbol{Z}^{CB} & \mathbf{0} \\ \mathbf{0} & \boldsymbol{Z}^{C} \end{bmatrix} \begin{bmatrix} \boldsymbol{u}^{CB} \\ \boldsymbol{u}^{C} \end{bmatrix} = \begin{bmatrix} \boldsymbol{f}^{CB} \\ \boldsymbol{f}^{C} \end{bmatrix} + \begin{bmatrix} \boldsymbol{g}^{CB} \\ -\boldsymbol{g}^{C} \end{bmatrix}$$

$$[\boldsymbol{B}^{CB} \quad \boldsymbol{B}^{C}] \begin{bmatrix} \boldsymbol{u}^{CB} \\ \boldsymbol{u}^{C} \end{bmatrix} = \mathbf{0} \tag{5}$$

$$[\boldsymbol{L}^{CB^T} \quad \boldsymbol{L}^{C^T}] \begin{bmatrix} \boldsymbol{g}^{CB} \\ \boldsymbol{g}^{C} \end{bmatrix} = \mathbf{0}$$

Employing the dual formulation for decoupling [16], the interface forces are satisfied a priori by choosing interface forces of the form of:

$$\boldsymbol{g} = -\boldsymbol{B}^T \boldsymbol{\lambda} \tag{6}$$

where $\boldsymbol{\lambda}$ are Lagrange multipliers, corresponding physically to the interface force intensities. The equilibrium condition in Eq. (4) thus becomes:

$$\boldsymbol{L^T g} = -\boldsymbol{L^T B^T \lambda} = \mathbf{0} \tag{7}$$

But by considering the fact that $\boldsymbol{L^T}$ is the null space of $\boldsymbol{B^T}$ [10], this condition is always satisfied. The decoupling methods can be categorized as collocated methods when both the compatibility and equilibrium are imposed at the same sets of DOFs ($\boldsymbol{C}^* = \boldsymbol{E}^*$) or non-collocated methods when different sets of DOFs ($\boldsymbol{C}^* \neq \boldsymbol{E}^*$) are used for imposing the compatibility and equilibrium conditions. The decoupling problem can therefore be formulated in a dual way as [15]:

$$\begin{bmatrix} \boldsymbol{Z}^{CB} & \mathbf{0} & \boldsymbol{E}^{CB^T} \\ \mathbf{0} & -\boldsymbol{Z}^{C} & \boldsymbol{E}^{C^T} \\ \boldsymbol{C}^{CB} & \boldsymbol{C}^{C} & \mathbf{0} \end{bmatrix} \begin{bmatrix} \boldsymbol{u}^{CB} \\ \boldsymbol{u}^{C} \\ \boldsymbol{\lambda} \end{bmatrix} = \begin{bmatrix} \boldsymbol{f}^{CB} \\ \mathbf{0} \\ \mathbf{0} \end{bmatrix} \tag{8}$$

By eliminating Lagrange multipliers $\boldsymbol{\lambda}$ in Eq. (8) and solving for decoupled DOF:

$$\begin{bmatrix} \boldsymbol{u}^{CB} \\ \boldsymbol{u}^{C} \end{bmatrix} = \left(\begin{bmatrix} \boldsymbol{H^{CB}} & \mathbf{0} \\ \mathbf{0} & -\boldsymbol{H^{C}} \end{bmatrix} - \begin{bmatrix} \boldsymbol{H^{CB}} & \mathbf{0} \\ \mathbf{0} & -\boldsymbol{H^{C}} \end{bmatrix} \begin{bmatrix} \boldsymbol{E^{CB^T}} \\ \boldsymbol{E^{C^T}} \end{bmatrix} \left([\boldsymbol{C^{CB}} \quad \boldsymbol{C^{C}}] \begin{bmatrix} \boldsymbol{H^{CB}} & \mathbf{0} \\ \mathbf{0} & -\boldsymbol{H^{C}} \end{bmatrix} \begin{bmatrix} \boldsymbol{E^{CB^T}} \\ \boldsymbol{E^{C^T}} \end{bmatrix} \right)^{+} [\boldsymbol{C^{CB}} \quad \boldsymbol{C^{C}}] \begin{bmatrix} \boldsymbol{H^{CB}} & \mathbf{0} \\ \mathbf{0} & -\boldsymbol{H^{C}} \end{bmatrix} \right) \boldsymbol{f} \tag{9}$$

which is the form of $\boldsymbol{u} = \boldsymbol{Hf}$, so that the decoupled FRF of substructure B in a general form can be found:

$$\boldsymbol{H^B} = \begin{bmatrix} \boldsymbol{H^{CB}} & \boldsymbol{0} \\ \boldsymbol{0} & \boldsymbol{-H^C} \end{bmatrix} - \begin{bmatrix} \boldsymbol{H^{CB}} & \boldsymbol{0} \\ \boldsymbol{0} & \boldsymbol{-H^C} \end{bmatrix} \begin{bmatrix} \boldsymbol{E^{CB^T}} \\ \boldsymbol{E^{C^T}} \end{bmatrix} \left(\begin{bmatrix} \boldsymbol{C^{CB}} & \boldsymbol{C^C} \end{bmatrix} \begin{bmatrix} \boldsymbol{H^{CB}} & \boldsymbol{0} \\ \boldsymbol{0} & \boldsymbol{-H^C} \end{bmatrix} \begin{bmatrix} \boldsymbol{E^{CB^T}} \\ \boldsymbol{E^{C^T}} \end{bmatrix} \right)^{+} \begin{bmatrix} \boldsymbol{C^{CB}} & \boldsymbol{C^C} \end{bmatrix} \begin{bmatrix} \boldsymbol{H^{CB}} & \boldsymbol{0} \\ \boldsymbol{0} & \boldsymbol{-H^C} \end{bmatrix} \tag{10}$$

where + denotes the (Moore–Penrose) pseudo-inverse, since the matrix in parentheses is not necessarily a square matrix. Eq. (10) is used throughout the paper for decoupling analysis.

3 FRF-BASED FINITE ELEMENT MODEL UPDATING

The form of the frequency response function (FRF) used in this study is accelerance which means acceleration response over force in the frequency domain. Accelerance FRF, $H_{a,b}(\omega)$, is the acceleration response at node a, $A_a(\omega)$, divided by the force at node b, $F_b(\omega)$, both in the frequency domain [17]:

$$H_{a,b}(\omega) = \frac{A_a(\omega)}{F_b(\omega)} \cong \sum_{i=1}^{m} \frac{-\omega^2 \hat{\phi}_{ai} \hat{\phi}_{bi}}{-\omega^2 + 2i\omega\Omega_i\xi_i + \Omega^2{}_i} \tag{11}$$

where m is the number of modes, ω is frequency, Ω_i is i^{th} natural frequency of the system, ξ_i is i^{th} damping ratio corresponding to i^{th} mode and $\hat{\phi}_{ai}$ and $\hat{\phi}_{bi}$ are the scalar values of mode shape i at response node a and excitation node b, respectively. The maximum number of modes, m, that can be used to construct the response is equal to the total number of degrees of freedom of the system. However, it is not feasible to measure all degrees of freedom and the entire range of natural frequencies during structural testing. Therefore, a reduced number of mode shapes can be used. Special care must be taken to include enough mode shapes in the formulation, typically more than measured [18]-[19]. For a rule of thumb, at least double the number of modes that are measured should be used for analytical FRF calculation [17].

From of FRF used for model updating is as follows and the values of the FRF magnitude is in dB scale:

$$\bar{H}_{a,b}(\omega) = 20\log_{10}\left(\left|H_{a,b}(\omega)\right|\right) \tag{12}$$

The goal of the FE model updating is to change the properties of a FEM such that the analytical response of the model matches that of measured data. The goal is to obtain an analytical FRF as close as possible to the experimental FRF in a desired frequency range. After developing the FE model, Eq. (12) and Eq. (11) are used to obtain the FRF at the response and excitation nodes corresponding to the response and excitation locations considered in the experiment. The problem then is a least squares problem where the difference between analytical and measured FRFs, the error or residual, is found and a scalar objective error function value is calculated [18]. With the scalar objective error function value, numerical optimization techniques are used to minimize the difference between the analytical and measured FRFs by modifying the parameters of the FEM such that the analytical FRF best matches the measured FRF [18].

Since all of the structural properties in the finite element can be modified, any combination of stiffness, mass, and damping updating may be performed. Stiffness, mass and damping parameter updating can also occur simultaneously. Substituting Eq. (11) into Eq. (12) and using modal responses as functions of the unknown updating parameters p results in Eq. **(13)** [18]:

$$\bar{H}_{a,b}(\omega, p) = 20\log_{10}\left(\left|\sum_{i=1}^{m} \frac{-\omega^2 \hat{\phi}_{ai}(p) \hat{\phi}_{bi}(p)}{-\omega^2 + 2i\omega\Omega_i(p)\xi_i(p) + \Omega^2{}_i(p)}\right|\right) \tag{13}$$

The error function, or residual e, is defined as:

$$e(\omega, p) = \bar{H}^{a}{}_{a,b}(\omega, p) - \bar{H}^{m}{}_{a,b}(\omega, p) \tag{14}$$

where $\bar{H}^{a}{}_{a,b}(\omega, p)$ and $\bar{H}^{m}{}_{a,b}(\omega, p)$ are analytical and measured FRF, respectively. Then, a scalar objective error function J is created and is the quantity that is minimized through bounded numerical optimization:

$$J(p) = e^{T}(\omega, p)e(\omega, p) \tag{15}$$

The purpose of optimization is to minimize $J(\omega, p)$ by considering the upper and lower bounds for p [18]. The scalar objective error function is normalized by the initial value of the scalar objective error function $J(p)_1$ so that the optimization starts at a value of 1 and the perfect match would be a value of 0.

$$J(p)_i = \frac{J(p)_i}{J(p)_1} \tag{16}$$

The parameter p is a unitless modifier that modifies any structural parameter.

4 CABLE-BEAM SYSTEM

The schematic of assembled cable-beam system (*CB*) and the cable substructure (*C*) is shown in Figure 2. The geometry of the (sub) structures is illustrated. The cantilever is a steel rectangular beam with cross section area of 46.67 mm^2 and the cable is a 7×19 steel stranded cable with a nominal diameter of 1/4 inch and linear density of 0.16667 kg/m. Three measurement points are considered for decoupling. In Figure 2-a, point 1 is a coupling DOF ($\boldsymbol{u}_{cou}^{CB}$ in Figure 1) and points 2 and 3 are the beam internal DOFs ($\boldsymbol{u}_{b}^{CB}$ in Figure 1) within the assembled system. There is no cable internal DOF ($\boldsymbol{u}_{a}^{CB}$ in Figure 1) since it was intended to need the least number of DOF from the numerical cable model. In Figure 2-b, the coupling point 1 ($\boldsymbol{u}_{cou}^{C}$ in Figure 1) is shown. All the degrees of freedom are along the *z* direction. The cable tension is 150 N when the cable is connected to the beam (in system *CB*) and when the cable-only system is considered.

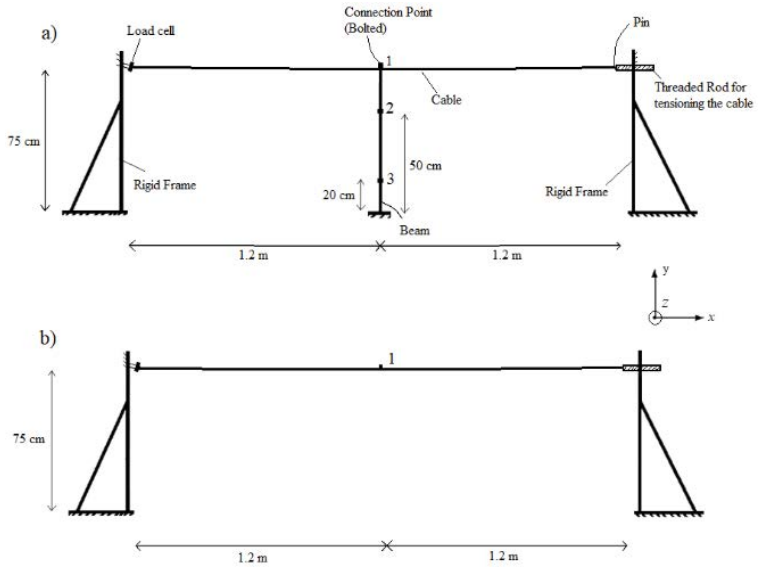

Figure 2. Schematic of a) Assembled cable-beam system (*CB*) b) Cable substructure (*C*)

FRFs of the assembled system ($\boldsymbol{H}^{CB}$ in Eq. (10)) are measured using modal testing and FRF of the cable at the coupling point ($\boldsymbol{H}^{C}$ in Eq. (10)) is obtained using a finite element model. Eq. (10) is then used to obtain the decoupled beam FRF, $\boldsymbol{H}^{B}$. The assembled system set up (*CB*) is shown in Figure 3. Two rigid frames were secured to the floor on the right and left sides. The natural frequencies of the frames were verified to be far away from the natural frequencies of the system. The right end of the cable was attached to a threaded rod to adjust the tension of the cable and an in-line load cell at the left end of the cable measured the longitudinal tension of the cable. Two U-bolts were used in the connection point of the cable and beam. Both ends of the cable are pinned and the beam is cantilevered. More details of the set up can be found in [3].

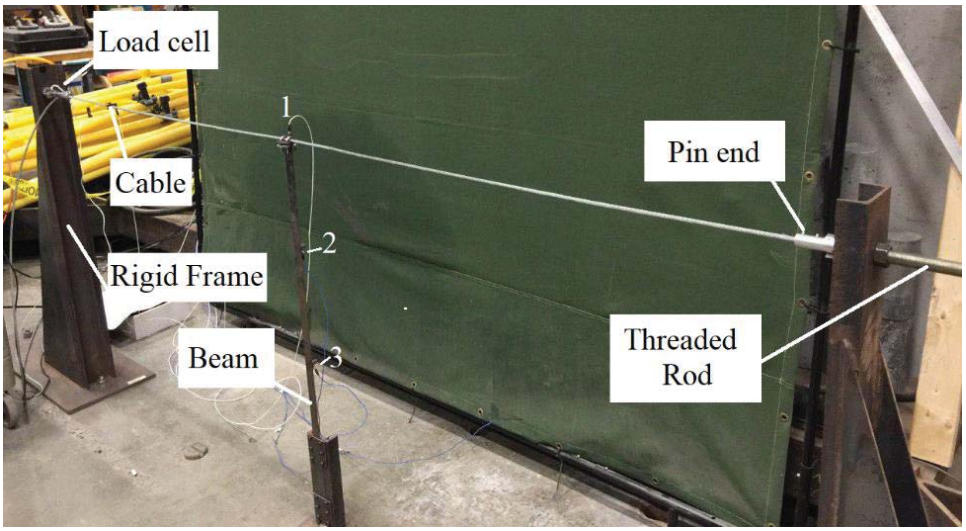

Figure 3. Experimental set up for cable-beam system

FRFs were obtained using a B&K 8205-002 impact hammer, a NI c-DAQ 9172 chassis and the software ModalView [20] was used to analyze the data.

4.1 Finite element model updating of the cable

In order to obtain the substructure *C* FRF matrix, $\boldsymbol{H}^{C}$ in Eq. (10), a finite element model for the cable is developed. The cable is modeled as pinned-pinned Euler beam with 100 finite elements. The bending stiffness (EI) of the cable was measured in the previous work of the authors [3] in different tensions and the measured value of 0.525 $Nm^2$is used in the FE model. The beam cross section area is 31.66 mm^2 and the linear density is 0.16667 kg/m.

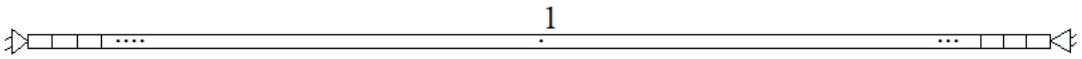

Figure 4. Finite element model of the cable

The FRF matrix $\boldsymbol{H}^{C}$ has only one array, ${H_{11}}^{C}$, since point 1 in Figure 2 is the only DOF on the cable substructure (*C*) that is being considered in the analysis. Therefore, in the FE model updating process, direct FRF of point 1 (excitation and response at the same place), ${H_{11}}^{C}$, that is obtained using Eq. (13) is updated based on the measured FRF. In the updating process, all the stiffness and mass elements are directly modified using the multipliers p in Eq. (13). Therefore, there are 100 multipliers (number of finite elements is 100) for the stiffness matrices and

100 multipliers for the mass matrices that need to be updated in each iteration. The nonlinear constrained optimization technique in MATLAB software is used. The lower and upper bounds for all the variables are considered to be 0.5 and 1.5, respectively. Figure 5 shows the updated and initial FRF compared to the FRF obtained from experiment. The magnitude of the updated FRF matches more with the experimental one and the sharpness of the peaks is closer to the experimental FRF in the updated FRF. There is still a slight discrepancy between the updated and experiment FRFs but the decoupling result in Section 5 shows that this discrepancy does not cause any unacceptable error in the final decoupling results.

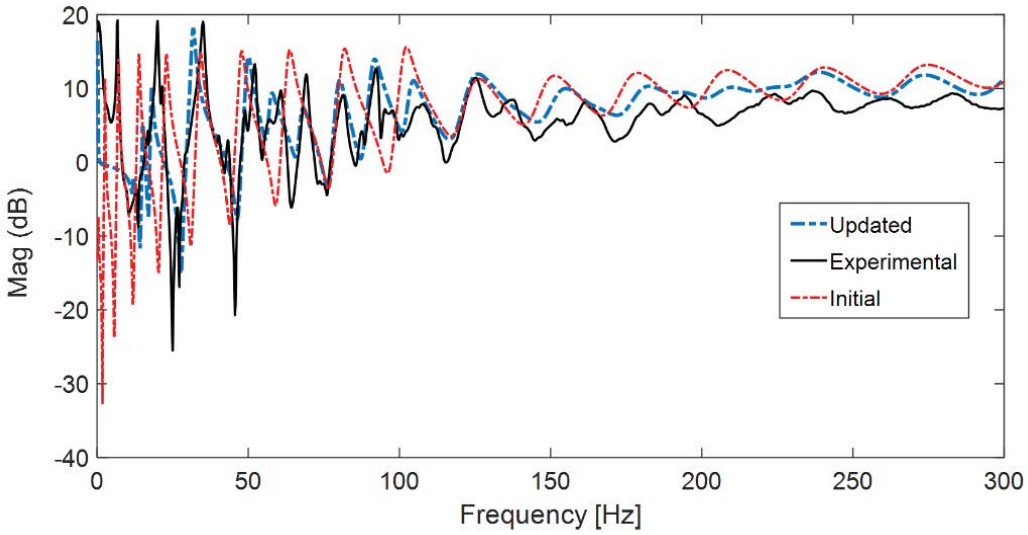

Figure 5. Comparison of updated and initial cable FRF with experimental FRF

5 DECOUPLING RESULTS

The measured FRFs from the assembled system and the calculated FRF from the finite element model are used in Eq. (10) to predict the decoupled beam FRF. Figure 6 shows the predicted FRF ${H_{33}}^{B}$ and ${H_{23}}^{B}$ compared to the directly-measured FRF. Decoupled FRFs show a good agreement with the measured FRFs. There is a spurious peak around 140 Hz which is probably due to numerical singularity that is common in dynamic substructuring [21]. A non-collocated approach [15] is used to obtain the results which means all the internal DOFs of the beam substructure were used for equilibrium condition.

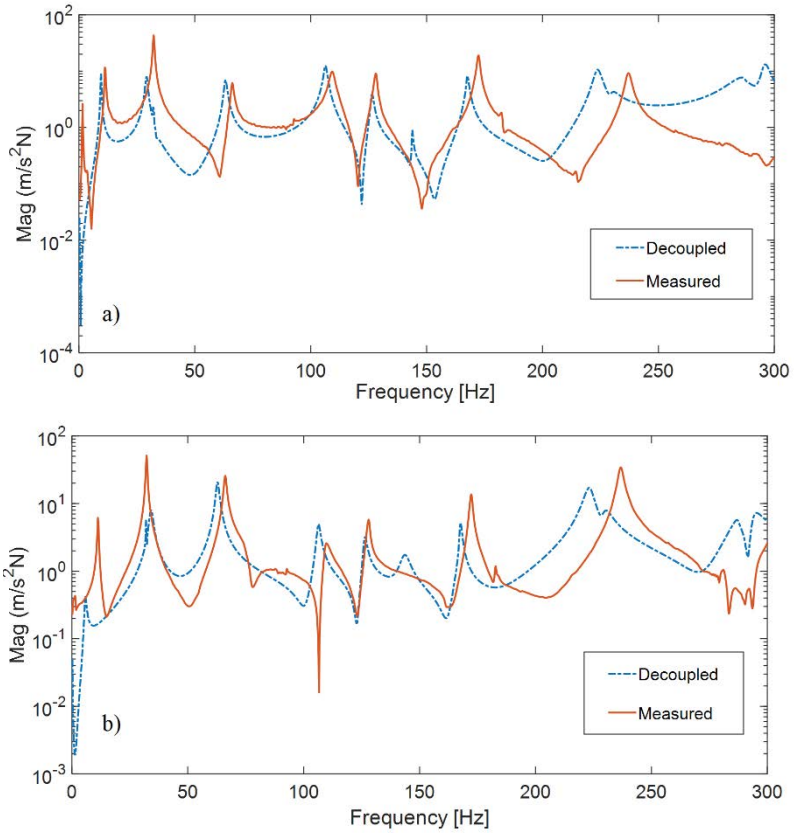

Figure 6. Comparison of decoupled beam FRF with measured FRF a) ${H_{23}}^B$ b) ${H_{33}}^B$

From the obtained FRFs, the modal properties of the beam can be extracted. Natural frequencies and damping ratios of the beam extracted from the predicted FRFs and measured FRFs are compared in Table 1. The 3 dB method [22] was used to extract the damping ratios from the FRF peaks. There is an acceptable agreement between the modal properties of the beam extracted from measured FRF and predicted FRF which shows that frequency based decoupling can be used to extract the modal properties of the beam in a cable-beam system with the cable effects filtered out. In some modes, the predicted and measured damping ratios differ which could be attributed to measurement error and difficulty in exciting the coupling point in the assembled and substructure at the same location. Damping ratio of the first mode was predicated with high error and it is not presented in the table.

Table 1. Natural frequencies (Hz) and damping ratios (%) of beam: predicted (decoupled) and measured

Mode	1		2		3		4		5		6		7		8	
	Hz	%	Hz	%	Hz	%	Hz	%	Hz	%	Hz	%	Hz	%	Hz	%
Measured	1.6	2.03	11.2	1.42	32.2	0.52	66.2	0.52	92.8	0.19	109.4	0.68	128	0.35	172.4	0.23
Decoupled	1.4	-	9.6	1.37	32	0.37	63.2	0.59	--	--	106.2	0.57	126.4	0.31	167.6	0.21

6 CONCLUSIONS

In this study, a cable-beam system was studied through the application of experimental-numerical FRF-based decoupling and the beam FRF was predicted. A finite element model for the cable was developed and updated using FRF-based nonlinear optimization and then was decoupled from the measured assembled system. It was shown that frequency-based decoupling can be applied in cable structures to extract the dynamics of a structure with the effects of cable filtered out. In the field, some parts of the system such as connection point of the conductors and electricity pole are inaccessible. In future, reliable simulation models should be developed for the assembled system so that FRFs of such inaccessible points be replaced by simulation results.

REFERENCES

[1] D. Rideout and O. F. Whelan, "Modeling of tapered cantilever beams for simulation of utility pole vibration," in *Proc. International Conference on Bond Graph Modeling and Simulation, Monterey, USA*, 2014, pp. 6–10.

[2] P. Ferreira Pinto and G. Rideout, "Development and validation of an in-situ utility pole simulation model for virtual modal testing," in *ASME 2016 International Mechanical Engineering Congress and Exposition*, 2016.

[3] M. H. Jalali and G. Rideout, "Analytical and experimental investigation of cable–beam system dynamics," *J. Vib. Control*, vol. 25, no. 19–20, pp. 2678–2691, 2019.

[4] M. H. Jalali and G. Rideout, "Development and Validation of a Numerical Model for Vibration of Power Lines," in *CSME International Congress Toronto, 2018*.

[5] M. H. Jalali and G. Rideout, "Three dimensional dynamic model development and validation for stranded cables," in *ASME 2019 International Mechanical Engineering Congress and Exposition*, 2019.

[6] V. Gattulli, M. Lepidi, F. Potenza, and U. Di Sabatino, "Dynamics of masonry walls connected by a vibrating cable in a historic structure," *Meccanica*, vol. 51, no. 11, pp. 2813–2826, 2016.

[7] F. Potenza, M. Lepidi, U. Di Sabatino, and V. Gattulli, "Nonlinear dynamics of a parametric analytical model for beam-cable-beam structures," *Procedia Eng.*, vol. 199, pp. 796–801, 2017.

[8] V. Gattulli, M. Lepidi, F. Potenza, and U. Di Sabatino, "Modal interactions in the nonlinear dynamics of a beam–cable–beam," *Nonlinear Dyn.*, vol. 96, no. 4, pp. 2547–2566, 2019.

[9] H.-N. Li, W.-L. Shi, G.-X. Wang, and L.-G. Jia, "Simplified models and experimental verification for coupled transmission tower–line system to seismic excitations," *J. Sound Vib.*, vol. 286, no. 3, pp. 569–585, 2005.

[10] D. de Klerk, D. J. Rixen, and S. N. Voormeeren, "General framework for dynamic substructuring: history, review and classification of techniques," *AIAA J.*, vol. 46, no. 5, pp. 1169–1181, 2008.

[11] M. Law, H. Rentzsch, S. Ihlenfeldt, and M. Putz, "Application of substructure decoupling techniques to predict mobile machine tool dynamics: numerical investigations," *Procedia CIRP*, vol. 46, pp. 537–540, 2016.

[12] S. Rahimi, D. de Klerk, and D. J. Rixen, "The Ampair 600 wind turbine benchmark: results from the frequency based substructuring applied to the rotor assembly," in *Topics in Experimental Dynamic Substructuring, Volume 2*, Springer, 2014, pp. 179–192.

[13] A. W. Otto, D. O. Elias, and R. L. Hatton, "Modeling transverse vibration in spider webs using frequency-based dynamic substructuring," in *Dynamics of Coupled Structures, Volume 4*, Springer, 2018, pp. 143–155.
[14] W. D'Ambrogio and A. Fregolent, "Use of experimental dynamic substructuring to predict the low frequency structural dynamics under different boundary conditions," *Math. Mech. Solids*, vol. 23, no. 11, pp. 1444–1455, 2018.
[15] S. N. Voormeeren and D. J. Rixen, "A family of substructure decoupling techniques based on a dual assembly approach," *Mech. Syst. Signal Process.*, vol. 27, pp. 379–396, 2012.
[16] D. de Klerk, D. J. Rixen, and J. de Jong, "The frequency based substructuring (FBS) method reformulated according to the dual domain decomposition method," in *24th International Modal Analysis Conference, St. Louis, MO*, 2006.
[17] D. J. Ewins, *Modal testing: theory and practice*, vol. 15. Research studies press Letchworth, 1984.
[18] J. D. Sipple and M. Sanayei, "Finite element model updating using frequency response functions and numerical sensitivities," *Struct. Control Heal. Monit.*, vol. 21, no. 5, pp. 784–802, 2014.
[19] M. H. Jalali, B. Shahriari, M. Ghayour, S. Ziaei-Rad, and S. Yousefi, "Evaluation of Dynamic Behavior of a Rotor-Bearing System in Operating Conditions," in *WASET, Dubai, 2014*.
[20] ABSignal, "ModalView." National Instrument, 2008.
[21] W. D'Ambrogio and A. Fregolent, "The role of interface DoFs in decoupling of substructures based on the dual domain decomposition," *Mech. Syst. Signal Process.*, vol. 24, no. 7, pp. 2035–2048, 2010.
[22] L. Meirovitch, *Fundamentals of vibrations*. Waveland Press, 2010.

EURODYN 2020
XI International Conference on Structural Dynamics
M. Papadrakakis, M. Fragiadakis, C. Papadimitriou (eds.)
Athens, Greece, 23–26 November 2020

CONTRIBUTION OF SEISMIC NOISE RECORDINGS TO THE NON-STRUCTURAL VULNERABILITY ASSESSMENT

Konstantinos G. Megalooikonomou[1]

[1] GFZ German Research Centre for Geosciences, Helmholtz Centre Potsdam, Section 2.6: Seismic Hazard and Risk Dynamics, Helmholtzstraße 7, 14467 Potsdam, Brandenburg, Germany
e-mail: kmegal@gfz-potsdam.de

Keywords: ambient vibrations, induced seismicity, non-structural components, masonry

Abstract. *Since the 1990s, the recordings of ambient vibrations in structures have gained interest in the civil engineering community due to technological improvements of portable sensors, allowing the recordings of small amplitude vibrations, and the possibility of processing a large amount of data even in real time. Many applications, based on the analysis of seismic noise, exist in the literature for checking the serviceability limit state of existing construction in the case of earthquakes. These applications can be extended to the case of occurrence of induced and triggered seismicity and its potential impact on the built environment. The latter impact has heightened both public concern and regulatory scrutiny, emphasizing the need for an integrated risk management framework. Considering the case of induced seismicity, the vulnerability assessment requires the expected damage to refer to non-structural components. In this study, some historical masonry buildings located in Alsace France are considered and the dynamic characteristics of these structures were estimated by the analysis of seismic noise recordings by sensors installed at each floor of the buildings under study. The estimated dynamic properties for small amplitude vibrations of these historical structures were used to derive simplified vulnerability models. Moreover, the Eurocode 8 defines the interstory drift limit of a building for non-structural damage, by looking at its displacement-sensitive non-structural components at the serviceability limit state. Therefore, by adopting these limits and the developed simplified vulnerability models, new fragility curves for typical historical masonry building types dominant in the region under study are proposed. The fragility curves have been calculated using incremental dynamic analysis for the seismic demands generally imposed upon linear and slightly non-linear models of single and multiple degrees of freedom, which is the case for the effects of induced seismicity. These results will prove useful for both local end-users and industrial stakeholders, with a clear perspective for a better understanding of the risk related to induced and triggered seismicity and its sound management.*

1 INTRODUCTION

Since the 1990s, the recordings of ambient vibrations in structures have gained interest in the civil engineering community due to technological improvements of portable sensors, allowing the recordings of small amplitude vibrations, and the possibility of processing a large amount of data even in real time. Many applications, based on the analysis of seismic noise, exist in the literature for checking the serviceability limit state of existing construction in the case of earthquakes. These applications can be extended to the case of occurrence of induced and triggered seismicity and its potential impact on the built environment. The latter impact has heightened both public concern and regulatory scrutiny, emphasizing the need for an integrated risk management framework. Considering the case of induced seismicity, the vulnerability assessment requires the expected damage to refer to non-structural components.

The ultimate goal of seismic design of a structure is to prevent structural collapse and human losses in case of an earthquake event. Over time, advances in earthquake engineering have led to a wide range of methodologies for earthquake resistant structural design. As a result, structures built with current methods are generally able to resist expected seismic activity and preserve their structural integrity. However, although a building remains structurally sound, it can be rendered unusable due to damage to its non-structural components. Additionally, the majority of the value of some specific buildings lies in their non-structural components. For instance, it has been shown that non-structural components account for 82%, 87% and 92% of building costs for offices, hotels and hospital buildings, respectively [1]. Therefore, building owners may still be burdened with high expenses due to the need to repair and replace non-structural components, despite applying the current seismic design standards.

The Eurocode 8 (Cl.4.4.3.2) [2] defines the maximum interstory drift (IDR) limit of a building for non-structural damage of its displacement-sensitive non-structural components for the serviceability limit state. The latter relates to structural performance for normal service conditions, under which the function of a building, its appearance, maintainability, durability and comfort for its occupants must be preserved. In that case, the IDR obtained from elastic analyses should be limited to the following values, set as a function of the non-structural typology/detailing and represented by θ_{ns}, which is the limiting story drift ratio, equal to the relative inter-story displacement divided by the story height:

- for buildings having non-structural components fixed in a way so as not to interfere with structural deformations: $\theta_{ns} \leq 1.0\%$;
- for buildings having ductile non-structural components: $\theta_{ns} \leq 0.75\%$;
- for buildings having non-structural components, realized with brittle materials, attached to the structure: $\theta_{ns} \leq 0.5\%$.

It is not clear from the above definitions in Eurocode 8 how ductile non-structural components are distinguished from the other mentioned types. In addition, a minimum required ductility capacity is not provided in these guidelines. Moreover, the drift limit of 1.0% for non-structural components fixed in a way not to interfere with structural deformations appears to be very high for masonry structures and there are not clear indications of how it is set to this value also for this case. However, the above criteria provide a test-bed for drift sensitive non-structural damage to be considered as damage thresholds in the analytical definition of fragility curves.

In this paper the focus will be on the rapid and efficient modeling of an urban area from the vulnerability point of view (considering only the possible damage to non-structural components), which is the key component for the efficient and reliable implementation of risk monitoring applications.

2 CASE STUDIES

In this study, some historical masonry buildings located in Alsace France are considered and the dynamic characteristics of these structures were estimated by the analysis of seismic noise recordings by sensors installed at each floor of the buildings under study (Fig. 1).

In the considered test site, the analysis of the collected exposure information indicates that traditional or historical masonry structures occur in large numbers near in the mostly rural areas close to the geothermal platforms in Alsace region in France [3]. Two general classes of structures, namely unreinforced masonry (URM) and timber-framed masonry (TFM) buildings have been considered, and the simple performance assessment models ([4], [5]) have been adopted in order to carry out a preliminary vulnerability assessment for these classes of structures. The objective is to rapidly identify buildings and their non-structural components that are at greater risk in the event of an induced earthquake, and to model their non-structural fragility.

The vulnerability modelling focused on buildings constructed of masonry, which may be more susceptible to the range of ground motion expected in the event of induced seismicity in the area. The measurements have been carried out using the MPwise (Multi-Parameter Wireless Sensing System) smart device [6], which has been designed to carry out rapid measurement activities by exploiting the computing and advanced networking capacities embedded in individual units. Based on measurements of environmental seismic noise, the fundamental frequency of vibration of the inspected buildings has been estimated and used to calibrate the respective fragility curves.

In collaboration with GFZ and ES-Géothermie a three-day acquisition campaign was organized which involved the installation of four sets of sensors in private houses located in villages located around the Soultz and Rittershoffen geothermal sites. The fundamental period of these structures was verified by analyzing the ambient noise measured using the MPwise sensors [6], with one sensor installed outside of the buildings, and the three others installed on each floor of the houses (basement, ground floor and first floor). The sensors were installed to record the ambient noise and to draw a vulnerability mode that allows the issuing of damage forecasts (Table 1, [7]). Finally, the main geometry required as input for the simplified vulnerability models was taken through field inspection of these buildings.

No	Building Type	Building Latitude	Building Longitude	Fundamental ESDOF Model Period (s)	Fundamental Frequency Sensor (Hz)
1	URM	48.964946	7.881095	0.17	5.5
2	URM	48.902075	7.874917	0.37	2.7
3	URM	48.905270	7.950266	0.11	9
4	TFM	48.914307	7.882233	0.15	6.7
5	URM	48.932865	7.874377	0.32	3.1

Table 1: Real URM and TFM buildings located near the geothermal platforms in Alsace region in France [7].

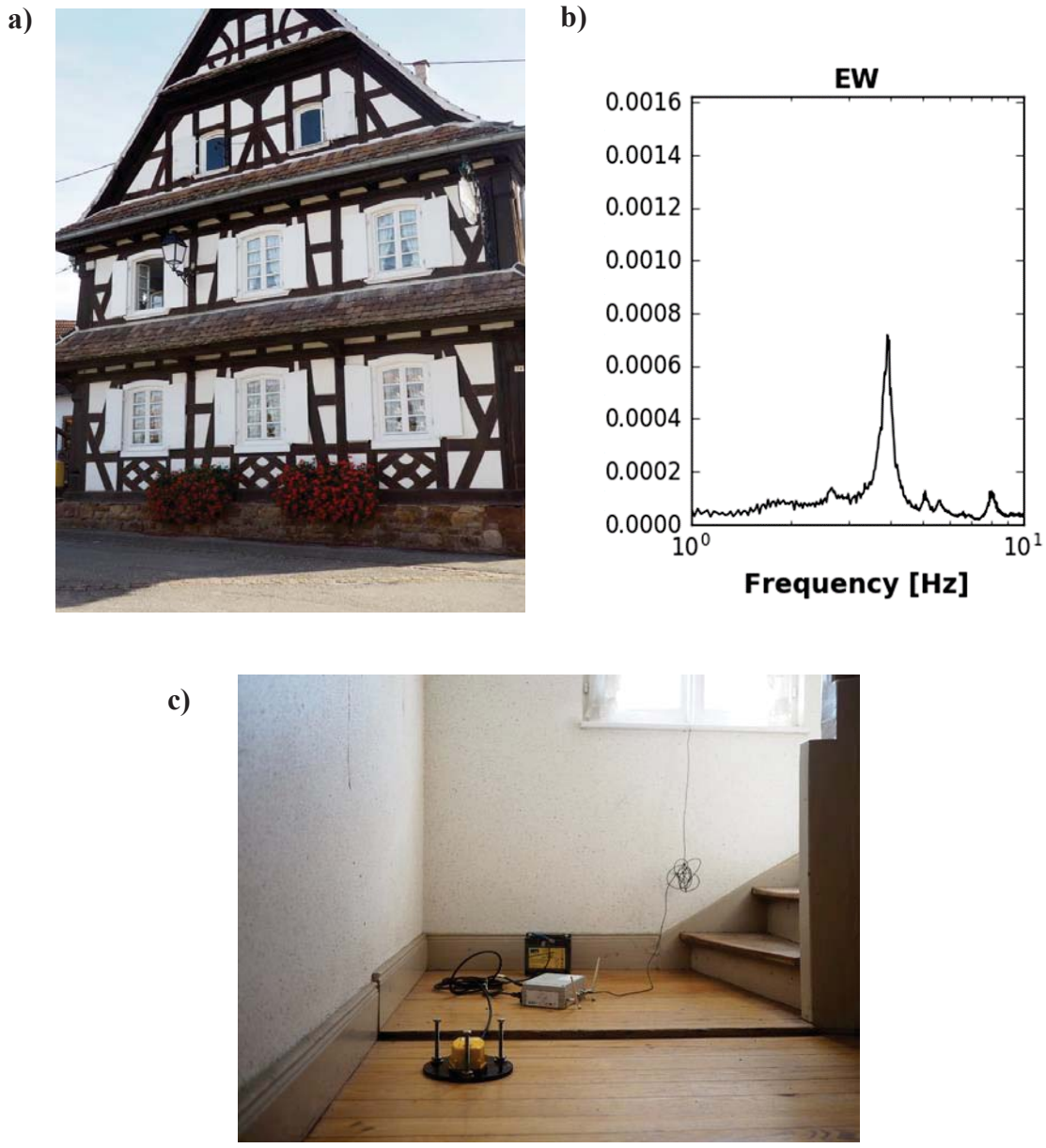

Figure 1: a) Example of timber-framed masonry building b) Measurements of the fundamental frequency of vibration estimated from the spectral analysis of environmental seismic noise. c) Installation of MPwise floor sensor

3 VALIDATION OF THE NUMERICAL MODEL

The estimated dynamic properties for small amplitude vibrations of these historical structures were used to derive simplified vulnerability models.

While steel or concrete frames are mostly lumped systems with stiff diaphragms, URM buildings have distributed mass and stiffness commonly in combination with flexible diaphragms. This fact obstructs the adoption of the established methodologies to URM buildings. Specifically, the fundamental mode shape of the latter buildings involves a low percentage of the total mass of the building below the 75% limit required for the good performance of ESDOF-based methods. In order to solve this issue, the simplified procedure of Vamvatsikos et al. (2015) [4] was adopted. In their procedure the dynamic URM building response is repre-

sented. Global response indices are transformed to local deformation measures in closed-form seismic assessment solution both for demand and supply in the critical structural locations. The solution involves the definition of the fundamental vibration mode, approximated by 3D shape function consistent with the building's boundary conditions. Strength and deformation indices are adopted for the evaluation of the acceptance criteria. Typical local failures are estimated through a local shape of deformation while the model captures the global dynamic characteristics. The adopted method allows the automation of the necessary calculations through closed-form expressions. The application of the methodology presented in this work to produce the analytical fragility curves for URM buildings is demonstrated here (Table 2) on a box-shaped unreinforced masonry structure of the townhall of Keffenach (URM building No.1 in Table 1) in Alsace region in France near the geothermal platforms of this region (Soultz-sous-Forêts and Rittershoffen).

Longitudinal wall length	9.14 m
Transverse wall length	12.04 m
Roof height	3.5 m
Wall thickness	0.25 m
Shear Modulus	930 MPa
Shear Strength	0.93 MPa
Wall mass	75.57 tn
Story mass	2.1 tn
Roof mass	3.27 tn
Total mass	80.94 tb
Horizontal "gravity" load	226.85 kN/m
Wall total area	10.59 m^2
Wall box moment of inertia	157.64 m^4
Resistance of wall plan	33.58 m^3
Wall plate stiffness factor	8470 kNm
Total crest acceleration at flexural cracking	2.7 g
Shear deformation	0.141 mm
In-plane flexural deformation	0.0044 mm
1st floor windows shear deformation	0.0006 mm
2nd floor doors shear deformation	0.002 mm
2nd floor windows shear deformation	0.01 mm
Out-of-plane flexural deformation	8.48 mm
In-plane deformation participation	0.025
Out-of-plane deformation participation	0.975
ESDOF generalized mass	7.98 tn
ESDOF generalized stiffness	10398.56 kN/m
ESDOF period	0.17 sec
ESDOF earthquake excitation factor	15.03 tn
ESDOF effective mass ratio	0.35
ESDOF participation factor	1.88

Table 2: Simplified model parameters for URM building (No.1 in Table 1) under transverse/short/weak building plan direction loading. Values are calculated based on Vamvatsikos et al. (2015) [4].

TFM walls are reinforced with timber elements, both horizontal and vertical but also X-type diagonal braces. It is evident historically, since the Bronze Age that the timber reinforcement into masonry walls is strongly related to seismic resistance in earthquake-prone areas. In TFM walls there is also recent experimental and numerical evidence [5] that the contribution of the diagonal braces is vital for walls' lateral behavior in the nonlinear range due to early detachment of the masonry infill from the surrounding timber frame in the event of an earthquake. In addition, it is observed that for very low horizontal displacement the diagonals in tension detach from the surrounding frame. Therefore, it is suggested [5] that the diagonals should contribute to the lateral behavior only in compression and moreover the infill masonry walls of the timber frame should not be considered in the analytical model. Based on these considerations, a macro-model was proposed ([5], [8]) where its input can be easily determined since it involves only the key geometric characteristics of the timber panels and the timber strength. The latter model facilitates the seismic assessment of TFM walls resulting in a valuable tool for simplified seismic vulnerability and risk analyses [9]. Based on the resulting pushover curves produced by pushover analysis [10] of the TFM walls' macro-model, a shape-function is defined for the derivation of the ESDOF properties which is similar to the methodology already described for URM buildings [4]. An example (TFM building No.4 in Table 1) of the resulting pushover curve [10] is given in Fig. 2 and the overall analysis results are tabulated below (Table 3).

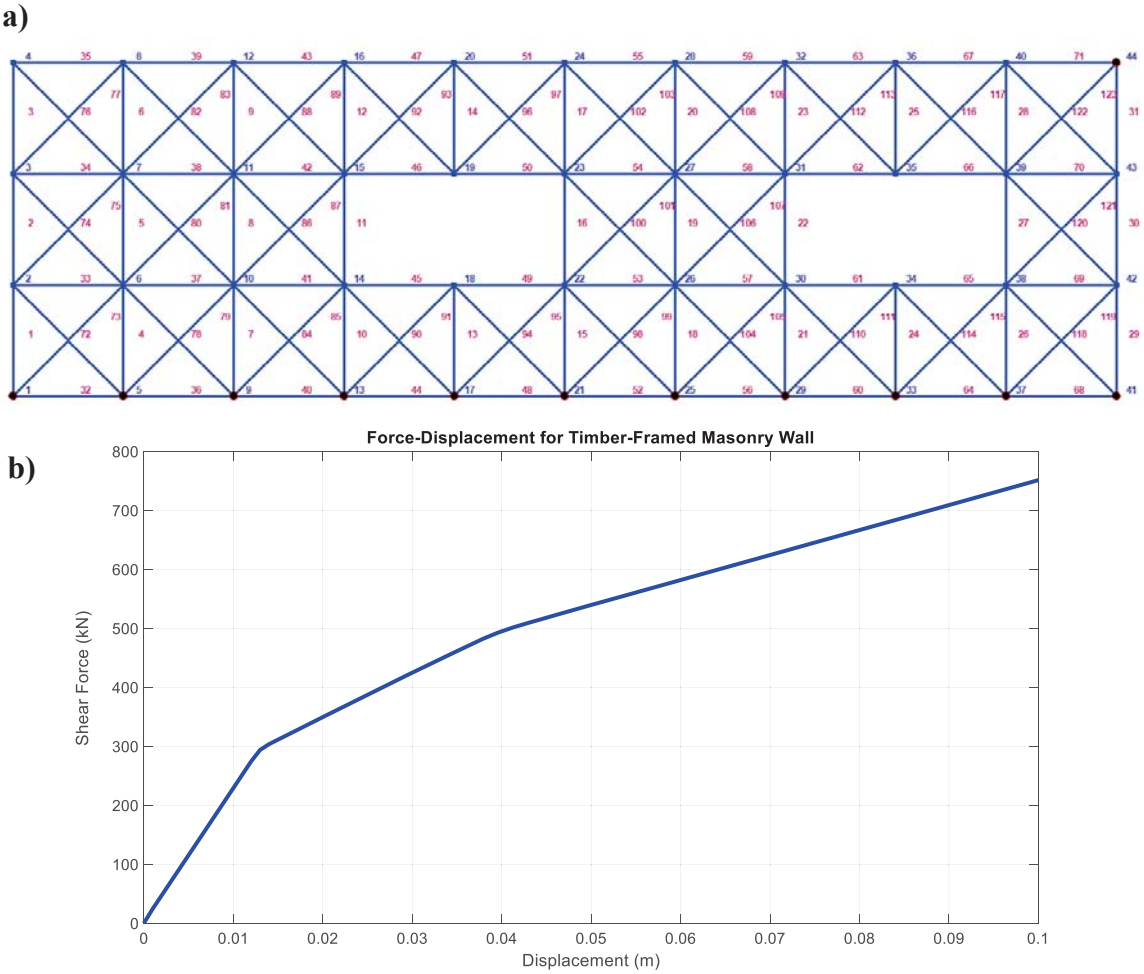

Figure 2: a) TFM wall model with panels incorporating X-type diagonal braces (No.4 in Table 1). b) Pushover curve from the methodology adopted by Kouris et al. (2014) [5].

Longitudinal wall length	7.7 m
Transverse wall length	17 m
Roof height	5.15 m
Wall thickness	0.2 m
Shear Modulus	930 MPa
Shear Strength	0.93 MPa
Wall mass	103.73 tn
Story mass	2.1 tn
Roof mass	3.27 tn
Total mass	109.1 tn
Horizontal "gravity" load	207.83 kN/m
Wall total area	9.88 m^2
Wall box moment of inertia	116.06 m^4
Resistance of wall plan	29.38 m^3
Wall plate stiffness factor	4340 kNm
In-plane deformation (Fig. 2b)	14 mm
Out-of-plane flexural deformation	60.54 mm
In-plane deformation participation	0.188
Out-of-plane deformation participation	0.812
ESDOF generalized mass	15.62 tn
ESDOF generalized stiffness	27653.24 kN/m
ESDOF period	0.15 sec
ESDOF earthquake excitation factor	31.38 tn
ESDOF effective mass ratio	0.58
ESDOF participation factor	2.01

Table 3: Simplified model parameters for TFM building (No.4 in Table 1) under transverse/short/weak building plan direction loading. Values are calculated based on Vamvatsikos et al. (2015) [4].

4 ESTIMATION OF THE NON-STRUCTURAL DAMAGE LEVEL

Considering these real TFM and URM building cases in Alsace France (Table 1) the corresponding fragility curves are derived in terms of peak ground acceleration (PGA) with the aid of structural analysis for a gradually increasing intensity (incremental dynamic analysis - IDA) [11]. The latter analysis of ESDOF of the building cases under study was performed with the MATLAB [12] toolbox FEDEAS Lab [13]. The correlation of the PGA values of the recordings used in the IDA analysis with the corresponding PGV values follows the rule that for very flexible structures (very high fundamental periods) the relative velocity response spectrum of the used record tends to the peak ground velocity (PGV). The induced ground motions obtained from the PEER database were employed and applied in the transverse/short/weak building plan direction ([7], [14]). The fundamental periods of these structures as already mentioned were verified with ambient noise vibration measurements using sensors [5] located at each floor of the buildings under study (Table 1). Moreover, the main geometry required as input for the simplified vulnerability models was taken through field inspection of these buildings. The results are shown in Fig. 3. It can be seen that the fragilities for URM buildings have more or less the same range of probability of damage while the more earthquake resistant TFM building is less fragile for low and medium intensities.

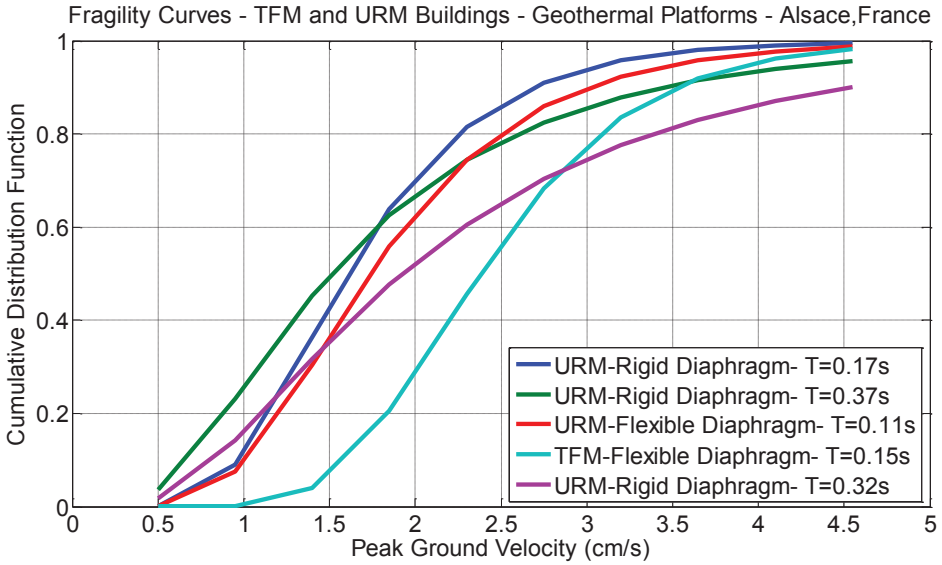

Figure 3: Proposed analytical fragility curves for first damage state (pre-yielding damage state –DS1-0.1% drift limit for non-structural damage) for Unreinforced Masonry Buildings (URM) and Timber-Framed Masonry Buildings (TFM). The buildings are located near the geothermal platforms in Alsace France and are loaded in the weak/short plan view direction of shaking. The fundamental period of these structures was verified with ambient noise measurements through applied sensors [7].

5 CONCLUSIONS

- The estimated dynamic properties for small amplitude vibrations of the historical structures near the geothermal platforms in Alsace, France considered in this work were used to derive simplified vulnerability models.
- Moreover, the Eurocode 8 defines the interstory drift limit of a building for non-structural damage, by looking at its displacement-sensitive non-structural components at the serviceability limit state.
- Therefore, by adopting these limits and the developed simplified vulnerability models, new non-structural fragility curves for typical historical masonry building types dominant in the region under study are proposed.
- The fragility curves have been calculated using incremental dynamic analysis for the seismic demands generally imposed upon linear and slightly non-linear models of single and multiple degrees of freedom, which is the case for the effects of induced seismicity.
- These results will prove useful for both local end-users and industrial stakeholders, with a clear perspective for a better understanding of the risk related to induced and triggered seismicity and its sound management.

REFERENCES

[1] Taghavi, S., Miranda, E. (2003). Response Assessment of Nonstructural Building Elements, *PEER Report 2003/05*, University of California Berkeley.

[2] CEN (2004) *Eurocode 8*: design of structures for earthquake resistance - Part I: general rules, seismic actions and rules for buildings. European Committee for Standardization (CEN). Brussels, Belgium.

[3] Pittore M, Haas M and Megalooikonomou KG (2018) Risk-Oriented, Bottom-Up Modeling of Building Portfolios with Faceted Taxonomies. *Front. Built Environ.* 4:41. doi: 10.3389/fbuil.2018.00041

[4] Vamvatsikos D., Pantazopoulou S. J. (2015) Development of a simplified mechanical model to estimate the seismic vulnerability of heritage unreinforced masonry buildings. *Journal of Earthquake Engineering*, Taylor & Fran, 20(2): 298-325. doi:10.1080/13632469.2015.1060583.

[5] Kouris LAS., Kappos AJ (2014) A practice – oriented model for pushover analysis of a class of timber-framed masonry buildings, *Engineering Structures Journal*, Elsevier, 75: 489-506. doi: 10.1016/j.engstruct.2014.06.012.

[6] Boxberger T, Fleming K, Pittore M, Parolai S, Pilz M, Mikulla S (2017) The Multi-Parameter Wireless Sensing System (MPwise): its description and application to earthquake risk mitigation. *Sensors* 17(10):2400. doi:10.3390/s17102400

[7] Megalooikonomou KG, Parolai S, Pittore M. (2018) Toward performance-driven seismic risk monitoring for geothermal platforms: development of ad hoc fragility curves, *Geothermal Energy*, 6(1):8 , doi: 10.1186/s40517-018-0094-3

[8] Kouris LAS., Kappos AJ (2012) Detailed and simplified non-linear models for timber-framed masonry structures, *Journal of Cultural Heritage*, Elsevier, 13 (1): 47-58. doi: 10.1016/j.culher.2011.05.009.

[9] Kouris L.A.S., Kappos A.J. (2015) Fragility Curves and Loss Estimation for Traditional Timber-Framed Masonry Buildings in Lefkas, Greece. In: Psycharis I., Pantazopoulou S., Papadrakakis M. (eds) Seismic Assessment, Behavior and Retrofit of Heritage Buildings and Monuments. *Computational Methods in Applied Sciences*, vol 37. Springer, Cham. doi: 10.1007/978-3-319-16130-3_8.

[10] Antoniou, S, Pinho, R (2004) Development and verification of a displacement-based adaptive pushover procedure, *Journal of Earthquake Engineering* 8(5), 643–661. doi: 10.1080/13632460409350504.

[11] Vamvatsikos D., Cornell C.A. (2002). Incremental Dynamic Analysis. *Earthquake Engineering and Structural Dynamics*, 31(3): 491-514. doi: 10.1002/eqe.141.

[12] Mathworks. (2017). MATLAB: User's Guide (r2017a).

[13] Filippou F.C., Constantinides M., (2004) FEDEAS Lab – Getting Started Guide and Simulation Examples, *NEESgrid Report 2004-22* and *SEMM Report 2004-05*.

[14] PEER-NGA-East Database (2017). Pacific Earthquake Engineering Research Center, University of California, Berkeley, CA, (http://peer.berkeley.edu/ngaeast/).

EURODYN 2020
XI International Conference on Structural Dynamics
M. Papadrakakis, M. Fragiadakis, C. Papadimitriou (eds.)
Athens, Greece, 23–26 November 2020

STRUCTURAL HEALTH MONITORING OF A PASSIVE VIBRATION CONTROLLED STRUCTURE

Tsutomu OCHIAI[1], **Tetsushi INUBUSHI**[2], **He MA**[3], **Manuel NAVARRO**[4], **and Takahisa ENOMOTO**[5]

[1] Department of Architecture and Engineering, Kanagawa University,
Kanagawa, Japan
e-mail: ochiai@kanagawa-u.ac.jp
[2] Faculty of Architecture, Kindai University,
Osaka, Japan
inubushi@arch.kindai ac.jp

[3] Architectural Engineering Institute, Hebei University,
Hebei, China
mahe@hebust.edu.cn

[4] Dept. de Quimicay Fisica, Almecia University
Almeria, Spain
mnavarro@ual.es
[5] Department of Architecture and Engineering, Kanagawa University,
Kanagawa, Japan
enomot01@kanagawa-u.ac.jp

Keywords: Structural health monitoring, Observation of strong motion, Primary natural frequency, Control of vibration structures, Secular change

Abstract. *Structural health monitoring, the observation of strong earthquake motions, is carried out at Kanagawa University, a low-rise steel structure. In this paper, a transfer function obtained from these observation records was examined. The results of microtremor and shaker experiments to determine the primary natural frequency, which we always conduct on the completion of a building, were almost the same. The natural frequency in the x-direction was 2.4–2.5 Hz. The natural frequency in the y-direction was 2.6–2.7 Hz. From the five years of monitoring data, we focused on 17 earthquakes, which had the greatest levels of vibration. For these earthquakes, where the maximum acceleration was large in the x-direction, the natural frequency tended to be slightly lower. However, such a trend could not be confirmed in the y-direction. We will continue observing and proceed with further analysis in the future.*

1 INTRODUCTION

After the 1995 South Hyogo Prefecture Earthquake, the number of strong earthquake ground motion observation sites in Japan rapidly increased, and today, this type of observation is conducted at a density unmatched worldwide, for example, at the National Research Institute for Earth Science and Disaster Prevention [1] and in Yokohama City [2]. Moreover, although not matching the extent of ground observations, there has been a steady increase in strong earthquake motion observations focusing on buildings, especially high-rise buildings. Although limited in scope, as part of business continuity planning, corporations use the results of building motion observation records for structural health monitoring by diagnosing the actual performance and soundness of their buildings [3].

The Kanagawa University Yokohama Campus Building 3 (Building 3) was completed in March 2014. Structural monitoring of Building 3 occurs through displacement meters installed on accelerometers and buckling-restrained braces. In addition, to determine the vibration characteristics of the building, microtremor measurements and shaker experiments were conducted in January 2015 [4–6].

In this paper, we outline the observation system, summarize the results of the analysis of the microtremor and shaker experiments, and, with special attention to the primary natural frequency of the building, compile a list of the results of the strong earthquake ground motion observations made during the 2015 to 2019 fiscal years.

2 TOPOGRAPHIC OUTLINE OF THE TARGET AREA

Kanagawa University Yokohama campus is located in Yokohama City in the northeastern part of Kanagawa prefecture (Figure 1). Yokohama City, an economic and industrial center, has a population of 3.7 million and is the second-largest city in Japan. It contains many historically valuable buildings because it has prospered as a port city since ancient times.

Figure 2 shows the topography of Kanagawa University and its surroundings [7]. The Yokohama campus is located on the Shimosueyoshi Plateau, which extends across the east side of the prefecture. The Shimosueyoshi Plateau is composed of Kazusa Group sediments overlain by a gravel layer and a Kanto Loam layer. Dendritic-shaped river valley lowlands have been cut into the plateau. A small valley is located to the north of the Yokohama campus, but the campus is located entirely on the plateau.

The northeastern part of Kanagawa prefecture, where the study area is located, suffered heavy damage from the 1923 Kanto Earthquake. Figure 3 shows the distribution of the destruction rate of wooden houses during the Kanto Earthquake. The destruction rate was high on the coast and extended to the south, and it was extremely high in the west (40%–50%). As shown by the administrative divisions of the time, the Yokohama campus is located near the border between the village of Shirosato and the former location of Yokohama City (Figure 3). In the former location of Yokohama City, relatively detailed damage investigations were conducted, and the destruction rate of wooden houses was as high as 20%–30%. However, the destruction rate of Shirosato is unknown.

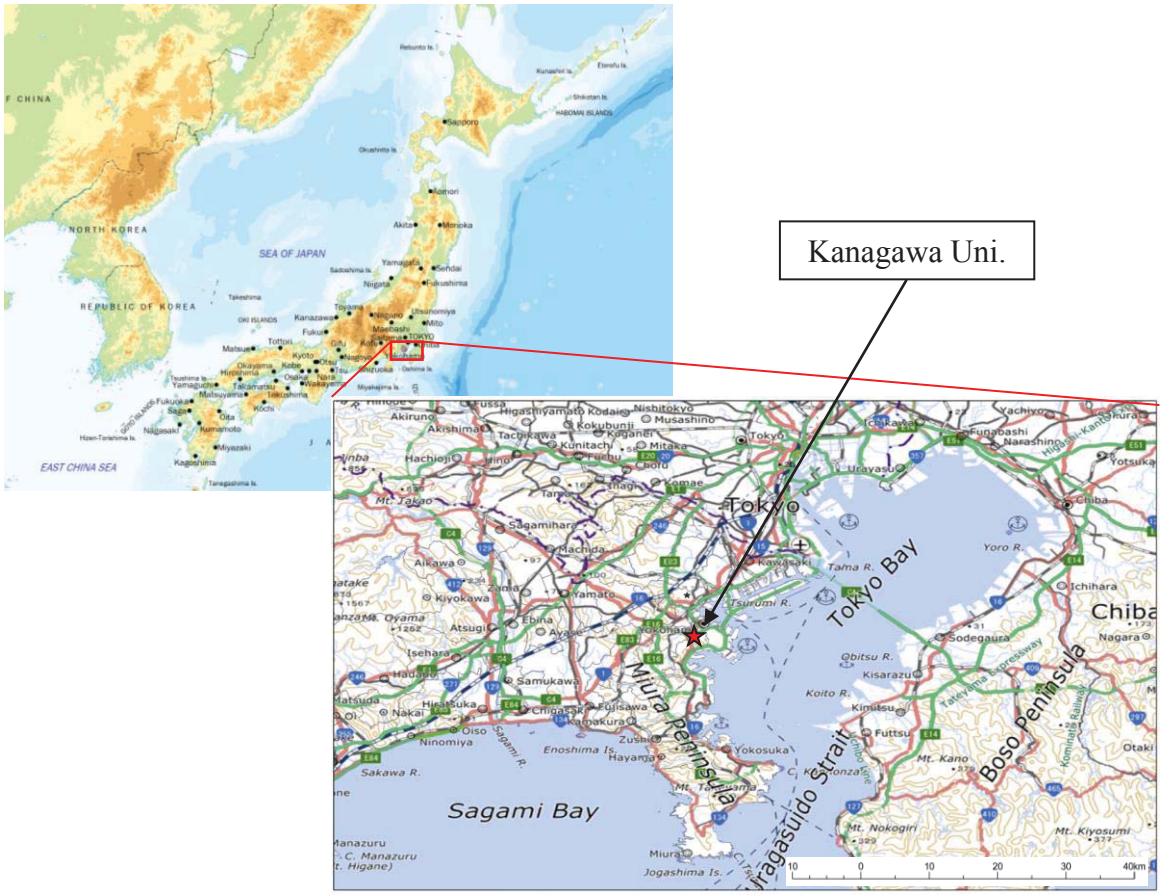

Figure 1: Location of Kanagawa University

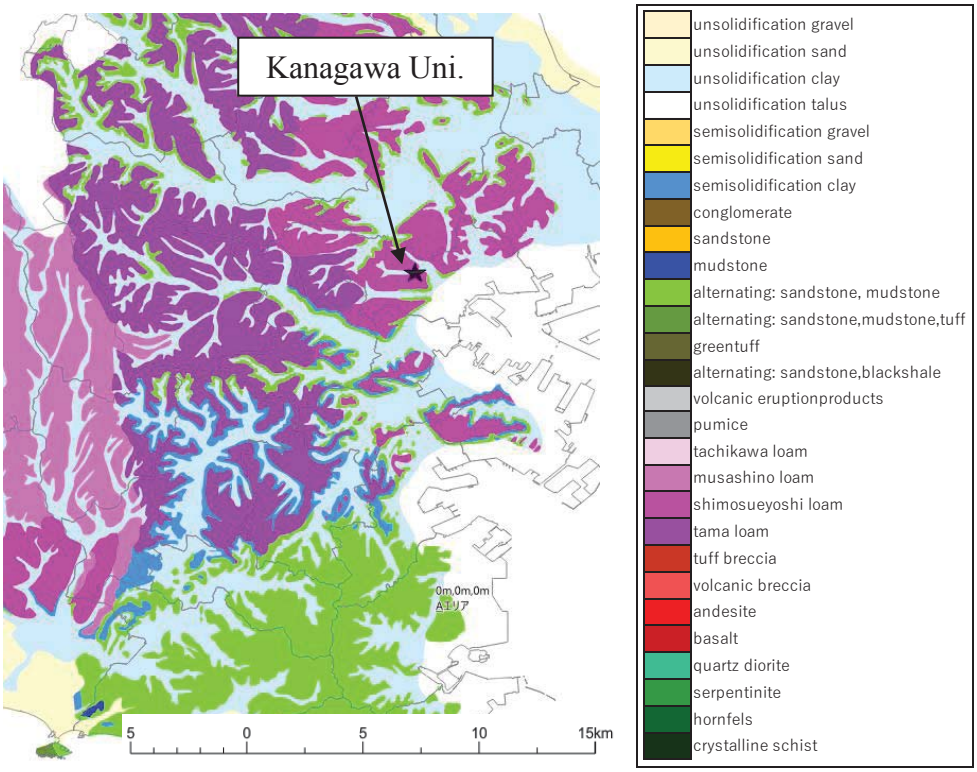

Figure 2: Topography of Kanagawa University and its surroundings [7]

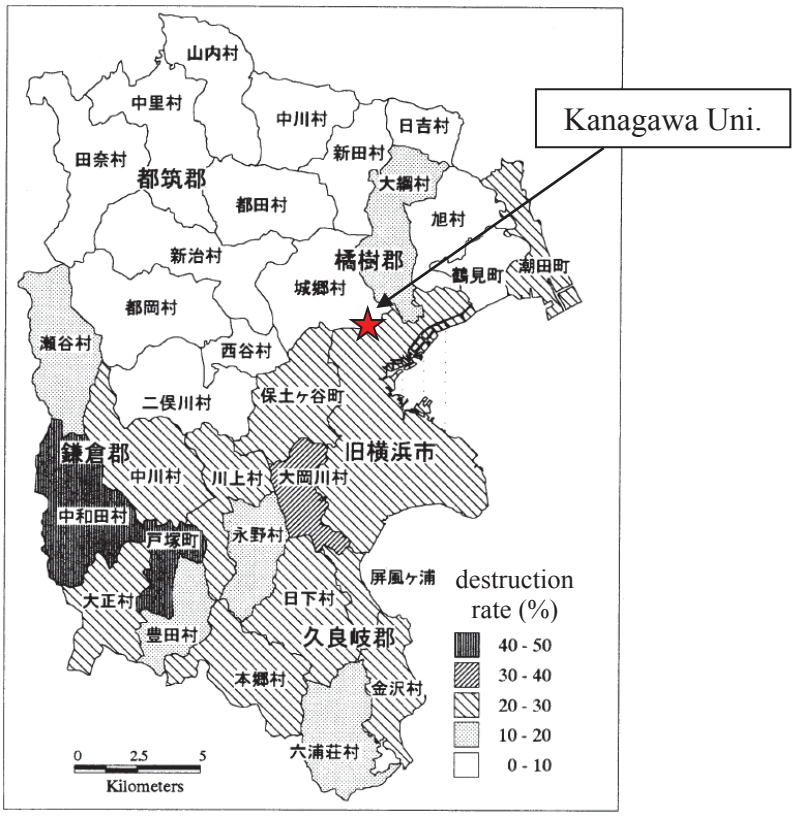

Figure 3: Distribution of the destruction rate of wooden houses during the 1923 Kanto Earthquake [8]. The divisions shown are the administrative divisions at the time.

3 STRUCTURAL MONITORING

3.1 Outline of the building

Building 3 has four floors above ground and two floors below ground. However, for the purposes of structural design, the building is deemed to be situated above ground, with five floors above and one floor below ground level.

Laterally, the structure has atriums on each floor, albeit they are approximately oblong shaped. Vertically, in its top-most section, the structure has pillars erected on beams, again almost oblong shaped. The short side of the building (X) has a span of 2.8 m, while the long side (Y) has a wider span of over 10 m to secure a large lecture room space. Moreover, although the building is a damage-controlled structure that uses buckling-restrained braces, its design is static, so the building is considered to be earthquake-resistant braced [9, 10].

- The main structure is a steel frame with partially reinforced concrete.
- The foundation structure is a spread foundation (the foundation ground is hard and the mudstone layer has an N value of 60 or more).
- There are four floors above ground and two floors below ground (the eave height is 20.45 m).
- The total floor area is 11,480 m2.
- The building area is 2,200 m2.

3.2 Outline of the structural monitoring system

For the structural monitoring, we conducted seismic observations using accelerometers and made displacement observations of the buckling-restrained braces in the building and surrounding ground. In the following, we outline the primarily seismic observations.

The earthquake observation system for this building comprises accelerometers installed in three locations of the building: 4th floor, 1st floor, and B2 floor (see Figure 4) and in two locations in the ground at distances of several tens of meters away from the building (i.e. on the ground surface, excluding the embankment, and at the engineering infrastructure depth). Each accelerometer has three components, two for bi-directional lateral (x, y) operation and one for vertical operation. Records are taken when the trigger level (1 gal) is exceeded at the engineering base position. Observation records are stored on a server and currently collected manually.

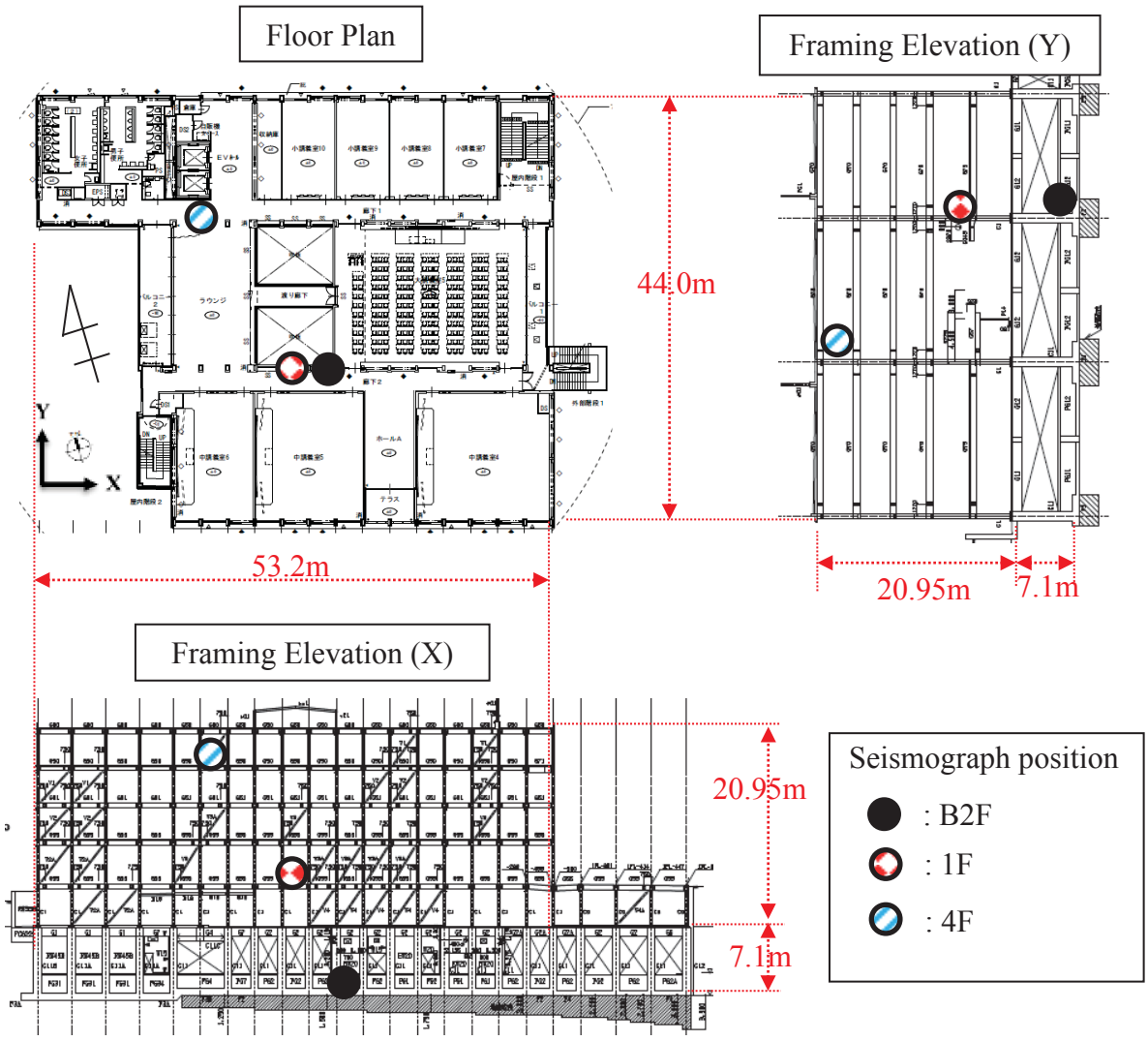

Figure 4: Seismograph positions in the target building (Building 3)

4 MICROTREMOR MEASUREMENT AND SHAKER EXPERIMENTS

4.1 Microtremor measurements

For the microtremor measurements, microtremor meters were installed at the approximate centers of the building's R and B1 floors. The x- and y-direction transfer function (R floor/B1 floor) was calculated from the Fourier spectrum of the measurement records.

The transfer function obtained using the microtremor measurements is shown in Figure 5. The peak frequencies of the transfer function were 2.52 Hz in the x-direction and 2.74 Hz in the y-direction; thus, they were slightly higher in the y-direction. The peak at 3.24 Hz is presumed to be due torsion.

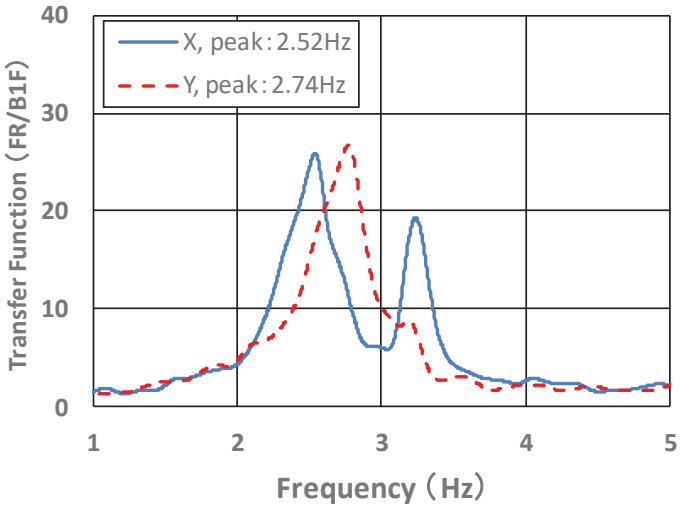

Figure 5: Transfer function from microtremor measurements

4.2 Shaker Experiments

For the shaker experiments, a small shaker with a linear motor was adapted from Aoki et al. [11] and Wen et al. [12]. In the experiments, the shaker was installed almost at the center of gravity on the R floor of the building with one-direction oscillation in each of the x- and y-directions. Measurements were taken at four points on the R floor. Figure 6 shows the resonance curve from the shaker experiment. The peak of the resonance curve was 2.38 Hz in the x-direction and 2.64 Hz in the y-direction; thus, it was slightly higher in the y-direction, as was the microtremor measurement. A peak of more than 3 Hz in the x-direction was conceivably due to a torsional component.

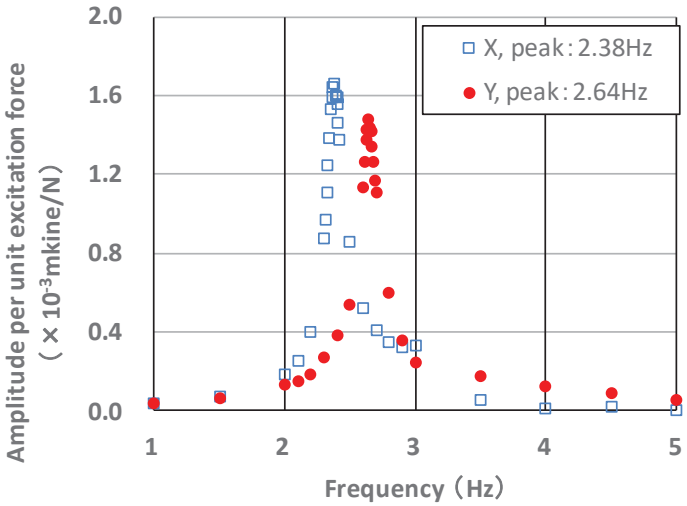

Figure 6: Resonance curve from the shaker experiment

4.3 Transfer function

Using the peak frequency of the transfer function and the peak of the resonance curve as the primary natural frequencies of the building, the primary natural frequencies are shown in Table 1. The results of the microtremor measurements and the shaker experiment were generally consistent. There are several possible causes for the slightly higher frequency in the y-direction. Conceivably, it is because the buildings' overall dimensions are longer in the x-direction (53 m) than in the y-direction (44 m).

Notably, a calculation using the natural period calculation formula of a general S structure (T = 0.02 x H) yields T = 0.409 s (2.44 Hz), which is largely consistent with the measured value.

Table 1: List of transfer functions

	Microtremor Measurement	Shaker Experimentation
X	2.52Hz (0.40s)	2.38Hz (0.42s)
Y	2.74Hz (0.36s)	2.64Hz (0.38s)

5 TARGET EARTHQUAKE

As part of the structural monitoring, Building 3 has been subject to strong earthquake motion and buckling-restrained brace displacement observations. In the following, we focus on the primary natural frequency of the building obtained from the transfer function from strong earthquake motion observation records and consider its secular change.

The target period ran from March 2015 (the start of the observations) to January 2020. The targeted earthquakes comprised 17 earthquakes with a seismic intensity of 2.5 or more

measured at K-NET Yokohama (KNG002), a strong ground motion observation point located relatively close to Kanagawa University. Table 2 lists the targeted earthquake motions and observation records, and Figure 7 shows the epicenter locations.

Of the targeted earthquakes, only the epicenter of the No. 2 earthquake was located off the western coast of the Ogasawara Islands to the south. This earthquake, at a depth of 682 km, somewhat differed from the other earthquakes, which were evenly distributed around the target location, from the north to the south. The majority of the epicenters were located at depths between 10 and 60 km; these earthquakes mainly occurred in shallow strata.

As an example, Figure 8 shows the time history waveform and response spectrum of the ground surface on May 25, 2015.

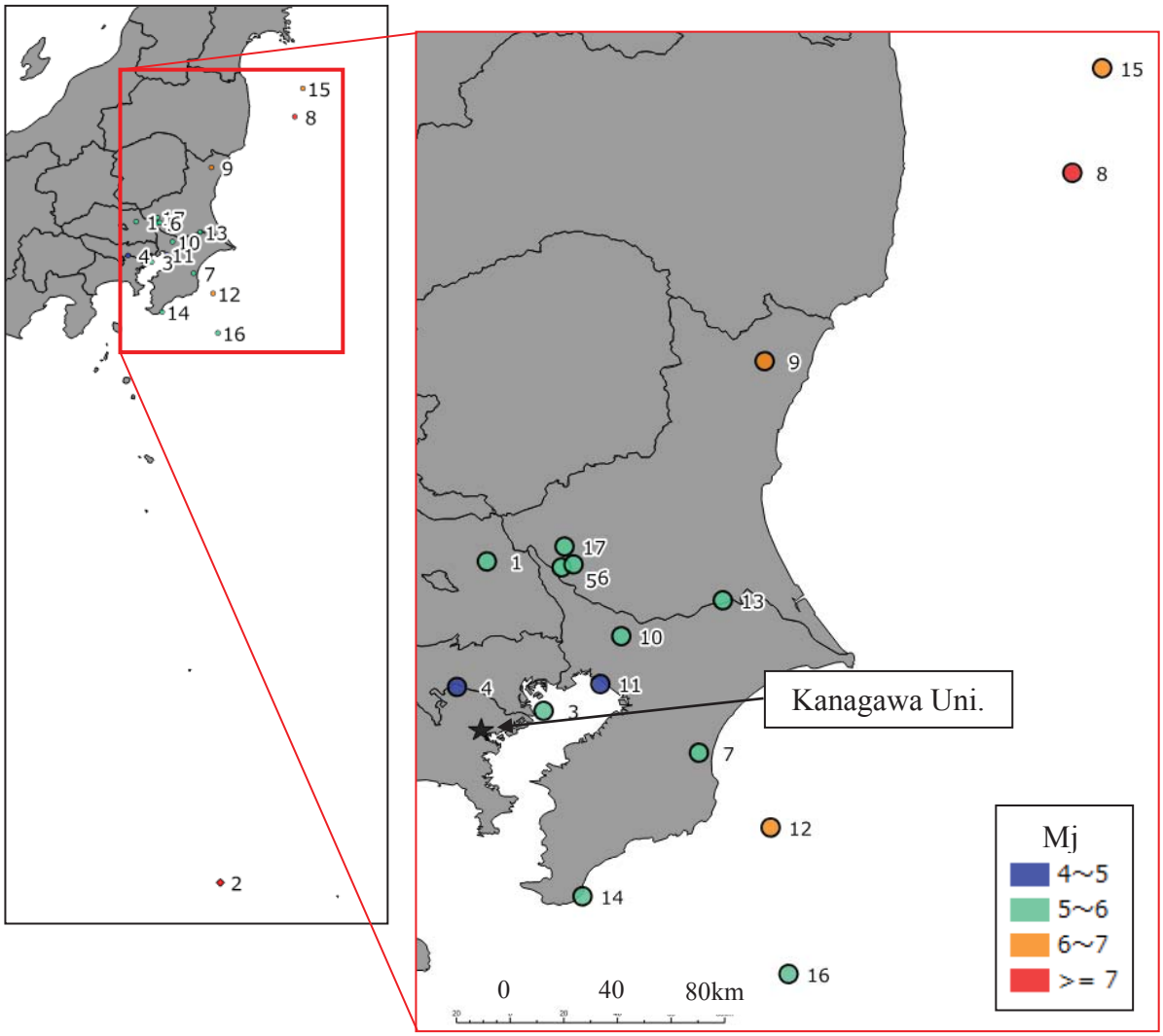

Figure 7: Distribution of the targeted earthquake epicenters

Table 2: List of targeted earthquakes

No.	data	soruce region	depth km	M_J	Ground PGA (gal)		Buliding PGA (gal) 4F/1F	
					X	Y	X	Y
1	2015/5/25	Saitama North	56	5.5	26.8	30.9	71.6/26.8	36.8/16.9
2	2015/5/30	Ogasawara Islands West	682	8.1	4.3	4.2	4.3/1.8	6.7/2.6
3	2015/9/12	Tokyo Bay	57	5.2	76.8	83.1	59.1/46.9	86.3/35.7
4	2016/2/5	Kanagawa West	26	4.6	69.3	83.5	16.3/30.8	22.4/30.3
5	2016/5/16	Ibaraki South	42	5.5	29.1	33.8	32.3/19.0	21.9/12.8
6	2016/7/17	Ibaraki South	42	5.0	14.9	15.2	14.2/11.0	35.7/11.4
7	2016/7/19	Chiba North	33	5.2	9.9	14.6	26.9/6.8	41.6/10.9
8	2016/11/22	Fukushima East	25	7.4	10.5	10.6	15.3/7.0	17.4/6.1
9	2016/12/28	Ibaraki North	11	6.3	7.1	6.8	11.7/4.1	14.3/4.5
10	2017/8/10	Chiba Northeast	64	5.0	41.1	33.1	13.1/11.9	24.4/18.1
11	2018/1/6	Tokyo Bay	71	4.7	41.9	43.2	36.5/25.5	26.6/22.4
12	2018/7/7	Chiba East	57	6.0	22.0	13.7	29.7/11.9	28.4/10.7
13	2019/1/18	Ibaraki South	54	5.3	9.6	8.0	14.0/5.3	14.3/4.6
14	2019/6/24	Chiba Southeast	61	5.2	44.8	42.4	22.6/21.0	45.1/21.5
15	2019/8/4	Fukushima East	50	6.2	7.3	7.1	5.9/6.2	5.9/5.9
16	2019/10/12	Chiba Southeast	75	5.4	13.9	8.6	5.5/5.5	5.5/5.5
17	2020/1/14	Ibaraki South	50	5.0	5.7	6.3	6.5/4.8	6.5/6.5

※Red：PGA is large earthquake (4F Max Acc. >20gal)

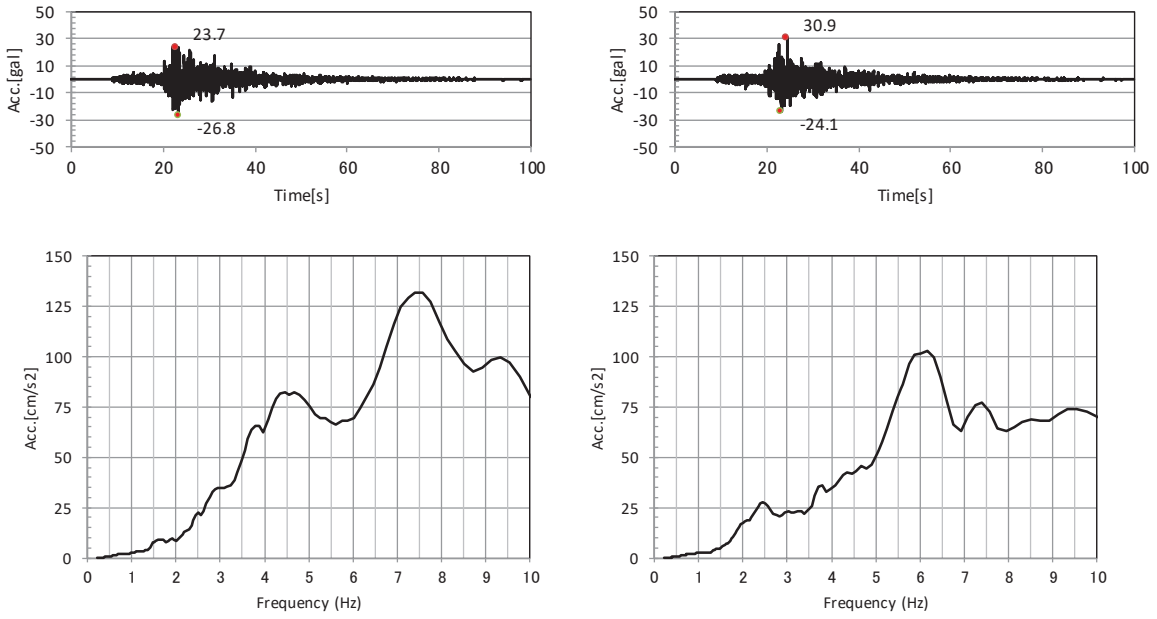

X-direction Y-direction

Figure 8: time history waveform and response spectrum (h = 5%) of the ground surface for the May 25, 2015 earthquake

6 STRUCTURAL HEALTH MONITORING

6.1 Primary natural frequency

Figure 9 presents the superposed transfer functions for each earthquake record. Earthquakes with a maximum acceleration (4F exceeding 20 gal in both directions) are shown in red. In the x-direction, when the maximum acceleration is large, the natural frequency tended to be slightly smaller (cycle prolongation). However, this tendency was not apparent in the y-direction.

Figures 10 shows the relationship between the primary natural frequency and the 4F maximum acceleration. It also presents the approximate curves and correlation coefficients. As described above, when the maximum acceleration was large, the natural frequency tended to be small. Variation in the x-direction was low overall, and the correlation coefficient of 0.84 indicates a relatively strong correlation between the two. As seen in the spectrum, for the y-direction, the overall variation was somewhat higher, and the correlation was weak, with a coefficient of 0.55.

We plan to conduct further analyses of differences in the characteristics of the x- and y-directions.

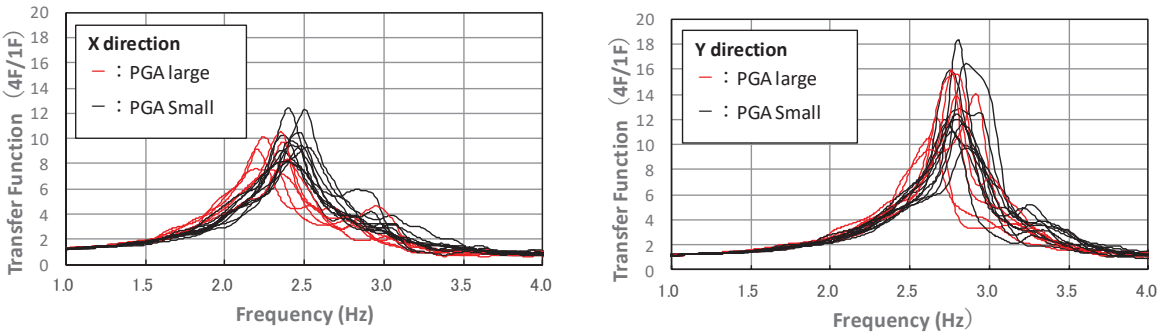

Figure 9: Transfer function (4F/1F)

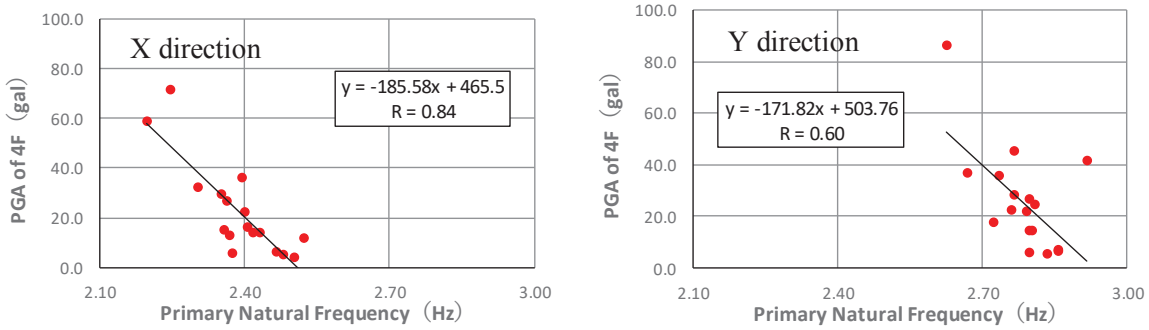

Figure 10: Peak accelerations (4F) and primary natural frequencies

6.2 Changes in primary natural frequency during the duration of an earthquake

Having confirmed the amplitude dependence of the primary natural frequency due to differences in the intensity of ground motion (section 5.1), we then analyzed whether the same tendency could be confirmed during the duration of a single targeted earthquake. The analysis target was the May 25, 2015 earthquake, which resulted in the building's largest acceleration. The earthquake was recorded for 100 seconds. The acceleration amplitude increased from around 20 seconds in both the x- and y- directions and then reduced after 60 seconds, up to about 6 gal at 4F.

Although the time history waveform cut out at 20.48 seconds, by shifting the start time by 2.0 seconds, a transfer function was obtained in the same manner as shown in Figure 9. Figure 11 shows the change in the primary natural frequency during the earthquake with the time history wave. The primary natural frequency in the x-direction for the first half of the 60 seconds, including the main motion, was 2.2 to 2.3 Hz. After 60 seconds, the primary natural frequency gradually increased from 2.3 to 2.6 Hz (micromotion: 2.52 Hz and shaker experimentation: 2.38 Hz). The primary natural frequency for the first 60 seconds in the y-direction was 2.6–2.7 Hz, and the second half was 2.7–2.9 Hz (micromotion: 2.74 Hz and shaker experimentation: 2.64 Hz). These results show that the natural frequency changed with amplitude level during the duration of the earthquake.

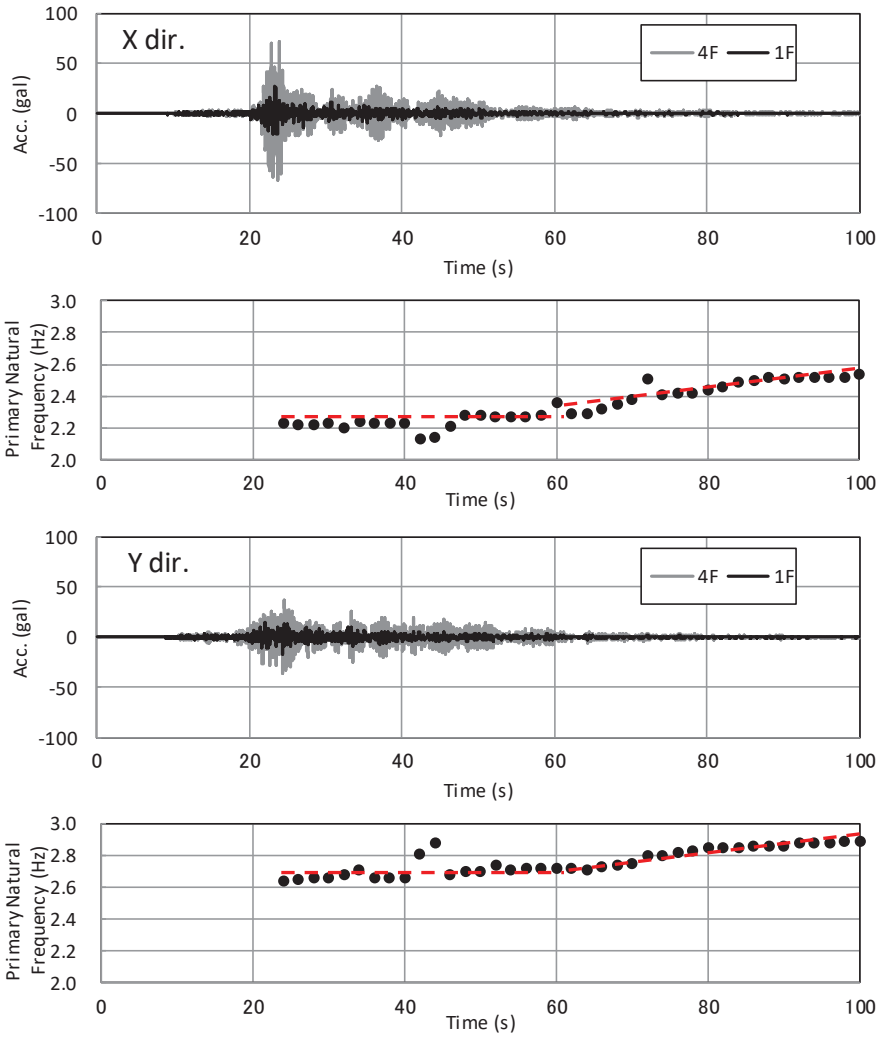

Figure 11: Changes in primary natural frequency during the duration of an earthquake

6.3 Time-dependent change in the primary natural frequency

Figure 12 shows the changes in the primary natural frequency over time, from the start of the observation period until the present. As described above, although there was some variation in the magnitude of the acceleration, the extent of the variation was small overall. Given that there has been almost no change in the natural frequency since immediately after the completion of construction, it was assumed that the soundness of the building has remained intact.

In the future, we plan to continue these observations and proceed with analyses that focus on questions around differences in changes due to external factors, such as seismic motion, and changes due to aging.

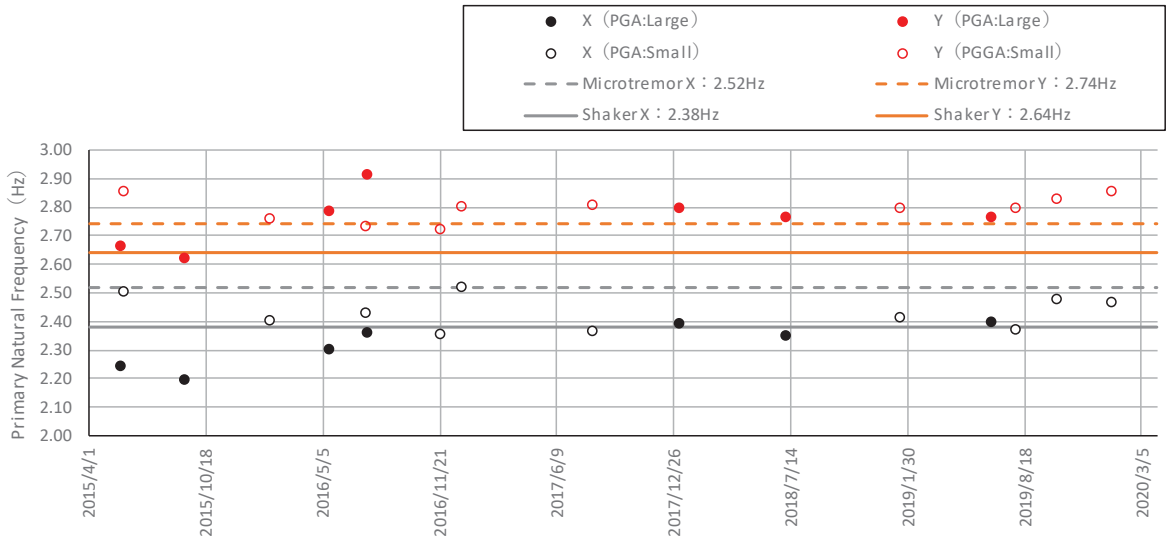

Figure 12: Time-dependent change of the primary natural frequency

7 SUMMARY

We examined the vibration characteristics of Kanagawa University Building 3 using microtremor measurements and a shaker experiment: the primary natural frequency data obtained were largely consistent for both methods.

The transfer function obtained from strong earthquake motion observation records evidenced time-dependent change in the primary natural frequency of the building. In the x-direction, the data showed that the natural frequency decreased when the maximum acceleration was large, and this correlation was strong. However, while a similar tendency was also observed in the y-direction, this correlation was weak. We will continue to analyze differences in vibration characteristics in the x- and y-directions. Currently, five years after the completion of construction, secular change is small, and conceivably, the soundness of the building remains intact.

In the future, based on the results of these analyses, we will focus on extracting indicators that can be used for structural health monitoring.

Notably, while this analysis has only treated primary natural frequency, in the future, we would like to also examine changes in attenuation characteristics.

REFERENCES

[1] National Research Institute for Earth Science and Disaster Resilience (NIED): Strong-motion Seismograph Networks (K-NET, KiK-net),

http://www.kyoshin.bosai.go.jp/ (Reading data: 2020.02.20)

[2] Yokohama City: Yokohama City High-Density Strong-Motion Seismograph Network

https://www.city.yokohama.lg.jp/kurashi/bousai-kyukyu-bohan/bousai-saigai/bosai/jishinjoho/eq.html (Reading data:2020.02.20)

[3] S. Ogawa, H. Kameda, H. Sato, and A. Mita: Development of Prototype System for Structural Health Monitoring Aimed at Practical Application, *Journal of Japan Association for Earthquake Engineering, Vol. 9, Issue 5*, 2009 (in Japanese)

[4] T. Inubushi, T. Enomoto S. Sato and T. Kuriyama: Vibration Characteristics Evaluation of Low-rise Steel Structure at Kanagawa University, *16th European Conference on Earthquake Engineering*, June 2018

[5] T. Enomoto, T. Inubushi, S. Sato T. Kuriyama and K. Koyano: Forced Vibration Experiment of Building No.3 Located in Yokohama Campus of Kanagawa University, *Summaries of technical papers of annual meeting (Kanto), Architectural Institute of Japan*, September 2015 (in Japanese)

[6] T. Enomoto, T. Inubushi, S. Sato, T. Kuriyama, and T. Ochiai: Evaluation of Vibration Characteristic of the Building No.3 in Yokohama Campus of Kanagawa University Based on Recorded Earthquake Motions, *Summaries of technical papers of annual meeting (Kyushu), Architectural Institute of Japan*, August 2016 (in Japanese)

[7] MLIT: Land Survey (Land Classification Basic Survey, Water Basic Survey, etc.),

http://nrb-www.mlit.go.jp/kokjo/inspect/inspect.html (Reading data:2020.02.20)

[8] T. Takahama, S. Midorikawa, H. Shinmo, and S. Abe: Damage Distribution of Wooden Houses in Yokohama City due to the 1923 Kanto Earthquake, *Proceedings of the JSCE Earthquake Engineering Symposium*, August 2001 (in Japanese)

[9] Yokohama City Architectural Joint Design Office: Kanagawa University Yokohama Campus (tentative name) New Building 3, Completion Drawing s, March 2014

[10] Yokohama Structural Design: Kanagawa University Yokohama Campus (tentative name) New Building 3, New Construction, Structural Calculation Documentation, October 2011

[11] Y. Aoki, T. Kikuchi, Y.K. Wen, J.Z. Shen T. Yamamoto, and T. Enomoto: Study on Estimation of Vibration Characteristics of Structures Using Small-Size Shakers - Part 1. Development and Performance Evaluation of Shakers Using Linear Motors -, *Summaries of technical papers of annual meeting (Kyushu), Architectural Institute of Japan*, August 2007 (in Japanese)

[12] Y.K. Wen, T. Kikuchi Y. Aoki, J.Z. Shen, T. Yamamoto, and T. Enomoto: Study on the Estimation of Vibration Characteristics of Structures by Using Small-Size Shakers - Part 2. Estimation Results of Building Vibration Characteristics by Shaker Experimentation -, *Summaries of technical papers of annual meeting (Kyushu), Architectural Institute of Japan*, August 2007 (in Japanese)

EURODYN 2020
XI International Conference on Structural Dynamics
M. Papadrakakis, M. Fragiadakis, C. Papadimitriou (eds.)
Athens, Greece, 23–26 November 2020

DYNAMIC RESPONSE OF TALL TIMBER BUILDINGS UNDER SERVICE LOAD – THE DYNATTB RESEARCH PROGRAM

Rune Abrahamsen[1], Magne A Bjertnæs[2], Jacques Bouillot[3], Bostjan Brank[4], Lionel Cabaton[5], Roberto Crocetti[6], Olivier Flamand[7], Fabien Garains[3], Igor Gavric[8], Olivier Germain[9], Ludwig Hahusseau[3], Stephane Hameury[7], Marie Johansson[10], Thomas Johansson[6], Wai Kei Ao[11], Blaž Kurent[4], Pierre Landel[10], Andreas Linderholt[12], Kjell Malo[13], Manuel Manthey[7], Petter Nåvik[2], Alex Pavic[11], Fernando Perez[14], Anders Rönnquist[13], Haris Stamatopoulos[13], Iztok Sustersic[8], Salue Tulebekova[13]

Corresponding Author: Olivier Flamand
CSTB
olivier.flamand@cstb.fr

Other addresses in the footnote below.

Keywords: Timber building, wind load, discomfort, modelling, damping, full scale.

Abstract. *Wind-induced dynamic excitation is becoming a governing design action determining size and shape of modern Tall Timber Buildings (TTBs). The wind actions generate dynamic loading, causing discomfort or annoyance for occupants due to the perceived horizontal sway – i.e. vibration serviceability failure. Although some TTBs have been instrumented and measured to estimate their key dynamic properties (natural frequencies and damping), no systematic evaluation of dynamic performance pertinent to wind loading has been performed for the new and evolving construction technology used in TTBs. The DynaTTB project, funded by the Forest Value research program, mixes on site measurements on existing buildings excited by heavy shakers, for identification of the structural system, with laboratory identification of building elements mechanical features coupled with numerical modelling of timber structures. The goal is to identify and quantify the causes of vibration energy dissipation in modern TTBs and provide key elements to FE modelers.*

The first building, from a list of 8, was modelled and tested at full scale in December 2019. Some results are presented in this paper. Four other buildings will be modelled and tested in spring 2021.

[1] Moelven Limtre, rune.abrahamsen@moelven.no, [2] Sweco, magne.bjertnaes@sweco.no, petter.navik@sweco.no, [3] Eiffage, jacques.bouillot@eiffage.com, ludwig.hahusseau@eiffage.com, [4] Uni Ljubjana, Bostjan.Brank@ikpir.fgg.uni-lj.si, bkurent@fgg.uni-lj.si, [5] Arbonis, lcabaton@arbonis.com, fgarains@arbonis.com, [6] Moelven SE, crocetti@kth.se, thomas.johansson@moelven.se, [7] CSTB, olivier.flamand@cstb.fr, stephane.hameury@cstb.fr, manuel.manthey@cstb.fr, [8] InnoRenew CoE, igor.gavric@innorenew.eu, iztok.sustersic@innorenew.eu, [9] Galeo, o.germain@galeo.fr, [10] RISE, marie.johansson@ri.se, pierre.landel@ri.se, [11] Uni Exeter, wka203@exeter.ac.uk, A.Pavic@exeter.ac.uk [12] LNU, andreas.linderholt@lnu.se, [13] NTNU, kjell.malo@ntnu.no, anders.ronnquist@ntnu.no, haris.stamatopoulos@ntnu.no, saule.tulebekova@ntnu.no [14] Smith&Wallwork, fernando.perez@smithandwallwork.com

1 INTRODUCTION

1.1 Background

Due to population expansion and concentration in urban regions, housing shortage is an increasing global issue, necessitating the efficient use of space in urban areas. One solution is an increased supply of tall buildings to optimize the best use of limited space. This has sustainability impacts surrounding the choice of materials and carbon footprint ramifications. Using more wood-based products in building construction, as a renewable raw material, could assist in the transition of society towards a circular based bio-economy, moving away from a dependence on fossil fuels and extractive materials, whilst helping meet the commitments contained within the UN Sustainable Development Goals. The use of tall buildings with timber structures would be an opportunity to create value and impact by encouraging the increased use of forest-based replenishable products. Tall Timber Buildings could provide cost effective, environmentally sustainable developments, maximising the limited space available in urban regions.

Tall Timber Buildings (> 10 storeys) is still a very new concept, some examples are:

- Murray Grove (London, UK (2009)) – 9 storeys,
- Forté (Melbourne, Australia (2012)) – 10 storeys,
- Treet (Bergen, Norway (2015)) – 14 storeys,
- Brook Commons (Vancouver, Canada (2017)) – 18 storeys,
- Origine (Quebec City, Canada (2018)) – 13 storeys and
- Mjøstårnet (Brumunddal, Norway (2019)) – 18 storeys.

The load-bearing system of these buildings are very different giving the buildings different properties. Building tall means several new challenges such as higher loads vertically and horizontally, earthquake loads, fire safety and increased needs regarding technical systems as some examples. One aspect that is of special interest is the dynamic behavior related to wind-loads that leads to a need to limit acceleration levels at the top of buildings. This is a factor that has shown to govern the design of the stabilization system of tall timber buildings from a height of 12-14 storeys and above, see [1] for example. The understanding of the wind-induced dynamic behaviour of Tall Timber Buildings (TTBs) and their components is till poor and results in a lack of confidence by designers in the use of timber as a construction material. A lack of reliable data for modelling is one of the main barriers in the further development of TTBs and wider utilisation of timber within construction.

This lack of reliable data regarding modelling wind-induced vibrations for tall timber buildings was the motivation for starting the ForestValue project "DynaTTB - Dynamic Response of Tall Timber Buildings under Service Loads". The project will be performed by partners from academia, research institutes and companies[2] from five different countries in Europe during 2019-2022. The research hypothesis for this project is that it is possible to create computational models for Tall Timber Buildings, based on system identification and calibration of advanced Finite Element (FE) models. This will be underpinned by data from full-scale tests of a number of representative mid-to-high rise timber buildings in Norway, Sweden, France, Slovenia and the UK. The project plan will utilize unique horizontal electro-dynamic sliding shakers from the University of Exeter (UK) and CSTB (France) to perform vibrational tests and use the data

[2] RISE Research Institutes of Sweden, NTNU Norwegian University of Science and Technology, University of Exeter, University of Ljubljana, InnoRenew Renewable Materials and Healthy Environments Research and Innovation Centre of Excellence (InnoRenew CoE), CSTB Centre Scientifique et Technique du Bâtiment, Linnaeus University, Moelven Töreboda AB, Moelven Limtre AS, SWECO Norge AS avd Lillehammer, Smith and Wallwork Engineers Ltd, Galeo, Eiffage Immobilier Sud Ouest, Arbonis.

to estimate Frequency Response Functions (FRFs) for a number of TTBs with different building systems.
The overall objective of the project is to experimentally identify a number of full-scale TTB structures within Europe and, based on these results, develop representative FE-models to predict the vibration response of TTBs exposed to wind-induced dynamic loading.
This paper will present the structure of the project and the first preliminary results from the first two tested buildings.

1.2 State-of-the-art

There are several all timber building systems that can be used for the stabilizing system in TTBs. In principle these systems can be made up of one-dimensional elements in the form of beams and columns, mostly made of glulam, or two-dimensional elements such as cross laminated timber (CLT) or laminated veneer lumber (LVL). The one-dimensional elements can be used in moment-resisting frames or as trusses while the two-dimensional elements are used as shear walls to stabilize the buildings, see Figure 1. It is also possible to use hybrid structures with parts of the building system in steel or concrete to help support the building against especially horizontal loads. CLT elements are typically connected using shear or tension angular steel brackets and self-tapping screws [2]. The glulam members are typically jointed using dowelled connections with slotted-in steel plates - a jointing technique successfully applied in large-span timber bridges and sport arenas.

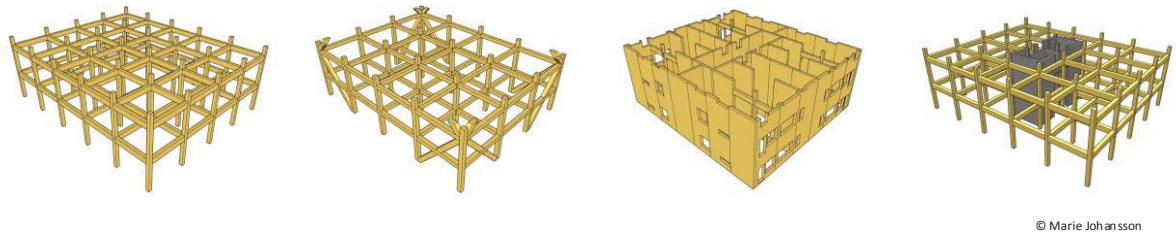

Figure 1: Principal buildings systems for Tall Timber Buildings, a) moment-resisting frames, b) truss-systems, c) shear wall systems and d) hybrid system combining timber with other materials.

TTBs have, in principle, sufficient strength capacity to resist lateral loads (e.g. wind, earthquake) for the ultimate limit state. However, instead the vibration serviceability limit state (SLS) governs the design, leading to the need to restrict wind-induced sway vibrations to within certain limits [4, 5]. The lowest natural frequencies, dependent on mass and stiffness, of the TTB sway motion is in the same frequency range as the wind spectra. The sway is, however, also largely dependent on the damping of the structure. Timber is a light material with only moderate stiffness and hence the fulfilment of the vibration SLS criteria, due to wind, results in restrictions to the total building height [6, 7].

The amount of sway/acceleration depends on the mass and stiffness distribution of TTB structures and the ability to dissipate vibrational energy from the structural system. Currently, the knowledge on structural stiffness and damping in TTBs is limited, particularly regarding the effects of different types of connections used in the load-carrying systems. These connections are crucial generators of stiffness and damping, yet little is known as to their impact on TTB structures. Current modal damping values used in the design of TTBs are based on guess work, with minimal underpinning rational or scientific basis.

Two major contributors to damping are: material damping and structural damping. Material damping arises from the internal friction within the material of a timber element, whilst structural damping is due to friction and energy dissipation in the connections. Non-structural elements and their connections are also assumed to contribute to the total damping. Timber structures are lightly damped systems and, therefore, due to the nature of resonant response calculations, a small change in the damping ratio can lead to significant changes in the vibration response and overall serviceability performance.

Although some TTBs have been instrumented and measured to estimate their key dynamical properties (natural frequencies, mode shapes and damping) [3], no systematic evaluation of dynamic performance pertinent to wind loading, has been performed for the innovative and evolving TTB construction technology. Knowing that the wind response calculations are highly sensitive to the damping values and natural frequencies, indicating that small variations in these uncertain modelling parameters may yield vastly different responses on either side of the acceptable vibration response values.

Full-scale tests on TTBs has been done using Operational Modal Analysis (OMA), also expressed as Ambient Vibration Testing (AVT), where the dynamic response is measured without knowledge of the load, [3, 8] for example). This technique gives relatively good results for natural frequencies and mode shapes but offers considerably less reliable values for damping. Using Forced Vibration Testing (FVT) gives the possibility of controlling the load level and thereby establishing Frequency Response Functions (FRFs) [9]. Using FVT gives the possibility of measuring over a range of frequencies and will result in better understanding of the dynamic response of TTBs as a function of excitation frequency, which is important for stochastic wind loading containing multiple frequencies. The FRFs also give a better base for model calibration of the FE-models of TTBs. The partners at University of Exeter and CSTB have unique equipment enabling measurements of dynamical properties of other types of large civil engineering structures, bridges and floors [10, 11] which will be used for TTBs in this project to provide excellent opportunities to establish unique and vital data.

FE models of full-scale TTBs have numerous uncertainties, for example, whereabouts stiffness and damping occur. Improved knowledge of the dynamic behaviour of TTBs can be developed through dynamic tests on full-scale building structures (in-situ), but these are time consuming and costly. The goal of this project is to limit the required number of tests and develop simulation tools such as reliable FE models.

2 PROJECT PLAN

The main objective of the project is to identify experimentally a number of full-scale TTB structures (existing or currently being built) and, based on these, develop representative FE-models for predicting the vibration response of TTBs exposed to dynamic loading due to wind. Figure 2 includes eight TTBs (plus a timber bridge) that have been identified as potential candidates. In most cases the companies designing and building the structures are involved in the project as industry partners making drawings and calculation models available. Table 1 gives some data for the buildings such as height, width and depth as well as their main building system.

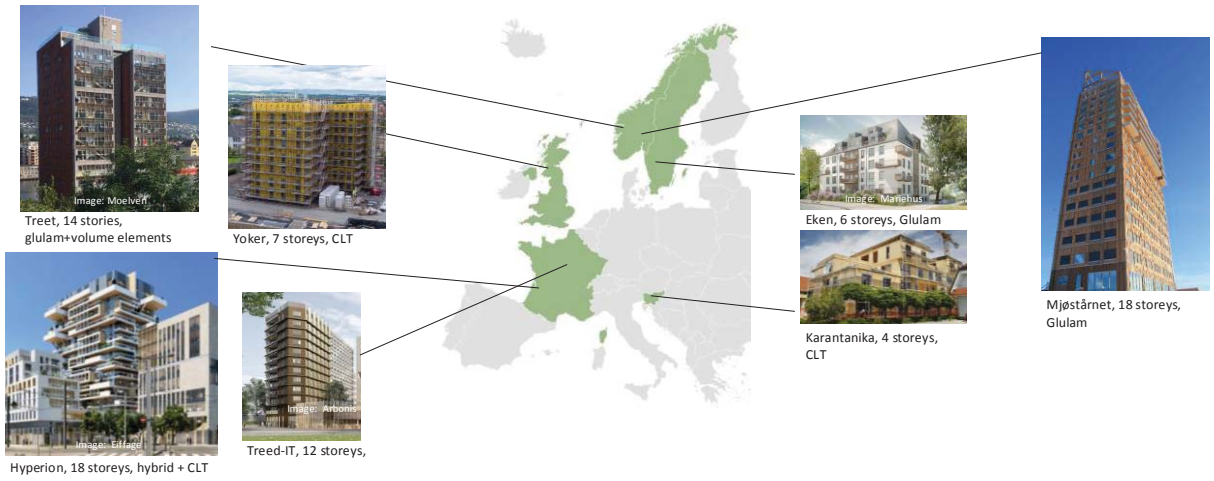

Figure 2: Map of Europe with the buildings that will be measured.

Building name	Country	Building height	Building width	Building depth	Load-bearing system	Stabilising elements
Mjøstårnet	Norway	85.4	36.8	16.3	Glulam	Trusses
Treet	Norway	46			Glulam+ strong concrete floors	Trusses
Timber bridge (Fjell-leet)	Norway	-			Glulam	Trusses
Hyperion	France	57	30.6	19.1	Glulam + CLT	Concrete Core
Treed It	France	36	47.4	18.6	Glulam + Timber Concrete Slab	Concrete Core
FlowerValley	Slovenia	12.7	14.5	21.2	CLT	Shear walls
Kv Eken	Sweden	24.4	27	19	Glulam	Trusses
Yoker	UK	22	31	28	CLT	CLT Shear walls

Table 1: Selected data about the building included measurements and main load-bearing system.

The buildings represent different modern timber building techniques and offer good examples of a variety of building types, providing a range in dynamic response for calibration and reliability in the modelling work. The buildings are dispersed across Europe providing a geographic spread. A bridge is included being an excellent example as to a similar type of glulam structure, including dowel connections, but with less non-structural elements. This will support research into the effect of connections versus non-structural elements.

The work in the project is divided into three interrelated main work-packages (WP2-4) and two supporting work-packages 1 and 5, see Figure 3. Work-packages 2 and 3 are experimentally based, to improve the understanding of the real behaviour of complete buildings measured in-situ (WP3) and parts of the structural system (components, connections and sub-assemblies), known to influence the dynamic response, as measured in the lab (WP2).

Work-package 4 includes the modelling aspects of the project, with a starting point from using best engineering judgement information to develop models of the buildings to predict load levels and initial estimates of the buildings dynamic responses. The data from WP2 will create detailed FE-models of the connections and sub-assemblies simulating the measured behaviour. These models will be simplified and used for model calibration of the FE-model for

the complete buildings, whilst also being calibrated against measurement data for the complete buildings.

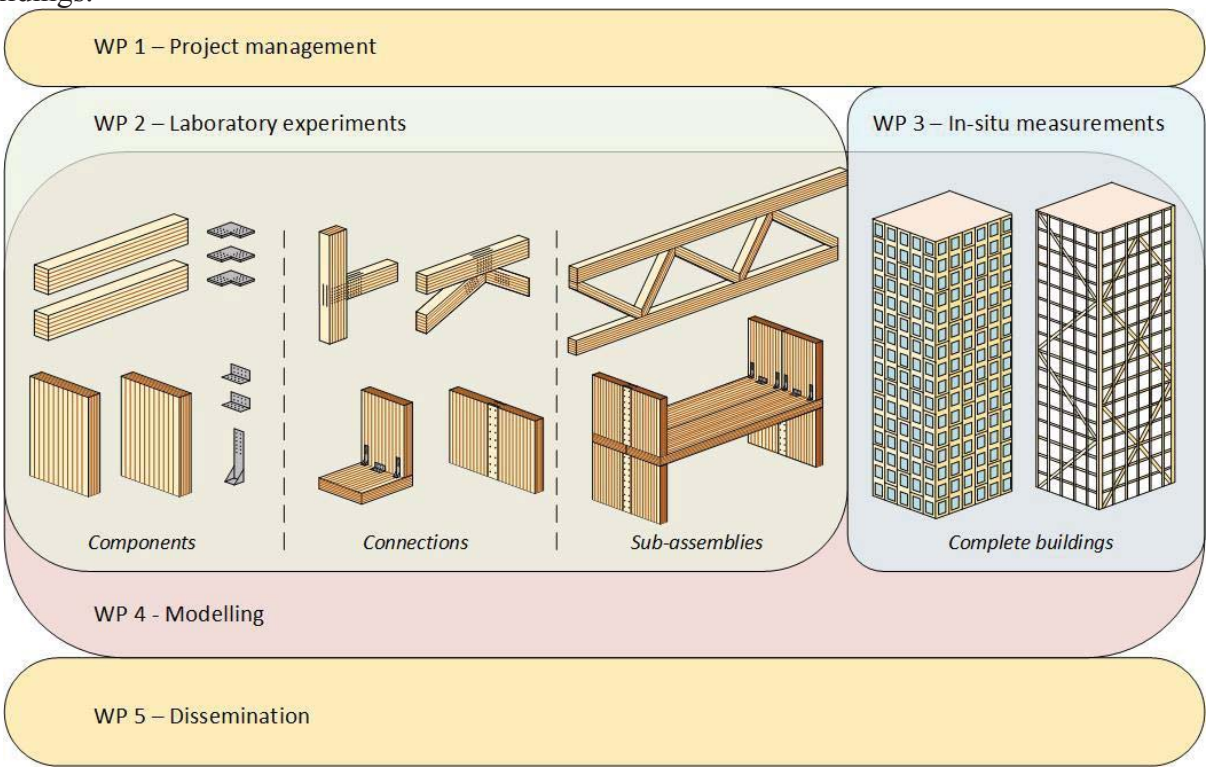

Figure 3: Project structure – WP2 - Laboratory experiments and WP3 - In-situ Measurements will run in parallel whilst WP4 - Modelling supports the measurement WPs and is calibrated with data from measurements. WP1 - Project management and WP5 - Dissemination will run during the whole project time for support and exploitation of the results.

The project is on-going and so far, measurements using forced vibrations have been conducted on two buildings, Treed-It in Paris and Yoker in Glasgow. Preliminary results from the measurements and modelling of these two buildings will be presented in this paper as well as an overview of the measurement techniques and modelling techniques used.

3 EXAMPLES OF BUILDINGS AND RESULTS

3.1 The Treed-It Building - structure

Treed-It is a 12 story building with the first podium story in concrete and then 11 stories with a glulam structure. The building is stabilized against horizontal loads with an elevator shaft in concrete. The building is located in Champs-sur-Marne and is constructed by Vinci Engineering with Arbonis as the main contractor for the timber parts of the structure. The main part of the construction work has been done during 2019 with the timber structure being raised during July to October 2019. The building was finished July 2020.

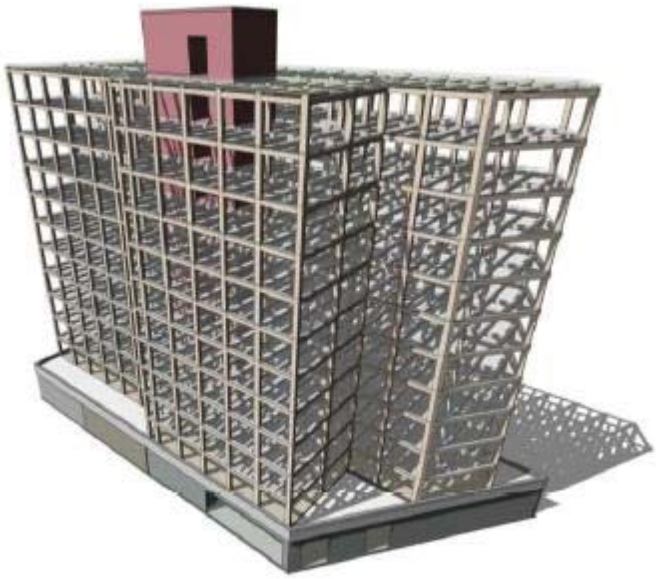

Figure 4: The structure of the Treed-It building with a concrete core and a glulam structure around it and mix timber-concrete floor slabs.

3.2 Modelling of Treed-It

An FE-model of the Treed-It building has been built using Ansys by CSTB. The structure is modelled using beams for the timber part and shells for the concrete and mix parts. As the building was not totally completed at the time of the dynamic measurements, the modelling takes into account the missing dead loads corresponding to inner partition that were not in place when natural frequencies have been measured. Oppositely, the stiffness of the structure was already the same as the final one. Cladding, that was already finished, is considered as bearing only load and no rigidity because façade is not contributing to the horizontal strength.

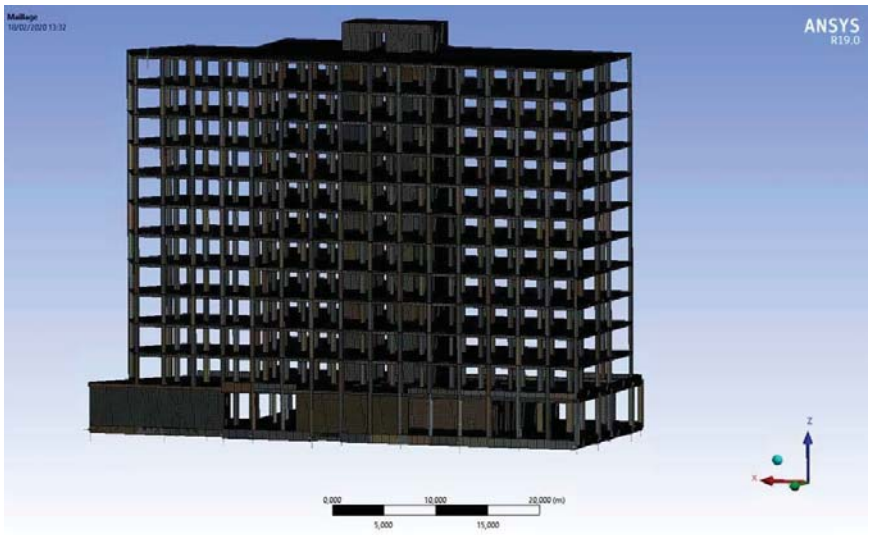

Figure 5: Ansys model of the Treed-It building by CSTB, using beam elements for the columns and beams and shells for the slabs and the concrete core.

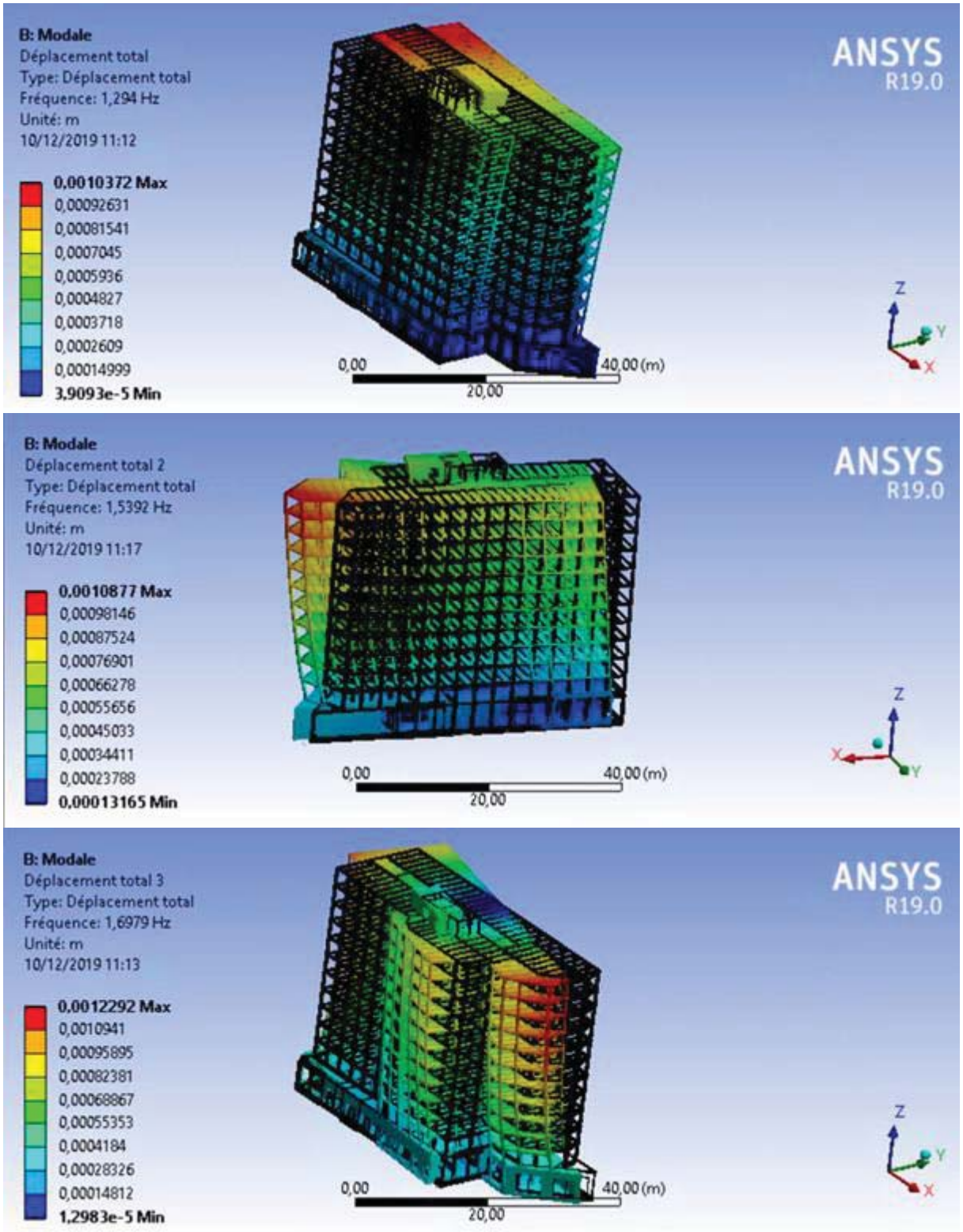

Figure 6: Dynamic analysis of the Treed-It Building performed by CSTB before the real testing.

3.3 Testing of Treed-It

The dynamic properties of the Treed-It Building was measured by CSTB using a horizontal mass shaker with a moving load of 500kg.The shaker was lifted in one piece to the top floor by a tower crane. With a stroke of 240mm the sinusoidal force applied to the building was up to 8000N. This applied force increases with the square of the frequency, as it is an inertial exciter. A first measurement campaign was conducted in December 2019 without internal partition.

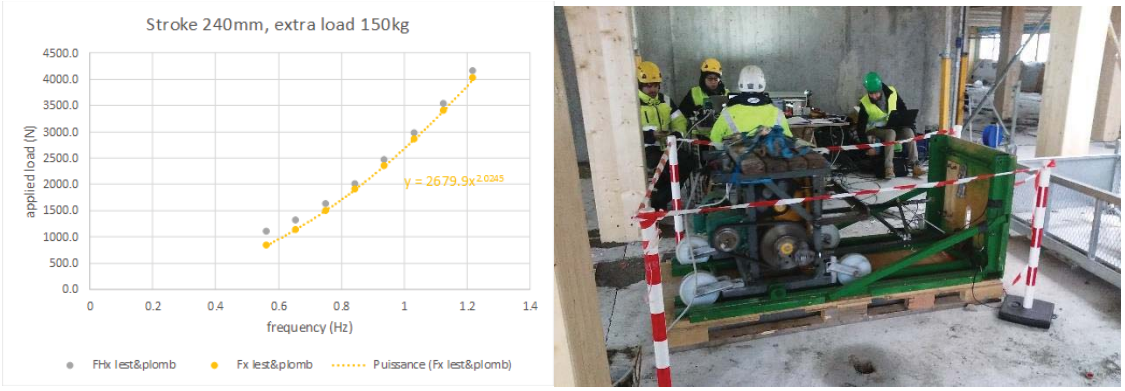

Figure 7: Horizontal force applied by the mass shaker for a given stroke (left) and shaker in operation on the Treed It Building (right)

Three locations of the shaker have been tested. Accelerometers were placed at three levels (11th, 7th and 2nd floor) to measure the amplitude of floor displacements, some displacement sensors (LVDTs) put between timber beam at the 7th level to measure the deformation of the structure. The preliminary analysis of the time domain signal show damping ratio close to 2% of critical, calculated from the decay of the acceleration signals. A more refined analysis shows damping is amplitude dependent. For large amplitudes (0.05m/s² to 0.1m/s²) the structural damping ranges from 2.5% to 3.5% of critical, depending on which mode is excited. For low amplitudes (less than 0.01m/s²) the damping ratio drops down to 1% of critical or less.

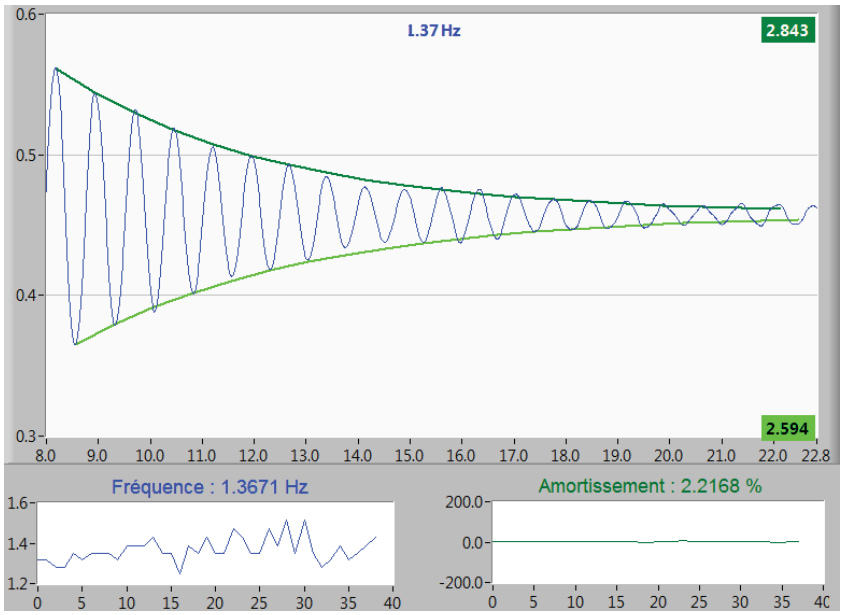

Figure 8: An example of decay of an accelerogram of shutdown test, amplitude in m/s²

A second measurement campaign on Treed It was achieved in June 2020, with all internal partitions done. These partitions added mass and stiffness at the same time : the balance of both gives a slight increase of frequency for the first bending mode, a more marked decrease for the second bending mode and the torsion one.

4 CONCLUSIONS

The DynaTTB research program will provide valuable information concerning the FE modelling of high-rise timber buildings, to be used by designers for assessing the comfort of final users. The modeling of structural damping of such structures is one of the main input of this European research.

5 FURTHER WORK

A FE-model of the Yoker building, which is a 7 storey building in Glasgow designed by Smith and Wallwork Ltd, made using a CLT structure, has been modelled using Ansys by University of Ljubljana. The dynamic properties of the Yoker building was measured Feb 2020 by University of Exeter using horizontal shaker. The Hyperion building in Bordeaux was first tested in July 2020 and will be tested again when completed in March 2021. Data processing is under way.

An extensive measurement campaign in Scandinavia is planned at spring 2021.

6 ACKNOWLEDGEMENT

The research leading to these results has received funding from the ForestValue Research Programme which is a transnational research, development and innovation programme jointly funded by national funding organisations within the framework of the ERA-NET Cofund ‘ForestValue – Innovating forest-based bioeconomy.

REFERENCES

[1] Malo, K.A., Abrahamsen, R.B. & Bjertnaes, M.A., 2016. Some structural design issues of the 14-storey timber framed building “Treet” in Norway. European Journal of Wood and Wood Products, 74(3), pp.407–424.

[2] Brandner, R., Flatscher, G., Ringhofer, A., Schickhofer, G., Thiel, A. 2015. Cross laminated timber (CLT): overview and development. Holz als Roh- und Werkstoff 74(3).

[3] Feldmann, A., Huang, H., Chang, W., Harris, R., Dietsch, P., Gräfe, M., Hein, C. 2016. Dynamic properties of tall timber structures under wind-induced vibration. In WCTE 2016 - Word Conference on Timber Engineering. Vienna, Austria.

[4] Anon 2005. SS EN 1991-1-4:2005 Eurocode 1: Actions on structures – Part 1-4: General Actions – Wind actions, SIS (2002).

[5] Anon 2008. SS-ISO 10137:2008, Basis for Design of Structures—Serviceability of Buildings and Walkways against Vibration, ISO (2008).

[6] Johansson, M. et al., 2016. Tall timber buildings – a preliminary study of wind- induced vibrations of a 22-storey building. In WCTE 2016 - Word Conference on Timber Engineering. Vienna, Austria.

[7] Reynolds, T., Casagrande, D. & Tomasi, R., 2016. Comparison of multi-storey cross-laminated timber and timber frame buildings by in situ modal analysis. Construction and Building Materials, 102, pp.1009–1017.

[8] Fjeld Olsen, M., Hansen, O. 2016. Measuring vibrations and assessing dynamic properties of tall timber buildings, Master thesis NTNU, Trondheim Norway.

[9] Ewins, D. J. (2000). Modal Testing: Theory, Practice and Application. Research Studies Press.

[10] Magalhães F., Caetano E., Cunha A., Flamand O., Grillaud G., Ambient and free vibration tests of the Millau Viaduct: Evaluation of alternative processing strategies, Engineering Structures, Volume 45, December 2012, Pages 372-384.

[11] Zivanovic S, Pavic A, Reynolds P. (2007) Finite Element Modelling and Updating of a Lively Footbridge: The Complete Process, *Journal of Sound and Vibration*, volume 301, pages 126-145

[12] On site testing of the Treed-It building – CSTB report.

EURODYN 2020
XI International Conference on Structural Dynamics
M. Papadrakakis, M. Fragiadakis, C. Papadimitriou (eds.)
Athens, Greece, 23–26 November 2020

SEISMIC RISK ASSESSMENT OF A MEDIEVAL TOWER: THE CASE STUDY OF CRACO

Michela Lerna[1], **Maria F. Sabbà**[2], **Mariella Diaferio**[3], **Leonarda Carnimeo**[4], **Salvador Ivorra**[5], **Dora Foti**[6]

[1] Politecnico di Bari
via E. Orabona 4, 70126, Bari, Italy
e-mail: michela.lerna@poliba.it

[2,3,4,6] Politecnico di Bari
via E. Orabona 4, 70126, Bari, Italy
{mariafrancesca.sabba, mariella.diaferio, leonarda.carnimeo, dora.foti}@poliba.it

[5]University of Alicante
Alicante, Spain,
e-mail: sivorra@ua.es

Keywords: Slender Structure, Risk assessment, historical buildings, seismic hazard.

Abstract. *In the present paper the risk assessment of the medieval Norman tower of Craco (Matera, Italy) is discussed. Craco is a totally abandoned little town because of the activation of landslide motions of its soil depth. The medieval tower is one of the few buildings still standing as it is built on a fixed stiff foundation ground. Nevertheless, the tower is, indirectly, subjected to the movements of the close landslide.*

The tower is located in the highest and more stable part of the hill where the old town was built in the XII century for protection from enemy attacks. It is 20 m tall and has a (11 x 11) m^2 square plan. The basement has a truncated pyramid shape; originally it had two masonry vaults, one barrel on the first floor, which no longer exists, and a still visible cruise at the second order, connected by a now destroyed internal staircase. In 1949 a reinforced concrete cistern was placed inside the tower.

Craco is classified as a town with a medium level seismic hazard. The main aim of the present study is to evaluate the seismic risk by means of a Finite Element model, calibrated through dynamic tests performed on the tower and considering the historical value of the structure and the context in which it stands. In fact, the structure is characterized by several peculiarities: the presence of a reinforced concrete cistern, the interaction with the surrounding buildings, the closeness to the landslide, the topographical exposition, etc. Moreover, the structure has a great impact on the society due to its touristic interest, as it is an emblem of the, so-called, "ghost town" of the Appennino mountains.

A new approach is proposed to evaluate the effects of all the previously cited features on the evaluation of the seismic risk of the tower, introducing also economical and sociological parameters.

1 INTRODUCTION

In Italy the preservation of architectural heritage towards seismic actions, occupies a prominent place in the social and scientific community priorities. The recent seismic events in Italy underlined the fragility of the historical heritage, which is vulnerable to horizontal forces. Such structures, as well known, were realized only in accordance with the rules of "good practice", which of course were defined considering the ordinary service conditions, i.e. the presence of vertical loads. Thus, in most of these structures a detailed analysis is required to safeguard this heritage, and, consequently, it is necessary to define procedures for evaluating their vulnerability. These procedures can be a tool for the Authorities, which have the responsibility of their maintenance, for judging and scheduling possible interventions. In recent years, the mechanical characteristics of the masonry walls, which make up a historical building, have been a topic of discussion in various studies; in fact, due to the historical value of such structures, the use of traditional tests for the evaluation of the mechanical properties is not allowed. As a consequence, the researchers' attention was devoted to the use of dynamic tests and the results are utilized to obtain the global mechanical characteristics of the structure [1-5].

However, for a complete evaluation of the seismic hazard of a historical structure more considerations/information are needed.

In the report Natural Disasters and Vulnerability Analysis [6], based on the Expert Meeting held in 1979, the scientific community proposed to unify the evaluation of disaster expected damage in any area of interest, through the definition of three parameters:

- *Hazard (H),* consisting in the probability that a disaster can occur;
- *Vulnerability (V),* consisting in the evaluation of the consequences of a disaster;
- *Exposition/Exposed elements (E),* consisting in the socio/economic evaluation of the consequences; this parameter is linked to the context of communities.

On such basis, in [6] the following relationship for the evaluation of the *Risk (R)* was suggested:

$$Risk = Hazard \bullet Vulnerability \bullet Exposition \quad (1)$$

In the last decades, on the basis of this general formulation, several conceptual approaches were developed for the risk assessment related to technological hazards (i.e., nuclear risk) [7, 8] and to natural disaster hazards (i.e., seismic, landslide, blast, flood) [9-13].

In particular, for seismic hazard several models are proposed in [14, 15] to evaluate and estimate the economic losses due to earthquakes for different Italian building typologies.

Recent seismic events highlighted that significant damages were attained in structural and non-structural components of Italian Heritage also under low-to-medium intensity earthquakes. For the purpose of improving the seismic safety of all existing Italian buildings, the Italian "Guidelines for the seismic risk classification of constructions" approved in February 2017 [16] provides technical principles for all seismic risk assessment.

Although several methodologies are available in literature, the evaluation of the risk for a historical building is still under discussion, because for this kind of structures the same procedures of a common building cannot be adopted, due to their peculiarities.

The present work is focused on such topic; in detail, the seismic risk evaluation and the expected damage computation due to a possible seismic event on a historical tower is discussed.

In this paper a new approach is suggested for extending the procedure proposed in [16] to typical buildings of the Mediterranean area, in particular to historic masonry buildings. Since the fragility functions of structural and non-structural components, which are defined for reinforced concrete and residential masonry structures, still need a calibration and validation for

other masonry buildings, in this paper the methodology of Italian legislation [16] is applied to the specific case of the Norman Tower of Craco.

2 PROPOSED APPROACH

The Italian guidelines approach for the evaluation of the seismic risk is described in detail in [17], which reports the fundamental principles and the procedures for determining the seismic risk class of a building and, moreover, for designing reinforcement interventions to reduce the seismic risk. The guidelines introduce several risk classes, from A to G, whose seismic risk increases passing from A^+ to G. To evaluate the risk class of a building, the document refers to a conventional approach and a simplified one. The conventional method, which requires a detailed seismic evaluation of the structural system for different limit states and is principally calibrated for the application to reinforced concrete structures, is the only one that allows improving the building risk class of two or more classes through adequately designed reinforcement interventions. However, the simplified approach, based on the European macro-seismic scale [17], is proposed for masonry buildings. The latter defines the seismic risk class based on the structural type and potential structural deficiencies. In this case, the local strengthening interventions allows to improve the seismic risk of only one class.

Based on the conventional approach and in accordance with eq. (1), the Seismic Risk Assessment (SRA) is identified by three parameters: *H* is the probability that an earthquake occurs considering the seismic zone in which the building is located, *V* is the vulnerability of the structure, in term of load-bearing capacity during the earthquake and *E* is a parameter which takes into account the socio/economic consequences of structural damages. In particular, the SRA of buildings is conducted at different Limit States: Operational Limit State and Damage at Serviceability Limit State; Life Safety and Collapse at Ultimate Limit State, according to the current Italian building code [16-18].

Following this approach, the seismic risk class of a building is defined as the minimum between two classes: one associated with the *Safety Index* of the structure at the Life Safety Limit State (namely *SI-LS*) and the other one related to the expected annual loss, in Italian code [16] namely *Perdita Annuale Media Attesa (PAM*).

In detail, the first index, *SI-LS*, of the structure is defined as the ratio between Peak Ground Acceleration capacity (PGA_C), which determines the achievement of the Life Safety Limit State, and the Peak Ground Acceleration design (PGA_D) referring to the Peak Ground Acceleration (PGA) of the Life Safety Limit State for the specific site where the construction is located, indicated by the Italian code for the design of a new building. Thus, the class associated with this parameter may be evaluated [16], namely $Class_{SI\text{-}LS}$.

The second index, *PAM*, estimates the overall behavior of the construction in terms of economic value (*PAM*) and computes the performance of the structure for different earthquake intensities/return periods T_r. Such index is obtained by plotting the percentage *Reconstruction Costs* (*RC*) vs. the mean annual frequency of exceedance (equal to $\lambda = 1/T_r$) and connecting the points representative of each limit state. The so-obtained broken line is the PAM-curve, the PAM value corresponds to the area under the broken line; the smaller the area subtended by this curve, the lower the expected average annual loss (see Figure 1). *RC* is defined considering the building collapse due to earthquake event and the relevant costs needed to rebuild (according to regional price lists).

Each PGA_C corresponds to a given return period and a mean annual frequency of exceedance, λ. Once the building performance associated with a specific limit state is known in terms of $\lambda = 1/T_r$, a reliable correspondence between each λ and the repair/reconstruction cost of structural and non-structural components expressed as a percentage of RC, is needed.

The return periods, T_{rC}, associated with the peak ground accelerations corresponding to the achievement of the Damage and Life Safety Limit States for the examined building may be evaluated adopting the following relationship:

$$T_{rC} = T_{rD} \, (PGA_C/PGA_D)^{\eta} \tag{2}$$

with η equal to:

$$\begin{aligned} \eta &= 1/0.49 && \text{for } a_g > 0.25g \\ \eta &= 1/0.43 && \text{for } 0.15\ g < a_g \leq 0.25\ g \\ \eta &= 1/0.356 && \text{for } 0.05\ g < a_g \leq 0.15\ g \\ \eta &= 1/0.34 && \text{for } a_g \leq 0.05\ g \end{aligned} \tag{3}$$

where a_g is the maximum acceleration on rigid soil for the considered site.

For each return period T_{rC} the average annual frequency of exceedance is defined by equation (4):

$$\lambda = 1/T_{rC} \tag{4}$$

To estimate the repair/reconstruction cost associated with each limit state, [16] provides conventional repair costs in terms of a percentage of RC for each limit state, properly calibrated to include all the repair actions associated with a specific damage level. Easy formulations to determine the capacity of the structure at Operational Limit State and Collapse Limit State are suggested in [16], once those at Damage Limit State and Life Safety Limit State are known. In particular, the annual frequency of exceedance at Operational Limit State and Collapse Limit State can be computed according to the following simplified formulations:

$$\begin{aligned} \lambda_{OLS} &= 1.67\lambda_{DLS} \\ \lambda_{CLS} &= 0.49\lambda_{LSLS} \end{aligned} \tag{5}$$

where λ_{OLS} is the annual frequency of exceedance at Operational Limit State, λ_{DLS} is the annual frequency of exceedance at Damage Limit State, λ_{CLS} is the annual frequency of exceedance at Collapse Limit State, λ_{LSLS} is the annual frequency of exceedance at Life Safety Limit State.

The percentages of RC were estimated according to the actual repair costs monitored in the reconstruction process of buildings. Based on the costs analysis and taking into account studies based on macro-seismic analyses as well as post-earthquake observational data reported in [3], the percentage of RC associated with Damage Limit State and Life Safety Limit State were set equal to 15% and 50%, respectively; moreover, the percentage of RC for Operational Limit State and Collapse Limit State were set equal to 7% and 80%, respectively. The repair costs associated with the Initial Damage Limit State and total loss or "Reconstruction" Limit States, conventionally related to a fixed λ = 10% and λ = 0%, were assumed equal to 0 and 100%, respectively (see Figure 1 and Table 1).

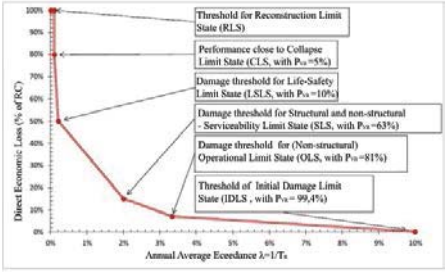

Figure 1: Trend of the curve that identifies PAM referring to a construction with a nominal life of 50 years and belonging to the use class II in according to [18].

Limit State	Percentage of RC [%]
Reconstruction	100
Collapse	80
Life Safety	50
Damage Limitation	15
Operational	7
Initial Damage	0

Table 1: Reconstruction/Repair Costs, expressed as percentage of RC, associated to each Limit State.

To determine the seismic risk class, the approach proposed in [16] requires evaluating PAM, according to the following equation:

$$PAM = \sum_{i=2}^{5} [\lambda(LS_i) - \lambda(LS_{i-1})] * [RC(LS_i) + RC(LS_{i-1})]/2 + \lambda(CLS) * RC(RLS) \quad (6)$$

where index "i" represents the generic limit state (i=5 for Collapse Limit State and i=1 for Initial Damage Limit State). Thus, the class associated with this parameter may be evaluated [16], namely $Class_{PAM}$.

Hence, the seismic risk class of the analyzed building corresponds to the worse risk class between $Class_{SI\text{-}LS}$ and $Class_{PAM}$.

The described procedure allows to simplify the seismic risk assessment and to have a design-oriented approach suitable for common practice applications. It is necessary to specify that the computation of the PAM class relies on the assumption that the repair costs at the different limit states are constant for private residential buildings without any distinction at component level.

This aspect obligates to calibrate the repair cost for different types of Italian construction heritage. In detail, for non-residential buildings the repair cost must be calibrated considering all their characteristics which lead to their proper value. In the following, a new approach is calibrated for the analysis of the case study of the Norman Tower of Craco.

2.1 Case of study

In this research the interest is centered on the Medieval Town of Craco, near Matera (Italy) and in particular on its tower. Today visiting Craco, the scenario is a village completely abandoned due to severe landslide motion, developed in the south-western part between 1959 and 1972, which damaged most part of the existing buildings. The Norman tower, object of the present study, was endowed with a defensive purpose and, for this reason, located on the highest point of the hill. The city has developed over time around it, thus creating the actual historic center (see Figure 2).

The Norman tower is one of the few structures remained unharmed by the effects of the landslide, until today. The defensive character of the tower is underlined by its robust appearance and by a quadrangular structure of 11 m size in compact masonry. The structure consists of an architrave opening on the East side at the first level, which allows access, and arched openings on the second level (12.5 m), one for each side, with the exception of the one facing North. Cracks arranged in three rows at the height of the crown (triangular in the lower rows and quadrangular in the third row) mark the horizontal closure placed at 20 m from the ground level, while the basement has a truncated pyramid shape.

Originally the structure had two masonry vaults, a barrel one (no longer existing) on the first floor and a cruise vault on the second level, connected by an internal staircase which was

destroyed. In relatively recent times, the inside of the tower has been subjected to manipulations, which have affected the general state of conservation. In 1949 the barrel vault and the staircase were demolished, and a municipal reinforced concrete tank of water with a cylindrical shape was realized. The cistern is not connected to the tower, but at some levels it is perfectly adherent to it.

Figure 2: South-East view of Craco with Normand tower.

A geometric survey was performed for evaluating the main characteristics of the structure: the wall thickness varies from 2.15 m at the base of the tower, to 1.70 m at the top. Based on a visual inspection and on the analysis of documents, it is assumed that the wall is realized by rubble masonry with a sand-interposed core. Externally the masonry base consists of a set of irregular river stones and shows conditions of advanced decay; the upper part of the tower, apparently in good conditions, consists of sandstones of varying sizes, with the exception of the cantons where cut stone blocks prevail, used for the double rings of the arched openings.

2.2 A new approach for the Reconstruction Cost calibration

The Reconstruction Cost [16] is the fundamental parameter for the evaluation of the PAM class, $Class_{PAM}$. In the specific case of the Norman Tower, it is not plausible to hypothesize a mere reconstruction cost which cannot take its significant historical and cultural value into account. In fact, even if the reconstruction could be economically estimable, however in no way it could replace the historical and cultural value lost in the event of its collapse and/or serious damage.

For this reason, the approach here proposed envisages the definition of a new *Reconstruction Cost* (*RC**), in accordance with equation (7), which, for the present case, is specified by introducing a new parameter, the *Usability Loss* (C_{UL}). Therefore:

$$RC^* = RC + C_{UL} \tag{7}$$

In the following, the evaluation of such parameter is proposed.

In the last decade, Craco has become a tourist attraction centre for its history, social value and historical and architectural heritage, becoming a symbolic ghost town. For this reason, the "Scenographic Museum of Craco" was realized with the aim of organizing touristic tours in the historic centre of Craco and in particular some visits of its symbolic structures, including the Tower.

It is possible to assume that the collapse of the Tower by seismic events and, therefore, the loss of a symbolic element of the historical centre would cause the non-usability of the latter. Consequently, the non-visitability would produce an economic loss during the whole period, which coincides with the "Recovery Time" of the structure. Such loss is here utilised for the evaluation of the proposed *Usability Loss* (UL) parameter, as a tool to estimate the historical-artistic value of the Tower.

The introduced parameter may be applied to any kind of structure with a historical/architectural value, by adopting a criterion able to describe the specific characteristics of the examined structure.
In this paper, the Usability Loss is quantified by calculating the monthly number of tickets sold (N_T), the time to rebuild the structure (t) and the average ticket price (C_T). In particular, the number of annual users of 2017 has been divided on a 12 months-period, so the monthly number N_T is equal to 1416.

The average ticket price C_T available from the "Parco Scenografico Museale di Craco" web, is equal to €10 [20]**.**

To identify the recovery time *(t)* and the Reconstruction Costs *(RC)* an intervention has been hypothesized, which foresees the faithful reconstruction of the "as it was, where it was" type, in accordance with the costs of [21]. It was therefore estimated that this intervention lasts 12 months, probably the shortest, to try to create the least possible discomfort at the museum.

Thus, *Norman Tower RC** is given in Table 2.

New Parameters	Acronym	Costs (€)
Cost of reconstruction	RC	€ 316,468.00
Loss of usability	C_{UL}	€ 170,000.00
Cost of reconstruction'	**RC***	**€ 486,468.00**

Table 2: New parameters and their economic value.

2.3 Seismic risk class of the Norman Tower

To evaluate the seismic risk class of the Norman Tower of Craco, the conventional method was applied as indicated by [16], adopting the prescription of the current Italian Technical Standards for Construction "NCT 2018" [18, 19].

The analysis of the structure was carried out by means of PROSAP software [22]. The structure was modelled through 12,160 shell elements, 12,470 nodes and a rigid floor. The following mechanical parameters for the masonry walls have been assumed:

- Young's modulus (E_m) equal to 1050 MPa
- Poisson's Modulus (ν_m) equal to 0.2
- Average specific weight of the masonry (w_m) equal to 19 kN/m^3,

while for the reinforced concrete elements the following values have been assumed:

- Young's modulus (E_c) equal to 27460 MPa
- Poisson's Modulus (ν_c) equal to 0.2
- Average specific weight of the masonry (w_c) equal to 24 kN/m^3

All the walls have been considered pinned at the base. The gravitational loads are the ones due to the structural masses, as no servicibility loads are acting on the tower.

In the following, the detailed procedure for the evaluation of the the Norman Tower seismic class is described. In the first part, the PAM graph is evaluted, while in the second part the safety index is discussed, and, finally, the risk class is defined.

The Italian building code [16] gives the design PGA for the Life Safety Limit State ($PGA_{D\text{-}LS\text{-}LS}$) and for the Damage Limit State ($PGA_{D\text{-}DLS}$), by using the Elastic Demand Spectrum for Craco town (Figure 3):

- $PGA_{D\text{-}LS\text{-}LS}$= 0.103g
- $PGA_{D\text{-}DLS}$= 0.048g

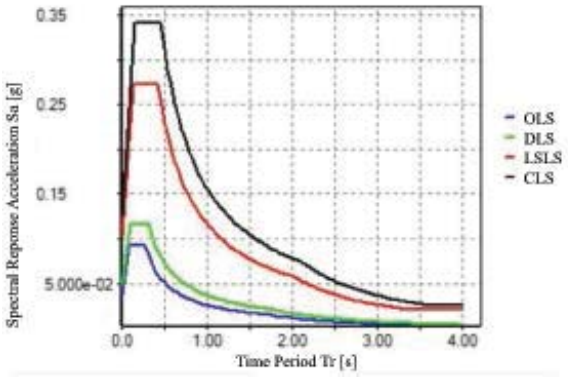

Figure 3: Elastic Demand Spectrum of Craco Town

The FE analysis allows the evaluation of the capacity peak ground acceleration related to the achievement of the Life Safety Limit State ($PGA_{C\text{-}LS\text{-}LS}$) and the Damage Limit State ($PGA_{C\text{-}DLS}$):

- $PGA_{C\text{-}LS\text{-}LS}$= 0.083g
- $PGA_{C\text{-}DLS}$= 0.0336g

The return periods, T_{rC}, associated with the considered limit states (LS-LS and DLS) were then evaluated by using the equation (2), where η was set equal to 1/0.43, in accordance with equation (3) (Craco lays in the seismic zone 2 [23]). In the following, the calculated T_{rC} values are reported:

- $T_{rC\text{-}LS\text{-}LS}$= 287 years
- $T_{rC\text{-}DLS}$= 22 years

Finally, in accordance with the Italian codes, the Annual Average Exceedance (λ) (see equations 4-5) and the minimum/maximum values of the economic loss for the reconstruction of the Tower were evaluated. The procedure adopts the same percentage.

For each considered Limit State, the value of the reconstruction cost percentage and the annual average exceedance values are reported in Table 3, which has been defined adopting the same percentages of Table 1.

Limit State	Percentage RC* [%]	Cost (€)	Annual Average Exceedance (λ)
Restoration	100%	€486,468.00	0
Collapse	80%	€389,174.00	0.0015
Safety Life	50%	€194,587.00	0.003
Damage	15%	€29,188.00	0.046
Operational	7%	€2,043.00	0.076
Initial damage	0%	€0.00	0.1

Table 3: Reconstruction/restoration costs (RC*) and Average annual frequency of exceedance, associated with the achievement of each Limit State for the Tower of Craco.

Finally, $Class_{PAM}$ is identified by means of Table 6 [16] which associates the class to the range of values assumed by PAM.

For the Tower studied in this paper, the *PAM*-value is equal to 2.07%, corresponding to C_{PAM}- class (see [16]).

The second step of the procedure, needs the evaluation of the safety index of the structures, which is defined as the ratio between the peak ground acceleration capacity PGA_C for which

the building reaches the Life Safety Limit State and the peak ground acceleration demand PGA_D of the site where the construction is built, with reference to the same limit state. In the case here examined, the first PGA is equal to *0.083g* while the second to *0.103g*, thus the safety index is equal to 81%.
The risk class associated with the Safety index can be derived through [16] and is equal to $A_{SI\text{-}LS}$.

On the basis of the aforementioned parameters, the Seismic Risk Class of the Tower is ***C***, that coincides with the worst/lowest class between the $Class_{PAM}$ and the $Class_{SI\text{-}LS}$, i.e. the one corresponding to the highest risk. It is useful to point out that the seismic risk class corresponds to the one associated with the PAM class, that is the one modified by the proposed procedure.

In conclusion, for the Norman Tower, being an asset with significant historical and cultural value, hypothesizing a cost of reconstruction alone is not plausible. Its reconstruction, however, economically estimable, can in no way being representative of the historical and cultural value lost in the event of its collapse. The identified approach, therefore, for the estimation of the RC* parameter represents a possible proposal for the determination of an economic value of PAM, associated with types of buildings with high historical and cultural value and accessible to the public.

3 CONCLUSIONS

A new methodology able to evaluate the seismic hazard of the medieval tower of Craco has been proposed, being this construction a historical-monumental building. The current Italian guidelines for seismic risk assessment provide a method based on both the indices PAM and SI-LS. However, this method is proposed for application to residential buildings in reinforced concrete, here such method is extended to the analysis of historical masonry structures.

In detail, the calibration of the *Reconstruction Cost* (RC), necessary to the PAM index calculation for the seismic classification, has been developed. PAM is evaluated by different parameters in the formulation of the new reconstruction cost (RC*). These parameters take into account the socio-economic, architectural, historical and cultural value of the structure. Specifically, in the study case of the Norman Tower, the Usability Loss has been considered as crucial parameter. This choice depends on the museum function of the tower and the *ghost town* of Craco.

From the analysis the tower *PAM*-value was equal to 2.07%, corresponding to C_{PAM}-class.

Further in-depth studies and analyzes are necessary for the validation of the proposed methodology. Additional parameters could be identified in order to take into account several aspects that can condition the value of the building.

ACKNOWLEDGEMENTS

The Italian project PRIN 2015 - “Mitigating the impacts of natural hazards on cultural heritage sites, structures and artefacts (MICHe)” is acknowledged for the support given to the present research.

REFERENCES

[1] S.Ivorra, F.Pallares, Dynamic investigations on a masonry bell tower, *Eng Struct*, 28(5), 660–667, 2006.

[2] M. Diaferio, D. Foti, N.I. Giannoccaro, Identification of the modal properties of a squat historic tower for the tuning of a FE model. in *Proceedings of the 6th International Operational Modal Analysis Conference, IOMAC 2015,* 12- 14 May 2015.

[3] L. Carnimeo, D. Foti, V. Vacca, On Damage Monitoring in Historical Buildings via Neural Networks, *in Proceedings of EESMS 2015- 2015 IEEE Workshop on Environmental, Energy and Structural Monitoring Systems*, Trento, Italy, July 9th -10th, 2015.

[4] D. Foti, A New Experimental Approach to the Pushover Analysis of Masonry Buildings, *Computers and Structures,* 147, 165-171, 2015.

[5] M. Diaferio, D. Foti, N.I. Giannoccaro, Modal parameters identification on environmental tests of an ancient tower and validation of its FE model, *International Journal of Mechanics* , 10, 80-89, 2016.

[6] UNDRO: 1980. Natural Disasters and Vulnerability Analysis, Report of Experts Group Meeting, UNDRO, Geneva.

[7] H. C. Hung, T. W. Wang, Determinants and mapping of collective perceptions of technological risk: the case of the second nuclear power plant in Taiwan. *Risk Analysis: An International Journal*, 31(4), 668-683, 2011.

[8] S. Tolo, E. Patelli, M. Beer, Risk assessment of spent nuclear fuel facilities considering climate change, *ASCE-ASME Journal of Risk and Uncertainty in Engineering Systems, Part A: Civil Engineering*, 3(2), G4016003, 2017.

[9] W. Kron. Keynote lecture: Flood risk= hazard× exposure× vulnerability.*Flood defence,* 82-9, .2002

[10] S. Tyagunov, L. Stempniewski, G. Grünthal, R. Wahlström, J. Zschau, Vulnerability and risk assessment for earthquake prone cities *in Proceedings of the 13th World Conference on Earthquake Engineering (13 WCEE)*, 2002.

[11] I. Alcántara-Ayala, K. Sassa, M. Mikoš, Q. Han, J. Rhyner, K. Takara, S. Briceño, The 4th World Landslide Forum: landslide research and risk reduction for advancing the culture of living with natural hazards, *International Journal of Disaster Risk Science*,8(4), 498-502, 2017.

[12] T. Glade, Vulnerability assessment in landslide risk analysis, *Erde*, 134(2), 123-146, 2003.

[13] M. L. Carreño, O. D. CardonaA. H. Barbat, Urban seismic risk evaluation: a holistic approach. *Natural Hazards*, 40(1), 137-172, 2007.

[14] P. Crespi, N. Giordano, G. Frascaro, Seismic Loss Estimation for an Old Masonry Building in Italy. *in proceeding 13th International Conference on Applications of Statistics and Probability in Civil Engineering*, ICASP13,2019.

[15] M. Bosio, M. E. Bressanelli, A. Belleri, Simplified models for the evaluation of the economic losses in precast structures due to earthquakes. *In Italian Concrete Days 2018*, 2018.

[16] Ministry Decree n.58 28/02/2017 Allegato A: linee guida per la classificazione del rischio sismico delle costruzioni (in Italian). Italian Ministry of Infrastructures and Transport, Italy: Updated with Ministry Decree n. 65 del 07/03/ 2017.

[17] Cosenza, E., Del Vecchio, C., Di Ludovico, M. et al. The Italian guidelines for seismic risk classification of constructions: technical principles and validation. Bull Earthquake Eng 16, 5905–5935, 2018. https://doi.org/10.1007/s10518-018-0431-8

[18] MI (2018) D.M. 17 Gennaio 2018 (D.M. 2018). Technical code for constructions (in Italian). G.U. n. 42 del 29/2/2018. Rome, Italy.

[19] Italian law: "Circolare n.7 del 21 gennaio 2019. "Istruzioni per l'applicazione dell'«Aggiornamento delle "Norme tecniche per le costruzioni"» di cui al decreto ministeriale 17 gennaio 2018.

[20] https://www.cracomuseum.eu/parco-museale-scenografico-di-craco/.

[21] Regional price list of the Basilicata Region: http://prezzariooperepubbliche.regione.basilicata.it/prezzarioop/prezzario/prezzari.xhtml

[22] 2S.I. ProSAP. PROfessional Structural Analysis Program 2017.

[23] The Order of the President of the Council of Ministers no. 3274 of 20th March 2003 published on the Official Gazette no. 105 of 8 May 2003.

EURODYN 2020
XI International Conference on Structural Dynamics
M. Papadrakakis, M. Fragiadakis, C. Papadimitriou (eds.)
Athens, Greece, 23–26 November 2020

DYNAMIC ANALYSIS OF A POMPEIAN DOMUS

M. Monaco[1], A. Iannuzzo[2], A. Tafuro[1] and A. Gesualdo[3]

[1]Department of Architecture and Industrial Design, University of Campania "Luigi Vanvitelli"
Via San Lorenzo 1, 81031 Aversa (CE), Italy
e-mail: {michela.monaco, anna.tafuro}@unicampania.it

[2]Institute of Technology in Architecture, ETH Zurich
Stefano-Franscini-Platz, 1, 8093 Zürich, Switzerland
iannuzzo@arch.ethz.ch

[2]Department of Structures for Engineering and Architecture, University of Naples “Federico II”
Via Claudio 21, 80125 Naples, Italy
gesualdo@unina.it

Keywords: Masonry, Pompeii, Restoration, Vulnerability

Abstract. *The archaeological site of Pompeii has been subjected to restoration interventions since the beginning of its excavation. After the second World War concrete structures replaced the old wooden roofs erected in the late XIX. A systematic study of these structures is lacking, despite the number and the significant role they play in the stress state of the ancient masonry. In particular, the structural role of atriums roofing structures in the Pompeii buildings is examined. The impact of the restoration interventions actually present in the archaeological area of Pompeii is analyzed. A dynamic analysis has been performed to assess the seismic vulnerability of the ancient buildings in their actual state. The paper shows that maintenance of the existing interventions is a fundamental topic and substitution of r.c. roofs with timber structures cannot be justified by structural reasons. As a case study the entire Domus of the Tragic Poet is analyzed. A simulation involving a wooden roof is compared with the actual structure of concrete roof building.*

1 INTRODUCTION

Pompeii, since its first excavation campaign, has been profoundly altered by successive mutilations, additions and transformations. In some cases strong interventions have been made in order to rebuild the original construction. This makes archaeological remains the object of complex, interdisciplinary studies involving archaeologists and applied scientists [1]. The balance between the respect of the ancient construction and the exigence of safety is a great challenge for the structural engineer [2, 3, 4]. Several different approaches for the interventions on Cultural heritage have been developed in these last decades [5, 6]. Different restoration materials have been in fact used during the decades, according the scientific approach to the structural technology of the time.

Fig. 1. Concrete Atrium roofs: Villa dei Misteri (left), Fabius Rufus (center) and Tragic Poet (right).

The first structural interventions in many Pompeian *Domus* involved the replacement of old wooden roofs with concrete structures similar to the old ones, especially in the two decades among 1960 and 1980, as the photo archives testify. Several of these roofs realized in particular on the atriums are nowadays visible (Figure 1) and the scientific debate is mainly about opportunity and durability of these interventions [7]. Reinforced concrete and wood are in fact the most diffused materials for the roofing structures of the atriums actually present in the archaeological area of Pompeii (Figure 2). A systematic study of these structures is lacking, despite the number and the significant role they play in the stress state of the ancient masonry.

Fig. 2. Wooden atrium roofs: Vettii Domus (left) and Domus on *Cardo V inferiore*

The use of steel structures in the atriums is limited, being extensively employed for quasi-provisional structures, therefore perhaps a more detailed analysis about the structural performance of both wood and r.c. in the seismic case could be a starting point in the scientific debate about the necessity of substitution of last with the first one [7]. It must be noted that all the upper part of the *Domus* atriums have been rebuilt and the ancient Pompeian masonry represents only the lower part of the walls [8], so that the seismic vulnerability should be regarded only from the point of view of the human safety and protection of original mosaics and paintings

[9]. An eventual collapse without damage to artworks could only bring back the walls to the original ruins state [10].

A Pompeian atrium is only a limited part of the complex structure of the *Domus*, so that the cultural discussion about the quality and scheme of the roof cannot be set apart from the structural analysis of the whole structure of the building and its history [11, 12]. The analysis of part of the structure, as successfully done in some cases [13, 14] cannot be applied to the Roman Domus, that is a complex arrangement of different materials and structures.

This paper deals with this last aspect, analyzing the whole *Tragic Poet Domus* by means of a finite element code. The influence of two distinct materials (wood and reinforced concrete) for the roof of the Tuscanic atrium. The structural behaviour is not significantly affected by the structural material chosen for restoration, so that the actual concrete roof (at present in perfect conditions) do not need an urgent replacement. The structural dynamic analysis of the whole Domus has shown that the atrium is the core structural element of the entire construction and the roofing technique do not significantly influence the vulnerability of the construction**.**

2 STRUCTURAL ANALYSIS

The Tragic Poet Domus in Pompeii, also known as the Domus of the "*Cave canem*" for its splendid black-white mosaic with a dog has been analyzed [15]. The case study is a corner building (Figure 13) with a Tuscanic atrium. The actual roofing structure is composed of r.c. beams, wooden rafters and clay shingles (Figure 1). The Domus has been chosen because it is a typical example of the Pompeian House [16] in which a key structural role is played by the large atrium, with a r.c. roofing structure in good conditions [7].

A finite element analysis has been performed in order to evaluate the role of the roofing structures' technologies in the structural behavior of the Domus (Figure 4).

Fig. 3. The "Cave canem" mosaic (left) and the Tragic Poet Domus (right) [7].

The linear analysis has been considered sufficient [17, 18] and has been carried out by means of a commercial finite element code [19], the whole structure has been modelled with solid tetrahedral elements C3D10 with medium dimensions 0.4 m. Different constitutive parameters have been taken into account, as reported in Table 1.

Mechanical properties	Masonry	R.C.	Wood	Wooden deck
Density, ρ [kg/m^3]	1937	2500	550	400
Elastic modulus, E [N/mm^2]	1140	30000	9800	6000
Poisson's ratio ν	0.2	0.16	0.2	0.2

Table 1. Mechanical properties.

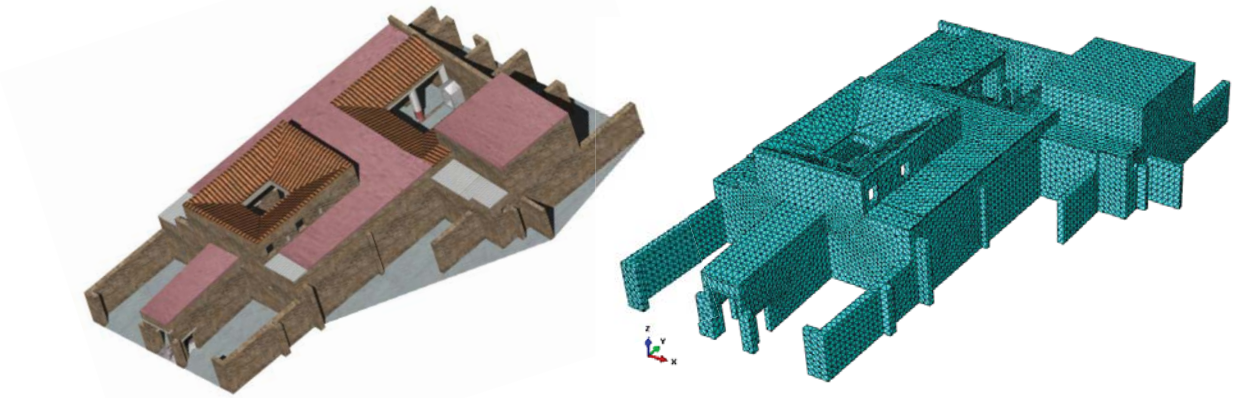

Fig. 4. Picture (left) and 3D mesh for the case study (right)

Two different roofing structures have been considered for the analysis: an ideal wooden structure and the actual r.c. one, leaving unaltered every other element of the Domus (geometry, material characteristics and self weight). The analysis results are reported in the following pictures, so to allow comparison in the two considered structural cases.

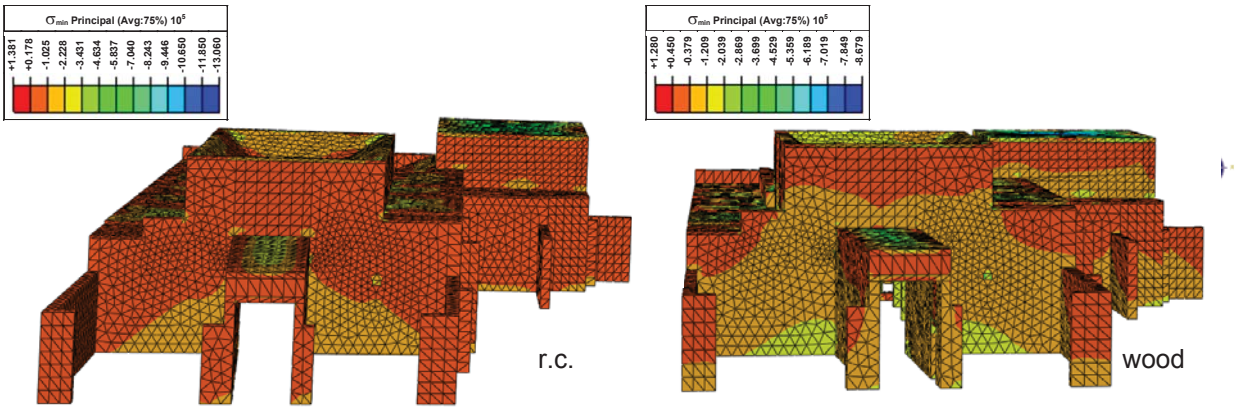

Fig. 5. Principal compressive stresses due to self weight. Detail of the front view

In Figure 5 a detail of the front view with a map of the principal compressive stresses due to the self weight is reported. Considering that the Roman masonry is only the lower part of the walls, its stress state in the two examined cases is similar, and this is true for all the ancient Domus masonry.

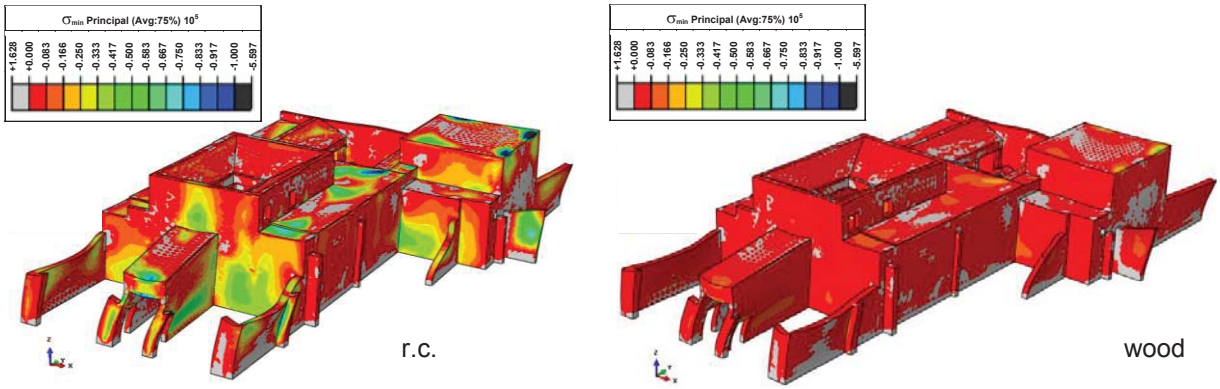

Fig. 6. Distribution of stresses in the case of selfweight and seismic action along x-axis.

Dynamic analyses have been performed considering the seismic action along the two principal axes of the Domus, involving a PGA 0.244 g and masonry tensile and compressive strength equal to 0.1 MPa and 3 MPa respectively [20, 21].

A similar condition can be evaluated in Figure 6 reporting the principal stress maps in the case of the combined actions of selfweight and seismic load along x-axis.

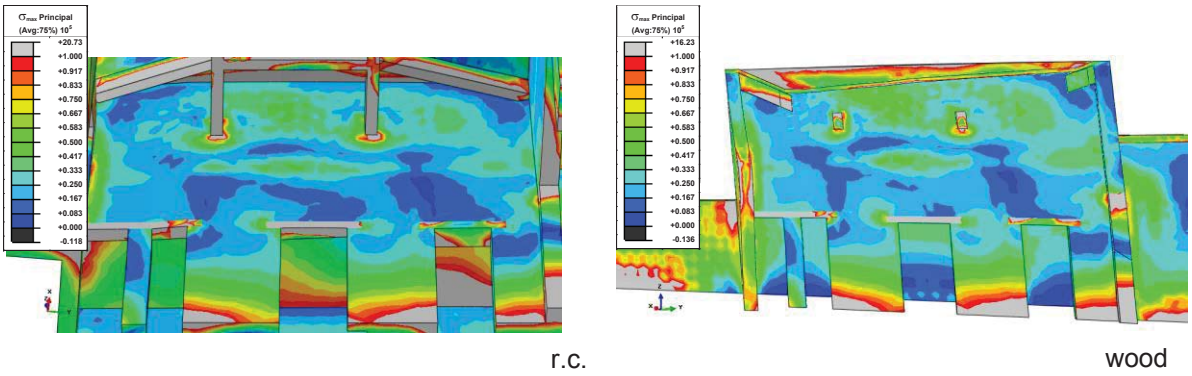

Fig. 7. Atrium distribution of stresses in the case of selfweight and seismic action along x-axis

In Figure 7 the stress state of the atrium is picted. As it can be note, the stress values are of the same order. The seismic analysis according the y-axis, reported in Figure 8, does not give more information, due to the larger inertia of the Domus in this direction.

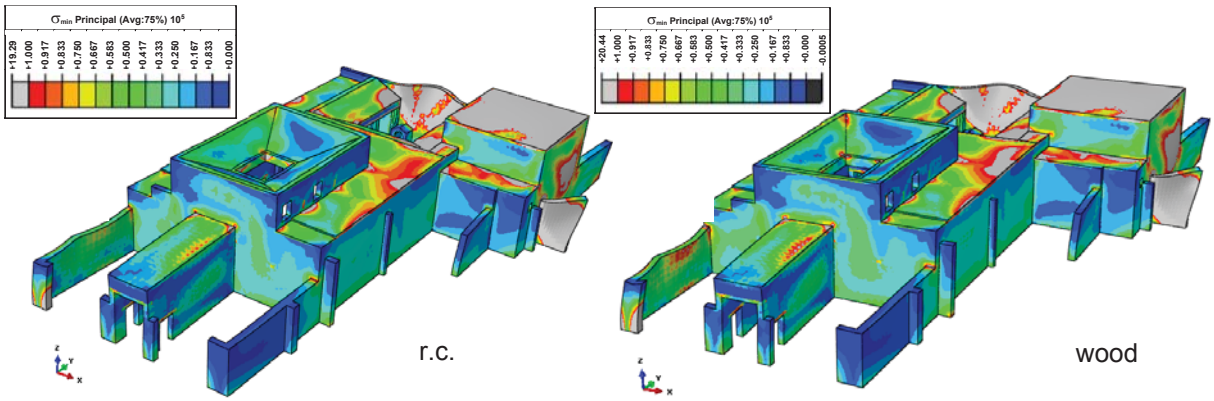

Fig. 8. Distribution of stresses in the case of selfweight and seismic action along y-axis

A dynamic modal analysis has been performed to assess the quality of response to seismic actions. The first 8 modes of vibration involve only limited structural elements: in general, all the masonry walls departing from the central block of rooms and the vestibulum. A representation of the first mode of vibration, where the vestibulum is involved, is reported in Figure 9.

The eventual collapse of the peripheral masonry elements makes the Domus become a more compact structure around the central atrium, since only the ninth mode of vibration involves almost all the domus structure, atrium and peristilium, as it can be seen in Figure 9.

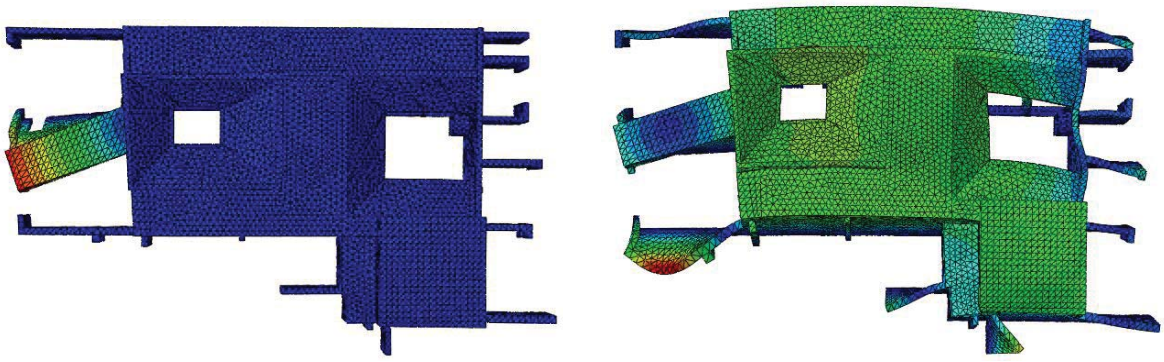

Fig. 9. First (left) and ninth (right) mode of vibration according the x-direction

These last considerations about the modes of vibration underline again the central role of the atrium in the overall behaviour of the Domus.

3 FINAL REMARKS

A Pompeian Domus is a complex arrangement of various structural elements, subjected in their previous life to heavy restoration interventions, in general respecting the original structural geometry only. Different restoration materials have been in fact used during the decades, according the scientific approach to the structural technology of the time. This paper analyzes the roofing interventions actually present in the atriums of the Pompeii archaeological area.

The entire structure of the Tragic Poet Domus (masonry walls and r.c. roof) is analyzed by means of a finite element code to evaluate the influence of structural material. Two cases have been examined: the actual r.c. roof structures, due to a post War intervention, and a geometrically similar timber structure. With regard to stress and strain maps, the two structures affect similarly the lower Roman masonry structures, so that substitution of r.c. roofs with timber structures cannot be justified with structural reasons.

Archaeological, aesthetical and durability considerations together with the restoration yard management, excluded in this approach, are the main aspects to take into account in a restoration program, since the stability and vulnerability questions depending on the roofing material assume limited importance as it has been shown in this paper.

4 ACKNOWLEDGEMENTS

The authors acknowledge the Ministry for Cultural Heritage and Activities and Tourism – Archaeological Park of Pompeii, for the permission of taking measurements and using images of the Pompeii site.

REFERENCES

[1] J. Ashurst (Ed.), Conservation of ruins, Butterworth-Heinemann, Elsevier, Oxford, U.K., 2007

[2] A. Gesualdo, M. Monaco, Seismic vulnerability reduction of existing masonry buildings. Modelling of retrofitting techniques, in: F.M. Mazzolani (Ed.), Urban Habitat Constructions Under Catastrophic Events: Proceedings of the COST C26 Action Final Conference, vol. 1, CRC Press, Taylor & Francis Group, London, New York, 853-858, 2010.

[3] G. De Matteis, V. Corlito, M. Guadagnuolo, A. Tafuro, Seismic Vulnerability Assessment and Retrofitting Strategies of Italian Masonry Churches of the Alife-Caiazzo Diocese in Caserta, International Journal Architectural Heritage, 2019.

[4] M. Orlando, M. Betti, P. Spinelli, Assessment of structural behaviour and seismic retrofitting for an Italian monumental masonry building. Journal of Building Engineering, 29, 101115, 2020.

[5] G. Buonocore, A. Gesualdo, M. Monaco, M.T. Savino, Improvement of Seismic Performance of Unreinforced Masonry Buildings using Steel Frames, in: B.H.V. Topping and P. Iványi (Eds.), Civil-Comp Proceedings of the Twelfth International Conference on Computational Structures Technology, Civil Comp Press, Kippen, Stirlingshire, U.K., 2014.

[6] M. Guadagnuolo, G. Faella, Simplified Design of Masonry Ring-Beams Reinforced by Flax Fibers for Existing Buildings Retrofitting, Buildings, Buildings, 10(1), 12, 2020.

[7] I. Bergamasco, A. Gesualdo, A. Iannuzzo, M. Monaco, An integrated approach to the conservation of the roofing structures in the Pompeian domus, Journal of Cultural Heritage, 31, 141-151, 2018.

[8] J.P. Adam, Roman Building: Materials and Techniques, Routledge, London, U.K., 2005.

[9] M. Guadagnuolo, M. Aurilio, G. Faella, Retrofit assessment of masonry buildings through simplified structural analysis, Frattura ed Integrità Strutturale, 14(51), 398-409, 2020.

[10] A. Gesualdo, M. Monaco, M.T. Savino, Seismic retrofitting techniques for masonry arch bridges, in: F.M. Mazzolani (Ed.), Urban Habitat Constructions Under Catastrophic Events Proceedings of the COST C26 Action Final Conference, vol. 1, CRC Press, Taylor & Francis Group, London, New York, 859-864, 2010.

[11] M.G. D'Amico, A. Flamini, La Casa dei Vettii e la casa VI, 15, 2: proposte per nuove coperture, in: Atti della Giornata di Studi Le coperture di aree e strutture archeologiche, Bologna, 2000.

[12] C.M. Salassa, Le coperture di restauro a Pompei, Rivista di studi Pompeiani, 10, 91-115, 1999.

[13] M. Monaco, I. Bergamasco, M. Betti, A no-tension analysis for a brick masonry vault with lunette, Journal of Mechanics of Materials and Structures, 13(5), 703-714, 2018.

[14] A. Gesualdo, B. Calderoni, A. Sandoli, M. Monaco, Minimum energy approach for the in-plane shear resistance of masonry panels, Ingegneria Sismica, 36(1), 42-53, 2019.

[15] D.R. Rochette, J.F. Bouchet, Pompéi, choix d'édifices inédits, vol. 1, Maison du poète tragique à Pompéi publiée avec ses peintures et ses mosaïques, Leconte, Paris, 1828.

[16] I.B. Bergmann, I. Victoria, The Roman house as memory theater: The house of the tragic poet in Pompeii, The Art Bulletin 76(2), 225-256, 1994.

[17] M. Lucchesi, B. Pintucchi, B., N. Zani, Normal elastic and elastoplastic materials: from a comprehensive approach a mixed method for masonry. Meccanica, 54(7), 1015-1028, 2019.

[18] A. Gesualdo, B. Calderoni, A. Iannuzzo, A. Fortunato, M. Monaco, Minimum energy strategies for the in-plane behaviour of masonry, Frattura ed Integrità Strutturale, 14(51), 376-385, 2020.

[19] Manual, Abaqus Users, Version 6.10, Abaqus Inc., 2010.

[20] L. Facchini, M. Betti, Time-history analysis of slender masonry towers: a parametric study on the reliability of a simplified Bouc and Wen approach. Meccanica, 52(13), 3181-3196, 2017.

[21] G. Faella, A. Giordano, M. Guadagnuolo, Unsymmetric-plan masonry buildings: pushover vs nonlinear dynamic analysis, Proc. 9th US National and 10th Canadian Conference on Earthquake Engineering, Toronto, July 25-29, 2010.

EURODYN 2020
XI International Conference on Structural Dynamics
M. Papadrakakis, M. Fragiadakis, C. Papadimitriou (eds.)
Athens, Greece, 23–26 November 2020

SHEAR PLASTIC DYNAMIC BEHAVIOUR OF WIND TURBINE TOWERS

A. Gesualdo[1], F. Penta[2], A. Iannuzzo[3] and M. Monaco[4]

[1]Department of Structures for Engineering and Architecture, University of Naples "Federico II"
Via Claudio 21, 80125 Naples, Italy
e-mail: gesualdo@unina.it

[2]Department of Industrial Engineering, University of Naples "Federico II"
Piazzale V. Tecchio 80, 80125 Naples, Italy
e-mail: penta@unina.it

[3]Institute of Technology in Architecture, ETH Zurich
Stefano-Franscini-Platz, 1, 8093 Zürich, Switzerland
iannuzzo@arch.ethz.ch

[4]Department of Architecture and Industrial Design, University of Campania "Luigi Vanvitelli"
Via San Lorenzo 1, 81031 Aversa (CE), Italy
michela.monaco@unicampania.it

Keywords: Nonlinear dynamics, Plastic shear failure, Modal approximation, Time history

Abstract. *The analysis of structures subjected to earthquake actions can be carried out by means of several methods with different levels of accuracy, among which the nonlinear dynamics is generally recognized as the most reliable one. This paper presents a general treatment to develop approximate solutions for rigid-plastic response of structures subjected to base harmonic pulse, by means of a numerical procedure on purpose developed. The case study is a vertical cantilever beam, with base support, constant mass and inertia distribution, subjected to only ground acceleration. The failure is assumed depending on the formation of a single shear hinge and the results are expressed in general terms. As a result, the motion proceeds through successive spreading and contractions of the plastic front and related elastic returns. Possible applications of the method to real structures can be envisaged.*

1 INTRODUCTION

The strong demand of sustainable energy has today led to build many aeolian park endowed of several wind turbine properly equipped for the production of electric power. A great number of these parks have been realised in seismic areas, and many of them have been established in Irpinia, a region in Southern Italy that was devastated by a strong earthquake in 1980. Observed collapse of several wind towers can be yield by a system of severe actions (see Fig. 1), mainly due to the action of the wind or earthquake. For the earthquake perturbation a nonlinear dynamic model presented in [1, 2, 3] constitutes a reliable tool to analyze this kind of problems.

Fig. 1. Collapsed wind tower [25].

A high level of expertise, high costs, and large amounts of calculation time are required to model the steel towers of these modern windmills. Constitutive and structural models with sufficient accuracy and low numerical complexity are generally adopted when elastic responses can be neglected, so that a rigid-plastic model, usually extensively employed in earthquake engineering, constitutes a simplified procedure [4, 5, 6, 7, 8]. The implementation of rigid-plastic models is a non-conventional stiffness-based computer method, because it exhibits a stiffness jump. Numerous constitutive models for rigid-plastic bending frames are largely widespread, while shear constitutive ones are quite rare. Nevertheless, the latter procedures have the advantage of a low computational complexity and a reduced number of mechanical parameters (yield property) [9, 10]. These advantages are the starting point of the present study because simple relationships between structure strength and parameters that are useful for design purposes can be established [11, 12]. Various authors analysed the dynamic plastic bending responses of structural elements in steel and reinforced-concrete structures and they found that bending hinges are the result of the general response characteristics of several structural elements under transverse loads. A concise number of studies have examined the dynamic of the plastic shear failure. An important issue in bending and shear problems is related to the localization and extension of plastic hinges [13, 14].

The structural dynamics has been largely analysed adopting the single-degree-of-freedom (SDOF) model that provides a first good evaluation of the response mode usually responsible of the collapse state [15]. A rigid-plastic cantilever beam can be an efficient structural scheme to clarify the nonlinear dynamic behavior of highly complex structures [16] and validate the reliability of numerical methods adopted in nonlinear dynamics [17, 18]. Generally, the stiffness of a structure is not uniform when strength and mass vary along the height of the structure. In several cases, such as those involving rigid bodies, efficient schematizations are required to solve complex dynamic problems [19, 20]. Wind turbine towers are structurally assimilable to cantilever beams so that the SDOF model constitutes indeed a powerful tool.

Near-fault ground motions are often characterized by pulse sequences with simple shapes that can be recognized in accelerograms via spectral analysis [21]. Generally, the development of elastic and inelastic response spectra is facilitated when accurate harmonic pulses are utilized to represent ground motions [22]. A sensitive analysis of elastic and inelastic responses induced by different simple pulse shapes has shown that local site effects on structures can be modeled with an appropriate pulse choice [23]. These considerations are the basis of the numerical analysis performed in this work because a harmonic pulse can be a suitable representation of near-fault ground motions [21]. Basically a numerical strategy developing an approximate solution of slender structures with base harmonic pulses is exposed. The fundamental equations are based on the rigid-plastic constitutive model and applied to the structure of a wind turbine tower, assimilated to a cantilever beam, having a harmonic forcing motion at the base support. Failure depend on the formation of shear hinges. The proposed model is an evolution of the SDOF cantilever beam because plastic hinges can form in each beam section.

2 NONLINEAR DYNAMIC MODEL

The validity of simplified constitutive models is limited when these models are applied to structures subjected to short-duration, high-intensity loading, given not extremely large deformations to cause strong geometry change effects and energy disturbance larger than the elastic one. This last consideration justifies the adoption of simplified models and the exclusion of elastic effects caused by large dynamic loads, although the results can also be refined to include the initially neglected aspects. The analysisi of rigid-plastic models is less difficult than that of elastic-plastic ones. In the following, geometry changes are small, and yield stress is assumed to be independent of the strain rate. Reference is made to the elastic-perfectly plastic body in Fig. 2.

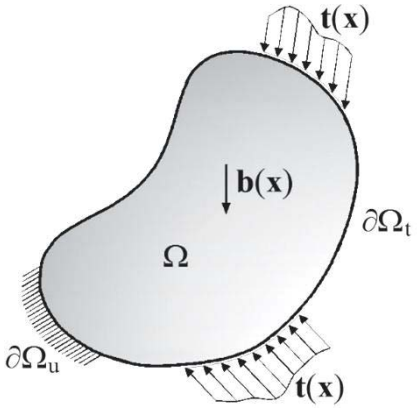

Fig. 2. Elastic-perfectly plastic body

where

$\partial\Omega = \partial\Omega_t \cup \partial\Omega_u$: total boundary of the body Ω and $\partial\Omega_t \cap \partial\Omega_u = \varnothing$,

$\partial\Omega_t$, $\partial\Omega_u$: free and constrained boundary of the body Ω,

$\lambda(t)\ \mathbf{t}(\mathbf{x})$: surface loads on the free boundary $\partial\Omega_t$,

$\lambda(t)\ \mathbf{b}(\mathbf{x})$: body forces in Ω,

$\dot{\boldsymbol{u}}_g(\boldsymbol{x},t)$: assigned velocity vector and $\dot{\mathbf{u}}(\mathbf{x},0) = \mathbf{0}$ on $\partial\Omega_u$,

$\lambda(t)$: time dependent load multiplier function.

The solution of the elastoplastic problem provides the strain rate $\dot{\mathbf{E}}(\mathbf{x},t)$ and velocity fields $\dot{\mathbf{u}}(\mathbf{x},t)$ satisfying the kinematical admissibility conditions and the stress field $\mathbf{T}(\mathbf{x},t)$ equilibrated with the applied loads $\lambda(t)\ \mathbf{t}(\mathbf{x})$, and the inertial forces $-\mu(\mathbf{x})\ddot{\mathbf{u}}^*(\mathbf{x},t)$, where $\mu(\mathbf{x})$ is the mass density function. The approximate response field [4] is assumed to be in the form:

$$\dot{\mathbf{u}}^*(\mathbf{x},t)=\boldsymbol{\Phi}(\mathbf{x})\,L(t) \tag{1}$$

with

$$\dot{\mathbf{u}}^*(\mathbf{x},t)=\dot{\mathbf{u}}_g(\mathbf{x},t) \text{ on } \partial\Omega_u \ ;\ \dot{\mathbf{u}}^*(\mathbf{x},t)=\mathbf{0} \text{ in } \Omega \text{ and } \partial\Omega_t,$$

where the assigned vector $\boldsymbol{\Phi}(\mathbf{x})$ depends on the initial position only and $L(t)$ is an unknown scalar function of the time to be determined.
The difference between the real stress field and the approximate one is in balance with the variation of the associate force fields and reduced to the difference between inertial forces.

The problem solution does not require $\mathbf{T}^*(\mathbf{x},t)$ and $\dot{\mathbf{E}}^*(\mathbf{x},t)$ to be associated by the plastic law. Thus, the stress field is dynamically admissible with respect to the D'Alembert principle. By applying the principle of virtual power, we obtain:

$$\int_\Omega \mu(\ddot{\mathbf{u}}-\ddot{\mathbf{u}}^*)\cdot(\dot{\mathbf{u}}-\dot{\mathbf{u}}^*)\,d\Omega+\int_\Omega(\mathbf{T}-\mathbf{T}^*)\cdot(\dot{\mathbf{E}}-\dot{\mathbf{E}}^*)\,d\Omega=0 \tag{2}$$

given that:

$$\Delta(t)=\frac{1}{2}\int_\Omega \mu(\dot{\mathbf{u}}-\dot{\mathbf{u}}^*)\cdot(\dot{\mathbf{u}}-\dot{\mathbf{u}}^*)\,d\Omega. \tag{3}$$

The first derivative of $\Delta(t)$ is calculated as:

$$\frac{d\Delta}{dt}=\int_\Omega \mu(\ddot{\mathbf{u}}-\ddot{\mathbf{u}}^*)\cdot(\dot{\mathbf{u}}-\dot{\mathbf{u}}^*)\,d\Omega. \tag{4}$$

From equations (4) and (2), we have:

$$\frac{d\Delta}{dt}=-\int_\Omega(\mathbf{T}-\mathbf{T}^*)\cdot(\dot{\mathbf{E}}-\dot{\mathbf{E}}^*)\,d\Omega=0$$

thus,

$$\frac{d\Delta}{dt}=-\int_\Omega\left[(\mathbf{T}-\mathbf{T}^*)\cdot\dot{\mathbf{E}}^*+(\mathbf{T}^*-\mathbf{T})\cdot\dot{\mathbf{E}}^*\right]d\Omega=\int_\Omega\left[(\mathbf{T}^*-\mathbf{T})\cdot\dot{\mathbf{E}}+(\mathbf{T}-\mathbf{T}^*)\cdot\dot{\mathbf{E}}^*\right]d\Omega. \tag{5}$$

Stress field $\mathbf{T}$ and strain rate $\dot{\mathbf{E}}$ are associated through the plastic flow rule, and $\mathbf{T}^*$ satisfies the plasticity condition. Drucker's stability postulate holds that

$$(\mathbf{T}-\mathbf{T}^*)\cdot\dot{\mathbf{E}}\geq 0. \tag{6}$$

In the regions where $\dot{\mathbf{E}}^*(\mathbf{x},t)\neq\mathbf{0}$, the generalized stress field $\mathbf{T}^*_{\dot{\mathbf{E}}^*}$ associated with $\dot{\mathbf{E}}^*$ through the flow rule satisfies the plasticity condition

$$(\mathbf{T}^*_{\dot{\mathbf{E}}^*}-\mathbf{T})\cdot\dot{\mathbf{E}}^*\geq 0. \tag{7}$$

By employing Drucker's stability postulate, relation (5) may be rewritten in the form:

$$\frac{d\Delta}{dt} = \int_{\Omega}\left[(\mathbf{T}^{*}-\mathbf{T})\cdot\dot{\mathbf{E}}+(\mathbf{T}-\mathbf{T}^{*})\cdot\dot{\mathbf{E}}^{*}\right]d\Omega = . \tag{8.a}$$

$$= \int_{\Omega}(\mathbf{T}^{*}-\mathbf{T})\cdot\dot{\mathbf{E}}\,d\Omega+\int_{\Omega}(\mathbf{T}-\mathbf{T}^{*}_{\dot{\mathbf{E}}^{*}})\cdot\dot{\mathbf{E}}^{*}d\Omega+\int_{\Omega}(\mathbf{T}^{*}_{\dot{\mathbf{E}}^{*}}-\mathbf{T}^{*})\cdot\dot{\mathbf{E}}^{*}d\Omega \le . \tag{8.b}$$

$$\le \int_{\Omega}(\mathbf{T}^{*}_{\dot{\mathbf{E}}^{*}}-\mathbf{T}^{*})\cdot\dot{\mathbf{E}}^{*}d\Omega = \Gamma(t) \;\Rightarrow\; \Gamma(t)\ge 0 . \tag{8.c}$$

The first and second integrals in expression 8(b) are less than or equal to zero. Hence, the last term in (8.c) is non-negative, such that:

$$\frac{d\Delta}{dt} \le \Gamma(t) . \tag{9}$$

The integration of the previous relation from 0 to time t provides the approximation measure $\Delta(t)$:

$$\Delta(t) \le \Delta^{+}(t) = \int_{0}^{t}\Gamma(t)\,dt . \tag{10}$$

The maximum value Δ_m of the non-decreasing time function $\Delta^{+}(t)$ is $\Delta^{+}(T)$, with T being the duration of the external forcing function. The function $L(t)$ satisfies the initial conditions:

$$L(0) = 0 . \tag{11}$$

Given the condition $\dot{\mathbf{u}}^{*}(\mathbf{x},0) = 0$, if $\boldsymbol{\Psi}(\mathbf{x})$ is a vector that involves the strain generalized components associated with modal vector $\boldsymbol{\Phi}(\mathbf{x})$, then acceleration $\ddot{\mathbf{u}}^{*}(\mathbf{x},t)$ and strain rate $\dot{\mathbf{E}}^{*}$ are given by:

$$\ddot{\mathbf{u}}^{*}(\mathbf{x},t) = \boldsymbol{\Phi}(\mathbf{x})\,\dot{L}(t) \;;\; \dot{\mathbf{E}}^{*}(\mathbf{x},t) = \boldsymbol{\Psi}(\mathbf{x})\,L(t) . \tag{12}$$

The principle of virtual velocity provides:

$$\int_{S_L}\mathbf{p}(\mathbf{x},t)\cdot\dot{\mathbf{u}}^{*}dS+\int_{\Omega}[\mathbf{F}(\mathbf{x},t)-\mu\ddot{\mathbf{u}}^{*}]\cdot\dot{\mathbf{u}}^{*}d\Omega = \int_{\Omega}\mathbf{T}^{*}(\mathbf{x},t)\cdot\dot{\mathbf{E}}^{*}(\mathbf{x},t)\,d\Omega \tag{13}$$

which can be manipulated with reference to relations (1) and (12):

$$\int_{S_L}\mathbf{p}^{T}(\mathbf{x},t)\,\boldsymbol{\Phi}(\mathbf{x})dS+\int_{\Omega}\mathbf{F}^{T}(\mathbf{x},t)\,\boldsymbol{\Phi}(\mathbf{x})d\Omega =$$

$$= \dot{L}(t)\int_{\Omega}\mu(\mathbf{x})\boldsymbol{\Phi}^{T}(\mathbf{x})\,\boldsymbol{\Phi}(\mathbf{x})d\Omega+\int_{\Omega}\mathbf{T}^{*}(\mathbf{x},t)\,\boldsymbol{\Psi}(\mathbf{x})d\Omega .$$

Hence, function $L(t)$ can be evaluated by the integration of the function:

$$\dot{L}(t) = \frac{\int_{S_L}\mathbf{p}^{T}(\mathbf{x},t)\,\boldsymbol{\Phi}(\mathbf{x})dS+\int_{\Omega}\mathbf{F}^{T}(\mathbf{x},t)\,\boldsymbol{\Phi}(\mathbf{x})d\Omega-\int_{\Omega}\mathbf{T}^{*}(\mathbf{x},t)\,\boldsymbol{\Psi}(\mathbf{x})d\Omega}{\int_{\Omega}\mu(\mathbf{x})\boldsymbol{\Phi}^{T}(\mathbf{x})\,\boldsymbol{\Phi}(\mathbf{x})d\Omega} . \tag{14}$$

This method can be applied to pulse loads with the following conditions: the tractions applied to $\partial\Omega_t$ are null and the initial velocities are prescribed over the entire structure at time $t=0$. Therefore, no external forces act on the structure.

3 SDOF MODEL FOR A WIND TURBINE

The SDOF model provides a good schematization of the dynamic behavior of various structures. Wind turbine towers can be easily represented by a cantilever beam supported at the base. As shown in [1, 2], a rigid-plastic cantilever beam can sufficiently approximate the nonlinear dynamic problem arising from sinusoidal excitation at the tower base. The problem is monodimensional, so that the parameters and relations developed in the previous section are scalar. The reference frame of the model has its origin in the support section and the z axis coincident with the wind tower one (Fig. 3a). The local yield kinematism corresponds to the activation of a shear hinge, in which total shear force $T(z,t)$ attains its bound value. The constitutive model is shown in Figs. 3b and 3c.

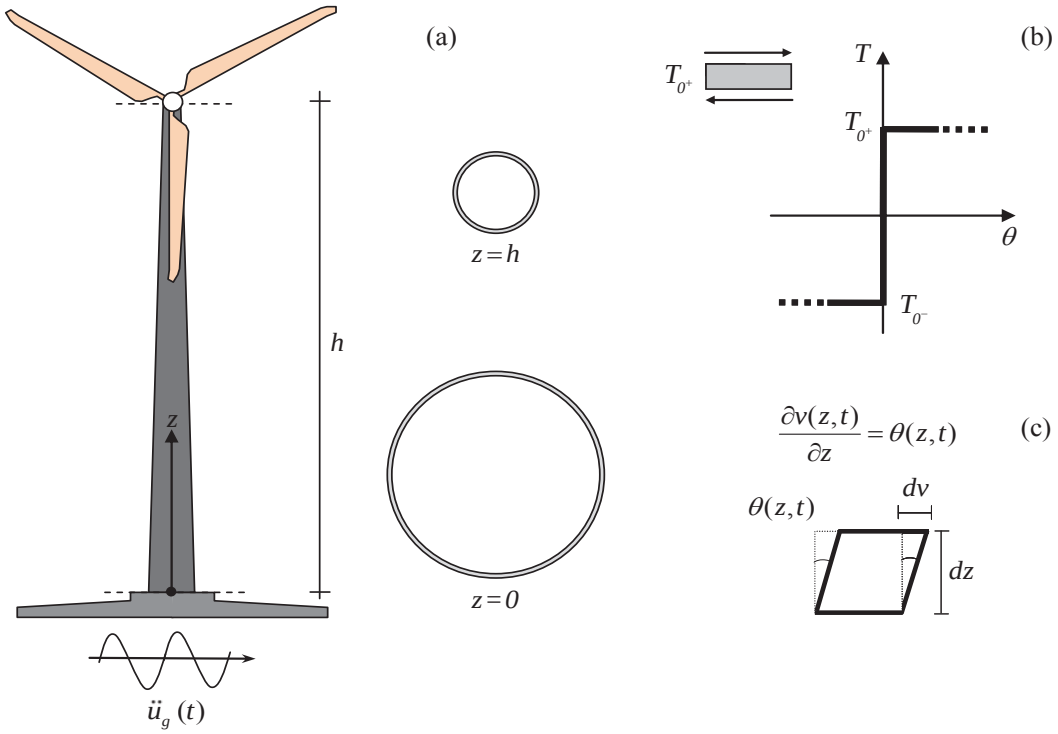

Fig. 3 Wind turbine tower geometry (a), rigid-plastic constitutive law (b), and shear strain representation (c)

where

$\mu(z)$:	linear mass density of the tower,
$u_g(t)$:	horizontal motion of the supported section,
$T(z,t)$:	shear stress whose bounds are $T_{0^+}(z)$ and $T_{0^-}(z)$
$\theta(z,t)$:	shear strain,
h:	total length of the tower.

The shear plastic constitutive relations are expressed as follows:

$$\begin{cases} \left[T(z,t) - T_{0^+}(z)\right]\left[T(z,t) + T_{0^-}(z)\right]\dot{\theta}(z,t) = 0 \\ -T_{0^-}(z) \le T(z,t) \le T_{0^+}(z) \end{cases}. \tag{15}$$

that is,

$$
\begin{aligned}
-T_{0^-} < T < T_{0^+} \quad & \dot{\theta} = 0 \quad \Rightarrow \quad \left[T - T_{0^+}\right]\dot{\theta} = 0 \ \text{ and } \ \left[T + T_{0^-}\right]\dot{\theta} = 0 \\
T = T_{0^+} \quad & \dot{\theta} \neq 0 \quad \Rightarrow \quad \left[T - T_{0^+}\right]\dot{\theta} = 0 \\
T = -T_{0^-} \quad & \dot{\theta} \neq 0 \quad \Rightarrow \quad \left[T + T_{0}\right]\dot{\theta} = 0
\end{aligned}
$$

in which plastic strain rate $\dot{\theta}$ depends on shear stress only. The dynamic equilibrium equation in the cross section at the z level involves inertial forces only:

$$\frac{\partial T(z,t)}{\partial z} = \mu(z)\,\ddot{u}(z,t) = \mu(z)[\ddot{u}_g(t) + \ddot{v}(z,t)]\,. \tag{16}$$

where

$$u(z,t) = u_g(t) + v(z,t)\,. \tag{17}$$

is the absolute displacement, and:

$$v(z,t) = \int_0^z \theta(x,t)dx = \int_0^z \int_0^t \dot{\theta}(x,\tau)d\tau\,dx\,. \tag{18}$$

is the relative one. A plastic shear hinge is formed when the limit value of shear stress is reached. One or more shear hinges can be activated in sections $z_1, z_2, ..., z_n$ during the plastic phase, and their abscissa varies according to time. Kinematic compatibility states that the plastic strain rate is non-null in active hinges only:

$$\dot{\theta}(z,t) = \frac{\partial\,\dot{v}(z,t)}{\partial z} = \dot{v}'(z,t)\,. \tag{19}$$

The relative displacement $v(z,t)$ in (18) can be deduced by integrating equation (19) with respect to z and by introducing the Heaviside function $H(z)$ ($H(z)=0$ for $z<0$, $H(z)=1 \ \ for \ \ z\geq 0$) as follows:

$$v(z,t) = \int_0^z v'(x,t)\,dx = \int_0^z \theta(x,t)\,dx = \int_0^h \theta\left(x,t\right)H(z-x)\,dx\,. \tag{20}$$

Double time derivation provides the relative acceleration $\ddot{v}(z,t)$:

$$\ddot{v}(z,t) = \int_0^z \ddot{\theta}(x,t)\,dx = \int_0^h \ddot{\theta}\left(x,t\right)H(z-x)\,dx\,. \tag{21}$$

When only one shear hinge is active, the time-dependent position is denoted by $z_0(t)$. Thus, the relative displacement velocity and the plastic strain rate have the form:

$$\dot{v}(z,t) = \dot{v}_1(t)\,H[z - z_0(t)],$$
$$\dot{\theta}(z,t) = \dot{v}'(z,t) = \dot{v}_1(t)\ \delta[z - z_0(t)],$$

being $\delta[z - z_0(t)]$ the Dirac function relative to the plastic hinge position. The shear stress becomes:

$$T(z,t) = \ddot{u}_g(t)\int_h^z \mu(x)\,dx + \int_h^z \mu(x)\,\ddot{v}(x,t)dx = \ddot{u}_g(t)\int_h^z \mu(x)\,dx + \ddot{v}_1(t)\int_h^z \mu(x)\,H[x-z_0(t)]dx\,.$$

The mass functions are:

$$m(z) = \int_h^z \mu(x)\,dx \quad ; \quad m_H[z,z_0(t)] = \int_h^z \mu(x)\,H[x-z_0(t)]\,dx\,. \tag{22}$$

The time derivative of (22.b) produces:

$$\frac{\partial m_H[z,z_0(t)]}{\partial t} = -\mu(z)\,\dot{z}_0(t)H[z-z_0(t)] = -\dot{z}_0(t)\frac{\partial m_H[z,z_0(t)]}{\partial z}.$$

Shear stress and its derivatives as functions of masses are:

$$T(z,t) = \ddot{u}_g(t)\,m(z) + \ddot{v}_1(t)\,m_H[z,z_0(t)]$$

$$\frac{\partial T(z,t)}{\partial z} = \mu(z)\,\ddot{u}_g(t) + \ddot{v}_1(t)\frac{\partial m_H[z,z_0(t)]}{\partial z}$$

$$\frac{\partial T(z,t)}{\partial t} = m(z)\,\dddot{u}_g(t) + \dddot{v}_1(t)\,m_H[z,z_0(t)] - \dot{z}_0(t)\,\ddot{v}_1(t)\frac{\partial m_H[z,z_0(t)]}{\partial z}.$$

Approximation by the Taylor series of shear stress proceeds as:

$$\begin{aligned} T(z_0+dz_0,t+dt) = T(z_0,t) &+ \left\{\mu(z_0)\,\ddot{u}_g(t) + \ddot{v}_1(t)\frac{\partial m_H[z,z_0(t)]}{\partial z}\bigg|_{z=z_0}\right\}dz_o + \\ &+ \left\{m(z_0)\,\dddot{u}_g(t) + \dddot{v}_1(t)\,m_H[z_0,z_0(t)] - \ddot{v}_1(t)\,\dot{z}_0(t)\frac{\partial m_H[z,z_0(t)]}{\partial z}\bigg|_{z=z_0}\right\}dt\,. \end{aligned} \tag{23}$$

We consider that shear is equal to the yield value $T(z_0,t) = T_0(z)$ in the plastic hinge. If at the instant $t+dt$ the position of the plastic shear hinge is z_0+dz_0, then $T(z_0+dz_0,t+dt) = T_0(z_0+dz_0)$ and $T(z_0+dz_0,t+dt) = T_0(z_0)+T_0'(z_0)\,dz_0$. Equation (23) in this case can be conveniently rewritten as:

$$\begin{aligned} &\left\{\mu(z_0)\,\ddot{u}_g(t) + \ddot{v}_1(t)\frac{\partial m_H[z,z_0(t)]}{\partial z}\bigg|_{z=z_0}\right\}dz_0 + \\ &+\left\{m(z_0)\,\dddot{u}_g(t) + \dddot{v}_1(t)\,m_H[z_0,z_0(t)] - \ddot{v}_1(t)\,\dot{z}_0(t)\frac{\partial m_H[z,z_0(t)]}{\partial z}\bigg|_{z=z_0}\right\}dt = T_0'(z_0)\,dz_0 \end{aligned} \tag{24}$$

and with $\dot{z}_0 = \dfrac{dz_0}{dt}$, we have:

$$[\mu(z_0)\,\ddot{u}_g(t) - T_0'(z_0)]\;\dot{z}_0(t) + m(z_0)\,\dddot{u}_g(t) + \dddot{v}_1(t)\,m_H[z_0,z_0(t)] = 0\,.$$

According to relations (22) the time evolution of the plastic shear hinge is governed by the relation:

$$\dot{z}_0(t) = -\frac{m(z_0)\ddot{u}_g(t) + \ddot{v}_1(t)\,H(0)\,m[z_0(t)]}{\mu(z_0)\ddot{u}_g(t) - T_0'(z_0)}. \tag{25}$$

When the plastic hinge moves, residual plastic deformations $\theta_r(z_0,t)$ can be detected in the previous position:

$$\theta_r(z_0,t) = \frac{\dot{v}_1(t)}{\dot{z}_0(t)}.$$

Their value do not vary until the plastic hinge forms again at the same position. Hence, the acceleration $\ddot{v}(z,t)$ can be determined as a function of shear:

$$T'(z,t) = T'_{0^+}(z) \Rightarrow \ddot{v}(z,t) = \frac{T'_{0^+}(\bar{z})}{\mu(z)} - \ddot{u}_g(t)$$
$$T'(z,t) = T'_{0^-}(z) \Rightarrow \ddot{v}(z,t) = \frac{T'_{0^-}(\bar{z})}{\mu(z)} - \ddot{u}_g(t).$$

At the abscissa z, the inertial force

$$q(z) = -\mu(z)[\ddot{u}_g(t) + \int_0^z \ddot{\theta}(x,t)\,dx]$$

allows the total shear to be written as:

$$T(z,t) = -\int_h^z q(x)\,dx = \ddot{u}_g(t)\,m(z) + \int_h^z \mu(x)\int_0^x \ddot{\theta}(y,t)\,dy\,dx \tag{26}$$

After some algebraic manipulations [2], the relations (26) can be rewritten in the form:

$$\begin{aligned} &[\ddot{u}_g(t) + \int_0^{z_1} \ddot{\theta}(y,t)\,dy - \frac{T_{0^+}(z_1)}{m(z_1)}][\ddot{u}_g(t) + \int_0^{z_1} \ddot{\theta}(y,t)\,dy - \frac{T_{0^-}(z_1)}{m(z_1)}] = 0 \\ &\frac{T_{0^-}(z)}{m(z)} < \ddot{u}_g(t) + \int_0^{z_1} \ddot{\theta}(y,t)\,dy < \frac{T_{0^+}(z)}{m(z)} \quad , \quad \forall z > z_1 \end{aligned} \tag{27}$$

according to relation (27), the plastic deformations stop at the abscissa z_p and cannot propagate upward. The abscissa z_p can be obtained by solving a minimum problem that is independent of time *t* and ground acceleration $\ddot{u}_g(t)$:

$$\left.\begin{aligned} z_{p1} \rightarrow \frac{T_{0^+}(z_{p1})}{m(z_{p1})} &= \min_{z\in(0,h)}\left[\frac{T_{0^+}(z)}{m(z)}\right] \\ z_{p2} \rightarrow \frac{T_{0^-}(z_{p2})}{m(z_{p2})} &= \min_{z\in(0,h)}\left[\frac{T_{0^-}(z)}{m(z)}\right] \end{aligned}\right\} \quad \Rightarrow \quad z_p = max(z_{p1}, z_{p2}) \tag{28}$$

When relation (28) is satisfied for $z_p = 0$, the beam response involves only one DOF.

4 NUMERICAL OUTCOMES

In general, pulses that occur during earthquakes have qualitative and quantitative characteristics that can adequately be approximated by specific functional expressions obtained by means of wavelet analysis [20]. Several strong ground motions contain in fact an acceleration pulse responsible for most of the inelastic deformations of structures. In the paper by Makris that distinguishable acceleration pulse has been determined with reference to the main world strong earthquakes in the last 50 years. The near fault ground motions are in fact often characterized by pulse sequences with simple shapes that can be recognized in the accelerograms by means of spectral analysis. In general, if accurate harmonic pulses are used to represent the ground motion the development of elastic and inelastic response spectra are facilitated [22]. The sensitive analysis of elastic and inelastic responses due to different simple pulse shapes has shown that local site effects on structures can be modelled with an appropriate choice of the pulse [23]. These considerations are the basis of the analysis performed on the turbine tower of Fig. 3, since the harmonic pulse can be a suitable representation of near-fault ground motion [21].

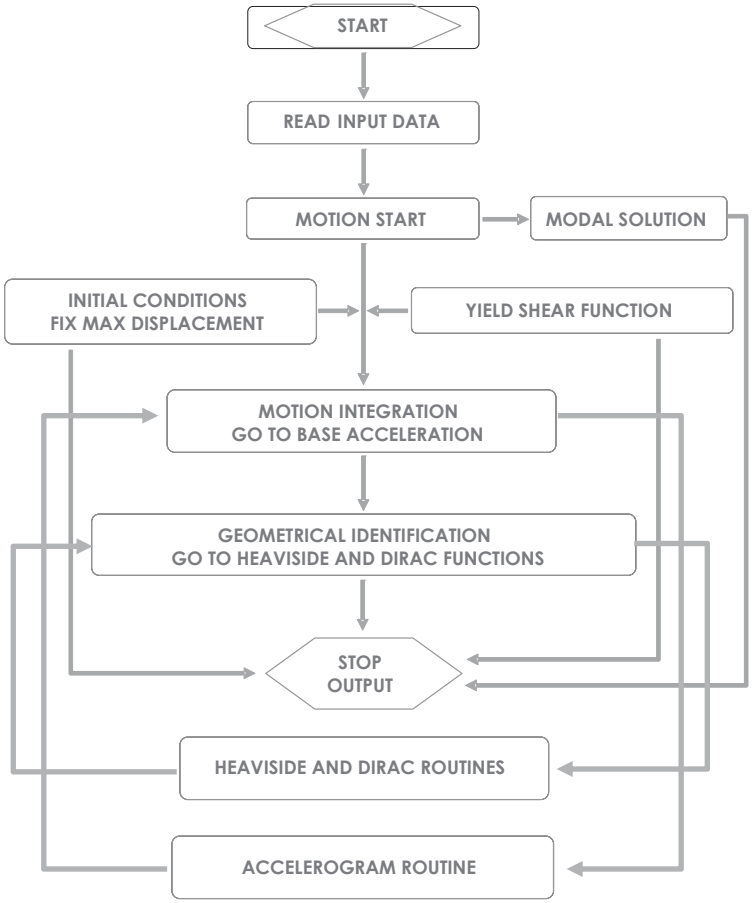

Fig. 4. Flow chart of the numerical procedure

From the numerical analyses (Fig. 4), successive extensions and contractions of the plastic front can be evaluated, according (25) and the forcing time history. In the following figures numerical results are reported: Fig. 5 contains the mechanical characteristics during the reduction of the plastic front, while Fig. 6 reports the situation at the final instant of the plastic process.

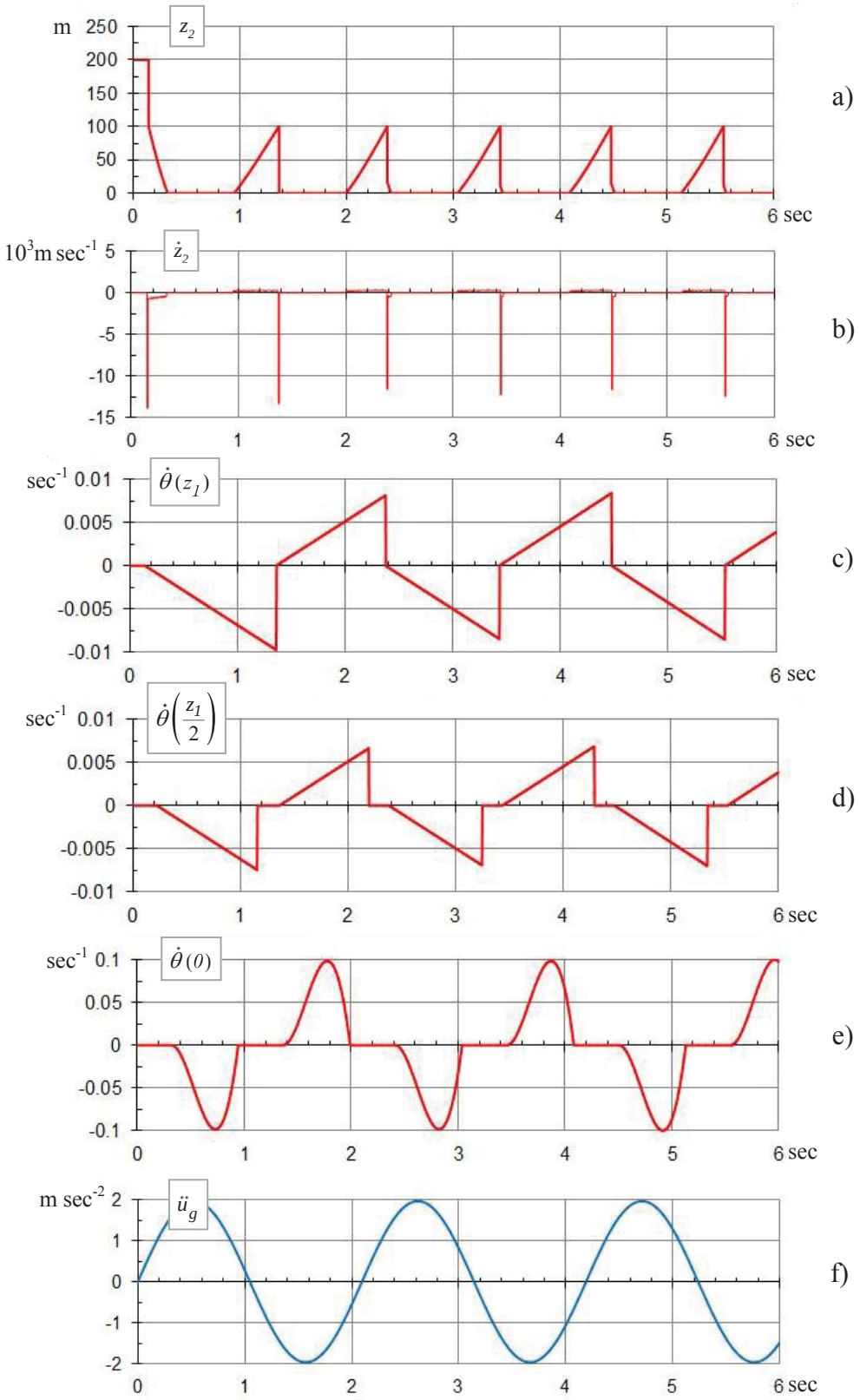

Fig. 5. Time histories of the functions: lower bound (a) and velocity of the plastic front (b); plastic shear rate at the upper bound (c), in the middle (d) and at the base support (e); base accelerogram (f);

The input data are derived with reference to a wind turbine tower with variable annular cross section and this choice implies a quadratic variation of the yield shear and the adopted pulse makes reference to near fault motion of Irpinia earthquake in 1980:

$$
\begin{cases}
h = 200\,m & (\textit{total height of the tower}) \\
\mu(z) = 5\times10^{4}\ kgm^{-1} & (\textit{mass linear density}) \\
\ddot{u}_g(t) = a_0 \sin\omega t & (\textit{base motion}) \\
\text{with} \quad a_0 = 0.2\,g\ ,\ \omega = 3\,\text{sec}^{-1} & \\
D = 6\ sec & (\textit{duration of the time history}) \\
T_0(z) = d\,z^2 + e\,z + f & (\textit{yield shear}) \\
\text{with} \quad d = 2\times10^{3}\ Nm^{-2} & e = -8\times10^{5}\ Nm^{-1},\quad f = 10^{8}\ N
\end{cases}
$$

The extension of the plastic boundary moves starting from the abscissa $z_1 = h/2$ and evolves until the plastic excursion stops, corresponding to the attainment of the plastic threshold. The extension of the elastic range is measured by the distance z_2 of the lower bound of the plastic zone from the base support. The motion proceeds through successive spreading and contractions of the plastic front and related elastic returns [11, 24]. This behaviour is represented in Fig. 5a, where the obscillation of the plastic hinge lower bound is represented. The maximum velocity lower bound corresponds to the attainment of the maximum spreading of the plastic front, as shown in Fig. 6b. The time histories corresponding to the evolution of the shear strain rate in three significant positions are picted respectively in Figs. 5c, 5d and 5e. A detailed analysis of the evolution of shear stress and deformed shape in a single pulse are reported in Fig. 6 together with a schematic picture of the cantilever beam with the actual plastic hinge extension.

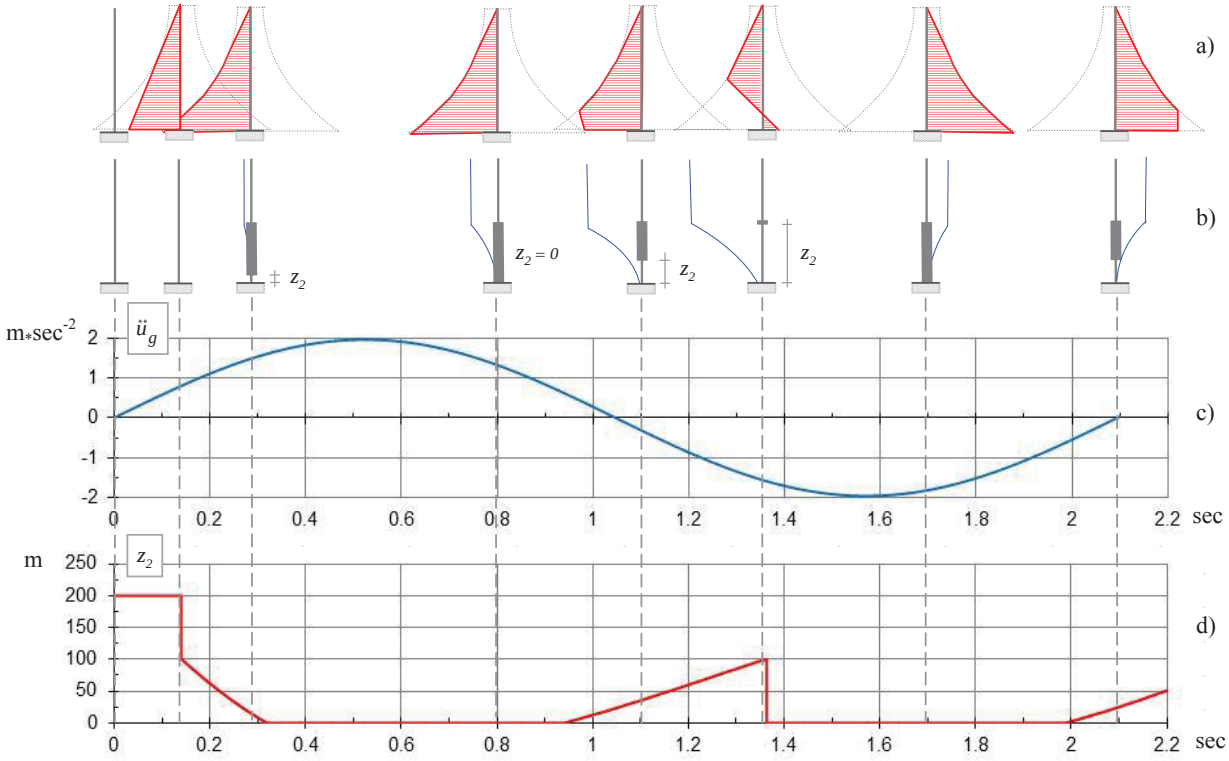

Fig. 6. Variation of the shear stress (a) and deformed shape (b) versus the base accelerogram (c) and the lower bound of the plastic hinge (d)

The inertial effects that cause the delay of the inversion of the displacements with regard to shear diagram are also shown. It is worth noting that both the diagrams have a sudden change of sign due to the inversion of the pulse sign.

5 CONCLUSIONS

The nonlinear dynamic response of rigid-plastic wind tower structures subjected to a base dynamic acceleration has been examined. The collapse mechanism obtained is due to the formation of shear hinges. A step-by-step integration procedure is employed to evaluate the dynamic response of a windmill in the time domain. The numerical analysis gives the plastic hinge patterns and the estimation of the maximum and minimum displacement under different base motions. The exposed method supplies a good interpretation of the tower post-elastic behavior and a realistic representation of fundamental response modes. Moreover, the procedure exhibits also a low computational effort and involves a low number of mechanical parameters. The proposed nonlinear dynamic procedure, with the localization of damage i.e. the extension of the plastic front, allows a designer to recognize the segment of tower that requires special attention. The same procedure can in fact applied to high rise buildings for which a cantilever beam model could represent with suitable accuracy the behavior.

REFERENCES

[1] A. Gesualdo, A. Iannuzzo, F. Penta., M. Monaco, Nonlinear dynamics of a wind turbine tower, Frontiers of Mechanical Engineering, 14(3), 342–350, 2019.

[2] C. Cennamo, A. Gesualdo, M. Monaco, Shear plastic constitutive behaviour for near-fault ground motion, Journal of Engineering Mechanics-ASCE, 143(9), 04017086, 2017.

[3] M. Monaco, A. Tafuro, B. Calderoni, M. Guadagnuolo, Shear plastic oscillations of a wind turbine tower. In COMPDYN 2019 7 th ECCOMAS Thematic Conference on Computational Methods in Structural Dynamics Earthquake Engineering, (Eds: M. Papadrakakis, M. Fragiadakis). 1, 409-421, ISBN 978-618-82844-6-3, 2019.

[4] J.B. Martin, The determination of mode shapes for dynamically loaded rigid-plastic structures, Meccanica, 16(1), 42-45, 1981.

[5] R.B. Schubak, D.L. Anderson, M.D. Olson, Simplified dynamic analysis of rigid-plastic beams, International Journal of Impact Engineering, 8(1), 27–42, 1989.

[6] A. Gesualdo, M. Monaco, Constitutive behaviour of quasi-brittle materials with anisotropic friction, Latin American Journal of Solids and Structures, 12(4): 695–710, 2015.

[7] F. Penta, M. Monaco, G.P. Pucillo, A. Gesualdo, Periodic beam-like structures homogenization by transfer matrix eigen-analysis: a direct approach, Mechanics Research Communications, 85, 81-88, 2017.

[8] A. Gesualdo, F. Penta, A model for the mechanical behaviour of the railway track in the lateral plane, International Journal of Mechanical Sciences, 146-147(October), 303-318, 2018.

[9] M. Fraldi, L. Nunziante, A. Gesualdo, F. Guarracino, On the bounding of multipliers for combined loading, Proceedings of the Royal Society A, 466, 493-514, 2010.

[10] M. Fraldi, A. Gesualdo, F. Guarracino, Influence of actual plastic hinge placement on the behavior of ductile frames. Journal of Zhejiang University-SCIENCE A, 15(7), 482-495, 2014.

[11] C. Málaga-Chuquitaype, A.Y. Elghazouli, R. Bento, Rigid-plastic models for the seismic design and assessment of steel framed structures, Earthquake Engineering and Structural Dynamics, 38(14), 1609–1630, 2009.

[12] A. Rutenberg, The seismic shear of ductile cantilever wall systems in multistorey structures, Earthquake Engineering and Structural Dynamics, 33(7), 881–896, 2004.

[13] P.S. Symonds, W.T. Fleming Jr., Parkes revisited: On rigid-plastic and elastic-plastic dynamic structural analysis, International Journal of Impact Engineering, 2(1), 1–36, 1984.

[14] M.T. Liang, B.J. Lee, S.S. Yang, On the rigid ideally plastic deformation of cantilever beam subjected to tip impact, Journal of Marine Science and Technology, 5(1), 39–46, 1997.

[15] Q.M. Li, Continuity conditions at bending and shearing interfaces of rigid, perfectly plastic structural elements. International Journal of Solids and Structures, 37(27), 3651–3665, 2000.

[16] S. Krishnan, M. Muto, Mechanism of Collapse of Tall Steel Moment-Frame Buildings under Earthquake Excitation, Journal of Structural Engineering, 138(11), 1361-1387, 2012.

[17] A. Paglietti, M.C. Porcu, Rigid-plastic approximation to predict plastic motion under strong earthquakes, Earthquake Engineering and Structural Dynamics, 30(1), 115–126, 2001.

[18] Y.T. Ren, X.M. Qiu, T.X. Yu, The sensitivity analysis of a geometrically unstable structure under various pulse loading, International Journal of Impact Engineering, 70, 62–72, 2014.

[19] A. Gesualdo, A. Iannuzzo, V. Minutolo, M. Monaco, Rocking of freestanding objects: theoretical and experimental comparisons, Journal of Theoretical and Applied Mechanics, 56(4), 977-991, 2018.

[20] M.S. Vassiliou, N. Makris, Estimating time scales and length scales in pulselike earthquake acceleration records with wavelet analysis, Bulletin of the Seismological Society of America, 101(2), 596–618, 2011.

[21] G.P. Mavroeidis, A.S. Papageorgiou, A mathematical representation of near-fault ground motions, Bulletin of the Seismological Society of America, 93(3), 1099–1131, 2003.

[22] S. Li, C. Zhai, L.L. Xie, Analysis on response of dynamic systems to pulse sequences excitation, International Journal of Advanced Structural Engineering, 1(1), 3–15, 2009.

[23] G. Mylonakis, E. Voyagaki, Yielding oscillator subjected to simple pulse waveforms: Numerical analysis and closed-form solutions, Earthquake Engineering and Structural Dynamics, 35(15), 1949–1974, 2006.

[24] A. Gesualdo, M. Guadagnuolo, F. Penta, Dynamic shear behaviour of truss towers for wind turbines. In Journal of Physics: Conference Series, 1141(1), 012078. IOP Publishing, 2018.

[25] https://www.dw.com/image/37017119_303.jpg (© by picture-alliance/dpa/P. Endig).

EURODYN 2020
XI International Conference on Structural Dynamics
M. Papadrakakis, M. Fragiadakis, C. Papadimitriou (eds.)
Athens, Greece, 23–26 November 2020

ON THE AXIAL FORCE IDENTIFICATION IN EULER-BERNOULLI BEAMS WITH UNKNOWN BOUNDARY CONDITIONS

Margaux Geuzaine[1] [2], Francesco Foti[1] [3], and Vincent Denoël[1]

[1]Structural & Stochastic Dynamics, University of Liège, Belgium
Allée de la Découverte 1, 4000 Liège, Belgium
e-mail: mgeuzaine@uliege.be, francesco.foti@polimi.it, v.denoel@uliege.be

[2] F. R. S.-FNRS, National Fund for Scientific Research, Belgium

[3] Department of Civil and Environmental Engineering, Politecnico di Milano, Italy

Keywords: Axial-force identification, Health-monitoring, Safety assessment, Rotational stiffness, Differential Evolution.

Abstract. *Identification of the tensile force in slender axially-loaded structural elements, such as stay cables, metallic bars and tie-rods, is of paramount importance for health monitoring and safety assessment purposes. Dynamic testing techniques provide the ground for quick and cheap identification strategies, based on the knowledge of: (a) a set of identified natural frequencies, and (b) a structural model that relates natural frequencies to the axial-force value. Within this framework, reliability of the identified axial force values depends, among other factors, on the predictive capabilities of the underlying structural model. Errors may arise, in particular, from the modeling of boundary conditions. The present paper analytically investigates the effect of boundary conditions on the modal properties of axially loaded Euler-Bernoulli beam elements. Starting from theoretical results obtained on this archetypal structural model, a numerical procedure for the identification of the axial force in beam elements with unknown bending stiffness and boundary conditions is then presented. Parametric analyses are carried out to quantitatively assess the accuracy of the proposed identification algorithm in the case of frequencies contaminated by measurement errors.*

1 INTRODUCTION

Dynamic testing techniques are widely used to get estimates of the modal properties of slender axially-loaded one-dimensional structural elements, such as stay cables, diagonal braces, truss elements and tie-rods of vaulted historical masonry structures. Knowledge of a set of measured natural frequencies of the beam, along with a suitable structural model updating strategy, then, can be used to identify the value of the axial force acting on the element, which is of paramount importance for structural health monitoring and safety assessment purposes. Within this framework, reliability of the identified axial force values depends, among the other factors, on the predictive capabilities of the underlying structural model.

Frequency-based axial force identification procedures often rely on the assumption of ideal boundary conditions, in the form of either perfectly hinged or perfectly clamped end sections (see e.g. [1, 7]). A more realistic structural scheme could be defined, however, by considering equivalent translational and rotational springs at the beam end sections to model the flexibility of the restraint devices and of the support structures (e.g. deck and tower for cables in stayed bridges). Proper definition of equivalent springs strongly depends on the particular technology adopted to realize the restraints and is inherently related to several different sources of uncertainties, such as those related to geometric imperfections and aging of the support devices.

The present paper presents an analytical investigation of the effects of the boundary conditions on the modal properties of axially-loaded Euler-Bernoulli beam elements whose end sections are restrained by rotational springs. Starting from theoretical results obtained on this archetypal structural model, a numerical procedure for the identification of the axial force in beam elements with unknown bending stiffness and boundary conditions is then presented. Parametric analyses are carried out to quantitatively assess the accuracy of the proposed identification algorithm in the case of frequencies contaminated by measurement errors.

2 FORMULATION OF THE PROBLEM

2.1 Free-vibrations of the Euler-Bernoulli beam model

Let us consider a straight axially-loaded one-dimensional structural element, with constant bending stiffness (EI) and mass per unit of length (m). Transverse displacements of the centerline are described through the function $v = v(x,t)$, where $x \in [0,l]$ is a coordinate spanning the free length (l) of the element and t is the time. By neglecting sag-extensibility and shear deformability effects, undamped planar transverse vibrations are governed by the partial differential equation (see e.g. [8]):

$$EI\partial_x^4 v - T\partial_x^2 v + m\partial_t^2 v = 0 \tag{1}$$

where $T > 0$ is the axial force (see Fig. 1).

By introducing the characteristic frequency ω_0 and the non-dimensional bending stiffness ε:

$$\omega_0 = \sqrt{\frac{T}{ml^2}},\ \varepsilon = \sqrt{\frac{EI}{Tl^2}}, \tag{2}$$

the Eq. (1) can be re-stated in the following non-dimensional form:

$$\varepsilon^2 \partial_\xi^4 \bar{v} - \partial_\xi^2 \bar{v} + \partial_\tau^2 \bar{v} = 0 \tag{3}$$

where $\xi = \frac{x}{l} \in [0,1]$, $\tau = \omega_0 t$ and $\bar{v}(\xi,\tau) = \frac{v(x(\xi),t(\tau))}{l}$.

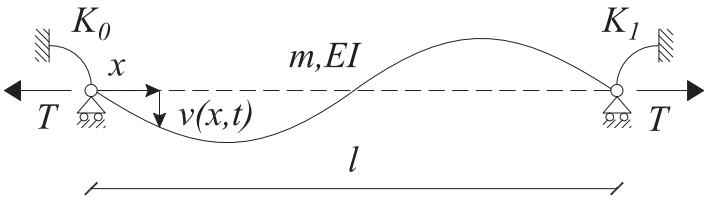

Figure 1: Schematic representation of a straight one-dimensional structural element subject to a tensile load T.

Values of ε typical of slender structural elements, such as stay cables and masts, are lower than 2% (see e.g. [1, 7, 15]). Thicker structural elements such as diagonal braces, truss elements, short cables and tie-rods of vaulted historical masonry structures, instead, can be characterized by values of non-dimensional bending stiffness in the broader range: $0.02 \lesssim \varepsilon \lesssim 1$ (see e.g. [11, 12, 13, 17]). It's worth noting that the governing equation (3) is singularly perturbed for small values of ε, typical of slender elements, hinting the existence of boundary layers in the mode shapes and possible ill-conditioning of numerical solvers (see e.g. [10, 5]).

General solutions of Eq. (3) can be expressed as $\bar{v}(\xi,\tau) = \phi(\xi)\sin(\bar{\omega}\tau - \theta)$, where $\bar{\omega}$ is a non-dimensional vibration frequency, θ is a phase angle depending on initial conditions and $\phi(\xi)$ is a mode shape function. The vibration frequencies $\bar{\omega}$ and shape functions $\phi(\xi)$ are the solutions of a fourth order boundary value problem defined by the ordinary differential equation:

$$\varepsilon^2 \phi^{IV} - \phi^{II} - \omega^2 \phi = 0,\ \xi \in [0,1] \tag{4}$$

along with suitable conditions modeling the cable restraints.

Ideal boundary conditions are often introduced, in the form of either perfectly hinged or perfectly clamped cable end sections. In many practical circumstances, however, this modeling strategy can lead to an oversimplified representation of the structural dynamics, naturally claiming for the adoption of elastically supported beam models (see e.g. [14, 16, 2]). In the present work, two rotational springs with stiffness K_i $(i = 1, 2)$ are assumed to be attached at the end sections of the element (see Fig. 1). The degree of fixity of the rotational restraints is then defined by introducing the non-dimensional parameters:

$$\rho_i = \frac{K_i}{K_i + \varepsilon T l},\ i = 0, 1 \tag{5}$$

It is worth noting that the parameter ρ_i can take values in the unit interval [0,1], being strictly equal to zero for $K_i = 0$, i.e. for a perfectly hinged end section. The upper bound

limit case $\rho_i = 1$, instead, is asymptotically approached as $K_i \to \infty$, i.e. for a perfectly clamped end section.

By accounting for the definitions in Eq. (5), the boundary conditions associated to Eq. (4) read:

$$\begin{cases} \phi(0) = 0 \\ \phi(1) = 0 \\ (1-\rho_0)\,\varepsilon^2\phi''(0) - \rho_0\varepsilon\phi'(0) = 0 \\ (1-\rho_1)\,\varepsilon^2\phi''(1) + \rho_1\varepsilon\phi'(1) = 0 \end{cases} \tag{6}$$

The general solution of Eq. (4) can be expressed as a combination of trigonometric and exponential functions:

$$\phi\left(\xi; z_1, z_2\right) = a_1 \sin\left(z_1\xi\right) + a_2 \cos\left(z_1\xi\right) + a_3 \exp\left(-z_2\xi\right) + a_4 \exp\left(-z_2\left(1-\xi\right)\right) \tag{7}$$

where a_i $(i = 1, ..., 4)$ are real integration constants and the arguments z_k $(k = 1, 2)$ are defined as:

$$z_i\left(\bar{\omega}; \varepsilon\right) = \frac{1}{\varepsilon\sqrt{2}}\sqrt{\left(-1\right)^i + \sqrt{1 + 4\varepsilon^2\bar{\omega}^2}},\ i = 1, 2 \tag{8}$$

Notice that the use of exponential instead of hyperbolic functions in Eq. (7) is more appropriate to highlight the existence of two boundary layers when $\varepsilon << 1$.

Substitution of Eqs. (7) and (8) in (6) yields the algebraic eigenvalue problem:

$$\mathbf{B}\left(\bar{\omega}; \varepsilon, \rho_0, \rho_1\right)\,\mathbf{a} = \mathbf{0} \tag{9}$$

where $\mathbf{a} = \left(A_1, ..., A_4\right)^T$, $\mathbf{0}$ is a null column matrix of size 4×1, and $\mathbf{B}$ is a 4×4 boundary condition matrix whose entries depend on both the non-dimensional bending stiffness ε and the degree of fixity parameters ρ_i $(i = 0, 1)$.

The non-dimensional natural frequencies $\bar{\omega}_k$ $(k \in \mathbb{N}^+)$ coincide with the roots of the characteristic equation $det\left(\mathbf{B}\left(\bar{\omega}; \varepsilon, \rho_0, \rho_1\right)\right) = 0$. Generally speaking, they will be a function of the non-dimensional bending stiffness ε and of the two variables ρ_0 and ρ_1, i.e. $\bar{\omega}_k = \bar{\omega}_k\left(\varepsilon, \rho_0, \rho_1\right)$, $k \in \mathbb{N}^+$. Symmetry, however, allows to conclude that the non-dimensional natural frequencies $\bar{\omega}_k$ should depend on a symmetric transformation of the variables ρ_0 and ρ_1 that can be arbitrarily, but conveniently, defined as:

$$p = \frac{1}{2}\left(\rho_0 + \rho_1\right),\ 0 \le p \le 1 \tag{10}$$

Dependency of the non-dimensional natural frequencies on p, then, can be fully highlighted by writing: $\bar{\omega}_k = \bar{\omega}_k\left(\varepsilon, p\right)$, $k \in \mathbb{N}^+$. It's worth noting that the ideal limit cases of doubly-hinged and doubly-clamped elements correspond, respectively, to set $p = 0$ and $p = 1$.

Exact closed-form solutions of the characteristic equation are only available for the doubly-hinged case (see e.g. [8]). Asymptotic closed-form solutions can also be derived, for small values of the non-dimensional bending stiffness parameters ε typical e.g. of stay cables. By extending the results firstly presented in [6] to deal with a beam element

supported by rotational springs at both end sections, indeed, the following result can be obtained:

$$\bar{\omega}_k = k\pi \left[1 + 2p\varepsilon + \left(\frac{(k\pi)^2}{2} + 4p^2\right)\varepsilon^2\right],\ k \in \mathbb{N}^+ + o(\varepsilon^2) \tag{11}$$

For arbitrary boundary conditions and non-dimensional bending stiffness values, the characteristic equation can be numerically solved e.g. through a sequential application of a root finding algorithm based on the bisection method. Within this context, it is worth noting that, thanks to the scaling of the governing equations adopted in the present work, the determinant of the boundary condition matrix $\mathbf{B}$ is bounded and with leading order terms of order one for vanishingly small values of ε. This makes simple numerical root finding algorithms well suited to find the natural frequencies of the system for over a wide interval of non-dimensional bending stiffness values, ranging from elements characterized by values of ε in the order of $0.5 - 1$ to very slender ones, with ε in the order of few percents or lower.

2.2 Parameter identification algorithm

Once the eigenvalues $\bar{\omega}_k = \bar{\omega}_k(\varepsilon, p)$ are known through an application of the semi-analytic model described in Section (2.1), multiplication by the characteristic frequency $\omega_0 = \omega_0(T, m, l)$ gives the natural frequencies:

$$\omega_k = \omega_0(T, m, l) \cdot \bar{\omega}_k(\varepsilon, p), k \in \mathbb{N}^+ \tag{12}$$

Standard vibration testing techniques (see e.g. [20, 9]) can be applied to obtain the first M natural frequencies of the beam: ω_k^* $(k = 1, ..., M)$. The difference between calculated and measured natural frequencies, then, can be quantitatively assessed by introducing the cost (or objective) function:

$$F_{obj} = \sqrt{\sum_{k=1}^{M}\left(1 - \frac{\omega_k}{\omega_k^*}\right)^2} \tag{13}$$

The unknown model parameters $\boldsymbol{X} = (\omega_0, \varepsilon, p)^T \in \mathbb{R}^3$ can be identified by solving the non-linear optimization problem:

$$\text{Find } \boldsymbol{X}_{opt} \text{ s.t. } F_{obj}(\boldsymbol{X}_{opt}) = \inf\{(\boldsymbol{X})\} \tag{14}$$

with the physical constraints: $\omega_0 > 0$, $\varepsilon > 0$, $0 \leq p \leq 1$. Once the optimal parameters ω_0, ε and p are known from the solution of (14), by assuming that the length (l) and the mass per unit of length (m) are known without uncertainties, the axial-force T can be easily calculated (see Eq. (2)) as $T = ml^2\omega_0^2$.

The non-linear optimization problem defined in Eq. (14) is characterized by several characteristic features that should guide the selection of an appropriate solution algorithm. Due to unavoidable measurement errors affecting the natural frequencies ω_k^* $(k = 1, ..., M)$, the landscape of the cost function (12) is characterized, in general, by many local minima. Moreover, the sensitivity of cost function (12) with respect to the parameter p tends to be substantially negligible for small values of the non-dimensional bending stiffness ε typical of slender elements, as it can be easily inferred by inspecting the asymptotic solution of the eigenvalue problem (Eq. (11)).

Gradient-based optimization algorithms, hence, are not well suited for the particular problem at hand, since they are prone to get trapped in local minima and their iteration operators could potentially be ill-conditioned for small values of ε. Within the class of gradient-free algorithms, the family of Differential Evolution algorithms, firstly proposed by Storn and Price [18, 19], has shown excellent performances in finding the global optimum of non-linear, non-convex, multi-modal and non-differentiable functions (see e.g. the review in [3]). DE is an Evolutionary Algorithm (EA) that iteratively operates on a population of candidate solutions made of NP parameter vectors. The initial population is randomly chosen and offsprings are generated by perturbing trial solutions with scaled differences of randomly selected population elements. As the number of iterations grows, the characteristic size of these differences tend to automatically adapt to the natural scales of the objective landscape [3]. It's worth noting that the peculiar strategy adopted to generate offsprings and evolve the population of candidate solution makes DE algorithms able to deal with objective functions characterized by low or moderately low sensitivity with respect to one ore more variables of the searching space without numerical problems. Selection of the better fitted elements of the population is performed through a one-to-one parent/offspring competition scheme. The physical constraint are enforced through a simple penalty criterion and the iterations are performed until a termination criterion is satisfied.

In the present work, a custom implementation of a well-known variant of the DE algorithm proposed by [4] has been adopted to solve the non-linear optimization problem in Eq. (14). The termination criterion has been defined such that iterations are stopped whenever one of the following conditions is satisfied: (a) the relative difference between the best and worst objective function values $\Delta = \frac{F_{obj}^{worst} - F_{obj}^{best}}{\max\left\{F_{obj}^{worst}, 1\right\}}$ of a population is below a given threshold $Toll$ (cf. the *Diff* termination criterion in [21]), (b) the value of the cost function is lower than a prescribed value V, (c) the number of iterations NIT is equal to the maximum number of iterations $MAXIT$.

3 APPLICATIONS

The performances of the proposed parameter identification strategy have been assessed through extensive numerical testing. Results will be presented in the following for an axially-loaded beam element characterized by $\omega_0 = 5.66$ rad/s and $T = 4000$ kN. Three different values of non-dimensional bending stiffness ($\varepsilon = 0.02, 0.1, 0.5$) have been considered, along with five different boundary conditions: (I) $p = 0$ (doubly-hinged beam), (II) $p = 0.25$, (III) $p = 0.50$, (IV) $p = 0.75$ and (V) $p = 1$ (doubly-clamped beam).

In order to simulate experimental input data, the eigenvalue problem (9) has been numerically solved to get the first five natural frequencies. These frequencies, then, have been corrupted by multiplying the nominal values by a unit-mean and low intensity Gaussian noise, to account for the effects of measurement errors. Different values of noise intensity, ranging from 0 to 2.5%, have been considered. For each noise intensity value, a sample of 10 sets of noisy natural frequencies has been randomly generated. The optimization problem (14) has been solved for each set of numerically generated input natural frequencies by running the DE algorithm ("DEGL/SAW/bin" scheme, with scale factor $F = 0.8$ and crossover parameter $CR = 0.9$, see [4] for further details), starting from a population of $NP = 30$ trial solutions randomly chosen in the initial search space $P \subset \mathbb{R}^3 : 10^{-5} \leq \omega_0 \leq 50,\ 10^{-5} \leq \varepsilon \leq 5,\ 0 \leq p \leq 1$. The parameters of the termination

criterion have been set up as: $V = 10^{-6}$, $Toll = 10^{-7}$ and $MAXIT = 1000$.

Figures (2)-(4) show the results of the proposed identification algorithm as a function of the noise intensity. The results are averaged over the number of runs NR of the algorithm for each different noise intensity level (i.e. $NR = 10$) and expressed in terms of: (a)-(c) the identified values of the parameters $\omega_{0,ave}$, ε_{ave} and p_{ave}; (d) the relative error on the element axial force, $\Delta T = \frac{T_{ave}-T^*}{T^*}$, where T_{ave} is the average identified value of the axial force and T^* is the target value (i.e. $T^* = 4000$ kN); (e) is the average value of the cost function associated to the identified optimal set of parameters (denoted as F_{obj}^{best} in the figures); (f) is the average number of iterations of the DE algorithm.

Figure 2 shows the results for a beam element with target bending stiffness value $\varepsilon = 0.02$ typical of slender elements, such as stay cables. The identification strategy gives fairly accurate results in terms of parameters ω_0 and ε for all values of noise intensity herein considered. As expected from the inspection of the asymptotic solution of the eigenvalue problem (Eq. (11)), the boundary conditions do not affect significantly the cost function of the optimization problem and, as a consequence, the identification algorithm is not able to correctly identifying the parameter p. As already noticed by the authors in [6], the identification procedure tends, for each value of noise intensity, to a mean value of p equal to about 0.5. This latter value coincides with the mean value of p within the randomly generated population members of the DE algorithm. On the overall, in spite of an highly inaccurate identification of the degree of fixity of the beam end sections, the procedure gives a good estimate of the axial force. Errors on the axial force obviously increase at the increase of the noise intensity and are higher for the two boundary conditions corresponding to the limit cases of doubly-hinged (label I, $p = 0$) and doubly-clamped (label V, $p = 1$) beams. Figure 2(e) allows to appreciate how measurements errors, herein associated to non-zero noise intensity values, determines a significant jump in the estimated minimum values of the cost function. Figure 2(f) allows to appreciate how for non-zero noise-intensity values iterations are mostly terminated because the maximum number of iterations ($MAXIT$) is reached. This is mainly due to the already discussed lacking of convergence on the degree of restraint parameter p (see also [6]).

Figure 3 shows the results for a beam element with target bending stiffness value $\varepsilon = 0.1$. The identification algorithm gives very accurate predictions of all parameters ω_0, ε and p for small values of the noise intensity (i.e. lower than 0.5%). By increasing the noise intensity, the accuracy in the predictions of the degree of restraint parameters p rapidly deteriorates, while the errors on both ω_0 and ε remain acceptable with maximum discrepancies from the target values in the order of $\pm 15\%$, depending on the boundary conditions. The maximum relative errors on the identified axial force are in the order of $\pm 15\%$ for small values of the noise intensity (i.e. lower than 0.5%), but rapidly increase up to about $\pm 25\%$ for a noise intensity value equal to 2.5%. Figures 3(a) and 3(d) also allows one to appreciate how, for the non-dimensional bending stiffness value herein considered, the proposed identification algorithm tends to systematically underestimate the axial force for the boundary conditions labeled (I) and (II), i.e. for p respectively equal to 0 (doubly-hinged beam) and 0.25; on the other hand, the axial force is systematically overestimated for the boundary conditions labeled (IV) and (V), i.e. for p respectively equal to 0.75 and 1 (doubly-clamped beam). The opposite trend is remarked for the non-dimensional bending stiffness ε (see Fig. 3(b)). These trends can be easily explained, through an inspection of Fig. 3(d), by noticing that the algorithm tends to: (a) overestimate the degree of fixity of the restraints in cases (I) and (II); and (b) underestimate the degree of

fixity of the restraints in cases (I) and (II).

Figure 4 shows the results for a beam element with target bending stiffness value $\varepsilon = 0.5$, that can be considered as representative e.g. of diagonal braces, truss elements and tie-rods. Differently than in the previous cases, the boundary conditions are identified with good accuracy for all values of noise intensity herein considered, except that for the case labeled as (I), corresponding to $p = 0$ (doubly-hinged beam), which is associated to errors on p in the order of 25%. More in details, the accuracy of the identified values of p decreases with the increasing of the flexibility of the restraints. The identified values of the parameters ω_0 and ε, on the other hand, are affected in general by significant discrepancies with respect to the target values. As a consequence, also the errors affecting the identified axial force are relevant. More in details, it is worth noting that errors on the non-dimensional bending stiffness parameter ε reach the 60%, depending on the boundary conditions and on the noise intensity value. Although difficult to evaluate in slender structural elements such as stay cables (associated to small values of ε), the bending stiffness of thicker structural elements such as diagonal braces, truss elements and tie-rods can often be easily estimated on the basis of available information on the geometric and mechanical properties of the structural element. Whenever the bending stiffness is known, however, the proposed algorithm can be easily re-formulated by assuming that ω_0 and p are the only unknown parameters, leading to a more precise evaluation of the beam axial force.

4 CONCLUSIONS

An analytical model for transverse vibrations of an axially loaded Euler-Bernoulli beam with partially restrained end conditions has been presented and used as the basis to develop a numerical parameter identification strategy. Parametric analyses have been carried out to quantitatively assess the performances of the proposed identification algorithm, for a broad range of structural configurations, characterized by different values of non-dimensional bending stiffness ε and boundary conditions, that cover a wide spectrum of applications, such as stay cables, diagonal braces, truss elements and tie-rods of vaulted historical masonry structures. On the overall, the proposed procedure gives accurate estimates of the beam axial force for small and moderately small values of ε, in the order of $\varepsilon \lesssim 0.1$. For higher values of ε, based on the critical discussion of the results of the proposed identification strategy, a simplified algorithm relying on a preliminary estimation of the bending stiffness of the beam is envisaged to reduce errors on the identified axial force.

ACKNOWLEDGMENTS

The project is funded by the Wallonia Public Service. It is carried out by the University of Liège and the company V2i (www.v2i.be). M.G. acknowledges the support of the FNRS (Belgian Fund for Scientific Research).

REFERENCES

[1] E. Caetano, Cable vibrations in cable-stayed bridges, *I. A. for B. and S. Engineering (IABSE) Ed.*, 2007.

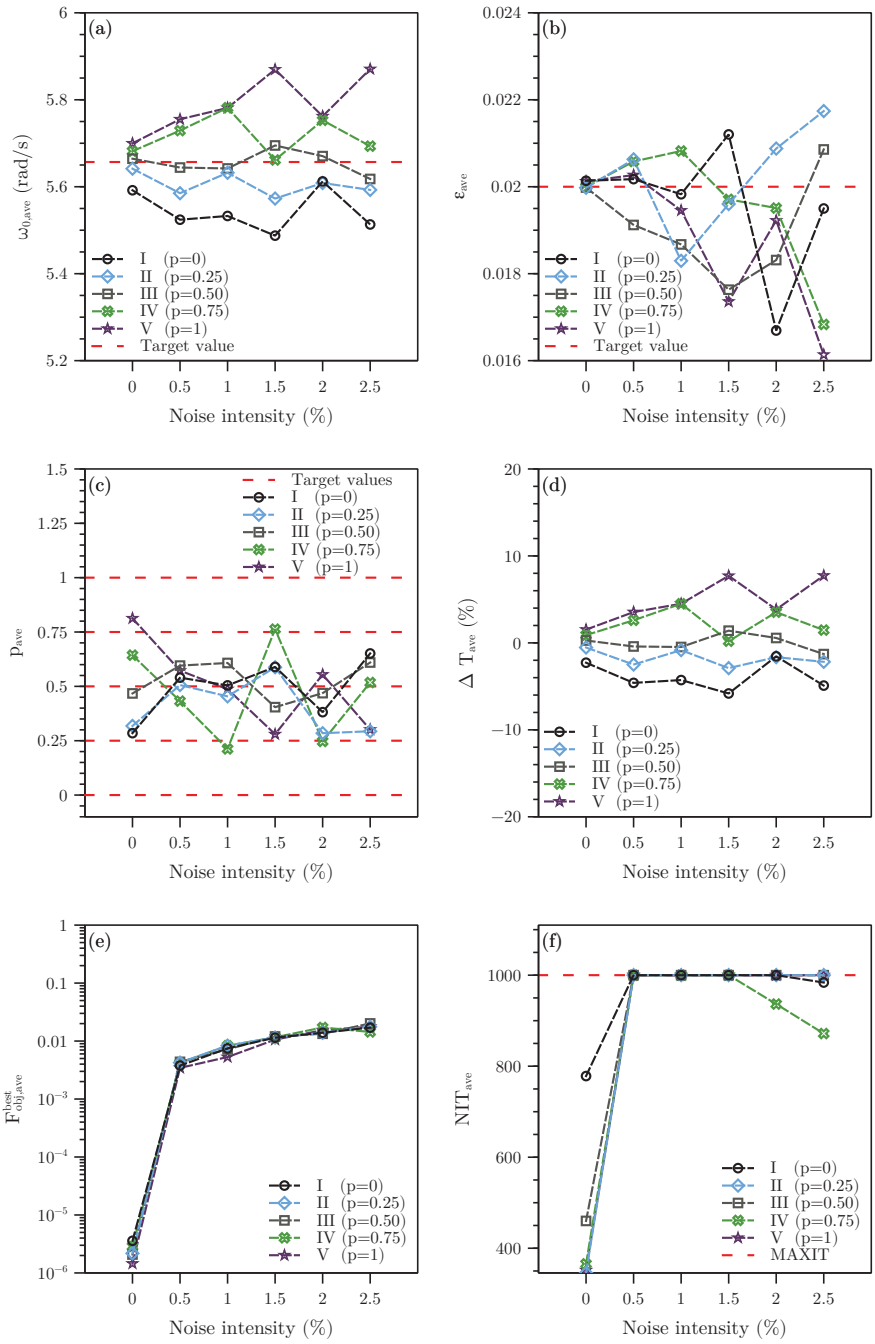

Figure 2: Results of the identification algorithm, averaged on ten runs, as a function of the noise intensity. (a) Characteristic frequency ω_0 (target value: $\omega_0 = 5.66$ rad/s), (b) non-dimensional bending stiffness ε (target value: $\varepsilon = 0.02$), (c) degree of fixity parameter p, (d) relative error on the axial force ΔT, (e) value of the cost function associated to the identified optimal set of parameters, F_{obj}^{best} (f) number of iteration (the maximum number is $MAXIT = 1000$).

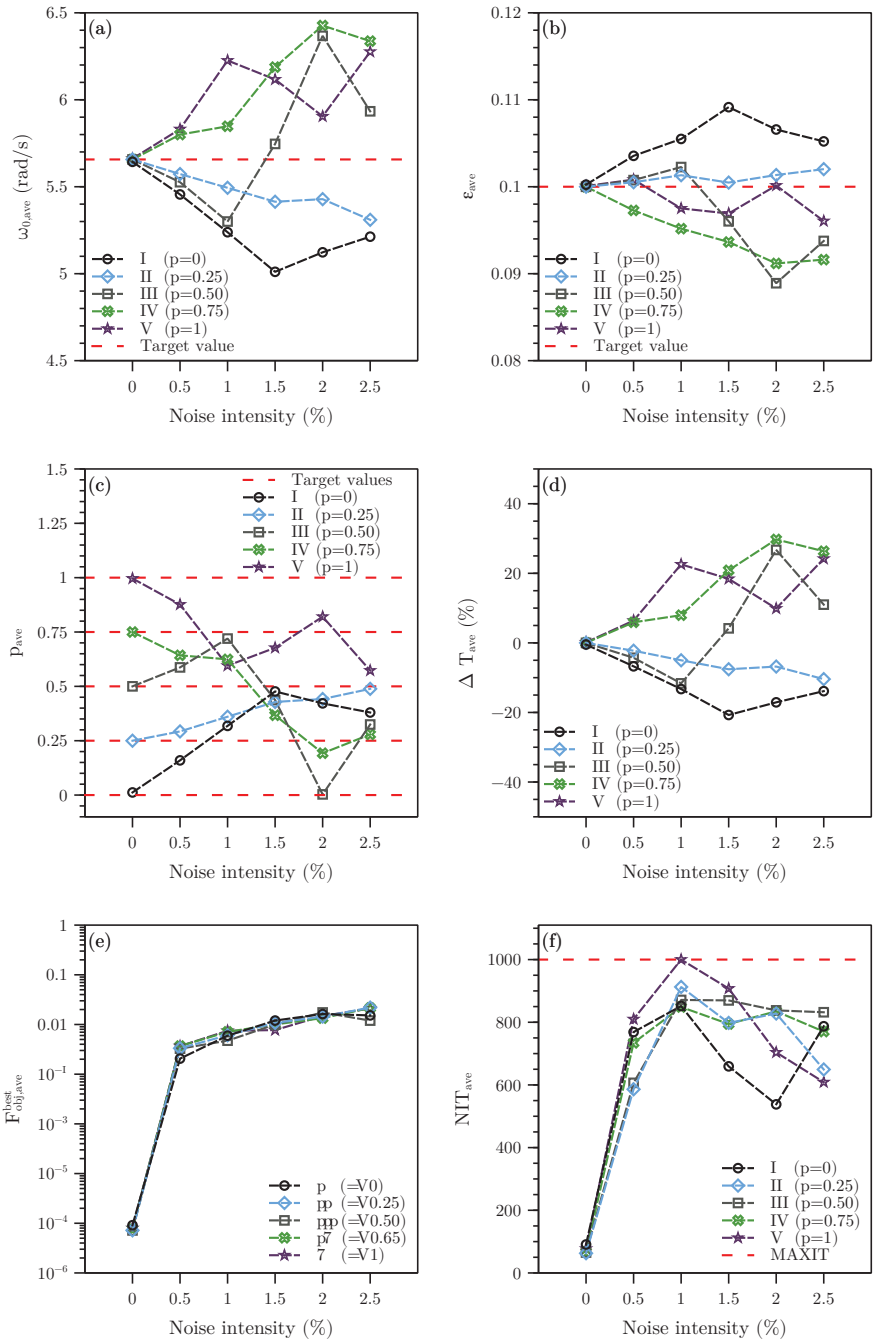

Figure 3: Results of the identification algorithm, averaged on ten runs, as a function of the noise intensity. (a) Characteristic frequency ω_0 (target value: $\omega_0 = 5.66$ rad/s), (b) non-dimensional bending stiffness ε (target value: $\varepsilon = 0.1$), (c) degree of fixity parameter p, (d) relative error on the axial force ΔT, (e) value of the cost function associated to the identified optimal set of parameters, F_{obj}^{best} (f) number of iteration (the maximum number is $MAXIT = 1000$).

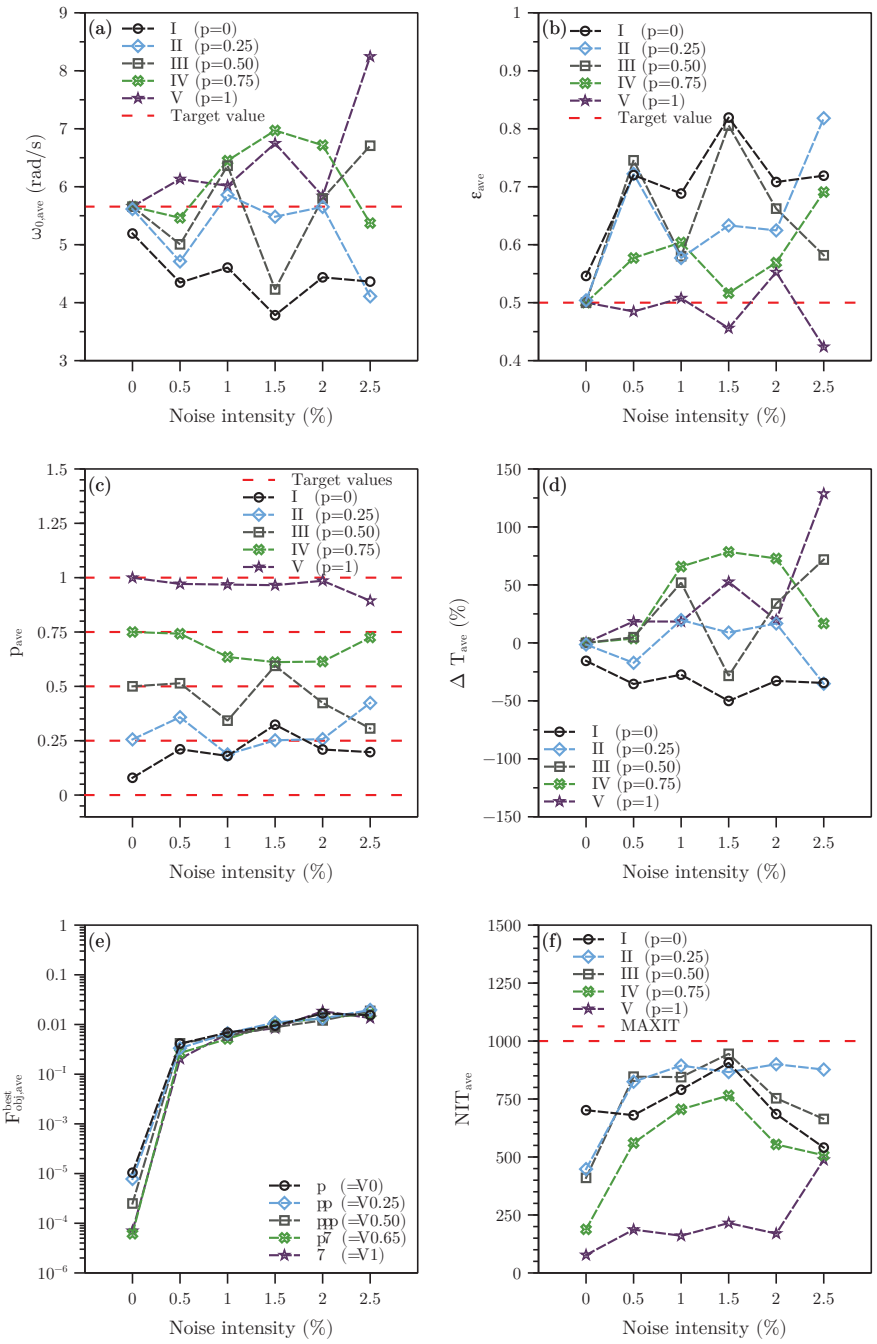

Figure 4: Results of the identification algorithm, averaged on ten runs, as a function of the noise intensity. (a) Characteristic frequency ω_0 (target value: $\omega_0 = 5.66$ rad/s), (b) non-dimensional bending stiffness ε (target value: $\varepsilon = 0.5$), (c) degree of fixity parameter p, (d) relative error on the axial force ΔT, (e) value of the cost function associated to the identified optimal set of parameters, F_{obj}^{best} (f) number of iteration (the maximum number is $MAXIT = 1000$).

[2] E. Caetano, R. Bartek, F. Magalhaes, C. Keenan, G. Trippick, Assessment of cable forces at the London 2012 Olympic Stadium roof, *Structural Engineering International*, **4**, 489–500, 2013.

[3] S. Das, S.S. Mullick, P.N. Suganthan, P.N., Recent advances in differential evolution - An updated survey, *Swarm and Evolutionary Computation*, **27**, 1–30, 2016.

[4] S. Das, A. Abraham, U.K. Chakraborty, A. Konar, Differential evolution using a neighborhood-based mutation operator, *IEEE Transactions on Evolutionary Computation*, **13**, 526–553, 2009.

[5] V. Denoël, E. Detournay, Multiple scales solution for a beam with a small bending stiffnes, *Journal of Engineering Mechanics*, **136**, 69–77, 2010.

[6] F. Foti, M. Geuzaine, V. Denoël, On the identification of the axial force in stay cables with unknown boundary conditions, *Proc. of the 8th UBT International Conference. on Civil Engineering, Infrastructure and Environment (IC-UBT)*, Pristine, Kosovo, 26th-28th October 2019.

[7] R. Geier, G.D. Roeck, R. Flesch, Accurate cable force determination using ambient vibration measurements, *Structure and Infrastructure Engineering*, **2**, 43–52, 2006.

[8] M. Géradin, D. Rixen, Mechanical vibrations, *John Wiley and Sons, Chichester (England)*, 1997.

[9] C.M. Harris, A.G. Piersol, Harris' shock and vibration handbook, *Vol. 5. New York: McGraw-Hill*, 2002.

[10] E.J. Hinch, *Perturbation methods, Cambridge University Press, Cambridge, U.S.*, 1991.

[11] T. Kernicky, M. Whelan, E. Al-Shaer, Dynamic identification of axial force and boundary restraints in tie rods and cables with uncertainty quantification using Set Inversion Via Interval Analysis, *Journal of Sound and Vibration*, **423**, 401–420, 2018.

[12] S. Lagomarsino, C. Calderini, The dynamical identification of the tensile force in ancient tie-rods, *Engineering Structures*, **27** 846–856, 2005.

[13] S. Li, E. Reynders, K. Maes, G. De Roeck, Vibration-based estimation of axial force for a beam member with uncertain boundary conditions, *Journal of Sound and Vibration*, **332**, 795–806, 2013.

[14] P. de Mars, D. Hardy, Mesure des Efforts dans les Structures a Cables, *Annales TP Belgique*, **6**, 515–531, 1985.

[15] A.B. Mehrabi, H. Tabatabai, Unified finite difference formulation for free vibration of cables, *Journal of Structural Engineering (ASCE)*, **124**, 1313–1322, 1998.

[16] U. Pabst, P. Hagedorn, Identification of boundary conditions as a part of model correction, *Journal of Sound and Vibration*, **182**, 565–575, 1995.

[17] G. Rebecchi, N. Tullini, F. Laudiero, Estimate of the axial force in slender beams with unknown boundary conditions using one flexural mode shape, *Journal of Sound and Vibration*, **332**, 4122–4135, 2013.

[18] R. Storn, K.V. Price, Differential evolution: a simple and efficient adaptive scheme for global optimization over continuous spaces, ICSI, USA, Tech. Rep. TR-95-012, 1995.

[19] R. Storn, K.V. Price, Differential evolution: a simple and efficient heuristic for global optimization over continuous spaces, *Journal of Global Optimization*, **11**, 341–359, 1997.

[20] P. Van Overschee, B. De Moor, Subspace algorithms for the stochastic identification problem, *Automatica*, **29**, 649–660, 1993.

[21] K. Zielinski, R. Laur, Stopping criteria for differential evolution in constrained single-objective optimization, *Advances in Differential Evolution, pp. 111–138, Springer-Verlag, Berlin*, 2008.

EURODYN 2020
XI International Conference on Structural Dynamics
M. Papadrakakis, M. Fragiadakis, C. Papadimitriou (eds.)
Athens, Greece, 23–26 November 2020

SEISMIC VULNERABILITY ASSESSMENT OF A ROMANIAN HISTORICAL MASONRY BUILDING UNDER NEAR-SOURCE EARTHQUAKE

N. Chieffo[1], A. Formisano[2], M. Mosoarca[1] and P.B. Lourenço[3]

[1] Faculty of Architecture and Urbanism
Politehnica University of Timisoara, Traian Lalescu Street 2/A, 300223 Timisoara, Romania
e-mail: nicola.chieffo@student.upt.ro, marius.mosoarca@upt.ro

[2] Department of Structures for Engineering and Architecture
School of Polytechnic and Basic Sciences, University of Naples "Federico II"
P.le V. Tecchio, 80125 Naples, Italy
e-mail: antoform@unina.it

[3] Department of Civil Engineering
University of Minho, ISISE, Institute of Science and Innovation for Bio-Sustainability (IB-S)
Azurém Campus, Guimaraes, Portugal
e-mail: pbl@civil.uminho.pt

Keywords: Vertical Ground Motion, Seismic Vulnerability Assessment, Historical Building, Time History Analysis, Damage Assessment

Abstract. *In the present research work, the effect of ground motion vertical component in case of near-source excitations on masonry buildings has been analysed. To this purpose, an investigation has been made on the Banloc Castle, a historical masonry construction damaged by the Banat-Voiteg earthquake occurred on December 1991 in the Romanian Region of Banloc. A FEM model of the building, setup using DIANA FEA analysis software, has been analysed in the non-linear dynamic field. In particular, the records have been referred to the Banloc site, characterized by a moment magnitude of 5.5 and a focal depth of 9 km. In order to estimate the influence of the vertical seismic motion on the case study building in terms of both displacement and internal forces, two different scenarios have been examined. The first scenario has taken into account the horizontal component only, whereas the second one has studied the simultaneous effects of three components of the seismic action. The comparison between the two scenarios has shown that the vertical ground motion significantly modifies the structural behaviour of the inspected building. Finally, numerical damage patterns have been plotted and compared to the real cracks detected in the case study after the considered seismic event.*

1 INTRODUCTION

Typically, the effect of the vertical component of earthquake ground motion on constructions has been ignored in the current studies of Earthquake Engineering. Gioncu and Mazzonlani have developed an important research activity concerning the influence of ground motion vertical component for the load-bearing masonry structures in the Banat seismic region [1, 2, 3]. In particular, the seismic design and assessment of Unreinforced Masonry (URM) structures is limited to the effects of the horizontal accelerations, neglecting the vertical component of the design ground motion [4, 5, 6]. The damages caused by disastrous earthquakes highlighted the brittle behaviour of several structural systems especially under seismic actions characterised by not negligible vertical components, which produced significant effects in cases of near-field events.

Generally, the ground motion vertical component is mainly associated to the arrival of vertically propagating compressive P-waves and secondary shear S-waves. However, the propagation direction of volume waves (P and S) is not influenced by the site geology, but by the site distance, the fault type and the magnitude. In these circumstances, it is evident that the effects induced by the ground motion vertical component are prominent in areas characterized by high hazard level and that they should be appropriately considered in the seismic behaviour analysis of existing masonry buildings, which have very low tensile resistance [7].

Generally, earthquakes occurring near an active seismogenic source contain pulse-like records (one or more consecutive peaks), characterised by a long period and a short duration [8]. These impulses, caused by the sliding of faults, release a large amount of seismic energy, which is transmitted abruptly to the structures. For this reason, the vertical component of these earthquakes is one of the determining factors to be taken into consideration for the correct safeguarding of buildings and design preventions.

In fact, as reported in [9, 10], it was shown that the ratio between vertical (V) and horizontal (H) components of ground motion in the near-source regions with high hazard earthquakes is considerably different than that expected at a smaller magnitude and greater distances; moreover, it was suggested that the V/H (empirical) limit of 2/3 should be re-evaluated in order to better foresee the effects of ground motion vertical component for design purposes. In particular, it was observed that these ratios near the seismogenic source can exceed the unitary value. The effects produced by the vertical component of the ground motion significantly influence the dynamic response of structures. In fact, as detailed in [11], the vertical component on masonry buildings provokes a reduction of load-bearing capacity of the wall panels and, consequently, an increase of lateral displacements. In particular, during the time history cycle, the vertical component acts alternately with compression and decompression peaks, that lead to a degradation of the stiffness of the masonry under dynamic action with the consequent increase of the local or global vulnerability.

Other studies [12, 13] inspected the behaviour of masonry buildings subjected to vertical seismic actions, asserting that the vertical component of the ground motion in epicentre areas characterized by a *Joyner and Boore* distance (R_{jb} <30 km) causes a variation of the axial stress regime in the walls. Consequentially, the dynamic amplification due to soil stratigraphy leads to a reduction in terms of the shear capacity of structural resistant elements, which show a deficit in terms of resistance, stability and ductility.

In this framework, focusing on the Banat-Voiteg seismic event occurred on December 1991, the Castle of Banloc has been selected as a case study. In order to take into account the influence of vertical accelerations on the seismic capacity of the examined building, nonlinear dynamic analyses have been carried out considering the ground motion records representative of the earthquake occurred in the region of Banat in Romania.

The displacements and foces regime of the investigated castle have been analysed in order to point out the influence of vertical component. Finally, the damages achieved from numerical modelling have been presented, discussed and compared to those really detected under the 1991 earthquake.

2 SEISMICITY OF BANAT REGION

The Western and South-Western part of Romania, well known as the Banat Region, is undoubtedly one of the most seismically active regions of the country, characterized by crustal earthquakes. Due to the presence of multiple vulnerability factors, such as old houses, areas with high population density, unprotected historic buildings, presence of factories, etc., the seismic risk of the region is very high.

The seismic history of this region is characterized by a high dispersion and variability of the epicentres and, therefore, of the events observed. Generally, the earthquakes in the Banat region occurred at the contact between the Carpathian and Pannonian plates (from Timisoara to S-W Jebel and Banloc and north of the Bega canal) and at the contact among irregular structures straddling Sânnicolau Mare, Nădlag-Jimbolia, Arad-Vinga- Calacea and Timis Valley in Faget. Moreover, the distributions of focal mechanisms associated to the earthquakes occurred in the South-West of Romania showed a reverse and strikes faults or the combination of the two. The focal depths of earthquakes in the western areas of Oltenia and Banat-Danube were between 5 and 33 km deep, as indicated in Figure 1 [14].

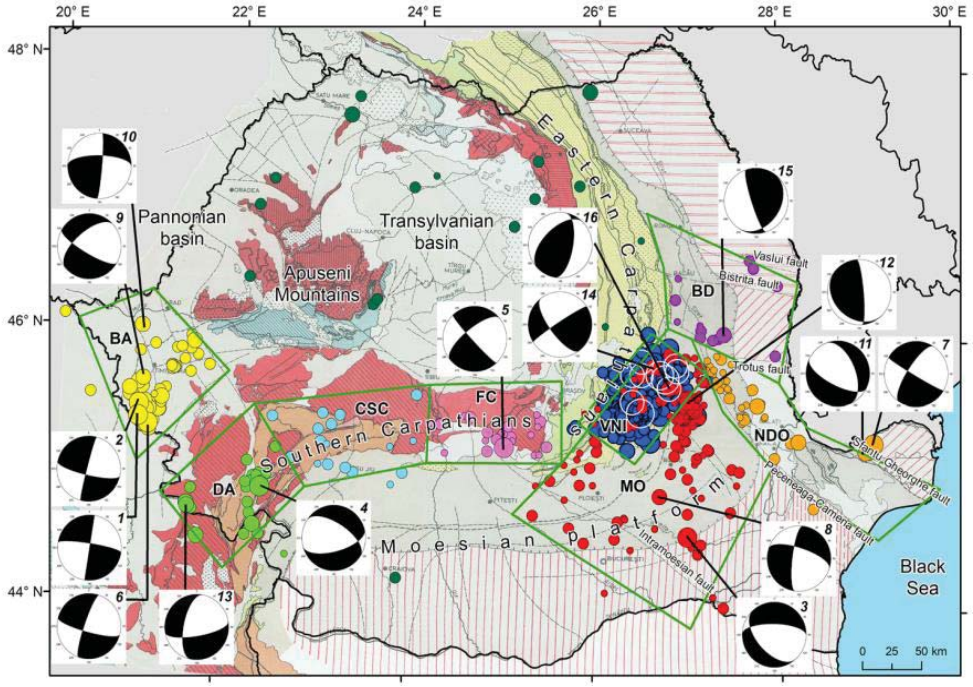

Figure 1: Focal mechanisms occurred in Romania [14].

The most significant earthquakes occurred in the Banat area were the two seismic events detected in Banloc in 1991 and denoted by moment magnitude of 5.5 and 5.6. These main records have been acquired by the INCERC seismic network (Banloc Town-Hall and Timisoara stations). In particular, the accelerometer records taken by INCERC for the cities of Timişoara and Banloc provided earthquakes with the following characteristics: (i) relatively short duration of 9-24 s and (ii) significant spectral values in the range 0.1-0.3 s, which extends up to 0.7 s for the Timişoara record and up to 1.2 s for the Banloc one.

Focusing on the event recorded in the city of Banloc, it is characterized by a reduced site-source distance (7.01 km far from the epicentre), which makes it as a near-source event.

This event showed an impulsive and high vertical peak acceleration of 1.2863 ms^{-2}, a focal depth of 9 km, a moment magnitude, M_w, of 5.5 and an intensity, I, of VIII according to Mercalli Intensity Scale (MCS).

The data provided by the SM-ROM-GL Earthquakes DB [15] related to the 1991 event occurred in the Banat Region are shown in Table 1.

Earthquake	Date	LatN	LongE	Depth - *h* (km)	M_w	Station
Banat-Voiteg	1991/12/02	45.45	21.12	9	5.5	BNL1

Table 1: Reference event occurred in the Banat seismogenic zone in December 1991.

Furthermore, the ShakeMap of the event occurred and the geolocation of the city of Banloc are shown in Figure 2.

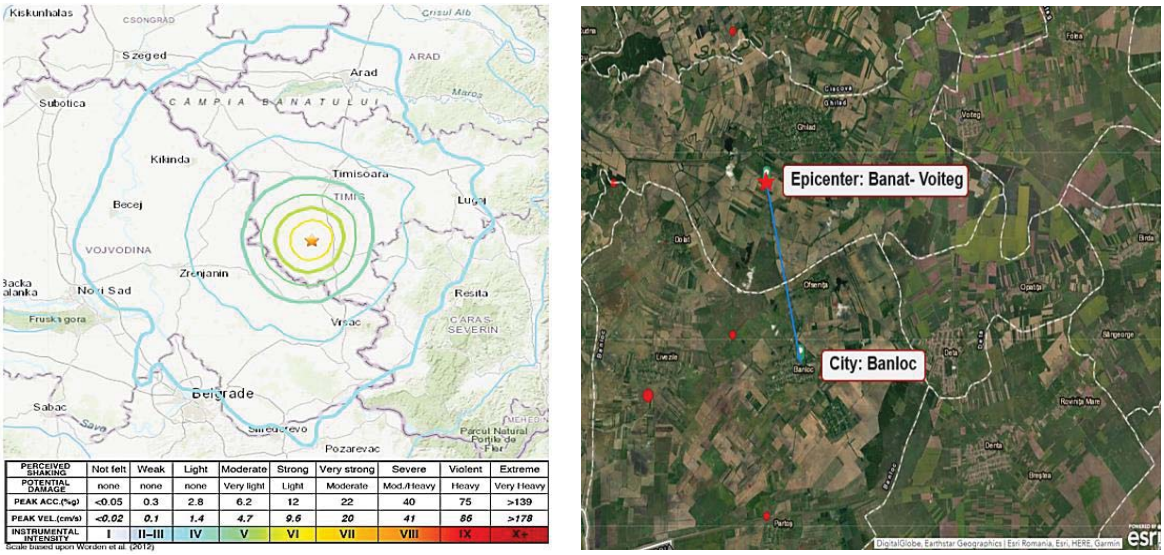

(a) (b)

Figure 2: ShakeMap of the Banat-Voiteg event (a) and geolocation of the city of Banloc (b).

3 PRELIMINARY ANALYSIS OF THE CASE STUDY BUILDING

3.1 Historical overview on the Banloc Castle

The municipality of Banloc is attested for the first time in May 1400, when the name "*Byallak*" was reported in a document provided to the clerk of Cenad.

For almost two centuries (1552–1716) Banloc was the summer residence of the Ottoman pasha of Temeşvar Eyalet. In 1716, the Banat region, where Banloc is located, was conquered by the Austrians and, in the census of the year later, the municipality was registered as "*Panloch*" in the district of Ciacova with 85 inhabited houses.

In 1759 the construction of the castle of Banloc was completed.

The castle (Figure 3) is the most important monument of the municipality. It is a massive building with a "U" in-plane shape built in the early nineteenth century. The main façade faces south, while on the opposite side the two wings border a terraced courtyard.

The castle is composed of very heavy perimeter brick and internal walls having thickness of 0.90 m and 0.80 m, respectively at ground level.

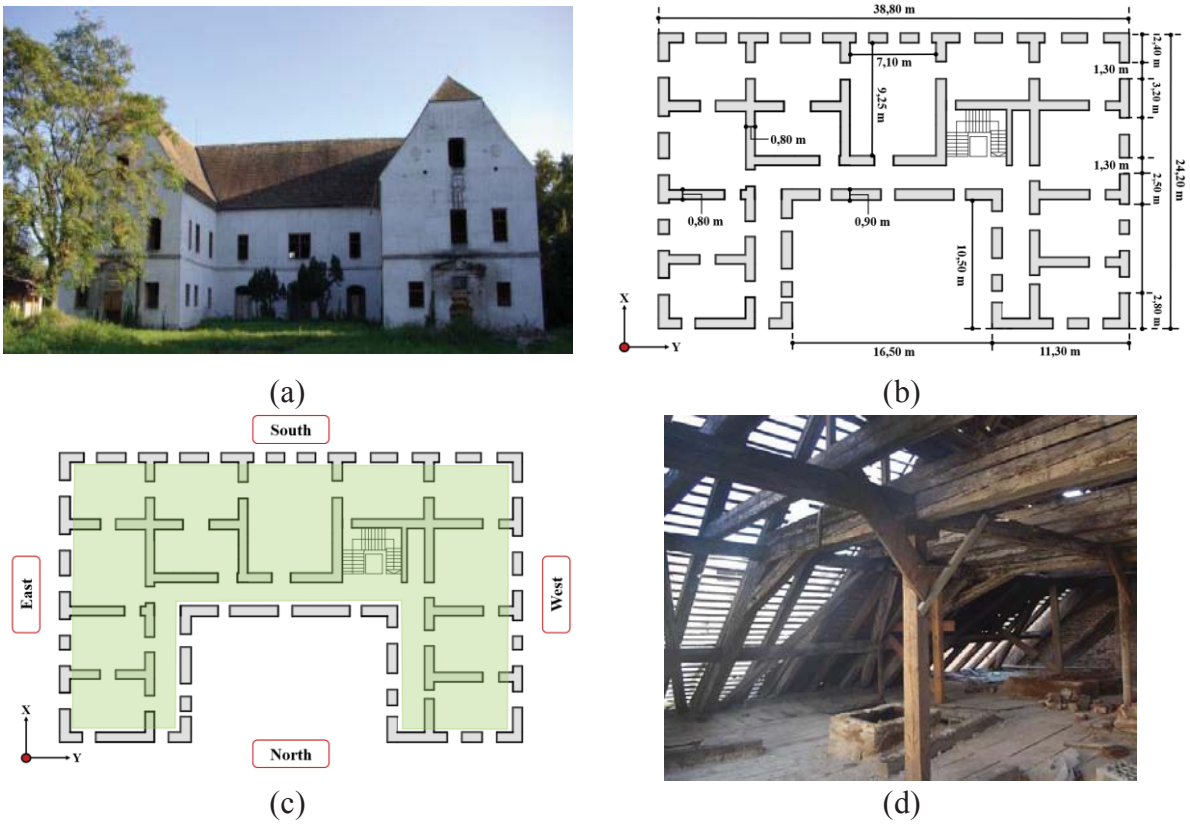

Figure 3: Castle of Banloc: (a) external view, (b) architectural plan layout, (c) geographical orientation and (d) timber roof structure.

On the top, vaulted ceilings with thickness of 0.25 m are present. The inter-storey heights of first and second floors are 4.00 m and 5.70 m, respectively. The roof is made of a solid timber supporting structure, whose construction technique was frequently used in the Banat region (Figure 3d).

3.2 Field evidence after the Banloc earthquake

The Banloc earthquake, occurred on 1991 December 2nd, was a very significant event in the seismic historicity of the Banat region. It was characterized by a focal depth of 9 km with the epicentre localized in Banloc. The released seismic energy produced a magnitude (M_w) of 5.5 on the Richter scale [15]. This earthquake can be classified as a medium-deep geological event. It caused slight damages to new designed structures, but several masonry buildings in the area were characterized by very serious damages, also with partial collapses. Referring to the case study building, the damage was detected through on-site inspections after the earthquake occurred. The achieved post-earthquake damages are presented in Figure 4 [16].

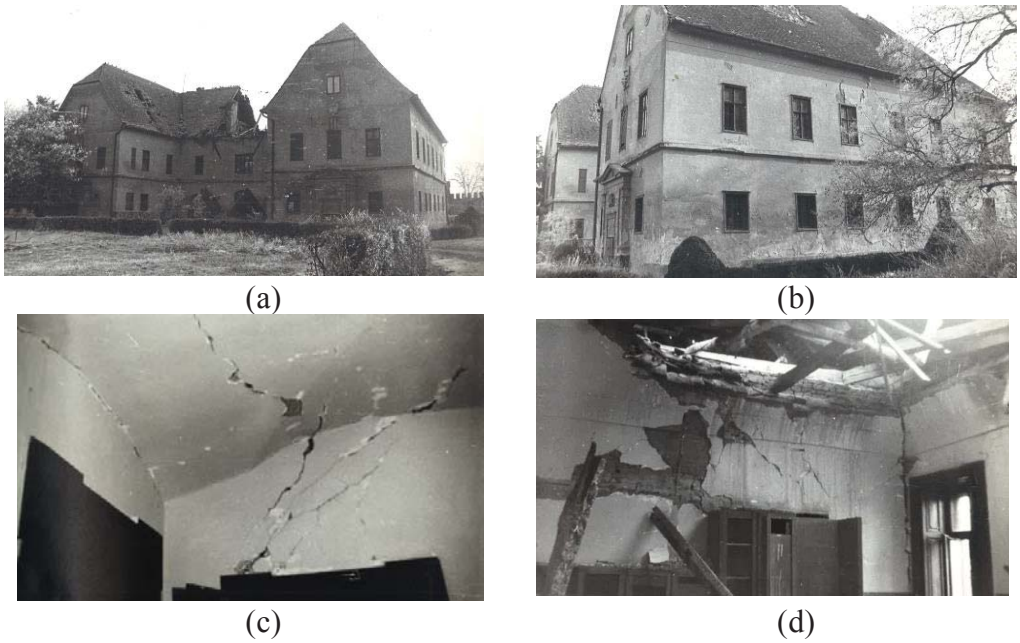

(a) (b) (c) (d)

Figure 4: Detected damages on the Banloc Castle after the 1991 earthquake: (a) North façade; (b) West façade; (c) first floor room; (d) second floor room [16]

As it is seen from the previous figures, the highest level of damage was localized in the vaults, which are elements characterized by large spans and resistance lower than that of vertical structures (Figures 4c). In particular, the cracks in the vaults were attributable to the impulsive vertical component, which produced very extensive damages. Contrary, large number of walls were affected by shear mechanisms induced by horizontal seismic components with widespread cracks [16].

4 STRUCTURAL ASSESSMENT

4.1 Analysis of the ground motion records

The accelerograms adopted are representative of the event occurred in Banloc in December 1991 considering the BNL1 seismometric station [15]. The accelerations are characterized by maximum components in X direction of 0,08g, in Y direction of 0,13g and in Z direction of 0,13g (Figure 5). The seismic phenomenon can be defined of near-source type, since the city of Banloc was located approximately 7 km far from the epicentre.

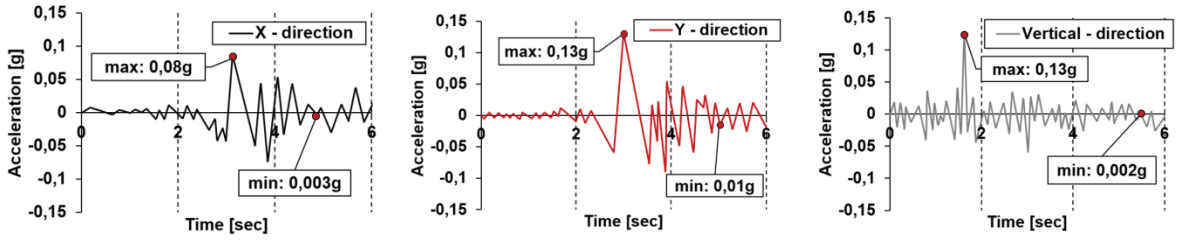

(a) (b) (c)

Figure 5: Accelerograms of the Banat-Voiteg seismic event.

As can be seen from the previous Figure, for numerical analyses, a 6 seconds time history has been considered and elaborated by means of the Seismosignal software [17]. This choice is dictated from the fact that, on one hand, in the first 6 seconds all the seismic energy input deriving from vertical component is manifested and, on the other hand, the analysis elaboration time is short.

The spectral ratios between vertical accelerations, V, and the corresponding horizontal ones, H, for the considered near-source ground motion, have been depicted in Figure 6. These results have shown how the vertical component effects are very important for earthquakes characterized by small site-source distances, where the V/H limit of 2/3 proposed in [9] is exceeded. In particular, Figure 6 shows that for short periods (less or equal than 0,2 seconds), the V/H ratio is greater than 1; this means that the rule imposed in [9] underestimates considerably the vertical component effects for low periods.

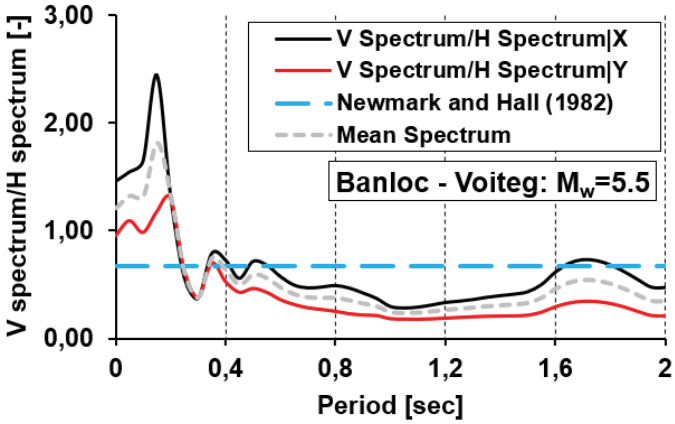

Figure 6: V/H spectral ratios for the Banloc-Voiteg event.

4.2 Non-linear dynamic analysis

Time-history analysis provides a global assessment of the castle dynamic structural response varying specified ground motion accelerograms. The implementation of the model has been set-up using the DIANA FEA software [18], where the structure has been conceived as set of shell elements (Figure 7).

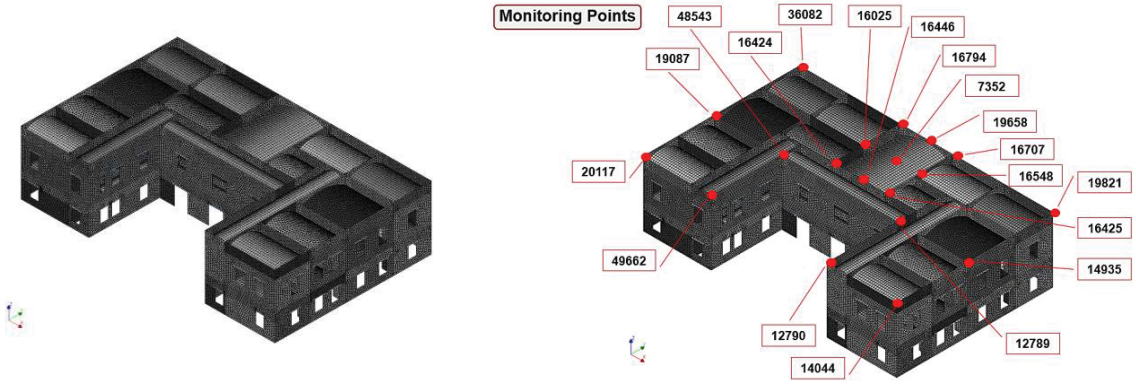

(a) (b)

Figure 7: 3D-shell element model of the castle (a) and selected monitoring points (b).

The masonry constitutive law is characterized by a non-linear response with a nonductile post-peak softening behaviour; tensile stresses are assumed to diminish exponentially, while the compression performance combines hardening and softening parabolic phases, as established in [19, 20]. Based on these assumptions, in Table 2 the masonry mechanical properties adopted in the analysis for the case study building have been reported according to NTC18 [21].

Mechanical Properties		
Modulus of elasticity	E [N/mm^2]	1500
Shear modulus	G [N/mm^2]	500
Compressive strength	f_m [N/mm^2]	2.40
Tensile strength	τ_0 [N/mm^2]	0.24
Specific weight	w [KN/m^3]	18
Poisson ratio	ν [-]	0.20
Fracture energy (compression)	G_{fc} [N/mm]	4.64
Fracture energy – Mode I (tensile)	G_{ft} [N/mm]	0.012

Table 2: Mechanical properties of masonry.

The results obtained have been represented, for the two scenarios considered, namely (H) and (H+V), in terms of dispersion of both mean displacements and resistances. They are referred to the monitoring points at the second floor (see Figure 7) and are summarized in Figure 8. Concerning displacements and strengths regime, positive and negative values of the points cloud denote the change of direction induced by the seismic input with respect to the straight line with equation x=y (bisector). Furthermore, in order to better highlight the influence of the vertical component, the upper (y=0,5x) and lower (y=2x) bounds of the dispersion range have been considered. In this way, the greater scatter with respect to the bisector, the larger effect of the ground motion vertical component [11].

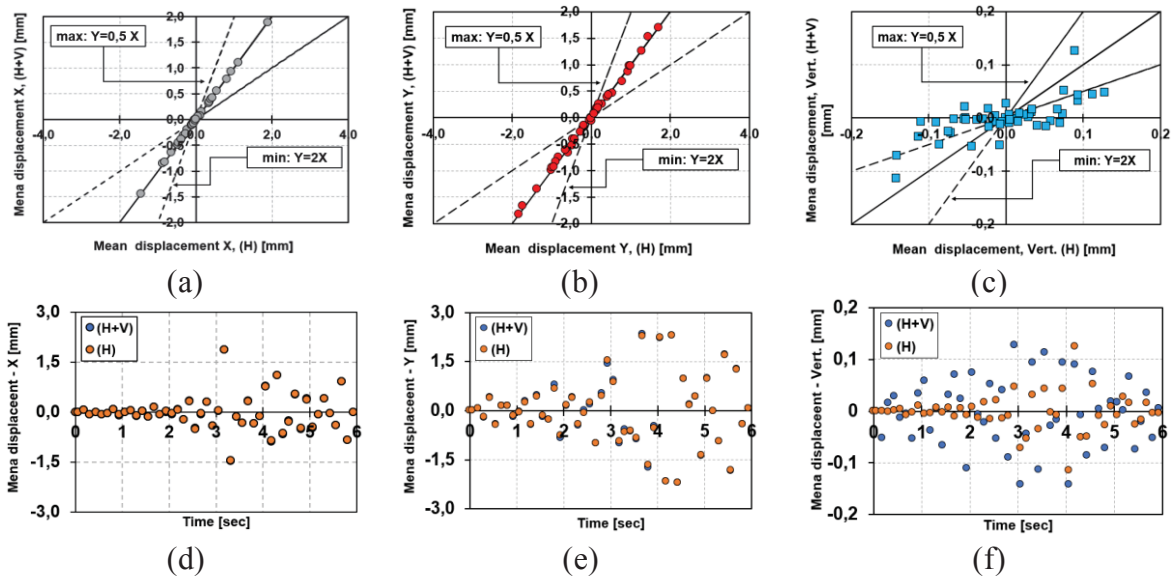

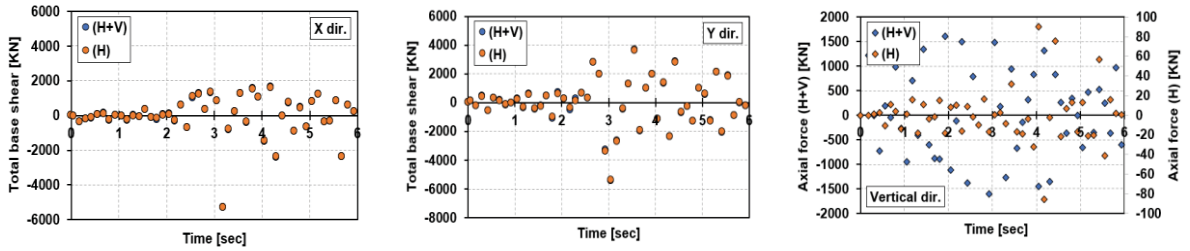

(g) (h) (i)

Figure 8: Scatter results in terms of displacements (a-f) and forces (g-i).

From the gotten results, it is worth noting how the average dispersions associated with the two main directions X and Y, in terms of displacements and base reactions, are not affected by the influence of the vertical component. However, in vertical direction, there is a marked average dispersion (Figures 8c and 8f) with respect to the case in which the vertical component is neglected (H).

It can be seen that in the first two seconds (in which the vertical component reached its maximum acceleration peak), the displacements are increased by about 6 times compared to the case in which the vertical component is neglected (H). Furthermore, in terms of axial stress, the same condition can be found by comparing the two scenarios, (H) and (H+V) mentioned above (Figure 8i).

Consequently, a time step of 2 seconds has been considered in order to consider the effect of ground motion vertical component in terms of both shear [22] and axial demands for one of the most stressed pier of the West façade. So, for the sake of representation, (H) and (H+V) scenarios have been compared and plotted according to the recommendations provided by EC8 [22], as reported in Figure 9.

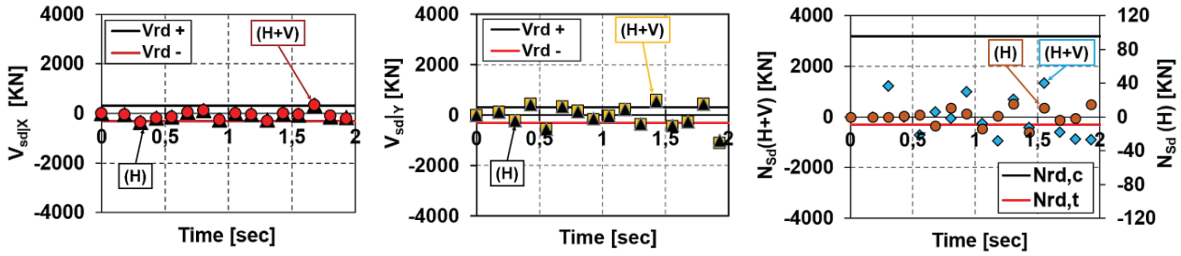

(a) (b) (c)

Figure 9: Safety checks for shear stresses (a-b) and axial loads (c) in case of (H) and (H+V) scenarios.

Firstly, in Figures 9a and 9b, it is possible to notice how the seismic vertical component in the two main directions, X and Y, does not produce any significant stress variation for both considered scenarios. Secondly, in Figure 9c, it is shown how the vertical component produces a significant increase in terms of axial load. In fact, at time step of 1.55 seconds (which corresponds to the maximum peak vertical acceleration), the difference between (H) and (H+V) is very high (more than two times). Moreover, it is detected that the axial load demands exceed averagely the corresponding tensile capacities ($N_{rd,t}$) of 2 times.

Subsequently, the force reduction factor, q, prescribed in almost all seismic design codes without taking into account the influence of the ground motion vertical component [23, 24], has been predicted for the examined building located in epicentral area of Romania.

The behaviour factor has been assessed both in terms of mean ductility values and areas equivalence criterion between the elastic system and the elasto-plastic one. Based on the energy dissipation criteria, the hysteretic cycles have been defined for the monitoring points

mentioned in Figure 7b, and, thus, the mean capacity curves, representative of the global behaviour of the structure in the two main directions, X and Y, have been considered (Figure 10a and 10b). Furthermore, with the same method, the behaviour factor has been calculated when the vertical component is neglected.

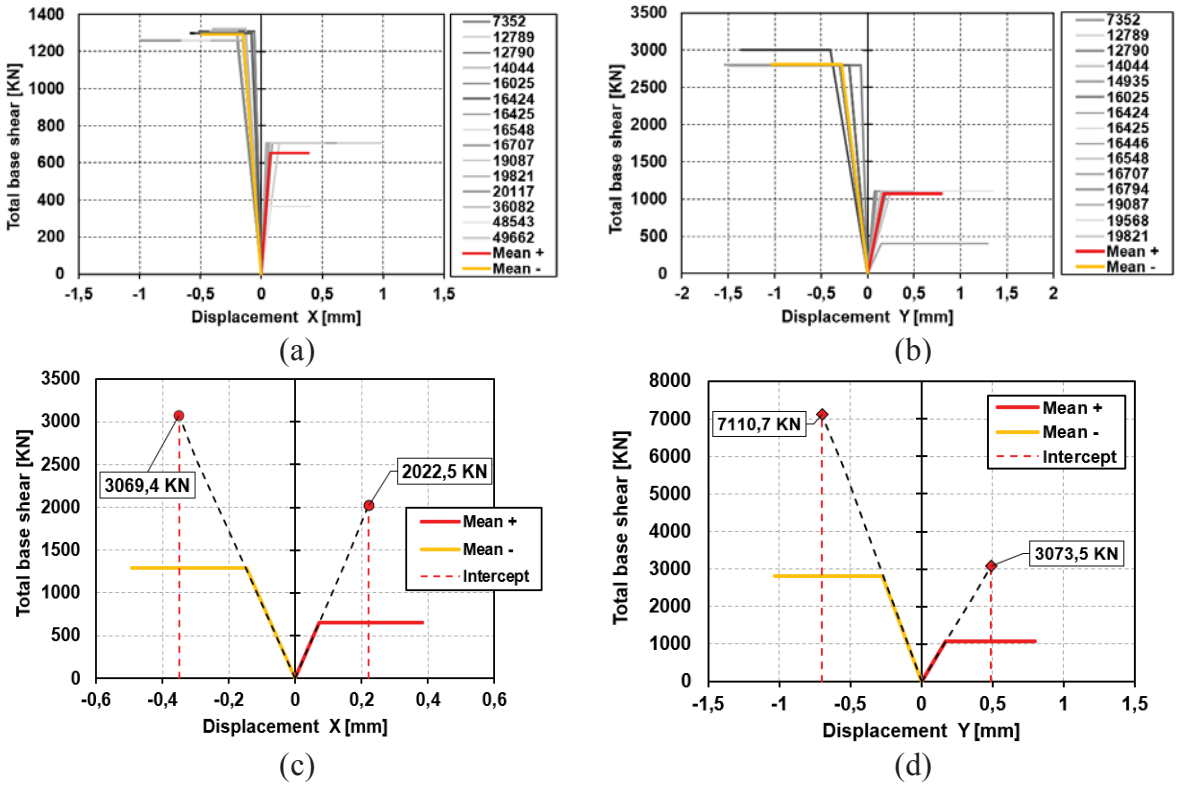

Figure 10: Mean capacity curves for (H+V) scenario in the two main directions X and Y in terms of energetic ductility (a, b) and equivalence criterion of areas (c, d).

From the results obtained, the proposed q-factor is intended as the absolute minimum of the values deriving from the scenarios (H) and (H+V) considered. It has been estimated as equal to 1.94, when the vertical acceleration associated to the case of maximum decompression reached at about 3 seconds in the time history is considered. This choice is based on the fact that, during the decompression phase, the structure presents the highest global vulnerability. Moreover, it is important to observe how the proposed value is contained in the range (1.5-2.5) established by EC8 [22]. Finally, the achieved value shows an increase of about 30% with respect to the value of 1.5 suggested by the Romanian Code [25] for masonry structural systems in case of design spectrum considering vertical acceleration components only.

4.3 Damage assessment

The damages detected in the castle after the Banloc earthquake were represented by a widespread distribution of cracks, that affected the vertical and horizontal structures, producing globally in the time the structure deterioration.

In particular, several failure mechanisms closely related to the seismic event were identified. More specifically, in the first two seconds of the time-history, the maximum vertical peak acceleration produced an extensive damage in the vaults, characterized by a brittle behaviour (Figure 11) [16].

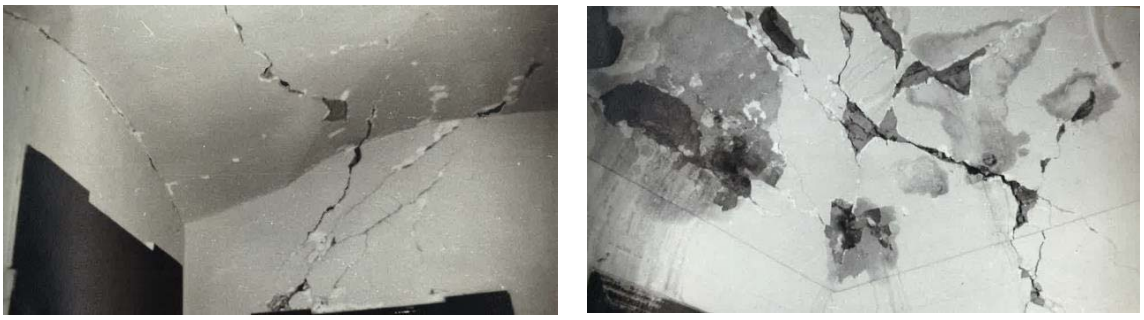

Figure 11: Damages detected in the second-floor vaults mainly due to ground motion vertical component [16].

Successively, following the impulsive action, the arrival of the horizontal components produced damage to the vertical structures, mainly represented by shear cracks in the spandrel beams, as shown in Figure 12 [16].

Figure 12: Vertical and diagonal shear cracks detected in the South façade of the case study building [16].

Finally, in the internal court of the building, a partial collapse of the roofing structure was observed. This collapse mechanism was triggered by the impulsive seismic action, as depicted in Figure 13 [16].

(a) – left view (b) – right view

Figure 13: Failure mechanisms observed in the internal court of the case study building [16].

The damages achieved from numerical analyses have been presented and compared to experimental ones in Figure 14.

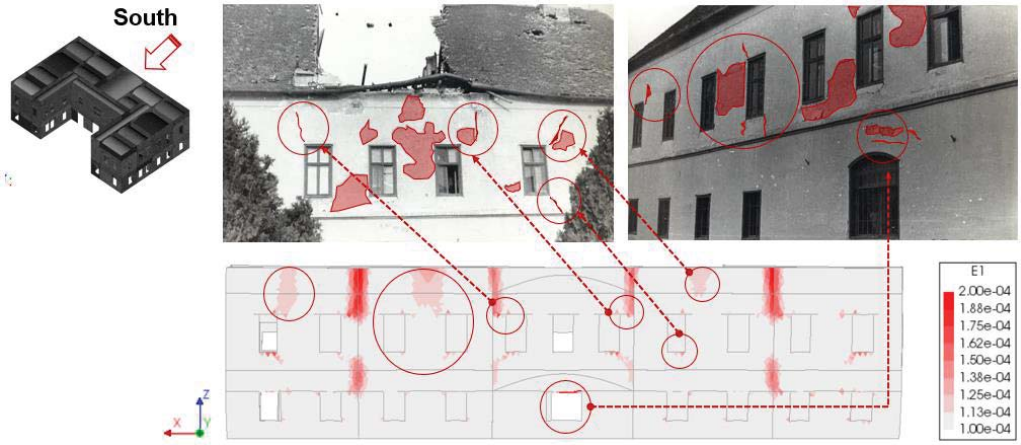

(a)

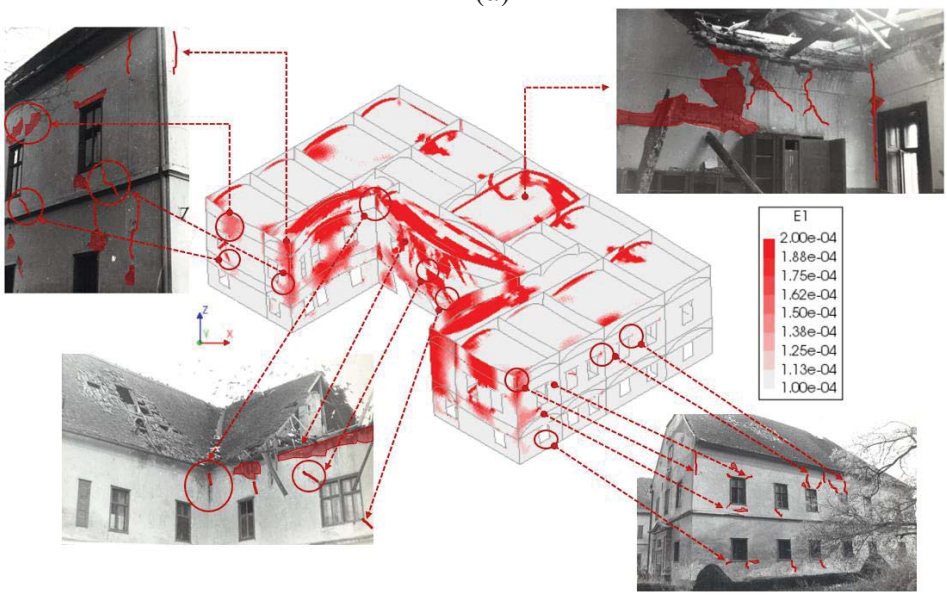

(b)

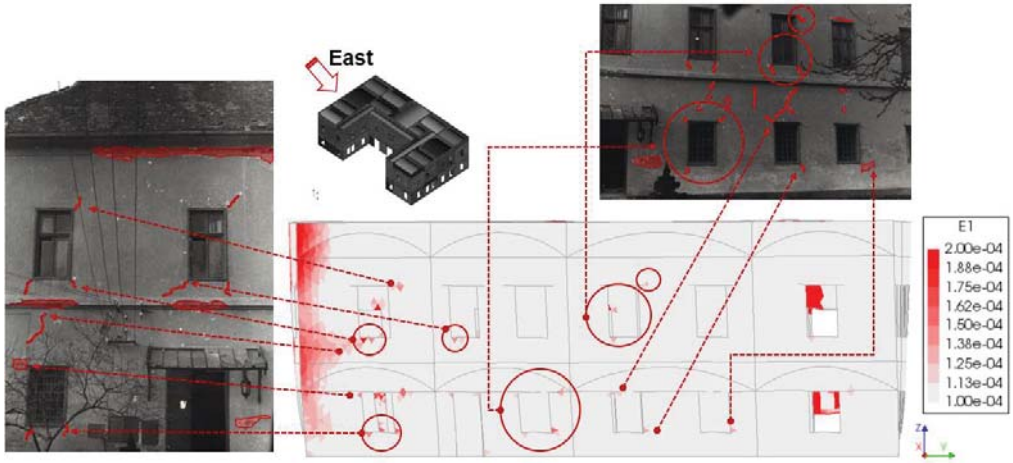

(c)

Figure 14: Numerical damages obtained simulating the Banloc-Voiteg event and comparison with experimental evidences.

From the above comparison, it appears that the non-linear analysis identified local damages very similar to those produced by the Banat-Voiteg earthquake.

The identification parameter used to evaluate the damage state in the numerical analysis is the *tensile fracture energy* (G_f), according to which, when the maximum principal stress reaches the defined cracking criterion, the fracture begins to distribute in the structural element. In particular, the numerical model catches in a satisfactory way the detected local damages and failure mechanisms, providing, as depicted in Figure 14, the right distribution of *Principal Total Strain* (E1).

5 CONCLUSIONS

The proposed work has analysed the effects induced by the vertical earthquake component on a historic masonry building located in the Romanian region of Banloc. The seismic event, occurred in December 1991 with a moment magnitude of 5.5, was characterised by a small (about 7 km) site-source distance. This impulsive event was identified by low frequency content and maximum PGAs comparable in vertical and horizontal directions. The accelerometric records were used to perform non-linear dynamic analyses on the case study building modelled with the DIANA FEA software using shell elements.

The effects of the ground motion vertical component were evaluated considering the comparison between two different scenarios: the first, named H, where only horizontal acceleration components were considered, and the second, called H+V, where also the vertical components were taken into account. The main results are summarized as follows:

- The considered record, due to the combination of medium magnitude and short site-to-source distance, had high energy in terms of vertical component in the first two seconds.
- There was a dispersion of the displacements induced by the vertical component in the first two seconds of the time-history, since the impulsive action releases a high input energy in that time period. The displacements increased about 6 times compared to the scenario in which the vertical component is neglected.
- In the first two seconds of time history, where the maximum vertical energy content of the seismic motion occurred, the comparison of the two scenarios (H and H+V) in terms of stress regime was done. In particular, in terms of shear strength the vertical component did not produce any significant variation of results in the two analysis directions. Conversely, referring to the axial stress regime, the vertical component induces a considerable increase of axial tensile loads, which exceeded averagely the corresponding tensile capacities of about 2 times.
- The q-factor for the study castle was predicted taking into account the influence of the ground motion vertical component. The achieved value was enclosed in the range established by EC8 and it is 30% greater than that provided by the Romanian Code for masonry structures in case of vertical acceleration design spectrum. Moreover, other research activity in this field will be study in future.
- The numerical damage assessment was carried out considering the *Principal Total Strains*, which take into account the overcoming of the tensile fracture energy in the structural elements. The numerical analysis results provided with satisfactory accuracy the same damage mechanisms really detected in the castle, namely cracks in the vaults (produced by vertical components) and vertical structures (mainly caused by horizontal components), as well as the out-of-plane horizontal bending mechanism in the façade facing the courtyard, which was produced by the partial collapse of the roof structures.

REFERENCES

[1] V. Gioncu, FM. Mazzolani, Influence of earthquake types on the design of seismic-resistant steel structures. Part 1: Challenges for new design approaches. Part 2: Structural response for different earthquake types. Behavior of Steel Structures in Seismic Areas. STESSA 2006 (eds. F.M. Mazzolani and A. Wada), Taylor & Francis, London, 113-120, 121-127.

[2] V. Gioncu, FM. Mazzolani, Earthquake Engineering for Structural Design, Spon Press, London, ISBN 0-203-84889-6 Master e-book ISBN, 2011.

[3] V. Gioncu, FM. Mazzolani, Ductility of Seismic Resistant Steel Structures, Spon Press, London, ISBN 9780367865313, 2002.

[4] M. Mosoarca, V. Gioncu, Failure mechanisms for historical religious buildings in Romanian seismic areas, *Journal of Cultural Heritage* 14, e65-e72, 2013.

[5] N. Chieffo, A. Formisano, The influence of geo-hazard effects on the physical vulnerability assessment of the built heritage: An application in a district of Naples, *Buildings* 9, 26.

[6] M. Mosoarca, I. Onescu, E. Onescu, B. Azap, N. Chieffo, M. Szitar-Sirbu, Seismic vulnerability assessment for the historical areas of the Timisoara city, Romania. *Engineering Failure Analysis* 101, 86-112, 2019.

[7] CJ. Collier, AS. Elnashai, A Procedure for Combining Vertical and Horizontal Seismic Action Effects, *Journal of Earthquake Engineering* 5, 521-539.

[8] PG. Somerville, Magnitude scaling of the near fault rupture directivity pulse, *Physics of the Earth and Planetary Interiors*, 137,201-12, 2003.

[9] N. Newmark, W. Hall, Earthquake Spectra and Design, EERI Monographs 1982.

[10] KW. Campbell, Y. Bozorgnia, Updated near-source ground-motion (attenuation) relations for the horizontal and vertical components of peak ground acceleration and acceleration response spectra, *Bulletin of the Seismological Society of America* 93, 1872.

[11] F. Di Michele, C. Cantagallo, E. Spacone, Effects of the vertical seismic component on seismic performance of an unreinforced masonry structures, *Bulletin of Earthquake Engineering* 18,1635–56, 2020.

[12] AJ. Papazoglou, AS. Elnashai, Analytical and field evidence of the damaging effect of vertical earthquake ground motion, *Earthquake Engineering and Structural Dynamics* 25, 1109-37, 1996.

[13] AS. Elnashai, L. Di Sarno, Fundamentals of Earthquake Engineering. 2008.

[14] A. Bala, D. Toma-Danila, M. Radulian, Focal mechanisms in Romania: statistical features representative for earthquake-prone areas and spatial correlations with tectonic provinces, *Acta Geodaetica et Geophysica* 39, 309-314, 2019.

[15] IS. Borcia, I. Craifaleanu, Examples of use of the SM-ROM-GL Database, *In 5th National Conference on Earthquake Engineering and 1st National Conference on Earthquake Engineering and Seismology–5CNIS & 1CNISS*, Bucharest, Romania, (2014), 1:165-172.

[16] IPROTIM TIMISOARA, Expertiza cu principii de consolidare (In Romanian), Pr. Nr. 35353/330, (1990).

[17] Seismosoft, SeismoSignal, User's Manual. 2018.

[18] DIANA FEA, Diana User's Manual, Release 10.2. DIANA FEA BV 2017.

[19] PB. Lourenço, Computations on historic masonry structures, *Progress in Structural Engineering and Materials* 4, 2002.

[20] PB. Lourenço, Structural Masonry Analysis: Recent Developments and Prospects, *J Proceedings of 14th International Brick and Block Masonry conference. University of Newcastle. Australia* 53, 2008.

[21] MD. 17 January 2018, Updating of Technical Codes for Constructions, Official Gazette n. 42 of 20/02/18, Ordinary Supplement n. 8, 2018.

[22] EN 1998-3 - Eurocode 8, Design of structures for earthquake resistance - Part 3: Assessment and retrofitting of buildings, CEN 2004:1–97.

[23] M. Tomaževič, P. Weiss, Displacement capacity of masonry buildings as a basis for the assessment of behavior factor: An experimental study, *Bulletin of Earthquake Engineering* 8, 1267-1294, 2010.

[24] D. Zonta, G. Zanardo, C. Modena, Experimental evaluation of the ductility of a reduced-scale reinforced masonry building, *Materials and Structures* 34, 636–44, 2001

[25] Technical University of Civil Engineering Bucharest, Cod de Proiectare Seismica-Partea I- Indicativ P100-1, 2013.

EURODYN 2020
XI International Conference on Structural Dynamics
M. Papadrakakis, M. Fragiadakis, C. Papadimitriou (eds.)
Athens, Greece, 23–26 November 2020

VIBRATION MONITORING OF CONSTRUCTION WORK AND INDUSTRIAL ACTIVITIES USING NEW SOLUTIONS OF INSTRUMENTATION

C. Moutinho[1], **and A. Cunha**[1]

[1] CONSTRUCT/ViBest - Faculty of Engineering (FEUP), University of Porto

R. Dr. Roberto Frias S/N, 4200-465 Porto, Portugal

moutinho@fe.up.pt; acunha@fe.up.pt

Keywords: Industrial activities, construction work, new generation of monitoring systems

Abstract. *Over the last years, the Laboratory of Vibrations and Structural Monitoring of the Faculty of Engineering of University of Porto (www.fe.up.pt/vibest) has been monitoring vibrations due to construction work and industrial activities. In these cases, several types of wired and wireless commercial systems were used. When the long term monitoring of vibrations is required, wired solutions are usually demanded because of the need of the continuous power supply to the sensors. However, these systems often present some difficulties such as: a) dependence on external power supply and cables spread throughout to the working area, and; b) difficulty in being physically integrated or attached to structures, especially in construction environment. This has motivated the ViBest research group in contributing to the development of a new generation of measurement systems offering the following advantages: a) cost attractive; b) wireless with high levels of autonomy (may run on batteries for several weeks); c) small size that facilitates the easy integration in the structures; d) possibility of installation of high number of sensors; e) may be easily customized. In this context, the objective of this paper is to share the experience of ViBest in this area by describing the developed instrumentation that may be used in the measurement of vibrations in industrial or construction environment.*

1 INTRODUCTION

In Civil Structures and Infrastructures, the continuous dynamic or static monitoring or certain quantities has lately assumed great importance. In the case of dynamic measurements, the main reason of this interest is related to the subject of Operational Modal Analysis (OMA), which aims to identify the modal parameters of a structure in operating conditions (particularly with regard to natural frequencies, damping ratios and mode shapes) taking into account the measured ambient vibrations at critical points. In these cases, the measurement of vibrations is performed without disturbing the normal functioning of the structures, which may be implemented in buildings, bridges (railway, roadway, highway), dams and offshore structures. Given the importance of this subject, the Laboratory of Vibrations and Structural Monitoring FEUP (CONSTRUCT-ViBest) has carried out consistent work in this area [1], both in the development of numerical tools for identifying modal parameters and in the continuous measurement of vibrations in actual structures (see www.fe.up.pt/vibest).

Parallel to this area, CONSTRUCT-ViBest has also been involved in the monitoring of construction work and industrial activities. In most of the cases, the measurement of dynamic quantities such as acceleration or velocity is requested. This is related to the area of the evaluation of human comfort and structural damage induced by machinery or construction equipment. The continuous monitoring of static variables is also requested in many situations, especially related to the measurement of displacements and slopes in geotechnical works.

In the previous described areas, traditional measurement systems based on commercial equipment from well-known manufacturers have been used for a long time. However, many times these systems present some difficulties, which include: a) high cost; b) excessive dependence on external power supply; c) frequent failures in data acquisition attributed to heavy operating systems; d) difficulty in being physically integrated into structures, taking up too much space and being barely manageable, and; e) when using cables, the number of sensors is limited due to the exponential complexity of the data acquisition system [2]. In contrast, systems based on a new generation of sensors offers the following advantages: a) cost attractive; b) enable wireless solutions; c) autonomous and small size (easily integrated into structures); d) possibility of installation of high number of sensors; e) low power consumption (can run on batteries or solar panels); f) simplicity of functioning and robustness; g) low maintenance, and; h) may be easily adapted and customized [3].

In this context, this paper intends to divulge the alternative measurement systems to the classic ones, which were developed in the scope of the research activities conducted at CONSTRUCT/ViBest in the area of the new data acquisition systems. This includes sensors like accelerometers, geophones, and inclinometers.

2 THE ROLE OF THE NEW GENERATION OF SENSORS

The interest of the research in the area emerged from the technological evolution of the last decades in the topic of sensors and data acquisition systems based on microcontrollers. This was encouraged by the easy access to this technology and by the easy access to information available in the internet. In fact, the quantity of tutorials and blogs around this topic is immense.

At same time, researchers who work in actual structures with data acquisition systems, often face many challenges and problems. The lack of robustness of some traditional instrumentation solutions is one of these difficulties. The failure of these systems when working for long periods is not the only cause of that lack of robustness. Sometimes there also external causes like power failures and adverse weather conditions, beyond to other causes of diverse origin. Some data acquisitions systems are also too complex, involving too many cables and

connections. The high cost of measurement systems is another factor that hinders the widespread use of these systems in common Civil Structures.

In this context, the objective of the research in this area is to develop instrumentation that meets the following characteristics: i) wireless and compact size, for easy integration and installation in structures; b) robust, allowing the functioning of the system for long periods with no crashes; c) long autonomy; d) flexible, by allowing a variety of different sensors in several mounting schemes; e) accurate, and; f) cost attractive.

The role of these systems is not certainly to substitute the traditional systems. However, there are many applications where these instruments have the same effectiveness as the traditional ones, with additional advantages. In fact, they can simplify the process of installation and operation; they can be custom-made, including the use of 3D printing; maintenance and replacement is facilitated, and; more interesting, their attractive cost may allow the generalization of dynamic monitoring systems in Civil Structures. Nevertheless, the implementation of these new data acquisition systems also raises some challenges. Particularly with regard to the following issues: a) power supply; b) data transmission; c) reduced energy consumption; d) miniaturization of the systems, and; e) reliability.

3 DEVELOPED INSTRUMENTATION

3.1 Accelerometers

Acceleration is easy to measure and there are a lot of accelerometers models available in the market. The most updated version of a device using these sensors is composed of a tri-axis MEM accelerometer which is operated by means on an ATmega328P Microcontroller. It includes a Real-Time-Clock (RTC) and a microSD card breakout for saving data. In general, files of a duration of 10 minutes are organized in a folder structure identified according to the date and time of the measurements.

The main issue of these systems (and in all systems as a general problem) is the power supply. If the device can be powered with electrical current, this issue is resolved. However, the need of avoiding electrical cables scattered throughout the structure or construction area makes alternative energy solutions desirable. In this sense, solutions based on solar energy or batteries were developed. Solar energy allows high levels of autonomy. However, it is necessary to bear in mind that solar panels usually take up more space and need to be cleaned frequently. Figure 1a) indicates an accelerometer powered by a solar panel that is being used especially in the dynamic monitoring of bridges [4].

On the other hand, systems based on batteries do not depend on solar exposure and can be used in a more aggressive environments if appropriate enclosures are used. In addition, the size of the sensor may be adapted according to the needed autonomy. Figure 1b) represents a model powered by 3xAAA size batteries, which allows a continuous operation for about 1 week. If more autonomy is required, the model shown in Figure 2a) equipped with 5 li-ion batteries of 18650 type, may guarantee an autonomy of 15 weeks, and the model indicated in Figure 2b), equipped with 9 batteries of the same type, may power the sensor for 6 months.

All previous model may be fixed to structures by mean of 4 screws tightened against the box flange. Figure 3 shows a specific model directed for short period measurements in industrial or construction environment. The weight of this device allows it to simply be placed on the floor for measurement.

a)  b) 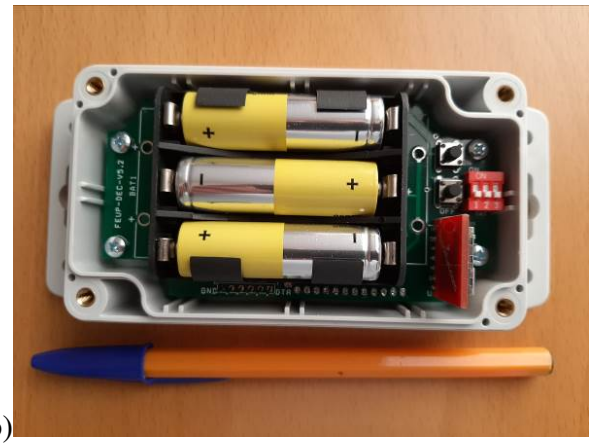

Figure 1: Accelerometer module: a) Solar powered; b) 3xAAA batteries.

a) 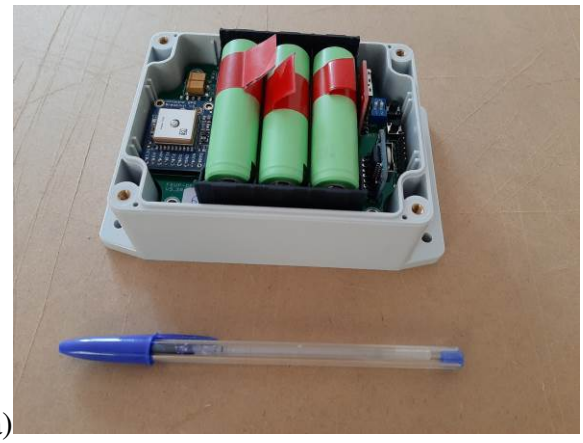 b) 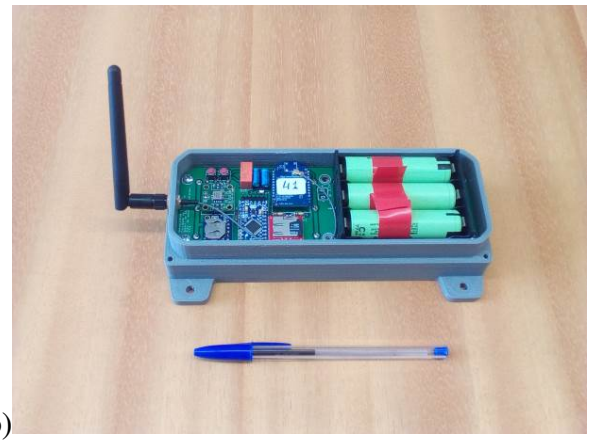

Figure 2: Accelerometer module: a) 5x18650 li-ion batteries; b) 9x18650 li-ion batteries.

Figure 3: Accelerometer used for short period measurements in industrial or construction environment.

3.2 Geophones

The measurement of velocity is many times required when evaluating the integrity of structures submitted to dynamic loads. This may happen essentially in construction work, when vibrations originated by construction machinery are propagated to nearby buildings. Standards like DIN 4150-3 [5] may be used for that evaluation in many countries.

In these measurements, the ideal situation is to have wireless solutions allowing data transmission, having at same time high autonomy. For this purpose, an integrated system was developed. It is composed of a set of sensors positioned in critical areas (see Figure 4a), which locally record the time histories of velocities in 3 axis, and periodically send the maximum vibration values via radio transmission to a receiver. In turn, the receiver shows the maximum values in an LCD to be observed by the person in charge (see Figure 4b). The LCD shows the maximum vibration levels in terms of total velocities of the last 10 minutes, of the last hour and of the last day. This way, it is possible to follow the history of the vibrations produced by the ongoing construction works. The maximum values are saved in a microSD located inside the receiver and may be accessed at any time. During the construction activities, if the maximum allowable values are exceeded, the device beeps and an alarm light.

This system is complemented with a device (Raspberry Pi, see Figure 4b) that sends the maximum vibration values to a server via the internet. This way, it is possible to remotely monitor the vibration levels of the construction, and draw graphs representing the history of the vibrations in the several measurement points.

One of the most important issue to be considered in this integrated solution, is the guarantee of the robustness of the system, as in this process some things may fail, especially with regard to the data transmission chain. Therefore, the recording of the original data inside the sensors is indispensable. In fact, data is recorded on a local microSD in each sensor, which may be accessed later to create a database of the signals.

The autonomy achieved with these sensors is about 1 month when using 6 li-ion batteries of 18650 type, which is considered a very good performance take into account that the signals are acquired continuously, with the exception of night and weekend periods.

At last, it must be mentioned that signals are primarily acquired in acceleration at a sampling frequency of 500Hz and integrated to velocity after applying the appropriate filters. The error in signals is less than 0.1 mm/s, which seams adequate for accessing vibrations admissibility.

a)  b) 

Figure 4: Measurement of velocities: a) Sensor unit; b) equipment for receiving and transmitting data.

3.3 Inclinometer

This sensor was developed for measuring the displacements profiles in the construction of pile walls. During the excavation process, it is often required to control the horizontal displacements of the wall in orthogonal directions. In this case, the topographic measurement of displacements is complemented with the measurement of displacements in tilt tubes placed on the back of the walls. The developed device is shown in Figure 5a). It consists of a probe that measures the inclination of the tube in 0.5-meter sections. The displacement profile of the wall is obtained by adding the contribution of each section from the base to the height of the tube. The measurement of the inclination is obtained by using a very precise 3 axis MEM accelerometer inside the probe, which enable the evaluation of the tilt by measuring the gravity acceleration in the 3 directions. It allows a resolution of the horizontal displacement 0.004mm/m and a maximum error of 0.02mm/m. The internal sampling rate of the accelerometer is 500 Hz, being each measurement of the slope obtained from the average of samples taken for 5 seconds.

The solution found for the data acquisition and storage module differs from commercial solutions, being able to be coupled directly to the tilt tube. This means that the device can only be operated by one technician, instead of the need of 2 persons, as is normally required (see Figure 5b). This module has an LCD for viewing records and internally contains a microSD card for saving the readings validated by the technician.

a)  b) 

Figure 5: Inclinometer: a) Probe and data acquisition module; b) One technician operating the device.

4 CONCLUSIONS

This paper describes the work developed at CONSTRUCT – ViBest research group located in FEUP, on the topic of a new generation of monitoring systems applied to Civil Structures, particularly related to dynamic and static measurements in industrial and construction environment.

It was pointed out that some traditional systems have some drawbacks, particularly related to the lack of robustness, complexity, and high cost. In the other hand, simpler systems based on new sensors may substitute that classical systems in certain applications, offering some advantages like the ease of installation and operation, less maintenance and attractive cost.

In this context, this document describes several measurement systems developed for the previously mentioned applications, which are shown to be sufficiently accurate when compared to commercial systems, which makes these systems a possible alternative solution to traditional systems in many practical cases.

ACKNOWLEDGMENTS

This work was financially supported by: Base Funding - UIDB/04708/2020 and Programmatic Funding - UIDP/04708/2020 of the CONSTRUCT - Instituto de I&D em Estruturas e Construções - funded by national funds through the FCT/MCTES (PIDDAC).

REFERENCES

[1] A. Cunha, E. Caetano, F. Magalhães and C. Moutinho, Dynamic identification and continuous dynamic monitoring of bridges: different applications along bridges life-cycle, *Structures and Infrastructures Engineering*, Vol.14, Issue 4, pp.445-467, 2017.

[2] C. Moutinho and A. Cunha, Contribution to new solutions of instrumentation of Civil structures for continuous dynamic monitoring, *IX ECCOMAS Thematic Conference on Smart Structures and Materials* (SMART 2019), Paris, France, 2019.

[3] C. Moutinho and A. Cunha, New solutions of sensors and instrumentation for dynamic monitoring of Civil structures: ViBest/FEUP experience, *14th International Workshop on Advanced Smart Materials and Smart Structures Technology* (ANCRiSST 2019), Rome, Italy, 2019.

[4] C. Moutinho, S. Pereira and A. Cunha, Continuous dynamic monitoring of human-induced vibrations at the Luiz I Bridge, *Journal of Bridge Engineering*, ASCE, Vol. 25, Issue 8, 2020.

[5] DIN 4150-3, Vibrations in buildings – Part 3: Effects on structures, 2016.

EURODYN 2020

Proceedings of the
XI International Conference on Structural Dynamics

M. Papadrakakis, M. Fragiadakis, C. Papadimitriou (Eds.)

First Edition, September 2020

ISBN (set): 978-618-85072-2-7
ISBN (vol II): 978-618-85072-1-0

Institute of Structural Analysis and Antiseismic Research
National Technical University of Athens, Greece